Available online at www.sciencedirect.com
ScienceDirect
Polyhedron 26 (2007) 1–5
POLYHEDRON
www.elsevier.com/locate/poly

Stabilization of the trivalent oxidation state of copper by tridentate imine–oxime–amine ligands

Mohamed A.-Z. Eltayeb, Yousif Sulfab *

Department of Chemistry and Earth Sciences, College of Arts and Sciences, Qatar University, P.O. Box 2713, Doha, Qatar

Received 1 March 2006; accepted 25 April 2006
Available online 30 April 2006

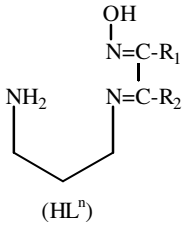
Abstract

Two tridentate imine–oxime–amine ligands have been synthesized and their corresponding copper(II) complexes have been isolated. These copper(II) complexes are readily oxidized both chemically and electrochemically to give relatively stable copper(III) complexes. In the pH range 1.5–3.0 the electron transfer process is electrochemically reversible with $\Delta E_p = 60$ mV and $i_{pa}/i_{pc} \sim 1$. Plots of $E_{1/2}$ versus pH are linear with a slope $= -60$ indicating the involvement of one proton in the electron transfer process. Aqueous solutions of copper(III) complexes have high molar absorption at λ_{max} with $\varepsilon > 10^4$ M^{-1} cm^{-1}. Solid samples of the complexes are diamagnetic consistent with a d^8 square planar geometry. It seems that only imine–oxime nitrogens are coordinated to copper(II) with the NH_2 group being free as indicated by i.r. spectra. Substitution of a $-CH_3$ group on the carbon atom adjacent to the oxime group by the more electron donating group $-CH(CH_3)_2$ lowers electrode potential by more than 90 mV. This is consistent with an earlier observation that electron-donating substituents on the carbon atom adjacent to the oxime group lower the potential of Cu^{III}/Cu^{II} couples and stabilize the higher oxidation state.
© 2006 Elsevier Ltd. All rights reserved.

Keywords: Imine–oxime–amine ligands; Diamagnetic copper(III); Proton-dependent electrochemically reversible $E_{1/2}$

1. Introduction

It is now very well established that the trivalent oxidation state copper is stabilized by several ligands [1,2]. The resolved X-ray structures of copper(III) complexes with various ligands as well as the diamagnetism of most of the others are consistent with prevalence of a square planar structure [3–10]. Few other reports have shown that other structures, square pyramidal and octahedral geometries are also possible [11,12]. The trivalent oxidation state of copper was found to be easily generated in aqueous solution by chemical oxidation of Cu^{II}(HDMG) (H_2DMG = dimethyglyoxime) [13]. We have previously reported the isolation and characterization of copper(III) complexes with tetradentate imine–oxime ligands [14]. These complexes are diamagnetic and hence are believed to be square planar. It was noticed that in coordinating solvents, these complexes undergo a colour change. It is believed that this may arise from weak axial coordination by a solvent molecule(s) forming either a five- or a six-coordinate species. The two tridentate imine–oxime–amine ligands of type (HL^n) and their corresponding copper(II) complexes have been synthesized



n	R_1	R_2
1	CH_3	CH_3
2	$CH(CH_3)_2$	CH_3

* Corresponding author. Tel.: +974 485 2193; fax: +974 485 1049.
E-mail address: yousifsulfab@yahoo.com (Y. Sulfab).

0277-5387/$ - see front matter © 2006 Elsevier Ltd. All rights reserved.
doi:10.1016/j.poly.2006.04.019

Copper(II) complexes were formed in the mole ratio 1:2 metal:ligand. The availability of six donating atoms around the copper ion may thus facilitate the formation of an octahedral complex. If this complex is oxidizable and also retains its structure it may lead to the formation of an octahedral copper(III) complex. Octahedral copper(III) complexes have been reported [15,16].

2. Experimental

2,3-Butanedione monoxime, 1,3-diaminopropane (pn), 4-methylpentan-2-one, ethyl acetate, copper(II) acetate, methanol, and ethanol were used as received. The keto-oxime 4-methyl-3-oximinopentan-2-one was prepared according to the literature method [17]. Buffer solutions were prepared from solutions with known concentrations. In the low pH range HCl/KCl solutions were used. Buffer solutions in the high pH range were prepared from CH_3CO_2H/NaOH solutions. Ionic strength was maintained at 0.10 M with $NaNO_3$.

The tridentate ligands, HL^1 and HL^2, were prepared following the same procedure. The keto-oxime was dissolved in ethyl acetate and was added drop wise to a stirred solution of (pn) dissolved in ethyl acetate at ~25 °C. The reaction mixture was kept overnight. The precipitate that was formed was filtered and washed with cold ethyl acetate and dried over P_2O_5. The diamine concentration was always greater than that of the keto-oxime (1.5:1 mol ratio) to avoid the formation of the tetradentate ligands. The copper(II) complexes, with the ligands HL^1 and HL^2, were prepared by refluxing the ligand with copper(II) acetate in a 2:1 mol ratio in methanol for 2 h. The complexes were precipitated by addition of solid $NaClO_4$. The products were recrystallized from methanol. Elemental analysis was performed at UMIST, Manchester (UK). Copper(III) solutions were generated by chemical oxidation of a buffered solution (pH ~ 4.0) of copper(II) complex using PbO_2.

Cyclic voltammetry of the complexes was measured with an Oxford Electrodes potentiostat and were recorded on an Allen X-Y recorder. The voltammograms were generated using a three-electrode system consisting of a carbon paste working electrode, a Pt wire auxiliary electrode and a saturated calomel reference electrode. Typically, votammograms were recorded at scan rates of 100 mV s^{-1} with a complex concentration of 5×10^{-4} M. Magnetic susceptibility was measured using a Johnson Matthy susceptibility balance at room temperature. A Nicolet 510P-FTIR spectrometer was used to record the i.r. spectra. Electronic spectra were recorded on a Lambda 25 UV–Vis spectrophotometer.

Copper(III) complexes with both ligands were readily formed in aqueous acidic solutions by chemical oxidation by PbO_2 to give intensely deep red coloured solutions. The visible absorption spectrum of the oxidized complex $[Cu^{III}(L_1)_2]^+$ is shown in Fig. 1. Solid copper(III) complexes were isolated by filtration after addition of solid $NaClO_4$ and cooling. The isolated complexes were dried over P_2O_5.

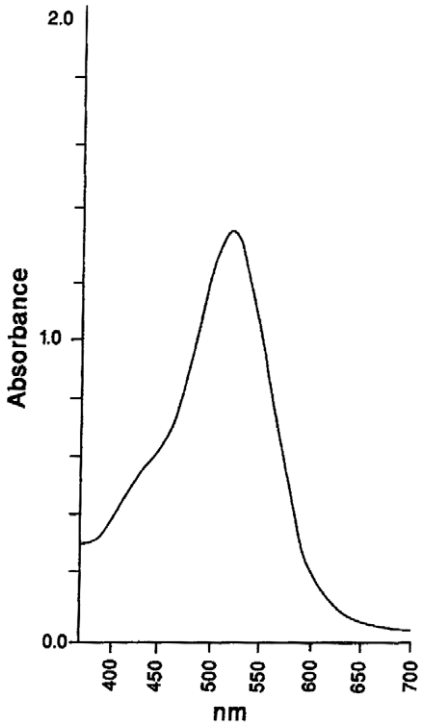


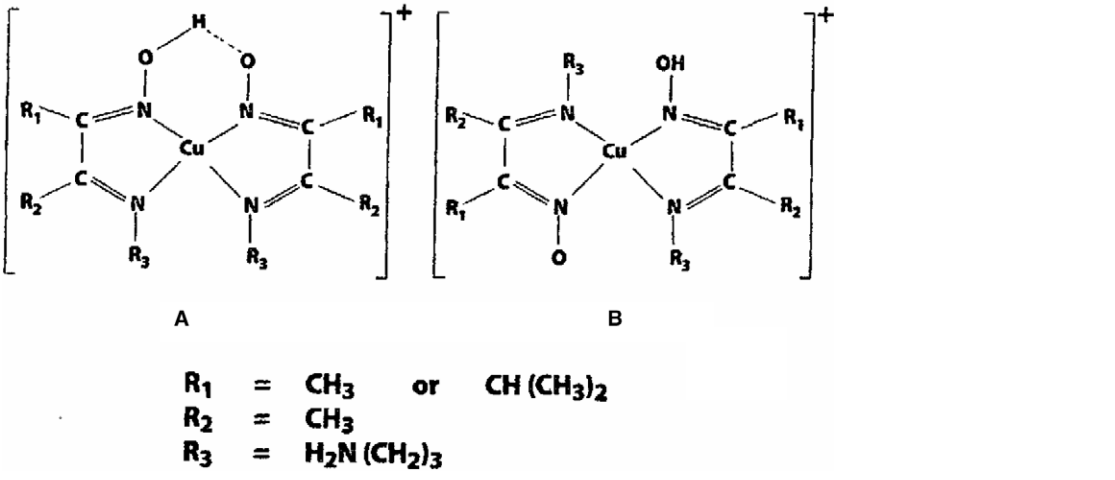
Fig. 1. Visible absorption spectrum of $[Cu^{III}(L^1)_2]^+$ in aqueous solution. $[Cu^{III}(L^1)_2^+] = 1.0 \times 10^{-4}$ M at pH 4.6.

3. Results and discussion

Elemental analysis of the two copper complexes are consistent with the formulations $[Cu^{II}(HL^1)(L^1)]ClO_4$. and $[Cu^{II}(HL^2)(L^2)]ClO_4.CH_3OH$ for the two complexes with the ligands HL^1 and HL^2, respectively. *Anal.* Calc. for $CuC_{14}H_{29}N_6O_6Cl$: C, 35.3; H, 6.1; N, 17.6. Found: C, 35.0; H, 5.6; N, 17.2% and Calc. for $CuC_{18}H_{41}N_6O_7Cl$: C, 40.4; H, 7.3; N, 14.9. Found: C, 40.7; H, 6.0; N, 14.9%. The inclusion of methanol in the crystal of a copper(II) imine–oxime complex has been observed before [18]. The copper(II) complexes with ligands HL^1 and HL^2 have m.p. of 173 and 195 °C, respectively. These values are lower by more than 30 °C than the m.p. of the corresponding tetradentate ligands. Copper(II) complexes with these tridentate ligands may lead to the formation of complexes in which the two nitrogen atoms of the oxime groups are *cis* or *trans* (A and B, respectively). Structure (B) seems to be favored as the i.r. spectra of the complexes displayed sharp bands at 3337 cm^{-1}. This is indicative of the absence of hydrogen-bonding between oxime oxygen atoms. The i.r. spectra of complexes with both ligands showed the presence of an NH_2 group confirming the addition of only one keto-oxime ligand to 1,3-diaminopropane (pn). The two copper(III) complexes show high molar absorption (ε_{max}) of 1.36×10^4 and 1.48 M^{-1} cm^{-1} at 518 nm, respectively. The band maxima positions are identical to those of the

tetradentate ligands [14]. It was observed that copper(III) complexes of the tridentate ligands are slightly less stable than the tetradentate ligands in aqueous acidic solutions. The high ε_{max} may be attributed to ligand to metal charge transitions (LMCT) by analogy to other complexes that display similar high absorption in this region. The visible spectra of the two copper(III) has a shoulder at ~440 nm. The isolated copper(III) complexes are diamagnetic; and this is consistent with a d^8 square planar structure. Aqueous acidic solutions of these complexes are very rapidly reduced by SO_3^{2-}, $S_2O_3^{2-}$, I^- and 1,2- and 1,4-dihydroxybenzene to give the initial copper(II) complexes.

donor ability and steric effects of substituents [10,14,19–21]. We have previously shown that substituents on the carbon atom adjacent to oxime group affect the magnitude of the electrode potential [14]. The electrode potentials of copper(III) complexes of tetradentate imine–oxime ligands are lowered on substituting $-CH_3$ by $-CH(CH_3)_2$. In the complexes considered here the same affect is observed. The electrode potential of the Cu^{III}/Cu^{II} couple with the ligand HL^2 having $-CH(CH_3)_2$ replacing $-CH_3$ in HL^1 is lowered by 90 mV. The lowering of $E_{1/2}$ is reflected in the greater stability of $[Cu^{III}(L^2)_2]^+$ relative to $[Cu^{III}(L^1)_2]^+$. The standard electrode potential, $E^0_{1/2}$, for the two complexes were calculated from Eq. (2) as 1.17 and 1.08 V (n.h.e.) for Cu^{III}/Cu^{II}



Cyclic voltammetry has established further evidence for the stabilization of the +3 oxidation state of copper by tridentate imine–oxime ligands. The voltammograms of the complexes $[Cu^{II}(L^1)(HL^1)]^+$ and $[Cu^{II}(L^2)(HL^2)]^+$ are electrochemically reversible at low pH values as shown in Fig. 2A. The anodic peak, E_{pa}, and the cathodic peak, E_{ca}, separation, $\Delta E_p = 60$ mV and $i_{pa}/i_{ca} \sim 1$ at pH 2.40. However, as the pH increases the electron process becomes less reversible and ΔE_p progressively increases (Fig. 2(B)). The electrode potential $E_{1/2}$ ($E_{1/2} = 0.5(E_{pa} + E_{pc})$) decreases with increasing pH. Plots of $E_{1/2}$ versus pH are linear for both complexes with slopes -60 ± 2 mV as shown in Fig. 3. This is consistent with the involvement of one proton in the electrochemical process. The electrode reaction for the copper(III) complexes can be described by Eq. (1)

$$[Cu^{III}(L^n)_2]^+ + H^+ + e \leftrightarrow [Cu^{III}(HL^n)(L^n)]^+ \quad (n = 1 \text{ or } 2) \tag{1}$$

The variation of the electrode potential with pH is given by Eq. (2)

$$E_{1/2} = E^0_{1/2} - 0.059\ \text{pH} \tag{2}$$

It has previously been reported that electrode potentials of copper(III) complexes are affected by both the electron couples with the ligands HL^1 and HL^2, respectively. These values are only slightly higher than values reported for $E^0_{1/2}$ for the tetradentate ligands synthesized using two equivalents of the same keto-oximes [14].

Previously it has been shown that the reaction designated in Eq. (1) may be separated into electron-transfer and proton-transfer processes as in Eqs. (3) and (4) [14,22]:

$$[Cu^{III}(L^n)_2]^+ + e \leftrightarrow [Cu^{II}(L^n)_2] \tag{3}$$

$$[Cu^{II}(L^n)_2] + H^+ \leftrightarrow [Cu^{II}(HL^n)(L^n)]^+ \tag{4}$$

The formal free energy change ΔG^0_T corresponding to Eq. (1) is given by

$$\Delta G^0_T = -nFE^0_T \tag{5}$$

A similar relation exit for Eq. (3) in which the free energy change and the formal electrode potential are represented by $(\Delta G^0_T)_{el}$ and $(E^0_T)_{el}$, respectively. The free energy associated with the proton transfer process (Eq. (4)) is given by Eq. (6), where K is the dissociation constant of $[Cu^{II}(HL^n)(L^n)]^+$ (K is the inverse of the dissociation constant of Eq. (4))

$$(\Delta G^0_T)_{pr} = RT \ln K \tag{6}$$

The relation for the free energy balance is given in Eq. (7) and this can be combined with Eqs. (5) and (6) to give Eq. (8):

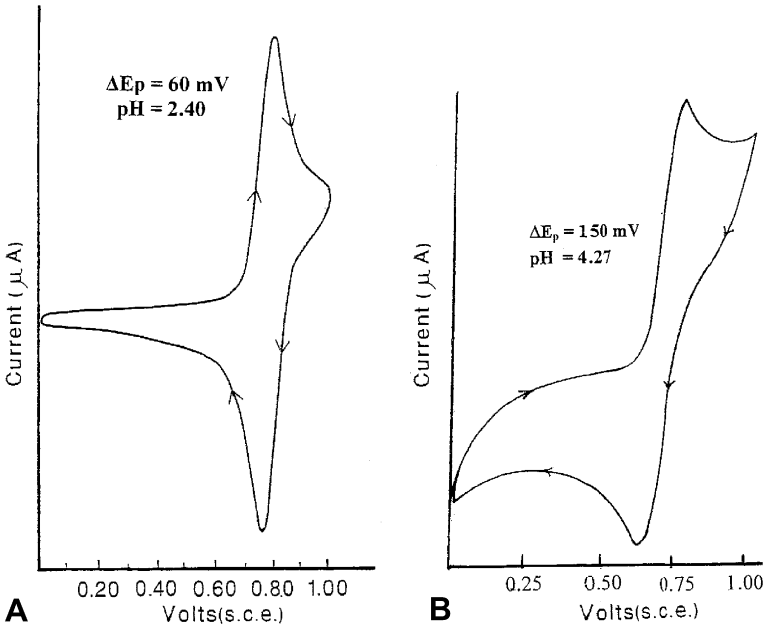


Fig. 2. Cyclic voltammogram of $[Cu^{II}(HL^1)(L^1)]^+$ in aqueous acidic solution at a carbon paste electrode. $[Cu^{II}(HL^1)(L^1)^+] = 5.0 \times 10^{-4}$ M, (A) pH 2.40, (B) pH 4.27, $I = 0.10$ M ($NaNO_3$) at a scan rate = 100 mV s^{-1}.

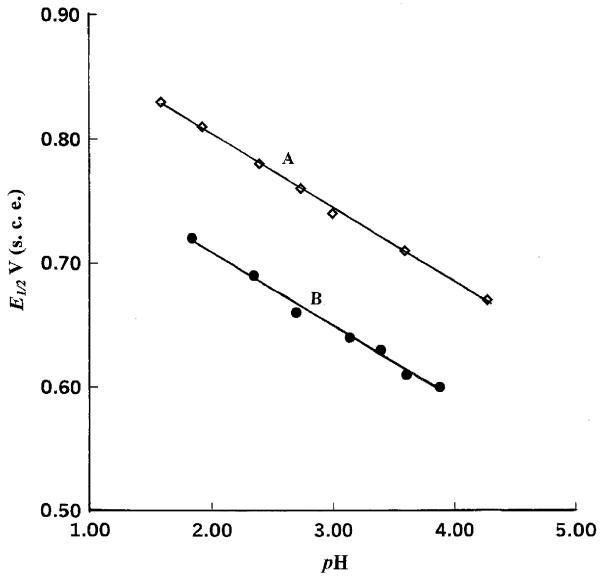


Fig. 3. Plot of $E_{1/2}$ vs. pH for $[Cu^{II}(HL^1)(L^1)]^+$ (A), and $[Cu^{II}(HL^2)(L^2)]^+$ (B).

$$\Delta G^0_T = \left(\Delta G^0_T\right)_{el} + \left(G^0_T\right)_{pr} \quad (7)$$

$$E^0_{1/2} = \left(E^0_{1/2}\right)_{el} + (0.059/n)pK \quad (8)$$

The pK_a value for the complex $[Cu^{II}(HL^1)(L^1)]^+$ has been determined by spectrophotometric titration as 11.2 and the value of pK_a for $[Cu^{II}(HL^2)(L^2)]^+$ is taken as 11.5 equal to that of the tetradentate ligand [14]. Using these values of pK_a and the standard $E^0_{1/2}$ in Eq. (8), the values of $(E^0_{1/2})_{el}$ are calculated as 0.51 and 0.39 V for Cu^{III}/Cu^{II} couples with HL^1 and HL^2 ligands, respectively. These values are very close to the values calculated for Cu^{III}/Cu^{II} couples with tetradentate ligands.

The two tridentate ligands coordinated to Cu^{III} seem to function only as bidentate ligands, with the amine group being free, and seem to form a square planar geometry as indicated by the diamagnetism of the Cu^{III} complexes. The formation of an octahedral complex Cu^{III} with either ligand would have resulted in the complexes being paramagnetic. It thus seems that with this type of ligands a square planar geometry is preferred. It has now been shown that the +3 oxidation state of copper(II) is stabilized by bidentate *vic*-dioximes as well as tridentate imine–oxime–amine and tetradentate imine–oxime ligands.

References

[1] W. Levason, M.D. Spicer, Coord. Chem. Rev. 76 (1987) 45, and references therein.
[2] D.W. Margerum, G.D. Owens, Metal Ions Biol. Syst. 12 (1981) 75.
[3] J.E.W.L. Smith, J.C. Taylor, Acta Crystallogr. 14 (1961) 407.
[4] L.L. Diaddro, W.R. Robinson, D.W. Margerum, Inorg. Chem. 22 (1983) 1021.
[5] I.O. Fritsky, H. Koziowski, P. Sadler, O.P. Yefetova, J. Swaitk-Koziowaska, V.A. Kalibabchuk, T. Giowiak, J. Chem. Soc., Dalton Trans. 3269 (1998).
[6] B. Cervera, J.L. Sanz, M.J. Ibanez, G. Vila, F. LLoret, M. Juve, R. Ruiz, X. Ottenwaelder, A. Aukauloo, S. Poussereau, Y. Journaux, M.C. Munoz, J. Chem. Soc., Dalton Trans. 781 (1998).
[7] J. Hanss, A. Beckmann, H.-J. Kruger, Eur. J. Inorg. Chem. 163 (1999).
[8] C. Bruckner, R.P. Brinas, J.A. Krause Bauer, Inorg. Chem. 42 (2003) 4495.
[9] X. Ribas, J.C. Dias, J. Morgado, K. Wurst, E. Molins, E. Ruiz, M. Almeida, J. Veciana, C. Rovira, Chem. Eur. J. 10 (2004) 1691.
[10] R. Xifra, X. Ribas, A. Llobet, A. Poater, M. Duran, M. Sola, T.D.P. Stack, J. Benet-Buchholz, B. Donnadieu, J. Mahia, T. Parella, Chem. Eur. J. 11 (2005) 5146.

[11] G.R. Clark, W.B. Skelton, T.N. Waters, J. Chem. Soc., Dalton Trans. 1528 (1976).
[12] L.F. Warren, M.A. Bennett, Inorg. Chem. 15 (1976) 3126.
[13] Y. Sulfab, Polyhedron 8 (1989) 2409.
[14] Y. Sulfab, F.M. Al-Sogair, Trans. Met. Chem. 27 (2002) 299.
[15] S.M. Abu-El-Wafa, R.M. Issa, C.A. McAuliffe, Inorg. Chim. Acta 99 (1985) 103.
[16] T. Krebs, E. Glaser, T. Bill, W. Meyer-Klaucke, K. Wieghradt, Angew. Chem., Int. Ed. 38 (1999) 359.
[17] A.F. Ferris, J. Org. Chem. 24 (1959) 580.
[18] J.A. Bertrand, J.H. Smith, D.G. VanDerveer, Inorg. Chem. 16 (1977) 1484.
[19] E. Kimura, T. Koike, R. Machida, R. Nagai, M. Kodama, Inorg. Chem. 23 (1984) 4181.
[20] A.R. Hendrickson, R.I. Martin, N.M. Rhode, Inorg. Chem. 15 (1976) 2115.
[21] F.B. Bossu, K.L. Chellappa, D.W. Margerum, J. Am. Chem. Soc. 99 (1985) 2159.
[22] J.G. Mohanty, A. Chakravorty, Inorg. Chem. 16 (1977) 1561.

Available online at www.sciencedirect.com
ScienceDirect
Polyhedron 26 (2007) 6–10
POLYHEDRON
www.elsevier.com/locate/poly

Binding of hydroxychromones with Al^{3+} in methanol

Nursen Binbuga [a], William P. Henry [a,*], Tor P. Schultz [b]

[a] Department of Chemistry, Mississippi State University, Box 9573, Mississippi State, MS 39762, United States
[b] Forest Products Department/FWRC, Mississippi State University, Box 9820, Mississippi State, MS 39762, United States

Received 26 May 2006; accepted 25 July 2006
Available online 10 August 2006

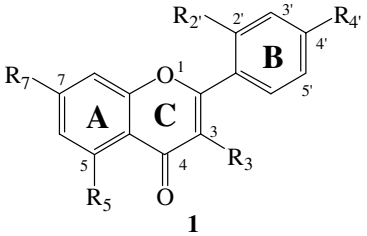
Abstract

The chelation of 3-hydroxy-, 5-hydroxy- and 5,7-dihydroxychromone with Al^{3+} was studied spectrophotometrically. Both the molar ratio method and method of continuous variation (Job's method) were used to determine the composition of the complexes. In all cases, complex formation involved 1:1 aluminum ion to hydroxychromone ratios. For the 5-hydroxy and 5,7-dihydroxy derivatives, this composition agrees with that for the corresponding hydroxyflavone. However, 3-hydroxyflavone (flavonol) forms a 2:1 complex with Al^{3+} in methanol in contrast to the results for 3-hydroxychromone in this study. The importance of the cinnamoyl mesomeric form for stabilizing the complex between flavonol and Al^{3+} is invoked to explain this discrepancy.
© 2006 Elsevier Ltd. All rights reserved.

Keywords: Hydroxychromones; Al^{3+}; Chelation; UV–Vis spectroscopy

1. Introduction

Flavonoids (specifically hydroxyflavonoids) have been extensively studied in recent years because of their antioxidant properties [1–9]. These studies have included reports of the effect of metal chelation on antioxidant activity [10–13] and determining binding strengths with metals ions [10,14–33]. For the hydroxyflavones (**1**), metal chelation occurs at the 3-hydroxy-4-keto binding site [17,27,34–40], 4-keto-5-hydroxy binding site [27,41] or, if present, at vicinal dihydroxy sites of the B ring [27,38,39] although it has also been postulated that the 1-ether-2′-hydroxy groups can bind Co^{2+} in morin (**1d**) [42,43].



1

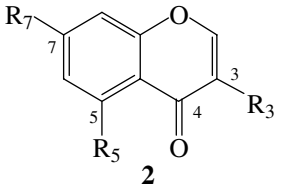
1a: R_3 = OH; $R_5 = R_7 = R_{2'} = R_{4'}$ = H: flavonol
1b: R_5 = OH; $R_3 = R_7 = R_{2'} = R_{4'}$ = H: 5-hydroxyflavone
1c: $R_5 = R_7$ = OH; $R_3 = R_{2'} = R_{4'}$ = H: 5,7-dihydroxyflavone
1d: $R_3 = R_5 = R_7 = R_{2'} = R_{4'}$ = OH: morin

Removal of the B ring from flavones gives the chromone (**2**) class of molecules. We became interested in these molecules to investigate the molecular properties important in protecting wood against fungal decay knowing that hydroxyflavones such as morin inhibit wood decaying fungi [44]. The postulate that a Fenton-type process is in

* Corresponding author. Tel.: +1 662 325 7606; fax: +1 662 325 1618.
E-mail address: wph1@ra.msstate.edu (W.P. Henry).

0277-5387/$ - see front matter © 2006 Elsevier Ltd. All rights reserved.
doi:10.1016/j.poly.2006.07.032

operation for the initial stages of fungal attack [45–52] suggests that both antioxidant activity and metal chelating properties are important in the development of effective and environmentally-benign wood protection systems to prevent fungal deterioration [53].



2

2a: R_3 = OH; $R_5 = R_7$ = H;
3-hydroxychromone
2b: R_5 = OH; $R_3 = R_7$ = H;
5-hydroxychromone
2c: $R_5 = R_7$ = OH; R_3 = H;
5,7-dihydroxychromone

In this paper, we report the results of complexation studies of chromone derivatives **2a**, **2b** and **2c** with Al^{3+} in methanol using the spectrophotometric method employed for the corresponding studies with hydroxyflavones [32,37–41]. The results obtained will be compared with those for the hydroxyflavones (**1a**–**c**) to determine the importance of the B ring on metal chelation at either the 3-hydroxy-4-keto or 4-keto-5-hydroxy binding site.

2. Experimental

Infrared spectra were obtained on a Midac FT-IR. NMR spectra were recorded using a Bruker AMX-300 spectrometer operating at 300 MHz.

2.1. Synthesis of hydroxychromones (*2a*–*c*)

Chromones (**2a**–**c**) were synthesized according to the literature procedures [54–56]. Melting points, infrared spectra and ^1H NMR spectra for compounds synthesized all agreed with those reported in the literature [57,58].

2.2. Spectroscopic studies

Spectroscopic studies were carried out on a Varian 50 Bio UV–Vis spectrometer at room temperature (21.5 ± 0.5 °C). A 1-cm pathlength quartz cell was used for all measurements. Two methods were used to study the binding of hydroxychromones with Al^{3+} in methanol solution. These are the molar ratio method and the method of continuous variation (Job's method [59]) as described by Cornard and co-workers [37]. In the former method, the molar ratio of $AlCl_3$/hydroxychromone (with constant hydroxychromone concentration) is varied between 0 and 3.0 and the UV–Vis spectrum is obtained at each ratio. A plot of absorbance at maximum wavelengths for complex and uncomplexed hydroxychromone versus molar ratio allows for the determination of the ratio of Al^{3+}/hydroxychromone in the complex. In Job's method, the mole fraction of hydroxychromone in a mixture with Al^{3+}, where the total concentration of Al^{3+} and hydroxychromone is held constant, is varied between 0 and 1 and the UV–Vis spectrum at each $\chi_{hydroxychromone}$ is obtained. A plot of λ_{max} (complex) (corrected for uncomplexed Al^{3+} and/or hydroxychromone) versus $\chi_{hydroxychromone}$ gives a maximum at the mole fraction of hydroxychromone in the complex. In both methods, the absorbance measurement was made 1 h after solution preparation to allow for complete complex formation. Each spectroscopic study was repeated twice.

3. Results and discussion

Fig. 1 shows the change in UV–Vis spectra (methanol solvent) as the ratio of Al^{3+}/5-hydroxychromone was varied. A similar behavior was observed for all hydroxychromone/$AlCl_3$ mixtures studied. The spectroscopic results for the chromones and their complexes with Al^{3+} are compiled in Table 1. The unsubstituted chromone was also studied as a possible ligand for Al^{3+}. At all ratios of Al^{3+}/chromone studied, the UV–Vis spectrum remained unchanged from that of the pure chromone, indicating no complex formation as anticipated.

Plotting the absorbances at the λ_{max} for the hydroxychromone and complex versus metal/ligand ratio results in a graph as shown in Fig. 2 for Al^{3+} with 3-hydroxychromone. The intercept of the lines drawn through the rising points and those on the plateau allows for a determination of the ratio in the complex. For 3-hydroxychromone with Al^{3+}, a 1:1 complex is formed. The method of continuous variation (Job's method) results in a graph such as is depicted in Fig. 3. This graph confirms the 1:1 nature of the complex for Al^{3+} with **2a**. Table 1 contains the ratio of Al^{3+}:hydroxychromone from the method of continuous variation and molar ratio experiments and the results for the corresponding hydroxyflavones.

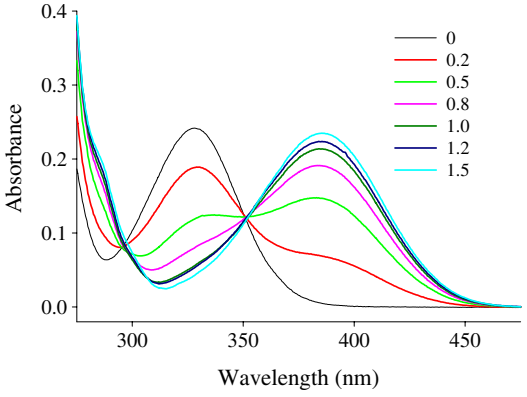


Fig. 1. UV–Vis spectra of 5-hydroxychromone (**2b**) and Al^{3+} in methanol at various ratios of Al^{3+}:**2b**.

Table 1
Spectroscopic results for the complexation of hydroxychromones and hydroxyflavones with Al^{3+} in methanol

Chromone or flavone	λ_{max} (uncomplexed) (nm)	λ_{max} (Al^{3+} complex) (nm)	Ratio Al^{3+}: hydroxychromone or – flavone in complex	Reference
1a	344	402	1:2	[37]
1b	336	397	1:1	[41]
1c	[b]	385[c]	1:1	[31]
	313	382	1:2	[30]
	[d]	383	1:1	[a]
2a	316	356	1:1	[a]
2b	336	397	1:1	[a]
2c	[d]	383	1:1	[a]

[a] This work.
[b] Not reported in reference.
[c] 1:1 Methanol/0.2 M acetate buffer.
[d] Absorbance of uncomplexed species not used in molar ratio method because of significant absorbance of Al^{3+} complex at λ_{max} (uncomplexed).

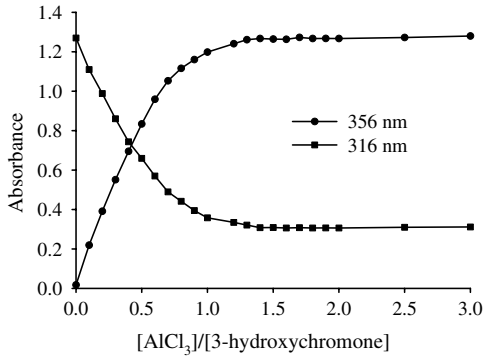


Fig. 2. Plot of absorbance at 356 and 316 nm vs. ratio of Al^{3+}:**2a** in methanol.

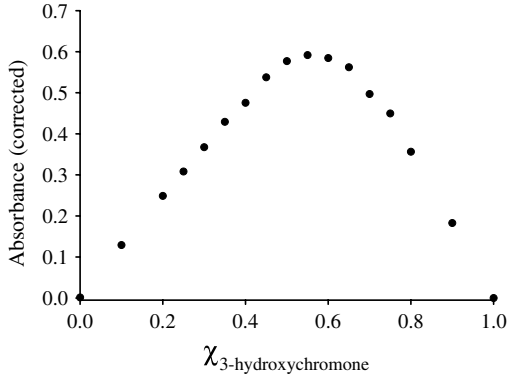


Fig. 3. Job's plot at 356 nm for mixtures of Al^{3+} and **2a** in methanol.

To verify the methods employed in this study, the spectroscopic experiments for the binding of hydroxyflavones with Al^{3+} in methanol were repeated. The results obtained matched those for **1a** and **1b** [37,41], but there is a discrepancy in the literature concerning the ratio of Al^{3+}:5,7-dihydroxyflavone (**1c**) with one group reporting a 1:1 ratio [31] while another a 1:2 ratio [30]. The present work clearly indicates a 1:1 ratio as expected from the behavior of **1b** with Al^{3+}.

The similarity of the results for the binding of **2b** and **2c** with Al^{3+} with those for the corresponding hydroxyflavones (**1b** and **1c**) suggests that the phenyl substituent has little effect when chelation occurs at the 4-keto-5-hydroxy site. On the other hand, the phenyl substituent has a significant effect on complexation when metal coordination occurs at the 3-hydroxy-4-keto site. Indeed, in the case of **1a** there are 2 flavonols bound to each Al^{3+}, whereas for **2a** only a single 3-hydroxychromone binds per metal. This insinuates that the metal complex is much more stable when the phenyl group is attached at the 2 position of the A ring.

This behavior can be readily explained by referring to the theoretical calculations performed on the complexes of **1a** and **1b** with Al^{3+} by Cornard and co-workers [37,41]. These calculations suggest that the metal complex is stabilized by the generation of negative charge on the 4-keto oxygen atom and that this can be done by invoking a number of mesomeric forms. The two most important ones are the pyronium and cinnamoyl forms (Fig. 4).

Obviously, in the case of the chromones the cinnamoyl form is not available. Therefore, the much greater binding of **1a** with Al^{3+} compared with **2a** can be rationalized by the fact that the cinnamoyl form contributes significantly to the stability of the complex when Al^{3+} is bound at the 3-hydroxy-4-keto position of **1a**. On the other hand, the similarity in the bonding strengths of **1b** and **2b** with Al^{3+} suggests that the cinnamoyl form is not an important contributor to the stability of the complex when complexation occurs at the 4-keto-5-hydroxy binding site.

It is interesting to note that the cinnamoyl form may be important in another property of hydroxyflavones. In unpublished work from this laboratory, the crystal structures of both **2a** and **2b** have been determined. While **2b** has an intramolecular hydrogen bond similar to what is observed for **1b** [60], **2a** does not show any indication of intramolecular hydrogen bonding in stark contrast to **1a** [61]. Thus, the cinnamoyl form is likely important in promoting intramolecular hydrogen bonding between the 3-hydroxy and 4-keto groups. The variation in dihedral angle observed between the B and C rings versus the

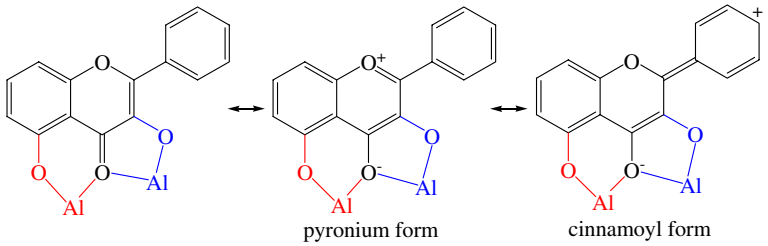


Fig. 4. Mesomeric forms invoked for stabilizing the Al^{3+} complex with **1a** (blue) or **1b** (red). (For interpretation of the references in color in this figure legend, the reader is referred to the web version of this article.)

intramolecular hydrogen bond formation in various 3-hydroxyflavone derivatives supports this hypothesis [61].

It is the goal of this research to correlate the ability of hydroxyflavone, hydroxychromone and other molecules to protect wood against fungal decay with their propensity for chelating metal centers [53,62,63]. Once accomplished, this allows for the rational design of molecules able to prevent the fungal destruction of woody materials for economical and environmentally-benign non-metallic preservatives.

4. Conclusions

The chelation of 3-hydroxychromone, 5-hydroxychromone and 5,7-dihydroxychromone with Al^{3+} was studied spectrophotometrically in methanol. All three molecules form 1:1 complexes with this metal ion. The results for the latter two molecules are in agreement with those for the corresponding hydroxyflavone. However, significant differences exist in the strength of the binding between the 3-hydroxy derivatives. In contrast to the present work, 3-hydroxyflavone forms a 2:1 complex with Al^{3+}. This reflects the importance of the cinnamoyl mesomeric form in the stabilization of the 3-hydroxyflavone complex.

Acknowledgements

This project was supported by the National Research Initiative of the USDA Cooperative State Research, Education and Extension Service, Grant Number 2003-35103-13616. Gratitude is also extended to Dr. John Young for graciously allowing his UV–Vis spectrometer to be used for these studies.

References

[1] C.A. Rice-Evans, N.J. Miller, Biochem. Soc. Trans. 24 (1996) 790.
[2] C.A. Rice-Evans, N.J. Miller, G. Paganga, Free Radical Biol. Med. 20 (1996) 933.
[3] S.A.B.E. van Acker, D.-J. van den Berg, M.N.J.L. Tromp, D.H. Griffioen, W.P. van Bennekom, W.J.F. van der Vijgh, A. Bast, Free Radical Biol. Med. 20 (1996) 331.
[4] S.V. Jovanovic, S. Steenken, M. Tosic, B. Marjanovic, M.G. Simic, J. Am. Chem. Soc. 116 (1994) 4846.
[5] J. Yu, L. Wang, R.L. Walzem, E.G. Miller, L.M. Pike, B.S. Patil, J. Agric. Food Chem. 53 (2005) 2009.
[6] O. Firuzi, A. Lacanna, R. Petrucci, G. Marrosu, L. Saso, Biochim. Biophys. Acta 1721 (2005) 174.
[7] C. Sanchez-Moreno, Food Sci. Tech. Int. 8 (2002) 121.
[8] M. Rajendran, P. Manisankar, R. Gandhidasan, R. Murugesan, J. Agric. Food Chem. 52 (2004) 7389.
[9] M. Furusawa, T. Tanaka, T. Ito, A. Nishiakwa, N. Yamzaki, K. Nakaya, N. Matsuura, H. Tsuchiya, M. Nagayama, M. Iinuma, J. Health Sci. 51 (2005) 376.
[10] S.A.B.E. van Acker, G.P. van Balen, D.-J. van den Berg, A. Bast, W.J.F. van der Vijgh, Biochem. Pharmacol. 56 (1998) 935.
[11] M.Y. Moridani, J. Pourahmad, H. Bui, A. Siraki, P.J. O'Brien, Free Radical Biol. Med. 34 (2003) 243.
[12] R.F.V. de Souza, E.M. Sussuchi, W.F. De Giovani, Synth. React. Inorg. Met. Org. Chem. 33 (2003) 1125.
[13] R.F.V. de Souza, W.F. De Giovani, Redox Rep. 9 (2004) 97.
[14] M. Satterfield, J.S. Brodbelt, Anal. Chem. 72 (2000) 5898.
[15] M.G. Barolli, R.A. Werner, L.D. Slep, A.B. Pomilio, Molecules 5 (2000) 516.
[16] G.M. Escandar, L.F. Sala, Can. J. Chem. 69 (1991) 1994.
[17] L. Barhacs, J. Kaizer, J. Pap, G. Speier, Inorg. Chim. Acta 320 (2001) 83.
[18] M. Yoshino, K. Murakami, Anal. Biochem. 257 (1998) 40.
[19] J.A. Kennedy, H.K.J. Powell, Aust. J. Chem. 38 (1985) 879.
[20] M. Thompson, C.R. Williams, G.E.P. Elliot, Anal. Chim. Acta 85 (1976) 375.
[21] L. Jurd, T.A. Geissman, J. Org. Chem. 21 (1956) 1395.
[22] G.M. Saxena, T.R. Seshadri, Proc. Indian Acad. Sci. 46A (1957) 218.
[23] L.J. Porter, K.R. Markham, Phytochemistry 11 (1972) 1477.
[24] T.A. Annan, C. Peppe, D.G. Tuck, Can. J. Chem. 68 (1990) 423.
[25] L. Mira, M.T. Fernandez, M. Santos, R. Rocha, M.H. Florencio, K.R. Jennings, Free Radical Res. 36 (2002) 1199.
[26] B. Bujonek, Pol. J. Chem. 67 (1993) 1339.
[27] M.D. Engelmann, R. Hutcheson, I.F. Cheng, J. Agric. Food Chem. 53 (2005) 2953.
[28] Y. Oka, M. Yanai, Bunseki Kagaku 13 (1964) 207.
[29] B. Buionek, M. Kopach, D. Novak, Zh. Obshch. Khim. 66 (1996) 1064.
[30] G.T. Castro, S.E. Blanco, Spectrochim. Acta, Part A 60 (2004) 2235.
[31] B. Alluis, O. Dangles, Helv. Chim. Acta 82 (1999) 2201.
[32] R.F.V. de Souza, W.F. De Giovani, Spectrochim. Acta, Part A 61 (2005) 1985.
[33] J.P. Cornard, L. Dangleterre, C. Lapouge, J. Phys. Chem. A 109 (2005) 10044.
[34] E. Balogh-Hergovich, J. Kaizer, G. Speier, G. Huttner, L. Zsolnai, Inorg. Chim. Acta 304 (2000) 72.
[35] G. Speier, V. Fulop, L. Parkanyi, J. Chem. Soc., Chem. Commun. (1990) 512.
[36] E. Balogh-Hergovich, J. Kaizer, G. Speier, G. Huttner, P. Rutsch, Acta Crystallogr., Sect. C 55 (1999) 557.
[37] A.-C. Boudet, J.-P. Cornard, J.-C. Merlin, Spectrochim. Acta, Part A 56 (2000) 829.
[38] J.P. Cornard, J.C. Merlin, J. Inorg. Biochem. 92 (2002) 19.
[39] J.P. Cornard, J.C. Merlin, J. Mol. Struct. 651–653 (2003) 381.
[40] J.P. Cornard, A.C. Boudet, J.C. Merlin, Spectrochim. Acta, Part A 57 (2001) 591.
[41] J.P. Cornard, J.C. Merlin, J. Mol. Struct. 569 (2001) 129.
[42] Y. Song, P. Yang, M. Yang, J. Kang, S. Qin, B. Lu, L. Wang, Transition Met. Chem. 28 (2003) 712.

[43] Z. Qi, L. Wang, L. Xiang, S. Li, F. He, Transition Met. Chem. 21 (1996) 23.
[44] T.P. Schultz, W.B. Harms, T.H. Fisher, K.D. McMurtrey, J. Minn, D.D. Nicholas, Holzforschung 49 (1995) 29.
[45] K.A.Jr. Jensen, C.J. Houtman, Z.C. Ryan, K.E. Hammel, Appl. Environ. Microbiol. 67 (2001) 2705.
[46] G. Xu, B. Goodell, J. Biotechnol. 87 (2001) 43.
[47] S.M. Hyde, P.M. Wood, Microbiology 143 (1997) 259.
[48] H. Tanaka, S. Itakura, A. Enoki, Mater. Org. 33 (2000) 91.
[49] W.P. Henry, ACS Symp. Ser. 845 (2003) 175.
[50] B. Halliwell, ACS Symp. Ser. 845 (2003) 10.
[51] B. Goodell, ACS Symp. Ser. 845 (2003) 97.
[52] J. Rodriguez, A. Ferraz, M.P. de Mello, ACS Symp. Ser. 845 (2003) 154.
[53] T.P. Schultz, D.D. Nicholas, W.P. Henry, C.U.Jr. Pittman, D.O. Wipf, B. Goodell, Wood Fiber Sci. 37 (2005) 175.
[54] R.M. Moriarty, O. Prokash, H.A. Musallam, J. Heterocyclic Chem. 22 (1985) 583.
[55] R.T. Borchardt, J.A. Huber, J. Med. Chem. 18 (1975) 120.
[56] G.F. Spencer, OPPI Briefs 23 (1991) 390.
[57] M.G. Constantino, V.L. Junior, G.V.J. da Silva, J. Heterocyclic Chem. 40 (2003) 369.
[58] G. Romussi, G. Ciarallo, J. Heterocyclic Chem. 13 (1976) 211.
[59] P. Job, Ann. Chim. 9 (1928) 113.
[60] M. Shoja, Acta Crystallogr., Sect. C 46 (1990) 517.
[61] M.C. Etter, Z. Urbanczyk-Lipkowska, S. Baer, P.F. Barbara, J. Mol. Struct. 144 (1986) 155.
[62] N. Binbuga, K. Chambers, W.P. Henry, T.P. Schultz, Holzforschung 59 (2005) 205.
[63] T.P. Schultz, D.D. Nicholas, W.P. Henry, Holzforschung 59 (2005) 370.

Available online at www.sciencedirect.com
ScienceDirect
Polyhedron 26 (2007) 11–16
POLYHEDRON
www.elsevier.com/locate/poly

Diverse coordination of two ligands in ferromagnetic $[Cu(\mu\text{-}HCO_2)_2(3\text{-}pyOH)]_n$ and $[Cu_2(\mu\text{-}HCO_2)_2(\mu\text{-}3\text{-}pyOH)_2(3\text{-}pyOH)_2(HCO_2)_2]_n$

Bojan Kozlevčar [a,*], Lea Glažar [a], Gordana Pirc [a], Zvonko Jagličić [b], Amalija Golobič [a], Primož Šegedin [a]

[a] Faculty of Chemistry and Chemical Technology, University of Ljubljana, Aškerčeva 5, P.O. Box 537, SI-1001 Ljubljana, Slovenia
[b] Institute of Mathematics, Physics and Mechanics, University of Ljubljana, Jadranska 19, Ljubljana, Slovenia

Received 8 June 2006; accepted 17 July 2006
Available online 4 August 2006

Abstract

Two novel polynuclear complexes with methanoate anions and 3-hydroxypyridine ligands $[Cu(\mu\text{-}HCO_2)_2(3\text{-}pyOH)]_n$ (**1**) and $[Cu_2(\mu\text{-}HCO_2)_2(\mu\text{-}3\text{-}pyOH)_2(3\text{-}pyOH)_2(HCO_2)_2]_n$ (**2**), respectively, were synthesized and characterized. The central copper atom in **1** is surrounded by four methanoates and a 3-pyOH molecule, forming a square-pyramidal CuO_3NO chromophore. All the methanoates are bidentate and serve as bridges between the adjacent copper ions via *syn-anti* and *anti–anti* coordination. The basal square coordination axes are formed by *O*(*syn*), *N*(3-pyOH) (1.974(2), 2.016(2) Å) and *O*(*anti*), *O*(*anti*) (1.945(2), 1.960(2) Å), while the third *O*(*anti*) (2.247(2) Å) is on the top of the pyramid. A ferromagnetic transition with an exchange constant $2J/k_B = 9.2\ cm^{-1}$ is found for **1** below 20 K. This interaction probably takes place through two *syn-anti* methanoates extended in a chain through the 2D structure. On the other hand, two monoatomic Cu–O–Cu intra-dinuclear asymmetric (1.986(2), 2.415(2) Å) bridges of two methanoates in $[Cu_2(HCO_2)_4(3\text{-}pyOH)_4]$ (**2**) are present. An elongated distorted octahedral coordination sphere around each copper(II) atom is completed by an additional monodentate terminal methanoate (1.975(2) Å), two *N*-coordinated 3-pyOH (2.005(2), 2.002(2) Å) and the third weakly *O*-coordinated 3-pyOH (2.732(2) Å). Although a shorter Cu···Cu distance is noticed in **2** than in **1** (4.690(1) Å **1**, 3.442(1) Å **2**), much weaker ferromagnetism is found in **2**.
© 2006 Elsevier Ltd. All rights reserved.

Keywords: 3-Hydroxypyridine; Methanoate; Copper; Ferromagnet; *Syn*; *Anti*

1. Introduction

Copper carboxylates are well known to form a variety of structures even with ligands of the same homologous series. Our recent investigations include efforts to find new synthetic routes for the preparation of copper carboxylates with additional *N*-donor ligands. A choice of ligands with a hydrogen-bonding functionality could lead to the formation of useful inorganic materials with desired physical properties. Some of them may serve also as bioinorganic models, since coordination compounds of the first-row transition metals are known to participate in multiple biological processes involving acid–base and redox reactions. In this sense, complexes of hydroxypyridine are of considerable interest [1,2]. However, only a few coordination compounds of copper(II) carboxylates with 3-hydroxypyridine (3-pyOH) have been structurally characterized so far. A two-dimensional network, linked by inter-molecular hydrogen bonds between trifluoroacetate and 3-pyOH ligands, is present in $[Cu(O_2CCF_3)_2(3\text{-}pyOH)_2(THF)_2]$ [2]. A similar 2D network is also reported for $[Cu(O_2CCF_3)_2(3\text{-}pyOH)_2]_n$ [3], however, 3-pyOH ligands serve as bridges (N, O) and intra-molecular H-bonding is present.

* Corresponding author.
E-mail address: bojan.kozlevcar@fkkt.uni-lj.si (B. Kozlevčar).

0277-5387/$ - see front matter © 2006 Elsevier Ltd. All rights reserved.
doi:10.1016/j.poly.2006.07.025

Replacement of the carboxylate ligand reveals structurally significantly different compounds. Due to tetradentate bridging oxalates, a 1D zig-zag chain structure of *cis*-$[Cu(\mu\text{-ox})(3\text{-pyOH})_2]_n$ [4] is formed. On the other hand, acetates coordinate bidentately, as in dinuclear *paddle-wheel* $[Cu_2(O_2CCH_3)_4(3\text{-pyOH})_2]$ [5] or in mononuclear $[Cu(O_2CCH_3)_2(3\text{-pyOH})_2]_n$ [6]. Only one example of 3-pyO, the deprotonated form of 3-pyOH, was found in the literature, in $\{[Cu(\mu\text{-3-pyO})(3\text{-pyO})(3\text{-pyOH})(H_2O)]\cdot 2H_2O\}_n$ [1]. For some of these complexes ferromagnetic or antiferromagnetic properties were reported, either through the carboxylate group or 3-pyO(H).

In this work, we present two novel coordination compounds with methanoate and 3-pyOH ligands. The methanoates show rather rare coordination modes in both cases, playing a distinguishing role in the magnetic properties of both complexes.

2. Experimental

2.1. Synthesis

Chemicals were readily available from commercial sources and were used as received without further purification.

$[Cu(\mu\text{-}HCO_2)_2(3\text{-pyOH})]_n$ (**1**). A mixture of $[Cu_2(OH)_2CO_3]$ (0.33 g, 1.5 mmol) and 3-pyOH (0.57 g, 6.0 mmol) in 30 mL CH_3OH and 3 mL HCOOH was refluxed in air for 1 h. A small amount of a solid residue was filtered off and the resulting solution was left at 279 K for 72 h. Light blue crystals of **1** were filtered off and dried in a desiccator over KOH for 24 h. Yield 57%. *Anal.* Calc. for $C_7H_7CuNO_5$: C, 33.8; H, 2.84; N, 5.63; Cu, 25.6. Found: C, 33.7; H, 3.02; N, 5.25; Cu, 26.1%. IR ($\bar{\nu}$/cm^{-1}): 1630 s $\nu_{as}(CO_2)$, 1580sh, 1564s $\nu_{as}(CO_2)$ + ν(ring), 1482 m ν(ring), 1369s $\nu_s(CO_2)$, 1344 s, 1297 s ν(C–O). UV/Vis (λ_{max}/nm): 225, 285, 610. EPR (295 K) g 2.150.

$[Cu_2(\mu\text{-}HCO_2)_2(\mu\text{-3-pyOH})_2(3\text{-pyOH})_2(HCO_2)_2]_n$ (**2**). The synthetic path for the dark blue compound **2** was the same as for **1**: $[Cu_2(OH)_2CO_3]$ (0.25 g, 1.1 mmol), 3-pyOH (1.1 g, 12 mmol), absolute C_2H_5OH (30 mL), HCOOH (2 mL). Yield 67%. *Anal.* Calc. for $C_{24}H_{24}Cu_2N_4O_{12}$: C, 41.9; H, 3.52; N, 8.15; Cu, 18.5. Found: C, 42.3; H, 3.79; N, 7.94; Cu, 18.3%. IR ($\bar{\nu}$/cm^{-1}): 1600 s $\nu_{as}(CO_2)$, 1557 m ν(ring), 1452 m ν(ring), 1370 m $\nu_s(CO_2)$, 1333 s, 1285 s ν(C–O). UV/Vis (λ_{max}/nm): 225, 285, 615. EPR (295 K) $g_\perp$ 2.100, $g_\parallel$ 2.257.

The single crystals of **1** and **2**, suitable for X-ray analysis, were obtained by a similar procedure, but at a lower concentration of the starting compounds.

2.2. X-ray structure analysis

Details of the crystal data, data collection and refinement parameters for **1** and **2** are listed in Table 1, and selected distances and angles in Table 2. The diffraction data were collected on a Nonius Kappa CCD diffractometer with graphite monochromated Mo Kα radiation. The data were processed using DENZO [7]. The structures were solved by direct methods using SIR97 [8] and refined using XTAL3.6 [9] by a full-matrix least-squares procedure based on F. All of the non-hydrogen atoms were refined anisotropically. The positions of the hydrogen atoms for both structures were located using difference Fourier maps. They were refined together with their isotropic displacement parameters for **1**. The H-atoms parameters of **2** were not refined.

Table 1
Relevant crystal data and data collection summary

Formula	$C_7H_7CuNO_5$ (**1**)	$C_{12}H_{12}CuN_2O_6$ (**2**)
Formula weight	248.68	343.78
Crystal system	orthorhombic	monoclinic
Space group	*Pbca*	$P2_1/c$
a (Å)	15.7293(3)	8.0710(1)
b (Å)	6.9881(1)	13.4048(3)
c (Å)	17.1409(4)	12.9065(2)
β (°)	90	100.1110(7)
V (Å^3)	1884.09(6)	1374.67(4)
Z	8	4
D_x (g/cm^3)	1.753	1.661
μ (mm^{-1})	2.313	1.618
T (K)	293	293
Crystal colour	light blue	dark blue
Crystal shape	plate	plate
Crystal size (mm)	0.30 × 0.15 × 0.10	0.30 × 0.10 × 0.10
θ Max (°)	27.47	27.47
R_{int}	0.051	0.030
Refined parameters	155	190
Total data	25445	17983
Independent data	2150	3153
Observed data [$F^2 > 2\sigma(F^2)$]	1707	2706
R[a] (observed)	0.031	0.032
wR[b] (observed)	0.019	0.024
$\Delta\rho_{min,\,max}$ (e Å^{-3})	−0.662, 0.503	−1.49, 0.65

[a] $R = \sum(||F_o| - |F_c||)/\sum|F_o|$.
[b] $wR = \sum(w||F_o| - |F_c||)/\sum|wF_o|$.

2.3. Physical measurements

The magnetic susceptibility data of powdered polycrystalline samples were measured with a Quantum Design SQUID magnetometer, equipped with a 5 T magnet. The molar magnetic susceptibility χ_M was investigated in the temperature interval between 300 and 2 K in a magnetic field strength $H = 50$ Oe. The data were corrected for the experimentally determined contribution of the sample holder. Corrections for the diamagnetic response of the compounds, due to closed atomic shells as estimated from the Pascal's constants, were applied [10].

Metal analysis was carried out electrogravimetrically with Pt electrodes. *C,H,N* analysis was performed with a Perkin–Elmer, Elemental Analyzer 2400 CHN. Infrared spectra were measured on mineral oil mulls, using a Perkin–Elmer FT-IR 1720X spectrometer. Electronic spectra were recorded as nujol mulls with a Perkin–Elmer UV/Vis/NIR spectrometer Lambda 19. EPR spectra of the powdered samples were recorded by a Bruker ESP-300

Table 2
Selected bond distances (Å), angles (°) and hydrogen-bonding geometries for complexes **1** and **2**

1					
Cu–O11	1.9454(14)	O11–Cu–O21′	93.19(5)	O11–Cu–O22	169.99(6)
Cu–O22	1.9600(14)	O11–Cu–N	87.18(6)	O11–Cu–O12′	94.44(5)
Cu–O21′	1.9740(13)	O12′–Cu–N	96.75(6)	O21′–Cu–O22	92.60(5)
Cu–N	2.0158(15)	O21′–Cu–N	175.13(6)	O12′–Cu–O21′	88.07(5)
Cu–O12′	2.2473(14)	O22–Cu–N	86.36(6)	O12′–Cu–O22	93.91(5)
O12–C1	1.240(2)	Cu–O11–C1	126.24(13)	Cu–O12′–C1′	124.67(13)
O22–C2	1.244(2)	Cu–O21′–C2′	114.30(12)	Cu–O22–C2	128.93(12)
O11–C1	1.248(2)				
O21–C2	1.258(2)				
2					
Cu–O31	1.9751(11)	O31–Cu–O41	162.89(4)	O31–Cu–N1	91.73(5)
Cu–O41	1.9855(10)	O31–Cu–N2	91.28(5)	O31–CuO41′	85.40(4)
Cu–N1	2.0049(12)	O22′–Cu–O31	88.67(4)	O41–Cu–N1	90.64(5)
Cu–N2	2.0023(13)	O41–Cu–N2	89.69(5)	O41–Cu–O41′	77.50(4)
Cu–O41′	2.4147(10)	O22′–Cu–O41	108.37(4)	N1–Cu–N2	168.64(5)
Cu–O22′	2.7324(14)	O41′–Cu–N1	95.66(4)	O22′–Cu–N1	87.37(4)
O31–C3	1.256(2)	O41′–Cu–N2	95.50(4)	O22′–Cu–N2	81.76(5)
O32–C3	1.222(3)	O22′–Cu–O41′	173.42(4)	Cu–O41–Cu′	102.50(4)
O41–C4	1.266(2)	Cu–O22′–C22′	141.53(11)	Cu–O31–C3	127.77(10)
O42–C4	1.226(2)	Cu–O41–C4	128.21(10)	Cu–O41′–C4′	129.16(10)
D–H···A (**1**)	D···A	D–H···A	D–H···A (**2**)	D···A	D–H···A
O(41)–H(41)···O(12)[a]	2.692(2)	172(4)	O(12)–H(12)···O(42)[b]	2.695(2)	171
			O(22)–H(22)···O(32)[c]	2.540(2)	159

[a] $1-x, 1-y, 1-z$.
[b] $1+x, y, z$.
[c] $x, 1/2-y, -1/2+z$.

spectrometer, operating at X-band at room temperature and at 100 K. The values of parameters g were calculated directly from the signal positions in the spectra.

3. Results and discussion

The crystal structure analysis of $[Cu(\mu\text{-}HCO_2)_2(3\text{-}pyOH)]_n$ (**1**) (*katena-bis-(μ-methanoato-O,O′)-(3-hydroxypyridine-N)copper(II)*) reveals a polynuclear structure of Cu and 3-hydroxypyridine (3-pyOH) moieties (Cu–N 2.016(2) Å) bridged by four methanoates (Fig. 1). Due to the symmetry relations, only two different methanoates are in the structure. One coordinates *syn-anti* (Cu–O21′ 1.974(2), Cu–O22 1.960(2), Cu···Cu (4.690(1) Å), while the other *anti-anti* (Cu–O11 1.945(2), Cu–O12′ 2.247(2), Cu···Cu 5.935(1) Å). The coordination sphere around the copper(II) atom is square-pyramidal with N–Cu–O21′ and O11–Cu–O22 coordination axes and O12′ on the top of the pyramid. The methanoate bridges enable a layered structure, while 3-pyOH is involved only in an inter-layer H-bonding network (O41(H41)···O12 2.692(2) Å).

Two copper(II) atoms in the dinuclear central core of $[Cu_2(\mu\text{-}HCO_2)_2(\mu\text{-}3\text{-}pyOH)_2(3\text{-}pyOH)_2(HCO_2)_2]_n$ (**2**) (*katena-bis-(μ-3-hydroxypyridine-O,N)-bis-(μ-methanoato-O)-(methanoato-O)-(3-hydroxypyridine-N)dicopper(II)*) are connected by two monoatomic non-symmetric methanoate bridges (Cu–O41 1.986(2), Cu′–O41 2.415(2) Å, Cu–O41–Cu′ 102.50(4)°; Fig. 2). Two additional monodentate methanoates (Cu–O31 1.975(2) Å) are on the terminal positions of the dinuclear unit, *trans* to the closer bridging methanoate oxygen atom (O41). Two 3-pyOH ligands are coordinated *trans* on each copper atom, and thus are perpendicular to the copper–methanoate plane (Cu–N1 2.005(2), Cu–N2 2.002(2) Å) and complete the dinuclear unit. The so far described coordination sphere of **2** is very similar to that reported for $[\{Cu(tzq)_2(HCO_2)\}_2((\mu\text{-}HCO_2)_2]\cdot 4H_2O$ (tzq = [1,2,3]triazolo[1,5-a]quinoline) [13]. A shorter intra-dinuclear Cu···Cu distance in the tzq complex (3.339(2) Å) than in **2** (3.442(1) Å) is likely to be due to a stronger π···π interaction (tzq complex: $12\pi e^-$/ligand;

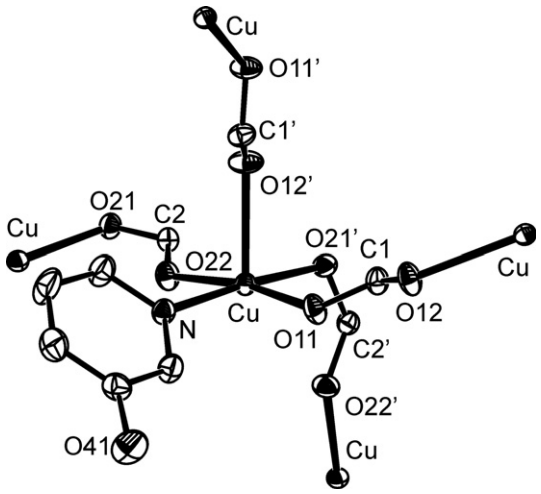


Fig. 1. Two types of four methanoate bridges among the Cu-3-pyOH moieties in the polymeric structure of **1** [11,12] (Cu···Cu: *syn–anti* 4.690(1) Å, *anti–anti* 5.935(1) Å). All H-atoms are omitted for clarity.

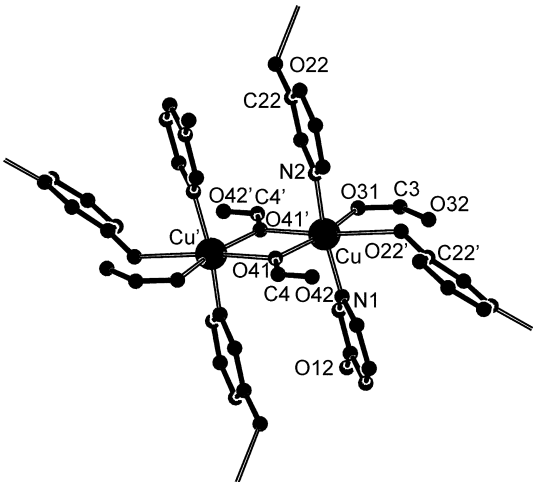


Fig. 2. A dinuclear unit in the structure of **2** bridged by 3-pyOH molecules, forming a 2D network (Cu···Cu′ 3.442(1) Å) [11,12]. All H-atoms are omitted for clarity.

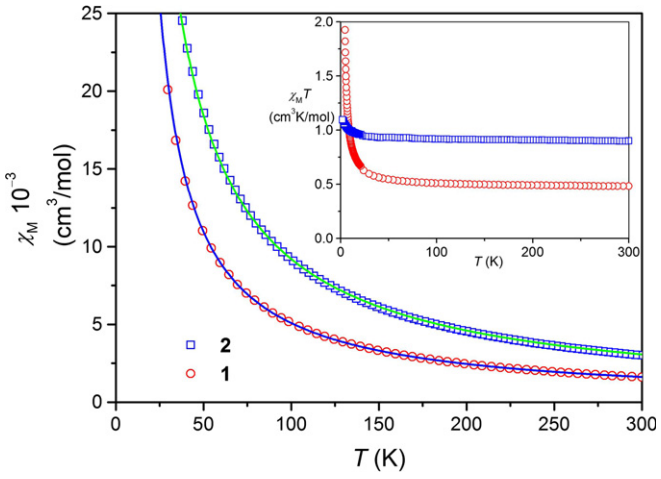


Fig. 3. The magnetic properties χ_M and $\chi_M T$ (inset) of the title compounds, measured in 50 kOe. The full lines in the graph χ_M correspond to the Curie–Weiss law.

2: 6πe⁻/ligand). The dinuclear units in the tzq complex are inter-molecularly H-bonded by water molecules, while in **2**, they are connected by 3-pyOH molecules. Two 3-pyOH molecules, strongly bonded inside one dimer in **2**, are thus additionally semi-coordinated to the apical position of the adjacent dimers (Cu–O22′ 2.732(2) Å) forming inter-dinuclear bridges. The hydroxo oxygen atom O22′ coordinates *trans* to the more distant bridging methanoate atom O41′, completing the elongated Jahn–Teller axis (Fig. 2, Table 2). This inter-dinuclear bridge is additionally strengthened by a strong H-bond between the hydroxo group and the non-coordinated terminal methanoato oxygen atom (O22′(H22′)···O32 2.540(2) Å). Such a poly-dinuclear structure shows a 2D network, H-bonded between adjacent layers via non-coordinated oxygen atoms of the bridging methanoates, and those 3-pyOH hydroxo groups not involved in the semi-coordination (O12(H12)···O42 2.695(2) Å). Additional stabilization inside the dinuclear units is found in π–π stacking (cg···cg 3.878(2) Å, mean interplanar separation 3.537, 3.506 Å) of the 3-pyOH rings.

The molar magnetic susceptibility χ_M of compounds **1** and **2**, increases with decreasing temperature, while the product $\chi_M \cdot T$ is approximately constant in the temperature interval from 300 K to 50 K, indicating a paramagnetic behaviour (Fig. 3) [14]. High temperature susceptibility data χ_M (above 50 K) were fitted with the Curie–Weiss law: $\chi_M = C/(T-\theta)$. The Curie constant C and the Weiss constant θ are 0.47, 0.92 cm^3 K/mol and 6.6, 0 K for **1** and **2**, respectively. Below 50 K, $\chi_M T$ remains almost constant for **2**, and only a very weak ferromagnetic interaction is noticed (inset in Fig. 3). On the contrary, $\chi_M T$ for **1** significantly increases below 20 K, and the magnetic susceptibility $\chi_M(M/H)_{H\to 0} = 14$ cm^3/mol (2 K) is much higher than expected for non-interacting $S = 1/2$ spins of Cu^{II}. In a small magnetic field strength H, the magnetization M_M of **1** linearly increases, however at 1 kOe the $\mu_a(H)$ dependence becomes non-linear and M_M saturates at $H \sim 20$ kOe (Fig. 4). The magnetization saturation is 1.07 μ_B per Cu^{II} atom, showing that all Cu^{II} atoms in the sample contribute to specific magnetic properties of the sample. No hysteresis loop for the $\mu_a(H)$ dependence was detected. Due to a large increase of χ_M below 20 K, $\theta = 6.6$ K, and an "S" shaped curve $\mu_a(H)$ at 2 K with an absence of hysteresis, a soft ferromagnetic behaviour at low temperature for **1** is clearly noticed.

Magnetic interactions among non-diluted copper(II) atoms have been described frequently, however mostly for dicopper tetracarboxylates with a strong antiferromagnetic interaction. In those *paddle-wheel* structures, the carboxylates coordinate bidentately in a *syn–syn* mode. The coordination sphere is square-pyramidal with the magnetic Cu^{II} orbital $d_{x^2-y^2}$ oriented towards four bridging carboxylates and the non-magnetic d_{z^2} towards the apical ligand [15–17]. This agrees with the magnetic interaction between

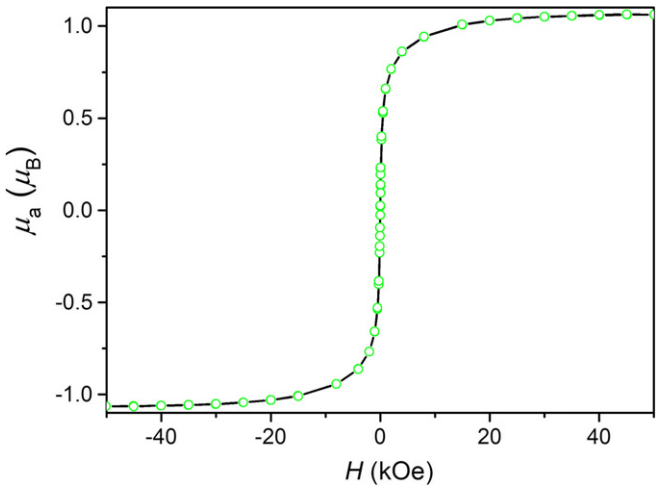


Fig. 4. The magnetization $\mu_a(H)$ for Cu^{II} (S = 1/2) species in **1**, calculated per 1 copper atom and measured at 2 K.

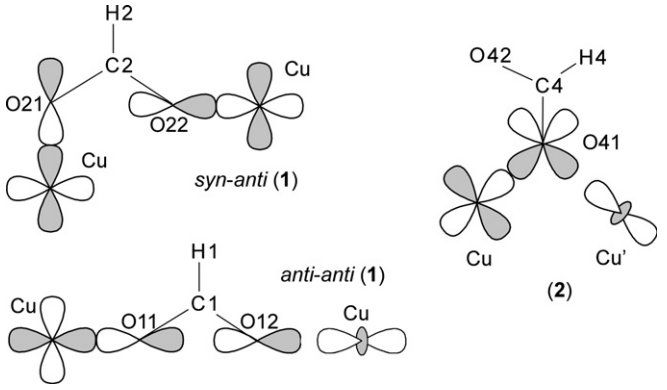
two $S = 1/2$ spins of two Cu^{II} always found only inside the dinuclear unit. Although such dinuclear moieties are often connected by various types of bridges, no inter-dinuclear interactions via $S = 1/2$ were confirmed, but sometimes suggested via $S = 1$ joint dinuclear spins ($2 \times Cu^{II}$) [18,19]. Some evidence for these interactions may be found in the EPR spectra. If less than four carboxylates bridge two Cu^{II} atoms, a significant reduction of the magnetic interaction is observed [17,20–22], despite the magnetic $d_{x^2-y^2}$ orbitals involved on both sides of the bridge. Theoretically, for the *syn-anti* carboxylate bridged models [17], a weak ferromagnetic interaction was calculated, while a weak antiferromagnetic for the *syn–syn* bridge and a moderate antiferromagnetic for the *anti–anti* models. The reported complexes with the less common *syn–anti* bridging mode show ferromagnetic or antiferromagnetic properties, with small magnitudes of their exchange coupling constants J [23–29]. Generally, the exchange interaction is a combination of two components, negative antiferromagnetic and positive ferromagnetic ($J = J_{AF} + J_F$) [30]. The J_{AF} magnitude is proportional to the square of the overlap integral between the magnetic orbitals centred on the adjacent metal atoms, while for the J_F, it is governed by the overlap density between the magnetic orbitals [31]. Polyatomic extended ligands thus reduce the ferromagnetic contribution. The unfavourable overlap of the *syn–anti* oriented ligand orbitals [23] and non-planarity of the bridging network significantly reduce especially the antiferromagnetic part, to the extent that the ferromagnetic one becomes predominant [27,32].

Such an explanation fits both the herein analyzed compounds **1** and **2**. In **1**, the *anti–anti* methanoates (Cu–O11–C1–O12–Cu) connect the non-magnetic d_{z^2} with the magnetic $d_{x^2-y^2}$ Cu^{II} orbitals, while the *syn–anti* type (Cu–O21–C2–O22–Cu) enables the ferromagnetic interaction, since it connects the $d_{x^2-y^2}$ magnetic orbitals only (Scheme 1). This interaction between the magnetic orbitals is not limited to two Cu atoms, but is extended in a chain, due to two *syn–anti* bridges from a *cis* position of each Cu atom to two adjacent Cu atoms (Fig. 1). The *syn–anti* connected Cu atoms are pushed out of the O–C–O bridge plane by 0.105(1) and 0.398(1) Å, respectively, thus the Cu–O21–C2–O22–Cu skeleton deviates from planarity, in accordance with an absence of an antiferromagnetic interaction in **1**. A weak interaction between the nearest Cu^{II} neighbours can be treated as a small perturbation added to the Zeeman term: $\widehat{H} = -z2J\widehat{S}_1 \cdot \widehat{S}_2$, where z is the number of nearest neighbours and $2J$ is the interaction parameter between them [33,34]. Due to the two magnetically interacting nearest neighbours ($z = 2$) found in the structure of **1**, $2J/k_B = 9.2\ cm^{-1}$ can be calculated (Eq. (1))

$$2J = \frac{3k_B\theta}{zS(S+1)} \tag{1}$$

In the structure of **2**, the monoatomic methanoate and the 3-pyOH molecule bridges are present, however they all connect the magnetic $d_{x^2-y^2}$ (Cu–O41(equatorial) 1.986(1) Å) and the non-magnetic d_{z^2} Cu^{II} orbitals (Cu′-O41(axial) 2.415 (1) Å) (Scheme 1). Therefore, they do not enable a magnetic interaction of the same magnitude as found in **1** despite the shorter Cu···Cu distance (4.690(1) Å **1**, 3.442(1) Å **2**). Actually, the inset in Fig. 3 shows a very weak ferromagnetism for **2**, and the interaction more likely takes place through the methanoates than 3-pyOH due to a shorter length of such bridges. This weak interaction may be possible by some admixture of d_{z^2} character with the $d_{x^2-y^2}$ type of Cu(II) orbital, where the unpaired electron lies primarily. A significant octahedral distortion of the copper coordination sphere in **2** (see Table 2) strongly supports such a theory. A very weak ferromagnetism in **2** and a weak antiferromagnetism in the related $[\{Cu(tzq)_2(HCO_2)\}_2(\mu\text{-}HCO_2)_2] \cdot 4H_2O$ [13] may be correlated with different distances and almost the same angle in their monoatomic Cu–O–Cu bridges (tzq: 1.950(4), 2.331(4) Å, 102.2(2)°; **2**: 1.986(1), 2.415(1) Å, 102.5(2)°). Longer distances in **2** reduce the magnetic orbital overlap, and thus the antiferromagnetic contribution to the extent that ferromagnetism predominates. A numerical analysis to predict the antiferromagnetic or the ferromagnetic properties of dicopper complexes with two monoatomic chlorine bridges has been introduced [22,29]. The higher value ϕ/R (angle Cu–Cl–Cu = ϕ, Cu–Cl axial distance = R) suggests antiferromagnetism, while lower value ferromagnetism. The ϕ/R values 42.4 (**2**) and 43.8 (tzq) °/Å thus fit with the measured magnetic properties of **2** and the tzq complex.

The EPR spectrum of **1** (298 K) shows one signal ($g = 2.150(3)$), revealing pseudo isotropic symmetry of the complex and the presence of an isolated paramagnet with $S = 1/2$. Similar was observed for another Cu ferromagnetic complex with a *syn–anti* carboxylate bridge [27]. On the other hand, two axial symmetry signals ($g_\parallel = 2.257(3)$, $g_\perp = 2.100(3)$) are found in the spectrum of **2**. Significantly longer Cu–L distances for the z-axis oriented ligands in **2** than in **1** are thus in agreement with the EPR spectra. The



Scheme 1. A relative orientation of the magnetic $d_{x^2-y^2}$ and non-magnetic d_{z^2} Cu^{II} orbitals and their interactions through the methanoate bridges in **1** and **2**. Every d_{z^2} orbital is shifted away from the ligand bonding p orbital to stress a longer Cu–O distance in the axial direction.

spectra of both compounds do not change by decrease of temperature to 100 K, and they are consistent with the magnetic susceptibility analysis. A full correlation was not done, due to unavailability of the EPR experiment below 100 K. On the other hand, some comparison was done for the structurally related $[Cu_2(\mu\text{-}HCO_2)_2(\mu\text{-}3\text{-}pyOH)_2(3\text{-}pyOH)_2(HCO_2)_2]_n$ (**2**) and $[\{Cu(tzq)_2(HCO_2)\}_2(\mu\text{-}HCO_2)_2]\cdot 4H_2O$ [13]. Different spectra were recorded at room temperature, only two signals ($H_{\|}$ and $H_{\perp}$) are found for **2**, while the $\Delta M_s \pm 2$ resonance and four $\Delta M_s \pm 1$ signals are reported for the tzq complex. These differences are related to the observations described by the magnetic susceptibility analysis.

4. Concluding remarks

The coordination compound $[Cu(\mu\text{-}HCO_2)_2(3\text{-}pyOH)]_n$ (**1**) shows triatomic methanoate bridges of *anti–anti* and *syn–anti* mode. On the other hand, $[Cu_2(\mu\text{-}HCO_2)_2(\mu\text{-}3\text{-}pyOH)_2(3\text{-}pyOH)_2(HCO_2)_2]_n$ (**2**) reveals only monoatomic methanoate coordination, either to one Cu atom or bridging inside the dinuclear moiety. Additionally, one half of the 3-pyOH molecules also serve as bridges, connecting the adjacent dinuclear units in **2** in a poly-dinuclear network. A ferromagnetic interaction is found in both complexes, however, this is significantly important only for **1** ($2J = 9.2\ cm^{-1}$). This interaction takes place via the *syn–anti* methanoates, due to the magnetic Cu(II) $d_{x^2-y^2}$ orbitals on both sides of the bridge. In all the other bridging cases in **1** and **2**, the non-magnetic d_{z^2} orbital is always involved. Such a ferromagnetic interaction in **1** is also in agreement with a medium sized length of the triatomic O–C–O *syn–anti* bridge and non-planarity of its Cu–O–C–O–Cu skeleton.

Acknowledgements

The financial support of the MVZT Republic of Slovenia, P1-0175-103 and X-2000, is gratefully acknowledged. We thank Dr. M. Šentjurc, EPR center, 'Jožef Stefan' Institute, Ljubljana, for EPR spectra.

Appendix A. Supplementary data

All atomic parameters and other crystallographic data have been deposited with the Cambridge Crystallographic Data Center as supplementary material with the deposition numbers CCDC 610244 **1** and 610245 **2**. These data can be obtained, free of charge via http://www.ccdc.cam.ac.uk/conts/retrieving.html. Supplementary data associated with this article can be found, in the online version, at doi:10.1016/j.poly.2006.07.025.

References

[1] O. Castillo, A. Luque, S. Iglesias, P. Vitoria, P. Román, New J. Chem. 24 (2000) 771.
[2] S.R. Breeze, S. Wang, Inorg. Chem. 32 (1993) 5981.
[3] S. Kawata, S.R. Breeze, S. Wang, J.E. Greedan, N.P. Raju, Chem. Commun. (1997) 717.
[4] O. Castillo, A. Luque, M. Julve, F. Lloret, P. Román, Inorg. Chim. Acta 315 (2001) 9.
[5] S. Gao, X.-F. Zhang, L.-H. Huo, H. Zhao, Acta Crystallogr. E60 (2004) m1405.
[6] S. Gao, Z.-Z. Lu, L.-H. Huo, X.-F. Zhang, H. Zhao, Acta Crystallogr. E60 (2004) m1353.
[7] Z. Otwinowski, W. Minor, Methods Enzymol. 276 (1997) 307.
[8] A. Altomare, M.C. Burla, M. Camalli, G. Cascarano, C. Giacovazzo, A. Guagliardi, A.G.G. Moliterni, G. Polidori, R. Spagna, J. Appl. Cryst. 32 (1999) 115.
[9] S.R. Hall, D.J. du Boulay, R. Olthof-Hazekamp (Eds.), XTAL3.6 System, University of Western Australia, 1999.
[10] R.L. Dutta, A. Syamal, Elements of Magnetochemistry, Affiliated East-West Pvt Ltd., New Delhi, 1993, pp. 6–11.
[11] A.L. Spek, PLATON, University of Utrecht, The Netherlands, 2003.
[12] L.J. Farrugia, J. Appl. Cryst. 30 (1997) 565.
[13] E. Escriva, J. Server-Carrio, L. Lezama, J.V. Folgado, J.L. Pizarro, R. Ballesteros, B. Abarca, J. Chem. Soc., Dalton Trans. (1997) 2033.
[14] N.W. Ashcroft, N.D. Mermin, Solid State Physics, Saunders College Publishing, 1976, p. 658.
[15] F.P.W. Agterberg, H.A.J. Provó Kluit, W.L. Driessen, H. Oevering, W. Buijs, M.T. Lakin, A.L. Spek, J. Reedijk, Inorg. Chem. 36 (1997) 4321.
[16] B. Kozlevčar, I. Leban, M. Petrič, S. Petriček, O. Roubeau, J. Reedijk, P. Šegedin, Inorg. Chim. Acta 357 (2004) 4220.
[17] A. Rodriguez-Fortea, P. Alemany, S. Alvarez, E. Ruiz, Chem. Eur. J. 7 (2001) 627.
[18] V.V. Gavrilov, Yu.V. Yablokov, L.N. Milkova, A.V. Ablov, Phys. Soc. Sol. 45B (1971) 603.
[19] J. Mrozińsky, E. Heyduk, J. Coord. Chem. 13 (1984) 291.
[20] I.A. Koval, P. Gamez, O. Roubeau, W.L. Driessen, M. Lutz, A.L. Spek, J. Reedijk, Inorg. Chem. 42 (2003) 868.
[21] K. Geetha, A.R. Chakravarty, J. Chem. Soc., Dalton Trans. (1999) 1623.
[22] K.-S. Bürger, P. Chaudhuri, K. Wieghardt, Inorg. Chem. 35 (1996) 2704.
[23] R.L. Carlin, K. Kopinga, O. Kahn, M. Verdaguer, Inorg. Chem. 25 (1986) 1786.
[24] M. Inoue, M. Kubo, Inorg. Chem. (1970) 2310.
[25] F. Sapiña, M. Burgos, E. Escriva, J.-V. Folgado, D. Marcos, A. Beltran, D. Beltran, Inorg. Chem. 32 (1993) 4337.
[26] D. Valigura, M. Melnik, M. Koman, L. Martiška, M. Korabik, J. Mrozińsky, T. Glowiak, Polyhedron 23 (2004) 2447.
[27] E. Colacio, J.M. Dominguez-Vera, R. Kivekäs, J.M. Moreno, A. Romerosa, J. Ruiz, Inorg. Chim. Acta 212 (1993) 115.
[28] S. Konar, P.S. Mukherjee, M.G.B. Drew, J. Ribas, N. Ray Chaudhuri, Inorg. Chem. 42 (2003) 2545.
[29] E. Colacio, M. Ghazi, R. Kivekäs, J.M. Moreno, Inorg. Chem. 39 (2000) 2882.
[30] O. Kahn, Inorg. Chim. Acta 62 (1982) 3.
[31] M. Julve, M. Verdaguer, A. Gleizes, M. Philoche-Levisalles, O. Khan, Inorg. Chem. 23 (1984) 3808.
[32] E. Colacio, J.M. Dominguez-Vera, J.P. Costes, R. Kivekäs, J.P. Laurent, J. Ruiz, M. Sundberg, Inorg. Chem. 31 (1992) 774.
[33] O. Kahn, Molecular Magnetism, VCH Publ. Inc., 1992, p 26.
[34] S. Hatscher, H. Schilder, H. Lueken, W. Urland, Pure Appl. Chem. 77 (2005) 497.

Available online at www.sciencedirect.com
ScienceDirect
Polyhedron 26 (2007) 17–23
POLYHEDRON
www.elsevier.com/locate/poly

Increasing transmission of electronic interaction in dinuclear unsymmetric mixed-valent ruthenium complexes

Florencia Fagalde [a], Mónica E. García Posse [a], Mónica M. Vergara [a], Mauricio Cattaneo [a], Néstor E. Katz [a,*], Isabel Romero [b], Teodor Parella [c], Antoni Llobet [*,d]

[a] *Instituto de Química Física, Facultad de Bioquímica, Química y Farmacia, Universidad Nacional de Tucumán, Ayacucho 491, (T4000INI) San Miguel de Tucumán, Argentina*
[b] *Departament de Química, Universitat de Girona, Campus de Montilivi, E-17071 Girona, Spain*
[c] *Servei de RMN, Universitat Autònoma de Barcelona, Bellaterra E-08193, Barcelona, Spain*
[d] *Departament de Química, Universitat Autònoma de Barcelona, Bellaterra, E-08193, Barcelona, Spain*

Received 10 April 2006; accepted 24 July 2006
Available online 3 August 2006

Abstract

The preparation and characterization by spectroscopic and electrochemical techniques of new dinuclear complexes of the type $[(tpm)(bpy)Ru^{II}(L)Ru^{II/III}(NH_3)_5]^{4+/5+}$ (bpy = 2,2′-bipyridine), tpm = tris(1-pyrazolyl)methane, L = pz (pyrazine), 4,4′-bpy (4,4′-bipyridine), BPE (*trans*-1,2-bis(4-pyridyl)ethylene) and PCA (= 4-pyridinecarboxaldehyde azine), are described in this work. The analysis of the visible spectral data for the metal-to-metal charge transfer (MMCT) bands in the corresponding mixed-valent species $[Ru_b^{II}, Ru_a^{III}]$ (Ru_b = Ru bonded to bpy; Ru_a = Ru bonded to NH_3) allows the determination of the reorganization energies λ and electronic coupling elements H_{AB} for the intramolecular electron transfers $Ru_b^{II} \rightarrow Ru_a^{III}$ mediated by L. An increased transmission of the metal-to-metal electronic interaction is disclosed for this series, when comparing the distance dependence of H_{AB} to that of the analogous series with trpy (2,2′:6′,2″-terpyridine) acting as a spectator ligand instead of tpm.
© 2006 Elsevier Ltd. All rights reserved.

Keywords: Mixed valence; Scorpionate ligands; Ruthenium dinuclear complexes; Electronic interaction; Intervalence transitions

1. Introduction

The distance dependence of intramolecular electron transfer parameters in mixed-valence complexes is an important issue in connection to artificial photosynthesis [1]. The magnitude and the mechanism of the donor–acceptor electronic interactions can be tuned by changing the bridge and/or the co-ligands [2].

We have recently described the syntheses and spectroscopic, electrochemical and photophysical properties of mononuclear complexes of the type $[Ru(bpy)(L)(tpm)]^{2+}$, with bpy = 2,2′-bipyridine, tpm = tris(1-pyrazolyl)methane, L = pz (pyrazine), 4,4′-bpy (4,4′-bipyridine) and BPE (*trans*-1,2-bis(4-pyridyl)ethylene) [3]. These species have now been used as building blocks for new unsymmetric ruthenium complexes of formulae $[(tpm)(bpy)Ru^{II}(L)Ru^{II}(NH_3)_5]^{4+}$, with L = pz (**1**), 4,4′-bpy (**2**), BPE (**3**) and PCA (**8**), and $[(tpm)(bpy)Ru^{II}(L)Ru^{III}(NH_3)_5]^{5+}$, with L = pz (**4**), 4,4′-bpy (**5**), BPE (**6**) and PCA (**9**), on which a few preliminary results were reported [3]. The additional bridging ligand PCA (4-pyridinecarboxaldehyde azine) has also been included for comparison purposes [4]. Besides, the new mononuclear complex $[Ru(bpy)(PCA)(tpm)]^{2+}$ (**7**), has been synthesized and characterized. The main objective in this work is the determination of the influence of metal–metal distance on the reorganization energies and electronic coupling elements for the L-mediated intramolecular electron transfers in the mixed-valent species $[Ru_b^{II}, Ru_a^{III}]$ (where Ru_b = Ru bonded to bpy; Ru_a = Ru bonded to NH_3).

* Corresponding author. Tel.: +54 381 4200960; fax: +54 381 4248169.
E-mail address: nkatz@arnet.com.ar (N.E. Katz).

0277-5387/$ - see front matter © 2006 Elsevier Ltd. All rights reserved.
doi:10.1016/j.poly.2006.07.021

In a previous work [5], we have studied the series $[(trpy)(bpy)Ru^{II}(L)Ru^{II/III}(NH_3)_5]^{4+/5+}$, with, trpy = 2,2′:6′, 2″-terpyridine, L = pz, 4,4′-bpy and BPE. In this work, we report the syntheses and characterization by spectroscopic and electrochemical techniques of the analogous tpm complexes, in order to establish the degree of influence of ligand electronic properties and geometry when going from a meridional (trpy) to a facial (tpm) coordination. Scheme 1 shows the structures of the ligands used in this work and Scheme 2 shows the structure of complex **2** as a representative example.

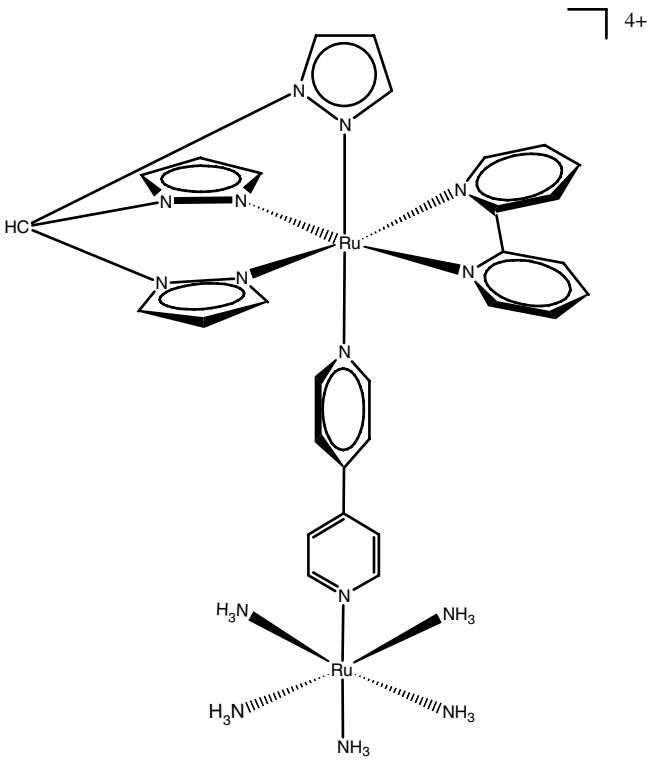
2. Experimental

2.1. Preparations

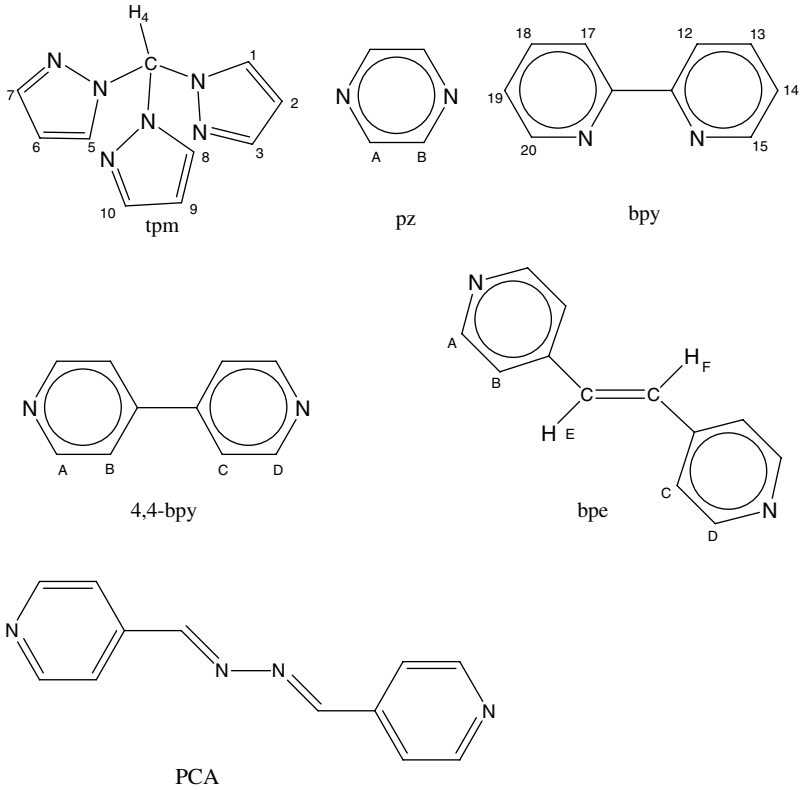
All synthetic manipulations were routinely performed under a nitrogen atmosphere using Schlenk tubes and vacuum line techniques. Electrochemical experiments were performed in the dark under a N_2 or Ar atmosphere with degassed solvents.

2.2. Syntheses

Complexes of formulae $[(tpm)(bpy)Ru^{II}(L)Ru^{II}(NH_3)_5](PF_6)_4$ (with L = pz (**1**), 4,4′-bpy (**2**), BPE (**3**) and PCA (**8**)) have been prepared by the following technique: 0.2 g of $[Ru(tpm)(bpy)(L)](PF_6)_2$, prepared as in Ref. [3], or by refluxing for 2 h $[Ru(tpm)(bpy)(H_2O)](PF_6)_2$ with an excess of L in MeOH, were mixed with an equimolar amount of $[Ru(NH_3)_5(H_2O)](PF_6)_2$, obtained as in Ref. [5], in 10 mL of acetone, under Ar in the dark and using



Scheme 2. Structure of complex **2**.



Scheme 1. Structure of the ligands.

Schlenk techniques. After stirring the mixture for 4 h at room temperature, the desired complexes were precipitated with 50 mL of ether, filtered, washed with ether and dried under vacuo over P_4O_{10}. Purification was achieved by chromatography in Sephadex LH-20. Yields were between 70% and 80%. Elution of the dinuclear species were performed with CH_3CN. After rotoevaporating to complete dryness, samples were re-precipitated from acetone/ether.

2.2.1. [(tpm)(bpy)Ru(pz)Ru(NH_3)$_5$](PF_6)$_4$·0.5(CH_3)$_2$CO (1)

Anal. Calc. for $C_{25.5}H_{40}F_{24}N_{15}O_{0.5}P_4Ru_2$ (1346.7): C, 22.7; H, 3.0; N, 15.6. Found: C, 22.5; H 2.9; N 15.7%.

2.2.2. [(tpm)(bpy)Ru(4,4′-bpy)Ru(NH_3)$_5$](PF_6)$_4$·(CH_3)$_2$CO (2)

Anal. Calc. for $C_{33}H_{47}F_{24}N_{15}OP_4Ru_2$ (1451.8): C, 27.3; H, 3.3; N 14.5. Found: C, 27.3; H 3.1; N 14.9%. ^{1}H NMR (500 MHz, CD_3CN, 25 °C): δ, 6.31 (dd, 1, $J_{9-10} = 3.0$ Hz, $J_{9-8} = 2.2$ Hz, H_9), 6.59 (d, 1, $J_{9-10} = 2.2$ Hz, H_{10}), 6.78 (dd, 1, $J_{2-1} = 2.1$ Hz, $J_{2-3} = 3.0$ Hz H_2), 7.50 (d, 2, $J_{C-D} = 6.8$ Hz, H_C), 7.54 (o, 2, H_B), 7.55 (o, 2, H_A), 7.57 (dd, 2, $J_{13-14} = 8.8$ Hz, $J_{15-14} = 6.0$ Hz, H_{14}), 7.95 (d, 2, $J_{3-2} = 2.1$ Hz, H_3), 8.23 (dd, 2, $J_{12-14} = 8.8$ Hz, $J_{12-13} = 8.1$ Hz, H_{13}), 8.38 (d, 1, $J_{8-9} = 3.0$ Hz H_8), 8.51 (d, 2, $J_{D-C} = 6.8$ Hz, H_D), 8.57 (d, 2, $J_{1-2} = 3.0$ Hz, H_1), 8.67 (d, 2, $J_{15-14} = 6.0$ Hz, H_{15}), 8.79 (d, 2, $J_{12-13} = 8.1$ Hz, H_{12}), 9.06 (s, 1, H_4) ppm. ^{13}C NMR (500 MHz CD_3CN, 25 °C): δ, 75.9 (C_4), 108.7 (C_9), 110 (C_2), 120.7 (C_B) 121.4 (C_C), 125.1 (C_{12}), 126.5 (C_{14}), 135.6 (C_8), 135.9 (C_1), 137.8 (C_{13}), 144.1 (C_{10}), 147.4 (C_3, C_D), 152.8 (C_{15}), 154.1 (C_A) ppm.

2.2.3. [(tpm)(bpy)Ru(BPE)Ru(NH_3)$_5$](PF_6)$_4$·(CH_3)$_2$CO (3)

Anal. Calc. for $C_{35}H_{49}F_{24}N_{15}OP_4Ru_2$ (1477.9): C, 28.5; H, 3.3; N 14.2. Found: C, 28.6; H 3.1; N, 15.0%. ^{1}H NMR (500 MHz, CD_3CN, 25 °C): δ, 6.30 (dd, 1, $J_{9-8} = 2.8$ Hz, $J_{9-10} = 2.0$ Hz H_9), 6.58 (dd, 1, $J_{9-10} = 2.0$ Hz, $J_{10-8} = 2.8$ Hz H_{10}), 6.77 (dd, 2, $J_{2-3} = 2.0$ Hz $J_{2-1} = 2.6$ Hz H_2), 7.27 (d, 2, $J_{B-A} = 6.75$Hz H_B), 7.35(d overlapped, 1, H_E), 7.39 (d overlapped, 1, H_F), 7.43 (d, 2, $J_{B-A} = 6.75$ Hz H_A), 7.47 (d, 2, $J_{C-D} = 6.0$ Hz, H_C), 7.54 (dd, 2, $J_{14-15} = 5.7$ Hz, $J_{14-13} = 7.8$ Hz, H_{14}), 7.96 (d, 2, $J_{2-3} = 2.0$ Hz H_3), 8.21 (dd, 2, $J_{14-13} = 7.8$ Hz, $J_{12-13} = 8.2$ Hz, H_{13}), 8.37 (t, 1, $J_{9-8} = 2.8$ Hz, H_8), 8.55 (d 2.6 Hz, 2, H_1), 8.59 (d, 2, $J_{C-D} = 6.0$ Hz, H_D), 8.65 (d, 2, $J_{14-15} = 5.7$ Hz, H_{15}), 8.76 (d, 2, $J_{12-13} = 8.2$ Hz H_{12}), 9.02 (s, 1, H_4) ppm. ^{13}C NMR (500 MHz, CD_3CN, 25 °C): δ, 76.0 (C_4), 108.7 (C_9), 110.0 (C_2), 122.1 (C_B), 125 (C_{12}), 126.4 (C_{14}), 128.0 (C_{12}), 128.7 ($C_{E,F}$), 135.7 (C_8), 135.8 (C_1), 138 (C_{13}), 143.8 (C_{10}), 147.3 (C_3), 150.7 (C_D), 152.9 (C_{15}), 153.3 (C_A) ppm.

The mixed-valent species [(tpm)(bpy)Ru^{II}(L)Ru^{III}-(NH_3)$_5$]$^{5+}$ (L = pz (**4**), 4,4′-bpy (**5**), and BPE (**6**)) were generated *in situ* by adding Br_2 vapour to an acetonitrile solution of (**1**), (**2**) and (**3**), respectively, or by bulk electrolysis at 0.5–0.8 V in CH_3CN, 0.1 M TBAH.

2.2.4. [(tpm)(bpy)Ru(PCA)](PF_6)$_2$·4H_2O (7)

Anal. Calc. for $C_{32}H_{36}F_{12}N_{12}O_4P_2Ru$ (1043.7): C, 36.8; H, 3.5; N 16.1. Found: C, 36.9; H, 3.0; N 15.4%.

The corresponding dinuclear complexes [(tpm)(bpy)-Ru^{II}(PCA)Ru^{II}(NH_3)$_5$]$^{4+}$ (**8**) and [(tpm)(bpy)Ru^{II}(PCA)-Ru^{III}(NH_3)$_5$]$^{5+}$ (**9**) were obtained and characterized in solution by procedures similar to those already described for the other complexes.

2.3. Equipments and techniques

All used chemicals were reagent grade. CH_3CN was freshly distilled for electrochemical measurements. UV–Vis spectra were recorded with Shimadzu UV-160A and Cary 50 spectrophotometers. IR spectra were performed on a Perkin–Elmer 983G spectrophotometer. Cyclic voltammetry experiments were carried out in CH_3CN, using a BAS Epsilon EC equipment, with Ag/AgCl (3 M KCl) as reference electrode, vitreous C as working electrode, Pt wire as auxiliary electrode and 0.1 M TBAH [tetrakis-(*n*-butyl)ammonium hexafluorophosphate] as supporting electrolyte. A special OTTLE cell designed by BAS was used for the spectroelectrochemical measurements. All NMR data were recorded in CD_3CN with a Bruker 500 MHz spectrometer. 2D COSY, 2D HSQC and 2D NOESY (mixing time 500 ms) experiments were collected in routine conditions. Chemical Analyses were carried out at INQUIMAE, UBA, Argentina, with an estimated error of ±0.5%.

3. Results and discussion

3.1. Synthesis and IR spectra

All dinuclear complexes of the type [(tpm)(bpy)Ru(L)-$Ru(NH_3)_5$](PF_6)$_4$ (with L = pz, 4,4′-bpy, BPE and PCA) were prepared by mixing stoichiometric amounts of [Ru(tpm)(L)(bpy)](PF_6)$_2$ and [$Ru(NH_3)_5(H_2O)$](PF_6)$_2$ in acetone under Ar for 2 h, with subsequent purification by standard chromatographic techniques, as described in the experimental section. The mixed-valent species were synthesized *in situ* by adding excess of bromine to CH_3CN solutions of the reduced complexes, since the redox potential of the Br_2/Br_2^- couple is higher than that of the Ru_b^{III}, Ru_a^{II} couple but lower than that of the Ru_a^{III}/Ru_b^{II} couple (vide infra) [6].

IR spectra (as KBr pelletes) of **1**, **2**, and **3** show characteristic ligand vibrations between 1600 and 600 cm^{-1}. The typical ammonia symmetric deformation frequencies $\delta_{sym}(NH_3)$ appear in these complexes at 1287, 1286 and 1286 cm^{-1}, respectively, indicating oxidation

states (II) for all ruthenium atoms bonded to amines (= Ru_a) [5].

3.2. NMR spectra

Fig. 1 shows the ^1H NMR spectrum of $[(tpm)(bpy)Ru^{II}(BPE)Ru^{II}(NH_3)_5]^{4+}$ in CD_3CN at 500 MHz, as a representative example. NMR chemical shifts are closely related to those reported [3] for the mononuclear species of the type $[Ru(tpm)(L)(bpy)]^{2+}$, confirming the molecular symmetry of the complexes and the relative position of each coordinating position of all N-containing ligands around the first Ru center. The effect of the additional $Ru(NH_3)_5$ moiety has minor effects on chemical shift values. All NMR data have been confirmed and fully assigned by using 2D COSY, HSQC and NOESY experiments.

3.3. Redox properties

The electrochemical measurements in CH_3CN (0.1 M TBAH) for complexes **1**, **2** and **3** show in the oxidative range of potentials two reversible redox waves that can be assigned to the couples Ru_b^{III}/Ru_b^{II} ($E_{1/2} = 1.30$, 1.21 and 1.19 V, versus SCE, for the species bridged by pz, 4,4′-bpy and BPE, respectively) and Ru_a^{III}/Ru_a^{II} ($E_{1/2} =$ 0.46, 0.35 and 0.35 V, versus SCE, for the same species, respectively). The redox potentials for the Ru_b^{III}/Ru_b^{II} couples decrease in the order pz > 4,4′-bpy > BPE, evidencing the decreasing order of π-backbonding effects from Ru_b to the L ligands, as demonstrated before for the corresponding mononuclear precursors $[Ru(tpm)(L)(bpy)]^{2+}$ ($E_{1/2} =$ 1.20, 1.15 and 1.10 V, versus SCE, for L = pz, 4,4′-bpy and BPE, respectively) [3]. The higher values obtained here for the dinuclear species can be attributed to their higher charges. On the other hand, the values of the redox potentials for the Ru_a^{III}/Ru_a^{II} couples are consistent with those already obtained in the analogous $[(trpy)(bpy)Ru^{II}(L)Ru^{II/III}(NH_3)_5]^{4+/5+}$ series ($E_{1/2} = 0.66$, 0.39 and 0.31 V, versus SCE, for L = pz, 4,4′-bpy and BPE, respectively) [5]. When comparing these values to those of the mononuclear complexes $[Ru(NH_3)_5(L)]^{2+}$, a small increase in $E_{1/2}$ is observed when pz is the bridging ligand, but almost no changes are detected when BPE is the bridging ligand [5]. Complex **8** (with PCA as a bridging ligand) exhibits values of $E_{1/2}$ at 1.21 and 0.41 V, versus SCE, for the Ru_b^{III}/Ru_b^{II} and Ru_a^{III}/Ru_a^{II} couples, respectively, indicating electronic π-backbonding effects intermediate between those of pz and 4,4′-bpy. Fig. 2 shows the CV of complex **8**, as a representative example of this series.

3.4. UV–Vis spectra

Fig. 3 shows the UV–Vis spectrum of complex **3** in CH_3CN, as a representative example.

Table 1 shows the UV–Vis absorption spectral data of complexes **1**, **2**, **3** and **8** in CH_3CN. The bands observed between 200 and 300 nm can be assigned to intraligand $\pi \rightarrow \pi^*$ absorptions [3,5]. The bands at $\lambda_{max} = 397$, 416, 420 and 444 nm (corresponding to L = pz, 4,4′-bpy, BPE and PCA, respectively) are readily assigned to MLCT (metal-to-ligand charge transfer) transitions $d_\pi(Ru_b) \rightarrow \pi^*(bpy)$ of lowest energy, since these values are similar to those obtained for the mononuclear species $[Ru(tpm)(L)(bpy)]^{2+}$ ($\lambda_{max} = 392$, 395, 410 and 430 nm, corresponding to L = pz, 4,4′-bpy, BPE and PCA, respectively) [3]. The bands at $\lambda_{max} = 510$, 514, 523 and 545 nm (for L = pz, 4,4′-bpy, BPE and PCA, respectively), which disappear upon addition of Br_2 vapour, can be assigned to MLCT transitions d_π (Ru_a) → $\pi^*(L)$. These latter bands, as the former ones, are shifted to lower energies than the corresponding ones in $[Ru(NH_3)_5L]^{2+}$ complexes ($\lambda_{max} = 455$, 470, 500 and 536 nm for pz, 4,4′-bpy, BPE and PCA, respectively) [4,7], indicating a considerable decrease in the energies of the d–π^* excited states when connecting a second metallic center to the free N of the bridging ligand.

In the mixed-valent species **4**, **5**, **6** and **9**, the lowest energy bands of **1**, **2**, **3** and **8** disappear completely and new bands appear at 790, 680, 674 and 630 nm (values determined by gaussian deconvolution) for L = pz, 4,4′-bpy, BPE and PCA, respectively, due to MMCT

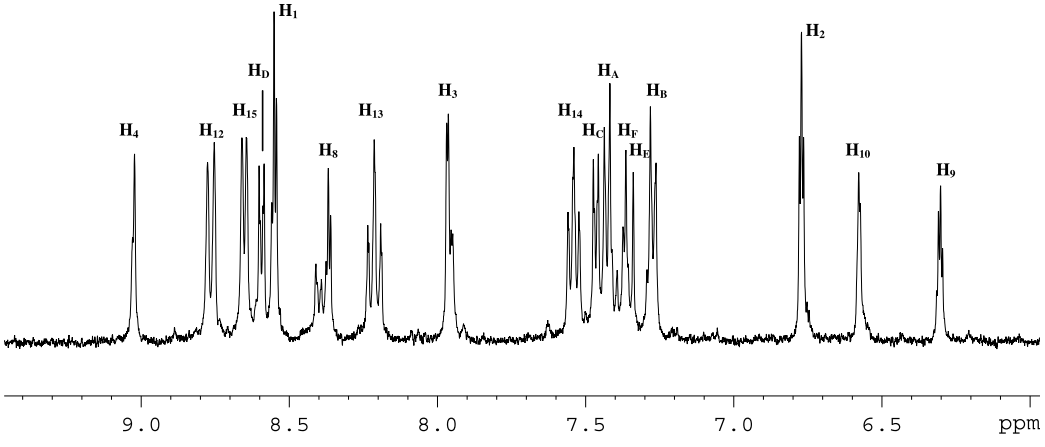


Fig. 1. ^1H NMR spectrum of $[(tpm)(bpy)Ru^{II}(BPE)Ru^{II}(NH_3)_5]^{4+}$, in CD_3CN, at 500 MHz.

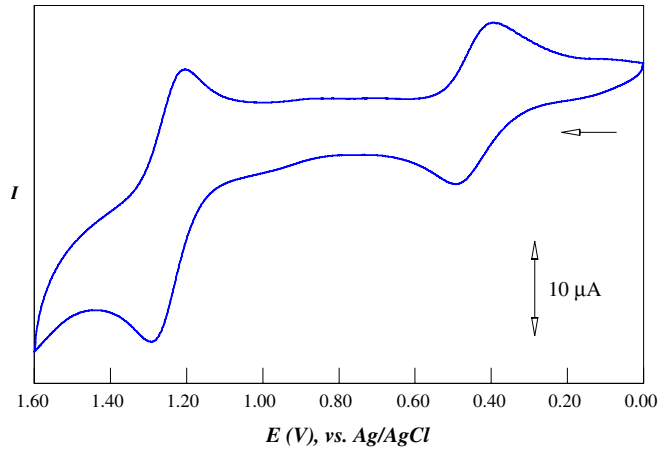


Fig. 2. Cyclic voltammogram of $[(tpm)(bpy)Ru^{II}(PCA)Ru^{II}(NH_3)_5]^{4+}$, in CH_3CN, 0.1 M TBAH, $v = 100$ mV s^{-1}.

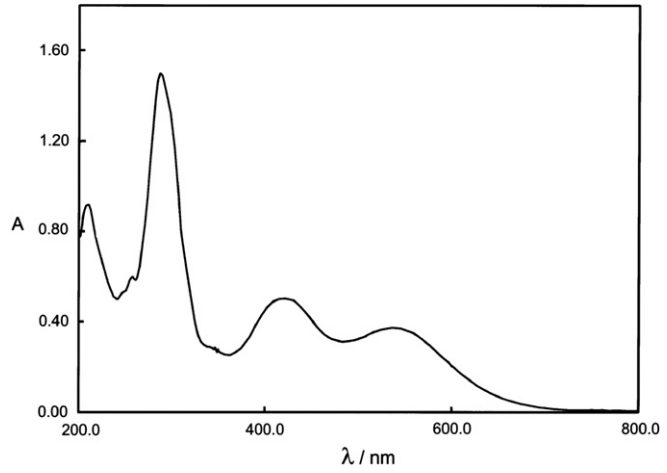


Fig. 3. UV–Vis spectra of $[(tpm)(bpy)Ru^{II}(BPE)Ru^{II}(NH_3)_5]^{4+}$, in CH_3CN, at room temperature ($C = 2.8 \times 10^{-5}$ M).

Table 1
Electronic spectral data in CH_3CN at 22 °C of complexes of the type: $[(tpm)(bpy)Ru(L)Ru(NH_3)_5]^{4+}$

L	Complex	λ_{max} (nm) ($\varepsilon_{max} \times 10^{-3}$ M^{-1} cm^{-1})
pz	**1**	510 (14.0), 397 (10.6), 338 (sh), 284 (31.1), 224 (18.9)
4,4′-bpy	**2**	508 (17.8), 416 (15.0), 337 (sh), 286 (33.6), 245 (30.4)
BPE	**3**	534 (13.3), 420 (17.9), 343 (sh), 288 (53.2), 209 (32.5)
PCA[a]	**8**	545 (10.1), 444 (10.4), 330 (sh), 285 (36.0), 256 (23.0)

[a] Values of ε_{max} are estimated by comparison with the UV bands of the mononuclear species **7**.

(metal-to-metal charge transfer) transitions $[Ru_b^{II} \rightarrow Ru_a^{III}]$. As a representative example, Fig. 4 shows the spectrum of **6** obtained after adding Br_2 vapour to a concentrated solution of **3** in CH_3CN. This assignment is confirmed by the detection of MMCT bands in similar ranges of the related complexes $[(trpy)(bpy)Ru^{II}(L)Ru^{III}(NH_3)_5]^{5+}$ and $\{(bpy)_2Ru^{II}[(L)Ru^{III}(NH_3)_5]_2\}^{8+}$, with L = CN^-, pz, 4-CNpy, 4,4′-bpy and BPE [5,8]. Controlled potential electrolyses at 0.5–0.8 V for the three complexes showed identical

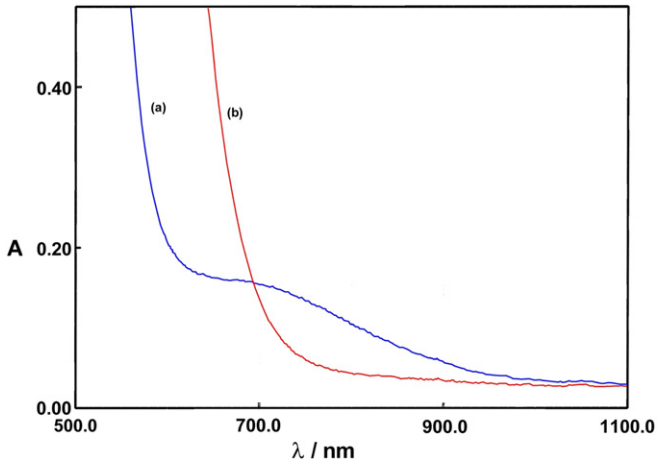


Fig. 4. UV–Vis spectra of: (a), $[(tpm)(bpy)Ru^{II}(BPE)Ru^{III}(NH_3)_5]^{5+}$ and (b), $[(tpm)(bpy)Ru^{II}(BPE)Ru^{II}(NH_3)_5]^{4+}$, in CH_3CN, at room temperature ($C = 2.8 \times 10^{-4}$ M). (a) was obtained from (b) by oxidation with bromine vapour.

results, as shown in Fig. 5, where the spectra of complexes **2** and **5** (the latter one obtained by electrolysis of **2**) are compared. These oxidation processes are reversible in a longer time-scale (*ca.* 1 h).

3.5. Intramolecular electron transfer parameters

Using the Marcus–Hush formalism [9,10] and the experimental spectral data of the MMCT bands in the mixed-valent species, the reorganization energy (λ) for the intramolecular electron transfer through the bridging ligand L and the electronic coupling element between both metal centers (H_{AB}) can be calculated as follows:

$$\lambda = E_{op} - \Delta G^0 - \Delta E_{ex} \quad (1)$$

$$H_{AB} = \frac{2.06 \times 10^{-2}}{r}(\varepsilon_{max} \cdot \Delta\tilde{\nu}_{1/2} \cdot \tilde{\nu}_{max})^{1/2} \quad (2)$$

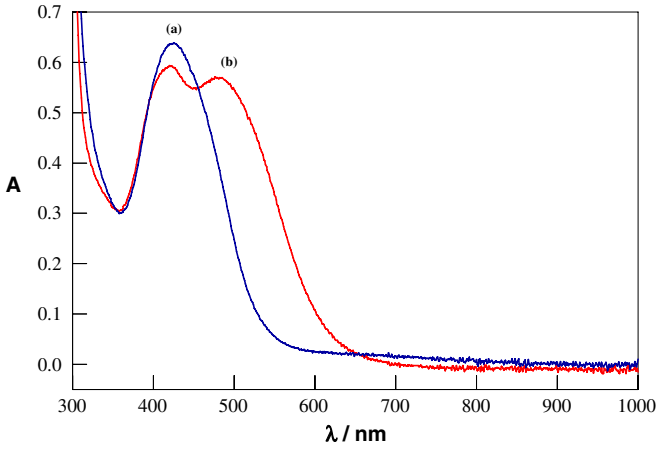


Fig. 5. UV–Vis spectra of: (a), $[(tpm)(bpy)Ru^{II}(4,4'\text{-}bpy)Ru^{III}(NH_3)_5]^{5+}$ and (b), $[(tpm)(bpy)Ru^{II}(4,4'\text{-}bpy)Ru^{II}(NH_3)_5]^{4+}$, in CH_3CN, 0.1 M TBAH, at room temperature ($C = 3.8 \times 10^{-5}$ M). (a) was obtained from (b) by electrolysis at $V = 0.5$ V.

where E_{op} is the energy of the absorption maximum (in eV), ΔG° is the free energy difference between both redox sites (approximated as the difference in the redox potentials $\Delta E_{1/2}$) and ΔE_{exc} is an excited-state energy difference, estimated as 0.25 eV [8]. ε_{max} is the absorption coefficient of the MMCT band, $\tilde{\nu}_{max}$ is the energy maximum of the same band (in cm^{-1}), $\Delta\tilde{\nu}_{1/2}$ is the bandwidth at half-height, and r is the metal–metal distance in Å [10].

Table 2 shows the obtained values for these parameters in the series of mixed-valent complexes **4**, **5**, **6** and **9**.

For all these mixed-valent species, the values of $H_{AB} \ll \lambda$; therefore, they can be classified as belonging to Class II according to Robin and Day nomenclature [10]. The reorganization energy λ increases with r in going from pz to PCA, as predicted by Marcus theory [11]. Moreover, this increment is reflected in the increasing values of E_{op} with r, as recently reported in unsymmetric mixed-valent Co^{III}–Fe^{II} complexes [12]. For L = pz and 4,4′-bpy, the reverse intramolecular electron transfers $Ru_a^{II} \rightarrow Ru_b^{III}$ are predicted to be in the Marcus inverted region, since $\lambda < -\Delta G^{\circ}$, while for L = BPE, the analogous charge recombination falls almost in the barrierless region ($\lambda \cong -\Delta G^{\circ}$). This trend is similar to that found for the corresponding species with trpy [5]. In the case of L = PCA, this charge recombination falls in the normal region, since $\lambda > -\Delta G^{\circ}$.

The electronic coupling H_{AB} decreases with increasing metal-to-metal distance, as expected from Marcus theory [11], but the obtained values are higher than those found in the trpy complexes by an average factor of *ca.* 1.3 [5]; for example, the value of H_{AB} is 750 cm^{-1} for $[(tpm)(bpy)Ru^{II}(L)Ru^{III}(NH_3)_5]^{5+}$ and 614 cm^{-1} for $[(trpy)(bpy)Ru^{II}(L)Ru^{III}(NH_3)_5]^{5+}$, pointing to a stronger electronic communication in the tpm series. Moreover, as shown in Fig. 6, the distance dependence is less steeper: a value of $\beta = 0.3$ $Å^{-1}$ is obtained (where β is the slope of $2\ln H_{AB}$ versus r), when considering the four ligands, which is 25% lower than the value determined for the series of the trpy complexes ($\beta = 0.4$ $Å^{-1}$) [5].

As stated before [13], the value of β determines the attenuation with distance of the electronic overlap between both metallic centers with the bridging ligand. Pure σ-connectors, such as polyprolines acting as bridges in ruthenium amines [14], have a slope $\beta = 0.6$ $Å^{-1}$. Pure π-connectors, such as polyenes acting as bridges in ruthenium amines [15], have a slope $\beta = 0.2$ $Å^{-1}$. Since the value of β obtained in this work is much closer to that of the pure π-connectors, we deduce that the facial geometry and poor π-acceptor character of tpm induce a better transmission of the metal-to-metal electronic interaction in these complexes. Connecting at least three metal centers may eventually lead to a molecular-wire behaviour [16].

Table 2
Intramolecular electron transfer parameters in the series of mixed-valent complexes of the type $[(tpm)(bpy)Ru^{II}(L)Ru^{III}(NH_3)_5]^{5+}$

L	Complex	r (Å)	E_{op} (eV)	ΔG° (eV)	λ (eV)	H_{AB} (cm^{-1})
pz	**4**	7.0	1.62	0.84	0.53	750
4,4′-bpy	**5**	11.3	1.82	0.86	0.71	350
BPE	**6**	13.8	1.84	0.84	0.75	320
PCA	**9**	14.9	1.97	0.80	0.92	200

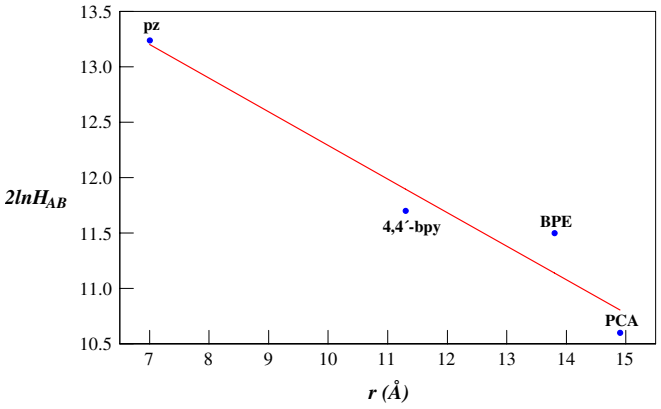


Fig. 6. Plot of $2\ln H_{AB}$ vs. r for the four mixed-valent species $[(tpm)(bpy)Ru^{II}(L)Ru^{III}(NH_3)_5]^{5+}$, in CH_3CN (L = pz, 4,4′-bpy, BPE and PCA).

4. Conclusions

We conclude that the distance dependence of the reorganization energies and the electronic coupling elements in the new mixed-valent unsymmetric complexes prepared and characterized in this work point to a stronger electronic communication between both metallic centers than in the analogous complexes with trpy. Moreover, an increased transmission of the electronic interaction is induced in these complexes by using tpm instead of trpy as a spectator ligand.

Acknowledgements

To CONICET, UNT, and ANPCyT (Argentina) for financial support. M.C. thanks CONICET for a graduate fellowship. N.E.K and F.F. are Members of the Research Career (CONICET). N.E.K. gratefully acknowledges support for a short stay as a Visiting Professor from the University of Girona, Spain.

References

[1] (a) N. Sutin, C. Creutz, Pure Appl. Chem. 52 (1980) 2717;
(b) T.J. Meyer, Acc. Chem. Res. 22 (1989) 163;
(c) V. Balzani, F. Scandola, Supramolecular Photochemistry, Ellis Horwood, Chichester, 1991;
(d) V. Balzani, A. Juris, M. Venturi, S. Campagna, S. Serroni, Chem. Rev. 96 (1996) 759;
(e) J.H. Alstrum-Acevedo, M.K. Brennaman, T.J. Meyer, Inorg. Chem. 44 (2005) 6802.
[2] (a) J.P. Launay, Chem. Soc. Rev. 30 (2001) 386;
(b) M.E. García Posse, M.M. Vergara, F. Fagalde, N.E. Katz, Polyhedron 22 (2003) 465;

(c) W.-Z. Chen, F.A. Cotton, N.S. Dalal, C.A. Murillo, C.M. Ramsey, T. Ren, X. Wang, J. Am. Chem. Soc. 127 (2005) 12691.
[3] N.E. Katz, I. Romero, A. Llobet, T. Parella, J. Benet-Buchholz, Eur. J. Inorg. Chem. (2005) 272.
[4] M. Cattaneo, F. Fagalde, N.E. Katz, A.M. Leiva, R. Schmehl, Inorg. Chem. 45 (2006) 127.
[5] F. Fagalde, N.E. Katz, Polyhedron 14 (1995) 1213.
[6] S. Plotkin, A. Haim, Inorg. Chim. Acta 270 (1998) 89.
[7] R.W. Callahan, G.M. Brown, T.J. Meyer, Inorg. Chem. 14 (1975) 1443.
[8] N.E. Katz, C. Creutz, N. Sutin, Inorg. Chem. 27 (1988) 1687.
[9] N. Hush, Coordin. Chem. Rev. 64 (1985) 135.
[10] C. Creutz, Prog. Inorg. Chem. 30 (1983) 1.
[11] R.A. Marcus, N. Sutin, Biochim. Biophys. Acta 811 (1985) 265.
[12] P. Pérez-Tejeda, G. López-Pérez, R. Prado-Gotor, F. Sánchez, D. González-Arjona, M. López-López, F. Bozoglián, G. González, M. Martínez, Inorg. Chim. Acta 359 (2006) 149.
[13] M.D. Newton, Chem. Rev. 91 (1991) 767.
[14] N. Sutin, Adv. Chem. Ser. 228 (1991) 25.
[15] S. Woitellier, J.P. Launay, C.W. Sprangler, Inorg. Chem. 28 (1989) 758.
[16] J.F. Berry, F.A. Cotton, T. Lu, C.A. Murillo, X. Wang, Inorg. Chem. 42 (2003) 3595.

Available online at www.sciencedirect.com
ScienceDirect
Polyhedron 26 (2007) 24–32
POLYHEDRON
www.elsevier.com/locate/poly

Three-dimensional supramolecular H-bonding network in the compounds containing hexamethylenetetramine and aquated Ni(II) or Cd(II) salts

Suparna Banerjee [a], Angshuman Roy Choudhury [b], T.N. Guru Row [b], Siddhartha Chaudhuri [c], Ashutosh Ghosh [a,*]

[a] *Department of Chemistry, University College of Science, University of Calcutta, 92, A.P.C. Road, Kolkata 700 009, India*
[b] *Solid State and Structural Chemistry Unit, Indian Institute of Science, Bangalore 560 012, India*
[c] *R.S.I.C, Bose Institute, Kolkata 700 009, India*

Received 13 June 2006; accepted 25 July 2006
Available online 1 August 2006

Abstract

To investigate the interactions between hydrogen bond donor and acceptor giving rise to three dimensional networks, compounds $[Ni(H_2O)_6](ClO_4)_2 \cdot 2\{(CH_2)_6N_4\} \cdot 2H_2O$ (**1**), $[Ni(H_2O)_6]Cl_2 \cdot 2\{(CH_2)_6N_4\} \cdot 4H_2O$ (**2**) and $[Cd(H_2O)_4\{(CH_2)_6N_4\}_2](ClO_4)_2 \cdot 2H_2O$ (**3**) (where $(CH_2)_6N_4$ = hexamethylenetetramine) have been prepared and their crystal structures were investigated. In all three complexes, the metal coordination is octahedral. The hexamine molecules are complexed in the cadmium compound, **3** but are free in the nickel salts, **1** and **2**. The supramolecular structures of **1** and **2** show $R_4^4(16)$ motif linking the cationic moieties with hexamine which are in turn interwoven with anionic moieties via water molecules. In contrast the supramolecular structure of **3** shows $R_2^2(12)$ motif.
© 2006 Elsevier Ltd. All rights reserved.

Keywords: Crystal structure; Nickel(II); Cadmium(II); Hexamethylenetetramine; H-bonding

1. Introduction

Understanding of charge assisted non-covalent interactions such as hydrogen bonding, π–π stacking, dipole–dipole, hydrophobic interactions, etc., collectively constitute a promising field of persistent research interest [1]. The weak intermolecular interactions between molecular building units enforce a self-assembling process to generate molecular networks of different dimensionality with specific architectural and functional behaviors [2]. Experimental generation of supramolecular aggregates based on H-bonding could be achieved via versatile donor–acceptor interactions among the metal coordinated N, O rich ligands and even with free partners (solvents, organic molecules) in the lattice [3]. Increasing the number of components, polar bridging groups with variable spacer and counter-ions definitely play a crucial role in deciding whether 1-D molecular chains are interlocked to form 2-D networks which in turn could be cross linked into 3-D networks. Therefore, the intricate association of molecular synthons through weak forces results in novel multidimensional structures [4]. Molecular assemblies possessing translational symmetry of one or several assembling units could be modeled by interplay of H-bonding and other weak forces depending upon the chemical environment. This implies the necessity of rational designing strategy known as crystal engineering [5], yet to be explored at its best, to obtain desired architecture. Higher stability, better dimensionality and complementary combination of donors and acceptors in H-bonding could be superiorly utilized in crystal engineering over the other intermolecular forces [6]. Transition metal ions can be incorporated into H-bonding networks by employing bi-functional ligands that contain

* Corresponding author.
E-mail address: ghosh_59@yahoo.com (A. Ghosh).

0277-5387/$ - see front matter © 2006 Elsevier Ltd. All rights reserved.
doi:10.1016/j.poly.2006.07.019

unaffected H-bonding functionalities in addition to chelating centres [7].

To substantiate these assumptions, we were encouraged to examine the interactive details in the crystal structures of two Ni(II) complexes and of a Cd(II) complex derived from hexamethylenetetramine, respective metal salts and water molecules. Herein, some striking observations have been accessed in the context of H-donor acidity, H-acceptor basicity, steric/electronic demands of counter-ions, conformational constraints of hexamine to inspire high nuclearity and metal contrast.

2. Experimental

2.1. Starting materials

$NiCl_2 \cdot 6H_2O$ and hexamine were purchased from spectrochem, India and used as received. $Ni(ClO_4)_2 \cdot 6H_2O$ and $Cd(ClO_4)_2 \cdot 2H_2O$ salts were prepared in our laboratory. *Caution:* Perchlorate salts are hazardous and may explode.

2.2. Synthesis of complexes

2.2.1. $[Ni(H_2O)_6](ClO_4)_2 \cdot 2\{(CH_2)_6N_4\} \cdot 2H_2O$ (**1**)

$Ni(ClO_4)_2 \cdot 6H_2O$ (0.165 g, 0.45 mmol) dissolved in minimum volume of water was added to an aqueous solution of hexamine (0.126 g, 0.90 mmol). On slow evaporation at room temperature single crystals appeared. Yield: 298 mg (79%). *Anal.* Calc. for $C_{12}H_{40}Cl_2N_8NiO_{16}$: C, 21.12; H, 5.86; N, 16.42. Found: C, 21.06; H, 5.83; N, 16.40%. IR (ν/cm^{-1}): 3495, 3417 (ν_{O-H}), 2984, 2889 (ν_{C-H}), 1662 (δ_{O-H}), 1089, 622 (ν_{ClO_4}).

2.2.2. $[Ni(H_2O)_6]Cl_2 \cdot 2\{(CH_2)_6N_4\} \cdot 4H_2O$ (**2**)

This complex was prepared by a similar procedure taking $NiCl_2 \cdot 6H_2O$ (0.107 g, 0.45 mmol) and hexamine (0.126 g, 0.90 mmol). Yield: 226 mg (82%). *Anal.* Calc. for $C_{12}H_{44}Cl_2N_8NiO_{10}$: C,24.40; H, 7.45; N, 18.97. Found: C, 24.37; H, 7.41; N, 18.92%. IR (ν/cm^{-1}): 3397 (ν_{O-H}), 2980, 2885 (ν_{C-H}), 1663 (δ_{O-H}).

2.2.3. $[Cd(H_2O)_4\{(CH_2)_6N_4\}_2](ClO_4)_2 \cdot 2H_2O$ (**3**)

This complex was prepared by a similar procedure taking $Cd(ClO_4)_2 \cdot 2H_2O$ (0.174 g, 0.5 mmol) and hexamine (0.140 g, 1.0 mmol) Yield: 297 mg (85%). *Anal.* Calc. for $C_{12}H_{36}CdCl_2N_8O_{14}$: C, 20.57; H, 5.14; N, 17.43. Found: C, 20.53; H, 5.09; N, 17.41%. IR (ν/cm^{-1}): 3435, 3413 (ν_{O-H}), 2982, 2885 (ν_{C-H}), 1633 (δ_{O-H}), 1096, 626 (ν_{ClO_4}).

2.3. Physical measurements

IR (KBr disc), Perkin–Elmer RXI FT-IR spectrometer and Nicolet Magna IR 750 Series II. A Perkin–Elmer 2400 Series II elemental analyzer was used for microanalysis (C, H, N). Thermal analysis (TG-DTA) were carried out on a Metler Toledo TGA/SDTA 851 thermal analyzer in a dynamic atmosphere of dinitrogen (flow rate: 30 cm^3 min^{-1}). The sample was heated in an alumina crucible at a rate of 5 °C min^{-1}.

2.4. Crystal structure determination

Single crystal X-ray diffraction data were collected on a Bruker AXS single crystal X-ray diffractometer using SMART APEX CCD detector. The X-ray generator was operated at 50 kV and 35 mA using Mo Kα radiation. Data were collected with a ω scan width of 0.3°. A total of 606 frames per sets were collected in three different settings of φ (0°, 90° and 180°) keeping the sample to detector distance of 6.03 cm and the 2θ value fixed at −25°. The data were reduced by SAINT-PLUS [8] and an empirical absorption correction was applied using the package SADABS [8]. All the structures were solved using SIR92 [9] and refined using SHELXL-97 [10]. Molecular and packing diagrams were generated by ORTEP-32 [11] and CAMERON [12] present in the WinGx (Version 1.64.03b) [13] program suite. The geometric calculations were done by PARST-95 [14] and PLATON [15]. In compound **1** the perchlorate ion is disordered. Details of crystallographic data and refinements of three complexes are summarized in Table 1 while selected bond lengths and bond angles are presented in Table 2. A list of H-bonds in the three complexes is given in Tables 3a–3c.

3. Results and discussion

The ions and ligands were chosen in such a way so as to generate a H-bonded supramolecular frameworks. The neutral ligand, hexamine was chosen along with perchlorate and chloride ions as hydrogen bond acceptor. The Ni(II) compounds, **1** and **2** were prepared by using the counterions perchlorate and chloride, respectively, whereas compound **3** was prepared by replacing the nickel salt with cadmium perchlorate.

3.1. Description of the structures of *1* and *2*

In complex **1** the crystallographic asymmetric unit, as illustrated in the ORTEP (Fig. 1a) of the molecule, consists of one half of the aquated cation, one perchlorate anion, one neutral hexamine molecule and one crystallized water molecule. The remaining portion of the cationic complex is generated via a centre of inversion (at 0.5, 0.5, 0) giving a distorted octahedral nickel centre. The Ni–O bond lengths vary in the range 2.03–2.06 Å and are more or less comparable to those of the similar compounds reported in the literature [16].

A supramolecular structure generated via hydrogen bonding patterns between the $[Ni(H_2O)_6]^{2+}$ and hexamine moities, and those between $[Ni(H_2O)_6]^{2+}$ and perchlorate ions are illustrated separately in Figs. 1b and 1c, respectively. The supramolecular structure can be described in terms of the following subunits: a $[Ni(H_2O)_6]^{2+}$ cationic 2-D assembly incorporating neutral hexamine molecules

Table 1
Crystal data and structure refinement for the structures

Compound	**1**	**2**	**3**
Formula	$C_{12}H_{40}Cl_2N_8NiO_{16}$	$C_{12}H_{44}Cl_2N_8NiO_{10}$	$C_{12}H_{36}CdCl_2N_8O_{14}$
M	681.79	590.16	699.78
Crystal system	triclinic	triclinic	monoclinic
Space group	$P\bar{1}$	$P\bar{1}$	$P2_1/c$
a (Å)	8.191 (3)	9.338(4)	7.997(4)
b (Å)	9.155(3)	9.400(4)	19.367(10)
c (Å)	10.734(3)	9.442(4)	8.454(4)
α (°)	94.094(5)	119.494(6)	90.00
β (°)	104.420(4)	94.180(7)	103.337(8)
γ (°)	113.881(4)	101.062(7)	90.00
V (Å^3)	699.2(4)	694.2(5)	1274.1(11)
D_{calc} (Mg m^{-3})	1.619	1.412	1.824
Z	1	1	2
μ (mm^{-1})	0.968	0.947	1.147
T (K)	293(2)	293(2)	293(2)
Measured reflections	5775	7451	10958
R_{int}	0.0158	0.0593	0.0204
Collected reflections	2931	2816	3055
R_1, wR_2 [$I > 2\sigma(I)$]	0.0288, 0.0763	0.0271, 0.0763	0.0322, 0.0872

Table 2
List of selected bond lengths and bond angles for compounds **1**, **2** and **3**

	Distances (Å)		Angles (°)	
Compound **1**	Ni1–O1W	2.036(2)	∠O1W–Ni1–O3W	89.78(6)
	Ni1–O3W	2.043(1)	∠O1W–Ni1–O2W	90.02(6)
	Ni1–O2W	2.068(1)	∠O3W–Ni1–O2W	89.68(6)
Compound **2**	Ni1–O3W	2.025(1)	O3W–Ni1–O2W	87.22(6)
	Ni1–O2W	2.046(1)	O3W–Ni1–O1W	89.39(6)
	Ni1–O1W	2.056(1)	O2W–Ni1–O1W	93.39(6)
Compound **3**	Cd1–O1W	2.284(2)	O1W–Cd1–O2W	91.16(10)
	Cd1–O2W	2.292(2)	O1W–Cd1–N1	86.28(8)
	Cd1–N1	2.400(2)	O2W–Cd1–N1	93.15(8)

and cation···anion interaction through hydrophilic porous channels together with the solvent molecules. The cationic structure is mainly dominated by three different types of hydrogen bonds. Of them, two interactions viz. [O(3W)–H(1W3)···N(4)] and [O(2W)–H(1W2)···N(2)] together constitute a 16-membered hydrogen bonded rings [graph set $R_4^4(16)$] [17]. These rings are repeated in the lattice by translation along the y-axis. The x-direction is characterized by the formation of a similar 16-membered rings [graph set $R_4^4(16)$] [17] comprised of the interactions [O(1W)–H(1W1)···N(1)] and [O(3W)–H(1W3)···N(4)] (Fig. 1b). Consequently, a 2-D network results via the interplay of [O(2W)–H(1W2)···N(2)] and [O(1W)–H(1W1)···N(1)] interactions within the 2D framework and the two sets of rings are interwoven utilizing the common [O(3W)–H(1W3)···N(4)] bonding. Therefore the 2-D network can be envisaged as having been generated by the O–H···N interactions involving two co-facial N atoms [N(1), N(2)] of hexamine and coordinated water molecules [O(1W), O(2W)]. The structural intricacy has been further enhanced by the active participation of O–H donor functionality of the uncoordinated lattice water. The H(1W4) atom of the uncoordinated water molecule O(4W) is engaged in a moderately strong H-bonding with the remaining nitrogen atom N(3) of the hexamine species [O(4W)–H(1W4)···N(3)], thereby defining the z-axis with the formation of a 16-membered H-bonded ring [O(3W)–H(1W3)···N(4)……N(3)···H(1W4)–O(4W)……] (Fig. 1b). Another type of intermolecular interaction has been noticed between the hydrogen H(2W4) of O(4W) and O(3A) of the counterion perchlorate [O(4W)–H(2W4)···O(3A)] (Fig. 1c). In conjunction with this interaction, an additional one existing between H(2W1) of coordinated oxygen O(1W) and O(1) of the anionic moiety results in the formation of a 20-membered ring [graph set $R_6^6(20)$]

Table 3a
A list of hydrogen bonds found in the crystal structure of **1**

D–H···A	D–H (Å)	D···A (Å)	H···A (Å)	∠D–H···A (°)
O(3W)–H(1W3)···N(4)	0.83(4)	2.836(3)	2.10(4)	175(3)
O(3W)–H(2W3)···O(4W)	0.77(3)	2.704(3)	1.93(3)	175(3)
O(4W)–H(2W4)···O(3A)	0.69(5)	2.852(6)	2.28(4)	143(5)
O(1W)–H(1W1)···N(1)^1	0.84(3)	2.771(2)	1.94(3)	170(3)
O(1W)–H(2W1)···O(1)^2	0.72(2)	2.931(3)	2.22(2)	175(3)
O(4W)–H(1W4)···N(3)^3	0.75(4)	2.870(3)	2.13(3)	169(4)
O(2W)–H(1W2)···N(2)^4	0.84(3)	2.794(3)	1.98(2)	163(3)

Symmetry equivalents: 1: $x-1$, y, z; 2: $-x$, $-y+1$, $-z$; 3: $-x+2$, $-y+1$, $-z+1$; 4: $-x+1$, $-y$, $-z$.

Table 3b
A list of hydrogen bonds found in the crystal structure of **2**

D–H···A	D–H (Å)	D···A (Å)	H···A (Å)	∠D–H···A (°)
O(1W)–H(1W1)···N(3)	0.77(4)	2.806(3)	2.05(3)	170(3)
O(1W)–H(2W1)···Cl(1)	0.78(2)	3.196(2)	2.45(2)	159(2)
O(3W)–H(1W3)···O(4W)	0.74(3)	2.709(2)	1.98(3)	167(3)
O(2W)–H(1W2)···O(5W)	0.79(2)	2.740 (3)	1.98(3)	160(2)
O(2W)–H(2W2)···N(4)[1]	0.77(2)	2.823 (2)	2.07(2)	170(3)
O(3W)–H(2W3)···N(2)[2]	0.83(3)	2.798(2)	1.99(3)	168(2)
O(4W)–H(1W4)···Cl(1)[3]	0.74(3)	3.174(2)	2.45(2)	169(3)
O(4W)–H(2W4)···N(1)[4]	0.85(3)	2.833(2)	1.99(3)	173(2)
O(5W)–H(1W5)···Cl(1)[5]	0.93(3)	3.201(2)	2.270(3)	177(3)
O(5W)–H(2W5)···Cl(1)[6]	0.73(4)	3.257(3)	2.537(4)	171(3)

Symmetry equivalents: 1: $x, y-1, z$; 2: $-x, -y, -z$; 3: $-x, -y-1, -z$; 4: $x-1, y-1, z$; 5: $-x+1, -y, -z+1$; 6: $x, y, z+1$.

Table 3c
A list of hydrogen bonds found in the crystal structure of **3**

D–H···A	D–H (Å)	D···A (Å)	H···A (Å)	∠D–H···A (°)
O(2W)–H(1W2)···O(3W)	0.77(5)	2.684(4)	1.92(5)	169(5)
O(3W)–H(2W3)···O(4)	0.90(7)	3.078(6)	2.23(7)	158(6)
O(1W)–H(1W1)···N(4)[1]	0.77(5)	2.778(3)	2.02(5)	172(6)
O(1W)–H(2W1)···O(1)[2]	0.66(6)	2.826(7)	2.34(6)	134(6)
O(2W)–H(2W2)···N(3)[3]	0.76(5)	2.884(3)	2.19(5)	153(5)
O(3W)–H(1W3)···N(2)[4]	0.75(5)	2.870(4)	2.23(5)	169(6)

Symmetry equivalents: 1: $x+1, y, z$; 2: $-x+2, -y, -z$; 3: $-x+2, -y, -z+1$; 4: $-x+2, y-1/2, -z+1/2$.

[17] (Fig. 1c) which serves as a linker between the graph sets propagating along the *x*- and *z*-directions.

In complex **2** the crystallographic asymmetric unit, as illustrated in the ORTEP (Fig. 2a) of the molecule, consists of one half of hexaaua Ni(II), one chloride anion, one uncoordinated neutral hexamine moiety and two molecules of water of crystallization. The remainder of the cation is generated by transformation through the inversion centre at 0, 0, 0 (the nickel atom location; site occupancy 0.5). The coordination geometry of nickel is distorted octahedral with Ni–O distances ranging from 2.02–2.05 Å [16].

Hydrogen bonding patterns between $[Ni(H_2O)_6]^{2+}$ and hexamine moieties, and those between $[Ni(H_2O)_6]^{2+}$ and chloride ions are shown in Figs. 2b and 2c, respectively. A 16-membered ring $[R_4^4(16)]$ [17] (Fig. 2b) formed by cations and hexamine moieties via the H-bonding interactions [O(3W)–H(2W3)···N(2) and O(1W)–H(1W1)···N(3)] propagates along the *z*-axis. A similar 16-membered ring formed by the interactions of N(3) and N(4) with hydrogens of the coordinated water molecules O(1W) and O(2W) [O(1W)–H(1W1)···N(3) and O(2W)–H(2W2)··· N(4)] is translated along the *y*-axis. The two sets of rings share the H-bonding

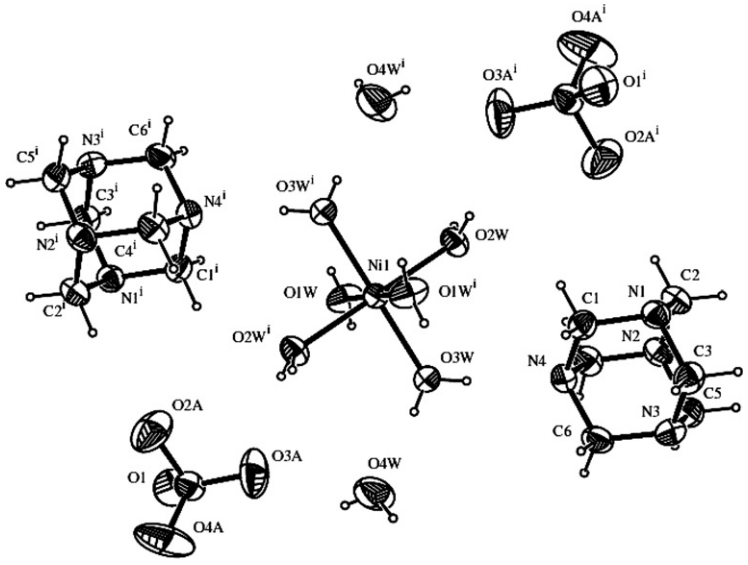


Fig. 1a. ORTEP-3 plot of the structure of $[Ni(H_2O)_6](ClO_4)_2 \cdot 2C_6H_{12}N_4 \cdot 2H_2O$. Atoms having superscripted labels are those generated by the centre of inversion at the Ni centre.

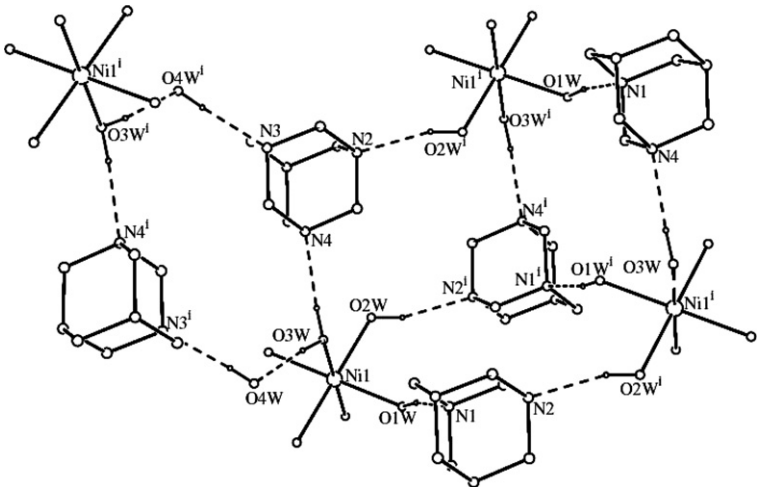


Fig. 1b. Hydrogen bonding patterns between the $[Ni(H_2O)_6]^{2+}$, the hexamine moieties and the included water molecule in the crystal structure of $[Ni(H_2O)_6](ClO_4)_2 \cdot 2C_6H_{12}N_4 \cdot 2H_2O$.

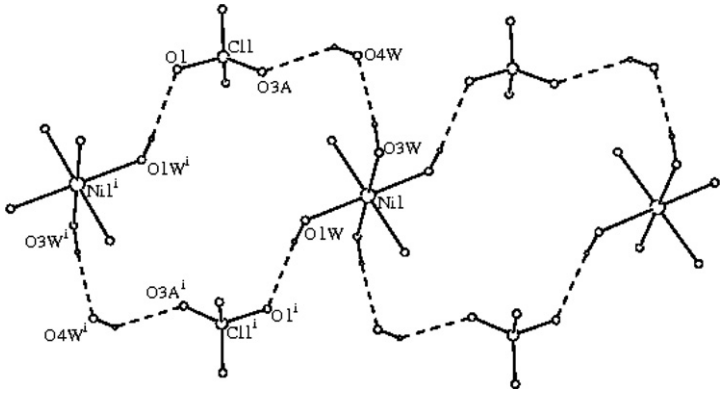


Fig. 1c. Hydrogen bonding patterns between the $[Ni(H_2O)_6]^{2+}$, the perchlorate ions and the included water molecule in the crystal structure of $[Ni(H_2O)_6](ClO_4)_2 \cdot 2C_6H_{12}N_4 \cdot 2H_2O$.

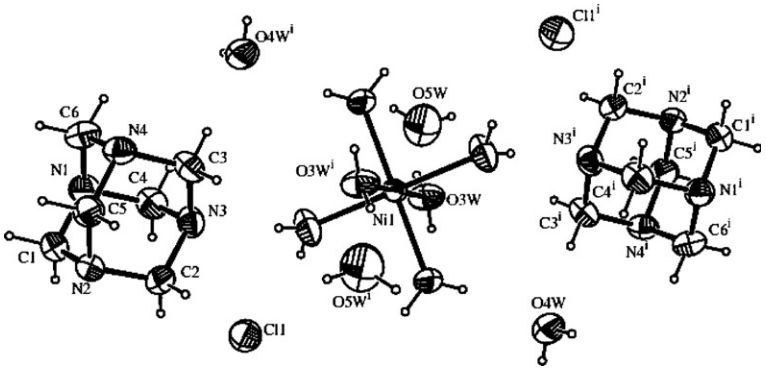


Fig. 2a. ORTEP-3 plot of the structure of $[Ni(H_2O)_6]Cl_2 \cdot 2C_6H_{12}N_4 \cdot 4H_2O$. Atoms having superscripted labels are those generated by the centre of inversion at the Ni centre.

link [O(1W)–H(1W1)···N(3)], thereby forming a 2-D network of graph sets. The remaining nitrogen atom N(1) of the hexamine moiety forms a strong H-bonding interaction with one of the hydrogen atom H(2W4) of the uncoordinated water molecule O(4W) along the *x*-direction, leading to the formation of a 20-membered ring [O(1W)–H(1W1)···N(3)……N(1)···H(2W4)–O(4W) ···H(1W3)–O(3W)……] $[R_6^6(20)]$ [17] (Fig. 2c). The chloride ion H-bonded with the uncoordinated water molecules gives rise to a number of anionic ring systems (Fig. 2c). One of the hydrogen atoms H(2W5) of the uncoordinated water molecule O(5W) connects the chloride ion and forms a 16-membered ring

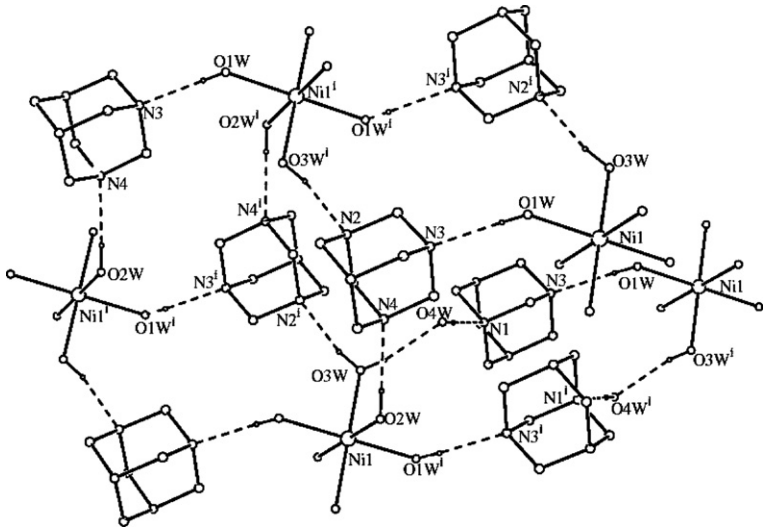


Fig. 2b. Hydrogen bonding patterns between the $[Ni(H_2O)_6]^{2+}$, the hexamine moieties and one of the included water molecules, O4W, in the crystal structure of $[Ni(H_2O)_6]Cl_2 \cdot 2C_6H_{12}N_4 \cdot 4H_2O$.

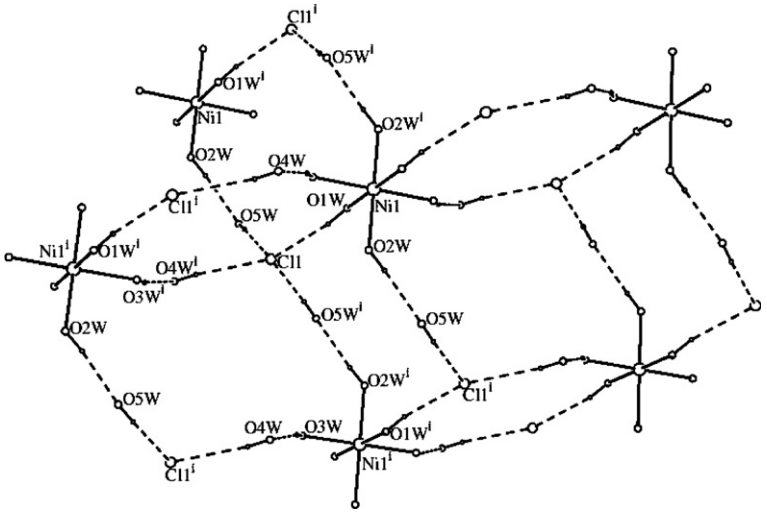


Fig. 2c. Hydrogen bonding patterns between the $[Ni(H_2O)_6]^{2+}$ and chloride ions and the included water molecules, O4W and O5W, in the crystal structure of $[Ni(H_2O)_6]Cl_2 \cdot 2C_6H_{12}N_4 \cdot 4H_2O$.

[O(1W)–H(2W1)···Cl1···H(2W5)–O(5W)···H(1W2)–O(2W) .....] propagating along the *z*-direction. The remaining hydrogen atom H(2W5) of O(5W) forms a similar ring system [O(2W)–H(1W2)···O(5W)–H(1W5)··· Cl1···H(2W1)–O(1W).....] $[R_6^4(16)]$ [17] propagating along the *x*-direction (Fig. 2c). One of the remaining hydrogen atoms H(1W4) of O(4W) connects the ring systems propagating along the *x*-direction with the system [O(3W)–H(1W3)···O(4W)–H(1W4)···Cl1···H(1W5)–O(5W)···H(1W2)–O(2W).....] $[R_8^6(20)]$ [17]. Interweaving of these anionic and cationic frameworks results in the formation of a three-dimensional network.

3.2. Effects of counterions in **1** and **2**

In both the structures **1** and **2** the counterions ClO_4^- and Cl^-, respectively, are uncoordinated. The significant differences, in, electronegativity of H-bond acceptor centres and polarizability arising from their differing sizes, affects the number and modes of H-bonds associated with them. In addition to the smaller size of counterion Cl^-, the extent of solvation is higher in **2** compared to that in **1** [four water of crystallization per metal centres in **2** versus two molecules in **1**], thereby dictating different H-bonding patterns in the complexes involving uncoordinated water molecules. In **1**, ClO_4^- is engaged in only one H-bonding interaction with the water oxygen O(4W) whereas for the chloride ion there are three interactions with the uncoordinated water oxygens in complex **2**, once with O(4W) and twice with O(5W). Thus, the weak interactions involving the ClO_4^- ion is only two, whereas there are four such interactions involving the Cl^- ion, thereby attesting to the better polarizability towards H-bond formation of the latter.

3.3. Description of structure of **3**

In compound **3**, the crystallographic asymmetric unit, as illustrated in the ORTEP-3 plot (Fig. 3a) of the molecule, consists of one half of a cation coordinated to two water molecules and one hexamine ligand, one perchlorate anion, and one uncoordinated water molecule. The remaining half of the cation complex is generated by the centre of inversion at the cadmium atom (located at 1, 0, 0), giving a distorted octahedral geometry around Cd^{2+}. The symmetry related second hexamine moiety, the perchlorate anion and the water molecule completes the molecular view.

The cations are linked through two principle hydrogen bonds between O(1W)–H(1W1) and N(4) and O(2W)–H(2W2) and N(3) involving the coordinated hexamine and water molecules of two adjacent moieties (Fig. 3b). The former H-bonding interactions lead to the formation of 12-membered rings [graph set $R_2^2(12)$] [17] which propagate through the lattice, translated along the *x*-direction. The latter interaction similarly gives rise to a 12-membered H-bonded ring defining the *z*-direction. As a consequence of the interaction of these two graph sets a third graph set is generated [O(1W)–H(1W1)……N(4)……N(3)……H(2W2)–O(2W)……]. Again a H-bond [O(3W)–H(1W3)···N(2)] between one of the uncoordinated water molecules and a glide related hexamine nitrogen interlink the graph sets giving rise to 3-D network. No significant graph set is formed by the perchlorate ion. It is engaged

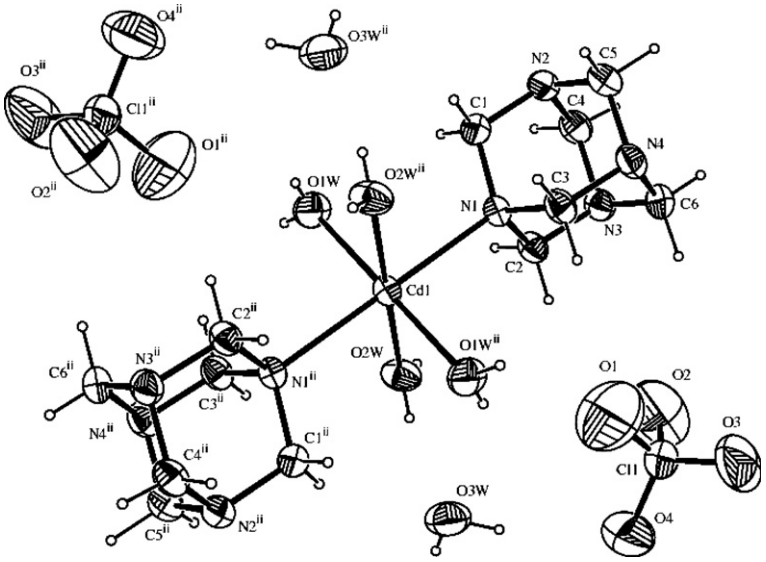


Fig. 3a. ORTEP-3 plot of the structure of $[Cd(H_2O)_4(C_6H_{12}N_4)_2](ClO_4)_2 \cdot 2H_2O$. Atoms having superscripted labels are those generated by the centre of inversion at the Cd centre.

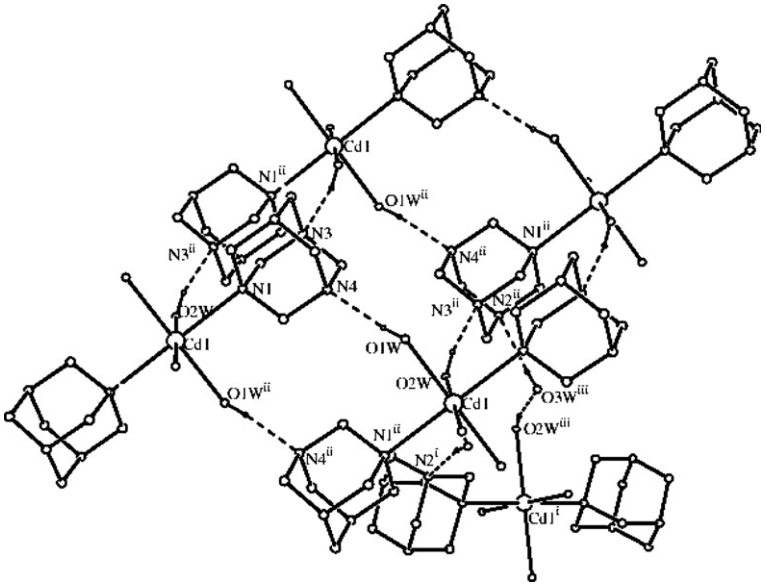


Fig. 3b. Hydrogen bonding patterns between hexamine and water molecules in the crystal structure of $[Cd(H_2O)_4(C_6H_{12}N_4)_2](ClO_4)_2 \cdot 2H_2O$ (**3**).

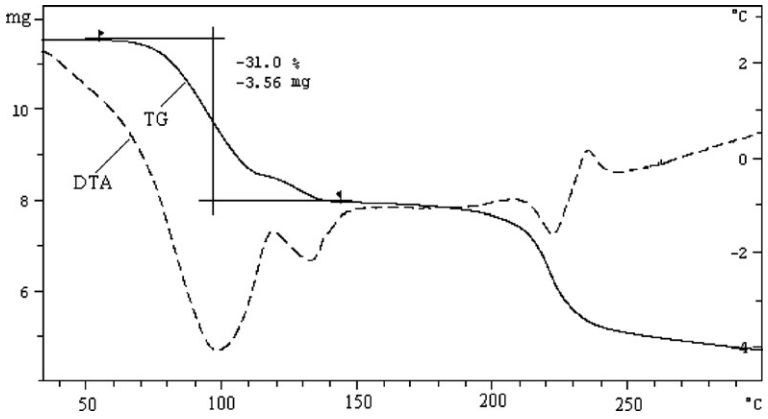


Fig. 4. TG-DTA curve of complex **2** (sample mass: 11.5 mg).

in simple H-bonding with the coordinated water molecule O(1W) and the uncoordinated water molecule O(3W), this pattern is extended throughout the crystal lattice.

Complex **3** has simpler H-bonding pattern compared to the other two structures due to the following reasons: (a) decrease in H-bond receptors of coordinated hexamine, (b) coordination induces decrease in the basicity of N-centres, and (c) induced stereochemical rigidity of methylene spacer due to chelation imposed decrease in rotational freedom.

3.4. Effect of metal ions on the structures

The structures of **1** and **3**, both containing perchlorate as counter ion, show an interesting difference. The two hexamine molecules are coordinated to Cd(II) in **3** to form octahedral $[Cd(H_2O)_4\{(CH_2)_6N_4\}_2]^{2+}$ species whereas in **1**, they remain uncoordinated resulting in hexaaqua nickel complex, $[Ni(H_2O)_6]^{2+}$. Hexamine molecules remain uncoordinated in the other nickle salt, **2** also. Ni(II) being a transition element, prefers strong field ligands to be coordinated to gain crystal field stabilization energy. Thus, its primary coordination sphere consists of six small water molecules leaving the two bulky hexamine molecules containing weakly coordinating tertiary amine nitrogen outside the coordination sphere. On the other hand, Cd(II) being larger and softer metal ion with no crystal field stabilization energy accommodates the two hexamine molecules into its coordination sphere. Therefore, for this kind of structures although the multi-point hydrogen bonding is a very important set of interaction, it is not the only one dominant set. The stability of structure as a whole governs the set of coordinating molecules, crystal packing and molecular stoichiometry. A similar conclusion has also been drawn for the hydrogen bonded sandwich structure for a range of aquated metal complexes with 18-crown-6 [18].

3.5. Thermogravimetry

The TGA trace of **1** shows that it starts to lose water molecules at 60 °C and becomes completely deaquated at 130 °C in two steps. The weight loss in the first step is 15.5% and in the second is 6.1%. The total weight loss corresponds to the loss of eight H_2O molecules per formula unit. The compound starts decomposing at 200 °C. The TGA trace of **2** also shows that the deaquation occurs in two overlapping steps in the temperature range 60–140 °C. A total weight loss of ca. 31.1%, corresponding to the loss of ten H_2O molecules per formula unit (Fig. 4). On further heating, the compound starts to decompose at 220 °C. The deaquation of **3** in the temperatrure range 60–145 °C is also a two-step process as that of **1** and **2**. The first loss of 12.5% and the second loss of 2.6% suggest that all the six H_2O molecules per formula unit are lost. The anhydrous species thus produced for all three compounds do not reabsorb any water molecule from the humid atmosphere suggesting that the framework integrity breaks down once the water molecule are lost.

4. Conclusion

The compounds studied, namely $[Ni(H_2O)_6](ClO_4)_2 \cdot 2C_6H_{12}N_4 \cdot 2H_2O$ (**1**), $[Ni(H_2O)_6]Cl_2 \cdot 2C_6H_{12}N_4 \cdot 4H_2O$ (**2**) and $[Cd(H_2O)_4(C_6H_{12}N_4)_2](ClO_4)_2 \cdot 2H_2O$ (**3**) exhibit 3-D H-bonding networks in the solid state. In the cases of the two Ni(II) compounds, the uncoordinated neutral hexamine and anionic counterparts behave as H-bond receptors in contrast to water molecules acting both as donors and acceptors. Similar donor–acceptor modes are witnessed in the cadmium complex also. Variation of counter-anions in **1** (ClO_4^-) and **2** (Cl^-) does not alter the potential to form rings, but does influence the pattern of interaction between the moieties to form networks. The impact of counter-anions in controlling the overall molecular assembly through H-bonding with $[Ni(H_2O)_6]^{2+}$ motif in **1** and **2** is worth mentioning. Interestingly, compound **2** is stabilized with four molecules of water of crystallization per metal centre unlike **1**, which enjoys lower degree of hydration with only two water molecules per metal centre, attributable to counter-anion change. Replacement of Ni^{2+} by Cd^{2+} in **3** has been attended with a notable change in the coordination sphere resulting in a different H-bonding pattern with fewer acceptor N atoms available for H-bond formation.

Acknowledgement

This work was supported by the University Grants Commission (UGC), India (Fellowship for S. Banerjee, Sanction No. UGC/548/jr. Fellow Sc 2001/2002).

Appendix A. Supplementary material

Crystallographic data for the structure reported in this paper have been deposited at the Cambridge Crystallographic Data Centre as supplementary publication No. CCDC 281949 (**1**), 281950 (**2**) and 281951 (**3**). Copies of the data can be obtained free of charge on application to CCDC, 12 Union Road, Cambridge CB2 1EZ, UK [fax: int. code +44(1223)336–033; e-mail: deposit@ccdc.cam.ac.uk]. Supplementary data associated with this article can be found, in the online version, at doi:10.1016/j.poly.2006.07.019.

References

[1] (a) M. Lansa, J. Huuskonen, K. Rissanen, J. Pursiainen, Chem. Eur. J. 4 (1998) 84;
(b) E. Ishow, A. Gourdon, J.-P. Launay, Chem. Commun. (1998) 1909.;
(c) H.-P. Wu, C. Janiak, L. Uehlin, P. Klufers, P. Mayer, Chem. Commun. (1998) 2637;
(d) D. Ranganathan, V. Haridas, R. Gilardi, I.L. Karle, J. Am. Chem. Soc. 120 (1998) 10793;
(e) S. Kawata, S.R. Breeze, S. Wang, J.E. Greedan, N.P. Raju, Chem. Commun. (1997) 717;
(f) J. Dai, M. Yamamoto, T. Kuroda-Sowa, M. Maekawa, Y. Suenaga, M. Munakata, Inorg. Chem. 36 (1997) 2688;
(g) D. Braga, L. Maini, M. Polito, F. Grepioni, Struct. Bond. 111 (2004) 1;
(h) J.S. Miller, Angew. Chem., Int. Ed. 42 (2003) 27;
(i) M.E. Itkis, X. Chi, A.W. Cordes, R.C. Haddon, Science 296 (2002) 1443;
(j) X.M. Ren, Y.C. Chen, C. He, S. Gao, J. Chem. Soc., Dalton Trans. (2002) 3915;
(k) C. Paraschiv, S. Ferlay, M.W. Hosseini, V. Bulach, J.-M. Planeix, Chem. Commun. (2004) 2270;
(l) T. Akutagawa, S. Takeda, T. Hasegawa, T. Nakamura, J. Am. Chem. Soc. 126 (2004) 291;
(m) X.M. Ren, S. Nishihara, T. Akutagawa, S. Noro, T. Nakamura, Inorg. Chem. 45 (2006) 2229;
(n) M. Pascu, G.J. Clarkson, B.M. Kariuki, M.J. Hannon, Dalton Trans. (2006) 2635;
(o) N. Sanyal, P.M. Lahti, Cryst. Growth Des. 6 (2006) 1253;
(p) J. Barbera, L. Puig, P. Romero, J.L. Serrano, T. Sierra, J. Am. Chem. Soc. 128 (2006) 4487.
[2] M. Munakata, T. Kuroda-Sowa, M. Maekawa, A. Hirota, S. Kitagawa, Inorg. Chem. 34 (1995) 2705.
[3] (a) J.-M. Lehn, M. Mascal, A. Decian, J. Fischer, J. Chem. Soc., Perkin Trans. 2 (1992) 461;
(b) G.M. Whitesides, E.E. Simanek, J.P. Mathias, C.T. Seto, D.N. Chin, M. Mammen, D.M. Gordan, Acc. Chem. Res. 28 (1995) 37;
(c) J.A. Zerkowski, G.M. Whitesides, J. Am. Chem. Soc. 116 (1994) 4298.
[4] (a) G.R. Desiraju, Angew. Chem., Int. Ed. Engl. 34 (1995) 2311;
(b) V.R. Thalladi, B.S. Goud, V.J. Hoy, F.H. Allen, J.A.K. Howard, G.R. Desiraju, J. Chem. Soc., Chem. Commun. (1996) 401;
(c) J.C. MacDonald, G.M. Whitesides, Chem. Rev. 94 (1994) 2383;
(d) C.B. Aakeroy, K.R. Seddon, Chem. Soc. Rev. (1993) 22, 397;
(e) M. Mascal, Contemp. Org. Synth. 1 (1994) 31;
(f) E.R.T. Tiekink, J.J. Vittal (Eds.), Frontiers in Crystal Engineering, Wiley, Chichester, 2006;
(g) S. Furukawa, H. Uji-i, K. Tahara, T. Ichikawa, M. Sonoda, F.C. De Schryver, Y. Tobe, S. De Feyter, J. Am. Chem. Soc. 128 (2006) 3502.
[5] J.L. Atwood, J.E.D. Davies, D.D. MacNicol, F. Vogtle (Eds.), Comprehensive Supramolecular Chemistry, vol. 6, Permagon Press, Oxford, 1996.
[6] (a) S.V. Kolotuchin, E.E. Fenlon, S.R. Wilson, C.J. Loweth, S.C. Zimmerman, Angew. Chem., Int. Ed. Engl. 34 (1995) 2654;
(b) O.M. Yaghi, H. Li, T.L. Groy, J. Am. Chem. Soc. 118 (1996) 9096;
(c) D. Braga, F. Grepioni, G.R. Desiraju, Chem. Rev. 98 (1998) 1375;
(d) S. Subramanian, M.J. Zaworotko, Coord. Chem. Rev. 137 (1994) 357.
[7] A.D. Burrows, C.-W. Chan, M.M. Chowdhry, J.E. McGrady, D.M.P. Mingos, Chem. Soc. Rev. 24 (1995) 329.
[8] Bruker, SMART, SAINT, SADABS, XPREP, SHELXTL, Bruker AXS Inc, Madison. WI, USA, 1998.
[9] A. Altomare, G. Cascarano, C. Giacovazzo, A. Guagliardi, J. Appl. Crystallogr. 26 (1993) 343.
[10] G.M. Sheldrick, SHELXL-97: Program for Crystal Structure Refinement, University of Göttingen, Göttingen, Germany, 1997.
[11] L.J. Farrugia, J. Appl. Crystallogr. 30 (1997) 565.
[12] D.M. Watkin, L. Pearce, C.K. Prout, CAMERON: A Molecular Graphics Package, Chemical Crystallography Laboratory, University of Oxford, England, 1993.
[13] L.J. Farrugia WINGX, J. Appl. Cryst. 32 (1999) 837.
[14] M. Nardelli, J. Appl. Crystallogr. 28 (1995) 569.
[15] A.L. Spek, Acta Crystallogr., Sect A 46 (1990) C34.
[16] J.C. Gallucci, R.E. Gerkin, Acta Crystallogr., Sect. C 46 (1990) 350, and references therein.
[17] (a) M.C. Etter, Acc. Chem. Res. 23 (1990) 120;
(b) M.C. Etter, J. Phys. Chem. 95 (1991) 4601;
(c) J. Bernstein, R.E. Davis, L. Shimoni, N.-L. Chang, Angew. Chem., Int. Ed. Engl. 34 (1995) 1555.
[18] J.W. Steed, B.J. McCool, P.C. Junk, J. Chem. Soc., Dalton Trans. (1998) 3417.

Available online at www.sciencedirect.com
ScienceDirect
Polyhedron 26 (2007) 33–38
POLYHEDRON
www.elsevier.com/locate/poly

Synthesis, characterization and structure of nickel(II) complexes of a 16-membered mixed-donor macrocyclic Schiff base ligand, potentially hexadentate, bearing two pendant alcohol functions

Ali Akbar Khandar [a,*], Seyed Abolfazl Hosseini-Yazdi [a], Masomeh Khatamian [a], Patrick McArdle [b], Seyed Amir Zarei [a]

[a] Department of Inorganic Chemistry, Faculty of Chemistry, University of Tabriz, Tabriz 51666-14766, Iran
[b] Department of Chemistry, NUI Galway, Galway, Ireland

Received 17 April 2006; accepted 24 July 2006
Available online 4 August 2006

Abstract

The reactions of $NiX_2 \cdot 6H_2O$ ($X = Cl^-$, ClO_4^-, NO_3^-) with a new macrocyclic Schiff base ligand (**L** = 8,9,18,19-tetrahydro-7*H*,17*H*-dibenzo[*f*,*o*][1,5,9,13]dioxadiaza cyclohexadecine-8,18-diol), potentially hexadentate containing two alcoholic pendant arms, have been investigated by template condensation of 2-[3-(2-formylphenoxy)-2-hydroxypropoxy]benzaldehyde and 1,3-diamino-2-propanol. The isolation of a selection of 1:1 (metal:ligand) complexes of nickel(II) has been carried out and IR and UV–Vis spectroscopy, conductance measurements and X-ray determination have been employed to probe the nature of the respective complexes in both solid and solution states. The UV–Vis spectra and X-ray determination indicate that the complexes are of the type [NiLX]X, with a distorted octahedral ligand field. However, the perchlorate complex of Ni(II) is of the $[NiL(solv)]^{2+}$ form in solution. In all complexes, the potentially hexadentate ligand behaves as a pentadentate ligand.
© 2006 Elsevier Ltd. All rights reserved.

Keywords: Pendant arm; Oxa-aza macrocycle; Schiff base; Nickel(II) complexes; X-ray structure

1. Introduction

In order to improve the understanding of the coordination geometry, electrochemical and magnetic behavior of nickel, many complexes of nickel with different macrocycles have been studied [1–3]. Macrocyclic ligands containing a heteroatom are important complexing agents for cations, anions and molecules [4–8]. The coordination chemistry of macrocyclic ligands is a fascinating area of intense study for inorganic chemists [9–14]. The aspect of interest in macrocyclic ligands is raised from features such as the nature, number and arrangement of ligand donors, as well as ligand conjugation, substitution and flexibility, which produce different types of macrocyclic molecules suitable for specific uses [15]. In general, a pendant arm enhances the binding strength of the macrocycle toward cations, by cooperative ring-side arm interaction, in comparison with the macrocycle analogues without pendant arms [16–20]. Therefore, the synthesis of pendant arm macrocycles has attracted considerable attention because of their unique coordination and structural properties [21–25] and their roles in bioinorganic chemistry as models of biomolecules and in modern chemical techniques such as magnetic resonance imaging [26–30]. Previously, we have reported the synthesis and structures of some nickel(II) complexes of one alcohol pendant arm macrocyclic Schiff base ligand [1 + 1] with a N_2O_3 donor set [21,22].

We report here the synthesis, structure and spectral properties of some Ni(II) complexes of a two alcohol pendant arms macrocyclic Schiff base, potentially a

* Corresponding author. Tel.: +98 411 3346494; fax: +98 411 3340191.
E-mail addresses: khandar@tabrizu.ac.ir, akhandar@yahoo.com (A.A. Khandar).

0277-5387/$ - see front matter © 2006 Elsevier Ltd. All rights reserved.
doi:10.1016/j.poly.2006.07.022

hexadentate ligand [1 + 1] with 16-members and mixed N_2O_4 donors, containing different counter ions.

2. Experimental

2.1. Materials

Solvents were dried and purified before being used according to published procedures [31]. Other reagents were purchased from Merck or Fluka and were used without further purification. Caution: Although no problems were encountered during this work with the perchlorate salt, it should be regarded as potentially explosive.

2.2. Physical measurements

CHN analyses were carried out using a Heraeus, CHN-O-RAPID elemental analyzer. The UV–Vis measurements were carried out in DMF solution using a Shimadzu 1650PC UV–Vis spectrophotometer. Infrared spectra were obtained on a Bomem, FT-IR MB-100 instrument as KBr pellets. Mass spectrum was recorded on a Finnigan mass spectrometer. Conductance measurements were performed using a Metrohm 712 conductometer.

2.3. X-ray crystallography

Single crystals of the $[NiLCl]Cl \cdot 0.75H_2O$ complex were obtained from acetonitrile solution by slow evaporation. The crystal was not of ideal quality, although it was the very best available. The structure was solved by direct methods and refined by full matrix least squares using SHELXL-97 [32,33]. SHELX operations were automated using ORTEX, which was also used to obtain the drawings [34]. Data were corrected for Lorentz and polarization effects but not for absorption. Hydrogen atoms were included in calculated positions with thermal parameters 30% larger than the atom to which they were attached. The non-hydrogen atoms were refined anisotropically. All calculations were performed on a Pentium PC.

The data was collected on a Marresearch image plate using monochromatized Mo Kα radiation (0.71069 Å) at 298 K: Molecular formula $C_{20}H_{21}NiCl_2N_2O_{4.75}$, M 495, triclinic, space group $P\bar{1}$, $a = 8.114(4)$ Å, $b = 13.482(9)$ Å, $c = 20.271(10)$ Å, $\alpha = 94.56(2)°$, $\beta = 90.96(2)°$, $\gamma = 100.58(2)°$, $V = 2172(2)$ Å^3, $Z = 4$, $D_{calc} = 1.514$ Mg/m^3, absorption coefficient $\mu = 1.172$ mm^{-1}, crystal dimensions: $0.48 \times 0.42 \times 0.31$ (mm), $F(000)$: 1020, θ range for data collection: 5.65–20.30 (°), index ranges: $-7 \leqslant h \leqslant 7$, $-12 \leqslant k \leqslant 13$, $-19 \leqslant l \leqslant 19$, reflections collected/unique: 7345/3616, significant unique reflections: 3289 with $I > 2\sigma(I)$, refinement method: full-matrix least-squares on F^2, data/parameters/restraints: 3616/540/0, goodness-of-fit on F^2: 1.022, final R indices $[I > 2\sigma(I)]$: $R_1 = 0.0517$, $wR_2 = 0.1287$, R indices (all data): $R_1 = 0.0564$, $wR_2 = 0.1321$, weighting scheme: $w = 1/[(\sigma F_o)^2 + (0.0419^*P)^2 + 5.3765^*P]$ where $P = (F_o^2 + 2F_c^2)/3$, largest difference peak and hole (e/Å^3): 0.528 and −0.372.

$R_1 = [\Sigma||F_o| - |F_c||]/\Sigma|F_o|$ (based on F),

$wR_2 = \left[[\Sigma_w(|F_o^2 - F_c^2|)2]/[\Sigma_w(F_o^2)^2]\right]^{1/2}$ (based on F^2).

2.4. Syntheses

2.4.1. 2-[3-(2-Formylphenoxy)-2-hydroxypropoxy] benzaldehyde (*1*)

Compound **1** was prepared in a way similar to the reported method [21,35] using salicylaldehyde and 1,3-dichloro-2-propanol.

2.4.2. Macrocycle (*L*)

1,3-Diamino-2-propanol (0.0905 g, 1 mmol) in methanol (20 mL) was added to a solution of **1** (0.3002 g, 1 mmol) in warm methanol (50 mL). The reaction mixture was then refluxed for 3 h. The mixture was cooled to room temperature and the solvent removed under reduced pressure until a solid product was formed that was washed with cold methanol. Yield (72.5%), Mp 90–92 °C. Selected FT-IR data, ν (cm^{-1}): 3377b, 3072w, 2888w, 1637s (C=N), 1595m, 1486s, 1242s, 1107m, 1034m, 754s. *Anal.* Calc. for $C_{20}H_{22}N_2O_4 \cdot 2H_2O$: C, 61.5; H, 6.7; N, 7.2. Found: C, 61.6; H, 6.1; N, 7.0%. Mass spectral parent ion; m/z 354.

2.4.3. Nickel complexes

A 1-butanol solution (120 mL) of 1,3-diamino-2-propanol (0.3694 g, 4 mmol) was added slowly with stirring to a 200 mL hot 1-butanol solution of **1** (1.206 g, 4 mmol) and $NiX_2 \cdot 6H_2O$ (4 mmol). The solution was refluxed for 2 h and then filtered. The volume of the resulting solution was reduced using a rotary evaporator. The resultant product was recrystallized and dried in a vacuum desiccator over P_4O_{10}.

$NiLCl_2$: Blue crystals were recrystallized from acetonitrile. Yield: 0.9 g (55.8%). Mp > 230°C (dec). Selected FT-IR data, ν (cm^{-1}): 3456w, 3361w, 3252w, 3029w, 2927w, 1637s (C=N), 1603m, 1492m, 1432m, 1283w, 1220s, 1128m, 985s, 804m, 771m, 627w, 584w, 534w, 472w. *Anal.* Calc. for $C_{20}H_{21}NiCl_2N_2O_{4.75}$: C, 48.5; H, 4.2; N, 5.6. Found: C, 49.0; H, 4.7; N, 4.8%. $\Lambda_m = 94$ cm^2 Ω^{-1} mol^{-1} in DMF. Electronic spectrum in DMF (λ, nm) (ε, M^{-1} cm^{-1}): 620(16.9), 798(shoulder) (2.4), 1075(8.1).

$NiL(ClO_4)_2$: Blue-green crystals were recrystallized from acetonitrile/methanol (1:1 v/v). Yield: 0.5 g (25%). Mp > 215°C (dec). Selected FT-IR data, ν (cm^{-1}): 3386b, 3078w, 2937w, 1639 s (C=N), 1604s, 1491m, 1446m, 1285w, 1216s, 1144s, 1113, 1088, 1019w, 988m, 796w, 766m, 630s, 475w. *Anal.* Calc. for $C_{20}H_{22}Cl_2NiN_2O_{12} \cdot 0.33CH_3OH$: C, 39.25; H, 3.62; N, 4.58. Found: C, 39.22; H, 3.78; N, 4.50%. $\Lambda_m = 125$ cm^2 Ω^{-1} mol^{-1} in DMF. Electronic spectrum in DMF (λ, nm) (ε, M^{-1} cm^{-1}): 613(5.9), 1089(5.7).

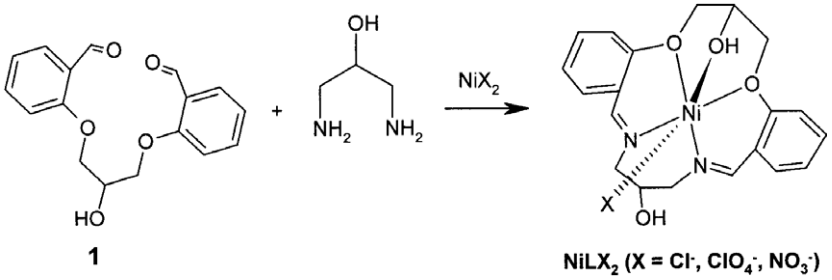
NiL(NO$_3$)$_2$: Blue crystals were recrystallized from acetonitrile. Yield: 0.79 g (41.5%). Mp > 235 °C (dec). Selected FT-IR data, ν (cm^{-1}): 3433w, 3068w, 2955w, 1637s (C=N), 1605m, 1483m, 1421s, 1384s, 1313s, 1223s, 1120w, 984m, 814m, 770m, 529w, 476w. *Anal.* Calc. for $C_{20}H_{22}NiN_4O_{10}\cdot 0.5H_2O$: C, 43.99; H, 4.2; N, 10.3. Found: C, 44.00; H, 4.3; N, 10.0%. $\Lambda_m = 86\ cm^2\ \Omega^{-1}\ mol^{-1}$ in DMF. Electronic spectrum in DMF (λ, nm) (ε, $M^{-1}\ cm^{-1}$): 598(10.8), 773(shoulder) (5), 1046(8.5).

3. Results and discussion

3.1. Syntheses and characterization

Since macrocycle **L** is not soluble in methanol, ethanol and 1-butanol, the complexes were prepared by template cyclocondensation reactions in the presence of $NiX_2\cdot 6H_2O$ ($X = Cl^-$, ClO_4^-, NO_3^-) salts and yielded solids according to Scheme 1, which were characterized by IR, elemental analysis, UV–Vis and conductance measurements.

The molar conductivity data for ca. 10^{-3} M of $NiLCl_2$ and $NiL(NO_3)_2$ in DMF solutions at room temperature are in accordance with those expected for a 1:1 electrolyte, while the measured value for $NiL(ClO_4)_2$ under the same conditions is as expected for a 2:1 electrolyte [36]. These observations imply that at least one of the anions in $NiLCl_2$ and $NiL(NO_3)_2$ is coordinated to the Ni atom, while the perchlorate anions in $NiL(ClO_4)_2$ solution does not participate in coordination. The IR spectra of all the complexes confirm the presence of imine bonds and each complex exhibits the ν(C=N) mode at ca. 1637 cm^{-1}, while no band attributable to a C=O stretching vibration is detected related to aldehyde which indicates that condensation and cyclization has occurred. The stretching mode of O–H in the $NiLCl_2$ complex (3456, 3361 and 3252 cm^{-1}) is split and shifted compared to that of the free macrocycle (3377 cm^{-1}) which may indicate the existence of three kinds of hydroxyl groups, two groups are alcohol pendant arms, one is coordinated to the Ni atom, and third one corresponds to lattice water as is found from the crystal structure of the $NiLCl_2$ complex, but the stretching mode of O–H in the case of the $NiL(NO_3)_2$ and $NiL(ClO_4)_2$ complexes is only shifted. The vibration band at 1242 cm^{-1}, assigned to ν(C–O–C) in the free ligand, was shifted toward lower frequency by ca. 26 cm^{-1}, indicating the complexation of the ether oxygen atoms to the nickel ion. The C=C vibration band of the aromatic ring at 1595 cm^{-1} of the free ligand was shifted towards higher frequency by ca. 10 cm^{-1} in the complex due to hindrance to the ring breathing vibration. The vibration bands of the ClO_4^- and NO_3^- groups provide some useful structural information [37]. The IR spectrum for the nitrate complex shows bands at ca. 1421 cm^{-1} (ν_5) and 1313 cm^{-1} (ν_1), suggesting the presence of a coordinated nitrate group, and a band at ca. 1384 cm^{-1} is attributable to ionic NO_3^-. The separation $\nu_5 - \nu_1$ can be used as a near criterion to distinguish between the degree of covalence of the nitrate coordination. The magnitude of this value (110 cm^{-1}) is indicative of a unidentate interaction. The perchlorate bands were assigned according to Refs. [21,24,25,38,39]. The IR spectrum of the perchlorate complex exhibits bands assignable to the asymmetric Cl–O stretching mode (ν_3) around 1100 cm^{-1} and the asymmetric Cl–O bending mode (ν_4) at 630 cm^{-1}. The higher energy band shows three well-resolved maxima of the perchlorate at 1144, 1113 and 1088 cm^{-1}. This may reflect different environments in this complex arising from crystal packing or hydrogen bonding and or lowering of the symmetry of the perchlorate group owing to coordination to nickel. It must be pointed out that the $\nu(C–O–C)_{ether}$ band also falls in this region. Thus it is not possible to precisely define the coordination mode of ClO_4^- [21,24,39]. The UV–Vis spectra of the nickel complexes in DMF solutions show two absorption bands in the regions of 1046–1100 and 598–620 nm. These absorption bands may be assigned to the $^3A_{2g} \rightarrow {}^3T_{2g}$ (F) (ν_1) and $^3A_{2g} \rightarrow {}^3T_{1g}$ (F) (ν_2) transitions, respectively, and reflect Ni(II) d^8 ions in an octahedral geometrical environment [21,24]. One absorption band near 800 nm is also present and is probably due to the spin forbidden transition $^3A_{2g} \rightarrow {}^1E_g$ observed in $NiLCl_2$ and $NiL(NO_3)_2$ complexes [21,40]. According to the molar conductivity data, the perchlorate ions do not participate in coordination in a $NiL(ClO_4)_2$ solution in DMF, but its UV–Vis spectrum shows Ni(II) has an octahedral geometry environment so that one can assume the participation of one solvent molecule in the sixth coordination position of Ni(II) due to the high donor capacity of DMF. The absorption bands for the complexes increase toward higher energies in the order



1 **NiLX$_2$ (X = Cl$^-$, ClO$_4^-$, NO$_3^-$)**

Scheme 1.

DMF < Cl^- < NO_3^-, indicating that the presence of these coordinated axial ligands affects the ligand field strength of the complexes. The 10 Dq values of $[NiL(DMF)]^{2+}$, $[NiLCl]^+$ and $[NiL(NO_3)]^+$ are 9182.7, 9302.3 and 9560 cm^{-1}, respectively. The observed disagreement in the order of DMF and Cl^- may arise from DMF-macrocycle steric effects.

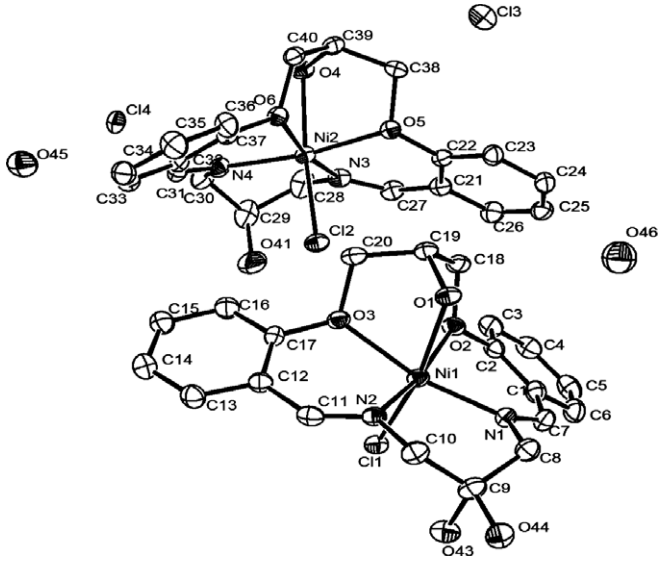


Fig. 1. ORTEP representation of the asymmetric unit for $NiLCl_2$. Hydrogen atoms are omitted for clarity.

In all the complexes, the ligand **L** behaves as pentadentate as a similar macrocycle with one alcohol pendant arm [21,22]. It seems that the second alcohol pendant arm cannot participate in coordination because of the rigidity of **L** in the region of the imine nitrogen bonds.

Table 1
Selected some bond lengths (Å) and bond angles (°) for $NiLCl_2$

Bond lengths			
Ni(1)–N(1)	1.994(5)	Ni(2)–N(3)	1.990(5)
Ni(1)–N(2)	2.008(5)	Ni(2)–N(4)	2.021(6)
Ni(1)–O(1)	2.139(4)	Ni(2)–O(4)	2.118(4)
Ni(1)–O(2)	2.069(4)	Ni(2)–O(5)	2.073(4)
Ni(1)–O(3)	2.091(4)	Ni(2)–O(6)	2.069(4)
Ni(1)–Cl(1)	2.327(2)	Ni(2)–Cl(2)	2.3448(19)
Bond angles			
N(1)–Ni(1)–N(2)	98.7(2)	N (3)–Ni(2)–N(4)	99.2(2)
N(1)–Ni(1)–O(1)	93.99(19)	N(3)–Ni(2)–O(4)	95.69(19)
N(2)–Ni(1)–O(1)	94.36(18)	N(4)–Ni(2)–O(4)	94.44(19)
N(1)–Ni(1)–O(2)	88.6(2)	N(3)–Ni(2)–O(5)	88.3(2)
N(2)–Ni(1)–O(2)	169.50(19)	N(4)–Ni(2)–O(5)	170.2 (2)
O(1)–Ni(1)–O(2)	77.48(16)	O(4)–Ni(2)–O(5)	78.50(16)
N(1)–Ni(1)–O(3)	167.71(19)	N(3)–Ni(2)–O(6)	169.3(2)
N(2)–Ni(1)–O(3)	88.39(19)	N(4)–Ni(2)–O(6)	88.2(2)
O(1)–Ni(1)–O(3)	75.37(17)	O(4)–Ni(2)–O(6)	75.84(17)
O(2)–Ni(1)–O(3)	83.19(16)	O(5)–Ni(2)–O(6)	83.59(16)
N(1)–Ni(1)–Cl(1)	96.07(16)	N(3)–Ni(2)–Cl(2)	94.75(16)
N(2)–Ni(1)–Cl(1)	95.33(15)	N(4)–Ni(2)–Cl(2)	93.65(17)
O(1)–Ni(1)–Cl(1)	164.81(11)	O(4)–Ni(2)–Cl(2)	165.60(12)
O(2)–Ni(1)–Cl(1)	91.40(13)	O(5)–Ni(2)–Cl(2)	91.94(12)
O(3)–Ni(1)–Cl(1)	93.23(13)	O(6)–Ni(2)–Cl(2)	92.55(13)

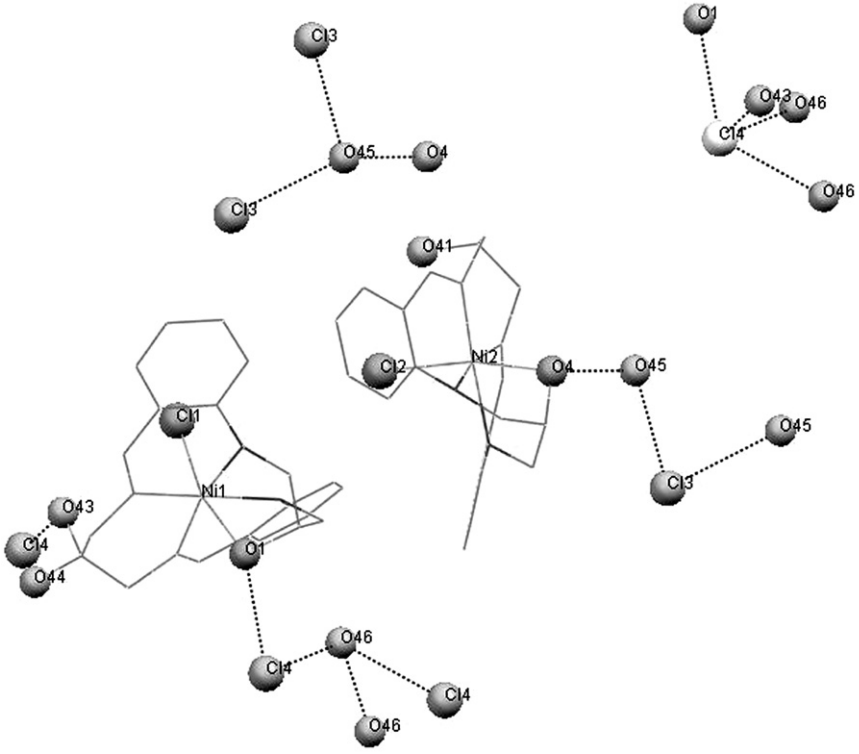


Fig. 2. H-Bonds in the asymmetric unit.

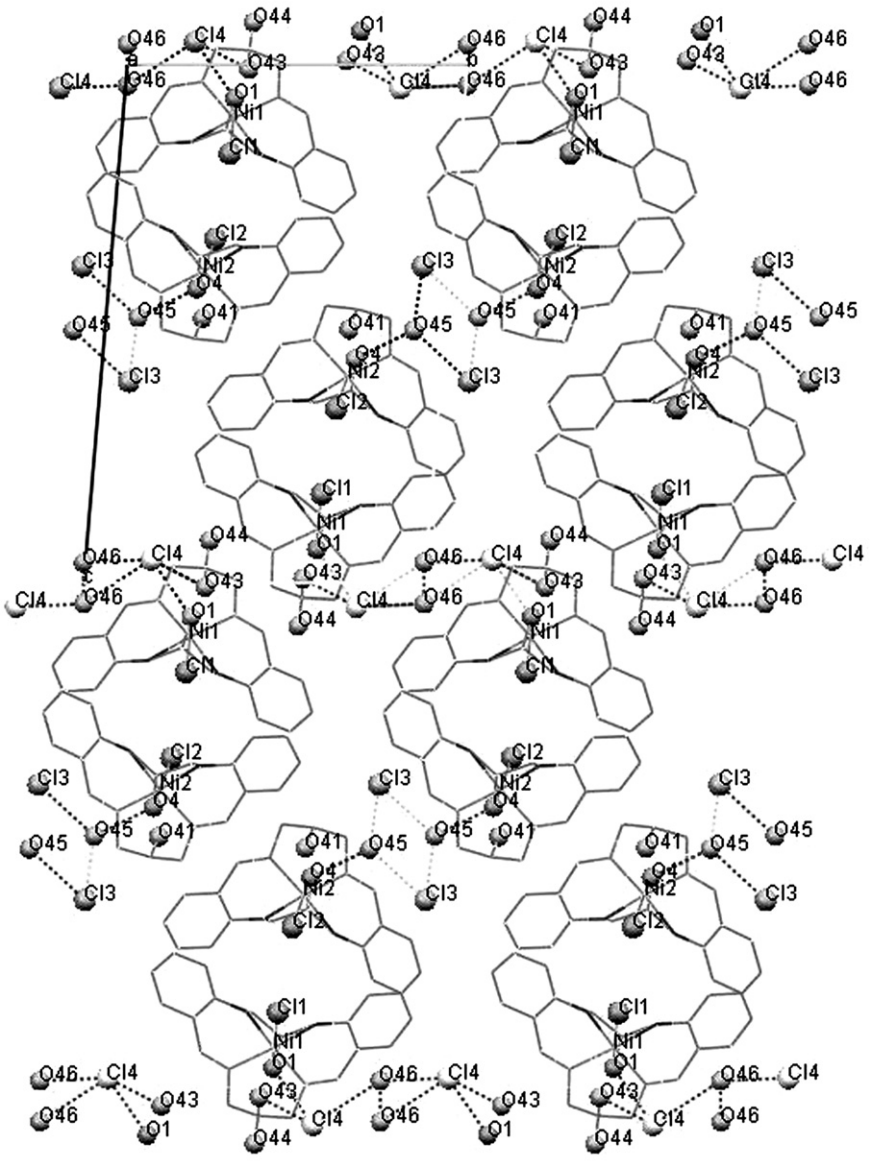


Fig. 3. H-Bonds and crystal packing along the *a*-axis.

3.2. X-ray structure of $NiLCl_2$

The asymmetric unit of the crystal is illustrated in Fig. 1, and selected bond distances and bond angles are listed in Table 1. There are two $[NiLCl]^+$ cations and two Cl^- counter ions per asymmetric unit. Each asymmetric unit has two water molecules (O45 and O46) of crystallization, one of which has half site occupancy. This gives a molecular formula of $[NiLCl]Cl \cdot 0.75H_2O$. The two molecules in the asymmetric unit are almost identical and they are almost coincident. There is also disorder in the position of one of the uncoordinated hydroxyl oxygens in one of the molecules over two positions (O43, O44) with occupancy ratios of 0.7 and 0.3. In both molecules it is clear that one of the hydroxyls (O1 in one molecule and O4 in the other) is coordinated to Ni while the other (O43–O44 and O41) is not, and that one Cl (Cl1 and Cl2) is coordinated to Ni and the other (Cl3 and Cl4) is not. The Ni atoms in the molecules are hexacoordinated with a distorted octahedral geometry. One Cl^- ion and one of the hydroxyl pendants on the etheric backbone occupy the apical positions and two imine nitrogen atoms and two ether oxygen atoms of the macrocycle occupy basal positions of the octahedron. The Ni–Cl bond lengths [2.327(2) and 2.3448(19) Å] are almost comparable to those of reported Ni–Cl complexes with an octahedral geometry [41,42]. The Ni–N bond distances [1.994(5), 2.008(5), 1.990(5) and 2.021(6) Å] and Ni–O bond distances [2.139(4), 2.069(4), 2.091(4), 2.118(4), 2.073(4) and 2.069(4) Å] are comparable to the corresponding values [2.007(4), and 2.008(4) Å] for Ni–N and [2.119(4), 2.080(3) and 2.085(3) Å] for Ni–O in our previous work on a N_2O_3 macrocyclic ligand [21]. The

conformation of the macrocycle is such that the two phenyl rings are tilted to the same side. Figs. 2 and 3 show the H-bonds in the asymmetric unit and crystal packing along *a*-axis respectively. O1 and O43 in one of the molecules are H-bonded to their corresponding adjacent uncoordinated Cl4s, while in the other molecule only the coordinated hydroxyl group, O4, is H-bonded to its corresponding adjacent water molecule O45. Both uncoordinated Cls are H-bonded to water molecules. However the water molecules are involved in H-bonding which is 3D in nature and thus not easy to describe in any simple way. The H-bond distances involved in the asymmetric unit are O45···O4 2.594, O45···Cl3 3.099 and O46···O46 2.596, O46···Cl4 3.093 Å. The Cl2···O41 and Cl1···O43 distances are 3.295(7) and 3.537(7) Å respectively.

4. Conclusion

The UV–Vis spectra, conductivity measurements and X-ray determination indicate that the complexes are of the type [NiLX]X with a distorted octahedral ligand field. However, the perchlorate complex of Ni(II) has the $[NiL(solv)]^{2+}$ form in solution. In all the complexes, the ligand **L**, potentially hexadentate, bearing two pendant alcohol arms, behaves as a pentadentate ligand.

Acknowledgements

We are grateful to the University of Tabriz Research Council for the financial support of this research. We are also grateful to Professor Patrick McArdle for the crystal structure determination.

Appendix A. Supplementary data

Crystallographic data for the structural analysis of $NiLCl_2$ have been deposited with Cambridge Crystallographic Data Centre, CCDC number 286163. Copies of this information may be obtained free of charge from the Director, CCDC, 12 Union Road, Cambridge, CB2 1EZ, UK. Fax: +44 1223 336033; email: deposit@ccdc.cam.ac.uk or http://www.ccdc.cam.ac.uk. Supplementary data associated with this article can be found, in the online version, at doi:10.1016/j.poly.2006.07.022.

References

[1] M. Yonemura, Y. Matsumura, H. Furutachi, M. Ohba, H. Okawa, D.E. Fenton, Inorg. Chem. 36 (1997) 2711.
[2] A.J. Blake, J. Casabo, F.A. Devillanova, L. Escriche, A. Garau, F. Isaia, V. Lippolis, R. Kivekas, V. Muns, M. Schroder, R. Sillanpaa, G. Verani, J. Chem. Soc., Dalton Trans. (1999) 1085.
[3] M.D. Santana, A.A. Lozano, G. Garcia, G. Lopez, J. Perez, J. Chem. Soc., Dalton Trans. (2005) 104.
[4] R.M. Izatt, J.S. Bradshaw, S.A. Nielsen, J.D. Lamb, J.J. Christensen, Chem. Rev. 85 (1985) 271.
[5] R. Izatt, K. Pawlak, J.S. Bradshaw, Chem. Rev. 91 (1991) 1721.
[6] R.M. Izatt, J.S. Bradshaw, K. Pawlak, R.L. Bruening, B.J. Tarbet, Chem. Rev. 92 (1992) 1261.
[7] R.M. Izatt, K. Pawlak, J.S. Bradshaw, Chem. Rev. 95 (1995) 2529.
[8] K. Choi, A.D. Hamilton, Coord. Chem. Rev. 240 (2003) 101.
[9] J.D. Chartres, L.F. Lindoy, G.V. Meehan, Coord. Chem. Rev. 216–217 (2001) 249.
[10] A. McAuley, S. Subramanian, Coord. Chem. Rev. 200–202 (2000) 75.
[11] A.I. Fallis, Annu. Rep. Prog. Chem., Sect. A (93) (1997) 339.
[12] A.I. Fallis, Annu. Rep. Prog. Chem., Sect. A (94) (1998) 351.
[13] A.I. Fallis, Annu. Rep. Prog. Chem., Sect. A (95) (1999) 313.
[14] A.I. Fallis, Annu. Rep. Prog. Chem., Sect. A (98) (2002) 321.
[15] J.S. Bradshaw, K.E. Karkowiak, R.M. Izatt, Aza-Crown Macrocycles, John Wiley and Sons Inc., New York, 1993.
[16] G.W. Gokel, L.J. Barbour, S.L. Wall, E.S. Meadows, Coord. Chem. Rev. 222 (2001) 127.
[17] R.D. Hancock, H. Maumela, A.S. Sousa, Coord. Chem. Rev. 148 (1996) 315.
[18] P. Jiang, Z. Guo, Coord. Chem. Rev. (2004).
[19] S.R. Collinson, D.E. Fenton, Coord. Chem. Rev. 148 (1996) 19.
[20] L. Tei, A.J. Blake, A. Bencini, B. Valtancoli, C. Wilson, M. Schroder, J. Chem. Soc., Dalton Trans. (2000) 4122.
[21] A.A. Khandar, S.A. Hosseini-Yazdi, Polyhedron 22 (2003) 1481.
[22] A.A. Khandar, S.A. Hosseini-Yazdi, Aust. J. Chem. 56 (2003) 1255.
[23] M. Vicente, R. Bastida, A. Macias, L. Valencia, C.F.G.C. Geraldes, C.D. Bronidino, Inorg. Chim. Acta 358 (2005) 1141.
[24] M. Vicente, C. Lodeiro, H. Adams, R. Bastida, A. Blas, D.E. Fenton, A. Macy'as, A. Rodry'guez, T. Rodry'guez-Blas, Eur. J. Inorg. Chem. (2000) 1015.
[25] M. Vicente, R. Bastida, C. Lodeiro, A. Macias, A.J. Parola, L. Valencia, S.E. Spey, Inorg. Chem. 42 (2003) 6768.
[26] V. Artero, M. Fontecave, Coord. Chem. Rev. 249 (15-16) (2005) 1518.
[27] S. Li, J. Xia, D. Yang, Y. Xu, D. Li, M. Wu, W. Tang, Inorg. Chem. 41 (2002) 1807.
[28] K.P. Wainwright, Adv. Inorg. Chem. 52 (2001) 293.
[29] L. Siegfried, A. Comparone, M. Neuburger, T.A. Kaden, J. Chem. Soc., Dalton Trans. (2005) 30.
[30] J. Costamagna, G. Ferraudi, B. Matsuhiro, M. Campos-Vallette, J. Canales, M. Villagra'n, J. Vargas, M.J. Aguirre, Coord. Chem. Rev. 196 (2000) 125.
[31] W.L.F. Armarego, D.D. Perrin, Purification of Laboratory Chemicals, Pergamon Press, Oxford, 1988.
[32] G.M. Sheldrick, Acta. Crystallogr. 46 (1990) 467.
[33] G.M. Sheldrick, SHELXL-97 A Computer Program for Crystal Structure Determination, University of Gottingen, 1997.
[34] P. McArdle, J. Appl. Cryst. 28 (1995) 65.
[35] L.F. Lindoy, L.G. Armstrong, Inorg. Chem. 14 (1975) 1322.
[36] W.J. Geary, Coord. Chem. Rev. 7 (1971) 81.
[37] K. Nakamoto, Infrared and Raman Spectra of Inorganic and Coordination Compounds, John Wiley and Sons Inc., New York, 1986.
[38] C. Platas, R. Bastida, A. de Blas, D.F. Fenton, A. Macias, A. Rodriguez, T. Rodriguez-Blas, Polyhedron 17 (10) (1998) 1759.
[39] C. Lodeiro, R. Bastida, E. Bertolo, A. Macías, A. Rodríguez, Polyhedron 22 (2003) 1701.
[40] M.J. Prushan, A.W. Anthony, R.J. Butcher, Inorg. Chim. Acta 300-302 (2000) 992.
[41] M. Vetrichelnan, Y.H. Lai, K.F. Mok, J. Chem. Soc., Dalton Trans. (2003) 295.
[42] A.S. Batsanov, A.E. Goeta, J.A.K. Howard, D. Maffeo, H. Puschmann, J.A.G. Williams, Polyhedron 20 (2001) 981.

Available online at www.sciencedirect.com
ScienceDirect
Polyhedron 26 (2007) 39–42
POLYHEDRON
www.elsevier.com/locate/poly

Synthesis and characterization of silver(III) complexes with tetradentate and tridentate ligands with imine-oxime groups

Mohamed A. Eltayeb, Yousif Sulfab *

Department of Chemistry and Earth Sciences, College of Arts and Sciences, Qatar University, P.O. Box 2713, Doha, Qatar

Received 9 May 2006; accepted 25 July 2006
Available online 4 August 2006

Abstract

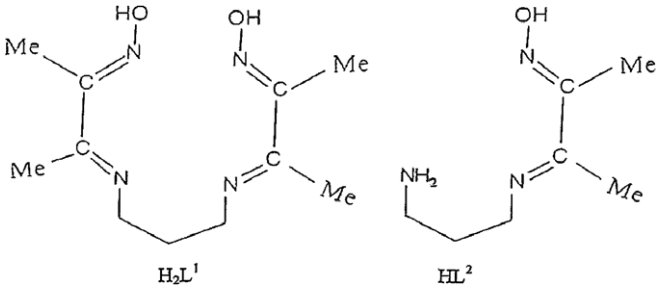
The trivalent oxidation state of silver is stabilized by tetradentate imine-oxime and tridentate imine-oxime-amine ligands. Silver(I), in the presence of these ligands, is readily oxidized by PbO_2 in acidic solutions or by $S_2O_8^{2-}$ to the corresponding silver(III) complexes. The isolated complexes were characterized by elemental analysis, IR, UV–Vis spectra, magnetic susceptibility, TG and cyclic voltammetry. The complexes are diamagnetic, consistent with the formation of spin-paired d^8 square planar or tetragonal structures. The complexes have a high molar absorption in the UV–Vis region with $\varepsilon > 10^4\ M^{-1}\ cm^{-1}$, that may be attributed to ligand to metal charge transfer (MLCT). The complexes seem to be stable in the solid state when kept dry and away from light. The complexes decompose very slowly in aqueous solutions. The rate of decomposition is accelerated by both acids and bases. The decomposition involves oxidation of the ligands by Ag^{III}.
© 2006 Elsevier Ltd. All rights reserved.

Keywords: Diamagnetic silver(III) complexes; Imine-oxime ligands; Ligand to metal charge transfer; Irreversible cyclic voltammograms

1. Introduction

Trivalent silver is often proposed as a transient species in silver catalyzed peroxydisulfate oxidations [1]. Complexes of Ag^{III} are considered to be unstable, rare and much more restricted than those of Ag^{II} [2]. However, several compounds and complexes of Ag^{III} have been isolated and are well characterized. These include the mixed-valent oxides AgO and Ag_3O_4 as well as the stoichiometric Ag_2O_3 [3,4]. Other complexes include diamagnetic four-coordinate and paramagnetic six-coordinate fluoro-complexes, diperiodato, ditellurato, dithioccarbamate, porphyrins, tetrazamacrocycles, biguanides, phosphines, arsines, *vic*-dioximes, polypeptides, hydroxide and aminoethylpyridine complexes [5–19]. Silver(III) complexes with biguanides, corroles and carboporphrins have been isolated and their structures resolved by X-ray crystallography [20–22].

Imine-oxime, pyridine-oxime and *vic*-dioxime ligands have been shown to be good ligands for the stabilization of uncommon high oxidation states of transition metals [23–28]. The ability of imine-oxime and *vic*-dioxime ligands to stabilize Cu^{III}, Ni^{III} and Ni^{IV} has been attributed to the oxime π-donor character as well as the negative charge on the oximato oxygen.



We have previously shown that *vic*-dioximes and tetradentate imine-oxime ligands such as H_2L^1 stabilize Cu^{III}. The tridentate imine-oxime-amine ligand, HL^2, has been synthesized and was shown to stabilize the +3 oxidation

* Corresponding author. Tel.: +974 485 2193; fax: +974 485 1049.
E-mail address: yousifsulfab@yahoo.com (Y. Sulfab).

0277-5387/$ - see front matter © 2006 Elsevier Ltd. All rights reserved.
doi:10.1016/j.poly.2006.07.026

state of copper [29]. It seems that ligands, such as periodate, tellurate, biuret, *vic*-dioximes and tetraazamacrocyclic ligands, which are capable of stabilizing Cu^{III} stabilize Ag^{III} as well. In this work, we report the synthesis, isolation and characterization of new Ag^{III} complexes using the ligands H_2L^1, HL^2.

2. Experimental

2-Oximinobutan-3-one (Sigma), 1,3-diaminopropane (Aldrich) and ethyl acetate (Aldrich) were used as received. All other organic solvents used were of reagent grade and were used as received. Tetrabutylammonium hexafluorophosphate, $(n\text{-Bu})_4NPF_6$(Fluka), was used as a supporting electrolyte.

The ligand H_2L^1 was synthesized as reported previously [23b,24]. The ligand HL^2 was prepared by adding 2-oximinobutan-3-one (2.02 g, 20 mmol) dropwise to a stirred solution of 1,3-diaminopropane (1.85 g, 25 mmol) at room temperature. Both reactants were dissolved in methyl acetate. The reaction product was collected the next day and was washed with cold ethyl ether and dried over P_4O_{10}. The Ag^I-imine-oxime complexes were formed in situ by mixing $AgNO_3$ solution with an aqueous suspension of the ligand of choice with metal:ligand mole ratios 1:1.1 for H_2L^1 and 1:2.2 HL^2 in water at room temperature. Typically 0.85 g of $AgNO_3$ was used with the appropriate amount of the ligand. The mixtures were stirred until pale yellow solutions were formed. To the stirred solution of the Ag^I complex with the ligand H_2L^1, 2.0 g of PbO_2 was added and the solution acidified with drops of glacial acetic acid. The intensely orange-red solution that was formed was filtered and the complex formed was precipitated by the addition of NH_4PF_6 solution. The precipitate was filtered, washed with diethyl ether and dried over P_4O_{10}. The Ag^I complex with the ligand HL^2 was oxidized by either PbO_2 or $S_2O_8^{2-}$. The Ag^{III} complex was also precipitated by addition of NH_4PF_6. The IR spectra of the metal complexes were measured as KBr pellets using a Nicolet 510P-FT-IR spectrometer. The electronic spectra were recorded on a Lambda 25 UV–Vis spectrophotometer. Magnetic susceptibilities were measured at room temperature (~25 °C) by the Gouy method using a Sherwood Instruments magnetic susceptibility balance. Cyclic voltammograms were generated using an EG&G Princeton Applied Research Instruments Model 394 Electrochemical Trace analyzer. A three electrode system consisting of a Pt working electrode, an auxiliary platinum electrode and Ag/Ag^+ (0.10 M $AgNO_3$) reference electrode for a non-aqueous medium was used. Elemental analyses were performed at the UMIST (UK) and at Ain Shams University (Egypt).

A Perkin–Elmer TG A7 unit was used to record TG and DTG curves in a static N_2 atmosphere at a heating rate of 10 °C/min in the 30–900 °C range using platinum crucibles. The conductivity of the complexes was measured at 25 °C in water because the complexes are very unstable in non-aqueous solvents.

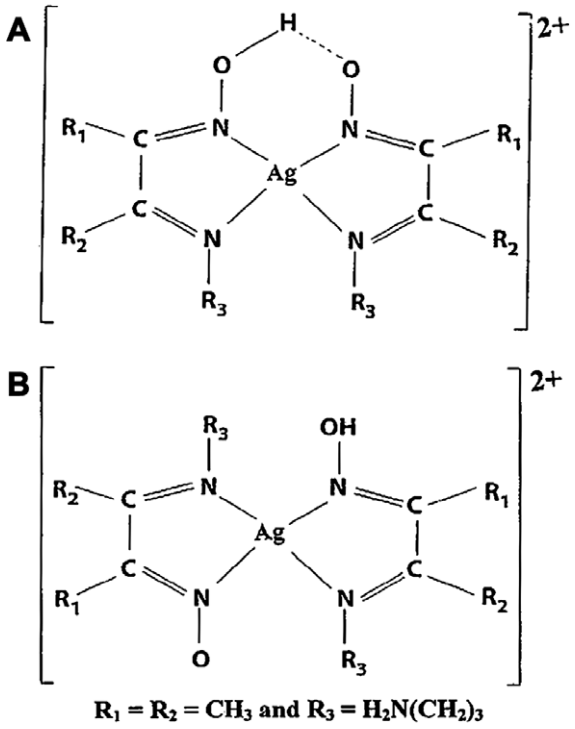
3. Results and discussion

The elemental analyses are consistent with the formation $[Ag^{III}HL^1](PF_6)_2 \cdot 4H_2O$ and $[Ag^{III}(HL^2)(L^2)](PF_6)_2 \cdot 3H_2O$. Elemental analyses for the complexes with the ligands H_2L^1 and HL^2 are: *Anal.* Calc.: C, 18.6; H, 3.8; N, 7.5. Found: C, 18.6; H, 3.6; N, 7.6% and *Anal.* Calc.: C, 22.0; H, 3.9; N, 11.0. Found: C, 21.8; H, 4.6; N, 9.9%, respectively. The thermal analysis curve for the complex with the ligand H_2L^1 showed that decomposition takes place in four stages in the 30–480 °C temperature range. The first endothermic stage corresponds to the dehydration process. The TG and DTG curves of the complex with the tetradentate ligand show a weight loss of 10.0%, which is in good agreement with the formula $[Ag^{III}HL^1](PF_6)_2 \cdot 4H_2O$. The weight loss of all four water molecules, calculated as 10.2%, occurs between 100 and 185 °C. The thermal decomposition of the complex with the ligand HL^2 proceeds in five stages. The first stage corresponds to the loss of three water molecules. The observed weight loss of 7.5% is in fairly good agreement with the loss of three water molecules (calc. 7.05%) from the formula $[Ag^{III}(HL^2)(L^2)](PF_6)_2 \cdot 3H_2O$. It seems that the ligands lose only one proton when coordinated to Ag^{III} unlike the case of Cu^{III} complexes with these same ligands where both protons are lost [23b,24]. The conductivity of the complexes $[Ag^{III}HL^1](PF_6)_2 \cdot 4H_2O$ and $[Ag^{III}(HL^2)(L^2)](PF_6)_2 \cdot 3H_2O$ was determined as 183 and 212 Ω^{-1} cm^2 mol^{-1}, respectively. This is consistent with the loss of only one proton and the formation of 1:2 electrolytes. The difference in the number of protons in the Cu^{III} and Ag^{III} complexes probably points the difference in the sizes of the +3 oxidation state of these metal ions, with the former being more polarizing than the latter due to its smaller size. The electronic spectrum of each complex is markedly affected by the nature of the solvent. This is indicative of the formation axial bonds. It also indicates that in the complex $[Ag^{III}(HL^2)(L^2)](PF_6)_2 \cdot 3H_2O$ the tridentate ligand is functioning only as a bidentate ligand. All the isolated complexes are diamagnetic, consistent with the formation of a low spin d^8 square planar or tetragonal structure with water molecules occupying axial positions.

The IR spectra of the two ligands showed the disappearance of the carbonyl band of the 2-oximinobutan-3-one and the appearance of sharp C=N bands. In the ligand HL^2 two bands appeared around 3256 cm^{-1} which are assigned to NH_2, confirming the 1:1 condensation between 1.3-diaminopropane and 2-oximinobutan-3-one. The C=N bands of the ligands are shifted to lower frequencies in the Ag^{III} complexes indicating bonding to the metal.

The UV–Vis absorption spectrum of the complex $[Ag^{III}HL^1]^{2+}$ is shown in Fig. 1. The complex $[Ag^{III}(HL^2)(L^2)]^{2+}$ showed a similar spectrum with slight variation in peak positions. A similar behavior was shown by the closely related Ag^{III}-dioximate complexes [16]. The high absorption in the visible region may be assigned to ligand to metal charge transfer (LMCT) by analogy to other

related complexes. Other Ag^{III}–N_4 ligand systems also exhibit similar LMCT bands in the visible region [21,22]. The positions of the UV bands in these complexes are very close to those of the free ligands and may be assigned to $\pi \rightarrow \pi^*$ transitions. The molar absorption of the complexes with the ligands H_2L^1 and HL^2 were measured at λ_{max} 486 nm as 1.76×10^4 and 1.12×10^4 M^{-1} cm^{-1}, respectively. Both complexes decompose slowly in aqueous solutions and the rate of decomposition is accelerated by both acid and base. A similar behavior was observed for the Cu^{III} complexes with the same ligands [23,24]. The complexes show marked color changes on dissolution of the complexes in coordinating solvents such as Me_2CO, Me_2SO and MeCN. This, most likely, is due to axial coordination to the four-coordinate Ag^{III} complex. Reported X-ray crystal structures have shown axial coordination by H_2O, NO_3^- as well as SO_4^{2-} [20]. Silver(III)-imine-oxime complexes decompose much more readily in non-aqueous solvents than in water. The d–d transition bands in these and other Ag^{III} complexes are not observed because they fall in the same spectral region as the charge-transfer bands.



The Ag^{III} complex with the ligand HL^2 may assume either structure A or B. However, all attempts to form crystals were unsuccessful because the complex decomposes slowly. Indeed both complexes decompose in the solid state if they are not kept dry and away from light.

The cyclic voltammograms of the complexes, shown in Figs. 2 and 3, indicate that the electron transfer processes are electrochemically irreversible and these generally involve a two-electron process [19]. This is not unexpected

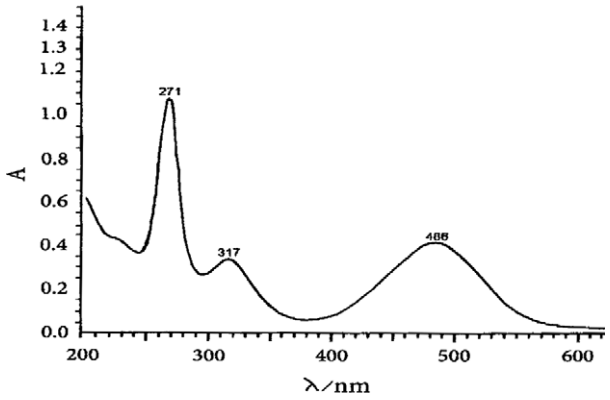


Fig. 1. UV–Vis absorption spectrum of $[Ag^{III}HL^1]^{2+}$ in aqueous solution at pH 4.60.

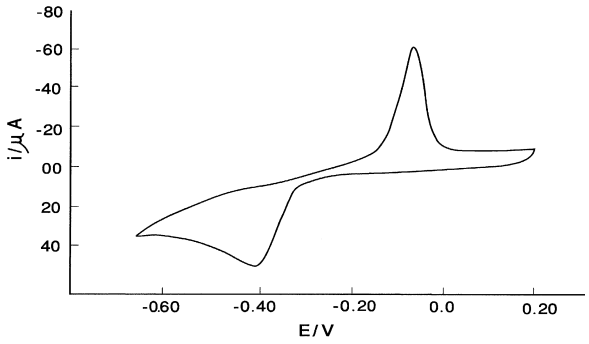


Fig. 2. Cyclic voltammogram of $[Ag^{III}HL^1]^{2+}$ in acetonitrile at $I = 0.10$ M $(n\text{-}Bu)_4NPF_6$ against Ag/Ag^+ (0.10 M $AgNO_3$) reference electrode for non-aqueous solvents.

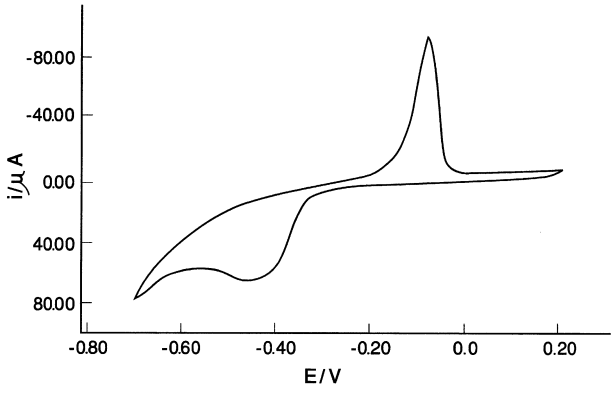


Fig. 3. Cyclic voltammogram of $[Ag^{III}HL^2]^{2+}$ in acetonitrile at $I = 0.10$ M $(n\text{-}Bu)_4NPF_6$ against Ag/Ag^+ (0.10 M $AgNO_3$) reference electrode for non-aqueous solvents.

as the conversion of $Ag^{III} \rightarrow Ag^{I}$ would be accompanied by structural changes. Electrochemically reversible cyclic voltammograms are only observed for $Ag^{III} \rightarrow Ag^{II}$ processes, where the electron transfer step is accompanied by only small structural changes [30]. Fig. 2 shows a cyclic voltammogram of the Ag^{III} complex with the ligand H_2L^1. The anodic, E_{pa}, and the cathodic, E_{pc}, potentials appear at −90 and −410 mV, respectively. The anodic and cathodic

potentials for the Ag^{III} complex with the ligand HL^2, shown in Fig. 3, appear at −83 and −440 mV, respectively, at a scan rate of 100 mV/s. Electrochemical irreversibility remained even at a scan rate of 20 mV/s. The i_a/i_c ratio is <1, thus confirming the irreversibility of the electron transfer. The peaks separations, ΔE_p, of 320 and 357 mV of the complexes with the tetradentate and tridentate ligands, respectively, are much higher than the 28 mV expected for a reversible two-electron transfer process. It may thus be concluded that tetradentate imine-oxime ligands stabilize higher oxidation states better than tridentate imine-oxime-amine ligands.

Acknowledgment

The authors thank Mr. Ahmed R. Abdelati of the Department of Chemistry and Earth Sciences for his assistance with cyclic voltammetry.

References

[1] D.A. House, Chem. Rev. 62 (1962) 185.
[2] W. Levason, M.D. Spicer, Coord. Chem. Rev. 76 (1987) 17.
[3] (a) T.P. Dirkak, J. Electrochem. Soc. 106 (1959) 453;
(b) M.B. Robin, P. Day, Adv. Inorg. Chem. Radiochem. 10 (1957) 167.
[4] (a) B. Standke, M. Jansen, Angew. Chem., Int. Ed. Engl. 25 (1986) 77;
(b) B. Standke, M. Jansen, Angew. Chem., Int. Ed. Engl. 24 (1985) 133.
[5] R. Hoppe, Rec. Trav. Chim. Pays-Bas. 75 (1956) 569.
[6] R. Hoppe, Z. Anorg. Allgem. Chem. 292 (1970) 28.
[7] L. Malaprade, Compt. Rend. 210 (1940) 504.
[8] L. Jenovsky, M. Skala, Z. Anorg. Allgem. Chem. 312 (1961) 26.
[9] T.J. Bergendahl, E.M. Bergendahl, Inorg. Chem. 11 (1972) 638.
[10] (a) K.M. Kadish, D.G. Davis, J.H. Fuhrhop, Angew. Chem. 84 (1972) 3388;
(b) , J. Am. Chem. Soc. 95 (1973) 5140.
[11] E.K. Barefield, M.T. Mocella, Inorg. Chem. 12 (1973) 2829.
[12] P. Ray, Nature 151 (1943) 643.
[13] K. Chakravorty, P. Ray, J. Ind. Chem. Soc. 21 (1944) 41, 47.
[14] P. Ray, Inorg. Synth. 6 (1960) 74.
[15] (a) L.F. Warren, M.A. Bennett, J. Am. Chem. Soc. 96 (1974) 3340;
(b) L.F. Warren, M.A. Bennett, Inorg. Chem. 15 (1976) 3126.
[16] L.J. Kirschenbaum, R.K. Panda, E.T. Borish, E. Mentasti, Inorg. Chem. 28 (1989) 3623.
[17] L.J. Kirschenbaum, D.J. Rush, J. Am. Chem. Soc. 106 (1984) 1003.
[18] G.L. Cohen, G. Atkinson, J. Electrochem. Soc. 115 (1968) 1236.
[19] A. Kahani, M. Abedini, M. Farnia, Transition Met. Chem. 25 (2000) 711.
[20] (a) N.R. Kunchur, Nature 217 (1968) 539;
(b) M.L. Simms, J.L. Atwood, D.A. Zatko, J. Chem. Soc., Chem. Commun. (1973) 46;
(c) L. Coghi, G. Pelizzi, Acta Crystallogr., Sect. B 31 (1975) 131.
[21] C. Bruckner, C.A. Barta, R.P. Brinas, J.A. Krause Bauer, Inorg. Chem. 42 (2003) 1673.
[22] T.D. Lash, D.A. Colby, L.F. Szczepura, Inorg. Chem. 43 (2004) 5258.
[23] (a) Y. Sulfab, M.A. Hussein, N.I. Al-Shatti, Inorg. Chim. Acta 67 (1982) L33;
(b) Y. Sulfab, N.I. Al-Shatti, Inorg. Chim. Acta 87 (1984) L23.
[24] Y. Sulfab, F.M. Al-Sogair, Transition Met. Chem. 27 (2002) 299.
[25] Y. Sulfab, Polyhedron 8 (1989) 2409.
[26] (a) J.G. Mohanty, R.P. Singh, A. Chakravorty, Inorg. Chem. 14 (1975) 2178;
(b) A.N. Singh, R.P. Singh, J.G. Mohanty, A. Chakravorty, Inorg. Chem. 6 (1977) 2597.
[27] (a) E.I. Baucom, R.S. Drago, J. Am. Chem. Soc. 93 (1971) 6469;
(b) R.S. Drago, E.I. Baucom, Inorg. Chem. 11 (1972) 2064.
[28] R.K. Panda, S. Acharga, G.N. Neogi, D. Ramaswamy, J. Chem. Soc., Dalton Trans. (1983) 225.
[29] M.A-Z. Eltayeb, Y. Sulfab, Polyhedron (in press).
[30] A. Harrima, M.C. Richoux, P. Neta, J. Phys. Chem. 87 (1983) 4957.

Available online at www.sciencedirect.com
ScienceDirect
Polyhedron 26 (2007) 43–48
POLYHEDRON
www.elsevier.com/locate/poly

Synthesis and characterisation of titanium pyridine- and pyrimidine-thiolates and their application as precursors to titanium disulfide

Claire J. Carmalt *, Emily S. Peters, Ivan P. Parkin, Derek A. Tocher

Department of Chemistry, University College London, 20 Gordon Street, London, WC1H 0AJ, UK

Received 19 June 2006; accepted 26 July 2006
Available online 2 August 2006

Abstract

The reaction of $TiCl_4$ with pyridine- and pyrimidine-thiol has been investigated. Reaction of $TiCl_4$ with 3 equiv. of 2-mercaptopyridine and 3 equiv. of *tert*-butylpyridine in toluene at room temperature resulted in the formation of the tris(pyridine-2-thiolate) complex $[TiCl(SC_5H_4N)_3]$ (**1**). The related reaction between $TiCl_4$ with 3 equiv. of 2-mercaptopyrimidine and 3 equiv. of *tert*-butylpyridine in toluene at room temperature resulted in the isolation of the complex $[TiCl(SC_4H_3N_2)_3]$ (**2**). Compound **2** has been characterised by X-ray crystallography. Low pressure CVD of **1** and **2** produced brown/gold films of TiS_2/TiO_2 on glass substrates at 550 and 600 °C.
© 2006 Elsevier Ltd. All rights reserved.

Keywords: Titanium thiolate; Titanium disulfide; Molecular precursor; CVD

1. Introduction

Early transition metal thiolate complexes represent a class of compound that have only been studied to a limited extent until recently [1]. Early routes to titanium thiolates involved the reaction of thiols with $[Ti(NR_2)_4]$ (R = Me or Et) resulting in the formation of complexes of the type $[Ti(SR')_4(HSR')_x(NHR_2)_y]$ (where $(x + y)$ varied from 0.8 to 1.33) [2]. We have recently shown that the reaction of $[Ti(NEt_2)_4]$ with C_6F_5SH and $PhCH_2SH$, resulted in the formation of ionic complexes of the type $[Et_2NH_2][Ti(SC_6F_5)_4(NEt_2)]$ and $[Et_2NH_2][Ti_2(\mu\text{-}SCH_2Ph)_3(SCH_2Ph)_6]$, respectively [3,4]. Similarly, reaction of $[Ti(NMe_2)_4]$ with CF_3CH_2SH afforded the salt $[Me_2NH_2]_2[Ti(SCH_2CF_3)_6]$ [5]. In contrast, addition of an excess of ^{t}BuSH to $[Ti(NEt_2)_4]$ resulted in the neutral complexes $[Ti(S^tBu)_4]$ and $[Ti(S^tBu)_3(NEt_2)]$ [6]. Titanium thiolates have also been prepared by reaction of an alkali metal thiolate with $TiCl_4$. For example, the titanium(III) thiolate $[Li(OEt_2)_3][Ti(S\text{–}2,4,6\text{–}^iPr_3C_6H_2)_4]$ was formed from the reaction of the lithiated thiol with $TiCl_3$ [7]. The homoleptic titanium thiolate $[Ti(S\text{-}2,3,5,6\text{-}Me_4C_6H)_4]$ resulted from reaction of $TiCl_4$ with 4 equiv. of $K[S\text{-}2,3,5,6\text{-}Me_4C_6H]$ [8]. The salt $[Et_4N]_2[Ti(SPh)_6]$ was isolated from $TiCl_4$, NaSPh and Et_4NBr [9]. In general, the isolation and purification of products from the reaction of $TiCl_4$ with alkali metal thiolates is difficult due to the strong interaction of titanium cations with halide ions. In order to avoid the purification problems associated with the route *via* alkali metal thiolates, trimethylsilylsulfides (Me_3SiSR) have also been used [10].

Early transition metal thiolates are of interest as potential precursors to transition metal disulfides, which in turn show a wide range of interesting characteristics from high temperature lubricating properties due to their layered structures to a variety of electronic properties (TiS_2 and MoS_2 are semiconductors; TaS_2 and NbS_2 are superconductors) [11–14]. However, most research has focussed on the use of TiS_2 as the cathode material in lithium rechargeable batteries [15,16]. TiS_2 has one of the highest

* Corresponding author. Tel.: +44 207 679 7528; fax: +44 207 679 7463.
E-mail address: c.j.carmalt@ucl.ac.uk (C.J. Carmalt).

0277-5387/$ - see front matter © 2006 Elsevier Ltd. All rights reserved.
doi:10.1016/j.poly.2006.07.017

intercalation energies when lithium diffuses into the van der Waal's gap between sulfur layers. TiS_2 is used as the cathode for lithium microbatteries, where formation of Li_xTiS_2 occurs on the discharge process. The surface area and morphology of the TiS_2 material is important as a large surface area, with the crystallographic *c*-axis of the TiS_2 parallel to the substrate, gives the highest lithium diffusion, which relates directly to the current density produced by the battery. In addition, a large surface area such as a thin film could improve intercalation rates.

In this paper the synthesis and structures of the pyridine- and pyrimidine-thiolate titanium(IV) complexes, $[TiCl(SC_5H_4N)_3]$ (**1**) and $[TiCl(SC_4H_3N_2)_3]$ (**2**) are reported. The pyridine- and pyrimidine-thiolate ligands were chosen in an attempt to stabilise neutral titanium(IV) thiolate complexes. The thermal decomposition of **1** and **2** has also been studied.

2. Experimental

2.1. General procedure

All manipulations were carried out under a dry, oxygen-free dinitrogen atmosphere using either standard Schlenk techniques or in a MBraun Unilab glove box. Dichloromethane was distilled from CaH_2 prior to use, toluene dried using sodium and hexanes were dried using sodium/benzophenone. All other reagents were procured commercially from Aldrich. Microanalytical data were obtained at University College London (UCL).

NMR spectra were recorded on a Bruker AMX400 spectrometer at UCL, referenced to CD_2Cl_2, which was dried and degassed over molecular sieves prior to use; ^1H and ^{13}C chemical shifts are reported relative to $SiMe_4$ (δ 0.00). Thermal gravimetric analysis (TGA) was performed under a dinitrogen atmosphere with a heating rate of 10 °C min^{-1} and obtained from the Thermal Methods Laboratory at Birkbeck College London. Raman spectra were acquired on a Renishaw Raman System 1000 using a helium–neon laser of wavelength 632.8 nm. The Raman system was calibrated against the emission lines of neon. EDAX was obtained on a JOEL 25 and SEM was obtained on a Hitachi S570 instrument using the KEVEX system. X-ray powder diffraction patterns were measured on a Siemens D5000 diffractometer using monochromated Cu $K\alpha_1$ radiation ($\lambda = 1.5406$ Å). The diffractometer used glancing incident radiation (1.5°). Samples were indexed using unit cell and compared to database standards. X-ray photoelectron spectra were recorded using a VG ESCALAB 220i XL instrument using focused (300 μm spot) monochromatic Al Kα radiation at a pass energy of 20 eV. Scans were acquired with steps of 50 meV. A flood gun was used to control charging and the binding energies were referenced to an adventitious C 1s peak at 284.8 eV. Depth profile measurements were obtained by using argon beam sputtering. Film solubility was assessed by immersing a 2 cm × 7 mm strip, cut from the substrate, into solvent (water, dichloromethane, ether, toluene, acetone and concentrated nitric and hydrochloric acids). Hardness scratch tests were conducted using a brass stylus and a stainless steel scalpel.

2.2. Preparation of compound *1*

2-Mercaptopyridine (0.35 g, 3.15 mmol) was added to a solution of $TiCl_4$ (1.05 cm^3 of 1 M solution in toluene, 1.05 mmol) in toluene (30 ml) with stirring. 4-*tert*-Butylpyridine (0.47 ml, 3.15 mmol) was added causing an immediate colour change from yellow to deep purple. Stirring was continued for 3 h and a dark purple precipitate had formed. The solution was removed by filtration and the solid was washed with 2×5 cm^3 of hexanes and dried *in vacuo*. Dark purple needle-like crystals (0.36 g, 84%) were formed over a week from diffusion of a concentrated dichloromethane solution with an overlayer of hexane at room temperature. ^1H NMR (CD_2Cl_2) δ 7.1 (1H, m, *m*, C_5H_4NS), 7.2 (1H, m, *p*, C_5H_4NS), 7.4 (1H, m, *m*, C_5H_4NS), 7.6 (1H, m, *o*, C_5H_4NS). $^{13}C\{^1H\}$ NMR (CD_2Cl_2) δ 118.4 (*m*, C_5H_4NS), 128.5 (*p*, C_5H_4NS), 129.3 (*o*, C_5H_4NS), 179.3 (*o*, C_5H_4NS). *Anal.* Calc. for $C_{15}H_{12}ClN_3S_3Ti$: C, 43.5; H, 2.9; N, 10.2. Found: C, 43.7; H, 2.7; N, 10.7%. Melting point: 70 °C.

2.3. Preparation of compound *2*

2-Mercaptopyrimidine (0.35 g, 3.15 mmol) was added to a solution of $TiCl_4$ (1.05 cm^3 of 1 M solution in toluene, 1.05 mmol) in toluene (30 ml) with stirring. 4-*tert*-Butylpyridine (0.47 ml, 3.15 mmol) was added causing an immediate colour change to deep red. Stirring was continued for 3 h and a dark red precipitate had formed. The solution was removed by filtration and the solid was washed with 2×5 cm^3 of hexanes and dried *in vacuo*. Dark red needle-like crystals (0.37 g, 86%) were formed over a week from a concentrated dichloromethane solution at room temperature. ^1H NMR (CD_2Cl_2) δ 1.4 (18H, s, $(CH_3)_3CC_5H_4NH$), 6.9 (1H, m, *p*-$C_4H_3N_2S$), 7.1 (2H, m, *m*-$C_4H_3N_2S$), 7.9 (4H, m, *m*-$(CH_3)_3CC_5H_4NH$), 8.7 (4H, m, *o*-$(CH_3)_3CC_5H_4NH$), 9.7 (2H, s, $(CH_3)_3CC_5H_4NH$). $^{13}C\{^1H\}$ NMR (CD_2Cl_2) δ 30.2 ($(CH_3)_3CC_5H_4NH$), 36.9 ($(CH_3)_3CC_5H_4NH$), 124.5(*m*-$(CH_3)_3CC_5H_4NH$), 125.6 (*p*-$C_4H_3N_2S$), 128.5 (*m*-$C_4H_3N_2S$), 129.3 (*i*-$C_4H_3N_2S$), 140.7 (*o*-$(CH_3)_3CC_5H_4NH$) 151.4 (*p*-$(CH_3)_3CC_5H_4NH$). *Anal.* Calc. for $C_{30}H_{37}Cl_3N_8S_3Ti$: C, 47.4; H, 4.9; N, 14.7. Found: C, 47.7; H, 5.1; N, 14.1%. Melting point: 147 °C.

2.4. Low pressure CVD experiments

The experimental apparatus was the same as that described previously although quantities of precursor and size of substrates were different as described below [20]. The same procedure was carried out for all compounds (**1**, **2**) shown here for **2**. A sample of compound **2** (0.3 g) was loaded into the end of a glass ampoule (40 cm

length × 16 mm diameter) in the glovebox. Glass substrates (10 cm × 7 mm – uncoated microscope slide) were placed carefully inside the ampoule. The ampoule was then placed in a furnace such that 30 cm was inside the furnace and the end containing the sample protruded by 4 cm. The ampoule was heated to a temperature of 500 and 600 °C under dynamic vacuum (3.0 kPa), except for the section of the tube containing the sample. The ampoule was slowly drawn into the furnace over a period of a few minutes until **2** started to melt. Once the compound had decomposed the furnace was allowed to cool to room temperature. Brown/gold films were deposited on the glass substrates. The films were analyzed by EDAX/SEM, powder X-ray diffraction, Raman and X-ray photoelectron spectroscopy.

2.5. Crystal structures determination and refinement

Crystals of **2** were isolated from dichloromethane at room temperature. A single crystal was mounted on a glass fibre and all geometric and intensity data were taken from this sample on a Bruker SMART APEX CCD diffractometer using graphite-monochromated Mo Kα radiation ($\lambda = 0.71073$ Å) at 150 ± 2 K. Data reduction and integration was carried out with SAINT+ and absorption corrections applied using the programme SADABS. The structure was solved by direct methods and developed using alternating cycles of least-squares refinement and difference-Fourier synthesis. All non-hydrogen atoms were refined anisotropically. Hydrogen atoms were placed in calculated positions and their thermal parameters linked to those of the atoms to which they were attached (riding model). Structure solution and refinement used the SHELXTL Plus v6.10 program package [17]. See Table 1 for selected crystal data.

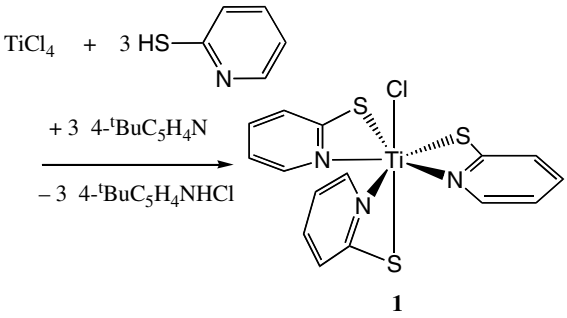
Table 1
Crystallographic data for compound **2**[a]

Data	**2**
Chemical formula	$C_{13}H_{11}Cl_3N_6S_3Ti$
Fw	501.71
T (K)	150(2)
Space group	$P2_1/n$
Unit cell dimensions	
a (Å)	8.6877(9)
b (Å)	10.3449(11)
c (Å)	21.851(2)
β (°)	101.387(2)
V (Å^3)	1925.2(4)
Z	4
ρ_{calc} (g cm^{-3})	1.731
λ (Å)	0.71073
μ (mm^{-1})	1.198
R_1[b]	0.0583
wR_2[c]	0.1415

[a] Bruker SMART APEX diffractometer ω rotation with narrow frames, graphite monochromated Mo Kα radiation, refinement based on F^2.
[b] $R_1 = \sum\|F_o| - |F_c\|/\sum|F_o|$.
[c] $wR_2 = \{\sum[w(F_o^2 - F_c^2)^2]/\sum[w(F_o^2)^2]\}^{1/2}$; $w^{-1} = \sigma^2(F_o^2) + (aP)^2 + bP$.

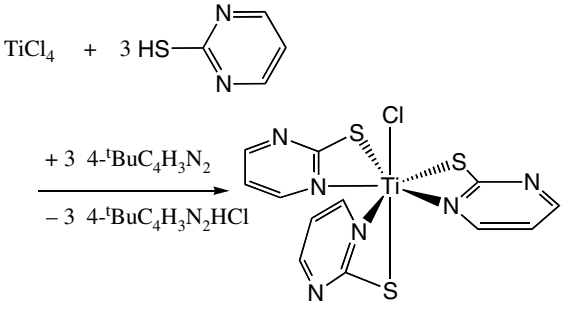
3. Results and discussion

Reaction of $TiCl_4$ and 3 equiv. of both HSC_5H_4N and 4-*tert*-butyl pyridine resulted in the isolation, after work up, of $[TiCl(SC_5H_4N)_3]$ (**1**). A dark purple precipitate of **1** formed in an 84% yield. Dark purple needle-like crystals of **1** suitable for X-ray analysis were formed by the diffusion of hexane into a concentrated dichloromethane solution at room temperature. Analytical and spectroscopic data for **1** were consistent with the formation of the tris(pyridine-thiolate) complex $[TiCl(SC_5H_4N)_3]$ (**1**) (Eq. (1)). The room temperature ^{1}H NMR spectrum of **1** in CD_2Cl_2 shows one set of resonances for the three thiolate ligand. These results are consistent with compound **1** being fluxional on the NMR time scale. Compound **1** has been prepared (in lower yield) and structurally characterised previously from the reaction of $TiCl_4$ and $Me_3SiSC_5H_4N$ [10]. Compound **1** has a distorted seven-coordinate pentagonal bipyramidal geometry at the titanium centre (Eq. (1)). The melting point of **1** was 70 °C which is sufficiently low to suggest that vaporisation and subsequent film growth could be possible by CVD.



(1)

1



(2)

2

The reaction of $TiCl_4$ with 3 equiv. of both $HSC_4H_3N_2$ and 4-*tert*-butyl pyridine was carried out in toluene at room temperature with the formation of a dark red precipitate. After work up of the reaction, red needle-like crystals were isolated, which were shown by a single crystal structure determination to consist of the pyrimidine-thiolate $[TiCl(SC_4H_3N_2)_3]$ (**2**) (Eq. (2)). The structure of compound **2** was determined by X-ray crystallography, the results are shown in Fig. 1; selected bond lengths and angles are shown in Table 2. Compound **2** crystallises into the monoclinic, $P2_1/n$ space group. The geometry adopted by titanium is a distorted seven-coordinate pentagonal bipyramidal with the Cl atom in an axial position, as for

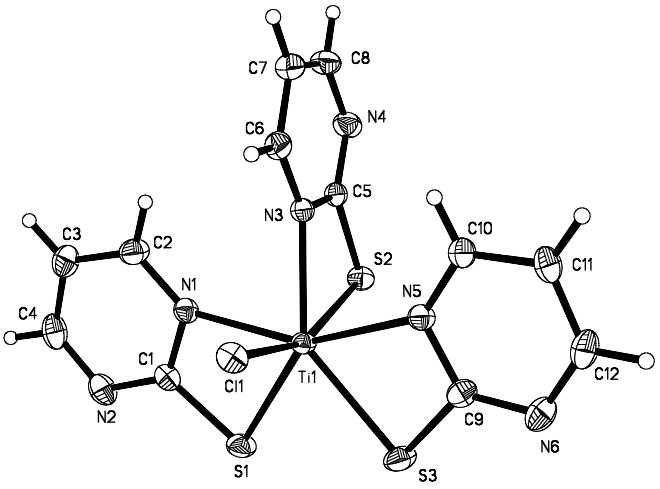


Fig. 1. X-ray structure of compound **2**.

Table 2
Selected bond lengths (Å) and angles (°) for $[TiCl(SC_4H_3N_2)_3]$ (**2**)

Bond lengths			
Ti(1)–N(3)	2.182(3)	Ti(1)–N(5)	2.202(3)
Ti(1)–N(1)	2.219(3)	Ti(1)–Cl(1)	2.2940(11)
Ti(1)–S(2)	2.4361(11)	Ti(1)–S(3)	2.4483(11)
Ti(1)–S(1)	2.4548(11)	S(1)–C(1)	1.733(4)
S(2)–C(5)	1.740(4)	S(3)–C(9)	1.733(4)
Bond angles			
N(3)–Ti(1)–N(1)	77.23(11)	N(3)–Ti(1)–N(5)	77.35(11)
N(3)–Ti(1)–Cl(1)	90.92(9)	N(5)–Ti(1)–N(1)	153.79(12)
N(1)–Ti(1)–Cl(1)	85.85(8)	N(5)–Ti(1)–Cl(1)	88.29(8)
N(5)–Ti(1)–S(2)	87.78(8)	N(3)–Ti(1)–S(2)	66.78(8)
Cl(1)–Ti(1)–S(2)	157.68(4)	N(1)–Ti(1)–S(2)	88.03(8)
N(5)–Ti(1)–S(3)	65.60(8)	N(3)–Ti(1)–S(3)	140.08(8)
Cl(1)–Ti(1)–S(3)	101.87(4)	N(1)–Ti(1)–S(3)	140.61(9)
N(3)–Ti(1)–S(1)	139.21(8)	S(2)–Ti(1)–S(3)	96.46(4)
N(1)–Ti(1)–S(1)	65.47(8)	N(5)–Ti(1)–S(1)	140.79(9)
S(2)–Ti(1)–S(1)	95.06(4)	Cl(1)–Ti(1)–S(1)	101.82(4)
C(1)–S(1)–Ti(1)	82.61(13)	S(3)–Ti(1)–S(1)	75.15(4)
C(9)–S(3)–Ti(1)	82.73(13)	C(5)–S(2)–Ti(1)	81.35(12)
C(1)–N(1)–Ti(1)	101.5(2)	C(2)–N(1)–Ti(1)	139.4(3)

compound **1**. The ligands are orientated such that the three S atoms are in all-*cis* positions on one triangular face of the pentagonal bipyramid. The Ti–S bond lengths are in the range 2.4361(11)–2.4548(11) Å and are comparable to those in **1** (2.4257(18)–2.4528(17) Å). A similar seven-coordinate structure incorporating dithiocarbamate ligands, namely $[TiCl(S_2CNMe_2)_3]$, where the chlorine atom adopts an axial position has previously been reported [18]. The Ti–S bond lengths in **1** and **2** are comparable to those reported for $[TiCl(S_2CNMe_2)_3]$ (2.473(3)–2.577(3) Å) and other titanium thiolate complexes [3–6,8–10,18]. The Ti–Cl bond length for compound **2** (2.2940(11) Å) is similar to that found in compound **1** and reported for $[TiCl(S_2CNMe_2)_3]$ (2.305(3) Å) [18]. The S–C bond lengths (1.733(4)–1.740(4) Å) are comparable to those in the dithiocarbamate $[TiCl(S_2CNMe_2)_3]$ (av. 1.715(10) Å) but shorter than other reported S–C(sp^2) bond lengths, for example the S–C bond lengths in $[Li(OEt_2)_3][Ti(S\text{-}2,4,6\text{-}^iPr_3C_6H_2)_4]$ were in the range 1.798(4)–1.806(5) Å [7]. The Ti–N bond lengths (2.182(3)–2.219(3) Å) in **2** are longer than that observed for a covalent Ti–N bond (e.g. 1.856(5) Å in $[Ti(NEt_2)(S^tBu)_3]$) but shorter than in titanium pyridine complexes such as $[Ti(N^tBu)Cl(N_3)(py)_2]_2$ (av. Ti–N 2.241(5) Å) [6,19]. The shorter Ti–N and S–C bond lengths suggest that there is some contribution from canonical form b, shown in Fig. 2, as was also observed for **1**. The spectroscopic and analytical data for **2** showed the presence of the side product $[^tBuC_5H_4NH]Cl$.

In order to study the decomposition pathway of compounds **1** and **2** thermal analyses were carried out. The TGA (thermal gravimetric analysis) of **1** (10 °C/min from 20 to 500 °C) shows a weight loss of 91%. The decomposition of **1** does not occur in clean, discrete stages but is continuous from the onset at *ca.* 150 °C throughout the temperature range studied. The mass loss of 91% is significantly higher than the calculated mass loss of 73% for **1** to form TiS_2. It is worth noting that TGA at atmospheric pressure only gives an indication of the potential of the precursors to form bulk titanium sulfide. Any sublimation of the precursor, a desirable characteristic for low pressure chemical vapour deposition (LPCVD) studies, would register as a further mass loss, as observed in the TGA of **1**. The DSC of **1** shows a sharp endotherm at 70 °C which corresponds to the melting point. The decomposition of **1** begins at a higher temperature than the melting point suggesting that transport of the intact molecule to the substrate could be successfully achieved. This would suggest that compound **1** would be a good CVD precursor. The TGA for **2** shows that the onset of decomposition is *ca.* 200 °C and continues over the entire temperature range up to 500 °C. As with compound **1** there are no discrete steps observed in the TGA, suggesting that the decomposition will not proceed cleanly. The measured mass loss of 57% is less than the required mass loss to produce TiS_2 (73%). This behaviour indicates an incomplete decomposition to TiS_2 up to 500 °C, although it is possible that the required weight loss could be attained at higher temperatures (the TGA set-up allows analysis only to 500 °C). The DSC of **2** shows a sharp endotherm at 147 °C signifying the melting point. This is significantly higher than the pyridine analogue, compound **1**.

LPCVD of **1** and **2** were investigated, the details of which are described in Section 2 [20]. The films produced

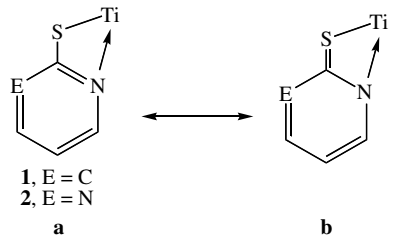


Fig. 2. Resonance forms of the mercapto-pyridine and -pyrimidine ligand.

were analyzed by EDAX/SEM, XPS, powder XRD and Raman spectroscopy. The films produced from **1** and **2** under LPCVD conditions were adhesive to the substrate in that they passed the Scotch Tape Test but were easily scratched by a brass or stainless steel stylus. Chemically, the films showed no reactivity to common organic solvents. Concentrated nitric acid digested a film within 30 s of immersion, whereas concentrated hydrochloric acid dissolved the film over 2 h. Brown/gold reflective films were deposited from compound **1** at 500 and 600 °C, 0.03 mm Hg. All the films deposited from **1** were sulfur deficient by EDAX with a titanium to sulfur ratio of 1:1.6 at 600 °C and 1:1 at 500 °C. No chlorine contamination was found by EDAX. The Ti:S ratios could indicate the formation of Ti_2S_3 and TiS (at 600 and 500 °C, respectively) or alternatively could be due to partial oxidation of the films with the formation of a mixture of TiS_2 and TiO_2. However, the XPS of the film deposited at 600 °C from **1** does not show the presence of TiO_2 in the Ti 2p spectrum [21]. The peaks at 456.8 and 462.4 eV correspond to Ti $2p_{3/2}$ and Ti $2p_{1/2}$, respectively, which match well with those previously reported for TiS_2 (Ti $2p_{3/2}$, 456.2 eV; Ti $2p_{1/2}$, 462.2 eV) [21]. The S 2p peaks in the XPS confirm that TiS_2 has been formed, with peaks observed at 161.6 and 163.4 eV (corresponding to S $2p_{3/2}$ and $2p_{1/2}$, respectively). Furthermore, the XPS shows that only one sulfur environment is present within the film and that this corresponds to sulfur in TiS_2. No chlorine contamination was observed in the XPS.

Further evidence for the formation of TiS_2 films from **1** were provided by Raman spectroscopy and powder XRD. The Raman patterns for the films deposited from **1** show the characteristic TiS_2 peak at 332 cm^{-1} and do not show the presence of TiO_2 peaks suggesting that the sulfur deficiency is not due to surface oxidation. Glancing angle XRD for the film deposited at 600 °C from **1** shows peaks which correspond well with the literature values for TiS_2. In contrast to the Raman patterns which did not show the presence of TiO_2, the glancing angle XRD for the film deposited from **1** at 500 °C shows peaks corresponding to TiS_2 and TiO_2 (anatase). The XRD suggests some preferential orientation. The SEM image for the film deposited at 600 °C shows a series of hexagonal platelets in a perpendicular orientation to the substrate (Fig. 3a). The platelets measure *ca.* 1.5 μm in diameter. The perpendicular orientation of this film would be particularly favoured for use in battery applications as intercalation is maximised, where films are perpendicular to the substrate. In addition, the platelets are indicative of film formation *via* an island growth type mechanism. The SEM image for the film deposited at 500 °C also shows platelets in a perpendicular orientation to the substrate which are *ca.* 3.7 μm in diameter (Fig. 3b). Small clusters are also observed on the surface of the substrate, which are 0.7 μm in diameter. This could explain the inconsistent XRD and Raman results for films deposited at 500 °C, in that there is a deposit of TiO_2 (clusters) on the surface, with TiS_2 platelets above. The Raman pattern does not show TiO_2, as this is a surface sensitive technique (with a penetration depth of *ca.* 600 nm), whereas XRD penetrates further. The EDAX results are also in agreement with these observations as EDAX measures a large area and penetrates into the film and therefore the titanium to sulfur ratio of 1:1 is explained by the mixed TiS_2/TiO_2 film. Therefore, the presence of TiO_2 is not a consequence of surface oxidation as TiO_2 peaks would be observed in the Raman pattern, instead it was formed at the time of deposition and could be due to reaction with the uncoated glass substrate. TiS_2 films were produced from **1** at 600 °C although some slight deviations were noted from this composition by EDAX, where breakthrough to the underlying glass was observed.

The films deposited from **2** had a titanium to sulfur ratio of 1:1.5 by EDAX showing them to be sulfur deficient which may be due to oxidation of the films. The XPS for Ti 2p gave a binding energy of 458.5 and 464.2 eV for Ti $2p_{3/2}$ and $2p_{1/2}$, respectively, which match well with those previously reported for TiS_2 [21]. The spectrum was particularly clean with no titanium peaks due to TiO_2 observed.

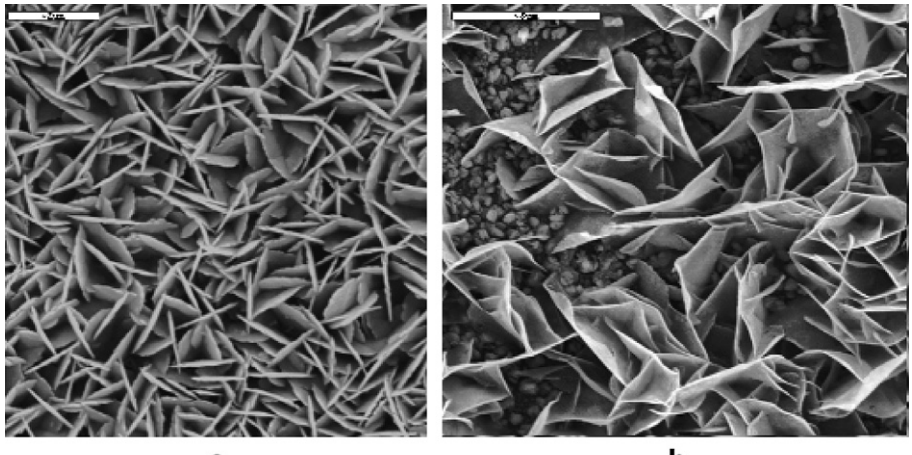


Fig. 3. SEM image for a film deposited by LPCVD from compound **1** at: (a) 600 °C and (b) 500 °C.

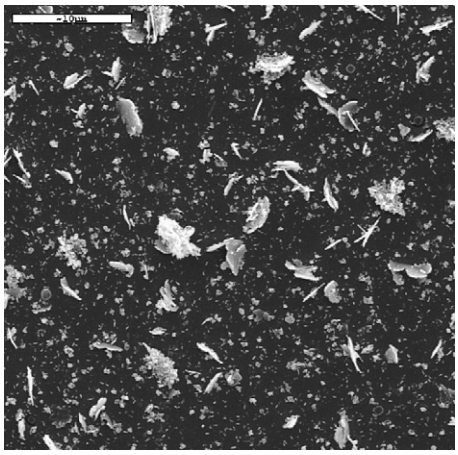


Fig. 4. SEM image for a film deposited by LPCVD from compound **2** at 600 °C.

The S 2p peaks in the XPS show one sulfur environment, which corresponds with that in TiS_2. The peaks at 161.7 and 163.2 eV can be attributed to S $2p_{3/2}$ and $2p_{1/2}$, respectively, the values matching well with those previously reported [21]. Chlorine contamination (*ca.* 4%) was found in the films by XPS. In addition, both carbon and nitrogen contamination was observed in the films suggesting that the decomposition mechanism of **2** is not particularly clean. These results are consistent with the TGA observed for **2**. The Raman pattern for the film deposited from **2** showed the presence of the TiS_2 peak at 329 cm^{-1} with a shoulder at 373 cm^{-1}. The XRD for these films showed them to be amorphous to X-rays. This is in contrast with films deposited from the pyridine analogue **1** which were crystalline even at 500 °C.

The SEM image for the films deposited from **2** shows hexagonal platelets in a perpendicular orientation to the substrate's surface (Fig. 4). This corresponds with the morphology of films grown from the pyridine analogue **1**. However, the image of the film produced from **2** shows that the platelets are much more dispersed than in the films deposited from **1**. The SEM image of the film grown from **2** shows small clusters (0.6 μm in diameter) and needle-like features (0.6 μm in length) between the platelets. This suggests that the growth rate of the films from **2** are significantly slower than from **1**. This supports the TGA data, where **2** decomposed further than **1** at the same temperature.

4. Conclusions

The titanium thiolate complexes, $[TiCl(SC_5H_3N)_3]$ and $[TiCl(SC_4H_3N_2)_3]$ have been synthesized and characterised. X-ray crystallography showed that $[TiCl(SC_4H_3N_2)_3]$ is monomeric with seven-coordinate titanium atoms. Low pressure CVD indicate that $[TiCl(SC_5H_3N)_3]$ is an effective titanium sulfide precursor resulting in TiS_2 films at 600 °C or TiS_2/TiO_2 films at 500 °C. In contrast, $[TiCl(SC_4H_3N_2)_3]$ was shown to be unsuitable as a precursor since amorphous TiS_2 films contaminated with C, N and Cl were obtained.

Acknowledgements

The EPSRC is thanked for a DTA studentship (ESP). We are also grateful to Dr. M. Odlyha (Birkbeck College) for the TGA.

Appendix A. Supplementary data

Supplementary data are available from the CCDC, 12 Union Road, Cambridge CB2 1EZ, UK, on request quoting deposition numbers CCDC 611365 and 611366. Supplementary data associated with this article can be found, in the online version, at doi:10.1016/j.poly.2006.07.017.

References

[1] D.W. Stephan, T.T. Nadasdi, Coordin. Chem. Rev. 147 (1996) 147.
[2] D.C. Bradley, P.A. Hammersley, J. Chem. Soc. A (1967) 1894.
[3] C.J. Carmalt, C.W. Dinnage, I.P. Parkin, A.J.P. White, D.J. Williams, J. Chem. Soc., Dalton Trans. (2000) 3500.
[4] C.J. Carmalt, C.W. Dinnage, I.P. Parkin, J.W. Steed, Inorg. Chem. 39 (2000) 2693.
[5] C.J. Carmalt, E.S. Peters, I.P. Parkin, D.A. Tocher, New J. Chem. 29 (2005) 620.
[6] C.J. Carmalt, C.W. Dinnage, I.P. Parkin, A.J.P. White, D.J. Williams, J. Chem. Soc., Dalton Trans. (2001) 2554.
[7] G. Sigel, P.P. Power, Inorg. Chem. 26 (1987) 2819.
[8] D.T. Corwin, J.F. Corning, S.A. Koch, M. Millar, Inorg. Chim. Acta 229 (1995) 335.
[9] J.T. Kim, J.W. Park, S.M. Koo, Polyhedron 19 (2000) 1139.
[10] Y. Nakayama, K. Miyamoto, N. Ueyama, A. Nakamura, Chem. Lett. (1999) 391.
[11] T.S. Lewkebandara, C.H. Winter, Adv. Mater. 6 (1994) 237.
[12] M. Bochmann, Chem. Vap. Depos. 2 (1996) 85.
[13] R.C. Bill, Wear 106 (1985) 283.
[14] R.H. Friend, A.D. Yoffe, Adv. Phys. 36 (1987) 1.
[15] K. Kanehori, F. Kirino, Y. Ito, K. Miyauchi, T. Kudo, J. Electrochem. Soc. 136 (1989) 1265.
[16] S.D. Jones, J.R. Akridge, F.K. Shokoohi, Solid State Ion. 69 (1994) 357.
[17] SHELTXTL V 6.10 Bruker AXS, 2000.
[18] A.N. Bhat, R.C. Fay, D.F. Lewis, A.F. Lindmark, S.H. Strauss, Inorg. Chem. 13 (1974) 886.
[19] C.J. Carmalt, S.R. Whaley, P.S. Lall, A.H. Cowley, R.A. Jones, B.G. McBurnett, J.G. Ekerdt, J. Chem. Soc., Dalton Trans. (1998) 553.
[20] C.J. Carmalt, A.C. Newport, I.P. Parkin, A.J.P. White, D.J. Williams, J. Chem. Soc., Dalton Trans. (2002) 4055.
[21] S.O. Said, J.L. Sullivan, T. Choudhry, C.G. Pearce, Vacuum 38 (1988) 917.

Available online at www.sciencedirect.com
ScienceDirect
Polyhedron 26 (2007) 49–58
POLYHEDRON
www.elsevier.com/locate/poly

Transition metal complexes with thiosemicarbazide-based ligands. Part LIV. Nickel(II) complexes with pyridoxal semi- (PLSC) and thiosemicarbazone (PLTSC). Crystal and molecular structure of $[Ni(PLSC)(H_2O)_3](NO_3)_2$ and $[Ni(PLTSC\text{-}H)py]NO_3$

Vukadin M. Leovac [a], Ljiljana S. Jovanović [a,*], Vladimir Divjaković [b], Andrej Pevec [c], Ivan Leban [c], Thomas Armbruster [d]

[a] *Department of Chemistry, Faculty of Sciences, University of Novi Sad, Trg D. Obradovića 3, 21000 Novi Sad, Serbia*
[b] *Department of Physics, Faculty of Sciences, University of Novi Sad, Trg D. Obradovića 3, 21000 Novi Sad, Serbia*
[c] *Faculty of Chemistry and Chemical Technology, University of Ljubljana, Aškerčeva cesta 5, 1000 Ljubljana, Slovenia*
[d] *Laboratory for Chemical and Mineralogical Crystallography, University of Bern, Freierstr. 3, CH-3012 Bern, Switzerland*

Received 3 May 2006; accepted 26 July 2006
Available online 7 August 2006

Abstract

This paper describes the synthesis of the first Ni(II) complexes with pyridoxal semicarbazone (PLSC), viz. $Ni(PLSC)Cl_2 \cdot 3.5H_2O$ (**1**), $[Ni(PLSC)(H_2O)_3](NO_3)_2$ (**2**), $Ni(PLSC)(NCS)_2 \cdot 4H_2O$ (**3**), $[Ni(PLSC\text{-}2H)NH_3] \cdot 1.5H_2O$ (**4**), as well as two new complexes with pyridoxal thiosemicarbazone (PLTSC), $[Ni(PLTSC\text{-}H)py]NO_3$ (**5**) and [Ni(PLTSC-H)NCS] (**6**). Complexes **1**–**3** are paramagnetic and have most probably an octahedral structure, for complex **2** this was proved by X-ray diffraction analysis. In contrast, complexes **4**–**6** are diamagnetic and have a square-planar structure, and in the case of complex **5** this was also confirmed by X-ray structural analysis. In all cases the Schiff bases are coordinated as tridentate ligands with an ONX (X = O, PLSC; X = S, PLTSC) set of donor atoms. With the complexes involving the neutral form of PLSC and the monoanionic form of PLTSC, the PL moiety is in the form of a zwitterion. In addition to the above-mentioned techniques, all the complexes were characterized by measuring their molar conductivities, UV–Vis and partial IR spectra.
© 2006 Elsevier Ltd. All rights reserved.

Keywords: Ni(II) complexes; Pyridoxal semi- and thiosemicarbazone; Spectral characteristics; X-ray analysis

1. Introduction

For some time, semi- and thiosemicarbazones have been a subject of interest to researchers of different profiles. In view of the fact that these compounds form with many metals complexes of diverse chemical, physical and structural characteristics, they are of special interest to coordination chemists [1–3]. In addition, many of these compounds as well as their metal complexes, especially those with thiosemicarbazones, have shown a wide spectrum of biological activity, so that they have also become a subject of intense research for pharmacologists [4].

One of the newer semicarbazone ligands, which is the subject of our research, is pyridoxal semicarbazone (PLSC), whose only complexes reported up to now are those with Cu(II), Fe(III) and Pt(IV) [5–8]. In contrast to PLSC, a number of pyridoxal thiosemicarbazone (PLTSC) complexes, involving not only transition metals (among them Ni(II) too) but also some non-transition metals, have been described [9].

* Corresponding author. Tel.: +381 21 4852752; fax: +381 21 454065.
E-mail address: lilij@ih.ns.ac.yu (L.S. Jovanović).

0277-5387/$ - see front matter © 2006 Elsevier Ltd. All rights reserved.
doi:10.1016/j.poly.2006.07.031

As a continuation of our study of the complexing properties of PLSC, we describe here the synthesis and some physico-chemical and structural characteristics of its first complexes with Ni(II), as well as two new Ni(II) complexes with PLTSC.

2. Experimental

All chemicals used for the synthesis and measurements were commercial products, except for the ligands, which were prepared according to the previously described procedures [6].

Elemental (C, H, N) analysis of air-dried samples was carried out by standard micromethods in the Center for Instrumental Analysis, Faculty of Chemistry, Belgrade.

2.1. Syntheses of complexes

2.1.1. Ni(PLSC)$X_2 \cdot nH_2O$ (**1–3**); (X = Cl, n = 3.5 (**1**); X = NO_3, n = 3 (**2**), X = NCS, n = 4 (**3**))

To a warm suspension of 0.26 g (1.0 mmol) of PLSC $\cdot$ $2H_2O$ in 10 cm^3 of EtOH 1.2 mmol of solid $NiX_2 \cdot 6H_2O$ (X = Cl, NO_3) was added and the content heated until the reactants were completely dissolved. In the case of the reaction with $Ni(NCS)_2 \cdot 2H_2O$ use was made of aqueous solutions of the reactants. The green solutions were left to evaporate at room temperature. The crystals were filtered and washed with EtOH. Yield: 50–70%.

2.1.2. [Ni(PLSC-2H)NH_3] $\cdot$ 1.5H_2O (**4**)

To a warm suspension of 0.26 g (1 mmol) of PLSC $\cdot$ $2H_2O$ in 10 cm^3 of EtOH, a warm EtOH (5 cm^3) solution of 0.35 g (1.2 mmol) of $Ni(NO_3)_2 \cdot 6H_2O$ was added, and the content heated to complete dissolution of the ligand. To the green solution NH_3(aq.) (1 cm^3) was added and the content heated for 2–3 min, whereby the solution became red. After 10 h the orange microcrystalline precipitate was filtered and washed with EtOH. Yield: 0.28 g (86%).

2.1.3. [Ni(PLTSC-H)py]NO_3 (**5**)

A mixture of 0.15 g (0.5 mmol) of PLTSC $\cdot$ $3H_2O$ and 0.17 g (0.6 mmol) of $Ni(NO_3)_2 \cdot 6H_2O$ was dissolved by heating in MeOH (10 cm^3), and pyridine (0.5 cm^3) was added to the solution. The red solution was left at room temperature for 24 h. The obtained red monocrystals were filtered and washed with MeOH. Yield: 0.10 g (44%).

2.1.4. [Ni(PLTSC-H)NCS] (**6**)

A warm solution of 0.12 g (0.6 mmol) of $Ni(NCS)_2 \cdot 2H_2O$ in H_2O (5 cm^3) was mixed with a warm solution of 0.15 g (0.5 mmol) of PLTSC $\cdot$ $3H_2O$ in DMF (2 cm^3) and heated mildly for 2–3 min. The complex started to crystallize immediately from the warm solution. After 10 h brown crystals were filtered and washed with H_2O and EtOH. Yield: 0.10 g (55%).

Data of microanalysis and measurements of magnetic susceptibility, molar conductivity, along with the description of colors and geometry of all the complexes, are given in Table 1.

2.2. Physical methods

Magnetic susceptibilities were measured at room temperature using a magnetic susceptibility balance MSB-MKL (Sherwood Scientific Ltd. Cambridge, England).

Molar conductivities of the freshly prepared 1×10^{-3} M aqueous or methanolic solutions were measured on a Jenway 4010 conductivity meter.

IR spectra (KBr disk) were recorded on a Thermo Nicolet (NEXUS 670 FT-IR) instrument.

Electronic spectra were recorded on a Secomam (Anthelie 2, Advanced, for the range 200–900 nm) and on a Thermo Nicolet instrument (NEXUS 670 FT-IR, for the range 900–1400 nm) in (2–4) $\times 10^{-4}$ mol dm^{-3} MeOH and DMF solutions of the complexes.

2.3. Crystal structure determination

Single crystals of the title compounds **2** (green) and **5** (dark red) were selected and glued on glass threads. Diffraction data were collected on a Bruker PLATFORM three-circle goniometer equipped with SMART 1K CCD detector for **2** and on a Nonius Kappa CCD diffractometer for **5**. The crystal to detector distances were 5.4 and

Table 1
Partial elemental analysis and some physical characteristics of the complexes

Complex	Found (calculated) %			Color	μ_{eff} (BM)	λ_M (S cm^2 mol^{-1}) (solvent)	Geometry
	C	H	N				
Ni(PLSC)$Cl_2 \cdot 3.5H_2O$ (**1**)	26.22 (25.93)	4.63 (4.59)	13.40 (13.44)	green	3.18	194 (H_2O) 156 (MeOH)	octahedral
[Ni(PLSC)$(H_2O)_3$]$(NO_3)_2$ (**2**)	23.72 (23.45)	4.01 (3.93)	18.10 (18.24)	green	3.07	201 (H_2O) 162 (MeOH)	octahedral
Ni(PLSC)$(NCS)_2 \cdot 4H_2O$ (**3**)	28.25 (28.04)	4.25 (4.28)	17.74 (17.84)	green	3.12	203 (H_2O) 120 (MeOH)	octahedral
[Ni(PLSC-2H)NH_3] $\cdot$ 1.5H_2O (**4**)	33.27 (33.26)	4.91 (4.96)	21.51 (21.56)	orange diamagnetic		6.7 (DMF)	square-planar
[Ni(PLTSC-H)py]NO_3 (**5**)	38.01 (38.29)	3.74 (3.67)	18.90 (19.14)	red diamagnetic		64 (DMF)	square-planar
[Ni(PLTSC-H)NCS] (**6**)	33.94 (33.73)	3.18 (3.11)	19.58 (19.67)	brown diamagnetic		18 (DMF)	square-planar

3.0 cm for **2** and **5**, respectively. Graphite monochromated Mo Kα radiation ($\lambda = 0.71073$ Å) was employed in both measurements. Frame widths of 0.3° and 2° in ω, with 10 and 200 s were used to acquire each frame for **2** and **5**, respectively. More than hemispheres of three-dimensional data were collected in both measurements. The data were reduced using the Bruker program SAINT for **2** and Nonius program COLLECT for **5**. A semiempirical absorption-correction based upon the intensities of equivalent reflections was applied, and the data were corrected for Lorentz polarization and background effects. Scattering curves for neutral atoms, together with anomalous-dispersion corrections, were taken from the International Tables for X-ray Crystallography [10]. The structures were solved by direct methods [11], and the figures were drawn using ORTEP [12]. Refinements were based on F^2 values and done by full-matrix least-squares [13] with all non-H atoms anisotropic. The positions of hydrogen atoms were found from the inspection of the difference Fourier maps. The final refinement included atomic positions and displacement parameters for all atoms. The non-H atoms were refined anisotropically, while all H sites were refined with isotropic displacement parameters. The crystal data and refinement parameters for the title compounds are listed in Table 2.

3. Results and discussion

3.1. Syntheses, physico-chemical characteristics and geometric structures of the complexes

Reactions of warm EtOH or H_2O solutions of PLSC and $NiX_2 \cdot nH_2O$ (X = Cl, NO_3, NCS) in a mole ratio of 1:1 yielded the paramagnetic green monoligand complexes of the general formula $Ni(PLSC)X_2 \cdot nH_2O$ (**1**, **2**, **3**) (Table 1). In the presence of NH_3(aq.) and pyridine (py), $Ni(NO_3)_2 \cdot 6H_2O$ forms with PLSC and PLTSC, respective diamagnetic complexes $[Ni(PLSC\text{-}2H)NH_3] \cdot 1.5H_2O$ (**4**), and [Ni(PLTSC-H)py]NO_3 (**5**). The other, also diamagnetic, complex with PLTSC, viz. [Ni(PLTSC-H)NCS] (**6**) was obtained in the reaction of an H_2O solution of $Ni(NCS)_2$ and DMF solution of PLTSC. The isolated complexes are crystalline substances that are stable in air. With the exception of $[Ni(PLSC\text{-}2H)NH_3] \cdot 1.5H_2O$, which is slightly soluble only in DMF, the other PLSC complexes, in addition to being soluble in DMF, are also soluble in H_2O, but are somewhat less soluble in MeOH and EtOH. The PLTSC complexes are soluble in DMF but dissolve poorly in H_2O and alcohols.

Some physical characteristics of the complexes that are relevant to their geometric structures are presented in

Table 2
Crystal data and refinement parameters for complexes **2** and **5**

Compound	$[Ni(PLSC)(H_2O)_3](NO_3)_2$	[Ni(PLTSC-H)py]NO_3
Empirical formula	$C_9H_{18}N_6O_{12}Ni$	$C_{14}H_{18}N_6O_5SNi$
Formula weight	461.00	441.12
Temperature(K)	293	293
Wavelength (Å)	0.71073	0.71073
Crystal system	triclinic	monoclinic
Space group	$P\bar{1}$	$P2_1/c$
Unit cell dimensions		
a (Å)	9.1392(2)	6.7290(1)
b (Å)	9.0566(2)	15.9620(3)
c (Å)	11.4737(3)	16.6520(3)
α (°)	97.196(1)	
β (°)	102.593(1)	95.064(1)
γ (°)	112.139(1)	
V (Å^3)	834.89	1781.63
Z	2	4
D_{calc} (g/cm^3)	1.834	1.645
Absorption coefficient (mm^{-1})	1.24	1.25
F(000)	476	921
Crystal size (mm)	$0.35 \times 0.50 \times 0.45$	$0.45 \times 0.25 \times 0.05$
Color	green	dark red
$2\theta_{max}$ for data collection (%)	57.3	55.0
Index ranges: $-h\ +h$; $-k\ +k$; $-l\ +l$	$-12\ +12$; $-11\ +11$; $-15\ +15$	$-8\ +8$; $-20\ +20$; $-21\ +21$
Reflections collected	9676	7868
Independent reflections (R_{int})	3906 (0.0497)	4058 (0.0187)
Refinement methods	full matrix least square on F^2	full matrix least square on F^2
Data/restraints/parameters	3906/0/325	4058/0/304
Goodness-of-fit on F^2	0.979	0.799
Final R indices [$F_o > 4\sigma F_o$]	$R_1 = 0.0251$	$R_1 = 0.0328$
R indices (all data)	$R_1 = 0.0306$, $wR_2 = 0.0671$	$R_1 = 0.0475$, $wR_2 = 0.1208$
Extinction coefficient	no	no
Largest difference in peak and hole (e/Å^3)	0.31 and −0.24	0.44 and −0.48

Table 1. First of all, the X-ray analysis of $[Ni(PLSC)(H_2O)_3](NO_3)_2$ (**2**) (vide infra) showed that it has an octahedral structure, formed by the tridentate ONO coordination of the PLSC ligand and three H_2O molecules. The Ni(II) complexes are of the characteristic green color and have the expected μ_{eff} values (Table 1). Based on this, the same geometric configuration could also be ascribed to the other two paramagnetic PLSC complexes **1** and **3**, this configuration being the most frequently observed for paramagnetic Ni(II) complexes [14]. Therefore, apart from the PLSC ligand, H_2O molecules or acid residues must participate in coordination. In the case of the $Ni(PLSC)(NCS)_2 \cdot 4H_2O$ complex, the coordination of the NSC group is also supported by the position of the ν(CN) band in the IR spectrum, which appears as a doublet at 2091 and 2104 cm^{-1}, i.e. in the region of a coordinated NCS-group [15], bonded through the nitrogen atom, as is usual with Ni(II) as a representative of medium-hard acids. The weak ν(CS) and δ(NCS) bands, appearing at lower energies, cannot be located as they are masked by the bands of the organic ligand. On the basis of the IR spectrum of complex **1**, it can be supposed that Cl^- does not participate in coordination. This assumption is based on the absence of the ν(Ni–Cl) band. The conclusion is also supported by the great similarity of the IR spectra of the octahedral $[Ni(PLSC)(H_2O)_3](NO_3)_2$ complex and the Cl-containing complex in the range below 350 cm^{-1}, i.e. at the wavelengths where one could expect the ν(Ni–Cl) bands [15,16].

Molar conductivities (λ_M) of H_2O solutions of the paramagnetic PLSC complexes (Table 1) indicate the presence of a 2:1 type of electrolyte [17]. The same also holds for the MeOH solutions of the Cl- and NO_3-containing complexes. In contrast to them, the λ_M values of MeOH solutions of the NCS complex correspond to a 1:1 type of electrolyte [17], which suggests partial replacement of the coordinated NCS group with solvent molecules. However, for the same complex in acetone solution $\lambda_M = 32\ \Omega^{-1}\ cm^2\ mol^{-1}$ was obtained, which is significantly lower than the usual value for a 1:1 electrolyte ($\lambda_M = 100$–$140\ \Omega^{-1}\ cm^2\ mol^{-1}$) [17], suggesting the coordination of both NCS groups is preserved in solution.

Concerning the exact formulas of the octahedral complexes **1** and **3**, it can be supposed that the structure of complex **1** is similar to that of complex **2**, which is also supported by the similarity of the values of their molar conductivities (electrolyte type 2:1). Hence, the probable formula involves a complex cation of the type $[Ni(PLSC)(H_2O)_3]^{2+}$. However, for complex **3**, for which a coordination of two NCS groups and one water molecule in crystal is supposed, the molar conductivity data indicate that the NCS-group coordination depends on the nature of the solvent: in the least polar solvent, acetone, both groups remain coordinated, in MeOH only one is coordinated, whereas in H_2O both are dissociated. Hence, this complex and complexes **1** and **2** in aqueous solution have the same complex cation, i.e. $[Ni(PLSC)(H_2O)_3]^{2+}$.

The diamagnetism and color of complex **4** and of two new PLTSC complexes **5** and **6** suggest their structure is square-planar [14]. In the case of **5**, this was proved by X-ray analysis (vide infra). In contrast to the other compounds, the PLSC complex **4** contains the ligand in a dianionic form, arising from the deprotonation of not only the enol-form of the semicarbazide moiety but also of the zwitter ion of the PL residue, which also explains its non-electrolytic nature. Both PLTSC complexes contain the ligand in its monoanionic form, resulting from the deprotonation of the thiol form of the thiosemicarbazide moiety. As is the case with the other complexes containing this ligand [9], both PLTSC complexes involve the ONS set of donor atoms; the fourth coordination site being occupied by a py or NCS group. The ν(CN) band of the coordinated NCS group is observed at 2113 cm^{-1}. The molar conductivity of this complex in DMF (Table 1) suggests partial replacement of the NCS group with solvent molecules.

In the example of the reactions of $Ni(NCS)_2$ with these two ligands it can be concluded that the TSC residue is a stronger acid than the SC residue, i.e. that PLTSC is more readily deprotonated than PLSC. The same conclusion can be made on the basis of the reaction of PLTSC with $Ni(NO_3)_2$ too, keeping in mind the fact that in this reaction Ferrari et al. [18] obtained a complex involving the monoanionic form of the ligand of the composition $Ni(PLTSC\text{-}H)NO_3 \cdot 2H_2O$. It should be noted that these authors also described the compound $Ni(PLTSC\text{-}2H) \cdot 2H_2O$, obtained from the reaction of PLTSC with $Ni(OAc)_2$.

3.2. Electronic spectra

Table 3 summarizes the electronic spectral data for the investigated complexes in two solvents, recorded in the range of 220–1200 nm (MeOH) and 270–1200 nm (DMF). As can be seen, the spectra display several electronic transitions. The strong peak at the blue end of the spectra of the complexes in MeOH (at about 240 nm) can be ascribed to $\pi \rightarrow \pi^*$ pyridine ring absorptions [19], which are, due to an increased conjugation in the complexes, shifted by about 10–20 nm to higher wavelengths compared to those of the ligands alone [20]. Other spectral characteristics are mainly influenced by the coordinated ligand and its deprotonation and only slightly by solvent effects.

The paramagnetic semicarbazone complexes are characterized by two main bands at about 300 and 400 nm (Fig. 1). Obviously, the bands are complex, each being composed of at least two close bands. The band at 300 nm comprises transitions $\pi \rightarrow \pi^*$ imine and $n \rightarrow \pi^*$ of both the imine and pyridine ring, which are also present in this range in the spectra of the ligand alone [21]. The other band (~400 nm) may be due mainly to LMCT transitions. In this spectral range, one would expect LM N → Ni and SCN → Ni charge transfers, but the band for Cl → Ni is usually observed at somewhat higher energies (around 330 nm) [22]. In addition, low intensity d–d

Table 3
Electronic spectral data for Ni(SCPL) and Ni(TSCPL) complexes in DMF and MeOH

Complex	Solvent	λ_{max}[a](log ε)[b] Intraligand and CT	λ_{max}[a](log ε)[b] d–d
Ni(PLSC)$Cl_2 \cdot 3.5H_2O$ (**1**)	MeOH	243(4.40), 297(3.90), 307(3.93), 321sh(3.80), 394(4.0), 405(4.0)	616(0.95), 720sh(0.70), 930(1.20)
	DMF	301(4.00), 325sh(3.83), 404(4.00)	588(1.07), 1198(1.30)
[Ni(PLSC)$(H_2O)_3$]$(NO_3)_2$ (**2**)	MeOH	242(4.44), 297(3.92), 305(3.90), 322sh(3.72), 394(4.02), 405(4.01)	606(0.48), 940(1.26), 1053(1.18)
	DMF	301(3.95), 327sh(3.75), 405(3.93)	587(1.09),720sh(0.78), 980bp(1.04), 1052(0.94), 1199(1.43)
Ni(PLSC)$(NCS)_2 \cdot 4H_2O$ (**3**)	MeOH	241(4.46), 298(3.89), 306(3.89) 322sh(3.73), 394(3.94), 405(3.94)	622(0.95), 938(1.18)
	DMF	297bp(4.01), 326sh(3.79), 399(3.86), 410(3.86)	608(1.0), 732sh(0.70), 972(1.32)
[Ni(PLSC-2H)NH_3] $\cdot 1.5H_2O$ (**4**)	MeOH	241(4.24), 297(3.82), 325(3.76), 393(3.83)	456sh(3.38), ~1195(2.30)
	DMF	305sh(3.86), 319(3.89), 341sh(3.93), 358(4.01)	408(3.78), ~1192(0.95)
[Ni(PLTSC-H)py]NO_3 (**5**)	MeOH	249(4.41), 293sh(3.92), 327sh(3.79), 407(4.04), 419(4.06)	~870(0.48)
	DMF	295sh(4.02), 325(3.96), 410(4.16), ~425(4.12)	475sh(3.53), ~950(0.5), 1068(0.58), 1200(1.30)
[Ni(PLTSC-H)NCS] (**6**)	MeOH	249(4.12), 283sh(3.67), 323sh(3.54), 399(3.75), 424(3.66)	476sh(2.95), ~920(1.79), 1200(2.01)
	DMF	302(4.00), ~325(3.92), 410(4.12), 433(4.14)	~500sh(1.81), 1198(1.36)

sh, shoulder; bp, broad peak.
[a] In nm.
[b] In M cm^{-1}.

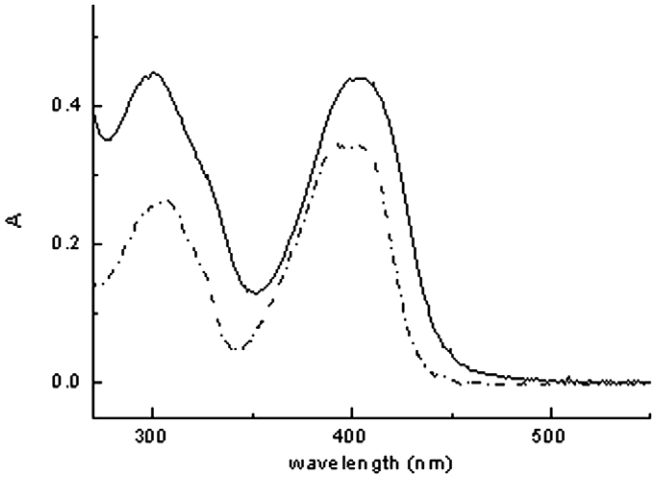


Fig. 1. Electronic spectra of Ni(PLSC)$Cl_2 \cdot 3.5H_2O$ in MeOH (------) and DMF (——).

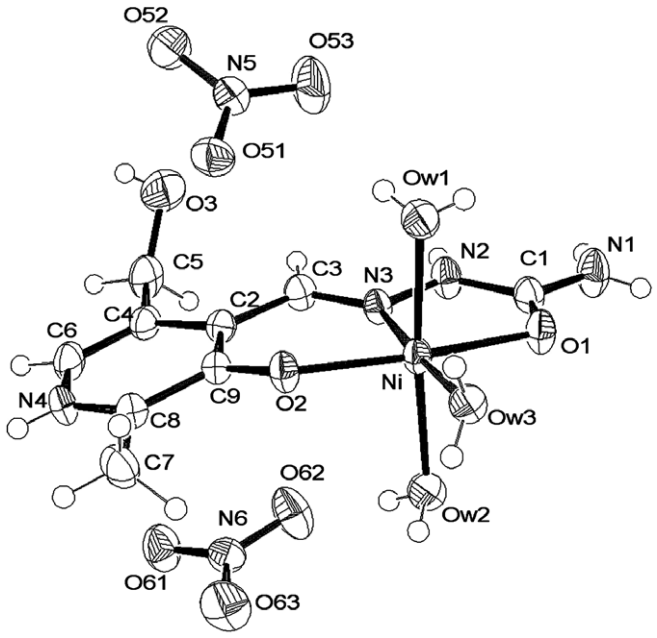


Fig. 2. ORTEP view of [Ni(PLSC)$(H_2O)_3$]$(NO_3)_2$.

bands (ν_3) should also be present in this range, but they are masked by the stronger CT absorptions.

Because of their low spectral intensities and the low solubilities of the complexes, the data on d–d transitions are difficult to assign unambiguously. However, having in mind the crystal structure of **2** and the paramagnetic characteristics of the complexes, their light yellow-greenish color of solutions and molar conductivity data, it is reasonable to presume a pseudo-octahedral configuration. Since the PLSC ligand in the crystal occupies three coordination sites in the equatorial plane, the other three sites in the meridional plane are occupied either by three water molecules (**1**, **2**) or, probably, two NCS^- and one water molecule (**3**). In solutions, partial replacement of the anion (NCS^-) with solvent molecules occurs, which was confirmed by the conductivity measurements (see above). However, the recorded spectra of all three complexes in d–d range are similar thus suggesting a presumption of a similar geometry of these compounds in solution.

A comparison of the spectral data in the two solvents suggests a red shift of the CT bands in the more polar solvent (DMF), arising as a consequence of a positive solvatochromic effect.

The diamagnetic non-electrolyic complex **4**, which is square-planar in the crystal, has probably the same configuration in solution. This assumption is supported by the

lack of bands in the visible region. In fact, a d–d band (456 nm, $\varepsilon = 2400\ M\ cm^{-1}$) appears in MeOH as a shoulder of a stronger CT band, but in DMF these bands overlap. The very poor solubility of this complex in both solvents may be the reason for an apparent absence of weak bands in the region of 900–1000 nm.

The thiosemicarbazone complexes have very broad and unresolved bands in the range 300–350 nm, which are of similar origin to those in the semicarbazone complexes. The other complex band at about 400 nm resulted from

Table 4
Selected bond distances (Å) and bond angles (°)

Compound		$[Ni(PLSC)(H_2O)_3](NO_3)_2$	$[Ni(PLTSC)py]NO_3$
Ni–OW1		2.0927(19)	
Ni–OW2		2.0539(11)	
Ni–OW3		2.1154(18)	
Ni–O1	Ni(II)	2.0681(14)	
Ni–O2	surrounding	1.9829(12)	1.8483(18)
Ni–N3		2.0161(12)	1.8574(21)
Ni–N			1.9193(21)
Ni–S			2.1345(7)
O1–C1		1.2431(18)	
S–C1			1.7259(25)
O2–C9		1.3036(15)	1.3002(29)
O3–C5		1.4145(32)	1.4194(42)
N1–C1		1.3281(25)	1.3472(34)
N2–N3		1.3675(20)	1.4016(27)
N2–C1		1.3706(20)	1.3100(31)
N3–C3	chelate ligand	1.2886(18)	1.3022(31)
N4–C6		1.3434(22)	1.3471(39)
N4–C8		1.3372(18)	1.3351(34)
C2–C3		1.4473(24)	1.4395(33)
C2–C4		1.4199(19)	1.4225(34)
C2–C9		1.4244(19)	1.4057(33)
C4–C5		1.5138(22)	1.4966(38)
C4–C6		1.3632(26)	1.3629(37)
C7–C8		1.4793(25)	1.4871(40)
C8–C9		1.4165(24)	1.4210(34)
N–C15			1.3509(36)
N–C11			1.3394(38)
C11–C12	Py-ring		1.4024(50)
C12–C13			1.3639(65)
C13–C14			1.3461(65)
C14–C15			1.3678(41)

$[Ni(PLSC)(H_2O)_3](NO_3)_2$	
OW1–Ni–OW3	86.95(6)
OW1–Ni–OW2	173.83(6)
OW1–Ni–O1	89.62(5)
OW1–Ni–O2	91.14(5)
OW1–Ni–N3	89.91(6)
OW3–Ni–OW2	87.80(5)
OW3–Ni–O1	98.82(5)
OW3–Ni–O2	92.46(5)
OW3–Ni–N3	176.22(5)
OW2–Ni–O1	87.99(5)
OW2–Ni–O2	92.32(5)
OW2–Ni–N3	95.22(6)
O1–Ni–O2	168.71(5)
O1–Ni–N3	79.06(5)
O2–Ni–N3	89.68(5)
Ni–O1–C1	112.50(10)
Ni–O2–C9	126.25(10)
N3–N2–C1	115.77(13)
Ni–N3–N2	111.70(10)
Ni–N3–C3	129.28(11)
N2–N3–C3	118.48(13)
C6–N4–C8	124.13(16)
O1–C1–N1	123.59(15)
O1–C1–N2	120.38(16)
N1–C1–N2	116.03(15)
C3–C2–C4	117.43(14)
C3–C2–C9	123.41(13)
C4–C2–C9	119.13(14)
N3–C3–C2	122.27(14)
C2–C4–C5	121.67(15)
C2–C4–C6	119.43(15)
C5–C4–C6	118.90(15)
O3–C5–C4	111.09(17)
N4–C6–C4	120.09(16)
N4–C8–C7	119.79(16)
N4–C8–C9	119.22(14)
C7–C8–C9	120.98(15)
O2–C9–C2	125.70(14)
O2–C9–C8	116.52(13)
C2–C9–C8	117.78(13)

$[Ni(PLTSC)py]NO_3$	
S–Ni–O2	175.49(6)
S–Ni–N	91.65(6)
S–Ni–N3	87.39(6)
O2–Ni–N	85.79(8)
O2–Ni–N3	95.36(8)
N–Ni–N3	176.84(9)
Ni–S–C1	96.24(9)
Ni–O2–C9	127.33(16)
N3–N2–C1	111.49(19)
Ni–N3–N2	121.97(15)
Ni–N3–C3	125.65(17)
N2–N3–C3	112.36(19)
C6–N4–C8	123.83(24)
S–C1–N1	118.76(20)
S–C1–N2	122.90(19)
N1–C1–N2	118.34(23)
C3–C2–C4	119.15(21)
C3–C2–C9	121.45(21)
C4–C2–C9	119.39(22)
N3–C3–C2	125.24(23)
C2–C4–C5	121.85(23)
C2–C4–C6	118.48(23)
C5–C4–C6	119.64(25)
O3–C5–C4	110.45(22)
N4–C6–C4	120.94(26)
N4–C8–C7	119.40(24)
N4–C8–C9	118.34(23)
C7–C8–C9	122.26(24)
O2–C9–C2	124.61(21)
O2–C9–C8	116.52(22)
C2–C9–C8	118.88(21)
Ni–N–C11	122.54(19)
Ni–N–C15	119.27(17)
C11–N–C15	117.85(24)
N–C11–C12	120.87(30)
C11–C12–C13	119.76(34)
C12–C13–C14	119.00(47)
C13–C14–C15	119.95(31)
N–C15–C14	122.55(26)

the overlapping absorptions of two transitions: LMCT (S → Ni) and the second n → π* of the deprotonated ligand [22]. The data obtained for d–d transitions, with the exception of the band at about 470–490 nm which appears as a shoulder of the stronger CT band, are ambiguous because of the mentioned low solubility and resultant low absorption intensity. However, on the basis of their diamagnetism, orange-to-red color in solutions and very weak bands (shoulders) in the range of 700–900 nm, a distorted square-planar configuration can be suggested. Furthermore, the existence of a mixture of these and pseudo-tetrahedral complexes cannot be completely excluded, especially in DMF solutions, as was observed in some previous cases [23].

3.3. Crystal structure of $[Ni(PLSC)(H_2O)_3](NO_3)_2$ (2)

The crystal lattice of compound **2** consists of discrete complex cations $[Ni(PLSC)(H_2O)_3]^{2+}$ and $(NO_3)^-$, bound together by hydrogen bonds. The coordination environment around the central ion is a distorted octahedron. In the equatorial position of the complex cation, the tridentate (ONO) neutral pyridoxal semicarbazone (PLSC) chelates the nickel atom, which is additionally surrounded by three water molecules in the meridional position (Fig. 2). The apical positions of the octahedron are occupied by two water oxygens at the distances Ni–Ow1 2.093(2) Å and Ni–Ow2 2.115(2) Å (Table 4). The Ni–O(2) (phenolic) bond of 1.983(2) Å is significantly shorter than Ni–O1 (2.068 Å) and Ni–Ow3 (2.054 Å), probably because of the presence of a negative charge on the phenolic deprotonated oxygen (the pyridoxal ring adopts the role of a zwitter ion). The zwitter ion form, i.e. pyridine nitrogen protonation is suggested by the angle of ~124° for C6–N4–C8 [9]. The octahedral bond angles Ow1–Ni–Ow2 (173.8°) and Ow3–Ni–N3 (176.2°) are close to each other and slightly different from the theoretical value of 180°, while the bond angle O1–Ni–O2 (168.7°) is significantly smaller due to the chelation ring strain. The whole ligand molecule deviates considerably from planarity. The

Table 5
Hydrogen-bonding geometry (Å, °)

D–H	D···A	H···A	D–H···A	
Hydrogen bonds of **2**				
OW1–H1W1	OW1···O53	H1W1···O53	OW1–H1W1···O53	(1)
0.72(3)	3.049(3)	2.36(3)	161(3)	
OW1–H2W1	OW1···O63	H2W1···O63	OW1–H2W1···O63	(2)
0.70(3)	2.958(2)	2.27(3)	170(3)	
OW2–H1W2	OW2···O62	H1W2···O62	OW2–H1W2···O62	(1)
0.73(2)	2.793(2)	2.06(2)	174(3)	
OW2–H2W2	OW2···O52	H2W2···O52	OW2–H2W2···O52	(3)
0.82(2)	2.811(2)	2.02(2)	162(2)	
OW3–H1W3	OW3···O2	H1W3···O2	OW3–H1W3···O2	(4)
0.86(2)	2.788(2)	1.95(2)	163(2)	
OW3–H2W3	OW3···O52	H2W3···O52	OW3–H2W3···O52	(3)
0.78(3)	2.866(2)	2.14(3)	156(2)	
N1–H1N1	N1···O53	H1N1···O53	N1–H1N1···O53	(5)
0.86(2)	3.004(2)	2.26(2)	144(2)	
N2–HN2	N2···O61	HN2···O61	N2–HN2···O61	(6)
0.82(2)	2.839(2)	2.03(2)	164(2)	
N4–HN4	N4···O51	HN4···O51	N4–HN4···O51	(8)
0.78(2)	2.853(2)	2.11(2)	161(2)	
O3–HO3	O3···O63	HO3···O63	O3–HO3···O63	(7)
0.67(4)	2.995(3)	2.33(4)	168(4)	

Equivalent positions: (1) x, y, z; (2) $x, +y+1, +z$; (3) $x+1, +y, +z$; (4) $-x+1, -y+1, -z$; (5) $-x, -y+1, -z-1$; (6) $-x, -y, -z-1$; (7) $x-1, +y, +z$; (8) $-x, -y, -z$

Selected hydrogen bonds of **5**				
N1–H2	N1···N2	H2···N2	N1–H2···N2	(2)
0.75(4)	3.211(3)	2.46(4)	173(4)	
N1–H10	N1···O53	H10···O53	N1–H10···O53	(3)
0.81(3)	3.155(4)	2.38(4)	162(3)	
N4–H14	N4···O51	H14···O51	N4–H14···O51	(1)
0.92(4)	2.814(3)	1.93(4)	161(3)	
N4–H14	N4···O52	H14···O52	N4–H14···O52	(1)
0.92(4)	3.098(3)	2.35(4)	139(3)	
O3–H11	O3···O51	H11···O51	O3–H11···O51	(4)
0.74(5)	2.765(3)	2.06(5)	159(5)	

Equivalent positions: (1) x, y, z; (2) $-x+1, -y, -z+1$; (3) $x+2, -y+1/2, +z+1/2$; (4) $-x-1, +y-1/2, -z+1/2$

dihedral angles between the mean planes of the pyridoxal moiety (A) and six- (B) and five-membered (C) chelate rings are A–B 12.3°, A–C 15.2° and B–C 3.5°. The basal plane of the coordination polyhedron is slightly tetrahedrally deformed, with a maximum distance from the least squares plane of 0.039(1) Å for N3. The nickel atom is displaced towards the apical Ow2 atom by 0.0208(3) Å. Bond distances and bond angles in PLSC are in good agreement with the corresponding values found in the structure of dibromo(pyridoxal semicarbazone-$\kappa^3N^1,O^3,O^{3'}$)copper(II) [5]. The geometry of the NO_3 groups do not deviate from the usual literature values. Possible hydrogen bonds are listed in Table 5. The packing (Fig. 3) of this compound is determined by a large network of hydrogen bonds, a few of which are bifurcated among the complex molecules, the nitrate ions and water molecules.

3.4. Crystal structure of [Ni(PLTSC-H)py]NO_3 (5)

Experimental details of the crystal structure of complex **5** are presented in Table 2. The asymmetric unit consists of the well-separated complex cation $[Ni(PLTSC\text{-}H)py]^+$ and the NO_3^- anion. The monodeprotonated PLTSC is coordinated to the Ni atom through the phenolic oxygen O2, imine nitrogen N3, and thiolato sulfur of the Schiff base. The pyridine nitrogen N completes the coordination plane (Fig. 4). Because of the different character of the atoms forming the environment around the Ni(II) ion, the coordination square is distorted, as is confirmed by the given interatomic distance values and bond angles (Table 4). The coordination plane is slightly tetrahedrally deformed with a maximum distance of 0.076(2) Å for O2. The Ni atom is displaced by −0.0173(3) Å from the least squares plane. The same square-planar arrangement around Ni(II) ion with very similar Ni-donor bond distances and angles can be found in the structure of the amine (salicylidenethiosemicarbazonato(2^-)) nickel(II) [24]. Bond distances and angles in the chelate ligand of complex **5** are in good agreement with those found for the free pyridoxal thiosemicarbazone molecule [18]. An exception is the C1–N2–N3 angle of the thiosemicarbazide fragment (112.5°), which is in **5** significantly smaller than 120°, due to deprotonated nitrogen N2. The whole chelate ligand is close to coplanarity. If the skeletal atoms are considered, the largest deviation from the least-squares plane is 0.116(3) Å for C4 atom. At the same time, the atoms C7, C5 and Ni deviate from this plane by 0.252(4), −0.287(4) and −0.0572(3) Å, respectively. The dihedral angles between the pyridoxal

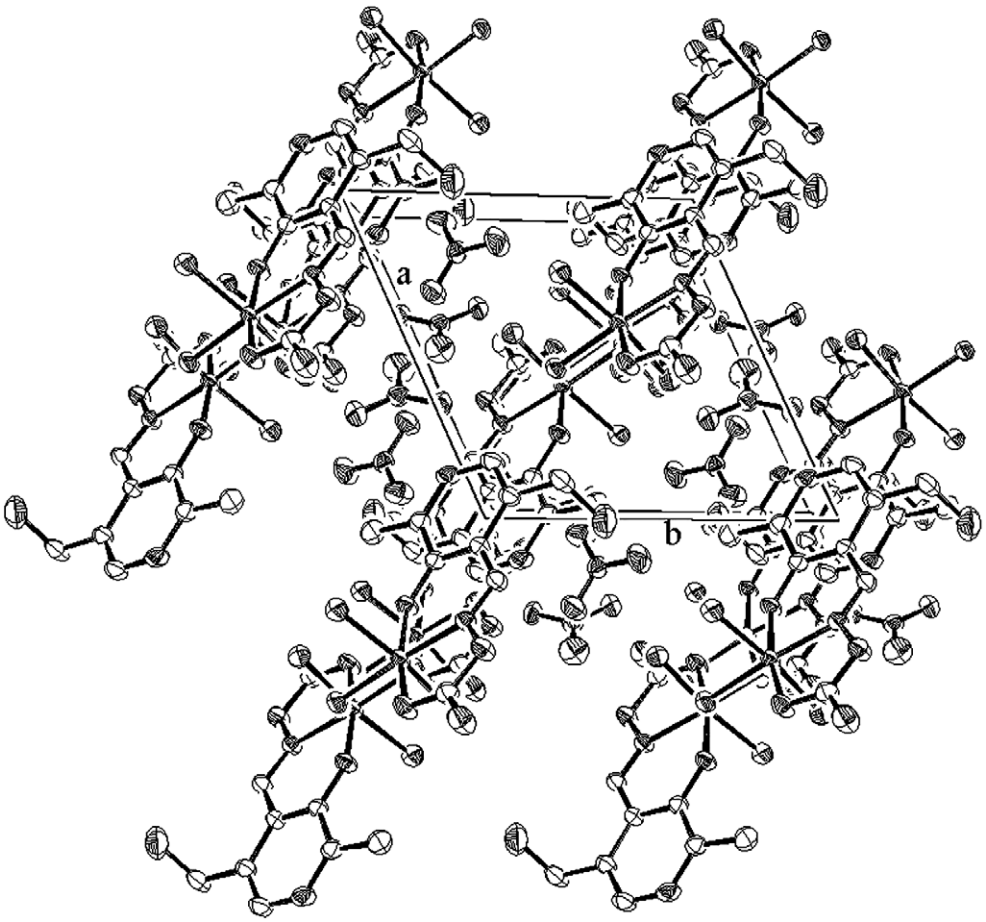


Fig. 3. The crystal structure of $[Ni(PLSC)(H_2O)_3](NO_3)_2$ viewed along the *c*-axis.

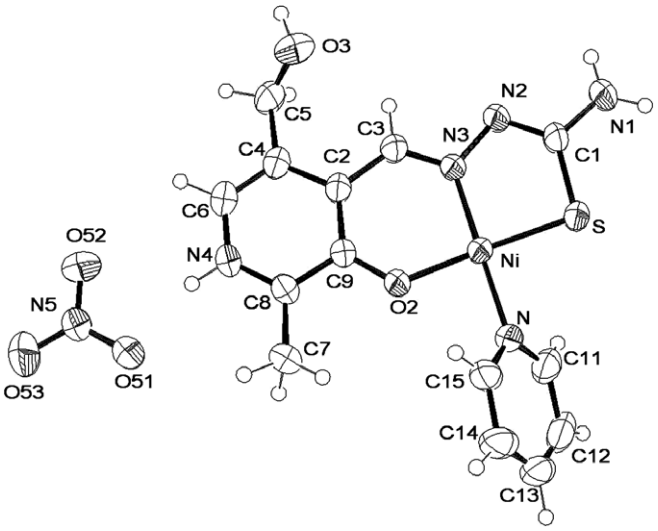


Fig. 4. ORTEP view of [Ni(PLTSC-H)py]NO_3.

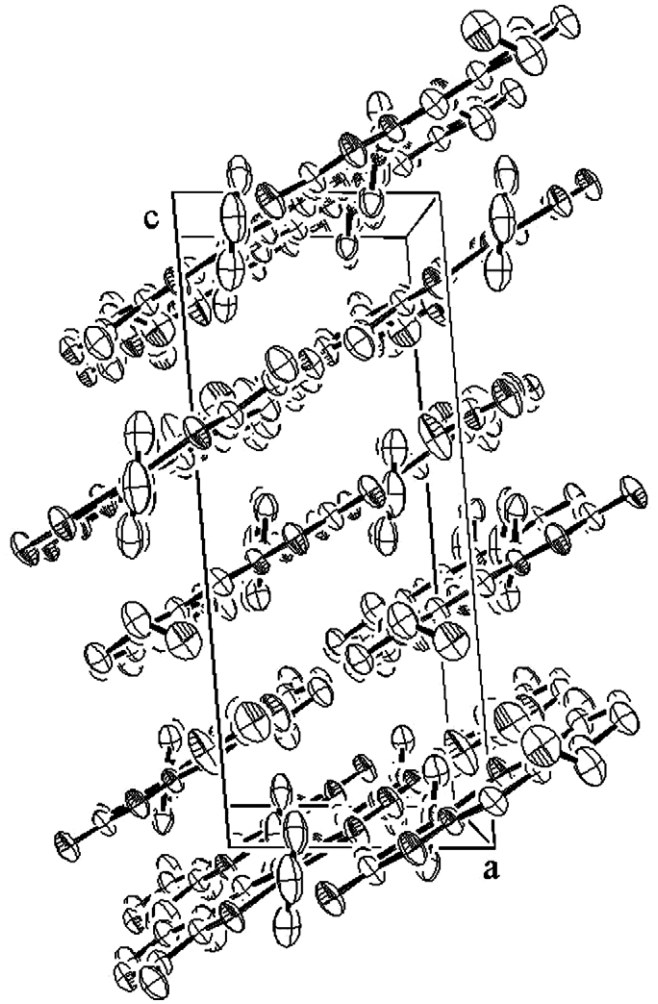


Fig. 5. The crystal structure of [Ni(PLTSC-H)py]NO_3 viewed along the *b*-axis.

moiety (A) and the six- (B) and five-membered (C) chelate rings are A–B 4.71(7)°, A–C 6.63(7)° and B–C 2.85(4)°. The pyridine nitrogen deviates from the ligand best plane by −0.224(2) Å. The dihedral angle between the pyridine and the chelate ligand best plane is about 52°. The angle of ∼124° for C6–N4–C8 suggests the protonation of the nitrogen from the PL moiety [9]. The nitrate group is strictly planar, and the NO_3 plane lies close to the ligand best plane, with a dihedral angle of 3.9(1)°. The packing (Fig. 5) is determined by an extended network of hydrogen bonding, as can bee seen from Table 5.

4. Supplementary material

Crystallographic data for the structures reported in this paper have been deposited with the Cambridge Crystallographic Data Center as CCDC 603421 for [Ni(PLSC)-$(H_2O)_3$]$(NO_3)_2$ and CCDC 603420 for [Ni(PLTSC-H)py]-NO_3. Copies of the available material can be obtained, free of charge, on application to the Director, CCDC, 12 Union Road, Cambridge CB2 1EZ, UK (fax: +44 1223 336 033 or e-mail: deposit@ccdc.cam.ac.uk).

Acknowledgements

This work was partly supported by the Ministry of Science and Environmental Protection of the Republic of Serbia (Grant No. 142028) and by the Provincial Secretariat for Science and Technological Development of AP Vojvodina.

The financial support of the Ministry of Higher Education, Science and Technology, Republic of Slovenia through Grants P1-0175 and X-2000 is also acknowledged.

References

[1] M.J.M. Campbell, Coord. Chem. Rev. 15 (1975) 279.
[2] S.B. Padhye, G.B. Kaufman, Coord. Chem. Rev. 63 (1985) 127.
[3] J.S. Casas, M.S. Garcia-Tasende, J. Sordo, Coord. Chem. Rev. 209 (2000) 197.
[4] H. Beraldo, D. Gambino, Mini Rev. Med. Chem. 4 (2004) 159.
[5] D. Poleti, Lj. Karanović, V.M. Leovac, V.S. Jevtović, Acta Crystallogr., Sect. C 59 (2003) m73.
[6] V.S. Jevtović, Lj.S. Jovanović, V.M. Leovac, L.J. Bjelica, J. Serb. Chem. Soc. 68 (2003) 929.
[7] Lj.S. Jovanović, V.S. Jevtović, L.J. Bjelica, V.M. Leovac, J. Serb. Chem. Soc. 70 (2005) 187.
[8] N.Ž. Knežević, V.M. Leovac, V.S. Jevtović, S. Grgurić-Šipka, T.J. Sabo, Inorg. Chem. Commun. 6 (2003) 561.
[9] V.M. Leovac, V.S. Jevtović, Lj.S. Jovanović, G.A. Bogdanović, J. Serb. Chem. Soc. 70 (2005) 393, and references therein.
[10] J.A. Ibers, W.C. Hamilton, International Tables for X-ray Crystallography, vol. IV, The Kynoch Press, Birmingham, 1974.
[11] M. Sheldrick SHELXS-86, Acta Crystallogr., Sect. A 46 (1990) 467.
[12] L.J. Farrugia, J. Appl. Crystallogr. 32 (1999) 837.
[13] M. Sheldrick, SHELXL-97, University of Göttingen, Göttingen, Germany, 1997.
[14] F.A. Cotton, G. Wilkinson, Advanced Inorganic Chemistry, Wiley, New York, 1988.
[15] K. Nakamoto, Infrared and Raman Spectra of Inorganic and Coordination Compounds, Wiley, New York, 1997.

[16] S.K. Jain, B.S. Garg, Y.K. Bhoon, Transition Met. Chem. 12 (1987) 73.
[17] W.J. Geary, Coord. Chem. Rev. 7 (1971) 81.
[18] M. Ferrari Belicchi, G. Fava Gaspari, E. Leporati, C. Pelizzi, P. Tarasconi, G. Tosi, J. Chem. Soc., Dalton Trans. (1986) 2455.
[19] A. Sreekanth, S. Sivakumar, M.R. Prathapachandra Kurup, J. Mol. Struct. 655 (2003) 47.
[20] Lj.S. Jovanović, V.M. Leovac, unpublished results.
[21] H. Beraldo, W.F. Nacif, L.R. Teixeira, J.S. Rebouças, Transition Met. Chem. 27 (2002) 85.
[22] D.X. West, I.S. Billeh, J.P. Jasinski, J.M. Jasinski, R.J. Butcher, Transition Met. Chem. 23 (1998) 209.
[23] A.B.P. Lever, Inorganic Electronic Spectroscopy (Russian Translation), Mir, Moskva, 1987, p. 2.
[24] E. Gyepes, F. Pavelčik, A. Beno, Coll. Czech. Chem. Commun. 46 (1981) 975.

Available online at www.sciencedirect.com
ScienceDirect
Polyhedron 26 (2007) 59–65
POLYHEDRON
www.elsevier.com/locate/poly

Complex formation of uranium(VI) with the amino acids L-glycine and L-cysteine: A fluorescence emission and UV–Vis absorption study

A. Günther *, G. Geipel, G. Bernhard

Forschungszentrum Rossendorf e.V., Institute of Radiochemistry, P.O. Box 510119, 01314 Dresden, Germany

Received 15 June 2006; accepted 26 July 2006
Available online 8 August 2006

Abstract

The complexation of uranium(VI) with the amino acids L-glycine and L-cysteine has been investigated by time-resolved laser-induced fluorescence spectroscopy (TRLFS) and UV–Vis spectroscopy at a low pH range. The identified 1:1 and 1:2 uranyl-L-glycine complexes fluoresce and have similar absorbance properties. In contrast to the glycine system, uranyl forms two different non-fluorescent 1:1 complexes with L-cysteine, showing individual absorbance properties under the given experimental conditions. The corresponding complex formation constants were calculated using the spectroscopic data.
© 2006 Elsevier Ltd. All rights reserved.

Keywords: Uranium; Complexation; Amino acid; TRLFS; UV–Vis spectroscopy

1. Introduction

For determination of uranium speciation in biosystems such as plants and bacteria, the investigation of the complexation behavior of uranium(VI) with biologically important organic ligands of relevant functionalities, like amino acids, is necessary. L-Glycine and L-cysteine (Fig. 1) are non-essential proteinogenic amino acids. Both amino acids have a carboxylic group and cysteine additionally has a sulfuryl functionality in the side chain of the molecule, which can bind heavy metals. Next to L-glutamic acid, L-glycine and L-cysteine are the ground elements of phytochelatines. These appear to be the primary metal-binding polypeptides of plants.

Some studies about uranium complexation by L-glycine [1–8] and L-cysteine [9–12] have been published. Generally a 1:1 and a 1:2 complex were found in the case of glycine using potentiometric titration, calorimetric investigations, spectrophotometric measurements or polarography. Treatment of the experimental data of Ramanujam et al. [1] and Bismondo et al. [2] has shown that glycine acts as unidentate ligand through the carboxylate group, while the amino moiety is not involved in the metal coordination. Contrary to this Lagrange et al. [3,4] and Cerfola et al. [5] favored the formation of a chelate complex between the uranyl cation and the amino acid. IR spectroscopic measurements carried out by Lagrange suggest the dissociation of a proton from the $-NH_3^+$ during the interaction with UO_2^{2+}. Szabo and Grenthe [6] could demonstrate the formation of uranyl glycine complexes in the form of a ''zwitterion'' without deprotonation at low pH and of a chelate with deprotonation at higher pH values. Alcock et al. [8] characterized a tetrakis(glycine)dioxo-uranium(VI) nitrate complex using absorption, luminescence and X-ray structural methods. All glycine ligands are in the zwitterionic form and act as O-donors in the triclinic structure with hexagonal bipyramidal coordination about the uranium atom. They observed both monodentate and bidentate coordination of the uranyl ion to the carboxyl group.

Iftekhar and Dubey [10] and Raghavan and Santappa [11,12] investigated the complex formation of U(VI) with L-cysteine using potentiometry. They found a 1:1 uranyl-cysteine species ML. The α-amino moiety and the carboxylic

* Corresponding author. Tel.: +49 351 2602433; fax: +49 351 2603553.
E-mail address: A.Guenther@fz-rossendorf.de (A. Günther).

0277-5387/$ - see front matter © 2006 Elsevier Ltd. All rights reserved.
doi:10.1016/j.poly.2006.07.030

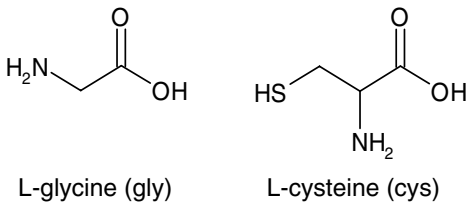


Fig. 1. Structure of the investigated amino acids.

group are coordinated to the uranyl cation. Iftekhar postulated further a stabilization of the complex by the S atom.

UV–Vis absorption and time-resolved laser-induced fluorescence spectroscopy are important experimental techniques for the investigation of uranium(VI) complexation behavior with a variety of ligands in aqueous systems. Detailed background information about uranyl ion absorption and uranyl ion emission spectroscopy is given in [13,14]. The aim of this work was to determine the absorption and fluorescence emission properties of uranium(VI) complexes with L-glycine and L-cysteine at low pH values. Further, the complex formation constants of the formed uranyl complexes were calculated based on the measured spectroscopic data.

2. Experimental

2.1. Solutions and reagents

A stock solution of uranium(VI) perchlorate (10^{-2} M) was prepared from sodium diuranate as described in [15] and analyzed using ICP-MS. Ligand stock solutions of L-glycine and L-cysteine (Merck) were prepared freshly for each experiment. The complex formation experiments were performed at pH 2, 3 and 4. The pH value of each reference and complex solution was adjusted with $HClO_4$ or NaOH. The possible influence of U(VI) hydrolytic species at pH 4 was considered in the analysis of the spectroscopic data.

2.2. TRLFS measurements

Laser pulses at 266 nm with an average pulse energy of 250 μJ (Nd:YAG laser system, Spectron Laser systems, SL 401-20, Rugby) were used for the excitation of the uranyl fluorescence (22 ± 1 °C). The emitted fluorescence light from the initial and complex solutions was focused into a fiber optic, deconvolved by an Acton Research 500 nm spectrograph (model 1236, provided by EG&G). The resulting spectra were measured in time-resolved mode using a digital delay generator (EG&G, model 9650) and a gated diode array (EG&G, model 1471A) of the same company. The TRLFS spectra from 407.3 to 634.8 nm were recorded by averaging 100 laser pulses using a gate time of 2 μs. Each sample was measured three times on every delay time. All functions of the laser spectrometer were computer controlled. A more detailed description of the equipment is given elsewhere [16].

The TRLFS experiments were carried out at constant uranium concentration of 5×10^{-5} M. The concentration of amino acids varied between 0 and 4×10^{-1} M. The measurements were performed at an ionic strength of 0.1 and 0.5 M ($NaClO_4$).

2.3. UV–Vis measurements

The absorption spectroscopy measurements were performed using a CARY5G UV–Vis–NIR Spectrometer (Varian Co.) at room temperature (22 ± 1 °C). The spectra were recorded between 200 and 600 nm. For the determination of the uranyl absorption signals, the spectra were background corrected and analyzed in the wavelength range from 360 to 480 nm.

The uranium concentration was always constant at 1×10^{-3} M. The concentration of amino acids varied between 0 and 3×10^{-1} M. All absorption spectra were measured at an ionic strength of $I = 0.5$ M ($NaClO_4$).

3. Results and discussion

3.1. TRLFS-measurements

Fig. 2 shows examples of the measured TRLFS spectra of uranium(VI) as a function of the total ligand concentration in the glycine (A) and cysteine (B) system.

The fluorescence emission spectra of the U(VI) glycine complex solutions showed an increase in the fluorescence intensity and a significant bathochromic shift of the emission maxima with increasing ligand concentration. Contrary to that, the U(VI)/cysteine system is characterized by a decrease of the fluorescence intensity without a shift of the emission bands in comparison to the uranyl test solution without cysteine at low pH values. This we found already at minor ligand excess. The fluorescence signal was completely quenched at an excess of ligand greater than 100.

The time dependency of the fluorescence signal represents the sum of the fluorescence intensities of all species in the solution with

$$E(t) = \sum E_i \cdot e^{-\frac{t}{\tau_i}} \quad (1)$$

where E is the total fluorescence intensity at time t, E_i the fluorescence intensity of the species i at $t = 0$ and τ_i the corresponding fluorescence lifetime.

The time-resolved fluorescence spectra of uranyl glycine complex solutions at ionic strengths of 0.1 M and 0.5 M showed a bi-exponential fluorescence decay in each case about the investigated pH range (Fig. 3(C)). That means two species are the main components in each complex solution. The averaged lifetimes are $\tau_1 = 1800 \pm 100$ ns and $\tau_2 = 3200 \pm 270$ ns for an ionic strength of 0.1 M and $\tau_1 = 1880 \pm 140$ ns and $\tau_2 = 3500 \pm 470$ ns for an ionic strength of 0.5 M, up to U(VI)/glycine concentration ratios of 1:1000. The shorter lifetime is typical for the free uranyl

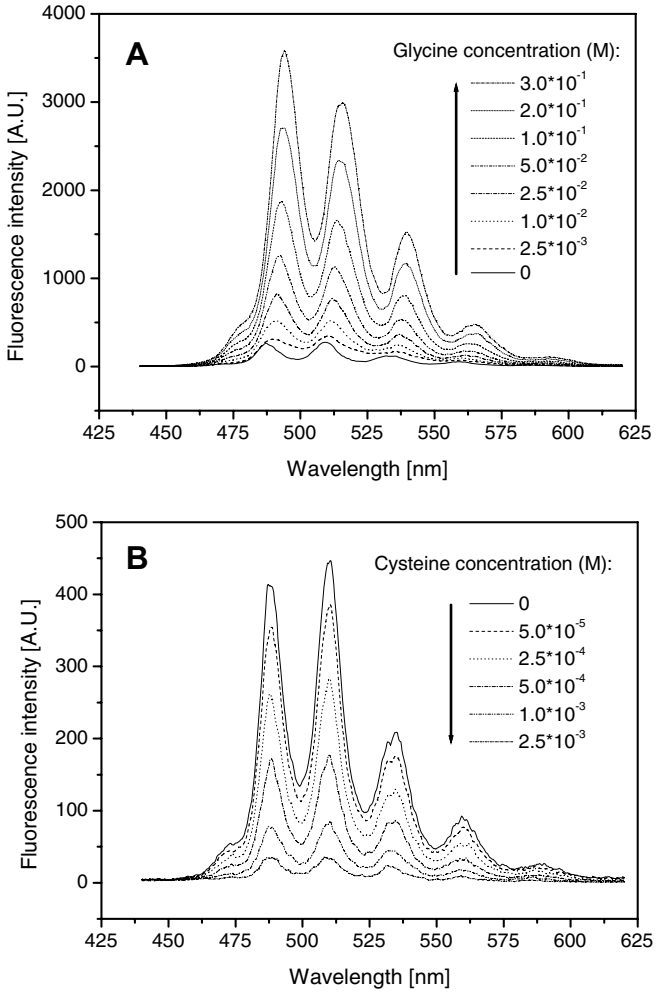


Fig. 2. Fluorescence emission spectra of uranium(VI) as a function of the ligand concentration: (A) glycine at pH 4 and $I = 0.5$ M, (B) cysteine at pH 3 and $I = 0.1$ M.

ion [17]. The marginal longer lifetime can be assigned to a first uranyl glycine complex.

At higher glycine excess ([U]:[glycine] < 1:1000) and pH 3 and 4 we found, additional to the first uranyl complex

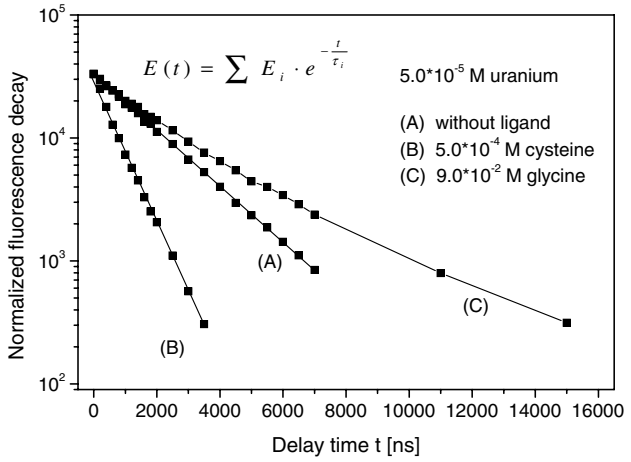


Fig. 3. Exponential fluorescence decay of uranium at pH 3 and $I = 0.1$ M: (A) monoexponential with $\tau_{UO_2^{2+}}$, (B) monoexponential with $\tau_{UO_2^{2+}\text{quenched}}$ and (C) bi-exponential with $\tau_{UO_2HGly^{2+}}$ and $\tau_{UO_2(Hgly)_2^{2+}}$.

species with τ_2, a further uranyl complex species which has an average lifetime of $\tau_3 = 690 \pm 240$ ns at an ionic strength of 0.1 M and $\tau_3 = 690 \pm 190$ ns at an ionic strength of 0.5 M. It is shorter than the lifetime of the free uranyl ion and the first uranyl glycine species.

We used the factor analysis program SPECFIT [18] for the analysis of the mixed spectra and their decomposition into single spectra of the different species. The program performs a global analysis of equilibrium and kinetic systems with singular value decomposition and non-linear regression modelling by the Levenberg–Marquardt method. The spectra of the uranium test solution without ligand and all complex solutions, the known total concentration of uranium and ligand, the pH value of each sample and the protonation constants for glycine were the input parameters for the spectra analysis and data fitting. The spectra were evaluated for each pH value separately. Besides the decomposition of the mixed spectra into single components, we determined the stoichiometry (x, y, z) of the formed uranyl complexes and the corresponding stability constants with this program (Eq. (2)).

The complex formation reaction of UO_2^{2+} with glycine can be written in general as

$$x UO_2^{2+} + y H^+ + z Gly^- \overset{\beta_{xyz}}{\rightleftarrows} \{(UO_2)_x H_y Gly_z\}^{(2x+y-z)+} \quad (2)$$

with $\beta_{xyz} = \frac{[(UO_2)_x H_y Gly_z^{(2x+y-z)+}]}{[UO_2^{2+}]^x [H^+]^y [Gly^-]^z}$.

The obtained stability constants of each uranyl glycine complex at each selected pH value were averaged over the whole investigated pH range.

The results of the factor analysis program demonstrated that the first formed uranyl glycine species is of the type MHL (fluorescence lifetime τ_2). The second uranyl glycine complex has a metal:proton:ligand ratio of 1:2:2 and is of the type $M(HL)_2$. The resulting stability constants are assigned to be $\log\beta_{111} = 10.84 \pm 0.10$ and $\log\beta_{122} = 21.19 \pm 0.13$ at an ionic strength of 0.1 M. In analogy to the analysis of the measurements at $I = 0.1$ M, the complex formation constants at an ionic strength of 0.5 M are calculated to be $\log\beta_{111} = 10.79 \pm 0.22$ and $\log\beta_{122} = 20.93 \pm 0.14$ (Table 1). For the direct reaction of UO_2^{2+} with the zwitterionic form $HGly^{+/-}$, the stability constants are $\log K_{111} = 1.26 \pm 0.11$ and $\log K_{122} = 2.03 \pm 0.14$ at an ionic strength of 0.1 M as an example. They are comparable with the values obtained by Bismondo [2] and Ramanujam [3] under slightly different experimental conditions (ionic strength, temperature).

The mathematical deconvolution of a mixed spectrum using the molar single spectra of the UO_2HGly^{2+} and $UO_2(HGly)_2^{2+}$ species obtained by the factor analysis procedure is shown in Fig. 4. The molar fluorescence yield of the uranyl complex species is clearly higher than the molar fluorescence yield of the free uranyl ion. The main emission bands of the 1:1:1 and 1:2:2 uranyl glycine complexes show a bathochromic shift of about 4 and 7 nm, respectively, in comparison to the bands of the free uranyl cation (Table 2).

Table 1
Relevant protonation constants of amino acids and formation constants for uranium(VI) glycine and uranium(VI) cysteine complexes

Species	xyz[a]	$\log\beta_{xyz}$	Ionic strength (M)	Method/references
HGly	011	9.58 ± 0.04	0.1	[19]
	011	9.54 ± 0.03	0.5	[19]
H_2Gly^+	021	11.92 ± 0.04	0.1	[19]
	021	11.93 ± 0.06	0.5	[19]
UO_2HGly^{2+}	111	10.84 ± 0.10	0.1	TRLFS/this work
	111	10.79 ± 0.22	0.5	TRLFS/this work
	111	10.74 ± 0.08	0.5	UV–Vis/this work
$UO_2(HGly)_2^{2+}$	122	21.19 ± 0.13	0.1	TRLFS/this work
	122	20.93 ± 0.14	0.5	TRLFS/this work
	122	20.91 ± 0.10	0.5	UV–Vis/this work
$HCys^-$	011	10.30 ± 0.08	0.1	[19]
	011	10.10 ± 0.04	0.5	[19]
H_2Cys	021	18.48 ± 0.11	0.1	[19]
	021	18.20 ± 0.07	0.5	[19]
H_3Cys^+	031	20.38 ± 0.15	0.1	[19]
	031	20.10 ± 0.31	0.5	[19]
$UO_2H_2Cys^{2+}$	121	20.05 ± 0.14	0.1	TRLFS/this work
	121	19.28 ± 0.04	0.5	UV–Vis/this work
UO_2HCys^+	111	15.28 ± 0.04	0.5	UV–Vis/this work

[a] x, y, z are the stoichiometric coefficients of the free ligands and complex corresponding to UO_2, proton and ligand.

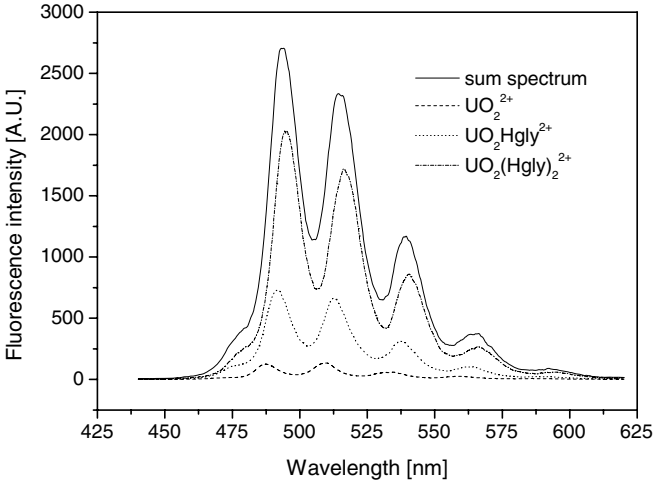


Fig. 4. Result of the peak deconvolution of the fluorescence spectrum of a solution containing 5×10^{-5} M uranium(VI) and 2×10^{-1} M glycine at pH 4 and $I = 0.5$ M.

The analysis of the time-resolved fluorescence measurements of the U(VI)/cysteine system showed a decrease of the fluorescence intensity with increasing cysteine concentration without a shift of the main emission bands. The fluorescence decay was monoexponential in all samples (Figs. 3(B) and 5).

This behavior is typical for static fluorescence quenching due to the complex formation and decrease of the free uranyl ion concentration. We therefore conclude that only the free uranyl ion is present in the complex solutions as fluorescent species and the formed uranyl cysteine complex(es) shows or show no fluorescence properties. The significant decreasing lifetime with increasing ligand concentration (Fig. 5) indicates additionally a dynamic quenching. The cause of the dynamic quenching in the presence of cysteine has not been clarified up to now. Fluorescence investigations with organic ligands which have such a quenching effect are little known. The process of dynamic quenching can be described quantitatively by a Stern–Volmer plot [20]. The averaged quenching constant for the cysteine system in the pH range from 2 to 4 was calculated to be $K_Q = 3840 \pm 40\ M^{-1}$, based on the obtained fluorescence lifetime values of free uranyl without and with ligand. Using the corresponding quenching constant and experimental lifetime data of each complex solution it was possible to calculate the fluorescence intensity of UO_2^{2+} if no dynamic quenching takes place. The corrected fluorescence spectra of each complex solution and corresponding fluorescence intensity of the free uranyl cation were used for the calculation of the realistic uranyl concentration in all complex solutions and the complex formation constants in the U(VI)/cysteine system with the factor analysis program SPECFIT.

In analogy to glycine, the reaction of UO_2^{2+} with cysteine can be formulated in the following equation:

$$x\mathrm{UO_2}^{2+} + y\mathrm{H}^+ + z\mathrm{Cys}^{2-} \overset{\beta_{xyz}}{\rightleftarrows} \{(\mathrm{UO_2})_x\mathrm{H}_y\mathrm{Cys}_z\}^{(2x+y-2z)+} \quad (3)$$

with $\beta_{xyz} = \frac{[(\mathrm{UO_2})_x\mathrm{H}_y\mathrm{Cys}_z^{(2x+y-2z)+}]}{[\mathrm{UO_2}^{2+}]^x[\mathrm{H}^+]^y[\mathrm{Cys}^{2-}]^z}$.

Using SPECFIT we could determine one uranyl cysteine species with a metal:proton:ligand ratio of 1:2:1 under the given experimental conditions. The formation constant was calculated to be $\log\beta_{121} = 20.05 \pm 0.14$ (Table 1). Due to

Table 2
Fluorescence properties of different U(VI) complexes in comparison to the free uranyl cation

Species	Fluorescence emission bands (nm)						Averaged lifetime (ns)
UO_2^{2+}	471.4	487.9	509.1	532.7	558.7	584.4	1800 ± 100[a] 1880 ± 140[b]
UO_2HGly^{2+}	475.8	492.1	513.1	537.3	562.4	587.0	3200 ± 270[a] 3500 ± 470[b]
$UO_2(HGly)_2^{2+}$	478.7	495.3	516.7	540.6	565.0	594.4	690 ± 240[a] 690 ± 190[b]
UO_2–Cys-complexes	no fluorescence at room temperature						

[a] $I = 0.1$ M.
[b] $I = 0.5$ M.

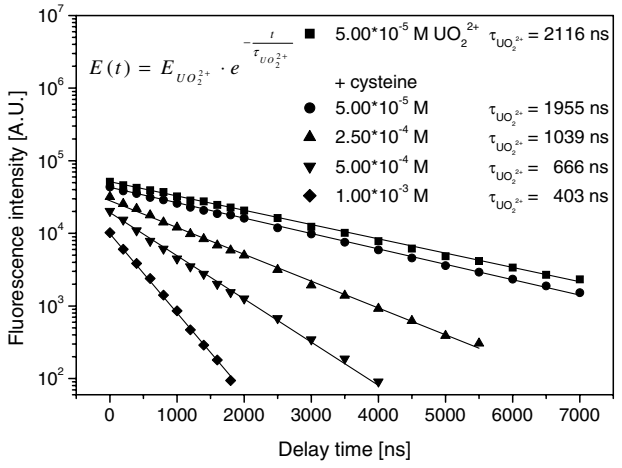


Fig. 5. Monoexponential fluorescence decay measured in the U(VI)/cysteine system at pH 3.

the existence of two functional protons in the uranyl cysteine complex species, a binding of the uranyl cation only on the deprotonated carboxyl group is very probably. The SH− and NH_3+ functionalities do not seem to be involved in the metal coordination by deprotonation and chelate formation.

3.2. UV–Vis measurements

Fig. 6 depicts a summary of the measured UV–Vis absorption spectra of uranium(VI) with glycine in comparison to cysteine as a ligand at different pH values. The detected significant increase in the absorption and a bathochromic shift of the absorption maxima compared to the free uranyl cation indicate complex formation between the uranyl cation and the amino acid glycine at pH 3 (Fig. 6(A)) as an example. The same results were obtained for the U(VI)/glycine system at pH 2 and 4. Contrary to this, the U(VI)/cysteine system is characterized by a change in the absorption behavior in the investigated pH range from 2 to 4. Additional to an increase of absorption with increasing cysteine concentration in the whole investigated pH range, a bathochromic shift at pH 2 and 3 (Fig. 6(B1)) and an increasing hypsochromic shift of the main absorption bands at pH 4 (Fig. 6(B2)) were detected. Therefore we can assume that species with different metal–proton–ligand ratio and/or different structure (binding of metal) are formed.

The measured UV–Vis absorptions of each test and complex solution can be described with the Lambert–Beer's law and is the summary of the absorption of each species in the solution. It is given by

$$A(\lambda) = \sum \varepsilon_{i,\lambda} \cdot c_i \tag{4}$$

where A is the absorption of light by the solution at wavelength λ, $\varepsilon_{i,\lambda}$ the molar absorption coefficient of the species i at the wavelength λ and c_i the concentration of the species i in the solution at a thickness of the cuvette of 1 cm. In analogy to the analysis of the fluorescence spectra, the mixed UV–Vis spectra of both U(VI) amino acid systems were decomposed in the single components and the metal:proton:ligand ratio in the formed complex species with corresponding constants were estimated using the factor analysis program SPECFIT. The molar ($c_i = 1$ M) absorption spectra of each species (uranyl and complex species) obtained from the factor analysis procedure are the basis for the determination of the wavelengths of the main absorption bands and the molar extinction coefficients $\varepsilon_{i,\lambda}$. From this information we could determine two different uranyl glycine species of the type MHL and $M(HL)_2$ with complex formation constants of $\log\beta_{111} = 10.74 \pm 0.08$ and $\log\beta_{122} = 20.91 \pm 0.10$. They are in good agreement with the corresponding data obtained by our fluorescence measurements (Table 1). The absorption properties of the uranyl glycine species in the UV range are very similar. The absorption wavelengths and the molar extinction coefficients of both uranyl glycine species differ only slightly and are summarized in Table 3.

The UV–Vis spectra of the U(VI) cysteine system were evaluated in the same way. Here we obtained, additional to the 1:2:1 species, a 1:1:1 species in the pH range from 3 to 4. This species has the same metal to ligand ratio, but lower proton number. It is generally accepted in the literature that deprotonation can occur simultaneously from SH and NH_3^+ groups. In combination with the large hypsochromic shift of the absorption bands of the system at pH 4 we assume that next to the deprotonated carboxyl group, the $-S^-$ or the $-NH_2$ group is already involved in the

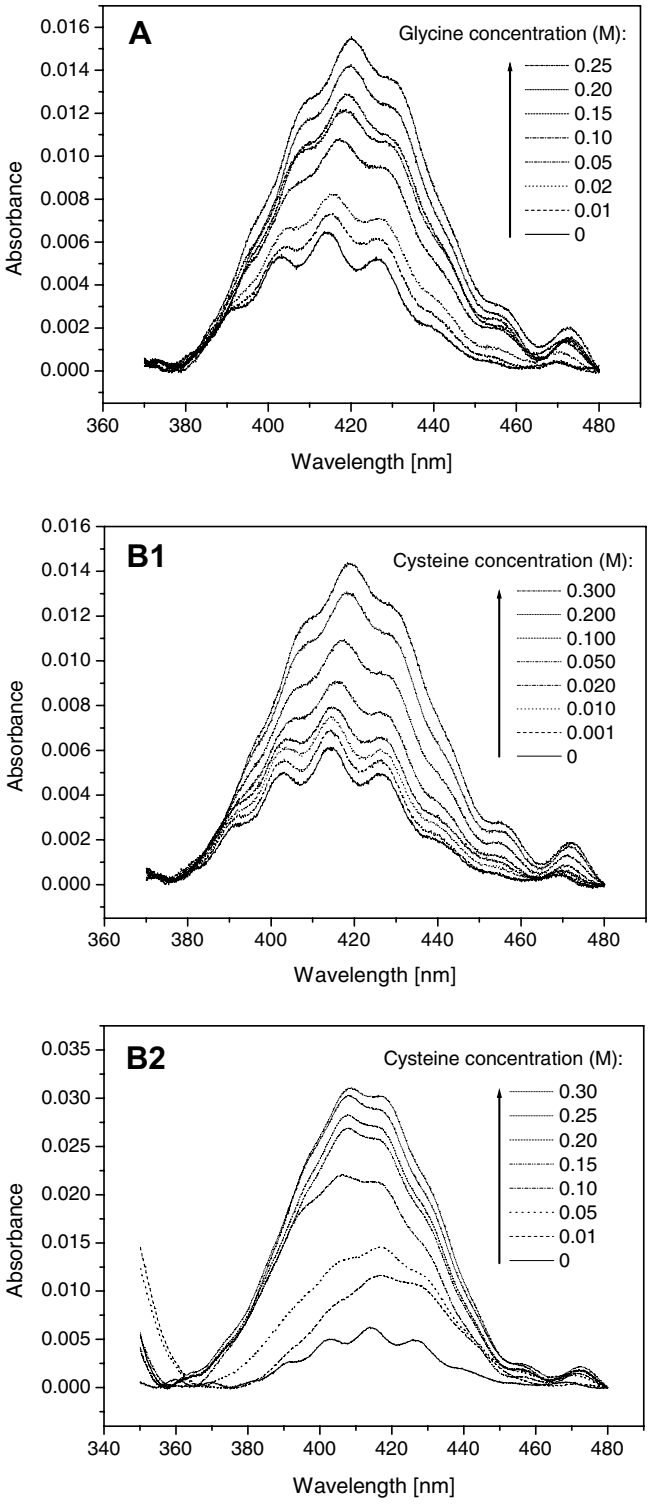


Fig. 6. Summary of UV–Vis spectra at 1×10^{-3} M uranium(VI) and $I = 0.5$ M ($NaClO_4$) as a function of the ligand concentration: (A) glycine system at pH 3, (B1) cysteine system at pH 2 and (B2) cysteine system at pH 4.

coordination of the uranyl cation. It could not be clarified by the applied methods which group is preferred for the metal coordination. The formation constants are $\log \beta_{121} = 19.28 \pm 0.04$ and $\log \beta_{111} = 15.28 \pm 0.04$ (Table 1). The value of $\log \beta_{111}$ is in the range of complex formation constants for the corresponding simple protonated 1:1 complexes with Ni^{2+} and Zn^{2+} at $I = 0.2$ M [21]. Fig. 7 shows examples for the spectra deconvolution of mixed spectra

Table 3
Main absorption bands and calculated molar extinction coefficients (in parenthesis) of the uranium species in the uranium(VI)/amino acid system in the pH range from 2 to 4

Species	Absorption bands (nm) (ε (L mol^{-1} cm^{-1}))					
UO_2^{2+}	391.2 (2.3)	402.5 (4.6)	414.2 (5.8)	426.8 (4.6)	439.5 (1.6)	452.5 (0.3)
UO_2HGly^{2+}	395.9 (6.7)	406.6 (10.6)	418.5 (16.1)	430.6 (11.5)	441.7 (6.8)	456.4 (2.4)
$UO_2(HGly)_2^{2+}$	396.9 (6.2)	408.0 (11.6)	419.5 (16.0)	431.8 (13.5)	443.7 (6.4)	456.8 (2.9)
$UO_2H_2Cys^{2+}$	395.9 (6.6)	407.3 (12.4)	418.0 (16.6)	430.8 (13.3)	442.1 (7.0)	455.9 (2.8)
UO_2HCys^{+}	385.7 (12.6)	396.4 (22.8)	407.4 (31.7)	418.8 (29.7)	430.2 (19.0)	441.0 (8.0)

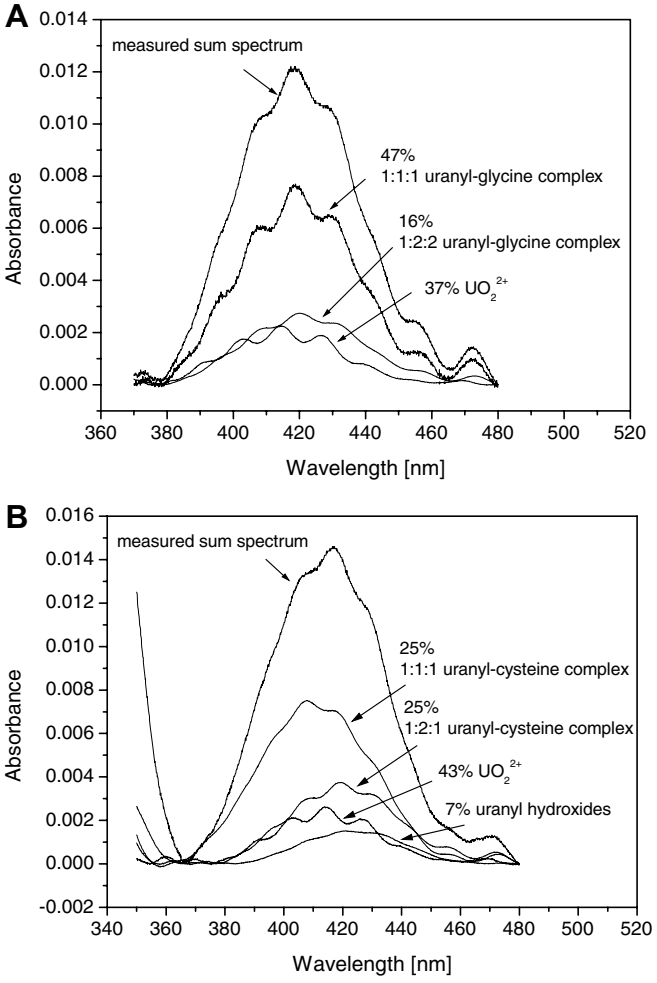


Fig. 7. Results of the peak deconvolution of the UV–Vis spectra of solutions containing 1×10^{-3} M uranium(VI) and (A) 1×10^{-1} M glycine at pH 3 and (B) 5×10^{-2} M cysteine at pH 4.

in the U(VI)/glycine and U(VI)/cysteine system using molar absorption spectra of several species. The deconvolution of the UV–Vis spectrum of a selected uranyl cysteine complex solution at pH 4 (Fig. 7(B)) demonstrates that a small quantity of uranyl hydroxides are formed at the uranium concentration 10^{-3} M and relatively high uranyl ligand concentration ratio (low excess of ligand) during the reaction of U(VI) and the amino acid.

4. Conclusion

U(VI) complexes with different amino acids can be formed on cell surfaces e.g., in biological systems like plants, algae and bacteria over a wide pH range. Time-resolved laser-induced fluorescence spectroscopy and UV–Vis spectroscopy were used to investigate the complex behavior of U(VI) with the amino acids L-glycine and L-cysteine in aqueous solution. Spectroscopic properties of the formed uranyl complexes were determined in comparison to the free uranyl cation. We found several protonated uranyl amino acids complexes with metal: ligand ratios of 1:1 (glycine and cysteine system) and 1:2 complexes (glycine system) at low pH values. The results showed a change of the complexation behavior of amino acids towards the uranyl cation and the spectroscopic properties of the system dependent on the presence of the functional groups ($-COOH/-COO^-$, $-SH/-S^-$, NH_2/NH_3^+). At relative high uranium concentration a 1:1 species in the U(VI)/cysteine system with a metal coordination through the deprotonated carboxyl group and –S or $-NH_2$ group was detected. This species has other absorption properties than the 1:1 species where the metal is bound only to the carboxyl group. TRLFS was applied at lower biological more relevant uranium concentration.

An important aspect is that in contrast to the uranyl glycine complexes the U(VI) complexes with cysteine do not fluoresce. The identification of uranyl cysteine species in biological systems seems to be not possible by TRLFS at room temperature.

Acknowledgment

The authors thank Tabea Birk for the samples preparation.

References

[1] V.V. Ramanujam, K. Rengaraj, B. Sivasankar, Bull. Chem. Soc. Jpn. 52 (9) (1979) 2713.
[2] A. Bismondo, L. Rizzo, G. Tomat, D. Curto, P. Di Bernardo, A. Cassol, Inorg. Chim. Acta 74 (1983) 21.
[3] P. Lagrange, M. Schneider, K. Zare, E. Lagrange, Polyhedron 13 (6/7) (1994) 861.
[4] P. Lagrange, M. Schneider, J. Lagrange, J. Chim. Phys. 95 (1998) 2280.
[5] M. Cerfola, R.C. Taylor, P.S. Gentile, A.V. Celiano, J. Phys. Chem. 66 (1962) 790.
[6] Z. Szabo, I. Grenthe, Inorg. Chem. 39 (2000) 5036.
[7] V.G. Dongre, D.G. Dhuley, Curr. Sci. 49 (8) (1980) 305.
[8] N.W. Alcock, D.J. Flanders, T.J. Kemp, M.A. Shand, J. Chem. Soc., Dalton Trans. (1985) 517.
[9] G. Berthon, Pure Appl. Chem. 67 (7) (1995) 1117.
[10] S. Iftekhar, K.P. Dubey, J. Indian Chem. Soc. LXI (1984) 702.
[11] A. Raghavan, M. Santappa, Curr. Sci. 39 (1972) 302.
[12] A. Raghavan, M. Santappa, J. Inorg. Nucl. Chem. 35 (1973) 3363.
[13] J.T. Bell, R.E. Biggers, J. Mol. Spectrosc. 25 (1968) 312.
[14] J.T. Bell, R.E. Biggers, J. Mol. Spectrosc. 18 (1965) 247.
[15] G. Bernhard, G. Geipel, V. Brendler, H. Nitsche, Radiochim. Acta 74 (1996) 87.
[16] G. Geipel, A. Brachmann, V. Brendler, G. Bernhard, H. Nitsche, Radiochim. Acta 75 (1996) 199.
[17] V. Eliet, G. Bidoglio, N. Omenetto, L. Parma, I. Grenthe, J.Chem. Soc., Faraday Trans. 91 (1995) 2275.
[18] SPECFIT 32, Spectrum Software – Associates, 2003.
[19] NIST Standard References Database 46 Version 5.0.
[20] H.-H. Perkampus, Encyclopedia of Spectroscopy, VCH Verlagsgesellschaft mbH, Weinheim, 1995.
[21] I. Sovago, A. Gergely, B. Harman, T. Kiss, J. Inorg. Nucl. Chem. 41 (1979) 1629.

Available online at www.sciencedirect.com
ScienceDirect
Polyhedron 26 (2007) 66–72
POLYHEDRON
www.elsevier.com/locate/poly

Redistribution reactions of heteroleptic barium iodide derivatives: Synthesis and structures of *trans*-BaI_2(DME)(triglyme), *cis*-BaI_2(DME)(tetraglyme) and [Ba(tetraglyme)$_2$]$I_2 \cdot C_7H_8$

Shashank Mishra [a,*], Liliane G. Hubert Pfalzgraf [a,*], Erwann Jeanneau [b]

[a] *Université Claude Bernard Lyon 1, IRC, 2 Avenue A. Einstein, 69626 Villeurbanne Cedex, France*
[b] *Université Claude Bernard Lyon 1, Centre de Diffractométrie, 69622 Villeurbanne Cedex, France*

Received 13 March 2006; accepted 2 August 2006
Available online 18 August 2006

Abstract

The reaction between $BaI_2 \cdot 2H_2O$ and NaHFIP [HFIP = $OCH(CF_3)_2$] in a 1:1 stoichiometry gave the heterometallic compound $NaBaI_2(HFIP)(H_2O)(THF)_{0.5}$ (**1**). Attempts to recrystallize **1** in the presence of N- or O-donor ligands lead to redistribution reactions. Barium iodide adducts such as $BaI_2(DME)_3$ (**2**), *trans*-BaI_2(DME)(triglyme) (**3**) and *cis*-BaI_2(DME)(tetraglyme) (**4**) were isolated with DME as solvent. A similar behavior was observed for the reaction between $BaI_2 \cdot 2H_2O$ and NaTFA (TFA = O_2CCF_3) in a 1:1 stoichiometry in THF, and [Ba(tetraglyme)$_2$]$I_2 \cdot C_7H_8$ (**6**) was isolated in the presence of excess tetraglyme. All compounds have been characterized by elemental analysis, IR and ^{1}H NMR as well as single crystal X-ray studies for **3**, **4** and **6**. Compounds **3** and **4** are covalent adducts with eight- and nine-coordinate barium, respectively. Compound **6** is an ionic compound where two tetraglyme ligands wrap the 10-coordinate barium cation in a helical fashion. The presence of DME actually allows the coordination number of barium in the mixed-ligand adducts **3** and **4** to be tuned. The average Ba–O bond lengths (2.80 for **3** to 2.87 Å for **6**) reflect the coordination number of the metal. The same observation is valid for the average Ba–I bond distance, 3.442 for **3** vs. 3.536 Å for **4**.
© 2006 Elsevier Ltd. All rights reserved.

Keywords: Barium; Iodide; Fluorocarboxylate; Hexafluoroisopropoxide; Complexes; Structure

1. Introduction

Barium derivatives with fluorinated ligands such as trifluoroacetate (TFA = $CF_3CO_2^-$) [1] have attracted attention due to their use for the elaboration of high T_c superconductors coatings by metal organic deposition (MOD). Their preferential decomposition into barium fluoride represents a means to avoid the formation of the highly stable barium carbonate, which is detrimental for the superconducting properties [2]. However, formation of corrosive hydrofluoric acid during decomposition is a drawback [3]. Barium iodide, along with yttrium and copper(I) iodides, has been used in all iodide routes to high T_c superconductors [4]. The lower stability of BaI_2 with respect to $BaCO_3$ (decomposition 660 vs. 1100 °C) and lower volatility of CuI in comparison to $Cu(TFA)_2$ could be more favorable than the TFA-MOD approach for $YBa_2Cu_3O_{7-x}$ films. However, barium iodide is a rather inert cluster due to its three-dimensional network structure [5] and its chemistry remains poorly known. Homoleptic barium derivatives supported by trifluoroacetate [6], trifluoromethane sulfonate [7] or fluoroisopropoxide ligands [8] are known but no heteroleptic barium iodide derivatives with these ligands have been reported, despite the fact that such compounds could reduce the hazard of hydrofluoric acid and provide better solubility than BaI_2 in organic media. The stability of heteroleptic alkaline earth metal derivatives depends on a delicate balance of steric effects,

* Corresponding authors. Tel.: +33 472445329.
E-mail address: mishrashashank74@rediffmail.com (S. Mishra).

0277-5387/$ - see front matter © 2006 Elsevier Ltd. All rights reserved.
doi:10.1016/j.poly.2006.08.007

metal size, ligand basicity and solubility equilibria [9]. A challenge for their isolation is the Schlenk-type equilibrium leading to rearrangement of heteroleptic species into their homoleptic counterparts [10]. To our knowledge, only five heteroleptic barium iodides stabilized by bulky anionic ligands, namely $\{[C_5(SiMe_3)_3H_2]BaI(THF)_2,\ 1/2C_7H_8\}_\infty$ [9], $Ba_2(\mu\text{-}I)_2(OC_6H_2Bu^t{}_2\text{-}2,6\text{-}Me\text{-}4)_2(THF)_6, (THF)_2$ [11], $Li_4BaI(\mu_4\text{-}OH)(\mu_3\text{-}OBu^t)_4(THF)_4$ [12], $[Ba\{\eta^2\text{-}(2,6\text{-}Pr^i{}_2\text{-}C_6H_3)NC(Bu^t)CH_2C(Bu^t)N(2,6\text{-}Pr^i{}_2C_6H_3)\}(\mu\text{-}I)]_2$ and $(\eta^5\text{-}L)_4Ba_4(\mu\text{-}I)_2(\mu\text{-}\eta^2{:}\eta^5\text{-}L)_2$ ($L = Bu^tNC(Me)(CHC(Me)NBu^t)$) [13], have been fully characterized.

We wish to present here our results on our attempts to isolate and characterize heteroleptic barium iodide derivatives with hexafluoroisopropoxide or trifluoroacetate ligands. The polar media needed for their crystallization afforded barium iodide complexes, namely $BaI_2(DME)_3$ (**2**), *trans*-BaI_2(DME)(triglyme) (**3**), *cis*-BaI_2(DME)(tetraglyme) (**4**) and $[Ba(tetraglyme)_2]I_2 \cdot C_7H_8$ (**6**), which were characterized by elemental analysis, IR and ^1H NMR spectroscopy as well as single crystal X-ray analysis for **3**, **4** and **6**.

2. Experimental

All reactions were carried out under argon using Schlenk tubes and vacuum line techniques. $BaI_2 \cdot 2H_2O$ and BaI_2 (Aldrich) were used as received. Solvents were purified by standard methods, hexafluoroisopropanol, trifluoroacetic acid and glymes $MeO(CH_2CH_2O)_xMe$ ($x = 1, 3, 4$) were stored over molecular sieves. ^1H NMR spectra were registered on a Bruker AC-300 spectrometer. FT-IR spectra were recorded as Nujol mulls on a Perkin–Elmer Paragon 500 spectrometer. Analytical data were obtained from the Service Central d'Analyses du CNRS.

2.1. Synthesis of $NaBaI_2(HFIP)(H_2O)(THF)_{0.5}$ (1)

Freshly prepared sodium hexafluoroisopropoxide (NaHFIP) [Na (0.084 g, 3.65 mmol) and $HOCH(CF_3)_2$ (0.4 ml, 3.70 mmol) in 10 ml THF] was added to a suspension of $BaI_2 \cdot 2H_2O$ (1.56 g, 3.65 mmol) in THF (10 ml). No sodium iodide or other derivative could be crystallized out and the solution was evaporated to dryness after 4 h to give **1** as a light yellow solid, 2.40 g (99%). *Anal.* Calc. for $C_5H_7F_6O_{2.5}NaBaI_2$: C, 9.30; H, 1.09, Na, 3.62. Found: C, 8.84; H, 1.09, Na, 3.50%. IR (Nujol, cm^{-1}): 3478, 3420 br (ν_{OH}), 1622 m, 1608 m (δ_{OH}), 1277 s, 1228 s, 1179 s, 1136 s, 1085 s (ν_{C-F}, ν_{C-O}), 1039 m, 891 m, 848 m, 801 m, 733 m, 680 m, 560 m; 514 m (ν_{Ba-I}), 442 m. ^1H NMR ($CDCl_3$, ppm): 4.58 [br, 1H, $CH(CF_3)_2$], 3.73 [m, 2H, α-H (THF)], 1.86 [m, 2H, β-H (THF)].

2.2. Synthesis of $BaI_2(DME)_3$ (2)

Dissolution of 0.5 g of **1** in DME and THF (10 ml each) at 70 °C, followed by filtration and crystallization gave **2** (0.22 g, 45%). *Anal.* Calc. for $C_{12}H_{30}O_6BaI_2$: C, 21.78, H, 4.53. Found: C, 20.87, H, 4.32%. IR (Nujol, cm^{-1}): 1282 m, 1243 m, 1191 m, 1115 s, 1064 s, 1024 m, 892 w, 855 s (ν_{C-O}), 722 w, 686 w, 569 m (ν_{Ba-I}), 429m (ν_{Ba-O}). ^1H NMR ($CDCl_3$, ppm): 3.41 [s, 18H, Me], 3.56 [s, 12H, OCH_2]. Monoclinic $P2_1/n$, $a = 8.668(2)$, $b = 9.886(1)$, $c = 13.651(3)$ Å, $\beta = 104.58(1)°$, $V = 1132.2(4)$ Å^3. Due to the poor quality of the crystals, the data could not be refined.

$BaI_2(DME)_3$ was also isolated along with sodium iodide adducts $[Na_2(H_2O)_2(PMDTA)_2]I_2$ and $Na_2I_2(PMDTA)_2$ at −20 ° C from the reaction between $BaI_2 \cdot 2H_2O$ (1.015 g, 2.73 mmol) in DME (7 ml) with $NaOCH(CF_3)_2$ (2.34 mmol) in 7 ml of THF in the presence of *N*,*N*,*N*′,*N*″,*N*″-pentamethyldiethylenetriamine (PMDTA) (0.7 ml, 3.35 mmol).

2.3. Synthesis of $BaI_2(DME)(triglyme)$ (3) and $BaI_2(DME)(tetraglyme)$ (4)

Triglyme (0.48 g, 2.69 mmol) was added to a DME (20 ml) solution of **1** (0.711 g, 1.58 mmol). After stirring for 6 h and filtration, **3** crystallized (0.3 g, 42%). FT-IR (Nujol, cm^{-1}): 1346 m, 1297 m, 1243 m, 1199 m (ν_{C-C}), 1085 s, 1062 s, 1016 m, 942 m, 858 m (ν_{C-O}), 720 m, 522 m (ν_{Ba-I}); ^1H NMR ($CDCl_3$, ppm): 3.40 [s, 6H, Me (DME)], 3.42 [s, 6H, Me (triglyme)], 3.54 [s, 4H, CH_2 (DME)], 3.61 [m, 4H, CH_2 (triglyme)], 3.7 [m, 8H, CH_2 (triglyme)].

Using the same procedure, **4** was obtained by reacting **1** (0.65 g, 1.44 mmol) and tetraglyme (0.48 g, 2.17 mmol) in DME (20 ml) (0.26 g, 40%). *Anal.* Calc. for $C_{14}H_{32}O_7BaI_2$: C, 23.89; H, 4.55. Found: C, 24.41; H, 4.78%. FT-IR (Nujol, cm^{-1}): 1458 s, 1376 m, 1351 m, 1283 m, 1249 m, 1200 m (ν_{C-C}), 1092 s, 1023 m, 945 m, 848 m (ν_{C-O}), 797 m, 719 w, 679 w, 527 w (ν_{Ba-I}). ^1H NMR ($CDCl_3$, ppm): 3.57 [s, 6H, Me (DME)], 3.58 [s, 6H, Me (tetraglyme)], 3.59 [s, 4H, CH_2 (DME)], 3.65 [m, 4H, CH_2 (tetraglyme)], 3.66 [m, 12H, CH_2 (tetraglyme)].

Compounds **3** and **4** were isolated in better yields at −20 °C from reactions in DME between BaI_2 (0.341 g, 0.87 mmol) and triglyme (15 ml) (0.4 g, 70%) or BaI_2 (0.35 g, 0.90 mmol) and tetraglyme (15 ml) (0.47 g, 75%), respectively.

2.4. Synthesis of $NaBaI_2(TFA)(THF)(H_2O)_{0.5}$ (5)

A freshly prepared solution of NaTFA [Na (0.076 g, 3.33 mmol) and TFAH (0.26 ml, 3.40 mmol) in 10 ml THF was added to a suspension of $BaI_2 \cdot 2H_2O$ (1.30 g, 3.33 mmol) in 10 ml of THF. The resulting solution was stirred for 5 h and since no solid could be precipitated out, evaporated to dryness giving a yellow solid **5** (2.0 g, 98%). *Anal.* Calc. for $C_6H_9F_3O_{3.5}NaBaI_2$: C, 11.88; H, 1.48, Na 3.78. Found: C, 12.4; H, 1.42, Na, 3.62%. FT-IR (Nujol, cm^{-1}): 3430 br (ν_{O-H}), 1677br ($\nu_{as}CO_2$), 1461 s, 1376 s, 1297 m, 1258 m, 1204 w, 1150 m (ν_{C-F}, ν_{C-O}), 1081 w, 1027 w, 964 w, 885 w, 850 w, 802 w, 724 s, 548 m.

Table 1
Crystallographic and refinement data of **3**, **4** and **6**

Compound	**3**	**4**	**6**
Empirical formula	$C_{12}H_{28}O_6BaI_2$	$C_{14}H_{32}O_7BaI_2$	$C_{27}H_{52}O_{10}BaI_2$
Formula weight	659.5	703.5	927.85
Crystal system	monoclinic	orthorhombic	triclinic
Space group	$P2_1$ (no. 4)	*Pcab* (no. 61)	$P\bar{1}$
a (Å)	8.3864(2)	14.2772(4)	16.88(3)
b (Å)	10.7060(3)	15.0526(5)	23.03(3)
c (Å)	12.2888(3)	21.5901(7)	39.41(8)
α (°)	90	90	89.07(3)
β (°)	96.041(2)	90	81.93(9)
γ (°)	90	90	76.53(2)
Volume (Å^3)	1097.22(5)	4639.9(3)	14750(5)
Z	2	8	16
Absorption coefficient (mm^{-1})	4.64	4.4	2.79
Temperature (*K*)	150	150	150
Unique data (R_{int})	6114 (0.039)	5463 (0.042)	74360 (0.071)
Data/restrains/parameters	4928/121/303	3593/138/345	34 209/581/2881
Goodness-of-fit	0.942	0.978	1.062
R_1 ($I > 2(\sigma)$)	0.041	0.043	0.073
R_1 (all data)	0.058	0.082	0.200
wR_2 ($I > 2(\sigma)$)	0.075	0.091	0.082
wR_2 (all data)	0.083	0.107	0.173
Residual electron density (e Å^{-3})	−1.61 to 2.27	−0.81 to 2.21	−4.80 to 5.53

2.5. Synthesis of $[Ba(tetraglyme)_2]I_2 \cdot C_7H_8$ (6)

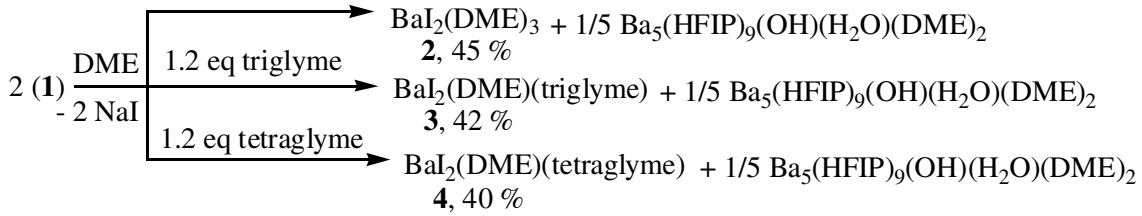
Tetraglyme (0.48 g, 2.16 mmol) was added to a solution of **5** (0.57 g, 1.44 mmol) in THF (8 ml) and toluene (7 ml). After stirring for 6 h, sodium iodide was filtered out. The filtrate afforded colorless crystals of **6**, 0.98 g (47%). After drying under *vacuo*, these lost half of their toluene molecules. *Anal.* Calc. for $C_{23.5}H_{48}O_{10}BaI_2$: C, 32.0; H, 5.44. Found: C, 32.08; H, 5.59%. FT-IR (Nujol, cm^{-1}): 1458 s, 1377 m, 1351 m, 1287 m, 1247 m, 1199 m, 1095 s, 1057 s, 1019 m, 948 m, 861 m, 846 m, 723 m, 689 w, 664 w, 532 w (ν_{Ba-I}). ^{1}H NMR ($CDCl_3$, ppm): 2.35 [s, 1.5H, Me (toluene)], 3.51 [s, 12H, Me (tetraglyme)], 3.68 [m, 8H, CH_2 (tetraglyme)], 3.78 [m, 24H, CH_2 (tetraglyme)], 7.23 [m, 2.5H, Ph].

2.6. X-ray structure determination of trans-$BaI_2(DME)(triglyme)$ (3), cis-$BaI_2(DME)(tetraglyme)$ (4) and $[Ba(tetraglyme)_2]I_2 \cdot C_7H_8$ (6)

Suitable crystals of **3**, **4** and **6** were obtained at room temperature from the reaction media. Data were collected at 150 K on a Nonius Kappa CCD diffractometer using the COLLECT software [14]. Reduction of the data was carried out with DENZO [15]. Frame scaling and unit-cell parameters refinement were made through SCALEPACK [15]. Absorption corrections were achieved with DIFABS [16]. The structures were solved by direct methods with SIR92 [17] and successive difference Fourier map analyses. Refinement on F^2 was carried out with CRYSTALS [18]. The hydrogen atoms were placed geometrically and included in the refinement using soft restraints on bond lengths and angles to regularize their geometry (C–H in the range 0.93–0.98 Å and O–H = 0.82 Å) and isotropic atomic displacement parameters (U(H) 1.2–1.5 times $U_{eq.}$ of the adjacent atom). Eight independent moieties were found in the asymmetric unit of compound **6**, generating thus a large number of data to refine. The maximum electron density peak was found at 0.851 Å from I(3). Crystallographic data and structure refinement are listed in Table 1.

3. Results and discussion

The reaction between $BaI_2 \cdot 2H_2O$ and sodium hexafluoroisopropoxide (NaHFIP) (1:1 stoichiometry) in THF gave a solution from which no sodium iodide could be precipitated out. Evaporation to dryness gave a compound having a formula $NaBaI_2(HFIP)(H_2O)(THF)_{0.5}$ (**1**) according to elemental analysis. Compound **1** is insoluble in non-polar media suggesting the formation of a polynuclear species, but soluble in THF and DME. However, these polar solvents favor redistribution reactions and formation of homoleptic species (Scheme 1). $BaI_2(DME)_3$ (**2**) crystallizes out as the first Ba species from DME solutions after elimination of sodium iodide due to its low solubility. Attempts to stabilize **1** by using other polyethers such as triglyme or tetraglyme in DME lead also to simple barium iodide adducts namely $BaI_2(DME)(triglyme)$ (**3**) and BaI_2-$(DME)(tetraglyme)$ (**4**). The elemental analysis and FT-IR spectra of the second barium compound isolated from all these media corresponds to that of $Ba_5(HFIP)_9(OH)(H_2O)(DME)_2$ (by comparison with the product of a 1:2 reaction of $BaI_2 \cdot 2H_2O$ with NaHFIP in DME and also with an authentic sample derived from $Ba_5(\mu_5\text{-}OH)$-$(\mu_3\text{-}HFIP)_4(\mu\text{-}HFIP)_4(HFIP)(THF)_4(H_2O) \cdot THF$ [8]). The use of non-polar solvents such as toluene was precluded by the insolubility of **1** even in the presence of an excess of glymes and by refluxing for several hours.



Scheme 1. Redistribution reactions of **1**.

N-donor ligands were also evaluated for stabilization of **1**. The reaction between $BaI_2 \cdot 2H_2O$ and $NaOCH(CF_3)_2$ (1:1 solution) in THF/DME in the presence of 1.5 equiv of *N*,*N*,*N*′,*N*″,*N*″-pentamethyldiethylenetriamine (PMDTA) afforded crystals of $BaI_2(DME)_3$ and of PMDTA adducts of sodium iodide $[Na_2(H_2O)_2(PMDTA)_2]I_2$ and Na_2I_2-$(PMDTA)_2$ [19]. These reactions indicate that BaI_2 adducts are more stable with O-donors, even only bidentate, than with even polydentate N-donors. **3** and **4** were also obtained, in better yields, directly from BaI_2.

The reaction between $BaI_2 \cdot 2H_2O$ (or BaI_2) and sodium trifluoroacetate (NaTFA) (1:1 stoichiometry) in THF afforded the heterometallic Na–Ba derivative **5**. Attempts to crystallize **5** from THF/toluene at room temperature gave $BaI_2 \cdot 2H_2O$ (43%). Attempts to stabilize **5** by excess tetraglyme resulted in crystallization of $[Ba(tetraglyme)_2]I_2 \cdot C_7H_8$ (**6**) (Eq. (1)):

$$BaI_2 \cdot 2H_2O + NaTFA \xrightarrow{THF,5\ h} \mathbf{5} \xrightarrow{1.5\ \text{equiv tetraglyme THF+toluene}} \underset{\mathbf{6},\ 47\%}{1/2\,[Ba(\text{tetraglyme})_2]\,I_2 \cdot C_7H_8} + 1/2m[Ba(TFA)_2]_m \quad (1)$$

Similar to lanthanide chemistry, formation of 'ate' complexes with alkali metals are not unusual for alkaline earth metal compounds and numerous examples of alkali-alkaline earth metal 'ate' complexes such as $LiBa(\eta^5\text{-}C_5Me_5)_2$-$[CH(SiMe_3)_2](THF)_2$, $LiBa(\eta^5\text{-}C_5Me_5)_2[N(SiMe_3)_2](THF)_2$, [20], $LiM(OSO_2R)_2[CH(SiMe_3)_2](THF)$ (M = Ca, Sr, Ba; R = C_6H_4Me-4, $C_6H_2Me_3$-2,4,6 and $C_6H_4Bu^t$-4) and $KM[CH(SiMe_3)_2]_3(THF)_3$ (M = Ca, Sr, Ba) [21] are known. The reactions between $BaI_2 \cdot 2H_2O$ and NaHFIP or NaTFA here are particularly reminiscent of that between $Ba(\eta^5\text{-}C_5Me_5)_2(THF)_2$ and $LiCH(SiMe_3)_2$ in which the formed $LiBa(\eta^5\text{-}C_5Me_5)_2[CH(SiMe_3)_2](THF)_2$, insoluble in toluene, regenerates the metallocene and alkyl anion in THF [20]. It can, however, be noted that the only other known heteroleptic alkali metal-barium iodide cluster, $Li_4BaI(\mu_4\text{-}OH)(\mu_3\text{-}OBu^t)_4(THF)_4$ [12], is stable in solution because of its hydroxo-bridged pentanuclear structure and stabilizing effect of bulky *tert*-butoxide groups.

3.1. Spectroscopic characterization

The FT-IR spectrum of **1** exhibits strong absorptions at 1278, 1239, 1215 and 1174 cm^{-1} for ν(C–F) and ν(C–O), vibrations respectively. The νBa–O frequency appears as a medium intensity band at 519 cm^{-1}. The heterometallic TFA derivative $NaBaI_2(TFA)(THF)(H_2O)_{0.5}$ (**5**) shows absorptions due to ν(O–H), ν_{as}(C=O) and ν(C–F) at 3432, 1656 and 1206–1083 cm^{-1}, respectively. Three characteristic strong absorptions for the TFA ligands are also found at 850, 800 and 728 cm^{-1}. The presence of DME, triglyme or tetraglyme is confirmed by their characteristic absorptions bands in the IR spectra of **2**, **3**, **4** and **6**. The solubility of **1** in $CDCl_3$ allowed characterization by ^1H NMR. Its spectrum displays a broad peak at 4.58 ppm for the CH proton of $OCH(CF_3)_2$ and multiplets at 3.72 and 1.86 ppm for the THF ligands. ^1H NMR spectra of the adducts $BaI_2(DME)_3$ (**2**), *trans*-BaI_2(DME)(triglyme) (**3**), *cis*-BaI_2(DME)(tetraglyme) (**4**) and $[Ba(tetraglyme)_2]$-$I_2 \cdot C_7H_8$ (**6**) are in agreement with those of coordinated polyethers. For example, two singlets in a 3:2 ratio are observed for **2** at 3.41 and 3.56 ppm for the Me and OCH_2– groups of DME, respectively.

Although structural prediction of **1** and **5** on the basis of elemental analysis and limited spectroscopic data would be highly speculative, the structures of these two compounds may well be related to either solvated ion-pairs, Na^+-$[BaI_2(X)]^-$ (X = $(CF_3)_2CHO^-$, $CF_3CO_2^-$), or bridged bimetallic compounds, as reported for $[Yb\{N(SiMe_3)_2\}$-$\{\mu\text{-}N(SiMe_3)_2\}_2Na]$ [22]. The secondary Ba–F bonds are likely to complete the coordination sphere of barium as observed for other barium compounds with fluorinated ligands [8,23].

3.2. X-ray structures of trans-BaI_2(DME)(triglyme) (3), cis-BaI_2(DME)(tetraglyme) (4) and $[Ba(tetraglyme)_2]I_2 \cdot C_7H_8$ (6)

All Ba iodide adducts with bidentate and/or polydendate glymes are monomeric. Selected bond lengths and angles are collected in Tables 2–4. The eight-coordinate Ba atom in *trans*-BaI_2(triglyme)(DME) (**3**) (Fig. 1) has a distorted hexagonal bipyramidal geometry. The six oxygens of the DME and triglyme ligands form a distorted hexagonal plane with the DME ligand being slightly tilted with respect to the equatorial plane. The angle between the DME and triglyme molecular planes is 39.6(2)°. The two iodide are in *trans* positions, the value of the I(1)–Ba–I(2) angle being 164.4(1)°. The Ba–I(1) and Ba–I(2) bond distances, 3.434(1) and 3.449(1) Å, respectively, are longer than those in other covalent monomeric barium iodide adducts such as $BaI_2(THF)_5$ (3.379 Å av.) for instance

Table 2
Selected bond lengths (Å) and angles (°) in BaI_2(DME)(triglyme) (**3**)

Bond lengths			
Ba(1)–I(1)	3.434(1)	Ba(1)–O(3)	2.832(6)
Ba(1)–I(2)	3.449(1)	Ba(1)–O(4)	2.772(6)
Ba(1)–O(1)	2.820(6)	Ba(1)–O(5)	2.807(5)
Ba(1)–O(2)	2.786(6)	Ba(1)–O(6)	2.793(6)
Bond angles			
I(1)–Ba(1)–I(2)	164.4(1)	O(1)–Ba(1)–O(3)	118.9(2)
I(1)–Ba(1)–O(1)	88.5(1)	O(1)–Ba(1)–O(4)	169.7(2)
I(1)–Ba(1)–O(2)	85.9(1)	O(1)–Ba(1)–O(5)	122.3(2)
I(1)–Ba(1)–O(3)	83.7(1)	O(1)–Ba(1)–O(6)	75.5(2)
I(1)–Ba(1)–O(4)	81.4(1)	O(2)–Ba(1)–O(3)	59.4(2)
I(1)–Ba(1)–O(5)	116.9(1)	O(2)–Ba(1)–O(4)	117.0(2)
I(1)–Ba(1)–O(6)	83.3(1)	O(2)–Ba(1)–O(5)	156.6(2)
I(2)–Ba(1)–O(1)	77.9(1)	O(2)–Ba(1)–O(6)	134.0(2)
I(2)–Ba(1)–O(2)	80.7(1)	O(3)–Ba(1)–O(4)	58.1(2)
I(2)–Ba(1)–O(3)	96.1(1)	O(3)–Ba(1)–O(5)	115.0(2)
I(2)–Ba(1)–O(4)	111.8(1)	O(3)–Ba(1)–O(6)	160.3(2)
I(2)–Ba(1)–O(5)	77.4(1)	O(4)–Ba(1)–O(5)	65.0(2)
I(2)–Ba(1)–O(6)	100.4(1)	O(4)–Ba(1)–O(6)	105.3(2)
O(1)–Ba(1)–O(2)	59.6(2)	O(5)–Ba(1)–O(6)	59.1(2)

Table 3
Selected bond lengths (Å) and angles (°) in BaI_2(DME)(tetraglyme) (**4**)

Bond lengths			
Ba(1)–I(1)	3.538(6)	Ba(1)–O(4)	2.858(5)
Ba(1)–I(2)	3.534(6)	Ba(1)–O(5)	2.831(4)
Ba(1)–O(1)	2.881(5)	Ba(1)–O(6)	2.793(4)
Ba(1)–O(2)	2.858(4)	Ba(1)–O(7)	2.846(4)
Ba(1)–O(3)	2.848(4)		
Bond angles			
I(1)–Ba(1)–I(2)	118.22(5)	O(1)–Ba(1)–O(5)	80.5(1)
I(1)–Ba(1)–O(1)	74.60(9)	O(1)–Ba(1)–O(6)	137.2(1)
I(1)–Ba(1)–O(2)	78.92(9)	O(1)–Ba(1)–O(7)	119.6(1)
I(1)–Ba(1)–O(3)	93.87(9)	O(2)–Ba(1)–O(3)	57.6(1)
I(1)–Ba(1)–O(4)	78.75(9)	O(2)–Ba(1)–O(4)	108.8(1)
I(1)–Ba(1)–O(5)	147.74(9)	O(2)–Ba(1)–O(5)	70.6(1)
I(1)–Ba(1)–O(6)	148.19(9)	O(2)–Ba(1)–O(6)	113.8(1)
I(1)–Ba(1)–O(7)	74.43(9)	O(2)–Ba(1)–O(7)	152.4(1)
I(2)–Ba(1)–O(1)	78.09(9)	O(3)–Ba(1)–O(4)	57.8(1)
I(2)–Ba(1)–O(2)	127.54(9)	O(3)–Ba(1)–O(5)	78.8(1)
I(2)–Ba(1)–O(3)	147.81(9)	O(3)–Ba(1)–O(6)	72.2(1)
I(2)–Ba(1)–O(4)	122.68(9)	O(3)–Ba(1)–O(7)	116.8(1)
I(2)–Ba(1)–O(5)	75.13(9)	O(4)–Ba(1)–O(5)	120.6(1)
I(2)–Ba(1)–O(6)	78.38(9)	O(4)–Ba(1)–O(6)	69.6(1)
I(2)–Ba(1)–O(7)	73.07(9)	O(4)–Ba(1)–O(7)	59.0(1)
O(1)–Ba(1)–O(2)	58.2(1)	O(5)–Ba(1)–O(6)	59.1(1)
O(1)–Ba(1)–O(3)	115.8(1)	O(5)–Ba(1)–O(7)	136.9(1)
O(1)–Ba(1)–O(4)	152.1(1)	O(6)–Ba(1)–O(7)	86.4(1)

Table 4
Selected bond lengths (Å) and angles (°) in $[Ba(tetraglyme)_2]I_2 \cdot C_7H_8$ (**6**)

Bond lengths			
Ba(1)–O(1)	2.851(9)	Ba(1)–O(6)	2.851(9)
Ba(1)–O(2)	2.830(8)	Ba(1)–O(7)	2.833(1)
Ba(1)–O(3)	2.842(9)	Ba(1)–O(8)	2.855(9)
Ba(1)–O(4)	2.801(1)	Ba(1)–O(9)	2.866(1)
Ba(1)–O(5)	2.842(9)	Ba(1)–O(10)	2.796(8)
Bond angles			
O(1)–Ba(1)–O(2)	57.5(2)	O(3)–Ba(1)–O(10)	74.6(3)
O(1)–Ba(1)–O(3)	113.3(2)	O(4)–Ba(1)–O(5)	58.4(3)
O(1)–Ba(1)–O(4)	158.0(3)	O(4)–Ba(1)–O(6)	79.9(3)
O(1)–Ba(1)–O(5)	139.9(3)	O(4)–Ba(1)–O(7)	68.3(4)
O(1)–Ba(1)–O(6)	78.1(3)	O(4)–Ba(1)–O(8)	112.2(3)
O(1)–Ba(1)–O(7)	100.2(3)	O(4)–Ba(1)–O(9)	127.7(3)
O(1)–Ba(1)–O(8)	73.6(2)	O(4)–Ba(1)–O(10)	98.6(3)
O(1)–Ba(1)–O(9)	73.9(3)	O(5)–Ba(1)–O(6)	128.9(3)
O(1)–Ba(1)–O(10)	97.7(3)	O(5)–Ba(1)–O(7)	78.1(3)
O(2)–Ba(1)–O(3)	57.4(2)	O(5)–Ba(1)–O(8)	71.7(3)
O(2)–Ba(1)–O(4)	114.6(3)	O(5)–Ba(1)–O(9)	71.1(3)
O(2)–Ba(1)–O(5)	149.0(3)	O(5)–Ba(1)–O(10)	79.4(3)
O(2)–Ba(1)–O(6)	72.3(3)	O(6)–Ba(1)–O(7)	58.7(3)
O(2)–Ba(1)–O(7)	130.0(3)	O(6)–Ba(1)–O(8)	102.9(3)
O(2)–Ba(1)–O(8)	131.0(2)	O(6)–Ba(1)–O(9)	149.7(3)
O(2)–Ba(1)–O(9)	101.4(3)	O(6)–Ba(1)–O(10)	139.5(3)
O(2)–Ba(1)–O(10)	71.8(3)	O(7)–Ba(1)–O(8)	58.5(3)
O(3)–Ba(1)–O(4)	57.7(3)	O(7)–Ba(1)–O(9)	115.2(3)
O(3)–Ba(1)–O(5)	104.4(3)	O(7)–Ba(1)–O(10)	157.4(3)
O(3)–Ba(1)–O(6)	70.6(3)	O(8)–Ba(1)–O(9)	58.1(2)
O(3)–Ba(1)–O(7)	110.2(3)	O(8)–Ba(1)–O(10)	114.6(3)
O(3)–Ba(1)–O(8)	168.3(2)	O(9)–Ba(1)–O(10)	57.4(2)
O(3)–Ba(1)–O(9)	131.9(2)		

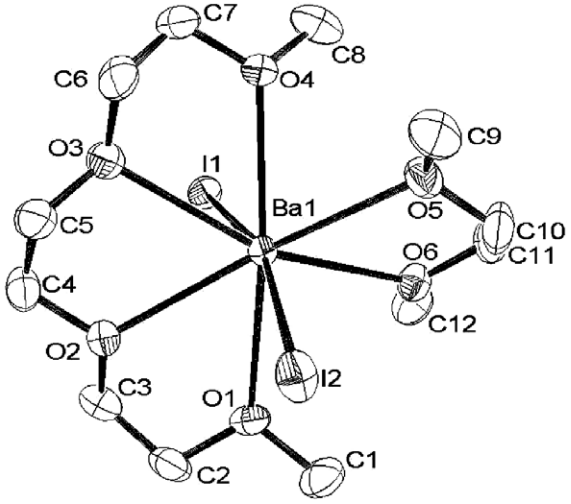


Fig. 1. Molecular structure of *trans*-BaI_2(DME)(triglyme) (**3**) (thermal ellipsoids at 50% probability). H atoms have been omitted for clarity.

[24] due to the higher coordination number of barium (eight in **3** vs. seven in $BaI_2(THF)_5$). They are the shortest among the structures reported here. The structure of **3** can be related to the recently reported samarium(II) compound *trans*-SmI_2(triglyme)(DME), which crystallises as two independent molecules (enantiomers) per asymmetric unit [25].

Assignment of the chiral space group $P2_1$ for **3** was unequivocal. The chirality in **3** stems from the presence of DME and triglyme ligands, which form odd numbers of five-membered rings upon coordination to the barium atom, the three rings of triglyme exhibiting alternate patterns of δ and λ chiral conformations. Another element of chirality in **3** is the orientation of the terminal methyl groups in the triglyme ligand; one methyl group is located below the triglyme plane while the other one is situated above it. However, a value of 0.57(4) for the Flack parameter suggests that there is substantial racemic twinning with

micro-domains of each enantiomer present in the same crystal.

Replacement of triglyme with tetraglyme gives a nine-coordinate barium atom in *cis*-BaI_2(tetraglyme)(DME) (**4**) (Fig. 2). As expected, the more bulky ligand causes DME and tetraglyme molecular planes to be inclined by 73.99(9)°. In contrast to **3**, the iodide ligands are in *cis* positions with a I–Ba–I angle of 118.22(5)°. The Ba–I bond distances [3.538(6) and 3.534(6) Å] are on average 0.095 Å longer than those in **3**, due to the higher coordination number as well as to the repulsion between the iodides in *cis*-positions [26]. The Ba–O(DME) bond lengths (2.81 Å av.) are shorter than the Ba–O(tetraglyme) ones (2.84 Å av.). It is quite surprising that both iodides occupy *cis* positions. In general, molecular alkaline earth metal halide complexes with coordination numbers equal or larger than six, preferentially exhibit a *trans* orientation of halide ligands [27,28]. Compound **4**, with SrI_2(diglyme)$_2$ [26], is the only example of a molecular alkaline earth metal iodide where the iodides are *cis*. For further comparison, both *cis*-SmI_2(diglyme)$_2$ and *trans*-SmI_2(diglyme)$_2$ have actually been isolated from the same solution [29]. It is worth mentioning that in the gas phase, BaI_2 is bent with an angle between 102° and 105° [30].

In contrast to **3** and **4** which are covalent, compound **6** is ionic with two iodide anions (Ba···I distance of 6.40 Å av.) and a $[Ba(tetraglyme)_2]^{2+}$ cation whose structure is shown in Fig. 3. The barium ion is coordinated by ten oxygen atoms of two tetraglyme ligands, the five oxygen atoms of each tetraglyme ligands lying approximately in a plane. The planes of the two tetraglymes are inclined to each other by 86.32(6)°. The Ba–O(tetraglyme) bond lengths (2.87 Å av.) in **6** are longer than the Ba–O(tetraglyme) ones (2.84 Å av.) in **4** due to the higher coordination number and the ionic character [27]. A similar helical wrapping of metals by tetraglyme has been reported for $[Sm(tetraglyme)_2]^{2+}$ [25] and $[Cs(tetraglyme)_2]^{+}$ [31]. Compound **6** is the first example of discrete ionic species of the heavier alkaline earth metal halide adducts with polyethers.

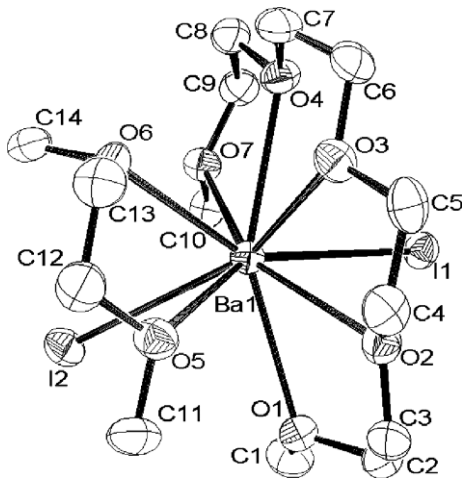


Fig. 2. Molecular structure of *cis*-BaI_2(DME)(tetraglyme) (**4**) (thermal ellipsoids at 50% probability). H atoms have been omitted for clarity.

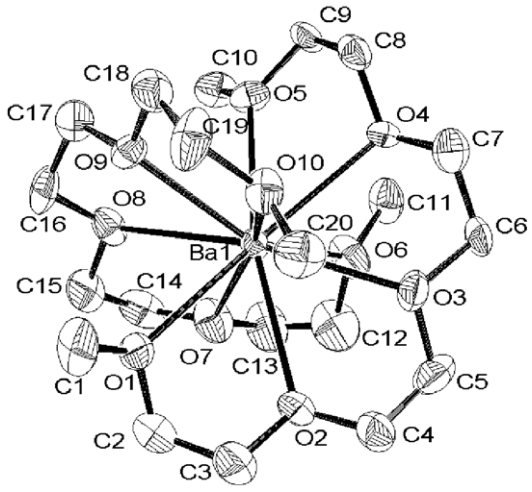


Fig. 3. Molecular structure of $[Ba(tetraglyme)_2]^{2+}$ of **6** (thermal ellipsoids at 50% probability). H atoms have been omitted for clarity.

The same heteroleptic Na–Ba species **1** and **5** were obtained using either $BaI_2 \cdot 2H_2O$ or BaI_2 as starting material, although the hydrate was more reactive. The presence of water ligands in the formula of **1** and **5** might be favored by the high Lewis acidity generated by the fluorinated ligands but does not preclude the presence of water ligands. The new barium iodide adducts **2**, **3**, **4** and **6** derived from **1** and **5** with bidentate and/or polydentate ethers, either covalent or ionic, are monomeric, mainly because of the absence of water in their coordination sphere. Indeed, it has been shown by Fromm et al. [32,33] that the number of water molecules in the coordination sphere of alkaline earth metal iodides directs their dimensionality by H-bonding, iodides acting as acceptors. BaI_2(triglyme)$_2$(H_2O), $[M(diglyme)_2(H_2O)_x]I_2$, ($M = Ca$, $x = 2$; $M = Ba$, $x = 3$) and $[Ca(triglyme)(H_2O)_4]I_2$, obtained from MI_2 and glymes containing 1% water, are thus 0D-, 1D-, 2D- and 3D-polymers, respectively [32,33].

4. Conclusions

Our attempts to isolate heteroleptic barium iodide derivatives with hexafluoroisopropoxide or trifluoroacetate ligands resulted into redistribution reactions where the use of DME and/or other polyethers such as triglyme or tetraglyme led to crystallization of simple barium iodide adducts with polyethers. Heteroleptic barium derivatives with sterically less demanding ligands have been shown to rearrange into their homoleptic counterparts via a Schlenk-type equilibrium [9,10]. Crystallization of barium iodide adducts with bidentate and/or polydentate ethers as either covalent or ionic compounds depends on the nature of the solvent(s). The use of DME as a solvent affords molecular adducts since the DME ligand allows the coordination number of the metal in the mixed-ligand adducts **3** and **4**

to be tuned. The absence of DME in the reaction medium and/or a large excess of tetraglyme favors the formation of the ionic species **6** in comparison to **4**.

Acknowledgements

We thank the region Rhone-Alpes for financial support and a fellowship to S.M. (Superflex). The help of Dr. D. Watkin (Chem. Dept., Oxford Univ., UK) in refinement of structure **6** is also gratefully acknowledged.

Appendix A. Supplementary material

CCDC 297973, 297974 and 298618 contains the supplementary crystallographic data (tables of coordinates, of thermal parameters, of bond lengths and angles) for **3**, **4** and **6**, respectively. These data can be obtained free of charge via http://www.ccdc.cam.ac.uk/conts/retrieving.html, or from the Cambridge Crystallographic Data Centre, 12 Union Road, Cambridge CB2 1EZ, UK; fax: (+44) 1223-336-033; or e-mail: deposit@ccdc.cam.ac.uk. Supplementary data associated with this article can be found, in the online version, at doi:10.1016/j.poly.2006.08.007.

References

[1] T. Araki, I. Hirabayashi, Supercond. Sci. Technol. 16 (2003) R71.
[2] (a) S. Sathyamurthy, K. Salama, J. Supercond. 11 (1998) 545;
(b) T. Araki, I. Hirabayashi, T. Niwa, Supercond. Sci. Technol. 17 (2004) 135.
[3] V.F. Solovoy, H.J. Wiesmann, L.J. Wu, Y.M. Zhu, M. Suenaga, Appl. Phys. Lett. 76 (2000) 1911.
[4] (a) R.H. Baney, D.F. Bergstrom, B.H. Justice, Chem. Mater. 4 (1992) 984;
(b) I. Matsubara, M. Paranthaman, A. Singhal, C. Vallet, D.F. Lee, P.M. Martin, R.D. Hunt, R. Feenstra, C.Y. Yang, S.E. Babcock, Physica C 319 (1999) 127.
[5] E.B. Brackett, T.E. Brackett, R.L. Sass, J. Phys. Chem. 67 (1963) 2132.
[6] (a) W.A. Wojtczak, P. Atanassova, M.J. Hampden-Smith, E. Duesler, Inorg. Chem. 35 (1996) 6995;
(b) W.A. Wojtczak, M.J. Hampden-Smith, E.N. Duesler, Inorg. Chem. 37 (1998) 1781;
(c) J. Zhang, L.G. Hubert-Pfalzgraf, D. Luneau, Polyhedron 24 (2005) 1185.
[7] K.M. Fromm, G. Bernardinelli, Z. Anorg. Allg. Chem. 627 (2001) 1626.
[8] H. Vincent, F. Labrize, L.G. Hubert-Pfalzgraf, Polyhedron 13 (1994) 3323.
[9] M.J. Harvey, T.P. Hanusa, Organometallics 19 (2000) 1556.
[10] (a) T.P. Hanusa, Organometallics 21 (2002) 2529;
(b) A.G. Avent, M.R. Crimmin, M.S. Hill, P.B. Hitchcock, J. Chem. Soc., Dalton Trans. (2005) 278.
[11] K.F. Tesh, D.J. Burkey, T.P. Hanusa, J. Am. Chem. Soc. 116 (1994) 2409.
[12] K.M. Fromm, E.D. Gueneau, H. Goesmann, Chem. Commun. (2000) 2187.
[13] H.M. El-Kaderi, M.J. Heege, C.H. Winter, Polyhedron 25 (2006) 224.
[14] Nonius, COLLECT. Nonius BV, Delft, The Netherlands, 1997–2001.
[15] Z. Otwinowski, W. Minor, in: C.W. CarterJr., R.M. Sweet (Eds.), Methods in Enzymology, vol. 276, Academic Press, New York, 1997, p. 307.
[16] N. Walker, D. Stuart, Acta Cryst. A 39 (1983) 158.
[17] A. Altomare, G. Cascarano, G. Giacovazzo, A. Guagliardi, M.C. Burla, G. Polidori, M. Camalli, J. Appl. Cryst. 27 (1994) 435.
[18] D.J. Watkin, C.K. Prout, L.J. Pearce, CAMERON, Chemical Crystallography Laboratory, Oxford, UK, 1996.
[19] E. Jeanneau, S. Mishra, L.G. Hubert-Pfalzgraf, Acta Cryst. E 61 (2005) 1528.
[20] S.C. Sockwell, T.P. Hanusa, J.C. Huffman, J. Am. Chem. Soc. 114 (1992) 3393.
[21] A.D. Frankland, M.F. Lappert, J. Chem. Soc., Dalton Trans. (1996) 4151.
[22] T.D. Tilley, R.A. Andersen, A. Zalkin, Inorg. Chem. 23 (1984) 2271.
[23] (a) A.P. Purdy, C.F. George, Inorg. Chem. 30 (1991) 1969;
(b) F. Labrize, L.G. Hubert-Pfalzgraf, J.-C. Daran, S. Halut, Polyhedron 15 (1996) 2707;
(c) J. Zhang, S. Mishra, L.G. Hubert-Pfalzgraf, D. Luneau, E. Jeanneau, unpublished results.
[24] K.M. Fromm, Angew. Chem., Int. Ed. 36 (1997) 2799.
[25] M. Vestergren, B. Gustafsson, A. Johansson, M. Hakansson, J. Organomet. Chem. 689 (2004) 1723.
[26] K.M. Fromm, W. Maudez, Eur. J. Inorg. Chem. (2003) 3440.
[27] K.M. Fromm, Cryst. Eng. Commun. 4 (2002) 318.
[28] K.M. Fromm, E.D. Gueneau, G. Bernardinelli, H. Goesmann, J. Weber, M.J. Mayor-Lopez, P. Boulet, H. Chermette, J. Am. Chem. Soc. 125 (2003) 3593.
[29] A. Sen, V. Chebolu, A.L. Rheingold, Inorg. Chem. 26 (1987) 1821.
[30] R.J. Gillespie, E.A. Robinson, Angew. Chem., Int. Ed. 35 (1996) 477.
[31] C. Nather, H. Bock, Z. Havlas, T. Hauck, Organometallics 17 (1998) 4707.
[32] K.M. Fromm, H. Goesmann, G. Bernardinelli, Polyhedron 19 (2000) 1783.
[33] (a) K.M. Fromm, Chem. Eur. J. 7 (2001) 2236;
(b) K.M. Fromm, E.D. Gueneau, A.Y. Robin, W. Maudez, J. Sague, R. Bergougnant, Z. Anorg. Allg. Chem. 631 (2005) 1725.

Available online at www.sciencedirect.com
ScienceDirect
Polyhedron 26 (2007) 73–84
POLYHEDRON
www.elsevier.com/locate/poly

Synthesis, characterization, and electrochemical, electrical and gas sensing properties of a novel *tert*-butylcalix[4]arene bridged bis double-decker lutetium(III) phthalocyanine

Tanju Ceyhan [a], Ahmet Altındal [b], Ali Rıza Özkaya [c], Mehmet K. Erbil [a], Özer Bekaroğlu [c,*]

[a] *Department of Biochemistry, Division of Organic Chemistry, Gülhane Medical Academy (GATA), Ankara, Turkey*
[b] *Department of Physics, Marmara University, 34722 Göztepe, Istanbul, Turkey*
[c] *Department of Chemistry, Marmara University, 34722 Göztepe, Istanbul, Turkey*

Received 23 May 2006; accepted 27 July 2006
Available online 12 August 2006

Abstract

A novel *tert*-butylcalix[4]arene bridged bis double-decker lutetium(III) phthalocyanine (Lu_2Pc_4) (**5**) has been synthesized by the reaction of dimeric lutetium(III) phthalocyanine (**4**) with two equiv. of dilithium octakis hexylthiophthalocyanine in amyl alcohol. The phthalonitrile derivative **1** was obtained through the displacement reaction of 4-nitrophthalonitrile with 1,3-dimethoxy-4-*tert*-butylcalix[4]arene and was converted to the isoindoline derivative **2** by bubbling ammonia gas in dry MeOH. Compound **4** was prepared from **2**, 4,5-bis(hexylthio)-1,2-diiminoisoindoline (**3**), and lutetium acetate in dry DMF. The new compounds and phthalocyanines were characterized by elemental analysis, IR, UV–Vis, ^{1}H NMR, ESR and MALDI-TOF MS spectra. The electrochemical properties of **4** and **5** have been examined by cyclic voltammetry, and compared. Distinctive differences between the voltammetric behaviour of **4** and **5** were detected. These differences were compatible with the structures of the compounds. A detailed study of the effect of temperature on the d.c. conductivity and impedance spectra (40–10^5 Hz) of spin coated films of **4** and **5** at temperatures between 290 K and 420 K was carried out. By analyzing the d.c. electrical behaviour of the **5** film, it was found that the experimental data are described by a thermally activated conductivity dependence on temperature with an activation energy of 0.77 eV. The a.c. results give a power law behaviour, $\sigma_{a.c.} = A(T)\omega^s$, in which the frequency exponent s decreases with temperature. The sensing behaviour of the film for the online detection of volatile organic solvent vapors was investigated by utilizing an AT-cut quartz crystal resonator. It was observed that the adsorption of the target molecules on the coating surface cause a reversible negative frequency shift of the resonator. Thus, a variety of solvent vapors can be detected by using the **5** film as sensitive coating, with sensitivity in the ppm and response times in the order of several seconds depending on the dipole moment of the organic solvent.
© 2006 Elsevier Ltd. All rights reserved.

Keywords: Phthalocyanine; Calix[4]arene; Double decker; Cyclic voltammetry; Gas sensing

1. Introduction

Phthalocyanines (Pcs) exhibit a number of unique properties that make them of great interest in different scientific and technological areas. Some technological applications of these macrocycles, such as electrophotography, photovoltaic and solar cells, semiconductive devices, rectifying devices, molecular electronics, electrochromic display devices, low-dimensional conductors, gas sensors, liquid crystals, non-linear optics, optical disks, photosensitizers in photodynamic cancer therapy and electrocatalytic agents, have been intensively investigated [1]. Among the classical Pcs, unsymmetrical ones are important for the development of new methods of synthesis. Although the synthesis of symmetrical tetra- or octa-substituted Pcs by cyclotetramerization of a suitable phthalonitrile as a single precursor can be accepted as a relatively straightforward method,

* Corresponding author. Tel.: +90 216 3590130; fax: +90 216 3860824.
E-mail address: obekaroglu@marmara.edu.tr (Ö. Bekaroğlu).

0277-5387/$ - see front matter © 2006 Elsevier Ltd. All rights reserved.
doi:10.1016/j.poly.2006.07.035

unsymmetrical Pcs containing different substituents on the benzo groups are difficult to obtain [2].

Our previous papers have described a series of symmetric and unsymmetric Pcs carrying various substituents. An essential shortcoming of the Pcs remains in their low solubility and spectroscopic measurement in organic solvents which hinders their application in solution. The introduction of different central metal ions or benzenoid rings turned out to be a powerful means of modifying the chemical and physical properties of Pcs [3,4]. Our group has been actively engaged in the synthesis of phthalocyanines with macrocyclic, acyclic or heterocyclic substituents, the immediate consequences of which are enhanced solubility and additional donor sites for alkali and/or transition metal ions [5–15]. Rare-earth diphthalocyanines, especially the lutetium derivatives, have become objects of intense investigations. The interest for this kind of compounds is actually increasing because of their electrochromic properties [16–29] and unusual conductivity [30–34]. Substituents on the periphery of a macrocycle ring like a Pc are known to affect its physicochemical properties. Many relationships between the chemical structure and properties like photoconductivity [35], electrocrystallization [36] and redox potentials [37] have been established. Chemical groups linked to the peripheral benzene rings not only modify the electronic properties of the phthalocyanines, but also those of the materials obtained from these molecular units [38,39]. The aim of the synthesis and study of substituted diphthalocyanines is the possibility to design molecules with two different phthalocyanine rings. These asymmetric dimeric compounds are interesting for different reasons. The delocalization of the electrons and the polarizability will be different from what is generally observed for the symmetrical diphthalocyanines, inducing perhaps unusual electrical or optical properties. The unsymmetrical derivatives, bearing hydrophilic and lipophilic groups, respectively, on each of the two units, are important for the preparation of oriented phases, using the Langmuir–Blodgett technique for example. Sandwich-type phthalocyaninato metal complexes, in which the large conjugated π systems are held in close proximity by metal ions, have found widespread applications in materials science [40]. The lutetium complex $LuPc_2$, for example, is an intrinsic molecular semiconductor with a conductivity of $5\times 10^{-5}\ \Omega^{-1}\ cm^{-1}$ in thin films [41] and shows promising electrochromic [42] and gas sensing properties [43]. As the bulk characteristics of a molecular material are largely related to the properties of individual molecules, various modifications have been made on these sandwich compounds with the goal of improving their performance as advanced materials [29–34].

There is an increasing demand for the detection of volatile organic solvents in the field of environmental analysis, industrial process control and work-place monitoring. A number of materials, e.g., Pc [44,45], PVC blended lipid membrane [46], ω functionalized alkanethiols [47], substituted azacyclophanes [48] and tetradentate dithioglyoximes [49] have been used as sensitive coatings for the recognition of organic solvent molecules. It is well established that a quartz crystal resonator (QCR) also known as a quartz crystal microbalance becomes a highly sensitive gas sensor when coated with the appropriate materials [50]. The application of the QCR in gas sensors is based on interactions between the surface of a quartz crystal coated with a thin layer of sensitive material and the target molecules. These interactions result in detectable changes in the fundamental resonant frequency (Δf) of the resonator. When a small mass (Δm) is deposited or sorbed into a coating layer on the surface of the QCR, it induces a decrease in the resonant frequency, which is a function of (Δm). According to Sauerbrey [51], the deposition of a homogeneous coating promotes a shift of the natural resonant frequency of the crystal, which, for assumed negligible mass increase and rigid layer behaviour, is described by the following linear relationship:

$$\Delta f = \frac{f_0}{A\rho_q h_q}\Delta m, \tag{1}$$

where f_0 is the fundamental resonant frequency of the quartz crystal, ρ_q is the density of the quartz crystal, h_q is thickness of the quartz and A is the surface area of the electrode.

We have previously synthesized a triazine carrying three phthalocyaninato zinc (II) macrocycles through amino groups [52] and a new type of sandwich dilutetium tetraphthalocyanine for the first time which exhibit variable range hopping conductivity as inorganic semiconductors and also have observed an electrochromic effect from cyclic voltammetry (CV) measurements [29].We have also reported on the synthesis and characterization of novel s-triazines bearing three oxygen-linked metallophthalocyanines and lutetium bisphthalocyanine sandwich complexes [53,54]. Synthesis, characterization, conduction and gas sensing properties of novel multinuclear metallophthalocyanines with alkylthio substituents were also reported in the literature [44].

In the present work, a novel *tert*-butylcalix[4]arene bridged bis double-decker lutetium(III) phthalocyanine (Lu_2Pc_4) (**5**) has been prepared by the reaction of compounds **3** and **4** in amyl alcohol in the presence of lithium metal at reflux temperature, and characterized. Also, the electrochemical properties of *tert*-butylcalix[4]arene bridged **4** and **5** in solution were investigated by cyclic voltammetry. In addition, the electrical (a.c. and d.c.) and gas sensing properties of **4** and **5** are discussed.

2. Experimental

2.1. Synthesis and characterization

All reagents and solvents obtained from commercial suppliers were of reagent-grade quality. The solvents were stored over molecular sieves (4 Å). 4-Nitrophthalonitrile [55] and 4,5-bis(hexylthio)-1,2-diimino-isoindoline (**3**) [56]

were prepared by the literature methods. Column chromatography was used for purification of the complexes.

Routine IR were recorded on a Mattison 1000 FTIR spectrometer using KBr pellets, electronic spectra were measured in $CHCl_3$ with a UNICAM UV 500 UV–Vis spectrometer. Elemental analysis was performed by the LECO CHNS 932 in the Instrumental Analysis Laboratory of TUBITAK Ankara Research Center. ^1H NMR spectra were recorded on a Bruker Avance DPX-400 spectrometer. The ESR spectra were carried out using a Varian E-L 9″ X-band ESR spectrometer operating at 9.5 GHz and equipped with a TE104 rectangular double cavity.

2.1.1. Preparation of 1,3-bis(3,4-dicyanophenoxy)-4-tert-butylcalix[4]arene (1)

1,3-Dimethoxy-4-*tert*-butylcalix[4]arene (1.9 g, 2.8 m mol) and 4-nitrophthalonitrile (0.972 g, 5.6 mmol) were added successively with stirring to dry DMSO (60 ml). After they were dissolved, anhydrous K_2CO_3 (1.16 g, 8.4 mmol) was added and the reaction mixture was stirred at 85 °C for 76 h. Reaction was monitored by TLC. Then, the reaction mixture was poured into 200 ml of cold water, acetic acid (2 ml) was added and it was stirred for 15 min. The precipitate was filtered off, flushed several times with cold water until the filtrate was neutral, and then dried in air at 70 °C. This compound was readily soluble in the majority of organic solvents such as ethanol, methanol, chloroform, THF, acetone, diethyl ether, DMF and DMSO. Yield: 2.26 g (87%), m.p. 165–168 °C; ^1H NMR ($CDCl_3$): δ, ppm 7.78–6.31 (m, 14H, arom.), 3.73–3.23 (m, 6H, OCH_3), 2.66 (s, 8H, Ar-CH_2), 1.63–1.12 (m, 36H, *t*-BuCH_3). IR (KBr): ν, cm^{-1} 3046, 2959–2869 (CH aliph.), 2822, 2357, 2323, 2229 (C≡N), 1734, 1596 (Ar C=C), 1476, 1359, 1290, 1245 (Ar–O–Ar), 1193, 1117, 1017, 949, 873, 834, 523. *Anal.* Calc. for $C_{62}H_{64}N_4O_4$ (928): C, 80.17; H, 6.89; N, 6.03. Found: C, 79.93; H, 6.68; N, 5.96%.

2.1.2. Preparation of 1,3-bis(3,4-tetra iminoisoindoline)-4-tert-butylcalix[4]arene (2)

To a solution of compound **1** (0.568 g, 0.612 mmol) in dry methanol (100 ml) under argon, sodium methoxide (0.017 g, 0.314 mmol) in dry methanol (5 ml) was added. Anhydrous ammonia was bubbled through the mixture for 6 h at reflux temperature, after which time the reaction was complete (TLC). The NH_3 inlet was stopped, the volume of the solution was reduced to 10 ml in vacuo and 40 ml of diethyl ether was added to the residue. After filtration, the filtrate was evaporated to dryness to give a pale yellow product. Yield: 0.551 g (93.5%). This product is soluble in diethyl ether, chloroform, acetone and DMF, m.p. 183–186 °C; ^1H NMR ($CDCl_3$): δ, ppm 7.27–6.20 (m, 14H, arom.), 3.64 (s, 6H, NH), 3.44–3.13 (m, 6H, OCH_3), 2.54 (s, 8H, Ar-CH_2), 1.58–1.23 (m, 36H, *t*-BuCH_3). IR (KBr): ν, cm^{-1} 3362 (NH), 3192 (NH), 3046 (CH arom.), 2958–2868 (CH aliph.), 2821, 2736, 2359, 1729, 1663 (NH bending), 1606 (Ar C=C), 1546, 1473, 1359, 1287, 1240 (Ar–O–Ar), 1199, 1117, 1019, 935, 872, 832, 793, 756, 713, 637, 522. *Anal.* Calc. for $C_{62}H_{70}N_6O_4$ (962): C, 77.33; H, 7.27; N, 8.73. Found: C, 76.94; H, 7.19; N, 8.35%.

2.1.3. Synthesis of 1,3-bis[2-oxa-9,10,16,17,23,24-hexa(hexylthio) phthalocyaninato lutetium(III) acetate]-4-tert-butylcalix[4]arene [$(LuOAc)_2(Pc)_2$] (4)

A mixture of compound **2** (0.162 g, 0.17 mmol), compound **3** (0.385 g, 1.02 mmol) and lutetium acetate (0.120 g, 0.34 mmol) was refluxed in dry DMF (2 ml) under argon for 24 h. The mixture was cooled, the dark green mixture was diluted with EtOH (20 ml) and the crude product precipitated. This was filtered off and washed several times with ethanol to remove unreacted organic materials. The precipitate was then heated at 80 °C with DMSO (3 × 15 ml) and at 60 °C with MeOH (3 × 15 ml) and filtered off. The dark green product was washed with acetone and EtOH and it was dried in vacuo. Then, the crude product was dissolved in ethyl acetate (40 ml), the solution was filtered and the filtrate was evaporated to a smaller volume (ca. 10 ml). Reprecipitation from the solution with ethanol, washing successively with water and with ethanol prior to drying in vacuo gave a dark green powder. Finally, pure **4** was obtained by chromatography with silica gel using $CHCl_3$ as eluent This compound is soluble in DCM, $CHCl_3$, CCl_4, THF, ethyl acetate, diethyl ether and DMF. Yield: 0.108 g, 18%, m.p. >300 °C. UV–Vis λ_{max} ($CHCl_3$, 14.99 μM) ($\log \varepsilon/dm^3\,mol^{-1}\,cm^{-1}$): 364 (5.187), 640 (4.713), 712 (5.262) nm. ^1H NMR ($CDCl_3$): δ, ppm 8.71–6.92 (m, 26H, arom.), 3.29–3.25 (t, 6H, OCH_3), 2.99 (d, 8H, Ar-CH_2), 2.59 (s, 6H, $COCH_3$), 1.99 (br s, 24H, SCH_2), 1.71–1.60 (t, 36H, *t*-BuCH_3), 1.27 (d, 96H, –CCH_2 C–), 0.84 (d, 36H, –CH_3). IR (KBr): ν, cm^{-1} 3046, 2919–2853 (CH aliph.), 2358, 2218, 1654 ($COCH_3$), 1585 (Ar C=C), 1540, 1508, 1453, 1401, 1283 (Ar–O–Ar), 1195, 1067, 1021, 939, 833, 755, 690, 540. *Anal.* Calc. for $C_{186}H_{238}N_{16}O_8S_{12}Lu_2$ (3556): C, 62.76; H, 6.69; N, 6.29; S, 10.79. Found: C, 62.27; H, 6.97; N, 5.94; S, 11.18%.

2.1.4. Synthesis of 1,3-bis[[2-oxa-9,10,16,17,23,24-hexa(hexylthio)][2,3,9,10,16,17,23,24-hexa(hexylthio)] phthalocyaninato lutetium(III)]-4-tert-butylcalix[4]arene [$Lu_2(Pc)_4$] (5)

Compound **3** (0.241 g, 0.64 mmol), 0.0082 g of lithium metal and dry amyl alcohol (3 ml) were stirred at 50 °C under an argon atmosphere until complete dissolution of Li. The mixture was then refluxed for 5 h more and to this reaction mixture compound **4** (0.114 g, 0.032 mmol) was added and refluxed for a further 24 h. Then, the reaction mixture was diluted with EtOH (15 ml), the precipitate was filtered off and washed with hot EtOH to remove unreacted organic materials. The dark green product was then heated at 80 °C with DMF (3 × 20 ml) and DMSO (3 × 20 ml) and filtered off, washed with EtOH, acetone and ethyl acetate, and it was dried. After that, the crude product was dissolved in $CHCl_3$ (40 ml) and the solution was filtered. After the filtrate had been evaporated to

dryness, the dark green residue was washed with EtOH, acetone and dried in vacuo. Pure **5** was isolated on a silica gel column with $CHCl_3$. This compound is soluble in DCM, $CHCl_3$ and diethyl ether but insoluble in ethyl acetate. Yield: 0.093 g, 46%, m.p. >300°C. UV–Vis λ_{max} ($CHCl_3$, 17.09 μM) ($\log \varepsilon/dm^3\,mol^{-1}\,cm^{-1}$): 328 (5.069), 360 (5.015), 430 (4.712), 636 (4.762), 669 (4.920), 702 (5.197), 732 (5.125) MS (MALDI-TOF): *m*/*z* 6319 $(M+H)^+$. ^1H NMR ($CDCl_3$): δ, ppm 8.37 (s, 42H, arom.), 3.35 (t, 6H, OCH_3), 3.05 (t, 8H, Ar-CH_2), 1.19–1.50 (t, 224H, –CCH_2C–), 1.99 (t, 56H, SCH_2), 1.7 (t, 36H, *t*-$BuCH_3$), 0.93 (t, 84H, –CH_3). IR (KBr): *v*, cm^{-1} 3046, 2920–2855 (CH aliph.), 2581, 2356, 1592 (Ar C=C), 1500, 1454, 1400, 1363, 1320, 1283 (Ar–O–Ar), 1111, 1070, 1017, 935, 865, 824, 745, 679, 537. *Anal*. Calc. for $C_{342}H_{456}N_{32}O_4S_{28}Lu_2$ (6318): C, 64.95; H, 7.21; N, 7.09; S, 14.18. Found: C, 65.21; H, 7.24; N, 7.64; S, 13.78%.

2.2. MALDI-TOF sample preparation

Supra molecular complex **5** was prepared at a concentration of 4 mg/ml in chloroform for MALDI-TOF MS analysis. 3,5-Dinitrobenzoic acid (DNB) was chosen as the best MALDI-TOF matrix and prepared in acetonitrile at a concentration of 20 mg/ml. MALDI-TOF samples were prepared by mixing the complex solution of **5** with the DNB matrix solution (1:10 v/v) in a 0.5 ml Eppendorf® microtube. Finally, 1 μL of these mixtures were deposited on the sample plate, dried at room temperature and then analyzed.

2.2.1. MALDI mass spectrometry

Mass spectra were acquired on a Voyager-DE™ PRO MALDI-TOF mass spectrometer (Applied Biosystems, USA) equipped with a nitrogen UV-Laser ($\lambda = 337$ nm) at 10^{-8} Torr using the delayed extraction mode (delay 375 ns) by changing the laser intensity, if necessary. The acceleration potential was 20 kV for the spectra recorded in the linear mode and all spectra were the average of 50 shots. Then, the data were transferred to a personal computer for further processing.

2.3. Electrochemical measurements

Tetrabutyammonium perchlorate (TBAP) (Electrochemical grade, Fluka Chemical Co.), as the supporting electrolyte, and triply distilled water and extra pure dichloromethane (DCM) (Fluka Chemical Co.) as the solvents were used in the voltammetric measurements. Electrochemical measurements were carried out with a Princeton Applied Research Model Versostat II potentiostat/galvanostat, controlled by an external PC, utilizing a three electrode configuration at 25 °C. A platinum spiral wire was used as the auxiliary electrode. The working electrode was platinum with an area of 0.12 cm^2 in the measurements in non-aqueous solution and an indium-tin oxide (ITO) conducting glass electrode (12 $\Omega\,cm^{-2}$) with an active area of 1.0 cm^2 in the measurements of cast film. The surface of the platinum working electrode was polished with an H_2O suspension of Al_2O_3 before each run. The last polishing was done with a particle size of 50 nm. The ferrocene/ferrocenium couple (Fc/Fc^+) was used as an internal standard, and potentials were also reported with respect to Fc/Fc^+. Solutions containing **4** and **5** were deoxygenated by a stream of high-purity nitrogen for at least 15 min prior to running the experiment, and the solution was protected from air by a blanket of nitrogen during the experiment. For the controlled-potential coulometry (CPC) studies, a platinum gauze working electrode, a platinum wire counter electrode separated with a bridge, a SCE as the reference electrode and a model 377/12 synchronous stirrer were used.

2.4. Electrical and gas sensing measurements

2.4.1. D.c conductivity and impedance spectra

The temperature dependence of the d.c. conductivity and impedance spectra of the films were measured by using an interdigital transducer structure with gold electrodes which consist of 10 finger pairs of electrodes having a width of 100 μm, spaced 100 μm from the adjacent electrode. A thin film of the compounds was obtained by spin-coating chloroform solutions of the compounds over the electrode arrays. For the spin coating of **4** and **5**, the compounds were dissolved in $CHCl_3$ at concentrations of $\sim 1 \times 10^{-3}$ M for both compounds. Fifteen microlitres of such solutions were added with a glass pipette onto the IDT structure held onto the spinner (Speciality Coatings Systems Inc., Model P6700 Series). The substrate spun at 2000 rpm for 10 s and then the films were dried under vacuum. The temperature of the samples was controlled with a Leybold LTC 60 temperature controller during the measurements. The measurement procedure for the temperature dependent d.c. conductivity and impedance spectra was described in [45].

2.4.2. Gas sensing measurements

Due to the best temperature coefficient in combination with the highest mass sensitivity, AT-cut quartz crystals vibrating in the thickness shear mode with a fundamental resonant frequency of 10 MHz with Au electrodes were used in the gas sensing measurements. The sensitive layer was generated on one side of the quartz crystals by the spin coating technique. Typical thicknesses ranged from 100 to 300 nm. The sensors were placed in a homemade teflon chamber with a volume of approximately 20 cm^3. A dry nitrogen flow of 100 ml min^{-1} was passed through the test chamber until stabilization. A volume of 25 ml of the organic solvent was deposited in a 150 ml flask. The solvents selected for this study were ethanol, acetone, chloroform and carbon tetrachloride. Then, an appropriate flow of dry nitrogen was passed for 5 min through the solvent and then conducted to the measurement chamber. The test gases were mixed with dry nitrogen (N_2) using computer

driven mass flow controllers (Heastings 200/202 series). The carrier gas (dry nitrogen) used in the experiments had a purity level of 99%. The vapour effect on the fundamental resonant frequency of **4** and **5** coated QCR was monitored sequentially by using a Keithley 776 programmable frequency counter. A typical experiment consisted of exposure to VOC vapors and subsequent purging with dry nitrogen. The shifts in resonant frequency of the QCR were recorded using an IEEE 488 data acquisition system incorporated to a personal computer. The results obtained under these conditions were reproducible with an uncertainty less than 2%.

3. Results and discussion

3.1. Synthesis and characterization

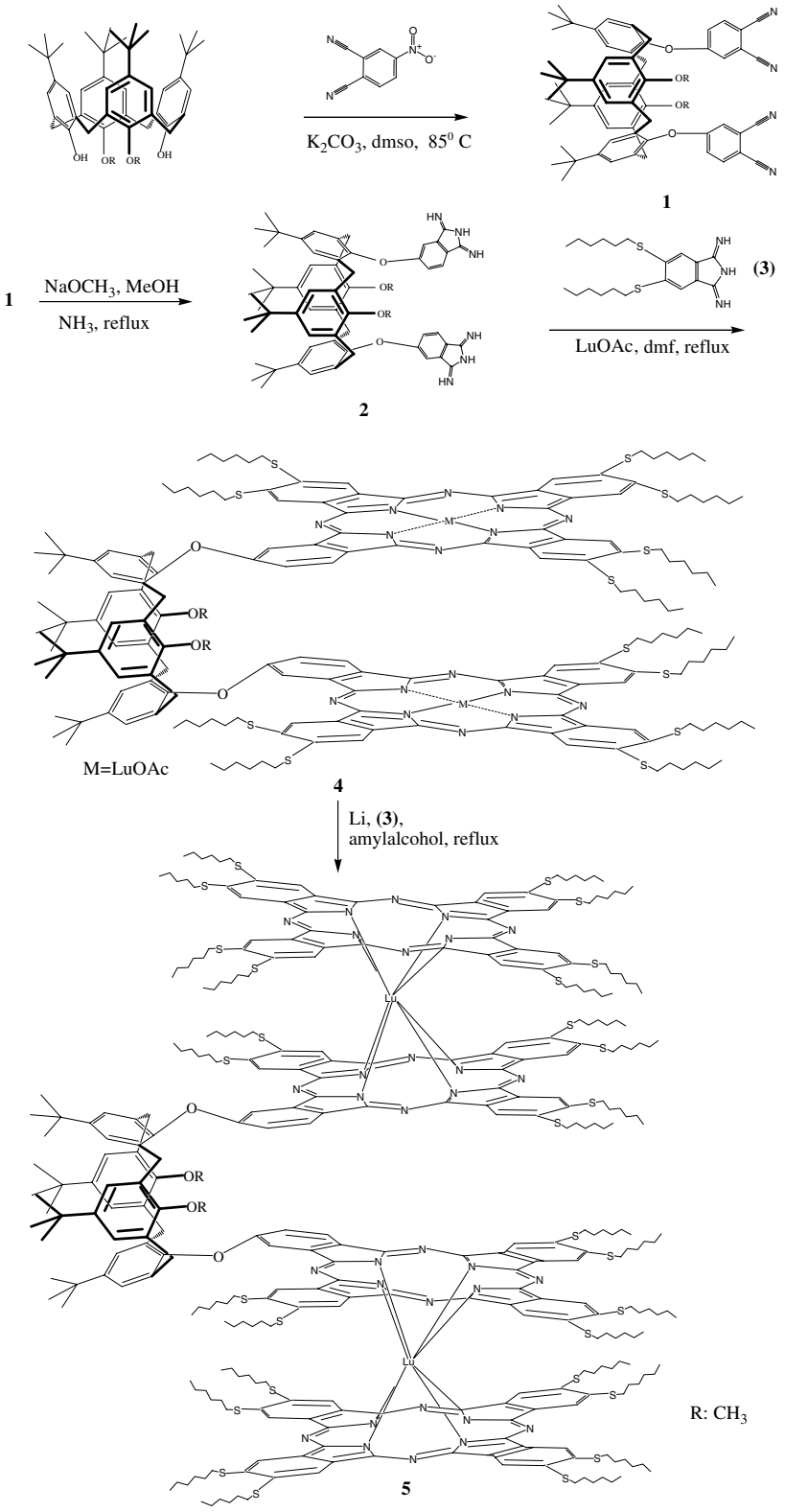
As a first step, compound **1** was prepared by the reaction with 1,3-dimethoxy-4-*tert*-butylcalix[4]arene and 4-nitrophthalonitrile in dry DMSO in the presence of K_2CO_3 as the base. The reaction sequence was followed clearly by TLC. Compound **1** was converted to isoindoline derivative **2** by bubbling ammonia gas in dry MeOH in the presence of $NaOCH_3$ at reflux temperature in high yield followed by the reaction with six equiv. of 4,5-bis(hexylthio)-1,2-diiminoisoindoline (**3**) and lutetium acetate in refluxing DMF for 24 h to give dimeric dilutetium phthalocyanine (**4**) in 18% yield, without forming a sandwich-type complex [57]. The synthesis of bis double-decker lutetium(III) phthalocyanine (Lu_2Pc_4), namely compound **5**, was the most important step in these reaction sequences as shown in Scheme 1. It was achieved in situ by the reaction of dimeric dilutetium phthalocyanine (**4**) with two equiv. of symmetrical dilithium octakishexylthio phthalocyanine, which was prepared by **3** in amyl alcohol in the presence of lithium metal at reflux temperature.

All the new compounds were obtained sufficiently pure and gave satisfactory analytical results. Characterization of the products involved a combination of methods including elemental analysis, IR, ^{1}H NMR, UV–Vis, MALDI-TOF MS and ESR spectroscopy. The IR spectra taken with KBr pellets showed an aromatic C=C peak at around 1606–1585 cm^{-1}, an aromatic –CH peak at 3046 cm^{-1} and a Ar–O–Ar peak at around 1283–1240 cm^{-1} for all of the compounds. In addition, the comparison of the IR spectrum of **1** to that of **2** confirmed the proposed structure by the disappearance of the C≡N band at 2229 cm^{-1} for compound **1** and the appearance of a new absorptions at 3362 and 3192 cm^{-1} attributable to NH groups in compound **2**. The stretching peaks at around 2959–2853 cm^{-1} and the bending peaks at around 1476–1320 cm^{-1} confirmed the presence of –CH and $–CH_3$ groups, respectively, for all of the compounds. The additional peak at 1654 cm^{-1} in the IR spectrum of compound **4** indicated the presence of a $–COCH_3$ group that disappeared in the case of the compound **5**.

In the ^{1}H NMR analysis of compound **1** and **2** in d-chloroform, the aromatic protons appeared as multiplets at 7.78–6.31 and 7.27–6.20 ppm, respectively. In the spectra of **1**, the $–OCH_3$ protons appeared at 3.73–3.23 ppm, $–CH_2$ protons at 2.66 ppm and *t*-BuCH_3 protons at 1.63–1.12 ppm. The ^{1}H NMR spectrum of **2** was similar to that of compound **1**. The $–OCH_3$ protons appeared at 3.44–3.13 ppm, $–CH_2$ protons at 2.54 ppm and *t*-BuCH_3 protons at 1.58–1.23 ppm. The only difference is the signal at 3.64 ppm, corresponding to the –NH group, as expected for compound **2** which disappeared on D_2O exchange. When the ^{1}H NMR spectra of **4** and **5** in d-chloroform was investigated, aromatic protons appeared as multiplets at 8.71–6.92 and as a singlet at 8.37 ppm, respectively. In the ^{1}H NMR spectrum of **4**, the peaks at 3.29–3.25, 2.99 and 1.71–1.60 ppm indicated the presence of $–OCH_3$, $–CH_2$ and *t*-BuCH_3 groups of 1,3-dimethoxy-4-*tert*-butylcalix[4]arene, respectively, in the structure. The $–CH_3$ protons at the end of the chain appeared at 0.84 ppm, $–CCH_2C–$ protons at 1.27 ppm and the $–SCH_2$ group neighboring an aromatic ring at 1.99 ppm. The aliphatic protons of **5** exhibited the $–OCH_3$, $–CH_2$ and *t*-BuCH_3 groups of 1,3-dimethoxy-4-*tert*-butylcalix[4]arene at 3.35, 3.05 and 1.7 ppm, respectively. The $–CH_3$ protons at the end of the chain were found at 0.93 ppm, $–CCH_2C–$ protons at 1.19–1.50 ppm and the $–SCH_2$ group neighbouring an aromatic ring at 1.99 ppm. The only difference, which was the most important information indicating the formation of a bis double-decker lutetium(III) phthalocyanine (**5**), was the presence of the signal at 2.59 ppm in **4**, corresponding to the $COCH_3$ group, which disappeared in the spectrum of **5**.

Electronic spectra are especially fruitful in establishing the structures of **4** and **5**. The typical UV–Vis spectrum of **4** exhibited a characteristic Q band in the visible region at 712 nm. It is attributed to the $\pi \rightarrow \pi^*$ transition from the highest occupied molecular orbital (HOMO) to the lowest unoccupied molecular orbital (LUMO) of the Pc^{2-} ring (Fig. 1, solid line).

Compounds **4** and **5** show an additional band centered at 640 and 636 nm, respectively, as a result of aggregation through exciton coupling of the Pc units [58]. When the electronic spectrum of **5** was investigated, some peculiarities were observed. The intense Q band at 702 and 732 nm are somewhat distorted leading a third band of lower intensity at 669 nm in $CHCl_3$ (Fig. 1, dot line). This result might be interpreted in terms of the formation of HOMO–HOMO interactions of the two phthalocyanine rings. This fully agrees with the observation for the analogous Pc anions [59]. A characteristic absorption band for the radical phthalocyanine anion appears as a shoulder in the 400–500 nm region [60,61]. The band at 430 nm in the spectrum of **5** is assigned to a transition of a full level to the semi-occupied molecular orbital (SOMO) [62–65]. The B bands of **4** and **5** arising from the deeper π levels → LUMO transitions are observed in the UV region



Scheme 1. Summary of the synthetic pathway for the preparation of compounds **1**, **2**, **4** and **5**.

at 364 nm and with two maxima at 360 and 328 nm, respectively.

A close investigation of the mass spectrum of **5** confirmed the proposed structure. In the MALDI-TOF MS analysis of **5**, the protonated molecular ion peak at 6319 Da was observed (Fig. 2).

The free-radical nature of the green $Lu(Pc)_2$ complex is characterized by its ESR spectrum [23]. The spectrum of a

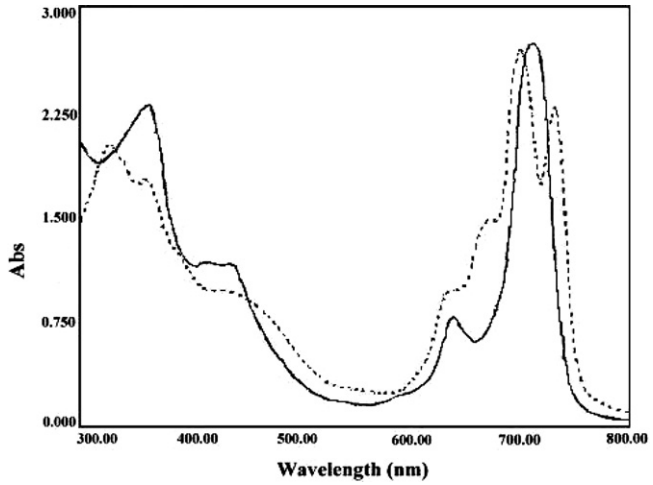


Fig. 1. UV–Vis spectra for **4** (——) and **5** (·····).

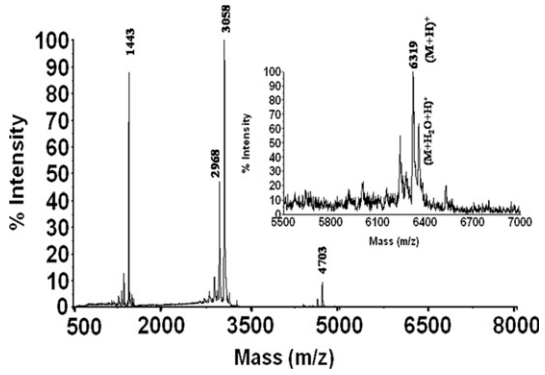


Fig. 2. Positive ion MALDI-MS spectrum of **5** in 3,5-dinitrobenzoic acid matrix.

solid sample of **5** at room temperature presented a strong signal at $g = 2.0022$ with a bandwidth of 5 G (Fig. 3). Very high signal intensity observed for the solid state of **5** likely witnesses the high amount of radicals per gram of this compound, producing an exchange narrowing on the linewidth. This confirms the presence of an unpaired spin, and thus is consistent with the occurrence of a phthalocyanine radical [66].

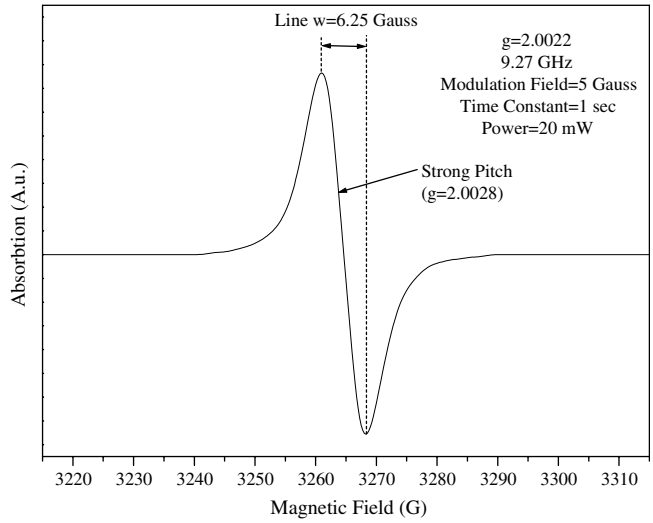


Fig. 3. ESR spectrum of **5**.

3.2. Electrochemistry

The voltammetric measurements for **4** and **5** were carried out on platinum in dichloromethane (DCM). The relevant data are given in Table 1.

Compound **4** undergoes up to two reductions at $E_{1/2} = -0.89$ V and $E_{1/2} = -1.15$ V versus SCE, and a single oxidation at $E_{1/2} = +0.65$ V versus SCE when dissolved in DCM. Controlled-potential coulometry studies showed that each redox process involves the transfer of two electrons. Typical cyclic voltammograms at several scan rates and a differential pulse voltammogram for **4** are shown in Fig. 4. All redox processes of **4** are related to ring-based processes because only the cerium derivatives in the series of lanthanide bis(phthalocyanines) and related double deckers display a metal-centered redox process.

The redox processes of **4** showed reversible or quasi-reversible behaviour at very slow scan rates but the cathodic to anodic peak separations, ΔE_p varied with scan rate indicating that the heterogeneous electron transfer rate was relatively slow at higher scan rates. The separation between the first ring oxidation and the first ring reduction, $\Delta E_{1/2}$ for **4** was found to be 1.54 V, a value approaching the average value for monomeric phthalocyanines [67].This value should be a consequence of very weak interactions between the phthalocyanine rings. The overall splitting of the molecular orbitals to a high degree are expected to occur only in the case where the rings are positioned in a face to face (cofacial) orientation as in the sandwich-type phthalocyanines. The weak interactions may be attributed to isolation of the two rings in **4** by the *tert*-butylcalix[4]arene bridge, and are compatible with the data reported recently for a similar lutetium phthalocyanine by our group [29b].

The voltammetric behaviour of **5** involving two sandwich-type diphthalocyanines differs from that of **4**. Typical cyclic voltammograms at different scan rates and a differential pulse voltammogram for **5** are shown in Fig. 5. Controlled-potential coulometry and cyclic voltammetry measurements indicated that at the positive potential side three one-electron redox couples were observed for **5** at $E_{1/2} = +0.13$ V, $E_{1/2} = +0.51$ V and $E_{1/2} = +0.77$ V versus SCE. On sweeping to negative potentials starting from 0.00 V, compound **5** displayed two two-electron redox processes at $E_{1/2} = -0.64$ V and $E_{1/2} = -0.86$ V versus SCE. All the redox processes are also ring-based. The voltammetric data for the redox processes are presented in Table 1. The peak separations and the variation of the peak potentials with the scan rate (Fig. 5) for these redox processes were usually within the range of quasi-reversible behaviour. As also was reported previously for $S_4(CH_2)_4$ bridged Lu_2Pc_2 and Lu_2Pc_4 compounds [29b], although in

Table 1
Voltammetric data for **4** and **5**

Compound	Redox couple	$E_{1/2}$[a] V vs. SCE and Fc/Fc^{+}[b]	ΔE_p[c]
4	$[Pc(-1)]_2/[Pc(-2)]_2$ (III)	0.65 (0.20)	0.07
	$[Pc(-2)]_2/[Pc(-3)]_2$ (I)	−0.89 (−1.34)	0.07
	$[Pc(-3)]_2/[Pc(-4)]_2$ (II)	−1.15 (−1.60)	0.12
5	$[Pc(-1)]_3Pc(-2)/[Pc(-1)Pc(-2)]_2$ (IV)	0.77 (0.32)	0.11
	$[Pc(-1)Pc(-2)]_2/Pc(-1)[Pc(-2)]_3$ (IIIA)	0.51 (0.06)	0.10
	$Pc(-1)[Pc(-2)]_3/[Pc(-2)]_4$ (IIIB)	0.13 (−0.32)	0.06
	$[Pc(-2)]_4/[Pc(-2)Pc(-3)]_2$ (I)	−0.64 (−1.09)	0.10
	$[Pc(-2)Pc(-3)]_2/[Pc(-3)]_4$ (II)	−0.86 (−1.31)	0.14

[a] $E_{1/2} = (E_{pa} + E_{pc})/2$ at 0.050 V s^{-1}.
[b] The values in parenthesis indicate the potentials vs. Fc/Fc^{+}.
[c] $\Delta E_p = E_{pa} - E_{pc}$ at 0.050 V s^{-1}.

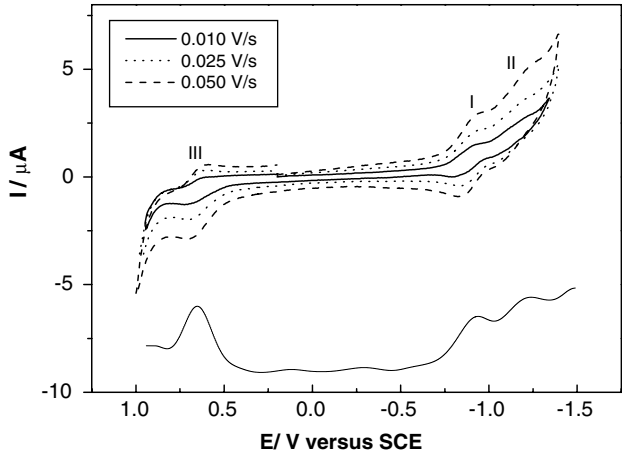


Fig. 4. Cyclic and differential pulse voltammograms of **4** (1.00×10^{-4} M) on Pt in DCM/TBAP.

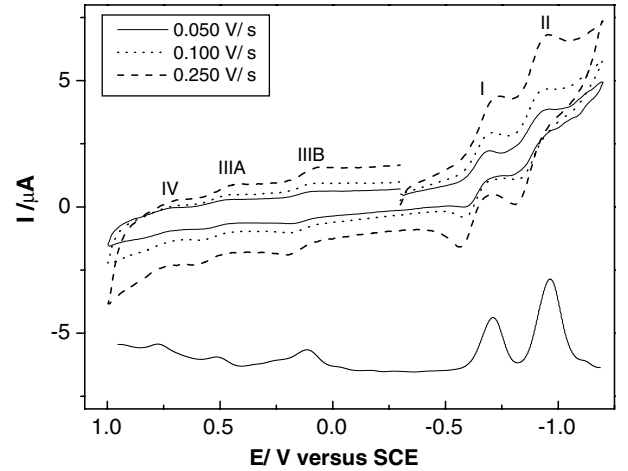


Fig. 5. Cyclic and differential pulse voltammograms of **5** (1.00×10^{-4} M) on Pt in DCM/TBAP.

the solid state compound **5** consists of two non-interacting free radicals, $[(Pc)(-1)Lu(Pc)(-2)]_2$, in solution at 0.00 V versus the SCE, it is in the form $[(Pc)(-2)Lu(Pc)(-2)]_2^{2-}$ with the extra two electrons per molecule coming from the electrode set–up in the cell. On scanning towards positive potentials, it is oxidized first to the original state, $[(Pc)(-1)Lu(Pc)(-2)]_2$ in two one-electron steps (IIIB and IIIA in Fig. 5), and then to $\{[(Pc)(-1)]_3Lu_2(Pc)(-2)\}^{+}$ (IV in Fig. 5), since it involves two phthalocyanine monoanions, $Pc(-1)$. Couple IV is well defined by the differential pulse voltammogram, and can be assigned to the oxidation of one of the sandwich units in the original compound. The couple for the oxidation of other sandwich unit is out of the solvent-limited potential range, and thus cannot be detected. We could not observe any oxidation couple for $S_4(CH_2)_4$ bridged Lu_2Pc_4 in the previous study for the same reason. The second and the third reduction couples (I and II, respectively), monitored for **5** at $E_{1/2} = -0.64$ V and $E_{1/2} = -0.86$ V versus SCE are also associated with the ring-based processes. Each of these couples was found to involve 2-electron transfer, suggesting that the two sandwich units are reduced at the same potential.

Half-wave potentials of *tert*-butylcalix[4]arene bridged Lu_2Pc_4, **5** are all more negative by 0.2–0.3 V than the measured $E_{1/2}$ values for previously reported $S_4(CH_2)_4$ bridged $Lu_2Pc_4(OAc)_2$ [29b]. This negative shift should be due to the benzene rings in the *tert*-butylcalix[4]arene bridges which increase the electron density of the phthalocyanine rings. Electrochemical measurements with cast films of **4** and **5** in aqueous and non-aqueous media on an ITO glass electrode are also continuing. These measurements suggest that the compounds display interesting electrochromic behaviour. The explicit discussion and comparison of electrochemical measurements in solution and in the film will be presented in a separate paper.

3.3. Electrical measurements

The dependence of the d.c. electrical conductivity of **4** and **5** versus inverse temperature, $\ln\sigma = f(1/T)$, were studied in the temperature range 290–420 K. The variation of d.c. conductivity with the inverse temperature at fixed voltage under forward bias (0.6 V) are shown in Fig. 6 for the films of **4** and **5** in a vacuum ($<10^{-3}$ mbar) in the dark. The

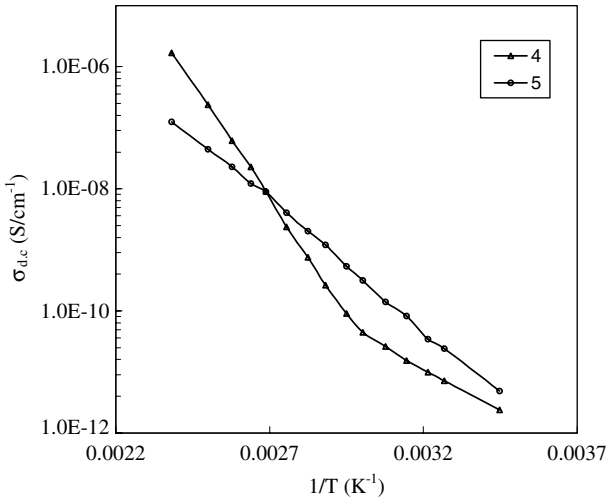


Fig. 6. Variation of d.c. conductivity as a function of temperature for the films of **4** and **5**.

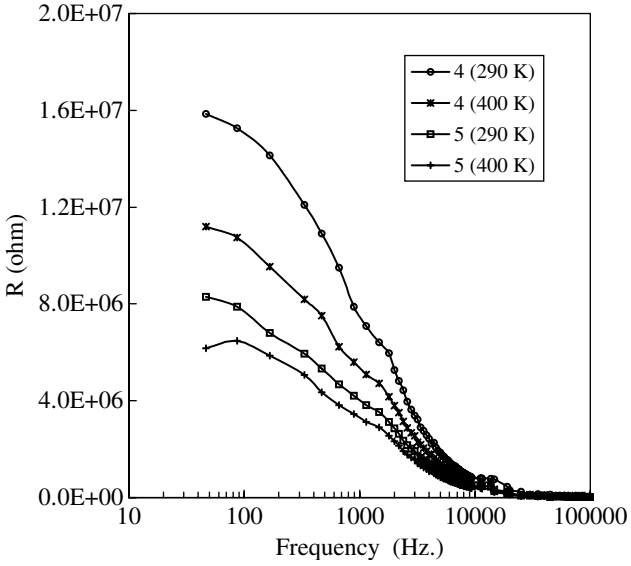


Fig. 7. Frequency dependence of the real part of the impedance for spin coated **4** and **5** films at the indicated temperatures.

conductivity measurements were carried out immediately after film deposition. The linear dependence in the Arrehenius plot suggests the presence of only one conduction mechanism, assuming that the dominant levels are the conduction and valence bands in the temperature range 290–420 K for film **5**.

In this case, it is reasonable to represent the temperature dependence of the conductivity for film **5** by the well known expression:

$$\sigma_{\mathrm{d.c.}} = \sigma_0 \exp(-E_{\mathrm{A}}/kT),$$

where E_{A} is the thermal activation energy of the electrical conduction, T is temperature, k is Boltzmann's constant and σ_0 is a parameter depending on the semiconductor nature. The value of the activation energy was derived from the slope of the $\log\sigma_{\mathrm{d.c.}}$ versus $1/T$ graph and is 0.77 eV for compound **5**. This E_{A} value for **5** matches well with that for the previously reported $S_4(CH_2)_4$ bridged Lu_2P-$c_4(OAc)_2$ [34]. There is a clear discontinuity in the $\log\sigma_{\mathrm{d.}c}$ versus $1/T$ plot at ~333 K for compound **4**. As can be seen from Fig. 6, the graph splits into two different linear regions, and each region can be ascribed to a different activation energy corresponding to a different dominant excitation. The activation energies obtained for region I and II were found to be 0.53 eV and 1.43 eV, respectively. A possible reason for the observed two different activation energy values in the Arrehenius plot could be a transition from extrinsic to intrinsic conduction. The variation of real part of impedance, $Z(\omega) = R(\omega) + \mathrm{i}X(\omega)$, as a function of frequency at room temperature and 400 K for the films of **4** and **5** is presented in Fig. 7. It becomes clear that there is a monotonic decrease in the real part of the impedance for the films at low frequencies. At higher frequency the value of $R(\omega)$ merges irrespective of temperature, which indicates the presence of space charge polarization. It can also be seen from Fig. 7 that the value of $R(\omega)$ is higher for the film of compound **4** than **5** for all frequencies. As the temperature rises, the value of $R(\omega)$ becomes less sensitive to frequency increase. Both the high impedance value at lower frequencies and the high frequency behaviour of $R(\omega)$ clearly indicate the presence of space charge polarization.

The temperature dependence of the imaginary part, $X(\omega)$, of the impedance (Fig. 8) of the films of **4** and **5** can be characterized by the following three important features: (i) at low temperatures, a monotonic decrease in the magnitude of the imaginary part, with increasing frequency without any peaks, (ii) presence of peaks at high temperatures, and (iii) a shift in the $X(\omega)$ peak to higher frequencies with increasing temperature. The decrease in $X(\omega)$ with the absence of any peak means that there is no

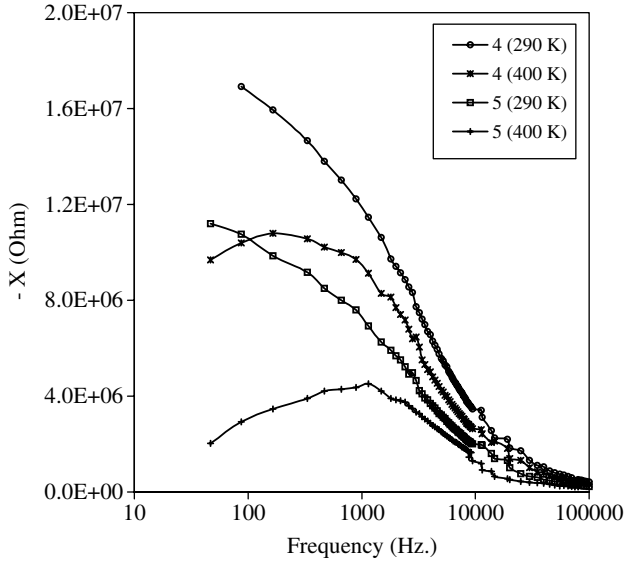


Fig. 8. The dependence of imaginary part of impedance on frequency for spin coated **4** and **5** films at room temperature and 400 K.

current dissipation in this temperature range. The appearance and broadening of peaks at high temperatures suggests the presence of an electrical relaxation phenomenon in the materials. The relaxation process can be attributed to the immobile species/electrons at low temperature and defects in the high temperature regions.

3.4. Sensor response for VOCs

In this part of the study, we concentrated on investigating the sensing properties of spin coated films of compounds **4** and **5** for VOCs vapors by using a quartz crystal microbalance transducer. The sensing principle of the quartz crystal microbalance sensor is based on changes in the fundamental resonant frequency, Δf, upon adsorption/absorption of molecules from the gas phase. In the adsorption experiments, the sensor response when exposed to different classes of organic solvent vapors over a wide range of concentrations (50–400 ppm) on the **4** and **5** coated sensors were examined. Typical responses of the 10 MHz QCM sensors coated with **4** and **5** to chloroform vapors are shown in Fig. 9. In this figure the frequency change Δf was plotted against time for six different chloroform concentrations. It can be seen from Fig. 9 that chloroform vapor causes a rapid frequency decrease, which represents a mass increase followed by saturation. It can also be seen that the response times for **4** and **5** coated sensors are typically one min. For example, in the case of 100 ppm of carbon tetrachloride, 90% of the maximum frequency change is attained in 68 s. The recovery times are also about one min. The sensor signals were completely reversible.

Fig. 10 shows the frequency change versus organic solvent vapor concentration for a **4** coated QCM sensor. The dependence of the frequency change on analyte concentration suggests that there are two kinds of adsorption behaviour onto the **4** coated sensor. The initial slopes in Fig. 10 indicate that the sensor responses linearly depend on organic solvent vapour concentration at the low concentration range. For a high concentration of analyte, the response of the **4** coated sensor does not increase any more with the increase of concentration. The high concentration region of Fig. 10 indicates that the analyte molecules were adsorbed as monolayers via hydrogen bonding. It is reasonable to assume that at higher concentration, the active adsorption sites on the surface of the coating (compound **4**) are occupied by the target molecules, and adsorption reaches a maximum.

The response characteristics of the **5** coated sensor was different from **4** (Fig. 11). A linear increase in the frequency

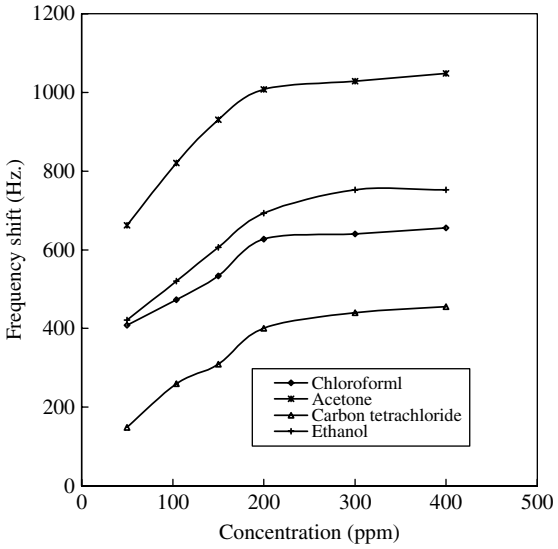


Fig. 10. Relationship between the solvent vapor concentration and frequency shift of the **4** coated QCM.

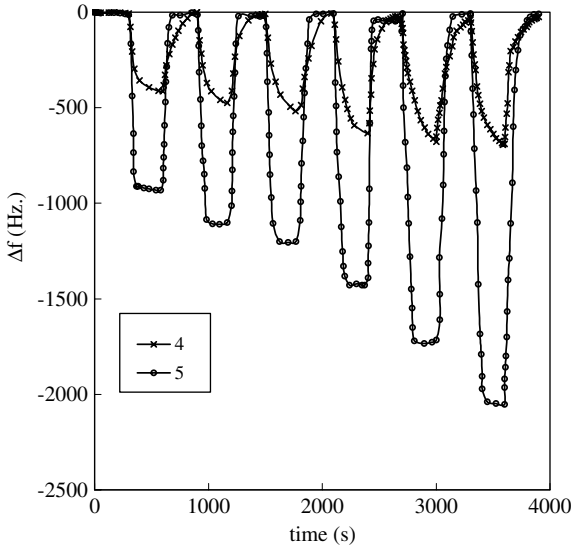


Fig. 9. Response of **4** and **5** coated QCM sensors to 50, 100, 150, 200, 300 and 400 ppm of chloroform vapors.

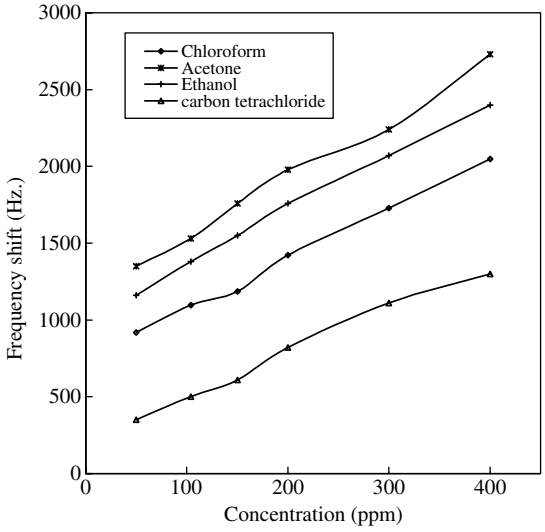


Fig. 11. Relationship between the solvent vapor concentration and frequency shift of the **5** coated QCM.

change with increase of vapour concentrations was obtained with the **5** coated sensor. The linear relationship between the frequency change and analyte concentration can be explained by multilayer adsorption. As the solvent vapour concentration increases, more analyte molecules are adsorbed on the sensitive layer by interacting with the previously trapped molecules on the surface of **5** to form multilayers.

We observed from aging experiments that the sensitive layers (**4** and **5**) were stable and have been used for three months without significant losses in sensitivity and selectivity.

The sensitivity S, which is an important parameter for any sensor, defined as

$$S = \frac{1}{C_V}\frac{\Delta f_V}{\Delta f_C}, \quad (2)$$

where Δf_V is the frequency change caused by exposure of the sensor to a concentration of an organic vapor, and Δf_C is the frequency shift in resonant frequency due to the coating. The results show less sensitivity for the non-polar organic molecules investigated, such as carbon tetrachloride. The higher sensor sensitivities are observed for the polar solvent molecules. The total response is in the order: acetone > ethanol > chloroform > carbon tetrachloride. This result may be due to dipole–dipole interactions between the adsorbed molecules and the coating material. The order of response is the same as that of the dipole moment of the analytes: acetone (2.91 D), ethanol (1.69 D), chloroform (1.08 D) and carbon tetrachloride (0 D).

4. Conclusions

In this study, a novel 1,3-bis(3,4-dicyanophenoxy)-4-*tert*-butylcalix[4]arene, namely compound **1** was prepared and used as a key compound for the preparation of a novel *tert*-butylcalix[4]arene bridged bis double-decker lutetium(III) phthalocyanine (**5**), which was achieved by the reaction of dimeric lutetium(III) phthalocyanine (**4**) with two equiv. of dilithium octakis (hexylthio) phthalocyanine in amyl alcohol, and produced in 46% yield. The ESR spectrum of **5** showed that this novel compound is radical in nature. The structures of the newly synthesized compounds were confirmed and characterized by elemental analysis as well as by IR, UV–Vis, ^{1}H NMR, MALDI-TOF MS and by ESR spectra. The electrochemical measurements suggested that π-orbital interactions between two Pc rings in **4** are very weak. On the other hand, the splitting of the first reduction process of a sandwich-type $LuPc_2$ was detected as a result of the strong HOMO–HOMO orbital interactions between the two rings of each sandwich unit in **5**. It can be concluded from the results of d.c., a.c. and gas sensing measurements performed on a spin coated film of **5** that the frequency dependent conductivity for the film can be represented by the power law relation. A QCR sensor showed high sensitivity for organic solvents with a high dipole moment, such as acetone.

Acknowledgments

We thank the Research Funds of the Gülhane Medical Academy (GATA), and Marmara University (Project No. SCIENCE-107/020603) for financial support. One of the authors Ö. Bekaroğlu is grateful to Turkish Academy of Science (TUBA) for their support. We are also grateful to Mr. M. Akyol, computer expert, Gülhane Medical Academy (GATA), Ankara for his valuable help.

References

[1] C.C. Leznoff, A.B.P. Lever (Eds.), Phthalocyanines: Properties and Applications, vols. 1–4, VCH, Weinheim, 1989–1996.
[2] J. Simon, J.J. Andre, Molecular Semiconductors, Springer, New York, 1985.
[3] M. Hanack, S. Deger, A. Lange, Coord. Chem. Rev. 83 (1988) 115.
[4] S.A. Mikhalenko, S.V. Barkanova, O.L. Lebedev, E.A. Luk'yanets, Zh. Obshch. Khim. 41 (1971) 2735.
[5] A.R. Koray, V. Ahsen, Ö. Bekaroğlu, J. Chem. Soc., Chem. Commun. (1986) 932.
[6] V. Ahsen, E. Yılmazer, M. Ertaş, Ö. Bekaroğlu, J. Chem. Soc., Dalton Trans. (1988) 401.
[7] V. Ahsen, A. Gürek, E. Musluoglu, A. Gül, Ö. Bekaroğlu, Helv. Chim. Acta 73 (1990) 174.
[8] M. Koçak, A. Cihan, A.I. Okur, Ö. Bekaroğlu, J. Chem. Soc., Chem. Commun. (1991) 578.
[9] A. Gürek, V. Ahsen, A. Gül, Ö. Bekaroğlu, J. Chem. Soc., Dalton Trans. (1991) 3367.
[10] G. Gümüş, Z.Z. Öztürk, V. Ahsen, A. Gül, Ö. Bekaroğlu, J. Chem. Soc., Dalton Trans. (1992) 2485.
[11] I. Yılmaz, Ö. Bekaroğlu, Chem. Ber. 129 (1996) 967.
[12] M. Koçak, A.I. Okur, Ö. Bekaroğlu, J. Chem. Soc., Dalton Trans. (1994) 323.
[13] A.G. Gürek, Ö. Bekaroğlu, Helv. Chim. Acta 77 (1994) 1616.
[14] A.G. Gürek, Ö. Bekaroğlu, J. Porphyr. Phthalocya. 1 (1997) 227.
[15] M. Kandaz, Ö. Bekaroğlu, Chem. Ber. 130 (1997) 833.
[16] N. Moskalev, I.S. Kirin, Russ. J. Inorg. Chem. 16 (1971) 57.
[17] N. Moskalev, I.S. Kirin, Russ. J. Inorg. Chem. 46 (1972) 1019.
[18] M. Nicholson, F.A. Pizarello, J. Electrochem. Soc. 126 (1979) 1490.
[19] A. Corker, B. Grant, N.J. Clecak, J. Electrochem. Soc. 126 (1979) 1339.
[20] T. Chang, J.C. Marchon, Inorg. Chim. Acta 53 (1981) L 241.
[21] C.S. Collins, D.J. Schiffrin, J. Electroanal. Chem. 139 (1982) 335.
[22] (a) M. L'Her, Y. Cosien, J. Courtot-Loupez, J. Electroanal. Chem. 157 (1983) 183;
(b) M. L'Her, Y. Cosien, J. Courtot-Loupez, C.R. Acad. Sci. Paris, Ser. II 302 (1986) 9.
[23] A. De Cian, M. Moussavi, J. Fisher, R. Weiss, Inorg. Chem. 24 (1985) 3162.
[24] M. M'Sadak, J. Roncali, F. Garnier, J. Electroanal. Chem. 189 (1985) 99.
[25] V.I. Gavrilov, A.P. Konstantinov, E.A. Luk'yanets, I.V. Shelepin, Sov. Electrochem. Engl. Transl. 22 (1986) 1562.
[26] (a) M.T. Riou, M. Auregan, C. Clarisse, J. Electroanal. Chem. 187 (1985) 349;
(b) M.T. Riou, C. Clarisse, J. Electroanal. Chem. 249 (1988) 181;
(c) C. Clarisse, M.T. Riou, S. Robinet, Synth. Met. 38 (1990) 121.
[27] F. Castenade, V. Plichon, C. Clarisse, M.T. Riou, J. Electroanal. Chem. 233 (1987) 77.
[28] M. Petty, D.R. Lovett, P. Townsed, J.M. O'Connor, J. Silver, J. Phys. D 22 (1989) 1604.
[29] (a) Ş. Abdurrahmanoğlu, A. Altındal, A.R. Özkaya, M. Bulut, Ö. Bekaroğlu, Chem. Commun. (2004) 2096;
(b) Ş. Abdurrahmanoğlu, A.R. Özkaya, M. Bulut, Ö. Bekaroğlu, J. Chem. Soc., Dalton Trans. (2004) 4022.

[30] J. Simon, J.J. Andre, Molecular Semiconductors, Springer, Berlin, 1985 (Chapter 3).
[31] J.J. Andre, K. Holczer, P. Petit, M.T. Riou, C. Clarisse, R. Even, M. Fourmigue, J. Simon, Chem. Phys. Lett. 115 (1985) 463.
[32] P. Turek, J.J. Petit, J.J. Andre, J. Simon, R. Even, B. Boudjema, G. Guillaud, M. Maitrot, J. Am. Chem. Soc. 109 (1987) 5119.
[33] M. Maitrot, G. Guillaud, B. Boudjema, J.J. Andre, H. Strzelecka, J. Simon, R. Even, Chem. Phys. Lett. 133 (1987) 59.
[34] A. Altındal, Ş. Abdurrahmanoğlu, M. Bulut, Ö. Bekaroğlu, Synth. Met. 150 (2005) 181.
[35] H. Meier, W. Albrecht, D. Wöhrle, A. Jahn, J. Phys. Chem. 90 (1986) 6349.
[36] Y. Orimashi, H. Ohno, E. Tsuchida, H. Matsuda, H. Nakanishi, M. Kato, Mol. Cryst. Liq. Cryst. 160 (1988) 139.
[37] A. Louati, M. El Meray, J.J. Andre, J. Simon, K.M. Kadish, M. Gross, A. Giraudeau, Inorg. Chem. 24 (1985) 1175, and ref. 9–20 herein.
[38] K. Ohta, L. Jacquemin, C. Sirlin, L. Bosio, J. Simon, New J. Chem. 12 (1988) 751.
[39] J. Simon, J.J. Andre, A. Skoulios, Nouv. J. Chim. 10 (1986) 295.
[40] (a) D.K.P. Ng, J. Jiang, Chem. Soc. Rev. 26 (1997) 433;
(b) J.W. Buchler, D.K.P. Ng, in: K.M. Kadish, K.M. Smith, R. Guilard (Eds.), The Porphyrin Handbook, 3, Academic Press, San Diego, 2000 (Chapter 20).
[41] M. Passard, J.P. Blanc, C. Maleysson, Thin Solid Film 271 (1995) 8.
[42] (a) M.M. Nicholson, in: C.C. Leznoff, A.B.P. Lever (Eds.), Phthalocyanines: Properties and Applications, vol. 3, VCH, New York, 1993, pp. 71–117;
(b) R. Jones, A. Krier, K. Davidson, Thin Solid Films 298 (1997) 228.
[43] (a) M. Trometer, R. Even, J. Simon, A. Dubon, J.Y. Laval, J.P. Germain, C. Maleysson, A. Pauly, H. Robert, Sensor Actuator B 8 (1992) 129;
(b) R.E. Clavijo, D. Battisti, R. Aroca, G.J. Kovacs, C.A. Jennings, Langmuir 8 (1992) 113;
(c) M.L. Rodriguez-Mendez, R. Aroca, J.A. De-Saja, Chem. Mater. 5 (1993) 933.
[44] T. Ceyhan, A. Altındal, M.K. Erbil, Ö. Bekaroğlu, Polyhedron 25 (2006) 737.
[45] M. Özer, A. Altındal, A.R. Özkaya, M. Bulut, Ö. Bekaroğlu, Synth. Met. 155 (2005) 222.
[46] A.K.M. Shafiqul Islam, Z. Ismail, M.N. Ahmad, B. Saad, A.R. Othman, A.Y. Md. Shakaff, A. Daud, Z. Ihsak, Sensor Actuator B 109 (2005) 238.
[47] X.C. Zhou, L. Zhong, S.F.Y. Li, S.C. Ng, H.S.O. Chan, Sensor Actuator B 42 (1997) 59.
[48] F.L. Dickert, A. Haunschild, V. Maune, Sensor Actuator B 12 (1993) 169.
[49] Z.Z. Öztürk, R. Zhou, V. Ahsen, Ö. Bekaroglu, W. Göpel, Sensor Actuator B 35–36 (1996) 404.
[50] R.L. Bunde, E.J. Jarvi, J.J. Rosentreter, Talanta 46 (1998) 1223.
[51] G. Sauerbrey, Z. Phys. 155 (1959) 206.
[52] N. Ozan, Ö. Bekaroğlu, Polyhedron 22 (2003) 819.
[53] T. Ceyhan, M. Korkmaz, T. Kutluay, Ö. Bekaroğlu, J. Porphyr. Phthalocya. 8 (2004) 1383.
[54] T. Ceyhan, M. Korkmaz, M.K. Erbil, Ö. Bekaroğlu, J. Porphyr. Phthalocya. 9 (2005) 423.
[55] J.G. Young, W. Onyebuagu, J. Org. Chem. 55 (1990) 2155.
[56] S. Dabak, Ö. Bekaroğlu, New J. Chem. 21 (1997) 269.
[57] Y. Liu, K. Shigehara, M. Hara, A. Yamada, J. Am. Chem. Soc. 113 (1991) 440.
[58] W.A. Nevin, W. Liu, M.R. Hempstead, S.M. Marcuccio, M. Melnik, C.C. Leznoff, A.B.P. Lever, Inorg. Chem. 26 (1987) 891.
[59] A. Iwase, C. Harnoode, Y. Kameda, J. Alloys Compd. 192 (1993) 280.
[60] M.L. Rodriguez-Mendez, R. Aroca, J.A. De Saja, Chem. Mater. 4 (1992) 1017.
[61] D. Battisti, L. Tomilova, R. Aroca, Chem. Mater. 4 (1992) 1323.
[62] V.M. Negrimovskii, M. Bouvet, E.A. Luk'yanets, J. Simon, J. Porph. Phthalocya. 5 (2001) 423.
[63] T. Tran-Thi, D. Markovitsi, R. Even, J. Simon, Chem. Phys. Lett. 139 (1987) 107.6.
[64] H. Sugimoto, T. Higashi, M. Mori, Chem. Lett. (1982) 801.
[65] H. Sugimoto, T. Higashi, A. Maeda, M. Mori, H. Masuda, T. Taga, J. Chem. Soc., Chem. Commun. (1983) 1234.
[66] C. Piechocki, J. Simon, J. Chem. Soc., Chem. Commun. (1985) 259.
[67] (a) A.B.P. Lever, E.R. Milaeva, G. Speier, in: C.C. Leznoff, A.B.P. Lever (Eds.), Phthalocyanines: Properties and Applications, vol. 3, VCH, Weinheim, 1993, pp. 1–69;
(b) A.R. Özkaya, A.G. Gürek, A. Gül, Ö. Bekaroğlu, Polyhedron 16 (1997) 1877;
(c) A.R. Özkaya, İ. Yılmaz, Ö. Bekaroğlu, J. Porphyr. Phthalocya. 2 (1998) 483;
(d) A.R. Özkaya, E. Hamuryudan, Z.A. Bayır, Ö. Bekaroğlu, J. Porphyr. Phthalocya. 4 (2000) 689;
(e) M. Kandaz, A.R. Özkaya, Ö. Bekaroğlu, Monats. Chem. 132 (2001) 1013.

Available online at www.sciencedirect.com
ScienceDirect
Polyhedron 26 (2007) 85–92
POLYHEDRON
www.elsevier.com/locate/poly

Synthesis, structures, electrochemistry and catalytic activities of copper(II) and palladium(II) complexes with asymmetric tetraazacycloannulenes

E.H. Kim [a], D.I. Kim [a], H.S. Lee [a], H.G. Na [b], J.C. Byun [c], J.H. Choi [d], Y.C. Park [a,*]

[a] *Department of Chemistry, Kyungpook National University, Daegu 702-701, Republic of Korea*
[b] *Department of Chemistry, Daejin University, Pochon 487-800, Republic of Korea*
[c] *Department of Chemistry, Cheju National University, Cheju 690-756, Republic of Korea*
[d] *Department of Chemistry, Andong National University, Andong 760-749, Republic of Korea*

Received 9 March 2006; accepted 26 July 2006
Available online 11 August 2006

Abstract

Copper(II) and palladium(II) complexes with 15-membered asymmetric 5,9-dihydro-2,4,10,12-tetramethyl-1,5,9,13-monobenzotetraazacyclo[15]tetradecine have been synthesized and characterized. The electrochemical behaviors of the complexes showed a reduction and two one-electron irreversible oxidation waves in given potential ranges due to the metal ion and macrocycle ring, respectively. The electrocatalytic reduction of dioxygen on glassy carbon electrodes electropolymerized by such 15-membered and 14-membered tetraazaannulene complexes occurred at 160–280 mV (versus SCE), less negative than on the bared one at pH 7.0. The catalytic activities of the copper(II) complexes in the oxidation of *p*-Xstyrene (X = OCH_3, CH_3, H, F, Cl) were higher than those of the palladium(II) ones. The structures of the 15-membered copper(II) and palladium(II) complexes were determined using the X-ray diffraction method.
© 2006 Elsevier Ltd. All rights reserved.

Keywords: Cu(II)- and Pd(II)-tetraazacycloannulene; Structure; Spectral and electrochemical properties; Electrocatalytic reduction

1. Introduction

The chemistry of transition metal complexes with the dibenzotetraazacyclo[14]annulene macrocycle has been much studied largely because of the interaction between substrates and metal centers in biological systems [1–5]. However, the complexes mostly reported are symmetric 14-membered macrocycle compounds. On the other hand, the synthesis, electrochemistry and catalytic activity of 15-membered asymmetric monobenzotetraazaannulene complexes have rarely been studied [6,7,12,15]. The 15-membered complexes are expected undergo easier attack on the metal center by an oxidant than the14-membered complexes because the 15-membered complexes show square pyramidal structures. Some square planar Ni(II) complexes of macrocyclic ligands such as cyclam have been shown to act as catalysts for epoxidation of alkenes when PhIO or NaOCl was used as a terminal oxidant [9,10]. Various efforts have been made to elucidate the mechanism in which a Ni(III) species is involved, although there are some controversies of high valent metal-oxo intermediates [11]. The Cu(II) and Pd(II) complexes with such asymmetric ligands might be expected to show mostly similar processes, depending on the effect of the structure and electronic properties of the metal complexes. The crystal structures and characteristics for transition metal complexes with 15-membered asymmetric monobenzotetraazaannulenes have scarcely been reported until now because it is not easy to prepare the free ligands compared to the symmetric ones [8]. Previously [12–15], we have synthesized and reported nickel(II) complexes with a series of 14-membered

* Corresponding author. Tel.: +82 53 950 5333; fax: +82 53 950 6330.
E-mail address: ychpark@mail.knu.ac.kr (Y.C. Park).

0277-5387/$ - see front matter © 2006 Elsevier Ltd. All rights reserved.
doi:10.1016/j.poly.2006.07.033

asymmetric tetraazaannulenes and also characterized the glassy carbon electrodes oxidatively electropolymerized by such complexes as modifiers.

In this paper, we have attempted to synthesize monobenzotetraazaannulene ligands with 15-membered asymmetric macrocyclic rings and then to synthesize the copper(II) and palladium(II) complexes from the reactions of the metal acetates with the free ligands in acetonitrile under nitrogen atmosphere. The spectral and electrochemical properties of the complexes prepared were characterized by means of infrared, mass, electronic absorption, ^{1}H and ^{13}C NMR spectra and cyclic voltammograms. The structures of the copper(II) and palladium(II) complexes with 2,4,10,12-tetramethyl-1,5,9,13-monobenzotetraazacyclo[15]tetradecine were identified by X-ray diffraction analysis. The catalytic activities of the metal complexes, varying with factors such as ring sizes and metal ions of the complexes and substituents of substrate, were preliminarily tested in the oxidation of *p*-Xstyrene (X = OCH_3, CH_3, H, F, Cl) in dichloromethane at room temperature. These studies will certainly help to better understand and summarize the properties and catalytic activities of tetraazaannulene metal complexes in the future.

2. Experiments

2.1. Materials and measurements

All chemicals used were obtained from commercial suppliers. The solvents such as CH_3OH, C_2H_5OH and CH_2Cl_2 were refluxed over calcium hydride under nitrogen, and their purities checked by GC just before use. Dimethylsulfoxide (DMSO) and acetonitrile (AN) were used as purchased without further purification. Tetraethylammoniumperchlorate (TEAP), used as a supporting electrolyte, was prepared and purified by the method described by Kolthoff and Coetzee [16]. All aqueous solutions for the measurements were prepared with deionized water purified using a Millipore Milli-Q water system (Bedford, MA).

Elemental analyses (C, H, N) of the complexes prepared were carried out on a Carlo-Ebra, EA 1108 instrument. Infrared spectra were recorded on a Matteson Instruments, Inc. Galaxy 7020A using KBr Pellets. ^{1}H and ^{13}C NMR (300 MHz) spectra were recorded on a Brucker instrument at room temperature and chemical shifts in $CDCl_3$ are given in ppm relative to tetramethylsilane as an internal reference. Electronic absorption spectra were obtained on a Shimadzu UV-265 spectrophotometer. EI mass spectra were determined with a JEOL MS-DX 300 GC–mass spectrometer at 70 eV using a direct inlet system.

Cyclic voltammetry was performed using a Bioanalytical System (BAS) CV-50W electrochemical analyzer and C2 cell stand at room temperature. The three-electrode system composed of a glassy carbon electrode (GCE) as a working electrode, Ag/Ag^+ (0.01 M $AgNO_3$ in 0.1 M TEAP-DMSO or AN solution) as a reference electrode and a platinum wire as an auxiliary electrode was used for the electrochemical measurements. Investigating the electrocatalytic activities of the modified electrodes, a saturated calomel electrode (SCE) was used as a reference electrode.

Analyses of organic products for the catalytic oxidation reaction were taken on a SHIMADZU GC-17A system. The column temperature was programmed from 80 to 100 °C (5–15 min) at rate of 5 °C/min. The products were identified by a comparison of their retention times with those of the pure compounds. *n*-Octane was used as an internal standard for the quantitative analysis of the product.

2.2. Synthesis

The nickel(II) complexes (**14-Ni** and **15-Ni**) as starting compounds and the free ligand (**L1**) and its 14-membered copper and palladium complexes were prepared as in processes described elsewhere [12,17–19].

The ligand 5,9-dihydro-2,4,10,12-tetramethylmonobenzo-1,5,9,13-tetraazacyclo[15]tetradecine (**L2**) was prepared by modifying the method previously used in **L1** [18,19]. At first, the starting complex **15-Ni** was dissolved in absolute ethanol and treated with excess anhydrous hydrochloric acid until the blue colored ligand salt precipitated. The reaction mixture was stirred at room temperature for 18 h. The solid was filtered, dissolved in water and neutralized by adding solid sodium cyanide. The bright yellow precipitate was recovered, washed with water and dried in vacuo. The yellow single crystal was obtained by recrystallisation from a 1:1 mixture of dichloromethane and methyl alcohol. Yield: 0.93 g (20% for **L2**). *Anal*. Calc. for $C_{19}H_{26}N_4$: C, 73.51; H, 8.44; N, 18.05; Found: C, 73.50; H, 8.40; N, 18.05%. IR (KBr disc, cm^{-1}): ν(C=C), 1552; ν(C=N), 1574; $\nu(C_6H_6)$, 723. UV–Vis: λ_{max} (nm) and ε_{max} ($M^{-1}\,cm^{-1}$) in $CHCl_3$ 316 and 37000. ^{1}H NMR ($CDCl_3$): 1.868 (s, 6H), 1.934 (s, 6H) (methyl); 4.613 (s, 2H) (methine); 2.152 (s, 2H), 3.415 (t, 4H, $J = 6.3$ Hz) (propylene); 6.812 ~ 6.965 (m, 4H) (aromatic); 11.220 (br, 2H) (N–*H*). ^{13}C NMR ($CDCl_3$): 19.721, 20.573 (methyl); 30.475, 45.841 (propylene); 95.378 (methine); 157.291, 162.421 (imine); 121.512, 122.370, 141.253 (aromatic). EIMS: *m*/*z* 310 $[M]^+$.

The 15-membered copper(II) and palladium(II) complexes could be prepared by modifying the method used for complexes **14-Cu** and **14-Pd**. The **15-Cu** and **15-Pd** complexes were prepared from the reaction of $M(OAc)_2 \cdot xH_2O$ ($M = Cu^{2+}$, Pd^{2+}) with **L2** in acetonitrile. The mixtures were heated under reflux for 2 h with stirring and bubbling of nitrogen gas to protect from moisture, and were then left to stand in a refrigerator for around 12 h. The solids were filtered and washed with acetonitrile. The products were chromatographed on aluminum oxide and eluted with chloroform. The effluents were collected, evaporated to dryness in vacuo and dried. The single crystals of **15-Cu**

and **15-Pd** obtained from 1:1 mixtures of dichloromethane and methyl alcohol were bright green and ruby red, respectively. Yield: 0.216 g (58% for **15-Cu**) and 0.228 g (55% for **15-Pd**). *Anal*. Calc. for $C_{19}H_{24}CuN_4$: C, 61.35; H, 6.50; N, 15.06; Found: C, 61.30; H, 6.50; N, 15.12%. IR (KBr disc, cm^{-1}): v(C=C), 1547; v(C=N), 1572; v(aromatic), 749. UV–Vis: λ_{max} (nm) and ε_{max} ($M^{-1}\,cm^{-1}$) in $CHCl_3$ 348 and 21 000, 675 and 800. EIMS: m/z 371 $[M]^+$. *Anal*. Calc. for $C_{19}H_{24}PdN_4$: C, 55.01; H, 5.83; N, 15.51; Found: C, 55.01; H, 5.81; N, 15.53%. IR (KBr disc, cm^{-1}): v(C=C), 1525; v(C=N), 1551; $v(C_6H_6)$, 740. UV–Vis: λ_{max} (nm) and ε_{max} ($M^{-1}\,cm^{-1}$) in $CHCl_3$ 380 and 20 000, 455 and 10 500. ^1H NMR ($CDCl_3$): 2.074 (s, 6H), 2.286 (s, 6H) (methyl); 4.779 (s, 2H) (methine); 2.174 (t, 2H, $J = 6.3$ Hz), 3.236 (t, 4H, $J = 6.3$ Hz) (propylene); 6.705–7.037 (m, 4H) (aromatic). ^{13}C NMR ($CDCl_3$): 22.306, 22.664 (methyl); 34.947, 52.463 (propylene); 102.925 (methine); 154.404, 158.943 (imine); 120.775, 121.410, 146.037 (aromatic). EIMS: m/z 414 $[M]^+$.

2.3. Electrochemical modification of GCE

In order to fabricate the polymer modified glassy carbon electrode (GCE), glassy carbon rods (BAS model MF-1000, 2.0 mm in diameter) were used. Prior to the modifications, the GCE was polished with alumina slurry (0.05 μm, Buehler) on a microcloth pad, washed with deionized water, and dried. After the polishing procedure, the residual polishing material was removed by sonication for 30 s, and then dried. Electropolymerization of the complexes on the GCE was carried out by cycling in the range of +1.0 to −2.0 V at 100 mV/s in freshly prepared AN solutions containing 1.0 mM copper(II)- or palladium(II)-tetraazaannulene complexes and 0.1 M TEAP at 25 °C under a nitrogen atmosphere. After one cycle, the electrode was removed from the solution, rinsed with water and dried in air.

2.4. Catalytic reactions

Styrene oxidations catalyzed by the complexes **14-Cu**, **15-Cu**, **14-Pd** and **15-Pd** were carried out in a 25 mL round bottom flask equipped with side neck fitted with a screw capped silicon septum. In a typical experiment, a complex (0.2 mmol) was put into the flask and then dichloromethane (4 mL) was added, and followed by a substituted styrene (2 mmol) as substrates. After stirring for a few minutes, a solution of 10% NaClO (5 mmol) as the terminal oxidant was injected at the controlled temperature. The reaction was monitored with GC by periodically sampling. Relative oxidation rates of the substrates were calculated from the concentration of products and the conversion yields (%) were calculated using the following equation:

$$\text{Conversion } \% = 100 \times \{[\text{initial styrene}] - [\text{final styrene}]/[\text{initial styrene}]\}.$$

2.5. X-ray diffraction analysis

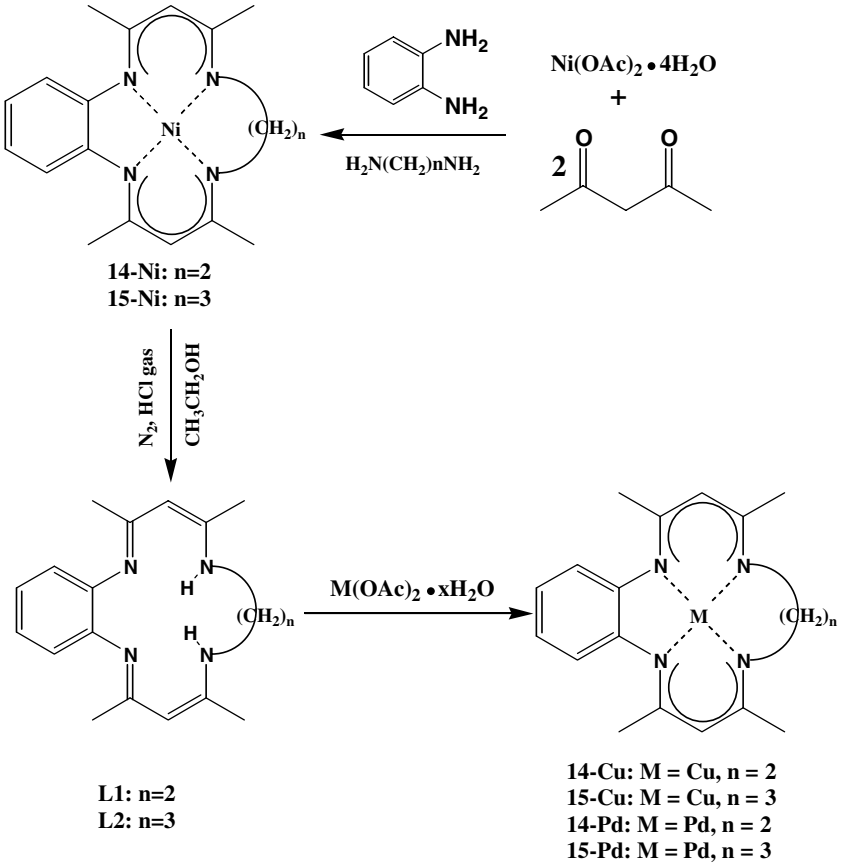
Preliminary examination and data collection for crystals of **15-Cu** and **15-Pd** were performed with Mo Kα radiation ($\lambda = 0.71069$ Å for **15-Cu** and $\lambda = 0.71073$ Å for **15-Pd**) on an Enraf-Nonius CAD4 computer controlled k-axis diffractometer equipped with a graphite crystal, incident-beam monochromator. Cell constants and orientation matrices for data collection were obtained from least-squares refinement, using the setting angles of 25 reflections. The data were collected for Lorentz-polarization and absorption corrections were applied to the data. The structure was solved by direct methods using SHELXS-86 [20] and refined by full-matrix least-squares calculations with SHELXL-97 [21]. The final cycles of the refinements for **15-Cu** and **15-Pd** converged with $R_1 = 0.0351$ and $wR_2 = 0.0727$ and $R_1 = 0.0189$ and $wR_2 = 0.0492$, respectively.

3. Results and discussion

The free ligands (**L1** and **L2**) were obtained by demetallating the asymmetric 14-membered and 15-membered nickel(II)-tetraazaannulene complexes, respectively (Scheme 1) and their copper(II) and palladium(II) complexes (**14-Cu** and **15-Cu** and **14-Pd** and **15-Pd**) in 20–58% yields were prepared from the corresponding ligands with the metal acetates in acetonitrile under nitrogen atmosphere. Elemental analyses and mass data of the new compounds, collected in Section 2, were consistent with their formulations.

3.1. Spectral properties

The C=N, C=C and aromatic vibrational modes for the **15-Cu** and **15-Pd** complexes were at around 1550, 1570 and 745 cm^{-1}, respectively. The electronic absorption spectrum of **L2** exhibited only a band at 316 nm ($\varepsilon_{max} =$ 3!7 000 $M^{-1}\,cm^{-1}$) and a band ($\lambda_{max} = 322$ nm, $\varepsilon_{max} =$ 36 000 $M^{-1}\,cm^{-1}$) for **L1** was consistent with that previously reported [18]. The bands could be attributed to the $\pi \rightarrow \pi^*$ transitions of the macrocycle. The $\pi \rightarrow \pi^*$ transition bands of the new complexes, **15-Cu** and **15-Pd** moved to around 35 nm and 55 nm longer than that of the free ligand, reflecting some difference between the interactions of copper(II) and palladium(II) with the ligand. The visible spectrum of the complexes also had a band, which might be attributed to ligand to metal charge transfer (LMCT) transitions from the highest occupied ligand molecular orbital to the lowest empty d-orbital of the copper or palladium. The values of ε_{max} are much larger than those commonly assigned to ligand field transitions. This behavior is comparable to that observed for other nickel(II)-tetraazaannulene complexes, which have two bands at around 370 and 550 nm [12–15]. The electronic transition band of the copper(II) complexes (606 and 675 nm for **14-Cu** and **15-Cu**, respectively) appeared at wavelengths longer than those of the palladium(II) ones (432 and 455 nm for



Scheme 1.

14-Pd and **15-Pd**, respectively), as expected. The interaction between metal and macrocyclic ligand definitely increases in the order of copper < nickel < palladium.

The methyl and methine proton NMR peaks of **14-Pd** and **15-Pd** shifted downfield by about 0.2 ppm compared to those of **L1** and **L2**. The amine proton NMR peaks of **L1** and **L2** disappeared in the palladium(II) complexes. The peaks for the copper(II) complexes could not be measured due to the paramagnetic property of the copper(II) ion.

3.2. Electrochemical studies

The redox potentials of the new complexes measured in TEAP-DMSO (0.1 M) solutions *vs* Ag/Ag^+ (0.01 M) at 25 °C and sweep rates of 100 mV s^{-1} are listed in Table 1, and the cyclic voltammograms in the range +1100 to −3000 mV versus Ag/Ag^+ are drawn in Fig. 1. All the complexes showed a reduction peak (E_r) for the metal and two oxidation peaks ($E_{0(1)}$ and $E_{0(2)}$) for the macrocyclic ligand in the ranges −2000 to −2710 and −70 to +700 mV, respectively. The reduction potential of the metal decreased in the order Cu > Ni > Pd. The order is in accordance with the sequence shown in the electronic absorption spectra. The reduction peaks of the complexes with the 15-membered macrocylic ring appeared at less negative potentials compared to those with the 14-membered ring. This reflects that the increase in ring size makes the reduction easier because the 15-membered ring may be better able to stabilize the large M(I) ion. The 15-membered ring with a propylene group was be found to be more flexible than the 14-membered one with an ethylene group. The interaction between the metal and the tetraaza group on the 15-membered complex might be somewhat weaker than that of the 14-membered complex, which would cause the electron density on the metal center to be lower. The effect of ring size on the oxidation peaks is also similar to that on the reduction potential of the metals.

Table 1
Redox potential data for the asymmetric tetraazacycloannulene ligands and their complexes

Complex	$E_{0(1)}$, mV 0 → +1	$E_{0(2)}$, mV +1 → +2	E_r, mV $M^{2+} \rightarrow M^+$
L1[a]	+170	+580	
14-Ni[b]	+96	+620	−2650
14-Cu	−92	+510	−2217
14-Pd[a]	+85	+698	−2710
L2	+125	+560	
15-Ni	+113	+615	−2433
15-Cu	−82	+471	−1999
15-Pd	+114	+619	−2642

[a] Ref. [19].
[b] Ref. [14].

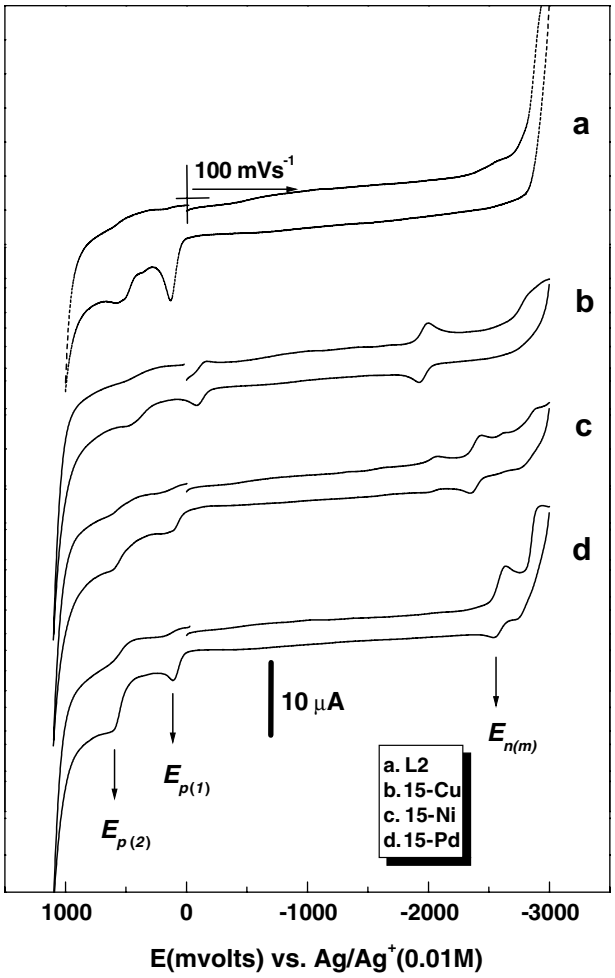


Fig. 1. Cyclic voltammograms of the new complexes in a 0.1 M TEAP-DMSO solution at 25 °C and 100 mV s^{-1}.

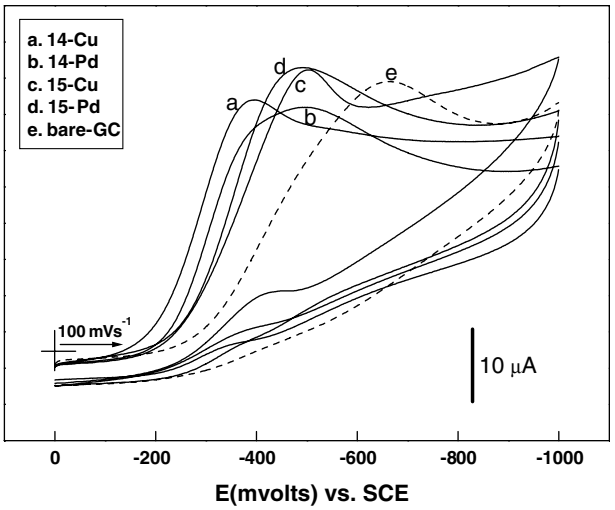


Fig. 2. Cyclic voltammograms of catalytic dioxygen reduction by the modified and bare-GC electrodes in a 0.1 M phosphate buffer (pH 7.0) water solution at 25 °C and 100 mV s^{-1}.

The GCEs modified by **14-Cu**, **15-Cu**, **14-Pd** and **15-Pd** were applied for dioxygen electroreduction, and the reduction potential differences between the modified and bare-GC electrodes were measured to evaluate the catalytic activity of the complexes as the electrode modifier. As shown in Fig. 2, the reduction potentials of dioxygen by the modified GCEs were reduced by 160–280 mV comparing to the bare-GCE. It could be shown that the electrodes modified by the new complexes have good catalytic activities for use of electrocatalytic reduction of dioxygen in water solution. The nucleophilic attack of dioxygen on the copper(II)-containing complex, **14-Cu**, might be readily available; that is the relatively hard metal Cu could effectively accept oxygen attack.

3.3. Epoxidation of styrene

To investigate the electronic effects of catalyst and substrate on the oxidation reaction, the copper(II)- and palladium(II)-tetraazaannulenes (**14-Cu**, **15-Cu**, **14-Pd** and **15-Pd**) and the styrene derivatives were used as catalysts and as substrate, respectively. The results of the reactions are listed in Table 2. As shown in Table 2, the % conversion by the copper(II) complexes were generally higher than those of the palladium(II) ones. Such an observation could be explained by the difference of the electron densities on the metal centers of the complexes, depending on the substituents, which affects the formation of the activated metal-olefin complexes as an intermediate. The about 40% conversion yield by the copper complexes for

Table 2
Catalytic activities of **14-**, **15-Cu** and **14-**, **15-Pd** for *p*-Xstyrene oxidation[a]

Catalyst	Substrate (*p*-Xstyrene)	Conversion (%)	Product		
			A (%)	B (%)	C (%)
14-Cu	X = OCH_3	70	10	81	9
	X = CH_3	55	28	67	5
	X = H	40	30	55	15
	X = F	33	27	60	13
	X = Cl	20	14	84	2
14-Pd	X = OCH_3	53	7	75	18
	X = CH_3	43	15	70	15
	X = H	33	28	55	17
	X = F	25	20	43	37
	X = Cl	14	12	48	40
15-Cu	X = OCH_3	75	17	75	8
	X = CH_3	63	20	71	9
	X = H	43	24	55	21
	X = F	38	32	54	14
	X = Cl	24	29	50	21
15-Pd	X = OCH_3	46	15	70	15
	X = CH_3	37	25	70	5
	X = H	25	16	53	31
	X = F	22	24	44	32
	X = Cl	11	35	38	27

[a] Experimental conditions: complex, 0.2 mmol; *p*-Xstyrene, 2 mmol; NaOCl, 5 mmol; solvent, dichloromethane 4 mL; temperature, 25 °C; reaction time, 48 h; product A, benzaldehyde; B, styreneoxide; C, phenylacetaldehyde + acetophenone; conversion (%) = 100 × [oxidation product]/[initial *p*-Xstyrene].

styrene indicated slightly better catalytic activities than the cyclam-nickel(II) one, which showed about a 30% conversion yield. The activities of the palladium complexes were similar to those of the Ni cyclam complex [9a]. The copper(II) complex can accept nucleophilic attack of styrene easier than the palladium(II) one due to the poor electron density. That is the π-electron in carbon double bond of styrene readily transfers to the copper(II) complex to form the activated metal-olefin. The palladium(II) complex, with rich electron density in comparison to the copper(II) complex, could not effectively manage the electrophilic attack on the olefin, therefore making the olefin less activated. The electronic effect of the complex on the conversion of substrate was in agreement with that for metal porphyrin complexes for olefin oxidation [25]. On the other hand, the substituent effect of *p*-Xstyrene on the substrate % conversion was consistent with the reverse order of the substituents σ_p values; X = *p*-OCH_3 (−0.27) < *p*-CH_3 (−0.17) < H (0) < *p*-F (+0.06) < *p*-Cl (+0.23) [22]. The electron withdrawing groups (F or Cl) of styrene decrease the electron density of the double bond in styrene, making it more difficult for nucleophilic attack on the metal center in comparison with the electron donating groups such as OCH_3 or CH_3. Thus the oxidation reaction of olefin should consider the electronic properties of the metal complexes together with those of olefins. Such basic experiments will certainly be useful to summarize the catalytic properties of the prepared teraazaannulene complexes in the future.

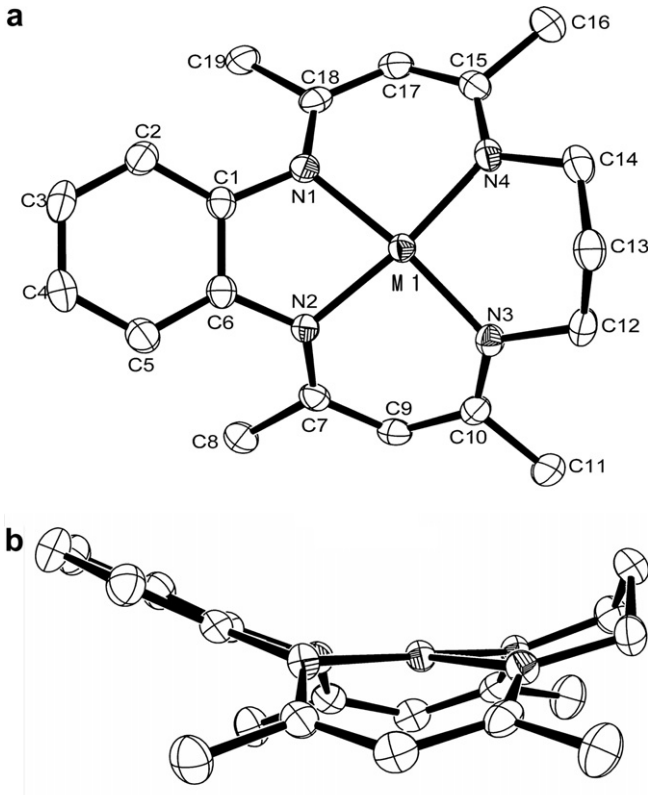


Fig. 3. Molecular structure (a) and side view (b) of **15-M** (M = Cu(II) or Pd(II)).

3.4. Crystal structures

The structures of 2,4,10,12-tetramethyl-1,5,9,13-monobenzotetraazacyclo[15]tetra-decinato(2-)copper(II) and -palladium(II) complexes were very similar and are illustrated in Fig. 3. Crystal data, details of the data collection and refinement parameters are listed in Table 3. Selected bond distances and bond angles are collected in Table 4. The **15-Cu** and **15-Pd** complexes have two molecules and a molecule in a cell, respectively, and both **15-Cu** and **15-Pd** showed like saddle-shaped structures. The average distances of N–Cu and N–Pd were 1.9692 ± 0.0066 and 2.0116 ± 0.0067 Å, respectively. The result is

Table 3
Crystal data and structure refinements for **15-Cu** and **15-Pd**

Empirical formula	$C_{38}H_{48}Cu_2N_8$	$C_{19}H_{24}PdN_4$
Formula weight	743.92	414.82
Temperature (K)	173(2)	173(2)
Wavelength (Å)	0.71069	0.71073
Crystal system	monoclinic	monoclinic
Space group	*C*2/*c*	*C*2/*c*
Unit cell dimensions		
a (Å)	22.833(5)	22.9504(15)
b (Å)	10.215(5)	10.2746(7)
c (Å)	14.869(5)	14.6978(10)
α (°)	90.000(5)	90
β (°)	101.200(5)	100.0930(10)
γ (°)	90.000(5)	90
V (Å^3)	3401(2)	3412.2(4)
Z	4	8
D_{calc} (Mg/m^3)	1.453	1.615
Absorption coefficient (mm^{-1})	1.292	1.095
F(000)	1560	1696
Crystal size (mm)	0.50 × 0.25 × 0.03	1.05 × 0.40 × 0.20
θ Range for data collection (°)	1.82–28.37	2.18–28.27
Index ranges	$-29 \leqslant h \leqslant 13$ $-13 \leqslant k \leqslant 13$ $-19 \leqslant l \leqslant 19$	$-30 \leqslant h \leqslant 24$ $-13 \leqslant k \leqslant 9$ $-18 \leqslant l \leqslant 19$
Reflections collected	10493	10486
Independent reflections [R_{int}]	4083 [0.0298]	4093 [0.0179]
Completeness to theta	95.8% (28.37°)	96.6% (28.27°)
Absorption correction	semi-empirical from equivalents	semi-empirical from equivalents
Maximum and minimum transmission	0.9623 and 0.5644	0.8107 and 0.3926
Refinement method	full-matrix least-squares on F^2	full-matrix least-squares on F^2
Data/restraints/parameters	4083/0/313	4093/0/313
Goodness-of-fit on F^2	1.028	1.046
Final *R* indices [$I > 2\sigma(I)$]	$R_1 = 0.0315$, $wR_2 = 0.0727$	$R_1 = 0.0189$, $wR_2 = 0.0492$
R indices (all data)	$R_1 = 0.0486$, $wR_2 = 0.0823$	$R_1 = 0.0203$, $wR_2 = 0.0501$
Largest difference in peak and hole (e Å^{-3})	0.450 and −0.358	0.552 and −0.591

Table 4
Selected bond distances (Å) and angles (°)

	15-Cu	15-Pd
N(1)–M(1)	1.9668(19)	1.9930(12)
N(2)–M(1)	1.9583(19)	1.9969(13)
N(3)–M(1)	1.0775(19)	2.0273(13)
N(4)–M(1)	1.974(2)	2.0292(13)
N(1)–C(1)	1.406(3)	1.4148(19)
N(1)–C(18)	1.335(3)	1.338(2)
N(2)–C(6)	1.413(3)	1.4169(19)
N(2)–C(7)	1.336(3)	1.336(2)
N(3)–C(10)	1.321(3)	1.321(2)
N(3)–C(12)	1.470(3)	1.4692(19)
N(4)–C(15)	1.324(3)	1.318(2)
N(4)–C(14)	1.467(3)	1.469(2)
C(7)–C(9)	1.391(3)	1.394(2)
C(9)–C(10)	1.409(3)	1.412(2)
C(12)–C(13)	1.510(4)	1.513(2)
C(13)–C(14)	1.507(4)	1.513(2)
C(15)–C(17)	1.404(3)	1.414(2)
C(17)–C(18)	1.399(3)	1.391(2)
N(1)–M(1)–N(3)	171.42(7)	173.13(5)
N(2)–M(1)–N(4)	172.63(7)	171.83(5)
N(1)–M(1)–N(2)	81.58(8)	81.48(5)
N(1)–M(1)–N(4)	91.05(8)	92.52(5)
N(2)–M(1)–N(3)	91.30(7)	92.12(5)
N(3)–M(1)–N(4)	96.04(8)	93.59(5)
M(1)–N(1)–C(1)	111.61(14)	111.20(9)
M(1)–N(1)–C(18)	122.37(15)	121.96(10)
M(1)–N(4)–C(15)	121.58(15)	121.05(11)
M(1)–N(4)–C(14)	121.09(15)	120.36(11)
N(1)–C(18)–C(17)	121.7(2)	122.45(14)
N(4)–C(15)–C(17)	124.1(2)	124.45(14)
N(4)–C(14)–C(13)	112.8(2)	111.96(13)
C(12)–C(13)–C(14)	113.4(2)	113.46(14)
C(15)–C(17)–C(18)	126.9(2)	128.67(15)

consistent with the sequence of the radius of the metal ion ($Pd^{2+} = 1.28$ Å, $Cu^{2+} = 1.17$ Å). The bond distances of N(1)–C(18) (1.335 Å for **15-Cu** and 1.338 Å for **15-Pd**) and N(2)–C(7) (1.336 Å for both **15-Cu** and **15-Pd**) were longer than N(3)–C(10) (1.321 Å for **15-Cu** and **15-Pd**) and N(4)–C(15) (1.324 Å for **15-Cu** and 1.318 Å for **15-Pd**), which might be due to smaller basicities of phenylenediamine (pK_{a1} and pK_{a2}, 1.81 and 4.61) than those of propylenediamine (pK_{a1} and pK_{a2}, 9.03 and 10.94) [27,28]. The bond angles of the asymmetric15-membered macrocyclic complexes, **15-Cu** and **15-Pd**, having a five-membered and three six-membered chelate rings, were appreciably different in comparison with those of asymmetric 14-membered tetraaza[14]annulene nickel(II) [23,24,26] and palladium(II) [10]. In the five-membered ring of the symmetric tetraaza[14]annulene complexes, the bond angles (N–M–N) were about 83° for palladium [10] and 85.5° for nickel [23]. The values (N(1)–M(1)–N(2)) of the five-membered ring of **15-Cu** and **15-Pd** were 81.48° and 81.58°. The N(3)–M(1)–N(4) angles of **15-Cu** and **15-Pd** were 96.04° and 93.59°, and the average angles of N(1)–M(1)–N(4) and N(2)–M(1)–N(3) were 91.18° and 92.32°, respectively, while the average N(2)–M(1)–N(4) and N(1)–M(1)–N(3) angles are similar (172.02° for **15-Cu** and 172.48° for **15-Pd**). It should be able to be explained from these results that the metal and four nitrogen atoms in the asymmetric complexes definitely display more square-pyramidal geometries comparing to the symmetric tetraaza[14]annulene complexes, as illustrated in Fig. 3, owing to ring strain of the propylenediamine group [10,23,24].

Acknowledgement

This work was supported by Korea Research Foundation Grant (KRF-2006-005-C00009).

Appendix A. Supplementary material

Crystallographic data for the structural analysis have been deposited at the CCDC, 12 Union Road, Cambridge CB2 1EZ, UK with the deposition numbers CCDC 222449 (**15-Pd**) and CCDC 222451 (**15-Cu**). Copies of this information can be obtained free of charge via, e-mail: deposit@ccdc.cam.ac.uk or http://www.ccdc.cam.ac.uk; fax: +44 1223 336 033. Supplementary data associated with this article can be found, in the online version, at doi:10.1016/j.poly.2006.07.033.

References

[1] K. Sakata, M. Shimoda, M. Hashimoto, J. Heterocyclic Chem. 33 (1996) 1593.
[2] D. Mandon, J.M. Giraudon, L. Toupet, J. Sala-Pala, J.E. Gurechais, J. Am. Chem. Soc. 109 (1987) 3490.
[3] E.V. Gaemelbecke, W. Kuntner, K.M. Kadish, Inorg. Chem. 32 (1993) 438.
[4] P.J. Hochgesang, R.D. Bereman, Inorg. Chim. Acta 162 (1989) 91.
[5] C.L. Bailey, R.D. Bereman, D.P. Rillema, R. Nowak, Inorg. Chim. Acta. 116 (1986) 697.
[6] (a) M. Hashimoto, K. Sakata, Polyhedron 16 (1997) 975;
(b) F. Lelj, G. Morelli, G. Ricciardi, M. Romanelli, A. Rosa, Polyhedron 10 (1991) 1911;
(c) M. Tsutsui, R.L. Bobsein, G. Cash, R. Pettersen, Inorg. Chem. 18 (1979) 758;
(d) P.J. Hochgesang, R.D. Bereman, Inorg. Chim. Acta. 156 (1989) 213.
[7] C.L. Bailey, R.D. Bereman, D.P. Rillema, Inorg. Chem. 25 (1986) 3149.
[8] J. Eilmes, Polyhedron 4 (1985) 943.
[9] (a) J.F. Kinneary, J.S. Albert, C.J. Burrows, J. Am. Chem. Soc. 110 (1988) 6124;
(b) J.D. Koola, J.K. Kochi, Inorg. Chem. 26 (1987) 908;
(c) J.F. Kinneary, T.R. Wagler, C.J. Burrows, Tetrahedron Lett. 29 (1988) 877.
[10] (a) H. Yoon, C.J. Burrows, J. Am. Chem. Soc. 110 (1988) 4087;
(b) M. Yamada, S. Ochi, H. Huzuki, A. Hisazumi, S. Kuroda, I. Shimao, K. Araki, J. Mol. Catal. 87 (1994) 195;
(c) T.R. Wagler, Y. Fang, C.J. Burrows, J. Org. Chem. 54 (1989) 1584.
[11] (a) Y. Yang, F. Diederich, J.S. Valentine, J. Am. Chem. Soc. 113 (1991) 7195;
(b) Y. Yang, F. Diederich, J.S. Valentine, J. Am. Chem. Soc. 112 (1990) 7826;
(c) W. Nam, J.S. Valentine, J. Am. Chem. Soc. 112 (1990) 4977.
[12] Y.C. Park, S.S. Kim, D.C. Lee, C.H. An, Polyhedron 16 (1997) 253.

[13] Y.C. Park, H.G. Na, J.H. Choi, J.C. Byun, E.H. Kim, D.I. Kim, J. Coord. Chem. 55 (2002) 505.
[14] Y.C. Park, J.C. Byun, J.H. Choi, J.W. Lim, D.C. Lee, H.G. Na, Polyhedron 21 (2002) 917.
[15] Y.C. Park, Z.U. Bae, S.S. Kim, S.K. Baek, Bull. Korean Chem. Soc. 16 (1995) 287.
[16] I.M. Kolthoff, J.F. Coetzee, J. Am. Chem. Soc. 79 (1957) 1852.
[17] F.A. L'Eplattenier, A. Pugin, Helv. Chim. Acta. 58 (1975) 917.
[18] Y.C. Park, J.H. Choi, Z.U. Bae, H.G. Na, D.I. Kim, J. Incl. Phenom. Macrocycl. Chem. 49 (2004) 107.
[19] Y.C. Park, J.H. Choi, J.C. Byun, Z.U. Bae, H.G. Na, E.H. Kim, D.I. Kim, Bull. Korean Chem. Soc. 25 (2004) 317.
[20] G.M. Sheldrick, Acta Crystallogr., Sect. A 46 (1990) 467.
[21] G.M. Sheldrick, SHELX-97, University of Goettingen, Goettingen, Germany, 1997.
[22] K.M. Kadish, M.M. Morrison, L.A. Constant, L. Dickens, D.G. Davis, J. Am. Chem. Soc. 98 (1976) 8387.
[23] E.M. Opozda, W. Lasocha, Inorg. Chem. Commun. 3 (2000) 239.
[24] J. Eilmes, M. Basato, G. Valle, Inorg. Chim. Acta. 290 (1999) 14.
[25] Y.C. Park, H.G. Na, S.S. Kim, J. Korean Chem. Soc. 38 (1994) 333.
[26] Y.C. Park, D. Yoshioka, M. Mikuriya, J.H. Choi, J.H. Choi, J.W. Lim, D.I. Kim, Inorg. Chim. Acta 358 (2005) 419.
[27] A. Mederos, A. Domínguez, R.H. Molina, J. Sanchiz, R. Brito, Coord. Chem. Rev. 193–195 (1999) 913.
[28] Robert C. Weast, Handbook of Chemistry and Physics, 53rd ed., CRC Press, Boca Raton, 1972–1973, D117-D118.

Available online at www.sciencedirect.com
ScienceDirect
Polyhedron 26 (2007) 93–100
POLYHEDRON
www.elsevier.com/locate/poly

Thermal behaviour of hexanuclear titanium(IV) oxo isopropoxide carboxylates, and their usability as a single-source TiO_2 CVD precursors

P. Piszczek *

Faculty of Chemistry, Nicolaus Copernicus University, 87-100 Toruń, ul. Gagarina 7, Poland

Received 16 May 2006; accepted 28 July 2006
Available online 24 August 2006

Abstract

Hexanuclear oxo titanium(IV) isopropoxide carboxylates, of the general formula $[Ti_6O_6(OPr^i)_6(O_2CR)_6]$ ($R = Bu^t$ (**1**), CH_2Bu^t (**2**)) and $[Ti_6O_6(OPr^i)_6(O_2CC(CH_3)_2Et)_6]\cdot 0.5(C_7H_8)$ (**3**), have been synthesized as polycrystalline powders in order to study their thermal properties and usability as TiO_2 CVD precursors. Analysis of thermogravimetric and variable temperature (VT-IR) data shows that the thermal stability of the synthesized complexes decreases as follows **3** > **2** > **1**. The composition of the vapors formed during the thermolysis of **1**–**3** were qualitatively analysed with VT-IR methods and mass spectrometry (MS-EI). According to obtained results, the decomposition of **1** and **2** proceeds with a partial decomposition and the formation of a volatile and stable titanium species, sufficient for their transport in vapors. The formation of volatile titanium-containing derivatives is an important factor that decides the application of **1** and **2** as precursors in CVD experiments. The high stability of **3** causes the thermal decomposition of this complex to be observed just above 573 K, and volatile titanium-containing derivatives were not detected in vapors. These results indicate that **3** could not be used as a precursor in CVD processes.
© 2006 Elsevier Ltd. All rights reserved.

Keywords: Ti(IV) complexes; Volatile titanium species; Thermal analysis; MS and VT-IR studies; CVD precursors

1. Introduction

Multinuclear titanium(IV) alkoxy complexes of the general formula $[Ti_xO_y(OR)_i(L)_j]$ ($R = Et$, Pr^i, Bu, Bu^t; L – β-diketonates, carboxylates) are an interesting group of compounds consisting of a Ti(IV) oxide core surrounded by alkoxy and bridge ligands. They are often applied as sol–gel precursors for the preparation of new materials containing titanium dioxide, which are mainly used in microelectronics, optics, optoelectronics technologies [1–5], and also in photocatalytical processes [6–8]. Moreover physico-chemical properties of selected multinuclear Ti(IV) complexes allow for their application also as potential precursors in chemical vapor deposition methods (CVD). The examples are hexanuclear Ti(IV) oxo isopropoxide carboxylates with the general formula $[Ti_6O_6(OPr^i)_6(O_2CR)_6]$ ($R = Bu^t$, CH_2Bu^t) [9]. The application of these compounds as CVD precursors require knowledge about their thermal decomposition mechanisms and gas phase reactions enables the fabrication of pure titanium dioxide layers.

X-ray studies exhibited that the crystallographic structure of $[Ti_6O_6(OPr^i)_6(O_2CR)_6]$ ($R = H$, C_6H_4OPh, Bu^t) consists of clusters, where three μ_3-oxo, two μ-carboxylate bridges and a terminal alkoxide ligand surround each central cation [10–12]. The prismatic hexamers are associated through van der Waals interactions between the isopropoxide and carboxylate ligands (Fig. 1). The network of the weak intermolecular interactions seems to be responsible for the promising volatility of this compound.

In this paper, the results of the thermal behaviour of complexes synthesized in the 1:1 reaction of $Ti(OPr^i)_4$ with HO_2CR ($R = Bu^t$ (**1**), CH_2Bu^t (**2**), $C(CH_3)_2Et$ (**3**)) are discussed. Thermogravimetric analysis (TG/DTG/DTA), mass spectrometry (MS-EI) and variable temperature

* Fax: +48 56 652 477.
E-mail address: piszczek@chem.uni.torun.pl.

0277-5387/$ - see front matter © 2006 Elsevier Ltd. All rights reserved.
doi:10.1016/j.poly.2006.07.037

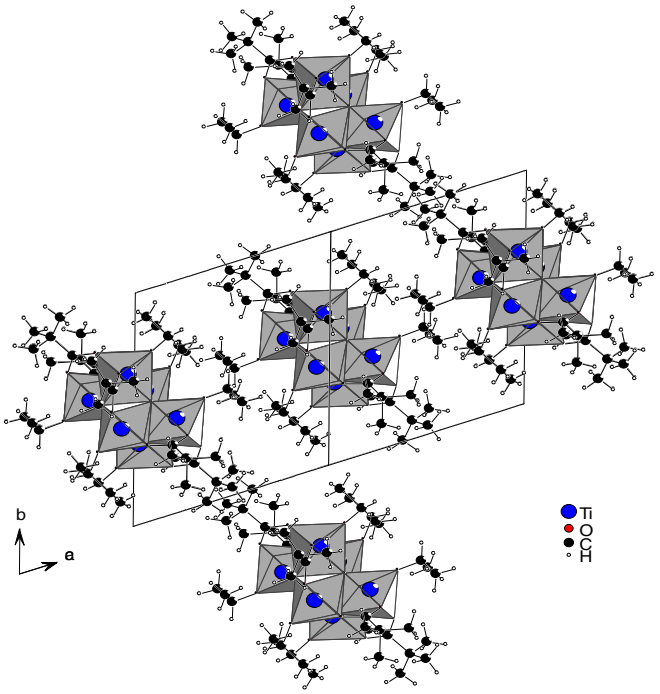


Fig. 1. The structure of $[Ti_6O_6(OPr^i)_6(O_2CBu^t)_6]$ (**1**).

infrared spectrometry (VT-IR) were used in order to study the thermolysis pathway and the identification of the vapor composition. The discussed results were compared with results of earlier CVD experiments [9].

2. Experimental

The studied complexes were synthesized as colourless polycrystalline powders in the direct reaction of titanium(IV) isopropoxide ($Ti(OPr^i)_4$) with the carboxylic acid (HO_2CR, R = Bu^t, CH_2Bu^t, $C(CH_3)_2Et$) in a 1:1 $Ti(OPr^i)_4$/RCO_2H molar ratio under the conditions described in the earlier report [12]. The powders were stored at room temperature under an argon atmosphere. The obtained compounds were slightly soluble in aromatic solvents. Themogravimetric analysis (TGA) was carried out using SDT 2960 TA Instruments, in nitrogen atmosphere from 298 to 773 K at a ramp rate of 3° min^{-1}. The complexes were characterized using IR and ^{13}C NMR spectroscopy. Infrared spectra (IR) were recorded on a Perkin Elmer Spectrum 2000 spectrometer within the range 400–4000 cm^1 with a medium slit width and a peak resolution of 4.0 cm^{-1}. The crystals were studied as a powder dispersed in a KBr pellet (400–4000 cm^{-1}). Solid state ^{13}C NMR spectra were recorded on a Bruker AMX 300. Solution ^1H NMR spectra (C_7D_8) were recorded using a 5 mm solution probe on a Varian Gemini 200.

The spectral data of $[Ti_6O_6(OPr^i)_6(OOCBu^t)_6]$ (**1**) were discussed in the earlier report [12], and therefore in this paper, only the spectral data of **2** and **3** have been presented. The elemental analysis (Vario Macro) has been used in order to determine carbon and hydrogen contamination. The % Ti was gravimetrically determined as TiO_2, according to the Meth-Cohn et al. method [13].

$[Ti_6O_6(OPr^i)_6(OOCCH_2Bu^t)_6]$ (**2**): *Anal.* Calc. for $C_{54}H_{108}O_{24}Ti_6$: C, 45.42; H, 7.10; Ti, 18.91. Found: C, 45.32; H, 6.90; Ti, 19.15%. TG/DTG/DTA 411–537 K (endotherm.), 573–681 K (endotherm.), overall weight loss: calculated: 66.4%, found: 66.9%, IR (KBr, cm^{-1}) 1577 (s, COO), 1538 (m, COO), 1455 (s, COO), 1416 (s, COO), 1209 (m, C–Me_3), 800 (m, Ti–O), 722 (m, Ti–O), 635 (m, Ti–O (OR)). ^{13}C NMR (solid, δ, ppm) 49.5 (CH_3), 29.9 (C–(CH_3)$_3$), 24.5 (CH_3–(Pr^i)), 81.5 (CH–(Pr^i)), 180.8, 178.4 (COO). ^1H NMR (C_7D_8, δ, ppm) 1.23 (s, CH_3), 5.13 (m, CH(Pr^i)).

$[Ti_6O_6(OPr^i)_6(OOC(CH_3)_2Et)_6]\cdot 0.5(C_7H_8)$ (**3**): *Anal.* Calc. for $C_{57.5}H_{112}O_{24}Ti_6$: C, 46.76; H, 7.59; Ti, 19.52. Found: C, 46.86; H, 7.36; Ti, 19.35%. TG/DTG/DTA 373–553 K (endotherm.), 553–693 K (endotherm.), overall weight loss: calculated: 65.7%, found: 66.9%, IR (KBr, cm^{-1}) 1584 (s, COO), 1528 (m, COO), 1479 (s, COO), 1428 (s, COO), 1215 (m, C–Me_2R), 750 (m, Ti–O), 600 (m, Ti–O (OR)). ^{13}C NMR (solid, δ, ppm) 9.0, 34.0 (Et), 24.6 (CH_3), 43.0, 44.5 (C–(CH_3)$_2$), 29.6 (CH_3–(Pr^i)), 82.4 (CH_3–(Pr^i)), 188.0, 185.2 (COO). ^1H NMR (C_7D_8, δ, ppm) 1.14 (t, CH_3(Et), J_{H-H} 7.0 Hz), 1.24 (s, CH_3 (C(Me)$_2$)), 1.54 (d, CH_3 (Pr^i), J_{H-H} 6.4 Hz), 1.67 (q, CH_2 (Et), J_{H-H} 8.2 Hz).

Variable temperature IR spectroscopic studies between 273 and 523 K, in the solid phase, were carried out with a SPECAC temperature variable cell. IR spectra of vapors transported with the carrier gas (Ar) were studied in the reactor described in the earlier report [14]. Mass spectra were recorded, in the temperature range 423–593 K with a MS AMD-604, MASPEC system using the EI method. The deposition experiments were carried out using a horizontal *hot-wall* CVD reactor as described in a previous publication [9,15].

3. Results and discussion

The results of the elemental analysis of polycrystalline powders suggest the formation of complexes of the general formula $[Ti_6O_6(OPr^i)_6(O_2CR)_6]$ (R = Bu^t (**1**), CH_2Bu^t (**2**), $C(CH_3)_2Et)_6$ (**3**). However, according to microanalysis data $[Ti_6O_6(OPr^i)_6(O_2CC(CH_3)_2Et)_6]\cdot 0.5(C_7H_8)$ as a general formula of **3** should be postulated. It is a consequence of the presence of toluene molecules in the crystal lattice of this complex. The structures of **2** and **3** were characterized by IR and ^{13}C NMR spectroscopy (detailed data are presented in the experimental part) and were compared with X-ray and spectroscopic data of **1** [12]. The medium intensity bands, which were detected in the IR spectra of **2** and **3** at 722–750 cm^{-1}, proved the formation of oxo bridges in the $[Ti_6O_6]$ clusters. The frequencies of stretching vibrations of the COO groups (ν_{as} = 1528–1574 cm^{-1} and ν_s = 1416–1479 cm^{-1}), and the chemical shifts of split peaks attributed to the carboxylate carbon (^{13}C NMR, δ = 178–188 ppm) indicates the formation of asymmetric

syn–syn carboxylate bridges. Moreover, both IR and ^{13}C NMR data confirm the presence of coordinated alkoxide ligands in the structure of **2** and **3**. Considering the spectroscopic data, in the structure of the studied complexes an analogous type of cluster is formed as is found in the crystal lattice of **1**.

3.1. Influence of temperature on the solid structure of $[Ti_6O_6(OPr^i)_6(O_2CR)_6]$ complexes

Thermogravimetric and variable temperature IR spectroscopy methods have been used in order to study the thermal changes in the solid structure of **1**–**3**. The results of TGA/DTG/DTA measurements are summarised in Table 1. The thermal decomposition (under an inert atmosphere) of **1**–**3** proceeds in three endothermic stages at 540–691 K, 499–689 K and 628–673 K (Table 1). In the case of **1** an additional weak decomposition stage at 365 K was also found. According to thermogravimetric data (Table 1), the thermal stability of the studied complexes decreases as follows: **3** > **2** > **1**. The complete weight loss reaches 64.7% (**1**), 64.5% (**2**) and 67.6% (**3**) at 703 K and is in agreement with the formation of titanium dioxide as the main decomposition product (theoretical weight loss: 64.3%, 66.4% and 66.4% for **1**–**3** respectively).

Variable temperature spectroscopy studies exhibit a significant frequency shift of the ν_{as}(COO) band from 1594 to 1590 cm^{-1}, and splitting of ν(Ti–OR) and ν_{as}(Ti–O–Ti) bands at ~1130 $cm^{-1}$and ~729 cm^{-1} respectively, during the heating of **1** between 293 and 523 K (Fig. 2). It was found that the dependence of ν_{as}(COO), ν(Ti–OR) and ν_{as}(Ti–O–Ti) frequencies versus temperature changes stepwise, the first step near 413 K and the second one at 473 K. Above effects can be assigned to phase transitions close to the above temperatures [16,17]. The analogous dependences of **2**, observed in VT-IR spectra between 373 and 523 K, were distinctly weaker.

Continuous changes of frequency and the integral intensity of bands assigned to vibrations of OOC, Ti–OR and Ti–O–Ti groups were observed in the spectra of **3**, which confirms its high thermal stability.

3.2. VT-IR studies of vapor composition

A potential application of **1**–**3** in CVD experiments requires the determination of changes in the composition of vapors formed during the thermolysis of these complexes under the conditions at which the deposition processes occur. The application of variable temperature IR spectroscopy enables the study of this problem and the obtained results have been presented in Fig. 3(a)–(c). Volatile titanium species containing the coordinated carboxylate or alkoxide groups were identified based on the presence of absorption bands at 1450–1700 cm^{-1} (ν_{as}(COO), ν_s(COO)), 1100–1200 cm^{-1} (ν(CO)) and 600–900 cm^{-1} (ν_{as}(TiOTi), ν_{as}(TiOR), δ(COO)) [18–21].

The overall studies of VT-IR spectra of the gas phase, formed during the thermolysis of **1**–**3**, make the determination of the temperature ranges in which the concentrations of volatile species are highest possible. This region was relatively narrow in spectra of **1**, strong bands of thermolysis products were detected in VT-IR spectra between 523 and 553 K (Fig. 3(a)). In the case of **2** they were found between 373 K and 533 K (Fig. 3(b)). Studies of **3** revealed that intense bands of volatile species appeared just above 573 K, as a result of the high thermal stability of this complex (Fig. 3(c)).

A detailed analysis of VT-IR spectra of **1** between 373 and 673 K (Fig. 3(a)) revealed changes in the vapor composition with the increase of the temperature. Weak bands of volatile species were detected in spectra registered near 413 K, which is the temperature region where, according to frequency changes in the solid structure of this complex, the first phase transition was observed. The hydrocarbon species (bands at 2890–3070, 1472, 1382, 1254 cm^{-1} assigned to vibrations of $-CH_2$, $=CH_2$ and $-CH_3$ groups), –OR and probable $Ti(OR)_4$ derivatives (bands at 1150, 1073, 953 cm^{-1}), have been identified as the main components of vapors at this temperature. Strong changes were noticed at 473 K (second phase transition). The appearances of bands at 1743, 1168 cm^{-1} (ester groups), 1117, 919 cm^{-1} (coordinated alkoxide groups) and also 1652, 1485 cm^{-1} (coordinated carboxylate groups) indicate the detachment of titanium alkoxides and titanium carboxylate

Table 1
Thermogravimetric results of the decomposition of hexanuclear oxo Ti(IV) carboxylate alkoxides

Complex	Stage	Temperature range (weight loss) [K]	DTA (K)
$[Ti_6O_6(OPr^i)_6(O_2CBu^t)_6]$ (**1**)	I	303–398 (4.4%)	365_{endo}
	II	398–573 (28.7%)	540_{endo}
	III	573–678 (22.3%)	672_{endo}
	IV	678–713 (9.3%)	691_{endo}
$[Ti_6O_6(OPr^i)_6(O_2CCH_2Bu^t)_6]$ (**2**)	I	343–523 (15.1%)	499_{endo}
	II	523–653 (38.2%)	641_{endo}
	III	653–713 (11.2%)	689_{endo}
$[Ti_6O_6(OPr^i)_6(O_2CC(CH_3)_2Et)_6]\cdot 0.5(C_7H_8)$ (**3**)	I	323–643 (32.6%)	628_{endo}
	II	643–683 (27.4%)	678_{endo}
	III	683–703 (7.6%)	673_{endo}

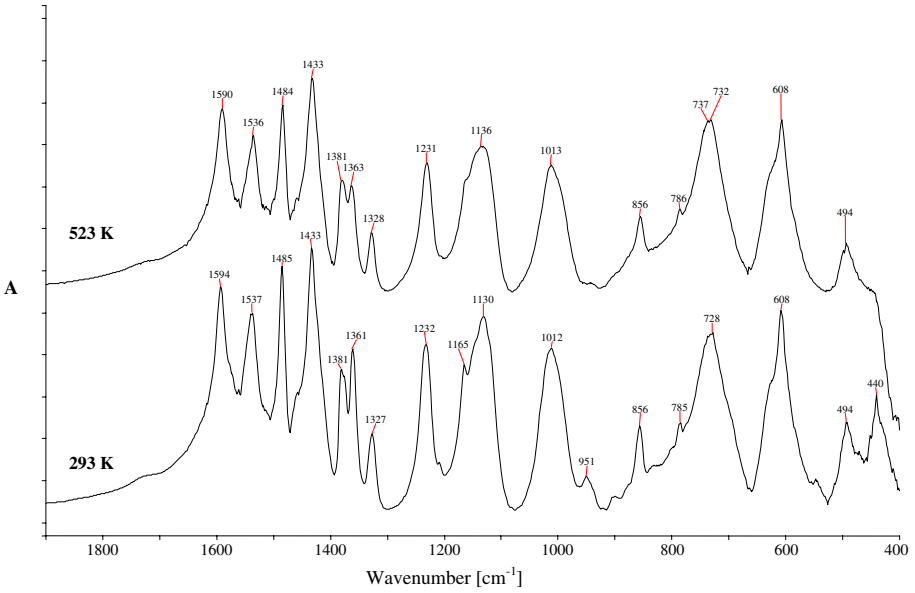


Fig. 2. IR spectra of $[Ti_6O_6(OPr^i)_6(O_2CBu^t)_6]$, registered at 293 and 523 K.

derivatives as well as esterification processes occurring. The intensities of the above mentioned bands are very weak at 473 K, but rapidly increase between 523 and 553 K. The complete decomposition of **1** at higher temperatures (613–673 K) causes the appearances of bands attributed to vibration of CO_2 (2360, 667 cm^{-1}), CO (2115, 2173 cm^{-1}), anhydride acid (1824, 1771 cm^{-1}), and also carboxylate and titaniumcarboxylate derivatives (1716, 1675, 1458 cm^{-1}). Considering the VT-IR data, the decomposition pathway of **1** as partial decomposition of this complex and formation of volatile and stable titanium-containing fragments (titanium alkoxide and titanium carboxylate derivatives), between 523 and 553 K has been proposed. Analysis of VT-IR data revealed that two potential sources of TiO_2 layers, of different thermal stability, are transported in vapors. The consequence of the postulated pathway is the deposition of TiO_2 films, which characterize the different polycrystalline structure. The formation of pure TiO_2 anatase films at lower deposition temperatures (713–753 K) can be caused by the majority of titanium alkoxide species in vapors. The presence of stable titanium carboxylate fragments in vapors, at higher temperatures, leads to deposition pure TiO_2 rutile layers between 833 and 873 K [9].

During the thermolysis of **2** only titanium alkoxide species (800–1120 cm^{-1}) and ester derivatives (1133, 1747 cm^{-1}) were found in the gas phase, in the wide temperature range 373–533 K (Fig. 3(b)). Appearances of the strong bands at 2360, 667 cm^{-1} (CO_2), 2050–2200 cm^{-1} (CO), and low intensity bands between 1830 and 1740 cm^{-1} (anhydride acid) indicate the complete decomposition of this compound above 573 K. Simultaneously absorption bands which can be assigned to volatile titanium carboxylate species, were not detected in the VT-IR spectra of the vapors. According to earlier reports [9] application of **2** as a CVD precursor allowed the deposition of pure TiO_2 anatase films (714–793 K) or a mixture of anatase/rutile films (>793 K). The pure TiO_2 rutile layers have not been obtained.

The high thermal stability of **3** caused only very weak bands, which can be attributed to titanium alkoxide (1034, 818 cm^{-1}), ester (1676, 1115 cm^{-1}) and other species containing carboxylate groups (1716 cm^{-1}), to be observed below 573 K (Fig. 3(c)). The intensity of absorption bands attributed to volatile decomposition fragments increases above 573 K. The appearance of a composite band between 1730 and 1770 cm^{-1}, which appears in IR spectra at 573–623 K can be assigned to vibrations of carboxylate groups of aldehyde, ketone or ester species. Bands derived from stretching vibrations of coordinated COO groups were not observed in spectra registered below 623 K. Spectral analysis of vapors formed during the thermolysis of **3** at 673 K shows that hydrocarbons, CO_2, CO and probable titanium carboxylate species (weak band at 1652 cm^{-1}) were the main components.

3.3. Results of MS studies

The main mass signals of titanium-containing fragments registered in the MS-EI spectra of **1**–**3** between 423 and 603 K and their relative intensities, are listed in Tables 2–4. Results of these investigations reveal clear differences in the way that complexes **1**–**3** fragment. In the case of **1** and **2**, the fragmentation of multinuclear clusters can be described as a result of the detachment of alkoxo, carboxylate ligands and the following volatile titanium derivatives: $[Ti(OPr^i)_4]$, $[TiO(OPr^i)_2]$, $[Ti(O_2CR)_2]$, $[OTi_2(O_2CR)_2]$ (Tables 2 and 3). According to data presented in Table 2 at 473–533 and 473–593 K for **1** and **2** respectively, the detachment of alkoxides and carboxylate

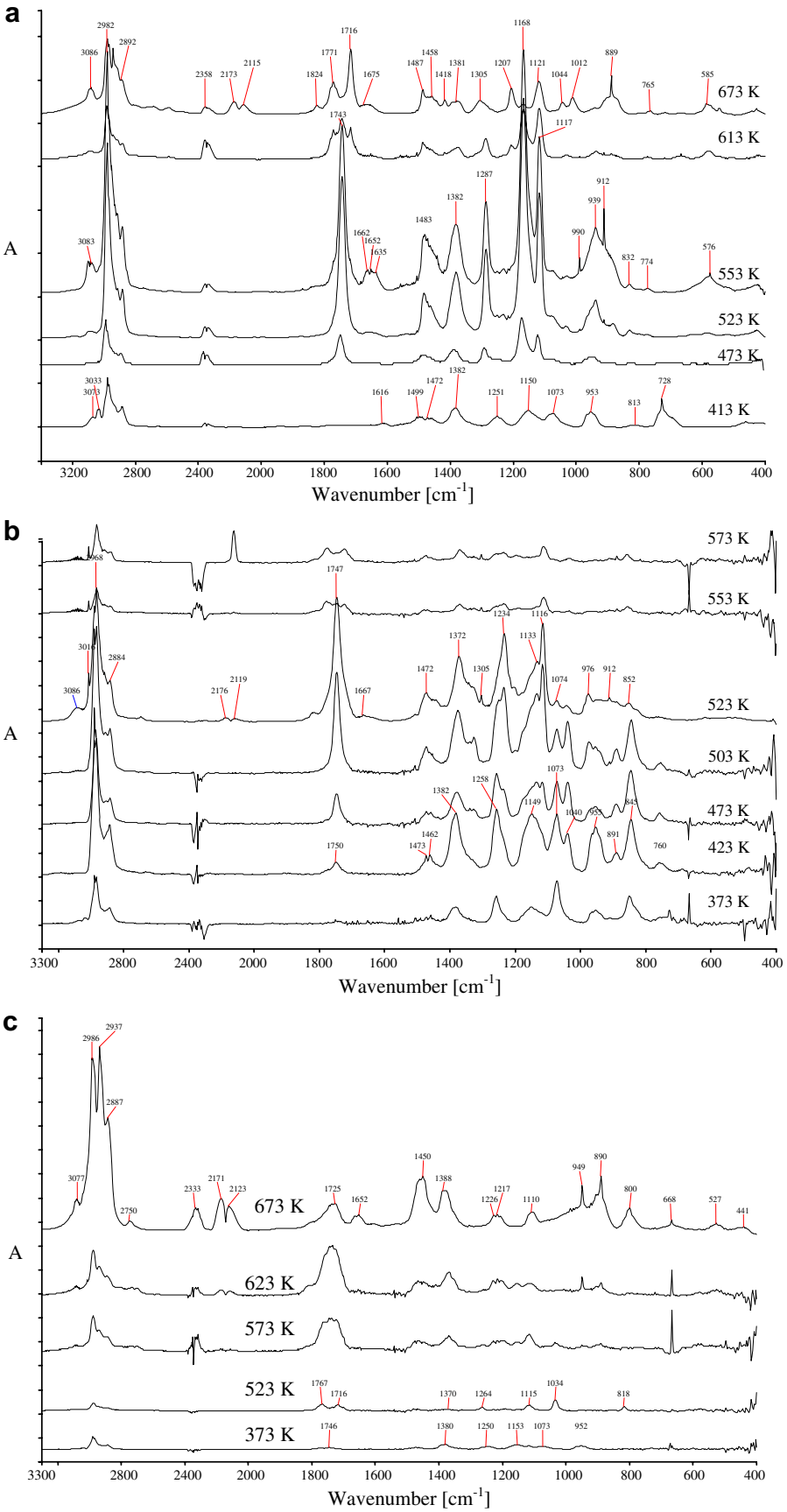


Fig. 3. Variable temperature IR spectra of vapors formed during the thermolysis of (a) **1**, (b) **2**, (c) **3** (VT-IR spectra registered between 353 and 693 K under Ar atmosphere and $p = 3$ mbar).

Table 2
Results of variable temperature MS studies of $[Ti_6O_6(O^iPr)_6(O_2CBu^t)_6]$ (**1**) (MS-EI 70 eV)

$[Ti_6O_6(O^iPr)_6(O_2CBu^t)_6]$ (**1**)	*m/z*	*T* (K)						
Fragmentation ion		423	473	493	533	553	573	593
$OOCBu^t$	101	2.5			100	100	100	100
$[TiO(OC_3H_6)]^+$	122	6.5			11.1	6.0	4.9	1.5
$[Ti(O_2CBu^t)]^+$	149	100	8.1	8.5	8.4	3.8	3.7	
$[Ti(OPr^i)_2(OC_2H_3)]^+$	209	4.1			10.7	4.1	5.6	7.7
$[Ti(OPr^i)_3(OC_2H_4)]^+$	267	2.9	3.1	5.2	50.7	32.6	10.5	6.1
$[Ti_2O_4(O_2CBu^t)_3]^+$	463	1.7			13.4		2.8	
$[Ti_3O_3(O_2CBu^t)_4]^+$	596	2.3	17.1	10.7	5.2	3.5		
$[Ti_3O_3(O_2CBu^t)_4(O_2CC_2H_3)]^+$	667	2.5	9.4	5.1	11.7	3.7		
$[Ti_3O_4(OPr^i)_2(O_2CBu^t)_4]^+$	731	2.6	10.4	4.6	11.1	4.2		2.3
$[Ti_3O_3(OPr^i)_3(O_2CBu^t)_4]^+$	773	3.3	12.7	9.9	16.8	5.3	3.3	
$[Ti_4O_5(O_2CBu^t)_5]^+$	777						5.9	12.2
$[Ti_4O_5(OPr^i)_3(O_2CBu^t)_4]^+$	853	2.9	11.5		12.4	4.5	2.5	2.2
$[Ti_5O_6(OPr^i)_4(O_2CBu^t)_3]^+$	875	4.7	26.2	23.7	27.4	7.7	3.9	3.6
$[Ti_5O_6(OPr^i)_2(O_2CBu^t)_4(Bu^t)]^+$	917	6.8	34.1	33.8	37.6	9.4	6.0	4.7
$[Ti_5O_6(OPr^i)_2(O_2CBu^t)_5]^+$	959	1.6	12.1	11.1	12.0	3.5		
$[Ti_6O_6(OPr^i)_5(O_2CBu^t)_5]^+$	1184	2.0	12.0	11.6	12.8	4.8	3.9	4.4
$[Ti_6O_6(OPr^i)_4(O_2CBu^t)_6]^+$	1226	9.5	67.3	68.4	65.8	12.8	6.6	5.3
$[Ti_6O_6(OPr^i)_6(O_2CBu^t)_5]^+$	1243	6.6	49.6	50.1	48.4	9.1	5.3	4.4
$[Ti_6O_6(OPr^i)_5(O_2CBu^t)_6]^+$	1285	12.2	100	100	100	19.5	12.1	9.1

Table 3
Results of variable temperature MS studies of $[Ti_6O_6(O^iPr)_6(O_2CCH_2Bu^t)_6]$ (**2**) (MS-EI 70 eV)

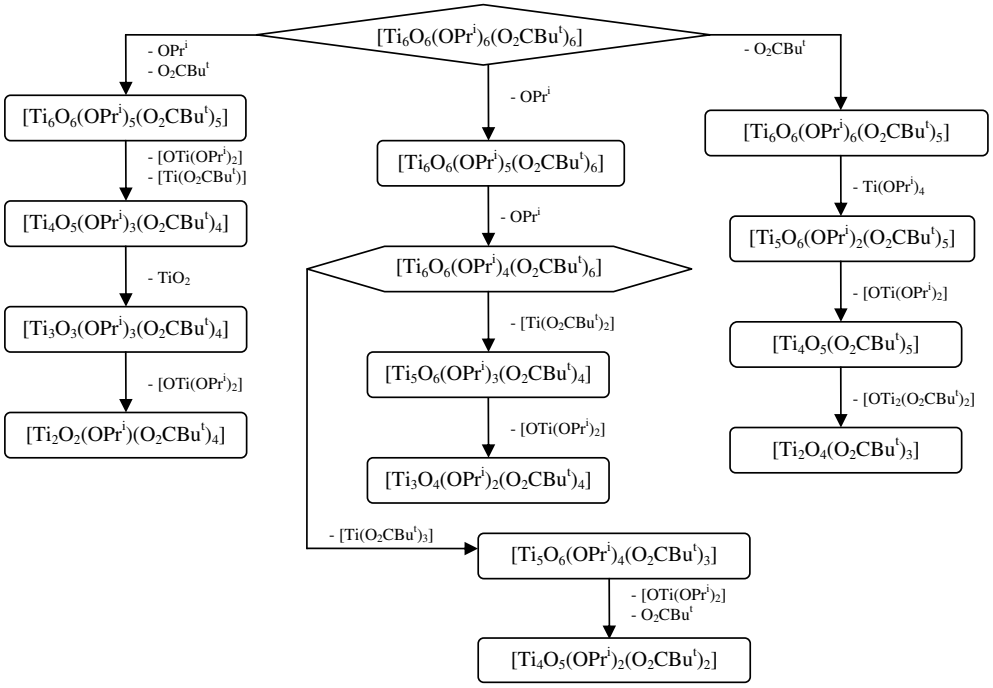
$[Ti_6O_6(O^iPr)_6(O_2CCH_2Bu^t)_6]$ (**2**)	*m/z*	*T* (K)						
Fragmentation ion		423	473	493	523	553	573	593
$OOCBu^t$	101	3.1	1.5	2.0	3.3	5.8	55.2	100
$[OTi(OPr^i)]^+$	123	12.2	2.5	2.4	1.8	3.0	8.4	5.0
$CH_3O_2CCH_2Bu^t$	130	1.3			2.1	8.6	43.1	81.4
$[OTi(O_2CC_3H_5)]^+$	149	100	12.4	8.5	3.9	4.7	6.5	7.8
$[Ti(OPr^i)_4]^+$	284		1.4	4.0	5.1	7.0	27.1	4.8
$[OTi(O_2CCH_2Bu^t)]^+$	294				2.6	4.7	15.4	23.6
$[Ti(OPr^i)(O_2CH_2Bu^t)_2]^+$	337			2.0	2.9	5.9	19.0	28.6
$[Ti_3O_3(OPr^i)_3(O_2CH_2Bu^t)_2]^+$	599		4.8	6.7	5.8	10.3	15.3	14.5
$[Ti_3O_3(OPr^i)_3(O_2CH_2Bu^t)_2(OCH)]^+$	628	1.4	13.7	16.1	15.6	18.7	35.7	32.7
$[Ti_3O_3(OPr^i)_3(O_2CH_2Bu^t)(O_2CCH)]^+$	656		10.2	12.6	12.4	15.3	25.7	23.2
$[Ti_3O_2(OPr^i)_6(O_2CH_2Bu^t)_2]^+$	760		4.1	4.7	5.4	9.0	11.9	10.9
$[Ti_3O_2(OPr^i)_4(O_2CH_2Bu^t)_4]^+$	793		2.6	4.7	5.0	7.8	11.3	11.3
$Ti_3O_4(OPr^i)_3(O_2CCH_2Bu^t)_3(O_2CC_3H_6)]^+$	816	1.5	6.5	8.4	8.4	13.6	17.1	16.6
$[Ti_5O_6(OPr^i)_5(O_2CCH_2Bu^t)_2(O_2CCH_2)]^+$	919		17.3	20.9	21.3	30.3	34.3	30.9
$[Ti_5O_6(OPr^i)_2(O_2CCH_2Bu^t)_5(O_2CCH_3)]^+$	973		25.6	30.5	32.2	40.4	45.1	44.6
$[Ti_5O_6(OPr^i)_2(O_2CCH_2Bu^t)_5]^+$	1031	1.2	11.5	13.3	14.1	16.8	20.3	19.6
$[Ti_6O_6(OPr^i)_6(O_2CCH_2Bu^t)_5(O_2CCH_2)]^+$	1256		11.9	11.7	11.8	12.1	13.3	12.0
$[Ti_6O_6(OPr^i)_6(O_2CCH_2Bu^t)_5]^+$	1313	4.2	99.4	95.8	96.2	96.1	94.9	83.6
$[Ti_6O_6(OPr^i)_6(O_2CCH_2Bu^t)_5(O_2CCH_2)]^+$	1371	4.0	100	100	100	100	100	91.7

ligands leads to the formation of the following multinuclear fragments; $[Ti_6O_6(OPr^i)_5(O_2CR)_6]^+$ ($m/z = 1285$ (**1**), 1363 (**2**), 92–100%), $[Ti_6O_6(OPr^i)_6(O_2CR)_5]^+$ ($m/z = 1243$ (**1**), 1313 (**2**), 48–99%) and $[Ti_6O_6(OPr^i)_5(O_2CR)_5]^+$ ($m/z = 1184$ (**1**), 1254 (**2**), 12–13%).

Moreover, the loss of such fragments as $[Ti(OPr^i)_4]$, $[TiO(OPr^i)_2]$, $[Ti(O_2CR)_2]$, $[OTi_2(O_2CR)_2]$ conduce the formation of species containing $\{Ti_mO_n\}$ clusters: e.g. $[Ti_5O_6(OPr^i)_2(O_2CCH_2Bu^t)_5(O_2CCH_3)]^+$ ($m/z = 973$, 26–45%), $[Ti_5O_6(OPr^i)_2(O_2CR)_5]^+$ ($m/z = 959$ (**1**), 1031 (**2**) 11–20%), $[Ti_5O_6(OPr^i)_2(O_2CCH_2Bu^t)_2(O_2CCH_3)]^+$ ($m/z = 919$, 21–34%), $[Ti_5O_6(OPr^i)_2(O_2CBu^t)_4(Bu^t)]^+$ ($m/z = 917$, 34–37%), $[Ti_5O_6(OPr^i)_4(O_3CBu^t)_5]^+$ ($m/z = 875$, 24–27%), $[Ti_3O_3(OPr^i)_3(O_2CBu^t)_4]^+$ ($m/z = 773$, 3–17%), $[Ti_3O_3(OPr^i)_3(O_2CCH_2Bu^t)_2(OCH)]^+$ ($m/z = 628$, 1–36%), $[Ti(OPr^i)(O_2CCH_2Bu^t)_2]^+$ ($m/z = 337$, 2–29%). The possible fragmentation pathway of **1** presented in Scheme 1 and it suggests that the main components of vapors are the simple titanium alkoxide or carboxylate derivatives ($[Ti(OPr^i)_4]$, $[TiO(OPr^i)_2]$, $[Ti(O_2CR)_2]$, $[OTi_2(O_2CR)_2]$) and probable multinuclear fragments containing $\{Ti_mO_n\}$ clusters ($m = 2$–4, $n = 2$–6). It confirms the results of VT-IR investigations. A similar degradation pathway may be proposed for **2**, however the obtained results suggest a difference in stability of volatile titanium-containing fragments of **1** and **2** (Table 3). In the case of **1**, intense peaks assigned

Table 4
Results of MS-EI studies of $[Ti_6O_6(OPr^i)_6(O_2CC(CH_3)_2Et)_6]\cdot 0.5(C_7H_8)$ (**3**)

$[Ti_6O_6(O^iPr)_6(O_2CC(CH_3)_2Et)_6]\cdot 0.5(C_7H_8)$ (**3**)	*m/z*	*T* (K)					
Fragmentation ion		423	473	493	513	573	593
$[Bu^tCOO]^+$	101		81.0	100	100	100	100
$[Ti(OPr^i)]^+$	107		1.1	2.0			
$[TiO_2C_2H_2]^+$, $[(Pr^i)_2O]$	118		10.6	12.8	10.9	9.4	9.8
$[Ti(O_2C(Me)_2Et)]^+$	163		2.6	3.5	2.6		
$[Ti(O_2CCH_2CH_3)(C_5H_6)]^+$	173		9.0	10.3	8.1		
$[Ti(O_2CCH_2CH_3)(C_5H_8)]^+$	175		3.2	3.3	2.6		
$[Ti(O_2C(Me)_2Et)(C_2H_4)]^+$	191		4.4	1.9	1.2		
$[Ti(OCH_2CH_3)(O_2CC(Me)_2Et)]^+$	208		9.9	3.1	1.7	1.1	6.1
$[Ti(O_2C(Me)_2Et)_2(OPr^i)]^+$	337		1.7	1.3	1.6		
$[Ti_6O_6(O_2CC(Me)_2Et)_5(OPr^i)_6(O_2CCH)]^+$	1370		<1	<1	<1		



Scheme 1. Proposed fragmentation pathway of **1**.

to multinuclear titanium species appear between 473 and 533 K, but at higher temperatures their intensity rapidly decreases. In MS spectra of **2**, the intense peaks attributed to fragments containing $\{Ti_xO_y\}$ clusters were registered between 473 and 593 K. It indicates higher thermal stability of volatile titanium-containing species in comparison with **1**.

Analysis of MS spectra of **3**, registered between 423 and 593 K, shows that the main fragmentation species are carboxylates ($m/z = 101$, 81–100), and the intensity of peaks attributed to titanium-containing fragments is less than 10% (Table 4).

4. Conclusions

In the presented study, the thermal decomposition and evaporation of hexanuclear Ti(IV) oxo isoproxide carboxylates (potential TiO_2 CVD precursors) of the general formula $[Ti_6O_6(OPr^i)_6(O_2CR)_6]$ ($R = Bu^t$ (**1**), CH_2Bu^t (**2**)) and $[Ti_6O_6(OPr^i)_6(O_2CC(CH_3)_2Et)_6]\cdot 0.5(C_7H_8)$ (**3**) were analysed using VT-IR and MS methods. Although, these complexes form a similar type of structure, their decomposition mechanisms are different. The partially thermal decomposition of **1** and **2** proceeds with the formation of volatile titanium-containing species and ester derivatives between 373 and 553 K. VT-IR studies of vapors formed during the thermolysis of **1** revealed that stable titanium alkoxide and titanium carboxylate derivatives are the main components (in terms of CVD processes) transported in vapors. However, only titanium alkoxide species were detected in vapors formed during the decomposition of **2**. The anhydride acids, aldehyde, ketone species, and also carboxylate derivatives (only in the case of **1**) were the main components of vapors formed at higher temperatures (>553 K). Analysis of spectral data revealed promising properties of **1** and **2** as TiO_2 precursors for thermal

inducted CVD methods. Variable temperature spectra indicate that thermolysis at 553 K will deliver titanium-containing fragments into the CVD reactor, as was confirmed in the earlier reports [9]. In contrast, the formation of the volatile and stable titanium derivatives during the thermolysis of **3** was not observed. The high thermal stability of this complex is the main reason why thermal decomposition occurs at just above 573 K, where stable titanium-containing fragments are not formed.

Acknowledgement

The authors wish to acknowledge the Polish Committee for Science Research for financial support grant No. 4T09A 152 23.

References

[1] T. Kamada, M. Kitagawa, M. Shibuya, T. Hirao, Jpn. J. Appl. Phys. 30 (1991) 3594.
[2] G.D. Wilk, R.M. Wallace, Appl. Phys. Lett. 74 (1999) 2854.
[3] D.A. Muller, G.D. Wilk, Appl. Phys. Lett. 79 (2001) 4195.
[4] A. Hagfeldt, M. Grätzel, Chem. Rev. 95 (1995) 49.
[5] M. Thelakkat, C. Schmitz, H.-W. Schmidt, Adv. Mater. 14 (2002) 577.
[6] A.L. Linsebigler, G. Lu, J.T. Yates Jr., Chem. Rev. 95 (1995) 735.
[7] S.M. Melponder, A.W. West, C.L. Barnes, T.N. Blanton, J. Mater. Sci. 26 (1991) 3585.
[8] J.-D. Grunwaldt, U. Göbel, A. Baiker, Fresenius J. Anal. Chem. 358 (1997) 96.
[9] P. Piszczek, M. Richert, A. Grodzicki, Chem. Vap. Deposition 11 (2005) 399.
[10] T.J. Boyle, T.M. Alam, C.J. Tafoya, B.L. Scott, Inorg. Chem. 37 (1998) 5588.
[11] R. Papiernik, L.G. Hubert-Pfalzgraf, J. Vaissermann, M.C. Henriques Baptista Goncalves, J. Chem. Soc., Dalton Trans. (1998) 2285.
[12] P. Piszczek, A. Grodzicki, M. Richert, A. Wojtczak, Inorg. Chim. Acta 357 (2004) 2769.
[13] O. Meth-Cohn, D. Thorpe, H.J. Twitchett, J. Chem. Soc. (C) (1970) 132.
[14] P. Piszczek, A. Grodzicki, M. Richert, A. Radtke, Mater. Sci.-Pol. 23 (2005) 663.
[15] E. Szłyk, P. Piszczek, I. Łakomska, A. Grodzicki, M. Chaberski, A. Goliński, J. Szatkowski, T. Błaszczyk, Chem. Vap. Deposition 6 (2000) 105.
[16] A.W. Rakov, Opt. Spectrosk. 10 (1961) 713.
[17] W. Bała, A. Grodzicki, P. Piszczek, M. Wojdyła, A. Bratkowski, M. Szybowicz, T. Runka, M. Drozdowski, J. Mol. Struct. 782 (2006) 177.
[18] K. Nakamoto, Infrared and Raman Spectra of Inorganic and Coordination Compounds, part B/V ed., Wiley, New York, 1997, p. 58, 172.
[19] G.B. Decon, R.J. Philips, Coord. Chem. Rev. 33 (1980) 227.
[20] P.D. Moran, A. Graham, G.A. Bowmaker, R.P. Cooney, K.S. Finnie, J.R. Bartlett, J.L. Woolfrey, Inorg. Chem. (1998) 2741.
[21] V. Koleva, D. Stoilova, J. Mol. Struct. 611 (2002) 1.

Available online at www.sciencedirect.com
ScienceDirect
Polyhedron 26 (2007) 101–106
POLYHEDRON
www.elsevier.com/locate/poly

Reaction of uranyl nitrate with carboxylic diacids under hydrothermal conditions. Crystal structure of complexes with L(+)-tartaric and oxalic acids

Pierre Thuéry

CEA/Saclay, DSM/DRECAM/SCM (CNRS URA 331), Bât. 125, 91191 Gif-sur-Yvette, France

Received 11 July 2006; accepted 28 July 2006
Available online 4 August 2006

Abstract

L(+)-tartaric acid reacts with uranyl nitrate in the presence of KOH, under mild hydrothermal conditions, to give the complex $[UO_2(C_4H_4O_6)(H_2O)]$ (**1**), the first uranyl tartrate to be crystallographically characterized. Each tartrate ligand bridges three uranyl ions, one of them in chelating fashion through proximal carboxylate and hydroxyl groups. The resulting assemblage is two-dimensional, with the uranyl pentagonal bipyramidal coordination polyhedra separated from one another. Prolonged heating of an uranyl tartrate solution resulted in oxidative cleavage of the acid and formation of the oxalate complex $[(UO_2)_2(C_2O_4)_2(OH)Na(H_2O)_2]$ (**2**). The bis-bidentate oxalate and bridging hydroxide groups ensure the formation of sheets with corner-sharing uranyl pentagonal bipyramidal coordination polyhedra, in which six-membered metallacycles encompass the sodium ions. These sheets are assembled into a three-dimensional framework through further oxo-bonding of the sodium ions.
© 2006 Elsevier Ltd. All rights reserved.

Keywords: Uranyl ion; Tartaric acid; Oxalic acid; Hydrothermal synthesis; Crystal structures

1. Introduction

The use of metal carboxylates in the design of open, porous assemblages has reached a high mark in recent years [1] and several groups were particularly active in the investigation of carboxylate-containing uranium-organic frameworks (UOFs), generally obtained via hydrothermal methods and in which uranium is in its most common dioxouranium(VI) (uranyl) form [2]. The peculiar geometric requirements of the linear uranyl ion also open many possibilities in molecular engineering, as illustrated by the synthesis of metallamacrocycles with a tetracarboxylic acid [3]. Most of the polymeric assemblages obtained with uranyl and polyacids involve diacids such as succinic [2b], glutaric [2b,2g], adipic [2c], 3,5-pyrazoledicarboxylic [2h], 2,4-, 2,6- and 3,4-pyridinedicarboxylic [2i,2l], 1,3- and 1,4-benzenedicarboxylic acids [2b,2j], and triacids such as benzene-1,3,5-tricarboxylic [2e], citric and tricarballylic acids [2n], with only one example of a tetra-acid, 1,2,4,5-benzenetetracarboxylic acid [2j,2m]. The assemblages formed with these polyfunctional ligands are one- [2b,2c,2e,2l], two- [2g,2h,2i,2j,2m,2n] or three-dimensional [2b,2c,2n], some of them incorporating also 3d-block [2h,2j,2l] or alkali metal ions [2n], and the uranium coordination polyhedron is always the usual pentagonal or hexagonal bipyramid. Considering the present development of uranyl structural chemistry, it appears somewhat surprising that the crystal structures of complexes with some common, naturally occurring polyacids have never been described. Such is the case of L(+)-tartaric [L(+)-2,3-dihydroxybutanedioic] acid which, being a chiral molecule, could give chiral UOFs, as recently reported for (1*R*,3*S*)-(+)-camphoric acid [4]. It was indeed possible to get crystals of uranyl tartrate under mild hydrothermal conditions, and the crystal structure of the complex is described herein. However, during the course of this study, it appeared that prolonged heating of uranyl

E-mail address: pierre.thuery@cea.fr

0277-5387/$ - see front matter © 2006 Elsevier Ltd. All rights reserved.
doi:10.1016/j.poly.2006.07.024

tartrate in the presence of NaOH resulted in the oxidation of the acid into oxalic (ethanedioic) acid. The crystal structure of the complex thus formed differs from those of the other polymeric forms of uranyl oxalate which are reported in the Cambridge Structural Database (CSD, Version 5.27) [5] and is also described herein.

2. Experimental

2.1. Synthesis

Uranyl nitrate hexahydrate and L(+)-tartaric acid were purchased from Prolabo and used without further purification.

2.1.1. $[UO_2(C_4H_4O_6)(H_2O)]$ (1)

Uranyl nitrate hexahydrate (205 mg, 0.41 mmol), L(+)-tartaric acid (62 mg, 0.41 mmol), KOH (46 mg, 0.82 mmol) and demineralized water (4.5 mL) were placed in a 15 mL tightly closed vessel and heated at 180 °C under autogenous pressure. Few light yellow crystals of complex **1** were obtained within 3 days. Attempts to increase the yield by lengthening the reaction time resulted in the deposition of an insoluble powder likely resulting from degradation of tartaric acid and in situ formation of oxalic acid, as described hereafter. It was thus not possible to isolate complex **1** in sufficiently large quantity to perform chemical analyses.

2.1.2. $[(UO_2)_2(C_2O_4)_2(OH)Na(H_2O)_2]$ (2)

Uranyl nitrate hexahydrate (200 mg, 0.40 mmol), L(+)-tartaric acid (60 mg, 0.40 mmol), NaOH (32 mg, 0.80 mmol) and demineralized water (3.2 mL) were placed in a 15 mL tightly closed vessel and heated at 140 °C under autogenous pressure. Few yellow crystals of complex **2** were obtained after 6 weeks.

2.2. Crystallography

Data were collected at 100(2) K with a Nonius Kappa-CCD area detector diffractometer [6] using graphite-monochromated Mo Kα radiation ($\lambda = 0.71073$ Å). The crystals were placed inside glass capillaries with a protecting "Paratone-N" oil (Hampton Research) coating. The unit cell parameters were determined from ten frames, then refined on all data. The data (φ- and ω-scans) were processed with HKL2000 [7]. The structures were solved by direct methods with SHELXS97 and subsequent Fourier-difference synthesis and refined by full-matrix least-squares on F^2 with SHELXL97 [8]. Absorption effects were corrected empirically with SCALEPACK [7]. All non-hydrogen atoms were refined with anisotropic displacement parameters. All the hydrogen atoms bound to oxygen atoms were found on Fourier-difference maps, except those of the water oxygen atom O9 in **1**. The other hydrogen atoms were introduced at calculated positions and all were treated as riding atoms with a displacement parameter equal to 1.2 times that of the parent atom. The absolute configuration determined for **1** from the value of the Flack parameter [9] matches that expected. Crystal data and structure refinement details are given in Table 1 and selected bond lengths and angles in Table 2. The structural plots were drawn with SHELXTL [10] and BALLS AND STICKS [11].

Table 1
Crystal data and structure refinement details

	Compound **1**	Compound **2**
Chemical formula	$C_4H_6O_9U$	$C_4H_5NaO_{15}U_2$
M (g mol^{-1})	436.12	792.13
Crystal system	monoclinic	orthorhombic
Space group	$P2_1$	$Pnma$
a (Å)	5.3614(3)	9.1506(4)
b (Å)	8.3366(6)	13.1912(8)
c (Å)	9.8186(7)	11.6910(6)
β (°)	99.268(5)	
V (Å^3)	433.12(5)	1411.19(13)
Z	2	4
D_{calc} (g cm^{-3})	3.344	3.728
μ(Mo Kα) (mm^{-1})	18.767	23.031
F(000)	388	1376
Total reflections	14739	61481
Independent reflections	1631	1396
Observed reflections [$I > 2\sigma(I)$]	1606	1323
R_{int}	0.034	0.064
Parameters	127	106
R_1 (observed data)	0.020	0.016
wR_2 (all data)	0.051	0.041
S	1.062	1.110
Flack parameter	−0.014(10)	
$\Delta\rho_{min}$ (e Å^{-3})	−1.63	−1.20
$\Delta\rho_{max}$ (e Å^{-3})	0.97	0.70

Table 2
Selected bond lengths (Å) and angles (°)

1	U–O1	1.755(4)	O1–U–O2	177.26(19)
	U–O2	1.778(4)	O3–U–O4′	72.30(15)
	U–O3	2.372(4)	O3–U–O5	64.03(14)
	U–O4′	2.357(5)	O4′–U–O9	78.05(15)
	U–O5	2.493(5)	O5–U–O7″	67.77(14)
	U–O7″	2.368(4)	O7″–U–O9	78.66(16)
	U–O9	2.407(4)		

Symmetry codes: ′ = 1 − x, y − 0.5, 1 − z; ″ = 1 − x, y − 0.5, 2 − z

2	U–O1	1.772(3)	O1–U–O2	179.36(12)
	U–O2	1.770(3)	O3–U–O5	66.49(10)
	U–O3	2.431(3)	O5–U–O4′	70.24(10)
	U–O4′	2.449(3)	O4′–U–O6′	66.44(9)
	U–O5	2.422(3)	O6′–U–O7	79.24(11)
	U–O6′	2.423(3)	O7–U–O3	77.47(11)
	U–O7	2.2867(14)	O1–Na–O1″	74.54(14)
	Na–O1	2.549(3)		
	Na–O5‴	2.728(3)		
	Na–O6‴	2.514(3)		
	Na–O8	2.334(5)		
	Na–O9	2.577(5)		

Symmetry codes: ′ = 1.5 − x, 1 − y, z + 0.5; ″ = x, 1.5 − y, z; ‴ = 1 − x, 1 − y, 1 − z.

3. Results and discussion

The crystal structure of the complex $[UO_2(C_4H_4O_6)(H_2O)]$ (**1**) is the first ever reported for uranyl tartrate. Complex **1** crystallizes in the chiral space group $P2_1$ with one uranyl ion, one tartrate and one coordinated water molecule in the asymmetric unit (Fig. 1a). The uranium atom is bound to the carboxylate atom O3 and to the proximal hydroxyl group O5 in chelating fashion, as previously observed in the uranyl complex with citric acid [2n], to two carboxylic groups from neighbouring molecules (O4′ and O7″) and to a water molecule (O9). The average U–O(carboxylate) and the U–O(hydroxyl) bond lengths, 2.366(6) and 2.493(5) Å, respectively, match those in the citric acid complex [2.38(2) and 2.496(10) Å], whereas the U–O(water) bond length, 2.407(4) Å, is intermediate between the values of 2.367(13) and 2.495(6) Å in the latter complex. The uranium environment is thus pentagonal bipyramidal, as very often observed in uranyl complexes with carboxylates, except when three bidentate carboxylate groups surround the metal to give a hexagonal bipyramidal environment, such as with tricarballylic acid [2n]. The five atoms O3, O5, O4′, O7″ and O9 define a plane with an r.m.s. deviation of 0.12 Å and the metal atom is located at 0.007(2) Å from this mean plane. As in the citric acid complex, the carboxylic, but not the hydroxyl groups, are deprotonated. The latter are involved in hydrogen bonds (Table 3): atom O5 is hydrogen bonded to the only uncoordinated carboxylate oxygen atom O8 of a neighbouring molecule whereas O6 is involved in a bifurcated hydrogen bond with atom O7 in the same molecule and atom O8 in a second neighbouring unit. The protons of the aqua ligand were not found, but two short contacts are indicative of hydrogen bonding, one with an uranyl oxo atom [O9···O2′ 2.798(6) Å, symmetry code $x-1, y, z$] and the other with the uncoordinated hydroxyl group of a neighbouring molecule [O9···O6″ 2.748(7) Å, symmetry code $x, y-1, z$].

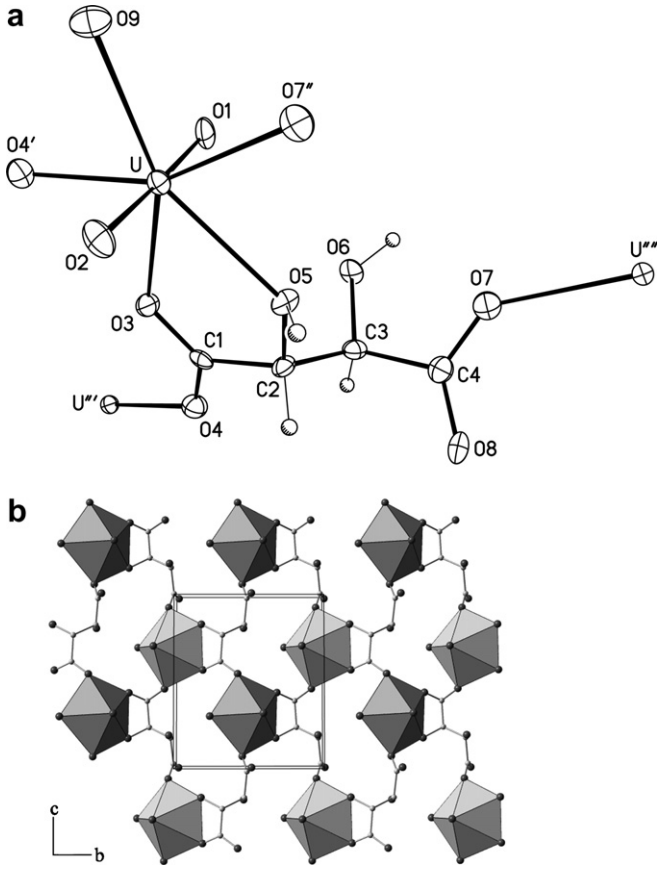


Fig. 1. (a) View of the complex $[UO_2(C_4H_4O_6)(H_2O)]$ (**1**). Displacement ellipsoids are drawn at the 70% probability level. Symmetry codes: $' = 1-x,\ y-0.5,\ 1-z$; $'' = 1-x,\ y-0.5,\ 2-z$; $''' = 1-x,\ y+0.5,\ 1-z$; $'''' = 1-x,\ y+0.5,\ 2-z$. (b) View of the bidimensional assemblage parallel to the *bc* plane. The uranium coordination polyhedra are represented. Other atoms are shown as spheres of arbitrary radii.

The three metal ions are bridged by the (μ_3-tartrato-1κ^2O,O':2$\kappa O''$:3$\kappa O'''$) species, a bridging mode which, to the best of our knowledge, has never before been observed with this ligand. The full metal-binding potential of the tartrate moiety is thus not reached, since one of the hydroxyl functions and one of the carboxylic oxygen atoms are not coordinated. This gives rise to the formation of undulated sheets parallel to the *bc* plane in which the uranium coordination polyhedra are separated from one another, having no edge or apex in common (Fig. 1b). Sheets stacked along the *a*-axis are tightly held by hydrogen bonds and the shortest U···U distance is along this axis [5.3614(3) Å] (the two metal atoms which are bound to the same carboxylate group are at a distance of 5.8966(3) Å from one another). No channel is formed in the packing, by contrast with the chiral channels formed in the uranyl complex with another enantiopure ligand, (1*R*,3*S*)-(+)-camphoric acid [4]. To the best of our knowledge, the present structure is the first for a tartrate of an actinide element. Eleven structures of lanthanide tartrates are reported in the CSD [5], in which three examples of chelation through one carboxylate and the proximal hydroxyl group are found [12], whereas all the other examples are mixed lanthanide/molybdenum chiral double helicates in which the lanthanide ion is bound to two ligands through one carboxylate oxygen atom [13]. In all cases, the hydration level is higher than in **1** since two to six water molecules are coordinated to the metal. It has been noted that hydrothermal methods generally yield

Table 3
Hydrogen bonding geometry: distances (Å) and angles (°)

		D···A	D–H	H···A	D–H···A
1	O1···O8′	2.599(6)	0.95	1.67	166
	O6···O7	2.633(6)	0.92	2.15	111
	O6···O8″	3.052(6)	0.92	2.28	141
Symmetry codes: $' = 2-x, y-0.5, 2-z$; $'' = x-1, y, z$					
2	O7···O9′	2.798(6)	0.88	1.99	153
	O8···O4″	2.979(4)	0.92	2.07	168
Symmetry codes: $' = x+1, y, z$; $'' = x-0.5, y, 0.5-z$					

phases with higher dimensionality and lower water coordination than room temperature methods [14] and a recent example concerns the synthesis of microporous lanthanide tartrates with only one aqua ligand per metal ion [15].

Prolonged heating of an aqueous solution of L(+)-tartaric acid, uranyl nitrate and NaOH (1:1:2) at 140 °C (i.e. at a temperature lower than that leading to crystallization of complex **1**) resulted in the oxidative cleavage of the acid and in situ formation of oxalic acid. Similar formation of oxalic acid from 3,5-pyrazoledicarboxylic acid under hydrothermal conditions has been mentioned [2h] but, to the best of our knowledge, no details have been published. It was also reported that quinolinic acid could be decarboxylated into nicotinic acid under similar conditions [2m]. Formation of oxalic acid from tartaric acid oxidation has been known for long [16]. However, the enantiomeric stability of L(+)-tartaric acid in neutral solutions at 160 °C for several days has been demonstrated by circular dichroism spectroscopy [15]. The present experiment was conducted at pH ~ 2–3 and in the presence of an uranyl salt and it is thus possible that the metal plays a role in the oxidation reaction.

The oxalate complex $[(UO_2)_2(C_2O_4)_2(OH)Na(H_2O)_2]$ (**2**) is different from the other polymeric uranyl oxalate complexes reported in the CSD. The asymmetric unit in **2** comprises one uranyl ion and one oxalate dianion in general position, and one sodium atom, one hydroxide ion and two aqua ligands located on the symmetry plane (x, 1/4, z) of space group *Pnma* (Fig. 2a). The uranyl ion is bound, in its equatorial plane, to two (μ-oxalato-1κ^2O,O':2κ^2O'',O''') ligands and one bridging μ-OH anion, which results in a pentagonal bipyramidal environment for the uranium atom, with the five atoms in equatorial positions defining a mean plane with an r.m.s. deviation of 0.015 Å. The bis-bidentate, (μ-oxalato-1κ^2O,O':2κ^2O'',O''') ligand is frequently encountered in uranyl complexes, either binuclear

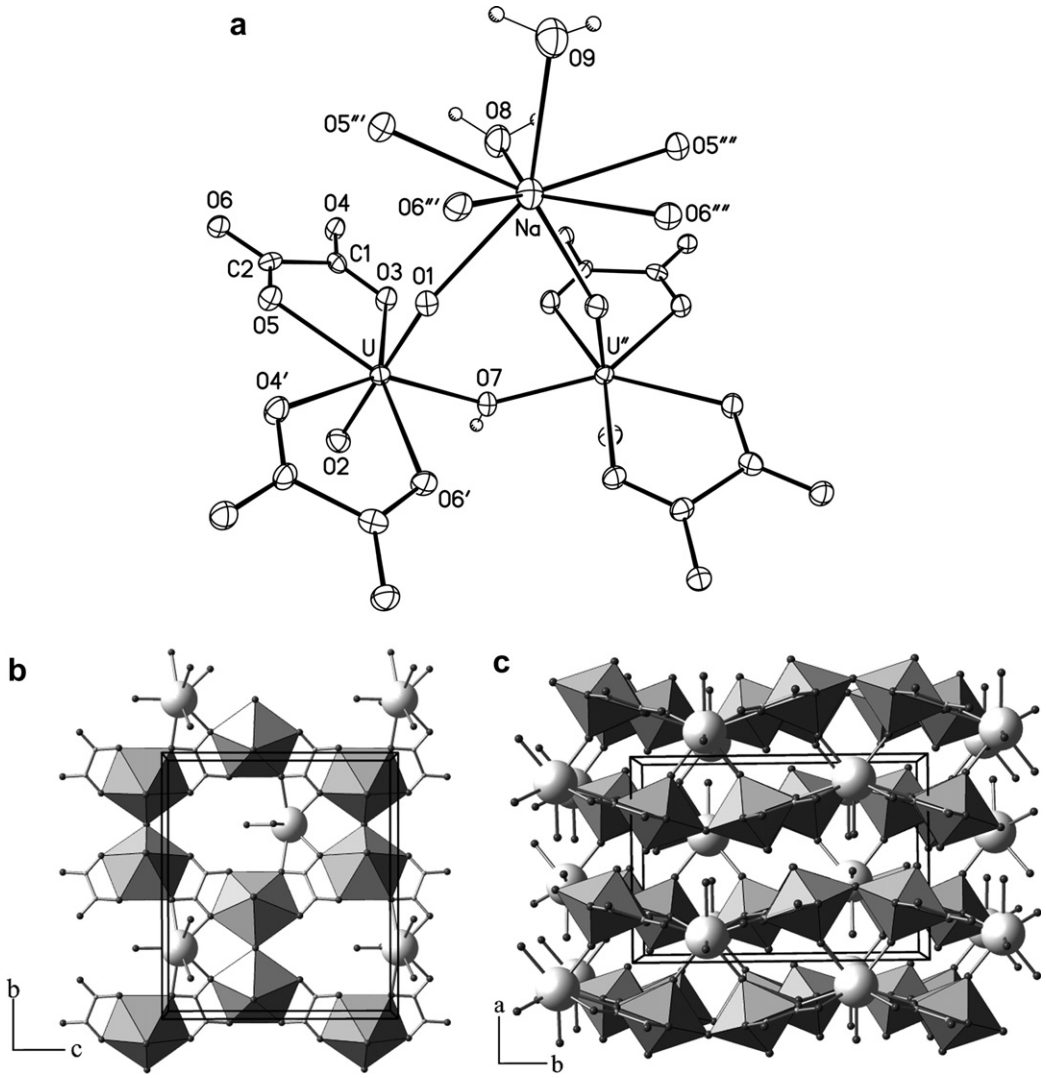


Fig. 2. (a) View of the complex $[(UO_2)_2(C_2O_4)_2(OH)Na(H_2O)_2]$ (**2**). Displacement ellipsoids are drawn at the 50% probability level. Symmetry codes: $' = 1.5 - x, 1 - y, z + 0.5$; $'' = x, 1.5 - y, z$; $''' = 1 - x, 1 - y, 1 - z$; $'''' = 1 - x, y + 0.5, 1 - z$. (b) Projection of one sheet in the *bc* plane. (c) View of the tridimensional assemblage. The uranium coordination polyhedra are represented. Other atoms are shown as spheres of arbitrary radii.

[17] or polymeric [18]. The average U–O(oxalate) and U–O(hydroxide) bond lengths in **2** are 2.431(11) and 2.2867(14) Å, in good agreement with the mean values from the CSD, 2.42(5) and 2.33(2) Å, respectively. The U–O–U angle around the hydroxide bridge is 138.67(19)° and the dihedral angle between the two corresponding mean O_5 equatorial planes is 37.58(5)°. This angle brings the uranyl oxo atom O1 and its image by the mirror plane at a rather short distance of 3.09 Å from one another and these atoms are thus apt to complex the sodium ion while forming a six-membered U_2NaO_3 ring. Such bonding of an alkali metal to the uranyl ion is possible due to the Lewis basicity of the oxo groups and has been previously observed in uranyl complexes with tricarballylic acid (although it was absent with citric acid in the same experimental conditions) [2n] or other ligands [19], as well as in other uranyl oxalate complexes [18c,18e,20]. Sodium bonding to neptunyl oxo groups is also found in a neptunium(V) oxalate complex [21]. The Na–O(oxo) bond length of 2.549(3) Å in **2** is in quite perfect agreement with that in $[(UO_2)_4(C_2O_4)_5Na_2(H_2O)_8]\cdot 2H_2O$, the other polymeric uranyl/sodium oxalate complex, which is 2.542 Å [18e] and both are intermediate between that measured in the tricarballylic acid complex [2.715(9) Å] [2n] and the mean value of 2.40(8) Å (2.20–2.50 Å range) for the other seven comparable bond lengths in the CSD. The sodium atom in **2** is located 0.593(5) Å from the mean plane defined by the uranium and oxygen atoms in the U_2NaO_3 ring (r.m.s. deviation of 0.015 Å). Its coordination sphere is completed by four carboxylate oxygen atoms, which are bridging the uranium and sodium atoms, and two water molecules, thus resulting in an eight-coordinate environment of very irregular geometry.

The hydroxide bridged uranyl groups in **2** can be considered as pseudo-dimeric basic units, which are further linked by oxalate ligands to form six-membered U_6 rings or metallacycles (Fig. 2b). Each of these rings contains one sodium ion bound to oxalate oxygen atoms and located on one side of the cavity. Larger, 10-membered rings were observed in the other polymeric uranyl/sodium complex [18e]. Conversely, the basic units in **2** can be viewed as oxalate-bridged chains directed along the *c*-axis, which are further linked by hydroxide ligands corresponding to the polyhedra apexes pointing out on each side of the chain. The oxalate- and hydroxide-bridged uranyl groups are thus arranged in sheets parallel to the *bc* plane. The U···U distances are 4.2791(4) Å for atoms separated by hydroxide links and 6.3004(3) Å for those separated by oxalate moieties; as expected, the former value is larger than those for double hydroxide bridges [mean value 3.84(7) Å from the CSD], but in good agreement with the value of 4.3152(12) Å reported for another oxalato/hydroxide complex [18f], whereas the latter value is in the range usually observed for oxalate-bridged UO_7 pentagonal bipyramids, ca. 6.08–6.55 Å [18f]. The sodium ions are bound both to oxalate groups of one sheet and to oxo groups from the neighbouring sheet along the *a*-axis, which results in the formation of a three-dimensional assemblage (Fig. 2c). The hydroxide and water moieties are involved in intra- or inter-sheets hydrogen bonds (Table 3). The three-dimensional organisation in **2**, as well as those previously described [18e,20], is at variance with the formation of a layered structure in the mixed uranyl/sodium complex of tricarballylic acid, in which the sodium ion has a higher hydration level, being bound to one oxo, one carboxylate and four water ligands and is thus less efficient an assembling unit than in **2** [2n].

4. Conclusion

The present work illustrates both the strengths and weaknesses of hydrothermal methods. On the first hand, crystallization under hydrothermal conditions permitted the first structural characterization of uranyl tartrate, in the form of a chiral two-dimensional assemblage in which the L(+)-tartrate ligand acts as a (μ_3-tartrato-1κ^2O,O':2$\kappa O''$:3$\kappa O'''$) assembler. On the other hand, oxidative cleavage of L(+)-tartaric acid on prolonged heating resulted in in situ formation of oxalic acid and crystallization of a mixed uranyl/sodium complex. A similar reaction was observed when replacing tartaric by citraconic (2-methyl-2-butenedioic) acid and heating at 180 °C in the presence of NaOH or KOH (1:1). In this case, the complex formed was $[(UO_2)_2(C_2O_4)(OH)_2(H_2O)_2]\cdot H_2O$, the synthesis (from oxalic acid) and crystal structure of which have recently been reported [18f]. Complex **2** is a rare example of a three-dimensional assemblage in the family of uranyl oxalates. The oxalate ligand is likely too small to give three-dimensional UOFs by itself. However, incorporation of oxo-bound sodium ions in the lattice increases the structure dimensionality. Both hydroxide complexation and sodium uptake are interesting features, considering the importance of uranyl oxalates in nuclear technology [17,18f].

Supplementary data

Crystallographic data for the structural analysis have been deposited with the Cambridge Crystallographic Data Centre, CCDC Nos. 614325 and 614326. Copies of this information may be obtained free of charge from The Director, CCDC, 12 Union Road, Cambridge CB2 1EZ, UK (Fax: +44 1223 336033; e-mail: deposit@ccdc.cam.ac.uk or www: http://www.ccdc.cam.ac.uk). Supplementary data associated with this article can be found, in the online version, at doi:10.1016/j.poly.2006.07.024.

References

[1] C.N.R. Rao, S. Natarajan, R. Vaidhyanathan, Angew. Chem., Int. Ed. Engl. 43 (2004) 1466.
[2] (a) J.Y. Kim, A.J. Norquist, D. O'Hare, Chem. Mater. 15 (2003) 1970;
(b) J.Y. Kim, A.J. Norquist, D. O'Hare, Dalton Trans. (2003) 2813;
(c) L.A. Borkowski, C.L. Cahill, Inorg. Chem. 42 (2003) 7041;

(d) W. Chen, H.M. Yuan, J.Y. Wang, Z.Y. Liu, J.J. Xu, M. Yang, J.S. Chen, J. Am. Chem. Soc. 125 (2003) 9266;
(e) L.A. Borkowski, C.L. Cahill, Acta Crystallogr., Sect. E 60 (2004) m198;
(f) Z.T. Yu, Z.L. Liao, Y.S. Jiang, G.H. Li, G.D. Li, J.S. Chen, Chem. Commun. (2004) 1814;
(g) L.A. Borkowski, C.L. Cahill, Acta Crystallogr., Sect. E 61 (2005) m816;
(h) M. Frisch, C.L. Cahill, Dalton Trans. (2005) 1518;
(i) Y.Z. Zheng, M.L. Tong, X.M. Chen, Eur. J. Inorg. Chem. (2005) 4109;
(j) Z.T. Yu, Z.L. Liao, Y.S. Jiang, G.H. Li, J.S. Chen, Chem. Eur. J. 11 (2005) 2642;
(k) W. Zhang, J. Zhao, Inorg. Chem. Commun. 9 (2006) 397;
(l) Y.S. Jiang, G.H. Li, Y. Tian, Z.L. Liao, J.S. Chen, Inorg. Chem. Commun. 9 (2006) 595;
(m) Y.S. Jiang, Z.T. Yu, Z.L. Liao, G.H. Li, J.S. Chen, Polyhedron 25 (2006) 1359;
(n) P. Thuéry, Chem. Commun. (2006) 853.

[3] P. Thuéry, C. Villiers, J. Jaud, M. Ephritikhine, B. Masci, J. Am. Chem. Soc. 126 (2004) 6838.

[4] P. Thuéry, Eur. J. Inorg. Chem., in press, doi:10.1002/ejic.200600358.

[5] F.H. Allen, Acta Crystallogr., Sect. B 58 (2002) 380.

[6] Kappa-CCD Software, Nonius BV, Delft, 1998.

[7] Z. Otwinowski, W. Minor, Methods Enzymol. 276 (1997) 307.

[8] G.M. Sheldrick, SHELXS97 and SHELXL97, University of Göttingen, 1997.

[9] H.D. Flack, Acta Crystallogr., Sect. A 39 (1983) 876.

[10] G.M. Sheldrick, SHELXTL, Version 5.1, Bruker AXS Inc., Madison, WI, 1999.

[11] S.J. Kang, T.C. Ozawa, BALLS AND STICKS. Available from: <www.toycrate.org>.

[12] (a) F.C. Hawthorne, I. Borys, R.B. Ferguson, Acta Crystallogr., Sect. C 39 (1983) 540;
(b) P. Starynowicz, G. Meyer, Z. Anorg. Allg. Chem. 626 (2000) 2441;
(c) C.D. Wu, X.P. Zhan, C.Z. Lu, H.H. Zhuang, J.S. Huang, Acta Crystallogr., Sect. E 58 (2002) m228.

[13] C.D. Wu, C.Z. Lu, S.F. Lu, H.H. Zhuang, J.S. Huang, Dalton Trans. (2003) 3192.

[14] S.S.Y. Chui, S.M.F. Lo, J.P.H. Charmant, A.G. Orpen, I.D. Williams, Science 283 (1999) 1148.

[15] S. Thushari, J.A.K. Cha, H.H.Y. Sung, S.S.Y. Chui, A.L.F. Leung, Y.F. Yen, I.D. Williams, Chem. Commun. (2005) 5515.

[16] J.B. McNair, Am. J. Botany 23 (1936) 629.

[17] A.E. Bradley, J.E. Hatter, M. Nieuwenhuyzen, W.R. Pitner, K.R. Seddon, R.C. Thied, Inorg. Chem. 41 (2002) 1692, and references therein.

[18] (a) N.W. Alcock, J. Chem. Soc., Dalton Trans. (1973) 1616;
(b) N.C. Jayadevan, D.M. Chackraburtty, Acta Crystallogr., Sect. B 28 (1972) 3178;
(c) N.C. Jayadevan, K.D. Singh Mudher, D.M. Chackraburtty, Acta Crystallogr., Sect. B 31 (1975) 2277;
(d) R.N. Shchelokov, Y.N. Mikhailov, A.G. Beirakhov, I.M. Orlova, Z.R. Ashurov, Russ. J. Inorg. Chem. 31 (1986) 1180;
(e) E.E. Baeva, Y.N. Mikhailov, Y.E. Gorbunova, L.B. Serezhkina, V.N. Serezhkin, Russ. J. Inorg. Chem. 48 (2003) 1651;
(f) L. Duvieubourg, G. Nowogrocki, F. Abraham, S. Grandjean, J. Solid State Chem. 178 (2005) 3437.

[19] (a) P. Thuéry, B. Masci, Dalton Trans. (2003) 2411, and references cited therein;
(b) P. Thuéry, B. Masci, Polyhedron 23 (2004) 649.

[20] E.E. Baeva, Y.N. Mikhailov, Y.E. Gorbunova, L.B. Serezhkina, V.N. Serezhkin, Russ. J. Inorg. Chem. 47 (2002) 1348.

[21] A.C. Bean, E. Garcia, B.L. Scott, W. Runde, Inorg. Chem. 43 (2004) 6145.

Available online at www.sciencedirect.com
ScienceDirect
Polyhedron 26 (2007) 107–114
POLYHEDRON
www.elsevier.com/locate/poly

Synthesis and crystal structures of three novel coordination polymers generated from AgCN and AgSCN with flexible N-donor ligands

Jian-Di Lin [a,b], Zhi-Hua Li [a], Jian-Rong Li [a], Shao-Wu Du [a,*]

[a] State Key Laboratory of Structural Chemistry, Fujian Institute of Research on the Structure of Matter, Chinese Academy of Sciences, Fuzhou, Fujian 350002, PR China
[b] Graduate School of Chinese Academy of Sciences, Beijing 100039, PR China

Received 21 April 2006; accepted 28 July 2006
Available online 11 August 2006

Abstract

The solvothermal reactions of AgX (X = CN, SCN) with mbix [mbix = 1,3-bis(imidazole-l-yl-methyl)benzene] or bix [bix = 1,4-bis(imidazole-l-yl-methyl)benzene] afforded the polymers $[AgCN(mbix)]_n$ (**1**), $[(AgCN)_4(bix)_2]_n$ (**2**) and $[(AgSCN)_2(mbix)]_n$ (**3**). They were all characterized by infrared spectroscopy, elemental analysis and X-ray single-crystal analysis. The structure of **1** contains a 3-fold-interpenetrated 2D network, while that of **2** exhibits 2-fold parallel interpenetration. There is no interpenetration observed in **3**. Compounds **2** and **3** show 3D supramolecular structures built from 2D networks through weak $\pi \cdots \pi$ interactions. The photoluminescent properties of the present compounds were also investigated.
© 2006 Elsevier Ltd. All rights reserved.

Keywords: Coordination polymers; Cyanide-bridging; Triply-bridged SCN ligand; Photoluminescent property; Interpenetration; Flexible N-donor ligands

1. Introduction

The design and synthesis of inorganic–organic hybrid coordination polymers are currently receiving much attention due to their fascinating network topologies and their potential application as functional materials [1–14]. The hydro(solvo)thermal technique is a powerful method for the construction of supramolecular polymers through their self-assembly. Self-assembly is a complicated process, highly influenced by lots of factors, such as the coordination nature of metal ions, the structural characterization of organic ligands, solvent system, temperature, pH value of the solution, the ratio of metal to ligand, the templates and the counter ions. Besides these aspects, other forces such as hydrogen-bonding, π–π interactions, metal–metal interactions can also greatly influence the supramolecular topology and its dimensionality [15–17]. Therefore, much work should be done to extend the area of the relevant structural types and to strive to find out proper synthetic strategies leading to the anticipated compounds.

The CN^- and SCN^- anions, with their ambidexterous character, show considerable flexible coordination modes in the construction of supramolecular architectures. Silver (I) is a good candidate as a soft acid tending to coordinate to soft bases such as ligands containing sulfur and nitrogen atoms. On the other hand, Ag(I) ions are apt to form silver–silver interactions which are propitious to control supramolecular architectures and dimensionality. Although cyanate and thiocyanate are well-known bridging ligands, their silver (I) coordination polymers are rare. To our knowledge, most of the AgCN and AgSCN polymers are those involving pyridine derivatives, organic amines and chelating ligands [18–20]. There are only two examples of AgCN and AgSCN polymers constructed from bridging dipodal N-donor ligands [21,22].

* Corresponding author. Tel.: +86 591 83709470; fax: +86 591 83709470.
E-mail address: swdu@ms.fjirsm.ac.cn (S.-W. Du).

0277-5387/$ - see front matter © 2006 Elsevier Ltd. All rights reserved.
doi:10.1016/j.poly.2006.07.034

The ligands mbix and bix, which have been considered to be highly flexible N-containing ligands, have been employed in recent years for the construction of numerous inorganic–organic hybrid supramolecular networks [23,24]. Enlightened from our previous work [25], we introduced mbix and bix into the silver cyanate or silver thiocyanate systems and isolated three polymeric compounds, namely, $[AgCN(mbix)]_n$ (**1**), $[(AgCN)_4(bix)_2]_n$ (**2**) and $[(AgSCN)_2(mbix)]_n$ (**3**).

2. Experimental

2.1. Materials

The ligands bix and mbix were synthesized according to the literature [24a]. Other chemicals were purchased from commercial sources and were used as received without further purification.

2.2. Physical measurements

The infrared spectra were recorded on a Perkin–Elmer FT-IR spectrophotometer in KBr matrices. Elemental analyses were carried out using a Perkin–Elmer 2400 II elemental analyser. Photoluminescence analyses were performed on an Edinburgh FLS920 fluorescence spectrometer.

2.3. Synthesis of the compounds

2.3.1. $[AgCN(mbix)]_n$ (1)

AgCN (33.47 mg, 0.25 mmol), mbix (30.00 mg, 0.13 mmol) and 2 mL of CH_3CN were placed in a 15 cm Pyrex tube. The tube was evacuated and sealed. The glass tube was heated at 120 °C for 24 h. After cooling to room temperature over 48 h, colorless crystals suitable for X-ray diffraction were formed, yielded: 13 mg, about 28% based on mbix. *Anal.* Calc. for $C_{15}H_{14}AgN_5$: C, 48.41; H, 3.79; N, 18.82. Found: C, 48.22; H, 3.98; N, 18.65%. FT-IR (cm^{-1}) (KBr disk): 3107m, 2102m, 2093m, 1611m, 1516vs, 1495s, 1450s, 1439s, 1392m, 1368m, 1274m, 1231m, 1242vs, 1112s, 1107vs, 1087m, 1076vs, 1030 m, 929m, 744s.

2.3.2. $[(AgCN)_4(bix)_2]_n$ (2)

Compound **2** was prepared in a similar manner as for **1** except that bix was used instead of mbix and the reaction was carried out at 160 °C. Yield: 21 mg, about 33% based on AgCN. *Anal.* Calc. for $C_{32}H_{28}Ag_4N_{12}$: C, 37.97; H, 2.79; N, 16.61. Found: C, 37.98; H, 3.09; N, 16.65%. FT-IR (cm^{-1}) (KBr disk): 3445m, 3134m, 3106m, 2928m, 2135s, 2113m, 2085m, 1512vs, 1437m, 1232vs, 1107vs, 1077vs, 757m, 720s, 656s, 618m.

2.3.3. $[(AgSCN)_2(mbix)]_n$ (3)

Pale yellow crystals of **3** were obtained in a similar way as for **1** except that AgSCN was employed instead of AgCN and the reaction temperature was 160 °C. Yield: 33 mg, about 46% based on AgSCN. *Anal.* Calc. for $C_{16}H_{14}Ag_2N_6S_2$: C, 33.70; H, 2.47; N, 14.74. Found: C, 34.03; H, 2.77; N, 14.73%. FT-IR (cm^{-1}) (KBr disk): 3435vs, 2104s, 2085s, 1631s, 1514s, 1441w, 1383w, 1368w, 1275w, 1236m 1103m, 1084m, 1078m, 830m, 770w, 743m, 657m.

2.4. X-ray crystallographic studies

Crystallographic data of **1**–**3** were collected on a Rigaku Mercury CCD diffractometer equipped with graphite monochromated Mo Kα radiation ($\lambda = 0.71073$ Å). Crystals of **1**–**3** suitable for X-ray crystallography were mounted on the top of a glass fiber with epoxy cement. The structure factors were obtained after Lorentz and polarization corrections. All the non-hydrogen atoms were located by the direct method and refined by full-matrix least-squares techniques. Crystallographic parameters, details of data collection and structure refinement for the crystals of **1**–**3** are summarized in Table 1.

3. Results and discussion

3.1. Syntheses and spectroscopic studies

The compounds $[AgCN(mbix)]_n$ (**1**), $[(AgCN)_4(bix)_2]_n$ (**2**) and $[(AgSCN)_2(mbix)]_n$ (**3**), were solvothermally prepared by mixing AgCN or AgSCN with corresponding ligands in vacuo. The reaction between AgSCN and bix failed to give any identified products. The IR spectra of **1**–**3** show characteristic CN groups around 2110 cm^{-1}. Other complicated peaks show the characteristic C–N and C–C vibrational frequencies for the bix and mbix ligands.

3.2. Structure of $[AgCN(mbix)]_n$ (1)

Fig. 1a shows the asymmetric unit of compound **1**, which consists of one Ag atom, one mbix ligand and one CN group. The Ag atom is in a deviated trigonal environment [the bond angles C1–Ag–N5A = 126.1(1)°, C1–Ag–N2 = 123.4(1)° and N5A–Ag–N2 = 103.46(9)°], coordinated by two different mbix ligands [Ag–N2 = 2.285(2), Ag–N5A = 2.284(2) Å], and one terminally bonded CN ligand [Ag–C1 = 2.113(3) Å, Ag–C1–N1 = 166.7(3)°] (Fig. 1b). The Ag ⋯ AgB distance is 2.888(1) Å, which is much shorter than twice the van der Waals radius of silver (3.4 Å), indicating significant silver–silver interactions [26–28]. The AgB–C1 distance is 2.87(3) Å, suggesting a non-negligible interaction compared to the Ag–C bond length [Ag2–C2B = 2.757(5) Å] found in $[Me_4N][Ag_2(CN)Cl]$ [26]. On the other hand, the direction of distortion from the terminal Ag–C1–N1 angle also indicates the existence of a weak interaction between AgB and C1. Thus, the cyanide group C1N1 can be described as having a semi-bridging coordination mode. Along the *a*-axis, the adjacent Ag

Table 1
Crystallographic data for compounds **1**–**3**

Compound	**1**	**2**	**3**
Formula	$C_{15}H_{14}AgN_5$	$C_{32}H_{28}Ag_4N_{12}$	$C_{16}H_{14}Ag_2N_6S_2$
Formula weight	372.18	1012.14	570.19
Crystal system	monoclinic	triclinic	triclinic
Space group	$P2_1/n$	$P\bar{1}$	$P\bar{1}$
Unit cell dimensions			
a (Å)	9.635(3)	9.6244(3)	8.0205(2)
b (Å)	7.550(2)	12.7147(1)	10.7058(4)
c (Å)	20.940(7)	14.6305(4)	11.7723(3)
α (°)	90	73.042(4)	83.61(1)
β (°)	100.135(7)	89.280(6)	71.540(9)
γ (°)	90	82.927(6)	80.64(1)
V (Å^3)	1499.4(8)	1698.96(7)	944.13(5)
Z	4	2	2
D_{calc} (g/cm^3)	1.649	1.979	2.006
$F(000)$	744	984	556
μ(Mo Kα) (mm^{-1})	1.344	2.314	2.308
Range (θ) for data collection (°)	$2.87 \leqslant \theta \leqslant 27.48$	$2.53 \leqslant \theta \leqslant 7.48$	$2.70 \leqslant \theta \leqslant 7.48$
Temperature (K)	293(2)	293(2)	293(2)
Limiting indices	$-12 \leqslant h \leqslant 12$, $-6 \leqslant k \leqslant 9$, $-27 \leqslant l \leqslant 26$	$-12 \leqslant h \leqslant 11$, $-16 \leqslant k \leqslant 15$, $-18 \leqslant l \leqslant 18$	$-8 \leqslant h \leqslant 10$, $-13 \leqslant k \leqslant 13$, $-15 \leqslant l \leqslant 15$
Reflections collected	9953	13 184	7308
Independent reflections (R_{int})	3388 (0.0177)	7667 (0.0125)	4257 (0.0146)
Parameter/restraints/data	238/0/2881	537/0/6442	291/0/3586
Goodness-of-fit	1.066	1.046	1.019
Final R indices [$I > 2\sigma(I)$][a,b]	$R_1 = 0.0353$, $wR_2 = 0.0851$	$R_1 = 0.0290$, $wR_2 = 0.0720$	$R_1 = 0.0292$, $wR_2 = 0.0711$
R indices (all data)	$R_1 = 0.0434$, $wR_2 = 0.0916$	$R_1 = 0.0368$, $wR_2 = 0.0764$	$R_1 = 0.0369$, $wR_2 = 0.0760$

[a] $R_1 = \sum ||F_o| - |F_c|| / \sum |F_o|$.

[b] $wR_2 = \left[\sum w(F_o^2 - F_c^2)^2 / \sum w(F_o^2)^2\right]^{0.5}$.

atoms are linked to each other through imidazole N atoms to form a zigzag chain with Ag ⋯ Ag separations along Ag ⋯ mbix ⋯ Ag being 14.93 Å (Fig. 1b). Two such zigzag chains are consolidated by silver–silver interactions to form a 2D layer structure with 50-membered rings, possessing an effective size of *ca.* 15 × 17 Å. It is worth mentioning that each layer network with (4, 4) topology is interlocked by two adjacent identical networks (above and below) as illustrated in Fig. 3c, forming a 3-fold-interpenetrated 2D framework. The nearest Ag ⋯ Ag separation between the 2D layers is 4.777 Å. There is no significant π ⋯ π stacking among these 3-fold-interpenetrated 2D networks (the centroid-centroid distance between benzene and imidazole rings being 4.802 Å).

3.3. Structure of $[(AgCN)_4(bix)_2]_n$ (**2**)

The asymmetric unit of compound **2** contains four crystallographically independent Ag atoms, four CN groups and two bix ligands. All the Ag atoms are in an approximately trigonal environment. The Ag1 atom is coordinated to N3 from the bix ligand [Ag1–N3 = 2.343(3) Å], C2 from the bridging cyanide [Ag1–C2 = 2.112(3) Å] and C1 from the μ-*C*,*C*-cyanide ligand [Ag1–C1 = 2.177(3) Å]. The Ag2 atom is surrounded by N5 from the other bix ligand [Ag2–N5 = 2.371(3) Å], N2 from the bridging cyanide [Ag2–N2 = 2.218(3) Å] and C1 from the μ-*C*,*C*-cyanide ligand [Ag2–C1 = 2.319(3) Å]. The distance of Ag1 ⋯ Ag2 [2.8462(4) Å] is a little shorter than that in **1**, but a little longer than that in the structure of $[Me_4N][Ag_2(CN)Cl]$ [26] and the compounds reported by Mak [29]. As shown in Fig. 2a, the bridging cyanide ligands and two pairs of Ag1 ⋯ Ag2 bonds form a 10-membered ring with the bond angles Ag2–C1–Ag1 78.5(1)° and Ag1–C2–N2A 171.1(3)°. The Ag3 atom is coordinated to C20 and N9 from the bridging cyanides [Ag3–C20 = 2.091(3), Ag3–N9 = 2.341(3) Å; Ag3–C20–N10D = 176.5(3), Ag3–N9–C21 = 176.8(3)°] and N8 from the bix ligand [Ag3–N8 = 2.215(3) Å]. The coordination environment of Ag4 is similar to that of Ag3. It is coordinated to C21 and N10 from the bridging cyanides [Ag4–C21 = 2.067(3), Ag4–N10 = 2.424(3) Å; Ag4–C21–N9 = 175.3(3), Ag4–N10–C20C = 175.1(3)°] and N11 from the bix ligand [Ag4–N11 = 2.195(2) Å]. As illustrated in Fig. 2b, the Ag3 atom set and Ag4 atom sets are bridged alternately by C20N10 and C21N9 group sets to make up an $[AgCN]_n$ infinite zigzag chain with the bond angles N10–Ag4–C21 116.41(1)° and N9–Ag3–C20 123.57(1)°. These zigzag chains connect the 10-membered rings through two bix

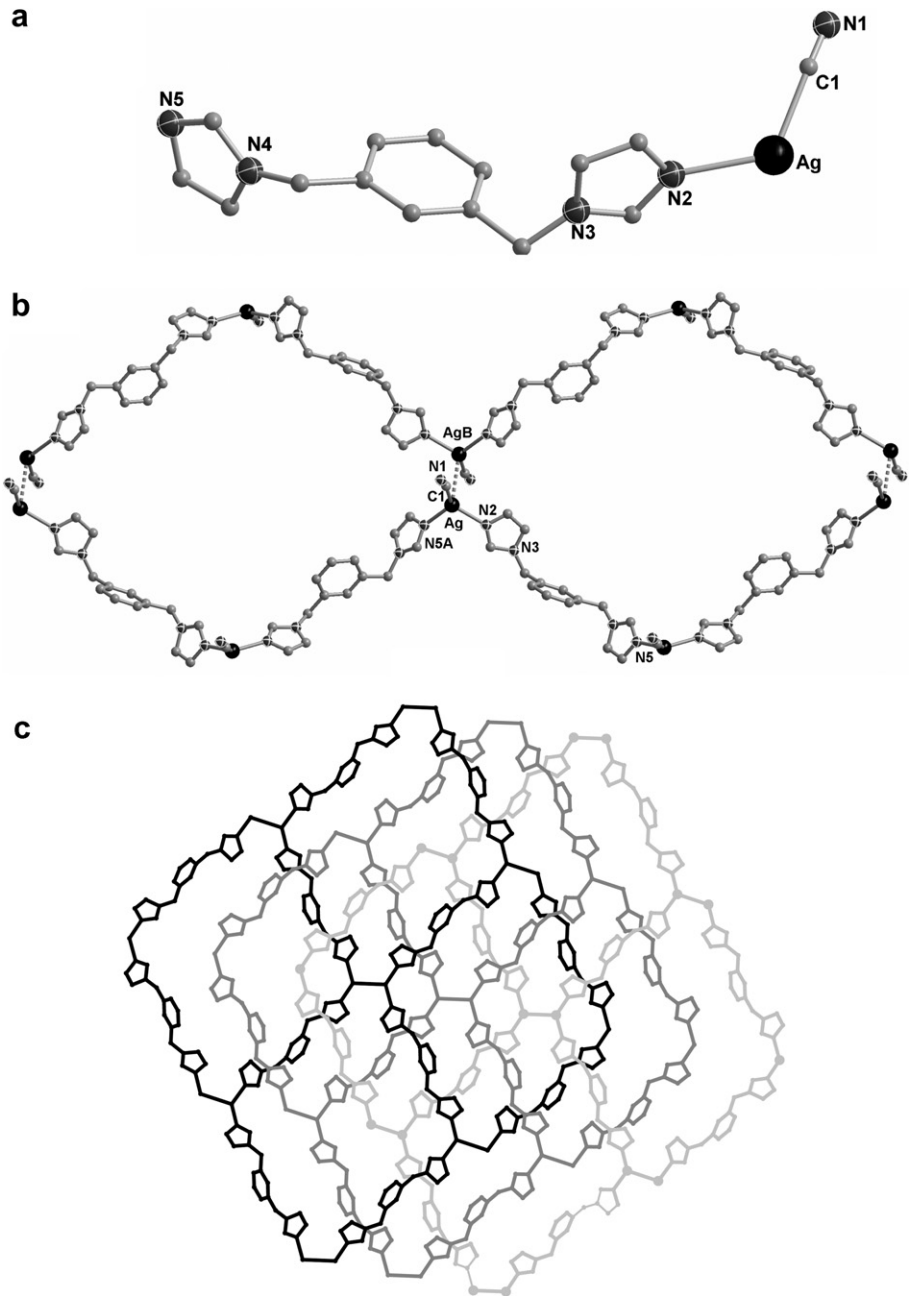


Fig. 1. (a) Representation of the asymmetric unit of **1**. (b) Representation of 50-membered rings in **1**. (c) View of the 3-fold interpenetrating 2D network, the CN groups are omitted for clarity. Hydrogen atoms are omitted for clarity. Symmetry codes: (A) $x - 1/2$, $-y + 1/2$, $z + 1/2$; (B) $-x + 2$, $-y + 2$, $-z + 1$.

ligands to generate a 2D framework with cavities (*ca.* 16×13 Å) along the *a*-axis.

It is interesting and worth mentioning that the structure contains two independent layers that interpenetrate in a parallel manner. As shown in Fig. 2c, the two undulating layers pass through each other to generate an interpenetrating double-layer structure. The corrugations in the layers, which make the interpenetration possible, arise from the flexible bix ligands that adopt a*syn*-conformation coordination mode. Upon interpenetration, the total effective pore sizes have been drastically decreased for those 10-membered rings that are located in the cavities along the *a*-axis. These 2-fold interpenetrating 2D networks are stacked into a 3D supramolecular structure through two types of weak $\pi \cdots \pi$ interactions (the centroid–centroid distance of imidazole rings between the adjacent layers being 4.1 and 3.992 Å, respectively) [30–32].

3.4. Structure of $[(AgSCN)_2(mbix)]_n$ (3)

The structure of **3** crystallizes in the triclinic space group $P\bar{1}$. Each asymmetric unit of **3** includes two Ag atoms, two

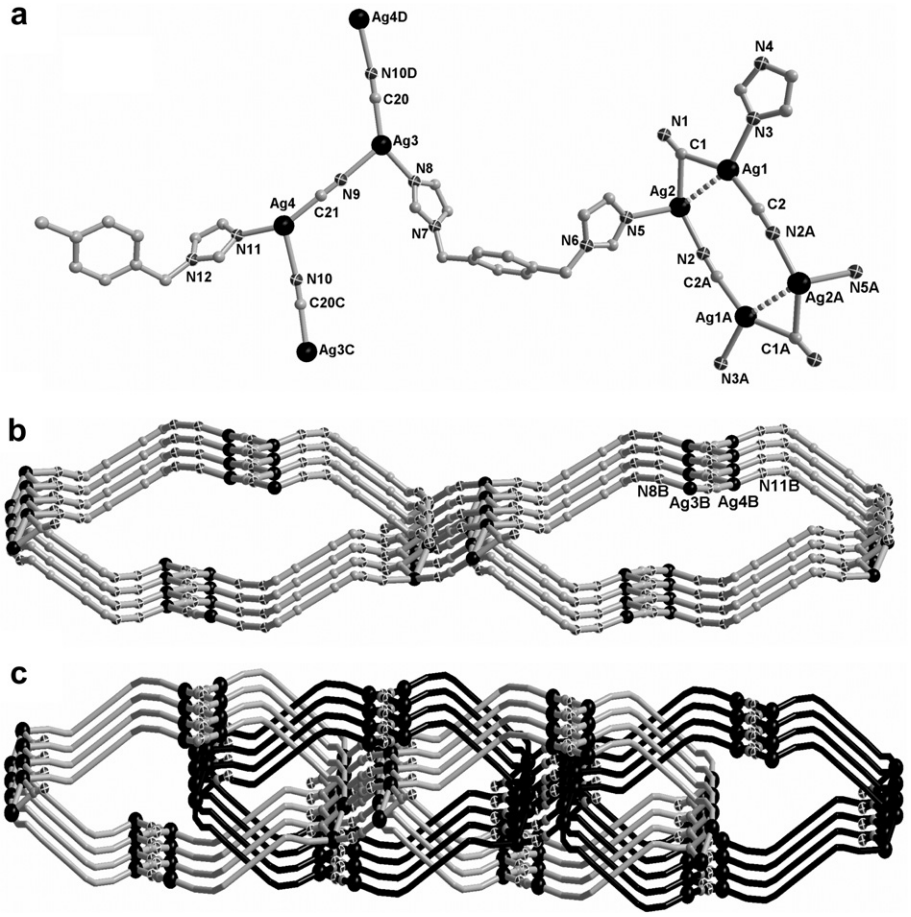


Fig. 2. (a) A portion of the structure of **2**. (b) View of the 2D framework extending along the *a*-axis, the bix ligand has been simplified as a wavelike line. (c) View of the 2-fold interpenetrating 2D network, the spacer stands for the bix ligand. Hydrogen atoms are omitted for clarity. Symmetry codes: (A) $-x+1, -y, -z-1$; (B) $-x+1, -y, -z+1$; (C) $x+1, y, z$; (D) $x-1, y, z$.

SCN groups and one mbix ligand. The Ag1 atom is coordinated to N3 from the mbix ligand [Ag1–N3 = 2.301 (2) Å], three different thiocyanate sulfur atoms [Ag1–S1 = 2.6133(8), Ag1–S2 = 2.6457(9) and Ag1–S2A = 2.6338(8) Å], resulting in a highly distorted tetrahedral coordination geometry for Ag1, with bond angles ranging from 92.09(3)° to 134.18(3)°. The environment of the Ag2 atom is also badly deviated from a tetrahedral coordination geometry, surrounded by two N and one S atoms from SCN groups [Ag2–N1C = 2.440(3), Ag2–N2B = 2.358(3) and Ag2–S1 = 2.5469(9) Å] and one N atom from the mbix ligand [Ag2–N5 = 2.211(2) Å], with bond angles in the range 87.38(1)–125.40(7)°.

The SCN groups act as triply-bridged ligands in the architecture of **3**. The Ag–S bond lengths varying from 2.5469(9)–2.6547(9) Å are in the normal range [18,33–35]. The Ag1 ⋯ Ag2 distance is 3.1882(4) Å, which is shorter than twice the van der Waals radius of silver (3.4 Å), suggesting the existence of an argentophilic interaction in **3** [18,26–28]. As shown in Fig. 3a, a pair of thiocyanate groups bridge a pair of Ag(I) atoms to form an eight-membered $Ag_2(SCN)_2$ macrocycle similar to the chair conformation of cyclohexane [Ag2–S1–C1 = 99.2(1), N1C–Ag2–S1 = 102.03(8) and S1–C1–N1 = 177.4(3)°]. Since the sulfur atoms of the SCN groups act in a bridging fashion, four Ag–S bonds make up a four-membered centrosymmetric Ag_2S_2 ring [Ag1–S2–Ag1A = 87.91(3), S2–Ag1–S2A = 92.086(3)°, Ag1 ⋯ Ag1A = 3.6708(5) Å]. The eight-membered macrocycle is connected to the four-membered ring through Ag1–S1 bonds and Ag2C–N2A–C2A–S2A edges to form a one-dimensional $[Ag_2(SCN)_2]_n$ chain, which is unprecedented in the literature. The chains are further interlinked by mbix ligands that bridge the Ag atoms to produce a two-dimensional $[(AgSCN)_2(mbix)]_n$ layer (Fig. 3c). Weak π ⋯ π interactions occur between adjacent layers to produce a 3D supramolecular structure (the centroid–centroid distance of the imidazole rings is *ca.* 4.048 Å, Fig. 3d) [30–32].

3.5. Luminescent properties

As illustrated in Fig. 4, **1** displays a sharp purple emission band in the solid state at 424 nm (λ_{ex} = 350 nm), while **2** exhibits a strong and broad emission band in the solid state at 440 nm (λ_{ex} = 376 nm). Compound **3** emits a very sharp and intense emission band in the solid state at 461 nm upon excitation at 380 nm. The origin of the emission bands of **1** and **2** is neither metal-to-ligand charge

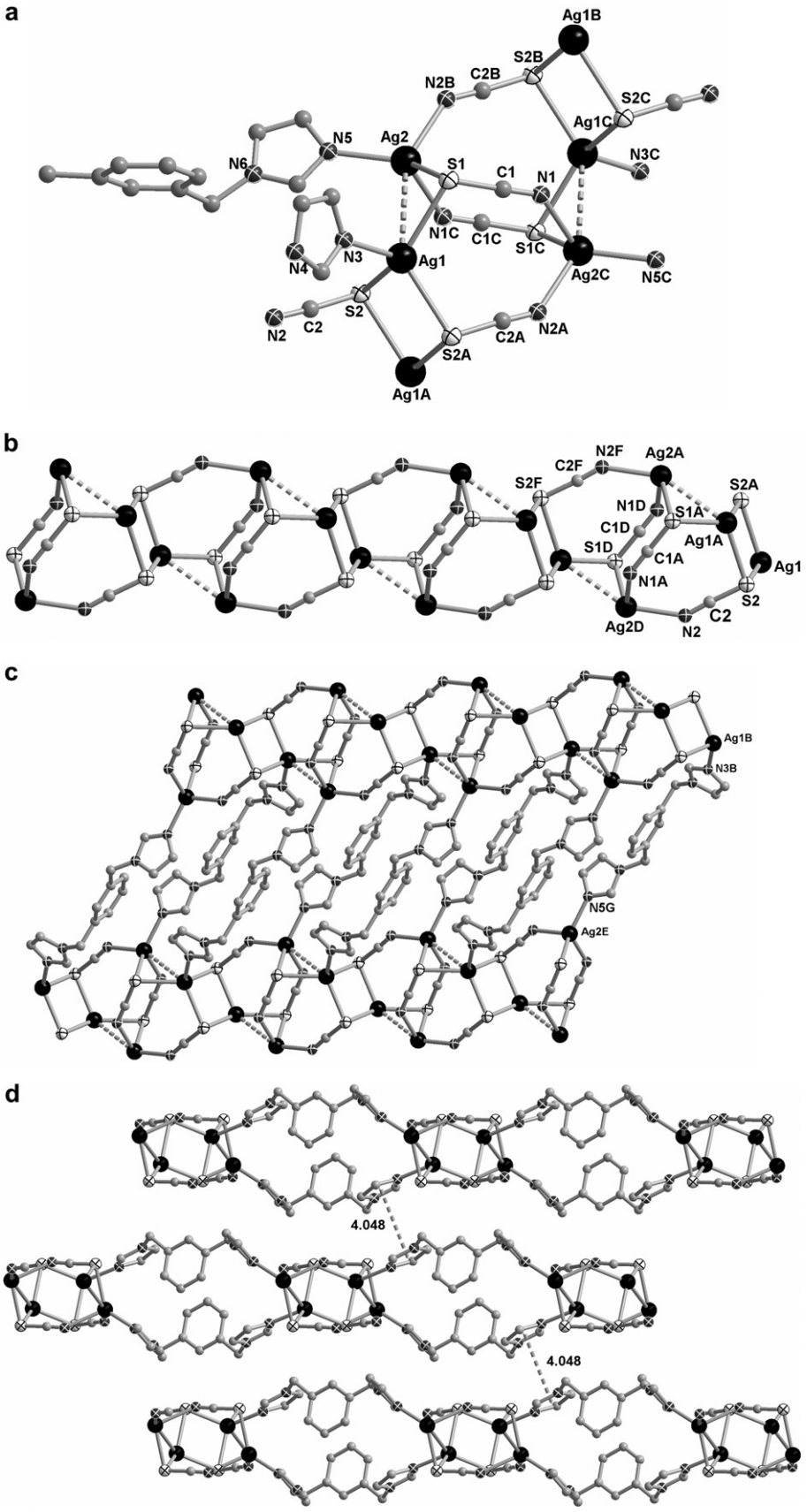


Fig. 3. (a) A portion of the structure of **3**. (b) Representation of a $[AgSCN]_n$ chain in **3**. (c) Representation of the 2D network of **3**. (d) Representation of the $\pi \cdots \pi$ interactions between adjacent layers. Hydrogen atoms are omitted for clarity. Symmetry codes: (A) $-x+1, -y+2, -z+1$; (B) $x+1, y, z$; (C) $-x+2, -y+2, -z+1$; (D) $x-1, y, z$; (E) $-x, -y+1, -z+2$; (F) $-x, 2-y, 1-z$; (G) $1-x, 1-y, 2-z$.

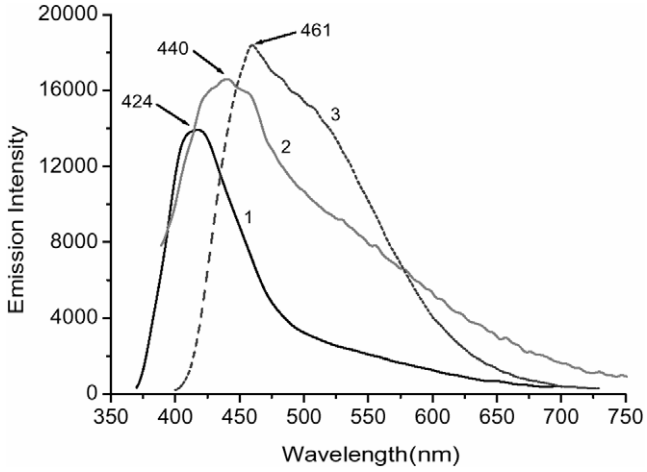


Fig. 4. Solid-state emission spectra of **1** ($\lambda_{ex} = 350$ nm), **2** ($\lambda_{ex} = 376$ nm) and **3** ($\lambda_{ex} = 380$ nm) at room temperature.

transfer (MLCT) nor ligand-to-metal charge transfer (LMCT) in nature and can be tentatively attributed to an intraligand emission because similar emissions are observed at 395 nm ($\lambda_{ex} = 334$ nm) for free mbix and 392 nm ($\lambda_{ex} = 340$ nm) for free bix ligands [24i]. The origin of the emission band of **3** may be attributed to the intraligand fluorescent emission where the electron is transferred from the π orbital of the thiocyanate groups to an unoccupied π^* orbital of the mbix ligands [36]. The clear red shift of the emission bands may be associated with aromatic $\pi \cdots \pi$ stacking interactions in the solid state.

4. Conclusion

The synthesis and crystal structures of **1**–**3** have been successfully synthesized via the solvothermal technique. In **1**, the 3-fold interpenetration of adjacent (4, 4) layers produces a 2D network structure in which the CN groups act as terminal ligands. In **2**, two undulating sheets interpenetrate each other to form a 2D network with the coexistence of linear-bridged CN groups and μ-*C*,*C*-cyanide bridging groups. In the structure of **3**, the SCN groups function as triply-bridging ligands and the structure of the $[AgSCN]_n$ subunit has not been previously observed for the silver thiocyanate system. The $\pi \cdots \pi$ interactions and silver–silver interactions play a significant role in the formation of the three polymers. Compounds **1**–**3** all exhibit strong photoluminescence at room temperature. The structures presented here show that the flexibility of the N-donor ligands can have dramatic effects on the structures of the silver–cyanide subunits. Further studies on the synthesis of related metal–cyanide polymers and their physical properties by using other imidazole ligands are already in progress.

Acknowledgements

This work was supported by grants from the State Key Laboratory of Structural Chemistry, Fujian Institute of Research on the Structure of Matter, Chinese Academy of Sciences (CAS), the Ministry of Science and Technology of China (001CB108906) and the National Science Foundation of China (20333070).

Appendix A. Supporting material

Supplementary data for the structures of **1**–**3** are available from the CCDC, 12 Union Road, Cambridge, CB2 1EZ, UK on request; fax: +44 1223 336 033; e-mail: deposit@ccdc.cam.ac.uk or http://www.ccdc.cam.ac.uk, quoting the deposition numbers 604652–604654. Supplementary data associated with this article can be found, in the online version, at doi:10.1016/j.poly.2006.07.034.

References

[1] O.M. Yaghi, H. Li, J. Am. Chem. Soc. 117 (1995) 10401.
[2] S.R. Batten, R. Robson, Angew. Chem., Int. Ed. 37 (1998) 1460.
[3] D.N. Reinhoudt, J.F. Stoddart, R. Ungaro, Chem. Eur. J. 4 (1998) 1349.
[4] J.K.M. Sanders, Chem. Eur. J. 4 (1998) 1378.
[5] D.H. Pierre, F. Daniel, Chem. Soc. Rev. 171 (1998) 351.
[6] M. Fujita, Y.J. Kwon, S.W. Ashizu, K. Ogure, J. Am. Chem. Soc. 116 (1994) 1151.
[7] M. Kondo, T. Yoshitomi, H. Matsuzaka, S. Kitagawa, K. Seki, Angew. Chem., Int. Ed. 36 (1997) 1725.
[8] C. Janiak, J. Chem. Soc., Dalton Trans. (2003) 2781.
[9] S.L. James, Chem. Soc. Rev. 32 (2003) 276.
[10] S. Kitagawa, R. Kitaura, S.-I. Noro, Angew. Chem., Int. Ed. 43 (2004) 2334.
[11] M. Eddaoudi, J. Kim, D. Vodak, A. Sudik, J. Wachter, M. O'Keeffe, O.M. Yaghi, PNAS 99 (2002) 4900.
[12] S.-L. Zheng, X.-M. Chen, Aust. J. Chem. 57 (2004) 703.
[13] D. Maspoch, D. Ruiz-Molina, J. Veciana, J. Mater. Chem. 14 (2004) 2713.
[14] S.R. Batten, K.S. Murray, Coordin. Chem. Rev. 246 (2003) 103.
[15] A.J. Blake, N.R. Champness, P. Hubberstey, W.-S. Li, M.A. Withersby, M. Schroder, Coordin. Chem. Rev. 183 (1999) 117.
[16] D.B. Leznoff, B.-Y. Xue, R.J. Batchelor, F.W.B. Einstein, B. Patrick, Inorg. Chem. 40 (2001) 6026.
[17] M. Munakata, L.P. Wu, T. Kuroda-Sowa, Adv. Inorg. Chem. 46 (1999) 173.
[18] C.-X. Ren, H.-L. Zhu, G. -Yang, X.-M. Chen, J. Chem. Soc., Dalton Trans. (2001) 85.
[19] N.K. Mills, A.H. White, J. Chem. Soc., Dalton Trans. (1984) 229.
[20] T. Pretsch, H. Hartl, Inorg. Chim. Acta 358 (2005) 1179.
[21] C.-X. Ren, B. -H Ye, F. He, L. Cheng, X.-M. Chen, Cryst. Eng. Comm. 6 (2004) 200.
[22] C.M. Hartshorn, P.J. Steel, Aust. J. Chem. 50 (1997) 1195.
[23] J. Fan, C. Slebodnick, D. Troya, R. Angel, B.E. Hanson, Inorg. Chem. 44 (2005) 2719.
[24] (a) B.F. Hoskins, R. Robson, D.A. Slizys, J. Am. Chem. Soc. 119 (1997) 2952;
(b) B.F. Hoskins, R. Robson, D.A. Slizys, Angew. Chem., Int. Ed. 36 (1997) 2336;
(c) H.-Y. Shen, D.-Z. Liao, Z.-H. Jiang, S.-P. Yan, G.-L. Wang, X.-K. Yao, H.-G. Wang, Acta Chem. Scand. 53 (1999) 387;
(d) B.F. Abrahams, B.F. Hoskins, R. Robson, D.A. Slizys, Cryst. Eng. Commun. 4 (2002) 478;
(e) L. Carlucci, G. Ciani, D.M. Prosepio, Chem. Commun. 4 (2004) 380;
(f) L. Carlucci, G. Ciani, D.M. Prosepio, L. Spadacini, Cryst. Eng. Commun. 6 (2004) 96;

(g) L. Carlucci, G. Ciani, D.M. Prosepio, Cryst. Growth Des. 5 (2005) 37;
(h) J. Kan, C. Slebodnick, R. Angel, B.E. Hanson, Inorg. Chem. 44 (2005) 552;
(i) L.-L. Wen, D.-B. Dong, C.-Y. Duan, Y.-Z. Li, Z.-F. Tian, Q.-J. Meng, Inorg. Chem. 44 (2005) 7161;
(j) T. Li, S.-M. Hu, S.-W. Du, Acta Crystallogr., Sect. C. 61 (2005) m409;
(k) L.-L. Wen, Y.-Z. Li, Z.-D. Lu, J.-G. Lin, C.-Y. Duan, Q.-J. Meng, Cryst. Growth Des. 6 (2006) 530.
[25] J.-D. Lin, Z.-H. Li, T. Li, J.-R. Li, S.-W. Du, Inorg. Chem. Commun. 9 (2006) 675.
[26] X. Liu, G.-C. Guo, M.-L. Fu, W.-T. Chen, Z.-J. Zhang, J.-S. Huang, J. Chem. Soc., Dalton Trans. (2006) 884.
[27] M.A. Omary, T.R. Webb, Z. Assefa, G.E. Shankle, H.H. Patterson, Inorg. Chem. 37 (1998) 1380.
[28] T. Dorn, K.M. Fromm, C. Janiak, Aust. J. Chem. 59 (2006) 22.
[29] G.-C. Guo, Thomas C.W. Mak, Angew. Chem., Int. Ed. 37 (1998) 3183.
[30] T. Kumar Maji, M. Ohba, S. Kitagawa, Inorg. Chem. 44 (2005) 9225.
[31] C. Janiak, J. Chem Soc., Dalton Trans. (2006) 3885.
[32] S. Aravinda, N. Shamala, C. Das, A. Sriranjini, I.L. Karle, P. Balaram, J. Am. Chem. Soc. 125 (2003) 5308.
[33] G.A. Bowmaker, Effendy, B.W. Skelton, A.H. White, J. Chem. Soc., Dalton Trans. (1998) 2123.
[34] G.A. Bowmaker, Effendy, P.J. Harvey, P.C. Healy, B.W. Skelton, A.H. White, J. Chem. Soc., Dalton Trans. (1996) 2449.
[35] Q.-P. Hu, D.-R. Chen, Y.-D. Meng, Y.-P. Fan, Jiegou Huaxue, J. Struct. Chem. 14 (1995) 206.
[36] X. Liu, G.-C. Guo, M.-L. Fu, X.-H. Liu, M.-S. Wang, J.-S. Huang, Inorg. Chem. 45 (2006) 3679.

Available online at www.sciencedirect.com
ScienceDirect
Polyhedron 26 (2007) 115–122
POLYHEDRON
www.elsevier.com/locate/poly

Synthesis and structure of copper (II) complexes with L–OH (L–OH = 2,6-bis-[*N*-(2-pyridylethyl)-formidoyl]-4-methyl-phenol)

Jorge Manzur [a,*], Ana María García [a], Andrés Vega [b], Andrés Ibañez [c]

[a] *Facultad de Ciencias Físicas y Matemáticas, Universidad de Chile, Departamento de Ciencia de los Materiales, Tupper 2069, Santiago, Chile*
[b] *Facultad de Ecología y Recursos Naturales, Departamento de Ciencias Químicas, Universidad Nacional Andrés Bello, República 275, Santiago, Chile*
[c] *Centro de Investigación Interdisciplinaria Avanzada en Ciencia de los Materiales, Facultad de Ciencias Físicas y Matemáticas, Universidad de Chile, Blanco Encalada, 2008 Santiago, Chile*

Received 9 June 2006; accepted 31 July 2006
Available online 5 August 2006

Abstract

The synthesis and molecular structures of three new copper (II) complexes with the ligand 2,6-bis-[*N*-(2-pyridylethyl)-formidoyl]-4-methyl phenol (L–OH) are reported. The complexes were prepared by reaction of L–OH with $CuX_2 \cdot nH_2O$, affording $[Cu_2(L–O)(\mu\text{-}OH)(\mu\text{-}ClO_4)](ClO_4)$ (**I**); $X = CLO_4^-$, with KOH in the reaction media; or $[Cu_2(L–O)(\mu\text{-}Cl)_2][Cu_2Cl_6]_{0.5}$ (**II**); X = Cl, in neutral conditions. The presence of methyl 3,4-dihydroxy-benzoate (CAT-$(OH)_2$) during the synthesis of **I** leads to the complex $[Cu_2(L–O)(\mu\text{-}OH)(CH_3OH)][Cu(CAT\text{-}O_2)_2]_{0.5}(ClO_4)$ (**III**). This compound exhibits an uncommon anion consisting of a bis-(catecholate) cuprate (II) moiety. The complete series of complexes show bridging phenoxo groups between the copper centers, together with hydroxo and perchlorate bridges found in **I** or two chlorides found in **II**. Compound **I** exhibit a rather low catalytic activity for the oxidation of 3,5-ditertbutyl catechol under aerobic conditions (12% quinone formation after 48 h at room temperature, in methanol solution 1×10^{-3} M in catalyst and 1×10^{-2} M in catechol), which could be ascribed to steric limitations of the catechol to coordinate the central Cu_2O_2 core.
© 2006 Elsevier Ltd. All rights reserved.

Keywords: Copper complexes; Molecular structure; Catecholase activity; Pyridyl Schiff-base ligand

1. Introduction

During the last years our group have been involved in the study of the oxidative catalytic properties of mono and binuclear copper complexes in the presence of molecular oxygen, with the final goal of designing new catalysts for the oxygenation of organic substrates with molecular oxygen, mimicking the activity of the metalloenzyme tyrosinase, Tyr [1]. This copper enzyme catalyses the *ortho*-hydroxylation of phenols (phenolase activity) and the further oxidation of the resulting catechols to quinones (catecholase activity) (Chart 1). It is responsible for the formation of melanin pigments and others polyphenolic natural products [2]. Catechol oxidase, CO [3] catalyses the oxidation of catechols to the corresponding quinones without acting on tyrosine. It has been proposed that the difference between both enzymes can be rationalized in terms of the more opened structure of the active site in tyrosinase compared with catechol oxidase.

It has been shown [4], using model systems, that the electron transfer from catechol to copper (II) can begin only after the catechol and the copper (II) species form a catecholate intermediate. The rate of the reaction is related to the redox potential and the steric match between the substrate and the complex. Substantial retardation of reactivity is evident if either steric or electronic factors do not match.

Numerous studies [5] have been reported on copper (II) complexes with different type of ligands, which mimic the catecholase activity of these two metalloproteins. Schiff-base ligands have also been used to study the activity of the resulting copper complexes in oxygenation and oxidation reactions [6]. 1,3-Benzene dicarboxaldehyde and 2,6-diformyl-4-methyl phenol have been used as building blocks

* Corresponding author.
E-mail address: jmanzur@dqb.uchile.cl (J. Manzur).

0277-5387/$ - see front matter © 2006 Elsevier Ltd. All rights reserved.
doi:10.1016/j.poly.2006.07.027

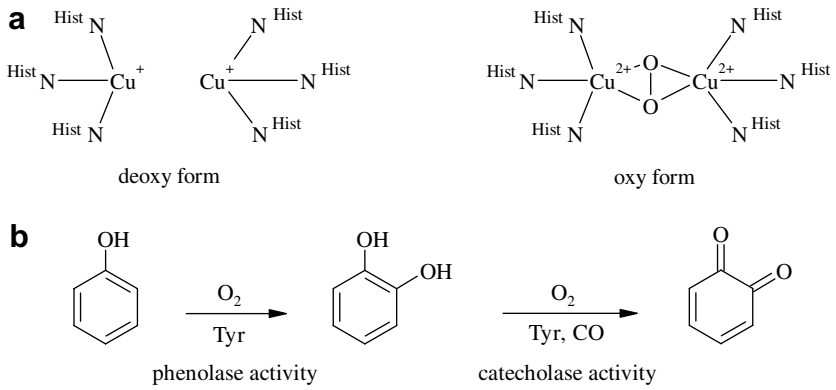
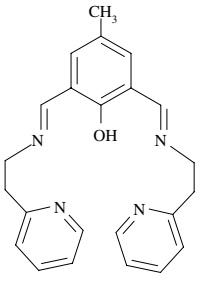


Chart 1. (a) Schematic diagram of the Cu coordination in the deoxy and oxy forms of tyrosinase and catechol oxidase and (b) pathway of the *o*-quinone formation from phenol precursors.

for the synthesis of macrocyclic and non-macrocyclic binucleating ligands. The copper complexes derived from these ligands have been the subject of numerous studies. We have reported the oxidation reaction of the copper (I) complexes with the binucleating Schiff-base ligand obtained from condensation of benzene-1,3-dicarboxaldehyde and di-(2-pyridyl)methyl amine [6a] and its methylated analogue [7].

Preliminary studies on the oxidation of 3,5-diterbutylcatechol using the copper (II) complexes obtained with the Schiff-base ligand derived from condensation of 2,6-diformyl-4-methyl phenol with (2-pyridyl)ethyl amine (L–OH) evidence a rather low catalytic activity. Since a catecholate intermediate is expected to be formed as a requirement for efficient catalytic activity, we tried to prepare and isolate such species in order to verify if the steric effect imposed by the ligand is responsible for the low activity. We used methyl 3,4-dihydroxybenzoate as the 'catechol' substrate, since the effect of the electron withdrawing ester group is known to prevent the oxidation to the quinone, making easier to isolate the proposed intermediate. Instead of the expected complex, we obtained a copper (II) species with an unusual anion consisting of a bis-(catecholate) cuprate (II) moiety. In this work, we wish to report the synthesis and molecular structure of this new copper (II) complex together with that obtained with copper (II) perchlorate and copper (II) chloride in the absence of the 'catechol'. In the last case we obtained a complex with a hexachloro dicuprate (II) anion, while the cation consist of a binuclear copper center bridged by the deprotonated phenol group of the ligand and two chloride atoms.



L-OH

2. Experimental

2.1. Materials and methods

All reagents were of reagent grade and were used without further purification unless stated otherwise. Solvents were of HPLC quality and were freshly distilled under nitrogen before use. Acetonitrile (CH_3CN) was distilled from calcium hydride. 3,4-Dihydroxy-benzoate (CAT-$(OH)_2$) was prepared by esterification of the acid in dry methanol in the presence of concentrated sulfuric acid as reported [8]. Elemental analysis for C, H, and N were performed at CEPEDEQ (University of Chile) on a Fison-Carlo Erba EA 1108 model analyzer. Copper was determined by Atomic Absorption Spectroscopy. IR spectra were obtained on a Bruker Vector 22 instrument. UV–Visible spectra were recorded in a Perkin–Elmer Lambda 11 equipment. ^1H NMR spectra were recorded in $CDCl_3$ on a Bruker AMX-300 NMR spectrometer. Chemical shifts are reported as δ values downfield an internal Me_4Si reference.

2.2. Synthesis of the ligand

The Schiff-base ligand 2,6-bis-[*N*-(2-pyridylethyl)-formidoyl]-4-methyl phenol (L–OH) was obtained as reported in reference [9] by reaction of 2,6-diformyl-4-methyl phenol with two equivalents of 2-aminoethyl pyridine in refluxing methanol. Evaporation of the solvent gives a yellowish oil that was characterized by IR and ^1H NMR spectroscopy.

IR (neat): 3386 (broad, ν OH) 1638 (ν C=N); 1591, 1569, 1474, 1460, 1436 (aromatic nuclei); 1255 (ν Ph–O), 760 (δ C–H).

^1H NMR ($CDCl_3$, 298 K): δ: 8.57 (2H, dd, pyridine alpha protons); 7.59 (2H, dt), 7.2 (2H, d), and 7.13 (2H, dd) (pyridine protons 3.96); (4H, t) and 3.12 (4H, t) (ethylene, $-CH_2-CH_2-$, protons); 2.2 (3H, s, methyl protons). 8.52 (~2H, s, broad, CH=N proton); 7.42 (~2H, s, broad, phenyl protons).

2.3. Syntheses of the complexes

2.3.1. $[Cu_2(L–O)(\mu\text{-}OH)(\mu\text{-}ClO_4)](ClO_4)$ (**I**)

1.48 g (4 mmol) of $Cu(ClO_4)_2(H_2O)_6$ were added to a solution of 2 mmol of the deprotonated (KOH) ligand in methanol (15 mL) and the mixture was refluxed for 30 min. Standing at room temperature affords a brown solid, yield 90%. Good quality crystals for X-ray diffraction studies were obtained by recrystallization from boiling methanol. *Anal.* Calc. for $C_{23}H_{24}N_4Cl_2O_{10}Cu_2$: C, 38.65; H, 3.39; N, 7.84; Cu, 17.78. Found: C, 38.12; H, 3.21; N, 7.64; Cu, 17.85%.

IR (KBr pellet): 1640, 1608, 1562, 1488, 1447, 1238, 1100, 770.

2.3.2. $[Cu_2(L–O)(\mu\text{-}Cl)_2][Cu_2Cl_6]_{0.5}$ (**II**)

To a solution of the ligand (2 mmol) in methanol (10 mL) were added $CuCl_2$ (0.54 g, 4 mmol) and the mixture was refluxed for 30 min. Standing at room temperature affords a brown solid, yield 70%. Recrystallization from hot acetonitrile gives crystals suitable for X-ray diffraction studies. *Anal.* Calc. for $C_{23}H_{23}N_4Cl_5OCu_3$: C, 37.34; H, 3.14; N, 7.58; Cu, 25.77. Found: C, 37.07; H, 3.10; N, 7.47; Cu, 25.58%.

IR (KBr pellet): 1638, 1607, 1564, 1485, 1445, 1237, 768.

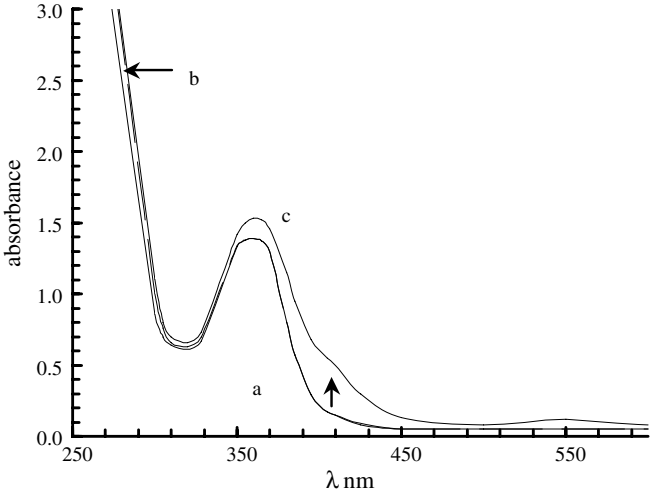


Fig. 1. (a) UV–Vis spectra of a 1.5×10^{-4} M solution of I in methanol and (b) in the presence of $DTBCH_2$ 2×10^{-3} M under nitrogen for 24 h (dotted line); (c) oxygen bubbled through the reaction mixture for 48 h.

2.3.3. $[Cu_2(L–O)(\mu\text{-}OH)(CH_3OH)][Cu(CAT\text{-}O_2)_2]_{0.5}(ClO_4)$ (**III**)

To a solution of the ligand (2 mmol) in methanol (10 mL) were added $Cu(ClO_4)_2(H_2O)_6$ (1.48 g, 4 mmol), 0.34 g of CAT-$(OH)_2$ (2 mmol) and 6 mL of a solution of KOH 1 M (6 mmol) in methanol and the reaction mixture was refluxed for 30 min. Standing overnight precipitate a crystalline green

Table 1
Structure and refinement details for **I**, **II**, and **III**

	I	**II**	**III**
Formula	$C_{23}H_{24}Cl_2Cu_2N_4O_{10}$	$C_{23}H_{23}Cl_5Cu_3N_4O$	$C_{32}H_{34}ClCu_{2.50}N_4O_{11}$
Weight	714.4	739.3	844.9
Color, habit	blue, block	green, plate	green, plate
Size/mm^3	$0.25 \times 0.19 \times 0.10$	$0.34 \times 0.10 \times 0.02$	$0.17 \times 0.13 \times 0.08$
Crystal system	orthorhombic	triclinic	triclinic
Space group	*P*bca	$P\bar{1}$	$P\bar{1}$
a (Å)	10.3233(7)	8.275(1)	10.693(3)
b (Å)	17.778(1)	10.977(1)	13.085(3)
c (Å)	29.112(2)	15.079(2)	14.033(4)
α (°)	90	84.451(2)	67.190(4)
β (°)	90	86.822(2)	73.252(5)
γ (°)	90	79.157(2)	70.755(5)
Volume (Å^3)	5342.8(6)	1337.9(3)	1679.4(8)
Z	8	2	2
D_c (kg m^{-3})	1.776	1.835	1.671
μ (mm^{-1})	1.857	2.888	1.721
T_{min}, T_{max}	0.6509, 0.8419	0.441, 0.934	0.755, 0.879
F(000)	2896	738	863
2θ Range	2.80–50.18	3.80–50.16	3.20–50.18
Index ranges	$-12 \leqslant h \leqslant 12$	$-9 \leqslant h \leqslant 9$	$-12 \leqslant h \leqslant 12$
	$-21 \leqslant k \leqslant 21$	$-13 \leqslant k \leqslant 12$	$-15 \leqslant k \leqslant 15$
	$-34 \leqslant l \leqslant 34$	$-17 \leqslant l \leqslant 17$	$-16 \leqslant ls \leqslant 16$
Reflection collected	4765	4708	5872
Observed reflections	3613	3007	3205
Parameters	369	326	456
R[a]	0.0563	0.0615	0.0732
wR[b]	0.1273	0.1298	0.1624
S	1.054	1.009	0.9980
Maximum, minimum difference (e – Å^{-3})	0.845, −0.447	0.838, −0.503	0.844, −0.515

[a] $R = \sum ||F_o| - |F_c|| / \sum |F_o|$.
[b] $wR = [\sum w(|F_o| - |F_c|)^2 / \sum w(F_o)^2]^{1/2}$, where $w = 1/\sigma^2(F_o)$. λ (Mo Kα) = 0.71073.

solid, that was collected, washed with cold methanol and vacuum dried, yield 90%. Green crystals suitable for X-ray diffraction studies were obtained by recrystallization in hot methanol. *Anal.* Calc. for $C_{32}H_{34}N_4ClO_{11}Cu_{2.5}$: C, 45.47; H, 4.06; N, 6.63; Cu, 18.80. Found: C, 45.02; H, 4.10; N, 6.47; Cu, 18.58%.

IR (KBr pellet): 1682, 1640, 1608, 1563, 1490, 1434, 1273, 1236, 1085, 770.

Caution! Perchlorate salts are potentially explosive and should be handled with care.

2.4. Preliminary oxidation studies

The capacity of complex **I** to achieve the stoichiometric or catalytic oxidation of 3,5-ditertbutylcatechol (DTBC) was studied using UV–Vis spectroscopy following the characteristic band of the expected product, 3,5-ditertbutylquinone, at 400 nm. Compound **I** (1.5×10^{-4} M) was added to a 2×10^{-3} M solution of DTBC in methanol under nitrogen, and the spectrum of the mixture was recorded. No changes were observed after 24 h under nitrogen. Oxygen gas was bubbled through the solution and the increase in the absorbance at 400 nm was monitored for a 48-hour period. Fig. 1 shows the observed changes.

In a separated experiment 10 mL of the reaction mixture (1×10^{-3} M in catalyst and 1×10^{-2} M in catechol) was bubbled with oxygen and quenched with HCl after 48 h The solvent was evaporated and the residue was extracted with hexane, the extracts were diluted to 25 mL and the spectrum was recorded. The absorbance at 400 nm was assumed to depend only on the concentration of the formed quinone. A control experiment shows no significant absorbance at 400 nm.

2.5. X-ray crystallographic data collection and refinement details

For each compound a single crystal was mounted on the tip of a glass fiber. Diffracted intensities were collected on a

Table 2
Selected bond lengths (Å) and angles (°) for **I**, **II**, and **III**

I		**II**		**III**	
Cu1–Cu2	2.9929(8)	Cu1–Cu2	2.970(1)	Cu1–Cu2	3.011(1)
Cu1–O1	1.960(3)	Cu1–O1	1.951(4)	Cu1–O1	1.960(5)
Cu2–O1	1.957(3)	Cu2–O1	1.936(4)	Cu2–O1	1.979(5)
Cu1–O2	1.912(3)	Cu1–Cl1	2.324(2)	Cu1–O2	1.901(5)
Cu2–O2	1.928(3)	Cu2–Cl1	2.802(2)	Cu2–O2	1.907(5)
Cu1–N1	1.945(4)	Cu1–Cl2	2.689(2)	Cu1–N1	1.928(6)
Cu2–N3	1.949(4)	Cu2–Cl2	2.335(2)	Cu2–N3	1.945(6)
Cu1–N2	2.005(4)	Cu1–N1	1.947(5)	Cu1–N2	1.998(6)
Cu2–N4	1.990(4)	Cu2–N3	1.945(6)	Cu2–N4	2.011(7)
Cu1–O3	2.610(4)	Cu1–N2	1.965(5)	Cu1–O5	2.879(6)
Cu2–O4	2.464(4)	Cu2–N4	1.974(5)	Cu2–O3	2.273(6)
C1–O1	1.314(6)	C1–O1	1.309(7)	Cu1–O8A	2.81(1)
				Cu1–O8B	2.66(2)
				C1–O1	1.329(8)
				Cu3–O4	1.903(5)
				Cu3–O5	1.938(5)
Cu1–O1–Cu2	99.6(1)	Cu1–O1–Cu2	99.6(2)	Cu1–O1–Cu2	99.7(2)
Cu1–O2–Cu2	102.4(2)	Cu1–Cl1–Cu2	70.11(5)	Cu1–O2–Cu2	104.5(2)
O2–Cu1–O1	78.7(1)	Cu2–Cl2–Cu1	72.09(5)	O2–Cu1–O1	78.2(2)
O2–Cu2–O1	78.4(1)	Cl1–Cu1–O1	84.7(1)	O2–Cu2–O1	77.5(2)
O2–Cu1–N1	168.9(2)	Cl1–Cu2–O1	72.7(1)	O2–Cu1–N1	169.5(2)
O2–Cu2–N3	167.1(2)	Cl2–Cu1–O1	74.6(1)	O2–Cu2–N3	166.1(2)
O2–Cu1–N2	95.6(2)	Cl2–Cu2–O1	84.0(1)	O2–Cu1–N2	94.2(2)
O2–Cu2–N4	94.7(2)	Cl1–N1–Cu1	145.0(2)	O2–Cu2–N4	94.4(2)
N1–Cu1–O1	91.4(2)	Cl1–N2–Cu1	94.1(2)	N1–Cu1–O1	91.7(2)
N3–Cu2–O1	91.5(2)	Cl2–N1–Cu1	119.1(2)	N3–Cu2–O1	91.2(2)
N2–Cu1–O1	172.3(2)	Cl2–N2–Cu1	95.9(2)	N2–Cu1–O1	170.4(3)
N4–Cu2–O1	173.0(2)	N3–Cu2–Cl1	118.4(2)	N4–Cu2–O1	165.5(2)
N1–Cu1–N2	94.7(2)	N4–Cu2–Cl1	92.3(2)	N1–Cu1–N2	96.2(3)
N3–Cu2–N4	95.5(2)	N3–Cu2–Cl2	148.7(2)	N3–Cu2–N4	94.7(3)
		N4–Cu2–Cl2	95.8(2)	N1–Cu1–O5	93.1(2)
		N1–Cu1–O1	90.1(2)	N2–Cu1–O5	97.0(2)
		N3–Cu2–O1	91.3(2)	N3–Cu2–O3	96.6(2)
		N2–Cu1–O1	170.3(2)	N4–Cu2–O3	104.0(2)
		N4–Cu2–O1	165.0(2)	O1–Cu1–O5	87.9(2)
		N1–Cu1–N2	96.3(2)	O2–Cu1–O5	83.7(2)
		N3–Cu2–N4	96.4(3)	O1–Cu2–O3	88.5(2)
		Cl1–Cu1–Cl2	92.84(6)	O2–Cu2–O3	91.4(2)
		Cl1–Cu2–Cl2	89.76(6)	O5–Cu3–O4	85.9(2)

Bruker Smart Apex diffractometer, using separations of 0.3° between frames and 10 s by frame. Data integration and absorption corrections were made using SAINT [10a]. The structures were solved using XS in SHELXTL [10a] by means of direct methods and completed (non-H atoms) by Fourier difference synthesis. The hydroxo hydrogen atom was located in the Fourier map and then fully refined for **I**, while could not be confidently located for **III**. During the last stages of refinement some disorder on the perchlorate oxygen atoms of **I** and **III** was evident. In the case of **I** it was modeled using two positions (A and B) for three of the oxygen atoms of the perchlorate counter anion, with partial occupancies of 0.55 and 0.45, respectively. For compound **III**, two equally occupied positions (A and B) were considered for all the oxygen atoms. Refinement until convergence was obtained using XL SHELXTL and SHELXL97 [10b]. Additional crystallographic and refinement details are given in Table 1 and selected bond lengths and angles are given in Table 2.

3. Results and discussion

3.1. Synthesis

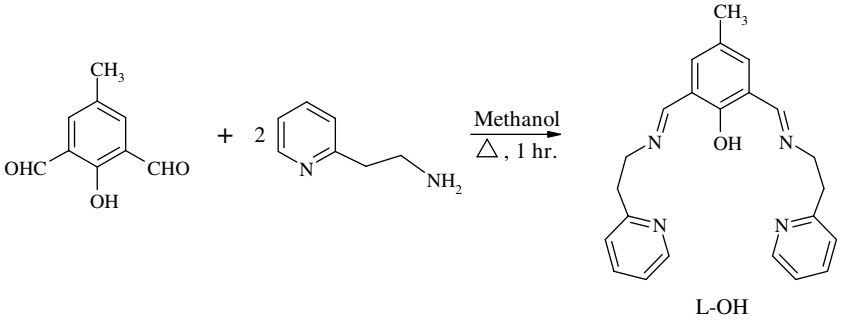
The synthesis of the ligand L–OH was described previously (Scheme 1) [9], but the free base was not characterized. In this work, after the reaction was completed, the solvent was evaporated giving an oil that was characterized by IR and ^{1}H NMR spectroscopy. The IR spectrum shows the absence of the band due to the aldehyde carbonyl stretching frequency (*ca.* 1690 cm^{-1}) indicating complete formation of the azomethine C=N bond, whose stretching band is observed at 1638 cm^{-1}. The ^{1}H NMR spectrum of the base, at 298 K, shows the signals due to the protons of the pyridylethyl and the methyl groups. Besides, two broad bands are observed at 8.52 and 7.42 δ that were assigned to the CH=N and the phenyl protons, respectively. These signals become best resolved at higher temperature (318 K) (see supplementary material, Figure S1). The exact reason for the broadening of these signals at low temperature remains unclear.

The copper complexes were obtained straightforward by reaction of a solution of the ligand, prepared *in situ*, with the proper copper salt in methanol (Scheme 2, see Section 2).

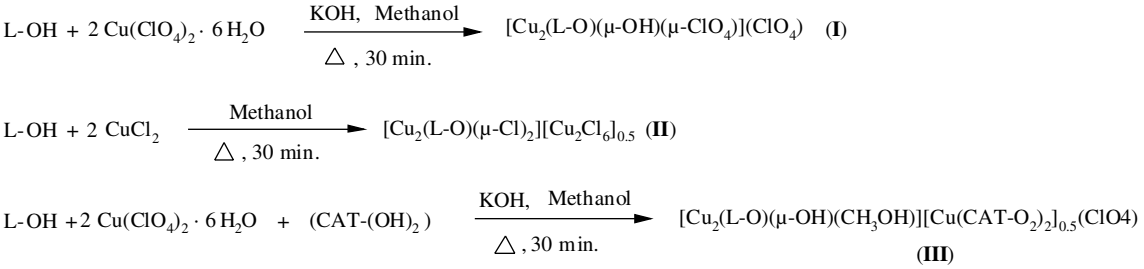
The elemental analysis support the given stoichiometries, and the IR spectra show the expected bands for the coordinated ligand. All three complexes show the azomethine stretching frequency in the range 1630–1640 cm^{-1}, as expected for this type of complexes [11], and the typical bands owing to the pyridine and phenyl nuclei at 1600–1400 cm^{-1}. Besides, complex **I** and **III** show the bands due to the perchlorate anion at 1100 and 1085 cm^{-1}, respectively. Complex **III** also shows a band at 1685 cm^{-1} that is assigned to the carbonyl ester group.

3.2. Structural description

The structure determined for every one of the complexes show a deprotonated molecule of the 2,6-bis-[*N*-(2-pyridylethyl)-formidoyl]-4-methyl phenol (L–OH) ligand coordinating two cupric centers, which results in a close vicinity, 2.9929(8), 2.970(1), and 3.011(1) Å for **I**, **II**, and **III**, respectively. The molecular structures present then a central bi cupric core bridged by the phenolic oxygen atom of L–O in all cases and additional bridge(s), a hydroxo



Scheme 1.



Scheme 2.

anion for **I** and **III**, two chloride anion for **II** and a O,O′ perchlorate for **I**, are observed. The coordination of each copper center is completed by two nitrogen atoms of each arm of L–O. The hydroxo-bridged compounds **I** and **III** show a planar Cu_2O_2 central core, while in **II** the chloride bridges lie out (and at opposite sides) of the Cu_2O plane.

For compound **III**, an oxygen atom from a methanol molecule and a catecholate oxygen atom additionally coordinate the vicinal cupric centers, as shown in Fig. 2. In this way, complexes **I** and **III** exhibits two cupric centers with square based pyramid as coordination geometry, while the copper centers in complex **II** are intermediate between pyramidal and trigonal bipyramidal geometry, been Cu1 the more distorted from an ideal square-based pyramid (τ [12] = 0.42 and 0.27 for Cu1 and Cu2, respectively).

The Cu–O(phenolic)–Cu angles are similar for all the compounds, being 99.6(1), 99.6(2), and 99.7(2)° for **I**, **II**, and **III**, respectively, which is the same value compared to the 99.2(3)° described for $[Cu_2(L'–O)(\mu\text{-}ClO_4)](ClO_4)$ (L′–OH = 2,6-bis-[*N*-(2-(2′-pyridyl)ethyl) formidoyl]-4-hydroxy-phenol) [13].

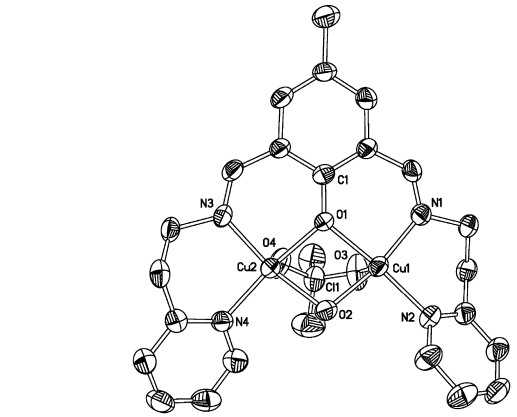
The chloride bridges in **II** are quite asymmetric. Two of the measured copper – chloride distances, (Cu1–Cl1, 2.324(2) and Cu2–Cl2, 2.335(2) Å), compare well with the ones observed for [2,6-bis-((2-pyridyl)-methyliminomethyl)-*p*-cresolato-(μ-chloro)-di-copper (II)] dichloride (2.297 and 2.310 Å) [14], while the another two are significantly longer, (Cu1–Cl2, 2.689(2) and Cu2–Cl1, 2.802(2) Å), suggesting that each chloride ligand is mainly coordinated to one cupric center of the binuclear unit.

The $Cu_2Cl_6^{2-}$ moiety has been previously described to be present as uncoordinated counter anion of cationic copper (II) complexes [15,16]. In the same way the complex anionic $[Cu(CAT\text{-}O_2)_2]^{2-}$ moiety has been described to bridge between cupric [17] or cuprous centers [18]. The shortest Cu ··· Cu(counter anion) distance measured in this work is 5.921 Å for **II** and 3.817 Å for **III**.

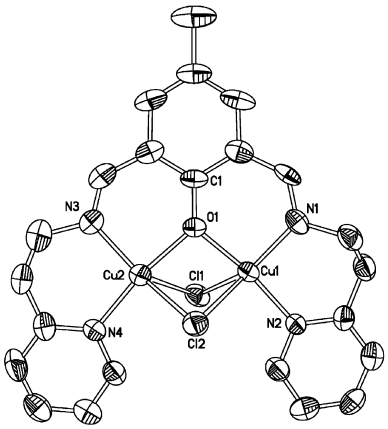
3.3. Catalytic activity

A large number of copper (II) complexes react with 3,5-ditertbutylcatechol to give the corresponding quinone and the reduced copper (I) complexes in a two-electron transfer reaction. Subsequent reaction with oxygen re-oxidizes the cooper (I) to copper (II) leading to the catalytic oxidation of the catechol mediated by the copper complexes. The need for two copper centers in a binuclear complex for the oxidation of catechol substrates in terms of the complementarity in the number of electrons transferred and the steric fit advantages have been discussed by several authors [19].

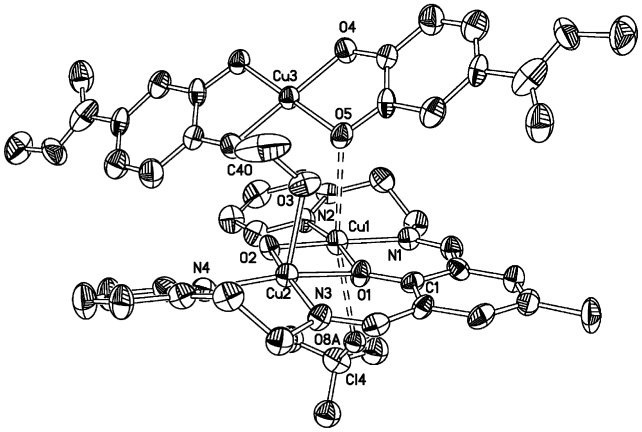
Fig. 1 shows the spectral changes observed when DTBC (2×10^{-3} M) was added to a 1.5×10^{-4} M solution of **I** in methanol, under anaerobic conditions. It can be seen that there is no major changes in the spectra even after reacting for 24 h, showing that the oxidation of the DTBC does not take place, in any significant extent. Bubbling the reaction mixture with oxygen produces the slow development of a band at 400 nm, indicative of the formation of the quinone. In a separated experiment (see Section 2) the amount of quinone formed, after reacting for a 48-hour period, was found to be roughly 12% of the theoretical value; a rather poor yield compared to other reported systems [5b,5c,19].



I



II



III

Fig. 2. Molecular structure diagram for **I**, **II**, and **III** with partial numbering scheme. Hydrogen atoms, perchlorate and hexachloro dicuprate (II) counter anions omitted for clarity. Displacement ellipsoids drawn at the 50% probability level.

A complex formulated as $Cu_2(L–O)(OH)(ClO_4)_2$, like complex **I**, was reported previously and the magnetic, electronic spectrum and conductance measurements were described. Reaction of this complex with sodium ascorbate in dearated aqueous solution gives an intense purple color that the authors attributed to the formation of a weak adduct $[(Cu_2L)OH]^{2+} \cdot (ascorbate)^-$. Qualitative O_2 uptake studies show that the complex catalyses the ascorbate oxidation, in air-saturated solution, but not as effectively as Cu^{2+} ions [9]. The oxidation of DTBC catalyzed by complex **I**, described in this work, is also a non-efficient process.

These results prompt us to study the reaction of the complex with methyl 3,4-dihydroxy benzoate, a 'catechol' that is not oxidized to the quinone due to the electron withdrawing effect of the ester group. Since many authors, on the base of mechanistic studies, have proposed a catecholate moiety as a key intermediate for an efficient catalytic activity, we tried to prepare such species to verify if the steric effect imposed by the ligand is responsible for the measured low catalytic activity of **I**. Efforts to isolate the proposed catecholate were unsuccessful. Instead, we isolate the binuclear copper (II) compound **III**, suggesting that the low catalytic activity may be due to the sterical limitation of the catechol to reach the first coordination sphere of **I**.

4. Conclusions

In conclusion, we have synthesized and structurally characterized three new copper (II) complexes with the Schiff-base binucleating ligand 2,6-bis-[*N*-(2-pyridylethyl)-formidoyl]-4-methyl phenol. The reported complexes show bridging phenoxo groups between the copper centers, and hydroxo and perchlorate bridges in **I** or two chlorides in **II**. The third complex **III** contains an uncommon bis-(catecholate) cuprate (II) complex species as the counter anion. Compound **I** exhibits a rather low catalytic activity for the oxidation of 3,5-ditertbutyl catechol under aerobic conditions, which could be ascribed to steric limitations of the catechol to coordinate the central Cu_2O_2 core.

Acknowledgements

Financial support from FONDECYT Project No. 1050484 is gratefully acknowledged. Authors gratefully acknowledge Fundación Andes for the purchase of the area detector diffractometer currently operating at the University of Chile.

Appendix A. Supplementary data

Figure S1 showing the ^1H NMR spectra of the free Schiff-base, 2,6-bis-[*N*-(2-pyridylethyl)-formidoyl]-4-methyl phenol, at 298 and 318 K. Crystallographic data for structural analysis have been deposited with the Cambridge Crystallographic Data Centre with CCDC numbers for **I**, **II**, and **III** of 610183, 610184, and 610185, respectively. Copies of this information may be obtained free of charge from The Director, CCDC, 12 Union Road, Cambridge CB2 1EZ, UK, fax: +44 1223 336 033; or deposit@ccdc.cam.ac.uk or http://www.ccdc.cam.ac.uk. Supplementary data associated with this article can be found, in the online version, at doi:10.1016/j.poly.2006.07.027.

References

[1] (a) J. Manzur, A.M. García, C. Córdova, O. Pizarro, V. Acuña, E. Spodine, Polyhedron 21 (2002) 181;
(b) J. Manzur, A.M. García, B. Gómez, E. Spodine, Polyhedron 19 (2000) 2367;
(c) J. Manzur, A.M. García, V. Rivas, A.M. Atria, J. Valenzuela, E. Spodine, Polyhedron 16 (1997) 2299.
[2] (a) D.A. Robb, in: R. Lontie (Ed.), Copper Proteins and Copper Enzymes, vol. 2, CRC Press, Boca Raton, FL, 1984, p. 207;
(b) M.G. Peter, Angew. Chem., Int. Ed. Engl. 28 (1989) 555.
[3] (a) R. Than, A.A. Feldman, B. Krebs, Coord. Chem. Rev. 182 (1999) 211;
(b) T. Klabunde, C. Eicken, J.C. Sacchettini, B. Krebs, Nat. Struct. Biol. 5 (1998) 1084.
[4] (a) N. Osishi, Y. Nishida, K. Ida, S. Ida, Bull. Chem. Soc. Jpn. 53 (1980) 2847;
(b) M.M. Rogic, M.D. Swerdloff, T.R. Demmin, in: K.D. Karlin, J. Zubieta (Eds.), Copper Coordination Chemistry; Biochemical and Inorganic Perspectives, Adenine Press, Guilderland, NY, 1983, p. 167;
(c) E.I. Solomon, U.M. Sundaram, T.E. Machonkin, Chem. Rev. 96 (1996) 2563.
[5] (a) See for example. K. Selmeczi, M. Règlier, M. Giorgi, G. Speier, Coord. Chem. Rev. 245 (2003) 191;
(b) A. Neves, L.M. Rossi, A.J. Bortoluzzi, B. Szpoganicz, C. Wiezbicki, E. Schwingel, W. Haase, S. Ostrovsky, Inorg. Chem. 41 (2002) 1788;
(c) E. Monzani, G. Battaini, A. Perotti, L. Casella, M. Gullotti, L. Santagostini, G. Nardin, L. Randaccio, S. Geremia, P. Zanello, G. Opromolla, Inorg. Chem. 38 (1999) 5359;
(d) L.M. Mirica, D.J. Rudd, M.A. Vance, E.I. Solomon, K.O. Hodgson, B. Hedman, T.D.P. Stack, J. Am. Chem. Soc. 128 (2006) 2654;
(e) S.P. Foxon, D. Utz, J. Astner, S. Schindler, F. Thaler, F.W. Heinemann, G. Liehr, J. Mukherjee, V. Balamurugan, D. Ghosh, R. Mukherjee, Dalton Trans. (2004) 2321.
[6] (a) A.M. García, J. Manzur, M.T. Garland, R. Baggio, O. González, O. Peña, E. Spodine, Inorg. Chim. Acta 248 (1996) 247;
(b) O.J. Gelling, F. van Bolhuis, A. Meetsma, B.L. Feringa, J. Chem. Soc., Chem. Commun. (1988) 552;
(c) S. Ryan, H. Adams, D.E. Fenton, M. Becker, S. Schindler, Inorg. Chem. 37 (1998) 2134.
[7] R. Calero, A. Vega, A.M. García, E. Spodine, J. Manzur, J. Chilean Chem. Soc. 48 (2003) 85.
[8] L. Casella, E. Monzani, M. Gullotti, D. Cavagnino, G. Cerina, L. Santagostini, R. Ugo, Inorg. Chem. 35 (1996) 7516.
[9] J.J. Grzybowski, P.H. Merrell, F.L. Urbach, Inorg. Chem. 17 (1978) 3078.
[10] (a) SHELXTL Version 5.1, Bruker AXS, Madison, WI, 1998.;
(b) G.M. Sheldrick, SHELXL-97, Program for Crystal Structure Refinement, University of Göttingen, Germany, 1997.
[11] H. Okawa, T. Toki, Y. Nonaka, Y. Muto, S. Kida, Bull. Chem. Soc. Jpn. 46 (1973) 1462.
[12] A.W. Adison, N.T. Rao, J. Chem. Soc., Dalton Trans. (1984) 1349.
[13] O.J. Gelling, A. Meetsma, B.L. Feringa, Inorg. Chem. 29 (1990) 2816.
[14] R.J. Majeste, C.L. Klein, E.D. Stevens, Acta Crystallogr. C39 (1983) 52.
[15] R. Kapoor, A. Kataria, P. Venugopalan, P. Kapoor, M. Corbella, M. Rodriguez, I. Romero, A. Llobet, Inorg. Chem. 43 (2004) 6699.
[16] E.W. Ainscough, A.M. Brodie, C.V. Depree, J. Chem. Soc., Dalton Trans. (1999) 4123.

[17] M. Kawahara, Md.K. Kabir, K. Yamada, K. Adachi, H. Kumagai, Y. Narumi, K. Kindo, S. Kitagawa, S. Kawata, Inorg. Chem. 43 (2004) 92.
[18] G. Speier, S. Tisza, Z. Tyeklar, C.W. Lange, C.C. Pierpont, Inorg. Chem. 33 (1994) 2041.
[19] (a) K. Selmeczi, M. Réglier, M. Giorgi, G. Speier, Coord. Chem. Rev. 245 (2003) 191;
(b) E. Monzani, L. Kinti, A. Perotti, L. Casella, M. Gullotti, L. Randaccio, S. Geremia, G. Nardin, P. Faleschini, G. Tabbi, Inorg. Chem. 37 (1998) 553.

Available online at www.sciencedirect.com
ScienceDirect
Polyhedron 26 (2007) 123–132
POLYHEDRON
www.elsevier.com/locate/poly

Synthesis, crystal structures and magnetic properties of five new metal(II) compounds constructed with isomers of aminobenzonitrile and dicyanamide ligands

Moumita Biswas [a], Georgina M. Rosair [b], Guillaume Pilet [c], M. Salah El Fallah [d,*], Joan Ribas [d], Samiran Mitra [a,*]

[a] Department of Chemistry, Jadavpur University, Kolkata 700 032, West Bengal, India
[b] Department of Chemistry, Heriot-Watt University, Edinburgh EH14 4AS, UK
[c] Groupe de Cristallographie et Ingénierie Moléculaire, Laboratoire des Multimatériaux et Interfaces – UMR 5615 CNRS-Université Claude Bernard Lyon 1, Bât. Jules Raulin 43 Bd du 11 Novembre 1918, 69622 Villeurbanne Cedex, France
[d] Department de Química Inorgànica, Universitat de Barcelona, Martí i Franquès, 1-11, 08028 Barcelona, Spain

Received 25 May 2006; accepted 2 August 2006
Available online 18 August 2006

Abstract

Five new compounds formulated as $[Ni^{II}(dca)_2(para\text{-}ABN)_2(H_2O)_2]$ (**1**), $[Cu^{II}(dca)_2(para\text{-}ABN)_2(H_2O)_2]$ (**2**), $[Cu^{II}(dca)_2(para\text{-}ABN)_2]_n$, (**3**), $[Cu^{II}(dca)_2(ortho\text{-}ABN)_2]_n$, (**4**) and $[Cd^{II}(dca)_2(meta\text{-}ABN)_2]_n$ (**5**), where dca = dicyanamide and ABN = aminobenzonitrile, have been synthesized and characterized by single crystal X-ray diffraction studies and low temperature (300–2 K) magnetic measurements. The structural analyses revealed that **1** and **2** are isomorphous where dca and *para*-ABN both act as monodentate ligands. **3** consists of infinite double stranded chains of Cu(II) ions connected through the *para*-ABN bridges whereas **4** and **5** consist of infinite double stranded chains of Cu(II) and Cd(II) respectively, connected through $\mu_{1,5}$-dca bridges. The compounds extend their geometries to three-dimensional for **1**–**3** and **5** and two-dimensional for **4** through hydrogen bonding interactions. All the metal ions Ni^{2+}, Cu^{2+} and Cd^{2+} are located on inversion centres and have distorted octahedral coordination geometries. The variable temperature magnetic susceptibility measurements show that the global feature of the $\chi_M T$ versus T curves for **3** and **4** is characteristic of very weak antiferromagnetic interactions and between 300 and 2 K the best fit parameters were determined as $J = -2.35$ and $-5.1\ cm^{-1}$, respectively.
© 2006 Elsevier Ltd. All rights reserved.

Keywords: Metal (nickel, copper, cadmium); Bridging ligands (dca, ABN); Supramolecular structures; Magnetic properties; First Cu–ABN compounds

1. Introduction

The bulk properties of a molecular material depend critically on its crystal structure and intermolecular interactions. Recently, enormous interests have been shown in coordination polymers, zeolitic structures, hydrogen-bonded networks and potentially important magnetic materials [1–3]. The main attractions for extended structures are their tunability and potential applications [4–6]. There is also an aesthetic perspective; chemists are attracted by the particular beauty and the intriguing diversity of the structures, which can be obtained by assembling metal ions and various multifunctional ligands. The coordination geometry of the metal ion is crucial in the self-assembling process [7–11]. Solvent molecules and counter ions will also influence the final supramolecular architectures. These can affect the size, shape and hydrophilic character of voids in zeolitic structures and hydrogen-bonded networks as well as the overall stability of the supramolecular systems [5,7,12,13]. Our study describes two types of ligands namely

* Corresponding authors. Fax: +91 33 24146414 (S. Mitra).
E-mail addresses: salah.elfallah@qi.ub.es (M.S. El Fallah), smitra_2002@yahoo.com (S. Mitra).

0277-5387/$ - see front matter © 2006 Elsevier Ltd. All rights reserved.
doi:10.1016/j.poly.2006.08.008

dicyanamide (dca) and aminobenzonitrile (ABN) isomers for coordination with M(II) ions (M = Ni, Cu and Cd) in order to construct new and varied metal frameworks. The coordination polymers are formed when divalent first-row transition metals are linked with the generally bidentate (monodentate and tridentate coordination is also possible) dicyanamide (dca, $N(CN)_2^-$) ligand. This ligand has significant current interest for their structural diversities and potentially interesting magnetic properties [14]. Aminobenzonitrile isomers can coordinate to a metal centre through either the amine or nitrile nitrogen. Accordingly, we have obtained five different structures where the above two ligands show different bonding modes to metal(II) ions.

In this paper, we report five compounds with the following formula $[Ni^{II}(dca)_2(para\text{-}ABN)_2(H_2O)_2]$ (**1**), $[Cu^{II}(dca)_2(para\text{-}ABN)_2(H_2O)_2]$ (**2**), $[Cu^{II}(dca)_2(para\text{-}ABN)_2]_n$, (**3**), $[Cu^{II}(dca)_2(ortho\text{-}ABN)_2]_n$, (**4**) and $[Cd^{II}(dca)_2(meta\text{-}ABN)_2]_n$ (**5**) using dicyanamido (dca) and three isomers of aminobenzonitrile (ABN) ligands. A CSD search [15,16] yielded only ten complex compounds with aminobenzonitriles. The present work contains the first coordination polymers of Cu(II) with ABN ligands. Two monomeric isomorphous compounds **1** and **2** and three polymeric frameworks **3**–**5** have been characterized. All except **4** (2D hydrogen bonding network) have an extensive 3D hydrogen bonding network.

2. Experimental

All reagents were of commercial grade and were used as received. $Na[N(CN)_2]_2$, was purchased from the Aldrich Company.

2.1. Preparations

2.1.1. Synthesis of $[Ni(dca)_2(para\text{-}ABN)_2(H_2O)_2]$ (*1*)

para-Aminobenzonitrile (0.0590 g, 0.5 mmol) was dissolved in 3 mL of methanol. The resultant solution was added to 3 mL of a methanolic solution of $Ni(NO_3)_2\cdot 6H_2O$ (0.1454 g, 0.5 mmol). It was stirred for 1 h at room temperature. Then the mixture was placed in an ice-bath and the temperature maintained at 0 °C. Next, 5 mL aqueous solution of $NaN(CN)_2$ (0.0445 g, 0.5 mmol) was added to the mixture. Green cubic crystals suitable for X-ray diffraction study were obtained from the mother liquor by slow evaporation at room temperature after 10 days. They were filtered off, washed with a small amount of water and dried in air. Elemental analysis: Calc. for $NiC_{18}H_{16}N_{10}O_2$: C 46.64, H 3.45, N 30.23%. Found: for **1** C 46.63, H 3.44, N 30.25%. Infrared spectrum: $[N(CN)]^-$, ν_{sym}(C≡N) 2195, ν_{asym}(C≡N) 2237, ν_{sym}(C–N) 922 and ν_{asym}(C–N) 1370; ABN, ν(N–H) 3444 cm^{-1}.

2.1.2. Synthesis of $[Cu(dca)_2(para\text{-}ABN)_2(H_2O)_2]$ (*2*)

The preparation of **2** was the same as stated for compound **1**, using $Cu(NO_3)_2\cdot 3H_2O$ (0.1208 g, 0.5 mmol) instead of $Ni(NO_3)_2\cdot 6H_2O$. Dark green crystals suitable for X-ray diffraction were formed after 10 days. They were filtered off, washed with a small amount of water and dried in air. Elemental analysis: Calc. for $CuC_{18}H_{16}N_{10}O_2$: C 46.16, H 3.42, N 29.92%. Found: for **2** C 46.14, H 3.41, N 29.94%. Infrared spectrum: $[N(CN)]^-$, ν_{sym}(C≡N) 2195, ν_{asym}(C≡N) 2227, ν_{sym}(C–N) 915 and ν_{asym}(C–N) 1345; ABN, ν(N–H) 3443 cm^{-1}.

2.1.3. Synthesis of $[Cu(dca)_2(para\text{-}ABN)_2]_n$ (*3*)

para-Aminobenzonitrile (0.0590 g, 0.5 mmol) was dissolved in 5 mL of methanol. The resultant solution was added to 5 mL of a methanolic solution of $Cu(NO_3)_2\cdot 3H_2O$ (0.1208 g, 0.5 mmol). The mixture was heated under reflux for half an hour at 45–50 °C after which it was cooled and to it 3 mL aqueous solution of $NaN(CN)_2$ (0.0445 g, 0.5 mmol) was added and the resultant solution was stirred for 1 h at room temperature. It was filtered off and the filtrate was kept at room temperature. Green cubic crystals suitable for X-ray diffraction study were obtained after two weeks. They were filtered off, washed with a small amount of water and dried in air. Yield 68% Elemental analysis: Calc. for $CuC_{18}H_{12}N_{10}$: C 50.01, H 2.78, N 32.41%. Found: for **3**: C 50.02, H 2.77, N 32.39%. Infrared spectrum: $[N(CN)]^-$, ν_{sym}(C≡N) 2190, ν_{asym}(C≡N) 2235, ν_{sym}(C–N) 935 and ν_{asym}(C–N) 1357; ABN, ν(N–H) 3440 cm^{-1}.

2.1.4. Synthesis of $[Cu(dca)_2(ortho\text{-}ABN)_2]_n$ (*4*)

This compound was synthesized as for **3** but from $Cu(NO_3)_2\cdot 3H_2O$ (0.1208 g, 0.5 mmol) and *ortho*-aminobenzonitrile (0.0590 g, 0.5 mmol). Green cubic crystals suitable for X-ray diffraction study were obtained from the mother liquor by slow evaporation at room temperature after 7 days. They were filtered off, washed with a small amount of water and dried in air. Yield 65%. Elemental analysis: Calc. for $CuC_{18}H_{12}N_{10}$: C 50.01, H 2.78, N 32.41%. Found: for **4**: C 50.03, H 2.79, N 32.38%. Infrared spectrum: $[N(CN)]^-$, ν_{sym}(C≡N) 2186, ν_{asym}(C≡N) 2230, ν_{sym}(C–N) 900 and ν_{asym}(C–N) 1371; ABN, ν(N–H) 3440 cm^{-1}.

2.1.5. Synthesis of $[Cd(dca)_2(meta\text{-}ABN)_2]_n$ (*5*)

This compound was synthesized as for **3** but from $Cd(NO_3)_2\cdot 4H_2O$ (0.1542 g, 0.5 mmol) and *meta*-aminobenzonitrile (0.0590 g, 0.5 mmol). Colourless crystals were formed after 3–4 weeks. They were filtered off, washed with small amount of water and dried in air. Yield 66%. Elemental analysis: Calc. for $CdC_{18}H_{12}N_{10}$: C 44.93, H 2.50, N 29.12%. Found: for **5**: C 44.90, H 2.49, N 29.14%. Infrared spectrum: $[N(CN)]^-$, ν_{sym}(C≡N) 2185, ν_{asym}(C≡N) 2230, ν_{sym}(C–N) 905 and ν_{asym}(C–N) 1355; ABN, ν(N–H) 3440 cm^{-1}.

2.2. Physical measurements

The elemental analyses (C, H, N) were carried out with a Perkin Elmer 2400 II elemental analyser. For each sample

the analyses were carried out in duplicate. The FT-IR spectra were recorded on Perkin Elmer RX I FT-IR spectrophotometer from KBr pellets in range 4000–400 cm^{-1}. It is important for the characteristic bands of the dca ligand and amino group.

Magnetic susceptibility measurements for **3** and **4** were carried out on polycrystalline samples, with a Quantum Design SQUID MPMS-XL susceptometer apparatus working in the range 2–300 K under a magnetic field of approximately 500 G (2–30 K) and 10 000 G (35–300 K). Diamagnetic corrections were estimated from Pascal tables.

2.3. Crystal data collection and refinement

Single crystal diffraction data for **1**–**3** and **5** were collected on a Bruker Nonius X8 Apex 2 CCD diffractometer at 100 K, cooled by an Oxford Cryosystems Cryostream. The crystals were covered in Paratone-N oil and mounted in cryoloops. The structures were solved and refined using the SHELXTL [17] suite of programs. Amine and water H atoms were located in the difference Fourier map and isotropic displacement parameters were freely refined for **1** and **5**, and riding for **3** and **2**. The data for **4** were collected on a Nonius KappaCCD diffractometer; [18] the lattice constants were refined by least-square refinement using 2005 reflections ($2.1° < \theta < 27.8°$). No absorption correction was applied to the data sets. The structure was solved by direct methods [19] and refined [20] against F using reflections with $[I/\sigma(I) > 3]$. All non-hydrogen atoms were successfully refined with anisotropic displacement factors. Further experimental details for all the compounds are summarized in Table 1.

3. Results and discussion

In the five compounds, both dca and ABN ligands show varied bonding modes, i.e. (i) dca acts as bridging ligand for **4** and **5**, (ii) *para*-ABN acts as bridging ligand for **3** and (iii) both the dca and *para*-ABN ligands act as monodentate ligands for **1** and **2**. *ortho*- and *meta*-ABN act as monodentate ligands in **4** and **5**, respectively. These resulted in four generally different structural frameworks. The formation of compounds **2** and **3** was highly dependent on the reaction conditions. In both cases the starting materials were used in the same ratio, $Cu(NO_3)_2$:dca:*para*-ABN of 1:1:1, but the different synthetic methods employed yielded two new compounds. In the synthesis of **3** when an aqueous solution of $NaN(CN)_2$ was added to a methanolic solution of $Cu(NO_3)_2$ and *para*-aminobenzonitrile, a deep-green precipitate was formed within a few minutes, during the stirring. On filtration a green coloured solution was obtained which on keeping yielded **3**. The deep-green precipitate was characterized by IR and X-ray powder diffraction study and the found results were identical with those of **2**. From this it was concluded that **3** was the major and thermodynamically controlled product, whereas **2** was the minor and kinetically controlled product in the preparative process of **3**. The low temperature preparative process produced **2** exclusively.

3.1. Crystal structure analyses

Crystal structure analyses show that **1** and **2** are monomeric compounds and form two-dimensional hydrogen bonded sheets through the interaction of the *para*-ABN and dicyanamide ligands which further extend

Table 1
Experimental parameters for the crystal structure analyses

Compound	**1**	**2**	**3**	**4**	**5**
Empirical formula	$NiC_{18}H_{16}N_{10}O_2$	$CuC_{18}H_{16}N_{10}O_2$	$CuC_{18}H_{12}N_{10}$	$CuC_{18}H_{24}N_{20}$	$CdC_{18}H_{12}N_{10}$
Formula weight	463.12	467.95	431.92	431.91	480.78
Temperature (K)	100(2)	100(2)	100(2)	293	100(2)
Crystal system	triclinic	triclinic	triclinic	triclinic	monoclinic
Space group	$P\bar{1}$	$P\bar{1}$	$P\bar{1}$	$P\bar{1}$	$P2_1/n$
a (Å)	7.1952(6)	7.2159(19)	7.2105(8)	7.1128(2)	7.7055(15)
b (Å)	7.6033(7)	7.600(2)	7.9475(9)	7.1730(4)	8.7676(17)
c (Å)	9.8968(9)	9.897(3)	9.4240(10)	9.8358(6)	13.806(3)
α (°)	104.674(3)	104.713(7)	99.740(4)	89.511(3)	90
β (°)	92.945(3)	92.879(7)	110.095(4)	85.069(3)	90.262(4)
γ (°)	101.929(3)	102.055(7)	109.258(4)	71.300(3)	90
Volume (Å^3)	509.37(8)	510.3(2)	453.83(9)	473.48(4)	932.7(3)
Z	1	1	1	1	2
D_c (Mg m^{-3})	1.510	1.523	1.580	1.515	1.712
μ (mm^{-1})	0.991	1.109	1.232	1.181	1.199
Reflections collected	10 555	6903	14 525	3405	23 446
Independent reflections [R_{int}]	3613 [0.0213]	3509 [0.0222]	3278 [0.0324]	2214 [0.0270]	2987 [0.0363]
Data/restraints/parameters	3613/0/158	3509/2/154	3278/0/139	1289/0/133	2987/0/141
R_1 [$I > 2\sigma(I)$]	0.0242	0.0394	0.0332	0.0411	0.0266
R_1 (all data)	0.0258	0.0450	0.0408	0.0940	0.0363
wR_2 [$I > 2\sigma(I)$]	0.0741	0.1142	0.0864	0.0476	0.0712
wR_2 (all data)	0.0749	0.1168	0.0885	0.0886	0.0727

the structures to three dimensions through weak π–π interactions from the aromatic group of *para*-ABN ligands. **3**–**5** revealed that one-dimensional double stranded polymeric chains were formed. These infinite chains were further connected via hydrogen bonding interactions to extend the network into 3D in **3** and **5** and 2D in **4**

Self-association has taken place in a variety of ways. Firstly intermolecular interactions have been propagated solely through ligand OH···N and NH···N hydrogen bonds (in **1** and **2**), secondly through two *trans*-coordinated dca ligands and two *cis* amine bonded *para*-ABN ligands (in **3**) and thirdly by *trans*-coordinated amine groups of two ABN and two *cis* dca ligands (in **4** and **5**). Selected bond lengths and angles for **1**–**5** are given in Tables 2–6, respectively. The compounds have an extensive 3D (**1**–**3** and **5**) or 2D (**4**) hydrogen bonding networks; these details are summarized in Table 7.

The structures of $[Ni(dca)_2(para\text{-}ABN)_2(H_2O)_2]$ (**1**) and $[Cu(dca)_2(para\text{-}ABN)_2(H_2O)_2]$ (**2**) are virtually identical and are exemplified by **1**. The crystal structure of **1** consists of centrosymmetric, mononuclear $[Ni(dca)_2(para\text{-}ABN)_2(H_2O)_2]$ entities. Both *para*-ABN and dicyanamide act as terminal ligands (Figs. 1 and 2). The *para*-ABN ligand is coordinated to the metal ion through the amine nitrogen atom. The Ni–N bond lengths are Ni–N(dca) = 2.0351 Å and Ni–N(*para*-ABN) = 2.1513 Å. The two Ni–O (aqua) distances are 2.0700 Å. The nickel(II) ion exhibits a *trans* distorted octahedral stereochemistry. The C–N–C angle of the dicyanamide is 120.91°. The most intriguing features of the crystal structure of the compound arise from interactions at the supramolecular level. The *para*-ABN ligand acts as both a hydrogen donor (through the amine group) and a hydrogen acceptor (through the nitrile group) while the dicyanamide ligand acts as a hydrogen acceptor and the aqueous ligand acts as a hydrogen donor. The hydrogen bonding network for both **1** and **2** consists of layers. Each layer consists of interlocked parallelograms. One set of parallel sides is doubly-bridging *para*-ABN and the other doubly-bridging dca. In the latter, the bridge is formed between dca and *para*-ABN rather than with the metal ion. This supramolecular architecture is shown in Fig. 3. The interlayer interactions are of a weak π–π nature

Table 2
Selected interatomic distances (Å) and angles (°) for **1**

Ni(1)–N(11)	2.0351(8)	Ni(1)–O(1)	2.0700(7)
Ni(1)–N(1)	2.1513(8)	N(1)–C(2)	1.4169(11)
N(1)–H(11N)	0.898(15)	N(1)–H(12N)	0.881(16)
O(1)–H(11W)	0.787(19)	O(1)–H(12W)	0.757(19)
C(8)–N(9)	1.1484(14)	C(11)–N(11)	1.1549(12)
C(11)–N(12)	1.3097(12)	C(12)–N(13)	1.1576(13)
C(12)–N(12)	1.3084(13)		
N(11)–Ni(1)–O(1)	89.14(3)	N(11)–Ni(1)–O(1)#1	90.86(3)
O(1)–Ni(1)–O(1)#1	180.0	N(11)–Ni(1)–N(1)	85.00(3)
O(1)–Ni(1)–N(1)	91.97(3)	O(1)#1–Ni(1)–N(1)	88.03(3)
N(11)–Ni(1)–N(1)#1	95.00(3)	C(2)–N(1)–Ni(1)	117.58(6)
C(2)–N(1)–H(11N)	111.2(9)	Ni(1)–N(1)–H(11N)	102.7(10)
C(2)–N(1)–H(12N)	108.1(10)	Ni(1)–N(1)–H(12N)	104.9(11)
H(11N)–N(1)–H(12N)	112.3(15)	Ni(1)–O(1)–H(11W)	110.6(12)
Ni(1)–O(1)–H(12W)	118.5(14)	H(11W)–O(1)–H(12W)	104.6(18)
C(12)–N(12)–C(11)	120.73(9)		

Symmetry transformations used to generate equivalent atoms: #1 $-x, -y+2, -z+2$.

Table 3
Selected interatomic distances (Å) and angles (°) for **2**

Cu(1)–N(11)	2.0318(15)	Cu(1)–O(1)	2.0748(12)
Cu(1)–N(1)	2.1481(14)	N(1)–C(2)	1.416(2)
N(1)–H(11N)	0.80(2)	N(1)–H(12N)	0.84(2)
O(1)–H(11W)	0.730(16)	O(1)–H(12W)	0.709(16)
C(8)–N(9)	1.147(2)	N(11)–C(12)	1.154(2)
C(12)–N(12)	1.307(2)	N(12)–C(13)	1.307(2)
C(13)–N(13)	1.158(2)		
N(11)#1–Cu(1)–O(1)	90.97(5)	N(11)–Cu(1)–O(1)	89.03(5)
O(1)–Cu(1)–O(1)#1	180.0	N(11)#1–Cu(1)–N(1)	94.84(5)
N(11)–Cu(1)–N(1)	85.16(6)	O(1)–Cu(1)–N(1)	92.09(5)
O(1)#1–Cu(1)–N(1)	87.91(5)	C(2)–N(1)–Cu(1)	117.86(10)
Cu(1)–N(1)–H(11N)	103.8(17)	Cu(1)–N(1)–H(12N)	106.2(16)
Cu(1)–O(1)–H(11W)	107.1(19)	Cu(1)–O(1)–H(12W)	121(2)
H(11W)–O(1)–H(12W)	107(3)	N(9)–C(8)–C(5)	177.68(19)
C(12)–N(12)–C(13)	120.91(14)		

Symmetry transformations used to generate equivalent atoms: #1 $-x+2, -y+1, -z+1$.

Table 4
Selected interatomic distances (Å) and angles (°) for **3**

Cu(1)–N(1)	2.0550(12)	Cu(1)–N(11)	1.9763(12)
Cu(1)–N(9)	2.497	N(1)–C(2)	1.4284(16)
N(1)–H(12N)	0.798(19)	C(2)–C(3)	1.3951(18)
C(2)–C(7)	1.3955(19)	C(3)–C(4)	1.3884(18)
C(3)–H(3)	0.9500	C(4)–C(5)	1.402(2)
C(4)–H(4)	0.9500	C(5)–C(6)	1.3932(19)
C(5)–C(8)	1.4453(18)	C(6)–C(7)	1.3893(18)
N(1)–H(11N)	0.780(18)		
N(11)–Cu(1)–N(11)#1	180.00(9)	N(11)–Cu(1)–N(1)#1	90.78(5)
N(11)#1–Cu(1)–N(1)#1	89.22(5)	N(11)–Cu(1)–N(1)	89.22(5)
N(11)#1–Cu(1)–N(1)	90.78(5)	N(1)#1–Cu(1)–N(1)	180.00(6)
C(2)–N(1)–Cu(1)	114.34(8)	C(2)–N(1)–H(11N)	111.2(13)
Cu(1)–N(1)–H(11N)	104.9(13)	C(2)–N(1)–H(12N)	114.9(13)
Cu(1)–N(1)–H(12N)	103.0(13)	H(11N)–N(1)–H(12N)	107.5(18)
C(3)–C(2)–C(7)	120.33(12)	C(3)–C(2)–N(1)	119.25(12)
C(7)–C(2)–N(1)	120.29(12)	C(4)–C(3)–C(2)	120.15(12)
C(4)–C(3)–H(3)	119.9	C(11)–N(12)–C(12)	118.35(12)

Symmetry transformations used to generate equivalent atoms: #1 $-x$, $-y$, $-z$.

Table 5
Selected interatomic distances (Å) and angles (°) for **4**

Cu(1)–N(1)	1.965(3)	Cu(1)–N(5)	1.989(3)
Cu(1)–N(11)	2.564(3)	N(11)–C(12)	1.396(5)
C(12)–C(13)	1.390(5)	C(13)–C(14)	1.386(6)
C(14)–C(15)	1.384(7)	C(15)–C(16)	1.361(6)
C(16)–C(17)	1.400(6)	C(17)–C(12)	1.401(5)
C(17)–C(18)	1.437(5)	C(18)–N(19)	1.147(5)
N(1)–C(2)	1.141(4)	C(2)–N(3)	1.299(4)
N(3)–C(4)	1.291(4)	C(4)–N(5)	1.149(4)
N(1)–Cu(1)–N(1)	179.994	N(1)–Cu(1)–N(5)	91.4(1)
N(1)–Cu(1)–N(5)	88.6(1)	N(5)–Cu(1)–N(5)	179.994
N(1)–Cu(1)–N(11)	89.4(1)	N(1)–Cu(1)–N(11)	90.6(1)
N(5)–Cu(1)–N(11)	93.0(1)	N(5)–Cu(1)–N(11)	87.0(1)
N(11)–Cu(1)–N(11)	179.996		

between the *para*-ABN aromatic rings which results in the third dimensions and in **1** and **2** the centroid–centroid distances are 3.8159(7) and 3.8141(15) Å, respectively.

Table 6
Selected interatomic distances (Å) and angles (°) for **5**

Cd(1)–N(2)	2.3259(15)	Cd(1)–N(11)	2.3326(15)
Cd(1)–N(1)	2.3737(15)	N(1)–C(1)	1.423(2)
N(1)–H(1N)	0.99(2)	N(1)–H(2N)	0.87(2)
N(11)–C(12)	1.162(2)	C(12)–N(13)	1.312(2)
N(13)–C(20)#2	1.302(2)	N(2)–C(20)	1.149(2)
C(20)–N(13)#3	1.301(2)		
N(2)–Cd(1)–N(11)	95.16(5)	N(2)#1–Cd(1)–N(11)	84.84(5)
N(2)–Cd(1)–N(1)#1	87.32(5)	N(11)–Cd(1)–N(1)#1	93.11(5)
N(2)–Cd(1)–N(1)	92.68(5)	N(11)–Cd(1)–N(1)	86.89(5)
N(1)#1–Cd(1)–N(1)	180.00(6)	C(1)–N(1)–Cd(1)	116.11(10)
C(1)–N(1)–H(1N)	108.2(13)	Cd(1)–N(1)–H(1N)	105.4(13)
C(1)–N(1)–H(2N)	109.0(14)	Cd(1)–N(1)–H(2N)	109.3(16)
H(1N)–N(1)–H(2N)	108.7(19)	N(7)–C(7)–C(5)	179.07(19)
C(12)–N(11)–Cd(1)	155.06(14)	C(20)#2–N(13)–C(12)	120.04(15)
C(20)–N(2)–Cd(1)	152.80(13)		

Symmetry transformations used to generate equivalent atoms: #1 $-x+1$, $-y+1$, $-z$; #2 $x+1$, y, z; #3 $x-1$, y, z.

Table 7
Hydrogen-bonding parameters

Compound	D–H···A	*d*(D–H)	*d*(H···A)	*d*(D···A)	(D–H···A)
1	N(1)–H(11N)···N(13)#5	0.898(15)	2.182(15)	3.0539(12)	163.8(13)
	O(1)–H(11W)···N(13)#5	0.787(19)	2.067(19)	2.8332(12)	164.4(17)
	N(1)–H(12N)···N(12)#6	0.881(16)	2.307(17)	3.1772(13)	169.7(15)
	O(1)–H(12W)···N(9)#7	0.757(19)	2.116(19)	2.8652(12)	170.7(18)
2	N(1)–H(11N)···N(13)#8	0.80(2)	2.28(2)	3.064(2)	164(2)
	N(1)–H(12N)···N(12)#9	0.84(2)	2.36(2)	3.185(2)	170(2)
	O(1)–H(11W)···N(13)#10	0.730(16)	2.112(17)	2.832(2)	169(3)
	O(1)–H(12W)···N(9)#4	0.709(16)	2.170(17)	2.862(2)	166(3)
3	N(1)–H(11N)···N(12)#1	0.780(18)	2.319(19)	3.0984(17)	176.7(17)
	N(1)–H(12N)···N(13)#2	0.798(19)	2.198(19)	2.9905(17)	171.8(17)
4	N(11)–H(5)···N(19)	0.91	2.42	3.257(5)	154
5	N(1)–H(1N)···N(13)#3	0.99(2)	2.81(2)	3.471(2)	125.0(16)
	N(1)–H(2N)···N(7)#4	0.87(2)	2.32(2)	3.121(2)	153(2)

Symmetry operator codes :#1 $-x+1$, $-y$, $-z$; #2 $x-1$, $y-1$, z; #3 $-x+3/2$, $y+1/2$, $-z+1/2$; #4 $-x+1/2$, $y+1/2$, $-z+1/2$; #5 $-x+1$, $-y+3$, $-z+2$; #6 $-x$, $-y+3$, $-z+2$; #7 $-x$, $-y+1$, $-z+1$; #8 $-x+3$, $-y+2$, $-z+1$; #9 $-x+2$, $-y+2$, $-z+1$; #10 $-x+2$, $-y$, $-z$.

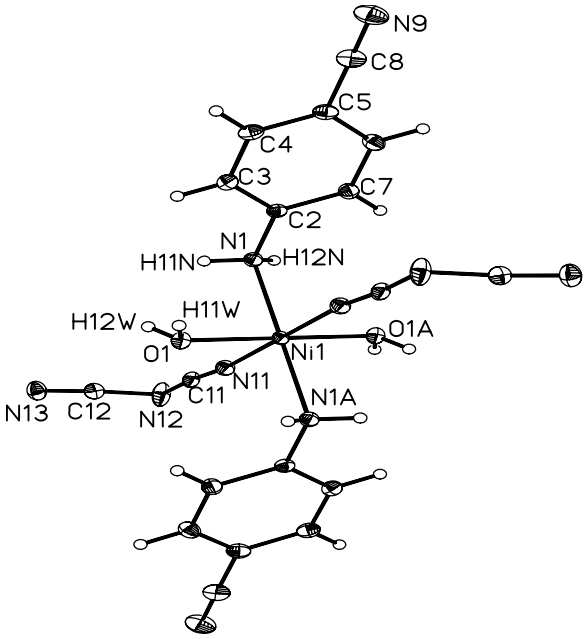


Fig. 1. Ortep view of **1** with the atom numbering scheme.

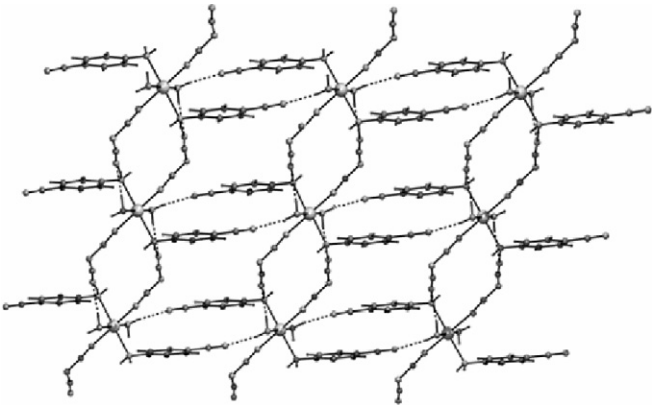


Fig. 3. Packing diagram of **1** with hydrogen bonding shown as a dotted line.

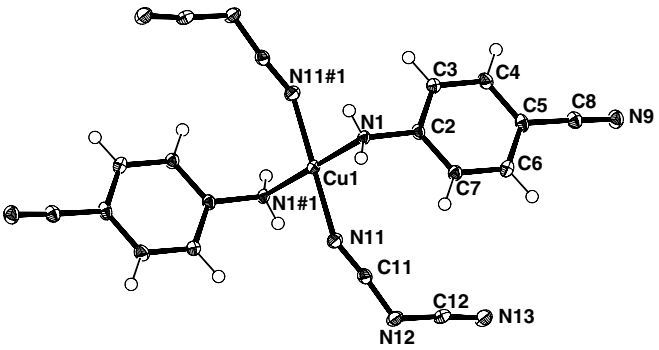


Fig. 4. Ortep view of **3** showing the atom numbering scheme.

Fig. 4 shows a perspective view of **3** which is found to be a $[Cu(dca)_2(para\text{-}ABN)_2]$ asymmetric unit. This unit contains two terminal dicyanamido ligands and four bridging *para*-ABN ligands which adopt a distorted octahedral coordination sphere. The terminal dca ligands coordinate through the nitrile N(11) atoms, occupying the axial positions with Cu(1)–N(11) 1.9763(12) Å, while the equatorial plane contains four nitrogen atoms from bridging *para*-ABN ligands which coordinate through the two amino N(1) atoms and two nitrile N(9) atoms [Cu(1)–N(1) 2.0550(12) and Cu(1)–N(9) 2.497 Å]. The $[Cu(dca)_2(para\text{-}ABN)_2]$ monomer units are linked through bridging *para*-ABN ligands to make a double stranded polymeric chain (Fig. 5). The coordination polymer runs parallel to

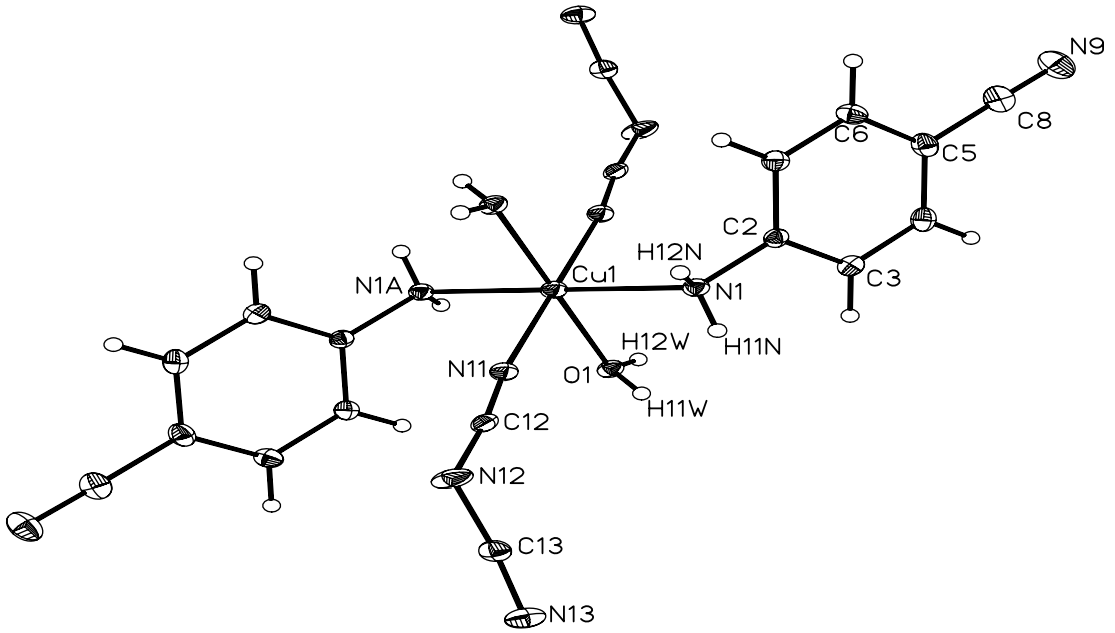


Fig. 2. Ortep view of **2** with the atom numbering scheme.

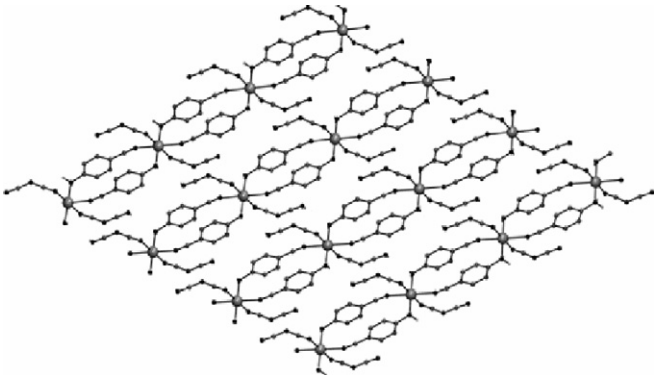


Fig. 5. Packing diagram of **3** omitting the H-bonding for clarity.

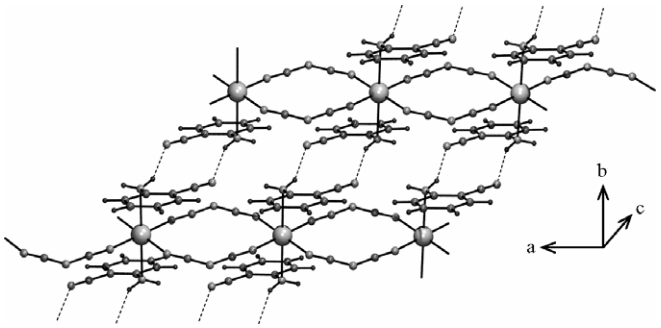


Fig. 7. View of the propagation of **4**.

the crystallographic *a*-axis (Fig. 5), which is also observed for compounds **4** and **5**. The metal–metal distance between adjacent Cu centres within one polymer strand is equal to 9.7020 Å, while the closest Cu···Cu distance between two neighbouring strands is 8.795 Å.

Compound **3** shows a rarely observed characteristic, namely doubly bridging of the *para*-ABN ligand which binds via both the amine and nitrile nitrogen atoms. Dicyanamide can also be considered as a doubly bridging ligand but the bridge is made by a NH···N hydrogen bond to a *para*-ABN amine, which extends the geometry into three dimensions (Supporting information 1). The cobalt and nickel thiocyanate complexes [11] also have double bridging ABN ligands and the SCN ligands remain terminally bound but are involved in NH···S hydrogen bonds.

In **4** (Fig. 6) the dca ligands form bridges and the *ortho*-ABN ligands are terminal in contrast to the coordination mode of dca and *para*-ABN ligands in **3**. The copper(II) ion coordination sphere is formed by two dca ligands bridging the pairs of Cu atoms while the amino groups from *ortho*-ABN ligands coordinate in the axial positions (Fig. 7). The metal–metal distance between adjacent Cu centres within one polymer strand is equal to 7.113 Å, while the closest Cu···Cu distance between two neighbouring strands is 7.173 Å. The NH···N hydrogen bond between two neighbouring polymer strands extend the structure of **4** into two-dimensions with the amine group from the *ortho*-ABN ligand acting as a hydrogen donor and nitrile group from the same ligand of another strand acting as a hydrogen acceptor (Fig. 7).

The structure of **5** (Fig. 8) is very similar to that of **4** and it is worthwhile to note that the metal–metal distance between adjacent Cd centres within the polymer strand is 7.705 Å, whilst the closest Cd···Cd distance between two neighbouring strands is 8.768 Å. The non-bridging *meta*-ABN ligands are bound to Cd with the amine group. They are orientated anti to each other with the torsion angle C(7A)–N(7A)–N(7)–C(7) being 180° as the Cd atom lies on an inversion centre.

The polymers strands of **3** and **5** are interconnected in three dimensions by an extensive network of NH···N hydrogen bonds. In **3** the amine group from the *para*-ABN ligand acts as the hydrogen donor and both nitrile and amide nitrogen atoms from dicyanamide ligands of another strand act as hydrogen acceptors (Fig. 5). While in **5** the amine group from *meta*-ABN acts as the hydrogen donor and the nitrogen atoms of the nitrile group from

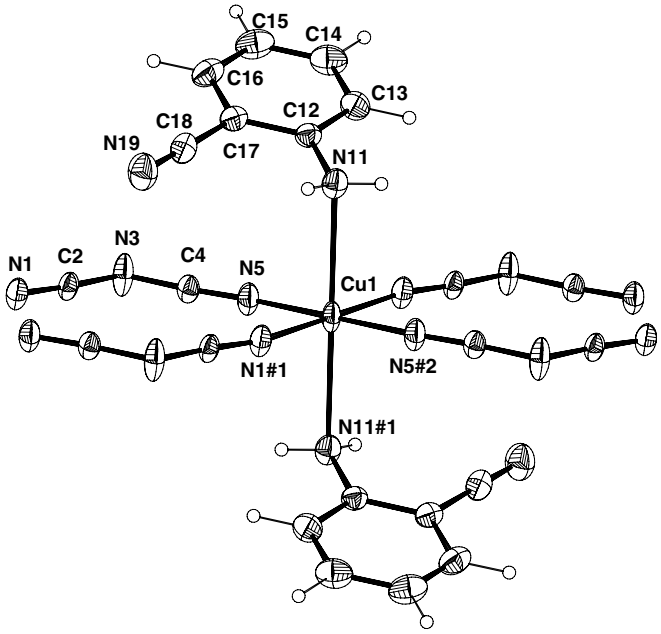


Fig. 6. Ortep view of **4** with the atom numbering scheme.

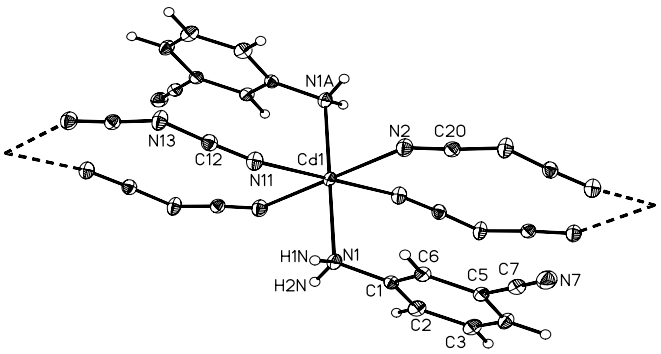


Fig. 8. Ortep view of **5** with the atom numbering scheme.

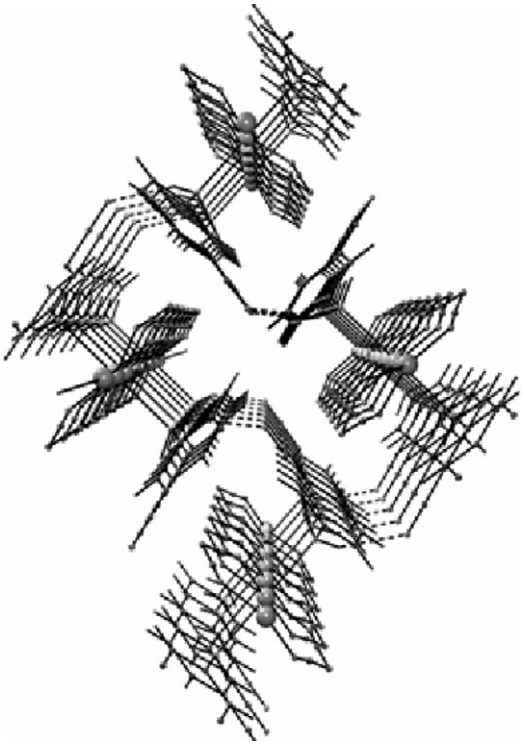


Fig. 9. Packing diagram of **5** with hydrogen bonding shown as a dotted line.

both *meta*-ABN and dicyanamide ligands of another strand act as hydrogen acceptors (Fig. 9). Although **4** and **5** show very similar connectivity, **4** has a hydrogen bonding network which extends into two dimensions and **5** extends into three dimensions. The position of the nitrile group of the ABN ligands for **4** and **5** is different i.e. *ortho*-ABN and *meta*-ABN respectively, so the *meta*-ABN isomer may be more able to form hydrogen-bonds compared to the *ortho*-ABN isomer, possibly for steric reasons.

3.2. Magnetochemistry

Variable temperature magnetic susceptibility measurements have been performed for **3** and **4**. The global feature of the $\chi_M T$ versus T curves in both compounds is characteristic of very weak antiferromagnetic interactions (Figs. 10 and 11). For **3** the value of $\chi_M T$ at 300 K is 0.384 cm^3 K mol^{-1} which is as expected for one uncoupled copper(II) ion (0.37 cm^3 K mol^{-1} per Cu(II) with $g = 2.0$). With decreasing temperature, the $\chi_M T$ value remains almost constant until ca. 70 K and then it decreases sharply, giving the minimum value of 0.170 cm^3 K mol^{-1} at 2 K. The drop in $\chi_M T$ at low temperatures indicates the presence of a very weak antiferromagnetic coupling between the copper(II) ions.

As is shown in Fig. 5, the structure of **3** consists of copper entities linked by two *para*-ABN ligands, which also acts as hydrogen donors via the amine groups, and both nitrile and amide nitrogen atoms of dicyanamide act as hydrogen acceptors to give a 3D compound. To interpret

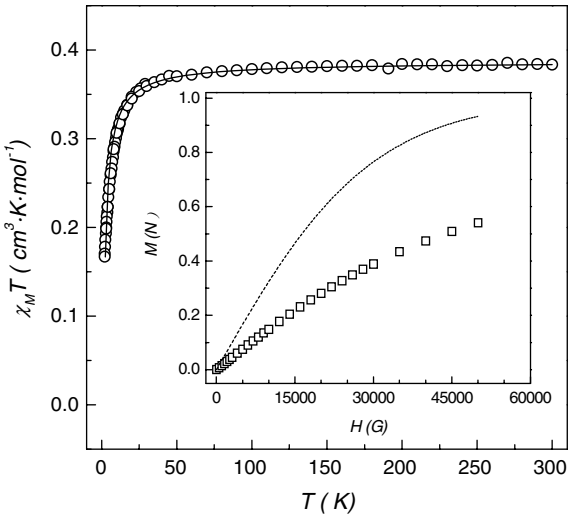


Fig. 10. Plot of $\chi_M T$ vs. T and $M(N_\beta)$ vs. $H(G)$ (inset) for **3**.

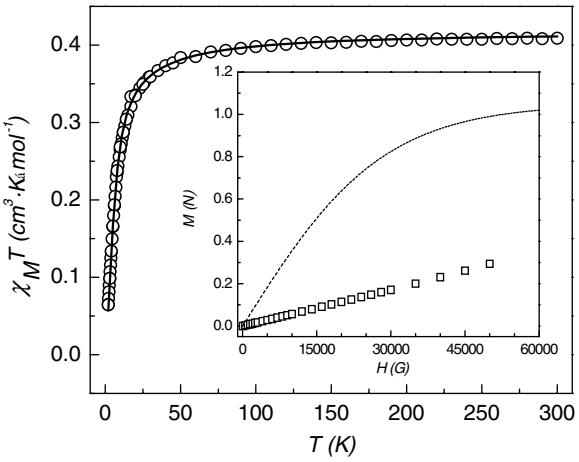


Fig. 11. Plot of $\chi_M T$ vs. T and $M(N_\beta)$ vs. $H(G)$ (inset) for **4**.

the magnetic behaviour of **3** we assume a negligible contribution from the interactions through the hydrogen bonding. The system may be treated in a simplified form as a uniform chain of Cu(II) atoms. Thus, only one coupling parameter (J) must be considered to interpret a possible magnetic interaction. The experimental magnetic data have been fitted using the equation, derived from the Bonner–Fisher [21] calculation based on the isotropic Heisenberg Hamiltonian: $H = -J\sum(S_i S_{i+1})$. The best fit parameters from 300 down to 2 K are found as $J = -2.35\ cm^{-1}$ and $g = 2.03$ with an error $R = 3.2 \times 10^{-5}$, where $R = \sum[(\chi_M T)_{exp} - (\chi_M T)_{calc}]^2 / \sum[(\chi_M T)_{exp}]^2$. The very low value of the superexchange parameter can be understood considering the large Cu···Cu distance (9.702 Å). The weak antiferromagnetic interaction was confirmed by magnetization measurements at 2 K up to an external field of 5 T. At higher field, the magnetization in M/Nβ units indicates a value of 0.54; (a quasi half saturated $S = 1/2$ system) (inset Fig. 10). Comparison of the overall shape

of the plot with the Brillouin plot (dashed plot) for one isolated ion with $S = 1/2$ system and $g = 2$ indicates slower magnetization which is consistent with a weak antiferromagnetic interaction.

For **4** the value of $\chi_M T$ at 300 K is 0.409 $cm^3\,mol^{-1}K$ which is as expected for one uncoupled copper(II) ion (0.413 $cm^3\,mol^{-1}$ K per one Cu^{II} with $g = 2.1$). The $\chi_M T$ values are constant over the temperature range, decreasing to 0.0644 $cm^3\,mol^{-1}$ K, at very low temperatures (2 K). The χ_M curve starts at 1.36×10^{-3} $cm^3\,mol^{-1}$ at room temperature and increases in a uniform way to 0.0322 $cm^3\,mol^{-1}$ at 2 K. The weak antiferromagnetic interaction was confirmed by magnetization measurements at 2 K up to an external field of 5 T. At higher field, the magnetization in M/Nβ units indicates a 0.2945 value for **4** (inset Fig. 11). Comparison of the overall shape of the plot with the Brillouin plot for one fully isolated ion with $S = 1/2$ system with $g = 2.1$ (dash curve) indicates very slow magnetization which consistent with a weak antiferromagnetic interaction.

Taking into account the structure of **4** (Fig. 7), which consists of copper ions linked by double $\mu_{1,5}$-dicyanamide groups in a 1D system, only one coupling parameter (J) was considered to interpret possible magnetic interactions in this compound (the interaction through the hydrogen bonding has not been considered). The experimental magnetic data have been fitted using the equation which was derived from the Bonner–Fisher [21] calculation based on the isotropic Heisenberg Hamiltonian: $H = -J\sum(S_i S_{i+1})$. The best fit parameters from 300 down to 2 K are found as $J = -5.1\ cm^{-1}$ and $g = 2.1$ with an error $R = 2.3 \times 10^{-5}$, where $R = \sum[(\chi_M T)_{exp} - (\chi_M T)_{calc}]^2/\sum[(\chi_M T)_{exp}]^2$. The low superexchange parameter value found can be understood perfectly, if we consider the data reported in the literature. Indeed, the dicyanamide ligand in the coordination mode $\mu_{1,5}$ normally leads to a very weak antiferromagnetic coupling in Mn(II) , Ni(II) or Cu(II) complexes and this interaction can even be zero or very weak ferromagnetic [22].

4. Conclusion

We have synthesized five new metal-organic frameworks including the first Cu(II) polymers with *para*- and *ortho*-ABN ligands. In these compounds dca and *para*-ABN ligands show the terminal as well as bridging bonding mode whereas *ortho*- and *meta*-ABN coordinated only in a monodentate fashion. The spin coupling constants, J, were estimated to be -2.35 and $-5.1\ cm^{-1}$ for **3** and **4**, respectively.

Acknowledgements

We acknowledge the financial support from the Council of Scientific and Industrial Research, New Delhi, India to Moumita Biswas. We also wish to acknowledge the use of the EPSRC's Chemical Database Service at Daresbury, Cheshire, UK and grants given by the Ministerio de Educación y Ciencia (Programa Ramón y Cajal) and BQU2003/00539.

Appendix A. Supplementary data

Crystallographic data have been deposited at the Cambridge Crystallographic Data Centre with deposition numbers 602010–602014. These data can be obtained free of charge via http://www.ccdc.cam.ac.uk/conts/retrieving.html or from the Cambridge Crystallographic Data Centre, 12 Union Road, Cambridge CB2 IEZ, UK; fax: +44 1223 336 033; or e-mail deposit@ccdc.cam.ac.uk. Supplementary data associated with this article can be found, in the online version, at doi:10.1016/j.poly.2006.08.008.

References

[1] B. Moulton, M.J. Zaworotko, Chem. Rev. 101 (2001) 1629.
[2] G.F. Swiegers, T.J. Malefetse, Chem. Rev. 100 (2000) 3483.
[3] M.J. Zaworotko, Chem. Commun. (2001) 1.
[4] T. Kuroda-Sowa, T. Horino, M. Yamamoto, Y. Ohno, M. Maekawa, M. Munakata, Inorg. Chem. 36 (1997) 6382.
[5] K. Biradha, Y. Hongo, M. Fujita, Angew. Chem., Int. Ed. 39 (2000) 3843.
[6] M.J. Zaworotko, Angew. Chem., Int. Ed. 39 (2000) 3052.
[7] M. Fujita, Y.J. Kwon, S. Washizu, K. Ogura, J. Am. Chem. Soc. 116 (1994) 1151.
[8] M. Fujita, K. Umemoto, M. Yoshizawa, N. Fujita, T. Kusukawa, K. Birdha, Chem. Commun. (2001) 509.
[9] M. Eddaoudi, D.B. Moler, H. Li, B. Chen, T.M. Reineke, M. O'Keeffe, O.M. Yaghi, Acc. Chem. Res. 34 (2001) 319.
[10] L.R. MacGillivary, S. Subramanian, M.J. Zaworotko, J. Chem. Soc., Chem. Commun. (1994) 1325.
[11] (a) L.J. Moitsheki, S.A. Bourne, L.R. Nassimbeni, Acta Cryst. Sect. E. 61 (2005) m2580;
(b) D. Vujovic, H.G. Raubenheimer, L.R. Nassimbeni, J. Chem. Soc., Dalton Trans. (2003) 631.
[12] (a) D. Venkataraman, G.B. Gardner, S. Lee, J.S. Moore, J. Am. Chem. Soc. 117 (1995) 11600;
(b) O.M. Yaghi, G. Li, H. Li, Nature 378 (1995) 703;
(c) C.J. Kepert, M.J. Rosseinsky, Chem. Commun. (1999) 375.
[13] (a) J.S. Miller, A.J. Epstein, Angew. Chem., Int. Ed. 33 (1994) 385;
(b) M. Ohba, H. Ökawa, Coord. Chem. Rev. 198 (2000) 313;
(c) K.R. Dunbar, R.A. Heintz, Progr. Inorg. Chem. 45 (1997) 283;
(d) E. Coronado, J.R. Galan-Mascaros, C.J. Gomez-Garcia, J. Ensling, P. Gutlich, Chem. Eur. J. 6 (2000) 552;
(e) E. Coronado, M. Clemete-León, J.R. Galán- Mascarós, C. Giménez-Saiz, C.J. Gómez-García, E. Martínez- Ferrero, J. Chem. Soc., Dalton. Trans. (2000) 3955.
[14] S.R. Batten, K.S. Murray, Coord. Chem. Rev. 246 (2003) 103.
[15] The United Kingdom Chemical Database Service D.A. Fletcher, R.F. McMeeking, D. Parkin, J. Chem. Inf. Comput. Sci. 36 (1996) 746.
[16] (a) F.H. Allen, Acta Crystallogr. B58 (2002) 380;
(b) I.J. Bruno, J.C. Cole, P.R. Edgington, M. Kessler, C.F. Macrae, P. McCabe, J. Pearson, R. Taylor, Acta Crystallogr. B58 (2002) 389.
[17] G.M. Sheldrick, SHELXTL version 5.1, Bruker Inc., Madison, Wisconsin, USA, 1999.
[18] Nonius COLLECT, DENZO, SCALEPACK, SORTAV: KappaCCD B.V., Delft, The Netherlands, 1999.
[19] G. Cascarano, A. Altomare, C. Giacovazzo, A. Guagliardi, A.G.G. Moliterni, D. Siliqi, M.C. Burla, G. Polidori, M. Camalli, Acta Crystallogr. A52 (1996) C-79.

[20] D.J. Watkin, C.K. Prout, J.R. Carruthers, P.W. Betteridge, CRYSTAL Issue 11, Chemical Crystallography Laboratory, Oxford, UK, 1999.
[21] O. Kahn, Molecular Magnetism, VCH, Weinheim, 1993, p. 252.
[22] (a) J. Carranza, C. Brennan, J. Sletten, F. Lloret, M. Julve, J. Chem. Soc., Dalton Trans. (2002) 3164;
(b) J. Carranza, J. Sletten, F. Lloret, M. Julve, Inorg. Chim. Acta 357 (2004) 3304;
(c) J. Luo, M. Hong, J. Weng, Y. Zhao, R. Cao, Inorg. Chim. Acta 329 (2002) 59;
(d) A. Escuer, F.A. Mautner, N. Sanz, R. Vicente, Inorg. Chem. 39 (2000) 1668;
(e) R. Karmakar, C.R. Choudhury, D.L. Hughes, Glenn P.A. Yap, M.S. El Fallah, C. Desplanches, J.-P. Sutter, S. Mitra, Inorg. Chim. Acta 359 (2006) 1184.

Available online at www.sciencedirect.com
ScienceDirect
Polyhedron 26 (2007) 133–141
POLYHEDRON
www.elsevier.com/locate/poly

Oxomolybdenum(VI) and (IV) complexes of pyrazole derived ONO donor ligands – synthesis, crystal structure studies and spectroelectrochemical correlation

Samik Gupta [a], Anil Kumar Barik [b], Sachindranath Pal [c], Arijit Hazra [a], Somnath Roy [a], Ray J. Butcher [d], Susanta Kumar Kar [a,*]

[a] Department of Chemistry, University College of Science, University of Calcutta, 92 A.P.C. Road, Kolkata 700 009, West Bengal, India
[b] Department of Chemistry, St. Paul's C.M. College, 33/1, Raja Rammohan Roy Sarani, Kolkata 700 009, West Bengal, India
[c] Department of Chemistry, Sree Chaitanya College, Habra, North 24 Parganas, West Bengal, India
[d] Department of Chemistry, Howard University, 2400 Sixth Street, N.W., Washington, DC 200 59, USA

Received 10 June 2006; accepted 3 August 2006
Available online 8 August 2006

Abstract

Four *cis*-dioxomolybdenum complexes of general formula $[MoO_2(L^n)EtOH]$ ($n = 1$–4) and one oxomolybdenum(IV) complex $[MoO(L^4)EtOH]$, with potentially tridentate Schiff bases derived from 5-methyl pyrazole-3-carbohydrazide and salicylaldehyde/substituted salicylaldehyde/*o*-hydroxy acetophenone have been prepared. The Mo(IV) complex is derived from the Mo(VI) dioxo complex by oxotransfer reaction with PPh_3. The complexes are characterized by elemental analysis, electronic spectra, IR, ^1H NMR, and by cyclic voltammetry. All the Mo(VI) species are crystallographically characterized. The complexes have a distorted octahedral structure in which the ligand behaves as a binegative donor one, leaving the pyrazole –N uncoordinated towards the metal center. It is also revealed from the crystal structure that the Mo(VI) center enjoys an NO_5 donor environment.
© 2006 Elsevier Ltd. All rights reserved.

Keywords: Dioxomolybdenum(VI); Oxomolybdenum(IV); Oxotransfer reaction; Pyrazole derived Schiff base ligands; Crystal structure; Structural correlation

1. Introduction

Recent years have witnessed a phenomenal growth in coordination chemistry literature of molybdenum(VI) because of its recently discovered biochemical significance [1–3] as well as involvement of Mo(VI) compounds in some industrial catalytic processes [4–6]. *cis*-Dioxomolybdenum cation is present in the oxidized form of certain oxotransferase enzymes like xanthine oxidase/dehydrogenase, DMSO reductase [7,8], etc. This has created a tremendous impetus in synthesis of a number of model complexes mimicking the oxotransferase molybdoenzymes [9–13]. In order to understand the activity of oxotransferase molybdoenzymes, several attempts have been made to monitor the oxotransfer reaction of dioxomolybdenum complexes to substrates such as PPh_3 [14]. Oxomolybdenum complexes have been isolated and characterized as end products of such reactions along with PPh_3O [15]. Some of these reactions have also been kinetically followed [16]. It is known that the molybdenum cycles between (VI) and (IV) states in the catalytic reaction of these molybdoenzymes [17,18] where Mo(V) coexists with Mo(VI) and Mo(IV) during the course of reaction [17,19,20]. Hence study of the redox properties of model dioxomolybdenum complexes has gained momentum steadily. Many dioxomolybdenum complexes of ligands having NS, SS, NSO (S– as common donor atom) [21–23] as well as ONO (non-sulfur donor atoms) have been prepared and characterized [24,25].

* Corresponding author. Tel.: +91 33 24322936; fax: +91 33 23519755.
E-mail address: skkar_cu@yahoo.co.in (S.K. Kar).

0277-5387/$ - see front matter © 2006 Elsevier Ltd. All rights reserved.
doi:10.1016/j.poly.2006.08.001

Although Schiff base complexes by and large dominate the chemistry of Mo(VI), dioxomolybdenum complexes of Schiff base ligands derived especially from heterocyclic bases are still ill-explored. In this work, we aim at the synthesis and characterization of a few dioxomolybdenum(VI) complexes of Schiff base ligands derived from 5-methyl pyrazole-3-carbohydrazide and salicylaldehyde/*o*-hydroxy acetophenone/substituted salicylaldehyde. Our goal is to arrive at a comparative study of the complexes regarding their structures, redox stability and spectral characteristics with the variation of electron donating nature of the ligands. Further we have studied the oxotransfer reaction of one of the representative complexes. The resultant Mo(IV) complex has been isolated and characterized.

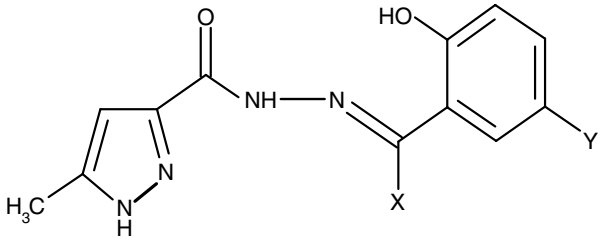
2. Experimental

$MoO_2(acac)_2$ was prepared as described in the literature [26]. Reagent grade solvents were used as received. 5-Methyl pyrazole-3-carbohydrazide was prepared as described in the literature [27]. Salicylaldehyde, 5-bromo salicylaldehyde, 5-nitro salicylaldehyde and *o*-hydroxy acetophenone were purchased from Aldrich Chemical Company, USA and used as received. Tetraethyl ammonium perchlorate (TEAP) used for electrochemical work was prepared as reported in the literature [28].

2.1. Synthesis

2.1.1. Synthesis of ligands

All the four ligands H_2L^1, H_2L^2, H_2L^3, H_2L^4 were synthesized in a similar way by refluxing an ethanolic solution (20 ml) of 5-methyl pyrazole-3-carbohydrazide (10 mmol, 1.4 g) with salicylaldehyde (10 mmol, 1.22 g), *o*-hydroxy acetophenone (10 mmol, 1.36 g), 5-bromo salicylaldehyde (10 mmol, 2.01 g) and 5-nitro salicylaldehyde (10 mmol, 1.67 g), respectively, also taken in ethanol (20 ml). Reflux was continued for ca. 2 h at water bath temperature during which a solid compound separated. It was filtered, washed with ethanol and dried over fused $CaCl_2$. The crude product was recrystallized from ethanol–water mixture (4:1 V/V) (see Fig. 1).



X=H, Y=H :H_2L^1
X=CH_3, Y=H :H_2L^2
X=H, Y=Br :H_2L^3
X=H, Y=NO_2 :H_2L^4

Fig. 1. Structure of the ligand H_2L^n ($n = 1, 2, 3, 4$).

H_2L^1. M.p. above 200 °C. Yield: 1.95 g (80%). IR (KBr pellet) cm^{-1}: ν(N–H) 3283, ν(O–H) 3175, ν(C=O) 1648.5, ν(C–N) 1619, ν(C=C) 1546.9. ^{1}H NMR (D_6-DMSO) δ, ppm: –(C_6H_4) (6.89–7.41)m(4), (–CH=N–) 8.67s(1), (aromatic-OH) 11.47s(1), (pyrazoleN–H), 11.99s(1), (pyrazoleC–H) 6.53m(1).

H_2L^2. M.p. above 200 °C. Yield: 2 g (80%). IR (KBr pellet) cm^{-1}: ν(N–H) 3274, ν(O–H) 3180 ν(C=O) 1637, ν(C=N) 1609, ν(C=C) 1537. ^{1}H NMR (D_6-DMSO) δ, ppm: –(C_6H_4) (6.8–7.6)m(4), (–CH=N–CH_3) 2.65s(3), (aromatic-OH) 11.47s(1), (pyrazoleN–H), 11.99s(1) (pyrazoleC–H) 6.53m(1).

H_2L^3. M.p. above 200 °C. Yield: 2.7 g (80%). IR (KBr pellet) cm^{-1} ν(N–H) 3318, ν(O–H) 3187 ν(C=O) 1652, ν(C–N) 1612, ν(C=C) 1535.2. ^{1}H NMR (D_6-DMSO) δ, ppm: –(C_6H_4) (6.9–7.6)m(3), (–CH=N–) 8.59s(1), (aromatic-OH) 11.42s(1), (pyrazoleN–H) 11.99s(1), (pyrazoleC–H) 6.53m(1).

H_2L^4. M.p. above 200 °C. Yield: 1.73 g (60%). IR (KBr pellet) cm^{-1} ν(N–H) 3278, ν(O–H) 3193 ν(C=O) 1649, ν(C–N) 1610, ν(C=C) 1528. ^{1}H NMR (D_6-DMSO) δ, ppm: –(C_6H_4) (7.1–8.75)m(3), (–CH=N–) 8.5s(1), (aromatic-OH) 12.1s(1), (pyrazoleN–H) 12.18s(1), (pyrazoleC–H) 6.53s(1).

2.1.2. Preparation of the complexes

The complexes [$MoO_2(L^1)$EtOH] (**1**), [$MoO_2(L^2)$EtOH] (**2**), [$MoO_2(L^3)$EtOH] (**3**), [$MoO_2(L^4)$EtOH] (**4**) were prepared in a similar way by refluxing an ethanolic solution (10 ml) of $MoO_2(acac)_2$ (0.5 mmol, 0.163 g) with ehthanolic solutions of H_2L^1 (0.5 mmol, 0.122 g), H_2L^2 (0.5 mmol, 0.129 g), H_2L^3 (0.5 mmol, 0.161 g) and H_2L^4 (0.5 mmol, 0.145 g), respectively. Initially on mixing the two components immediately an orange yellow color was observed. The mixture was refluxed for 1 h. The respective complex separated as an orange microcrystalline compound during reflux or afterwards on slow evaporation of the reaction mixture. It was filtered, washed with ethanol and dried over fused $CaCl_2$.

[$MoO_2(L^1)$EtOH] (**1**): Yield: 0.124 g (60%). Elemental analysis: *Anal*. Calc. for $C_{14}N_4O_5H_{16}Mo$: C, 40.57; H, 3.63; N, 13.3. Found: C, 39.51; H, 3.72; N, 13.30%. X-ray quality crystals of the composition [$MoO_2(L^1)H_2O$] (**1a**) were prepared from compound **1** by slow diffusion of *n*-hexane into a saturated solution of **1** in acetone. (The water molecule may have come from the solvents, acetone or *n*-hexane, as we used only purified solvents and not dehydrated solvents.)

[$MoO_2(L^2)$EtOH] (**2**): Yield: 0.107 g (50%). Elemental analysis: *Anal*. Calc. for $C_{15}N_4O_5H_{18}Mo$: C, 42.05; H, 4.20; N,13.08. Found: C, 42.1; H, 3.95; N, 12.95%.

[$MoO_2(L^3)$EtOH] (**3**): Yield: 0.12 g (50%). Elemental analysis: *Anal.* Calc. for $C_{14}N_4O_5H_{15}BrMo$: C, 34.07; H, 2.83; N, 11.35. Found: C, 33.8; H, 2.56; N, 11.53%. The crystals of **2** and **3** obtained from the reaction mixture were found suitable for X-ray diffraction.

[$MoO_2(L^4)$EtOH] (**4**): Yield: 0.116 g (50%). Elemental analysis: *Anal.* Calc. for $C_{14}N_5O_7H_{15}Mo$: C, 36.52; H,

3.26; N, 15.21. Found: C, 36.05; H, 3.57; N, 15.27%. X-ray quality crystals of **4a** were grown by slow evaporation of a solution of **4** in a mixed solvent of DMF–diethyl ether (1:3 V/V) at refrigerator temperature.

[MoO(L^4)EtOH] (**5**): Complex **4** (0.25 mmol, 0.115 g) was taken in a suspension of 40 ml degassed acetonitrile, PPh_3 (2.25 mmol, 5.5 g) was added and the mixture was refluxed at water bath temperature under dinitrogen atmosphere for 1 h. The green compound obtained as a residue was filtered on a sintered gooch crucible and washed with acetonitrile. It was dried in a vacuum desiccator over concentrated H_2SO_4. Yield: 0.055 g (52%). Elemental analysis: *Anal.* Calc. for $C_{14}N_5O_6H_{14}Mo$: C, 37.9; H, 3.16; N, 15.80. Found: C, 36.8; H, 3.55; N, 14.01%.

2.2. Physical measurements

Elemental analyses were performed at IACS, Kolkata on a Perkin–Elmer 2400 CHN analyzer. The ^1H NMR spectra of the complexes and the ligands were recorded on a Bruker AM300L (300 MHz) superconducting FT-NMR. IR spectra were recorded as a KBr pellet on a Perkin–Elmer FTIR spectrophotometer. UV–Vis spectra and DRS were measured on a Hitachi U-3501 spectrophotometer. Cyclic Voltammetry was carried out using a Sycopel model AEW2 1820F/L instrument. The measurements were carried out at 293 K in DMF solutions containing 0.2 M TEAP as supporting electrolyte and 10^{-3}–10^{-4} M solution of the respective complex deoxygenated by bubbling with nitrogen. The working, counter and reference electrodes used were a Pt wire, platinum coil and an SCE, respectively.

2.3. Crystallographic measurements

The crystals were measured on an Bruker SMART 1K CCD diffractometer using Mo Kα radiation ($\lambda = 0.71073$ Å) and a graphite monochromator at −80 °C. Unit cell and reflection data were obtained by standard methods [29,30] and are summarized in Table 1. The structures were solved, refined, and prepared for publication using the SHEXTL package [31] (structure solution refinements and molecular graphics).

The structures were solved using direct methods and refined on F^2 using full matrix least squares techniques with anisotropic displacement factors for all non-hydrogen

Table 2
Selected bond distances (Å) and bond angles (°) for **1a**, **2**, **3**, **4a**

	1a	**2**	**3**	**4a**
Bond distance				
Mo–O(1)	1.908(4)	1.934(15)	1.922(3)	1.959(3)
Mo–O(2)	2.009(4)	2.005(15)	1.989(3)	2.012(3)
Mo–O(3)	1.700(5)	1.718(15)	1.709(3)	1.710(3)
Mo–O(4)	1.664(6)	1.700(17)	1.691(4)	1.713(3)
Mo–O(1S)	2.359(13)	2.301(15)	2.306(3)	2.263(4)
Mo–N(1)	2.224(4)	2.250(18)	2.240(3)	2.257(3)
N(1)–N(2)	1.391(6)	1.405(2)	1.391(5)	1.401(6)
N(1)–C(7)	1.297(7)	1.306(3)	1.295(6)	1.287(5)
N(2)–C(8)	1.294(7)		1.295(6)	1.305(5)
N(2)–C(9)		1.295(3)		
C(8)–O(2)	1.309(6)		1.328(5)	1.325(5)
C(9)–O(2)		1.330(2)		
C(7)–C(1)	1.411(7)	1.469(3)	1.424(6)	1.462(6)
C(1)–C(2)	1.411(7)	1.412(3)	1.416(7)	1.425(6)
C(2)–O(1)	1.352(6)	1.355(2)	1.333(6)	1.337(5)
C(3)–C(4)	1.398(8)	1.387(3)	1.391(8)	1.382(7)
Bond angle				
O(3)–Mo–N(1)	150.9(2)	159.85(7)	158.48(14)	158.87(13)
O(3)–Mo–O(4)	106.3(3)	105.03(7)	105.20(18)	105.12(15)
O(4)–Mo–O(1S)	171.0(2)	170.23(6)	171.78(16)	168.61(15)
O(2)–Mo–O(1)	154.49(16)	148.54(6)	149.18(14)	151.97(13)
O(1S)–Mo–N(1)	70.70(3)	78.71(6)	76.90(12)	74.38(12)
C(2)–O(1)–Mo	138.3(3)	131.22(13)	136.7(3)	135.7(3)
C(8)–O(2)–Mo	119.9(3)		120.1(3)	119.3(2)
C(9)–O(2)–Mo		119.07(12)		

Table 1
Crystallographic data for the single crystals of **1a**, **2**, **3**, **4a**

	1a	**2**	**3**	**4a**
Empirical formula	$C_{12}H_{11}MoN_4O_5$	$C_{15}H_{18}MoN_4O_5$	$C_{14}H_{15}BrMoN_4O_5$	$C_{18}H_{23}MoN_7O_8$
Formula weight	387.19	430.27	495.14	561.37
Temperature (K)	293	293(2)	293	293(2)
Crystal system	orthorhombic	monoclinic	monoclinic	triclinic
Space group	*Pmcn*	*P*2(1)/*c*	*P*2(1)/*c*	$P\bar{1}$
a (Å)	6.5940(9)	8.2534(15)	8.4994(9)	9.923(3)
b (Å)	10.6624(15)	13.150(2)	15.4088(19)	10.058(4)
c (Å)	19.040(3)	15.957(3)	11.1125(11)	13.163(5)
α (°)		90	90	74.181(6)
β (°)		104.411(3)	92.424(2)	75.178(6)
γ (°)		90	90	67.536(5)
V (Å^3)	1338.6(3)	1677.4(5)	1737.2(3)	1151.0(7)
Z	4	4	4	2
F(000)	772	872	976	572
Data/restraints/parameters	1732/5/224	4086/0/230	4221/0/231	5337/0/312
Goodness-of-fit on F^2	1.275	1.07	1.03	1.071
Final *R* indices [$I > 2\sigma(I)$]	$R_1 = 0.0605$, $wR_2 = 0.1413$	$R_1 = 0.0269$, $wR_2 = 0.0638$	$R_1 = 0.0451$, $wR_2 = 0.1241$	$R_1 = 0.0619$, $wR_2 = 0.1700$
Largest difference peak and hole (e Å^{-1})	0.746 and −2.337	0.54 and −0.601	1.04 and −1.05	2.766 and −2.09

Table 2A
H-bonding distances and angles (Å and °)

Complex	D–H···A	*d*(D–H)	*d*(H···A)	*d*(D···A)	∠DHA	Symmetry transformations used to generate equivalent atoms
1a	O(1s)–H(1W1)···O(4)#2	0.82	2.440(6)	2.950(7)	121.2(2)	#1 $-x+1/2, y, z$; #2 $x-1, y, z$
	O(1s)–H(1W2)···N(2)#3	0.82	2.069(4)	2.833(4)	155.09(18)	#3 $-x, -y+1, -z$; #4 $x, y+1, z$
	N(4)–H(4B)···O(1)#4	0.86	2.45	3.295(6)	169.0	
2	O(1s)–H(1s)···N(3)#1	0.82	1.9700	2.791(2)	174.0	#1 $-x, -y+2, -z+2$
	N(4)–H(4B)···O(3)#2	0.86	2.1900	2.949(2)	147.0	#2 $-x, y+1/2, -z+3/2$
3	O(1s)–H(5)···N(3)#1	0.95(7)	1.78(7)	2.720(5)	169(6)	#1 $-x, -y+2, -z+2$
	N(4)–H(4B)···O(3)#2	0.86	1.99	2.847(5)	174	#2 $-x, y+1/2, -z+3/2$
4a	N(3)–H(3B)···O(2s)	0.86	1.92	2.746(6)	161	

atoms. Positions of the hydrogen atoms were calculated from the geometry of the molecular skeleton and their thermal displacement parameters were refined isotropically on a groupwise basis. Selected bond lengths and angles are reported in Table 2. H-bonding distances and angles are shown in Table 2A.

3. Results and discussion

3.1. Syntheses

All the four Schiff base ligands and their complexes were synthesized in a very facile and essentially identical way. Each ligand acts as a tridentate dianionic ONO donor one towards the MoO_2^{2+} core. All the Mo(VI) complexes were obtained from a refluxing mixture of the respective ligand and the bis(acetylacetonato)dioxomolybdenum(VI) precursor, taken in 1:1 molar proportion in purified ethanol. Complexes of the general formula $[MoO_2(L^n)EtOH]$ ($n = 1$–4, complexes **1**–**4**) were isolated as orange–yellow compounds from reaction mixture by slow evaporation at room temperature. These complexes were found to be fairly soluble in most of the common organic solvents. Magnetic susceptibility and molar conductance data show that the complexes are diamagnetic and electrically non-conducting in nature. The ligand H_2L^1 has been earlier employed by Syamal and Maurya to prepare the complex $[MoO_2(L^1)MeOH]$ from a methanol solution in a similar way [32]. Among the dioxomolybdenum(VI) complexes, the complex $[MoO_2(L^4)EtOH]$ (**4**) was found to be the most easily reducible by electrochemical studies and was chosen for the study of oxotransfer reaction. It undergoes oxoabstraction reaction at a fairly rapid rate at room temperature even at small concentration of about 10^{-4} mol/dm^3. The reaction progress was followed with respect to time in an acetonitrile solution using a UV–Vis spectrophotometer. The solid oxomolybdenum(IV) complex, $[MoO(L^4)EtOH]$ (**5**), was isolated from a refluxing mixture of **4** and excess PPh_3 in degassed acetonitrile at water bath temperature under dinitrogen atmosphere.

3.2. ^1H NMR studies

^{1}H NMR data of the ligands (cited in the experimental section) when compared with those of the complexes (Table 3) reveal that in every case the ligand serves as

Table 3
Characterization of the complexes **1**–**4**

Complex	IR (ν/cm^{-1}) (Mo=O)	NMR (^{1}H/δ TMS)	CV (E_{pc}/V) [Mo(VI)/Mo(V), Mo(V)/Mo(IV)]	UV–Vis (λ_{max}/nm) (ε/dm^3 mol^{-1} cm^{-1})	DRS (λ_{max}/nm)
1	903, 936	8.85(s)(–N=CH–) 1.13(t)(C*H*$_3$CH$_2$OH) 3.58(m)(CH$_3$C*H*$_2$OH) 3.50(s)(CH$_3$CH$_2$O*H*)	−1.15, −1.04	401.50(3597) 319.50(18481) 297.5(21021) 286.0(19206)	436
2	904, 929	2.92(s)[–N=C(CH3)–] 1.13(t)(C*H*$_3$CH$_2$OH) 3.58(m)(CH$_3$C*H*$_2$OH) 3.50(s)(CH$_3$CH$_2$O*H*)	−1.27, −1.15	389(4545) 315(19126) 293(19826) 282(19029)	411
3	901, 935	8.86(s)(–N=CH–) 1.13(t)(C*H*$_3$CH$_2$OH) 3.58(m)(CH$_3$C*H*$_2$OH) 3.50(s)(CH$_3$CH$_2$O*H*)	−1.12, −1.02	409(1977) 331(14023) 299.5(19990) 288.5(19456)	441
4	904, 939	9.06(s)(–N=CH–) 1.13(t)(C*H*$_3$CH$_2$OH) 3.59(m)(CH$_3$C*H*$_2$OH) 3.43(s)(CH$_3$CH$_2$O*H*	−1.02, −0.83	413.5(5189) 338(15700) 294.5(25690)	413

tridentate binegative ONO donor and the pyrazole unit remains free. The pyrazole residue of each ligand shows signal for N–H at δ12 ppm, C_5–CH_3 protons at δ2.3 ppm and ring C_4–H proton at δ6.58 ppm [33,34]. These signals are found unperturbed in the complexes.

The disappearance of the signal at δ3.34 ppm in the free ligands upon complexation suggests that during complexation the [–CO–NH–] group undergoes tautomerization to [–C(OH)=N–] followed by deprotonation of the –OH group. The absence of low field signal characteristic of aromatic –OH is ascribed to the fact that during complexation the ligand also undergoes deprotonation from phenolic –OH group.

The azomethine C–H signal in **1**, **3**, **4** is shifted downfield from its original position in the free ligands upon coordination of the (C=N–) group, on account of reduction of electron density at the azomethine C–H. The coordination of the nitrogen of (C=N–) group in **2** is supported by the shifting of CH_3 protons of acetophenone part in H_2L^2 towards the lower field, on complexation. The aromatic protons of salicylaldehyde or *o*-hydroxy acetophenone part appearing at δ6.7–7.9 ppm [35] also show a maximum deviation of δ0.25 ppm in the complexes as compared to free ligands since in the complexes they are in direct conjugation to the coordinated O and N of the hydrazone ligands. Appearance of characteristic signals for O–H at δ3.54 ppm, CH_2 at δ3.58–3.61 ppm and CH_3 at δ1.13 ppm indicates that the sixth coordination position is occupied by a solvent molecule (EtOH).

However, it has been observed that –OH signals of ligated ethanol are not affected by the difference in donating properties of the ligands.

3.3. IR spectral studies

IR spectra of the free ligands show multiple bands at 3274–3318 cm^{-1} for ν(N–H) of secondary amide group, 1652–1637.5 cm^{-1} for ν(C=O) and 3175–3193 cm^{-1} for ν(O–H) [36]. These peaks are absent in the spectra of complexes as each ligand binds in binegative mode losing protons from both carbohydrazide and phenolic O–H group. On the other hand strong peaks at 1602–1619 cm^{-1} (ν(C=N)) and another weak peak at 1528–1569 cm^{-1} (ν(C=C)) appear in both the spectra of complexes and the free ligands [37].

In addition to that all the four Mo(VI) complexes exhibit two characteristic bands at 900–904 cm^{-1} and 936–939 cm^{-1} for symmetric and antisymmetric stretching of *cis* MoO_2^{2+} core, respectively [38–40]. It has been found that the MoO_2^{2+} symmetric and antisymmetric stretching vibrations are independent of the donating capacity of the ligands. The ν(C=C) in the ligands are found to appear at ca. 20 cm^{-1} higher frequency compared to free ligands. However no real deviation was observed for values of ν(C=N). The absence of strong peaks at 1050 cm^{-1} indicates the nonparticipation of tertiary N of pyrazole end of the ligands in complexation [41], which is also further substantiated by crystal structure studies. In the complex [MoO(L^4)EtOH] (**5**) the ν(Mo=O) shows a single band at 912 cm^{-1}. The lower value compared to the Mo(VI) complex is due to the lowering of the Mo oxidation state [15]. Other peaks do not show any notable deviation from that of Mo(VI) complex.

3.4. UV–Vis, DRS spectral studies

Electronic spectra of the complexes recorded in DMF solution display two strong absorption bands in the regions 389–413 and 294–319 nm. These peaks are assigned as charge transfer transitions of the type N($p\pi$)–Mo($d\pi$) LMCT and O($p\pi$)–Mo($d\pi$) LMCT, respectively [42–44], as the ligand based orbitals are either N or O donor types. The slight change of λ values within each set of peaks may be due to the difference of electron donating capacity of the ligands. Between ligands H_2L^1 and H_2L^2, as the latter is more electron rich, the HOMO of H_2L^2 is of lower energy compared to that of H_2L^1. Thus in the complex **2**, HOMO(L) to LUMO(M) transition occurs at higher energy.

Again when H_2L^1 is compared to H_2L^3 and H_2L^4, i.e., salicylaldehyde derived ligand compared to its 5-bromo salicylaldehyde and 5-nitro salicylaldehyde counterparts, the ligands are progressively less electron rich due to the electron withdrawing nature of the substituents. This makes HOMO of H_2L^3 and H_2L^4 higher in energy compared to that of H_2L^1 for which the electronic transitions in the respective complex (**3** and **4**) suffer a red shift, compared to **1**. The DMF solution of each complex exhibits some additional bands in the electronic absorption spectra in the higher energy region 297–292 and 288–282 nm characteristic for intraligand transitions.

The spectrum of the individual complex **1**–**4** recorded in acetone (non-coordinating solvent) shows no substantial change in peak positions indicating that the coordinating nature of DMF does not grossly affect the coordination atmosphere of the complex in the solution.

The complex [MoO(L^4)EtOH] (**5**) shows a single, moderately intense, low energy charge transfer band at 623 nm in DMF solution, characteristic of Mo(IV)O^{2+} species [24]. Charge transfer absorption bands for the corresponding Mo(VI) complex **4** at 413.5 nm was found to be absent. This indicates that the Mo(VI) complex **4** has been completely reduced to a Mo(IV) complex during the course of oxo transfer reaction towards PPh_3. However bands lying around 260–340 nm are due to intraligand transition.

The changes in the spectral behavior of complex **4** as a result of oxoabstraction reaction, can be studied as a function of time, when spectral data are recorded at 5 min interval in a 10^{-4} M solution of **4** in acetonitrile with a 10-fold excess of PPh_3. Progress of the reaction was marked by gradual appearance of a band at 623 nm (Fig. 2a) and disappearance of a shoulder band at 413.5 nm (Fig. 2b). An interesting feature is that the reaction seems to complete within a time span of 40 min at room temperature (296 K) even at such low concentration.

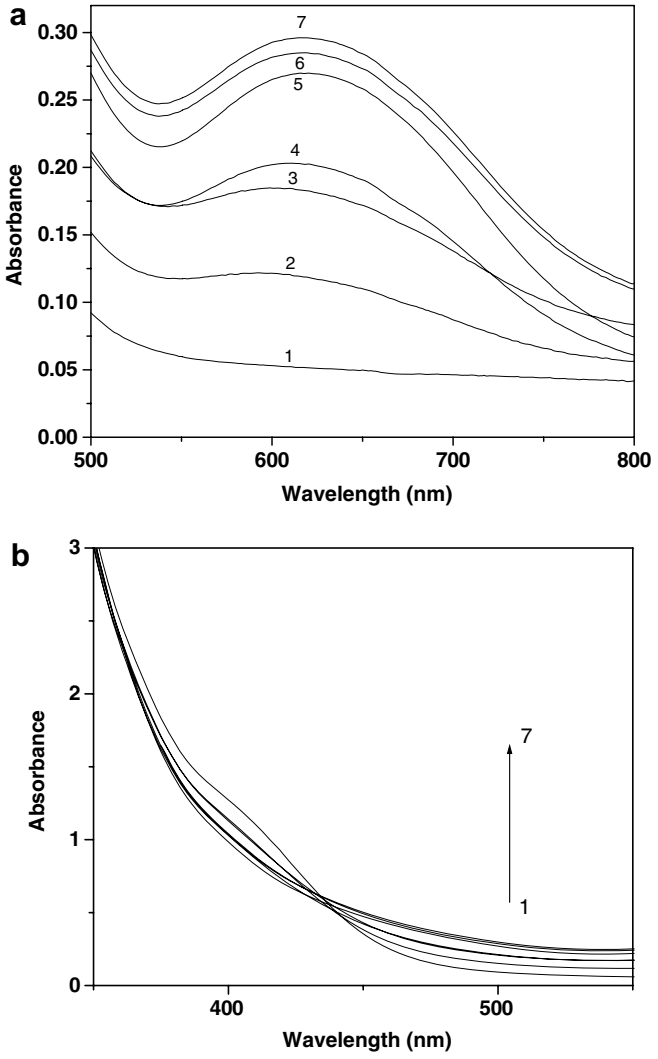


Fig. 2. Change in spectral behavior of complex **4** with time in a 10^{-4} M solution on addition of 10-folds excess of PPh_3 in acetonitrile at 298 K. Spectra taken at 5 min (1), 10 min (2), 15 min (3), 20 min (4), 25 min (5), 30 min (6), 35 min (7) shows gradual appearance of a peak at 623 nm (in **2a**) and disappearance of a shoulder at 413.5 nm (in **2b**).

The diffuse reflectance spectra of the complexes **1**–**4** show one broad band in the regions 413–444 nm. However, it is observed that complexes **1**–**3** show absorption band at lower energy compared to those in solution. This may be attributed to more destabilization of metal LUMO than the ligand HOMO in DMF solution. However in case of complex **4** no such deviations occur. Probably in this case, the ligand HOMO is destabilized to the same degree as the metal LUMO in solution. (Highly charge separated structures in resonance hybrid of the ligand.) The electron donating capacity of the ligands seems to have the same effect in diffuse reflectance spectra as in solution.

3.5. Electrochemistry

The electrochemical behavior of all the complexes $[MoO_2(L^n)EtOH]$ $(n = 1, 2, 3, 4)$, i.e., complexes **1**–**4** and complex **5** were examined in DMF solution using cyclic voltammetry at a platinum electrode with 0.1 M TEAP as supporting electrolyte. The corresponding data are supplied in Table 3. In the potential range −0.8 to 1.5 V the complexes show two irreversible reductive responses during a cathodic scan for Mo(VI)/Mo(V) and Mo(V)/Mo(IV). Each one is assigned to a one electron process established by comparison of current height with authentic one electron process. The corresponding oxidation peaks were found absent during an anodic scan. The ligands H_2L^1, H_2L^2, H_2L^3, H_2L^4 do not have any reductive response in the same potential window. Between H_2L^1 and H_2L^2, the latter is more electron donating. This results in an increase of electron density at the Mo(VI) center in **2** compared to **1**. As a consequence, the complex **2** is comparatively difficult to be reduced. E_{pc}s are shifted to more negative potential. Again among H_2L^1, H_2L^3 and H_2L^4 the ligands are gradually less electron donating. As the substituents at the 5- position of the phenyl ring in the ligands (–H, –Br, $–NO_2$, respectively) become more electron withdrawing, the e-density is shifted away from Mo(VI) center, the complexes (**1**, **3**, **4**) become easy to be reduced and the E_{pc}s are shifted towards the anodic direction. Though the substituents at the phenyl ring or azomethine carbon are not directly bonded to the MoO_2^{2+}, their effect is transmitted to the Mo-oxo core through the extended conjugation [45,46]. This is in direct correlation with the observation from the electronic spectra.

The redox behavior of the complex **5** has been shown in Table 4. It has to be mentioned here that the reduction potentials are only cathodic reduction potential not standard reduction potentials as the reductions are irreversible in nature.

3.6. Description of structures

The perspective view of the complexes **1a**, **2**, **3** and **4a** together with the atom numbering scheme are shown in Figs. 3–6 (atoms labeled O1S and O2S in the tables appears as O1s and O2s, respectively, in Figs. 3–6). Crystal parameters are presented in Table 1 and selected bond angles and bond distances are shown in Table 2.

The coordination geometry around the molybdenum(VI) atom in all the four complexes reveals a distorted octahedral environment with an NO_5 chromophore. Each ligand molecule behaves as dianionic tridentate one

Table 4
Characterization of complex **5**

IR (ν/cm^{-1}) (Mo=O)	UV–Vis (λ_{max}/nm) (ε/dm^3 mol^{-1} cm^{-1})	CV (E/V)
912	623(290)	[Mo(VI)/Mo(IV)] $E_{pa} = 1.53$ [Mo(IV)/Mo(III)] $E_{pc} = -1.18$ $E_{pa} = -0.67$ $\Delta E_p = 0.51$, $E_{1/2} = 0.925$

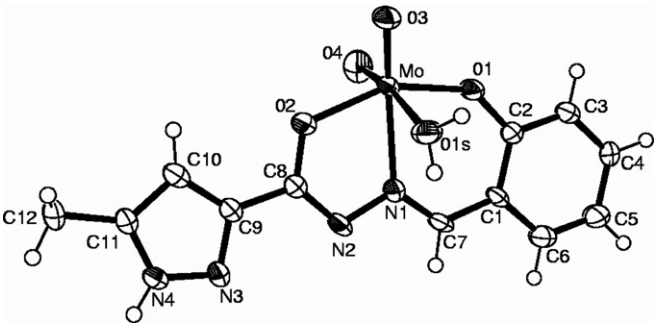


Fig. 3. ORTEP diagram of complex **1a** (50% thermal ellipsoid).

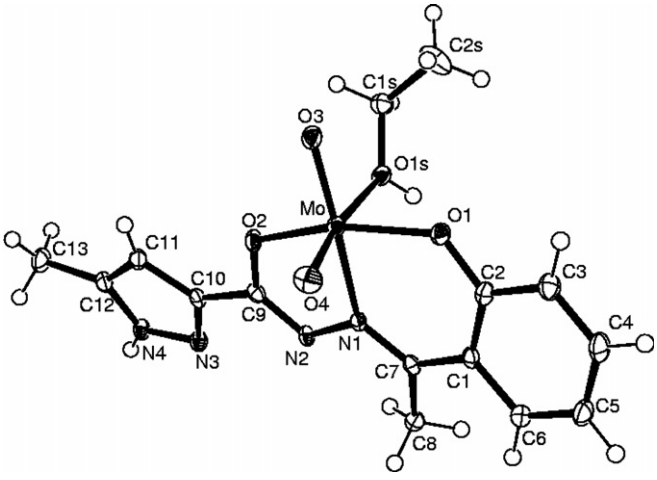


Fig. 4. ORTEP diagram of complex **2** (50% thermal ellipsoid).

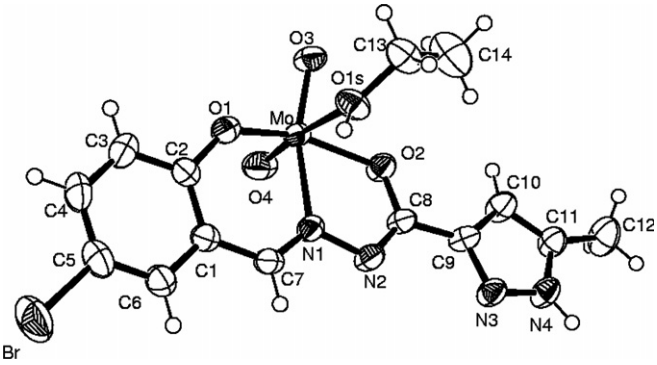


Fig. 5. ORTEP diagram of complex **3** (50% thermal ellipsoid).

binding through the phenolate oxygen (O1), the enolate oxygen (O2) and the imine nitrogen (N1) and occupies three positions in the meridional *XY* plane [43,47]. One oxo group (O3) is located *trans* to the imine nitrogen in the same plane. The other oxo group (O4) is located in the axial plane with the solvent molecule (EtOH, H_2O or DMF). The molybdenum is found to be deviated from the mean equatorial plane of O3, O2, O1 and N1 by 0.278–0.310 Å. The maximum deviation was observed in structure **2** and the minimum in structure **1a**. The Mo–O (H_2O, EtOH) bond lengths in structures **1a**, **2**, **3** are all

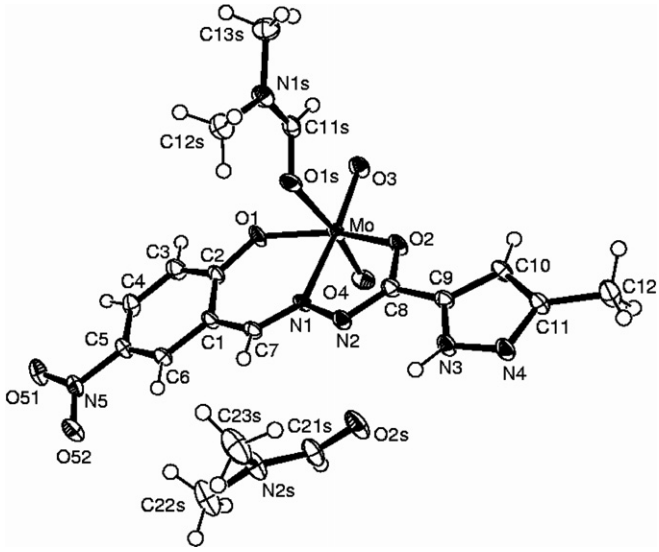


Fig. 6. ORTEP diagram of complex **4a** (50% thermal ellipsoid).

longer than the normal single bond lengths (2.30–2.35 Å against 1.9–2.0 Å). This shows that the solvent molecule is loosely attached to the Mo(VI) center. In structure **4a** the Mo–O (DMF) bond is comparatively shorter (2.26 Å) indicating that DMF acts as a better coordinating ligand. This also explains the exchange of solvent molecule (EtOH by DMF) in a DMF solution of complex **4** to give crystals of **4a**. The Mo–O(3), Mo–O(4) bond lengths are similar to other MoO_2^{2+} cores [3,48,49]. The bond between Mo and the azomethine nitrogen (N1) in the complexes are within a range of 2.22–2.25 Å which is comparatively longer than other Mo–N single bonds. This is due to the *trans* effect generated by the oxo group *trans* to the Mo–N(1) bond. The C(8)–O(2) bond length in **1a**, **3**, **4a** and the corresponding C(9)–O(2) length in **2** are 1.318–1.325 Å, which is closer to single bond length rather than C–O double bond length. However, the shorter length compared to C–O single bond may be attributed to extended electron delocalization in the ligands. Similarly shortening of C(8)–N(2) length in **1a**, **3**, **4a** and the corresponding C(9)–N(2) in **2** (1.306–1.29 Å instead of normal 1.385 Å) together with the elongation of N(2)–N(1) length also supports the electron cloud delocalization in the ligand system [50,51]. Each ligand molecule forms a five-membered and a six-membered ring with the Mo center. The electron donating capacity of the ligands does not influence the bond distances of the coordination sphere.

While examining the packing pattern in the crystals it was observed that in the crystals of **2** and **3** the heterocyclic pyrazole residue plays a vital role in building the H-bonded supramolecular structure of the crystals. The tertiary N atom of the pyrazole moiety is found to be intermolecularly H-bonded to the H atom of the coordinated O–H group of the weakly bonded ethanol. Again the H atom of the secondary nitrogen (N4) is found to be H-bonded with one of the oxo group of the MoO_2^{2+} core (Fig. 7).

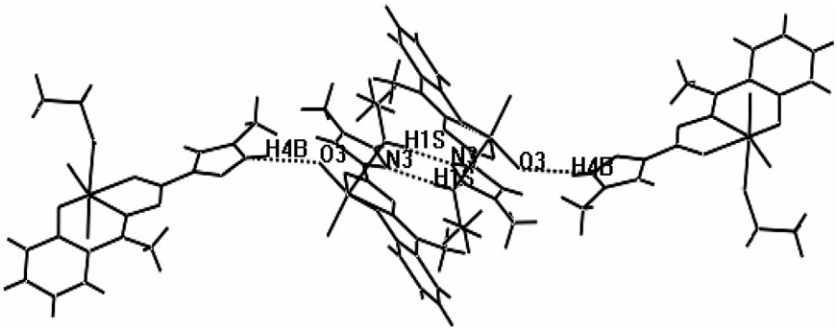


Fig. 7. Hydrogen bonding in complex **2** showing two types of interaction between [N(4)–H(4B)–O(3)] and [O(1S)–H(1S)–N(3)].

Packing pattern in the other two crystals (**1a**, **4a**) is quite different which may be attributed to the difference in their sixth coordination position. In **1a**, three intermolecular H-bonding interaction may be perceived between H atom of H_2O and azomethine nitrogen (N2) of another molecule, between H atom of water and the axial oxo atom (O4) and another weaker one between H atom of pyrazole nitrogen (N4) and the ligated phenolate oxygen (O1) (Table 2A). The packing in the crystals is also governed by a supramolecular π–π interaction involving the stacking of benzene rings as well as the pyrazole ring systems. This is observed when the molecules subjected through a translation symmetry operation along the X-axis (see Supplementary material).

The crystal structure **4a** contains one solvated DMF molecule along with one ligated DMF molecule per unit. The solvated DMF molecule is engaged in a H-bonding interaction involving the H atom of secondary pyrazole nitrogen (N3) and its oxygen (O2S). On a closer inspection, it is observed that solvated and ligated DMF molecules make solvent channels in this crystal.

4. Conclusion

A very common but facile way has been employed to synthesize the four Mo(VI) complexes. In all the complexes, the various Schiff base ligands differ only in the carbonyl part (in **1** and **2**) or by bearing different substituents at the phenyl ring (in **1**, **3** and **4**). The electron donating capacity of the ligands is related to the nature of the substituents. As the electron withdrawing capacity among H, Br and NO_2 follows the sequence H (in **1**) < Br (in **3**) < NO_2 (in **4**), in the corresponding complex, the Mo(VI) center becomes gradually electron poor. As a consequence, a less negative potential is necessary for reduction of the metal center. Again, between H (in **1**) and $-CH_3$ (in **2**), the latter being more electron donating, the metal center in **2** becomes more electron rich compared to that in **1**, for which **2** demands more negative potential to carry out the reduction process. Thus, since **4** is found to be most easily reducible Mo(VI) complex, we have chosen it to follow the oxotransfer reaction at room temperature leading to the Mo(IV) complex.

Acknowledgements

Acknowledgement is made to the University Grants Commission, New Delhi, India, for awarding a major research project in science [F. 30-65/2004(SR)] to S.K. Kar. Acknowledgement is also made to Mercury 1.4.1 (CCDC) free crystallographic programme for Fig. 7.

Appendix A. Supplementary material

CCDC numbers 610031, 610032, 610033 and 610034 contain the supplementary crystallographic data for the complexes **3**, **1a**, **2** and **4a**, respectively. These data can be obtained free of charge via http://www.ccdc.cam.ac.ac.uk/conts/retrieving.html, or from the Cambridge Crystallographic Data Center, 12, Union Road, Cambridge CB2 1EZ, UK; fax: +44 1223 336 033; or e-mail: deposit@ccdc.cam.ac.uk. Supplementary data associated with π stacking of **1a** is available in .Lis file format, generated from Platon. Supplementary data associated with this article can be found, in the online version, at doi:10.1016/j.poly.2006.08.001.

References

[1] E.I. Stiefel, in: M.P. Coughlan (Ed.), Molybdenum and Molybdenum containing Enzymes, Pergamon Press, Oxford, England, 1979, p. 43.
[2] R. Hill, Chem. Rev. 96 (1996) 2757.
[3] J. Liimatainen, A. Lehtonen, R. Sillanpää, Polyhedron 19 (2000) 1133.
[4] R.K. Grasselli, Catal. Today 49 (1999) 141.
[5] R.J. Cross, P.D. Newman, R.D. Peacock, D. Stirling, J. Mol. Catal. 144 (1999) 273.
[6] K.J. Ivin, J.C. Mol, Olefin Metathesis and Metathesis Polymerization, Academic Press, London, 1997.
[7] G.C. Tucci, J.P. Donahue, R.H. Holm, Inorg. Chem. 37 (1998) 1602.
[8] B.E. Schultz, S.F. Gheller, M.C. Muetterties, M.J. Scott, R.H. Holm, J. Am. Chem. Soc. 115 (1993) 271.
[9] R.H. Holm, Chem. Rev. 87 (1987) 1401.
[10] F. Bottmley, L. Sutin, Adv. Organomet. Chem. 28 (1998) 339.
[11] J.T. Spence, Coord. Chem. Rev. 48 (1983) 59.
[12] E.I. Stiefel, Prog. Inorg. Chem. 22 (1979) 1.
[13] (a) A. Lehtonen, M. Wasberg, R. Sillanpää, Polyhedron 25 (2006) 767;
(b) A. Lehtonen, R. Sillanpää, Polyhedron 24 (2005) 257.
[14] R.H. Holm, Coord. Chem. Rev. 100 (1990) 183.

[15] (a) A. Rana, R. Dinda, S.P. Ghosh, A.J. Blake, Polyhedron 22 (2003) 3075;
(b) N.R. Pramanik, S.P. Ghosh, T.K. Raychaudhuri, S. Ray, R.J. Butcher, S.S. Mandal, Polyhedron 23 (2004) 1595.
[16] K. Unoura, Y. Abiko, A. Yamazaki, Y. Kato, D.C. Coomber, G.D. Fallon, K. Nakahara, A.M. Bond, Inorg. Chim. Acta 333 (2002) 41.
[17] R.C. Bray, Enzymes 12 (1975) 299.
[18] R.C. Bray, in: W.E. Newton, S. Otsuka (Eds.), Molybdenum Chemistry of Biological Significance, Plenum Press, New York, 1980, p. 117.
[19] E.I. Stiefel, Prog. Inorg. Chem. 22 (1977) 1.
[20] R.C. Bray, S.P. Vincent, D.J. Lowe, R.A. Clegg, P.B. Garland, Biochem. J. 155 (1976) 201.
[21] O.A. Rajan, A. Chakraborty, Inorg. Chem. 20 (1981) 660.
[22] D.A. Smith, F.A. Schultz, Inorg. Chem. 21 (1982) 3035.
[23] M. Chaudhury, Inorg. Chem. 24 (1985) 3011.
[24] R. Dinda, P. Sengupta, S.P. Ghosh, H. Mayer-Figge, W.S. Sheldrick, J. Chem. Soc., Dalton. Trans. (2002) 4434.
[25] H. Arzoumanian, R. Lopez, G. Agrifoglio, Inorg. Chem. 33 (1994) 3177.
[26] G.J.J. Chen, J.W. McDonald, W.E. Newton, Inorg. Chem. 15 (1976) 2612.
[27] N. Saha, K.M. Dutta, J. Inorg. Nucl. Chem. 43 (1981) 1405.
[28] D.T. Sawyer, J.L. Roberts, Experimental Electrochemistry for Chemists, Wiley, New York, 1974, p. 212.
[29] Bruker, SMART (Version 5. 624) and SAINT (Version 6. 04) Programs Using the Windows NT System, Bruker AXS Inc., Madison, WI, USA, 2001.
[30] Ray J. Butcher, Jeffrey C. Bottaro, R. Gilardi, Acta Crystallogr., Sect. E 59 (2003) m591–m593.
[31] G.M. Sheldrick, SHELXTL, Version 5.10, Bruker AXS Inc., Madison, WI, USA, 1997.
[32] A. Syamal, M.R. Maurya, Transition Met. Chem. 11 (1986) 172.
[33] A.K. Barik, S. Paul, S.K. Kar, R.J. Butcher, C.J. Bryan, Polyhedron 18 (1999) 571.
[34] A.K. Barik, P. Bandopadhyay, S.K. Kar, Polyhedron 18 (1999) 1.
[35] R. Dinda, P. Sengupta, T.C.W. Mak, S.P. Ghosh, Inorg. Chem. 41 (2002) 1684.
[36] (a) W. Kemp, Organic Spectroscopy, Macmillan, Hamshire, 1987, p. 62;
(b) K. Nakamoto, Infrared and Raman Spectra of Inorganic and Coordination Compounds, Wiley, New York, 1986, p. 241.
[37] N.S. Biradar, B.R. Havinale, Inorg. Chim. Acta 17 (1976) 157.
[38] F.J. Arnaiz, R. Aguado, M.R. Podrosa, A.D. Cian, J. Fischer, Polyhedron 19 (2000) 2141.
[39] M. Kato, K. Nakajima, Y. Yoshikawa, M. Hirotsu, M. Kojima, Inorg. Chim. Acta 311 (2000) 619.
[40] S.A. Attia, S.F. El-Mashtoly, M.F. El-Shahat, Polyhedron 22 (2003) 895.
[41] A. Mitra, T. Banerjee, P. Roychoudhury, S. Chaudhury, P. Bera, N. Saha, Polyhedron 16 (1997) 3735.
[42] S. Purohit, S.P. Ghosh, J. Chem. Res. (s) (1988) 158.
[43] R. Hahn, U. Kusthardt, W. Scherer, Inorg. Chim. Acta 210 (1993) 177.
[44] R. Mattes, V. Mikloweit, Inorg. Chim. Acta 122 (1986) L19.
[45] J. Topich, Inorg. Chem. 20 (1981) 3704.
[46] J. Topich, J.T. Lyon, Inorg. Chem. 23 (1984) 3202.
[47] J.A. Craig, E.W. Harlan, B.S. Snyder, M.A. Whitener, R.H. Holm, Inorg. Chem. 28 (1989) 2082.
[48] J.M. Berg, R.H. Holm, J. Am. Chem. Soc. 106 (1984) 3035.
[49] S.K. Dutta, D.B. McConville, W.J. Youngs, M. Chaudhury, Inorg. Chem. 36 (1997) 2517.
[50] M.W. Bishop, J. Chatt, J.R. Dilworth, M.B. Hursthouse, S. Amarasiri, A. Jayaweera, A. Quick, J. Chem. Soc., Dalton. Trans. (1979) 914.
[51] M.W. Bishop, J. Chatt, J.R. Dilworth, M.B. Hursthouse, M. Motevealli, J. Chem. Soc., Dalton. Trans. (1979) 1603.

Available online at www.sciencedirect.com
ScienceDirect
Polyhedron 26 (2007) 142–148
POLYHEDRON
www.elsevier.com/locate/poly

Mitigating repulsions in close quarters: Copper tells us how!

Ritu Ahuja, M. Nethaji, A.G. Samuelson *

Department of Inorganic and Physical Chemistry, Indian Institute of Science, Bangalore 560012, India

Received 28 September 2005; accepted 8 August 2006
Available online 11 August 2006

Abstract

Four copper(I) complexes of short bite ligands, bis(diphenylphosphino)amine (dppa) and bis(diphenylphosphino)isopropylamine (dppipa) were synthesized from appropriate precursors. All complexes were characterized by single crystal X-ray crystallography and spectroscopic techniques. In each of these complexes, two filled shell cations are forced into close proximity (≈2.7–2.8 Å). With no strong π acid ligands to siphon electron density from the filled d shell, the unavoidable repulsive d^{10}–d^{10} interaction is mitigated when an unsymmetrical coordination environment around the copper atoms exists. The coordinatively saturated copper ion functions as a donor to the coordinatively unsaturated copper. A Cambridge Structural Database (CSD) search reveals the greater propensity of clusters with short contacts to adopt unsymmetrical coordination.
© 2006 Elsevier Ltd. All rights reserved.

Keywords: Copper; Cambridge Structural Database (CSD) analysis; Diphosphinoamine; Metal–metal interactions; Short bite ligand; Unsymmetrical coordination

1. Introduction

Closed shell interactions in inorganic chemistry have been a challenge to experimental and theoretical chemists alike [1,2]. Group 11 monocations have been the subject of innumerable studies for they form many polynuclear complexes and extended lattices with short contacts in the solid state despite the formally closed shell (d^{10}) electronic configuration of the metals involved. The nature of this closed shell interaction has been an area of considerable debate. In the case of gold, the attractive nature of this interaction has been particularly well documented and accepted. The term ''aurophilicity'' is used to collectively describe Au–Au interactions [3–6]. Some of these interactions are unsupported by exogenous ligands. This attractive interaction has found its theoretical justification in the ligand-induced [7] and relativistically-supported [8] stabilization, which leads to favorable mixing of the empty 6s with 5d states to effectively reduce the population of the 5d valence shell. Whereas in the lighter congeners, the existence of analogous cuprophilicity and argentophilicity [1,4,5,9] have not been substantiated by many ligand-unsupported M(I)–M(I) (M = Cu, Ag) contacts in coordination compounds. Very short distances, for example 2.42 Å between two copper centers has been observed by White et al. [10] in a complex with a short bite ligand 2-((6-methyl)pyridyl)trimethylsilylamine. Another example of an unusually short Cu(I)–Cu(I) distance (2.35 Å) [11] is found in [Cu(tolyl-*NNNNN*-tolyl)]$_3$. This complex has been analyzed at different levels of theory and the Cu–Cu interaction has been shown to be attractive as a result of $s + p_z + d_{z^2}$ mixing [12]. In the few unsupported short contacts, strong electrostatic interactions between the subunits cloud the analysis. This has resulted in a controversy about the degree of stabilization, if any, offered by metal–metal contacts in ligand supported cases.

We have examined in this study, four complexes of a diphosphinoamines of the type $Ph_2PN(R)PPh_2$ (dppa; R = H, dppipa; R = ^{i}Pr). These ligands are well known for their short bite [13], which force short metal–metal contacts. There would be considerable difficulty in accommodating

* Corresponding author. Fax: +91 80 2360 1552.
E-mail address: ashoka@ipc.iisc.ernet.in (A.G. Samuelson).

0277-5387/$ - see front matter © 2006 Elsevier Ltd. All rights reserved.
doi:10.1016/j.poly.2006.08.004

the short-bite of the ligand with the closed shell repulsion of Cu(I). Yet copper(I) adopts another route for relieving the repulsive interactions in these examples. Unsymmetrical coordination makes one copper electron rich relative to the other by the presence of an extra ligand. This makes one copper a donor and the other an acceptor and masks the otherwise repulsive interaction. The generality of this phenomenon in complexes with a short contact was brought out by analysis of data readily available in the Cambridge Structural Database (CSD) [14].

2. Results and discussion

2.1. X-ray crystal structure determinations

Complex **1** consists of a cationic dppa bridged dimer with an unsymmetrical coordination. The perspective view is represented in Fig. 1. Although Cu1 and Cu2 have 3 and 4 coordinating atoms around them respectively, including the distant copper in the coordination sphere makes the description easy to follow. Cu1 has a distorted tetrahedral geometry with P1, P3, N3 and Cu2 around it. Cu1 is merely 0.2336(1) Å from the plane formed by two P atoms (P1 and P3) and the N3 of acetonitrile. The sum of the three angles in this trigonal plane is approximately equal to 360° (see Table 1). The tetrahedral coordination is provided by the second copper atom (Cu2). Cu2 is found to adopt a severely distorted trigonal bipyramidal geometry. It has two P atoms P2, P4 and an oxygen atom of the perchlorate anion in the equatorial plane. Cu2 deviates from this plane by 0.227(1) Å. The axial ligands around Cu2 are the oxygen atom of the water (Ow1) and Cu1 subtending an angle of 166.3(2)° along this axis. Cu1 and Cu2 deviate by −2.6182(1) Å and −0.010(1) Å from the P2, P4, and O5a plane respectively, while Cu2 has a deviation of 2.9766(1) Å from the P1 P3 N3 plane. The two trigonal planes P1, P3, N3 and P2, P4, O5a, have a dihedral angle of 14.82(6) Å. The eight membered ring formed by the two PNP bridges adopts a twist boat conformation. Nitrogen atoms of the ligand are almost planar with the angles not very different from those of the free ligand. There is no significant change in the metrical parameters of the ligand on complexation (P–N bond length in the free ligand is 1.692 Å with a PNP angle of 118.9°).

Table 1
Selected bond distances (Å) and bond angles (°) for complex **1**

Bond distances			
Cu1–Cu2	2.7483(9)	Cu2–Ow1	2.189(5)
Cu1–P1	2.235(1)	Cu2–O5a	2.172(19)
Cu1–P3	2.2213(12)	P1–N1	1.676(3)
Cu1–N3	1.965(4)	P2–N1	1.676(3)
Cu2–P2	2.2645(12)	P3–N2a	1.673(3)
Cu2–P4	2.2632(13)	P4–N2a	1.688(3)
Bond angles			
P1–Cu1–P3	131.95(5)	P2–Cu2–P4	139.46(5)
P1–Cu1–N3	107.56(13)	P2–Cu2–Ow1	101.50(15)
P3–Cu1–N3	116.87(13)	P4–Cu2–Ow1	98.80(14)
P1–Cu1–Cu2	95.87(4)	O5a–Cu2–Ow1	58.4(5)
P3–Cu1–Cu2	98.69(4)	O5a–Cu2–Cu1	108.4(5)
N3–Cu1–Cu2	93.49(14)	Ow1–Cu2–Cu1	166.31(17)
P2–Cu2–O5a	111.1(5)	P1–N1–P2	122.2(2)
P2–Cu2–Cu1	81.65(3)	P3–N2a–P4	121.8(2)
P4–Cu2–O5a	109.4(5)		

The second ClO_4^- is found outside the coordination sphere. The counter anion ClO_4^- shows weak intermolecular hydrogen bonding interactions with the aromatic protons, H of the acetonitrile and the NH protons. The bound water is found to have a short contact with a phenylic proton as well. Some of the short contacts are listed in the Supplementary information (Table S1).

The ORTEP plot of the dication of complex **2** is given in Fig. 2 and shows that complexes **1** and **2** are similar. Cu1 is

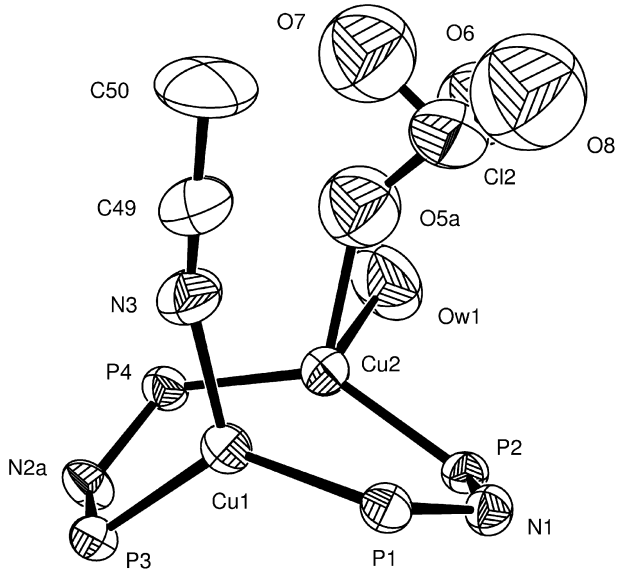


Fig. 1. Cationic fragment of complex **1** $[Cu_2(dppa)_2(CH_3CN)(H_2O)(OClO_3)]ClO_4$ with a Cu–Cu distance of 2.7483(9) Å (phenyl rings on phosphorus and hydrogen atoms removed for clarity).

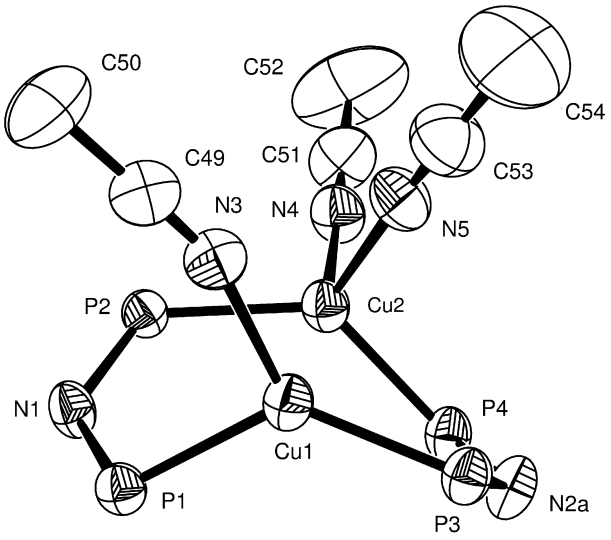


Fig. 2. Cationic fragment of complex **2** $[Cu_2(dppa)_2(CH_3CN)_3](BF_4)_2$ with a Cu–Cu distance of 2.8215(8) Å (phenyl rings on phosphorus and hydrogen atoms removed for clarity).

found in a severely distorted tetrahedral geometry. Cu1 deviates by −0.2237(5) Å from the P1, P3, N3 plane and Cu2 forms the fourth coordination site of the tetrahedron. The second metal atom Cu2 adopts an irregular trigonal bipyramidal geometry with Cu2 being −0.352(1) Å away from the P2, P4, N5 plane. The axial sites are occupied by Cu1 and N4 (CH_3CN) subtending an angle of 166.92(9)° at Cu2 (Table 2). The two counter anions lie far from the metal center.

Cu1 and Cu2 deviate by 2.4525(5) Å and −0.352(1) Å from the P2, P4, N5 plane respectively, −0.2237(5) Å and −3.043(1) Å from the P1, P3, N3 plane respectively. The two planes P1, P3, N3 and P2, P4, N5 have a dihedral angle of 6.92(7) Å. The short contacts formed by BF_4^- with phenylic protons and NH protons do not appear to affect the structure significantly and are listed in the Supplementary information (Table S2).

The movement of the two Cu atoms in complex **1** towards one other is quite striking. Complex **1** is also remarkable for it is the first example of a Cu(I) complex having a water molecule and a phosphine in the coordination sphere. Surprisingly, in spite of very similar synthetic conditions, they have different ancillary donors and Cu–Cu distances. Recently, an analogous complex with PF_6^- was characterized in both symmetrical (Cu–Cu distance = 3.341(2) Å) and unsymmetrical environments (Cu–Cu distance = 2.869(4) Å) [15]. Significantly, the shorter distance is associated with the unsymmetrical structure. While the unsymmetrical structure has donors similar to **2**, an entirely different orientation of the ligand leads to shorter Cu–Cu distance (2.8215(8) Å) in **2**. In **1** and **2**, the complex is coordinatively unsaturated in one of the metal centers although excess acetonitrile is present during the synthesis.

In a related study with the ligand dppipa, we isolated complexes **3** and **4**. The ORTEP plot of the dppipa complexes **3** and **4** are shown in Figs. 3 and 4 respectively. The two halide (chloride and bromide) dimers have highly unsymmetrical structures. There are two dppipa units, out of which one is found in a chelating and the other one in a bridging mode. Important bond lengths and bond angles for complex **3** and **4** are given in Tables 3 and 4 respectively. Both complexes have Cu–Cu distances within the sum of the Van der Waal's radii. The chloride complex **3** has two copper centers at a distance of 2.7664(14) Å and the bromide complex **4** has a Cu–Cu distance of 2.7675(8) Å.

In complex **3**, Cu1 has three of its coordination sites occupied by P1, P4 and Cl1 (bridged). The fourth coordination site is held by P3 at a comparatively longer distance of 2.263(1) Å. The other copper, Cu2 is trigonal planar with Cl1, Cl2 and P2 in its coordination sphere with sum of the three angles close to 360°. The two trigonal planes P2, Cl1, Cl2 and P1, P4, Cl1 are hinged by a chloride bridge, Cl1 and the dihedral angle is 69.59(2)°. The deviations of Cu1 and Cu2 from P1, P4, Cl1 planes are −0.358(1) Å and 2.115(1) Å respectively. On the other hand, Cu1 and Cu2 deviate by 2.161(1) Å and 0.1883(6) Å from P2, Cl1, Cl2 plane respectively. This indicates that Cu2 moves towards Cu1 in a cuprophilic fashion.

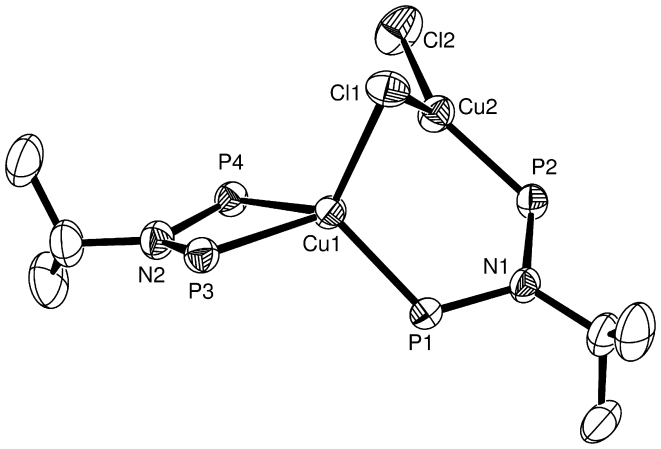


Fig. 3. Complex **3** $[Cu_2(dppipa)_2(Cl)_2]$ with a Cu–Cu distance of 2.7664(14) Å (phenyl rings on phosphorus and hydrogen atoms removed for clarity).

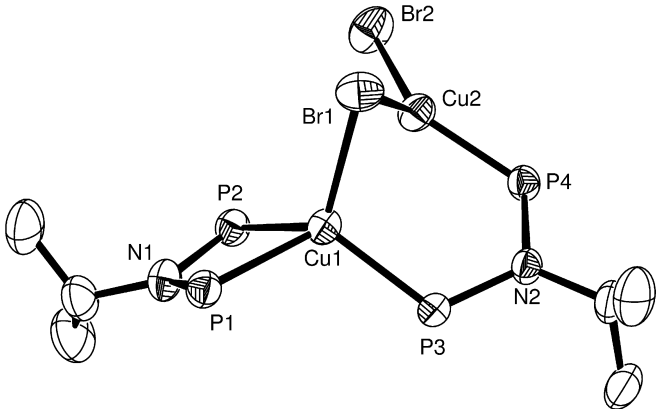


Fig. 4. Complex **4** $[Cu_2(dppipa)_2(Br)_2]$ with a Cu–Cu distance of 2.7675(8) Å (phenyl rings on phosphorus and hydrogen atoms removed for clarity).

Table 2
Selected bond distances (Å) and bond angles (°) for complex **2**

Bond distances			
Cu1–Cu2	2.8215(8)	Cu2–N4	2.073(3)
Cu1–P1	2.2725(10)	Cu2–N5	2.046(3)
Cu1–P3	2.2316(11)	P1–N1	1.687(3)
Cu1–N3	2.023(3)	P2–N1	1.677(3)
Cu2–P2	2.273(1)	P3–N2a	1.680(3)
Cu2–P4	2.2723(11)	P4–N2a	1.693(3)
Bond angles			
P1–Cu1–P3	129.87(4)	P4–Cu2–N5	103.33(9)
P1–Cu1–N3	96.07(9)	P2–Cu2–N4	95.71(9)
P3–Cu1–N3	130.71(8)	P4–Cu2–N4	105.55(9)
P1–Cu1–Cu2	97.93(3)	N4–Cu2–N5	96.15(12)
P3–Cu1–Cu2	93.66(3)	N4–Cu2–Cu1	166.92(9)
N3–Cu1–Cu2	96.87(8)	P1–N1–P2	123.31(15)
P2–Cu2–P4	130.68(4)	P3–N2a–P4	124.92(16)
P2–Cu2–N5	118.21(9)		

Table 3
Selected bond distances (Å) and bond angles (°) for complex **3**

Bond distances			
Cu1–Cu2	2.7664(14)	Cu2–Cl1	2.363(1)[c]
Cu1–P1	2.2604(12)[a]	Cu2–Cl2	2.1824(12)[d]
Cu1–P3	2.339(1)[b]	P1–N1	1.708(3)
Cu1–P4	2.301(1)[b]	P2–N1	1.720(3)
Cu1–Cl1	2.320(1)[c]	P3–N2	1.709(3)
Cu2–P2	2.186(1)[a]	P4–N2	1.721(3)
Bond angles			
P1–Cu1–P3	111.60(4)	P2–Cu2–Cl1	108.49(4)
P1–Cu1–P4	126.51(4)	P2–Cu2–Cl2	134.33(4)
P3–Cu1–P4	71.95(4)	Cl1–Cu2–Cl2	114.97(4)
P1–Cu1–Cl1	108.72(4)	P1–N1–P2	115.10(13)
P3–Cu1–Cl1	115.10(4)	P3–N2–P4	105.27(14)
P4–Cu1–Cl1	117.47(4)		

[a] Bridging dppipa.
[b] Chelating dppipa.
[c] Bridging Cl^-.
[d] Terminal Cl^-.

Table 4
Selected bond distances (Å) and bond angles (°) for complex **4**

Bond distances			
Cu1–Cu2	2.7675(8)	Cu2–Br1	2.4437(8)[c]
Cu1–P1	2.3404(12)[a]	Cu2–Br2	2.3094(8)[d]
Cu1–P2	2.2956(13)[a]	P1–N1	1.706(4)
Cu1–P3	2.263(1)[b]	P2–N1	1.722(4)
Cu1–Br1	2.4496(7)[c]	P3–N2	1.703(3)
Cu2–P4	2.1853(13)[b]	P4–N2	1.715(3)
Bond angles			
P1–Cu1–P3	112.11(4)	P4–Cu2–Br1	109.24(4)
P1–Cu1–P2	72.23(4)	P4–Cu2–Br2	132.91(4)
P2–Cu1–P3	126.21(5)	Br1–Cu2–Br2	114.64(3)
P1–Cu1–Br1	114.18(4)	P1–N1–P2	105.7(2)
P3–Cu1–Br1	108.49(4)	P3–N2–P4	115.47(19)
P2–Cu1–Br1	118.10(4)		

[a] Bridging dppipa.
[b] Chelating dppipa.
[c] Terminal Br^-.
[d] Bridging Br^-.

Similarly in case of complex **4**, there are two trigonal planes Br1, Br2, P4 and P2, P3, Br1 (common vertex at Br1) at a dihedral angle of 67.66(2)°. Cu1 is four coordinate with three coordination sites, Br1, Br2 and P3 almost in a plane with a weak interaction at a distance of 2.3404(12) Å with P1. Cu1 and Cu2 deivate by 0.3613(4) Å and −2.1246(6) Å from P2, P3, Br1 plane respectively. The three coordinate Cu2 deviates by 0.2346(6) Å from Br1, Br2, P4 plane with Cu1 deviating by 2.2484(4) Å from the same plane. In this case also, one can find Cu2 moving towards Cu1.

One would expect the Cu–Cu distance in the case of the bromide bridged dimer to be longer than in the case of analogous chloride complex due to larger size of the bridging bromide ion. Surprisingly the two Cu–Cu distances are not very different. This behavior is reminiscent of the behavior of copper in trimeric complexes [16]. The greater π-donation of bridging chloride ligands leads to larger Cu–Cu distances.

2.2. Solution behavior

One expects that complex **1** would exhibit conductivity corresponding to a 1:1 electrolyte and complex **2** would show conductivity corresponding to that of a 1:2 electrolyte [17]. Indeed complex **2** showed a conductivity value of 220.64 S cm^{-1} mol^{-1} (10^{-3} M in acetone), which shows that it is a 1:2 electrolyte. On the other hand complex **1** gave a value of 203.64 S cm^{-1} mol^{-1} (10^{-3} M in acetone), which was considerably higher than that of a 1:1 electrolyte suggesting significant dissociation in solution. This observation clearly indicates that the perchlorate anion, which is η^1-bound to the metal center, dissociates in solution and a 1:2 electrolyte is formed. The dissociation of the perchlorate in solution suggests that the structure in solution could be symmetrical even though the solid state structure is unsymmetrical.

2.3. Cambridge Structural Database analysis

To probe the frequency of unsymmetrical coordination, we explored the CSD and found 1227 instances where Cu–Cu distances were below 2.8 Å. Out of these, 829 fragments were obtained when the search was limited to "symmetrical" dimers with coordination numbers 2,2; 3,3 and 4,4, etc. Among these symmetrically coordinated fragments, 530 of them have coordination numbers up to 4,4. The remaining have higher coordination numbers. Fragments with coordination number of four each (221) were analyzed in detail. Although the CSD lists them as having the same coordination number, and it was found that about 76% (163) have an unsymmetrical coordination by virtue of different coordinating atoms or very different bond distances around the metal centers. In addition, these apparently "symmetrically bridged" compounds several (143 out of 221) have single atom bridges with acute angles in structures that lead to 3c–$2e^-$ bonds and so promote attractive Cu–Cu interactions.

On the contrary, unsymmetrical coordination occurred in 398 cases, which accounts for about one-third of the total number. Of these, 305 fragments have coordination number less than or equal to 4. There are 142 hits for coordination number 3 and 4, 119 hits with coordination numbers 2 and 3 and the remaining 44 have 2 and 4 coordinate Cu^I ions. Fig. 5 represents the distribution of M–M distances in complexes with coordination numbers 3/4 and 2/3 respectively. The histograms clearly reflect a well-defined interaction between the metal ions around 2.6–2.7 Å. This is below the sum of the van der Waal's radii for two Cu^I ions (2.8 Å) suggesting the presence of an attractive interaction between the two copper(I) centers. A similar analysis of structures having Cu–Cu distances above 2.8 Å shows that the probability of encountering unsymmetrical coordination is less (1/4th).

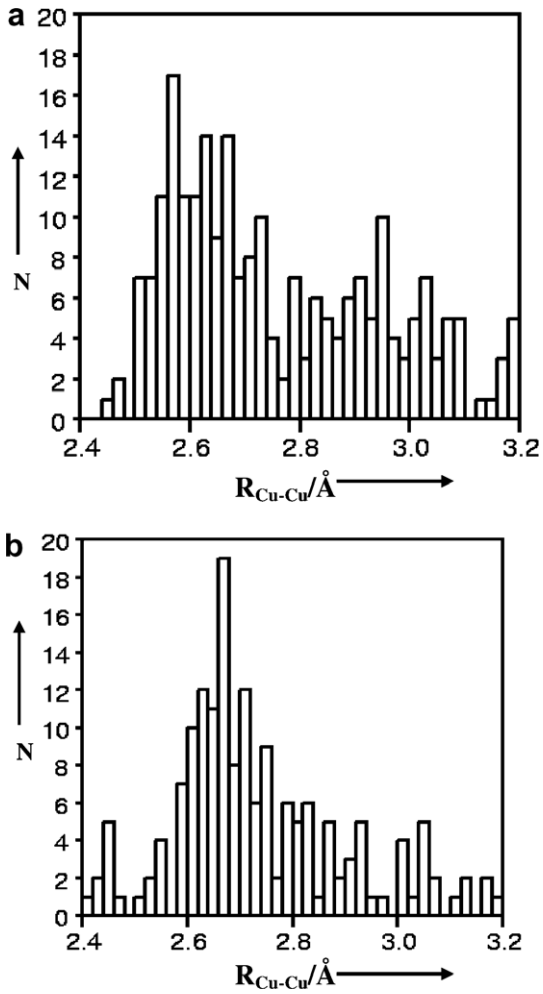


Fig. 5. Histograms of Cu–Cu distances in (a) CuL_3 and CuL_4 and (b) CuL_2 and CuL_3 complexes.

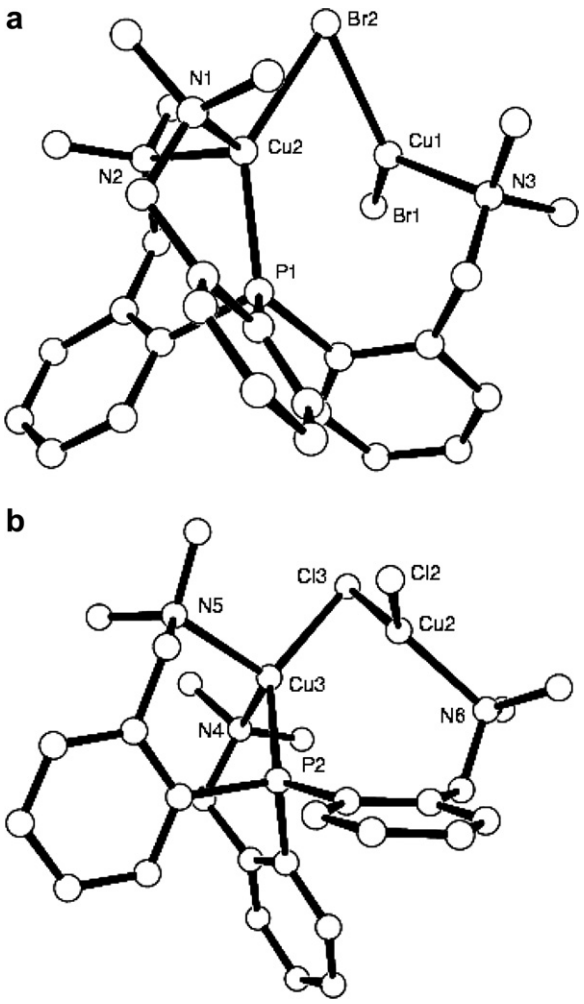


Fig. 6. Two unsymmetrical copper(I) dimers in wireframe style with refcodes: (a) CAGBIW and (b) ODODAM.

Among the complexes short listed from the CSD search, two complexes closely related to **3** and **4** were encountered with CCDC refcodes CAGBIW [18] and ODODAM [19] (Fig. 6(a) and (b)). These two structures have very similar coordination environments to those observed in the present study. The former has one copper having a coordination number of four with one bromide, two nitrogen atoms and one phosphorus bound to it. The three coordinate copper has two bromides (one terminal and one bridging) and one nitrogen in its coordination sphere. Similarly the latter structure has the three coordinate copper with two chlorides, one nitrogen and the four coordinate copper with one chloride, two nitrogen atoms and one phosphorus. The Cu–Cu distances are 2.658 and 2.665 Å respectively. These two examples again augment the fact that complexes that have Cu–Cu distances within the sum of the Van der Waal's radii of two copper centers tend to be unsymmetrically coordinated. A survey of short metal–metal contacts in systems with incomplete d shells, invariably reflected lesser preference for forming unsymmetrical dimers in comparison with the formation of symmetrical structures.

3. Conclusions

As expected for the short bite dppa as well as dppipa ligands, dinuclear copper(I) complexes formed have two copper(I) centers close to each other. In the absence of significant π-acceptor character in the ligand, such a short Cu–Cu distance is clearly repulsive and is forced by the ligand. Due to the plasticity of the coordination sphere in monovalent group 11 complexes, a change in the coordination number is energetically accessible. Hence, the coordination environment around only one of the copper(I) ions is altered to give a 4 coordinate–3 coordinate system. The four coordinate copper(I) can act as an electron donor and pump some electron density into a coordinatively unsaturated three coordinate copper. Computational work to justify this statement is underway. A CSD analysis reveals more frequent occurrence of unsymmetrical coordination in complexes with short contacts. Four complexes investigated in the present study along with two of the closely related copper(I) dimers with ((dimethylaminomethyl)phenyl)phosphine-*N*,*N*′,*N*″,*P* ligand and analogous

hexafluorophosphate copper(I) dppa dimers reinforce the importance of unsymmetrical coordination in relieving the repulsion between two closed shells. In spite of closed shell repulsions, a close contact results because the resourceful copper(I) adopts unsymmetrical coordination!

4. Experimental

4.1. General remarks

Dichloromethane, diethyl ether, acetonitrile, petroleum ether (b.p. 60–80 °C) and benzene (Caution: benzene is carcinogenic and should be handled with extreme caution!) were purified and dried under nitrogen atmosphere by conventional methods [20]. Bis(diphenylphosphino)amine [21] and bis(diphenylphosphino)isopropylamine [22] were synthesized using existing procedures and were further purified using column chromatography. $[Cu(CH_3CN)_4]ClO_4$ [23], $[Cu(CH_3CN)_4]BF_4$ [24], CuCl [25] and CuBr [26] were prepared by reported methods. All manipulations were carried out under an atmosphere of purified N_2 using a standard double manifold and Schlenk ware.

4.2. Physical measurements

^1H NMR spectra were recorded either on a Bruker ACF 200 MHz or AMX 400 MHz spectrometer with tetramethylsilane (TMS) as the internal reference. $^{31}P\{^1H\}$ NMR spectra were recorded either on a Bruker AMX 400 MHz spectrometer operating at 162.2 MHz or a Bruker ACF 200 MHz operating at 81.1 MHz with H_3PO_4 (85%) as the external reference. IR spectra were recorded in the solid state as KBr pellets on an Equinox 55 Bruker spectrometer. Elemental analyses were recorded with a Carlo Erba Elemental Analyzer model 1106 and HRESMS on Micromass Q-Tof micro. The conductivity measurements were carried out with a Control Dynamics Conductivity Meter with KCl (10^{-3} M) used as a standard solution.

4.3. Synthesis of complexes

Complex **1**: dppa (0.19 g, 0.5 mmol) was added to 15 ml CH_2Cl_2 containing $[Cu(CH_3CN)_4]ClO_4$ (0.16 g, 0.5 mmol) and stirred for 1 h at room temperature. Subsequently the solution was concentrated to about 7 and 15 ml of diethyl ether was allowed to diffuse through the solution to obtain colorless crystals (yield: 86%). ^1H NMR ($CDCl_3$, 25 °C): $\delta = 1.98$ (s, 3H, CH_3CN), 4.13 (s, 2H, NH), 7.12–7.43 (m, 40H, Ph); $^{31}P\{^1H\}$ NMR ($CDCl_3$): $\delta = 46.3$ (s); IR (KBr, cm^{-1}): 2303 (w), 2270 (w) (CH_3CN); 1099 (vs, br) 1064 (br) (ClO_4^-). Elemental *Anal.* Calc. for $Cu_2C_{50}H_{45}N_3P_4Cl_2O_8 \cdot H_2O \cdot CH_2Cl_2$: C, 49.15; H, 3.74; N, 3.16. Found: C, 49.3; H, 3.95; N, 3.38%.

Complex **2**: A similar procedure was adopted except that $[Cu(CH_3CN)_4]BF_4$ (0.15 g, 0.5 mmol) was used for the reaction which afforded colorless crystals (yield: 88%). ^1H NMR ($CDCl_3$, 25 °C): $\delta = 1.98$ (s, 9H, CH_3CN), 4.63 (s, 2H, NH), 7.12–7.45 (m, 40H, Ph). $^{31}P\{^1H\}$ NMR ($CDCl_3$): $\delta = 47.8$ (s). IR (KBr, cm^{-1}): 2303 (w), 2264 (w) (CH_3CN); 1102, 1052 (vs, br) (BF_4^-). HRESMS: $[M-(CH_3CN)_3]^{2+}$ obsd. m/z 448.0487, calc. for $C_{48}H_{42}N_2P_4$ 448.0445.

Complex **3**: To 15 ml of CH_2Cl_2 was added dppipa (0.22 g, 0.50 mmol) followed by the addition of CuCl (0.025 g, 0.25 mmol). The reaction was stirred at room temperature for half an hour. Subsequently the obtained yellow colored solution was concentrated to 2 ml and about 7 ml of petroleum ether was allowed to diffuse through the dichloromethane solution. Bright yellow colored shaped crystal were obtained in about 10–12 h (yield: 91%). ^1H NMR ($CDCl_3$, 25 °C): $\delta = 0.06$, 0.50 (d, 6H, Me of ^{i}Pr) (1:1), 3.57 (sep., 2H, br, –CH of ^{i}Pr), 6.98–7.49 (m, 40H, Ph). $^{31}P\{^1H\}$ NMR: $\delta = 77.1$ (w), 55.9 (s). Elemental *Anal.* Calc. for $Cu_2C_{54}H_{54}N_2P_4Cl_2 \cdot 0.5CH_2Cl_20.5H_2O$: C, 59.26; H, 5.07; N, 2.54. Found: C, 59.28; H, 5.06; N, 2.53%.

Complex **4**: A similar procedure was adopted except that CuBr (0.036 g, 0.25 mmol) was used for the reaction that gave bright yellow single crystals (yield: 91%). ^1H NMR ($CDCl_3$, 25 °C): $\delta = 0.05$, 0.44 (d, 6H, Me of ^{i}Pr) (1:1), 3.54 (sep., 2H, br, –CH of ^{i}Pr), 6.97–7.51 (m, 40H, Ph). $^{31}P\{^1H\}$ NMR: $\delta = 77.1$ (w), 55.9 (s). Elemental *Anal.* Calc. for $Cu_2C_{54}H_{54}N_2P_4Br_2 \cdot CH_2Cl_2$: C, 53.84; H, 4.57; N, 2.28. Found: C, 53.78; H, 4.69; N, 2.20%.

4.4. X-ray crystallographic study

Single crystals of complex **1**, **3** and **4** were mounted in a Lindemann capillary with paraffin oil and crystal of complex **2** was glued to the tip of a glass fiber along the largest dimension and coated with paraffin oil. Data were collected on a Bruker AXS single crystal diffractometer equipped with SMART APEX CCD detector and a sealed Mo Kα source working at 1.75 kW. Intensity data were collected at room temperature. Crystallographic computations were performed using the WINGX package [27]. The data were corrected for Lorentz and polarization effects. Absorption correction was applied using Psi-Scan [28] for complex **1**, **3** and **4** and SADABS [29] for complex **2**. The positions of heavy atoms were determined by SHELXS86 [30]. The remaining atoms were located from the difference Fourier map using SHELXL-97 [31]. Hydrogen atoms were geometrically fixed for all four complexes.

Single crystal structure of complex **1** ($C_{51}H_{49}Cl_4Cu_2N_3O_9P_4$): ($0.42 \times 0.40 \times 0.38$ mm^3); triclinic; $P\bar{1}$; $a = 11.0536(16)$ Å, $b = 12.3546(18)$ Å, $c = 22.106(3)$ Å, $\alpha = 78.332(3)°$, $\beta = 84.031(2)°$, $\gamma = 68.189(2)°$; $V = 2743.5(7)$ Å^3; $Z = 2$; $\rho_{calc.} = 1.502$ Mg/m^3; $\mu_{calc.} = 1.143$ mm^{-1}; $R = 0.0594$ for 10753 independent reflections with ($I > 2\sigma(I)$).

Complex **2**: $C_{54}H_{51}B_2Cu_2F_8N_5P_4$: ($0.36 \times 0.32 \times 0.20$ mm^3); triclinic; $P\bar{1}$; $a = 11.169(3)$ Å, $b = 12.349(4)$ Å, $c = 22.083(7)$ Å, $\alpha = 94.374(5)°$, $\beta = 95.555(5)°$, $\gamma = 106.850(4)°$; $Z = 2$; $\rho_{calc.} = 1.376$ Mg/m^3; $\mu_{calc.} = 0.914$ mm^{-1}; $R = 0.0519$ for 13298 independent reflections ($I > 2\sigma(I)$).

Complex **3**: $C_{55}H_{56}Cl_4Cu_2N_2P_4$: ($0.45 \times 0.4 \times 0.38$ mm^3); monoclinic; $P21/c$; $a = 21.042(10)$ Å, $b = 13.733(7)$ Å, $c = 20.649(10)$ Å, $\alpha = 90°$, $\beta = 114.365(8)°$, $\gamma = 90°$; $V = 5435(5)$ Å^3; $Z = 4$; $\rho_{calc.} = 1.390$ Mg/m^3; $\mu_{calc.} = 1.135$ mm^{-1}; $R = 0.0502$ for 12748 independent reflections with ($I > 2\sigma(I)$).

Complex **4**: $C_{55}H_{56}Br_2Cl_2Cu_2N_2P_4$: ($0.24 \times 0.22 \times 0.21$ mm^3); monoclinic; $P21/c$; $a = 21.287(3)$ Å, $b = 13.678(2)$ Å, $c = 20.660(3)$ Å, $\alpha = 90°$, $\beta = 114.071$ (2)°, $\gamma = 90°$; $V = 5492.5(15)$ Å^3; $Z = 4$; $\rho_{calc.} = 1.483$ Mg/m^3; $\mu_{calc.} = 2.481$ mm^{-1}; $R = 0.0545$ for 13015 independent reflections with ($I > 2\sigma(I)$).

Acknowledgements

We acknowledge the financial support of CSIR, New Delhi, DST for CCD facility, Bioinformatics, IISc for the CSD and Prof. Dr. Frenking and Dr. Sivasankar for useful discussions.

Appendix A. Supplementary material

CCDC-200619, CCDC-200620, CCDC-191476, CCDC-247449 contain the supplementary crystallographic data for **1**, **2**, **3** and **4**. These data can be obtained free of charge via www.ccdc.cam.ac.uk/conts/retrieving.html (or from the Cambridge Crystallographic Data Center, 12 Union Road, Cambridge CB2 1EZ, UK; fax (+44) 1223 336 033; or e-mail: deposit@ccdc.cam.ac.uk).

Weak hydrogen bonding interactions of ClO_4^- and BF_4^- ions in complex **1** and **2**, list of "refcodes" having Cu–Cu distances (<2.8 Å) with unsymmetrical coordination, histogram of short contacts in CuL_2 and CuL_4, and references dealing with apparent "cuprophilic" interactions. Supplementary data associated with this article can be found, in the online version, at doi:10.1016/j.poly.2006.08.004.

References

[1] P. Pyykkö, Chem. Rev. 97 (1997) 597.
[2] M. Jansen, Angew. Chem. 99 (1987) 1136.
[3] H. Schmidbaur, Gold Bull. 23 (1990) 11.
[4] P. Pyykkö, Y.-F. Zhao, Angew. Chem., Int. Ed. Engl. 30 (1991) 604.
[5] P. Pyykkö, J. Li, Chem. Phys. Lett. 197 (1992) 586.
[6] P. Pyykkö, J. Li, Inorg. Chem. 32 (1993) 2630.
[7] O.D. Häberlen, H. Schmidbaur, N. Rosch, J. Am. Chem. Soc. 116 (1994) 8241.
[8] P. Pyykkö, Chem. Rev. 88 (1988) 563.
[9] M.A. Omary, R.R. Webb, Z. Assefa, G.E. Shankle, H.H. Patterson, Inorg. Chem. 37 (1998) 1380.
[10] L.M. Engelhardt, G.E. Jacobsen, W.C. Patalinghug, B.W. Skelton, C.L. Raston, A.H. White, J. Chem. Soc., Dalton Trans. (1991) 2859.
[11] J. Beck, J. Strähle, Angew. Chem., Int. Ed. Engl. 24 (1985) 409.
[12] K.M. Merz Jr., R. Hoffmann, Inorg. Chem. 27 (1988) 2120.
[13] J.T. Mague, J. Cluster Sci. 6 (1995) 217.
[14] F.H. Allen, O. Kennard, Chem. Des. Autom. News. 8 (1993) 31.
[15] H. Liu, M.J. Calhorda, M.G.B. Drew, V. Félix, J. Novosad, L.F. Verios, F.F. de Biani, P. Zanello, J. Chem. Soc., Dalton Trans. (2002) 4365.
[16] J.K. Bera, M. Nethaji, A.G. Samuelson, Inorg. Chem. 38 (1999) 218.
[17] W.J. Geary, Coord. Chem. Rev. 7 (1971) 81.
[18] H. Lang, M. Leschke, H.A. Mayer, M. Melter, C. Weber, G. Rheinwald, O. Walter, G. Huttner, Inorg. Chim. Acta 324 (2001) 266.
[19] M. Leschke, H. Lang, M. Melter, G. Rheinwald, C. Weber, H.A. Mayer, H. Pritzkow, L. Zsolnai, A. Driess, G. Huttner, Z. Anorg. Allg. Chem. 628 (2002) 349.
[20] D.D. Perin, W.L.F. Armarego, Purification of Laboratory Reagents, 3rd ed., Pergamon Press, London, 1988.
[21] V.H. Nöth, L. Meinel, Z. Anorg. Allg. Chem. 5–6 (1967) 225.
[22] M.S. Balakrishna, T.K. Prakasha, S.S. Krishnamurthy, U. Siriwardane, S.N.J. Hosmane, Organomet. Chem. 390 (1990) 203.
[23] B.J. Hathaway, D.G. Holah, J.D. Postlethwaite, J. Chem. Soc. (1961) 3215.
[24] G.J. Kubas, Inorg. Synth. 19 (1979) 90, and references therein.
[25] R.N. Keller, H.D. Wycoff, Inorg. Synth. 50 (1946) 1.
[26] R.N. Keller, H.D. Wycoff, Inorg. Synth. 50 (1946) 3.
[27] L.J. Farrugia, G.X. Win, J. Appl. Crystallogr. 32 (1999) 837.
[28] A.C.T. North, D.C. Phillips, F.S. Mathews, Acta Crystallogr. Sect. A 24 (1968) 351.
[29] R.H. Blessing, Acta Crystallogr. Sect. A 51 (1995) 33.
[30] G.M. Sheldrick, SHELXS-86, Program for Crystal Structure Determination, University of Cambridge, Cambridge, England, 1986.
[31] G.M. Sheldrick, SHELXL-97, Program for Crystal Structure Refinement, University of Göttingen, Germany, 1997.

Available online at www.sciencedirect.com
ScienceDirect
Polyhedron 26 (2007) 149–153
POLYHEDRON
www.elsevier.com/locate/poly

CuO micro plates from a 3D metallo-organic framework (MOF) of a binary copper(II) complex of *N*,*N*-bis(2-hydroxyethyl)glycine

Harjyoti Thakuria, Gopal Das *

Department of Chemistry, Indian Institute of Technology Guwahati, Guwahati 781039, Assam, India

Received 25 May 2006; accepted 4 August 2006
Available online 18 August 2006

Abstract

The crystal structure of $[Cu(Bic)_2]$ (**1**) ($Bic^- = N,N$-bis(2-hydroxyethyl)glycinate), was determined by single-crystal X-ray diffraction techniques. $[Cu(Bic)_2]$: monoclinic system, space group $P21/n$. In the complex, the copper atom is tetra coordinated by two oxygen atoms of the carboxylato groups and two nitrogen atoms of the bicinate ligand, forming a distorted square planar coordination geometry. The molecular structure of the complex in solution is the same as that of the crystalline state, as supported by ESR and electronic spectra in solution. The blue complex **1** on heating at ~500 °C for 6 h results in the formation of black CuO (Tenorite) micro plates.
© 2006 Elsevier Ltd. All rights reserved.

Keywords: Copper complexes; Bicine; Metallo-organic framework; CuO micro plates

1. Introduction

Formation of metal-organic framework (MOF) structures [1] is an active area of research, as these compounds can be potentially useful in several applications [2]. In constructing MOFs, carboxylate ligands are usually selected because they may act as both counteranions and bridging ligands to extend the architecture to 1-D chain, 2-D layer and 3-D network [3].

N,*N*-bis(2-hydroxyethyl)glycine (Bicine) is popularly known as a buffer substance through the work of Good et al., after being prepared by Kiprianov in 1926 [4]. The metal ion coordinating properties of the anion of bicine, i.e. bicinate ($Bicy^-$), having two hydroxyl oxygen atoms, one carboxyl oxygen atom and one nitrogen atom, have long been recognized. Bicinate act as a tetradentate ligand. Indeed, many stability constants of binary complexes have been determined [5,6]. However, no such binary metal complex of bicinate in the solid state has been studied yet to best of our knowledge. For constructing open frameworks, a tripodal ligand bearing one carboxylate group and two alcohol groups from the bridgehead tertiary amine nitrogen has been used (Bicine).

In this work, the binary complex $[Cu(Bic)_2]$ is prepared and characterized by X-ray single crystal structural analysis. The tetra-coordinate distorted square-planer structure for this copper(II) complex is studied in detail. Formation of micro plates CuO from this metallocycle has been studied with SEM, powder X-ray diffraction.

2. Experimental

2.1. Chemicals and reagents

$Cu(OH)_2$ was freshly prepared from $CuCl_2$. The metal salt and Bicine were obtained from Aldrich and were used as received. The solvents were purified prior to use by standard procedures.

2.2. Physical measurements

The IR spectra were recorded on a Perkin Elmer-Spectrum One FT-IR spectrometer with KBr disks in the range 4000–400 cm^{-1}. The thermogravimetric analyses (TGA) of the compounds were performed by using an

* Corresponding author. Tel.: +91 361 2582313; fax: +91 361 2582349.
E-mail address: gdas@iitg.ernet.in (G. Das).

0277-5387/$ - see front matter © 2006 Elsevier Ltd. All rights reserved.
doi:10.1016/j.poly.2006.08.012

SDTA 851 e TGA thermal analyzer (Mettler Toledo) with a heating rate of 2 °C per min in a N_2 atmosphere. Scanning electron micrograph (SEM) images were obtained by means of a *LEO-1430 VP* electron microscope on samples glued on an aluminum stub and gold sputtered. PXRD data were recorded with Seifert powder X-ray diffractometer (XRD 3003TT) with Cu Kα source ($\lambda = 1.54$ Å) on glass surface of an air-dried sample. X-band EPR spectra were recorded with a Jeol JES-FA series EPR spectrometer equipped with a dual cavity and operating at X-band with 100 kHz modulation frequency. TCNE ($g = 2.0028$) was used as the field marker. Optical spectra were recorded in CH_3CN on a Perkin–Elmer-Lambda 25-UV–Visible spectrometer at 298 K. The solid-state magnetic susceptibility of the complex at room temperature was recorded using a Sherwood Scientific balance MSB-1. Solution electrical conductivity measurements were made with a Systronics Conductivity meter 306. Elemental analyses were done using a Carlo Erba 1108 and also by using a Perkin–Elmer series II 2400 instrument.

2.3. Preparation of the title complex, 1

A mixture of bicine (0.326 g, 2 mmol) and freshly prepared copper hydroxide (1 mmol, 0.097 g) were ground thoroughly with a pestle in an open mortar at room temperature in air. The mixture was ground occasionally for 30 min until the mixture turned into a melt. X-ray quality blue single crystals of the Cu(II) complex (**1**) were grown from ethanol/water (1:1) mixture within two days at room temperature in quantitative yield. *Anal*. Calc. for $Cu(C_6H_{12}NO_4)_2$: C, 37.15; H, 6.23; N, 7.22. Found: C, 37.74; H, 6.41; N, 7.36%.

2.4. X-ray crystallography

The intensity data for **1** were collected using a Bruker SMART APEX-II CCD diffracto-meter, equipped with fine focus 1.75 kW sealed tube Mo Kα radiation ($\lambda = 0.71073$ Å) at 273(3) K, with increasing ω (width of 0.3° per frame) at a scan speed of 3 s/frame. SMART software was used for data acquisition and SAINT software for data extraction. Absorption corrections were done using SDABS. The structure was solved and refined using SHELX 97. All non-hydrogen atoms were refined anisotropically. The hydrogen atoms were located from the difference Fourier maps and refined. Selected crystallographic data are summarized in Table 1.

Table 1
Crystal data of complex **1**

Compound	**1**
CCDC No.	607756
Empirical formula	$C_{12}H_{24}N_2O_8Cu$
F_w	387.87
Temperature (K)	298(2)
Radiation	Mo Kα
Wavelength (Å)	0.71073
Size (mm)	$0.20 \times 0.15 \times 0.11$
Crystal system	monoclinic
Space group	$P2(1)/c$
a (Å)	9.5164(8)
b (Å)	12.3042(11)
c (Å)	7.1922(6)
α (°)	90.00
β (°)	111.328(5)
γ (°)	90.00
V (Å^3)	784.47(12)
Z	2
ρ_{calc} (Mg/m^3)	1.625
μ	1.435
$F(000)$	398
Refinement method	[a]
Goodness-of-fit	1.205
Final R indices [$I > 2\sigma(I)$]	$R_1 = 0.0461$
	$wR_2 = 0.1459$
R indices (all data)	$R_1 = 0.0575$
	$wR_2 = 0.1639$

[a] Full-matrix least-squares on F^2.

3. Results and discussion

The complex **1** was synthesized using a simple acid–base reaction in the solid phase and blue crystals were obtained from an ethanol/water (1:1) mixture. The structure of the title compound was determined by single-crystal X-ray crystallography. The structure is best described as a 3-D framework of $[Cu(Bic)_2]_n$. Selected bond lengths and angles are collected in Table 2.

The molecular structure, with the atomic numbering scheme, of complex **1** is shown in Fig. 1. In complex **1** the Cu(II) atom is in an N_2O_2 coordination environment. It is ligated by four atoms: two carboxylato oxygen atoms and two bridge head tertiary amine nitrogen atoms of bicinate.

The carboxylato oxygen atoms bond more strongly with the copper atom than the bridge head tertiary amine nitrogen atoms. The complex has two five-membered N,O-chelate rings which consist of one copper atom, one carboxylato oxygen atom, one nitrogen atom and two carbon atoms. Bond angles and distances of the mononuclear complex indicate a slightly distorted square-planar coordination with a *trans*-structure. The bond distances and bond angles involving the metal ions (Table 2) are within normal statistical errors [7,8]. The shortening of the Cu–O bond lengths agree with the stronger chelating ability of the carboxylate oxygen compared to tertiary amine nitrogen atoms. All the coordination atoms and the Cu atom lie

Table 2
Selected bond lengths (Å) and angles (°) of **1**

Cu(1)–O(1)#1	1.947(2)	Cu(1)–N(1)#1	2.057(3)
Cu(1)–O(1)	1.948(2)	Cu(1)–N(1)	2.057(3)
O(1)#1–Cu(1)–O(1)	180.0	N(1)#1–Cu(1)–N(1)	180.0
O(1)#1–Cu(1)–N(1)#1	85.56(9)	O(1)#1–Cu(1)–N(1)	94.44(9)
O(1)–Cu(1)–N(1)#1	94.44(9)	O(1)–Cu(1)–N(1)	85.56(9)

Symmetry transformations used to generate equivalent atoms: #1 $-x$, $y + 1/2$, $-z + 1/2$; #2 $-x$, $-y$, $-z$; #3 x, $-y - 1/2$, $z - 1/2$.

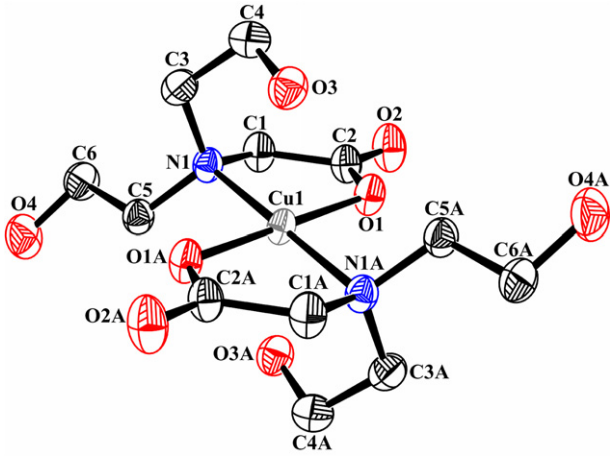


Fig. 1. Coordination environment of **1**. All hydrogen atoms are omitted for clarity.

Table 3
Non-bonding distances (Å) and angles (°) of **1**

D–H···A	H···A (Å)	D···A	∠D–H···A (°)
O3–H3···O1	2.668	3.488	150.31
O3–H3···O2	1.864	2.711	153.82
O4–H4···O2	1.907	2.726	176.71
C1–H1B···O4	2.454	3.415	170.90
C4–H4A···O3	2.565	3.356	138.74
C6–H6a···O4	2.578	3.543	173.28

exactly on the N_2O_2 mean plane. There is no deviation of the donor atoms from the basal plane. This is consistent with a square planar structure of the metal centre. The conventional strong O–H···O and unconventional weaker C–HO type intermolecular hydrogen bonding plays a major role in stabilizing the molecules in the solid state (Table 3). It forms a linear array along the *c*-axis via C–H···O type interactions involving the alcohol group (O3) nearer to the Cu atom. Each of the parallel linear arrays propagates along the *a*-axis to form a 2D network via O–H···O type interactions (see supporting information).

The overall structure looks like (Fig. 2) an array of metallocycles joined via carboxylate groups of the podand extending along the crystallographic *ab*-plane in a zig-zag fashion. In the metallocyclic units, the two Cu(II) ions show a distance of either 7.126 or 9.516 Å while the distance between the bridgehead N atoms is 6.726 Å, forming an oval-shaped cavity.

The Cu(II) complex in acetonitrile solution shows a d–d band in the region 21 881 cm^{-1} due to a $^2B_{1g} \rightarrow {}^2A_{1g}$ transition which supports the square-planar geometry. The magnetic moment of the Cu(II) complex is 1.51 BM which shows the presence of one unpaired electron. This value is lower than the spin-only value and is due to mixing of orbital angular momentum from an excited state via spin-orbit coupling. The FT-IR spectrum of the complex shows two strong and sharp bands at 3310 cm^{-1} and 3140 cm^{-1} due to O–H and N–H stretching vibrations [9]. The bands at

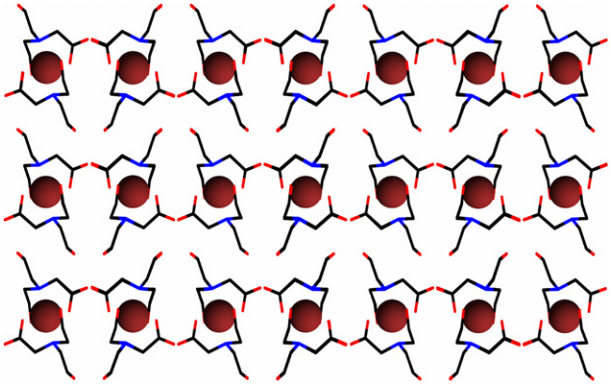


Fig. 2. Perspective view of the metallo-macrocyle in **1**, viewed along the *c*-axis.

1610 and 1405 cm^{-1} are attributed to the COO^- antisymmetric and symmetric stretching vibrations, respectively, which is confirmed by the crystal structural analysis; the carboxylato oxygen atom O(2) forms two hydrogen bonds with the hydroxyl hydrogen atoms of the neighboring units. Several new peaks appeared in the NIR region, which were absent in the ligand spectrum. The bands at 382 cm^{-1} and 318 cm^{-1} are assigned to the Cu–N and Cu–O stretching vibrations respectively. The molar conductivity measurements supported the non-electrolytic nature of complex **1**. EPR spectra of complex **1** were recorded in DMSO at 300 and 77 K. The spectrum of complex **1** at 300 K shows one intense absorption band in the high field region and is isotropic due to the tumbling motion of the molecules. However, this complex in the frozen state at 77 K shows four well-resolved peaks of low intensities in the low-field region and one intense peak in the high-field region. No band corresponding to the $Ms = \pm 2$ transition was observed in the spectrum, ruling out any Cu–Cu interactions, in the solution state. In square-planar complexes unpaired electrons lying in the $d_{x^2-y^2}$ orbital give $^2B_{1g}$ as the ground state with $g_{\|} > g_{\perp}$ while an unpaired electron lying in the d_{z^2} orbital gives $^2A_{1g}$ as the ground state with $g_{\perp} > g_{\|}$. The experimental values, $g_{\|}$ (2.341) > $g_{\perp}$ (2.041), indicates that the structure of the complex is square-planar and that the unpaired electron is predominantly in the $d_{x^2-y^2}$ orbital. The coordination in solution is thus the same as in the solid.

The PXRD patterns also confirm the crystalline nature of the complex. The macroscopic crystal shape and color of **1** remain unchanged after heating the crystals at 100 ± 1 °C for 3 h at atmospheric pressure. New powder X-ray data are collected every hour after the heat treatment. The PXRD data reveal that the crystalline nature of the complex framework is retained.

The robustness of the framework is reflected in the thermogravimetric analysis of **1** which shows negligible weight loss until about 140 °C. The sample decomposed in a number of steps. Two molecules of CO_2 were released in two well separated steps from coordinated carboxylic acid groups (150–168 °C; Δm = 11.34% calc.; 12.01% found; 176–205 °C; Δm = 12.79% calc.; 13.19% found), which is

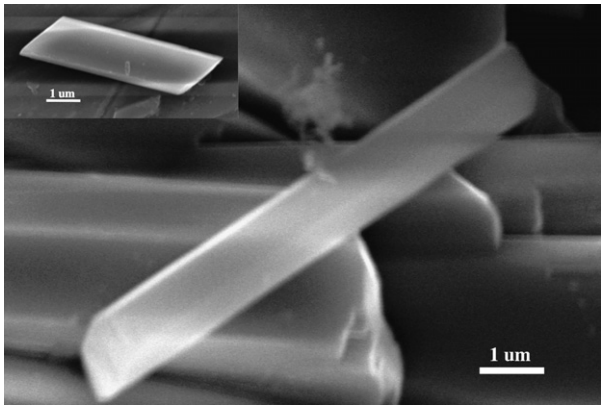


Fig. 3. Scanning electron micrograph of CuO after thermolysis of **1** at 500 °C (6 h).

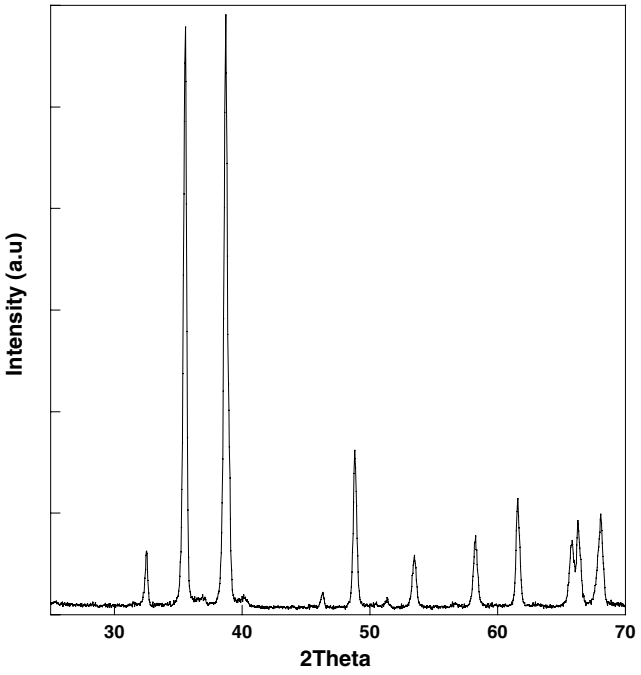


Fig. 4. Powder XRD pattern of CuO (tenorite) micro plates.

in good agreement with the X-ray crystal structure. Complete decomposition occurred at ~ 370 °C resulting in the formation of black CuO. The DSC-plot shows two exothermic peaks at 160 °C and 190 °C due to the loss of CO_2 molecules. It also shows an exothermic peak at 370 °C due to the decomposition of the complex.

Thermal decomposition of the blue colored complex **1** was carried out at 500 °C for 6 h in a muffle furnace. The reaction product, black colored copper(II) oxide, was obtained in micro-plates morphology (Fig. 3). The length and breadth of these plates range from 3 to 12 μm and 0.5 to 3 μm respectively. The average size and shape of these plates remains unchanged with longer reaction time, up to 14 h. SEM images taken of several batches of samples showed that the entire surface of the plates are clean without any fracture.

The crystallinity of these micro plates was analyzed by powder X-ray diffraction techniques. The diffraction peaks (Fig. 4) can be indexed as the Tenorite structure of CuO mineral (PDF No. 00-005-0661), indicating that the Cu(II)–bicine complex has been thermally decomposed into CuO.

X-ray diffraction pattern shows two enhanced (−111) and (111) peaks at 2θ values 35.554 and 38.731, resulting from the linear orientation of the micro plates.

4. Conclusion

We were able to synthesize and structurally characterize a binary Cu(II)–bicine complex of distorted square planar geometry. This geometry is retained in the solution too. It forms a 3D MOF made of an infinite array of Cu(II)-metallocycles in the solid state. We have also demonstrated a precursor synthesis of the Tenorite structure of CuO micro plates. The technique demonstrated here can be extended for synthesizing a wide range of inorganic materials having similar structures, which are currently ongoing in our laboratory.

Acknowledgements

The financial support from the Council of Scientific and Industrial Research (CSIR) of India to GD and HT (Grant no. 01(1948)/04/EMR-II) is gratefully acknowledged. We thank the Central Instrument Facility, Centre for Nanotechnology and Department of Chemistry IIT Guwahati for SEM, powder XRD and single crystal XRD measurements.

Appendix A. Supplementary data

Crystallographic data are available from the CCDC, 12 Union Road, Cambridge CB2 1EZ, UK on request, CCDC No. 607756. IR, TGA and X-ray powder diffraction patterns of complex **1** and the CuO, and data associated with this article can be found in the supplementary data. Supplementary data associated with this article can be found, in the online version, at doi:10.1016/j.poly.2006.08.012.

References

[1] (a) M. Eddaoudi, J. Kim, N. Rosi, D. Vodak, J. Wachter, M. O_Keeffee, O.M. Yaghi, Science 295 (2002) 469;
(b) R. Kitaura, K. Seki, G. Akiyama, S. Kitagawa, Angew. Chem., Int. Ed. 42 (2003) 428;
(c) B. Moulton, M.J. Zaworotko, Chem. Rev. 101 (2001) 1629.
[2] (a) J.S. Seo, D. Whang, H. Lee, S.I. Jun, J. Oh, Y. Jin, Y.J. Jeon, K. Kim, Nature 404 (2000) 982;
(b) F. Millange, C. Serre, G. Ferey, Chem. Commun. (2002) 822.
[3] (a) X.M. Zhang, M.L. Tong, M.L. Gong, X.M. Chen, Eur. J. Inorg. Chem. (2003) 138;
(b) H.X. Zhang, B.S. Kang, A.W. Xu, Z.N. Chen, Z.Y. Zhou, A.S.C. Chan, K.B. Yu, C. Ren, J. Chem. Soc., Dalton Trans. (2001) 2559;
(c) P. Ayyappan, O.R. Evans, W.B. Lin, Inorg. Chem. 40 (2001) 4627.

[4] N.E. Good, G.D. Winget, W. Winter, T.N. Connolly, S. Izawa, R.M.M. Singh, Biochemistry 5 (1966) 467.
[5] C.R. Krishnamoorthy, R. Nakon, J. Coord. Chem. 23 (1991) 233.
[6] H. Sigel, Coord. Chem. Rev. 122 (1993) 227.
[7] A.J. Hanss, A. Beckmann, H.-J. Kruger, Eur. J. Inorg. Chem. (1999) 163.
[8] B L.F. Szczepura, J.G. Muller, C.A. Bessel, R.F. See, T.S. Janik, M.R. Churchill, K.J. Takeuchi, Inorg. Chem. 31 (1992) 859.
[9] M.R. Ullah, P.K. Bhattachaya, Indian J. Chem. 30A (1991) 976.

Available online at www.sciencedirect.com
ScienceDirect
Polyhedron 26 (2007) 154–162
POLYHEDRON
www.elsevier.com/locate/poly

Synthesis, spectral characterization, properties and structures of copper(I) complexes containing novel bidentate iminopyridine ligands

Saeed Dehghanpour [a,*], Nouri Bouslimani [b], Richard Welter [b], Fresia Mojahed [c]

[a] Department of Chemistry, Alzahra University, P.O. Box 1993891176, Tehran, Iran
[b] Laboratoire DECOMET, LC003 7177 CNRS-ULP, Louis Pasteur University, Strasbourg I, F-67070 Strasbourg Cedex, France
[c] Department of Chemistry, Faculty of Science, Tarbiat Modares University, P.O. Box 14115-175, Tehran, Iran

Received 4 July 2006; accepted 7 August 2006
Available online 18 August 2006

Abstract

Four new ligands, (4-methyl-phenyl)-pyridin-2-ylmethylene-amine (A), (2,3-dimethyl-phenyl)-pyridin-2-ylmethylene-amine (B), (2,4-dimethyl-phenyl)-pyridin-2-ylmethylene-amine (C) and (2,5-dimethyl-phenyl)-pyridin-2-ylmethylene-amine (D), and their corresponding copper(I) complexes, $[Cu(A)_2]ClO_4$ (**1a**), $[Cu(B)_2]ClO_4$ (**1b**), $[Cu(C)_2]ClO_4$ (**1c**), $[Cu(D)_2]ClO_4$ (**1d**), $[Cu(A)(PPh_3)_2]ClO_4$ (**2a**), $[Cu(B)(PPh_3)_2]ClO_4$ (**2b**), $[Cu(C)(PPh_3)_2]ClO_4$ (**2c**) and $[Cu(D)(PPh_3)_2]ClO_4$ (**2d**), have been synthesized and characterized by CHN analyses, ^1H and ^{13}C NMR, IR and UV–Vis spectroscopy. The crystal structures of $[Cu(B)_2]ClO_4$ (**1b**), $[Cu(C)_2]ClO_4$ (**1c**) and $[Cu(A)(PPh_3)_2]ClO_4 \cdot 1/2CH_3CN$ (**2a**) were determined from single crystal X-ray diffraction. The coordination polyhedron about the copper(I) center in the three complexes is best described as a distorted tetrahedron. A quasireversible redox behavior is observed for the complexes.
© 2006 Elsevier Ltd. All rights reserved.

Keywords: 2-Pyridinecarbaldehyde; Diimine ligands; Copper(I) complexes; Distorted tetrahedral structure

1. Introduction

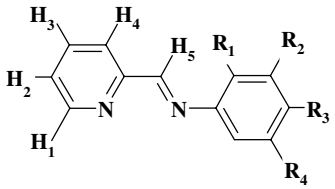
Monovalent copper (d^{10}) chemistry has drawn special attention because of its instability, unusual structural features, utility in solar energy and supramolecular devices, catalytic activity in photoredox reactions and the biological relevance of high potential copper complexes [1–8]. Most of the studies have been on four-coordinated tetrahedral Cu(I) complexes of the type $[Cu(LL)_2]^+$ or $[Cu(LL)(P)_2]^+$ where LL is a diimine and P is a phosphine, because of interdependence of their coordination geometry and their redox and photochemical behavior [9–12]. Recent reports have indicated that steric crowding and π-acidity in a well designed ligand are the most important prerequisites for the stability of copper(I) complexes and their redox, photophysical and photochemical behavior [13–16].

Although the coordination chemistry of symmetrical chelating diimines [e.g., 2,2-bipyridine, 1,10-phenanthroline and 2,9-dimethyl-1,10-phenanthroline] with copper(I) has been extensively studied [9,17–20], there are few data on complexes with unsymmetrical diimine ligands containing iminopyridine [21–26].

In a continuation of our work on the preparation of copper(I) diimine complexes with low lying MLCT transitions [27–29], here we report the synthesis and characterization of four ligands with extended conjugation, and their copper(I) complexes (Fig. 1). The structures, spectral properties and redox chemistry of these complexes are also discussed.

* Corresponding author. Tel./fax: +98 21 88041344.
E-mail address: dehghanpour_farasha@yahoo.com (S. Dehghanpour).

0277-5387/$ - see front matter © 2006 Elsevier Ltd. All rights reserved.
doi:10.1016/j.poly.2006.08.011



Ligand	R_1	R_2	R_3	R_4
A	H	H	CH_3	H
B	CH_3	CH_3	H	H
C	CH_3	H	CH_3	H
D	CH_3	H	H	CH_3

$[CuL_2]ClO_4$		$[CuL(PPh_3)_2]ClO_4$	
Complex	Ligand (L)	Complex	Ligand (L)
1a	A	**2a**	A
1b	B	**2b**	B
1c	C	**2c**	C
1d	D	**2d**	D

Fig. 1. Chemical formula of ligands (A–D), and Cu(I) complexes **1a**–**2d**.

2. Experimental

2.1. General

Caution! Perchlorate salts of metal complexes with organic ligands are potentially explosive and should be handled with care.

All chemicals used were reagent grade and used as received. Solvents used for the reactions were purified by literature methods [30]. $[Cu(CH_3CN)_4]ClO_4$ was prepared according to the literature procedure [31].

Elemental analyses were performed by using a Heraeus CHN-O-RAPID elemental analyzer. Infrared spectra were recorded on a Bruker Tensor 27 instrument. Electronic absorption spectra were recorded on a JASCO V-570 spectrophotometer; λ_{max} ($\log\varepsilon$). NMR spectra were obtained on a BRUKER AVANCE DRX500 (500 MHz) spectrometer. Proton chemical shifts are reported in part per million (ppm) relative to an internal standard of Me_4Si. All voltammograms were recorded with a three electrodes system consisting of an Ag/AgCl reference electrode, a platinum wire counter electrode, and Au as a working electrode. A Metrohm multipurpose instrument model 693 VA processor with 694A Va stand was used. In all electrochemical experiments the test solution was purged with argon gas for at least 5 min.

2.2. Synthesis

2.2.1. (4-Methyl-phenyl)-pyridin-2-ylmethylene-amine (A)

To a solution of pyridine-2-carbaldehyde (107 mg, 1 mmol) in 10 ml diethylether was added a solution of 4-methylaniline (107 mg, 1 mmol) in 10 ml diethylether and the resulting mixture was stirred for 2 h. The ligand (4-methyl-phenyl)-pyridin-2-ylmethylene-amine was obtained as a white microcrystalline precipitate. It was then filtered off, washed with cold diethylether, and dried in air. Yield: 172 mg (90%). IR (KBr): 1623 cm^{-1} ν(C=N). ^1H NMR (500 MHz, $CDCl_3$): 2.31 (s, 6H, $2CH_3$), 6.85–7.15 (m, 3H, ArH, amine ring), 7.32 (dd, 1H, $J_{H1,2} = 4.75$, $J_{H2,3} = 7.50$, H_2), 7.79 (*t*, 1H, $J_{H3,2} = 7.50$, $J_{H3,4} = 7.75$, H_3), 8.19 (d, 1H, $J_{H4,3} = 7.75$, H_4), 8.62 (s, 1H, H_5), 8.69 (d, 1H, $J_{H2,1} = 4.75$, H_1). ^{13}C {^1H} NMR (500 MHz, $CDCl_3$): 21.04 ($^{13}CH_3$), 121.12, 121.74, 124.91, 129.85, 136.54, 136.69, 148.37, 149.63, 154.77, 159.62 (^{13}C=N). *Anal.* Calc. for $C_{13}H_{12}N_2$: C, 79.56; H, 6.16; N, 14.27. Found: C, 79.55; H, 6.17; N, 14.28%.

2.2.2. (2,3-Dimethyl-phenyl)-pyridin-2-ylmethylene-amine (B)

This ligand was prepared by a procedure similar to **1** using 121 mg (1 mmol) of 2,3-dimethylaniline. Yield: 190 mg (90%). IR (KBr): 1630 cm^{-1} ν(C=N). ^1H NMR (500 MHz, $CDCl_3$): 2.31 (s, 6H, $2CH_3$), 6.85–7.15 (m, 3H, ArH, amine ring), 7.32 (dd, 1H, $J_{H1,2} = 4.12$, $J_{H2,3} = 7.30$, H_2), 7.76 (*t*, 1H, $J_{H3,2} = 7.30$, $J_{H3,4} = 7.90$, H_3), 8.24 (d, 1H, $J_{H4,3} = 7.90$, H_4), 8.50 (s, 1H, H_5), 8.68 (d, 1H, $J_{H2,1} = 4.12$, H_1). ^{13}C {^1H} NMR (500 MHz, $CDCl_3$): 13.90 (3-$^{13}CH_3$), 21.12 (2-$^{13}CH_3$), 115.43, 121.62, 124.98, 126.16, 127.98, 130.77, 136.58, 137.56, 149.56, 150.10, 155.01, 159.77 (^{13}C=N). *Anal.* Calc. for $C_{14}H_{14}N_2$: C, 79.97; H, 6.71; N, 13.32. Found: C, 79.99; H, 6.70; N, 13.35%.

2.2.3. (2,4-Dimethyl-phenyl)-pyridin-2-ylmethylene-amine (C)

This ligand was prepared by a procedure similar to **1** using 121 mg (1 mmol) of 2,4-dimethylaniline. Yield: 185 mg (88%). IR (KBr): 1629 cm^{-1} ν(C=N). ^1H NMR ($CDCl_3$; δ): 2.33 (s, 3H, 4-CH_3), 2.37 (s, 3H, 2-CH_3), 6.93–7.05 (m, 3H, ArH, amine ring), 7.33 (dd, 1H, $J_{H1,2} = 4.5$, $J_{H2,3} = 7.50$, H_2), 7.76 (*t*, 1H, $J_{H3,2} = 7.50$, $J_{H3,4} = 8.00$, H_3), 8.24 (d, 1H, $J_{H4,3} = 8.00$, H_4), 8.50 (s, 1H, H_5), 8.68 (d, 1H, $J_{H2,1} = 4.12$, H_1). ^{13}C {^1H} NMR (500 MHz, $CDCl_3$): 17.78 (4-$^{13}CH_3$), 20.96 (2-$^{13}CH_3$), 117.28, 121.54, 124.86, 127.3, 131.21, 132.49, 136.26, 136.55, 147.43, 149.53, 155.08, 159.03 (^{13}C=N). *Anal.* Calc. for $C_{14}H_{14}N_2$: C, 79.97; H, 6.71; N, 13.32. Found: C, 79.96; H, 6.70; N, 13.35%.

2.2.4. (2,5-Dimethyl-phenyl)-pyridin-2-ylmethylene-amine (D)

This ligand was prepared by a procedure similar to **1** using 121 mg (1 mmol) of 2,5-dimethylaniline. Yield:

200 mg (95%). IR (KBr): 1629 cm^{-1} ν(C=N). ^1H NMR ($CDCl_3$; δ): 2.34 (s, 3H, $2CH_3$), 6.83–7.13 (m, 3H, ArH, amine ring), 7.34 (dd, 1H, $J_{H1,2} = 4.8$, $J_{H2,3} = 7.65$, H_2), 7.79 (*t*, 1H, $J_{H3,2} = 7.65$, $J_{H3,4} = 7.90$, H_3), 8.24 (d, 1H, $J_{H4,3} = 7.90$, H_4), 8.50 (s, 1H, H_5), 8.69 (d, 1H, $J_{H2,1} = 4.80$, H_1). ^{13}C {^1H} NMR (500 MHz, $CDCl_3$): 17.70 (5-$^{13}CH_3$), 20.99 (2-$^{13}CH_3$), 118.31, 121.57, 124.97, 127.09, 129.08, 130.25, 136.35, 136.60, 149.50, 149.92, 154.91, 159.59 (^{13}C=N). *Anal.* Calc. for $C_{14}H_{14}N_2$: C, 79.97; H, 6.71; N, 13.32. Found: C, 79.96; H, 6.70; N, 13.34%.

2.2.5. *[Cu^I(A)$_2$]ClO$_4$ (**1a**)*

To a stirring solution of (4-methyl-phenyl)-pyridin-2-ylmethylene-amine, A (19.6 mg, 0.1 mmol) in 5 ml acetonitrile was added $[Cu(CH_3CN)_4]ClO_4$ (16.4 mg, 0.05 mmol) in 5 ml acetonitrile and the resulting mixture was stirred for 10 min. The solution turned dark red rapidly. The volume of the solvent was reduced under vacuum to about 4 ml. The diffusion of diethyl ether vapor into the concentrated solution gave dark-red crystals. The resulting crystals were filtered off, washed with a mixture of diethylether–acetonitrile (9:1 v/v), and dried under vacuum. Yield: 25 mg (92%). IR (KBr): 1582 cm^{-1} ν(C=N), 1090 cm^{-1} ν(Cl–O). ^1H NMR ($CDCl_3$; δ): 2.28 (s, 3H, CH_3), 7.09–7.40 (m, 4H, ArH, amine ring), 7.60 (*t*, 1H, H_2), 8.04–8.21 (m, 2H, H_3, H_4), 8.48 (d, 1H, $J_{H2,1} = 4.0$, H_1), 9.20 (s, 1H, H_5). ^{13}C {^1H} NMR (500 MHz, $CDCl_3$): 21.10 ($^{13}CH_3$), 118.21, 122.48, 123.49, 128.60, 130.40, 131.25, 138.47, 139.93, 144.05, 149.09, 151.28, 156.28 (^{13}C=N). *Anal.* Calc. for $C_{26}H_{24}ClCuN_4O_4$: C, 56.22; H, 4.35; N, 10.09. Found: C, 56.23; H, 4.34; N, 10.10%.

2.2.6. *[Cu^I(B)$_2$]ClO$_4$ (**1b**)*

This complex was prepared by a procedure similar to **1a** using 21 mg (0.1 mmol) of (2,3-dimethyl-phenyl)-pyridin-2-ylmethylene-amine, B. Dark-red crystals were collected by filtration and dried *in vacuo*. Yield: 27 mg (93%). IR (KBr): 1578 cm^{-1} ν(C=N), 1095 cm^{-1} ν(Cl–O). ^1H NMR ($CDCl_3$; δ): 2.03 (s, 3H, 3-CH_3), 2.22 (s, 3H, 2-CH_3), 6.58–7.06 (m, 3H, ArH, amine ring), 7.74 (*t*, 1H, H_2), 7.98–8.12 (m, 2H, H_3, H_4), 8.59 (s, 1H, H_5), 8.65 (d, 1H, $J_{H2,1} = 4.5$, H_1). ^{13}C {^1H} NMR (500 MHz, $CDCl_3$): 14.90 (3-$^{13}CH_3$), 20.12 (2-$^{13}CH_3$), 116.52, 122.01, 126.98, 127.14, 128.08, 132.78, 136.58, 138.56, 150.50, 154.12, 156.32, 159.90 (^{13}C=N). *Anal.* Calc. for $C_{28}H_{28}ClCuN_4O_4$: C, 57.63; H, 4.84; N, 9.60. Found: C, 57.62; H, 4.86; N, 9.61%.

2.2.7. *[Cu^I(C)$_2$]ClO$_4$ (**1c**)*

This complex was prepared by a procedure similar to **1a** using 21 mg (0.1 mmol) of (2,4-dimethyl-phenyl)-pyridin-2-ylmethylene-amine, C. Dark-red crystals were collected by filtration and dried *in vacuo*. Yield: 25 mg (86%). IR (KBr): 1585 cm^{-1} ν(C=N), 1090 cm^{-1} ν(Cl–O). ^1H NMR ($CDCl_3$; δ): 2.09 (s, 3H, 4-CH_3), 2.28 (s, 3H, 2-CH_3), 6.69-6.91 (m, 3H, ArH, amine ring), 7.68 (*t*, 1H, H_2), 8.01–8.11 (m, 2H, H_3, H_4), 8.54 (d, 1H, $J_{H2,1} = 4.75$, H_1), 8.60 (s, 1H, H_5). ^{13}C {^1H} NMR (500 MHz, $CDCl_3$): 17.80 (4-$^{13}CH_3$), 20.90 (2-$^{13}CH_3$), 120.54, 127.65, 128.14, 128.88, 130.57, 131.66, 137.67, 138.53, 154.52, 149.21, 150.47, 159.91 (^{13}C=N). *Anal.* Calc. for $C_{28}H_{28}ClCuN_4O_4$: C, 57.63; H, 4.84; N, 9.60. Found: C, 57.62; H, 4.85; N, 9.59%.

2.2.8. *[Cu^I(D)$_2$]ClO$_4$ (**1d**)*

This complex was prepared by a procedure similar to **1a** using 21 mg (0.1 mmol) of (2,5-dimethyl-phenyl)-pyridin-2-ylmethylene-amine, D. Dark-red crystals were collected by filtration and dried *in vacuo*. Yield: 26 mg (89%). IR (KBr): 1590 cm^{-1} ν(C=N), 1091 cm^{-1} ν(Cl–O). ^1H NMR ($CDCl_3$; δ): 2.05 (s, 3H, 3-CH_3), 2.12 (s, 3H, 2-CH_3), 6.50–7.16 (m, 3H, ArH, amine ring), 7.65 (*t*, 1H, H_2), 7.99–8.10 (m, 2H, H_3, H_4), 8.59 (s, 1H, H_5), 8.68 (d, 1H, $J_{H2,1} = 4.5$, H_1). ^{13}C {^1H} NMR (500 MHz, $CDCl_3$): 13.85 (5-$^{13}CH_3$), 20.10 (2-$^{13}CH_3$), 116.86, 122.21, 125.98, 126.18, 128.17, 131.70, 135.49, 139.01, 151.10, 153.99, 156.88, 160.00 (^{13}C=N). *Anal.* Calc. for $C_{28}H_{28}ClCuN_4O_4$: C, 57.63; H, 4.84; N, 9.60. Found: C, 57.62; H, 4.83; N, 9.59%.

2.2.9. *[Cu^I(A)(PPh$_3$)$_2$]ClO$_4$ (**2a**)*

To a 3 ml MeCN solution of $[Cu(CH_3CN)_4]ClO_4$ (32.8 mg, 0.1 mmol), 2 equivalent of Ph_3P (52.2 mg, 0.2 mmol) were added, and the solution was stirred for 15 min. The solvent was evaporated under vacuum at room temperature. The dry product $[Cu(CH_3CN)_2(PPh_3)_2]ClO_4$ was added to a stirring solution of 19.6 mg (0.1 mmol) pyridin-2-ylmethylene-p-tolyl-amine, A, in 3 ml MeCN. The solution rapidly turned yellow and it was stirred for 20 min at room temperature. The reaction medium was concentrated under vacuum, until the first crystals appeared in the liquid phase. Bright-yellow crystals were obtained by diffusion of Et_2O vapor into the concentrated solution. Yield: 80 mg (91%). IR (KBr): 1580 cm^{-1} ν(C=N), 1092 cm^{-1} ν(Cl–O), ^1H NMR (500 MHz, $CDCl_3$): ^1H NMR ($CDCl_3$; δ): 2.33 (s, 3H, CH_3), 6.96–7.40 (m, 35H, ArH, amine ring, PPh_3), 8.04 (m, 2H, H_3, H_4), 8.38 (d, 1H, $J_{H2,1} = 7.5$, H_1), 9.01 (s, 1H, H_5). ^{13}C {^1H} NMR (500 MHz, $CDCl_3$): 21.1 ($^{13}CH_3$), 122.71, 126.25, 127.59, 128.32 (d, $J = 4.2$, *ipso*-C of PPh_3), 128.94, 130.04, 130.32, 133.15, 138.48, 139.55, 148.70, 149.12, 150.12, 162.69 (^{13}C=N). *Anal.* Calc. for $C_{49}H_{42}ClCuN_2O_4P_2$: C, 66.59; H, 4.79; N, 3.17. Found: C, 66.58; H, 4.80; N, 3.16%.

2.2.10. *[Cu^I(B)(PPh$_3$)$_2$]ClO$_4$ (**2b**)*

This complex was prepared by a procedure similar to **1** using 21 mg (1 mmol) of (2,3-dimethyl-phenyl)-pyridin-2-ylmethylene-amine, B. Yellow-orange crystals were collected by filtration and dried *in vacuo*. Yield: 70 mg (79%). IR (KBr): 1591 cm^{-1} ν(C=N), 1088 cm^{-1} ν(Cl–O), ^1H NMR (500 MHz, $CDCl_3$): ^1H NMR ($CDCl_3$; δ): 1.55 (s, 3H, CH_3), 2.17 (s, 3H, CH_3), 6.74–7.39 (m, 34H, ArH, amine ring, PPh_3), 7.53 (*t*, 1H, H_2), 8.23 (m, 2H, H_3, H_4), 8.42 (d, 1H, $J_{H2,1} = 7.75$, H_1), 8.60 (s, 1H, H_5). ^{13}C {^1H} NMR (500 MHz, $CDCl_3$): 14.12 (4-$^{13}CH_3$), 21.1 (2-$^{13}CH_3$), 119.45, 126.02, 127.50, 128.47 (d, $J = 4.2$,

ipso-C of PPh3), 128.94, 130.24, 130.38, 133.14, 138.57, 139.87, 148.77, 149.66, 150.08, 162.98 (^{13}C=N). *Anal.* Calc. for $C_{50}H_{44}ClCuN_2O_4P_2$: C, 66.89; H, 4.94; N, 3.12. Found: C, 66.87; H 4.95; N, 3.11%.

2.2.11. $[Cu^{I}(C)(PPh_3)_2]ClO_4$ (**2c**)

This complex was prepared by a procedure similar to **1** using 21 mg (0.1 mmol) of (2,4-dimethyl-phenyl)-pyridin-2-ylmethylene-amine, C. Yellow-orange crystals were collected by filtration and dried *in vacuo*. Yield: 80 mg (90%). IR (KBr): 1595 cm^{-1} ν(C=N), 1091 cm^{-1} ν(Cl–O), ^{1}H NMR (500 MHz, $CDCl_3$): 1.45 (s, 3H, CH_3), 2.10 (s, 3H, CH_3), 6.70–7.59 (m, 34H, ArH, amine ring, PPh_3), 7.50 (*t*, 1H, H_2), 8.20 (m, 2H, H_3, H_4), 8.41 (d, 1H, $J_{H2,1} = 7.8$, H_1), 8.63 (s, 1H, H_5). ^{13}C {^{1}H} NMR (500 MHz, $CDCl_3$): 18.35 (4-$^{13}CH_3$), 20.30 (2-$^{13}CH_3$), 123.60, 124.30, 126.63, 128.28 (d, $J = 4.0$, *ipso*-C of PPh_3), 129.12, 130.56, 132.32, 133.23, 137.60, 139.12, 147.91, 149.56, 150.24, 162.55 (^{13}C=N). *Anal.* Calc. for $C_{50}H_{44}ClCuN_2O_4P_2$: C, 66.89; H, 4.94; N, 3.12. Found: C, 66.88; H, 4.95; N, 3.12%.

2.2.12. $[Cu^{I}(D)(PPh_3)_2]ClO_4$ (**2d**)

This complex was prepared by a procedure similar to **1** using 21 mg (0.1 mmol) of (2,5-dimethyl-phenyl)-pyridin-2-ylmethylene-amine, D. Yellow-orange crystals were collected by filtration and dried *in vacuo*. Yield: 75 mg (84%). IR (KBr): 1590 cm^{-1} ν(C=N), 1091 cm^{-1} ν(Cl–O), ^{1}H NMR (500 MHz, $CDCl_3$): ^{1}H NMR ($CDCl_3$; δ): 1.68 (s, 3H, CH_3), 1.92 (s, 3H, CH_3), 6.90–7.40 (m, 34H, ArH, amine ring, PPh_3), 7.53 (*t*, 1H, H_2), 8.24 (m, 2H, H_3, H_4), 8.43 (d, 1H, $J_{H2,1} = 7.25$, H_1), 8.63 (s, 1H, H_5). ^{13}C {^{1}H} NMR (500 MHz, $CDCl_3$): 17.30 (5-$^{13}CH_3$), 20.54 (2-$^{13}CH_3$), 123.00, 125.55, 127.84, 128.42 (d, $J = 4.1$, *ipso*-C of PPh3), 128.99, 130.40, 131.42, 133.12, 136.58, 139.87, 148.15, 149.64, 150.14, 162.70 (^{13}C=N). *Anal.* Calc. for $C_{50}H_{44}ClCuN_2O_4P_2$: C, 66.89; H, 4.94; N, 3.12. Found: C, 66.90; H, 4.93; N, 3.11%.

2.3. X-ray analysis

Crystals of **1b**, **1c** and **2a** suitable for X-ray analysis were obtained as described above. The single crystals were mounted on a Nonius Kappa-CCD area detector diffractometer (Mo Kα $\lambda = 0.71073$ Å). The complete conditions of data collection (Denzo software) and structure refinements are given below. The cell parameters were determined from reflections taken from one set of 10 frames (1.0° steps in phi angle), each at 20 s exposure. The structures were solved using direct methods (SHELXS97) and refined against F^2 using the SHELXL97 software [32]. The absorption was not corrected. All non-hydrogen atoms were refined anisotropically. Hydrogen atoms were generated according to stereochemistry and refined using a riding model in SHELXL97. The crystal data and refinement details are summarized in Table 1.

Table 1
Crystal data and single crystal X-ray diffraction refinement details for compounds **1b**, **1c** and **2a**

Formula	$C_{28}H_{28}ClCuN_4O_4$	$C_{28}H_{28}ClCuN_4O_4$	$C_{100}H_{87}Cl_2Cu_2N_5O_8P_4$
Formula weight	583.53	583.53	1808.61
Crystal system	monoclinic	monoclinic	triclinic
Space group	*P*2/*n*	*C*2/*c*	$P\bar{1}$
a (Å)	12.350(4)	34.062(5)	11.0500(10)
b (Å)	8.238(3)	8.938(2)	12.676(2)
c (Å)	13.201(4)	22.760(5)	32.847(5)
α (°)	90.00	90.00	79.13(5)
β (°)	91.348(2)	128.33(5)	81.31(4)
γ (°)	90.00	90.00	85.21(7)
V (A^3)	1342.7(8)	5435.6(42)	4459.3(14)
Z	2	8	2
Density (g cm^{-3})	1.443	1.426	1.347
μ(Mo Kα) (mm^{-1})	0.954	0.943	0.669
F(000)	604	2416	1876
Data collection			
Temperature (K)	173(2)	173(2)	173(2)
θ minimum–maximum	2.91–30.02	1.52–27.45	1.27–27.49
Dataset [*h*,*k*,*l*]	−17/11, −11/11, −18/18	−43/44, −11/10, −25/29	−9/14, −16/16, −42/42
Total, unique data, R_{int}	3920, 2479, 0.0503	6206, 3739, 0.0955	19 850, 10 524, 0.0956
Observed data	>2σ(*I*)	>2σ(*I*)	>2σ(*I*)
Refinement			
No. of reflections, no. of parameters	3920, 173	6207, 370	19 850, 1075
R_1, R_2	0.0437, 0.0892	0.0685, 0.1877	0.0860, 0.1931
wR_1, wR_2	0.0994, 0.1126	0.1526, 0.1963	0.1809, 0.2144
Goodness-of-fit	1.078	1.040	1.070
Maximum and average shift/error	0.001, 0.000	0.003, 0.000	0.002, 0.000
Minimum, maximum resolved density (e/A^3)	−0.484, 0.390	−0.708, 0.696	−1.403, 1.518

3. Results and discussion

3.1. General characterization

The IR spectra of the free ligands exhibit the characteristic band of the imine group, which appears in the region 1623–1630 cm^{-1}. This band is shifted to lower frequencies in the IR spectra of the corresponding complexes due to the coordination of the imine nitrogen [33], and appears in the region 1580–1595 cm^{-1}. A strong band at about 1085 cm^{-1} in the IR spectra of the complexes is characteristic of the asymmetric Cl–O stretching mode of the perchlorate anion [34].

The electronic absorption spectra of the ligands and the corresponding complexes are presented in Table 2. Since no d–d transitions are expected for a d^{10} complex, the UV–Vis bands are assigned to metal to ligand charge transfer (MLCT) or ligand-centered $\pi \rightarrow \pi^*$ transitions [35].

The absorption spectrum of $[Cu(A)_2]ClO_4$ (**1a**), in chloroform features a band with a true maximum at 518 nm, whereas $[Cu(A)(PPh_3)_2]ClO_4$ (**2a**), shows a clear shoulder at 419 nm, which is shifted considerably (ca. 99 nm) relative to that of complex **1a**. A similar shift (90 nm) has been reported in going from $[Cu(dmp)_2]^+$ ($\lambda_{MLCT} = 454$ nm) to $[Cu(dmp)(PPh_3)_2]^+$ ($\lambda_{MLCT} = 365$ nm) [36] and also similar shifts were observed in the other $Cu(L)_2^+$ complexes **1b**–**1d** relative to the $Cu(L)(PPh_3)_2^+$ complexes **2b**–**2d** (Table 2).

The considerable red shift in the position of the first MLCT band of complexes **1a**–**1d** as compared to that of other bis(diimine) copper(I) complexes is quite interesting and points to the possible application of these complexes as more efficient charge transfer photosensitizers in the visible region. Additional absorption bands are also observed in the spectra of **1a**–**2d** in chloroform in the UV region (Table 2). The intensity of these bands are consistent with being assigned as ligand-centered $\pi \rightarrow \pi^*$ or/and charge-transfer transitions.

The ^1H NMR spectra and peak assignments are presented in the experimental section in each complex. These peaks are assigned based on the splitting of the resonance signals, spin coupling constants and the literature, and are clearly in accordance with the molecular structure determined by X-ray crystal structure analysis. The ^1H resonances of the coordinated ligands are commonly observed in complexes **1a**–**2d**. In complexes **2a**–**2d**, however, the aromatic H atoms of the coordinated Ph_3P ligands overlap to some extent with those of the phenyl H atoms of ligands A–D. Aside from the aromatic H-atoms, which appear at 7.00–8.15 ppm in the complexes, the imine protons appear as a singlet at 8.60–9.50 ppm in the complexes. The downfield shift of the iminic protons relative to the free ligands can be attributed to the deshielding effect resulting from the coordination of the ligands [29]. The singlet at about 2 ppm in the compounds is assigned to the CH_3 substitutions of the phenyl ring.

The sharp NMR peaks are indicative of diamagnetic Cu(I) complexes. The appearance of a unique signal for each type of proton in $CDCl_3$ solution indicates that the symmetry of the molecules is retained in solution, and only one isomer or exchange processes within the NMR timescale are present.

3.2. X-ray structures of $[Cu(B)_2]ClO_4$ (**1b**), $[Cu(C)_2]ClO_4$ (**1c**) and $[Cu(A)(PPh_3)_2]ClO_4 \cdot 1/2CH_3CN$ (**2a**)

The crystallographic data are summarized in Table 1 and selected bond distances and angles are given in Table 3. No classical H-bonding occurs in these three crystal structures.

A view of the cation of complex **1b**, including the atom-numbering scheme is illustrated in Fig. 2. While a tetrahedral geometry might be expected for a four coordinated copper(I) center, the coordination sphere around the metal ion in this complex is distorted by the restricting bite angles of the chelating ligand. The intraligand N1–Cu–N2 angle is much less than 109.5°, being only 81.07(7)°. On the contrary the N2–Cu–N2b and N1–Cu–N2b angles (134.31(10)°, 122.41(7)°) are much larger than those of a tetrahedral complex. The average Cu–N bond distance (2.037 Å) is similar to that found in the $[Cu(dpdmp)_2]^+$ cation (2.047 Å) at room temperature [37], and other Cu(I) pseudotetrahedral complexes (typical $Cu–N_{av} = 2.055$ Å) [38].

Table 2
IR, UV–Vis spectral data and cyclic voltammetric data of ligands and complexes

Compound	ν(C=N)/cm^{-1}	ν(Cl–O)/cm^{-1}	λ_{max}/nm (Log ε/M^{-1} cm^{-1})	E_p^a	E_p^c
A	1623		241 (4.05), 283 (3.97), 329 (3.92)		
B	1630		245 (4.29), 281 (4.20), 332 (3.90)		
C	1629		239 (4.68), 275 (4.58), 341 (4.44)		
D	1629		241 (4.86), 273 (4.75), 339 (4.45)		
1a	1582	1090	249 (4.52), 339 (4.55), 518 (3.74)	0.41	0.84
1b	1578	1095	255 (4.49), 328 (4.17), 500 (3.59)	0.46	0.67
1c	1585	1090	248 (4.54), 341 (4.23), 500 (3.61)	0.46	0.66
1d	1580	1091	254 (4.37), 315 (4.08), 485 (3.51)	0.48	0.67
2a	1580	1092	243 (4.09), 342 (4.37), 419 (4.01)	0.29	1.73
2b	1591	1088	243 (4.53), 273 (4.41), 414 (3.54)	0.41	1.71
2c	1595	1091	241 (4.60), 275 (4.31), 418 (3.65)	0.39	1.69
2d	1590	1091	243 (4.66), 268 (3.57), 414 (3.72)	0.37	1.68

Table 3
Selected bond lengths (Å) and bond angles ° for **1b**, **1c** and **2a**

1b		**1c**		**2a**			
				I		II	
Cu–N1	2.0180(16)	Cu1–N1	2.021(4)	Cu1–N1	2.064(4)	Cu2–N3	2.085(6)
Cu–N2	2.0564(16)	Cu1–N2	2.067(4)	Cu1–N2	2.103(5)	Cu2–N4	2.142(5)
Cu–N1b	2.0179(16)	Cu1–N3	2.039(4)	Cu1–P1	2.2447(18)	Cu2–P3	2.2359(19)
N1–C1	1.279(2)	Cu1–N4	2.018(4)	Cu1–P2	2.2489(19)	Cu2–P4	2.275(2)
N1–C7	1.439(3)	N2–C1	1.283(6)	N1–C5	1.438(6)	N3–C54	1.407(8)
C1–C2	1.460(3)	N2–C7	1.427(6)	N1–C8	1.285(7)	N3–C57	1.320(8)
		N4–C15	1.284(6)	N2–C9	1.343(7)	N4–C58	1.346(9)
		N4–C21	1.427(6)	N2–C13	1.349(7)	N4–C62	1.330(9)
		C1–C2	1.453(7)	C8–C9	1.456(8)	C57–C58	1.417(10)
		C2–C3	1.386(7)	P1–C14	1.825(6)	P3–C75	1.830(7)
N1–Cu–N2	81.07(7)	N1–Cu1–N2	82.06(17)	N1–Cu–N2	79.39(18)	N3–Cu–N4	79.6(2)
N1–Cu–N1b	121.27(10)	N1–Cu1–N3	125.27(16)	N1–Cu–P1	118.13(14)	N3–Cu–P3	120.04(15)
N1–Cu–N2b	122.41(7)	N1–Cu1–N4	126.21(18)	N1–Cu–P2	114.76(13)	N3–Cu–P4	104.66(14)
N2–Cu–N2b	134.31(10)	N2–Cu1–N3	105.68(17)	N2–Cu–P1	105.35(14)	N4–Cu–P3	115.11(15)
Cu–N1–C1	113.79(14)	N2–Cu1–N4	140.10(16)	N2–Cu–P2	111.81(13)	N4–Cu–P4	98.79(14)
Cu–N1–C7	126.23(11)	N3–Cu1–N4	81.65(17)	P1–Cu–P2	119.22(7)	P3–Cu–P4	126.99(8)
Cu–N2–C2	111.30(13)	Cu1–N1–C2	111.3(4)	Cu1–N1–C5	126.1(3)	Cu2–N3–C54	128.7(4)
Cu–N2–C6	131.61(13)	Cu1–N1–C6	130.2(4)	Cu1–N1–C8	113.9(4)	Cu2–N3–C57	112.2(5)
C1–N1–C7	119.97(16)	Cu1–N2–C1	110.3(3)	Cu1–N2–C9	112.0(4)	Cu2–N4–C58	110.1(5)
C2–N2–C6	117.08(16)	Cu1–N2–C7	126.1(3)	Cu1–N2–C13	129.7(4)	Cu2–N4–C62	131.1(6)
		C1–N2–C7	119.3(4)	C5–N1–C8	119.4(5)	C54–N3–C57	119.1(6)
		C2–N1–C6	118.3(5)	C9–N2–C13	118.2(5)	C58–N4–C62	118.0(7)

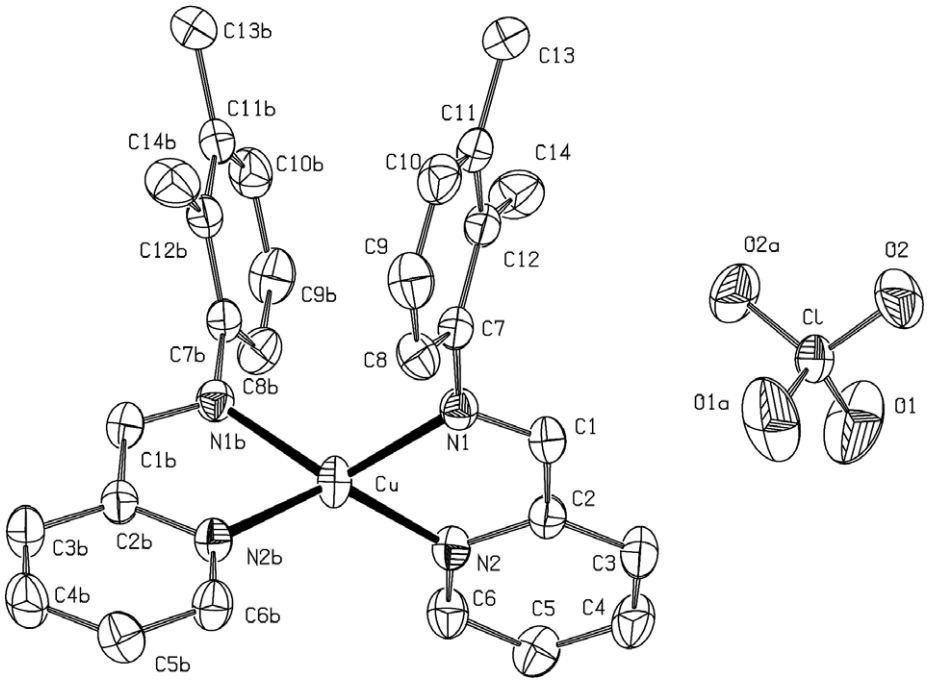


Fig. 2. ORTEP view of the crystal structure of $[Cu(B)_2]ClO_4$ (**1b**) showing the atom labelling scheme. The thermal ellipsoids enclose 50% of the electronic density. Hydrogen atoms are omitted for clarity.

The dihedral angle between the two chelate rings is 85(1)°. The value for the dihedral angle of N1–C1–C2–N2 is 0.00(3)°, and comparison of the dihedral angles between the chelate rings and pyridine groups indicate the coplanarity of these moieties, resulting in a bite size of 3.233 Å of d(N(1)–N(2)) for the chelating ligand. The environment of the imine and pyridine nitrogen atoms is planar. The planarity is measured by three N atom bond angles ($\sum$N). For **1b**, the sum of these angles is 359.99° for N1 and N2. Despite the fact that the nitrogen atoms in **1b** are sp^2 hybridized, some strain in the chelate ring is suggested by the deviation from the 120° angle about the

nitrogen, Cu–N1–C1 (113.79(14)°), Cu–N1–C7 (126.23(11)°), C1–N1–C7 (119.97(16)°), Cu–N2–C2 (111.30(13)°), Cu–N2–C6 (131.61(13)°) and C2–N2–C6 (117.08(16)°). The dihedral angle of the chelate ring and phenyl ring (C7 → C12) is 69.4(3)°.

The cation of complex **1c**, along with the atom-numbering scheme, is shown in Fig. 3. As in complex **1b**, the geometry about Cu(I) in **1c** is also distorted by the restricting bite angles of the chelating ligand. The N1–Cu1–N2 and N3–Cu1–N4 angles are 82.1(2)° and 81.7(2)°, respectively. However, the N2–Cu1–N4, N1–Cu1–N4 and N1–Cu1–N3 angles are 140.0(2)°, 126.3(2)° and 125.3(2)° respectively.

The average Cu–N bond distance (2.0375 Å) is similar to that found in other Cu(I)(diimine) pseudotetrahedral complexes [37–39].

The dihedral angle between the two chelate rings is 83(1)°. Torsion angles in the chelating rings and the pyridine groups are listed in Table 4. This result demonstrates that the chelating rings are nearly planar and the pyridine groups are coplanar with the chelate rings. Despite the fact that the chelate ring are planar, the sum of three N atom bond angles is 359.4° for N1, 359.9 for N2, 360 for N3, and 359.3 N4, however, some strain in the chelate ring is suggested by the deviation from the 120° angle about the nitrogen, for example; Cu1–N1–C6 (130.2(4)°), Cu1–N2–C7 (126.3(4)°) and Cu1–N3–C20 (130.2(4)°). The planarity of the chelate rings results in a bite size of 3.233 Å for d(N(1)–N(2)) and 3.248 for d(N(3)–N(4)) for the two chelating ligands.

The cation of complex **2a**, along with the atom-numbering scheme, is shown in Fig. 4, and selected bond distances and angles are listed in Table 3. The compound **2a** crystallizes with two molecules per asymmetric unit, probably due to some small conformational differences. As in complex **1b** and **1c**, the coordination environment around the metal ion in this complex is pseudotetrahedral with large angular distortion arising from the low intraligand N1–Cu–N2 chelate angle, 79.39(18)° in I and N3–Cu–N4 chelate angle, 79.6(2)° in II. However, the P1–Cu–P2, 119.22(7)° angle in I and the P3–Cu–P4, 126.99(8)° angle in II have opened

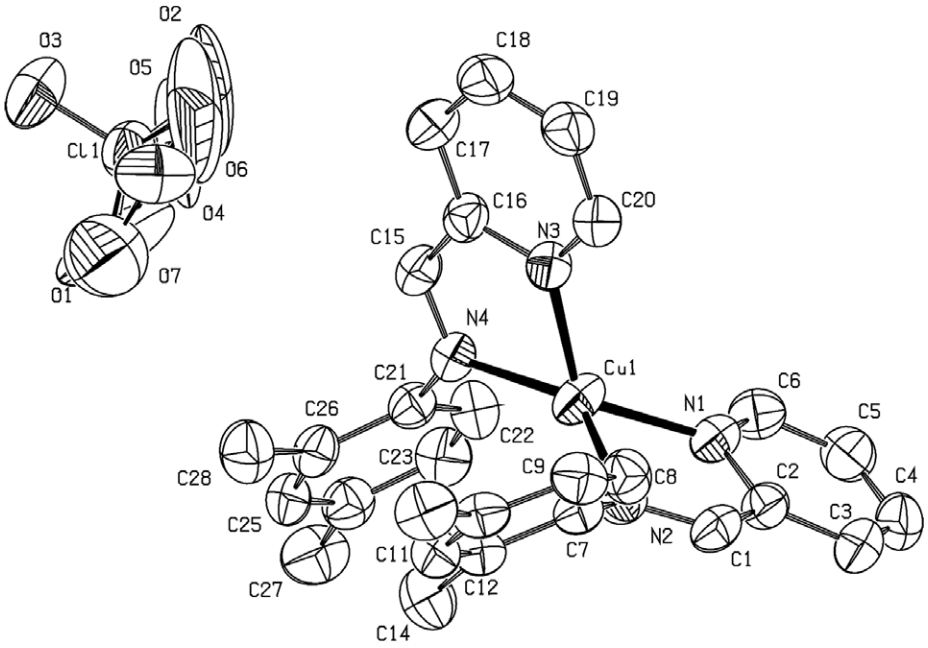


Fig. 3. ORTEP view of the crystal structure of $[Cu(C)_2]ClO_4$ (**1c**) showing the atom labelling scheme. The thermal ellipsoids enclose 50% of the electronic density. Hydrogen atoms are omitted for clarity.

Table 4
Torsion angles for chelating rings

1b		**1c**		**2a**			
				I		II	
N1–C1–C2–N2	0.0(3)	N2–C1–C2–N1	−12.8(7)	N1–C8–C9–C10	174.4(5)	N3–C57–C58–N4	4.2(9)
N1–C1–C2–C3	178.3(2)	N2–C1–C2–C3	169.1(5)	N1–C8–C9–C10	174.4(5)	N3–C57–C58–C59	−171.4(6)
Cu–N1–C1–C2	3.6(3)	Cu1–N1–C2–C1	4.3(5)	Cu1–N1–C8–C9	4.1(6)	Cu2–N3–C57–C58	0.1(7)
C1–C2–C3–C4	−177.0(2)	C1–C2–C3–C4	−179.2(5)	C1–C2–C3–C4	179.8(6)	C57–C58–C59–C60	175.9(7)
Cu–N2–C2–C1	−3.4(2)	Cu1–N2–C1–C2	13.7(6)	Cu1–N2–C9–C8	2.7(6)	Cu2–N4–C58–C59	169.7(6)
N1–Cu–N2–C2	4.01(14)	N2–Cu1–N1–C2	2.03(3)	N1–Cu1–N2–C9	−0.5(4)	Cu2–N3–C57–C58	0.1(7)

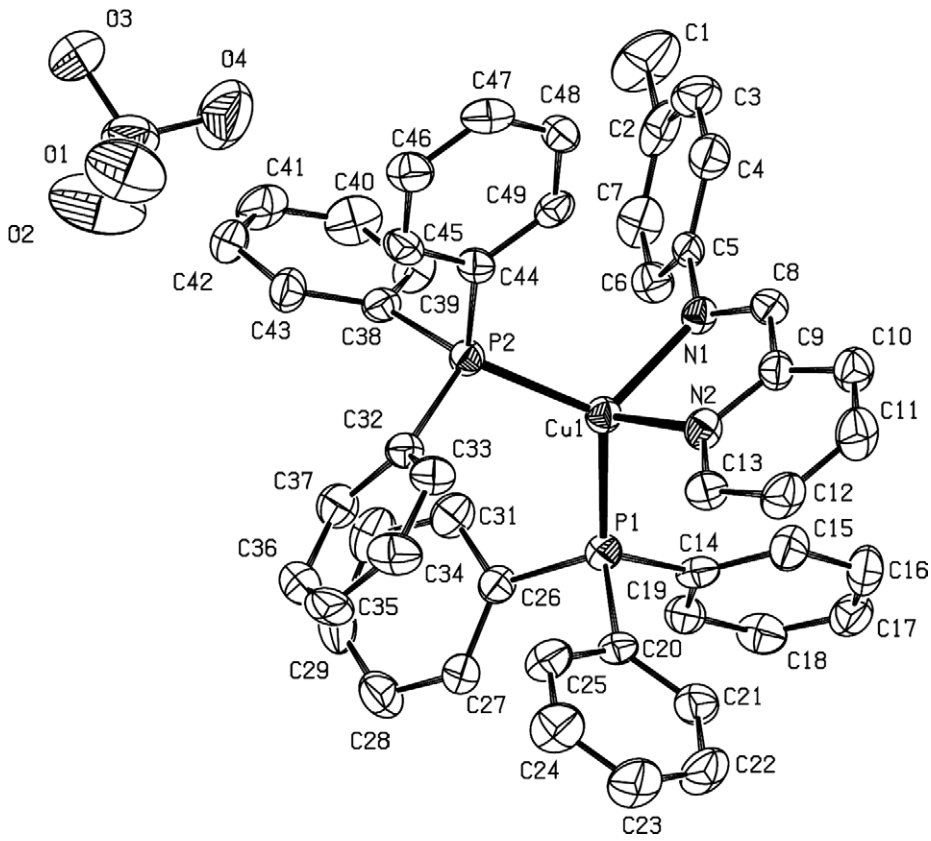


Fig. 4. ORTEP view of the crystal structure of $[Cu(A)(PPh_3)_2]ClO_4$ (**2a**) showing the atom labelling scheme. The thermal ellipsoids enclose 50% of the electronic density. Solvent molecules and hydrogen atoms are omitted for clarity.

up due to the steric effects from the bulky Ph_3P ligands. The average Cu–N and Cu–P bond distances are 2.098 and 2.251 Å, respectively, and are comparable to those reported for $[Cu(dmp)(PPh_3)_2]NO_3$ (2.117(6) and 2.294(2) Å) [29,40].

The chelate ring in complex **2a** is also nearly planar (Table 4) with some strain caused by the deviation from 120° angle about the N-atom (Cu1–N1–C5 126.1(3)°; Cu1–N2–C13 129.7(4)° in I; Cu2–N3–C54 128.7(4)°; Cu2–N4–C62 131.1(6)° in II). The dihedral angle between the chelate ring (Cu–N–C–C–N) and the plane defined by P1–Cu1–P2 is 75(1)° (and 73(1)° in the other molecule of the asymmetric unit) and agrees well with the 82.2° value for $[Cu(dmp)(PPh_3)_2]NO_3$ [25,36].

3.3. Electrochemistry

The electrochemical behavior of the complexes was examined by means of cyclic voltammetry in CH_2Cl_2. The four ligands are electroinactive in the working potential region. The complexes show a quasireversible $Cu^{II/I}$ couple (Table 2) and the ratio of the anodic and cathodic peak currents (i_{pa}/i_{pc}), approaches 1 as the scan rate increases. The peak-to-peak separations increase as the scan rate is changed from 50 mV/s to 500 mV/s.

The $Cu^{II/I}$ potential in a $Cu^{I}N_4$ chromophore is believed to increase with increasing π-acidity of the ligands and the resistance to tetrahedral distortion occurring in the corresponding $Cu^{II}N_4$ chromophore [20,41]. Although, a higher degree of conjugation exists in **1a**–**1d** relative to **2a**–**2d**, the existence of bulkier ligands in **2a**–**2d** which prevent the inner-sphere reorganization to a flattened tetrahedral, more appropriate to Cu(II) oxidation state, play a key role in shifting the oxidation potential to higher values for complexes **2a**–**2d** relative to **1a**–**1d**. However, the potential is approximately insensitive to the methyl substituents on the phenyl ring of ligands in the complexes **1a**–**1d** and/or **2a**–**2d**.

Acknowledgement

S. D. would like to acknowledge the Alzahra University Research Council for partial support of this work.

Appendix A. Supplementary material

Crystallographic data (excluding structure factors) for the structures **1b**, **1c** and **2a** reported in this paper have been deposited with the Cambridge Crystallographic Data Center, no. CCDC 612098–612100, respectively. Copies of the data can be obtained free of charge on application to CCDC, 12 Union Road, Cambridge CB2 1EZ, UK (fax: +44 1223 336033; e-mail: deposit@ccdc.cam.ac.uk or http://www.ccdc.cam.ac.uk/conts/retrieving.html). Supplementary data

associated with this article can be found, in the online version, at doi:10.1016/j.poly.2006.08.011.

References

[1] N. Armaroli, Chem. Soc. Rev. 30 (2001) 113.
[2] D.R. McMillan, J.R. Kirchhoff, K.V. Goodwin, Coord. Chem. Rev. 64 (1985) 83.
[3] Y. Lei, Z. Tyeklar (Eds.), Bioinorganic Chemistry of Copper, Chapman & Hall, New York, 1993.
[4] B.G. Malmstrom, in: R.J.P. Williams, J.R.R.F. De Silva (Eds.), New Trends in Bioinorganic Chemistry, Academic Press, New York, 1978, p. 59.
[5] S. Sakaki, T. Kuroki, T. Hamada, J. Chem Soc., Dalton Trans. (2002) 840.
[6] G.A. Hogan, A.A. Gallo, K.M. Nicholas, R.S. Srivastava, Tetrahedron Lett. 43 (2002) 9505.
[7] S. Mahadevan, M. Palaniandavar, Inorg. Chem. 37 (1998) 693.
[8] F. Liu, K.A. Meadows, D.R. McMillin, J. Am. Chem. Soc. 115 (1993) 6699.
[9] M. Ruthkosky, C.A. Kelly, F.N. Castellano, G.J. Meyer, Coord. Chem. Rev. 171 (1998) 309.
[10] M. Ruthkosky, F.N. Castellano, G.J. Meyer, Inorg. Chem. 35 (1996) 6406.
[11] A.K.I. Gushurst, D.R. McMillin, C.O. Dietrich-Buchecker, J.P. Sauvage, Inorg. Chem. 28 (1989) 4070.
[12] A.K. Ichinaga, J.R. Kirchhof, D.R. McMillin, C.O. Dietrich-Buchecker, P.A. Marnot, J.P. Sauvage, Inorg. Chem. 26 (1987) 4290.
[13] M. Ruthkosky, C.A. Kelly, M.C. Zaros, G.J. Meyer, J. Am. Chem. Soc. 119 (1997) 12004.
[14] D.R. McMillin, M.T. Buckner, B.T. Ahn, Inorg. Chem. 16 (1977) 943.
[15] C.O. Dietrich-Buchecker, J.-P. Sauvage, Chem. Rev. 87 (1987) 795.
[16] C.C. Phifer, D.R. McMillin, Inorg. Chem. 25 (1986) 1329.
[17] A.K. Ichinaga, J.R. Kirchhoff, D.R. McMillin, C.O. Dietrich-Buchecker, P.A. Marnot, J.-P. Sauvage, Inorg. Chem. 26 (1987) 4290.
[18] R.M. Everly, D.R. McMillin, J. Phys. Chem. 95 (1991) 9071.
[19] C.T. Cunningham, K.L.H. Cunningham, J.F. Michalec, D.R. McMillin, Inorg. Chem. 38 (1999) 4388.
[20] M.T. Miller, P.K. Gantzel, T.B. Karpishin, Inorg. Chem. 38 (1999) 3414.
[21] V. Desvergnes-Breuil, V. Hebbe, C. Dietrich-Buchecker, J-P. Sauvage, J. Lacour, Inorg. Chem. 42 (2003) 255.
[22] G.C. Van Stein, G. van Koten, B. Debok, L.C. Taylor, K. Vrieze, C. Brevard, Inorg. Chim. Acta 89 (1984) 29.
[23] X.H. Zhou, T. Wu, D. Li, Inorg. Chim. Acta 359 (2006) 1442.
[24] J.A. Garciavazquez, M. Lopezbecerra, J.R. Masaguer, Polyhedron 10 (1983) 1081.
[25] P.R. Shukla, R. Takroo, J. Indian Chem. Soc. 57 (1980) 556.
[26] R.E. Rulke, J.G.P. Delis, A.M. Groot, C.J. Elsevier, P.W.N.M. van Leeuwen, K. Vrieze, K. Goubitz, H. Schenk, J. Organomet. Chem. 508 (1996) 109.
[27] S. Meghdadi, M. Amirnasr, K.J. Schenk, S. Dehghanpour, Helv. Chim. Acta 85 (2002) 2807.
[28] R. Hadjikhani, S. Dehghanpour, A. Mahmoudi, F. Mojahed, Z. Anorg. Allg. Chem. 632 (2006) 723.
[29] M. Amirnasr, G. Kickelbick, S. Dehghanpour, Helv. Chim. Acta 89 (2006) 274.
[30] D.D. Perrin, W.L. Armarego, D.R. Perrin, Purification of Laboratory Chemicals, 2nd ed., Pergamon, New York, 1990.
[31] P. Hemmerich, C. Sigwart, Experientia 15.IX (1963) 488.
[32] G.M. Sheldrick, in: SHELXL-93, Program for Crystal Structure Refinement, University of Göttingen, Göttingen, 1993.
[33] C.T. Cunnighum, J.J. Moore, K.L.H. Cunningham, P.E. Fanwick, D.R. McMillin, Inorg. Chem. 39 (2000) 3638.
[34] K. Nakamoto, Infrared and Raman Spectra of Inorganic and Coordination Complexes, 4th ed., John Wiley & Sons, USA, 1992.
[35] A.A. Del Paggio, D.R. McMillin, Inorg. Chem. 22 (1983) 691.
[36] R.A. Rader, D.R. McMillin, M.T. Buckner, T.G. Matthews, D.J. Casadonte, R.K. Lengel, S.B. Whittaker, L.M. Darmon, F.E. Lytle, J. Am. Chem. Soc. 103 (1981) 5906.
[37] M.T. Miller, P.K. Gantzel, T.B. Karpishin, Inorg. Chem. 37 (1998) 2285.
[38] D.A. Bradwell, J.C. Jeffery, C.A. Otter, M.D. Ward, Polyhedron 15 (1996) 191.
[39] P.K. Santra, D. Das, T.K. Misra, R. Roy, C. Sinha, S.-M. Peng, Polyhedron 18 (1999) 1909.
[40] J.R. Kirchhoff, D.R. McMillin, W.R. Robinson, D.R. Powell, A.T. McKenzie, S. Chen, Inorg. Chem. 24 (1985) 3928.
[41] M.T. Miller, P.K. Gantzel, T.B. Karpishin, Angew. Chem., Int. Ed. 37 (1998) 1556.

Available online at www.sciencedirect.com
ScienceDirect
Polyhedron 26 (2007) 163–168
POLYHEDRON
www.elsevier.com/locate/poly

Synthesis, structural and spectroscopic characterization of novel zinc(II) complexes with *N*-methylsulfonyldithiocarbimato and *N*-methylsulfonyltrithiocarbimato ligands

Marcelo R.L. Oliveira [a,*], Genivaldo J. Perpétuo [b], Jan Janczak [c], Mayura M.M. Rubinger [a]

[a] *Departamento de Química, Universidade Federal de Viçosa, Viçosa, Minas Gerais, CEP 36571-000, Brazil*
[b] *Departamento de Física, Instituto de Ciências Exatas e Biológicas, Universidade Federal de Ouro Preto, Ouro Preto MG, CEP 35400-000, Brazil*
[c] *Institute of Low Temperature and Structure Research, Polish Academy of Science, P.O. Box 1410, 50-950 Wrocław, Poland*

Received 27 June 2006; accepted 8 August 2006
Available online 11 August 2006

Abstract

Two new zinc(II)-complexes, dithiocarbimato $(Ph_4P)_2[Zn(CH_3SO_2N{=}CS_2)_2]$ (**1**) and trithiocarbimato $(Ph_4P)_2[Zn(CH_3SO_2N{=}CS_3)_2]$ (**2**), were obtained in the crystalline form by the reaction of potassium *N*-methylsulfonyldithiocarbimate ($RSO_2N{=}CS_2K_2$) with zinc(II) acetate dihydrate and tetraphenylphosphonium chloride in dimethylformamide. Both complexes crystallize in the monoclinic system. The central Zn(II) ion has a distorted tetrahedral coordination in both compounds. In **1** the dithiocarbimato ligand coordinates via two S atoms while in **2** the trithiocarbimato ligand coordinates via S and N atoms. Both complexes were also characterized by IR, ^1H NMR and ^{13}C NMR spectroscopies. Compound **2** is the first example of a zinc(II)-trithiocarbimato complex.
© 2006 Elsevier Ltd. All rights reserved.

Keywords: Dithiocarbimate; Trithiocarbimate; Zinc complexes; Crystal structure

1. Introduction

Compounds containing zinc–sulfur-coordinated ligands have a wide range of applications. For example, several dithiocarbamate complexes and salts have been used as fungicides mainly due to their high efficiency in controlling plant fungal diseases, showing relatively low toxicity [1–7]. Furthermore, zinc(II)–dithiocarbamato complexes are worldwide used in the vulcanization process [7–14]. Anionic zinc(II)–dithiocarbamato complexes are also active, and the $[Zn(R_2NCS_2)_3]^-$ ($R = CH_3CH_2$) was found to be a fast accelerator for rubber vulcanization [8]. Zinc(II)–polythiocarbamato complexes that have one or more sulfur atoms inserted in the zinc–dithiocarbamato bond such as $[Zn(Me_2NCS_3)_2]$ are very important intermediates in the vulcanization process [8]. It is also known that correlate nickel(II)–bis(dithiocarbimato) complexes are anionic species, which can also react with sulfur [15,16]. Considering these facts we decided to prepare and study zinc(II) analogues. In a recent work we reported on the structures of compounds $(Ph_4P)_2[Zn(C_6H_5SO_2N{=}CS_2)_2]$ and $(Ph_4P)_2[Zn(4\text{-}CH_3C_6H_4SO_2N{=}CS_2)_2]$ that contain dithiocarbimate anions from aromatic sulfonamides [17].

In the present work, we investigate two new tetraphenylphosphonium salts of anionic zinc(II) complexes with dithio and trithiocarbimate: $(Ph_4P)_2[Zn(CH_3SO_2N{=}CS_2)_2]$ (**1**) and $(Ph_4P)_2[Zn(CH_3SO_2N{=}CS_3)_2]$ (**2**). To our knowledge **2** is the first example of a zinc(II)-trithiocarbimato complex.

2. Experimental

2.1. Methods and materials

The solvents were purchased from Merck and used without further purification. The methanesulfonamide, zinc

* Corresponding author. Tel.: +55 31 3899 3059; fax: +55 31 3899 3065.
E-mail address: marcelor@ufv.br (M.R.L. Oliveira).

0277-5387/$ - see front matter © 2006 Elsevier Ltd. All rights reserved.
doi:10.1016/j.poly.2006.08.002

acetate dihydrate and tetraphenylphosphonium chloride were purchased from Aldrich. Carbon disulfide and potassium hydroxide were purchased from Vetec. The *N*-methylsulfonyldithiocarbimate potassium salt dihydrate was prepared in dimethylformamide from methanesulfonamide analogously as described in the literature [18,19]. Melting point was determined with a Mettler FP5 equipment. Microanalyses for C, H and N were obtained from a Perkin–Elmer 2400 CHN elemental analyzer. Zinc was analyzed by atomic absorption with a Hitachi Z-8200 Atomic Absorption Spectrophotometer. The IR spectra (4000–400 cm^{-1}) were recorded with a Perkin–Elmer 283 B infrared spectrophotometer using CsI pellets. Far-IR spectra (550–100 cm^{-1}) were recorded on a Bruker-IFS 113 V FT-IR spectrometer (polyethylene disks). The ^{1}H (400 MHz) and ^{13}C (100 MHz) NMR spectra were recorded with a Bruker Advance DRX-400 spectrophotometer in $CDCl_3$ with TMS as internal standard.

2.2. Syntheses

Zinc(II) acetate dihydrate (0.7 mmol) was added to a suspension of potassium *N*-methylsulfonyldithiocarbimate dihydrate (1.5 mmol) in DMF (15 mL). The mixture was stirred for 1.5 h at room temperature and filtered. Water (15 mL) and tetraphenylphosphonium chloride (1.5 mmol) was added to the solution obtained. The mixture was stirred for 15 min and the solid product was filtered, washed with distilled water and dried under reduced pressure for 1 day. The solid product was resolved in a mixture dichloromethane/methanol/water. After slowly evaporation of the solution two different crystals were obtained. The transparent colourless crystals are bis(tetraphenylphosphonium) bis(*N*-methylsulfonyldithiocarbimato)-zincate(II): $(Ph_4P)_2$-$[Zn(CH_3SO_2N{=}CS_2)_2]$ (**1**) (ca. 60%) while the other yellow crystals are bis(tetraphenylphosphonium) bis(*N*-methylsulfonyltrithiocarbimato)zincate (II): $(Ph_4P)_2[Zn(CH_3SO_2N{=}CS_3)_2]$ (**2**) (ca. 40%).

Elemental analysis for (**1**): found (calculated for $C_{52}H_{46}N_2O_4P_2S_6Zn$): C, 57.31 (57.69); H, 4.40 (4.28); N, 2.68 (2.59); O, 5.98 (5.91); P, 5.81 (5.72); S, 17.69 (17.77); Zn, 6.14 (6.04). Mp (°C): 187.8–189.1 with decomposition. IR (most intense bands) (cm^{-1}): 1375 ν(C=N); 1286, 1273 $\nu_{ass}(SO_2)$; 1131 $\nu_{sym}(SO_2)$; 957, 947, 936, 925 $\nu_{ass}(CS_2)$ and 328 ν(ZnS); most intense tetraphenylphosphonium cation bands: 1437, 1108, 997, 763, 724, 692, 528. ^{1}H NMR (δ): 7.84–7.63 (m, 40H, Ph_4P^+); 2.96 (s, 6H, CH_3); $^{13}C\{^{1}H\}$ NMR (δ): 208.71 (N=CS_2); 39.30 (CH_3); tetraphenylphosphonium cation signals (J (Hz)): 117.38 (d, $J = 88.9$, C1); 130.70 (d, $J = 12.8$, C2 and C6); 134.44 (d, $J = 10.3$, C3 and C5); 135.62 (d, $J = 3.0$, C4).

Elemental analysis for (**2**): found (calculated for $C_{52}H_{46}N_2O_4P_2S_8Zn$): C, 54.52 (54.47); H, 4.02 (4.00); N, 2.39 (2.44); O, 5.62 (5.58); P, 5.38 (5.42); S, 22.33 (22.37); Zn, 5.75 (5.71). Mp (°C): 185.8–187.4 with decomposition. IR (most intense bands) (cm^{-1}): 1374 ν(C=N); 1288, 1271 $\nu_{ass}(SO_2)$; 1132 $\nu_{sym}(SO_2)$; 959, 948, 924 $\nu(CS_3)$; 505 ν(S–S); 431 ν(ZnN) and 334 ν(ZnS); most intense tetraphenylphosphonium cation bands: 1437, 1109, 998, 764, 723, 693, 527. ^{1}H NMR (δ): 7.84–7.63 (m, 40H, Ph_4P^+); 2.99 (s, 6H, CH_3); $^{13}C\{^{1}H\}$ NMR (δ): 208.78 (N=CS_2); 39.10 (CH_3); tetraphenylphosphonium cation signals (J (Hz)): 117.38 (d, $J = 88.9$, C1); 130.70 (d, $J = 12.8$, C2 and C6); 134.44 (d, $J = 10.3$, C3 and C5); 135.62 (d, $J = 3.0$, C4).

2.3. X-ray crystallography

X-ray intensity data for both crystals were collected using graphite monochromatic Mo Kα radiation on a four-circle κ-geometry KUMA KM-4 diffractometer with a two-dimensional area CCD detector at room temperature. The ω-scan technique with $\Delta\omega = 0.75°$ for each image was used for data collection. The 960 images for six different runs covered about 95% of the Ewald sphere were performed. Initially the lattice parameters were refined on about 150 reflections obtained from 40 images for eight runs with different orientation in the reciprocal space. Finally the lattice parameters were refined by least-squares methods based on all the reflections with $I > 2\sigma(F^2)$. One image was used as a standard for monitoring of the stability of the crystals as well as for monitoring the data collection after every 40 images, and no correction on the relative intensity variation was necessary. Integration of the intensities, correction for Lorenz and polarization effects were performed using a KUMA KM-4 CCD program system [20]. The face-indexed analytical absorption was calculated using the SHELXTL program [21]. The structures were solved by direct methods using the SHELXS of the SHELXL97 program [22]. The calculated E map revealed the Zn, S, P, O, N and most of the C atoms. The remaining C atoms were located from the difference Fourier synthesis. The structures were refined with the anisotropic thermal parameters for all non-hydrogen atoms. Difference Fourier maps gave electron density concentrations approximately located for all hydrogen atoms positions; these positions were idealized (HFIX 43 for all H atoms of the phenyl rings with isotropic thermal parameters of $1.2U_{eq}$ of the carbon atoms joined directly to the hydrogen atoms, and HFIX 137 for the CH_3 group in the compound **2** with isotropic thermal parameters of $1.5U_{eq}$ of the methyl carbon atom). Final difference Fourier maps showed no peaks of chemically significance. Details of the data collection parameters and final agreement factors are collected in Table 1. Selected bond lengths and angles and torsion angles are listed in Table 2.

3. Results and discussion

Compounds **1** and **2** are quite stable in the solid state at the ambient conditions. They are insoluble in water, slightly soluble in ethanol and are soluble in methanol, chloroform and dichloromethane. Compounds **1** and **2** were obtained by recrystallization of the crude product. The obtained crystals have different colours (colourless

Table 1
Crystallographic data and structure refinement parameters

Crystal data	**1**	**2**
Formula	$C_{52}H_{46}N_2O_4P_2S_6Zn$	$C_{52}H_{46}N_2O_4P_2S_8Zn$
Molecular weight (g mol^{-1})	1082.58	1146.70
Crystal system	monoclinic	monoclinic
Space group	$P2_1/c$ (no. 14)	$C2/c$ (no. 15)
Lattice parameters		
a, b, c (Å)	28.344(6), 7.623(2), 24.506(5)	24.934(5), 11.648(2), 19.351(4)
β (°)	106.40(3)	110.60(3)
Volume, V (Å^3)	5080(2)	5261(2)
Z	4	4
$D_{Calc.}$; $D_{obs.}$ (flotation) (g cm^{-3})	1.416; 1.41	1.448; 1.44
Radiation, λ (Å)	Mo Kα (0.71073)	
Absorption coefficients μ (mm^{-1})	0.840	0.892
Transmission factor, T_{max}; T_{min}	0.901; 0.792	0.942; 0.825
Data collection		
h, k, l Range	−38 to 39, −10 to 7, −32 to 33	−34 to 32, −15 to 15, −24 to 26
Collected reflections	46801	25033
Unique reflections	13081	6873
Observed reflections (>2$\sigma(I)$)	5826	2778
Refinement		
R ($F_o^2 > 2\sigma(F_o^2)$)	0.0479	0.0464
wR (F_o^2, all reflections)[a,b]	0.0851	0.0648
$\Delta\rho_{min}$; $\Delta\rho_{max}$ (e Å^{-3})	−0.573; +0.785	−0.924; +0.406
Goodness-of-fit(S)	1.012	1.003

[a] $w = 1/[\sigma^2(F_o^2) + (0.0150P)^2 + 0.0000P]$ where $P = (F_o^2 + 2F_o^2)/3$.
[b] $w = 1/[\sigma^2(F_o^2) + (0.0063P)^2 + 0.0000P]$ where $P = (F_o^2 + 2F_o^2)/3$.

Table 2
Selected bond lengths (Å), bond angles (°) and torsion angles (°)

Compound **1**				Compound **2**	
Zn1–S1	2.360(1)	Zn1–S4	2.380(1)	Zn1–S4	2.285(1)
Zn1–S2	2.321(1)	Zn1–S5	2.334(1)	Zn1–N1	2.021(2)
S1–C1	1.725(3)	S4–C3	1.726(3)	C2–S2	1.751(3)
S2–C1	1.722(3)	S5–C3	1.750(4)	C2–S3	1.683(4)
C1–N1	1.319(4)	C3–N2	1.295(4)	C2–N1	1.328(3)
N1–S3	1.621(3)	N2–S6	1.626(3)	N1–S1	1.646(2)
S3–O1	1.428(2)	S6–O3	1.429(2)	S1–O1	1.434(2)
S3–O2	1.442(2)	S6–O4	1.446(2)	S1–O2	1.438(2)
S3–C2	1.758(3)	S6–C4	1.760(3)	S1–C1	1.760(3)
				S2–S4	1.999(2)
S1–Zn1–S2	76.81(4)	S4–Zn1–S5	76.44(4)	S4–Zn1–N1	92.9(1)
S1–C1–S2	115.0(2)	S4–C3–S5	114.1(2)	S4–Zn1–S4^i	117.7(1)
S1–C1–N1	127.8(2)	S5–C3–N2	127.0(3)	N1–Zn1–N1^i	125.2(1)
S2–C1–N1	117.1(2)	S4–C3–N2	118.9(3)	S3–C2–S2	112.0(2)
C1–N1–S3	123.1(2)	C3–N2–S6	124.9(2)	S3–C2–N1	131.7(3)
O1–S3–O2	115.9(1)	O3–S6–O4	115.9(2)	O1–S1–O2	117.9(1)
O1–S3–N1	114.2(1)	O3–S6–N2	109.5(2)	O1–S1–N1	112.7(1)
O1–S3–N1–C1	51.3(2)	O3–S6–N2–C3	−86.3(2)	O1–S1–N1–C2	56.4(2)
O2–S3–N1	105.9(2)	O4–S6–N2	115.1(1)	O2–S1–N1	104.3(1)
O2–S3–N1–C1	180.0(2)	O4–S6–N2–C3	46.3(2)	O2–S1–N1–C2	−174.6(2)
C2–S3–N1	106.1(2)	C4–S6–N2	98.8(2)	C1–S1–N1	106.3(2)
C2–S3–N1–C1	−67.1(2)	C4–S6–N2–C3	159.6(2)	C1–S1–N1–C2	−61.9(2)

Symmetry operation code i: $-x$, y, $1/2 - z$.

and yellow) and morphologies, therefore it was possible to separate and characterize them. All intense bands of the Ph_4P^+ ion vibrations are present in the infrared spectrum of both **1** and **2** compounds. In the spectrum of **1** a strong band at 1375 cm^{-1} was assigned to the νCN vibration of the RSO_2NC group. Some vibrational bands due to the SO_2 group are observed between 1300 and 1100 cm^{-1}. A multiple band centred at 936 cm^{-1} observed in the

spectrum of **1** was assigned to $\nu_{ass}CS_2$. The spectrum also shows the expected band at 328 cm^{-1} assigned to the ZnS stretching vibration [23]. The IR spectrum of the complex **2** is similar to the spectrum of the compound **1** and shows some additional bands. The band at 505 cm^{-1} was assigned to ν(S–S). Due to N and S coordination of the trithiocarbimato ligand to Zn in **2** the band at 431 was assigned to ν(ZnN).

The ^1H NMR spectra of the compounds **1** and **2** showed the expected signals for the hydrogen atoms of the tetraphenylphosphonium cation, and the hydrogen atoms of the CH_3 group. The integration curves were consistent with a 2:1 proportion between the tetraphenylphosphonium cation and the bis(*N*-methylsulfonyldithiocarbimato)zincate(II) or bis(*N*-methylsulfonyltrithiocarbimato) zincate(II) anions.

The ^{13}C NMR spectra of the compounds **1** and **2** showed the expected doublets for the signals of the tetraphenylphosphonium cation in the aromatic region. The signal at 208.71 δ in the spectrum of **1**, assigned to the dithiocarbimate group (NCS_2), was observed in the same region of other zinc(II)–*R*-sulfonyldithiocarbimate complexes [17]. The methyl group signal of compound **1** was observed at 39.30 δ. The ^{13}C NMR spectrum of the compound **2** shows signals at 208.78 and 39.10 δ, which were assigned to the carbons of the NCS_3 and CH_3 groups.

The molecular structures of **1** and **2** are shown in Figs. 1 and 2, respectively. In both compounds the central Zn(II) atom has a distorted tetrahedral coordination. The asymmetric unit of **1** consists of two chemical equivalents but crystallographically independent *N*-methylsulfonyldithiocarbimate ligands coordinated to the Zn atom, and two tetraphenylphosphonium cations. The *N*-methylsulfonyldithiocarbimate ligands have similar bond lengths but different bond angles and torsion angles (Table 2) due to the interactions with the adjacent cations (Fig. 1). The distortion from the ideal tetrahedral geometry around Zn(II) in **1** is due to the coordination by the two sulfur atoms of each chelating ligand leading to the considerably smaller S1–Zn1–S2 and S4–Zn1–S5 bond angles when compared to the other S–Zn–S bond angles. The two Zn–S_2–C four membered rings are almost planar with a dihedral angle of 79.1(1)°. The average value of 1.731 Å for the C–S bonds within the rings is similar to those observed for other Ni(II) and Zn(II) *N*-*R*-sulfonyldithiocarbimate complexes [17,24]. The average length of 2.349 Å for the Zn–S bonds are also in the range of analogous Zn(II) complexes [17]. The chemical equivalent and crystallographic independent C1–N1 and C3–N3 bond lengths are equal within three e.s.d. and

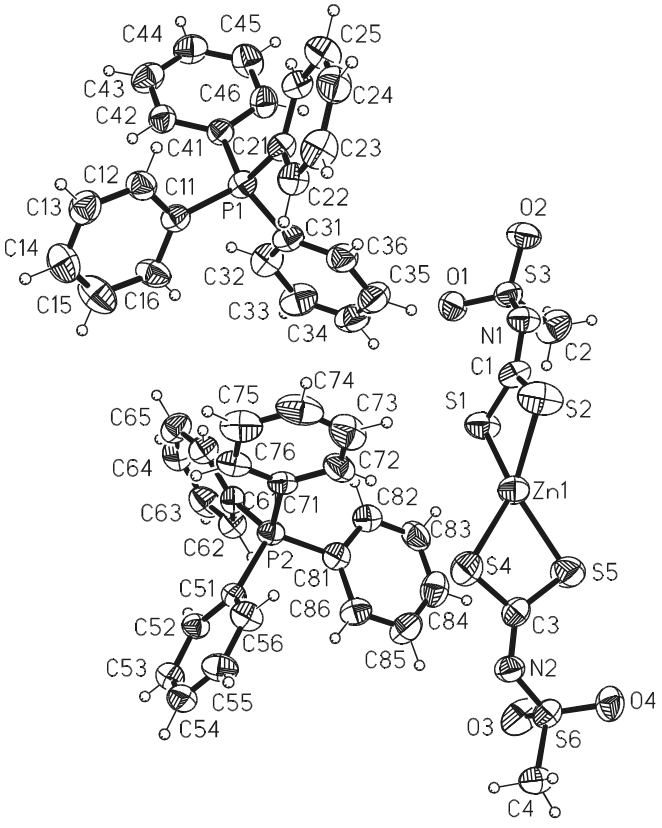


Fig. 1. X-ray molecular structure of tetraphenylphosphonium bis-(*N*-methylsulfonyldithiocarbimato)zincate(II).

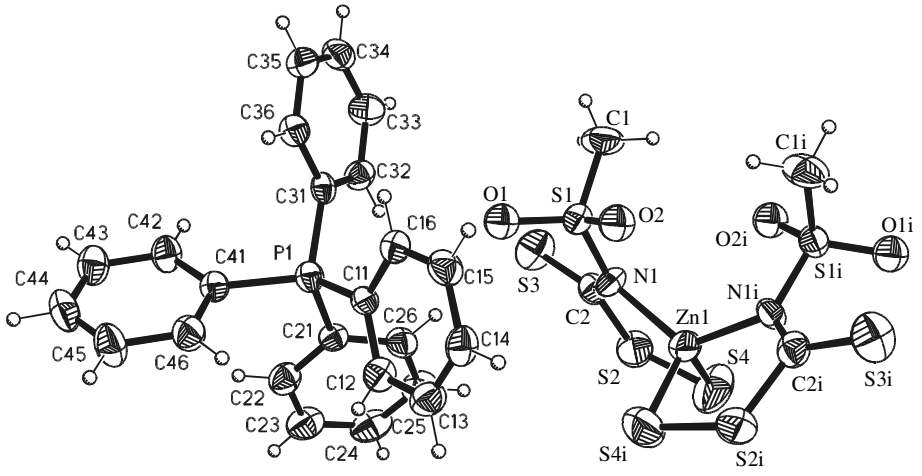
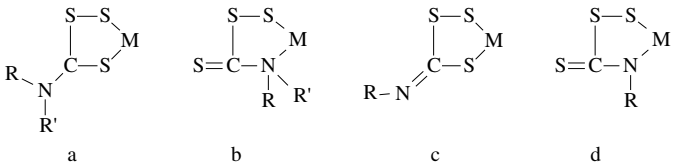


Fig. 2. X-ray molecular structure of tetraphenylphosphonium bis(*N*-methylsulfonyltrithiocarbimato)zincate(II), symmetry code: i = $-x$, y, 1/2 $-z$.

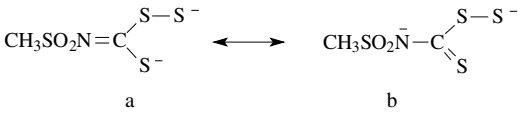
indicate a C(sp^2)–N(sp^2) double-bond character [25]. The S1–C1–N1 and S5–C3–N2 angles are about 10° greater than S2–C1–N1 and S4–C3–N2 due to the interaction between the two CH_3SO_2 groups and S1 and S5 atoms, respectively, which are in *cis* positions in relation to the C1–N1 and C3–N2 bonds. The steric effects of the two CH_3SO_2 groups are greater than the effects of non-bonding lone-pair of electrons at the N1 and N2 atoms, since the C1–N1–S3 and C3–N2–S6 angles are greater than 120°, differently than it would be predicted by the VSEPR theory [26,27].

The asymmetric unit of **2** consists of a half *N*-methylsulfonyltrithiocarbimate zincate(II) anion and a tetraphenylphosphonium cation (Fig. 2). The central zinc lies on a twofold axis and is coordinated by two nitrogen N1 and two sulfur S4 atoms of the anions $CH_3SO_2N{=}CS_3^{2-}$, in a considerably distorted tetrahedral geometry, with very distinct bond angles S–Zn–S, N–Zn–N and N–Zn–S (Table 2). However, the five-membered ring defined by Zn1–N1–C2–S2–S4 atoms is almost planar (maximum deviation atom to mean plane 0.11 Å) and forms a dihedral angle of 87.5° with its crystallographic equivalent plane Zn1–$N1^i$–$C2^i$–$S2^i$–$S4^i$. The Zn1–S4 bond length is slightly smaller than the Zn-S bond lengths in compound **1**, whereas the S2–C2 bond length is similar to the corresponding values observed in **1**. The bond length of S2–S4 is typical for single bond values observed in several organic compounds (2.03 Å) and the S3–C2 bond length is similar to those observed for thioureas S=C bonds [25]. The Zn1–N1 bond length of 2.021(2) Å is in the usual range for Zn–N coordination bonds [28]. The bond lengths and bond angles within the N-methylsulfonyl group are very similar to those in the structure of **1**. Different contributing forces count to the stabilization of the molecular structure of **2**: the oxygen atom O2 is approximately on the mean plane minimizing the stereo repulsion to S3; further repulsion between the sulfur and C1 and O1 can be seen in the bond angles on the C_{ring} carbon, namely, an enhancement of the S3–C2–N1 bond angle in comparison to S3-C2–S2; on the other hand, two equivalent H1c···O2···$H1c^i$ intermolecular contacts (2.72(1) Å) indicate an attractive interaction between the oxygen O2 and two methyl hydrogen atoms.

Some sulfur-rich dithiocarbamato complexes are known [29–31]. The osmium(II) dithiocarbamato complex $[Os_2(S_3CNMe_2)_2(S_2CNMe_2)_3]^+$ is an example of such compounds [30]. The single-crystal X-ray analysis of this cation showed that the trithiocarbamato ion is coordinated to de osmium cation by two sulfur atoms as shown in Scheme 1a. The same coordination mode was proposed for the structures of zinc(II)–trithiocarbamato complexes [31]. Examples of sulfur-rich-nickel(II)–dithiocarbimato complexes have been synthesized and in these cases the coordination of the trithiocarbimate anion can be as represented by the structure in Scheme 1c [15,16]. So, to our knowledge, compound **2** is the first example of a sulfur-rich-zinc(II)–dithiocarbimato, and also the first example of a sulfur-rich-trithio-complex where the metal is coordinated by the sulfur and nitrogen atoms (Scheme 1d).



Scheme 1. Possible ways of coordination of the sulfur-rich-dithiocarbamato (a, b) and sulfur-rich-dithiocarbimato (c, d) ligands.



Scheme 2. Two canonical forms for *N*-methylsulfonyltrithiocarbimate anion.

The strong electron withdrawing property of the SO_2 group might be important for this coordination fashion. The SO_2 neighbouring group stabilizes the negative charge in the nitrogen atom, and the canonical form (b) (Scheme 2) contributes appreciably to the resonance hybrid.

The structure determination of the compound **2** is very important since it has been proposed that correlated trithiocarbamate ligands ($R_2NCS_3^-$) are key intermediates in rubber vulcanization accelerated by zinc dithiolate compounds [8,31]. The formation of the compound **2** is under investigation. The potassium *N*-methylsulfonyldithiocarbimate precursor is not very stable. The oxidation of analogous salts, for example, potassium phenylsulfonyldithiocarbimate, involves dimerization of the anion by the formation of a S–S bond, followed by an intramolecular cyclization with elimination of sulfur [32]. This is a possible source of the third sulfur atom that gives rise to the trithiocarbimato ligand in compound **2**.

4. Conclusion

Two new zinc(II) complexes with dithiocarbimato (**1**) and trithiocarbimato (**2**) ligands as tetraphenylphosphonium salts were obtained in crystalline form and their structures were determined by single crystal X-ray diffraction technique. The compound **2** is the first example of a zinc–trithiocarbimato complex. Furthermore, it is the first example of a sulfur-rich-dithiolate in which the ligand coordinates to the metal cation by sulfur and nitrogen atoms, and not only by the sulfur atoms. The structure determination of **2** is very important since it has been proposed that trithiocarbamate ligands ($R_2NCS_3^-$) are key intermediates in rubber vulcanization accelerated by zinc dithiocarbamate compounds.

Acknowledgements

This work has been supported by CNPq, CAPES and FAPEMIG (Brazil).

Appendix A. Supplementary material

CCDC Nos. 605156 and 605157 contain the supplementary crystallographic data for **1** and **2**, respectively. These data can be obtained free of charge via http://www.ccdc.cam.ac.uk/conts/retrieving.html, or from the Cambridge Crystallographic Data Centre, 12 Union Road, Cambridge CB2 1EZ, UK; fax: (+44) 1223 336 033; or e-mail: deposit@ccdc.cam.ac.uk. Supplementary data associated with this article can be found, in the online version, at doi:10.1016/j.poly.2006.08.002.

References

[1] K.H. Gustafsson, C.H. Fahlgren, J. Agric. Food Chem. 31 (1983) 461.
[2] Y. Jianren, Z. Yongquan, J. Shuzshen, W. Zhengguo, Z. Fuzhen, Sci. Agric. Sin. 22 (1989) 76.
[3] G.D. Thorn, R.A. Ludwig, in: The Dithiocarbamates and Related Compounds, Elsevier Publishing Co., Amsterdam, The Netherlands, 1962.
[4] M.J. Burkitt, H.S. Bishop, L. Milne, S.Y. Tsang, G.J. Provan, C.S.I. Nobel, S. Orrenius, A.F.G. Slater, Arch. Biochem. Biophys. 353 (1998) 73.
[5] A.K. Malik, W. Faubel, Pestic. Sci. 55 (1999) 965.
[6] E. Humeres, N.A. Debacher, M.M.de S. Sierra, J. Org. Chem. 64 (1999) 1807.
[7] D. Coucouvanis, Prog. Inorg. Chem. 11 (1969) 233.
[8] P.J. Nieuwenhuizen, J. Reedijk, M. van Duin, W.J. McGill, Rubber Chem. Technol., Rubber Rev. 70 (1997) 368.
[9] M.J. Cox, E.R.T. Tiekink, Rev. Inorg. Chem. 17 (1997) 1.
[10] W. Hofmann, in: Rubber Technology Handbook, Carl Hanser Verlag, Munich, 1989, pp. 242–259.
[11] L. Bateman, C.G. Moore, M. Porter, B. Saville, in: L. Bateman (Ed.), The Chemistry and Physics of Rubber-like Substances, first ed., Maclaren & Sons Ltd., London, 1963, pp. 449–561.
[12] P.J. Nieuwenhuizen, S. Timal, J.G. Haasnoot, A.L. Spek, J. Reedijk, Chem. Eur. J. 3 (1997) 1846.
[13] P.J. Nieuwenhuizen, A.W. Ehlers, J.G. Haasnoot, S.R. Janse, J. Reedijk, E.J. Baerends, J. Am. Chem. Soc. 121 (1999) 163.
[14] D. Hogarth, Prog. Inorg. Chem. 53 (2005) 71.
[15] J.P. Fackler Jr., D. Coucouvanis, J. Am. Chem. Soc. 89 (1967) 1745.
[16] J.P. Fackler Jr., D. Coucouvanis, J. Am. Chem. Soc. 88 (1966) 3913.
[17] G.J. Perpétuo, M.R.L. Oliveira, J. Janczak, H.P. Vieira, F.F. Amaral, V.M. De Bellis, Polyhedron 22 (2003) 3355.
[18] K. Hartke, Archiv der Pharmazie 299 (1966) 164.
[19] H.U. Hummel, U. Korn, Z. Naturforsch 44B (1989) 24.
[20] KUMA Diffraction, KUMA KM-4 CCD program package, Ver. 171.2, 2002, Wroclaw, Poland.
[21] G.M. Sheldrick, SHELXTL Program, Siemens Analytical X-ray Instrument Inc., Madison, WI, 1991.
[22] G.M. Sheldrick, SHELXL-97, Program for the Solution and Refinement of Crystal Structures, University of Göttingen, Göttingen, Germany, 1997.
[23] K. Nakamoto, in: Infrared and Raman of Inorganic and Coordination Compounds, third ed., John Wiley & Sons, Inc., New York, 1978, p. 339.
[24] M.R.L. Oliveira, H.P. Vieira, G.J. Perpétuo, J. Janczak, V.M. De Bellis, Polyhedron 21 (2002) 2243.
[25] F.H. Allen, O. Kennard, D.G. Watson, L. Brammer, A.G. Orpen, J. Chem. Soc., Perkin Trans. 2 (1987) S1–S19.
[26] R .J. Gillespie, J. Chem. Educ. 40 (1963) 295.
[27] R.J. Gillespie, Chem. Soc. Rev. 21 (1992) 59.
[28] F.H. Allen, Acta Crystallogr. B58 (2002) 380–388.
[29] L.J. Maheu, L.H. Pignolet, Inorg. Chem. 18 (12) (1979) 3626.
[30] L.J. Maheu, L.H. Pignolet, J. Am. Chem. Soc. 102 (1980) 6348.
[31] P.J. Nieuwenhuizen, A.W. Ehlers, J.W. Hofstraar, S.R. Janse, M.W.F. Nielsen, J. Reedijk, E.J. Baerends, Chem. Eur. J. 4 (9) (1998) 1816.
[32] H.U. Hummel, U. Korn, P. Otto, Inorg. Chim. Acta 165 (1989) 99.

Available online at www.sciencedirect.com
ScienceDirect
Polyhedron 26 (2007) 169–177
POLYHEDRON
www.elsevier.com/locate/poly

Kinetics and mechanism of the chromic oxidation of *myo*-inositol

Mabel Santoro [a], Evangelina Caffaratti [a], Juan Manuel Salas-Peregrin [b], Laszlo Korecz [c], Antal Rockenbauer [c], Luis F. Sala [a,*], Sandra Signorella [a,*]

[a] *Departamento de Química-Física, Facultad de Ciencias Bioquímicas y Farmacéuticas, UNR, Suipacha 531, 2000 Rosario, Argentina*
[b] *Departamento de Química Inorgánica, Facultad de Ciencias, Universidad de Granada, Fuentenueva s/n, 18071 Granada, Spain*
[c] *Chemical Research Center, Pusztaszeri street 59-67, H-1025 Budapest, Hungary*

Received 5 July 2006; accepted 8 August 2006
Available online 11 August 2006

Abstract

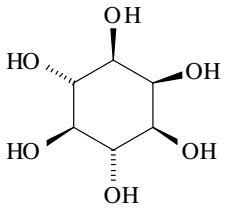
The oxidation of D-*myo*-inositol (Myo) by Cr^{VI} yields the inosose and Cr^{3+} as final products when an excess of cyclitol over Cr^{VI} is used. The redox reaction takes place through the combination of $Cr^{VI} \rightarrow Cr^{IV} \rightarrow Cr^{II}$ and $Cr^{VI} \rightarrow Cr^{IV} \rightarrow Cr^{III}$ pathways. Intermediacy of Cr^{IV} was evidenced by the detection of CrO_2^{2+}, formed by reaction of Cr^{II} with O_2. The EPR spectra show that five- and six-coordinated oxo-Cr^{V} intermediates are formed, with the cyclitol acting as bidentate ligand. Penta-coordinated oxo-Cr^{V} species are present at any $[H^+]$, whereas hexa-coordinated ones are only observed at $pH < 1$, where rapidly decompose to the redox products. At higher pH, where hexa-coordinated oxo-Cr^{V} species are not observed, oxo-Cr^{V} bischelates are stable enough to remain long time in solution.
© 2006 Elsevier Ltd. All rights reserved.

Keywords: Chromate; *myo*-Inositol; Redox chemistry; Complexation chemistry

1. Introduction

Cr^{VI} is a well-established carcinogen and mutagen, and can be reduced to lower states with a wide variety of biological reductants [1–3]. Cr^{V} and Cr^{IV} intermediates have been observed in the selective oxidation of organic substrates by Cr^{VI} and might be implicated in the mechanism of Cr-induced cancers [4–6]. Ligands that posses two oxygen atoms able to form five-membered rings about the metal ion, such as 1,2-diols and α-hydroxy-acids, are effective as non-enzymatic reductants (at low pH) and complexation agents towards high valent chromium and can stabilize the labile oxidation states of chromium [7–10].

Inositols are essential growth factors for rapidly dividing cells and a simple polyol precursor in a second messenger system important in the brain [11,12]. In particular, *myo*-inositol (Myo) is a naturally occurring inositol found in all plant and animal tissues. In this work, we have chosen Myo as a model for investigating the coordination and redox chemistry of chromium with cyclitols, and compare the ability of this kind of compounds to reduce and stabilize high valent chromium with that of other polyols, such as aldoses and alditols.



Myo-inositol (Myo)

* Corresponding authors. Tel./fax: +54 341 4350214 (S. Signorella).
E-mail addresses: lsala@fbioyf.unr.edu.ar (L.F. Sala), signorel@infovia.com.ar (S. Signorella).

0277-5387/$ - see front matter © 2006 Elsevier Ltd. All rights reserved.
doi:10.1016/j.poly.2006.08.003

2. Experimental

2.1. Materials

myo-Inositol, D-gluconic acid sodium salt, D-glucose, acrylamide (Sigma grade), 2,4-dinitrophenylhydrazine (Riedel-de Haën c.a.), potassium dichromate (Cicarelli c.a.), glutathione (GSH), perchloric acid, and sulfuric acid (Merck) were used without purification.

Aqueous solutions were prepared in double-distilled deionized water. In experiments performed at pH $\leqslant$ 3, the pH of the solution was adjusted by addition of 2.0 M $HClO_4$. The concentration of stock solutions of $HClO_4$ was determined using standard analytical methods [13]. 4-(2-Hydroxyethyl)-1-piperazineethanesulfonic acid (HEPES) buffer was used to adjust the pH value of the solution to 7.4. Acetate buffer was used for experiments at pH 4.4. The stability of the organic substrate under conditions used in the kinetic studies was tested by paper chromatography and high performance liquid chromatography (HPLC).

Caution: Cr^{VI} are human carcinogens, and Cr^{V} complexes are mutagenic and potential carcinogens [14]. Contact with skin and inhalation must be avoided. Acrylamide is a carcinogen and must be handled in a well-ventilated fume hood [15].

3. Spectrophotometric measurements

Kinetic measurements were performed by monitoring absorbance changes using a Jasco V-530 spectrophotometer with fully thermostated cell compartment (±0.2 °C). The reactions were followed under pseudo-first-order conditions, using an excess of substrate over Cr^{VI}. Reactant solutions were previously thermostated and transferred into a 1-cm path length cell immediately after mixing. Experiments were performed at 33 °C unless otherwise stated and mixtures of sodium perchlorate and perchloric acid were used to maintain a constant ionic strength (I) of 1.0 M.

The disappearance of Cr^{VI} was followed at 350 nm until at least 80% of the Cr^{VI} was consumed. In the kinetic measurements, the initial concentration of Cr^{VI} was kept constant at 6.0×10^{-4} M, while [Myo] and [H^+] were varied from 0.06 to 0.24 M and from 0.1 to 0.4 M, respectively. The observed pseudo-first-order rate constants were averages of multiple determinations and were within ±8% of each other. The first-order dependence of the rate upon [Cr^{VI}] was verified in a set of experiments where the $[Cr^{VI}]_0$ was varied but temperature, $[Myo]_0$, [H^+] and I were kept constant.

The formation of Cr^{III} from mixtures of 15×10^{-3} M Cr^{VI} and 24×10^{-2} M Myo in 0.10–0.40 M $HClO_4$, was monitored by following the growth of the 570 nm absorption band The final absorption spectrum of the reaction solution showed two d–d bands at $\lambda_{max} = 408$ nm ($\varepsilon = 18\ M^{-1}\ cm^{-1}$) and 574 nm ($\varepsilon = 15\ M^{-1}\ cm^{-1}$), which are distinctive of the free Cr^{3+} aqua-ion [16], and are attributable to the octahedral $^4A_{2g} \rightarrow {}^4T_{1g}$ and $^4A_{2g} \rightarrow {}^4T_{2g}$ transitions in O_h symmetry.

Chromate esters were investigated by UV–Vis spectrophotometry in the 350–400 nm region in which they show characteristic absorption bands. Reactions were performed at pH 3.0, where the redox reaction is slow enough to enable the observation of the ester formation. The instrument was zeroed to an arrangement of the reference and sample beams passing through matched cells, both containing Cr^{VI} at pH = 3.0. The solution in the sample cell was replaced with the reaction solution containing 6×10^{-4} M Cr^{VI} and 0.03–0.24 M Myo at pH 3, $I = 1.0$ M, and $T = 33$ °C. Spectra obtained within 30 min after mixing revealed a distinctive absorption band at 371 nm.

The formation of CrO_2^{2+} (Cr^{III} superoxide) was examined by periodic scanning of O_2-saturated solutions containing 0.13 M Myo and 0.03 mM Cr^{VI} in 0.40 M $HClO_4$. The band at 350 nm decreased in intensity over a period of 30 min, while two new peaks at 290 nm and 249 nm grew in and then slowly decreased. These two peaks were attributed to CrO_2^{2+} [17], formed as a long-lived intermediate.

3.1. Polymerization test

The presence of free radicals in the reactions of Myo with Cr^{VI} was tested by the acrylamide polymerization test. In a typical experiment, acrylamide (0.5 g) was added to a solution of Cr^{VI} (0.024 mmol) and Myo (1.25 mmol) in $HClO_4$ 0.1 M (5 mL). After a few minutes a white precipitate appeared. Control experiments (without Cr^{VI} or reductant present) did not show the formation of a precipitate. The possible reaction of Cr^{V} or Cr^{IV} with acrylamide was tested with $Na[Cr^{V}O(ehba)_2]$ [18] and $[Cr^{IV}O(ehba)_2]$ [19] (ehba = 2-ethyl-2-hydroxybutanoic acid). No precipitation occurred on mixing the Cr^{V} or Cr^{IV} complexes with acrylamide under the same conditions as those used in the Cr^{VI} + Myo reaction.

3.2. Product analysis

HPLC was employed to detect the reaction products under the conditions used in the kinetic measurements (excess of Myo over Cr^{VI}). The chromatograms were obtained on a KNK-500A chromatograph provided with a 7125 HPLC pump. The separation was carried out on Aminex HPX-87H HPLC column (300 × 7.8 mm, Bio-Rad Laboratories) using 3.2×10^{-2} M H_2SO_4 as eluent and a flow rate of 0.4 mL/min, at 33 °C. The effluent was monitored with refractive index (ERC-7522, ERMA INC) and UV (115 UV Gilson, $\lambda = 220$ nm) detectors. Standard solutions and reaction mixtures were prepared in 0.2 M $HClO_4$. All the samples were thermostated at 33 °C during 2 h, and filtered through a 0.2 μm membrane prior to injection into the chromatographic system.

Standard solutions of Myo, D-*epi*-inosose (synthesized according to a described method [20]), D-glucose and D-gluconic acid were prepared individually in 0.2 M

$HClO_4$ and chromatographed separately to determine the chromatographic retention times (t_R) of each sample: t_R(Myo) = 8′41″, t_R(D-*epi*-inosose) = 13′22″, t_R(D-glucose) = 8′48″, t_R(D-gluconic acid) = 12′40″.

Reaction solutions containing 0.075–0.15 M Myo and 0.015 M Cr^{VI} in 0.2 M $HClO_4$ were stirred at 33 °C during 2 h and then chromatographed. The chromatograms of the reaction mixtures showed one peak at t_R = 13′22″ in addition to the peak of excess Myo at t = 8′41″. The retention time of the new peak is coincident with that of the standard solution of D-*epi*-inosose. Furthermore, co-chromatography of a Cr^{VI}/Myo reaction mixture with added D-*epi*-inosose resulted in the increase of the peak at 13′22″. This result indicates that Cr^{VI} oxidizes one of the C–OH groups of the ring to yield the inosose as the reaction product (Scheme 1).

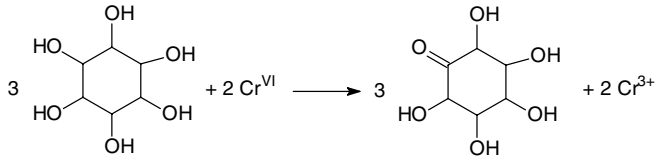
The formation of the inosose as the reaction product was confirmed spectrophotometrically. The final electronic spectrum of mixtures of 0.075 M Myo + 0.015 M Cr^{VI} in 0.2 M $HClO_4$, showed one absorption band with λ_{max} = 271 nm in the 200–350 nm spectral region, analogous to that observed for a solution of D-*epi*-inosose (λ_{max} = 271 nm, ε = 45 M^{-1} cm^{-1}). The possible chromic oxidation of the inosose formed in the Myo + Cr^{VI} reaction mixture through a competitive pathway was also checked. Treatment of 0.015 M D-*epi*-inosose with 0.003 M Cr^{VI} in 0.2 M $HClO_4$ yields a product with a 20-times more intense band at λ_{max} 310 nm. The absence of this band in the reaction mixture of excess of Myo and Cr^{VI} indicates that the inosose does not compete with Myo for Cr^{VI}. Alternatively, the formation of the inosose as the reaction product was tested spectrophotometrically by addition of 2,4-dinitrophenylhydrazine to the Cr^{VI}/Myo reaction mixtures, following a method described in the literature [21]. The ketone was identified by the observation of two absorbance bands at 430 and 510 nm characteristic of the 2,4-dinitrophenylhydrazone derivative.

Under all experimental conditions, CO_2 and HCOOH were never observed as reaction products, indicating the absence of C–C bond cleavage.

3.3. EPR measurements

The EPR spectra were obtained on a Bruker Elexsys spectrometer operating at X-band frequencies (~9–10 GHz). Spectra were recorded as first derivatives of the microwave absorption of a total of 5–20 scans, at 25 ± 1 °C, using 10 mW microwave power, modulation frequency = 100 kHz, modulation amplitude = 0.4–4 G and conversion time = 5.12 ms. g-Values were determined by reference to diphenylpicrylhydrazyl radical (g = 2.0036) as an external standard. Spectra were obtained from mixtures of 8.0 mM Cr^{VI} and 510 mM Myo in 0.2 M $HClO_4$ or from reactions carried out by addition of 1.0 mM Cr^{VI} + 1.0 mM GSH to 25–500 mM solutions of Myo in 100 mM acetate buffer (pH 4.4) or 100 mM HEPES buffer (pH 7.4). Aqueous stock solution (100 mM) of GSH was freshly prepared before each series of experiments.

All the EPR spectra were simulated with the PEST WinSIM [22] program using 100% Lorentzian line shapes. The spectral parameters for each Cr^{V} species were similar in all simulations, with maximum deviations of ±0.0001 units in the g_{iso} values. In the simulations, values for a_{iso} (^{1}H) were included only when they were greater than the line width of the Cr^{V} species.



Scheme 1.

4. Results and discussion

4.1. Myo + Cr^{VI} reaction intermediates

4.1.1. Intermediate Cr^{VI}ester

Differential UV–Vis spectra of mixtures of Cr^{VI} and Myo exhibit an absorption band with λ_{max} = 371 nm, consistent with that ascribed to Cr^{VI} oxo-esters [23,24]. At pH 3.0, the redox reaction of Cr^{VI} with Myo proceeds very slowly, with negligible reduction of Cr^{VI} within the first hour. Thus, at this pH the ester formation step can be distinguished clearly from the electron transfer reaction. Spectra obtained within 2 min after mixing revealed a distinctive absorption band at 371 nm. Continued scanning for 30 min showed no further change in the spectra. Varying the excess concentration of Myo at pH 3.0 showed that the absorbance at 371 nm increased with increasing [Myo] (Fig. 1), probably as result of a shift toward the ester in the esterification equilibrium.

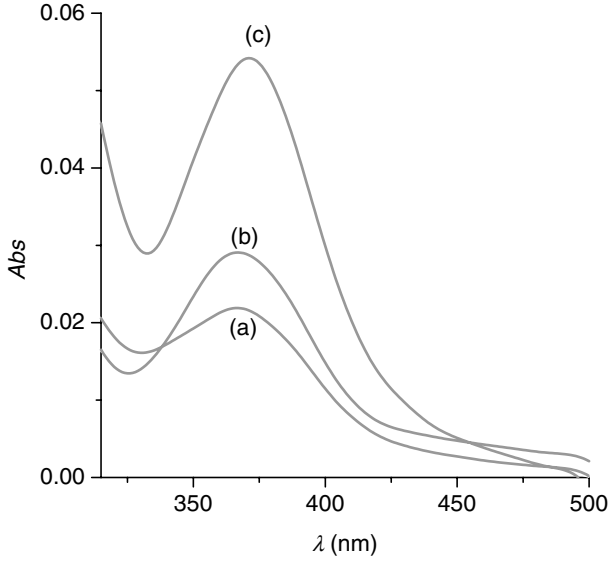


Fig. 1. UV–Vis difference spectra of Cr^{VI}/Myo solutions at pH 3.0, showing the increasing band at 371 nm with increasing [Myo]: (a) 0.06, (b) 0.12, and (c) 0.18 M. [Cr^{VI}] = 6.0×10^{-4} M, T = 33 °C, I = 1.0 M. Spectra taken 20 min after preparation of solutions.

4.1.2. Intermediacy of Cr^{II}

It is known that Cr^{IV} oxidizes alcohols as a two-electron oxidant to yield Cr^{II} and the oxidized organic product [17,25–27]. The participation of Cr^{II} in the mechanism of the oxidation of several alcohols by Cr^{IV} and Cr^{VI} in $HClO_4$ has been demonstrated by conversion to CrO_2^{2+} upon reaction with molecular oxygen [17,25]. At high $[O_2]$ and low $[Cr^{VI}]$ the reaction of Cr^{II} with O_2 can compete successfully with the reaction of Cr^{II} with Cr^{VI}, and if formed, Cr^{II} should yield the CrO_2^{2+} product [25,27]. The presence of intermediate Cr^{II} in the reaction of Myo with Cr^{VI} was examined by monitoring the formation of CrO_2^{2+}, using a $[Cr^{VI}]_0$ lower than employed in the kinetic studies. A periodic scanning of the O_2-saturated solution (1.26 mM O_2) of a Cr^{VI} + Myo reaction mixture in 0.40 M $HClO_4$ showed the appearance of two bands at 290 and 245 nm (Fig. 2). These two bands are characteristic of CrO_2^{2+} and persisted in solution after all the Cr^{VI} had been consumed. These spectroscopic results reveal that Cr^{II} forms in the redox reaction, and can be taken as evidence that Cr^{IV} is implied in the redox mechanism of the reaction between Cr^{VI} and Myo, such as observed in the reduction of Cr^{VI} by alcohols, linear polyols, saccharides, and hydroxyacids [17,25–29].

The yield of CrO_2^{2+} is expected to approach 100% if the reaction should take place exclusively through the $Cr^{VI} \rightarrow Cr^{IV} \rightarrow Cr^{II}$ pathway [27]. In the Myo + Cr^{VI} reaction, the percent yield of CrO_2^{2+} reaches a value of 50% suggesting that one half of the $HCrO_4^-$ is reacting through a pathway that involves Cr^{II}.

4.1.3. Intermediacy of Cr^{V}

EPR spectroscopy was used to detect intermediate Cr^{V} species formed in the reaction of Myo with Cr^{VI}. In 0.2 M $HClO_4$, the EPR spectra of Myo + Cr^{VI} reaction mixtures consist of one major signal at $g_{iso} = 1.9800$ and a weak (<10% of total Cr^{V}) signal at $g_{iso} = 1.972$. At this $[H^+]$, a modulation amplitude of ≈4 G was required to observe the Cr^{V} species; therefore, the superhyperfine (shf) pattern of the EPR signal (the ^1H shf splitting (a_H) for Cr^{V}-alcoholato species is usually <1 G) could not be resolved. The structure of the Cr^{V} intermediates was then analyzed from the EPR spectral features of 25–500 times excess of Myo over a mixture of chromate with GSH (1:1 ratio) at pH 4.4 and 7.4. Under these conditions, Cr^{V} generated by rapid reaction of GSH with Cr^{VI} was trapped by the inositol yielding Cr^{V}–Myo species that remain long time in solution. At pH 7.4 and 25–500:1:1 Myo:Cr^{VI}:GSH ratio, the EPR spectra were composed (signals were deconvoluted by fitting the spectra to Lorentzian derivatives) of one triplet at $g_{iso} = 1.9801$ ($a_H = 1.03 \times 10^{-4}$ cm^{-1}) and one doublet at $g_{iso} = 1.9799$ ($a_H = 0.95 \times 10^{-4}$ cm^{-1}) (Fig. 3(a)). The same two components were observed at pH 4.4 in 1:1: > 100 GSH:Cr^{VI}:Myo reaction mixtures (Fig. 3(b)). At this pH, and [Myo] = 25–100 mM, a third weak signal was observed at $g_{iso} \sim 1.979$ (Fig. 3(c) and (d)).

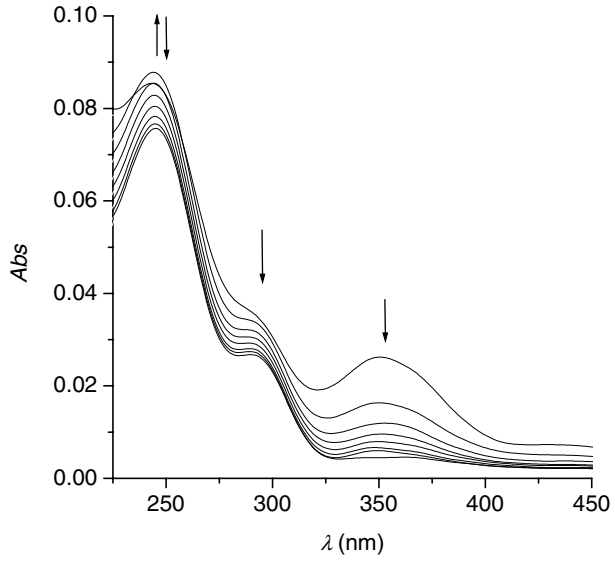


Fig. 2. Formation of CrO_2^{2+} (λ_{max} 290, 249) from the reaction between 0.130 M Myo, 1.26 mM O_2 and 3.0×10^{-2} mM Cr^{VI}, in 0.40 M $HClO_4$.

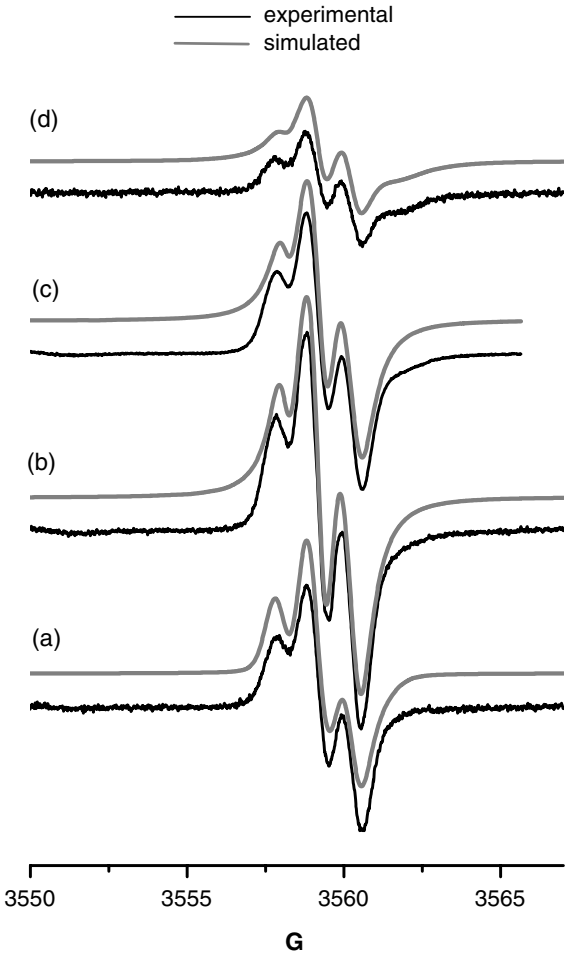


Fig. 3. Experimental and simulated X-band EPR spectra from mixtures of 1 mM GSH + 1 mM Cr^{VI} and: (a) 100 mM Myo, pH 7.4; (b) 250 mM Myo, pH 4.4; (c) 100 mM Myo, pH 4.4; (d) 25 mM Myo, pH 4.4. Frequency = 9.8640 GHz, mod. ampl. = 0.4 G.

4.2. Characterization of intermediate Cr^V species by EPR spectroscopy

The EPR spectral parameters together with the proton shf coupling have been shown to be useful in determining the binding modes of O-donor ligands in Cr^V complexes [7,12]. The g_{iso} value of the EPR signal of Cr^V complexes depends on the coordination number and the nature of the donor groups bound to Cr^V [30]. The estimation of Cr^V species present in solution was made taking into account empirical correlations between the structure of the Cr^V complexes and the EPR parameters together with [substrate] and pH dependencies of the EPR signals of the Cr^V complexes formed in Cr^{VI}/GSH/Myo mixtures.

It has been found that the multiplicity of the EPR signal of Cr^V-diolato complexes is dependent upon whether the ligand is cyclically strained or not. It was observed that in Cr^V-diolato complexes formed with linear diols, all the protons are equivalent in the isotropic EPR spectra [31], but the strain of a six membered rings imparts inequivalence to the magnetic environment of the protons in the second coordination sphere [32]. Thus, the EPR spectra of $[CrO(cis\text{-}1,2\text{-cyclohexanediol})_2]^-$ and $[CrO(trans\text{-}1,2\text{-cyclohexanediol})_2]^-$ exhibit a triplet and a singlet, respectively, and the difference was explained by arguing that only when the protons lie in the Cr^V-ligand plane there is a maximal overlap between the proton orbital and the Cr^V orbital containing the unpaired electron density.

It is known that five-membered Cr^V chelates are favored over six-membered ones [7,33,34]. Therefore, any of the *vic*-diolato groups of Myo are potential binding modes to afford five-membered Cr^V species. The two components at g_{iso} 1.9801 and 1.9799 of the EPR signal observed in the reaction of Cr^{VI} with GSH (1:1 ratio) in the presence of 25- to 500-times molar excess of Myo, at pH 7.4, correspond to those calculated for five-coordinated oxochromate(V) complexes with four alcoholato donors ($g_{calc} = 1.9800$) [30]. The shf splitting found for the two components of the EPR signal are in agreement with those expected for oxo-Cr^V-diolato$_2$ species with one and two (one from each chelate ring) carbinolic protons coupled to the Cr^V electronic spin [33]. The triplet can be attributed to the bis-chelate with oxo-Cr^V bound to the *cis*-diolato moiety of two Myo ligands $[Cr(O)(cis\text{-}O,O\text{-Myo})_2]^-$ (**I**), while the doublet can correspond to the $[Cr(O)(trans\text{-}O,O\text{-Myo})(cis\text{-}O,O\text{-Myo})]^-$ (**II**) bis-chelate (Fig. 4). At any [Myo], the ratio of the triplet (Cr^V-*cis*/*cis*-diol$_2$) to the doublet (Cr^V-*cis*/*trans*-diol$_2$) was 30:70, which means that 65% of the ligand is bound to Cr^V through the *cis*-diolato moiety. However, the ratio of *cis*:*trans* diol sites in Myo is 2:4. The marked preference of the CrO^{3+} ion for binding *cis*-rather than *trans*-diolato groups of cyclic diols explains the higher proportion of the Cr^V-*cis*-diolato binding mode in the mixture [33].

At pH 4.4, the EPR spectra of mixtures of 1:1: > 100 GSH:Cr^{VI}:Myo are composed of the same two signals at g_{iso} 1.9801 and 1.9799, in 30:70 ratio. But when [Myo] ⩽ 100 mM, the EPR spectra show, besides the two main components, a minor unresolved signal at $g_{iso} \sim 1.979$. The proportion of this third signal decreases from 20% to 3% of total Cr^V present in solution, when [Myo] varies from 25 to 100 mM. Although the lack of resolution disable the assignment of this signal, the decrease of its proportion with increasing [Myo] suggests that this species corresponds to a Cr^V monochelate (i.e. oxo-Cr^V–Myo) that transforms into the bis-chelate as the [Myo] increases.

In 0.2 M $HClO_4$ and 500:1 Myo:Cr^{VI} ratio, ($[Cr^{VI}]_0 = 8.0$ mM), one additional signal at $g_{iso} = 1.972$ appeared along with the signal centered at $g_{iso} = 1.9800$. At this $[H^+]$, rapid redox reaction between Cr^V and the ligand takes place affording a low intensity EPR signal that can be observed over a short time period. Therefore, to obtain good signal/noise ratios, a high modulation amplitude value is required and the shf pattern of the signals is not observed. The signal at g_{iso} 1.9800 corresponds to $[Cr(O)(vic\text{-}O,O\text{-diolato})_2]^-$ species (**I**, **II**), also observed at higher

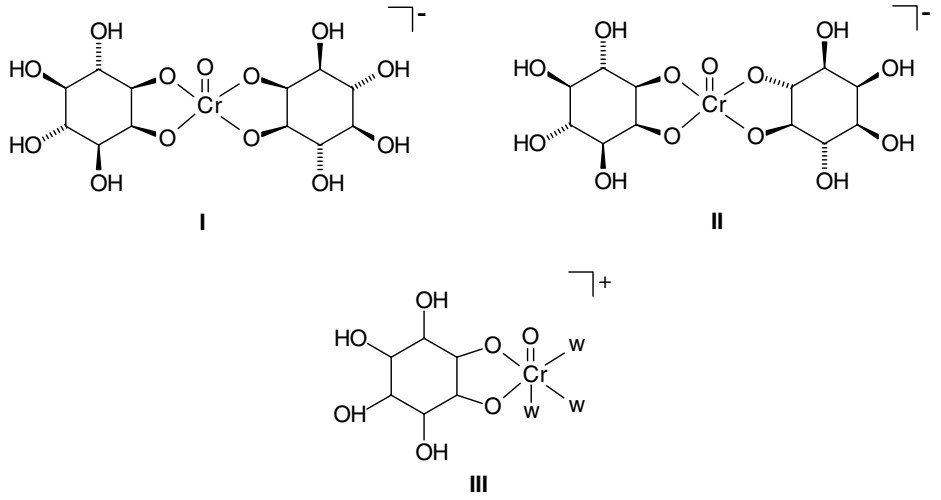


Fig. 4. Proposed structures of Cr^V complexes formed with Myo. For each complex only one of the possible binding isomers is shown.

pH values. The g-value of the weak signal at g_{iso} 1.972 and its observation at high [H^+], affords some information on its nature. Firstly, the low g_- value suggests a six-coordinated oxo-Cr^V species, possibly $[Cr(O)(O,O\text{-Myo})(H_2O)_3]^+$ (**III**, Fig. 4), since the calculated g_{iso} value for a six-coordinated oxo-Cr^V species with one *vic*-diolato donor and three water molecules (1.972) is in agreement with the observed g_{iso} value [30]. Furthermore, the positive charge is consistent with its appearance at high [H^+].

4.3. Rate studies

The reduction of Cr^{VI} by Myo is strongly dependent on pH. Although the reaction is slow at pH > 1, Cr^{VI} is rapidly consumed when the [H^+] > 0.1 M. For this reason, the 0.10–0.40 M [H^+] range was chosen to study the kinetics of this reaction. In 0.1–0.4 M $HClO_4$, the time-dependent UV–Vis spectra showed that the reaction of Myo with Cr^{VI} resulted in an absorbance band at 350 nm and a shoulder at 420–500 nm, characteristic of Cr^{VI} in acidic medium. The absorbance vs. time curves exhibited a monotonic decrease of absorbance at 350 nm that could not be described by a single exponential decay. It is known that Cr^V species absorb strongly at 350 nm and may superimpose Cr^{VI} absorbance. This Cr^V contribution to Abs^{350} becomes significant especially when the Cr^{VI} and Cr^V decay rates are of the same order [35]. In the redox reaction between Cr^{VI} and Myo relatively long-lived Cr^V species were observed in the EPR spectra. Therefore, the kinetic profiles for the Myo/Cr^{VI} system were fitted on the basis of the formation of Cr^V intermediate species and the reaction could be adequately described by the two consecutive first-order reactions of Scheme 2.

$$2\,Cr^{VI} \xrightarrow{k_6} Cr^{V} \xrightarrow{k_5} Cr^{III}$$
$$+$$
$$Cr^{III}$$

Scheme 2.

Taking into account the Cr^V and Cr^{VI} absorption superimposition, the absorbance at 350 nm, at any time during the reaction, is given by

$$Abs^{350} = \varepsilon^{VI}[Cr^{VI}] + \varepsilon^{V}[Cr^{V}] \quad (1)$$

Combining Eq. (1) with rate expressions [36] derived from Scheme 2 yields

$$Abs^{350} = Abs_o e^{-2k6t} + k_6\varepsilon^{V}[Cr^{VI}]_o(e^{-k5t} - e^{-2k6t})/(2k_6 - k_5) \quad (2)$$

In this equation, ε^V refers to the molar absorptivity of Cr^V at 350 nm. Values of ε^V depend on pH and were assumed to be the same as those found for the complex $[Cr^VO(ehba)_2]^-$ in the same [H^+] range (ε^V = 900–1100 M^{-1} cm^{-1}) [28]. Parameters k_6 and k_5 refer to the rate of disappearance of Cr^{VI} and Cr^V, respectively, and were evaluated from a non-linear iterative computer fit of Eq. (2). In this equation, k_6 appears in the numerator of the pre-exponential term and $2k_6$ appears in the denominator and in the exponential term because, according to the proposed reaction scheme, only one half of the Cr^{VI} reaches Cr^{III} through a Cr^V intermediate. Fig. 5(a) shows a typical curve for one run at 350 nm and the curve fit according to Eq. (2). The calculated kinetic parameters, k_6 and k_5, for various concentrations of Myo at fixed concentrations of $HClO_4$ are summarized in Table 1.

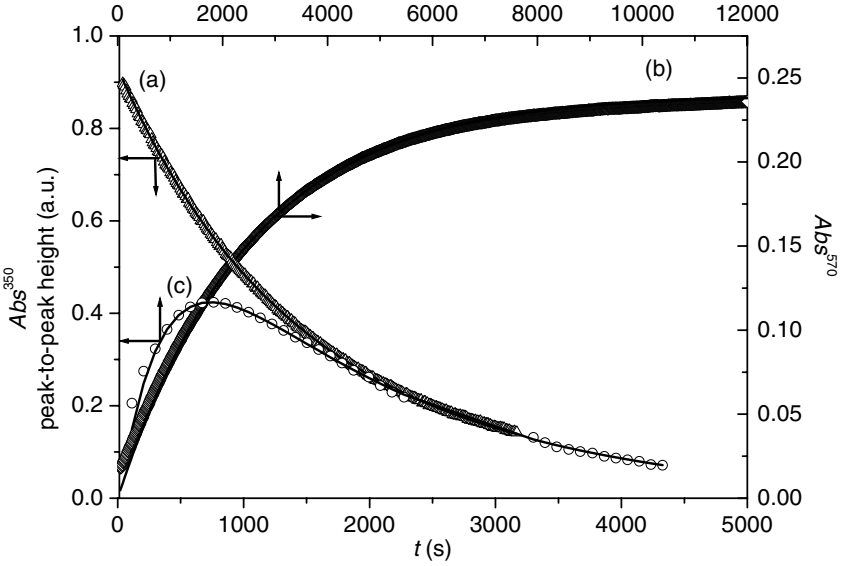


Fig. 5. Curves showing absorbance and EPR signal height vs. time for the oxidation of Myo by Cr^{VI}, I = 1.0 M, [H^+] = 0.20 M. (a) λ = 350 nm, [Cr^{VI}] = 6.0×10^{-4} M, [Myo] = 0.24 M; T = 33 °C; (b) λ = 570 nm, [Cr^{VI}] = 1.5×10^{-2} M, [Myo] = 0.24 M, T = 33 °C; (c) g_{iso} = 1.9800, [Cr^{VI}] = 8.0×10^{-3} M, [Myo] = 0.51 M, T = 20 °C. Fitted lines were calculated using Eqs. (2)–(4).

Table 1
Observed pseudo-first-order rate constants (k_6 and k_5) for different concentrations of $HClO_4$ and Myo

[Myo] (M)	0.06	0.12	0.15	0.18	0.24	
					350 nm	570 nm[a]
$[HClO_4]$ (M) 10^4k_6 (s^{-1})						
0.10	0.31 (1)	0.59 (1)	0.71 (1)	1.02 (1)	1.67 (1)	1.24 (2)
0.20	1.10 (1)	2.25 (6)	2.56 (4)	3.76 (3)	4.93 (1)	4.39 (3)
0.25	1.40 (5)	3.00 (1)	4.80 (9)	5.34 (9)	7.50 (9)	7.15 (5)
0.30	1.82 (6)	3.90 (9)	5.34 (2)	6.55 (5)	8.70 (9)	9.36 (8)
0.40	3.90 (1)	7.20 (8)	10.0 (1)	12.1 (3)	15.2 (1)	16.2 (1)
$[HClO_4]$ (M) 10^4k_5 (s^{-1})						
0.10	0.69 (1)	1.17 (1)	1.92 (1)	2.04 (1)	2.30 (8)	2.00 (7)
0.20	1.62 (8)	2.90 (9)	3.19 (9)	3.79 (3)	5.08 (1)	4.31 (2)
0.25	2.38 (3)	4.43 (3)	5.64 (9)	6.11 (4)	7.66 (9)	6.74 (5)
0.30	3.34 (9)	5.91 (9)	7.18 (4)	9.80 (1)	12.5 (1)	11.5 (1)
0.40	7.95 (1)	9.31 (3)	13.4 (7)	15.4 (6)	23.9 (1)	19.6 (1)

$T = 33$ °C; $[Cr^{VI}]_0 = 6 \times 10^{-4}$ M; $I = 1$ M.
[a] $[Cr^{VI}] = 15 \times 10^{-3}$ M.

The possible contribution of a Cr^{IV} intermediate species to Abs^{350} was disregarded because the rate constant for the formation of CrO_2^{2+} (k_f) equals $k_6 - k_f$ was calculated from the $Abs^{245}(CrO_2^{2+})$ vs. time curve, where $Abs^{245}(CrO_2^{2+}) = Abs^{245} - Abs^{245}(Cr^{VI} + Cr^{V})-$. This result means that the $Cr^{IV} \rightarrow Cr^{II}$ is a fast step in the $Cr^{VI} \rightarrow Cr^{IV} \rightarrow Cr^{II}$ pathway and Cr^{IV} reacts much rapidly than forms.

The electronic and EPR spectra show that the final Cr species in the reaction mixture is the free aqueous Cr^{3+}. At 570 nm, where only Cr^{3+} absorbs, the experimentally observed Cr^{3+} growth curves could be fitted to the expression derived from Scheme 2 for the Cr^{3+} present in the mixture at any time (Eq. (3))

$$Abs^{570} = Abs_\infty\{1 + [(k_5 - k_6)e^{-2k6t} - k_6e^{-k5t}]/(2k_6 - k_5)\} \quad (3)$$

Values of k_5 and k_6 obtained with Eq. (3) are in good agreement with those calculated from Eq. (2), for 0.24 M Myo and 0.10 to 0.40 M $HClO_4$ (Table 1). A typical fit of experimental data at 570 nm by using Eq. (3) is shown in Fig. 5(b).

The values of k_6 and k_5 were independently confirmed by monitoring the redox reaction by EPR spectroscopy. In 0.20 M $HClO_4$ and 500:1 Myo:Cr^{VI} molar ratio, the Cr^{V} EPR signal at $g_{iso} = 1.9800$ was found to grow, reach a maximum and then decay (Fig. 5(c)). The peak-to-peak height of the EPR signal as a function of time could be fitted to the expression derived from Scheme 2 for the total Cr^{V} present in the reaction mixture (Eq. (4))

$$EPR_{height} = k_6[Cr^{VI}]_0U(e^{-k5t} - e^{-2k6t})/(2k_6 - k_5) \quad (4)$$

In this equation, the U parameter depends on the EPR spectrometer acquisition conditions (gain, power, modulation, etc.). The calculated rate constants for the formation and disappearance of the intermediate Cr^{V}, k_6, and k_5, are consistent with those obtained from the spectrophotometric measurements. The lower temperature (25 °C, instead of 33 °C) used in the EPR measurements accounts for the slightly delayed t_{max} observed by this technique. The intensity of the minor signal decayed with time at the same rate as the major one.

4.4. k_6 and k_5 dependencies on [Myo] and [H^+]

In the range of $[H^+]$ used in the kinetic studies, plots of k_6 vs. [Myo] gave good straight lines from which values of k_{6H} were determined (Fig. 6). The bimolecular rate constant k_{6H} varied with $[H^+]$ (inset in Fig. 6) according to Eq. (5)

$$k_{6H} = k_I[H^+] + k_{II}[H^+]^2 \quad (5)$$

where $k_I = (3.22 \pm 1.3) \times 10^{-3}$ M^{-2} s^{-1}, and $k_{II} = (31.9 \pm 4.5) \times 10^{-3}$ M^{-3} s^{-1}.

At constant $[H^+]$, plots of k_5 vs. [Myo] showed a linear dependence on [Myo] (Fig. 7), from which the bimolecular rate constants k_{5H} were calculated. k_{5H} showed a second-order dependence on $[H^+]$ (inset in Fig. 7), with a slope $k_{III} = (56.67 \pm 1.83) \times 10^{-3}$ M^{-3} s^{-1}.

The complete rate laws for the Cr^{VI} and Cr^{V} disappearance are then given by

$$-d[Cr^{VI}]/dt = 2k_6[Cr^{VI}] = 2(k_I[H^+] + k_{II}[H^+]^2)[Myo][Cr^{VI}] \quad (6)$$

$$-d[Cr^{V}]/dt = k_5[Cr^{V}] = k_{III}[H^+]^2[Myo][Cr^{V}] \quad (7)$$

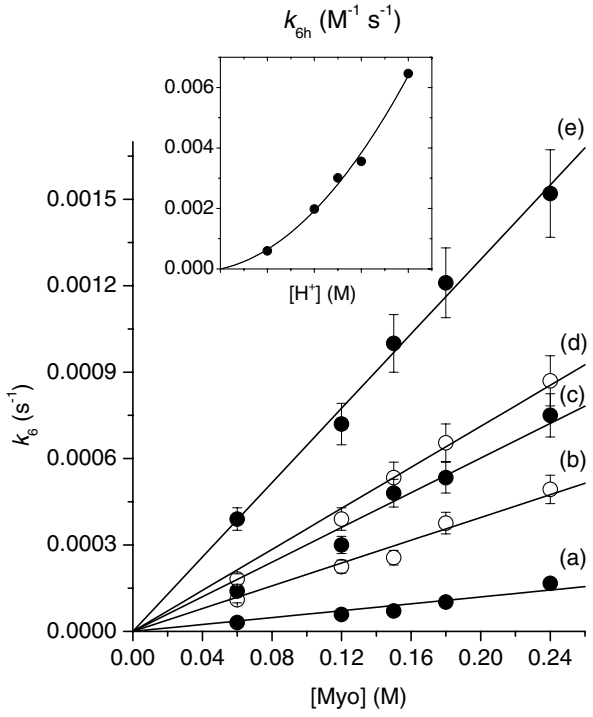


Fig. 6. Effect of [Myo] on k_6 at 33 °C, $I = 1.0$ M and $[H^+]$: (a) 0.10; (b) 0.20; (c) 0.25; (d) 0.30 and (e) 0.40 M. Inset: dependence of k_{6h} on $[H^+]$.

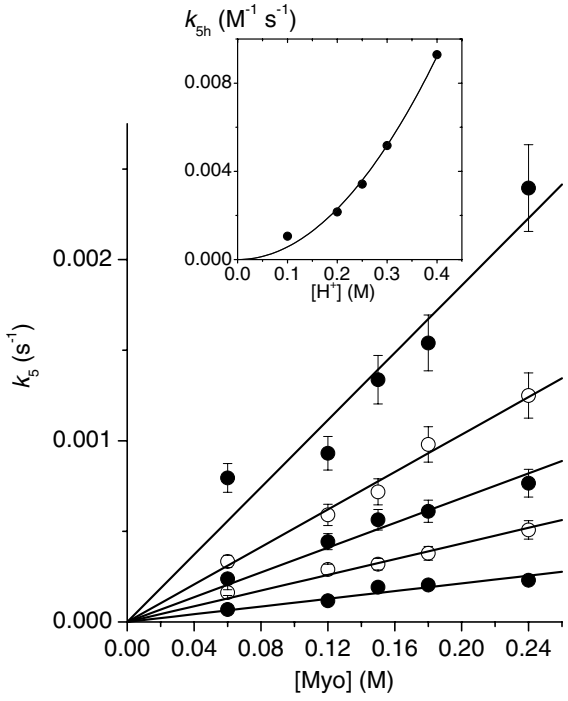
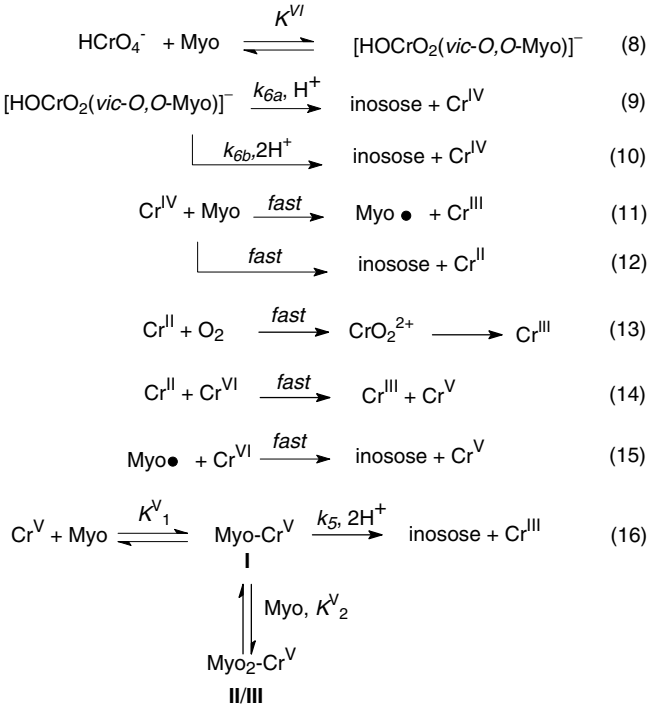


Fig. 7. Effect of [Myo] on k_5 at 33 °C, $I = 1.0$ M and [H^+]: (a) 0.10; (b) 0.20; (c) 0.25; (d) 0.30 and (e) 0.40 M. Inset: effect of acidity on k_{5h}.



Scheme 3.

4.5. Mechanism of the oxidation of Myo by Cr^{VI} and Cr^V

In the range of substrate and acid concentration used in this work, the oxidation of Myo by Cr^{VI} is a complex multistep reaction yielding Cr^{3+} and inosose as final redox products. In Scheme 3, we propose a mechanism that takes into account (a) the kinetic results, (b) the polymerization of acrylamide added to the reaction mixture, (c) the detection of an intermediate Cr^{VI} ester and oxochromate(V) species, (d) the reaction products, and (e) the 50% yield of CrO_2^{2+}.

In the [H^+] range under study, Cr^{VI} may exist as $HCrO_4^-$ [37], and this species is proposed as the reactive form of Cr^{VI}, in agreement with the first-order dependence of the reaction rate on [Cr^{VI}]. It is known that the chromic oxidation of alcohols and glycols are preceded by the formation of a chromate ester [23,24]. The observation of the absorbance band characteristic of chromate ester around 371 nm a few minutes after mixing Myo and Cr^{VI}, under conditions where the redox reaction is extremely slow, reveals that such an intermediate Cr^{VI} complex is rapidly formed prior to the redox step. Thus, the first step of the mechanism proposed in Scheme 3 (Eq. (8)) can be interpreted as the formation of a Myo–Cr^{VI} monochelate, with the cyclitol acting as a bidentate ligand bound to Cr^{VI} via any pair of appropriately disposed hydroxyl groups.

The two terms in the rate law result from the fact that there are at least two transition states, through which the reduction of Cr^{VI} can proceed. Thus, the oxidation of Myo by Cr^{VI} is proposed to occur through two parallel slow steps, catalyzed by one or two protons, respectively, leading to the redox products (Eqs. (9) and (10)). These slow steps are proposed to involve a two-electron intramolecular transfer to yield Cr^{IV} and the inosose. The formation of Cr^{IV} is consistent with the observation of CrO_2^{2+}, the product of the reaction of Cr^{II} with O_2, which is taken as evidence of the Cr^{IV} formation [17,25].

After the slow redox steps, Cr^{IV} is predicted to react with excess Myo to yield Cr^{III} and a Myo radical or Cr^{II} and inosose through two competitive fast steps (Eqs. (11) and (12)). The first is supported by the observed polymerization of acrylamide when it is added to the reaction mixture, while the second, by the formation of CrO_2^{2+}. Cr^{IV} + Myo is proposed to be faster than reaction Cr^{VI} + Myo, a fact supported by the $[CrO_2^{2+}]/[Cr^{VI}]_0$ ratio of 0.5. The 50% yield of CrO_2^{2+} means that Eqs. (11) and (12) are fast reactions and that CrO_2^{2+} and Myo radical are formed at the rate of Cr^{VI} consumption (slow step).

Cr^V can form by fast reaction of Cr^{II} with Cr^{VI} (Eq. (14)) – the [Cr^{VI}] used in the kinetic experiments is higher than used for the detection of CrO_2^{2+}, therefore Cr^{VI} can successfully compete with O_2 for Cr^{II} –, and, alternatively, by rapid reaction of the Myo radical with Cr^{VI} (Eq. (15)). Under the experimental conditions used in the kinetic experiments (more diluted Cr^{VI} solutions than used to detect CrO_2^{2+}), Eq. (13) can be neglected [25].

The kinetic data indicate that Cr^V formed in the fast steps can further oxidize Myo through an acid catalyzed step to yield Cr^{III} and the inosose as the final redox products. In the scheme, it is proposed that Cr^V reacts with Myo to form an oxo-Cr^V–Myo monochelate (species **III**

observed in the EPR spectra) that yield the redox products through an acid catalyzed step (Eq. (16)). At higher pH, this redox path is much slower than reaction with a second Myo molecule to yield the oxo-Cr^{V}–Myo_2. This proposal is in agreement with the EPR spectra at pH 4.4 and 7.4 that show the oxo-Cr^{V}–Myo_2 species (**I**, **II**) as the main Cr^{V} species present in the mixture.

5. Conclusions

The present study shows that Myo is able to stabilize Cr^{VI} and Cr^{V} species at pH 4–7, but at higher $[H^+]$ redox reaction occurs and Cr^{III} and the inosose are the final redox products. The kinetic results show that all the redox steps, involving either Cr^{VI} or Cr^{V}, require one or two protons, thus explaining the lack of redox reaction at the higher pH and the formation of oxo-Cr^{VI}/Myo and oxo-Cr^{V}/Myo species that remain in solution long time (days to months). This behavior is analogous to that of alditols [38] and aldoses [39], which are oxidized by Cr^{VI} (and Cr^{V}) at pH < 1 – at rates similar to Myo –, and form stable Cr^{VI} and Cr^{V} chelates at pH > 2.

Acknowledgements

This work was supported by the National Research Council of Argentina (CONICET), the National Agency for Sciences Promotion (ANPCyT), the National University of Rosario (UNR) and the Grant HU/A01/EV1/01 (Scientific Co-operation Project between Argentina and Hungary).

References

[1] C.B. Klein, in: L.W. Chang (Ed.), Toxicology of Metals, CRS-Lewis Publishers, New York, 1996, p. 205.
[2] S.A. Katz, H. Salem, in: The Biological and Environmental Chemistry of Chromium, VCH Publishers, New York, 1994.
[3] J. Barnhart, Chromium in soil: perspectives in chemistry, health, and environmental regulation, J. Soil Contamination (special issue) 6 (1997) 561.
[4] P.C. Grevat, Toxicological Review of Hexavalent Chromium (CAS No. 18540-29-9), US Environmental Protection Agency, Washington, DC, 1998.
[5] X. Shi, A. Chiu, C.T. Chen, B. Halliwell, V. Castranova, V. Vallyathan, J. Toxicol. Environm. Health, Part B (1999) 87.
[6] M. Costa, Crit. Rev. Toxicol. 27 (1997) 431.
[7] R. Cood, C.T. Dillon, A. Levina, P.A. Lay, Coord. Chem. Rev. 216–217 (2001) 537.
[8] E.S. Gould, Coord. Chem. Rev. 135–136 (1994) 651.
[9] D.K. Geiger, Coord. Chem. Rev. 164 (1997) 261.
[10] S. Signorella, C. Palopoli, M. Santoro, S. García, V. Daier, J.C. González, V. Roldán, M.I. Frascaroli, M. Rizzotto, L.F. Sala, Res. Trends 7 (2001) 197.
[11] K. Othmer, Encycl. Chem. Technol. 24 (1983) 50.
[12] T. Levine, Eur. Neuropsychopharmacol. 7 (1997) 147.
[13] I.M. Kolthoff, E.B. Sandell, E.J. Meehan, S. Bruchenstein, in: S.R.L. Nigar (Ed.), Análisis Químico Cuantitativo, 1988, p. 806.
[14] International Agency for Research on Cancer (IARC), Monogr. Eval. Carcinog. Risk Chem. Hum. Suppl. 7 (1987) 165.
[15] R. Feldman, Occupational and Environmental Neurotoxicology, Lippincott-Raven Publishers, Philadelphia, 1999, p. 337.
[16] A.B.P. Lever, Inorganic Electronic Spectroscopy, second ed., Elsevier, Amsterdam, 1984, p. 419.
[17] S.I. Scott, A. Bakac, J.H. Espenson, J. Am. Chem. Soc. 113 (1991) 7787.
[18] M. Krumpolc, J. Rocek, Inorg. Synth. 20 (1980) 63.
[19] M.C. Ghosh, E.S. Gould, Inorg. Chem. 30 (1991) 491.
[20] G.E. McCasland, in: R.L. Whistler, M.L. Wolfrom (Eds.), Methods in Carbohydrate Chemistry, vol. 1, Academic Press, New York, 1962, p. 289.
[21] F. Snell, C. Snell, Colorimetric Methods of Analysis, vol. IIB., Van Nostrand, New York, 1961, p. 353.
[22] WinSIM EPR calculations for MS-Windows, version 0.96, National Institute of Environmental Health Sciences, 1995.
[23] J.K. Beattie, G.P. Haight, in: J.O. Edwards (Ed.), Inorganic Reaction Mechanisms Part II, Wiley, New York, 1972.
[24] M. Mitewa, P. Bontchev, Coord. Chem. Rev. 61 (1985) 241.
[25] S. Scott, A. Bakac, J. Espenson, J. Am. Chem. Soc. 114 (1992) 4205.
[26] A. Al-Ajlouni, A. Bakac, J.H. Espenson, Inorg. Chem. 33 (1994) 1011.
[27] J.C. González, S. García, N. Mamana, L.F. Sala, S. Signorella, Inorg. Chem. Commun. 9 (2006) 437.
[28] V. Roldán, M. Santoro, J.C. González, J.M. Salas Peregrin, S. Signorella, L.F. Sala, J. Inorg. Biochem. 98 (2004) 347.
[29] J.C. González, V. Daier, S. García, B. Goodman, A.M. Atria, L.F. Sala, S. Signorella, J. Chem. Soc., Dalton Trans. (2004) 2288.
[30] G. Barr-David, M. Charara, R. Codd, R.P. Farrell, J.A. Irwin, P.A. Lay, P. Bramley, S. Brumby, J.Y. Ji, G.R. Hanson, J. Chem. Soc., Faraday Trans. 91 (1995) 1207.
[31] R. Brambley, J.Y. Li, P.A. Lay, Inorg. Chem. 30 (1991) 1557.
[32] R. Codd, P.A. Lay, J. Am. Chem. Soc. 121 (1999) 7864.
[33] S. Signorella, J.C. González, L.F. Sala, J. Argentine Chem. Soc. 90 (2002) 1.
[34] M. Branca, G. Micera, Inorg. Chim. Acta 156 (1988) 61.
[35] G.P. Haight, G.M. Jursich, M.T. Kelso, P.J. Merrill, Inorg. Chem. 24 (1985) 2740.
[36] R.G. Wilkins, The Study of Kinetics and Mechanism of Reactions of Transition Metal Complexes, Allyn & Bacon, Boston, 1974, p. 20.
[37] N.E. Brasch, D.A. Buckingham, A.B. Evans, C.R. Clark, J. Am. Chem. Soc. 118 (1996) 7969.
[38] V. Roldán, V. Daier, B. Goodman, M. Santoro, J.C. González, N. Calisto, S. Signorella, L.F. Sala, Helv. Chim. Acta 83 (2000) 3211.
[39] S. Signorella, V. Daier, S. García, R. Cargnello, J.C. González, M. Rizzotto, L.F. Sala, Carbohydr. Res. 316 (1999) 14.

Available online at www.sciencedirect.com
ScienceDirect
Polyhedron 26 (2007) 178–183
POLYHEDRON
www.elsevier.com/locate/poly

Synthesis, characterization and reactivity of a novel ruthenium(II) complex containing polypyridyl ligand

Debabrata Chatterjee *, Ayon Sengupta, Anannya Mitra

Chemistry Group, Central Mechanical Engineering Research Institute, M.G. Avenue, Durgapur, West Bengal 713 209, India

Received 17 June 2006; accepted 9 August 2006
Available online 12 August 2006

Abstract

The $[Ru^{II}(trpy)(pic)(H_2O)]^+$ (**1**) was synthesized and characterized by analytical, spectral (UV–Vis and IR), molar conductivity, magnetic moment and electrochemical studies. Complex **1** catalyzes the epoxidation of styrene and stilbenes in presence of *tert*-butyl hydroperoxide (*t*-BuOOH) in dichloromethane at room temperature. No epoxide formation was observed in presence of the radical trapping agent (benzoquinone). A mechanism involving formation of [Ru–O(*t*-Bu)–O]˙ type of radicaloid intermediate as an active intermediate responsible for epoxide formation is proposed for the catalytic epoxidation process.
© 2006 Elsevier Ltd. All rights reserved.

Keywords: Ruthenium(II)-complex; Ruthenium(IV)-complex; Terpyridine ligand; *t*-BuOOH; Alkene epoxidation

1. Introduction

Over the past two decades it has been shown that the polypyridyl complexes of ruthenium are of great significance as they are coordinatively stable both in higher and lower oxidation states, and a variety of polypyridyl complexes of ruthenium are reportedly known to be effective stoichiometric and/or catalytic reagents toward oxidation of a variety organic and inorganic substrates. In this regard ruthenium-oxo-polypyridyl complexes such as $[Ru(bipy)_2(py)(O)]^{2+}$ (biy = 2,2′-bipyridine) [1] and $[Ru^{IV}(trpy)(bipy)(O)]^{2+}$ (tpy = 2,2′,6′,2″-terpyridine) [2] are reportedly known to be a very powerful oxidants toward oxidation of various organic substrates. However, catalytic application of $[Ru^{II}(tpy)(XY)(H_2O)]$ type of complexes toward hydrocarbon oxidation using a terminal oxidant has not been reported till date. Recently, we have been engaged in developing [Ru(TDL)(XY)(H_2O)] type of ruthenium(III) catalyst complexes (where TDL = tridentate ligands; XY = bidentate ligands) that exhibit selectivity toward oxo-functionalization of saturated and unsaturated hydrocarbons [3]. The use of mixed-ligand complexes of ruthenium of the type $[Ru^{III}(TDL)(XY)(H_2O)]$ are particularly intriguing in view of exploiting a combined effects with regards to the metal redox chemistry and geometry. Incorporation of nearly 'flat' TDL in the metal complexes could afford a near planar geometry for the catalytic species for which side-on-approach for the organic substrate would be easier stereochemically. Moreover, TDL's provide sites that can undergo stereogenic as well as chiral substitution, thus rendering promising chiral controlling shapes for asymmetric catalysis [3c,3d]. Secondly, the electrophilicity of the ruthenium center could be tuned by changing the ancillary ligand (XY). The present investigation is undertaken to examine the catalytic properties of $[Ru^{II}(tpy)(XY)(H_2O)]$ type of complexes toward olefin epoxidation using a terminal oxidant. We wish to report herein, the synthesis and characterization of a new $[Ru^{II}(tpy)(pic)(H_2O)]^+$ ($pic^- =$ picolinate) complex and its catalytic application, first instance of any $[Ru^{II}(tpy)(XY)(H_2O)]$ complex, toward epoxidation of various alkenes (viz. styrene and substituted styrenes, stilbenes, cyclohexene, 1,2-dihydronaphthalene) in presence of *t*-BuOOH as a terminal

* Corresponding author. Tel.: +91-343-5510263; fax: +91-343-2546745.
E-mail address: dchat57@hotmail.com (D. Chatterjee).

0277-5387/$ - see front matter © 2006 Elsevier Ltd. All rights reserved.
doi:10.1016/j.poly.2006.08.005

oxidant under ambient conditions. The use of *t*-BuOOH is of significance in regard to its by-product, environmentally friendliness and price.

2. Experimental

2.1. Materials

The starting compound $[Ru(tpy)Cl_3]\cdot 2H_2O$ was prepared by following the literature procedure [4] and characterized by elemental analysis and spectral data which were in agreement with data reported in the literature [4]. $[Ru^{II}(trpy)(pic)H_2O]ClO_4$ (**1**) was synthesized by adopting the procedure reported for $[Ru^{II}(trpy)(bipy)H_2O]ClO_4$ [5]. All other chemicals used were of AR grade and doubly distilled H_2O was used to prepare all solutions.

2.2. Synthesis of $[Ru^{II}(trpy)(pic)H_2O]ClO_4$ (1)

To a solution of $[Ru(tpy)Cl_3]\cdot 2H_2O$ (442.5 mg, 1 mmol) in water–ethanol mixture (40 ml, 75:25) containing LiCl (0.25 g, 6 mmol) and triethylamine (0.25 ml) was added picolinic acid (123.1 mg, 1 mmol), and the resultant mixture was refluxed for 4 h and filtered hot. The filtrate was cooled and the volume was reduced in rotary evaporator. A dark brown precipitate so obtained was collected on a frit and washed with chilled 3 M HCl followed by washing with acetone and finally by ether. The product [Ru(trpy)-(pic)Cl] so obtained was treated with $AgClO_4$ to obtain the desired aquo-product, $[Ru(trpy)(pic)H_2O]ClO_4$. To a hot solution of $[Ru(trpy)(pic)Cl]\cdot 3H_2O$ (1 mmol, 550.5 mg) was added $AgClO_4$ (1 mmol, 225.3 mg) and the reaction mixture was heated for 15 min. AgCl produced was filtered off and the volume of the filtrate was reduced in rotary evaporator. A brown mass was obtained which was washed with a minimum amount of cold water and dried in air. Yield. (65%). *Anal.* Calc. for $C_{21}H_{17}N_4O_7RuCl$: Calc. C, 43.9; H, 2.96; N, 9.76. Found. C, 44.2; H, 3.1; N, 9.5%. Λ_M ($\Omega^{-1}\,M^{-1}\,cm^2$) in $H_2O = 86$. $m/z = 473.98$. UV–Vis in H_2O: λ_{max} (ε_{max}): 495 (5234), 361s (5800), 316 (20 746), 284 (18 000), 268 (20 200); UV–Vis in CH_3CN: λ_{max} (ε_{max}): 540 (3600), 380 (5250), 316 (12 700), 240 (16 000); IR: ν_{COO^-} 1626 cm^{-1}, $\nu_{C=N}$ 1595 cm^{-1}. ^1H NMR (in CD_3CN, δ ppm): 8.54 (t, 2H, $J = 7.3$, H3′), 8.29 (t, 3H, $J = 7.8$, H3 + a), 8.05 (t, 1H, $J = 8.0$, H4′), 7.92 (td, 2H, $J_1 = 7.7$, $J_2 = 1.3$, H4), 7.61 (d, $J = 6.7$, Hb), 7.26 (d, 2H, $J = 5.8$, Hc), 6.92 (d, $J = 5.7$, Hd).

2.3. Instrumentation

The UV–Vis electronic absorption spectra were obtained on a Perkin–Elmer (Model Lambda 35) spectrophotometer. IR spectra were collected on a Perkin–Elmer (Model 783) spectrometer using KBr pellets. NMR studies were performed on a Bruker 300AC NMR spectrometer. Cyclic voltammetric experiments were conducted in a glass cell equipped with a glassy carbon working electrode, platinum-wire auxiliary electrode and standard calomel electrode (SCE) as reference electrode. A CH Electrochemical Instruments (CHI-660B) was used for this purpose. Coulometric experiments were performed using a platinum gauge working electrode. A sample of **1** (5 mg) dissolved in 25 ml of an aqueous solution of $NaClO_4$ (0.2 M) was used for constant potential electrolysis. Electrolysis of the bulk solution was carried out at pH 6.7. The values of '*n*' estimated from the coulomb readings were found to lie in the range 0.95–0.98. The oxidized solution was suitably diluted for spectrophotometric measurements. Magnetic susceptibility was measured by using a PAR-155 vibrating sample magnetometer. A Perkin–Elmer 240C elemental analyzer was used to collect microanalytical (C,H,N) data.

2.4. Kinetic studies

The kinetics of the reaction of **1** with terminal oxidant *t*-BuOOH was studied spectrophotometrically under pseudo-first order condition of excess oxidant (10–40 times) at 500 nm where appreciable spectral changes exist. The solution temperature was maintained to within ±0.1 °C using a circulating water bath (JEIO TECH RW-1025G). The pH of the solutions was measured with a Mettler Delta 350 pH meter. Phosphate buffer was used to maintain the pH at 6.2 during the kinetic studies.

2.5. Procedure of catalytic studies

In a typical experiment 0.01 mmol of the catalyst complex (**1**), 1.0 mmol of 70% aqueous *t*-BuOOH oxidant and 1.0 mmol of substrate in 5 ml of CH_2Cl_2 were rapidly magnetically stirred at room temperature (25 °C). For radical trapping experiments 1.0 mmol of benzoquinone (used as radical trapping agent) was added to the above catalytic system. At the end of the reaction an internal standard (decane) was added and an aliquot was taken for GC analysis. GC analysis was performed with a Carlo Erba GC 8000^{Top} series on Tenax column fitted with FID. GC parameters were quantified with authentic samples of product prior to the analysis.

3. Results and discussion

3.1. Characterization of ruthenium complexes

Complex **1** together with the NMR numbering scheme is pictorially represented in Fig. 1. A strong band in the IR spectra of the **1** appeared in the region 1590–1600 cm^{-1} is assigned to ν(C=N) stretching, whereas, the strong band in the region 1630–1635 cm^{-1} is assigned to the coordinated carboxylate group. The absorption spectrum of **1** in H_2O exhibited a number of bands in the UV–Vis region. The bands appearing in the UV region are characterized by intra-ligand ($\pi \rightarrow \pi^*$) charge transition, whereas, spectral features in the visible region (Fig. 2a) are attributed to the metal to ligand, $d\pi(Ru) \rightarrow \pi^*$(polypyridyl) charge

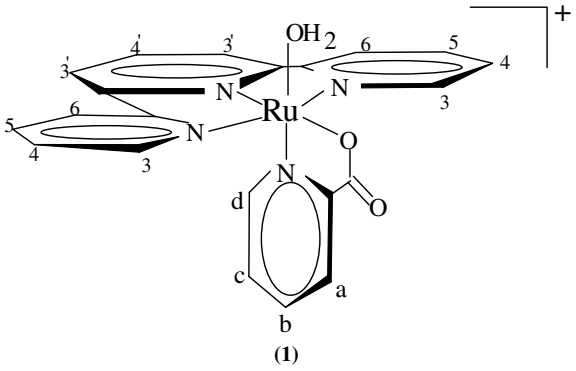


Fig. 1. Pictorial representation of $[Ru^{II}(tpy)(pic)(H_2O)]^+$ (**1**).

transitions. In the ^1H NMR spectrum of the **1**, signals for the 'tpy' ring protons as well as for the pyridyl protons of 'pic$^-$' appeared in a narrow chemical shift range (6.92–8.54 ppm). It had been reported earlier that in the $[Ru(tpy)(bipy)Cl]^+$ the two pyridyl rings of the 'bipy' moiety are non-equivalent, while the 'tpy' ligand is split into two equivalent parts by a plane of symmetry. The 6′ proton of the 'bipy' ligand which is closest to coordinated CD_3CN, has a quite low field chemical shift (9.6 ppm) with regard to other bipy protons [2a]. Absence of resonance in such a low field region plausibly indicates that the coordinated pyridyl moiety of the 'pic$^-$' is positioned *trans* to the H_2O in **1**, as shown in Fig. 1. Conductance data (see Section 2) established the 1:1 electrolyte nature of **1**.

Cyclic voltammogram of **1** in aqueous solution buffered at pH 3.8 displayed two distinct reversible waves (Fig. 3) and, the $E_{1/2}$ values corresponding to the Ru^{IV}/Ru^{III} and Ru^{III}/Ru^{II} redox couples estimated from cyclic voltammetric studies are 0.60 and 0.41 V, respectively. The potentials for two redox waves varied with the pH of the solution as recorded in Table 1. The reversibility of the Ru(IV)/(III)/(II) couples observed in the present studies is consistent with one electron, one proton transfer process as proposed in Scheme 1.

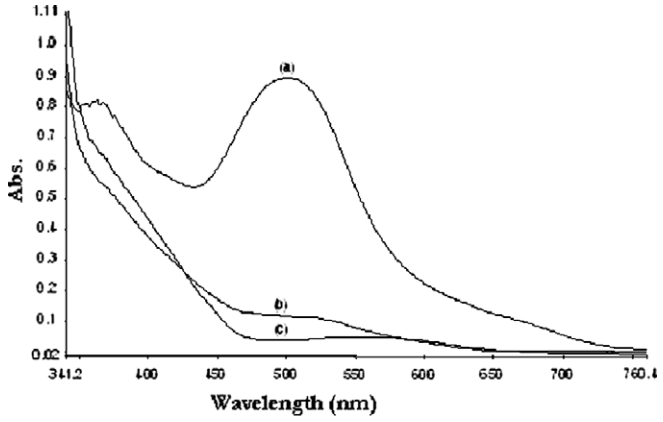


Fig. 2. Absorption spectra (a) $[Ru^{II}(tpy)(pic)(H_2O)]^+$, (b) $[Ru^{III}(tpy)(pic)(OH)]^+$ and (c) $[Ru^{IV}(tpy)(pic)(O)]^+$ in H_2O at pH 6.2.

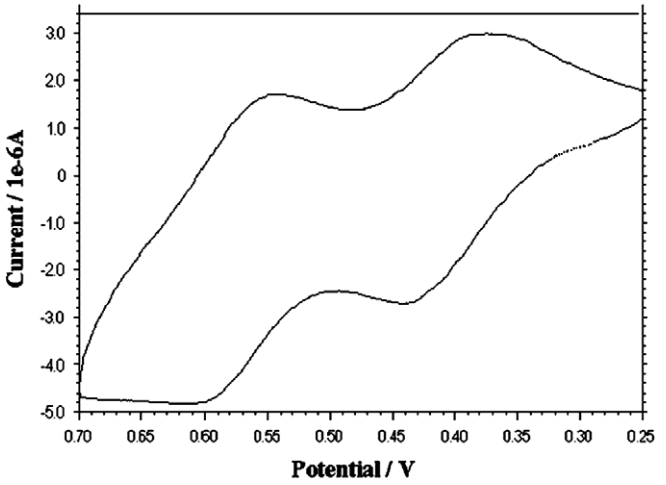


Fig. 3. Cyclicvoltammogram of $[Ru^{II}(tpy)(pic)(H_2O)]^+$ (**1**) in H_2O at pH 3.8, scan rate = 100 mV s^{-1}.

Table 1
Results of cyclic voltammetric studies of **1** at different pH[a]

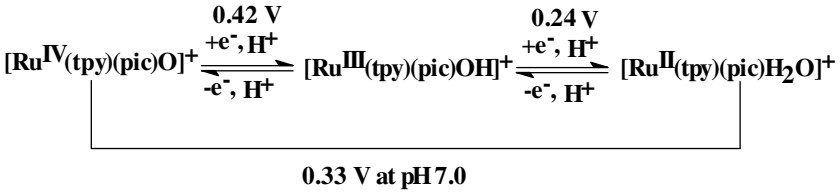
	Ru^{IV}/Ru^{III}				Ru^{III}/Ru^{II}			
pH	E_p	E_c	ΔE_p	$E_{1/2}$	E_p	E_c	ΔE_p	$E_{1/2}$
3.8	0.63	0.57	60	0.60	0.44	0.38	70	0.41
5.1	0.58	0.52	60	0.55	0.40	0.34	50	0.37
7.0	0.45	0.39	70	0.42	0.27	0.21	60	0.24
9.2	0.38	0.31	70	0.345	0.18	0.12	60	0.15

[a] Potentials are expressed against SCE; scan rate 100 mV s^{-1}.

The spectrum of $[Ru^{III}(tpy)(pic)OH]^+$ species generated electrochemical oxidation (bulk electrolysis at 0.42 V , pH 3.8) is shown in Fig. 2b.

3.2. Catalysis of alkene epoxidation

Prior to the catalytic experimentation we performed a brief kinetic study of the reaction of **1** with *t*-BuOOH demonstrated by the spectral changes as shown in Fig. 4. The rate of the reaction was found to be first order with respect to [**1**] and the values of pseudo-first order rate constant (k_{obs}) increased linearly by increasing [*t*-BuOOH]. The temperature dependence studies of the reaction yielded rate-constant (k) values of 3.26, 3.85, 4.46, 5.31 and 6.20 M^{-1} s^{-1} at 25, 30, 35, 40 and 45 °C, respectively at pH 6.2. The values of activation parameters obtained from the above studies are $\Delta H^{\neq} = 21 \pm 0.4$ kJ mol^{-1} and $\Delta S^{\neq} = -161 \pm 1.3$ J mol^{-1} deg^{-1}. Comparison of the spectral feature of the resultant solution at the end of the reaction (Fig. 4) with that of shown in Fig. 2b, indicative of the formation of ruthenium(III)-species in the solution. The results of epoxidation of selected alkenes catalyzed by **1** using *t*-BuOOH as a precursor oxidant are summarized in Table 2. In all cases, epoxides were found to be the major product, however, minor amounts of benzaldehyde was also obtained in each case (Table 2). In presence of the radical trap (BQ) negligible amount of product (<1%) formation was observed after 10 h of reaction. A mixture



Scheme 1.

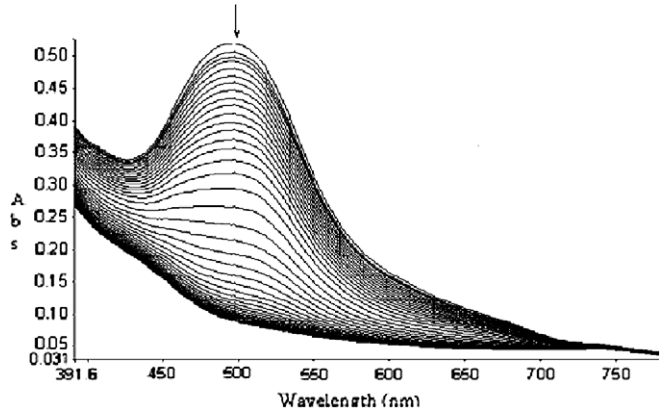


Fig. 4. Spectral changes that occurs in the reaction of **1** (1×10^{-4} M) with *t*-BuOOH (1×10^{-2} M) in H_2O at 25 °C, pH 6.0.

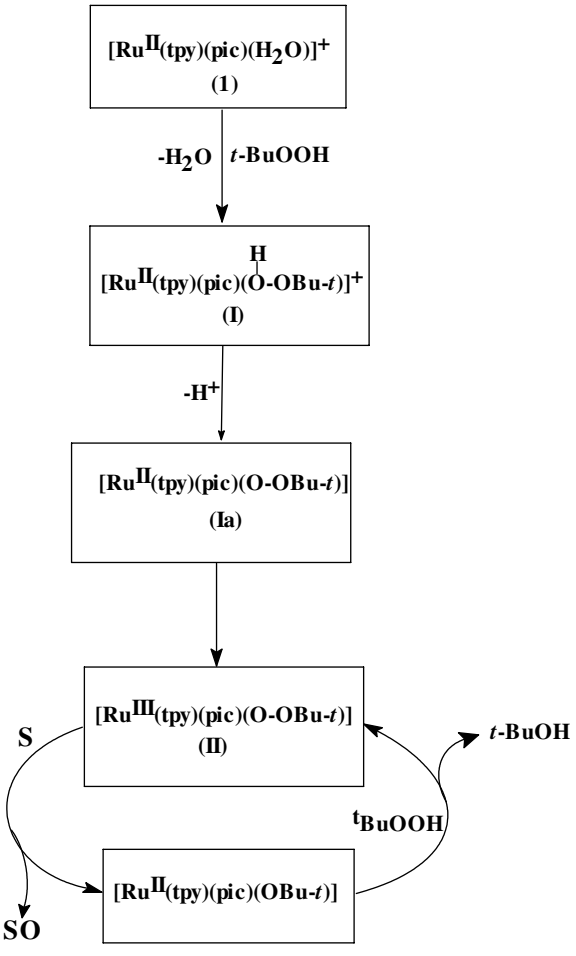
Table 2
Results of epoxidation of *cis*-stilbene, *trans*-stilbene and styrenes catalyzed by the **1** at ambient conditions[a]

Substrate	Product	Yield (%)[b]
Styrene	styrene oxide	54
	benzaldehyde	14
4-Chlorostyrene	4-chlorostyrene oxide	51
	4-chlorobenzaldehyde	13
4-Methylstyrene	4-methylstyrene oxide	59
	4-methylbenzaldehyde	15
4-Methoxystyrene	4-methoxystyrene oxide	57
	4-methoxybenzaldehyde	13
cis-Stilbene	*cis*-stilbeneoxide	16
	trans-stilbeneoxide	34
	benzaldehyde	15
trans-Stilbene	*cis*-stilbeneoxide	not detected
	trans-stilbeneoxide	55
	benzaldehyde	13
Cyclohexene	cyclohexene oxide	43
1,2-Dihydronaphthalene	1,2-dihydronapthalene oxide	54

[a] Identification and quantification of epoxides of stilbenes were carried out by following an earlier report on the ^{1}H NMR analysis of stilbene epoxides [13], wherein, the peaks at 3.90 and 4.31 ppm were assigned to *trans*-stilbene oxide and *cis*-stilbene oxide, respectively.
[b] Based on alkene taken. Reaction time 5 h.

of *cis*- and *trans*-epoxides was produced (Table 2) during epoxidation of *cis*-stilbene. The loss of stereoselectivity necessarily indicates the radicaloid character of the intermediate species formed during epoxidation, which allowed a limited amount of rotation through –C–C– bond prior to the epoxide formation. The results of the above investigation taken together provide a qualitative picture of the alkene epoxidation in presence of **1** and *t*-BuOOH in dichloromethane. The formation of a [Ru–O(*t*-Bu)–O]$^{\bullet}$ type of radicaloid intermediate species in resemblance to that of reported earlier in the catalytic oxidation of alkanes with *t*-BuOOH using *cis*-$[Ru^{II}(L)_2(H_2O)_2]^{2+}$ (L = polypyridyl ligands) [6a] and $[Ru^{III}(Me_3tacn)(H_2O)(CF_3CO_2)]^{2+}$ [6b] as catalysts, is proposed in the plausible stepwise mechanisms (Scheme 2) for complex-**1** catalyzed epoxidation of alkenes in the present case. No product formation in presence of BQ (radical trap) further substantiates the formation such intermediate.

In the first step of the proposed mechanism (Scheme 2), **1** reacts with *t*-BuOOH to form an intermediate $[Ru^{II}(tpy)(pic)(OHO^tBu)]^+$ (**I**) species in a rate determining aquo-substitution step. Coordinated *t*-BuOOH undergoes



Scheme 2.

Table 3
Comparison of **1** with other Ru-based catalytic system for epoxidation of *trans*-stilbene using *t*-BuOOH as precursor oxidant

Catalyst	Yield (%)	Time (h)	Reference
1	55	5	present work
$[Ru^{II}(terpy)(pydic)]$[a]	81	24	[7]
$[Ru^{II}(S,S'\text{-}Ph_2\text{-}pybox)(pydic)]$[b]	45	12	[8]
cis-$[Ru^{II}Cl(CH_3CN)\{\kappa^4\text{-}(1R,2R)\text{-}P(NH)(NH)P\}]^+$[c]	no epoxide	16	[9]
$[Ru^{II}(dppm)_3]^+$[d]	67	5	[10]
$[Ru^{II}(bipy)_2Cl_2]$[e]	54	24	[11]
$[Ru^{III}(Me_3tacn)(OH_2)_2(CF_3CO_2)]^{2+}$[f]	54	8	[6b]
$[Ru^{III}(Me_3tacn)(OH_2)_2(CF_3CO_2)]^{2+}$–$SiO_2$[g]	75	14	[12]

[a] terpy = 2,2′,6′,2″-terpyridine; pydic = pyridyl dicarboxylate. Reaction conditions: catalyst = 0.025 mmol, oxidant = 2.0 mmol, substrate = 0.5 mmol, solvent = CH_2Cl_2, temp. = room temperature.

[b] pybox = pyridinebisoxazoline. Reaction conditions: catalyst = 0.025 mmol, oxidant = 1.5 mmol, substrate = 0.5 mmol, solvent = CH_2Cl_2, temp. = room temperature.

[c] [(1*R*,2*R*)-P(NH)(NH)P] = (1*R*,2*R*)-*N*,*N*′-bis(diphenylphosphanyl)benzylidene]-1,2-diaminocyclohexane]. Reaction conditions: catalyst = 0.001 mmol, oxidant = 3.2 mmol, substrate = 1.5 mmol, solvent = benzene, temp. = ambient temperature; major reaction products are 2,3-diphenyloxirane (58%), benzoic acid (17%) and benzaldehyde (15%).

[d] dppm = diphenylphosphinomethane. Reaction conditions: catalyst = 12 μmol, oxidant = 5.8 mmol, substrate = 10 mmol, solvent = CH_3Cl, temp. = 50 °C.

[e] bipy = 2,2′-bipyridine. Reaction conditions: catalyst = 0.05 mmol, oxidant = 6.0 mmol, substrate = 3 mmol, solvent = CH_2Cl_2, temp. = 0 °C.

[f] Me_3tacn = 1,4,7-trimethyl-1,4,7-triazacyclononane. Reaction conditions: catalyst = 0.01 mmol, oxidant = 1 mmol, substrate = 1 mmol, solvent = CH_2Cl_2, temp. = 25 °C.

[g] Reaction conditions: catalyst = 600 mg (1% w/w), oxidant = 2.3 mmol, substrate = 1 mmol, solvent = CH_2Cl_2, temp. = room temperature.

deprotonation **Ia** and oxidize metal center to from the radicaloid intermediate **II** through an inner-sphere electron transfer pathway. Interaction between **II** and alkene appears to be the plausible route for the catalytic epoxidation of styrenes and stilbenes studied in the present work. The catalytic cycle is further repeated by the generation of **II** in the reaction between $[Ru^{II}(tpy)(pic)(OBu^t)]$ and another molecule of *t*-BuOOH as shown in Scheme 2.

The efficacy of the present system is shown with that of other reported Ru-complex/*t*-BuOOH catalytic system, taking *trans*-stilbene as a test substrate (Table 3). Since, product yield and selectivity are dependent on so many factors like, variability of solvent, reaction time and most importantly the nature of the active intermediate formed in the catalytic process, it is difficult to make any significant comparison of one system with another. However, the efficacy of the present catalytic system in terms of product yield and selectivity seems to be prospective.

4. Conclusions

The results of the present studies reveal that the $[Ru^{II}(tpy)(pic)(H_2O)]^+$ can effect alkene epoxidation in presence of *t*-BuOOH (as precursor oxidant). This work taken collectively with those on Ru-complex/*t*-BuOOH catalytic systems [6b–12] indicate the intermediacy of a radicaloid species, [Ru–O(t-Bu)–O•] in the catalytic oxidation process. This is regardless of the fact that the high-valent Ru-oxo species is capable of transferring O-atom to the alkenes, or not.

Acknowledgements

We gratefully acknowledge the financial support (No. SR/S1/IC-33/2003) obtained from Department of Science and Technology, Govt. of India. We are thankful to Dr. G. P. Sinha, Director of this institute for his encouragement to this work. AM thanks C.S.I.R. for research associateship.

Appendix A. Supplementary data

Supplementary data associated with this article can be found, in the online version, at doi:10.1016/j.poly.2006.08.005.

References

[1] (a) B.A. Moyer, M.S. Thompson, B.K. Sipe, T.J. Meyer, Inorg. Chem. 20 (1981) 1475;
(b) L. Roecker, J.C. Dobson, W.J. Vining, T.J. Meyer, Inorg. Chem. 26 (1987) 779;
(c) L.K. Stulz, M.H.V. Huynh, R.A. Binstead, M. Curry, T.J. Meyer, J. Am. Chem. Soc. 117 (1995) 2520;
(d) W.K. Seok, T.J. Meyer, J. Am. Chem. Soc. 110 (1988) 7358;
(e) L. Roecker, T.J. Meyer, J. Am. Chem. Soc. 109 (1987) 746;
(f) L.K. Stulz, M.H.V. Huynh, R.A. Binstead, M. Curry, T.J. Meyer, J. Am. Chem. Soc. 122 (2000) 5984;
(g) J.R. Bryant, J.M. Mayer, J. Am. Chem. Soc. 125 (2003) 10351.
[2] (a) W.K. Seok, M.Y. Kim, Y. Yokomori, D.J. Hodgson, T.J. Meyer, Bull. Korean Chem. Soc. 16 (1995) 619;
(b) M.S. Thompson, T.J. Meyer, J. Am. Chem. Soc. 104 (1982) 4106;
(c) M.S. Thompson, T.J. Meyer, J. Am. Chem. Soc. 104 (1982) 5070;
(d) W.K. Seok, T.J. Meyer, Inorg. Chem. 44 (2005) 3931;
(e) B.A. Moyer, M.S. Thompson, T.J. Meyer, J. Am. Chem. Soc. 102 (1980) 2310;
(f) M.S. Thompson, W.F. De Giovani, B.A. Moyer, T.J. Meyer, J. Org. Chem. 25 (1984) 4972;
(g) M. Navarro, W.F. De Giovani, J.R. Romero, J. Mol. Catal. 135 (1998) 249.
[3] (a) D. Chatterjee, A. Mitra, R.E. Shepherd, Inorg. Chim. Acta 357 (2004) 980;
(b) S. Lujan, J.M. Slocik, D. Chatterjee, A. Mitra, R.E. Shepherd, Inorg. Chim. Acta 357 (2004) 785;
(c) D. Chatterjee, S. Basak, A. Mitra, A. Sengupta, J. Le Bras, J. Muzart, Inorg. Chim. Acta 359 (2006) 1325;

(d) D. Chatterjee, S. Basak, A. Mitra, A. Sengupta, J. Le Bras, J. Muzart, J. Mol. Catal. A: Chem. 255 (2006) 283.
[4] F.P. Dwyer, H.A. Goodwin, F.C. Gyarfas, Aust. J. Chem. 16 (1963) 42.
[5] K.J. Takeuchi, M.S. Thompson, D.W. Pipes, T.J. Meyer, Inorg. Chem. 23 (1984) 1845.
[6] (a) T.C. Lau, C.-M. Che, W.O. Lee, C.K. Poon, J. Chem. Soc., Chem. Commun. (1988) 1406;
(b) W.-C. Cheng, W.-H. Fung, C.-M. Che, J. Mol. Catal A: Chem. 113 (1996) 311.
[7] H. Nishiyama, T. Shimada, H. Itoh, H. Sugiyama, Y. Motoyama, Chem. Commun. (1997) 1863.
[8] S. Bhor, M.K. Tse, M. Klawonn, C. Doebler, W. Maegerlein, M. Beller, Adv. Synth. Catal. 346 (2004) 263.
[9] W.-K. Wong, X.-P. Chen, T.-W. Chik, W.-Y. Wong, J.-P. Guo, F.-W. Lee, Eur. J. Inorg. Chem. 19 (2003) 3539.
[10] A.S. Kanmani, S. Vancheesan, J. Mol. Catal. A: Chem. 150 (1999) 95.
[11] G.A. Barf, H.D. Van den, R.A. Sheldon, Tetrahedron 52 (1996) 12971.
[12] W.-H. Cheung, W.-Y. Yu, W.-P. Yip, N.-Y. Zhu, C.-M. Che, J. Org. Chem. 67 (2002) 7716.
[13] R.E. Shepherd, Inorg. Chim. Acta 209 (1993) 201.

Available online at www.sciencedirect.com
ScienceDirect
Polyhedron 26 (2007) 184–196
POLYHEDRON
www.elsevier.com/locate/poly

Uranyl ion complexes with long chain aminoalcoholbis(phenolate) [O,N,O,O′] donor ligands

Harri Sopo, Ari Väisänen, Reijo Sillanpää *

Department of Chemistry, University of Jyväskylä, P.O. Box 35, FIN-40351 Jyvaskyla, Finland

Received 21 July 2006; accepted 8 August 2006
Available online 15 August 2006

Abstract

The reaction between uranyl nitrate hexahydrate and phenolic ligand precursor [(*N*,*N*-bis(2-hydroxy-3,5-dimethylbenzyl)-4-amino-1-butanol) · HCl], $H_3L1 \cdot HCl$, leads to a uranyl complex $[UO_2(H_2L1)_2]$ (**1a**) and $[UO_2(H_2L1)_2] \cdot 2CH_3CN$ (**1b**). The ligand [(*N*,*N*-bis-(2-hydroxy-5-*tert*-butyl-3-methylbenzyl)-4-amino-1-butanol)$H_3L2 \cdot HCl$], $H_3L2 \cdot HCl$, yields a uranyl complex with a formula $[UO_2(H_2L2)_2] \cdot CH_3CN$ (**2**). The ligand [(*N*,*N*-bis(2-hydroxy-3,5-dimethylbenzyl)-5-amino-1-pentanol) · HCl], $H_3L3 \cdot HCl$, produces a uranyl complex with a formula $[UO_2(H_2L3)_2] \cdot 2CH_3CN$ (**3**) and the ligand [(*N*,*N*-bis(2-hydroxy-5-*tert*-butyl-3-methylbenzyl)-5-amino-1-pentanol) · HCl], $H_3L4 \cdot HCl$, leads to a uranyl complex with a formula $[UO_2(H_2L4)_2] \cdot 2CH_3CN$ (**4**). The ligand [(*N*,*N*-bis(2-hydroxy-5-*tert*-butyl-3-methylbenzyl)-6-amino-1-hexanol) · HCl], $H_3L5 \cdot HCl$, leads to a uranyl complex with a formula $[UO_2(H_2L5)_2] \cdot 4$toluene (**5**). The complexes **1**–**5** are obtained using a molar ratio of 1:2 (U to L) in the presence of a base (triethylamine). The molecular structures of **1a**, **1b**, **3**, **4** and **5** were verified by X-ray crystallography. All complexes are neutral zwitterions and have similar centrosymmetric, mononuclear, distorted octahedral uranyl structures with the four coordinating phenoxo ligands in an equatorial plane. In uranyl ion extraction studies from water to dichloromethane with ligands $H_3L1 \cdot HCl$–$H_3L5 \cdot HCl$, ligands $H_3L1 \cdot HCl$, $H_3L4 \cdot HCl$ and $H_3L5 \cdot HCl$ are the most effective ones.
© 2006 Elsevier Ltd. All rights reserved.

Keywords: Uranyl ion; Uranyl ion extraction; Crystal structures; NMR studies; Phenolate ligands

1. Introduction

The world production of uranium over the past few years has been about 36 000 t (about 42 000 t of U_3O_8). This is used mainly as fuel for nuclear reactors and in different kinds of military uses, small amounts have been used as a pigment to color ceramics and glass [1]. The production and consumption of uranium on this scale causes different kinds of needs for its removal from e.g. wastes or the human body because it poses a threat to human health and environment due to its toxicity and radioactivity [2]. After an exposure to uranium, the treatment of the person afflicted consist of chelation therapy, which is aimed at binding the metal and subsequently favoring its excretion as a metal–chelate complex [3]. For that purpose chelating agents such as catechols, β-diketones and hydroxy ketones have been proposed [4]. Also other kinds of chelators which contain nitrogen in addition to oxygen have been studied in certain laboratories [5]. A common feature in these is that they are organic multidentate ligands with hard oxygen donor atoms and possibly nitrogen atoms.

The coordination chemistry of the linear UO_2^{2+} ion is dominated by between four to six donor atoms, all occupying equatorial positions resulting in octahedral, pentagonal bipyramidal or hexagonal bipyramidal coordination, respectively, for U(VI). Typical hard Lewis bases such as F^- or O-donors like phenolate O are good ligands for the hard UO_2^{2+} ion [6,7]. However, the Lewis basicity of uranyl oxo ligands is generally quite weak and they very

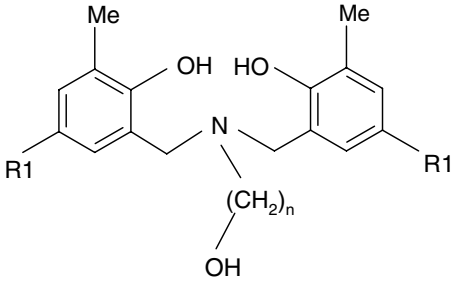
* Corresponding author. Fax: +358 14 260 2501.
E-mail address: resillan@jyu.fi (R. Sillanpää).

0277-5387/$ - see front matter © 2006 Elsevier Ltd. All rights reserved.
doi:10.1016/j.poly.2006.08.006

rarely produce, for example, polynuclear complex units by forming an oxo bridge between the U(VI) ions [8]. For uranyl extraction many kinds of ligands have been prepared and are in current use. For example, organic phosphorous oxides are used in a commercial uranyl extraction system [9] and other functional groups bound to a solid matrix have also been used for the extraction of uranyl and actinide ions [10,11]. Agents specific for sequestering the uranyl ion from biological systems are generally based on ligands containing catecholate functional groups and ligands containing keto and hydroxyl groups like hydroxypyridinones [5] and -pyridones [4]. Calixarenes and modified calixarenes have also been prepared for uranyl extraction [12]. The uranyl complexes of calixarenes possess several phenolato ligands, many such complexes have been prepared and their structures have been reviewed recently [13].

We have earlier prepared and reported on four aminoalcohol (2-aminoethanol and 3-aminopropanol) based bisphenolate ligands, which easily form complexes with the UO_2^{2+}-ion [14]. In this paper we report a set of five new ligands of a similar series, which are potential uranium chelators and have better uranyl ion extraction properties than those reported earlier. Each of the ligands contains two phenol oxygens, one alcohol oxygen and one amine nitrogen, thus there is the possibility of the ligand functioning as up to a tetradentate ligand (Scheme 1).

The syntheses of these new ligands and their uranyl ion complexes are reported below. The X-ray diffraction structures are given for five uranyl complexes. Information about the ability of these ligands to extract uranyl ions from water to dichloromethane is also presented.



Ligand	*R1*	*n*
H_3L1	Me	4
H_3L2	*t*-butyl	4
H_3L3	Me	5
H_3L4	*t*-butyl	5
H_3L5	*t*-butyl	6

Scheme 1. The ligands under study.

2. Experimental

2.1. General information

4-Amino-1-butanol (98%), 5-amino-1-pentanol (97%), 6-amino-1-hexanol (97%) (Aldrich), 4-*tert*-butyl-2-methylphenol (98%) (Fluka), triethylamine (Riedel), 2,4-dimethylphenol, 37% formaldehyde and uranyl nitrate hexahydrate (Merck) were used as supplied. The ligands were synthesized by following a procedure for methylamino-*N*,*N*-bis(1-methylene-2-naphthol) [15], but in the separation process we treated the ligands with HCl making the relevant salt of the ligand. This helped the separation of the ligand from the starting materials and byproducts. Syntheses of the ligands ($H_3L1 \cdot HCl$–$H_3L5 \cdot HCl$) were not optimized. The NMR spectra were recorded on a Bruker AVANCE DPX 250 FT-NMR spectrometer or a Bruker AVANCE DRX 500 FT-NMR spectrometer. ^1H and ^{13}C NMR spectra were recorded either in $CDCl_3$, MeOD-d_4 or DMSO-d_6 at 30 °C. Chemical shifts are reported in parts per million and referenced internally using the residual protio solvent resonances relative to tetramethylsilane ($CDCl_3$ δ 7.26, ^1H NMR; δ 77.0, ^{13}C NMR; MeOD-d_4 δ 3.30, ^1H NMR; δ 49.15, ^{13}C NMR and DMSO-d_6 δ 2.50, ^1H NMR; δ 39.50, ^{13}C NMR). Mass spectrometric measurements were performed using a Micromass LCT time of flight (TOF) mass spectrometer with electrospray ionization (ESI). Elemental analysis was performed using a VarioEl III elemental analyzer. Single crystal X-ray measurements were performed using an Enraf Nonius Kappa CCD diffractometer. Melting points were measured by a Mettler Toledo FP62 Melting Point instrument. The uranyl extraction samples were analyzed with inductively coupled plasma optical emission spectrometry (ICP-OES) at 385.958 nm using a Perkin Elmer Optima 4300DV instrument.

2.2. $H_3L1 \cdot HCl$ [(*N*,*N*-bis(2-hydroxy-3,5-dimethylbenzyl)-4-amino-1-butanol) · HCl]

To a solution of 2,4-dimethylphenol (2.44 g, 0.020 mol) in ethanol (15 ml) and water (3 ml) was added aqueous formaldehyde (37%, 3.26 g, 0.040 mol), 4-amino-1-butanol (0.89 g, 0.010 mol) and triethylamine (0.5 ml, 0.004 mol). The resulting solution was kept in a water bath (50 °C) for 118 h. The solution was then cooled down and 5 ml of 6 M HCl was added. To that solution was added 300 ml of water and it was then extracted three times with 20 ml of diethyl ether. The water phase was left to evaporate down to 100 ml of solution and it was then extracted three times with 40 ml of $CHCl_3$. The chloroform phase was evaporated and the remaining white solid was filtered, washed with diethyl ether (40 ml) and recrystallized from a mixture of CH_3CN (3 ml) and MeOH (1 ml). The solid was filtered off, washed with 10 ml of diethyl ether and dried. The yield was 0.52 g (13%). The white solid ($H_3L1 \cdot HCl$) is soluble in MeOH, EtOH and DMSO. Mp 197–199 °C.

^{1}H NMR (MeOD-d_4, 250 MHz): 1.51 (m, 2H, NCH_2CH_2), 1.90 (m, 2H, OCH_2CH_2), 2.19 (s, 6H, aryl-*Me*), 2.21 (s, 6H, aryl-*Me*), 3.18 (t, $J = 7.5$ Hz, 2H, NCH_2CH_2), 3.50 (t, $J = 6.1$ Hz, 2H, OCH_2CH_2), 4.33 (s, 4H, N–CH_2-aryl), 6.91 (s, 2H, aryl), 6.99 (s, 2H, aryl). ^{13}C NMR (MeOD-d_4, 63 MHz): 16.50, 20.53 (aryl-*Me*), 22.24, 30.26 (NCH_2CH_2, OCH_2CH_2), 54.84, 56.90, 61.88 (NCH_2CH_2, N–CH_2-aryl, OCH_2CH_2), 118.83, 126.39, 131.03, 131.41, 134.78, 152.93 (aryl). The ESI-MS measurement showed the following ion for H_3L1: $m/z = 358.20$ $[H_3L1 + H]^+$. The calculated figure was: $m/z = 358.24$ $[H_3L1 + H]^+$. Elemental *Anal.* Calc. for $C_{22}H_{32}NO_3Cl$: C, 67.07; H, 8.19; N, 3.56. Found: C, 66.67; H, 8.28; N, 3.36%.

2.3. $H_3L2 \cdot HCl \cdot H_2O$ [(N,N-bis(2-hydroxy-5-tert-butyl-3-methylbenzyl)-4-amino-1-butanol) · HCl · H_2O]

To a solution of 4-*tert*-butyl-2-methylphenol (4.55 g, 0.028 mol) in ethanol (15 ml) and water (3 ml) was added aqueous formaldehyde (37%, 3.26 g, 0.040 mol), 4-amino-1-butanol (0.89 g, 0.010 mol) and triethylamine (0.5 ml, 0.004 mol). The resulting solution was kept in a water bath (50 °C) for 118 h. The solution was then cooled down and 5 ml of 6 M HCl was added, leading to the formation of a white precipitate. This latter was filtrated, washed with cold water (200 ml), hot water (300 ml), diethyl ether (80 ml) and recrystallized from ethanol (4 ml). The solid was filtered off, washed with 10 ml of diethyl ether and dried. The yield was 1.69 g (35%). The product is soluble in $CHCl_3$, MeOH, EtOH, DMSO and acetone. Mp 180–181 °C. ^{1}H NMR ($CDCl_3$, 250 MHz): 1.25 (s, 18H, aryl-*t-bu*), 1.59 (m, 2H, NCH_2CH_2), 1.95 (m, 2H, OCH_2CH_2), 2.41 (s, 6H, aryl-*Me*), 3.18 (t, $J = 6.1$ Hz, 2H, NCH_2CH_2), 3.59 (t, $J = 5.6$ Hz, 2H, OCH_2CH_2), 4.21 (s, 4H, N–CH_2-aryl), 6.98 (s, 2H, aryl), 7.18 (s, 2H, aryl). ^{13}C NMR ($CDCl_3$, 63 MHz): 17.10, 21.97, 29.30, 31.45, 33.94 (aryl-*Me*, NCH_2CH_2, OCH_2CH_2, aryl-$C(CH_3)_3$, aryl-$C(CH_3)_3$), 54.40, 56.60, 61.03 (NCH_2CH_2, N–CH_2-aryl, OCH_2CH_2), 116.03, 125.64, 126.13, 130.29, 143.44, 151.28 (aryl). The ESI-MS measurement showed the following ion for H_3L2: $m/z = 442.35$ $[H_3L2 + H]^+$. The calculated value was: $m/z = 442.33$ $[H_3L2 + H]^+$. Elemental *Anal.* Calc. for $C_{28}H_{46}NO_4Cl$: C, 67.79; H, 9.35; N, 2.83. Found: C, 67.98; H, 9.27; N, 2.63%.

2.4. $H_3L3 \cdot HCl \cdot 0.5H_2O$ [(N,N-bis(2-hydroxy-3,5-dimethylbenzyl)-5-amino-1-pentanol) · HCl · $0.5H_2O$]

To a solution of 2,4-dimethylphenol (5.49 g, 0.045 mol) in methanol (25 ml) was added paraformaldehyde (1.65 g, 0.055 mol) and 5-amino-1-pentanol (2.66 g, 0.025 mol) with stirring. The resulting solution was refluxed for 25 h. After that the solution was evaporated, the resulting oil was dissolved in 15 ml CH_2Cl_2 and extracted three times with 10 ml of water. CH_2Cl_2 was evaporated, the obtained oil was dissolved in 10 ml of MeOH and to that solution was added 4 ml of 6 M HCl with stirring. The MeOH was evaporated and the resulting oil was dissolved in 10 ml of CH_3CN, during which a white solid separated. The solid was filtered and recrystallized with a solution of CH_3CN (8 ml) and EtOH (6 ml). The yield was 1.60 g (18%). The product is soluble in MeOH and DMSO. Mp 186–188 °C. ^{1}H NMR (MeOD-d_4, 250 MHz): 1.42 (m, 4H, $NCH_2CH_2CH_2$), 1.82 (m, 2H, OCH_2CH_2), 2.20 (s, 6H, aryl-*Me*), 2.22 (s, 6H, aryl-*Me*), 3.14 (t, $J = 7.6$ Hz, 2H, NCH_2CH_2), 3.50 (t, $J = 6.1$ Hz, 2H, OCH_2CH_2), 4.32 (s, 4H, N–CH_2-aryl), 6.90 (s, 2H, aryl), 7.00 (s, 2H, aryl). ^{13}C NMR (MeOD-d_4, 63 MHz): 16.47, 20.51 (aryl-*Me*), 23.84, 25.11, 32.75 ($NCH_2CH_2CH_2CH_2$), 54.80, 57.13, 62.44 (NCH_2CH_2, N–CH_2-aryl, OCH_2CH_2), 118.85, 126.40, 130.98, 131.46, 134.82, 152.91 (aryl). The ESI-MS measurement showed the following ion for H_3L3: $m/z = 372.23$ $[H_3L3 + H]^+$. The calculated figure was: $m/z = 372.25$ $[H_3L3 + H]^+$. Elemental *Anal.* Calc. for $C_{23}H_{35}NO_{3.5}Cl$: C, 66.25; H, 8.46; N, 3.36. Found: C, 66.75; H, 8.48; N, 3.25%.

2.5. $H_3L4 \cdot HCl \cdot 0.5H_2O$ [(N,N-bis(2-hydroxy-5-tert-butyl-3-methylbenzyl)-5-amino-1-pentanol) · HCl · $0.5H_2O$]

To a solution of 4-*tert*-butyl-2-methylphenol (3.28 g, 0.020 mol) in ethanol (15 ml) and water (3 ml) was added aqueous formaldehyde (37%, 3.26 g, 0.040 mol), 5-amino-1-pentanol (1.03 g, 0.010 mol) and triethylamine (0.5 ml, 0.004 mol). The resulting solution was kept in a water bath (50 °C) for 118 h. The solution was then cooled down and 5 ml of 6 M HCl was added, leading to the formation of a white precipitate. This latter was filtrated, washed with cold water (200 ml), hot water (200 ml), diethylether (80 ml) and recrystallized from ethanol (4 ml). The solid was filtered off, washed with 20 ml of diethylether and dried. The yield was 1.65 g (34%). The product is soluble in $CHCl_3$, MeOH, EtOH and DMSO. Mp 179–182 °C. ^{1}H NMR ($CDCl_3$, 250 MHz): 1.25 (s, 18H, aryl-*t-bu*), 1.36–1.59 (m, 4H, $NCH_2CH_2CH_2$), 1.87 (m, 2H, OCH_2CH_2), 2.42 (s, 6H, aryl-*Me*), 3.14 (t, 2H, NCH_2CH_2), 3.63 (t, $J = 5.0$ Hz, 2H, OCH_2CH_2), 4.24 (s, 4H, N–CH_2-aryl), 6.98 (s, 2H, aryl), 7.18 (s, 2H, aryl). ^{13}C NMR (CDCl3, 126 MHz): 17.16 (aryl-*Me*), 22.65, 23.84, 31.32, 31.45, 33.97 ($NCH_2CH_2CH_2CH_2$, aryl-$C(CH_3)_3$, aryl-$C(CH_3)_3$), 53.34, 56.93, 61.36 (NCH_2CH_2, N–CH_2-aryl, OCH_2CH_2), 115.85, 125.33, 126.17, 130.38, 143.58, 151.04 (aryl). The ESI-MS measurement showed the following ion for H_3L4: $m/z = 456.28$ $[H_3L4 + H]^+$. The calculated figure was: $m/z = 456.35$ $[H_3L4 + H]^+$. Elemental *Anal.* Calc. for $C_{29}H_{47}NO_{3.5}Cl$: C, 69.50; H, 9.45; N, 2.79. Found: C, 69.18; H, 9.44; N, 2.60%.

2.6. $H_3L5 \cdot HCl \cdot 0.5H_2O$ [(N,N-bis(2-hydroxy-5-tert-butyl-3-methylbenzyl)-6-amino-1-hexanol) · HCl · $0.5H_2O$]

To a solution of 4-*tert*-butyl-2-methylphenol (3.28 g, 0.020 mol) in ethanol (15 ml) and water (3 ml) was added

aqueous formaldehyde (37%, 3.26 g, 0.040 mol), 6-amino-1-hexanol (1.17 g, 0.010 mol) and triethylamine (0.5 ml, 0.004 mol). The resulting solution was kept in a water bath (50 °C) for 118 h. The solution was then cooled down and 6 ml of 6 M HCl was added, leading to the formation of a white precipitate. This latter was filtrated, washed with cold water (200 ml), hot water (300 ml), diethylether (80 ml) and recrystallized from ethanol (4 ml). The solid was filtered off, washed with 10 ml of diethylether and dried. The yield was 1.78 g (35%). The product is soluble in $CHCl_3$, MeOH, EtOH and DMSO. Mp 180–182 °C. ^{1}H NMR ($CDCl_3$, 250 MHz): 1.25 (s, 18H, aryl-*t-bu*), 1.33 (m, 4H, $NCH_2CH_2CH_2CH_2$), 1.55 (m, 2H, NCH_2CH_2), 1.83 (m, 2H, OCH_2CH_2), 2.44 (s, 6H, aryl-*Me*), 3.07 (t, $J = 7.0$ Hz, 2H, NCH_2CH_2), 3.62 (t, $J = 6.1$ Hz, 2H, OCH_2CH_2), 4.21 (s, 4H, N–CH_2-aryl), 6.95 (s, 2H, aryl), 7.19 (s, 2H, aryl). ^{13}C NMR ($CDCl_3$, 63 MHz): 17.25, 23.85, 24.90, 25.63, 31.46, 31.67, 33.98 (aryl-*Me*, $NCH_2CH_2CH_2CH_2CH_2$, aryl-$C(CH_3)_3$, aryl-$C(CH_3)_3$,), 53.18, 56.96, 61.79 (NCH_2CH_2, N–CH_2-aryl, OCH_2CH_2), 115.85, 125.13, 126.63, 130.48, 143.62, 151.16 (aryl). The ESI-MS measurement showed the following ion for H_3L5: $m/z = 470.36$ $[H_3L5 + H]^+$. The calculated value was: $m/z = 470.36$ $[H_3L5 + H]^+$. Elemental *Anal.* Calc. for $C_{30}H_{49}NO_{3.5}Cl$: C, 69.94; H, 9.59; N, 2.72. Found: C, 69.74; H, 9.60; N, 2.54%.

2.7. $[UO_2(H_2L1)_2]$ (**1a**)

The complex **1a** was prepared by dissolving 0.036 g (0.090 mmol) of $H_3L1 \cdot HCl$, 0.023 g (0.045 mmol) of $UO_2(NO_3)_2 \cdot 6H_2O$ and 25.0 μl (0.180 mmol) of NEt_3 in 5 ml of CH_3CN. $H_3L1 \cdot HCl$ does not dissolve in CH_3CN but after addition of NEt_3 it is soluble. To that solution was added $UO_2(NO_3)_2 \cdot 6H_2O$ which immediately turned the solution orange-red. The resulting orange-red solution was kept at room temperature for 3 weeks leading to the formation of orange crystals. The crystals were filtered off and washed once with 5 ml of cold diethyl ether and air-dried. The yield was 0.027 g (61%). The crystals are soluble in DMSO. ^{1}H NMR (DMSO-d_6, 250 MHz) 0.91, 1.32 (m, 4H, NCH_2CH_2), 1.56 (m, 4H, OCH_2CH_2), 2.09, 2.15, 2.31, 2.59 (s, 24H, aryl-*Me*), 2.40, 2.83 (t, 4H, NCH_2CH_2), 3.13, 3.31 (t, 4H, OCH_2CH_2), 3.60 (s, 4H, N–CH_2-aryl), 4.20 (m, 4H, N–CH_2-aryl), 6.73, 6.78, 6.91, 6.98 (s, 8H, aryl). ^{13}C NMR (DMSO-d_6, 63 MHz): 16.07, 16.15, 16.99, 20.03, 20.06, 21.80, 30.20, 30.48 (aryl-*Me*, $NCH_2CH_2CH_2$), 49.80, 52.42, 54.29, 59.16, 60.35, 60.57 (NCH_2CH_2, N–CH_2-aryl, OCH_2CH_2), 122.67–164.74 (aryl). The ESI-MS measurement showed the following ion for **1**: $m/z = 983.73$ $[\mathbf{1} + H]^+$. The calculated value for **1** was: $m/z = 983.49$ $[\mathbf{1} + H]^+$. Elemental *Anal.* Calc. for $C_{44}H_{60}N_2O_8U$: C, 53.76; H, 6.15; N, 2.85. Found: C, 53.10; H, 6.09; N, 3.18%. Single crystal X-ray analysis was performed on one of these crystals.

2.8. $[UO_2(H_2L1)_2] \cdot 2CH_3CN$ (**1b**)

During the preparation of $[UO_2(H_2L1)_2]$ also an other type of crystals formed. After keeping for more than 3 weeks the solution for the preparation of **1a** produced also other type of orange crystals, an X-ray measurement showed those to be an acetonitrile adduct of **1a** i.e. $[UO_2(H_2L1)_2] \cdot 2CH_3CN$ **(1b)**.

2.9. $[UO_2(H_2L2)_2] \cdot CH_3CN$ (**2**)

The complex **2** was prepared by dissolving 0.043 g (0.090 mmol) of $H_3L2 \cdot HCl$, 0.023 g (0.045 mmol) of $UO_2(NO_3)_2 \cdot 6H_2O$ and 25.0 μl (0.180 mmol) of NEt_3 in 10 ml of CH_3CN. $H_3L2 \cdot HCl$ does not dissolve in CH_3CN but after addition of NEt_3 it is soluble. To that solution was added $UO_2(NO_3)_2 \cdot 6H_2O$ which immediately turned the solution orange-red. The resulting orange-red solution was kept at room temperature for 3 weeks leading to the formation of orange crystals. The crystals were filtered off and washed twice with 5 ml of diethyl ether and air-dried. The yield was 0.036 g (69%). The crystals are soluble in DMSO. ^{1}H NMR (DMSO-d_6, 250 MHz): 0.84, 1.32 (m, 4H, NCH_2CH_2), 1.22, 1.28 (s, 36H, aryl-*t-bu*), 1.57 (m, 4H, OCH_2CH_2), 2.13, 2.62 (s, 12H, aryl-*Me*), 2.41, 2.75 (t, 4H, NCH_2CH_2), 3.11, 3.31 (t, 4H, OCH_2CH_2), 3.64 (s, 4H, N–CH_2-aryl), 4.18 (m, 4H, N–CH_2-aryl), 6.94, 6.99, 7.13, 7.19 (s, 8H, aryl). ^{13}C NMR (DMSO-d_6, 63 MHz): 16.21, 16.39, 17.36, 22.03, 30.25, 31.36, 31.87, 33.15, 33.45 (aryl-*Me*, aryl-*t-bu*, $NCH_2CH_2CH_2$), 49.52, 52.47, 54.36, 59.50, 60.35, 60.81 (NCH_2CH_2, N–CH_2-aryl, OCH_2CH_2), 122.10–164.80 (aryl). The ESI-MS measurement showed the following ions for **2**: $m/z = 1151.97$ $[\mathbf{2} + H]^+$, 1173.93 $[\mathbf{2} + Na]^+$. The calculated values for **2** are: $m/z = 1151.68$ $[\mathbf{2} + H]^+$, 1173.66 $[\mathbf{2} + Na]^+$. Elemental *Anal.* Calc. for $C_{58}H_{87}N_3O_8U$: C, 58.42; H, 7.35; N, 3.52. Found: C, 57.55; H, 7.28; N, 3.57%.

2.10. $[UO_2(H_2L3)_2] \cdot 2CH_3CN$ (**3**)

The complex **3** was prepared by dissolving 0.037 g (0.090 mmol) of $H_3L3 \cdot HCl$, 0.023 g (0.045 mmol) of $UO_2(NO_3)_2 \cdot 6H_2O$ and 25.0 μl (0.180 mmol) of NEt_3 in 10 ml of CH_3CN. $H_3L3 \cdot HCl$ does not dissolve in CH_3CN but after addition of NEt_3 it is soluble. To that solution was added $UO_2(NO_3)_2 \cdot 6H_2O$ which immediately turned the solution orange-red. The resulting orange-red solution was kept at room temperature for two days leading to the formation of orange crystals. The crystals were filtered off which caused almost immediate decomposition of crystals due to the escape of acetonitrile. The yield was 0.030 g (63%). The crystals are soluble in DMSO. ^{1}H NMR (DMSO-d_6, 250 MHz): 0.79, 1.14, 1.33, 1.52 (m, 12H, $NCH_2CH_2CH_2CH_2$), 2.09, 2.15, 2.31, 2.59 (s, 24H, aryl-*Me*), 2.39, 2.84 (t, 4H, NCH_2CH_2), 3.20, 3.32 (t, 4H, OCH_2CH_2), 3.60 (s, 4H, N–CH_2-aryl), 4.16 (m, 4H, N–CH_2-aryl), 6.72, 6.79, 6.91, 6.98 (s, 8H, aryl). ^{13}C NMR

(DMSO-d_6, 63 MHz): 16.07, 16.99, 19.07, 20.02, 20.06, 23.17, 23.26, 25.02, 32.00, 32.17 (aryl-*Me*, NCH_2CH_2-CH_2CH_2), 49.69, 52.46, 54.41, 59.21, 60.46 (NCH_2CH_2, N–CH_2-aryl, OCH_2CH_2), 122.70–164.77 (aryl). The ESI-MS measurement showed the following ions for **3**: $m/z = 1011.78$ $[\mathbf{3} + H]^+$, 1033.73 $[\mathbf{3} + Na]^+$. The calculated values for **3** are: $m/z = 1011.52$ $[\mathbf{3} + H]^+$, 1033.51 $[\mathbf{3} + Na]^+$. Elemental *Anal.* Calc. for $C_{46}H_{64}N_2O_8U$: C, 54.65; H, 6.38; N, 2.77. Found: C, 53.73; H, 6.34; N, 3.08%. Single crystal X-ray analysis was performed on one of these crystals.

2.11. $[UO_2(H_2L4)_2] \cdot 2CH_3CN$ (4)

The complex **4** was prepared by dissolving 0.045 g (0.090 mmol) of $H_3L4 \cdot HCl$, 0.023 g (0.045 mmol) of $UO_2(NO_3)_2 \cdot 6H_2O$ and 25.0 μl (0.180 mmol) of NEt_3 in 5 ml of CH_3CN. $H_3L4 \cdot HCl$ does not dissolve in CH_3CN but after addition of NEt_3 it is soluble. To that solution was added $UO_2(NO_3)_2 \cdot 6H_2O$ which immediately turned the solution orange-red. The resulting orange-red solution was kept at room temperature for two days leading to the formation of the orange crystals, which were filtered off. The yield was 0.036 g (64%). The crystals decompose easily, but are soluble in DMSO and THF. ^{1}H NMR (DMSO-d_6, 250 MHz): 0.71, 1.17, 1.32, 1.53 (m, 12H, $NCH_2CH_2CH_2CH_2$), 1.22, 1.28 (s, 36H, aryl-*t-bu*), 2.13, 2.62 (s, 12H, aryl-*Me*), 2.40, 2.70 (t, 4H, NCH_2CH_2), 3.16, 3.32 (t, 4H, OCH_2CH_2), 3.64 (s, 4H, N–CH_2-aryl), 4.13 (m, 4H, N–CH_2-aryl), 6.94, 6.99, 7.13, 7.19 (s, 8H, aryl). ^{13}C NMR (DMSO-d_6, 63 MHz): 16.40, 17.35, 23.23, 23.39, 25.18, 31.35, 31.87, 32.20, 32.44, 33.14, 33.45 (aryl-*Me*, aryl-*t-bu*, $NCH_2CH_2CH_2CH_2$), 49.42, 51.66, 52.49, 54.48, 59.54, 60.50 (NCH_2CH_2, N–CH_2-aryl, OCH_2CH_2), 122.14–164.84 (aryl). The ESI-MS measurement showed the following ions for **4**: $m/z = 1180.04$ $[\mathbf{4} + H]^+$, 1202.03 $[\mathbf{4} + Na]^+$. The calculated values for **4** are: $m/z = 1179.71$ $[\mathbf{4} + H]^+$, 1201.69 $[\mathbf{4} + Na]^+$. Elemental *Anal.* Calc. for $C_{58}H_{88}N_2O_8U$: C, 59.07; H, 7.52; N, 2.38. Found: C, 57.39; H, 7.31; N, 2.09%. Single crystal X-ray analysis was performed on one of these crystals.

2.12. $[UO_2(H_2L5)_2] \cdot 4$toluene (5)

The complex **5** was prepared by dissolving 0.046 g (0.090 mmol) of $H_3L5 \cdot HCl$, 0.023 g (0.045 mmol) of $UO_2(NO_3)_2 \cdot 6H_2O$ and 25.0 μl (0.180 mmol) of NEt_3 in 20 ml of CH_3CN. $H_3L5 \cdot HCl$ does not dissolve in CH_3CN but after addition of NEt_3 it is soluble. To that solution was added $UO_2(NO_3)_2 \cdot 6H_2O$ which immediately turned the solution orange-red. This solution was kept at room temperature for three days leading to formation of orange starlike crystals. These crystals were filtered off (yield 0.032 g (59%)) and dissolved in toluene and this solution was left to evaporate slowly at room temperature. Better shaped orange crystals were formed and they were filtered off. The crystals are soluble in DMSO, $CHCl_3$, THF and toluene.^{1}H and ^{13}C NMR were made from crystals obtained from CH_3CN. ^{1}H NMR (DMSO-d_6, 250 MHz): 0.69, 1.02. 1.17, 1.52 (m, 16H, $NCH_2CH_2CH_2CH_2CH_2$), 1.22, 1.28 (s, 36H, aryl-*t-bu*), 2.13, 2.62 (s, 12H, aryl-*Me*), 2.40, 2.74 (t, 4H, NCH_2CH_2), 3.21, 3.32 (t, 4H, OCH_2CH_2), 3.64 (s, 4H, N–CH_2-aryl), 4.17 (m, 4H, N–CH_2-aryl), 6.94, 6.99, 7.13, 7.19 (s, 8H, aryl). ^{13}C NMR (DMSO-d_6, 63 MHz): 16.50, 17.43, 25.27, 25.41, 31.41, 31.92, 33.20, 33.52 (aryl-*Me*, aryl-*t-bu*, NCH_2CH_2-$CH_2CH_2CH_2$), 54.52, 59.57, 60.51, 60.60 (NCH_2CH_2, N–CH_2-aryl, OCH_2CH_2), 122.20–164.87 (aryl). The ESI-MS measurement showed the following ions for **5**: $m/z = 1208.03$ $[\mathbf{5} + H]^+$, 1230.05 $[\mathbf{5} + Na]^+$. The calculated values for **5** are: $m/z = 1207.74$ $[\mathbf{5} + H]^+$, 1229.73 $[\mathbf{5} + Na]^+$. Elemental *Anal.* Calc. for $C_{60}H_{92}N_2O_8U$: C, 59.68; H, 7.68; N, 2.32. Found: C, 57.63; H, 7.41; N, 2.02%. Single crystal X-ray analysis was performed on one of the crystals, which was obtained by crystallization from toluene.

2.13. Uranyl extraction

Two-phase extraction studies were performed to determine the UO_2^{2+} cation uptake from water layer to CH_2Cl_2 layer by the ligands $H_3L1 \cdot HCl$, $H_3L2 \cdot HCl$, $H_3L3 \cdot HCl$, $H_3L4 \cdot HCl$, $H_3L5 \cdot HCl$, $H_3L6 \cdot 1/3$toluene, H_3L7 and $H_3L8 \cdot HCl$ (the results for three last ones were published in our earlier paper [14]). The experimental setup was as follows: into the bottom of a test tube was placed 3 ml of CH_2Cl_2 with ligand (0.210 mmol), and 0.210 mmol NEt_3 to neutralize HCl was added except in cases of H_3L6 and H_3L7, which were used as neutral ligands. At the top of the organic layer was placed 2 ml of water with uranyl nitrate ($c(U) = 6.25$ mg/ml, $n(U) = 0.0525$ mmol) leading to a ratio of U to ligand of 1:4. Furthermore one test tube with CH_2Cl_2 containing no ligand was prepared. The samples for ICP (V = 50 μl, diluted to 10 ml) were taken from the water layer over 54 h period of time. The samples were analyzed with ICP-OES at 385.958 nm using a Perkin Elmer Optima 4300DV instrument.

2.14. X-ray crystallography

Crystals suitable for single crystal X-ray measurements were obtained directly from the reaction vessels. The crystal data for compounds **1a**, **1b**, **3**–**5** along with other experimental details, are summarized in Table 1. The crystallographic data were collected at 173 K on an Enraf Nonius Kappa CCD area-detector diffractometer using graphite monochromatized Mo Kα radiation ($\lambda = 0.71073$ Å). Data collection was performed using φ and ω scans and the data processed using DENZO-SMN V0.93.0 [16]. SHELXA [17] absorption correction was applied to the data of **1a**, **3**–**5**. The structures were solved by direct methods using the SHELXS-97 program [18] and full-matrix least-squares refinements on F^2 were performed using the SHELXL-97 program [18]. For all compounds the heavy atoms were refined

Table 1
Summary of crystallographic data for **1a**, **1b**, **3**–**5** at 173(2) K

	1a	**1b**	**3**	**4**	**5**
Formula	$C_{44}H_{60}N_2O_8U$	$C_{48}H_{66}N_4O_8U$	$C_{50}H_{70}N_4O_8U$	$C_{62}H_{94}N_4O_8U$	$C_{88}H_{124}N_2O_8U$
M_r	982.97	1065.08	1093.13	1261.44	1574.91
Crystal system	triclinic	triclinic	triclinic	triclinic	monoclinic
Space group (no.)	$P\bar{1}$ (2)	$P\bar{1}$ (2)	$P\bar{1}$ (2)	$P\bar{1}$ (2)	$C2/c$ (15)
a (Å)	9.5394(2)	8.8922(2)	9.1043(3)	9.4243(3)	15.3013(3)
b (Å)	9.6303(2)	11.7134(2)	10.9246(4)	12.9906(3)	24.3376(4)
c (Å)	11.7396(3)	12.2525(3)	13.0396(4)	14.2802(5)	23.6905(5)
α (°)	106.850(1)	74.976(1)	93.197(2)	109.058(2)	90
β (°)	91.995(1)	69.694(1)	108.741(2)	99.946(2)	108.254(1)
γ (°)	91.001(1)	79.265(1)	93.142(2)	104.502(2)	90
V (Å^3)	1031.13(4)	1149.42(4)	1222.62(7)	1536.70(8)	8378.30(3)
Z	1	1	1	1	4
$D_{calc.}$ (g cm^{-1})	1.583	1.539	1.485	1.363	1.249
μ(Mo Kα) (cm^{-1})	39.90	35.87	33.74	26.95	19.90
Observed reflections	4958	5568	4541	6728	7831
R_{int}	0.028	0.040	0.053	0.047	0.029
Parameters	256	290	297	346	463
R_1[a]	0.028 (0.028)[b]	0.029 (0.029)	0.028 (0.027)	0.037 (0.035)	0.051 (0.028)
wR_2[c]	0.057 (0.057)	0.059 (0.059)	0.061 (0.061)	0.066 (0.065)	0.064 (0.058)
Peak, hole (e Å^{-3})	0.61, −0.52	0.49,−0.68	1.39, −1.08	0.71, −0.84	0.61, −0.86

[a] $R_1 = \sum\|F_o| - |F_c\|/\sum|F_o|$.
[b] Values in parentheses for reflections with $I > 2\sigma(I)$.
[c] $wR_2 = \left\{\sum\left[w(F_o^2 - F_c^2)^2\right]/\sum[w(F_o^2)^2]\right\}^{1/2}$ and $w = 1/\left[\sigma^2(F_o^2) + (aP)^2 + (bP)\right]$, where $P = (2F_c^2 + F_o^2)/3$.

anisotropically. The CH hydrogen atoms were included at fixed distances using fixed displacement parameters from their host atoms whilst other H atoms were refined using fixed displacement parameters. Structure figures were drawn using ORTEP-3 for *Windows* [19].

3. Results and discussion

3.1. Syntheses of ligands and uranyl complexes

The details of the ligand syntheses are described in Section 2. Generally, the yields of the new ligands were quite low. One reason for this is the fact that the solubility properties of the product and the phenol in question are quite similar. Also, the reaction itself does not readily go to completion and intermediates with only one phenol moiety attached to the aminoalcohol were present. Thus the separation of the product from the sticky oil (especially with 2,4-dimethylphenol derivatives), which was generally formed at the end of the reaction, was quite difficult and as a result part of the product was lost together with the starting phenol during the separation process.

In order to make the separation process easier the reaction mixtures were treated with HCl (6 M) in order to make the product more polar with respect to the phenol (the formation of the hydrochloride). This led to an immediate formation of a white solid (the hydrochloride) with 4-*tert*-butyl-2-methylphenol derivatives. In the case of 2,4-dimethylphenol the white solid formed slowly and it seems to be more soluble during the separation process and thus 4-*tert*-butyl-2-methylphenol derivatives gave better yields than 2,4-dimethylphenol derivatives.

Generally, the crystals of the uranyl complexes formed quite easily following the dissolution of the uranyl nitrate hexahydrate in acetonitrile together with an appropriate amount of the ligand. The quick formation of the complex was clearly indicated by the immediate change in color of the solution from the yellow of uranyl nitrate to red. The reaction vessels, however, were left to stand at room temperature from two days to up to 3 weeks to allow for the formation of crystals. The filtrates, though, were still red or orange in color after removal of the crystals indicating that the crystallization was incomplete. The crystals of compounds **3** and **4** decompose quite quickly after they are removed from the reaction solution indicating that acetonitrile molecules are quite loosely bonded in these crystals. Furthermore, it seems that ligands $H_3L1 \cdot HCl$ and $H_3L2 \cdot HCl$ form two kinds of crystals with the uranyl ion from acetonitrile, with or without acetonitrile. This leads to some discrepancy in the results of elemental analysis as it was difficult to separate these crystals on the basis of their outlook. In order to get homogeneous crystals of **1a**, ethanol was tried as solvent but the crystals formed were not better than the crystals from acetonitrile as they contained loosely bonded ethanol molecules.

The solubility of the complexes into organic solvents was best in the case of **5**, which dissolved easily at room temperature in DMSO, $CHCl_3$, THF and toluene.

The ESI-MS measurements for compounds **1**–**5** were done in a solution of CH_2Cl_2 and CH_3OH. In this procedure the compounds **1**–**5** mainly broke down to the corresponding ligands but the complex ions of compounds **1**–**5** could still be identified, although the peaks were of very low intensity.

3.2. NMR studies

Although some of the complexes are slightly soluble in $CHCl_3$ (or other NMR solvents), the NMR spectra were recorded in DMSO where all the complexes dissolve readily making possible comparisons of the spectra 1–5. In the compounds where CH_3CN molecules were present in the crystal structure it could be identified from the NMR spectra.

The NMR spectra of compounds **1**–**5** were quite similar indicating that all the complexes behave similarly in DMSO. The ^1H NMR spectrum of **1** in DMSO is presented in Fig. 1a.

In order to find out what happens to these uranyl complexes in a DMSO solution we did a thorough NMR-analysis for **1**. Its DMSO solution was analyzed with ^1H, ^{13}C, ^1H–^1H COSY, NOESY, HMQC and HMBC NMR techniques. Furthermore, in order to find out if other uranyl complexes form during the reactions of uranyl ion with H_3Ln ($n = 1$–5) ligands in DMSO, we followed with the ^1H NMR spectroscopy the stepwise reaction of $H_3L1 \cdot HCl$ with $UO_2(NO_3)_2 \cdot 6H_2O$ in DMSO in the presence of

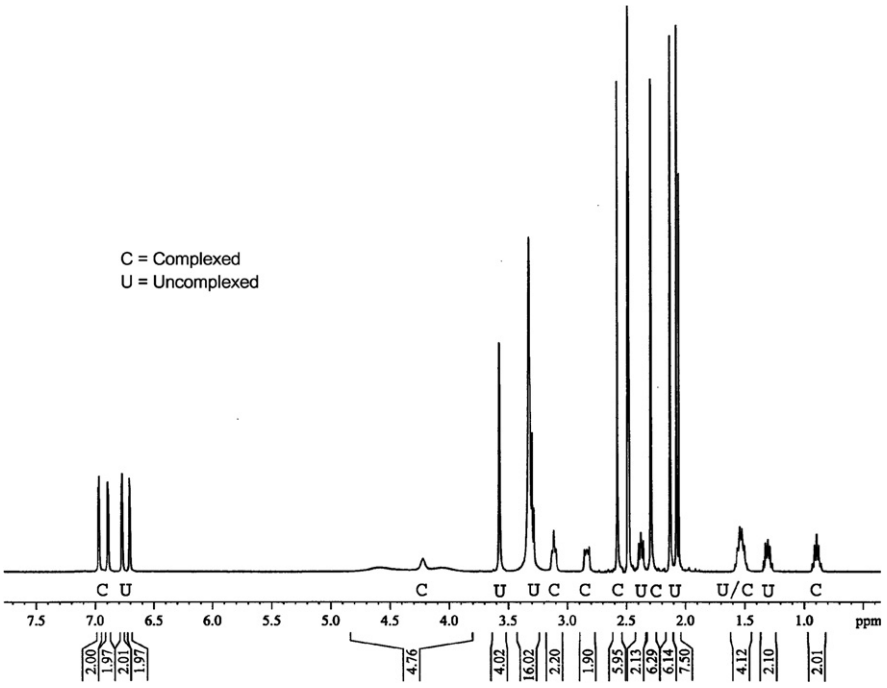


Fig. 1a. The ^1H NMR spectrum of compound **1** in DMSO.

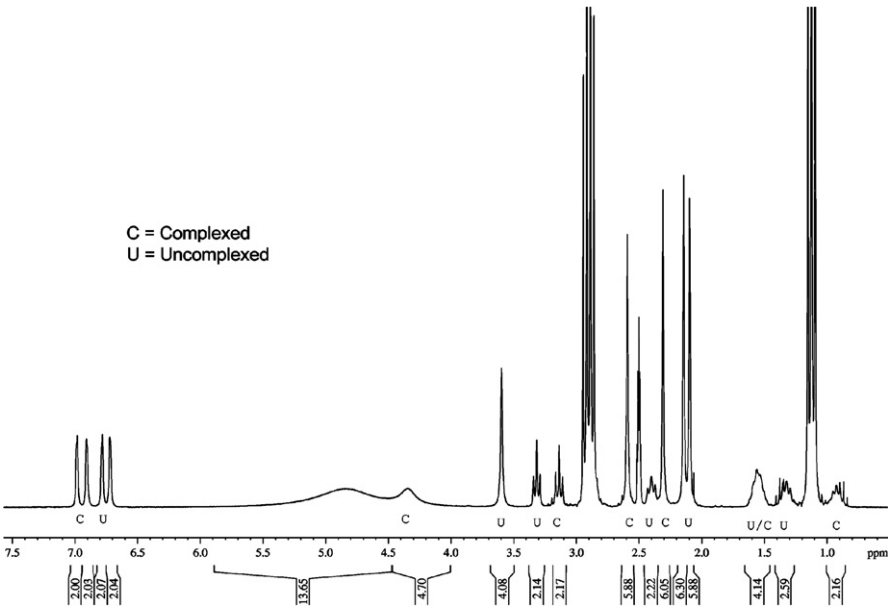


Fig. 1b. The ^1H NMR spectrum of the DMSO solution, where the ratio of $[UO_2]^{2+}$:$H_3L1 \cdot HCl$:NEt_3 is 1:2:4.

NEt_3, which was used as a base in order to avoid extra use of $H_3L1 \cdot HCl$. We started from pure $UO_2(NO_3)_2 \cdot 6H_2O$ in DMSO and then gradually added $H_3L1 \cdot HCl$ and NEt_3 (to produce H_3L1 and H_2L1^-). The main interesting compositions are the $[UO_2]^{2+}$:$H_3L1 \cdot HCl$:NEt_3 being 1:1:2 and 1:2:4. In Fig. 1b is presented a ^1H NMR spectrum of this stepwise reaction follow-up where the $[UO_2]^{2+}$:$H_3L1 \cdot HCl$:NEt_3 composition is 1:2:4.

From these data it seems obvious that at first mainly the $[UO_2(H_2L1)(DMSO)_x]^+$ complex (x is 2 or 3) is formed when the ratio $[UO_2]^{2+}$:H_2L1^- is 1:1. The addition of H_2L1^- up to a ratio of $[UO_2]^{2+}$:H_2L1^- of 1:2 does not lead to the formation of $[UO_2(H_2L1)_2]$ complex, but instead the peaks of the free H_2L1^- ligand grow, leading to the ratio $[UO_2(H_2L1)(DMSO)_x]^+$:H_2L1^- being 1:1.

In Fig. 1b the extra peaks, compared to the spectrum in Fig. 1a, are from NEt_3 (δ 1.1 and 2.9) and in Fig. 1a the peak in δ 3.30 originates from HOD, which is not seen in the spectra 1b, possibly due to the presence of the $[NH(Et)_3]^+$ ion. In NOESY of **1** there is a strong correlation between the NH^+–CH_2-aryl group peaks of the coordinated ligand and the HOD peaks, due to the hydrogen bond between the NH^+ hydrogen of the ligand and the HOD oxygen atom. The round shape of the signals of the NH^+–CH_2-aryl hydrogens of the coordinated ligand (δ 4.10–4.30) is possibly due to conformational changes of the $PhCH_2NCH_2Ph$ chains in the coordinated ligand in the DMSO solution.

The similar stepwise reaction follow-up was done also with ligand H_3L7 (*N*,*N*-bis(2-hydroxy-3,5-dimethylbenzyl)-3-amino-1-propanol), for which the uranyl complex was prepared earlier [14], the results were in accordance with the observations for compound **1**.

On the basis of the previously mentioned data, two types of the ligands, complexed (C) and uncomplexed (U), seem to be present in a DMSO solution of complexes prepared in this study. It means that only one type of uranyl complex is found in a DMSO solution, and in the dissolution of $[UO_2(H_2L1)_2]$ in DMSO the following reaction occurs [reaction (1)]:

$$[UO_2(H_2L1)_2] + nDMSO \rightarrow [UO_2(H_2L1)(DMSO)_x]^+ + H_2L1^- + (n\text{-}x)DMSO \quad (1)$$

3.3. Structural studies of the uranyl complexes

The solid-state structures of compounds **1a**, **1b**, **3**–**5** were verified by single crystal X-ray analysis. The crystals of **1a**, **1b**, **3**–**5** were obtained from an acetonitrile solution. The triclinic unit cell of **1a** contains one complex unit. The triclinic unit cells of **1b**, **3** and **4** contain one complex unit and two acetonitrile molecules and the monoclinic (C-type) unit cell of **5** contains four complex units and 16 toluene molecules.

The complexes have a centrosymmetric structure in which the uranium ion has a compressed octahedral symmetry (Figs. 2–5). Selected bonding parameters for these five molecules are compared in Table 2. The asymmetric unit of all compounds contains a UO unit with a negative H_2L^- ligand, which binds to the UO unit via two phenoxide groups. The aliphatic nitrogen atom accepts a proton and thus it does not form a bond with the U(VI) ion. The proton on the nitrogen atom, however, forms weak intramolecular H-bonds to O2 and O3. The complexes are neutral zwitterionic units with four negative charges at the oxygen atoms, two positive charges at the uranyl ion and two positive charges on the nitrogen atoms (one per nitrogen). The aliphatic alcohol groups do not take part in bonding with the uranyl ion, but do form H-bonds in all compounds (Table 3). The overall structures are similar to the uranyl homoazacalixarene complex [20], where the uranyl ion is located inside the cage, and to the earlier reported complexes of uranyl ion with the similar shorter chain aminoalcohol ligands [14].

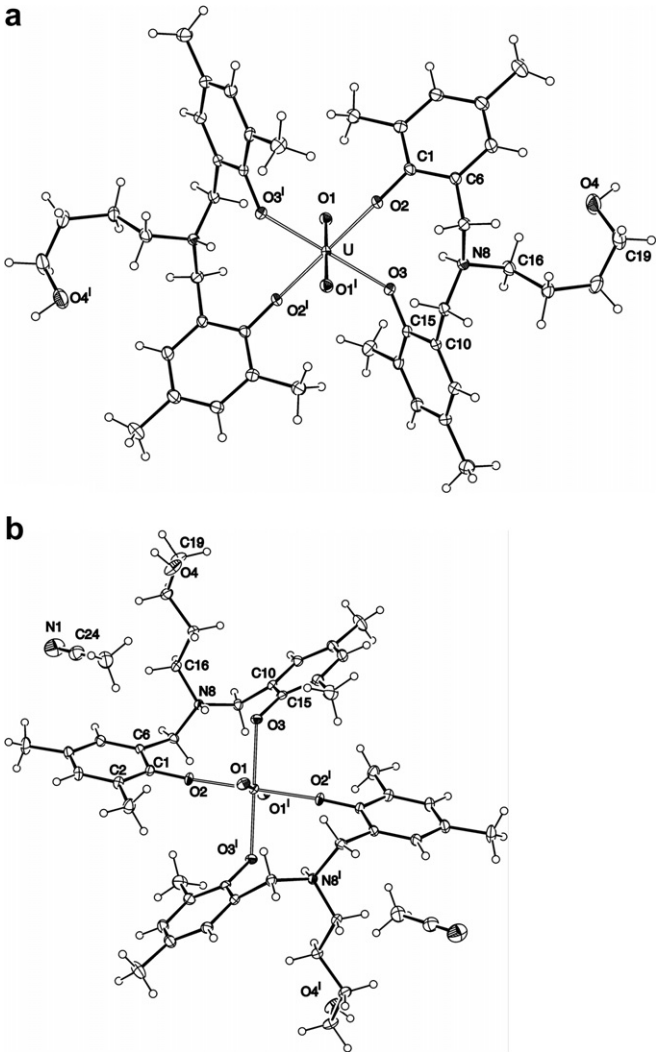


Fig. 2. (a) Molecular structure of $[UO_2(H_2L1)_2]$ (**1a**). (b) Molecular structure of $[UO_2(H_2L1)_2] \cdot 2CH_3CN$ (**1b**). Thermal ellipsoids have been drawn at 30% probability level. Symmetry operation i = $-x$, $-y$, $-z$.

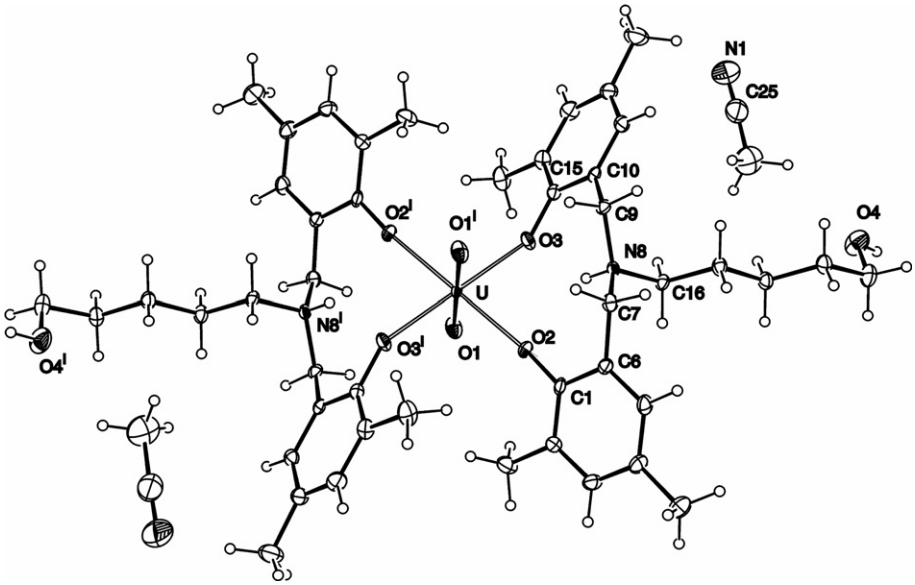


Fig. 3. Molecular structure of $[UO_2(H_2L3)_2]\cdot 2CH_3CN$ (**3**). Thermal ellipsoids have been drawn at 30% probability level. Symmetry operation i = $-x$, $-y$, $-z$.

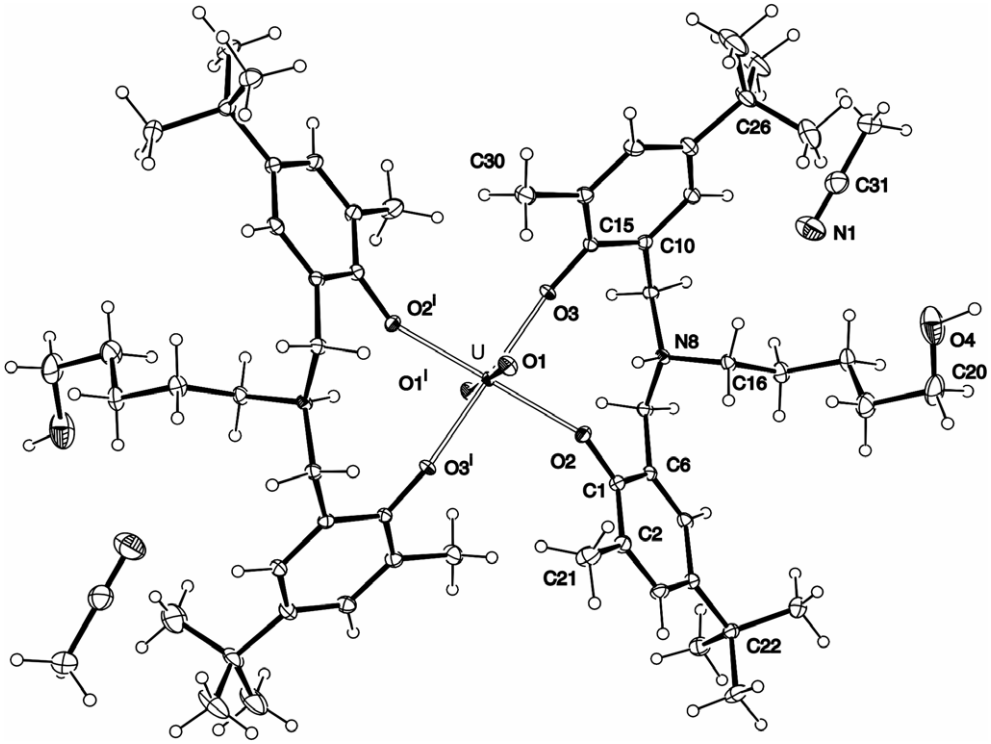


Fig. 4. Molecular structure of $[UO_2(H_2L4)_2]\cdot 2CH_3CN$ (**4**). Thermal ellipsoids have been drawn at 30% probability level. Symmetry operation i = $-x$, $-y$, $-z$.

The U=O distances are almost the same in all studied compounds; they range from 1.795(2) to 1.807(2) Å. Only compound **5** forms a hydrogen bond to O1 (see Table 3), and as the U=O bond length in **5** is near the average of all five compounds, the hydrogen bonding does not significantly influence the U=O bond lengths.

The extreme values of the U–O(phenoxide) bond distances are from 2.202(2) to 2.307(2) Å in the studied compounds. These values are near the estimated "ideal" value of 2.2 Å found in U(VI) compounds with unrestricted, unidentate alkoxide ligands [13,21]. Also in U(VI) compounds with Schiff base ligands similar values have been found [22]. This suggests that now reported ligands bind to the UO_2^{2+} ion quite effectively.

The U–O–C bond angles in **1b** are 132.2(2)° and 175.5(2)°. The relevant U–O(phenoxide) bond distances

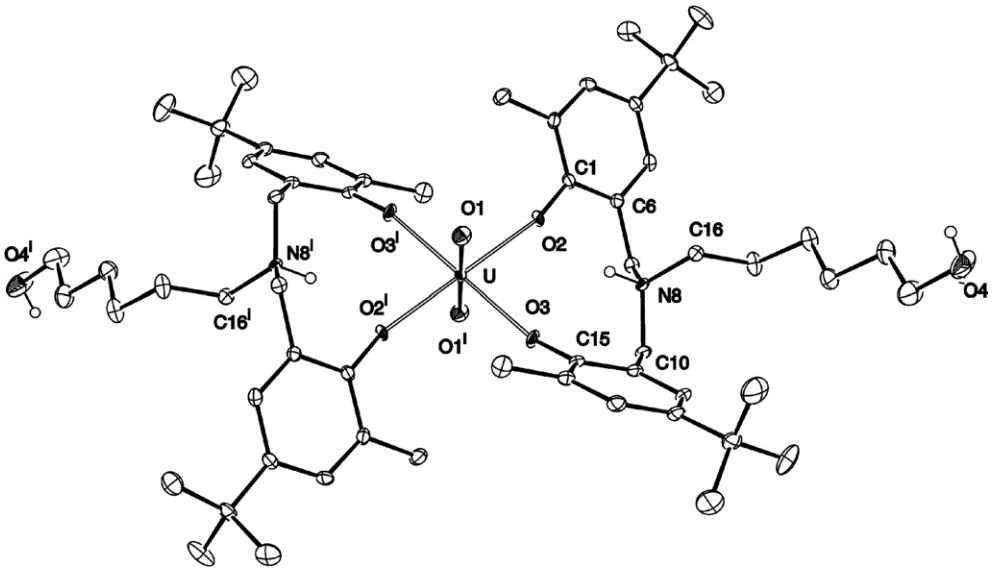


Fig. 5. Molecular view of $[UO_2(H_2L5)_2]$ in the solvate $[UO_2(H_2L5)_2]\cdot 4$toluene (**5**). Thermal ellipsoids have been drawn at 30% probability level. Toluene molecules are not shown and the CH hydrogen atoms have been omitted for clarity. Symmetry operation i = $-x$, $-y$, $-z$.

Table 2
Selected bond lengths (Å) and angles (°) for **1a**, **1b**, **3**–**5**

	1a	1b	3	4	5
Bond lengths (Å)					
U–O1	1.795(2)	1.807(2)	1.796(2)	1.798(2)	1.800(2)
U–O2	2.242(2)	2.202(2)	2.250(2)	2.266(2)	2.245(2)
U–O3	2.307(2)	2.303(2)	2.250(2)	2.251(2)	2.227(2)
C1–O2	1.339(3)	1.335(3)	1.332(4)	1.353(4)	1.338(4)
C15–O3	1.354(3)	1.351(4)	1.348(4)	1.339(3)	1.331(4)
Bond angles (°)					
O1–U–O2	90.26(9)	89.43(9)	88.36(12)	88.87(9)	89.03(10)
O1–U–O3	89.34(9)	90.39(8)	90.48(11)	90.89(9)	90.46(10)
O2–U–O3	84.96(7)	82.52(8)	82.72(9)	84.54(8)	84.03(10)
O2–U–O3[a]	95.04(7)	97.48(8)	97.28(9)	95.46(8)	95.97(8)
C1–O2–U	151.9(2)	175.5(2)	167.2(2)	150.9(2)	159.7(2)
C15–O3–U	135.8(2)	132.2(2)	149.8(2)	154.4(2)	156.7(2)
τ_1 vs. τ_2[b]	57.3(1)	37.8(1)	32.3(1)	60.6(1)	59.1(1)

[a] Atom generated by inversion.
[b] Dihedral angle between the planes C1,...,C6 and C10,...,C15.

Table 3
Intermolecular hydrogen bond parameters (Å, °)

Compound	D–H ··· A	*d*(D–H)	*d*(H ··· A)	*d*(D ··· A)	∠(D–H ··· A)
1a	O(4)–H(4) ··· O(3)^{i}	0.95(6)	1.86(6)	2.766(4)	159(5)
1b	O(4)–H(4) ··· O(3)^{ii}	0.77(4)	2.02(4)	2.742(3)	158(5)
3	O(4)–H(4) ··· O(2)^{iii}	0.98(6)	2.09(6)	3.048(5)	164(5)
4	O(4)–H(4) ··· O(2)^{iv}	0.98(2)	2.04(3)	2.945(4)	153(4)
5	O(4)–H(4) ··· O(1)^{v}	0.81(5)	1.98(5)	2.776(4)	168(5)

Symmetry codes: i = $-x$, $-y$, $-z-1$, ii = $-x$, $-y+1$, $-z$, iii = $-x+2$, $-y+1$, $-z+1$, iv = $-x$, $-y-1$, $-z$, v = $-x$, y, $-z+1/2$.

are 2.303(2) and 2.202(2) Å. In the rest of the compounds the U–O–C angles vary from 135.8(2)° to 167.3(2)° and roughly we can say that if the U–O–C angles are about 130°, 150° and 170°, then the U–O(phenoxide) distances are about 2.30, 2.25 and 2.20 Å. Thus the general finding: the larger the U–O–C angle is, the shorter is the U–O bond distance, is valid in these compounds and also in $[Na(THF)_2]_2[UO_2(O\text{-}2,6Me_2C_6H_3)_4]$ [21]. The found distortions of the U–O(phenoxide) bond angles and distances are caused mainly by packing effects as reasoned below.

Table 4
Selected torsion angles (°) for **1a**, **1b**, **3**–**5**

	1a	1b	3	4	5
C(5)–C(6)–C(7)–N(8)	108.0(3)	109.5(3)	125.0(3)	126.6(3)	123.0(3)
C(1)–C(6)–C(7)–N(8)	−73.9(3)	−72.4(3)	−58.1(4)	−52.3(3)	−57.0(4)
N(8)–C(9)–C(10)–C(11)	−126.6(3)	−137.4(3)	−134.8(3)	−110.3(3)	−108.8(3)
N(8)–C(9)–C(10)–C(15)	55.7(3)	50.9(4)	52.8(4)	66.3(3)	70.7(4)
C(16)–N(8)–C(7)–C(6)	−81.2(3)	−74.4(3)	−60.9(4)	−55.8(3)	−62.9(3)
C(9)–N(8)–C(7)–C(6)	147.9(2)	159.8(2)	166.6(3)	172.8(2)	166.3(2)
C(16)–N(8)–C(9)–C(10)	61.3(3)	80.5(3)	59.5(4)	69.7(3)	67.1(3)
C(7)–N(8)–C(9)–C(10)	−169.6(2)	−156.6(2)	−168.1(3)	−158.2(2)	−162.5(3)

Conformational differences of the coordinated ligands in **1a**, **1b**, **3**–**5** were evident in the analysis of the torsion and dihedral angles in the structures (see Tables 2 and 4). In particular, the dihedral angles between the phenyl rings (formed by the atoms C1,...,C6 and C10,...,C15) vary and the angles between these planes in **1a**, **1b**, **3**–**5** are from 32.1(1)° to 60.6(1)° (Table 2). These deviations indicate that the frameworks of the ligands are flexible and have enough freedom to accommodate slightly different arrangements in the solid state for packing reasons. In compounds **1a** and **1b** there is the same ligand, but **1b** contains in the unit cell two acetonitrile molecules. This presence of acetonitrile molecules causes several conformational changes to the ligand as the dihedral angles between the phenyl rings are 57.1(3)° for **1a** and 37.8(1)° for **1b**. Also the aminoalcohol chains have different conformations as seen from Fig. 2. These conformational changes influence on the bond parameters of the uranyl ion in **1a** and **1b** (see Table 2). Especially the U–O2 bonds are slightly different. In **1a** and **1b** there are also similar, moderately strong intermolecular hydrogen bonds to O3 from the aminoalcohol hydrogen atoms (at O4) and these H-bonds can influence on the U–O3 bond distances and U–O3–O15 bond angles.

3.4. Uranyl ion extraction studies

The decrease of the uranyl ion concentration in water layer during the extraction studies at room temperature (22–23 °C) with the ligands $H_3L1 \cdot HCl$–$H_3L8 \cdot HCl$ (H_3L6 = *N*,*N*-bis(2-hydroxy-3,5-dimethylbenzyl)-2-aminoethanol · 1/3toluene, H_3L7 = *N*,*N*-bis(2-hydroxy-3,5-dimethylbenzyl)-3-amino-1-propanol and H_3L8 = *N*,*N*-bis(2-hydroxy-5-*t*-butyl-3-methylbenzyl)-3-amino-1-propanol · HCl) [14] are shown in Table 5 and Fig. 6. The extraction was done without mixing the extraction tube at the pH of the uranyl nitrate in water solution (around 3). The concentration ratio of the uranyl ion to the ligand was 1:4 during the extraction process. The concentration of the uranyl ion in the water layer of the control sample was constant after the 54 h follow-up.

With ligands $H_3L1 \cdot HCl$, $H_3L3 \cdot HCl$, $H_3L4 \cdot HCl$, $H_3L5 \cdot HCl$, $H_3L6 \cdot 1/3$toluene, H_3L7 and $H_3L8 \cdot HCl$ red or orange crystals formed into the CH_2Cl_2 layer. The crystals of $H_3L1 \cdot HCl$, $H_3L3 \cdot HCl$, $H_3L4 \cdot HCl$, $H_3L5 \cdot HCl$ in CH_2Cl_2 layer were not of X-ray quality, but we assume that they have the formula of $[UO_2(H_2Ln)_2]$, the same as the uranyl complexes with the ligands $H_3L6 \cdot 1/3$toluene and H_3L7 was found [14]. The reason for the low quality is possibly the fact that generally $[UO_2(H_2Ln)_2]$ crystals contain two acetonitrile molecules in the lattice per one $UO_2(H_2Ln)_2$ molecule, and as the extraction system does not contain acetonitrile these type of crystals cannot form. On the other hand there is a possibility that the uranyl complexes in dichloromethane are the 1:1 complexes, for example the $[UO_2(H_2Ln)(NO_3)]$ complexes, which are suggested by the formation of the $[UO_2(H_2L1)(solvent)_x]^+$ complexes (solvent = DMSO, acetonitrile, alcohol or other hard Lewis base).

Fig. 6 (Table 5) shows that the transfer of the uranyl ion from the water layer to the CH_2Cl_2 during the 54 h was

Table 5
Decrease of the uranium concentration (%) in the water layer as a function of time during the extraction process

Time (h)	$H_3L1 \cdot HCl$	$H_3L2 \cdot HCl$	$H_3L3 \cdot HCl$	$H_3L4 \cdot HCl$	$H_3L5 \cdot HCl$	$H_3L6 \cdot 1/3$toluene	H_3L7	$H_3L8 \cdot HCl$
0	100	100	100	100	100	100	100	100
1	53.7	52.5	44.6	74.9	62.2	80.3	64.3	65.8
2	30.1	36.6	31.4	66.6	61.1	61.6	41.8	61.1
3	22.7	28.0	24.6	61.1	46.9	65.4	26.9	59.0
4	20.5	24.5	20.3	48.3	49.4	62.2	22.6	55.0
6	12.2	23.8	16.5	39.4	44.0	68.2	21.0	52.2
24	8.0	13.6	8.6	13.1	9.6	38.2	10.4	29.3
30	8.3	12.8	8.6	10.2	8.2	36.0	9.1	26.4
48	7.2	10.1	7.0	7.5	6.2	29.1	8.6	18.7
54	6.7	9.1	6.9	6.4	6.1	25.9	8.3	16.6

$H_3L6 \cdot 1/3$toluene, *N*,*N*-bis(2-hydroxy-3,5-dimethylbenzyl)-2-aminoethanol · 1/3toluene; H_3L7, *N*,*N*-bis(2-hydroxy-3,5-dimethylbenzyl)-3-amino-1-propanol; $H_3L8 \cdot HCl$, *N*,*N*-bis(2-hydroxy-5-*t*-butyl-3-methylbenzyl)-3-amino-1-propanol · HCl.

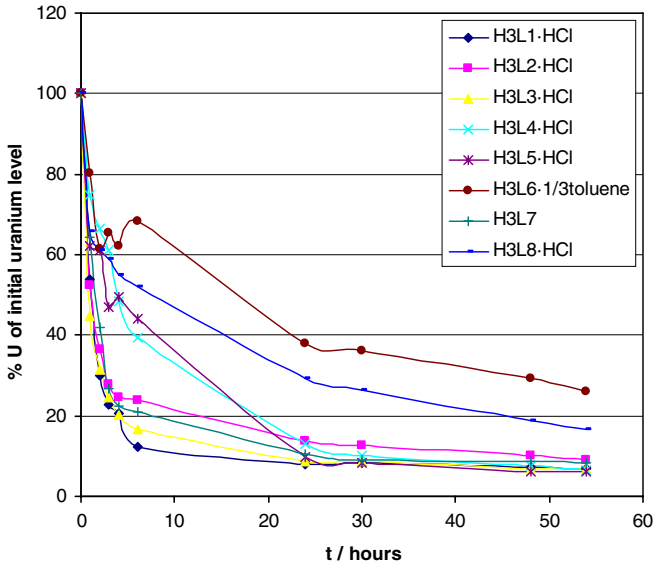


Fig. 6. Decrease of the uranium concentration (%) in the water layer as a function of time during extraction process.

best with $H_3L5 \cdot HCl$ (93.9%) although the ligands $H_3L1 \cdot HCl$, $H_3L3 \cdot HCl$ and $H_3L4 \cdot HCl$ were at the same efficiency level (93.3%, 93.1% and 93.6%, respectively).

However, already after 4 h extraction with $H_3L1 \cdot HCl$ and $H_3L3 \cdot HCl$, 80% of uranyl ions were in the CH_2Cl_2. About the same extraction level after 4 h was obtained also with ligands $H_3L2 \cdot HCl$ and H_3L7 (76% and 77%, respectively), but the ligands $H_3L4 \cdot HCl$ and $H_3L5 \cdot HCl$ had transferred only 52% and 51%. After 24 h all these ligand had extracted over 90% of the uranyl ions. The lower solubility of $H_3L5 \cdot HCl$ in water possibly explains its low extraction speed.

The uranyl ion extraction efficiency of the ligands in a equilibrium situation can be described by using the distribution coefficient (D), which expresses the ratio of the total mass of the extracted substance in all of its possible forms in the organic and aqueous layers. It was calculated modifying the equation given in Ref. [23]:

$$D = \frac{m(U)_o}{m(U)_w}, \quad (2)$$

where $m(U)_o = m(U)$ in all possible forms in the CH_2Cl_2 layer at equilibrium (54 h), $m(U)_w = m(U)$ in the water layer at equilibrium (54 h).

The D values given in Table 6 are calculated from the numerical values presented in Table 5. Table 6 gives the efficiency of each ligand in the extraction uranyl ions from water to organic solvent (CH_2Cl_2) during 54 h. The best ligand, $H_3L5 \cdot HCl$ has $D = 15.4$ and the second, $H_3L4 \cdot HCl$ has $D = 14.7$. The worst extractor is $H_3L6 \cdot 1/3$toluene ($D = 2.9$). On the other hand the extraction speed of the ligands is also important and that point has been discussed earlier.

4. Conclusions

In the solid state the neutral uranyl complexes form structures in which the uranyl ion is almost ideally bonded to four phenolato oxygen atoms of two ligands. The formed complex is a zwitterion as one of the phenolic protons moves to the nitrogen atom. By formulating the aminoalcohol part of the ligands it is possible to regulate the solubility of ligands and their complexes, but the actual coordination sphere around the uranyl ion changes only slightly. Although the yields of the ligand syntheses are low, compared to yields of some calixarene molecules, these ligands are reasonably easy to prepare; furthermore, the complexation of the new ligands mainly produce only one crystalline complex of type $[UO_2(H_2L1)_2]$ with a similar structure. It is shown that in the solution $[UO_2(H_2L1)(solvent)_x]^+$ complexes are also present. The solvent can be DMSO, acetonitrile, alcohol or other hard Lewis base solvent.

It seems obvious that the ligand with good extraction properties for UO_2^{2+} from water layer to organic water immiscible solvent needs to have a good balance between its hydrophilic and hydrophobic properties [24,25]. The three fastest ligands (about 50–60% extraction level after 1 h) have medium length carbon chains (4–5 carbons) in the aliphatic alcohol (Scheme 1 describes the ligands). If the ligand is too hydrophobic (*tert*-butyl-group in the phenyl ring and long CH_2 chain in the aliphatic alcohol) it cannot migrate to the water layer very quickly; this leads to a slower extraction rate, although the extraction level after 54 h can be good (in this case best with $H_3L5 \cdot HCl$). In this respect all the ligands presented in this article seem quite suitable for the extraction of uranyl ion from water to organic solvents: $H_3L1 \cdot HCl$ is the quickest and almost as effective as $H_3L5 \cdot HCl$.

Although some of these ligands are quite good uranyl ion extractors, the search for new better ligands, as well as optimizing studies of the uranyl extraction process are still under way. The selectivity of these new ligands towards uranyl ion in the presence of other metals has not yet been studied. This is an important point, as other metal ions are always present in the elimination process of uranyl ions from biological systems. We have started uranyl ion selectivity studies with these ligands under extraction process in the presence of other metal ions such as iron(III).

Table 6
Distribution coefficients (D) of the uranyl ion by the ligands $H_3L1 \cdot HCl$–$H_3L8 \cdot HCl$ (pH 3–4, $T = 296$ K, $t = 54$ h)

	$H_3L1 \cdot HCl$	$H_3L2 \cdot HCl$	$H_3L3 \cdot HCl$	$H_3L4 \cdot HCl$	$H_3L5 \cdot HCl$	$H_3L6 \cdot 1/3$ toluene	H_3L7	$H_3L8 \cdot HCl$
D	13.9	10.0	13.5	14.7	15.4	2.9	11.0	5.0

H_3L6–H_3L8 as in Table 5.

Acknowledgements

We are grateful to Prof. Matti Nurmia for correction of the language, to Elina Hautakangas for her help in the synthetic and elemental analysis work and to Reijo Kauppinen for his assistance with NMR measurements.

Appendix A. Supplementary data

CCDC 615461, 615462, 615463, 615464 and 615465 contains the supplementary crystallographic data for **1a**, **1b**, **3**, **4** and **5**. These data can be obtained free of charge via http://www.ccdc.cam.ac.uk/conts/retrieving.html, or from the Cambridge Crystallographic Data Centre, 12 Union Road, Cambridge CB2 1EZ, UK; fax: (+44) 1223-336-033; or e-mail: deposit@ccdc.cam.ac.uk. Supplementary data associated with this article can be found, in the online version, at doi:10.1016/j.poly.2006.08.006.

References

[1] M. Yazzie, S.L. Gamble, E.R. Civitello, D.M. Stearns, Chem. Res. Toxicol. 16 (2003) 524.
[2] M. Sawicki, J.-M. Siaugue, C. Jacopin, C. Moulin, T. Bailly, R. Burgada, S. Meunier, P. Baret, J.-L Pierre, F. Taran, Chem. Eur. J. 11 (2005) 3689.
[3] M. Carrière, L. Avoscan, R. Collins, F. Carrot, H. Khodja, E. Ansoborlo, B. Gouget, Chem. Res. Toxicol. 17 (2004) 446.
[4] C. Drouza, V. Gramlich, M.P. Sigalas, I. Pashalidis, A.D. Keramidas, Inorg. Chem. 43 (2004) 8336.
[5] J. Xu, K.N. Raymond, Inorg. Chem. 38 (1999) 308.
[6] A.E. V Gorden, J. Xu, K.N. Raymond, P. Durbin, Chem. Rev. 103 (2003) 4207.
[7] N.N. Greenwood, A. Earnshaw, Chemistry of the Elements, Pergamon Press, Exeter, UK, 1984, pp. 1477–1479.
[8] M.P. Wilkerson, C.J. Burns, H.J. Dewey, J.M. Martin, D.E. Morris, R.T. Paine, B.L. Scott, Inorg. Chem. 39 (2000) 5277.
[9] P.D. Wilson (Ed.), Nuclear Fuel Cycle, From Ore to Waste, Oxford Science Publications, Oxford, UK, 1996, p. 373.
[10] K.A. Venkatesan, V. Sukumaran, M.P. Antony, P.R.V. Rao, J. Radioanal. Nucl. Chem. 260 (2004) 443.
[11] N. Koshino, M. Harada, Y. Morita, T. Kiikuchi, Y. Ikeda, Progr. Nucl. Energy 47 (2005) 406.
[12] (a) P.D. Beer, G.D. Brindley, D.O. Fox, A. Grieve, M.I. Ogden, F. Szemes, M.G.B. Drew, J. Chem. Soc., Dalton Trans. 16 (2002) 3101;
(b) S. Shinkai, H. Koreishi, K. Ueda, T. Arimura, O. Manabe, J. Am. Chem. Soc. 109 (1987) 6371;
(c) C. Dinse, N. Baglan, C. Cossonnet, J.F. Le Du, Z. Asfari, J. Vicens, J. Alloys Compd. 271–273 (1998) 778.
[13] (a) J. Harrowfield, Gazz. Chim. Ital. 127 (1997) 663;
(b) P. Thuéry, M. Nierlich, J. Harrowfield, J. Vicens (Eds.), Calixarenes 2001, Kluwer Academic Publishers, Dordrecht, 2001.
[14] H. Sopo, J. Sviili, A. Valkonen, R. Sillanpää, Polyhedron 25 (2006) 1223.
[15] W.J. Burke, M.J. Kolbezen, C.W. Stephens, J. Am. Chem. Soc. 74 (1952) 3601.
[16] Z. Otwinowski, W. Minor, Methods Enzymol. 276 (1997) 307.
[17] G.M. Sheldrick, (anon) SHELX-97 (Release 97-2). A program for Crystal Structure Refinement, University of Göttingen, Germany, 1998.
[18] G.M. Sheldrick, SHELXS-97 and SHELXL-97. Programs for Crystal Structure Refinement, University of Göttingen, Germany, 1997.
[19] L.J. Farrugia, J. Appl. Crystallogr. 32 (1999) 837.
[20] P. Thuéry, M. Nierlich, J. Vicens, H. Takemura, Polyhedron 20 (2001) 3183.
[21] D.M. Barnhart, C.J. Burns, N.N. Sauer, J.G. Watkin, Inorg. Chem. 34 (1995) 4079.
[22] D.J. Evans, P.C. Junk, M.K. Smith, Polyhedron 21 (2002) 2421.
[23] F. Barbette, F. Rascalou, H. Chollet, J.L. Babouhot, F. Denat, R. Guilard, Anal. Chim. Acta 502 (2004) 179.
[24] Y. Ikeda, E. Wada, M. Harada, T. Chikazawa, T. Kikuchi, H. Mineo, Y. Morita, M. Nogami, K. Suzuki, J. Alloys Compd. 374 (2004) 420.
[25] M. Baaden, R. Schurhammer, G. Wipff, J. Phys. Chem. B 106 (2002) 434.

Available online at www.sciencedirect.com
ScienceDirect
Polyhedron 26 (2007) 197–203
POLYHEDRON
www.elsevier.com/locate/poly

Ni(II)-mediated synthesis of the novel tripodal aminopyridyl ligand *tamepyr*: Coordination geometry and rigidity of complexes with the divalent 3d metals Fe–Zn and with In(III)

Daniel P. Kennedy [a], Antonio G. DiPasquale [b], Arnold L. Rheingold [b], Roy P. Planalp [a,*]

[a] *Department of Chemistry, University of New Hampshire, Parsons Hall, 23 College Road, Durham, NH 03824-3598, United States*
[b] *Department of Chemistry, University of California, San Diego, CA 92093, United States*

Received 27 May 2006; accepted 13 August 2006
Available online 3 September 2006

Abstract

The synthesis of the novel chelator 'tamepyr' (*N*,*N*′,*N*″-tris(2-pyridylmethyl)-1,1,1-tris(aminomethyl)ethane) and properties of its complexes with Fe(II), Co(II), Ni(II), Cu(II), Zn(II) and In(III) are reported. Tamepyr was prepared as a complex with Ni(II) by the $NaBH_4$ reduction of the tamepyr-trisimine complex, $[Ni((2\text{-py-}C(H){=}NCH_2)_3CMe)]^{2+}$. The decomposition of $[Ni(tamepyr)]^{2+}$ with excess sodium cyanide affords tamepyr in 40% overall yield from tame. Structural study of $[Zn(tamepyr)](ClO_4)_2$ shows similar Zn–N distances with reference to the aminopyridyl tripod tachpyr (*N*,*N*′,*N*″-tris(2-pyridylmethyl)-*cis*,*cis*-1,3,5-triaminocyclohexane), being $d(Zn\text{–}N_{amine,py}) = 216.9(2)$, 212.8(2) pm versus 216.0(3), 216.5(4) pm for $[Zn(tachpyr)](ClO_4)_2$. However, the $[Zn(tamepyr)]^{2+}$ data indicate a greater propensity to octahedral coordination in a tame-framework chelator compared to a tach-framework chelator: the trigonal twist angle in the ZnN_6 coordination sphere of $[Zn(tamepyr)]^{2+}$ is 46.5(2)° versus 43.7(2)° for $[Zn(tachpyr)]^{2+}$. When presented with larger metals such as In(III), tamepyr shows greater flexibility than tachpyr, thus, $[In(tamepyr)]^{3+}$ is completely fluxional at ambient temperature while $[In(tachpyr)]^{3+}$ is static up to 107 °C as shown by ^1H NMR in DMSO-d_6.
© 2006 Elsevier Ltd. All rights reserved.

Keywords: Tripodal chelator; Templating reaction; Fe(II); Ni(II); Zn(II)

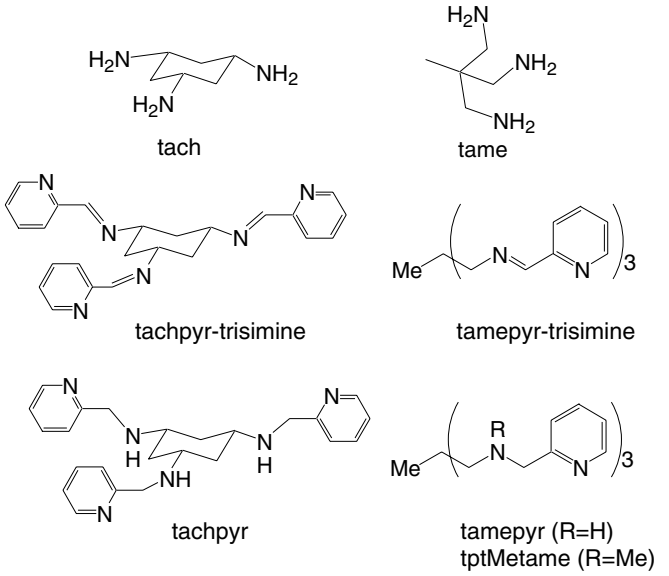
1. Introduction

In the design of metal chelators, the ligand geometry and conformational properties as well as the donor atom character are key to controlling thermodynamics and kinetics of the metal–ligand interaction [1–4]. A number of chelators that are based on triamines with zero to three pendant donor groups have been studied, with objectives that include modulating the reactivity of a supported metal (in analogy to the cyclopentadienyl or tris(pyrazolylborate) ligands), sequestering a metal (analogous to DTPA or DOTA) and the synthesis of polynuclear structures [5–17]. An understanding of metal-binding dynamics and structure is essential to tailor these chelators to such applications. We report the preparation of the novel hexadentate tripod tris(2-pyridylmethyl)-1,1,1-tris(aminomethyl) ethane (tamepyr) and complexation, structural and dynamic information for the metal ions Fe(II), Co(II), Ni(II), Cu(II), Zn(II) and In(III).

The particular motivation to develop tamepyr derived from our studies of tripodal aminopyridyl chelators such as tachpyr (Scheme 1) as intracellular Fe- and Zn-complexing agents [18,19]. We determined that air oxidation plays a role in Fe(II) complexation by tachpyr, leading to Fe-imino species including Fe–tachpyr-trisimine via iron-mediated oxidative dehydrogenation [20,21]. These complexes liberate iron by hydrolysis due to structural strain. We observed this strain in the structure of an Fe(II)-tachpyr-trisimine derivative [22] and saw that it arises from the strong

* Corresponding author. Tel.: +1 603 862 2471; fax: +1 603 862 4278.
E-mail address: roy.planalp@unh.edu (R.P. Planalp).

0277-5387/$ - see front matter © 2006 Elsevier Ltd. All rights reserved.
doi:10.1016/j.poly.2006.08.020



Scheme 1. The tripodal amines tach and tame and their corresponding methinyl-2-py and methyl-2-py derivatives.

preference of tachpyr-trisimine for trigonal-prismatic geometry, for example in $[Zn(tachpyr\text{-}trisimine)]^{2+}$, which has a trigonal twist angle of 4.6°, where values of an ideal trigonal-prism are 0° and of an octahedron, 60° [23–26]. Fe(II) in the low-spin state prefers the octahedral geometry and so its geometry preferences are in opposition to the tachpyr-trisimine ligand. In order to retain and sequester iron as Fe(II), it was thus desirable to prepare chelators whose products of iron-mediated oxidative dehydrogenation would bind Fe(II) well. The structure of Fe(tamepyr-trisimine) is known and is quite octahedral (trigonal twist angle = 43°) [27], but surprisingly the hexahydro analogue tamepyr has not been previously reported, although an *N*-methylated derivative of tamepyr, tptMetame is known (Scheme 1). Herein, we describe use of Ni(II) templating to stabilize the tris-imine condensation product of tame with pyridine-2-carboxaldehyde which then allows synthesis of the novel ligand tamepyr by reduction of Ni(II)-tamepyr-trisimine (Scheme 2). The coordination chemistry of tamepyr with Fe(II), Co(II), Ni(II), Cu(II), Zn(II) and In(III), and comparison of its rigidity to tachpyr are presented.

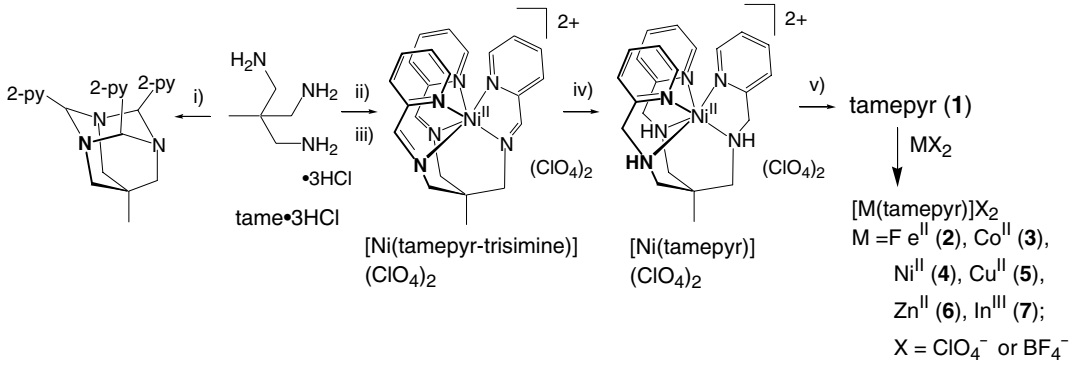
2. Results and discussion

The direct condensation of tame with 3 equiv. of pyridine-2-carboxaldehyde yielded a triazaadamantane, whereas reaction of tame, Ni(II) and 3 equiv. of pyridine-2-carboxaldehyde affords $[Ni(tamepyr\text{-}trisimine)]^{2+}$, according to the template reaction previously reported [28]. However, reduction of $[Ni(tamepyr\text{-}trisimine)]^{2+}$ with $NaBH_4$ forms $[Ni(tamepyr)]^{2+}$, accompanied by a color change from orange to pink and disappearance of a C=N stretching frequency at 1650 cm^{-1}. Workup with $HClO_4$ and recrystallization from $MeCN/Et_2O$ provides fuchsia prisms of $[Ni(tamepyr)](ClO_4)_2$ (40% yield) from which free tamepyr is displaced in 96% yield with aqueous NaCN.

The Fe(II), Co(II), Cu(II), Zn(II) and In(III) tamepyr complexes are prepared straightforwardly by reactions of the metal salts and the ligand in MeOH with Et_2O cosolvent to improve precipitation and yields, followed by recrystallization from a $MeCN/Et_2O$ solvent system. A 1:1 M:L composition was verified for all complexes by elemental analysis and electrospray mass spectrometry. Work with Fe(II) was conducted under inert atmosphere, due to the tendency of Fe to mediate oxidative dehydrogenation of aminopyridyl ligands [20,29].

2.1. Structural study

Crystallographic study of $[Zn(tamepyr)](ClO_4)_2$ helps elucidate the influence of the ligand on the metal ion coordination geometry, because Zn(II) has no electronic geometry preferences (Fig. 1) [30]. The cation possesses crystallographic C_3 symmetry where the C_3 axis passes through C9, C8 and Zn1. Tame appears better suited to providing an octahedral geometry, because $[Zn(tamepyr)](ClO_4)_2$ has



Scheme 2. Left of tame · 3HCl, formation of a triazaadamantane; right of tame · 3HCl, synthesis of $[Ni(tamepyr\text{-}trisimine)](ClO_4)_2$ and $[Ni(tamepyr)](ClO_4)_2$. (i) 3 equiv. NaOH, 2-pyridinecarboxaldehyde, $-H_2O$; (ii) 3 equiv. NaOH, EtOH; (iii) 2-pyridinecarboxaldehyde, $Ni(ClO_4)_2 \cdot 6H_2O$; (iv) $NaBH_4$, H_2O, EtOH; (v) NaCN(aq), CH_2Cl_2 extraction and evaporation.

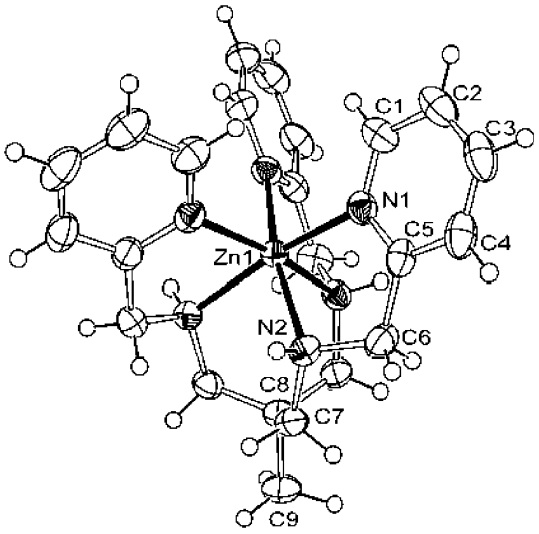


Fig. 1. Structure of $[Zn(tamepyr)](ClO_4)_2$ (ORTEP; 50% probability ellipsoids) showing the atom-numbering scheme. Selected bond lengths (Å) and angles (°): Zn–N(2) = 2.169(2), Zn–N(1) = 2.128(2), N(2)–Zn–N(1) = 79.16(8), trigonal twist angle = 46.47°.

a larger trigonal twist angle (46.5(2)°) than $[Zn(tachpyr)](ClO_4)_2$ (43.7(2)° [30]). Complex $[Zn(tamepyr)](ClO_4)_2$ also has significantly shorter Zn–N_{py} bond lengths than $[Zn(tachpyr)](ClO_4)_2$ (2.128(2) Å versus 2.165(4) Å). A greater twist angle is consistent with shorter bond lengths to the metal ion because steric interactions between coordinating pyridines are reduced. The other striking comparison is with $[Fe(tptMetame)](ClO_4)_2$, the Fe(II) complex of the tri-*N*-methylated tamepyr analog tptMetame (Scheme 2) [31]. This complex was structurally characterized at 153 K, where it Fe(II) is in the low-spin state and the trigonal twist angle is nearly octahedral at 51.0°.

The ability of tamepyr to attain a conformation close to octahedral is clearly attributable to twisting of the framework and so an analysis according to the formalisms that Al-Obaidi et al. applied to $[Fe(tptMetame)]^{2+}$ [31] is appropriate. There are multiple conformational possibilities in tamepyr chelates because left- and right-handed twists with respect to the C_3-axis of both the tame cap (atoms C8, C7, C7A, C7B) and the three aminopyridyl arms are possible. The twist configuration of the three six-membered rings in the tame cap portion of $[Zn(tamepyr)]^{2+}$ is assigned as δ^{cap}. Further, λ or δ configurations of the five-membered aminopyridyl chelate rings (e.g., Zn1–N2–C6–C5–N1) are possible, and finally, the three aminopyridyl arms may have a Λ or a Δ twist. In $[Zn(tamepyr)]^{2+}$, the conformations of the five-membered chelate rings are λλλ and the twist of the three aminopyridyl arms is Δ. Together these last two constraints require an *SSS* stereochemistry at the three chiral nitrogen (amine) donor atoms, as is observed. The complex crystallizes in the chiral space group $P2_13$. Because the Flack parameter refined to a value of 0.015(14), the enantiomer reported in this paper is the correct one. While the crystal studied is of the δ^{cap}–Δ(λλλ) enantiomer, crystals of the λ^{cap}–Λ(δδδ) enantiomer are probably also present. In sum, crystallography shows that the pyridyl-pendant chelator of the tame framework has a greater tendency to octahedrality than the tach framework, accompanied by shorter Zn–N bond lengths and consistent with previous results findings for $[Fe(tptMetame)](ClO_4)_2$.

2.2. Electronic structure

The solution spectra of $[M(tamepyr)]^{2+}$ are fully consistent with a pseudooctahedral coordination geometry and strong metal–ligand interactions including effective $d\pi \rightarrow p\pi$ metal–ligand donation. The room temperature ^1H NMR spectrum of $[Fe(tamepyr)]^{2+}$ (CD_3CN solvent) is not paramagnetically shifted, indicating a low spin electronic configuration ($^1A_1$ ground-state). Whereas, spin-crossover behavior is exhibited by $[Fe(tptMetame)]^{2+}$ in propionitrile solution or the solid-state at temperatures greater than 153 K [31]. Thus, tertiary coordinating amines are substantially more hindered than secondary amines in the tamepyr system, as we observed in the tach system, where the Fe(II) complex of *N*,*N*′,*N*″-trimethyltachpyr ($[Fe((N\text{-}Me)_3tachpyr)](ClO_4)_2$) is a high-spin Fe(II) complex while $[Fe(tachpyr)]^{2+}$ is a low-spin complex [20,32].

The electronic structures of the Fe(II), Co(II), Ni(II), and Cu(II) complexes of tamepyr have been assessed with UV–Vis–NIR spectroscopy. The complex $[Fe(tamepyr)]^{2+}$ exhibits an absorption band at 24 000 cm^{-1} (Table 1). This absorption is often assigned as a metal to ligand charge transfer band (MLCT) characteristic of LS Fe(II) complexes [33,34]. The MLCT band masks all d–d transitions of low-spin Fe(II) except for a low-energy shoulder (18 000 cm^{-1}, $\varepsilon = 300\ cm^{-1}\ M^{-1}$), which is often assigned as an obscured $^1A_{1g} \rightarrow {}^1T_{1g}$ transition [34]. The $[Ni(tamepyr)]^{2+}$ spectrum compares well with other octahedral d^8 metal complexes, although only two of the three possible d–d bands could be assigned. The third band ($^3A_{2g} \rightarrow {}^3T_{1g}$) was obscured by a charge transfer band beginning at

Table 1
Spectral properties of tamepyr complexes[a]

M(II)	ν, cm^{-1} (ε, $M^{-1}\ cm^{-1}$)	Transition	Δ_o (cm^{-1})	Color
Fe	24 000 (70 000)	MLCT		bronze
Co	21 100(63), 18 400(28), 10 650(21)	$^4T_{1g} \rightarrow {}^4A_{2g}$, $^4T_{1g} \rightarrow {}^4T_{1g}(P)$, $^4T_{1g} \rightarrow {}^4T_{2g}$	11 100	orange
Ni	19 600(16), 12 600(12)	$^3A_{2g} \rightarrow {}^3T_{1g}$, $^3A_{2g} \rightarrow {}^3T_{2g}$		pink
Cu	16 100(107)	$^2E_g \rightarrow {}^2T_{2g}$		blue

[a] Recorded at ambient temperature in MeCN for all complexes except Fe where the spectrum was recorded in degassed H_2O; assignments in octahedral pseudosymmetry.

approximately 27 000 cm^{-1}. The $^3A_{2g} \rightarrow {}^3T_{1g}(F)$ transition in $[Ni(tamepyr)]^{2+}$ occurs at 19 600 cm^{-1}. The corresponding transition for $[Ni(ampy)_3]^{2+}$ is red-shifted and occurs at 18 800 cm^{-1} [35]. This is consistent with the additional field strength imparted to $[Ni(tamepyr)]^{2+}$ via a chelate-effect originating from the presence of the tame framework. The $^3A_{2g} \rightarrow {}^3T_{2g}$ transition is mixing with the spin-forbidden $^3A_{2g} \rightarrow {}^1E_g$ transition, so the value of Δ_o reported in Table 1 is only approximate [35]. The energy of this transition is similar to those found for $[Ni(trenpyr)]^{2+}$ and $[Ni(tachpyr)]^{2+}$ [36,37]. The spectrum of $[Cu(tamepyr)]^{2+}$ is typical of distorted octahedral Cu(II) complexes, with the presence of one asymmetric band at 16 100 cm^{-1} [37]. The asymmetry in this band can be attributed to Jahn–Teller distortions of this complex in solution. All three possible d–d transitions are seen in the spectrum of $[Co(tamepyr)]^{2+}$. The $^4T_{1g} \rightarrow {}^4A_{2g}$ band often lies under the $^4T_{1g}(P)$ transition, but in the case of $[Co(tamepyr)]^{2+}$ both transitions can be seen at 21 100 cm^{-1} and 18 400 cm^{-1} respectively. The lowest energy transition, which is equal to Δ_o, lies at 10 650 cm^{-1}, which is consistent with the reported range of 6500–10 500 cm^{-1} [38]. A ligand field strength $\Delta_o \geqslant 15\,000$ cm^{-1} can cause a LS octahedral Co(II) complex, which would however be Jahn–Teller distorted [39]. It is possible that the octahedral-enforcing nature of tamepyr would lead to additional strain in a Jahn–Teller distorted complex which would outweigh the stabilization difference of low-spin d^7 relative to high-spin d^7 electron configurations.

2.3. Solution conformation

Proton NMR spectra show that tamepyr maintains a rigid pseudooctahedral geometry at room temperature when coordinated to 3d metal ions, but as the metal–ligand size fit worsens (in the case of In(III)) the tamepyr coordination sphere is apparently more flexible than that of tachpyr. The ^1H NMR of the Fe(II) and Zn(II) tamepyr complexes show a sharp doublet of doublet spin pattern for the pyridyl-CH_2–N protons, indicative of conformational rigidity in solution at room temperature [40]. The ^1H NMR spectrum for $[In(tamepyr)]^{3+}$ (DMSO-d_6) shows a single doublet for each of the two types of CH_2 (pyridyl–methylene and aminomethylene), thus the geminal H's are chemically equivalent but split by the neighboring amino proton. This is consistent with the racemization of the chelate rings between the Λ and Δ forms, and is not observed in the ^1H NMR spectrum of $[In(tachpyr)]^{3+}$ (DMSO-d_6) until the temperature of the solution is raised to 107 °C [40].

3. Conclusions

We have synthesized the novel ligand tamepyr and studied its coordination chemistry with several 3d transition-metal elements. Investigations of aqueous metal ion complexation processes and thermodynamics of tamepyr's interaction with 3d-transition metals are underway.

4. Experimental section

4.1. General

All the materials listed below were of a research grade or a spectro-grade in the highest purity available and were generally used without further purification except diethyl ether, which was distilled from sodium benzophenone. Anhydrous methanol, acetonitrile, and the salts $Zn(ClO_4)_2 \cdot 6H_2O$, $Cu(ClO_4)_2 \cdot 6H_2O$, $Ni(ClO_4)_2 \cdot 6H_2O$, $Co(BF_4)_2 \cdot 6H_2O$, and $Fe(ClO_4)_2 \cdot 6H_2O$ were obtained from Aldrich. Anhydrous grade EtOH was obtained from Pharmco. DMSO-d_6, $CDCl_3$, CD_3CN, and D_2O were obtained from Cambridge Isotope Laboratories. All of the UV–Vis spectra were measured using a Varian Cary 50 Bio spectrometer with 1 cm^3 quartz cuvettes (1 cm path-length). Electrospray ionization (ESI) mass spectra in the positive ion detection mode were obtained on a Finnegan LCQ Classic instrument with dual optical Paul traps and Picoview nanospray source. Assignments were based on calculations by the program developed by Scientific Instrument Services (http://www.sisweb.com/cgi-bin/mass10.pl, accessed 8 August 2006). ^1H and ^{13}C NMR were obtained using a Varian Mercury 400 MHz NMR instrument and chemical shifts are reported in ppm on the δ scale relative to TMS or DSS. Proton chemical shifts are annotated as follows: ppm (integral, multiplicity, coupling constant (Hz), assignment). The magnetic moment was measured by Evan's method using residual CD_2HCN or CD_2HSOCD_3 as indicator in both the sample and closed capillary. Elemental analysis was performed by Atlantic Microlabs (Atlanta, Georgia). Drying was accomplished under a stream of nitrogen or under reduced pressure (*ca.* 10^{-2} Torr) with a standard Schlenk line. Anaerobic manipulations were accomplished under a nitrogen atmosphere in a glovebox (VAC model HE-43 with HE-493 purifier).

Caution: perchlorate salts can be explosive and should be handled with care. No explosions occurred during the course of this work.

4.2. Preparations of compounds

4.2.1. *[Ni(tamepyr)](ClO$_4$)$_2$ (**4**)*

An aqueous solution of NaOH (265 mg, 6.63 mmol) was added to 1,1,1-tris(aminomethyl)ethane · 3HCl (0.500 g, 2.21 mmol). The resulting solution was then brought to dryness on a rotary evaporator affording colorless oily solids. Absolute ethanol (25 mL) was then added to the solids, and the mixture was sonicated for 5 min and cooled to 4 °C for 1 h. The cold ethanolic solution was filtered through a glass frit. The filtrate was then diluted with 100 mL of water and transferred to a flask that contained $Ni(ClO_4)_2 \cdot 6H_2O$ (808 mg, 2.21 mmol). The resulting sky blue solution

was stirred with slow addition of an ethanolic solution (40 mL) of 2-pyridinecarboxaldehyde (710 mg, 6.63 mmol). The resulting solution was stirred under nitrogen for 16 h where a color change from blue to orange took place. The reaction mixture afforded significant amounts of orange colored precipitate, which was collected on a glass frit and dried under vacuum to afford 614 mg of [Ni(tamepyr-trisimine)]-$(ClO_4)_2$. This complex was added to a mixture of 150 mL of doubly distilled water and 20 mL of EtOH (0.5 g, 0.8 mmol) and $NaBH_4$ (2.2 g, 58 mmol). The reaction mixture was stirred for 16 h to give a pale pink solution. The pH of the mixture was dropped to 6.7 with addition of 70% perchloric acid. The pink precipitate that formed was collected on a glass frit and washed with small portions of Et_2O. The resulting powder was recrystallized by Et_2O diffusion from CH_3CN yielding fuchsia colored prisms. The prisms were isolated and dried under vacuum to give 473 mg (40%) of the product. (*Anal.* Calc. for $C_{23}H_{30}N_6NiCl_2O_8$: C, 42.62; H, 4.67; N, 12.97. Found: C, 42.68; H, 4.71; N, 12.94%.) MS(ESI/methanol): *m*/*z* 547 ($M - ClO_4^-$). $\mu_{eff} = 3.2$ BM at 23 °C. λ_{max}/cm^{-1} (MeCN) 12600 (12.0 cm^{-1} M^{-1}), 19600 (15.8 cm^{-1} M^{-1}). IR (KBr/Nujol): 3275 s, 1611 s, 1576 m, 1095 s, br.

4.2.2. *N,N′,N″-tris(2-pyridylmethyl)-1,1,1-tris(aminomethyl)ethane (tamepyr) (**1**)*

To a sample of $[Ni(tamepyr)](ClO_4)_2$ (50 mg, 80 μmol) was added 5 mL of hot aqueous sodium cyanide (21 mg, 420 μmol). The mixture was shaken for 5 min affording a pale yellow solution. The solution was extracted with methylene chloride (3 × 5 mL); the organic fractions were combined, and dried over anhydrous Na_2SO_4. The supernatant was decanted and the solvent was removed on a rotary evaporator. The resulting colorless oil was dried further under vacuum to afford 30 mg (96%) of the product. ^1H NMR [$CDCl_3$]: δ 8.51 (3H, m, pyridyl H); 7.60 (3H, m, pyridyl H); 7.33 (3H, d, $^3J = 7.6$ Hz, pyridyl H); 7.13 (3H, m, pyridyl H); 3.91 (6H, s, pseudobenzylic H); 2.62 (6H, s, methylene H); 2.50 (3H, s, N*H*); 0.95 (3H, s, methyl H). ^{13}C NMR [$CDCl_3$]: δ 160.6, 149.3, 136.6, 122.4, 122.0, 56.9, 56.2, 38.7, 22.1.

4.2.3. *[Fe(tamepyr)](ClO4)2 (**2**)*

A pale yellow degassed methanolic solution (1 mL) of $Fe(ClO_4)_2 \cdot 6H_2O$ (29 mg, 80 μmol) was added to a colorless degassed methanolic solution (1 mL) of tamepyr (31 mg, 80 μmol) under the protection of a nitrogen atmosphere. The reaction mixture was allowed to deposit solids for 16 h. The supernatant was removed and the resulting dark colored crystalline solids were washed with small portions of degassed Et_2O, and then dried under a stream of nitrogen. The solids were then recrystallized by Et_2O diffusion from CH_3CN affording chestnut colored prisms. The crystals of the complex were stable to air indefinitely whereas a sealed oxygenated aqueous solution of the complex decomposed when incubated at 37 °C overnight. ^1H NMR [CD_3CN degassed]: δ 7.81 (3H, m, pyridyl H); 7.52 (6H, m, pyridyl H); 7.20 (3H, t, $^3J = 6.4$ Hz, pyridyl H); 4.46 (3H, m, N*H*); 4.31 (3H, dd, diastereotopic pseudobenzylic H); 4.05 (3H, dd, diastereotopic pseudobenzylic H); 2.97 (3H, dd, diastereotopic methylene H); 2.49 (3H, dd, diastereotopic methylene H); 0.812 (3H, s, methyl H). IR (CsI pellet): 3267 m, 1615 w, 1577 w, 1088 s, br, 761 s, 624 s. (*Anal.* Calc. for $C_{23}H_{30}N_6FeCl_2O_8$: C, 42.81; H, 4.69; N, 13.02. Found: C, 43.10; H, 4.75; N, 13.13%.)

4.2.4. *[Co(tamepyr)](BF4)2 (**3**)*

A pale red degassed methanolic solution (1 mL) of $Co(BF_4)_2 \cdot 6H_2O$ (19 mg, 55 μmol) was added to a colorless degassed methanolic solution (1 mL) of tamepyr (21 mg, 55 μmol) under the protection of a nitrogen atmosphere. The reaction mixture was then subjected to Et_2O diffusion for 5 days to afford orange colored prismatic crystals. The supernatant was removed and the resulting crystalline solids were washed with small portions of degassed Et_2O, and then dried under a stream of nitrogen to give 21 mg (63%) of the product. The crystals of the complex were stable to air indefinitely but decomposed rapidly in CH_3CN when exposed to air. (*Anal.* Calc. for $C_{23}H_{30}N_6CoB_2F_8$: C, 44.34; H, 4.85; N, 13.49. Found: C, 44.28; H, 5.05; N, 13.35%.) $\mu_{eff} = 4.9$ BM at 23 °C. IR (CsI pellet): 3172 m, 1606 m, 1565 w, 729 s, 478 s. IR (KBr/Nujol): 3275 s, 1611 s, 1576 m, 1095 s, br. λ_{max}/cm^{-1} (CH_3CN degassed) 10650 (21 cm^{-1} M^{-1}), 18400 (28 cm^{-1} M^{-1}), 21100 (63 cm^{-1} M^{-1}).

4.2.5. *[Cu(tamepyr)](ClO4)2 (**5**)*

A pale blue isopropanolic solution (1 mL) of $Cu(ClO_4)_2 \cdot 6H_2O$ (30 mg, 80 μmol) was added to a colorless isopropanolic solution (1 mL) of tamepyr (31 mg, 80 μmol) resulting in the formation of a sky blue powder. The solvent was removed on a rotary evaporator and the resulting powder was recrystallized by Et_2O diffusion from CH_3CN, isolated and dried under vacuum, to afford 47 mg (91%) of the product as royal blue needles. (*Anal.* Calc. for $C_{23}H_{30}N_6CuCl_2O_8$: C, 42.31; H, 4.63; N, 12.87. Found: C, 42.21; H, 4.58; N, 12.77%.) MS(ESI/methanol): *m*/*z* 552 ($M - ClO_4^-$). $\mu_{eff} = 2.1$ BM at 23 °C. IR (KBr/Nujol): 3249 m, 1613 m, 1574 w, 1096 s, br. λ_{max}/cm^{-1} (CH_3CN) 16100 (107 cm^{-1} M^{-1}) asymmetric peak.

4.2.6. *[Zn(tamepyr)](ClO4)2 (**6**)*

A colorless methanolic solution (1 mL) of $Zn(ClO_4)_2 \cdot 6H_2O$ (30 mg, 80 μmol) was added to a colorless methanolic solution (1 mL) of tamepyr (31 mg, 80 μmol) resulting in the formation of a colorless precipitate. The solvent was diluted with a small portion of Et_2O and the solids were isolated, washed with additional ether, and then recrystallized by Et_2O diffusion from CH_3CN to afford 30 mg (58%) of colorless prisms. ^1H NMR [CD_3CN]: δ 8.07 (3H, m, pyridyl H); 7.88 (3H, d, $^3J = 4.8$ Hz, pyridyl H); 7.57 (3H, d, $^3J = 8$ Hz, pyridyl H); 7.46 (3H, t, $^3J = 6.8$ Hz, pyridyl H); 4.35 (3H, dd, pseudobenzylic H); 3.95 (3H, dd, diastereotopic H); 3.53 (3H, m, N*H*); 3.32 (3H, dd, diastereotopic methylene H);

2.85 (3H, dd, diastereotopic methylene H); 0.77 (3H, s, methyl H). IR (KBr/Nujol): 3249 m, 1613 m, 1574 w, 1096 s, br. (*Anal*. Calc. for $C_{23}H_{30}N_6ZnCl_2O_8$: C, 42.19; H, 4.62; N, 12.83. Found: C, 41.90; H, 4.60; N, 12.68%.) MS(ESI/methanol): *m/z* 553 ($M - ClO_4^-$). Suitable crystals for X-ray crystallography were prepared by slow Et_2O diffusion into an CH_3CN solution of the complex.

4.2.7. *[In(tamepyr)](NO$_3$)$_3$ · MeOH (7)*

A colorless methanolic solution (0.90 mL) of $In(NO_3)_3 \cdot 5H_2O$ (8.0 mg, 20 μmol) was added to a colorless methanolic solution (0.90 mL) of tamepyr (7.8 mg, 20 μmol) resulting in the formation of a colorless solution. The solution was allowed to stand for 18 h. The complex was crystallized from solution as feather-like white needles by Et_2O diffusion. The needles were isolated and dried under vacuum to afford 10.1 mg (73%) of the desired product. ^{1}H NMR [DMSO-d_6]: δ 8.25–8.21 (3H, m, pyridyl H); 8.04 (3H, s, pyridyl H); 7.79 (3H, d, $^3J = 8.0$ Hz, pyridyl H); 7.66 (3H, t, $^3J = 6.0$ Hz, pyridyl H); 5.86 (3H, m, N*H*); 4.31 (6H, d, $^3J = 6.0$ Hz, pseudobenzylic H); 3.17 (6H, d, $^3J = 7.2$ Hz, methylene H); 0.84 (3H, s, methyl H). IR (KBr pellet): 3163, 1609 m, 1571 w, 1365 vs, 1279 s. (*Anal*. Calc. for $C_{23}H_{30}N_6InN_3O_9$: C, 39.85; H, 4.74; N, 17.43. Found: C, 39.99; H, 4.47; N, 17.72%.)

4.3. Crystallography

Crystallographic data for [Zn(tamepyr)]$(ClO_4)_2$: colorless prisms, crystal dimensions $0.30 \times 0.40 \times 0.40$ mm, $C_{23}H_{30}Cl_2N_6O_8Zn$, cubic, space group $P2_13$, $a = b = c = 13.9397(3)$ Å, $\alpha = \beta = \gamma = 90°$, $V = 2708.70(10)$ Å^3, $Z = 4$, $\lambda = 0.71073$ Å, $D_{calc} = 1.606$ g/cm^3, $T = 213(2)$ K, μ(Mo Kα) = 1.163 mm^{-1}. A total of 2147 independent reflections were used with $2.53° < \theta < 28.26°$, of which 2041 reflections had $I > 2\sigma(I)$. Final results: $R(F, I > 2\sigma(I)) = 0.0326$, $R_w(F,\ I > 2\sigma(I)) = 0.0944$, Goodness-of-fit = 1.020, maximum residual electronic density = 0.530 e Å^{-3}.

Acknowledgement

We thank a reviewer for helpful suggestions on the structure of **6**.

Appendix A. Supplementary data

The CIF file for the structural analysis of [Zn(tamepyr)]$(ClO_4)_2$ has been deposited with the Cambridge Crystallographic Data Centre, CCDC No. 280055. These data can be obtained free of charge via http://www.ccdc.cam.ac.uk/conts/retrieving.html or from the Director, CCDC, 12 Union Road, Cambridge, CB2 1EZ, UK; fax: +44 1233 336033; e-mail deposit@ccdc.cam.ac.uk. Supplementary data associated with this article can be found, in the online version, at doi:10.1016/j.poly.2006.08.020.

References

[1] A.E. Martell, R.D. Hancock, Metal Complexes in Aqueous Solutions, Plenum Press, New York, 1996.
[2] Z.D. Liu, R.C. Hider, Coord. Chem. Rev. 232 (2002) 151.
[3] J. Romba, D. Kuppert, B. Morgenstern, C. Neis, S. Steinhauser, T. Weyhermuller, K. Hegetschweiler, Eur. J. Inorg. Chem. (2006) 314.
[4] S.J. Archibald, A.K. Nairn, P. Timmins, P.H. Walton, Tetrahedron Lett. 46 (2005) 6441.
[5] U. Brand, H. Vahrenkamp, Inorg. Chim. Acta 198–200 (1992) 663.
[6] B. Greener, M. Moore, P. Walton, J. Chem. Soc., Chem. Commun. (1996) 27.
[7] K.A. Deal, G. Park, J. Shao, N.D. Chasteen, M.W. Brechbiel, R.P. Planalp, Inorg. Chem. 40 (2001) 4176.
[8] C.C. Cummins, J. Lee, R.R. Schrock, W.D. Davis, Angew. Chem., Int. Ed. Engl. 31 (1992) 1501.
[9] L. Turculet, T.D. Tilley, Organometallics 21 (2002) 3961.
[10] D.T. Puerta, M. Botta, C.J. Jocher, E.J. Werner, S. Avedano, K.N. Raymond, S.M. Cohen, J. Am. Chem. Soc. 128 (2006) 2222.
[11] M.W. Brechbiel, O.A. Gansow, J. Chem. Soc., Perkin Trans. I (1992) 1173.
[12] F. Xiao, D.v.d. Helm, R. Hider, P. Dobbin, J. Chem. Soc., Dalton Trans. (1992) 3265.
[13] S. Steinhauser, U. Heinz, M. Bartholoma, T. Weyhermuller, H. Nick, K. Hegetschweiler, Eur. J. Inorg. Chem. (2004) 4177.
[14] G.J.T. Cooper, D.-L. Long, L. Cronin, Inorg. Chem. Commun. 8 (2005) 737.
[15] C.E. Dube, S. Mukhopadhyay, P.J. Bonitatebus Jr., R.J. Staples, W.H. Armstrong, Inorg. Chem. 44 (2005) 5161.
[16] S. Mann, G. Huttner, L. Zsolnai, K. Heinze, Angew. Chem., Int. Ed. Engl. 35 (1997) 2808.
[17] R. Shaw, I.S. Tidmarsh, R.H. Laye, B. Breeze, M. Helliwell, E.K. Brechin, S.L. Heath, M. Murrie, S. Ochsenbein, H.-U. Güdel, E.J.L. McInnes, Chem. Commun. (2004) 1418.
[18] S.V. Torti, F.M. Torti, S.P. Whitman, M.W. Brechbiel, G. Park, R.P. Planalp, Blood 92 (1998) 1384.
[19] R. Zhao, R.P. Planalp, R. Ma, B. Greene, B. Jones, M. Brechbiel, F.M. Torti, S.V. Torti, Biochem. Pharmacol. 67 (2004) 1677.
[20] G. Park, F. Lu, N. Ye, M. Brechbiel, S. Torti, F. Torti, R. Planalp, JBIC, J. Biol. Inorg. Chem. 3 (1998) 449.
[21] R.P. Planalp, A.M. Przyborowska, G. Park, N. Ye, F.H. Lu, R.D. Rogers, G.A. Broker, S.V. Torti, M.W. Brechbiel, Biochem. Soc. Trans. 30 (2002) 758.
[22] G. Lu, D.P. Kennedy, S. Lai, G. Park, A.M. Przyborowska, M.W. Brechbiel, G.A. Broker, R.D. Rogers, R. Ma, F.M. Torti, S.V. Torti, R.P. Planalp, Inorg. Chim. Acta, submitted for publication.
[23] W. Gillum, J. Huffman, W. Streib, R. Wentworth, J. Chem. Soc., Chem. Commun. (1969) 843.
[24] J.E. Parks, B.E. Wagner, R.H. Holm, J. Am. Chem. Soc. 92 (1970) 3500.
[25] E. Larsen, G.N. La Mar, B.E. Wagner, J.E. Parks, R.H. Holm, Inorg. Chem. 11 (1972) 2652.
[26] R. Kirchner, C. Mealli, M. Bailey, N. Howe, L. Torre, L. Wilson, L. Andrews, N. Rose, E. Lingafelter, Coord. Chem. Rev. 77 (1987) 89.
[27] E.B. Fleischer, A.E. Gebala, D.R. Swift, P.A. Tasker, Inorg. Chem. 11 (1972) 2775.
[28] S.O. Wandiga, J.E. Sarneski, F.L. Urbach, Inorg. Chem. 11 (1972) 1349.
[29] M. Holanda, P. Krumholz, H. Chum, Inorg. Chem. 15 (1976) 890.
[30] G. Park, N. Ye, R. Rogers, M. Brechbiel, R. Planalp, Polyhedron 19 (2000) 1155.
[31] A.H.R. Al-Obaidi, K.B. Jensen, J.J. McGarvey, H. Toftlund, B. Jensen, S.E.J. Bell, J.G. Carroll, Inorg. Chem. 35 (1996) 5055.

[32] G. Park, A.M. Przyborowska, N. Ye, N. Tsoupas, C.B. Bauer, G.A. Broker, R.D. Rogers, M.W. Brechbiel, R.P. Planalp, J. Chem. Soc., Dalton Trans. (2003) 318.
[33] M. Tamura, Y. Urano, K. Kikuchi, T. Higuchi, M. Hirobe, T. Nagano, J. Organomet. Chem. 611 (2000) 586.
[34] M. Goto, N. Koga, Y. Ohse, H. Kurosaki, T. Komatsu, Y. Kuroda, J. Chem. Soc., Chem. Commun. (1994) 2015.
[35] R.D. Hancock, G.J. McDougall, J. Chem. Soc., Dalton Trans. (1977) 67.
[36] J.R. Hartman, R.W. Vachet, J.H. Callahan, Inorg. Chim. Acta 297 (2000) 79.
[37] N. Ye, G. Park, A.M. Przyborowska, P.E. Sloan, T. Clifford, C.B. Bauer, G.A. Broker, R.D. Rogers, R. Ma, S.V. Torti, M.W. Brechbiel, R.P. Planalp, J. Chem. Soc., Dalton Trans. (2004) 1304.
[38] L. Banci, A. Bencini, C. Benelli, D. Gatteschi, C. Zanchini, Struct. Bonding (Berlin) 52 (1982) 37.
[39] F. Cotton, G. Wilkinson, C. Murillo, M. Bochmann, Advanced Inorganic Chemistry, Wiley, New York, 1999, pp. 821.
[40] K.A. Hilfiker, R.D. Rogers, M.W. Brechbiel, R.P. Planalp, Inorg. Chem. 36 (1997) 4600.

Available online at www.sciencedirect.com
ScienceDirect
Polyhedron 26 (2007) 204–213
POLYHEDRON
www.elsevier.com/locate/poly

Synthesis, characterisation and biological activity of cycloaurated organogold(III) complexes with imidate ligands

Kelly J. Kilpin, William Henderson *, Brian K. Nicholson

Department of Chemistry, University of Waikato, Private Bag 3105, Hamilton, New Zealand

Received 13 June 2006; accepted 14 August 2006
Available online 18 August 2006

Abstract

The reactions of the cycloaurated gold(III) complexes (2-bp)$AuCl_2$ (2-bp = 2-benzylpyridyl) or (damp)$AuCl_2$ (damp = Me_2NCH_2-C_6H_4) with an excess of sodium saccharinate (Nasacc), potassium phthalimidate (Kphth), or with isatin and trimethylamine in refluxing methanol results in the successful isolation of a series of new gold(III) imidate complexes. These were characterised by NMR and IR spectroscopies, and by X-ray structure determinations on (2-bp)Au(sacc)$_2$ and (2-bp)Au(phth)$_2$. In both structures, the planes of the saccharinate and the phthalimidate ligands are orientated almost perpendicular to the gold coordination plane. As expected from *trans*-influence considerations, the Au–$N_{(imidate)}$ bond lengths *trans* to the aryl carbon atoms are longer than the Au–$N_{(imidate)}$ bond lengths *trans* to the pyridyl groups. The complexes have also been characterised by electrospray ionisation MS; in the presence of halide ligands, one imidate ligand is readily displaced. Anti-tumour (P388 murine leukemia) and selected anti-microbial data for the new complexes are reported. Surprisingly, all three damp complexes had low anti-tumour activity, which is likely to be a consequence of the poor solubility of these complexes. The synthesis and characterisation of a related gold(III) bis(amidate) complex derived from sulfathiazole is also described.
© 2006 Elsevier Ltd. All rights reserved.

Keywords: Gold complexes; Imidate ligands; Crystal structures; Electrospray mass spectrometry; Biological activity

1. Introduction

The search for potent anti-tumour activity has been one of the driving forces for recent activity in the chemistry of cycloaurated gold(III) complexes [1–3], in light of the well-developed medicinal chemistry of platinum(II), and the similarities between this metal centre and gold(III), imparted by their isoelectronic nature. In cycloaurated complexes, the ligand, typically a bidentate nitrogen–carbon donor, stabilises the square-planar gold(III) state towards reduction. Most work has been carried out with the damp complex **1** [1], because of its typical good solubility characteristics and tendency to promote good anti-tumour activity in the corresponding acetate derivative. Developments in this area have been thoroughly reviewed [4,5].

We have been investigating the synthesis and biological properties of cycloaurated complexes that contain a range of ancillary ligands, derived from both the damp system as well as other cycloaurated complexes that are more readily prepared in one step from $HAuCl_4$. Complexes containing chelating thiosalicylate ($SC_6H_4CO_2$) ligands have been found, by ourselves [6,7] and others [8], to show promising biological activity, and we have recently turned our attention to the investigation of complexes with nitrogen and oxygen donor ligands. Examples of catecholate [9], amidophenolate [9], ureylene [10], lactam [11], and auracyclic bis(amidate) [12] complexes have all been prepared, with a number showing promising anti-tumour activity. In this paper, we report studies on the synthesis, characterisation and biological activity of cycloaurated gold(III) complexes containing monodentate imidate ligands derived from saccharin, phthalimide and isatin.

Although imidate derivatives of cycloaurated complexes are new, gold(III) imidate complexes have a long

* Corresponding author. Fax: +64 7 838 4219.
E-mail address: w.henderson@waikato.ac.nz (W. Henderson).

0277-5387/$ - see front matter © 2006 Elsevier Ltd. All rights reserved.
doi:10.1016/j.poly.2006.08.009

history. As long ago as 1929, Pope filed a patent claiming to have synthesised a range of gold(III) succinimidate complexes [13]. Subsequently, Kharasch and Isbell reported [14] the formation of gold(III) imidate complexes $[Au(imidate)_4]^-$ (imidate = anion of succinimide, phthalimide, saccharin or diethyl barbituric acid), which were reformulated by Tyabji and Gibson [15]. Malik et al. [16] demonstrated that the product of the reaction between $[AuCl_4]^-$ and *N*-methylhydantoin was actually a gold(I) complex, and suggested that Kharasch's original Au(III) tetrasuccinimidate complex was also a gold(I) bis(imidate) complex. Only recently, a stable gold(III) complex **2** was reported [17], containing four deprotonated hydantoin ligands, an arrangement thought to be impossible (on steric grounds) by Tyabji and Gibson. Few other gold(III) imidate complexes have been reported, though there are many examples of both gold(I) [18–23] and platinum(II) [24–29] imidate complexes, derived from a range of ligands such as saccharin, phthalimide, and isatin.

2. Results and discussion

2.1. Synthesis and characterisation of gold(III) imidate complexes derived from saccharin, phthalimide and isatin

The reactions of (damp)$AuCl_2$ (**1**) or (2-bp)$AuCl_2$ (**3**) with an excess of either sodium saccharinate (Nasacc), potassium phthalimidate (Kphth) or isatin (Hisa) in refluxing methanol afforded products **4**–**9** in good yields. The reactions involving isatin required the use of Me_3N to remove the imide proton whereas preformed salts of saccharin and phthalimide were used, and additional base was unnecessary for these ligands. The products **4**–**9** were characterised by ESI MS, NMR and IR spectroscopies, together with elemental microanalysis. The damp complexes **5** and **9** were, surprisingly, only sparingly soluble in $(CH_3)_2SO$ and $CDCl_3$, but the other complexes were soluble in common organic solvents such as dichloromethane, acetone and $(CH_3)_2SO$.

^{1}H NMR spectroscopy of the 2-benzylpyridyl derivatives was used to determine sample purity, however full assignment proved difficult due to the presence of four non-equivalent aromatic rings and hence the presence of complex multiplets in the aromatic region. The methylene protons of the benzylpyridyl ligand are expected to appear as a doublet of doublets, due to geminal coupling between protons in equatorial and axial environments of a puckered six-membered ring, as previously described by Fuchita et al. [30] In the phthalimide **6** and isatin **8** derivatives, the CH_2 signals were very broad and barely visible above the baseline, as illustrated in Fig. 1 for (2-bp)Au(phth)$_2$ (**6**); heating effected convergence of the two broad methylene proton signals, giving a broad singlet (Fig. 1). For the saccharin derivative **4** the CH_2 resonances were resolved into two broad doublets.

The ^{1}H NMR spectrum of (damp)Au(phth)$_2$ (**7**) showed two singlets at δ 3.32 and 4.53 due to the methyl and

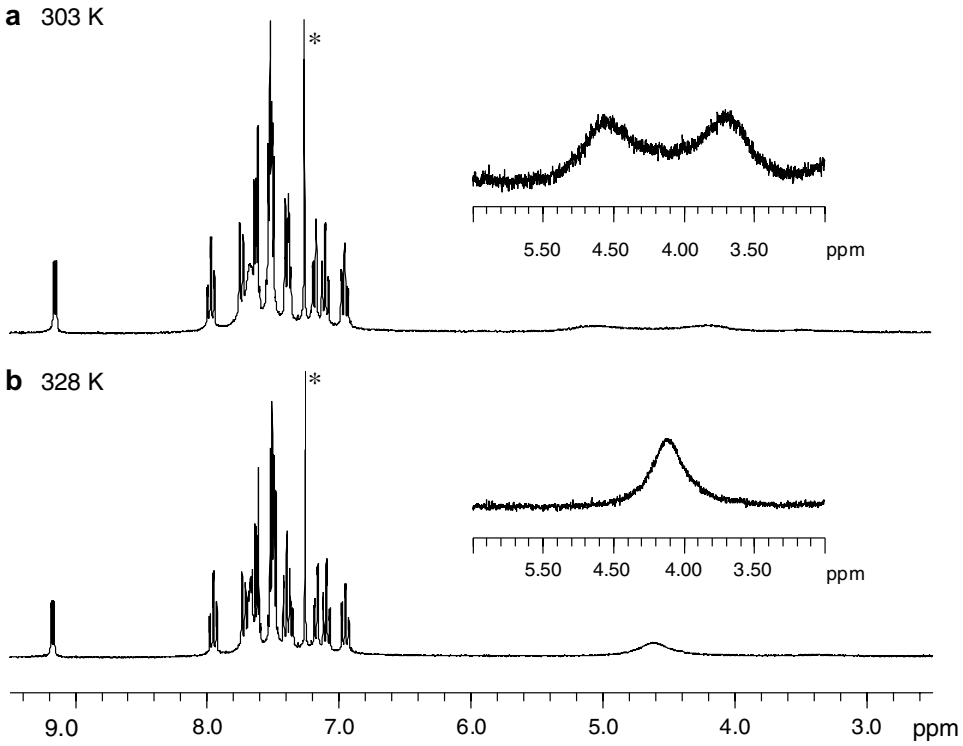


Fig. 1. ^{1}H NMR spectra (300 MHz) of the complex (2-bp)Au(phth)$_2$ (**6**) at temperatures of (a) 303 K and (b) 328 K, in $CDCl_3$ solution, showing the fluxionality of the benzylpyridyl group. The peaks marked * are due to $CHCl_3$ (7.26 ppm).

methylene protons of the damp ligand, respectively; this complex contains a plane of symmetry co-planar to the gold coordination plane. However, both (damp)Au(sacc)$_2$ (**5**) and (damp)Au(isa)$_2$ (**9**) were poorly soluble in all common NMR solvents with the exception of $CDCl_3$, in which they were soluble enough to acquire very weak spectra. In contrast to the bis(phthalimidate) species, these complexes do not have a plane of symmetry through the Au plane, due to the unsymmetrical nature of the saccharin and isatin ligands. As a result, the methylene and methyl group protons are in different chemical environments giving rise to two singlets from the methyl protons and two doublets (due to geminal H–H coupling) from the methylene protons.

The IR spectrum of isatin shows strong absorptions in the carbonyl region at 1748, 1728 and 1617 cm^{-1}; coordination to gold results in a decrease in the stretching frequency of these bands to 1736, 1692 and 1605 cm^{-1} for the benzylpyridyl derivative **8**, and to 1730, 1701, 1682 and 1603 cm^{-1} for the damp derivative **9**. The NH stretch, present at 3192 cm^{-1} in the free ligand, is absent in the spectra of the gold complexes, indicating coordination through the nitrogen atom. This effect was less pronounced in the saccharin and phthalimide complexes, as the regions of interest contained a large number of strong overlapping bands.

The imidate complexes have also been characterised by ESI MS. As the bis(imidate) complexes **4**–**9** are neutral, NaCl was typically added as an ionisation aid. However, along with the anticipated $[M+Na]^+$ ions, a common ion assigned as $[M\text{-imidate}+Cl+Na]^+$ was visible, even at low cone voltages. This ion could either arise from the mono(imidate) complex (as an impurity in the sample) or displacement of an imidate ligand by chloride during ESI MS analysis. The fragment ion $[M\text{-imidate}]^+$ was also often observed and, in some cases, $[M\text{-imidate} + OMe + Na]^+$. In order to ascertain if the chloride ion was displacing the imidate ligand a small amount of $NaBPh_4$ was added as a (chloride-free) sodium source to complex **6**. The ion $[M\text{-imidate}+Cl+Na]^+$ was no longer detected, suggesting that such species are only formed when chloride ions are present. Addition of small amounts of Et_4NX (X = Cl, Br) to **6** also produced additional ions corresponding to $[M\text{-imidate}+X+Et_4N]^+$, providing further evidence that halide ions can displace the imidate ligand. Table 1 details the range of ions observed when complex **6** was analysed in the presence of various ionisation aids. Addition of pyridine (py) exclusively produced the ion $[M-phth+py]^+$. Together, these ESI MS investigations appear to suggest that one of the monodentate imidate ligands is labile towards displacement by halide and other ligands. This is likely to be the imidate ligand *trans* to the high *trans*-influence aryl carbon; studies of the dissociation of acetate from (damp)Au(OAc)$_2$ have previously shown that one acetate, presumably the one *trans* to the aryl group, was also readily labilised [31]. Labilisation of one amidate donor ligand by halide was previously observed for certain auracyclic bis(amidate) species [7], but in general, auracyclic systems are much more robust towards MS-induced fragmentation, or reaction with halide ligands [6,7,9–11].

Table 1
Ions observed in positive-ion ESI mass spectra for the complex (2-bp)Au(phth)$_2$ (**6**) (=M) at a cone voltage of 20 V

Ionisation aid	Observed ions (*m*/*z*)
NaCl	680 (100%, $[M+Na]^+$), 565 (78%, $[M-phth+MeO+Na]^+$), 569 (35%, $[M-phth+Cl+Na]^+$), 1337 (28%, $[2M+Na]^+$)
Pyridine (py)	590 (100%, $[M-phth+py]^+$)
$NaBPh_4$	680 (100%, $[M+Na]^+$), 511 (60%, $[M-phth]^+$)
Et_4NCl	676 (100%, $[M-phth+Cl+Et_4N]^+$), 787 (85%, $[M+Et_4N]^+$), 511 (63%, $[M-phth]^+$)
Et_4NBr	787 (100%, $[M+Et_4N]^+$), 722 (67%, $[M-phth+Br+Et_4N]^+$)

At a cone voltage of 20 V, the compound (damp)Au(sacc)$_2$ (**4**) showed a strong peak in the ESI mass spectrum at *m*/*z* 465 (100% relative intensity) which was assigned as the cation $[(damp)_2Au]^+$. This ion was not observed at higher cone voltages (>40 V), and had considerably reduced intensity when NaCl was added to promote ionisation of the neutral **4**. The cation $[(damp)_2Au]^+$ was not detected in the ^1H NMR spectrum but is visible in the ESI spectrum due to it having a high ionisation efficiency, exacerbated by the low solubility of **4**. The analogous methoxy-substituted cation $[(MeO\text{-}damp)_2Au]^+$ has previously been observed in ESI MS analyses [32].

2.2. Synthesis and characterisation of a gold(III) sulfathiazole complex

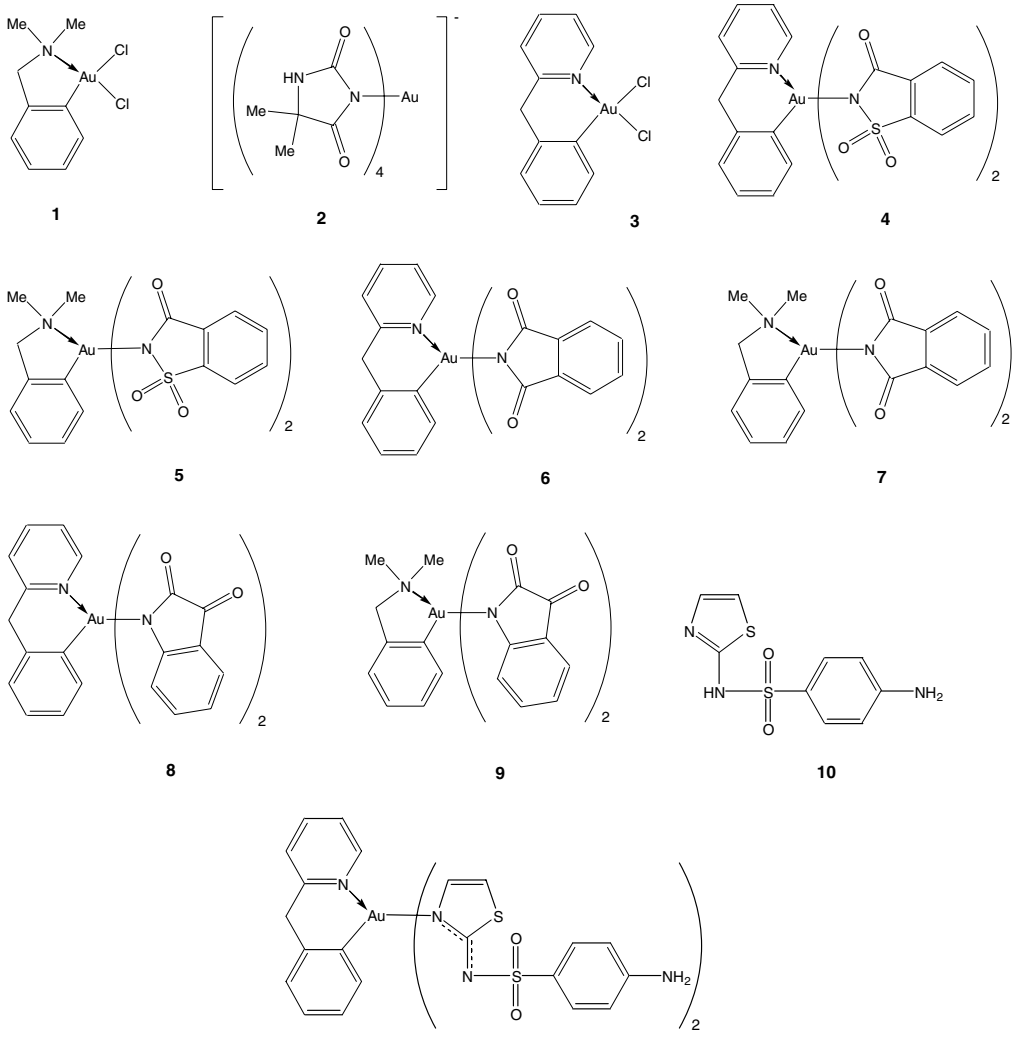
The complex (2-bp)AuCl$_2$ (**3**) was also reacted with sulfathiazole [4-amino-*N*-(thiazol-2-yl)benzenesulfonamide, stzH (**10**)], giving the bis(sulfathiazole) complex **11** in excellent yield as a yellow solid. This complex was poorly soluble in all solvents with the exception of $(CH_3)_2SO$ and $HC(O)NMe_2$ (DMF), but was successfully characterised by NMR, ESI MS, IR, and elemental microanalysis. The mode of co-ordination to the gold is unclear, as sulfathiazole has three available nitrogen binding sites. Attempts at growing X-ray quality single crystals (by slow evaporation of a saturated DMF solution, or by vapour diffusion of methanol into a DMF solution) were unsuccessful thus the structure was unable to be assigned unambiguously. An X-ray crystal structure of the isoelectronic platinum(II) sulfathiazole complex *cis*-[Pt(stz)$_2$(PPh$_3$)$_2$] has confirmed bonding of the sulfathiazole anions through the thiazole nitrogen [33]. Structures of other transition metal [Co(II) [34] and Cu(II) [35]] sulfathiazole complexes indicate the ligand bonded to the metal centre via the thiazole nitrogen. However, an X-ray crystal structure has also been solved showing sulfathiazole bridging two independent Cu atoms through amide and thiazole nitrogens [36].

The ^{1}H NMR spectrum of complex **11** was very complicated, however the signal from the amino (NH_2) protons was visible, only very slightly shifted ($\delta = 5.69$) from free sulfathiazole ($\delta = 5.75$), indicating that bonding to the gold centre is not through the amino group. The IR spectrum of **11** provides evidence for coordination to the gold through the thiazole nitrogen. Sulfathiazole has a strong absorption at 3350 cm^{-1} due to NH_2 stretching and **11** also has absorptions in this region (3430 cm^{-1}) suggesting that the NH_2 group remains intact. Likewise, the absorptions due to SO_2 stretching and bending modes are not greatly shifted upon coordination (1136 and 1323 cm^{-1} in sulfathiazole compared with 1131 and 1323 cm^{-1} in **11**). However, the S–N stretching frequency of the thiazole ring has decreased from 1531 to 1459 cm^{-1} upon coordination, indicating that coordination probably occurs through $N_{thiazole}$. The values obtained are very comparable to the Pt(II) sulfathiazole complexes, again supporting binding through the thiazole nitrogen. This observation has been noted before in other metal-sulfathiazole compounds [37,38].

2.3. X-ray crystal structures of (2-bp)Au(sacc)$_2$ (4) and (2-bp)Au(phth)$_2$ (6)

Structure determinations of **4** and **6** were carried out in order to ascertain the geometry and orientation of the saccharinate and phthalimidate ligands around the gold centre. Views of the structures are shown in Figs. 2–5 along with the atom numbering schemes. A comparison of important bond lengths and angles is presented in Table 2, while comparisons of the geometric parameters of the coordinated ligands with free saccharin [39] and phthalimide [40] are given in Tables 3 and 4, respectively.

In both cases, the geometry around the gold atom is essentially square-planar. No atom deviates from the least-squares plane [defined by N(1), N(2), N(3), Au(1) and C(41) for the saccharin derivative **4**; N(1), N(2), N(3), Au(1) and C(12) for the phthalimide derivative **6**] by more than 0.040 or 0.0675 Å, respectively. The Au–$N_{imidate}$ bond lengths in the structures are very comparable; as expected, the Au–$N_{imidate}$ bond lengths *trans* to the benzylpyridyl



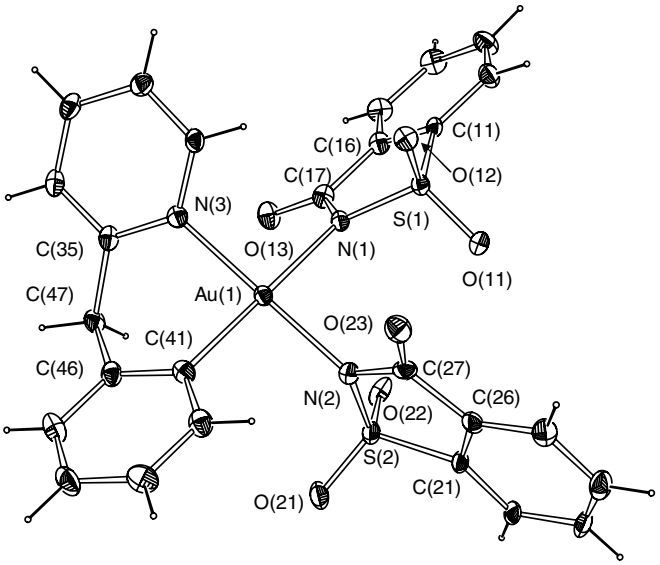


Fig. 2. Perspective view of the X-ray crystal structure of the complex (2-bp)Au(sacc)$_2$ (**4**) showing the atom labelling scheme. Thermal ellipsoids are shown at the 30% probability level. The solvent of crystallisation has been omitted for clarity.

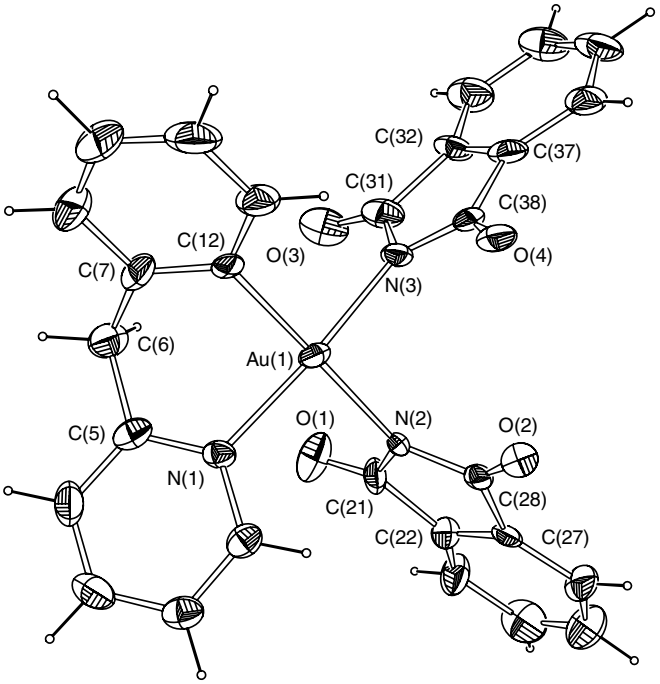


Fig. 3. Perspective view of the X-ray crystal structure of the complex (2-bp)Au(phth)$_2$ (**6**) showing the atom labelling scheme. Thermal ellipsoids are shown at the 50% probability level. The dichloromethane of crystallisation has been omitted.

carbon are longer than those *trans* to the benzylpyridine nitrogen due to the phenyl ligand having a higher *trans* influence than the pyridyl nitrogen ligand [41].

Both saccharinate and phthalimidate ligands are essentially planar. Tables 3 and 4 compare selected bond lengths of the free saccharin and phthalimide molecules with those of the coordinated ligands. Upon coordination to gold, the

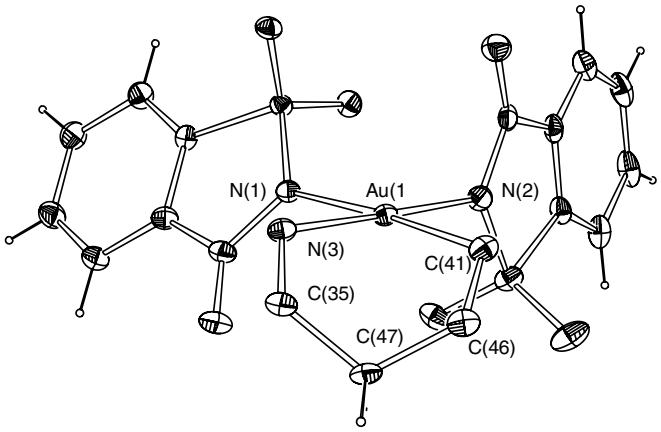


Fig. 4. Side view of the X-ray crystal structure of the complex (2-bp)Au(sacc)$_2$ (**4**) showing the orientation of the saccharinate ligands with respect to the gold coordination plane. Thermal ellipsoids are shown at the 30% probability level. Solvent of crystallisation and the atoms completing the benzyl and pyridyl rings have been omitted for clarity.

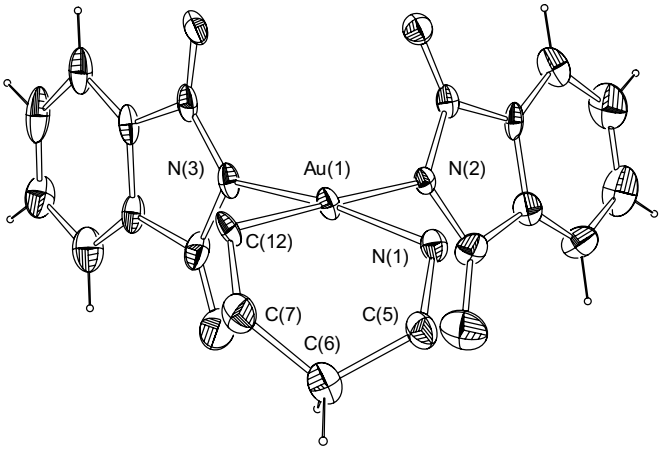


Fig. 5. Side view of the X-ray crystal structure of the complex (2-bp)Au(phth)$_2$ (**6**) showing the orientation of the phthalimidate ligands with respect to the gold coordination plane. Dichloromethane of solvation and atoms completing the benzyl and pyridyl rings have been omitted for clarity. Thermal ellipsoids are shown at the 40% probability level.

C=O and S=O bond lengths in the saccharin ligand significantly increase. This effect is less pronounced in the phthalimidate complex.

In both structures, the planes of the saccharin and the phthalimide ligands are orientated almost perpendicular to the coordination plane of the gold (Figs. 4 and 5), most probably to reduce steric interactions between the bulky imidate ligands. This particular ligand orientation has been observed previously in the similar square-planar platinum(II) isatin complex *cis*-[Pt(isat)$_2$(PPh$_3$)$_2$] [42]. In the structure of the saccharin complex **4**, the plane of the ligand coordinated through N(1) has a dihedral angle of 58.70° relative to the gold co-ordination plane, whereas the ligand coordinated through N(2) has an angle of 85.21°. The bis(phthalimide) structure is such that the plane of the phthalimide ligand co-ordinated through

Table 2
Comparison of selected bond lengths (Å) and angles (°) between (2-bp)Au(sacc)$_2$ (**4**) and (2-bp)Au(phth)$_2$ (**6**)

	4	**6**
Bonds		
Au–$N_{benzylpyridyl}$	2.041(4)	2.046(10)
Au–$C_{benzylpyridyl}$	2.021(4)	2.041(11)
Au–$N_{trans\ to\ C}$	2.118(4)	2.117(9)
Au–$N_{cis\ to\ C}$	2.015(4)	2.007(9)
Angles		
$N_{benzylpyridyl}$–Au–$C_{benzylpyridyl}$	89.4(2)	88.3(4)
$N_{cis\ to\ C}$–Au–$N_{trans\ to\ C}$	90.4(2)	90.5(4)
$C_{benzylpyridyl}$–Au–$N_{cis\ to\ C}$	90.5(2)	90.2(4)
$N_{benzylpyridyl}$–Au–$N_{trans\ to\ C}$	89.8(2)	91.1(4)

Table 3
Comparison of selected bond lengths (Å) between saccharin and the coordinated saccharinate ligands of **4**

Bond	Saccharin [28]	Ligand co-ordinated through N(1)	Ligand co-ordinated through N(2)
C=O	1.214	1.221(5)	1.216(6)
S=O	1.409	1.444(3)	1.434(3)
	1.429	1.444(3)	1.443(3)
N–C	1.369	1.389(6)	1.383(6)
N–S	1.633	1.647(4)	1.662(4)

Table 4
Comparison of selected bond lengths (Å) between phthalimide and the coordinated phthalimidate ligands of **6**

Bond	Phthalimide [29]	Ligand co-ordinated through N(2)	Ligand co-ordinated through N(3)
C=O	1.216	1.212(15)	1.228(17)
	1.222	1.237(16)	1.235(16)
C–N	1.381	1.367(14)	1.363(16)
	1.395	1.382(16)	1.387(17)

N(2) is at an angle of 71.60°, while the N(3)-coordinated ligand is at an angle of 89.53°, with respect to the gold coordination plane.

Interestingly, the saccharin ligands are orientated so that the SO_2 groups are *trans* to each other, as seen in Fig. 4. Although no crystal structures of square-planar bis(saccharin) metal complexes could be found in the literature, the arrangement of the two SO_2 groups *trans* to each other appears to be a common trend. Examples of six co-ordinate octahedral structures where the SO_2 groups occupy opposite binding sites in a *trans* configuration are vast [43]. In square pyramidal complexes there are examples of both *cis* [44] and *trans* [45] arrangements of the saccharinate ligands. Interestingly, in the linear Hg(saccharinate)$_2$ molecule the saccharinate ligands are orientated so the SO_2 groups are positioned on the same side [46].

3. Biological activity

The anti-tumour and anti-microbial activities of the bis(imidate) complexes were determined and data are reported in Table 5. The benzylpyridyl complexes **6** and **8** have IC_{50} values that are very comparable to the auracyclic bis(amidate) products reported by us in a previous paper [12]. The other bis(imidate) complexes show low anti-tumour activity towards the P388 murine leukaemia cell line. There are two likely reasons for this. Firstly, the damp complexes **5**, **7** and **9** all have surprisingly low solubilities in common solvents when compared to other damp complexes reported in the literature, where there are many examples often showing excellent anti-tumour activity [1–5]. Secondly, the greater lability of monodentate ligands relative to the more stable and less labile metallacyclic products may have an influence on the biological activity. ESI MS results indicate that one imidate ligand is lost very easily, and such reactions might prevent the complex from reaching its biological target. Continuing the analogy with platinum(II) systems, it is known that replacement of monodentate ligands (such as chloride in cisplatin) with a bidentate chelating ligand (such as cyclobutane-1,1-dicarboxylate in carboplatin) slows the rate of hydrolysis and moderates the toxicity of the platinum-based drug [47].

4. Conclusions

New gold(III) bis(imidate) complexes (imidate = anion of saccharin, phthalimide, isatin) have successfully been synthesised and characterised. To the best of our knowledge, these are the first gold compounds of this type to

Table 5
Anti-tumour (P388) and anti-microbial activities for gold(III) bis(imidate) derivatives

Compound	Anti-tumour IC_{50}[a]		Anti-microbial[b] activity[c]					
	ng mL^{-1}	μM	Ec	Bs	Pa	Ca	Tm	Cr
(2-bp)Au(sacc)$_2$ (**4**)	>25000	>34.3	2	7	2	5	2	–
(damp)Au(sacc)$_2$ (**5**)	>25000	>36.0	1	4	–	–	3	–
(2-bp)Au(phth)$_2$ (**6**)	3258	5.0	N/T	10	N/T	5	5	N/T
(damp)Au(phth)$_2$ (**7**)	>25000	>40.1	2	5	–	4	3	–
(2-bp)Au(isa)$_2$ (**8**)	6894	10.5	4	8	6	4	5	–
(damp)Au(isa)$_2$ (**9**)	>25000	>40.1	1	4	–	–	3	–

N/T = not tested.

[a] The concentration of the sample required to reduce the cell growth of the P388 leukaemia cell line (ATCC CCL 46) by 50%.

[b] Ec = *Escherichia coli*, Bs = *Bacillus subtilis*, Pa = *Pseudomonas aeruginosa*, Ca = *Candida albicans*, Tm = *Trichophyton mentagrophytes*, Cr = *Cladosporium resinae*.

[c] Inhibition zone as an excess radius (mm) from a 6 mm disc containing 2 μg of sample; – denotes no observed activity.

be reported. The X-ray crystal structures of (2-bp)Au(sacc)$_2$ (**4**) and (2-bp)Au(phth)$_2$ (**6**) have been solved and indicate that the imidate anions are co-ordinated to the gold centre through Au–N bonds. In both cases, the planar imidate ligands are orientated perpendicular to the gold co-ordination plane.

5. Experimental

5.1. General

General experimental techniques were as previously described [9]; routine ESI mass spectra were recorded on a VG Platform II instrument, using methanol as the mobile phase. Assignment of mass spectrometric isotope patterns was aided by the ISOTOPE program [48]. All NMR spectra were acquired in $CDCl_3$, with the exception of **11** [$(CD_3)_2SO$]. Integration of the ^{1}H NMR spectra indicated that **7** and **8** crystallised with approximately 1.0 and 0.12 mol of dichloromethane, respectively.

All reactions were carried out with no attempts to exclude light or air. The solvents used were LR grade. Trimethylamine (Eastman, 25% aqueous solution), sodium saccharinate (Aldrich), potassium phthalimidate (Merck), isatin (BDH) and sulfathiazole (BDH) were used as supplied. The cycloaurated gold(III) complexes (2-bp)$AuCl_2$ (**3**) [49] and (damp)$AuCl_2$ (**1**) [50,51] were prepared by modified literature methods.

5.2. Synthesis of (2-bp)Au(sacc)$_2$ (4)

The complex (2-bp)$AuCl_2$ (**3**) (100 mg, 0.23 mmol) and sodium saccharinate (190 mg, 93 mmol) were added to methanol (25 mL) and refluxed with stirring for 2 h. After cooling to room temperature, water (50 mL) was added, resulting in the rapid deposition of white microcrystals. These were filtered, washed with water (2 × 10 mL) and diethyl ether (10 mL) and dried under vacuum to give 158 mg (93%) of product. For microanalysis the crude product was recrystallised by vapour diffusion of diethyl ether into a dichloromethane solution of the product at room temperature to give white crystals. M.p. 131–134 °C. *Anal.* Calc. for $C_{26}H_{18}N_3O_6S_2Au$: C, 42.8; H, 2.5; N, 5.8. Found: C, 42.2; H, 2.8; N, 5.5%. IR: υ(C=O) 1686 cm^{-1} (s); $\upsilon(SO_2$, sym) 1291 cm^{-1} (s), $\upsilon(SO_2$, asym) 1155 cm^{-1} (br s). ESI MS: Cone voltage 20 V: NaCl added, *m*/*z* 605 (100%, [M-sac+Cl+Na]$^+$). ^{1}H NMR, δ 4.17 (d, 1H), 5.11 (d, 1H), 7.01–8.04 (m, 15H), 9.26 (d, 1H). ^{13}C–{^{1}H} NMR, δ 47.5 (CH_2), 120.5–157.3 (aryl C), 182.7, 184.5 (*C*=O).

5.3. Synthesis of (damp)Au(sacc)$_2$ (5)

The complex (damp)$AuCl_2$ (**1**) (100 mg, 0.25 mmol) and sodium saccharinate (206 mg, 1 mmol) were dissolved in refluxing methanol (30 mL) to give a colourless solution. During two hours of refluxing with stirring, white microcrystals were deposited. These were filtered, washed with water (2 × 10 mL) and diethyl ether (10 mL) then dried under vacuum to give 142 mg (84%) of product. M.p. 196–198 °C (decomp.). *Anal.* Calc. for $C_{23}H_{20}N_3O_6S_2Au$: C, 39.7; H, 2.9; N, 6.0. Found: C, 39.7; H, 3.1; N, 5.9%. IR: υ(C=O) 1695 cm^{-1}; $\upsilon(SO_2$, sym) 1317, 1291 cm^{-1}; $\upsilon(SO_2$, asym) 1159, 1167 cm^{-1}. ESMS: Cone voltage 20 V: NaCl added, *m*/*z* 571 (100%, [M-sac+Cl+Na]$^+$), 465 (30%, [(damp)$_2$Au]$^+$), 718 (10%, [M+Na]$^+$); pyridine added, *m*/*z* 592 (100%, [M-sac+py]$^+$). ^{1}H NMR, δ 3.43 (s, 3H), 3.49 (s, 3H), 4.20 (br d, 1H), 5.06 (br d, 1H), 7.09 (t, 1H), 7.13–7.24 (m, 4H), 7.68–7.71 (m, 6H), 8.0 (d, 1H). The compound was too insoluble for a satisfactory ^{13}C–{^{1}H} NMR spectrum.

5.4. Synthesis of (2-bp)Au(phth)$_2$ (6)

The complex (2-bp)$AuCl_2$ (**3**) (200 mg, 0.46 mmol) and potassium phthalimidate (340 mg, 1.8 mmol) were added to methanol (50 mL) and refluxed with stirring for 1 h, during which time a pale yellow solution formed. Water (30 mL) was added, resulting in the immediate deposition of white microcrystals. After cooling to room temperature, the suspension was filtered, washed with water (2 × 10 mL) and diethyl ether (10 mL) then dried under vacuum to give 254 mg (84%) of product. *Anal.* Calc. for $C_{28}H_{18}N_3O_4Au$: C, 51.2; H, 2.8; N, 6.4. Found: C, 50.4; H, 2.8; N, 6.4%. IR: υ(C=O) 1690 cm^{-1} (s) and 1664 cm^{-1} (s). ESI MS: Cone voltage 20 V, NaCl added: *m*/*z* 680 (100%, [M+Na]$^+$), 565 (78%, [M−phth+MeO+Na]$^+$), 569 (35%, [M−phth+Cl+Na]$^+$), 1337 (27%, [2M+Na]$^+$). ^{1}H NMR, δ 4.15 (br d, 1H), 5.15 (br d, 1H), 6.95 (t, 1H), 7.10 (t, 1H), 7.17 (d, 1H), 7.38 (m, 3H), 7.51 (m, 5H), 7.62 (m, 2H), 7.69 (d, 1H), 7.97 (t, 1H), 9.15 (d, 1H). ^{13}C–{^{1}H} NMR, δ 47.6 (CH_2), 122.1–157.8 (aryl *C*), 177.3, 172.8 (*C*=O).

5.5. Synthesis of (damp)Au(phth)$_2$ (7)

The complex (damp)$AuCl_2$ (**1**) (100 mg, 0.25 mmol) and potassium phthalimidate (186 mg, 1 mmol) were added to methanol (30 mL) and refluxed with stirring for 2 h, during which time white microcrystals were deposited. The mixture was cooled, filtered then washed with methanol (2 × 10 mL) and diethyl ether (10 mL). The crude product was recrystallised by vapour diffusion of pentane into a dichloromethane solution of the crude product. The colourless crystals were filtered, washed (petroleum spirits) then dried under vacuum to give 133 mg (86%) of product. M.p. 192 °C (decomp.). *Anal.* Calc. for $C_{25}H_{20}N_3O_4Au \cdot 1.06CH_2Cl_2$: C, 43.9; H, 3.1; N, 5.9. Found: C, 44.3; H, 3.1; N, 6.1%. IR: υ(C=O) 1686 cm^{-1} (s) and 1655 cm^{-1} (s). ESI MS: Cone voltage 20 V: *m*/*z* 646 (100%, [M+Na]$^+$), 477 (82%, [M−phth]$^+$), 1269 (27%, [2M+Na]$^+$). ^{1}H NMR, δ 3.32 (s, 6H), 4.53 (s, 2H), 5.30 (s, 2.11H, from CH_2Cl_2), 6.69 (d, 1H), 7.01 (t, 1H), 7.19, (d, 1H), 7.25 (t, 1H), 7.56 (m, 4H), 7.68 (m, 4H).

^{13}C–{^{1}H} NMR, δ 53.5 (CH_2Cl_2), 53.0 (CH_3), 75.5 (CH_2), 122.4–144.5 (aryl *C*), 172.7, 177.5 (*C*=O).

5.6. Synthesis of (2-bp)Au(isa)$_2$ (**8**)

The complex (2-bp)$AuCl_2$ (**3**) (200 mg, 0.46 mmol) and isatin (270 mg, 1.84 mmol) were added to refluxing methanol (40 mL). While stirring, trimethylamine (2 mL, excess) was added, resulting in the solution changing from deep red to bright orange. The solution was further refluxed with stirring for 20 min. Water (50 mL) was added, resulting in the deposition of orange microcrystals which were collected by filtration. The crude product was recrystallised from dichloromethane and pentane, filtered, washed with water (2 × 10 mL) and diethyl ether (10 mL) and dried under vacuum to give 266 mg (88%) of **8**. M.p. 225 °C (decomp.). *Anal.* Calc. for $C_{28}H_{18}N_3O_4Au \cdot 0.12CH_2Cl_2$: C, 50.6; H, 2.8; N, 6.3. Found: C, 49.7; H, 3.0; N, 6.3%. IR: υ(C=O) 1736 cm^{-1} (s), 1692 cm^{-1} (s) and 1605 cm^{-1} (s). ESI MS: Cone voltage 20 V: *m*/*z* 680 (100%, $[M+Na]^+$), 569 (67%, [M-isa + Cl + Na]), 565 (56%, $[M\text{-isa}+MeO+Na]^+$). ^{1}H NMR, δ 4.35 (br. s, 2H), 5.33 (s, 0.24H, from CH_2Cl_2), 6.87 (t, 1H), 6.95 (t, 1H), 7.01 (d, 1H), 7.18–7.51 (m, 11H), 7.81 (d, 1H), 8.06 (t, 1H). ^{13}C–{^{1}H} NMR, δ 47.7 (CH_2), 53.5 (CH_2Cl_2), 112.4–157.3 (aryl *C*), 162.9, 166.8, 185.1, 189.0 (*C*=O).

5.7. Synthesis of (damp)Au(isa)$_2$ (**9**)

The complex (damp)$AuCl_2$ (**1**) (100 mg, 0.25 mmol) and isatin (148 mg, 1 mmol) were stirred in refluxing methanol (30 mL). Trimethylamine (2 mL, excess) was added, resulting in the solution turning from orange to deep red, and the mixture was refluxed for a further 10 min during which time orange microcrystals were deposited. After cooling to room temperature, the product was filtered, washed with water (2 × 10 mL) and diethyl ether (10 mL) and dried under vacuum to give 117 mg (75%) of product. M.p. 210–212 °C (decomp.). *Anal.* Calc. for $C_{25}H_{20}N_3O_4Au$: C, 48.2; H, 3.2; N, 6.7. Found: C, 47.7; H, 3.4; N, 6.7%. IR: υ(C=O) 1730 cm^{-1} (s), 1701 cm^{-1} (m), 1682 cm^{-1} (s), 1603 cm^{-1} (s). ESI MS: Cone voltage 20 V: *m*/*z* 646 (100%, $[M+Na]^+$), 465 (55%, $[(damp)_2Au]^+$), 678 (35%, $[M+Na+MeOH]^+$), 1269 (27%, $[2M+Na]^+$). ^{1}H NMR, δ 3.24 (s, 3H), 3.48 (s, 3H), 4.17 (d, 1H), 4.89 (d, 1H), 6.85 (t, 1H), 6.92 (t, 1H), 7.06–7.39 (m, 13H), 7.43 (t, 1H). The compound was too insoluble for a satisfactory ^{13}C–{^{1}H} NMR spectrum.

5.8. Synthesis of (2-bp)Au(stz)$_2$ (**11**)

The complex (2-bp)$AuCl_2$ (**3**) (200 mg, 46 mmol) and sulfathiazole (**10**) (257 mg, 1 mmol) were stirred in refluxing methanol (25 mL). Trimethylamine (2 mL, excess) was added, resulting in the rapid deposition of pale yellow microcrystals. The mixture was refluxed with stirring for a further 2 h before being cooled in ice and filtered. The product was then washed with ice-cold methanol (2 × 10 mL) and diethyl ether (10 mL) before being dried under vacuum giving 324 mg (81%) of **11**. M.p. 194–196 °C (decomp.). *Anal.* Calc. for $C_{30}H_{26}N_7O_4S_4Au$: C, 41.2; H, 3.0; N, 11.2. Found: C, 40.8; H, 3.0; N, 10.9%. IR: υ(NH) 3430 cm^{-1} (w), υ(SN) 1459 cm^{-1} (vs), υ(SO_2, sym) 1323 cm^{-1} (s), υ(SO_2, asym) 1131 cm^{-1} (s). ESI MS: Cone voltage 20 V: NaCl added, *m*/*z* 677 (100%, $[M\text{-stz}+Cl+Na]^+$), 896 (72%, $[M+Na]^+$). ^{1}H NMR, δ 4.64 (br s, 2H), 5.69 (s, 4H, NH_2), 5.75 (br s, 2H), 6.51 (d, 2H), 6.56 (d, 1H), 6.66 (d, 1H), 6.77 (d, 1H), 6.90 (t, 1H), 7.13 (d, 1H), 7.21 (t, 1H), 7.31 (d, 1H), 7.36 (d, 1H), 7.52 (t, 1H), 8.02 (d, 1H), 8.22 (t, 1H), 8.55 (d, 1H). The compound was too insoluble for a satisfactory ^{13}C–{^{1}H} NMR spectrum.

6. X-ray crystallography

X-ray intensity data were collected on a Bruker CCD diffractometer using standard procedures and software. Empirical absorption corrections were applied (SADABS) [52]. Structures were solved by direct methods and developed and refined on F_o^2 using the SHELX programmes [53] operating under WinGX [54,55]. Hydrogen atoms were included in calculated positions. For both structures there was potential pseudo symmetry which could have led to disorder between the phenyl and pyridyl rings of the cyclometallated ligand. However, as found for other examples [12], the assignment of the metallated C and N atoms could be done unambiguously, showing there was no disorder. As discussed earlier [12]: (i) the N position was revealed with higher electron density than the C in the difference map; (ii) the U_{iso} values for the atoms were similar when refined as allocated, but were quite different if the assignment was reversed, and R_1 values increased in each case on changing the assignment; (iii) the differences in the Au–N distances to the sacc or phth ligands were consistent with the expected *trans* influences of C and N as assigned.

6.1. Structure of (2-bp)Au(sacc)$_2$ (**4**)

White prism crystals of **4** (M.p. 131–134 °C) were obtained from CH_2Cl_2/Et_2O.

Crystal data: $C_{26}H_{18}AuN_3O_6S_2 \cdot 0.5CH_2Cl_2 \cdot 0.5C_4H_{10}O$, $M = 809.04$, orthorhombic, space group *Pccn*, $a = 15.7051(2)$, $b = 18.7045(3)$, $c = 19.5764(1)$ Å, $V = 5750.7(1)$ Å^3, $T = 84(2)$ K, $Z = 8$, $D_{calc} = 1.869$ g cm^{-3}, μ(Mo Kα) = 5.405 mm^{-1}, $F(000) = 3168$; 32 131 reflections collected with $2° < \theta < 26°$, 5862 unique ($R_{int} = 0.0309$) used after correction for absorption ($T_{max,min} = 0.521$, 0.385). Crystal dimensions = 0.22 × 0.20 × 0.14 mm^3.

When the main molecule had been refined, there was significant residual electron density around special positions with 2-fold symmetry at $\frac{1}{4}, \frac{1}{4}, z$. These appeared to be a mixture of CH_2Cl_2 and Et_2O, but were very disordered and could not be sensibly modelled. This electron density was

excluded using the SQUEEZE procedure of PLATON [56] and refinement was continued against the modified *hkl* data with just the main molecule.

Refinement on F_o^2 converged at $R_1 = 0.0327$ [$I > 2\sigma(I)$] and $wR_2 = 0.0569$ (all data), GoF = 1.140. The structure of **4** is illustrated in Fig. 2, with selected bond parameters summarised in Tables 2 and 3.

6.2. Structure of (2-bp)Au(phth)$_2$ (6)

White plate-like crystals of **6** were obtained from CH_2Cl_2/pentane at 4 °C.

Crystal data: $C_{28}H_{18}AuN_3O_4 \cdot CH_2Cl_2$, $M = 742.35$, monoclinic, space group $P2_1/c$, $a = 12.1739(11)$, $b = 11.9101(9)$, $c = 21.597(2)$ Å, $\beta = 104.58(3)°$, $V = 3030.4(5)$ Å^3, $T = 84(2)$ K, $Z = 4$, $D_{calc} = 1.627$ g cm^{-3}, μ(Mo Kα) = 5.06 mm^{-1}, $F(000) = 1440$; 32 727 reflections collected with $2° < \theta < 26°$, 6333 unique ($R_{int} = 0.0779$) used after correction for absorption ($T_{max,min} = 0.687, 0.230$). Crystal dimensions $0.41 \times 0.20 \times 0.08$ mm^3.

Residual electron density once the main molecule had been refined appeared to come from CH_2Cl_2 in the lattice. Although these features were not very well defined, they could be reasonably successfully modelled as two half-solvent molecules over two sites.

Refinement on F_o^2 converged at $R_1 = 0.0717$ [$I > 2\sigma(I)$] and $wR_2 = 0.1942$ (all data), GoF = 1.219. The structure of **6** is illustrated in Fig. 3, with selected bond parameters summarised in Tables 2 and 4.

7. Biological assays

Details of the biological assays have been published previously [9].

Acknowledgements

We thank the University of Waikato (UW) for financial support of this work, including a scholarship to K.J.K. We also thank Dr. Tania Groutso (University of Auckland) and Dr. Jan Wikaira (University of Canterbury) for collection of the X-ray data sets, and Gill Ellis (University of Canterbury) for the biological assay data. Professor Alistair Wilkins is thanked for NMR expertise, and Pat Gread for technical support with mass spectrometry.

Appendix A. Supplementary data

CCDC 610499 and 610498 contain the supplementary crystallographic data for (**4**) and (**6**). These data can be obtained free of charge via www:http://www.ccdc.cam.ac.uk/conts/retrieving.html, or from the Crystallographic Data Centre, 12 Union Road, Cambridge CB2 1EZ, UK; fax: +44 1223 336 033; or e-mail deposit@ccdc.cam.ac.uk. Supplementary data associated with this article can be found, in the online version, at doi:10.1016/j.poly.2006.08.009.

References

[1] W. Henderson, Adv. Organomet. Chem. 54 (2006) 207.
[2] E.R.T. Tiekink, Gold Bull. 36 (2003) 117.
[3] E.R.T. Tiekink, Crit. Rev. Oncol./Hematol. 42 (2002) 225.
[4] R.V. Parish, Metal-Based Drugs 6 (1999) 271.
[5] S.P. Fricker, Metal-Based Drugs 6 (1999) 291.
[6] W. Henderson, B.K. Nicholson, S.J. Faville, D. Fan, J.D. Ranford, J. Organomet. Chem. 631 (2001) 41.
[7] M.B. Dinger, W. Henderson, J. Organomet. Chem. 560 (1998) 233.
[8] Y. Zhu, B. Song, B.R. Cameron, R.T. Skerlj, in: Proceedings of Gold 2003 Conference, Vancouver, 2003.
[9] C.H.A. Goss, W. Henderson, A.L. Wilkins, C. Evans, J. Organomet. Chem. 679 (2003) 194.
[10] M.B. Dinger, W. Henderson, J. Organomet. Chem. 557 (1998) 231.
[11] W. Henderson, B.K. Nicholson, A.G. Oliver, J. Organomet. Chem. 620 (2001) 182.
[12] K.J. Kilpin, W. Henderson, B.K. Nicholson, Polyhedron, submitted for publication.
[13] W.J. Pope, Brit. Pat. (1929) 338506.
[14] M.S. Kharasch, H.S. Isbell, J. Am. Chem. Soc. 53 (1931) 3059.
[15] A.M. Tyabji, C.S. Gibson, J. Chem. Soc. (1952) 450.
[16] N.A. Malik, P.J. Sadler, S. Neidle, G.L. Taylor, J. Chem. Soc., Chem. Commun. (1978) 711.
[17] K. Oyaizu, Y. Ohtani, A. Shiozawa, K. Sugawara, T. Saito, M. Yuasa, Inorg. Chem. 44 (2005) 6915.
[18] S.J. Berners-Price, M.J. DiMartino, D.T. Hill, R. Kuroda, M.A. Mazid, P.J. Sadler, Inorg. Chem. 24 (1985) 3425.
[19] F. Bonati, A. Burini, B.R. Pietroni, B. Bovio, J. Organomet. Chem. 317 (1986) 121.
[20] D.M.L. Goodgame, C.A. O'Mahoney, S.D. Plank, D.J. Williams, Polyhedron 12 (1993) 2705.
[21] C.K. Mirabelli, D.T. Hill, L.F. Faucette, F.L. McCabe, G.R. Girard, D.B. Bryan, B.M. Sutton, J.O. Leary Bartus, S.T. Crooke, R.K. Johnson, J. Med. Chem. 30 (1987) 2181.
[22] F. Bonati, A. Burini, B.R. Pietroni, E. Giorgini, B. Bovio, J. Organomet. Chem. 344 (1988) 119.
[23] A.V. Churakov, L.G. Kuz'mina, J.A.K. Howard, K.I. Grandbery, Acta Crystallogr., Sect. C 54 (1998) 54.
[24] W. Henderson, B.K. Nicholson, L.J. McCaffrey, Inorg. Chim. Acta 285 (1999) 145.
[25] D.M. Roundhill, Inorg. Chem. 9 (1970) 254.
[26] A. Shaver, R.D. Lai, Inorg. Chem. 27 (1988) 4664.
[27] S. Cenini, F. Porta, M. Pizotti, J. Organomet. Chem. 296 (1985) 291.
[28] J.M. Law, W. Henderson, B.K. Nicholson, J. Chem. Soc., Dalton Trans. (1997) 4587.
[29] D.A. Clarke, M.M. Hunt, R.D.W. Kemmitt, J. Organomet. Chem. 175 (1979) 303.
[30] Y. Fuchita, H. Ieda, Y. Tsunemune, J. Kinoshita-Nagaoka, H. Kawano, J. Chem. Soc., Dalton Trans. (1998) 791.
[31] R.V. Parish, J. Mack, L. Hargreaves, J.P. Wright, R.G. Buckley, A.M. Elsome, S.P. Fricker, B.R.C. Theobald, J. Chem. Soc., Dalton Trans. (1996) 69.
[32] M.B. Dinger, W. Henderson, J. Organomet. Chem. 560 (1998) 233.
[33] J.M. Law, W. Henderson, B.K. Nicholson, J. Chem. Soc., Dalton Trans. (1997) 4587.
[34] S. Bellú, E. Hure, M. Trapé, C. Trossero, G. Molina, C. Drogo, P.A.M. Williams, A.M. Atria, J.C. Muñoz Acevedo, S. Zacchino, Polyhedron 24 (2005) 501.
[35] J. Casanova, G. Alzuet, J. Borrás, J. Latorre, M. Sanaú, S. Garcia-Granda, J. Inorg. Biochem. 60 (1995) 219.
[36] J. Casanova, G. Alzuet, J. Borras, O. Carugo, J. Chem. Soc., Dalton Trans. (1996) 2239.
[37] S. Bellú, E. Hure, M. Trapé, M. Rizotto, E. Sutrich, E. Sigrist, V. Moreno, Quím. Nova 26 (2003) 188.
[38] J. Casanova, G. Alzuet, J. Latorre, J. Borrás, Inorg. Chem. 36 (1997) 2052.

[39] P. Naumov, G. Jovanovski, O. Grupče, B. Kaitner, A.D. Rae, S.W. Ng, Angew. Chem., Int. Ed. Engl. 44 (2005) 1251.
[40] C.M. Zakaria, J.N. Low, C. Glidewell, Acta Crystallogr., Sect. C 58 (2002) 9.
[41] T.G. Appleton, H.C. Clark, L.E. Manzer, Coord. Chem. Rev. 10 (1973) 335.
[42] J.M. Law, W. Henderson, B.K. Nicholson, J. Chem. Soc., Dalton Trans. (1997) 4587.
[43] F.A. Cotton, L.R. Falvello, C.A. Murillo, A.J. Schultz, Eur. J. Solid State Inorg. Chem. 29 (1992) 311.
[44] P. Naumov, G. Jovanovski, S.W. Ng, Acta Crystallogr., Sec. E 58 (2002) m16.
[45] P. Naumov, G. Jovanovski, M.G.B. Drew, S.W. Ng, Inorg. Chim. Acta 314 (2001) 154.
[46] B. Kamenar, G. Jovanovski, D. Grdenic, Cryst. Struct. Commun. 11 (1982) 263.
[47] E. Wong, C.M. Giandomenico, Chem. Rev. 99 (1999) 2451.
[48] L.J. Arnold, J. Chem. Educ. 69 (1992) 811.
[49] M.A. Cinellu, A. Zucca, S. Stoccoro, G. Minghetti, M. Manassero, M. Sansoni, J. Chem. Soc., Dalton Trans. (1995) 2865.
[50] P.-A. Bonnardel, R.V. Parish, J. Organomet. Chem. 515 (1996) 221.
[51] J. Vicente, M.T. Chicote, M.D. Bermudez, J. Organomet. Chem. 268 (1984) 191.
[52] R.H. Blessing, Acta Crystallogr., Sect. A 51 (1995) 33.
[53] G.M. Sheldrick, SHELX97 Programs for the Solution and Refinement of Crystal Structures, University of Göttingen, Germany, 1997.
[54] L.J. Farrugia, WinGX, Version 1.70.01, University of Glasgow, UK.
[55] L.J. Farrugia, J. Appl. Cryst. 32 (1999) 837.
[56] A.L. Spek, J. Appl. Cryst. 36 (2003) 7.

Available online at www.sciencedirect.com
ScienceDirect
Polyhedron 26 (2007) 215
POLYHEDRON
www.elsevier.com/locate/poly

Preface

It is a great pleasure for us to see the completion of this special issue of *Polyhedron* showcasing the current status of inorganic chemistry in Australia and New Zealand. The idea for this issue came from the recognition that the nature of inorganic chemistry research in these countries has undergone a major change over the last decade or so, for the obvious reason, of course, that this period has seen significant changes to the Australasian inorganic chemistry community. A rash of university appointments in the late 1950s and 1960s has now resulted in the partial or full retirement of a large number of academics over the past 10 or so years. In their place has been appointed a new generation of people with their own new research ideas and directions, and they are currently helping to shape the future of inorganic chemistry in Australasia. The calibre of the people they have replaced can be conveniently recognised with reference to previous winners of the Burrows Award, awarded jointly by the Royal Australian Chemistry Institute (RACI) and the New Zealand Institute of Chemistry (NZIC). The list of winners since the inception of the award in 1975 is as follows (in alphabetical order):

Martin A. Bennett
Alan M. Bond
Michael I. Bruce
David A. Buckingham
Ian G. Dance
Brian N. Figgis
Hans C. Freeman
Clifford J. Hawkins
David L. Kepert
Peter A. Lay
Leonard F. Lindoy
Raymond L. Martin
Keith S. Murray
Colin L. Raston
Richard Robson
Warren R. Roper
Alan M. Sargeson
Donald R. Stranks
Bruce O. West
Alan White

Many of these chemists are now either semi- or fully retired, while Don Stranks passed away at a tragically early age. The names on this impressive list are known worldwide, as indeed are those of a previous age in Australasian inorganic chemistry who acted as mentors to many of the above: Eustace Turner, George Burrows, Ronald Nyholm, Frank Dwyer and Arthur Birch. In addition, many recent retirees do not appear on this list, but their loss is felt no less keenly. It might therefore be thought that this enormous loss of experience would be difficult to overcome. However, as this special issue of *Polyhedron* shows, the currently active researchers of all ages are continuing to ensure that inorganic chemistry in Australia and New Zealand maintains an extremely healthy state. Indeed, the new generation of inorganic chemists are upholding the considerable reputation that Australasian inorganic chemistry has always enjoyed and are, like those before them, creating a legacy to be passed on to succeeding generations.

George Christou
Department of Chemistry,
University of Florida,
Gainesville, FL, USA
E-mail address: christou@chem.ufl.edu

Allan Blackman
Department of Chemistry,
University of Otago,
Dunedin, New Zealand

Available online 12 November 2006

0277-5387/$ - see front matter © 2006 Elsevier Ltd. All rights reserved.
doi:10.1016/j.poly.2006.11.004

Available online at www.sciencedirect.com
ScienceDirect
Polyhedron 26 (2007) 216–221
POLYHEDRON
www.elsevier.com/locate/poly

Solid-state anion interactions in the diastereoisomers of dinuclear ruthenium complexes based on 2,2′-bipyrimidine

Deanna M. D'Alessandro, Fiona M. Foley, Murray S. Davies, Peter C. Junk [1], F. Richard Keene *

School of Pharmacy and Molecular Sciences, James Cook University Townsville, Qld 4811, Australia

Received 7 November 2005; accepted 31 March 2006
Available online 18 April 2006

Abstract

The cations in the solid-state structures of *meso*-(ΛΔ)-[{Ru(bpy)$_2$}$_2$(μ-bpm)](PF$_6$)$_4$, *meso*-(ΛΔ)-[{Ru(Me$_2$bpy)$_2$}$_2$(μ-bpm)](tos)$_4$ · 2CH$_3$OH · 4H$_2$O and *meso*-(ΛΔ)-[{Ru(Me$_4$bpy)$_2$}$_2$(μ-bpm)](tos)$_4$ · 26H$_2$O (bpm = 2,2′-bipyrimidine; bpy = 2,2′-bipyridine; Me$_2$bpy = 4,4′-dimethyl-2,2′-bipyridine; Me$_4$bpy = 4,4′,5,5′-tetramethyl-2,2′-bipyridine; tos$^-$ = toluene-4-sulfonate anion) exhibit similar features including comparable bond lengths and angles, and metal–metal separations of 5.56–5.59 Å. The counter-ions present in the structures reside in the clefts above and below the plane of the bridging ligand, but show considerable variation in location compared with their known occupancy in solution.
© 2006 Elsevier Ltd. All rights reserved.

Keywords: Stereochemistry; Dinuclear; Ruthenium; Anion interactions

1. Introduction

A rigid dinuclear ligand-bridged complex containing a symmetrical di-bidentate bridging group {such as 2,2′-bipyrimidine (bpm); point group symmetry D_{2h}} and symmetrical bidentate terminal ligands {such as 2,2′-bipyridine (bpy); point group symmetry C_{2v}} may exist in three possible stereoisomeric forms – *meso* (ΔΛ ≡ ΛΔ; point group symmetry C_{2h}), and *racemic* (*rac*) (point group symmetry D_2), where the latter comprises an enantiomeric pair ΔΔ and ΛΛ (Fig. 1) [1]. While the identity and coordination environments of the metal centres are identical in the two diastereoisomeric forms, a significant difference may be discerned between them in terms of the nature of the "clefts" formed between the planes of the terminal bpy ligands. "Interior clefts" are formed between the bpy ligands immediately above and below the plane of the bridging ligand, which are approximately orthogonal in the *meso* form and parallel in the *rac* form. In addition, "exterior clefts" are evident between the planes of the terminal bpy ligands at either end of the complex, but these are identical for two diastereoisomeric forms.

The description is somewhat more complicated if the orientation of the axes of the two "bites" of the bridging ligands is angular or stepped-parallel (rather than linear, as in the case of bpm), or if the two metal centres are no longer equivalent because of different metal centres or different coordination environments, but the general principles remain pertinent [1].

We have developed a general cation-exchange chromatographic method for the separation of stereoisomeric mixtures of the genre of complexes, using SP Sephadex C-25 as the support [1,2]. The mechanism for the separation involves the differential association between the diastereoisomers of the same complex and eluent anions such as toluene-4-sulfonate {CH$_3$(C$_6$H$_4$)SO$_3^-$; tos$^-$}, and the nature of the interaction has been ascribed to a combination of

* Corresponding author. Tel.: +61 7 47814433; fax: +61 7 4781 6078.
E-mail address: Richard.Keene@jcu.edu.au (F.R. Keene).
[1] Present address: School of Chemistry, Monash University, Clayton, Vic. 3800, Australia.

0277-5387/$ - see front matter © 2006 Elsevier Ltd. All rights reserved.
doi:10.1016/j.poly.2006.03.030

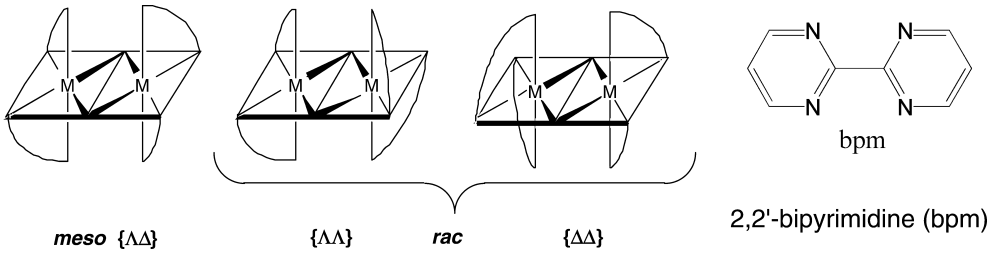


Fig. 1. Stereoisomeric forms of $[\{Ru(bpy)_2\}_2(\mu\text{-bpm})]^{4+}$.

specific π-stacking and hydrophobic effects [3]. Detailed solution-phase NMR titration studies on the diastereoisomers of $[\{Ru(Me_2bpy)_2\}_2(\mu\text{-bpm})]^{4+}$ ($Me_2bpy = 4,4'$-dimethyl-2,2′-bipyridine) revealed that the hydrophobic aryl ring of the toluene-4-sulfonate counter-ion is positioned within the interior cleft, with the SO_3^- terminus orientated away from the bridging ligand [3,4]. Exterior associations also occur in the cavities created by the terminal ligands, but such interactions are identical for the diastereoisomers [3]. However, the associations are different for the interior clefts – arising from the access available as a consequence of the shape of the cavity (illustrated schematically in Fig. 2) – and this allows the observed chromatographic separation on the basis of the overall charge of the complex-anion entity.

A limited number of crystal structures of dinuclear polypyridylruthenium complexes have been reported to date. Three examples of dinuclear species containing symmetrical linear bridging ligands have been described [5–7] where crystallisation afforded the *meso* forms preferentially, and Ward and coworkers [8,9] described the isolation of the *rac* form of an alkoxide-bridged species. Keene et al. [4] reported the first example of a crystal structure in which the *meso* diastereoisomer of $[\{Ru(Me_2bpy)_2\}_2(\mu\text{-bpm})]^{4+}$ was isolated via chromatography prior to crystal growth.

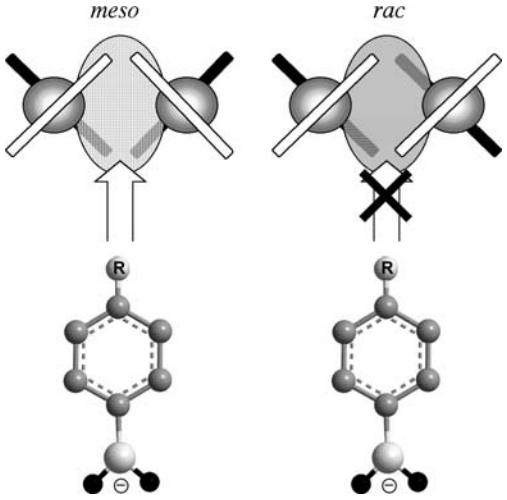
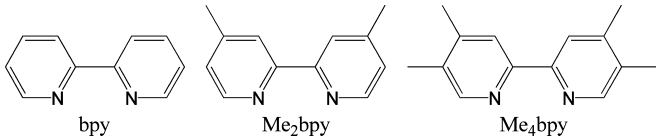


Fig. 2. A schematic representation of the discrimination by the diasatereoisomers of $[\{Ru(bpy)_2\}_2(\mu\text{-bpm})]^{4+}$ for the toluene-4-sulfonate anion (R = H), based on the dimension of the interior cavity above (and below) the bridging bpm ligand [3].



Scheme 1. 2,2′-bipyridine (bpy), 4,4′-dimethyl-2,2′-bipyridine (Me_2bpy) and 4,4′,5,5′-tetramethyl-2,2′-bipyridine (Me_4bpy) terminal ligands.

Structures of complexes involving angular [10,11] and stepped-parallel [12] bridging ligands have recently been reported, as well as examples of dinuclear species incorporating unsymmetrical bridges [13–15], including two containing the 3,5-bis(2-pyridyl)-1,2,4-triazolate (bpt^-) bridging ligand.

We were interested in whether the strong specific complex-anion interactions observed in solution were reflected in the solid-state structures. There is significant interest in the observation of stereochemically-directed anion interactions and the influence of such "supramolecular" effects on the intramolecular electron transfer properties of polymetallic assemblies [11]. The present study reports an examination of the interactions between toluene-4-sulfonate (tos^-) and hexafluorophosphate (PF_6^-) anions in the solid-state structures of the *meso* diastereoisomers of $[\{Ru(pp)_2\}_2(\mu\text{-bpm})]^{4+}$ {pp = bpy, Me_2bpy, and 4,4′,5,5′-tetramethyl-2,2′-bipyridine (Me_4bpy); Scheme 1}. In the case of *meso*-$[\{Ru(Me_2bpy)_2\}_2(\mu\text{-bpm})]^{4+}$, the results are contrasted with those obtained from previous solution-phase NMR titration studies [3,4].

2. Experimental

2.1. Materials

DOWEX® 1 × 8, 50–100 mesh anion exchange resin (Aldrich) and QAE Sephadex A-25 anion exchanger (Amersham Pharmacia Biotech), 2,2,2-trifluoroethanol (TFE; Aldrich) and laboratory reagent solvents were used as received.

2.2. Synthesis and diastereoisomer separation

The synthesis, separation and structural characterisation of the diastereoisomeric forms of $[\{Ru(pp)_2\}_2(\mu\text{-bpm})](PF_6)_4$ (pp = bpy, Me_2bpy, Me_4bpy) were performed as

described previously [4,16,17]. In all cases, the identity of the first band eluted in the diastereoisomer separation as the *meso* form (consistent with a previous literature report) [4] was confirmed by determination of the crystal structures reported herein.

2.3. X-ray crystallography

Crystals of *meso*-[{Ru(bpy)$_2$}$_2$(μ-bpm)](PF$_6$)$_4$ were grown by slow evaporation of a 70:30 TFE/H$_2$O solution of the complex under ambient conditions in the absence of light. The rod-shaped dichroic crystals were deep green/red: a single crystal of dimensions $0.2 \times 0.2 \times 0.15$ mm was coated with paratone-N and mounted onto a glass fibre.

Single crystals of the related complex *meso*-[{Ru(Me$_2$-bpy)$_2$}$_2$(μ-bpm)](tos)$_4$ were obtained by preliminary anion exchange of the PF_6^- to the toluene-4-sulfonate salt using QAE Sephadex A-25 anion-exchanger in the tos^- form. An aqueous solution of the Cl^- form of *meso*-[{Ru(Me$_2$-bpy)$_2$}$_2$(μ-bpm)]$^{4+}$ (ca. 10 mg in 2 cm^3) – obtained by stirring a suspension of the hexafluorophosphate salt in water/methanol with DOWEX® anion-exchange resin – was subsequently loaded onto the Sephadex column. The narrow green band of the dinuclear complex was eluted with water and the eluate permitted to evaporate under ambient conditions the absence of light for several weeks to yield dichroic dark green/red plate-like crystals. A single crystal of dimensions $0.15 \times 0.15 \times 0.15$ mm was quickly coated with polyacrylamide (to avoid rapid methanol loss) and mounted onto a glass fibre for X-ray structural determination.

Single crystals of the complex *meso*-[{Ru(Me$_4$bpy)$_2$}$_2$-(μ-bpm)](tos)$_4$ were obtained in the same manner. A single crystal of dimensions $0.20 \times 0.20 \times 0.15$ mm was sealed in a capillary to avoid solvent loss during the structural determination.

For each structure, a hemisphere of data was collected at room temperature on a Bruker SMART CCD diffractometer using the omega scan mode with total reflections and unique data listed below. The data sets were corrected for absorption using the program SADABS [18]. Structural solution and refinement was carried out using SHELXL-97 [19] and SHELXS97 [19] utilising the graphical interface WINGX [20] (bpy and Me$_2$bpy complexes) or X-Seed [21] (Me$_4$bpy complex). All non-hydrogen atoms were located and were refined with anisotropic thermal parameters. Due to a low data:parameters ratio, the structure of *meso*-[{Ru(bpy)$_2$}$_2$(μ-bpm)](PF$_6$)$_4$ was refined with the C atoms isotropic. This resulted in an increase in R and wR_2, and a data:parameter ratio of 8.14. Hydrogen atoms were placed in calculated positions (riding model) and were not refined, except for the hydrogen atoms on the lattice water molecules which were not located. For the Me$_4$bpy complex, the sulfonate oxygen atoms on the anions were rotationally disordered and these were successfully modelled over two sites, although the oxygen atoms maintained large thermal envelopes, as did the oxygen atoms of the lattice water molecules. Such disorder was less significant for the Me$_2$bpy analogue. Crystal data and a summary of data collection appear below; the full details are provided Table S1 (Supplementary Material).

2.4. [{Ru(bpy)$_2$}$_2$(μ-bpm)](PF$_6$)$_4$

Crystal data for $C_{48}H_{38}N_{12}F_{24}P_4Ru_2$, $M = 1564.9$, $0.2 \times 0.2 \times 0.15$ mm, monoclinic, space group C_2/c (no. 15), $a = 19.367(5)$ Å, $b = 17.679(4)$ Å, $c = 18.321(5)$ Å, $\beta = 111.228(5)°$, $V = 5847(3)$ Å^3, $Z = 4$, $D_c = 1.778$ g/cm^3, $F_{000} = 3096$, Mo Kα radiation, $\lambda = 0.71069$ Å, $T = 293$ K, $2\theta_{max} = 53.0°$, 6054 reflections collected, 6054 unique ($R_{int} = 0.1967$). Final Goodness-of-fit = 0.869, $R_1 = 0.0681$, $wR_2 = 0.2073$, R indices based on 2355 reflections with $I > 2\sigma(I)$ (refinement on F^2), 289 parameters, $\mu = 0.750$ mm^{-1}.

2.5. [{Ru(Me$_2$bpy)$_2$}$_2$(μ-bpm)](tos)$_4$ · 2CH$_3$OH · 4H$_2$O

Crystal data for $C_{86}H_{98}N_{12}O_{18}Ru_2S_4$, $M = 1918.14$, $0.15 \times 0.15 \times 0.15$ mm, orthorhombic, space group *Pcab* (no. 61), $a = 13.681(5)$ Å, $b = 19.968(5)$ Å, $c = 33.090(5)$ Å, $V = 9040(4)$ Å^3, $Z = 4$, $D_c = 1.409$ g/cm^3, $F_{000} = 3911.4$, Mo Kα radiation, $\lambda = 0.71069$ Å, $T = 293$ K, $2\theta_{max} = 50.6°$, 8194 reflections collected, 8194 unique ($R_{int} = 0.1305$). Final Goodness-of-fit = 1.129, $R_1 = 0.0653$, $wR_2 = 0.1987$, R indices based on 4899 reflections with $I > 2\sigma(I)$ (refinement on F^2), 558 parameters, $\mu = 0.499$ mm^{-1}.

2.5.1. [{Ru(Me$_4$bpy)$_2$}$_2$(μ-bpm)](tos)$_4$ · 26H$_2$O

Crystal data for $C_{92}H_{150}N_{12}O_{38}Ru_2S_4$, $M = 2362.62$, $0.20 \times 0.20 \times 0.15$ mm, triclinic, space group $P\bar{1}$ (no. 2), $a = 13.0310(13)$ Å, $b = 14.6320(15)$ Å, $c = 15.1356(15)$ Å, $\alpha = 104.240(2)°$, $\beta = 96.112(2)°$, $\gamma = 98.970(2)°$, $V = 2731.2(5)$ Å^3, $Z = 1$, $D_c = 1.436$ g/cm^3, $F_{000} = 1242$, Mo Kα radiation, $\lambda = 0.71073$ Å, $T = 296(2)$ K, $2\theta_{max} = 46.6°$, 12 832 reflections collected, 7855 unique ($R_{int} = 0.0568$). Final Goodness-of-fit = 1.046, $R_1 = 0.0578$, $wR_2 = 0.1442$, R indices based on 5951 reflections with $I > 2\sigma(I)$ (refinement on F^2), 733 parameters, 72 restraints. Lp and absorption corrections applied, $\mu = 0.440$ mm^{-1}.

3. Results and discussion

Meso-(ΛΔ)-[{Ru(bpy)$_2$}$_2$(μ-bpm)](PF$_6$)$_4$ crystallised in the monoclinic space group C_2/c, *meso*-(ΛΔ)-[{Ru(Me$_2$-bpy)$_2$}$_2$(μ-bpm)](tos)$_4$ · 2CH$_3$OH · 4H$_2$O in the orthorhombic space group *Pcab*, and *meso*-(ΛΔ)-[{Ru(Me$_4$bpy)$_2$}$_2$-(μ-bpm)](tos)$_4$ · 26H$_2$O in the triclinic space group $P\bar{1}$. The asymmetric units of all three complexes contain one half of the dinuclear cation, which resides on a crystallographic axis, along with two anions and associated lattice water molecules for the tosylate complexes.

The ORTEP structures of the dinuclear cations *meso*-(ΛΔ)-[{Ru(bpy)$_2$}$_2$(μ-bpm)]$^{4+}$, *meso*-(ΛΔ)-[{Ru-(Me$_2$-bpy)$_2$}$_2$(μ-bpm)]$^{4+}$ and *meso*-(ΛΔ)-[{Ru(Me$_4$bpy)$_2$}$_2$-(μ-bpm)]$^{4+}$ are shown in Figs. 3(a), 4(a) and 5(a), respectively, and the full atom labelling is provided in Figures S1–S3 (Supplementary Material). The cations in the three structures *meso*-(ΛΔ)-[{Ru(pp)$_2$}$_2$(μ-bpm)]$^{4+}$ (pp = bpy, Me$_2$bpy, Me$_4$bpy) exhibit comparable Ru–N distances and N–Ru–N angles which are consistent with those reported previously for *meso*-(ΛΔ)-[{Ru(Me$_2$bpy)$_2$}$_2$-(μ-bpm)](Cl)$_4$ [4] and related polypyridyl complexes of ruthenium [5,6,8,9,13,14]. In all structures, the Ru centres reside in slightly distorted octahedral environments. The "bite angles" of the terminal chelating ligands vary between ca 78° and 79°, which is typical for the polypyridyl ligands bpy and Me$_2$bpy [13,22–24], and the metal centres

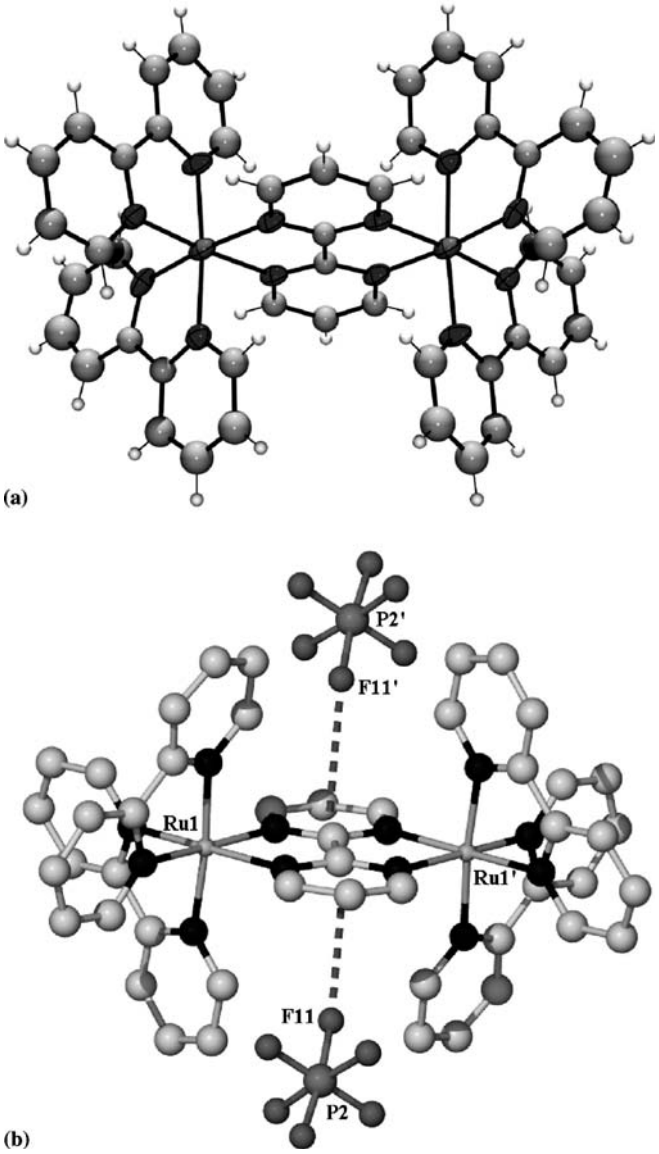


Fig. 3. (a) ORTEP view (30% probability) of the cation in *meso*-(ΛΔ)-[{Ru(bpy)$_2$}$_2$(μ-bpm)](PF$_6$)$_4$. (b) A perspective view showing the position of the PF$_6^-$ anions (two shown) relative to the clefts between the ligands.

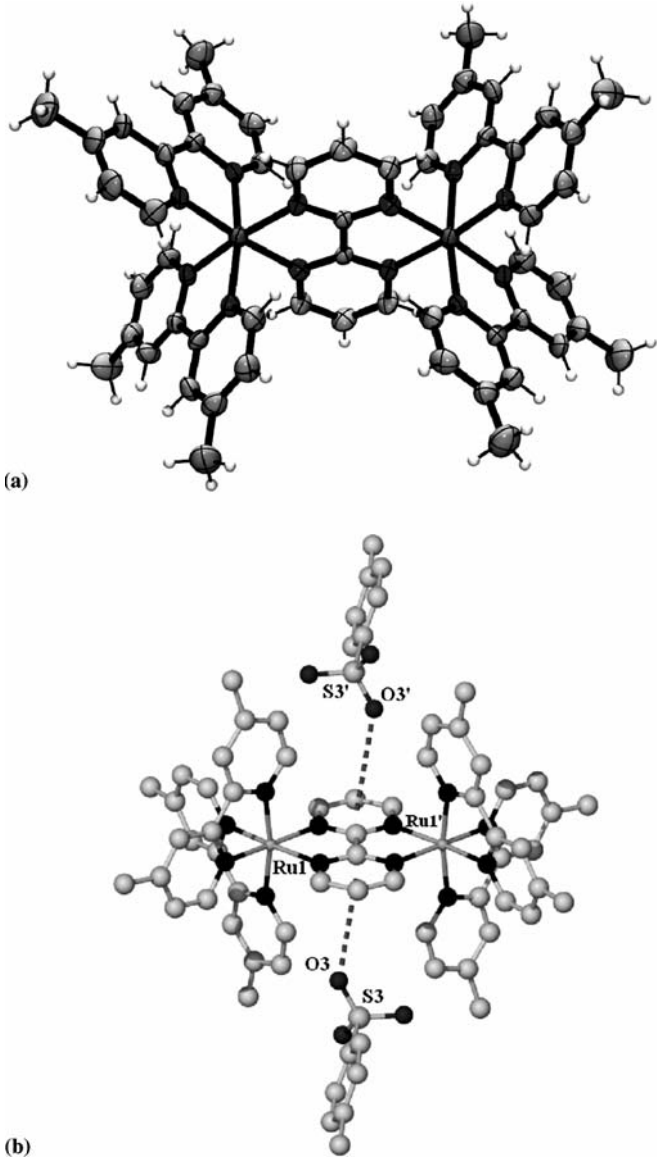


Fig. 4. (a) ORTEP view (50% probability) of the cation in *meso*-(ΛΔ)-[{Ru(Me$_2$bpy)$_2$}$_2$(μ-bpm)](tos)$_4$. (b) A perspective view showing the position of the tos$^-$ anions (two shown) relative to the clefts between the ligands.

are coordinated at each bidentate coordination site of bpm with average N–Ru–N angles of 79.9(3)°, 80.2(3)° and 79.6(3)° , for the complexes incorporating the bpy, Me$_2$bpy and Me$_4$bpy terminal ligands, respectively. The bridging bpm ligand maintains planarity in all three structures, with Ru···Ru separations of 5.565(5), 5.564(5) and 5.586(5) Å, for the bpy, Me$_2$bpy and Me$_4$bpy complexes.

As shown in Fig. 3(b), two PF$_6^-$ counter-ions are located close to the clefts between the bpy ligands above and below the bridging bpm ligand in *meso*-(ΛΔ)-[{Ru-(bpy)$_2$}$_2$(μ-bpm)](PF$_6$)$_4$. The distance of 3.050 Å between F(11) and the centroid of bpm confirms that the PF$_6^-$ anions are involved in van der Waals interactions with the complex cation. The crystal packing diagram reveals that the additional PF$_6^-$ counter-ions reside in layers

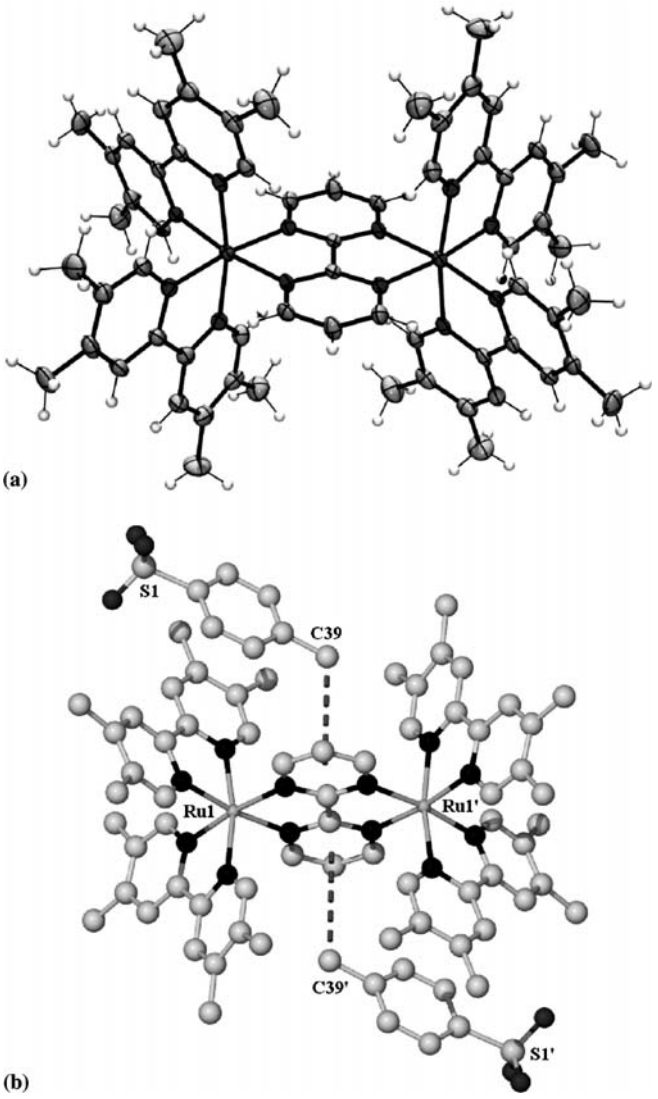


Fig. 5. (a) ORTEP view (50% probability) of the cation in *meso*-(ΛΔ)-[{Ru(Me$_4$bpy)$_2$}$_2$(μ-bpm)](tos)$_4$. (b) A perspective view showing the position of the tos$^-$ anions (two shown) relative to the clefts between the ligands.

between the predominantly organic layers of the complex. The presence of these distinct layers may account for the brittle nature of the crystals. Similar observations were noted previously in the crystal structure determination of *meso*-(ΛΔ)-[{Ru(Me$_2$bpy)$_2$}$_2$(μ-bpm)](Cl)$_4$ [4], and may account for the limited number of crystal structures for complexes of this genre in the literature.

The positions of two toluene-4-sulfonate counter-ions relative to the cations in *meso*-(ΛΔ)-[{Ru(Me$_2$bpy)$_2$}$_2$-(μ-bpm)](tos)$_4$ and [{Ru(Me$_4$bpy)$_2$}$_2$(μ-bpm)](tos)$_4$ are shown in Figs. 4(b) and 5(b), respectively. For the Me$_2$bpy complex, two tos$^-$ anions are located symmetrically either side of the plane of the bridging ligand, with the hydrophilic SO_3^- termini of the anions oriented inwards towards the relatively open orthogonal shaped cavities of the cation. The O(3)···centroid distance of 3.568 Å is consistent with van der Waals interactions between the counter-ions and the complex cation. The additional tos$^-$ counter-ions do not engage in any intermolecular interactions with the cation.

In the Me$_4$bpy complex the two tos$^-$ anions are also located symmetrically either side of the bridging ligand plane; however, the CH_3 termini of the counter-ions are directed inwards towards the ruthenium centres. The C(39)···centroid and H(39B)···centroid distances are 3.988 and 3.095 Å, respectively. The aromatic moiety of the counter-ion engages in π-stacking interactions with the bpy ligands which are oriented along the long axis of bpm. The SO_3^- termini are directed towards the periphery of the dinuclear cation and experience extensive H-bonding interactions with water molecules which are located in layers between the predominantly organic layers of the complex. While H-bonding interactions between the tos$^-$ counter-ions and water molecules are also evident in the structure involving the Me$_2$bpy terminal ligands, the water molecules do not form discernable layers and are evenly distributed about periphery of the complex.

The orientation adopted by the toluene-4-sulfonate counter-ions in the solid-state structure of the Me$_4$bpy complex is analogous to that determined by solution-phase NMR titration studies for complexes of this type, where the counter-ion is positioned with the hydrophobic aryl ring in the cavity and the SO_3^- terminus orientated away from the bridge [3,4]. This contrasts to the situation for the Me$_2$bpy complex where the orientation of the tos$^-$ anions in the solid state is different to that in the solution phase.

4. Conclusions

The cations in the solid-state structures of *meso*-(ΛΔ)-[{Ru(bpy)$_2$}$_2$(μ-bpm)](PF$_6$)$_4$, *meso*-(ΛΔ)-[{Ru(Me$_2$bpy)$_2$}$_2$-(μ-bpm)](tos)$_4$ and *meso*-(ΛΔ)-[{Ru(Me$_4$bpy)$_2$}$_2$(μ-bpm)]-(tos)$_4$ exhibit similar features including comparable bond lengths and angles, and metal-metal separations of 5.56–5.59 Å. The counter-ions present in the structures reside within the clefts formed between the planes of the terminal polypyridyl ligands in each case. For the methylated-bpy derivatives, the tos$^-$ counter-ions adopt different orientations, contrary to their location in solution-phase deduced from NMR titration studies [3,4]. Accordingly, despite strong specific anion associations, these examples illustrate that the packing forces in the solid state are significant, and provide a salutary warning on the comparison of interactions in the two phases.

5. Supplementary material

Crystallographic data (excluding structure factors) for the structures reported in this paper have been deposited with the Cambridge Crystallographic Data Centre as supplementary publications nos. CCDC-288380 for [{Ru- (bpy)$_2$}$_2$(μ-bpm)](PF$_6$)$_4$, CCDC-288379 for [{Ru(Me$_2$-bpy)$_2$}$_2$(μ-bpm)](tos)$_4$ · 2CH$_3$OH.4H$_2$O, and CCDC-288378

for $[\{Ru(Me_4bpy)_2\}_2(\mu\text{-bpm})](tos)_4 \cdot 26H_2O$. Copies of the data can be obtained free of charge on application to the CCDC, 12 Union Road, Cambridge, CB2 1EZ, UK, fax: +44 1223 336 033, email: deposit@ccdc.cam.ac.uk.

Acknowledgement

This work was supported by the Australian Research Council.

Appendix A. Supplementary data

Supplementary data associated with this article can be found, in the online version, at doi:10.1016/j.poly.2006.03.030.

References

[1] F.R. Keene, Chem. Soc. Rev. 27 (1998) 185.
[2] F.R. Keene, Coord. Chem. Rev. 166 (1997) 122.
[3] N.C. Fletcher, F.R. Keene, J. Chem. Soc., Dalton Trans. (1999) 683.
[4] N.C. Fletcher, P.C. Junk, D.A. Reitsma, F.R. Keene, J. Chem. Soc., Dalton Trans. (1998) 133.
[5] S. Baitalik, U. Flörke, K. Nag, J. Chem. Soc., Dalton Trans. (1999) 719.
[6] H. Masui, A.L. Freda, M.C. Zerner, A.B.P. Lever, Inorg. Chem. 39 (2000) 141.
[7] S.D. Bergman, I. Goldberg, A. Barbieri, F. Barigelletti, M. Kol, Inorg. Chem. 43 (2004) 2355.
[8] D. Bardwell, J.C. Jeffery, L. Joulie, M.D. Ward, J. Chem. Soc., Dalton Trans. (1993) 2255.
[9] D.A. Bardwell, L. Horsburgh, J.C. Jeffery, L.F. Joulié, M.D. Ward, I. Webster, L.J. Yellowlees, J. Chem. Soc., Dalton Trans. (1996) 2527.
[10] C. Richardson, P.J. Steel, D.M. D'Alessandro, P.C. Junk, F.R. Keene, J. Chem. Soc., Dalton Trans. (2002) 2775.
[11] D.M. D'Alessandro, P.C. Junk, F.R. Keene, Supramol. Chem. 17 (2005) 529.
[12] J.A. Zampese, F.R. Keene, P.J. Steel, Dalton Trans. (2004) 4124.
[13] R. Hage, J.G. Haasnoot, H.A. Nieuwenhuis, J. Reedijk, D.J.A. De Ridder, J.G. Vos, J. Am. Chem. Soc. 112 (1990) 9245.
[14] V. Balzani, D.A. Bardwell, F. Barigelletti, F.L. Cleary, M. Guardigli, J.C. Jeffery, T. Sovrani, M.D. Ward, J. Chem. Soc., Dalton Trans. (1995) 3601.
[15] D. Gut, I. Goldberg, M. Kol, Inorg. Chem. 42 (2003) 3483.
[16] D.M. D'Alessandro, F.R. Keene, Chem. Phys. DOI: 10.1016/j.chemphys.2005.09.016 (in press).
[17] B.T. Patterson, J.G. Collins, F.M. Foley, F.R. Keene, J. Chem. Soc., Dalton Trans. (2002) 4343.
[18] R.H. Blessing, Acta Crystallogr., Sect. A 51 (1995) 33.
[19] G.M. Sheldrick, SHELX97 – Programs for Crystal Structure Analysis, Institüt für Anorganische Chemie der Universitat Gottingen, Gottingen, 1997.
[20] L.J. Farrugia, J. Appl. Crystallogr. 32 (1999) 837.
[21] L.J. Barbour, J. Supramol. Chem. 1 (2001) 189.
[22] R. Hage, J.P. Turkenburg, R.A.G. de Graaff, J.G. Haasnoot, J. Reedijk, Acta Crystallogr. 45 (1989) 381.
[23] D.P. Rillema, D.G. Taghdiri, D.S. Jones, C.D. Keller, L.A. Worl, T.J. Meyer, H.A. Levy, Inorg. Chem. 26 (1987) 578.
[24] D.P. Rillema, D.S. Jones, H.A. Levy, J. Chem. Soc., Chem. Commun. 849–851 (1979) 849.

Available online at www.sciencedirect.com
ScienceDirect
Polyhedron 26 (2007) 222–236
POLYHEDRON
www.elsevier.com/locate/poly

Effect of ring substituents on crystal packing and H-bonding in a series of halobis(phen)copper(II) arylphosphonic acid complexes

Kay Latham [a,*], Anne M. Coyle [a], Colin J. Rix [a], Alan Fowless [a], Jonathan M. White [b]

[a] *Applied Chemistry, RMIT University, 124 LaTrobe Street, Melbourne, Vic. 3001, Australia*
[b] *School of Chemistry, University of Melbourne, Melbourne, Vic. 3010, Australia*

Received 31 March 2006; accepted 20 April 2006
Available online 13 May 2006

Abstract

The synthesis and crystal structures of five new analogues of the supramolecular copper(II) organophosphonate $[Cu^{II}(phen)_2Cl][(C_6H_5PO(OH)_2)((OH)O_2PC_6H_5)]$ (**1**) are presented. The structures contain substituted phenylphosphonic acids, and are of the general formula $[Cu^{II}(phen)_2Cl][(XPO(OH)_2)((OH)O_2PX)]\cdot Z$, where $X = o\text{-}CH_3(C_6H_5)$ (**2**); $X = p\text{-}CH_3(C_6H_5)$, $Z = H_2O\cdot 2CH_3CH_2OH$ (**4**); $X = o\text{-}NO_2(C_6H_5)$, $m\text{-}NO_2(C_6H_5)$ (**5**); $X = m\text{-}NO_2(C_6H_5)$ (**6**); $X = C_{10}H_7$ (**7**).

Single-crystal analysis revealed structures of similar molecular unit to **1**, with the exception of **4** which contained lattice solvent. The general assembly strategy of 'ribbons' of $[Cu^{II}(phen)_2Cl]^+$ cations interleaved with dimeric H-bonded anionic acid 'chains' seen in **1** was maintained in some form for **2**, **4**, **5** and **6**. Perturbations to packing were found largely to be related to the position of the substituent (rather than the chemical nature), where the *para* substituent was the most disruptive. This forced the adoption of alternate π–π bonding motifs between the anion and cation, which was especially apparent in the grid-like assembly of the naphthyl group in **7**. A sixth product **3** containing $m\text{-}CH_3(C_6H_5)$ was atypical to the series, having phosphonic acid bound to the metal centre and no halide.
© 2006 Elsevier Ltd. All rights reserved.

Keywords: Copper(II) complexes; Arylphosphonic acids; Ring substituents; Supramolecular networks; H-bonding

1. Introduction

One of the lesser studied functionalities in crystal engineering is the phosphonate group ($R–P(O)(OH)_2$). Like sulphonic acids, phosphonic acids are strong acids, with the first $pK_a \approx 1–2$, and so they remain ionised over a wide pH range in aqueous media. Each phosphonic acid group can provide one-, two- or three-oxygen atoms to coordinate metal ions, and thus the principal uses of these acids include chelation, e.g. to remove heavy metals from bleaching solutions in the paper, pulp and textile industry, and also scale inhibition [1]. Another fertile area of research has been the development of metal phosphonates, a class of organic–inorganic hybrid materials with a wide range of applications encompassing ion-exchange, intercalation, catalysis, light-harvesting, molecular magnetic devices, and the ability to form thin films [2]. Phosphonic acids also form extremely strong hydrogen bonds. However, the rapid growth of metal phosphonates has overshadowed the potential of phosphonic acids to form supramolecular arrays. Although this ability has been well-studied in nucleic acids and other biological molecules, crystal engineers have not invoked the use of phosphonate groups for the design of organic and organic–inorganic solids, in comparison to its carbon counterpart, the carboxylate group.

Structural studies on phosphonate groups, with the aim of designing organic solids, have only recently been reported in the literature. These studies have examined only a small selection of acids, principally phenylphosphonic acid $[C_6H_5PO(OH)_2]$ [3–5], and those acids that have multiple functionalities and may form zwitterions, e.g. *N*-nitrilotri(methylphosphonic) acid, NTMP [6–8]. Some work has also been carried out on diphosphonic

* Corresponding author. Tel.: +161 3 9925 2117; fax: +161 3 9639 3747.
E-mail address: kay.latham@rmit.edu.au (K. Latham).

0277-5387/$ - see front matter © 2006 Elsevier Ltd. All rights reserved.
doi:10.1016/j.poly.2006.04.028

acids [9]. Deprotonation of organophosphonic acids, by amines (e.g. aniline, phenanthrolines, etc.) [3–7] or metal(II) salts (e.g. Mn, Co, Cu, Ni, Zn, Cd and mixtures of these ions) [3,4,8], appears to trigger a self-assembly process and lead to the formation of very strong and predictable aggregates.

We have recently reported the synthesis of a range of copper(II)amine arylphosphonates with supramolecular architecture. These materials have the general formula: $[Cu^{II}(phen)_2X][((OH)_2OPC_6H_5)((OH)O_2P_6H_5)]$ (where X = I, Br, Cl (**1**), NCS), and contain a 5-coordinate copper(II) cation, counterbalanced by a hydrogen-bonded phenylphosphonic acid dimer anion [4]. The complexes are associated through hydrogen bonding interactions between the phosphonic acids, and π–π interactions between phen–phen, phen–acid, and acid–acid aromatic rings, resulting in 'ribbons' of copper cations interleaved between 'sheets' of phosphonate anions. The supramolecular motifs observed in these systems are shown in Chart 1: (a) symmetrical O···H···O hydrogen bonds, with the classic R2,2(8) ring motif – analogous to that found in carboxylic and sulphonic acids [10–12]; and (b) hydrogen-bonded dimers – a less common motif. The H-bonds in the dimers are exceptionally short, perfectly linear, and strong (typical O···O distances of 2.44–2.46 Å). Indeed, these bonds have stabilisation energies ten times those of normally occurring hydrogen bonds.

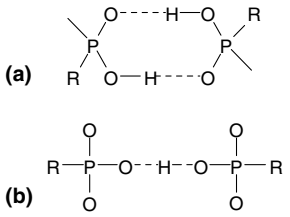


Chart 1. Supramolecular synthons of phenylphosphonic acid observed in the halobis(phen)copper(II) phenylphosphonate series [4]: (a) paired, regular H-bonds (R2,2(8) ring) and (b) hydrogen-bonded dimer.

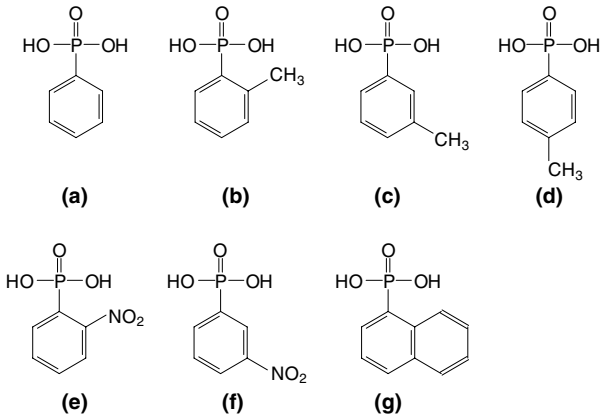


Chart 2. The acids used in this study: (a) phenylphosphonic; (b) *o*-tolylphosphonic; (c) *m*-tolylphosphonic; (d) *p*-tolylphosphonic; (e) *o*-nitrophenylphosphonic; *m*-nitrophenylphosphonic; and (f) 1-naphthylphosphonic acid.

The aims of the present study were to synthesise analogues of $[Cu^{II}(phen)_2Cl][((OH)_2OPC_6H_5)((OH)O_2P_6H_5)]$ (**1**), containing a range of substituted phenylphosphonic acids, and to explore the hydrogen-bonding and packing characteristics of the new structures. Whilst some work has been done on the effect of substituents on the pK_a values of arylphosphonic acids [13], to our knowledge, this has not been considered in the context of crystal engineering. The introduction of substituents on the acid ring will have several impacts: (a) on the ability of the phosphonic acid to form hydrogen bonds, due to changes in electron density; (b) on the π–π interactions observed between acids, and those between acid and phen; and (c) on spatial requirements for the substituent for crystal packing. Hence, a global impact on structure may be expected.

The seven acids used in this preliminary study (Chart 2a–g) were chosen because they represent a range of characteristics. The possible impacts of the substituents on intermolecular interactions (based on the criteria above) are summarised in Table 1. Substituents on an aromatic

Table 1
Characteristics of substituent groups on the aromatic ring

Substituent	P(O)(OH)$_2$ (**1**)	*o*-CH$_3$ (**2**)	*m*-CH$_3$ (**3**)	*p*-CH$_3$ (**4**)	*o*-NO$_2$ (**5**)	*m*-NO$_2$ (**6**)	1-Naphthyl (**7**)
H bonding influence							
Directing	*meta*	*ortho/para*	*ortho/para*	*ortho/para*	*meta*	*meta*	
Activating/deactivating	activating	activating	activating	activating	deactivating	deactivating	
Electron withdrawal/donation to ring	donation [13]	donation	donation	donation	withdrawal	withdrawal	
Induction	strong	weak	weak	weak	strong	strong	
Resonance	strong	none	none	none	strong	strong	
H bonding by substituent							
Donor group	O–H	C–H	C–H	C–H			
Acceptor atom	O				O	O	
Potential strength	strong	weak	weak	weak	strong	strong	
Steric influence							
Position		*ortho*	*meta*	*para*	*ortho*	*meta*	
Likely influence		low	medium	high	low	medium	
Additional π–π interactions							yes

ring affect the electron density of the ring, either via withdrawal or donation of electrons. This can occur through induction (movement of σ electrons) and/or resonance (movement of π electrons). The influence of the substituent on the electronic distribution of the ring may extend to the phosphonate group, which in turn may affect its hydrogen bonding character. The closer the substituent is to the phosphonate, the stronger the influence may be (i.e. *ortho* > *meta* > *para*). Whether this serves to create a stronger or weaker H-bond can only be postulated at this point. However, if the substituent is to have any significant influence, its activating/deactivating capacity must be fairly strong compared to the phosphonate group. Thus, the nitro group might be expected to have the greatest impact in the current series. The π–π interactions may also be perturbed via the steric influence of both the bulk and position of the substituent. A *para* substituent is protruded, an *ortho* substituent is more discreet, and the *meta* position intermediate. Finally, one must also consider the potential for the substituent itself to participate in intermolecular interactions: the nitro group oxygen atoms can participate in H bonding; the methyl group C–H can also undergo very weak H bonding; and the extended aromatics can undergo additional OFF (Offset-Face-to-Face) and EF (Edge-to-Face) π–π dispersion interactions [32].

2. Experimental

2.1. Materials

Copper(I) chloride was prepared according to published procedures [14]. *m*-Bromotoluene was prepared by the bromination of *p*-toluidine followed by deamination [15]. All starting materials were obtained from Aldrich and were used without any further purification (~98–99% pure).

2.2. Preparation of substituted phenylphosphonic acids

2.2.1. *o*-Tolylphosphonic acid [*o*-CH_3–$C_6H_4PO(OH)_2$]

ortho-Tolylphosphonic acid was prepared via the diethyl phosphonate, using the procedure of Mateeva et al. [16]. The ester was then hydrolysed according to Grabiak [17]. Yield: 0.44 g (40%); white solid; m.p. 138–141 °C.

2.2.2. *m*-Tolylphosphonic acid [*m*-CH_3–$C_6H_4PO(OH)_2$]

Under an atmosphere of dry argon, a solution of *m*-bromotoluene (5.13 g, 0.03 mol) in ether (20 mL) was stirred at −78 °C. To this, butyl lithium (1.6 M in hexanes, 18.7 mL, 0.03 mol) was added dropwise, and the resulting pale yellow solution stirred for 30 min., then allowed to warm to room temperature. This solution of *m*-tolyl lithium was added dropwise to a cooled solution (−78 °C) of diethyl chlorophosphate (10.35 g, 0.06 mol) in ether (40 mL). After stirring at −78 °C for 2 h the solution was warmed to room temperature and left to stir overnight. The turbid mixture was washed with dilute hydrochloric acid and the organic layer separated. This was washed with water, dried with $MgSO_4$, and the solvent removed to give a pale yellow oil which was distilled in vacuo to give diethyl *m*-tolylphosphonate as a colourless oil (b.p. 87–90 °C/0.1 mm Hg). The diethyl ester was suspended in concentrated hydrochloric acid (15 mL) and refluxed overnight. The pale yellow solution was evaporated to dryness and the solid recrystallised from hot concentrated hydrochloric acid. The white precipitate obtained was filtered, washed with concentrated hydrochloric acid and air dried. Finally, drying over P_2O_5 gave *m*-tolylphosphonic acid. Yield 3.5 g (68%); white solid; m.p. 122–124 °C. ^{1}H NMR (300 MHz, $CDCl_3$): δ 7.2–7.4, 7.5–7.7 (m, 4H, aromatic); δ 4.07 (m, 4H, $POCH_2C$); δ 2.35 (s, 3H, CH_3); δ 1.28 (t, $J_{HH} = 7.1$ Hz, 6H, $POCCH_3$). ^{31}P NMR (121 MHz, d^6-DMSO): δ 14.32 (s).

2.2.3. *p*-Tolylphosphonic acid [*p*-CH_3–$C_6H_4PO(OH)_2$]

The preparation initially required the synthesis of the appropriate diazonium salt, using the method of Broxton et al. [18]. The acid was then prepared via the Diazo reaction [19], using the modification suggested by Ashby and Kosolapoff [20]. Yield = 8.6 g (41%); white solid; m.p. 184–186 °C.

2.2.4. *o*-/*m*-Nitrophosphonic acid [*o*-NO_2–$C_6H_4PO(OH)_2$]/[*m*-NO_2–$C_6H_4PO(OH)_2$] (15:85%)

The mixed isomer acid was prepared by direct nitration of phenylphosphonic acid [21]. Yield: 61.4 g (96%); pale-yellow flakes; m.p. 138–140 °C. ^{31}P NMR (121 MHz, NaOD/D_2O): δ 8.37 (s), δ 4.69 (s) (85% *m*-NO_2:15% *o*-NO_2).

2.2.5. *m*-Nitrophosphonic acid [*m*-NO_2–$C_6H_4PO(OH)_2$]

The pure acid was prepared via the Diazo reaction [19]. Yield: 4.9 g (16%); white solid; m.p. 150–154 °C.

2.2.6. 1-Naphthylphosphonic acid [$C_{10}H_7PO(OH)_2$]

1-Naphthyl phosphonic acid was prepared via the diethyl phosphonate [17], followed by hydrolysis. Yield: 0.95 g (32%); white solid; m.p. 204–206 °C.

2.3. Preparation of supramolecular copper complexes

2.3.1. [$Cu^{II}(phen)_2Cl$][($C_6H_5PO(OH)_2$)-(($OH)O_2PC_6H_5$)] (**1**)

Compounds **1**–**7** were prepared according to a published method [4]. The general procedure is as follows: to a suspension of copper(I) chloride (0.19 g, 0.00095 mol, 20 mL ethanol) was added an ethanolic solution of 1,10-phenanthroline (0.73 g, 0.0040 mol, 20 mL). The mixture was stirred for 2 h at room temperature, and then phenylphosphonic acid solution (0.64 g, 0.0040 mol, 20 mL EtOH) was added to the red-brown suspension, and stirred for 1 h. The resulting olive-green precipitate was filtered, then recrystallised from milli-Q water (40 mL), giving aqua needle-like

crystals of **1**. These were filtered off, washed with cold milli-Q water and dried over P_2O_5. Yield: 0.186 g (13%).

*2.3.2. ($[Cu^{II}(phen)_2Cl][(o\text{-}CH_3)C_6H_4PO(OH)_2)$-$((OH)O_2PC_6H_4(o\text{-}CH_3))]$ (**2**)*

Similar procedure to **1**, using *o*-tolylphosphonic acid. The resulting aqua-green powdery precipitate was filtered, and recrystallised from ethanol (99%) to give a grass-green solution. On standing three days, the solution produced aqua block-like crystals, which were washed in cold ethanol and dried over P_2O_5. Yield: 0.1 g (20%).

*2.3.3. $[Cu^{II}(phen)((m\text{-}CH_3)C_6H_4PO_2(OH))$-$((OH)O_2PC_6H_4(m\text{-}CH_3))]$ (**3**)*

Similar procedure to **1**, using *m*-tolylphosphonic acid. Fine aqua-green solid was produced from the aqua-blue solution on standing for three days. This solid was collected by filtration and recrystallised from ethanol/water. After two weeks, small, blue, slab-like crystals formed, which were washed in cold ethanol and dried over P_2O_5. Yield: 0.1 g (20%).

*2.3.4. $([Cu^{II}(phen)_2Cl][(p\text{-}CH_3)C_6H_4PO(OH)_2)$-$((OH)O_2PC_6H_4(p\text{-}CH_3))] \cdot H_2O \cdot 2CH_3CH_2OH$ (**4**)*

Similar procedure to **1** except that *p*-tolylphosphonic acid was added and stirred for $3\frac{1}{2}$ h. The resultant solution was rotary evaporated to dryness, the remaining oily-solid was then dissolved in 40 mL of hot 1:2 ether:ethanol (95%) solution. On standing undisturbed at room temperature for one month, the solution produced several large green diamond-shaped crystals of $([Cu^{II}(phen)_2Cl][(p\text{-}CH_3)C_6H_4PO(OH)_2)((OH)O_2PC_6H_4(p\text{-}CH_3))] \cdot H_2O \cdot 2CH_3CH_2OH$ (**4**). The crystals were carefully removed, washed in water and ethanol, and due to their instability towards solvent loss, stored in a sample vial containing a 5 mL volume of filtered reaction solution. Yield: 0.024 g (2%). Elemental *Anal.* Calc.: C, 55.3; H, 5.2; N, 6.1; P, 6.8. Found: C, 56.2; H, 4.2; N, 6.8; P, 7.4%.

*2.3.5. $([Cu^{II}(phen)_2Cl][(m\text{-}NO_2)C_6H_4PO(OH)_2)$-$((OH)O_2PC_6H_4(o\text{-}NO_2))]$ (**5**)*

Similar procedure to **1**, using *o*-/*m*-nitrophosphonic acid. A pale aqua powder was filtered from the pale green solution, the volume was then reduced by 25 mL on a rotary evaporator. On standing undisturbed for one week, the solution yielded mid-green square crystals of **5**. Yield: 9.3%.

*2.3.6. $([Cu^{II}(phen)_2Cl][(m\text{-}NO_2)C_6H_4PO(OH)_2)$-$((OH)O_2PC_6H_4(m\text{-}NO_2))]$ (**6**)*

Similar procedure to **1**, using pure *m*-nitrophenylphosphonic acid. Following filtration of the grey precipitate, the volume of the pale green-aqua solution was reduced by 20 mL on a rotary evaporator. On standing, green rhomboid crystals of **6** were produced within a few days. Yield: 0.009 g (1.3%).

*2.3.7. $[Cu^{II}(phen)_2Cl][(H_7C_{10}PO(OH)_2)$-$((OH)O_2PC_{10}H_7)]$ (**7**)*

Similar procedure to **5**, using 1-naphthylphosphonic acid. The resultant aqua-powder was filtered off, and also the first crop of crystalline material. The filtrate was then reheated to boiling. Green rectangular shard crystals of **7** were formed after 3 days. Yield: 0.051 g (7.4%).

2.4. Spectroscopic measurements

All solids were analysed by FTIR, which provided an excellent initial qualitative means to identify the phen ligand (which was nearly always present due to its strong co-ordinating nature) and most importantly, the likely presence of the intercalated acid. Spectra could generally be used to indicate the similarity, or otherwise, of two products where there was a difference in crystal habit or colour. It was also discovered, notably with the nitro series, that subtle differences in similar spectra could indicate polymorphism. FTIR spectra were obtained on a Perkin–Elmer 1725X spectrometer, using KBr disks, with a spectral resolution of 4 cm^{-1}. ^1H, ^{13}C and ^{31}P NMR spectra were collected on a Bruker Avance DRX 300 MHz instrument. Chemical shifts are given in ppm relative to TMS or phosphoric acid.

2.5. Crystal structure determination

In the present study, the structures of products **2**–**7** were determined and analysed for the first time by single crystal X-ray diffraction. Crystal data was collected at 293 K for structures **1** and **6**, and 130 K for structures **2**–**5** and **7**, using graphite monochromated Mo Kα radiation for compounds **1**–**5**, **7** and Cu Kα radiation for **6** (see Table 2). Data for **2** and **6** were collected and integrated using an Enraf–Nonius CAD4 diffractometer [22], whilst for compounds **1**, **3**–**5** and **7** the data were collected and integrated using a Bruker SMART CCD area detector system [23]. In all cases, structures were solved by direct methods, using SHELXS-97 [24] (**2** and **6**) or SHELXTL [25] (**1**, **3**–**5** and **7**), and refined using SHELXL-97 [24] (**2** and **6**) or SHELXTL [25] (**1**, **3**–**5** and **7**). A mixed strategy was used for the refinement of hydrogen atoms. Hydrogen atoms attached to carbon were placed in calculated positions with a C–H distance of 0.93 Å, whilst hydrogen atoms attached to oxygen were located from difference Fourier maps, and refined without constraint. Molecular graphics were performed using ZORTEP [26], SHELXTL [25] and MERCURY [27] programs.

3. Results and discussion

3.1. Synthesis

The reaction of copper(I) chloride with 1,10-phenanthroline and the substituted phenylphosphonic acids shown in Chart 2, led to the corresponding supramolecular

Table 2
Crystal data and structure refinement details for compounds **1**–**7**

Crystal data	**1**	**2**	**3**	**4**	**5**	**6**	**7**
Compound formula	$C_{24}H_{16}N_4ClCu \cdot C_{12}H_{13}O_6P_2$	$C_{24}H_{16}N_4ClCu \cdot C_{14}H_{17}O_6P_2$	$C_{26}H_{24}N_2O_6P_2Cu$	$C_{24}H_{16}N_4Cl\ Cu \cdot C_{14}H_{17}O_6P_2 \cdot 2C_2H_5OH \cdot H_2O$	$C_{24}H_{16}N_4ClCu \cdot C_{14}H_{11}N_4O_8P_2$	$C_{24}H_{16}N_4ClCu \cdot C_{14}H_{11}N_4O_8P_2$	$C_{48}H_{32}N_8Cl_2Cu_2 \cdot C_{40}H_{34}O_{12}P_4$
Crystal class	monoclinic	monoclinic	orthorhombic	triclinic	monoclinic	triclinic	monoclinic
Space group	$C2/c$	$C2/c$	$Pbca$	$P\bar{1}$	$P2(1)/c$	$P\bar{1}$	$C2/c$
a (Å)	25.057(3)	26.084(4)	10.2372(5)	12.748(5)	10.033(3)	9.9936(7)	42.595(2)
b (Å)	8.3700(10)	8.2515(11)	18.9029(9)	12.922(5)	13.164(4)	13.155(2)	8.0817(4)
c (Å)	16.546(3)	16.325(2)	25.5159(13)	15.183(6)	26.944(9)	14.8687(9)	33.1336(17)
α (°)	90.00	90.00	90.00	100.922(7)	90.00	73.347(7)	90.00
β (°)	103.370(10)	96.156(3)	90.00	104.499(7)	96.546(6)	75.667(6)	100.8940(10)
γ (°)	90.00	90.00	90.00	114.595(6)	90.00	83.129(9)	90.00
V (Å^3)	3376.1(8)	3493.4(9)	4937.7(4)	2075.6(13)	3535.4(19)	1812.0(3)	11200.5(10)
Z	4	8	8	4	4	2	4
Colour, habit	block, blue	block, blue-green	slab, blue	block, blue	block, green	block, green	block, green
Size (mm)	$0.65 \times 0.54 \times 0.25$	$0.10 \times 0.20 \times 0.20$	$0.10 \times 0.30 \times 0.50$	$0.3 \times 0.35 \times 0.50$	$0.3 \times 0.15 \times 0.1$	$0.4 \times 0.3 \times 0.2$	$0.10 \times 0.15 \times 0.20$
λ (Å)	Mo Kα, 0.71069	Mo Kα, 0.71073	Mo Kα, 0.71073	Mo Kα, 0.71073	Mo Kα, 0.71073	Cu Kα, 1.54180	Mo Kα, 0.71073
Reflections used	25	1542	7410	5151	1334	25	5985
θ Min–max	15–25	2.59–22.52	2.3–27.23	2.34–27.25	2.17–19.21	20–30	2.50–27.08
μ (mm^{-1})	0.875	0.741	1.061	0.729	0.854	2.958	0.801
T (K)	293(2)	130(2)	130(2)	130(2)	130(2)	293(2)	130(2)
Absorption correction	analytical [28]	none	none	none	none	none	none
T_{min}–T_{max}	0.6391–0.8257						
Reflections	3017	10668	29497	13184	17890	7907	34205
Independent	2947	3965	5662	9140	6224	7461	12723
Reflections with $I > 2\sigma(I)$	2508	2450	4320	6957	3586	6310	9043
R_{int}	0.0129	0.0642	0.0590	0.047	0.0828	0.047	0.0815
θ Min–max	2.53–24.98	1.57–27.50	2.15–27.55	1.47–27.62	1.52–25.00	3.18–75.19	0.97–27.56
R_1 [$F^2 > 2\sigma(F^2)$]	0.0375	0.0464	0.0396	0.0569	0.0486	0.0481	0.0451
wR [F^2]	0.1028	0.0913	0.1045	0.1664	0.0704	0.1377	0.1047
S	1.074	0.879	0.978	1.024	0.737	1.047	0.938
Parameters	233	242	344	551	517	518	802
CCDC no.	216752	602676	602677	602678	602679	602680	602681

copper(II) structures **2**, **4**–**7**. The parent compound, $[Cu^{II}(phen)_2Cl][(C_6H_5PO(O\ H)_2)((OH)O_2PC_6H_5)]$ (**1**) (Fig. 1a), was prepared according to Clarke et al. [4]. The *o*-tolyl product, $([Cu^{II}(phen)_2Cl][(o\text{-}CH_3)C_6H_4PO(OH)_2)((OH)O_2PC_6H_4(o\text{-}CH_3))]$ (**2**), was synthesised with relative ease, forming blue-green block-like crystals within a few days. Blue slab crystals of the *m*-tolyl product, $[Cu^{II}(phen)(m\text{-}CH_3)C_6H_4PO_2(OH))((m\text{-}CH_3)C_6H_4PO_3)]$ (**3**), were also readily synthesised, but their formula and structure (Fig. 1b) were the least typical of the series. The first attempt at producing a *p*-tolylphosphonic acid derivative yielded a crystalline product with no intercalated acid, as well as the desired product **4**. The former were poorly diffracting but are believed to have the formula $[Cu^{II}(phen)_2Cl][OH]\cdot 6H_2O\cdot CH_3CH_2OCH_2CH_3$, and a structure and unit-cell size similar to the reported structures: $[Cu^{II}(phen)_2Cl][OH]\cdot 2CH_3OH\cdot 6H_2O$ [29]; $[Cu^{II}(phen)_2Cl][OH]\cdot 6H_2O$ [30]; and $[Cu^{II}(phen)_2Cl][Cl]\cdot 2CH_3OH\cdot 4.5H_2O$ [31]. Product **4** was difficult to isolate and analyse (unstable in air), and gave an early indication of the disruptive influence of a *para*-oriented substituent. X-ray analysis revealed a solvated product $[Cu^{II}(phen)_2Cl][(p\text{-}CH_3)C_6H_4PO_2(OH)][(p\text{-}CH_3)C_6H_4PO(OH)_2]\cdot 2C_2H_5OH\cdot H_2O$.

Two attempts were made to produce *m*-nitrophenylphosphonic acid. The first approach [21] yielded a mixed isomer acid, determined to be 85% *m*-NO_2 plus 15% *o*-NO_2 via ^{31}P NMR. This approach led to product **5** which contained a mixed *o*-/*m*-NO_2 acid dimer, $([Cu^{II}(phen)_2Cl][(o\text{-}NO_2)C_6H_4PO(OH)_2)((OH)O_2PC_6H_4(m\text{-}NO_2))]$. The second synthesis [19] produced a pure *m*-nitro acid, which led to product **6**. The major solid product obtained from this synthesis was a grey powder, which on recrystallisation from ethanol yielded green needles (**6a**) (10% yield). Meanwhile, the pale aqua mother liquor was concentrated and also produced crystalline material. The latter were of two types, needles (**6a***) and block-like crystals. This difference in crystal habit was further supported by differences in FTIR spectra. The needle specimens of **6a** and **6a*** gave similar spectra (in terms of spectrum shape and peak positions) and were thus considered the same product; while the spectrum of the block-like crystals exhibited subtle, but key, differences (Table 3), suggesting polymorphism. However, despite the quantity and apparent quality of the needle crystals of **6a**/**6a***, they did not diffract sufficiently to obtain a crystal structure. Fortunately, the block crystals did diffract, and were subsequently identified as $([Cu^{II}(phen)_2Cl][(m\text{-}NO_2)C_6H_4PO(OH)_2)((OH)O_2PC_6H_4$-

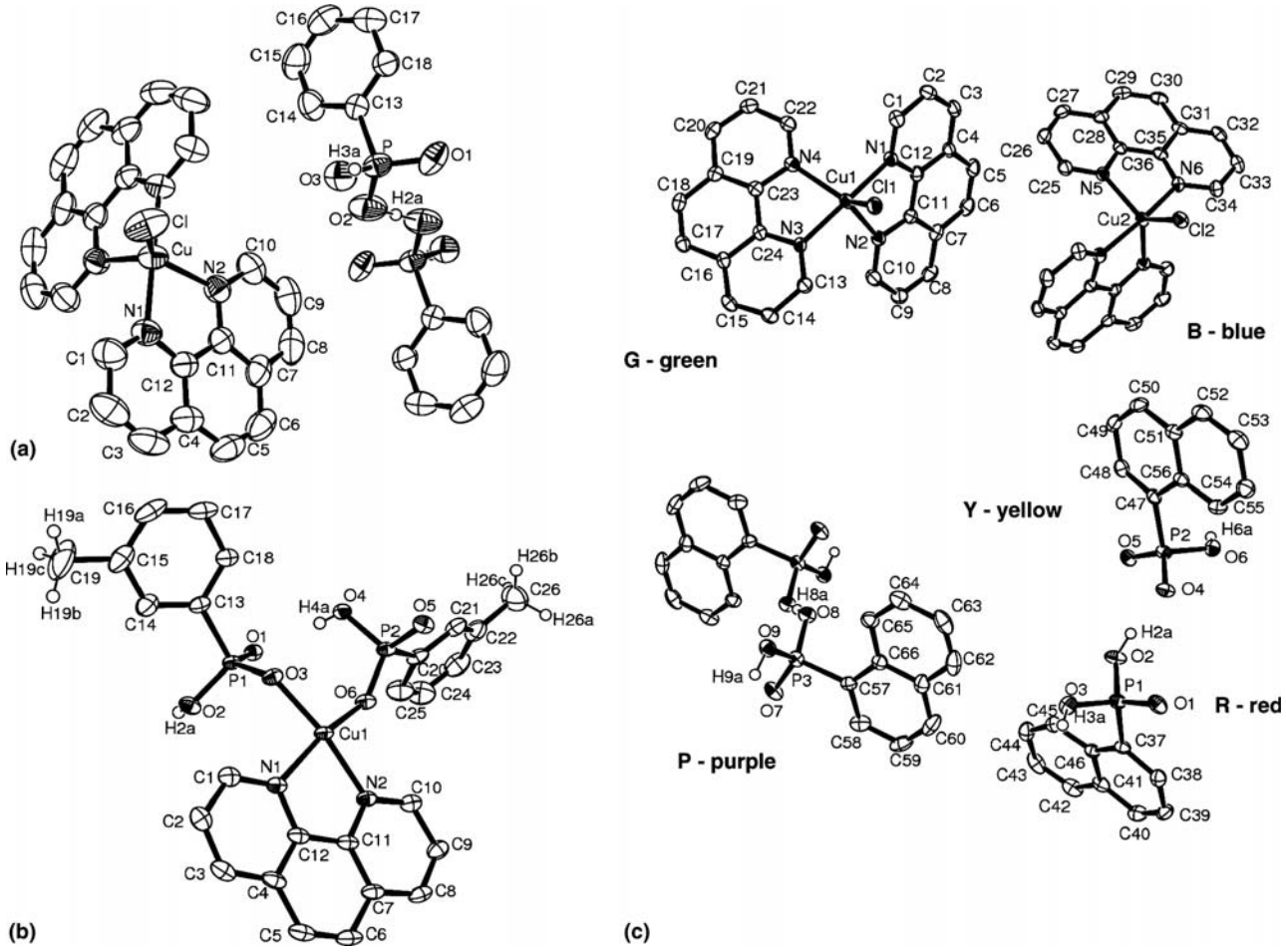


Fig. 1. Molecular units of: (a) **1**, (b) **3**, and (c) **7** (G = green phen; B = blue phen; R = red neutral acid; Y = yellow neutral acid; P = purple acid dimer), showing the co-ordination environment of the Cu atom and the numbering of atoms in text and tables.

Table 3
FTIR data for nitro analogues

Peak assignment	5	6a	6a*	6
C–H stretch of phen	3066 m	3061 w	3061 w	3077 w
PO–H stretch	2855 b	2865 b	2865 b	2858 b
PO–H stretch	2327 b	2304 b	2320 b	2323 b
C–C vibration of aromatic	1626 w	1626 w	1626 w	1626 w
C–C and C–N stretch of phen	1532, 1519 s	1524 s	1523 s	1531, 1521 s
C=N stretch of phen	1471 w	1471 w	1471 w	1472 w
C–H bend of aromatic	1427 s	1430 s	1430 s	1428 s
O–N–O symmetric stretch	1359, 1348 s	1351 s	1351 s	1362, 1348 s
C–C and C–N stretch of phen	*1141 m*	*1152 m*	*1152 m*	*1145 m*
P=O, P–O stretch	1200–800 b	1200–800 b	1200–800 b	1200–800 b
P=O, P–O stretch	*954 m*	*952 m*	*953 m*	*937 m*
P=O, P–O stretch	*937 m*	*917 m*	*916 m*	*m*
C–N stretch of phen	860 s	870 s	870 s	870 s
C–H out of plane vibration of aromatic	734 m	734 m	733 m	733 m
C–H out of plane vibration of aromatic	725 s	724 s	724 s	723 s
O–P–O	*554 m*	*558 m*	*558 m*	*550 m*
O–P–O	*539 m*	*538 m*	*538 m*	*512 w*

(m-NO_2))] (**6**). Thus, at this stage, the presence of polymorphism cannot be proven, but the differences in crystal habit and FTIR provide persuasive evidence for its existence. While **6** and **6a** were both recrystallised from ethanol, **6** was formed from a concentrated reaction mixture – i.e. a more dynamic system which is more conducive to the formation of polymorphs. The naphthyl product, [Cu^{II}-$(phen)_2Cl$][$(H_7C_{10}PO(OH)_2)((OH)O_2PC_{10}H_7)$] (**7**) (Fig. 1c), formed as rectangular shard crystals from the mother liquor on standing for 10 days.

3.2. Structure

3.2.1. Structure of *1*

The crystal structure of **1** was previously solved by Clarke et al. [4]. The molecular unit consists of a 5-coordinate $[Cu(phen)_2Cl]^+$ cation, counterbalanced by a phenylphosphonic "dimer" anion (Fig. 1a). The Cu(II) ion exhibits distorted trigonal bipyramidal stereochemistry, in which the equatorial Cu–Cl bond lies along a 2-fold crystallographic axis. Each phen ligand occupies an axial (N2) and equatorial (N1) position. This 'symmetrical' complex is assembled into 'ribbons' via a continuous OFF interaction between the outer surfaces of the phen rings (Fig. 2a). This is a common motif for phenanthroline complexes, which has been explored and quantified by Dance [32]. Looking closely, the phen overlap involves the perfectly parallel overlap of the middle rings (C4–C5–C6–C7–C11–C12) giving the ribbon a circular cross-section when viewed down the c-axis (Fig. 3a). Adjacent ribbons are perfectly aligned.

The acid dimer consists of a hydroxyl proton (H2a) shared equally (centrosymmetric) between the O2 and O2′ atoms, resulting in an ionic, strong, perfectly linear hydrogen-bond (d(O···H) = 1.21(7) Å, O2–H2a–O2 = 180.00°), with H2a lying on a centre of inversion. Adjacent acid dimers are connected through pairs of regular strength H-bonds (d(H3a···O1) = 1.784 Å, O3–H3a–O1 = 169.22°), see Fig. 4a and Table 4. The alternation of these motifs forms H-bonded acid 'chains', which further associate via EF interactions of the phenyl rings (E = H14, H15), to form acid 'sheets' (Fig. 5a). Further EF interaction is seen between the acid phenyl and phen rings, as shown in Fig. 6a. Overall, the packing is that of anionic acid sheets interleaved by cationic phen ribbons (Fig. 7a), with the assembly assisted by electrostatic attraction and dispersion forces.

3.2.2. Substituted acid products

3.2.2.1. Overview. Apart from the m-tolyl derivative **3** (Fig. 1b), the structures of compounds **2**, **4**–**7** exhibit an analogous molecular unit to the parent **1**. With regard to packing, changes were subtle to significant. While the phosphonate oxygen and HO– groups continued to participate in the formation of acid chains, a range of variation was observed. Likewise, there was much diversity in the π–π motifs of the substituted acid phenyl rings. The phen OFF "ribbon" being maintained in all but products **3** and **7**.

Product **2**, the o-tolyl derivative, is the most similar analogue to **1**, both in terms of the molecular unit and the packing strategy. The nitro-substituted products **5** and **6** have similar molecular units to **1** and **2**, but contain a phosphonic acid and phosphonate anion linked by a strong H-bond, i.e. the proton is not shared equally. The effect of the naphthyl group on packing is quite profound. The usual alternation of two-dimensional regions of acid and phen are not seen in **7**. Rather, there is a more intimate and intricate interlocking of the two components, through an extensive range of OFF and EF interactions. The assembly is best described as a grid of intersecting planes (Fig. 8a and b). The packing of the p-tolyl derivative **4** is very different to both **1** and **2** since it contains cavities constructed from acid and solvent, filled by metal–phen ribbons. However, by far the most puzzling structure is that of the m-tolyl derivative **3**, which contains only one phen molecule,

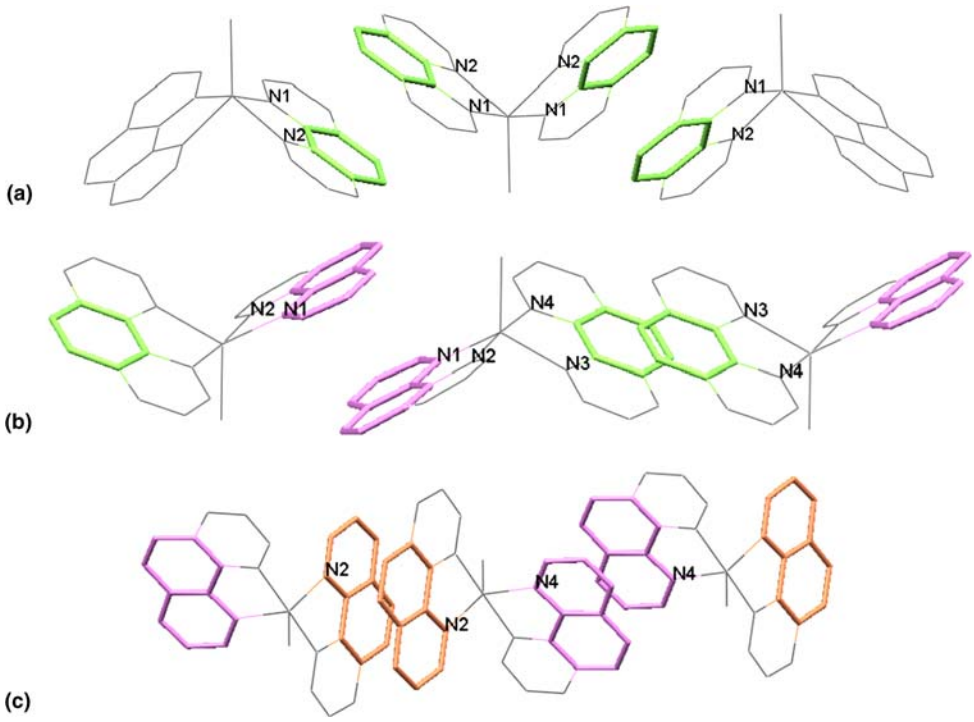


Fig. 2. (a) The 'outer OFF phen ribbon' of **1**, showing the middle ring overlap, in comparison to the phen ribbons of (b) **5**, showing the alternation of middle- and 2-ring OFF overlaps, and (c) **4**, showing the alternation of two different two ring OFF overlaps.

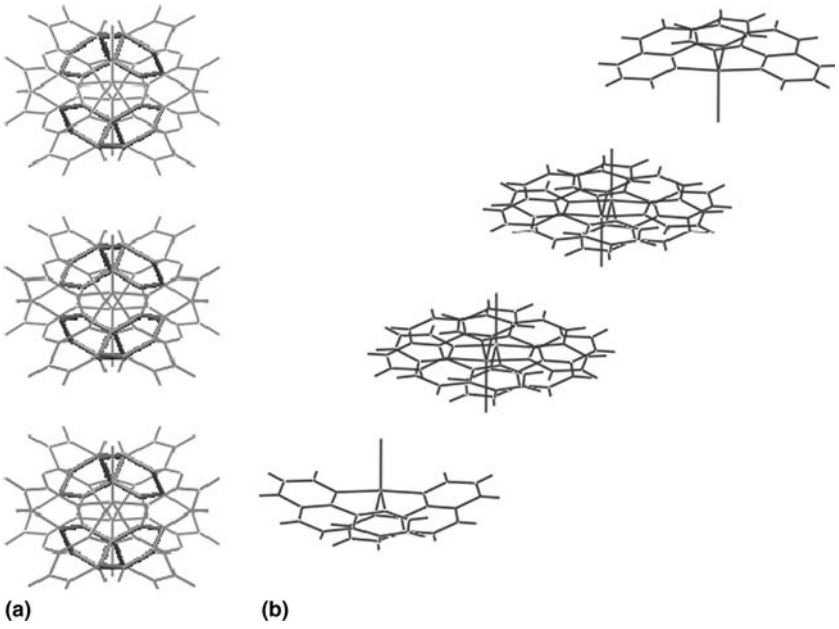


Fig. 3. (a) In **1**, the perfect alignment of phen ribbons via alignment of Cu–Cl bonds leads to a circular type ribbon cross-section. (b) The offset arrangement of phen ribbons in **5** and **6** leads to elliptical cross-sections, which are stacked diagonally.

no halogen, and two 'bound' acids per molecular unit. Product **3** serves as a reminder that there can be quite surprising outcomes in crystal design, and that we still have a way to go until crystal engineering becomes an 'exact' science. However, we must realise that in such multi-component synthetic systems a multitude of chemical equilibria exist, so that temperature, solvent, structure of nucleation interfaces, and concentration factors often lead to the kinetically controlled product being isolated as it precipitates from solution. Thus, in most instances it is the least soluble species that is isolated, and this may be the case in **3**.

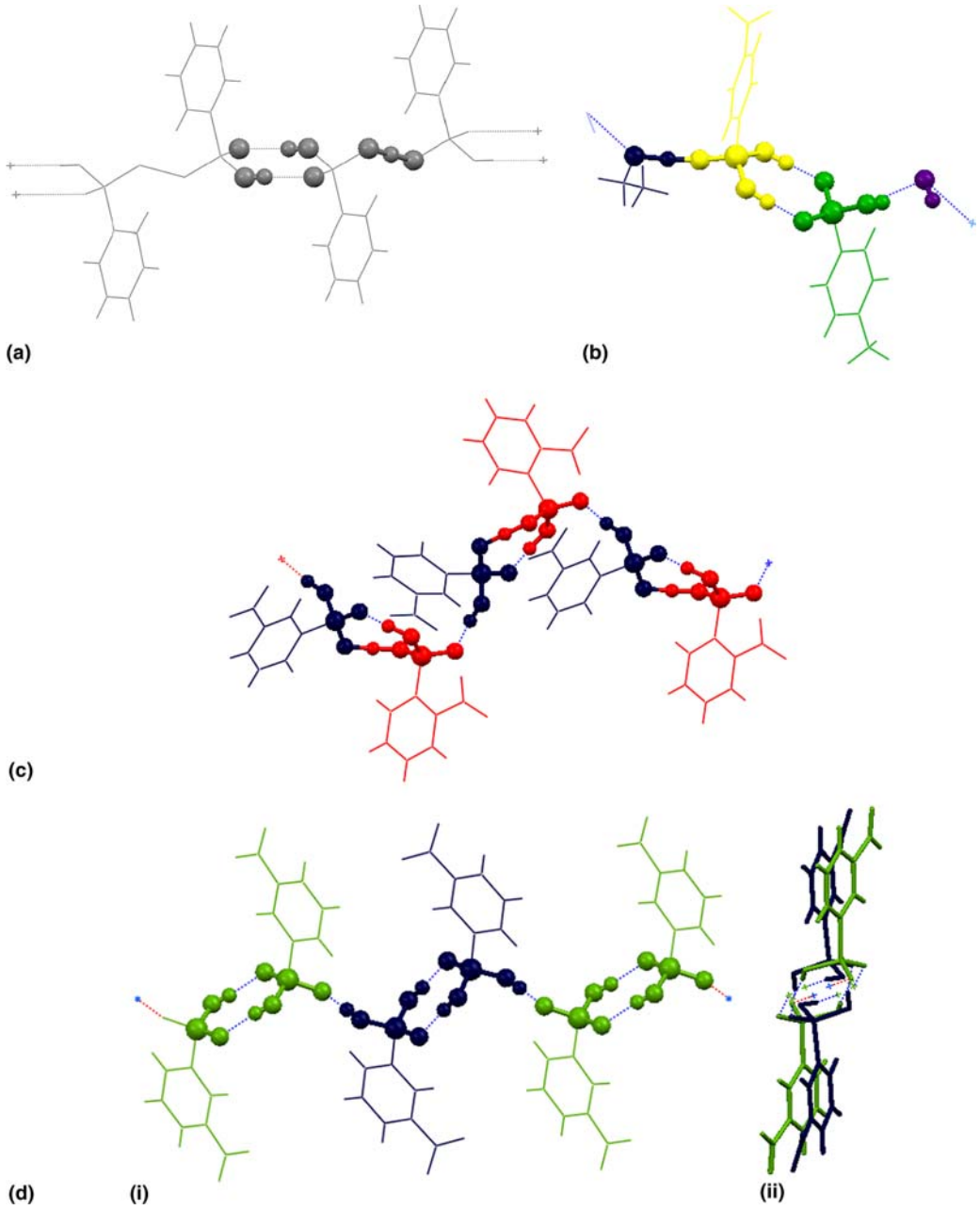


Fig. 4. (a) Acid chain of **1** showing alternation of strong H-bonded dimer and pair of symmetrical H-bonds. (b) The pair of non-symmetrical H-bonds between the anionic (green) and neutral (yellow) *p*-tolyl acids of **4** – anion donates both protons and paired acids are connected by a H-bonded bridging system with water (purple) and ethanol (blue). (c) The alternation of the doubly H-bonded acid dimer with a single H-bond in **5** forms a 'zigzag' acid chain – *meta* rings (blue) occupy the centre of the chain. (d) (i) Pairs of anionic (green) acids are connected to pairs of neutral (blue) acids in the acid chain of **6**, (ii) rings are angled gently in plane, with the anionic ring at a sharper angle. (For interpretation of the references to colour in this figure legend, the reader is referred to the web version of this article.)

3.2.2.2. The copper cation. In the case of the $[Cu^{II}(phen)_2Cl]^+$ cation component, it was generally observed that the equatorial N–Cu–N angles became more regular (approaching 120°), improving the trigonal bipyramidal stereochemistry of **1**. The 2-fold axis of symmetry along the Cu–Cl bond was maintained in only two cases **2** and **7** – the other cations exhibited non-equivalent phen rings. Other angles (i.e. the phen bite angles) were found to vary insignificantly. Changes were also observed in the OFF interactions of the phen rings, which was unexpected. All interactions involved the parallel overlap of planes, but the two-ring overlaps were generally stronger interactions, with closer centroid-to-plane distances, than those of the single-ring overlaps.

The $[Cu^{II}(phen)_2Cl]^+$ cation in **2** has similar geometry to **1**. The cation is still symmetric about the Cu–Cl bond, and the phen rings also participate in a middle-ring OFF interaction to yield a fairly circular ribbon cross-section. In

Table 4
Hydrogen bond parameters for compounds **1**–**7**

	D–H	*d*(D–H) (Å)	*d*(H···A) (Å)	∠DHA (°)	*d*(D···A) (Å)	*A*	Symmetry operator
1	O2–H2a	1.21(7)	1.21(7)	180	2.43(5)	O2	$[-x+1/2, -y-1/2, -z+1]$
	O3–H3a	0.67(2)	1.86(0)	165(4)	2.53(2)	O1	$[-x+1/2, -y+1/2, -z+1]$
2	O2–H2a	1.20(5)	1.20(5)	180	2.41(0)	O2	$[-x+1/2, -y+1/2, -z+1]$
	O3–H3a	0.90(3)	1.60(4)	177(7)	2.50(6)	O1	$[-x+1/2, -y+3/2, -z+1]$
3	O2–H2a	0.69(5)	1.78(9)	170(3)	2.47(7)	O5	
	O4–H4a	0.67(1)	0.94(3)	176(1)	2.61(3)	O1	$[x-1/2, -y+1/2, -z+1]$
4	O4–H4a	0.66(6)	1.95(8)	159(6)	2.59(2)	O10	
	O10–HO10	0.91(7)	1.86(1)	144(1)	2.65(9)	O7	
	O1–H7	1.23(6)	1.32(6)	174(1)	2.55(9)	O7	
	O3–H3a	0.93(0)	1.51(4)	176(3)	2.44(2)	O5	
	O2–H2a	0.91(0)	1.58(2)	161(7)	2.46(3)	O6	
5	O2–H2a	1.09(0)	1.39(4)	176(3)	2.48(3)	O7	
	O3–H3a	1.19(5)	1.25(8)	176(8)	2.45(2)	O6	$[-x+2, y-1/2, -z+3/2]$
	O8–H8a	0.94(0)	1.58(2)	172(3)	2.51(7)	O1	
6	O2–H2a	0.93(9)	1.50(1)	171(6)	2.43(4)	O7	
	O3–H3a	0.88(7)	1.57(7)	169(8)	2.45(5)	O1	$[-x+1, -y+1, -z+1]$
	O6–H6a	0.80(0)	1.72(3)	171(4)	2.51(7)	O8	$[-x, -y+2, -z+1]$
7	O2–H2a	0.86(2)	1.61(2)	167(0)	2.45(9)	O4	
	O6–H6a	0.72(5)	1.84(6)	174(3)	2.56(9)	O1	$[x, y+1, z]$
	O3–H3a	1.00(8)	1.51(9)	165(8)	2.50(8)	O5	$[x, y-1, z]$
	O8–H8a	1.22(4)	1.22(4)	180	2.44(9)	O8	$[-x+2, -y+1, -z+1]$
	O9–H9a	0.91(6)	1.63(3)	174(7)	2.54(7)	O7	$[-x+2, -y, -z+1]$

contrast, the cations of **4**, **5** and **6** are asymmetric. In each case, the non-equivalent phen rings form two outer OFF interactions, which alternate to give the ribbon. The overlaps are quite different (Fig. 2). In **4**, two different, two-ring OFF interactions are observed: middle and N2 (*d*(plane to centroid) = 3.41(6) Å), and middle and N3 (*d*(plane to centroid) = 3.38(0) Å). In **5** and **6** a two-ring overlap alternates with a significantly weaker one-ring overlap. The former involves the middle and N2 rings (*d*(plane to centroid) = 3.41(2) Å) in **5**, and the middle and N1 rings in **6** (*d*(plane to centroid) = 3.574 Å). Whilst the latter involves the N3 rings in **5** (*d*(plane to centroid) = 3.56(9) Å), and the middle rings in **6** (*d*(plane to centroid) = 3.68(3) Å). The alternation of stronger and weaker interactions in **5** and **6** have broadened the ribbon, forming an elliptical rather than circular cross-section. These ribbons are not aligned along the Cu–Cl axis as in **1**, rather they are offset, giving a diagonal type stacking (Fig. 3b). The naphthyl product **7** contains two different $[Cu^{II}(phen)_2Cl]^+$ cations: symmetric (G), and asymmetric (B), with Cu2 (B) lying on a 2-fold axis at 0, *y*, 1/4. Neither cation undergoes continuous outer face OFF interactions to form ribbons – the first clue to the dominance of the acid in the structure – or more specifically, the important role of the naphthyl group in building π–π connections that replace the usual phen ribbon motif.

3.2.2.3. The acid. The acid dimer (O2–H2a···O2) in the *o*-tolyl derivative **2**, is almost identical to **1**, with H-bonded pairs (O3–H3a–O1′) more linear by 8°. The EF interaction between acid chains also appears to involve the methyl hydrogens (edge atoms H19a, H19c), rather than the unsubstituted edge interacting with the face.

The acid dimer anion of the *o*-NO_2/*m*-NO_2 derivative **5**, contains one strong H bond (O3–H3a···O6), and one weaker bond (O2–H2a···O7). In the former, the proton is not shared equally as in **1**, but lies closer to the *o*-acid (*d*(O3–H3a) = 1.19(5) Å, *d*(H3a···O6) = 1.25(8) Å), and the paired dimers are connected via regular H bonding (O8–H8a···O1, *d*(H8a···O1) = 1.582 Å, 172.34°) to form exaggerated 'zigzag' chains, Fig. 4c. This conformation is very different to the usual linear conformation seen. The pure *m*-NO_2 derivative **6**, also contains one acid anion and one neutral acid joined by a strong H-bond. The anion forms a pair of equivalent H-bonds with another anion; and the neutral acid forms a weaker pair with another neutral acid. Both pairs are stronger than the pairing of **1** (Fig. 5d(i–ii)). In both **5** and **6**, some weak H-bonding is observed between the phen protons and the NO_2 groups (C8–H8···O4 *d*(H8···O4) = 2.503 Å, 164.99°; C13–H13···O10 *d*(H13···O10) = 2.713 Å, 137.10° in **5**). However, this is thought to be a less important contributor to assembly.

The *p*-tolyl derivative **4** contains an acid anion, a neutral acid, together with ethanol and water. Consequently, the H-bonding networks are very different to those in other products: the usual strong acid dimer connection being replaced by a bridging system of H-bonds with solvent molecules (Fig. 4b). A pair of H-bonds exists between the anionic and neutral acid, where the neutral species donates both protons. The (neutral) O3–H3a···O5 (anion) bond

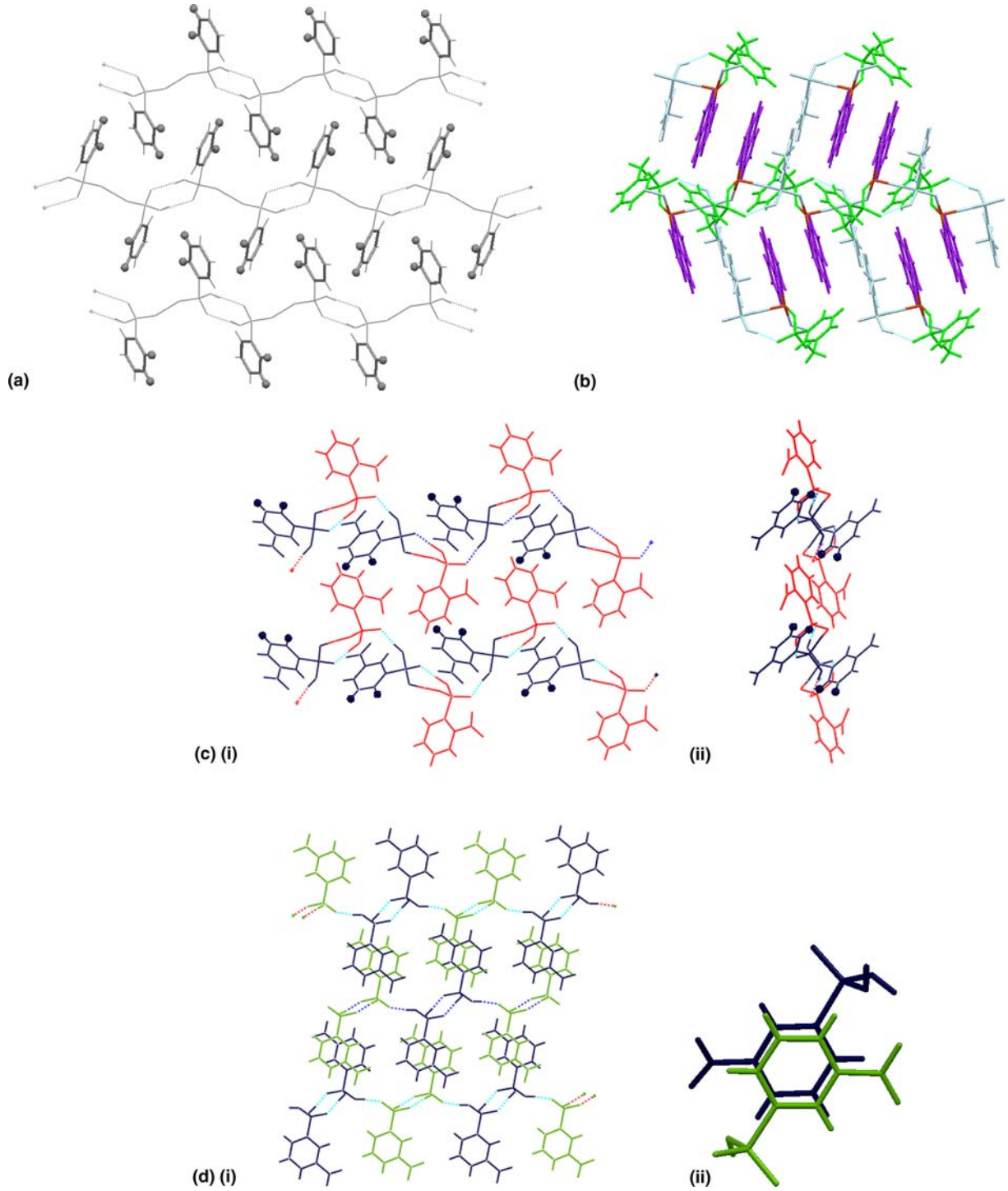


Fig. 5. (a) The H-bonded acid chains of **1** are assembled into sheets via EF interaction of phenyl rings – 'edge' H-atoms shown as spheres; aromatic 'face' as bolded ring. (b) The OFF pairing of phen–phen (purple–purple) and phen–acid (purple–blue) in **3**. (c) (i) The zigzag acid chains of **5** meshed together via non-continuous EF interaction to form a sheet, (ii) the *meta* rings (blue) protrude from the layer, while the *ortho* rings (red) are in-plane. (d) (i) Acid chains of **6** are connected into sheets via OFF overlapping of the rings, (ii) the overlap is noticeably offset, with nitro groups *trans* to one another. (For interpretation of the references to colour in this figure legend, the reader is referred to the web version of this article.)

(176.31°) is significantly more linear than the (neutral) O2–H2a···O6 (anion) (161.74°).

There are two acid species in the naphthyl derivative **7**: a dimer acid anion (P) (O8–H8a···O8, d(O8···H8a) = 1.22(4) Å) which forms pairs of identical H-bonds (O9–H9a···O7, d(H9a···O7) = 1.633 Å, 174.69°); and a pair of neutral (R) and anionic (Y) acids connected by a regular H bond (O2–H2a···O4, d(H2a···O4) = 1.612 Å, 167.00°) (Fig. 1c). The pairing of the P dimer anion is stronger then in **1** and **2**. In both YR and P acid chains, the naphthyl

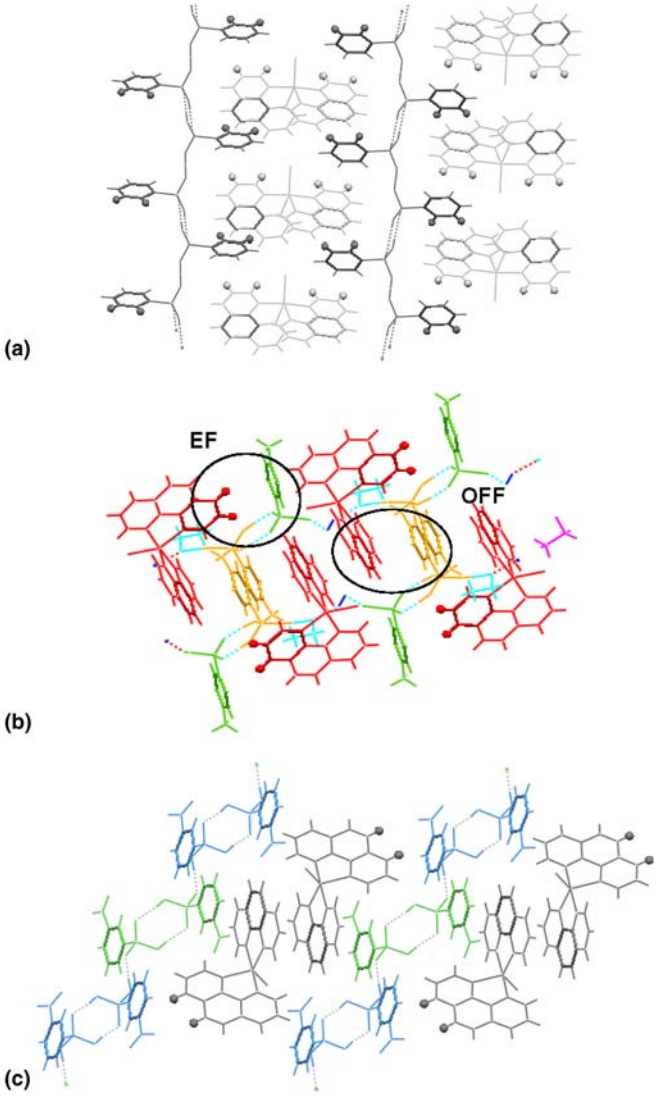


Fig. 6. (a) The continuous EF interactions between acid chains and phen in **1**. (b) EF and OFF interactions between phen and acid in **4**. (c) OFF stacking between anionic (green) acid rings and phen, and the EF interaction between neutral (blue) acid rings and phen in **6**. (For interpretation of the references to colour in this figure legend, the reader is referred to the web version of this article.)

groups are angled from the linear type chains in a similar orientation to the phenyl rings of **1**. This orientation, and the fact the naphthyl group gives a wider face and edge to undergo π–π interactions, are thought responsible for the range of EF and OFF motifs seen.

In summary, whilst the acid participates in three H-bonding motifs in all structures, there are some notable variations in bond lengths and angles. Examining the data in Table 4, it appears that only the centrosymmetric inter-dimer bonds of **1**, **2** and **7** satisfy Jeffrey's criteria [33] for a strong (almost covalent) hydrogen bond: H···A = 1.2–1.5 Å; D···A = 2.2–2.5 Å; DHA = 170–180 °; and X–H ∼ H···A. Amongst the remaining structures, the H-bonds of the mixed *o*-/*m*-NO_2 derivative **5**, the *m*-NO_2 derivative **6**, and the P═O1···H7–O7 bonds between ethanol and the *p*-tolyl acid in **4** are the strongest, but can only be classified as moderate with respect to their X–H:H···A ratios. From current evidence, the *o*-NO_2 bond of **5** appears to have formed stronger H-bonds than its *m*-NO_2 partner and **1**. This tends to support the notion that electronic 'inductive' effects have a role to play in the overall structure assembly.

However, the effects on H-bonding motifs might be better traced to steric reasons, i.e. that the acid chains orient to place the substituted ring in a position where the π–π networking can self-assemble. This conclusion is supported by Nagarajan et al. [13] who determined the acid dissociation constants of 36 substituted phenylphosphonic acids, and also in the work of Russell and Ward on substituted arylsulphonic acids [10]. Nagarajan found that unlike benzoic acid, where virtually any *ortho* group has an acid strengthening effect, in the majority of cases, substituted arylphosphonic acids are either slightly weaker acids (*ortho*-) or have pK_{a1} and pK_{a2} values comparable (*meta*- and *para*-) to the unsubstituted form (H $pK_a = 1.86$; *o*-CH_3 $pK_a = 2.08$; *m*-CH_3 $pK_a = 1.95$; *p*-CH_3 $pK_a = 2.00$ [13]). The only exceptions being NO_2-substituted acids, which have significantly lower dissociation constants (*o*-NO_2 $pK_a = 1.28$; *m*-NO_2 $pK_a = 1.20$, *p*-NO_2 $pK_a = 1.19$ [13]). Therefore, as we have observed, alkyl groups are fairly benign in their effect on the hydrogen bonding ability of the acid, whereas acids substituted with electron-withdrawing groups, such as NO_2, may form slightly stronger hydrogen bonds.

3.2.2.4. Global observations. Looking along the *c*-axis, the overall packing of **2** is extremely similar to **1** (Fig. 7b). The *ortho*-position results in the methyl substituent being contained within the acid layer, so the EF acid-to-phen interactions are not disrupted. The unit cell is more square than **1** (*β* more acute by 7.2°), but otherwise only a slight expansion is observed.

The symmetry of the overall packing in **5** has been disrupted (Fig. 7e). Adjacent acid sheets are not aligned, being rotated 54° in the *a*–*b* plane with respect to one another. The phen layers are not aligned either – there is a 70° rotation in the *a*–*b* plane. If viewed along the *b*-axis, the *meta*-acids protrude sharply either side of the chain, while the *ortho*- are more in line (Fig. 5c(i)). One might expect that the protruding *meta*-acids would be more favourable participants in acid–phen π–π interactions, but this does not appear to occur. They are actually projected into the spacings between ribbons, which is possible because of the offset arrangement of the phen ribbons and the previously mentioned plane rotations. It is the *ortho*-acid ring, rather than the *meta*-, which undergoes an EF interaction with phen protons (H20, H21) (Fig. 6c). In summary, the *ortho*-acid ring is the greater contributor to assembly – participating in both the assembly of acid sheets and the binding of acid to phen.

The rings of **6** are angled gently in-plane (Fig. 4d), and the nitro groups are '*trans*' to one another. This enables an OFF interaction between acid rings of adjacent chains

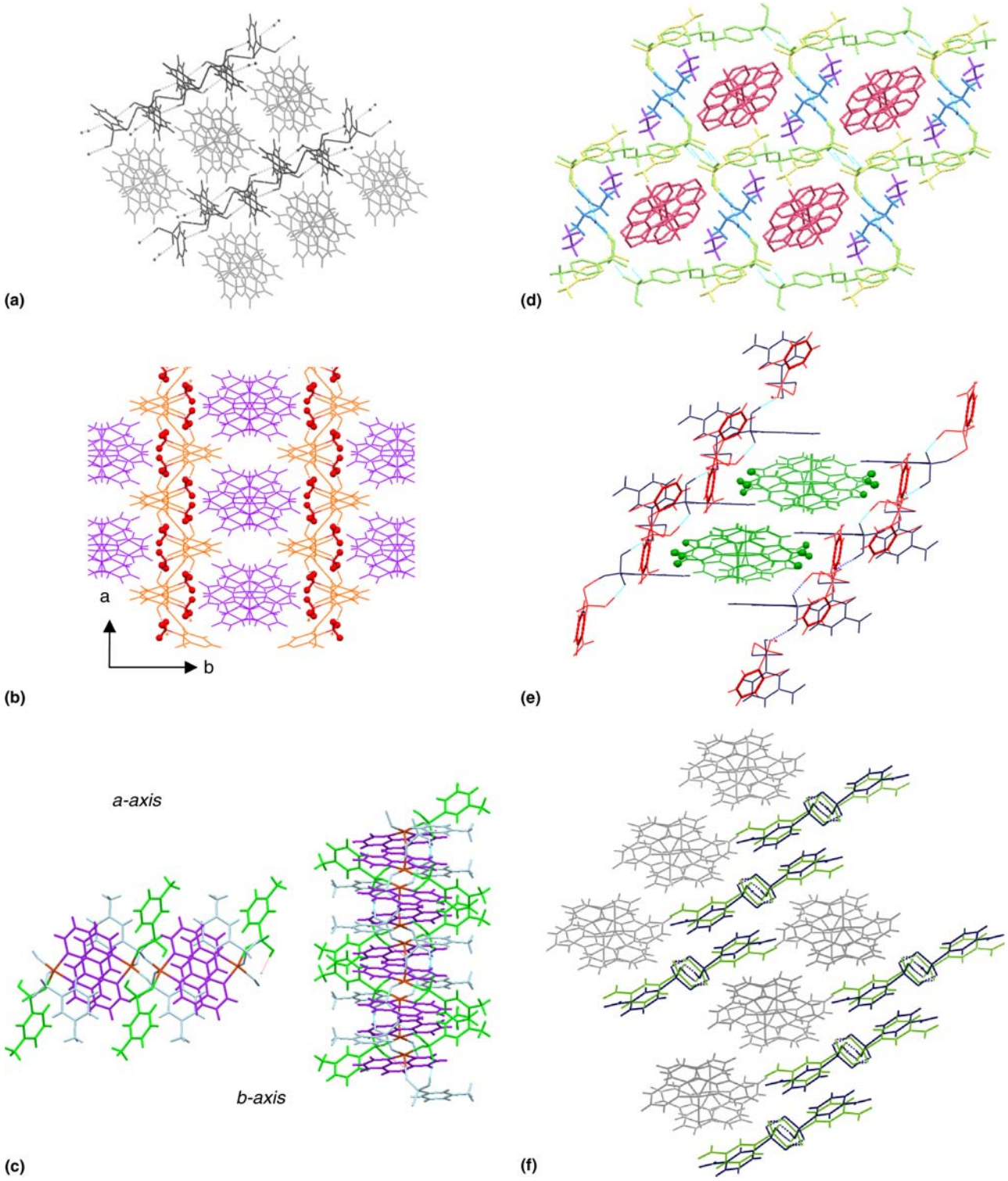


Fig. 7. Overall packing for: (a) **1** showing the acid layers interleaved by phen ribbons. (b) **2** – The presence of the methyl substituent has not interfered with the continuous EF interactions between acid chains and phen. (c) **3** Along the *a* and *b*-axes. (d) **4** – The methyl groups protrude to create cavities, which are filled by the phen ribbons. (e) **5** – The acid sheets and adjacent phen sheets are rotated with *meta* (blue) rings projected between ribbons, while the *ortho* (red) rings EF interact with phen. (f) **6** Where the phen ribbons run in the same direction as the acid chains. (For interpretation of the references to colour in this figure legend, the reader is referred to the web version of this article.)

(Fig. 5d), as opposed to the usual continuous EF interaction. The OFF assembly has major effects on overall packing. Firstly, the acid sheet is thicker, and consequently the spacing between adjacent phen layers is expanded. Secondly, the acid chains now run in the same direction as the phen ribbons (Fig. 7f). The anionic and neutral acid

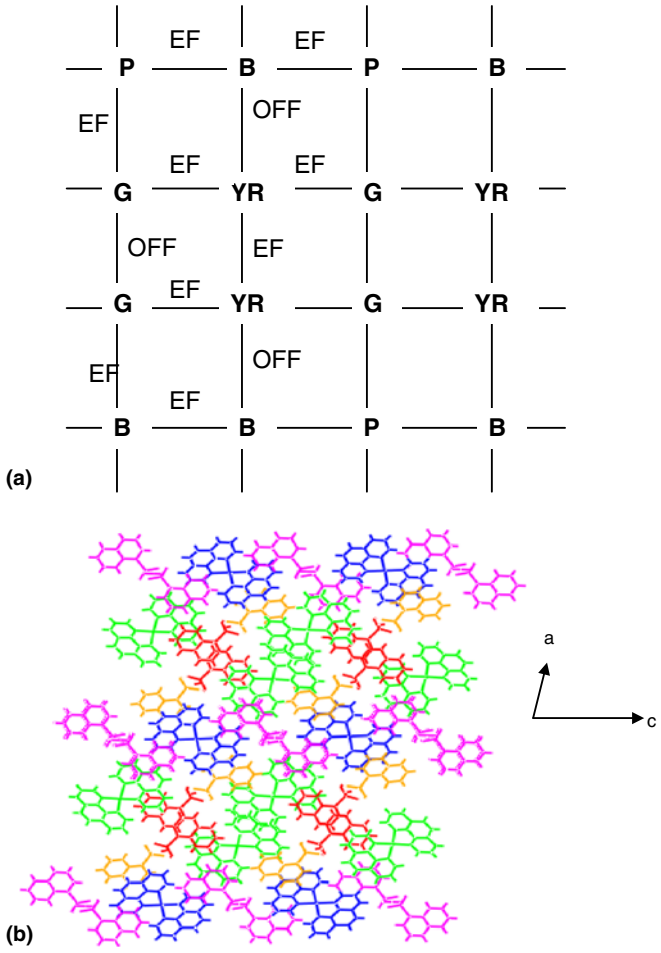


Fig. 8. (a) The structure of **7** contains multiple OFF/EF interactions and is best represented graphically as an intersecting grid (P, B, G, and YR are defined in Fig. 1c). (b) Packing in the *a*–*c* plane reveals four unique, intersecting lines of π–π interactions.

rings protrude between the phen ribbons. The anion forming an OFF interaction with the middle ring of phen (*d*(plane to centroid) = 3.729 Å, 3.39°), and the neutral acid forming a weaker EF interaction with the phen edge of H3, H5 (angle = 64.74°). Thus, the assembly of **6** is dominated by OFF interactions.

No π–π interactions are observed between adjacent chains of acid/solvent in **4**. The methyl groups are not orientated to allow this, rather they protrude to create cavities (Fig. 7d). These stack behind one another to give two-dimensional voids, which are filled by the phen ribbons. This is possible because of two types of π–π interactions between the acid and phen, which are best viewed along the *b*-axis (Fig. 6b). There is an OFF overlap between the neutral acid and the middle ring of the N3/N4 phen (*d*(centroid to plane) = 3.47(3) Å, 5.2°); while an EF interaction exists between the N1/N2 phen (edge = H8, H9) and the anionic acid plane.

When observed in the *a*–*c* plane (Fig. 8a and b), the unit cell of **7** contains a series of interlocking planes. In Plane 1: B–YR–RY–B–YR, the B acid forms OFF pairs with the Y acid. This is a one-ring overlap between the middle phen ring and the Y 'original' ring, which is a strong interaction (3.381 Å, 5.19° divergence). Adjacent acid chains are connected by a continuous EF interaction between R acid groups. In Plane 2: YR–G–YR–G–YR–G, on one side of the acid chain, a continuous EF interaction occurs between R acid and G phen, and on the other side, there is a continuous EF interaction between Y acid and D phen. In Plane 3: B–P–B–P–B–P, there is a continuous EF interaction between the B phen and P acid. Finally, in Plane 4: P–G–G–P–G–G, the G phens form perfectly parallel OFF pairs, involving the two ring overlap of middle and N4 rings (*d*(plane to centroid) = 3.462 Å). These pairs form continuous EF interactions with the P acid. In total, the naphthyl group in product **7** participates in 11 different π–π interactions, with approximately half involving the 'fused' ring.

3.2.3. *Molecular structure and packing of* ***3***

As mentioned previously, the structure of **3** is very different from the rest of the series, and consists of a neutral molecule instead of an ion pair (Fig. 1b). Trigonal bipyramidal stereochemistry is retained, as is typical of copper(II) compounds, but the copper is connected to one phen molecule (N1 and N2), and three phosphonate oxygens: two from the two phosphonate ions in the molecular unit (O3 and O6); and one from a P1 phosphonate ion (O1′) in an adjacent molecular unit. The latter connecting neighbouring molecular units, via a P1–O3–Cu1–O1′–P1′ link, which results in a mixed inorganic/organic polymeric chain in the *a*-direction (Fig. 7c).

There are two hydrogen bonding interactions: an intramolecular strong H-bond between O2–H2a···O5 (*d*(O2···O5) = 2.477 Å); and an intermolecular H-bond of moderate strength between O4–H4a···O1′ (*d*(O4···O1′) = 2.613 Å). Both bonds are almost linear with angles of 170.34° and 176.08°, respectively.

There are three different π–π interactions: an intramolecular OFF interaction between the N2 phen ring and the C13–C18 acid ring (*d*(centroid to plane) = 3.391 Å; 5.23 °); an intermolecular, parallel OFF interaction between phen molecules in adjacent molecular units, via overlap of the N1 and N2 rings (*d*(centroid to plane) = 3.387 Å; and a weak intermolecular EF interaction 45.03 °) between methyl protons H26a and H26b of the P2 acid, and the acid ring of P2′ (*d*(H26a to H20′–H25′ centroid) = 4.40 Å; *d*(H26b to H20′–H25′ centroid) = 4.842 Å). All of the former are single, not continuous interactions, such that only phen–phen, phen–acid and acid–acid pairing occurs (Fig. 5b).

4. Conclusion

The successful synthesis and structure determination of the six new compounds reported here has provided valuable data for the investigation of the variety of supramolecular motifs of phen and phenylphosphonic acid metal derivatives. Most importantly, they have emphasised the

potential of phenylphosphonic acids (the $P(O)(OH)_2$ group and the unsubstituted/substituted aromatic rings) to be used in the context of intermolecular design, rather than, or in addition to, the well known use of phosphonates in co-ordination networks. With the exception of the *m*-tolyl derivative **3**, the structural unit – a 5-coordinate $[Cu^{II}(phen)_2Cl]^+$ cation, with two acids functioning as counter-anion, was maintained in the series – indicating that the major role of the acid has not changed. The general assembly strategy of acid sheets with phen ribbons interleaved, seen in **1**, has been maintained in four structures (*o*-tolyl (**2**), *o*-/*m*-NO_2 (**5**–**6**) and naphthyl (**7**)). In three cases (*m*-tolyl (**3**), *p*-tolyl (**4**) and naphthyl (**7**)), the substituent has disrupted the symmetry of overall packing, and has greatly impacted on the arrangement of phen ribbons. This disruption can be traced to moderate to strong perturbations of the H-bonding motifs, and π–π interactions. The substituent *type* had a lesser influence on the structure than the substituent *position*. The substituent *type* had only minor effects on H-bonding character, with the strongest intra- and inter-dimer H-bonds being observed in the nitro acids. The *position* of the substituent had a considerable influence on π–π motifs, and hence on global packing. The degree of disruption to packing increased from *ortho* to *meta* to *para*. The *o*-CH_3 structure **2** is a very close structural analogue to the unsubstituted parent **1**, where the phen–acid EF motifs were maintained, but in structure **4** a completely different packing style was adopted due to the protruding *p*-CH_3 group. The inadvertent formation of the mixed isomer product **5** provided an opportunity to study *ortho* versus *meta* substitution. The *o*-NO_2 group appeared to adopt the assembly roles seen in **2**, whilst the *m*-NO_2 group had to be accommodated. Therefore, in the pure *m*-NO_2 product **6**, a different assembly strategy was required, which utilised more OFF interactions. Significant changes were observed in π–π interactions in the naphthyl product **7**. The larger aromatic group forms a range of EF and OFF motifs, to create a completely different assembly. Attempts to produce a *p*-phenyl acid derivative were unsuccessful, lending further evidence for the disruption of the structure by *para* substituents. The need to satisfy π–π networking requirements of the acid, appears to indicate that the substituted acid has a more dominant role in the overall assembly then the unsubstituted form, i.e. the substituent has given the acid greater control in the self-assembly of the supramolecular structure.

Appendix A. Supplementary data

CCDC Reference Nos. 602676–602681 contain the supplementary crystallographic data for this paper. These data are available free of charge from The Cambridge Crystallographic Data Centre via www.ccdc.cam.ac.uk/data_request/cif. Product **1** has been previously reported (CCDC No. 216752) [4]. Supplementary data associated with this article can be found, in the online version, at doi:10.1016/j.poly.2006.04.028.

References

[1] B. Nowack, Water Res. 37 (2003) 2533.
[2] B. Bujoli, S.M. Lane, G. Nonglaton, M. Pipelier, J. Léger, D.R. Talham, C. Tellier, Chem. Eur. J. 11 (2005) 1980.
[3] R. Clarke, K. Latham, C. Rix, M. Hobday, J. White, CrystEngComm 6 (10) (2004) 42.
[4] R. Clarke, K. Latham, C. Rix, M. Hobday, J. White, CrystEngComm 7 (3) (2005) 28.
[5] A.M. Mahmoudkhani, V. Langer, J. Mol. Struct. 609 (2002) 97.
[6] C.V.K. Sharma, A. Clearfield, J. Am. Chem. Soc. 122 (18) (2000) 4394.
[7] C.V.K. Sharma, A.J. Hessheimer, A. Clearfield, Polyhedron 20 (2001) 2095.
[8] C.V.K. Sharma, A. Clearfield, J. Am. Chem. Soc. 123 (12) (2001) 2885.
[9] E. Matczak-Jon, V. Videnova-Adrabińska, Coord. Chem. Rev. 249 (2005) 2458.
[10] V.A. Russell, M.D. Ward, Chem. Mater. 8 (8) (1996) 1654.
[11] D.A. Haynes, J.A. Chisholm, W. Jones, W.D. Motherwell, CrystEngComm 6 (95) (2004) 584.
[12] B. Abrahams, M.G. Haywood, T.A. Hudson, R. Robson, Angew. Chem. Int. Ed. 43 (2004) 6157.
[13] K. Nagarajan, K.P. Shelly, R.R. Perkins, R. Stewart, Can. J. Chem. 65 (1978) 1729.
[14] R.N. Keller, H.D. Wycoff, in: W.C. Fernelius (Ed.), Inorganic Syntheses, vol. 2, McGraw-Hill Book Company, 1946, p. 1.
[15] A.I. Vogel, Textbook of Practical Organic Chemistry, 4th ed., Longman, 1978, p. 709.
[16] E.D. Matveeva, T.A. Podrugina, N.Yu. Morozkina, O.N. Zefirova, I.V. Seregin, S.O. Bachurin, R. Pellicciari, N.S. Zefirov, Russ. J. Org. Chem. 38 (12) (2002) 1769.
[17] R.C. Grabiak, J.A. Miles, G.M. Schwenzer, Phosphorus Sulphur 9 (1980) 197.
[18] T.J. Broxton, J.F. Bunnett, C.H. Paik, J. Org. Chem. 42 (1977) 643.
[19] G.O. Doak, L.D. Freedman, J. Am. Chem. Soc. 73 (1951) 5658.
[20] E.C. Ashby, G.M. Kosolopoff, J. Am. Chem. Soc. 75 (1953) 4903.
[21] L.D. Freedman, G.O. Doak, J. Am. Chem. Soc. 77 (1955) 6221.
[22] Enraf–Nonius, CAD4 Software, Version 5.0, 1989.
[23] Siemens SMART and SAINT, Version 4.0, Siemens Analytical X-ray Instruments Inc., Madison, WI, USA, 1995.
[24] G.M. Sheldrick, SHELXS-97 and SHELXL-97, University of Göttingen, Germany, 1997.
[25] Bruker SHELXTL, Version 6.12, Bruker AXS Inc., Madison, WI, USA, 2001.
[26] L. Zsolnai, ZORTEP, University of Heidelberg, Germany, 1994.
[27] I.J. Bruno, J.C. Cole, P.R. Edgington, M.K. Kessler, C.F. Macrae, P. McCabe, J. Pearson, R. Taylor, Acta Crystallogr. B58 (2002) 389.
[28] N.W. Alcock, PLATON, Cryst. Comput. (1970) 271.
[29] H. Mao, X. Shen, G. Li, H. Zhang, C. Xu, H. Liu, E. Wang, Q. Wu, H. Hou, Y. Zhy, Polyhedron 23 (2004) 1961.
[30] B. Ma, S. Gao, T. Yi, C. Yan, G. Xu, Inorg. Chem. Commun. 3 (2000) 93.
[31] L. Lu, S. Qin, P. Yang, M. Zhu, Acta Crystallogr. E60 (2004) m574.
[32] I. Dance, in: G. Desiraju (Ed.), Supramolecular Inorganic Chemistry, The Crystal as a Supramolecular Entity, Wiley, 1996.
[33] G.A. Jeffrey, An Introduction to Hydrogen Bonding, Oxford University Press, Oxford, 1997.

Available online at www.sciencedirect.com
ScienceDirect
Polyhedron 26 (2007) 237–243
POLYHEDRON
www.elsevier.com/locate/poly

Stabilisation of heterobimetallic networks by crown ethers and hydrogen-bonding in $[Ni(H_2O)_6][Cu_3Cl_8(H_2O)_2] \cdot (15\text{-crown-}5)_2 \cdot 2H_2O$: Structure and magnetism

Peter C. Junk *, Boujemaa Moubaraki, Keith S. Murray

School of Chemistry, Monash University, Clayton, Vic. 3800, Australia

Received 28 March 2006; accepted 8 May 2006
Available online 16 May 2006

Abstract

$[Ni(H_2O)_6][Cu_3Cl_8(H_2O)_2] \cdot (15\text{-crown-}5)_2 \cdot 2H_2O$ can be conveniently prepared by the interaction of $NiCl_2 \cdot 6H_2O$, $CuCl_2 \cdot 2H_2O$ and 15-crown-5 in water. The X-ray crystal structure reveals an ionic complex involved in a hydrogen-bonded two dimensional network with the $[Ni(H_2O)_6]^{2+}$ and $[Cu_3Cl_8(H_2O)_2]^{2-}$ ions sandwiched between the 15-crown-5 macrocycles. The magnetic susceptibility data (4–300 K) and magnetisation isotherms (2–5.5 K; 0–5 T) are best interpreted in terms of intra-trimer ferromagnetic coupling within the $[Cu_3Cl_8(H_2O)_2]^{2-}$ moieties, with $J \sim 6\ cm^{-1}$, and antiferromagnetic coupling between the trimers, the latter mediated by H-bonding pathways. Comparisons are made to other reported quaternary ammonium salts of $[Cu_3Cl_8]^{2-}$ and $[Cu_3Cl_{12}]^{6-}$, most of which display structures that involve close stacking of such Cu(II) trimers, rather than being of the present isolated, albeit H-bonded, types.
© 2006 Elsevier Ltd. All rights reserved.

Keywords: Heterobimetallics; Crown ethers; Hydrogen bonding; Magnetochemistry; Nickel; Copper

1. Introduction

Molecular based magnets have been the subjects of intense interest in heterobimetallic complexes in recent years. Paramagnetic metal based compounds offer distinct advantages over organic radical counterparts in this respect due to the magnetic nature being tunable based on choices of metal, ligands and bridging groups, electron spin being reserved to each metal centre and the possibility of networks being constructed by judicious choice of stereochemistry about the metal centres [1].

As part of our research into the coordination of metal ions with crown ethers [2] and in particular the stabilisation of unusual $[(H_2O)_5Fe(\mu\text{-}O)Fe(OH_2)_5]^{4+}$ species in $[(H_2O)_5Fe–O–Fe(OH_2)_5][NO_3]_4 \cdot (18\text{-crown-}6)_2$ [3] and second sphere coordination complexes of the transition metals [4], we now present the synthesis, structure and magnetism of a heterobimetallic, non-covalent species involving Ni^{2+}, Cu^{2+} and 15-crown-5; viz the trinuclear anionic copper species $[Ni(H_2O)_6][Cu_3Cl_8(H_2O)_2] \cdot (15\text{-crown-}5)_2 \cdot 2H_2O$. The crown ether and associated hydrogen-bonding has enabled the halide-rich trinuclear Cu(II) cluster to be stabilised and, in contrast to the situation commonly found in crystalline $[Cu_3Cl_8]^{2-}$ compounds that do not contain a crown ether, the trinuclear $[Cu_3Cl_8(H_2O)_2]^{2-}$ moiety does not stack to neighbours via semi-coordinate 2.9 Å long Cu···Cl interactions along the apical Cu(II) direction [5,6].

2. Results and discussion

Treatment of equimolar amounts of $NiCl_2 \cdot 6H_2O$ and $CuCl_2 \cdot 2H_2O$ with 15-crown-5 in water resulted in a brown solution from which large brown crystals and small green acicular crystals deposited. Manual separation of the two sets of crystals was possible and the latter were shown by unit cell determination to be the previously reported

* Corresponding author. Tel.: +61 3 9905 4570; fax: +61 3 9905 4597.
E-mail address: peter.junk@sci.monash.edu.au (P.C. Junk).

0277-5387/$ - see front matter © 2006 Elsevier Ltd. All rights reserved.
doi:10.1016/j.poly.2006.05.004

$[\{Ni(H_2O)_4\}_2(\mu\text{-}Cl)_2]Cl_2 \cdot$ 15-crown-5 [4c]. An infrared spectrum of the brown material showed strong broad bands around 3360 and 1650 cm^{-1} attributable respectively to OH stretches and bending of either water ligands or water of crystallization. The presence of the crown ether is indicated by moderate to high intensity C–O stretches in the 1000–1500 cm^{-1} region. To ascertain the true nature of the brown crystals, they were subjected to an X-ray crystal structure determination and their composition found to be $[Ni(H_2O)_6][Cu_3Cl_8(H_2O)_2] \cdot (15\text{-crown-}5)_2 \cdot 2H_2O$. Microanalysis of the bulk sample confirmed this composition.

$[Ni(H_2O)_6][Cu_3Cl_8(H_2O)_2] \cdot (15\text{-crown-}5)_2 \cdot 2H_2O$ crystallises in the triclinic space group *P*-1 with one half of the structural entity comprising the asymmetric unit. The complex ions do not exist as discrete ionic units, rather they are involved in extended hydrogen bonding networks. The $[Ni(H_2O)_6]^{2+}$ octahedral cation which resides on an inversion centre is unexceptional (Table 1). The water ligands are however, multiply hydrogen bonded to two 15-crown-5 molecules, resulting in the complex ion being sandwiched centrally between two of the macrocyclic ligands in a second sphere coordination mode (Fig. 1). Thus, the $[Ni(H_2O)_6]^{2+}$ ion is involved in six hydrogen bonds with two 15-crown-5 hydrogen bond acceptors (Fig. 1), being closely related to the type of interaction in $[Ni(H_2O)_6](ClO_4)_2 \cdot (15\text{-crown-}5) \cdot 2H_2O$ [4c]. In a similar fashion, the $[Cu_3Cl_8(H_2O)_2]^{2-}$ anion is also sandwiched between two 15-crown-5 molecules through hydrogen bonding between the coordinated water molecules and the O atoms of the crown ether (Fig. 2). The $[Cu_3Cl_8(H_2O)_2]^{2-}$ polynuclear anion has been previously structurally characterised in $[Mg(H_2O)_6][Cu_3Cl_8(H_2O)_2] \cdot (15\text{-crown-}5)_2 \cdot 2H_2O$ [7] which is isomorphous to the present nickel analogue. Thus, the anion has a central $CuCl_2(H_2O)_2$ unit which has very close to square planar geometry (Table 1), but Cl(2) and its symmetry generated partner are predisposed in axial positions (relative to the $CuCl_2(H_2O)_2$ plane) at a "semi-coordinate" distance of 2.862(1) Å, representing extreme Jahn–Teller distortion about Cu(2). Cu(1) is coordinated by four chloride ligands in a flattened tetrahedral array (see Fig. 2, Table 1). The geometric parameters of this ion are very similar to the previous Mg analogue [7]. While both the $[Ni(H_2O)_6]^{2+}$ and the $[Cu_3Cl_8(H_2O)_2]^{2-}$ ions are sandwiched between 15-crown-5 molecules, they take up alternate positions in the overall structure, such that the 15-crown-5 molecules bridge successive $[Ni(H_2O)_6]^{2+}$ and the $[Cu_3Cl_8(H_2O)_2]^{2-}$ ions (Fig. 3). These $[Ni(H_2O)_6]^{2+}$–15C5–$[Cu_3Cl_8(H_2O)_2]^{2-}$–15C5 ladders are cross-linked through a Cl···H–O hydrogen bond arising through Cl(3) and a proton on O(3s), an equatorial water ligand on $[Ni(H_2O)_6]^{2+}$ (see Fig. 3). Thus, overall, the structure is a two dimensional hydrogen bonded grid.

Magnetic susceptibilities of polycrystalline $[Ni(H_2O)_6][Cu_3Cl_8(H_2O)_2] \cdot (15\text{-crown-}5)_2 \cdot 2H_2O$ were measured in a field of 1 T over the temperature range 4–300 K. The susceptibilities over the range 4–300 K showed a Curie–Weiss temperature dependence ($C = 2.16\ cm^3\ mol^{-1}\ K^{-1}$; $\theta = -1.0$ K) and the corresponding plot of $\chi_M T$ versus temperature, shown in Fig. 4, varies from 2.43 $cm^3\ mol^{-1}$ K (4.40 μ_B), per $NiCu_3$, at 300 K, to a broad maximum of 2.53 $cm^3\ mol^{-1}$ K, at ~40 K, before decreasing rapidly to reach 1.60 $cm^3\ mol^{-1}$ K (3.56 μ_B) at 5.4 K, and still decreasing. There appears to be a very broad, gentle minimum in $\chi_M T$ at ~200 K, such observations being sometimes indicative of ferrimagnetic coupling. This seems unlikely to be the case here in view of the Ni(II) $S = 1$ centres being not covalently bonded to the Cu(II) ions, even though they are H-bonded via the long Cl(3)···O(3S)(H_2O) interactions. It more likely reflects the superposition of $\chi_M T$ contributions

Table 1
Selected (i) bond distances (Å), (ii) angles (°), for $[Ni(H_2O)_6][Cu_3Cl_8(H_2O)_2] \cdot (15\text{-crown-}5)_2 \cdot 2H_2O$

Atoms	Distance	Atoms	Distance
(i)			
Ni(1)–O(1S)	2.044(4)	Cu(1)–Cl(1)	2.3226(13)
Ni(1)–O(2S)	2.031(4)	Cu(1)–Cl(2)	2.2493(14)
Ni(1)–O(3S)	2.058(4)	Cu(1)–Cl(3)	2.2264(14)
Cu(2)–O(4S)	1.935(3)	Cu(1)–Cl(4)	2.2075(14)
Cu(2)–Cl(1)	2.3400(11)	Cu(2)···Cl(2)	2.862(1)
Cu(1)···Cu(2)	3.563(1)	Ni(1)···Cu(1)	6.418(1)
Atoms	Angle	Atoms	Angle
(ii)			
O(1S)–Ni(1)–O(2S)	90.37(19)	O(1S)–Ni(1)–O(2S)#1	89.63(19)
O(1S)–Ni(1)–O(3S)	88.2(2)	O(1S)–Ni(1)–O(3S)#1	91.8(2)
O(2S)–Ni(1)–O(3S)	90.56(18)	O(2S)–Ni(1)–O(3S)#1	89.44(18)
Cl(1)–Cu(1)–Cl(2)	93.71(5)	O(4S)–Cu(2)–O(4S)#2	180.0
Cl(1)–Cu(1)–Cl(3)	96.65(5)	O(4S)–Cu(2)–Cl(1)	90.38(11)
Cl(1)–Cu(1)–Cl(4)	138.36(6)	O(4S)–Cu(2)–Cl(1)#2	89.62(11)
Cl(2)–Cu(1)–Cl(3)	141.38(6)	Cu(1)–Cl(1)–Cu(2)	99.65(4)
Cl(2)–Cu(1)–Cl(4)	100.52(6)		
Cl(3)–Cu(1)–Cl(4)	96.04(6)		
Cl(1)–Cu(2)–Cl(1)#2	180.0		

Symmetry transformations used to generate equivalent atoms: #1 $-x+1, -y+1, -z+1$; #2 $-x, -y, -z+2$.

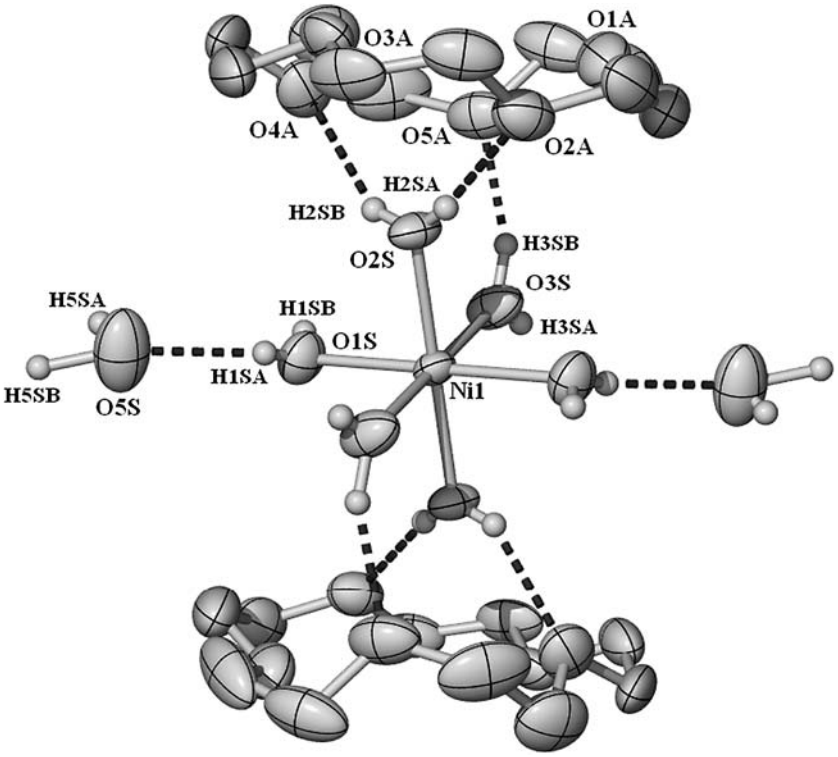


Fig. 1. Structure of the $[Ni(H_2O)_6]^{2+}$ ion sandwiched by hydrogen bonding between two 15-crown-5 molecules and hydrogen bonded to two water molecules.

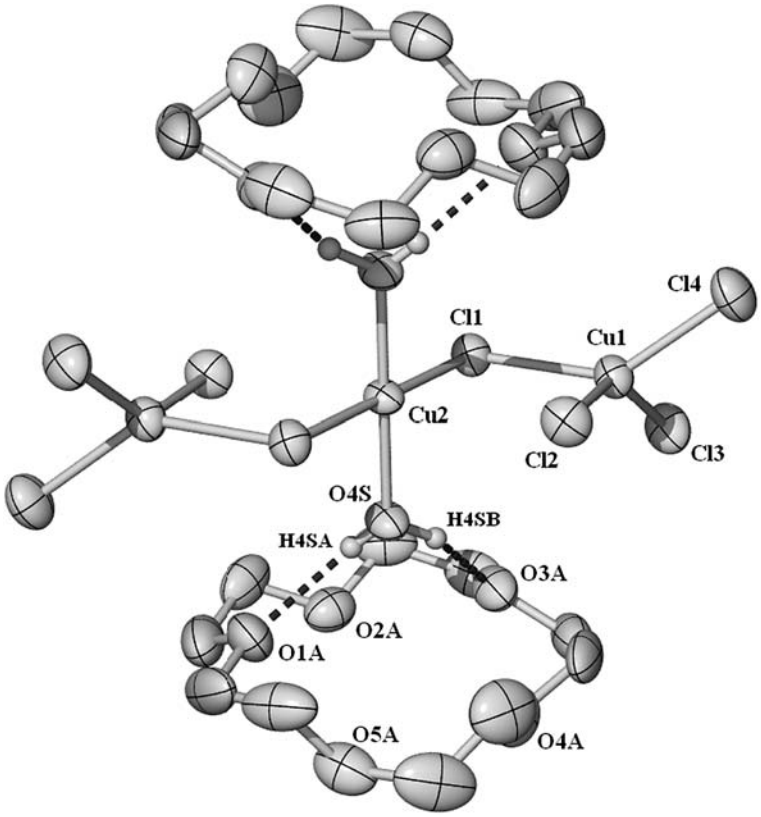


Fig. 2. X-ray structure of the $[Cu_3Cl_8(H_2O)_2]^{2-}$ polynuclear anion sandwiched by hydrogen bonding between two 15-crown-5 molecules.

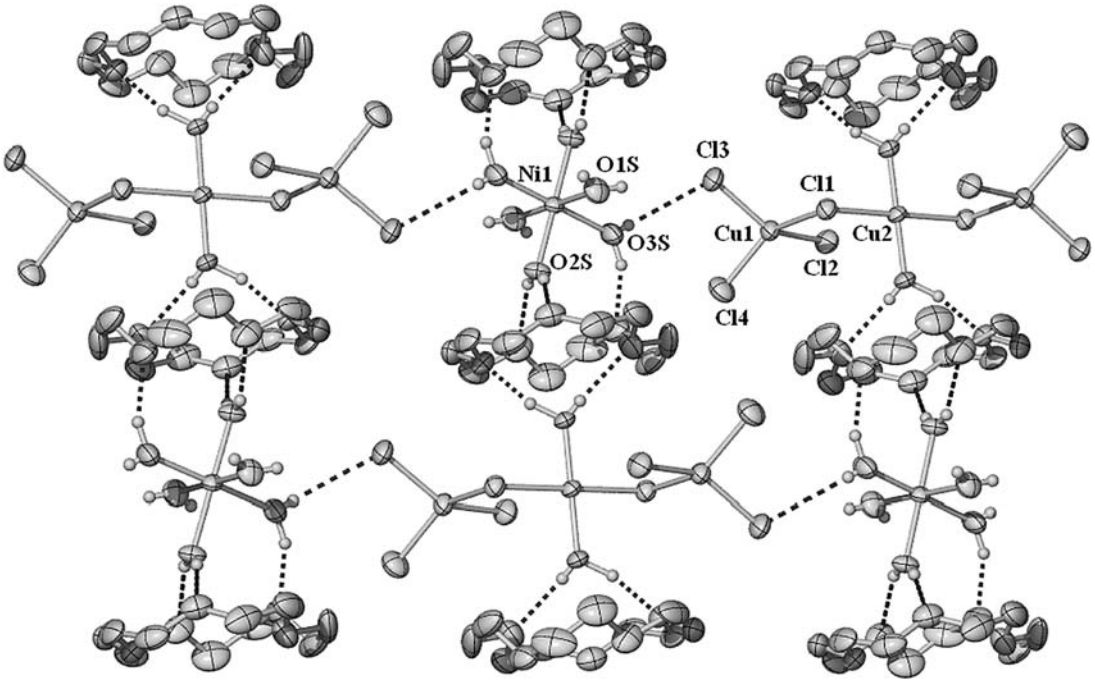


Fig. 3. Crystal packing diagram of $[Ni(H_2O)_6][Cu_3Cl_8(H_2O)_2]\cdot(15\text{-crown-}5)_2\cdot 2H_2O$ showing the extensive hydrogen bonding network.

from the $S = 1$ ions and from the $Cu_3Cl_8^{2-}$ trinuclear spin-coupled moieties. The overall shape of the $\chi_M T$ plot, particularly in the range 300–40 K, is suggestive of weak ferromagnetic coupling, with a combination of zero-field splitting of the ground state(s) and antiferromagnetic trimer–trimer coupling being responsible for the rapid decrease observed below 40 K.

Probing the low temperature region, further, by measurements of magnetisation (M) isotherms (2–5.5 K) yielded the plots shown in Fig. 5. The M versus H dependence is almost linear at 2 K and shows a slight downward curvature for the 3–5.5 K isotherms. Clearly, saturation in M does not occur and the behaviour is indicative of either paramagnetic (i.e. M proportional to H) or, more likely, of antiferromagnetic coupling occurring in this temperature region, as was seen in the $\chi_M T$ plot. An M value of 3.37 Nβ obtained at 2 K and $H = 5$ T, is less than the expected value of ~5 Nβ if all four metal ions are uncoupled and, also, saturation would also be anticipated under these conditions. A similar M value of ~5 Nβ would be anticipated if the $[Cu_3Cl_8(H_2O)_2]^{2-}$ unit had a coupled $S = 3/2$ ground state at 2 K, combined with M for the $S = 1$ Ni(II) aqua ion. Whereas, if the $[Cu_3Cl_8(H_2O)_2]^{2-}$ unit has a $S = 1/2$ ground state, a value of ~3 Nβ would be expected. The observed value, together with the linear behaviour and lack of saturation noted in Fig. 5, is also probably indicative of the thermal population of M_S Zeeman levels that are close to the ground state, rather than being indicative of an isolated ground state.

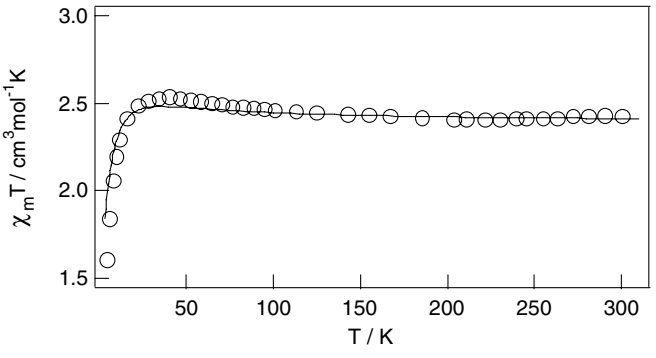


Fig. 4. Plot of $\chi_M T$ (per $NiCu_3$) vs. temperature, in a field of 1 T, for $[Ni(H_2O)_6][Cu_3Cl_8(H_2O)_2]\cdot(15\text{-crown-}5)_2\cdot 2H_2O$. The solid line is that calculated using a linear $S = 1/2$ trimer model plus a Curie-like Ni(II), $S = 1$ contribution, with the best-fit parameters discussed in the text. The trimer model includes a trimer–trimer interaction parameter, θ'.

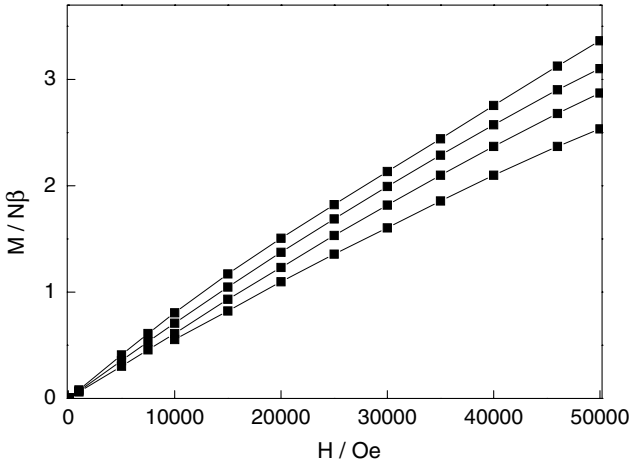


Fig. 5. Magnetisation isotherms for $[Ni(H_2O)_6][Cu_3Cl_8(H_2O)_2]\cdot(15\text{-crown-}5)_2\cdot 2H_2O$ at temperatures of 2 (top), 3, 4 and 5.5 K (bottom) in the field range shown. The solid lines simply join the points.

The $\chi_M T$ data of Fig. 4 could be fitted well by use of a linear $S = 1/2$ trimer model (employing a $-2J\,\mathbf{S}_1 \cdot \mathbf{S}_2$ Hamiltonian) [8] plus a Curie susceptibility contribution ($\chi_M T = 1.20\ \mathrm{cm^3\ mol^{-1}\ K}$) for the $S = 1$ $[Ni(H_2O)_6]^{2+}$ centre. The best fit parameters were $g = 2.06(1)$, $J = 13.8(1)\ \mathrm{cm^{-1}}$ and $\theta' = -7.3(1)$ K. J is the coupling parameter between the terminal Cu(1) atoms and the central Cu(2), across the Cu(1)–Cl(1)–Cu(2) bridges. Importantly, the θ' term that is incorporated as $(T - \theta')$ in the trimer susceptibility equation, represents a trimer–trimer interaction and allows the simulation of the maximum and the low temperature decrease in $\chi_M T$ (Fig. 4). The inclusion of θ' has a significant correlative effect upon the value of J needed to reproduce the 300–40 K data as well as the 4–40 K region. This can be seen in Fig. 6, where θ' is not included in the susceptibility equation and the best fit J is now $6.0(1)\ \mathrm{cm^{-1}}$. The rapidly increasing calculated $\chi_M T$ plot at low temperatures would level to a $S = 3/2(Cu_3) + 1(Ni(aq))$ value of $\sim 3.1\ \mathrm{cm^3\ mol^{-1}\ K}$. Interestingly, it is also possible to get a good fit of the data, over the whole 300–4 K range, by use of a positive J(Cu(1)–Cu(2)) $= 16.6(1)\ \mathrm{cm^{-1}}$, and a negative J(Cu(1)–Cu(1′)) $= -12.0(1)\ \mathrm{cm^{-1}}$, but there is no structural or exchange-pathway reason for such a (Cu(1)–Cu(1′)) interaction.

In making comparisons with related trimeric $Cu_3Cl_n^{x-}$ species, we note that Willett et al. [5] have reported ferromagnetic coupling in $[Cu_3Cl_{12}]^{6-}$, and related 'semi-coordinate' Cu···Cl–Cu bridged compounds in which the central, square-planar disposed $CuCl_4^{2-}$ moiety is weakly bridged in the axial positions (Cu···Cl = ~2.9 Å; Cu···Cl–Cu angle = ~117°) to the distorted tetrahedral $CuCl_4^{2-}$ terminal groups; J values of 7–20 $\mathrm{cm^{-1}}$ being noted in such cases. Weak, antiferromagnetic trimer–trimer coupling was again noted, but the magnetisation isotherm at 2 K showed $S = 3/2$ saturation occurring in fields near 5 T, different, therefore, to the present case. In contrast, the present compound displays symmetrical/bent Cl bridging via the in-plane Cl of the central planar $CuCl_2(H_2O)_2$ group bonding directly to the distorted tetrahedral $CuCl_3^-$ terminal groups (with d(Cu–Cl) ~ 2.33 Å; Cu(1)–Cl(1)–Cu(2) angle = 99.65(4)°). As indicated in the structural discussion, semi-coordinate Cu(2)···Cl(2) separations of ~2.8 Å do occur in both axial positions around the central Cu(2), thus giving potential magnetic exchange pathways using a $\{Cu(2)(d_{x^2-y^2})$–Cl(1)–Cu(1)$(d_{xy})\}$ orbital overlap combination as well as the weaker $\{Cu(2)(d_{z^2})\cdots Cl(2)$–Cu$(d_{xy})\}$ combination.

$[Cu_3Cl_8]^{2-}$ trimeric units are also known in pyridinium salts such as (1,1,4-trimethylpiperazinium)$[Cu_3Cl_8]$ [6] but these have structures involving stacking of the trimer units, via semi-coordinate ~2.8 Å long Cu···Cl links, in to ladder type motifs. Planar $CuCl_4^{2-}$ groups in such trimers are joined by di-μ-chloro bridging (Cu–Cl–Cu angle ~94°) and are coplanar, yielding approximate D_{2h} symmetry within the linear trimer. The present compound possesses much more isolated trimeric Cu(II) units by virtue of the H-bonded $\{$crown ether $Ni(H_2O)_6^{2+}\}$ millieu surrounding the trimers. The magnetism of Fig. 4 is quite different to the antiferromagnetic behaviour noted for these stacked $[Cu_3Cl_8]^{2-}$ species for which was found $J = -23\ \mathrm{cm^{-1}}$ and a $S = 1/2$ ground state within the trimer.

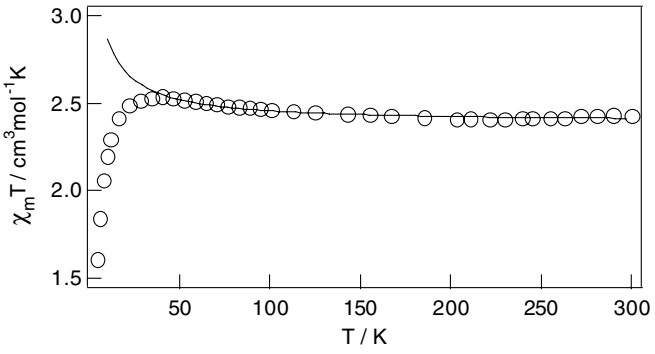


Fig. 6. Plot of $\chi_M T$ (per $NiCu_3$) vs. temperature, in a field of 1 T, for $[Ni(H_2O)_6][Cu_3Cl_8(H_2O)_2]\cdot(15\text{-crown-}5)_2\cdot 2H_2O$. The solid line is that calculated using a linear $S = 1/2$ trimer model plus a Curie contribution from Ni(II) of 1.20 $\mathrm{cm^3\ mol^{-1}\ K}$; with $g = 2.06$ and $J = 6.0\ \mathrm{cm^{-1}}$. It does not include the θ' parameter.

3. Conclusion

$[Ni(H_2O)_6][Cu_3Cl_8(H_2O)_2]\cdot(15\text{-crown-}5)_2\cdot 2H_2O$ can be conveniently prepared by the reaction of $NiCl_2\cdot 6H_2O$, $CuCl_2\cdot 2H_2O$ and 15-crown-5 in water. The X-ray crystal structure reveals an ionic complex involved in a hydrogen-bonded two dimensional network with the cations and trinuclear anions sandwiched between the crown macrocycles. The magnetic susceptibility and magnetisation data result from a combination of the spin-coupled $[Cu_3Cl_8(H_2O)_2]^{2-}$ moiety and the magnetically isolated $S = 1$ Ni(II) hexaaqua cation. While different in detail to a recently reported Cu(II) trimer, [5] $[Cu_3Cl_{12}]^{6-}$, as far as the structure and bridging is concerned, the magnetism of the two systems are not too dissimilar, both displaying ferromagnetic coupling. The present compound shows a stronger antiferromagnetic trimer–trimer interaction, presumably modulated by the intricate H-bonding pathways to the $[Ni(H_2O)_6]^{2+}$ cations.

4. Experimental

Nickel chloride hexahydrate, copper chloride dihydrate and 15-crown-5 were purchased from Aldrich and used without further purification. Deionised water was used as solvent. The infrared spectrum was recorded as a Nujol mull using sodium chloride plates on a Nicolet Nexus FTIR spectrophotometer. Microanalysis (C, H) was undertaken at the University of Otago, P.O. Box 56, Dunedin, New Zealand. Magnetic susceptibility was measured on a powdered sample contained in a calibrated gelatine capsule using a Quantum Design MPMS 5 SQUID magnetometer operating in a field of 1 T. The instrument was calibrated

against a standard Pd sample supplied by the company and against a chemical calibrant $CuSO_4 \cdot 5H_2O$.

4.1. Synthesis of $[Ni(H_2O)_6][Cu_3Cl_8(H_2O)_2] \cdot (15\text{-crown-}5)_2 \cdot 2H_2O$

Samples of $NiCl_2 \cdot 6H_2O$ (0.125 g, 0.53 mmol), $CuCl_2 \cdot 2H_2O$ (0.09 g, 0.53 mmol) and 15-crown-5 (0.33 g, 1.5 mmol) were dissolved in H_2O (5 cm^3) forming a brown solution which was allowed to evaporate at room temperature. Large brown crystals of the title compound were isolated amongst green crystals of $[\{Ni(H_2O)_4\}_2(\mu\text{-}Cl)_2]Cl_2 \cdot$ 15-crown-5. The brown crystals were collected manually for analysis. FTIR (Nujol)/cm^{-1}: 3364s (br), 1711m, 1654m, 1295m, 1256m, 1092vs, 943s, 839m. *Anal.* Calc. for $C_{20}H_{60}Cl_8Cu_3NiO_{20}$: C, 20.82; H, 5.24. Found: C, 21.22; H, 5.10%.

5. Crystal structure determination

A crystal of $[Ni(H_2O)_6][Cu_3Cl_8(H_2O)_2] \cdot (15\text{-crown-}5)_2 \cdot 2H_2O$ was mounted on a glass fibre using epoxy resin, and a hemisphere of data were collected at room temperature on a Bruker SMART CCD diffractometer using the omega scan mode with total reflections and unique data listed below. Data were collected to a 2θ value of 23.3°, and at this value the structure solution and refinement were very satisfactory. Data were corrected for absorption using the program SADABS [9]. The position of the heavy atoms were found using the Patterson method and refined on F^2 using SHELXL 97-2 [10] with X-SEED [11] as a graphics interface. All non-hydrogen atoms were located and were refined with anisotropic thermal parameters. All hydrogen atoms on water molecules were located and refined with isotropic thermal parameters while those on the crown ether were placed in calculated positions (riding model) and were not refined. Selected bond distances and angles appear in Table 1 and hydrogen bonding parameters are compiled in Table 2.

Table 2
Hydrogen bond distances (Å), and angles (°), for $[Ni(H_2O)_6][Cu_3Cl_8(H_2O)_2] \cdot (15\text{-crown-}5)_2 \cdot 2H_2O$

D–H···A	*d*(D–H)	*d*(H···A)	*d*(D···A)	∠(DHA)
O(1S)–H(1SA)···O(5S)#2	0.73(6)	1.98(6)	2.670(8)	159(6)
O(2S)–H(2SA)···O(2A)#4	0.67(6)	2.20(6)	2.857(6)	168(6)
O(2S)–H(2SB)···O(4A)#4	0.78(9)	2.08(9)	2.791(5)	153(9)
O(3S)–H(3SA)···Cl(3)#2	0.64(7)	2.62(7)	3.262(5)	170(7)
O(3S)–H(3SB)···O(5A)#4	0.85(8)	1.90(9)	2.701(6)	158(8)
O(4S)–H(4SA)···O(1A)#5	0.74(9)	1.99(9)	2.719(5)	169(10)
O(4S)–H(4SB)···O(3A)#5	1.04(6)	1.69(6)	2.702(5)	163(5)
O(5S)–H(5SA)···Cl(4)#4	0.66(7)	2.90(8)	3.354(6)	129(7)
O(5S)–H(5SA)···Cl(2)#4	0.66(7)	2.90(7)	3.499(7)	154(8)
O(5S)–H(5SB)···Cl(3)#1	1.03(11)	2.13(10)	3.131(6)	163(8)

Symmetry transformations used to generate equivalent atoms: #1 $-x+1$, $-y+1$, $-z+1$; #2 x, y, z; #3 $-x$, $-y$, $-z+2$; #4 $-x$, $-y+1$, $-z+1$; #5 $-x$, $-y+1$, $-z+2$.

5.1. Crystal data for $[Ni(H_2O)_6][Cu_3Cl_8(H_2O)_2] \cdot (15\text{-crown-}5)_2 \cdot 2H_2O$

$C_{20}H_{60}Cl_8Cu_3NiO_{20}$, $M = 1153.61$, $0.35 \times 0.30 \times 0.25$ mm, triclinic, space group $P\bar{1}$ (No. 2), $a = 8.4480(11)$ Å, $b = 11.1378(14)$ Å, $c = 12.3026(16)$ Å, $\alpha = 95.990(2)°$, $\beta = 97.761(2)°$, $\gamma = 99.505(2)°$, $V = 1121.7(2)$ $Å^3$, $Z = 1$, $D_c = 1.708$ g/cm^3, $F_{000} = 591$, Mo Kα radiation, $\lambda = 0.71073$ Å, 5191 reflections collected, 3199 unique ($R_{int} = 0.0432$). Final Goodness-of-fit = 1.065, $R_1 = 0.0554$, $wR_2 = 0.1489$, R indices based on 2823 reflections with $I > 2\sigma(I)$ (refinement on F^2), 280 parameters, 0 restraints. Lp and absorption corrections applied, $\mu = 2.358$ mm^{-1}.

Acknowledgements

We are grateful to the Australian Research Council for continued support.

Appendix A. Supplementary material

Crystallographic data (excluding structure factors) for the structure reported in this paper have been deposited with the Cambridge Crystallographic Data Centre as supplementary publication number CCDC 602886. Copies of the data can be obtained free of charge on application to CCDC, 12 Union Road, Cambridge CB2 1EZ, UK (fax: +44 1223 366 033, e-mail: deposit@ccdc.ac.uk or on the web www: http://www.ccdc.cam.ac.uk). Supplementary data associated with this article can be found, in the online version, at doi:10.1016/j.poly.2006.05.004.

References

[1] (a) For recent examples see O. Kahn, Adv. Inorg. Chem. 43 (1995) 179;
(b) J.S. Miller, M. Drillon, Magnetism: Molecules to Materials, Wiley-VCH, Germany, 2005.
[2] (a) P.C. Junk, J.W. Steed, J. Chem. Soc., Dalton Trans. (1999) 407;
(b) J.W. Steed, P.C. Junk, J. Chem. Soc., Dalton Trans. (1999) 2141;
(c) C. Jones, P.C. Junk, M.K. Smith, R.C. Thomas, Z. Anorg. Allg. Chem. 626 (2000) 2491;
(d) P.C. Junk, M.K. Smith, J.W. Steed, Polyhedron 20 (2001) 2979;
(e) P.C. Junk, L.M. Louis, M.K. Smith, Z. Anorg. Allg. Chem. 628 (2002) 1196;
(f) P.C. Junk, M.K. Smith, Inorg. Chem. Commun. 5 (2002) 1082.
[3] (a) P.C. Junk, B.J. McCool, B. Moubaraki, K.S. Murray, L. Spiccia, Angew. Chem., Int. Ed. Engl. 38 (1999) 2224;
(b) P.C. Junk, B.J. McCool, B. Moubaraki, K.S. Murray, L. Spiccia, J.D. Cashion, J.W. Steed, J. Chem. Soc., Dalton Trans. (2002) 1024.
[4] (a) P.C. Junk, S.M. Lynch, B.J. McCool, Supramol. Chem. 9 (1998) 151;
(b) J.W. Steed, B.J. McCool, P.C. Junk, J. Chem. Soc., Dalton Trans. (1998) 3417;
(c) J.W. Steed, P.C. Junk, M.K. Smith, Chem. Euro. J. 7 (2001) 1240.
[5] M. Wei, R.D. Willett, Inorg. Chem. 43 (2004) 4534.
[6] M.R. Bond, R.D. Willett, R.S. Rubins, P. Zhou, C.E. Zaspel, S.L. Hutton, J.E. Drumheller, Phys. Rev. B 42 (1990) 10280.
[7] T.B. Rubtsova, O.K. Kineva, B.M. Bulychev, N.P. Streltsova, V.K. Belsky, B.P. Tarasov, Polyhedron 11 (1992) 1929.

[8] L. Spiccia, B. Graham, M.T.W. Hearn, G. Lazarev, B. Moubaraki, K.S. Murray, E.R.T. Tiekink, Dalton Trans. 4089 (1997), and references therein.
[9] R.H. Blessing, Acta Cryst. A51 (1995) 33.
[10] G.M. Sheldrick, SHELXL-97, University of Gottingen, 1997.
[11] L.J. Barbour, J. Supramol. Chem. 1 (2001) 189.

Available online at www.sciencedirect.com
ScienceDirect
Polyhedron 26 (2007) 244–249
POLYHEDRON
www.elsevier.com/locate/poly

High temperature synthesis of some strontium and barium 2,6-dibenzylphenolates

Marcus L. Cole [a,b], Glen B. Deacon [a], Craig M. Forsyth [a], Peter C. Junk [a,c,*], Kathryn M. Proctor [c], Janet L. Scott [c], Christopher R. Strauss [c]

[a] School of Chemistry, Monash University, Clayton, Vic. 3800, Australia
[b] School of Chemistry and Physics, University of Adelaide, Adelaide, SA 5005, Australia
[c] Special Research Centre for Green Chemistry, Monash University, Vic. 3800, Australia

Received 27 March 2006; accepted 8 May 2006
Available online 16 May 2006

Abstract

Direct treatment of HOdbp (= 2,6-dibenzylphenol) with strontium or barium metal in the absence of solvent at high temperature provides the corresponding phenolates $Sr(Odbp)_2$ and $Ba(Odbp)_2$. Recrystallisation of $Ba(Odbp)_2$ from THF gave a good yield of the crystalline dimer $[Ba(Odbp)_2(THF)]_2 \cdot 2THF$. Attempted recrystallisation of $Sr(Odbp)_2$ from THF mostly yielded microcrystalline material characterized as $[Sr(Odbp)_2]_n$ but on one occasion gave a small crop of crystalline $[Sr_9(Odbp)_8(O_2SiMe_2)_4(OH)_2(THF)_6(OH_2)_2] \cdot 6THF$ derived from the adventitious reaction of $Sr(Odbp)_2$ with dimethylsilicone grease ($\{OSiMe_2\}_\infty$). In the solid-state $[Ba(Odbp)_2(THF)]_2 \cdot 2THF$ displays significant intramolecular Ba···π-arene interactions with the pendant benzyl substituents. $[Sr_9(Odbp)_8(O_2SiMe_2)_4(OH)_2(THF)_6(OH_2)_2] \cdot 6THF$ features a square prismatic $[Sr(O_2SiMe_2)_4]^{6-}$ core capped by two *inverse crown*-like square $[Sr_4(Odbp)_4(OH)(L)_4]^{3+}$ units, where L = OH_2 or THF, that are staggered with respect to the cuboidal core.
© 2006 Elsevier Ltd. All rights reserved.

Keywords: Strontium; Barium; Phenolates; X-ray crystal structures

1. Introduction

There has been significant recent interest in alkaline earth phenolate chemistry, focussing particularly on strontium and barium, due to their potential use as precursors to form binary and ternary oxides via sol–gel or MOCVD processes [1]. By a judicious choice of ligands, complexes may be isolated that have significant but weak M···π-arene interactions. These interactions can have implications for reactivity due to their potential displacement by stronger binding, small molecules. Phenolate ligands with aryl groups in the 2,6-positions have the inherent functionality to induce such interactions and this has been the subject of many of our previous investigations. Primarily we have been concerned with the 2,6-diphenylphenolate (Odpp) ligand and have uncovered some interesting interactions in the solid state with both rare earth [2,3] and alkaline earth metals [4].

The phenolate chemistry of strontium and barium is dominated by the formation of aggregates or insoluble polymeric material, particularly when relatively non-bulky phenolate ligands are used. In most cases, isolable material is only obtained when polar donor solvents such as THF [5], HMPA (= hexamethylphosphoramide) [6,7] or TMEDA (=*N*,*N*′-tetramethylethylenediamine) [7] are used to de-aggregate the clustered compounds. When bulkier phenols such as 2,6-di-*tert*-butyl-4-X-phenol (X = methyl, *tert*-butyl) are used, monomeric and dimeric complexes can be isolated, but again, solvated species dominate [8]. We have recently shown that homoleptic calcium, strontium and barium 2,6-diphenylphenolate (Odpp) complexes can be synthesised by the high temperature, solvent-free

* Corresponding author. Tel.: +61 3 9905 4570; fax: +61 3 9905 4597.
E-mail address: peter.junk@sci.monash.edu.au (P.C. Junk).

0277-5387/$ - see front matter © 2006 Elsevier Ltd. All rights reserved.
doi:10.1016/j.poly.2006.05.003

reactions of the metals with HOdpp. In the absence of coordinating solvent these compounds display M···π-interactions with the adjacent phenyl rings [4]. The Odpp ligand has shown great versatility in displaying π-arene interactions in homoleptic complexes, and more recently we have been pursuing the chemistry of a closely related ligand system; 2,6-dibenzylphenolate (Odbp) where the 2,6-positions of the phenol are occupied by functional groups that not only possess the capacity for π-arene coordination, but also the rotational flexibility to occupy spatial voids about the metal centre [9]. We now turn our attention to Odbp chemistry involving the heavier alkaline earth metals strontium and barium, and describe the direct high temperature treatment of these elements with the phenol (HOdbp) in the absence of solvent.

2. Experimental

2.1. General procedures

2,6-Dibenzylphenol was prepared via literature procedures [10]. The alkaline earth metals used were purchased from Aldrich Chemical Co. as metal ingots which were manually filed into metal powder in an inert atmosphere for use in reactions. Hexane, toluene and THF were dried over sodium and distilled over sodium or sodium benzophenone ketyl prior to use. All manipulations were performed using conventional Schlenk or glovebox procedures under an atmosphere of high purity dinitrogen in flame-dried glassware. IR spectra were recorded as Nujol mulls on sodium chloride plates on a Perkin–Elmer 1600 FTIR spectrophotometer. ^{1}H NMR spectra were recorded at 300.13 MHz and ^{13}C{^{1}H} NMR spectra were recorded at 75.46 MHz using a Bruker DPX 300 spectrometer with chemical shifts referenced to the residual ^{1}H or ^{13}C resonances of the *deutero*-benzene solvent (δ 7.16 and 128.39 ppm, respectively). Melting points were determined in sealed glass capillaries under dinitrogen and are uncalibrated. Satisfactory microanalyses for compounds **1** and **3** could not be obtained due to consistent solvent loss for **3** and problems associated with incomplete combustion of the samples [11].

2.2. Synthesis of $Sr(Odbp)_2$ (**1**)

HOdbp (0.20 g, 0.729 mmol), strontium metal (0.063 g, 0.364 mmol) and Hg metal (two drops) were sealed in an evacuated Carius tube. The reaction vessel was heated at 180 °C for 4 days yielding a pale yellow solid. The solid was extracted into THF (30 ml) and concentrated (2 ml). The solution changed to pale green upon standing at room temperature and very small colourless crystals of **1** deposited (0.18 g, 40%) m.p.: 159–162 °C. ^{1}H NMR (C_6D_6, 298 K): δ 7.16–6.92 (m, 20H, *o*,*m*,*p*-H(Ph)), 6.89 (m, 4H, *m*-H central ring), 6.75 (m, 2H, *p*-H central ring), 3.76 (s, 8H, CH_2–Ph); ^{13}C{^{1}H} NMR (C_6D_6, 298 K): δ 147.9, 139.0, 128.3, 127.8, 127.6, 126.5, 125.3, 119.7 (s, Ar*C*), 35.5 (s, *C*H_2–Ph); IR (Nujol) ν/cm^{-1}: 1601m, 1452m, 1389s, 1326m, 1270s, 1229s, 1073m, 1030s, 977s, 911s, 856w, 822w, 793w, 756s, 699s.

2.3. Isolation of $[Sr_9(Odbp)_8(O_2SiMe_2)_4(OH)_2(THF)_6(OH_2)_2]\cdot 6THF$ (**2**)

In one reaction involving the synthesis of compound **1** (0.23 g, 0.839 mmol HOdbp, 0.037 g, 0.419 mmol strontium metal), several small diamond shaped crystals grew during recrystallisation from THF over several weeks. Other than the crystal structure there was insufficient material for further analysis.

2.4. Synthesis of $[Ba(Odbp)_2(THF)]_2\cdot 2THF$ (**3**)

HOdbp (0.20 g, 0.729 mmol) was heated to 180 °C for 4 days with barium metal (0.05 g, 0.36 mmol) and Hg metal (two drops) in an evacuated and sealed Carius tube resulting in the formation of a pale yellow solid. This was extracted into THF (30 ml) and concentrated (2 ml). Colourless rectangular-shaped crystals formed at room temperature (0.26 g, 43%) m.p.: 238–242 °C. ^{1}H NMR (C_6D_6, 298 K): δ 7.16–6.86 (m, 48H, *Ph* + *m*-H central ring), 6.72 (m, 4H, *p*-H central ring) (s, 16H, CH_2–Ph), 3.59 (m, 8H, OCH_2, THF), 1.44 (m, 8H, CH_2, THF); ^{13}C{^{1}H} NMR (C_6D_6, 298 K): δ 155.6, 151.8, 129.7, 127.9, 126.3, 120.2, 119.2, 109.4 (s, Ar*C*), 71.0, 35.7 (s, THF), 29.7 (s, *C*H_2–Ph); IR (nujol) ν/cm^{-1}: 1600m, 1451m, 1389s, 1311m, 1264s, 1230s, 1073m, 1030s, 950w, 922w, 895w, 848w, 830w, 794w, 755s, 734m, 698s.

2.5. X-ray crystallography

Crystalline samples of compounds **2** and **3** were mounted on glass fibres in highly viscous silicone oil at 123(2) K. A summary of crystallographic data can be found below. Hydrogen atoms were refined in calculated positions (Riding model) for both compounds. Data were collected on an Enraf-Nonius Kappa CCD diffractometer using graphite monochromated Mo Kα X-ray radiation ($\lambda = 0.71073$ Å). Data were corrected for absorption by the DENZO-SMN package [12]. Lorentz polarisation and absorption corrections were applied. Structural solution and refinements were carried out using the SHELX suite of programs [13] with the graphical interface X-Seed [14].

2.6. X-ray crystal data for $[Sr_9(Odbp)_8(O_2SiMe_2)_4(OH)_2(THF)_6(OH_2)_2]\cdot 6THF$ (**2**)

$C_{216}H_{256}O_{32}Si_4Sr_9$, $M = 4265.14$, diamond-shaped pale yellow, $0.20 \times 0.20 \times 0.20$ mm, monoclinic, space group $P2_1/n$ (no. 14), $a = 23.393(5)$ Å, $b = 17.550(4)$ Å, $c = 24.936(5)$ Å, $\beta = 99.59(3)°$, $V = 10094(4)$ Å^3, $Z = 2$ (nonanuclear units), $D_c = 1.403$ g/cm^3, $F_{000} = 4412$, $2\theta_{max} = 50°$, 65469 reflections collected, 17708 unique ($R_{int} = 0.1916$). Final GooF = 1.012, $R_1 = 0.0984$, $wR_2 = 0.1932$, R indices based on 8005 reflections with $I > 2\sigma(I)$ (refinement on F^2),

Table 1
Selected bond lengths (Å) for $[Sr_9(Odbp)_8(O_2SiMe_2)_4(OH)_2(THF)_6(OH_2)_2]\cdot 6THF$ (**2**)

Atoms	Lengths	Atoms	Lengths
Sr1–O1	2.657(7)	Sr4–O1	2.489(6)
Sr1–O2	2.645(6)	Sr4–O4	2.532(7)
Sr1–O3	2.654(7)	Sr4–O5#	2.547(7)
Sr1–O4	2.660(6)	Sr4–O8	2.559(8)
Sr2–O2	2.516(6)	Sr4–O12	2.567(12)
Sr2–O4#	2.504(7)	Sr4–O13	2.519(7)
Sr2–O5	2.512(7)	Sr5–O1	2.503(7)
Sr2–O6	2.526(7)	Sr5–O3#	2.474(7)
Sr2–O9	2.592(9)	Sr5–O7#	2.497(8)
Sr2–O13#	2.557(6)	Sr5–O8	2.531(8)
Sr3–O2	2.487(7)	Sr5–O11	2.671(7)
Sr3–O3	2.517(6)	Sr5–O13	2.582(6)
Sr3–O6	2.509(6)	Si1–O1	1.611(7)
Sr3–O7	2.521(8)	Si1–O2	1.612(7)
Sr3–O10	2.551(10)	Si2–O3	1.614(7)
Sr3–O13#	2.606(7)	Si2–O4	1.615(8)

Symmetry operation used to generate equivalent (#) atoms: $-x, -y, -z$.

1135 parameters, 153 restraints. Lp and absorption corrections applied, $\mu = 2.451$ mm^{-1} (see Table 1).

Variata. The dataset was poor but the connectivity is irrefutable. The phenyl group of one benzyl group of one phenolate was disordered over two sites of partial occupancy that are coincident at the *ipso* carbon (C722). These were refined with partial occupancies of 55 and 45%. To obtain satisfactory thermal parameters an ISOR refinement (0.01) was necessary for carbon atoms 82, 86, 121, 122, 123, 124, 726, 727, 762–767, 861, and THF oxygen O12. The hydrogen atoms on O10 and O13 were not located from difference maps despite repeated attempts to do so.

2.7. X-ray crystal data for $[Ba(Odbp)_2(THF)]_2\cdot 2THF$ (**3**)

$C_{48}H_{50}BaO_4$, $M = 828.22$, colourless rectangular prism, $0.20 \times 0.10 \times 0.10$ mm, triclinic, space group $P\bar{1}$ (no. 2), $a = 10.179(2)$ Å, $b = 12.514(3)$ Å, $c = 16.174(3)$ Å, $\alpha = 82.26(3)°$, $\beta = 73.54(3)°$, $\gamma = 85.21(3)°$, $V = 1955.6(7)$ Å^3, $Z = 2$, $D_c = 1.407$ g/cm^3, $F_{000} = 852$, $T = 2\theta_{max} = 56.4°$, 22 763 reflections collected, 9427 unique ($R_{int} = 0.0675$). Final GooF = 1.024, $R_1 = 0.0520$, $wR_2 = 0.0986$, R indices based on 7022 reflections with $I > 2\sigma(I)$ (refinement on F^2), 488 parameters, 0 restraints. Lp and absorption corrections applied, $\mu = 1.060$ mm^{-1}.

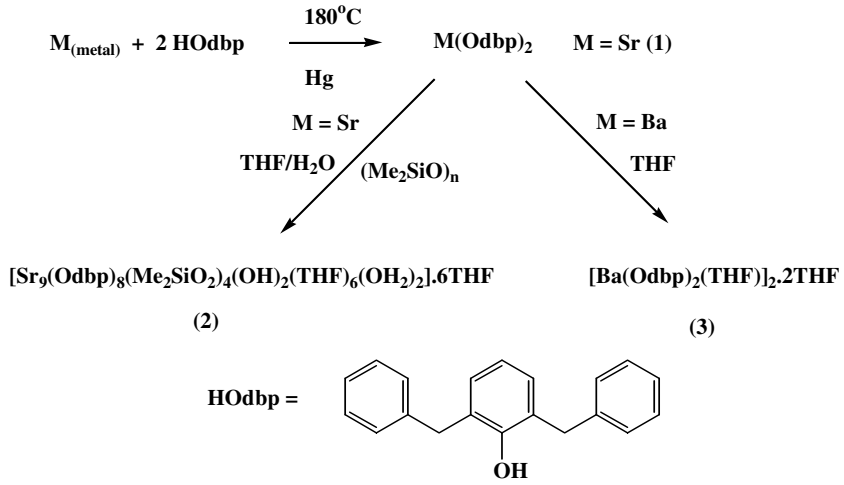
Variata. There was disorder in one THF carbon (C42) and this was modelled over two sites with 75:25% occupancy.

3. Results and discussion

The high temperature (180 °C) treatment of strontium or barium metal with HOdbp (ratio 1:2) in the presence of two drops of mercury for four days in a sealed Carius tube results in the complete consumption of metal to yield pale yellow solids (Scheme 1). Several drops of mercury metal were added to the reaction mixture to form a reactive group 2 amalgam. After extraction of the residues from the Carius tubes using THF (both compounds had negligible solubility in the relatively non-polar solvents hexane or toluene) $Sr(Odbp)_2$ (**1**) and $[Ba(Odbp)_2(THF)]_2\cdot 2THF$ (**3**) (latter composition based on X-ray crystallography) were isolated in moderate yields. Both compounds were characterised by IR, ^{1}H and ^{13}C{^{1}H} NMR spectroscopy. ^{1}H and ^{13}C{^{1}H} NMR spectra were performed in *deuterated* benzene in which the compounds had only slight solubility. The ^{1}H NMR spectra of both compounds showed no resonances for the phenolic protons at approximately 4.6 ppm and the IR spectra also had no indication of O–H stretching at 3560 cm^{-1} [9b] demonstrating complete deprotonation of 2,6-dibenzylphenol in both reactions. The ^{1}H NMR spectrum of compound **1** did not display any resonances for THF, indicating that any THF of solvation was easily lost upon isolation. The integration of the ^{1}H NMR spectrum of compound **3** shows a THF to phenolate ratio of 1:2, indicating that lattice THF was lost during isolation from the mother liquor. Although observation of a single set of ^{1}H resonances is inconsistent with the dimeric structure of **3** (below), which has both terminal and bridging Odbp ligands, and the likely structure of **1**, analogous behaviour has been observed for $[M(Odpp)_2]_2$ (M = Ca, Sr, Ba [4], Yb [2]). Thus, either the bridging and terminal resonances are not resolved, there is rapid ligand exchange, or C_6D_6 cleaves the bridges to give symmetrical monomeric structures. π-Interactions from benzene rings to the heavier alkaline earth metals are receiving increasing attention [15], e.g. $[Ba(\eta^6\text{-PhMe})_2\{Zn(SiMe_3)(CH_2SiMe_3)_2\}_2]$ [15c], hence bridge cleavage at high dilution in C_6D_6 is plausible. We have also found that monomeric Ca and Sr formamidinates with unsymmetrical solid state environments also show a single set of ^{1}H (and ^{13}C) resonances in solution [16].

In one reaction involving the synthesis of compound **1** a few small crystals of $[Sr_9(Odbp)_8(O_2SiMe_2)_4(OH)_2(THF)_6(OH_2)_2]\cdot 6THF$ (**2**) were isolated after leaving the product in THF over several weeks (see Section 2.3). The presence of O_2SiMe_2 groups in the structure is indicative of reaction between $Sr(Odbp)_2$ and the high vacuum dimethylsilicone grease used to seal ground glass joints. This grease is generally regarded as chemically inert, though there are a number of examples in the literature where $OSiMe_2$ and $O(SiMe_2O)_n$ groups have been incorporated into structures [17]. The presence of water and hydroxide in the structure highlights the water sensitivity of these complexes and indicates that **2** was isolated following partial hydrolysis.

The strontium phenolate–siloxane cluster/cage complex, $[Sr_9(Odbp)_8(O_2SiMe_2)_4(OH)_2(THF)_6(OH_2)_2]\cdot 6THF$ (**2**) (Fig. 1), Table 1 for selected bond lengths and angles crystallised in the monoclinic space group $P2_1/n$. Half of the molecule is symmetry generated to give a nonanuclear



Scheme 1.

species (Fig. 1a) comprised of a central $[Sr(O_2SiMe_2)_4]^{6-}$ (see Fig. 1b) core surrounded by eight $Sr(Odbp)^+$ units and two hydroxide ligands (O(13), O(13′)) bound in central clefts of two square faces of the cage. THF and water molecules complete the coordination spheres of the strontium atoms (Fig. 1a). The core (Fig. 1b) consists of an eight coordinate close to ideal cuboid strontium ion, Sr1, which is chelated by four O_2SiMe_2 groups. The oxygen atoms of

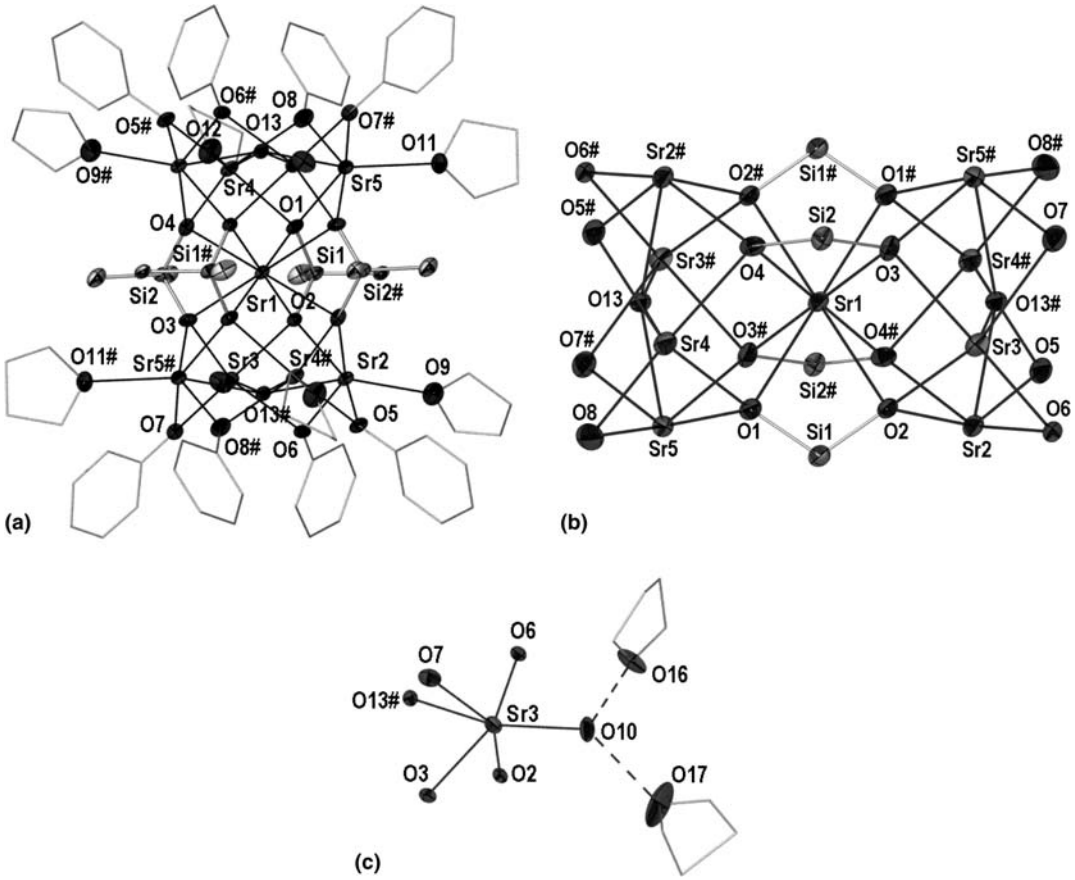


Fig. 1. Molecular structure of the centrosymmetric nonanuclear $[Sr_9(Odbp)_8(O_2SiMe_2)_4(OH)_2(THF)_6(OH_2)_2] \cdot 6THF$ (**2**). Thermal ellipsoids are shown at the 40% level. (a) Entire molecule. '#' Atoms generated using symmetry transformation $-x, -y, -z$. All hydrocarbons (except methyl groups of O_2SiMe_2) groups represented as wire frames. Benzyl groups of phenolates, lattice THF molecules and hydrogen atoms omitted for clarity. (b) Central cage (side view). '#' Atoms generated using symmetry transformation $-x, -y, -z$. All neutral donors, O_2SiMe_2 methyl groups and phenolate hydrocarbon groups omitted. (c) Illustration depicting proposed H-bonding interaction between O10 (coordinated OH_2 on Sr3) and two lattice THF molecules. Distances (Å) and angles (°): O10···O16 2.713(17), O10···O17 2.754(27); O16···O10–Sr3 125.5(6), O17···O10–Sr3 138.1(9), O16···O10···O17 99.6(9).

the O_2SiMe_2 groups μ_3-bridge to the remaining eight strontium ions on the exterior of the central SrO_8. These strontium ions are in two square units (each with two symmetry generated and two non-symmetry generated Sr atoms) that sandwich and are staggered with respect to the cuboidal $[Sr(O_2SiMe_2)_4]^{6-}$ core. Four phenolate ligands bridge the four edges of each square tetrastrontium unit. Within these, Sr2 is bound to a THF molecule and a phenolate bridges to Sr3. Sr3 is bound to two oxygen atoms of the O_2SiMe_2 groups, as well as to a phenolate that bridges to Sr5, which is bound to a terminal THF molecule, two oxygen atoms (O_2SiMe_2) and a bridging phenolate (to Sr4). Sr4 is bound to two bridging phenolates (bridging to Sr2 and Sr5) and three oxygen atoms. Two belong to O_2SiMe_2 groups and one to a lone hydroxide oxygen atom O13. Each of the four exterior Sr atoms is six coordinate and has distorted octahedral geometry. O10 is considered to be a water molecule bound to Sr3 and is hydrogen bonded to two THF molecules using the two water protons (Fig. 1c). This implies that the μ_4-O O13 is an OH^- ion for correct charge balance (see Table 1).

Compound **3**, $[Ba(Odbp)_2(THF)]_2 \cdot 2THF$ (Fig. 2, Table 2a), crystallises in the triclinic space group $P\bar{1}$ with one half of the centrosymmetric dimer as the asymmetric unit. The dimer is comprised of one terminal phenolate, one terminal THF molecule and two bridging phenolates generating an oxygen coordination number of four for the barium atom. Supplementing the O–Ba bonds are Ba···π-arene interactions from one of the pendant phenyl rings on the bridging phenolate, and another from a phenyl ring on the terminal phenolate, increasing the coordination number formally to seven. The Ba–O (bridging phenolate) bond distances are 2.649(3) and 2.655(3) Å, respectively. The Ba–O (terminal) bond distance is 2.475(3) Å, which is shorter than the bridging Ba–O bond distances as expected. The structural motif of compound **3** is significantly different from that of $[Ba(Odpp)_2]_2$ which contains three bridging phenolates between the two metal centres and one terminal phenolate at one barium, leaving the second barium atom formally 'naked' on one face [4]. The Ba–O (terminal) bond distance for $[Ba(Odpp)_2]_2$ is 2.488(2) Å, whilst the average

Table 2a
Selected bond lengths (Å) and angles (°) for $[Ba(Odbp)_2(THF)]_2 \cdot 2THF$ (**3**)

Atoms	Lengths	Atoms	Angles
Ba1–O2	2.475(3)	O1–Ba1–O2	103.56(9)
Ba1–O1	2.649(3)	O1–Ba1–O2#	95.84(8)
Ba1–O1#	2.655(3)	O1–Ba1–O3	91.81(9)
Ba1–O3	2.796(3)	O1–Ba1–O1#	74.83(9)
Ba1···Ba1#	4.213(1)	O2-Ba1–O3	78.59(9)
		O1–Ba1–O3#	164.05(9)
		Ba1–O1–C1	114.9(2)
		Ba1–O1–C1#	137.7(2)
		Ba1–O2–C21	157.2(2)
		Ba1–O1–Ba1#	105.17(9)

Symmetry transformations used to generate equivalent (#) atoms: $-x+2$, $-y+2$, $-z+1$.

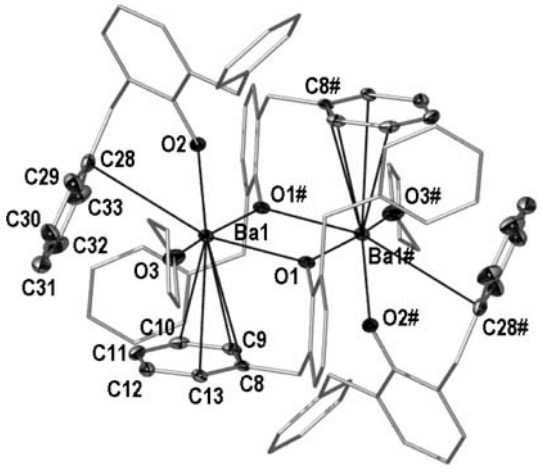


Fig. 2. Molecular structure of the centrosymmetric dimer $[Ba(Odbp)_2(THF)]_2 \cdot 2THF$ (**3**). Hydrogen atoms have been omitted for clarity. All hydrocarbons groups, excepting those involved in Ba···π-arene interactions, represented as wire frames. Thermal ellipsoids are shown at the 40% level. '#' Atoms generated using symmetry transformation: $-x+2$, $-y+2$, $-z+1$.

Ba–O (bridging) bond distance is 2.750(2) Å which is significantly longer than in **3**. The metal oxygen array leaves the metal naked allowing arene interactions to occur between the pendant phenyl rings on the bridging phenolates (η^1 and η^6). The Ba···C average distance is 3.33(4) Å, with the longest distance being 3.434(4) Å. A cut-off distance of distance for Ba···π-arene interactions of 3.48 Å was formulated based on limits set for $[(\eta^6\text{-PhMe})BaSn_3(\mu\text{-PSiBu}^t_3)_4]$ [18]. If these limits are used for compound **3**, then there would be only an η^2 interaction between Ba1 and C8, C9 of the phenyl group on the bridging phenolate. However, closer inspection of the Ba···C distances (Table 2b) indicates that there are further plausible contacts. Thus, if the limit is extended beyond 3.48 Å to ca. 3.52 Å, then the barium atom is bound in an η^4 fashion to one aromatic ring and η^1 to another. Further inspection of the Ba···C distances indicates a demarcation in distances at this point (Table 2b), wherein any further Ba···C contacts would be considerably longer. An interesting feature of compound **3** is that the barium atom involves itself in π-arene interactions preferentially over further THF coordination. This has been previously been observed in alkali metal complexes involving these ligands [9c]. The only other barium phenolate Lewis acid adduct that does not contain other donor

Table 2b
Barium–carbon distances (Å) of π-phenyl–metal interactions in **3**

Atoms	Distance	Atoms	Distance
Ba1–C8	3.394(4)	Ba1–C28	3.501(4)
Ba1–C9	3.382(4)	Ba1–C29[a]	3.638(5)
Ba1–C10	3.508(4)	Ba1–C30[a]	3.981(5)
Ba1–C11[a]	3.641(4)	Ba1–C31[a]	4.183(5)
Ba1–C12[a]	3.646(4)	Ba1–C32[a]	4.045(5)
Ba1–C13	3.524(4)	Ba1–C33[a]	3.708(5)

[a] Not considered as a 'bonding' interaction.

atoms (e.g. I, Br, Cl) is the monomeric complex $[Ba(OC_6H_2Bu^t_2\text{-}2,6\text{-}Me\text{-}4)_2(THF)_3] \cdot THF$ of Hanusa et al. [8b] The three Ba–O(THF) bond distances for $[Ba(OC_6H_2Bu^t_2\text{-}2,6\text{-}Me\text{-}4)_2(THF)_3] \cdot THF$ are 2.72(1), 2.73(1) and 2.75(1) Å and are shorter than the Ba–O(THF) distance found in compound **3** (2.796(3) Å), which has a higher formal coordination number.

4. Conclusions

$M(Odbp)_2$(M = Sr, Ba) complexes were prepared by the solvent-free, high temperature reaction between Sr or Ba metal and HOdbp. Extraction and crystallisation of the compounds from THF resulted in the isolation of $Sr(Odbp)_2$ and $[Ba(Odbp)_2(THF)]_2 \cdot 2THF$. Crystals of the former of suitable quality for X-ray structure determination were not obtained but the absence of THF from the compound was evidenced spectroscopically. A small yield of $[Sr_9(Odbp)_8(O_2SiMe_2)(OH)_2(THF)_6(OH_2)_2] \cdot 6THF$ was obtained from one recrystallisation of $Sr(Odbp)_2$. The X-ray crystal structures of $[Sr_9(Odbp)_8(O_2SiMe_2)_4(OH)_2(THF)_6(OH_2)_2] \cdot 6THF$ and $[Ba(Odbp)_2(THF)]_2 \cdot 2THF$ show interesting features. The former is constructed from a $[Sr(O_2SiMe_2)_4]^{6-}$ core surrounded by eight THF/H_2O coordinated "$Sr(Odbp)^{+}$" units with two hydroxide ligands residing in clefts. $[Ba(Odbp)_2(THF)]_2 \cdot 2THF$ displays significant Ba···π-arene interactions with pendant benzyl substituents on both bridging and terminal phenolates.

5. Supplementary material

Crystallographic data (excluding structure factors) for **2** and **3** have been deposited with the Cambridge Crystallographic Data Centre as supplementary numbers CCDC – 601930 for compound **2** and CCDC – 601929 for compound **3**. Copies of the data can be obtained free of charge on application to CCDC, 12 Union Road, Cambridge, CB2 1EZ, UK (fax: +44 1223 336 033; e-mail: deposit@ccdc.cam.ac.uk).

Acknowledgements

The authors acknowledge the Australian Research Council, the Special Research Centre for Green Chemistry at Monash University for their financial support and postgraduate scholarship (K.M.P.) and the CSIRO for supporting one of us (C.R.S.) on secondment. We also acknowledge significant input from Ms. K. Konstas.

References

[1] D.C. Bradley, R.C. Mehrotra, I.P. Rothwell, A. Singh, Alkoxo and Aryloxo Derivatives of Metals, Academic Press, London, UK, 2001.
[2] G.B. Deacon, C.M. Forsyth, P.C. Junk, B.W. Skelton, A.H. White, Chem. Euro. J. 5 (1999) 1452.
[3] G.B. Deacon, T. Feng, C.M. Forsyth, A. Gitlits, D.C. Hockless, Q. Shen, B.W. Skelton, A.H. White, J. Chem. Soc., Dalton Trans. (2000) 961.
[4] G.B. Deacon, C.M. Forsyth, P.C. Junk, J. Organomet. Chem. 607 (2000) 112.
[5] (a) S.R. Drake, W.E. Streib, M.H. Chisholm, K.G. Caulton, Inorg. Chem. 29 (1990) 2707;
(b) K.G. Caulton, M.H. Chisholm, S.R. Drake, K. Folting, Chem. Commun. (1990) 1349;
(c) P. Miele, J.-D. Foulon, N. Hovnanian, Polyhedron 12 (1993) 209.
[6] K.G. Caulton, M.H. Chisholm, S.R. Drake, K. Folting, J.C. Huffman, Inorg. Chem. 32 (1993) 816.
[7] K.G. Caulton, M.H. Chisholm, S.R. Drake, K. Folting, J.C. Huffman, W.E. Streib, Inorg. Chem. 32 (1993) 1970.
[8] (a) S.R. Drake, D.J. Otway, M.B. Hursthouse, K.M.A. Malik, Polyhedron 11 (1992) 1995;
(b) K.F. Tesh, T.P. Hanusa, J.C. Huffman, C.J. Huffman, Inorg. Chem. 31 (1992) 5572;
(c) T.R. Belderrain, J.P. Espinos, A. Fernandez, A.R. Gonzalez-Elipe, D. Leinen, A. Monge, M. Paneque, C. Ruiz, E. Carmona, J. Chem. Soc., Dalton Trans. (1995) 1529.
[9] (a) M.L. Cole, L.T. Higham, P.C. Junk, K.M. Proctor, J.L. Scott, C.R. Strauss, Inorg. Chim. Acta 358 (2005) 3159;
(b) M.L. Cole, G.B. Deacon, P.C. Junk, K.M. Proctor, J.L. Scott, C.R. Strauss, Eur. J. Inorg. Chem. (2005) 4138;
(c) M.L. Cole, P.C. Junk, K.M. Proctor, J.L. Scott, C.R. Strauss, Dalton Trans. (in press).
[10] E.C. Horning, J. Org. Chem. 10 (1945) 263.
[11] M.J. McCormack, S.C. Sockwell, C.E.H. Davies, T.P. Hanusa, J.C. Huffman, Organometallics 8 (1989) 2044.
[12] Z. Otwinowski, W. Minor, Processing of X-ray diffraction data collected in oscillation mode, in: Methods in Enzymology, in: C.W. Carter, R.M. Sweet (Eds.), Macromolecular Crystallography, Part A, vol. 276, Academic Press, New York, 1997, p. 307.
[13] G.M. Sheldrick, SHELX-97, University of Göttingen, Germany, 1997.
[14] L.J. Barbour, J. Supramol. Chem. 1 (2001) 189.
[15] (a) T.P. Hanusa, Coord. Chem. Rev. 210 (2000) 329;
(b) J.S. Alexander, K. Ruhlandt-Senge, Eur. J. Inorg. Chem. (2002) 2761, and references therein;
(c) M. Westerhausen, C. Gückel, T. Habereder, M. Vogt, M. Warchhold, H. Nöth, Organometallics 20 (2001) 893.
[16] M.L. Cole, G.B. Deacon, C.M. Forsyth, K. Konstas, P.C. Junk, Dalton Trans. (in press).
[17] I. Haiduc, Organometallics 23 (2004) 3.
[18] M. Westerhausen, M. Krofta, N. Wiberg, J. Knizck, H. Noth, A. Pfitzner, Z. Naturforsch. B 53 (1998) 1489.

Available online at www.sciencedirect.com
ScienceDirect
Polyhedron 26 (2007) 250–265
POLYHEDRON
www.elsevier.com/locate/poly

Iron–carbon clusters: Geometric structures and interconversions

Hugh H. Harris [1], Ian G. Dance *

School of Chemistry, University of New South Wales, Sydney, NSW 2052, Australia

Received 30 March 2006; accepted 8 May 2006
Available online 16 May 2006

Abstract

We report density functional theoretical investigations of the experiments described by Pilgrim and Duncan [J.S. Pilgrim, M.A. Duncan, J. Am. Chem. Soc., 115 (1993) 6958] in which $[Fe_xC_y]^+$ clusters are generated by laser vapourisation of Fe atoms in a plasma containing acetylene. Many possible structures for the clusters $[Fe_{12}C_{12}]$, $[Fe_{10}C_{12}]$, $[Fe_8C_{12}]$, $[Fe_6C_{12}]$, $[Fe_4C_{12}]$, $[Fe_3C_{12}]$ and $[Fe_2C_{12}]$ are evaluated, with the following conclusions: $[Fe_{12}C_{12}]$ is a slightly distorted $2 \times 3 \times 4$ nanocrystallite fragment of a face-centered cubic FeC lattice; $[Fe_{10}C_{12}]$ is distorted $[Fe_{12}C_{12}]$ depleted by two three-coordinate Fe atoms; $[Fe_8C_{12}]$, with the prototypical composition for metallocarbohedrenes, has a C_{3v} structure containing only C_2 groups and with a short axial Fe—Fe bond; $[Fe_6C_{12}]$ has the $[Fe_8C_{12}]$ structure but without the two axial Fe atoms, such that each C_2 group has two end-on Fe—σ—C_2 bonds and one side-on Fe—π—C_2 interaction; at $[Fe_4C_{12}]$ there are two cumulenic C_6 chains separated by four Fe atoms; $[Fe_3C_{12}]$ is a monocyclic alternation of cumulenic C_4 chains and Fe atoms, while $[Fe_2C_{12}]$ is a monocyclic alternation of cumulenic C_6 chains and Fe atoms. Mechanisms are proposed for the experiments in which photodissociation of Fe atoms converts $[Fe_{12}C_{12}]$ to $[Fe_8C_{12}]$, and in which $[Fe_8C_{12}]$ photodissociates to $[Fe_6C_{12}]$, $[Fe_4C_{12}]$, and $[Fe_2C_{12}]$. The formation of C—C bonds and of C_n chains initiated by the withdrawal of Fe atoms in these processes is related to the Fe catalysed formation of carbon nanotubes.
© 2006 Elsevier Ltd. All rights reserved.

Keywords: Cluster; Metallocarbohedrene; Nanocrystallite; Gas-phase; Photodissociation; Mechanism; Theory; Density functional; Mass spectrometry; Carbon; Iron

1. Introduction

In the last decade a variety of types and instances of metal carbon binary molecules have been uncovered experimentally, including (1) endohedral, exohedral, and networked metallofullerenes MC_n [1–9], (2) graphitic and ring structures MC_n [1,5,7,10], (3) metallocarbohedrenes (metcars) M_xC_y with C_2 groups [11–52] and (4) nanodimensional fragments of MC lattices containing C atoms [25,28,30,40–42,52–55]. These unprecedented and unpredictable systems raise many fundamental questions, and suggest opportunities for further scientific and technological development. All of this experimental work has involved molecules or ions in the gas phase: the principal experimental information on them involves their stabilities to dissociation [19,21,35,45,53], and their reactions with a range of molecules including oxygen, water, acetonitrile, ammonia, benzene, alkyl halides, alcohols, and acetone [14,15,26,31–33,37,39,42,45,55,56]. Bowers et al. have determined their collisional cross-sections, measured as drift times through inert gas [57–59]. Wang et al. have applied a photoelectron spectroscopic technique to measure electron affinities of a range of species [47,49]. Duncan and coworkers have reported IR data for several M_xC_y species [60–63].

Since the first report of Ti_8C_{12} in 1992 [13], most attention has concentrated on the dominant metallocarbohedrene $M_8(C_2)_6$, and on the nanocrystallite class of clusters M_xC_y in which $y/x \sim 1$. The metallocarbohedrenes are polyhedral frameworks of M atoms and C_2 groups

* Corresponding author. Tel.: +612 9415 8404.
E-mail addresses: h.harris@chem.usyd.edu.au (H.H. Harris), i.dance@unsw.edu.au (I.G. Dance).
[1] Current address: School of Chemistry, University of Sydney, NSW 2006, Australia.

0277-5387/$ - see front matter © 2006 Elsevier Ltd. All rights reserved.
doi:10.1016/j.poly.2006.05.005

(in some cases with C_n higher than C_2). In contrast, the gas-phase nanocrystallites are regarded as fragments of the face-centered cubic lattice adopted by the non-molecular solid MC compounds, and are believed to contain only (or predominantly) C atoms bonded to M. Experimentally the classification of M_xC_y clusters as metallocarbohedrenes or nanocrystallites is based largely on the stable compositions observed mass spectrometrically, and on their dissociation behavior. The structural differentiation (not proven experimentally) is that metallocarbohedrenes possess C—C bonds while nanocrystallites do not, although this is an oversimplification because it is likely that many observed clusters contain both isolated C atoms and C—C bonded groups. A significant type of experiment is the photoextrusion of metal atoms from M_xC_y, because these processes must at some stage involve C—C bond formation. The sequence of photoextrusions from $[Ti_{14}C_{13}]^+$ to $[Ti_8C_{13}]^+$ has been described experimentally [53] and theoretically [64]. This paper models photoextrusion experiments for $[Fe_xC_y]^+$ clusters [35].

One of the questions in this research is the influence of the electronic properties of the metal in the formation and stabilisation of the various types of M_xC_y clusters. Early first transition series metals such as titanium show super-abundance of the composition $[M_8C_{12}]^+$ and to a lesser extent the composition $[M_{14}C_{13}]^+$. Tantalum shows only compositions with $y/x \sim 1$ [65,66], while Nb [54,40] and Fe [35] have complicated abundance distributions that are highly sensitive to formation conditions.

The $[Fe_xC_y]$ clusters are generated in pulsed laser vapourisation sources, in which ablated Fe atoms aggregate while cooling in the presence of hydrocarbon, which is dehydrogenated [35]. The experimental distribution of cations $[Fe_xC_y]^+$ (Fig. 1) has a range of abundant species with a C/Fe ratio between 1 and 1.5. The most abundant $[Fe_xC_y]^+$ species have $x/y = 7/8$, 8/9, 8/10, 8/11, 8/12, 9/10, 10/11, 11/12 and 12/12. While the 8/12 composition

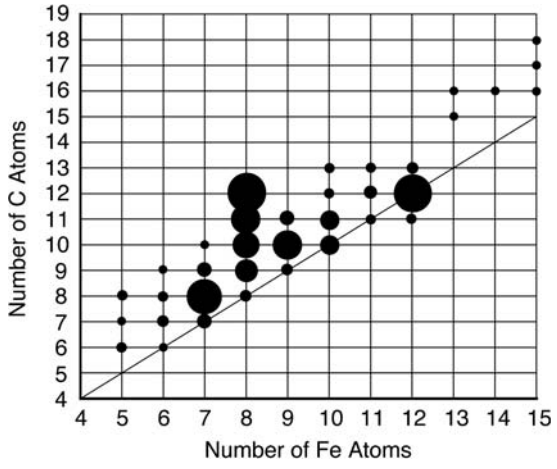


Fig. 1. Map of the observed compositions of binary $[Fe_xC_y]^+$ clusters produced by laser vapourisation of Fe metal and cooling/clustering in acetylene (from Ref. [35]). Dot size indicates observed relative abundance. The diagonal line emphasises the 1:1 Fe:C ratio.

is strong for Fe it does not display the super-abundant behaviour observed for Ti, V, Hf, and Cr. The $[Fe_{14}C_{13}]^+$ species is not observed, while $[M_{14}C_{13}]^+$ is often particularly abundant for earlier transition metals.

Pilgrim and Duncan [35] have made photodissociation measurements on $[Fe_{12}C_{12}]^+$ and $[Fe_8C_{12}]^+$ and report the following results:

$$[Fe_{12}C_{12}]^+ \rightarrow [Fe_8C_{12}]^+ \text{ (major)},\ [Fe_7C_{12}]^+ \text{ and } [Fe_6C_{12}]^+ \text{ (both minor)}$$

$$[Fe_8C_{12}]^+ \rightarrow [Fe_xC_{12}]^+ \quad \text{for } x = 7, 6, 5, 4, 3, 2.$$

Each of the intermediates in the photoextrusion sequence from $[Fe_8C_{12}]^+$ to $[Fe_2C_{12}]^+$ is observable, but intermediates in the $[Fe_{12}C_{12}]^+ \rightarrow [Fe_8C_{12}]^+$ transformation were not observed. Similar results were obtained for photodissociation of $[Cr_8C_{12}]^+$ [35]. The long sequences of metal dissociation from $[M_8C_{12}]^+$ when M is Fe and Cr are not observed for other metals Ti, V, Mo [35]. The photodissociation experiments were not time-resolved and so differentiation between sequential and concerted loss of metal atoms was not possible.

The observed $[Fe_xC_y]$ clusters (Fig. 1) and their photodissociation behaviour raise the following questions: (1) What are the probable geometric structures of the observed $[Fe_xC_y]$ clusters, and what are the important structural principles for these species? (2) What are the general bonding principles of these species? (3) What are the mechanisms for the dissociative rearrangements of these clusters and why is carbon–carbon bond formation seemingly more efficient in the iron and chromium systems?

In this paper we report density functional calculations on $[Fe_{12}C_{12}]$, $[Fe_{10}C_{12}]$, $[Fe_8C_{12}]$, $[Fe_6C_{12}]$, $[Fe_4C_{12}]$, $[Fe_3C_{12}]$, and $[Fe_2C_{12}]$, with the primary aim of determining the most favourable structures for the $[Fe_xC_{12}]^+$ compositions observed in the dissociation series, and the probable mechanisms for the transformations between these compositions. The $[Fe_xC_{12}]$ species discussed here are larger than those already treated theoretically in the literature. For smaller $[Fe_xC_y]$ clusters ($x = 1,2,3$, $y = 2$–8), gas phase ion mobility experiments have yielded some structural information, and favour segregation of atoms of the same element in cyclic or bicyclic structures [57].

We note that C—C bond formation catalysed by Fe clusters is a significant part of the generation of carbon nanotubes. While the systems described here are smaller than those involved in catalysed nanotube growth, the extrusion of Fe atoms concomitant with C—C bond formation is analogous to the process where the growing nanotube is separating from the Fe nanoparticle [67,68].

2. Methodology

The general strategy for structure investigation involved postulation of possible structures for each composition, optimisation of those structures by energy minimisation, and comparison of binding energies for each isomer: this

follows previous investigations of MnS [69] and NbC clusters [70]. The postulation of structures for the $[Fe_xC_y]$ clusters was based on knowledge of: (1) geometrical isomerism for other carbohedrenes of the early transition metals; (2) the structural principles for Nb_xC_y clusters [71]; (3) the regular fragments of the cubic MC lattice, as suggested by Duncan [53]. In addition, we use the similarities between the structures of clusters M_xE_y for E = S, O and $E = C_2$ [71].

Density functional calculations used the program DMol, v2.36 and v960 [72–74]. The density functionals used are the Lee–Yang–Parr functional for correlation [75] and Becke for exchange [76], including non-local corrections which were applied post-SCF: this has been validated for metal acetylide clusters [77]. Double numerical basis sets [74] included polarisation functions for metals and carbon. Calculations were spin-restricted, and core orbitals were frozen. The electronic states of the molecules were not specified in the initial calculations: by use of smearing of electron population close to the Fermi level, the optimisation was allowed access to low-lying electronic states. This is desirable in the initial investigation of the gross features of the geometry–energy surfaces, where various electronic states could be involved, and the objective is to locate the most stable structures. Subsequent energy minimisation for each principal geometrical isomer focussed on its electronic ground state, by reducing any population smearing to zero. Energy surfaces for specific ground or excited electronic states have not been explicitly evaluated.

Postulated structures were initially optimised in the highest possible Abelian symmetry. For each structure, once the overall geometry was optimised in this symmetry, the structure was evaluated further by optimisation after distortion and reduction of symmetry. This provided insight into the quality of the stationary point on the energy hypersurface (saddle point or minimum), and the steepness of the gradients. The energies presented and tabulated do not include zero-point or thermal corrections.

In order to locate transition states and determine activation energies, a reaction path following (RPF) methodology was employed. Our procedure started by testing various structures near a postulated transition state until two structures were found, one (**P**) which optimised without constraints to the product and one (**R**) which optimised to the reactant. The geometrical average of these two structures (**A1**) was then optimised, resulting in the geometry of either the product or reactant via **P** or **R**. The geometrical average of **A1** and the member of the set **P**, **R** to which **A1** does not optimise is the next estimate of the transition state, **A2**. This hill-climbing algorithm is repeated until two consecutive geometrically averaged structures (**Ax** and **Ax + 1**) are identical.

3. Results

The results for the geometric structures of species in the dissociation series are presented in sequence from the largest composition $[Fe_{12}C_{12}]$ to the smallest $[Fe_2C_{12}]$, as many of the structures for smaller species are conceived in terms of depletion of larger structures. Isomeric structures for the composition Fe_xC_y are labelled as **x/yA**, **x/yB**, **x/yC**, etc., in order of decreasing stability for each x/y. The energies E_R (kcal mol^{-1}) are for the uncharged species, relative to the most stable isomer for each composition. In the figures (Fe black, C grey throughout), Fe—Fe bonds are generally not drawn in order to clarify the figures and to emphasise the Fe—C and C—C bonding. Relatively short Fe—Fe distances occur in many structures, and are given on the figures or in captions.

3.1. $Fe_{12}C_{12}$

The $[M_{12}C_{12}]$ composition is of particular interest as it is either not abundant or unobserved for M other than Fe, and because feasible structures (in terms of coordination number and geometry) may be generated both as nanocrystallite fragments and as metallocarbohedrene analogues. The regular nanocrystallite structure is simply the $2 \times 3 \times 4$ fragment of the cubic crystal lattice, while several distinct metallocarbohedrene structures are generated by capping the M_4 faces of a cuboctahedron of metal atoms with C_2 groups. As in the series of $[Ti_8C_{12}]$ metcar isomers [30], the $[Fe_{12}C_{12}]$ metallocarbohedrene isomers are conceptually related by ca. 90° rotations of C_2 groups. The nanocrystallite structures are calculated to be most stable overall, with relative energies $E_R < 15$ kcal mol^{-1}. The metcar analogues lie in several groupings from 40 to 170 kcal mol^{-1} higher in energy than the nanocrystallite structures. Other less regular species are energetically well above these two structure types.

For $[Fe_{12}C_{12}]^0$ the most stable structure is the $2 \times 3 \times 4$ face-centred cubic crystal fragment with C_{2h} symmetry **12/12A**. However there are two closely related local energy minima, **12/12B** and **12/12C** (Fig. 2), that result from the breaking of Fe—C bonds in **12/12A** (two bonds broken in **12/12B**, four in **12/12C)**, and **12/12C** attains threefold rotational symmetry. The energy minima for these three structures differ by less than 2 kcal mol^{-1}. There is a gap of ~15 kcal mol^{-1} to the next most stable isomer found, **12/12D**, which is generated by removal of the central Fe atom and two apical C atoms from a standard $3 \times 3 \times 3$ nanocrystallite, and results in a structure with D_{3d} symmetry which can also be described as a cuboctahedron of Fe atoms with all six Fe_4 faces capped with a C atom and six of the eight Fe_3 faces capped with a C atom. Capping a regular icosahedron in similar fashion generates **12/12N** which is 200 kcal mol^{-1} less stable; however, if **12/12N** is modified to form six C—C bonds, with retention of symmetry, optimisation leads to **12/12I** which is more than 100 kcal mol^{-1} more stable.

The lowest energy of the metallocarbohedrene structures with C_2 groups is **12/12E**, at $E_R = 42$ kcal mol^{-1}. The six Fe_4 faces of an Fe_{12} cuboctahedron provide likely coordination sites for six C_2 units. It is evident that the C_2 units

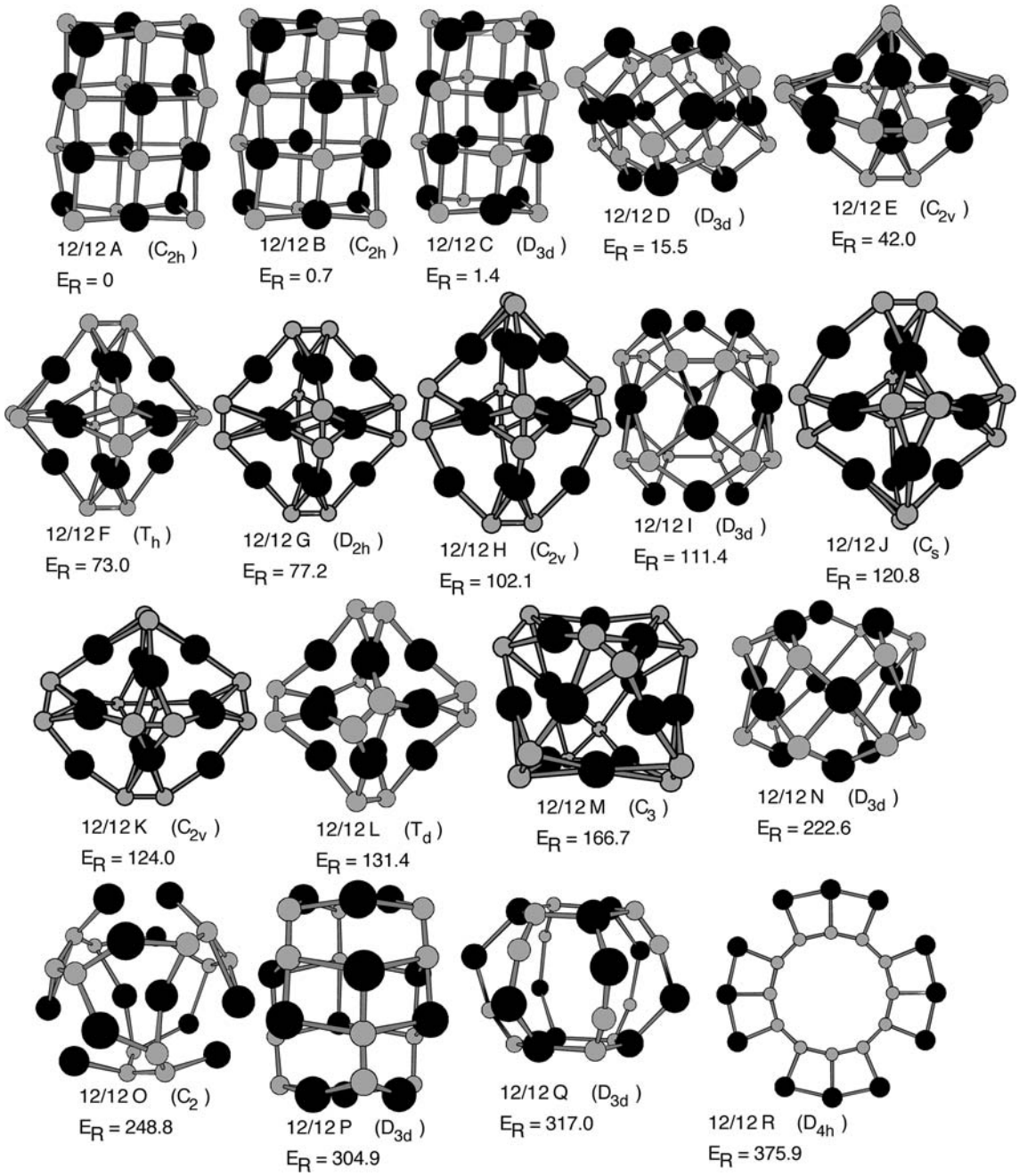


Fig. 2. Optimised structures for $[Fe_{12}C_{12}]^0$ (Fe black, C grey), arranged in order of decreasing stability. E_R is the energy (kcal mol^{-1}) of the uncharged species, relative to that of the most stable structure. Primary symmetry elements of each structure are oriented approximately vertically and in the plane of the page, except as follows: **12/12A** and **B**, horizontal and in the plane of the page; **12/12J** vertical and perpendicular to the plane of the page; **12/12R** perpendicular to the plane of the page. Shortest Fe—Fe distances (Å) are: **12/12A**, **12/12B**, and **12/12C**, upwards from 2.48 to 2.50; **12/12D**, 2.50 around the equator and 2.49 between equatorial and polar Fe atoms; **12/12E**, 2.49 and 2.53; **12/12F** all 20 immediate Fe—Fe distances (edges of icosahedral Fe_{12}) are 2.35 Å; **12/12G**, 2.35, 2.39 for Fe_{equat}—Fe_{polar}, 2.46 for Fe_{polar}—Fe_{polar}; **12/12H**, Fe_{equat}—$Fe_{polar} = 2.46$, Fe_{polar}—$Fe_{polar} = 2.42$; **12/12I**, Fe_{equat}—$Fe_{equat} = 2.41$, Fe_{equat}—$Fe_{polar} = 2.40$, Fe_{polar}—$Fe_{polar} = 2.47$; **12/12J**, Fe_{equat}—$Fe_{polar} = 2.38$, 2.47, Fe_{polar}—$Fe_{polar} = 2.45$, 2.49; **12/12K**, Fe_{equat}—$Fe_{polar} = 2.42$, 2.45, Fe_{polar}—$Fe_{polar} = 2.42$, 2.46; **12/12L**, 2.29, 2.42; **12/12M**, 2.31, 2.37, 2.41.

aligned with the long diagonal of Fe_4 faces provides much greater stability than C_2 bound parallel to the edge of an Fe_4 face (i.e. **12/12L**, $E_R = 131$ kcal mol^{-1}): this agrees with the principle established for the orientations of C_2 groups in $M_8(C_2)_6$ structures [30,78,79]. The other polyhedral metallocarbohedrene structures, **12/12F**, **12/12G**, **12/12H**, **12/12J**, **12/12K**, and **12/12M** have relative energies ranging from 73 to 167 kcal mol^{-1}. Structure **12/12F**, with the high symmetry T_h, is the $M_{12}C_{12}$ analog of the highly symmetric T_d isomer for M_8C_{12}. What is remarkable about **12/12F** is the short Fe—Fe distance, 2.35 Å, indicative of strong Fe—Fe bonding and occurring 20 times in the

icosahedral cluster. Fe—Fe distances of order 2.4–2.5 Å occur throughout all of the stable structures shown in Fig. 2. The shortest Fe—Fe interaction, 2.29 Å, occurs in **12/12L** (neglecting the uncompetitive structures **12/12O** to **12/12R**), which is appreciably less stable, and the most stable metallocarbohedrene structure, **12/12E**, has Fe—Fe distances of 2.48, 2.53 Å, so there is not a correlation between overall stability and short Fe—Fe distances in the range 2.3–2.5 Å. This conclusion is supported by the Fe—Fe distances in the more stable nanocrystallite structures, which are fewer and upwards of 2.48 Å, and suggests the unknown Fe—Fe bonding energy in the $Fe_{12}C_{12}$ clusters is maximized at about 2.45 Å.

The calculated HOMO–LUMO gap for the neutral of **12/12A** is extremely small at 0.02 eV. In fact the orbital manifolds of all three isomers **12/12A**, **B** and **C** in the vicinity of the Fermi level are extremely complex. For **12/12A**$^+$ there are 10 orbitals lying within a range of 0.3 eV at the Fermi level and many other orbitals within 2 eV above and below this. This complex electronic structure complicates determination of the barriers between the isomers as the interconversions may traverse several electronic states. Calculation of the size of the barrier between the isomers is complicated further by the result that optimisation of the geometrical average of **12/12A** and **12/12C** yields **12/12B**. The distortions required to interconvert these three 12/12 isomers are not the same as the distortions noted for the Nb_xC_y nanocrystallites [70] (indeed such distortions are not evident in the Fe_xC_y series). The differences between **12/12A**, **12/12B** and **12/12C** seem to be a compromise between the number of Fe—C bonds and the amount of stereochemical strain at each atom.

In attempt to rationalise the pronounced abundance of $[Fe_{12}C_{12}]$ in the $[Fe_xC_y]^+$ spectra we have calculated the binding energies per atom and ionisation energies (IE) of the $2\times3\times4$ and $3\times3\times3$ nanocrystallites for Fe, in comparison with Ti (Table 1). The calculated normalised binding energies for $[M_{12}C_{12}]$ and $[M_{14}C_{13}]$ are very similar for M = Fe and Ti. The reason for the superabundance of $[Ti_{14}C_{13}]^+$ is traced to the low ionisation energy of the neutral, which is almost identical to the calculated IE for $[Ti_8C_{12}]^0$ of 4.42 eV. While the calculated IE of $[Fe_{14}C_{13}]$ is much closer to that of the more experimentally abundant $[Fe_{12}C_{12}]$, it is still the lower of the two by almost 0.5 eV, and therefore the reason behind the disparate relative abundances of $[Fe_{12}C_{12}]^+$ and $[Fe_{14}C_{13}]^+$ remains unclear.

Table 1
Calculated ionisation energies (eV) and binding energies (kcal mol^{-1}) per atom for titanium and iron nanocrystallites, assuming the favourable regular nanocrystallite geometries

Species	Binding energy per atom (uncharged species)	Ionisation energy
$Ti_{12}C_{12}$	−136.4	5.64
$Ti_{14}C_{13}$	−137.6	4.41
$Fe_{12}C_{12}$	−110.9	6.81
$Fe_{14}C_{13}$	−112.9	6.35

3.2. $Fe_{10}C_{12}$

The cluster $[Fe_{10}C_{12}]^+$ is not observed in the photodissociation spectrum of $[Fe_{12}C_{12}]^+$ and has only minor abundance in the nascent ablation spectrum. It is, however, a possible intermediate in the dissociation process $[Fe_{12}C_{12}]^+ \rightarrow [Fe_8C_{12}]^+$, and the structures proposed (Fig. 3) are generated with this transformation in mind.

Isomers **10/12B** and **10/12C** are generated by the removal of one Fe atom from each end of **12/12A**. Isomer **10/12A** is generated from **10/12C** by displacing two end C atoms towards nearby C atoms (see Fig. 3) to form C_2 groups. Formation of these new C—C bonds during energy minimisation results in the breaking of two Fe—C bonds along the short axis of the molecule. A similar result is achieved if the same steps are performed on **10/12B**, again resulting in the breaking of the two Fe—C bonds through the centre of the molecule, again with **10/12A** as the resultant geometry. The relationship between **10/12B** and **10/12C** is similar to that between **12/12A** and **12/12C**, indeed **10/12A** may be generated from **12/12C** by removing Fe atoms and bringing the appropriate C atoms into close proximity, followed by optimisation. The binding energies are very similar for **10/12A** which contains two C_2 units and **10/12B** which does not.

3.3. Fe_8C_{12}

The majority of the isomers (all except **8/12L**, **N**, and **P**) considered for Fe_8C_{12} have been previously considered for Nb_8C_{12} [70]. Two of the new isomers that are proposed for Fe_8C_{12} (**8/12N** and **P**) are based on depleted $Fe_{12}C_{12}$ structures.

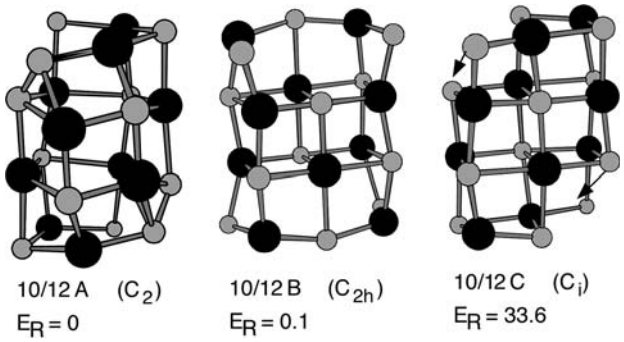


Fig. 3. Optimised structures for $[Fe_{10}C_{12}]$: E_R is the relative energy (kcal mol^{-1}) of the uncharged species. Primary symmetry elements of each structure are oriented horizontally and in the plane of the page, except **10/12A** whose C_2 axis is perpendicular to the plane of the page. **10/12A** is generated from **10/12C** by displacement of two C atoms as marked by the arrows.

Surprisingly, of the 19 structures evaluated (see Fig. 4), two structures, **8/12A** (C_{3v}) and prolate **8/12B** (D_{3d}) are calculated to be 11 kcal mol^{-1} more stable than the T_d tetracapped tetrahedron structure **8/12D** found to be so stable for earlier transition metals [30,70,78,80], and the C_s isomer **8/12C** is also slightly more stable than the T_d structure. All seven isomers (**8/12B-H)** which are generated by 45° rotations of the C_2 groups in Castleman's T_h isomer [30] **8/12K**, are within 17 kcal mol^{-1} of **8/12A**. This is a small energy range in comparison with that of these isomers of Nb_8C_{12} where the range is roughly 54 kcal mol^{-1} [70]. **8/12F** with symmetry D_{3d} is not a true minimum, because when optimised in symmetry C_{3v} structure **8/12A** is obtained (discussed in more detail below). There is a gap in energy of more than 40 kcal mol^{-1} from **8/12H** to the next most stable isomer, **8/12I**. **8/12I** contains C_3 groups arranged over an Fe_5 face and has greater relative stability for Fe_8C_{12} than calculated for the same isomer of Nb_8C_{12} [70]. The structures proposed for M_8C_{12} by Castleman [13] (**8/12K**), and Fowler [81] (**8/12M**), have unfavourable binding energies, whilst Khan's [82] structure **8/12R** reverts to **8/12O** on optimisation, and Pauling's [83] structure **8/12S** attains the same geometry as **8/12K**. A 3° rotation of the C_2 groups of **8/12K** (rotating opposite groups in different directions yielding a structure with threefold rotational symmetry) followed by optimisation results in **8/12A**: the

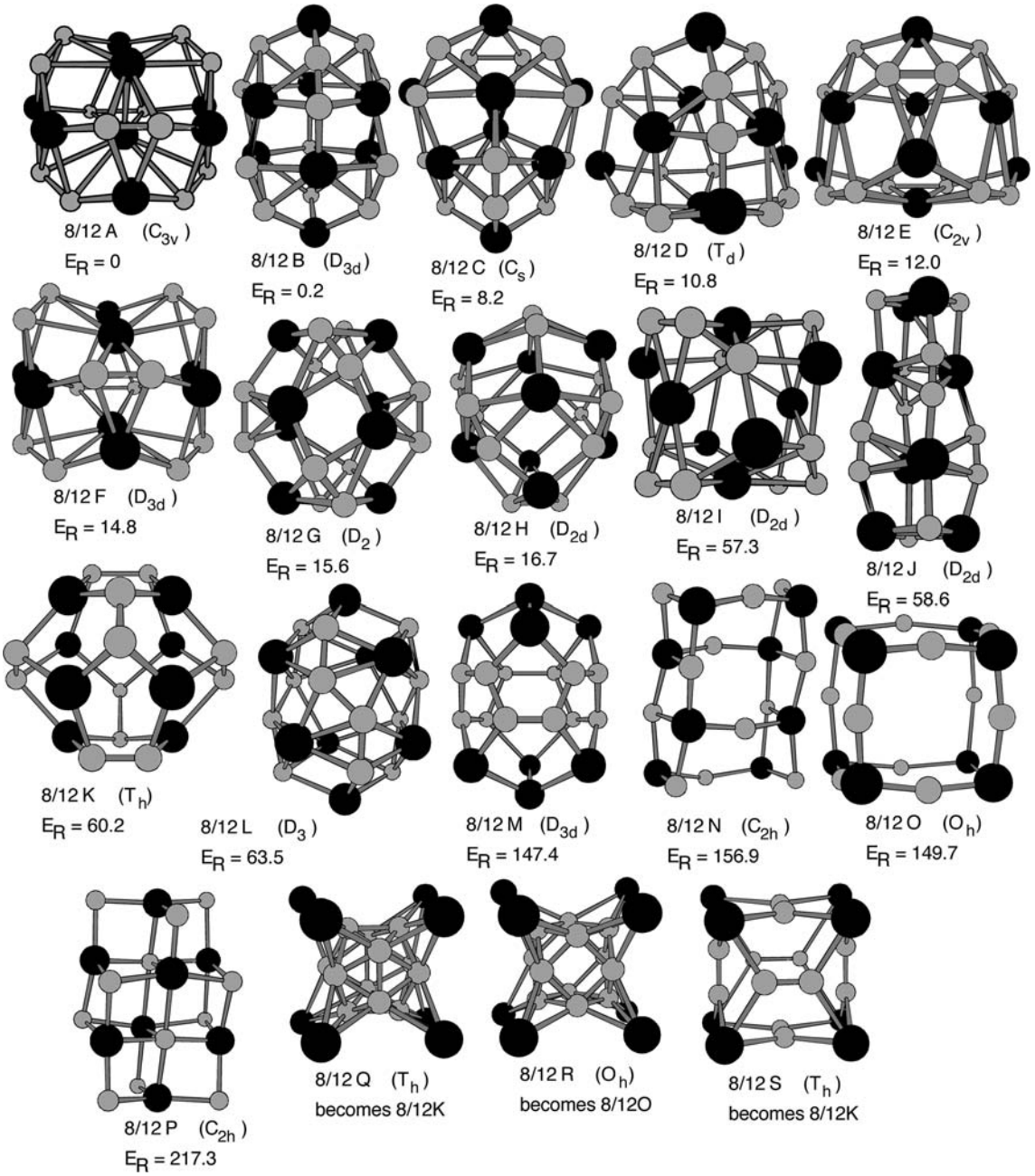


Fig. 4. Optimised structures for $[Fe_8C_{12}]^0$, arranged in order of decreasing stability: E_R is the relative energy (kcal mol^{-1}) of the uncharged species.

energy change associated with this initial distortion is 9 kcal mol^{-1}, and the barrier for conversion of **8/12K** to **8/12A** is estimated to be of similar magnitude. **8/12L** is generated from **8/12B** by removal of the vertical mirror planes and the formation of three new C—C bonds by a slight rotation of one of the horizontal halves of the molecule. Note from **8/12Q** and **8/12R** that a symmetrical C_{12} core with multiple C—C bonds is unstable to C—C bond breaking. **8/12O**, **N**, and **P** are depleted nanocrystallites, **8/12O** from the $3\times3\times3$ nanocrystallite, **8/12N** and **8/12P** from the $2\times3\times4$ nanocrystallite: these last two are important intermediates in consideration of the transformation from $[Fe_{12}C_{12}]$ to $[Fe_8C_{12}]$ (see Section 4, below).

We delve further into reasons for the energetic ordering of the more stable isomers for $[Fe_8C_{12}]$. The calculated structure for **8/12A** has one very short Fe—Fe bond (2.27 Å) along the threefold axis. It is the shortening of this bond that drives the energy minimisation from **8/12F** to **8/12A** on symmetry reduction from D_{3d} to C_{3v}, as shown in Fig. 5. One consequence of this is a straining of the associated Fe—C_2 bonding. A characteristic of many metallocarbohedrene structures is the occurrence of local cradle structures, in which a C_2 group lies over the diagonal of an M_4 rhombus, forming two M—σ—C_2 bonds and two M—π—C_2 bonds (Fig. 6). Normal cradle geometry is **1A**. The shortening of one Fe—Fe bond in **8/12A** causes a contraction of the Fe^{π}—Fe^{π} distances in three Fe_4C_2 cradles, distorting them to **1B**, and introducing angular distortion of the ideally linear C_2—σ—Fe bonding: in addition the Fe^{π}—C—Fe^{π} angles are distorted from 84.9° in **8/12F** to 72.4° in **8/12A**.

The stability of **8/12A** and **8/12B** relative to **8/12D** can be correlated with more general shortening of Fe—Fe distances, with implied Fe—Fe bonding. Distances are presented in Table 2, and Fig. 5. In the T_d isomer **8/12D** all 18 Fe—Fe bonds are about 2.77 Å in length, for **8/12B** (D_{3d}) six of these shorten to 2.5 Å and six lengthen to 3.1 Å. In **8/12A** (C_{3v}) three are shortened to 2.4 Å and three lengthen to 3.4 Å, together with the formation of a very short new Fe—Fe bond at 2.3 Å. Thus the stabilisation **8/12D** ⇒ **C** ⇒ **B** ⇒ **A** appears to be associated with a strengthening of Fe—Fe bonds, and it is understandable that this effect is greater than would occur with the early transition metals. A caveat is that the energies of the short Fe—Fe interactions in these structures are not known.

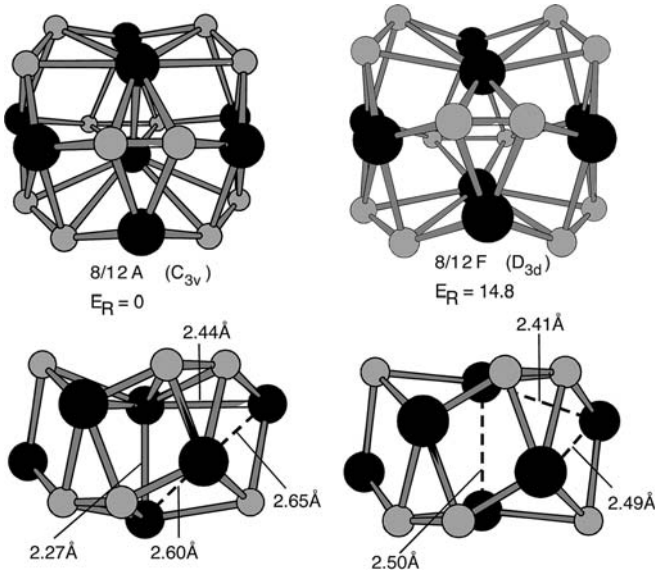


Fig. 5. Comparison of the two closely related structures **8/12A** (left) and **8/12F** (right): the lower left picture is upside down relative to the upper left picture. **8/12F** optimises to **8/12A** on removal of the D_{3d} symmetry constraint. Both lower views are normal to a mirror plane, and so two rear Fe atoms and six rear C atoms are obscured by front atoms.

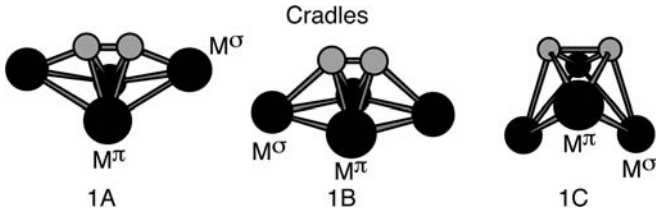


Fig. 6. The cradle motif **1A** commonly present in calculated $[M_xC_y]$ structures, and increasingly distorted forms **1B** and **1C**.

3.4. Fe_6C_{12}

The structures considered and optimised for $[Fe_6C_{12}]$ are shown in Fig. 7. There is a very wide range of stability, and some of the structures that are intriguing and symmetrical (such as the monocycles **6/12K** and **6/12L**, the chain **6/12P**, and the O_h polyhedron **6/12N**) are energetically uncompetitive. The polyhedron **6/12F** (D_{6h}) with two C_6 hexagons and all atoms four-coordinate is probably destabilised by the stereochemistry at C and Fe. We will focus attention on the more stable isomers. Six of the more stable structures, **6/12A**, **B**, **C**, **D**, **G** and **H**, are generated by the removal of Fe atoms from stable isomers of $[Fe_8C_{12}]$. Structure **6/12A**, which is 40 kcal mol^{-1} more stable than all of the others, is generated by the removal of the two Fe atoms on the threefold rotation axis of **8/12A**.

The depletion by two Fe atoms, $[Fe_8C_{12}]$ to $[Fe_6C_{12}]$, means that C_2 groups in the more stable structures for $[Fe_6C_{12}]$ are not all fully coordinated by four Fe atoms, as they are in the more stable $[Fe_8C_{12}]$ structures. Thus each of the C_2 groups in **6/12A** has two Fe—σ—C_2 bonds but only one Fe—π—C_2 bond: the cradles (Fig. 6) are

Table 2
Fe—Fe distances (Å) for the four most stable isomers of $[Fe_8C_{12}]^0$

8/12D T_d	**8/12C** C_s	**8/12B** D_{3d}	**8/12A** C_{3v}
6 at 2.779	1 at 2.422	6 at 2.525	1 at 2.266
12 at 2.764	2 at 2.477	6 at 2.709	3 at 2.441
	2 at 2.480	6 at 3.085	3 at 2.581
	2 at 2.518		3 at 2.600
	2 at 2.533		
	2 at 2.750		
	2 at 3.048		

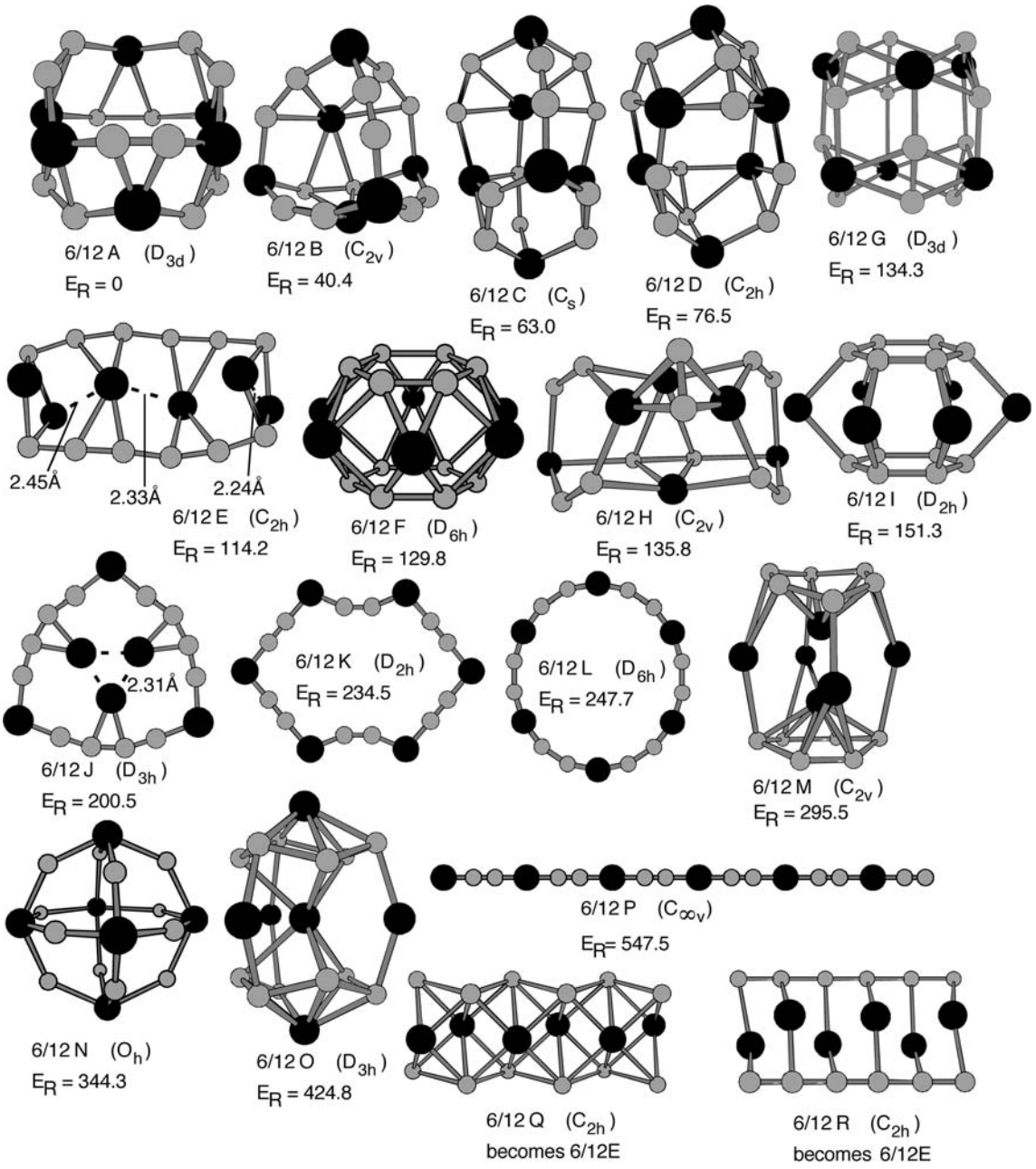


Fig. 7. Optimised structures for $[Fe_6C_{12}]^0$. Primary symmetry elements of each structure are oriented close to vertically and in the plane of the page, except as follows; **6/12C**, vertical and perpendicular to the plane of the page; **6/12D**, horizontal and in the plane of the page; **6/12H**, **6/12J**, **K**, **L**, perpendicular to the plane of the page. E_R is the relative energy (kcal mol^{-1}) of the uncharged species.

metal-deficient. The decreasing stability of the structures with C_2 groups in the sequence **6/12A**, **B**, **C**, **D**, **G**, **H**, **K**, **L** correlates with the nature and degree of Fe deficiency around C_2: **6/12B** has one less Fe—π—C_2 bond than **6/12A**, at a cost of 40 kcal mol^{-1}; further degradation of the Fe—π—C_2 bonding in **6/12C** costs an additional 20 kcal mol^{-1}; **6/12D** has more Fe—π—C_2 bonding, but two Fe—σ—C_2 bonds are missing, while in **6/12G** all of the C_2 groups are fully Fe—π—C_2 bonded but only half Fe—σ—C_2 bonded, which costs 134 kcal mol^{-1} relative to **6/12A**. In general the Fe—σ—C_2 bonding contributes more to the overall stability than does the Fe—π—C_2 bonding. Comparison of the binding energies of **6/12A** (with 12 Fe—σ—C_2 bonds and six Fe—π—C_2 bonds) and **6/12G** (with six Fe—σ—C_2 bonds and 12 Fe—π—C_2 bonds) suggests that a Fe—σ—C_2 bond contributes roughly 20 kcal mol^{-1} more than a Fe—π—C_2 bond.

The general openness of the stable 6/12 structures is due to the favourability of the extended Fe—σ—C_2—σ—Fe bonding. Structure **6/12E**, the most stable with C_6 chains, is generated by optimisation of **6/12Q** and **R** in which Fe atoms bridge the chains. Because Fe—Fe is longer than

C—C, the central Fe_6 set in **6/12E** zig-zags through the central domain, with relatively tight Fe—Fe bonding.

3.5. Fe_4C_{12}

A further significant change in structures occurs in the transition from $[Fe_6C_{12}]$ to $[Fe_4C_{12}]$. For $[Fe_6C_{12}]$ metal-depleted metallocarbohedrenes are the most stable, but this is not the case for Fe_4C_{12}. Instead, **4/12A** (see Fig. 8) which contains two C_6 chains is 48 kcal mol^{-1} more stable than any other structure. The second most stable structure, **4/12B**, contains C_3 chains with Fe—σ—C_3 bonding, but the low coordination of Fe will be a destabilising influence: the related non-cyclic structure, **4/12J**, is much less stable. The most metallocarbohedrene-like structure is **4/12C**, with complete Fe—σ—C_2 bonding but no Fe—π—C_2 bonding, and is 54 kcal mol^{-1} less stable than **4/12A**. We note in passing that the highly symmetric T_d structure **4/12K**, which complements **4/12C** in having only Fe—π—C_2 bonding and no Fe—σ—C_2 bonding, is almost 300 kcal mol^{-1} less stable, reinforcing the earlier conclusion that a Fe—σ—C_2 bond contributes roughly 20 kcal mol^{-1} more than a Fe—π—C_2 bond.

We describe the consequences of the three distinct ways to remove two Fe atoms from **6/12A**. (1) Removal of two adjacent Fe atoms followed by optimisation yields **4/12I** (see below for transformation of **4/12I** to **4/12A**). (2) Removal of two Fe atoms which are related by a threefold rotation axis yields **4/12E**. (3) Removal of two opposite Fe atoms results in **4/12F** after rearrangement of two C_2 groups to increase the number of Fe—σ—C_2 interactions. The most stable of these three product isomers is **4/12E** which gains its stability from the spontaneous formation of two new C—C bonds on optimisation. **4/12F** is also generated directly by removal of two Fe atoms from either **6/12B** or **C** followed by optimisation.

While both **4/12B** and **4/12C** contain metal atoms which are Fe—σ—C_n bound to all nearby carbon units, the lower energy **4/12A** has all metal atoms side bound to carbon chains. It seems likely that the stability of **4/12A** is due to an increased number of C—C bonds, ten for **4/12A** versus six for other stable structures. **4/12D** which contains two C_6 rings now has a competitive stability, in comparison to that of those $[Fe_6C_{12}]$ structures that contain C_6 rings.

3.6. Fe_3C_{12}

Optimised structures for $[Fe_3C_{12}]$ are shown in Fig. 9. Two characteristic features are extended carbon chains (in **3/12A**, **B**, **F**, **H**, **I**) or C_n cycles, mainly C_6. The two most stable structures, **3/12A** and **3/12B**, contain cumulenic C_4 and C_6 chains respectively, slightly bent or kinked. Structures containing C_6 cycles are generally less stable, and **3/12J**, inspired by established $(\eta^6\text{-}C_6H_6)_2M$ complexes, is clearly not a structure type to be considered in the present

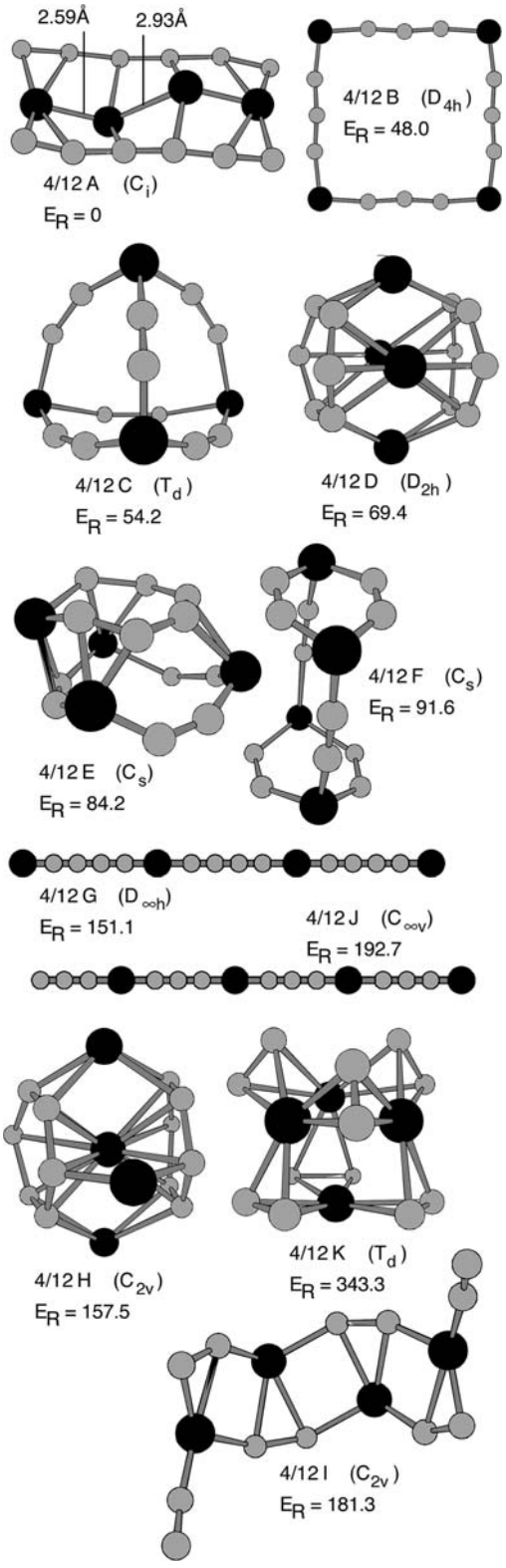


Fig. 8. Optimised structures for $[Fe_4C_{12}]^0$. Primary symmetry elements of each structure are oriented approximately vertically and in the plane of the page, except as follows; **4/12B**, **H**, and **I**, perpendicular to the plane of the page; **4/12F**, vertical and perpendicular to the plane of the page; **4/12G** and **J**, horizontal and in the plane of the page. E_R is the relative energy (kcal mol^{-1}) of the uncharged species.

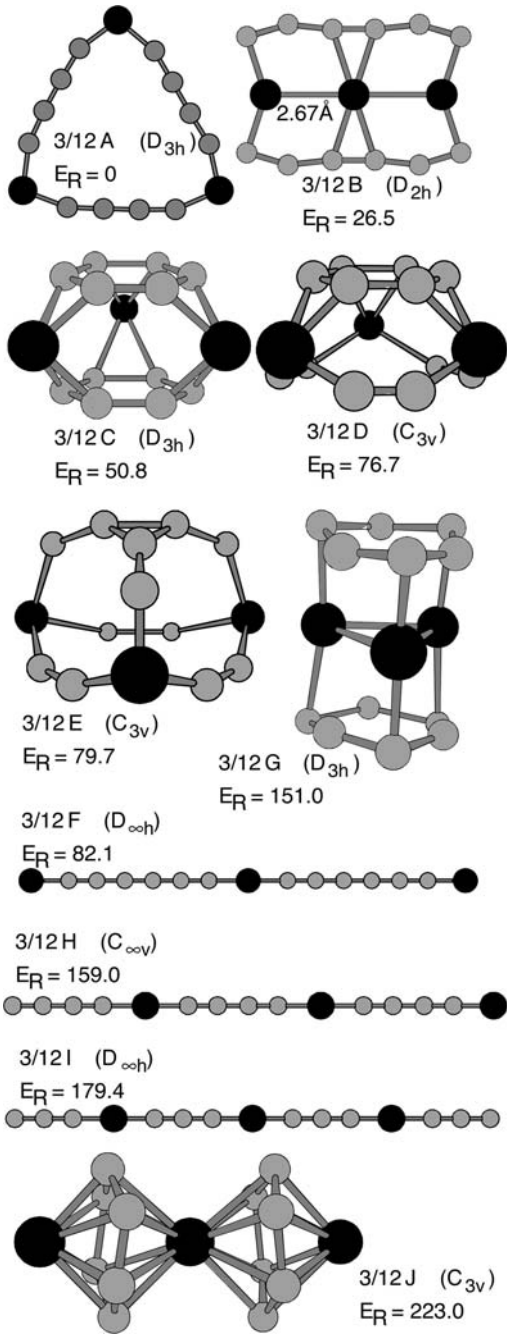


Fig. 9. Optimised structures for $[Fe_3C_{12}]^0$. Primary symmetry elements of each structure are oriented close to vertically and in the plane of the page, except as follows; **3/12A**; perpendicular to the plane of the page; **3/12F**, **H**, **I**, and **J**, horizontal and in the plane of the page. In **3/12A** the C—C distances are 1.30, 1.31 Å; C—C distances in **3/12B** alternate 1.30, 1.35, 1.29, 1.35, 1.30 Å; C—C distances in **3/12H** and **3/12I** are in the range 1.28–1.32 Å. E_R is the relative energy (kcal mol^{-1}) of the uncharged species.

context. Some insight into the bonding of three Fe to cyclic C_6 is obtained from the fact that **3/12C** with widely separated (>4 Å) Fe atoms is obtained on optimisation of the same connectivity with a smaller (2.9 Å) Fe_3 triangle. The difference in energy between **3/12D** and **3/12C** is probably a consequence of the fewer C—C bonds in **3/12D**.

The basis for the relative stabilities of the favourable structures **3/12A** and **3/12B** is probably the occurrence of Fe—σ—C_n bonding in **A** but not **B**, countered by the occurrence of some Fe—Fe bonding in **B** but not in **A**. We note that the two most stable structures for $[Fe_3C_{12}]$ resemble in connectivity the two most stable structures for $[Fe_4C_{12}]$, but that the stability ordering is reversed. Why might this be? The lengths of the C_n chains are relevant, because C_{even} chains (C_4 and C_6) occur in the relatively stable isomers **4/12A**, **3/12A** and **3/12B** while the less stable isomer **4/12B** contains C_3. The relative energies of the linear isomers **3/12F**, **3/12H**, **3/12I** with C_6, C_4, C_3, respectively, also manifest the favourable influence of C—C bonds and C_{even} chains.

3.7. Fe_2C_{12}

The most stable structure found for $[Fe_2C_{12}]$ is the planar monocyclic structure, **2/12A** (Fig. 10), consisting of two Fe atoms (separated by >7 Å) connected by two slightly curved cumulenic C_6 chains. This is analogous to the best structure for $[Fe_3C_{12}]$. Two tricyclic versions of **2/12A** are **2/12B** and **2/12C**, retaining bent cumulenic C_{even} chains and Fe—σ—C_n bonding, and are ca. 25 kcal mol^{-1} less stable. The linear structures **2/12D** and **2/12K** clearly demonstrate the importance of terminating C_n chains with Fe atoms. Structures **2/12E** and **2/12F** were initiated by placing an Fe_2 unit over a C_{12} group which is two C_5 rings fused to opposite edges of a C_6 ring: the two starting structures differed by a 90° rotation of the Fe_2 unit. Optimisation of **2/12G′** results in the destruction of the two ring-shared C—C bonds giving the near planar **2/12G**. The differences between the three related structures **2/12E**, **F** and **G** are in the numbers of Fe—C and C—C bonds, which when maximized in **2/12E** provide an energetic advantage. **2/12F** is related to **4/12A** by the removal of the two central Fe atoms.

Before moving to investigation of a structural interpretation of the experimental photodissociations of Fe atoms, we summarise the main principles that have evolved so far for the structures of $[Fe_xC_{12}]$ clusters. With the largest complement of Fe atoms, $[Fe_{12}C_{12}]$ and $[Fe_{10}C_{12}]$, the stable structures contain isolated C atoms in a distorted nanocrystallite fragment. The stability associated with C_2 groups is intimated at $[Fe_{10}C_{12}]$, and is dominant in the metallocarbohedrene isomers of $[Fe_8C_{12}]$ and the Fe-deficient metallocarbohedrene structures of $[Fe_6C_{12}]$. At composition $[Fe_4C_{12}]$ there are longer C_n chains, decorated or terminated by Fe atoms, while for $[Fe_3C_{12}]$ and $[Fe_2C_{12}]$ the stable structures are monocycles containing cumulenic C_4 and C_6 chains respectively. It appears that Fe—Fe bonding, at distances <ca. 2.5 Å, is significant in the metallocarbohedrene structures, but the C—C and Fe—C bonds contribute greater stabilisation, and the stable structures tend to maximize the number of C—C and Fe—C bonds. In metallocarbohedrene structures the Fe—σ—C_2 bonding is more favourable than Fe—π—C_2 bonding.

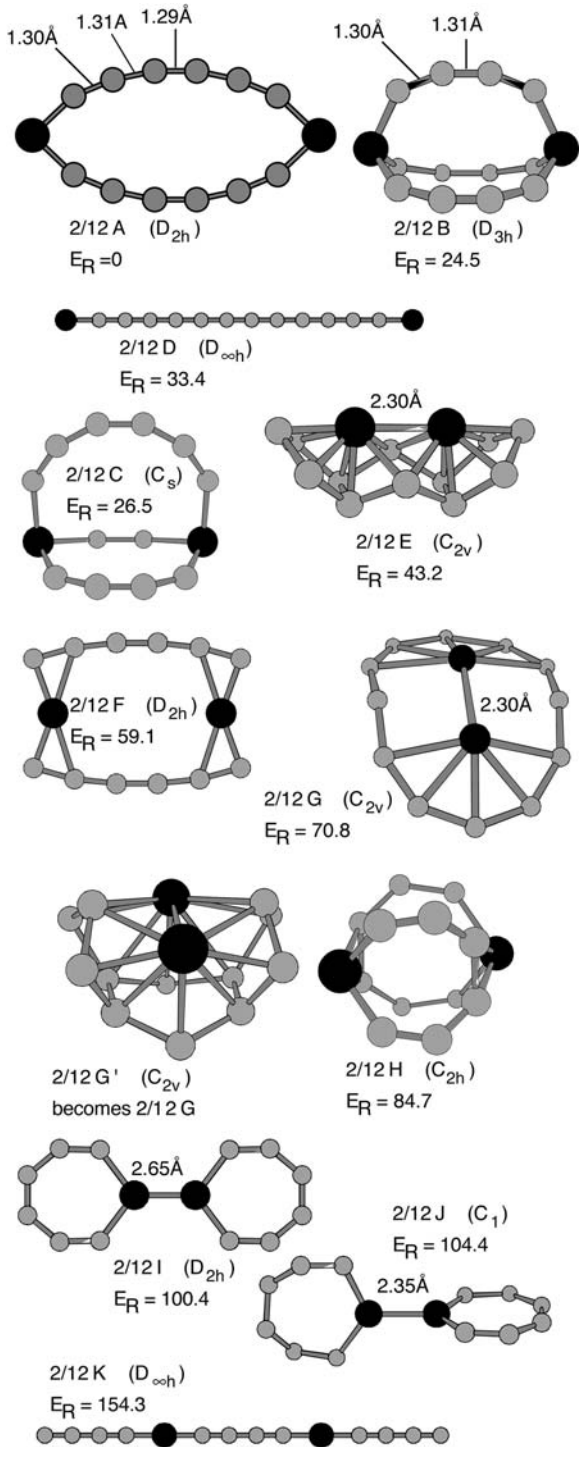


Fig. 10. Optimised structures for $[Fe_2C_{12}]^0$. Primary symmetry elements of each structure are oriented approximately vertically and in the plane of the page, except as follows; **2/12A**, **2/12G**, perpendicular to the plane of the page; **2/12B**, **C**, **D**, and **K** horizontal and in the plane of the page. E_R is the relative energy (kcal mol^{-1}) of the uncharged species.

4. Dissociation mechanisms

4.1. $Fe_{12}C_{12}$ to Fe_8C_{12}

Whilst the photodissociation spectrum of $[Ti_{14}C_{13}]^+$ clearly shows the presence of the intermediates with progressively lost Ti atoms, intermediate compositions are not clearly resolved in the dissociation spectrum of $[Fe_{12}C_{12}]^+$. The transformation $[Fe_{12}C_{12}]^+$ to $[Fe_8C_{12}]^+$ is considered in two possible compositional pathways, one-step concerted dissociation, and sequential dissociation from $[Fe_{12}C_{12}]^+$ to $[Fe_{10}C_{12}]^+$ to $[Fe_8C_{12}]^+$. The $[Fe_{11}C_{12}]^+$ and $[Fe_9C_{12}]^+$ intermediates are ignored to retain the convenience of twofold symmetry throughout the calculations of the process.

Fig. 11 illustrates the proposed mechanism for the concerted transformation of **12/12A** to **8/12A**. The first step in this process is the removal of the four apical Fe atoms, giving **8/12P′** with C_{2h} symmetry. Note that it is the three-coordinate Fe atoms that are proposed to dissociate, while the retained Fe atoms are four-coordinate. Loss of these four Fe atoms allows the retention of C_2 symmetry and yields an Fe_8 framework which is similar in topology to that in **8/12A**. Optimisation of **8/12P′** gives **8/12P** along with a net stabilisation of ca. 80 kcal mol^{-1}, very little geometric change occurs during this optimisation. If **8/12P′** is to be converted to a metallocarbohedrene then six new C—C bonds must be formed, and this is modeled by moving the positions of six C atoms in the directions indicated on **8/12P′** in Fig. 11. The transition state **8/12TS** shown in Fig. 11 for the transformation between **8/12P′** and the final product **8/12A** was calculated by the RPF method, and lies 25 kcal mol^{-1} above **8/12P′** and ca. 320 kcal mol^{-1} above **8/12A**. In the transition state the six nascent C—C interactions are ca. 2.1 Å. Details of the geometry and energy changes during the transformation from the transition state to the product, including the change in symmetry, are provided in the Supplementary material.

A mechanism proposed for sequential transformation of $[Fe_{12}C_{12}]$ to $[Fe_8C_{12}]$ via $[Fe_{10}C_{12}]$ is illustrated in Fig. 12. It is based on the observation that the central Fe_6C_6 segments of structures of **12/12C, 10/12A** and **8/12B** are very similar. The first stage (Fig. 12(a)) involves the removal of two three-coordinate Fe atoms from **12/12C**, followed by conversion through the transition state which involves moving only one symmetry independent C atom, to the product **10/12A**. This conversion has an activation barrier of at least 70 kcal mol^{-1}, while the product is 165 kcal mol^{-1} below the transition state. Two C—C bonds are formed (2.79 to 2.08 to 1.36 Å), with minor changes elsewhere. The second stage (Fig. 12(b)) involves removal of two three-coordinate Fe atoms, leaving two dangling C atoms, but then shortening four C—C distances and two Fe—Fe distances as shown in Fig. 12(b) and performing an RPF transition state search gives a transition state which lies 133 kcal mol^{-1} above the undistorted structure, and 400 kcal mol^{-1} above the product **8/12B**.

In comparing this sequential mechanism for the photodissociation of $[Fe_{12}C_{12}]$ to form $[Fe_8C_{12}]$ with the concerted mechanism suggested above, we note that the reactant nanocrystallite **12/12C** is only 1.4 kcal mol^{-1} less stable than **12/12A**, the intermediate **10/12A** is the most stable for this composition, and the product **8/12B** is only

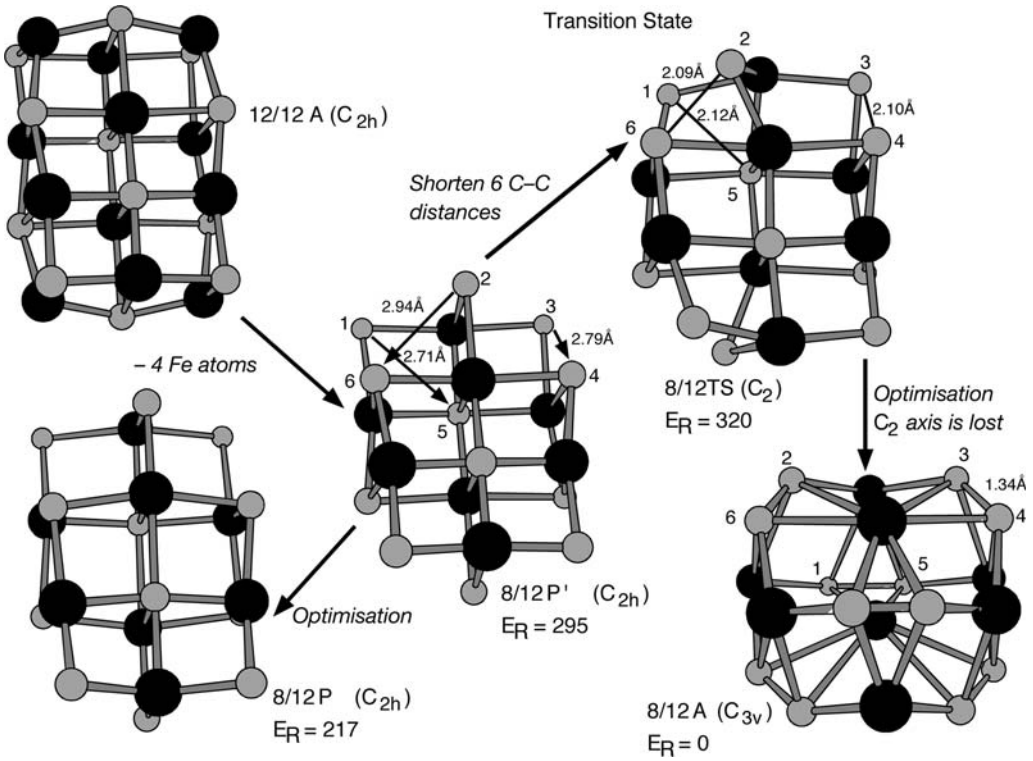


Fig. 11. Proposed mechanism for the concerted transformation of $[Fe_{12}C_{12}]$ to $[Fe_8C_{12}]$. Relative energies E_R are given in kcal mol^{-1}. The primary symmetry elements of all species are aligned horizontally and in the plane of the page except **8/12M** whose C_3 axis is vertical (the molecule is not rotated in space but the horizontal C_2 axis is lost whilst a perpendicular C_3 axis is gained). The calculated transition state is **8/12TS**.

0.2 kcal mol^{-1} less stable than **8/12A**. However, the activation barriers for the sequential mechanism are significantly larger, favouring the concerted mechanism, which is consistent with the non-observation of $[Fe_{10}C_{12}]^+$ in the photodissociation experiment [35].

4.2. Fe_8C_{12} to Fe_2C_{12}

This process requires formation of C—C bonds, concomitant with the dissociation of Fe atoms. Based on the results of the structure determinations described above, we propose a mechanism for the conversion of **8/12A** to **6/12A** to **4/12A** to **2/12A**. It is likely that the formation of these species occurs via distinct concerted single-step or cascading processes that occur after the absorption of one or more photons and may be perpetuated by stabilising rearrangement energy at each step: however modelling as a sequence of 2Fe losses allows for easier calculation and comprehension of the process. The proposed mechanism is illustrated in Fig. 13. The Fe atoms most easily removed from **8/12A** are probably those that lie on the threefold rotation axis because they are involved in Fe—π—C_2 bonding only, and subsequent optimisation gives the most stable structure found for $[Fe_6C_{12}]$, **6/12A**. If two adjacent Fe atoms are removed from **6/12A** and the resultant structure is optimised without alteration, the opened structure **4/12I** is the product. It seems likely that the removal of two adjacent Fe atoms where only two Fe—Fe bonds must be broken, will be a lower energy process than the removal of two non-adjacent Fe atoms where four Fe—Fe bonds are destroyed. The conversion of **4/12I** to **4/12A** is the next step and requires the formation of four new C—C bonds. The only uphill component of this conversion is the requirement that eight Fe—C bonds (marked "X" in Fig. 13) be converted from end-bound Fe—σ—C_2 bonds to side-bound Fe—π—C2 bonds. The exact transition state has not been determined, but it is likely that the activation barrier associated with this process is considerably less than that for the loss of Fe atoms throughout the process. Conversion of **4/12A** to **2/12F** requires only the removal of the two central Fe atoms followed by optimisation. The final step to yield stable **2/12A** requires only the breaking of four side-bound Fe—π—C bonds, which is achieved by moving C atoms as shown in Fig. 13. The transition state for this process has not been determined, but as it is only a slight rearrangement requiring the breaking of only four relatively weak bonds while forming four stronger Fe—σ—C bonds, the activation barrier is assumed to be readily overcome.

5. Discussion and summary

While we have not investigated probable structures for all of the observed $[Fe_xC_y]$ clusters, and have focused on the species involved in the photodissociation experiments, our results provide insight into the structural principles for the larger $[Fe_xC_y]$ clusters. It is clear that when $x \sim y$

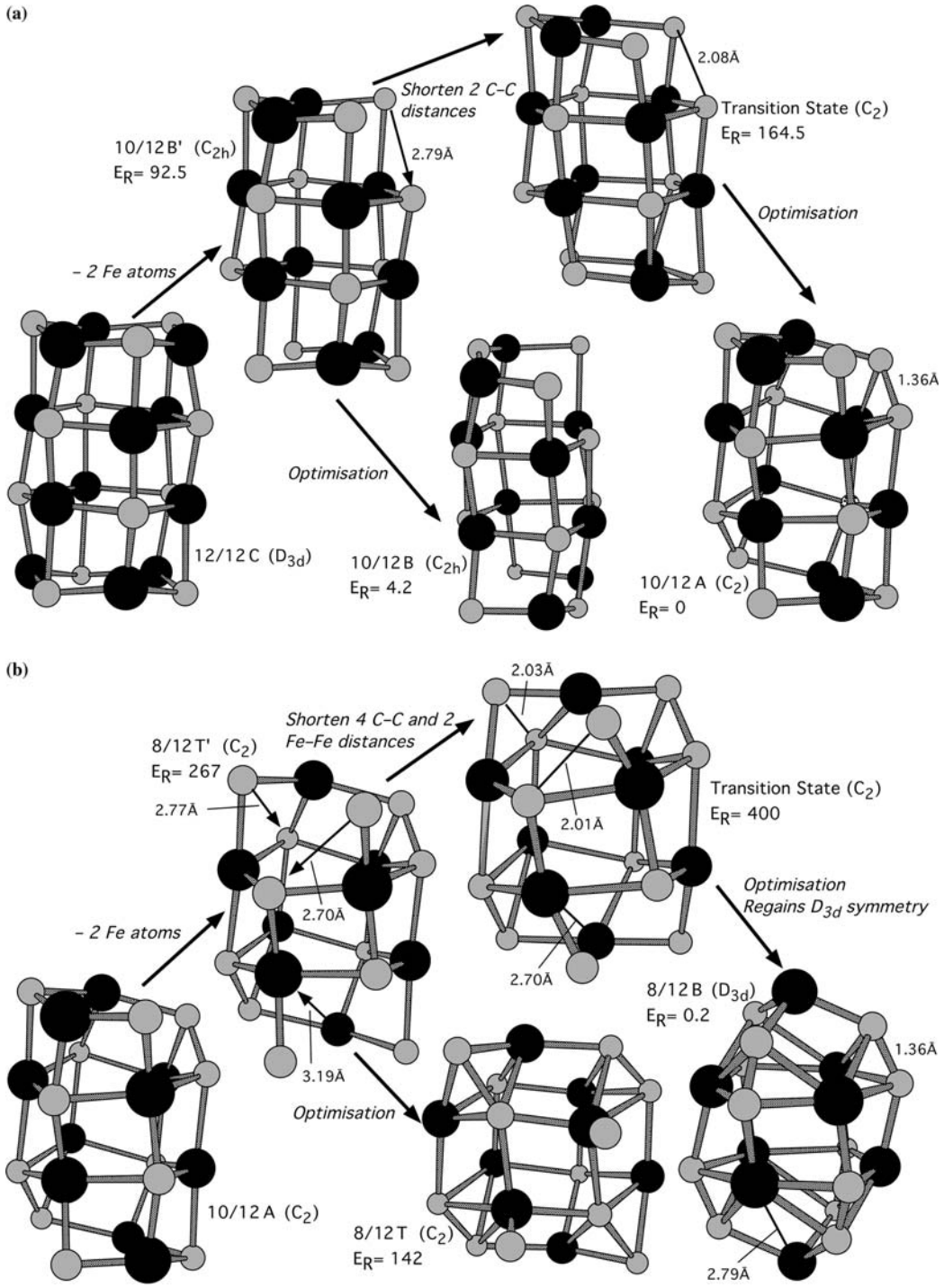


Fig. 12. The two stages in the mechanism for sequential dissociation of two pairs of Fe atoms in the conversion of $[Fe_{12}C_{12}]$ to $[Fe_{10}C_{12}]$ to $[Fe_8C_{12}]$. (a) The first stage conversion from **12/12C** to **10/12A** involves the loss of two three-coordinate Fe atoms, and progresses via the transition state pictured, which was calculated by the RPF method. The threefold rotation axis of **12/12C** is aligned vertically and in the plane of the page, whilst the twofold rotation axes of the remaining species are perpendicular to the plane of the page. (b) In the second stage two three-coordinate Fe atoms are removed from **10/12A**, leading to the transition state shown (determined by the RPF method), which leads to the product **8/12B**. The primary symmetry elements of all species are perpendicular to the plane of the page, except **8/12B** whose C_3 axis is vertical and in the plane of the page.

the probable structures contain isolated C atoms, and that cluster stability derives principally from Fe—C bonding. For the prototypical composition $[Fe_8C_{12}]$, and probably for closely related compositions, carbon is present only in C_2 groups that are bound end-on (i.e. σ) and side-on (i.e. π) to Fe, with the metal array approximating a regular polyhedron. It appears that the Fe—σ—C_2 bonding is stronger than Fe—π—C_2 bonding. As the y/x ratio changes from 2 to 3 (i.e. $[Fe_6C_{12}]$, $[Fe_4C_{12}]$) the C_n chains lengthen, and by $[Fe_3C_{12}]$ and $[Fe_2C_{12}]$ the stable structures are

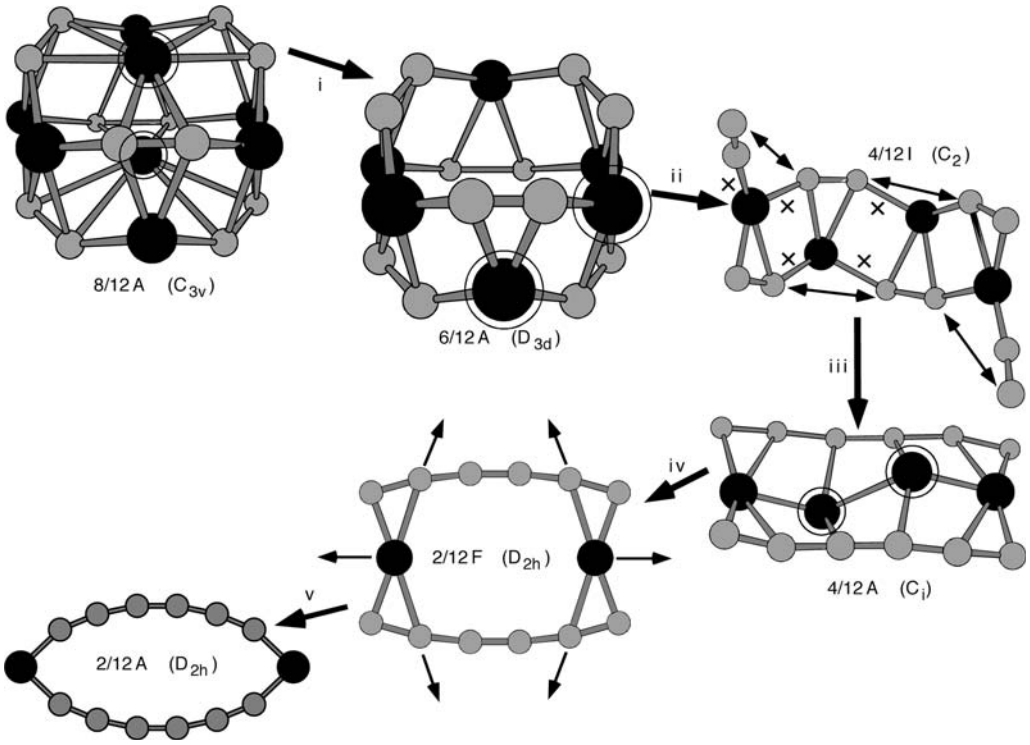


Fig. 13. Proposed sequential mechanism for the transformation of **8/12A** to **2/12A**. (i) **8/12A** is converted to **6/12A** by removal of the two Fe atoms (circled) that lie on the threefold axis, followed by optimisation. (ii) Removal of two adjacent Fe atoms (circled) from **6/12A** followed by optimisation yields **4/12I**. (iii) It is envisaged that the conversion of **4/12I** to **4/12A** may be achieved by small atomic displacements in the directions indicated followed by optimisation. The energy and geometry of the transition state has not been investigated. (iv) **2/12F** is generated from **4/12A** by removal of the two central Fe atoms followed by optimisation. (v) The conversion of **2/12F** to **2/12A** is achieved by elongation of the Fe—Fe distance in **2/12F**. The energy and geometry of the transition state has not been investigated.

monocycles containing long cumulenic C_{even} chains and Fe—σ—C bonds.

These principles are similar to those presented previously for over 50 $[Nb_xC_y]$ clusters [70], with the significant exception that Fe—Fe bonding at shorter distances is more influential than Nb—Nb interactions at longer distances. The influence of Fe—Fe bonding is evident through comparison of the structures 8/12A (C_{3v}) with one variable axial M—M interaction and 8/12D (T_d) with four necessarily equivalent M—M interactions (see Fig. 4). When M = Fe the C_{3v} structure is the more stable by 11 kcal mol^{-1} with Fe—Fe = 2.27 Å, while when M = Nb the C_{3v} structure is less stable by 46 kcal mol^{-1} and Nb—Nb = 3.30 Å. The role of Fe—Fe bonding in determining the structures of $[Fe_xC_y]$ metallocarbohedrenes is evident in a number of the results described above.

Bowers et al. used gas phase ion-mobility measurements to obtain experimental information on the structures of small $[Fe_xC_y]^+$ clusters ($x = 1,2,3$, $y = 2$–8) [57]. While no compositions are common to this investigation and to our calculations reported here, there is general agreement that mono- or bi-cyclic structures occur for the smaller carbon-rich species.

The proposed mechanisms for the observed photodissociative transformations of $[Fe_{12}C_{12}]^+$ to $[Fe_8C_{12}]^+$, and of $[Fe_8C_{12}]^+$ to $[Fe_6C_{12}]^+$, of $[Fe_6C_{12}]^+$ to $[Fe_4C_{12}]^+$, and of $[Fe_4C_{12}]^+$ to $[Fe_2C_{12}]^+$, all pass through energy minima (possibly global minima) for each composition. The mechanisms involve the loss of metal atoms followed by exergonic and low activation energy rearrangements. Other pathways with odd numbers of metal atoms may exist.

In the photodissociation of Fe atoms from $[Fe_{12}C_{12}]^+$ and from $[Fe_8C_{12}]^+$, we can speculate about three types of reaction:

(i) absorption of one or more photons, followed by the concerted loss of the required number of Fe atoms, followed by structural rearrangements activated by the excess energy from the initial absorption;
(ii) absorption of one or more photons, followed by cascading sequential single Fe atom losses, each with associated structural rearrangements. The activation energy for each Fe atom expulsion is provided by the previous exergonic structural rearrangement;
(iii) absorption of one or more photons, each absorption event being followed by sequential single Fe atom loss and associated structural rearrangements. The activation energy for each Fe atom loss is provided by the multiple distinct photon absorption events.

Reaction types (i) and (ii) cannot be ruled out because the original experiment does not provide definite

information about the number of photons absorbed by each molecule, although Pilgrim and Duncan [35] argue that the photodissociation involves multiple photons. The photodissociation experiments are not time-resolved which also leaves pathway (iii) as a distinct possibility. Further experimental data such as the effect of variation of laser energy and pulse duration should provide elucidation of this issue. At this point the cascading pathway seems favourable as it does not rely as heavily on initial energy absorbed nor on the need for multiple absorption events.

Acknowledgments

This research was supported by the Australian Research Council and the University of New South Wales. Hugh Harris acknowledges an Australian Postgraduate Award.

Appendix A. Supplementary data

Supplementary data associated with this article can be found, in the online version, at doi:10.1016/j.poly.2006.05.005.

References

[1] K.B. Shelimov, D.E. Clemmer, M.F. Jarrold, J. Phys. Chem. 98 (1994) 12819.
[2] D.E. Clemmer, J.M. Hunter, K.B. Shelimov, M.F. Jarrold, Nature 372 (1994) 248.
[3] D.E. Clemmer, K.B. Shelimov, M.F. Jarrold, Nature 367 (1994) 718.
[4] K.B. Shelimov, M.F. Jarrold, J. Am. Chem. Soc. 117 (1995) 6404.
[5] K.B. Shelimov, D.E. Clemmer, M.F. Jarrold, J. Phys. Chem. 99 (1995) 11376.
[6] S. Suzuki, H. Torisu, H. Kubota, T. Wakabayashi, H. Shiromaru, Y. Achiba, Int. J. Mass Spectrom. Ion Process. 138 (1994) 297.
[7] D.E. Clemmer, M.F. Jarrold, J. Am. Chem. Soc. 117 (1995) 8841.
[8] H. Shinohara, Rep. Prog. Phys. 63 (2000) 843.
[9] T. Sugai, M. Inakuma, R. Hudgins, P. Dugourd, J.L. Fye, M.F. Jarrold, H. Shinohara, J. Am. Chem. Soc. 123 (2001) 6427.
[10] D.E. Clemmer, K.B. Shelimov, M.F. Jarrold, J. Am. Chem. Soc. 116 (1994) 5971.
[11] S. Wei, B.C. Guo, J. Purnell, S. Buzza, A.W. Castleman, J. Phys. Chem. 96 (1992) 4166.
[12] S. Wei, B.C. Guo, J. Purnell, S. Buzza, A.W. Castleman, Science 256 (1992) 818.
[13] B.C. Guo, K.P. Kerns, A.W. Castleman, Science 255 (1992) 1411.
[14] B.C. Guo, S. Wei, J. Purnell, S. Buzza, A.W. Castleman, Science 256 (1992) 515.
[15] B.C. Guo, K.P. Kerns, A.W. Castleman, J. Am. Chem. Soc. 115 (1993) 7415.
[16] Y. Yamada, A.W. Castleman, Chem. Phys. Lett. 204 (1993) 133.
[17] B.C. Guo, S. Wei, Z. Chen, K.P. Kerns, J. Purnell, S. Buzza, A.W. Castleman, J. Chem. Phys. 97 (1992) 5243.
[18] A.W. Castleman, B.C. Guo, S. Wei, Z.Y. Chen, Plasma Phys. Controlled Fusion 34 (1992) 2047.
[19] J.S. Pilgrim, M.A. Duncan, J. Am. Chem. Soc. 115 (1993) 4395.
[20] A.W. Castleman, Z. Phys. D D26 (1993) 159.
[21] S. Wei, B.C. Guo, J. Purnell, S.A. Buzza, A.W. Castleman, J. Phys. Chem. 97 (1993) 9559.
[22] Z.Y. Chen, G.J. Walder, A.W. Castleman, Phys. Rev. B 49 (1994) 2739.
[23] S.F. Cartier, B.D. May, A.W. Castleman, J. Chem. Phys. 100 (1994) 5384.
[24] S.F. Cartier, B.D. May, A.W. Castleman, J. Am. Chem. Soc. 116 (1994) 5295.
[25] J.S. Pilgrim, M.A. Duncan, Adv. Metal Semicond. Clusters 3 (1995) 181.
[26] K.P. Kerns, B.C. Guo, H.T. Deng, A.W. Castleman, J. Am. Chem. Soc. 117 (1995) 4026.
[27] A.W. Castleman, K.H. Bowen, J. Phys. Chem. 100 (1996) 12911.
[28] M.A. Duncan, J. Cluster Sci. 8 (1997) 239.
[29] M.M. Rohmer, M. Benard, J.M. Poblet, in: P. Braunstein, L.A. Oro, P.R. Raithby (Eds.), Metal Clusters in Chemistry, VCH-Wiley, Weinheim, Germany, 1999, pp. 1664–1710.
[30] M.M. Rohmer, M. Benard, J.M. Poblet, Chem. Rev. 100 (2000) 495.
[31] Y.G. Byun, S.A. Lee, S.Z. Kan, B.S. Freiser, J. Phys. Chem. 100 (1996) 14281.
[32] Y.G. Byun, B.S. Freiser, J. Am. Chem. Soc. 118 (1996) 3681.
[33] Y.G. Byun, S.Z. Kan, S.A. Lee, Y.H. Kim, M. Miletic, R.E. Bleil, S. Kais, B.S. Freiser, J. Phys. Chem. 100 (1996) 6336.
[34] Z.Y. Chen, G.J. Walder, A.W. Castleman, J. Phys. Chem. 96 (1992) 9581.
[35] J.S. Pilgrim, M.A. Duncan, J. Am. Chem. Soc. 115 (1993) 6958.
[36] S.F. Cartier, B.D. May, B.J. Toleno, J. Purnell, S. Wei, A.W. Castleman, Chem. Phys. Lett. 220 (1994) 23.
[37] C.S. Yeh, S. Afzaal, S.A. Lee, G. Byun, B.S. Freiser, J. Am. Chem. Soc. 116 (1994) 8806.
[38] J. Purnell, S. Wei, A.W. Castleman, Chem. Phys. Lett. 229 (1994) 105.
[39] H.T. Deng, B.C. Guo, K.P. Kerns, A.W. Castleman, J. Phys. Chem. 98 (1994) 13373.
[40] J.S. Pilgrim, L.R. Brock, M.A. Duncan, J. Phys. Chem. 99 (1995) 544.
[41] J.S. Pilgrim, M.A. Duncan, Int. J. Mass Spectrom. Ion Process. 138 (1994) 283.
[42] C.S. Yeh, Y.G. Byun, S. Afzaal, S.Z. Kan, S. Lee, B.S. Freiser, P.J. Hay, J. Am. Chem. Soc. 117 (1995) 4042.
[43] S.F. Cartier, B.D. May, A.W. Castleman, J. Chem. Phys. 104 (1996) 3423.
[44] S.F. Cartier, B.D. May, A.W. Castleman, J. Phys. Chem. 100 (1996) 8175.
[45] S.Z. Kan, S.A. Lee, B.S. Freiser, J. Mass Spectrom. 31 (1996) 62.
[46] L.R. Brock, M.A. Duncan, J. Phys. Chem. 100 (1996) 5654.
[47] L.S. Wang, S. Li, H. Wu, J. Phys. Chem. 100 (1996) 19212.
[48] K.P. Kerns, B.C. Guo, H.T. Deng, A.W. Castleman, J. Phys. Chem. 100 (1996) 16817.
[49] S. Li, H. Wu, L.S. Wang, J. Am. Chem. Soc. 119 (1997) 7417.
[50] K.J. Auberry, Y.G. Byun, D.B. Jacobson, B.S. Freiser, J. Phys. Chem. A 103 (1999) 9029.
[51] J. Zhao, B. Liu, H.-J. Zhai, R. Zhou, G. Ni, Z. Xu, Solid State Commun. 124 (2002) 253.
[52] J.M. Lightstone, H.A. Mann, M. Wu, P.M. Johnson, M.G. White, J. Phys. Chem. B 107 (2003) 10359.
[53] J.S. Pilgrim, M.A. Duncan, J. Am. Chem. Soc. 115 (1993) 9724.
[54] S. Wei, B.C. Guo, H.T. Deng, K. Kerns, J. Purnell, S.A. Buzza, A.W. Castleman, J. Am. Chem. Soc. 116 (1994) 4475.
[55] Y.G. Byun, C.S. Yeh, Y.C. Xu, B.S. Freiser, J. Am. Chem. Soc. 117 (1995) 8299.
[56] Y.G. Byun, S.A. Lee, S.Z. Kan, B.S. Freiser, J. Am. Chem. Soc. (1995).
[57] G.v. Helden, N.G. Gotts, P. Maitre, M.T. Bowers, Chem. Phys. Lett. 227 (1994) 601.
[58] M.T. Bowers, Acc. Chem. Res 27 (1994) 324.
[59] S. Lee, N.G. Gotts, G.v. Helden, M.T. Bowers, Science 267 (1995) 999.
[60] D. van Heijnsbergen, G. von Helden, M.A. Duncan, A.J.A. van Roji, G. Meijer, Phys. Rev. Lett. 83 (1999) 4983.
[61] G. von Helden, A.G.G.M. Tielens, D. Van Heijnsbergen, M.A. Duncan, S. Hony, L.B.F.M. Waters, G. Meijer, Science 288 (2000) 313.
[62] G. von Helden, D. Van Heijnsbergen, M.A. Duncan, G. Meijer, Chem. Phys. Lett. 333 (2001) 350.

[63] D. van Heijnsbergen, M.A. Duncan, G. Meijer, G. von Helden, Chem. Phys. Lett. 349 (2001) 220.
[64] I.G. Dance, J. Am. Chem. Soc. 118 (1996) 2699.
[65] C.J. Cassady, S.W. McElvany, J. Am. Chem. Soc. 112 (1990) 4788.
[66] S.W. McElvany, C.J. Cassady, J. Phys. Chem. 94 (1990) 2057.
[67] S. Ramesh, B. Brinson, M.P. Johnson, Z. Gu, R.K. Saini, P. Willis, T. Marriott, W.E. Billups, J.L. Margrave, R.H. Hauge, R.E. Smalley, J. Phys. Chem. B 107 (2003) 1360.
[68] F. Ding, K. Bolton, A. Rosen, J. Phys. Chem. B 108 (2004) 17369.
[69] I.G. Dance, K.J. Fisher, J. Chem. Soc., Dalton Trans. (1997) 2563.
[70] H.H. Harris, I.G. Dance, J. Phys. Chem. A 105 (2001) 3340.
[71] I. Dance, J. Chem. Soc., Chem. Commun. (1998) 523.
[72] B. Delley, J. Chem. Phys. 92 (1990) 508.
[73] B. Delley, New J. Chem. 16 (1992) 1103.
[74] B. Delley, in: J.M. Seminario, P. Politzer (Eds.), Modern Density Functional Theory: A Tool for Chemistry, Elsevier, Amsterdam, 1995, pp. 221–254.
[75] C. Lee, W. Yang, R.G. Parr, Phys. Rev. B 37 (1988) 785.
[76] A.D. Becke, Phys. Rev. A 38 (1988) 3098.
[77] I.G. Dance, E. Wenger, H.H. Harris, Chem. Eur. J. 8 (2002) 3497.
[78] I.G. Dance, J. Chem. Soc., Chem. Commun. (1992) 1779.
[79] I.G. Dance, J. Am. Chem. Soc. 118 (1996) 6309.
[80] H. Hou, J.T. Muckerman, P. Liu, J.A. Rodriguez, J. Phys. Chem. A 107 (2003) 9344.
[81] A. Ceulemans, P.W. Fowler, J. Chem. Soc., Faraday Trans. 1 88 (1992) 2797.
[82] A. Khan, J. Phys. Chem. 97 (1993) 10937.
[83] L. Pauling, Proc. Natl. Acad. Sci. USA 89 (1992) 8175.

Available online at www.sciencedirect.com
ScienceDirect
Polyhedron 26 (2007) 266–274
POLYHEDRON
www.elsevier.com/locate/poly

Binuclear ruthenium and osmium mixed-valence complexes containing fused and flexible polypyridyl bridging ligands

Matthew I.J. Polson, Allan G. Blackman *, Keith C. Gordon *

University of Otago, Chemistry Department, Union Place West, Cnr Union and Cumberland, Dunedin, New Zealand

Received 21 March 2006; accepted 8 May 2006
Available online 19 May 2006

Abstract

$\{Os(bpy)_2\}^{2+}$ and $\{Ru(CN)_4\}^{2-}$ mononuclear and binuclear complexes with ligands 2,3-di-(2-pyridyl)quinoxaline (dpq) and dipyrido[2,3-*a*:3′,2′-*c*]phenazine (ppb) have been prepared. For the binuclear complexes a splitting in oxidation potentials is observed consistent with the formation of mixed-valence species with comproportionation constants (K_{com}) ranging from 2.5×10^4 to 1.8×10^6. The electronic absorption spectra of the mixed-valence species reveal IVCT transitions in the near infrared region. The absorption maximum for the IVCT band ranges from 5800 to 9980 cm^{-1} and the extinction coefficients from 80 to 6300 M^{-1} cm^{-1}. In general the $\{Os(bpy)_2\}^{2+}$ complexes show larger K_{com} values and more intense IVCT bands than the corresponding $\{Ru(CN)_4\}^{2-}$ complexes.
© 2006 Elsevier Ltd. All rights reserved.

Keywords: Mixed-valent states; Osmium; Ruthenium; Spectroelectrochemistry

1. Introduction

The chemistry of ligand-bridged binuclear metal complexes is dictated to a significant extent by the nature of the ligand(s) that bridge the two metal centres. Of particular interest over the past few decades has been the elucidation of the electronic nature of mixed valent binuclear complexes through studies of the way in which the bridging ligand in such complexes facilitates or hinders electronic communication between the metal centres [1–19]. Bridging ligands which allow unimpeded communication between the metal centres result in completely delocalised (Class III) metal complexes, while conversely, bridging ligands which contain orbitals orthogonal to those on the metal ions and which thus cannot effect electron transfer between the two centres give localised (Class I) complexes [20]. We have been interested in attempting to identify and understand the features of bridging ligands that are important in determining the overall electronic nature of mixed valent binuclear metal complexes in which the metal ions are bridged by polypyridyl-type ligands [1,21–24] and in this paper we report our findings concerning the optical and electrochemical properties of a number of binuclear Os(II) and Ru(II) complexes. The bridging ligands used, dpq and its fused planar counterpart ppb (Fig. 1), were chosen because of their interesting steric characteristics. dpq and its derivatives undergo significant distortion on coordination to metal ions, so as to avoid steric clashes between protons on the pyridyl substituents [25–27] while ppb, despite its significantly more rigid nature, also displays large deviations from planarity in its complexes [28,29] and we were interested to see what, if any, effects such distortions would have on the electronic nature of the mixed valent Os_2 and Ru_2 species.

2. Results and discussion

2.1. Synthesis

The binuclear Os complex $[(bpy)_2Os(ppb)Os(bpy)_2](PF_6)_4$ was prepared by reaction of equimolar amounts of $[(bpy)_2OsCl_2]$ and ppb in refluxing ethylene glycol, a method similar to that previously used for the preparation of

* Corresponding authors. Tel.: +64 3 479 7931; fax: +64 3 479 7906.
E-mail addresses: blackman@chemistry.otago.ac.nz (A.G. Blackman), kgordon@chemistry.otago.ac.nz (K.C. Gordon).

0277-5387/$ - see front matter © 2006 Elsevier Ltd. All rights reserved.
doi:10.1016/j.poly.2006.05.012

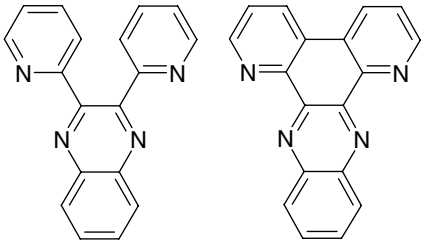


Fig. 1. The bridging ligands ppb and dpq.

$[(bpy)_2Os(dpq)Os(bpy)_2](PF_6)_4 \cdot 2H_2O$ [30]. In this case, however, purification was achieved by chromatography on Sephadex SP-C25 cation exchange resin with sodium *p*-tolylsulfonate as eluent. Subsequent addition of NH_4PF_6 gave the complex in moderate (48%) yield. ^1H NMR spectral data were consistent with the isolated material being an essentially equimolar mixture of two diastereoisomers, each of which contains an axial mirror plane bisecting the ppb ligand, and all attempts to separate these isomers were unsuccessful. The mononuclear complexes $[(bpy)_2Os(dpq)](PF_6)_2$ and $[(bpy)_2Os(ppb)](PF_6)_2$ were prepared as previously reported [29,31].

The $\{Ru(CN)_4\}^{2-}$ complexes were prepared as their sodium salts by an adaptation of the synthesis of $K_2[(bipy)Ru(CN)_4] \cdot 2H_2O$ [32] and related complexes [33] involving 254 nm irradiation of a mixture of $Na_4[Ru(CN)_6]$ and the appropriate ligand in aqueous methanol, and subsequent purification using Sephadex DEAE A-25 anion exchange resin. Use of excess ligand gave predominantly the monomeric species while excess $Na_4[Ru(CN)_6]$ was used to obtain the binuclear complexes.

2.2. Electrochemistry

Electrochemical data for the mononuclear and binuclear Os and Ru complexes in MeCN, MeOH and DMF are presented in Table 1.

Reduction potentials in MeCN of −1.27 V and −1.56 V (versus SCE) for ppb and dpq, respectively, have been reported previously [29,34], and increases in these potentials have been observed on coordination to either one or two metal ions. For example the reduction potentials for the dpq ligands in $[(bpy)_2Ru(dpq)]^{2+}$ and $[(bpy)_2Ru(dpq)Ru(bpy)_2]^{4+}$ in MeCN are −0.8 V and −0.37 V versus SCE, respectively [34–36]. The magnitude of the increase in ligand reduction potential is a function of the metal moiety and the ability of the metal to facilitate metal(dπ) to ligand(π^*) mixing [37].

$[(bpy)_2Os(dpq)]^{2+}$ and $[(bpy)_2Os(dpq)Os(bpy)_2]^{4+}$ (Table 1, MeCN solvent) show increases in the ligand reduction potentials of 650 mV and 1100 mV, respectively, relative to the free ligand, while the corresponding values for $[(bpy)_2Os(ppb)]^{2+}$ and $[(bpy)_2Os(ppb)Os(bpy)_2]^{4+}$ are 760 mV and 900 mV. The binuclear complexes were also examined in MeOH in which the increase in reduction potential is 50–100 mV less than in MeCN.

Similar trends are also observed in the $[(CN)_4Ru(L)]^{2-}$ and $[(CN)_4Ru(L)Ru(CN)_4]^{4-}$ (L = dpq, ppb) complexes (Table 1). The reduction potential is increased by 300–350 mV in the mononuclear complexes, but, in contrast to the Os complexes above, the binuclear systems display essentially identical reduction potentials to the mononuclear complexes. This behaviour is unusual and differs from that usually observed in similar systems. For example, $[(CO)_3ClRe(dpq)]$ and $[(CO)_3ClRe(dpq)Re(CO)_3Cl]$ display reduction potential increases of 800 mV and 1200 mV, respectively, relative to the free dpq ligand [38,39]. In the heterobimetallic system $[(tpy)RuCl(dpq)PtCl_2]$ (tpy = 2,2′:6′,2″-terpyridine), reported by Williams et al. [40] the reduction potential showed a cathodic shift of 1000 mV relative to dpq. This increase in potential was attributed to the presence of an electron-rich Ru centre bound to five polyazine nirogens. For heterobimetallic systems such as $[(bpy)_2Ru(dpq)Cu(PPh_3)_2]^{3+}$ the second metal, in this case Cu, increases the potential by 100 mV. This small increase was

Table 1
Electrochemical data for the Ru and Os complexes

	Solvent	*E*/(V) vs. Ag/AgCl			
		Oxidation		Reduction	
		M(III)/M(III)	M(III)/M(II)	L	L
$[(bpy)_2Os(dpq)]^{2+}$	MeCN		1.00	−0.89	
$[(bpy)_2Os(ppb)]^{2+}$	MeCN		1.07	−0.51	
$[(bpy)_2Os(dpq)Os(bpy)_2]^{4+}$	MeCN	1.35	1.05	−0.44	−1.03
$[(bpy)_2Os(ppb)Os(bpy)_2]^{4+}$	MeCN	1.33	0.96	−0.30	−0.90
$[(bpy)_2Os(dpq)Os(bpy)_2]^{4+}$	MeOH	1.33	0.98	−0.46	−1.03
$[(bpy)_2Os(ppb)Os(bpy)_2]^{4+}$	MeOH	1.33	0.89	−0.39	−0.95
$[(CN)_4Ru(dpq)]^{2-}$	MeOH		0.75		
$[(CN)_4Ru(ppb)]^{2-}$	MeOH		0.79		
$[(CN)_4Ru(dpq)]^{2-}$	DMF		0.49	−1.21	
$[(CN)_4Ru(ppb)]^{2-}$	DMF		0.49	−1.00	−1.55
$[(CN)_4Ru(dpq)Ru(CN)_4]^{4-}$	MeOH	0.81	0.55		
$[(CN)_4Ru(ppb)Ru(CN)_4]^{4-}$	MeOH	0.80	0.50		
$[(CN)_4Ru(dpq)Ru(CN)_4]^{4-}$	DMF	0.65	0.37	−1.19	
$[(CN)_4Ru(ppb)Ru(CN)_4]^{4-}$	DMF	0.7	0.36	−1.01	−1.51

attributed to the weak π-acid character of $\{Cu(PPh_3)_2\}^+$ [25]. One possible explanation for the trends in the reduction potentials of the $\{Ru(CN)_4\}^{2-}$ complexes is that the coulombic effect of the negatively charged metal moieties counterbalances the metal(dπ) to ligand(π*) mixing. The mixing increases the reduction potential.

The mononuclear Os complexes show a single oxidation wave assigned to oxidation of the Os(II) centre (Table 1) [29,41]. The binuclear Os complexes show two oxidation waves separated by 300–400 mV, which are assigned to the Os(II)Os(II)/Os(III)Os(II) and Os(III)Os(II)/Os(III)-Os(III) couples [30]. The product of the first oxidation is a mixed-valent state. The first oxidation potential for the binuclear complexes is <100 mV shifted from that of the corresponding mononuclear complex, indicating that addition of a second metal ion has little effect on the energy of the valence orbitals of the mononuclear complex. The effect of solvent on these potentials is modest, with shifts of <100 mV observed. The observation of two separate one-electron oxidation processes indicates a degree of inter-metal coupling in the binuclear complexes, which may be quantified by the comproportionation constant (K_{com})[1] and these data are presented in Table 4. K_{com} for $[(bipy)_2Os(ppb)Os(bipy)_2]^{4+}$ is an order of magnitude greater than that for $[(bipy)_2Os(dpq)Os(bipy)_2]^{4+}$ suggesting that the ppb ligand offers a communication conduit which facilitates production of a more stable mixed-valence species.

The mononuclear Ru complexes display a single oxidation wave that is insensitive to the bridging ligand, and which is assigned to oxidation of the Ru(II) centre, by comparison with previously reported data (Table 1) [32]. However, these oxidation potentials shift to significantly more positive potentials on changing the solvent from DMF to MeOH, and such behaviour appears to be a feature of Ru(II) complexes containing cyano ancillary ligands. Timpson et al. found that the π* MOs on the CN^- ligands in solvents of high acceptor number are stabilised. This causes the metal dπ MOs to shift to higher energy thus decreasing the oxidation potential [42].

The binuclear complexes show sequential one-electron oxidations and, in contrast to the Os complexes, the first oxidation is 130–200 mV less than that of the corresponding mononuclear compound, showing that the presence of the second metal has an effect on the redox orbitals of the mononuclear metal–ligand assembly. The K_{com} values for the binuclear $[Ru(CN)_4]^{2-}$ complexes in MeOH (Table 4) show that $[(CN)_4Ru(ppb)Ru(CN)_4]^{4-}$ is more stable than the analogous dpq complex, and both complexes display larger K_{com} values in DMF.

[1] The comproportionation constant may be evaluated from the electrochemical data by application of the equation $K_{com} = e^{\Delta E_{1/2}/25.69}$, where $\Delta E_{1/2}$ is the splitting (mV) between the sequential oxidation potentials.

2.3. Electronic absorption spectroscopy

The electronic absorption spectra of the mononuclear and binuclear $[Os(bpy)_2]^{2+}$ complexes and their oxidation products are presented in Table 2, while data for the analogous $[Ru(CN)_4]^{2-}$ complexes are given in Table 3.

The lowest energy transitions of the $[Os(bpy)_2]^{2+}$ complexes are charge-transfer in nature, and both ^{3}MLCT and ^{1}MLCT transitions (Os → ppb or Os → dpq) are observed [31]. Os → bpy MLCT transitions are also observed over the wavelength range 430–450 nm [43].

In the visible region the $[Ru(CN)_4]^{2-}$ complexes show strong MLCT transitions which are very solvatochromic. The MLCT transitions of $[(CN)_4Ru(dpq)]^{2-}$ and $[(CN)_4Ru(ppb)]^{2-}$ complexes show shifts of ~2100 cm^{-1} to longer wavelength when the solvent is changed from water to MeOH, and 4600 and 4800 cm^{-1}, respectively, on going from water to DMF. The binuclear complex $[(CN)_4Ru(ppb)Ru(CN)_4]^{4-}$ shows similar behaviour (a shift of ~4400 cm^{-1}) but the shift observed for $[(CN)_4Ru(dpq)Ru(CN)_4]^{4-}$ (~2500 cm^{-1}) is markedly smaller.

A plot of the electronic absorption band energies for the lowest energy MLCT transition, M → L (E_{op}) against the difference between first oxidation and first reduction potentials (ΔE) for each of the complexes (Fig. 2) reveals a correlation between these parameters.

A number of researchers have investigated the relationship between the energy of the optical transition (E_{op}) and the electrochemical parameters of the metal and ligand involved in the optical transition (ΔE) [44–46]. For a series of related complexes the plots of E_{op} versus ΔE are often linear. The slope may be altered by the extent of mixing between the donor, in these systems metal(dπ), and acceptor, ligand(π*), MOs [47]. Meyer et al. showed that the gradient is $1/(1-\Delta\alpha)$ where $\Delta\alpha$ is the change in extent of mixing between donor and acceptor orbitals caused by the charge-transfer process [47]. For our data the gradient for the osmium complexes is 0.7 ± 0.1 but for the ruthenium complexes is 1.2 ± 0.4. This implies that the $\Delta\alpha$ is greater in the osmium complexes than in the ruthenium, consistent with the electrochemical data which suggest little stabilisation of the ligands in the presence of the ruthenium moiety.

2.4. Spectroelectrochemistry

The electrochemical oxidation of $[(CN)_4Ru(dpq)]^{2-}$ in MeOH and DMF leads to a depletion of the MLCT transition with the concomitant growth of a less intense blue-shifted transition (Fig. 3 and Table 3). This new absorption is similar to those observed in oxidised Os and Ru dpq complexes [31,36,48] which are attributed to an LMCT transition. The LMCT transition shifts to lower energy in MeOH relative to DMF. This solvatochromic behaviour is in the opposite direction to that observed for the MLCT transition of the parent complex. This is consistent with

Table 2
Electronic absorption data for the Os complexes and their corresponding oxidised species

	Solvent	λ/nm ($\varepsilon/10^3$ M^{-1} cm^{-1})							
		IVCT Os–Os	^{3}MLCT Os–L	^{1}MLCT Os–L	1MLCT Os–bpy	LMCT L–Os	π–π* L	π–π* bpy	π–π* bpy
$[(bpy)_2Os(dpq)]^{2+}$	MeCN		765(1.2)	531(7.5)	432(7.2)		350(14.6)		286(54.7)
$[(bpy)_2Os(ppb)]^{2+}$	MeCN		817(2.0)	557(13.0)	442(9.0)		358(21.3)		284(75.3)
$[(bpy)_2Os(dpq)]^{3+}$	MeCN					590(1.3)	369(8.8)	315(30.9)	302(35.9)
						394(7.6)			
$[(bpy)_2Os(ppb)]^{3+}$	MeCN					574(1.2)	376(14.1)	315(55.1)	305(58.1)
						453(2.8)	391(13.8)		
$[(bpy)_2Os(dpq)Os(bpy)_2]^{4+}$	MeCN		924(4.0)	629(20.9)	450(19.6)				287(90.5)
$[(bpy)_2Os(ppb)Os(bpy)_2]^{4+}$	MeCN		1023(12.0)	690(29.5)	441(17.3)		371(28.0)		285(125)
$[(bpy)_2Os(dpq)Os(bpy)_2]^{5+}$	MeCN	1011(2.3)		626(9.9)		739(2.4)		316(38.8)	283(56.6)
$[(bpy)_2Os(ppb)Os(bpy)_2]^{5+}$	MeCN	1092(6.3)		666(24.5)		766(5.4)	377(21.4)	311(51.7)	280(74.1)
$[(bpy)_2Os(dpq)Os(bpy)_2]^{6+}$	MeCN					626(2.1)		316(38.5)	305(42.3)
$[(bpy)_2Os(ppb)Os(bpy)_2]^{6+}$	MeCN					643(3.3)	412(9.8)	314(70.4)	304(68.7)
						513(10.3)			

Table 3
Electronic absorption data for the Ru complexes and their corresponding oxidised species

	Solvent	λ/nm ($\varepsilon/10^3$ M^{-1} cm^{-1})						
		IVCT Ru–Ru	^{1}MLCT Ru–BL	LMCT BL–Ru	π–π* BL	π–π* BL	π–π* BL	π–π* BL
$[(CN)_4Ru(dpq)]^{2-}$	H_2O		497(3.4)			336(8.7)		283(15.5)
$[(CN)_4Ru(ppb)]^{2-}$	H_2O		522(4.2)		357(10.8)		303(19.4)	291(19.9)
			393(4.3)					
$[(CN)_4Ru(dpq)]^{2-}$	MeOH		555(4.2)			339(10.7)		288(14.8)
$[(CN)_4Ru(ppb)]^{2-}$	MeOH		590(3.6)		366(8.3)	349(6.5)	306(14.6)	293(14.8)
			430(1.4)					
$[(CN)_4Ru(dpq)]^{2-}$	DMF		643(5.5)			349(11.5)		291(14.0)
			457(2.1)					
$[(CN)_4Ru(ppb)]^{2-}$	DMF		699(4.4)		371(7.8)	354(5.7)	308(13.0)	296(14.6)
			488(1.9)					
$[(CN)_4Ru(dpq)]^{-}$	MeOH			484(2.3)	389(7.7)			266(20.4)
$[(CN)_4Ru(ppb)]^{-}$	MeOH			513(2.2)	390(3.2)sh	354(6.7)		291(13.8)
$[(CN)_4Ru(dpq)]^{-}$	DMF			437(2.9)	357(11.1)			277(22.0)
$[(CN)_4Ru(ppb)]^{-}$	DMF			436(2.1)	389(6.1)	373(6.2)		
				579(0.6)				
$[(CN)_4Ru(dpq)Ru(CN)_4]^{4-}$	H_2O		551(2.6)		386(3.1)	370(3.3)	303(7.8)	
$[(CN)_4Ru(ppb)Ru(CN)_4]^{4-}$	H_2O		593(5.3)		419(2.0)	364(9.2)	303(16.1)	
$[(CN)_4Ru(dpq)Ru(CN)_4]^{4-}$	MeOH		603(2.1)		389(1.8)	361(2.3)	311(5.8)	
$[(CN)_4Ru(ppb)Ru(CN)_4]^{4-}$	MeOH		666(6.0)		443(2.4)	369(8.5)	307(15.5)	
$[(CN)_4Ru(dpq)Ru(CN)_4]^{4-}$	DMF		641(1.4)		396(1.6)	358(3.1)	314(4.2)	
$[(CN)_4Ru(ppb)Ru(CN)_4]^{4-}$	DMF		805(5.9)		502(2.6)	375(7.2)	308(14.6)	
$[(CN)_4Ru(dpq)Ru(CN)_4]^{3-}$	MeOH	1318(0.08)	615(1.7)	615(1.7)		354(2.5)	310(5.0)	
$[(CN)_4Ru(ppb)Ru(CN)_4]^{3-}$	MeOH	1481(0.7)	672(3.0)	557(2.1)		368(8.7)	304(16.9)	
$[(CN)_4Ru(dpq)Ru(CN)_4]^{3-}$	DMF	1469(0.2)	690(0.9)	690(0.9)		371(1.3)	315(2.5)	
$[(CN)_4Ru(ppb)Ru(CN)_4]^{3-}$	DMF	1710(1.6)	786(2.6)	614(1.8)		372(7.5)	310(15.5)	
$[(CN)_4Ru(dpq)Ru(CN)_4]^{2-}$	MeOH			542(1.2)	385(1.8)	368(1.9)	303(4.6)	
$[(CN)_4Ru(ppb)Ru(CN)_4]^{2-}$	MeOH			582(3.1)		367(8.6)	303(15.7)	
$[(CN)_4Ru(dpq)Ru(CN)_4]^{2-}$	DMF			632(1.1)		367(1.5)	317(4.1)	
$[(CN)_4Ru(ppb)Ru(CN)_4]^{2-}$	DMF			609(1.9)		372(8.0)	309(15.0)	
				703(2.3)				

the LMCT assignment for the oxidised species as the metal(dπ) orbitals are *acceptor* MOs in this transition; they are destabilised in DMF relative to MeOH thus increasing the transition energy. Similar changes are observed for $[(CN)_4Ru(ppb)]^{2-}$ (Table 3).

The spectral changes that accompany the oxidation of $[(bpy)_2Os(ppb)]^{2+}$ are similar to those observed for the previously reported complex $[(bpy)_2Os(dpq)]^{2+}$ and are presented in Table 2 [31].

The binuclear complexes show a depletion of their MLCT transitions upon oxidation (Table 2). The first oxidation leads to the formation of a mixed-valent state and an IVCT band is observed at 1092 nm for $[(bpy)_2Os(ppb)Os(bpy)_2]^{5+}$. This is slightly red-shifted from the corresponding

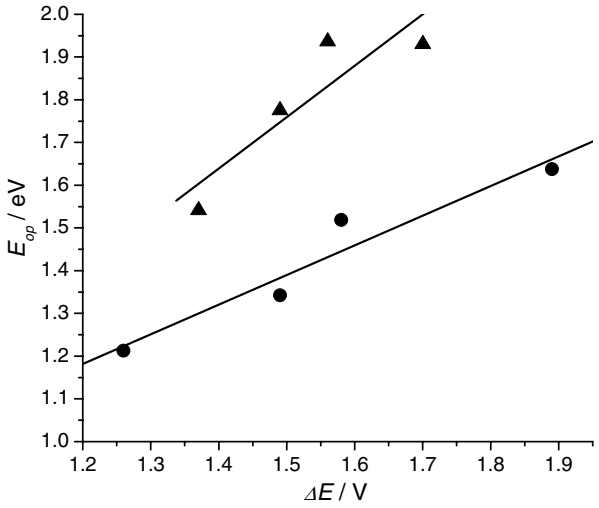


Fig. 2. Plots of the energy of the lowest energy ^{3}MLCT transition (E_{op}) vs. the thermodynamic energy difference between first oxidation and first reduction potentials (ΔE) for $\{Os(bpy)_2\}^{2+}$ (●) and Ru (▲) complexes. Plotted lines are the least squares regression for each data set.

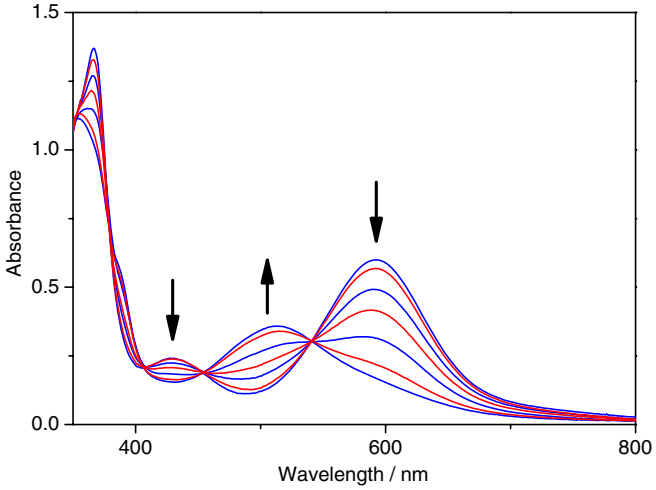


Fig. 3. The electronic absorption spectral changes (indicated by arrows) for $[Ru(CN)_4(ppb)]^{2-}$ in MeOH with application of an oxidising potential.

$[(bpy)_2Os(dpq)Os(bpy)_2]^{5+}$ IVCT band and is about 3 times more intense [30]. Further oxidation results in depletion of the IVCT transition and the growth of new features attributed to LMCT transitions [24,30]. The electrochemically prepared mixed-valence species $[(CN)_4Ru(dpq)Ru(CN)_4]^{3-}$ shows a weak IVCT transition which is red-shifted on going from MeOH (1318 nm) to DMF (1469 nm). The IVCT transition of $[(CN)_4Ru(ppb)Ru(CN)_4]^{3-}$ also red-shifts on going from MeOH to DMF and the transitions are an order of magnitude more intense than in the dpq complex. However, the IVCT transitions observed in the ruthenate complexes are significantly less intense than those observed for the Os complexes (Tables 2 and 3).

Subsequent oxidation of the mixed-valent ruthenate complexes causes the bleaching of the IVCT transitions and formation of new bands (Table 3) that are assigned as LMCT transitions. These transitions, red-shift, in DMF (relative to MeOH) in contrast to those observed in the mononuclear complexes.

The bandwidth (full width half height, $\nu_{1/2}$/cm^{-1}) values for the IVCT transition in a mixed-valence species can be used to obtain information about the nature of the mixed valence state [5,49–51] and such data for the Os and Ru complexes are given in Table 4. For each of the $\{Ru(CN)_4\}^{2-}$ complexes, the bandwidth of the IVCT band is close to that predicted by Hush theory [52–54]. For $[Ru(CN)_4(dpq)]^{2-}$, $\nu_{1/2}$ is 4500 and 4000 cm^{-1} in MeOH and DMF, respectively, close to the predicted values of 4200 and 4000 cm^{-1}. For $[Ru(CN)_4(ppb)]^{2-}$ the observed (and predicted) values are 3400 (4000) cm^{-1} in MeOH and 4300 (3700) cm^{-1} in DMF. However, both $[Os(bpy)_2(dpq)]^{2+}$ (2500 cm^{-1}) and $[Os(bpy)_2(ppb)]^{2+}$ (1700 cm^{-1}) complexes display significantly narrower transitions than predicted (>4000 cm^{-1}) (Table 4). Hush theory is generally considered to be very effective in accurately predicting the IVCT transition bandwidths of weakly coupled Class II systems [55–58] and the observation of transitions narrower than those predicted by the theory suggests strong coupling and hence Class III systems. Thus our data suggest that the Os complexes are Class III while the Ru complexes are weakly coupled Class II systems (see Fig. 4).

The spectroscopic and electrochemical data show that the ppb complexes form more stable mixed-valence systems than the dpq complexes, as evidenced by more intense and spectrally narrower IVCT transitions. The increase in stability ranges between 4 and 15 times (Table 4). Comparing dpq and ppb ruthenate complexes, the IVCT transitions of the ppb complex are 8 times more intense – the effect is less for the Os systems (about 2.5 times).

We were unable to obtain crystallographic structural data for these systems but the structure of the ruthenate complexes may be modelled using density functional theory. These calculations reveal that the ppb complex is

Table 4
Electrochemical and spectroscopic parameters for the binuclear mixed-valence species

	Solvent	ΔE (mV)	K_{com} ($\times 10^{-4}$)	λ_{max} (cm^{-1})	$\nu_{1/2}$ (cm^{-1})	$\nu_{1/2(calc)}$ (cm^{-1})	ε_{max} (M^{-1}cm^{-1})
$[(CN)_4Ru(dpq)Ru(CN)_4]^{4-}$	MeOH	260	2.5	7587	4474	4186	80
$[(CN)_4Ru(ppb)Ru(CN)_4]^{4-}$	MeOH	300	10	6752	3380	3949	700
$[(CN)_4Ru(dpq)Ru(CN)_4]^{4-}$	DMF	280	5.4	6807	3959	3965	200
$[(CN)_4Ru(ppb)Ru(CN)_4]^{4-}$	DMF	340	56	5848	4259	3679	1600
$[(bpy)_2Os(dpq)Os(bpy)_2]^{4+}$	MeCN	300	12	9988	2539	4803	2300
$[(bpy)_2Os(ppb)Os(bpy)_2]^{4+}$	MeCN	370	180	9143	1684	4596	6300

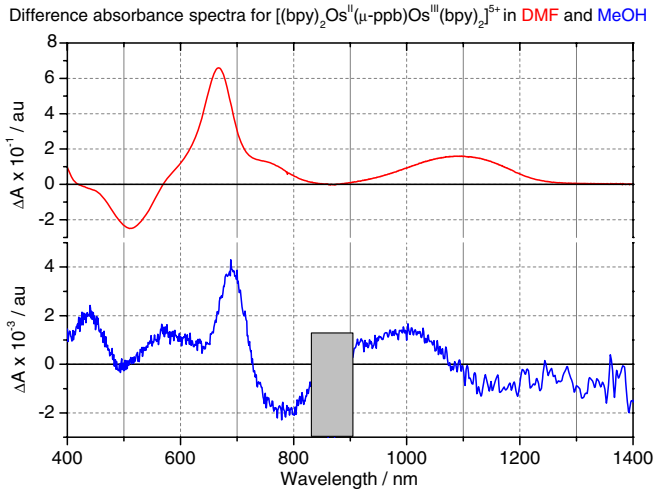


Fig. 4. Absorbance difference spectra for $[(bpy)_2Os^{III}(\mu\text{-ppb})Os^{II}(bpy)_2]^{5+}$ minus $[(bpy)_2Os^{II}(\mu\text{-ppb})Os^{II}(bpy)_2]^{4+}$ in DMF (top trace) and MeOH (bottom trace). Spectra were generated in a spectroelectrochemical cell using the parent species as the background trace. A strong MeOH solvent feature has been blocked in the lower trace difference spectrum.

much more planar than that with dpq (Fig. 5). In the case of $[(CN)_4Ru(ppb)Ru(CN)_4]^{4-}$ the axial CN groups on adjacent Ru centres are essentially co-linear; however, for $[(CN)_4Ru(dpq)Ru(CN)_4]^{4-}$ these groups are rotated 42°. The dpq ligand is also non-planar with the pyridyl rings splayed 70° apart. This loss of planarity in the case of dpq is consistent with the reduction in inter-metal coupling as evidenced in the IVCT transitions.

3. Conclusions

The behaviours of mixed valence complexes prepared from binuclear complexes of $[Ru(CN)_4]^{2-}$ and $[Os(bpy)_2]^{2+}$ differ as a function of metal and bridging ligand. The $[Os(bpy)_2]^{2+}$ complexes appear to be Class III in nature with those of $[Ru(CN)_4]^{2-}$ being closer to Class II. It is clear for these data that the $[Os(bpy)_2]^{2+}$ complexes are more strongly coupled than those of $[Ru(CN)_4]^{2-}$. The effect of the bridging ligand is also pronounced, with the less sterically flexible bridging ligand providing greater inter-metal stabilisation (by an order of magnitude in K_{com}), as evidenced by increases in the intensity of the IVCT and by the width of the IVCT. These data provide an example of control of the structure giving control over electronic properties. Calculations suggest that the ppb ligand has a much less distorted structure than that of dpq, this may explain the greater coupling in the case of complexes with the former bridging ligand.

4. Experimental

Synthetic reagents were LR or AR grade and were used without further purification unless otherwise specified. All solvents used for spectroscopic and electrochemical measurements were Aldrich spectroscopic or HPLC grade and were used without further purification.

$[(bpy)_2OsCl_2]$ [59] and ppb [29] were prepared by the literature methods. $[(bpy)_2Os(dpq)Os(bpy)_2](PF_6)_4$ was prepared by the method of Richter and Brewer [31] while

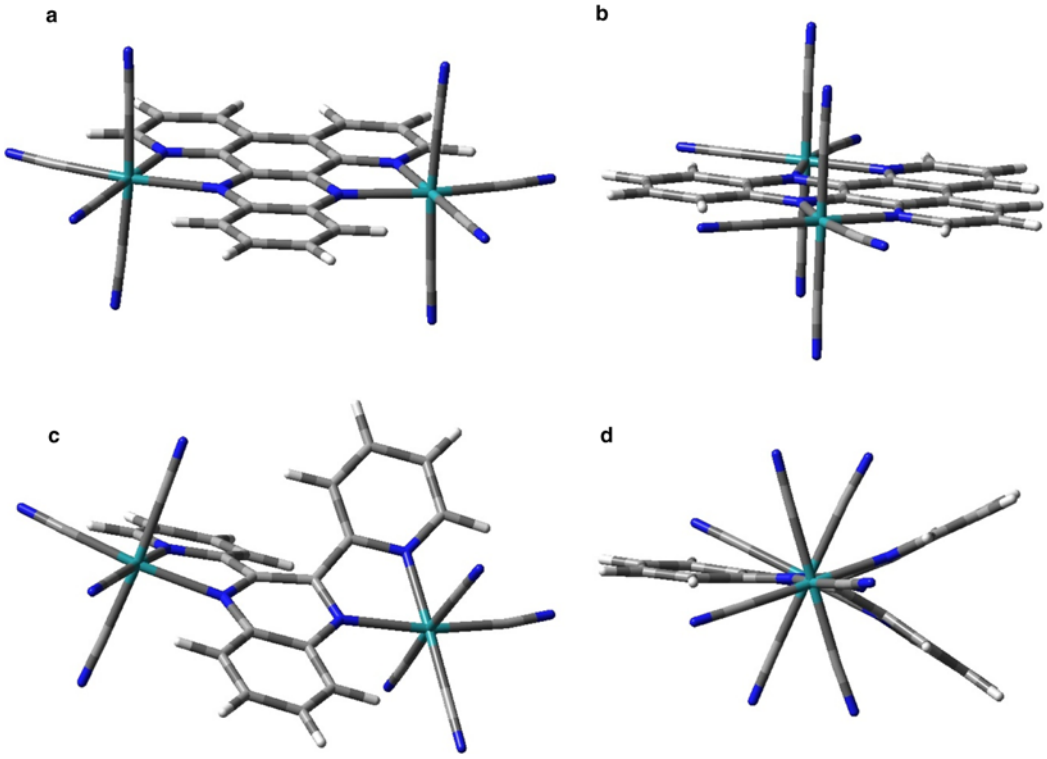


Fig. 5. Calculated structures of $[(CN)_4Ru(ppb)Ru(CN)_4]^{4-}$ (a, b) and $[(CN)_4Ru(dpq)Ru(CN)_4]^{4-}$ (c, d).

$[(bpy)_2Os(ppb)](PF_6)_2$ and $[(bpy)_2Os(dpq)](PF_6)_2$ were prepared as previously described [29]. The samples of $[(bpy)_2Os(dpq)Os(bpy)_2](PF_6)_4$, $[(bpy)_2Os(ppb)](PF_6)_2$ and $[(bpy)_2Os(dpq)](PF_6)_2$ were used from our previous study [29].

5. Instrumentation

Spectroscopic and electrochemical data were obtained as previously reported [29]. Calculations (B3LYP/3-21G) were performed using the GAUSSIAN-03W suite of programmes [60].

5.1. $[(bpy)_2Os(ppb)Os(bpy)_2](PF_6)_4$

$[(bpy)_2OsCl_2]$ (200 mg, 0.349 mmol) and ppb (100 mg, 0.354 mmol) were gently heated in ethylene glycol (50 ml) until completely dissolved. The solution was then heated to reflux for 2 h. On cooling, dichloromethane (100 ml) and water (200 ml) were added. The organic layer was separated and discarded and the aqueous layer again extracted with dichloromethane (100 ml). The aqueous layer was diluted, loaded on to a Sephadex SP-C25 column (10 cm × 2 cm diameter) and washed well with water and 0.05 M sodium *p*-tolylsulfonate to remove an uncharged species. The binuclear complex was eluted with 0.3 M sodium *p*-tolylsulfonate. The complex was separated from the eluant by addition of solid NH_4PF_6 (1 g) followed by extraction with 5 × 100 ml of dichloromethane. The resulting intensely coloured organic solution was taken to dryness (rotavap), dissolved in a minimum volume of acetonitrile and reprecipitated by addition to an aqueous NH_4PF_6 solution. The solid was collected by filtration, dissolved in acetonitrile and reprecipitated by addition to ether. Yield: 120 mg (48%). *Anal.* Calc. for $C_{58}H_{42}N_{12}Os_2P_4F_{24}$: C, 37.30; H, 2.27; N, 9.00. Found: C, 37.00; H, 2.85; N, 8.81%. ^{1}H NMR (500 MHz, MeCN-d_3): 9.14 (d, $J^d = 8.5$ Hz, 1H), 9.09 (d, $J^d = 8.5$ Hz, 1H), 8.75 (d, $J^d = 8.5$ Hz, 1H), 8.68 (d, $J^d = 8.5$ Hz, 1H), 8.64 (d, $J^d = 8.0$ Hz, 1H), 8.57 (d, $J^d = 8.0$ Hz, 1H), 8.54 (d, $J^d = 8.0$ Hz, 1H), 8.50 (d, $J^d = 8.5$ Hz, 1H), 8.30 (d, $J^d = 8.5$ Hz, 1H), 8.12 (m, 2H), 8.05 (m, 6H), 7.96 (ddd, $J^{d1} = 8.5$ Hz, $J^{d2} = 8.0$ Hz, $J^{d3} = 1.0$ Hz, 1H), 7.88 (m, 4H), 7.79 (d, $J^d = 5.5$ Hz, 1H), 7.67 (m, 2H), 7.56 (d, $J^d = 5.0$ Hz, 1H), 7.50 (m, 7H), 7.37 (AA′BB′, $J = 3.5$ Hz, 1H), 7.31 (d, $J^d = 5.0$ Hz, 1H), 7.23 (m, 3H), 7.16 (d, $J^d = 8.5$ Hz, 1H), 7.12 (ddd, $J^{d1} = 5.0$ Hz, $J^{d2} = 4.0$ Hz, $J^{d3} = 1.0$ Hz, 1H), 6.97 (ddd, $J^{d1} = 7.5$ Hz, $J^{d2} = 6.0$ Hz, $J^{d3} = 1.0$ Hz, 1H), 6.71 (d, $J^d = 5.0$ Hz, 1H). ES-MS: *m/z* 1723, $\{M-PF_6\}^+$; 789, $\{M-2PF_6\}^{2+}$; 477.7, $\{M-3PF_6\}^{3+}$; 322, $\{M-4PF_6\}^{4+}$.

5.2. $Na_4Ru(CN)_6$

$RuCl_3 \cdot xH_2O$ (1.00 g) was dissolved in the minimum volume of water (10 ml) and added to a solution of NaCN (10 g) in ethylene glycol (50 ml). The solution was refluxed for 30 min, cooled and added to methanol (100 ml) to precipitate the crude product. This was collected by filtration, dissolved in the minimum volume of water and filtered. NaI (5 g) was added to the aqueous solution which was layered with methanol (200 ml) and left undisturbed for one week. Large crystals formed which were filtered, washed with ether and air dried. Yield: 1.25 g. ^{13}C NMR (50 MHz, D_2O): 164.0. IR (KBr disc): 2064 cm^{-1}. ES-MS: *m/z* 278, $\{M-(Na_2CN)\}^-$; 255, $\{M-(Na_3CN)\}^-$; 229, $\{M-(Na_3(CN)_2)\}^-$; 206, $\{M-(Na_4(CN)_2)\}^-$; 180, $\{M-(Na_4(CN)_3)\}^-$; 154, $\{M-(Na_4(CN)_3)\}$.

5.3. $Na_2[Ru(CN)_4(L)]$

To the appropriate ligand (270 mg, 0.96 mmol) in methanol (250 ml) was added $Na_4Ru(CN)_6$ (200 mg, 0.57 mmol) dissolved in water (250 ml). The resulting clear solution was thoroughly purged with argon in a quartz reaction vessel and irradiated with 254 nm light in a Rayonet reactor for 32 h. The now red (dpq) or purple (ppb) solution was concentrated and extracted 3 times with dichloromethane (50 ml). The desired product was separated from unreacted $Na_4Ru(CN)_6$ and the binuclear product on a Sephadex DEAE-A25 column, the red product eluting with 0.3 M NaI. The solution was concentrated and the product precipitated by slow addition to acetone. This was repeated to ensure no NaI remained.

5.4. $Na_2[Ru(CN)_4(ppb)]$

Yield: 220 mg (72%). *Anal.* Calc. for $Na_2[Ru(CN)_4(ppb)]1.5NaI \cdot 4H_2O$ ($C_{22}H_{18}I_{1.5}N_8Na_{3.5}O_4Ru$): C, 31.82; H, 2.19; N, 13.50. Found: C, 31.41; H, 1.99; N, 14.08% [61,62]. ^{1}H NMR (300 MHz, D_2O): 9.54 (d, $J^d = 9.0$ Hz, 2H), 9.40 (d, $J^d = 5.5$ Hz, 2H), 8.04 (m, 4H), 7.86 (d, $J^d = 8.0$ Hz, 1H), 7.70 (dd, $J^{d1} = 6.0$ Hz, $J^{d2} = 5.5$ Hz, 1H), 7.59 (d, $J^d = 8.0$ Hz, 1H), 7.51 (t, $J^t = 5.5$ Hz, 1H), 6.99 (d, $J^d = 7.5$ Hz, 1H). ^{13}C NMR (50 MHz, D_2O): 164.7, 163.9, 163.4, 163.2, 156.3, 154.5, 151.5, 150.8, 149.9, 144.8, 141.3, 141.2, 140.7, 137.2, 134.4, 133.2, 13.4, 129.4, 129.3, 127.3, 127.1, 126.9. ES-MS: *m/z* 513, $\{M-Na\}^-$; 491, $\{M-2Na\}^-$; 465, $\{M-(Na_2CN)\}$. IR (KBr disc): 2097(w), 2068(w), 2059(m), 2044(m).

5.5. $Na_2[Ru(CN)_4(dpq)]$

Yield: 270 mg (88%). *Anal.* Calc. for $Na_2[Ru(CN)_4(dpq)]1.7NaI \cdot 4H_2O$ ($C_{22}H_{20}I_{1.7}N_8Na_{3.7}O_4Ru$): C, 30.64; H, 2.34; N, 12.99. Found: C, 30.34; H, 2.15; N, 14.10%. ^{1}H NMR (300 MHz, D_2O): 9.94 (d, $J^d = 8.0$ Hz, 1H), 9.60 (d, $J^d = 4.0$ Hz, 2H), 8.41 (d, $J^d = 10.0$ Hz, 1H), 8.22 (m, 3H), 8.03 (m, 2H), 7.66 (t, $J^t = 8.0$ Hz, 1H), 6.44(t, $J^t = 7.0$ Hz, 1H). ^{13}C NMR (50 MHz, D_2O): 164.7, 163.8, 163.3, 162.1, 154.3, 151.7, 148.1, 145.9, 145.8, 144.0, 143.7, 142.2, 134.5, 133.8, 133.2, 132.0, 131.7, 131.0, 128.9, 127.4, 125.5, 125.0. ES-MS: *m/z* 511,

{M−Na}$^-$; 489, {M−2Na}$^-$; 462, {M−(Na_2CN)}$^-$. IR (KBr disc): 2100(w), 2077(w), 2066(m), 2052(m).

5.6. $Na_4[Ru(CN)_4(ppb)Ru(CN)_4]$

To dpq (155 mg) in methanol (200 ml) was added $Na_4Ru(CN)_6$ (400 mg) dissolved in water (300 ml). The resulting clear solution was thoroughly purged with argon in a quartz reaction vessel and irradiated with 254 nm light in a Rayonet reactor for 48 h. The now purple solution was concentrated and extracted 3 times with dichloromethane (50 ml). The desired product was separated from unreacted $Na_4Ru(CN)_6$, the mononuclear product and a contaminating possibly trinuclear complex on a Sephadex DEAE-A25 column, the purple product eluting with 1.0 M NaI. The solution was concentrated and the oily product precipitated by slow addition to acetone. This solid was redissolved in methanol and reprecipitated by addition to acetone. Yield: 180 mg (48%). *Anal*. Calc. for $Na_4[Ru(CN)_4(ppb)Ru(CN)_4]0.5NaI \cdot 11H_2O$ ($C_{26}H_{32}I_{0.5}N_{12}Na_{4.5}O_{11}Ru_2$): C, 29.53; H, 3.05; N, 15.89. Found: C, 29.91; H, 3.06; N, 15.24%. ^{1}H NMR (300 MHz, D_2O): 9.31 (m, 4H), 8.05 (d, $J^d = 8.5$ Hz, 2H), 8.00 (AA′BB′, $J = 3.0$ Hz, 2H), 7.75 (t, $J^t = 8.0$ Hz, 2H), 7.53 (t, $J^t = 6.0$ Hz, 2H). ^{13}C NMR (50 MHz, D_2O): 163.3, 162.7, 162.1, 162.0, 157.4, 153.9, 152.6, 143.6, 136.9, 133.4, 131.6, 129.8, 126.9. ES-MS: *m/z* 347, {M}$^{2-}$; 334, {M−CN}$^{2-}$. IR (KBr disc): 2099(w), 2068(w), 2050(m), 2046(m).

5.7. $Na_4[Ru(CN)_4(dpq)Ru(CN)_4]$

To ppb (155 mg) in methanol (200 ml) was added $Na_4Ru(CN)_6$ (400 mg) dissolved in water (300 ml). The resulting clear solution was thoroughly purged with argon in a quartz reaction vessel and irradiated with 254 nm light in a Rayonet reactor for 48 h. The now blue solution was concentrated and extracted 3 times with dichloromethane (50 ml). The desired product was separated from unreacted $Na_4Ru(CN)_6$ and the mononuclear product on a Sephadex DEAE-A25 column, the purple product eluting with 1.0 M NaI. The solution was concentrated and the product precipitated by slow addition to acetone. This solid was found to contain a green, possibly trinuclear contaminant which was removed by size exclusion chromatography on a Sephadex LH-20 column by eluting with methanol. Yield: 27 mg (7%). *Anal*. Calc. for $Na_4[Ru(CN)_4(dpq)Ru(CN)_4]0.5NaI \cdot 11H_2O$ ($C_{26}H_{34}I_{0.5}N_{12}Na_{4.5}O_{11}Ru_2$): C, 29.47; H, 3.23; N, 15.86;. Found: C, 29.84; H, 3.16; N, 15.13%. ^{1}H NMR (300 MHz, D_2O): 9.97 (AA′BB′, $J = 3.5$ Hz, 2H), 9.63 (d, $J^d = 4.5$ Hz, 2H), 8.66 (d, $J^d = 5.5$ Hz, 2H), 8.28 (AA′BB′, $J = 3.5$ Hz, 2H), 7.75 (dd, $J^{d1} = 5.5$ Hz, $J^{d2} = 4.5$ Hz, 2H). ^{13}C NMR (50 MHz, D_2O): 165.4, 163.5, 162.0, 161.2, 154.3, 148.2, 146.2, 145.9, 133.7, 131.9, 131.5, 127.8, 126.9. ES-MS: *m/z* 346, {M}$^{2-}$; 333, {M−CN}$^{2-}$. IR (KBr disc): 2099(w), 2081(w), 2072(m), 2051(m).

References

[1] K.C. Gordon, J.J. McGarvey, Chem. Phys. Lett. 173 (1990) 443.
[2] K.D. Demadis, T.J. Meyer, P.S. White, Inorg. Chem. 36 (1997) 5678.
[3] T. Ito, T. Hamaguchi, H. Nagino, T. Yamaguchi, J. Washington, C. Kubiak, Science 277 (1997) 660.
[4] K.D. Demadis, G.A. Neyhart, E.M. Kober, T.J. Meyer, J. Am. Chem. Soc. 120 (1998) 121.
[5] C.E.B. Evans, M.L. Naklicki, A.R. Rezvani, C.A. White, V.V. Kondratiev, R.J. Crutchley, J. Am. Chem. Soc. 120 (1998) 13096.
[6] T.E. Keyes, R.J. Forster, P.M. Jayaweera, C.G. Coates, J.J. McGarvey, J.G. Vos, Inorg. Chem. 37 (1998) 5925.
[7] S. Roche, J.A. Thomas, L.J. Yellowlees, Chem. Commun. (1998) 1429.
[8] K.D. Demadis, G.A. Neyhart, E.M. Kober, P.S. White, T.J. Meyer, Inorg. Chem. 38 (1999) 5948.
[9] M. Glockle, W. Kaim, Angew. Chem., Int. Ed. 38 (1999) 3072.
[10] T. Ito, T. Hamaguchi, H. Nagino, T. Yamaguchi, H. Kido, I.S. Zavarine, T. Richmond, J. Washington, C.P. Kubiak, J. Am. Chem. Soc. 121 (1999) 4625.
[11] M. Ketterle, W. Kaim, J.A. Olabe, A.R. Parise, J. Fiedler, Inorg. Chim. Acta 291 (1999) 66.
[12] S. Klokishner, K. Boukheddaden, F. Varret, Phys. Rev. B 60 (1999) 150.
[13] Y.J. Chen, D.-S. Pan, C.-F. Chiu, J.-X. Su, S.J. Lin, K.S. Kwan, Inorg. Chem. 39 (2000) 953.
[14] K.D. Demadis, G.A. Neyhart, E.M. Kober, P.S. White, T.J. Meyer, Inorg. Chem. 39 (2000) 3430.
[15] S. Chellamma, M. Lieberman, Inorg. Chem. 40 (2001) 3177.
[16] T. Yamaguchi, N. Imai, T. Ito, C.P. Kubiak, Bull. Chem. Soc. Jpn. 73 (2000) 1205.
[17] J.V. Lockard, J.I. Zink, A.E. Konradsson, M.N. Weaver, S.F. Nelsen, J. Am. Chem. Soc. 125 (2003) 13471.
[18] S. Chakraborty, R.H. Laye, P. Munshi, R.L. Paul, M.D. Ward, G. Kumar Lahiri, J. Chem. Soc., Dalton Trans. (2002) 2348.
[19] T.P. Ortiz, J.A. Marshall, L.A. Emmert, J. Yang, W. Choi, A.L. Costello, J.A. Brozik, Inorg. Chem. 43 (2004) 132.
[20] M.B. Robin, P. Day, Adv. Inorg. Radiochem. 10 (1967) 247.
[21] L.C. Abbott, C.J. Arnold, K.C. Gordon, R.E. Hester, J.N. Moore, R.N. Perutz, T.Q. Ye, Laser Chem. 19 (1999) 279.
[22] P.D.W. Boyd, A.K. Burrell, W.M. Campbell, P.A. Cocks, K.C. Gordon, G.B. Jameson, D.L. Officer, Z.D. Zhao, Chem. Commun. (1999) 637.
[23] C.A. Bignozzi, R. Argazzi, J.R. Schoonover, K.C. Gordon, R.B. Dyer, F. Scandola, Inorg. Chem. 31 (1992) 5260.
[24] K.C. Gordon, A.K. Burrell, T.J. Simpson, S.E. Page, G. Kelso, M.I.J. Polson, A. Flood, Eur. J. Inorg. Chem. (2002) 554.
[25] S.M. Scott, K.C. Gordon, A.K. Burrell, J. Chem. Soc., Dalton Trans. (1999) 2669.
[26] A. Ferretti, A. Lami, G. Villani, Inorg. Chem. 37 (1998) 4460.
[27] K.C. Gordon, A.H.R. Al-Obaidi, P.M. Jayaweera, J.J. McGarvey, J.F. Malone, S.E.J. Bell, J. Chem. Soc., Dalton Trans. (1996) 1591.
[28] S.L. Howell, B.J. Matthewson, M.I.J. Polson, A.K. Burrell, K.C. Gordon, Inorg. Chem. 43 (2004) 2876.
[29] M.I.J. Polson, S.L. Howell, A. Flood, A.G. Blackman, K.C. Gordon, Polyhedron 23 (2004) 1427.
[30] M.M. Richter, K.J. Brewer, Inorg. Chem. 32 (1993) 2827.
[31] M.M. Richter, K.J. Brewer, Inorg. Chim. Acta 180 (1991) 125.
[32] C.A. Bignozzi, C. Chiorboli, M.T. Indelli, M.A. Rampi Scandola, G. Varani, F. Scandola, J. Am. Chem. Soc. 108 (1986) 7872.
[33] S.L. Howell, K.C. Gordon, J.J. McGarvey, J. Phys. Chem. A 109 (2005) 2948.
[34] J. Sherborne, S.M. Scott, K.C. Gordon, Inorg. Chim. Acta 260 (1997) 199.
[35] G.N.A. Nallas, K.J. Brewer, Inorg. Chim. Acta 257 (1997) 27.

[36] J.B. Cooper, D.B. MacQueen, J.D. Petersen, D.W. Wertz, Inorg. Chem. 29 (1990) 3701.
[37] J.F. Endicott, H.B. Schlegel, M.J. Uddin, D.S. Seniveratne, Coord. Chem. Rev. 229 (2002) 95.
[38] M.R. Waterland, T.J. Simpson, K.C. Gordon, A.K. Burrell, J. Chem. Soc., Dalton Trans. (1998) 185.
[39] T.J. Simpson, K.C. Gordon, Inorg. Chem. 34 (1995) 6323.
[40] R.L. Williams, H.N. Toft, B. Winkel, K.J. Brewer, Inorg. Chem. 42 (2003) 4394.
[41] S.C. Rasmussen, M.M. Richter, E. Yi, H. Place, K.J. Brewer, Inorg. Chem. 29 (1990) 3926.
[42] C.J. Timpson, C.A. Bignozzi, B.P. Sullivan, E.M. Kober, T.J. Meyer, J. Phys. Chem. 100 (1996) 2915.
[43] P. Huber, H. Yersin, J. Phys. Chem. 97 (1993) 12705.
[44] R.A. Metcalfe, E.S. Dodsworth, S.S. Fielder, D.J. Stufkens, A.B.P. Lever, W.J. Pietro, Inorg. Chem. 35 (1996) 7741.
[45] E.I. Solomon, A.B.P. Lever, et al. (Eds). Inorganic Electronic Structure and Spectroscopy: Applications and Case Studies, vol. II, 1999.
[46] H. Masui, A.L. Freda, M.C. Zerner, A.B.P. Lever, Inorg. Chem. 39 (2000) 141.
[47] J.C. Curtis, B.P. Sullivan, T.J. Meyer, Inorg. Chem. 22 (1983) 224.
[48] M.M. Richter, K.J. Brewer, Inorg. Chem. 31 (1992) 1594.
[49] K.D. Demadis, C.M. Hartshorn, T.J. Meyer, Chem. Rev. 101 (2001) 2655.
[50] W. Kaim, A. Klein, M. Gloeckle, Acc. Chem. Res. 33 (2000) 755.
[51] A.C. Benniston, A. Harriman, P. Li, C.A. Sams, M.D. Ward, J. Am. Chem. Soc. 126 (2004) 13630.
[52] N.S. Hush, J.R. Reimers, Chem. Rev. 100 (2000) 775.
[53] N.S. Hush, J.R. Reimers, Coord. Chem. Rev. 177 (1998) 37.
[54] N.S. Hush, Prog. Inorg. Chem. 8 (1967) 391.
[55] S.F. Nelsen, Chem.-Eur. J. 6 (2000) 581.
[56] T. Nishiumi, Y. Nomura, Y. Chimoto, M. Higuchi, K. Yamamoto, J. Phys. Chem. B 108 (2004) 7992.
[57] J.E. Sutton, H. Taube, Inorg. Chem. 20 (1981) 3125.
[58] C. Creutz, M.D. Newton, N. Sutin, J. Photochem. Photobiol. A 82 (1994) 47.
[59] D.A. Buckingham, F.P. Dwyer, H.A. Goodwin, A.M. Sargeson, Aust. J. Chem. 17 (1964) 325.
[60] M.J. Frisch, G.W. Trucks, H.B. Schlegel, G.E. Scuseria, M.A. Robb, J.R. Cheeseman, J.A. Montgomery Jr., T. Vreven, K.N. Kudin, J.C. Burant, J.M. Millam, S.S. Iyengar, J. Tomasi, V. Barone, B. Mennucci, M. Cossi, G. Scalmani, N. Rega, G.A. Petersson, H. Nakatsuji, M. Hada, M. Ehara, K. Toyota, R. Fukuda, J. Hasegawa, M. Ishida, T. Nakajima, Y. Honda, O. Kitao, H. Nakai, M. Klene, X. Li, J.E. Knox, H.P. Hratchian, J.B. Cross, C. Adamo, J. Jaramillo, R. Gomperts, R.E. Stratmann, O. Yazyev, A.J. Austin, R. Cammi, C. Pomelli, J.W. Ochterski, P.Y. Ayala, K. Morokuma, G.A. Voth, P. Salvador, J.J. Dannenberg, V.G. Zakrzewski, S. Dapprich, A.D. Daniels, M.C. Strain, O. Farkas, D.K. Malick, A.D. Rabuck, K. Raghavachari, J.B. Foresman, J.V. Ortiz, Q. Cui, A.G. Baboul, S. Clifford, J. Cioslowski, B.B. Stefanov, G. Liu, A. Liashenko, P. Piskorz, I. Komaromi, R.L. Martin, D.J. Fox, T. Keith, M.A. Al-Laham, C.Y. Peng, A. Nanayakkara, M. Challacombe, P.M.W. Gill, B. Johnson, W. Chen, M.W. Wong, C. Gonzalez, J.A. Pople, GAUSSIAN-03, Gaussian, Inc., Pittsburgh, PA, 2003.
[61] Microanalyses of cyano complexes can be complicated by incomplete combustion as reported by Brewer et al. K.J. Brewer, W.R. Murphy Jr., J.D. Petersen, Inorg. Chem. 26 (1987) 3376.
[62] The presence of NaI has also been observed by Posse et al. M.E.G. Posse, F. Fagalde, M.M. Vergara, N.E. Katz, Polyhedron 17 (1998) 2733, Despite rigorous purification measures they found microanalysis on N was out by up to 1% for complexes similar to those reported herein.

Available online at www.sciencedirect.com
ScienceDirect
Polyhedron 26 (2007) 275–283
POLYHEDRON
www.elsevier.com/locate/poly

The molecular structure of selected minerals of the rosasite group – An XRD, SEM and infrared spectroscopic study

Ray L. Frost *, Daria L. Wain, Wayde N. Martens, B. Jagannadha Reddy

Inorganic Materials Research Program, School of Physical and Chemical Sciences, Queensland University of Technology, 2 George Street, GPO P.O. Box 2434, Brisbane, Qld 4001, Australia

Received 22 March 2006; accepted 18 May 2006
Available online 13 July 2006

Abstract

Minerals in the rosasite mineral group namely rosasite, glaucosphaerite, kolwezite, mcguinnessite have been studied by powder X-ray diffraction, scanning electron microscopy and infrared spectroscopy. X-ray diffraction shows the minerals to be complex mixtures with more than one rosasite mineral observed in each sample. SEM analysis shows the minerals to be fibrous in nature and the use of EDAX enabled the chemical composition of the minerals to be determined. The spectral patterns for the minerals rosasite, glaucosphaerite, kolwezite and mcguinnessite are similar to that of malachite implying the molecular structure is similar to malachite. A comparison is made with the spectrum of malachite. The rosasite mineral group is characterised by two OH stretching vibrations at ~3401 and 3311 cm^{-1}. Two intense bands observed at ~1096 and 1046 cm^{-1} are assigned to v_1 $(CO_3)^{2-}$ symmetric stretching vibration and the δ OH deformation mode. Multiple bands are found in the 800–900 and 650–750 cm^{-1} regions attributed to the v_2 and v_4 bending modes confirming the symmetry reduction of the carbonate anion in the rosasite mineral group as C_{2v} or C_s. A band at ~560 cm^{-1} is assigned to a CuO stretching mode.
© 2006 Elsevier Ltd. All rights reserved.

Keywords: Glaucosphaerite; Kolwezite; Mcguinnessite; Nullaginite; Rosasite; Hydroxycarbonate; Infrared spectroscopy

1. Introduction

The carbonates are a group of over 60 naturally occurring minerals containing the essential structural building block $(CO_3)^{2-}$. Most of these minerals are relatively rare and often in association with other building blocks such as hydroxyls, halogens, sulphate, silicate, phosphate, etc. The common simple rock-forming carbonates can be divided into three main groups: (a) the calcite group, (b) the dolomite group and (c) the aragonite group. Peter Williams reports that whilst metal substitution in azurite is extremely uncommon, such is not the case for malachite [1]. Substitution of Cu(II) by other cations gives rise to the rosasite mineral group. In minerals related to malachite, ions identified together with Cu(II) are: Zn(II), Co(II), Ni(II) and Mg(II). The rosasite mineral group is monoclinic or triclinic hydroxy carbonates with the general formula $A_2(CO_3)(OH)_2$ or $AB(CO_3)(OH)_2$ where A and B is cobalt, copper, magnesium, nickel and zinc [2]. The most common congener of malachite is rosasite. Rosasite forms in the oxidation zones of zinc–copper deposits and the crystals are often fibrous and found in tufted aggregates. No single crystal study of rosasite has been forth coming. Powder diffraction studies of rosasite suggest the mineral is triclinic [3]. The chemical composition of the rosasite minerals means that the minerals are highly colourful, often green to blue. Minerals in the rosasite group are related to the mineral malachite [4,5]. Minerals in this group include rosasite $[(Cu,Zn)_2(CO_3)(OH)_2]$ [6–8], glaucosphaerite $[(Cu,Ni)_2(CO_3)(OH)_2]$ [9–11], kolwezite $[(Cu,Co)_2(CO_3)(OH)_2]$ [12], mcguinnessite $[(Mg,Cu,)_2(CO_3)(OH)_2]$ [13–16], and nullaginite $[(Ni)_2(CO_3)(OH)_2]$ [17–19]. Apart from rosasite the minerals are rare secondary minerals.

* Corresponding author. Tel.: +61 7 3864 2407; fax: +61 7 3864 1804.
E-mail address: r.frost@qut.edu.au (R.L. Frost).

0277-5387/$ - see front matter © 2006 Elsevier Ltd. All rights reserved.
doi:10.1016/j.poly.2006.05.046

Besides the chemical composition, the structural relationships between these minerals are demonstrated by the similarity of their powder diffraction patterns [20]. The space group symmetry and cell parameters are mainly derived from powder pattern indexing. Apart from that of malachite, no other structural determinations are available for the rosasite minerals. Rosasite as with the other minerals of this group form spheroidal aggregates in extremely thin fibrous crystals. Rosasite may be associated with aurichalcite, smithsonite and hemimorphite.

Infrared and Raman spectroscopy have been used to investigate carbonates including azurite and malachite [21,22]. A detailed single crystal Raman study has been undertaken [5,21]. However the vibrational spectroscopy of minerals of the rosasite group has not been undertaken. No infrared spectra of the minerals of the rosasite group have been forthcoming [22–25]. Also no NIR research on these minerals has been reported. An infrared stretching vibration of the hydroxyl unit of azurite was observed at 3425 cm^{-1}, whereas two bands were reported for malachite at 3400 and 3320 cm^{-1}. The observation of two bands for malachite suggests coupling of the hydroxyl stretching vibrations [5]. This coupling was not observed for azurite [5]. Azurite and malachite form the basis of pigments in samples of an archaeological or medieval nature [26–29]. Malachite has a characteristic intense band at ~430 cm^{-1} and for azurite an intense band at ~400 cm^{-1}. The deformation modes of azurite were reported at 1035 and 952 cm^{-1} and at 1045 and 875 cm^{-1} for malachite [22,30]. Thus even though the two carbonate minerals have the same space group, the molecular structure of the minerals is sufficiently different to show infrared bands at slightly different wavenumbers. Differences between the spectra of malachite and azurite may be explained by the molecular structure of azurite being based upon a distorted square planar arrangement compared with a distorted octahedral arrangement about the copper in malachite.

The symmetric stretching bands of carbonate for azurite and malachite were observed at 1090 and 1095 cm^{-1}. Goldsmith and Ross reported the infrared bending modes of carbonate at 837 and 817 cm^{-1} for azurite and at 820 and 803 cm^{-1} for malachite [21]. Two v_3 modes were observed at 1490 and 1415 cm^{-1} for azurite and at 1500 and 1400 cm^{-1} for malachite [4,5]. The observation of these two bands shows a loss of degeneracy. Such a conclusion is also supported by the observation of two v_4 modes at 769 and 747 cm^{-1} for azurite and 710 and 748 cm^{-1} for malachite. The vibrational spectroscopy of these two minerals is complicated by this loss of degeneracy. Schmidt and Lutz report some vibrational spectroscopic data [31]. Two infrared bands at 3415 and 3327 cm^{-1} were observed for malachite. Although the Raman spectra of the mineral brochantite [$Cu_4(OH)_6SO_4$] have been reported, the Raman spectra of malachite and azurite were not [31].

In this work we report the X-ray diffraction, SEM analysis and infrared spectroscopy of minerals of the rosasite group and relate the spectroscopy to the mineral structure.

2. Experimental

2.1. Minerals

The minerals, their formula and origin used in this study are listed in Table 1. Selected minerals were obtained from the Mineral Research Company and other sources including Museum Victoria. The samples were phase analysed by X-ray diffraction for phase analysis and for chemical composition by EDX measurements.

2.2. X-ray diffraction

X-ray diffraction (XRD) patterns were recorded using Cu Kα radiation ($n = 1.5418$ Å) on a Philips PANalytical X' Pert PRO diffractometer operating at 40 kV and 40 mA with 0.125° divergence slit, 0.25° anti-scatter slit, between 3° and 15° (2θ) at a step size of 0.0167°. For low angle XRD, patterns were recorded between 1° and 5° (2θ) at a step size of 0.0167° with variable divergence slit and 0.5° anti-scatter slit.

2.3. SEM analysis

Mineral samples of the rosasite were coated with a thin layer of evaporated carbon and secondary electron images were obtained using an FEI Quanta 200 scanning electron microscope (SEM). For X-ray microanalysis (EDX), three

Table 1
Table of the hydroxycarbonate minerals, their chemical formulae and origin

Mineral	Locality of origin	Formulae	Analysis (% by mass)
Rosasite	Mapimi, Durango, Mexico	$(Cu,Zn)_2(CO)_3(OH)_2$	CuO 35.7 ZnO 36.5
Glaukosphaerite	Carr Boyd Nickel Mine, Carr Boyd Rocks, W.A. [17,19]	$(Cu,Ni)_2(CO_3)(OH)_2$	CuO 41.6 NiO 25.2
Kolwezite	Mupine, Shaba Province, Zaire [33]	$(Cu,Co)_2(CO)_3(OH)_2$	CuO 48.4 CoO 23.0
McGuinnessite	Red Mountain, Mendocino County, CA [16]	$(Mg,Cu)_2(CO_3)(OH)_2$	CuO 39.6 MgO 23.7

samples were embedded in Araldite resin and polished with diamond paste on Lamplan 450 polishing cloth using water as a lubricant. The samples were coated with a thin layer of evaporated carbon for conduction and examined in a JEOL 840A analytical SEM at 25 kV accelerating voltage. Preliminary analyses of the rosasite mineral samples were carried out on the FEI Quanta SEM using an EDAX microanalyser, and microanalysis of the clusters of fine crystals was carried out using a full standards quantitative procedure on the JEOL 840 SEM using a Moran Scientific microanalysis system. Oxygen was not measured directly but was calculated using assumed stoichiometries to the other elements analysed.

2.4. Mid-IR spectroscopy

Infrared spectra were obtained using a Nicolet Nexus 870 FTIR spectrometer with a smart endurance single bounce diamond ATR cell. Spectra over the 4000–525 cm^{-1} range were obtained by the co-addition of 64 scans with a resolution of 4 cm^{-1} and a mirror velocity of 0.6329 cm/s. Spectra were co-added to improve the signal to noise ratio.

Spectral manipulation such as baseline adjustment, smoothing and normalisation were performed using the Spectracalc software package GRAMS (Galactic Industries Corporation, NH, USA). Band component analysis was undertaken using the Jandel 'Peakfit' software package

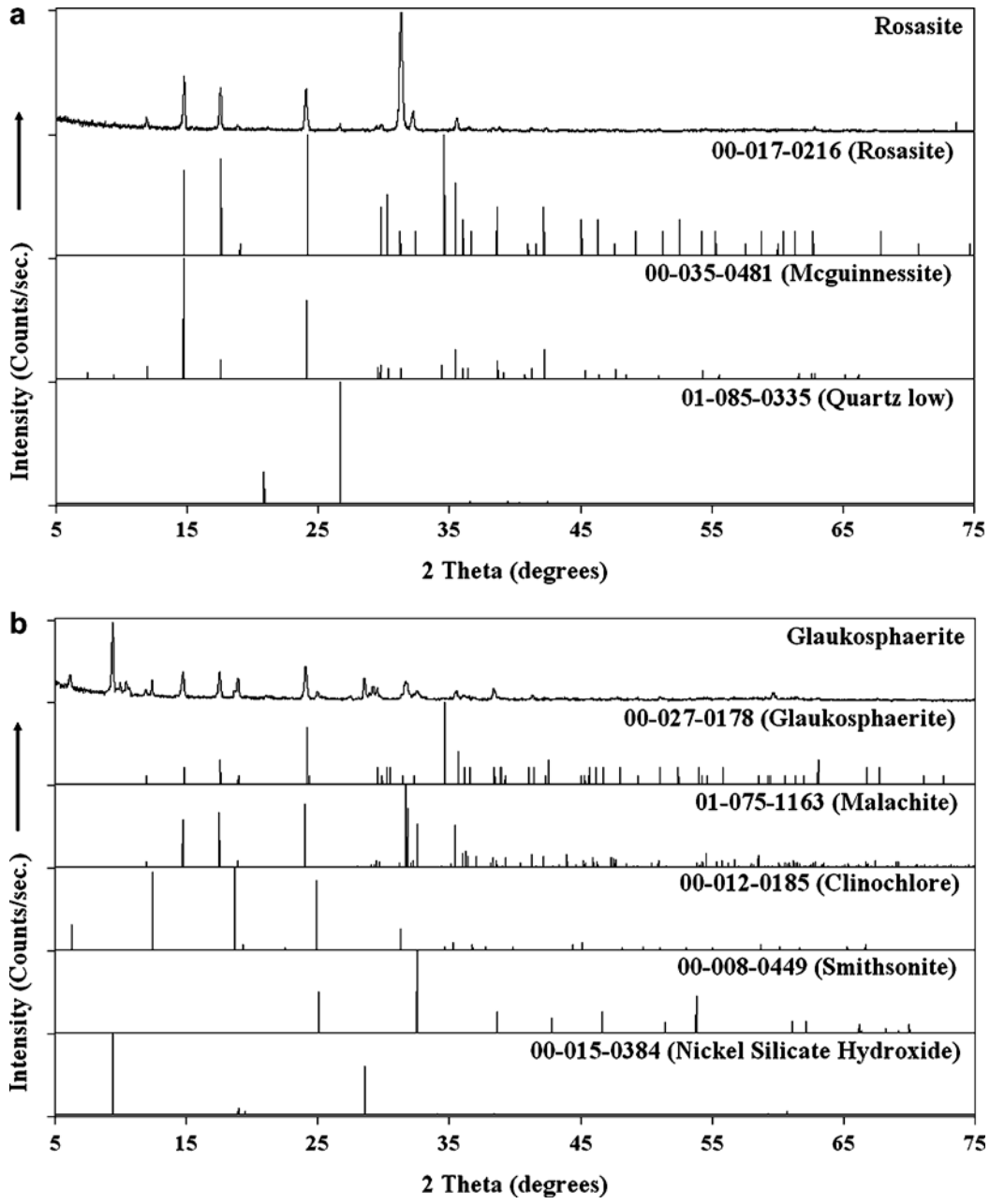


Fig. 1. (a and b) XRD patterns for rosasite and glaukosphaerite.

which enabled the type of fitting function to be selected and allows specific parameters to be fixed or varied accordingly. Band fitting was done using a Lorentz–Gauss cross-product function with the minimum number of component bands used for the fitting process. The Gauss–Lorentz ratio was maintained at values greater than 0.7 and fitting was undertaken until reproducible results were obtained with squared correlations of r^2 greater than 0.995.

3. Results and discussion

3.1. X-ray diffraction

The XRD patterns of the rosasite mineral group are illustrated by those of rosasite and glakosphaerite which are shown in Fig. 1a and b. What is observed from the XRD patterns is that the mineral rosasite appears to be a mixture of rosasite, quartz and mcguinnessite. Glaukosphaerite appears to be a mixture of glaukosphaerite with some malachite and other impurities. In order to run an XRD pattern the mineral is scraped off a host rock and is ground before the XRD pattern is collected. This means that all minerals present will be collected and analysed. In terms of SEM and spectroscopy a more judicious selection can be made and only specific crystals analysed. In this instance the correct mineral is obtained. Roberts et al showed that the mineral rosasite was monoclinic [32].

3.2. SEM images

SEM images of rosasite, glaucosphaerite, kolwezite and pokrovskite are shown in Fig. 2a–d. The crystals of the three minerals are acicular and may be up to 0.5 mm in length. The minerals appear to be fibrous in nature. The images show the hydroxycarbonates to be botryoidal and forming crusts. This is best illustrated by the SEM image of pokrovskite (Fig. 2d). Fig. 3 show the typical EDAX analyses of rosasite, gluakosphaerite, kolwezite and mcguinessite. The results of the analyses are reported in Table 1.

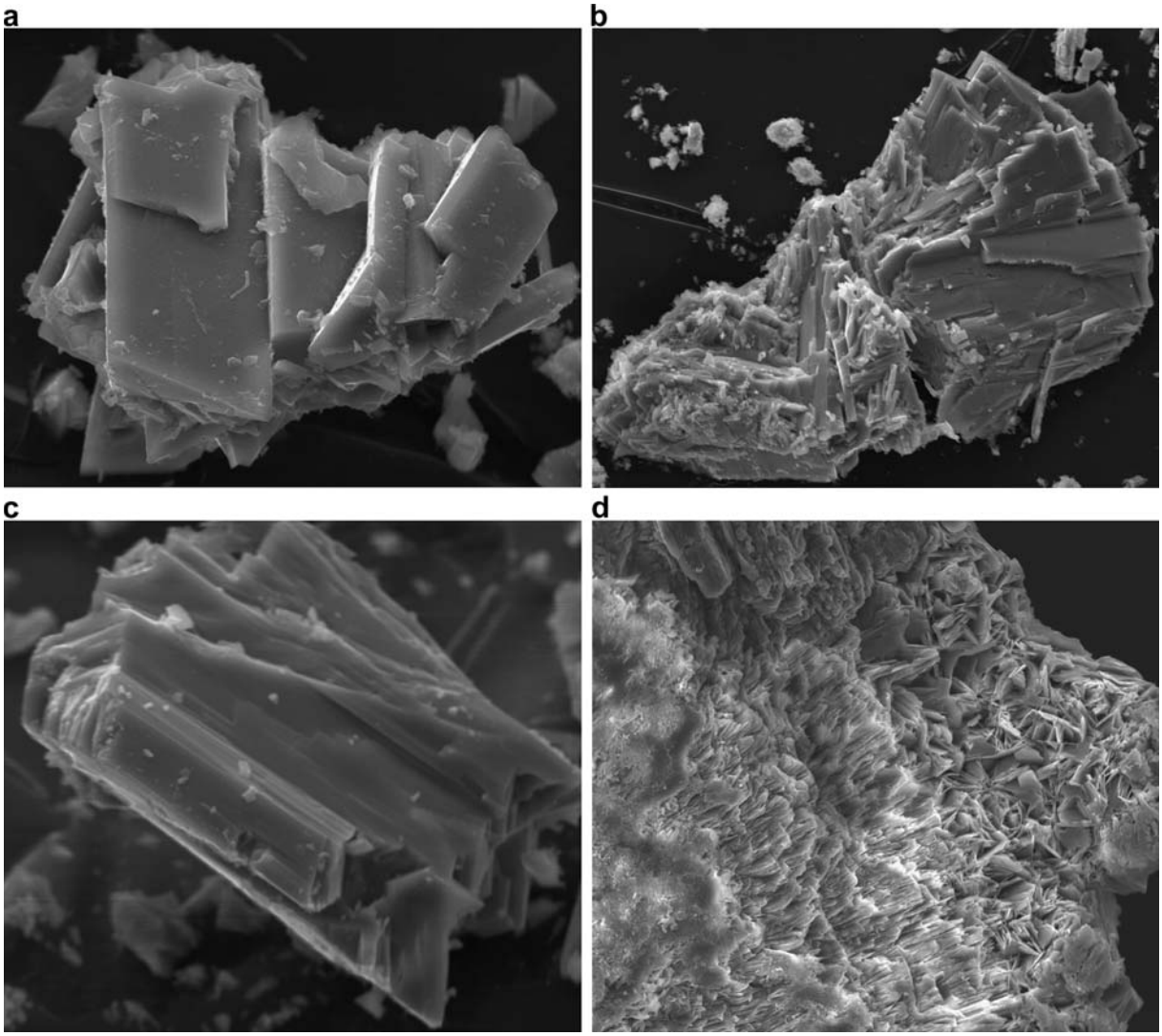


Fig. 2. (a–d) SEM images of rosasite, glaucosphaerite, kolwezite and pokrovskite (magnification 1500×).

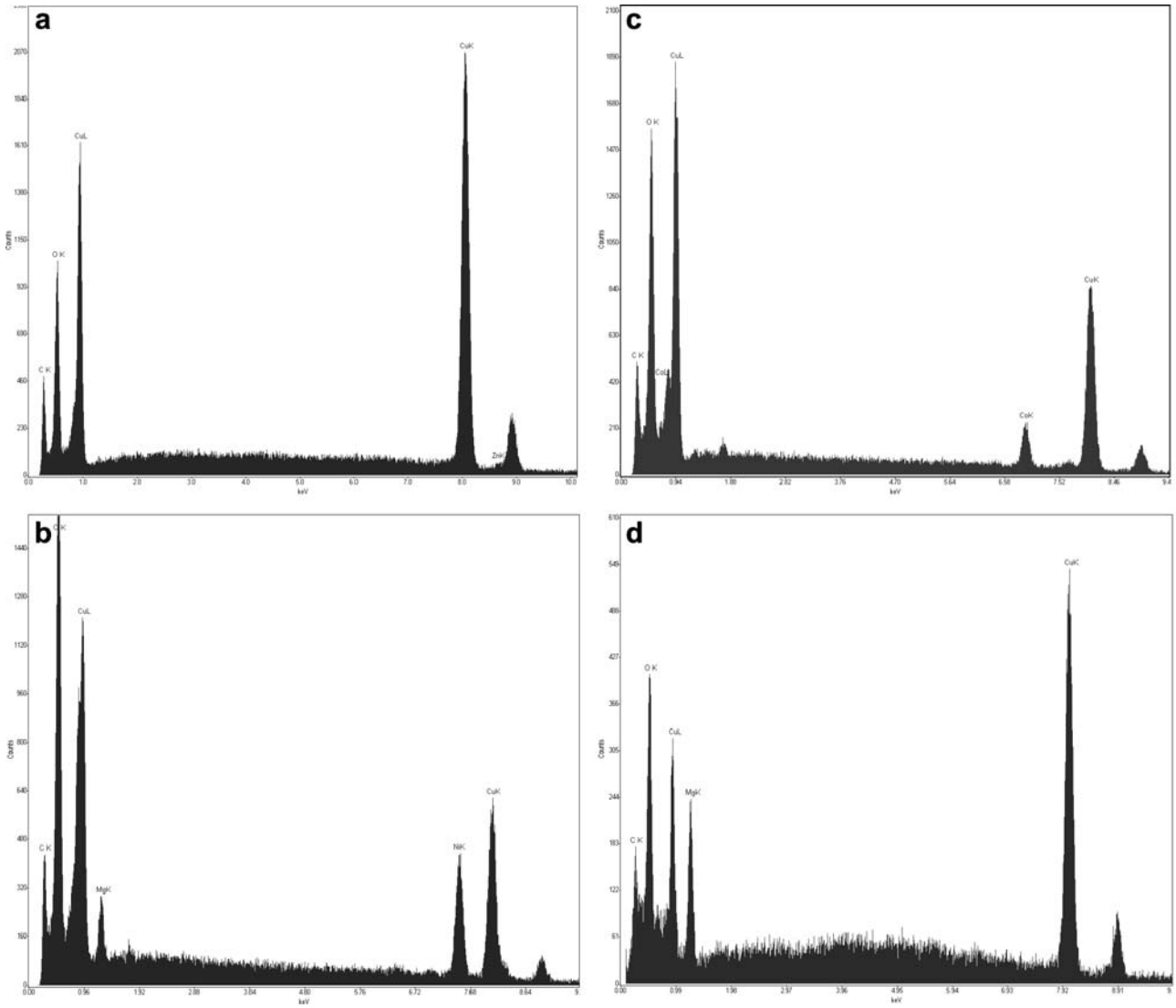


Fig. 3. (a–d) EDAX spectra of rosasite, glaucosphaerite, kolwezite and mcguinessite.

The rosasite sample used in this work analysed to a Cu/Zn ratio of close to 1:1. As such if the atom ratio of Cu/Zn is 1:1 then every second position in the model will be taken up by a Zn atom. Rosasite does not necessarily maintain a ratio of 1:1. For example the rosasite from Rosas mine, Narcao, Cagliari, Sardegna (Sardinia), Italy analyses as CuO 53.7% and ZnO 18.3%. This gives a formula of the Narcao rosasite as $(Cu_{1.5}Zn_{0.5})_2(CO)_3(OH)_2$. According to Anthony et al. a glaucosphaerite sample from Kasompi, Congo gave a formula of $(Cu_{1.23}Zn_{0.71})_2(CO)_3(OH)_2$ [33]. It is noted that the Cu/Zn ratio is not 1:1 and the total cations is not 2.0, but 1.94. The mineral glaucosphaerite from the Carr Boyd Nickel mine analyses as CuO 41.6% and NiO 25.2%. This gives the formula of glaucosphaerite as $(Cu_{1.1}Ni_{0.7}Mg_{0.06})_2(CO)_3(OH)_2$. A similar formula exists for the mineral kolwezite from Zaire namely $(Cu_{1.33}Co_{0.67})_2(CO)_3(OH)_2$. The fact that the two cation ratio is not 1:1 may have implications for the structure of the mineral and therefore for the vibrational spectroscopy of the mineral. The mcguinnessite from California gives a cation ratio of Cu/Mg as 1:1. Other measurements record a ratio of Mg/Cu as 1.5/0.5.

3.3. Infrared spectroscopy

The minerals of the rosasite group have not been studied by single crystal X-ray diffraction. Invariably because most of the crystals are composed of thin fibres. Extensive powder X-ray diffraction suggests the minerals are triclinic, although Anthony et al. states the minerals are monoclinic [33]. This statement is apparently based upon the assumption the structures are similar to that of malachite. The structure shows that two of the three oxygens bond to separate copper atoms but one carbonate oxygen bonds to two copper atoms. The OH unit serves to bridge two copper atoms. The model of the structure of malachite shows that the carbonate anion is of C_{2v} symmetry if the two cations bonding to the carbonate anion are identical [4,5]. If however the two cations are different (e.g. Cu and Ni or Cu and Zn) then the symmetry of the carbonate anion would be C_s.

The mineral glaucosphaerite is equally enigmatic and may be monoclinic. Williams reported the structure of the rosasite group of minerals to be triclinic [1]. It is not neccessarily true that rosasite has the same structure as malachite [1]. In the structure of rosasite some of the copper atoms in the model of malachite are replaced by zinc atoms.

The infrared spectra of selected minerals of the rosasite group in the OH stretching region are shown in Fig. 4. The results of the band component analysis of the infrared spectra are reported. Rosasite is characterised by two intense bands at 3401 and 3311 cm^{-1} with two additional bands at 3139 and 3486 cm^{-1}. The bands at 3486, 3401 and 3311 cm^{-1} are attributed to OH stretching vibrations whereas the bands at 3228 and 3139 cm^{-1} are ascribed to adsorbed water. If we use a Libowitzky type empirical formula [34] calculation of the hydrogen bond distances in the structure can be estimated. The bands at 3486, 3401, 3311 and 3139 cm^{-1} lead to hydrogen bond distances of 2.877, 2.80, 2.75 and 2.68 Å. The conclusion may be made that there are three different hydrogen bond distances of the OH units which are a weaker hydrogen bond strength than the hydrogen bond formed from adsorbed water. The mineral glaukosphaerite has infrared bands at 3529, 3402, 3309, 3191 and 3022 cm^{-1}. The bands at 3402 and 3309 cm^{-1} are in almost identical positions to those of rosasite. Because of the broad spectral profile in the OH stretching region variation in the bands at 3191 and 3022 cm^{-1} may occur. This makes the fitting of bands difficult. Similarly for the mineral kolwezite the two OH stretching vibrations are observed at 3401 and 3307 cm^{-1}. The infrared spectrum of mcguinnessite appears different. The two bands at 3407 and 3316 $cm^{-1}$are in common with the spectra of the other minerals. The other intense band at 3545 cm^{-1} may be due to an impurity. Powder X-ray diffraction shows that these minerals are not 100% pure and are often mixed with other minerals of the rosasite group or related minerals.

The infrared spectra of selected rosasite minerals in the 900–1200 cm^{-1} region are shown in Fig. 5. For rosasite two intense bands are observed at 1096 and 1046 cm^{-1}. The first band is assigned to the ν_1 symmetric stretching mode of the carbonate unit. Bands have been observed in the infrared spectra of malachite at 1095 and 1090 cm^{-1} for azurite [4,5]. The infrared spectrum of hydrocerrusite showed an intense band at 1090 cm^{-1} [35]. Interestingly the $(CO_3)^{2-}$ ν_1 band of the rosasite minerals should not

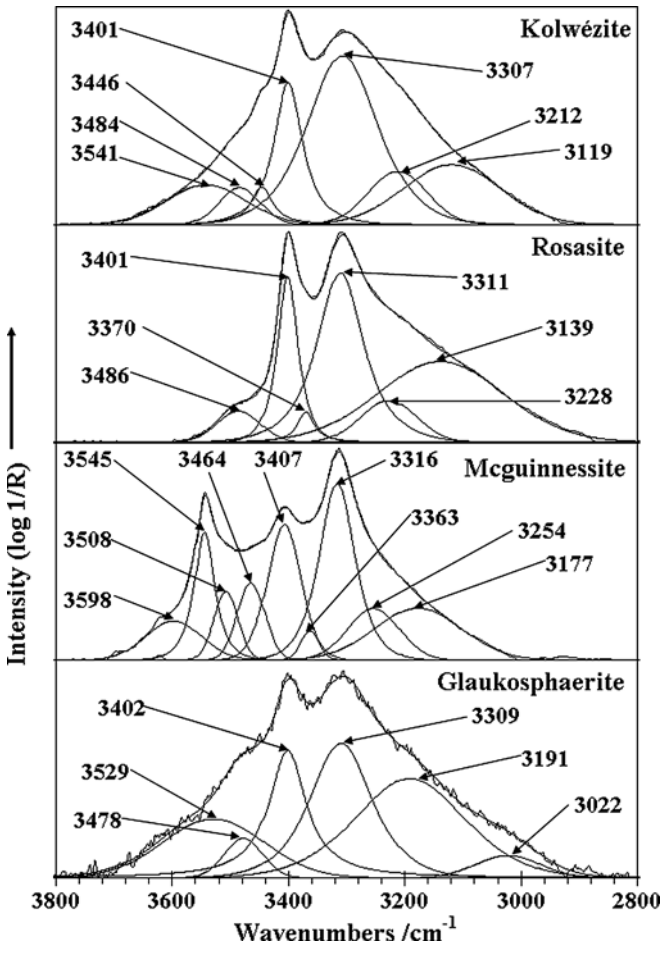


Fig. 4. Infrared spectra of rosasite, glaukosphaerite, kolwezite and mcguinessite in the 2800–3800 cm^{-1} region.

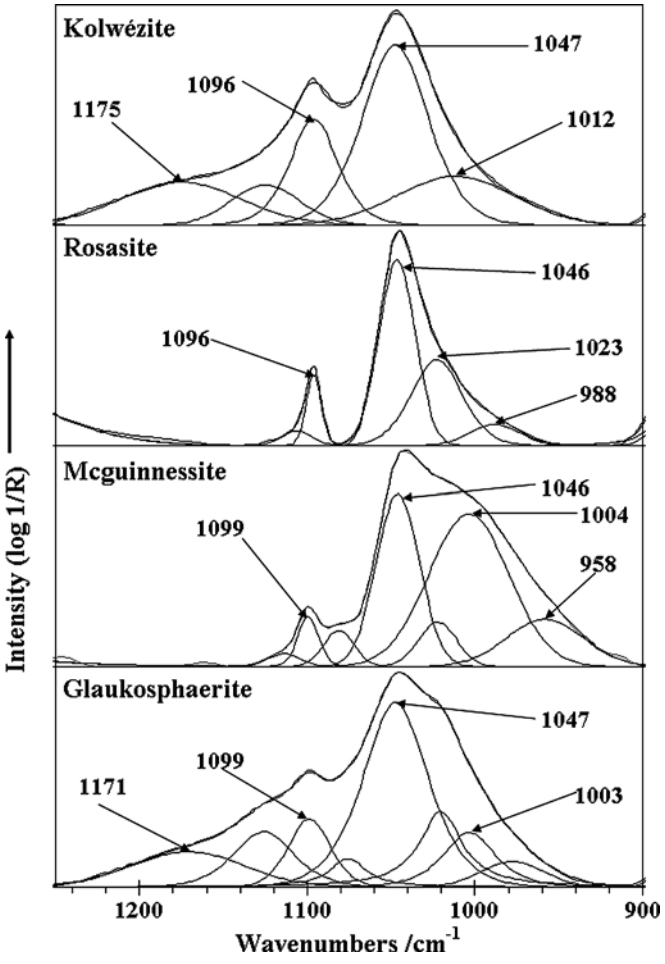


Fig. 5. Infrared spectra of rosasite, glaukosphaerite, kolwezite and mcguinessite in the 900–1200 cm^{-1} region.

be infrared active [5,36–38]. However because of symmetry reduction of the carbonate anion the band becomes activate. An intense Raman band is observed at 1096 cm^{-1} for rosasite and is assigned to the v_1 $(CO_3)^{2-}$ symmetric stretching vibration [5,36–38]. The intense band at 1046 cm^{-1} is assigned to the δ OH deformation mode. For malachite two bands attributed to OH deformation modes are found at 1045 and 875 cm^{-1} [5]. For hydrocerrusite the OH deformation modes were observed at 1047 and 1040 cm^{-1}. It is noted that in the infrared spectrum of rosasite an intense shoulder occurs at 1023 cm^{-1}. This band is also assigned to an OH deformation mode [39,40]. In the Raman spectrum of rosasite a low intensity band is observed at 1056 cm^{-1} and is ascribed to this vibrational mode [5,36,38,41].

For the mineral kolwezite two intense infrared bands are observed at 1096 and 1047 cm^{-1}. The first band is assigned to the v_1 $(CO_3)^{2-}$ vibrational mode and the second band to a δ OH deformation mode. As for rosasite in the infrared spectrum a long tail on the low wavenumber side is observed and a component band may be resolved at 1012 cm^{-1}. This band is a second δ OH deformation mode. The position of this second band appears to vary between the rosasite minerals. In the IR spectrum of mcguinnessite, two bands are observed at 1046 and 1004 cm^{-1}. Both bands are ascribed to δ OH deformation modes. The v_1 $(CO_3)^{2-}$ symmetric stretching mode is observed at 1099 cm^{-1}. A second band is observed at 1084 cm^{-1}. The observation of a second band supports the concept of two different carbonate units in the mcguinnessite structure. In the Raman spectrum the intensity of bands assigned to δ OH deformation modes is low and for mcguinnessite a band is observed at 1060 cm^{-1}. In the infrared spectrum of glaukosphaerite the δ OH deformation mode is observed at 1047 cm^{-1}. However the spectral profile on the lower wavenumber side of this band is complex and may be resolved into a series of overlapping bands. Two bands are observed at 1099 and 1078 cm^{-1} and are assigned to the v_1 symmetric stretching modes; again supporting the concept of two different carbonate units in the glaukosphaerite structure. Only a single v_1 symmetric stretching mode band for rosasite was observed.

The infrared spectra of selected rosasite minerals in the 1225–1625 cm^{-1} region are shown in Fig. 6. The infrared spectrum of rosasite in this spectral region are characterised by strong bands centered upon 1488 and 1388 cm^{-1} which may be resolved into four bands at 1522, 1488, 1425 and 1388 cm^{-1}. These bands are attributed to the v_3 antisymmetric $(CO_3)^{2-}$ stretching modes. In the IR spectrum of malachite two bands are observed at around 1500 and 1400 cm^{-1} [5]. For hydrozincite two bands are observed at 1515 and 1400 cm^{-1}. It would appear that there are two pairs of bands for rosasite namely (1522 and 1425 cm^{-1}) and (1488 and 1388 cm^{-1}). The observation of two sets of bands for rosasite suggests that there are two independent carbonate units in the crystal structure. Such sets of bands are also observed for each of the

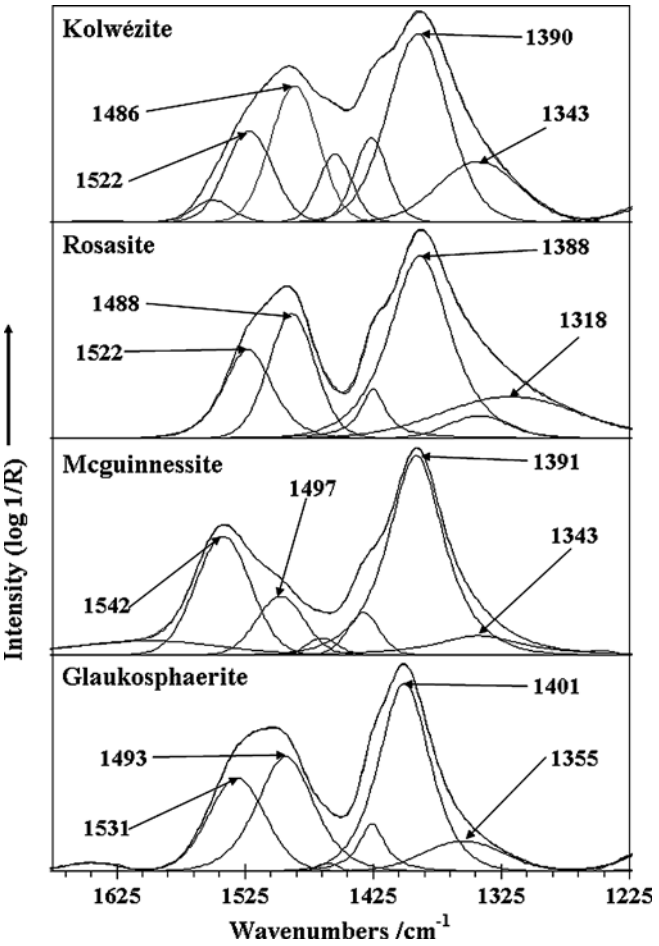


Fig. 6. Infrared spectra of rosasite, glaukosphaerite, kolwezite and mcguinessite in the 1225–1625 cm^{-1} region.

other rosasite minerals. For kolwezite two sets of bands are found at (1522 and 1426 cm^{-1}) and (1486 and 1390 cm^{-1}) and for glaukosphaerite (1531 and 1425 cm^{-1}) and (1493 and 1401 cm^{-1}). The intensities for mcguinnessite are opposite to that of rosasite in this spectral region; bands are observed for this mineral at (1542 and 1432 cm^{1}) and (1497 and 1391 cm^{-1}).

The infrared spectrum of the low wavenumber region are shown in Fig. 7. The infrared spectrum is limited to the cut-off point at 550 cm^{-1} at which point the diamond ATR cell absorbs the infrared radiation. However such a cut off point does not effect the infrared spectroscopy of minerals containing carbonate as all of the bands are above 550 cm^{-1}. The mineral rosasite shows two intense infrared bands at 870 and 818 cm^{-1}. These bands are assigned to the v_2 bending modes of the $(CO_3)^{2-}$ units. The observation of two v_2 bands is in harmony with the observation of two sets of bands in the v_3 antisymmetric stretching region. The infrared spectrum of malachite shows two bands at 820 and 803 cm^{-1} ascribed to v_2 bending modes as does azurite at 837 and 817 cm^{-1}[5]. Hydrocerrusite infrared spectrum shows two bands at 850 and 834 cm^{-1}. The ~880 cm^{-1} band for rosasite is not symmetrical and may be resolved

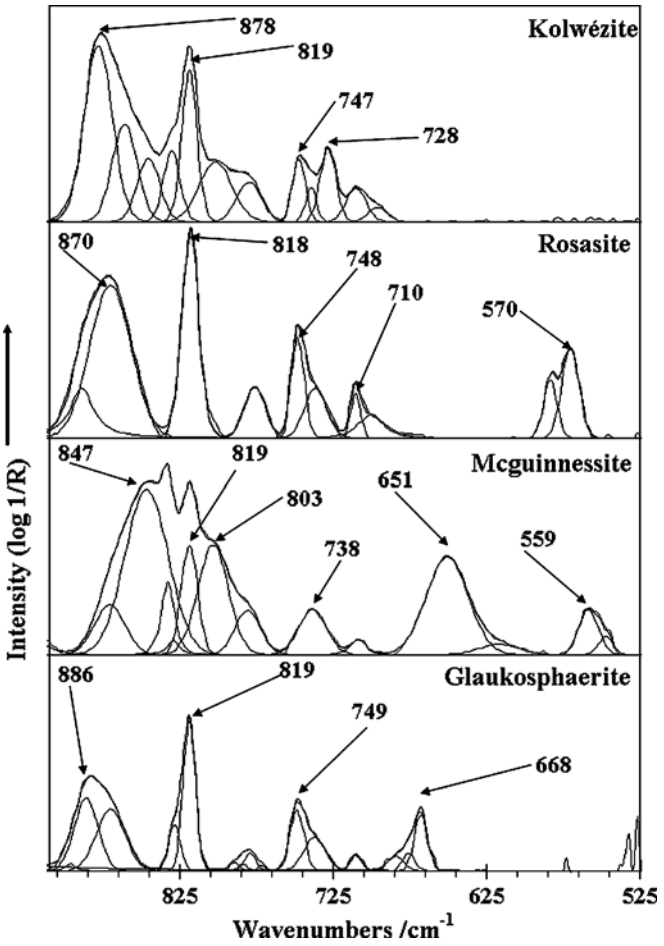


Fig. 7. Infrared spectra of rosasite, glaukosphaerite, kolwezite and mcguinessite in the 525–900 cm^{-1} region.

into two component bands at 889 and 870 cm^{-1}. The infrared spectrum of the mineral glaucosphaerite is very similar to that of rosasite with two bands observed at 886 and 819 cm^{-1}. The infrared spectrum of the mineral kolwezite is also similar in this spectral region, even though the profile is more complex. The spectrum of mcguinnessite is more complex with a number of bands observed at 870, 847, 833, 819 and 803 cm^{-1}. The bands at 870 and 819 cm^{-1} are related to the v_2 bending modes. The other bands may be due to impurities.

For rosasite a number of bands are observed at 781, 748 and 710 cm^{-1}. These bands are assigned to the v_4 $(CO_3)^{2-}$ bending modes. For malachite two infrared bands are observed at 748 and 710 cm^{-1} which are assigned to this vibration [4,5]. Another mineral with similar formulation to rosasite, hydrozicite has bands in this region at 738 and 710 cm^{-1}. The infrared spectrum of hydrocerrusite has v_4 $(CO_3)^{2-}$ bending modes at 700, 687 and 676 cm^{-1}. Two bands are observed around 570 cm^{-1} for rosasite; it is not known if these bands are due to v_4 $(CO_3)^{2-}$ bending modes. However this assignment seems unlikely. These bands are due to CuO stretching vibrations [41–45]. The infrared spectrum of kolwezite displays bands at 747, 728 and 710 cm^{-1}. The results for glaukosphaerite include bands at 749, 737 and 668 cm^{-1}. A low intensity band is observed at 570 cm^{-1} and is ascribed to the CuO stretching vibration. The IR spectrum of mcguinnessite also shows an intense band at 559 cm^{-1} which is assigned to CuO stretching vibration [42,43,45,46].

4. Conclusions

XRD studies of the rosasite mineral group showed the minerals are mixtures of members of the rosasite mineral group. Normally one of the rosasite minerals is predominant. EDAX has been used to determine the chemical composition of the mineral. The rosasite from Rosas mine, Narcao, Cagliari, Sardegna (Sardinia), Italy analysed as CuO 53.7% and ZnO 18.3% giving rise to the formula $(Cu_{1.5}Zn_{0.5})_2(CO)_3(OH)_2$. Glaucosphaerite from the Carr Boyd Nickel mine analysed as CuO 41.6% and NiO 25.2% giving rise to the formula $(Cu_{1.1}Ni_{0.7}Mg_{0.06})_2(CO)_3(OH)_2$. Similarly the mineral kolwezite from Zairehas a formula $(Cu_{1.33}Co_{0.67})_2(CO)_3(OH)_2$.

The infrared spectral patterns for the minerals rosasite, glaucosphaerite, kolwezite and mcguinnessite are similar and may be compared with that of malachite. This implies the molecular structure is similar to malachite. The single crystal structure of the members of the rosasite mineral group remains undetermined. The question arises as to why there are similar infrared spectral patterns for the rosasite minerals. It means the minerals must have the same structure or at least related structures. Malachite is monoclinic with point group 2/*m*. Therefore it can be inferred that the structure of the rosasite group of minerals is monoclinic. This conclusion is in agreement with the assumptions of Anthony et al. who state that rosasite and related minerals have monoclinic structure by analogy with malachite [33].

Acknowledgements

The financial and infra-structure support of the Queensland University of Technology Inorganic Materials Research Program is gratefully acknowledged. The Australian Research Council (ARC) is thanked for funding the instrumentation.

References

[1] P.A. Williams, Oxide Zone Geochemistry, Ellis Horwood Ltd, Chichester, West Sussex, England, 1990.
[2] J.A. Mandarino, Fleischer's Glossary of Mineral Species, The Mineralogical Record Inc., Tucson, 1999.
[3] J.L. Jambor, Paper – Geol. Surv. Can. 76-1C (1976) 97.
[4] R.L. Frost, Z. Ding, J.T. Kloprogge, W.N. Martens, Thermochim. Acta 390 (2002) 133.
[5] R.L. Frost, W.N. Martens, L. Rintoul, E. Mahmutagic, J.T. Kloprogge, J. Raman Spectrosc. 33 (2002) 252.
[6] D. Lovisato, Atti. accad. Lincei 17 (2) (1910) 723.
[7] G.P. Bolgov, N.A. Rozybakieva, Sbornik Nauch. Trudov Kazakh. Gorno-Met. Inst. (1956) 34.

[8] C. Perrier, Am. Mineral. 6 (1921) 166.
[9] M.W. Pryce, J. Just, Mineral. Mag. 39 (1974) 737.
[10] L.B. Railsback, Carbonate Evaporite 14 (1999) 1.
[11] J.L. Jambor, Can. Mineral. 14 (Pt. 4) (1976) 574.
[12] M. Deliens, P. Piret, Bull. Mineral. 103 (1980) 179.
[13] A.J. Read, Mineral. Mag. 48 (1984) 457.
[14] W. Postl, P. Golob, Mitteilungsblatt - Abteilung fuer Mineralogie am Landesmuseum Joanneum 49 (1981) 293.
[15] S. Matsubara, A. Kato, Ganko 88 (1993) 517.
[16] R.C. Erd, F.P. Cesbron, F.E. Goff, J.R. Clark, Mineral. Record 12 (1981) 143.
[17] E.H. Nickel, J.A. Hallbert, R. Halligan, J. Geol. Soc. Aust. 26 (1979) 61.
[18] E.H. Nickel, L.G. Berry, Can. Mineral. 19 (1981) 315.
[19] E.H. Nickel, J.F.M. Clout, B.J. Gartrell, Mineral. Record 25 (1994) 283.
[20] F. Zigan, W. Joswig, H.D. Schuster, S.A. Mason, Z. Kristallogr. Krist. 145 (1977) 412.
[21] J.A. Goldsmith, S.D. Ross, Spectrochim. Acta, Part A: Mol. Biomol. Spectrosc. 24 (1968) 2131.
[22] P.C. Rodriguez, B. Soc. Quim. del Peru 35 (2) (1969) 38.
[23] K. Wada, Kanzei Chuo Bunsekishoho 19 (1978) 133.
[24] P. Tarte, in: Proceedings of the fourth International Meeting on Molecular Spectroscopy, Bologna, 1959, vol. 3, p. 1041 (publ. 1962).
[25] P. Tarte, M. Deliens, Bull. Soc. R. Sci. Liege 43 (1974) 96.
[26] R.J.H. Clark, J. Mol. Struct. 480–481 (1999) 15.
[27] L. Burgio, D.A. Ciomartan, R.J.H. Clark, J. Raman Spectrosc. 28 (1997) 79.
[28] M. Bouchard, D.C. Smith, Asian Chem. Lett. 5 (2001) 157.
[29] B. Guineau, Stud. Conserv. 29 (1984) 35.
[30] C. Rocchiccioli, Compt. Rend. 259 (1964) 4581.
[31] M. Schmidt, H.D. Lutz, Phys. Chem. Miner. 20 (1993) 27.
[32] A.C. Roberts, J.L. Jambor, J.D. Grice, Powder Diffr. 1 (1986) 56.
[33] J.W. Anthony, R.A. Bideaux, K.W. Bladh, M.C. Nichols, Handbook of Mineralogy, vol. 5, Mineral Data Publishing, Tiscon, AZ, 2003.
[34] E. Libowitzky, Monatsh. Chem. 130 (1999) 1047.
[35] R.L. Frost, W. Martens, J.T. Kloprogge, Z. Ding, Spectrochim. Acta, Part A 59A (2003) 2705.
[36] R.L. Frost, P.A. Williams, W. Martens, Mineral. Mag. 67 (2003) 103.
[37] R.L. Frost, D.A. Henry, K. Erickson, J. Raman Spectrosc. 35 (2004) 255.
[38] R.L. Frost, K.L. Erickson, M.L. Weier, O. Carmody, J. Cejka, J. Mol. Struct. 737 (2005) 173.
[39] W.N. Martens, L. Rintoul, J.T. Kloprogge, R.L. Frost, Am. Mineral. 89 (2004) 352.
[40] B.J. Reddy, R.L. Frost, Neues Jahrb. Mineral. Monatsh. (2004) 525.
[41] R.L. Frost, M.L. Weier, Thermochim. Acta 409 (2004) 79.
[42] Z. Ding, R.L. Frost, J.T. Kloprogge, J. Mater. Sci. Lett. 21 (2002) 981.
[43] R.L. Frost, Z. Ding, W.N. Martens, T.E. Johnson, Thermochim. Acta 398 (2003) 167.
[44] R.L. Frost, M.L. Weier, Thermochim. Acta 406 (2003) 221.
[45] R.L. Frost, Z. Ding, Thermochim. Acta 405 (2003) 207.
[46] R.L. Frost, M.L. Weier, M.E. Clissold, P.A. Williams, Spectrochim. Acta, Part A 59 (2003) 3313.

Available online at www.sciencedirect.com
ScienceDirect
Polyhedron 26 (2007) 284–289
POLYHEDRON
www.elsevier.com/locate/poly

Organometallic complexes for nonlinear optics. 37: Synthesis and third-order nonlinear optical properties of a hexaruthenium triplatinum dendrimer

Clem E. Powell [a], Marie P. Cifuentes [a], Mark G. Humphrey [a,*], Anthony C. Willis [b], Joseph P. Morrall [a,c], Marek Samoc [c]

[a] Department of Chemistry, Australian National University, Canberra, ACT 0200, Australia
[b] Research School of Chemistry, Australian National University, Canberra, ACT 0200, Australia
[c] Laser Physics Centre, Research School of Physical Sciences and Engineering, Australian National University, Canberra, ACT 0200, Australia

Received 22 March 2006; accepted 8 May 2006
Available online 16 May 2006

Contribution to the Special Issue "Modern Inorganic Chemistry in Australia and New Zealand".

Abstract

The complexes *trans*-[Pt(C≡CC$_6$H$_4$-4-C≡CPh)Cl(PMe$_2$Ph)$_2$] (**1**), 1,3,5-C$_6$H$_3${C≡CC$_6$H$_4$-4-C≡C-*trans*-[PtCl(PMe$_2$Ph)$_2$]}$_3$ (**2**) and 1,3,5-C$_6$H$_3$(C≡CC$_6$H$_4$-4-C≡C-*trans*-[Pt(PMe$_2$Ph)$_2$]C≡C-4-C$_6$H$_4$C≡C-3,5-C$_6$H$_3$-{C≡C-*trans*-[Ru(C≡CPh)(dppe)$_2$]}$_2$)$_3$ (**3**) have been synthesized and the identity of **1** confirmed by a single-crystal X-ray diffraction study. The optical limiting merit of **1** and **2** has been assessed at 523 nm employing 40 ns pulses; the effective absorption cross-section for **1** is low, while that of **2** is larger, but the complex is susceptible to photo-damage. The third-order nonlinearity of the Ru$_6$Pt$_3$ dendrimer **3** has been examined at 800 nm using 150 fs pulses; it is larger than that of a related Ru$_6$ dendrimer, but smaller than that of a Ru$_9$ dendrimer under the same conditions, suggesting that increasing metal content and electron richness is correlated to increased nonlinearity in these complexes.
© 2006 Elsevier Ltd. All rights reserved.

Keywords: Ruthenium; Platinum; Dendrimer; Nonlinear optics; Optical limiting

1. Introduction

Organotransition metal dendrimers have attracted enormous interest over the past few years [1]. Although most examples are peripherally-metallated organic dendrimers, several dendrimers with metals in each generation and an arylethynyl-derived framework have been reported. The focus of our studies has been ruthenium-containing arylalkynyl dendrimers [2–10], while other groups have reported related platinum-containing examples [11–15]. We report herein the synthesis of a mixed-metal arylalkynyl dendrimer incorporating both ruthenium and platinum, together with an assessment of its third-order nonlinear optical (NLO) properties.

2. Experimental

2.1. General conditions and reagents

All reactions were performed under a nitrogen atmosphere with the use of Schlenk techniques. Dichloromethane was dried by distilling over calcium hydride; other solvents were used as received. Chromatography was performed on ungraded basic alumina.

* Corresponding author. Tel.: +61 2 6125 2927; fax: +61 2 6125 0760.
E-mail address: Mark.Humphrey@anu.edu.au (M.G. Humphrey).

0277-5387/$ - see front matter © 2006 Elsevier Ltd. All rights reserved.
doi:10.1016/j.poly.2006.05.007

The following were prepared by literature procedures: HC≡CC$_6$H$_4$-4-C≡CPh [16], 1,3,5-C$_6$H$_3$(C≡CC$_6$H$_4$-4-C≡CH)$_3$ [9], 1,3-{*trans*-[(dppe)$_2$(PhC≡C)RuC≡C]}$_2$-5-(HC≡C-4-C$_6$H$_4$C≡C)C$_6$H$_3$ [6]. PtCl$_2$(PMe$_2$Ph)$_2$ was a gift from Dr E. Wenger and Prof. A.F. Hill, RSC, Australian National University. CuCl (J.T. Baker) was used as received.

Microanalyses were carried out at the Australian National University. UV–Vis spectra of solutions in tetrahydrofuran in 1 cm cells were recorded using a Cary 5 spectrophotometer. Infrared spectra were recorded as dichloromethane solutions using a Perkin–Elmer System 2000 FT-IR. ^{1}H (300 MHz) and ^{31}P NMR (121 MHz) spectra were recorded using a Varian Gemini-300 FT NMR spectrometer and are referenced to residual chloroform (7.24 ppm) or external H_3PO_4 (0.0 ppm), respectively. Fast atom bombardment mass spectra (FAB MS) were recorded on a VG ZAB-2SEQ hybrid sector (BEqQ) MS instrument (30 kV Cs^+ ions, current 1 mA, accelerating potential 8 kV, matrix 3-nitrobenzyl alcohol) at the ANU.

2.2. Syntheses

2.2.1. *trans*-[Pt(C≡CC$_6$H$_4$-4-C≡CPh)Cl(PMe$_2$Ph)$_2$] (**1**)

A solution of *cis*-[PtCl$_2$(PMe$_2$Ph)$_2$] (45 mg, 0.083 mmol), HC≡CC$_6$H$_4$-4-C≡CPh (8.8 mg, 0.044 mmol) and CuCl (6.6 mg, 0.067 mmol) in CH_2Cl_2 (10 mL) and NEt_3 (10 mL) was stirred for 17 h. The reaction mixture was passed through a short pad of alumina with CH_2Cl_2, and the eluate was taken to dryness under reduced pressure. Diffusion of MeOH into a CH_2CH_2 solution of the residue afforded yellow needles (28 mg, 90%). *Anal.* Calc. for $C_{32}H_{31}ClP_2Pt$: C, 54.28; H, 4.41. Found: C, 54.21; H, 3.82%. IR: ν(C≡C) 2119 cm^{-1}. UV–Vis: λ 342 nm, ε 33 600 M^{-1} cm^{-1}. ^{1}H NMR: δ 1.93 (12H, t, 4 Hz, Me), 6.98–7.81 (19H, m, phenyl). ^{31}P NMR: δ −6.84 (s, J_{PtP}: 2396 Hz). FAB MS; *m*/*z* (fragment, relative intensity): 708 ([M]$^+$, 100), 672 ([M]$^+$−Cl, 20), 471 ([Pt(PMe$_2$Ph)]$^+$, 100).

2.2.2. 1,3,5-C$_6$H$_3${C≡CC$_6$H$_4$-4-C≡C-*trans*-[PtCl(PMe$_2$Ph)$_2$]}$_3$ (**2**)

A solution of *cis*-[PtCl$_2$(PMe$_2$Ph)$_2$] (48 mg, 0.089 mmol), 1,3,5-C$_6$H$_3$(C≡CC$_6$H$_4$-4-C≡CH)$_3$ (7.4 mg, 0.016 mmol) and CuCl (15 mg, 0.15 mmol) in CH_2Cl_2 (15 mL) and NEt_3 (10 mL) was stirred for 17 h. The reaction mixture was passed through a short pad of alumina with CH_2Cl_2 as eluent, and the eluate was taken to dryness under reduced pressure. The residue was purified by solvent diffusion of MeOH into a CH_2Cl_2 solution to afford a pale yellow powder (27 mg, 83%). *Anal.* Calc. for $C_{84}H_{81}Cl_3P_6Pt_3$: C, 51.27; H, 4.15. Found: C, 51.01; H, 4.23%. IR: ν(C≡C) 2117 cm^{-1}. UV–Vis: λ 345 nm, ε 123 000 M^{-1} cm^{-1}. ^{1}H NMR: δ 1.94 (36 H, t, 4 Hz, Me), 6.98–7.84 (45 H, m, phenyl). ^{31}P NMR: δ −6.84 (s, J_{PtP}: 2400 Hz). FAB MS; *m*/*z* (fragment, relative intensity): 1970 ([M]$^+$, 2), 471 ([Pt(PMe$_2$Ph)]$^+$, 40).

2.2.3. 1,3,5-C$_6$H$_3$(C≡CC$_6$H$_4$-4-C≡C-*trans*-[Pt(PMe$_2$Ph)$_2$]C≡C-4-C$_6$H$_4$C≡C-3,5-C$_6$H$_3$-{C≡C-*trans*-[Ru(C≡CPh)(dppe)$_2$]}$_2$)$_3$ (**3**)

A solution of **2** (21 mg, 11 μmol), 1,3-{*trans*-[(dppe)$_2$(PhC≡C)RuC≡C]}$_2$-5-(HC≡C-4-C$_6$H$_4$C≡C)C$_6$H$_3$ (73 mg, 0.034 mmol) and CuCl (15 mg, 0.15 mmol) in CH_2Cl_2 (20 mL) and NEt_3 (5 mL) was stirred for 19 h. The reaction mixture was passed through a short pad of alumina with CH_2Cl_2 as eluent, and the eluate was taken to dryness under reduced pressure. The residue was purified by vapour diffusion of MeOH into a solution in CH_2Cl_2 to afford a yellow powder (53 mg, 56 %). *Anal.* Calc. for $C_{504}H_{420}P_{30}Pt_3Ru_6$: C, 70.41; H, 4.92. Found: C, 69.51; H, 5.02%. IR: ν(C≡CPt) 2101 cm^{-1}, ν(C≡CRu) 2060 cm^{-1}. UV–Vis: λ 357 nm, ε 52 300 M^{-1} cm^{-1}. ^{1}H NMR: δ 2.13 (36 H, t, 4 Hz, Me), 2.68 (48 H, m, CH_2), 6.67–7.90 (336 H, m, phenyl). ^{31}P NMR: δ −11.62 (6 P, s, J_{PtP}: 2380 Hz), 54.25 (24 P, s). FAB MS; *m*/*z* (fragment, relative intensity): 898 ([Ru(dppe)$_2$]$^+$, 55), 471 ([Pt(PMe$_2$Ph)$_2$]$^+$, 35).

2.3. X-ray structural study of **1**

A suitable crystal of **1** was obtained by slow diffusion of hexane into a dichloromethane solution. A single crystal was mounted on a fine glass capillary, and data collected on a Nonius KappaCCD diffractometer using graphite-monochromated Mo Kα radiation ($\lambda = 0.7107_3$ Å). The unit cell parameters were obtained by least-squares refinement [17] of 31 726 reflections with $3 \leqslant \theta \leqslant 27°$. The reduced data were corrected for absorption using numerical methods [18] implemented from within maXus [19]; equivalent reflections were merged. The structure was solved by heavy atom methods [20], and refined using the software package CRYSTALS [21].

Crystal/refinement data: $C_{32}H_{31}ClP_2Pt$, $M = 708.09$. Triclinic, space group *P*-1, $a = 5.9924(1)$ Å, $b = 9.6522(1)$ Å, $c = 25.7727(3)$ Å, $\alpha = 91.905(1)°$, $\beta = 95.940(1)°$, $\gamma = 105.910(1)°$, $V = 1422.93(3)$ Å^3. D_c ($Z = 2$) = 1.653 g cm^{-3}. $\mu_{Mo} = 5.156$ mm^{-1}; specimen: 0.48 × 0.34 × 0.21 mm; $T_{min/max} = 0.23/0.45$. $2\theta_{max} = 55°$; $N_{total} = 28\,704$ (CCD diffractometer, monochromatic Mo Kα radiation, $\lambda = 0.7107_3$ Å; T 200 K) merging to $N = 6513$ unique ($R_{int} = 0.04$), $N_o = 5067$ ($I > 3\sigma(I)$) refining to $R = 0.020$, $R_w = 0.020$. The crystallographic asymmetric unit consists of one [Pt(C$_{16}$H$_9$)(C$_8$H$_{11}$P)$_2$Cl] molecule. The largest peaks in the final difference electron density map were located near the Pt atom.

2.4. Z-scan measurements

Z-scan measurements [29] were performed using a femtosecond laser system based on a Coherent Mira-900D Ti–sapphire oscillator and including a chirped pulse

Ti–sapphire amplifier operating at a repetition rate of 30 Hz. This system operated at a wavelength of 800 nm and provided ca. 150 fs FWHM pulses. The Z-scan set-up used lenses with the focal lengths suitable for creating focal spots with the $1/e^2$ radius, w_0, being in the range 40–65 μm. This resulted in the Rayleigh lengths, $z_R = \frac{\pi w_0^2}{\lambda}$, being greater than 3 mm; the measurements of tetrahydrofuran solutions in 1 mm thick glass cells with ca. 1 mm thick glass walls could therefore be treated in the thin sample approximation. All measurements were calibrated against Z-scans taken on the pure solvent and on silica and glass plates of thicknesses in the range 1–2.5 mm; the value $n_2 = 3 \times 10^{-16}$ cm^2 W^{-1} was adopted for silica nonlinear index. Nonlinear phase shifts for the measured samples were in the range 0.5–1.0 rad, corresponding to peak intensities of the order of 100 GW cm^{-1}.

2.5. Optical limiting measurements

The measurements were performed using the Z-scan technique at 523 nm, with about 5 μJ, 40 ns pulses from a frequency-doubled Q-switched Nd:YLF diode-pumped laser. Solutions of both compounds were placed in 1 mm path length glass cells. The open-aperture Z-scans were converted into transmission–fluence plots using an assumption of Gaussian beam propagation and the spot size determination made on the basis of numerical fitting of the closed-aperture Z-scan obtained simultaneously with the open-aperture measurement (the signal in the closed-aperture Z-scan was due to thermal nonlinearity of the solutions). The data were analyzed assuming that excited-state absorption is responsible for the effect.

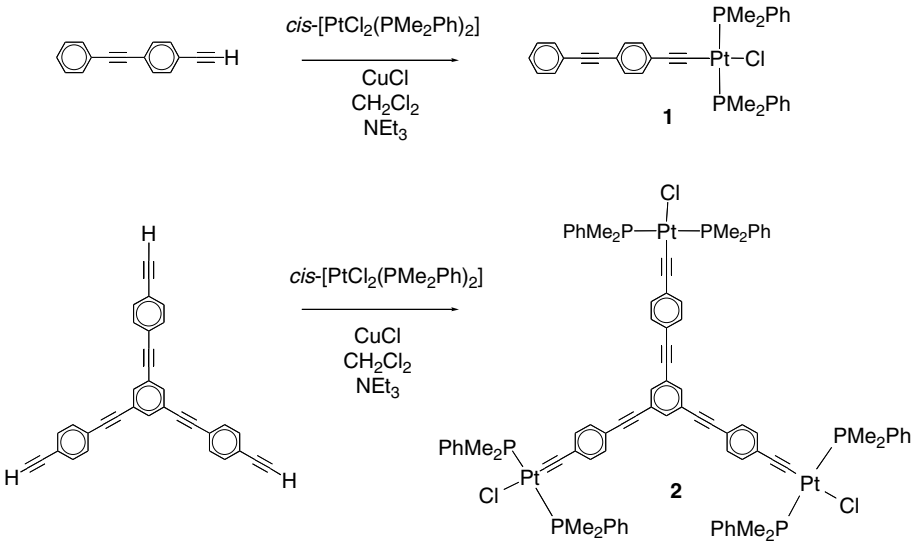
3. Results and discussion

The bis(phosphine)platinum-containing core of the dendrimer (**2**), together with a linear analogue (**1**), was synthesized by reaction of *cis*-[$PtCl_2(PMe_2Ph)_2$] with the relevant alkynyl ligand in the presence of a CuCl catalyst (Scheme 1). There is no inherent means of avoiding generation of the bis-alkynyl complex – to minimize its formation, an excess of *cis*-[$PtCl_2(PMe_2Ph)_2$] was added, no trace of the bis-alkynyl product being observed in the ^{31}P NMR spectrum. The products were characterized by ^{1}H and ^{31}P NMR, UV–Vis, IR, FAB mass spectrometry and (in the case of the linear analogue) a single-crystal X-ray diffraction study.

Selected bond distances and angles are listed in Table 1, and an ORTEP plot is displayed in Fig. 1. The crystallographic asymmetric unit consists of one molecule of **1**. The complex shows square-planar geometry around the metal center, with only small deviations from the idealized geometry. An example of an octupolar platinum–alkynyl complex incorporating a C≡CC_6H_4-4-C≡CPh motif, 1,3,5-[Cl(PEt_3)$_2$PtC≡CC_6H_4-4-C≡C]$_3C_6H_3$, has been reported previously and structurally characterized [22]. Reported bond lengths for this octupolar complex [Pt–Cl: 2.358(6) Å, Pt–C: 1.95(2) Å, Pt–P: 2.276(9)–2.297(8) Å and C≡C: 1.14(3) Å] are similar to those observed with **1**.

Table 1
Selected bond distances (Å) and angles (°) for **1**

Pt1–C1	1.953(3)	Pt1–Cl1	2.3588(8)
Pt1–P1	2.3051(8)	Pt1–P2	2.3059(8)
C1–C2	1.200(4)	C9–C10	1.200(5)
C2–C3	1.441(4)	C10–C11	1.432(4)
P1–C17	1.813(3)	P1–C18	1.807(3)
P2–C19	1.810(3)	P2–C20	1.817(3)
P1–C21	1.819(3)	P2–C27	1.817(3)
Cl–Pt1–P1	87.70(3)	Cl1–Pt1–P2	91.52(3)
P1–Pt1–P2	177.16(3)	Cl1–Pt1–C1	177.25(9)
Pt1–C1–C2	178.7(3)	C1–C2–C3	177.4(3)
C6–C9–C10	178.7(4)	C9–C10–C11	177.7(4)



Scheme 1. Syntheses of **1** and **2**.

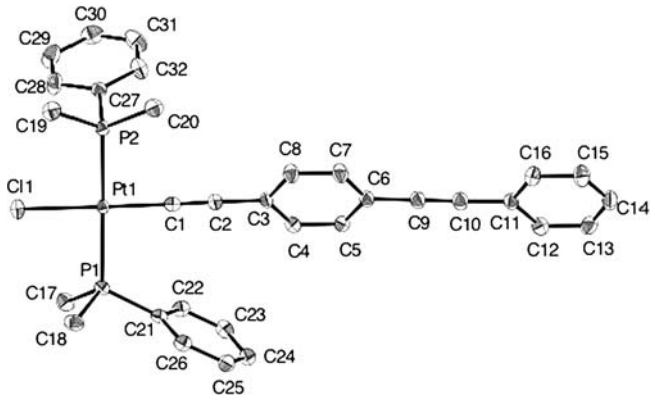


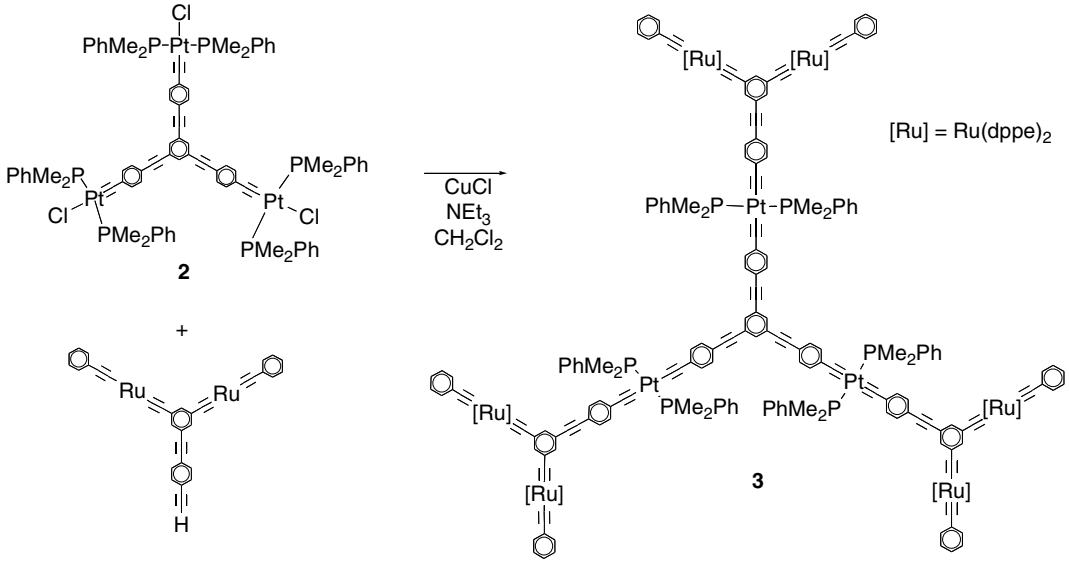
Fig. 1. Thermal ellipsoid diagram of *trans*-[Pt(C≡CC$_6$H$_4$-4-C≡CPh)Cl(PMe$_2$Ph)$_2$] with labeling of selected atoms. Ellipsoids show 30% probability levels. H atoms have been omitted for clarity.

The triplatinum dendritic core, **2**, was reacted with the wedge, 1,3-{*trans*-[(dppe)$_2$(PhC≡C)RuC≡C]}$_2$-5-(HC≡C-4-C$_6$H$_4$C≡C)C$_6$H$_3$, in the presence of CuCl to give the mixed-metal dendrimer complex, 1,3,5-C$_6$H$_3$(C≡CC$_6$H$_4$-4-C≡C-*trans*-[Pt(PMe$_2$Ph)$_2$]C≡C-4-C$_6$H$_4$C≡C-3,5-C$_6$H$_3$-{C≡C-*trans*-[Ru(C≡CPh)(dppe)$_2$]}$_2$)$_3$ (**3**) (Scheme 2). The dendrimer was characterized by ^{1}H and ^{31}P NMR, UV–Vis, IR, and FAB mass spectrometry.

Examination of the ^{31}P NMR spectroscopic data for **1**, **2** and **3** reveals a ^{31}P chemical shift of −6.8 ppm in the case of complexes containing a chloro-ligand (**1** and **2**), which moves to −11.6 ppm upon replacement of the chloro ligand by an alkynyl group on conversion of **2** to **3**. These figures are consistent with literature values for *trans*-[Pt(C≡CPh)-Cl(PMe$_2$Ph)$_2$] and *trans*-[Pt(C≡CPh)$_2$(PMe$_2$Ph)$_2$], which have ^{31}P NMR spectral shifts of −7.5 and −12.4 ppm, respectively [23]. Complex **3** also contains a resonance at 54.4 ppm, consistent with a bis-alkynyl ruthenium unit; the integral of the resonances is 1:2, as expected. The IR spectra of the platinum-containing complexes **1** and **2** each show a band at approximately 2119 cm^{-1}, which is consistent with similar platinum complexes: *trans*-[Pt(C≡CPh)$_2$(PMe$_2$Ph)$_2$]-2106 cm^{-1} [24], *trans*-[Pt(C≡CCH$_2$OH)$_2$(PMe$_2$Ph)$_2$] 2120 cm^{-1}, *trans*-[Pt(C≡CCH$_2$CH$_2$OH)$_2$(PMe$_2$Ph)$_2$] 2110 cm^{-1} and *trans*-[Pt(C≡CCH$_2$OPh)$_2$(PMe$_2$Ph)$_2$] 2115 cm^{-1} [25]. The mixed platinum/ruthenium dendrimer **3** contains two bands at 2060 and 2101 cm^{-1}, assigned to the ruthenium- and platinum-bound alkynyl groups, respectively.

Measurement of the third-order molecular nonlinearity of **3** was performed using the Z-scan technique at 800 nm; results are presented in Table 2, together with previously-reported data for related ruthenium-containing dendrimers. The mixed-metal dendrimer, **3**, possesses a $|\gamma_{800}|$ of $7200 \pm 2900 \times 10^{-36}$ esu. This is substantially higher than that of the phenylalkynyl-containing dendrimer 1,3,5-{3,5-(*trans*-[(dppe)$_2$(PhC≡C)RuC≡C])$_2$C$_6$H$_3$C≡CC$_6$H$_4$-4-C≡C}$_3$C$_6$H$_3$ ($1600 \pm 2400 \times 10^{-36}$ esu) [26], but lower than that of 1,3,5-C$_6$H$_3$(C≡CC$_6$H$_4$-4-C≡C-*trans*-[Ru(dppe)$_2$]-C≡C-3,5-C$_6$H$_3$-{C≡CC$_6$H$_4$-4-C≡C-*trans*-[Ru(C≡CPh)-(dppe)$_2$]}$_2$)$_3$ ($20700 \pm 2000 \times 10^{-36}$ esu) [3]. Increasing the metal loading (proceeding from the Ru$_6$ to Ru$_6$M$_3$ dendrimers, M = Ru, Pt) and increasing electron richness (proceeding from Ru$_6$Pt$_3$, with a mixture of 18 and 16 valence electron metals, to Ru$_9$, with 18 electron metal centers only) both result in an increase in $|\gamma_{800}|$.

Platinum-alkynyl complexes possess interesting optical properties [22,26–28]. Of particular relevance to the current studies, *trans*-[Pt(C≡CC$_6$H$_4$-4-C≡CPh)$_2$(PBu$_3$)$_2$] has been shown to act as a broadband optical limiter [28]. In view of the close structural similarities between the linear platinum complex *trans*-[Pt(C≡CC$_6$H$_4$-4-C≡CPh)Cl(PMe$_2$Ph)$_2$] (**1**), its octupolar analogue **2**, and *trans*-[Pt(C≡CC$_6$H$_4$-4-



Scheme 2. Synthesis of **3**.

Table 2
Experimental nonlinear optical response parameters

Complex	γ_{real} (10^{-36} esu)	γ_{imag} (10^{-36} esu)	$\lvert\gamma\rvert$ (10^{-36} esu)	Ref.
1,3,5-{3,5-(*trans*-[(dppe)$_2$(PhC≡C)RuC≡C])$_2$C$_6$H$_3$C≡CC$_6$H$_4$-4-C≡C}$_3$C$_6$H$_3$	−1600 ± 2400	0 ± 0	1600 ± 2400	[6]
1,3,5-C$_6$H$_3$(C≡CC$_6$H$_4$-4-C≡C-*trans*-[Pt(PMe$_2$Ph)$_2$]C≡C-4-C$_6$H$_4$-3,5-C$_6$H$_3$-{C≡C-*trans*-[Ru(C≡CPh)(dppe)$_2$]}$_2$)$_3$ (**3**)	−6700 ± 2600	−2500 ± 1300	7200 ± 2900	this work
1,3,5-C$_6$H$_3$(C≡CC$_6$H$_4$-4-C≡C-*trans*-[Ru(dppe)$_2$]C≡C-3,5-C$_6$H$_3$-{4-C≡CC$_6$H$_4$C≡C-*trans*-[Ru(C≡CPh)(dppe)$_2$]}$_2$)$_3$	−5050 ± 500	20100 ± 2000	20700 ± 2000	[3]

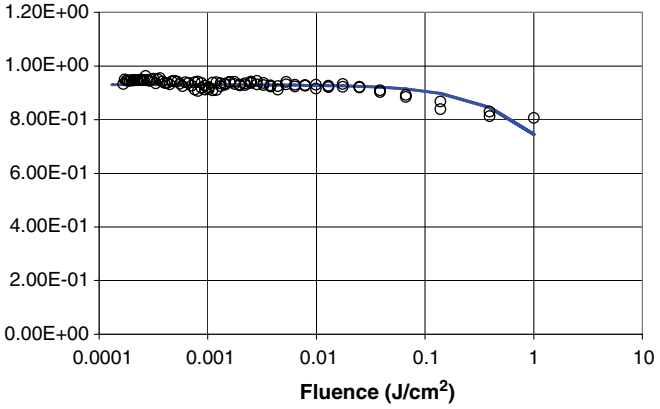


Fig. 2. Transmission–fluence plot for **2**.

C≡CPh)$_2$(PBu$_3$)$_2$], the optical limiting performance of **1** and **2** was examined at 523 nm.

Only poor optical limiting behavior was exhibited by **1**; the effective excited state absorption cross-section at 523 nm was determined to be no larger than 4×10^{-20} cm^2. In comparison, the effective absorption cross-section of *trans*-[Pt(C≡CC$_6$H$_4$-4-C≡CPh)$_2$(PBu$_3$)$_2$] is reported to be 7×10^{-17} cm^2 [28]. The octupolar platinum–alkynyl complex **2** shows a considerably larger effective absorption cross-section than its linear analogue (7×10^{-19} cm^2). However, it is still significantly smaller than the effective absorption cross-section of *trans*-[Pt(C≡CC$_6$H$_4$-4-C≡CPh)$_2$(PBu$_3$)$_2$]. A plot of transmission versus fluence for complex **2** is shown in Fig. 2, illustrating the drop-off in transmission as the fluence increases. A significant problem, however, exists in photodecomposition of the sample. The effective absorption cross-section value reported above applies to a fresh sample. Subsequent measurements on the same spot of the solution cell show considerably stronger changes of transmission, consistent with the formation of absorbing species. Similar photodecomposition is observed for *trans*-[Pt(C≡CC$_6$H$_4$-4-C≡CPh)$_2$(PBu$_3$)$_2$] [28].

4. Conclusion

The mono- and triplatinum complexes reported herein are readily accessible by straightforward syntheses, but their low optical limiting merit and lack of photostability mitigate against potential use. The triplatinum complex is a dendritic core in convergent dendrimer synthesis. Coupling the triplatinum core complex **2** to three equivalents of the triruthenium dendron complex has afforded a hexaruthenium triplatinum dendrimer. The cubic optical nonlinearity of this dendrimer is lower than that of a nonaruthenium dendrimer that we reported previously [3], suggesting that a search for organometallic dendrimers with larger NLO coefficients should focus on those with electron-rich (18 valence electron) metal centers. The synthetic methodology that we have employed in the current studies is, in principle, applicable to higher generation species, which will be the subject of a future report.

Acknowledgements

We thank the Australian Research Council for support of this work and Johnson-Matthey Technology Centre for the generous loan of ruthenium salts. M.G.H. is an ARC Australian Professorial Fellow. M.P.C. is an ARC Australian Research Fellow.

Appendix A. Supplementary material

Final atomic positional coordinates, with estimated standard deviations, bond lengths and angles, and anisotropic thermal parameters have been deposited at the Cambridge Crystallographic Data Centre and allocated the deposition number 602009. Copies of this information may be obtained free of charge from the Director, CCDC, 12 Union Road, Cambridge, CB2 1EZ, UK (fax: +44 1223 336 033, email: deposit@ccdc.cam.ac.uk, or www: http://www.ccdc.cam.ac.uk). Supplementary data associated with this article can be found, in the online version, at doi:10.1016/j.poly.2006.05.007.

References

[1] P.A. Chase, R.J.M. Klein Gebbick, G. van Koten, J. Organomet. Chem. 689 (2004) 4016.
[2] A.M. McDonagh, M.G. Humphrey, M. Samoc, B. Luther-Davies, S. Houbrechts, T. Wada, H. Sasabe, A. Persoons, J. Am. Chem. Soc. 121 (1999) 1405.
[3] A.M. McDonagh, M.G. Humphrey, M. Samoc, B. Luther-Davies, Organometallics 18 (1999) 5195.
[4] M.P. Cifuentes, C.E. Powell, M.G. Humphrey, G.A. Heath, M. Samoc, B. Luther-Davies, J. Phys. Chem. A 105 (2001) 9625.
[5] S.K. Hurst, M.G. Humphrey, T. Isoshima, K. Wostyn, I. Asselberghs, K. Clays, A. Persoons, M. Samoc, B. Luther-Davies, Organometallics 21 (2002) 2024.

[6] S. Hurst, M.P. Cifuentes, M.G. Humphrey, Organometallics 21 (2002) 2353.
[7] S.K. Hurst, N.T. Lucas, M.G. Humphrey, T. Isoshima, K. Wostyn, I. Asselberghs, K. Clays, A. Persoons, M. Samoc, B. Luther-Davies, Inorg. Chim. Acta 350 (2003) 62.
[8] C.E. Powell, M.G. Humphrey, M.P. Cifuentes, J.P. Morrall, M. Samoc, B. Luther-Davies, J. Phys. Chem. A 107 (2003) 11264.
[9] A.M. McDonagh, C.E. Powell, J.P. Morrall, M.P. Cifuentes, M.G. Humphrey, Organometallics 22 (2003) 1402.
[10] C.E. Powell, J.P.L. Morrall, S.A. Ward, M.P. Cifuentes, E.G.A. Notaras, M. Samoc, M.G. Humphrey, J. Am. Chem. Soc. 126 (2004) 12234.
[11] S. Leininger, P.J. Stang, S. Huang, Organometallics 17 (1998) 3981.
[12] K. Onitsuka, A. Iuchi, M. Fujimoto, S. Takahashi, Chem. Commun. (2001) 741.
[13] K. Onitsuka, M. Fujimoto, N. Ohshiro, S. Takahashi, Angew. Chem., Int. Ed. Engl. 38 (1999) 689.
[14] K. Onitsuka, S. Takahashi, Top. Curr. Chem. 228 (2003) 39.
[15] K. Onitsuka, A. Shimizu, S. Takahashi, Chem. Commun. (2003) 280.
[16] O. Lavastre, S. Cabioch, P.H. Dixneuf, J. Vohlidal, Tetrahedron 53 (1997) 7595.
[17] Z. Otwinowski, W. Minor, in: C.W. Carter, R.M. Sweet (Eds.), Methods in Enzymology, vol. 276, Academic Press, New York, USA, 1997, p. 307.
[18] P. Coppens, in: F.R. Ahmed, S.R. Hall, C.P. Huber (Eds.), Crystallographic Computing, Munksgaard, Copenhagen, Denmark, 1970, p. 255.
[19] S. Mackay, C.J. Gilmore, C. Edwards, M. Tremayne, N. Stewart, K. Shankland, maXus Computer Program for the Solution and Refinement of Crystal Structures, Nonius, The Netherlands, MacScience, Japan, and The University of Glasgow, UK, 2000.
[20] P.T. Beurskens, G. Admiraal, W.P. Bosman, R.S. de Gelder, S. Garcia-Granda, R.O. Gould, J.M.M. Smits, The DIRDIF96 Program System. Technical Report of the Crystallographic Laboratory, University of Nigmegen, The Netherlands, 1996.
[21] D.J. Watkin, C.K. Prout, J.R. Carruthers, P.W. Betteridge, R.I. Cooper, CRYSTALS, issue 11, Chemical Crystallography Laboratory, Oxford, UK, 2001.
[22] V.W.-W. Yam, C.-H. Tao, L. Zhang, K.M.-C. Wong, K.-K. Cheung, Organometallics 20 (2001) 453.
[23] R.J. Cross, M.F. Davidson, J. Chem. Soc., Dalton Trans. (1986) 1987.
[24] S. Yamazaki, Polyhedron 11 (1983) 1983.
[25] H.D. Empsall, B.L. Shaw, A.J. Stringer, J. Organomet. Chem. 94 (1975) 131.
[26] T.J. McKay, J.A. Bolger, J. Staromlynska, J.R. Davy, J. Chem. Phys. 108 (1998) 5537.
[27] T.J. McKay, J. Staromlynska, P. Wilson, J.R. Davy, J. Appl. Phys. 85 (1999) 1337.
[28] J. Staromlynska, T.J. McKay, P. Wilson, J. Appl. Phys. 88 (2000) 1726.
[29] M. Sheik-Bahae, A.A. Said, T. Wei, D.J. Hagan, E.W. van Stryland, IEEE J. Quantum Electron. 26 (1990) 760.

Available online at www.sciencedirect.com
ScienceDirect
Polyhedron 26 (2007) 290–299
POLYHEDRON
www.elsevier.com/locate/poly

Cluster chemistry in the solid state: Structured diffuse scattering, oxide/fluoride ordering and polar behaviour in transition metal oxyfluorides

Ray L. Withers *, F.J. Brink, Yun Liu, Lasse Norén

Research School of Chemistry, Australian National University, Building 35, Science Road, Canberra, ACT 0200, Australia

Received 28 March 2006; accepted 8 May 2006
Available online 6 June 2006

Abstract

Oxide/fluoride ordering in three families of 'disordered' transition metal oxyfluoride compounds is carefully investigated and used to obtain insight into why the constituent inherently acentric octahedral units do not usually order in a long range ordered polar sense. Observed highly structured diffuse intensity distributions are used in each case to analyze the local crystal chemistry and orientational ordering rules governing the way in which the dipole moments from the individual polar pseudo-octahedral units add together. The common local oxide/fluoride ordering rules, the consequences of these rules for polar behaviour on the local scale as well as the role of configurational entropy and energy minimization in suppressing long range polar order are highlighted.
© 2006 Elsevier Ltd. All rights reserved.

Keywords: Structured diffuse scattering; Oxide/fluoride ordering; Transition metal oxyfluorides; Polar behaviour; Orientational disorder; Order/disorder

1. Introduction

The synthesis and control of polar behaviour in crystalline materials is an increasingly important objective for solid state chemists as a result of the strong correlation of polarity with a range of useful physical properties including pyroelectricity, ferroelectricity, piezoelectricity and second harmonic generation (SHG) [1–3]. Early transition metal d^0 cations in octahedral environments (such as *e.g.* the Ti^{4+} ion in the TiO_6 octahedra of $BaTiO_3$, $KTiOPO_4$, *etc.* or the Nb^{5+} ion in the NbO_6 octahedra of $LiNbO_3$) have a well known susceptibility to move off-centre in a correlated fashion as a result of a second-order Jahn–Teller (SOJT) effect [3] giving rise to inherently polar materials and technologically very useful physical properties – in particular, ferroelectricity and SHG. An important strategy for synthesizing new polar materials is therefore to include transition metal MO_6 octahedral units susceptible to such a SOJT distortion [3].

An alternative, closely related approach is to use inherently polar, or acentric, anions such as, for example, pseudo-octahedral $Nb^{V}OF_5^{2-}$, (*cis*-)$Mo^{VI}O_2F_4^{2-}$ or (*fac*-)$Mo^{VI}O_3F_3^{3-}$ (see Fig. 1) to mimic such off-centre behaviour [4–9]. The arrangement of strong π-donor oxygen atoms to the unoccupied t_{2g}-type d orbitals of the transition metal atom required for the maximization of p_π—d_π bonding in pseudo-octahedral units typically leads to the *cis*-dioxo and *fac*-trioxo isomers shown in Fig. 1b and c being preferred to their respective *trans*-dioxo and *mer*-trioxo isomers in transition metal oxyfluoride structures [10,11]. Such anions are inherently strongly polar, particularly the (*fac*-)MO_3F_3 anion [1]. They might therefore be expected to be capable of giving rise to strongly polar materials upon their incorporation into non-centrosymmetric crystalline compounds, provided that it is possible to control the relative orientations of the inherently polar anions from one octahedral unit to the next *i.e.* to prevent

* Corresponding author.
E-mail address: withers@rsc.anu.edu.au (R.L. Withers).

0277-5387/$ - see front matter © 2006 Elsevier Ltd. All rights reserved.
doi:10.1016/j.poly.2006.05.021

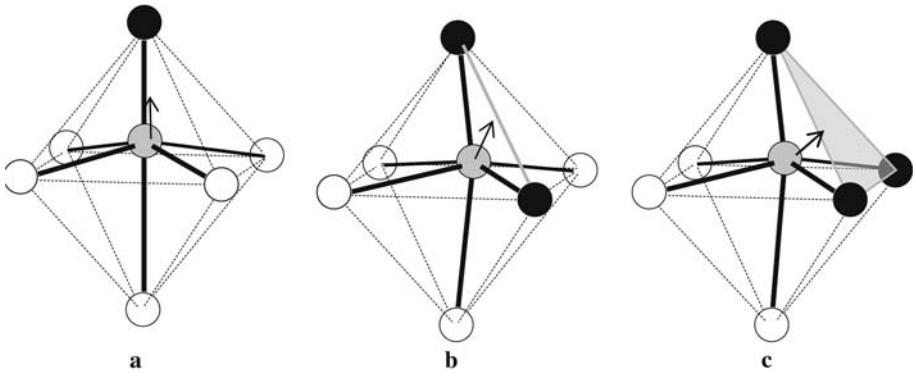


Fig. 1. Shows the inherently polar pseudo-octahedral (a) MOF_5^{2-}, (b) (*cis*-)$MO_2F_4^{2-}$ and (c) (*fac*-)$MO_3F_3^{3-}$ transition metal oxyfluoride anions. The initially central transition metal ion moves off-centre away from the fluoride ions and towards the oxide ions.

the dipole moments of separate octahedra from cancelling each other [1].

In practice, however, many if not most transition metal oxyfluoride compounds incorporating such polar anions have turned out to be inherently orientationally disordered [4–9,12–25] giving rise to crystal structures where there is no resultant polarity and where there appears to be no oxide/fluoride ordering at all, at least from a conventional 3-d crystallographic point of view. Examples include $(NH_4)_3MoO_3F_3$ [12], $CsMMoO_3F_3$ [13], $A_2BMoO_3F_3$, $A, B =$ Na, K, Rb, Cs [14–16], FeOF [17], *etc.*

In order to obtain insight into strategies for the design and synthesis of polar transition metal oxyfluoride compounds, it is helpful to characterize the oxide/fluoride and orientational ordering rules in a range of such apparently 'disordered' transition metal oxyfluorides in order to understand why the constituent inherently acentric octahedral units do not usually want to order up in a long range ordered sense. In this contribution, we review recent results obtained via the analysis of highly structured diffuse intensity distributions in some relatively simple, high symmetry, 'disordered' transition metal oxyfluorides. The aim is to highlight the common local oxide/fluoride ordering rules, the consequences of these rules for polar behaviour on the local scale as well as the roles of configurational entropy and free energy in suppressing long range polar order.

2. The M^{3+}OF family of transition metal oxyfluorides

One disordered family of transition metal oxyfluoride compounds containing locally polar pseudo-octahedral units is the family of M^{3+}OF ($M =$ Fe, Ti, V, *etc.*) oxyfluoride compounds [26–30]. They crystallize in the well-known tetragonal $P4_2/mnm$, rutile type average structure (see Fig. 2a). A single crystal X-ray diffraction study of one member of this family, FeOF, reported no evidence for oxide/fluoride ordering [17]. Mössbauer spectroscopy studies of FeOF, on the other hand, clearly show a single unique environment of $3O^{2-}$ ions and $3F^-$ ions surrounding each Fe^{3+} cation [28,29].

Furthermore, a bond valence sum analysis of FeOF using the refined average structure again showed that O^{2-} is significantly under-bonded while F^- is significantly over-bonded in the average structure anion position [31]. From the crystal chemical point of view, this implies that opposite corners of each FeO_3F_3 octahedron must necessarily be of opposite type *i.e.* if one corner is occupied by a F^- ion then the opposite corner is necessarily occupied by an O^{2-} ion thus allowing the central Fe^{3+} ion to move off-centre away from the local F_3 octahedral face and towards the opposite O_3 octahedral face with a shift magnitude estimated to be of ~0.12–0.13 Å [31]. Taken in conjunction with the Mossbaüer results, is clear that FeOF is composed of a network of locally polar *fac*-type octahedral ($M^{III}O_3F_3$) units.

As for the majority of the oxyfluorides discussed in this paper, direct evidence as to the nature of oxide/fluoride ordering on the local scale in these compounds is to be found in the existence of a highly structured diffuse intensity distribution – this time in the form of continuous 1-d rods of diffuse intensity running along the $[1\,1\,0]^*$ and $[1\,\bar{1}\,0]^*$ directions of reciprocal space through the $(h + k + l)$ odd parent rutile type Bragg reflections [31] (see Fig. 3a and b). Continuous $\langle 1\,1\,0\rangle^*$ rods of diffuse intensity in reciprocal space require the existence of 2-d, long range oxide/fluoride ordered $\{1\,1\,0\}$ planes in real space that are uncorrelated from one such $\{1\,1\,0\}$ plane to the next.

There are two distinct patterns of 2-d, oxide/fluoride ordering compatible with the bond valence sum implied constraint that an O^{2-} ion must always be opposite a F^- ion and these are shown in Figs. 3c and d [31]. Note that the tetragonal symmetry of the rutile average structure type divides the 8 potential faces of the *fac*-type pseudo-octahedral ($M^{III}O_3F_3$) units (which might be thought of as potential directions for the local dipole moment) into two sets of 4 crystallographically equivalent faces. The two distinct patterns of oxide/fluoride ordering shown in Figs. 3c and d correspond to the central Fe cation moving towards one or other of these two sets of crystallographically inequivalent faces. Only the latter (Fig. 3d), however, is compatible with the observed diffraction evidence that the diffuse rods only run through the $(h + k + l)$ odd parent rutile type Bragg reflections [31]. The tetragonal strain distortion of the individual *fac*-type pseudo-octahedral

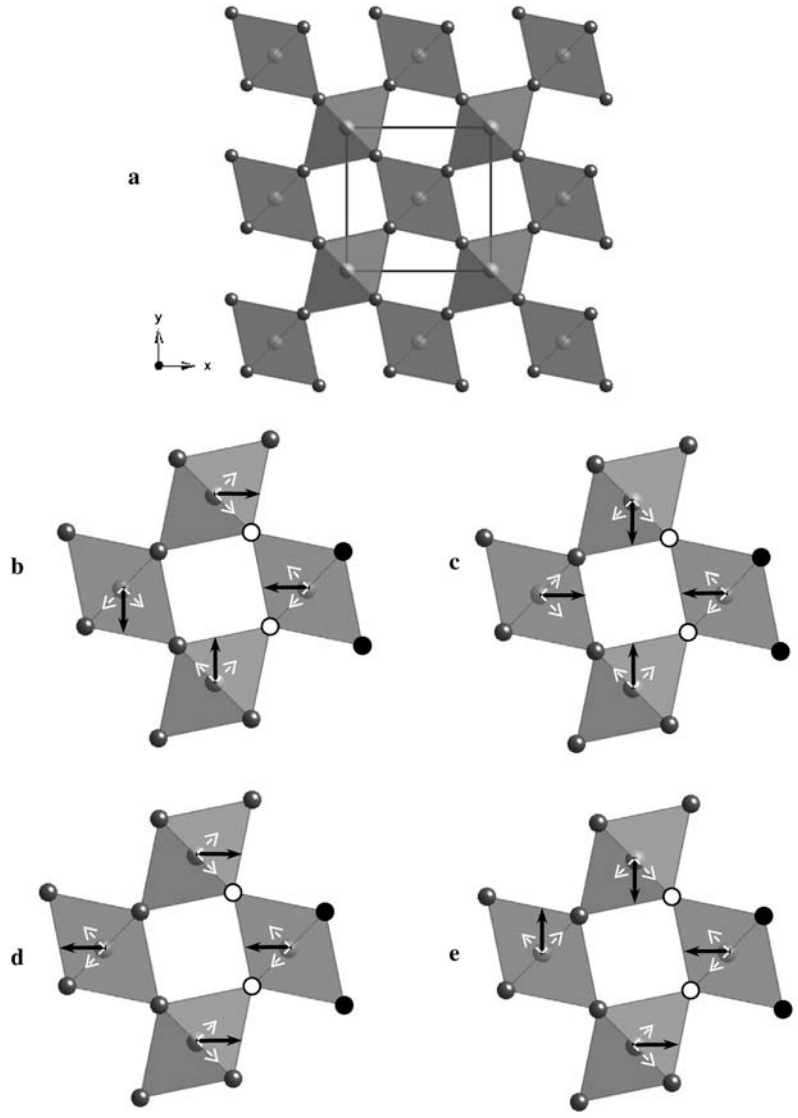


Fig. 2. (a) Shows the well-known tetragonal $P4_2/mnm$, rutile type average structure in which the family of M^{3+}OF (M = Fe, Ti, V, *etc.*) oxyfluoride compounds crystallize in projection along the [0 0 1] direction. The unit cell is outlined. Figs. 4b–e show the four distinct local configurations possible having chosen an initial displacement direction for the right hand pseudo-octahedral unit. Note that the sum of the dipole moments of the 4 polar ($M^{III}O_3F_3^{3-}$) units sum to zero in each of these 4 cases.

($M^{III}O_3F_3$) units associated with crystallizing in the rutile type average structure has thus selectively differentiated between the original 8 possible faces.

On the local scale, the Fe^{3+} (and hence the local dipole moment) can thus only point along either ±**a** or ±**b** *i.e.* towards one or other of four crystallographically equivalent faces of the *fac*-type pseudo-octahedral ($M^{III}O_3F_3$) units (see Fig. 2). Given the constraints imposed by Fig. 3d, it is not difficult to show that the sum of the dipole moments of any four polar ($M^{III}O_3F_3$) units immediately surrounding any 4_2 axis in the average structure type must necessarily always add to zero. Having chosen an initial displacement direction for the octahedral unit on the right hand side of these four pseudo-octahedral units, there are only four local configurations possible and these are shown in Fig. 2b–e, respectively. Note that the sum of the dipole moments is zero in each case. There are, in general, 16 possible local configurations for each cluster of four *fac*-type pseudo-octahedral ($M^{III}O_3F_3$) units. All, however, have the property that the sum of their dipole moments is zero. It is thus not possible to have a resultant polar structure of this type. The observed diffuse distribution ensures that the inherent dipole moments associated with each (*fac*)-FeO_3F_3 octahedral unit not only sum to zero macroscopically but also on the local unit cell scale. Indeed this is a recurrent theme for oxyfluoride compounds.

3. The *Re*O_3-type oxyfluorides $MO_{3-x}F_x$ ($M^{IV,V,VI}$ = Nb, Ta, Ti, Mo and W)

A further disordered (non-polar) family of transition metal oxyfluoride compounds containing locally polar

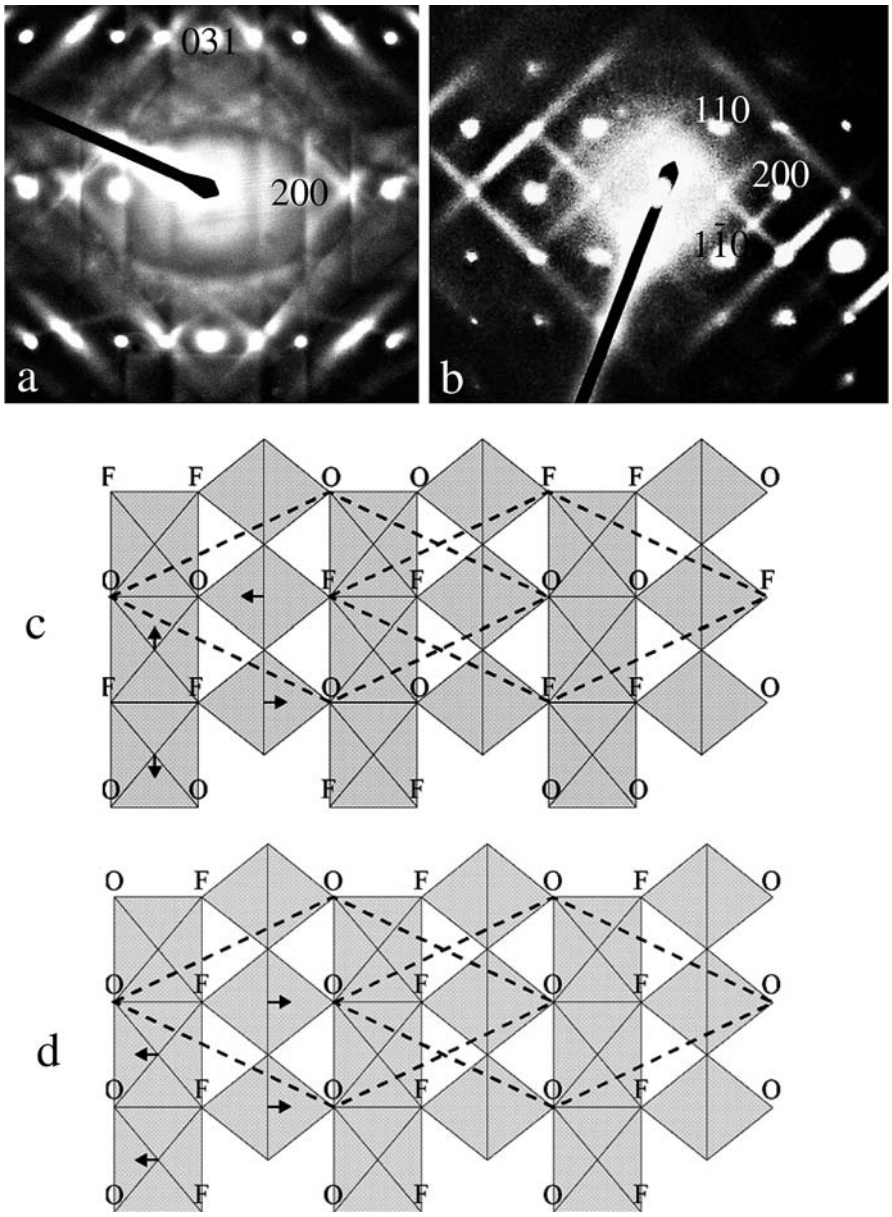


Fig. 3. Typical (a) ⟨0 1 3⟩ and (b) close to [0 0 1] zone axis EDP's of FeOF showing the continuous rods of diffuse intensity running along the ⟨1 1 0⟩* directions of reciprocal space through the $(h+k+l)$ odd parent rutile type Bragg reflections. These continuous ⟨1 1 0⟩* rods of diffuse intensity in reciprocal space require the existence of 2-d, long range oxide/fluoride ordered {1 1 0} planes in real space that are uncorrelated from one such {1 1 0} plane to the next. (c,d) show the two distinct patterns of 2-d, oxide/fluoride ordering in the {1 1 0} planes compatible with the constraint that an oxide ion must always be opposite a fluoride ion. Only the latter, however, is compatible with the observation that the diffuse rods only run through the $(h+k+l)$ odd parent rutile type Bragg reflections.

pseudo-octahedral units is the family of $MO_{3-x}F_x$ (M = Nb, Ta, Ti, Mo, W) oxyfluoride compounds which crystallize in the well known cubic $Pm\bar{3}m$, ReO_3 average structure-type (see Fig. 4a). Until recently, all of these transition metal oxyfluoride compounds were again reported as exhibiting random anion site occupation [26,32,33]. Bond valence sum calculations on the disordered average structures of $Nb^{V}O_2F$ and $Ta^{V}O_2F$, however, show clearly that O^{2-} is significantly under-bonded whilst F^- is again over-bonded in the average structure anion position [34,35]. Hence one should again expect that F^- ions will, as far as is possible, always occupy corners opposite to O^{2-} in each octahedra, thus allowing the central cation to move off-centre and thereby simultaneously improve the underbonding of the O^{2-} as well as the overbonding on the F^- ions.

Direct evidence for oxide/fluoride ordering is again found in a structured diffuse distribution, this time in the form of characteristic transverse polarized planes of diffuse intensity running through the $\mathbf{G} \pm \langle hk\,1/3\rangle^*$ (h,k continuous) regions of reciprocal space (see *e.g.* the ⟨1 1 6⟩ zone axis EDP of NbO_2F shown in Fig. 4b). Diffuse sheets in reciprocal space imply the existence of 1-d, long range O^{2-}/F^- ordered ⟨0 0 1⟩ columns of atoms in real space that are

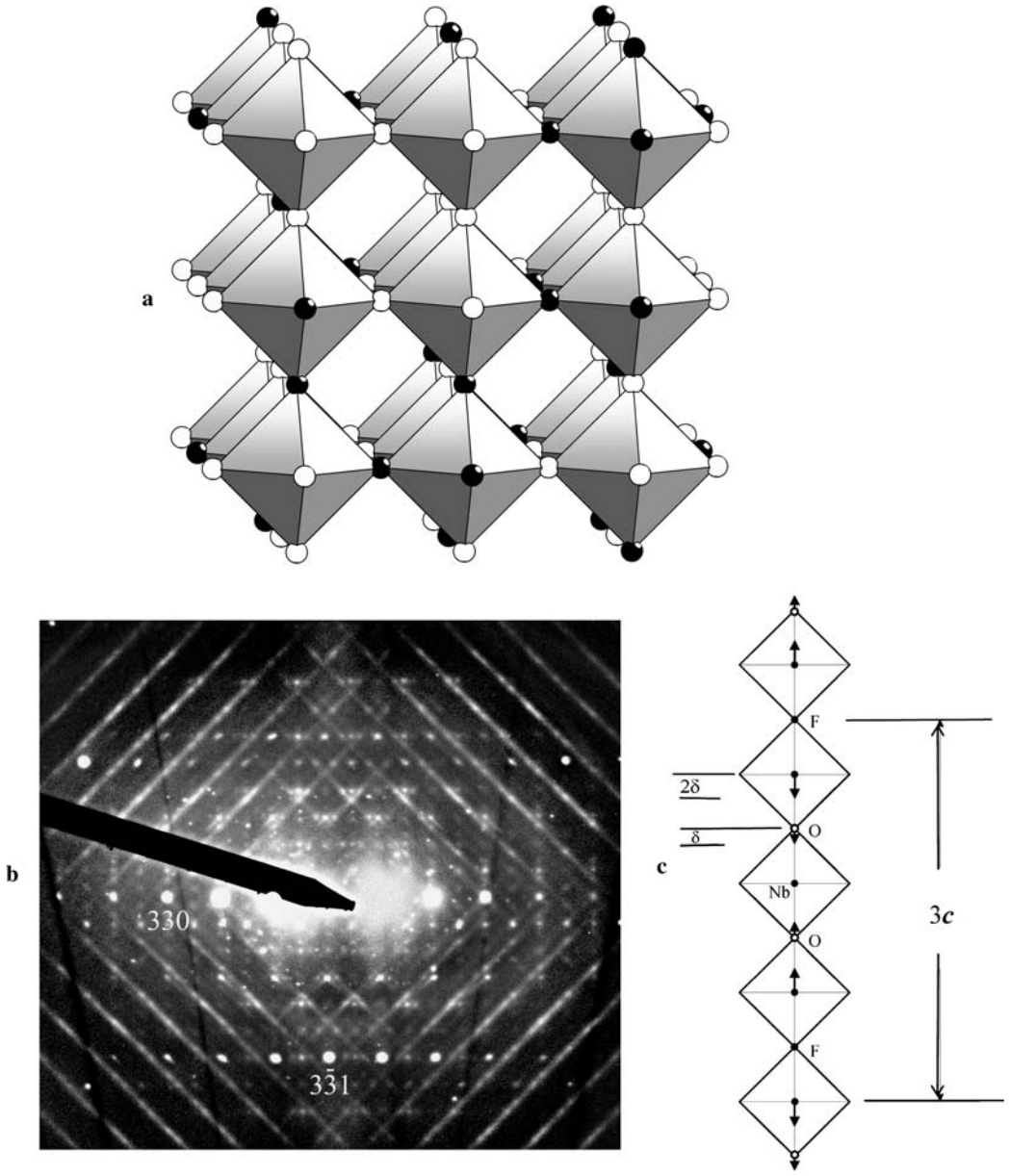


Fig. 4. (a) Shows a $3\times3\times3$ array of the cubic $Pm\bar{3}m$, ReO_3 type average structure of the family of $MO_{3-x}F_x$ (M = Nb, Ta, Ti, Mo, W) oxyfluoride compounds. The small black balls represent F^- ions while the small open circles represent O^{2-} ions. (b) A $\langle 1\,1\,6\rangle$ zone axis EDP of NbO_2F showing typical diffuse streaking along $\langle h\,0\,l\rangle^*$ directions of reciprocal space perpendicular to the $\langle 0\,1\,0\rangle$ directions of real space. (c) the ordered along $\langle 0\,0\,1\rangle$ ...$O^{2-}O^{2-}F^-$... arrangement implied by the observed diffuse distribution along with the associated induced atom shifts. Note that the component of the net dipole moment of three neighbouring octahedral units along the column direction is necessarily zero.

uncorrelated from one such column to the next while the $1/3\langle 0\,0\,1\rangle^*$ component of the diffuse distribution repeat implies an ordered —OOFOOFOOF— anion arrangement along the $\langle 0\,0\,1\rangle$ column direction (see Fig. 4c). Bond valence sum considerations suggest that the magnitude of the shift parameter, 2δ, in Fig. 4c is ~0.14 Å [34]. Note furthermore that the component of the net dipole moment of three neighbouring octahedral units along the column direction is necessarily zero.

Given the diffraction evidence for perfect 1-d, ...OOF... ordering along each of the three $\langle 0\,0\,1\rangle$ directions without any correlation from anion string to anion string running along the same $\langle 0\,0\,1\rangle$ direction or between anion strings of differing $\langle 0\,0\,1\rangle$ directions, the probability of an inherently polar (*cis*-)$Nb^VO_4F_2$ octahedral unit is $3\cdot(1/3)\cdot(2/3)^2 = 12/27$, of an inherently polar (*fac*-)$Nb^VO_4F_2$ octahedral unit is $(2/3)^3 = 8/27$, of an inherently polar Nb^VO_5F octahedral unit is $3\cdot(2/3)\cdot(1/3)^2 = 6/27$ while the probability of a non-polar Nb^VO_6 unit is 1/27. Thus the Nb^VO_2F and Ta^VO_2F compounds can be described as a corner-connected network of (overwhelmingly) inherently polar octahedral units. Nonetheless, the sum of the dipole moments of the 27 octahedra in any $3\times3\times3$ array (see Fig. 4a) necessarily must always sum to zero given Fig. 4c *i.e.* it is again

the case that the inherent dipole moments associated with the constituent $Nb^{V}O_{6-n}F_n$ octahedral units not only sum to zero macroscopically but also on the smallest possible $(3\times3\times3)$ local unit cell scale.

4. The $A_2BMoO_3F_3$, A,B = Na, K, Rb, Tl and Cs, family of oxyfluorides

A final disordered (non-polar) family of transition metal oxyfluoride compounds containing locally polar pseudo-octahedral units is the relatively large family of $A_2{}^{+}B^{+}M^{VI}O_3F_3$ (A,B = Na, K, Rb, Tl, Cs; M^{VI} = Mo, W) oxyfluoride compounds which crystallize at high temperature in the ideal cubic, $Fm\bar{3}m$, A_2BMX_6, structure type shown in Fig. 5a, or in closely related displacive variants thereof at lower temperatures [12–23]. A ⟨0 0 1⟩ projection of one half of the unit cell of this orientationally disordered, high temperature polymorphic form is shown in Fig. 5a. (The second half of the unit cell is exactly the same as that shown, just translated by $1/2(\mathbf{a}_p+\mathbf{c}_p)$, subscript p for parent. It has not been shown for the purposes of clarity). The octahedra shown represent the isolated, orientationally disordered $M^{VI}O_3F_3{}^{3-}$ octahedra while the large (open) and medium (shaded) balls represent the interstitial A and B alkali ions respectively.

Bond valence sum calculations performed on this average, ideal cubic structure type for several such materials, *e.g.* $K_3MoO_3F_3$ [24] and $Rb_2KMoO_3F_3$ [25], finds clear evidence of the need for large amplitude octahedral rotations as well as evidence that the F^- ions are invariably significantly over-bonded while the O^{2-} ions are invariably significantly under-bonded in the average structure anion positions [24,25]. The latter strongly suggests that opposite vertices in each $Mo^{VI}O_3F_3{}^{3-}$ octahedra will again always be occupied the one by O^{2-} and the other by F^-, thus confirming the existence of local *fac*-type octahedral $M^{VI}O_3F_3{}^{3-}$ units in these materials. As there are eight distinct octahedral faces associated with each *fac*-$M^{VI}O_3F_3{}^{3-}$ pseudo-octahedral unit, there are therefore eight different possible ⟨1 1 1⟩ real space directions along which the local dipole moment can point. There is thus plenty of scope for local orientational disorder.

On cooling, this high temperature γ polymorph typically undergoes two instantaneously reversible, displacive structural phase transitions – at temperature T_2 to a β polymorph and at temperature T_1 to a lowest temperature, usually room temperature, α polymorph [13–16,18–25]. The instantaneously reversible nature of these phase transitions shows that they are purely displacive in nature (associated with octahedral rotations and associated displacements of the interstitial A and B cations) but not with oxide/fluoride ordering and associated structural relaxation. This has recently been confirmed by the fact that the room temperature polymorphic form of K_3AlF_6 [36] exhibits exactly the same complex superstructure unit cell and space group symmetry as the α polymorph of $K_3MoO_3F_3$ [25]. In the case of K_3AlF_6, there is of course no possibility of oxide/fluoride ordering and associated off-centre transition metal shifts being responsible for the observed additional satellite reflections.

Evidence for oxide/fluoride ordering and associated off-centre displacements of the Mo ions in these $A_2{}^{+}B^{+}M^{VI}O_3F_3$ compounds is not to be found in the sharp additional satellite reflections associated with these lower temperature polymorphic forms but rather in the existence of a highly structured, quite sharp, continuous diffuse intensity distribution with inherent cubic symmetry (see the right hand sides of the four panels shown in Fig. 6) [25]. A virtually identical 3-d diffuse distribution has been found for $K_3MoO_3F_3$ [25], $Tl_3MoO_3F_3$ [37] as well as $Rb_2KMoO_3F_3$ [37]. It thus appears to be quite characteristic of $A_2{}^{+}B^{+}M^{VI}O_3F_3$ oxyfluoride compounds except in the special case where A and B = Na (see below).

The shape of this sharp, highly structured, diffuse intensity distribution takes the form

$$\exp 2\pi i\mathbf{q}\cdot\tfrac{1}{2}\mathbf{a}+\exp 2\pi i\mathbf{q}\cdot\tfrac{-1}{2}\mathbf{a}+\exp 2\pi i\mathbf{q}\cdot\tfrac{1}{2}\mathbf{b}+\exp 2\pi i\mathbf{q}\cdot\tfrac{-1}{2}\mathbf{b}+\exp 2\pi i\mathbf{q}\cdot\tfrac{1}{2}\mathbf{c}+\exp 2\pi i\mathbf{q}\cdot\tfrac{-1}{2}\mathbf{c}=2(\cos\pi h+\cos\pi k+\cos\pi l)=0$$

(where $\mathbf{q}=h\mathbf{a}^*+k\mathbf{b}^*+l\mathbf{c}^*$) [24,25]. The local constraint responsible for the observed diffuse distribution thus necessarily corresponds to a six-body octahedral cluster relationship involving atoms located at $\pm1/2$ $\mathbf{a}_p$, $\pm1/2$ $\mathbf{b}_p$ and $\pm1/2$ $\mathbf{c}_p$ around a central atom, specifically to a requirement that the sum of the dipole moments of the six $Mo^{VI}O_3F_3{}^{3-}$ octahedra surrounding any central B ion (equivalently the sum of the associated off-centre displacements of the Mo ions) must always sum to zero (see *e.g* Figs. 5b and c). Note that there are six, inherently acentric $M^{VI}O_3F_3{}^{3-}$ octahedra surrounding each central B cation (and vice-versa) at $\pm1/2$ $\mathbf{a}_p$, $\pm1/2$ $\mathbf{b}_p$ and $\pm1/2$ $\mathbf{c}_p$ respectively (see Fig. 5a).

Monte–Carlo simulation of Mo ion distributions satisfying such a local rule give corresponding diffraction patterns in excellent agreement with the experimentally observed diffuse distributions (*cf. e.g.* the coloured left hand side of the four panels shown in Fig. 6 with the corresponding right hand side of the same panels) [24]. Thus the inherent dipole moments associated with each (*fac*-)$MoO_3F_3{}^{3-}$ octahedra not only sum to zero macroscopically but also on the local unit cell scale (see *e.g.* Figs. 5b and c). This very strong local ordering rule, while extremely restrictive, nonetheless does not lead to conventional long range 3-d order (see Fig. 6). The reason is the numerous distinct local configurations which can still satisfy the required constraint.

Given that there are eight orientations possible for each local octahedron and six octahedra in each local cluster, there are therefore $8^6=262\,144$ distinct local configurations possible. Of these $8^6=262\,144$ local configurations possible for a random distribution, only some 8000 (or 3.05 %) satisfy the local constraint that the sum of the dipole moments must be zero (one out of these 8000

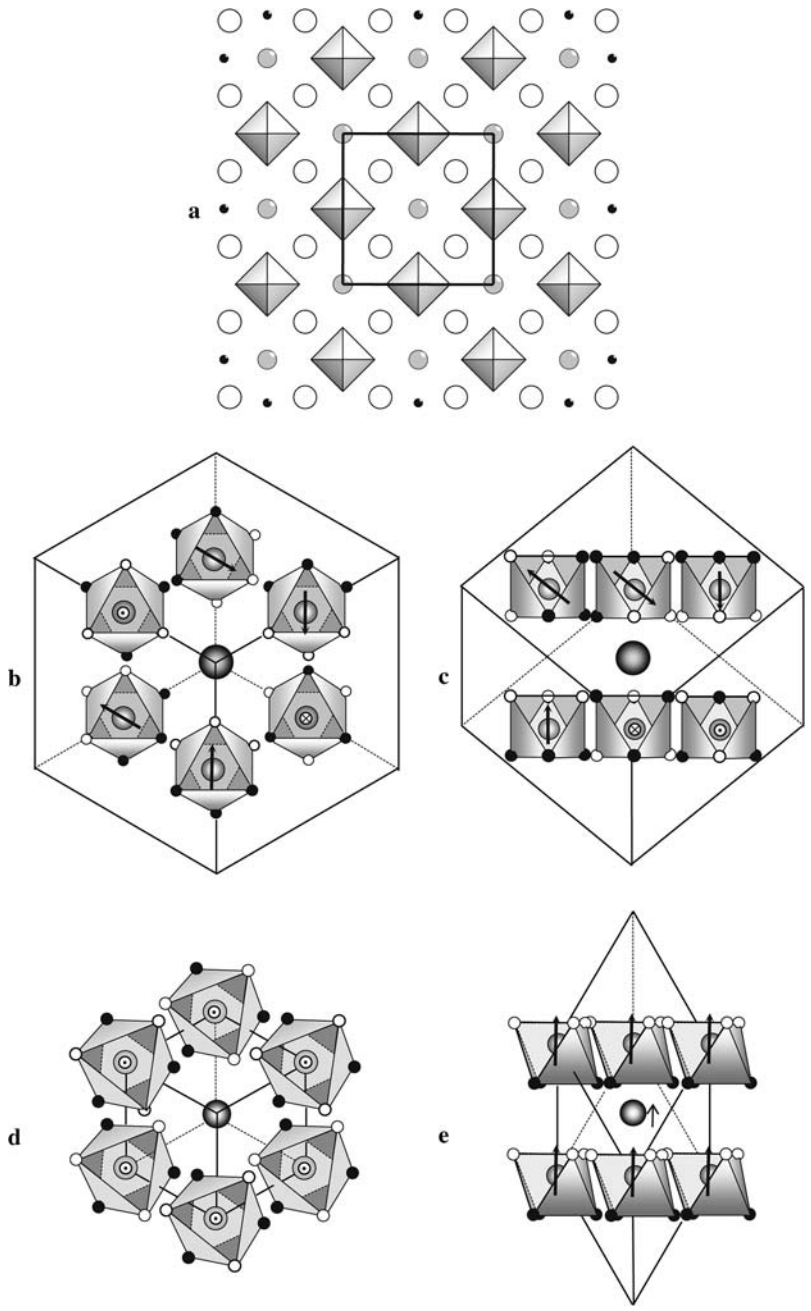


Fig. 5. (a) An ⟨0 0 1⟩ projection of one half of the unit cell of the ideal cubic $Fm\bar{3}m$, high temperature polymorphic form of the $A_2{}^{+}B^{+}M^{VI}O_3F_3$ family of transition metal oxyfluoride compounds. (The second half of the unit cell is exactly the same as that shown, just translated by 1/2 ($\mathbf{a}_p + \mathbf{c}_p$), subscript p for parent.) The octahedra represent the isolated, orientationally disordered, $M^{VI}O_3F_3{}^{3-}$ octahedra while the large (open) and medium (shaded) balls represent the interstitial *A* and *B* alkali ions, respectively. (b,c) Show one of the 8000 possible local configurations which satisfy the local constraint that the sum of the dipole moments of the six $Mo^{VI}O_3F_3{}^{3-}$ octahedra surrounding any central *B* ion (equivalently the sum of the off-centre displacements of the Mo ions) must sum to zero. The F^- ions are represented by the small dark balls while the O^{2-} ions are represented by the small open balls. The induced off-centre shifts of the metal ions are represented by the arrows. The projection axis is along a [1 1 1] direction in (b) and along the orthogonal [1 $\bar{1}$ 0] direction in (c). (d,e) Show equivalent projections of the fully dipole ordered α-$Na_3MoO_3F_3$ compound along and perpendicular to the polar axis.

possible local configurations is shown in projection along a ⟨1 1 1⟩ direction in Fig. 5b and along an orthogonal ⟨1 $\bar{1}$ 0⟩ direction in Fig. 5c). The configurational entropy associated with complete orientational disorder of the (*fac*-)$MoO_3F_3{}^{3-}$ octahedra is thus very considerably reduced by the imposition of the local constraint. It is not, however, removed altogether. The removal of ~97% of the potential local configurations shows that there must clearly be a genuine energy lowering, rather than entropy, advantage which explains why the local constraint is so strongly obeyed. Possibilities include the minimization of the overall dipole–dipole interaction energy, minimization of the dipole–interstitial B^+ monopole interaction energy or even mimization of local strain.

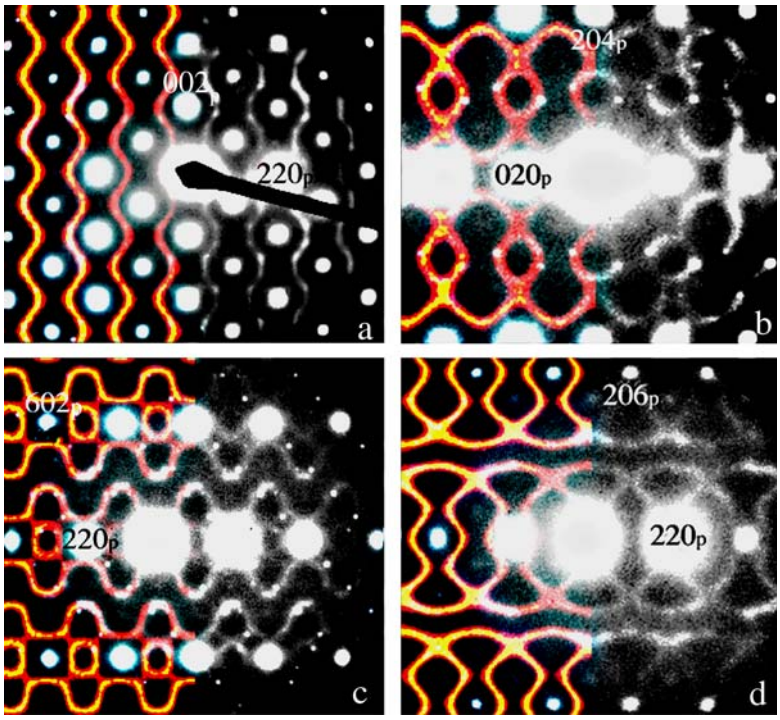


Fig. 6. Shows experimental (on the right hand side) and simulated (coloured on the left hand side) zone axis EDP's of $K_3MoO_3F_3$ at the (a) $\langle 1\,1\,0\rangle_p$, (b) $\langle 2\,0\,1\rangle_p$, (c) $\langle 1\,1\,3\rangle_p$ and (d) $\langle 3\,3\,1\rangle_p$ zone axis orientations [25]. Note the highly structured, quite sharp, continuous diffuse intensity distribution characteristic of the oxide/fluoride ordering and associated displacive shifts in these $A_2{}^+B^+M^{VI}O_3F_3$ compounds.

From the point of view of designing inherently polar transition metal oxyfluorides, the observed constraint that the inherent dipole moments associated with each (*fac*-)$MoO_3F_3{}^{3-}$ octahedra not only sum to zero macroscopically but also on the local unit cell scale is not a very encouraging result. There is, however, one counter-example from this family of compounds. The recent discovery of a fully dipole ordered $A_2{}^+B^+M^{VI}O_3F_3$ compound of this type, namely $Na_3MoO_3F_3$ (see Fig. 5d and e), demonstrates that it is quite possible for the constituent (*fac*-)$MoO_3F_3{}^{3-}$ octahedra in materials of this type to orientationally order if the local crystal chemistry (size of the interstitial alkali ions and the amplitude of octahedral rotation) is appropriate [38]. It is interesting in this context to note that a similar phenomenon also appears to take place in the case of the $A_2WO_2F_4$ oxyfluorides in that the $[WO_2F_4]^{2-}$ anion is orientationally disordered when the alkali ion is large, $A = Cs$, but becomes orientationally ordered when the much smaller alkali ion $A = Na$ is used [9].

That the room temperature polymorph of α-$Na_3MoO_3F_3$ is indeed inherently polar had already been shown by Chaminade *et al.* [21] who performed non linear optical testing and reported the harmonic yield to be about 40 times that of α-quartz. Note that neutron refinement of the crystal structure of α-$Na_3MoO_3F_3$ shows that the oxide-fluoride ordering is also accompanied by relatively large amplitude octahedral rotation of the constituent (*fac*-)$MoO_3F_3{}^{3-}$ octahedra around the resultant $[1\,1\,1]_R$, *R* for rhombohedral, axis [38], displacive shifts of the interstitial Na^+ ions along the same $[1\,1\,1]_R$ axis as well as significant rhombohedral metric distortion of the underlying cubic unit cell.

5. Conclusions

Whilst we have by no means covered, nor even attempted to cover, the wide and ever-growing spectrum of known transition metal oxyfluoride compounds ([1,2,26,39–41] and references contained therein), there are nonetheless valuable conclusions that can be drawn from the results of this paper.

First, bond valence sum calculations performed on available refined average crystal structures of 'disordered' oxyfluorides provide invaluable insight into local transition metal co-ordination environments if interpreted carefully (preferably in conjunction with spectroscopic and chemical evidence, if available [28,29,40–42]). In the three classes of transition metal oxyfluorides discussed above, such calculations invariably show O^{2-} ions to be significantly underbonded and F^- ions significantly overbonded in the average structure anion positions. A logical consequence of this is that O^{2-} and F^- ions should, as far as is possible, locally arrange themselves to be at opposite corners of each pseudo-octahedral unit. This allows the transition metal ions to move off-centre towards the O^{2-} and away from the F^- ions thereby simultanuously decreasing the overbonding of the F^- ion and the underbonding of the O^{2-} as well as providing a strong driving force for local O^{2-}/F^- ordering. It also generally leads to the expected, and desired, polar pseudo-octahedral units shown in Fig. 1.

Second, such oxide/fluoride ordering is rarely contained to the immediate co-ordination environment of the transition metal ions but usually extends considerably further depending upon factors such as the topological connectivity of the polar pseudo-octahedral units (corner- or face-sharing *etc.*) or, if not directly connected to one another, to their immediate co-ordination environment. Orientational 'ordering' of the individual polar pseudo-octahedral units rarely takes a conventional long range ordered crystallographic form (presumably as a result of configurational entropy). It rather usually manifests itself in the form of a highly structured diffuse intensity distribution. Electron diffraction, with its proven ability to detect weak, highly structured features of reciprocal space, is an invaluable tool in the search for such longer range orientational ordering rules.

Third, the concept of 'order' is a much richer concept than is usually thought. In this paper, examples have been provided of 3-d, 2-d, 1-d and 0-d order (see Table 1). In each case, the dimensional order (D) of the diffuse features of reciprocal space has implied a (3-D) dimensional order in real space. In the case of FeOF, for example, 1-d rod like diffuse was observed ($D = 1$) in reciprocal space corresponding to long range 2-d order (*i.e.* 3–1) in real space. Likewise, in the case of NbO_2F, planar diffuse ($D = 2$) implied 1-d order (*i.e.* 3–2) in real space. In the more complex case of $K_3MoO_3F_3$, a complex diffuse surface was observed in reciprocal space ($D = 3$) implying 0-d order in real space. This does not mean there is no order but rather that the extent of the order is localized in all 3 real space directions. Lastly, in the case of $Na_3MoO_3F_3$, sharp Bragg reflections in reciprocal space ($D = 0$) imply conventional 3-d long range order in real space.

Finally, the presence of inherently polar pseudo-octahedral units in transition metal oxyfluorides by no means guarantees polar macroscopic behaviour. Indeed, it would seem without appropriate intervention or clever adjustment of local crystal chemistry [1], that the local dipole moments associated with the constituent polar pseudo-octahedral units invariably not only sum to zero macroscopically but also on a very close to the average structure unit cell scale. This was the general case for each of the three classes of transition metal oxyfluorides discussed above and is clearly so for a very definite energy reason.

Table 1
Relationship between the dimensional order of real and reciprocal space

Oxyfluoride system	Dimensional order of weak scattering in reciprocal space	Implied dimensional order in real space
	(D)	(3-D)
$Na_3MoO_3F_3$	0	3
FeOF	1	2
NbO_2F	2	1
$K_3MoO_3F_3$, $Tl_3MoO_3F_3$, $Rb_2KMoO_3F_3$	3	0

Acknowledgement

R.L.W. and Y.L. acknowledge the Australian Research Council (ARC) for financial support in the form of an ARC Discovery Grant.

References

[1] Paul A. Maggard, Tiffany S. Nault, Charlotte L. Stern, Kenneth R. Poeppelmeier, J. Solid State Chem. 175 (2003) 27.
[2] Margaret E. Welk, Alexander J. Norquist, Frederick P. Arnold, Charlotte L. Stern, Kenneth R. Poeppelmeier, Inorg. Chem. 41 (2002) 5119.
[3] P. Shiv Halasyamani, Kenneth R. Poeppelmeier, Chem. Mater. 10 (1998) 2753.
[4] Kevin R. Heier, Alexander J. Norquist, Christopher G. Wilson, Charlotte L. Stern, Kenneth R. Poeppelmeier, Inorg. Chem. 37 (2002) 76.
[5] Alexander J. Norquist, Charlotte L. Stern, Kenneth R. Poeppelmeier, Inorg. Chem. 38 (1999) 3448.
[6] Margaret E. Welk, Alexander J. Norquist, Charlotte L. Stern, Kenneth R. Poeppelmeier, Inorg. Chem. 39 (2000) 3946.
[7] P. Shiv Halasyamani, Kevin R. Heier, Charlotte L. Stern, Kenneth R. Poeppelmeier, Acta Cryst. C 53 (1997) 1240.
[8] P. Shiv Halasyamani, Kevin R. Heier, Alexander J. Norquist, Charlotte L. Stern, Kenneth R. Poeppelmeier, Inorg. Chem. 37 (1998) 369.
[9] Margaret E. Welk, Alexander J. Norquist, Charlotte L. Stern, Kenneth R. Poeppelmeier, Inorg. Chem. 40 (2001) 5479.
[10] W.J. Casteel, D.A. Dixon, N. LeBlond, H.P.A. Mercier, G.J. Schrobilgen, Inorg. Chem. 37 (1998) 340.
[11] M. Gerken, H.P.A. Mercier, G.J. Schrobilgen, in: T. Nakajima, B. Zemva, A. Tressaud (Eds.), Advanced Inorganic Fluorides: Synthesis, Characterization and Applications, Elsevier, 2000 (Chapter 5).
[12] L.J. Pauling, J. Am. Chem. Soc. 46 (1924) 2738.
[13] D. Babel, G. Pausewang, W. Viebahn, Z. Naturforsch. 22 (1967) 1219.
[14] Z.G. Ye, J. Ravez, J.-P. Rivera, J.-P. Chaminade, H. Schmid, Ferroelectrics 124 (1991) 281.
[15] G. Pausewang, W. Rüdorff, Z. Anorg. Allg. Chem. 364 (1969) 69.
[16] S.C. Abrahams, J.L. Bernstein, J. Ravez, Acta Cryst. B 37 (1981) 1332.
[17] M. Vlasse, J. Massies, G. Demazeau, J. Solid State Chem. 8 (1973) 109.
[18] G. Péradeau, J. Ravez, A. Tressaud, P. Hagenmuller, H. Arend, G. Chanussot, Solid State Commun. 23 (1977) 543.
[19] G. Péradeau, J. Ravez, H. Arend, Solid State Commun. 27 (1978) 515.
[20] J. Ravez, G. Péradeau, H. Arend, S.C. Abrahams, P. Hagenmuller, Ferroelectrics 26 (1980) 767.
[21] J.P. Chaminade, M. Cervera-Marzal, J. Ravez, P. Hagenmuller, Mat. Res. Bull. 21 (1986) 1209.
[22] J.P. Chaminade, M. Cervera-Marzal, J. Ravez, Mater. Sci. Eng. B3 (1989) 497.
[23] M. Fouad, J.P. Chaminade, J. Ravez, A. Sadel, J. Solid State Chem. 124 (1996) 123.
[24] R.L. Withers, T.R. Welberry, F.J. Brink, L. Norén, J. Solid State Chem. 170 (2003) 211.
[25] F.J. Brink, R.L. Withers, K. Friese, G. Madariaga, L. Norén, J. Solid State Chem. 163 (2002) 267.
[26] P. Hagenmuller, in: K.J. Rao (Ed.), Perspectives in Solid State Chemistry, Narosa, New Delhi, 1995, p. 66.
[27] P. Hagenmuller, J. Portier, J. Cadiou, R. de Pape, C. R. Acad. Sci. 260 (1965) 4768.
[28] J. Chappert, J. Portier, Solid State Commun. 4 (1966) 185.
[29] J. Chappert, J. Portier, Solid State Commun. 4 (1966) 395.
[30] B.L. Chamberland, A.W. Sleight, J. Solid State Chem. 2 (1970) 49.

[31] F.J. Brink, R.L. Withers, J.G. Thompson, J. Solid State Chemistry 155 (2000) 359.
[32] L.K. Frevel, H.W. Rinn, Acta Cryst. 9 (1956) 626.
[33] A.W. Sleight, Inorg. Chem. 8 (1969) 1764.
[34] F.J. Brink, R.L. Withers, L. Norén, J. Solid State Chemistry 166 (2002) 73.
[35] F.J. Brink, L. Norén, R.L. Withers, J. Solid State Chem. 177 (2004) 2177.
[36] A.M. Abakumov, M.D. Rossell, A.M. Alekseeva, S.Y. Vassiliev, S.N. Mudrezova, G. Van Tendeloo, E.V. Antipov, J. Solid State Chem. 179 (2006) 421.
[37] F.J. Brink, L. Norén, R.L. Withers, J. Solid State Chem. 174 (2003) 44.
[38] F.J. Brink, L. Norén, D.J. Goossens, R.L. Withers, Y. Liu, C. Xu, J. Solid State Chem. 174 (2003) 450.
[39] J. Ravez, J. Phys. III France 7 (1997) 1129.
[40] L.-S. Du, F. Wang, C.P. Grey, J. Solid State Chem. 140 (1998) 285.
[41] L.-S. Du, R.W. Schurko, N. Kim, C.P. Grey, J. Phys. Chem. A 106 (2002) 7876.
[42] K.R. Heier, K.R. Poeppelmeier, J. Solid State Chem. 133 (1997) 576.

Available online at www.sciencedirect.com
ScienceDirect
Polyhedron 26 (2007) 300–304
POLYHEDRON
www.elsevier.com/locate/poly

The structure-directing influence of guanidinium cations in the crystal structures of $[C(NH_2)_3]_2[M^{II}(H_2O)_4(VO_3)_4]\cdot 4H_2O$ (M = Mn, Co, Ni)

Brendan F. Abrahams *, Marissa G. Haywood, Richard Robson *

School of Chemistry, University of Melbourne, Vic. 3010, Australia

Received 13 April 2006; accepted 21 May 2006
Available online 13 June 2006

Abstract

The combination of guanidinium, vanadate and the divalent transition metals Mn^{II}, Co^{II} and Ni^{II} in aqueous solution leads to the generation of crystals of formula $[C(NH_2)_3]_2[M^{II}(H_2O)_4(VO_3)_4]\cdot 4H_2O$ (M = Mn, Co, Ni). The structures consist of undulating anionic $[M^{II}(H_2O)_4(VO_3)_4{}^{2-}]$ sheets which stack in an ABAB fashion. Guanidinium ions bind pairs of sheets together by a combination of electrostatic attraction and hydrogen bonding to generate a 3D coordination/hydrogen-bonded network. TGA studies of the compounds reveal that upon heating, water molecules are first lost and this process is followed by the decomposition of the guanidinium ion.
© 2006 Elsevier Ltd. All rights reserved.

Keywords: Crystal engineering; Hydrogen-bonded networks; Guanidinium cations

1. Introduction

The guanidinium cation is a very versatile hydrogen bonding building block showing much promise for the construction of a variety of network structures. Reports from Ward and co-workers [1–3], describing the elegant crystal engineering of a series of guanidinium sulphonates with reliable and predictable connectivities, suggested that the guanidinium ion might possess a much more widely applicable potential for framework construction. We have been attempting to exploit some of these possibilities and have reported (a) a very extensive series of carbonate-based networks with cubic symmetry and with a topology based on that of sodalite [4,5], in which the guanidinium cation behaves as a 3-connecting node in a very predictable manner, (b) a series of composition $[C(NH_2)_3][N(CH_3)_4][XO_4]$ (X = S, Cr and Mo) again with cubic symmetry but with the (10,3)-*a* topology [6], in which the guanidinium cation plays a similar 3-connecting role, (c) a series of composition $\{[B(OCH_3)_4]_3[C(NH_2)_3]_4\}^+X^-$ (X^- = a range of anions) in which the guanidinium cation yet again plays a very similar role and yet again the crystals have cubic symmetry, but in this case the topology is that of the boracite net [7] and (d) the structure of guanidinium rhodizonate in which the guanidinium ion plays essentially the same 3-connecting role, but in which the network nevertheless adopts an unexpected and new type of 3D topology [8]. In all of these examples, including those of Ward [1–3], the guanidinium ion forms three pairs of hydrogen bonds to three separate oxyanions as depicted in Fig. 1. In the present report, we describe a new series of guanidinium transition metal vanadates, in which the guanidinium cation cements undulating anionic sheets together (see Table 1).

2. Results and discussion

The reaction of sodium metavanadate, guanidinium chloride and metal(II) nitrate in water affords crystals of formula, $[C(NH_2)_3]_2[M(H_2O)_4(VO_3)_4]\cdot 4H_2O$ (M = Mn, Co, Ni) which were orange–red in the Mn and Co cases

* Corresponding authors. Tel.: +61 3 8344 0341; fax: +61 3 9347 5180.
E-mail address: bfa@unimelb.edu.au (B.F. Abrahams).

0277-5387/$ - see front matter © 2006 Elsevier Ltd. All rights reserved.
doi:10.1016/j.poly.2006.05.033

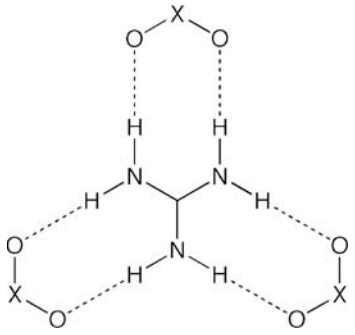


Fig. 1. The interaction of the guanidinium ion with three anions. The XO_2 units are part of oxyanions, such as sulphonate, sulphate, chromate, molbydate, tungstate, tetramethylborate, carbonate and rhodizonate. In rhodizonate, X represents a C–C link.

Table 1
Crystallographic data for $[C(NH_2)_3]_2[M(H_2O)_4(VO_3)_4]\cdot 4H_2O$ [M = Co, Ni]

	M = Co	M = Ni
Colour	orange	green
Habit	needle	needle
Size (mm)	$0.27\times0.05\times0.05$	$0.27\times0.05\times0.05$
Formula	$C_2H_{28}N_6CoO_{20}V_4$	$C_2H_{28}N_6NiO_{20}V_4$
a (Å)	3.6273(10)	3.6261(6)
b (Å)	16.374(5)	16.327(3)
c (Å)	19.248(6)	19.253(4)
β (°)	94.950(5)	94.819(3)
V (Å^3)	1138.9(6)	1135.8(3)
λ (Å)	0.71073	0.71073
Crystal system	monoclinic	monoclinic
Space group	$C2/c$	$C2/c$
Z	2	2
Reflections measured	3539	3552
Unique reflections	1307	1298
R_{int}	0.0330	0.0243
Observed reflections $I > 2\sigma(I)$	1174	1171
Completeness of data ($0° \leqslant 2\theta \leqslant 55°$) (%)	99.2	99.2
wR_2[a]	0.1198	0.0988
R_1[b]	0.0478	0.0356

[a] $wR_2 = \{\sum[w(F_o^2 - F_c^2)^2]/\sum[w(F_o^2)^2]\}^{1/2}$.
[b] $\sum\|F_o| - |F_c\|/\sum|F_o|$.

and green in the Ni case; yellow crystals of guanidinium decavanadate which also formed were easily distinguished and separated. Full X-ray single crystal structural analyses were performed on the Co and Ni compounds which showed that the compounds were isomorphous. The crystals of the Mn analogue were too small for a full structure determination but its powder diffraction pattern revealed the same structure.

Within the structure, the vanadate ion exists in the form of ladder-like chains that extend in the *a*-direction (Fig. 2). The vanadium centre is coordinated by five oxygen atoms with a coordination geometry somewhere between trigonal bipyramidal and square pyramidal. The sides of the ladder are formed from –V–O–V– chains involving oxygen atoms that lie in the axial coordination sites of a distorted trigonal bipyramid. Vanadium–oxygen links between these chains

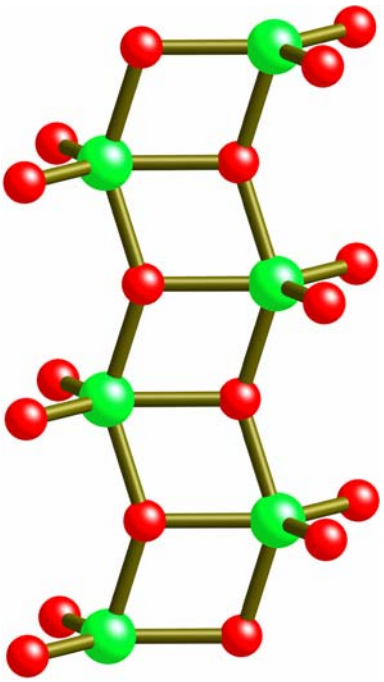


Fig. 2. A $[VO_3^-]_n$ ladder within $[C(NH_2)_3]_2[M(H_2O)_4(VO_3)_4]\cdot 4H_2O$ [M = Mn, Co, Ni]. The large spheres represent vanadium atoms, small spheres represent oxygen atoms.

form the rungs of the ladder. These ladder-like chains are common in 1D, 2D and 3D vanadium(V) oxide materials [9–13] including V_2O_5 itself [14]. Individual ladders are linked through $M^{II}(H_2O)_4$ units to form an undulating 2D network as depicted in Fig. 3. Intra-sheet hydrogen bonding between terminal oxo groups and coordinated water molecules, shown in Fig. 3, strengthens the connections between ladders within a sheet.

The fact that the vanadate ion is present as ladder-like units prevents the types of highly symmetrical interactions between the anion and guanidinium, which were a feature of the cubic networks mentioned in Section 1. As a consequence the vanadate structures described in the manuscript do not possess cubic symmetry.

Fig. 3 indicates two types of vanadium centre, one type with two terminal oxo groups and the second type with only a single terminal oxo group and an oxo bridge to the M^{II} centre. Despite this difference in coordination, both types of vanadium centres are crystallographically equivalent, with the $M^{II}(H_2O)_4$ units disordered over two symmetry related positions. As a consequence of this disorder the relative positions of the $M^{II}(H_2O)_4$ units on either side of a ladder are not certain. One possible arrangement is depicted in Fig. 3.

The mean planes of the $[VO_3^-]_n$ ladders within a sheet are equally inclined to the mean plane of the sheet, however the ladders in adjacent sheets are inclined in opposite directions as shown in Fig. 4. The sheets stack in the ABAB fashion with adjacent sheets related by a 2-fold axis. The troughs in one sheet are directly opposed to crests in the sheet below creating expanded and narrowed regions

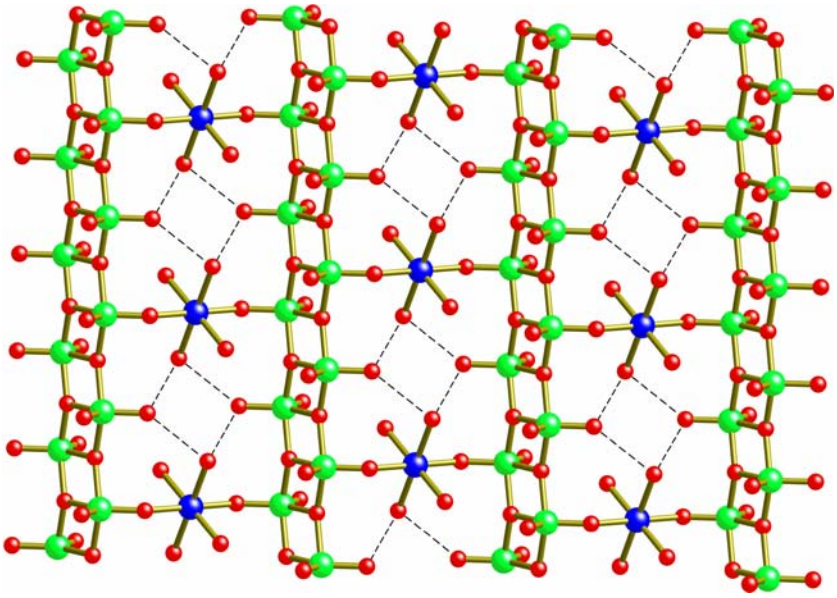


Fig. 3. A $[M(H_2O)_4(VO_3)_4^{2-}]$ (M = Co, Ni) sheet. The large pale spheres, large dark spheres and small dark spheres represent V, M and O atoms, respectively. Hydrogen bonds are represented by dashed lines. Hydrogen atoms are not shown.

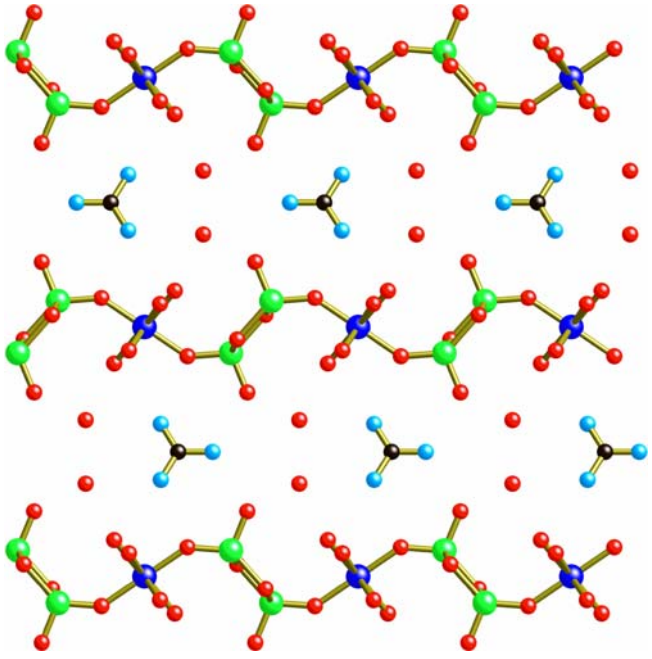


Fig. 4. The arrangement of the anionic sheets in $[C(NH_2)_3]_2[M(H_2O)_4(VO_3)_4]\cdot 4H_2O$ [M = Mn, Co, Ni]. The trigonal units between the sheets are guanidinium ions. The isolated spheres represent the oxygen atoms of non-coordinated water molecules. Hydrogen atoms are not shown.

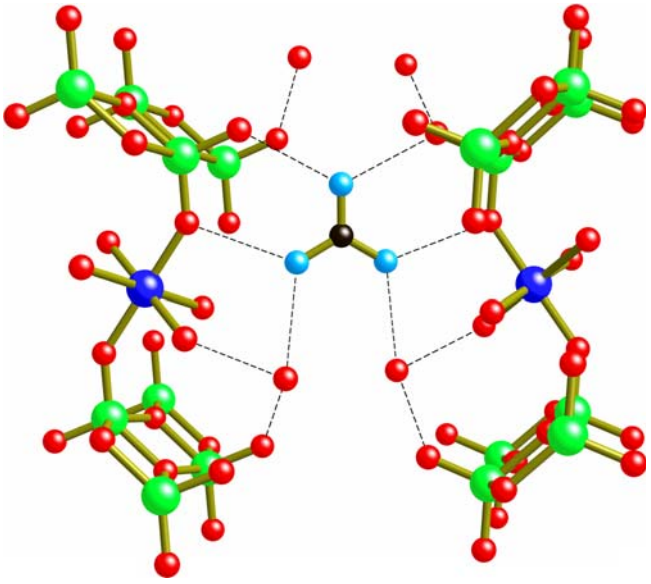


Fig. 5. A representation of the hydrogen bonding between the guanidinium ions, the anionic sheets and non-coordinated water molecules. Hydrogen atoms are not shown.

between the sheets. The guanidinium cations are situated near the narrow regions, oriented in a plane that is almost perpendicular to the mean plane of the sheets. Non-coordinated water molecules lie in the expanded regions.

Each guanidinium ion lies on a 2-fold axis and participates in six hydrogen bonds as indicated in Fig. 5. Pairs of hydrogen bonds extend to vanadate units belonging to different sheets. The guanidinium ions are further hydrogen bonded to pairs of uncoordinated water molecules which in turn are hydrogen bonded to water molecules coordinated to the divalent metal ions. The hydrogen bonding role played by the guanidinium cation seen here is closely similar to that seen in Fig. 1. It appears that this interaction plays a major role in the relative orientation of adjacent sheets within the structure.

Thermogravimetric analysis of $[C(NH_2)_3]_2[Mn(H_2O)_4(VO_3)_4]\cdot 4H_2O$ shows two distinct mass losses up to 350 °C (see Fig. 6). The first mass loss is already underway at 25 °C and is complete at 120 °C. This corresponds to the

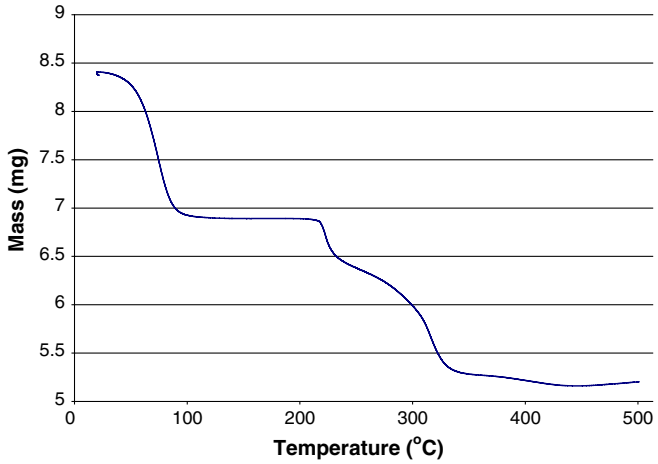


Fig. 6. TGA trace for $[C(NH_2)_3]_2[Mn(H_2O)_4(VO_3)_4]\cdot 4H_2O$.

loss of the uncoordinated and coordinated water molecules (18.0% found, 20.2% calculated). At 200 °C a second mass loss begins which is likely to correspond to the decomposition of the guanidinium ion. This is a multi-step process, occurring in the range 200–350 °C and is consistent with the loss of ammonia followed by cyanamide and water. It is proposed that the water molecule lost in this process is formed from an oxide anion and guanidinium protons. Similar behaviour is observed with the Co and Ni compounds although the second mass loss process is less well-defined. Further thermogravimetric details are presented in the Supplementary data.

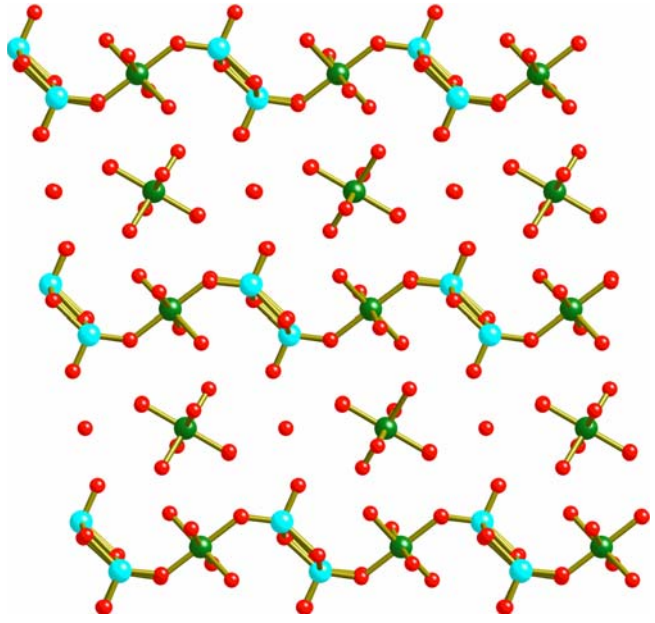


Fig. 7. The structure of $[Mg(H_2O)_6]_2[Mg(H_2O)_4(VO_3)_4]$ (dickthomsenite). The large pale spheres, large dark spheres and small dark spheres represent V, Mg and O atoms, respectively. Hydrogen atoms are not shown. (Dickthomsenite cell dimensions and space group: $a = 38.954(2)$, $b = 7.2010(4)$, $c = 16.3465(9)$ Å, $\beta = 97.602(1)°$, $C2/c$.)

The structures reported here are related to that of dickthomsennite [15], but differ from it in an important respect which reveals the structure-directing role played by the guanidinium cation. One view of the structure of dickthomsennite, $[Mg(H_2O)_6][Mg(H_2O)_4(VO_3)_4]$ is shown in Fig. 7, in which it can be seen that the individual $[Mg(H_2O)_4(VO_3)_4^{2-}]$ sheets stack in what may be described as an AAAA fashion. In this case the average planes of all the ladders in all the sheets are parallel to each other, in contrast to the ABAB-stacked structures reported above. The origin of the different stacking is plain – only by having alternating A and B sheets related by a 2-fold axis are the hydrogen bonding capabilities of the guanidinium cation maximised in the manner seen in Fig. 5.

3. Experimental

3.1. $[C(NH_2)_3]_2Mn(H_2O)_4(VO_3)_4\cdot 4H_2O$ (1)

A solution of $Mn(NO_3)_2\cdot 4H_2O$ (200 mg, 1.12 mmol) and $C(NH_2)_3Cl$ (530 mg, 5.6 mmol) in H_2O (5 ml) was added to a slurry of NH_4VO_3 (260 mg, 2.24 mmol) in H_2O (10 ml) to produce a soupy yellow suspension. After several days, orange crystals of (**1**) were separated from an inhomogeneous reaction mixture by repeated washing and decanting finer solid, leaving the larger, more dense desired product free of impurity. The crystals were washed with water and dried in air. *Anal.* Calc.: C, 3.3; H, 3.9; N, 11.7. Found: C, 3.5; H, 3.9; N, 11.7%.

3.2. $[C(NH_2)_3]_2Co(H_2O)_4(VO_3)_4\cdot 4H_2O$ (2) and $[C(NH_2)_3]_2Ni(H_2O)_4(VO_3)_4\cdot 4H_2O$ (3)

Cobalt and nickel analogues were prepared in a similar manner, differing by only replacing $Mn(NO_3)\cdot 4H_2O$ with either $Co(CH_3COO)_2\cdot 4H_2O$ or $Ni(NO_3)_2\cdot 6H_2O$. After a few days, red crystals of (**2**) and green crystals of (**3**), which selectively adhered to the walls, were isolated by flushing away the finer suspended material with water. *Anal.* Calc. for (**2**): C, 3.3; H, 3.9; N, 11.7. Found: C, 3.6; H, 4.0; N, 12.1%. *Anal.* Calc. for (**3**): C, 3.3; H, 3.9; N, 11.7 . Found: C, 3.5; H, 4.0; N, 11.7%. Powder diffraction patterns are consistent with single crystal data although there is perhaps evidence of very minor contamination of the product by the co-precipitated solid (see supplementary data).

Single crystal X-ray data were collected on a Bruker CCD diffractometer. The structures were solved using direct methods and refined using a full-matrix least-squares refinement procedure based on F^2 [16]. All data were used in the refinement process. Absorption corrections were applied using the multi-scan procedure [17].

Acknowledgements

The authors gratefully acknowledge the support of the Australian Research Council.

Appendix A. Supplementary data

CCDC Nos. 604416 (2) and 604417 (3) contain the supplementary crystallographic data for this paper. These data can be obtained free of charge at www.ccdc.cam.ac.uk [or from Cambridge Crystallographic Data Centre, 12 union Road, Cambridge CB2 1EZ, UK; e-mail: deposit@ccdc.cam.ac.uk]. Powder diffraction patterns and TGA results relating to compounds 1, 2 and 3 have been deposited. Supplementary data associated with this article can be found, in the online version, at doi:10.1016/j.poly.2006.05.033.

References

[1] K.T. Holman, A.M. Pivovar, M.D. Ward, Science 294 (2001) 1907.
[2] K.T. Holman, S.M. Martin, D.P. Parker, M.D. Ward, J. Am. Chem. Soc. 123 (2001) 4421.
[3] V.A. Russell, M.D. Ward, Chem. Mater. 8 (1996) 1654.
[4] B.F. Abrahams, A. Hawley, M.G. Haywood, T.A. Hudson, R. Robson, D.A. Slizys, J. Am. Chem. Soc. 126 (2004) 2894.
[5] B.F. Abrahams, M.G. Haywood, R. Robson, D.A. Slizys, Angew. Chem., Int. Ed. 42 (2003) 1111.
[6] B.F. Abrahams, M.G. Haywood, T.A. Hudson, R. Robson, Angew. Chem., Int. Ed. 43 (2004) 6157.
[7] B.F. Abrahams, M.G. Haywood, R. Robson, J. Am. Chem. Soc. 127 (2005) 816.
[8] B.F. Abrahams, M.G. Haywood, R. Robson, CrystEngComm 7 (2005) 629.
[9] A. Bjoernberg, B. Hedman, Acta Chem. Scand., Ser. A 31 (1977) 579.
[10] V. Legagneur, J.H. Liao, Y. An, A. le Gal la Salle, A. Verbaere, Y. Piffard, D. Guyomard, Solid State Ionics 133 (2000) 161.
[11] E. Baudrin, M. Touboul, G. Nowogrocki, J. Solid State Chem. 152 (2000) 511.
[12] M.M. Borel, J. Chardon, A. Leclaire, B. Raveau, J. Solid State Chem. 145 (1999) 634.
[13] J.H. Liao, T. Drezen, F. Leroux, D. Guyomard, Y. Piffard, Eur. J. Solid State Inorg. Chem. 33 (1996) 411.
[14] H.G. Bachmann, F.R. Ahmed, W.H. Barnes, Zeitschrift fuer Kristallographie, Kristallgeometrie, Kristallphysik, Kristallchemie 115 (1961) 110.
[15] J.M. Hughes, F.E. Cureton, J. Marty, R.A. Gault, M.E. Gunter, C.F. Campana, J. Rakovan, A. Sommer, M.E. Brueseke, Can. Mineral. 39 (2001) 1691.
[16] G.M. Sheldrick, SHELX-97 Programs for crystal structure analysis (Release 97-2), Institüt für Anorganische Chemie der Universität, Tammanstrasse 4, D-3400 Göttingen, Germany, 1998.
[17] SADABS Area Detector Absorption Correction; Siemens Industrial Automation, Madison, WI, USA.

Available online at www.sciencedirect.com
ScienceDirect
Polyhedron 26 (2007) 305–317
POLYHEDRON
www.elsevier.com/locate/poly

Synthesis, crystal structure and magnetism of a single-molecule magnet, $[Mn_{16}O_{16}(OMe)_6(OAc)_{16}(MeOH)_3(H_2O)_3]\cdot 6H_2O$, and of a mixed bridge 1D chain, $[Mn(\mu\text{-}OMe)(\mu\text{-}OAc)_2]_n$

David J. Price [1], Stuart R. Batten, Boujemaa Moubaraki, Keith S. Murray *

School of Chemistry, Monash University, Building 23, Clayton, Vic. 3800, Australia

Received 31 March 2006; accepted 19 May 2006
Available online 11 July 2006

Abstract

The syntheses, structures and magnetic characterisations of the hexadecanuclear manganese(III/IV) carboxylate cluster $[Mn_{16}O_{16}(OMe)_6(OAc)_{16}(MeOH)_3(H_2O)_3]\cdot 6H_2O$ (**1** · $6H_2O$) and a linear chain Mn^{III} complex $[Mn(\mu\text{-}OMe)(\mu\text{-}OAc)_2]_n$ (**2**) are reported. AC magnetic susceptibility measurements confirm **1** to be a single-molecule magnet with relaxation parameters of $\tau_0 = 3.00\times10^{-9}$ s and energy barrier, ΔE, of 52.2 cm^{-1}. Complexes **1** · $6H_2O$ and **2** were obtained by reaction of *n*-Bu_4NMnO_4 with $Mn(NO_3)_2\cdot 4H_2O$ in a mixture of methanol and acetic acid. Complex **1** · $6H_2O$ crystallises in the triclinic space group $P\bar{1}$ and the cluster structure consists of six Mn^{IV} and 10 Mn^{III} ions held together by 14 μ_3-O^{2-}, two μ_2-O^{2-}, four μ_2-OMe^- and two μ_2-OAc^- groups to give a roughly elliptical planar $[Mn_{16}O_{16}(OMe)_4(OAc)_2]^{16+}$ core. Peripheral ligation consists of the remaining 14 μ_2-OAc^-, two μ_2-OMe^- groups and three axial water and methanol molecules. Complex **2** crystallises in the orthorhombic space group *Pbcn* and consists of infinite linear 1D chains of manganese(III) atoms bridged by two μ-OAc^- ligands and one μ-OMe^-. The magnetic data on **1** · $6H_2O$ and **2** are compared with those of other recently reported Mn_{16} and Mn(III) μ-carboxylate chain analogues.
© 2006 Elsevier Ltd. All rights reserved.

Keywords: Single-molecule magnet; Mixed-valent manganese carboxylate clusters; 1D chain manganese(III) complexes; Magnetism; Crystal structures

1. Introduction

The discoveries of magnetically coupled clusters of d-block ions that display nanoscale magnetism of the single-molecule magnetic (SMM) type continue apace. In the case of the most abundant metal to form such molecular species, manganese, the carboxylate clusters known to display SMM behaviour include particular examples of Mn_4 [1,2], Mn_9 [3–5], Mn_{10} [6], Mn_{12} [7], Mn_{18} [8], Mn_{21} [9], Mn_{22} [10], Mn_{26} [11,12], Mn_{30} [13] and Mn_{84} (the largest Mn carboxylate cluster isolated to date) [14]. Other nuclearities such as Mn_3, Mn_6 [15,16], Mn_7 [17] Mn_8 [5,16,18,19], Mn_{13} [20] $(Ba_8Na_2)Mn_{16}$(II/III) [21] and Mn_{21} [22] do not, even though some have high-spin ground states, one of the key prerequisites for being an SMM. Another key prerequisite for SMM behaviour is a negative anisotropy in the axial zero-field splitting term *D*, which in the Mn clusters is introduced into the cluster ground state by Mn^{III} single-ion centres. A limited number of examples of SMM clusters containing metals other than manganese also exist. These include Fe_4 [23], Fe_8 [24–28], Fe_{10} [29,30], Fe_{19} [31] and V_4 [32] complexes, and recently, particular Ni_{12} [33], Ni_{21} [34], Co_4 [35] and Ni_4 [36] clusters have been reported to display SMM behaviour, albeit in the millikelvin temperature range. The SMM materials are not limited to oxo/carboxylato-based species, and now include a few examples of cyano-bridged clusters [37,38].

During attempts to link Mn_3 or Mn_4 carboxylate clusters together using the dicyanamide ($N(CN)_2^-$) ligand, in work aimed at making long-range ordered cluster arrays,

* Corresponding author. Tel.: +61 3 9905 4512; fax: +61 3 9905 4597.
E-mail address: keith.murray@sci.monash.edu.au (K.S. Murray).
[1] Present address: School of Chemistry, University of Melbourne, Parkville, Vic. 3010, Australia.

0277-5387/$ - see front matter © 2006 Elsevier Ltd. All rights reserved.
doi:10.1016/j.poly.2006.05.044

a new manganese(III/IV) carboxylate cluster $[Mn_{16}O_{16}(OMe)_6(OAc)_{16}(MeOH)_3(H_2O)_3]\cdot 6H_2O$ (**1** · $6H_2O$) and a new linear chain Mn^{III} complex $[Mn(\mu\text{-}OMe)(\mu\text{-}OAc)_2]_n$ (**2**) were obtained, neither of which contained the dicyanamide group! Our preliminary results were communicated [39]. The deliberate synthesis and detailed physical properties of these compounds are now described and the results are compared to those of related species including the family of new Mn_{16} carboxylate/alkoxo SMM clusters $[Mn_{16}O_{16}(OMe)_6(O_2CCH_2R)_{16}(MeOH)_6]$, where R = Ph, Cl and Br, recently discovered by Christou et al. during a study of the use of reductive aggregation methods, in methanol, to make high nuclearity Mn(III)/(IV) clusters [40].

2. Experimental

All manipulations were performed under aerobic conditions using chemicals as received, unless otherwise stated. *n*-Bu_4NMnO_4 was prepared as previously reported [41].

Warning. Extreme caution should be taken in the use of organic permanganates.

2.1. Synthesis of $[Mn_{16}O_{16}(OMe)_6(OAc)_{16}(MeOH)_3(H_2O)_3]\cdot 6H_2O$ (**1** · $6H_2O$)

To a stirred methanolic solution (120 mL) of $Mn(NO_3)_2\cdot 4H_2O$ (2.90 g, 11.57 mmol), and glacial acetic acid (10 mL), *n*-Bu_4NMnO_4 (1.14 g, 3.15 mmol) was added in small portions over a period of 30 min. The solution was then left to stand. After several weeks a small amount of block-like black crystals of **1** · $6H_2O$ formed. The solution was decanted, the crystals collected by filtration and washed quickly with methanol (0.20 g, 8% based on total available Mn). IR (Nujol, cm^{-1}): 3600 m, 3387 mbr, 1558 s, 1335 m, 1027 w, 960 vw. Many repeats of the reaction show that crystals of **1** · $6H_2O$ decompose with time to yield species containing low content of carbon and poor diffraction quality despite a good external morphology. Presumably slow hydrolysis of OMe^- and OAc^- groups occurs in the solid state. Analysis of a fresh sample, Calc. for $C_{41}H_{96}Mn_{16}O_{66}$ (hexahydrate): C, 19.6; H, 3.8; N, 0.0 [Calc. for $C_{41}H_{96}Mn_{16}O_{66}\cdot 14H_2O$: C, 18.5: H, 4.2; N, 0.0]. Found: C, 18.8; H, 3.8; N, 0.0%.

2.2. Synthesis of $[Mn(\mu\text{-}OMe)(\mu\text{-}OAc)_2]_n$ (**2**)

When the above reaction also had sodium dicyanamide (2.23 g, 25.0 mmol) and Me_4NBr (3.85 g, 25.0 mmol) added, black crystals of **1** · $6H_2O$ formed first, followed by smaller red rectangular block-like crystals of **2**. They were obtained free of the larger black **1** · $6H_2O$ crystals by successive filtration of the reaction to remove mixtures of **1** · $6H_2O$ and **2** that formed, and leaving the filtrate to stand until the product appeared homogenous with respect to the smaller red crystals by inspection under microscope. The crystals were collected by filtration and washed quickly with methanol. (Typical yield 0.25 g, 8% based on total available Mn.) IR (Nujol, cm^{-1}): 3603 vw, 1568 s, 1401 s, 1355 m, 1340 s, 1018 w, 992 m, 945 w. *Anal*. Calc. for $C_5H_9O_5Mn$: C, 29.4; H, 4.4; N, 0.0. Found: C, 29.2; H, 4.6; N, 0.0%.

2.3. X-ray crystallographic studies

Crystal data for **1** · $6H_2O$ and **2** are summarised in Table 1. Data were collected using a Nonius KappaCCD diffractometer with graphite monochromated Mo Kα radiation ($\lambda = 0.71073$ Å). Integration was carried out by the program DENZO-SMN [42], and data were corrected for Lorentz polarisation effects using the program SCALEPACK [42]. No absorption corrections were applied. Solutions were obtained by direct methods (SHELXS 97) [43] followed by successive Fourier difference methods, and refined by full-matrix least-squares on F^2_{obs} (SHELXL 97) [43] with the aid of the graphical interface program X-SEED [44]. All non-hydrogen atoms were refined anisotropically unless otherwise stated. All hydrogen atoms attached to carbons for **1** · $6H_2O$ and **2** were included at calculated positions with isotropic thermal parameters fixed at 1.5 times the U_{eq} of the adjoining carbon atom. For **1** · $6H_2O$, the hydrogens (where assigned) attached to oxygen atoms were located in the difference maps and refined isotropically. The O–H

Table 1
Summary of crystal data

Compound	**1** · $6H_2O$	**2**
Formula	$C_{41}H_{96}Mn_{16}O_{66}$	$C_5H_9MnO_5$
M	2524.22	204.06
Crystal system	triclinic	orthorhombic
Space group	$P\bar{1}$	*Pbcn*
a (Å)	12.8547(2)	14.2547(5)
b (Å)	14.4366(2)	7.1796(2)
c (Å)	14.4590(2)	6.8865(2)
α (°)	108.276(1)	
β (°)	116.273(1)	
γ (°)	96.900(1)	
U (Å^3)	2176.49(5)	704.79(4)
Z	1	4
ρ_{calc} (g cm^{-3})	1.926	1.923
T (K)	123(2)	123(2)
μ(Mo Kα) (mm^{-1})	2.343	1.842
Crystal habit, colour	irregular block, black	pyramidal plate, red-orange
Crystal size (mm)	0.2 × 0.15 × 0.15	0.09 × 0.05 × 0.03
Index ranges	$-17 \leqslant h \leqslant 17$, $-18 \leqslant k \leqslant 18$, $-19 \leqslant l \leqslant 19$	$-18 \leqslant h \leqslant 18$, $-9 \leqslant k \leqslant 8$, $-9 \leqslant l \leqslant 9$
Completeness to $2\theta = 55°$ (%)	99.6	99.8
Data collected	37016	9731
Unique data (R_{int})	10573 (0.0609)	873 (0.0703)
Observed reflections [$I > 2\sigma(I)$]	8648	632
Parameters	669	66
Final R_1, wR_2 [$I > 2\sigma(I)$][a]	0.0424, 0.1032	0.0337, 0.0613
(all data)	0.0580, 0.1101	0.0601, 0.0679
Goodness-of-fit, S	1.051	1.082
$\Delta\rho_{min}$, $\Delta\rho_{max}$ (e Å^{-3})	−0.687, 1.794	−0.449, 0.410

[a] $R_1 = \sum ||F_o| - |F_c|| / \sum |F_o|$, $wR_2 = \{\sum[w(F_o^2 - F_c^2)^2] / \Sigma[w(F_o^2)^2]\}^{1/2}$.

bond distances were restrained with the SHELX [43] (anti-bumping restraint) DFIX instruction to be 0.90(2) Å.

The asymmetric unit of $\mathbf{1}\cdot 6H_2O$ was found to contain half a Mn_{16} complex as well as three water molecules. Two of the water molecules were disordered. The first disordered water was modelled over two positions, O(540) and O(541), with site occupancies refined to be 0.702 and 0.298, respectively. O(540) and O(541) were refined with isotropic and anisotropic thermal parameters, respectively. The second disordered water was modelled over three positions: O(530), O(531) and O(532), with site occupancies of 0.33(1), 0.36(1) and 0.38(1), respectively. The sum of the occupancies was restrained to be 1.00(1) (calculated 1.07) using the SHELX [43] SUMP instruction. O(530–532) were refined with anisotropic thermal parameters. The third water, O(52), was ordered and refined with anisotropic thermal parameters. Its hydrogen atoms, H(52A) and H(52B), were located in successive iterations of least-squares refinements and difference Fourier maps and refined isotropically with the aforementioned anti-bumping restraints on the O–H bond distances. No hydrogen atom positions were assigned for the two disordered lattice water molecules.

Three areas of disorder were located within the cluster. Firstly, an axial μ-OAc^- and an adjacent methanol ligand, both on the outer Mn^{III}_{10} perimeter, were disordered over two positions. The three oxygen donor atoms O(39), O(41) and O(44) were refined at full occupancy. The positions of the two carbon atoms of the acetate group, C(420) and C(421), C(430) and C(431), and the two positions for the methyl carbon of the methanol, C(400) and C(401), were refined to site occupancies in the ratio of 0.684/0.316.

Secondly, two coordinated oxygens (O(45) and O(47)) were initially assigned as two water ligands, however peaks near each oxygen were located at positions consistent with partially occupied methanol carbon atoms. They were consequently assigned as such and site occupancies of these carbon atoms and the attached hydrogen atoms were fixed at 0.25. Thus over the entire cluster four axial positions are occupied by three waters and one methanol. One hydrogen atom for O(45) and two hydrogen atoms for O(47) were located and refined isotropically with the aforementioned anti-bumping restraints applied. Finally, the carbon atom of the μ-OMe^- bridging between Mn(6) and Mn(7) was disordered over two positions. The site occupancies of these carbon atoms (C(260) and C(261)), and the attached hydrogen atoms, were refined to the ratio of 0.496/0.504, respectively.

As O(1) and C(2) of the bridging methoxide of **2** lie along a 2-fold rotational axis the methyl hydrogens are disordered over two positions with equal site occupancies.

2.4. Magnetic measurements

DC susceptibilities were measured using a Quantum Design Magnetic Properties Measurement System (MPMS 5) SQUID magnetometer calibrated by use of a standard palladium sample (Quantum Design) of accurately known magnetisation or by use of magnetochemical calibrants such as $CuSO_4\cdot 5H_2O$ and $[Ni(en)_3]S_2O_3$. AC susceptibilities were measured with a Quantum Design Physical Property Measurement System (PPMS 7) fitted with an Option P-500 (ACMS) attachment, with an AC field of 1 Oe and frequencies varying over the range 10–1500 Hz, at temperatures between 1.75 and 4 K. Powder samples were dispersed in vaseline, contained in a calibrated gelatine capsule held at the centre of a drinking straw fixed to the end of the sample rod in order to avoid torquing of the crystallites. Crystalline samples of $\mathbf{1}\cdot 6H_2O$ were removed from their mother liquor (and briefly washed with methanol) immediately prior to placement in the cooled sample chamber of the instrument in order to minimise the amount of decomposition undergone by the sample before being measured.

3. Results and discussion

3.1. Synthesis and characterisation

As previously reported [39], $\mathbf{1}\cdot 6H_2O$ was initially obtained accidentally when attempting to expand our dicyanamide (dca^-, $N(CN)_2^-$) molecule-based magnet work into networks of Mn_3 or Mn_4 clusters bridged by dca^- ligands. It was subsequently found that dca^- was not necessary for its formation. Thus, addition of solid *n*-Bu_4NMnO_4 to a stirred solution of $Mn(NO_3)_2\cdot 4H_2O$ in a mixture of methanol and acetic acid yielded a dark brown solution which was allowed to stand for several weeks, with the formation of black block-like crystals of $\mathbf{1}\cdot 6H_2O$. If Na(dca) and Me_4NBr are included in the reaction, $\mathbf{1}\cdot 6H_2O$ is formed first followed by small red crystals of **2**. Successive filtrations of the reaction to remove the product mixture formed, and subsequent standing yields a pure sample of **2**. Infrared spectra show an absorption due to ν(C=O) at 1558 and 1568 cm^{-1} for $\mathbf{1}\cdot 6H_2O$ and **2**, respectively. The crystals of the two products are readily differentiated by visual inspection. In similar work with a related pseudohalide ligand, dicyanonitrosomethanide ($dcnm^-$, $^-ONC(CN)_2$) we reported the synthesis of a linear chain complex, $\{[Mn(\mu\text{-}OH)(\mu\text{-}OAc)_2]\cdot HOAc\cdot H_2O\}_n$ [45], that also did not contain the $dcnm^-$ ligand. Christou et al. [46] simultaneously reported $\{[Mn(\mu\text{-}OH)(\mu\text{-}OAc)_2]\cdot HOAc\cdot H_2O\}_n$, prepared by reacting $Mn(OAc)_2\cdot 4H_2O$ with $KMnO_4$, in a 2.5 to 1 ratio, in methanol–acetic acid mixtures.

Attempts were made to synthesise the benzoate analogue of the $\mathbf{1}\cdot 6H_2O$ complex. One method involved using similar reaction conditions to those for $\mathbf{1}\cdot 6H_2O$, but replacing benzoic acid for acetic acid. Another route explored was to attempt to replace the acetate groups of $\mathbf{1}\cdot 6H_2O$ with benzoate, in a similar method utilised by Christou et al. and other groups to synthesise a series of $[Mn_{12}O_{12}(O_2CR)_{16}(H_2O)_4]$ derivatives of Mn_{12}-acetate, where R groups include Ph, CH_2Ph, CH_2Bu^t, Et, *p*-Tol, and *m*-Cl-Ph, by substituting acetate groups on Mn_{12}-acetate [47–50]. However, these attempts were unsuccessful

and were not pursued further. The latter method presents difficulties as the $\mathbf{1}\cdot 6H_2O$ complex decomposes when removed from its mother liquor, and it did not dissolve in a range of common solvents tried.

The synthetic method utilised here differs in a number of ways from that employed by Christou and co-workers to prepare their $[Mn_{16}O_{16}(OMe)_6(O_2CCH_2R)_{16}(MeOH)_6]$ complexes, where R = Ph, Cl and Br [40]. Most notably, their method uses a single source of Mn, viz. n-Bu_4NMnO_4, and reactions were performed in solutions of comparatively higher concentration. It is clear from our experience and that of Christou and Hendrickson [5,7,51,52] that these reactions affording high nuclearity Mn clusters are complex, with several variables, which perhaps, with only minor shifts such as slightly higher or lower Mn^{II}/Mn^{VII} ratios can result in widely different outcomes, such as the formation of Mn oxides as opposed to the desired large Mn clusters. The roles of Na(dca) and Me_4NBr, here, in the sequential formation of $\mathbf{1}\cdot 6H_2O$ and the chain complex, **2**, are not known.

3.2. Crystal structures

3.2.1. $[Mn_{16}O_{16}(OMe)_6(OAc)_{16}(MeOH)_3(H_2O)_3]\cdot 6H_2O$ ($\mathbf{1}\cdot 6H_2O$)

$\mathbf{1}\cdot 6H_2O$ crystallises in the triclinic space group $P\bar{1}$. The cluster lies on an inversion centre relating one half of the cluster to the other. The asymmetric unit contains half of the molecule and three lattice water molecules. The complex consists of six Mn^{IV} and 10 Mn^{III} ions held together by 14 μ_3-O^{2-}, two μ-O^{2-}, four μ-OMe^- and two μ-OAc^- groups to give an approximately elliptical planar $[Mn_{16}O_{16}(OMe)_4(OAc)_2]^{16+}$ core (Fig. 1). Peripheral ligation consists of the remaining 14 μ-OAc^-, two μ-OMe^- groups and three axial water and methanol molecules.

The Mn_{16} core can be divided into two sub-units, a central $[Mn^{IV}_6O_6(OMe)_4]^{8+}$ unit connected to an outer perimeter of 10 Mn^{III} ions by 10 μ_3-O^{2-} ions in the plane of the molecule and two μ-OAc^- groups perpendicular (above and below) to the plane of the molecule. The central unit contains six Mn^{IV} ions in two rows of three (Mn(1),

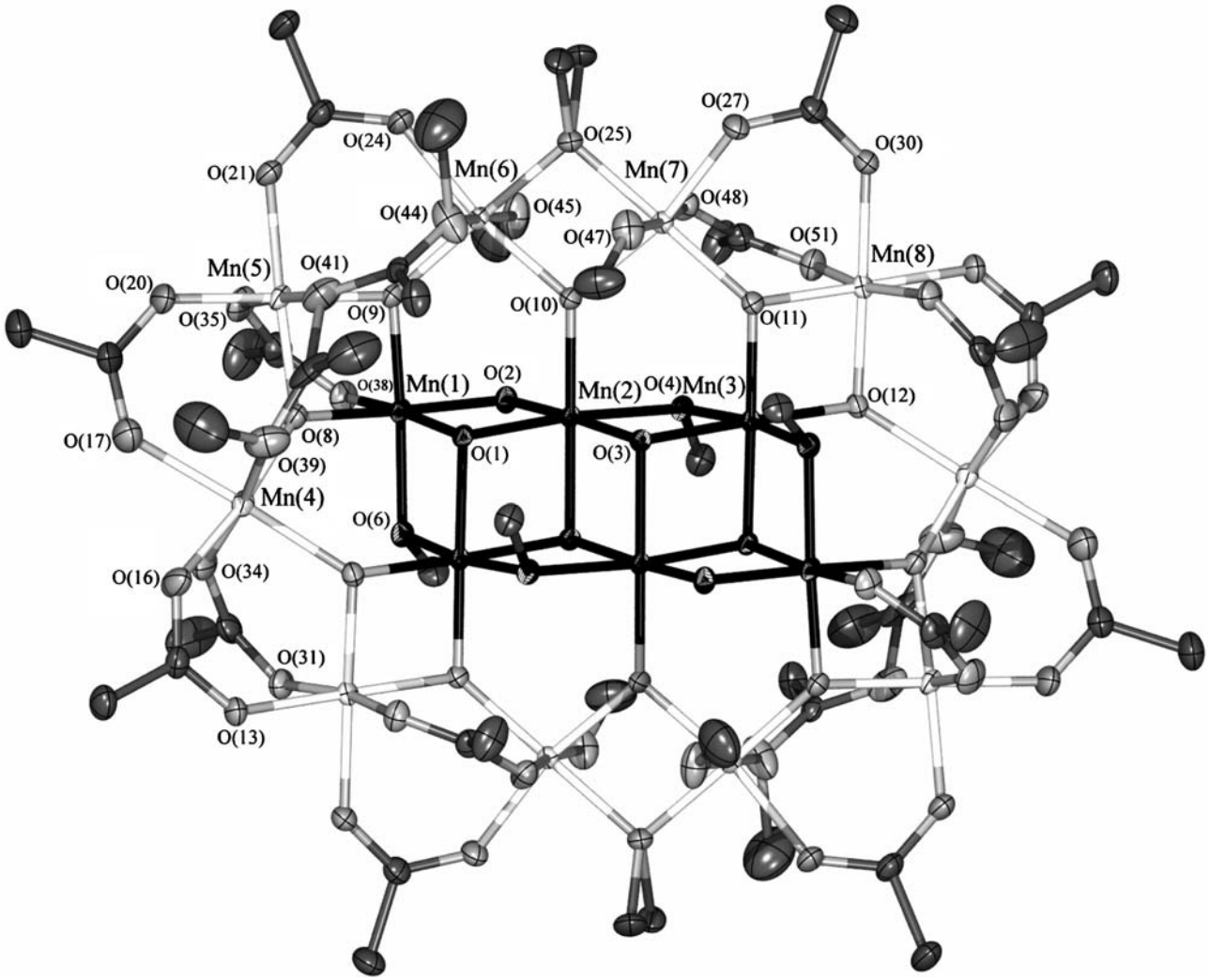


Fig. 1. The crystal structure of $[Mn_{16}O_{16}(OMe)_6(OAc)_{16}(MeOH)_3(H_2O)_3]\cdot 6H_2O$ ($\mathbf{1}\cdot 6H_2O$) with atom labelling scheme of manganese and oxygen atoms only (hydrogen atoms are omitted for clarity and thermal ellipsoids shown at 50% probability). The central $[Mn^{IV}_6O_6(OMe)_4]^{8+}$ sub-unit is emphasised in black with octant slices.

Mn(2), Mn(3) and the symmetry related Mn(1^i), Mn(2^i), Mn(3^i)) lying in a plane that is sandwiched between two planes of oxygen atoms. Each oxygen plane contains two μ_3-O^{2-}, one μ-O^{2-} and two μ-OMe^- ions. One oxygen plane contains O(1) and O(3) (μ_3-O^{2-}), O(2^i) (μ-O^{2-}) and O(4^i) and O(6^i) (μ-OMe^-). The other oxygen plane contains O(1^i) and O(3^i) (μ_3-O^{2-}), O(2) (μ-O^{2-}) and O(4) and O(6) (μ-OMe). The Mn^{IV} ions occupy distorted octahedral sites between these two hexagonal close-packed O layers, in the manner seen in many layered manganese oxide minerals [53–55], metal dihalides, dihydroxides and disulphides [56]. A recent review by Winpenny [33] describes this phenomenon, whereby the cores of many large polynuclear complexes adopt a layered mineral or general CdI_2 type structure. For example, two Fe_{17} and Fe_{19} oxyhydroxide clusters are related to fragments of goethite or lepidocrocite [31,57]. The CdI_2 structure is also present in several examples of manganese clusters, $Mn_6^{III}Na$ [58], Mn_7 ($4Mn^{II}$, $3Mn^{III}$) [17], Mn_{10} [51], and Mn_{19} (albeit all Mn^{II}) [59] clusters and in a recently reported Mn_{21} ($12Mn^{III}$, $9Mn^{IV}$) cluster [22]. Winpenny et al. reported a large Co_{24} cluster, in which the core bears a very obvious relationship to $Co(OH)_2$ [60]. Therefore, just as the Fe_{17} and Fe_{19} complexes have been termed "captured rusts" or "crusts" [31,57], $\mathbf{1}\cdot 6H_2O$ could be thought of as a captured portion of a manganese oxide mineral. The Mn_{12}-acetate cluster, $[Mn_{12}O_{12}(OAc)_{16}(H_2O)_4]\cdot 2HOAc\cdot 4H_2O$ [61], can be described as consisting of two subunits, a central $[Mn_4^{IV}O_4]^{8+}$ cubane unit connected to an outer ring of $[Mn_8^{III}O_8]^{8+}$.

Peripheral ligation around the Mn_{10}^{III} perimeter in the $\mathbf{1}\cdot 6H_2O$ cluster consists of eight equatorial μ-OAc^- groups, six axial μ-OAc^- groups (three either side of the cluster in an alternating up–down–up fashion) and two μ-OMe^- ligands (bridging Mn(6) and Mn(7)). In addition there are three axially coordinated monodentate water and methanol molecules. Eight of the 10 perimeter Mn^{III} ions experience Jahn-Teller (JT) axial elongation in the direction perpendicular to the plane of the cluster (Fig. 2).

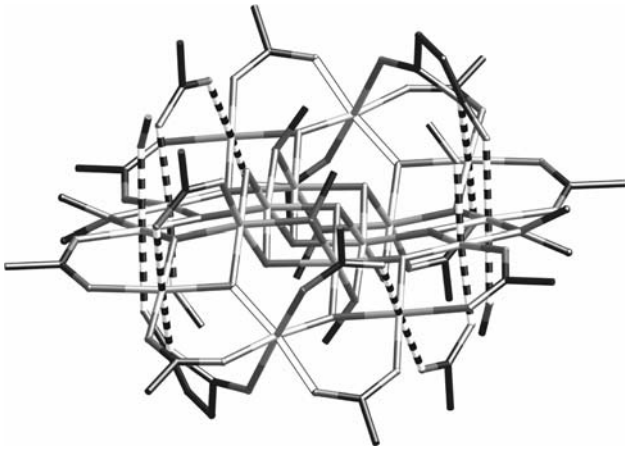


Fig. 2. The crystal structure of $\mathbf{1}\cdot 6H_2O$ showing Jahn-Teller elongation (dashed bonds) and compression (open bonds) distortions, of the perimeter Mn^{III} atoms of $\mathbf{1}\cdot 6H_2O$.

The remaining two (Mn(4) and Mn(4^i)) experience JT axial compression roughly parallel to the plane of the cluster in the direction of a μ-OAc^- and a core μ_3-O^{2-}. Christou and co-workers' three Mn_{16} carboxylate clusters are essentially isostructural with $\mathbf{1}\cdot 6H_2O$ with some notable exceptions [40]. Firstly, here there are three terminal H_2O and MeOH ligands as opposed to their six MeOH ligands. More significantly perhaps, in terms of the magnetic properties, are the disposition of the JT axes of the perimeter 10 Mn^{III} ions. Christou observes all 10 elongation JT axes aligning roughly parallel to each other and perpendicular to the plane of the molecule [40]. The orientation of the JT axes of SMMs has been shown to be important to the overall cluster magnetic anisotropy and consequently the AC χ'' behaviour [62], described later (see Tables 2 and 3 for Mn–O bond distances and Table 6 for SMM parameters).

Several regions of disorder were observed in $\mathbf{1}\cdot 6H_2O$ and in the lattice waters. Full details of this disorder are given in Section 2. There is positional disorder of the peripheral ligands. In particular, three terminal water ligands and one methanol ligand are disordered over four axial coordination sites (O(45), O(47) and symmetry related partners). Also, another terminal methanol and adjacent acetate group are disordered over two positions (Fig. 3). A similar type of disorder has also been seen in mixed carboxylate derivatives of Mn_{12}-acetate, observed by ^1H NMR solution studies by Christou et al. Axial H_2O and RCO_2^- ligands exchange rapidly at room temperature [63].

Several hydrogen bonding interactions were located in the $\mathbf{1}\cdot 6H_2O$ structure (Table 4). They can be divided into two types: intra-cluster and inter-cluster. Intra-cluster hydrogen bonding exists on the Mn_{10}^{III} perimeter (Fig. 3). The axially coordinated terminal disordered water/methanol (O(45)) on Mn(6) hydrogen bonds to the adjacent μ-OAc^- oxygen (O(48)) coordinated to Mn(7). In addition, the coordinated water/methanol (O(47)) on Mn(7) (*trans* to the aforementioned acetate) hydrogen bonds to the adjacent disordered methanol/acetate oxygen (O(44)) on Mn(6). Each Mn_{16} cluster is hydrogen bonded to two adjacent Mn_{16} clusters through two lattice water molecules (O(52)) located between each cluster. The lattice waters hydrogen bond to adjacent clusters via the axial water/methanol, O(47), on Mn(7) and an axial μ-OAc^- oxygen, O(31) on Mn(6). The lattice water molecules also hydrogen bond to their symmetry related neighbour. These hydrogen-bonded chains of clusters propagate parallel to the *c*-axis direction (Fig. 4). The role that hydrogen-bonding might play in the properties of these high-spin polynuclear manganese clusters is now being studied more closely. Recently Cornia and Gatteschi et al. reported the crystal structure of $[Mn_{12}O_{12}(OAc)_{16}(H_2O)_4]\cdot 2HOAc\cdot 4H_2O$ at 83 K [64,65] in an effort to explain the significant magnetic anisotropy displayed by this complex despite it being highly structurally symmetrical (S_4 crystallographic symmetry). They found the two disordered acetic acid molecules of solvation transfer this disorder to the cluster by hydrogen bonding interactions thus lowering the effective

Table 2
Selected interatomic distances (Å) and angles (°) for the central $[Mn_6^{IV}O_6(OMe)_4]^{8+}$ unit and surrounds of $\mathbf{1}\cdot 6H_2O$

Mn(1)–O(1)	1.898(2)	Mn(2)–O(1)	1.893(2)	Mn(3)–O(1^i)	1.917(2)
Mn(1)–O(2)	1.827(2)	Mn(2)–O(2)	1.835(2)	Mn(3)–O(3)	1.920(2)
Mn(1)–O(6)	1.937(2)	Mn(2)–O(3)	1.941(2)	Mn(3)–O(4)	1.942(2)
Mn(1)–O(8)	1.920(2)	Mn(2)–O(3^i)	1.916(2)	Mn(3)–O(6^i)	1.926(2)
Mn(1)–O(9)	1.857(2)	Mn(2)–O(4)	1.945(2)	Mn(3)–O(11)	1.860(2)
Mn(1)–O(38)	1.924(2)	Mn(2)–O(10)	1.896(2)	Mn(3)–O(12)	1.861(2)
Mn(1)···Mn(2)	2.7593(6)	Mn(2)···Mn(3^i)	2.8906(6)	Mn(3)···Mn(1^i)	2.8644(6)
Mn(1)···Mn(3^i)	2.8644(6)	Mn(2)···Mn(2^i)	2.9082(9)	Mn(3)···Mn(2^i)	2.8906(6)
		Mn(2)···Mn(3)	2.9149(6)		

O(2)–Mn(1)–O(9)	93.9(1)	O(1)–Mn(2)–O(3)	96.80(9)
O(2)–Mn(1)–O(1)	84.33(9)	O(10)–Mn(2)–O(3)	90.40(9)
O(9)–Mn(1)–O(1)	91.90(9)	O(3^i)–Mn(2)–O(3)	82.13(9)
O(2)–Mn(1)–O(8)	172.9(1)	O(2)–Mn(2)–O(4)	96.87(9)
O(9)–Mn(1)–O(8)	82.44(1)	O(1)–Mn(2)–O(4)	174.33(9)
O(1)–Mn(1)–O(8)	89.77(9)	O(10)–Mn(2)–O(4)	91.87(9)
O(2)–Mn(1)–O(38)	92.4(1)	O(3^i)–Mn(2)–O(4)	92.28(9)
O(9)–Mn(1)–O(38)	94.2(1)	O(3)–Mn(2)–O(4)	81.79(9)
O(1)–Mn(1)–O(38)	173.2(1)	O(11)–Mn(3)–O(12)	85.19(9)
O(8)–Mn(1)–O(38)	93.7(1)	O(11)–Mn(3)–O(1^i)	176.90(9)
O(2)–Mn(1)–O(6)	91.56(9)	O(12)–Mn(3)–O(1^i)	96.73(9)
O(9)–Mn(1)–O(6)	172.4(1)	O(11)–Mn(3)–O(3)	96.73(9)
O(1)–Mn(1)–O(6)	83.47(9)	O(12)–Mn(3)–O(3)	178.02(9)
O(8)–Mn(1)–O(6)	91.52(9)	O(1^i)–Mn(3)–O(3)	81.37(9)
O(38)–Mn(1)–O(6)	90.7(1)	O(11)–Mn(3)–O(6^i)	94.36(9)
O(2)–Mn(2)–O(1)	84.22(9)	O(12)–Mn(3)–O(6^i)	88.84(9)
O(2)–Mn(2)–O(10)	92.86(9)	O(1^i)–Mn(3)–O(6^i)	83.26(9)
O(1)–Mn(2)–O(10)	93.63(9)	O(3)–Mn(3)–O(6^i)	91.44(9)
O(2)–Mn(2)–O(3^i)	94.73(9)	O(11)–Mn(3)–O(4)	91.09(9)
O(1)–Mn(2)–O(3^i)	82.08(9)	O(12)–Mn(3)–O(4)	97.12(9)
O(10)–Mn(2)–O(3^i)	170.85(9)	O(1^i)–Mn(3)–O(4)	91.08(9)
O(2)–Mn(2)–O(3)	176.51(9)	O(3)–Mn(3)–O(4)	82.43(9)
		O(6^i)–Mn(3)–O(4)	172.24(9)

Symmetry transformation: (i) $1-x$, $1-y$, $1-z$.

symmetry of the cluster, hence increasing magnetic anisotropy. They also reported that the water of solvation hydrogen bonds to a water ligand coordinated to one of the peripheral Mn^{III} atoms. The water ligand also hydrogen bonds to an adjacent bridging acetate. This pattern of hydrogen bonding is very similar to that seen in $\mathbf{1}\cdot 6H_2O$. However, no mention is made of inter-cluster hydrogen bonding interactions in the Mn_{12}-OAc structure [64,65].

In the context of cluster–cluster effects, Wernsdorfer and Christou et al. have also reported a supramolecular dimer of Mn_4 SMMs [1,2]. They find that due to antiferromagnetic coupling between the two components, the dimer displays quantum behaviour different from that of the individual tetranuclear components, possibly via six C–H···Cl hydrogen bonds and a Cl···Cl interaction. Importantly, the dimer displays an exchange-bias of the quantum tunnelling transition with no tunnelling (i.e. no hysteresis step) at $H = 0$. Hendrickson et al. [35,36] have also made similar observations on M_4 cubane clusters of Co^{II} and Ni^{II}.

3.2.2. $[Mn(\mu\text{-}OMe)(\mu\text{-}OAc)_2]_n$ (2)

Complex **2** crystallises in the orthorhombic space group *Pbcn*. The asymmetric unit contains one bridging acetate ligand, half a manganese(III) atom and half a bridging methoxide ligand. The structure (Fig. 5) consists of infinite linear 1D chains of manganese(III) atoms bridged by two μ-OAc^- ligands and one μ-OMe^-. Each manganese(III) is coordinated in a distorted octahedral environment. As expected for a high-spin d^4 ion, the metal centres are Jahn-Teller distorted with elongation of the axial bonds to one oxygen atom each of the two μ-OAc^- ligands (Mn(1)–O(6^{ii}) = 2.171(2) Å). The equatorial coordination plane consists of two oxygen atoms from two μ-OMe^- ligands (Mn(1)–O(1) = 1.946(1) Å) and the other two oxygens of the two μ-OAc^- ligands (Mn(1)–O(3) = 1.932(2) Å). The hydrogen atoms of the bridging methoxide group are disordered over two positions due to the methoxide lying on a rotational 2-fold axis. The chains run parallel to the *c*-axis direction. The intra-chain Mn···Mn distance is equal to half the unit cell length *c* (3.4433(1) Å). The inter-chain Mn···Mn distance to adjacent chains in the *b*-axis direction is equal to the unit cell length *b* (7.1796(2) Å). The next shortest inter-chain Mn···Mn distance is equal to half the diagonal of the *ab*-unit cell face (7.9803(2) Å). Fig. 6 shows five chains viewed parallel to the *c*-axis (see Table 5 for selected bond distances and angles).

The structure of **2** is similar to a related complex, $\{[Mn(\mu\text{-}OH)(\mu\text{-}OAc)_2]\cdot HOAc\cdot H_2O\}_n$, reported previously by ourselves [45] and by Christou et al. [46]. This

Table 3
Selected interatomic distances (Å) and angles (°) for the outer Mn_{10}^{III} perimeter of $\mathbf{1} \cdot 6H_2O$

Mn(4)–O(8)	1.863(2)	Mn(5)–O(41)	2.203(3)	Mn(7)–O(11)	1.900(2)
Mn(4)–O(16)	1.948(3)	Mn(5)–O(35)	2.244(3)	Mn(7)–O(25)	1.934(2)
Mn(4)–O(34)	2.029(3)	Mn(6)–O(9)	1.869(2)	Mn(7)–O(27)	1.941(2)
Mn(4)–O(12^i)	2.049(2)	Mn(6)–O(25)	1.908(2)	Mn(7)–O(48)	2.216(2)
Mn(4)–O(17)	2.093(3)	Mn(6)–O(10)	1.917(2)	Mn(7)–O(47)	2.237(3)
Mn(4)–O(39)	2.125(3)	Mn(6)–O(24)	1.964(2)	Mn(8)–O(12)	1.883(2)
Mn(5)–O(9)	1.879(2)	Mn(6)–O(44)	2.217(3)	Mn(8)–O(11)	1.905(2)
Mn(5)–O(8)	1.883(2)	Mn(6)–O(45)	2.269(3)	Mn(8)–O(13^i)	1.959(2)
Mn(5)–O(20)	1.914(2)	Mn(6)–Mn(7)	2.9321(6)	Mn(8)–O(30)	1.974(2)
Mn(5)–O(21)	1.956(2)	Mn(7)–O(10)	1.897(2)	Mn(8)–O(51)	2.169(2)
Mn(4)···Mn(5)	3.3818(7)	Mn(4)···Mn(1)	3.4746(7)	Mn(8)–O(31^i)	2.191(2)
Mn(5)···Mn(6)	3.3509(7)	Mn(5)···Mn(1)	2.8066(7)	Mn(7)···Mn(3)	3.3965(6)
Mn(6)···Mn(7)	2.9321(6)	Mn(6)···Mn(1)	3.3761(7)	Mn(8)···Mn(3)	2.7845(6)
Mn(7)···Mn(8)	3.3330(6)	Mn(6)···Mn(2)	3.4126(6)	Mn(4^i)···Mn(3)	3.5317(6)
Mn(8)···Mn(4^i)	3.3828(7)	Mn(7)···Mn(2)	3.4521(6)		

O(8)–Mn(4)–O(16)	172.2(1)	O(25)–Mn(6)–O(44)	87.7(1)
O(8)–Mn(4)–O(34)	91.4(1)	O(10)–Mn(6)–O(44)	90.3(1)
O(16)–Mn(4)–O(34)	91.1(1)	O(24)–Mn(6)–O(44)	90.6(1)
O(8)–Mn(4)–O(12^i)	94.71(9)	O(9)–Mn(6)–O(45)	87.4(1)
O(16)–Mn(4)–O(12^i)	92.4(1)	O(25)–Mn(6)–O(45)	90.1(1)
O(34)–Mn(4)–O(12^i)	95.39(9)	O(10)–Mn(6)–O(45)	87.4(1)
O(8)–Mn(4)–O(17)	90.1(1)	O(24)–Mn(6)–O(45)	91.4(1)
O(16)–Mn(4)–O(17)	82.6(1)	O(44)–Mn(6)–O(45)	177.0(1)
O(34)–Mn(4)–O(17)	88.1(1)	O(10)–Mn(7)–O(11)	99.45(9)
O(12^i)–Mn(4)–O(17)	174.0(1)	O(10)–Mn(7)–O(25)	79.94(9)
O(8)–Mn(4)–O(39)	93.4(1)	O(11)–Mn(7)–O(25)	178.8(1)
O(16)–Mn(4)–O(39)	83.4(1)	O(10)–Mn(7)–O(27)	167.4(1)
O(34)–Mn(4)–O(39)	172.8(1)	O(11)–Mn(7)–O(27)	92.7(1)
O(12^i)–Mn(4)–O(39)	89.6(1)	O(25)–Mn(7)–O(27)	88.0(1)
O(17)–Mn(4)–O(39)	86.5(1)	O(10)–Mn(7)–O(48)	89.96(9)
O(9)–Mn(5)–O(8)	82.86(9)	O(11)–Mn(7)–O(48)	93.25(9)
O(9)–Mn(5)–O(20)	176.9(1)	O(25)–Mn(7)–O(48)	85.66(9)
O(8)–Mn(5)–O(20)	97.6(1)	O(10)–Mn(7)–O(47)	88.9(1)
O(9)–Mn(5)–O(21)	93.41(1)	O(11)–Mn(7)–O(47)	92.4(1)
O(8)–Mn(5)–O(21)	175.2(1)	O(25)–Mn(7)–O(47)	88.7(1)
O(20)–Mn(5)–O(21)	86.0(1)	O(27)–Mn(7)–O(47)	87.1(1)
O(9)–Mn(5)–O(41)	92.9(1)	O(48)–Mn(7)–O(47)	174.4(1)
O(8)–Mn(5)–O(41)	92.0(1)	O(12)–Mn(8)–O(11)	83.32(9)
O(20)–Mn(5)–O(41)	90.1(1)	O(12)–Mn(8)–O(13^i)	96.8(1)
O(21)–Mn(5)–O(41)	91.3(1)	O(11)–Mn(8)–O(13^i)	178.6(1)
O(9)–Mn(5)–O(35)	85.6(1)	O(12)–Mn(8)–O(30)	178.6(1)
O(8)–Mn(5)–O(35)	86.4(1)	O(11)–Mn(8)–O(30)	95.42(9)
O(20)–Mn(5)–O(35)	91.5(1)	O(13^i)–Mn(8)–O(30)	84.4(1)
O(21)–Mn(5)–O(35)	90.2(1)	O(12)–Mn(8)–O(51)	90.79(9)
O(41)–Mn(5)–O(35)	177.91(9)	O(11)–Mn(8)–O(51)	94.74(9)
O(9)–Mn(6)–O(25)	177.2(1)	O(13^i)–Mn(8)–O(51)	83.85(9)
O(9)–Mn(6)–O(10)	98.60(9)	O(30)–Mn(8)–O(51)	89.9(1)
O(25)–Mn(6)–O(10)	80.09(9)	O(12)–Mn(8)–O(31^i)	94.46(9)
O(9)–Mn(6)–O(24)	91.1(1)	O(11)–Mn(8)–O(31^i)	93.26(9)
O(10)–Mn(6)–O(24)	170.2(1)	O(13^i)–Mn(8)–O(31^i)	88.1(1)
O(9)–Mn(6)–O(44)	94.8(1)	O(30)–Mn(8)–O(31^i)	84.97(9)
		O(51)–Mn(8)–O(31^i)	170.89(9)

Symmetry transformation: (i) $1-x, 1-y, 1-z$.

chain also consists of a triply bridged linear chain of manganese(III) atoms and these chains hydrogen bond to adjacent chains via the μ-OH and lattice acetic acid and water molecules to form pseudo 2D sheets. It displays long-range antiferromagnetic order ($T_N = 6.1$ K) that is probably facilitated by the hydrogen bonding pathways. The lack of magnetic order in the complex described here would seem to support this conclusion, as it is superficially identical but without the hydrogen bonding network.

3.3. Magnetism

3.3.1. $[Mn_{16}O_{16}(OMe)_6(OAc)_{16}(MeOH)_3(H_2O)_3] \cdot 6H_2O$ ($\mathbf{1} \cdot 6H_2O$)

DC magnetic susceptibilities were measured as a function of temperature on freshly isolated samples of $\mathbf{1} \cdot 6H_2O$ in a field of 1 T over the range 2–300 K (Fig. 7). The same results were obtained on neat powders and on Vaseline mulls. The effective magnetic moment, per Mn_{16}, decreases gradually

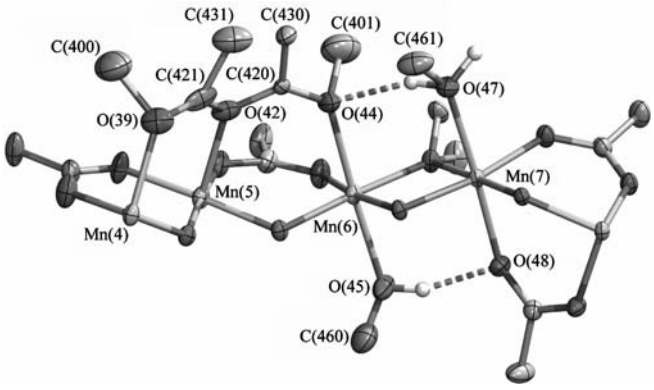


Fig. 3. The crystal structure of a portion of the Mn^{III} perimeter of $\mathbf{1}\cdot 6H_2O$, showing intra-cluster hydrogen bonding (dashed), and disordered methanol/acetate and water/methanol (see text).

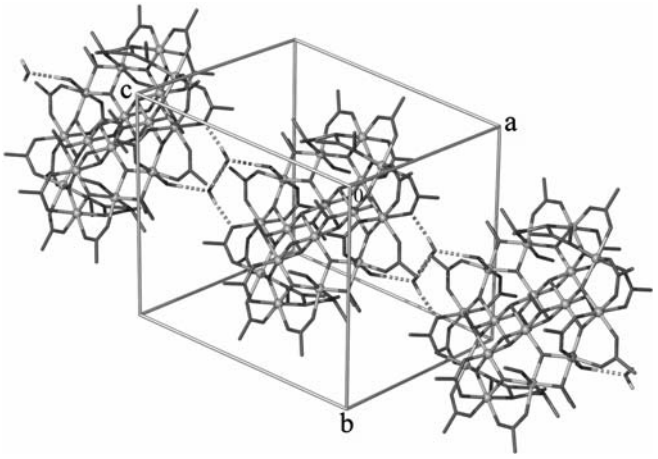


Fig. 4. A single hydrogen-bonded chain of $\mathbf{1}\cdot 6H_2O$ running parallel to the *c*-axis direction (hydrogen bonds shown in dashed bonds).

from 14.0 μ_B ($\chi_M T = 24.53\ cm^3\ mol^{-1}\ K$) at 300 K to ca. 10.5 μ_B at ~30 K, then more rapidly, reaching 5.7 μ_B ($\chi_M T = 4.06\ cm^3\ mol^{-1}\ K$) at 2 K and still decreasing. The value of μ_{eff} at 300 K compares to the value of 18.16 μ_B (41.25 $cm^3\ mol^{-1}\ K$) calculated for six uncoupled Mn^{IV} ($S = 3/2$) and 10 Mn^{III} ($S = 4/2$) and is thus indicative of overall antiferromagnetic coupling. The Mn_{16}-O_2CCH_2R analogues of Christou et al. show very similar $\mu_{eff}(\chi_M T)$ versus temperature behaviour to $\mathbf{1}\cdot 6H_2O$ [40].

To try to identify the ground spin state of $\mathbf{1}\cdot 6H_2O$, magnetisation (M) measurements were made in the ranges of $H = 0$–5 T and temperature = 2–20 K (Fig. 8). It can be seen that, at 2 K, the M values increase in a smooth, curved fashion between 0 and 5 T to reach ca. $7N\beta$ in the 5 T field. The M values are still increasing and saturation is not achieved. This is most likely due to thermal population of the ground-state and of other low lying spin-states occurring even at 2 K. Zero-field splitting and Zeeman effects will also influence the shape and size of the M versus H plots. Weak cluster–cluster interactions, via hydrogen bonding pathways, may also play a part. It is therefore not possible, without fitting of the M/H data, to unambiguously assign the ground state spin and the weaknesses of using DC magnetisations to obtain S in this way have been recognised previously [40]. When the M/H data are plotted as M versus H/temperature, in the way commonly employed by Hendrickson and Christou, Fig. 9 is obtained. The separation of the lines indicates zero-field splitting is occurring.

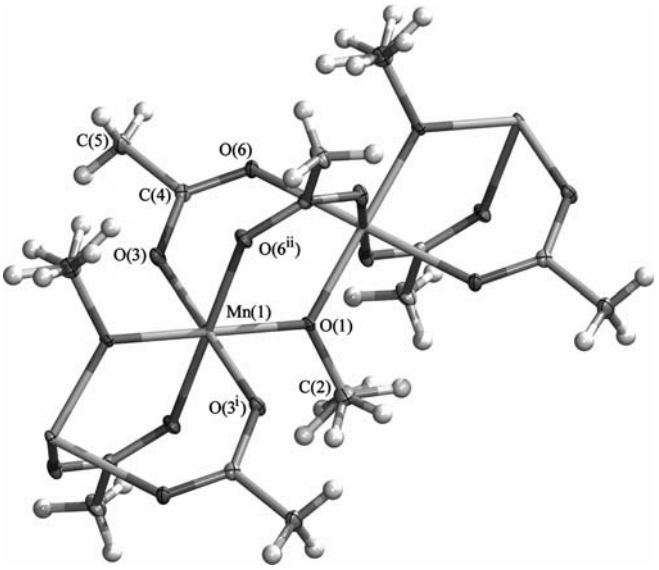


Fig. 5. The crystal structure of $[Mn(\mu\text{-}OMe)(\mu\text{-}OAc)_2]_n$ (**2**) with atom labelling scheme shown (thermal ellipsoids shown at 50% probability). Disorder of methoxide hydrogen atoms is due to site symmetry (see text).

Table 4
Hydrogen bonding distances (Å) angles (°) for $\mathbf{1}\cdot 6H_2O$

O(45)–H(45)	0.87(2)	O(47)–H(47A)	0.95(7)
H(45)···O(48)	1.90(3)	H(47A)···O(52)	1.81(7)
O(45)···O(48)	2.734(3)	O(47)···O(52)	2.732(4)
O(52)–H(52A)	0.89(2)	O(52)–H(52B)	0.90(2)
H(52A)···O(52^{ii})	1.96(4)	H(52B)···O(31^{iii})	1.89(2)
O(52)···O(52^{ii})	2.768(8)	O(52)···O(31^{iii})	2.781(4)
O(47)–H(47B)	0.87(2)		
H(47B)···O(44)	2.01(3)		
O(47)···O(44)	2.851(4)		
O(45)–H(45)···O(48)	159(5)	O(47)–H(47A)···O(52)	163(6)
O(52)–H(52A)··· O(52^{ii})	150(6)	O(52)–H(52B)···O(31^{iii})	168(5)
O(47)–H(47B)···O(44)	160(6)		

Symmetry transformations: (ii) $1-x, 1-y, -z$; (iii) $x, y, z-1$.

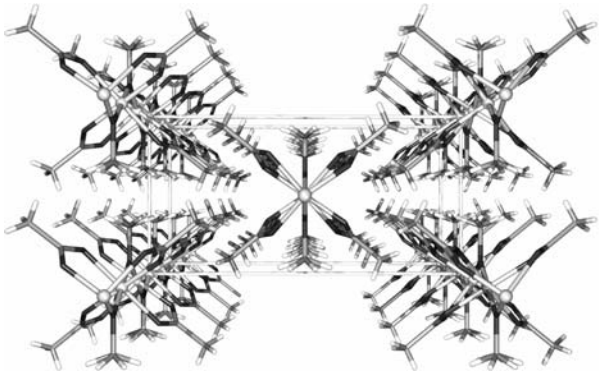


Fig. 6. Packing diagram of **2** viewed parallel to the *c*-axis (spheres represent Mn ions).

Table 5
Selected interatomic distances (Å) and angles (°) for **2**

Mn(1)–O(1)	1.946(1)
Mn(1)–O(3)	1.932(2)
Mn(1)–O(6^{ii})	2.171(2)
O(1)–Mn(1)–O(3)	93.15(6)
O(1)–Mn(1)–O(6^{ii})	90.54(6)
O(1)–Mn(1)–O(6^{iii})	90.54(6)
O(1)–Mn(1)–O(3^{i})	86.85(6)
O(3)–Mn(1)–O(6^{ii})	91.54(8)
O(3)–Mn(1)–O(6^{iii})	88.46(8)

Symmetry transformations: (i) $1-x, 1-y, -z$; (ii) $1-x, y, 1/2-z$; (iii) $x, 1-y, z-1/2$.

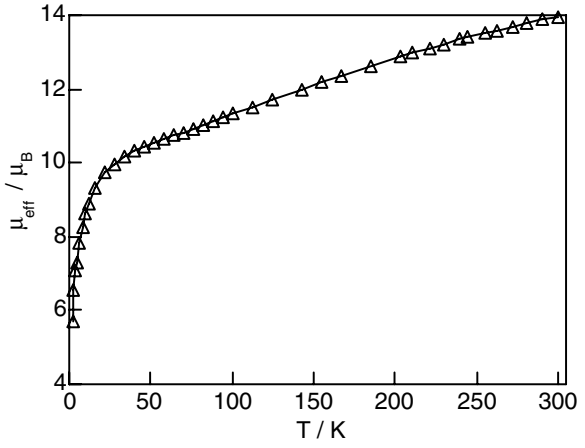


Fig. 7. Plot of μ_{eff} vs. temperature in $H = 1$ T for $\mathbf{1} \cdot 6H_2O$. The solid line just joins the points.

A hysteresis loop measured in low fields (±0.2 T) on a neat powder at 2 K shows a rapid increase in M in the ±250 Oe region with very small coercive field (Fig. 10). To observe the characteristic 'stepped' hysteresis loops of SMMs, due to quantum tunnelling, requires the use of single crystals or collections of oriented crystals and so, despite using a powder, this rapid increase through zero field might be such a step because of its similarity to those observed using a micro-Squid system on the $PhCH_2CO_2^-$ analogue of **1**, measured between 1.0 and 0.04 K at a field sweep rate of 0.07 T/s [40].

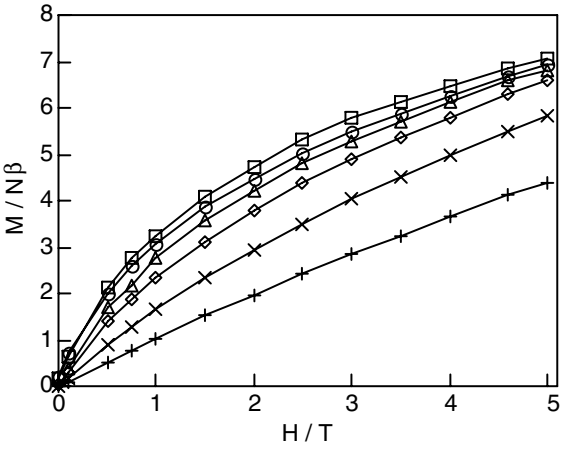


Fig. 8. Plots of magnetisation, M vs. applied field (Tesla) for $\mathbf{1} \cdot 6H_2O$, at various temperatures 2 K (□), 3 K (○), 4 K (△), 5.5 K (◇), 10 K (×), and 20 K (+). The solid lines simply join the isothermal points and are not fitted curves.

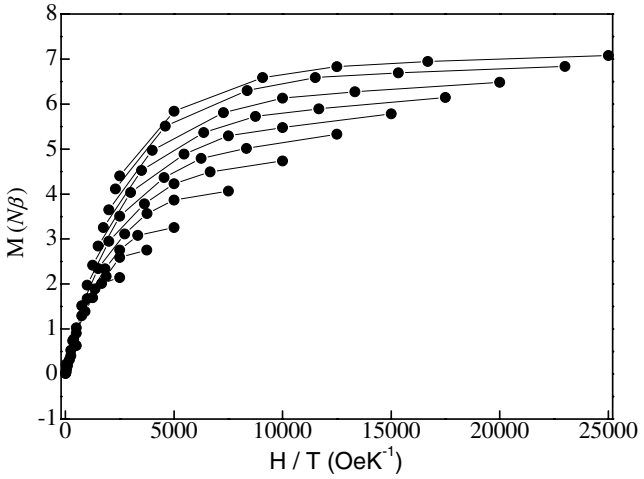


Fig. 9. Plots of magnetisation, M vs. H/T for $\mathbf{1} \cdot 6H_2O$ for the field values (from top): $H = 5$, 4.6, 4, 3.5, 3, 2.5, 2, 1.5, 1, 0.75 and 0.5 T, at temperatures 2–20 K.

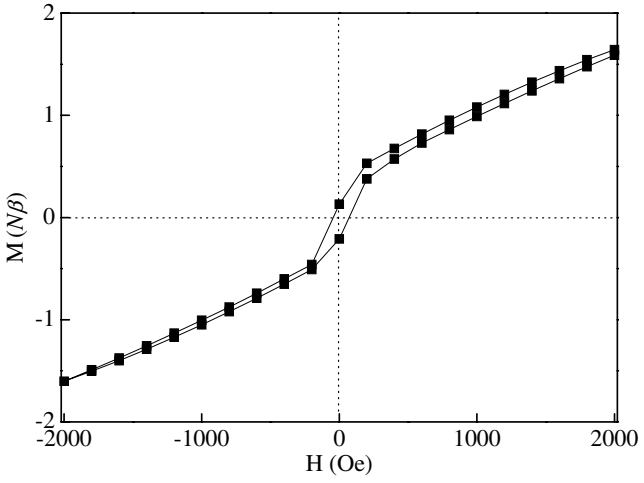


Fig. 10. Hysteresis plot of a powder sample of $\mathbf{1} \cdot 6H_2O$ dispersed in Vaseline, at 2 K.

Detailed AC susceptibility studies were made as a function of frequency (50–1500 Hz) in the temperature range 2–10 K, and these are plotted as $\chi'_M T$ versus T and χ''_M versus T in Fig. 11. The $\chi'_M T$ values between 8 and 10 K (~8.5 $cm^3\ mol^{-1}\ K$) are independent of frequency and are of similar magnitude to the DC values of $\chi_M T$ in this temperature range. If all the Mn_{16} molecules were populating an isolated $S = 3$ ground state, and assuming $g = 2.0$, the $\chi'_M T$ value would be 6.01 $cm^3\ mol^{-1}\ K$, while population of only an $S = 4$ ground state would yield $\chi'_M T$ = 10.01 $cm^3\ mol^{-1}\ K$. The observed $\chi'_M T$ value is of an intermediate value, as is the DC magnetisation value, M, at a temperature of 2 K and a field of 5 T ($M \sim 7N\beta$). Thus, as indicated earlier, the data suggest that there is not an isolated ground S level, but that levels are close together and zero-field splitting and Zeeman level thermal depopulation effects play a part. Below 8 K the $\chi'_M T$ values for $\mathbf{1} \cdot 6H_2O$ decrease rapidly, indicative of the onset of slow magnetic relaxation. At higher frequencies, the decrease in $\chi'_M T$ occurs at higher temperatures. The Mn_{12}-carboxylates behave similarly [7,62]. There is a hint of another such decrease in $\chi'_M T$ occurring below ~3 K. In Fig. 11(b), the out-of-phase χ''_M values show maxima in the region 5–7 K, which vary in position, width and magnitude as the frequency is varied, typical of SMM behaviour and similar to that in Mn_{12}-acetate type clusters. In contrast to the Mn_{12} species, the values of the maxima in χ''_M, of 0.25–0.20 $cm^3\ mol^{-1}$, are much smaller than in the Mn_{12} clusters but of similar size to those observed for a Mn_{30} cluster [13]. It is possible that a second series of maxima occur below 2 K, but further measurements on an ultra low temperature instrument would be required to confirm this and to obtain the relative intensity compared to the 5–7 K maxima. Two such series of maxima, at 4–7 and 2–3 K, have been observed in some of the Mn_{12}-carboxylate clusters [47,66] and these originated from the presence of two Jahn-Teller isomers in the samples. In that study each isomer could be isolated separately and assigned to the relevant series of maxima in χ''_M. More recently, Mn_{12} clusters have been isolated the structures of which have axial (tetragonal) symmetry and contain a majority, individual Jahn-Teller isomer [67]. It is possible that such isomers can exist in $\mathbf{1} \cdot 6H_2O$, as can be seen in the structural discussion (see above). Perusal of the $\chi'_M T$ and χ''_M data for the $PhCH_2CO_2^-$ analogue [40] (shown at 5, 10 and 50 Hz, measured to 1488 Hz) reveal no frequency dependent drop in $\chi'_M T$ between 5 and 7 K, but show a similar start of a decrease below 2 K to that shown in Fig. 11. Likewise, there are no maxima in χ''_M in the 5–7 K range, but just the beginnings of such below 2 K. This is intriguing and, in view of the different Jahn-Teller axes patterns noted between the acetate ($\mathbf{1} \cdot 6H_2O$) and phenylacetate Mn_{16} derivatives, lends support to the observation of two sets of maxima in χ''_M and to SMM behaviour in the acetate cluster.

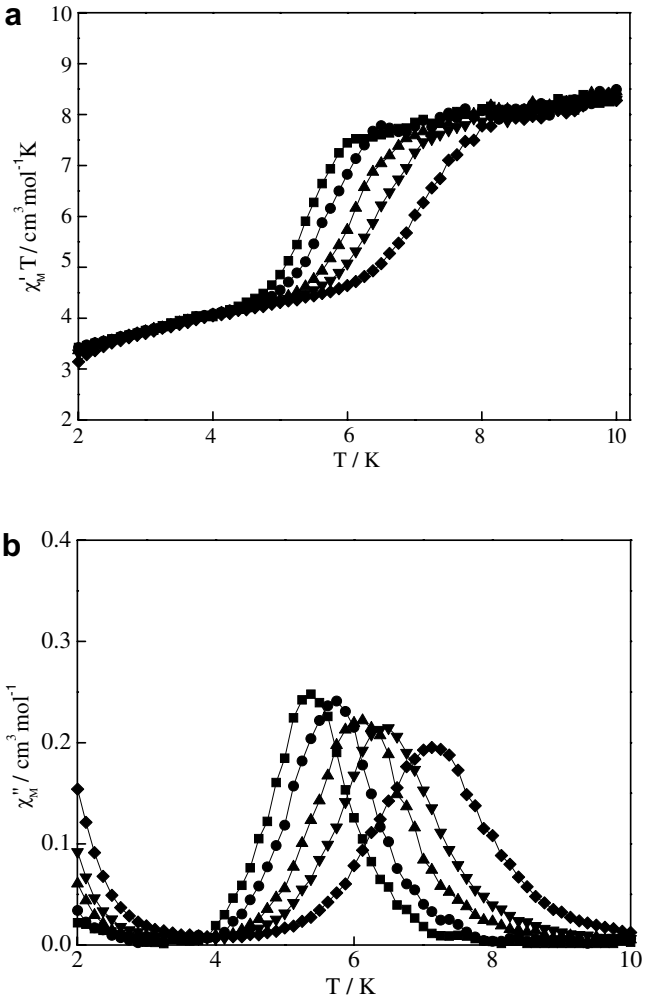


Fig. 11. (a) In-phase AC susceptibilities, $\chi'_M T$ vs. temperature and (b) out-of-phase AC susceptibilities, χ''_M vs. temperature for $\mathbf{1} \cdot 6H_2O$ measured at frequencies 50 (■), 100 (●), 250 (▲), 500 (▼), 1500 (◆) Hz in a DC field of 10 Oe.

The magnetisation relaxation data for $\mathbf{1} \cdot 6H_2O$ were analysed using the Arrhenius law for the relaxation time, τ (Eq. (1)):

$$\tau = \tau_0 e^{-\Delta E/kT}. \quad (1)$$

The values of T are the temperatures of the maxima in Fig. 11(b). The relaxation times, τ, are obtained from the frequencies (ν in Hz) of each χ''_M measurement using the relation $\tau = 1/(2\pi\nu)$, since at each maximum the relaxation frequency of an SMM is equal to the operating AC frequency, ν (τ_0 = pre-exponential factor, k = Boltzmann constant). From the least-squares fit to a plot of $\ln(1/\tau)$ versus $1/T$, the energy barrier, ΔE, was found to be 52.2 cm^{-1} (c.f. Mn_{12}-acetate 43 cm^{-1} = 62 K) [52,62] with a pre-exponential factor of 3.00×10^{-9} s. Table 6 compares these values with those of other SMMs of Mn.

In the absence of fitting of the M/H data to an appropriate Spin Hamiltonian it is possible to estimate the size of $|D|$, the axial zero-field splitting parameter for the coupled ground state, by use of the relationship $|D|S_z^2 = \Delta E$, where ΔE is the barrier height [68,69]. Since the precise value of S is not known, it was assumed to be 4. Thus a $|D|$ value of

Table 6
Effective energy barrier energies, ΔE, and pre-exponential factors, τ_0, for some Mn SMM clusters

Cluster	ΔE (cm^{-1})	τ_0 (s)	References
$[Mn_9O_7(OAc)_{11}(thme)(py)_3(H_2O)_2]$[a]	18.9	not given	[3,4]
$[Mn_{12}O_{12}(O\text{-}p\text{-}Me\text{-}Bz)_{16}(H_2O)_4]\cdot 3H_2O$[b]	45.0	7.7×10^{-9}	[47]
$[Mn_{12}O_8Cl_4(OBz)_8(hmp)_6]$[c]	21.1	2.5×10^{-9}	[7]
$[Mn_{16}O_{16}(OMe)_6(OAc)_{16}(MeOH)_3(H_2O)_3]\cdot 6H_2O$	52.2	3.0×10^{-9}	tw

tw, this work.
[a] H_3thme = 1,1,1-tris(hydroxymethyl)ethane.
[b] O-*p*-Me-Bz = *p*-methylbenzoate.
[c] hmpH = 2-(hydroxymethyl)pyridine.

$52/16 = 3.2\ cm^{-1}$ is predicted, which is much larger than those determined for Mn_{12}-acetate systems having a ground $S = 10$ and $D \approx -0.5\ cm^{-1}$. It is much more akin to values obtained for Mn^{III} monomeric complexes [70]. Christou et al. [40] were not able to deduce $|D|$ in the $PhCH_2CO_2^-$ and other haloacetate cases that were thought to have $S = 2$ ground states, but concluded that $|D|$ was larger than in Mn_{12}-OAc.

Use of the above ΔE relationship assumes that only the ground S state, and its M_S components 0, ±1, ±2,..., ±S, are thermally populated. In the present $\mathbf{1}\cdot 6H_2O$ cluster there are other low-lying S states as indicated by the nature of the M versus H isotherms in Fig. 8. In attempts to try to simulate the M/H data and thus obtain the ground state levels and the D values in a more direct manner, it is clear, despite the limitations mentioned earlier, that calculations of M, at 2 K and 5 T, for an $S = 4$ level yield, as expected, $8N\beta$ for $D = 0$; $6.3N\beta$ for $D = -1\ cm^{-1}$ and $4N\beta$ for $D = -3.5\ cm^{-1}$. Thus, the D value obtained from the AC relaxation data, assuming it is negative ($-3.2\ cm^{-1}$), is not compatible with the Brillouin calculation of M which limits D to being less than $\sim -1\ cm^{-1}$. The $S = 3$ (or $S = 2$) calculations gave an even bigger discrepancy, and hence there appears to be a dilemma.

Güdel et al. [34] have recently discussed somewhat related anomalies in a Ni_{21}-citrate SMM cluster in which an $S = 3$ state was lowest, but with many other excited states (up to $S = 9$) close in energy and thermally populated in high-fields (up to 8 T) at temperatures below 1 K. The ΔE value obtained from the χ''_M versus frequency Arrhenius plot was ~3 K in this Ni_{21}-cluster and D was estimated to be $-0.22\ cm^{-1}$ (along the crystallographic *c*-axis). Rhombic ligand-field terms, E, were thought to be partly responsible for differences in the D value compared to that of Mn_{12}-acetate, and transverse anisotropy terms were also thought to be important, thus rendering the relationship $\Delta E = |D|S^2$ invalid because of admixture of M_S levels. It is also interesting to note that excited S states are now thought to be important in the Mn_{12}-acetate system, e.g. $S = 9$ close to $S = 10$ and $S > 10$ under very high fields [62].

A possible, though unlikely explanation for the AC data and the consequent estimated $|D|$, is that traces of Mn_{12}-acetate are present in the samples and responsible for the frequency dependent AC behaviour. Certainly, there is no evidence for Mn_{12} in the μ_{eff}/T plot of Fig. 7, since it would show a ferromagnetic-like increase in μ_{eff} as the temperature is decreased towards 2 K. A powder XRD measured on one sample showed, by comparison to calculated line positions that $\mathbf{1}\cdot 6H_2O$ was the major species present, with traces of the chain **2** and only a hint of Mn_{12}-acetate. Finally, these Mn_{16} clusters would benefit from detailed probing by single crystal micro-Squid measurements [1,2,5,8,14] as well as by high frequency/high field EPR studies, at variable temperatures, to attempt to better delineate the ground and nearby energy levels and elucidate any trace impurities that contribute.

3.3.2. *[Mn(μ-OMe)(μ-OAc)$_2$]$_n$ (**2**)*

The variation of susceptibility and effective magnetic moment, per Mn^{III}, with temperature is given in Fig. 12. A broad maximum in χ_M occurs at ~70 K typical of the behaviour of a Heisenberg antiferromagnetically coupled $S = 2$ chain [71]. The rapid increase in χ_M at low temperature could be due to monomer impurity or to ferromagnetic chain–chain interactions. The corresponding μ_{eff} values decrease gradually from 4.16 μ_B at 300 K (less than the uncoupled 4.87 μ_B value) to 0.98 μ_B at 2 K. The inflection below 10 K is due to monomer impurity or chain–chain effects.

The data were fitted to an $S = 2$ Fisher chain ($-2JS_i\cdot S_j$) model [72], modified by a $(T-\theta)$ term to give an approximate way of expressing inter-chain interactions. The fit is good and is shown in Fig. 12. The parameters are

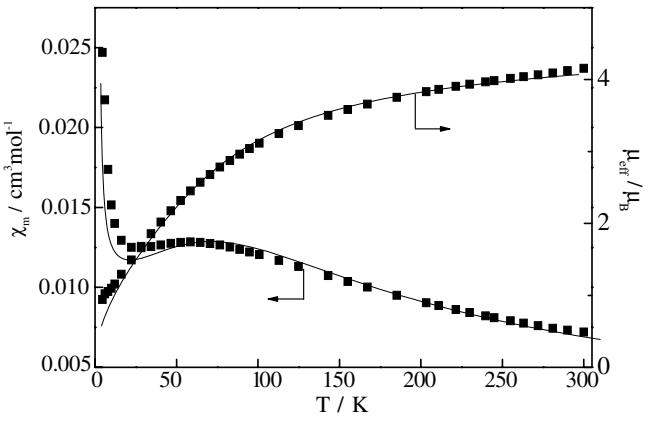


Fig. 12. Plots of μ_{eff} (■) and χ_M (●), per Mn, vs. temperature for **2**. The solid lines are the calculated best-fits using the Heisenberg, $-2JS_i\cdot S_j$, linear chain model (see text).

$g = 1.91$, $J = -7.0\ cm^{-1}$ and $\theta = +1.95$ K. The J value is of similar magnitude to those of some $[Mn^{III}(Schiff\text{-}base)X]_n$ chains ($X = OAc^-$, N_3^-) [68,69], but much bigger than those obtained in the dca^- bridged $[Mn^{III}(Schiff\text{-}base)(dca)]_n$ systems [73].

Complex **2** resembles $\{[Mn(\mu\text{-}OH)(\mu\text{-}OAc)_2] \cdot HOAc \cdot H_2O\}_n$ [45,46], which displays hydrogen bonding between ligands on adjacent chains to form a 2D sheet structure. Probably as a result of these hydrogen-bonding pathways the complex displays long-range antiferromagnetic order, whereas **2** displays antiferromagnetic coupling with no subsequent magnetic order. The benzoate analogue of **2**, $[Mn(\mu\text{-}OMe)(\mu\text{-}O_2CPh)_2]_n$, has recently been isolated from methanol solution using a reductive aggregation method and shown to adopt the same 1-D chain structure with π-stacking occurring between benzoate rings of neighbouring chains [74]. The magnetic data were very similar to those of **2** and were likewise indicative of medium strength antiferromagnetic coupling, with no evidence for long-range magnetic order.

Acknowledgements

K.S.M. acknowledges the receipt of an Australian Research Council Discovery Grant and D.J.P. was the grateful recipient of a Sir J. McNeil postgraduate scholarship.

Appendix A. Supplementary material

Crystallographic data in CIF format have been deposited at the Cambridge Crystallographic Data Centre with CCDC numbers 176429 (**1** · $6H_2O$) and 603080 (**2**). Copies of this information may be obtained free of charge from the Director, CCDC, 12 Union Road, Cambridge, CB2 1EZ, UK (fax: +44 1223 336033; e-mail: deposit@ccdc.cam.ac.uk; or www:http://www.ccdc.cam.ac.uk). Supplementary data associated with this article can be found, in the online version, at doi:10.1016/j.poly.2006.05.044.

References

[1] W. Wernsdorfer, N. Aliaga-Alcalde, D.N. Hendrickson, G. Christou, Nature 416 (2002) 406.
[2] L.M. Wittick, K.S. Murray, B. Moubaraki, S.R. Batten, L. Spiccia, K.J. Berry, Dalton Trans. 1003 (2004).
[3] E.K. Brechin, M. Soler, J. Davidson, D.N. Hendrickson, S. Parsons, G. Christou, Chem. Commun. (2002) 2252.
[4] E.K. Brechin, Chem. Commun. (2005) 5141.
[5] C. Boskovic, W. Wernsdorfer, K. Folting, J.C. Huffman, D.N. Hendrickson, G. Christou, Inorg. Chem. 41 (2002) 5107.
[6] J. Kortus, T. Baruah, N. Bernstein, M.R. Pederson, Phys. Rev. B 66 (2002) 092403.
[7] C. Boskovic, E.K. Brechin, W.E. Streib, K. Folting, J.C. Bollinger, D.N. Hendrickson, G. Christou, J. Am. Chem. Soc. 124 (2002) 3725.
[8] E.K. Brechin, C. Boskovic, W. Wernsdorfer, J. Yoo, A. Yamaguchi, E.C. Sañudo, T.R. Concolino, A.L. Rheingold, H. Ishimoto, D.N. Hendrickson, G. Christou, J. Am. Chem. Soc. 124 (2002) 9710.
[9] E.C. Sañudo, W. Wernsdorfer, K.A. Abboud, G. Christou, Inorg. Chem. 43 (2004) 4137.
[10] M. Murugesu, J. Raftery, W. Wernsdorfer, G. Christou, E.K. Brechin, Inorg. Chem. 43 (2004) 4203.
[11] L.F. Jones, E.K. Brechin, D. Collison, A. Harrison, S.J. Teat, W. Wernsdorfer, Chem. Commun. (2002) 2974.
[12] L.F. Jones, G. Rajaraman, J. Brockman, M. Murugesu, E.C. Sañudo, J. Raftery, S.J. Teat, W. Wernsdorfer, G. Christou, E.K. Brechin, D. Collison, Chem. Eur. J. 10 (2004) 5180.
[13] M. Soler, E. Rumberger, K. Folting, D.N. Hendrickson, G. Christou, Polyhedron 20 (2001) 1365.
[14] A.J. Tasiopoulos, A. Vinslava, W. Wernsdorfer, K.A. Abboud, G. Christou, Angew. Chem. Int. Ed. 43 (2004) 2117.
[15] G. Aromi, J.-P. Claude, M.J. Knapp, J.C. Huffman, D.N. Hendrickson, G. Christou, J. Am. Chem. Soc. 120 (1998) 2977.
[16] C.S. Alvarez, A.D. Bond, D. Cave, M.E.G. Mosquera, E.A. Harron, R.A. Layfield, M. McPartlin, J.M. Rawson, P.T. Wood, D.S. Wright, Chem. Commun. (2002) 2980.
[17] M.A. Bolcar, S.M.J. Aubin, K. Folting, D.N. Hendrickson, G. Christou, Chem. Commun. (1997) 1485.
[18] E. Libby, K. Folting, C.J. Huffman, J.C. Huffman, G. Christou, Inorg. Chem. 32 (1993) 2549.
[19] M.W. Wemple, H.-L. Tsai, S. Wang, J.P. Claude, W.E. Streib, J.C. Huffman, D.N. Hendrickson, G. Christou, Inorg. Chem. 35 (1996) 6437.
[20] Z. Sun, P.K. Gantzel, D.N. Hendrickson, Inorg. Chem. 35 (1996) 6640.
[21] M.M. Grush, J. Chen, T.L. Stemmler, S.J. George, C.Y. Ralston, R.T. Stibrany, A. Gelasco, G. Christou, S.M. Gorun, J.E. Penner-Hahn, S.P. Cramer, J. Am. Chem. Soc. 118 (1996) 65.
[22] J.T. Brockman, J.C. Huffman, G. Christou, Angew. Chem. Int. Ed. 41 (2002) 2506.
[23] A.L. Barra, A. Caneschi, A. Cornia, F.F. de Biani, D. Gatteschi, C. Sangregorio, R. Sessoli, L. Sorace, J. Am. Chem. Soc. 121 (1999) 5302.
[24] K. Wieghardt, K. Pohl, I. Jibril, G. Huttner, Angew. Chem. Int. Ed. 23 (1984) 77.
[25] A.L. Barra, P. Debrunner, D. Gatteschi, C.E. Schulz, R. Sessoli, Europhys. Lett. 35 (1996) 133.
[26] S. Hill, S. Maccagnano, K. Park, R.M. Achey, J.M. North, N.S. Dalal, Phys. Rev. B 65 (2002) 224410.
[27] A.L. Barra, D. Gatteschi, R. Sessoli, Chem. Eur. J. 6 (2000) 1608.
[28] A.-L. Barra, B. Fabio, A. Caneschi, D. Gatteschi, C. Paulsen, C. Sangregorio, R. Sessoli, L. Sorace, ChemPhysChem 2 (2001) 523.
[29] C. Benelli, S. Parsons, G.A. Solan, R.E.P. Winpenny, Angew. Chem. Int. Ed. 35 (1996) 1825.
[30] C. Benelli, J. Cano, Y. Journaux, R. Sessoli, G.A. Solan, R.E.P. Winpenny, Inorg. Chem. 40 (2001) 188.
[31] J.C. Goodwin, R. Sessoli, D. Gatteschi, W. Wernsdorfer, A.K. Powell, S.L. Heath, J. Chem. Soc., Dalton Trans. (2000) 1835.
[32] S.L. Castro, Z. Sun, C.M. Grant, J.C. Bollinger, D.N. Hendrickson, G. Christou, J. Am. Chem. Soc. 120 (1998) 2365.
[33] R.E.P. Winpenny, J. Chem. Soc., Dalton Trans. (2002) 1.
[34] S.T. Ochsenbein, M. Murrie, E. Rusanov, H. Stoeckli-Evans, C. Sekine, H.U. Güdel, Inorg. Chem. 41 (2002) 5133.
[35] E.-C. Yang, D.N. Hendrickson, W. Wernsdorfer, M. Nakano, L.N. Zakharov, R.D. Sommer, A.L. Rheingold, M. Ledezma-Gairaud, G. Christou, J. Appl. Phys. 91 (2002) 7382.
[36] M. Nakano, G.-E. Matsubayashi, T. Muramatsu, T.C. Kobayashi, K. Amaya, J. Yoo, G. Christou, D.N. Hendrickson, Mol. Cryst. Liq. Cryst. 376 (2002) 405.
[37] J.J. Sokol, A.G. Hee, J.R. Long, J. Am. Chem. Soc. 124 (2002) 7656.
[38] C.P. Berlinguette, D. Vaughn, C. Cañada-Vilalta, J.R. Galan-Mascaros, K.R. Dunbar, Angew. Chem. Int. Ed. 42 (2003) 1523.
[39] D.J. Price, S.R. Batten, B. Moubaraki, K.S. Murray, Chem. Commun. (2002) 762.
[40] P. King, W. Wernsdorfer, K.A. Abboud, G. Christou, Inorg. Chem. 43 (2004) 7315.
[41] T. Sala, M.V. Sargent, Chem. Commun. (1978) 253.
[42] Z. Otwinowski, W. Minor, Methods Enzymol. 276 (1997) 307.

[43] G.M. Sheldrick, SHELX 97, University of Göttingen, Göttingen, Germany, 1997.
[44] L.J. Barbour, J. Supramol. Chem. 1 (2001) 189.
[45] D.J. Price, S.R. Batten, B. Moubaraki, K.S. Murray, Polyhedron 22 (2003) 2161.
[46] A.J. Tasiopoulos, N.C. Harden, K.A. Abboud, G. Christou, Polyhedron 22 (2003) 133.
[47] S.M.J. Aubin, Z. Sun, H.J. Eppley, E. Rumberger, I.A. Guezei, K. Folting, P.K. Gantzel, A.L. Rheingold, G. Christou, D.N. Hendrickson, Inorg. Chem. 40 (2001) 2127.
[48] J. An, Z.D. Chen, J. Bian, J.T. Chen, S.X. Wang, S. Gao, G.X. Xu, Inorg. Chim. Acta 299 (2000) 28.
[49] Z. Sun, D. Ruiz, E. Rumberger, C.D. Incarvito, K. Folting, A.L. Rheingold, G. Christou, D.N. Hendrickson, Inorg. Chem. 37 (1998) 4758.
[50] H.J. Eppley, H.-L. Tsai, N. de Vries, K. Folting, G. Christou, D.N. Hendrickson, J. Am. Chem. Soc. 117 (1995) 301.
[51] C. Boskovic, J.C. Huffman, G. Christou, Chem. Commun. (2002) 2502.
[52] G. Aromi, S.M.J. Aubin, M.A. Bolcar, G. Christou, H.J. Eppley, K. Folting, D.N. Hendrickson, J.C. Huffman, R.C. Squire, H.-L. Tsai, S. Wang, M.W. Wemple, Polyhedron 17 (1998) 3005.
[53] T. Kohler, T. Armbruster, E. Libowitzky, J. Solid State Chem. 133 (1997) 486.
[54] A.D. Wadsley, Acta Crystallogr. 5 (1952) 676.
[55] A.D. Wadsley, Acta Crystallogr. 8 (1955) 165.
[56] A.F. Wells, Structural Inorganic Chemistry, 3rd ed., Oxford University Press, London, 1962.
[57] A.K. Powell, Struct. Bond. 88 (1997) 1.
[58] G.L. Abbati, A. Cornia, A.C. Fabretti, A. Caneschi, D. Gatteschi, Inorg. Chem. 37 (1998) 1430.
[59] I.A.M. Pohl, L.G. Westin, M. Kritikos, Chem. Eur. J. 7 (2001) 3438.
[60] E.K. Brechin, S.G. Harris, A. Harrison, S. Parsons, A.G. Whittaker, R.E.P. Winpenny, Chem. Commun. (1997) 653.
[61] T. Lis, Acta Crystallogr. Sect. B 36 (1980) 2042.
[62] D. Gatteschi, R. Sessoli, Angew. Chem. Int. Ed. 42 (2003) 268.
[63] S.M.J. Aubin, Z. Sun, L. Pardi, J. Krzystek, K. Folting, L.-C. Brunel, A.L. Rheingold, G. Christou, D.N. Hendrickson, Inorg. Chem. 38 (1999) 5329.
[64] A. Cornia, A.C. Fabretti, R. Sessoli, L. Sorace, D. Gatteschi, A.-L. Barra, C. Daiguebonne, T. Roisnel, Acta Crystallogr. Sect. C 58 (2002) m371.
[65] A. Cornia, R. Sessoli, L. Sorace, D. Gatteschi, A.L. Barra, C. Daiguebonne, Phys. Rev. Lett. 89 (2002) 257201.
[66] S.M.J. Aubin, Z. Sun, H.J. Eppley, E.M. Rumberger, I.A. Guzei, K. Folting, P.K. Gantzel, A.L. Rheingold, G. Christou, D.N. Hendrickson, Polyhedron 20 (2001) 1139.
[67] S. Hill, N. Anderson, A. Wilson, S. Takahashi, K. Petukhov, N.E. Chakov, M. Murugesu, J.M. North, E. delBarco, A.D. Kent, N.S. Dalal, G. Christou, Polyhedron 24 (2005) 2284.
[68] A. Caneschi, D. Gatteschi, C. Sangregorio, R. Sessoli, L. Sorace, A. Cornia, M.A. Novak, C. Paulsen, W. Wernsdorfer, J. Magn. Magn. Mater. 200 (1999) 182.
[69] G. Christou, D. Gatteschi, D.N. Hendrickson, R. Sessoli, MRS Bull. 25 (2000) 66.
[70] B.J. Kennedy, K.S. Murray, Inorg. Chem. 24 (1985) 1552.
[71] T. Smith, S.A. Friedberg, Phys. Rev. 176 (1968) 660.
[72] M.E. Fisher, Am. J. Phys. 32 (1964) 343.
[73] D.J. Price, S.R. Batten, B. Moubaraki, K.S. Murray, Indian J. Chem. Sect. A 42 (2003) 2256.
[74] A.J. Tasiopoulos, W. Wernsdorfer, K.A. Abboud, G. Christou, Inorg. Chem. 44 (2005) 6324.

Available online at www.sciencedirect.com
ScienceDirect
Polyhedron 26 (2007) 318–328
POLYHEDRON
www.elsevier.com/locate/poly

Synthesis of a heterodinuclear ruthenium(II)–platinum(II) complex linked by L-cysteine methyl ester

Sarah J. Yousouf, Craig R. Brodie, Nial J. Wheate, Janice R. Aldrich-Wright *

School of Biomedical and Health Sciences, University of Western Sydney, Campbelltown, NSW 2560, Australia

Received 22 March 2006; accepted 2 June 2006
Available online 10 June 2006

Abstract

A potential anticancer heterodinuclear ruthenium(II)–platinum(II) complex, [ruthenium(II)(4,4′-dimethyl-2,2′-bipyridine)$_2$(5-(L-cysteine-methyl ester)-1,10-phenanthroline)-*trans*-chlorodiammineplatinum(II)] chloride, [Ru(Me$_2$bipy)$_2$(5-(L-cysteine-Me)-phen)-*trans*-Pt(NH$_3$)$_2$Cl]Cl$_3$, was synthesised. L-Cysteine methyl ester was used to link the two metal centres, as more conventional straight chain diaminoalkanes and 2-mercaptoethylamine failed to couple to the phenanthroline ligand. From the precursor mononuclear ruthenium(II) complexes, which were separated into their Δ- and Λ-isomers by column chromatography, the dinuclear complex was synthesised and characterised by ^{1}H and ^{13}C NMR, UV–Vis, circular dichroism, fluorescence and electrospray ionisation mass spectrometry.
© 2006 Elsevier Ltd. All rights reserved.

Keywords: Ruthenium(II); Platinum(II); Heterodinuclear; L-Cysteine methyl ester; Phenanthroline; Anticancer

1. Introduction

Cisplatin, carboplatin and oxaliplatin are the only platinum-based drugs widely approved for the treatment of human cancers [1]. Over the last decade, multi-nuclear platinum drugs, like BBR3464 (a novel trinuclear complex having two mono-functional *trans*-[PtCl(NH$_3$)$_2$] units coupled by a central *trans*-[Pt(NH$_3$)$_2$(H$_2$N(CH$_2$)$_6$NH$_2$)$_2$] linker), have demonstrated clinical potential, but are limited by toxic side-effects and in vivo degradation before reaching their cellular target, DNA [1,2]. Both mono- and multi-nuclear drugs derive their anticancer activity by forming coordinate covalent adducts with DNA, thereby preventing replication and transcription [3]. By changing the structure of the DNA adducts, or increasing the DNA binding affinity, new complexes may be developed that are able to overcome drug resistance.

Over the last 20 years many researchers have examined the synergistic properties of combining a DNA intercalating compound with a moiety capable of covalent binding to DNA. These new complexes include: organic intercalators linked to cisplatin-like molecules [4–21], octahedral metal intercalators coupled to cisplatin-like molecules [22–27], and organic intercalators linked to DNA-alkylating agents like mustards [28–32]. Recently, carborane cages have been attached to intercalators for use in radiation therapy [33–36]. These synergistic compounds have been developed to increase the DNA binding affinity and drug transport properties of conventional chemotherapeutic drugs and/or to modify their DNA adducts and sequence selectivity. There has been little research, however, into heteronuclear metal complexes which link platinum groups capable of forming DNA coordinate covalent adducts to other groups capable of DNA groove binding.

In this paper we report the synthesis of a heterodinuclear ruthenium(II)–platinum(II) metal complex, [Ru(Me$_2$bipy)$_2$(5-(L-cysteine-Me)-phen)-*trans*-Pt(NH$_3$)$_2$Cl]Cl$_3$,

* Corresponding author. Present address: School of Biomedical and Health Sciences, University of Western Sydney, Locked Bag 1797, Penrith South DC, NSW 1797, Australia. Tel.: +61 2 4620 3218; fax: +61 2 4620 3025.
E-mail address: j.aldrich-wright@uws.edu.au (J.R. Aldrich-Wright).

0277-5387/$ - see front matter © 2006 Elsevier Ltd. All rights reserved.
doi:10.1016/j.poly.2006.06.004

Table 1
Synthetic yield and characterisation data for the heterodinuclear ruthenium(II)–platinum(II): $[Ru(Me_2bipy)_2(5\text{-}(L\text{-cysteine-Me})\text{-phen})\text{-}trans\text{-}Pt(NH_3)_2Cl]^{3+}$ and its mononuclear precursors for the racemic and Δ- and Λ-isomer solutions

Metal complex	% Yield	ESI-MS (m/z)	CD λ_{max} nm ($\Delta\varepsilon$)	UV–Vis λ_{max} nm (ε)	Fluorescence quantum yield
Δ,Λ-$[Ru(Me_2bipy)_2(5\text{-Cl-phen})](PF_6)_2$	77	341.7		451 (8.91×10^3) 261 (4.58×10^4)	
Δ-$[Ru(Me_2bipy)_2(5\text{-Cl-phen})](PF_6)_2$			285 (−246)		0.035
Λ-$[Ru(Me_2bipy)_2(5\text{-Cl-phen})](PF_6)_2$			285 (+301)		0.035
Δ,Λ-$[Ru(Me_2bipy)_2(5\text{-(L-cysteine-MeBOC)-phen})](PF_6)_2$	54	1028.0			
Δ-$[Ru(Me_2bipy)_2(5\text{-(L-cysteine-MeBOC)-phen})](PF_6)_2$			285 (1955)	456 (1.11×10^3) 334 (9.21×10^2) 279 (7.69×10^3)	0.086
Λ-$[Ru(Me_2bipy)_2(5\text{-(L-cysteine-MeBOC)-phen})](PF_6)_2$			285 (+1998)	456 (1.61×10^3) 334 (1.38×10^3) 267 (3.39×10^4)	0.157
Δ,Λ-$[Ru(Me_2bipy)_2(5\text{-(L-cysteine-Me)-phen})\text{-}trans\text{-}Pt(NH_3)_2Cl]Cl_3$	78	342.1			
Δ-$[Ru(Me_2bipy)_2(5\text{-(L-cysteine-Me)-phen})\text{-}trans\text{-}Pt(NH_3)_2Cl]Cl_3$			285 (−2808)	456 (1.55×10^4) 334 (1.25×10^4) 257 (3.17×10^4) 282 (3.17×10^4) 206 (6.95×10^4)	
Λ-$[Ru(Me_2bipy)_2(5\text{-(L-cysteine-Me)-phen})\text{-}trans\text{-}Pt(NH_3)_2Cl]Cl_3$			285 (+2505)	456 (1.45×10^4) 334 (1.17×10^4) 257 (2.88×10^4) 282 (6.09×10^4) 206 (6.03×10^4)	

containing a platinum moiety attached to a DNA groove binding ruthenium moiety via a modified amino acid linker. This metal complex was designed as a potential anticancer agent that may display increased DNA binding affinity compared to native mononuclear platinum complexes (Table 1).

2. Experimental

2.1. Materials and methods

2.1.1. Materials

Deuterated acetonitrile (d_3-CD_3CN) and dimethylsulphoxide (d_6-DMSO) were obtained from Cambridge Isotope Laboratories. (−)-*O*,*O*′-dibenzoyl-L-tartaric acid and Sephadex® LH20 were obtained from Fluka. Silica gel 60 was obtained from Merck. 2-Mercaptoethylamine hydrochloride, 1,6-diaminohexane, 1,3-diaminopropane, L-cysteine methyl ester (*tert*-butoxy)carbonate (L-cysteine-MeBOC), DOWEX® 550A OH^- anion exchange resin (DOWEX®), Amberlite® IRA-400(Cl^-) ion exchange resin (Amberlite®), potassium hexafluorophosphate, SP Sephadex® C25, 4,4′-dimethyl-2,2′-bipyridine (Me_2bipy), 5-chloro-1,10-phenanthroline (5-Cl-phen) and deuterated methanol (d_4-CD_3OD) were all purchased from Aldrich. Ruthenium(II) trichloride hydrate {$RuCl_3\cdot xH_2O$ (Ru 40–43%)} and *trans*-diamminedichloroplatinum(II) (transplatin) were purchased from Precious Metals Online. $[Ru(Me_2bipy)_2Cl_2]$ was prepared as previously described [37,38]. All other reagents and solvents were of analytical grade and were used as received, except trifluoroacetic acid (TFA) which was redistilled before use. Aqueous solutions were prepared with Milli-Q water (Millipore, MA).

2.1.2. Nuclear magnetic resonance spectroscopy

^1H NMR spectra were obtained with a 300 MHz Varian Mercury VX spectrometer, a 400 MHz Varian Mercury VX spectrometer, or a Varian 300 MHz Unity*Plus* spectrometer. All spectra were recorded at 25 °C, unless otherwise stated and were internally referenced to the solvent resonances. All final and precursor metal complexes were characterised using NOESY, g-DQCOSY, HMBC and HMQC experiments. Spectra were obtained over a spectral width of 4200 Hz with a mixing time of either 300 or 800 ms using 2048 points in the t_2 dimension with 256 increments and a total recycle time of 1.5 s.

2.1.3. UV–Vis spectrophotometry

Absorption spectra were measured with a Varian Cary 300 Bio UV–Vis double-beam spectrophotometer. Spectra were obtained over the range of 200–800 nm with samples in 1 cm quartz cells, which were referenced to water. A scan rate of 600 nm/min, data interval of 1 nm and average time of 0.1 s were utilised. Extinction coefficients were determined by repeated measurement of the absorbance of known concentrations of the metal complexes (as PF_6^- salts) in a 3% acetone/water solution. All absorbances were within the range 0.3–0.8, and the average of repeated measurements at λ_{max} gave the extinction coefficient, ε_{max}.

2.1.4. Circular dichroism spectropolarimetry

CD spectra were acquired with a JASCO J-810 spectropolarimeter equipped with J-800 for Windows®. Samples were prepared in either 3% acetone/water or in water and were placed in 0.1 cm cylindrical quartz cells. Data collection was performed at room temperature, between 200 and 650 nm, and at a speed of 500 nm/min. A sensitivity setting of 100 mdeg, data pitch of 0.5 nm, response time of 1 s and bandwidth of 1 s were used. Spectra are given as an average of 10 scans. From the angle of ellipticity (θ, mdeg), the molar absorptivity ($\Delta\varepsilon$, mdeg/M cm) was calculated using Eq. (1), where c is the concentration (mol/L) and l is the path length

$$\Delta\varepsilon = \frac{\theta}{32\,982 \times c \times l} \tag{1}$$

2.1.5. Fluorescence spectroscopy

Fluorescence spectra were acquired with a Varian Cary Eclipse spectrofluorimeter with Windows® based software, at an excitation wavelength of 450 nm. The emission was monitored over the range 500–800 nm. Slit widths of 5 nm were used for both the excitation and emission slits, with a medium scan speed and voltage over an average of five scans. Quartz cuvettes (1 cm pathlength) were used and the metal complex samples were dissolved in acetonitrile (~0.167 mg/mL) at room temperature.

Fluorescence quantum yields were calculated using ratios of the integrated fluorescence intensities to that of $[Ru(Me_2bipy)_3]^{2+}$ in acetonitrile ($\Phi_r = 0.062$) [39], using Eq. (2) [40]:

$$\Phi_{unk} = \Phi_{std}\left(\frac{I_{unk}}{A_{unk}}\right)\left(\frac{A_{std}}{I_{std}}\right)\left(\frac{\eta_{unk}}{\eta_{std}}\right)^2 \tag{2}$$

where Φ_{unk} is the radiative quantum yield of the sample, Φ_{std} is the radiative quantum yield of the standard, and I_{unk} and I_{std} are the integrated emission intensities of the sample and standard, respectively. A_{unk} and A_{std} are the absorbances of the sample and standard, respectively, at a common excitation wavelength (nm), and η_{unk} and η_{std} are the indexes of refraction of the sample and standard solutions, respectively. Values of η corresponding to the pure solvent were used, and as all measurements were performed in the same solvent, therefore $\eta_{unk}/\eta_{std} = 1$.

2.1.6. Electrospray ionisation mass spectrometry

Mass spectra were acquired with a Micromass (Wyntheshaw, UK) Qtof 2 spectrometer with a Z-spray probe. All samples were diluted with 5 mM ammonium acetate (pH 6.8) in acetonitrile, to a final concentration of approximately 1 μM. These were injected directly into the spectrometer using a Harvard model 22 syringe pump (Natick, MA, USA) at a flow rate of 20 mL min^{-1}. Positive ion ESI mass spectra were acquired using a probe tip potential of 2500 V, a cone voltage of either 40 or 50 V, and the source block and desolvation temperatures were set to 60 and 150 °C, respectively. The transport and aperture were set to 2.0 and 13.0, respectively. In most experiments spectra were acquired over the range 200–2000 m/z. Typically, 50–70 scans were summed to obtain representative spectra. The data points were calibrated against a standard CsI solution (750 mM) over the same m/z range.

2.1.7. Elemental analysis

Elemental analysis (C, H, and N) were conducted using a Carlo Erba 1106 automatic analyser by the Microanalytical Unit, Research School of Chemistry, of the Australian National University.

2.2. Metal complex synthesis

2.2.1. $[Ru(Me_2bipy)_2(5\text{-}Cl\text{-}phen)](PF_6)_2 \cdot H_2O$

$[Ru(Me_2bipy)_2Cl_2]$ (0.30 g, 0.56 mmol) and 5-Cl-phen (0.13 g, 0.58 mmol) were dissolved in methanol (100 mL) and refluxed for 45 min. Once cooled, the solvent was removed under reduced pressure yielding the product as a red solid. Purification was achieved by applying the product, dissolved in a minimal amount of water, to an SP Sephadex® C-25 column (5 × 10 cm). The metal complex was eluted with a sodium chloride gradient (0.1–0.3 M) using 0.1 M increments. KPF_6 was then added to the fractions to induce precipitation. The resulting precipitate was extracted into dichloromethane (3 × 30 mL), the extracts dried over anhydrous sodium sulphate and the organic solvent removed under reduced pressure. Yield: 0.42 g (77%). *Anal.* Calc. for $C_{37}H_{34}F_{12}N_6P_2RuCl \cdot H_2O$: C, 44.12; H, 3.61; N, 8.35. Found: C, 44.12; H, 3.43; N, 8.29%. λ_{max}/nm (ε/mol^{-1} dm^3 cm^{-1}) (H_2O/$(CH_3)_2CO$): 451 (8.91×10^3); 261 (4.58×10^4). MS (ESMS, CH_3CN, MW $[Ru(Me_2bipy)_2(5\text{-}Cl\text{-}phen)](PF_6)_2 = 974.12$) m/z: 341.7 $[M-(1H+2PF_6)]^{2+}$. Φ (CH_3CN) = 0.035. ^1H NMR (300 MHz, CD_3CN) δ: 8.80 (H4; 1H, dd, $J_1 = 1.27$ Hz, $J_2 = 8.56$ Hz), 8.51 (H7; 1H, dd, $J_1 = 1.11$ Hz, $J_2 = 8.24$ Hz), 8.39 (H6; 1H, s), 8.38 (A/B3; 2H, s), 8.34 (A/B3; 2H, s), 8.16 (H2; 1H, dd, $J_1 = 1.11$ Hz, $J_2 = 5.23$ Hz), 8.09 (H9; 1H, dd, $J_1 = 1.11$ Hz, $J_2 = 5.23$ Hz), 7.82 (H3; 1H, dd, $J_1 = 5.22$ Hz, $J_2 = 8.57$ Hz), 7.73 (H8; 1H, dd, $J_1 = 5.22$ Hz, $J_2 = 8.29$ Hz), 7.63 (A/B6; 2H, m), 7.31 (A/B6; 2H, m), 7.27 (A/B5; 2H, m), 7.04 (A/B5; 2H, m), 2.55 (A/BMe; 6H, s), 2.46 (A/BMe; 6H, s). ^{13}C NMR (400 MHz, CD_3CN) δ: 154.2 (C2; CH), 153.8 (C11; CH), 152.3 (C26; CH), 152.0 (C20; CH), 151.50 (C18; QC), 151.4 (C24; QC), 136.7 (C9; CH), 134.5 (C4; CH), 132.6 (C8; QC), 129.3 (C19; CH), 129.1 (C25; CH), 128.2 (C7; CH), 127.6 (C3; CH), 127.6 (C10; CH), 125.9 (C23; CH), 125.8 (C17; CH), 21.4 (C18Me; CH_3), 21.3 (C24Me; CH_3).

2.2.2. Resolution of isomers

Rac-$[Ru(Me_2bipy)_2(5\text{-}Cl\text{-}phen)](PF_6)_2 \cdot H_2O$ (0.25 g, 0.26 mmol) was converted to the chloride salt by dissolving in acetone, diluting with water, then stirring with Amberlite® anion exchange beads (Cl^- form) for 1 h. The solution was filtered to remove the beads, and the

resin washed with water to elute any residual metal complex. The solvent was then removed by rotary evaporation before the red coloured residue was dissolved in water.

Rac-[Ru(Me_2bipy)$_2$(5-Cl-phen)]Cl_2 was loaded onto an SP Sephadex® column (2.6 × 100 cm). The isomers were eluted with 75 mM disodium-*O*,*O*′-dibenzoyl-L-tartrate (pH 8), which was prepared by neutralising *O*,*O*′-dibenzoyl tartaric acid with sodium hydroxide. The solution was also filtered prior to use through 0.45 μm nylon membranes. Extraction of each fraction into dichloromethane (3 × 30 mL) after the addition of KPF_6 gave each isomer. Optical purity was then established by circular dichroism. Δ-[Ru(Me_2bipy)$_2$(5-Cl-phen)](PF_6)$_2$: *Anal*. Calc. for $C_{37}H_{34}F_{12}N_6P_2RuCl$: C, 44.93; H, 3.46; N, 8.50. Found: C, 45.12; H, 3.69; N, 8.00%. CD λ_{max} nm (Δε mdeg/M cm) (H_2O/$(CH_3)_2CO$): 210 (−41); 226 (+40); 264 (+118); 285 (−246); 410 (+11). Λ-[Ru(Me_2bipy)$_2$(5-Cl-phen)]-(PF_6)$_2$: *Anal*. Calc. for $C_{37}H_{34}F_{12}N_6P_2RuCl$: C, 44.93; H, 3.46; N, 8.50. Found: C, 44.67; H, 3.51; N, 8.13%. CD λ_{max} nm (Δε mdeg/M cm) (H_2O/$(CH_3)_2CO$): 210 (+41); 226 (−56); 264 (−151); 285 (+301); 410 (−24).

2.2.3. *Rac*-[*Ru*(*Me*$_2$*bipy*)$_2$(5-(L-*cysteine-MeBOC*)-*phen*)](PF_6)$_2$

[Ru(Me_2bipy)$_2$(5-Cl-phen)](PF_6)$_2$ (0.03 g, 0.03 mmol) and L-cysteine methyl ester butoxy carbamate (L-cysteine-MeBOC) (22 μL, 0.30 mmol) were dissolved in DMF (3 mL) and de-aerated for 5 min under N_2, after which time a degassed solution of Na_2CO_3 (0.030 g, 0.30 mmol) in water (3 mL) was added via syringe. The solution was then heated to 55 °C for 1.5 h. The reaction mixture was allowed to cool to room temperature and the solvent removed under reduced pressure. The product was purified by silica gel chromatography [41] with an eluent of 1–3% KNO_3 in 10% water/acetonitrile. The eluted product was rotary evaporated to dryness, dissolved in a minimum amount of water then KPF_6 added. The resultant precipitate was extracted into dichloromethane and dried over sodium sulphate. The solvent was removed and the residue dried under reduced pressure. Yield: 19 mg (54%). MS (ESMS, CH_3CN, [Ru(Me_2bipy)$_2$(5-(L-cysteine-MeBOC)-phen)]-(PF_6)$_2$ = 1173.17) *m*/*z*: 829.1 (M−{1(PF_6)$^-$ + $C_9H_{16}NO_4$}$^+$). ^{1}H NMR (400 MHz, CD_3CN) *δ*: 8.81 (H4; 1H, dd, $J_1 = 1.32$ Hz, $J_2 = 8.42$ Hz), 8.50 (H7; 1H, dd, $J_1 = 1.11$ Hz, $J_2 = 8.31$ Hz), 8.39 (H6; 1H, s), 8.36 (A/B3; 2H, s), 8.32 (A/B3; 2H, s), 8.14 (H2; 1H, dd, $J_1 = 1.06$ Hz, $J_2 = 5.22$ Hz), 8.08 (H9; 1H, dd, $J_1 = 1.22$ Hz, $J_2 = 5.22$ Hz), 7.80 (H3; 1H, dd, $J_1 = 5.20$ Hz, $J_2 = 8.55$ Hz), 7.71 (H8; 1H, dd, $J_1 = 5.20$ Hz, $J_2 = 8.36$ Hz), 7.62 (A/B6; 2H, m), 7.31 (A/B6; 2H, m), 7.27 (A/B5; 2H, m), 7.03 (A/B5; 2H, m), 5.90 (Δ-NH; 1H, bs), 5.72 (Λ-NH; 1H, bs), 5.42 (OCH_3; 3H, s), 4.48 (Δ-N–CH; 1H, bs), 4.38 (Λ-N–CH; 1H, bs), 3.22 (Δ-CH_2; 2H, m), 2.96 (Λ-CH_2; 2H, m), 2.55 (A/BMe; 6H, s), 2.46 (A/BMe; 6H, s), 1.40 (BOC; 9H, s). ^{13}C NMR (400 MHz, CD_3CN) *δ*: 154.2 (C2; CH), 153.8 (C11; CH), 152.3 (C26; CH), 152.0 (C20; CH), 151.5 (C18; QC), 151.4 (C24; QC), 136.7 (C9; CH), 134.5 (C4; CH), 132.6 (C8; QC), 129.3 (C19; CH), 129.1 (C25; CH), 128.2 (C7; CH), 127.6 (C3; CH), 127.6 (C10; CH), 125.9 (C23; CH), 125.8 (C17; CH), 56.6 (Cys; CH), 53.0 (BOC; CH_3), 28.5 (BOC; CH_3), 27.2 (Cys; CH_2), 21.4 (C18Me; CH_3), 21.3 (C24Me; CH_3).

2.2.3.1. *Δ-[Ru(Me*$_2$*bipy)*$_2$*(5-(L-cysteine-MeBOC)-phen)]-(PF*$_6$*)*$_2$.

Experimental conditions were the same as those in Section 2.2.3. CD λ_{max} nm (Δε mdeg/M cm) (H_2O/$(CH_3)_2CO$): 210 (−254); 227.5 (+172); 271 (+716); 285 (−1955); 410 (+77). λ_{max}/nm (ε/mol^{-1} dm^3 cm^{-1}) (H_2O/$(CH_3)_2CO$): 456 (1.11×10^3); 334 (9.21×10^2); 279 (7.69×10^3). *Φ* (CD_3CN) = 0.086. ^{1}H NMR (400 MHz, CD_3CN) *δ*: 8.73 (H4; 1H, dd, $J_1 = 1.41$ Hz, $J_2 = 8.66$ Hz), 8.43 (H7; 1H, dd, $J_1 = 1.21$ Hz, $J_2 = 8.26$ Hz), 8.36 (A/B3; 2H, s), 8.31 (A/B3; 2H, s), 8.08 (H2; 1H, dd, $J_1 = 1.21$ Hz, $J_2 = 5.13$ Hz), 7.94 (H9; 1H, dd, $J_1 = 1.21$ Hz, $J_2 = 5.13$ Hz), 7.91 (H6; 1H, s), 7.71 (H3; 1H, dd, $J_1 = 5.33$ Hz, $J_2 = 8.54$ Hz), 7.65 (H8; 1H, dd, $J_1 = 5.55$ Hz, $J_2 = 8.38$ Hz), 7.62 (A/B6; 2H, m), 7.32 (A/B6; 2H, m), 7.26 (A/B5; 2H, m), 7.03 (A/B5; 2H, m), 5.98 (NH; 1H, bs), 5.42 (OCH_3; 3H, s), 4.54 (N–CH; 1H, bs), 3.20 (CH_2; 2H, m), 2.55 (A/BMe; 6H, s), 2.46 (A/BMe; 6H, s), 1.41 (BOC; 9H, s).

2.2.3.2. *Λ-[Ru(Me*$_2$*bipy)*$_2$*(5-(L-cysteine-MeBOC)-phen)]-(PF*$_6$*)*$_2$.

Experimental conditions were the same as those in Section 2.2.3. CD λ_{max} nm Δε mdeg/M cm (H_2O/$(CH_3)_2CO$): 210 (+210); 227.5 (−248); 271 (−726); 285 (+1999); 410 (−214). λ_{max}/nm (ε/mol^{-1} dm^3 cm^{-1}) (H_2O/$(CH_3)_2CO$): 456 (1.63×10^3); 334 (1.38×10^3); 267 (3.39×10^4). *Φ* (CD_3CN) = 0.157. ^{1}H NMR (400 MHz, CD_3CN) *δ*: 8.73 (H4; 1H, dd, $J_1 = 1.41$ Hz, $J_2 = 8.66$ Hz), 8.43 (H7; 1H, dd, $J_1 = 1.21$ Hz, $J_2 = 8.26$ Hz), 8.36 (A/B3; 2H, s), 8.31 (A/B3; 2H, s), 8.08 (H2; 1H, dd, $J_1 = 1.21$ Hz, $J_2 = 5.13$ Hz), 7.94 (H9; 1H, dd, $J_1 = 1.21$ Hz, $J_2 = 5.13$ Hz), 7.91 (H6; 1H, s), 7.71 (H3; 1H, dd, $J_1 = 5.33$ Hz, $J_2 = 8.54$ Hz), 7.65 (H8; 1H, dd, $J_1 = 5.55$ Hz, $J_2 = 8.38$ Hz), 7.62 (A/B6; 2H, m), 7.32 (A/B6; 2H, m), 7.26 (A/B5; 2H, m), 7.03 (A/B5; 2H, m), 5.75 (NH; 1H, bs), 5.42 (OCH_3; 3H, s), 4.33 (N–CH; 1H, bs), 2.94 (CH_2; 2H, m), 2.55 (A/BMe; 6H, s), 2.46 (A/BMe; 6H, s), 1.41 (BOC; 9H, s).

2.2.4. *Deprotection of rac-[Ru(Me*$_2$*bipy)*$_2$*(5-(L-cysteine-MeBOC)-phen)](PF*$_6$*)*$_2$

Rac-[Ru(Me_2bipy)$_2$(5-(L-cysteine-MeBOC)-phen)](PF_6)$_2$ (50 mg, 0.040 mmol) was dissolved in dichloromethane (2 mL) and added to a solution of trifluoroacetic acid/dichloromethane (1:1, 2.2 mL) containing water (40 μL) which was stirred for 1.5 h. The reaction was monitored by TLC {3% KNO_3 in 10 % H_2O/CH_3CN, ninhydrin stain (0.2% w/v in ethanol)}. Upon completion, the solvent was removed under reduced pressure and the residue stirred with DOWEX® 550A OH^- anion exchange resin

(148 mg, loading capacity 3.44 mmol/g, washed with methanol). The solution was filtered to remove the resin, and the solvent removed to yield a red solid that was dried under vacuum. Yield: 46 mg (100%). ^{1}H NMR (300 MHz, CD_3CN) δ: 8.81 (H4; 1H, dd, $J_1 = 1.32$ Hz, $J_2 = 8.42$ Hz), 8.50 (H7; 1H, dd, $J_1 = 1.11$ Hz, $J_2 = 8.31$ Hz), 8.39 (H6; 1H, s), 8.36 (A/B3; 2H, s), 8.32 (A/B3; 2H, s), 8.14 (H2; 1H, dd, $J_1 = 1.06$ Hz, $J_2 = 5.22$ Hz), 8.08 (H9; 1H, dd, $J_1 = 1.22$ Hz, $J_2 = 5.22$ Hz), 7.80 (H3; 1H, dd, $J_1 = 5.20$ Hz, $J_2 = 8.55$ Hz), 7.71 (H8; 1H, dd, $J_1 = 5.20$ Hz, $J_2 = 8.36$ Hz), 7.62 (A/B6; 2H, m), 7.31 (A/B6; 2H, m), 7.27 (A/B5; 2H, m), 7.03 (A/B5; 2H, m), 5.42 (OCH_3; 3H, s), 4.48 (Δ-N–CH; 1H, bs), 4.38 (Λ-N–CH; 1H, bs), 3.22 (Δ-CH_2; 2H, m), 2.96 (Λ-CH_2; 2H, m), 2.55 (A/BMe; 6H, s), 2.46 (A/BMe; 6H, s), 1.26 (NH_2; 2H, s).

2.2.5. *Rac-[Ru(Me$_2$bipy)$_2$(5-(L-cysteine-Me)-phen)-trans-Pt(NH$_3$)$_2$Cl]Cl$_3$*

Trans-[$PtCl_2(NH_3)_2$] (0.013 g, 0.040 mmol) was suspended in water (5 mL), acidified with 1 M HCl to pH 5, then heated to ~95 °C to dissolve the metal complex. Over a period of 1.5 h, [$Ru(Me_2bipy)_2$(5-(L-cysteine-Me)-phen)]-Cl_2 (0.037 g, 0.040 mmol) in water (10 mL) was added drop wise to the solution, in the dark, after which time the temperature (95 °C) was maintained for 5 h. The solution was then cooled to 0 °C and filtered to remove any precipitate. The solution volume was reduced under vacuum and the remaining water removed by lypholysation. The red/orange precipitate was dissolved in a minimum of methanol and applied to a Sephadex® LH20 column (3 × 15 cm, 70 g packing material). Fractions (3 mL) were collected and monitored by TLC (3% saturated potassium nitrate, 10% water/acetonitrile, ninhydrin stain). *Rac*-[$Ru(Me_2bipy)_2$(5-(L-cysteine-Me)-phen)-*trans*-$Pt(NH_3)_2Cl]^{3+}$ eluted first, and fractions containing the product were combined before the solvent was removed under reduced pressure. Yield: 37 mg (78%). MS (ESMS, CH_3CN, MW [$Ru(Me_2bipy)_2$(5-(L-cysteine-Me)-phen)-*trans*-$Pt(NH_3)_2$-$Cl]^{3+} = 1045$) *m/z*: 342.1 ($M/3 - 1NH_3^+$, $1H^+$). ^{1}H NMR (400 MHz, d_6-DMSO) δ: 8.84 (H4; 1H, dd, $J_1 = 1.02$ Hz, $J_2 = 8.46$ Hz), 8.71 (H7; 1H, dd, $J_1 = 1.11$ Hz, $J_2 = 8.31$ Hz), 8.36 (A/B3; 2H, s), 8.69 (A/B3; 2H, s), 8.73 (H6; 1H, s), 8.22 (H2; 1H, d, $J = 5.22$ Hz), 8.14 (H9; 1H, d, $J = 4.90$ Hz), 7.96 (H3; 1H, dd, $J_1 = 5.29$ Hz, $J_2 = 8.42$ Hz), 7.87 (H8; 1H, dd, $J_1 = 5.09$ Hz, $J_2 = 8.23$ Hz), 7.62 (A/B6; 2H, m), 7.40 (A/B6; 2H, m), 7.35 (A/B5; 2H, m), 7.14 (A/B5; 2H, m), 4.35 (NH_2; 1H, s), 4.07 (N–CH; 1H, q, $J_1 = 4.93$ Hz, $J_2 = 10.01$ Hz), 3.50 (OCH_3; 3H, s), 3.16 (CH_2; 2H, d, $J = 4.78$ Hz), 2.53 (A/BMe; 6H, s), 2.45 (A/BMe; 6H, s).

2.2.5.1. *Δ-[Ru(Me$_2$bipy)$_2$(5-(L-cysteine-Me)-phen)-trans-Pt(NH$_3$)$_2$Cl]Cl$_3$.*

Experimental conditions were the same as those in Section 2.2.5. CD λ_{max} nm (Δε mdeg/M cm) (H_2O): 210 (−289); 228.5 (+334); 270.5 (+1044); 285 (−2808); 410 (+250). λ_{max}/nm (ε/mol^{-1} dm^3 cm^{-1}) (H_2O/$(CH_3)_2CO$): 456 (1.55×10^4); 334 (1.25×10^4); 257 (3.17×10^4); 282 (7.12×10^4); 206 (6.95×10^4). ^{1}H NMR (400 MHz, d_6-DMSO) δ: 8.74 (H4; 1H, dd, $J_1 = 1.20$ Hz, $J_2 = 8.56$ Hz), 8.72 (A/B3; 2H, s), 8.68 (A/B3; 2H, s), 8.61 (H7; 1H, dd, $J_1 = 1.20$ Hz, $J_2 = 8.38$ Hz), 8.14 (H2; 1H, dd, $J_1 = 1.16$ Hz, $J_2 = 5.22$ Hz), 8.11 (H6; 1H, s), 7.98 (H9; 1H, dd, $J_1 = 1.31$ Hz, $J_2 = 5.37$ Hz), 7.87 (H3; 1H, dd, $J_1 = 5.22$ Hz, $J_2 = 7.88$ Hz), 7.80 (H8; 1H, dd, $J_1 = 5.22$ Hz, $J_2 = 8.27$ Hz), 7.61 (A/B6; 2H, m), 7.38 (A/B6; 2H, m), 7.32 (A/B5; 2H, m), 7.15 (A/B5; 2H, m), 3.95 (N–CH; 1H, d, $J = 8.77$ Hz), 3.89 (NH_2; 1H, s), 3.73 (CH_2; 2H, dd, $J_1 = 7.10$ Hz, $J_2 = 14.20$ Hz), 2.81 (OCH_3; 3H, s), 2.53 (A/BMe; 6H, s), 2.44 (A/BMe; 6H, s).

2.2.5.2. *Λ-[Ru(Me$_2$bipy)$_2$(5-(L-cysteine-Me)-phen)-trans-Pt(NH$_3$)$_2$Cl]Cl$_3$.*

Experimental conditions were the same as those in Section 2.2.5. CD λ_{max} nm (Δε mdeg/M cm) (H_2O): 210 (+289); 228.5 (−243); 270.5 (−895); 285 (+2505); 410 (−210). λ_{max}/nm (ε/mol^{-1} dm^3 cm^{-1}) (H_2O/$(CH_3)_2CO$): 456 (1.45×10^4); 334 (1.17×10^4); 257 (2.88×10^4); 282 (6.09×10^4); 206 (6.03×10^4). ^{1}H NMR (400 MHz, d_6-DMSO) δ: 8.74 (H4; 1H, dd, $J_1 = 1.20$ Hz, $J_2 = 8.56$ Hz), 8.72 (A/B3; 2H, s), 8.68 (A/B3; 2H, s), 8.61 (H7; 1H, dd, $J_1 = 1.20$ Hz, $J_2 = 8.38$ Hz), 8.14 (H2; 1H, dd, $J_1 = 1.16$ Hz, $J_2 = 5.22$ Hz), 8.11 (H6; 1H, s), 7.98 (H9; 1H, dd, $J_1 = 1.31$ Hz, $J_2 = 5.37$ Hz), 7.87 (H3; 1H, dd, $J_1 = 5.22$ Hz, $J_2 = 7.88$ Hz), 7.80 (H8; 1H, dd, $J_1 = 5.22$ Hz, $J_2 = 8.27$ Hz), 7.61 (A/B6; 2H, m), 7.38 (A/B6; 2H, m), 7.32 (A/B5; 2H, m), 7.15 (A/B5; 2H, m), 3.95 (N–CH; 1H, d, $J = 8.77$ Hz), 3.89 (NH_2; 1H, s), 3.73 (CH_2; 2H, dd, $J_1 = 7.10$ Hz, $J_2 = 14.20$ Hz), 2.81 (OCH_3; 3H, s), 2.53 (A/BMe; 6H, s), 2.44 (A/BMe; 6H, s).

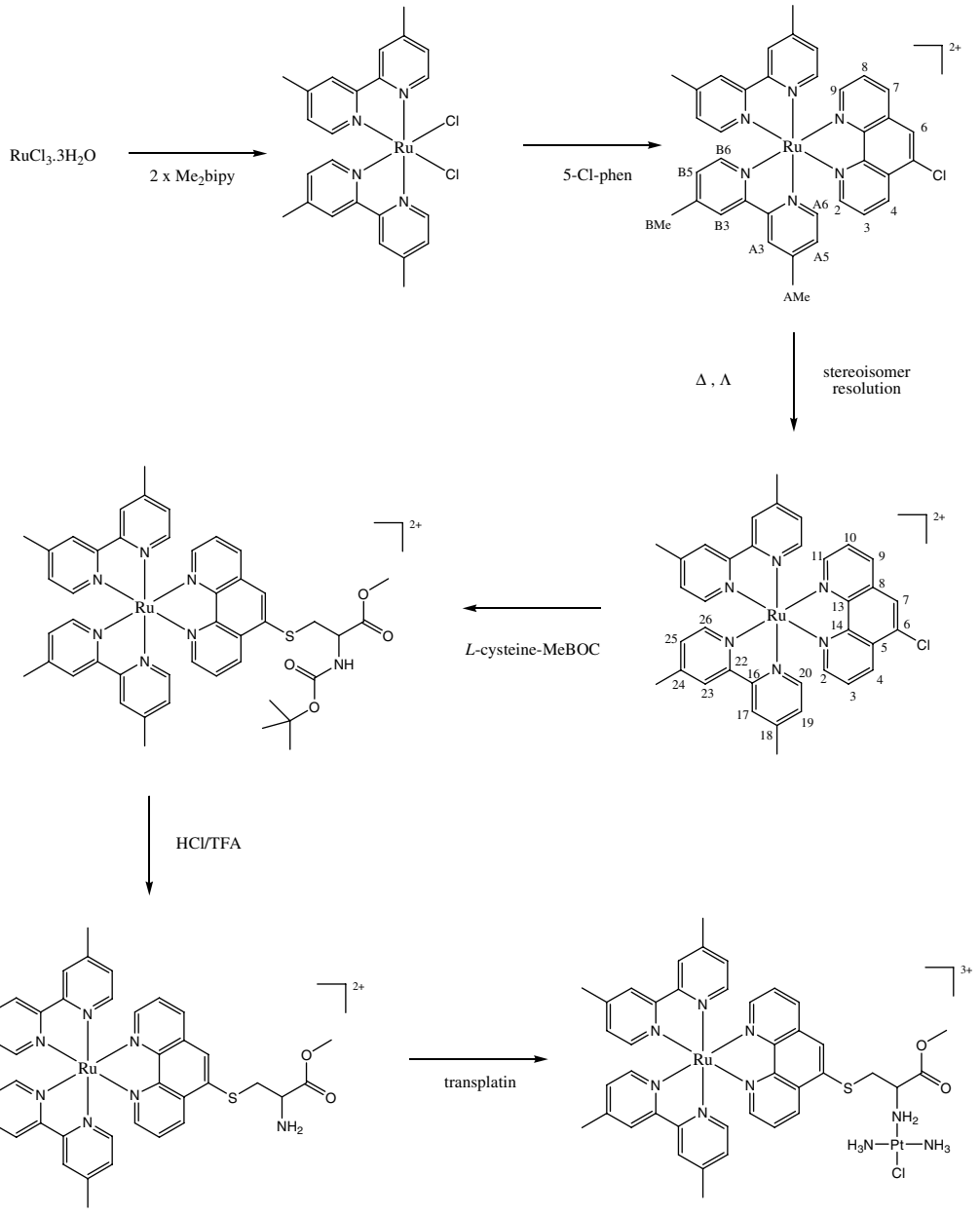
3. Results and discussion

3.1. Metal complex synthesis

The heterodinuclear metal complex was synthesised using a six step method as shown in Scheme 1 (where the proton numbering scheme is shown after step 2 and the carbon numbering scheme is shown after step 3). All reactions were initially performed with unresolved mononuclear complexes then repeated with the Δ- and Λ-isomers once the reaction conditions had been optimised.

[$Ru(Me_2bipy)_2Cl_2$] was synthesised using alternative methods [37,38]. The phenanthroline ligand was then coordinated to the [$Ru(Me_2bipy)_2Cl_2$] complex by refluxing in methanol for approximately half an hour. Completion of the reaction was signified by a change in colour of the solution from deep purple to red. Upon removal of the solvent a red/brown solid resulted.

Two methods of purifying *rac*-[$Ru(Me_2bipy)_2$(5-Cl-phen)][PF_6)$_2$ were trialed. Dissolution of the ruthenium complex as a hexafluorophosphate salt in acetonitrile and elution through an aluminum oxide column produced an impure product; however, further purification on a cation exchange column enabled isolation of the desired purified metal complex. Purification using an



Scheme 1.

SP Sephadex® C-25 column alone (sodium chloride eluent) was also trialed. Before loading onto the Sephadex column, the ruthenium complex was converted to the chloride salt by stirring with Amberlite® anion exchange beads. The first band to be eluted with water from the column was a golden brown colour, followed by a yellow band that eluted with 0.1 M NaCl. The remaining deep red band eluted with 0.3 M NaCl and was the desired product. A residual brown band, thought to comprise $[Ru(Me_2bipy)_2Cl_2]$, remained bound to the column head. A column 10–15 cm in length and 5 cm in width was found to be sufficient to attain separation between the bands. The metal complex was isolated by the addition of potassium hexafluorophosphate and extracted into dichloromethane.

The isomers of $[Ru(Me_2bipy)_2(5\text{-Cl-phen})]^{2+}$ were resolved using solvent-recycled solution cation exchange chromatography [42]. Using SP Sephadex® C25 and 75 mM disodium-*O*,*O*′-dibenzoyl-L-tartrate as the eluent, two discreet bands were observed after an effective column length of 0.9 m, indicating baseline-to-baseline separation. After collection, the metal complexes were precipitated by the addition of potassium hexafluorophosphate and extracted into dichloromethane, to remove the tartrate salt.

Two diaminoalkanes of varying carbon chain lengths were protected using BOC [43], with the intention of observing the effect of linker length on the DNA binding affinity of the heterodinuclear complex. Diaminoalkanes were selected for their flexibility, which would allow the different metal centres to bind at preferential DNA structures,

and because of their relevance in multi-nuclear platinum agents [44–46]. Attempts were made to couple the single amine BOC-protected linkers 1,6-diaminohexane, 1,3-diaminopropane and 2-mercaptoethylamine to free 5-Cl-phen before addition of the ligand to $[Ru(Me_2bipy)_2Cl_2]$. Unfortunately the coupling attempts were unsuccessful as the phenanthroline-linker bond was degraded upon coordination of the ligand to the metal centre. Subsequent attempts were made to couple the linkers to phenanthroline in $[Ru(Me_2bipy)_2(5\text{-Cl-phen})]^{2+}$, however, degradation of the phenanthroline-linker C–N bond was again observed.

The method of Hurley et al. [47] which involved the coupling of L-cysteine to 3-bromo-1,10-phenanthroline containing ruthenium complexes under mildly basic conditions was therefore attempted, but instead using BOC-protected L-cysteine methyl ester (L-cys-MeBOC) to couple to the phenanthroline ligand of $[Ru(Me_2bipy)_2(5\text{-Cl-phen})]^{2+}$. After the reaction, two distinct bands were observed with silica gel column chromatography, one eluting with 1% ($R_f = 0.57$) and the other with 3% ($R_f = 0.33$) saturated potassium nitrate solutions. Excess L-cys-MeBOC moved with the solvent front. ^{1}H NMR spectra subsequently showed that the desired compound was contained within the second fraction.

The BOC-protecting group was cleaved from $[Ru(Me_2bipy)_2(5\text{-(L-cysteine-MeBOC)-phen})](PF_6)_2$ using strongly acidic conditions. Initially, de-protection was achieved using a solution of concentrated hydrochloric acid in methanol (48 h) to isolate the amine as a hydrochloride salt. Alternatively, the use of trifluoroacetic acid (TFA) in dichloromethane also achieved de-protection, in a shorter length of time (1 h) with 100% recovery of $[Ru(Me_2bipy)_2(5\text{-(L-cysteine-Me)-phen})](PF_6)_2$, and was thus the preferred option of the two reactions. Stirring over DOWEX® Monosphere 550A® (OH^- form) in methanol neutralised the TFA/amine salt complex.

The coupling of transplatin {*trans*-diamminedichloroplatinum(II)} to the amine group of $[Ru(Me_2bipy)_2(5\text{-(L-cysteine-Me)-phen})]^{2+}$ proved more difficult than first anticipated. After purification on Sephadex® LH20, the presence of light during the reaction was found to result in a very low yield of $[Ru(Me_2bipy)_2(5\text{-(L-cysteine-Me)-phen})\text{-}trans\text{-}Pt(NH_3)_2Cl]Cl_3$. Repeated experiments with altered exposure to light demonstrated that formation of the heterodinuclear complex was photosensitive. Consequently, the synthesis and purification of the final metal complex were performed in the dark.

The separation of the mononuclear reactant and the heterodinuclear product was achieved using Sephadex® LH20 support media as the stationary phase with methanol. TLC was used to verify the contents of the fractions, with *rac*-$[Ru(Me_2bipy)_2(5\text{-(L-cysteine-Me)-phen})\text{-}trans\text{-}Pt(NH_3)_2Cl]Cl_3$ displaying an R_f value of 0.67 and the unreacted *rac*-$[Ru(Me_2bipy)_2(5\text{-(L-cysteine-Me)-phen})]^{2+}$ stained purple with ninhydrin at R_f 0.38.

The final product was precipitated by the addition of potassium hexafluorophosphate, and extracted into dichloromethane. Conversion to the water soluble chloride salt was then achieved by stirring with Amberlite® anion exchange beads, followed by filtration in order to remove the resin, and finally freeze drying, which yielded the heterodinuclear complex as a red solid.

3.2. Characterisation

The heterodinuclear metal complex and the precursor mononuclear complexes were fully characterised by ^{1}H and ^{13}C NMR, circular dichroism, and electrospray ionisation mass spectrometry, and are described in more detail in Sections 3.2.1, 3.2.2, 3.2.3. UV–Vis spectra were measured to determine the molar extinction coefficients, fluorescence spectra were used to determine quantum yields and elemental analysis to confirm bulk purity. Unfortunately, the use of Eq. (2) for the determination of the quantum yields of fluorescent samples in comparison to a standard, at a common excitation wavelength, was not applicable for the heterodinuclear complex. This was because its excitation wavelength had shifted dramatically from the excitation wavelength of tris(bipyridine) ruthenium(II) (the standard). The method is thus limited in use, and another standard of known quantum yield is required to calculate the relative fluorescence of $[Ru(Me_2bipy)_2(5\text{-(L-cysteine-Me)-phen})\text{-}trans\text{-}Pt(NH_3)_2Cl]Cl_3$. Elemental analysis demonstrated bulk purity of *Rac*-$[Ru(Me_2bipy)_2(5\text{-Cl-phen})]\cdot 2PF_6$ with one water of crystallisation, but which is lost upon separation into its isomers. Bulk purity of the boc-protected ruthenium complex and the final heterodinuclear complex could not be obtained by elemental analysis; however, purity is indicated by both ^{1}H and ^{13}C NMR and high resolution mass spectrometry. Bulk and isomeric purity was also confirmed by CD with the spectrum of each isomer of all metal complexes synthesised showing peaks in almost equal proportion, in opposite directions, at the same wavelength. In addition, the CD spectra also confirm the purity of the samples through the presence of isosbestic points, where the two spectra intercept on the *x*-axis.

3.2.1. NMR spectroscopy

All metal complexes in this study were characterised using one-dimensional ^{1}H and ^{13}C NMR and two-dimensional NOESY, g-DQCOSY experiments. ^{13}C assignments were made using heteronuclear multiple quantum correlation spectroscopy (HMQC) and heteronuclear multiple bond correlation spectroscopy (HMBC) experiments. Full details of the ^{1}H NMR spectrum of the heterodinuclear complex, *rac*-$[Ru(Me_2bipy)_2(5\text{-(L-cysteine-Me)-phen})\text{-}trans\text{-}Pt(NH_3)_2Cl]Cl_3$, including proton assignments are presented here as an example of how all the metal complexes were characterised.

The ^{1}H NMR spectrum of *rac*-$[Ru(Me_2bipy)_2(5\text{-(L-cysteine-Me)-phen})\text{-}trans\text{-}Pt(NH_3)_2Cl]Cl_3$ displays 13 resonances in the aromatic region and six resonances in the

aliphatic region. The two singlets at 2.46 and 2.54 ppm each integrate for six protons, and are assigned as the two methyl groups on the Me_2bipy rings. The NOESY spectrum shows NOE cross-peaks from the A/BMe resonance at 2.54 ppm to the singlet at 8.38 ppm and a multiplet at 7.27 ppm, which are assigned as the A/B3 and A/B5 protons, respectively. In the g-DQCOSY spectrum, the A/B5 resonance also displays cross-peaks with a multiplet 7.63 ppm, which is assigned as the A/B6 proton (Fig. 1). Similar cross-peaks were observed from the A/BMe resonance at 2.46 ppm, to the A/B3 resonance at 8.34 ppm, A/B5 at 7.04 ppm and from this latter resonance to the A/B6 at 7.31 ppm. It was hoped that cross-peaks might be observed in the NOESY spectrum from the A/B6 resonances to either H2 or H9 on the phenanthroline ring, allowing the definitive assignments of the Me_2bipy proton resonances to particular protons, but no NOE cross-peaks were observed.

The substitution of a chloro group at the 5-position in 1,10-phenanthroline results in seven separate proton resonances for this ligand. The H6 proton resonance couples to no other proton (δ 8.39 ppm), and is the only aromatic singlet in the spectrum integrating for one proton. Both H3 and H8 each have two neighbouring protons and can be identified by their doublet of doublet resonances (see Fig. 1). The remaining resonances for the H2, H4, H7 and H9 protons all appear as doublets. Definitive assignments can be made using NOESY spectra. The H6 resonance gives one NOE cross-peak to the resonance at 8.50 ppm (assigned as H7), which in turn gives an NOE to H8 at 7.73 ppm, and from H8 to H9 at 8.10 ppm. The remaining doublet of doublet resonance at 7.82 is assigned as the H3 proton. The H2 and H4 resonances can be assigned based on the coupling constants. In pyridine rings, the proton nearest the nitrogen atom exhibits the smallest coupling constant (typically 5–6 Hz), whilst a proton further away exhibits a larger coupling constant (typically 7–9 Hz) [48]. On this basis, the resonance at 8.81 ppm is assigned as H4 and the resonance at 8.16 ppm as H2. The remaining unassigned proton resonances in the spectrum are the $–NH_2$, –CH, $–OCH_3$, and $–CH_2$ protons of the L-cysteine methyl ester. The resonance at 4.35 ppm is assigned to $–NH_2$, due to its broadness, the singlet at 3.50 ppm to $–OCH_3$, the triplet at 3.16 ppm to $–CH_2$ and the multiplet at 4.07 ppm to –CH proton. Coordination of the platinum to the cystiene-NH_2 group is confirmed

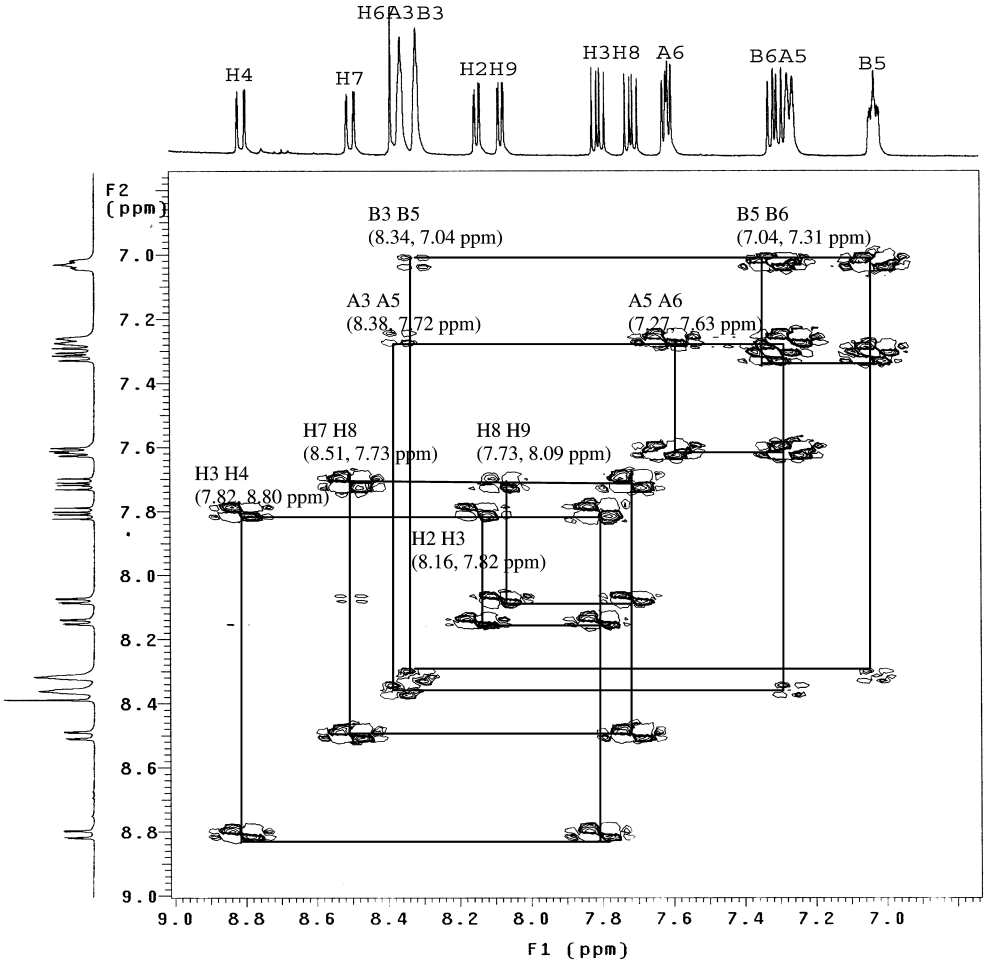


Fig. 1. ^{1}H g-DQCOSY NMR spectrum showing the assignment of the aromatic proton resonances of $[Ru(Me_2bipy)_2(5\text{-(L-cysteine-Me)-phen})\text{-}trans\text{-}Pt(NH_3)_2Cl]^{3+}$.

by the large downfield movement of the proton resonance, which moves from 1.26 to 4.35 ppm, upon reaction with transplatin.

It is of note that there are slight differences in the ^{1}H NMR spectra of the Δ- and Λ-ruthenium complexes compared to that of the racemic solutions for all metal complexes synthesised in this study. For instance, a significant chemical shift change of the H6 resonance (8.29–7.91 ppm) is observed in the spectra of the resolved isomers of $[Ru(Me_2bipy)_2(5\text{-(L-cysteine-MeBOC)-phen})]^{2+}$ in comparison to the spectrum of the racemic complex (Fig. 2). There is also a large movement of the $-NH_2$ resonance (4.35–3.89 ppm). All other resonances undergo less significant chemical shift changes upon resolution of the isomers.

3.2.2. Circular dichroism spectrophotometry

CD spectra were recorded for each of the metal complex isomers by plotting the angle of ellipticity (θ mdeg) versus wavelength (nm). This was converted to the change in molar absorptivity by Eq. (1). All metal complexes synthesised in this study show four major peaks at 210, 226, 264 and 285 nm, and one broad peak at 410 nm (Fig. 3). In comparison to $[Ru(Me_2bipy)_2(5\text{-Cl-phen})]^{2+}$, attachment of the amino acid and then the platinum metal centre do not change either the wavelength, nor shape of the CD peaks, however, the intensities are increased.

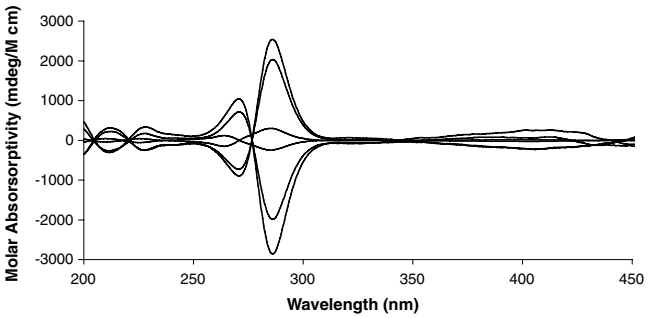


Fig. 3. Circular dichroism spectra of the isomeric complexes from top to bottom (at 285 nm): Λ-$[Ru(Me_2bipy)_2(5\text{-(L-cysteine-Me)-phen})\text{-}trans\text{-}Pt(NH_3)_2Cl]Cl_3$, Λ-$[Ru(Me_2bipy)_2(5\text{-(L-cysteine-MeBOC)-phen})](PF_6)_2$, Λ-$[Ru(Me_2bipy)_2(5\text{-Cl-phen})](PF_6)_2$, Δ-$[Ru(Me_2bipy)_2(5\text{-Cl-phen})](PF_6)_2$, Δ-$[Ru(Me_2bipy)_2(5\text{-(L-cysteine-MeBOC)-phen})](PF_6)_2$ and Δ-$[Ru(Me_2bipy)_2(5\text{-(L-cysteine-Me)-phen})\text{-}trans\text{-}Pt(NH_3)_2Cl]Cl_3$.

The assignments of the absolute configuration of the metal complexes are based on previous studies of analogous compounds [42]. The metal complex exhibiting a positive value of θ at 250 nm corresponds to the Δ-isomer, while the Λ-isomer exhibits a negative peak at the same wavelength. The elution profile of the isomers from the Sephadex® column further supported this finding, with the Δ-isomer eluting prior to the Λ-isomer.

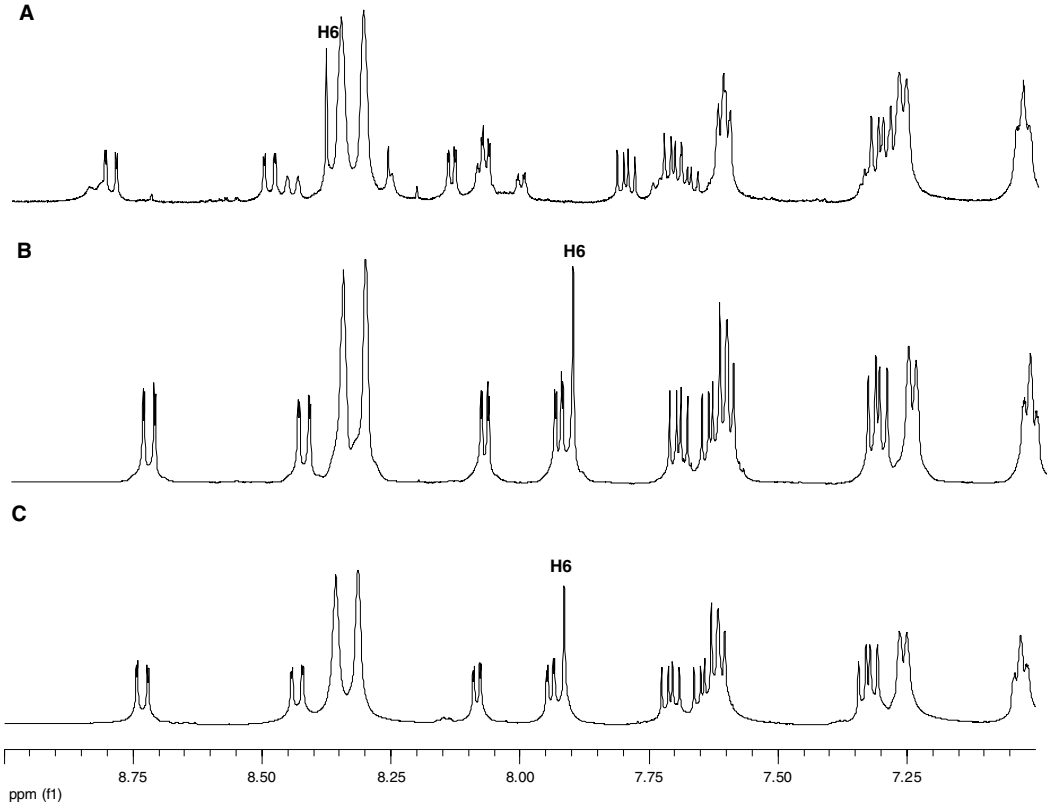


Fig. 2. ^{1}H NMR spectra of (a) *rac*-$[Ru(Me_2bipy)_2(5\text{-(L-cysteine-MeBOC)-phen})](PF_6)_2$ (b) Λ-$[Ru(Me_2bipy)_2(5\text{-(L-cysteine-MeBOC)-phen})](PF_6)_2$ (c) Δ-$[Ru(Me_2bipy)_2(5\text{-(L-cysteine-MeBOC)-phen})](PF_6)_2$ demonstrating the chemical shift change of the phenanthroline H6 proton resonance in a racemic solution and when separated into its Δ- and Λ-isomers.

3.2.3. Mass spectrometry

The synthesis of the precursor mononuclear complexes and the final heteronuclear complexes were also confirmed by electrospray ionisation mass spectrometry. $[Ru(Me_2bipy)_2(5\text{-Cl-phen})]^{2+}$ shows a molecular ion at 341.7 m/z which corresponds to the metal complex with a 2+ charge and the loss of one proton and both hexafluorophosphate counter ions. For $[Ru(Me_2bipy)_2(5\text{-(L-cysteine-MeBOC)-phen})]^{2+}$, five peaks are observed for the parent and daughter ion fragments. For instance, a molecular ion at 1028.2 m/z is consistent with the $[Ru(Me_2bipy)_2(5\text{-(L-cysteine-MeBOC)-phen})]^{2+}$ cation and one PF_6^- counterion. Finally, the heterodinuclear complex was confirmed by the observance of a molecular ion at 342.1 m/z, corresponding to the charged parent ion minus both counterions and one ammine group. This is characteristic of charged metal complexes of this type and matched the expected isotopic pattern for a ruthenium(II)–platinum(II) complex.

4. Summary

The heterodinuclear complex, $[Ru(Me_2bipy)_2(5\text{-(L-cysteine-Me)-phen})\text{-}trans\text{-}Pt(NH_3)_2Cl]Cl_3$, was synthesised using a six step method, as a potential agent to overcome platinum resistance in human cancer treatment. The heterodinuclear complex, and its mononuclear precursors were characterised by ^1H and ^{13}C NMR, UV–Vis, circular dichroism, fluorescence and electrospray ionisation mass spectrometry. The cytotoxicity and DNA binding studies of $[Ru(Me_2bipy)_2(5\text{-(L-cysteine-Me)-phen})\text{-}trans\text{-}Pt(NH_3)_2Cl]Cl_3$ are currently under examination, with the results to be used to develop a family of heterodinuclear complexes with anticancer activity.

Acknowledgements

This work was supported by an Australian Research Council Grant (No. DP0343480) and the University of Western Sydney. We thank Assoc. Prof. S. Ralph (University of Wollongong) for assistance with the mass spectrometry and Prof. W.S. Price and M. van Holst (University of Western Sydney) and Dr. D.M. D'Alessandro (University of Sydney) for helpful discussions.

References

[1] N.J. Wheate, J.G. Collins, Curr. Med. Chem. – Anti-Cancer Agents 5 (2005) 267.
[2] N.J. Wheate, J.G. Collins, Coord. Chem. Rev. 241 (2003) 133.
[3] N. Farrell, Met. Ions Biol. Sys. 42 (2004) 251.
[4] V. Murray, H. Motyka, P.R. England, G. Wickham, H.H. Lee, W.A. Denny, W.D. McFadyen, J. Biol. Chem. 267 (1992) 18805.
[5] C. Cullinane, G. Wickham, W.D. McFadyen, W.A. Denny, B.D. Palmer, D.R. Phillips, Nucl. Acids Res. 21 (1993) 393.
[6] L.C. Perrin, P.D. Prenzler, C. Cullinane, D.R. Phillips, W.A. Denny, W.D. McFadyen, J. Inorg. Biochem. 81 (2000) 111.
[7] L.C. Perrin, C. Cullinane, W.D. McFadyen, D.R. Phillips, Anti-Cancer Drug Des. 14 (1999) 243.
[8] C. Ciatto, M.L. D'Amico, G. Natile, F. Secco, M. Venturini, Biophys. J. 77 (1999) 2717.
[9] M.D. Temple, P. Recabarren, W.D. McFadyen, R.J. Holmes, W.A. Denny, V. Murray, Biochim. Biophys. Acta-Gene Struct. Express. 1574 (2002) 223.
[10] R.J. Holmes, M.J. McKeage, V. Murray, W.A. Denny, W.D. McFadyen, J. Inorg. Biochem. 85 (2001) 209.
[11] J. Whittaker, W.D. McFadyen, B.C. Baguley, V. Murray, Anti-Cancer Drug Des. 16 (2001) 81.
[12] M.D. Temple, W.D. McFadyen, R.J. Holmes, W.A. Denny, V. Murray, Biochemistry 39 (2000) 5593.
[13] B.D. Palmer, H.H. Lee, P. Johnson, B.C. Baguley, G. Wickham, L.P.G. Wakelin, W.D. McFadyen, W.A. Denny, J. Med. Chem. 33 (1990) 3008.
[14] H.H. Lee, B.D. Palmer, B.C. Baguley, M. Chin, W.D. McFadyen, G. Wickham, D. Thorsbourne-Palmer, L.P.G. Wakelin, W.A. Denny, J. Med. Chem. 35 (1992) 2983.
[15] B.E. Bowler, S.J. Lippard, Biochemistry 25 (1986) 3031.
[16] B.E. Bowler, S. Hollis, S.J. Lippard, J. Am. Chem. Soc. 106 (1984) 6102.
[17] B.E. Bowler, K.J. Ahmed, W.I. Sundquist, L.S. Hollis, E.E. Whang, S.J. Lippard, J. Am. Chem. Soc. 111 (1989) 1299.
[18] M.E. Budiman, R.W. Alexander, U. Bierbach, Biochemistry 43 (2004) 8560.
[19] J.M. Perez, I. Lopez-Solera, E.I. Montero, M.F. Brana, C. Alonso, S.P. Robinson, C. Navarro-Ranninger, J. Med. Chem. 42 (1999) 5482.
[20] C.G. Barry, H. Baruah, U. Bierbach, J. Am. Chem. Soc. 125 (2003) 9629.
[21] F. Zunino, G. Savi, A. Pasini, Cancer Chemother. Pharmacol. 18 (1986) 180.
[22] A. Petitjean, J.K. Barton, J. Am. Chem. Soc. (2004) 14728.
[23] K. van der Schilden, F. Garcia, H. Kooijman, A.L. Spek, J.G. Haasnoot, J. Reedijk, Angew. Chem., Int. Ed. 43 (2004) 5668.
[24] Z. Fang, S. Swavey, A. Holder, B. Winkel, K.J. Brewer, Inorg. Chem. Commun. 5 (2002) 1078.
[25] M. Milkevitch, B.W. Shirley, K.J. Brewer, Inorg. Chim. Acta 264 (1997) 249.
[26] R.L. Williams, H.N. Toft, B. Winkel, K.J. Brewer, Inorg. Chem. 42 (2003) 4394.
[27] M. Milkevitch, H. Storrie, E. Brauns, K.J. Brewer, B.W. Shirley, Inorg. Chem. 36 (1997) 4534.
[28] G. Wickham, A.S. Prakash, L.P.G. Wakelin, W.D. McFadyen, Biochim. Biophys. Acta 1073 (1991) 528.
[29] V. Murray, C. Matias, W.D. McFadyen, G. Wickham, Biochim. Biophys. Acta-Gene Struct. Express. 1305 (1996) 79.
[30] T.A. Gourdie, K.K. Valu, G.L. Gravatt, T.J. Boritzki, B.C. Baguley, L.P. Wakelin, W.R. Wilson, P.D. Woodgate, W.A. Denny, J. Med. Chem. 33 (1990) 1177.
[31] K.K. Valu, T.A. Gourdie, T.J. Boritzki, G.L. Gravatt, B.C. Baguley, W.R. Wilson, L.P.G. Wakelin, P.D. Woodgate, W.A. Denny, J. Med. Chem. 33 (1990) 3014.
[32] A.S. Prakash, W.A. Denny, T.A. Gourdie, K.K. Valu, P.D. Woodgate, L.P.G. Wakelin, Biochemistry 29 (1990) 9799.
[33] J.A. Todd, L.M. Rendina, Inorg. Chem. 41 (2002) 3331.
[34] S.L. Woodhouse, E.J. Ziolkowski, L.M. Rendina, Dalton Trans. (2005) 2827.
[35] E.L. Crossley, D. Caiazza, L.M. Rendina, Dalton Trans. (2005) 2825.
[36] J.A. Todd, P. Turner, E.J. Ziolkowski, L.M. Rendina, Inorg. Chem. 44 (2005) 6401.
[37] P.A. Anderson, R.F. Anderson, M. Furue, P.C. Junk, F.R. Keene, B.T. Patterson, B.D. Yeomans, Inorg. Chem. 39 (2000) 2721.
[38] T. Togano, N. Nagao, M. Tsuchida, H. Kumakura, K. Hisamatsu, F.S. Howell, M. Mukaida, Inorg. Chim. Acta 195 (1992) 221.
[39] J.V. Casper, T.J. Meyer, J. Am. Chem. Soc. 105 (1983) 5583.
[40] J.N. Demas, G.A. Crosby, J. Phys. Chem. 78 (1971) 991.
[41] W.C. Still, M. Kahn, A. Mitra, J. Org. Chem. 43 (1978) 2923.

[42] T.J. Rutherford, P.A. Pellegrini, J. Aldrich-Wright, P.C. Junk, F.R. Keene, Eur. J. Inorg. Chem. (1998) 1677.
[43] A.P. Krapcho, C.S. Kuell, Synth. Commun. 20 (1990) 2559.
[44] T.D. McGregor, Z. Balcarova, Y. Qu, M.-C. Tran, R. Zaludova, V. Brabec, N. Farrell, J. Inorg. Biochem. 77 (1999) 43.
[45] Y. Qu, N. Farrell, J. Inorg. Biochem. 40 (1990) 255.
[46] N.P. Farrell, S.G. de Almeida, K.A. Skov, J. Am. Chem. Soc. 110 (1988) 5018.
[47] D.J. Hurley, J.R. Roppe, Y. Tor, Chem. Commun. (1999) 993.
[48] R.M. Silverstein, F.X. Webster, Spectrometric Identification of Organic Compounds, 6th ed., John Wiley, New York, 1998, p. 212.

Available online at www.sciencedirect.com
ScienceDirect
Polyhedron 26 (2007) 329–337
POLYHEDRON
www.elsevier.com/locate/poly

Ruthenium complexes that incorporate a *chiro*-inositol derived diphosphinite ligand as catalysts for asymmetric hydrogenation reactions

Andrew Falshaw [a], Graeme J. Gainsford [a], Cornelis Lensink [a], Angela T. Slade [b], L. James Wright [b,*]

[a] *Industrial Research Limited, P.O. Box 31-310, Lower Hutt, New Zealand*
[b] *Department of Chemistry, The University of Auckland, Private Bag 92019, 23 Symonds Street, Auckland 1020, New Zealand*

Received 5 May 2006; accepted 21 June 2006
Available online 30 June 2006

Abstract

The diol, 1D-1,2,5,6-tetra-*O*-methyl-*chiro*-inositol (**D-9**), can be conveniently prepared from 1D-*chiro*-inositol using a series of standard protection/deprotection steps. Treatment of **D-9** with Ph_2PCl gives the chiral diphosphinite, 1D-3,4-bis(*O*-diphenylphosphino)-1,2,5,6-tetra-*O*-methyl-*chiro*-inositol (**D-10**). The structure of **D-10** has been determined by X-ray crystallography. Using 1L-*chiro*-inositol as starting material and following the same synthetic sequence used to produce **D-10**, the other enantiomer of this diphosphinite, 1L-3,4-bis(*O*-diphenylphosphino)-1,2,5,6-tetra-*O*-methyl-*chiro*-inositol (**L-10**) can also be obtained. Ruthenium complexes of these diphosphinite ligands can be conveniently prepared through ligand substitution reactions with appropriate substrate complexes. Thus, treatment of $[RuCl_2(COD)]_n$ with **D-10** in the presence of triethylamine produces the bis(diphosphinite) complex, $RuHCl\{\kappa^2(P,P)$-1D-3,4-bis(*O*-diphenylphosphino)-1,2,5,6-tetra-*O*-methyl-*chiro*-inositol$\}_2$ (**11**). In addition, reaction between $RuCl_2(PPh_3)_3$, **D-10** and (1*R*,2*R*)-(+)-1,2-diphenylethylenediamine gives the mono(diphosphinite) complex, $RuCl_2\{\kappa^2(P,P)$-1D-3,4-bis(*O*-diphenylphosphino)-1,2,5,6-tetra-*O*-methyl-*chiro*-inositol$\}\{\kappa^2(N,N)$-(1*R*,2*R*)-(+)-1,2-diphenylethylenediamine$\}$ (**12**). The closely related complex $RuCl_2\{\kappa^2(P,P)$-1D-3,4-bis(*O*-diphenylphosphino)-1,2,5,6-tetra-*O*-methyl-*chiro*-inositol$\}\{\kappa^2(N,N)$-(1*S*,2*S*)-(−)-1,2-diphenylethylenediamine$\}$ (**13**) can be obtained in a similar manner using (1*S*,2*S*)-(−)-1,2-diphenylethylenediamine in place of the corresponding (+)-isomer. These new chiral, diphosphinite complexes catalyse the hydrogenation of the ketones acetophenone and 3-quinuclidinone to give the corresponding alcohols with low to moderate enantiomeric excesses. The complexes are not catalytically active for the hydrogenation of the olefin dimethylitaconate or the α-ketoester methyl benzoylformate.
© 2006 Elsevier Ltd. All rights reserved.

Keywords: Ruthenium; Catalytic asymmetric hydrogenation of ketones; *chiro*-Inositol; Chiral diphosphinite ligand; X-ray crystal structure

1. Introduction

The study of transition metal complex catalysed asymmetric transformations of prochiral substrates is an active area of research that is of both fundamental and practical significance. Although this was recently emphasised by the award of the 2004 Nobel Prize for Chemistry to Knowles, Noyori and Sharpless [1] for their seminal work in this area, there are still no universal ligands and catalysts for asymmetric transformations [2]. Even within a specific reaction type such as metal-catalysed asymmetric hydrogenation of prochiral alkenes, catalysts incorporating a given chiral ligand will not form products of high enantiomeric purity with all prochiral substrates. Therefore, the synthesis of new classes of chiral ligands, especially those in which the electronic and steric properties can be easily and rationally modified, is an important goal.

* Corresponding author. Tel.: +64 9 373 7999x88257; fax: +64 9 373 7422.
E-mail address: lj.wright@auckland.ac.nz (L.J. Wright).

0277-5387/$ - see front matter © 2006 Elsevier Ltd. All rights reserved.
doi:10.1016/j.poly.2006.06.016

A wide range of chiral, phosphorus-donor ligands have been synthesised and these are the most common ligands that are used in the formation of metal complexes that catalyse asymmetric transformations [2,3]. A number of these ligands have been derived from carbohydrate molecules [4–9], although factors that often reduce the efficacy of carbohydrate-based ligands are the complexity of the syntheses, the reactivity of the masked acetal groups present in reducing sugar derivatives, and the difficulty in obtaining both enantiomers of the carbohydrate. *Chiro*-inositol is a carbohydrate with C_2 symmetry that does not suffer from these potential drawbacks. The cyclohexane backbone is chemically robust, both the D- and L-enantiomers are readily available from the natural products 1D-pinitol (**1**) and 1L-quebrachitol (**2**), respectively (see Chart 1), and the six hydroxyl groups provide extensive scope for selective functionalisation. Despite these attractive features, chiral inositols have been rarely studied in the context of chiral ligand synthesis for transition metal catalysed asymmetric transformations [10]. In an earlier communication we briefly described the syntheses and properties of some new *chiro*-inositol based phosphinite ligands [11]. In this paper, which extends and expands this work, we present full details of: (i) the synthesis and characterisation of the chiral ligands 1D-3,4-bis(*O*-diphenylphosphino)-1,2,5,6-tetra-*O*-methyl-*chiro*-inositol (**D-10**) and 1L-3,4-bis(*O*-diphenylphosphino)-1,2,5,6-tetra-*O*-methyl-*chiro*-inositol (**L-10**) which are the two enantiomers of a diphosphinite ligand based on D- and L-*chiro*-inositol, respectively; (ii) the X-ray crystal structure of **D-10**; (iii) the synthesis of the ruthenium complexes $RuHCl\{\kappa^2(P,P)$-1D-3,4-bis(*O*-diphenylphosphino)-1,2,5,6-tetra-*O*-methyl-*chiro*- inositol$\}_2$ (**11**), $RuCl_2\{\kappa^2(P,P)$-1D-3,4-bis(*O*-diphenylphosphino)-1,2,5,6-tetra-*O*-methyl-*chiro*-inositol$\}\{\kappa^2(N,N)$-(1*R*,2*R*)-(+)-1,2-diphenylethylenediamine$\}$ (**12**), and $RuCl_2\{\kappa^2(P,P)$-1D-3,4-bis(*O*-diphenylphosphino)-1,2,5,6-tetra-*O*-methyl-*chiro*-inositol$\}\{\kappa^2(N,N)$-(1*S*,2*S*)-(−)-1,2-diphenylethylenediamine$\}$ (**13**) that all incorporate the chiral ligand **D-10**; and (iv) the results of catalytic asymmetric hydrogenation studies of the prochiral ketones acetophenone, 3-quinuclidinone and methyl benzoyl formate, as well as the prochiral alkene dimethyl itaconate, in the presence of **11**, **12** or **13**.

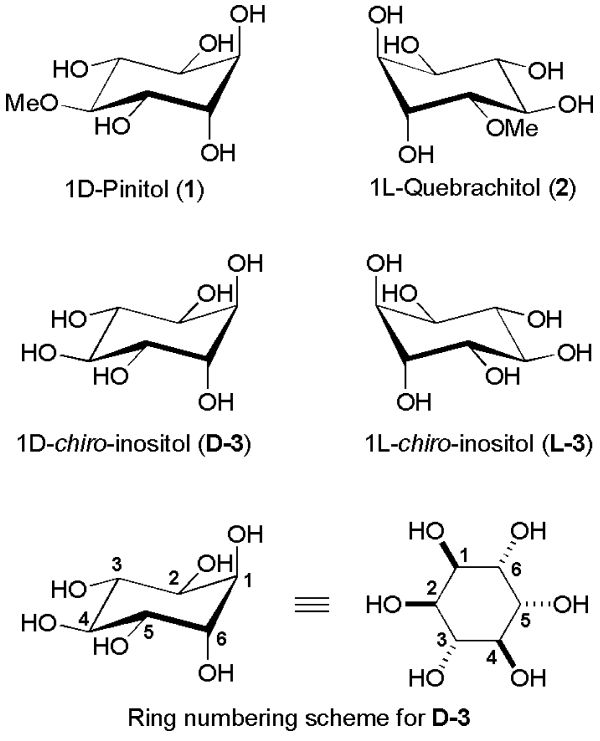


Chart 1.

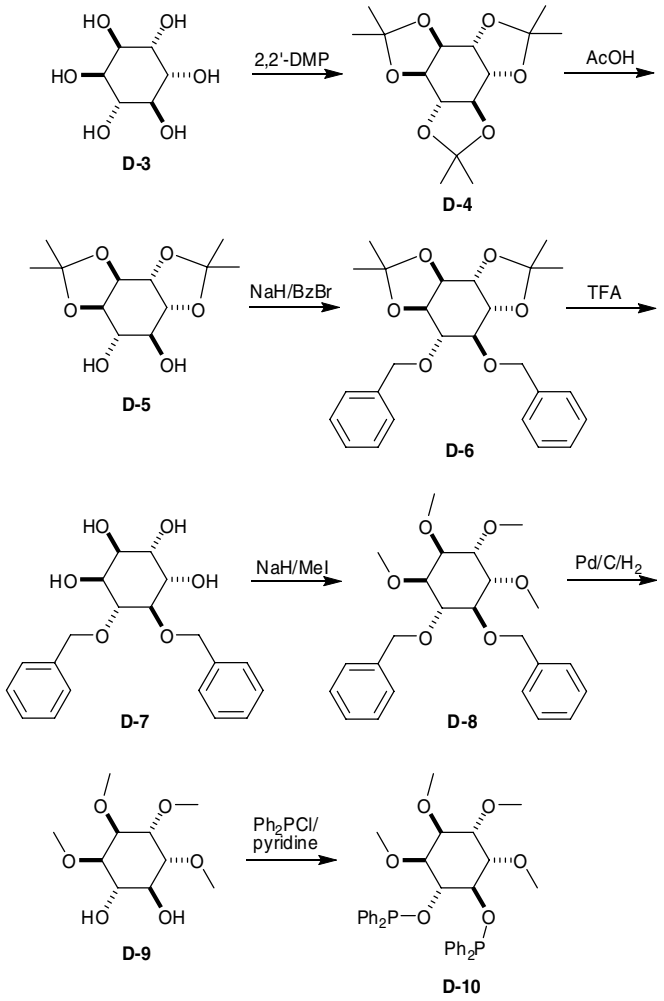
2. Results and discussion

2.1. Syntheses of the chiro-inositol derived diphosphinite ligands, 1D-3,4-bis(O-diphenylphosphino)-1,2,5,6-tetra-O-methyl-chiro-inositol (D-10) and 1L-3,4-bis(O-diphenylphosphino)-1,2,5,6-tetra-O-methyl-chiro-inositol (L-10), and the crystal structure of D-10

The synthetic pathway that was employed to obtain the diphosphinite ligands **D-10** and **L-10** that have C_2 symmetry is depicted in Scheme 1. Starting from 1D-*chiro*-inositol (**D-3**), which can be obtained from naturally occurring 1D-pinitol, and by utilising the different reactivities of the six hydroxyl groups, selective attachment of diphenylphosphine groups to the oxygen atoms at ring positions 3 and 4, and methyl groups to the other four ring oxygen atoms can be conveniently achieved. The first step in the reaction sequence involves treatment of **D-3** with 2,2′-dimethoxypropane to yield the tris-isopropylidene derivative, **D-4** [12]. The 3,4-isopropylidene group is then selectively removed by treatment with acetic acid to produce 1,2: 5,6-di-*O*-isopropylidene-(D)-*chiro*-inositol (**D-5**) [12]. Protection of the two hydroxyl groups in **D-5** by benzylation and subsequent removal of the remaining isopropylidene groups yields **D-7**. Methylation of **D-7** with NaH/MeI followed by removal of the protecting benzyl groups yields the diol, **D-9**. Treatment of this diol with Ph_2PCl/pyridine then smoothly gives the chiral diphosphinite ligand, 1D-3,4-bis(*O*-diphenylphosphino)-1,2,5,6-tetra-*O*-methyl-*chiro*-inositol (**D-10**).

If 1L-*chiro*-inositol (which can be obtained from naturally occurring 1L-quebrachitol) is used as starting material and the same synthetic sequence described above is followed, 1L-3,4-bis(*O*-diphenylphosphino)-1,2,5,6-tetra-*O*-methyl-*chiro*-inositol (**L-10**), the enantiomer of **D-10**, is obtained. The ready availability of both enantiomers of the diphosphinite ligand, **10**, in principle means that for catalytic asymmetric transformations of prochiral substrates either *R*- or *S*-products could be selectively obtained depending on which enantiomer of ligand **10** is incorporated in the chiral catalyst.

Spectroscopic data for **D-10** and all other new compounds reported in this paper are collected in Section 4. In the ^1H NMR spectrum of **D-10** singlet signals at 2.67



Scheme 1. Synthesis of 1D-3,4-bis(*O*-diphenylphosphino)-1,2,5,6-tetra-*O*-methyl-*chiro*-inositol (**D-10**).

and 3.46 ppm that each integrate for six protons are assigned to the four methyl groups. Signals each integrating for two protons are observed for the saturated ring protons at 3.38 (multiplet, H-2 and H-5), 3.67 (doublet, $J(HH) = 1.7$ Hz, H-1 and H-6) and 4.35 (multiplet, H-3 and H-4) ppm. In the ^{13}C NMR spectrum two methyl carbon resonances are observed at 56.6 and 59.8 ppm. All these data are consistent with the C_2 symmetry of the molecule. In the ^{31}P NMR spectrum of **D-10**, a singlet resonance at 113.4 ppm is observed for the two equivalent phosphorus atoms. Solutions of **D-10** in chloroform slowly react with the oxygen in air (over a period of minutes) to give several products with the major one having a characteristic resonance in the ^{31}P NMR spectrum at 21.4 ppm. This oxidised product has not been fully characterised, but the chemical shift of the new phosphorus resonance is consistent with the phosphorus atoms having undergone oxidation to P(V).

A colourless crystal of **D-10** suitable for X-ray crystallographic structure determination was obtained from diethylether solution under nitrogen. Crystallographic data for **D-10** are listed in Section 4. The molecular structure is depicted in Fig. 1 and selected bond distances and angles are presented in Table 1. The inositol ring adopts a chair conformation with Q 0.565(3) Å, θ 171.4(3)° and φ 133.9(3)° [13]. All bond lengths and bond angles fall within normal ranges and do not warrant further discussion. The molecules are packed utilising weak C–H···π-bond interactions to form dimer units (see Table 2). All other close contacts are intramolecular H···O interactions, e.g. C5–H5···O1 where H···O is 2.49 Å and the angle C–H–O is 101°.

*2.2. Synthesis of RuHCl{κ²(P,P)-1D-3,4-bis(O-diphenylphosphino)-1,2,5,6-tetra-O-methyl-chiro-inositol}₂ (**11**), $RuCl_2${κ²(P,P)-1D-3,4-bis(O-diphenylphosphino)-1,2,5,6-tetra-O-methyl-chiro-inositol}{κ²(N,N)-(1R,2R)-(+)-1,2-diphenylethylenediamine} (**12**) and $RuCl_2${κ²(P,P)-1D-3,4-bis(O-diphenylphosphino)-1,2,5,6-tetra-O-methyl-chiro-inositol}{κ²(N,N)-(1S,2S)-(−)-1,2-diphenylethylenediamine} (**13**)*

Ruthenium complexes containing chiral diphosphinite ligands (i.e. $R_2PO–X–OPR_2$, where X is a chiral bridging group) are very rare, although complexes of these ligands with other metals, especially rhodium, are well known [14]. Nevertheless, ruthenium complexes of the chiral diphosphinite ligand, **D-10**, can be conveniently prepared by direct reaction between appropriate ruthenium substrate complexes and **D-10**. Thus, treatment of $[RuCl_2(COD)]_2$ with **D-10** and triethylamine in toluene at reflux for 12.5 h produces the yellow/orange complex RuHCl{κ²(*P*,*P*)-1D-3,4-bis(*O*-diphenylphosphino)-1,2,5,6-tetra-*O*-methyl-*chiro*-inositol}₂ (**11**) in 34% yield after column chromatography (see Scheme 2). The triethylamine was added to help dissolve the $[RuCl_2(COD)]_n$ [15], but under the vigorous conditions employed it may also have been responsible for the formation of the hydride ligand in the product, perhaps through β-hydride elimination from coordinated triethylamine.

In the ^1H NMR spectrum, the hydride ligand in **11** is observed at a characteristically high field position (−16.26 ppm) and has the appearance of a second order, seven line, multiplet signal. This signal collapses to a singlet in the ^{31}P decoupled ^1H NMR spectrum. The methyl signals of the two diphosphinite ligands are observed as four singlet signals at 2.49, 3.31, 3.37 and 3.67 ppm that each integrate for six protons. In the ^{13}C NMR spectrum the methyl carbon resonances are also observed as four singlet signals at 58.6, 58.6, 59.0 and 59.7 ppm. In the ^{31}P NMR spectrum, two, three-line multiplet signals with very similar shapes are observed at 120.4 and 148.6 ppm. The structure of **11** in solution cannot be unambiguously assigned on the basis of this NMR information. However, the results are consistent with octahedral coordination geometry about ruthenium where the hydride and chloride ligands are arranged mutually *trans* and the two bidentate diphosphinite ligands are positioned in the equatorial plane (see representation of **11** in Scheme 2). The two phosphorus

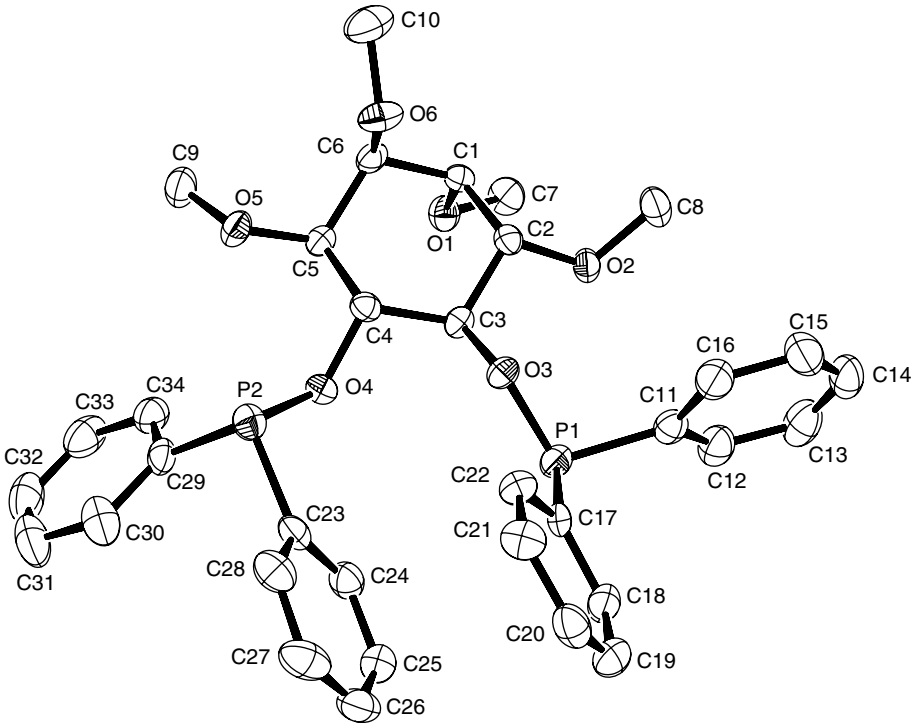


Fig. 1. The molecular structure of 1D-3,4-bis(*O*-diphenylphosphino)-1,2,5,6-tetra-*O*-methyl-*chiro*-inositol (**D-10**) with the non-hydrogen atom labelling scheme. The thermal ellipsoids are scaled to 50% probability. Selected bond lengths and bond angles are given in Table 1.

Table 1
Selected bond lengths (Å) and angles (°) for **D-10**

P1–O3	1.6514(18)
P2–O4	1.6607(18)
P2–C23	1.836(3)
P2–C29	1.859(3)
O3–P1–C17	97.38(11)
O3–P1–C11	104.05(11)
C23–P2–C29	99.28(12)
C3–O3–P1	119.70(15)

Table 2
Hydrogen-bonding geometry (Å) and (°) for compound **D-10**

D–H···A[a]	D–H (Å)	H···A (Å)	D···A (Å)	∠D–H···A (°)
C7–H7A···Cg1[i]	0.98	2.76	3.731(3)	174
C8–H8C···Cg2[ii]	0.98	2.84	3.749(3)	154

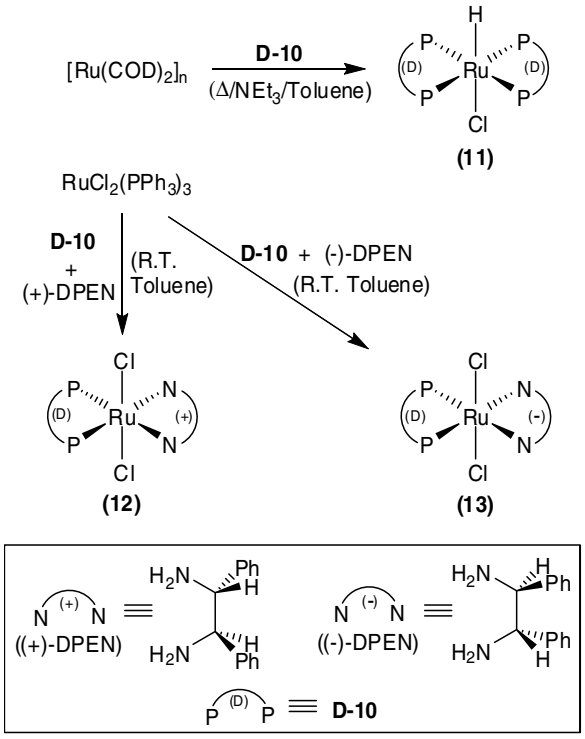
Symmetry codes: (i) $x - 1/2, 3/2 - y, 1 - z$. (ii) $x - 1/2, 1/2 - y, 1 - z$.
[a] C–H···π-bond interactions where Cg1 and Cg2 are the centres of phenyl rings C29–C34 and C11–C16, respectively.

atoms within any one of the two bidentate diphosphinite ligands are not related by a C_2 axis as they are in the free diphosphinite ligand, **D10**. Therefore, the two phosphorus atoms within each of the two bidentate diphosphinite ligands are inequivalent. There is a C_2 axis that passes through H, Ru and Cl in the idealised structure drawn in Scheme 2. This means that the four equatorial phosphorus atoms form an AA′BB′ spin system and the two multiplet signals observed in ^{31}P NMR spectrum of **11** are entirely consistent with this.

In other work we have prepared the closely related complex, RuHCl{κ^2(*P*,*P*)-1,2-bis(*O*-diphenylphosphino)cyclohexane}$_2$ in which the phosphorus donors of each of the two bidentate, diphosphinite ligands are attached to a cyclohexane ring instead of a six-membered inositol ring. The hydride resonance of RuHCl{κ^2(*P*,*P*)-1,2-bis(*O*-diphenylphosphino)cyclohexane}$_2$ in the ^{1}H NMR spectrum and the phosphorus resonances in of this complex in the ^{31}P NMR spectra are strikingly similar in multiplicity and chemical shifts to the corresponding signals observed for **11**. The crystal structure of RuHCl{κ^2(*P*,*P*)-1,2-bis-(*O*-diphenylphosphino)cyclohexane}$_2$ has been determined and in the solid state the ligands form an approximately octahedral arrangement about ruthenium with the hydride and chloride ligands arranged mutually *trans*. The two diphosphinite ligands are positioned approximately in the equatorial plane [16]. The adoption of a similar structure for **11** in solution would be consistent with the observed NMR data, and it is therefore tentatively proposed that the structure of **11** is similar to this complex, as is depicted in Scheme 2.

In the solid state, **11** can be exposed to air for extended periods (months), although in solution **11** is degraded by atmospheric oxygen over a period of hours. Nevertheless, solutions of **11** can be exposed to the atmosphere for short periods of time (minutes) during procedures such as column chromatography and recrystallisation without significant degradation occurring.

Treatment of $RuCl_2(PPh_3)_3$ with **D-10** and (1*R*,2*R*)-(+)-1,2-diphenylethylenediamine ((1*R*,2*R*)-(+)-DPEN) in



Scheme 2. Syntheses of the ruthenium complexes RuHCl{κ²(*P*,*P*)-1D-3,4-bis(*O*-diphenylphosphino)-1,2,5,6-tetra-*O*-methyl-*chiro*-inositol}$_2$ (**11**), $RuCl_2${κ²(*P*,*P*)-1D-3,4-bis(*O*-diphenylphosphino)-1,2,5,6-tetra-*O*-methyl-*chiro*-inositol}{κ²(*N*,*N*)-(+)-1,2-diphenylethylenediamine} (**12**) and $RuCl_2$ {κ²(*P*,*P*)-1D-3,4-bis(*O*-diphenylphosphino)-1,2,5,6-tetra-*O*-methyl-*chiro*-inositol}{κ²(*N*,*N*)-(−)-1,2-diphenylethylenediamine} (**13**).

toluene at room temperature for 30 min produces the yellow complex, $RuCl_2${κ²(*P*,*P*)-1D-3,4-bis(*O*-diphenyl phosphino)-1,2,5,6-tetra-*O*-methyl-*chiro*-inositol}{κ²(*N*,*N*)-(1*R*,2*R*)-(+)-1,2-diphenylethylenediamine} (**12**) in 71% yield after chromatography. Under the milder reaction conditions used for the synthesis of this compound and with no triethylamine present, neither of the chloride ligands in $RuCl_2(PPh_3)_3$ are replaced by hydride during the reaction to produce **12** (see Scheme 2). In the ^{1}H NMR spectrum of **12** the methyl signals of the single diphosphinite ligand are observed as two singlets at 3.13 and 3.39 ppm. In the ^{13}C NMR spectrum the methyl carbon resonances are observed as two singlets at 59.0 and 59.7 ppm. A singlet resonance at 150.4 ppm is observed for the two equivalent phosphorus atoms in the ^{31}P NMR spectrum. The equivalence of two phosphorus atoms in the ^{31}P NMR spectrum strongly supports the structure depicted in Scheme 2 in which the two chloride ligands are mutually *trans*. Complex **12** is much more resistant to reaction with atmospheric oxygen than **11**, both in the solid state and in solution. Solutions of **12** are only degraded by oxygen over a period of days.

Reaction between $RuCl_2(PPh_3)_3$, **D-10** and (1*S*,2*S*)-(−)-1,2-diphenylethylenediamine ((1*S*,2*S*)-(−)-DPEN) under the same conditions used for the synthesis of **12** produces the closely related complex, $RuCl_2${κ²(*P*,*P*)-1D-3,4-bis(*O*-diphenylphosphino)-1,2,5,6-tetra-*O*-methyl-*chiro*-inositol}{κ²(*N*,*N*)-(1*S*,2*S*)-(−)-1,2-diphenylethylenediamine} (**13**). The NMR spectral properties of **13** are very similar to those observed for **12**. Also, the stability of **13** to atmospheric oxygen, both in solution and in the solid state, is very similar to that of complex **12**.

2.3. Investigation of the catalytic activity of the ruthenium complexes 11, 12 and 13 for asymmetric hydrogenation reactions of selected prochiral substrates

Preliminary investigations of the catalytic activity of the complexes **11**, **12** and **13** towards asymmetric hydrogenation reactions were carried out on the ketones acetophenone (to give *sec*-phenylethyl alcohol) and 3-quinuclidinone (to give 3-quinuclidinol), the α-ketoester methyl benzoylformate (to give methyl mandelate) and the alkene dimethyl itaconate (to give dimethyl methyl succinate) (see Chart 2 for structures of the substrates). 3-Quinuclidinone is an important pharmaceutical intermediate and the other three substrates are frequently used in profiling studies of potential metal hydrogenation catalysts [17].

The hydrogenation reactions were carried out in toluene/isopropanol solution (1:1) for acetophenone and 3-quinuclidinone and in toluene solution for methyl benzoylformate and dimethyl itaconate with a substrate to catalyst ratio of 200:1, hydrogen pressure of 1000 psi, temperature of 60 °C and a time period of 3 h. In addition, KO^{t}Bu (2 mole equivalent versus the ruthenium complex) was added to each reaction since it has been shown that the presence of this base can significantly improve the yield of product formed in hydrogenation reactions, especially with catalysts that incorporate a diamine ligand [18]. Indeed this was found to be the case for complexes **12** and **13** where no conversion of acetophenone was observed in reactions without added KO^{t}Bu.

The results of the hydrogenation reactions are collected in Table 3. The prochiral alkene dimethyl itaconate was not hydrogenated in the presence of any of the three complexes, **11**, **12** or **13** under the stated conditions. This suggests that in general the catalytic activity of these

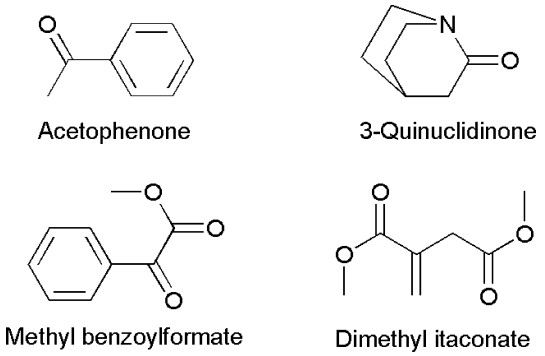


Chart 2.

Table 3
Results of the hydrogenation studies

Complex	Substrate	Conversion (%)	ee (%)
11	acetophenone	20	2
	3-quinuclidinone	97	2
	methyl benzoylformate	7	20
	dimethyl itaconate	0	
12	acetophenone	100	25
	3-quinuclidinone	100	20
	methyl benzoylformate	0	
	dimethyl itaconate	0	
13	acetophenone	100	24
	3-quinuclidinone	100	50
	methyl benzoylformate	0	
	dimethyl itaconate	0	

Conditions: Substrate:catalyst ratio, 200:1; hydrogen pressure 1000 psi; temperature, 60 °C; time, 3 h; solvent, toluene/isopropanol (1:1) (3 mL) for acetophenone and 3-quinuclidinone and toluene (3 mL) only for methyl benzoylformate and dimethyl itaconate; KO^{t}Bu, 2 mole equivalent vs. the ruthenium complex.

three complexes for alkene hydrogenation may be low or non-existent. Clearly the study of other alkene substrates is needed to confirm this, and work in this area is planned for the future. The α-ketoester, methyl benzoylformate, was also not hydrogenated in the presence of **12** or **13** and only very small conversions were observed in the presence of **11**. In contrast to these results, hydrogenation reactions of the ketones acetophenone and 3-quinuclidinone to the corresponding alcohols were catalysed by all three complexes, **11**, **12** or **13** under the reported reaction conditions. Complex **11** was not very effective as a catalyst for acetophenone hydrogenation (20% conversion, no enantioselectivity), but complete hydrogenation of this ketone with low enantioselectivity (ca. 25%) was observed in the presence of **12** or **13**. For 3-quinuclidinone, complete conversion (97–100%) was observed in the presence of all three catalysts, **11**, **12** or **13**. However, in each case the products were formed with very different enantioselectivities. The hydrogenation of 3-quinuclidinone in the presence of **11** proceeded with no enantioselectivity. In the presence of **12**, the product was formed with 20% ee, and in the presence of **13**, product with 50% ee was obtained.

The higher enantioselectivity observed for the catalytic hydrogenation of 3-quinuclidinone in the presence of **13** as opposed to **12** indicates that in **13**, the chiral diphosphinite ligand derived from D-pinitol and the chiral (1*S*,2*S*)-(−)-DPEN ligand work in concert as a "matched pair" to effect asymmetric hydrogenation. In **12**, the same chiral diphosphinite ligand does not form such an effective combination with the chiral (1*R*,2*R*)-(+)-DPEN ligand, and the product is formed with significantly lower enantioselectivity. The large difference in enantioselectivities of product formation for these reactions catalysed by **12** and **13** suggests that both chiral ligands are still coordinated to ruthenium in the active catalytic species.

3. Conclusions

It has been demonstrated that the carbohydrate *chiro*-inositol is a very useful building-block from which chiral, diphosphinite ligands can be conveniently prepared. *chiro*-Inositol has a number of features that makes its use in the construction of chiral ligands very attractive. For example, the two enantiomers of *chiro*-inositol are both readily available in high purity from natural resources, the cyclohexane ring is chemically robust and the six hydroxyl groups present important opportunities for extensive, selective functionalisation. The chiral diphosphinite ligands **D-10** and **L-10** reported in this paper can be used to synthesise the chiral complexes **11**, **12** and **13** through simple ligand substitution reactions of appropriate ruthenium substrate complexes. Asymmetric hydrogenation of the prochiral ketones acetophenone and 3-quinuclidinone is catalysed by **11**, **12** and **13**. Although only low (25%) to modest (50%) ee values were observed for some of the products, these results are significant in that they demonstrate chiral diphosphinite ligands based on *chiro*-inositol can successfully be used to produce asymmetric hydrogenation catalysts.

It is well established that key factors that influence the enantioselectivity of transition metal catalysed hydrogenation reactions include the stereochemistry, steric bulk, and electronic properties of the chiral ligands [6,19]. Importantly, it is possible in principle to synthesise analogues of the diphosphinite ligands **D-10** and **L-10** in which all these properties are changed in a rational way through the selective use of alternate substituents in place of the O-bound methyl groups and the phenyl groups on the two phosphorus atoms. Compound **7** (see Scheme 1) could serve as a convenient starting point from which these alternate substituents could be introduced to facilitate the production of a wide range of new chiral diphosphinite ligands with C_2 symmetry that are related to **D-10** and **L-10**. Work in this area is currently underway.

4. Experimental

4.1. General synthetic procedures and instruments

Manipulations of air sensitive materials were conducted in an argon atmosphere by using either Schlenk techniques or an Innovative Technology inert atmosphere glove box. Tetrahydrofuran, ether and toluene were distilled from sodium benzophenone ketyl under nitrogen and stored over activated 4 Å molecular sieves. Dichloromethane was distilled from calcium hydride. Triethylamine was distilled from calcium hydride and stored over potassium hydroxide. Flash column chromatography [20] was carried out on 230-400 silica (Scharlau). ^{1}H, ^{13}C, and ^{31}P NMR spectra were obtained on a Bruker Avance 300 at 25 °C operating at 300.13 (^{1}H), 75.48 (^{13}C), and 121.5 (^{31}P) MHz, respectively. Resonances are quoted

in ppm and the ^{1}H NMR is referenced to the proteo-impurity in the solvent (7.25 ppm for $CDCl_3$) or TMS (0.00 ppm). ^{13}C NMR spectra were referenced to $CDCl_3$ (77.00 ppm) and ^{31}P NMR spectra to 85% orthophosphoric acid (0.00 ppm) as an external standard. Elemental analyses were obtained from the Microanalytical Laboratory, University of Otago. FAB+ mass spectra were obtained from a VG-70SE machine. (1*R*,2*R*)-(+)-DPEN and (1*S*,2*S*)-(−)-DPEN were obtained commercially, 1L-quebrachitol was obtained from the Rubber Research Instiutute of Malaysia, Kuala Lumpur, Malaysia, 1D-pinitol was obtained from New Zealand Pharmaceuticals Ltd., Palmerston North, New Zealand. 1D-*chiro*-Inositol (**D-3**) and 1L-*chiro*-inositol (**L-3**) were prepared from 1D-pinitol and 1L-quebrachitol, respectively [21]. 1D-1,2: 3,4: 5,6-tri-*O*-isopropylidene-*chiro*-inositol (**D-4**), 1L-1,2: 3,4: 5,6-tri-*O*-isopropylidene-*chiro*-inositol (**L-4**) [12], 1D-1,2: 5,6-di-*O*-isopropylidene-*chiro*-inositol (**D-5**), and 1L-1,2: 5,6-di-*O*-isopropylidene-*chiro*-inositol (**L-5**) [12] were all prepared according to the literature methods. 1L-3,4-Di-*O*-benzyl-1,2: 5,6-di-*O*-isopropylidene-*chiro*-inositol (**L-6**) and 1L-3,4-di-*O*-benzyl-*chiro*-inositol (**L-7**) were prepared using the same procedures that were reported for the corresponding D-isomers and the spectroscopic properties of **L-6** and **L-7** are identical to those of the corresponding D-isomers apart from the optical rotations which are of opposite sign [22]. $[RuCl_2(COD)]_n$ [23] and $RuCl_2(PPh_3)_3$ [24] were prepared according to the literature methods.

4.2. General procedures and instruments employed for the hydrogenation reactions

Hydrogenations were carried out in 12 mL glass vials equipped with a magnetic stirrer bar. The vials were filled with catalyst (0.005 mmol), substrate (1.0 mmol), KO^{t}Bu (0.01 mmol) and 1:1 toluene/isopropanol (3 mL) for acetophenone and 3-quinuclidinone, and toluene only (3 mL) for dimethyl itaconate and methyl benzoyl formate inside an inert atmosphere glove box (Innovative technologies) and then placed inside a 300 mL Parr autoclave made from Hastelloy C. In this way several hydrogenation experiments could be carried out at the same time. The autoclave was sealed, taken outside the glovebox and heated to 60 °C using a thermostatic heating mantle. The autoclave was then flushed with hydrogen 3 times before being filled with hydrogen (1000 psi).

After the required reaction time the autoclave was cooled, and the pressure reduced to atmospheric pressure. The autoclave was then opened, and samples of the crude reaction mixture were analysed by GC. The GC analysis to obtain conversion and enantiomeric excess values were performed on a HP 6890 Series gas chromatography apparatus using a capillary Supelco GAMMA-DEX 225 (30 m × 0.25 mm × 0.25 μm) column or a SGE CYDEX-B (2 m × 0.32 mm × 0.25 μm) column.

4.3. Preparation of 1L-3,4-di-O-benzyl-1,2,5,6-tetra-O-methyl-chiro-inositol (*L-8*)

Compound **L-7** (10.0 g, 28 mmol) was dissolved in dry DMF (200 mL) under argon and the flask was cooled to 0 °C. Sodium hydride (2.99 g of a 60% w/w suspension in oil, 75 mmol) was added followed by iodomethane (5.18 mL, 83.2 mmol) under argon and the flask was allowed to warm to room temperature and stand for 1 h. The flask was cooled to 0 °C and another portion of sodium hydride (2.99 g of 60% w/w in oil, 75 mmol) was added followed by another portion of iodomethane (5.18 mL, 83.2 mmol) under argon. The flask was warmed to room temperature and stirred overnight under argon. Ethanol (100 mL) was added to quench the reaction and the solvents were removed under vacuum. The residue was purified by Flash Chromatography (EtOAc:hexanes, 1:2) to give pure **L-8** (7.50 g, 95%) as a pale yellow oil; $[\alpha]_D$ +20.3 (*c* 1.1, $CHCl_3$). *Anal*. Calc. for $C_{24}H_{32}O_6$: C, 69.21; H, 7.74. Found: C, 68.82; H, 7.75%. MS (*m*/*z*, referred to the most abundant isotopes): (NBA/DCM): Calcd. for $C_{24}H_{31}O_6$ ($M-H^+$) 415.2121 *m*/*z*. Found: 415.2111. ^{1}H NMR ($CDCl_3$, δ): 3.49 (s, 6H, Me), 3.51 (2H, H-3 and H-4), 3.53 (s, 6H, Me), 3.73 (dd, 2H, *J* 7.1, 2.6 Hz, H-2 and H-5), 3.75 (d, 2H, *J* 2.6 Hz, H-1 and H-6), 4.79 (d, 2H, *J* 10.8 Hz, CH*H*′), 4.85 (d, 2H, *J* 10.8 Hz, C*H*H′), 7.22–7.36 (m, 10H, Ar). ^{13}C NMR ($CDCl_3$, δ): 59.4 (Me), 59.5 (Me), 76.1 (CH_2), 76.2 (C-1 and C-6), 82.2 (C-3 and C-4), 82.3 (C-2 and C-5), 127.7, 128.3, 128.6, 139.2 (Ar).

4.4. Preparation of 1L-1,2,5,6-tetra-O-methyl-chiro-inositol (*L-9*)

Compound **L-8** (7.50 g, 18.0 mmol) in ethanol (64 mL) and trifluoroacetic acid (7 mL) was hydrogenated at atmospheric pressure for 24 h at room temperature in the presence of palladium on carbon catalyst (2.3 g, 10% w/w). The catalyst was removed by filtration through Celite (pre-washed with ethanol) and the solvents were removed from the filtrate under vacuum. The residue was purified by Flash Chromatography (CH_2Cl_2:EtOAc:MeOH, 5:4:1) to give pure **L-9** (3.80 g, 89%). *Anal*. Calc. for $C_{10}H_{20}O_6$: C, 50.84; H, 8.53. Found: C, 49.94; H, 8.41%. $[\alpha]_D$ −67 (*c* 1.4, $CHCl_3$); ^{1}H NMR ($CDCl_3$, δ): 3.38 (br s, 2H, H-2 and H-5), 3.49 (s, 6H, Me), 3.51 (s, 6H, Me), 3.78 (dd, 2H, *J* 6.8, 2.1 Hz, H-3 and H-4), 3.82 (d, 2H, *J* 2.1 Hz, H-1 and H-6). ^{13}C NMR ($CDCl_3$, δ): 58.5 (Me), 59.7 (Me), 72.6 (C-3 and C-4), 75.4 (C-1 and C-6), 81.5 (C-2 and C-5).

4.5. Preparation of the compounds *D-6*–*D-9*

The D-enantiomers of compounds **L-6**–**L-9**, were prepared using the same procedures that are detailed in Sections 4.3–4.6, only using the corresponding D-enantiomer starting materials in each case. The spectral properties for all the compounds **D-6**–**D-9** are identical within experimental error to those reported for **L-6**–**L-9**.

4.6. Preparation of 1D-3,4-bis(O-diphenylphosphino)-1,2,5,6-tetra-O-methyl-chiro-inositol (**D-10**)

The diol **D-9** (536 mg, 2.27 mmol) (which had been predried azeotropically with dry toluene (2 × 5 mL)) and dry pyridine (410 μL, 5.07 mmol) were added to dry THF (5 mL). The resulting solution was transferred by cannula into a Schlenk tube containing freshly distilled chlorodiphenyl phosphine (830 μL, 4.62 mmol) in dry THF (3.5 mL) under argon. The resulting suspension was stirred at room temperature overnight. The solution was filtered under argon and the solvent removed from the filtrate under vacuum. The remaining solid was washed with dry toluene and filtered. The filtrate was collected and the solvent removed under vacuum to give the diphosphinite **D-10** as a white solid (1.30 g, 95%). Compound **D-10** was used in subsequent metal complex synthesis without further purification. ^{1}H NMR ($CDCl_3$, δ): 2.67 (s, 6H, Me), 3.38 (m, 2H, H-2 and H-5), 3.46 (s, 6H, Me), 3.67 (d, 2H, J 1.7 Hz, H-1 and H-6), 4.35 (m, 2H, H-3 and H-4), 6.96–7.55 (m, 20H, Ar). ^{13}C NMR ($CDCl_3$, δ): 56.6 (Me), 59.8 (Me), 74.5 (C-1 and C-6), 81.4 (C-2 and C-5), 127.9, 128.2, 128.3, 129.0, 129.2, 129.5, 130.9, 131.2 (Ar). ^{31}P NMR ($CDCl_3$, δ): 113.4.

4.7. Preparation of RuHCl(1D-3,4-bis(O-diphenylphosphino)-1,2,5,6-tetra-O-methyl-chiro-inositol)$_2$ (**11**)

Compound **D-10** (0.20 g, 0.33 mmol), $[RuCl_2(COD)]_n$ (0.043 g, 0.16 mmol) and triethylamine (0.10 mL, 0.74 mmol) were added to toluene (20 mL) under nitrogen and the mixture heated under reflux for 12.5 h. The toluene was then removed under reduced pressure and the resulting residue dissolved in a minimum amount of acetone and purified by column chromatography on basic alumina using acetone as eluant. The yellow/orange band was collected and the acetone was removed under reduced pressure. The resulting residue was recrystallised from dichloromethane/*n*-hexane to give pure **11** as yellow/orange crystals (0.080 g, 34%). *Anal*. Calc. for $C_{68}H_{77}ClO_{12}P_4Ru$: C, 60.64; H, 5.76. Found: C, 60.03; H, 5.74%. ^{1}H NMR ($CDCl_3$, δ): −16.26 (m, 1H, hydride), 2.49 (s, 6H, Me), 3.31 (s, 6H, Me), 3.37 (s, 6H, Me), 3.67 (s, 6H, Me), 3.70 (m, 2H, –CH–), 3.89 (m, 2H, –CH–), 3.89 (m, 2H, –CH–), 3.95 (m, 2H, –CH–), 4.82 (m, 2H, –CH–), 5.58 (m, 2H, –CH–), 6.55–7.81 (m, 40H, Ph). ^{13}C{^{1}H} NMR ($CDCl_3$, δ): 58.6 (s, Me), 58.6 (s, Me), 59.0 (s, Me), 59.7 (s, Me), 63.6 (s, –CH–), 74.3 (s, –CH–), 76.3 (s, –CH–), 77.2 (s, –CH–), 80.4 (s, –CH–), 80.5 (s, –CH–), 123.2–138.9 (Ph). ^{31}P{^{1}H} NMR ($CDCl_3$, δ): 120.4 (m), 148.6 (m).

4.8. Preparation of RuCl$_2$(1D-3,4-bis(O-diphenylphosphino)-1,2,5,6-tetra-O-methyl-chiro-inositol){(1R,2R)-(+)-DPEN} (**12**)

Compound **D-10** (0.336 g, 0.556 mmol) and $RuCl_2(PPh_3)_3$ (0.266 g, 0.278 mmol) were added to toluene (10 mL) under nitrogen and the resulting mixture stirred at room temperature for 5 min, (1*R*,2*R*)-(+)-DPEN (0.0580 g, 0.273 mmol) was then added and the solution was stirred at room temperature for an additional 25 min. The toluene was removed under reduced pressure to give a green residue. This was dissolved in a minimum amount of dichloromethane and purified by column chromatography on basic alumina using dichloromethane as eluant. The bright yellow band was collected and the dichloromethane removed under reduced pressure. The resulting residue was recrystallised from diethylether/*n*-hexane to give pure **12** as yellow crystals (0.195 g, 71%). *Anal*. Calc. for $C_{48}H_{54}Cl_2N_2O_6P_2Ru$: C, 58.30; H, 5.50; N, 2.83. Found: C, 58.32; H, 5.68; N, 2.55%. ^{1}H NMR ($CDCl_3$, δ): 3.13 (s, 6H, Me), 3.39 (s, 6H, Me), 3.45 (m, 2H, –CH–), 3.63 (m, 2H, –CH–), 4.39 (m, 2H, –CH–), 4.79 (m, 2H, –CH–), 6.96–7.76 (30H, Ph). ^{13}C{^{1}H} NMR ($CDCl_3$, δ): 59.0 (s, Me), 59.7 (s, Me), 62.9 (s, –CH–), 76.2 (s, –CH–), 77.0 (s, –CH–), 80.7 (s, –CH–), 126.9–140.2 (m, Ph). ^{31}P{^{1}H} NMR ($CDCl_3$, δ): 150.4 (s).

4.9. Preparation of RuCl$_2$(1D-3,4-bis(O-diphenylphosphino)-1,2,5,6-tetra-O-methyl-chiro-inositol){(1S,2S)-(−)-DPEN} (**13**)

The same procedure that was used for the synthesis of **12** in Section 4.8 was followed except that (1*S*,2*S*)-(−)-DPEN was used instead of (1*R*,2*R*)-(+)-DPEN. After recrystallisation from chloroform/*n*-hexane, pure **13** was obtained as yellow crystals (0.0667 g, 76%). *Anal*. Calc. for $C_{48}H_{54}Cl_2N_2O_6P_2Ru \cdot 0.5CHCl_3$: C, 55.53; H, 5.28; N, 2.67. Found: C, 55.23; H, 5.31; N, 2.56%. ^{1}H NMR ($CDCl_3$, δ): 3.12 (s, 6H, Me), 3.38 (s, 6H, Me), 3.44 (m, 2H, –CH–), 3.63 (m, 2H, –CH–), 4.40 (m, 2H, –CH–), 4.76 (m, 2H, –CH–), 6.9–7.75 (30H, Ph). ^{13}C{^{1}H} NMR ($CDCl_3$, δ): 59.0 (s, Me), 59.8 (s, Me), 64.1 (s, –CH–), 76.3 (s, –CH–), 76.9 (s, –CH–), 80.7 (s, –CH–), 127.0–140.2 (m, Ph). ^{31}P{^{1}H} NMR ($CDCl_3$, δ): 151.6 (s) ppm.

4.10. X-ray crystal structure determination for compound **D-10**

A suitable crystal of compound **D-10** was isolated from diethylether. X-ray data were collected on a Siemens SMART CCD diffractometer using graphite monochromated Mo Kα ($\lambda = 0.71073$ Å). Data collection method: ω-scan, range 0.8°, crystal to detector distance 5 cm. Data reduction and cell determination were carried out with the SAINT and XPREP (SMART) programs [25]. Absorption corrections were applied by the use of the SADABS program [26]. The structures were determined and refined using the SHELXS-97 and SHELXL-97 program packages [27]. All non-H atoms were refined with anisotropic thermal parameters. All carbon-bound H atoms were constrained to their expected geometries (C–H 0.95, 0.98 and 1.0 Å) and refined with U_{iso} 1.2 times the U_{eq} of their parent atom.

Crystal data for $C_{34}H_{38}O_6P_2$ (**D-10**): $M = 604.58$, orthorhombic, $P2_12_12_1$, $a = 10.6945(11)$ Å, $b = 13.5855(14)$ Å,

$c = 21.992(2)$ Å, $V = 3195.3(6)$ Å^3, $Z = 4$, $D_{calc} = 1.257$ Mg m^{-3}, $\mu = 0.179$ mm^{-1}, $T = 163(2)$ K, measured 40719 reflections (6492 unique) in θ range 1.8–26.4°. $R_{int} = 0.087$. Final R indices $[I > 2\sigma(I)]$ $R_1 = 0.041$, $wR_2 = 0.070$. Absolute structure parameter (Flack [28]) = 0.11(8).

Acknowledgements

We thank the Tertiary Education Commission, administered by Auckland UniServices Limited, for granting an Enterprise Scholarship to A.T.S. and Industrial Research Limited New Zealand for partial support of this work. We also thank The University of Auckland Research Committee for partial support of this work through Grants-in-Aid.

Appendix A. Supplementary material

Crystallographic data (excluding structure factors) for the compound **D-10** have been deposited with the Cambridge Crystallographic Data Centre as supplementary publication No. 294672. Copies of this information can be obtained free of charge from the Director, CCDC, 12 Union Road, Cambridge CB2 1EZ, UK (fax: +44 1223 336 033; e-mail: deposit@ccdc.cam.ac.uk or www: http://www.ccdc.cam.ac.uk). Supplementary data associated with this article can be found, in the online version, at doi:10.1016/j.poly.2006.06.016.

References

[1] (a) W.S. Knowles, Angew. Chem., Int. Ed. 41 (2002) 1998;
(b) R. Noyori, Angew. Chem., Int. Ed. 41 (2002) 2008;
(c) K.B. Sharpless, Angew. Chem., Int. Ed. 41 (2002) 2024.
[2] X. Zhang, Tetrahedron Asymmetry 15 (2004) 2099.
[3] T.T.-L. Au-Yeung, A.S.C. Chan, Coord. Chem. Rev. 248 (2004) 2151.
[4] S. Castillon, C. Claver, Y. Diaz, Chem. Soc. Rev. 34 (8) (2005) 702.
[5] R. Selke, J. Organomet. Chem. 370 (1989) 249.
[6] T.V. RajanBabu, T.A. Ayers, G.A. Halliday, K.K. You, J.C. Calabrese, J. Org. Chem. 62 (1997) 6012.
[7] R. Selke, in: H.U. Blaser, E. Schmidt (Eds.), Asymmetric Catalysis on Industrial Scale, Wiley–VCH, New York, 2004, p. 39.
[8] M. Diéguez, O. Pàmies, C. Claver, Chem. Rev. 104 (2004) 3189.
[9] M. Diéguez, O. Pàmies, A. Ruiz, Y. Díaz, S. Castillón, C. Claver, Coord. Chem. Rev. 248 (2004) 2165.
[10] V.N. Azev, M. d'Alarcao, J. Org. Chem. 69 (2004) 4839.
[11] K. Ishii, C. Lensink, J.B. Hart, A. Falshaw, Jpn. Kokai Tokkyo Koho (2003), JP 2003155293.
[12] G. Cousins, A. Falshaw, J.O. Hoberg, Carbohydr. Res. 338 (9) (2003) 995.
[13] D. Cremer, J.A. Pople, J. Am. Chem. Soc. 97 (1975) 1354.
[14] (a) E. Guimeta, J. Paradab, M. Diéguez, A. Ruiz, C. Claver, Appl. Catal. A 282 (2005) 215;
(b) A. Fuerte, M. Iglesias, F. Sánchez, J. Organomet. Chem. 588 (1999) 186;
(c) T.V. RajanBabu, T.A. Ayers, Tetrahedron Lett. 35 (1994) 4295.
[15] (a) T. Ikariya, Y. Ishii, H. Kawano, T. Arai, M. Saburi, S. Yoshikawa, S. Akutagawa, J. Chem. Soc., Chem. Commun. (1985) 922;
(b) V. Ratovelomanana-Vidal, J. Genet, J. Organomet. Chem. 567 (1998) 163;
(c) T. Ohta, H. Takaya, R. Noyori, Inorg. Chem. 27 (1988) 566.
[16] A. Falshaw, G.J. Gainsford, C. Lensink, A.T. Slade, L.J. Wright (unpublished results).
[17] F. Spindler, C. Malan, M. Lotz, M. Kesselgruber, U. Pittelkow, A. Rivas-Nass, O. Briel, H. Blaser, Tetrahedron Asymmetry 15 (2004) 2299.
[18] C.A. Sandoval, T. Ohkuna, K. Muniz, R. Noyori, J. Am. Chem. Soc. 125 (2003) 13490.
[19] T.V. Rajanbabu, T.A. Ayers, A.L. Casalnuovo, J. Am. Chem. Soc. 116 (1994) 4101.
[20] W.C. Still, M. Kahn, A. Mitra, J. Org. Chem. 43 (1978) 2923.
[21] S.J. Angyal, N.K. Matheson, J. Am. Chem. Soc. 77 (1955) 4343.
[22] A. Falshaw, J.B. Hart, P.C. Tyler, Carbohydr. Res. 329 (2000) 301.
[23] (a) M.A. Bennett, G. Wilkinson, Chem. Ind. (1959) 1516;
(b) J. Chatt, L.M. Venzanzi, J. Chem. Soc. (1957) 4735.
[24] L.A. Ortiz-Frade, L. Ruiz-Ramirez, I. Gonzalez, A. Marin-Becerra, M. Alcarazo, J.G. Alvarado-Rodriguez, R. Moreno-Esparza, Inorg. Chem. 42 (2003) 1825.
[25] Siemens. SMART and SAINT. Versions 4.0. Siemens Analytical X-ray Instruments Inc., Madison, WI, USA., 1996.
[26] G.M. Sheldrick, SADABS: Program for Semi-Empirical Absorption Correction, University of Göttingen, Göttingen, Germany, 1996.
[27] G.M. Sheldrick, SHELXL-97 and SHELXS-97: Programs for Crystal Structure Determination and Refinement, University of Göttingen, Göttingen, Germany, 1997.
[28] H.D. Flack, Acta Crystallogr., Sect. A 39 (1983) 876.

Available online at www.sciencedirect.com
ScienceDirect
Polyhedron 26 (2007) 338–343
POLYHEDRON
www.elsevier.com/locate/poly

Synthesis, characterisation and X-ray structure of a novel porphyrin array employing Zn–O and O–H...O bonding motifs

Steven J. Langford *, Clint P. Woodward

School of Chemistry, Monash University, Wellington Road, Clayton, Melbourne, Vic. 3800, Australia

Received 4 April 2006; accepted 2 June 2006
Available online 10 June 2006

Abstract

The preparation and characterisation of the free-base and zinc metallated derivatives of 5,10,15,20-tetrakis(4-(2-(2-hydroxyethoxy)ethoxy)phenyl)porphyrin **1** is described. The X-ray crystal structure of the Zn(II) adduct **2** dimerises in the solid state *via* an intermolecular polyether oxygen–Zn(II) interaction (O...Zn = 2.124(4) Å). The porphyrin dimers form discrete layers defined by a distance of 5.10 Å between the porphyrin planes in adjacent layers. A bilayer sheeting arrangement of the porphyrin macrocyclic units is achieved through cooperative hydrogen bonding of the ethoxyethanol arms to form 11-membered macrocycles containing four hydrogen bonds.
© 2006 Elsevier Ltd. All rights reserved.

Keywords: Metalloporphyrins; Zn(II) complex; Hydrogen bonding; Coordination network; X-ray structure

1. Introduction

Controlling the arrangement of porphyrin macrocycles into well-defined solid-state arrays through the processes of self-assembly and self-organisation is necessary to advance the development of surface bound porphyrin devices with applications in surface sensing, size exclusion, light harvesting and heterogeneous porphyrin catalysis [1–6]. Desired control may be executed by utilising ''intelligent'' porphyrins in which non-covalent interactions are pre-programmed into the porphyrin structure to aid molecular alignment in either a *pseudo* 1-D or 2-D and 3-D arrays [7–10]. In particular, new porphyrin systems capable of forming either hydrogen bonded or coordinative 2D sheet networks from a single molecular entity are desirable. In this paper we report on preliminary studies using ethoxyethanol side chains for this goal (Fig. 1). Such functionality could potentially self-assemble at the porphyrin periphery in a non-covalent way cooperatively, forming two distinct intermolecular hydrogen bonds per ethoxyethanol set leading to discrete assemblies or 2-D supramolecular arrays.

2. Results and discussion

5,10,15,20-Tetrakis(4-(2-(2-hydroxyethoxy)ethoxy)phenyl)porphyrin (**1**, H_2TEEP) was prepared in 83% yield by the alkylation of 5,10,15,20-tetrakis(4-hydroxyphenyl)porphyrin with 2-(2-chloroethoxy)ethanol [11]. Compound **1** is surprisingly insoluble in the usual aprotic solvents used for dissolving porphyrins ($CHCl_3$, CH_2Cl_2, toluene, etc). This insolubility can be attributed to extensive intermolecular hydrogen bonding interactions, which are desirable but uncontrolled to this point. The problem is alleviated by the addition of a small amount of a solvent capable of interfering with hydrogen bonding (e.g., methanol or pyridine)[1]. Zinc metallation of **1** was achieved using the acetate method [12] producing 5,10,15,20-tetrakis(4-(2-(2-hydroxyethoxy)ethoxy)phenyl)porphinato zinc(II) (**2**, ZnTEEP) in 89% yield as a light purple solid. Solubility of the porphy-

* Corresponding author. Tel.: +61 3 9905 4569; fax: +61 3 9905 4597.
E-mail address: Steven.Langford@sci.monash.edu.au (S.J. Langford).

[1] Despite this fix, crystals of **1** suitable for X-ray crystallography have not been forthcoming.

0277-5387/$ - see front matter © 2006 Elsevier Ltd. All rights reserved.
doi:10.1016/j.poly.2006.06.002

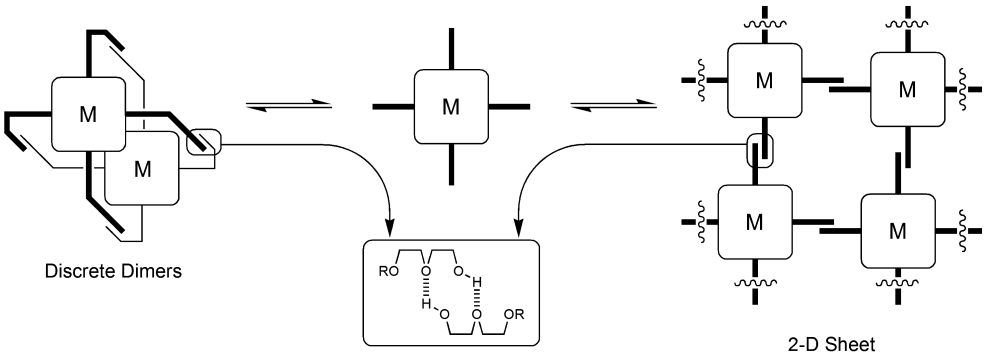
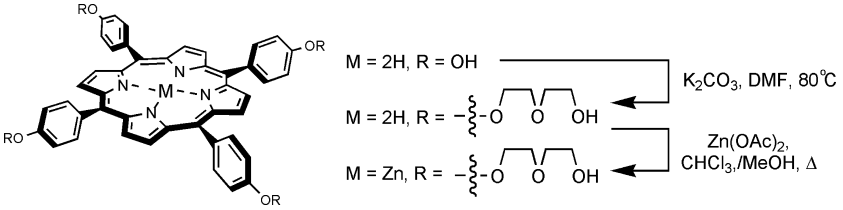


Fig. 1. Utilising the potential of ethoxyethanol groups on the porphyrin periphery could lead to a range of supramolecular constructs through concentration and surface dependency.



Scheme 1.

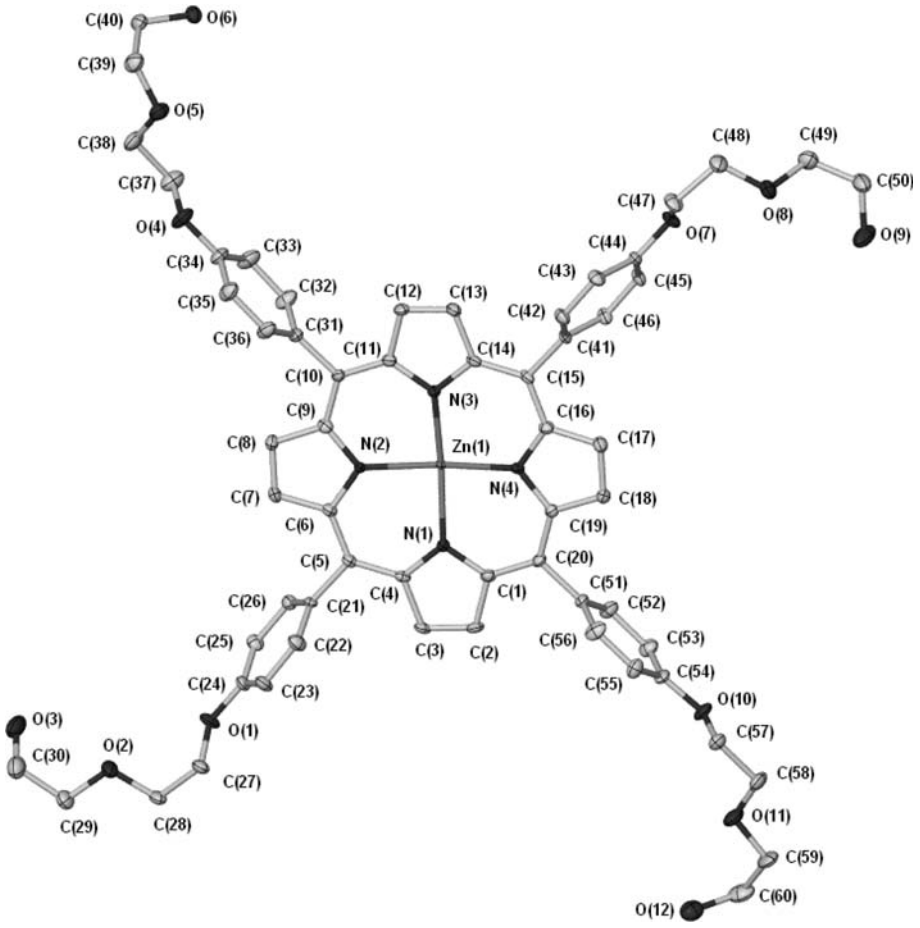


Fig. 2. ORTEP diagram of the molecule displaying the atom labelling scheme used with in paper. Ellipsoids are drawn at 50% probability level. Coordinating alcohol removed for clarity.

Table 1
Selected bond lengths (Å) and bond angles (°) for **2**

Bond distances			
M–N(1)	2.056(4)	M–N(4)	2.071(4)
M–N(2)	2.059(4)	M–O(6)	2.124(4)
M–N(3)	2.050(4)		
Bond angles			
N1–Zn1–N2	88.76(14)	N3–Zn1–O6	99.34(14)
N1–Zn1–N3	163.25(15)	N1–Zn1–O6	97.41(14)
N1–Zn1–N4	88.86(14)	N2–Zn1–O6	97.84(14)
N2–Zn1–N3	89.23(14)	N4–Zn1–O6	98.35(14)
N2–Zn1–N4	163.80(15)		
N3–Zn1–N4	88.45(14)		

rin **2** was also only possible in a mixed solvent system in which a solvent capable of competing with ethoxyethanol hydrogen bonding was employed. Using this technique, crystals suitable for X-ray crystallography were grown by the slow diffusion of diethyl ether into dichloromethane/methanol (see Scheme 1).

ZnTEEP (**2**) crystallises in the triclinic space group $P\bar{1}$. The molecular structure of **2** is shown in Fig. 2 and selected bond distances and angles for **2** are listed in Table 1. The square pyramidal Zn(II) centre is somewhat distorted with the four inner peripheral nitrogens of the porphyrin defining the pyramid base and the apical position occupied by a coordinated (intermolecularly) alcohol side chain (see Fig. 3). The metal to nitrogen bond distances vary from 2.050(4) to 2.071(4) Å (average value 2.059 Å), with the axially coordinated Zn–O bond displaying a longer distance of 2.124(4) Å. These values fall into the ranges observed in other Zn(II) porphyrin systems [13]. The Zn(II) metal ion resides 0.29 Å above the porphyrin least squares plane and toward the coordinating alcohol. The large dihedral angles observed between the *meso* phenyl rings and the mean porphyrin plane (69.9–88.3°) are also typical, the difference from orthogonal attributed to crystal packing forces [14]. Despite their inherent flexibility, the ethoxyethanol chains are extended and relatively well ordered. Each

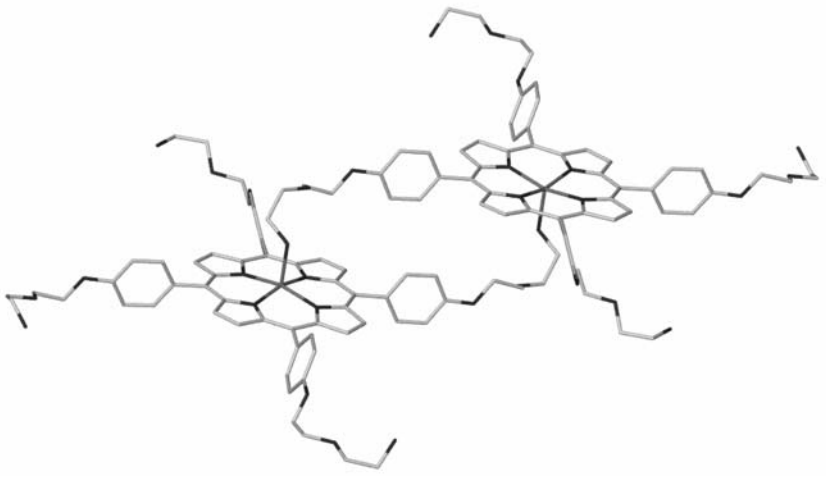


Fig. 3. Representation of the dimer formed in the crystal structure of **2** (H-atoms and CH_2Cl_2 solvent molecule have been omitted for clarity).

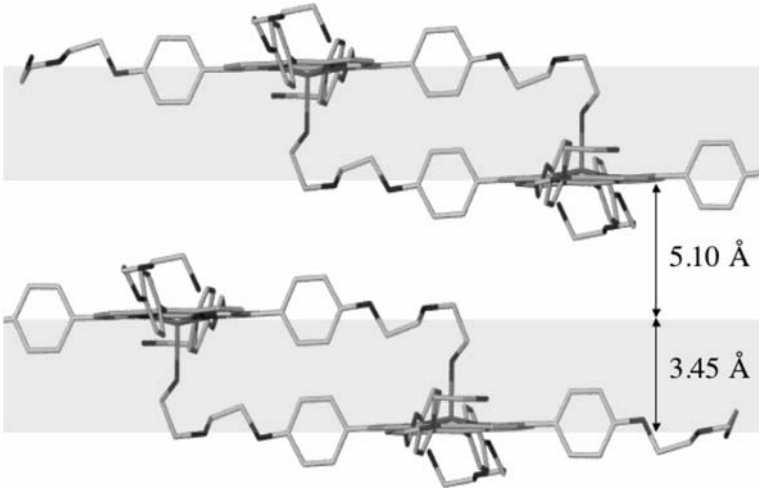


Fig. 4. Bilayer sheeting arrangement observed in the crystal structure of **2**. The shaded area highlights the organisation and intra-layer thickness (3.45 Å), with inter-layer separation of 5.10 Å (H-atoms have been omitted for clarity).

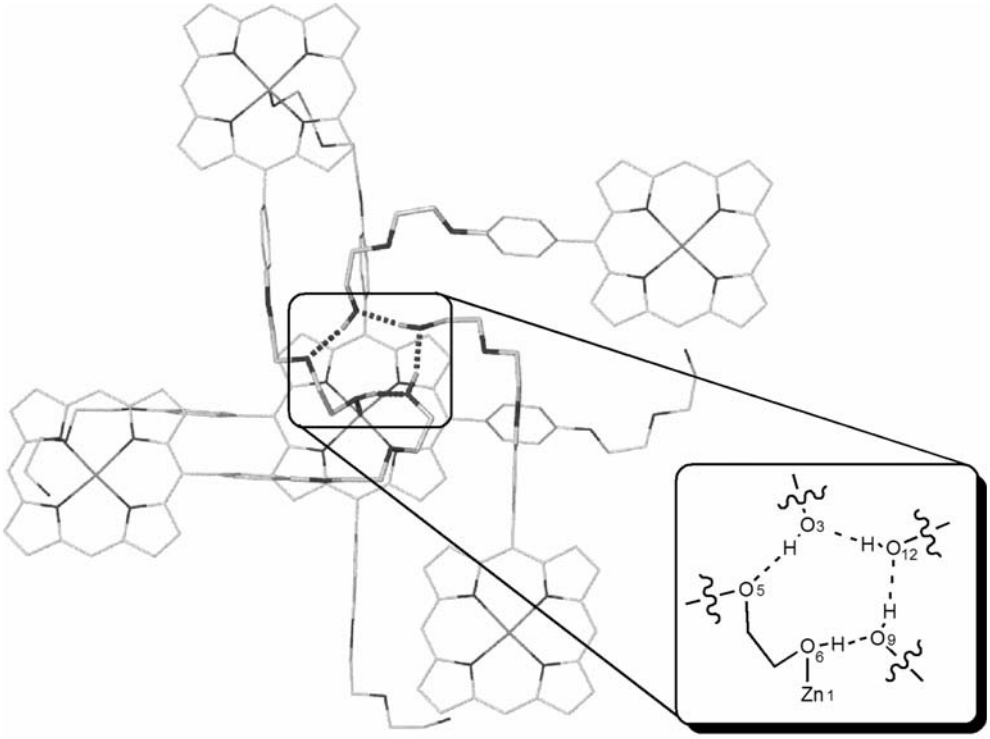


Fig. 5. Representation of the hydrogen bonding motif observed above the zinc coordination site (hydrogen atoms have been omitted for clarity).

Table 2
Hydrogen bonding parameters of **2**

O–H	O	O–H (Å)[a]	H···O (Å)	O···O (Å)	O–H···O (°)
O–H(3)	O5	0.84	2.16	2.791(6)	132.2
O–H(6)	O9	0.84	1.92	2.626(6)	159.8
O–H(9)	O12	0.84	1.89	2.677(6)	155.9
O–H(12)	O3	0.84	1.82	2.686(6)	150.2

[a] All non-hydrogen atoms were refined anisotropic, while all hydrogen atoms were fixed in idealised positions and allowed to ride on the atom to which they are attached.

OCH_2CH_2OH group forms a staggered *gauche* arrangement while the internal OCH_2CH_2O groups are not as well defined, forming both *extended* and *gauche* arrangements.

Interestingly, ZnTEEP forms a C_2 symmetric dimer in which the OH group from the ethoxyethanol side chain of one porphyrin coordinates to the Zn(II) centre of an adjacent porphyrin molecule [15]. A representation of this dimer is shown in Fig. 3. The observed Zn...Zn separation between the two porphyrins within the dimer is 13.39 Å, with the mean plane of the porphyrins aligned parallel to one another at a distance of 3.45 Å (Fig. 3). The two *meso* phenyl groups used to form the 28-membered macrocycle are parallel to each other but do not provide further Van der Waals stabilisation through π–π interactions.

The dimeric arrays occur within a plane represented by the grey regions in Fig. 4 and alternate in an up-and-down fashion. Each bilayer is separated by an intervening space of thickness 5.10 Å (porphyrin plane to porphyrin plane). The dimers within one layer are interconnected through a hydrogen bonding motif involving the ethoxyethanol chains not involved in dimerisation. A representation of this motif and the extended layer is shown in Fig. 5. Selected hydrogen bonding data are listed in Table 2.

The bilayer sheeting arrangement of the porphyrin macrocyclic units is achieved through cooperative hydrogen bonding of the ethoxyethanol arms to form 11-membered macrocycles containing four hydrogen bonds. Hence, all ethoxyethanol groups are employed in the formation of the overall structure. The longest of the hydrogen bonds O3–H...O5 differs from the others (Table 2) in that it is an ether oxygen rather than hydroxy oxygen atom that partakes in the noncovalent bonding.

3. Concluding remarks

A novel supramolecular structure utilising hydrogen bonding and Zn(II)–N and Zn(II)–O coordination was determined. Despite the use of hydrogen bonding (avail-

able through the ethoxyethanol side chains) to form a layered structure, this present result was more complex than anticipated by design. We are continuing our quest to form hydrogen bonded arrays based on the ethoxyethanol motif for surface adhesion, but recognise that the use of free-base or metalloporphyrins in which axial coordination is not possible (i.e. using four coordinate metal ions or strong donor ligands) may be necessary to achieve this goal. These experiments are underway.

4. Experimental

4.1. General

Synthesis reagents including solvents were used as purchased. Melting points (m.p.) were measured on a Stuart Scientific SMP 3 melting point apparatus. UV–Vis spectra were recorded on a Varian model Cary 100 Bio UV–Visible Spectrophotometer, with the solvent systems used stated in the synthesis description. ^{1}H and ^{13}C nuclear magnetic resonance (n.m.r.) spectra were recorded using a Bruker DPX 300 MHz spectrometer (300 MHz ^{1}H, 75 MHz ^{13}C) or a Bruker DRX 400 MHz spectrometer (400 MHz ^{1}H, 100 MHz ^{13}C), as solutions in the deuterated solvents specified. Deuterated chloroform ($CDCl_3$) was base washed with anhydrous Na_2CO_3 prior to use. High-resolution electrospray mass spectra (HRMS) were recorded on a Bruker BioApex 47e Fourier transform mass spectrometer.

4.1.1. 5,10,15,20-Tetrakis(4-(2-(2-hydroxyethoxy) ethoxy)phenyl)porphyrin (*1*)

To a stirred DMF solution (50 mL) of 5,10,15,20-tetrakis(4-hydroxyphenyl)porphyrin (100 mg, 0.15 mmol), anhydrous K_2CO_3 (410 mg, 2.96 mmol) and 2-(2-chloroethoxy)ethanol (0.2 mL, 1.89 mmol) were added and the resulting solution was heated to 80 °C and left to stir for 4 days. After cooling, the porphyrin was precipitated by the addition of water (50 mL), filtered and washed with water (3 × 5 mL). Further purification by column chromatography (SiO_2, $CHCl_3$/MeOH, 9:1 ratio) eluted **1** as a purple solid (128.5 mg, 83%). m.p. 261–262 °C, UV–Vis ($CHCl_3$/MeOH, 9:1) λ_{max} (log ε): 403 sh (4.79); 422 (560); 520 (4.16); 556 (4.09); 594 (3.88); 649 nm (3.90). ^{1}H n.m.r (400 MHz, $CDCl_3$/MeOH, 4:1): δ 3.66 (m, 8H, OCH_2); 3.72 (m, 8H, OCH_2); 3.19 (t, *J* 4.6 Hz, 8H, OCH_2); 4.29 (t, *J* 4.5 Hz, 8H, OCH_2); 7.17 (ABq, *J* 8.2 Hz, 8H, ArH); 7.98 (ABq, *J* 8.2 Hz, 8H, ArH); 8.69 (s, 8H, β-pyrrolic-H); inner NH not observed. HR-MS (ESI, +ve, DCM/MeOH): calculated *m*/*z* 1053.4262; observed *m*/*z* 1053.4230 $[M+Na]^+$.

4.1.2. [5,10,15,20-Tetrakis(4-(2-(2-hydroxyethoxy) ethoxy)phenyl)porphinato]zinc(II) (*2*)

To a solution of **1** (15 mg, 0.015 mmol) in $CHCl_3$/MeOH (3 mL, 4:1 ratio) was added a saturated $Zn(OAc)_2$ in MeOH (5 mL) and stirred at reflux for 3 h in darkness. Upon completion, the solvent system was removed by rotary evaporation. Water and THF were added and the THF was removed by rotary evaporation to precipitate the porphyrin. The purple suspension was filtered and washed with water (3 × 5 mL). The sample was dried under high vacuum pump to remove the residual solvent giving **2** as a purple solid (14.2 mg, 89%). X-ray quality crystals were grown by the slow diffusion of diethyl ether into a CH_2Cl_2/MeOH solvent system (4:1), resulting in elongated hexagonal red plates. m.p. 223–225 °C. UV–Vis (THF) λ_{max} (log ε): 406 sh (4.63); 426 (6.07); 558 (4.94); 599 nm (4.60). ^{1}H n.m.r (400 MHz, $CDCl_3$/MeOD 9:1): δ 3.53 (m, 16H, OCH_2); 3.76 (m, 8H, OCH_2); 4.14 (m, 8H, OCH_2); 7.00 (ABq, *J* 8.6 Hz, 8H, ArH); 7.83 (ABq, *J* 8.6 Hz, 8H, ArH); 8.56 (s, 8H, β-pyrrolic-H). ^{13}C n.m.r (75 MHz, $CDCl_3$/MeOD 9:1): δ 61.5, 67.8, 69.9, 73.0, 112.6, 120.1, 131.5, 135.6, 136.4, 150.3, 158.2. HR-MS (ESI, +ve, DCM/MeOH): calculated *m*/*z* 1115.3397; observed *m*/*z* 1115.3414 $[M+Na]^+$.

4.1.3. X-ray structure determination

4.1.3.1. Data collection and processing. X-ray measurements were made using a Bruker X8 Apex II CCD diffractometer using monochromated Mo Kα radiation (0.71073 Å). The collection temperature was maintained at 123 K using an Oxford Cryostream open-flow N_2 cryostat. Solution was obtained by direct methods (SHELXS 97)[15] followed by successive Fourier-difference methods, and refined by full matrix least squares on F^2_{obs} (SHELXL 97) [16]. Hydrogen atom thermal parameters were tied to those of the atom to which they are attached.

Crystal data for **2**: $C_{61}H_{62}Cl_2N_4O_{12}Zn$, $M = 1179.42$, red plate, $0.20 \times 0.20 \times 0.02$ mm, triclinic, space group $P\bar{1}$, $a = 11.6110(5)$, $b = 13.3604(5)$, $c = 17.6703(8)$ Å, $\alpha = 87.943(2)$, $\beta = 86.938(2)$, $\gamma = 88.317(2)°$, $V = 2734.4(2)$ Å^3, $Z = 2$, $D_c = 1.432$ g/cm^3, $F_{000} = 1232$, $T = 123(2)$ K, $2\theta_{max} = 55.1°$, 60 320 reflections collected, 12 539 unique ($R_{int} = 0.0751$). Final Goodness-of-fit = 1.117, $R_1 = 0.0891$, $wR_2 = 0.1995$, *R* indices based on 9409 reflections with $I > 2\sigma(I)$ (refinement on F^2), 721 parameters. Lp and absorption corrections applied, $\mu = 0.616$ mm^{-1}.

Acknowledgements

We gratefully acknowledge Dr. Craig Forsyth and Dr. Paul Jensen for their contributions to structure determination. This research was supported by the Australia Research Council Discovery Grant (DP0556313). C.P.W. thanks the Monash University Faculty of Science for support through a Dean's postgraduate scholarship.

Appendix A. Supplementary material

Crystallographic data for the structure analyses have been deposited with the Cambridge Crystallographic Data Centre, CCDC (awaiting No.) for structures of **2**. Copies of this information may be obtained free of charge from The Director, CCDC, 12 Union Road, Cambridge, CB2 1EZ,

UK (fax: +44 1223 336033; e-mail: deposit@ccdc.cam.ac.uk or http://www.ccdc.cam.ac.uk). The ^{1}H n.m.r. spectrum of **2** is also presented. Supplementary data associated with this article can be found, in the online version, at doi:10.1016/j.poly.2006.06.002.

References

[1] (a) N.A. Rakow, K.S. Suslick, Nature 406 (2000) 710;
(b) M.E. Kosal, K.S. Suslick, J. Solid State Chem. 152 (2000) 87.
[2] I. Goldberg, Chem. Commun. (2005) 1243.
[3] (a) J.E. Redman, J.K.M. Sanders, Org. Lett. 2 (2000) 4141;
(b) X.-L. Guo, Z.-C. Dong, A.S. Trifonov, K. Miki, S. Mashiko, T. Okamoto, Nanotechnology 15 (2004) S402;
(c) H. Spillmann, A. Kiebele, M. Stöhr, T.A. Jung, D. Bonifazi, F. Cheng, F. Diederich, Adv. Mater. 18 (2006) 275.
[4] K. Kobayashi, M. Koyanagi, K. Endo, H. Masuda, Y. Aoyama, Chem. Eur. J. 4 (1998) 417.
[5] S.J. Langford, M.J. Latter, Inorg. Chem. Commun. 8 (2005) 920.
[6] A. Hosseini, M.C. Hodgson, F.S. Tham, C. Reed, P.D.W. Boyd, Cryst. Growth Des. 6 (2006) 397.
[7] (a) M. Vinodu, I. Goldberg, CrystEngComm. 6 (2004) 215;
(b) M. Vinodu, I. Goldberg, CrystEngComm. 7 (2005) 133.
[8] Y. Diskin-Posner, G.K. Patra, I. Goldberg, Eur. J. Inorg. Chem. (2001) 2515.
[9] G.D. Fallon, M.A.-P. Lee, S.J. Langford, P.J. Nichols, Org. Lett. 4 (2002) 1895.
[10] M.E. Kosal, J.-H. Chou, S.R. Wilson, K.S. Suslick, Nat. Mater. 1 (2002) 118.
[11] An alternative method has been described for securing alcohol side chains onto 5,10,15,20-tetrakis(4-hydroxyphenyl)porphyrins, see: S.P. Songca, B.S. Mbatha, Afr. J. Chem. 53 (2000) 113.
[12] J.W. Buchler, in: D. Dolphin (Ed.), The Porphyrins, vol. 1, Academic Press, New York, 1978.
[13] Y. Diskin-Posner, G.K. Patra, I. Goldberg, J. Chem. Soc., Dalton Trans. (2001) 2775.
[14] C. Raptopoulou, D. Daphnomili, A. Karamalides, M. Di Vaira, A. Terzis, A.G. Coutsolelos, Polyhedron 23 (2004) 1777.
[15] (a) For examples of Zn–O bonds in porphyrin systems see: R.K. Kumar, S. Balasubramanian, I. Goldberg, Inorg. Chem. 37 (1998) 541;
(b) J.T. Fletcher, M.J. Therien, J. Am. Chem. Soc. 122 (2000) 12393.
[16] G.M. Sheldrick, SHELXS-97, University of Göttingen, 1997.

Available online at www.sciencedirect.com
ScienceDirect
Polyhedron 26 (2007) 344–355
POLYHEDRON
www.elsevier.com/locate/poly

Syntheses, structures and hydrolytic properties of copper(II) complexes of asymmetrically *N*-functionalised 1,4,7-triazacyclononane ligands

Matthew J. Belousoff, Andrew R. Battle, Bim Graham [1], Leone Spiccia *

School of Chemistry, Monash University, Vic. 3800, Australia

Received 24 April 2006; accepted 21 June 2006
Available online 11 July 2006

Abstract

A series of new asymmetrically *N*-substituted derivatives of the 1,4,7-triazacyclononane (tacn) macrocycle have been prepared from the common precursor 1,4,7-triazatricyclo[5.2.1.$0^{4,10}$]decane: 1-ethyl-4-isopropyl-1,4,7-triazacyclononane (**L1**), 1-isopropyl-4-propyl-1,4,7-triazacyclononane (**L2**), 1-(3-aminopropyl)-4-benzyl-7-isopropyl-1,4,7-triazacyclononane (**L3**), 1-benzyl-4-isopropyl-1,4,7-triazacyclononane (**L4**) and 1,4-*bis*(3-aminopropyl)-7-isopropyl-1,4,7-triazacyclononane **(L5)**. The corresponding monomeric copper(II) complexes were synthesised and were found to be of composition: $[Cu(\mathbf{L1})Cl_2]\cdot 1/2\,H_2O$ (**C1**), $[Cu(\mathbf{L4})Cl_2]\cdot 4H_2O$ (**C2**), $[Cu(\mathbf{L3})(MeCN)](ClO_4)_2$ (**C3**), $[Cu(\mathbf{L5})](ClO_4)_2\cdot MeCN\cdot NaClO_4$ (**C4**) and $[Cu(\mathbf{L2})Cl_2]\cdot 1/2\,H_2O$ (**C5**). The X-ray crystal structures of each complex revealed a distorted square-pyramidal copper(II) geometry, with the nitrogen donors on the ligands occupying 3 (**C1** and **C2**), 4 (**C3**) or 5 (**C4**) coordination sites on the Cu(II) centre. The metal complexes were tested for the ability to hydrolytically cleave phosphate esters at near physiological conditions, using the model phosphodiester, *bis*(*p*-nitrophenyl)phosphate (BNPP). The observed rate constants for BNPP cleavage followed the order $k_{C1} \approx k_{C2} > k_{C5} \gg k_{C3} > k_{C4}$, confirming that tacn-type Cu(II) complexes efficiently accelerate phosphate ester hydrolysis by being able to bind phosphate esters and also form the nucleophile necessary to carry out intramolecular cleavage. Complexes **C1** and **C2**, featuring asymmetrically disubstituted ligands, exhibited rate constants of the same order of magnitude as those reported for the Cu(II) complexes of symmetrically tri-*N*-alkylated tacn ligands ($k \sim 1.5\times10^{-5}\ s^{-1}$).
© 2006 Elsevier Ltd. All rights reserved.

Keywords: 1,4,7-triazacyclononane derivatives; Macrocyclic ligands; Copper(II) complexes; X-ray crystal structures; Phosphate esters hydrolysis

1. Introduction

The coordination chemistry of 1,4,7-triazacyclononane (tacn) has been a fertile field of endeavour over the last 30 years, with over 1400 publications describing the chemistry of this ligand and its derivatives. Recognition that this macrocycle could mimic functional groups that bind metals in many proteins, particularly histidine residues, led to its use in numerous bio-inorganic chemistry studies [1–7]. Moreover, the possibility that bridged metal complexes could also be conveniently assembled using tacn-based ligands attracted the attention of magnetochemists [8–12]. These interests led to the modification of the tacn macrocycle, primarily but not exclusively through *N*-functionalisation, and to the detailed study of the coordination properties of the resulting derivatives. Initially, the focus was on symmetric, tri-substituted derivatives, since these could be readily prepared directly from the parent macrocycle [13], however a number of partially substituted or asymmetrically functionalised tacn derivatives soon began to appear in the scientific literature [14–16]. Early syntheses of these types of ligands generally yielded mixtures of products and/or involved complicated preparative routes utilising, for example, *p*-tosyl protecting groups [14]. Introduction of the highly versatile synthon, 1,4,7-triazatri-

* Corresponding author. Tel.: +61 3 9905 4526; fax: +61 3 9905 4597.
E-mail address: leone.spiccia@sci.monash.edu.au (L. Spiccia).
[1] Present address: Department of Medicinal Chemistry, Victorian College of Pharmacy, Monash University, Vic. 3800, Australia.

0277-5387/$ - see front matter © 2006 Elsevier Ltd. All rights reserved.
doi:10.1016/j.poly.2006.06.029

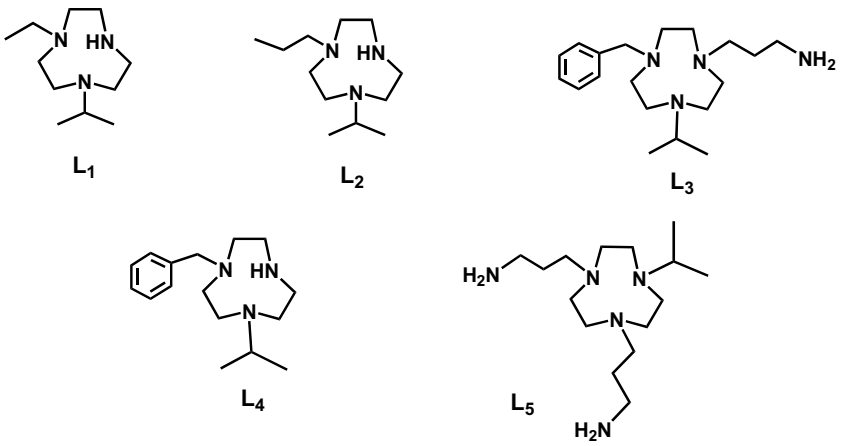


Fig. 1. Derivatives of 1,4,7-triazacyclononane investigated in this study.

cyclo[5.2.1.$0^{4,10}$]decane (''tacn orthoamide''), subsequently revolutionised the field, providing much more clean and efficient routes to tacn derivatives incorporating different functional groups [17,18], in addition to multi(tacn) assemblies that can simultaneously bind two or more metal ions [8,19]. As well as yielding interesting systems for magnetochemists to study [20,8,19,21], the complexes of these ligands have recently begun to be explored as models for phosphatase enzymes with significant success [22–30].

The possibility of attaching different functional groups to the tacn macrocycle in a highly controlled fashion has been the stimulus for much of our recent work in the area of tacn coordination chemistry. For example, we have recently reported the structure and properties of complexes formed by 'amino acid' derivatives of tacn, our ultimate interest being the incorporation of the macrocycle into natural peptide sequences [18,31]. In addition, exciting reports that the copper(II) complexes of *N*-alkylated derivatives of tacn, *viz.*, $[Cu(Me_3tacn)(OH_2)_2]^{2+}$ and $[Cu(^{i}Pr_3tacn)(OH_2)_2]^{2+}$ (Me_3tacn = 1,4,7-trimethyl-1,4,7-triazacyclononane and $^{i}Pr_3tacn$ = 1,4,7-triisopropyl-1,4,7-triazacyclononane) [26,32], are able to cleave phosphate esters much more efficiently than $[Cu(tacn)(OH_2)_2]^{2+}$ recently led us to begin to explore the hydrolytic activity of the copper(II) complexes of symmetrically and asymmetrically functionalised derivatives of tacn [22]. As part of this work, we now report the synthesis and characterisation of five new asymmetrically functionalised ligands (**L1**–**L5**) (see Fig. 1) and their copper(II) complexes, together with an examination of the ability of the copper(II) complexes to hydrolyse the model phosphate ester, *bis*(*p*-nitrophenyl)phosphate (BNPP).

2. Experimental

Reagent or analytical grade chemicals were used as supplied. Acetonitrile, DMF and chloroform were dried over 4 Å molecular sieves and used without further purification. THF was pre-dried with sodium, distilled from Na/benzophenone and used immediately. Distilled H_2O was used throughout. 1,4,7-triazatricyclo[5.2.1.$0^{4,10}$]decane was synthesised according to published methods [33]. The synthesis of 1-benzyl-4-formyl-1,4,7-triazacyclononane has been described by Warden et al. [18] and the syntheses of 1-ethyl-4,7-diaza-1-azoniatricyclo[5.2.1.0^{10}]decane iodide and 1-propyl-4,7-diaza-1-azoniatricyclo[5.2.1.0^{10}]decane iodide have been described by Battle and Spiccia [34].

Instrumentation and methods: Organic solutions were dried with anhydrous $MgSO_4$ before concentration, which were performed under reduced pressure at 50 °C (water bath). All NMR spectra were recorded using Bruker and Varian Spectrometers. ^{1}H and ^{13}C spectra were performed in $CDCl_3$ or D_2O at 25 °C using 200, 300 or 400 MHz instruments. Samples were calibrated using TMS as an internal standard. Electrospray ionisation (ESI) mass spectra were recorded on a Micromass Platform *II* quadrupole mass spectrometer fitted with an ESI source. The capillary voltage was at 3.5 eV and the cone voltage at 35 V. UV–Vis spectra were recorded using Varian Cary 300 or Cary 5G spectrophotometers. IR spectra were recorded using a Perkin–Elmer FTIR 1600 series spectrometer at 4.0 cm^{-1} resolution, using either KBr discs, nujol mulls, or neat liquid as listed. Cation exchange chromatography of complexes was performed using Sephadex™ SP C25 columns of 30 mm diameter. Column chromatography of ligands was performed using Merck 60 silica gel. 10 mL fractions were collected and analysed by TLC, using silica gel 60 F-254 (Merck) plates, with detection of species present by UV irradiation or $KMnO_4$ spray.

!!Caution!! Although no problems were encountered in this work, transition metal perchlorates are potentially explosive and should be prepared in small quantities and handled with care.

2.1. 1-Ethyl-4-isopropyl-1,4,7-triazacyclononane trihydrochloride (*L1* · 3HCl)

1-Ethyl-4,7-diaza-1-azoniatricyclo[5.2.1.0^{10}]decane iodide (8.29 g, 28.1 mmol) was dissolved in 50 mL H_2O and refluxed for 24 h. The solvent was then removed under

reduced pressure to yield a colourless oil. Yield of 1-ethyl-4-formyl-1,4,7-triazacyclononane: 4.94 g, 95%. ^{1}H NMR spectrum (D_2O): δ 8.14 (s, 1H, formyl C*H*), 3.36–2.78, (m, 2H, ethyl CH_2; 12H, CH_2 tacn ring), 1.11 (t, 3H, ethyl CH_3). ^{13}C NMR spectrum ($CDCl_3$): δ 165.8 (d, *C*H formyl), 52.3–43.6 (m, *C*H_2, ring atoms, 6C, ethyl *C*H_2, 1C) 12.16 (s, 1C, ethyl *C*H_3).

1-Ethyl-4-formyl-1,4,7-triazacyclononane (4.94 g, 26.6 mmol) was dissolved in 50 mL acetonitrile, and to this solution was added 7.5 g of Na_2SO_4 (drying agent) and 10 equivalents of Na_2CO_3. A solution of 2-iodopropane in 10 mL acetonitrile was then added to this solution, and the mixture stirred at 60 °C for 72 h. The mixture was then cooled to room temperature and filtered through celite, resulting in an orange filtrate. The solvent was removed under reduced pressure to yield an orange oil containing a white precipitate. Chloroform was added to the mixture, and the solution filtered to remove any inorganic salts. The solvent was removed *in vacuo* to afford 1-ethyl-4-formyl-7-isopropyl-1,4,7-triazacyclononane as a yellow oil. Yield: 4.74 g, 80%. ^{1}H NMR spectrum (D_2O): δ 8.05 (d, 1H, formyl CH), 3.57 (m, 2H, ethyl CH_2), 3.33 (m, 1H, ^{i}Pr C*H* group), 3.1–2.5 (m, 12H, CH_2 tacn ring), 1.01 (m, 6H, ethyl and ^{i}Pr CH_3). ^{13}C NMR spectrum (D_2O): δ 164.32 (d, *C*H formyl), 54.23 (s, ^{i}Pr*C*H,) 54.75–46.93 (m, 6C, *C*H_2 ring), 18.80 (s, ethyl *C*H_3), 18.47 (2C, ^{i}Pr*C*H_3). ESI mass spectrum (H_2O): $m/z = 228.2$, $[M + H]^+$.

1-Ethyl-4-formyl-7-isopropyl-1-4-7-triazacyclononane (4.70 g, 20.7 mmol) was dissolved in 5 M HCl (50 mL) and the solution was refluxed while stirring for 18 h. The solvent was removed under reduced pressure after this time. The resulting brown oily solid was dissolved in 100 mL water, and the pH adjusted to 11 using a 5 M NaOH solution. The desired 1-ethyl-4-isopropyl-1,4,7-triazacyclononane was extracted into chloroform (3×50 mL) and the chloroform layer dried over Na_2SO_4. The solvent was removed under reduced pressure to yield a yellow oil. Suspension of this oil in water, followed by drop wise addition of conc. HCl and concentration of the solution afforded 1-ethyl-4-isopropyl-1,4,7-triazacyclononane · 3HCl. Yield: 4.11 g, 64%. ^{1}H NMR spectrum (D_2O): δ 3.54 (septet, $J = 6.6$ Hz, 1H, ^{i}Pr C*H*), 3.23–3.42 (m, 12H, CH_2 tacn ring), 3.06 (q, $J = 7.2$ Hz, 2H, ethyl CH_2), 1.28 (d, $J = 6.6$ Hz, 6H, ^{i}Pr CH_3), 1.19 (t, $J = 7.2$ Hz, 3H, ethyl CH_3). ^{13}C NMR spectrum (D_2O): δ 58.98 (1C, ^{i}Pr *C*H), 51.5–42.5 (6C, *C*H_2 tacn ring), 17.02 (ethyl *C*H_3), 9.48 (^{i}Pr *C*H_3). ESI mass spectrum (H_2O): $m/z = 200.2$, $[M + H]^+$.

2.2. 1-Isopropyl-4-propyl-1,4,7-triazacyclononane trihydrochloride (*L2* · 3HCl)

1-Propyl-4,7-diaza-1-azaniatricyclo[5.2.1.0^{10}] decane iodide (7.41 g, 23.9 mmol) [34] was dissolved in 50 mL H_2O and stirred under reflux for 24 h. The solvent was then removed under reduced pressure, affording 1-formyl-4-propyl-1,4,7-triazacyclononane as a colourless oil. Yield: 4.49 g, 94%.

Reaction of 1-formyl-4-propyl-1,4,7-triazacyclononane with 2-iodopropane followed by hydrolysis in 5 M HCl and work-up as described above for 1-ethyl-4-isopropyl-1,4,7-triazacyclononane gave the product as a trihydrochloride salt. Yield: 2.81 g, 60%. ^{1}H NMR spectrum (D_2O): δ 3.53 (septet, $J = 6.7$ Hz, 1H, ^{i}Pr C*H*), 3.38–3.22 (m, 12H, tacn ring CH_2), 2.933–2.878 (m, 2H, Pr CH_2), 1.654–1.575 (m, 2H, Pr CH_2), 1.264 (d, $J = 6.7$ Hz, 6H, ^{i}Pr CH_3), 0.86 (t, $J = 7.4$ Hz, 3H, Pr CH_3). ESI mass spectrum (D_2O): $m/z = 214.3$, $[M + H]^+$.

2.3. 1-(3-Aminopropyl)-4-benzyl-7-isopropyl-1,4,7-triazacyclononane tetrahydrochloride (*L3* · 4HCl) and 1-benzyl-4-isopropyl-1,4,7-triazacyclononane (*L4*)

1-Benzyl-4-formyl-1,4,7-triazacyclononane (3.25 g, 13.1 mmol) was reacted with 2-iodopropane and, following work-up as described in the multi-step synthesis of **L1**, afforded 1-benzyl-4-formyl-7-isopropyl-1,4,7-triazacyclononane. Yield: 2.91 g, 76%. ^{1}H NMR spectrum ($CDCl_3$): δ 8.04 (s, 1H, formyl C*H*), 7.31–7.22 (m, 5H, benzyl C*H*), 3.66 (d, $J = 3.86$ Hz, 2H, benzyl CH_2), 3.48–2.38 (m, 12H, CH_2 tacn ring), 0.952 (dt, 6H, CH_3 isopropyl).

Acid hydrolysis of 1-benzyl-4-formyl-7-isopropyl-1,4,7-triazacyclononane (2.91 g, 10.1 mmol) and work-up as in the case of 1-ethyl-4-formyl-7-isopropyl-1-4-7-triazacyclononane gave the desired 1-benzyl-4-isopropyl-1,4,7-triazacyclononane as a yellow oil. Some of this product was used for coordination to copper(II), the rest being used for further derivatisation reactions. Yield of 1-benzyl-4-isopropyl-1,4,7-triazacyclononane (**L4**): 1.93 g, 73%. ^{1}H NMR spectrum (D_2O): δ 7.48 (m, 5H, benzylic), 3.97 (s, 2H, benzylic CH_2), 3.66–3.60 (m, 4H, tacn ring CH_2), 3.39–3.28 (m, 4H, tacn ring CH_2), 3.20–3.08 (m, 4H, tacn ring CH_2), 1.36–1.30 (m, 1H, ^{i}Pr C*H*), 1.30 (d, $J =$ 6.6 Hz, 6H, ^{i}Pr CH_3).

Reaction of 1-benzyl-4-isopropyl-1,4,7-triazacyclononane (1.00 g, 3.83 mmol) with a 1.5 molar equivalent of 3-bromopropylphthalimide, as described for **L1**, gave 1-(3-phthalimidopropyl)-4-benzyl-7-isopropyl-1,4,7-triazacyclononane as an orange/yellow oily solid. Yield: 1.65 g, 96%. Hydrolysis and work-up as described for 1-ethyl-4-formyl-7-isopropyl-1-4-7-triazacyclononane gave 1-(3-aminopropyl)-benzyl-7-isopropyl-1,4,7-triazacyclononane as a yellow-brown oil. This impure oil, containing *bis*(3-aminopropyl)-7-isopropyl-1,4,7-triazacyclononane (**L5**) as a side-product, was used in the synthesis of copper(II) complexes **C3** and **C4** (*vide infra*). In order to purify the ligand, this oil was then suspended in water and conc. HCl was added dropwise until no more white solid precipitated. Yield of **L3** · 4HCl: 0.83 g, 45%. ^{1}H NMR spectrum (D_2O): δ 7.34–7.18 (5H, m, benzylic C*H*), 3.64 (s, 2H, benzylic CH_2), 2.95–2.39 (m, 17H, tacn ring CH_2, amine arm CH_2 and ^{i}Pr C*H*), 1.06–0.95 (m, 2H, amine arm CH_2), 0.94 (d,

$J = 5.2$ Hz, 6H, ^{i}Pr CH_3). ESI mass spectrum (H_2O): $m/z = 319.3$ $[M + H]^+$.

2.4. [Cu(L1)Cl$_2$] · 1/2 H$_2$O (C1)

A 10 mL solution of $CuCl_2 \cdot 2H_2O$ (1.53 g, 9.04 mmol) in water was added to a solution of **L1** (1.60 g, 8.03 mmol) in 10 mL absolute ethanol, resulting in a pale green solution. Dropwise addition of 3 M NaOH to increase the pH to 9 caused the colour to deepen to royal blue, with precipitation of $Cu(OH)_2$. The solution was filtered, and the solvent removed under reduced pressure to yield a dark blue solid. Addition of absolute ethanol to this solid caused it to dissolve, affording a bright green solution with a white solid. The solution was filtered and diethyl ether diffused into it to afford dark green crystals of **C1**. Yield: 1.02 g, 33%.

Microanalysis Calc. for **C1**, $C_{11}H_{26}N_3O_{0.5}Cl_2Cu$: C, 38.5; H, 7.6; N, 12.3. Found: C, 38.2; H, 7.1; N, 12.6%. Selected IR bands (ATR) ν (cm^{-1}): 3227s, 2967s, 2920s, 2875s, 1644m, 1493m, 1451m, 1379m, 1352w, 1290w, 1165m, 1135m, 1101m, 1038m, 1024w, 958m, 888m, 827w, 744w. ESI mass spectrum (EtOH): $m/z = 297.3$ $[Cu(\mathbf{L1})Cl]^+$, 307.3 $[Cu(\mathbf{L1})(OEt)]^+$. UV–Vis spectrum (MeCN: λ_{max} (nm) [ε_{max}] ($M^{-1}\,cm^{-1}$)): 1110 [60], 799 [100], 685 [140], 350 [980], 298 [3600], 273 [4200], 216 [1300].

2.5. [Cu(L4)Cl$_2$] · 4H$_2$O (C2)

This complex was prepared in an analogous fashion to **C1**, starting from a solution of **L4** (1.22 g, 4.67 mmol) in 10 mL absolute ethanol and a solution of $CuCl_2 \cdot 2H_2O$ (0.87 g, 5.1 mmol in 10 mL of absolute ethanol). Vapor diffusion of ether into this solution afforded dark green crystals suitable for X-ray crystallography. Yield: 1.18 g, 64%.

Microanalysis Calc. for **C2**, $C_{16}H_{35}N_3O_4Cl_2Cu_2$: C, 36.4; H, 5.9; N, 8.0. Found: C, 36.5; H, 5.8; N, 8.5%. ESI mass spectrum (EtOH): $m/z = 323.3$ $[Cu(\mathbf{L4})]^+$, 369.3 $[Cu(\mathbf{L4})(OEt)]^+$, 279.2 $[Cu\mathbf{L4}(-^{i}Pr)]^+$. Selected IR bands (ATR) ν (cm^{-1}): 3404s br., 3202s br., 2967s, 2931s, 2874s, 1596s, 1490m, 1453s, 1367s, 1288m, 1129w, 1098w, 980w, 870w, 706m. UV–Vis spectrum (MeCN: λ_{max} (nm) [ε_{max}] ($M^{-1}\,cm^{-1}$)): 609 [140], 247 [5100].

2.6. [Cu(L3)(MeCN)](ClO$_4$)$_2$ (C3) and [Cu(L5)](ClO$_4$)$_2$ · MeCN · NaClO$_4$ (C4)

A solution of $Cu(ClO_4)_2 \cdot 6H_2O$ (1.82 g, 4.94 mmol) in 10 mL H_2O was added dropwise to a solution of crude **L3** (1.43 g, 4.45 mmol) in 10 mL absolute ethanol, resulting in a pale blue solution. The pH was increased to 9 using 3 M NaOH solution, resulting in a darker blue solution. Any precipitated $Cu(OH)_2$ was removed via filtration, and the solution diluted to 1 L with water. The solution was loaded onto a Sephadex SP C25 column (Na^+ form) and then eluted with $NaClO_4$. A pale blue band of $[Cu(OH_2)_6]^{2+}$ eluted first, followed by a pale purple band (which upon concentration did not produce appreciable crystals). A royal blue band of $[Cu(\mathbf{L3})(MeCN)](ClO_4)_2$ eluted with 0.3–0.4 M $NaClO_4$ solution, followed by a further blue band of $[Cu(\mathbf{L5})](ClO_4)_2$ with 0.6 M $NaClO_4$. For each of the collected fractions, excess $NaClO_4$ was removed by successive concentrations of solvent, and removal of the precipitated sodium perchlorate. Blue crystals formed upon cooling when the solvent had been almost evaporated to dryness. These were dissolved in acetonitrile and ether diffused into the resulting solution, yielding royal blue crystals. These were collected at the pump and washed with ether, then air dried. Yield of **C3**: 0.95 g, 34%. Yield of **C4**: 0.59 g, 22%.

Microanalysis Calc. for **C3**, $C_{21}H_{37}N_5Cl_2O_8Cu$: C, 40.6; H, 6.0; N, 11.3. Found: C, 40.8; H, 5.9; N, 11.3%. ESI mass spectrum (H_2O): 409.3 $[Cu(\mathbf{L3})(OH)_2(ClO_4)]^+$. Selected IR bands (ATR) ν (cm^{-1}): 3274m, 2945m, 1587m, 1496m, 1456m, 1396w, 1352w, 1292m, 1051s br., 931m, 850w, 724m, 708m, 622m. UV–Vis spectrum (MeCN: λ_{max} (nm) [ε_{max}] ($M^{-1}\,cm^{-1}$)): 599 [90], 292 [4200].

Microanalysis Calc. for **C4**, $C_{17}H_{38}N_6Cl_3O_{12}CuNa$: C, 28.7; H, 5.4; N, 11.8. Found: C, 28.6; H, 5.6; N, 11.0%. ESI mass spectrum (H_2O/EtOH): $m/z = 347.0$ $[Cu(\mathbf{L5})]^+$. Selected IR bands (KBr) ν (cm^{-1}): 3480s, 3410s, 3230m, 2955m, 3920m, 1618s, 1460m, 1380m, 1086s br, 940m, 630m, 480m. UV–Vis spectrum (MeCN: λ_{max} (nm) [ε_{max}] ($M^{-1}\,cm^{-1}$)): 625 [70], 282 [3500].

2.7. [Cu(L2)Cl$_2$] · 1/2 H$_2$O (C5)

This complex was prepared in an analogous fashion to **C1**, starting from a solution of **L2** (2.55 g, 12 mmol) in 10 mL of absolute ethanol and a solution of $CuCl_2 \cdot 2H_2O$ (2.24 g, 13.0 mmol) in 10 mL of water. Yield: 2.20 g, 54%.

Microanalysis Calc. for **C5**, $C_{12}H_{28}N_3O_{0.50}Cl_2Cu$: C, 40.4; H, 7.9; N, 11.8. Found: C, 40.1; H, 7.7; N, 11.8%. ESI mass spectrum (MeOH/formic acid): $m/z = 321.2$ $[(Cu(\mathbf{L2}))(\mu\text{-}Cl)_2(Cu(\mathbf{L2}))(OH_2)]^{2+}$. Selected IR bands (ATR) ν (cm^{-1}): 3480m br., 3230s br., 2963s, 2873s, 1636w br., 1492m, 1454s, 1385m, 1289w, 1163w, 1133w, 1098m, 1057m, 1014m, 977m, 910w, 826w, 719w. UV–Vis spectrum (MeCN: λ_{max} (nm) [ε_{max}] ($M^{-1}\,cm^{-1}$)): 1110 [68], 802 [103], 686 [153], 351 [1000], 297 [3700], 275 [4100].

2.8. Kinetic studies

The rate of cleavage of *bis*(*p*-nitrophenyl)phosphate (BNPP) by the Cu(II) complexes was measured at pH 7.4 (MOPS buffer) and $T = 50$ °C by following the formation of *p*-nitrophenylate ion in a solution containing 15 μM BNPP, 1 mM Cu(II) complex and $I = 0.15$ M ($NaClO_4$). The experimental procedure and data analysis has been described in detail elsewhere [25,32]. Briefly, in each experiment, a solution of the Cu(II) complex (3 mM, 1 mL) and buffer MOPS (pH 7.4, $T = 50$ °C, $I = 0.382$ M, 1 mL) were placed into a 1 cm cuvette, the cuvette stoppered with a Teflon stopper was inverted to allow the solutions to mix.

The solution temperature was allowed to come to equilibrium (10 min) before the solution of BNPP (0.045 mM, 1 mL) was added to the cuvette. The release of *p*-nitrophenylate from BNPP was followed by monitoring the formation of the *p*-nitrophenylate ion ($\lambda_{max} = 400$ nm, $\varepsilon_{max} = 18\,700\ M^{-1}cm^{-1}$) [35] at 400 nm on a Varian Cary 300 spectrophotometer. Absorbance measurements were commenced after 2 min and were continued for 8000 min with a reading taken every 5 min. As the complex was in large excess compared to BNPP, for complexes **C1**, **C2** and **C5** the appearance of NP (and cleavage of BNPP) was modelled as a first order process $Abs = A + Be^{-k_{obs}t}$, as done in these previous studies [25,32]. These reactions were followed for at least three-half lives and excellent fits to the data were obtained as indicated by the low errors in the first order rate constants. For the complex **C3**, the extremely slow reaction was followed for 5–10% conversion of BNPP and the variation in absorbance with time appeared to be linear. In this case, the initial rates method, applied by Burstyn et al. [26] was used to determine the initial rate constants, which were then converted to first order rate constants.

2.9. Crystal structure determinations

Intensity data for a dark green crystal of **C1** (0.21 × 0.20 × 0.17 mm), a dark green crystal of **C2** (0.75 × 0.65 × 0.20 mm), a royal blue crystal of **C3** (0.19 × 0.18 × 0.15 mm) and dark blue crystal of **C4** (0.31 × 0.27 × 0.19 mm) were measured at 123 K on a Nonius Kappa CCD fitted with graphite-monochromated Mo Kα radiation (0.71073 Å). The data were collected to a maximum 2θ value of 55° and processed using the Nonius software. Crystal parameters and details of the data collection and refinement for **C1**–**C4** are summarised in Table 1.

Each structure was solved by direct methods and expanded using standard Fourier routines in the SHELX-97 software package [36,37]. All non-hydrogen atoms were refined anisotropically and all hydrogen atoms were placed and refined in idealised positions. The structure of **C1** had a small disorder on one of the isopropyl pendant arms of the complex cations in the ASU, consequently C(20) and C(22) were modeled as half occupancy. For **C4**, there was a 11% disorder of the complex cation, with it residing in another position. The site occupancies of the two components were refined against each other and the disorder was successfully modeled, with the bond lengths and angles of the 11% part restricted with the SAME restriction to the 89% part, also all the isotropic displacement parameters of the 11% part were assumed to be similar and the SIMU restriction was placed upon them. The anisotropically refined Cu1′ (11% disordered copper) also had an isotropic restriction placed upon it. The other atoms in the 11% disordered part were refined isotropically (see Table 2).

3. Results and discussion

Despite the higher activities of $[Cu(Me_3tacn)(OH_2)_2]^{2+}$ and $[Cu(^iPr_3tacn)(OH_2)_2]^{2+}$ in affecting phosphate ester hydrolysis when compared to the non-substituted analogue, $[Cu(tacn)(OH_2)_2]^{2+}$ [25,32,26], little attention has been paid thus far to examining the activity of further copper(II) complexes of substituted tacn ligands, particularly those of the asymmetrically-functionalised kind. We thus set out in this study to prepare a series of new tacn derivatives, incorporating alkyl, aryl and amine pendant groups, in order to elucidate the structure–activity relationship between the type and degree of *N*-alkylation of the tacn ligand and the ability of its corresponding copper complex to perform phosphate ester bond scission.

Table 1
Crystal data for **C1**–**C4**

Compound	**C1**	**C2**	**C3**	**C4**
Empirical formula	$C_{11}H_{25}Cl_2CuN_3$	$C_{16}H_{27}Cl_2CuN_3$	$C_{21}H_{37}Cl_2CuN_5O_8$	$C_{17}H_{38}Cl_2CuN_6O_8$
M (g mol^{-1})	333.79	395.85	622.00	588.97
Crystal system	monoclinic	monoclinic	monoclinic	monoclinic
Space group	$P2_1/c$	$P2_1/n$	$P2_1/c$	$P2_1/c$
a (Å)	15.097(3)	13.017(3)	9.3755(19)	9.756(2)
b (Å)	15.299(3)	7.4966(15)	14.540(3)	12.983(3)
c (Å)	14.460(3)	17.908(4)	19.989(4)	20.356(4)
β (°)	115.33(3)	99.18(3)	95.34(3)	99.46(3)
Volume (Å^3)	3018.7(10)	1725.1(6)	2713.1(9)	2543.2(9)
Z	8	4	4	4
μ (Mo Kα) (mm^{-1})	1.785	1.576	1.055	1.121
D_{calc} (g cm^{-3})	1.467	1.524	1.523	1.528
Number of data measured	23 837	11 291	15 645	17 736
Unique data (R_{int})	7158 (0.0996)	4194 (0.0673)	6571 (0.0676)	6219 (0.0518)
Observed data [$I > 2\sigma(I)$]	3586	2625	3652	4368
Final R_1[a], wR_2[b] (observed data)	0.0583, 0.1246	0.0748, 0.1399	0.0481, 0.0861	0.0510, 0.1233
Final R_1, wR_2 (all data)	0.1577, 0.1507	0.1336, 0.1599	0.1241, 0.1046	0.0849, 0.1402
$\rho_{min,max}$ (e Å^3)	−0.634, 1.213	−0.688, 0.768	−0.539, 0.491	−0.904, 1.215

[a] $R_1 = \sum||F_o| - |F_c||/\sum|F_o|$.
[b] $wR_2 = [\sum w(F_o^2 - F_c^2)^2/\sum w(F_o^2)^2]^{1/2}$.

Table 2
Bond lengths (Å) and angles (°) for **C1** (esd values in parentheses)

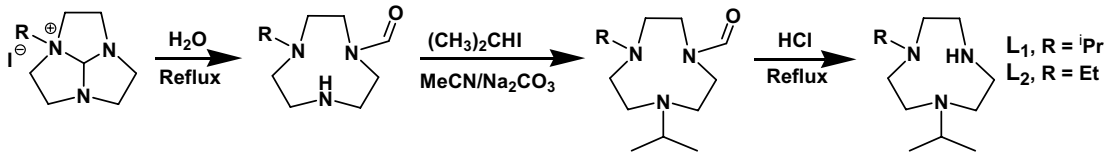
Cu(1)–N(3)	2.015(4)	N(3)–Cu(1)–N(2)	83.3(2)
Cu(1)–N(2)	2.137(4)	N(3)–Cu(1)–Cl(2)	173.7(2)
Cu(1)–Cl(2)	2.246(1)	N(2)–Cu(1)–Cl(2)	94.6(1)
Cu(1)–N(1)	2.275(5)	N(3)–Cu(1)–N(1)	82.3(2)
Cu(1)–Cl(1)	2.299(2)	N(2)–Cu(1)–N(1)	83.0(2)
Cu(2)–N(6)	2.029(4)	Cl(2)–Cu(1)–N(1)	103.3(1)
Cu(2)–N(4)	2.145(4)	N(3)–Cu(1)–Cl(1)	87.0(1)
Cu(2)–N(5)	2.234(4)	N(2)–Cu(1)–Cl(1)	164.3(1)
Cu(2)–Cl(4)	2.258(1)	Cl(2)–Cu(1)–Cl(1)	93.7(5)
Cu(2)–Cl(3)	2.301(2)	N(1)–Cu(1)–Cl(1)	108.0(1)
		N(6)–Cu(2)–N(4)	82.3(2)
		N(6)–Cu(2)–N(5)	82.9(2)
		N(4)–Cu(2)–N(5)	84.2(2)
		N(6)–Cu(2)–Cl(4)	176.3(1)
		N(4)–Cu(2)–Cl(4)	94.0(1)
		N(5)–Cu(2)–Cl(4)	97.0(1)
		N(6)–Cu(2)–Cl(3)	89.5(1)
		N(4)–Cu(2)–Cl(3)	155.4(1)
		N(5)–Cu(2)–Cl(3)	118.0(1)
		Cl(4)–Cu(2)–Cl(3)	93.8(5)

Ligands **L1** and **L2** were prepared using a standard procedure from the respective amidinium salts (Scheme 1), which were available from a previous study [34]. The synthesis of **L3**–**L5** used 1-benzyl-4-formyl-1,4,7-triazacyclononane as starting material [18]. This was reacted with 2-iodopropane to give 1-benzyl-4-formyl-7-isopropyl-1,4,7-triazacyclononane. Acid hydrolysis of this product then gave **L4**. Further reaction with 3-bromopropylphthalimide, followed by acid hydrolysis, yielded **L3** (Scheme 2), which could be isolated in pure form as its hydrochloride salt. The products were obtained in good yields and all returned satisfactory spectroscopic data (see Section 2). **L5** was found to be an impurity in the crude oil from which **L3** was obtained.

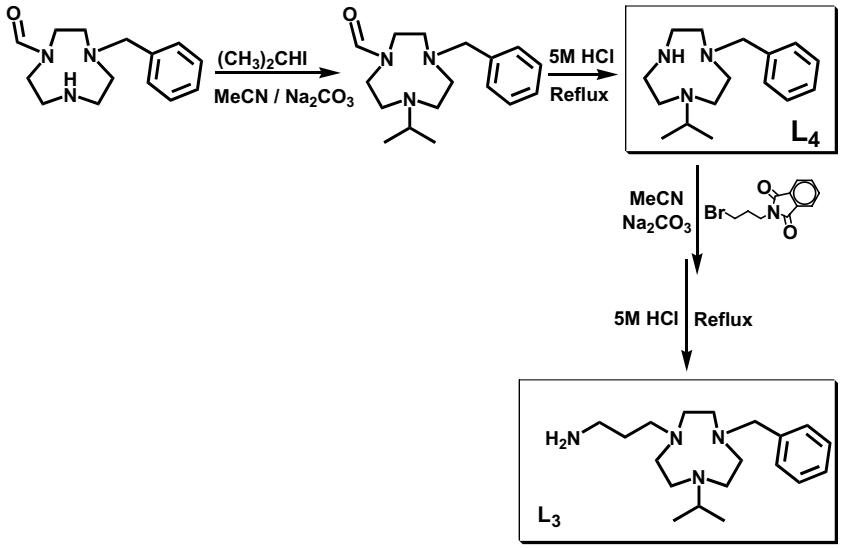
Copper(II) complexes of ligands **L1**–**L5** (see Fig. 2) were formed by reacting the ligands (usually dissolved in ethanol) with an aqueous or alcohol solution of a copper(II) salt and adjustment of the pH to ~9. In some cases the complexes were isolated directly from solution (**C1**, **C2** and **C5**), while in other cases purification by cation-exchange chromatography was necessary prior to isolation of the products as their perchlorate salts. In the case of the preparation of the Cu(II) complex of **L3** from a batch of crude ligand, cation exchange chromatography yielded two copper(II) complexes, corresponding to **C3** and **C4**. The formation of **C4** can only have occurred as a result of partial loss of the benzylic side arm from the 1-benzyl-4-formyl-1,4,7-triazacyclononane intermediate formed during the synthesis of **L3**. We have recently reported a crystallographic and kinetic study on the hydrolysis of tacn amidinium salts in water to their corresponding formyl derivatives, which indicated faster rates of hydrolysis for salts containing the benzyl group [34].

3.1. Crystal structure determinations

The asymmetric unit of **C1** contains two molecules, both of the composition [Cu**L2**Cl_2] and both featuring



Scheme 1. Synthetic route to L_1 and L_2.



Scheme 2. Synthetic route to **L3**–**L4**.

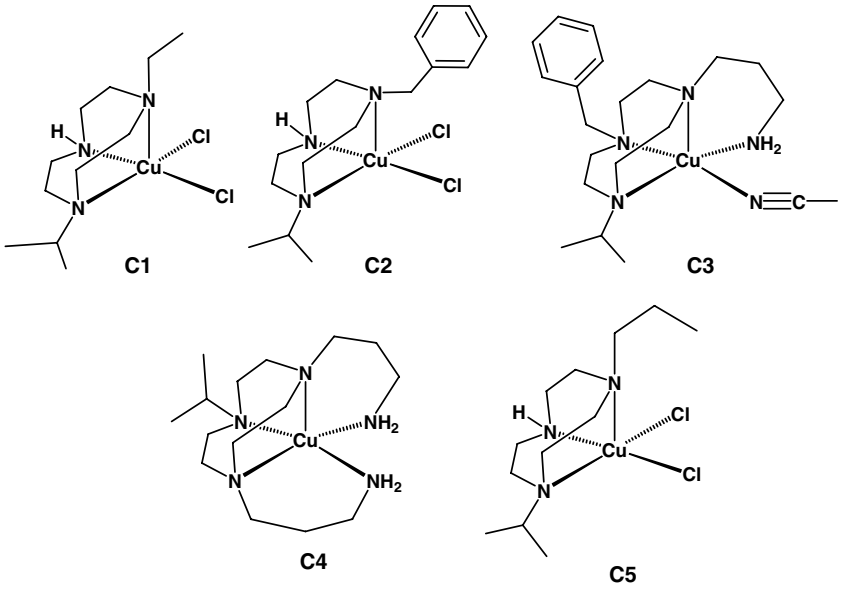


Fig. 2. Copper(II) complexes of asymmetrically-functionalised tacn ligands reported herein.

square-planar CuN_3Cl_2 coordination polyhedra, with the tacn ring facially coordinating the copper(II) centre in a tridentate manner. One of the complex units is distinguished by the fact that the ethyl and isopropyl arms are disordered between two locations (50% occupancy) (Fig. 3). As a consequence, atoms C(20) and C(22) have each been modeled with 50% occupancy. In the figure, the two complexes are discriminated by the labels 'A' and 'B' for the ordered and disordered complexes, respectively. The basal plane coordination environments (defined by two amine donors of the macrocycle and the two chloro ligands) are identical for both complex units, however the mean deviation from the least-squares basal plane in complex A is significantly lower than that of complex B (0.0949 and 0.2119 Å, respectively). The apex of the square-pyramid is occupied by a tertiary nitrogen in each case (involving the ethyl pendant in complex A and the disordered ethyl/isopropyl arm in complex B), with the Cu–N(apical) bond distances being 2.227(5) and 2.234(4) Å for complexes A and B, respectively (Table 3). The complex units exhibit the usual distortion from idealised square planar geometry found for tacn complexes, with all the N–Cu–N angles lying well below 90°, as a result of the constraints imposed by the tridentate coordination mode of the tacn ring. This distortion is evident from the value of the geometric parameter, $\tau = 0.12$, used by Addison et al. [38] to measure the degree of distortion from ideal square-pyramidal geometry ($\tau = 0$) towards trigonal bipyramidal geometry ($\tau = 1$). Adjacent molecular units in the crystal lattice of **C1** are paired up in a "head-to-head" arrangement (Fig. 4), due to two intermolecular

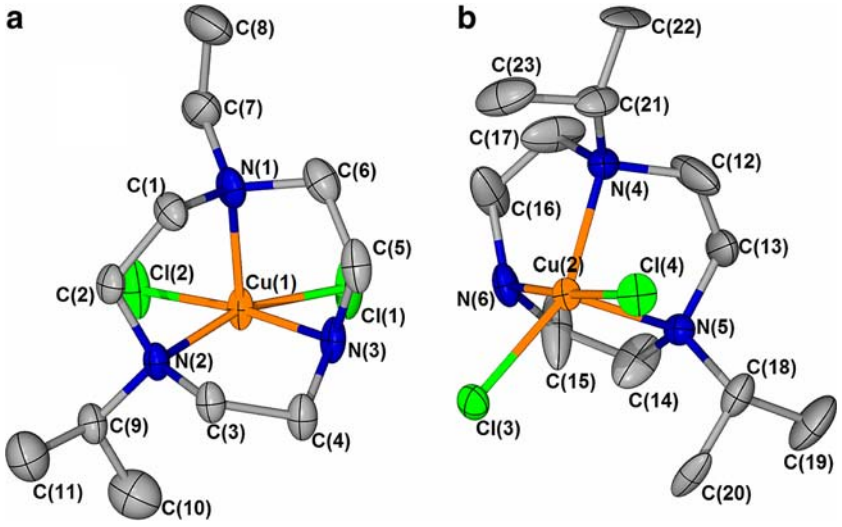


Fig. 3. Thermal ellipsoid plot of the asymmetric unit of **C1**, with ellipsoids drawn at the 50% probability level. The alkyl substituents in molecule 'B' are disordered over two locations (50% occupancy).

Table 3
Selected bond lengths (Å) and angles (°) for **C2** (esd values in parentheses)

Cu(1)–N(2)	2.016(5)	N(2)–Cu(1)–N(1)	82.1(2)
Cu(1)–N(1)	2.163(4)	N(2)–Cu(1)–Cl(2)	178.6(1)
Cu(1)–Cl(2)	2.251(2)	N(1)–Cu(1)–Cl(2)	96.5(1)
Cu(1)–N(3)	2.282(5)	N(2)–Cu(1)–N(3)	81.9(2)
Cu(1)–Cl(1)	2.338(2)	N(1)–Cu(1)–N(3)	82.3(2)
		Cl(2)–Cu(1)–N(3)	98.1(1)
		N(2)–Cu(1)–Cl(1)	88.7(1)
		N(1)–Cu(1)–Cl(1)	151.7(1)
		Cl(2)–Cu(1)–Cl(1)	92.48(6)
		N(3)–Cu(1)–Cl(1)	122.9(1)

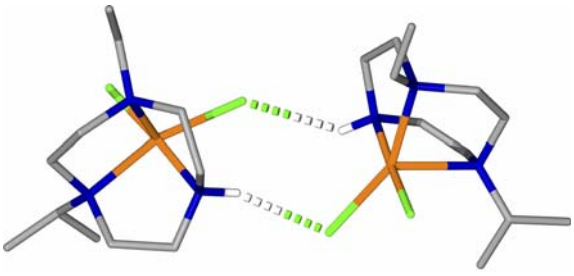


Fig. 4. Stick representation of the hydrogen bonding in **C1** (view down *b* axis).

hydrogen bonding interactions (N(3)–H(3)...Cl(3): 3.234(4) Å, 145.1°; Cl(1)...(H6)–N(6): 3.345(5) Å, 142.1°) (see Table 4).

As for **C1**, an X-ray crystal structure determination of **C2** established that the distorted square-pyramidal copper(II) coordination sphere of the neutral complex is occupied by three amine donors from the macrocycle, which are located on a triangular face of the polyhedron, and two chloride ligands (Fig. 5). There is a distortion from ideal square-pyramidal geometry with $\tau = 0.09$. Within the base of the square-pyramidal coordination sphere, the N(1)–Cu(1)–N(2) bond angle is 81.8(2)°, the contraction resulting from the 5-membered chelate ring, while the Cl(1)–Cu(1)–Cl(2) angle is slightly larger than expected (92.44(5)°). The deviation of the copper centre from the least-squares basal plane (defined by the atoms N(1), N(2), Cu(1), Cl(1) and Cl(2)) towards the apical nitrogen (N(3)) is 0.2505 Å. The apical position is occupied by the nitrogen bearing the isopropyl group, the Cu(1)–N(3) bond

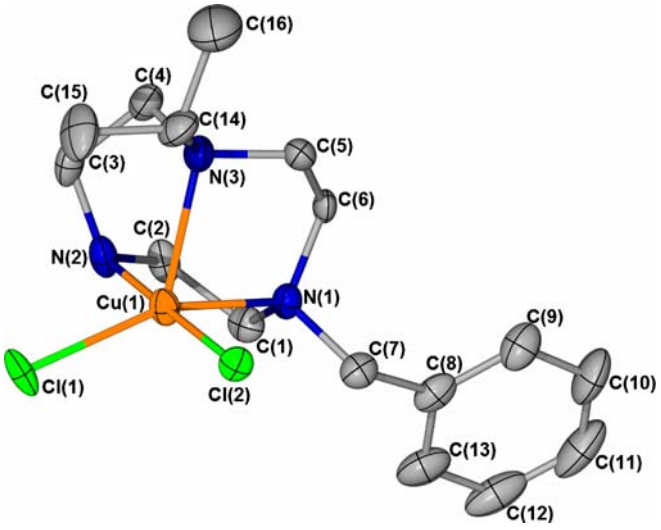


Fig. 5. Thermal ellipsoid plot of **C2**, thermal ellipsoids drawn at the 50% probability level.

length being 2.281(5) Å. All other bond lengths are within the expected ranges, and are detailed in Table 3. Pairs of hydrogen bonds occur between adjacent molecules in the crystal lattice of **C2** (N(2)–H(2)...Cl(1)* and N(2)*–H(2)*...Cl(1), with heteroatom-to-heteroatom distances of 3.317(5) Å, * denoting the symmetry operator ($-x$, $1-y$, $-z$)). This is depicted in Fig. 6, which shows the head-to-head arrangement of the molecules in the crystal lattice.

In the crystal structure of **C3**, shown in Fig. 7, the asymmetric unit consists of a cationic copper complex and two perchlorate anions that balance the charge. The distorted square-pyramidal coordination sphere consists of five nitrogen donors, three from the facially coordinating tacn ring, one from the pendant aminopropyl arm and one from an *N*-coordinated acetonitrile molecule. In this case, the apex of the square-pyramid is occupied by the amine bearing the benzyl arm, with a Cu(1)–N(1) distance of 2.21(1) Å. All other bond lengths and angles are within the expected range. The out-of-plane distance of the copper centre from the least-squares basal plane defined by N(2), N(3), N(4) and N(5) (0.072 Å) is less than in **C2** (0.2505 Å), most likely due to the presence of the N donor atom from the acetonitrile molecule in place of the larger

Table 4
Selected bond lengths (Å) and angles (°) for **C3** (esd values in parentheses)

Cu(1)–N(4)	2.008(2)	N(4)–Cu(1)–N(5)	85.2(1)
Cu(1)–N(5)	2.010(3)	N(4)–Cu(1)–N(2)	95.2(1)
Cu(1)–N(2)	2.026(2)	N(5)–Cu(1)–N(2)	176.6(1)
Cu(1)–N(3)	2.075(2)	N(4)–Cu(1)–N(3)	169.7(1)
Cu(1)–N(1)	2.215(2)	N(5)–Cu(1)–N(3)	92.5(1)
		N(2)–Cu(1)–N(3)	86.5(1)
		N(4)–Cu(1)–N(1)	106.2(1)
		N(5)–Cu(1)–N(1)	97.2(1)
		N(2)–Cu(1)–N(1)	86.0(1)
		N(3)–Cu(1)–N(1)	84.0(1)

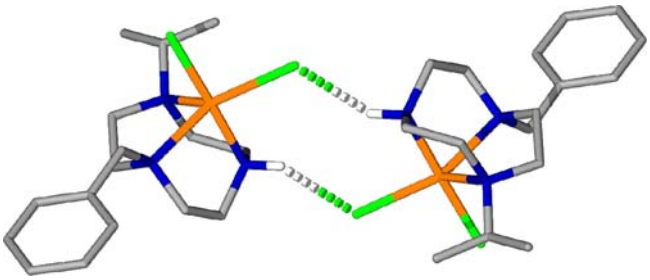


Fig. 6. Stick representation of the hydrogen bonding in **C2** (view down *b* axis).

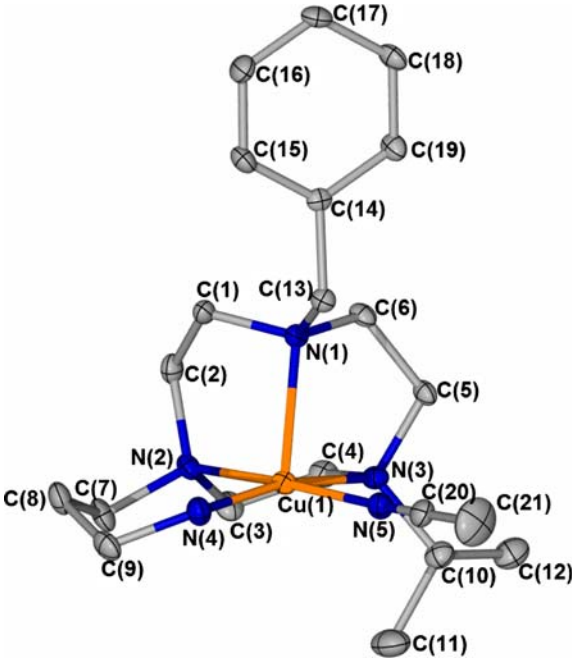


Fig. 7. Thermal ellipsoid plot of the complex cation in **C3**, with ellipsoids drawn at the 50% probability level (hydrogens and counter anions omitted for clarity).

chloro group. The six-membered ring defined by the aminopropyl arm coordinating to the copper centre is in a chair-like conformation. The degree of distortion from ideal square-pyramidal geometry about metal centre is given by the parameter $\tau = 0.18$. Within the crystal lattice, there are hydrogen bonds formed between the amino group of the aminopropyl pendant and neighbouring perchlorate anions (N(4)–H(36)...O(8): 2.971(4) Å, 143.2°; N(4)–H(37)...O(2): 3.129(3) Å, 158.6°) (Fig. 8).

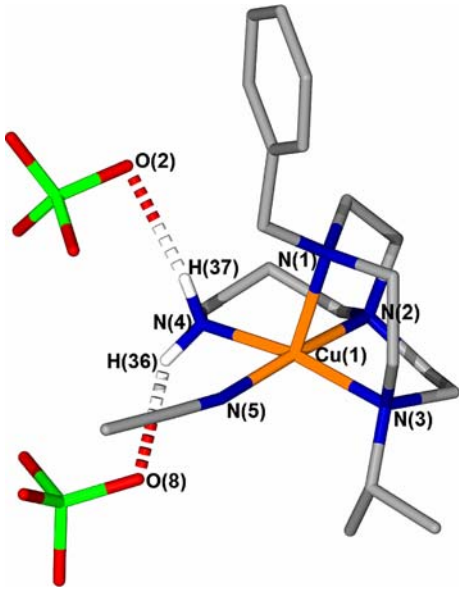


Fig. 8. Stick representation of the H-bonding in **C3**.

The asymmetric unit of **C4** (Fig. 9) contains a square-pyramidal Cu(II) complex in which the Cu(II) coordination sphere is occupied by five nitrogen donors, three from the tacn ring and two from the two aminopropyl pendant groups, i.e., in contrast to **C1**–**C3**, all the sites in the coordination sphere are occupied by the ligand. The divalent cation charge is balanced by two perchlorate anions. As with **C3**, the chelate rings involving the aminopropyl arms adopt a chair conformation. The apex of the square-pyramid is occupied by the tacn nitrogen atom bearing the isopropyl pendant, giving a very long Cu(1)–N(1) bond length of 2.37(1) Å (see Table 5). The degree of deviation from ideal square-pyramidal geometry for this complex is the largest of the complexes reported in this study ($\tau = 0.2$). As in **C3**, hydrogen bonding occurs, between the amino groups of the aminopropyl pendants and the oxygens located on the perchlorate anions (see Table 6 and Fig. 10).

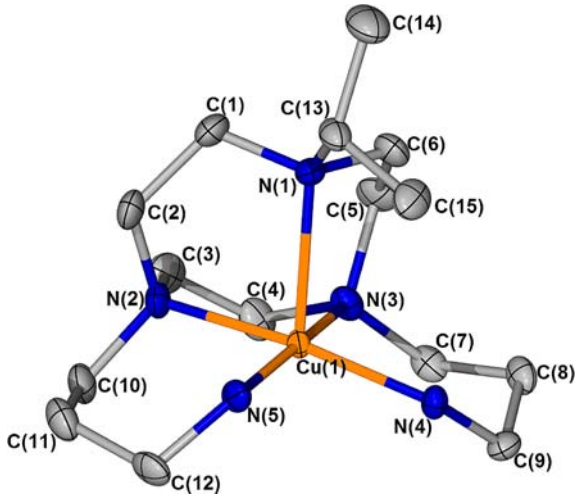


Fig. 9. Thermal ellipsoid plot of the complex cation in **C4**, with ellipsoids drawn at the 50% probability level.

Table 5
Bond lengths (Å) and angles (°) for **C4** (esd values in parentheses)

Cu(1)–N(4)	2.032(3)	N(4)–Cu(1)–N(5)	90.8(1)
Cu(1)–N(5)	2.039(3)	N(4)–Cu(1)–N(3)	93.2(1)
Cu(1)–N(3)	2.062(4)	N(5)–Cu(1)–N(3)	172.1(1)
Cu(1)–N(2)	2.082(4)	N(4)–Cu(1)–N(2)	172.3(1)
Cu(1)–N(1)	2.356(3)	N(5)–Cu(1)–N(2)	91.0(2)
		N(3)–Cu(1)–N(2)	84.2(2)
		N(4)–Cu(1)–N(1)	105.2(1)
		N(5)–Cu(1)–N(1)	100.2(1)
		N(3)–Cu(1)–N(1)	85.4(1)
		N(2)–Cu(1)–N(1)	81.90(1)

Table 6
Hydrogen bonds for **C4** (Å and °)

D–H...A	*d*(D–H)	*d*(H...A)	*d*(D...A)	∠(DHA)
N(4)–H(20)...O(4)	0.92	2.54	3.064(4)	116.4
N(4)–H(20)...O(3)	0.92	2.36	3.252(4)	162.4
N(5)–H(27)...O(3)	0.92	2.07	2.962(4)	162.8
N(5)–H(28)...O(6)	0.92	2.26	3.164(5)	166.1

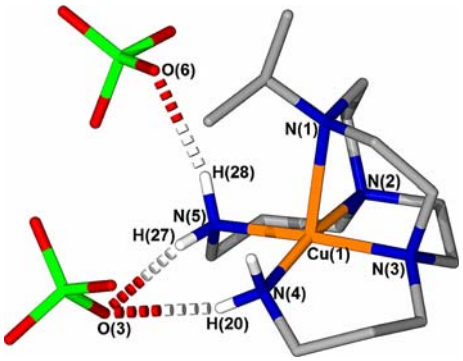
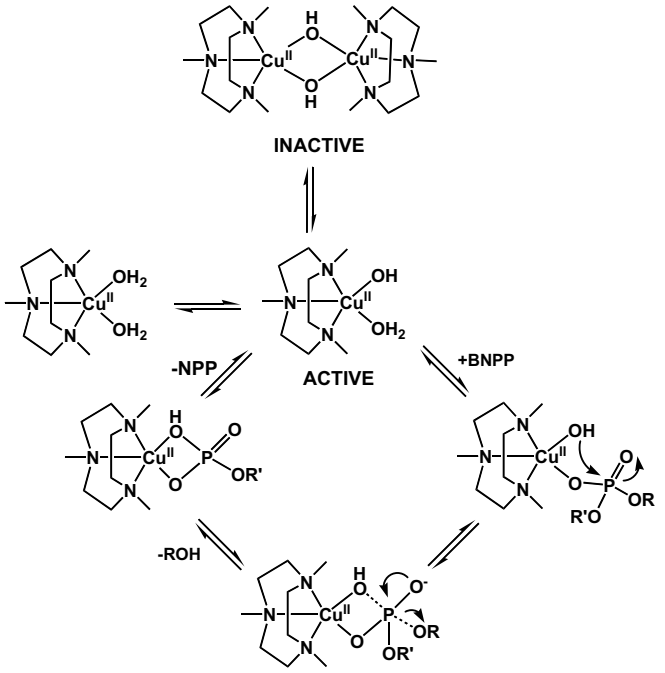


Fig. 10. Stick representation of the H-bonding in **C4**.

3.2. Phosphate ester cleavage studies

The established ability of the copper(II) complexes of the trialkylated tacn ligands, Me_3TACN and $^iPr_3TACN$ [32,26], to effectively cleave phosphate esters prompted us to explore the cleavage characteristics of the complexes reported herein. The complexes were examined for their ability to cleave BNPP, a model phosphate ester whose cleavage releases the *p*-nitrophenolate ion, a chromophore which absorbs strongly at 400 nm. As indicated in the experimental section, the rates of BNPP hydrolysis were estimated from plots of absorbance versus time following the procedure elaborated in the literature by Burstyn et al. [25] and Fry et al. [27]. Four of the copper(II) complexes (**C4** being the exception) demonstrated some ability to hydrolyse BNPP (Table 7). However, the rate of appearance of NP varied from complex to complex and indicated that some complexes were more efficient at accelerating BNPP cleavage than others.

A mechanism for the hydrolytic cleavage of phosphate esters by Cu(II) complexes has been proposed by Burstyn and co-workers (Scheme 3) [30]. According to this mechanism, for a complex to be active (in its monomeric form) it needs to possess one aqua ligand that can be deprotonated to generate a coordinated hydroxyl nucleophile, as well as at least one weakly binding ligand that can be displaced by the phosphate ester to enable substrate binding. This hypothesis is consistent with the observed BNPP hydrolysis rate constants for complexes **C1**–**C5** (Table 7). In complexes **C3** and **C4**, four or five of the coordination sites about the square-pyramidal copper centre (a common geometry for Cu(II) complexes of such ligands) are occupied by the supporting tacn-type ligand. This leaves only one site for the binding of either the phosphate ester substrate or a metal-bound hydroxo group in **C3**, and none in the case of **C4** (see Section 2.9). As a consequence, for these complexes there is no possibility for *intra*molecular attack of a metal-bound hydroxo group on a coordinated phosphate ester, and therefore they are inactive or poorly active.



Scheme 3. Mechanism for the cleavage of BNPP by Cu(II) tacn-type complexes [30].

In contrast to the case for **C3** and **C4**, the aqua complexes formed from **C1, C2** and **C5** were found to significantly accelerate the rate of BNPP hydrolysis, with observed rate constants within 10-fold of those reported for the Cu(II)–Me_3TACN and Cu(II)–$^iPr_3TACN$ complexes. Burstyn and co-workers have suggested that the enhanced hydrolytic activities of these latter complexes relative to the Cu(II) complex of tacn might be due to the three alkyl substituents hindering dimerisation of monomeric aquo forms of the complexes in solution to produce hydrolytically-inactive species (see Scheme 3). Our results suggest that the attachment of only two substituents to the tacn ring is sufficient to significantly suppress such

Table 7
Rates of BNPP hydrolysis by monomeric copper(II) tacn-type complexes[a]

Compound	k_{obs} ($\times 10^5$ s^{-1})	Ref.
C1, $[Cu(\mathbf{L1})(OH_2)_2]^{2+}$[b]	1.43 ± 0.01	this work
C2, $[Cu(\mathbf{L4})(OH_2)_2]^{2+}$[b]	1.53 ± 0.01	this work
C3, $[Cu(\mathbf{L3})(OH_2)_2]^{2+}$[b]	0.0480 ± 0.0001	this work
C4, $[Cu(\mathbf{L5})]^{2+}$	no reaction	this work
C5, $[Cu(\mathbf{L2})(OH_2)_2]^{2+}$[b]	0.44 ± 0.01	this work
$[Cu(^iPr_3tacn)(OH_2)_2]^{2+}$[b]	4.3	[32]
$[Cu(Me_3tacn)(OH_2)_2]^{2+}$[b]	3.7	[32]
$[Cu(Me_2tacn)(OH_2)_2]^{2+}$[b]	1.24	[22]
$[Cu(BzMe_2tacn)(OH_2)_2]^{2+}$[b,c]	7.01	[22]
$[Cu(NCBz_3tacn)(OH_2)_2]^{2+}$[b,c]	30.2	[22]
$[Cu(Me_3tacn)(OH_2)_2]^{2+}$[b,c]	11.2	[22]
OH^- @ 100 °C	0.04	[32]

Abbreviations: Me_2tacn = 1,4-dimethyl-1,4,7-triazacyclononane, $BzMe_2$-tacn = 1-benzyl-4,7-dimethyl-1,4,7-triazacyclononane, $NCBz_3tacn$ = 1,4,7-*tris*(3-cyanobenzyl)-1,4,7-triazacyclononane.

[a] Conditions: pH 7.4 (MOPS buffer), [BNPP] = 15 μM, [Complex] = 1 mM, $I = 0.15$ M ($NaClO_4$), $T = 50$ °C.

[b] Aquo-complexes formed on dissolution in aqueous solution.

[c] Solvent mixture 1:3 MeCN/H_2O.

dimerisation, leading to enhanced rates of BNPP hydrolysis relative to that of the parent Cu(II)-tacn complex. Complex **C2**, incorporating a benzyl group, displayed the fastest rate under the screening conditions. This is consistent with results from our previous work, which showed that the copper(II) complex of 1,4,7-*tris*(3-cyanobenzyl)-1,4,7-triazacyclononane is the fastest monomeric copper(II)-based tacn system for phosphate ester cleavage [22]. The benzyl group may be the most effective at sterically inhibiting the formation of inactive dihydroxo-bridged dimeric species in solution. It may also contribute to substrate binding via hydrophobic interactions with the aromatic rings of BNPP.

In addition to steric effects, the lower rate constants observed for **C1** and **C2** relative to that of the Cu(II)-Me_3tacn complex could also be due partly to electronic effects. It has been shown that the pK_a of the coordinated water in $[LCu(OH_2)_2]^{2+}$ (L = tacn, Me_3tacn, $^iPr_3$tacn) increases on progressing from the native tacn ligand to the Me_3tacn and $^iPr_3$tacn analogues, and that pK_{dim} (dimerisation constant) decreases similarly [32]. The lowering in the pK_a could be due to the poorer binding ability of the bulky tertiary nitrogens, which cause the metal centre to coordinate water more strongly. The observed decrease in pK_a, and hence in pK_{dim}, would lead to an increase in observed rate constant. In the case of **C1** and **C2**, the presence of a secondary nitrogen could result in slightly higher pK_a and pK_{dim} values, leading to a slightly higher concentration of inactive species of complex at the pH of the BNPP hydrolysis reaction.

4. Conclusion

A series of new asymmetrically *N*-substituted tacn ligands were synthesised and used to prepare the corresponding copper(II) complexes. These complexes were structurally characterised via X-ray crystallography, confirming that the Cu(II) centres reside in square-pyramidal geometries, with one face of the coordination polyhedron occupied by the three nitrogen donors from the tacn ring. This structural information was then used to rationalise the ability to of these complexes carry out hydrolysis on a model phosphodiester (BNPP). The copper(II) complexes of the disubstituted ligands, 1-benzyl-4-isopropyl-1,4,7-triazacyclononane (**L4**) and 1-ethyl-4-isopropyl-1,4,7-triazacyclononane (**L1**), were found to exhibit the fastest rates of hydrolysis at near physiological conditions ($k = 1.5 \times 10^{-5}\ s^{-1}$ and $1.4 \times 10^{-5}\ s^{-1}$, respectively). These rates are only three times slower than those found for the copper complexes of Me_3tacn and $^iPr_3$tacn. This level of hydrolytic activity is encouraging, since disubstituted ligands are ideal candidates for attachment, via the sole remaining secondary amine, to oligonucleotides and peptides targeting specific biomolecules. The resultant bioconjugates could then be used to selectively cleave these biomolecules, leading to new therapeutic agents for the treatment of various diseases.

5. Supplementary material

Crystallographic data for the structural analysis have been deposited with the Cambridge Crystallographic Data Centre, CCDC # 604324 for **C1**, 604325 for **C2**, 604326 for **C3**, and 604327 for **C4**. Copies of this information may be obtained free of charge from The Director, CCDC, 12 Union Road, Cambridge, CB2 1EZ, UK (fax: +44 1223 336 033; e-mail: deposit@ccdc.cam.ac.uk or http://www.ccdc.cam.ac.uk).

Acknowledgments

This work was supported by the Australian Research Council (ARC) and by an Australian Postgraduate Award to M.J.B.

References

[1] C.S. Rossiter, R.A. Mathews, J.R. Morrow, Inorg. Chem. 44 (2005) 9397.
[2] B. Graham, L. Spiccia, B.W. Skelton, A.H. White, D.C.R. Hockless, Inorg. Chim. Acta 358 (2005) 3974.
[3] H.-C. Liang, Y. Zhang, S.K. Das, S.M. Sato, J.R. McClean, J.R. Galvan, L.N. Zakharov, A.L. Rheingold, K.A. Wheeler, Abstracts of Papers, 229th ACS National Meeting, San Diego, CA, United States, March 13–17, 2005, INOR-947.
[4] V.L. Pecoraro, M. Scarpellini, S. Sherman, J.W. Kampf, Abstracts of Papers, 228th ACS National Meeting, Philadelphia, PA, United States, August 22–26, 2004, INOR-441.
[5] Y. Zhang, E. Oldfield, J. Am. Chem. Soc. 126 (2004) 9494.
[6] B.A. Jazdzewski, A.M. Reynolds, P.L. Holland, V.G. Young, S. Kaderli, A.D. Zuberbuehler, W.B. Tolman, J. Bio. Inorg. Chem. 8 (2003) 381.
[7] S. Delagrange, R. Delgado, F. Nepveu, J. Bio. Inorg. Chem. 81 (2000) 65.
[8] A.R. Battle, B. Graham, L. Spiccia, B. Moubaraki, K.S. Murray, B.W. Skelton, A.H. White, Inorg. Chim. Acta 359 (2006) 289.
[9] J.-N. Rebilly, L. Catala, E. Riviere, R. Guillot, W. Wernsdorfer, T. Mallah, Inorg. Chem. 44 (2005) 8194.
[10] M. Li, D. Bonnet, E. Bill, F. Neese, T. Weyhermueller, N. Blum, D. Sellmann, K. Wieghardt, Inorg. Chem. 41 (2002) 3444.
[11] R.J. Parker, L. Spiccia, B. Moubaraki, K.S. Murray, D.C.R. Hockless, A.D. Rae, A.C. Willis, Inorg. Chem. 41 (2002) 2489.
[12] B. Graham, L. Spiccia, G.D. Fallon, M.T.W. Hearn, F.E. Mabbs, B. Moubaraki, K.S. Murray, J. Chem. Soc., Dalton Trans. (2002) 1226.
[13] G. Haselhorst, S. Stoetzel, A. Strassburger, W. Walz, K. Wieghardt, B. Nuber, J. Chem. Soc., Dalton Trans. (1993) 83.
[14] J.A. Halfen, W.B. Tollman, K. Wieghardt, Inorg. Synth. 32 (1998) 75.
[15] J.E.W. Scheuermann, F. Ronketti, M. Motevalli, D.V. Griffiths, M. Watkinson, New J. Chem. 26 (2002) 1054.
[16] P. Rossi, F. Felluga, P. Scrimin, Tetrahedron Lett. 39 (1998) 7159.
[17] S.P. Creaser, S.F. Lincoln, S.M. Pyke, J. Chem. Soc., Perkin Trans. 1 (1999) 1211.
[18] A. Warden, B. Graham, M.T.W. Hearn, L. Spiccia, Org. Lett. 3 (2001) 2855.
[19] B. Graham, L. Spiccia, G.D. Fallon, M.T.W. Hearn, F.E. Mabbs, B. Moubaraki, K.S. Murray, J. Chem. Soc., Dalton Trans. (2001) 1226.
[20] K. Wieghardt, P. Chaudhuri, D. Ventur, E.-M. Peters, K. Peters, A. Simon, Angew. Chem., Int. Ed. 24 (1985) 58.
[21] L. Spiccia, B. Graham, M.T.W. Hearn, G. Lazarev, B. Moubaraki, K.S. Murray, E.R.T. Tiekink, J. Chem. Soc., Dalton Trans. (1997) 4089.
[22] M.J. Belousoff, M.B. Duriska, B. Graham, S.R. Batten, B. Moubaraki, K.S. Murray, L. Spiccia, Inorg. Chem. 47 (2006) 3746.

[23] J.N. Burstyn, K.A. Deal, Inorg. Chem. 32 (1993) 3585.
[24] K.A. Deal, Inorg. Chem. 40 (2001) 4176.
[25] K.A. Deal, J.N. Burstyn, Inorg. Chem. 35 (1996) 2792.
[26] K.M. Deck, T.A. Tseng, J.N. Burstyn, Inorg. Chem. 2002 (2002) 669.
[27] F.H. Fry, Ph.D., Monash University, 2002.
[28] F.H. Fry, P. Jensen, C.M. Kepert, L. Spiccia, Inorg. Chem. 42 (2003) 5637.
[29] O. Iranzo, T. Elmer, J.P. Richard, J.R. Morrow, Inorg. Chem. 42 (2003) 7737.
[30] E.L. Hegg, J.N. Burstyn, Coord. Chem. Rev. 173 (1998) 133.
[31] A.C. Warden, L. Spiccia, M.T.W. Hearn, J.F. Boas, J.R. Pilbrow, Dalton Trans. (2005) 1804.
[32] F. Fry, A.J. Fischmann, M.J. Belousoff, L. Spiccia, J. Brugger, Inorg. Chem. 44 (2005) 941.
[33] T.J. Atkins, J. Am. Chem. Soc. 102 (1980) 6365.
[34] A.R. Battle, L. Spiccia, Tetrahedron 61 (2005) 7499.
[35] D.A. Pot, J.E. Dixon, J. Biol. Chem. 267 (1992) 140.
[36] G.M. Sheldrick, SHELXL-97, University of Göttingen, Germany, 1997.
[37] G.M. Sheldrick, SHELXS-97, University of Göttingen, Germany, 1997.
[38] A.W. Addison, T.N. Rao, J. Reedijk, J. van Rijn, G.C. Verschoor, J. Chem. Soc., Dalton Trans. (1984) 1349.

Available online at www.sciencedirect.com
ScienceDirect
Polyhedron 26 (2007) 356–368
POLYHEDRON
www.elsevier.com/locate/poly

Opal and inverse opal photonic crystals: Fabrication and characterization

Geoffrey I.N. Waterhouse [a,b], Mark R. Waterland [b,*]

[a] Department of Chemistry, University of Auckland, Private Bag 92019, Auckland, New Zealand
[b] Nanomaterials Research Centre and MacDiarmid Institute for Advanced Materials and Nanotechnology, Massey University, Private Bag 11222, Palmerston North, New Zealand

Received 14 April 2006; accepted 21 June 2006
Available online 5 July 2006

Abstract

Three-dimensional photonic crystals made of close-packed polymethylmethacrylate (PMMA) spheres or air spheres in silica, titania and ceria matrices have been fabricated and characterized using SEM, XRD, Raman spectroscopy and UV–Vis transmittance measurements. The PMMA colloidal crystals (opals) were grown by self-assembly from aqueous suspensions of monodisperse PMMA spheres with diameters between 280 and 415 nm. SEM confirmed the PMMA spheres crystallized uniformly in a face-centred cubic (fcc) array, and UV–Vis measurements show that the colloidal crystals possess pseudo photonic band gaps in the visible and near-IR regions. Inverse opals were prepared by depositing silica (SiO_2), titania (TiO_2) or ceria (CeO_2) in the voids of the PMMA colloidal crystals using sol-gel procedures, then calcining the resulting structure at 550 °C to remove the polymer template. The resulting macroporous materials showed fcc ordering of air spheres separated by thin frameworks of amorphous silica, nanocrystalline titania or nanocrystalline ceria particles, respectively. Optical measurements confirmed the photonic nature of the inverse opal arrays. UV–Vis data collected for the opals and inverse opals obeyed a modified Bragg's law expression that considers both diffraction and refraction of light by the photonic crystal architectures. The versatility of the colloidal crystal template approach for the fabrication of macroporous oxide structures is demonstrated.
© 2006 Published by Elsevier Ltd.

Keywords: Colloidal crystals; Opals; Inverse opals; Macroporous oxides; Photonic band gaps

1. Introduction

Photonic crystals are highly ordered materials that possess a periodically modulated dielectric constant, with periods on the scale of visible light wavelengths (380–750 nm). Periodicity affects the propagation of electromagnetic waves in the material due to Bragg reflections on lattice planes. The result is a photonic band gap (PBG or stop band), a band of frequencies where light propagation in the photonic crystal is forbidden (the optical analogue of electronic band gaps in semiconductors). A complete photonic band gap occurs when a range of wavelengths is forbidden for every state of polarization and propagation direction [1]. Ever since Yablonovitch [2] and John [3] first demonstrated the possibility of a photonic band gap in such periodic structures, there has been determined effort from the scientific community to develop materials with complete photonic band gaps in various optical regimes and in particular in the visible region [4]. Complete photonic band gap materials could potentially be used to produce waveguides, laser resonant cavities, or to inhibit spontaneous emission [5]. Before their full potential can be realized, improved methods for the fabrication of highly ordered three-dimensional photonic crystals must be developed.

Experimentalists have traditionally used two approaches to fabricate photonic crystals: nanolithography and self-assembly of colloidal crystals. Engineers have used nanolithography (the so-called "top-down" approach) to etch

* Corresponding author. Tel.: +64 6 350 5799; fax: +64 6 350 5682.
E-mail address: M.Waterland@massey.ac.nz (M.R. Waterland).

0277-5387/$ - see front matter © 2006 Published by Elsevier Ltd.
doi:10.1016/j.poly.2006.06.024

successively smaller features into various solid substrates with remarkable precision [6,7]. However, this method is expensive, slow and capable only of producing materials of a few structural layers thickness. The self-assembly of colloidal crystals (the so-called "bottom-up" approach) is the more preferred route as it is simpler, inexpensive and can yield crystalline samples of a few to several hundred structural layers thickness [8,9]. This approach involves the crystallization of a colloidal dispersion of monodisperse spheres of silica, polystyrene or polymethylmethacrylate (PMMA) to form a material with a three-dimensional periodic structure in which 24% of the volume is air (a colloidal crystal or opal). Natural opal is an example of such a periodic colloidal crystal, and is composed of face-centred cubic (fcc) arrays of monodisperse amorphous silica spheres with average diameter in the range 15–900 nm. Theoretical [2,3,10–13] and experimental [8,9] studies have shown that a pseudo photonic band gap exists in the [1 1 1] direction for fcc arrangements of silica or polymer spheres. These opals do not possess a complete photonic band gap, since the band gap position, and hence frequencies of light allowed to propagate within the crystal, vary with the angle of incidence of incoming photons. Most of the technological applications envisaged for photonic crystals require materials that possess a complete photonic band gap. Theoretical requirements to achieve a complete band gap in opaline structures include a refractive index contrast higher than 2.9 and long range three-dimensional crystalline order (see above). The refractive index ratios for colloidal crystals of silica ($n_{silica}/n_{air} = 1.45$), polystyrene ($n_{PS}/n_{air} = 1.59$) and PMMA ($n_{PMMA}/n_{air} = 1.492$) are all well below the value of 2.9 needed for the realization of a full gap, thus they exhibit only pseudo photonic band gaps. A complete PBG is more easily achievable in materials with inverse opal structures, comprising fcc arrays of air spheres in materials with high refractive indices (e.g. Si $n = 3.5$ or Ge $n = 4.5$). The filling fraction of the dielectric in such structures is around 26%. A silicon inverse opal with a complete three-dimensional PBG at 1460 nm has been demonstrated [14]. Inverse opal structures can readily be fabricated from colloidal crystal (opal) templates, by filling the voids in the opal with a dielectric material, and then removing the original opal template by wet chemical etching in the case of SiO_2 or calcination in the case of polymer spheres [9]. The failure to date of researchers to realize a complete PBG in systems other than silicon is due to experimental difficulties in fabricating inverse opals with a large enough refractive index contrast and the required degree of crystalline order.

Macroporous oxides fabricated using the colloidal crystal template approach may also prove useful in other areas of materials science. Recently, dye-sensitized solar cells of the Grätzel type, based on inverse opal TiO_2 films, have been developed [15–17]. The cells show improved power conversion efficiency under simulated solar light compared to Grätzel cells prepared by conventional methods using nanocrystalline titania particles. The improved performance is attributed to the inherent uniformity and macroporosity of inverse opal TiO_2 architectures. Efficiencies could be further improved if technical difficulties related to the fabrication of inverse opal TiO_2 films with uniform thickness and large area could be overcome. The combination of high surface area and macroporosity (hence facile gas flux) suggest that inverse opal structures may also be useful in the field of heterogeneous catalysis [18–20]. It is envisaged that the colloidal crystal template approach could be used to fabricate highly efficient TiO_2 photocatalysts or CeO_2-based catalysts for CO oxidation, the water-gas shift reaction (WGS), the reforming of hydrocarbons and the partial oxidation of methane. To our knowledge, only one previous study of inverse opal ceria has appeared in the literature [21] justifying further research in this area.

In view of the discussion above, we have commenced a comprehensive programme aimed at the fabrication opal and inverse opal thin films with ordered structure extending over large areas. Here we describe the synthesis and characterization of PMMA colloidal crystals (opals) with long range three-dimensional order, and then show how the colloidal crystals can be used as templates for the fabrication of macroporous SiO_2, TiO_2 and CeO_2 structures (inverse opals) possessing comparable order and strong photonic behaviour in the visible and near-IR regions.

2. Experimental

2.1. General

Methyl methacrylate (MMA, 99%), 2,2′-azobis(2-methylpropionamidine) dihydrochloride (97%), tetraethylorthosilicate (TEOS, 98%), titanium (IV) isopropoxide (97%), concentrated HCl (37% in water), $Ce(NO_3)_3 \cdot 6H_2O$ (99%), hexamethylenetetramine (99%), TiO_2 powder (99%, anatase form) and CeO_2 powder (99.9%, <5 μm) were all obtained from Aldrich and used without further purification. CeO_2 nanoparticles were prepared from $Ce(NO_3)_3 \cdot 6H_2O$ and hexamethylenetetramine using a literature procedure [22]. The CeO_2(1 1 1) single crystal was obtained from Commercial Crystal Laboratories Inc. (USA).

2.2. Synthesis of polymethylmethacrylate spheres

Batches of monodisperse PMMA spheres with diameters between 280 and 415 nm were prepared by the method of Schroden et al. [9]. The size of the PMMA spheres produced using this method is highly dependent on the composition of the synthesis mixture and the reaction temperature (see Section 3.1). Syntheses were carried out in a 5-necked round-bottomed flask (3 L volume), fitted with a mechanical stirrer (glass shaft with Teflon stirrer blade), thermometer, water-cooled reflux condenser, nitrogen bubbler and a glass quickfit stopper. The procedure used is outlined below. Milli Q water (1.6 L) and methyl methacrylate (MMA, 200–400 mL) were added to the 5-necked round-bottomed flask.

Nitrogen gas was then slowly bubbled through the resulting two-phase system and vigorous mechanical stirring of the mixture commenced. The mixture was then heated to either 70, 75 or 80 °C, whereupon 2,2′-azobis(2-methylpropionamidine) dihydrochloride (0.75–3 g) was added as an azo initiator and polymerisation of the MMA commenced. The temperature of the reaction mixture increased initially on introduction of the initiator, but then stabilized after approximately 30 min. After stabilization, the reaction mixture was maintained at the initial temperature of either 70, 75 or 80 °C for 2 h. Heating was then discontinued, and the reaction mixture allowed to cool to room temperature over 3–4 h under a nitrogen purge. The resulting colloidal suspensions of PMMA spheres were then filtered through a glass wool plug to remove any large agglomerates and then stored in PET plastic bottles for later use.

2.3. Colloidal crystal preparation

Colloidal crystals of PMMA spheres were fabricated by three methods. Several preparation methods were used in order to determine which method afforded colloidal crystals of the best quality.

(1) *Gravitational sedimentation*: PMMA colloidal suspensions (typically 50 mL) were left in open glass beakers at 25 °C. After 3–5 weeks, water in the colloidal suspensions evaporated to leave well-ordered PMMA photonic crystals. The colloidal crystals were then left to dry in air at 25 °C for a further 1–2 weeks.
(2) *Centrifugation*: PMMA colloidal suspensions were loaded into 50 mL plastic falcon tubes, then centrifuged at 1500 rpm (rcf 369) and 10 °C for 24 h. The supernatant was then carefully removed by decantation, and the colloidal crystals left to dry in air at 25 °C for 1–2 weeks.
(3) *A flow-controlled vertical deposition method* [23,24]: This method was used to deposit thin PMMA colloidal crystals on glass microscope slides for UV–Vis transmittance measurements. Briefly, a colloidal suspension of PMMA spheres was prepared (200 mL, 1–10 wt% PMMA in H_2O) and ultrasonicated for 1 h to break up any agglomerated particles. The colloidal suspension was then poured into a clean glass beaker. Several pre-cleaned glass microscope slides were immersed vertically in the colloidal suspension, after which a peristaltic pump was used to remove the colloidal suspension (pump rate about 0.2 mL min^{-1}). As the liquid level in the beaker decreased, a thin colloidal crystal layer was deposited on the glass slide. This technique proved very effective for uniformly covering large areas. Film thickness could be varied by changing the concentration of PMMA in the colloidal suspension or by changing the pump speed. The 3D colloidal crystals were dried in air for 1–2 weeks before optical measurements.

2.4. Inverse opal preparation

Inverse opals of were prepared by filling the voids in PMMA colloidal crystal templates with SiO_2 or TiO_2 sol-gel precursors, or CeO_2 nanoparticles, then carefully calcining the resulting composite structure to remove the PMMA template. Filling of the voids in the colloidal crystal template was achieved using vacuum assisted infiltration of a sol-gel precursor. Briefly, PMMA colloidal crystals (10 g) prepared by gravitational sedimentation or centrifugation were lightly crushed with a metal spatula to give fractured pieces of size <2 mm, which were then deposited in a thin layer on filter paper in a Büchner funnel. With a strong vacuum applied to the Büchner funnel, a solution of either silica precursor (6 mL TEOS, 4 mL Abs. EtOH, 3 mL H_2O and 1 mL conc. HCl), titania precursor (6 mL titanium (IV) isopropoxide and 6 mL Abs. EtOH) or ceria nanoparticles (12 nm diameter, 10 wt% in ethanol) was applied dropwise over the surface of the PMMA layer. Infiltrated samples were then left to dry in air at 25 °C for 24 h. PMMA templates were then removed by calcination in air using the following protocol; samples were ramped from 25 to 300 °C at 2 °C min^{-1}; held at 300 °C for 5 h; then ramped from 300 to 550 °C at 2 °C min^{-1}; held at 550 °C for 12 h; then finally allowed to cool to room temperature over 3–4 h. The resulting products all displayed strong opalescence under incident light.

For UV–Vis measurements, inverse opals of SiO_2 were prepared from thin film PMMA colloidal crystals grown on glass microscope slides using the flow-controlled vertical deposition method. PMMA templates were infiltrated by carefully placing a few drops of a silica precursor (6 mL TEOS, 4 mL Abs. EtOH, 3 mL H_2O and 1 mL conc. HCl) on each edge of the colloidal crystal. Capillary forces quickly drew the sol-gel mixture into the voids in the PMMA template. The infiltrated crystal was then aged for 24 h under ambient conditions, and then calcined in accordance with procedure described above.

2.5. Product characterization

2.5.1. Particle size determination

PMMA sphere size and polydispersity were determined by dynamic light scattering on a Zetasizer Nano ZS (Malvern Instruments Limited). PMMA colloidal suspensions were diluted approximately 1000-fold with Milli Q water before measurements.

2.5.2. SEM

Opal and inverse opal morphologies were examined using a Philips XL-30 field emission gun scanning electron microscope (FEGSEM). All micrographs were collected at an electron gun accelerating voltage of 5 kV. Specimens were mounted on black carbon tape and platinum sputter coated for analysis.

2.5.3. UV–Vis

UV–Vis transmittance spectra were recorded over the range 200–1000 nm on Shimadzu U-3101PC spectrophotometer, equipped with a custom-built sample holder for angle-resolved UV–Vis measurements.

2.5.4. XRD

Powder X-ray diffraction patterns were acquired using a Philips PW-1130 diffractometer, equipped with a Cu anode X-ray tube and curved graphite filter monochromator. XRD data were collected at room temperature, using monochromatised Cu Kα X-rays ($\lambda = 1.5418$ Å). Additional acquisition parameters were: 2θ range, 2–90°; step size, 0.02°; and scan rate, 2° min^{-1}. Diffraction patterns were referenced against the JCPDS database for sample identification.

2.5.5. Raman

Raman spectra were taken on a Renishaw RM-2 Raman microscope system, fitted with an Olympus 20× objective lens. Raman spectra were excited using 785 nm radiation from a diode laser, and scattered light collected in the 180° backscattering sampling geometry. The laser power at the sample for data collection was ~5 mW. Spectra were collected over the range 200–2000 cm^{-1} and at a resolution of ca. 2 cm^{-1}.

3. Results and discussion

3.1. Synthesis of monodisperse PMMA spheres

The optical quality of colloidal crystals (opals) and their inverted structures is highly dependent on the size uniformity of the spheres used to fabricate the colloidal crystal. In this study, uniformly sized PMMA spheres where fabricated by the free radical induced polymerization of MMA in water. Table 1 shows the effect of synthesis conditions on the size and polydispersity of the PMMA spheres obtained by this method.

Results show that the reaction parameters can be adjusted to produce PMMA spheres of average size, Z_D, from 280 to 415 nm. Small spheres are prepared by using less MMA, higher temperatures or more azo initiator. Conversely, large spheres are obtained by using more MMA, lower temperatures or less azo initiator. The polydispersity of the preparations may be gauged from two indices; the polydispersity index (PDI) which measures width of the particle size distribution (the relative variance in the particle size)

$$\mathrm{PDI} = \frac{\sigma^2}{Z_D^2} \tag{1}$$

and the % polydispersity (%Pd) which measures the coefficient of variation

$$\%\mathrm{PD} = \sqrt{\mathrm{PDI}} \times 100. \tag{2}$$

As a rule of thumb, samples with PDI <0.04 and thus %PD <20% are considered to be monodisperse. From the PDI and %PD values given in Table 1, it is apparent that each PMMA sphere preparation is monodisperse and thus suitable for colloidal crystal construction.

3.2. Fabrication and characterization of PMMA colloidal crystals (opals)

PMMA colloidal crystals (opals) were fabricated by three different methods in order to determine that which afforded the best quality three-dimensional structures. Methods used were gravitational sedimentation, centrifugation and a flow-controlled vertical deposition method (see Section 2.3 for details). All three methods produced high quality colloidal crystals, as determined by SEM and evidenced by the visual colour play of the prepared samples under incident white light. We conclude that preparation method had little effect on the quality of PMMA colloidal crystals, at least for the three methods used here. On account of their shorter fabrication time, centrifugation and the flow-controlled vertical deposition method are preferred.

Fig. 1 shows SEM micrographs for PMMA colloidal crystals deposited on glass microscope slides using the flow-controlled vertical deposition method. Three different PMMA sphere preparations were used to fabricate the colloidal crystals shown in the images. In all cases, close-packed arrays of PMMA spheres are observed, whose (1 1 1) planes are parallel to the underlying substrate. Interestingly, the images show necking of the spheres to their nearest neighbours. Fig. 1f shows the arrangement of spheres in the underlying layer, and clearly demonstrates the close-packed nature of the packing. Sphere diameters measured directly from the SEM images were smaller than those determined by dynamic light scattering (see Table 1)

Table 1
Effect of synthesis conditions on the size and polydispersity of PMMA spheres

Preparation #	Volume MMA (L)	Volume H_2O (L)	Mass initiator (g)	Temperature (°C)	Mean diameter, Z_D (nm)[a]	PDI[a]	% PD
1	0.3	1.6	1.5	80	316	0.019	13.8
2	0.4	1.6	1.5	70	415	0.016	12.6
3	0.3	1.6	1.5	70	364	0.034	18.4
4	0.2	1.6	3	80	280	0.015	12.2
5	0.4	1.6	0.75	75	408	0.025	15.8

[a] Determined by dynamic light scattering.

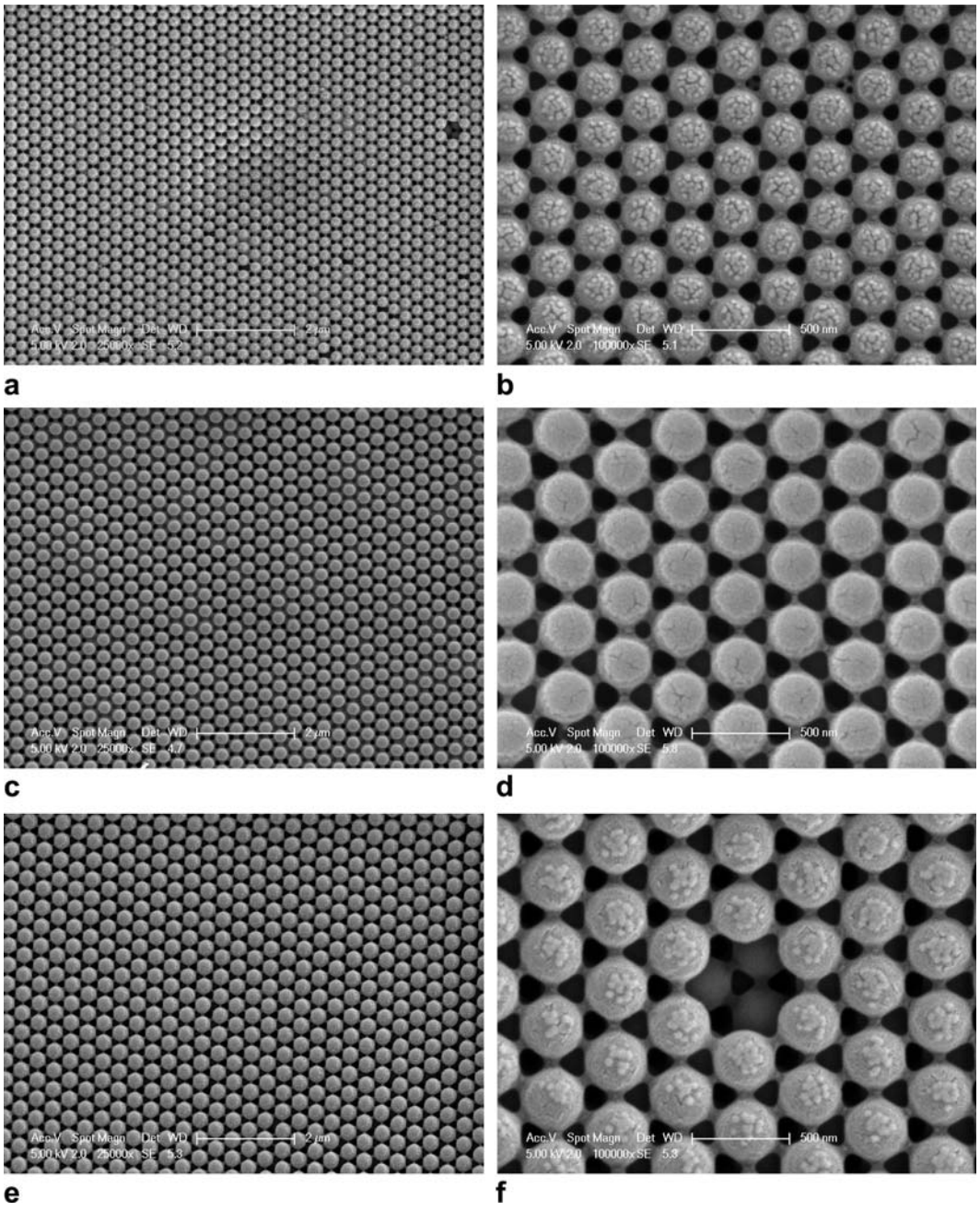


Fig. 1. SEM images of PMMA colloidal crystals fabricated using the flow-controlled vertical deposition method from (a), (b) Prep. 4 PMMA spheres; (c), (d) Prep. 3 PMMA spheres; and (e), (f) Prep. 5 PMMA spheres. Images on the left were taken at 25000× magnification and demonstrate close-packed (1 1 1) planes and long range order, images on the right were taken at 100000× magnification and reveal necking of the individual PMMA spheres to their nearest neighbours.

by approximately 20–22%. This difference is attributed to shrinkage of the PMMA spheres on drying in the colloidal crystal.

Although the images of Fig. 1 confirm a regular close-packed sphere arrangement, they cannot be used to distinguish between the face-centred cubic (ABCABC...) and hexagonal close-packed (ABABAB...) structures. Energetically the fcc structure is preferred over the hcp structure [25], although the energy difference is small. Valuable information about the packing structure of the colloidal crystals can be gained by examining images of a fractured colloidal crystal surface. Fig. 2a was taken from a colloidal crystal prepared by gravitational sedimentation, and exhibits structures that are consistent with the fcc packing arrangement. Note that the close-packed order extends throughout the colloidal crystal, and that fractures occur along well-defined planes in the lattice. All these points reflect the high degree of crystalline order achieved in PMMA colloidal crystals.

In a few of the colloidal crystals prepared, domains of both (1 1 1) and (1 0 0) orientation were observed on the same surface (Fig. 2b). It is unclear why (1 0 0) domains form, although the thermodynamic stability of the (1 1 1)

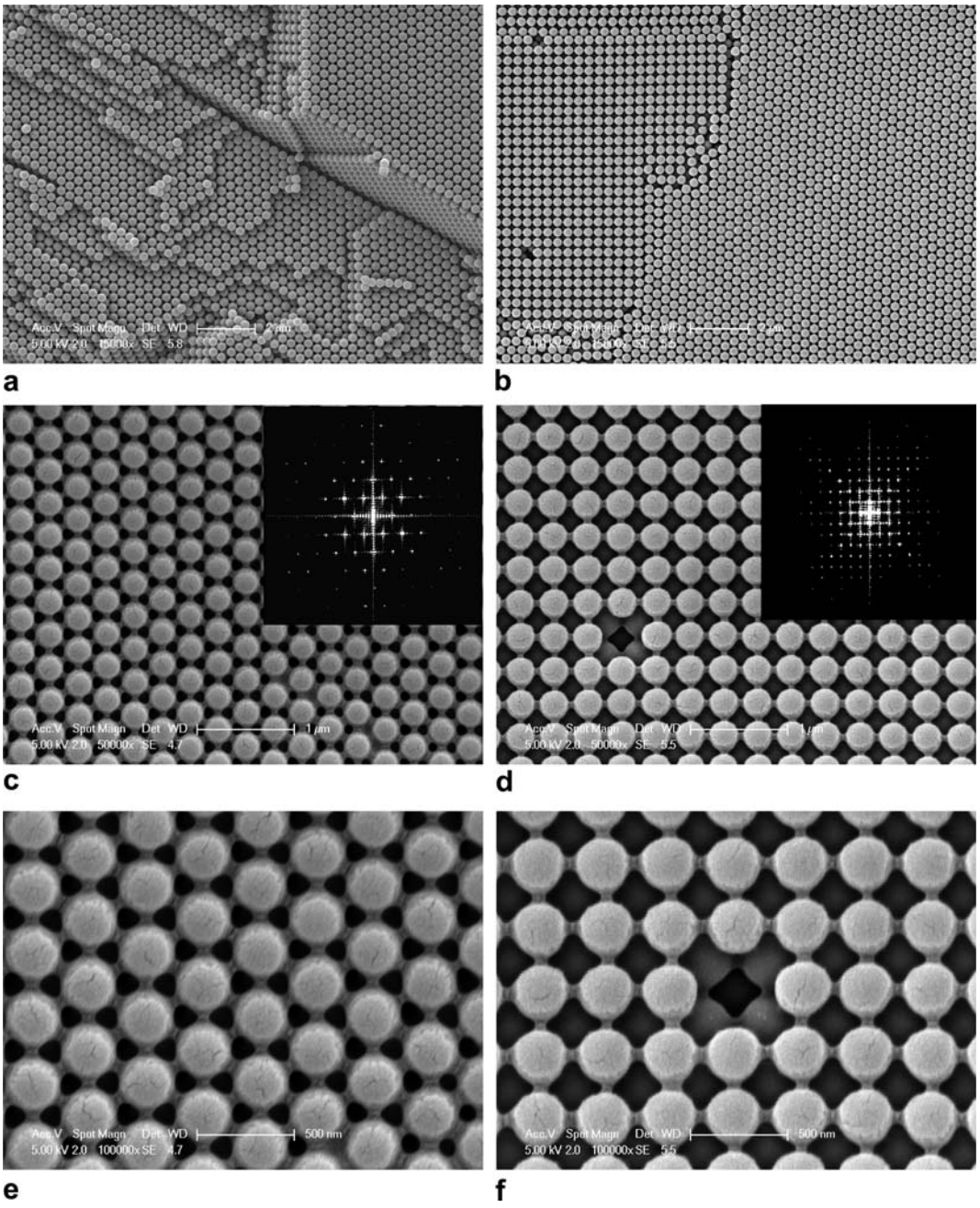


Fig. 2. SEM images of PMMA colloidal crystals fabricated using gravitational sedimentation and Prep 3 PMMA spheres. (a) Fractured surface showing fcc array of spheres, 15000×; (b) colloidal crystal exhibiting domains of both (1 1 1) and (1 0 0) orientations, 15000×; (c), (d) magnified views of the (1 1 1) and (1 0 0) domains, respectively, 50000×; insets show Fourier transforms performed on the images; (e), (f) further magnified views of the (1 1 1) and (1 0 0) domains, respectively, showing the of necking of spheres, 100000×.

and (1 0 0) structures are known to be similar. Figs. 2c and d show magnified views of the (1 1 1) and (1 0 0) faces, respectively. The insets show Fourier transforms (FT) of Fig. 2c and d, performed to examine the geometric structure in the spatial domain of each image. The FTs confirm the hexagonal and square registry, respectively, of the (1 1 1) and (1 0 0) crystallographic domains. The sharpness of the points on the reciprocal lattice and the absence of noise elsewhere indicate the extent of the long-range order. Figs. 1d and 2e demonstrate the similarity between colloidal crystals prepared using two different fabrication methods, while Fig. 2f shows the underlying structure in the (1 0 0) domains.

3.3. Optical properties of the PMMA colloidal crystals (opals)

The position of stop bands (band gaps) in fcc photonic crystals can be estimated using a modified form of Bragg's law (3) which takes into account refraction of light in the composite structure and the incident angle of the incoming light.

$$\lambda_{max} = \frac{2d_{hkl}}{m}\sqrt{n_{avg}^2 - \sin^2\theta}, \quad (3)$$

where λ_{max} is the wavelength of the reflectance peak maximum (i.e. the position of the photonic band gap), d_{hkl} is the interplanar spacing between hkl planes, m is the order of the Bragg diffraction, n_{avg} is the average refractive index of the photonic structure and θ is the angle between the incident light and the surface normal of the sample. For a PMMA colloidal crystal in air at 25 °C, $n_{avg} = n_{PMMA} f_{PMMA} + n_{air} f_{air}$, where $n_{PMMA} = 1.492$, $n_{air} = 1.000$, and f_{PMMA} and f_{air} are the volume fractions occupied by PMMA spheres and air in the structure (generally taken as 74% and 26%, respectively, for a fcc lattice). The SEM micrographs of Fig. 1 show the PMMA colloidal crystals to expose predominantly (1 1 1) planes. In the case of first order Bragg diffraction from fcc (1 1 1) planes, $d_{hkl} = 0.8165D$, where D is the average centre-to-centre distance between spheres on the (1 1 1) planes. Thus, Eq. (3) simplifies to give

$$\lambda_{max} = 1.633D\sqrt{n_{avg}^2 - \sin^2\theta}. \quad (4)$$

For fcc arrays of spheres, D would generally be taken as $2r$, where r is the sphere radius. Here, however, our PMMA spheres are necked. Necking increases the distance between spheres and hence increases the interplanar spacing in the [1 1 1] direction. For this reason, our D values will exceed $2r$. Eq. (4) shows that by using monodisperse spheres of different size, we can vary the wavelengths of light allowed to propagate through the photonic crystal. Experimentally d_{hkl} and n_{avg} are determined by measuring the position of the reflectance maximum (λ_{max}) at different angles of incidence, and plotting λ_{max}^2 against $\sin^2\theta$. If Bragg diffraction conditions are satisfied, a straight line will result with slope $= -(2d_{hkl})^2$ and y-axis intercept $= (2d_{hkl})^2 n_{avg}^2$.

Table 2 summarizes physical and UV–Vis transmittance data for colloidal crystals fabricated from the 5 PMMA preparations described in Table 1. The second and third columns of Table 2 give PMMA sphere diameters and centre-to-centre distances between spheres on the (1 1 1) planes (D), respectively, measured directly from SEM images. Column 4 gives a calculated λ_{max} for diffraction at normal incidence ($\theta = 0°$) from the (1 1 1) planes, obtained using Eq. (4), D values from column 3 and assuming an average refractive index of 1.364. Columns 5–9 give physical parameters determined experimentally from angle-resolved UV–Vis transmittance measurements on the colloidal crystals (see text below). The contents of Table 2 are discussed in conjunction with Figs. 3–5.

UV–Vis transmittance spectra collected at normal incidence ($\theta = 0°$) from colloidal crystals fabricated using preparation 1, 3 and 5 PMMA spheres are shown in Fig. 3a. D values determined experimentally for each preparation are 299, 347, 397 nm (see Table 2 and text below for their determination), respectively. For each preparation, five distinct stop bands are observed (reflectance maxima appear as dips in the transmittance spectra), superimposed on a background of intense sample absorption at low wavelengths. The most intense stop band in each spectrum, located at 689, 774 and 857 nm, respectively, arises from first order Bragg diffraction from (1 1 1) planes of the fcc colloidal crystal lattices. The other bands, with wavelength ratios with respect to the (1 1 1) stop band wavelength of 0.483, 0.500, 0.522, 0.556, are tentatively assigned to diffraction from other planes of the fcc lattice. The stop bands are red-shifted as D (and hence the interplanar spacing in the [1 1 1] direction) increases. According to Eq. (4), a direct proportionality should exist between the two parameters. Fig. 3b shows that the experimentally determined λ_{max} increases linearly with D (open triangles), satisfying the Bragg diffraction criteria. Stop band positions calculated using D values measured directly from SEM images and $n_{avg} = 1.364$ are also shown (closed triangles). Both sets of data are in excellent accord, demonstrating the close association between the geometric and optical properties of the colloidal crystals. At normal incidence, the ratio of the FWHM of the stop band reflection peak (ΔE) to the position of the stop band reflection peak (E) gives a normalised measure of the photonic band gap. For all PMMA colloidal crystal samples prepared, $\Delta E/E$ values between 0.085 and 0.1 were observed.

Figs. 4a and b show UV–Vis transmittance spectra measured at different angles of incidence with respect to the surface normal for colloidal crystals fabricated from Prep. 1 and Prep. 5 PMMA spheres ($\theta = 0°$, $\lambda_{max} = 689$ and 857 nm, respectively). The reflectance maxima for diffraction from the (1 1 1) planes shift to shorter wavelengths as θ increases, as predicted by Eqs. (3) and (4). These samples do not possess a complete photonic band gap, since wavelengths of incident light forbidden at normal incidence can

Table 2
Summarized physical and optical data for the PMMA colloidal crystals prepared in this work

Preparation #	Sphere diameter[a] (nm)	D[a] (nm)	Calculated λ_{max} $\theta = 0°$ (nm)	Experimental d_{111} (nm)	Experimental D (nm)	Experimental n_{avg}	Experimental f_{PMMA}	Experimental λ_{max} $\theta = 0°$ (nm)
1	252	300	668	244	299	1.410	0.83	689
2	325	388	864	325	398	1.32	0.65	863
3	289	347	773	283	347	1.364	0.74	774
4	224	267	595	220	269	1.39	0.79	611
5	317	384	855	324	397	1.32	0.65	857

[a] Measured directly from SEM images.

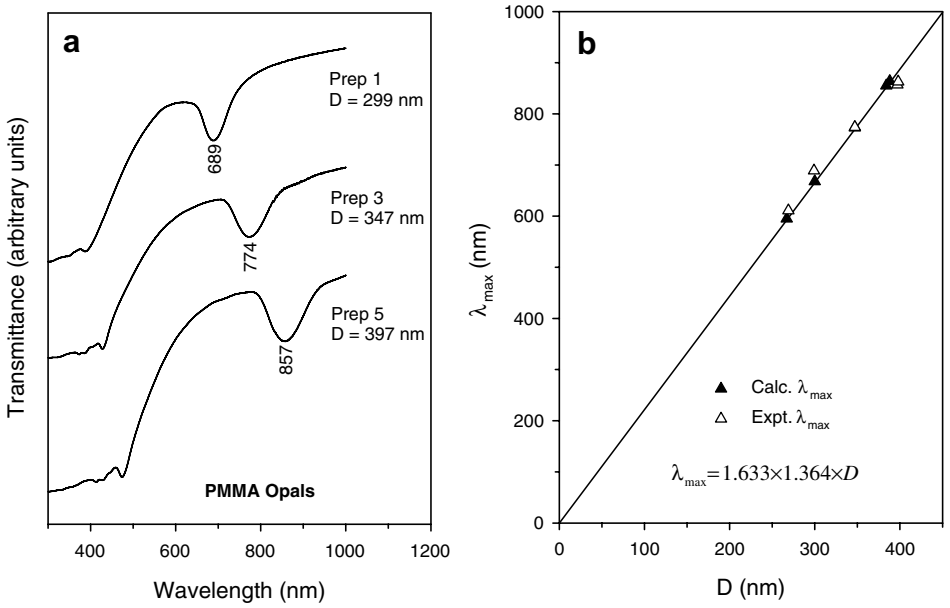


Fig. 3. (a) UV–Vis transmittance spectra collected from PMMA colloidal crystals of different sphere size. D values indicate the centre-to-centre distance between spheres on the (1 1 1) planes, determined from angle-resolved UV–Vis transmittance measurements. Spectra were taken at normal incidence to the (1 1 1) plane, and show the positions of the pseudo photonic band gaps in the colloidal crystals. (b) shows the position of the reflectance maximum (λ_{max}) for diffraction from (1 1 1) planes versus D for colloidal crystals fabricated from our five different PMMA preparations. λ_{max} values calculated from D values measured directly from SEM images are also shown (solid triangles). The linearity of the plot indicates Bragg diffraction conditions are satisfied (see Eq. (4)).

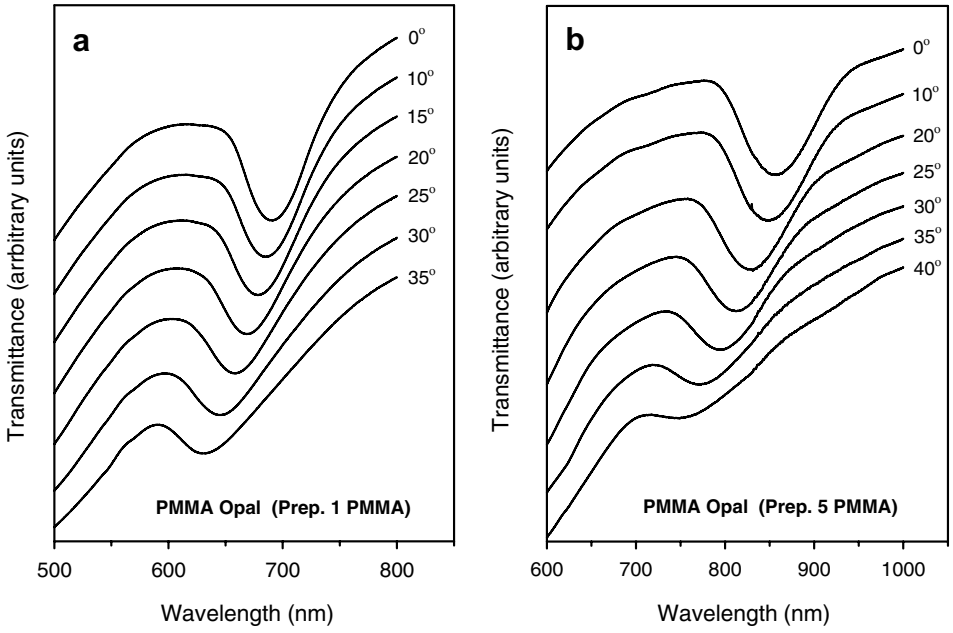


Fig. 4. UV–Vis transmittance spectra recorded at different angles of incidence from colloidal crystals of (a) Prep. 1 PMMA spheres ($D = 299$ nm) and (b) Prep. 5 PMMA spheres ($D = 397$ nm). Angles of incidence were measured with respect to the surface normal of the (1 1 1) planes. The figures show that the position of λ_{max} shifts to shorter wavelength as the angle of incidence increases, as predicted by Eq. (4).

transmit easily through the crystal at other angles. The interplanar spacing d_{111} and average refractive index of the photonic crystals can be determined from a plot of λ^2_{max} versus $\sin^2\theta$, as shown in Fig. 5. As mentioned above, if Bragg diffraction conditions are satisfied, a straight line will result with slope $= -(2d_{111})^2$ and y-axis intercept $= (2d_{111})^2 n^2_{avg}$. The data clearly obey the modified Bragg's law expression given in Eq. (3). From the experimentally determined d_{111}, the average centre-to-centre distance (D) between spheres on the (1 1 1) planes can be calculated ($D = d_{111}/0.8165$). Similarly, the volume fractions of PMMA and air in the colloidal structure can be calculated

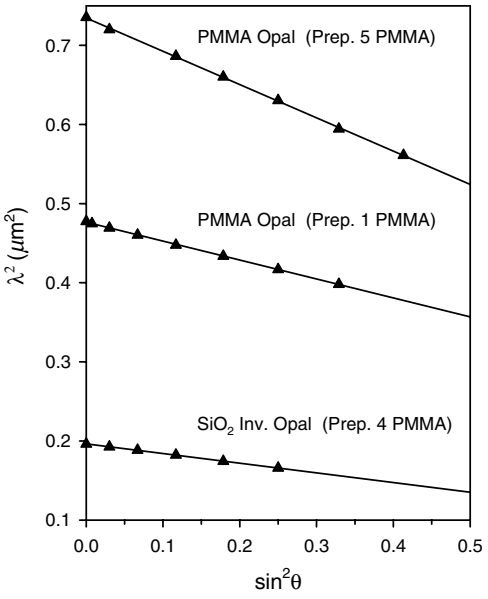


Fig. 5. Plot of λ^2_{max} versus $\sin^2\theta$, where λ_{max} is the reflectance maximum for diffraction from (1 1 1) planes and θ is the angle of incidence with respect to the surface normal of the (1 1 1) plane. Data for a SiO_2 IO are also given. A linear-least squares fit has been applied to each data set. From Eq. (3), it can be shown that the slope of the lines $= -(2d_{111})^2$ and the y-axis intercept $= (2d_{111})^2 n^2_{avg}$.

once the average refractive index is known. Data extracted from Fig. 5, and similar figures for colloidal crystals fabricated from our 5 PMMA sphere preparations, were used to complete the right-hand side of Table 2.

3.4. Fabrication and characterization of SiO_2, TiO_2 and CeO_2 inverse opals

Using the self-assembled PMMA colloidal crystals as a starting point, fcc lattices of air spheres embedded within SiO_2, TiO_2 or CeO_2 matrices were fabricated. PMMA colloidal crystals were first infiltrated with a sol-gel precursor, then carefully calcined at 550 °C to remove the PMMA template (see Section 2 for full details). All samples exhibited strong opalescence under light illumination, confirming the success of the inversion procedure.

Silica inverse opals from three different colloidal crystal templates, each of a different PMMA sphere size, are shown in the SEM micrographs of Fig. 6. PMMA templates were prepared by the centrifugation method, then crushed lightly with a metal spatula before SiO_2 infiltration. At low magnification, well-defined terrace structures can be discerned on the colloidal crystals (Figs. 6a, c and e). These structures are the result of crushing the PMMA crystals before infiltration (cf. Fig. 2a, which shows a fractured surface of a PMMA crystal). At high magnification, well-ordered inverse opal structures are observed (Figs. 6b, d and f), comprising fcc arrays of air spheres in silica. XRD showed the walls to be composed of amorphous silica (XRD pattern not shown). According to theory, the SiO_2 inverse opal should be approximately 24% silica and 76% air by volume. Note the small holes that connect each air sphere to its nearest neighbours. These holes conveniently indicate the position of the air spheres in the underlying layer of the inverse opal, and are the result of necking between spheres in the original PMMA template (cf. Fig. 1). The silica fraction of the inverse opals varies depending on infiltration conditions. The inverted part of the structure densified with additional infiltrations of sol-gel precursor into the PMMA template. Removal of the polymer template by calcination causes a large shrinkage of the inverted framework. This can be seen by directly comparing Figs. 1b, d and f with Figs. 6b, d and f, respectively (all images were taken at the same magnification). For each inverse opal preparation, the centre-to-centre distance between neighbouring air spheres (D) was 10–20% smaller than that between the spheres in the original PMMA template. Similar results have been reported for inverse opals prepared from polystyrene colloidal crystal templates [26].

Angle-resolved UV–Vis transmittance spectra for a SiO_2 inverse opal fabricated from a colloidal crystal of Prep. 4 PMMA spheres ($D = 269$ nm) are shown in Fig. 7. At normal incidence ($\theta = 0°$), the inverse opal exhibited a reflectance maximum (hence transmittance minimum) at 443 nm. We assign this feature to first order Bragg diffraction from the (1 1 1) planes of the fcc inverse opal structure (λ_{max}). The normalized band gap width in the inverse opal is $\Delta E/E = 0.1$, and of similar size to that of the PMMA template ($\Delta E/E = 0.85$). In agreement with behaviour observed for the PMMA colloidal crystals, the position of λ_{max} shifted to shorter wavelengths as the incident angle increased from 0° to 30°. Following the procedure above, we plotted λ^2_{max} versus $\sin^2\theta$ and achieved a straight line fit (see Fig. 5). From the plot, a d_{111} spacing of 174 nm and n_{avg} of 1.267 were obtained. A value $D = 214$ nm was calculated from the d_{111} spacing ($D = d_{111}/0.8165$). This value is in excellent agreement with a value of $D = 217$ nm measured directly from Fig. 6b. Comparing the values of D for the polymer template ($D = 269$ nm) and the SiO_2 inverse opal ($D = 214$ nm), it can be shown that the centre-to-centre distance between spheres in the fcc arrays decreased by approx 20% on inversion. The average refractive index of the inverse opal structure was higher than that predicted by theory ($n_{avg} = 0.74 \times 1 + 0.26 \times 1.45 = 1.117$), and suggests a silica fraction of 60%. Thickening of the silica walls, caused by lattice shrinkage during inversion, could be expected increase the silica content. However, the SEM images of Fig. 6 show that the filling fraction of silica in similar preparations to be significantly less than 60%, suggesting an alternative explanation is required. The presence of residual PMMA template in the voids of the inverse opal, instead of air, is one possible explanation.

To achieve a complete PBG for the visible and infrared regions, inverse opal structures with refractive index contrast of at least 2.9 are required. Inverse opals of TiO_2 ($n = 2.5$) and CeO_2 ($n = 2.4$) are interesting materials in

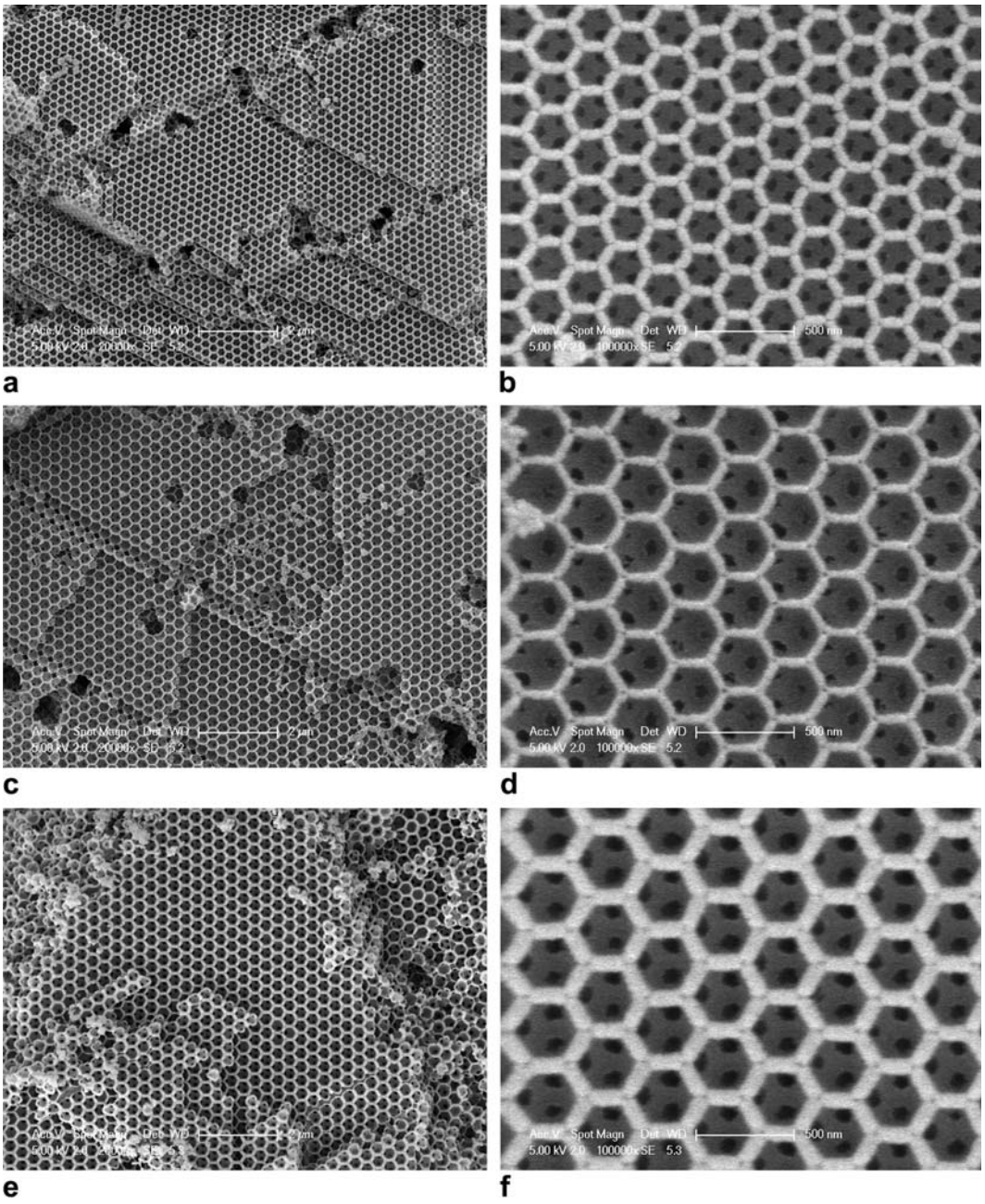


Fig. 6. SEM images showing SiO_2 inverse opals made from colloidal crystals templates of (a), (b) Prep. 4 PMMA spheres; (c), (d) Prep. 3 PMMA spheres; and (e), (f) Prep. 5 PMMA spheres. Images on the left were taken at 20 000× magnification, images on the right were taken at 100 000× magnification. Note the holes in the walls of the inverse opals where necks existed between PMMA spheres in the colloidal crystal templates.

this regard as their refractive contrasts are just below the required threshold. Potential also exists to exploit these materials in photovoltaic systems and catalytic applications, justifying a thorough investigation of their properties. Fig. 8 shows SEM micrographs of the TiO_2 and CeO_2 inverse opals fabricated from Prep. 3 PMMA colloidal crystals ($D = 347$ nm). The same template was used to fabricate the SiO_2 inverse opal shown in Figs. 6c and d. As was observed for SiO_2, the TiO_2 and CeO_2 inverse opals exhibited well-ordered fcc arrays of air spheres. Note the "clover leaf" like structure in the lower part of Fig. 8d, showing where a single PMMA sphere was positioned on top of an underlying (1 1 1) plane of PMMA spheres in the polymer template. Interestingly, all the inverse opal structures underwent a comparable degree of shrinkage during the inversion process (D decreased by approx. 15%).

Of interest were the structural forms of TiO_2 and CeO_2 in the inverted structures, since for many envisaged applications nanocrystalline titania and ceria are preferred. The XRD pattern for a TiO_2 inverse opal (Fig. 9a) was consistent with the anatase form of TiO_2 (space group $I4_1/amd$, $Z = 4$). Peak-widths were considerably broader than those determined for an anatase powder of micron-sized particles (Fig. 9b). The line broadening indicates the

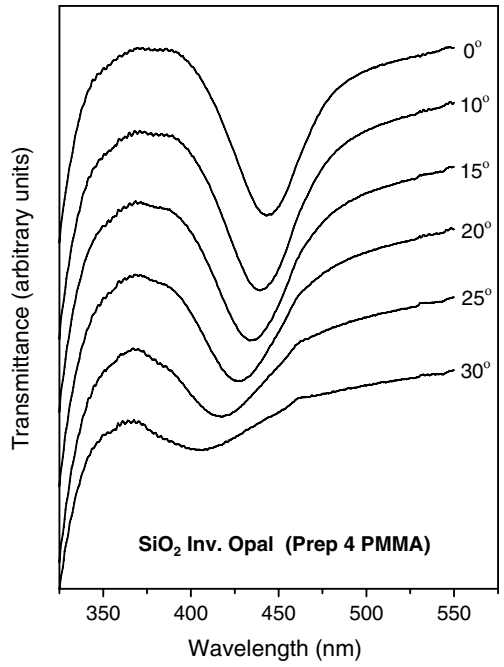


Fig. 7. UV–Vis transmittance spectra recorded at different angles of incidence from a SiO_2 inverse opal prepared from a colloidal crystal template of Prep. 4 PMMA spheres. The spectra show that the position of λ_{max} shifts to shorter wavelength as the angle of incidence increases, as predicted by Eq. (4).

TiO_2 network is composed of anatase nanoparticles. Line broadening for particles of nanometer dimension is well understood, and is caused by size-induced lattice relaxation and an increase in the lattice parameter(s). The average crystallite size of the TiO_2 nanoparticles was determined using the Scherrer equation

$$D_{avg} = \frac{K\lambda}{\beta \cos\theta}, \tag{5}$$

where D_{avg} is the mean crystallite diameter (in metres), K is the shape factor (typically 0.89), λ is the wavelength of the X-ray source (here $\lambda = 1.5148$ Å), θ is the Bragg angle of the diffraction peak (in degrees) and β is the linewidth of the diffraction peak corrected for instrument broadening (in radians)

$$\beta = \sqrt{B_M^2 - B_I^2}, \tag{6}$$

where B_M is the measured linewidth (in radians) and B_I is the instrumental broadening (also in radians). B_I is determined by measuring the linewidth for any standard particle of size >200 nm. From the FWHM of the anatase (1 0 1) reflections in Figs. 9a and b, we determined the TiO_2 particle size in the inverse opals to be approximately 31 nm. Inverse opals of ceria were also composed of nanocrystalline CeO_2, as evidenced by the relative linewidths of the

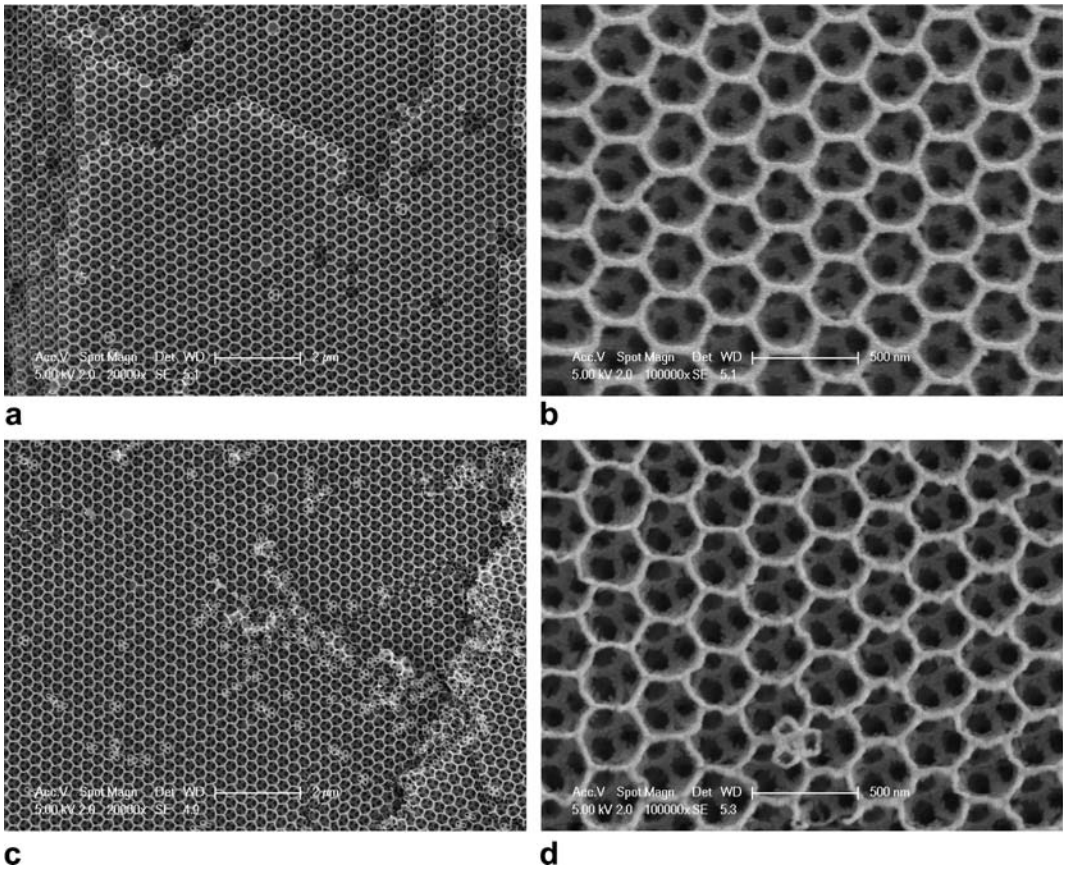


Fig. 8. SEM images showing inverse opals of (a), (b) TiO_2 and (c), (d) CeO_2 made from colloidal crystals templates of Prep. 3 PMMA spheres. Images on the left were taken at 20000× magnification, images on the right were taken at 100000× magnification.

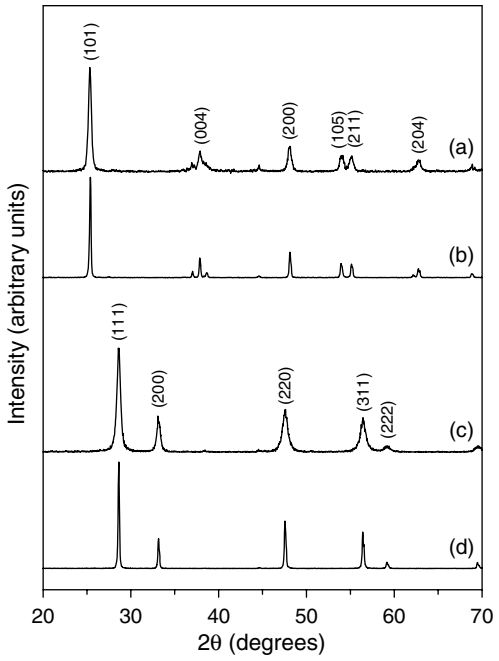


Fig. 9. XRD patterns for (a) TiO_2 inverse opal; (b) TiO_2 micron size powder (anatase form); (c) CeO_2 inverse opal; and (d) CeO_2 micron size powder. Line broadening observed for the inverse opals indicates the presence of nanocrystalline particles.

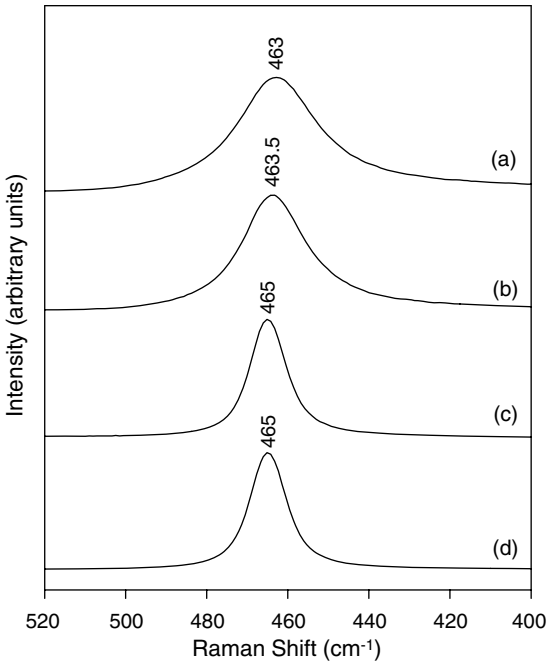


Fig. 10. Raman spectra for (a) CeO_2 nanoparticles of average size 12 nm; (b) CeO_2 inverse opal; (c) CeO_2 micron size powder; and (d) CeO_2(1 1 1) single crystal.

XRD patterns shown in Figs. 9c and d. Using the FWHM of the (1 1 1) reflections, the average size of ceria particles in inverse opal network was determined to be around 17 nm. This is an interesting result, since nanocrystalline CeO_2 has been shown to increase the activity of ceria-based catalysts for the WGS reaction and CO oxidation by several orders of magnitude.

Line broadening caused by the presence of nanocrystalline ceria in the CeO_2 inverse opal networks is also evidenced by Raman spectroscopy. CeO_2 crystallizes with the fluorite structure, space group $Fm3m$ (O_h^5) with $Z = 4$. On account of the high symmetry, the CeO_2 lattice shows only one infrared active phonon (T_{1u} symmetry) and one Raman active phonon (T_{2g} symmetry). The triply degenerate Raman active phonon is reported to appear at 465 cm^{-1} for micron-sized CeO_2 powders [27]. Raman spectra collected from CeO_2 nanoparticles of average size 12 nm, the CeO_2 inverse opal, a micron-sized CeO_2 powder and a CeO_2(1 1 1) single crystal are shown in Figs. 10a–d, respectively. All samples exhibit a single Raman band centred between 463 and 465 cm^{-1}, the position, FWHM and symmetry of the band being highly sample dependent. For the ceria nanoparticles and the ceria inverse opals, broad asymmetric peaks are observed at low energy, reflecting size-induced relaxation effects and an increase in the lattice parameter (i.e. Ce–O bonds are weakened due to lattice relaxation) [28,29]. For the micron-sized CeO_2 powder and the CeO_2(1 1 1) single crystal (Figs. 10c and d), sharp symmetric peaks of high energy are seen on account of the high crystalline order and rigidity in the bulk. In future work, the optical properties of the TiO_2 and CeO_2 inverse opal will be examined, and potential applications for these materials explored.

4. Conclusions

The fabrication of well-ordered photonic crystals with opal and inverse opal structures has been demonstrated. These materials have intrinsically interesting optical properties (such as photonic band gaps) that may be exploited in applications such as solar energy conversion or light-emitting devices. We are currently developing conducting polymer and piezoelectric oxides with inverse opal structures. In general, the well-ordered colloidal crystal templates provide an excellent route for the preparation of a wide variety of macroporous inorganic oxides.

Acknowledgements

G.I.N.W. thanks the Foundation for Research Science and Technology for the award of a New Zealand Science and Technology Postdoctoral Fellowship (Contract No. UOAX0412). This work was supported by the MacDiarmid Institute for Advanced Materials and Nanotechnology.

References

[1] J.D. Joannopoulos, R.D. D Meade, Joshua N. Winn, Photonic Crystals: Molding the Flow of Light, Princeton University Press, Princeton, 1995.
[2] E. Yablonovitch, Phys. Rev. Lett. 58 (1987) 2059.
[3] S. John, Phys. Rev. Lett. 58 (1987) 2486.
[4] See for instance, V.L. Colvin, MRS Bull. 26 (2001) 637.

[5] L. Bechger, P. Lodahl, W.L. Vos, J. Phys. Chem. B 109 (2005) 9980.
[6] S. Noda, K. Tomoda, N. Yamamodo, A. Chutinan, Science 289 (2000) 604.
[7] M. Qi, E. Lidorikis, P.T. Rakich, S.G. Johnson, J.D. Joannopoulos, E.P. Ippen, H.I. Smith, Nature 429 (2004) 538.
[8] P. Jiang, K.S. Hwang, D.M. Mittleman, J.F. Bertone, V.L. Colvin, J. Am. Chem. Soc. 121 (1999) 11630.
[9] R.C. Schroden, M. Al-Daous, C.F. Blanford, A. Stein, Chem. Mater. 14 (2002) 3305.
[10] K. Busch, S. John, Phys. Rev. E 58 (1998) 3896.
[11] R. Biswas, M.M. Sigalas, G. Subramania, K.-M. Ho, Phys. Rev. B 57 (1998) 3701.
[12] R. Biswas, M.M. Sigalas, G. Subramania, C.M. Soukoulis, K.-M. Ho, Phys. Rev. B 61 (2000) 4549.
[13] K.M. Ho, C.T. Chan, C.M. Soukoulis, Phys. Rev. Lett. 65 (1990) 3152.
[14] A. Blanco, E. Chomski, S. Grabtchak, M. Ibisate, S. John, S.W. Leonard, C. Lopez, F. Meseguer, H. Miguez, J.P. Mondia, G.A. Ozin, O. Toader, H.M. van Driel, Nature 405 (2000) 437.
[15] L.I. Halaoui, N.M. Abrams, T.E. Mallouk, J. Phys. Chem. B 109 (2005) 6334.
[16] S. Nishimura, N. Abrams, B.A. Lewis, L.I. Halaoui, T.E. Mallouk, K.D. Benkstein, J. van de Lagemaat, A.J. Frank, J. Am. Chem. Soc. 125 (2003) 6306.
[17] P.R. Somani, C. Dionigi, M. Murgia, D. Palles, P. Nozar, G. Ruani, Sol. Energy Mater. Sol. Cell. 87 (2005) 513.
[18] S. Carrettin, P. Concepcion, A. Corma, J.M. Lopez Nieto, V.F. Puntes, Angew. Chem. Int. Ed. 43 (2004) 2538.
[19] Q. Fu, S. Kudriavtseva, H. Saltsburg, M. Flytzani-Stephanopoulos, Chem. Eng. J. 93 (2003) 41.
[20] A. Fuerte, M.D. Hernandez-Alonso, A.J. Maira, A. Martinez-Arias, M. Fernandez-Garcia, J.C. Conesa, J. Soria, Chem. Commun. (2001) 2718.
[21] X.Y. Zhang, T.W. Wang, W.Q. Jiang, D. Wu, L. Liu, A.H. Duan, Chin. Chem. Lett. 16 (2005) 1109.
[22] F. Zhang, S.-W. Chan, J.E. Spanier, E. Apak, Q. Jin, R.D. Robsinson, I.P. Herman, Appl. Phys. Lett. 80 (2002) 127.
[23] Z. Zhou, X.S. Zhao, Langmuir 20 (2004) 1524.
[24] Z. Zhou, X.S. Zhao, Langmuir 21 (2005) 4717.
[25] P. Bolhuis, D. Frenkel, S.-C. Mau, D.A. Huse, Nature 388 (1997) 235.
[26] G. Subramania, R. Biswas, K. Constant, M.M. Sigalas, K.M. Ho, Phys. Rev. B 63 (2001) 235111.
[27] V.G. Keramidas, W.B. White, J. Chem. Phys. 59 (1973) 1561.
[28] J.E. Spanier, R.D. Robinson, F. Zhang, S.-W. Chan, I.P. Herman, Phys. Rev. B 64 (2001) 245407-1.
[29] F. Zhang, Q. Jin, S.-W. Chan, J. Appl. Phys. 95 (2004) 4319.

Available online at www.sciencedirect.com
ScienceDirect
Polyhedron 26 (2007) 369–377
POLYHEDRON
www.elsevier.com/locate/poly

Incorporation of a tripodal ligand with a (N,O,O)-donor set into a new family of nickel and cobalt spin clusters

Kerwyn G. Alley [a], Roland Bircher [b], Hans U. Güdel [b], Boujemaa Moubaraki [c], Keith S. Murray [c], Brendan F. Abrahams [a], Colette Boskovic [a,*]

[a] School of Chemistry, University of Melbourne, Vic. 3010, Australia
[b] Department of Chemistry and Biochemistry, University of Berne, Freiestrasse 3, CH-3012 Berne, Switzerland
[c] School of Chemistry, Building 23, Monash University, Clayton, Vic. 3800, Australia

Received 13 April 2006; accepted 21 June 2006
Available online 8 July 2006

Abstract

The reaction of $Ni(OAc)_2$, NiX_2 (X = Cl, Br) or $CoCl_2$ with the proligand 2-amino-2-methyl-1,3-propanediol ($ampdH_2$) affords a new family of tetranuclear complexes. The syntheses of $[Ni_4(OAc)_4(ampdH)_4]$ (**1**) and $[M_4X_4(ampdH)_4]$ (M = Ni, X = Cl, **2**; M = Ni, X = Br, **3**; M = Co, X = Cl, **4**) are reported, together with the single crystal X-ray structures of **1**, **2** and **4** and the magnetochemical characterization of **1**, **3** and **4**. Each member of this family of complexes displays a low symmetry structure that incorporates a $\{M_4O_4\}$ core unit based on a distorted cubane. Magnetic measurements reveal ferromagnetic exchange interactions for **1**, **3** and **4**. These give rise to $S = 4$ ground state spins for the tetranuclear Ni complexes and an anisotropic effective $S' = 2$ ground state for the Co complex.
Crown Copyright © 2006 Published by Elsevier Ltd. All rights reserved.

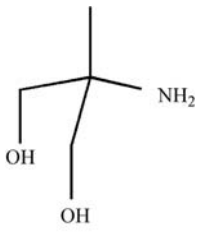
Keywords: Spin clusters; Polynuclear complexes; Nickel; Cobalt; Tripodal ligands; Magnetochemistry

1. Introduction

Polynuclear complexes of paramagnetic metal centers, or "spin clusters", are key components of the active sites of a number of metalloproteins and are therefore of considerable interest to the field of bioinorganic chemistry [1]. In addition, an important new branch of molecular materials chemistry is concerned with the investigation of spin clusters that act as "single-molecule magnets" (SMMs) [2–6]. These species display slow magnetic relaxation at low temperature that arises from the molecular properties of a high ground state spin and an easy-axis (Ising) type of magnetic anisotropy. The synthesis and investigation of new spin clusters is of fundamental importance to both these research fields, with the accessibility of new complexes, and particularly examples with novel structures, relying on the exploitation of new families of ligands. The potentially polynucleating tripodal proligand 2-amino-2-methyl-1,3-propanediol ($ampdH_2$) contains an (N,O,O)-donor set and is suitable for binding to a range of transition metals. Although tripodal triol-based ligands have been successfully incorporated in spin clusters [7], the coordination potential of $ampdH_2$ has been little explored, with only a single Mo_2 complex [8] having been structurally characterized prior to our recent reports of Fe_7, Co_6 and $\{Co_8\}_n$ complexes [9]. As part of our exploration of new spin clusters that contain polyalcohol/alkoxide ligands [4,9–11], we report here a new family of tetranuclear Co and Ni complexes that incorporate the monoanionic ligand $ampdH^-$. It is noteworthy that tetranuclear spin clusters of Mn, Fe, V, Ni and Co have been found to act as SMMs [3–6]

* Corresponding author. Tel.: +61 383444971; fax: +61 393475180.
E-mail address: c.boskovic@unimelb.edu.au (C. Boskovic).

0277-5387/$ - see front matter Crown Copyright © 2006 Published by Elsevier Ltd. All rights reserved.
doi:10.1016/j.poly.2006.06.028



ampdH$_2$

2. Experimental

2.1. Compound preparation

All manipulations were performed under aerobic conditions, using materials as received.

2.1.1. [$Ni_4(OAc)_4(ampdH)_4$] (**1**)

$Ni(OAc)_2 \cdot 4H_2O$ (3.00 g, 12.1 mmol) was added to a solution of $ampdH_2$ (1.26 g, 12.1 mmol) in ^iPrOH (50 cm^3) and the resulting mixture was stirred overnight, evaporated to dryness and recrystallized by layering a concentrated MeCN solution with Et_2O. Blue-green cuboidal crystals formed after one week. The crystals were isolated by filtration and washed with MeCN/MeOH; yield 9%. *Anal.* Calc. for $[Ni_4(OAc)_4(ampdH)_4]$, $C_{24}H_{52}N_4Ni_4O_{16}$: C, 32.48; H, 5.91; N, 6.31. Found: C, 32.45; H, 5.90; N, 6.34%. Selected IR data (cm^{-1}): 3333 (s), 3302 (s), 3265 (s), 3161 (s), 2956 (s), 2935 (s), 2879 (s), 2850 (s), 2703 (m), 2598 (m), 2019 (m), 1918 (m), 1589 (s), 1466 (s), 1416 (s), 1385 (s), 1336 (s), 1328 (s), 1290 (m), 1226 (w), 1203 (w), 1187 (w), 1157 (m), 1151 (m), 1065 (s), 1018 (s), 1004 (s), 945 (m), 914 (s), 899 (m), 794 (m), 736 (w), 711 (m), 690 (m), 666 (s), 652 (s), 616 (m), 606 (m), 536 (m), 483 (m), 445 (m), 420 (s).

2.1.2. [$Ni_4Cl_4(ampdH)_4$] (**2**)

$NiCl_2 \cdot 6H_2O$ (2.00 g, 8.42 mmol) was added to solution of NEt_3 (1.17 ml, 8.42 mmol) and $ampdH_2$ (0.88 g, 8.4 mmol) in MeOH (40 cm^3) and the resulting mixture was stirred overnight, evaporated to dryness and recrystallized by layering a concentrated MeOH solution with Et_2O. Light-green cuboidal crystals formed after three weeks. The crystals were isolated by filtration and washed with MeOH/Et_2O; yield 25%. A sample for crystallography was maintained in contact with mother liquor to prevent the loss of interstitial solvent. The sample was vacuum dried overnight at room temperature to remove the solvent of crystallization, but appears to be hygroscopic. *Anal.* Calc. for $[Ni_4Cl_4(ampdH)_4] \cdot 3H_2O$, $C_{16}H_{46}N_4Ni_4O_{11}Cl_4$: C, 22.69; H, 5.47; N, 6.61. Found: C, 22.81; H, 5.51; N, 6.23%. The hydration level was confirmed by thermogravimetric analysis. Selected IR data (cm^{-1}): 3436 (s), 3310 (s), 3247 (s), 2960 (s), 2860 (s), 2758 (m), 2567 (w), 2097 (w), 1633 (m), 1600 (m), 1475 (m), 1465 (m), 1385 (m), 1343 (m), 1291 (m), 1229 (w), 1202 (w), 1147 (m), 1105 (m), 1059 (s), 1018 (s), 996 (s), 957 (m), 917 (m), 898 (m), 793 (s), 734 (m), 659 (s), 606 (s), 527 (m), 483 (m), 419 (s).

2.1.3. [$Ni_4Br_4(ampdH)_4$] (**3**)

This was synthesized in a manner analogous to that employed for **2** using $NiBr_2 \cdot 3H_2O$ in place of $NiCl_2 \cdot 6H_2O$; yield 16%. Drying under vacuum at room temperature afforded a fully desolvated sample. *Anal.* Calc. for $[Ni_4Br_4(ampdH)_4]$, $C_{16}H_{40}N_4Ni_4O_8Br_4$: C, 19.79; H, 4.15; N, 5.77. Found: C, 19.71; H, 4.23; N, 5.75%. Selected IR data (cm^{-1}): 3401 (s), 3325 (s), 3271 (s), 3233 (s), 2962 (s), 2933 (s), 2860 (s), 2743 (m), 1653 (m), 1635 (m), 1589 (m), 1465 (m), 1383 (m), 1338 (m), 1290 (m), 1223 (w), 1199 (w), 1148 (m), 1052 (s), 1014 (m), 996 (s), 914 (m), 897 (m), 789 (m), 656 (m), 603 (s), 526 (m), 484 (m), 418 (s).

2.1.4. [$Co_4Cl_4(ampdH)_4$] (**4**)

$CoCl_2 \cdot H_2O$ (0.71 g, 3.0 mmol) was added to a solution of NEt_3 (0.425 ml, 3.00 mmol) and $ampdH_2$ (0.32 g, 3.0 mmol) in MeCN (60 cm^3). Stirring the resulting mixture overnight afforded a pink precipitate, which was recrystallized by layering a concentrated EtOH solution with Et_2O. After five days, purple plate-like crystals formed. These were isolated by filtration and washed with Et_2O; yield 20%. A sample for crystallography was maintained in contact with mother liquor to prevent the loss of interstitial solvent. Drying under vacuum at room temperature afforded a fully desolvated sample. *Anal.* Calc. for $[Co_4Cl_4(ampdH)_4]$, $C_{16}H_{40}N_4Co_4O_8Cl_4$: C, 24.19; H, 5.08; N, 7.05. Found: C, 24.11; H, 5.02; N, 6.97%. Selected IR data (cm^{-1}): 3435 (s), 3324 (s), 3276 (s), 3246 (s), 2962 (m), 2936 (m), 2883 (m), 2858 (m), 2750 (w), 2092 (w), 1632 (m), 1595 (m), 1466 (m), 1384 (m), 1340 (w), 1293 (w), 1229 (w), 1183 (w), 1147 (m), 1054 (s), 995 (m), 914 (w), 898 (w), 790 (m), 633 (m), 600 (m), 515 (m), 474 (m), 411 (m).

2.2. General and physical measurements

Infrared spectra (KBr disk) were recorded on a BioRad 175 FTIR spectrometer. Elemental analyses were performed at Chemical and Microanalytical Services, Belmont, Australia. Thermogravimetric analyses were performed on a Mettler Toledo thermal analyser.

Variable temperature magnetic susceptibility and magnetization measurements were performed with Quantum Design MPMS SQUID magnetometers equipped with a 5 T magnet. Data were collected on small dried crystals restrained in petroleum jelly. Two sets of DC magnetic susceptibility data were collected with magnetic fields of 0.1 T and 0.01 T. Pascal's constants were used to estimate the diamagnetic correction for each complex. The experimental susceptibility data for complexes **1** and **3** were fit using MAGMUN [12]. AC magnetic susceptibility measurements were performed on **4** at frequencies up to 1000 Hz.

2.3. X-ray crystallography

The intensity data of all compounds were collected on a Bruker CCD diffractometer using graphite monochromated Mo Kα radiation ($\lambda = 0.71073$ Å). Crystals were transferred directly from the mother liquor to a protective oil, which was used to prevent solvent loss. The structures were solved using direct methods and refined using a full-matrix least squares procedure based on F^2 using all data [13] (see Table 1).

3. Results and discussion

3.1. Syntheses

The overnight treatment of an ^{i}PrOH solution of $Ni(OAc)_2$ with one equivalent of ampdH_2 affords a dark green solution. Evaporation of this to dryness, re-dissolution of the residue in the minimum volume of MeCN and layering the resulting solution with Et_2O, yields crystals of **1** in 9% yield after one week. The reaction may be written as:

$$4Ni(OAc)_2 + 4ampdH_2 \rightarrow [Ni_4(OAc)_4(ampdH)_4] + 4AcOH \quad (1)$$

Formation of **1** involves loss and protonation of acetate ligands in conjunction with deprotonation and coordination of the polyalcohol ampdH_2 proligand. This process commonly occurs during the formation of polynuclear metal complexes with mixed carboxylate and chelating alkoxide ligands from metal carboxylate complexes and is likely driven by the chelate effect associated with the polynuclear product [9,10]. Addition of one equivalent of base (NEt_3 or NaOMe) to the above reaction also affords crystals of **1**, albeit with lower yield. In addition the product is contaminated with a white solid, which is probably NaOAc or Et_3NHOAc. In either case a highly concentrated MeCN solution is required to produce a crystalline sample of **1** in moderate yield, due to its high solubility. A similar reaction between $Co(OAc)_2$ and ampdH_2 in MeOH affords a hexanuclear complex that is reported elsewhere [9b].

Overnight treatment of a methanolic solution of NiX_2 (X = Cl, Br) with one equivalent each of ampdH_2 and NEt_3 results in a light green solution. Evaporation of this to dryness, re-dissolution of the residue in the minimum volume of MeOH, and layering the resulting solution with Et_2O, yields crystals of **2** and **3** in 25% and 16% yield, respectively, after three weeks. The reaction may be written as:

$$4MX_2 + 4ampdH_2 + 4Et_3N \rightarrow [M_4X_4(ampdH)_4] + 4Et_3NHX \quad (M = Ni, Co; X = Cl, Br) \quad (2)$$

After several additional weeks, the formation of a white precipitate of Et_3NHX can be observed. Again the high solubility of the products necessitates highly concentrated MeCN solutions to produce crystalline samples in moderate yield. Analogous reactions without base do not yield crystalline samples of **2** and **3**.

A similar reaction between $CoCl_2$ and one equivalent each of ampdH_2 and NEt_3 in MeCN produces a pink precipitate. Recrystallization from EtOH layered with Et_2O provides purple crystals of **4** in 20% yield after approximately five days. The formation of **4** is also summarized in reaction (2). A crystalline sample of **4** can also be

Table 1
Crystallographic data for **1**, **2** · 4.25MeOH and **4** · 3EtOH · Et_2O

Parameter	**1**	**2** · 4.25MeOH	**4** · 3EtOH · Et_2O
Formula	$C_{24}H_{52}N_4Ni_4O_{16}$	$C_{20.25}H_{57}Cl_4N_4Ni_4O_{12.25}$	$C_{26}H_{68}Cl_4Co_4N_4O_{12}$
Formula weight	887.54	929.34	1006.36
Space group	*Pbca*	*C*2/*c*	$P2_1/c$
Unit cell dimensions			
a (Å)	13.813(1)	40.501(5)	21.658(1)
b (Å)	19.700(1)	14.121(2)	14.4378(9)
c (Å)	28.277(2)	13.904(2)	14.1721(8)
α (°)	90	90	90
β (°)	90	107.043(2)	102.245(1)
γ (°)	90	90	90
V (Å^3)	7694(1)	7603(2)	4330.8(4)
Z	8	8	4
T (K)	130(1)	130(1)	130(1)
ρ_{calc} (g cm^{-3})	1.532	1.607	1.543
μ (mm)	1.995	2.287	1.807
Data with $I > 2\sigma(I)$	6619	4816	8650
Reflections measured	45 543	18 521	26 708
Unique reflections	8825	6693	9824
Observed data [$I > 2\sigma(I)$]	6619	4816	8650
R_1w[a]	0.0541	0.0800	0.0379
wR_2[b]	0.1308	0.1996	0.0982

[a] $I > 2\sigma(I)$.
[b] F^2, all data.

isolated from similar reactions without the addition of base, although the yields are around one quarter of those obtained with base. Crystals of complex **4** always appear simultaneously with a pale-colored amorphous precipitate of Et_3NHCl and efforts to remove this by washing typically also dissolve the crystals of **4**. Fortunately in batches where large crystals of **4** form, the precipitate can be removed by suspending it in Et_2O and removing the Et_2O by decantation. Repeating this several times affords analytically pure samples.

Table 2
Selected interatomic distances (Å) and angles (°) for **1**, **2** · 4.25MeOH and **4** · 3EtOH · Et_2O

Parameter	**1**	**2** · 4.25MeOH	**4** · 3EtOH · Et_2O
M···M	3.0459(8)–3.1308(8)	3.085(2)–3.103(2)	3.132(5)–3.176(4)
M–O[a]	2.040(3)–2.089(3)	2.034(6)–2.086(6)	2.062(2)–2.139(2)
M–O–M	95.2(1)–98.8(1)	96.3(2)–98.4(2)	96.61(7)–99.57(7)
M–O–O–M[b]	168.2(1)–173.0(1)	168.9(6)–170.4(3)	168.23(9)–170.27(9)

[a] μ_3-O atoms.
[b] Dihedral angles.

3.2. Description of structures

Labeled structural diagrams of complexes **1**, **2** and **4** are presented in Fig. 1. A summary of the interatomic distances and angles is provided in Table 2, while a more extensive listing is available in the Supplementary Information.

Complex **1** crystallizes in the orthorhombic space group *Pbca* with one tetranuclear complex in the asymmetric unit. Four Ni and four O atoms occupy the vertices of a distorted $\{Ni_4(\mu_3\text{-}O)_4\}$ cubane core, where the μ_3-O atoms (O4, O5, O11, O12) are from the deprotonated arms of four ampdH$^-$ ligands. Bond valence sum (BVS) calculations (Supplementary Material) are consistent with four Ni^{II} centers [14]. In addition to the three μ_3-O(alkoxo) O atoms, the coordination sphere of each Ni center is completed by one N(amino) atom and one O(alcohol) atom from the ampdH$^-$ ligands and an O atom from the monodentate acetate ligands, to give a distorted octahedral geometry. All four ampdH$^-$ ligands bind to the Ni atoms in a $\eta^1{:}\eta^1{:}\eta^3{:}\mu_3$-fashion (Fig. 2a). The ampdH$^-$ ligands are disposed in an asymmetrical manner about the cubane, such

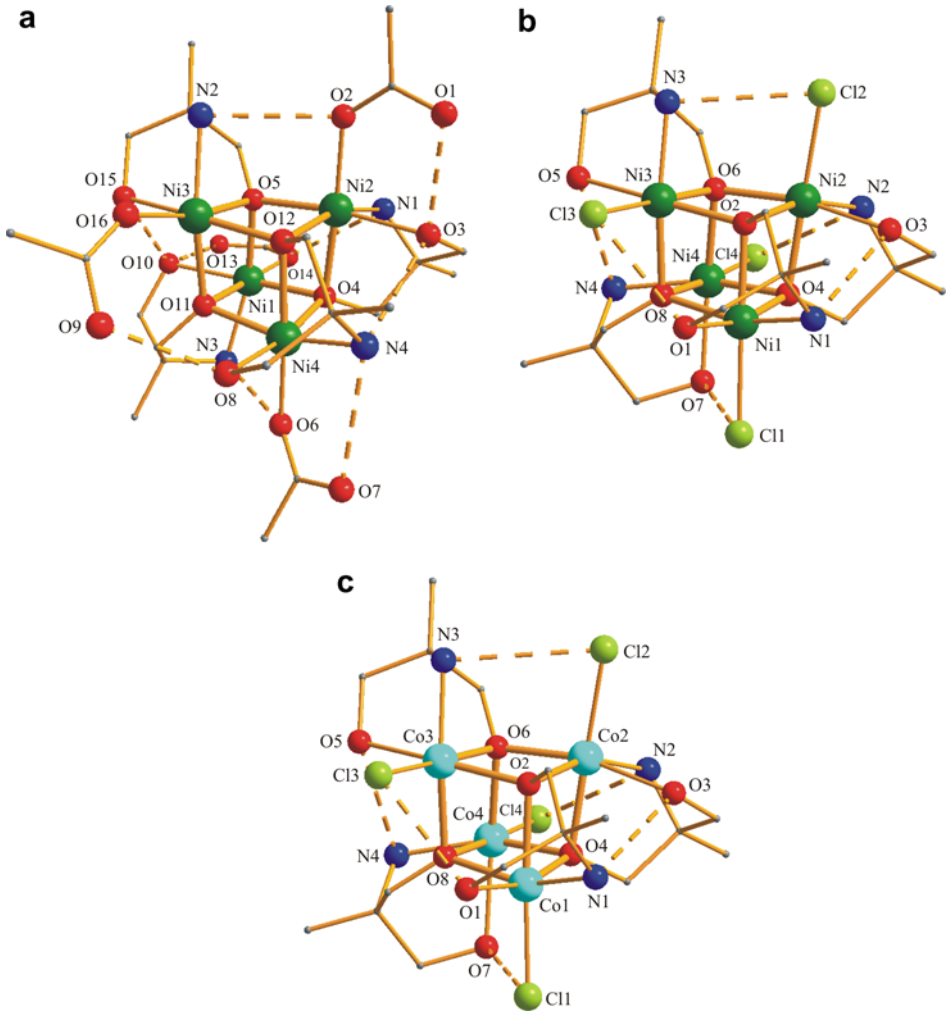


Fig. 1. Molecular structures of (a) **1**, (b) **2** in **2** · 4.25MeOH and (c) **4** in **4** · 3EtOH · Et_2O.

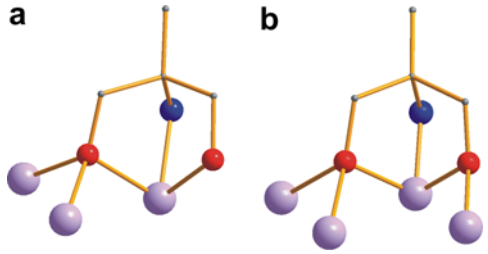


Fig. 2. Binding modes of (a) ampdH$^-$ in **1**–**4** and (b) ampd^{2-} in reported Co and Fe complexes [9].

that two bridging O atoms (O5 and O12) are each bound *trans* to a single N atom, one bridging O atom (O11) is *trans* to two N atoms and the remaining bridging O atom (O4) has no *trans*-N atoms. The four acetate ligands all bind in a terminal monodentate manner and the molecule has C_1 point symmetry. Multiple intramolecular N–H···O and O–H···O hydrogen bonds are evident (Table 3), involving O atoms from both alcohol and acetate moieties. In addition, extensive intermolecular hydrogen bonding is observed **1** between the non-coordinated O(acetate) atoms and the N(amino) atoms, with N···O distances of 2.602(5)–3.071(5) Å (Supplementary Material). Each tetranuclear complex is hydrogen bonded to six neighbouring complexes to form a three-dimensional cubic network.

Compounds **2** · 4.25MeOH and **4** · 3EtOH · Et_2O crystallize in the monoclinic space groups $C2/c$ and $P2_1/c$, respectively, each with one tetranuclear complex in the asymmetric unit. The structural data reveal that complexes **2** and **4** are isostructural. The strong similarity between the infrared spectra of **2** and **3** (Supplementary Material) and the elemental analysis data for **3** are consistent with isostructural character for **3** also. Four M (M = Ni, **2**; M = Co, **4**) and four O atoms occupy the vertices of a distorted {$M_4(\mu_3\text{-}O)_4$} cubane core, where the μ_3-O atoms (O2, O4, O6, O8) are from the deprotonated arms of four ampdH$^-$ ligands. BVS calculations (Supplementary Material) are consistent with four M^{II} centers for both complexes. In addition to the three μ_3-O(alkoxo) O atoms, the distorted octahedral coordination sphere of each metal center is completed by one N(amino) atom and one O(alcohol) atom from the ampdH$^-$ ligands and a chloro ligand. All four ampdH$^-$ ligands bind in a similar $\eta^1{:}\eta^1{:}\eta^3{:}\mu_3$-fashion (Fig. 2) to that observed in **1**. The ampdH$^-$ ligands are also arranged in a manner similar to that observed in **1**, such that two bridging O atoms (O2 and O4) are each *trans* to one N atom, one bridging O atom (O8) is *trans* to two N atoms and the remaining bridging O atom (O6) has no *trans*-N atoms. The molecules both have C_1 point symmetry. Multiple intramolecular hydrogen bonding is again evident in the structures of both **2** and **4** as N–H···Cl and O–H···Cl interactions (Table 3). Complexes **2** and **4** each display intermolecular O–H···N hydrogen bonds between O(alcohol) atoms and N(amino) atoms of the ampdH$^-$ ligands, with O···N separations of 3.047(11) and 3.005(3) Å for **2** and **4**, respectively (Supplementary Material). Each complex is bound to two neighbours to form extended chains along the *c*-direction. In addition, numerous hydrogen bonds are also evident between the ligands of **2** and **4** and the solvent molecules of crystallization.

Table 3
Intramolecular hydrogen bonding distances (Å) for **1**, **2** · 4.25MeOH and **4** · 3EtOH · Et_2O

Parameter	**1**	**2** · 4.25MeOH	**4** · 3EtOH · Et_2O
O···O	2.496(5)–2.681(5)		
N···O	2.939(5)–3.043(5)	2.95(1)–3.02(1)	2.967(3)–3.050(3)
O···Cl		2.990(8)–3.068(8)	3.025(2)–3.038(2)
N···Cl		3.225(8)–3.284(8)	3.356(2)–3.371(2)

The complexes reported here display a coordination mode that has not been previously reported for the coordinatively versatile tripodal amino-alcohol proligand $ampdH_2$ (Fig. 2). A $\eta^1{:}\eta^1{:}\eta^3{:}\mu_3$ binding mode is evident for monodeprotonated ampdH$^-$ in complexes **1**–**4**, while a $\eta^1{:}\eta^2{:}\eta^3{:}\mu_4$ binding mode is displayed by dianionic ampd^{2-} in $Fe^{II}Fe^{III}_6$, $Co^{II}_4Co^{III}_2$ and $\{Co^{II}_5Co^{III}_3\}_n$ complexes that we have reported elsewhere [9]. All of these complexes possess structures comprised of complete or face-sharing monovacant distorted cubane units and it appears that these structural units are favored by the tripodal nature of the ligand. The only other complex of ampd^{2-} whose structure has been reported is a Mo^{VI}_2 species featuring a $\eta^1{:}\eta^1{:}\eta^2{:}\mu_2$ binding mode [8].

3.3. Magnetochemistry

Variable temperature DC susceptibility measurements were performed at 0.01 and 0.1 T on a collection of randomly oriented small crystals of **1** and **3**, in the temperature range 2.0–300 K. Magnetic data were collected and analyzed for **3** rather than **2** due to complications associated with the hygroscopic nature of **2**. As discussed above, the two complexes are assumed to be isostructural. The data obtained at 0.1 T are plotted as $\chi_M T$ and χ_M versus T in Figs. 3a and 4a for **1** and **3**, respectively. For **1** $\chi_M T$ increases progressively from a value of 4.8 $cm^3\ mol^{-1}\ K$ at 300 K to 10.4 $cm^3\ mol^{-1}\ K$ at 8 K before decreasing to 9.5 $cm^3\ mol^{-1}\ K$ at 2.0 K. For **3** $\chi_M T$ increases progressively from a value of 4.8 $cm^3\ mol^{-1}\ K$ at 300 K to 9.3 $cm^3\ mol^{-1}\ K$ at 14 K before decreasing to 5.5 $cm^3\ mol^{-1}\ K$ at 2.0 K. The spin-only value of $\chi_M T$ for four non-interacting Ni^{II} centers is 4.8 $cm^3\ mol^{-1}\ K$ ($g = 2.2$) and the observed behavior is consistent with overall ferromagnetic intramolecular interactions for both species. The data collected above 20 K for **1** and **3** were fit to the exchange Hamiltonian:

$$\hat{H}_{ex} = -2J(\hat{S}_1\hat{S}_4 + \hat{S}_2\hat{S}_3 + \hat{S}_1\hat{S}_2 + \hat{S}_1\hat{S}_3 + \hat{S}_2\hat{S}_4 + \hat{S}_3\hat{S}_4) \quad (3)$$

where a single coupling constant, J, characterizes exchange across the six faces of the cubane. Although the C_1 point symmetry of these molecules strictly demands six different coupling constants, the minimal variation in crystallographically determined Ni···Ni distances and Ni–O–Ni angles (Table 2) is consistent with the use of a single coupling

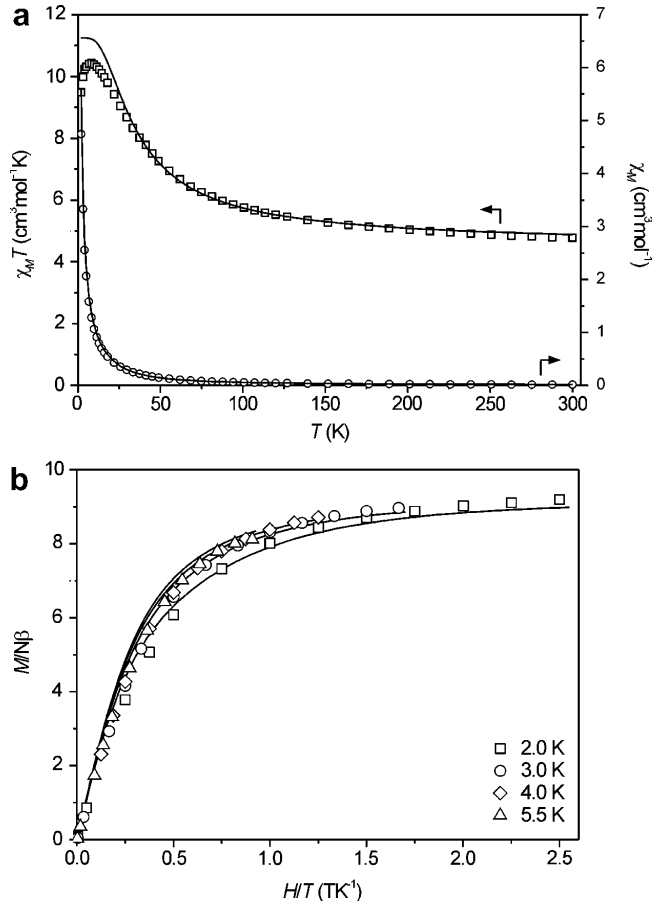


Fig. 3. Plots of magnetic data for **1**: (a) χ_M and $\chi_M T$ vs. T with an applied magnetic field of 0.1 T; and (b) $M/N\beta$ vs. H/T; the solid lines are fits or simulations as described in the text.

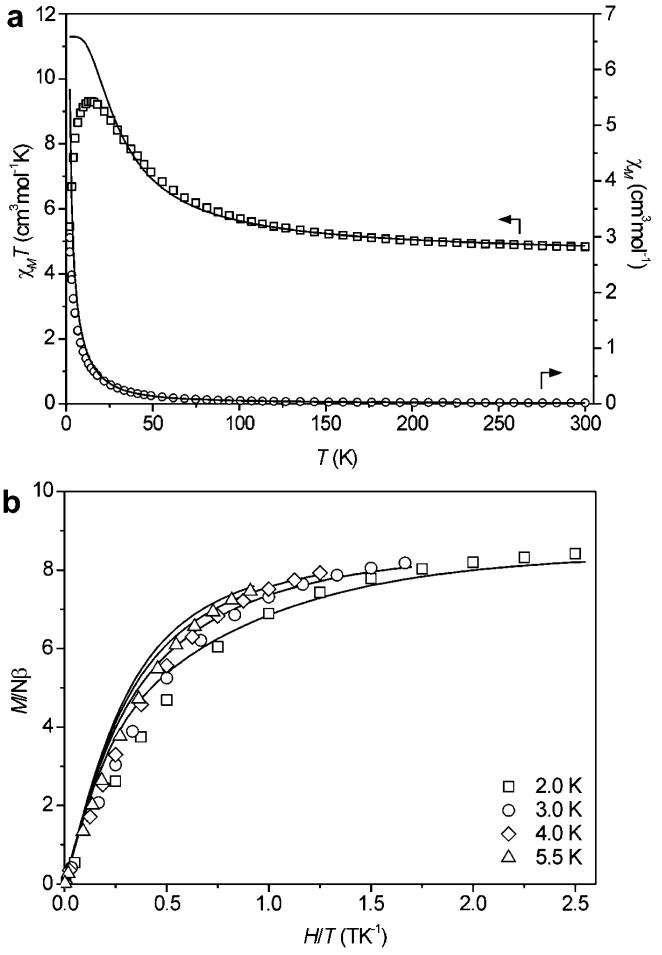


Fig. 4. Plots of magnetic data for **3**: (a) χ_M and $\chi_M T$ vs. T with an applied magnetic field of 0.1 T; and (b) $M/N\beta$ vs. H/T; the solid lines are fits or simulations as described in the text.

constant to fit the susceptibility data for both complexes. The data below 20 K were excluded from the fit, with the decrease in $\chi_M T$ at low temperatures consistent with the effects of zero field splitting (ZFS) and/or antiferromagnetic intermolecular interactions. The fits yielded the parameters $J = 4.3(2)$ cm^{-1} and $g = 2.12(2)$ for **1** and $J = 3.9(1)$ cm^{-1} and $g = 2.13(2)$ for **2**. These afford an $S = 4$ ground state for both complexes, which is the maximum possible for a Ni_4^{II} complex. The determined values of g are consistent with those typically observed for Ni^{II} complexes ($g = 2.1$–2.3) [11,15]. The study of a number of Ni_4 complexes with distorted cubane structures and bridging O atoms has revealed that the observed exchange interactions between Ni centers makes a transition from ferromagnetic to antiferromagnetic as the Ni–O–Ni bridging angles increase above ~98° and the Ni–O–O–Ni dihedral angles increase above ~170° [11,15]. The relevant angles (Table 2) observed for **1** and **2** apparently just fall within this range for ferromagnetic exchange. Ferromagnetic coupling constants are typically less than 20 cm^{-1} for Ni_4 complexes and the values determined for **1** and **3** are consistent with this [11,15].

Variable temperature magnetization measurements were performed on **1** and **3** in the temperature range 2.0–10 K, with fields up to 5 T. The data are presented in Figs. 3b and 4b as plots of $M/N\beta$ versus H/T. Magnetization values of 9.2 and 8.4 $N\beta$ were obtained at 5 T and 2.0 K for **1** and **3**, respectively, and are consistent with $S = 4$ ground states for both complexes. It was possible to simulate the data for the two compounds using the ZFS Hamiltonian:

$$\hat{H}_{ZFS} = D\left[\hat{S}_z^2 - \frac{1}{3}S(S+1)\right] \quad (4)$$

assuming axial anisotropy and a well-isolated $S = 4$ ground state. Two sets of parameters were found to give a reasonable reproduction of the data for each compound, one with $D > 0$ and one with $D < 0$. These parameters are: $g = 2.29(7)$, $D = -0.33(9)$ cm^{-1} and $g = 2.29(8)$, $D = 0.38(9)$ cm^{-1} for **1**; $g = 2.13(3)$, $D = -0.43(6)$ cm^{-1} and $g = 2.09(3)$, $D = 0.44(11)$ cm^{-1} for **3**. An examination of the literature suggests that $D < 0$ is more commonly observed for Ni_4 complexes with similar structures based on distorted cubanes [5], so the simulations provided in Figs. 3b and 4b are for the parameter sets with $D < 0$. The equivalent plots with $D > 0$ are available in the Supplementary Material. As the sign and magnitude of D values cannot

be unequivocally determined from powder magnetic measurements, further studies involving magnetic measurements on oriented single crystals, high field EPR spectroscopy or inelastic neutron scattering would be required to ascertain the D values for **1** and **3**. In addition, the simulations do not reproduce the data exceptionally well, particularly in the low H/T regime. Moreover, close examination of the plots, especially that of **3**, reveals a slight sigmoidal shape to the magnetization curves in the low H/T region. This is consistent with the presence of antiferromagnetic intermolecular interactions [4], which likely account for the deviations between the simulated and experimentally observed behavior. Given that extensive hydrogen bonding is observed crystallographically, multiple pathways probably exist to mediate such interactions. Some unaccounted for rhombic ZFS may also contribute to the discrepancy. Finally, the Ni_4 complexes that have been reported to act as SMMs have been found to do so only at temperatures significantly less than 1 K [5], so ultra-low temperature ac magnetic susceptibility or magnetization relaxation measurements would be required to investigate this possibility.

Variable temperature DC susceptibility measurements were performed at 0.01 and 0.1 T on a collection of randomly oriented small crystals of **4** in the temperature range 2.0–300 K. The data measured at 0.1 T are plotted as $\chi_M T$ and χ_M versus T in Fig. 5a. As the temperature decreases, $\chi_M T$ increases gradually from 13.2 cm^{-3} mol^{-1} K at 300 K. Between 50 and 30 K $\chi_M T$ exhibits a plateau, followed by a steep increase with a maximum value of $\chi_M T =$ 15.2 cm^{-3} mol^{-1} K at 10 K. Further cooling produces an abrupt decrease in $\chi_M T$ to 11.8 cm^{-3} mol^{-1} K at 2 K.

Complex **4** consists of four octahedrally coordinated Co^{II} ions. The ground state of high spin Co^{II} in O_h symmetry is $^4T_{1g}$. Spin–orbit coupling splits the ground state, and this first order effect considerably complicates the analysis of magnetic data of Co^{II} compounds. The room temperature value of $\chi_M T = 13.2$ cm^{-3} mol^{-1} K observed for **4** is much higher than the spin only value of 7.5 cm^{-3} mol^{-1} K calculated for four Co^{II} ($S_i = 3/2$) with $g = 2$ (A in Fig. 5a). The measured high temperature value compares well with the value of 13.6 cm^{-3} mol^{-1} K (B in Fig. 5a) calculated for four uncoupled Co^{II} ions with both spin and orbital contributions to the magnetic susceptibility [16,17]. However, this is not physically reasonable as part of the orbital contribution is undoubtedly quenched due to the distorted octahedral coordination geometries of the Co^{II} centers in **4**. Thus, a second effect has to be jointly responsible for the high $\chi_M T$ value measured at 300 K. The gradual increase in $\chi_M T$ with decreasing temperature is consistent with ferromagnetic intramolecular interactions, which need to be strong to influence the susceptibility at room temperature. The behavior of **4** is similar to that observed previously for another cuboidal Co_4^{II} complex [18], where a high $\chi_M T$ value at room temperature is attributed to the effect of strong intramolecular ferromagnetic interactions on two opposite faces of the cubane (J estimated to be > 300 cm^{-1}). This leads to a hypothetical molecule comprised of two coupled $S = 3$ moieties. Neglecting orbital contributions in this case, a room temperature $\chi_M T$ value of 12.0 cm^{-3} mol^{-1} K is calculated with $g = 2$ (C in Fig. 5a), which is close to the value obtained experimentally for **4**. We conclude that above 30 K the magnetic behavior of **4** originates from the interplay of ferromagnetic intramolecular interactions and spin–orbit coupling, as has been suggested for related complexes [18,19]. As is the situation for the related Ni complexes, the Co–O–Co bond angles in **4** (Table 2) are consistent with ferromagnetic interactions.

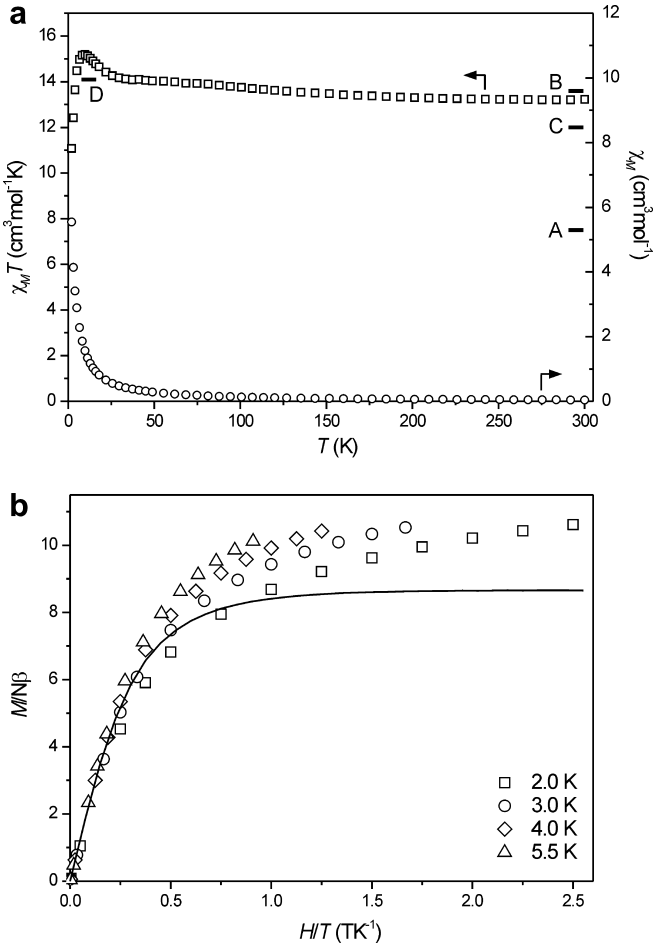


Fig. 5. Plots of magnetic data for **4**: (a) $\chi_M T$ vs. T and χ_M vs. T with an applied magnetic field of 0.1 T, A to D correspond to calculated $\chi_M T$ values as mentioned in the text; and (b) $M/N\beta$ vs. H/T, the solid line is a simulation of the 2 K data calculated with an effective cluster spin $S' = 2$ and $g' = 13/3$.

The sharp increase of $\chi_M T$ as the temperature is decreased below 33 K emphasizes the overall ferromagnetic interactions within the cluster. At temperatures below 30 K only the lowest lying doublet of the spin–orbit split $^4T_1$ ground state of the Co^{II} single ions is occupied. A model with an effective spin $S_i' = 1/2$ per Co^{II} with large g values ($g' = 13/3$ in O_h symmetry) is thus appropriate [17]. For an $S' = 2$ (ferromagnetic coupling of four $S_i' = 1/2$ centers) cluster ground state with isotropic $g' = 13/3$, $\chi_M T =$ 14.1 cm^{-3} mol^{-1} K (D in Fig. 5a), which is close to the

observed experimental maximum. This is a very crude estimate, because the distorted geometry of the Co^{II} positions in **4** will lead to anisotropy splitting of the $S' = 2$ cluster ground state, as well as anisotropic g tensors. However the present data do not allow the introduction of more parameters. The sharp decrease of $\chi_M T$ below 10 K is consistent with anisotropy splitting of the $S' = 2$ ground state and likely also weak antiferromagnetic intermolecular interactions.

Variable temperature magnetization measurements were performed on **4** at four different temperatures with fields up to 5 T. The data are shown in Fig. 5b as $M/N\beta$ versus H/T. The magnetization curve measured at 2 K is not saturated at the high-field limit of our instrument and at 5 T the experimental value is 10.6 $N\beta$. A simulation of the magnetization at 2 K for an $S' = 2$ ground state with $g' = 13/3$ is shown as a solid line in Fig. 5b. The shape of the simulated curve deviates significantly from the experimental data, saturating at 3 T with a saturation value of 8.7 $N\beta$ that is considerably lower than the highest value measured at 2 K. A model with O_h symmetry is oversimplified and distortions and consequently magnetic anisotropy need to be introduced for a quantitative description of the system. The presence of anisotropy is clearly indicated by the differences between the isothermal magnetization plots and their deviation from the calculated curve in Fig. 5b. They indicate splitting of the $S' = 2$ ground state and a higher average g value. Based on the observed magnetization value of 10.6 $N\beta$ at 2 K and 5 T an average g' of 5.3 or higher can be deduced. This order of magnitude is not uncommon for Co^{II} compounds [20].

The large magnetic anisotropy intrinsic to systems with distorted Co^{II} centers in combination with the observed ferromagnetic ground state raises the question whether complex **4** could act as a SMM, as has been observed for another Co_4^{II} cuboidal complex [6]. However, AC magnetic measurements did not show any sign of a peak in the out-of-phase magnetic susceptibility down to 1.8 K. Thus measurements at lower temperatures would be necessary to definitively answer this question.

4. Conclusions

An investigation of the coordination chemistry of the tripodal ligand ampdH_2 with 3d transition metals has afforded a new family of tetranuclear nickel and cobalt spin clusters. A novel binding mode for ampdH^- has been identified and the tendency of this ligand to provide polynuclear species with structures based on cuboidal units has become apparent. This structural preference promotes ferromagnetic exchange interactions in these complexes due to orthogonality of the magnetic orbitals.

Acknowledgement

This work was supported by the Australian Research Council.

Appendix A. Supplementary material

Crystallographic data in cif format have been deposited at the Cambridge Crystallographic Data Center. Copies of the data can be obtained free of charge on request from the CCDC, 12 Union Road, Cambridge CB2 1EZ, UK (fax: +44 1223 336408, email: deposit@ccdc.cam.ac.uk or http://www.ccdc.cam.ac.uk) quoting the deposition numbers 603849 (**1**), 603850 (**2** · 4.25MeOH) and 603851 (**4** · 3EtOH · Et_2O). Tables of selected interatomic distances (Å) and angles (°) for **1**, **2** · 4.25MeOH and **4** · 3EtOH · Et_2O; bond valence sum calculations for **1**, **2** · 4.25MeOH and **4** · 3EtOH · Et_2O; infrared spectra of **2** · $3H_2O$ and **3**; and plots of $M/N\beta$ versus H/T for **1** and **3**, including simulations with $D > 0$ are provided. Supplementary data associated with this article can be found, in the online version, at doi:10.1016/j.poly.2006.06.028.

References

[1] (a) K. Fukuyama, in: A. Messerschmidt (Ed.), Handbook of Metalloproteins, vol. 1, Wiley, Chichester, UK, 2001, p. 543;
(b) C.W. Carter, in: A. Messerschmidt (Ed.), Handbook of Metalloproteins, vol. 1, Wiley, Chichester, UK, 2001, p. 602;
(c) J.S. Vrettos, G.W. Brudwig, in: J.A. McCleverty, T.J. Meyer (Eds.), Comprehensive Coordination Chemistry II, vol. 8, Elsevier, New Haven, USA, 2004, p. 507.
[2] D. Gatteschi, R. Sessoli, Angew. Chem., Int. Ed. 42 (2003) 268, and references therein.
[3] (a) S.M.J. Aubin, M.W. Wemple, D.M. Adams, H.-L. Tsai, G. Christou, D.N. Hendrickson, J. Am. Chem. Soc. 118 (1996) 7746;
(b) S.L. Castro, Z. Sun, C.M. Grant, J.C. Bollinger, D.N. Hendrickson, G. Christou, J. Am. Chem. Soc. 120 (1998) 2997;
(c) A.-L. Barra, A. Caneschi, A. Cornia, F.F. deBiani, D. Gatteschi, C. Sangregorio, R. Sessoli, L. Sorace, J. Am. Chem. Soc. 121 (1999) 5302;
(d) J. Yoo, E.K. Brechin, A. Yamaguchi, M. Nakano, J.C. Huffman, A.L. Maniero, L.-C. Brunel, K. Awaga, H. Ishimoto, G. Christou, D.N. Hendrickson, Inorg. Chem. 39 (2000) 3615;
(e) H. Oshio, N. Hoshino, T. Ito, J. Am. Chem. Soc. 120 (2000) 2997;
(f) L.M. Wittick, K.S. Murray, B. Moubaraki, S.R. Batten, L. Spiccia, K.J. Berry, Dalton Trans. 7 (2004) 1003.
[4] C. Boskovic, R. Bircher, P.L.W. Tregenna-Piggott, H.U. Güdel, C. Paulsen, C.W. Wernsdorfer, A.L. Barra, E. Khatsko, A. Neels, H. Stoeckli-Evans, J. Am. Chem. Soc. 125 (2003) 14046.
[5] (a) E.-C. Yang, W. Wernsdorfer, S. Hill, R.S. Edwards, M. Nakano, S. Maccagnano, L.N. Zakharov, A.L. Rheingold, G. Christou, D.N. Hendrickson, Polyhedron 22 (2003) 1727;
(b) R.S. Edwards, S. Maccagnano, E.-C. Yang, S. Hill, W. Wernsdorfer, D. Hendrickson, J. Christou, J. Appl. Phys. 93 (2003) 7807;
(c) M. Moragues-Cánovas, M. Helliwell, L. Ricard, E. Rivière, W. Wernsdorfer, E.K. Brechin, T. Mallah, Eur. J. Inorg. Chem. (2004) 2219;
(d) C. Kirman, J. Lawrence, S. Hill, E.-C. Yang, D.N. Hendrickson, J. Appl. Phys. 97 (2005), 10M501-1.
[6] E.-C. Yang, D.N. Hendrickson, W. Wernsdorfer, M. Nakano, L.N. Zakharov, R.D. Sommer, A.L. Rheingold, M. Ledezma-Gairaud, G. Christou, J. Appl. Phys. 91 (2002) 7382.
[7] E.K. Brechin, Chem. Commun. (2005) 5141, and references therein.
[8] V. McKee, C.J. Wilkins, J. Chem. Soc., Dalton Trans. (1987) 523.
[9] (a) G. Labat, C. Boskovic, H.U. Güdel, Acta Crystallogr. E61 (2005) m611;
(b) K.G. Alley, R. Bircher, O. Waldmann, S.T. Ochsenbein, H.U.

Güdel, B. Moubaraki, K.S. Murray, F. Fernandez-Alonso, B.F. Abrahams, C. Boskovic (submitted for publication).
[10] (a) C. Boskovic, A. Sieber, G. Chaboussant, H.U. Güdel, J. Ensling, W. Wernsdorfer, A. Neels, G. Labat, H. Stoeckli-Evans, S. Janssen, Inorg. Chem. 43 (2004) 5053;
(b) C. Boskovic, H.U. Güdel, G. Labat, A. Neels, W. Wernsdorfer, B. Moubaraki, K.S. Murray, Inorg. Chem. 44 (2005) 3181.
[11] A. Sieber, C. Boskovic, R. Bircher, O. Waldmann, S.T. Ochsenbein, H.U. Güdel, N. Kirchner, J. van Slageren, W. Wernsdorfer, A. Neels, H. Stoeckli-Evans, S. Janssen, F. Juranyi, H. Mutka, Inorg. Chem. 44 (2005) 4315.
[12] L.K. Thompson, O. Waldmann, Z. Xu, Coord. Chem. Rev. 249 (2005) 2677.
[13] G.M. Sheldrick, SHELX97 Programs for Crystal Structure Analysis, Institut fur Anorganische Chemie der Universitat, Tammanstrasse 4, D-3400 Gottingen, Germany, 1998.
[14] N.E. Brese, M. O' Keefe, Acta Crystallogr. B47 (1991) 192.
[15] (a) P.D.W. Boyd, R.L. Martin, G. Schwarzenbach, Aust. J. Chem. 41 (1988) 1449;
(b) K.S. Murray, Adv. Inorg. Chem. 43 (1995) 261;
(c) M.A. Halcrow, J.S. Sun, J.C. Huffman, G. Christou, Inorg. Chem. 34 (1995) 4167;
(d) M.S. ElFallah, E. Rentschler, A. Caneschi, D. Gatteschi, Inorg. Chim. Acta 247 (1996) 231;
(e) A. Escuer, M. Font-Bardia, S.B. Kumar, X. Solans, R. Vicente, Polyhedron 18 (1999) 909;
(f) S. Mukherjee, T. Weyhermuller, E. Bothe, K. Wieghardt, P. Chaudhuri, Eur. J. Inorg. Chem. (2003) 863;
(g) J.M. Clemente-Juan, B. Chansou, B. Donnadieu, J.P. Tuchagues, Inorg. Chem. 39 (2000) 5515.
[16] O. Kahn, Molecular Magnetism, VCH Publishers, New York, 1993, p. 38.
[17] F.E. Mabbs, D.J. Machin, Magnetism and Transition Metal Complexes, Chapman & Hall, London, 1973, p. 87.
[18] J.F. Berry, F.A. Cotton, C.Y. Liu, T. Lu, C.A. Murillo, B.S. Tsukerblat, D. Villagrán, X. Wang, Inorg. Chem. 127 (2005) 4895.
[19] G.S. Papefstathiou, A. Escuer, F.A. Mautner, C. Raptopolou, A. Terzis, S.P. Perlepes, R. Vicente, Eur. J. Inorg. Chem. (2005) 879.
[20] (a) J.M. Clemente-Juan, H. Andres, J.J. Borras-Almenar, E. Coronado, H.U. Güdel, M. Aebersold, G. Kearly, H. Büttner, M. Zolliker, J. Am. Chem. Soc. 121 (1999) 10021;
(b) H. Andres, J.M. Clemente-Juan, M. Aebersold, H.U. Güdel, E. Coronado, H. Buttner, G. Kearly, J. Melero, R. Burriel, J. Am. Chem. Soc. 121 (1999) 10028;
(c) H. Andres, J.M. Clemente-Juan, R. Basler, M. Aebersold, H.U. Güdel, J.J. Borras-Almenar, A. Gaita, E. Coronado, H. Büttner, S. Janssen, Inorg. Chem. 40 (2001) 1943;
(d) J.M. Clemente-Juan, E. Coronado, A. Gaita-Arino, C. Gimenez-Saiz, H.U. Güdel, A. Sieber, R. Bircher, H. Mutka, Inorg. Chem. 44 (2005) 3389.

Available online at www.sciencedirect.com
ScienceDirect
Polyhedron 26 (2007) 378–384
POLYHEDRON
www.elsevier.com/locate/poly

A new series of potentially hexadentate ligands derived from 2,2′-bipyridine

Lynton J. Baird, Cory A. Black, Allan G. Blackman *

Department of Chemistry, University of Otago, P.O. Box 56, Dunedin, New Zealand

Received 5 April 2006; accepted 23 June 2006
Available online 30 June 2006

Abstract

Reaction of 2,2′-bipyridine-6-carboxaldehyde with the appropriate aliphatic diamine in MeOH and subsequent reduction with $NaBH_4$ gives the new, potentially hexadentate, ligands *N*,*N*′-bis(2,2′-bipyridin-6-ylmethyl)ethane-1,2-diamine (bmet), *N*,*N*′-bis-(2,2′-bipyridin-6-ylmethyl)propane-1,3-diamine (bmpp) and *N*,*N*′-bis(2,2′-bipyridin-6-ylmethyl)hexane-1,6-diamine (bmhx). The syntheses and characterisation of these ligands are reported; the ligands are isolated as the hydrochloride salts, with purification effected by either recrystallisation or cation exchange chromatography. $[Co(bmet)](ClO_4)_3 \cdot H_2O$ is obtained on reaction of bmet $\cdot$ 4.25HCl $\cdot$ 2.5H_2O with $Na_3[Co(O_2CO)_3] \cdot 3H_2O$, and X-ray structural analysis shows this to have a pair of very short Co–N bonds. The synthesis and characterisation of the first coordination complex containing 6-(aminomethyl)-2,2′-bipyridine (amb) is also described.
© 2006 Elsevier Ltd. All rights reserved.

Keywords: Hexaamine; Hexadentate ligand; Co(III); Crystal structure; 2,2′-Bipyridine

1. Introduction

The concept of ligand design has become increasingly important in all facets of coordination chemistry [1–5]. Rational ligand design now allows some degree of control over the nuclearity, geometry, magnetic behaviour, spectroscopic properties and reactivity of transition metal complexes, and the advent of metallosupramolecular chemistry has further emphasised the importance of ligand design in the synthesis of transition metal assemblies. One area of that has received particular attention is the synthesis of multidentate ligands that are predisposed to form helical complexes on coordination to two or more metal ions. Oligopyridine-based ligands have shown particular utility in this respect, and ligands such as 2,2′:6′,2″:6″,2‴:6‴,2⁗-quinquepyridine [6,7] and 2,2′:6′,2″:6″,2‴:6‴,2⁗:6⁗,2⁗′-sexipyridine [8,9] have been shown to form double-helical dimeric complexes with a variety of metal ions. These ligands were chosen as likely candidates for the formation of helical complexes because of their inherent structural limitations; rotation within the ligands is restricted to the interannular C–C bond, and this places significant constraints on the possible positionings of the N donor atoms, therefore limiting the ways in which the ligands can coordinate to a metal ion.

As part of our investigations into the synthesis of new multidentate N-donor ligands [10,11], we herein report the synthesis and characterisation of a new series of potentially hexadentate ligands which contain terminal 2,2′-bipyridine units and central aliphatic diamine spacers whose length can be easily varied. These ligands are more flexible than the corresponding hexadentate oligopyridine 2,2′:6′,2″:6″,2‴:6‴,2⁗:6⁗,2⁗′-sexipyridine, and should therefore be able to adopt a wider variety of binding modes to one or more transition metal ions. We also report the synthesis and crystal structure of the mononuclear complex $[Co(bmet)](ClO_4)_3 \cdot H_2O$, which displays two remarkably short Co–N bonds and, in addition, we undertake the first investigation of the coordination chemistry of 6-(aminomethyl)-2,2′-bipyridine.

* Corresponding author. Tel.: +64 3 4797931; fax: +64 3 4797906.
E-mail addresses: blackman@chemistry.otago.ac.nz, blackman@alkali.otago.ac.nz (A.G. Blackman).

0277-5387/$ - see front matter © 2006 Elsevier Ltd. All rights reserved.
doi:10.1016/j.poly.2006.06.018

2. Experimental

2.1. General

All chemicals used were of LR grade or better. ^{1}H and ^{13}C NMR spectra were obtained using either a Varian VXR 300 MHz or Varian Europa 500 MHz spectrophotometer. All spectra were recorded at room temperature with chemical shifts reported in ppm relative to NaTSP (^{1}H, 0.00 ppm) and dioxane (^{13}C, 67.8 ppm). Visible spectra were recorded in H_2O on a Varian Cary 500 Scan UV–vis NIR spectrophotometer at room temperature. Electrospray mass spectra were obtained on a Shimadzu LCMS-QP8000α (mass range m/z 10–2000, resolution $R = 2$ M, 50% valley) using direct infusion via a manual Rheodyne injector (5 μL loop). Positive ionisation techniques were used on an ESI probe (H_2O mobile phase, 0.2 m/min, CDL temp 250 °C, 4.5 kV). Elemental analyses were performed by the Campbell Microanalytical Laboratory, University of Otago. Reported elemental percentages (C, H, N, Cl, Br) are accurate to within ±0.4%.

Caution: Although no difficulties were experienced with the perchlorate complexes described herein, all perchlorate species should be treated as potentially explosive and handled with care.

2.2. X-ray data collection and refinement

X-ray data for $[Co(bmet)](ClO_4)_3 \cdot H_2O$ were recorded using a Bruker SMART diffractometer at 98(2) K. The structure was solved by direct methods using SIR97 [12] running within the WINGX package [13], with the resulting Fourier map revealing the location of all non-hydrogen atoms. Weighted full matrix refinement on F^2 was carried out using SHELXL-97 [14] with all non-hydrogen atoms being refined anisotropically. With the exceptions noted below, hydrogen atoms were included in calculated positions and were refined as riding atoms with individual (or group, if appropriate) isotropic displacement parameters. H10A and H10B, the hydrogen atoms of the water molecule, were located in a search of the Fourier map and were allowed to refine freely. Crystal data and collection parameters are given in Table 1.

Table 1
Crystal data and structure refinement for $[Co(bmet)](ClO_4)_3 \cdot H_2O$

Empirical formula	$C_{24}H_{26}Cl_3CoN_6O_{13}$
Formula weight	771.79
T (K)	98(2)
λ (Å)	0.71069
Crystal system	triclinic
Space group	$P\bar{1}$
Unit cell dimensions	
a (Å)	10.992(5)
b (Å)	11.267(5)
c (Å)	12.831(5)
α (°)	81.754(5)
β (°)	70.248(5)
γ (°)	75.023(5)
V (Å^3)	1442.0(11)
Z	2
D_{calc} (Mg m^{-3})	1.777
Absorption coefficient (mm^{-1})	0.954
$F(000)$	788
Crystal size (mm)	0.40 × 0.33 × 0.26
θ Range for data collection (°)	1.87 to 26.38
Index ranges	$-13 \leqslant h \leqslant 12$, $-14 \leqslant k \leqslant 13$, $-15 \leqslant l \leqslant 15$
Reflections collected	12474
Independent reflections (R_{int})	5705 (0.0273)
Completeness to $\theta = 25.00°$	97.5%
Absorption correction	semi-empirical from equivalents
Maximum and minimum transmission	1.000000 and 0.846643
Refinement method	full-matrix least-squares on F^2
Data/restraints/parameters	5705/0/432
Goodness-of-fit on F^2	1.061
Final R indices ($I > 2\sigma(I)$)	$R_1 = 0.0307$, $wR_2 = 0.0736$
R indices (all data)	$R_1 = 0.0386$, $wR_2 = 0.0766$
Largest difference in peak and hole (e Å^{-3})	0.322 and −0.448

2.3. Syntheses

$Na_3[Co(O_2CO)_3] \cdot 3H_2O$ [15], 6-methyl-2,2′-bipyridine [16], 6-(bromomethyl)-2,2′-bipyridine [17] and 2,2′-bipyridine-6-carbaldehyde [17,18] were prepared as described. 6-(Dibromomethyl)-2,2′-bipyridine was prepared by modification of the reported method [17], with the product being separated from 6-(bromomethyl)-2,2′-bipyridine by chromatography on partially deactivated (5% v/v H_2O) silica gel (CH_2Cl_2 eluent). 6-(Aminomethyl)-2,2′-bipyridine (amb) was prepared by the method of Ziessel and Lehn [19], and was isolated as amb.2HCl · H_2O.

2.3.1. N,N′-bis(2,2′-bipyridin-6-ylmethyl)ethane-1,2-diamine · 4HCl · H_2O (bmet · 4HCl · H_2O)

A solution of 1,2-diaminoethane (9.06 μL, 0.136 mmol) and 2,2′-bipyridine-6-carbaldehyde (50.0 mg, 0.271 mmol) in MeOH (2 mL) was heated at reflux for 10 min with stirring. $NaBH_4$ (12.1 mg, 0.321 mmol) was then added slowly to the cooled solution and the mixture was stirred for 2 h. After this time, the solution was reduced (rotavap) to dryness yielding a white solid, which was dissolved in water (10 mL) and extracted with $CHCl_3$ (3 × 5 mL). The organic fractions were combined, dried over $MgSO_4$ and reduced (rotavap) to dryness. The resulting white solid was dissolved in 1 M HCl (1 mL) and reduced (rotavap) to dryness. The product was recrystallised by dissolution in the minimum volume of EtOH and cooling to ca. −20 °C for 72 h to give a white solid which was filtered, washed with cold ethanol and dried under vacuum (29.0 mg, 54%): MS (H_2O/MeCN): $m/z = 397$ $[M + 1\ H]^+$. *Anal.* Calc. for $C_{24}H_{30}N_6OCl_4$: C, 51.44; H, 5.40; N, 15.00; Cl, 25.31. Found: C, 51.55; H, 5.63; N, 14.80; Cl, 25.07%. ^{1}H NMR (500 MHz, D_2O): δ 8.91 (2H, t d, $J = 1$, 6 Hz), 8.77 (4H, m), 8.41 (2H, d, $J = 8$ Hz), 8.23 (2H, t,

$J = 8$ Hz), 8.14 (2H, m), 7.78 (2H, d, $J = 8$ Hz), 4.78 (4H, s), 3.90 (4H, s) ppm; ^{13}C NMR (500 MHz, D_2O): δ 152.1, 148.6, 147.8, 146.3, 142.2, 141.1, 128.0, 126.6, 125.1, 123.3, 51.5, 43.7 ppm.

Purification of the ligand could also be effected by chromatography on Dowex 50 W-X2 cation exchange resin instead of recrystallisation. The product was eluted from the column using 4 M HCl, and removal of solvent (rotavap) gave the product bmet · 4.25HCl · 2.5H_2O as a pale-brown solid in 76% yield. *Anal*. Calc. for $C_{24}H_{33.25}N_6O_{2.5}Cl_{4.25}$: C, 48.33; H, 5.58; N, 14.10; Cl, 25.28. Found: C, 48.05; H, 5.63; N, 14.20; Cl, 25.67%.

2.3.2. *N,N′-bis(2,2′-bipyridin-6-ylmethyl) propane-1,3-diamine · 4.25HCl · 2.5H_2O (bmpp · 4.25HCl · 2.5H_2O)*

A solution of 1,3-diaminopropane (22.7 μL, 0.271 mmol) and 2,2′-bipyridine-6-carbaldehyde (100 mg, 0.542 mmol) in MeOH (2 mL) was heated at reflux with stirring for 10 min. $NaBH_4$ (24.3 mg, 0.642 mmol) was added slowly to the cooled solution and the mixture was stirred for 2 h. After this time the solution was reduced (rotavap) to dryness. The crude product was dissolved in 1 M HCl (1.00 mL) and reduced (rotavap) to dryness to give a white solid which was dissolved in H_2O (200 mL) and loaded onto a Dowex 50 W-X2 cation exchange column. The product was eluted with 4 M HCl (aq) and the band was reduced to dryness (rotavap) to give a pale pink solid (90.0 mg, 54%): ^{1}H NMR (300 MHz, D_2O): δ 9.00 (2H, d, $J = 6$ Hz), 8.82 (4H, m), 8.44 (2H, d, $J = 8$ Hz), 8.26 (2H, t, $J = 8$ Hz), 8.21 (2H, dt, $J = 3$, 6 Hz), 7.82 (2H, d, $J = 8$ Hz), 4.76 (4H, s), 3.55 (4H, t, $J = 8$ Hz), 2.58 (2H, d, $J = 6$ Hz) ppm; ^{13}C NMR (300 MHz, D_2O): δ 152.5, 148.5, 147.7, 146.1, 142.3, 141.0, 128.0, 126.7, 125.0, 123.2, 51.2, 45.3, 23.5 ppm. MS (MeOH): m/z = 411 $[M + 1H]^+$, 206 $[M + 2H]^{2+}$. *Anal*. Calc. for $C_{25}H_{35.25}N_6O_{2.5}Cl_{4.25}$: C, 49.19; H, 5.78; N, 13.77; Cl, 24.70. Found: C, 49.33; H, 5.70; N, 13.79; Cl, 24.35%.

2.3.3. *N,N′-bis(2,2′-bipyridin-6-ylmethyl)hexane-1,6-diamine · 4.5HCl· 2H_2O(bmhx · 4.5HCl · 2H_2O)*

A solution of 1,6-diaminohexane (31.5 mg, 0.271 mmol) and 2,2′-bipyridine-6-carbaldehyde (100 mg, 0.542 mmol) in MeOH (2.00 mL) was heated at reflux with stirring for 10 min. $NaBH_4$ (24.3 mg, 0.642 mmol) was added slowly to the cooled solution and the mixture was stirred for 2 h. After this time, the solution was reduced (rotavap) to dryness. The crude product was dissolved in 1 M HCl (1.00 mL) and reduced (rotavap) to dryness to give a white solid which was dissolved in H_2O (200 mL) and loaded onto a Dowex 50 W-X2 cation exchange column. The product was eluted with 4 M HCl (aq) and the band was reduced to dryness (rotavap) to give a pale green solid (162 mg, 92%): ^{1}H NMR (300 MHz, D_2O): δ 8.93 (2H, d, $J = 6$ Hz), 8.77 (4H, m), 8.40 (2H, d, $J = 8$ Hz), 8.22 (2H, t, $J = 8$ Hz), 8.16 (2H, dt, $J = 3$, 6 Hz), 7.76 (2H, d, $J = 8$ Hz), 4.63 (4H, s), 3.29 (4H, t, $J = 8$ Hz), 1.89 (4H, m), 1.52 (4H, m) ppm; ^{13}C NMR (300 MHz, D_2O): δ 152.8, 148.5, 148.0, 146.3, 142.3, 140.9, 128.0, 126.7, 125.1, 123.1, 51.0, 48.2, 26.1, 26.0 ppm; MS (H_2O/MeCN): $m/z = 453$ $[M + 1H]^+$, 227 $[M + 2\ H]^{2+}$. *Anal*. Calc. for $C_{28}H_{40.5}N_6O_2Cl_{4.5}$: C, 51.53; H, 6.21; N, 12.88; Cl, 24.47. Found: C, 51.36; H, 6.16; N, 12.76; Cl, 24.10%.

2.3.4. *[Co(bmet)](ClO$_4$)$_3$*

$Na_3[Co(O_2CO)_3] \cdot 3H_2O$ (30.4 mg, 83.9 μmol) was added to a solution of bmet · 4.25HCl · 2.5H_2O (50.0 mg, 83.9 μmol) in H_2O (2 mL). The mixture was heated at 65 °C until the colour changed to orange (ca. 5 min). The mixture was then filtered through celite and the filtrate was diluted to 500 mL with distilled water and loaded onto a Sephadex SP C-25 cation exchange column. Elution with 0.3 M $NaClO_4$(aq) removed a yellow band which was reduced to low volume (rotavap) and cooled. The resulting yellow solid was filtered off, washed with MeOH and Et_2O and dried under vacuum. (29.0 mg, 46%): MS (H_2O/MeCN): $m/z = 453$ $[M - 2H]^+$, 227 $[M - 1H]^{2+}$, 151 $[M]^{3+}$. *Anal*. Calc. for $C_{24}H_{24}N_6O_{12}Cl_3Co$: C, 38.23; H, 3.19; N, 11.15; Cl, 14.12. Found: C, 38.00; H, 3.49; N, 10.81; Cl, 13.83%. ^{1}H NMR (500 MHz, D_2O): δ 8.82 (2H, d, $J = 8$ Hz, H_a), 8.74 (2H, t, $J = 8$ Hz, H_b), 8.66 (2H, dd, $J = 8$, 1 Hz, H_d), 8.36 (2H, dt, $J = 1$, 8 Hz, H_e), 8.21 (2H, d, $J = 8$ Hz, H_c), 7.59 (2H, ddd, $J = 8$, 6, 1 Hz, H_f), 7.40 (2H, dd, $J = 6$, 1 Hz, H_g), 5.20 (2H, d, $J = 19$ Hz, $-C^{11}H_2$), 4.72 (1H, d, $J = 19$ Hz, $-C^{11}H_2$), 3.03 (1H, m, $-C^{12}H_2$) ppm; ^{13}C NMR (500 MHz, D_2O): δ 164.4 (C^{10}), 158.1 (C^5), 155.8 (C^6), 151.9 (C^1), 144.7 (C^8), 143.7 (C^3), 130.4 (C^2), 126.8 (C^4), 126.1 (C^7), 125.0 (C^9), 63.0 (C^{11}), 55.5 (C^{12}) ppm; UV–vis (H_2O) (λ_{max}, nm): 440. Crystals of [Co(bmet)]$(ClO_4)_3 \cdot H_2O$ suitable for X-ray structural determination were obtained by slow cooling of a hot, concentrated aqueous solution of the product.

The complex was also obtained as the more soluble chloride salt by elution with 0.3 M NaCl(aq) (Sephadex) and 3 M HCl(aq) (Dowex).

2.3.5. *[Co(amb)$_2$](ClO$_4$)$_3$*

$Na_3[Co(O_2CO)_3] \cdot 3H_2O$ (32.8 mg, 0.0906 mmol) was added to a solution of amb · 2HCl · H_2O (50.0 mg, 0.181 mmol) in H_2O (2 mL) with stirring. The mixture was heated at 65 °C until the colour changed to orange (ca. 10 min). The mixture was filtered through celite, the filtrate was diluted to 200 mL with distilled water and loaded onto a Sephadex SP C-25 cation exchange column. The yellow band that eluted with 0.3 M NaCl (aq) was loaded onto a Dowex 50 W-X2 cation exchange column, eluted with 3 M HCl (aq) and the elaute was reduced to dryness (rotavap). The product was dissolved in H_2O (1.00 mL) and a saturated solution of $NaClO_4$ (aq) was added dropwise until no more yellow solid precipitated. The yellow solid was filtered and washed with isopropanol. The product was recrystallised by dissolution in the minimum volume of hot water and cooling at 4 °C overnight. The product was filtered off, washed with isopropanol and

Et_2O and dried under vacuum (46.1 mg, 70%): ^1H NMR (500 MHz, DMSO-d^6): δ 8.98 (2H, d, $J = 8$ Hz, H_a), 8.82 (2H, d, $J = 8$ Hz, H_d), 8.72 (2H, t, $J = 8$ Hz, H_b), 8.36 (2H, dt, $J = 1$, 8 Hz, H_e), 8.16 (2H, d, $J = 8$ Hz, H_c), 7.54 (2H, ddd, $J = 6$, 3, 2 Hz, H_f), 7.37 (2H, d, $J = 6$ Hz, H_g), 5.95 (2H, br s, $–CH_2–NH_2$), 5.83 (2H, br s, $–CH_2–NH_2$), 4.77 (2H, br d, bipy-CH_2–), 4.51 (2H, br d, bipy-CH_2–) ppm; ^{13}C NMR (500 MHz, DMSO-d^6): δ 166.0 ($C^{5,6,10}$), 157.0 ($C^{5,6,10}$), 154.2 ($C^{5,6,10}$), 150.9 (C^1), 142.6 (C^8), 142.0 (C^3), 129.1 (C^2), 125.4 (C^4), 124.7 (C^7), 123.5 (C^9), 52.4 (C^{11}) ppm; UV–vis (H_2O) (λ_{max}, nm): 440; MS (H_2O/MeCN): $m/z = 427$ $[M - 2H]^+$. *Anal.* Calc. for $C_{22}H_{22}N_6O_{12}Cl_3Co$: C, 36.29; H, 3.02; N, 11.54; Cl, 14.62. Found: C, 36.43; H, 3.06; N, 11.42; Cl, 14.41%.

3. Results and discussion

3.1. Synthesis of bmet, bmpp and bmhx

The new ligands bmet, bmpp and bmhx (Fig. 1) were prepared by the reaction, in methanol, of two equivalents of 2,2′-bipyridine-6-carboxaldehyde with 1,2-diaminoethane, 1,3-diaminepropane and 1,6-diaminohexane, respectively, with reduction of the resulting diimine effected by $NaBH_4$ (Scheme 1). Initial attempts to prepare the ligands utilised the reaction of 6-(bromomethyl)-2,2′-bipyridine with the appropriate diamine, but these reactions proved unsuccessful, in contrast to the previous work, where 6-(bromomethyl)-2,2′-bipyridine was used as the starting material for the synthesis of a number of 2,2′-bipyridin-6-ylmethyl-appended multidentate amine ligands [19]. The ligands were isolated in moderate yields as hydrochloride salts, with purification being achieved by either crystallisation from ethanol, or cation exchange chromatography. Microanalytical data were in all cases consistent with the proposed formulations of the ligands, and both ^1H and ^{13}C NMR data were consistent with a symmetrical structure in which the two halves of the ligands are equivalent.

While the ligands bmet, bmpp and bmhx each contain six N donor atoms, they are not all expected to exhibit the same modes of coordination to transition metals. Each ligand contains, in effect, two tridentate binding domains, linked by an aliphatic carbon chain, and it is the length of this carbon chain which may determine the mode of binding of the ligand. Coordination of the two aliphatic N atoms to the same metal ion will form a chelate ring having 5, 6 and 9 members for bmet, bmpp and bmhx, respectively. Formation of the latter is very unlikely, as evidenced by the mere six examples of a chelated $–N(CH_2)_6N–$ fragment in the Cambridge Structural Database [20–24] (this contrasts with 11 156 examples of a chelated $–N(CH_2)_2N–$ fragment) and therefore it would be expected that the bmhx ligand should bind separately to two metal ions in preference to acting as a hexadentate ligand towards a single metal ion. In contrast, the relatively unstrained 5- and 6-membered chelate rings formed by chelation of the aliphatic N atoms of bmet and bmpp should allow these ligands to coordinate to a single metal ion, but will not necessarily preclude formation of dimeric species. With this in mind, we undertook preliminary investigations of the coordination behaviour of the bmet ligand.

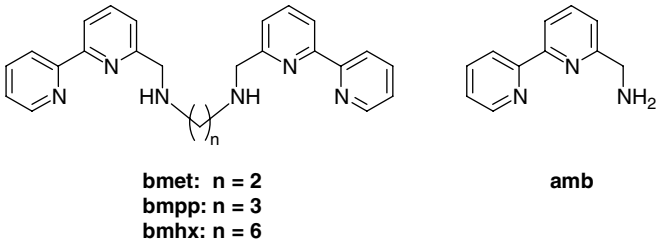
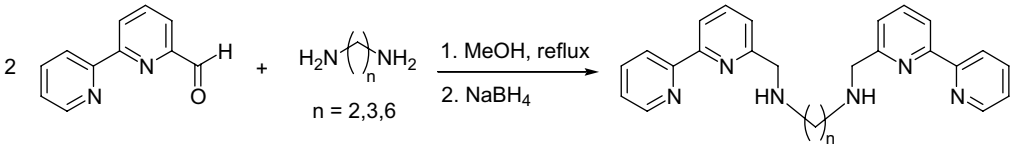


Fig. 1. Structures of the hexadentate ligands bmet, bmpp and bmhx, and the tridentate ligand amb.

3.2. Synthesis and characterisation of $[Co(bmet)](ClO_4)_3$

The mononuclear complex $[Co(bmet)](ClO_4)_3$ was prepared by the reaction of $Na_3[Co(O_2CO)_3] \cdot 3H_2O$ with one equivalent of bmet $\cdot$ 4.25HCl $\cdot$ 2.5H_2O in hot water. The reaction was evidenced by a colour change from dark green to orange over 5 min and purification of the product was achieved by chromatography on Sephadex SP-C25 cation exchange resin ($NaClO_4$ eluent) and subsequent crystallisation on reduction of the volume of the eluate. The complex moved as a 3+ ion on the column, suggesting that it was a mononuclear, rather than binuclear, species. X-ray quality crystals of the monohydrate were obtained on slow cooling of a hot, concentrated aqueous solution and the identity of the complex was confirmed by successful solution and refinement of the structure. Fig. 2 shows an ORTEP diagram of the $[Co(bmet)]^{3+}$ cation, while selected bond lengths and angles are given in Table 2. The structure consists of a central Co^{3+} ion coordinated to all six N atoms of a bmet ligand. The charge is balanced by three ClO_4^- counterions, and a single water of crystallisation is involved in H-bonding interactions with one of the ClO_4^- counterions. While there are potentially a number of ways in which the bmet ligand could fold about the metal ion,



Scheme 1. The synthesis of the hexadentate ligands.

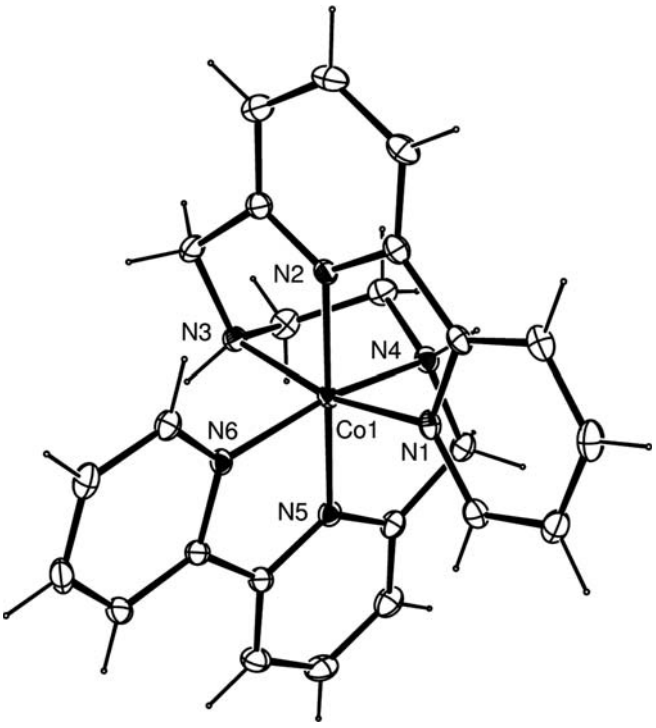


Fig. 2. ORTEP diagram of the $[Co(bmet)]^{3+}$ cation. Thermal ellipsoids are drawn at the 50% probability level.

Table 2
Selected bond lengths (Å) and angles (°) for $[Co(bmet)](ClO_4)_3 \cdot H_2O$

Co(1)–N(1)	1.9436(18)
Co(1)–N(2)	1.8653(19)
Co(1)–N(3)	1.9744(18)
Co(1)–N(4)	1.9702(19)
Co(1)–N(5)	1.8636(19)
Co(1)–N(6)	1.9421(19)
N(1)–Co(1)–N(3)	166.49(8)
N(1)–Co(1)–N(4)	91.19(8)
N(2)–Co(1)–N(1)	82.52(8)
N(2)–Co(1)–N(3)	84.26(8)
N(2)–Co(1)–N(4)	93.99(8)
N(2)–Co(1)–N(6)	98.97(8)
N(4)–Co(1)–N(3)	86.98(8)
N(5)–Co(1)–N(1)	99.36(8)
N(5)–Co(1)–N(2)	177.57(8)
N(5)–Co(1)–N(3)	93.79(8)
N(5)–Co(1)–N(4)	84.45(8)
N(5)–Co(1)–N(6)	82.49(8)
N(6)–Co(1)–N(1)	93.60(8)
N(6)–Co(1)–N(3)	91.18(8)
N(6)–Co(1)–N(4)	166.66(7)

the presence of the terminal 2,2′-bipyridine fragments essentially constrains the CH_2 groups at the 6′ positions to be coplanar with the attached pyridine ring. This means that both N3 and N4 must, of necessity, coordinate in a *meridional* manner with respect to their neighbouring 2,2′-bipyridine fragments and the overall conformation of the complex can therefore be described as *mffm* [25]. Such a conformation gives rise to the possibility of a single enantiomeric pair, and both enantiomers are observed in the crystal structure. The Co^{3+} ion displays a distorted octahedral geometry; the Co(1)–N(2) (1.8653(19) Å) and Co(1)–N(5) (1.8636(19) Å) bonds involving the non-terminal pyridine rings are significantly shorter than the other four, and in fact are amongst the shortest known Co^{III}–N_{amine} bonds. A search of the Cambridge Structural Database for Co^{III} bonded to amine N found 826 structures containing 8660 Co–N bonds ($R_1 < 5\%$, no errors and not disordered) with the average distance being 1.967 Å (standard deviation 0.031 Å). Only 29 of the 8660 bonds were shorter than 1.867 Å, with all of these being bonds to deprotonated N atoms. It therefore appears that the Co–N bonds to the non-terminal pyridine rings in $[Co(bmet)](ClO_4)_3 \cdot H_2O$ are remarkably short, and this is presumably due to steric constraints imposed by the ligand. Similar shortening of the Co–N bonds to non-terminal pyridine rings has also been observed in $[Co(terpy)_2]Cl_3.$"$11H_2O$" [26], and appears to be a feature of metal complexes of terpy in general. The quarterpy complex $[Co(quaterpy)(OH_2)(SO_3)]NO_3 \cdot H_2O$ also exhibits short Co–N bonds to the two N atoms of the central pyridine rings [27]. The pair of very short Co–N bonds in $[Co(bmet)](ClO_4)_3 \cdot H_2O$ help to make the average Co–N bond length (1.927 Å) in this CoN_6 system shorter than any reported in an extensive review of CoN_6 complexes [28], and the very strong-field nature of the bmet ligand is further reflected in the λ_{max} value of 440 nm found in the UV/vis spectrum, a shorter wavelength than previously found in CoN_6 complexes [28]. The bond angles around the metal ion in $[Co(bmet)](ClO_4)_4 \cdot H_2O$ attest to the deviations from strict octahedral geometry, with the angles subtended by the N atoms of the two sets of neighbouring pyridine rings (82.52(8)° and 82.49(8)°) typical of the angles found in Co(III) complexes containing bipyridine [29–31]. In contrast to the solid-state structure, the ^1H and ^{13}C NMR spectra of $[Co(bmet)]^{3+}$ are consistent with a solution structure having a C_2 rotation axis; the ^1H NMR spectrum exhibits 11 well-separated signals, while the ^{13}C NMR spectrum shows 12 peaks. A combination of HSQC and gCOSY spectra allowed complete assignment of the ^1H and ^{13}C spectra, and the assignments are given in Section 2, according to the numbering scheme given in Fig. 3.

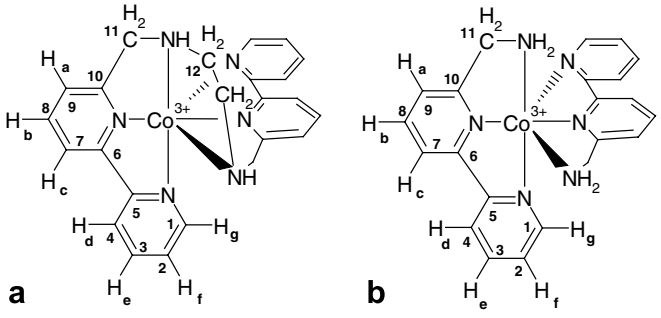


Fig. 3. Numbering schemes for: (a) $[Co(bmet)]^{3+}$ and (b) $[Co(amb)_2]^{3+}$.

3.3. Synthesis and characterisation of $[Co(amb)_2](ClO_4)_3$

The amb ligand (Fig. 1) represents essentially half of the bmet ligand, and we were therefore interested in comparing the coordination chemistry of amb to bmet, to see what, if any, effect the ethyl linker in bmet had on the geometry of the respective Co(III) complexes. Reaction of 2 equivalents of amb · 2HCl · H_2O with $Na_3[Co(O_2CO)_3] \cdot 3H_2O$ in water at elevated temperature and subsequent purification using cation exchange chromatography gave $[Co(amb)_2](ClO_4)_3$ in good yield. Elemental analysis and ESI-MS data were consistent with the formulation of the complex as a 6-coordinate Co(III) complex containing two tridentate amb ligands, and the complex was further characterised by ^1H and ^{13}C NMR spectroscopy. Unfortunately, crystals of the complex suitable for X-ray crystallography could not be obtained.

To the best of our knowledge $[Co(amb)_2](ClO_4)_3$ represents the first reported transition metal complex of the amb ligand, although complexes of ligands derived from amb are known [32,33]. The amb ligand is constrained to coordinate in a *meridional* tridentate fashion as found above for the two tridentate binding domains of bmet. Both the ^1H and ^{13}C NMR spectra are consistent with a solution structure in which the complex cation contains a C_2-axis. The rigid nature of the coordinated amb ligand is reflected in the ^1H NMR spectrum of $[Co(amb)_2]^{3+}$; the $-CH_2-$ protons appear as separate geminally coupled signals at 4.77 and 4.51 ppm, each of which also show coupling to one of the neighbouring $-NH_2$ protons. The $-NH_2$ protons are observed as separate broad signals at 5.95 ppm and 5.83 ppm in DMSO-d^6, and these signals are absent when the spectrum is obtained in D_2O. The ^{13}C NMR spectra of both $[Co(amb)_2]^{3+}$ and $[Co(bmet)]^{3+}$ are similar, the one distinct difference being the peak due to the isolated methylene carbon C11, which appears at 52.4 ppm and 63.0 ppm in the amb and bmet complexes, respectively. Like bmet, amb also appears to act as a very strong-field ligand, with $[Co(amb)_2]^{3+}$ displaying a λ_{max} value of 440 nm, possibly again indicative of a very short Co–N bond to the central pyridine ring. It therefore appears that both $[Co(amb)_2]^{3+}$ and $[Co(bmet)]^{3+}$ display similar spectral properties and hence similar geometries.

4. Conclusions

The successful synthesis of bmet, bmpp and bmhx should allow the synthesis of many other potentially hexadentate ligands using the same synthetic scheme, simply by changing the aliphatic diamine. We are currently investigating the synthesis of such ligands. We are also extending our studies into the coordination chemistry of the bmpp and (particularly) bmhx ligands with a variety of metal ions, in the hope of preparing dinuclear helical systems. Finally, we have shown that the amb ligand is useful as a very strong-field *meridional* tridentate ligand, and its coordination chemistry deserves further investigation.

Acknowledgements

We thank Professor Ward Robinson and Dr. Jan Wikaira (University of Canterbury) for X-ray data collection. This work was supported by the Department of Chemistry, University of Otago.

Appendix A. Supplementary material

CCDC 603573 contains the supplementary crystallographic data for this paper. These data can be obtained free of charge via www.ccdc.cam.ac.uk/data_request/cif, by emailing data_request@ccdc.cam.ac.uk, or by contacting the Cambridge Crystallographic Data Centre, 12, Union Road, Cambridge, CB2 1EZ, UK; fax: +44 1223 3360333. Supplementary data associated with this article can be found, in the online version, at doi:10.1016/j.poly.2006.06.018.

References

[1] M.J. Wilkinson, P.W.N.M. van Leeuwen, J.N.H. Reek, Org. Biomol. Chem. 3 (2005) 2371.
[2] P.J. Steel, Acc. Chem. Res. 38 (2005) 243.
[3] A.L. Gavrilova, B. Bosnich, Chem. Rev. (Washington, DC, US) 104 (2004) 349.
[4] C.J. Elsevier, J. Reedijk, P.H. Walton, M.D. Ward, Dalton Trans. (2003) 1869.
[5] W.B. Tolman, D.J.E. Spencer, Curr. Opin. Chem. Biol. 5 (2001) 188.
[6] E.C. Constable, M.G.B. Drew, M.D. Ward, J. Chem. Soc., Chem. Commun. (1987) 1600.
[7] P.K.-K. Ho, K.-K. Cheung, C.-M. Che, Chem. Commun. (1996) 1197.
[8] E.C. Constable, M.D. Ward, D.A. Tocher, J. Am. Chem. Soc. 112 (1990) 1256.
[9] E.C. Constable, M.D. Ward, D.A. Tocher, J. Chem. Soc., Dalton Trans. (1991) 1675.
[10] R.L. Fanshawe, A.G. Blackman, Inorg. Chem. 34 (1995) 421.
[11] A.J. Clarkson, A.G. Blackman, Polyhedron 25 (2006) 373.
[12] A. Altomare, M.C. Burla, M. Camalli, G.L. Cascarano, C. Giacovazzo, A. Guagliardi, A.G.G. Moliterni, G. Polidori, R. Spagna, J. Appl. Crystallogr. 32 (1999) 115.
[13] L.J. Farrugia, J. Appl. Crystallogr. 32 (1999) 837.
[14] G.M. Sheldrick, T.R. Schneider, Method. Enzymol. 277 (1997) 319.
[15] H.F. Bauer, W.C. Drinkard, Inorg. Syn. 8 (1966) 202.
[16] K.J. Schmalzl, L.A. Summers, Aust. J. Chem. 30 (1977) 657.
[17] K. Nakatani, S. Hagihara, S. Sando, H. Miyazaki, K. Tanabe, I. Saito, J. Am. Chem. Soc. 122 (2000) 6309.
[18] F.R. Heirtzler, M. Neuburger, M. Zehnder, E.C. Constable, Liebigs Annalen/Recueil (1997) 297.
[19] R. Ziessel, J.M. Lehn, Helv. Chim. Acta 73 (1990) 1149.
[20] M. Sugimoto, J. Fujita, H. Ito, K. Toriumi, T. Ito, Inorg. Chem. 22 (1983) 955.
[21] S. Imajo, K. Nakanishi, M. Roberts, S.J. Lippard, T. Nozoe, J. Am. Chem. Soc. 105 (1983) 2071.
[22] W.M. Davis, M.M. Roberts, A. Zask, K. Nakanishi, T. Nozoe, S.J. Lippard, J. Am. Chem. Soc. 107 (1985) 3864.
[23] L.H. Doerrer, S.J. Lippard, Inorg. Chem. 36 (1997) 2554.
[24] B.S. Jaynes, L.H. Doerrer, S. Liu, S.J. Lippard, Inorg. Chem. 34 (1995) 5735.
[25] R.M. Hartshorn, D.A. House, J. Chem. Soc., Dalton Trans. (1998) 2577.

[26] B.N. Figgis, E.S. Kucharski, A.H. White, Aust. J. Chem. 36 (1983) 1563.
[27] E.N. Maslen, C.L. Raston, A.H. White, J.K. Yandell, J. Chem. Soc., Dalton Trans. (1975) 327.
[28] P. Hendry, A. Ludi, Adv. Inorg. Chem. 35 (1990) 117.
[29] E.C. Niederhoffer, A.E. Martell, P. Rudolf, A. Clearfield, Inorg. Chem. 21 (1982) 3734.
[30] I. Strenger, T. Rosu, M. Negoiu, Z. Kristallogr, New Cryst. Struct. 215 (2000) 489.
[31] Z. Tao, Q. Zhu, W.G. Jackson, Z.-Y. Zhou, X.-G. Zhou, Polyhedron 22 (2003) 263.
[32] C. Stroh, E. Belorizky, P. Turek, H. Bolvin, R. Ziessel, Inorg. Chem. 42 (2003) 2938.
[33] C. Stroh, R. Ziessel, Chem. Commun. (2002) 1916.

Available online at www.sciencedirect.com
ScienceDirect
Polyhedron 26 (2007) 385–391
POLYHEDRON
www.elsevier.com/locate/poly

Synthesis and structure of the two-dimensional coordination networks $[Ln(PDC)(N\text{-}HPDC)]_\infty$ (PDC = pyridine-3,4-dicarboxylate, Ln = La, Ce, Pr)

Desmond Ang, Glen B. Deacon *, Peter C. Junk *, David R. Turner

School of Chemistry, Monash University, Clayton, Vic. 3800, Australia

Received 5 April 2006; accepted 23 June 2006
Available online 18 July 2006

Abstract

The title compounds, $[Ln(PDC)(HPDC)]_\infty$ (H_2PDC = pyridine-3,4-dicarboxylic acid, Ln = La, Ce, Pr), have been prepared and have been characterised by IR, MS, TGA, X-ray crystallography and powder diffraction. These isostructural complexes display both bridging and chelating carboxylate binding modes including a highly unusual chelation in which both carboxylate substituents bind to the same Pr atom, imparting chirality around the metal despite the non-chiral crystal setting. This system represents the first fully characterised metal complex containing the N-protonated ligand derivative ($N\text{-}HPDC^-$). A polymorph of the ligand precursor, pyridine-3,4-dicarboxylic acid is also reported.
© 2006 Elsevier Ltd. All rights reserved.

Keywords: Coordination network; Rare-earth; Dicarboxylate; π-Stacking; Lanthanum; Praseodymium

1. Introduction

Metal-organic coordination networks are increasingly coming under the spotlight for their potential to exhibit useful bulk properties such as nonlinear optical (NLO) behaviour [1], novel magnetism [2] and guest sorption [3]. On top of these properties they often possess aesthetically attractive architectures, a factor which adds to their appeal for many researchers. The deliberate design of functional materials, crystal engineering, has seen many metal-organic networks formed that utilise the rigidity provided by predictable metal coordination geometries combined with 'semi-predictable' bridging ligands, such as dicarboxylates, bipyridyls and poly-alcohols [4–6]. Lanthanoids have received somewhat less attention in the crystal engineering field due to their less predictable coordination geometries, however, many properties of rare-earths, such as luminescence and some magnetic properties, are worth harnessing in solid-state networks [7,8].

Carboxylate networks in particular have received a great deal of attention due to their ability to both chelate to a metal and simultaneously bridge to an adjacent metal, especially with the larger and less rigid coordination spheres of rare-earth elements [9]. More recently, complexes of bi-functional ligands containing both the carboxylate appended to a pyridyl ring have been examined structurally. Within our own sphere of research, mixed functionality pyridyl/carboxylate ligands have been employed as corrosion inhibitors when part of rare-earth coordination complexes [10] and cerium carboxylates are known to be less toxic alternatives to chromate-based inhibitors to steel corrosion [11,12].

One of the least studied pyridyl/carboxylate ligands is that derived from the unsymmetrical pyridine-3,4-dicarboxylic acid (H_2PDC). Several structures are known of the related pyridine-3,5-dicarboxylate with rare-earth metals [13–15], including a Tm structure with an N-protonated

* Corresponding authors.
E-mail address: glen.deacon@sci.monash.edu.au (G.B. Deacon).

0277-5387/$ - see front matter © 2006 Elsevier Ltd. All rights reserved.
doi:10.1016/j.poly.2006.06.030

ligand [16]. Pyridine-2,6-dicarboxylate (dipicolinate) has also been well studied forming anionic [17,18], cationic [19] and neutral [20] networks with rare-earths including ones that incorporate mixed carboxyl/carboxylate ligands, $[NC_5H_3(CO_2)(CO_2H)]^-$ [21,22]. The first structures containing PDC ligated rare-earths have only emerged very recently [23] (structurally characterised transition metal PDC complexes are better known [24–28]). These first rare-earth/PDC complexes are heteroleptic, incorporating either nitrate or oxalate anions into the coordination network, e.g., $[La_2(PDC)_2(NO_3)_2(H_2O)_3]_n$. The hetero-anions bridge between metals to form 'dimers' which are then repeated in 2D sheets held together by the PDC^{2-} ligands. Since completion of this present study, a compound class resulting from hydrothermal synthesis was reported to be of the form $[Ln(III)(PDC)_2]_\infty$ (Ln = La, Nd) [29]. However, this represents a system with an unbalanced charge across the coordination framework.

Herein, we report the synthesis and structure of an 'isostructural' series, synthesised by standard aqueous chemistry, and determine that the correct formulation of these compounds is $[Ln(PDC)(HPDC)]_\infty$ (Ln = La, Ce, Pr), with protonation of a pyridine of one of the PDC ligands.

2. Experimental

2.1. General

Starting materials and solvents were of standard reagent grade and used as purchased with no further purification. Prior to analyses, products were dried under vacuum for 2 h, over a steam bath for a further 2 h and in a desiccator for a minimum of 24 h. IR data were collected of Nujol mulls with a Perkin–Elmer 1600 FTIR instrument in the range 500–4000 cm^{-1}. TGA analyses were obtained with a Perkin–Elmer Pyris 1 instrument under flowing N_2 at a heating rate of 10 °C/min. Microanalyses were conducted by the Campbell Microanalytical Laboratories at the University of Otago, New Zealand. Lanthanoid content was determined by EDTA titration with xylenol orange indicator following acid digestion and buffering with hexamine. XRD powder diffraction data were collected at ambient temperature using a Phillips 1140 diffractometer equipped with a monochromated Cu source (1.5418 Å). X-ray powder simulation of **3** was generated using the program PULVERIX from experimental single crystal data [30].

2.2. Synthesis

A standard solution of Na_2PDC was prepared and used in all subsequent syntheses. Sodium hydroxide (2.81 g, 70.3 mmol) was added to a stirred solution of pyridine-3,4-dicarboxylic acid (6.60 g, 39.26 mmol) in water (350 ml). Further NaOH (0.5 M solution in H_2O) was added until the pH of the solution was ~7. The solution was diluted to give a final concentration of 0.079 mol dm^{-3}.

2.2.1. $\{[La(PDC)(N\text{-}HPDC)]\cdot xH_2O\}_\infty$ (**1**)

A solution of Na_2PDC (85 ml, 6.67 mmol) was added to a solution containing an excess of $LaCl_3\cdot 6H_2O$ (3.56 g, 9.70 mmol) in water (100 ml). The pH was adjusted to 5.0 (using 0.5 M NaOH) and the solution stirred for 8 h at 90 °C. Upon cooling a pale yellow precipitate was isolated, washed with water and dried. Yield, 2.61 g, 79% (based on Na_2PDC). *Anal.* Calc. for $C_{14}H_{11}N_2O_{10}La$ ($[La(PDC)(N\text{-}HPDC)]\cdot 2H_2O$): C, 33.22; H, 2.19; N, 5.53; La, 27.44. Found: C, 33.40; H, 2.26; N, 5.46; La, 28.45%. IR (ν/cm^{-1}): 3420(s), 2243(w), 2200(m), 1997(w), 1957(w), 1557(s), 1493(s), 1417(s), 1282(s), 1172(m), 1121(s), 1061(s), 880(s), 839(s). XRD *d*-spacings (Å, relative intensity in parentheses): 14.00(m), 7.14(m), 6.61(m), 6.11(s), 4.92(m), 4.61(m), 4.17(s), 3.39(s), 3.33(m), 3.14(w), 3.00(w).

2.2.2. $\{[Ce(PDC)(N\text{-}HPDC)]\cdot xH_2O\}_\infty$ (**2**)

The compound was prepared in a similar manner to **1** from a solution of Na_2PDC (85 ml, 6.67 mmol) and $CeCl_3\cdot 7H_2O$ (3.91 g, 10.49 mmol) in water (100 ml) giving a yellow precipitate. Yield, 2.39 g, 71% (based on Na_2PDC). *Anal.* Calc. for $C_{14}H_{11}N_2O_{10}Ce$ ($[Ce(PDC)(N\text{-}HPDC)]\cdot 2H_2O$): C, 33.14; H, 2.18; N, 5.52; Ce, 27.6. Found: C, 32.13; H, 2.05; N, 5.25; Ce, 28.54%. IR (ν/cm^{-1}): 3425(m), 2239(w), 2188(w), 1996(w), 1957(w), 1601(s), 1571(s), 1550(s), 1418(s), 1378(s), 1164(s), 1129(w), 1060(s), 878(s), 840(s), 813(m). XRD *d*-spacings (Å, relative intensity in parentheses): 14.37(m), 7.21(w), 6.68(m), 6.13(s), 4.94(m), 4.62(m), 4.19(s), 3.39(s), 3.34(m), 3.14(w), 2.99(w).

2.2.3. $\{[Pr(PDC)(N\text{-}HPDC)]\cdot xH_2O\}_\infty$ (**3**)

The compound was prepared in a similar manner to **1** from a solution of Na_2PDC (50 ml, 3.93 mmol) and $Pr(NO_3)_3\cdot 6H_2O$ (2.01 g, 4.62 mmol) in water (100 ml) giving a pale green precipitate. Yield, 1.56 g, 78%. *Anal.* Calc. for $C_{14}H_{11}N_2O_{10}Pr$ ($[Pr(PDC)(N\text{-}HPDC)]\cdot 2H_2O$): C, 33.09; H, 2.18; N, 5.51; Pr, 27.70. Found: C, 33.33; H, 2.18; N, 5.56; Pr, 27.16%. IR (ν/cm^{-1}): 3416(m), 2250(w), 2201(m), 1997(w), 1957(w), 1602(s), 1574(s), 1568(s), 1551(s), 1419(m), 1311(m), 1169(m), 1120(w), 1062(w), 900(w), 840(m), 818(w). XRD *d*-spacings on bulk powder (Å, relative intensity in parentheses): 14.40(m), 7.23(m), 6.68(m), 6.15(s), 4.95(m), 4.62(m), 4.18(m), 3.39(s), 3.33(m), 3.15(w), 2.99(w). Single crystals were obtained by crystallisation from aqueous ethanol (1:1, v/v), vide infra. Calculated XRD *d*-spacings from single crystal data (Å, relative intensity in parentheses): 14.43(s), 7.22(m), 6.65(m), 6.10(s), 4.93(m), 4.59(m), 4.16(m), 3.37(s), 3.33(m), 3.14(w), 2.97(w).

2.3. X-ray crystallography

Crystals were mounted on a fine glass fibre using viscous hydrocarbon oil. Data were collected on a Bruker X8 Apex II CCD diffractometer using monochromated Mo Kα

radiation (0.71073 Å). The collection temperature was maintained at 123 K using a Oxford Cryosystem open-flow N_2 cryostat. Data sets were corrected for Lorentz and polarisation effects and for the effects of absorption. Structures were solved by Patterson synthesis (Pr complex) or direct methods (pyridine-3,4-dicarboxylic acid) using SHELXS-97 [31] and refined using conventional alternating cycles of least-squares refinement with SHELXL-97 [32] and difference Fourier synthesis with the aid of the graphical interface program X-Seed [33,34]. In all cases non-hydrogen atoms were refined anisotropically. Hydrogen atoms attached to carbon were fixed in idealised positions and allowed to ride on the atom to which they are attached. Hydrogen atom thermal parameters were tied to those of the atom to which they are attached. In both structures the pyridinium NH could be experimentally located, however these were fixed in calculated positions for refinement purposes. The OH proton in the structure of pyridine-3,4-dicarboxylic acid was also placed in a fixed position (see Section 3).

Crystal data for $\{[(PDC)(HPDC)Pr]\cdot H_2O\}_n$: $C_{14}H_9N_2O_9Pr$, $M = 490.14$, colourless block, $0.12 \times 0.12 \times 0.10$ mm^3, monoclinic, space group $P2_1/m$ (No. 11), $a = 7.2439(14)$ Å, $b = 6.7374(13)$ Å, $c = 14.488(3)$ Å, $\beta = 94.13(3)°$, $V = 705.3(2)$ Å^3, $Z = 2$, $D_c = 2.308$ g/cm^3, $F_{000} = 476$, $2\theta_{max} = 54.9°$, 5707 reflections collected, 5725 unique ($R_{int} = 0.0438$). Final GooF = 1.107, $R_1 = 0.0348$, $wR_2 = 0.0961$, R indices based on 5410 reflections with $I > 2\sigma(I)$ (refinement on F^2), 173 parameters, 0 restraints, $\mu = 3.516$ mm^{-1}. All of the crystals in the sample displayed evidence of twinning (see Section 3). The initial solutions were conducted on a simulated HLKF-4 file and final refinements were carried out using the full HLKF-5 data.

Crystal data for pyridine-3,4-dicarboxylic acid: $C_7H_5NO_4$, $M = 167.12$, colourless block, $0.20 \times 0.17 \times 0.12$ mm^3, monoclinic, space group $P2_1/c$ (No. 14), $a = 7.564(3)$ Å, $b = 7.305(3)$ Å, $c = 12.120(5)$ Å, $\beta = 104.310(10)°$, $V = 648.9(5)$ Å^3, $Z = 4$, $D_c = 1.711$ g/cm^3, $F_{000} = 344$, $2\theta_{max} = 50.0°$, 1585 reflections collected, 1103 unique ($R_{int} = 0.0280$). Final GooF = 1.095, $R_1 = 0.0699$, $wR_2 = 0.1840$, R indices based on 866 reflections with $I > 2\sigma(I)$ (refinement on F^2), 123 parameters, 1 restraint, $\mu = 0.144$ mm^{-1}. One oxygen atom, O(3), is disordered over two positions with refined occupancies of 66:34.

3. Results and discussion

The reaction of disodium pyridine-3,4-dicarboxylate with $LnX_3 \cdot xH_2O$ salts (X = Cl, NO_3) in water at pH 5 resulted in the precipitation of pure samples of the title complexes, $[Ln(PDC)(N\text{-}HPDC)]_\infty$ (Ln = La **1**, Ce **2** and Pr **3**). A publication in the recent literature reports the structure of the charge-unbalanced complex "$[Nd(PDC)_2]_\infty$" obtained through the hydrothermal reaction of pyridine-3,4-dicarboxylic acid and $Nd(NO_3)_3$ [29]. The harsh, hydrothermal synthesis gives rise to decarboxylated side-products, whereas our aqueous synthesis affords the present pure complexes in good yields. An examination of the crystal structure of "$[Nd(PDC)_2]_\infty$"[1] compared to that of our own complex $[Pr(PDC)(N\text{-}HPDC)]_\infty$ (**3**) shows that these two compounds are essentially isostructural, hence the neodymium complex is $[Nd(PDC)(N\text{-}HPDC)]_\infty$.

Infra-red analysis of the series $[Ln(PDC)(N\text{-}HPDC)]_\infty$ shows, in all cases, a very weak band attributable to the pyridinium NH^+ group at around 2200 cm^{-1} [35], making the complex charge neutral. There is no absorption in the region of 1700 cm^{-1} confirming that carboxylate groups are not protonated. The pyridinium proton was also observable by X-ray crystallography, as described later. The IR spectra of the three complexes all display several peaks corresponding to carboxylate stretching absorptions in the region 1300–1600 cm^{-1}, suggestive of several binding modes in the structure, and also peaks suggestive of the presence of water. Thermo-gravimetric analyses carried out on the precipitated products (powders) confirm the presence of water of crystallisation (all products were dried thoroughly before analysis). Complexes **1** and **3** show weight losses of 7.63% and 6.87%, respectively, within one steady process that occurs between approximately 110 and 300 °C. TGA carried out on a sample of the crystals of **3** showed a similar weight loss of 7.96%. These values correspond to the loss of two water molecules per formula unit if the empirical formula of the complex is taken to be $[Ln(PDC)(N\text{-}HPDC)]\cdot 2H_2O$ (calculated loss for $2H_2O$ = La (7.11%), Ce (7.10%), Pr (7.09%); if formulations were $[Ln(PDC)(N\text{-}HPDC)]\cdot H_2O$ the loss should be ~3.37%). Elemental analyses (C, H, N, Ln) also strongly support this formulation. TGA of complex **2** shows a somewhat lower weight loss of 5.96%, although the temperature range involved is the same. This may be due to a lesser degree of hydration in the structure. As one of the water molecules is not structurally significant/detectable, see below, partial occupancy is plausible. The slight spread of weight-loss values for **1**–**3** also suggests that this may be the case.

X-ray quality single crystals were obtained of the praseodymium complex **3** and the structure was determined by X-ray crystallography. Only one molecule of water per formula unit, $[Pr(PDC)(N\text{-}HPDC)]\cdot H_2O$, could be located. However, the possibility of a second lattice water in the crystal structure exists, as discussed below and the TGA data from both crystals and powder of **3** indicate that two water molecules are present. The La and Ce complexes were only obtained as microcrystalline powders and were determined to be isostructural with the Pr complex by comparison of the calculated powder pattern from the single crystal diffraction data of **3** with the experimental XRD patterns of **1** and **2** (see Section 2). The bulk product of **3** obtained before recrystallisation was also determined to be identical with the crystals by XRD data.

The polymeric complex $[Pr(PDC)(N\text{-}HPDC)]\cdot xH_2O$ crystallises from water/ethanol (1:1) in the space group

[1] Reported cell parameters of $[Nd(PDC)_2]$: $P2_1/c$, $a = 14.424(1)$ Å, $b = 6.761(1)$ Å, $c = 14.522(1)$ Å, $\beta = 94.25(1)°$, $V = 1412.22(15)$ Å^3.

$P2_1/m$. The asymmetric unit contains half of one repeating chemical unit ([Pr(PDC)(N-HPDC)]) due to the presence of the mirror plane, upon which the N-HPDC ligand lies and which the PDC ligand straddles. Each praseodymium ion is charge balanced by one fully deprotonated ligand (PDC^{2-}) and one N-protonated ligand ($N\text{-}HPDC^{-}$) (Fig. 1). The two ligands each have only one mode of coordination. To the best of our knowledge these systems represent the first examples of structurally characterised coordination complexes containing the N-protonated version of the PDC ligand. The previously known structure of the free acid, H_2PDC, contains the molecule in one of its potential zwitterionic forms, with the *para*-carboxylate group deprotonated [36] and the new polymorph of this di-acid also exists in this zwitterionic form, vide infra.

The praseodymium atoms are nine coordinate with a distorted tri-capped trigonal prismatic geometry. Each praseodymium atom has attached two chelating carboxylates, one oxygen atom from each of four bridging carboxylates and one pyridyl nitrogen, (Fig. 2). There are no aqua ligands within the structure, despite the syntheses being carried out in aqueous media and there was no nitrate coordination from the counter-ions by contrast with earlier studies [23]. The Pr–O bond lengths for the chelating carboxylate groups lie within the expected range with lengths of 2.554(5)–2.612(3) Å. These Pr–O lengths are comparable to those observed in $[Pr(H_2O)_9]^{3+}$ with an average of 2.525 Å, value obtained from the structures of $[Pr(H_2O)_9](CF_3SO_3)_3$ [37] and $[Pr(H_2O)_9](EtOSO_3)_3$ [38]. The Pr–O distances involving bridging carboxylates are, in all cases, shorter than their chelating counterparts, within the range 2.393(5)–2.486(5) Å (Table 1).

The long-range structure consists of pseudo-2D sheets, aligned parallel to the 0 0 1 plane, in which offset rows of Pr atoms are connected by both PDC^{2-} and $N\text{-}HPDC^{-}$ ligands, (Fig. 3). These ligands exist in distinct environments with the $N\text{-}HPDC^{-}$ ions located exclusively on the exterior of the sheets and the PDC^{2-} ions located within the sheets. Along the 'outside' of the 2D sheets the

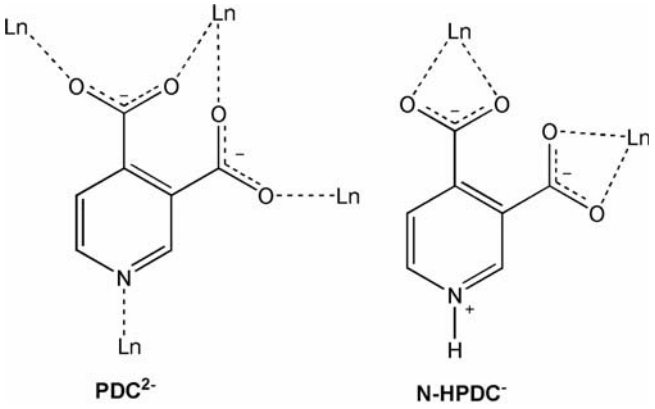


Fig. 1. The two pyridine-3,4-dicarboxylate ligands observed in the structure of **3** and their observed binding modes; μ_4-(η^1:η^1:η^2:η^1) and μ-η^2(*m*-CO_2):η^2(*p*-CO_2).

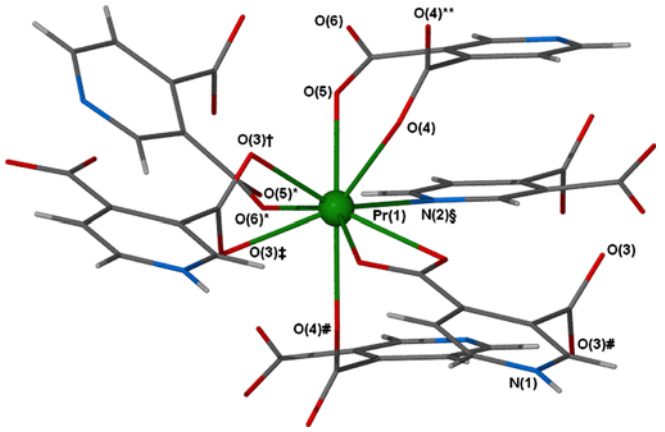


Fig. 2. The immediate environment around one praseodymium atom within the structure of [(PDC)(N-HPDC)Pr]. Symmetry equivalents used: $^{\dagger}1+x, y, z$; $^{\ddagger}1+x, 3/2-y, z$; $^{\S}-x-1, y-1/2, 3-z$; $^{\#}x, 3/2-y, z$; $^{*}-x, y-1/2, 3-z$; $^{**}x, 5/2-y, z$. Selected bond lengths and angles are shown in Table 1.

Table 1
Selected bond lengths (Å) and angles (°) observed in the structure of $\{[(PDC)(HPDC)Pr]\cdot H_2O\}_n$

Pr(1)–O(1)	2.554(4)
Pr(1)–O(2)	2.583(4)
Pr(1)–O(3)	2.612(3)
Pr(1)–O(4)	2.438(3)
Pr(1)–O(5)	2.486(5)
Pr(1)–O(6)	2.393(5)
Pr(1)–N(2)	2.640(4)
O(4)–Pr(1)–O(5)	63.18(16)
O(1)–Pr(1)–O(2)	50.90(12)
$O(3)^{\dagger}$–Pr(1)–$O(3)^{\ddagger}$	50.33(12)

Symmetry equivalents used are shown in Fig. 2.

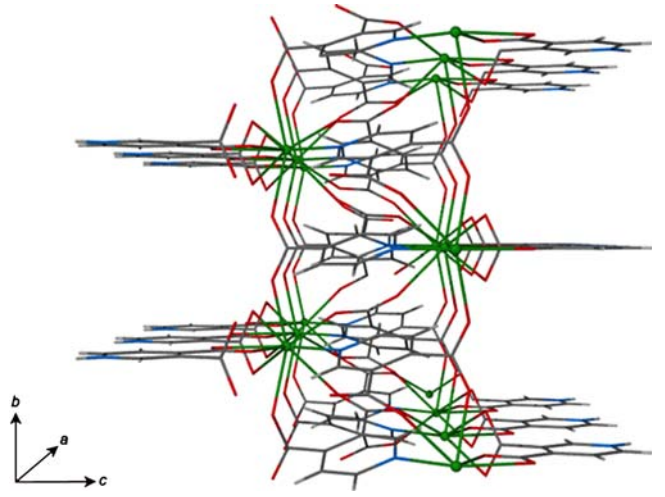


Fig. 3. The pseudo-2D sheets propagate parallel to the *a*/*b* plane and are held together by the ligands PDC^{2-} (internally) and $N\text{-}HPDC^{-}$ (externally). Pr atoms are represented by spheres.

$N\text{-}HPDC^{-}$ ligands bridge between pairs of adjacent Pr atoms by means of chelating carboxylates that are orientated perpendicular with respect to each other, effectively

'zipping' together the Pr atoms within rows. These ligands adopt a μ-η^2(*m*-CO_2):η^2(*p*-CO_2) binding geometry, bridging between lanthanoid atoms using only a bidentate chelating binding mode at each metal centre (Fig. 1). The pyridinium ring of this ligand lies on a crystallographic mirror plane with the protonated nitrogen atom facing towards carboxylate groups on the exterior of the adjacent sheets.

The interior of the sheets contains the doubly deprotonated PDC^{2-} ligands, connecting the offset Pr rows exclusively through bridging carboxylates and the Pr–N interaction. Overall the PDC^{2-} ligand displays μ_4 binding. Each carboxylate group is in a μ_2 bridging mode between two lanthanoid atoms. One Ln atom is common to both carboxylate groups, chelating within a seven-membered [OCCCCOLn] ring (Fig. 1). This mode of metal chelation between the two adjacent carboxylates has only been observed previously in $[Zn(PDC)]_\infty$ [26,39] and $[Mn_2(PDC)_2(4,4'\text{-bipy})_2]$ [40]. The nitrogen bonds to a further Ln atom to complete the μ_4 coordination; μ_4-(η^1:η^1:η^2:η^1). Each ligand links four metal atoms between three rows; two adjacent Pr atoms within the same row and one Pr each on the offset rows above and below (Fig. 4a). The PDC^{2-} ligand is disordered 50:50 across a mirror plane upon which the nitrogen, *p*-carbon and the *p*-carboxylate carbon atom lie. The pyridyl ring is rotated approximately 23° from this mirror plane. The *p*-carboxylate is perpendicular to the mirror plane and bridges between Pr atoms that lie directly over each other. The disorder of the ligand results in chelation to one of two praseodymium atoms, either above or below, (Fig. 4a). The PDC^{2-} ligands lie in stacks perpendicular to the *b*-axis and when the disorder in the structure is rationalised it can be seen that ligands within each stack are orientated in the same direction. The orientations of the PDC^{2-} ligands alternate throughout the stacks that comprise the 2D sheets (Fig. 4b).

A fascinating aspect of the structure is the interaction between adjacent 2D sheets. The exterior of each individual sheet consists of parallel pyridinium groups. When the sheets are viewed next to each other, these pyridinium groups are observed to interdigitate by means of face-to-face π–π interactions, (Fig. 5). There are also donor bifurcated CH···O_2C hydrogen bonds [41] between the pyridyl ring and a carboxylate group. The observed water molecule in the structure exists in the void between sheets and assists in the hydrogen bonding that holds the sheets together. The water molecule receives hydrogen bonds from both the protonated pyridinium nitrogen and a CH donor and appears to hydrogen bond to carboxylate acceptors, although the hydrogen atoms of the water could not be experimentally located by X-ray diffraction. The weak interactions holding the sheets together may explain the twinned nature of all of the crystalline samples that were obtained. Analysis of the twin components shows that they are related by a 180° rotation about the *c*-axis. This can readily be seen to correspond to the 2D sheets being rotated by 180°. As previously mentioned, TGA and microanalytical results are suggestive of a second water molecule being present within the structure. It is believed that this may exist within the centre of the 2D sheets in a shared position with a carboxylate ligand although the disorder that is manifest within the structure makes any definitive assignment impossible and no large residual Fourier peaks are evident.

During the course of our investigation, crystals were also obtained of a second polymorph of pyridine-3,4-dicarboxylic acid whilst attempting the synthesis of an ytterbium complex of PDC^{2-}. The existing compound crystallises in the chiral space group $P2_12_12_1$ and exists in a zwitterionic form, with the carboxylate in the *para*-position being deprotonated, and forms an interpenetrating hydrogen-bonded network [36]. The new polymorph exists in the space group $P2_1/c$, with the pyridinium rings all lying parallel to one another. As with the previously known

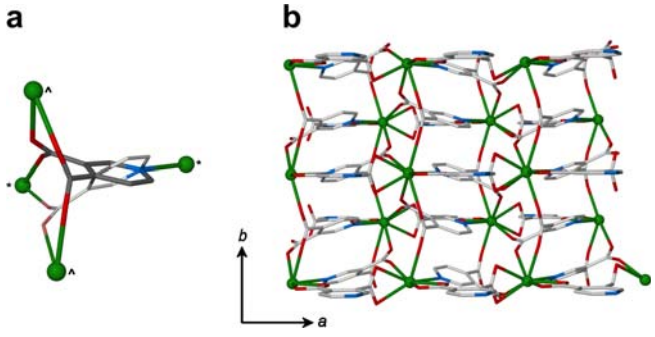


Fig. 4. (a) The PDC^{2-} ligand is disordered over two positions rotated around the N···CO_2^- axis (one unique position shown in bold). The μ_4 ligand bridges between two adjacent Pr atoms in the same row (*) and two Pr atoms in the offset rows immediately above and below (^). (b) The orientation of the ligands within one stack along the *b*-axis remains the same with alternate stacks in the a-direction having opposing orientations. The disorder is removed for clarity.

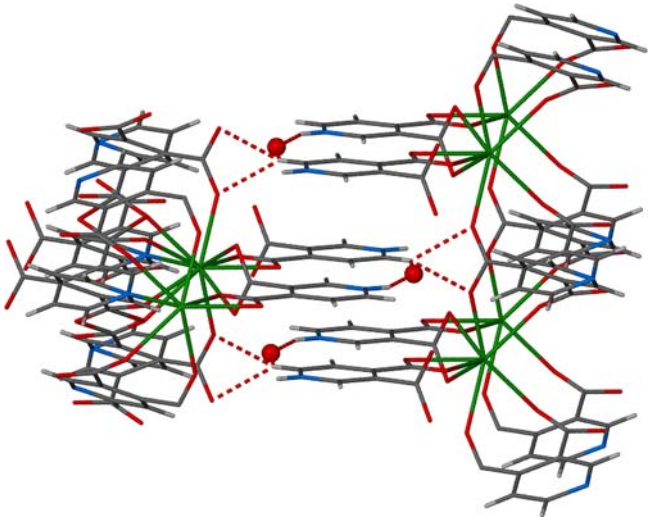


Fig. 5. Adjacent sheets interdigitate by means of π–π stacking and hydrogen bonding involving enclathrated water (shown as spheres).

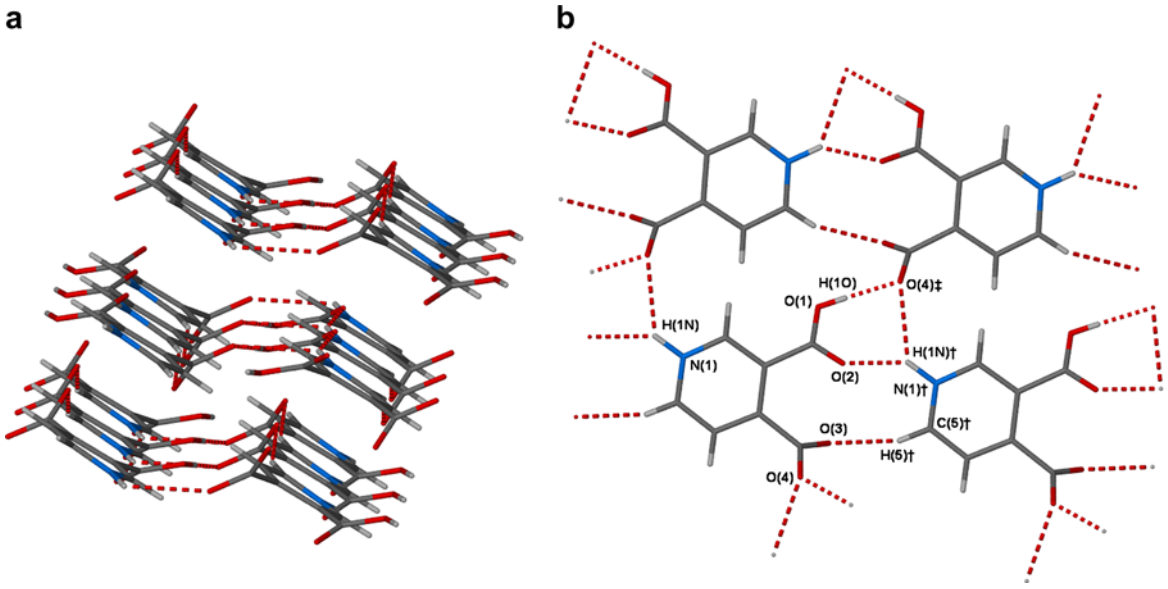


Fig. 6. (a) 2D sheets in the structure of H_2PDC viewed along the *b*-axis and (b) the hydrogen bonding motif within one sheet (only one of the disordered O(3) positions is shown for clarity). Symmetry equivalents used: $^{\dagger}x, 1+y, z$; $^{\ddagger}x, -y+3/2, z-1/2$. Selected hydrogen bond lengths (D···A) (Å): N(1)†···O(2), 2.797(5); N(1)†···O(4)‡, 3.217(5); C(5)†···O(3A), 3.23(3); C(5)†···O(3B), 2.78(8); O(1)···O(4)‡, 2.470(4); O(1)···O(3A)‡, 3.281(9); O(1)···O(3B)‡, 3.19(3).

structure the molecule exists as a zwitterion, deprotonated at the same position.[2] The structure forms 2D hydrogen-bonded sheets held together predominantly by NH···O and OH···O interactions (Fig. 6), of which the major interaction is the $R_2^2(6)$ interaction (using Graph Set notation [42]) involving the pyridinium proton as a bifurcated hydrogen-bond donor group.

4. Conclusions

We have presented the first fully characterised rare-earth complexes using exclusively ligands derived from pyridine-3,4-dicarboxylic acid. The structure displays interesting bonding modes of the dicarboxylate ligand and is held together by virtue of weak interactions between infinite 2D sheets. A second polymorph of pyridine-3,4-dicarboxylic acid is also reported.

5. Supplementary information

Full crystallographic data have been deposited with the CCDC (603746 and 603747). These data may be obtained free of charge via www.ccdc.cam.ac.uk/conts/retrieving.html or from the Cambridge Crystallographic Data Centre, 12 Union Road, Cambridge, CB2 1EZ, UK (fax: +44 1223 336 033 or e-mail: deposit@ccdc.cam.ac.uk).

[2] The quality of the crystallographic data, whilst not excellent, is sufficient to show a residual peak present almost midway between the *meta*- and *para*-carboxylate groups of two adjacent molecules. This peak lies closest to the *m*-carboxylate and has therefore been fixed in this position.

Acknowledgements

The authors thank the Australian Research Council for research funding through the Centre for Green Chemistry. We also thank an ARC LIEF grant, Monash University and the Victorian Institute for Chemical Sciences for funding the Bruker X8 diffractometer.

References

[1] S. Di Bella, Chem. Soc. Rev. 30 (2001) 355.
[2] J. Mrozinski, Coord. Chem. Rev. 249 (2005) 2534.
[3] U. Mueller, M. Schubert, F. Teich, H. Puetter, K. Schierle-Arndt, J. Pastré, J. Mater. Chem. 16 (2006) 626.
[4] K. Biradha, CrystEngComm 5 (2003) 374.
[5] D. Braga, L. Brammer, N.R. Champness, CrystEngComm 7 (2005) 1.
[6] L. Brammer, Chem. Soc. Rev. 33 (2004) 476.
[7] J.-C.G. Bünzli, Acc. Chem. Res. 39 (2006) 53.
[8] R.J. Hill, D.-L. Long, P. Hubberstey, M. Schröder, N.R. Champness, J. Sol. State Chem. 178 (2005) 2414.
[9] A. Ouchi, Y. Suzuki, Y. Ohki, Y. Koizumi, Coord. Chem. Rev. 92 (1988) 29.
[10] D.A. Ang, Conference Presentation at OZOM3, Gippsland, Austalia, 2006.
[11] M. Bethencourt, F.J. Batana, J.J. Calvino, M. Marcos, M.A. Rodrigeuz-Chacon, Corrosion Sci. 40 (1998) 1803.
[12] K. Wilson, T. Behrsing, C.M. Forsyth, G.B. Deacon, A. Phanasgoanker, M. Forsyth, Corrosion 58 (2002) 953.
[13] Z. Liu, D. Zhang, C. Liu, D. Zhu, Chem. Lett. 33 (2004) 180.
[14] D. Min, S.W. Lee, Inorg. Chem. Commun. 5 (2002) 978.
[15] S. Si, C. Li, R. Wang, Y. Li, J. Coord. Chem. 57 (2004) 1545.
[16] J.-Y. Kim, A.J. Norquist, D. O'Hare, J. Am. Chem. Soc. 125 (2003) 12688.
[17] J.M. Harrowfield, Y. Kim, B.W. Skelton, A.H. White, Aust. J. Chem. 48 (1995) 807.
[18] P.A. Brayshaw, A.K. Hall, W.T.A. Harrison, J.M. Harrowfield, D. Pearce, T.M. Shand, B.W. Skelton, C.R. Whitaker, A.H. White, Eur. J. Inorg. Chem. (2005) 1127.

[19] P. Starynowicz, Acta. Cryst., Sect. C: Cryst. Struct. Commun. 48 (1992) 1428.
[20] S.K. Ghosh, P.K. Bharadwaj, Inorg. Chem. 43 (2004) 2293.
[21] B. Zhao, L. Yi, Y. Dai, X.-Y. Chen, P. Cheng, D.-Z. Liao, S.-P. Yan, Z.-H. Jiang, Inorg. Chem. 44 (2005) 911.
[22] S.K. Ghosh, P.K. Bharadwaj, Inorg. Chem. 42 (2003) 8250.
[23] C. Qin, X. Wang, E. Wang, L. Xu, Inorg. Chim. Acta 359 (2006) 417.
[24] W. Chen, Q. Yue, C. Chen, H.-M. Yuan, W. Xu, J.-S. Chen, S.-N. Wang, Dalton Trans. (2003) 28.
[25] E.E. Sileo, D. Vega, R. Baggio, M.T. Garland, M.A. Blesa, Aust. J. Chem. 52 (1999) 205.
[26] X. Wang, C. Qin, E. Wang, Y. Li, N. Hao, C. Hu, L. Xu, Inorg. Chem. 43 (2004) 1850.
[27] S.-Q. Xia, S.-M. Hu, J.-C. Dai, X.-T. Wu, J.-J. Zhang, Z.-Y. Fu, W.-X. Du, Inorg. Chem. Commun. 7 (2004) 51.
[28] Y.-F. Zhou, D.-Q. Yuan, B.-L. Wu, R.-H. Wang, M.-C. Hong, New J. Chem. (Nouv. J. Chim.) 28 (2004) 1590.
[29] Z.-B. Han, X.-N. Cheng, X.-F. Li, X.-M. Chen, Z. Anorg. Allg. Chem. 631 (2005) 937.
[30] K. Yvon, W. Jeitschko, E. Parthé, J. Appl. Crystallogr. 10 (1977) 73.
[31] G.M. Sheldrick, SHELXS-97, University of Göttingen, 1997.
[32] G.M. Sheldrick, SHELXL-97, University of Göttingen, 1997.
[33] L.J. Barbour, XSEED, University of Missouri, Columbia, 1999.
[34] L.J. Barbour, J. Supra. Chem. 1 (2001) 189.
[35] L.J. Bellamy, The Infra-red Spectra of Complex Molecules, Methuen & Co. Ltd., London, 1964.
[36] F. Takusagawa, K. Hirotsu, A. Shimida, Bull. Chem. Soc. Jpn. 46 (1973) 2669.
[37] A. Chatterjee, E.N. Maslen, K.J. Watson, Acta Crystallogr. Sect. B: Struct. Sci. 44 (1988) 381.
[38] R.E. Gerkin, W.J. Reppart, Acta Crystallogr. Sect. C: Cryst. Struct. Commun. 40 (1984) 781.
[39] Y.-F. Zhou, D.-Q. Yuan, B.-L. Wu, R.-H. Wang, M.-C. Hong, New J. Chem. 28 (2004) 1590.
[40] Q.-Z. Zhang, C.-Z. Lu, C.-K. Yia, Inorg. Chem. Commun. 8 (2005) 304.
[41] G.R. Desiraju, Chem. Commun. (2005) 2995.
[42] J. Bernstein, R.E. Davis, L. Shimoni, N.-L. Chang, Angew. Chem. Int. Ed. Engl. 33 (1994) 143.

Available online at www.sciencedirect.com
ScienceDirect
Polyhedron 26 (2007) 392–399
POLYHEDRON
www.elsevier.com/locate/poly

Macrocyclic cobalt(III) complexes as precursors for metal-polythiophene hybrid materials

Paul V. Bernhardt *, Nathan L. Kilah

Department of Chemistry, University of Queensland, Brisbane, Qld 4072, Australia

Received 31 March 2006; accepted 6 July 2006
Available online 14 July 2006

Abstract

A thiophene-functionalised macrocyclic ligand *trans*-6,13-dimethyl-6-((thiophen-3-ylmethyl)amino)-1,4,8,11-tetraazacyclotetradecane-13-amine (L^1) has been prepared and complexed with Co^{III}. The ligand L^1 binds as a pentadentate in the crystallographically characterised complexes $[CoL^1(OAc)](ClO_4)_2$ and $[CoL^1Cl]Cl_2$. Electro-copolymerisation of $[CoL^1Cl]Cl_2$ with 3,4-ethylenedioxythiophene (EDOT) in a 1:2 ratio on a preformed poly-3,4-ethylenedioxythiophene (PEDOT) film resulted in metal–polymer hybrid films of high quality, consistency and uniformity in appearance. The copolymerised films were characterised by XPS indicating a 1:11 ratio of incorporation of complex to EDOT. Electrochemistry of the Co-PEDOT film (cast on an indium-doped tin oxide working electrode) in water revealed a $Co^{III/II}$ redox couple at a potential ca. −600 mV (vs Ag/AgCl) which is similar to that seen in solution for the monomeric aqua complex $[CoL^1(OH_2)]^{3+}$.
© 2006 Elsevier Ltd. All rights reserved.

Keywords: Macrocycle; Conducting polymer; Electrochemistry; Cobalt

1. Introduction

Functional materials based on conductive (conjugated) polymers have received much attention in the years following the discovery of conductive polyacetylene to include many π-conjugated organics such as polythiophene, polypyrrole and polyaniline [1–4]. These polymeric materials are often referred to as synthetic metals due to their high conductivity when doped with appropriate agents. The range of dopants has developed from simple counter ions to a wide range of specialised transition metal complexes.

Polythiophene is a particularly popular scaffold for the development of functional materials [5–7]. The incorporation of redox active and/or spectroscopically active metal ions into a poly-thiophene architecture may engender useful properties to the polymer [8,9]. To mention but a few, these including light harvesting [10] and electrochemoluminescent materials [11] and sensors [12]. The metal may be dispersed within a polythiophene polymer or precomplexed with a thiophene-modified monomer which then undergoes a polymerisation or copolymerisation reaction with a different monomer [10–20].

Substituents on the thiophene ring influence the electronic bandgap and hence the observed colour of the polymer film. The commercially available monomer 3,4-ethylenedioxythiophene (EDOT, Chart 1) has been used extensively in polymerisation and copolymerisation reactions [21]. The ethylenedioxy bridge restricts polymerisation to the 2- and 5-positions while the ether O-atoms also alter the electronic properties of the polymer e.g. lowering the band gap energy.

Oxidative polymerisation may be achieved by chemical or electrochemical means [22], with anodic electrochemical growth of hybrid materials being an effective route when the polymer is to be integrated with an electrical circuit. This is most commonly achieved on a platinum electrode or optically transparent indium-doped tin oxide (ITO) electrode deposited as a thin layer on a glass support.

The redox properties of the film vary depending on the interactions between the metal centre and the conjugated organic chain. These varying morphologies have been

* Corresponding author. Tel.: +61 7 3365 4266; fax: +61 7 3365 4299.
E-mail address: P.Bernhardt@uq.edu.au (P.V. Bernhardt).

0277-5387/$ - see front matter © 2006 Elsevier Ltd. All rights reserved.
doi:10.1016/j.poly.2006.07.001

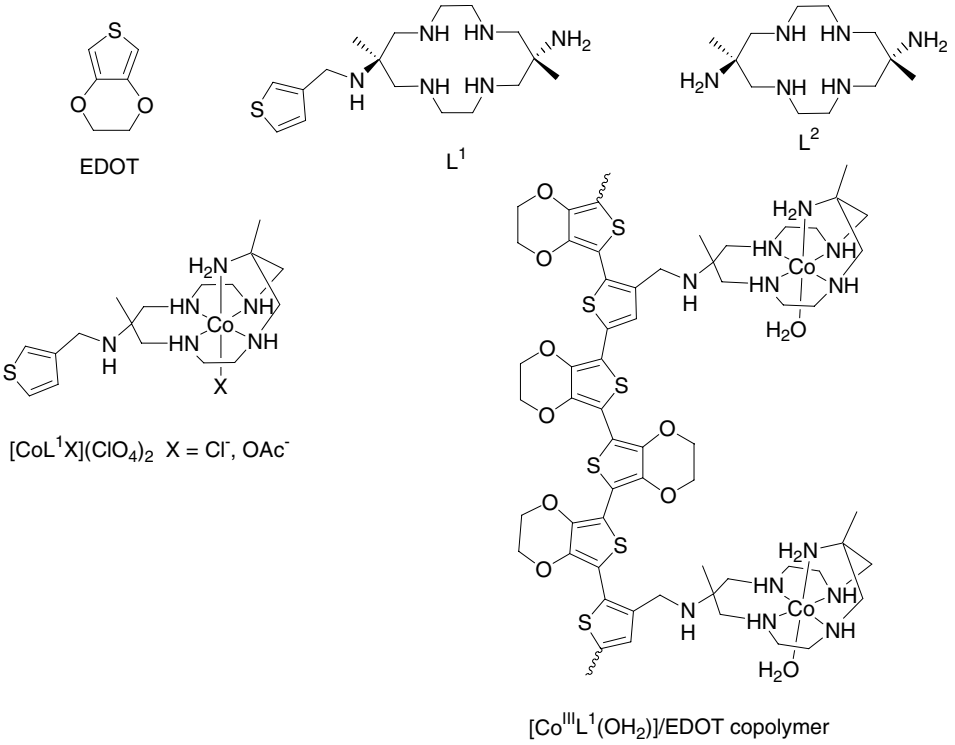


Chart 1.

classified into three types [8]. Briefly, the metal centres may be connected to the polymeric chain through a saturated link (Type I), attached through an unsaturated link to the conjugated backbone (Type II) or form part of the polymeric chain (Type III). Here we demonstrate that the new thiophene-appended macrocycle L^1 (Chart 1) can be utilised in the covalent incorporation of tightly bound transition metal ions into a Type I conductive polymer film. This was achieved through copolymerisation of a Co^{III} complex of L^1 with EDOT by electrochemical oxidation.

2. Experimental

2.1. Safety notes

Perchlorate salts are potentially explosive. Although no problems were experienced with the compounds synthesised, they should only be handled in small quantities, never scraped from sintered glass frits, nor heated in the solid state. Solutions containing sodium cyanoborohydride liberate toxic HCN gas when acidified and should only be used in a well ventilated fume hood.

2.2. Precursors

The precursors *trans*-6,13-dimethyl-1,4,8,11-tetraazacyclotetradecane-6,13-diamine hexahydrochloride ($L^2 \cdot 6HCl$) [23] and sodium triscarbonatocobaltate trihydrate ($Na_3[Co(CO_3)_3] \cdot 3H_2O$) [24] were prepared from the literature procedures. All remaining chemicals were used as purchased.

2.3. The monomeric ligand L^1 and its Co^{III} complexes

2.3.1. *trans*-6,13-Dimethyl-13-((thiophen-3-ylmethyl)-amino)-1,4,8,11-tetraazacyclo-tetradecane-6-amine, L^1

The parent hexamine $L^2 \cdot 6HCl$ (4.77 g, 10 mmol) was suspended in $EtOH/H_2O$ (9:1 v/v, 300 mL) with dissolution occurring upon adjustment of the pH to 5.5 with NaOH (3 M). Sodium cyanoborohydride (1.88 g, 30 mmol) was added and the pH readjusted to 5.5 with further NaOH solution (3 M). Thiophene-3-carboxaldehyde (0.912 mL, 10 mmol) was added with stirring, and the resulting mixture was kept at pH 5.5 through the periodic addition of aliquots of HCl solution (1 M) for 3 h. After 16 h of stirring at room temperature a precipitate of the crude disubstituted by product *trans*-6,13-bis((thiophen-3-ylmethyl)amino)-6,13-dimethyl-1,4,8,11-tetraaza-cyclotetradecane as its $[BH_3(CN)]^-$ salt was filtered off and not characterised further. Ethanol was evaporated from the filtrate at reduced pressure and water (200 mL) added. The solution was acidified to ca. pH 2 through the addition of HCl solution (1 M) and extracted with CH_2Cl_2 (3×75 mL) to remove the contaminant thiophen-3-ylmethanol. The pH of the aqueous phase was adjusted to ca. 12 with NaOH solution (3 M) and the free ligand L^1 now in its charge neutral form was extracted with CH_2Cl_2 (3×100 mL). The combined extracts were dried over anhydrous sodium sulfate and evaporated at reduced pressure to leave an oil (1.2 g, 3.38 mmol, 34%). MeCN (50 mL) and CH_2Cl_2 (10 mL) were added to the oil with gentle warming to assist dissolution. The mixture was evaporated at reduced pressure to remove CH_2Cl_2, and Et_2O (50 mL) was added, resulting in precipitation of

the desired product. X-ray quality crystals were obtained through slow evaporation of a 1:5 $MeCN/CH_2Cl_2$ solution of the ligand. Elemental *Anal.* Calc. for $C_{17}H_{34}N_6S \cdot 2.5H_2O$: C, 51.51; H, 9.84; N, 21.03. Found: C, 51.51; H, 9.69; N, 20.72%. ^1H NMR ($CDCl_3$): δ (ppm vs TMS) 1.01 (s, 3H, CH_3), 1.04 (s, 3H, CH_3), 2.05 (broad s, 6H, NH), 2.42–2.67 (m, 16H, CH_2-macrocyclic), 3.70 (s, 2H, linker CH_2), 7.01 (dd, 1H, thiophene) 7.11 (dd, 1H, thiophene), 7.19 (dd, 1H, thiophene). ^{13}C NMR ($CDCl_3$): δ (ppm vs TMS) 22.92, 27.25, 41.12, 48.62, 48.66, 51.28, 54.99, 57.64, 60.61, 121.07, 125.46, 127.70, 142.29.

2.3.2. Chloro(trans-6,13-dimethyl-6-((thiophen-3-ylmethyl)-amino)-1,4,8,11-tetra-azacyclo-tetradecane-6-amine)-cobalt(III) chloride, $[CoL^1Cl]Cl_2$

L^1 (1.20 g, 3.38 mmol) was dissolved in water (400 mL) through the addition of aliquots of HCl solution (1 M) to bring the pH to ca. 8. $Na_3[Co(CO_3)_3] \cdot 3H_2O$ (1.45 g, 4.00 mmol) was added with stirring. The resulting mixture was heated at ca. 60 °C for 16 h. A black precipitate of cobalt oxide was filtered off, the filtrate was diluted to 10 L and loaded onto a Sephadex C-25 cation exchange column (75 cm × 2.5 cm, Na^+ form). Elution was achieved with 0.2 M NaCl, resulting in three bands; yellow (minor), orange (major) and finally yellow (minor). The first and third bands were not characterised further. The dominant orange band was concentrated to 100 mL which led to substitution of the aqua ligand by chloride to give a red solution. On standing a coprecipitate of NaCl and $[CoL^1Cl]Cl_2$ (as crystals suitable for X-ray work) formed. These crystals were removed by hand and the remaining mixture was purified by washing on a sintered glass frit under vacuum filtration with a minimal quantity of water. Elemental *Anal.* Calc. for $CoN_6C_{17}H_{34}SCl_3 \cdot H_2O$: C, 37.98; N, 15.62; H, 6.75. Found: C, 38.10; N, 15.71; H, 6.64%. Electronic spectrum (H_2O, pH 5): λ_{max}, nm (ε, M^{-1} cm^{-1}) 522 (75), 428 (43), 324 (149). ^1H NMR (D_2O): δ (ppm vs TSP) 1.28 (s, 3H, CH_3), 1.30 (s, 3H, CH_3), 2.23–3.71 (m, 16H, macrocyclic CH_2), 3.88 (s, 2H CH_2), 7.26 (t, 1H, thiophene), 7.46 (m, 2H, thiophene). ^{13}C NMR (D_2O): δ (ppm vs TSP) 20.67, 23.72, 43.11, 54.76, 55.01, 58.97, 60.53, 62.38, 68.12, 125.50, 129.51, 131.26, 144.43. The yield of isolated complex was limited by the amount of complex that crystallised from the NaCl solution and ultimately isolation of further crops of pure complex was prevented by contamination with NaCl. However, on the basis of the solution absorbance of the orange band obtained from the column, the yield of complex (based on L^1) was greater than 75%.

2.3.3. Acetato(trans-6,13-dimethyl-6-((thiophen-3-ylmethyl)amino)-1,4,8,11-tetra-azacyclotetradecane-6-amine)cobalt(III) perchlorate, $[CoL^1(OAc)](ClO_4)$

This complex was prepared in an identical manner to the chloro complex except the eluent for chromatography was 0.2 M NaOAc solution. Upon concentrating the orange eluent, crystallisation was achieved by the addition of excess $NaClO_4$ to afford X-ray quality crystals of the desired product. Elemental *Anal.* Calc. for $CoC_{19}H_{37}N_6SCl_2O_{10}$: C, 33.99; N, 12.52; H, 5.55; S, 4.78. Found: C, 33.47; N, 12.31; H, 5.58; S, 4.64%. Electronic spectrum (H_2O): λ_{max}/nm (ε/M^{-1} cm^{-1}) 489 (58), 352 (83). ^1H NMR (D_2O): δ (ppm vs TSP) 1.24 (s, 3H, CH_3), 1.32 (s, 3H, CH_3), 1.99 (s, 3H, acetato) 2.34–3.62 (m, 16H, macrocyclic CH_2) 3.90 (s, 2H CH_2), 7.22 (dd, 1H, thiophene), 7.42 (dd, 1H, thiophene), 7.48 (dd, 1H, thiophene). ^{13}C NMR (D_2O): δ (ppm vs TSP) 23.06, 26.13, 29.58, 45.32, 56.87, 57.31, 61.55, 62.48, 64.16, 70.12, 127.31, 131.96, 133.28, 147.10, 190.67. As above, the yield of complex was in excess of 75% but limited by co-precipitation with $NaClO_4$.

2.4. Electropolymerisation

Electropolymerisation of 3,4-ethylenedioxythiophene (EDOT) was adapted from a published procedure [22] employing cyclic voltammetry of a solution containing 0.1 M EDOT, 0.2 M sodium dodecylsulfate (SDS) and 0.1 M $NaClO_4$ as electrolyte in deionised water with a transparent indium tin oxide (ITO) glass slide as the working electrode. A Pt counter and Ag/AgCl reference electrode were also employed. Electrodeposition was preceded by a conditioning procedure which involved 10 cycles to successively positive potentials i.e. −200 to 600, then −200 to 700 and finally −200 to 800 mV (vs Ag/AgCl) at a scan rate of 50 mV s^{-1}. Polymerisation was finally achieved through sweeping the potential between −200 and 900 mV for five complete cycles, resulting in the oxidation and electrodeposition of a polymer thin film on the electrode.

This preformed poly-3,4-ethylenedioxythiophene (PEDOT) film cast on the ITO electrode was placed in a solution of $[CoL^1Cl]Cl_2$ (0.015 M), 3,4-ethylenedioxythiophene (0.030 M) and *n*-Bu_4NBF_4 (0.1 M) in freshly distilled MeCN. The potential was swept between −200 and 600 mV (vs the non-aqueous reference electrode Ag/$AgNO_3$ 0.01 M in MeCN) for 10 complete cycles at a scan rate of 50 mV s^{-1}. Further series of 10 cycles were completed in +100 mV increments to a limit of 1000 mV (−200 to 700, 800, 900 and 1000 mV, respectively).

2.5. Physical methods

Electronic spectra were recorded on a Perkin–Elmer Lambda 40 spectrophotometer. Nuclear magnetic resonance spectra were measured on a Bruker AC400 at 400.13 MHz for ^1H and 100.62 MHz for ^{13}C. Samples run in D_2O were referenced through the addition of sodium-(trimethylsilyl)propionate while spectra run in $CDCl_3$ were referenced to residual $CHCl_3$ peaks and cited vs TMS. Electrochemical examination of metal complexes was undertaken with a BAS100B/W potentiostat utilising an auxiliary platinum wire, Ag/AgCl reference electrode (+196 mV vs NHE) and either a glassy carbon (BAS C2 cell stand) or mercury drop working electrode (EG and G PARC Model 202 SMDE). Solutions contained approximately millimolar

concentrations of analyte and 0.1 M $NaClO_4$ in H_2O, and *n*-Bu_4NBF_4 or Et_4NClO_4 electrolyte in acetonitrile respectively. XPS data were acquired using a Kratos Axis ULTRA X-ray Photoelectron Spectrometer incorporating a 165 mm hemispherical electron energy analyser and utilising incident monochromatic Al X-rays (1486.6 eV) at 150 W (15 kV, 10 mA). Survey (wide) scans were taken at analyser pass energy of 160 eV and multiplex (narrow) high-resolution scans at 20 eV. Base pressure in the analysis chamber was 1.0×10^{-9} torr and during sample analysis was of 10^{-8} torr in magnitude.

2.6. Crystallography

Cell constants were determined by a least-squares fit to the setting parameters of 25 independent reflections measured on an Enraf-Nonius CAD4 four-circle diffractometer employing graphite-monochromated Mo Kα radiation (0.71073) and operating in the ω–2θ scan mode. Data reduction and empirical absorption corrections (ψ-scans) [25] were performed with the WINGX [26] package. Structures were solved with SHELXS 86 [27] through heavy atom methods for metal complexes and direct methods for the free ligand then refined by a full-matrix least-squares analysis with SHELXL-97 [28]. All non-hydrogen atoms were modelled with anisotropic thermal parameters. Hydrogen atoms were modelled for all water molecules where apparent from the difference map. All other H atoms were included at estimated positions using a riding model. Drawings of all molecules were prepared with ORTEP3 [26]. Crystal data are summarised in Table 1. The data have been deposited in CIF format with the Cambridge Crystallographic Data Centre (CCDC Nos. 603168–603170).

3. Results and discussion

3.1. Characterisation of the free ligand L^1

The reductive alkylation of the parent hexaamine L^2 with 3-thiophene carbaldehyde proceeded efficiently to give the monosubstituted ligand L^1. The procedure followed well established methods in our laboratory that have been used in the past to introduce a variety of substituents such as crown ethers [29], polycyclic aromatics [30–35], ferrocenes [36,37], aromatic and aliphatic carboxylic acids [38,39] onto an exocyclic primary amine. Despite the presence of six potentially reactive amines on L^2, the desired monosubstitution procedure requires no formal protecting groups other than protons. We have reported the first five protonation constants of the parent hexaamine to be 11.0, 9.9, 6.3, 5.4 and 2.9 [40], and through crystallography it is known that the third and fourth protonation constants are associated with the two exocyclic amines [41]. Therefore, control of the reaction pH at approximately 5.5 permits only one primary amine (in its free base form) to react with 3-thiophenecarbaldehyde. Cyanoborohydride is a selective reductant for imines over aldehydes at this pH and thus can be present at the start of the reaction. Nevertheless a small amount of disubstituted macrocycle was identified as an unwanted byproduct, but it was not characterised further.

The crystal structure of the free ligand $L^1 \cdot 2H_2O$ was determined and a view of the compound is shown in Fig. 1. The structure contains no unusual features. Intra- and intermolecular H-bonds abound; in fact all six N-atoms and two O-atoms are paired in H-bonding interactions with either water or amine protons. The asymmetric

Table 1
Crystal data

	$L^1 \cdot 2H_2O$	$[CoL^1Cl]Cl_2$	$[CoL^1(OAc)](ClO_4)_2$
Formula	$C_{17}H_{38}N_6O_2S$	$C_{17}H_{34}Cl_3CoN_6S$	$C_{19}H_{37}Cl_2CoN_6O_{10}S$
Formula weight	390.59	519.84	671.44
Temperature (K)	293	293	293
Wavelength (Å)	0.71073	0.71073	0.71073
Crystal system	monoclinic	monoclinic	orthorhombic
Space group	$P2_1/n$	$P2_1/n$	$P2_12_12_1$
a (Å)	13.023(2)	13.029(3)	11.545(4)
b (Å)	9.883(1)	12.7248(9)	15.326(2)
c (Å)	17.909(3)	14.262(4)	15.502(1)
α (°)			
β (°)	108.78(1)	107.83(2)	
γ (°)			
Volume (Å^3)	2182.3(5)	2250.9(8)	2743(1)
Z	4	4	4
Absorption coefficient (mm^{-1})	0.171	1.228	0.96
Measured reflections	4014	4131	3469
Independent reflections	3834	3946	3270
R_{int}	0.067	0.028	0.040
Observed reflections	1883	3077	2853
Parameters	235	253	354
Goodness-of-fit	1.017	1.041	1.07
$R_1(I > 2\sigma(I))$	0.059	0.035	0.040
wR_2 (all data)	0.1941	0.099	0.1047

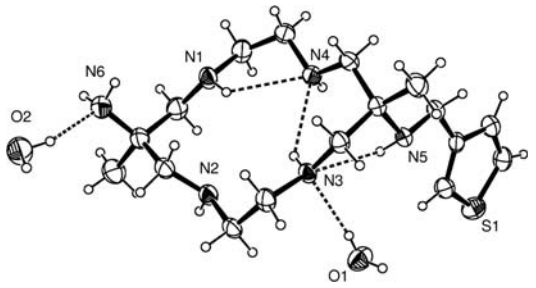


Fig. 1. ORTEP view of $L^1 \cdot 2H_2O$ (30% probability ellipsoids) showing intramolecular and selected intermolecular H-bonds. N1–H1···N4 2.37 Å, 124.0°; N3–H3···N4 2.40 Å, 132.5°; N5–H5···N3 2.43 Å, 110.2°; O1–H1C···N3 2.13 Å, 170.6°; O2–H2C···N6 1.93 Å, 164.7°.

conformation of the macrocycle is similar to that seen previously in structures of other unprotonated, metal free derivatives of L^2 [36,37]. Intramolecular N–H···N contacts within the macrocyclic ligand are apparent and determine the overall ring conformation. The lone pairs of N1 and N2 accept H-bonds from N–H groups of adjacent macrocycles (not shown).

3.2. Coordination chemistry

Coordination of the ligand L^1 to Co^{III} was straightforward and led initially to a complex $[CoL^1(OH_2)]^{3+}$ where the macrocycle was bound in a pentadentate manner. The substituted exocyclic amine remains free from the metal. The two complexes isolated as solids $[CoL^1Cl]^{2+}$ and $[CoL^1(OAc)]^{2+}$ formed through anation reactions in the presence of high concentrations of chloride and acetate respectively following column chromatography. The two isolated complexes exhibited electronic spectra consistent with $Co^{III}N_5Cl$ and $Co^{III}N_5O$ chromophores respectively. The coordination sphere of these two ions are consistent with their electronic spectra as the lowest energy spin allowed electronic transition of Co^{III} complexes ($^1T_{1g} \leftarrow {}^1A_{1g}$, O_h) is very sensitive to changes in the donor atoms. Asymmetric broadening of this transition is due to the influence of the low symmetry ligand field. The spectrum of the chloro complex was run in weakly acidic solution to suppress base catalysed hydrolysis of the monodentate ligand. It has generally been found [29,31,32] that attachment of bulky substituents onto the exocyclic amines of ligands such as L^2 precludes their participation as donor atoms and here again the pentadentate coordinated form is the dominant product.

Pentadentate coordination of the ligand L^1 to Co^{III} was confirmed by X-ray crystallographic analysis of $[CoL^1Cl]Cl_2$ (Fig. 2) and $[CoL^1(OAc)](ClO_4)_2$ (Fig. 3). The structures of each complex cation are rather similar and each find the monodentate ligand *trans* to the exocyclic primary amine. The four macrocyclic amines are coplanar with the metal and all macrocyclic amine H-atoms appear on the same side of the ring; the so-called *trans*-I configuration. The bond lengths and angles within the two complexes are very similar (see captions of Figs. 2 and 3).

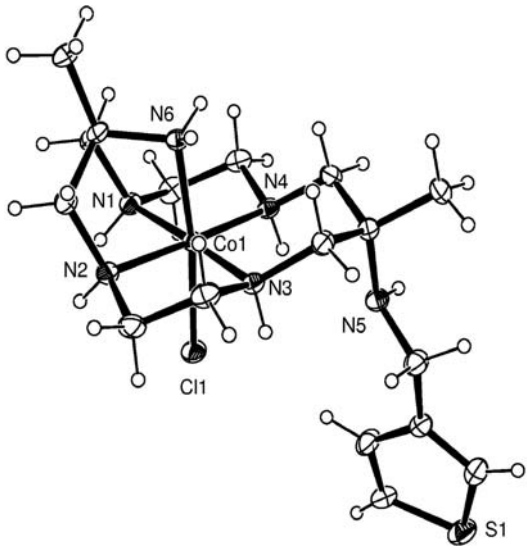


Fig. 2. ORTEP view of the $[CoL^1Cl]^{2+}$ cation (30% probability ellipsoids). Selected bond lengths (Å): Co1–N1 1.938(2), Co1–N2 1.943(2), Co1–N3 1.948(2), Co1–N4 1.954(2), Co1–N6 1.961(2), Co1–Cl1 2.2469(9).

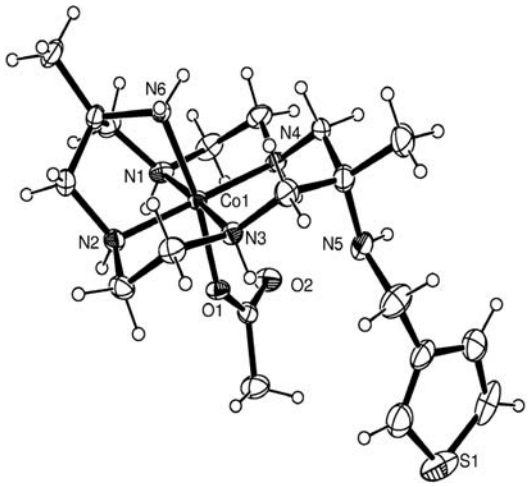


Fig. 3. ORTEP view of the $[CoL^1(OAc)]^{2+}$ cation (30% probability ellipsoids). Selected bond lengths (Å): Co1–N1 1.951(4), Co1–N2 1.954(4), Co1–N3 1.957(4), Co1–N4 1.939(4), Co1–N6 1.961(3), Co1–O1 1.898(3).

Cyclic voltammetry of $[CoL^1(OH_2)]^{3+}$ in aqueous solution at pH 7 was conducted on a static Hg drop working electrode (Fig. 4). A reversible $Co^{III/II}$ couple was identified at −550 mV vs Ag/AgCl. The voltammetry at pH 12 revealed a shift in the couple to −704 mV vs Ag/AgCl which is consistent with deprotonation of the aqua ligand to give the hydroxo analogue $[CoL^1(OH)]^{2+}$.

3.3. Electropolymerisation

Polymerisation of micellular 3,4-ethylenedioxythiophene (EDOT) was undertaken as listed in Section 2. Typical cyclic voltammograms for this stepwise polymerisation are shown in Fig. 5. Sweeping the potential to increasingly positive values resulted in a gradual increase in current

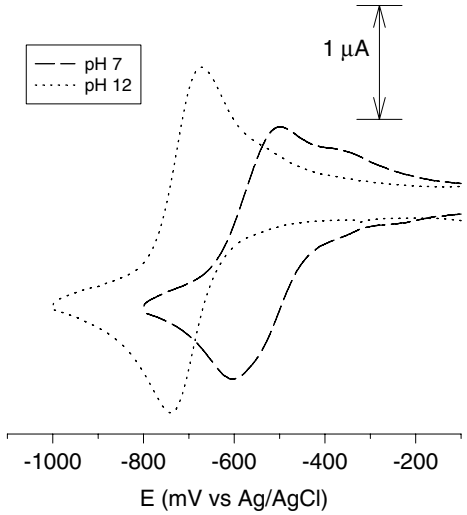


Fig. 4. Cyclic voltammograms of $[CoL^1(OH_2)]^{3+}$ (at pH 7, dashed curve) and $[CoL^1(OH)]^{2+}$ (at pH 12, dotted curve) on a static Hg drop electrode (sweep rate 100 mV s^{-1}). The minor peaks at −400 mV on the voltammogram at pH 7 are due to adsorption of the complex on the Hg electrode.

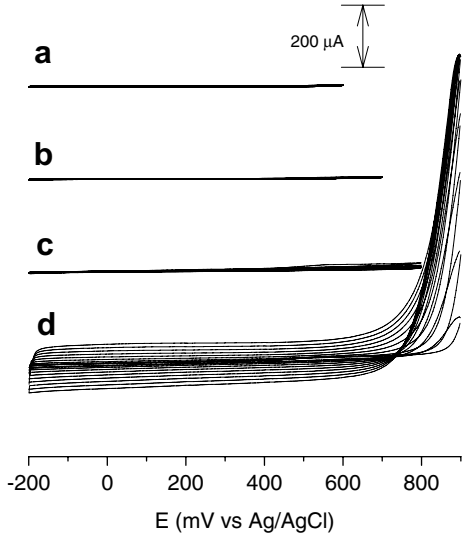


Fig. 5. Electropolymerisation of EDOT on an ITO working electrode. The three conditioning voltammograms (a)–(c) show the successive increase in the anodic potential limit leading eventually to polymerisation (d).

flow, increasing dramatically upon oxidation and electrodeposition of the polymer film. This is observed in the thousand-fold increase of current with the change in oxidative potential from +800 mV to +900 mV (lower panels Fig. 5). Homogeneous growth of the polymer film is observed with an incremental increase in current with subsequent cycles.

Metal–polymer hybrid films of uniform colour, surface coverage and strength were produced through an incremental increase in the anodic potential limit in a similar fashion to that of the PEDOT base layer. The resulting electrodeposited copolymeric film of EDOT and $[CoL^1Cl]^{2+}$ was blue as expected for polythiophene and can be described as a Type I hybrid material [8]. Attempted polymerisation of $[CoL^1Cl]^{2+}$ as the sole monomer in the absence of EDOT resulted in no electrodeposition onto the electrode surface.

Analysis of the copolymer film was assisted through the use of X-ray photoelectron spectroscopy (XPS), which has been shown to be an exceptionally powerful technique in the analysis of electropolymerised films [42]. The XPS spectrum of the $[CoL^1Cl]Cl_2$/EDOT copolymer film was charge corrected to the sulfur $2p^{3/2}$ photoelectron (thiophene, 164.3 eV), with reported values rounded to the nearest electron volt [43]. Observed photoelectrons for the $[CoL^1Cl]^{2+}$/EDOT copolymer film included: Co^{III} 797 eV ($2p^{1/2}$), 783 eV ($2p^{3/2}$); oxygen 534 eV (1s); nitrogen 401 eV (1s); carbon 286 eV (1s); sulfur 170 eV ($2p^{1/2}$), 165 eV ($2p^{3/2}$). The ratio of Co^{III} to sulfur was calculated at 1:12, indicating an incorporation of one complex unit per 11 EDOT monomer in the polymer film. Direct comparison of the initial monomer concentrations in solution and within the final polymer film reveals a preference for inclusion of EDOT monomer over $[CoL^1Cl]Cl_2$, (ca. 1:11 (complex:EDOT) from a 1:2 solution). This preference for EDOT inclusion is thought to be due to steric hinderance, however electrostatic interactions between the cationic complex and the oxidising electrode surface may also represent an important contribution.

Cyclic voltammetry of the CoL^1/EDOT copolymer film in neutral aqueous solution (Fig. 6) revealed the presence of the expected $Co^{III/II}$ redox couple at a similar potential to that seen in the solution voltammetry of the monomer $[CoL^1(OH_2)]^{3+}$ (Fig. 4). That is, the chloro ligand present during polymerisation appears to have been substituted by an aqua ligand during the electrochemical experiment. The peak currents increased linearly with sweep rate which is consistent with the voltammetric response to a surface confined molecule [44].

The broad nature of the anodic and cathodic maxima is indicative of a dispersion of orientations of the complex

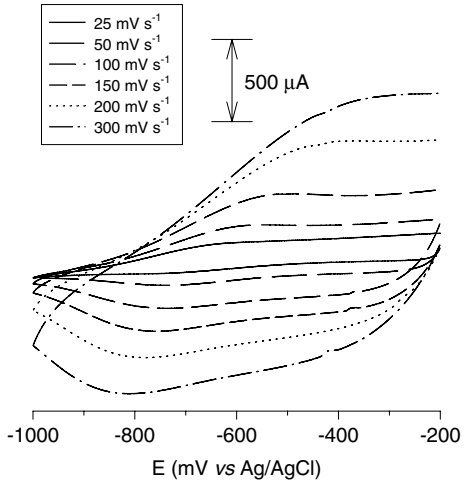


Fig. 6. Cyclic voltammograms (aqueous solution) of the $[CoL^1(OH_2)]^{3+}$/EDOT copolymer film at sweep rates between 25, 50, 100, 150, 200 and 300 mV s^{-1} (currents increase with sweep rate).

within the film, each with a slightly different apparent redox potential. Furthermore the peak potentials shift considerably with sweep rate which is indicative of sluggish heterogeneous electron transfer with the Co centres appended to the polymer.

We have found that preconditioning of the ITO surface through an incremental increase in the voltammetric positive potential limit was important in ensuring homogeneity of the initial PEDOT film deposited on the electrode. Films produced through either poising the potential at a polymerising voltage or sweeping directly over the range for oxidation resulted in opaque films with poor homogeneity. Polymerisation and electrodeposition of the highly uniform PEDOT films involves initial electrostatic attraction of the negatively charged micelles towards the positively charged surface of the oxidative working electrode. At a suitable oxidation potential, EDOT contained within this micelle undergoes polymerisation and electrodeposition onto the ITO electrode. This process can be repeated through continuing cycles, increasing the thickness of the PEDOT layer. The polymerisation of EDOT within micelles has a number of advantages in the generation of high quality films, such as lowering the oxidation potential and increasing the solubility of the monomer in aqueous solution [45–48].

Copolymerisation of EDOT and $[CoL^1(OH_2)]^{3+}$ onto a preformed PEDOT film was straightforward and resulted in a film of consistent colour and also uniform surface coverage. Attempts to copolymerise films directly onto bare ITO coated glass from acetonitrile solution produced films of uneven coverage and thickness. Nucleation of polymer growth was observed with these films as isolated regions of growth across the surface of the ITO coated glass slide. Continuation of electrochemical cycling to improve the surface coverage led to darkening (film growth) at the nucleated regions without a noticeable improvement in surface coverage. This is consistent with previous attempts to produce polythiophene films from acetonitrile solution, which were reported to give brittle or powdery deposits [1,49].

It is believed that precoating the ITO slide with PEDOT allows for surface grafting and homogeneous electrodeposition. This is achieved through the conducting PEDOT layer acting as the working electrode, oxidising EDOT monomer (or thiophene appended transition metal complex) directly for inclusion in the growing chain. This technique could potentially be applied to a number of systems, such as where a complex of interest cannot be directly polymerised to a conductive surface or in the production of metal–polymer hybrid films in a reproducible manner.

4. Conclusions

A versatile method has been reported for the incorporation of transition metal ions into a polythiophene film. Using well established chemistry, a thiophene monomeric residue has been introduced to the non-coordinating exocyclic amine of a macrocyclic ligand. This group is able to undergo co-polymerisation with 3,4-ethylenedioxythiophene to produce a redox active film laid down on an ITO electrode. Electroactivity of the Co complex within the polymer film has been demonstrated. One particularly important feature is that the macrocyclic ring not only binds its metal tightly, but it is also capable of binding to a number of other transition metal ions in various oxidation states. The ability to construct polymeric films with tunable redox potentials is apparent and the subject of ongoing work.

Acknowledgement

We are grateful for financial support to P.V.B from the Australian Research Council

Appendix A. Supplementary data

Supplementary data associated with this article can be found, in the online version, at doi:10.1016/j.poly.2006.07.001.

References

[1] J. Roncali, Chem. Rev. 92 (1992) 711.
[2] G. Barbarella, M. Melucci, G. Sotgiu, Adv. Mater. 17 (2005) 1581.
[3] A. Bhattacharya, A. De, Prog. Solid State Chem. 24 (1996) 141.
[4] A.J. Heeger, Angew. Chem., Int. Ed. 40 (2001) 2591.
[5] L.M. Goldenberg, M.R. Bryce, M.C. Petty, J. Mater. Chem. 9 (1999) 1957.
[6] T. Otsubo, Y. Aso, K. Takimiya, J. Mater. Chem. 12 (2002) 2565.
[7] E.R. Van Keuren, R.C. White, Nonlinear Opt., Quant. Opt. 33 (2005) 63.
[8] M.O. Wolf, Adv. Mater. 13 (2001) 545.
[9] T.L. Stott, M.O. Wolf, Coord. Chem. Rev. 246 (2003) 89.
[10] C. Li, T. Hatano, M. Takeuchi, S. Shinkai, Tetrahedron 60 (2004) 8037.
[11] A. O'Riordan, E. O'Connor, S. Moynihan, P. Nockemann, P. Fias, R. Van Deun, D. Cupertino, P. Mackie, G. Redmond, Thin Solid Films 497 (2006) 299.
[12] M. Schaeferling, P. Baeuerle, J. Mater. Chem. 14 (2004) 1132.
[13] S. Burnet, M.-H. Choi, P.S. Donnelly, J.M. Harrowfield, I. Ivanova, S.-H. Jeong, Y. Kim, M. Mocerino, B.W. Skelton, A.H. White, C.C. Williams, Z.-L. Zeng, Eur. J. Inorg. Chem. (2001) 1869.
[14] J. Hjelm, R.W. Handel, A. Hagfeldt, E.C. Constable, C.E. Housecroft, R.J. Forster, Inorg. Chem. 44 (2005) 1073.
[15] J.-C. Lepretre, A. Deronzier, O. Stephan, Synth. Met. 131 (2002) 175.
[16] R. Das Rupasree, C.-L. Lee, Y.-Y. Noh, J.-J. Kim, Opt. Mater. 21 (2003) 143.
[17] D.M. DeLongchamp, M. Kastantin, P.T. Hammond, Chem. Mater. 15 (2003) 1575.
[18] T. Hatano, A.-H. Bae, K. Sugiyasu, N. Fujita, M. Takeuchi, A. Ikeda, S. Shinkai, Org. Biomol. Chem. 1 (2003) 2343.
[19] A. O'Riordan, E. O'Connor, S. Moynihan, X. Llinares, R. Van Deun, P. Fias, P. Nockemann, K. Binnemans, G. Redmond, Thin Solid Films 491 (2005) 264.
[20] S.-M. Seo, J.H. Kim, J.-Y. Park, H.H. Lee, Appl. Phys. Lett. 87 (2005) 183501.
[21] J. Roncali, P. Blanchard, P. Frere, J. Mater. Chem. 15 (2005) 1589.
[22] A. Hamnett, P.A. Christensen, D.C. Read, PCT Int. Appl. (1993) 31.
[23] P.V. Bernhardt, G.A. Lawrance, T.W. Hambley, J. Chem. Soc., Dalton Trans. (1989) 1059.

[24] H.F. Bauer, W.C. Drinkard, Inorg. Synth. 8 (1966) 202.
[25] A.C.T. North, D.C. Phillips, F.S. Mathews, Acta Crystallogr., Sect. A 24 (1968) 351.
[26] L.J. Farrugia, J. Appl. Crystallogr. 32 (1999) 837.
[27] G.M. Sheldrick, Acta Crystallogr., Sect. A: Found. Crystallogr. 46 (1990) 467.
[28] G.M. Sheldrick, SHELXL-97: Program for Crystal Structure Refinement, University of Goettingen, Goettingen, 1997.
[29] P.V. Bernhardt, E.J. Hayes, Inorg. Chem. 41 (2002) 2892.
[30] P.V. Bernhardt, B.M. Flanagan, M.J. Riley, J. Chem. Soc., Dalton Trans. (1999) 3579.
[31] P.V. Bernhardt, E.G. Moore, M.J. Riley, Inorg. Chem. 40 (2001) 5799.
[32] P.V. Bernhardt, E.G. Moore, M.J. Riley, Inorg. Chem. 41 (2002) 3025.
[33] E.G. Moore, P.V. Bernhardt, A. Pigliucci, M.J. Riley, E. Vauthey, J. Phys. Chem. (2003) 8396.
[34] E.G. Moore, P.V. Bernhardt, A. Fuerstenberg, M.J. Riley, E. Vauthey, J. Phys. Chem. A 109 (2005) 11715.
[35] E.G. Moore, P.V. Bernhardt, M.J. Riley, T.A. Smith, Inorg. Chem. 45 (2006) 51.
[36] P.D. Beer, P.V. Bernhardt, J. Chem. Soc., Dalton Trans. (2001) 1428.
[37] P.V. Bernhardt, N.L. Creevey, Dalton Trans. (2004) 914.
[38] P.V. Bernhardt, N.L. Kilah, A.P. Meacham, P. Meredith, R. Vogel, Dalton Trans. (2005) 2508.
[39] P.V. Bernhardt, P.C. Sharpe, Inorg. Chem. 39 (2000) 4123.
[40] P.V. Bernhardt, G.A. Lawrance, M. Maeder, M. Rossignoli, T.W. Hambley, J. Chem. Soc., Dalton Trans. (1991) 1167.
[41] P.V. Bernhardt, T.W. Hambley, G.A. Lawrance, Aust. J. Chem. 43 (1990) 699.
[42] K.S. Ryder, L.F. Schweiger, A. Glidle, J.M. Cooper, J. Mater. Chem. 10 (2000) 1785.
[43] B.J. Lindberg, K. Hamrin, G. Johansson, U. Gelius, A. Fahlman, C. Nordling, K. Siegbahn, Phys. Scr. 1 (1970) 286.
[44] A.J. Bard, L.R. Faulkner, Electrochemical Methods: Fundamentals and Applications, 2nd ed., Wiley, New York, 2001.
[45] N. Sakmeche, E.A. Bazzaoui, M. Fall, S. Aeiyach, M. Jouini, J.C. Lacroix, J.J. Aaron, P.C. Lacaze, Synth. Met. 84 (1997) 191.
[46] N. Sakmeche, J.-J. Aaron, S. Aeiyach, P.-C. Lacaze, Electrochim. Acta 45 (2000) 1921.
[47] S. Sadki, C. Chevrot, Electrochim. Acta 48 (2003) 733.
[48] Y. Kudoh, K. Akami, Y. Matsuya, Synth. Met. 98 (1998) 65.
[49] G. Tourillon, F. Garnier, J. Electroanal. Chem. Interfac. Electrochem. 135 (1982) 173.

Available online at www.sciencedirect.com
ScienceDirect
Polyhedron 26 (2007) 400–405
POLYHEDRON
www.elsevier.com/locate/poly

Synthesis and X-ray structures of two discrete metal complexes of 2,2′-bi-1,5-naphthyridine, a new ambivergent ligand

Christopher M. Fitchett, Peter J. Steel *

Department of Chemistry, University of Canterbury, Christchurch, New Zealand

Received 5 April 2006; accepted 28 June 2006
Available online 14 July 2006

Abstract

A new synthesis of 2,2′-bi-1,5-naphthyridine (**1**) is described along with its reactions with copper(II) nitrate, silver(I) tetrafluoroborate and palladium(II) chloride. X-ray crystal structures are described of a mononuclear copper complex, in which **1** acts as a convergent ligand chelating through the two internal nitrogens, and an unusual M_4L_3 silver complex containing both two- and three-coordinate silvers and with ligand **1** acting in two different bridging modes.
© 2006 Elsevier Ltd. All rights reserved.

Keywords: Copper; Silver; Crystal structures; Bridging ligands; Naphthyridines

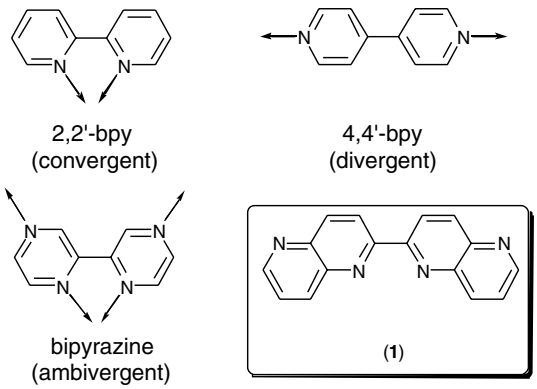
1. Introduction

Metallosupramolecular chemistry [1] involves the use of combinations of metal ions and multidentate organic ligands for the construction of both discrete and polymeric assemblies that possess diverse topologies. By far the most commonly employed ligands are those containing aromatic nitrogen heterocycles [2]. Two archetypal ligands are 2,2′-bipyridine, which has been classified [3] as a *convergent* ligand wherein the two nitrogen donors chelate to a single metal, and 4,4′-bipyridine, which is a *divergent* ligand that acts as a bridge between two metals (Scheme 1). However, some ligands can perform both these roles and we call these *ambivergent* ligands. A well-known example is bipyrazine, which can chelate to a single metal through the central more hindered nitrogen donors but also use the external nitrogens to bridge other metals. Many structurally-diverse supramolecular architectures have been assembled using this ligand [4], which can display a variety of coordination modes, including a recently reported case of μ_4-coordination [5].

An important aspect for control of the topology within metallosupramolecular architectures is the spatial arrangement of the binding domains in multidentate ligands. In particular, the distance between the donor groups and their angular disposition determine the size and shape of the assembly. In a continuation of our work on the design and synthesis of heterocyclic ligands [1c,1d], we now report the use of 2,2′-bi-1,5-naphthyridine (**1**) as a ligand. This compound was prepared almost half a century ago [6] and reported to form a copper complex, but has not been studied since. It is potentially an ambivergent ligand related to bipyrazine, but has the external bridging nitrogens separated by a greater distance. The most closely related ligand recently studied is 2,2′-bi-1,6-naphthyridine, which was shown to produce both interpenetrated coordination nets and helical coordination polymers [7]. However, this ligand differs in that the external bridging nitrogens are arranged in a linear fashion, rather than the 60° angular arrangement in **1**. We describe below the preparations of three metal complexes of **1** and the X-ray structures of two discrete coordination compounds, including an intriguing M_4L_3 tetranuclear silver complex.

* Corresponding author.
E-mail address: peter.steel@canterbury.ac.nz (P.J. Steel).

0277-5387/$ - see front matter © 2006 Elsevier Ltd. All rights reserved.
doi:10.1016/j.poly.2006.06.033



Scheme 1.

2. Experimental

2.1. General procedures

NMR spectra were recorded with a Varian INOVA 500 spectrometer at 23 °C with a 3 mm probe and operating at 500 MHz. Melting points were determined using an Electrothermal melting point apparatus and are uncorrected. Elemental analyses were performed by the Campbell Microanalytical laboratory at the University of Otago. 1-Methyl-1,5-napthyridin-2(1H)-one [8] and nickel(II) bistriphenylphosphine bromide [9] were prepared by literature procedures. Solvents were purified according to standard procedures. Other reagents were obtained from commercial sources and used as supplied.

2.2. Ligand synthesis

2.2.1. Preparation of 2-chloro-1,5-naphthyridine

1-Methyl-1,5-naphthyridin-2(1H)-one (0.96 g, 6.0 mmol) and phosphorus pentachloride (1.25 g, 6.0 mmol) were refluxed in phosphorus oxychloride (50 mL) for 24 h. The solvent was evaporated *in vacuo* to give a brown solid. This was suspended in water (75 mL) and neutralized ($NaHCO_3$). This suspension was extracted with $CHCl_3$ (2×75 mL) and the organic phase washed (2×20 mL H_2O, 20 mL brine), dried (Na_2SO_4) and the solvent evaporated *in vacuo*. The solid formed was recrystallized from 1:1 pet-ether/ethyl acetate to give 2-chloro-1,5-naphthyridine as an orange solid. Yield 0.58 g (59%). M.p. 109–111 °C (lit. [10] 112°). ^{1}H NMR (500 MHz, $CDCl_3$): 8.98 (H, dd, H6), 8.34 (2H, m, H8, H4), 7.63 (2H, m, H3, H7).

2.2.2. Preparation of 2,2′-bi-1,5-naphthyridine (1)

Nickel(II) bistriphenylphosphine bromide (0.79 g, 1.1 mmol), zinc powder (0.45 g, 6.9 mmol) and tetraethylammonium iodide (0.90 g, 3.4 mmol) were stirred at room temperature in dry THF (15 mL) under argon for 30 min. 2-Chloro-1,5-naphthyridine (0.57 g, 3.5 mmol) was added in dry THF (10 mL) and the mixture stirred at 50 °C for 22 h under argon. The mixture was poured onto 100 mL 2 M aq. NH_3 and extracted with $CHCl_3$ (2×75 mL). The organic phase was washed (H_2O, 50 mL), dried (Na_2SO_4) and the solvent removed *in vacuo* to give a brown solid. This was purified via chromatography (10 g Silica, EtOAc), and the product recrystallized (1:1 pet ether/EtOAc) to give a yellow solid. Yield 0.10 g (22%). M.p. 275–276 °C (lit. [6] 282–284 °C) ^{1}H NMR (300 MHz, $CDCl_3$): 9.08 (2H, d, H3), 9.03 (2H, d, H6), 8.58 (2H, d, H4), 8.55 (2H, d, H8), 7.71 (2H, dd, H7).

2.3. Complex synthesis

2.3.1. Preparation of copper(II) nitrate complex 2

Reaction of **1** (13.0 mg, 0.05 mmol) dissolved in hot acetonitrile with copper(II) nitrate (25.1 mg, 0.10 mmol) dissolved in hot acetonitrile gave a green solution. Crystals suitable for X-ray diffraction were deposited after 4 h. Yield 15.7 mg (70%). M.p. >270 °C (dec.). *Anal.* Calc. for $C_{16}H_{10}N_6O_6Cu$: C, 43.10; H, 2.43; N, 18.85. Found: C, 42.93; H, 2.43; N, 19.00%.

2.3.2. Preparation of silver(I) tetrafluoroborate complex 3

Reaction of **1** (13.0 mg, 0.05 mmol) dissolved in hot acetonitrile with silver tetrafluoroborate (20.5 mg, 0.11 mmol) dissolved in hot acetonitrile gave a light yellow solution. Crystals suitable for X-ray diffraction were obtained by diffusion of pentane into the reaction mixture. Yield 11.19 mg (29%). M.p. >200 °C (dec.). *Anal.* Calc. for $C_{52}H_{36}N_{14}Ag_4B_4F_{16}$: C, 38.18; H, 2.22; N, 11.99. Found: C, 38.59; H, 2.19; N, 11.82%.

Table 1
Crystal data for **2** and **3**

Compound	**2**	**3**
Empirical formula	$C_{18}H_{13}N_7O_6Cu$	$C_{52}H_{36}B_4F_{16}N_{14}Ag_4$
Formula weight	486.89	1635.67
Temperature (K)	168(2)	168(2)
Crystal system	triclinic	triclinic
Space group	$P\bar{1}$	$P\bar{1}$
Unit cell dimensions		
a (Å)	8.889(4)	10.639(4)
b (Å)	9.778(4)	10.704(4)
c (Å)	13.041(5)	12.821(5)
α (°)	102.165(5)	83.767(5)
β (°)	97.835(5)	67.201(5)
γ (°)	114.229(5)	83.379(5)
Volume (Å^3)	978.3(7)	1333(1)
Z	2	1
D_{calc} (Mg/m^3)	1.653	2.036
Absorption coefficient (mm^{-1})	1.171	1.558
$F(000)$	494	798
Crystal size (mm)	$0.55 \times 0.16 \times 0.02$	$0.21 \times 0.14 \times 0.06$
Theta range (°)	2.39–26.52	2.08–26.41
Reflections collected	12,431	17,035
Independent reflections [R_{int}]	3936 [0.0388]	5337 [0.0305]
Observed reflections [$I > 2\sigma(I)$]	2993	4111
Data/restraints/parameters	3936/0/290	5337/0/407
Goodness-of-fit on F^2	1.017	1.022
R_1 [$I > 2\sigma(I)$]	0.0385	0.0379
wR_2 (all data)	0.1057	0.1133

*2.3.3. Preparation of palladium(II) chloride complex **4***

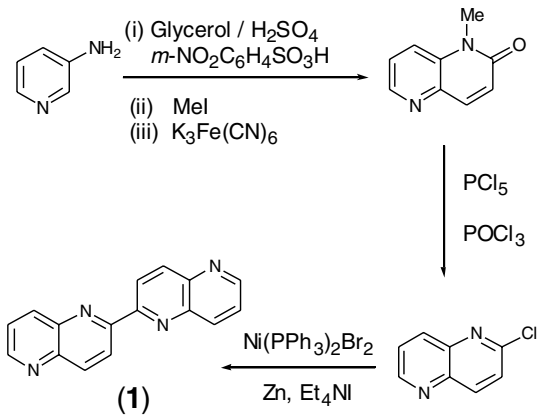
Reaction of **1** (12.0 mg, 0.047 mmol) in methanol with a methanolic solution of 0.1511 M Li_2PdCl_4 (0.7 ml, 0.10 mmol) gave a yellow solid. Yield 13.0 mg (42%). M.p. >300 °C (dec.). *Anal.* Calc. for $C_{16}H_{10}N_4Pd_2Cl_4$: C, 31.35; H, 1.64; N, 9.14. Found: C, 31.49; H, 1.74; N, 9.14%.

2.4. X-ray crystallography

The crystal data and details of the data collections and refinements for the two structures are listed in Table 1. Measurements were made with a SMART CCD area detector using graphite-monochromatized Mo Kα ($\lambda = 0.71073$ Å) radiation. The structures were solved by direct methods using SHELXS [11] and refined on F^2 using all data by full-matrix least-squares procedures with SHELXL-97 [12]. All non-hydrogen atoms were refined with anisotropic displacement parameters. Hydrogen atoms were included in calculated positions with isotropic displacement parameters 1.2 times the isotropic equivalent of their carrier atoms. The functions minimised were $\sum w(F_o^2 - F_c^2)$, with $w = [\sigma^2(F_o^2) + aP^2 + bP]^{-1}$, where $P = [\max(F_o)^2 + 2F_c^2]/3$.

3. Results and discussion

The only literature reference to 2,2′-bi-1,5-naphthyridine involves its formation, in very low yield, by the oxidative dimerization of 1,5-naphthyridine using activated Pd/C at 220 °C [6]. We have prepared it by the method outlined in (Scheme 2). Thus, 3-aminopyridine was converted to 1,5-naphthyridine by a Skraup reaction and this was reacted in a methylation, oxidation, chlorination sequence to afford 2-chloro-1,5-naphthyridine, which was then subjected to the Ni^0-catalyzed coupling procedure pioneered by Iyoda et al. [13]. The downfield position (9.08 ppm) of H3 in the ^1H NMR spectrum clearly showed that the free ligand exists in the conformation, shown in Scheme 2, with a s-*trans* arrangement about the central inter-ring bond. This is the normal conformation observed in both solution and the solid state for biheterocycles of this type [14].



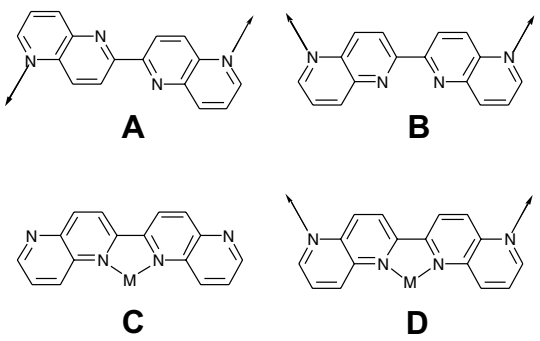
Scheme 2.

The conformation of the ligand has important consequences for the topology of any metal complexes. One could envisage *inter alia* several possible coordination modes for **1** (Scheme 3). When acting as a divergent ligand, the s-*trans* conformation would result in a stepped-linear bridging arrangement (A), whereas the s-*cis* conformation would provide a 60° angular bridge (B). In a convergent mode (C) or ambivergent mode (D) the s-*cis* conformation is enforced.

In a continuation of our long-standing interest in the study of copper(II) [15], silver(I) [16] and palladium(II) [17] complexes, we reacted **1** with two equivalents of salts of each of these metals. Reaction with copper(II) nitrate in acetonitrile solution furnished a green crystalline product (**2**) in 70% yield, which elemental analysis showed to be a 1:1 M:L complex. The complex crystallizes in the triclinic space group $P\bar{1}$, with one molecule of **1**, one copper(II) nitrate and an acetonitrile solvate molecule in the asymmetric unit. The mononuclear structure of **2** is shown in Fig. 1, and has one molecule of **1** chelating one copper atom through the most hindered internal nitrogen atoms. The ligand (**1**) is held in a s-*cis* planar conformation, with a mean deviation of 0.041(5) Å from planarity. The nitrate anions chelate the copper atom asymmetrically, with each having one short and one long bond. This gives the copper atom a severely distorted octahedral geometry. The bond lengths and angles are within normal ranges for a complex of this type [18].

The molecules pack in ribbons with adjacent molecules held together by centrosymmetric pairs of C–H···N interactions [19] involving the non-coordinated external nitrogens of **1** and hydrogen atoms of adjacent molecules, the shortest being 2.416(6) Å between H4 and N5 (Fig. 2). Further π–π stacking interactions exist between adjacent ribbons, with the aromatic molecules coplanar and in an offset stacked arrangement. The slight offset has C4 of one ligand lying above the centre of the N1–C8 ring, at a distance of 3.440(4) Å. The acetonitrile solvate molecule occupies the spaces between the stacks of molecules. Thus, we have shown that ligand **1** readily acts as a chelating convergent ligand (Scheme 3, mode C).

Silver(I) salts have been extensively used as versatile synthons for the construction of a diverse myriad of metallo-supramolecular assemblies [20]. Multidentate ligands



Scheme 3.

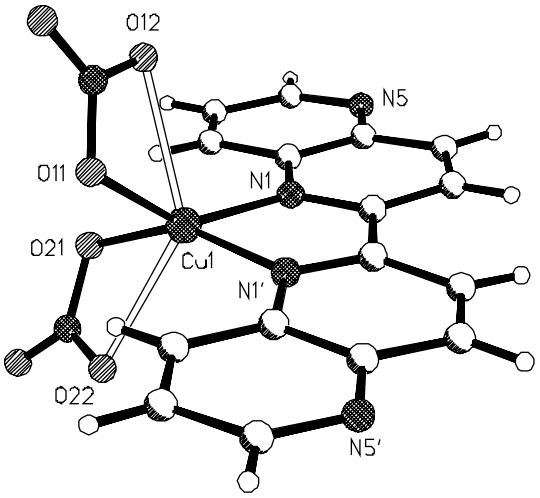


Fig. 1. Perspective view of the crystal structure of **2**, with the long Cu–O bonds of the chelating nitrate anions shown as hollow bonds. The non-coordinated acetonitrile molecule is not shown. Selected bond lengths (Å) and bond angles (°): Cu1–N1′ 1.983(2), Cu1–N1 2.004(2), Cu1–O21 1.984(2), Cu1–O11 2.005(2), Cu1–O22 2.371(2), Cu1–O12 2.461(2), N1′–Cu1–O21, 152.29(10), N1′–Cu1–N1 82.40(9), O21–Cu1–N1 102.58(9), N1′–Cu1–O11 97.2(1), N1–Cu1–O11 143.45(10), N1′–Cu1–O22 96.38(9), N1–Cu1–O22 123.54(9).

usually react with silver to produce 1-, 2- or 3-dimensional coordination polymers. With the expectation that ligand **1** would act in an ambidentate fashion with silver, we react it with two equivalents of silver tetrafluoroborate and obtained a crystalline product (**3**) that elemental analysis showed to have an intriguing M_4L_3 stoichiometry. In order to determine unambiguously the structure of this compound a single-crystal X-ray structure analysis was carried out.

Once again this complex crystallizes in the triclinic space group $P\bar{1}$ and has two silver tetrafluoroborates, one and a half molecules of **1** and a coordinated acetonitrile molecule in the asymmetric unit. The structure of **3** (Fig. 3) is a remarkable discrete tetranuclear complex with four silver atoms bridged by three molecules of **1**. The central ligand lies on a centre of inversion and hence has a s-*trans* planar conformation. It bridges two silver atoms, separated by 12.759(7) Å, using the least hindered external nitrogens. Thus, it acts as a stepped-linear divergent ligand (Scheme 3, mode A). The two remaining ligands are in a s-*cis* planar conformation, and chelate one silver atom and bridge to another through one external nitrogen; these silvers are separated by 7.716(7) Å. The internal silver atom, Ag2, is coordinated by two molecules of **1** with a distorted linear geometry [N5C-Ag2-N5B 167.9(1)°]. The external silver atom, Ag1, is chelated by one molecule of **1** and coordinated to a molecule of acetonitrile with an overall trigonal-planar geometry. The full tetranuclear structure is remarkably planar, with a mean deviation of only 0.092(7) Å from the non-hydrogen atom meanplane.

The tetranuclear units stack in a coplanar fashion, with two linear Ag2 atoms adjacent to one another (Fig. 4). The silver atoms are separated by a distance of 3.556(4) Å, indicating a relatively weak interaction [21]. Adjacent units are offset by one molecule of **1**, such that the s-*cis* ligands stack atop the s-*trans* ligands. The distance between the planes of the tetranuclear units is only 3.258(7) Å, indicating strong face-to-face π–π interactions between the aromatic ligands [22]. Such combinations of Ag···Ag and π–π interactions between heterocyclic ligands have often been observed in silver coordination polymers [4b]. The tetrafluoroborate counterions are held in place via numerous weak

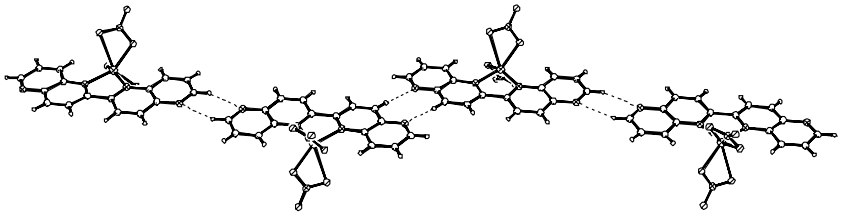


Fig. 2. Perspective view of a hydrogen bonded ribbon of **2**.

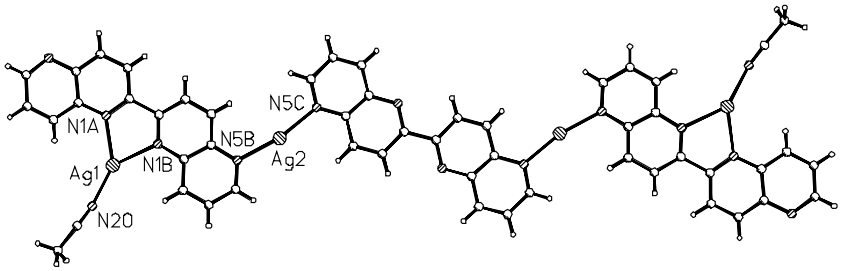


Fig. 3. Perspective view of the tetranuclear silver complex **3**. Tetrafluoroborate counterions have been omitted for clarity. Selected bond lengths (Å) and bond angles (°): Ag1–N20 2.114(4), Ag1–N1A 2.293(4), Ag1–N1B 2.292(4), Ag2–N5C 2.175(4), Ag2–N5B 2.181(4), N20–Ag1–N1A 144.9(1), N20–Ag1–N1B 142.8(1), N1A–Ag1–N1B 72.3(1), N5C–Ag2–N5B 167.9(1).

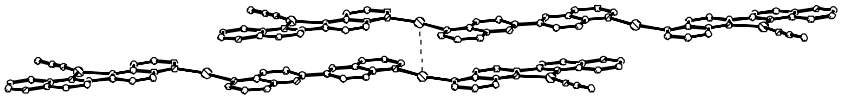


Fig. 4. View showing the association of two adjacent molecules of **3** with the Ag–Ag interaction indicated by a dashed line. Hydrogen atoms and tetrafluoroborate counterions are not shown.

C–H···F interactions, the shortest being 2.40(5) Å. In this novel discrete tetranuclear complex each of the two components acts in two different modes; the silver atoms have linear two-coordinate and trigonal three-coordinate geometries and the bridging ligands show stepped-linear divergent and ambivergent behaviours.

Finally, the reaction of **1** with two equivalents of palladium(II) chloride was investigated. This reaction furnished a highly insoluble complex that was shown, by elemental analysis, to have a 2:1 M:L stoichiometry. Since palladium(II) almost invariably adopts a square planar four-coordinate geometry, this would suggest that this complex is a coordination polymer in which the ligand **1** acts in an ambivergent manner using all four of its donor nitrogens.

4. Conclusion

2,2′-Bi-1,5-naphthyridine (**1**) has been prepared by a new synthetic route and shown to act in a variety of coordination modes. Reaction with copper(II) nitrate produced a discrete mononuclear complex in which the copper atom is chelated to the central internal nitrogens. Reaction with silver(I) tetrafluoroborate gave an intriguing discrete M_4L_3 tetranuclear complex with both two- and three-coordinated silvers and the ligand acting in two different bridging modes.

5. Supplementary material

Full tables of atom coordinates, thermal parameters, and bond lengths and angles have been deposited at the Cambridge Crystallographic Data Centre. CCDC 603159 and 603160 contains the supplementary crystallographic data for this paper. These data can be obtained free of charge at www.ccdc.cam.ac.uk/conts/retrieving.html [or from the Cambridge Crystallographic Data Centre, 12 Union Road, Cambridge CB2 1EZ, UK; fax: +44 1223 336 033; e-mail: deposit@ccdc.cam.ac.uk].

Acknowledgements

We thank the Royal Society of New Zealand Marsden Fund for financial support.

References

[1] (a) E.C. Constable, Chem. Ind. (1994) 56;
(b) P.J. Steel, Chem. New Zealand 67 (2003) 57;
(c) P.J. Steel, Molecules 9 (2004) 440;
(d) P.J. Steel, Acc. Chem. Res. 38 (2005) 243.

[2] (a) S. Leininger, B. Olenyuk, P.J. Stang, Chem. Rev. 100 (2000) 853;
(b) G.F. Swiegers, T.J. Malefetse, Chem. Rev. 100 (2000) 3483;
(c) B. Moulton, M.J. Zaworotko, Chem. Rev. 101 (2001) 1629;
(d) M. Fujita, K. Umemoto, M. Yoshizawa, N. Fujita, T. Kusukawa, K. Biradha, Chem. Commun. (2001) 509;
(e) D.W. Johnson, K.N. Raymond, Supramol. Chem. 13 (2001) 639;
(f) B.J. Holliday, C.A. Mirkin, Angew. Chem. Int. Ed. 40 (2001) 2022;
(g) G.F. Swiegers, T.J. Malefetse, Coord. Chem. Rev. 225 (2002) 91;
(h) L. James, Chem. Soc. Rev. 32 (2003) 276;
(i) M.J. Hannon, L.J. Childs, Supramol. Chem. 16 (2004) 7;
(j) F. Würthner, C.-C. You, C.R. Saha-Möller, Chem. Soc. Rev. 33 (2004) 133;
(k) H. Hofmeier, U.S. Schubert, Chem. Soc. Rev. 33 (2004) 373;
(l) A.L. Gavrilova, B. Bosnich, Chem. Rev. 104 (2004) 349;
(m) P. Thanasekaran, R.-T. Liao, Y.-H. Liu, T. Rajendran, S. Rajagopal, K.-L. Lu, Coord. Chem. Rev. 249 (2005) 1085;
(n) M.W. Hosseini, Acc. Chem. Res. 38 (2005) 313.

[3] E.C. Constable, D. Morris, S. Carr, New J. Chem. (1998) 287.

[4] (a) J.A.R. Navarro, B. Lippert, Coord. Chem. Rev. 222 (2001) 219, and references therein;
(b) A.N. Khlobystov, A.J. Blake, N.R. Champness, D.A. Lemenovskii, A.G. Majouga, N.V. Zyk, M. Schröder, Coord. Chem. Rev. 222 (2001) 155, and references therein.

[5] T.-T. Yeh, J.-Y. Wu, Y.-S. Wen, H.-S. Liu, J. Twu, Y.-T. Tao, K.-L. Lu, Dalton Trans. (2005) 656.

[6] H. Rapoport, R. Iwamoto, J.R. Tretter, J. Org. Chem. 25 (1960) 372.

[7] H.-P. Wu, C. Janiak, L. Uehlin, P. Klufers, P. Mayer, Chem. Commun. (1998) 2637.

[8] (a) H. Rapoport, A.D. Batcho, J. Org. Chem. 28 (1963) 1753;
(b) A. Albert, J. Org. Chem. 25 (1960) 1790.

[9] L.M. Venanzi, J. Chem. Soc. (1958) 719.

[10] E.V. Brown, A.C. Plasz, J. Org. Chem. 32 (1967) 241.

[11] G.M. Sheldrick, Acta Crystallogr., Sect A 46 (1990) 467.

[12] G.M. Sheldrick, SHELXL-97, University of Göttingen, 1997.

[13] M. Iyoda, H. Otsuka, K. Sato, N. Nisato, M. Oda, Bull. Chem. Soc. Jpn. 63 (1990) 80.

[14] (a) P.J. Steel, Adv. Heterocycl. Chem. 67 (1997) 1;
(b) C.M. Fitchett, C. Richardson, P.J. Steel, Org. Biomol. Chem. 3 (2005) 498.

[15] (a) A.A. Watson, D.A. House, P.J. Steel, Polyhedron 8 (1989) 1345;
(b) R.J. Anderson, P.H. Hagback, P.J. Steel, Inorg. Chim. Acta 284 (1999) 273;
(c) C. Richardson, P.J. Steel, Dalton Trans. (2003) 992;
(d) M.R.A. Al-Mandhary, P.J. Steel, Inorg. Chim. Acta 351 (2003) 7;
(e) P.J. Steel, C.J. Sumby, Dalton Trans. (2003) 4505;
(f) M.R.A. Al-Mandhary, P.J. Steel, Eur. J. Inorg. Chem. (2004) 329;
(g) P. Børsting, P.J. Steel, Eur. J. Inorg. Chem. (2004) 376;
(h) D.A. McMorran, C.M. Hartshorn, P.J. Steel, Polyhedron 23 (2004) 1055.

[16] (a) C.M. Hartshorn, P.J. Steel, Inorg. Chem. 35 (1996) 6902;
(b) C.M. Fitchett, P.J. Steel, New J. Chem. 24 (2000) 945;
(c) C.J. Sumby, P.J. Steel, Chem. Commun. (2002) 322;
(d) P.J. Steel, N.C. Webb, Eur. J. Inorg. Chem. (2002) 2257;
(e) D.A. McMorran, P.J. Steel, Chem. Commun. (2002) 2120;
(f) C.J. Sumby, P.J. Steel, New J. Chem. 29 (2005) 1077;
(g) W. Lewis, P.J. Steel, Supramol. Chem. 17 (2005) 579;
(h) C.M. Fitchett, P.J. Steel, Aust. J. Chem. 59 (2006) 19;
(i) J. Burgess, J.R.A. Cottam, P.J. Steel, Aust. J. Chem. 59 (2006) 296;
(j) M.R.A. Al-Mandhary, C.M. Fitchett, P.J. Steel, Aust. J. Chem. 59 (2006) 307.

[17] (a) P.J. Steel, Acta Crystallogr. C39 (1983) 1623;
(b) D.A. House, P.J. Steel, A.A. Watson, Aust. J. Chem. 39 (1986) 1525;
(c) A.J. Downard, P.J. Steel, J. Steenwijk, Aust. J. Chem. 48 (1995) 1625;
(d) C.M. Hartshorn, P.J. Steel, Chem. Commun. (1997) 541;
(e) C.M. Hartshorn, P.J. Steel, J. Chem. Soc., Dalton Trans. (1998) 3927;
(f) A.J. Downard, I.G. Phillips, P.J. Steel, Aust. J. Chem. 57 (2004) 865.
[18] M. Melnik, M. Kabesova, L.U. Macaskova, C.E. Holloway, J. Coord. Chem. 45 (1998) 31.
[19] (a) G.R. Desiraju, Acc. Chem. Res. 35 (2002) 565;
(b) A. Nangia, Cryst. Eng. Commun. 4 (2002) 93;
(c) M. Mazik, D. Blaser, R. Boese, Tetrahedron Lett. 41 (2000) 5827;
(d) V.R. Thalladi, A. Gehrke, R. Boese, New. J. Chem. 24 (2000) 463;
(e) J.J.M. Amoore, L.R. Hanton, M.D. Spicer, Dalton Trans. (2003) 1056, and references therein.
[20] (a) C.M. Hartshorn, P.J. Steel, J. Chem. Soc., Dalton Trans. (1998) 3935, and references therein;
(b) M. Munakata, L.P. Wu, T. Kuroda-Sowa, Adv. Inorg. Chem. 46 (1999) 173;
(c) S.-L. Zheng, M.-L. Tong, X.-M. Chen, Coord. Chem. Rev. 246 (2003) 185;
(d) C.-L. Chen, B.-S. Kang, C.-Y. Su, Aust. J. Chem. 59 (2006) 3.
[21] P. Pyykkö, Chem. Rev. 97 (1997) 597.
[22] (a) C.A. Hunter, K.R. Lawson, J. Perkins, C.J. Urch, J. Chem. Soc., Perkin Trans. 2 (2001) 651;
(b) W.B. Jennings, B.M. Farrell, J.F. Malone, Acc. Chem. Res. 34 (2001) 885;
(c) E.A. Meyer, R.K. Castellano, F. Diederich, Angew. Chem. Int. Ed. 42 (2003) 1210.

Available online at www.sciencedirect.com
ScienceDirect
Polyhedron 26 (2007) 406–414
POLYHEDRON
www.elsevier.com/locate/poly

Aqueous chemistry of the five-coordinate zirconocene dichloride $PhP(CH_2CH_2–\eta^5\text{-}C_5H_4)_2ZrCl_2$: X-ray structure of the sulfato complex $PhP(CH_2CH_2–\eta^5\text{-}C_5H_4)_2Zr(\eta^2\text{-}SO_4)$

James R. Butchard, Owen J. Curnow *

Department of Chemistry, University of Canterbury, Private Bag 4800, Christchurch, New Zealand

Received 3 April 2006; accepted 28 June 2006
Available online 14 July 2006

Abstract

ES-MS of dilute solutions of $(bcep)ZrCl_2$ (**1**) (bcep = $PhP(CH_2CH_2–\eta^5\text{-}C_5H_4)_2$) in acetonitrile–water indicates the presence of three species in solution: $[(bcep)Zr(H_2O)_2]^{2+}$ (**2**), $[\{(bcep)Zr(\mu\text{-}OH)\}_2]^{2+}$ (**3**), and the singly deprotonated form of dimer **3**, $[\{(bcep)Zr\}_2(\mu\text{-}O)(\mu\text{-}OH)]^+$ (**4**). In aqueous solutions, reactivity studies investigated largely by ^{31}P NMR spectroscopy support the presence of **2**, **3** and **4**. One equivalent of fluoride was found to react immediately with **2**, but slowly with **3** and **4**, to give the monofluoro complex $[(bcep)ZrF]^+$ which was isolated as the BPh_4^- salt. Addition of aqueous sodium sulphate gave insoluble crystals of the sulfato complex $(bcep)Zr(SO_4)$ which was characterised by X-ray crystallography. Addition of acids HX (X = Br, NO_3, HSO_4, HCO_3) to aqueous solutions of **1** gave species observed by ES-MS corresponding to $[(bcep)ZrX]^+$.
© 2006 Elsevier Ltd. All rights reserved.

Keywords: Zirconocene; Phosphine; Sulfato complex; Fluoro complex; Aqueous chemistry

1. Introduction

The chemistry of zirconocene dichlorides is currently one of the most significant areas of research in organometallic chemistry [1]. The area of functionalised bis(cyclopentadienyl) ligands capable of chelation is an active field of organometallic chemistry [2–4]. Notable zirconocenes are the complexes $MeN(CH_2CH_2C_5H_4)_2ZrCl_2$ and $\{C_5H_3N(CH_2C_5H_4)_2\text{-}2,6\}ZrCl_2$ in which amine and pyridine coordination, respectively, is proposed on the basis of ^1H NMR spectroscopy and XPS studies [2]. A crystallographically characterized hydrolysis product of $\{C_5H_3N(CH_2C_5H_4)_2\text{-}2,6\}ZrCl_2$ is the cationic chloro-aqua complex $[\{C_5H_3N(CH_2C_5H_4)_2\text{-}2,6\}ZrCl(H_2O)]^+$ in which the pyridine substituent is coordinated to the metal center [3].

Ansa-metallocenes with a P bridging atom directly bonded to the C_5 ring are known for a number of iron [5] and zirconium [6] complexes. The number of bis(cyclopentadienyl) phosphine ligands capable of chelation is very small [7,8]. The ligand $C_6H_{11}P(CHMe\text{-}2\text{-}PPh_2C_5H_3^-)_2$ [7] could exhibit phosphine chelation, but this has not yet been demonstrated. We recently communicated the preparation of $PPh(CH_2CH_2C_5H_5)_2$ ($bcepH_2$) and the synthesis of ferrocene complexes derived from this compound in which the P atom is not coordinated to the Fe center [8]. The P atom can, however, coordinate to a second metal center as in the complex *trans*-$PdCl_2\{(bcep)Fe\}_2$ [8].

The aqueous chemistry of zirconocenes has been investigated by a small number of workers (in contrast to that of the titanocenes [9]) with the identification of species in solution largely dependent upon crystallographic characterisation of the compounds isolated in the solid state. Addition of two equivalents of water to $Cp_2Zr(C_7H_7SO_3)_2$ gives the toluenesulfonatodiaqua cation $[Cp_2Zr(C_7H_7SO_3)(H_2O)_2]^+$ [10], whereas addition of three equivalents of water to the bistriflate complex $Cp_2Zr(CF_3SO_3)_2$ (THF) gives the triaqua dication $[Cp_2Zr(H_2O)_3]^{2+}$ [11] and addition of six

* Corresponding author. Tel.: +64 3 364 2819; fax: +64 3 364 2110.
E-mail address: owen.curnow@canterbury.ac.nz (O.J. Curnow).

0277-5387/$ - see front matter © 2006 Elsevier Ltd. All rights reserved.
doi:10.1016/j.poly.2006.06.031

equivalents gives a 30% yield of the dinuclear hydroxo-bridged complex $[Cp_2Zr_2(\mu\text{-}OH)_2(H_2O)_6]^{4+}$ in which one Cp ligand has been hydrolysed from each Zr atom [12]. Other zirconocene dichloride hydrolysis products have been reported by Thewalt and co-workers in which one Cp ligand has been hydrolysed and there are oxo/hydroxo bridges: $\{CpZr(NO_3)_2\}_2(\mu\text{-}OH)_2$ was isolated from nitric acid in chloroform [13] and $[Cp_3Zr_3(\mu_3\text{-}O)(\mu\text{-}OH)_3(\mu\text{-}PhCOO)_3]^+$ was isolated from sodium benzoate in water/chloroform [14]. Fischer and co-workers obtained the dicationic dinuclear di-μ-hydroxo complex $[\{Cp_2Zr(\mu\text{-}OH)(n\text{-}PrCN)\}_2]^{2+}$ by addition of *n*-PrCN to a mixture they formulated as $[\{Cp_2Zr(H_2O)\}_2O][BPh_4]_2 \cdot pH_2O$ and/or $[Cp_2Zr(OH)(H_2O)_n][BPh_4] \cdot mH_2O$ (this was prepared by addition of $Na[BPh_4]$ to Cp_2ZrCl_2 dissolved in water) [15]. A related neutral dinuclear di-μ-hydroxo complex, $[Cp_2Zr(\mu\text{-}OH)(CF_3COO)]_2$, was obtained by Klima and Thewalt by treatment of Cp_2ZrCl_2 with CF_3COOH in a $CHCl_3/H_2O$ two-phase system [16]. Erker and co-workers reported that treatment of $[Cp_2ZrCH_3(THF)]^+$ with excess water in CH_2Cl_2/THF gave the trinuclear cluster $[(Cp_2Zr)_3(\mu\text{-}OH)_3(\mu_3\text{-}O)]^+$ in which the cyclopentadienyl ligands are still intact [17]. Using chloride potentiometry, Toney and Marks studied the aqueous chemistry of Cp_2ZrCl_2: the rate of the second chloride loss was found to be 1.31 h^{-1} for 1–3.5 mM solutions with an equilibrium $[Cl^-]$:[Zr] ratio of 1.75 [18]. Thus, significant amounts of $[Cp_2ZrCl(H_2O)_x]^+$ and $[Cp_2Zr(H_2O)_x]^{2+}$ are present in these solutions. Some aqueous polymerisation studies of styrene and methyl methacrylate using Cp_2ZrCl_2 have also been reported [19]. Hillhouse and Bercaw have reported some stoichiometric reactions of bis(pentamethylcyclopentadienyl)-zirconium and -hafnium hydrides to give a variety of hydroxo and oxo complexes [20].

We recently reported the preparation and structure of $(bcep)ZrCl_2$ (**1**) along with some initial chemical investigations [21]: crystals of $[(bcep)ZrCl(H_2O)]Cl$ were isolated by evaporation of a wet methanol solution of **1**; the ES-MS of a CH_3CN/H_2O solution of **1** with added HCl(aq) gave peaks corresponding to the expected species $[(bcep)Zr(OH)]^+$ and $[(bcep)ZrCl]^+$ in addition to species of the formulae $[(bcep)Zr(OH)O]^+$ and $[(bcep)ZrClO]^+$ (no peak corresponding to the crystallographically characterised cation $[(bcep)ZrCl(H_2O)]^+$ has been observed).

In this paper, we detail further aqueous chemistry of complex **1** which has been studied using ^{31}P NMR spectroscopy, ES-MS, and X-ray crystallography.

2. Results and discussion

Positive-ion ES-MS of dilute (ca. 10^{-4} M) solutions of complex **1** in 1:1 acetonitrile–water shows the presence of three species (Fig. 1). The masses are consistent with the hydroxo complex $[(bcep)Zr(OH)]^+$ (**5**) (derived from the diaqua dicationic complex $[(bcep)Zr(H_2O)_2]^{2+}$ (**2**)) and its dimer $[\{(bcep)Zr(\mu\text{-}OH)\}_2]^{2+}$ (**3**), as well as the singly-deprotonated form of **3**, $[\{(bcep)Zr\}_2(\mu\text{-}O)(\mu\text{-}OH)]^+$ (**4**) (Scheme 1). Although the diaqua dication $[(bcep)Zr(H_2O)_2]^{2+}$ (**2**) is not observed directly by ES-MS, this is not surprising: under ES-MS conditions, as the solvent evaporates and the charge density increases, the dication **2** can both lose solvent and reduce charge by the loss of H_3O^+ to give the hydroxo complex **5**. There is no evidence in these dilute solutions for any chloro complexes such as the crystallographically-characterised cation $[(bcep)ZrCl(H_2O)]^+$ [21].

The aqueous chemistry of **1** was investigated with reactivity studies that were followed by ^{31}P NMR spectroscopy. Results are summarised in Table 1. Three major species, in a 14:2:1 ratio, are observed. These are proposed to be the diaqua dication $[(bcep)Zr(H_2O)_2]^{2+}$ (**2**) (δ 32.32), and the dinuclear complexes **3** (δ 33.14) and **4** (δ 34.36). The assignment of the resonance at δ 32.32 as the diaqua dication **2** rather than the mononuclear hydroxo complex **5**, as is observed under ES-MS conditions, or the hydroxo-aqua complex

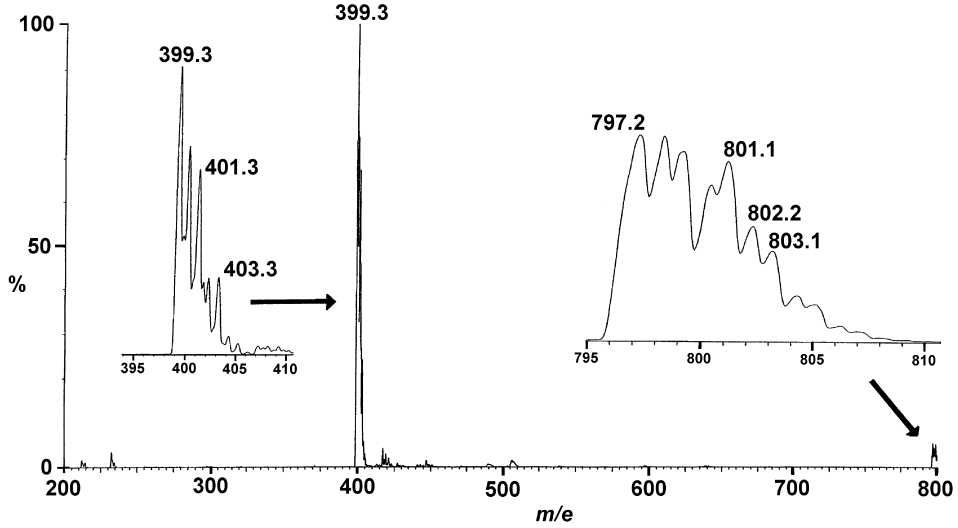
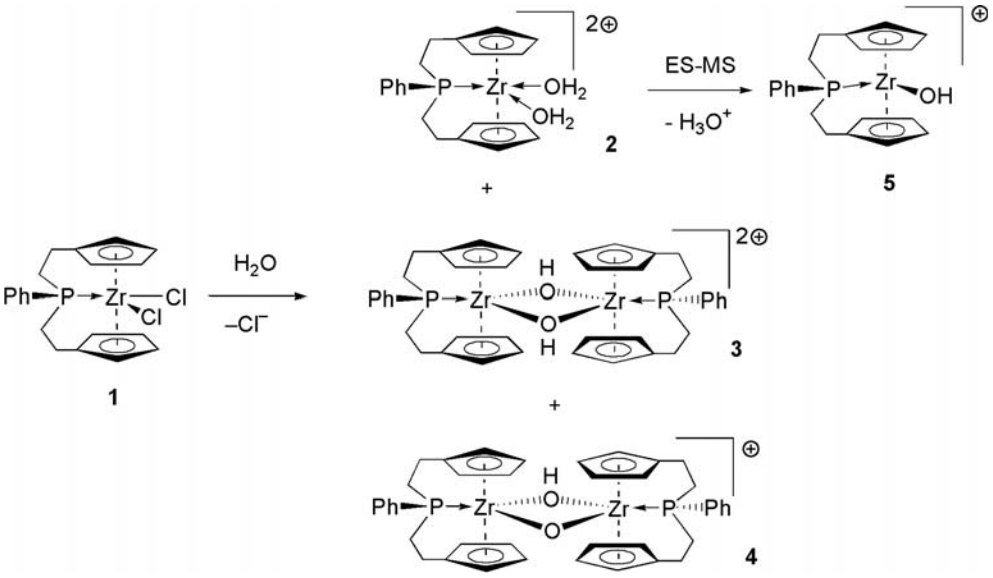


Fig. 1. ES-MS of $(bcep)ZrCl_2$ (**1**) in H_2O/CH_3CN (cone voltage of 20 V).



Scheme 1. (Bcep)$ZrCl_2$ (**1**) in H_2O.

Table 1
^{31}P NMR spectra of aqueous solutions of **1**[a]

Solvent	$[(bcep)_2Zr_2(O)(OH)]^+$	$[\{(bcep)Zr(OH)\}_2]^{2+}$	$[(bcep)Zr(H_2O)_2]^{2+}$
H_2O	34.36 (0.11)	33.14 (0.18)	32.32 (0.71)
D_2O	34.25 (0.10)	33.01 (0.22)	32.46 (0.68)
1:1 H_2O/D_2O	34.34 (0.10)	33.18 (0.05)	32.40 (0.70)
		33.15 (0.05)	
		33.12 (0.05)	
		33.09 (0.05)	
2:1 H_2O/D_2O	34.34 (0.11)	33.18 (0.02)	32.40 (0.71)
		33.15 (0.04)	
		33.12 (0.04)	
		33.09 (0.08)	
25:75 H_2O/CH_3CN	33.16 (0.15)	33.03 (0.22)	29.12 (0.63)
			$w_{1/2} \sim 83$ Hz
50:50 H_2O/CH_3CN	33.11	33.01	31.38
			$w_{1/2} \sim 50$ Hz
65:35 H_2O/CH_3CN	34.10 (0.12)	33.09 (0.22)	32.09 (0.66)
			$w_{1/2} = 23$ Hz
75:25 H_2O/CH_3CN	34.17 (0.11)	33.12 (0.20)	32.15 (0.69)
			$w_{1/2} = 9$ Hz
H_2O + 10HCl (5 min)	34.36 (0.01)	33.14 (0.14)	32.68 (0.85)
H_2O + 10HCl (30 min)			32.68 (1.00)

[a] Chemical shift in ppm, integral given in parentheses.

$[(bcep)Zr(OH)(H_2O)]^+$ (**6**) is based on the following observations: addition of one half equivalent of NaOH(aq) rapidly converts **2** to **3** and **4** (more than one equivalent of hydroxide rapidly leads to hydrolysis of bcep from the complex) whereas addition of aqueous HCl converts **3** and **4** to **2** over several minutes – a possible equilibrium between **3** and its monomer **5** (or a complex such as **6**) would not be affected by addition of acid or base. Balzarek et al. have reported that the monomer/dimer equilibrium between $[Cp_4Mo_2(\mu\text{-}OH)_2]^{2+}$ and $[Cp_2Mo(OH)(H_2O)]^+$ (equivalent to an equilibrium between **3** and **6**) is independent of pH [22]. Dicationic species such as **2** also have precedence in the form of the triaqua complex $[Cp_2Zr(H_2O)_3]^{2+}$ [11]. Dissolving complex **1** in 0.1 M HCl(aq) gives only **2**.

The assignment of the resonance at δ 33.14 to the di-μ-hydroxo complex **3**, with the phosphorus atoms *trans* about the $Zr_2(OH)_2$ core, is supported by its ^{31}P NMR spectrum in 2:1 D_2O/H_2O which shows four peaks in a 4:2:2:1 ratio (Fig. 2). The downfield resonance at 32.94 ppm is assigned to $[\{(bcep)Zr(\mu\text{-}OD)\}_2]^{2+}$, the resonances at 32.91 and 32.88 ppm to the mixed species $[\{(bcep)Zr\}_2(\mu\text{-}OH)(\mu\text{-}OD)]^{2+}$, and the resonance at 32.85 ppm to $[\{(bcep)Zr(\mu\text{-}OH)\}_2]^{2+}$. Complex **4** could also give four peaks in this solvent mixture, but they would be in a 2:2:1:1 ratio. Accidental degeneracy of two of these peaks could give a 1:3:2 pattern, unfortunately, we have been unable to resolve the resonances at ca. 34 ppm sufficiently well to confirm this unambiguously. The resonance due to **2** is essentially

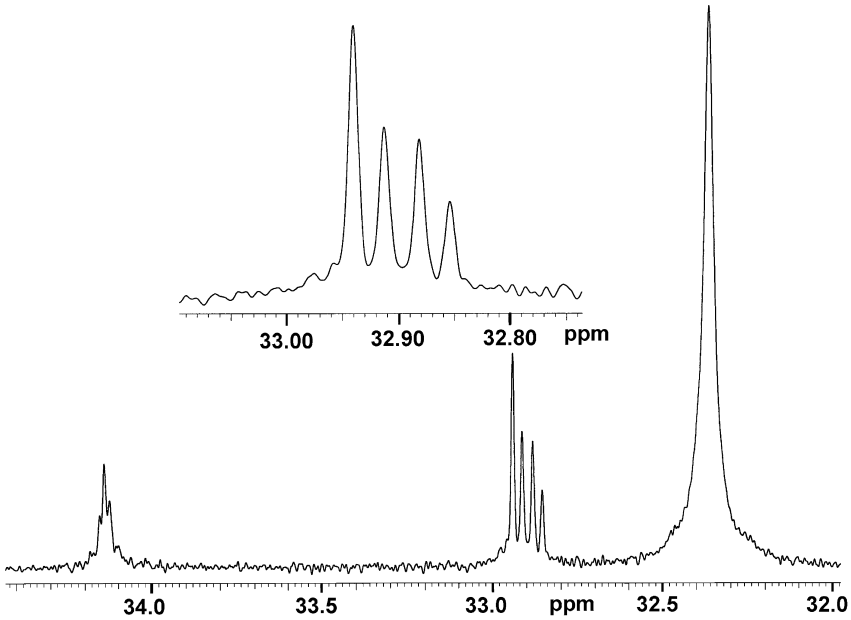


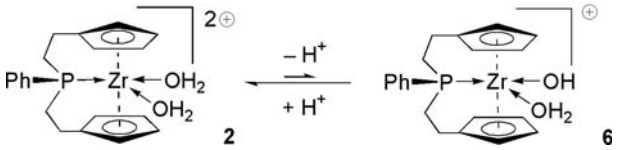
Fig. 2. ^{31}P NMR spectrum of complex **1** dissolved in a 2:1 D_2O/H_2O mixture.

unchanged, as would be expected for rapid proton exchange in this complex. In a 1:1 solvent mixture, both **3** and **4** would have four peaks in a 1:1:1:1 ratio; this is observed for **3** but, again, is unresolved for **4**. The related complex $[\{Cp_2Zr(n\text{-PrCN})(\mu\text{-OH})\}_2]^{2+}$, has been crystallographically characterized and also found to have the *n*-PrCN substituents *trans* about the $Zr_2(OH)_2$ core [15]. The observation of this isotope effect deserves some comment. The average isotope effect on the ^{31}P NMR chemical shift is 0.045 ppm per H/D substitution, which is quite significant considering that the substitution is made three bonds away from the P atoms. A comparison can be made with $P(CH_3)_3$ versus $P(CD_3)_3$ in which the chemical shifts are −61.9 and −64.9 ppm, respectively [23]. This is an average isotope effect of 0.33 ppm per H/D exchange, for which the P atom is two bonds from the H/D atoms.

To confirm the absence of chloro complexes, $Ag(NO_3)$-(aq) was added to the aqueous solution of **1**. Although the expected precipitate of AgCl rapidly formed, there was no change in the ^{31}P NMR spectrum. Thus, the presence of chloro complexes can be ruled out.

Further evidence in support of the proposed structures for **2**, **3** and **4** is provided by the treatment of aqueous **1** with aqueous $HClO_4$. One equivalent immediately precipitates out only **3** and **4**, as is expected from their larger size and hydrophobic exterior (the Zr_2O_2 cores are sterically shielded by the four cyclopentadienyl rings and two phenyl groups, as evidenced by the slow rate of proton exchange in the mixed D_2O/H_2O solvent systems). The concentration of **2** is unaffected and it seems reasonable to suggest that hydrogen bonding with the solvent keeps this species in solution.

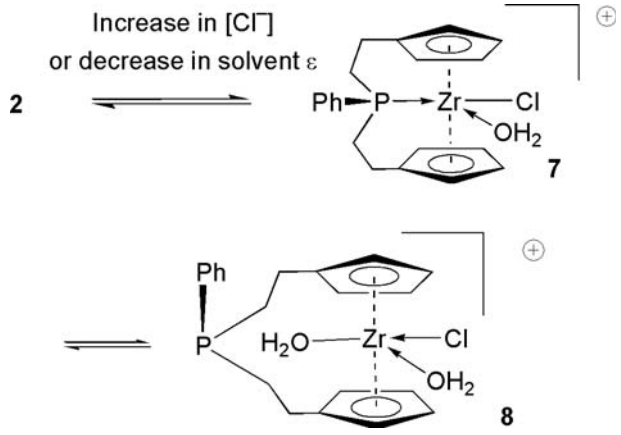
Potentiometry measurements were also carried out to support the proposed mixture of compounds. Complex **1** dissolves in water over several minutes to give an acidic solution for which a stable pH reading can be taken after about 30 min. For a 10^{-3} M solution, the equilibrium pH is 3.3. This is lower than the expected pH calculated using the ^{31}P NMR peak ratios, which gives a pH of 3.7, but is higher than would be expected if **2** was in fact a hydroxo species like **5** or **6**, in which case, the expected pH would be less than 3.0. Similarly, a 10^{-2} M solution gives a pH of 2.2, rather than 2.7. The discrepancy could be accounted for by an equilibrium between **2** and **6**, which would be expected to be rapid and which could also provide a proton exchange mechanism. Attempts to measure the free chloride concentration using a chloride-ion selective electrode were prevented by chronic electrode fouling.



2 **6**

In an attempt to observe a species such as $[(bcep)ZrCl(H_2O)]^+$ (**7**), aqueous NaCl was added to an aqueous solution of **1**. Although no new peaks were observed in the ^{31}P NMR spectrum and the peaks assigned to **3** and **4** remained unchanged, the peak assigned to **2** at ca. 32 ppm broadened from 6 Hz with no added chloride to 60 Hz at 1.2 M chloride. A similar broadening effect was seen upon addition of acetonitrile (Table 1). We believe that this broadening is due to the formation of an equilibrium in which the **7** is in rapid equilibrium with the dication **2**. The chloroaqua cation may also have a largely non-coordinated phosphorus atom as in complex **8** since a non-coordinated P atom would be expected to have a

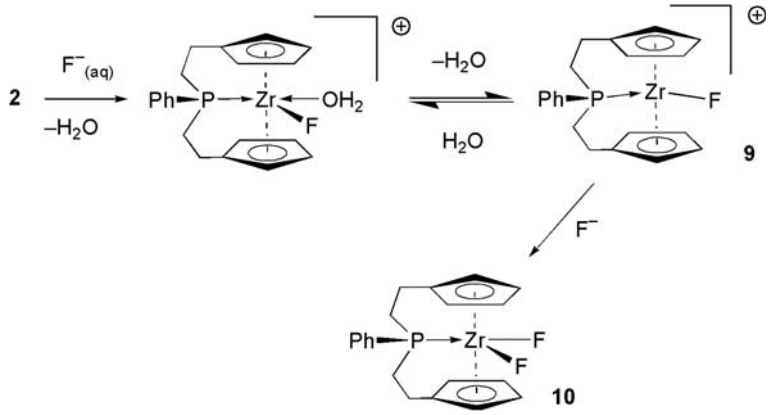
chemical shift considerably upfield of **2** and similar to that of the ferrocene complex (bcep)Fe at −16.8 ppm [8].



Unlike the addition of chloride, the addition of one equivalent of fluoride to aqueous solutions of **1** immediately converts **2** to the monofluoro species $[(bcep)ZrF(H_2O)_x]^+$ (**9**) ($x = 0$ or 1), while **3** and **4** react only slowly to give the same product (Scheme 2). Following the reaction by ^{31}P NMR spectroscopy, a doublet is observed for **9** at 27.3 ppm with a P–F coupling constant of 67 Hz. A small doublet of doublets is also observed at 18.3 ppm with coupling constants of 95 and 84 Hz. This compound is assigned as the difluoro complex $PhP(CH_2CH_2C_5H_4)_2ZrF_2$ (**10**). This compound disappears after several minutes and attempts to isolate a difluoro complex failed: only the oxide of the free ligand is observed in solution and a white precipitate that forms after addition of a second equivalent of fluoride contains no carbon or hydrogen. ES-MS of aqueous **1** with added CsF(aq) gives cation **9** as the major species with the difluoride observed as a Cs^+ adduct, $[PhP(CH_2CH_2C_5H_4)_2ZrF_2Cs]^+$ ($m/e = 553$) with a relative intensity of 8%. Significant peaks for hydrolysis products $[PHPh(CH_2CH_2C_5H_5)_2]^+$ (75%) and $[C_{20}H_{22}FPO]^+$ (50%) are also observed. The chemistry with fluoride contrasts with that of isothiocyanate in which the diisothiocyanato complex readily forms, but the monoisothiocyanato complex cannot be isolated, even with only one equivalent of thiocyanate [21]. This difference in chemistry can be attributed to the π-donor effect of fluoride which disfavours (relative to isothiocyanate) coordination of an additional ligand.

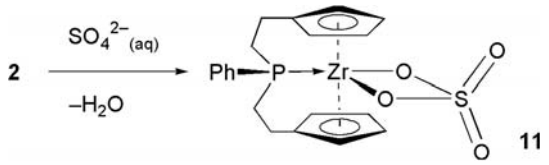
The fluoro complex **9** was precipitated from aqueous solution as the tetraphenylborate salt. It is important to do this reaction in the presence of added acid (as HCl(aq)), otherwise, an increase in pH as F^- substitutes OH^- in **3** and **4** eventually leads to hydrolysis of the zirconocene. Spectroscopic evidence indicates that there is no water coordinated in the solid state: no υ_{OH} in the infrared spectrum or additional proton resonances in the ^1H NMR spectrum (CD_3CN solvent) were observed and TGA/DSC shows no changes below 175 °C – above 175 °C, there are significant mass losses (>25%). In solution, however, a weakly coordinated water molecule cannot be ruled out. Fluoride is a much better π-donor ligand than chloride and, thus, electronic factors may disfavour coordination of water. As would be expected for ES-MS conditions, the highest mass ion (401 m/e (^{90}Zr isotopomer) for $[PhP(CH_2CH_2C_5H_4)_2ZrF]^+$) does not contain coordinated water.

Treatment of an acidified aqueous solution of (bcep)$ZrCl_2$ with sulfate gives a precipitate of (bcep)$Zr(SO_4)$ (**11**) that is insoluble in common solvents. Fortunately, the precipitate appears over several minutes and X-ray quality crystals were obtained directly from the reaction mixture. The infrared S=O stretch was observed at 1263 cm^{-1}, similar to other Zr(IV) complexes [24]. Under dilute conditions, complex **11** can be observed by ES-MS at 479 m/e as a bisulfato complex, $[(bcep)Zr(SO_4H)]^+$. A single crystal of **11** was subjected to an X-ray crystallographic analysis. The structure contains one independent molecule in the asymmetric unit. The structure is similar to other mononuclear (bcep)Zr complexes: the zirconium atom is approximately trigonal bipyramidal with the two cyclopentadienyl rings and one oxygen atom of the sulfato ligand occupying the equatorial positions and the axial positions occupied by the phosphorus atom and another sulfato oxygen atom. The sulfato ligand is O,O′ chelated. Fig. 3 shows an ORTEP plot of **11** with the atomic



Scheme 2. Reaction of aqueous **1** with fluoride.

labelling scheme and selected bond distances and angles. Table 2 gives the crystallographic data and structure refinement details.



The Zr–O distances in **11** are very similar with the axial distance of 2.2010(12) Å only very slightly longer than the equatorial distance of 2.1944(12) Å. These distances are similar to those found in other chelated Zr(IV) sulfato complexes, for example, in $[Zr(SO_4)_4]^{4-}$, the Zr–O distances range from 2.180(4) to 2.220(5) Å [25] and in $[\{CpCo(P(OEt)_2O)_3\}Zr(NO_3)_2(SO_4)]^-$, the Zr–$O_{sulfato}$ distances are 2.232(3) and 2.164(4) Å [24]. The Zr–P distance of 2.7793(5) Å is in the middle of the range of distances found in other (bcep)Zr complexes: 2.7810(8), 2.7499(7) and 2.794(2) Å for $(bcep)ZrCl_2$, $(bcep)Zr(NCS)_2$ and $[(bcep)ZrCl(H_2O)]Cl$, respectively [21]. Similarly, the Zr–CNT distances and the CNT–Zr–CNT angle are typical of (bcep)Zr complexes reported to date [21]. The *trans* angle, P–Zr–O2, of 139.54(3)° is small compared to the other (bcep)Zr complexes in which the smallest *trans* angle of 148.55(8)° is found in $(bcep)Zr(NCS)_2$ [11]. However, this is simply due to the chelating nature of the sulfato ligand since the P–Zr–O1 angle of 75.68(3)° is actually larger than the corresponding angle in $(bcep)Zr(NCS)_2$ (71.14(8)°). Notably, the *trans* angles in the five-coordinate di-μ-hydroxo complexes $[Cp_2Zr(CF_3COO)(\mu\text{-}OH)]_2$ [16] and $[\{Cp_2Zr(^nPrCN)(\mu\text{-}OH)\}_2]^{2+}$ [15] are similar (141.9° and 139.5°, respectively) to those found in **11**. The ligand conformation is similar to that found in $[(bcep)ZrCl(H_2O)]^+$ in which $\alpha_x = -69.8°$ and 95.9° (α_x = Cl–Zr–CNT(x)–C(x2), (CNT(x) = centroid of atoms C(x3) to C(x7)) and $\beta = 2.6°$ (β = Cl–Zr–P–C11) [21]. The corresponding angles in **11** are $\alpha_2 = -67.3°$, $\alpha_3 = 98.7°$ and $\beta = -3.1°$. The difference in $|\alpha_x|$ of 31.4° corresponds to staggered cyclopentadienyl rings. The most significant difference is that in $[(bcep)ZrCl(H_2O)]^+$ the phenyl plane lies between the chloro ligand and a cyclopentadienyl ring which forces one ring to be further from the equatorial chloro ligand than the other: CNT–Zr–Cl angles of 120.0° and 111.9°. In **11**, the phenyl ring is approximately perpendicular to the $ZrPO_2$ plane (Zr–P–C(11)–C(12) = −94.7°) and the CNT–Zr–O1 angles are consequently similar to each other (116.44° and 115.42°).

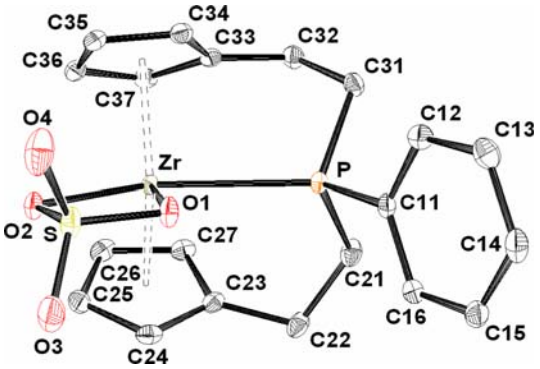


Fig. 3. ORTEP of $(bcep)Zr(SO_4)$ (**11**) with 40% thermal ellisoids. Selected bond distances and angles are Zr–O1 = 2.1944(12), Zr–O2 = 2.2010(12), Zr–P = 2.7793(5), Zr–CNT(C23–C27) = 2.225(1), Zr–CNT(C33–C37) = 2.223(1), S–O1 = 1.5341(12), S–O2 = 1.5209(12), S–O3 = 1.4382(15), S–O4 = 1.4412(16) Å, O1–Zr–O2 = 63.87(4)°, O1–Zr–P = 75.68(3)°, O2–Zr–P = 139.54(3)°, Zr–P–C11 = 125.05(5)°, Zr–P–C21 = 105.91(6)°, Zr–P–C31 = 108.57(6)°, CNT–Zr–CNT = 128.13°, CNT(2)–Zr–O1 = 116.44°, CNT(2)–Zr–O2 = 100.24°, CNT(2)–Zr–P = 96.82°, CNT(3)–Zr–O1 = 115.42°, CNT(3)–Zr–O2 = 102.91°, CNT(3)–Zr–P = 94.62°.

Table 2
Crystallographic data and structure refinement parameters for $(bcep)Zr(SO_4)$ (**11**)

Empirical formula	$C_{20}H_{21}O_4PSZr$
Formula weight	479.62
Crystal colour	colourless
Crystal size (mm)	$0.39 \times 0.12 \times 0.07$
Temperature (K)	93(2)
Wavelength (Å)	0.71073
Crystal system	monoclinic
Space group	$P2_1/c$
Unit cell dimensions	
a (Å)	11.6805(13)
b (Å)	8.9775(13)
c (Å)	17.800(2)
α (°)	90
β (°)	93.110(2)
γ (°)	90
$F(000)$	976
Volume (Å^3)	1863.8(4)
Z	4
D_{calc}	1.709
Absorption coefficient (mm^{-1})	0.812
θ Range (°)	1.75–33.41
Limiting indices	$-15 \leqslant h \leqslant 16$ $-11 \leqslant k \leqslant 13$ $-23 \leqslant l \leqslant 23$
Reflections collected	23474
Independent reflections ($>2\sigma$)	4733
R indices ($I > 2\sigma(I)$)	$R_1 = 0.0269$, $wR_2 = 0.0589$
R indices (all data)	$R_1 = 0.0366$, $wR_2 = 0.0656$
Largest difference in peak/hole (e Å^{-3})	0.477/−0.422

2.1. Other electrospray mass spectrometry studies

Addition of acids HX (X = Br, NO_3, HSO_4, HCO_3) to 10^{-4} M CH_3CN/H_2O solutions of **1** eliminates the peaks due to the dinuclear complexes **3** and **4** and gives only peaks corresponding to **2** and $[(bcep)ZrX]^+$ (Table 3). Since the structure of $(bcep)Zr(SO_4)$ contains a chelated sulfato ligand, it seems reasonable that the complexes $[(bcep)Zr(HCO_3)]^+$, $[(bcep)Zr(HSO_4)]^+$, and $[(bcep)Zr(NO_3)]^+$ would also contain chelated ligands to give five-coordinate

Table 3
Summary of ES-MS experiments with H_2O/CH_3CN solutions of **1** at low cone voltage (20 V)

Reagent added	*m/e* (rel. int.)	Assignment
None	399(100)	$[\{(bcep)Zr(OH)\}_n]^{n+}$ ($n = 1, 2$)[a]
	797(6)	$[\{(bcep)Zr\}_2(O)(OH)\}]^+$
CO_2(aq)	399(10)	$[(bcep)Zr(OH)]^+$
	443(100)	$[(bcep)Zr(CO_3H)]^+$
HBr	399(45)	$[(bcep)Zr(OH)]^+$
	463(100)	$[(bcep)ZrBr]^+$
	479(8)	$[(bcep)ZrOBr]^+$
HBr (after 1 h)	399(13)	$[(bcep)Zr(OH)]^+$
	415(65)	$[(bcep)Zr(OH)O]^+$
	463(10)	$[(bcep)ZrBr]^+$
	479(100)	$[(bcep)ZrBrO]^+$
H_2SO_4	399(35)	$[(bcep)Zr(OH)]^+$
	479(100)	$[(bcep)Zr(SO_4H)]^+$
HNO_3	399(15)	$[(bcep)Zr(OH)]^+$
	444(100)	$[(bcep)Zr(NO_3)]^+$
CsF	553(8)	$[PhP(CH_2CH_2C_5H_4)_2ZrF_2Cs]^+$
	401(100)	$[PhP(CH_2CH_2C_5H_4)_2ZrF]^+$
	328(50)	$[C_{20}H_{22}PFO]^+$
	295(75)	$[PHPh(CH_2CH_2C_5H_5)_2]^+$

[a] Ratio of approximately 1:2 for $n = 1$ and 2, respectively.

zirconocene complexes. After 1 h, the solution containing added HBr has additional peaks corresponding to $[(bcep)ZrOBr]^+$ (479 *m/e*, rel. int. = 100) and $[(bcep)ZrO(OH)]^+$ (415 *m/e*, rel. int. = 65), which may contain oxidised phosphine, while $[(bcep)ZrOH]^+$ and $[(bcep)ZrBr]^+$ are now much weaker with relative intensities of 13 and 10, respectively. Similar behaviour was observed for solutions containing added HCl [21].

3. Conclusions

In this paper, we have described some aqueous chemistry of the five-coordinate zirconocene dichloride complex **1**. Its speciation in water and water/acetonitrile solvents was investigated by ^{31}P NMR and ES-MS studies and shown to give three species in solution. Some reactivity studies were also carried out: treatment of aqueous solutions of **1** with various acids HX produced cationic complexes $[(bcep)ZrX]^+$ which were observed by ES-MS; addition of fluoride allowed the isolation of the monofluoro complex **9**, but not the difluoro complex **10**; addition of sulphate allowed the isolation of the sulfato complex **11** which was crystallographically characterised. These reactions thus demonstrate the potential to carry out reactions of this zirconocene in aqueous solutions.

4. Experimental

4.1. General considerations

Solvents were distilled prior to use. Complex **1** was prepared by the published procedure [21]. ^1H, $^{13}C\{^1H\}$ and $^{31}P\{^1H\}$ NMR data were collected on a Varian XL-300 spectrometer operating at 300, 75 and 121 MHz, respectively. Unless otherwise stated, spectra were measured at ambient temperature with residue solvent peaks as internal standard for ^1H and $^{13}C\{^1H\}$ NMR. $^{31}P\{^1H\}$ NMR chemical shifts are reported relative to external 85% H_3PO_4, positive shifts representing deshielding. ES-MS were collected on a VG Platform MS8 and *m/e* are reported for the ^{90}Zr isotopomer. IR spectra were obtained on a Shimadzu FTIR-8201PC spectrophotometer. Elemental analyses were done by Campbell Microanalysis Services, University of Otago, Dunedin.

4.2. Speciation of 1 in H_2O, D_2O and CD_3CN solutions by ^{31}P NMR spectroscopy

In a typical NMR experiment, **1** (2.5 mg) was dissolved in the solvent (0.6 mL) to give a 10^{-2} M solution in Zr. H_2O solutions were locked with a D_2O insert. A 10 s delay was used to ensure accurate determination of integrals. The results for a variety of solvent mixtures are given in Table 1.

4.3. Reactions of 1 followed by ^{31}P NMR spectroscopy

(a) Addition of one half equivalent of NaOH(aq) gave only peaks at δ 34.4 and 33.1 in the ratio 1:1.6.
(b) Addition of one equivalent of $AgNO_3$(aq) immediately gave a white precipitate of AgCl. The ^{31}P resonances were unchanged.
(c) Addition of one equivalent of $HClO_4$(aq) gave an immediate precipitate with loss of the ^{31}P resonances of the dinuclear complexes while the resonance due to $[(bcep)Zr(H_2O)_2]^{2+}$ was unchanged.
(d) Addition of NaCl broadens the resonance of the diaqua dication while the other resonances are unaffected: $[Zr] = 1.4 \times 10^{-2}$; $[Cl^-]$ ($w_{1/2}$): 2.8×10^{-2} M (6 Hz), 5.4×10^{-2} M (8 Hz), 16.8×10^{-2} M (14 Hz), 60×10^{-2} M (27 Hz), 120×10^{-2} (60 Hz).

4.4. Speciation and reactions of 1 in CH_3CN/H_2O solutions by ES-MS

In a typical experiment, a dilute solution of the reagent was added to 10^{-4} M solutions of **1** in 1:1 CH_3CN/H_2O. The reagents and results are summarised in Table 3.

4.5. Preparation of $[PhP(CH_2CH_2C_5H_4)_2ZrF]BPh_4$ (9)

Complex **1** (0.0339 g, 0.0745 mmol) was dissolved in water and HCl(aq) (0.55 mmol) added after the complex had dissolved. One equivalent of NaF (1 mL of a 0.0313 g/10 mL solution, 0.0745 mmol) was slowly added and the solution stirred at ambient temperature for 1 h. $^{31}P\{^1H\}$ NMR (H_2O): δ 27.3 (d, $^2J_{PF} = 62$ Hz) (s). An aqueous solution of $NaBPh_4$ (0.0291 g, 0.0850 mmol) was slowly added to give immediately a white precipitate, this was stirred for 1 h before collection by filtration and drying in air to give 0.050 g (93% yield) of **9**. ^1H NMR (CD_3CN): δ 7.75 (m, 3H, Ph), 7.52 (m, 2H, Ph), 7.27 (m,

8H, BPh_4^-), 6.98 (t, $J = 7.5$ Hz, 8H, BPh_4^-), 6.83 (t, $J = 7.2$ Hz, 4H, BPh_4^-), 6.53 (m, 2H, Cp), 6.20 (m, 2H, Cp), 6.13 (m, 2H, Cp), 5.97 (m, 2H, Cp), 3.2–2.7 (m, 8H, CH_2); $^{13}C\{^1H\}$ NMR (CD_3CN): δ 137.0 (s, BPh_4^-), 133.7 (d, $J_{PC} = 9$ Hz, Ph), 132.3 (s, Ph), 130.1 (d, $J_{PC} = 9$ Hz, Ph), 126.7 (m, BPh_4^-), 123.7 (s, Cp), 122.9 (s, BPh_4^-), 113.0 (s, Cp), 111.9 (s, Cp), 104.3 (s, Cp), 32.7 (d, $^1J_{PC} = 23$ Hz, PCH_2), 25.5 (d, $^2J_{PC} = 11$ Hz, PCH_2CH_2), (*i*-Ph and *i*-Cp not observed); $^{31}P\{^1H\}$ NMR (CD_3CN): δ 24.3 (d, $^2J_{PF} = 55$ Hz). *Anal.* Calc. for $C_{44}H_{41}BFPZr$: C, 73.22; H, 5.73. Found: C, 72.41; H 5.59%.

4.6. Attempted preparation of (bcep)ZrF_2 (**10**)

Complex **1** (0.015 g, 0.033 mmol) was dissolved in D_2O and one equivalent of NaF added (1.4 mg, 0.033 mmol). The ^{31}P resonance at 32.77 ppm, assigned as the dication **2**, rapidly disappeared with the formation of a doublet due to the monofluoro complex **9** and a small doublet of doublets at 18.31 ppm ($^2J_{PF} = 95$ and 84 Hz), assigned as the difluoro complex **10**. This doublet of doublets disappeared after several minutes as the resonances due to the dinuclear complexes **3** and **4** slowly converted to that of **9**. Addition of a second equivalent of NaF rapidly gave an insoluble white precipitate and resonances consistent with the oxide of the free ligand (^{31}P NMR: δ 40.28, 40.12 and 39.96 in a ratio of 1:2:1).

4.7. Preparation of $PhP(CH_2CH_2C_5H_4)_2ZrSO_4$ (**11**)

Complex **1** (0.011 g, 0.024 mmol) was dissolved in aqueous HCl (3 mL of 0.1 M HCl). After 20 min, Na_2SO_4 (0.0034 g, 0.024 mmol) was added. Over several minutes, small colourless plates of the product **11** appeared (0.01 g, 87%). The product was found to be insoluble in common solvents. IR (KBr) (cm^{-1}): 1263 (s), 1155 (s) 935 (s), 918 (s). *Anal.* Calc. for $C_{20}H_{21}O_4PSZr$: C, 50.08; H, 4.41. Found: C, 50.06; H, 4.62%.

4.8. Potentiometry experiments

Dissolution of complex **1** (0.227 g, 0.5 mmol) in H_2O (50 mL) to give a 10^{-2} M solution was followed by pH measurement. Total dissolution occurred within 10 min and a stable pH reading (pH 3.3) was obtained after about 30 min. Neutralisation required two equivalents of NaOH(aq) with a white precipitate forming at this pH (7–8). Attempts to follow the dissolution process or to measure chloride-ion equilibria using a chloride-ion selective electrode were prevented by chronic electrode fouling.

4.9. Crystal structure determination

X-ray crystallographic data for **11** were collected from a single crystal sample which was mounted on a glass fibre. Data were collected using an APEX-II diffractometer equipped with a Bruker SMART CCD area detector (using the program SMART [26]). Processing was carried out by use of the program SAINT [26] which applied Lorentz and polarisation corrections to three-dimensionally integrated diffraction spots. The program SADABS [26] was utilised for the scaling of diffraction data, the application of a decay correction, and empirical absorption correction based on redundant reflections. The structure was solved by the direct methods procedure [27] and refined by least-squares methods on F^2 with anisotropic thermal parameters for all non-hydrogen atoms. Hydrogen atoms were added as riding contributors, at calculated positions with isotropic thermal parameters based on the attached carbon atom. Crystal data and structure refinement parameters are given in Table 2.

5. Supplementary material

Crystallographic data for the structural analysis have been deposited with the Cambridge Crystallographic Data Centre, CCDC reference number 299554. Copies of this information may be obtained free of charge from The Director, CCDC, 12 Union Road, Cambridge, CB2 1EZ, UK, fax: +44 1223 366 033, e-mail: deposit@ccdc.ac.uk or on the web: http://www.ccdc.cam.ac.uk.

Acknowledgements

We thank Professor Brian K. Nicholson, University of Waikato, for assistance with the ES-MS work and Dr. Cees Lensink, Industrial Research Laboratories, Lower Hutt, New Zealand, for the TGA/DSC results.

References

[1] (a) P. Binger, S. Podabrin, in: E.W. Abel, F.G.A. Stone, G.W. Wilkinson (Eds.), Comprehensive Organometallic Chemistry II, vol. 4, Elsevier, 1995, p. 439 (Chapter 7);
(b) E.J. Ryan, in: E.W. Abel, F.G.A. Stone, G.W. Wilkinson (Eds.), Comprehensive Organometallic Chemistry II, vol. 4, Elsevier, 1995, p. 465 (Chapter 8);
(c) E.J. Ryan, in: E.W. Abel, F.G.A. Stone, G.W. Wilkinson (Eds.), Comprehensive Organometallic Chemistry II, vol. 4, Elsevier, 1995, p. 483 (Chapter 9);
(d) E. Hey-Hawkins, in: E.W. Abel, F.G.A. Stone, G.W. Wilkinson (Eds.), Comprehensive Organometallic Chemistry II, vol. 4, Elsevier, 1995, p. 501 (Chapter 10);
(e) S. Gambarotta, J. Jubb, J. Song, D. Richeson, in: E.W. Abel, F.G.A. Stone, G.W. Wilkinson (Eds.), Comprehensive Organometallic Chemistry II, vol. 4, Elsevier, 1995, p. 543 (Chapter 11);
(f) A.S. Guran, R.F. Jordan, in: E.W. Abel, F.G.A. Stone, G.W. Wilkinson (Eds.), Comprehensive Organometallic Chemistry II, vol. 4, Elsevier, 1995, p. 589 (Chapter 12).
[2] C. Qian, J. Guo, C. Ye, J. Sun, P. Zheng, J. Chem. Soc. D (1993) 3441.
[3] K.-H. Thiele, Ch. Schliessburg, B. Neumüller, Z. Anorg. Allg. Chem. 621 (1995) 1106.
[4] (a) For examples, see: U. Siemeling, Chem. Rev. 100 (2000) 1495;
(b) D.W. Macomber, W.P. Hart, M.D. Rausch, Adv. Organomet. Chem. 21 (1982) 1;
(c) N.J. Coville, K.E. du Plooy, W. Pickl, Coordin. Chem. Rev. 116 (1992) 1;

(d) P.J. Shapiro, Coordin. Chem. Rev. 231 (2002) 67;
(e) C. Qian, Z. Xie, Y. Huang, J. Organomet. Chem. 323 (1987) 285;
(f) J. Gräper, R.D. Fischer, G. Paolucci, J. Organomet. Chem. 471 (1994) 87;
(g) C. Qian, D. Zhu, J. Chem. Soc. D (1994) 1599;
(h) G. Paolucci, F. Ossola, M. Bettinelli, R. Sessoli, M. Benetollo, G. Bombieri, Organometallics 13 (1994) 1746;
(i) T. Kauffmann, J. Ennen, H. Lhotak, A. Rensing, F. Steinseifer, A. Woltermann, Angew. Chem., Int. Ed. Engl. 19 (1980) 328;
(j) T. Kauffmann, J. Ennen, K. Berghus, Tetrahedron Lett. 25 (1984) 1971.

[5] (a) T. Mizuta, T. Yamasaki, H. Nakazawa, K. Miyoshi, Organometallics 15 (1996) 1093;
(b) D. Seyferth, H.P. Withers, Organometallics 1 (1982) 1275;
(c) T. Mizuta, M. Onishi, K. Miyoshi, Organometallics 19 (2000) 5005;
(d) C.H. Honeyman, T.J. Peckham, J.A. Massey, I. Manners, J. Chem. Soc., Chem. Commun. (1996) 2589;
(e) C.H. Honeyman, D.A. Foucher, F.Y. Dahman, R. Rulkens, A.J. Lough, I. Manners, Organometallics 14 (1995) 5503;
(f) H.P. Withers, D. Seyferth, J.D. Fellmann, P.E. Garrou, S. Martin, Organometallics 1 (1982) 1283;
(g) T.J. Peckham, A.J. Lough, I. Manners, Organometallics 18 (1999) 1030;
(h) A.G. Osborne, R.H. Whiteley, R.E. Meads, J. Organomet. Chem. 193 (1980) 345;
(i) H. Stoeckli-Evans, A.G. Osborne, R.H. Whiteley, J. Organomet. Chem. 194 (1980) 91;
(j) I.R. Butler, W.R. Cullen, S.J. Rettig, Organometallics 6 (1987) 872.

[6] (a) J.H. Shin, B.M. Bridgewater, G. Parkin, Organometallics 19 (2000) 5155;
(b) N. Leyser, K. Schmidt, H.-H. Brintzinger, Organometallics 17 (1998) 2155;
(c) J.H. Shin, T. Hascall, G. Parkin, Organometallics 18 (1999) 6;
(d) C.J. Schaverien, R. Ernst, W. Terlouw, P. Schut, O. Sudmerijer, P.H.M. Budzelaar, J. Mol. Catal. A: Chem. 128 (1998) 245;
(e) H.G. Alt, M. Jung, J. Organomet. Chem. 568 (1998) 127;
(f) G.K. Anderson, M. Lin, Organometallics 7 (1988) 2285.

[7] P. Barbaro, A. Togni, Organometallics 14 (1995) 3570.
[8] O.J. Curnow, G. Huttner, S.J. Smail, M.M. Turnbull, J. Organomet. Chem. 524 (1996) 267.
[9] K. Doppert, Naturwissenschaften 77 (1990) 19, and references therein.
[10] W. Lasser, U. Thewalt, J. Organomet. Chem. 302 (1986) 201.
[11] U. Thewalt, W. Lasser, J. Organomet. Chem. 276 (1984) 341.
[12] W. Lasser, U. Thewalt, J. Organomet. Chem. 311 (1986) 69.
[13] W. Lasser, U. Thewalt, J. Organomet. Chem. 275 (1984) 63.
[14] U. Thewalt, K. Döppert, W. Lasser, J. Organomet. Chem. 308 (1986) 303.
[15] H. Aslan, S.H. Eggers, R.D. Fischer, Inorg. Chim. Acta 159 (1989) 55.
[16] S. Klima, U. Thewalt, J. Organomet. Chem. 354 (1988) 77.
[17] M. Niehues, G. Erker, O. Meyer, R. Fröhlich, Organometallics 19 (2000) 2813.
[18] J.H. Toney, T.J. Marks, J. Am. Chem. Soc. 107 (1985) 947.
[19] (a) B.N. Patra, M. Bhattacharjee, J. Poly. Sci., Part A: Poly. Chem. 43 (2005) 3707;
(b) B.N. Patra, M. Bhattacharjee, J. Poly. Sci., Part A: Poly. Chem. 43 (2005) 3797.
[20] G.L. Hillhouse, J.E. Bercaw, J. Am. Chem. Soc. 106 (1984) 5472.
[21] J.R. Butchard, O.J. Curnow, S.J. Smail, J. Organomet. Chem. 541 (1997) 407.
[22] C. Balzarek, T.J.R. Weakley, L.Y. Kuo, D.R. Tyler, Organometallics 19 (2000) 2927.
[23] P.J. Desrosiers, R.S. Shinomoto, T.C. Flood, J. Am. Chem. Soc. 108 (1986) 7964.
[24] Q.-F. Zhang, T.C.H. Lam, X.-Y. Li, E.Y.Y. Chan, W.-Y. Wong, H.H.Y. Sung, I.D. Williams, W.-H. Leung, Chem. Eur. J. 11 (2005) 101.
[25] Y.-L. Fu, Z.-W. Xu, J.-L. Ren, S.W. Ng, Acta Crystallogr. E 61 (2005) 1520.
[26] APEX-II v 2.02, SMART, XPREP, SAINT, SADABS, Bruker AXS Inc., Madison, Wisconsin, USA, 2005.
[27] SHELXTL v 6.12, Bruker AXS Inc., Madison, Wisconsin, USA, 2000.

Available online at www.sciencedirect.com
ScienceDirect
Polyhedron 26 (2007) 415–429
POLYHEDRON
www.elsevier.com/locate/poly

A systematic study of ligand intermolecular interactions in crystals of copper(II) complexes of bidentate guanidino derivatives

Michael M. Bishop [a,b], Leonard F. Lindoy [a,*], Mary McPartlin [a], Andrew Parkin [a,c], Oliver T. Thorn-Seshold [b], Peter Turner [a]

[a] *Centre for Heavy Metals Research, School of Chemistry, University of Sydney, NSW 2006, Australia*
[b] *Sydney Grammar School, College Street, Darlinghurst, NSW 2010, Australia*
[c] *Department of Chemistry, University of Glasgow, Glasgow G12 8QQ, UK*

Received 29 April 2006; accepted 23 June 2006
Available online 22 July 2006

Abstract

The synthesis and X-ray structures of four neutral copper(II) complexes and one cationic complex incorporating bidentate alkyl *N*-(4-oxo-5,5-diphenyl-4,5-dihydro-1*H*-imidazol-2-yl)imidocarbamate ligands are reported. The neutral complexes, which possess potential doublet (DA) hydrogen bonding motifs, form supramolecular structures based on synthons involving hydrogen bonding or phenyl embraces. The formation of sheets within the crystal through combination of these synthons, and the occurrence of guest molecules trapped in cavities between the sheets, are described. The cationic complex forms an extended hydrogen-bonded structure that incorporates nitrate ions. The structures of the five complexes are compared with others reported previously for complexes of related ligands.
© 2006 Elsevier Ltd. All rights reserved.

Keywords: Crystal engineering; Self-assembly; Supramolecular; Hydrogen bonding; Copper(II)

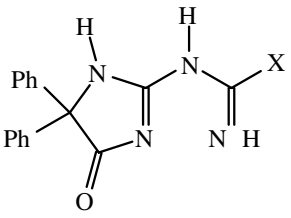
1. Introduction

In recent times there has been a growing interest in the rational design of crystals containing linked transition metal complexes, both by the formation of coordination polymers [1–4] as well as by using hydrogen bonding and other weak interactions between coordinated ligands [5–10]. In earlier papers we have described the incorporation of a number of transition metal complexes into supramolecular arrays using complementary hydrogen bonding motifs [11–13]. The complexes were based on the structurally similar bidentate ligands *N*-(4-oxo-5,5-diphenyl-4,5-dihydro-1*H*-imidazol-2-yl)alkanimidamide (where alk = Me, Et), methyl *N*-(4-oxo-5,5-diphenyl-4,5-dihydro-1*H*-imidazol-2-yl)imidocarbamate, *N*,*N*-dimethyl-*N*′-(4-oxo-5,5-diphenyl-4,5-dihydro-1*H*-imidazol-2-yl)guanidine and *N*-(4-oxo-5,5-diphenyl-4,5-dihydro-1*H*-imidazol-2-yl)-*N*′-phenyl guanidine (Scheme 1). These ligands, which are structurally related to biguanide, readily form neutral pseudo-macrocyclic complexes with self-complementary DA hydrogen bonding motifs and hence are well suited for use in structural studies concerned with investigating supramolecular interactions in crystals of transition metal complexes.

The above ligand type possesses a number of features that can be synthetically altered to affect significantly the supramolecular assembly of their complexes [11–13]. As a consequence, investigation of structural and electronic aspects of their complexation behaviour has the potential to contribute to a better understanding of rational crystal design. A common feature of these systems is that the anionic forms of the ligands that occur in the corresponding neutral divalent metal complexes exhibit self-complementary doublet donor–acceptor (DA) hydrogen bonding motifs. Also, the potential for hydrogen bonding between neighbouring complexes is restricted to the use of these motifs because the remaining ligand hydrogen bond donors and acceptors are

* Corresponding author. Tel.: +61 2 9351 4400; fax: +61 2 9351 3329.
E-mail address: lindoy@chem.usyd.edu.au (L.F. Lindoy).

0277-5387/$ - see front matter © 2006 Elsevier Ltd. All rights reserved.
doi:10.1016/j.poly.2006.06.043



I

X = Me, Et [11]

X = OMe, NMe2 [12]

X = NHPh [13]

X = OMe, OPr^n, OPr^i, OBu^n [this paper]

Scheme 1. The ligands.

used in the formation of pseudo-macrocyclic rings. Where intermolecular interaction between the potential doublet hydrogen bonding motifs is not prevented by solvation of the motif or by steric hindrance involving ligand substituents, the complexes link together into chains by $R_2^2(8)$ hydrogen bond patterns. While the complex units forming the hydrogen-bonded chains were often found to be approximately coplanar, twisting of the chains was also observed in particular instances. It is noted that in these species, conformational changes involving the bound ligands are required to allow efficient hydrogen bond formation to occur [11–13].

In addition to the above, the geminal diphenyl motif on the ligand provides an alternative means of assembling the complexes into chains through the formation of phenyl embraces [14,15]. The phenyl embraces consist of complementary CH to π-facial interactions (CHπ) and offset face-to-face (OFF) interactions between pairs of aromatic rings on adjacent ligands. Although such an assembly is clearly based on weak interactions, it is noted that in favourable cases such phenyl embraces can be as significant as hydrogen bonds [14–16]. There are two ways in which embraces can form in these systems (see Fig. 1) and both have been observed in our studies so far.

The –X and –OR (alkoxy) substituents in ligands of the present type (Scheme 1) have different steric requirements that may preclude the formation of the hydrogen-bonded rings, and will also to some degree vary the electronic properties of the ligand.

The potential doublet hydrogen bonding motif may also be extended to a potential triplet. Namely, when X was made a –NHR group the corresponding pseudo-macrocyclic complex contains a potential DAD triplet hydrogen bonding motif [13]. Co-crystallisation with 1,8-naphthalimide, a molecule with a complementary ADA motif, resulted in the component units assembling into chains using phenyl embraces. When the complex was crystallised in the absence of 1,8-naphthalimide, the structure obtained then consisted of twisted hydrogen-bonded chains linked by $R_2^2(8)$ patterns formed by self-complementary DA–AD motifs. There are two ways in which a triplet DAD motif might do this and both were observed to occur experimentally on growing the crystals from different solvents (benzonitrile and

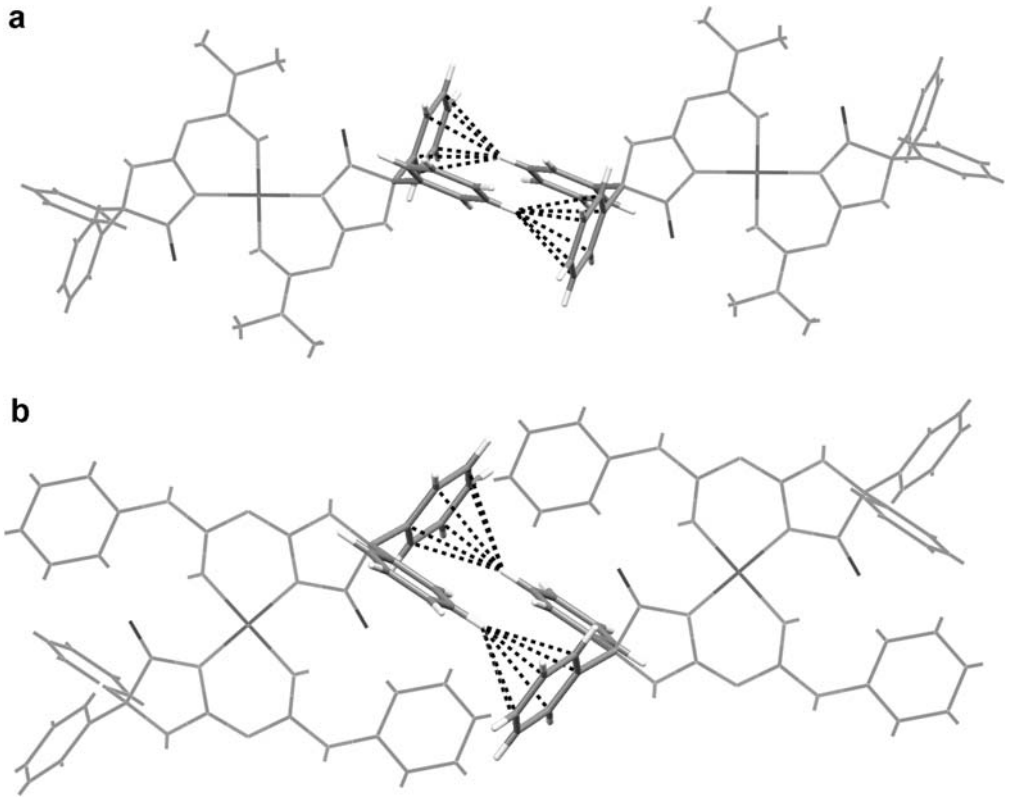
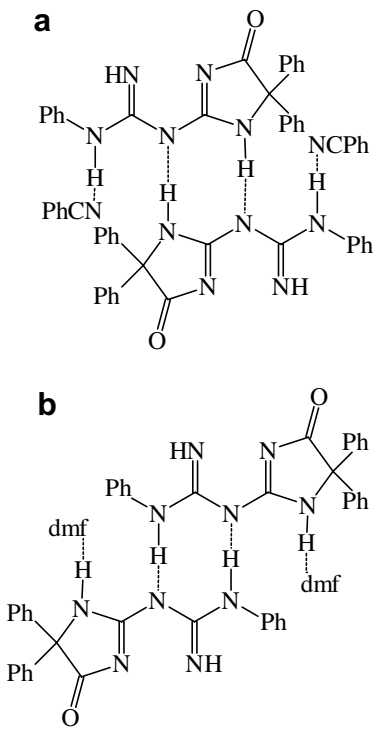


Fig. 1. Two types of phenyl embrace that may form between the gem diphenyl groups on adjacent macrocycles [11,12].



Scheme 2. The two ways in which the potential DAD triplet may form self-complementary DA–AD motifs.

N,*N*-dimethylformamide, respectively); both crystalline complex species were found to incorporate the corresponding solvent molecules (see Scheme 2, which also shows the respective hydrogen bonding patterns).

Two further features of these systems are of relevance to the discussion that follows. First, complexes of different ligands differed in the ease with which the hydrogen-bonded form could be obtained from a solution of the strong hydrogen bond acceptor, dimethylsulfoxide. Second, it was frequently observed that methyl groups attached to heteroatoms (O, N, S) showed a tendency to form contacts with the faces of adjacent phenyl rings.

In this paper, by employing a series of alkyl *N*-(4-oxo-5,5-diphenyl-4,5-dihydro-1*H*-imidazol-2-yl)imidocarbamate ligands (Scheme 1, X = –OR) for copper(II) complexation we keep the potential hydrogen bonding motif as a doublet (DA) while introducing side-chains with different steric requirements. In addition, we examine the inclusion of nitrate ions in an extended structure that incorporates a cationic pseudo-macrocyclic complex showing a potential DD hydrogen bonding motif.

2. Experimental

2.1. Synthesis

4-Oxo-5,5-diphenyl-4,5-dihydro-1H-imidazol-2-ylcyanamide was prepared in good yield (66%) from benzil and dicyandiamide as described in the literature [17].

2.1.1. (Dimethylformamide)bis(methyl N-(4-oxo-5,5-diphenyl-4,5-dihydro-1H-imidazol-2-yl)imidocarbamato)-copper(II) (**1**)

This complex was prepared as reported previously [12] and recrystallised from *N*,*N*-dimethylformamide. *Anal.* Calc. for $C_{37}H_{37}CuN_9O_5 \cdot 1/4H_2O$: C, 58.79; H, 5.00; N, 16.68. Found: C, 58.61; H, 4.83; N, 16.46%.

2.1.2. General methods

Method A. 4-Oxo-5,5-diphenyl-4,5-dihydro-1*H*-imidazol-2-ylcyanamide (0.138 g, 0.5 mmol) dissolved in the required hot alcohol (15 mL) was added to $Cu(NO_3)_2 \cdot 21/2H_2O$ (0.058 g, 0.25 mmol) in similar hot alcohol (20 mL). The solution was heated under reflux for 2–3 h during which time the colour turned deep blue. The solution was allowed to cool and concentrated aqueous ammonia added until precipitation was complete. The solid product was filtered off, washed with alcohol and ether, then air dried. The solid was recrystallised from *N*,*N*-dimethylformamide before microanalysis.

Method B. 4-Oxo-5,5-diphenyl-4,5-dihydro-1*H*-imidazol-2-ylcyanamide (0.138 g, 0.5 mmol) in the required hot alcohol (15 mL) was added to $Cu(NO_3)_2 \cdot 21/2H_2O$ (0.058 g, 0.25 mmol) in similar hot ethanol (20 mL). The solution was heated under reflux for 2–3 h during which the colour turned deep blue. The solution was allowed to cool and let stand until the blue (or blue-green) crystals formed. The crystals were isolated by filtration and air dried before microanalysis.

*2.1.2.1. Bis(isopropyl N-(4-oxo-5,5-diphenyl-4,5-dihydro-1H-imidazol-2-yl)imidocarbamato)copper(II) · 2dimethylformamide (**2**). Method A*. Yield 33 mg, 15%. *Anal.* Calc. for $C_{44}H_{52}CuN_{10}O_6$: C, 59.44; H, 5.34; N, 17.05. Found: C, 59.44; H, 5.34; N, 17.05%.

*2.1.2.2. Bis(1-butyl N-(4-oxo-5,5-diphenyl-4,5-dihydro-1H-imidazol-2-yl)imidocarbamato)copper(II) · 2dimethylformamide (**3**). Method A*. Yield 21 mg, 9%. *Anal.* Calc. for $C_{43}H_{49}CuN_9O_5$: C, 61.81; H, 5.91; N, 15.09. Found: C, 61.91; H, 6.06; N, 15.06%.

*2.1.2.3. (1-Butanol)bis(1-butyl N-(4-oxo-5,5-diphenyl-4,5-dihydro-1H-imidazol-2-yl)imidocarbamate)copper(II) nitrate (**4**). Method B*. Yield 15 mg, 6%. *Anal.* Calc. for $C_{44}H_{54}CuN_{10}O_{11}$: C, 54.91; H, 5.65; N, 14.55. Found: C, 55.15; H, 5.33; N, 14.63%.

*2.1.2.4. (1-Propanol)bis(1-propyl N-(4-oxo-5,5-diphenyl-4,5-dihydro-1H-imidazol-2-yl)imidocarbamato)copper(II) · 1/4(1-propanol) · 1/4water (**5**). Method A*. Sample was recrystallised from 1-propanol not *N*,*N*-dimethylformamide; yield 15 mg, 7%. *Anal.* Calc. for $C_{38}H_{38}CuN_8O_4$: C, 62.15; H, 5.22; N, 15.26. Found: C, 62.59; H, 5.19; N, 15.40%.

*2.1.2.5. (1-Propanol)bis(1-propyl N-(4-oxo-5,5-diphenyl-4,5-dihydro-1H-imidazol-2-yl)imidocarbamate)copper(II) nitrate (**6**). Method B*. yield 15 mg, 7%. *Anal.* Calc. for

$C_{41}H_{46}CuN_{10}O_{11}$: C, 53.61; H, 5.05; N, 15.25. Found: C, 53.59; H, 5.32; N, 15.17%.

2.2. X-ray crystal structure determinations

Single crystal diffraction data were collected with a Bruker SMART 1000 CCD diffractometer employing graphite monochromated Mo Kα radiation from a sealed tube, and equipped with an Oxford Cryosystems Cryostream. In general the data collections were undertaken at 150(2) K, with the exception of complex **2** for which data were collected at 200 K as the crystals were found to undergo a destructive phase transition between 150 and 200 K. Cell constants were obtained from a least squares refinement against at least 1000 reflections located between 4° and 56°, 2θ, and data were collected with ω scans to at least 56°, 2θ.

The data integration and reduction were undertaken with SAINT and XPREP [18], and in general subsequent computations were carried out with the WINGX [19] and XTAL [20] graphical user interfaces. The XP SHELXTL-PLUS [18] graphical user interface was used to model the structure for complex **1**. A recollection of the first 50 CCD frames at the end of each collection showed no evidence for crystal decay. A Gaussian absorption correction [18,21] was applied to the data for all but that of complex **1**, for which a multi-scan correction was applied with SADABS [22].

In general the structures were solved by direct methods with SIR-97 [23], and extended and refined with SHELXL-97 [24]. The solution for complex **1** was obtained with SHELXS-97 [24]. Full occupancy non-hydrogen atom sites were modelled with anisotropic displacement parameters, and partially occupied sites were modelled with isotropic displacement parameters. In general a riding atom model with group displacement parameters was used for the hydrogen atoms. Hydrogen atoms were not included for water solvate molecules. ORTEP [25] depictions for complexes **1**–**5** with 20% displacement ellipsoids were created (Figs. 2–4, 5a, 5b, 6a, 6b).

2.2.1. Complex *1*

Data were obtained from a purple plate-like crystal. The asymmetric unit contains the complex molecule together with a site modelled as the oxygen of a partial occupancy water molecule.

2.2.2. Complex *2*

Data were obtained from a purple tablet-like crystal. The asymmetric unit contains half a complex molecule centred on an inversion site, together with a DMF solvate molecule linked to the complex through hydrogen bonding to the N(2) hydrogen. An ether residue on the complex is disordered about two locations related by rotation about the C(4)–O(2) bond, with site occupancies refined and then fixed at 0.5.

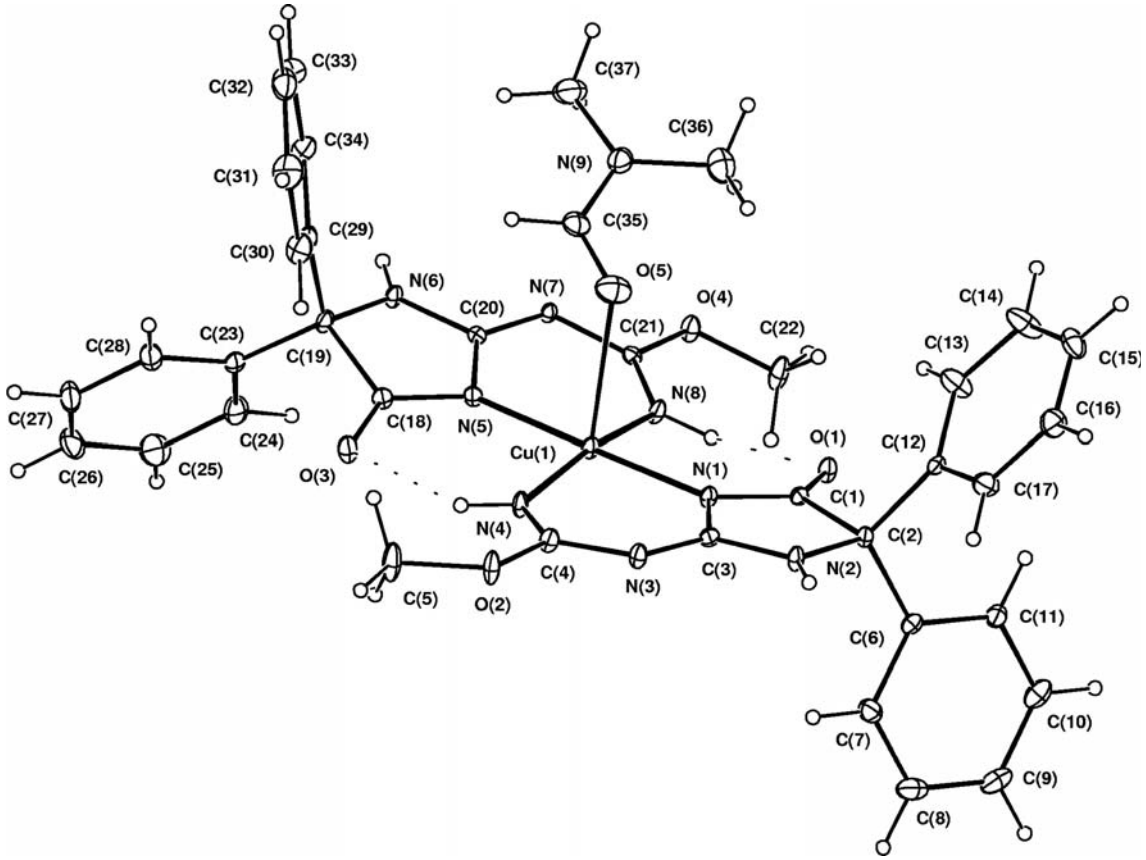


Fig. 2. An ORTEP [25] depiction of the complex in **1**. Displacement parameters are drawn at the 20% level.

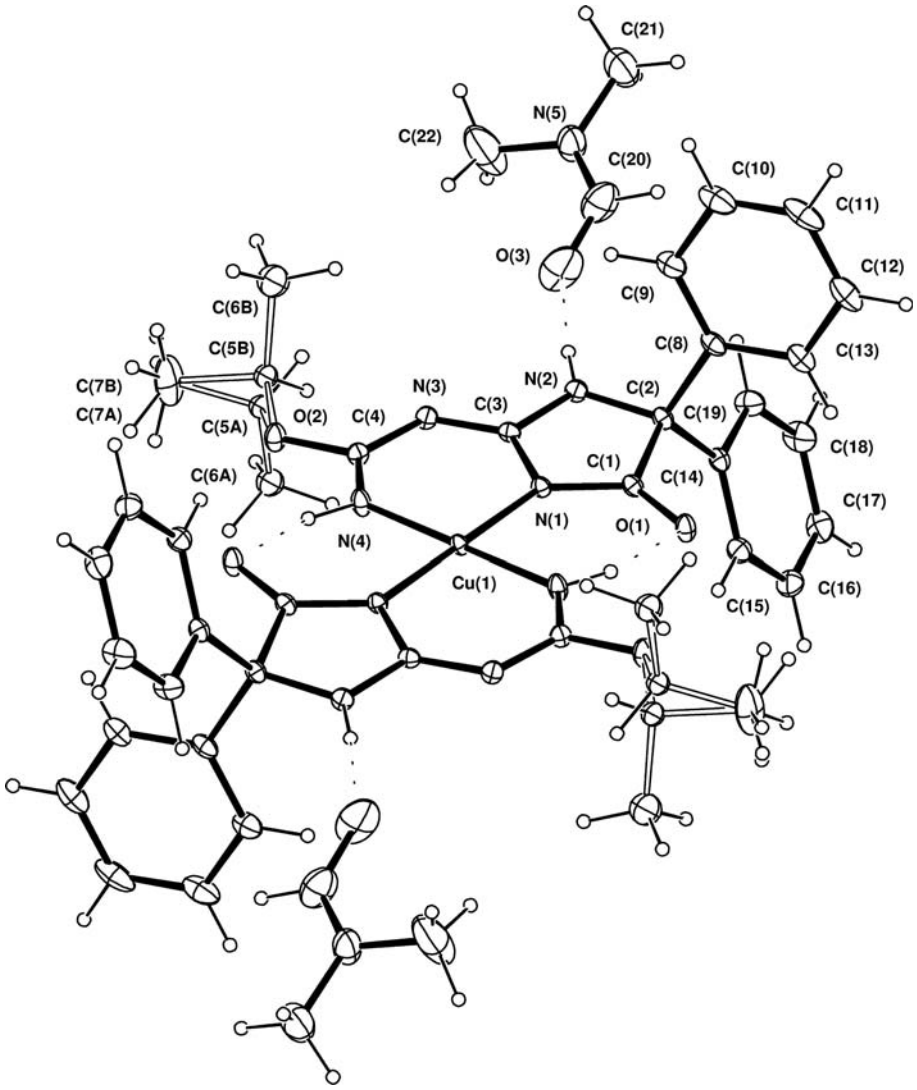


Fig. 3. An ORTEP [25] depiction of the complex in **2**. Displacement parameters are drawn at the 20% level.

*2.2.3. Complex **3***

Data were obtained from a purple tablet-like crystal. The asymmetric unit contains half a complex molecule centred on an inversion site, together with a DMF solvate molecule linked to the complex through hydrogen bonding to the N(2) hydrogen. The amine hydrogen sites were located and modelled with isotropic displacement parameters and weak distance restraints. A terminal ethyl residue on the complex is disordered about two locations related by bond rotation about C(5)–C(6), with site occupancies refined and then fixed at 0.7 and 0.3 respectively.

*2.2.4. Complex **4***

Data were obtained from a blue plate-like crystal. The asymmetric unit contains two crystallographically independent complex molecules and their nitrate counterions. A butanol molecule is axially coordinated to each complex to complete a square pyramidal coordination environment. One of the axial ligands is disordered about two orientations with site occupancies refined and then fixed at 0.6 and 0.4. The butyl ether residues of one of the complexes are similarly disordered. The structure was treated as an inversion twin, with the Flack parameter [26] refining to 0.374(7). An attempt to model the structure in the centrosymmetric space group $P\bar{1}(\#2)$ (with the origin shifted to −0.31020, −0.49160, −0.03150) was unsatisfactory with, for instance, the butyl ether residues of the complex not being resolved. The statistics for the reflections were intermediate between centric and non-centric and were interpreted as pseudo-centric.

*2.2.5. Complex **5***

Data were obtained from a purple prismatic crystal. The asymmetric unit contains a complex molecule that includes a weakly coordinated propanol ligand disordered over 3 closely spaced orientations with occupancies refined and then fixed at 1/3. A set of persistent residual density peaks near an inversion site were modelled as a partially occupied propanol solvate molecule site and a partially occupied water site, with occupancies refined and then fixed at

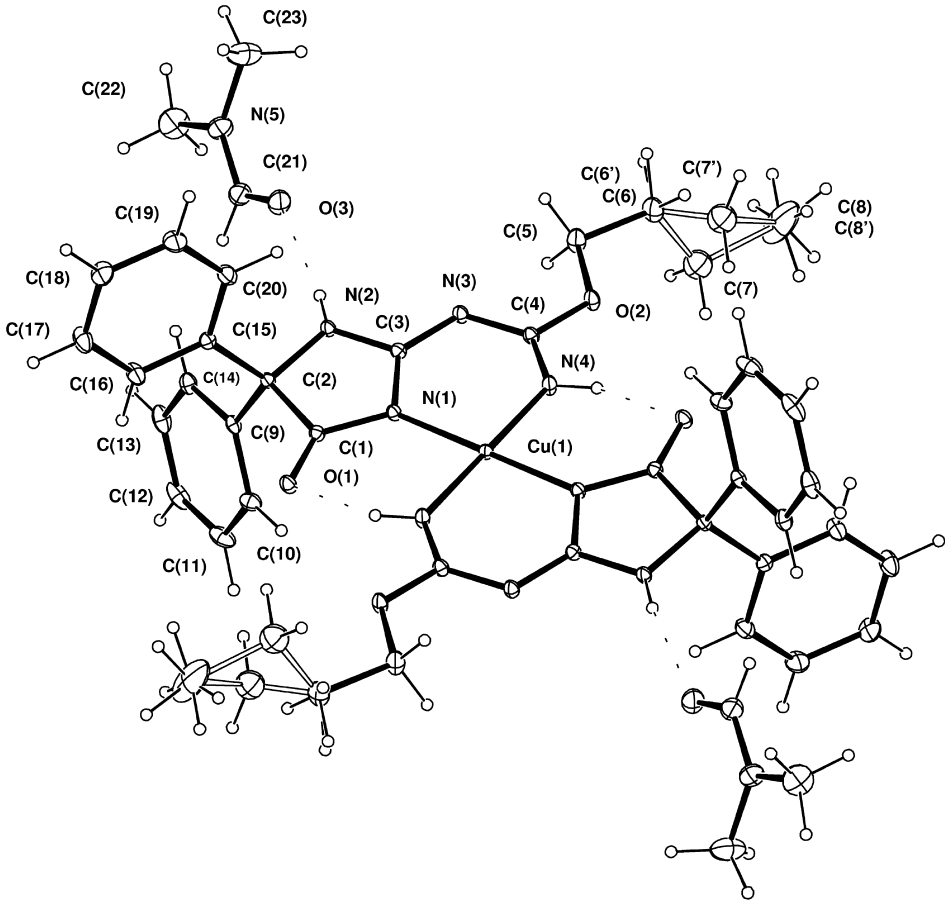


Fig. 4. An ORTEP [25] depiction of the complex in **3**. Displacement parameters are drawn at the 20% level.

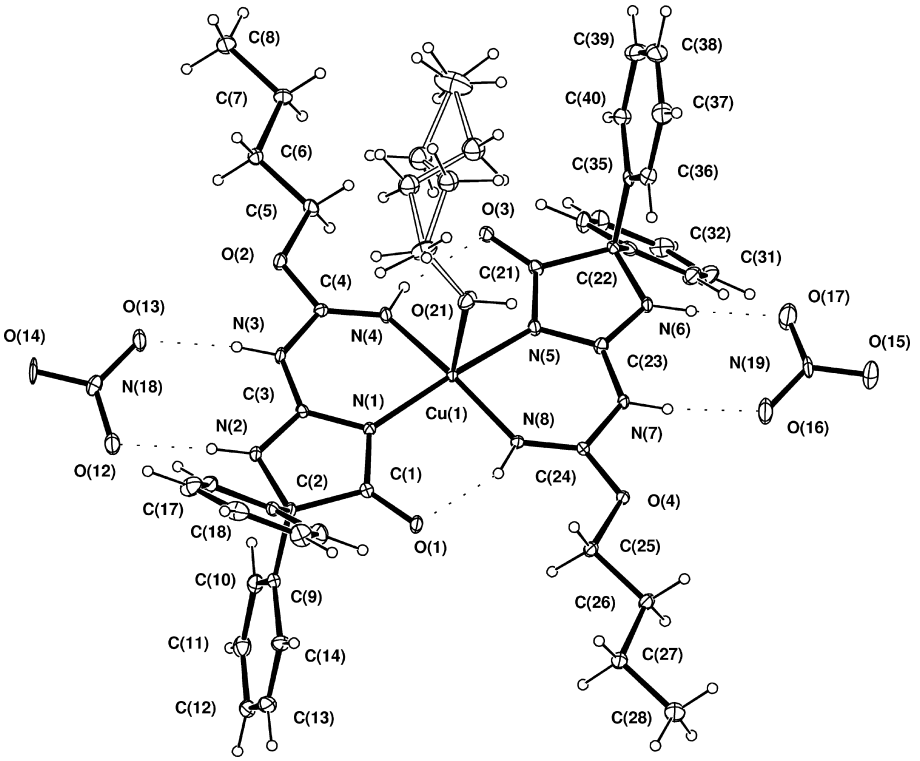


Fig. 5a. An ORTEP [25] depiction of the Cu(1) complex in **4**. Displacement parameters are drawn at the 20% level.

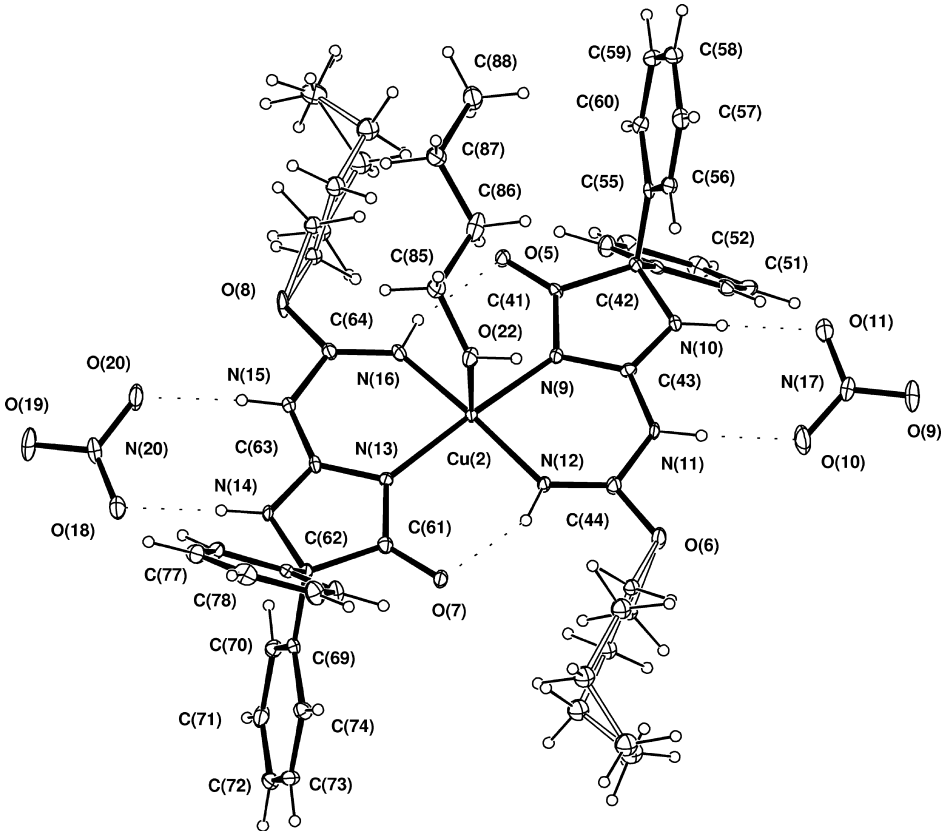


Fig. 5b. An ORTEP [25] depiction of the Cu(2) complex in **4**. Displacement parameters are drawn at the 20% level.

0.25. The model is somewhat unsatisfactory, as it results in unrealistically short hydrogen to hydrogen contacts between the solvate and a neighbouring complex molecule. Repeated attempts to avoid these contacts without the appearance of further significant residual density were unsuccessful. The contacts could be removed by swapping the identity of the terminal oxygen and carbon atoms, however this model seems even less likely. The contacts are attributed as artefacts of a limited model for disorder about an inversion site.

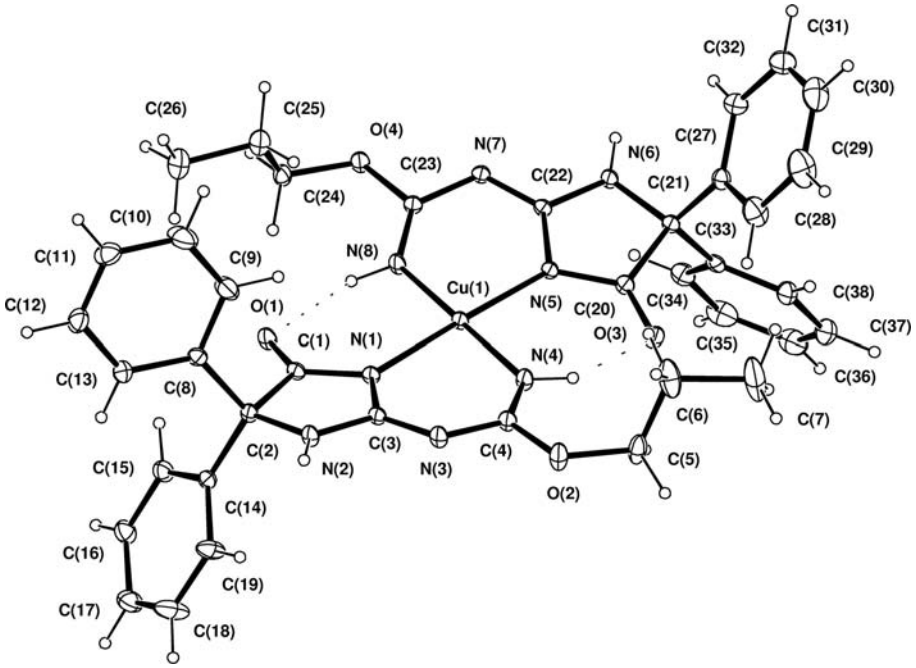


Fig. 6a. An ORTEP [25] depiction of the complex in **5**; the coordinated propanol is not shown (see Fig. 6b). Displacement parameters are drawn at the 20%

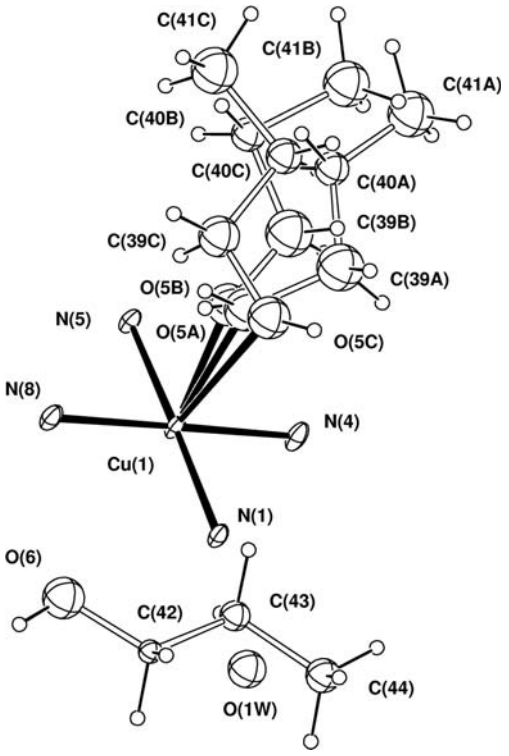


Fig. 6b. An ORTEP [25] depiction of the coordinated propanol and the guest molecules in **5**. The copper ion and its nitrogen donor atoms are shown for reference. Displacement parameters are drawn at the 20% level.

3. Results and discussion

3.1. Synthesis and X-ray studies

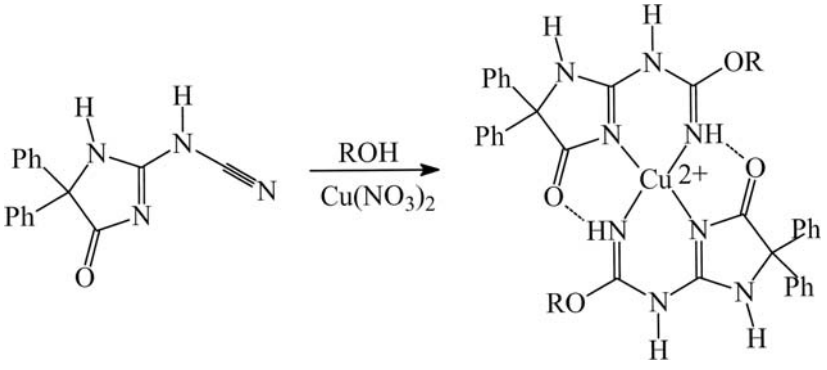
The synthetic method used to obtain the neutral complexes **1**, **2**, **3** and **5** is similar to that used for the cationic complex **4** (illustrated in Scheme 3) save that strong ammonia was added to the reaction solution to induce deprotonation of the bound ligands. The procedure for **4** incorporating neutral **I** (X = OBu^n) seems from the evidence of elemental analysis also to have been successful for **6** (X = OPr^n).

Crystallographic details for the structures determined during the study are listed in Table 1. Coordination bond lengths are presented in Table 2 and hydrogen bond interactions appear in Table 3. Metallaring bond lengths for the complexes of the neutral and anionic forms of the ligands (X = OBu^n) are compared in Table 4. ORTEP depictions are provided in Figs. 2–4, 5a, 5b, 6a, 6b.

3.2. Structure of *1*

The copper(II) species **1** was prepared for comparison with similar products reported earlier [12]. For these latter cases complex crystallisation occurred from methanol or dimethylsulfoxide. When crystallisation occurred from methanol, the pseudo-macrocyclic complexes yielded hydrogen-bonded chains, with similar chain formation also being observed in one of the crystal forms obtained from dimethylsulfoxide. In a minor phase obtained from the above dimethylsulfoxide crystallisation, the two hydrogen bond donors present in the potential DA motif were observed to be hydrogen bonded to dimethylformamide molecules rather than forming an $R_2^2(8)$ hydrogen bond ring pattern. In the present study, product **1** was found to resemble the major crystalline product obtained above from dimethylsulfoxide. The copper(II) is five-coordinate, with a dimethylformamide molecule occupying its apical site at a distance of 2.5475(27) Å from the metal. The maximum and minimum deviations of the four nitrogen donor atoms from their least squares plane are 0.0915(14) and 0.0927(14) Å and Cu(1) lies 0.0800(15) Å from the plane. In addition there is a site partially occupied (0.25) by water. The O(5)–O(6) distance is 2.91 Å, consistent with the water being hydrogen bonded to the coordinated dimethylformamide oxygen. The copper ion lies 0.2077(39) and 0.3960(38) Å from the mean planes of the ligand atoms that make up the metallarings; and these planes make an angle of 19.02(16)° with one another.

The individual pseudo-macrocyclic complexes are linked together into chains by $R_2^2(8)$ rings formed by the complementary DA motifs on the bound ligands. The hydrogen bond rings are approximately planar with the maximum deviation from the plane being 0.0918(25) Å. The coordinated dimethylformamide molecules all lie on the same side of the chain (Fig. 7) and in this respect the chains differ from those formed by the neutral pseudo-macrocyclic copper(II) complexes formed by **I** (X = OMe) and **I**



Scheme 3.

Table 1
Crystallographic data

	1	2	3	4	5
Formula of the refinement model	$C_{37}H_{37.5}CuN_9O_{5.25}$	$C_{44}H_{52}Cu_1N_{10}O_6$	$C_{46}H_{56}CuN_{10}O_6$	$C_{44}H_{54}CuN_{10}O_{11}$	$C_{41.75}H_{48}CuN_8O_5$
Model molecular weight	755.80	880.50	908.55	962.51	813.42
Crystal system	triclinic	triclinic	monoclinic	triclinic	monoclinic
Space group	*P*1 (#2)	*P*1 (#2)	$P2_1/c$ (#14)	*P*1 (#1)	$P2_1/n$ (#14)
a (Å)	9.2510(4)	9.897(5)	9.4916(14)	8.7224(19)	16.590(4)
b (Å)	9.9463(4)	10.774(5)	21.697(3)	15.281(3)	15.723(3)
c (Å)	20.2137(10)	11.584(5)	11.3286(16)	17.148(4)	16.677(4)
α (°)	84.444(3)	96.145(5)		92.775(5)	
β (°)	82.980(3)	97.423(5)	94.693(5)	91.764(5)	106.851(4)
γ (°)	74.809(3)	111.506(5)		100.694(5)	
V (Å^3)	1777.40(14)	1123.5(9)	2325.1(6)	2241.4(9)	4163.3(16)
D_c (g cm^{-3})	1.412	1.301	1.298	1.426	1.298
Z	2	1	2	2	4
Crystal size (mm)	$0.52 \times 0.27 \times 0.06$	$0.610 \times 0.452 \times 0.186$	$0.550 \times 0.480 \times 0.165$	$0.462 \times 0.284 \times 0.089$	$0.378 \times 0.254 \times 0.222$
Crystal colour	purple	purple	purple	blue	purple
Crystal habit	plate	tablet	tablet	plate	prism
Temperature (K)	150(2)	200 (2)	150(2)	150(2)	150(2)
λ(Mo Kα) (Å)	0.71073	0.71073	0.71073	0.71073	0.71073
μ(Mo Kα) (mm^{-1})	0.672	0.544	0.528	0.560	0.579
T(GAUSSIAN)$_{min,max}$	0.801,1.000 (SADABS)	0.7340, 0.9016	0.7762, 0.9215	0.8032, 0.9511	0.7519, 0.8997
$2\theta_{max}$ (°)	56.98	56.66	56.58	56.70	56.70
h,*k*,*l* range	−12 to 10, −13 to 12, −26 to 22	−12 to 12, −14 to 14, −15 to 15	−12 to 12, −28 to 28, −15 to 15	−11 to 11, −19 to 20, −22 to 22	−21 to 21, −20 to 20, −21 to 22
N	16026	11219	22634	22293	40391
N_{ind} (R_{merge})	8009 (0.0602)	5228 (0.0329)	5546 (0.0347)	18721 (0.0284)	9983 (0.0407)
N_{obs} ($I > 2\sigma(I)$)	4783	4757	4767	15077	7453
N_{var}	477	275	290	1152	516
Residuals[a] $R_1(F)$, $wR_2(F^2)$	0.0557, 0.1136	0.0405, 0.1020	0.0511, 0.1263	0.0397, 0.0911	0.0586, 0.1692
Goodness-of-fit (all)	0.992	1.286	1.296	1.161	1.320
Residual extrema (e Å^{-3})	−0.352, 0.435	−0.524, 0.638	−1.075, 1.412	−0.437, 0.699	−0.882, 1.445

[a] $R_1 = \sum ||F_o| - |F_c|| / \sum |F_o|$ for $F_o > 2\sigma(F_o)$; $wR_2 = (\sum w(F_o^2 - F_c^2)^2 / \sum (wF_c^2)^2)^{1/2}$ all reflections $w = 1/[\sigma^2(F_o^2) + (AP)^2 + BP]$ where $P = (F_o^2 + 2F_c^2)/3$.
Product **1**: $A = 0.038$, $B = 0.0$; **2**: $A = 0.03$, $B = 0.05$; **3**: $A = 0.03$, $B = 3.0$; **4**: $A = 0.03$, $B = 0.2$; **5**: $A = 0.05$, $B = 5.0$.

Table 2
A comparison of coordination bond lengths (Å)

(a) In five-coordinate complexes	
1	
Cu(1)–N(1)	2.029(2)
Cu(1)–N(4)	1.927(3)
Cu(1)–N(5)	2.038(3)
Cu(1)–N(8)	1.929(2)
Cu(1)–O(5)	2.548(3)
4	
Cu(1)–N(1)	2.056(3)
Cu(1)–N(4)	1.945(3)
Cu(1)–N(5)	2.065(3)
Cu(1)–N(8)	1.940(3)
Cu(1)–O(21)	2.303(2)
Cu(2)–N(9)	2.062(3)
Cu(2)–N(12)	1.960(3)
Cu(2)–N(13)	2.059(3)
Cu(2)–N(16)	1.941(4)
Cu(2)–O(22)	2.332(2)
5	
Cu(1)–N(1)	2.028(2)
Cu(1)–N(4)	1.925(3)
Cu(1)–N(5)	2.033(2)
Cu(1)–N(8)	1.920(3)
Cu(1)–O(5A)	2.506(9)
Cu(1)–O(5B)	2.445(9)
Cu(1)–O(5C)	2.824(13)
(b) In four-coordinate complexes	
2	
Cu(1)–N(1)	2.0316 (15)
Cu(1)–N(4)	1.9020 (18)
3	
Cu(1)–N(1)	2.0320(18)
Cu(1)–N(4)	1.9069(19)

(X = Me) with dimethylsulfoxide in the apical position; where, in the former case the dimethylsulfoxide molecules alternate above and below the chain and in the latter they alternate pair wise two above, two below and so on [11,12].

There are CHπ and OFF interactions between neighbouring phenyl groups and methyl-π–facial interactions between the ligand methoxy methyl groups and phenyl groups. The *O*-methyl groups on the ligands are in the *anti* conformation, which, although it is expected to be less favourable energetically than the *syn*, is necessary for the formation of the $R_2^2(8)$ hydrogen bonding patterns [27].

3.3. Complexes linked by phenyl embraces

As mentioned above, products **2** and **3** are neutral copper(II) pseudo-macrocyclic complexes based on **I** (X = OPr^i) and **I** (X = OBu^n) respectively. In both cases, although the ligands possess complementary DA doublet motifs, chains in which the complexes are linked by $R_2^2(8)$ hydrogen bonding patterns are not present. Instead, molecules of dimethylformamide act as hydrogen bond acceptors for the imidazole NH donors and the complexes are linked into chains by phenyl embraces of the type shown in Fig. 1a.

It is interesting that the only occasion on which we have seen the second type of embrace (Fig. 1b) has been with a ligand that contains a further phenyl group that also interacts with the aryl groups that make up the phenyl embrace. It is possible that collectively these interactions are sufficient to stabilise this latter type of embrace over the more frequently observed embrace. This above structure type, in which the potential doublet motif is solvated, has been observed previously when the formation of $R_2^2(8)$ hydrogen bonding patterns is prevented by steric hindrance (X = NMe_2) and also as a minor phase present amongst crystals containing hydrogen-bonded chains (X = NHPh).

In both **2** and **3**, the *O*-alkyl groups are in the *syn* conformation, which is expected to be more energetically favourable than the *anti* [17]. The copper(II) ion is four-coordinate and square planar in both these complex species and in each case Cu(1) lies on an inversion centre so that there is only one crystallographically distinct ligand. In **2**, the maximum deviation of a ligand atom in the metallaring from the least squares plane is 0.0377(11) Å, and the Cu(1) lies 0.1124(21) Å from this plane. In **3**, the maximum deviation is 0.0431(14) Å, with the Cu(1) lying 0.1651(24) Å from the plane.

Interpreting these structures in the light of the 'best donor joining with the best acceptor rule' suggests that the formation of the hydrogen-bonded chains depends on successful competition between the N(3) hydrogen bond acceptor and the solvent for the imidazole NH hydrogen bond donor. It would be expected on this basis that the choice of solvent might influence the adoption of one or other of these arrangements; that is, between forming hydrogen-bonded chains or chains formed through phenyl embraces.

3.4. The inclusion of an anion

Product **4** is composed of cationic pseudo-macrocyclic copper(II) complexes of **I** (X = OBu^n). There are two crystallographically distinct complexes per unit cell and both are five-coordinate square pyramidal, with a butanol molecule occupying the apical site; Cu(1)–O(21) and Cu(2)–O(22) distances are 2.2993(25) and 2.3252(26) Å respectively. Cu(1) and Cu(2) lie 0.1220(20) and 0.1265(21) Å from the least squares planes of their respective nitrogen donor atoms. The ligand metallarings within each complex are effectively coplanar, with the least squares planes making angles of just 0.57(0.20)° and 0.95(0.21)° with each other.

The ligands that form the pseudo-macrocycle now have a DD hydrogen bonding motif, and each ligand is hydrogen bonded to two oxygen atoms of a nitrate ion in a $R_2^2(8)$ pattern. The third oxygen on one of the two nitrate ions acts as a hydrogen bond acceptor, with the coordinated butanol in a neighbouring complex being the donor. The third oxygen of the other of the two nitrates is not involved in any short interactions and lies 4.2 Å from the copper ion in a neighbouring complex. The hydrogen-bonded chains interact with neighbouring chains through offset face-to-face phenyl interactions (Fig. 8). The atoms

Table 3
Hydrogen bond geometry

Donor	Hydrogen	Acceptor	D–H (Å)	H–A (Å)	D–A (Å)	DHA angle (°)
1						
N(8)	H(8N)	O(1)	0.88	2.00	2.739(3)	140.9
N(4)	H(4N)	O(3)	0.88	2.01	2.794(3)	147.0
N(2)	H(2N)	N(7[a])	0.88	2.14	2.950(3)	153.0
N(6)	H(6N)	N(3[b])	0.88	2.05	2.918(3)	168.4
2						
N(2)	H(2N)	O(3)	0.88	2.01	2.883(3)	173.9
N(4)	H(4N)	O(1[a])	0.88	1.98	2.772(2)	149.5
3						
N(4)	H(4N)	O(1[a])	0.843(17)	2.00(2)	2.755(3)	149(3)
N(2)	H(2N)	O(3)	0.860(18)	2.088(19)	2.931(3)	166(3)
4						
N(4)	H(4)	O(3)	0.88	1.97	2.757(4)	149.0
N(8)	H(8)	O(1)	0.88	1.97	2.773(4)	151.8
N(12)	H(12)	O(7)	0.88	1.95	2.752(4)	150.4
N(16)	H(16)	O(5)	0.88	1.98	2.783(4)	150.6
N(10)	H(10)	O(11)	0.88	1.88	2.756(4)	179.0
N(11)	H(11)	O(10)	0.88	1.83	2.706(5)	175.2
N(14)	H(14)	O(18)	0.88	1.91	2.786(4)	173.5
N(15)	H(15)	O(20)	0.88	1.91	2.786(5)	175.5
N(2)	H(2)	O(12)	0.88	1.91	2.785(4)	175.5
N(3)	H(3)	O(13)	0.88	1.85	2.727(4)	171.3
N(6)	H(6)	O(17[a])	0.88	1.84	2.717(5)	175.6
N(7)	H(7)	O(16[a])	0.88	1.88	2.757(5)	171.3
O(21)	H(21O)	O(19[a])	0.95	1.98	2.826(4)	166.0
O(22)	H(22O)	O(14)	0.91(4)	1.90(4)	2.726(4)	150(4)
5						
N(4)	H(4N)	O(3)	0.88	1.97	2.764(3)	149.3
N(8)	H(8N)	O(1)	0.88	2.01	2.777(3)	145.4
N(2)	H(2N)	N(7[a])	0.88	2.11	2.959(3)	163.2
N(6)	H(6N)	N(3[b])	0.88	2.08	2.918(3)	158.6

Symmetry operators. For **1**: (a) $x, y+1, z$ and (b) $x, y-1, z$; **2**: (a) $-x+1, -y, -z+1$; **3**: (a) $-x, -y, -z$; **4**: (a) $x, y-1, z-1$; **5**: (a) $x-1/2, -y+1/2, z-1/2$ (b) $x+1/2, -y+1/2, z+1/2$.

Table 4
Comparison of bond lengths (Å) in the metallarings in the anionic and neutral forms of the ligand (X=OBu^n)

Complex **3** *(anionic ligand)*	
Cu(1)–N(1)	2.0320(18)
N(1)–C(3)	1.381(3)
N(3)–C(3)	1.321(3)
N(3)–C(4)	1.341(3)
N(4)–C(4)	1.296(3)
Cu(1)–N(4)	1.9069(19)
Complex **4** *(neutral ligand)*	
Cu(1)–N(1)	2.056(3)
N(1)–C(3)	1.354(5)
N(3)–C(3)	1.333(5)
N(3)–C(4)	1.381(5)
N(4)–C(4)	1.257(5)
Cu(1)–N(4)	1.945(3)
Cu(1)–N(5)	2.065(3)
N(5)–C(23)	1.340(5)
N(7)–C(23)	1.348(5)
N(7)–C(24)	1.375(5)
N(8)–C(24)	1.277(5)
Cu(1)–N(8)	1.940(3)
Cu(2)–N(9)	2.062(3)
N(9)–C(43)	1.359(5)
N(11)–C(43)	1.354(5)
N(11)–C(44)	1.374(5)
N(12)–C(44)	1.277(5)
Cu(2)–N(12)	1.960(3)
Cu(2)–N(13)	2.059(3)
N(13)–C(63)	1.340(5)
N(15)–C(63)	1.330(5)
N(15)–C(64)	1.381(5)
N(16)–C(64)	1.267(5)
Cu(2)–N(16)	1.941(4)

forming the hydrogen bonded $R_2^2(8)$ patterns are effectively planar. The maximum deviations from the least squares planes of the six non-hydrogen atoms in each ring are 0.1388(28) and 0.1499(29) Å for the rings in which all three nitrate oxygen atoms are hydrogen bond acceptors and 0.0850(30) and 0.1229(33) Å in the other two respectively.

Product **6** with X = OPr^n was also prepared and, although its structure was not determined, the microanalysis is consistent with it adopting a structure analogous to that of **4**.

The incorporation of anions into these arrays requires that the anion be a sufficiently weak base such that the 'acidic' N(3) proton remains attached to the ligand. If this nitrogen were deprotonated on addition of the anion one

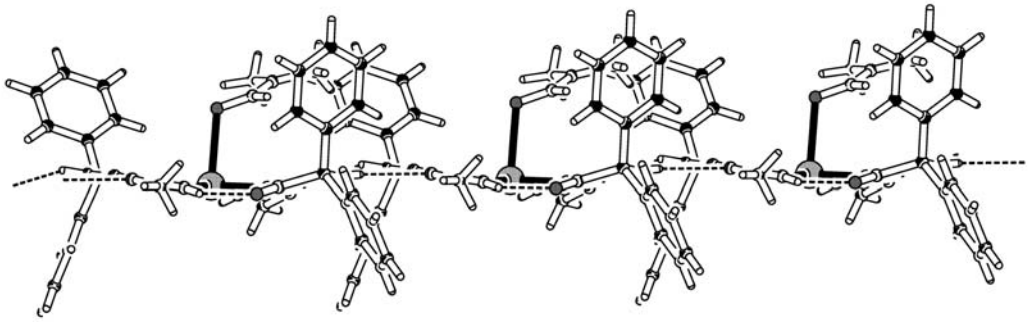


Fig. 7. A PLATON [28] depiction of a side-on view of the hydrogen-bonded chains in **1**. All the apical dmf molecules can be seen to be on the same side of the chain.

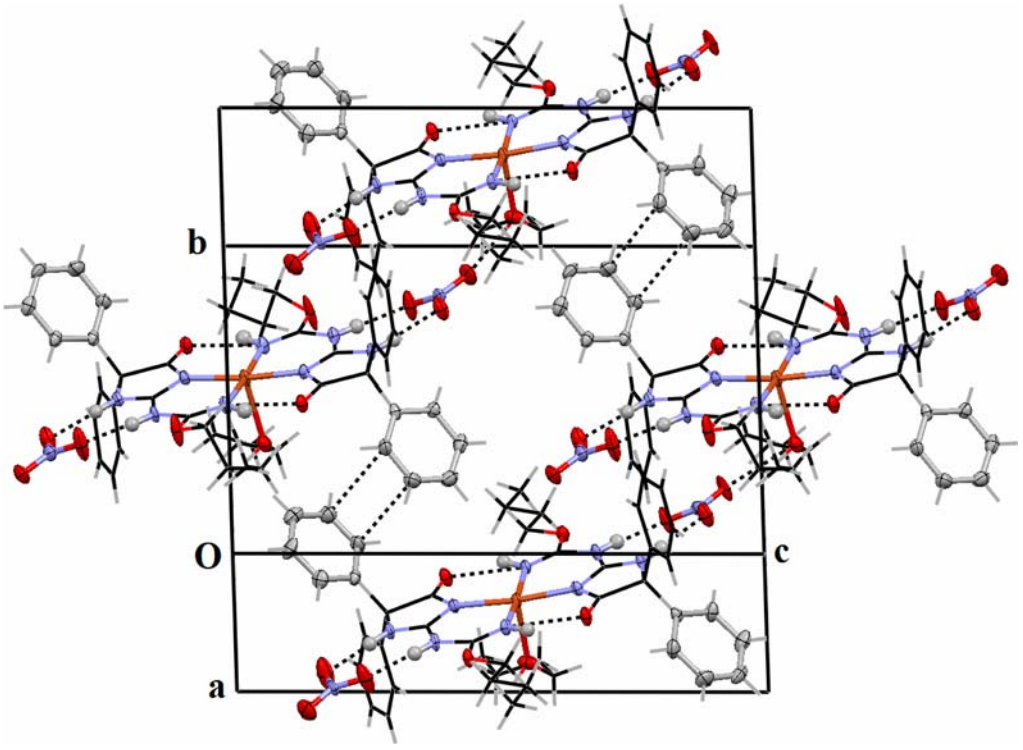
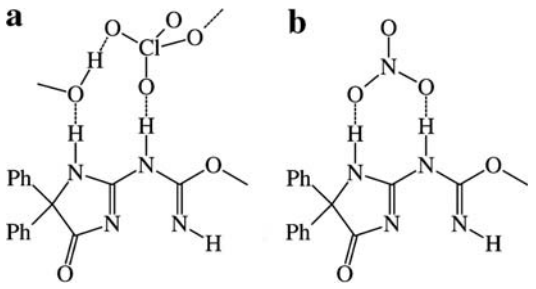


Fig. 8. A Mercury v1.4.1 [29] depiction of hydrogen bonding and phenyl–phenyl interactions in **4**. Hydrogen bonds and offset face-to-face (OFF) interactions are shown with dotted lines; the disorder, present in some of the butyl groups, is not shown. Heteroatoms are shown as thermal ellipsoids at 50% level as are the phenyl rings involved in OFF phenyl–phenyl interactions.

would expect the neutral complex to link into chains through the complementary DA motifs generated.

We have previously described the incorporation of a perchlorate ion into an array based on **I** (X = OMe) [12]. In this product each ligand formed a $R_3^3(10)$ hydrogen bonding pattern which included two of the perchlorate oxygens and the –OH group from a methanol (Scheme 4). This product, when left in the mother liquor, transformed spontaneously into a material consisting of chains of neutral pseudo-macrocyclic complexes linked by hydrogen bonding between the complementary motifs; the crystals of the new phase contained solvent methanol that was neither coordinated nor involved in hydrogen bonding interactions. One of the other two perchlorate oxygens formed a long contact with a copper(II) ion in a neighbouring complex. The nitrate ions in **4** do not interact directly with the copper ions.



Scheme 4. (a) Diagram showing the $R_3^3(10)$ ring formed by a perchlorate ion, methanol molecule and the ligand (X = OMe) in the cationic complex [12]. A perchlorate oxygen atom forms a long (2.816 Å) contact with a copper ion in a neighbouring complex. (b) Diagram of the $R_2^2(8)$ ring formed by a nitrate ion in **4**. There are different types of nitrate in the crystal; in one, the third nitrate oxygen is hydrogen bonded to a propanol molecule in an adjacent complex; in the other, it does not form a hydrogen bond.

3.5. The inclusion of guest molecules

Crystals of **5** were prepared by crystallisation of the corresponding neutral pseudo-macrocyclic complex from 1-propanol. The copper ions in this product are five-coordinate square pyramidal with a propanol molecule occupying the apical site; as shown in Fig. 6b, this coordinated propanol molecule is highly disordered. Cu(1) lies 0.0331(17) Å from the least squares plane of the nitrogen donors. The ligand atoms in the metallarings are effectively planar with the maximum deviations from the least squares planes being respectively 0.0372(29) and 0.0217(25) Å; Cu(1) lies 0.2936(46) and 0.3490(44) Å out of these planes. The planes make an angle of 23.10(9)° with each other.

The bound ligands are linked by hydrogen bonding between the complementary DA pairs on neighbouring complexes via $R_2^2(8)$ hydrogen bonding patterns. The six non-hydrogen atoms in these patterns are approximately coplanar with the maximum deviation from the least squares plane being 0.1668(24) Å. In addition, there are alkyl-to-π-facial contacts between the ligand propyl groups

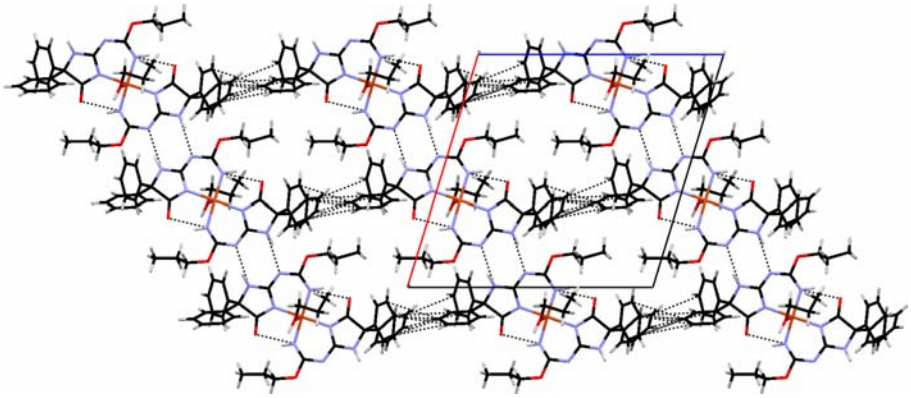


Fig. 9. A Mercury 1.4.1 [29] depiction of a supramolecular sheet of complexes in **5**. The view is along the *b*-axis and the guest molecules are not shown; neither is the disorder associated with the coordinated propanol molecules. Hydrogen bonds and phenyl–phenyl interactions are shown as dotted lines. The horizontal axis is the *c*-axis.

and phenyl rings on the neighbouring hydrogen-bonded complex. Thus chains of complexes are formed that run through the crystal. The position of the apical propanol molecules alternates on opposite sides of the chain. As well as being linked by hydrogen bonds, the pseudo-macrocycles are linked by phenyl embraces (based on edge to face interactions) into chains running parallel to the *c*-axis. As a result, the complexes form sheets that run perpendicular to the *b*-axis. Phenyl edge-to-face interactions occur between complexes in adjacent sheets (Fig. 9).

As shown in Fig. 10, the hydrogen-bonded chains lie directly one above another so that there are channels running through the crystal. Within these channels lie coordinated propanol molecules and non-coordinated guest molecules. The guests sit within centrosymmetric cavities, the walls of which are formed by both complex units and phenyl rings. Coordinated propanol molecules lie at the ends of each cavity. The occupancy of these cavities by propanol guests is 0.25; water molecules are also found in the cavities with this same occupancy. The centre of symmetry means that there are two possible orientations of the guest propanol molecules, the oxygen atoms (O6) of which lie 3.47 Å from Cu(1). The guests are not centrally placed within the cavity, but lie closer to one pair of adjacent faces. A view of the environment of one of the guest propanol molecules is shown in Fig. 11, which also depicts some of the short contacts between a propanol molecule and the walls of the cavity. A side-on view of the cavity is shown in Fig. 12.

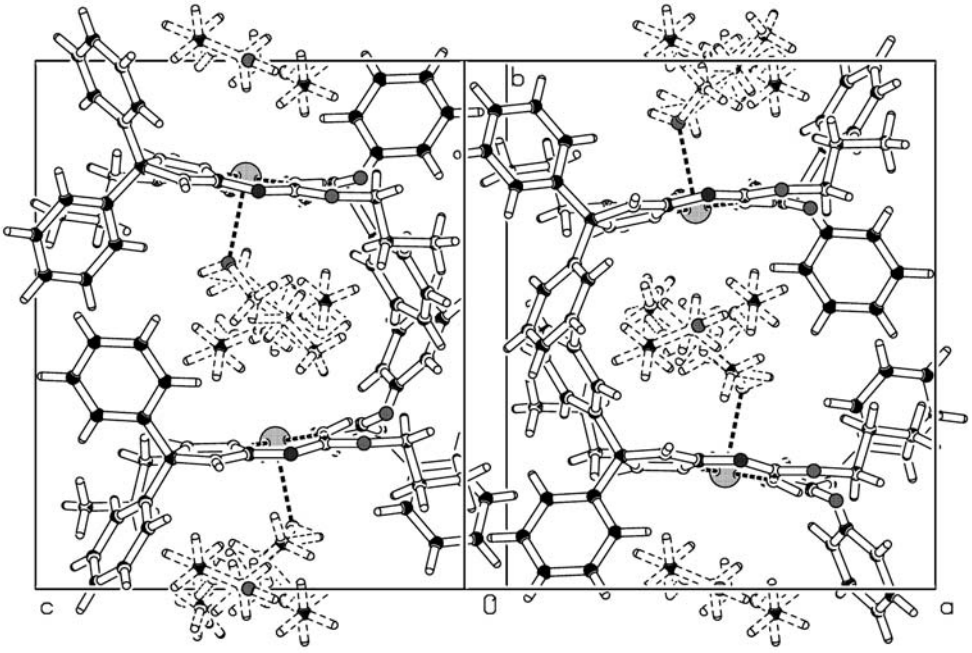


Fig. 10. A PLATON [28] depiction of the unit cell of **5** showing the view down the channels between adjacent supramolecular sheets of complexes.

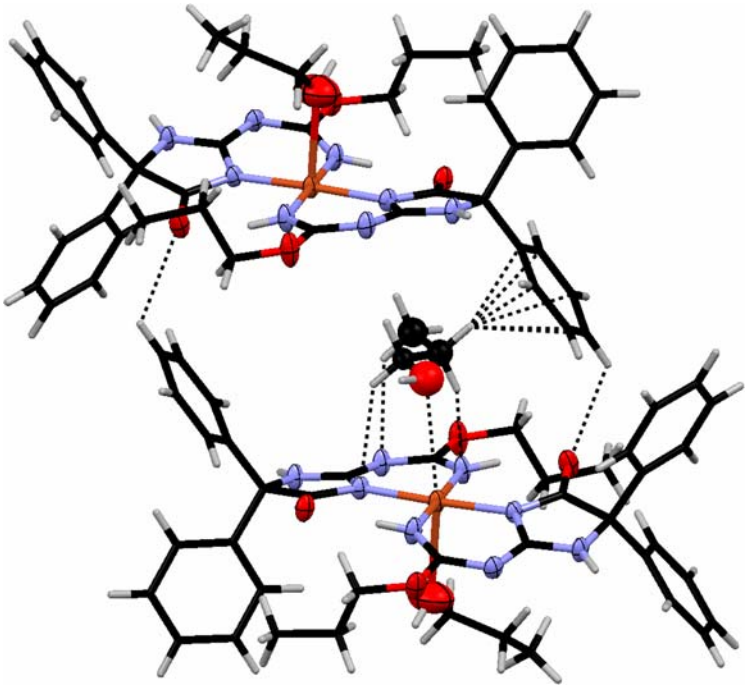


Fig. 11. A view, generated by Mercury v1.4.1 [29], of the environment of a guest propanol in a cavity in product **5**. The heteroatoms are drawn as thermal ellipsoids at the 50% level and no disorder has been shown.

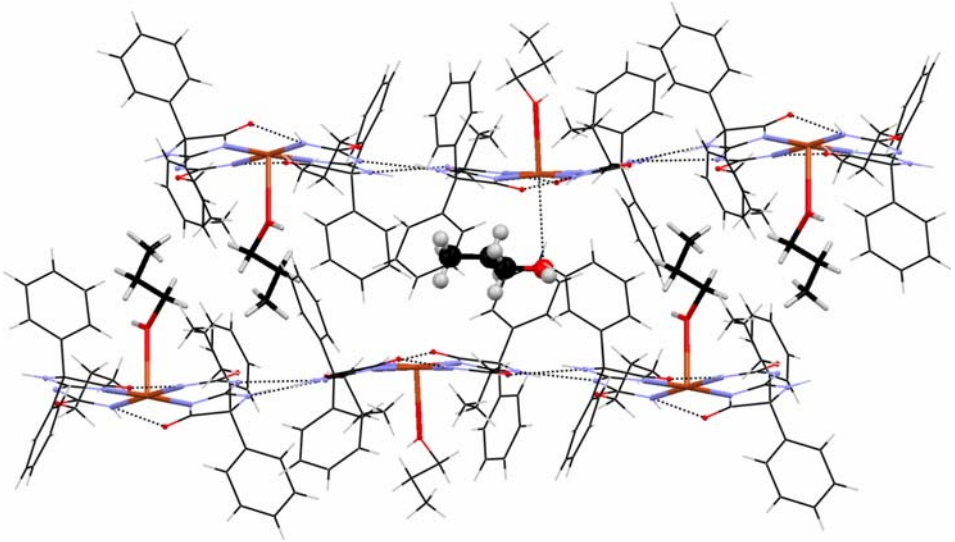


Fig. 12. A view, generated by Mercury v1.4.1 [29], that shows a side on view of a cavity containing a guest propanol molecule (shown in ball and stick mode in one of the two possible orientations) in product **5**. Coordinated propanols are drawn in capped stick mode, other atoms in wireframe. The long interaction between the guest oxygen and a copper is shown with a dotted line. No disorder is shown.

4. Final remarks

In this study we have examined the supramolecular structures of a series of copper complexes of bidentate guanidino derivatives. The anionic forms of the ligands, as present in the neutral complexes, possess a doublet (DA) hydrogen bonding motif, and were shown to form extended supramolecular structures linked by either hydrogen bonding or phenyl embraces (or both). The synthons were also observed to assemble into sheets, in some instances with the inclusion of guest molecules in cavities between the sheets. In the case of the cationic complex, the doublet (DD) hydrogen bonding motif allowed the incorporation of linking hydrogen-bonded nitrate ions in its structure.

5. Supplementary data

CIF files for all structures are deposited with the Cambridge Crystallographic Data Centre, CCDC Nos.

605940–605944, 12 Union Road, Cambridge CB2 1EZ, UK [fax: +44 1223 336 033, e-mail:deposit@ccdc.cam.ac.uk, or on the web http://www.ccdc.cam.ac.uk].

Acknowledgement

We thank the Australian Research Council for support.

References

[1] O.M. Yaghi, H. Li, C. Davis, D. Richardson, T.L. Groy, Acc. Chem. Res. 31 (1998) 474.
[2] M. O' Keeffe, O.M. Yaghi, Science 295 (2002) 469.
[3] L. Carlucci, G. Ciani, D.M. Proserpio, CrystEngComm. 5 (2003) 269.
[4] G.J. Halder, C.J. Kepert, J. Am. Chem. Soc. 127 (2005) 7891.
[5] S. Subramanian, M.J. Zaworotko, Coord. Chem. Rev. 137 (1994) 357.
[6] R. Desiraju, Angew. Chem. Int. Ed. Engl. 34 (1995) 2311.
[7] C.B. Aakeröy, A.M. Beatty, Aust. J. Chem. 54 (2001) 409.
[8] T. Steiner, Angew. Chem. Int. Ed. 41 (2002) 48.
[9] A.D. Burrows, Struct. Bond. 108 (2004) 55.
[10] P. Hubberstey, U. Suksangpanya, Struct. Bond. 111 (2004) 33.
[11] M.M. Bishop, L.F. Lindoy, D.J. Miller, P. Turner, J. Chem. Soc., Dalton Trans. (2002) 4128.
[12] M.M. Bishop, L.F. Lindoy, A. Parkin, P. Turner, J. Chem. Soc., Dalton Trans. (2005) 2563.
[13] M.M. Bishop, S.J. Coles, L.F. Lindoy, A. Parkin, Inorg. Chim. Acta, 359 (2006) 3565.
[14] I. Dance, CrystEngComm. 5 (2003) 208.
[15] I. Dance, New J. Chem. 27 (2003) 22.
[16] G.R. Desiraju, Acc. Chem. Res. 35 (2002) 565.
[17] L. Call, Monatsch. Chem. 101 (1970) 344.
[18] Bruker, SMART, SAINT, XPREP and SHELXTL-PLUS. Area Detector Control and Data Integration and Reduction Software, Bruker Analytical X-ray Instruments Inc., Madison, WI, USA, 1995.
[19] WINGX L.J. Farrugia, J. Appl. Crystallogr. 32 (1999) 837.
[20] S.R. Hall, D.J. du Boulay, R. Olthof-Hazekamp (Eds.), XTAL3.6 System, University of Western Australia, 1999.
[21] P. Coppens, L. Leiserowitz, D. Rabinovich, Acta Crystallogr. 18 (1965) 1035.
[22] (a) R.H. Blessing, Acta Crystallogr. A 51 (1995) 33;
(b) G.M. Sheldrick, SADABS. Empirical Absorption Correction Program for Area Detector Data, University of Göttingen, Germany, 1996.
[23] A. Altomare, M.C. Burla, M. Camalli, G.L. Cascarano, C. Giacovazzo, A. Guagliardi, A.G.G. Moliterni, G. Polidori, R. Spagna, J. Appl. Crystallogr. 32 (1998) 115.
[24] G.M. Sheldrick, SHELX97 Programs for Crystal Structure Analysis, University of Göttingen. Institüt für Anorganische Chemie der Universität, Göttingen, Germany, 1998.
[25] C.K. Johnson, ORTEPII. Report ORNL-5138, Oak Ridge National Laboratory, Oak Ridge, TN, 1976.
[26] (a) H.D. Flack, Acta Crystallogr., Sect. A 39 (1983) 876;
(b) G. Bernardinelli, H.D. Flack, Acta Crystallogr., Sect. A 41 (1985) 500;
(c) H.D. Flack, G. Bernardinelli, Acta Crystallogr. A 55 (1999) 908;
(d) H.D. Flack, G. Bernardinelli, J. Appl. Crystallogr. 33 (2000) 1143.
[27] I.M. Atkinson, M.M. Bishop, L.F. Lindoy, S. Mahadev, P. Turner, Chem. Commun. (2002) 2818.
[28] (a) A.L. Spek, Acta Crystallogr., Sect. A C34 (1990) 46;
(b) A.L. Spek, PLATON, a Multipurpose Crystallographic Tool, Utrecht University, Utrecht, The Netherlands, 1998.
[29] I.J. Bruno, J.C. Cole, P.R. Edgington, M. Kessler, C.F. Macrae, F. McCabe, J. Pearson, R. Taylor, Acta Crystallogr. B 58 (2002) 389.

Available online at www.sciencedirect.com
ScienceDirect
Polyhedron 26 (2007) 430–433
POLYHEDRON
www.elsevier.com/locate/poly

A manganese carbonyl complex derived from the P,N-bonding ligand (2-aminophenyl)diphenylphosphine

Victor D. Fester, Paul J. Houghton, Lyndsay Main, Brian K Nicholson *

Department of Chemistry, University of Waikato, Private Bag 3105, Hamilton, New Zealand

Received 5 April 2006; accepted 23 June 2006
Available online 14 July 2006

Abstract

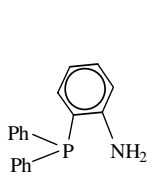
Thermal reaction of $[H_3Mn_3(CO)_{12}]$ with $Ph_2PC_6H_4NH_2$-2 gives good yields of $[Mn_2(CO)_6(PPh_2C_6H_4NH)_2]$, an X-ray single crystal structure determination of which reveals a P,N-chelating ligand with each of the NH groups, formed by deprotonation of the amine groups, bridging the two metal atoms.
© 2006 Elsevier Ltd. All rights reserved.

Keywords: Manganese carbonyl; Hemilabile; X-ray crystal structure; 2-Aminophenyldiphenylphosphine

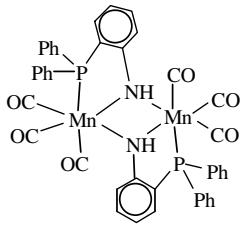
1. Introduction

Many bidentate hemilabile ligands have been explored for their ability to combine a stabilising effect on the metal centre with the possibility of readily generating a vacant coordination site for catalysis [1–5]. The most common ligating atom combinations are P,O or P,N which exploit the mismatch in bonding tendencies between soft P and hard O or N. Recent summaries giving examples are available [6–8].

One readily prepared ligand which has had some application in organometallic chemistry is $Ph_2PC_6H_4NH_2$-2 (**1**), which not only includes a soft-hard P,N combination but also retains potentially reactive N–H bonds [9,10].



1



2

Metal carbonyl complexes derived from **1** have been reported for both mononuclear and cluster compounds [11–18]. However, there are as yet no reports that we are aware of where derivatives of manganese have been prepared with **1**. Our longer term interest stems from the possibility of controlling the reactivity of the Mn–C bond in cyclomanganated compounds with such ancillary ligands [19], but here we describe a novel complex (**2**) from initial explorations of the reactions of **1** with simpler manganese carbonyls.

2. Experimental

2.1. General

Reactions were carried out under a nitrogen atmosphere using Schlenk techniques and solvents that were distilled under nitrogen from appropriate drying agents before use. Electrospray mass spectra were recorded on a VG Platform II spectrometer, operated as detailed elsewhere [20,21]. Assignments were confirmed by simulation of the characteristic isotope patterns using the ISOTOPE program [22]. NMR spectra were obtained on a Bruker AC300 instrument operating under standard conditions. IR spectra were recorded on a Digilab Scimitar instrument.

* Corresponding author. Fax: +64 7 838 4219.
E-mail address: b.nicholson@waikato.ac.nz (B.K Nicholson).

0277-5387/$ - see front matter © 2006 Elsevier Ltd. All rights reserved.
doi:10.1016/j.poly.2006.06.034

$Ph_2PC_6H_4NH_2$-2 and $[H_3Mn_3(CO)_{12}]$ were prepared by the literature methods [23,24].

2.2. Preparation of 2

$[H_3Mn_3(CO)_{12}]$ (40 mg, 0.079 mmol) was dissolved in heptane (5 mL) in a Schlenk flask. (2-Aminophenyl)diphenylphosphine (45 mg, 0.16 mmol) was added to the flask and the temperature of the reaction mixture was gradually increased to between 80 and 90 °C over a period of 50 min. During this time a colour change from orange–red to orange–yellow was observed, with a yellow precipitate starting to form at 80 °C. After cooling to room temperature, the solvent was removed in vacuo and the residue was redissolved in a small amount of dichloromethane. A similar volume of diethyl ether was added and the mixture was placed in the freezer. After one week, yellow crystals of **2** were obtained (40 mg, 61%). M.p. 110–116 °C. *Anal.* Calc. for $C_{42}H_{30}N_2O_6P_2Mn_2$ ($M_r = 830$) requires C, 60.74; H, 3.65; N, 3.37. Found: C, 59.99; H, 3.62; N, 3.38%. ν_{CO} (CH_2Cl_2) 2002 (s), 1923(s), 1898(s); ESI-MS, (MeOH, added NaOMe [20,21]), positive ion *m/z* 853 $[M+Na]^+$, 825 $[M+Na-CO]^+$, negative ion *m/z* 801 $[M-H-CO]^-$, 773 $[M-H-2CO]^-$. NMR ($CDCl_3$; 300 MHz): ^1H: δ 7.0–8.5 (m); the NH signal was either too broad to be observed or was amongst the aryl proton signals and could not be assigned. ^{13}C: owing to decomposition over the period of accumulation, the spectrum was poor and singlet signals were not resolved; doublet signals assigned to the ring carbons *ortho* and *para* to the amino group were at 111.0 ($J = 7$ Hz) and 118.9 ppm ($J =$ 11 Hz), the remainder overlapping at 128–135 ppm. ^{31}P: 65.4 ppm.

2.3. X-ray crystallography

X-ray intensity data were collected on a Siemens SMART CCD diffractometer using standard procedures and software. Multiscan absorption corrections were applied (SADABS [25]). Structures were solved by direct methods and developed and refined on F^2 using the SHELX programmes [26] operating under WINGX [27,28]. Hydrogen atoms were included in calculated positions, except for the hydrogen attached to N(1), which was located as the highest peak in a penultimate difference map and was refined with an isotropic temperature factor.

2.3.1. Structure of $[Mn_2(CO)_6(Ph_2PC_6H_4NH)_2] \cdot CH_2Cl_2$ ($2 \cdot CH_2Cl_2$)

Yellow crystals of **2** as the mono-solvate were obtained from CH_2Cl_2.

Crystal data: $C_{42}H_{30}N_2O_6P_2Mn_2 \cdot CH_2Cl_2$, $M = 1000.36$, monoclinic, space group $P2_1/n$, $a = 10.8871(1)$, $b = 14.7066(1)$, $c = 14.1506(2)$ Å, $\beta = 97.744(1)°$, $U =$ 2245.0(1) Å^3, $T = 190$ K, $Z = 2$, $D_{calc} = 1.48$ g cm^{-3}, μ(Mo Kα) = 0.921 mm^{-1}, $F(000)$ 1016; 12 596 reflections collected with $2° < \theta < 26°$, 4520 unique ($R_{int} = 0.0433$) used after correction for absorption ($T_{max,min} = 0.7697$, 0.7329). Crystal dimensions $0.36 \times 0.30 \times 0.30$ mm^3. Refinement on F^2 gave R_1 0.0563 [$I > 2\sigma(I)$] and $wR_2 = 0.1580$ (all data), GoF = 1.027. The structure of **2** is illustrated in Fig. 1, with selected bond parameters summarised in the caption to the figure.

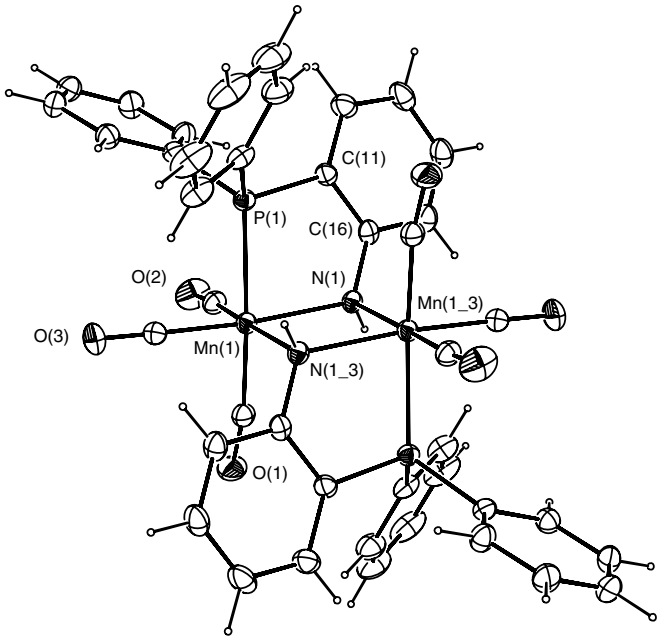


Fig. 1. The structure of the centrosymmetric dimer **2**. Bond parameters include bond lengths (Å): Mn–P 2.317(1), Mn–N(1) 2.084(3), Mn–N(1)′ 2.150(3), Mn...Mn 3.267(1); bond angles (°): Mn–P–C(11) 101.3(2), N(1)–Mn–N(1)′ 79.0(2), Mn–N(1)–Mn′ 100.9(2), Mn–N(1)–C(16) 112.1(2).

3. Results and discussion

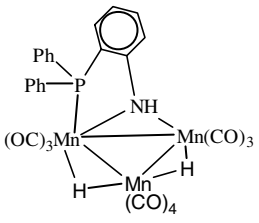
3.1. Synthesis and properties of 2

We were unable to isolate any new compounds from the thermal reaction between the ligand **1** and $Mn_2(CO)_{10}$, decomposition to insoluble brown residues taking place under conditions needed for reaction. However, the trinuclear species $H_3Mn_3(CO)_{12}$ underwent a smooth reaction at 80 °C with **1** to give good yields of a new species as yellow crystals. These were reasonably air-stable as a solid, but solutions tended to decompose giving a green product. ^1H and ^{13}C NMR of **2** gave little useful information, while ^{31}P NMR gave a signal at δ 65.4, well-shifted from that of the free ligand at δ −19.6. This indicated that a five-membered chelate ring had formed [29], though the shift of 75 ppm is unusually large [30]. The ESI mass spectrum suggested a mass of 830 from an $[M+Na]^+$ ion at *m/z* 853, corresponding to an empirical formula of $[Mn_2(CO)_6(Ph_2PC_6H_4NH)_2]$. To characterise the complex a single crystal X-ray determination was carried out. The structure is shown in Fig. 1. This shows a centrosymmetric molecule consisting of two $Mn(CO)_3$ units each coordinated to a phosphorus atom of a mono-deprotonated form of the

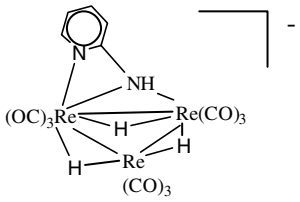
ligand **1**. The two halves of the molecule are linked only by the N atoms from the two ligands; the Mn...Mn distance of 3.267 Å precludes any direct metal–metalbond. The central Mn_2N_2 core of the molecule has strict planarity imposed by the space group symmetry, while the five-membered metallocyclic ring formed by Mn(1)P(1)C(11)-C(16)N(1) has a slightly folded envelope conformation, with deviations up to 0.18 Å from the least-squares plane. The Mn–N bonds differ slightly with Mn(1)–N(1) and Mn(1)–N(1)′ being 2.084(3) and 2.150(3) Å, respectively.

Deprotonation of the ligand **1** to provide a bridging amido group has been observed before, notably in reactions with $[Ru_3(CO)_{12}]$ and $[Os_3(CO)_{12}]$ [16–18]. However in these cases the clusters remain intact and the amido group bridges a formal M–M bond. A doubly bridged Rh–Rh bond is also retained in the complex $[Rh_2Cl_2(CO)_2(Ph_2PC_6H_4NH)_2]$ [31]. Structural characterisation of two metal carbonyl centres linked only by two amido groups appears to be unique to compound **2**, though a related rhenium example derived from 2-aminopyridine has been spectroscopically established [32].

The route to **2** presumably involves initial replacement of a CO ligand on $[H_3Mn_3(CO)_{12}]$ by the P atom of **1**. Oxidative addition of an N–H bond of the $-NH_2$ group across a metal-metal bond, followed by elimination of H_2 would give a species **3**, which would be related to the known rhenium anion **4** [32].



3



4

Repeating the process with a second ligand molecule apparently leads to fragmentation of the cluster and formation of **2**.

Other species can be detected in the reaction mixture, for example ESI-MS of the reaction mixture shows additional peaks to those associated with **2** at *m*/*z* 665 corresponding to the formula $[Mn(CO)_2(Ph_2PC_6H_4NH_2)_2]^+$, undoubtedly containing two intact bidentate ligand molecules, but we have as yet been unable to isolate this in a pure form for characterisation. This cation would be isoelectronic with the structurally characterised $[W(CO)(NO)(Ph_2PC_6H_4NH_2)_2]^+$ [33].

Acknowledgements

We thank Associate Professor Cliff Rickard, University of Auckland, for collection of X-ray intensity data and Ms. Kelly Kilpin for assistance with NMR spectroscopy.

Appendix A. Supplementary material

Crystallographic data for the structural analyses have been deposited with the Cambridge Crystallographic Data Centre, CCDC no. 603564. Copies of this information may be obtained free of charge from the Director, CCDC, 12 Union Rd., Cambridge CB2 1EZ, UK, fax: +44 1223 336 033, e-mail: deposit@ccdc.cam.ac.uk or http://www.ccdc.cam.ac.uk. Supplementary data associated with this article can be found, in the online version, at doi:10.1016/j.poly.2006.06.034.

References

[1] A. Bader, E. Lindner, Coord. Chem. Rev. 108 (1991) 27.
[2] M. Dieguez, O. Pamies, A. Ruiz, Y. Diaz, S. Castillion, C. Claver, Coord. Chem. Rev. 248 (2004) 2165.
[3] P. Laurent, N.L. Bris, H. des Abbayes, Trends Organometal. Chem. 4 (2002) 131.
[4] H. Werner, Dalton Trans. (2003) 3829.
[5] C.S. Slone, D.A. Weinberger, C.A. Mirkin, Prog. Inorg. Chem. 48 (1999) 233.
[6] P. Braunstein, Y. Chauvin, J. Nahring, Y. Dusausoy, D. Bayeul, A. Tiripicchio, F. Ugozzoli, J. Chem. Soc., Dalton Trans. (1995) 851.
[7] P. Braunstein, F. Naud, Angew. Chem., Int. Ed. Eng. 40 (2001) 680.
[8] J.A. Cabeza, Eur. J. Inorg. Chem. (2002) 1559.
[9] M.K. Cooper, J.M. Downes, Inorg. Chem. 17 (1978) 880.
[10] G.J. Organ, M.K. Cooper, K. Henrick, M. McPartlin, J. Chem. Soc., Dalton Trans. (1984) 2377.
[11] L. Dahlenburg, K. Herbst, H. Berke, J. Organometal. Chem. 585 (1999) 225.
[12] J. Pietsch, L. Dahlenburg, M. Moll, H. Berke, D. Veghini, I.L. Eremenko, J. Organometal. Chem. 472 (1994) 55.
[13] L. Dahlenburg, K. Herbst, G. Liehr, Acta Crystallogr., Sect. C 53 (1997) 1545.
[14] L. Dahlenburg, K. Herbst, A. Zahl, J. Organometal. Chem. 616 (2000) 19.
[15] H.-F. Klein, R. Beck, H.-J. Haupt, Eur. J. Inorg. Chem. (2003) 240.
[16] C.J. Adams, M.I. Bruce, P.A. Duckworth, P.A. Humphrey, O. Kuhl, E.R.T. Tiekink, W.R. Cullen, P. Braunstein, S.C. Cea, B.W. Skelton, A.H. White, J. Organomet. Chem. 467 (1994) 251.
[17] C.J. Adams, M.I. Bruce, B.W. Skelton, A.H. White, J. Organomet. Chem. 513 (1996) 255.
[18] E.W. Ainscough, A.M. Brodie, S.L. Ingham, J.M. Waters, J. Organomet. Chem. 468 (1994) 229.
[19] L. Main, B.K. Nicholson, Adv. Metal-Org. Chem. 3 (1994) 1.
[20] W. Henderson, B.K. Nicholson, L.J. McCaffrey, Polyhedron 17 (1998) 4291.
[21] W. Henderson, J.S. McIndoe, B.K. Nicholson, P.J. Dyson, J. Chem. Soc., Dalton Trans. (1998) 519.
[22] L.J. Arnold, J. Chem. Educ. 69 (1992) 811.
[23] M.K. Cooper, J.M. Downes, P.A. Duckworth, Inorg. Synth. 25 (1989) 129.
[24] B.F.G. Johnson, R.D. Johnston, J. Lewis, B.H. Robinson, Inorg. Synth. 12 (1970) 44.
[25] R.H. Blessing, Acta Crystallogr., Sect. A 51 (1995) 33.
[26] G.M. Sheldrick, SHELX 97 Programs for the Solution and Refinement of Crystal Structures, University of Göttingen, Germany, 1997.
[27] L. J. Farrugia, WINGX, Version 1.70.01, University of Glasgow, UK.
[28] L.J. Farrugia, J. Appl. Cryst. 32 (1999) 837.
[29] P.E. Garrou, Chem. Rev. 81 (1981) 229.

[30] M.A. Leeson, B.K. Nicholson, M.R. Olsen, J. Organomet. Chem. 579 (1999) 243.
[31] M.K. Cooper, G.J. Organ, P.A. Duckworth, K. Henrick, M. McPartlin, J. Chem. Soc., Dalton Trans. (1988) 2287.
[32] J.A. Cabeza, A. Llamazares, V. Riera, R. Trivedi, Organometallics 17 (1998) 5580.
[33] J. Pietsch, L. Dahlenburg, A. Wolski, H. Berke, I.L. Eremenko, J. Organometal. Chem. 495 (1995) 113.

Available online at www.sciencedirect.com
ScienceDirect
Polyhedron 26 (2007) 434–447
POLYHEDRON
www.elsevier.com/locate/poly

Organogold(III) complexes containing chelating bis(amidate) ligands: Synthesis, characterisation and biological activity

Kelly J. Kilpin, William Henderson *, Brian K. Nicholson

Department of Chemistry, University of Waikato, Private Bag 3105, Hamilton, New Zealand

Received 18 April 2006; accepted 23 June 2006
Available online 14 July 2006

Abstract

Reactions of cycloaurated gold(III) dichloride complexes, with 1,2-$C_6H_4(NHCOMe)_2$ and silver(I) oxide, or with $C_2H_4(NHSO_2Tol)_2$ (Tol = *p*-tolyl) or 1,2-$C_6H_4(NHSO_2Tol)_2$ and trimethylamine, give a series of new auracyclic complexes containing the Au–NR–CH_2CH_2–NR (R = SO_2Tol) and Au–NR–C_6H_4–NR (R = COMe or SO_2Tol) five-membered ring systems. An X-ray structure determination on (2-bp)Au{N(COMe)C_6H_4N(COMe)} (2-bp = cycloaurated 2-benzylpyridine) shows the presence of puckered metallacyclic rings, with both acetyl substituents positioned below the Au(III) coordination plane. The complex (2-bp)Au{N(COMe)C_6H_4N(COMe)} undergoes ring cleavage in the presence of halide and water, to give the complex (2-bp)Au{N(COMe)C_6H_4NH(COMe)}Cl, which was characterised crystallographically, and shown to contain a monodentate amidate ligand. Biological activity studies of the new auracyclic complexes are also reported, against P388 murine leukaemia cells and a range of bacteria and fungi, with a number of complexes showing high activity.
© 2006 Elsevier Ltd. All rights reserved.

Keywords: Gold complexes; Metallacylic complexes; Crystal structures; Electrospray mass spectrometry; Anti-tumour activity

1. Introduction

The chemistry of cyclometallated gold(III) complexes has been attracting recent interest [1], in part due to the isoelectronic nature of this metal centre with platinum(II), and the thoroughly established anticancer activity of the latter [2–7]. Since gold(III) is considerably more labile than platinum(II) [8,9], we have been investigating the synthesis and biological activity of cycloaurated complexes that also contain a chelating ligand, and have found that certain systems, notably thiosalicylate **1** [10,11] and catecholate **2** [12] derivatives show promising anticancer activity. To date, little is known about the chemistry of cycloaurated complexes that also contain ancillary amidate ligands, with the only Au(III) cyclometallated species containing a chelating bis(amidate) ligand being the ureylene complexes **3**, and an insertion product thereof with PhNCO [13]. In this contribution we report the synthesis and characterisation of some auracyclic derivatives containing the phenylenediamide and ethylenediamide moieties, with the nitrogen atoms bearing electron-withdrawing COMe or SO_2Tol (Tol = *p*-tolyl) groups. Although they are formally similar to the catecholate complexes **2**, the presence of a (variable) group on the amide nitrogen introduces the possibility of tuning the physical (e.g. solubility) and chemical properties of the ligands. Isoelectronic platinum(II) complexes containing such ligands have been well described, and many have been tested for anticancer activity [14,15]. Complexes containing chelating sulfonamide ligands have attracted much interest; there is a vast literature on the application of chiral metal–sulfonamide complexes as catalysts for organic transformations such as asymmetric hydrogenation (Ru) [16], amination [17] and alkylation [18] (Ti), Diels–Alder [19] and [2+2] cycloaddition [20] (Al), Claisen rearrangements (B) [21], and the synthesis of aryl glycines (Mg) [22]. Tungsten Schrock-type complexes, containing

* Corresponding author. Fax: +64 7 838 4219.
E-mail address: w.henderson@waikato.ac.nz (W. Henderson).

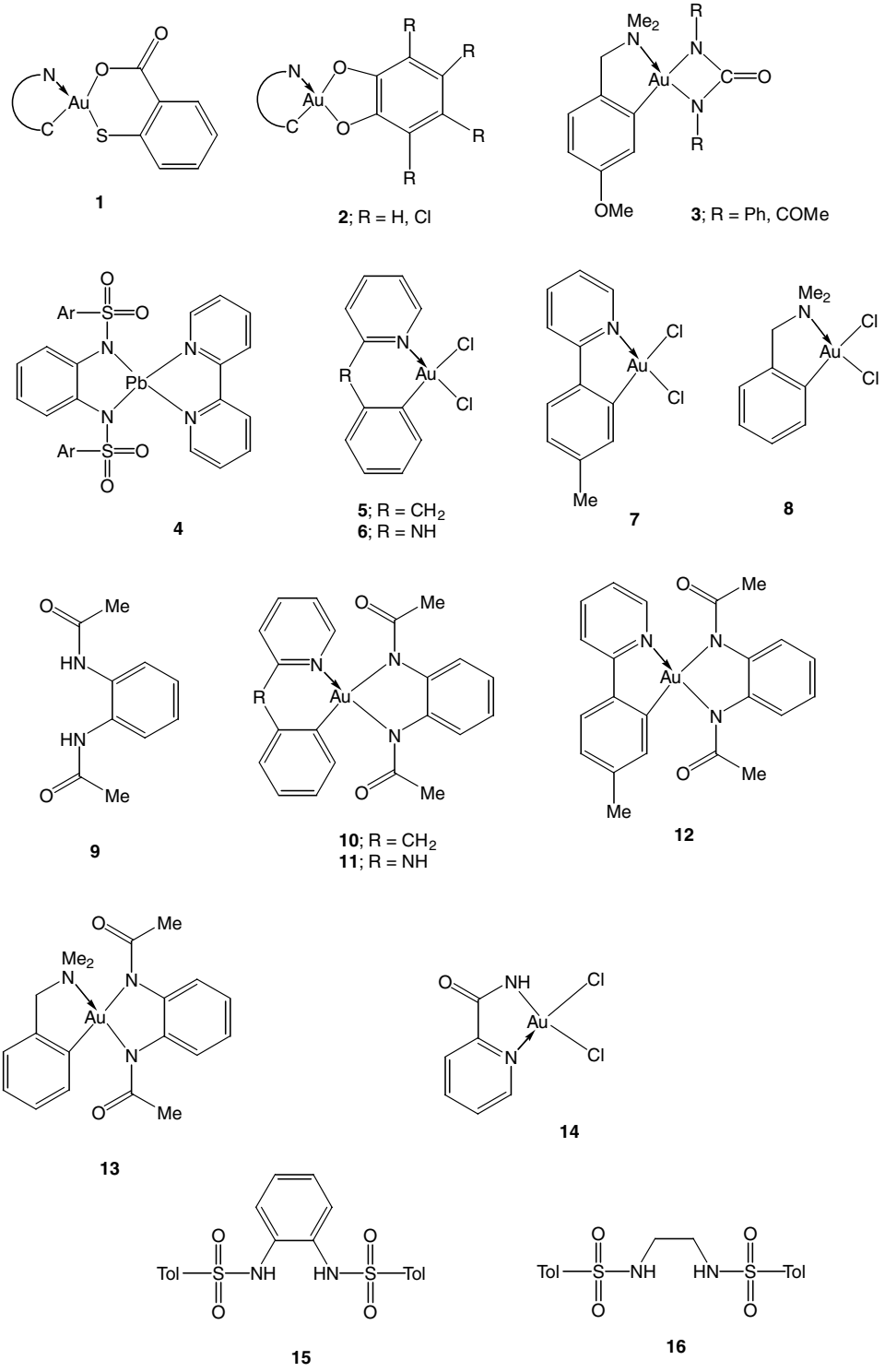
0277-5387/$ - see front matter © 2006 Elsevier Ltd. All rights reserved.
doi:10.1016/j.poly.2006.06.036

a W–N sulfonamide bond to increase the stability of the complex, have been developed to cleave hydrazine to ammonia [23]. Bis(sulfonamides) have also been explored as ligands for the extraction of lead(II) from aqueous to organic solutions via synergistic ion-exchange mechanisms with 2,2′-bipyridine, giving species such as **4** [24]; incorporation of the dansyl group gives derivatives that allow sensing of lead ions by fluorescence quenching [25].

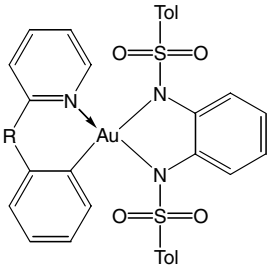
2. Results and discussion

2.1. Synthesis and characterisation of auracyclic amidate complexes

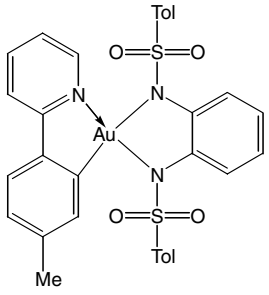
The reaction of the cycloaurated gold(III) dihalide starting materials (2-bp)$AuCl_2$ (**5**), (2-anp)$AuCl_2$ (**6**), (tolpy)-$AuCl_2$ (**7**) and (damp)$AuCl_2$ (**8**) with 1,2-diacetamidobenzene



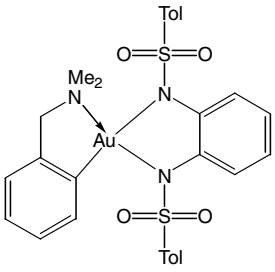
(**9**) and silver(I) oxide in refluxing dichloromethane gave the auracyclic products **10**–**13**, in moderate yields as pale yellow to yellow solids. The reaction time of 24 h was notably longer than the 2 h previously required for similar gold(III) ureylene systems [13] synthesised by the same method. When the same gold(III) dihalide starting materials, together with the cycloaurated picolinamide complex **14** was reacted with the sulfonamide ligand **15** or **16** in refluxing methanol with excess trimethylamine, the auracyclic complexes **17**–**25** were readily isolated in good yields, by precipitation with water. This suggests that the more strongly electron-withdrawing sulfonamide group facilitates proton removal from the amide nitrogen, and stabilises the Au–N bond. Reaction times were considerably less than those required for analogous platinum compounds [15]. The attempted synthesis of diacetamidobenzene complexes using trimethylamine in refluxing methanol was unsuccessful.



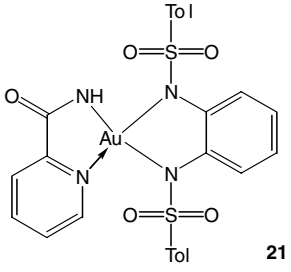
17; R = CH_2
18; R = NH



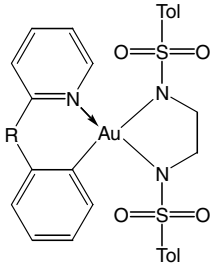
19



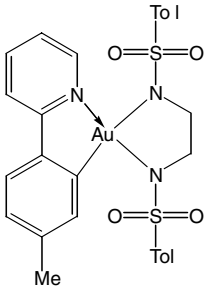
20



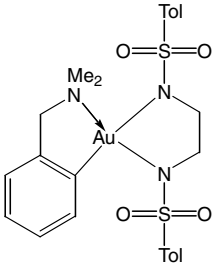
21



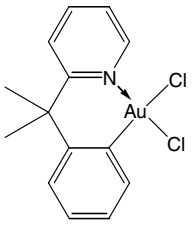
22; R = CH_2
23; R = NH



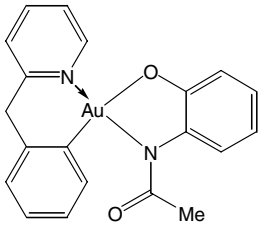
24



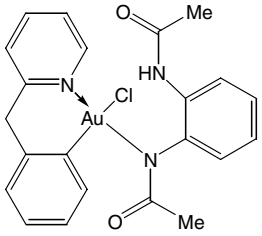
25



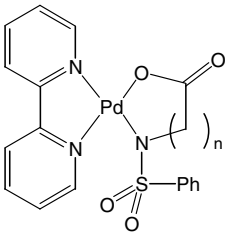
26



27



28



29, n=2
30, n=1

^{1}H, ^{13}C and DEPT135 NMR spectra were acquired for all compounds with the exception of the anilinopyridine complexes **11**, **18** and **23** which were too insoluble in common deuterated solvents [$CDCl_3$, D_2O and $(CD_3)_2SO$] to acquire satisfactory spectra. The low solubility of complexes containing this ligand has been noted previously [1,12]. Due to the complex overlapping of signals in the aromatic regions of the ^{1}H spectra, full NMR assignments were not made, however, integration of the aromatic region was used to ascertain that the expected number of signals were present, and hence as an indication of sample purity. Compounds **10**, **17** and **22** containing the benzylpyridyl ligand displayed the characteristic AB doublet of doublets due to the two methylene protons having different chemical environments in a puckered six-membered ring; Fuchita et al. have previously discussed the ring inversion process in the Au–benzylpyridyl system [26]. The pattern indicates that there is no inversion (at 30 °C, on the NMR timescale) between the two boat conformations. The compounds containing the damp ligand (**13**, **20** and **25**) contained two singlets corresponding to the *N*-methyl and -methylene protons. This was as expected, as all three compounds contain a plane of symmetry through the Au co-ordination plane.

The 1,2-diacetamidobenzene derivatives **10**–**13** showed strong stretches in the C=O region (1603–1630 cm^{-1}), at a lower wavenumber than the ν(C=O) in the free ligand **9** (1668 cm^{-1}). The sulfonamide derivatives **17**–**25** showed the expected strong peaks in the S=O stretching regions of the spectra, i.e. ~1160 cm^{-1} (symmetric) and ~1350 cm^{-1} (asymmetric) [27]. Upon co-ordination of the sulfonamide ligands to the gold(III) centre, the band due to NH stretching (3222 cm^{-1} and 3289 cm^{-1} for the free phenylenediamide and ethylenediamide ligands **15** and **16**, respectively) was lost, confirming that the ligands bind in the deprotonated form.

The auracyclic complexes have also been characterised by electrospray ionisation mass spectrometry (ESI-MS). At low cone voltages (20 V) complexes **10**–**13** all showed strong ions due to either $[M+H]^+$ or $[M+Na]^+$ (from adventitious Na^+ ions) with much less intense $[2M+H]^+$ and $[2M+Na]^+$ species. Increasing the cone voltage (40–60 V) produced fragmentation and the loss of $COCH_2$, possibly as ketene (Scheme 1, shown for (2-bp)Au{N(COMe)C_6H_4N(COMe)} (**10**)) as observed with the free ligand [28]. The ESI-MS behaviour of these complexes in the presence of added alkali metal halides is described later.

At low cone voltages (20 V) the sulfonamide complexes **17**–**25** showed ions assigned as $[M+Me_3NH]^+$ (presumably from the Me_3N used in synthesis, although not present in ^{1}H NMR) along with less intense $[M+Na]^+$ and $[M+H]^+$ adducts. Addition of NaCl as an ionisation aid produced much cleaner spectra, dominated by $[M+Na]^+$ ions. Aggregate ions $[2M+Na]^+$ and $[3M+Na]^+$ were also present at lower intensities. At higher cone voltages the Me_3NH^+ adduct disappeared and fragmentation of the parent ion by successive loss of *p*-toluenesulfonyl moieties was observed, as shown for complex **17** in Fig. 1. Oxidation produced radical cations, as proposed in Scheme 2. Confirmation of these ions was achieved using a Bruker Daltonics MicrOTOF high-resolution mass spectrometer; data are summarised in Table 1, and show excellent agreement between observed

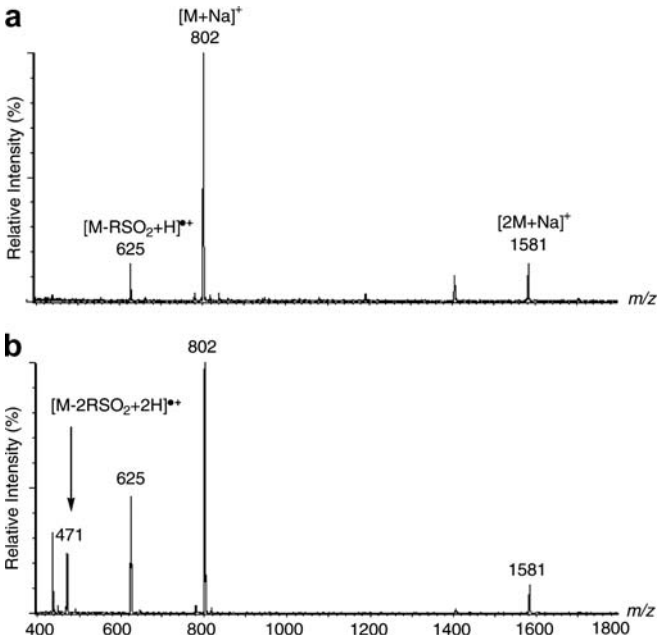
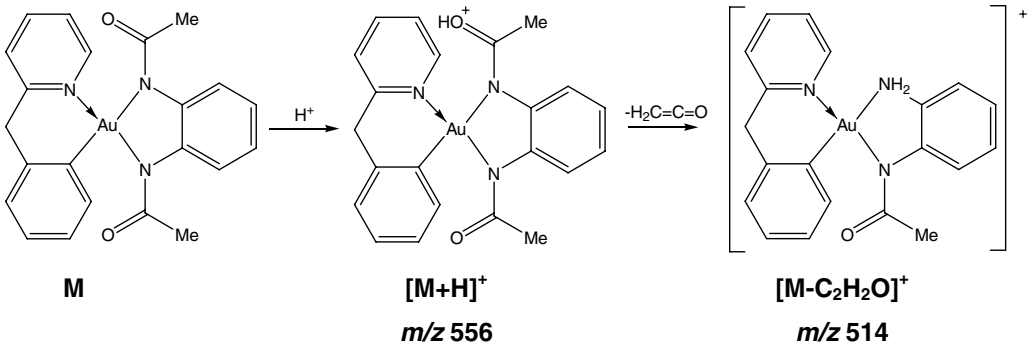
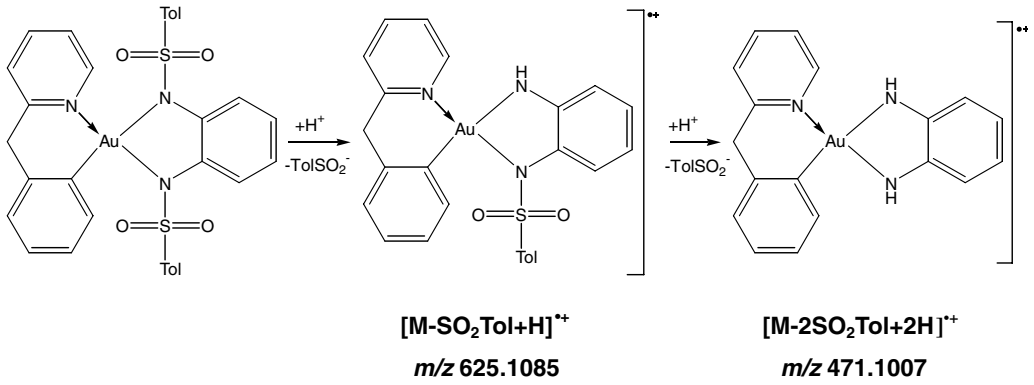


Fig. 1. ESI-MS Spectra of (2-bp)Au{N(SO_2Tol)C_6H_4N(SO_2Tol)} (**17**) (=M) in MeOH, recorded at cone voltages of: (a) 20 V; (b) 80 V, showing successive losses of *p*-toluenesulfonyl moieties, and the formation of radical cation fragment ions.



Scheme 1. Postulated ESMS fragmentation scheme for the compound (2-bp)Au{N(COMe)C_6H_4N(COMe)} (**10**) (=M).



Scheme 2. Postulated ESMS fragmentation and oxidation scheme for the compound (2-bp)Au{N(SO_2Tol)C_6H_4N(SO_2Tol)} (**17**) (=M).

Table 1
Comparison between calculated and observed accurate masses[a] of ions observed in the ESI mass spectrum of (2-bp)Au{N(SO_2Tol)C_6H_4N(SO_2Tol)} (**17**) (=M)

Ion	Formula	Observed *m/z*	Calculated *m/z*	σ[b]
$[M+Na]^+$	$C_{32}H_{28}N_3O_4S_2AuNa$	802.1087	802.1079	0.01
$[2M+Na]^+$	$C_{64}H_{56}N_3O_8S_4Au_2Na$	1581.2205	1581.2266	0.03
$[M-SO_2Tol+H]^{\bullet+}$	$C_{25}H_{22}N_3O_2SAu$	625.1085	625.1093	0.17
$[M-2SO_2Tol+2H]^{\bullet+}$	$C_{18}H_{16}N_3Au$	471.1007	471.1004	0.01

[a] Obtained using a Bruker Daltonics MicrOTOF mass spectrometer.
[b] A combined value for the standard deviation of masses and the intensities of all peaks in the isotopic envelope, compared to the calculated values.

and calculated accurate masses for the major observed ions. To determine if the added hydrogen originates from the solvent, spectra were obtained in CD_3OD solution; the ions at *m/z* 625 and 471 produced isotope patterns containing peaks respectively 1 or 2 mass units heavier which were tentatively assigned as the deuterium adducts (hence protonation from the solvent). However, due to the overlapping nature of the isotope patterns (from species containing hydrogen or deuterium) precise assignment was difficult.

It is well established that the metal electrospray capillary can act as an electrochemical cell allowing neutral molecules to be oxidised (when in positive ion mode); oxidation of the analyte is promoted by a low mobile phase flow rate, which increases the time the compound has to diffuse to the surface of the capillary [29,30]. Decreasing the rate of injection of **17** into the mass spectrometer, in the absence of added NaCl ionisation aid, resulted in the appearance of a small peak at *m/z* 779 (corresponding to the radical cation $[M]^{\bullet+}$ [M = (2-bp)Au{N(SO_2Tol)C_6H_4N(SO_2Tol)} (**17**)]), in addition to the $[M+H]^+$ ion at *m/z* 780, indicating that the parent metallacycle could also be oxidised. The same effect has been seen previously with analogous Pt(II) compounds [15] and oxidation of coordinated phenylenediamine ligands is well documented [31,32]. As expected, this was not seen for the gold–sulfonamide derivatives containing the ethylene backbone.

2.2. X-ray crystal structure determination of (2-bp)Au{N(COMe)C_6H_4N(COMe)} (**10**)

The crystal structure of **10** was determined in order to verify that the complex was the predicted auracycle. This was confirmed with the 1,2-diacetamidobenzene ligand coordinated to the gold through the amidate nitrogen donors. Views of the structure are shown in Figs. 2 and 3 along with the atom numbering scheme; selected bond lengths and bond angles are given in Table 2. The geometry around the gold atom is approximately square planar, with slight deviations; no atom deviates from the least-squares plane defined by N(1), N(2), Au(1), N(3) and C(31) by more than 0.0612(12) Å. Due to C(31) having a higher *trans*-influence than N(3) [33], the Au(1)–N(2) bond

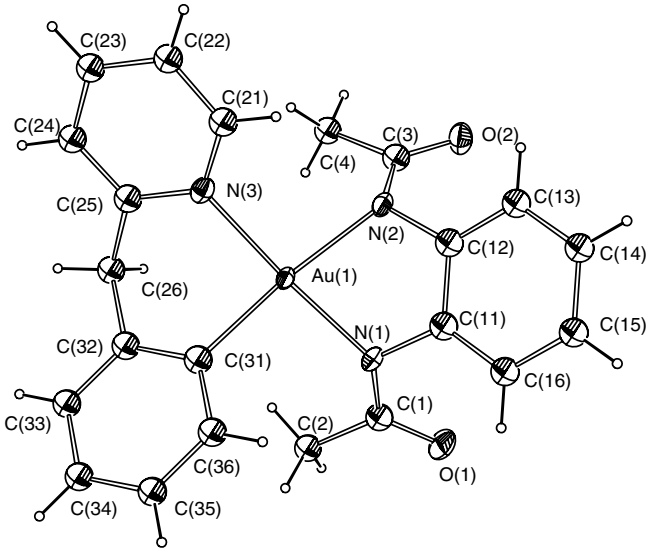


Fig. 2. Perspective view of the X-ray crystal structure of the complex (2-bp)Au{N(COMe)C_6H_4N(COMe)} (**10**), showing the atom labelling scheme. Thermal ellipsoids are shown at the 50% probability level.

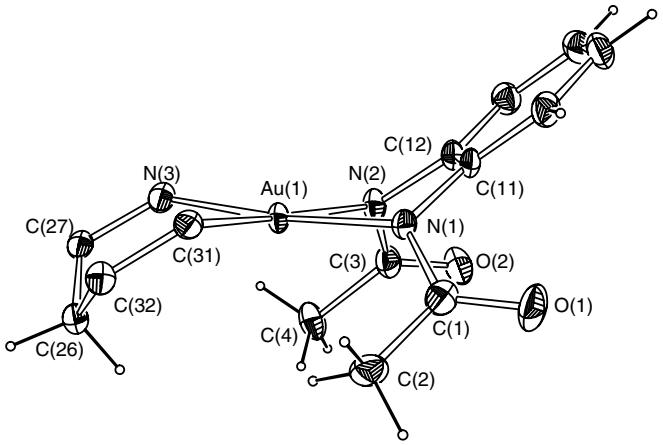


Fig. 3. Side view of the X-ray crystal structure of the complex (2-bp)Au{N(COMe)C_6H_4N(COMe)} (**10**), showing the non-planarity of 1,2-diacetamidobenzene nitrogen atoms and the orientation relative to the benzylpyridine ring system. Thermal ellipsoids are shown at the 50% probability level and atoms completing the benzyl and pyridyl rings have been omitted for clarity.

Table 2
Selected bond lengths (Å) and bond angles (°) (estimated standard deviations in parentheses) for (2-bp)Au{N(COMe)C_6H_4N(COMe)} (**10**)

Bond	Length (Å)	Bond	Angle (°)
Au(1)–N(1)	2.022(3)	N(1)–Au(1)–C(31)	94.76(12)
Au(1)–N(2)	2.089(3)	N(3)–Au(1)–N(2)	97.23(11)
Au(1)–N(3)	2.058(3)	C(31)–Au(1)–N(3)	88.11(12)
Au(1)–C(31)	2.031(3)	N(1)–Au(1)–N(2)	79.61(11)
1,2-Diacetamidobenzene ligand			
N(1)–C(1)	1.366(4)	C(1)–N(1)–C(11)	118.6(3)
N(1)–C(11)	1.435(4)	C(1)–N(1)–Au(1)	129.8(2)
N(2)–C(12)	1.433(4)	C(11)–N(1)–Au(1)	107.3(2)
N(2)–C(3)	1.356(5)	C(3)–N(2)–C(12)	118.0(3)
		C(3)–N(2)–Au(1)	129.1(2)
		C(12)–N(2)–Au(1)	105.9(2)

[2.089(3) Å] *trans* to C(31) is significantly longer than the Au(1)–N(1) bond [2.022(3) Å] *trans* to N(3). The benzylpyridyl moiety has a puckered boat configuration (Fig. 3), as seen with similar gold systems. Both acetyl moieties of the metallacycle are positioned below the Au(III) coordination plane (Fig. 3), in contrast to the uncoordinated ligand where the two acetyl groups are orientated in opposite directions [34]. Due to the puckering of the metallacycle, the aromatic ring of the amidate ligand [C(11)–C(16)] is orientated *trans* to the benzylpyridyl system, possibly to reduce steric interactions between acetyl groups of the acetamidobenzene ligand and the *ortho* ring protons of the benzylpyridyl ligand. The bite angle of the benzylpyridine ligand is 88.11(12)°. This is greater than that observed in compound **26** [35] (85.8°) which has two monodentate chloride ligands attached, but smaller than when a similar *O*,*N*-donor bidentate ligand is coordinated in **27** [89.7(3)°] [12]. The bite angle of the 1,2-diacetamidobenzene ligand is 79.61(11)°, which is less than the idealised 90° of a square-planar complex. This is a general feature of metallacyclic complexes.

The sums of the bond angles around the amidate nitrogens N(1) and N(2) are 355.7° and 353.0°, respectively, indicating a slight deviation from the planarity expected for formally sp^2 hybridised nitrogen atoms. Fully planar sp^2 nitrogen atoms would result in the auracyclic ring [defined by Au(1)–N(1)–C(11)–C(12)–N(2)] being planar, hence the distortion of the amidate nitrogen towards a tetrahedral geometry is most probably to reduce steric interactions. Non-planarity of formally sp^2 nitrogens was first reported in the Re–amide system CpRe(NO)(PPh_3)(NHPh) [36] and has since been observed in similar Pt(II) [15] and Zn [37] sulfonamide compounds along with Pd(II) *N*-sulfonylamino acid complexes [38]. X-ray crystal structures of bis-coordinated sulfonamide complexes of Ru(IV) [39], Os(VI) [40], Cu(II) [32,41,42], Ni(II), Zn(II) and Cd(II) [42] have been reported, however, no comments were offered on the geometry of the coordinating amide nitrogen. Investigation into the geometry around the nitrogen atoms in these structures was conducted using MERCURY [43] and defined as being in a planar environment.

2.3. Synthesis and characterisation of the monodentate amidate complex *28*

Addition of 1 molar equivalent of NaCl to a $CDCl_3$ solution of the auracyclic complex **10** (with monitoring by NMR spectroscopy) resulted in no reaction, but with subsequent addition of 1 molar equivalent of benzoic acid, reaction took place readily giving a new set of signals, subsequently identified as the monodentate complex **28**. Furthermore, this species was also observed in ESI mass spectra of **10**, in the presence of alkali metal halides, added as an ionisation aid. Here, it is significant to note that the electrospray process is known to result in a pH decrease [44,45], so the ESI-MS observations of ring cleavage do parallel those from NMR. Thus, in addition to the expected $[\mathbf{10}+\text{cation}]^+$ and $[2(\mathbf{10})+\text{cation}]^+$ ions (cation = Na or K), an additional ion 36 mass units higher was observed, which by analysis of the isotope pattern, was shown to contain a chloride ion. Fig. 4 shows the spectrum observed for complex **10** upon addition of NaCl. Interestingly, this effect was seen for all the acetamidobenzene metallacycles with the exception of **11**. Addition of small amounts of either Me_4NCl or Me_4NBr to the metallacycle **10** also resulted in cleavage of one Au–amidate bond in the ESI mass spectra.

When (2-bp)$AuCl_2$ (**5**) was reacted with **9** and Ag_2O using a shorter reaction time (2 h) than for the synthesis of the metallacycle **10**, a mixture of the monodentate amidate complex **28** with some metallacyclic complex was obtained. Unambiguous characterisation of **28** was achieved by carrying out a single-crystal X-ray structure determination. The structure of complex **28** is shown in Figs. 5 and 6, along with the atom numbering scheme; selected bond lengths and bond angles are given in Table 3. The structure confirms monodentate coordination of the 1,2-diacetamidobenzene ligand to the Au(III) centre

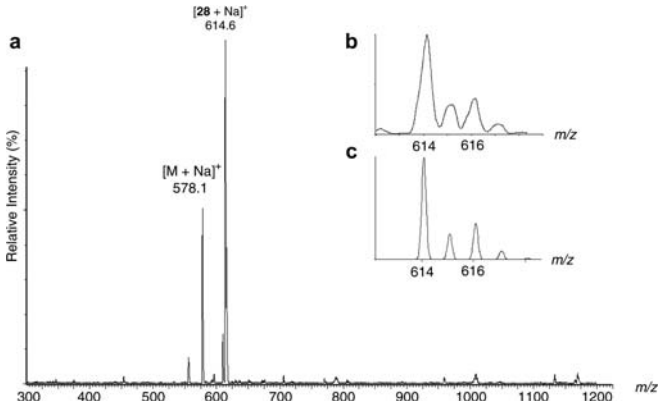


Fig. 4. (a) Positive-ion ESMS spectrum of (2-bp)Au{N(COMe)C_6H_4N-(COMe)} (**10**) (=M) in MeOH, recorded at a cone voltage of 20 V with aqueous NaCl added; (b) and (c) experimental and calculated isotope patterns of *m*/*z* 614 ion, [**28**+Na]$^+$.

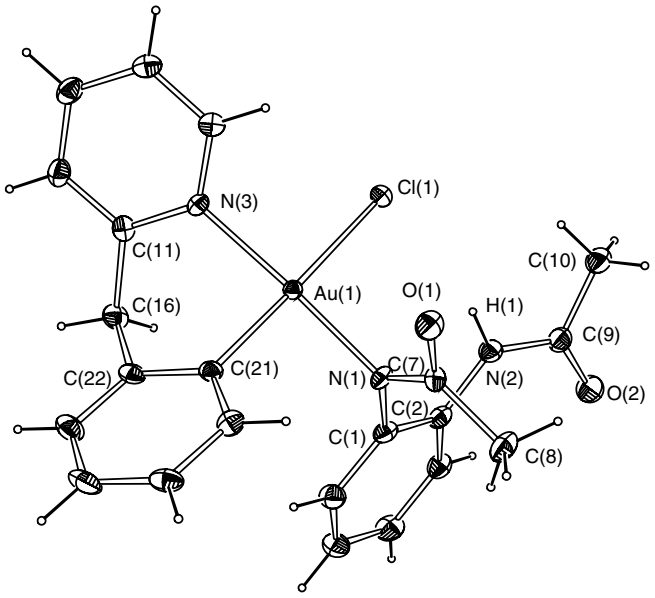


Fig. 5. Perspective view of the X-ray crystal structure of the complex (2-bp)Au{N(COMe)C_6H_4NH(COMe)}Cl (**28**), showing the atom labelling scheme. Thermal ellipsoids are shown at the 50% probability level.

through an Au–N bond. The geometry around the gold atom is essentially square-planar and the sum of the angles around the gold is 359.95°. No atom deviates from the least-squares plane that is defined by N(1), C(21), N(3), Cl(1) and Au(1) by more than 0.0229(7) Å. H(1) is in a position to form a hydrogen bond with Cl(1) (Fig. 6). The H···Cl and N···Cl distances are 2.48(4) Å and 3.302(2) Å, respectively, and the N···H···Cl angle is 153(3)°. These parameters are comparable to those which have recently been characterised as strong hydrogen bonds in organic compounds [46]. The benzylpyridyl moiety is in the expected puckered boat conformation. The bite angle of the benzylpyridine ligand is 87.41(9)° which is not significantly less than in the metallacyclic species **10**. The plane of the 1,2-diacetamidobenzene ligand [defined by C(1)–

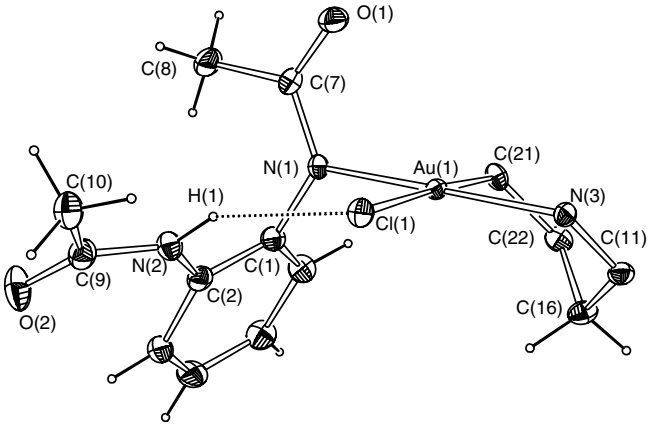


Fig. 6. Side view of the X-ray crystal structure of the complex (2-bp)Au{N(COMe)C_6H_4NH(COMe)}Cl (**28**), showing the puckering of the benzylpyridine ligand, orientation of the 1,2-diacetamidobenzene ligand and the hydrogen bond between H(1) and Cl(1). Thermal ellipsoids are shown at the 50% probability level and atoms completing the benzyl and pyridyl rings have been omitted for clarity.

Table 3
Selected bond lengths (Å) and bond angles (°) (estimated standard deviations in parentheses) for (2-bp)Au{N(COMe)C_6H_4NH(COMe)}Cl (**28**)

Bond	Length (Å)	Bond	Angle (°)
Au(1)–N(3)	2.053(2)	N(1)–Au(1)–C(21)	89.95(9)
Au(1)–C(21)	2.013(3)	C(21)–Au(1)–N(3)	87.41(9)
Au(1)–N(1)	2.014(2)	Cl(1)–Au(1)–N(3)	90.87(6)
Au(1)–Cl(1)	2.3941(6)	N(1)–Au(1)–Cl(1)	91.73(7)
1,2-Diacetamidobenzene ligand			
N(1)–C(1)	1.434(3)	Au(1)–N(1)–C(1)	119.6(2)
N(1)–C(7)	1.353(3)	C(1)–N(1)–C(7)	124.8(2)
N(2)–C(2)	1.410(3)	C(7)–N(1)–Au(1)	115.6(2)
N(2)–C(9)	1.366(4)		

C(6)] is perpendicular to the plane of the gold atom and the two acetyl groups point in opposite directions which differs from that in **10** but not in the free ligand [34].

The geometry around the coordinated nitrogen N(1) is essentially planar, with the sum of the angles adding to 360.03°. This differs from the metallacyclic species where both of the amidate nitrogen atoms show significant deviations from planarity, suggesting that the formation of a five-membered ring forces the nitrogen atoms towards a tetrahedral geometry in an effort to reduce strain on the ring. Digression towards a tetrahedral structure has been reported in Pd(II) complexes where decreasing the ring size from six atoms in **29** to five in **30** resulted in the sum of the bond angles around the sulfonamide nitrogen decreasing from 352.7(8)° to 332.2(3)° [38]. The Au(1)–N(1) bond of 2.014(2) Å in **28** is shorter than the Au(1)–N(2) (2.089 Å) and Au(1)–N(1) (2.022 Å) bonds in the metallacyclic complex **10**. The chlorine atom is in a position *trans* to C(21); this is presumably due to C having a higher *trans* effect than N, making the rate of ligand substitution *trans* to the C higher. The two low *trans* influence ligand atoms, Cl(1) and N(3), are also mutually *cis* due to antisymbiosis

[47]. This effect has been seen in many gold(III) cyclometallated compounds [1] including thiosalicylate [10,11], auralactam [48], and amidophenolate [12] systems, as well as in the interesting structurally characterised thiocyanate complex [LAu(NCS)(SCN)] (L = cycloaurated 2-phenylpyridyl), where the thiocyanate ligand *cis* to the aryl carbon is *S*-bonded, but the other thiocyanate is *N*-bonded [49].

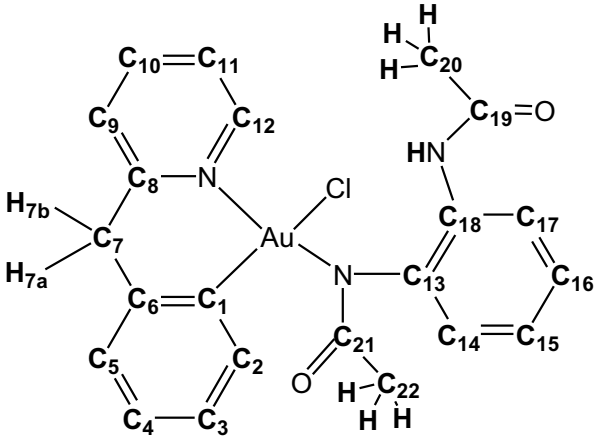
^{1}H NMR of the impure product containing **10** and **28** clearly indicated the presence of two sets of CH_2 AB resonances in the region δ 3.7–4.7 and all other signals showing a less intense partner. Peaks arising from **28** were more poorly resolved, which may be indicative of the auracyclic species **10** being more rigid. The ^{1}H NMR spectrum of **28** was fully assigned using a combination of ^{1}H, ^{13}C, DEPT135, ^{1}H–^{1}H COSY, HSQC, HMBC and 2D-NOESY experiments; data and the NMR atom numbering scheme are summarised in Table 4. A singlet peak at δ 9.43 in the ^{1}H spectrum was assigned to the amide NH proton, which shows no correlation to any other proton or carbon signals in the COSY or HSQC spectra, respectively. It did, however, show a weak correlation in the HMBC spectrum to a carbon in the phenylenediamido aromatic ring.

The ^{1}H–^{1}H COSY spectrum of **28** showed three distinct aromatic ring systems with most protons showing ^3J and ^4J coupling. In conjunction with HSQC and HMBC experiments, the chemical shifts of the ring protons and carbons could be assigned. The 2D-NOESY experiment was used to differentiate between the two acetyl moieties. The methyl protons at δ 2.30 produced a correlation to the amide proton whereas those at δ 1.88 showed correlations to the amide proton and protons in both the phenylenediamine and benzyl rings. The uncoordinated $NHC(O)CH_3$ group is located too far from the phenyl ring of the benzylpyridyl ligand to show an NOE correlation, but the coordinated $NC(O)CH_3$ group, in closer proximity, does show a correlation, placing the coordinated amidate ligand *cis* to the cycloaurated phenyl ring. As expected, the proton at δ 7.60 (H9, Table 4) showed a strong NOE to the proton at δ 7.96 (H10), its neighbour in the pyridyl ring. Inspection of the crystal structure revealed that H9 is closer to the methylene proton in the *pseudo*-equatorial position than in the *pseudo*-axial position. The larger NOE to the proton at δ 3.87 suggests it is the *pseudo*-equatorial proton, leaving the proton at δ 4.26 in the *pseudo*-axial position, assuming that the structure in solution is the same as in the crystalline state. This is to be expected, as the *pseudo*-axial proton is in closer proximity to the gold atom and thus more deshielded.

Two independent samples of **28**, recrystallised from dichloromethane and diethyl ether and dried under vacuum prior to analysis, produced microanalytical data with

Table 4
^{1}H and ^{13}C NMR chemical shift data, and NMR atom numbering scheme of (2-bp)Au{N(COMe)C_6H_4NH(COMe)}Cl (**28**)[a]

Atom	Type	^{13}C	^{1}H	
1	C	131.5		
2	CH	132.9	7.72	d, $J = 9.7$ Hz
3	CH	128.8	7.23	t, $J = 7.2$ Hz
4	CH	128.9	7.13	m, overlapping with H5, H16
5	CH	127.9	7.09	m, overlapping with H4, H16
6	C	141.4		
7	CH_2	48.0	3.87 (H_{ax})	d, $J = 15$ Hz
			4.26 (H_{eq})	d, $J = 15$ Hz
8	C	157.1		
9	CH	125.9	7.60	d, $J = 6.4$ Hz
10	CH	142.3	7.96	t, d, $J = 7.7$, 1.5 Hz
11	CH	124.3	7.49	t, $J = 6.3$ Hz
12	CH	152.6	9.30	br d, $J = 5.3$ Hz
13	C	135.7		
14	CH	122.2	8.30	br d, $J = 7.9$ Hz
15	CH	124.6	6.71	br t, $J = 7.1$ Hz
16	CH	128.2	7.11	m, overlapping with H4, H5
17	CH	128.7	6.35	br d, $J = 7.5$ Hz
18	C	136.6		
19	C=O	170.0		
20	CH_3	25.2	2.30	s
21	C=O	173.0		
22	CH_3	22.7	1.88	s
23	NH		9.43	br s



[a] 400 MHz, 300 K in $CDCl_3$. Protons are numbered after the carbon atoms to which they are bonded.

Table 5
Anti-tumour (P388) activities for metallacyclic gold(III) amidate derivatives

Compound	Anti-tumour IC_{50}[a]	
	ng mL^{-1}	μM
(2-bp)Au{N(COMe)C_6H_4N(COMe)} (**10**)	2434	4.38
(2-anp)Au{N(COMe)C_6H_4N(COMe)} (**11**)	3479	6.26
(tolpy)Au{N(COMe)C_6H_4N(COMe)} (**12**)	441	0.80
(damp)Au{N(COMe)C_6H_4N(COMe)} (**13**)	7546	14.47
(2-bp)Au{N(SO_2Tol)C_6H_4N(SO_2Tol)} (**17**)	236	0.30
(2-anp)Au{N(SO_2Tol)C_6H_4N(SO_2Tol)} (**18**)	>62 500	>80.13
(tolpy)Au{N(SO_2Tol)C_6H_4N(SO_2Tol)} (**19**)	41 201	52.89
(damp)Au{N(SO_2Tol)C_6H_4N(SO_2Tol)} (**20**)	4974	6.68
(pic)Au{N(SO_2Tol)C_6H_4N(SO_2Tol)} (**21**)	160	0.22
(2-bp)Au{N(SO_2Tol)C_2H_4N(SO_2Tol)} (**22**)	243	0.33
(2-anp)Au{N(SO_2Tol)C_2H_4N(SO_2Tol)} (**23**)	1156	1.58
(tolpy)Au{N(SO_2Tol)C_2H_4N(SO_2Tol)} (**24**)	3182	4.35
(damp)Au{N(SO_2Tol)C_2H_4N(SO_2Tol)} (**25**)	762	1.09
(TolSO_2)NHC_2H_4NH(SO_2Tol) (**16**)	>25 000	>67.93
Cisplatin	2583	8.15

[a] The concentration of the sample required to reduce the cell growth of the P388 leukaemia cell line (ATCC CCL 46) by 50%.

Table 6
Anti-microbial activities for metallacyclic gold(III) amidate derivatives

Compound	Anti-bacterial[a] and anti-fungal[b] activity[c]					
	Ec	Bs	Pa	Ca	Tm	Cr
(tolpy)Au{N(COMe)C_6H_4N(COMe)} (**12**)	6	11	10	13	14	9
(damp)Au{N(COMe)C_6H_4N(COMe)} (**13**)	10	15	10	10	11	1
(2-bp)Au{N(SO_2Tol)C_6H_4N(SO_2Tol)} (**17**)	–	1	–	–	–	–
(damp)Au{N(SO_2Tol)C_6H_4N(SO_2Tol)} (**20**)	5	10	3	8	13	1
(pic)Au{N(SO_2Tol)C_6H_4N(SO_2Tol)} (**21**)	–	2	1	2	2	–
(2-bp)Au{N(SO_2Tol)C_2H_4N(SO_2Tol)} (**22**)	1	2	1	–	–	–
(damp)Au{N(SO_2Tol)C_2H_4N(SO_2Tol)} (**25**)	8	15	8	10	15	1
(MeCO)NHC_6H_4NH(COMe) (**9**)	–	–	–	–	–	–

[a] Ec = *Escherichia coli*, Bs = *Bacillus subtilis*, Pa = *Pseudomonas aeruginosa*.
[b] Ca = *Candida albicans*, Tm = *Trichophyton mentagrophytes*, Cr = *Cladosporium resinae*.
[c] Inhibition zone as an excess radius (mm) from a 6 mm disc containing 5 μg of sample; – = no activity measured.

carbon, nitrogen and hydrogen compositions lower than expected. The difference in composition does not appear to be due to organic solvents as the ^{1}H NMR spectra lack signals due to dichloromethane or diethyl ether.

2.4. Biological activity

The anti-tumour activity of all compounds was determined against a P388 leukemia cell line, and results are reported in Table 5. The results show no clearly discernible pattern in anti-tumour activity. However, as a group the *N*,*N*′-bis(*p*-toluenesulfonyl)ethylenediamide derivatives appear to have a higher activity, possibly due to greater solubility. IC_{50} values were very comparable to those of catecholate, ureylene and thiosalicylate Au(III) metallacycles. With the exception of complexes **13**, **18** and **19**, all of the gold(III) amidate complexes demonstrated anti-tumour activity that was higher than cisplatin, under the screening conditions. The anti-microbial activities of the damp derivatives, and a selection of other complexes which showed good anti-tumour activity (defined by $IC_{50} < 500$ ng mL^{-1}) was also determined, and are listed in Table 6. The acetamido derivatives **12** and **13** show a broad spectrum activity which appears higher than other derivatives. It is also apparent that a higher anti-cancer activity gives lower anti-microbial activity although the reasons are unclear. Again, anti-microbial activity is probably due to the gold metallacycle as the 1,2-diacetamidobenzene (**9**) ligand itself shows no anti-microbial activity.

3. Conclusions

A series of new gold(III) metallacyclic complexes containing Au–N–C–C–N rings has been synthesised and characterised by NMR, ESI-MS, IR and micro-elemental analysis. Auracycles containing the acetamidobenzene ligand undergo protonolysis to give the monodentate amidate complex; in the case involving the benzylpyridyl ligand this was also synthesised as an intermediate in the Ag_2O-mediated reaction, and characterised by X-ray crystallography. All new auracyclic compounds were assayed in order to assess their anti-tumour activity. Seven of the complexes had an activity higher than cisplatin in the P388 assay, with the more soluble ethylenediamide derivatives showing the best activity. Three of the compounds also show good broad-spectrum anti-microbial activity.

4. Experimental

4.1. General

All reactions were carried out with no efforts at excluding air or light. Solvents were LR grade with the exception of dichloromethane (which was distilled from P_4O_{10}) when used in the workup. The sulfonamides [15] and silver(I) oxide [50] were prepared by the literature methods, the former from *p*-toluenesulfonyl chloride and *o*-phenylenediamine, or ethylenediamine (BDH) as appropriate. 1,2-Diacetamidobenzene was prepared by acetylation of 1,2-diaminobenzene (*o*-phenylenediamine, BDH) using acetic anhydride. Trimethylamine (Eastman, 25% aqueous solution) was used as supplied. The cycloaurated gold(III) complexes (2-bp)$AuCl_2$ (**5**) [35], (2-anp)$AuCl_2$ (**6**) [51], (tolpy)$AuCl_2$ (**7**) [10], (damp)$AuCl_2$ (**8**) [52,53], and (pic)$AuCl_2$ (**14**) [54] were prepared by modified literature methods.

General experimental techniques were as previously described [12]; routine ESI mass spectra were recorded on a VG Platform II instrument, using methanol as the mobile phase. A small quantity of aqueous NaCl solution was often added as an ionisation aid. Confirmation of the formation of oxidised ions was achieved using a Bruker Daltonics MicrOTOF high-resolution mass spectrometer, capable of achieving an accurate *m*/*z* value to ±5 ppm; calibration was achieved using a sodium formate solution. Assignment of mass spectrometric isotope patterns was aided by the ISOTOPE program [55].

4.2. Synthesis of (2-bp)Au{N(COMe)C_6H_4N(COMe)} (*10*)

The complex (2-bp)$AuCl_2$ (**5**) (200 mg, 0.45 mmol), 1,2-diacetamidobenzene (**9**) (88 mg, 0.45 mmol) and silver(I) oxide (400 mg, excess) were added to dichloromethane (30 mL) and refluxed with stirring for 24 h. The resulting

solution was filtered to give a pale yellow solution which was evaporated to give yellow crystals. These were dissolved in dichloromethane (~5 mL) and filtered through an alumina column. Slow addition of diethyl ether to the filtrate resulted in formation of yellow microcrystals which were filtered, washed with water (2 × 10 mL) and diethyl ether (10 mL) and dried under vacuum to give 178 mg (69%) of the product. *Anal.* Calc. for $C_{22}H_{20}N_3O_2Au$: C, 47.6; H, 3.6; N, 7.6. Found: C, 47.8; H, 3.8; N, 7.5%. M.p. 176–178 °C (dec.). IR: ν(C=O) region: 1611 cm^{-1}. ESI-MS: cone voltage 20 V; *m/z* 578 (100%, $[M+Na]^+$), 556 (45%, $[M+H]^+$), 1133 (30% $[2M+Na]^+$). ^1H NMR: δ 1.87 (s, 3H), 2.14 (s, 3H), 4.03 (d, 1H), 4.67 (d, 1H), 6.9–7.2 (m, 6H), 7.38 (t, 1H), 7.48 (d, 1H), 7.68 (d, 1H), 7.95 (t 1H), 8.98 (d, 1H). $^{13}C–\{^1H\}$ NMR: δ 23.0 (CH_3), 27.7 (CH_3), 47.7 (CH_2), 122.1–156.1 (aryl C), 173.5 (C=O), 174.1 (C=O).

4.3. Synthesis of (2-anp)Au{N(COMe)C_6H_4N(COMe)} (**11**)

The complex (2-anp)$AuCl_2$ (**6**) (201 mg, 0.46 mmol), 1,2-diacetamidobenzene (**9**) (89 mg, 0.46 mmol) and silver(I) oxide (400 mg, excess) were added to dichloromethane (30 mL) and refluxed with stirring for 24 h. The solution was filtered, and the filtrate evaporated under reduced pressure to give orange crystals. These were dissolved in dichloromethane (~5 mL) and the solution filtered through a column of neutral alumina. Diethyl ether was slowly added to the filtrate, resulting in the formation of yellow crystals which were filtered, washed with water (2 × 10 mL) and diethyl ether (10 mL) and dried under vacuum to give 142 mg (55%) of the product. *Anal.* Calc. for $C_{21}H_{19}N_4O_2Au$: C, 45.3; H, 3.4; N, 10.1. Found: C, 45.3; H, 3.6; N, 10.0%. M.p. 232–236 °C (dec.). IR: ν(C=O) region: 1604 cm^{-1}. ESI-MS: cone voltage 20 V; *m/z* 579 (100%, $[M+Na]^+$), 1135 (30%, $[2M+Na]^+$). The complex was too insoluble in the common deuterated solvents [$(CD_3)_2SO$, D_2O and $CDCl_3$] to acquire satisfactory NMR spectra.

4.4. Synthesis of (tolpy)Au{N(COMe)C_6H_4N(COMe)} (**12**)

The complex (tolpy)$AuCl_2$ (**7**) (100 mg, 0.23 mmol), 1,2-diacetamidobenzene (**9**) (44 mg, 0.23 mol) and silver(I) oxide (200 mg, excess) were suspended in dichloromethane (30 mL) and refluxed with stirring for 24 h. The resulting mixture was filtered and the filtrate evaporated to give yellow crystals. These were then dissolved in dichloromethane (~5 mL) and the solution filtered through an alumina column to remove remaining silver impurities. Addition of diethyl ether to the filtrate resulted in formation of pale yellow fluffy crystals which were filtered, washed with water (2 × 10 mL) and diethyl ether (2 × 10 mL) and dried under vacuum to give 86 mg (68%) of the product. *Anal.* Calc. for $C_{22}H_{20}N_3O_2Au$: C, 47.6; H, 3.6; N, 7.6. Found: C, 46.3; H, 3.8; N, 7.4%. M.p. 270–273 °C (dec.). IR: ν(C=O) region: 1607 cm^{-1}. ESI-MS: cone voltage 20 V; *m/z* 578 (100%, $[M+Na]^+$), 556 (50%, $[M+H]^+$), 1133 (25%, $[2M+Na]^+$). ^1H NMR: δ 2.23 (s, 3H), 2.36 (s, 3H), 2.44 (s, 3H) 6.9–7.4 (m, 8H), 7.77 (d, 1H), 9.46 (s, 1H). $^{13}C–\{^1H\}$ NMR: δ 14.1 (CH_3), 22.2 (CH_3), 22.4 (CH_3), 119.5–164.8 (aryl C), 173.6 (C=O), 174.7 (C=O).

4.5. Synthesis of (damp)Au{N(COMe)C_6H_4N(COMe)} (**13**)

The complex (damp)$AuCl_2$ (**8**) (100 mg, 0.25 mmol), 1,2-diacetamidobenzene (**9**) (48 mg, 0.25 mol) and silver(I) oxide (200 mg, excess) were suspended in dichloromethane (30 mL) and refluxed for 24 h. The solution was filtered and evaporated to give yellow crystals. These were dissolved in a minimum amount of dichloromethane and slow addition of diethyl ether resulted in the formation of yellow crystals which were filtered, washed with diethyl ether (10 mL) and water (2 × 10 mL) and dried under vacuum to give 64 mg (50%) of the product. *Anal.* Calc. for $C_{19}H_{22}N_3O_2Au \cdot 0.15CH_2Cl_2$: C, 43.1; H, 4.2; N, 7.9. Found: C, 42.3; H, 4.4; N, 7.7%. M.p. 202 °C (dec.). IR: ν(C=O) region: 1612 cm^{-1}. ESI-MS: cone voltage 20 V; *m/z* 544 (100%, $[M+Na]^+$), 522 (78%, $[M+H]^+$), 580 (68%, $[M+HCl+Na]^+$), 1065 (45%, $[2M+Na]^+$), 1101 (38%, $[2M+HCl+Na]^+$), 1043 (25%, $[2M+H]^+$). ^1H NMR: δ 2.15 (s, 3H), 2.23 (s, 3H), 3.39 (s, 6H), 4.21 (s, br, 2H), 5.32 (s, CH_2Cl_2), 6.86–6.89 (m 4H), 6.97–7.00 (m, 2H), 7.05 (m, 2H), 7.17 (m, 2H), 7.60 (d, 1H). $^{13}C–\{^1H\}$ NMR: δ 22.7 (CH_3), 52.6 (NCH_3), 53.4 (CH_2Cl_2), 74.9 (CH_2), 122.2–146.6 (aryl C), 173.5 (C=O), 174.1 (C=O).

4.6. Synthesis of (2-bp)Au{N(SO_2Tol)C_6H_4N(SO_2Tol)} (**17**)

The complex (2-bp)$AuCl_2$ (**5**) (100 mg, 0.229 mmol) and bis(sulfonamide) (**15**) (142 mg, 0.341 mmol) were stirred in refluxing methanol (30 mL). Aqueous trimethylamine (2 mL, excess) was added and the resulting bright orange solution was further refluxed for 15 min. Distilled water (50 mL) was added, resulting in the formation of a milky yellow suspension. This was stirred until cool, filtered, and the product washed with water (2 × 10 mL) and diethyl ether (10 mL) then dried under vacuum to give (88 mg, 49%) of bright yellow solid. *Anal.* Calc. for $C_{32}H_{28}N_3O_4S_2Au$: C, 49.3; H, 3.6; N, 5.4. Found: C, 48.0; H, 3.7; N, 5.5%. M.p. 151–155 °C. IR: ν(SO_2, asym) 1301 cm^{-1}; ν(SO_2, sym) 1145 cm^{-1}. ESI-MS: cone voltage 20 V; *m/z* 802 (100%, $[M+Na]^+$), 1581 (20%, $[2M+Na]^+$). Cone voltage 60 V: *m/z* 802 (100%, $[M+Na]^+$), 625 (20%, $[M-SO_2Tol+H]^{\bullet+}$), 471 (15%, $[M-2SO_2Tol+2H]^{\bullet+}$), 1581 (20%, $[2M+Na]^+$). ^1H NMR: δ 2.33 (s, 3H), 2.39 (s, 3H), 4.08 (d, 1H), 4.77 (d, 1H), 6.8–7.5 (m, 15H), 7.56 (d, 1H), 7.70 (d, 2H), 7.80 (t, 1H), 9.15 (d, 1H). $^{13}C–\{^1H\}$ NMR: δ 21.6 (CH_3), 21.7 (CH_3), 48.1 (CH_2), 121.6–156.8 (aryl C).

4.7. Synthesis of (2-anp)Au{N(SO$_2$Tol)C$_6$H$_4$N(SO$_2$Tol)} (**18**)

The complex (2-anp)AuCl$_2$ (**6**) (100 mg, 0.229 mmol) and bis(sulfonamide) (**15**) (143 mg, 342 mmol) were mixed in refluxing methanol (30 mL). Aqueous trimethylamine (2 mL, excess) was added, resulting in the rapid formation of yellow/brown micro-crystals. The mixture was refluxed for a further 20 min then left to cool and filtered. The yellow solid was washed with water (2 × 10 mL) and diethyl ether (10 mL) and then dried under vacuum to give 150 mg (84%) of product. *Anal*. Calc. for $C_{31}H_{27}N_4O_4S_2Au$: C, 47.7; H, 3.5; N, 7.2. Found: C, 47.5; H, 3.6; N, 7.2%. M.p. 264–265 °C (dec.). IR: ν(SO$_2$, asym) 1284 cm^{-1}, ν(SO$_2$, sym) 1140 cm^{-1}; ν(NH) 3294 cm^{-1}. ESI-MS: cone voltage 20 V; *m*/*z* 803 (100%, [M+Na]$^+$), 1583 (20%, [2M+Na]$^+$). Cone voltage 60 V: *m*/*z* 803 (100%, [M+Na]$^+$), 625 (20%, [M−SO$_2$Tol+H]$^{\bullet+}$), 471 (15%, [M−2SO$_2$Tol+2H]$^{\bullet+}$), 1583 (20%, [2M+Na]$^+$). ^{1}H NMR: δ 2.36 (s, 3H), 2.44 (s, 3H), 6.84 (t, 1H), 6.77 (t, 1H), 6.93–7.25 (m, 6H), 7.36 (d, 1H), 7.55 (d, 1H), 7.63 (d, 2H), 7.80 (t, 1H), 8.02 (d, 2H), 8.87 (d, 1H), 8.76 (s, NH). Due to the insolubility of this compound in common deuterated NMR solvents [(CD$_3$)$_2$SO, D$_2$O, CDCl$_3$], satisfactory ^{13}C NMR spectra could not be acquired.

4.8. Synthesis of (tolpy)Au{N(SO$_2$Tol)C$_6$H$_4$N(SO$_2$Tol)} (**19**)

The complex (tolpy)AuCl$_2$ (**7**) (100 mg, 0.231 mmol) and bis(sulfonamide) (**15**) (144 mg, 0.290 mmol) were mixed in refluxing methanol (30 mL). Aqueous trimethylamine (2 mL, excess) was added, resulting in the rapid deposition of yellow microcrystals. The solution was left to cool, then filtered, washed with water (2 × 10 mL) and diethyl ether (10 mL) then dried under vacuum to give 117 mg (65%) of yellow solid. *Anal*. Calc. for $C_{32}H_{28}N_3O_4S_2Au$: C, 49.3; H, 3.6; N, 5.4. Found: C, 49.5; H, 3.7; N, 5.5%. M.p. 262 °C (dec.). IR: ν(SO$_2$, asym) 1300 cm^{-1}; ν(SO$_2$, sym) 1140 cm^{-1}. ESI-MS: cone voltage 20 V; *m*/*z* 802 (100%, [M+Na]$^+$). Cone voltage 60 V: *m*/*z* 802 (100%, [M+Na]$^+$), 1581 (20%, [2M+Na]$^+$). ^{1}H NMR: δ 2.36 (s, 3H), 2.39 (s, 3H), 2.41 (s, 3H), 6.82 (t, 1H), 6.89 (t, 1H), 7.06 (d 1H), 7.18–7.24 (m, 3H), 7.34 (d, 1H), 7.40 (d, 1H), 7.72 (d, 2H), 7.79–7.81 (m, 3H), 8.00 (t, 1H), 9.31 (d, 1H). ^{13}C–{^{1}H} NMR: δ 21.8 (*C*H$_3$), 21.9 (*C*H$_3$), 23.4 (*C*H$_3$), 120–165 (aryl *C*).

4.9. Synthesis of (damp)Au{N(SO$_2$Tol)C$_6$H$_4$N(SO$_2$Tol)} (**20**)

The complex (damp)AuCl$_2$ (**8**) (75 mg, 0.19 mmol) and bis(sulfonamide) (**15**) (120 mg, 0.28 mmol) were mixed in refluxing methanol (30 mL), resulting in a clear yellow solution. Aqueous trimethylamine (2 mL, excess) was added resulting in a rapid colour change to give an orange solution which was further refluxed for 5 min. Water (75 mL) was added, resulting in the immediate formation of yellow microcrystals. After cooling, the mixture was filtered and the product washed with water (2 × 10 mL) and diethyl ether (10 mL) and dried under vacuum giving 57 mg (41%) of product. *Anal*. Calc. for $C_{29}H_{30}N_3O_4S_2Au$: C, 46.7; H, 4.1; N, 5.6. Found: C, 46.6; H, 3.9; N, 5.7%. M.p. 196–198 °C (dec.). IR: ν(SO$_2$, asym) 1302 cm^{-1}; ν(SO$_2$, sym) 1147 cm^{-1}. ESI-MS: cone voltage 20 V; *m*/*z* 767 (100%, [M+Na]$^+$), 465 (100%, unidentified), 1511 (32%, [2M+Na]$^+$). Cone voltage 60 V: *m*/*z* 767 (100%, [M+Na]$^+$), 591 (32%, [M−SO$_2$Tol+H]$^{\bullet+}$), 1511 (30%, [2M+Na]$^+$). ^{1}H NMR: δ 2.39 (s, 3H), 2.42 (s, 3H), 3.36 (s, 6H), 4.30 (s, 2H), 6.70 (t, 1H), 6.86 (t, 1H), 6.93 (d, 1H), 7.11 (m 2H), 7.2–7.3 (m, 6H), 7.70 (d, 2H), 7.80 (d, 2H), 8.02 (d, 1H). ^{13}C–{^{1}H} NMR: δ 21.5 (*C*H$_3$), 21.5 (*C*H$_3$), 53.2 (N*C*H$_3$), 75.7 (*C*H$_2$), 121.6–144.0 (aryl *C*).

4.10. Synthesis of (pic)Au{N(SO$_2$Tol)C$_6$H$_4$N(SO$_2$Tol)} (**21**)

The complex (pic)AuCl$_2$ (**14**) (75 mg, 0.19 mmol) and bis(sulfonamide) (**15**) (120 mg, 0.28 mmol) were mixed in refluxing methanol (30 mL), resulting in a colour change to give a red solution. Aqueous trimethylamine (2 mL, excess) was added, resulting in the rapid deposition of red/brown microcrystals. The solution was left to cool while stirring and then filtered, washed with water (2 × 10 mL) and diethyl ether (10 mL) then dried under vacuum to give 101 mg (72%) of red solid. *Anal*. Calc. for $C_{26}H_{23}N_4O_5S_2Au$: C, 42.6; H, 3.2; N, 7.7. Found: C, 41.6; H, 3.2; N, 7.4%. M.p. 226 °C. IR: ν(SO$_2$, asym) 1326 cm^{-1}, ν(SO$_2$, sym) 1154 cm^{-1}; ν(NH) 3368 cm^{-1}, ν(C=O) 1658 cm^{-1}. ESI-MS: cone voltage 20 V; *m*/*z* 755 (100%, [M+Na]$^+$), 1487 (30%, [2M+Na]$^+$), 1121 (25%, [3M+2Na]$^{2+}$). Cone voltage 60 V: *m*/*z* 755 (100%, [M+Na]$^+$), 1487 (25%, [2M+Na]$^+$). ^{1}H NMR: δ 2.40 (s, 3H), 2.41 (s, 3H), 6.7–7.5 (m, 8H), 7.60 (d, 2H), 7.71 (d, 2H), 7.95 (t, 1H), 8.17 (d, 1H), 8.36 (t, 1H), 9.61 (d, 1H). ^{13}C–{^{1}H} NMR: δ 21.6 (*C*H$_3$), 21.7 (*C*H$_3$), 118.3–150.0 (aryl C), 170.4 (*C*=O).

4.11. Synthesis of (2-bp)Au{N(SO$_2$Tol)C$_2$H$_4$N(SO$_2$Tol)} (**22**)

The complex (2-bp)AuCl$_2$ (**5**) (100 mg, 0.23 mmol) and bis(sulfonamide) (**16**) (100 mg, 28 mmol) were suspended in refluxing methanol (30 mL). Aqueous trimethylamine (2 mL, excess) was added and the solution further refluxed for 15 min. Water (50 mL) was added which resulted in the deposition of a white precipitate. After cooling to room temperature, the solid was filtered, washed with water (2 × 10 mL) and diethyl ether (10 mL) to give a pale grey solid. This was further purified by dissolving in minimal dichloromethane and filtering through a Pasteur pipette containing florisil. The compound was then isolated by slow addition of diethyl ether, filtered and washed with water (2 × 10 mL) and diethyl ether (10 mL) to give

59 mg (35%) of white microcrystals. *Anal.* Calc. for $C_{28}H_{28}N_3O_4S_2Au$: C, 46.0; H, 3.9; N, 5.8. Found: C, 45.9; H, 4.0; N, 5.8%. M.p. 215–219 °C (dec.). IR: $\nu(SO_2$, asym) 1280 cm^{-1}; $\nu(SO_2$, sym) 1139 cm^{-1}. ESI-MS: cone voltage 20 V; *m/z* 791 (100%, $[M+Me_3NH]^+$), 732 (95%, $[M+H]^+$), 754 (80%, $[M+Na]^+$), 1485 (35%, $[2M+Na]^+$), 1463 (30%, $[2M+H]^+$). Cone voltage 60 V: *m/z* 732 (100%, $[M+H]^+$), 754 (95%, $[M+Na]^+$), 1485 (40%, $[2M+Na]^+$). ^{1}H NMR: δ 2.37 (s, 3H), 2.38 (s, 3H), 3.10 (m, 2H), 3.51 (m, 2H), 4.01 (d, 1H), 4.55 (d, 1H), 6.80 (t, 1H), 7.06–7.33 (m, 9H), 7.42 (t, 1H), 7.63 (d, 1H), 7.75 (d, 2H), 7.94 (t, 1H), 9.16 (d, 1H). ^{13}C–{^{1}H} NMR: δ 21.4 (CH_3), 21.5 (CH_3), 47.9 (CH_2), 51.0 (CH_2), 56.6 (CH_2), 123.2–156.0 (aryl *C*).

4.12. Synthesis of (2-anp)Au{N(SO$_2$Tol)C$_2$H$_4$N-(SO$_2$Tol)} (*23*)

The complex (2-anp)$AuCl_2$ (**6**) (100 mg, 0.23 mmol) and bis(sulfonamide) (**16**) (100 mg, 0.28 mmol) were added to refluxing methanol (30 mL). While stirring, aqueous trimethylamine (2 mL, excess) was added and the solution was refluxed for a further 15 min. Water (50 mL) was added resulting in the formation of a pale yellow precipitate. After cooling, the solid was filtered and washed with water (2 × 10 mL) and diethyl ether (10 mL), and dried under vacuum to give 111 mg (54%) of yellow product. *Anal.* Calc. for $C_{27}H_{27}N_4O_4S_2Au$: C, 44.3; H, 3.7; N, 7.7. Found: C, 44.1; H, 3.8; N, 7.8%. M.p. 244–246 °C (decomp). IR: $\nu(SO_2$, asym) 1276 cm^{-1}, $\nu(SO_2$, sym) 1140 cm^{-1}; ν(NH) 3295 cm^{-1}. ESI-MS: cone voltage 20 V; *m/z* 755 (100%, $[M+Na]^+$), 1487 (20%, $[2M+Na]^+$), 1121 (20%, $[3M+2Na]^{2+}$). Cone voltage 60 V: *m/z* 755 (100%, $[M+Na]^+$), 1487 (25%, $[2M+Na]^+$). ^{1}H NMR: δ 2.44 (s, 6H), 3.29 (m, 2H), 3.62 (m, 2H), 6.69 (t, 1H), 6.76 (t, 1H), 7.03 (m, 2H), 7.22–7.35 (m, 4H), 7.45 (d, 1H), 7.63 (m, 3H), 7.42 (t, 1H), 7.90 (d, 2H), 8.73 (d, 1H), 8.83 (s, NH). Due to the insolubility of this compound in common deuterated NMR solvents [$(CD_3)_2SO$, D_2O, $CDCl_3$], satisfactory ^{13}C NMR spectra could not be acquired.

4.13. Synthesis of (tolpy)Au{N(SO$_2$Tol)C$_2$H$_4$N(SO$_2$Tol)} (*24*)

The complex (tolpy)$AuCl_2$ (**7**) (100 mg, 23 mmol) and bis(sulfonamide) (**16**) (100 mg, 0.23 mmol) were stirred in refluxing methanol (30 mL) and aqueous trimethylamine (2 mL, excess) was added, and the solution refluxed for 5 min. Water (50 mL) was added and the mixture cooled. The resulting pale yellow precipitate was filtered and washed with water (2 × 10 mL) and diethyl ether (10 mL) and dried under vacuum to give 135 mg (80%) of pale yellow microcrystals. *Anal.* Calc. for $C_{28}H_{28}N_3O_4S_2Au$: C, 46.0; H, 3.9; N, 5.8. Found: C, 45.7; H, 3.9; N, 5.8%. M.p. 186–188 °C (dec.). IR: $\nu(SO_2$, asym) 1303 cm^{-1}; $\nu(SO_2$, sym) 1138 cm^{-1}. ESI-MS: cone voltage 20 V; *m/z* 754 (100%, $[M+Na]^+$), 1485 (25%, $[2M+Na]^+$), 791 (20%, $[M+Me_3NH]^+$), 732 (15%, $[M+H]^+$). Cone voltage 60 V: *m/z* 754 (100%, $[M+Na]^+$), 732 (50%, $[M+H]^+$), 1485 (20%, $[2M+Na]^+$). ^{1}H NMR: δ 2.30 (s, 3H), 2.41 (s, 3H), 2.94 (s, 3H), 3.20 (d, 2H), 3.27 (d, 2H), 7.13–7.43 (m, 7H), 7.55 (s 1H), 7.77–7.86 (m, 5H), 8.03 (t, 1H), 9.45 (d, 1H). ^{13}C–{^{1}H} NMR: δ 21.56 (CH_3), 21.74 (2 × CH_3), 51.1 (CH_2), 57.7 (CH_2), 119.6–165.1 (aryl *C*).

4.14. Synthesis of (damp)Au{N(SO$_2$Tol)C$_2$H$_4$N(SO$_2$Tol)} (*25*)

The complex (damp)$AuCl_2$ (**8**) (75 mg, 0.19 mmol) and bis(sulfonamide) (**16**) (83 mg, 0.26 mmol) were mixed in refluxing methanol (30 mL), producing a pale yellow solution. Aqueous trimethylamine (2 mL, excess) was added and the mixture refluxed for 5 min. Water (75 mL) was added, resulting in the deposition of pale yellow microcrystals which were cooled, filtered and washed with water (2 × 10 mL) and diethyl ether (10 mL) and then dried under vacuum to give 115 mg (88%) of **25**. *Anal.* Calc. for $C_{25}H_{30}N_3O_4S_2Au$: C, 43.0; H, 4.3; N, 6.0. Found: C, 42.9; H, 4.3; N, 5.9%. M.p. 184–187 °C (dec.). IR: $\nu(SO_2$, asym) 1276 cm^{-1}; $\nu(SO_2$, sym) 1138 cm^{-1}. ESI-MS: cone voltage 20 V; *m/z* 719 (100%, $[M+Na]^+$), 1415 (35%, $[2M+Na]^+$). Cone voltage 60 V: *m/z* 719 (100%, $[M+Na]^+$), 1415 (30%, $[2M+Na]^+$). ^{1}H NMR: δ 2.40 (s, 6H), 3.13 (m, 2H), 3.18 (m, 2H), 3.40 (s, 6H), 4.34 (s, 2H), 6.97 (t, 1H), 7.12 (d, 1H), 7.17–7.25 (m, 5H), 7.38 (d, 1H), 7.65 (d, 2H), 7.73 (d, 2H). ^{13}C–{^{1}H} NMR: δ 21.5 (CH_3), 21.5 (CH_3), 52.0 (CH_2), 52.5 (NCH_3), 58.1 (CH_2), 77.1 (CH_2), 123.0–147.4 (aryl *C*).

4.15. Synthesis of (2-bp)Au{N(COMe)C$_6$H$_4$NH-(COMe)}Cl (*28*)

The complex (2-bp)$AuCl_2$ (**5**) (200 mg, 0.46 mmol), 1,2-diacetamidobenzene (**9**) (90 mg, 0.46 mmol) and silver(I) oxide (400 mg, excess) were added to dichloromethane (50 mL) and refluxed with stirring for 2 h. The solution was then filtered and the filtrate evaporated to dryness under reduced pressure. The resulting yellow crystals were dissolved in the minimum amount of dichloromethane and filtered through an alumina column. Slow addition of diethyl ether gave a pale yellow precipitate which was subsequently filtered and washed with diethyl ether (10 mL) and water (2 × 10 mL). ^{1}H NMR of the sample showed it to be a mixture of mainly **28** plus the metallacyclic complex **10**. X-ray quality crystals of **28** were grown by vapour diffusion of diethyl ether into a dichloromethane solution of the mixture at room temperature. M.p. 180–182 °C (dec.). *Anal.* Calc. for $C_{22}H_{21}N_3O_2AuCl$: C, 44.6; H, 3.5; N, 7.10. Found: C, 42.1; H, 3.4; N, 6.1%. *Anal.* Calc. for $C_{22}H_{21}N_3O_2AuCl \cdot 2H_2O$: C, 42.1; H, 3.4; N, 6.7%. IR: ν(N–H) 3303 cm^{-1}, ν(C=O) region 1693, 1611 cm^{-1}. ESI-MS: cone voltage 20 V; *m/z* 614

(100%, $[M+H]^+$), 556 (85%, $[M-HCl+Na]^+$), 578 (20%, $[M+Na]^+$).

4.16. Alternative synthesis of **28**

To the metallacyclic complex **10** (16.6 mg, 0.03 mmol) in dichloromethane (5 mL), sodium chloride (1.7 mg, 0.03 mmol) in methanol (2 mL) was added and stirred for 24 h. Benzoic acid (3.6 mg, 0.03 mmol) was then added, resulting immediately in the solution changing from dark to pale yellow. The solution was then filtered, reduced in volume and diethyl ether was added forming a precipitate that was identified as **28** by ^{1}H NMR.

4.17. X-ray crystal structure of (2-bp)Au{N(COMe)-C_6H_4N(COMe)} (**10**)

Yellow needles (m.p. 178 °C (dec.)) were obtained by vapour diffusion of diethyl ether into a dichloromethane solution of the crude product, at room temperature. Intensity data and unit cell dimensions were obtained on a Bruker SMART CCD diffractometer. Crystal size: $0.24 \times 0.10 \times 0.10$ mm, 23 180 total reflections, 3991 unique reflections (R_{int} 0.0378), range: $1.49° < \theta < 26.88°$, empirical absorption correction $T_{max,min}$: 0.518, 0.264. *Crystal data*: $C_{22}H_{20}AuN_3O_2$, M_r 555.38, tetragonal, space group $I4_1/a$. $a = 14.721(3)$ Å, $c = 35.971(1)$ Å, $V = 7795.4(3)$ Å^3, $D_{calc} = 1.893$ g cm^{-3}, $Z = 16$, $F(000) = 4288$, μ(Mo Kα) = 7.6 mm^{-1}.

The structure was solved using the direct methods option of SHELXS-97 [56]. The gold atom was initially located and then all other non-hydrogen atoms were located (SHELXL-97) by a series of difference maps. The full-matrix least-squares refinement was based upon F_o^2 with all non-hydrogen atoms anisotropic and hydrogen atoms in calculated positions; convergence gave $R_1 = 0.0214$ $[I \geqslant 2\sigma(I)]$, $wR_2 = 0.0427$ (all data), goodness-of-fit = 1.144. A final difference map showed no feature greater than 0.76 e Å^{-3}.

Due to potential *pseudo* symmetry in the molecule it was expected that the benzyl and pyridyl rings could show disorder. This was discounted since N(3) and C(31) were found to be in well-defined positions, based upon the following:

1. In the initial difference map the peak assigned to N(3) was 10 e Å^{-3} whereas for C(31) it was 8.8 e Å^{-3}.
2. When both positions were refined as carbon atoms, the U_{iso} values were 0.02 for the C(31) position and 0.07 for the N(3) (which are very similar to the other N atoms in the molecule when they were treated as carbon atoms).
3. The Au(1)–N(3) distance of 2.058 Å was significantly longer than the Au(1)–C(31) distance of 2.031 Å. The Au(1)–N(2) bond *trans* to C(31) was 2.089 Å, which is longer than the Au(1)–N(1) distance *trans* to N(3) of 2.022 Å. If the molecule had shown disorder presumably these distances would have been similar.
4. When the assignment of C(31) and N(3) was reversed the R factors increased from 0.0214 and 0.0427 to 0.0227 and 0.0466 for R_1 and wR_2, respectively.

4.18. X-ray crystal structure of (2-bp)Au{N(COMe)C_6H_4NH(COMe)}Cl (**28**)

Colourless prisms were obtained by vapour diffusion of diethyl ether into a dichloromethane solution containing the crude product at room temperature. M.p. 180–182 °C (dec.). Intensity data and unit cell dimensions were obtained on a Bruker SMART CCD diffractometer. Crystal size: $0.04 \times 0.32 \times 0.32$ mm, total reflections 11 252, unique reflections 4764 (R_{int} 0.0359), range: $1.73° < \theta < 27.13°$, empirical absorption correction $T_{max,min}$: 0.466, 0.389. *Crystal data*: $C_{22}H_{21}AuClN_3O_2$, M_r 591.83, triclinic, space group $P\bar{1}$. $a = 9.0334(1)$ Å, $b = 10.7766(1)$ Å, $c = 12.3915(1)$ Å, $\alpha = 88.846(1)°$, $\beta = 72.812(1)°$, $\gamma = 72.057(1)°$, $V = 1093.040(18)$ Å^3, $D_{calc} = 1.798$ g cm^{-3}, $Z = 2$, $F(000) = 572$, μ(Mo Kα) = 6.9 mm^{-1}.

The structure was solved by the direct methods option of SHELXS-97 [56], with the gold atom being located. All other non-hydrogen atoms were located by a series of difference maps. Full-matrix least-squares refinement (SHELXL-97) was based upon F_o^2 with all non-hydrogen atoms anisotropic and hydrogen atoms in calculated positions (with the exception of H(1) which was located by a difference map) converged with $R_1 = 0.0170$ $[I \geqslant 2\sigma(I)]$, $wR_2 = 0.0417$ (all data), goodness-of-fit = 1.072. A final difference map showed no feature greater than 0.99 e Å^{-3}. All calculations were carried out by the SHELX-97 suite of programs.

4.19. Biological assays

Details of the biological assays have been published previously [12].

Acknowledgements

We thank the University of Waikato (UW) for financial support of this work, including a scholarship to K.J.K. We also thank Tania Groutso (University of Auckland) for collection of the X-ray data sets, and Gill Ellis (University of Canterbury) for the biological assay data. Professor Alistair Wilkins is thanked for NMR expertise, and Pat Gread for technical support with mass spectrometry.

Appendix A. Supplementary information

Crystallographic data have been deposited with the Cambridge Crystallographic Data Centre, CCDC Nos. 602835 (**10**) and 602836 (**28**). Copies of this information can be obtained free of charge from The Director, CCDC, 12 Union Road, Cambridge CB2 1EZ, UK (fax: +44 1223 336 033; e-mail: deposit@ccdc.cam.ac.uk or www: http://www.ccdc.cam.ac.uk). Supplementary data associated with

this article can be found, in the online version, at doi:10.1016/j.poly.2006.06.036.

References

[1] W. Henderson, Adv. Organomet. Chem. 54 (2006) 207.
[2] A selection of the significant number of reviews on this topic: S.P. Fricker (Ed.), Metal Compounds in Cancer Chemotherapy, Chapman & Hall, London, 1994.
[3] C.W. Schwietert, J.P. McCue, Coord. Chem. Rev. 184 (1999) 67.
[4] Z. Guo, P.J. Sadler, Angew. Chem., Int. Ed. 38 (1999) 1512.
[5] Z. Guo, P.J. Sadler, Adv. Inorg. Chem. 49 (2000) 183.
[6] E. Wong, C.M. Giandomenico, Chem. Rev. 99 (1999) 2451.
[7] T.W. Hambley, J. Chem. Soc., Dalton Trans. (2001) 2711.
[8] B. Brønnum, H.S. Johansen, L.H. Skibsted, Inorg. Chem. 31 (1992) 3023.
[9] J.J. Pesek, W.R. Mason, Inorg. Chem. 22 (1983) 2958.
[10] W. Henderson, B.K. Nicholson, S.J. Faville, D. Fan, J.D. Ranford, J. Organomet. Chem. 631 (2001) 41.
[11] M.B. Dinger, W. Henderson, J. Organomet. Chem. 560 (1998) 233.
[12] C.H.A. Goss, W. Henderson, A.L. Wilkins, C. Evans, J. Organomet. Chem. 679 (2003) 194.
[13] M.B. Dinger, W. Henderson, J. Organomet. Chem. 557 (1998) 231.
[14] J. Kuduk-Jaworska, Transition Met. Chem. 19 (1994) 296.
[15] C. Evans, W. Henderson, B.K. Nicholson, Inorg. Chim. Acta 314 (2001) 42.
[16] K. Okano, K. Murata, T. Ikariya, Tetrahedron Lett. 41 (2000) 9277.
[17] N. Hazari, P. Mountford, Acc. Chem. Res. 38 (2005) 839.
[18] C. Guo, J. Qiu, X. Zhang, D. Verdugo, M.L. Larter, R. Christie, P. Kenney, P.J. Walsh, Tetrahedron 53 (1997) 4145.
[19] E.J. Corey, M.A. Letavic, J. Am. Chem. Soc. 117 (1995) 9616.
[20] Y. Tamai, H. Yoshiwara, M. Someya, J. Fukumoto, S. Miyano, J. Chem. Soc., Chem. Commun. (1994) 2281.
[21] H. Ito, A. Sato, T. Taguchi, Tetrahedron Lett. 38 (1997) 4815.
[22] D.A. Evans, S.G. Nelson, J. Am. Chem. Soc. 119 (1997) 6452.
[23] S. Cai, R.R. Schrock, Inorg. Chem. 30 (1991) 4105.
[24] K. Kavallieratos, J.M. Rosenberg, J.C. Bryan, Inorg. Chem. 44 (2005) 2573.
[25] K. Kavallieratos, J.M. Rosenberg, W.-Z. Chen, T. Ren, J. Am. Chem. Soc. 127 (2005) 6514.
[26] Y. Fuchita, H. Ieda, Y. Tsunemune, J. Kinoshita-Nagaoka, H. Kawano, J. Chem. Soc., Dalton Trans. (1998) 791.
[27] J.N. Baxter, J. Cymerman-Craig, J.B. Willis, J. Chem. Soc. (1955) 585.
[28] Y.-P. Tu, A.G. Harrison, J. Am. Soc. Mass Spectrom. 9 (1998) 454.
[29] G.J. Van Berkel, F. Zhou, J. Am. Soc. Mass Spectrom. 7 (1996) 157.
[30] G.J. Van Berkel, J.M.E. Quirke, R.A. Tigani, A.S. Dilley, T.R. Covey, Anal. Chem. 70 (1998) 1544.
[31] G.S. Hall, R.H. Soderberg, Inorg. Chem. 7 (1968) 2300.
[32] P.-H. Cheng, H.-Y. Cheng, C.-C. Lin, S.-M. Peng, Inorg. Chim. Acta 169 (1990) 19.
[33] T.G. Appleton, H.C. Clark, L.E. Manzer, Coord. Chem. Rev. 10 (1973) 335.
[34] A. Shivanyuk, K. Rissanen, S.K. Körner, D.M. Rudkevich, J. Rebek Jr., Helv. Chim. Acta 83 (2000) 1778.
[35] M.A. Cinellu, A. Zucca, S. Stoccoro, G. Minghetti, M. Manassero, M. Sansoni, J. Chem. Soc., Dalton Trans. (1995) 2865.
[36] M.A. Dewey, A.M. Arif, J.A. Gladysz, J. Chem. Soc., Chem. Commun. (1991) 712.
[37] S.E. Denmark, S.P. O'Connor, S.R. Wilson, Angew. Chem., Int. Ed. Engl. 37 (1998) 1149.
[38] A.B. Corradi, E. Gozzoli, L. Menabue, M. Saladini, L.P. Battaglia, P. Sgarabotto, J. Chem. Soc., Dalton Trans. (1994) 273.
[39] W.-H. Leung, J.L.C. Chim, H. Hou, T.S.M. Hun, I.D. Williams, W.-T. Wong, Inorg. Chem. 36 (1997) 4432.
[40] W.-H. Leung, E.K.-F. Chow, Polyhedron 12 (1993) 1635.
[41] H.-Y. Cheng, P.-H. Cheng, C.-F. Lee, S.-M. Peng, Inorg. Chim. Acta 181 (1991) 145.
[42] J. Sánchez-Piso, J.A. García-Vázquez, J. Romero, M.L. Durán, A. Sousa-Pedrares, E. Labisbal, O.R. Nascimento, Inorg. Chim. Acta 328 (2002) 111.
[43] MERCURY, version 1.4.1, Cambridge Crystallographic Data Centre, 2005.
[44] H. Wang, G.R. Agnes, Anal. Chem. 71 (1999) 3785.
[45] H. Wang, G.R. Agnes, Anal. Chem. 71 (1999) 4166.
[46] P. Frohberg, G. Drutkowski, C. Wagner, Eur. J. Org. Chem. (2002) 1654.
[47] R.G. Pearson, Inorg. Chem. 12 (1973) 712.
[48] W. Henderson, B.K. Nicholson, A.G. Oliver, J. Organomet. Chem. 620 (2001) 182.
[49] D. Fan, C.-T. Yang, J.D. Ranford, J.J. Vittal, P.F. Lee, Dalton Trans. (2003) 3376.
[50] H.L. Riley, H.B. Baker, J. Chem. Soc. (1926) 2510.
[51] Y. Fuchita, H. Ieda, A. Kayama, J. Kinoshita-Nagaoka, H. Kawano, S. Kameda, M. Mikuriya, J. Chem. Soc., Dalton Trans. (1998) 4095.
[52] P.-A. Bonnardel, R.V. Parish, J. Organomet. Chem. 515 (1996) 221.
[53] J. Vicente, M.T. Chicote, M.D. Bermudez, J. Organomet. Chem. 268 (1984) 191.
[54] D.T. Hill, K. Burns, D.D. Titus, G.R. Girard, W.M. Reiff, L.M. Mascavage, Inorg. Chim. Acta 346 (2003) 1.
[55] L.J. Arnold, J. Chem. Educ. 69 (1992) 811.
[56] G.M. Sheldrick, SHELX Suite of Programs, University of Göttingen, Göttingen, Germany, 1997.

Available online at www.sciencedirect.com
ScienceDirect
Polyhedron 26 (2007) 448–455
POLYHEDRON
www.elsevier.com/locate/poly

Electronic structure and near-IR transitions of FcC_2R and FcC_4R dyads

A.H. Flood [a], C.J. McAdam [b], K.C. Gordon [b], H.G. Kjaergaard [b], A.M. Manning [c], B.H. Robinson [b,*], J. Simpson [b]

[a] *Chemistry Department, Indiana University, 800 East Kirkwood Avenue, Bloomington, IN 47401, USA*
[b] *Department of Chemistry, University of Otago, P.O. Box 56, Dunedin, New Zealand*
[c] *Department of Chemistry, University College Dublin, Belfield, Dublin 4, Ireland*

Received 16 May 2006; accepted 6 July 2006
Available online 14 July 2006

Abstract

This paper describes the orbital configuration which provides a basis for the understanding of the electronic structure and spectroscopic properties of 17e and 18e FcC_2R and FcC_4R dyads, where R is H, 1-naphthyl, 9-anthryl, 3-pyrenyl, perylenyl. DFT calculations show that destabilisation of the ferrocenyl π orbitals upon binding a C≡CR group to a Cp ring leads to the metal-based a_1 orbital dropping below the e_1-a so that the frontier orbital configuration is $(e_2'\text{-a},\pi)^2(e_2'\text{-b},\text{metal})^2(e_1'\text{-a},\pi)^2$, $(a_1,\text{metal})^2$. The contribution of the aryl group to the π e_2-a and e_1-a orbitals varies with the annelation of the ring. The LUMO is aryl based. The calculations are consistent with the spectroscopic data for the 18e species. Oxidation to the 17e cations does not change the orbital configuration but the orbital energies are lowered by the positive charge centred on the Fe. A strongly solvatochromic transition in the near-IR, a signature for the 17e cations, is best described as an LMCT transition but the contribution of C_2R and C_4R to the donor and acceptor levels depends on the ionization energy of the aryl π orbital. LMCT energies decrease from FcC_2R to FcC_4R dyads.
© 2006 Elsevier Ltd. All rights reserved.

Keywords: Electronic structure; DFT calculations; Ferrocenylaryl dyads; Ferroceniumaryl dyads; NIR spectra

1. Introduction

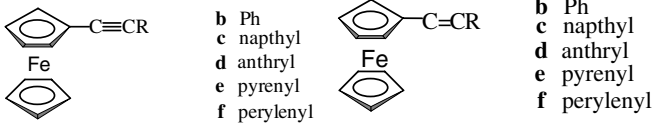
Many aspects of the electronic structure of closed shell metallocenes, especially ferrocene [1–5], have been investigated, both theoretically and experimentally. With the current focus on ferrocenyl materials with second-order NLO properties [6,7], these studies have extended into ferrocenyl derivatives where electron acceptors are bound to one or two cyclopentadienyl rings, especially via a π-linkage [2,8–10]. A detailed description of the electronic structure for this class of compound has evolved, the salient features being an understanding of the ferrocenyl-(π-link)-acceptor energy levels and consequential optical transitions. The electronic structure of compounds with strong donors on a Cp ring [11] or dyads with a ferrocenyl-(π-link)-donor motif [12] have not received the same attention. Barlow and Marder [2] have commented that a $D_{5h/5d}$ metallocene can interact with a π-bridge both via a cyclopentadienyl ring and through a metal-based orbital when an organic acceptor was involved. Whether this situation also pertains in electron-rich π-linked dyads, and/or with ferrocenium analogues, is the thrust of this paper. This was of interest to us as any change in the electronic structure, either in the neutral or oxidized molecule, may enable the classical quenching effect of the metallocene to be modified if a fluorophore is bound to a cyclopentadienyl ring via a π-conjugated bridge. This has been achieved where the fluorophore is a strong electron acceptor [13–15].

In a previous paper [16] we reported the synthesis and molecular structure of the ferrocenyl dyads **1a**–**f** and **2a**–**f** and [FcC═C–C═CR]. Spectroscopic and structural data indicated that there was little mutual perturbation of the Fc and aryl groups via the unsaturated link in the ground

* Corresponding author. Tel.: +64 3 4797912; fax: +64 3 4797906.
E-mail address: brobinson@alkali.otago.ac.nz (B.H. Robinson).

0277-5387/$ - see front matter © 2006 Elsevier Ltd. All rights reserved.
doi:10.1016/j.poly.2006.07.002

state of the dyad. But this was not true when the ferrocenyl group was oxidized to the ferrocenium analogue. Absorption bands in the 400–700 nm region of the visible spectrum were not typical of ferrocenium compounds and all oxidized dyads had weak bands in the near-IR. Similar NIR bands have been reported for a number of ferrocenium derivatives [10,11,17] and the effects of donors on the ferrocenium LMCT band have been documented [17]. We subsequently found that these near-IR bands were also a feature of dyads with FcC≡C– or FcC=C-group, even when R was a strong acceptor (e.g. naphthalimide [16]). They were also observed in oxidized dyads of general type, Mc^{+}–C≡C–R or Mc^{+}–C≡C–R, where Mc is a donor metallocene fragment such as the isolobal η-$C_5H_4Co(Ph_4C_4)$. In order to gain an insight into the origin of the NIR bands, DFT calculations were performed on the dyads **1a**–**f** [18] and **2a**–**f**. The π link between the ferrocenyl and aryl groups significantly perturbs the ferrocenyl energy levels leading to a different orbital configuration to that of ferrocene. This one-electron configuration provides an explanation of the interesting spectroscopic properties and electrochromism displayed by these dyads



2. Results and discussion

2.1. DFT calculations on 18e dyads

Density functional theory (DFT), which is well-performed for ferrocene [4,5] and derivatives [9b], was used to probe the influence of the –C≡C and aryl group on the frontier orbitals of ferrocene. B3LYP calculations were carried out on **1a**–**f** and **2a**–**f**. Iso-surfaces for the frontier orbitals for **1d** are represented in Fig. 1a; surfaces for the other molecules are available from the authors. Calculated orbital energies are given in Table 1 and schematically represented in Fig. 2. B3LYP/6.31G(d) calculations of the optimised geometries were in good agreement with those found in the X-ray crystal structures [16]. An eclipsed geometry for the Cp rings was found for all dyads so the appropriate ferrocenyl point group is D_{5h} but the subgroup D_5 is adequate. For the dyads the symmetry is C_{2v}.

Ferrocene (D_5) has an e_2' (x^2-y^2, xy) HOMO, which is predominately a δ bond and metal in character. The e_2' lies 0.35 eV above the metal-based a_1 (d_{z^2}) orbital. The e_1' ($Cp + d_{xz/yz}$) is the strongest bonding interaction. Ionization potentials for the e_2, a_1, e_1 frontier orbitals of ferrocene are, respectively, 6.88, 7.23 and 8.72 eV [4]. The addition of a C≡C to an aromatic ring raises the ionization energy of the π HOMO and for HC≡CR the IP's range from 9.12 eV for ethynylbenzene to 8.12 eV for the larger annelated rings [19]. Consequently, the π orbitals of the C≡CR group are ideally placed for a strong π interaction with ferrocene orbitals, with the aromatic HOMO having a stronger interaction with the e_2 orbital as the ring size increases; this was confirmed by the B3LYP calculations (vide infra). The DFT calculations show that the introduction of a conjugated substituent does indeed have a significant impact on the relative energies of the ferrocene orbitals, particularly the strongly bonding e_1' level (Fig. 2).

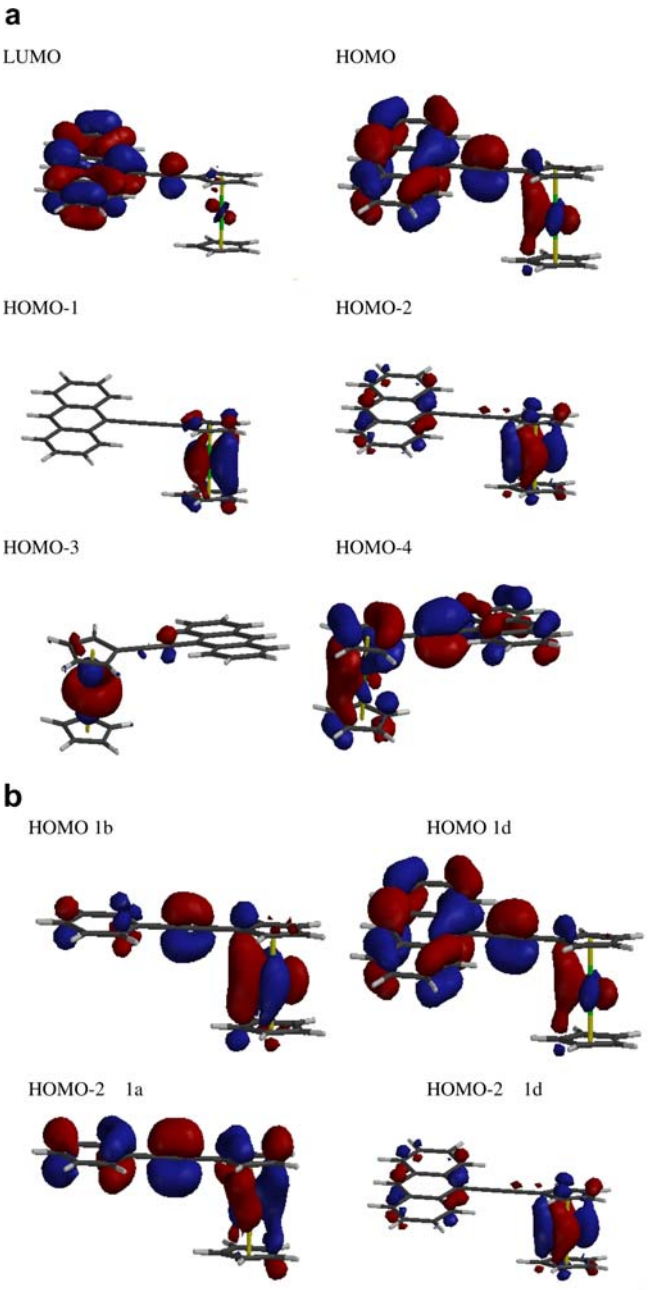


Fig. 1. (a) Frontier orbitals of **1d**; (b) comparison of HOMO and HOMO − 2 frontier orbitals for **1b** and **1d**.

Table 1
Molecular orbital energies[a]

Molecule	HOMO − 3	HOMO − 2	HOMO − 1	HOMO	LUMO
	e'_1	a'_1	e'_2	e'_2	e'_1
FcH	−0.2487	−0.22228	−0.18981	−0.18980	0.00784
	e'_1-a/a_1	e'_1-a/a_1	e'_2-b	e'_2-a	
1a	−0.23194	−0.22827	−0.19687	−0.19560	−0.00892
2a	−0.2257	−0.2219	−0.1922	−0.1900	−0.0120
	a_1	e'_1-a	e'_2-b	e'_2-a	
1b	−0.22892	−0.21229	−0.19605	−0.19184	−0.03386
1c	−0.22958	−0.20519	−0.19699	−0.19011	−0.05012
1d	−0.23850	−0.19965	−0.19763	−0.18173	−0.06893
1e	−0.22985	−0.19986	−0.19704	−0.18435	−0.06393
	e'_1	a'_1	e'_2	e'_2	e'_1
$[FcH]^{+b}$	−0.4281(α)	−0.4281(α)	−0.3916(β)	−0.3916(β)	−0.2862(β)

[a] Energies in au.
[b] Energies are given for the α or β one-electron orbitals.

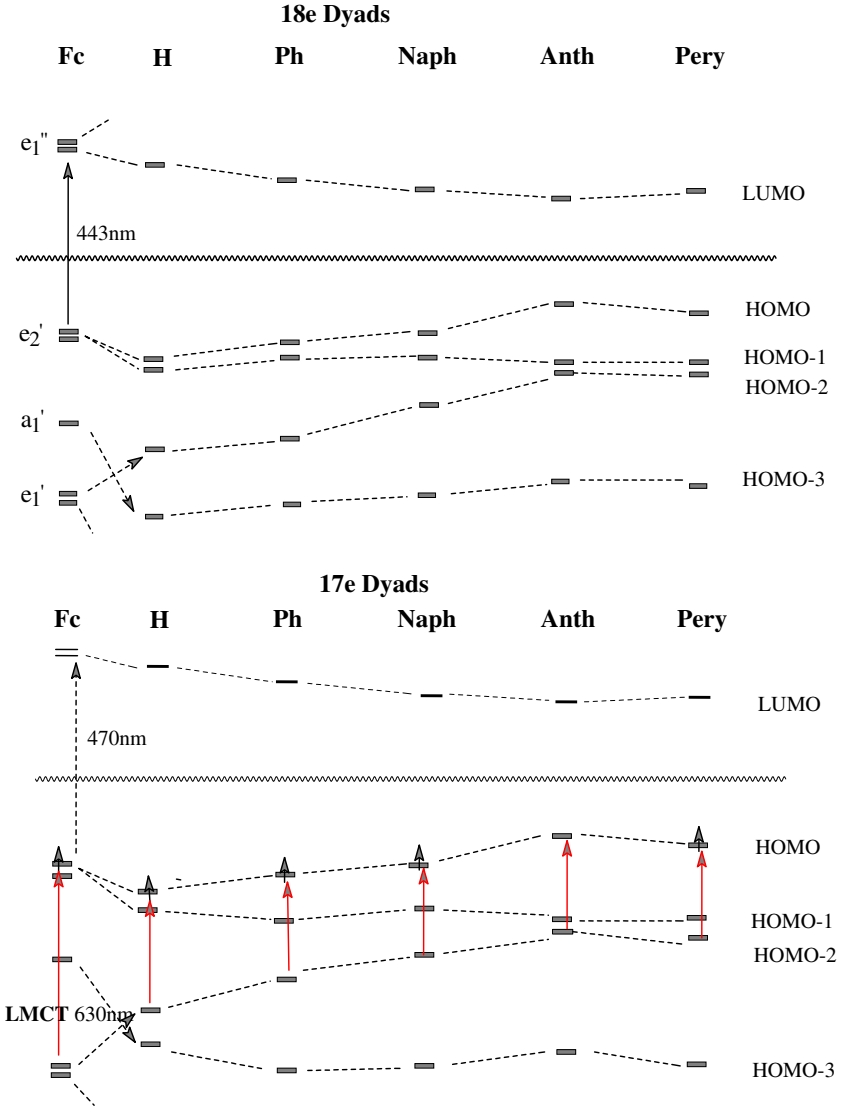


Fig. 2. Calculated orbital energies for 18e and 17e dyads compared to ferrocene.

For ease of tracing the perturbation of the ferrocenyl orbitals, the dyad frontier orbitals arising from the degenerate ferrocenyl orbitals in lower symmetry will be designated as e'_2-a/e'_2-b and e'_1-a/e'_1-b rather than a formal C_{2v} designation. One of the degenerate e'_2 or e'_1 orbitals has the correct nodal symmetry (e'_2-a and e'_1-a) to interact with the HOMO of the C≡CR substituent.

We first consider the effect of adding a –C≡CH group to the Cp ring of ferrocene. The energies of both orbital pairs, e'_2-a/e'_2-b and e'_1-a/e'_1-b, are lowered relative to the parent ferrocene orbital. There is an orbital mismatch for the ferrocenyl-π-substituent interaction (Fig. 1) and the orbital involved in the π interaction, the e'_2-a, is slightly destabilised relative to the e'_2-b orbital which is entirely metal-based. This is the reverse of that found when the C_1 substituent is an electron-withdrawing group [9b]. Similarly the strongly interacting e'_1-a orbital is higher in energy than the metal-based e'_1-b. This destabilisation of the π e'_1-a orbital has an extremely important consequence for the relative energy of the e'_1-a and a_1 (d_{z^2}) orbitals. For **1a**, mixing of these two orbitals occurs with the result that the one-electron HOMO − 2 and HOMO − 3 both have d_{z^2} and d_{xz} character. The orbital configuration for **1b–f** is more simple. For these dyads the increase in energy of the π (e'_1-a) orbital leads to a *crossover of energy such that the HOMO − 2 orbital is now the* e'_1-a *combination and the HOMO − 3 the* a_1 (see Fig. 2). The frontier orbital configuration for **1b–f** is thus $(e'_2\text{-a})^2$, $(e'_2\text{-b})^2$, $(a_1)^2$, $(e'_1\text{-a})^2$, $(e'_1\text{-b})^2$ (Figs. 2 and 5).

There is a progressive destabilisation of the HOMO e'_2-a π orbital as the annelation of the aryl ring increases. Since there is little variation in the energy of e'_2-b, the energy difference between HOMO and HOMO − 1 increases as the ionization energy of the aryl decreases, 0.035 eV (**1a**) to 0.43 eV (**1d**), although it is still relatively small. More significant is the increasing destabilisation of the strongly bonding HOMO − 2 (e'_1-a) orbital such that the HOMO − 2/HOMO − 3 separation increases from 0.45 eV for **1a** to 1.06eV for **1e**; in fact, the HOMO − 1/HOMO − 2 orbitals for **1e** are almost degenerate (separation 0.05 eV) (Table 1). Concomitant with the increase in energy of the HOMO, there is an increasing –C≡CR contribution to the HOMO; by **1d** the HOMO has a large –C≡CR component. This trend nicely correlates with the decreasing ionization potential of the C≡CR group. Conversely, there is an increase in the metal character of HOMO − 2 (e'_1-a) (Fig. 1b).

Calculations on the ethenyl dyads **2a**, **2c** and **2d** indicated that the orbital configuration $(e'_2\text{-a},\pi)^2(e'_2\text{-b, metal})^2$-$(e_1\text{-a},\pi)^2$, $(a_1$, metal$)^2$ also held for the ethenyl series. An ethenyl group interacts more strongly with the ferrocene moiety than an ethynyl group and this is reflected in the higher energy of the π orbitals for the ethenyl series. As a consequence, the HOMO for ferrocene and **2a** have almost the same energy which accounts for the observation that the potentials for the $[Fc]^{+/0}$ couple for ferrocene and **2a** are similar (0.55 V and 0.52 V, respectively) whereas that the ethynyl dyad **1a** is more difficult to oxidise (0.63 V).

Calculations show that the LUMO in all the dyads is entirely aryl-based and this is consistent with experimental data. Their reduction potentials were similar to the free arene in the same solvent and simulation of the EPR spectra of the radical anions **1**(**b–f**)$^{-\cdot}$ and **2**(**a–e**)$^{-\cdot}$ was achieved using the values obtained from EPR spectra of the HC≡CR$^{-\cdot}$ and HC=CR$^{-\cdot}$ radical anions.

3. Electronic spectra

Identification of the lowest energy bands in the UV–Vis spectra was hampered by the overlap with the very intense π–π* transition of the aryl group. Nevertheless, the weak lowest energy band does not change significantly in energy as the annelation of the ring increases; the energies are all $22\,500 \pm 200$ cm^{-1} compared to 22 700 cm^{-1} for ferrocene. These bands can be given an assignment analogous to the lowest energy spin-allowed d–d transition ($^1A_1 \rightarrow aE_1$) of ferrocene [1] and the invariant character of this transition is consistent with the relatively constant HOMO–LUMO band gap across the series. Resonance Raman spectra ($\lambda_{exc} = 457.9$ nm) supported this assignment for the low-energy band as there was a weak enhancement of the $\nu_{C\equiv C}$ band, the ferrocenyl ring breathing mode at 1100 cm^{-1} and ν_{Fe-C} at 298 cm^{-1} and aryl modes. As noted previously [16], the small red-shift in the π–π* transition of the C≡CR group shows that there was not strong perturbation by the ferrocenyl moiety.

Electrochemical oxidation of **1a–f** and **2a–f** at the potential of their $[Fc]^{+/0}$ couple generated the respective green-blue [**1a–f**]$^+$ and green [**2a–f**]$^+$ 17e cations. The C_4 species, $[Fc\text{-}(CH{=}CH)_2R]^+$ (R = Ph, naph, pyr, anthryl), were also produced to study the effect of extending the unsaturated link. For [**1b–f**]$^+$ constant isosbestic points, complete spectral reversibility when the potential is cycled in an OTTLE experiment, and the fact that identical spectra were obtained by controlled chemical oxidation, attest to the stability of the 17e species. There was spectroscopic evidence that the lifetime of **1a**$^+$ was much shorter due to decomposition to the butadiene species $(FcC{\equiv}C)_2$. Representation of the cations as $Fc^+C{\equiv}CR$ in the ground state is vindicated by the vibrational data which show that shifts in the ferrocenyl vibrational bands are similar to those that occur with the formation of a ferrocenium ion [20]. For example, the Raman spectrum of **1d**$^+$ shows a shift of the Fc ring-breathing mode of +7 cm^{-1} and there is a typical Fc^+ band at 1113 cm^{-1} in the infrared spectrum.

In the ferrocenium cation [1,21–23], the $^2E_2$ state is 0.46 eV more stable than $^2A_1$ state and the ground state configuration is $e_2^3\,(xy, x^2-y^2)a_1^2\,(z^2)$. Previous calculations on ferrocenium derivatives [9b], and PE data indicate that the orbital ranking does not change from that in the 18e parent. Our DFT calculations on [**1a–b**]$^+$, and preliminary results for the ethenyl series, also confirmed that the frontier orbital energy sequence was also unchanged upon oxidation, $[(e'_2\text{-a})^1(e'_2\text{-b})^2(e_1\text{-a})^2, (a_1)^2]$, and that aryl contribution to the one-electron orbitals in the 17e and

18e species was similar. Overall, the energies of the occupied orbitals are lower than in the 18e analogues due to the coulombic effect of the positive charge. The HOMO–LUMO gap is significantly smaller than for the corresponding neutral species and it decreases from Fc^+ to $\mathbf{1a}^+$ and as the ring size increases.

Broad ($v_{1/2} \sim 2100\ cm^{-1}$), weak bands ($\varepsilon$ 700–1550 $M^{-1}cm^{-1}$), with energies from 7600 to 14 300 cm^{-1} (band **A**, Fig. 3, Table 2), were a feature of the electronic spectra of all 17e C_2 and C_4 dyads. The energies for the ethenyl compounds are red-shifted relative to the ethynyl series (Table 2) indicative of a stronger π interaction. Interestingly, the intensity and energy of these bands *increased* from the C_2 to the C_4 analogue; that is, with the interpolation of another –C=C group between the donor arene and acceptor (Table 2). So rather than distance reducing the increase in the energy of the e_1-a orbital, it has the opposite effect, implying that longer conjugated-chain ferrocenium dyads could have significantly more intense NIR bands. The anomalous behaviour of $\mathbf{2e}^+$ in the trend data, discussed elsewhere [16], is probably due to steric hindrance involving the ethenyl α-H atoms restricting the π interaction.

Support for an LMCT assignment for these NIR bands came from several sources. (1) The energy of **A** was dependent on the annelation of the aryl group (Table 2) and plots of these energies against the first vertical ionization energy of the respective aryl group are linear. The intensity also increases as the IP of the aryl group decreases. (2) A large negative solvatochromic shift ΔE_{solv} of 900–1200 cm^{-1} between CH_2Cl_2 ($\varepsilon = 9.1$) to MeCN ($\varepsilon = 37.5$) is indicative of a larger dipole in the ground state of the cations than the excited state. This is consistent with a CT assignment as in the excited state configuration of the cations have the

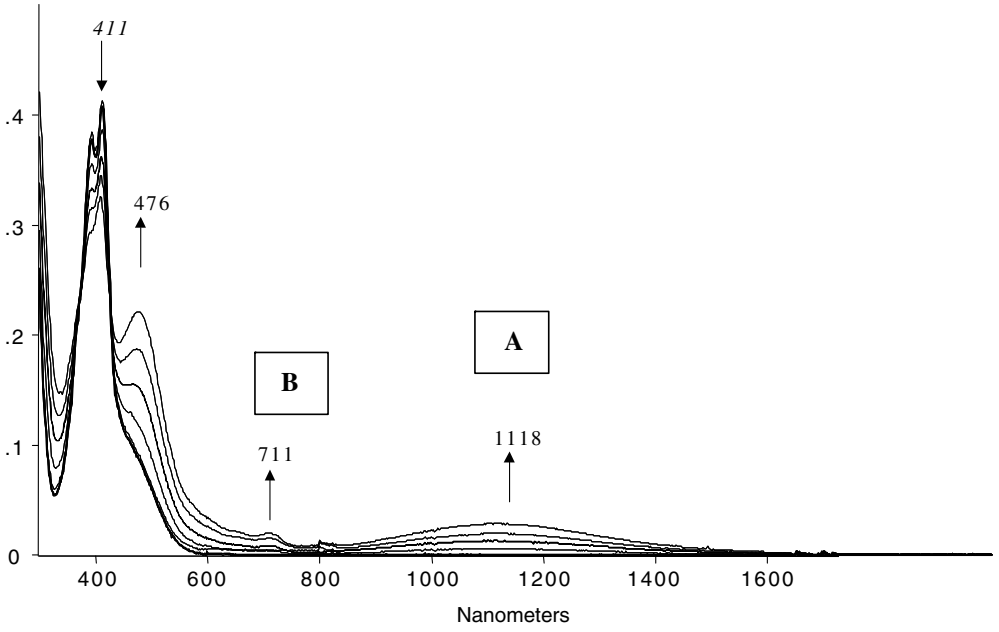


Fig. 3. OTTLE spectrum of **1d**, typical of the aryl dyads; 0.7 V on Pt, CH_2Cl_2, 293 K.

Table 2
Representative data for LMCT (A) and HOMO–LUMO (B) transitions[a]

R	Fc^+–C≡C–R			Fc^+–CH=CH–R			$Fc^+(CH=CH)_2R$	
	λ_{max}(A)	ε(A)	λ(B)	λ_{max}(A)[b]	ε(A)		λ_{max}(A)[b]	ε(A)
H	14.3		17.2	13.9		17.1		
Phenyl	12.6	0.7	17.4	11.1	0.6	17.1	9.5	0.5
1-Naphthyl	11.5	0.8	17.1	10.5	0.7	17.2		
2-Naphthyl	11.8	0.7	17.2	10.4	1.3	17.2	9.1	0.4
Phenanthryl	11.1	0.7	17.0	10.5	1.3	17.2		
Anthryl	8.9[b]	0.9	[d]	9.52	0.7	[d]	9.3	1.2
Pyrenyl	9.8[c]	1.3	17.5	9.0	1.6	17.5	8.3	1.9
Perylenyl	8.3	1.4	[d]	7.6	1.5	[d]		

[a] λ_{max}(A), ε(A), λ_{max}(B), refer to the data for bands A and B labelled in Fig. 3. $\lambda_{max} \times 10^{-2}\ cm^{-1}$; $\varepsilon \times 10^{-2}\ M^{-1}\ cm^{-1}$. Recorded in CH_2Cl_2.
[b] In MeCN, 9.7.
[c] In MeCN, 10.6.
[d] Obscured by π–π^* tail.

positive charge spread throughout the π system; in the ground state it is localised on the ferrocenyl acceptor. (3) For a CT transition the energy should be related to the electrochemical parameters of the donor and acceptor moieties; this is indeed the case (Fig. 4). (4) The Raman spectrum resonant with these bands shows an enhancement of modes associated with both Fc^+ and aryl units. The ring-breathing modes of the Fc/Fc^+ component show an *increase* in resonance enhancement on going from **1b–f** → $[\mathbf{1b–f}]^+$ whereas there is a threefold *decrease* in enhancement in the equivalent modes for FcH to FcH^+. These data imply that the Fc-based modes are deriving enhancement from an additional electronic transition that is not isolated on the metallocene.

Assignment of the lowest energy transition at 15900 cm^{-1} (in CH_2Cl_2) in the visible spectrum of the ferricenium ion and ferrocenium derivatives to a LMCT ($^2E_2 \rightarrow {}^2E_1$), corresponding to a $e_1 \rightarrow e_2$ one-electron transition, is well-founded [1,21,22]. Clearly, the same one-electron assignment e_1-a → e_2-a (Fig. 5) can be made for the lowest energy transition observed for these 17e dyads. What makes the LMCT energies so remarkable is the magnitude of their red-shift from the $^2E_2 \rightarrow {}^2E_1$ transition in Fc^+ (e.g. 8200 cm^{-1} for $\mathbf{2f}^+$). Previous work has found that the 'ferrocenium' transition is red-shifted by *donor* Cp-substituents [17]. Substitution by two butyl groups causes a red-shift of 800 cm^{-1} for example [20], and with the strong donor, N(*p*-tol)$_2$ the red-shift is 3250 cm^{-1} in CH_3CN with negative solvatochromism $\Delta E_{solv} = 427$ cm^{-1} for CH_2Cl_2/CH_3CN [11]. Aryl groups are not strong donors so we need to look to the electronic configuration for an explanation of the large red shifts. From the DFT calculations both the singly occupied HOMO and, especially the HOMO − 2, are the strongly perturbed orbitals because of conjugation of a C≡C–R group to the ferrocenyl ring. It is reasonable to assign the donor energy level as one related to the e_1-a orbital and the energy of this will be heavily dependant on the ionization potential of the C≡CR group. In the excited state the acceptor energy level, approximated by the $[Fc]^{+/0}$ potential, while perturbed strongly by the incorporation of the C≡C, is relatively invariant with aryl group. Therefore, the linear correlation of the CT energies seen in Fig. 4 is consistent with an assignment of a HOMO − 3 (donor) → HOMO (acceptor) CT transition. While a description as an LMCT transition is appropriate it is important to recognise that the contribution of the C≡CR π orbital to the donor and acceptor levels depends on the ionization energy of this π orbital. For the small ring aryl, the donor level has a significant input from the C≡CR π orbital; the reverse holds for the acceptor level.

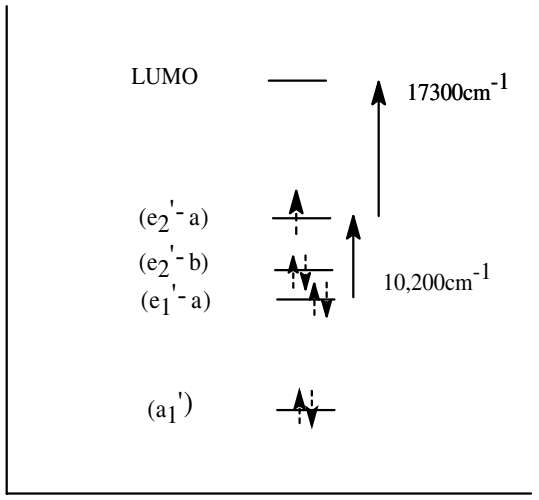


Fig. 5. NIR band assignment for $1d^+$; CH_2Cl_2, 15000–8000 cm^{-1}.

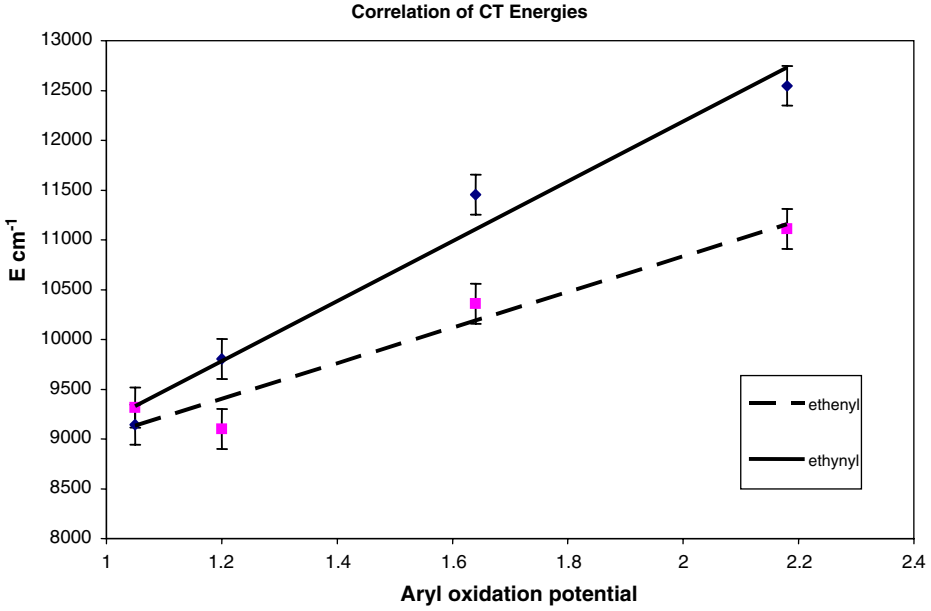


Fig. 4. Correlation of CT energies with oxidation potential of aryl group; CH_2Cl_2.

New bands in the OTTLE UV–Vis spectra above 22 000 cm^{-1} were generally shoulders on the intense aryl transitions and were not studied in detail nor were the weak transitions which were observed (Fig. 3) from 20 000 cm^{-1} to the LMCT band. The energy of some was dependent on the annelation of the ring and were solvatochromatic. Of greatest interest were the weak bands at ~17 200 cm^{-1} the energy of which varied little with aryl and were not solvatochromic (Table 2). These weak bands are assigned to HOMO–LUMO transitions (Fig. 5) but because both energy levels have considerable aryl character they cannot be described as spin-allowed d–d transitions as is the case for FcH^+ [1,21,22,24]. The calculated HOMO–LUMO gap for the 17e species is significantly smaller than for the corresponding 18e, consistent with the lower energy for the HOMO–LUMO transition in the 17e species.

4. Conclusion

Perturbation of a ferrocenyl moiety by an unsaturated RC_2 or RC_4 (R = aryl) group leads to an increase in the energy of the ferrocenyl π bonding orbitals such that the frontier orbital configuration for both 17e and 18e species has the dyad π orbitals at HOMO and HOMO − 2. The relative importance of the aryl contribution to the π orbitals is dependent on the ionization potential of the –C≡CR group and the HOMO has a significant aryl contribution with large annelated rings. Both the HOMO and HOMO − 2 provide a delocalised system for communication between the ferrocenyl and aryl groups but the experimental data suggest that there is not a strong π interaction in the ground state. Low-energy LMCT are ubiquitous in 17e $(metallocenyl)^+$-C_nR systems; R is a formal π donor and includes aromatic derivatives such as naphthalimide [13] generally regarded as acceptors. A wide range of metallocenyl groups, e.g. η-$C_5H_4Ni(PPh_3)$ [25], η-$C_5H_4Co(Ph_4C_4)$ [26] can be involved. As the LMCT energies range from 12 500 to 4000 cm^{-1} these systems represent a tunable electrochromic series. The challenge is to increase the intensity of the LMCT bands.

5. Experimental

The synthesis and characterisation of the compounds discussed herein have been published elsewhere [16]. *Calculations:* All *ab initio* calculations were performed using the B3LYP hybrid density functional theory with a 6-31G(d) basis set. All calculations were run within Spartan '02 and then QChem quantum module. The unrestricted B3LYP was used for calculations on the non-18 electron systems. *Spectroelectrochemistry:* Cyclic and square wave voltammetry in CH_2Cl_2 were performed for all compounds using a three-electrode cell with a polished disk, Pt (2.27 mm^2) as the working electrode; solutions were ~10^{-3} M in electroactive material and 0.10 M in supporting electrolyte (triply recrystallised $TBAPF_6$). Data were recorded on an EG&G PAR 273A computer-controlled potentiostat. Scan rates of 0.05–1 V s^{-1} were typically employed for cyclic voltammetry and for Osteryoung square-wave voltammetry, square-wave step heights of 1–5 mV, a square amplitude of 15–25 mV with a frequency of 30–240 Hz. All potentials are referenced to decamethylferrocene; $E_{1/2}$ for sublimed ferrocene was 0.55 V. EPR spectra were obtained using a Bruker EMX X-band spectrometer equipped with a Bruker variable temperature accessory, a Systron-Donner microwave frequency counter and a Bruker gaussmeter; ca 5 mM THF/$TBAPF_6$ solutions of the compound were reduced electrochemically *in situ*.

Acknowledgements

We thank Dr. A Rieger and the late Prof. P Rieger (Brown University) for assistance in recording and analysing the epr spectra and Dr. B. James (University of Auckland) for attempting to record UPS spectra of the dyads.

References

[1] Y.S. Sohn, D.N. Hendrickson, H.B. Gray, J. Am. Chem. Soc. 92 (1970) 3233.
[2] S. Barlow, S.R. Marder, J. Chem. Soc., Chem. Commun. (2000) 1555.
[3] (a) S. Evans, M.L.H. Green, B. Jewitt, A.F. Orchard, C.F. Pygall, J. Chem. Soc., Faraday Trans. 2 (68) (1972) 1847;
(b) C. Cauletti, J.C. Green, M.R. Kelly, P. Powell, J. van Tilburg, J. Robbins, J.C. Smart, J. Electron. Spectrosc. Rel. Phenom. 19 (1980) 327.
[4] M. Lein, J. Frunzke, A. Timoshkin, G. Frenking, Chem. Eur. J. 7 (2001) 4155.
[5] Z-F. Xu, Y. Xie, W-L. Feng, H.F. Schafer III, J. Phys. Chem. A 107 (2003) 2716.
[6] (a) N.J. Long, Angew. Chem., Int. Ed. Engl. 34 (1995) 21;
(b) A. Togni, T. Hayashi, Ferrocenes, VCH, Weinheim, 1995.
[7] I.R. Whitall, A.M. McDonagh, M. Samoc, M.G. Humphrey, Adv. Organometal. Chem. 42 (1998) 291.
[8] S. Barlow, H.E. Bunting, C. Ringham, J.C. Green, G.U. Bublitz, S.G. Boxer, J.W. Perry, S.R. Marder, J. Am. Chem. Soc. 121 (1999) 3715.
[9] (a) A.R. Pike, L.C. Ryder, B.R. Horrocks, W. Clegg, M.R.J. Elsegood, B.A. Connolly, A. Houlton, Chem. Eur. J. 8 (2002) 2891;
(b) M. Hocek, P. Stepnicka, J. Ludvik, I. Cisarova, I. Votruba, D. Reha, P. Hobza, Chem. Eur. J. 10 (2004) 2058;
(c) L. Lin, A. Berces, H-B. Kraatz, J. Organometal. Chem. 556 (1998) 11.
[10] M. Malaun, R. Kowallick, A.M. McDonagh, M. Marcaccio, R.L. Paul, I. Asselberghs, K. Clays, A. Persoons, B. Bildstein, C. Fiorini, J-M. Nunzi, M.D. Ward, J.A. McCleverty, J. Chem. Soc., Dalton Trans. (2001) 3025.
[11] (a) A. Mendiratta, S. Barlow, M.W. Day, S.R. Marder, Organometallics 18 (1999) 454;
(b) J. Ruiz, F. Ogliaro, J-Y. Saillard, J-F. Halet, F. Varret, D. Astruc, J. Am. Chem. Soc. 120 (1998) 1169.
[12] S-G. Liu, I. Perez, N. Martin, L. Echegoyen, J. Org. Chem. 65 (2000) 9092.
[13] C.J. McAdam, J.L. Morgan, B.H. Robinson, J. Simpson, P.H. Rieger, A.L. Rieger, Organometallics 22 (2003) 5126.
[14] (a) C.J. McAdam, B.H. Robinson, J. Simpson, Organometallics 19 (2000) 3644;
(b) E.M. McGale, B.H. Robinson, J. Simpson, Organometallics 22 (2003) 931.
[15] (a) S. Fery-Forgues, B. Delavaux-Nicot, J. Photochem. Photobiol. A 132 (2000) 137;
(b) M.D. Ward, J.A. McCleverty, J. Chem. Soc., Dalton Trans. (2002) 275;

(c) M. Murata, M. Yamada, T. Fujita, K. Kojima, M. Kurihara, K. Kubo, Y. Kobayashi, H. Nishihara, J. Am. Chem. Soc. 123 (2001) 12903.
[16] L. Cuffe, R.D.A. Hudson, J.F. Gallagher, S. Jennings, C.J. McAdam, R.B.T. Connelly, A.R. Manning, B.H. Robinson, J. Simpson, Organometallics 24 (2005) 2051.
[17] S. Toma, A. Gaplovsky, M. Hudecek, Z. Langfelderova, Monatsh. fur Chemie 116 (1985) 357.
[18] A low-level calculation on **1a** has been reported T. Lixandru, C. Ghirvu, L. Tataru, I. Mazilu, Buletin. Institut. Politehnic din Iasi, Chimie 23 (1977) 65.
[19] E.B. Ledesma, M.J. Wornat, Anal. Chem. 72 (2000) 5437.
[20] P.K. Dutta, M.A. Thomson, Chem. Phys. Lett. 131 (1986) 435.
[21] R. Prins, Chem. Commun. (1970) 280.
[22] R. Prins, Mol. Phys. 19 (1970) 603.
[23] (a) C. Kollmar, O. Khan, J. Chem. Phys. 96 (1992) 2988;
(b) A. Berces, T. Ziegler, L. Fan, J. Phys. Chem. 98 (1994) 1584.
[24] C. Levanda, K. Bechgaard, D.O. Cowan, J. Org. Chem. 41 (1976) 2700.
[25] C.J. McAdam, A.R. Manning, B.H. Robinson, J. Simpson, Inorg. Chim. Acta 358 (2005) 1673.
[26] C.J. McAdam, A.R. Manning, B.H. Robinson, J. Simpson, unpublished work.

Available online at www.sciencedirect.com
ScienceDirect
Polyhedron 26 (2007) 456–459
POLYHEDRON
www.elsevier.com/locate/poly

Radiotracer studies of the antitumor metallocene molybdocene dichloride with biomolecules

Kate S. Campbell [a], Carolyn T. Dillon [b], Suzanne V. Smith [c,*], Margaret M. Harding [d,*]

[a] School of Chemistry, The University of Sydney, NSW 2006, Australia
[b] Department of Chemistry, University of Wollongong, NSW 2522, Australia
[c] Institute of Materials and Engineering Science, Australian Nuclear Science and Technology Organization, Private Mail Bag 1, Menai, NSW 2234, Australia
[d] School of Chemistry, The University of New South Wales, Sydney, NSW 2052, Australia

Received 1 April 2006; accepted 10 July 2006
Available online 15 July 2006

Abstract

Neutron irradiation of Cp_2MoCl_2 for 24 h afforded the radiotracer $Cp_2{}^{99}MoCl_2$ which was characterised by UV–Vis spectroscopy and thin layer chromatography. Binding experiments with the thiol containing protein human serum albumin (HSA) or calf thymus DNA, were monitored for ^{99}Mo using a gamma counter. Under the conditions investigated, molar ratios of binding of 0.2:1 (Cp_2MoCl_2:DNA) and 9.4:1 (Cp_2MoCl_2:HSA) were calculated. The results are consistent with in vitro coordination studies that have shown strong preferential interaction of Cp_2MoCl_2 with thiols versus other donor sites in biomolecules including DNA.
© 2006 Elsevier Ltd. All rights reserved.

Keywords: Molybdocene dichloride; Antitumor metallocene; Genotoxicity; ^{99}Mo-radiotracer; DNA; Human serum albumin

1. Introduction

The development of new inorganic and organometallic complexes that interact with DNA and other biomolecules in a different way to cisplatin is an important goal in current medicinal chemistry [1–3]. A number of metallocene dihalides (Cp_2MCl_2, M = Ti, V, Mo, Nb) have provided promising lead compounds [4–6], notably titanocene dichloride, which completed phase II clinical trials [7,8]. While the mechanism of antitumor action of titanocene dichloride is not fully understood, current evidence suggests that the Cp ligands serve as hydrophobic ligands that protect the metal centre by allowing hydrolytic release of Ti into the vacant Fe binding sites of transferrin [9] which delivers the active metal species into the cell and the chromatin [10–12]. In contrast, molybdocene dichloride does not target transferrin as the Cp ligands in Cp_2MoCl_2 are stable to hydrolysis at physiological pH [13–15] (Fig. 1). This complex exhibits a different profile of biological activity to Cp_2MCl_2 (M = Ti, V, Nb) [4,16] and a number of studies have shown that, despite their structural similarity, each of the metallocene dihalides exhibits different bioinorganic chemistry [17,18].

We have performed detailed studies on the bioorganometallic chemistry of molybdocene dichloride in order to provide insight into the mechanism of antitumor action and to aid in the design of second generation derivatives that may have improved biological activity [18–24]. These studies have demonstrated that biological activity is dependent on generation of "Cp_2Mo^{2+}" as the putative active species in vivo [20] which rapidly and irreversibly coordinates with deprotonated thiols in preference to N-donor, O-donor and phosphate binding sites in DNA and proteins [21]. A number of thiol derivatives, $Cp_2Mo(SR_2)$, designed to maximize cell uptake and release the active species, were prepared and tested for activity [20]. Graphite furnace atomic absorption spectroscopy (GFAAS) [20] and X-ray fluorescence (XRF) studies [22] were used to study the uptake and cellular distribution of Mo derived from these

* Corresponding authors. Tel.: +61 2 9717 3125/9385 5638; fax: +61 2 9717 9225/9385 5949.
E-mail addresses: svs@ansto.gov.au (S.V. Smith), harding@unsw.edu.au (M.M. Harding).

0277-5387/$ - see front matter © 2006 Elsevier Ltd. All rights reserved.
doi:10.1016/j.poly.2006.07.004

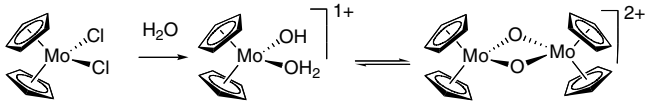


Fig. 1. Aqueous chemistry of molybdocene dichloride. The general formula $Cp_2MoCl_{2(aq)}$ is used as the relative amounts of aquated monomer and dimer and the exact species present in each solution depends on the concentration, salt and ionic strength.

complexes in V79 Chinese hamster lung cells. While the results were consistent with Mo being distributed fairly uniformly throughout the cells including in the nucleus, the sensitivity of the X-ray fluorescence images did not allow accumulation of Mo in specific organelles to be determined, or allow conclusions to be made regarding whether Mo targeted nuclear proteins or nucleic acids within the nucleus.

In this paper, the potential of radiotracer techniques for studying the interactions of $Cp_2{}^{99}MoCl_2$ with biomolecules was assessed by performing studies with calf thymus DNA and HSA. These biomolecules were chosen to parallel previous studies of Mo using GFAAS and inductively coupled plasma mass spectrometry (ICP-MS) [20,25,26]. While the preparation of the radioactive form of Cp_2MoCl_2 has been reported [27], there have been no applications of this chemistry in biological studies. The results with isolated biomolecules demonstrate that the use of radiotracers for monitoring the cellular distribution of Cp_2MoCl_2 warrants further study and has potential to providing new mechanistic information on molybdocenes.

2. Results

2.1. Characterisation of $Cp_2{}^{99}MoCl_2$

^{99}Mo has a half life of 65.94 h and decays predominantly to ^{99m}Tc ($t_{1/2} = 6.02$ h) as illustrated by Fig. 2a. The radiotracer $Cp_2{}^{99}MoCl_2$ was prepared by neutron irradiation of Cp_2MoCl_2 for 24 h. The gamma spectrum of the irradiated product in buffer showed there were no significant contaminating radionuclides (Fig. 2b). Characterisation of the radiotracer was required to ensure that structural integrity was maintained and to ensure that neutron irradiation and subsequent radioactive decay reactions had not led to the breakage of bonds.

TLC analysis of the radiotracer, $Cp_2{}^{99}MoCl_2$, showed a strong aromatic chromophore that fluoresced at 254 nm, consistent with aromatic cyclopentadienyl rings and an intact Cp–Mo bond. Degradation of Cp–Mo bonds leading to the formation of free cyclopentadiene would result in the absence, or significant reduction, of the aromatic chromophore.

Comparison of the UV spectra of buffered solutions of the resultant $Cp_2{}^{99}MoCl_{2(aq)}$ and control $Cp_2MoCl_{2(aq)}$ gave similar results, taking into account slight differences that result in the UV spectrum due to the concentration dependent monomer–dimer equilibrium [14,15] (Fig. 1). A standard curve of the $Cp_2MoCl_{2(aq)}$ concentration versus

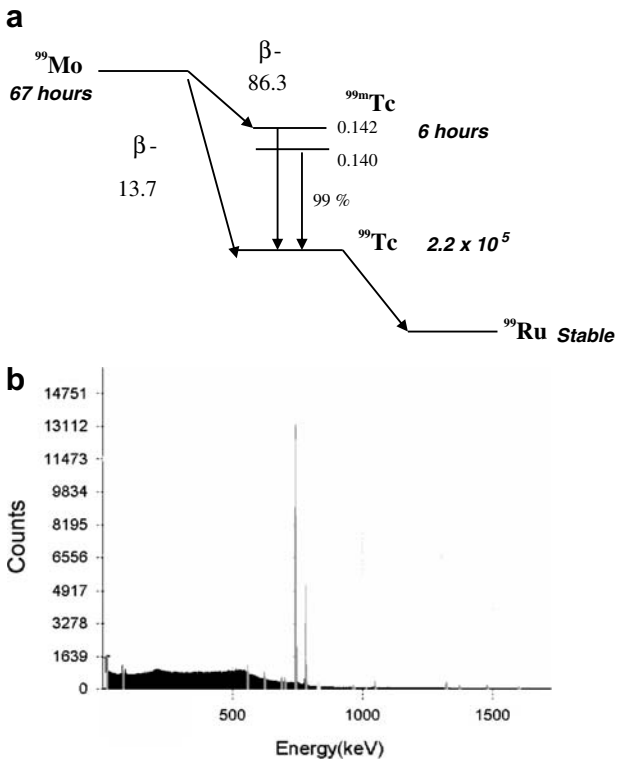


Fig. 2. (a) Decay scheme for ^{99}Mo. (b) Gamma spectrum of irradiated Cp_2MoCl_2 showing ^{99}Mo peak at 739.5 and 788 keV emissions (^{99m}Tc emission was shielded using a thin wall lead container).

UV absorption at 210 nm was generated and used to determine the concentration of $Cp_2{}^{99}MoCl_2$ in the $Cp_2{}^{99}MoCl_{2(aq)}$ solutions added to the HSA and DNA samples.

2.2. Binding studies of $Cp_2{}^{99}MoCl_2$ with HSA versus DNA

The results of binding studies of $Cp_2{}^{99}MoCl_2$ with HSA or DNA for 3 h are shown in Fig. 3. The results, reported as nmol of bound Cp_2MoCl_2, show that despite much higher concentrations of DNA, there is significantly more binding of Cp_2MoCl_2 to HSA than to DNA. There was no non-specific binding to DNA at $t = 0$ and with the exception of the data point that represents 18.75 nmol, binding to DNA increased with concentration and to a lesser extent, with incubation time. All errors were within 10%, with the exception of the 18.75 nmol sample of DNA at $t = 0.5$, which was attributed to experimental error.

In the case of HSA, a high degree of non-specific binding was present at all concentrations of HSA, as shown by binding at $t = 0$ (Fig. 3). HSA binding peaked at $t = 0.5$ h for most concentrations with a maximum binding of 102 nmol of Cp_2MoCl_2. In contrast, after 3 h incubation, maximum binding of Cp_2MoCl_2 was reached at only 1 nmol of HSA. The precipitation of protein at lower concentrations may not be as efficient as precipitation at higher concentrations where nucleation of small amounts of precipitate assists in extensive precipitation of the rest of the protein, and also aids in the formation of a tight pellet during centrifugation. For these reasons, the results from the highest

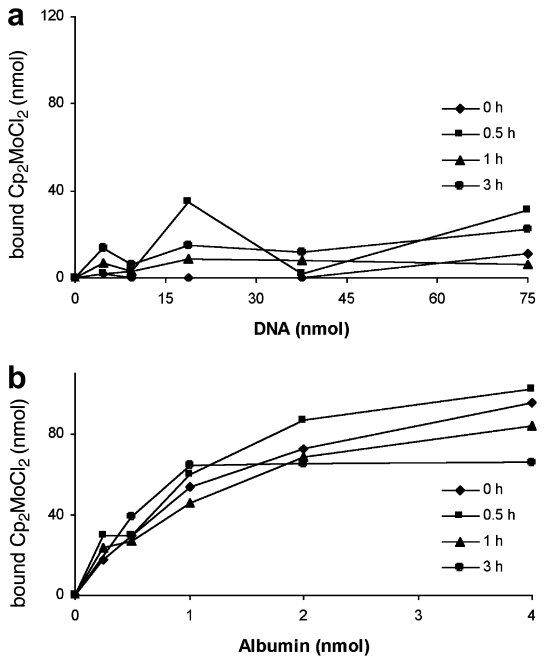


Fig. 3. Comparison of moles of $Cp_2{}^{99}MoCl_2$ bound to (a) DNA and (b) HSA over time at 37 °C. The concentration of Cp_2MoCl_2 in the reaction mixture was 298 nmol.

concentrations of HSA and DNA, were considered to be the most reliable data to illustrate the Mo binding trends.

Under the conditions investigated, molar ratios of binding of 0.2:1 (Cp_2MoCl_2:DNA) and 9.4:1 (Cp_2MoCl_2:HSA) were calculated. These ratios demonstrate that DNA binding is extremely low in comparison to HSA. Immediate, non-specific binding to HSA is followed by a small increase at $t = 0.5$ h, after which binding decreases by approximately 29 nmol, equivalent to 10%, over 3 h.

3. Discussion

Definitive tests that monitor the localisation of metal ions derived from metal based drugs in vivo are essential tools for mapping the uptake and distribution of drugs in cells and hence providing insight into the mechanism(s) of antitumor activity. In the case of Cp_2MCl_2 (M = Ti, V, Nb), a number of these techniques including GFAAS, ICP-MS, atomic emission spectroscopy, and electron energy loss spectroscopy have been used to study binding with biomolecules and cell update [20,22,25,26,28]. The use of radiolabelled metal complexes offers a potentially rapid, convenient and highly sensitive method of determining the binding of metals to biomolecules and monitoring their cellular distribution.

While the preparation and characterisation of radioactive Cp_2MoCl_2 has been reported [27] previously, to our knowledge the radiotracer has not been used in any applications to date. It was reported that the technetium-99 m daughter product $Cp_2{}^{99m}TcCl_2$ that resulted from decay to the ^{99}Mo retained the molecular structure of the parent complex. Any evidence of decomposition products were the direct result of 'shake-off' process rather than the beta decay. In the present study only the behaviour of the $Cp_2{}^{99}MoCl_2$ species was monitored.

The subcellular localisation of molybdenum is an important step in determining the molecular targets of molybdocene dichloride. While XRF studies have shown that Mo does enter the nucleus [22], we have hypothesised that Mo observed in the nucleus is associated with nuclear proteins, and not nucleic acids [22,24]. We have also highlighted the need for additional assays that distinguish between DNA damage and tubulin damage as related to the genotoxicity of molybdocene dichloride [24].

The binding studies (Fig. 3) showed clear preferential interaction of $Cp_2MoCl_{2(aq)}$ with HSA versus DNA, a result that correlates well with recently reported ICP-MS results that showed <5% binding of $Cp_2MoCl_{2(aq)}$ to DNA [26]. These results with isolated biomolecules also agree with our NMR studies with oligonucleotides and amino acids that show clear preferential coordination to deprotonated thiols under physiological conditions [21,29] and show no evidence for hydrolysis of the Cp ligands. The internal consistency between the results of this study and independent studies with other techniques, strongly suggests that further application of the assay to studies with cancer cells and the analysis of specific organelles and subcellular fractions, will provide informative data on the localisation of Mo derived from $Cp_2MoCl_{2(aq)}$ within cancer cells.

4. Conclusions

A direct measure of the Mo content in samples from gamma emissions of Mo-99 showed minimal association between $Cp_2{}^{99}MoCl_{2(aq)}$ and calf thymus DNA. In contrast, significantly higher binding to HSA, a protein with a free cysteine thiol group, was detected. These results are consistent with in vitro coordination studies that have demonstrated formation of irreversible adducts between $Cp_2MoCl_{2(aq)}$ with deprotonated thiols compared with other donor sites present in DNA and proteins.

While handling radioactive material requires access to a suitable laboratory, the binding studies of $Cp_2MoCl_{2(aq)}$ with DNA and HSA have demonstrated that this technique offers significant potential for the analysis of subcellular fractions such as mitochondria and other organelles at a higher sensitivity and improved time-scale compared with the measurement of metal concentrations in cell samples using traditional techniques such as GFAAS and ICP-MS. This methodology would allow the uptake and distribution of molybdocene dichloride in different cancer cell types to be monitored, and may also yield invaluable information on the pharmacology of the complex in vivo.

5. Experimental

5.1. Materials

Cp_2MoCl_2 was purchased from the Sigma–Aldrich Chemical Company and used as provided. All solutions

were prepared by sonication in sterile Milli-Q water, phosphate buffered saline (PBS, pH 7.4, 0.172 M, Oxoid) or 0.1 M Tris–HCl/10 mM NaCl buffer (pH 7.4), as specified.

5.2. Preparation of molybdocene dichloride radiotracer

Cp_2MoCl_2 (~50 mg) was irradiated in a thermal neutron flux of 1×10^{13} n cm^{-2} s^{-1} for 24 h in the High Flux Australian Reactor at the Australian Nuclear Science and Technology Organization. At the end of bombardment, the irradiated sample was left to decay for 9 h to eliminate any short-lived high energy gamma emitting radioisotopes. $Cp_2{}^{99}MoCl_2$ was sonicated in buffer (6 mL) for 2 h and the resultant dark maroon solution was filtered (0.2 μm, Millipore). The radioisotopic purity of $Cp_2{}^{99}MoCl_2$ was assessed by gamma spectrometry. Radioactivity measurements were performed on a Perkin–Elmer/Wallac 1480 gamma counter equipped with a thallium activated sodium iodide detector. The 739.5 and 778 keV gamma emission was monitored over the range 710–750 keV on the gamma counter as it represented a unique signal of ^{99}Mo in the region. The UV spectra of the irradiated sample (diluted with buffer 1:100 and 1:1000) were compared to spectra of Cp_2MoCl_2 (10–100 μM). The concentration of Cp_2MoCl_2 in the solution of irradiated $Cp_2{}^{99}MoCl_2$ was determined from a standard curve of Cp_2MoCl_2 at 210 nm. TLC of Cp_2MoCl_2 and $Cp_2{}^{99}MoCl_2$ dissolved in buffer were performed on F_{254} silica plates (Merck) (chloroform:methanol:ammonia, 80:18:2).

5.3. Radiotracer binding studies of $Cp_2{}^{99}MoCl_2$ with DNA or proteins

Stock solutions of human serum albumin (HSA) (0.15 mM, Tris–HCl) and calf thymus DNA (2.5 mM, Tris–HCl) were prepared. The purity of the DNA solution was determined from the $A_{260\,nm}/A_{280\,nm}$ ratio (1.85) and the concentration determined using the absorbance value $A_{260\,nm}$, ($\sum = 6600$ M^{-1} cm^{-1}). Stock solutions were serially diluted with buffer 1:2, to produce DNA solutions of 36, 18, 9, 4.5 and 2.25 mg/mL and HSA solutions of 0.30, 0.15, 0.075, 0.038 and 0.019 mg/mL. Each of these solutions (30 μL) (in quadruplicate) was diluted with buffer (30 μL) in low-protein binding micro centrifuge tubes and stored at 4 °C. An aliquot of the irradiated metallocene in buffer (20 μL) was added to each of the DNA and HSA solutions which were then vortexed and incubated at 37 °C. After set intervals ($t = 0$, 1 and 3 h) the DNA or HSA was precipitated by the addition of ammonium acetate (50 μL, 3 M) and ethanol (1 mL). The suspension was centrifuged (14000 rpm, 5 min) and aliquots (100 μL × 3) of the supernatant were removed and monitored for ^{99}Mo using a gamma counter. Radioactive standards were prepared in an identical manner, except that buffer was substituted for DNA or HSA solutions. The portion of $Cp_2{}^{99}MoCl_2$ associated with the DNA or the protein precipitate for each time interval was determined by the following equation

$$R_P = \frac{R_S \text{ at } T_0 - R_S \text{ at } T_X}{R_S \text{ at } T_0} \quad (1)$$

where R_S is the $Cp_2{}^{99}MoCl_2$ counts in solution, R_P is $Cp_2{}^{99}MoCl_2$ counts in pellet, T_0 is time zero and T_X is time at varying time intervals. The $Cp_2{}^{99}MoCl_2$ counts were correlated with the concentration of Cp_2MoCl_2 in solution (determined by UV spectroscopy) and hence the moles of Cp_2MoCl_2 associated with the protein or DNA were calculated.

Acknowledgements

This research was supported by the Australian Institute of Science and Engineering Award No. 04/072. We thank Alex Fuchs for assistance with the radiolabelling experiments.

References

[1] Z. Guo, P.J. Sadler, Angew. Chem., Int. Ed. 38 (1999) 1512.
[2] T. Pieper, K. Borsky, B.K. Keppler, in: M.J. Clarke, P.J. Sadler (Eds.), Metallopharmaceuticals I: DNA Interactions, vol. 1, Springer, New York, 1999, pp. 171–199.
[3] D. Wang, S.J. Lippard, Nature Rev. Drug Discov. 4 (2005) 307.
[4] P. Köpf-Maier, H. Köpf, Struct. Bond. 70 (1988) 103.
[5] P. Köpf-Maier, Eur. J. Clin. Pharmacol. 47 (1994) 1.
[6] P. Köpf-Maier, in: B.K. Keppler (Ed.), Metal Complexes In Cancer Chemotherapy, VCH Verlagsgesellschaft, Weinheim, 1993, pp. 259–296.
[7] G. Lümmen, S. Sperling, H. Luboldt, T. Otto, H. Rübben, Cancer Chemother. Pharmacol. 42 (1998) 415.
[8] N. Kröger, U.R. Kleeberg, K. Mross, L. Edler, G. Saß, D.K. Hossfeld, Onkologie 23 (2000) 60.
[9] A.D. Tinoco, A.M. Valentine, J. Am. Chem. Soc. 127 (2005) 11218.
[10] M. Guo, H. Sun, P.J. Sadler, J. Inorg. Biochem. 74 (1999) 150.
[11] M. Guo, P.J. Sadler, Dalton Trans. (2000) 7.
[12] M. Guo, H. Sun, H.J. McArdle, L. Gambling, P.J. Sadler, Biochemistry 39 (2000) 10023.
[13] L.Y. Kuo, M.G. Kanatzidis, M. Sabat, A.L. Tipton, T.J. Marks, J. Am. Chem. Soc. 113 (1991) 9027.
[14] C. Balzarek, D.R. Tyler, Angew. Chem., Int. Ed. Eng. 38 (1999) 2406.
[15] C. Balzarek, T.J.R. Weakley, L.Y. Kuo, D.R. Tyler, Organomet. 19 (2000) 2927.
[16] P. Köpf-Maier, M. Leitner, R. Voigtländer, H. Köpf, Z. Naturforscher c 34 (1979) 1174.
[17] M.M. Harding, G. Mokdsi, Curr. Med. Chem. 7 (2000) 1289.
[18] J.B. Waern, M.M. Harding, J. Organomet. Chem. 689 (2004) 4655.
[19] G. Mokdsi, M.M. Harding, J. Inorg. Biochem. 86 (2001) 611.
[20] J.B. Waern, C.T. Dillon, M.M. Harding, J. Med. Chem. 48 (2005) 2093.
[21] J.B. Waern, M.M. Harding, Inorg. Chem. 43 (2004) 206.
[22] J.B. Waern, H. Harris, B. Lai, Z. Zhai, M.M. Harding, C.T. Dillon, J. Biol. Inorg. Chem. 10 (2005) 443.
[23] J.B. Waern, P. Turner, M.M. Harding, Organomet. 25 (2006) 3417.
[24] K.S. Campbell, A.J. Foster, C.T. Dillon, M.M. Harding, J. Inorg. Biochem. 100 (2006) 1194.
[25] M.L. McLaughlin, J.M. Cronan Jr., T.R. Schaller, R.D. Snelling, J. Am. Chem. Soc. 112 (1990) 8949.
[26] J.L. Vera, F.R. Roman, E. Melendez, Anal. Bioanal. Chem. 379 (2004) 399.
[27] R. Blackburn, T. Yassine, Radiat. Phys. Chem. (1992) 263.
[28] P. Köpf-Maier, H. Köpf, Drugs Future 11 (1986) 297.
[29] M.M. Harding, G. Mokdsi, J.P. Mackay, M. Prodigalidad, S.W. Lucas, Inorg. Chem. 37 (1998) 2432.

Available online at www.sciencedirect.com
ScienceDirect
Polyhedron 26 (2007) 460–471
POLYHEDRON
www.elsevier.com/locate/poly

Copper complexes with 1,10-phenanthrolines tethered to a cyclotriphosphazene platform

Eric W. Ainscough *, Andrew M. Brodie *, Geoffrey B. Jameson, Carl A. Otter

Chemistry Department, Institute of Fundamental Sciences, Massey University, Private Bag 11 222, Palmerston North, New Zealand

Received 10 May 2006; accepted 10 July 2006
Available online 18 July 2006

Abstract

The synthesis of two ligands, L^1 and L^2, each containing two 2-oxy-1,10-phenanthroline moieties attached to the same phosphorus atom of a substituted cyclotriphosphazene ring via an oxy-bridge, but differing in substitution on the biphenyl capping groups, is described. The single-crystal X-ray structure of $L^1 \cdot 2CH_2Cl_2$ shows an ordered structure in the lattice with channels, containing dichloromethane molecules, running parallel to the *a*-axis. The reactions of L^1 and L^2 with $[Cu(MeCN)_4](PF_6)$ afford the dimetallic copper(I) derivatives, $[(CuL^1)_2](PF_6)_2 \cdot CH_2Cl_2$ and $[(CuL^2)_2](PF_6)_2$. The single-crystal X-ray structure of the former complex shows that the L^1 ligands of the cation $[(CuL^1)_2]^{2+}$ act as a bridges coordinating to the two copper(I) centres in a helical fashion. The copper atoms have distorted tetrahedral geometries with the interligand dihedral angle being 85°. With copper(II) chloride and copper(II) perchlorate, the monomeric copper(II) complexes, $[CuL^1Cl]Cl \cdot 2CH_2Cl_2$, $[CuL^2Cl]Cl \cdot CH_2Cl_2$, $[CuL^1(OMe)]PF_6 \cdot 2H_2O$, $[CuL^2(OMe)]PF_6 \cdot 2H_2O$, $[CuL^1(OH_2)](ClO_4)_2$ and $[CuL^2(OH_2)](ClO_4)_2 \cdot H_2O$ are obtained. The single-crystal X-ray structure of $[CuL^1Cl]Cl \cdot 2CH_2Cl_2$ shows the copper to be in a square-base pyramidal distorted trigonal-bipyramidal (SBPDTB) environment ($\tau = 0.57$) with L^1 acting as a κ^4N donor, coordinating via the four nitrogen atoms of the two tethered 1,10-phenanthrolines. In CH_3CN, this complex undergoes hydrolysis via the presence of adventitious water losing one oxyphenanthroline arm to form the centrosymmetric dimetallic species, $[(CuL^3Cl)_2] \cdot 4CH_3CN \cdot 3H_2O$ ($L^3 = [N_3P_3(biph)_2(ophen)O]^-$ where biph = 2,2′-dioxybiphenyl and O replaces an oxyphenanthroline and is attached to the phosphorus of the phosphazene ring). The two monomeric units, which are linked by bridging chlorine atoms, have a distorted square-based pyramidal geometry about the copper with the basal plane made by the 'ON_2Cl' ligand set. Spectroscopic (mass spectral, electronic and ESR) and magnetic moment data for the complexes are discussed.
© 2006 Elsevier Ltd. All rights reserved.

Keywords: Cyclotriphosphazene; 1,10-Phenanthroline; Copper(I); Copper(II); X-ray structures

1. Introduction

The ability of cyclotriphosphosphazenes to engage in coordination to transition metals is a developing area of interest [1] and a great variety of complexes can be attained by attaching different pendant donor groups to the phosphazene skeleton. For example, we have placed 2-oxypyridine groups onto the cyclotriphosphazene skeleton, hence demonstrating that *hexakis*(2-pyridyloxy)cyclotriphosphazene is a versatile multimodal ligand which displays a range of coordination modes such as uni-, bi-, tri-, tetra- and pentadentate [2–5]. Others have attached six [6], four [7,8] and two [9] 3,5-dimethylpyrazolyl groups to the cyclophosphazene ring and the predominant mode of binding is *non-gem*-κ^3N tridentate, using one phosphazene ring nitrogen while the hexa-substituted cyclotriphosphazene samarium complex displays the *gem*-κ^3N_5 mode [10].

The coordination chemistry of cyclic phosphazenes that contain polydentate ligand moieties is less established.

* Corresponding authors. Tel.: +64 6 3569099x3536; fax: +64 6 350 5682.
E-mail addresses: E.Ainscough@massey.ac.nz (E.W. Ainscough), A.Brodie@massey.ac.nz (A.M. Brodie).

0277-5387/$ - see front matter © 2006 Elsevier Ltd. All rights reserved.
doi:10.1016/j.poly.2006.07.007

Several phosphazene ligand systems based on 2-pyridylalkylamines have been prepared [11–18] that demonstrate coordination modes using various combinations of amine, pyridine and ring nitrogens. More recently, a lanthanum complex prepared from a phosphazene containing two pyrazolylpyridine ligands was reported [19].

There has been interest in ligands containing two 2,2′-bipyridine or 1,10-phenanthroline units linked at their ortho carbon atoms by linkers such as $–CH_2OCH_2–$ [20–22], $–CH_2CH_2–$ [23,24] or $–OCH_2CH(NH_2)CH_2O–$ and related bridges [25]. Their copper(II) and copper(I) complexes have been explored because of their interesting redox behaviour, luminescence properties, ability to form double-helicates and, in the presence of hydrogen peroxide, ability to mediate the single-strand cleavage of double-stranded DNA by oxidative attacks at C-1′ and C-4′ of 2-deoxyribose units. By tethering phenanthrolines to a cyclotriphosphazene platform and by investigating their coordinating properties towards copper, we can extend these previous studies. The phenanthroline substitutions would be expected to lead to conformational rigidity in these chelating systems.

Hence we have synthesised cyclotriphosphazene ligands containing two 2-oxyphenanthroline (ophen) moieties, which are attached to the same phosphorus atom via the oxy-bridge, effectively producing an OPO bridged bis-phenanthroline ligand. The remaining two ring phosphorus atoms are blocked with 5,5′-di-*tert*-butyl-2,2′-dioxybiphenyl (^{t}Bubiph) or 2,2′-dioxybiphenyl (biph) groups giving the new ligands $[N_3P_3(biph)_2(ophen)_2]$ and $[N_3P_3(^tBubiph)_2(ophen)_2]$ (L^1 and L^2, Scheme 1).

In this paper we examine the coordinating behaviour of these new ligands with copper(I) and (II) and compare their behaviour with the un-hinged diimine counterparts. Whether this ligand type forms a double helicate structure with copper(I) and copper(II), and whether the tethered phenanthroline moieties give more strained structures, and hence are more reactive will be addressed. These studies may also provide model systems for the interaction of copper ions with the phenanthroline-substituted linear-chain polymeric phosphazenes, in the quest for new metal-rich materials.

2. Experimental

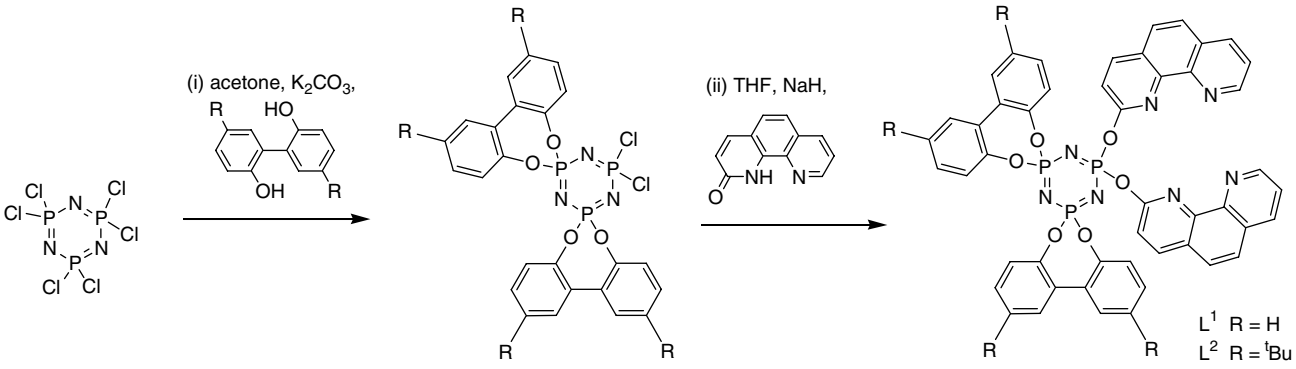
2.1. Materials and instrumentation

Analytical grade solvents were used without further purification with the exception of tetrahydrofuran (THF), which was distilled from sodium/benzophenone. $CuCl_2 \cdot xH_2O$ was dehydrated at 140 °C before use, $Cu(ClO_4)_2 \cdot 6H_2O$, $Cu(CH_3COO)_2 \cdot H_2O$, $NaPF_6$ and $[N_3P_3Cl_6]$ were used as supplied. 2-Methoxy-1,10-phenanthroline [26] was prepared from 2-chloro-1,10-phenanthroline [27] and demethylated [28] to give 2-hydroxy-1,10-phenanthroline (HOphen). 5,5′-Di-*tert*-butyl-2,2′-dihydroxybiphenyl (^{t}BubiphH$_2$) [29], $[N_3P_3(biph)_2Cl_2]$ [30] and $[Cu(MeCN)_4]PF_6$ [31] were prepared according to literature procedures. All manipulations were carried out under nitrogen using standard Schlenk techniques. Microanalyses were performed by the Campbell Microanalytical Laboratory, University of Otago. NMR spectra were recorded on a Bruker Avance A400 spectrometer; ^{1}H data were referenced internally to TMS; $^{31}P\{^1H\}$ data were referenced to an external sample of 85% aqueous H_3PO_4. IR spectra were run as KBr discs on a Perkin–Elmer FT-IR Paragon 1000 spectrometer and electronic absorption spectra were recorded using a Shimadzu UV-310-310PC scanning spectrometer. Electrospray mass spectra were obtained from MeCN solutions on a Micromass ZMD spectrometer run in positive ion mode. Listed peaks correspond to the most abundant isotopomer; assignments were made by a comparison of observed and simulated spectra. Magnetic susceptibility measurements were performed on a Faraday balance at room temperature. X-band EPR spectra were recorded at 113 K on a Varian E-104A spectrometer equipped with a E-257 variable-temperature controller and operating at about 9.0 GHz. The spectral g values were calibrated with (diphenylpicryl)hydrazyl (DPPH) as a standard.

2.2. Ligand syntheses

2.2.1. $[N_3P_3(^tBubiph)_2Cl_2]$

To a solution of ^{t}BubiphH$_2$ (859 mg, 2.9 mmol) in acetone (15 mL), cooled to 0 °C, was added K_2CO_3 (1 g, 7.2 mmol)



Scheme 1. Syntheses of L^1 and L^2.

and $[P_3N_3Cl_6]$ (500 mg, 1.4 mmol). The mixture was stirred at room temperature for 2 h and then taken to dryness on a rotary evaporator. The residue was extracted with CH_2Cl_2 (125 mL) and taken to dryness to give a white solid. Recrystallisation from CH_2Cl_2/hexane afforded analytically pure material. Yield: 522 mg (45%). ^{31}P NMR ($CDCl_3$): δ 30.3 (t, P, $J_{PP} = 79$ Hz), 20.6 (d, 2P, $J_{PP} = 78$ Hz). ^1H NMR ($CDCl_3$): δ 7.52 – 7.46 (m, 8H), 7.26 (s, 4H), 1.37 (s, 36H). IR ν_{max} (cm^{-1}): 1254, 1232, 1203, 1188. *Anal.* Required for $C_{40}H_{48}Cl_2N_3O_4P_3$: C, 60.15; H, 6.06; N, 5.26. Found: C, 60.40; H, 6.22; N, 5.30%.

2.2.2. $[N_3P_3(biph)_2(ophen)_2] \cdot CH_2Cl_2$ ($L^1 \cdot CH_2Cl_2$)

To a solution of HOphen (310 mg, 1.5 mmol) in THF (60 mL), NaH (63 mg of a 60% dispersion in oil, 1.6 mmol NaH) was added. The mixture was allowed to stir at room temperature for 3 h, during which time a white precipitate of NaOphen developed. $[N_3P_3(biph)_2Cl_2]$ (430 mg, 0.75 mmol) was added and the mixture was heated at reflux over 20 h. The crude reaction mixture was filtered through Celite and the filtrate was discarded. The Celite pad was washed well with CH_2Cl_2 and the washings were taken to dryness on a rotary evaporator to give the crude phosphazene. Recrystallisation from CH_2Cl_2/hexane affords the solvated material, which was then dried under vacuum. Yield 380 mg (55%). ^{31}P NMR ($CDCl_3$): δ 25.39 (d, 2P, $J_{PP} = 99$ Hz), 7.66 (t, P, $J_{PP} = 99$ Hz). ^1H NMR ($CDCl_3$): δ 9.20 (dd, 2H, Ophen H^{11}), 8.33 (d, 2H, Ophen H^4), 8.24 (dd, 2H, Ophen H^9), 8.09 (d, 2H, Ophen H^3), 7.77 (m, 4H, Ophen H^6 and H^7), 7.62 (dd, 2H, Ophen H^{10}), 7.44 (m, 4H, biphenyl), 7.31–7.17 (m, 12H, biphenyl). IR ν_{max} (cm^{-1}): 1230, 1174. *m/z* (ESMS): 894 $[MH]^+$. *Anal.* Required for $C_{49}H_{32}Cl_2N_7O_6P_3$: C, 60.14; H, 3.30; N, 10.02. Found: C, 60.12; H, 3.28; N, 9.97%. Crystals of $L^1 \cdot 2CH_2Cl_2$ suitable for X-ray diffraction were grown from a CH_2Cl_2/hexane solution of the ligand.

2.2.3. $[N_3P_3(^tBubiph)_2(ophen)_2] \cdot CHCl_3$ ($L^2 \cdot CHCl_3$)

To a solution of HOphen (600 mg, 3.1 mmol) in THF (60 mL), NaH (122 mg of a 60% dispersion in oil, 3.1 mmol NaH) was added. The mixture was allowed to stir at room temperature for 3 h, during which time a white precipitate of NaOphen developed. $[N_3P_3(^tBubiph)_2Cl_2]$ (1200 mg, 1.5 mmol) was added and the mixture was heated at reflux over 20 h. The mixture was filtered through Celite and the THF removed from the filtrate on a rotary evaporator. Chromatography on alumina using CH_2Cl_2/MeOH (96:4) as eluent yields a spectroscopically clean fraction of L^2. Yield: 1000 mg (58%). An analytical sample of $L^1 \cdot CHCl_3$ was obtained by vapour diffusion of pentane into a $CHCl_3$ solution of the phosphazene. ^{31}P NMR ($CDCl_3$): δ 25.32 (d, 2P, $J_{PP} = 97$ Hz), 7.80 (t, P, $J_{PP} = 97$ Hz). ^1H NMR ($CDCl_3$): δ 9.20 (dd, 2H, Ophen H^{11}), 8.33 (d, 2H, Ophen H^4), 8.24 (dd, 2H, Ophen H^9), 8.12 (d, 2H, Ophen H^3), 7.77 (m, 4H, Ophen H^6 and H^7), 7.62 (dd, 2H, Ophen H^{10}), 7.40 (m, 4H, biphenyl), 7.19 – 7.13 (m, 8H, biphenyl), 1.30 (s, 36H, ^{t}Butyl). ν_{max} (cm^{-1}): 1230, 1182. *m/z* (ESMS): 1118 $[MH^+]$. *Anal.* Required for $C_{65}H_{63}Cl_3N_7O_6P_3$: C, 63.09; H, 5.13; N, 7.92. Found: C, 63.18; H, 4.95; N, 7.97%.

2.3. Complex syntheses

2.3.1. $[(CuL^1)_2](PF_6)_2 \cdot CH_2Cl_2$ (**1** $\cdot CH_2Cl_2$)

To a solution of L^1 (90 mg, 0.1 mmol) in CH_2Cl_2 (6 mL) was added $[Cu(MeCN)_4]PF_6$ (40 mg, 0.1 mmol) dissolved in CH_2Cl_2 (6 mL). The solution was allowed to stir at room temperature for 1 h. Hexane was added to produce an orange precipitate that was collected by filtration and dried under vacuum. Yield: 87 mg (74%). ^{31}P NMR (CD_3CN): δ 25.36 (d, 2P, $J_{PP} = 96$ Hz), 7.40 (t, P, $J_{PP} = 96$ Hz), −143.38 (sept, P, $J_{PF} = 706$ Hz). IR ν_{max} (cm^{-1}): 1227(s), 1175(vs). *m/z* (ESMS): 956 $[CuL^1]^+$. *Anal.* Required for $C_{49}H_{32}Cl_2CuF_6N_7O_6P_4$: C, 49.57; H, 2.72; N, 8.26. Found: C, 49.87; H, 2.75; N, 8.34%. Crystals of **1** $\cdot 6CH_2Cl_2$ suitable for X-ray diffraction were grown from the slow evaporation of a CH_2Cl_2/hexane solution of the complex.

2.3.2. $[(CuL^2)_2](PF_6)_2$ (**2**)

To a solution of L^2 (112 mg, 0.1 mmol) in CH_2Cl_2 (10 mL) was added $[Cu(MeCN)_4]PF_6$ (47 mg, 0.1 mmol) dissolved in CH_2Cl_2 (10 mL). The solution was allowed to stir at room temperature for 20 min. Hexane was added to produce an orange precipitate that was collected by filtration and air dried. Yield 108 mg (82%). A purple microcrystalline analytically pure sample was prepared by vapour diffusion of diethylether into an acetonitrile solution of the complex. ^{31}P NMR ($CDCl_3$): δ 24.84 (d, P, $J_{PP} = 96$ Hz), 5.21 (d, P, $J_{PP} = 96$ Hz), −142.43 (sept, P, $J_{PF} = 712$ Hz). *m/z* (ESMS): 1180 $[CuL^2]^+$. IR ν_{max} (cm^{-1}): 1228(s), 1182(vs). *Anal.* Required for $C_{64}H_{62}CuF_6N_7O_6P_4$: C, 57.94; H, 4.71; N, 7.39. Found: C, 57.83, H, 4.56; N, 7.27%.

2.3.3. $[CuL^1Cl]Cl \cdot 2CH_2Cl_2$ (**3** $\cdot 2CH_2Cl_2$)

To a solution of L^1 (275 mg, 0.31 mmol) in CH_2Cl_2 (20 mL), $CuCl_2$ (41 mg, 0.3 mmol) was added. The mixture was heated at reflux for 24 h producing a green precipitate that was collected by filtration, washed with CH_2Cl_2, Et_2O and dried under vacuum. Yield 160 mg (43%). IR ν_{max} (cm^{-1}): 1277(s), 1227(s), 1170(vs). *m/z* (ESMS): 991 $[CuL^1Cl]^+$. *Anal.* Required for $C_{50}H_{34}Cl_6CuN_7O_6P_3$: C, 50.13; H, 2.86; N, 8.18. Found: C, 50.37; H, 2.92; N, 8.38%. Crystals of **3** $\cdot 2CH_2Cl_2$ suitable for X-ray diffraction were obtained from CH_2Cl_2. Crystals of **9** $\cdot$ 4MeCN $\cdot 3H_2O$, the hydrolysis product of **3**, were obtained in low yield by dissolving the complex **3** in hot CH_3CN and allowing the solution to stand for 2–3 weeks.

2.3.4. $[CuL^2Cl]Cl \cdot CH_2Cl_2$ (**4** $\cdot CH_2Cl_2$)

To a solution of L^2 (112 mg, 0.1 mmol) in CH_2Cl_2 (20 mL), $CuCl_2$ (13 mg, 0.1 mmol) was added. The mixture was heated at reflux for 24 h producing a green solution that was filtered and reduced in volume by approximately half. Hexane was added and the solution refrigerated

overnight to produce a green precipitate that was collected by filtration and dried under vacuum. Yield 104 mg (78%). *m/z* (ESMS): 1217 $[CuL^2Cl]^+$ IR ν_{max} (cm^{-1}): 1228(s), 1182(vs). *Anal.* Required for $C_{65}H_{64}Cl_4CuN_7O_6P_3$: C, 58.37; H, 4.82; N, 7.33. Found: C, 58.38; H, 4.91; N, 7.34%.

2.3.5. $[CuL^1(OMe)]PF_6 \cdot 2H_2O$ (**5** · $2H_2O$)

A mixture of L^1 (195 mg, 0.22 mmol) and $Cu(MeCOO)_2 \cdot H_2O$ (39 mg, 20 mmol) in MeOH (10 mL) was heated at reflux for 2 h. The turquoise solution was filtered and a solution of $NaPF_6$ in methanol was added to produce a pale turquoise precipitate that was collected by filtration, washed with Et_2O and dried under vacuum. Yield 161 mg (63%). *m/z* (ESMS): 987 $[CuL^1(OMe)]^+$. IR ν_{max} (cm^{-1}): 1227(s), 1193(s), 1172(vs). *Anal*. Required for $C_{49}H_{37}CuF_6N_7O_9P_4$: C, 50.33; H, 3.19; N, 8.39. Found: C, 50.34; H, 2.82; N, 8.35%.

2.3.6. $[CuL^2(OMe)]PF_6 \cdot 2H_2O$ (**6** · $2H_2O$)

A solution of L^2 (120 mg, 0.11 mmol) and $Cu(MeCOO)_2 \cdot H_2O$ (21 mg, 0.11 mmol) in methanol (10 mL) was heated at reflux for 2 h. The turquoise solution was filtered and a solution of $NaPF_6$ in methanol was added to produce a pale turquoise precipitate that was collected by filtration, washed with Et_2O and dried under vacuum. Yield 55 mg (36%). IR ν_{max} (cm^{-1}): 1230(s), 1196(s), 1181(vs). *m/z* (ESMS): 1211 $[CuL^2(OMe)]^+$. *Anal*. Required for $C_{65}H_{69}CuF_6N_7O_9P_4$: C, 56.02; H, 4.99; N, 7.03. Found: C, 56.00; H, 4.81; N, 7.10%.

2.3.7. $[CuL^1(OH_2)](ClO_4)_2$ (**7**)

To a solution of L^1 (46 mg, 0.05 mmol) in CH_2Cl_2 (10 mL), $Cu(ClO_4)_2 \cdot 6H_2O$ (20 mg, 0.05 mmol) was added. The mixture was allowed to stir at room temperature for 4 days during which time a pale green precipitate developed. The precipitate was filtered, washed with Et_2O and air dried. Yield 35 mg (58%). IR ν_{max} (cm^{-1}): 1285(s), 1225(s), 1175(vs). *Anal*. Required for $C_{48}H_{32}Cl_2CuN_7O_{15}P_3$: C, 49.10; H, 2.75; N, 8.35. Found: C, 49.18; H, 2.66; N, 8.31%.

2.3.8. $[CuL^2(OH_2)](ClO_4)_2 \cdot H_2O$ (**8** · H_2O)

To a solution of L^2 (50 mg, 0.045 mmol) in CH_2Cl_2 (10 mL), $Cu(ClO_4)_2 \cdot 6H_2O$ (17 mg, 0.045 mmol) was added. The mixture was allowed to stir at room temperature for 4 days during which time a pale green precipitate developed. The precipitate was filtered, washed with Et_2O and dried under vacuum. Yield 33 mg (52%). IR (cm^{-1}) 1227(s), 1184(vs). *Anal*. Required for $C_{64}H_{66}Cl_2CuN_7O_{16}P_3$: C, 54.26; H, 4.70; N, 6.92. Found: C, 54.15; H, 4.74; N, 6.91%.

2.4. Crystallography

The X-ray data were collected on a Siemens P4 four circle diffractometer, using a Siemens SMART 1 K CCD area detector. The crystals were mounted in an inert oil and irradiated with graphite monochromated Mo Kα ($\lambda = 0.71073$ Å) X-rays. The data were collected by the SMART program and processed with SAINT to apply Lorentz and polarisation corrections to the diffraction spots (integrated three dimensionally). Crystal data are given in Table 1. The structures were solved by direct methods and refined using the SHELXTL program [32]. Hydrogen atoms were calculated at ideal positions. Complexes **1** and **3** contained disordered solvent that could not be modelled satisfactorily.

Table 1
Crystal and refinement data for the compounds

Compound	$L^1 \cdot 2CH_2Cl_2$	**1** · $6CH_2Cl_2$	**3** · $2CH_2Cl_2$	**9** · $4CH_3CN \cdot 3H_2O$
Molecular formula	$C_{50}H_{34}Cl_4N_7O_6P_3$	$C_{102}H_{72}Cl_{12}Cu_2F_{12}N_{14}O_{12}P_8$	$C_{50}H_{34}Cl_6CuN_7O_6P_3$	$C_{80}H_{64}Cl_2Cu_2N_{14}O_{15}P_6$
M	1063.55	2714.07	1198.03	1845.26
T (K)	192(2)	200(2)	168(2)	83(2)
Crystal system	monoclinic	triclinic	triclinic	triclinic
Space group	$P2_1/c$	$P\bar{1}$	$P\bar{1}$	$P\bar{1}$
a (Å)	11.9732(3)	16.0425(7)	10.541(4)	9.0154(1)
b (Å)	39.3234(8)	18/1803(9)	15.679(6)	12.5223(2)
c (Å)	10.4878(2)	22.6989(12)	16.387(6)	19.1056(2)
α (°)		66.726(2)	105.509(6)	74.940(1)
β (°)	102.998(1)	75.683(2)	93.840(6)	77.095(1)
γ (°)		77.201(2)	99.076(6)	82.864(1)
V (Å^3)	4811.42(18)	5835.4(5)	2560.00(17)	2025.18(4)
Z	4	2	2	2
μ(Mo Kα) (mm^{-1})	0.405	0.832	0.891	0.785
ρ_{calc} (g cm^{-3})	1.468	1.544	1.553	1.513
$2\theta_{max}$ (°)	51.36	51.36	50.04	52.74
Number of unique reflections	9113	21080	9033	8090
Data/restraints/parameters	9113/42/654	21080/4/1357	9033/464/596	8090/0/541
Final *R* indices [$I > 2\sigma(I)$]	$R_1 = 0.0777$	$R_1 = 0.0539$	$R_1 = 0.0565$	$R_1 = 0.0728$
	$wR_2 = 0.2052$	$wR_2 = 0.1466$	$wR_2 = 0.1181$	$wR_2 = 0.1572$
R indices (all data)	$R_1 = 0.1025$	$R_1 = 0.0765$	$R_1 = 0.1202$	$R_1 = 0.1235$
	$wR_2 = 0.2231$	$wR_2 = 0.1582$	$wR_2 = 0.1345$	$wR_2 = 0.1836$
Goodness-of-fit on F^2	1.083	1.057	0.903	1.049

The contributions in each case were removed using PLATON/SQUEEZE [33]. In the case of **3**, the chloride anion is disordered over three positions and a site with low occupancy is in the disordered solvent region. The contribution from this anion was also removed. Complex **1**: 331 electrons per cell corresponding to four CH_2Cl_2 molecules were removed and 1260.8 Å^3 was left by the void. The remaining two solvent molecules were modelled satisfactorily. The reported formula is $\mathbf{1}\cdot 6CH_2Cl_2$. Complex **3**: 109 electrons per cell corresponding to $2CH_2Cl_2$ molecules and one Cl anion per molecule were removed and 521.3 Å^3 was left by the void.

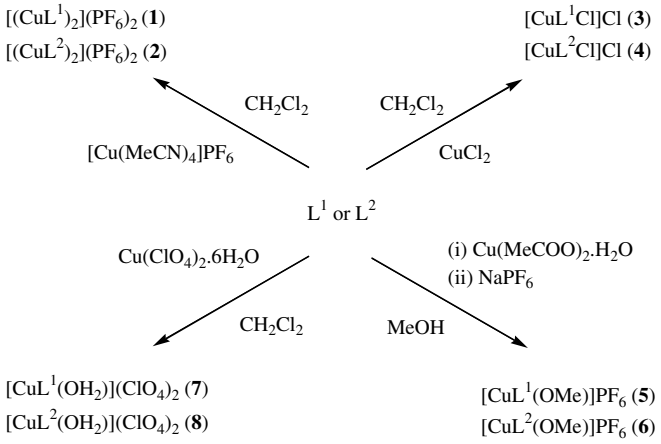
3. Results and discussion

3.1. Ligand syntheses

The bis-spiro derivatives $[N_3P_3(biph)_2Cl_2]$ or $[N_3P_3(^tBubiph)_2Cl_2]$ were reacted with two mole equivalents of the sodium salt of 2-hydroxy-1,10-phenanthroline (Hophen) in THF to give L^1 or L^2, respectively. Analytically pure samples of the ligands were obtained by recrystallisation. The ability of cyclotriphosphazenes with aromatic substituents to entrap solvents and form inclusion compounds is a common feature [34–39] and the ligands remained solvated even after drying under vacuum. The presence of solvent was confirmed by microanalyses and ^{1}H-NMR spectra and for L^1, X-ray crystallography. The ^{31}P NMR spectra for the ligands were, as expected, first order. The resonances for the two equivalent phosphorus atoms with biph or ^{t}Bubiph groups attached were observed as doublets at 23.39 and 25.32 ppm ($^2J_{PP} = 99$ and 97 Hz) while the resonance arising from third phosphorus was observed as a triplet at 7.66 and 7.80 ppm ($^2J_{PP} = 99$ and 97 Hz). The ^{1}H NMR resonances for the phenanthroline moieties were assigned using 2D correlation experiments. For both L^1 and L^2 the *m*/*z* peaks observed under ESMS conditions correspond to the protonated parent ions at 894 and 1118 mass units, respectively.

3.2. Complex syntheses

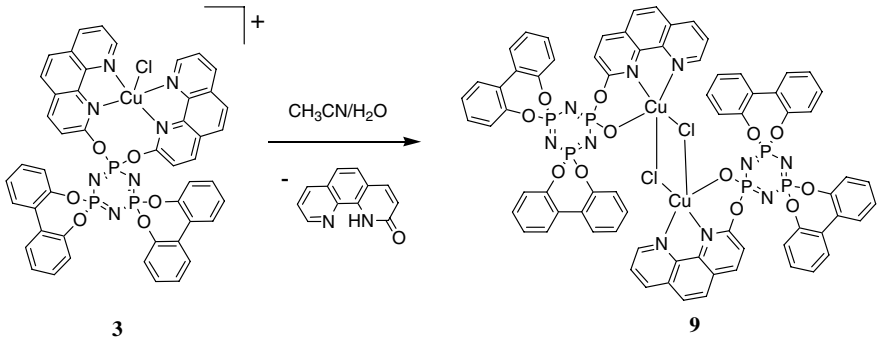
The reactions of L^1 and L^2 with copper salts reported here are shown in Scheme 2. The helical copper(I) complexes, $[(CuL^1)_2](PF_6)_2$ (**1**) and $[(CuL^2)_2](PF_6)_2$ (**2**), were prepared in high yield by reacting the appropriate ligand with $[Cu(MeCN)_4]PF_6$ at room temperature in CH_2Cl_2. ^{31}P NMR spectra were recorded for **1** and **2** in CD_3CN and $CDCl_3$, respectively, and the expected resonances for the phosphazene and hexafluorophosphate phosphorus atoms are observed (see Section 2). The room temperature ^{1}H NMR spectra of **1** in CD_3CN and **2** in either CD_3CN or $CDCl_3$ exhibit broad, poorly resolved signals. When samples of **1** were prepared in $CDCl_3$ to collect NMR data, a gel formed. The formation of a gel in the chlorinated solvent can be understood in terms of the layered structure (see Section 3.3.2) with its many intermolecular interactions which would persist in the less polar solvent but be broken by the polar acetonitrile molecules as the sample dissolves.



Scheme 2. The reactions of L^1 and L^2 with copper salts.

The ligands L^1 and L^2 react with anhydrous $CuCl_2$ in CH_2Cl_2 to give the copper(II) complexes, $[CuL^1Cl]Cl$ (**3**) and $[CuL^2Cl]Cl$ (**4**). The crystal structure of $\mathbf{3}\cdot 2CH_2Cl_2$ shows the complex to have a square-based pyramidal-distorted trigonal-bipyramidal geometry. When allowed to stand in acetonitrile, complex **3** undergoes hydrolysis (Scheme 3) to form the bimetallic species $[(CuL^3Cl)_2]$ (**9**, $L^3 = [N_3P_3(biph)_2(ophen)O]^-$). Ab initio molecular orbital calculations [40,41] on cyclophosphazene rings show the ring skeleton to be highly polar with a build up of charge density on the nitrogen atoms and nodes at the phosphorus atoms. This is in line with the experimental observation that the more positive phosphorus atoms are the preferred sites for nucleophilic attack [42]. Therefore hydrolysis is likely to occur at the phosphorus atom with a hydroxide ion replacing an oxyphenanthroline pendant group. Proton exchange followed by the formation of the ring oxygen copper(II) bond and dimerization through the two bridging chloro groups would give the final product, **9**. The observation that 2-hydroxy-1,10-phenanthroline is observed in the reaction mixture is consistent with this reaction scheme.

When L^1 or L^2 react with $Cu(MeCOO)_2$ in methanol followed by metathesis with $NaPF_6$, pale turquoise precipitates are formed, the elemental analyses of which are consistent with the formulations $[CuL^1(OMe)]PF_6\cdot 2H_2O$ ($\mathbf{4}\cdot 2H_2O$) and $[CuL^2(OMe)]\ PF_6\cdot 2H_2O$ ($\mathbf{5}\cdot 2H_2O$). In the presence of the acetate ion, the methoxide anion appears to be abstracted from the methanol solution and coordinates to the copper. The $[CuL^1(OMe)]^+$ and $[CuL^2(OMe)]^+$ species are also observed in the electrospray mass spectra and we have observed the formation of the corresponding ethoxide complexes from the reactions in ethanol. Although unusual, the abstraction of alkoxide ions during the reactions of copper acetate in alcohols is not unprecedented. Bimetallic complexes of the form $[Cu_2(bpy)_2(\mu\text{-}OAc)_2(\mu\text{-}OR)]$ (R = Me, Et) from the reaction of copper(II) acetate with bpy have been reported previously [43]. The reactions of L^1



Scheme 3. Hydrolysis of **3** to the dimetallic species **9**.

and L^2 with $Cu(ClO_4)_2 \cdot 6H_2O$ produces the complexes $[CuL^1(OH_2)](ClO_4)_2$ (**7**) and $[CuL^2(OH_2)](ClO_4)_2 \cdot H_2O$ (**8** $\cdot H_2O$). These complexes are obtained cleanly as precipitates from CH_2Cl_2.

3.3. Description of structures

3.3.1. $L^1 \cdot 2CH_2Cl_2$

The single-crystal structure of L^1 is shown in Fig. 1 and selected bond lengths and angles are given in Table 2. The P–N bond lengths [1.578(4)–1.591(4) Å] and both N–P–N and P–N–P angles [117.9(2)–118.11(19)° and 120.9(2)–121.2(3)°, respectively] are typical for cyclotriphosphazenes. The mean deviation of atoms from the plane of the N_3P_3 phosphazene ring is 0.0728 Å and the maximum deviation is 0.112 Å for P(3).

Intermolecular π-stacking interactions between phenanthroline rings are prevalent in the crystalline structure. For example, C(7) lies approximately 3.4 Å from the centre of the C(6)–C(9) bond on an adjacent molecule and the centroid of the fused pyridine ring containing N(4) is ca. 3.5 Å from C(19) of another molecule. The planes of the phenanthroline rings belonging to the same molecule lie at about 52° to one another. A consequence of these geometrical arrangements in the crystal packing is that two structurally distinct regions occur. Two-dimensional layers are generated by the stacked phenanthroline moieties while biphenyl groups on adjacent molecules are involved in π–π and π-H interactions which gives rise to 'back-to-back' layering of the phosphazene rings (Fig. 2). The arrangement creates channels running parallel to the *a*-axis that contain two molecules of dichloromethane per molecule of L^1. Also the nitrogen atoms N(4) and N(5) from one phenanthroline moiety participate in hydrogen bonds in a chelating manner with H(90A) of one of the dichloromethane molecules [N(4)···H(90A) and N(5)···H(90A) are 2.759 and 2.392 Å]. In this, and other work, we have often found it difficult to drive volatile solvents, such as CH_2Cl_2, from solid samples of both our phosphazene ligands and complexes [5]. It is likely that this is due to the persistence of packing motifs and non-covalent interactions such as those just described. The ability of cyclic phosphazenes bearing aromatic substituents to act as clathrates and inclusion compounds is well documented [34–39].

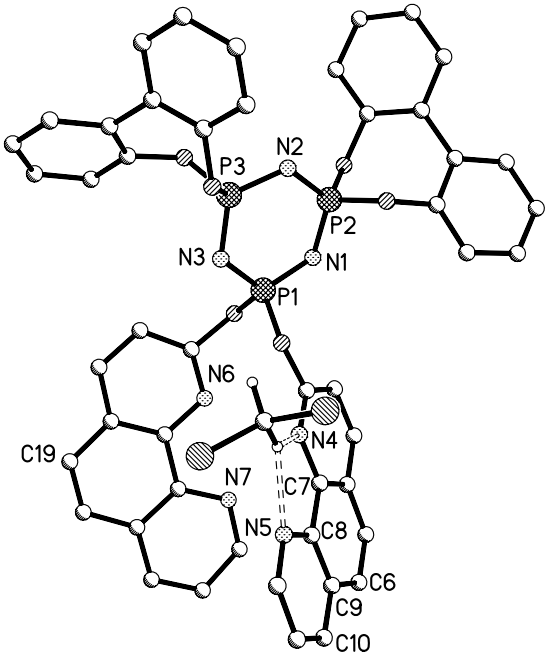


Fig. 1. Structure of the cyclotriphosphazene L^1, showing hydrogen bonding interaction with a CH_2Cl_2 solvate molecule. Most hydrogen atoms have been removed for clarity.

Table 2
Selected bond lengths (Å) and angles (°) for $L^1 \cdot 2CH_2Cl_2$

N(1)–P(1)	1.585(4)	N(2)–P(3)	1.588(4)
N(1)–P(2)	1.583(4)	N(3)–P(1)	1.591(4)
N(2)–P(2)	1.582(4)	N(3)–P(3)	1.578(4)
P(1)–N(1)–P(2)	121.0(2)	N(2)–P(2)–N(1)	118.1(2)
P(1)–N(3)–P(3)	120.9(2)	N(2)–P(3)–N(3)	117.9(2)
P(2)–N(2)–P(3)	121.2(3)	N(3)–P(1)–N(1)	118.11(19)
O(2)–P(1)–O(1)	104.97(16)	O(3)–P(2)–O(4)	102.06(17)
O(5)–P(3)–O(6)	102.55(16)		

3.3.2. Structure of $[(CuL^1)_2](PF_6)_2 \cdot 6CH_2Cl_2$ ($\mathbf{1} \cdot 6CH_2Cl_2$)

The structure of the $[(CuL^1)_2]^{2+}$ dication is shown in Fig. 3 and selected bond lengths and angles are given in Table 3. In this complex L^1 acts as a bridging ligand with two ligands coordinating to two copper(I) centres in a

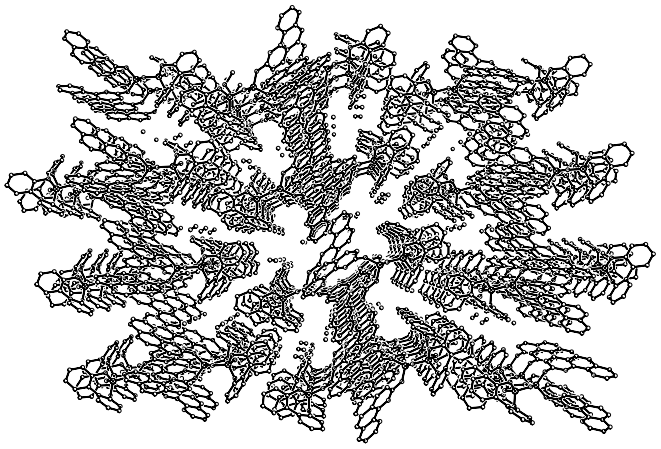


Fig. 2. Packing diagram of $L^1 \cdot 2CH_2Cl_2$ showing the channels along the *a*-axis. Individual carbon atoms of the CH_2Cl_2 solvate molecules occupying the channels are shown; chlorine atoms are omitted for clarity.

helical fashion similar to that observed for other bis-phenanthroline ligands that are linked by a spacer through the 2,2′-positions [20–25]. Both copper(I) centres have highly distorted tetrahedral geometry. The interligand N–Cu–N bond angles vary between 112.81(11)° and 143.14(12)° for Cu(1) and between 112.02(12)° and 134.02(12)° for Cu(2). Similarly there is a wide range in the Cu–N bond lengths: between 2.009(3) and 2.087(3) Å for Cu(1) and between 1.996(3) and 2.066(3) Å for Cu(2). The dihedral angles are 85.2° and 85.7° for Cu(1) and Cu(2). There is also a strong intramolecular π–π stacking interaction between the phenanthroline ring containing N(6) and N(7) and the phenanthroline ring containing N(13) and N(14); the angle between the mean planes of these rings is 8° and the closest contact between atoms in the rings is 3.364 Å for C(18)···C(65). Secondary intermolecular interactions within the crystal are numerous and give rise to an interesting longer range structural motif:

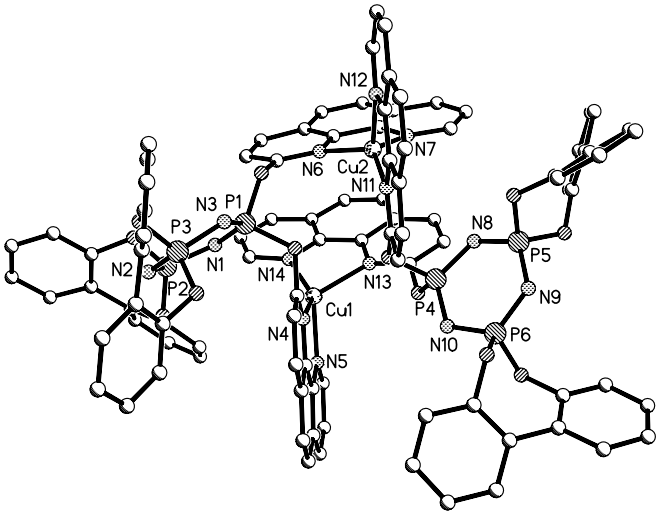


Fig. 3. Structure of the complex cation of $[(CuL^1)_2](PF_6)_2$ (**1**) with the hydrogen atoms removed for clarity.

Table 3
Selected bond lengths (Å) and angles (°) for $[(CuL^1)_2](PF_6)_2 \cdot 6CH_2Cl_2$ (**1** · $6CH_2Cl_2$)

Cu(1)–N(4)	2.013(3)	Cu(2)–N(6)	2.051(3)
Cu(1)–N(5)	2.087(3)	Cu(2)–N(7)	2.022(3)
Cu(1)–N(14)	2.009(3)	Cu(2)–N(11)	1.996(3)
Cu(1)–N(13)	2.073(3)	Cu(2)–N(12)	2.066(3)
N(1)–P(1)	1.583(3)	N(8)–P(4)	1.576(3)
N(1)–P(2)	1.586(3)	N(8)–P(5)	1.583(3)
N(2)–P(2)	1.588(3)	N(9)–P(5)	1.587(3)
N(2)–P(1)	1.586(3)	N(9)–P(6)	1.579(3)
N(3)–P(1)	1.577(3)	N(10)–P(4)	1.571(3)
N(3)–P(3)	1.588(3)	N(10)–P(6)	1.583(3)
N(4)–Cu(1)–N(5)	81.80(11)	N(6)–Cu(1)–N(7)	82.84(12)
N(4)–Cu(1)–N(13)	125.25(11)	N(6)–Cu(1)–N(11)	130.40(11)
N(4)–Cu(1)–N(14)	143.14(12)	N(6)–Cu(1)–N(12)	118.01(11)
N(5)–Cu(1)–N(13)	112.81(11)	N(7)–Cu(1)–N(11)	134.02(12)
N(5)–Cu(1)–N(14)	117.29(12)	N(7)–Cu(1)–N(12)	112.02(12)
N(13)–Cu(1)–N(14)	82.10(12)	N(11)–Cu(1)–N(12)	82.16(12)
N(1)–P(1)–N(3)	118.63(16)	N(8)–P(5)–N(9)	117.30(16)
N(1)–P(2)–N(2)	117.96(15)	N(8)–P(4)–N(10)	118.42(16)
N(2)–P(3)–N(3)	117.62(16)	N(9)–P(6)–N(10)	117.82(16)
P(1)–N(1)–P(2)	120.98(18)	P(4)–N(8)–P(5)	120.94(19)
P(2)–N(2)–P(3)	122.07(19)	P(5)–N(9)–P(6)	121.65(19)
P(3)–N(3)–P(1)	120.99(18)	P(6)–N(10)–P(4)	121.03(18)
O(1)–P(1)–O(2)	98.13(12)	O(7)–P(4)–O(8)	99.05(12)
O(3)–P(2)–O(4)	103.73(13)	O(9)–P(5)–O(10)	103.32(13)
O(5)–P(3)–O(6)	103.61(13)	O(11)–P(6)–O(12)	104.11(13)

the view along the *c*-axis is shown in Fig. 4. The cations are arranged so that they create continuous sheets of molecules that undulate along *b*-axis and stack along the *a*-axis. Many intermolecular contacts between adjacent cations occur from the close packing of the cations within the sheets. For example, in contrast to the phenanthroline rings described above, the phenanthroline rings containing N(11), N(12) and N(4), N(5) are involved in intermolecular stacking interactions with the equivalent phenanthroline rings on adjacent molecules. In the case of the ring containing N(11) and N(12), further stacking is observed with the phenyl ring bonded to O(6) resulting in a four ring interlocking stack (Fig. 5). This array is strengthened further by hydrogen bonds from phenanthroline H(58) to phosphazene N(3). In a direction roughly perpendicular to these interlinking stacking interactions there are close approaches between biphenyl rings; for instance, the distance between H(82) and O(6) is 2.384 Å and between C(88) and O(12) is 3.384 Å in adjacent molecules.

Between the sheets lie the hexafluorophosphate anions and solvent molecules [Fig. 4(b) is the view in Fig. 4(a) but with carbon and hydrogen atoms removed]. Both of the unique hexafluorophosphate anions have well defined atomic coordinates with the fluorine atoms being involved in numerous hydrogen-bonding interactions with aromatic hydrogen atoms, some of which cause the anions to bridge the sheets while others bridge cations within the sheets. In contrast only two of the six dichloromethane molecules have atomic coordinates defined well enough to include in the model and the remaining four molecules are disordered in the large voids left between the sheets. The self

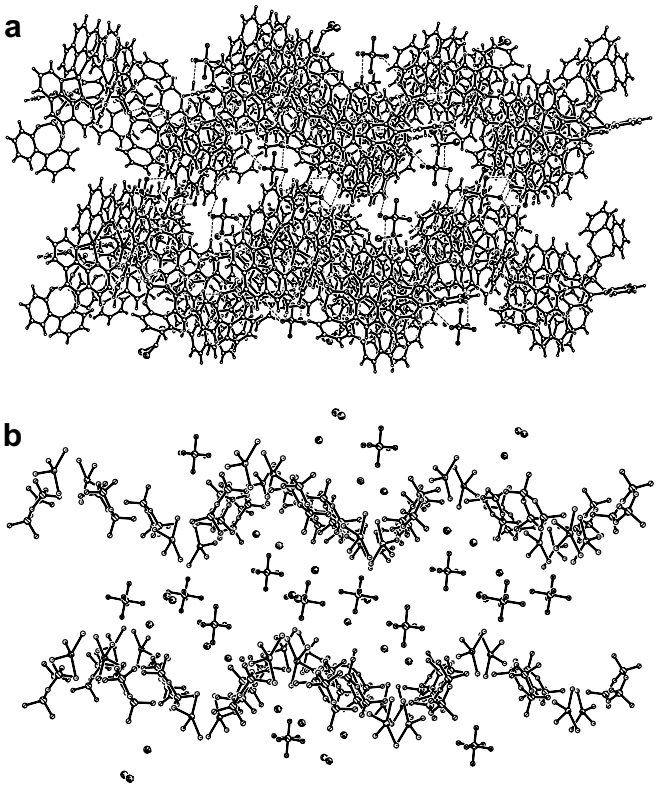


Fig. 4. (a) View along the *c*-axis of **1** showing the undulating sheets of $[(CuL^1)_2]^{2+}$ cations and the channels between the sheets containing PF_6^- anions and CH_2Cl_2 solvate molecules. (b) The same view with the carbon atoms removed.

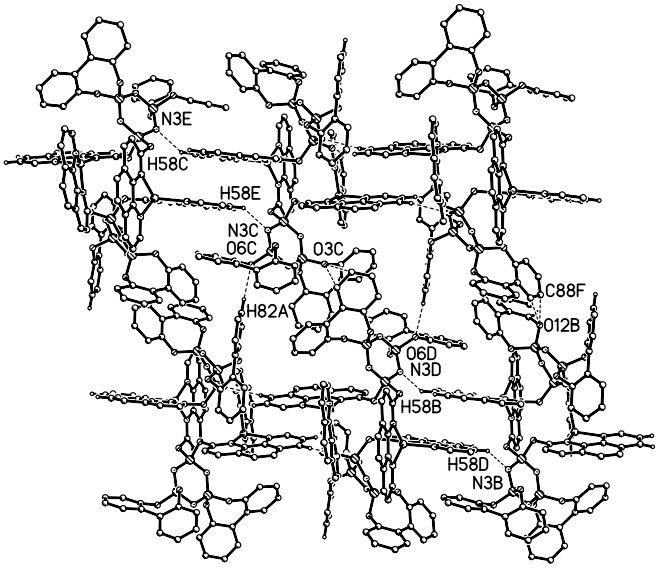


Fig. 5. Packing diagram showing the intermolecular close contacts and hydrogen bonding within the sheets of $[(CuL^1)_2]^{2+}$ cations in **1**.

assembly of cations and anions here is reminiscent of the motifs we reported previously for the structures of two silver(I) coordination polymers of *hexakis*(2-pyridyloxy)cyclotriphosphazene ligands [4].

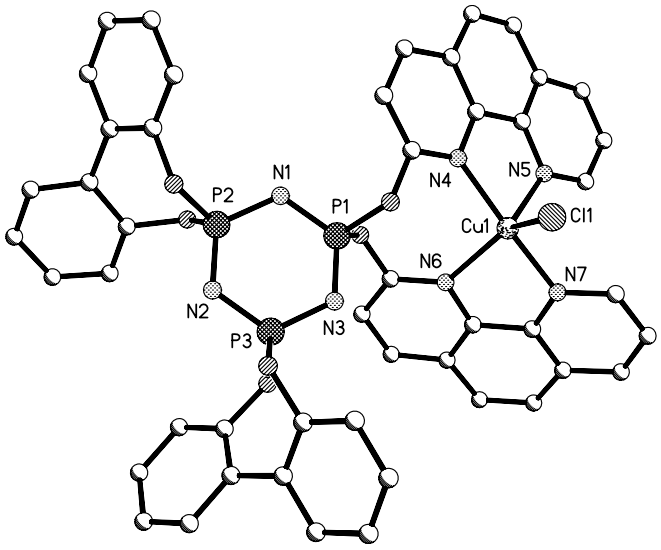


Fig. 6. Structure of the complex cation of $[CuL^1Cl]Cl$ (**3**) with the hydrogen atoms removed for clarity.

3.3.3. Structure of $[CuL^1Cl]Cl \cdot 2CH_2Cl_2$ ($\mathbf{3} \cdot 2CH_2Cl_2$)

The crystal structure of the $[CuL^1Cl]^+$ cation is shown in Fig. 6 and selected bond lengths and angles are given in Table 4. The copper(II) centre is five-coordinate with a 'N_4Cl' donor set arising from the two phenanthroline arms of L^1 and a chloride ion. The value of the structural index, τ [44], measured for this complex is 0.57 ($\tau = 1$ for perfect trigonal bipyramid, $\tau = 0$ for a perfect square-based pyramid) implying square-based pyramidal-distorted trigonal-bipyramidal (SBPDTB) geometry. However, the geometry about the copper differs from many reported $[Cu(phen)_2Cl]^+$ chromophores [45,46] in that the largest equatorial angle does not lie opposite the longest equatorial Cu–N bond length. The Cu–N(5) distance of 2.145(4) Å, opposite N(6)–Cu(1)–Cl(1) [137.24(10)°], is comparatively long and similar to the distance of 2.166(4) Å for Cu–N(6) opposite N(5)–Cu(1)–Cl(1) [112.58(11)°]. The contribution of crystal packing forces on the coordination geometry of this structure may be important. The cations are arranged such that the spirocyclic biphenyl ring bonded to P(3) forms an offset intermolecular π–π stack (ca. 3.48 Å) with its inversion related symmetry equivalent. Hence, a phenyl ring from the biphenyl moiety bound to P(3) is sandwiched between the phenanthroline ring bound through O(2) and the biphenyl moiety bound to P(3) of an adjacent molecule and the steric clash causes slightly larger thermal motion in the atoms of the participating phenanthroline.

The phosphazene ring in this structure is essentially planar and P–N bonds, P–N–P and N–P–N angles are unremarkable. There are small but concerted changes in the bond lengths of the oxyphenanthroline moieties upon coordination compared with the free ligand. The P–O(phen) bonds in L^1 have an average length of ca. 1.592 Å but in the complex they are slightly longer at an average of ca. 1.615 Å. The C(phen)–O(phen) bond lengths are slightly

Table 4
Selected bond lengths (Å) and angles (°) for $[CuL^1Cl]Cl \cdot 2CH_2Cl_2$ ($\mathbf{3} \cdot 2CH_2Cl_2$) and $[(CuL^3Cl)_2] \cdot 4CH_3CN \cdot 3H_2O$ ($\mathbf{9} \cdot 4CH_3CN \cdot 3H_2O$)

3		**9**	
Cu(1)–N(4)	1.998(3)	Cu(1)–N(4)	2.026(5)
Cu(1)–N(5)	2.145(4)	Cu(1)–N(5)	1.990(4)
Cu(1)–N(6)	2.166(4)	Cu(1)–O(2)	1.931(3)
Cu(1)–N(7)	1.977(4)	Cu(1)–Cl(1A)	2.2538(15)
Cu(1)–Cl(1)	2.3077(16)	Cu(1)–Cl(1)	2.7085(15)
N(1)–P(1)	1.578(3)	N(1)–P(1)	1.602(4)
N(1)–P(2)	1.601(4)	N(1)–P(2)	1.569(4)
N(2)–P(2)	1.577(4)	N(2)–P(2)	1.583(4)
N(2)–P(3)	1.594(3)	N(2)–P(3)	1.587(4)
N(3)–P(1)	1.571(4)	N(3)–P(1)	1.597(5)
N(3)–P(3)	1.603(4)	N(3)–P(3)	1.574(4)
N(4)–Cu(1)–N(5)	80.18(15)	N(4)–Cu(1)–N(5)	82.27(8)
N(4)–Cu(1)–N(6)	98.57(14)	N(4)–Cu(1)–Cl(1)	166.23(13)
N(4)–Cu(1)–N(7)	171.14(16)	N(4)–Cu(1)–O(2)	88.89(16)
N(5)–Cu(1)–N(6)	110.04(14)	N(5)–Cu(1)–Cl(1)	96.37(14)
N(5)–Cu(1)–N(7)	92.07(17)	N(5)–Cu(1)–O(2)	170.22(18)
N(6)–Cu(1)–N(7)	79.95(18)	Cl(1)–Cu(1)–O(2)	93.21(12)
N(4)–Cu(1)–Cl(1)	91.92(11)	N(4)–Cu(1)–Cl(1A)	96.81(13)
N(5)–Cu(1)–Cl(1)	112.58(11)	N(5)–Cu(1)–Cl(1A)	86.55(13)
N(6)–Cu(1)–Cl(1)	137.24(10)	Cl(1)–Cu(1)–Cl(1A)	96.78(5)
N(7)–Cu(1)–Cl(1)	95.05(14)	O(2)–Cu(1)–Cl(1A)	90.37(11)
		Cu(1)–Cl(1)–Cu(1A)	83.22(5)
		Cl(1)–Cu(1)–Cl(1A)	96.78(5)
N(1)–P(1)–N(3)	120.38(19)	N(1)–P(1)–N(3)	115.0(2)
N(1)–P(2)–N(2)	118.07(18)	N(1)–P(2)–N(2)	118.1(2)
N(2)–P(3)–N(3)	118.22(18)	N(2)–P(3)–N(3)	118.4(2)
P(1)–N(1)–P(2)	119.8(2)	P(1)–N(1)–P(2)	121.2(3)
P(2)–N(2)–P(3)	121.4(2)	P(2)–N(2)–P(3)	119.5(3)
P(3)–N(3)–P(1)	119.9(2)	P(3)–N(3)–P(1)	122.4(3)
O(1)–P(1)–O(2)	101.69(15)	O(1)–P(1)–O(2)	106.50(19)
O(3)–P(2)–O(4)	103.61(15)	O(3)–P(2)–O(4)	102.83(19)
O(5)–P(3)–O(6)	104.00(15)	O(5)–P(3)–O(6)	102.28(19)

shorter on coordination, average ca. 1.391 Å compared with an average of ca. 1.417 Å in the free ligand.

3.3.4. Structure of $[(CuL^3Cl)_2] \cdot 4CH_3CN \cdot 3H_2O$ ($\mathbf{9} \cdot 4CH_3CN \cdot 3H_2O$)

The hydrolysis product of $[CuL^1Cl]Cl$ (**3**) is the chloro-bridged bimetallic species $[(CuL^3Cl)_2]$ ($L^3 = [N_3P_3(biph)_2(ophen)O]^-$ (**9**)) (Scheme 3) and crystals of $\mathbf{9} \cdot 4CH_3CN \cdot 3H_2O$ grew from acetonitrile in the presence of adventitious water. The structure of **9** is depicted in Fig. 7 and selected bond lengths and angles are given in Table 4. The copper(II) ions have a 'N_2OCl_2' coordination sphere that arises from phenanthroline, phosphazenate and chloride ligands. The geometry about the copper is distorted square-based pyramidal with the Cu–Cl(1A) bond forming the apex. The atoms in the basal plane made by the 'N_2OCl' ligand set have a mean deviation of 0.1517 Å from planarity and Cu(1) lies 0.1011 Å out of this plane towards Cl(1A). The copper(II) ions are 3.313 Å apart with the copper(II) environment being similar to the polymeric compound $[Cu_2(phen)_2Cl_2(C_6H_8O_4)]_n \cdot 4H_2O$ [47].

The phosphazene ring in **9** is only slightly more distorted from planarity [the mean deviation of atoms from the plane of the N_3P_3 phosphazene ring is 0.089 Å and the maximum deviation is ca. 0.152 Å for P(1)] than those in L^1 and **3**, although the P–N bond lengths, P–N–P and P–N–P angles fall within the expected ranges. The most significant changes in geometry compared with the above two structures occur around P(1) of phosphazene ring. The P–O(phen) bond length in **9** is 1.657 Å and longer than the average 1.615 Å seen in **3**. The P–O(Cu) bond length of 1.502 Å is considerably shorter and comparable with the P–O(Cu) bond length of 1.520(2) Å observed in the copper(II) bound phosphazenate tetraanion, $[Cu\{(PO_2NH)_3\}_2]^{4-}$ [48].

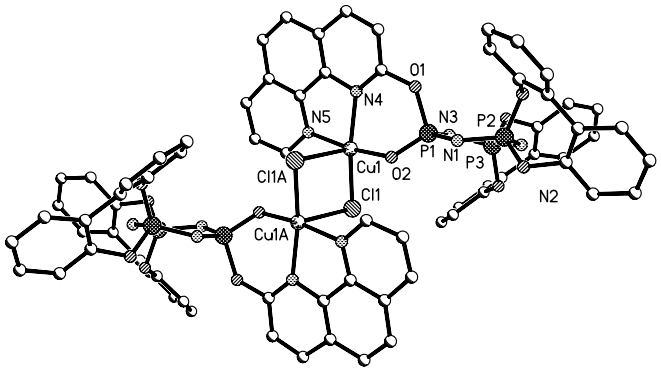


Fig. 7. Crystal structure of the bimetallic complex $[(CuL^3Cl)_2]$ (**9**) with the hydrogen atoms removed for clarity.

As with the structure of the parent ligand, L^1, an interesting feature of the long-range order in this structure is the existence of distinct regions in the crystal lattice as a result of non-covalent interactions. Both of the phenanthroline units in the dimer are involved in intermolecular stacking interactions with adjacent molecules which effectively result in a two-dimensional layer containing the copper ions. The biphenoxy residues of each ligand are involved in non-covalent interactions with the biphenoxy moieties of adjacent layers in a direction roughly perpendicular to the interactions between the phenanthroline moieties. The overall effect is a series of alternating layers of biphenoxy, phosphazene ring and copper-rich regions (Fig. 8).

3.4. Physicochemical studies

3.4.1. IR and electronic spectroscopy

The $P–N_{phosphazene}$ stretching frequencies for L^1 at 1230(s) and 1170(vs) cm^{-1} are altered only a little in the complexes, the ranges being 1226–1227 cm^{-1} for the first and 1170–1175 cm^{-1} for the second band. Similar changes occur in the $P–N_{phosphazene}$ stretching frequencies of L^2, at 1230(s) and 1182(vs) cm^{-1}, upon coordination to the copper centres. These data are consistent with the phosphazene rings not being distorted significantly from planarity upon copper coordination to the phenanthroline moieties [3].

The electronic spectra for the complexes are given in Table 5. For the copper(I) double-helicate compounds,

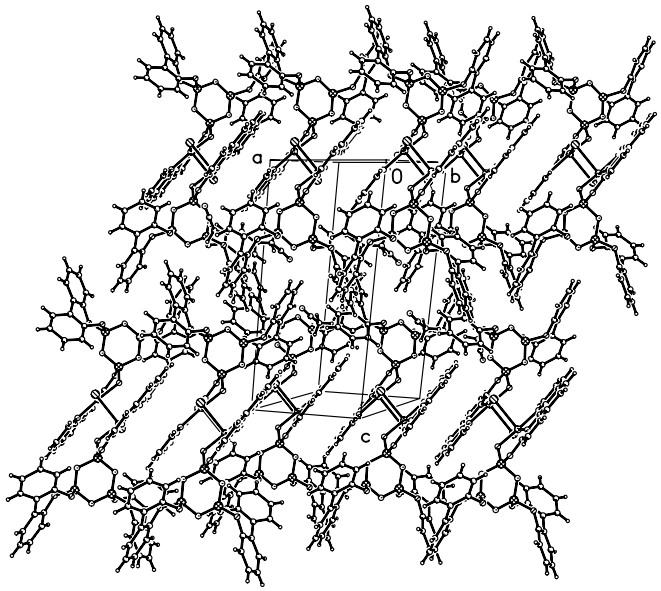


Fig. 8. Packing diagram of **9** showing alternating copper(II) and oxybiphenyl regions.

Table 5
Electronic spectral and ESR data for the complexes[a]

Complex	λ_{max}/nm (ε/l mol^{-1} cm^{-1})		ESR		
	d–d	MLCT	$g_{\parallel}$	$g_{\perp}$	$A_{\parallel}$ (cm^{-1})
1		465, 540sh[b] 444 (6250) 518 (4370)[c]			
2		402, 528[b] 450 (3890) 528 (2890)[c]			
3	820[d]		2.33	2.13	135×10^{-4}
4	828 (235) 980sh (175)		2.33	2.14	130×10^{-4}
5	704 (50) 921sh (40)		2.23	2.08	170×10^{-4}
6	709 (95) 905sh (55)		2.29	2.08	171×10^{-4}
7	834 (60) 980sh (45)		2.01[e,f] 2.42[e,g,h]	2.23 2.09	67×10^{-4} 142×10^{-4}
8	800br (200)		2.26	2.09	158×10^{-4}

[a] In CH_2Cl_2 unless otherwise indicated; sh = shoulder, br = broad.
[b] As nujol mull.
[c] In acetone.
[d] Not sufficiently soluble to determine ε.
[e] In CH_3CN/CH_2Cl_2.
[f] Major species.
[g] Minor species
[h] In acetone the parameters are $g_{\parallel} = 2.43$, $g_{\perp} = 2.09$ and $A_{\parallel} = 141 \times 10^{-4}$ cm^{-1}.

$[(CuL^1)_2](PF_6)_2$ (**1**) and $[(CuL^2)_2](PF_6)_2$ (**2**) bands in the 400–550 nm region can be assigned to metal-to-ligand charge-transfer (MLCT) [49]. For **1** in the solid state, the presence of a maximum at 465 nm with a weak shoulder at ca. 540 nm is typical of a so-called Class I spectrum [49,50] and implies a slight distortion from tetrahedral which is consistent with the single-crystal X-ray structure where the interligand dihedral angle at 85° is close to 90°. In acetone solution, the conductivity of **1** is 260 S cm^2 mol^{-1}, which is consistent with a 2:1 electrolyte [51], and confirms the retention of the double helicate structure. However, the solution displays two distinct bands at 444 and 518 nm which, with the well-formed band at a wavelength longer than 500 nm, are typical of a Class II type $[Cu(NN)_2]X$ compound [49,50] with the interligand dihedral angle considerably less than 90°. In the solid state, examples are given by $[Cu(phen)_2]ClO_4$ (dihedral angle 49.9°) and $[Cu(dpdmp)_2]PF_6$ (dpdmp = 2,9-diphenyl-4,7-dimethyl-1,10-phenanthroline) (dihedral angle 68.4°) [50]. The origin of the two bands in monomeric copper(I) diimine systems has been addressed [49,50] where the emphasis was placed on the variance of the dihedral angle between the equivalent ligands. If the copper centres show large distortions from D_{2d} symmetry then the d_{π} orbitals are non-degenerate and the two absorptions $b_2(xz) \rightarrow b_2(\pi^*)$ and $b_3(yz) \rightarrow b_3(\pi^*)$ are observed. For compound **2** in both the solid and acetone solution, the observation of two well resolved bands is consistent with a Class II spectrum and would suggest that the interligand dihedral angle is far removed from 90° in both states.

The copper(II) compounds all display d–d bands at wavelengths greater than 700 nm. In both the solid and dichloromethane solution, the complex $[CuL^1Cl]Cl$ (**3**) displays a broad d–d band at about 820 nm, which tails into the infrared, characteristic of a trigonal-bipyramidal geometry around copper(II) in solution [47]. A 10^{-3} M solution of **3** in CH_2Cl_2 has a conductivity of 23 S cm^2 mol^{-1} typical of a 1:1 electrolyte [51] supporting the retention of a monomeric structure in solution. The spectra of **4**, and of compounds **7** and **8** (where H_2O replaces the chloride ion) can be similarly assigned. However, each of the compounds **5** and **6** displays a single d–d band near 700 nm as well as in the 905–920 nm region with the shorter wavelength band having a greater extinction coefficient. These data are more characteristic [52] of a square-pyramidal distortion in the structures.

3.4.2. Magnetic moments and electron spin resonance spectra

The room temperature magnetic moments for **3**, **4**, **5** and **7** are 1.80, 1.93, 2.06 and 2.20 μ_B, respectively, consistent with the normal spin-only values for copper(II) [53].

X-Band ESR spectra (Table 5) of the complexes were generally recorded in CH_2Cl_2 at liquid nitrogen temperature. The spectra of **3**, **4**, **5**, **6** and **8** are similar and typical for monomeric axial copper(II) complexes with $d_{x^2-y^2}$ ground states with $g_{\parallel} > g_{\perp}$ ($g_{\parallel}$ 2.23–2.33, $g_{\perp}$ 2.08–2.14 and $A_{\parallel}$ in the range $130–171 \times 10^{-4}$ cm^{-1}). Well-resolved copper hyperfine lines in the $g_{\perp}$ region were not observed. These data are consistent with a square-based distortion

of a trigonal-bipyramidal structure [52], as found in the X-ray crystal structure of $[CuL^1Cl]Cl$ (**3**) described above. The ESR spectrum for **7** in a CH_3CN/CH_2Cl_2 glass was more complex, showing the presence of two species. The major one exhibited two identifiable magnetic g values, together with the corresponding copper ($I = 3/2$) hyperfine splitting constants ($g_\perp = 2.23$, $A_\perp = 105 \times 10^{-4}\,cm^{-1}$; $g_\parallel = 2.01$, $A_\parallel = 67 \times 10^{-4}\,cm^{-1}$). The g and A values match other reported examples of trigonal bipyramidal copper(II) complexes [24,25] which have 'reversed' axial spectra, i.e. $g_\perp > g_\parallel$ and $A_\perp > A_\parallel$. For the minor species, $g_\parallel = 2.42$, $g_\perp = 2.09$ and $A_\parallel = 142 \times 10^{-4}\,cm^{-1}$. These g and A values are in agreement with an axial spectrum with a $d_{x^2-y^2}$ ground state and suggest a species that has a square-based distortion of a trigonal-bipyramidal structure [52]. Hence in the glass, it appears that cation distortion isomerism exists with the two structures in equilibrium with each other. The equilibrium may be altered by the nature of the solvent, e.g. in acetone glass the major species now has very similar ESR parameters to the minor species in the CH_3CN/CH_2Cl_2 glass, which is the square-based isomer, while the minor species is the trigonal-bipyramidal isomer. The equilibrium is also affected by the substituents on the biphenolato moiety.

4. Conclusions

The new compounds, L^1 and L^2, represent the first examples of ligands with two 1,10-phenanthroline moieties tethered to a cyclotriphosphazene platform. A series of five-coordinate copper(II) complexes has been prepared by reacting L^1 or L^2 with copper chloride and copper perchlorate, and the single-crystal X-ray structure of one of these, i.e. $[CuL^1Cl]Cl \cdot 2CH_2Cl_2$ (**3** $\cdot 2CH_2Cl_2$) shows the copper to have a SBPDTB environment ($\tau = 0.57$) with L^1 acting as a κ^4N donor. The conformational rigidity of L^1 probably aids in the hydrolysis of **3** where one phenanthroline ligand is cleaved from L^1 to afford $[(CuL^3Cl)_2]$ (**9**). We have previously observed a P–O bond cleavage, coupled with a redox reaction, of the coordinated phosphazene ligand, hexakis(2-pyridyloxy)cyclotriphosphazene [4], and recently Chandrasekhar et al. have reported another such reaction [54]. The rigidity of the ligands, L^1 and L^2, does give good control over dihelicate copper(I) formation seen in $[(CuL^1)_2](PF_6)_2$ (**1**) and $[(CuL^2)_2](PF_6)_2$ (**2**) but not with copper(II) with its higher coordination number requirement.

Acknowledgements

We acknowledge financial support, including a postdoctoral fellowship (to C.A.O.), from the RSNZ Marsden Fund (MAU208). We thank Dr. C.V. Depree for some initial experimental data and the Otsuka Chemical Co. Ltd for a gift of hexachlorocyclotriphosphazene.

Appendix A. Supplementary material

Crystallographic data for the structural analysis has been deposited with the Cambridge Crystallographic Data Centre, CCDC Nos. 606780–606783. Copies of this information may be obtained free of charge from: The Director, CCDC, 12 Union Road, Cambridge, CB2 1EZ, UK (fax: +44 1223 336033; e-mail: deposit@ccdc.cam.ac.uk or www: http://www.ccdc.cam.ac.uk). Supplementary data associated with this article can be found, in the online version, at doi:10.1016/j.poly.2006.07.007.

References

[1] M. Gleria, R. De Jaeger (Eds.), Applicative Aspects of Cyclophosphazenes, Nova Science Publishers, Inc., New York, 2004.
[2] E.W. Ainscough, A.M. Brodie, C.V. Depree, J. Chem. Soc., Dalton Trans. (1999) 4123.
[3] E.W. Ainscough, A.M. Brodie, C.V. Depree, B. Moubaraki, K.S. Murray, C.A. Otter, Dalton Trans. (2005) 3337.
[4] E.W. Ainscough, A.M. Brodie, C.V. Depree, G.B. Jameson, C.A. Otter, Inorg. Chem. 44 (2005) 7325.
[5] E.W. Ainscough, A.M. Brodie, C.V. Depree, C.A. Otter, Polyhedron 25 (2006) 2341.
[6] K.R.J. Thomas, V. Chrandrasekhar, P.S. Pai, S.R. Scott, R. Hallford, A.W. Cordes, Inorg. Chem. 32 (1993) 606.
[7] K.R.J. Thomas, P. Tharmaraj, V. Chandrasekhar, C.D. Byran, A.W. Cordes, Inorg. Chem. 33 (1994) 5382.
[8] K.R.J. Thomas, V. Chandrasekhar, K. Vivekanandan, G.T.S. Andavan, S. Nagendran, S. Kingsley, E.R.T. Tiekink, Inorg. Chim. Acta 286 (1999) 127.
[9] A. Chandrasekaran, S.S. Krishnamurthy, M. Nethaji, Inorg. Chem. 32 (1993) 6102.
[10] B.H. Koo, Y. Byun, E. Hong, Y. Kim, Y. Do, Chem. Commun. (1998) 1227.
[11] U. Diefenbach, H.R. Allcock, Inorg. Chem. 33 (1994) 4562.
[12] U. Diefenbach, M. Kretschmann, O. Cavdarci, Phosphorus Sulfur 93–94 (1994) 415.
[13] U. Diefenbach, K.M. Retschmann, B. Stromburg, Chem. Ber. 129 (1996) 1573.
[14] M. Kretschmann, U. Diefenbach, Z. Anorg. Allg. Chem. 624 (1998) 335.
[15] U. Diefenbach, P. Adamaszek, M. Bloy, M. Kretschmann, S.Z. Scholz, Anorg. Allg. Chem. 624 (1998) 1679.
[16] U. Diefenbach, M. Kretschmann, B. Stromburg, Phosphorus Sulfur 124–25 (1997) 143.
[17] M. Bloy, M. Kretschmann, S. Scholz, M. Teichert, U. Diefenbach, Z. Anorg. Allg. Chem. 626 (2000) 1946.
[18] U. Diefenbach, M. Bloy, B. Stromburg, Phosphorus Sulfur 144 (1999) 65.
[19] M. Harmjanz, I.M. Piglosiewicz, B.L. Scott, C.J. Burns, Inorg. Chem. 43 (2004) 642.
[20] J.-M. Lehn, A. Rigault, J. Siegel, J. Harrowfield, B. Chevrier, D. Moras, Proc. Natl. Acad. Sci. USA 84 (1987) 2565.
[21] J.-M. Lehn, A. Rigault, Angew. Chem. Int. Ed. Engl. 27 (1988) 1095.
[22] T.M. Garett, U. Koert, J.-M. Lehn, A. Rigault, D. Meyer, J. Fischer, J. Chem. Soc., Chem. Commun. (1990) 557.
[23] M.-T. Youinou, R. Ziessel, J.-M. Lehn, Inorg. Chem. 30 (1991) 2144.
[24] Y. Yao, M.W. Perkovic, D.P. Rillema, C. Woods, Inorg. Chem. 31 (1992) 3956.
[25] M. Pitié, C. Boldron, H. Gornitzka, C. Hemmert, B. Donnadieu, B. Meunier, Eur. J. Inorg. Chem. (2003) 528.
[26] K.G. Claus, J.V. Rund, Inorg. Chem. 8 (1969) 59.
[27] C.R. Rice, K.M. Anderson, Polyhedron 19 (2000) 495.
[28] D.E. Zacharias, F.H. Case, J. Org. Chem. 27 (1962) 3878.

[29] T. Yamato, K. Hasegawa, Y. Saruwatarai, L.K. Doamekpor, Chem. Ber. 126 (1993) 1435.
[30] G.A. Carriedo, L. Fernádez-Catuxo, F.J. García Alonso, P. Gómez-Elipe, P.A. González, Macromolecules 29 (1996) 5320.
[31] G.J. Kubas, Inorg. Synth. 28 (1990) 68.
[32] G.M. Sheldrick, SHELXL Suite of Programs for Crystal Structure Analysis, Institüt für Anorganische Chemie der Universität, Göttingen, Germany, 1998.
[33] P. van der Sluis, A.L. Spek, Acta Crystallogr. A46 (1990) 194.
[34] H.R. Allcock, L.A. Siegel, J. Am. Chem. Soc. 86 (1964) 5140.
[35] H.R. Allcock, M.L. Levin, R.R. Whittle, Inorg. Chem. 25 (1986) 41.
[36] L.A. Siegel, J.H. van der Hende, J. Chem. Soc. A (1967) 817.
[37] H.R. Allcock, J. Am. Chem. Soc. 96 (1974) 49.
[38] H.R. Allcock, A.P. Primrose, E.N. Silverberg, K.B. Visscher, A.L. Rheingold, I.A. Guzei, M. Parvez, Chem. Mater. 12 (2000) 2530.
[39] E.W. Ainscough, A.M. Brodie, A. Derwhal, Polyhedron 22 (2003) 189.
[40] R. Jaeger, M. Debowski, I. Manners, G.J. Vancso, Inorg. Chem. 38 (1999) 1153.
[41] V. Luaňa, A.M. Pendás, A. Costales, G.A. Carriedo, G.J. García-Alonso, J. Phys. Chem. A 105 (2001) 5280.
[42] C.W. Allen, Coord. Chem. Rev. 130 (1994) 137.
[43] S.P. Perlepes, J.C. Huffman, G. Christou, S. Paschalidou, Polyhedron 14 (1995) 1073.
[44] A.W. Addison, T.N. Rao, J. Reedijk, J. Van Rijn, G.C. Verschoor, J. Chem. Soc., Dalton Trans. (1984) 1349.
[45] Y. Yamada, H. Sakurai, Y. Miyashita, K. Fujisawa, K. Okamoto, Polyhedron 21 (2002) 2143.
[46] G. Murphy, P. Nagle, B. Murphy, B. Hathaway, J. Chem. Soc., Dalton Trans. (1997) 2645.
[47] Y. Zheng, J. Sun, J.-L. Lin, Z. Anorg. Allg. Chem. 627 (2001) 90.
[48] S. Correll, W. Schnick, Z. Anorg. Allg. Chem. 626 (2000) 2347.
[49] A.Y. Kovalevsky, M. Gembicky, I.V. Novozhilova, P. Coppens, Inorg. Chem. 42 (2003) 8794.
[50] C.T. Cunningham, J.J. Moore, K.L.H. Cunningham, P.E. Fanwick, D.R. McMillin, Inorg. Chem. 39 (2000) 3638.
[51] W.J. Geary, Coord. Chem. Rev. 7 (1971–1972) 81.
[52] A.K. Patra, M. Ray, R. Mukherjee, J. Chem. Soc., Dalton Trans. (1999) 2461.
[53] B.J. Hathaway, in: G. Wilkinson (Ed.), Comprehensive Coordination Chemistry, Pergamon Press, 1987, p. 656 (Chapter 53).
[54] V. Chandrasekhar, B.M. Pandian, R. Azhakar, Inorg. Chem. 45 (2006) 3510.

Available online at www.sciencedirect.com
ScienceDirect
Polyhedron 26 (2007) 472–478
POLYHEDRON
www.elsevier.com/locate/poly

Encapsulating beryllium – Synthesis, characterisation and modelling of a chiral binaphthyldiimine-Be(II) complex

Paul G. Plieger [a,*], Kevin D. John [b,*], Anthony K. Burrell [b]

[a] Massey University, Department of Chemistry, Private Bag 11 222, Palmerston North, New Zealand
[b] Chemistry Division, MS J582, Los Alamos National Laboratory, Los Alamos, NM 87545, United States

Received 31 May 2006; accepted 25 July 2006
Available online 3 August 2006

Abstract

Beryllium has been successfully incorporated into a naphthalene containing Schiff base ligand. Evidence from ^{9}Be and ^{1}H NMR data and model compounds indicate that the ligand completely encapsulates the beryllium cation via tetra-dentate tetrahedral coordination using both phenol and imine donors. Calculated ^{9}Be NMR data at the B3LYP/6-311G+(2d,p) DFT level of theory is in agreement with this conclusion.
© 2006 Elsevier Ltd. All rights reserved.

Keywords: Beryllium; Encapsulation; GIAO; DFT; Schiff base; NMR; Complex

1. Introduction

Despite the well established toxicity of beryllium [1], it is employed in a variety of industrial applications due to the fact that it is three times lighter than aluminium, six times stiffer than steel and displays remarkable heat/corrosion resistance. Inhalation of beryllium particles and alloys is directly linked to chronic beryllium disease (CBD) [2] and skin contact with small particles of beryllium has been reported to lead to beryllium sensitisation [3]. Current treatment for beryllium exposure involves the application of immunosuppressive drugs to control the Be(II) induced immune response; this treatment only serves to slow the advance of CBD [4]. At present, no cure exists for this sometimes fatal disease. Chelation therapies are commonly employed to treat other forms of metal toxicity; however no selective chelating agent presently exists for the Be(II) cation. For example, EDTA which binds most other metals with some degree of strength, has been established to be a poor binder of beryllium [5]. A suitably selective encapsulating agent for Be(II) would therefore serve as a notable advance in the areas of Be(II) chelation therapy and environmental remediation.

We have observed that ligands with mixed N/O donors such as pyridine-phenol and 10-hydroxybenzoquinoline sulphate (HBQS) show promise as selective coordinators of beryllium (Fig. 1) [6].

Bidentate ligands that bind the Be(II) cation (such as those shown in Fig. 1) are quite common; however, ligands which completely chelate beryllium providing all four donor atoms are extremely rare. Complex ligand architectures that provide all four coordination sites for the beryllium tetrahedron in a small binding pocket are likely to be the key elements in the design of a Be(II)-specific chelator. An extensive search of the literature and the Cambridge Crystallographic Database Centre found only two examples (Fig. 2) of ligands providing the complete coordination sphere for the Be(II) cation [7]. The Be-phthalocyanine structure seems to be an unlikely geometry given the fact that no other square planar structure of Be(II) has been reported [8]. The nitrilotripropionate (NTP) structure creates an ideal tetrahedral binding environment however, the flexibility of the alkyl backbone will reduce the ability

* Corresponding authors. Tel.: +64 6 356 9099; fax: +64 6 350 5682 (P.G. Plieger).
E-mail addresses: p.g.plieger@massey.ac.nz (P.G. Plieger), kjohn@lanl.gov (K.D. John).

0277-5387/$ - see front matter © 2006 Elsevier Ltd. All rights reserved.
doi:10.1016/j.poly.2006.07.020

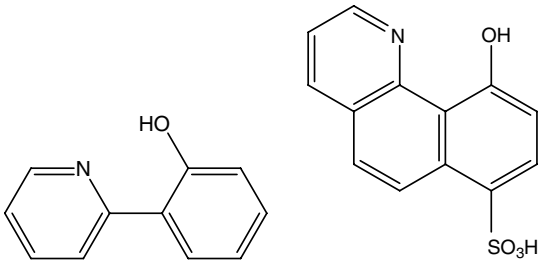
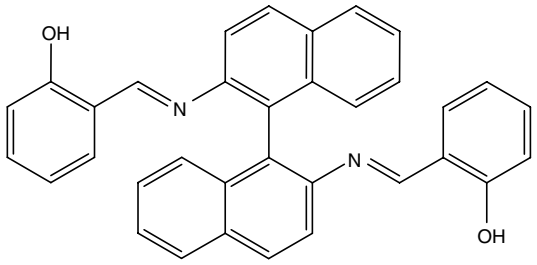


Fig. 1. Proven binders of Be(II).

of NTP to act as a selective sequestering agent for beryllium [9].

In this report, we describe our investigations on the rotationally hindered 2,2-disubstituted 1,1-binapthalene as a beryllium complexing agent (Fig. 3). Ligands containing 2,2-iminobiphenyl (or 2,2-iminobinapthalene) are well suited for binding tetrahedral metal cations. The steric repulsion of the opposing α-protons adjacent to the 1,1 aromatic linker forces the aromatic rings to sit perpendicular to one another, predisposing the ligand for a tetrahedral arrangement of donors, given a metal (for example, Be(II) or Zn(II)) that prefers such an arrangement. Our choice of binapthalene over the analogous biphenyl was dictated by its commercially available precursors and higher energy barrier to rotation. This ligand contains two hard phenolate donors in addition to the slightly softer imine donor atoms and potentially provides a fully encapsulating ligand donor set for beryllium (Fig. 4). The N/O mixed donor set is similar to HBQS, potentially forming a six-membered chelate ring on binding beryllium. In addition, incorporation of beryllium within this molecule would result in a neutral complex, eliminating the need for an attendant anion and the potential complication of competition with the ligand for the beryllium cation.

We have used density functional theoretical (DFT) methods in past studies to predict the NMR properties of



H_2L

Fig. 3. The ligand used in the present study.

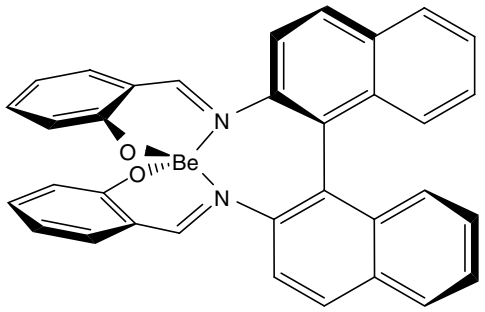


Fig. 4. Schematic of the binding of beryllium by **L**.

a variety of beryllium complexes [10]. We will employ these same techniques to predict the geometries and NMR chemical shifts (^{9}Be and ^{1}H) of this complex (Fig. 4).

2. Experimental

2.1. Starting materials and reaction procedures

(*R*)-(+)-2,2′-diamino-1,1′-binaphthalene (9%) and 2-hydroxybenzaldehyde (99%) were purchased from Acros Organics and used without further purification.

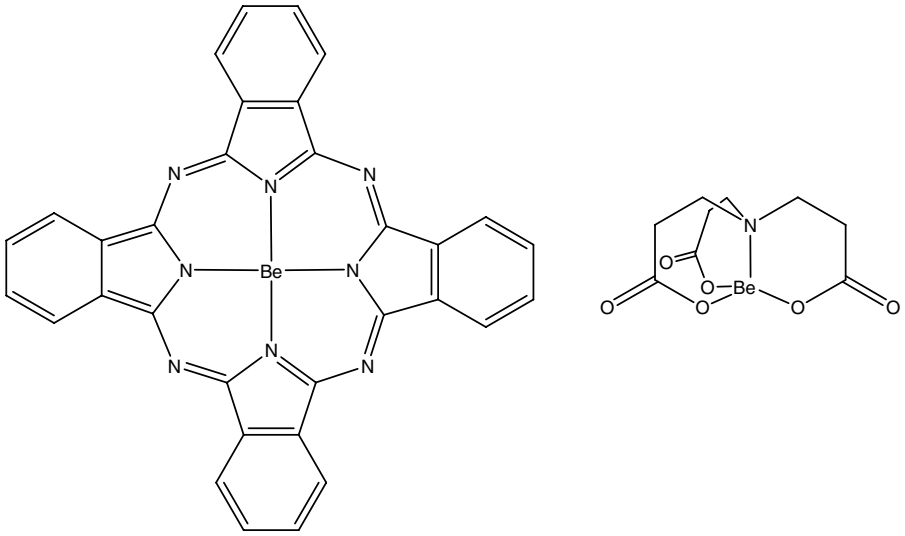


Fig. 2. Previously known tetra-chelating complexes of beryllium(II) as determined by X-ray crystallography.

Basic beryllium acetate was prepared via the synthesis of Moeller et al. [11].

Caution! Beryllium salts are extremely toxic and should be handled with appropriate care. All beryllium solid manipulations were handled in a Plas-Labs 818 Series, HEPA filtered (0.4 μm prefilter), reversed-pressure glove box. All beryllium solution work was performed in a dedicated HEPA filtered chemical hood. ^{9}Be NMR spectra were recorded on a Bruker Avance 300 at 42.17 MHz and referenced to an internal standard of $Be(H_2O)_4^{2+}$ (as the sulfate salt). All NMR samples containing beryllium were contained within Teflon sleeves in addition to the standard NMR glass tube. The alternative synthesis of $\mathbf{H_2L}$ has been reported previously [12].

2.2. H_2L

To a solution of *R*-(+)-2,2′-diamino-1,1-binapthalene (0.500 g, 1.76 mmol) in ethanol (40 mL) was added a solution of 2-hydroxy-benzaldehyde (0.434 g, 3.516 mmol) in ethanol (10 mL). The resulting orange solution was brought to reflux and within minutes an orange precipitate was formed. Refluxing was continued for 4.5 h. The solution was cooled and the resulting orange precipitate was filtered, washed with ice cold ethanol and dried (0.553 g). Reduction of the supernatant (10 mL) resulted in a further precipitation which was treated as above (0.256 g). Total yield: 0.804 g, 93%. M.p. > 300 °C. The data for this compound have been reported previously [12]. ^{1}H NMR ($CDCl_3$, TMS, 300 MHz) δ 12.08 (s, 2H, OH), 8.66 (s, 2H, H_{imine}), 8.10 (d, $J = 8.8$ Hz, 2H), 7.96 (d, $J = 8.8$ Hz, 2H), 7.64 (d, $J = 8.8$ Hz, 2H), 7.45 (dd, $J = 8.1$, 8.4, 2H), 7.31–7.15 (m, 8H), 6.77 (t, $J = 7.8$, 2H), 6.70 (d, $J = 7.8$, 2H); ^{13}C NMR ($CDCl_3$, 75 MHz) δ 162.1, 161.0, 144.0, 133.4, 133.0, 132.7, 132.4, 130.2, 129.8, 128.5, 127.2, 126.7, 126.1, 119.5, 118.9, 117.3, 117.1.

2.3. BeL

To a bright yellow solution of $\mathbf{H_2L}$ (0.121 g, 0.246 mmol) in a 1:1 ethanol (25 mL):chloroform (25 mL) mixture was added a few crystals of $Be_4O(COOCH_3)_6$ (0.025 g, 61.5 μmol). The beryllium crystals quickly dissolved and the solution was left to reflux doing which time the solution colour reduced in intensity to a pale yellow. After 5 h the solution was left to cool, then covered and left to evaporate. Yield: 25.4% based on NMR analysis. ^{1}H NMR ($CDCl_3$, TMS, 300 MHz) δ 8.27 (s, 2H, H_{imine}), 7.97 (d, $J = 8.4$ Hz, 2H), 7.53 (d, $J = 8.4$ Hz, 2H), 7.49–7.35 (m, 2H), 7.32–7.08 (m, 6H), 7.04 (d, $J = 8.4$ Hz, 2H), 6.86 (d, $J = 8.5$, 2H), 6.55 (t, $J = 7.4$, 2H); ^{9}Be NMR ($CDCl_3$, $Be(H_2O)_4^{2+}$, 42.17 MHz) δ 4.84 (complex), 0.90 ($Be_4O(OAc)_6$).

3. Computational

Computational calculations were performed using the program Gaussian 03 [13]. We found that Becke's three-parameter hybrid exchange correlation functional [14] containing the non-local gradient correction of Lee, Yang and Parr (B3LYP) [15], in conjunction with the 6-31(d) basis set, gave a satisfactory geometry for the most part. All optimized structures were confirmed as minima by calculation of the vibration frequencies. NMR shieldings for beryllium were evaluated at the minima using B3LYP with 6-311+G(2d,p) as the basis set and the GIAO (gauge-including atomic orbital) NMR method [16] as implemented by Cheeseman et al. [17] in the Gaussian 03 package. The complex $Be(H_2O)_4^{2+}$ is the standard reference for ^{9}Be NMR spectroscopy and is defined as 0.00 ppm. Structure determination for this complex (B3LYP/6-31(d)) followed by calculation of the magnetic shielding (B3LYP/6-311G+(2d,p)) gave a value of 108.96 ppm. The calculated chemical shift reported in this study is in relation to $Be(H_2O)_4^{2+}$, using the expression $\delta_{complex} = \sigma_{reference} - \sigma_{complex}$.

4. Results and discussion

4.1. Synthesis of H_2L

The ligand was easily prepared by the Schiff-base condensation of the commercially available precursors. Successful condensation was confirmed by the lack of a carbonyl proton signal and the presence of a new proton signal at 8.66 ppm in the ^{1}H NMR.

4.2. Molecular structure of H_2L

At the time this work was done, no single crystal X-ray determination had been reported for $\mathbf{H_2L}$, so we determined this structure to both aid in the characterisation of this ligand and more importantly so that we could compare the free ligand with that of our modelled beryllium structure to give an indication of the accuracy (as measured by C–C bond lengths) of the computed structure of the complexed model (see later). During the preparation of this manuscript however, Gao et al. [18] published a lower temperature crystal structure determination of $\mathbf{H_2L}$ which upon analysis had a slightly better fit of the data than our own determination. Therefore it is the structural parameters of Gao that we will use for our comparison with our calculated structure.

4.3. Complexation of H_2L

Complexing beryllium to ligand systems in organic media is challenging. Not withstanding the issue of toxicity but in addition, finding a suitable beryllium organic soluble starting material is somewhat limited given both the lack of availability and also the inherent inertness to

substitution of the few examples that do exist. For instance, $\mathbf{H_2L}$ was refluxed for some days in ethanol with the organic soluble starting material $Be(acac)_2$ with no reaction as monitored by ^{9}Be NMR analysis. In contrast, basic beryllium acetate can be used as a suitable source for Be(II) if it is reacted in the presence of an alcoholic reaction medium [19]. Subsequently, reaction of $\mathbf{H_2L}$ with basic beryllium acetate in an equal volume $CHCl_3$/ethanol mix lead to the formation of the neutral chloroform soluble complex Be**L**. Attempts to grow single crystals from the slow evaporation of a chloroform solution of Be**L** were unsuccessful.

4.4. ^{9}Be NMR of Be**L**

Analysis of the ^{9}Be NMR spectrum (Fig. 5) reveals that the chemical shift of 4.84 and a line width of ~40 Hz is consistent with a 4-coordinate complex [10b].

4.5. Modelling (structural)

We have shown that computational calculations can be a useful prediction of both structure and properties for beryllium complexes [10b]. In an effort to provide further evidence for beryllium complexation of $\mathbf{H_2L}$, the predicted structure of the complex was optimised and the ^{9}Be NMR chemical shift calculated. The calculated geometry is shown in Fig. 7 and the space filling model is provided in Fig. 8. Optimisation of the gas phase model at the B3LYP/6-31G(d) level was in good agreement with solid state data (as measured by bond lengths) from both the free ligand [18] and previously reported structural determinations of non-beryllium containing complexes and also with comparison to the much smaller sample size of related beryllium complexes (see Table 1 and Fig. 6) [7].

Comparison of the Be–X, (X = N, O) donor bond lengths of the model are in excellent agreement (<0.2% difference), within those of known beryllium containing complexes with similar heteroatom donor sets (Table 1). Examining one bond length further from the coordination sphere shows that the model still has very good agreement with comparable solid state bond lengths (<4% difference

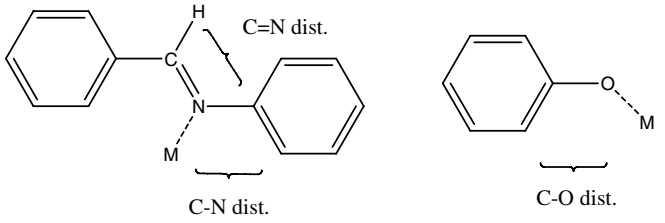


Fig. 6. Bond distances from the CCDC used for comparison with the model complex and the free ligand $\mathbf{H_2L}$.

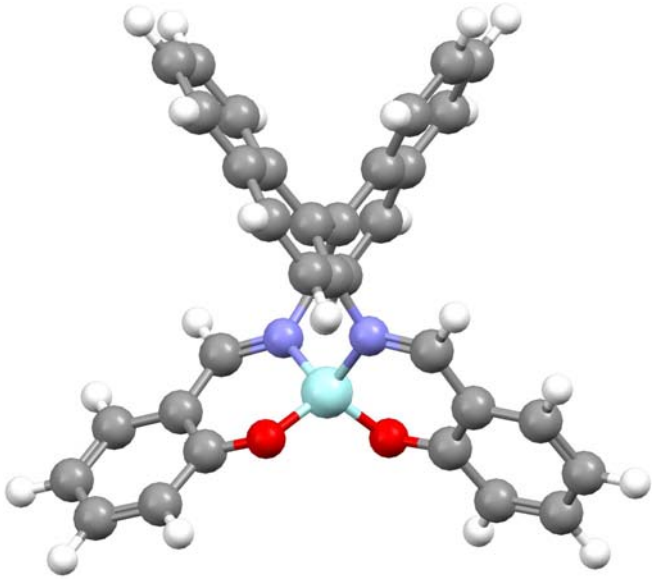


Fig. 7. Optimised structure of Be**L** showing the tetrahedral coordination of beryllium.

for the C–O and C=N bond lengths). The C–O bond length of the Be**L** model is 3.7% shorter than that of the corresponding average distance for solid state structures containing this bond in the presence of oxygen bound metal. We believe this is not significant as this difference is comparable to the difference between Gao's solid state structure of $\mathbf{H_2L}$ with that of the corresponding average C–O bond length in the absence of any coordinating metal (2.2% shorter). The beryllium atom adopts a near ideal tetrahedral geometry with angles (N/O–Be–N/O) of 104.2–

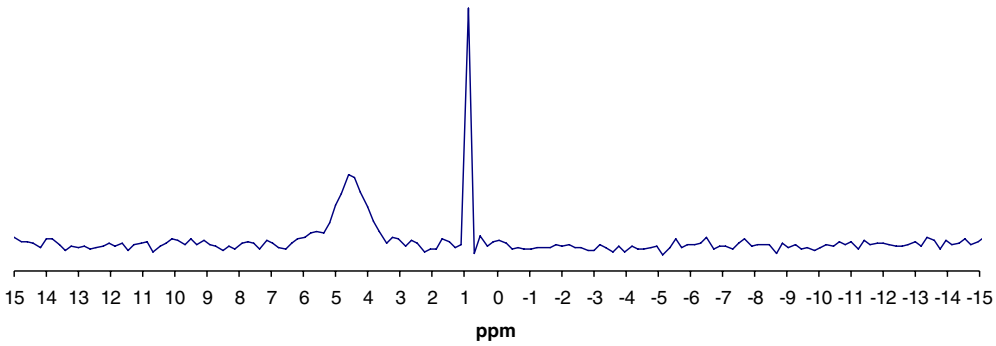


Fig. 5. ^{9}Be NMR spectrum of Be**L**. The $Be_4O(CH_3COO)_6$ cluster at 0.90 ppm is included as reference. ($CDCl_3$, 42.17 MHz, $T = 298.2$ K).

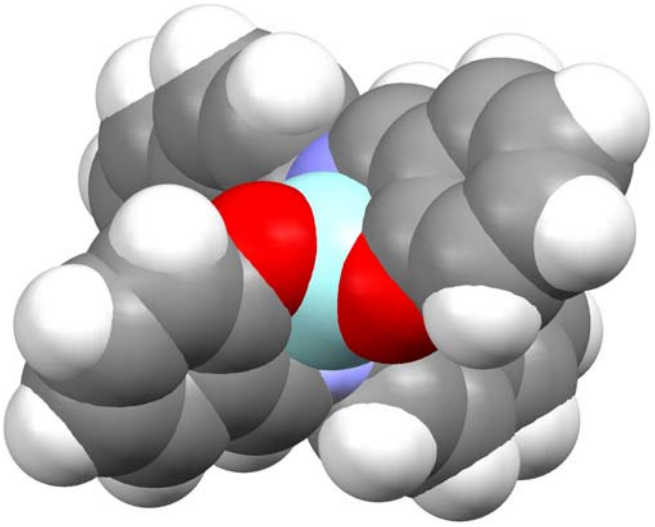


Fig. 8. Space filling model of Be**L** looking towards the beryllium binding site and showing the protection around the beryllium atom by the donor atoms (red = oxygen, blue = nitrogen) and the aromatic rings (grey = carbon, white = hydrogen). (For interpretation of the references to colour in this figure legend, the reader is referred to the web version of this article.)

115.1° (average 109.5). The naphthalene groups are at an angle of 65° to one another, with the N···N and O···O distances now at 2.759 and 2.651 Å, respectively.

The space filling model shows that beryllium sits well within the coordination pocket and is almost completely encapsulated by the ligand (Fig. 8).

A search of the Cambridge structural database indicates that tetrahedral metal coordination to this ligand type is surprisingly rare. Even cations of similar size to beryllium, such as Al(III) prefer to adopt an octahedral donor set with $\mathbf{H_2L}$, utilising deprotonated solvent (methoxide) and/or a second equivalence of $\mathbf{H_2L}$ to make this possible, this suggests that selective binding of beryllium in a metal-rich competitive environment may be possible. In fact of the seventeen known metal complexes crystallographically characterised using **L** or a slight derivation of **L**, only one example, a cobalt(II) complex, adopts a heavily distorted tetrahedral geometry (av. 110.0°, range 94.4–128.3) [20]. In contrast to these crystallographically characterised complexes, the beryllium gas phase model complex (**BeL**) adopts a slightly distorted tetrahedral geometry (Fig. 7 and Table 1).

4.6. Modelling (NMR)

Due to the toxic nature of solid beryllium and beryllium dust the manipulation of beryllium solids should be handled with extreme caution or not at all. Unfortunately many characterisation techniques used to determine the nature and structure of inorganic complexes require the manipulation of solids. An alternative to working with these solids is to use solution-based characterisation techniques. We have shown that NMR prediction using computational chemistry, coupled with ^{9}Be experimental solution data can be a valuable tool in predicting the binding motif of beryllium complexes in solution for simple molecules [10]. The accuracy of the NMR prediction largely lies with the accuracy by which the complexes can be structurally optimised. We and others [10a,21] have shown that good agreement between calculated structural parameters with crystallographic data is a prerequisite for accurate NMR predictions. In addition, it has been shown previously that the NMR prediction is also dependent on the level of theory employed for the calculation with a more complete basis set increasing the accuracy of the predicted NMR results [17].

The ^{9}Be NMR chemical shift has been determined for Be**L** at two different levels of theory. In addition, at the higher level of theory (6-311G+(2d,p)), a second

Table 1
Comparison of Be–X bond distances for Be**L** with corresponding Be–X donors from the Cambridge Crystallographic Data Centre

	[a] Freq.	Av. Be–O Å	Av. C–O Å	Av. Be–N Å	Av. C=N Å	Av. C–N Å
Be**L** model	2[b]	1.589	1.303	1.735	1.304	1.422
X-ray $\mathbf{H_2L}$ ligand	4[c]		1.343		1.270	1.410
CCDC						
Be–O phenol	8	1.589				
C–O phenol[d] (M)	10000+		1.340			
C–O phenol[e] (NM)	10000+		1.365			
all Be–O	294	1.617				
Be–N imine						
C=N[d] (M)	1480				1.292	
C=N[e] (NM)	109				1.295	
all Be–N	178			1.732		
C–N imine[d] (M)	2240					1.433
C–N[e] (NM)	212					1.431

[a] Frequency defined as the number of unique occurrences for a given parameter.
[b] Two occurrences of each kind present in structure.
[c] Four occurrences of each kind present in structure.
[d] Values reported for all metal bound species.
[e] Values reported for all non-metal containing species.

Table 2
Calculated ^{9}Be NMR parameters using the GIAO method and B3LYP as implemented in GAUSSIAN03™ [13]

Basis set	Solvent model	$\delta_{complex}$	δ_{ref}	NMR shift (ppm)[b]
6-31G(d)		107.32	114.21	6.89
6-311G+(2d,p)		103.50	108.96	5.46
6-311G+(2d,p)	SCRF=$CHCl_3$	103.62	108.96[a]	5.34

[a] Experimentally the aqueous reference $Be(H_2O)_4^{2+}$ is sealed and does not make contact with the $CHCl_3$ solution.
[b] The experiment NMR chemical shift value for Be**L** is 4.84 ppm.

calculation was performed with the inclusion of a solvent ($CHCl_3$) model, to determine the effect that this has on the predicted chemical shift value (Table 2).

The NMR chemical shift calculation for Be**L** is least accurate at the 6-31G(d) level of theory and most accurate at the 6-311G+(2d,p) level of theory incorporating the solvent $CHCl_3$ model, however it must be noted that the difference between solution and the gas phase model is only very slight (~0.1 ppm). The difference in the ^{9}Be chemical shift value between the more accurate calculations and that of the experiment value is approx. 0.5 ppm, a typical discrepancy in these types of calculations [10,22].

5. Conclusion

We have shown that the rotationally hindered bis-imino/phenol naphthalene ligand **H_2L** binds to beryllium resulting in an encapsulated environment. ^{1}H and ^{9}Be NMR data provide evidence for a 4-coordinate Be(II) centre. DFT modelling indicates that this structure is a tetra-dentate complex whereby all four of the donors are bound to beryllium, therefore, beryllium appears to bind to **H_2L** in a nearly ideal tetrahedral geometry as compared to other metal cations. The GIAO NMR prediction corroborates this interpretation. This geometry has been shown to be an extremely rare Be(II)-ligand binding motif and promises to be instrumental as a synthetic platform for the development of Be(II) chelators for physiological and environmental applications. The zero-point energy calculation of this complex will be compared to other Be(II) complexes for which binding constants are known – a process that once tested may provide the basis for *in silico* screening of potential candidates. Work continues on competition studies, synthesis of water soluble derivatives and more rigid systems that will serve to prevent larger cations from competing for the binding pocket provided by this ligand.

Acknowledgements

The authors thank the Laboratory Directed Research and Development program of the Los Alamos National Laboratory, operated by the University of California under contract to the US Department of Energy for funding. In addition P.G.P. thank Massey University for granting leave and Los Alamos National Laboratory for hosting him to allow the preparation of this manuscript.

Appendix A. Supplementary data

Supplementary data associated with this article can be found, in the online version, at doi:10.1016/j.poly.2006.07.020.

References

[1] L.S. Newman, Chem. Eng. News 81 (2003) 38.
[2] M. Eisenbud, Appl. Occup. Environ. Hyg. 13 (1998) 25.
[3] (a) D.A. Basketter, L.J. Lea, K. Cooper, J. Stocks, A. Dickens, I. Pate, R.J. Dearman, I. Kimber, Food Chem. Toxicol. 37 (1999) 1167; (b) S.S. Tinkle, J.M. Antonini, B.A. Rich, J.R. Roberts, R. Salmen, K. DePree, E.J. Adkins, Env. Health Per. 11 (2003) 1202.
[4] (a) A. Sood, W.S. Beckett, M.R. Cullen, Chest 126 (2004) 2000; (b) L.A. Hart, M. Conron, R.M. du Bois, Int. J. Tuberc. Lung Dis. 5 (2001) 791.
[5] L. Alderighi, P. Gans, S. Midollini, A. Vacca, in: A.G. Sykes, A.H. Cowley (Eds.), Advances in Inorganic Chemistry: Main Group Chemistry, vol. 50, Academic Press, New York, 2000, pp. 109–172.
[6] (a) A. Burrell, G. Collis, K. John, P. Plieger, Acta Crystallogr., Sect C 59 (2003) o443; (b) T.M. McCleskey, D.S. Ehler, K.D. John, A.K. Burrell, G. Collis, E.M. Minogue, B.P. Warner, Quantitative method of determining beryllium or a compound thereof in a sample, US Patent Application 20050221498, Filed March 2004.
[7] ConQuest, version 1.7, new software for searching the Cambridge Structural Database and visualizing crystal structures I.J. Bruno, J.C. Cole, P.R. Edgington, M. Kessler, C.F. Macrae, P. McCabe, J. Pearson, R. Taylor, Acta Crystallogr., Sect. B 58 (2002) 389.
[8] R.P. Linstead, J.M. Robertson, J. Chem. Soc. (1936) 1736.
[9] E. Chinea, S. Domínguez, A. Mederos, F. Brito, J.M. Arrieta, A. Sánchez, G. Germain, Inorg. Chem. 34 (1995) 1579.
[10] (a) P.G. Plieger, D.S. Ehler, B.L. Duran, T.P. Taylor, K.D. John, T.S. Keizer, T.M. McCleskey, A.K. Burrell, J.W. Kampf, T. Haase, P.G. Rasmussen, J. Karr, Inorg. Chem. 44 (2005) 5761; (b) P.G. Plieger, T.S. Keizer, K.D. John, T.M. McCleskey, A.K. Burrell, R.L. Martin, J. Am. Chem. Soc. 126 (2004) 14651.
[11] T. Moeller, A.J. Cohen, E. Marvell, Inorg. Synth. III (1950) 9.
[12] (a) M. Shi, C.-J. Wang, A.S.C. Chan, Tetrahedron: Asymmetry 12 (2001) 3105; (b) K.D.S. Bernardo, A. Robert, F. Dahan, B. Meunier, New J. Chem. 19 (1995) 129.
[13] M.J. Frisch, G.W. Trucks, H.B. Schlegel, G.E. Scuseria, M.A. Robb, J.R. Cheeseman, J.A. Montgomery Jr., T. Vreven, K.N. Kudin, J.C. Burant, J.M. Millam, S.S. Iyengar, J. Tomasi, V. Barone, B. Mennucci, M. Cossi, G. Scalmani, N. Rega, G.A. Petersson, H. Nakatsuji, M. Hada, M. Ehara, K. Toyota, R. Fukuda, J. Hasegawa, M. Ishida, T. Nakajima, Y. Honda, O. Kitao, H. Nakai, M. Klene, X. Li, J.E. Knox, H.P. Hratchian, J.B. Cross, V. Bakken, C. Adamo, J. Jaramillo, R. Gomperts, R.E. Stratmann, O. Yazyev, A.J. Austin, R. Cammi, C. Pomelli, J.W. Ochterski, P.Y. Ayala, K. Morokuma, G.A. Voth, P. Salvador, J.J. Dannenberg, V.G. Zakrzewski, S. Dapprich, A.D. Daniels, M.C. Strain, O. Farkas, D.K. Malick, A.D. Rabuck, K. Raghavachari, J.B. Foresman, J.V. Ortiz, Q. Cui, A.G. Baboul, S. Clifford, J. Cioslowski, B.B. Stefanov, G. Liu, A. Liashenko, P. Piskorz, I. Komaromi, R.L. Martin, D.J. Fox, T. Keith, M.A. Al-Laham, C.Y. Peng, A. Nanayakkara, M. Challacombe, P.M.W. Gill, B. Johnson, W. Chen, M.W. Wong, C. Gonzalez, J.A. Pople, GAUSSIAN 03, Revision C.02, Gaussian Inc., Wallingford, CT, 2004.
[14] A.D. Becke, J. Chem. Phys. 98 (1993) 5648.
[15] C. Lee, W. Yang, R.G. Parr, Phys. Rev. B 37 (1988) 785.

[16] (a) R. Ditchfield, Mol. Phys. 27 (1974) 789;
(b) K. Wolinski, J.F. Hinton, P. Pulay, J. Am. Chem. Soc. 112 (1990) 8251.
[17] J.R. Cheeseman, G.W. Trucks, T.A. Keith, M.J. Frisch, J. Chem. Phys. 104 (1996) 5497.
[18] J. Gao, J.H. Reibenspies, R.A. Zingaro, F.R. Woolley, A.E. Martell, A. Clearfield, Inorg. Chem. 44 (2005) 232.
[19] A.I. Grigor'ev, A.V. Novoselova, K.N. Semenenko, Zh. Neorg. Khim. 2 (1957) 2067.
[20] Y. Shen, W. Duan, M. Shi, J. Org. Chem. 68 (2003) 1559.
[21] G. Schreckenbach, Y. Ruiz-Morales, T. Ziegler, J. Chem. Phys. 104 (1996) 8605.
[22] J.A. Tossell, J. Mag. Res. 135 (1998) 203.

Available online at www.sciencedirect.com
ScienceDirect
Polyhedron 26 (2007) 479–485
POLYHEDRON
www.elsevier.com/locate/poly

Synthesis and X-ray crystal structures of some mononuclear and dinuclear complexes of 4-isobutyl-3,5-di(2-pyridyl)-4*H*-1,2,4-triazole

Marco H. Klingele [a], Andy Noble [a], Peter D.W. Boyd [b], Sally Brooker [a,*]

[a] *Department of Chemistry, University of Otago, P.O. Box 56, Dunedin, New Zealand*
[b] *Department of Chemistry, The University of Auckland, Private Bag 92019, Auckland, New Zealand*

Received 19 June 2006; accepted 25 July 2006
Available online 1 August 2006

Abstract

In order to probe the ability of the bis-bidentate ligand 4-isobutyl-3,5-di(2-pyridyl)-4*H*-1,2,4-triazole (ibdpt) to form mononuclear complexes of the 1:2 type, $[M^{II}(ibdpt)_2(X)_2]^{y+}$, a metal-to-ligand molar ratio of 1:2 has been employed in reactions with $Co(ClO_4)_2 \cdot 6H_2O$, $Ni(ClO_4)_2 \cdot 6H_2O$ and $Zn(ClO_4)_2 \cdot 6H_2O$. A high yield of the pure mononuclear complex $[Zn^{II}(ibdpt)_2(ClO_4)_2]$ is obtained when $Zn(ClO_4)_2 \cdot 6H_2O$ is employed. In contrast, when $Co(ClO_4)_2 \cdot 6H_2O$ is employed a mixture of mono- and dinuclear complexes, $[Co^{II}(ibdpt)_2(X)_2]^{y+}$ and $[Co^{II}_2(ibdpt)_2(X)_4]^{y+}$, respectively, results. Even more dramatically, when $Ni(ClO_4)_2 \cdot 6H_2O$ is employed, no mononuclear $[Ni^{II}(ibdpt)_2(X)_2]^{y+}$ complex is obtained despite the 1:2 ratio. It is clear from these studies that stoichiometry alone does not control the outcome of such complexation reactions but that other factors, including the nature of the N^4 substituent and the relative solubility of the various possible products, also influenced by the N^4 substituent, are also important. The X-ray crystal structures of the mononuclear complexes $[Co^{II}(ibdpt)_2(H_2O)_2](ClO_4)_2 \cdot Et_2O$, $[Zn^{II}(ibdpt)_2(ClO_4)_2]$ and $[Zn^{II}(ibdpt)_2(H_2O)_2](ClO_4)_2 \cdot 3MeCN$ and of the dinuclear complex $[Zn_2(ibdpt)_2(H_2O)_4](ClO_4)_2$ are presented. In all of these complexes the metal centres are octahedrally N_4O_2 coordinated by two in-plane ibdpt molecules and axial H_2O or ClO_4^- co-ligands. The *trans*-$(N',N^1)_2$ coordination mode is adopted in all three mononuclear complexes and the *trans*-$(N',N^1,N^2,N'')_2$ double bridging coordination mode is adopted in the dinuclear complex.
© 2006 Elsevier Ltd. All rights reserved.

Keywords: 1,2,4-Triazoles; N ligands; Cobalt; Nickel; Zinc

1. Introduction

Among the handful of 4-substituted 3,5-di(2-pyridyl)-4*H*-1,2,4-triazole ligands known before our work [1] only NH_2dpt [2,3] and pldpt [4] (Fig. 1) were reported to afford dinuclear complexes, while dinucleating behaviour was not observed for 4-aryl-3,5-di(2-pyridyl)-4*H*-1,2,4-triazoles [5–13] until very recently when a dinuclear silver(I) complex of ppdpt (Fig. 1) was structurally characterised [14]. It is important to note that in all of the structurally characterised complexes of 4-aryl-3,5-di(2-pyridyl)-4*H*-1,2,4-triazoles, all but one of which is mononuclear, the aryl substituents on N^4 form angles of about 68–84° with the triazole ring so no significant π-interactions are expected between them [5–14]. Given our interest in preparing 1,2,4-triazole-bridged dinuclear complexes we decided to develop access to a new group of such ligands, specifically those featuring an alkyl substituent on N^4, *i.e.* an electron-donating group, as it was anticipated that this should increase the electron density of the central triazole ring and hence promote the dinucleating ability of the ligand. We recently reported the first examples of 4-alkyl-3,5-di(2-pyridyl)-4*H*-1,2,4-triazoles [15]. Our studies of the coordination chemistry of one of these ligands, namely 4-isobutyl-3,5-di(2-pyridyl)-4*H*-1,2,4-triazole (ibdpt) (Fig. 1), have shown that, unlike their 4-aryl-substituted congeners, such ligands can readily form dinuclear complexes [16]. However, even though those studies employed a metal-to-ligand molar ratio of 2:2, in one case,

* Corresponding author. Tel.: +64 3 479 7919; fax: +64 3 479 7906.
E-mail address: sbrooker@alkali.otago.ac.nz (S. Brooker).

0277-5387/$ - see front matter © 2006 Elsevier Ltd. All rights reserved.
doi:10.1016/j.poly.2006.07.018

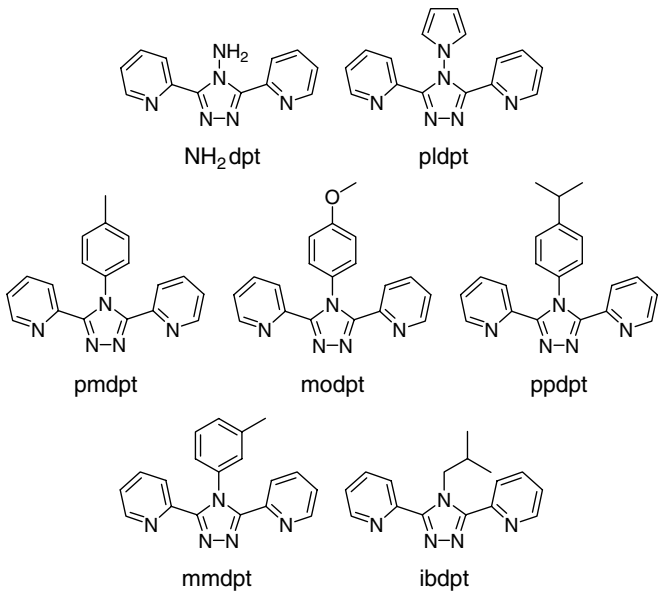


Fig. 1. Existing 4-substituted 3,5-di(2-pyridyl)-4*H*-1,2,4-triazole ligands along with our new 4-alkyl substituted ligand ibdpt.

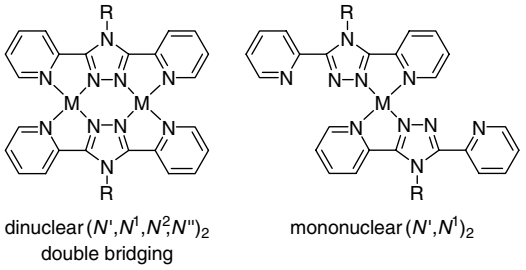


Fig. 2. The two most common coordination modes observed for 4-substituted 3,5-di(2-pyridyl)-4*H*-1,2,4-triazole ligands.

specifically using $Cu(ClO_4)_2 \cdot 6H_2O$, a small amount of a mononuclear complex, $[Cu^{II}(ibdpt)_2(ClO_4)_2]$, was obtained along with the desired dinuclear product [16]. This indicates that an electron-rich substitutent on N^4 can promote concomitant coordination of both N^1 and N^2 of the central triazole ring to metal ions, and thus the formation of dinuclear complexes, but that mononuclear complexes are also accessible. It should also be noted that the 4-isobutyl substituent gives rise to highly soluble complexes. Here we explore the possibility of using reaction stoichiometry to encourage the formation of mononuclear ibdpt complexes of the $[M^{II}(ibdpt)_2(X)_2]^{y+}$ type (Fig. 2).

2. Experimental

2.1. General

$Co(ClO_4)_2 \cdot 6H_2O$, $Ni(ClO_4)_2 \cdot 6H_2O$ and $Zn(ClO_4)_2 \cdot 6H_2O$ were purchased from Aldrich and used as received. The ibdpt ligand was prepared as described elsewhere [15]. All solvents used were laboratory reagent grade. Elemental analyses were carried out by the Campbell Microanalytical Laboratory at the University of Otago.

Caution: While no problems were encountered in the course of this work, perchlorate salts are potentially explosive and should be handled with appropriate care!

2.2. Reaction of $Co(ClO_4)_2 \cdot 6H_2O$ with ibdpt in a 1:2 molar ratio: synthesis of $[Co^{II}(ibdpt)_2(H_2O)_2](ClO_4)_2 \cdot Et_2O$

An orange solution of $Co(ClO_4)_2 \cdot 6H_2O$ (183 mg, 0.50 mmol) in MeCN (5 mL) was added to a colourless solution of ibdpt (279 mg, 1.00 mmol) in MeCN (35 mL). The resulting orange solution was stirred at room temperature for 2 h before it was subjected to vapour diffusion of Et_2O. This resulted in the formation of a mixture of orange and yellow crystals along with some orange oily drops. The yellow material was identified by X-ray diffraction as the mononuclear complex $[Co^{II}(ibdpt)_2(H_2O)_2](ClO_4)_2 \cdot Et_2O$. A sample of the yellow material could be collected and gave, after drying in vacuo (188 mg, 44% yield), an elemental analysis consistent with the composition $Co^{II}(ibdpt)_2(H_2O)_2(ClO_4)_2$. *Anal.* Calc. for $C_{32}H_{38}Cl_2CoN_{10}O_{10}$ (852.54 g mol^{-1}): C, 45.08; H, 4.49; N, 16.43. Found: C, 45.42; H, 4.65; N 16.38%. A sample of the solid orange material was dried in vacuo (46 mg, 8% yield) and subsequently analysed as a dinuclear complex with the composition $Co_2^{II}(ibdpt)_2(MeCN)_2(H_2O)(ClO_4)_4$. *Anal.* Calc. for $C_{36}H_{42}Cl_4Co_2N_{12}O_{17}$ (1174.48 g mol^{-1}): C 36.82, H 3.60, N 14.31. Found: C 36.50, H 3.77, N 14.26%.

2.3. Reaction of $Ni(ClO_4)_2 \cdot 6H_2O$ with ibdpt in a 1:2 molar ratio

A blue solution of $Ni(ClO_4)_2 \cdot 6H_2O$ (183 mg, 0.50 mmol) in MeCN (5 mL) was added to a colourless solution of ibdpt (279 mg, 1.00 mmol) in MeCN (35 mL). The resulting pink solution was stirred at room temperature for 2 h before it was subjected to vapour diffusion of Et_2O. This afforded purple crystals which were identified by X-ray diffraction as the known dinuclear complex $[Ni_2^{II}(ibdpt)_2(MeCN)_4](ClO_4)_4$ [16]. A sample of this material gave, after drying in air (133 mg, 23% yield), an elemental analysis consistent with the composition $Ni_2^{II}(ibdpt)_2(H_2O)_4(ClO_4)_4$. *Anal.* Calc. for $C_{32}H_{42}Cl_4N_{10}Ni_2O_{20}$ (1145.93 g mol^{-1}): C, 33.54; H, 3.69; N, 12.22. Found: C, 33.65; H, 3.74; N, 12.22%.

2.4. Reaction of $Zn(ClO_4)_2 \cdot 6H_2O$ with ibdpt in a 1:2 molar ratio: synthesis of $[Zn^{II}(ibdpt)_2(ClO_4)_2]$

A colourless solution of $Zn(ClO_4)_2 \cdot 6H_2O$ (20 mg, 0.053 mmol) in MeCN (3 mL) was added to a colourless solution of ibdpt (30 mg, 0.107 mmol) in MeCN (3 mL). The resulting yellowish solution was stirred at room temperature for 2 h before it was subjected to vapour diffusion of Et_2O. This resulted in the formation of colourless crystals which were identified by X-ray diffraction as the

mononuclear complex $[Zn^{II}(ibdpt)_2(ClO_4)_2]$. A sample of this material gave, after drying in vacuo (35 mg, 80% yield), an elemental analysis consistent with the composition $[Zn^{II}(ibdpt)_2(ClO_4)_2]$. *Anal.* Calc. for $C_{32}H_{34}Cl_2N_{10}O_8Zn$ (822.97 g mol^{-1}): C, 46.70; H, 4.16; N, 17.02. Found: C, 46.91; H, 4.12; N, 17.05%.

2.5. Reaction of $Zn(ClO_4)_2 \cdot 6H_2O$ with ibdpt in a 1:1 molar ratio: synthesis of $[Zn_2^{II}(ibdpt)_2(H_2O)_4](ClO_4)_4$ and $[Zn^{II}(ibdpt)_2(H_2O)_2](ClO_4)_2 \cdot 3MeCN$

A colourless solution of $Zn(ClO_4)_2 \cdot 6H_2O$ (40 mg, 0.107 mmol) in MeCN (3 mL) was added to a colourless solution of ibdpt (30 mg, 0.107 mmol) in MeCN (3 mL). The resulting yellowish solution was stirred at room temperature for 2 h before it was subjected to vapour diffusion of Et_2O. This resulted in the formation of two colourless crystal forms, namely blocks and rods. The blocks were found to be the major product with trace amounts of rods. Both crystal types were studied by X-ray diffraction. The blocks were found to be the dinuclear complex $[Zn_2^{II}(ibdpt)_2(H_2O)_4](ClO_4)_4$ and the rods were found to be the mononuclear complex $[Zn^{II}(ibdpt)_2(H_2O)_2](ClO_4)_2 \cdot 3MeCN$. A bulk sample gave, after drying in air (50 mg, 81% yield), an elemental analysis consistent with the composition $[Zn_2^{II}(ibdpt)_2(H_2O)_4](ClO_4)_4$. *Anal.* Calc. for $C_{32}H_{42}Cl_4N_{10}O_{20}Zn_2$ (1159.31 g mol^{-1}): C 33.15, H 3.65, N 12.08. Found: C 33.19, H 3.57, N 11.96%.

2.6. X-ray crystallography

Data were collected on a Bruker SMART {$[Co^{II}(ibdpt)_2(H_2O)_2](ClO_4)_2 \cdot Et_2O$, $[Zn^{II}(ibdpt)_2(ClO_4)_2]$ and $[Zn^{II}(ibdpt)_2(H_2O)_2](ClO_4)_2 \cdot 3MeCN$} or Bruker Kappa Apex II {$[Zn_2^{II}(ibdpt)_2(H_2O)_4](ClO_4)_4$} CCD area detector diffractometer using graphite-monochromated Mo Kα radiation ($\lambda = 0.71073$ Å). The structures of mononuclear complexes were all solved by direct methods with SIR-92 [17] while the structure of $[Zn_2^{II}(ibdpt)_2(H_2O)_4](ClO_4)_4$ was solved using SHELXS-97 [18]. All structures (Table 1) were refined against F^2 using all data by full-matrix least-squares techniques with SHELXL-97 [19]. All non-hydrogen atoms were refined anisotropically. Hydrogen atoms, except those of the H_2O co-ligands, were placed at calculated positions and refined using a riding model with thermal parameters 1.2 times the equivalent isotropic thermal parameters of the atom to which they were bonded. The hydrogen atoms of the H_2O co-ligands were located from the difference maps and allowed to refine freely.

3. Results and discussion

3.1. Complex syntheses (Table 2)

With the intention of preparing a mononuclear complex, $Co(ClO_4)_2 \cdot 6H_2O$ was reacted with ibdpt in a 1:2 molar

Table 1
Crystallographic data for $[Co^{II}(ibdpt)_2(H_2O)_2](ClO_4)_2 \cdot Et_2O$, $[Zn^{II}(ibdpt)_2(ClO_4)_2]$, $[Zn^{II}(ibdpt)_2(H_2O)_2](ClO_4)_2 \cdot 3MeCN$ and $[Zn_2^{II}(ibdpt)_2(H_2O)_4](ClO_4)_4$

	$[Co^{II}(ibdpt)_2(H_2O)_2](ClO_4)_2 \cdot Et_2O$	$[Zn^{II}(ibdpt)_2(ClO_4)_2]$	$[Zn^{II}(ibdpt)_2(H_2O)_2](ClO_4)_2 \cdot 3MeCN$	$[Zn_2^{II}(ibdpt)_2(H_2O)_4](ClO_4)_4$
Empirical formula	$C_{36}H_{48}Cl_2CoN_{10}O_{11}$	$C_{32}H_{34}Cl_2N_{10}O_8Zn$	$C_{38}H_{47}Cl_2N_{13}O_{10}Zn$	$C_{38}H_{42}Cl_4N_{10}O_{20}Zn_2$
Formula weight (g mol^{-1})	926.67	822.96	982.16	1231.38
Crystal system	monoclinic	monoclinic	triclinic	triclinic
Space group	$P2_1/c$	$P2_1/c$	$P\bar{1}$	$P\bar{1}$
a (Å)	11.925(5)	10.1790(2)	9.8052(2)	8.2781(4)
b (Å)	14.889(5)	7.6873(1)	10.9046(2)	11.3976(5)
c (Å)	12.197(5)	21.6334(2)	11.4893(3)	12.1986(6)
α (°)	90	90	87.584(1)	93.271(2)
β (°)	103.269(5)	92.878(1)	83.904(1)	104.753(2)
γ (°)	90	90	67.391(1)	94.331(2)
V (Å^3)	2107.8(14)	1690.66(4)	1127.64(4)	1106.34(9)
Z	2	2	1	1
ρ_{calc} (g cm^{-3})	1.460	1.617	1.446	1.740
μ (mm^{-1})	0.604	0.954	0.733	1.417
Temperature (K)	83(2)	83(2)	83(2)	89(2)
$F(000)$	966	848	510	592
Crystal colour and shape	yellow prism	colourless needle	colourless block	colourless block
Crystal size (mm)	$0.42 \times 0.28 \times 0.28$	$0.32 \times 0.20 \times 0.16$	$0.60 \times 0.50 \times 0.30$	$0.12 \times 0.12 \times 0.06$
$\Theta_{min}/\Theta_{max}$ (°)	1.75/27.06	1.89/25.65	1.78/25.69	1.80/26.45
Reflections collected/R_{int}	4574/0.035	3195/0.0201	10378/0.029	4528/0.0450
Data/restraints/parameter	4574/0/300	3195/0/241	4241/0/314	4528/0/325
Goodness-of-fit	1.085	1.081	1.076	1.060
R_1/wR_2 [$I > 2\sigma(I)$]	0.0381/0.0820	0.0269/0.0655	0.0348/0.0901	0.0321/0.0851
R_1/wR_2 (all data)	0.0527/0.0894	0.0306/0.0676	0.0361/0.0910	0.0383/0.0885
Maximum difference in peak/hole (e Å^{-3})	0.462/−0.471	0.351/−0.397	0.841/−0.579	0.913/−0.411

Table 2
Summary of the results of 2:2 and 1:2 complexation reactions between cobalt(II), nickel(II), copper(II) and zinc(II) perchlorate hexahydrate and ibdpt

Metal ion	M:L ratio employed	Coordination mode observed in product(s)[a]	Colour	Yield	Reference
Co^{2+}	2:2	dinuclear *trans*-(N',N^1,N^2,N'')$_2$ double bridging	orange	95%	[16]
	1:2	mononuclear *trans*-(N',N^1)$_2$ AND	yellow	44%[b]	this work
		dinuclear *trans*-(N',N^1,N^2,N'')$_2$ double bridging	orange	8%	this work
Ni^{2+}	2:2	dinuclear *trans*-(N',N^1,N^2,N'')$_2$ double bridging	purple	98%	[16]
	1:2	dinuclear *trans*-(N',N^1,N^2,N'')$_2$ double bridging	purple	23%	this work
Cu^{2+}	2:2	dinuclear *trans*-(N',N^1,N^2,N'')$_2$ double bridging AND	blue-green	86%	[16]
		mononuclear *trans*-(N',N^1)$_2$	steel blue	trace	[16]
	1:2	mononuclear *trans*-(N',N^1)$_2$	steel blue	48%[b]	[16]
Zn^{2+}	2:2	dinuclear *trans*-(N',N^1,N^2,N'')$_2$ double bridging AND	colourless	81%	this work
		mononuclear *trans*-(N',N^1)$_2$	colourless	trace	this work
	1:2	mononuclear *trans*-(N',N^1)$_2$	colourless	80%	this work

[a] See Fig. 2.
[b] The yields of these experiments were not optimised.

ratio in MeCN. Vapour diffusion of Et_2O into the orange reaction mixture resulted in the separation of some orange oily drops, a small amount of orange crystalline material and clusters of bushy yellow crystals. A specimen of the latter, the main product present, was found to be suitable for an X-ray diffraction study which revealed the identity of this material to be the mononuclear complex $[Co^{II}(ibdpt)_2(H_2O)_2](ClO_4)_2 \cdot Et_2O$ (Figs. 3 and 4, Table 1). After the crystallographic sample was returned, samples of both the yellow and the orange crystalline material were obtained by physical separation. After drying in vacuo the elemental analysis of the yellow material was in very good agreement with a mononuclear composition of $Co^{II}(ibdpt)_2(H_2O)_2(ClO_4)_2$, thus confirming the result of the X-ray diffraction study (see below). The orange sample, after drying in vacuo, was found to have the dinuclear composition $Co^{II}_2(ibdpt)_2(MeCN)_2(H_2O)(ClO_4)_4$. It is noteworthy that on repeating this reaction on a smaller scale and at lower concentrations, *i.e.* after diffusion of Et_2O into a more dilute reaction solution, the yellow mononuclear complex was found to be the almost exclusive product, with only trace amounts of the orange dinuclear material present.

Allowing $Ni(ClO_4)_2 \cdot 6H_2O$ to react with ibdpt in a 1:2 molar ratio in MeCN afforded a pink solution, in contrast to the more intense purple solution obtained when a 2:2 molar ratio was employed [16]. Nevertheless, vapour diffusion of Et_2O into this solution afforded purple crystals. Several of these single crystals were studied by X-ray diffraction which unambiguously revealed that the product was the dinuclear complex $[Ni^{II}_2(ibdpt)_2(MeCN)_4](ClO_4)_4$ which had previously been obtained from the 2:2 reaction

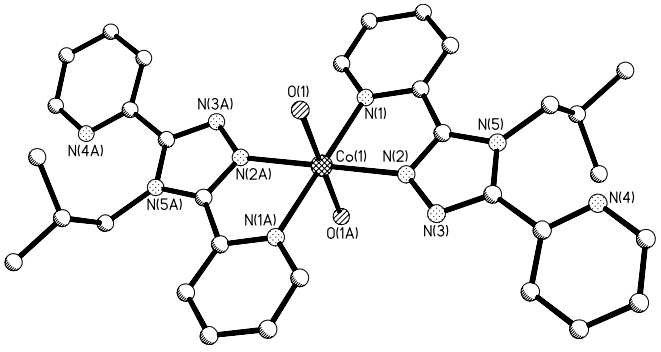


Fig. 3. View of the molecular structure of the cation of $[Co^{II}(ibdpt)_2(H_2O)_2](ClO_4)_2 \cdot Et_2O$. Hydrogen atoms have been omitted for clarity. Selected distances (Å): Co(1)–N(1) 2.1373(18), Co(1)–N(2) 2.0900(18), Co(1)–O(1) 2.0907(17). Selected angles (°): N(1)–Co(1)–N(2) 76.32(7), N(1)–Co(1)–N(2A) 103.68(7), N(1)–Co(1)–O(1) 88.25(6), N(1)–Co(1)–O(1A) 91.75(6), N(2)–Co(1)–O(1) 89.58(7), N(2)–Co(1)–O(1A) 90.42(7). Symmetry operation used to generate equivalent atoms: (A) $-x+1$, $-y$, $-z$.

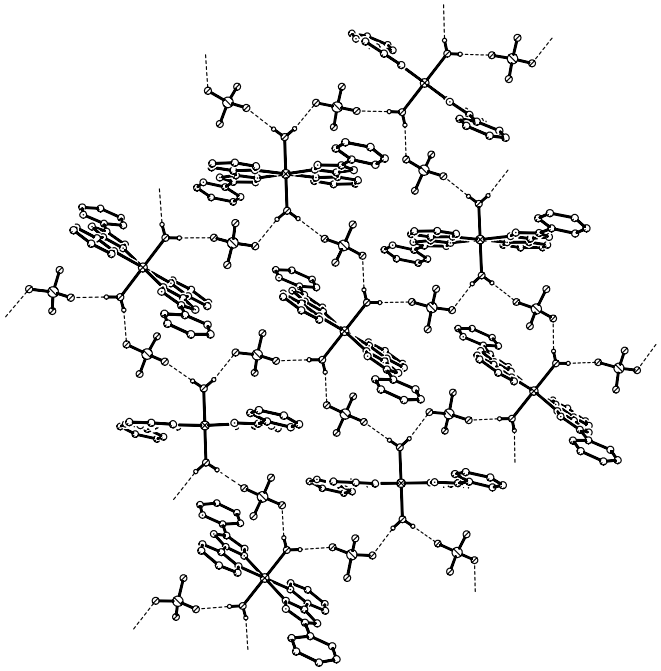


Fig. 4. Hydrogen bonding in $[Co^{II}(ibdpt)_2(H_2O)_2](ClO_4)_2 \cdot Et_2O$. Hydrogen atoms, except those involved in hydrogen bonding, have been omitted for clarity. The isobutyl groups and the Et_2O solvates are not shown.

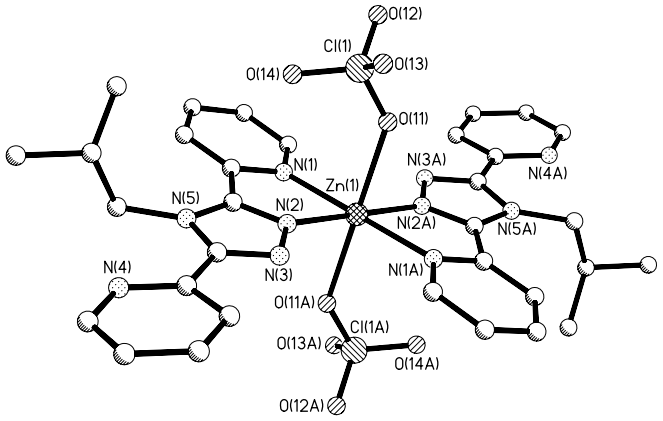


Fig. 5. View of the molecular structure of the cation of $[Zn^{II}(ibdpt)_2(ClO_4)_2]$. Hydrogen atoms have been omitted for clarity. Selected distances (Å): Zn(1)–N(1) 2.1494(14), Zn(1)–N(2) 2.0574(14), Zn(1)–O(11) 2.2609(13). Selected angles (°): N(1)–Zn(1)–N(2) 77.60(6), N(1)–Zn(1)–N(2A) 102.40(6), N(1)–Zn(1)–O(11) 89.32(5), N(1)–Zn(1)–O(11A) 90.68(5), N(2)–Zn(1)–O(11) 93.98(5), N(2)–Zn(1)–O(11A) 86.02(5). Symmetry operation used to generate equivalent atoms: (A) $-x+1$, $-y$, $-z+1$.

of ibdpt and $Ni(ClO_4)_2 \cdot 6H_2O$ [16]. Subsequently, after the crystallographic sample was returned, the elemental analysis of an air-dried sample of the purple material confirmed the dinuclear nature of these crystals, with a composition of $Ni^{II}_2(ibdpt)_2(H_2O)_4(ClO_4)_4$. Hence, using $Ni(ClO_4)_2 \cdot 6H_2O$, there was no evidence of the formation of any solid mononuclear complex of the $[Ni^{II}(ibdpt)_2(X)_2]^{y+}$ type, although its presence in solution certainly cannot be ruled out. This is in contrast to the above observations using the cobalt(II) salt, to our earlier reported observations for the reaction of ibdpt with $Cu(ClO_4)_2 \cdot 6H_2O$ [16] and to the observations reported below for $Zn(ClO_4)_2 \cdot 6H_2O$.

The 1:2 molar reaction of $Zn(ClO_4)_2 \cdot 6H_2O$ with ibdpt led to the clean formation of almost colourless needles of $[Zn^{II}(ibdpt)_2(ClO_4)_2]$ in high yield (Fig. 5). This is in stark contrast to the results obtained with $Co(ClO_4)_2 \cdot 6H_2O$ and $Ni(ClO_4)_2 \cdot 6H_2O$ as in the case of the zinc(II) salt no evidence of any formation of a dinuclear complex was observed, although it must be noted that it would not be as easily identified, especially if it formed in trace amounts (see below).

For completeness, the reaction of $Zn(ClO_4)_2 \cdot 6H_2O$ with ibdpt in a 2:2 molar ratio in MeCN was also carried out. By subjecting the resulting yellowish solution to vapour diffusion of Et_2O two forms of colourless crystals, namely rods and blocks, were obtained. The blocks were found to be the major, almost exclusive, product while only trace amounts of the rods were isolated. Single crystals of both crystal forms were found to be suitable for X-ray diffraction studies. The rod-like crystals (minor product) were found to be the mononuclear complex $[Zn^{II}(ibdpt)_2(H_2O)_2](ClO_4)_2 \cdot 3MeCN$ (Fig. 6) while the block like crystals (major product) were found to be the dinuclear complex $[Zn^{II}_2(ibdpt)_2(H_2O)_4](ClO_4)_4$ (Fig. 7). Physical separation of the two crystal types was impossible as the mononuclear complex was present in such negligible quantities. The elemental analysis of the bulk material gave results which were entirely consistent with the dinuclear formulation.

The results obtained from the 1:2 and 2:2 molar ratio reactions of $Zn(ClO_4)_2 \cdot 6H_2O$ with ibdpt are entirely consistent with those observed by this group for $Cu(ClO_4)_2 \cdot 6H_2O$ [16]. Specifically, when a 2:2 molar ratio is employed the bulk product is the dinuclear complex but a small amount of the mononuclear $[M^{II}(ibdpt)_2(X)_2]^{y+}$ complex forms along with it. That this had occurred was more easily identified in the case of the copper(II) salt

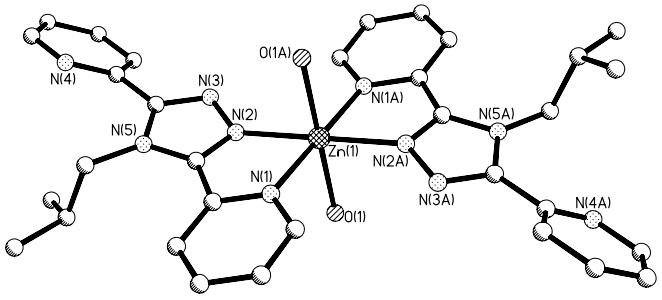


Fig. 6. View of the molecular structure of the cation of $[Zn^{II}(ibdpt)_2(H_2O)_2](ClO_4)_2 \cdot 3MeCN$. Hydrogen atoms have been omitted for clarity. Selected distances (Å): Zn(1)–N(1) 2.1502(15), Zn(1)–N(2) 2.0961(15), Zn(1)–O(1) 2.1551(14). Selected angles (°): N(1)–Zn(1)–N(2) 77.24(6), N(1)–Zn(1)–N(2A) 102.76(6), N(1)–Zn(1)–O(1) 85.93(6), N(1)–Zn(1)–O(1A) 94.07(6), N(2)–Zn(1)–O(1) 92.86(6), N(2)–Zn(1)–O(1A) 87.14(6). Symmetry operation used to generate equivalent atoms: (A) $-x$, $-y+1$, $-z$.

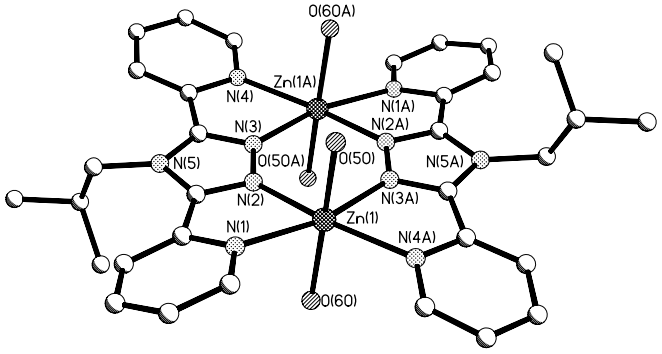


Fig. 7. View of the molecular structure of the cation of $[Zn^{II}_2(ibdpt)_2(H_2O)_4](ClO_4)_4$. Hydrogen atoms have been omitted for clarity. Selected distances (Å): Zn(1)–N(1) 2.190(2), Zn(1)–N(2) 2.1119(19), Zn(1)–N(3) 2.1192(19), Zn(1)–N(4) 2.184(2), Zn(1)–O(50) 2.0921(19), Zn(1)–O(60) 2.089(2). Selected angles (°): N(1)–Zn(1)–N(2) 75.16(7), N(1)–Zn(1)–N(3A) 165.39(8), N(1)–Zn(1)–N(4A) 119.35(7), N(1)–Zn(1)–O(50) 89.12(8), N(1)–Zn(1)–O(60) 84.94(8), N(2)–Zn(1)–N(3A) 90.81(7), N(2)–Zn(1)–N(4A) 164.37(7), N(2)–Zn(1)–O(50) 97.40(8), N(2)–Zn(1)–O(60) 87.51(8), N(3A)–Zn(1)–N(4A) 75.05(7), N(3A)–Zn(1)–O(50) 88.69(8), N(3A)–Zn(1)–O(60) 98.71(8), N(4A)–Zn(1)–O(50) 89.05(8), N(4A)–Zn(1)–O(60) 88.08(8), O(50)–Zn(1)–O(60) 171.09(8). Symmetry operation used to generate equivalent atoms: (A) $-x+1$, $-y+2$, $-z+1$.

due to the significantly different colour and crystal form of the mono- and dinuclear complexes.

When a metal-to-ligand molar ratio of 1:2 was employed, both the copper(II) and the zinc(II) salts cleanly formed the anticipated mononuclear $[M^{II}(ibdpt)_2(X)_2]^{y+}$ complex while $Co(ClO_4)_2 \cdot 6H_2O$ formed mostly the expected mononuclear complex with only a trace of the dinuclear complex present (Table 2). In contrast, and rather surprisingly, with $Ni(ClO_4)_2 \cdot 6H_2O$ there was no evidence of the formation of a mononuclear $[Ni^{II}(ibdpt)_2(X)_2]^{y+}$ complex despite the 1:2 ratio employed (Table 2). The difficulties sometimes experienced in trying to obtain a completely clean bulk sample of a complex of desired stoichiometry simply by employing the correct metal-to-ligand molar ratio are consistent with a tendency of first row transition metal ions and ibdpt to set up a complex set of equilibria in solution. Supporting evidence for this comes from the fact that often the colour of the reaction solution is different from the colour of the solid state products isolated, as noted here for cobalt(II) and nickel(II) and previously noted for copper(II) [16]. Along with M:L stoichiometry, the relative concentrations of the many possible products in solution and their relative solubilities appear to be important factors in determining the nature of the solid products obtained.

3.2. Description of the crystal structures

The distances and angles of the N_4O_2 coordination sphere about the cobalt centre in the yellow complex $[Co^{II}(ibdpt)_2(H_2O)](ClO_4)_2 \cdot Et_2O$ (Figs. 3 and 4) are very similar to those observed in analogous complexes incorporating 4-aryl-3,5-di(2-pyridyl)-4*H*-1,2,4-triazoles [12,13]. As could be expected from the fact that this complex adopts the *trans*-(N',N^1)$_2$ coordination mode (Fig. 2), the Co–N_{pyr} distance [2.1373(18) Å] is longer than the Co–N_{trz} distance [2.0900(18) Å]. The bidentate pyridine–triazole moiety is almost perfectly planar [1.5(1)°] while the non-coordinated pyridine ring, whose nitrogen atom faces towards the isobutyl group, is tilted by 15.4(1)° with respect to the triazole mean plane. The ClO_4^- ion forms hydrogen bonds to the H_2O co-ligand of its own and a neighbouring unit in a bridging fashion [O(1)···O(11) 2.78 and O(1)···O(12B) 2.77 Å] giving rise to a two-dimensional network of interlinked mononuclear units (Fig. 4). The shortest Co···Co separation between neighbouring units within this network is 9.6235(25) Å to each of four equally distant cobalt(II) centres.

Prior to this work only one mononuclear zinc(II) complex incorporating a 4-substituted 3,5-di(2-pyridyl)-4*H*-1,2,4-triazole, specifically $[Zn^{II}(NH_2dpt)_2(H_2O)_2](ClO_4)_2$ reported by Hartmann and Vahrenkamp in 1995 [20], was known. In this study we obtained two different mononuclear zinc(II) complexes of ibdpt, namely $[Zn^{II}(ibdpt)_2(ClO_4)_2]$ (Fig. 5) and $[Zn^{II}(ibdpt)_2(H_2O)_2](ClO_4)_2 \cdot 3MeCN$ (Fig. 6). In both of these complexes, and in $[Zn^{II}(NH_2dpt)_2(H_2O)_2](ClO_4)_2$, the *trans*-($N'$,$N^1$)$_2$ coordination mode (Fig. 2) is realised and the zinc(II) centre resides within an N_4O_2 coordination sphere made up of two bidentate 1,2,4-triazole-based ligands and of two axial oxygen donors (either ClO_4^- or H_2O co-ligands). The Zn–N_{pyr} and Zn–N_{trz} distances {2.1494(14) and 2.0574(14) Å, respectively, in $[Zn^{II}(ibdpt)_2(ClO_4)_2]$ and 2.1502(15) and 2.0961(15) Å, respectively, in $[Zn^{II}(ibdpt)_2(H_2O)_2](ClO_4)_2 \cdot 3MeCN$} are in good agreement with the corresponding distances observed in $[Zn^{II}(NH_2dpt)_2(H_2O)_2](ClO_4)_2$ [2.169(3) and 2.067(3) Å, respectively]. The coordinated pyridine–triazole moieties in $[Zn^{II}(ibdpt)_2(ClO_4)_2]$ and $[Zn^{II}(ibdpt)_2(H_2O)_2](ClO_4)_2 \cdot 3MeCN$ show relatively large deviations from planarity [11.20(11) and 16.77(13)°, respectively]. The non-coordinated pyridine rings of each complex are tilted by 7.97(12) and 30.61(10)° with respect to the triazole mean plane, each with the non-coordinated nitrogen atom pointing towards the isobutyl group. The axial co-ligands for $[Zn^{II}(ibdpt)_2(ClO_4)_2]$ are ClO_4^- ions while in $[Zn^{II}(ibdpt)_2(H_2O)_2](ClO_4)_2 \cdot 3MeCN$ they are H_2O molecules. Their respective Zn–O distances are 2.2609(13) and 2.1551(14) Å. The H_2O molecules in $[Zn^{II}(ibdpt)_2(H_2O)_2](ClO_4)_2 \cdot 3MeCN$ are also hydrogen bonded to one of the oxygen atoms of the non-coordinated ClO_4^- counterions and to the nitrogen atom of one of the MeCN solvates in the crystal lattice [O(1)···O(11) 2.82 and O(1)···N(20) 2.88 Å, respectively].

The dinuclear zinc(II) complex of ibdpt (Fig. 7) also has an octahedral N_4O_2 coordination sphere. The zinc(II) centres are bridged by the two triazole moieties. The ibdpt ligand adopts the common *trans*-(N',N^1,N^2,N'')$_2$ double bridging coordination mode (Fig. 2). The Zn–N_{trz} distances are shorter than the Zn–N_{pyr} distances (Fig. 7). This is due to the double bridging coordination mode of the triazole ring which results in a distortion of the octahedral geometry. This distortion is a feature common to all of the dinuclear complexes previously characterised by this group [16]. The distortion also causes a slight twist in the ibdpt ligand which can be seen by examining the angles between the mean plane of the triazole ring and each of the flanking pyridine rings [14.53(5) and 10.20(9)°]. The Zn··· Zn separation in this dinuclear complex is 4.353(2) Å. There are two axial H_2O co-ligands on each zinc(II) centre. These are engaged in hydrogen bonding interactions with the four non-coordinated ClO_4^- counterions.

4. Conclusion

Unlike most other 4-substituted 3,5-di(2-pyridyl)-4*H*-1,2,4-triazole ligands, ibdpt has been found to show a remarkable ability to form dinuclear 2:2 complexes. With $Co(ClO_4)_2 \cdot 6H_2O$, $Ni(ClO_4)_2 \cdot 6H_2O$, $Cu(ClO_4)_2 \cdot 6H_2O$ and $Zn(ClO_4)_2 \cdot 6H_2O$ predominantly the dinuclear complexes, $[Co^{II}_2(ibdpt)_2(MeCN)_2(H_2O)_2](ClO_4)_4$, $[Zn^{II}_2(ibdpt)_2(H_2O)_4](ClO_4)_4$, $[Ni^{II}_2(ibdpt)_2(MeCN)_4](ClO_4)_4$, and $[Cu^{II}_2(ibdpt)_2(MeCN)_2(ClO_4)_2](ClO_4)_2 \cdot 2MeCN$ are isolated from reactions employing a metal-to-ligand molar ratio of 2:2, but for cobalt(II), copper(II) and zinc(II) small to negligible

amounts of their respective mononuclear complexes, $[Co^{II}(ibdpt)_2(H_2O)_2](ClO_4)_2 \cdot Et_2O$, $[Zn^{II}(ibdpt)_2(H_2O)_2](ClO_4)_2 \cdot 3MeCN$ and $[Cu^{II}(ibdpt)_2(ClO_4)_2]$, are also isolated. Analytically pure samples of these mononuclear complexes are readily obtained when the zinc(II) or copper(II) salts are employed in a 1:2 molar ratio. In contrast, the cobalt(II) salt, employing the same 1:2 molar ratio, affords small amounts of the dinuclear complex in addition to the desired mononuclear complex, with the amount obtained depending on the concentrations of the reactants in solution. Surprisingly, the use of the nickel(II) salt, in the same 1:2 molar ratio, results in the isolation of the 2:2 dinuclear complex, albeit in low yield, with no evidence of the formation of a mononuclear $[Ni^{II}(ibdpt)_2(X)_2]^{y+}$ complex. This variable behaviour of ibdpt towards different metal salts warrants further attention as it clearly indicates that in addition to factors such as the reaction stoichiometry and the electronic effect of the N^4 substituent, other factors such as the relative solubilities of the many and various possible products, also influenced by the N^4 substituent, and relative concentration in solution also play a part in determining the nature of the solid products obtained. Our focus is currently on exploring the rich iron(II) coordination chemistry of this and related ligands and the magnetochemistry of the resulting complexes [21].

Acknowledgements

This work was supported by the University of Otago with a number of grants including a University of Otago Postgraduate Scholarship (M.H.K.), a Bridging Grant (M.H.K. and S.B.) and a University of Otago Research Grant (A.N. and S.B.). Dr. J. Klingele (née Hausmann) and Mr. J. A. Kitchen (University of Otago) are thanked for helpful discussions. J.A.K. is also thanked for his practical help.

Appendix A. Supplementary data

CCDC 608291, 608292, 608293 and 611425 contain the supplementary crystallographic data for $[Co^{II}(ibdpt)_2(H_2O)_2](ClO_4)_2 \cdot Et_2O$, $[Zn^{II}(ibdpt)_2(ClO_4)_2]$, $[Zn^{II}(ibdpt)_2(H_2O)_2](ClO_4)_2 \cdot 3MeCN$ and $[Zn_2^{II}(ibdpt)_2(H_2O)_4](ClO_4)_4$, respectively. These data can be obtained free of charge at www.ccdc.cam.ac.uk/data_request/cif or from the Cambridge Crystallographic Data Centre, 12 Union Road, Cambridge CB2 1EZ, UK (e-mail: data_request@ccdc.cam.ac.uk). Supplementary data associated with this article can be found, in the online version, at doi:10.1016/j.poly.2006.07.018.

References

[1] M.H. Klingele, S. Brooker, Coord. Chem. Rev. 241 (2003) 119.
[2] F.S. Keij, R.A.G. deGraaff, J.G. Haasnoot, J. Reedijk, J. Chem. Soc., Dalton Trans. (1984) 2093.
[3] P.J. van Koningsbruggen, D. Gatteschi, R.A.G. de Graaff, J.G. Haasnoot, J. Reedijk, C. Zanchini, Inorg. Chem. 34 (1995) 5175.
[4] S.K. Mandal, H.J. Clase, J.N. Bridson, S. Ray, Inorg. Chim. Acta 209 (1993) 1.
[5] S.-C. Shao, D.-R. Zhu, X.-H. Zhu, X.-Z. You, S.S.S. Raj, H.-K. Fun, Acta Crystallogr., Sect. C 55 (1999) 1412.
[6] S.C. Shao, D.R. Zhu, T.W. Wang, Y. Zhang, S.S.S. Raj, H.K. Fun, Chin. Chem. Lett. 11 (2000) 93.
[7] D. Zhu, Y. Xu, Y. Mei, Y. Shi, C. Tu, X. You, J. Mol. Struct. 559 (2001) 119.
[8] D. Zhu, Y. Xu, Z. Yu, Z. Guo, H. Sang, T. Liu, X. You, Chem. Mater. 14 (2002) 838.
[9] D.-R. Zhu, T.-W. Wang, S.-L. Zhong, Y. Xu, X.-Z. You, Chin. J. Inorg. Chem. 20 (2004) 508.
[10] S.-C. Shao, S.-D. Liu, H.-L. Zhu, Acta Crystallogr., Sect. E 60 (2004) m1815.
[11] S.-P. Zhang, S.-C. Shao, Z.-D. Liu, H.-L. Zhu, Acta Crystallogr., Sect. E 61 (2005) m799.
[12] D.-R. Zhu, Y. Song, Y. Xu, Y. Zhang, S.S.S. Raj, H.-K. Fun, X.-z. You, Polyhedron 19 (2000) 2019.
[13] D. Zhu, Y. Song, Y. Liu, Y. Xu, Y. Zhang, X. You, S.S.S. Raj, H.-K. Fun, Transit. Metal Chem. 25 (2000) 589.
[14] S.-C. Shao, Z.-L. You, S.-P. Zhang, S.W. Ng, H.-L. Zhu, Acta Crystallogr., Sect. E 61 (2005) m265.
[15] M.H. Klingele, S. Brooker, Eur. J. Org. Chem. (2004) 3422.
[16] M.H. Klingele, P.D.W. Boyd, B. Moubaraki, K.S. Murray, S. Brooker, Eur. J. Inorg. Chem. (2005) 910.
[17] A. Altomare, G. Cascarano, C. Giacovazzo, A. Guagliardi, M.C. Burla, G. Polidori, M. Camalli, J. Appl. Cryst. 27 (1994) 435.
[18] G.M. Sheldrick, Methods Enzymol. 276 (1997) 628.
[19] G.M. Sheldrick, T.R. Schneider, Methods Enzymol. 277 (1997) 319.
[20] U. Hartman, H. Vahrenkamp, Inorg. Chim. Acta 239 (1995) 13.
[21] J.A. Kitchen, A. Noble, C.D. Brandt, B. Moubaraki, K.S. Murray, S. Brooker, unpublished results.

Available online at www.sciencedirect.com
ScienceDirect
Polyhedron 26 (2007) 486–492
POLYHEDRON
www.elsevier.com/locate/poly

Theoretical investigations into trioxo group 7 compounds LRO_3 with perfluorated ligands

Matthias Lein *, Anton Hammerl [1], Holger L. Hermann [2], Peter Schwerdtfeger

Centre of Theoretical Chemistry and Physics, Institute of Fundamental Sciences, Massey University Auckland, Private Bag 102904, North Shore MSC, Auckland, New Zealand

Received 23 May 2006; accepted 8 August 2006
Available online 22 August 2006

Abstract

Group 7 trioxides LRO_3 with perfluorated ligands L (L = CF_3, C_5F_5 and C_6F_5) are investigated using density based (BP86) and wavefunction based (MP2) methods together with energy-adjusted scalar relativistic pseudopotentials for the metal atoms Mn, Tc and Re. The C_6F_5 compounds have short metal-carbon bond distances and are more stable than the η^1-C_5F_5 and the CF_3 compounds. The perfluorinated cyclopentadienyl compounds, $C_5F_5MO_3$, all are η^1 coordinated in contrast to the $C_5Me_5MO_3$ homologues. Our calculations indicate that $C_6F_5MnO_3$ might be a stable complex and therefore a promising target for future synthesis.
© 2006 Elsevier Ltd. All rights reserved.

Keywords: Group 7 compounds; Perfluorated ligands; Density functional calculations; NBO analysis

1. Introduction

Transition metal complexes containing terminal oxo ligands are very important as both oxidants and catalysts in organic synthesis [1]. One reason is that oxo ligands stabilize high oxidation states of transition element complexes, e.g. organic vanadium (V), molybdenum (VI) or rhenium (VII) oxo complexes have been prepared in the past [1]. After the synthesis of CH_3ReO_3 [2–4] and (η^5-CMe_5)ReO_3 [5,6] high oxidation state rhenium oxides have been studied intensively in the past [7,8]. Rhenium trioxide complexes have shown catalytic activity for a variety of reactions, including the oxidation of olefins and aromatic systems as well as metathesis reactions and olefination of aldehydes [9,10]. The homologous technetium compounds CH_3TcO_3 [11,12] and (η^5-CMe_5)TcO_3 [11,13] are known while the reported (η^5-CMe_5)Tc_2O_3 [15] was unfortunately a misinterpretation of X-ray data [16]. Compared to the rhenium species the technetium compounds have far greater oxidizing strengths and Lewis acidities [11,12]. Homologous manganese trioxo compounds should have greater oxidizing strengths and Lewis acidities compared to their heavier congeners. Unfortunately, these manganese trioxo organyl complexes are experimentally not known and have eluded synthesis so far. The known inorganic compounds MnO_4^- and $FMnO_3$ are a strong oxidant or very explosive [17]. CH_3MnO_3 and (η^5-CMe_5)MnO_3 have been predicted to be unstable on the basis of HF results [13,14]. DFT calculations on CH_3MnO_3 have also been performed [18]. The group 7 tetroxide anions [19,25], trioxide chlorides [20] and different organyl group 7 trioxides [21], rhenium compounds in particular [22], have been the subject of various theoretical studies [23–25].

The purpose of this study is to determine the influence of perfluorated ligands on the structure and stability of group 7 trioxo compounds. Transition metal complexes with perfluorated ligands often show increased thermal stability compared to the unfluorinated complexes [26] because of the high electronegativity of the ligand L. This is often

* Corresponding author.
E-mail addresses: m.lein@massey.ac.nz (M. Lein), p.a.schwerdtfeger@massey.ac.nz (P. Schwerdtfeger).
[1] Present address: Inorganic Chemistry, LMU Munich, Germany.
[2] Present address: Lonza Ltd., Visp, Switzerland.

0277-5387/$ - see front matter © 2006 Elsevier Ltd. All rights reserved.
doi:10.1016/j.poly.2006.08.013

Table 1
Optimised parameters for the $LMnO_3$ compounds

		r(M, O)	r(M, L)	α(O, M, O)	α(L, M, O)	E	ZPE
$HMnO_3$	BP86[a]	1.570	1.517	116.3	101.3	−330.79136	0.01704
	BP86[b]	1.571	1.521	116.5	110.9	−330.73014	0.01701
	MP2[a]	1.576	1.625	113.8	104.6	−330.26176	0.05049
	MP2[b]	1.567	1.637	113.0	105.7	−330.05888	0.05051
$MnO4^-$	BP86[a]	1.614		109.5	109.5	−405.57458	0.01287
	MP2[a]	1.567		109.5	109.5	−404.84925	0.02015
	Exp.[c]	1.610					
$FMnO_3$	BP86[a]	1.572	1.712	110.1	108.9	−430.09870	0.01261
	MP2[a]	1.526	1.679	112.0	106.8	−429.41787	0.03774
	Exp.[c]	1.586	1.724		108.5		
CH_3MnO_3	BP86[a]	1.574	1.978	1.094	103.9	−370.13300	0.04532
	MP2[a]	Diss.					
CF_3MnO_3	BP86[a]	1.572	2.035	115.6	102.4	−667.96519	0.02333
	MP2[a]	1.575	2.113	115.0	103.1	−666.95681	0.05681
$C_5F_5MnO_3$	BP86[b]	1.580	2.037	2 × 115.4	2 × 102.0	−1019.83886	0.05127
				114.1	105.1		
	MP2[b]	Diss.					
$C_6F_5MnO_3$	BP86[b]	1.575	1.940	2 × 113.6	2 × 106.0	−1057.98500	0.05806
				112.9	103.9		
	MP2[b]	2 × 1.564	2.035	2 × 113.1	2 × 105.7	−1055.57581	0.09277
				112.1	106.4		

Distances (r) are given in Å and angles (α) are given in degrees. The electronic total energies (E) and zero point vibrational energies (ZPE) are given in atomic units.
[a] Basis set 1.
[b] Basis set 2.
[c] Ref. [17].

attributed both to thermodynamic and kinetic factors, which include a higher bond dissociation energy of the metal–ligand bond. A stabilisation of the resulting trioxo compounds leading to a manganese trioxo organyl complex that can be isolated experimentally is desired. CF_3, C_5F_5 and C_6F_5 are chosen as perfluorated ligands. CF_3 acts as a σ-acceptor, the other two compounds are also involved in π-bonding. For comparison, the stable inorganic FMO_3 and MO_4^- compounds as well as the CH_3MO_3 compounds are also investigated.

2. Computational details

All calculations were performed with GAUSSIAN98 [27]. For the group 7 metal atoms, scalar relativistic pseudopotentials of the Stuttgart group with their respective valence basis sets were employed in all calculations, i.e. (311111s/22111p/411d/1f) [28] for manganese, (311111s/22111p/411d) for technetium [29], and (311111s/22111p/411d) for rhenium [29]. For the lighter elements H, C, O and F all electron basis sets were used, and Dunning's cc-pVTZ basis sets for the smaller molecules (basis set 1) and the cc-pVDZ basis sets [30,31] for the C_5F_5 and C_6F_5 compounds (basis set 2). We mention that it was often difficult to achieve SCF convergence for some of the Mn compounds in the Hartree–Fock calculations, as the wavefunction becomes multi-reference in character.

We optimized all geometries at the density functional theory (DFT) using the BP86 functional and second-order Møller–Plesset perturbation theory (MP2). The molecules LMO_3 (L = H, F, CH_3, CF_3; M = Mn, Tc, Re) were optimized within the restriction of C_{3v} symmetry, while for the MO_4^- (M = Mn, Tc, Re) anions T_d symmetry was assumed. The C_6F_5 compounds were optimized with C_2 symmetry with the BP86 functional, but the MP2 calculations gave only transition states for the C_2 symmetric compounds. As a consequence the C_6F_5 compounds at the MP2 level and the C_5F_5 compounds were optimized without symmetry constraints. Frequencies, calculated at all levels of theory, confirmed the calculated structures to be true minima. A natural bond orbital analysis (NBO) [32,33] has been performed at the BP86 level in order to discuss the importance of metal s- and d-contributions for the ligand-to-metal bonding.[3] The charge distribution of a natural population analysis (NPA) in the LMO_3 compounds is also addressed in this context.

3. Results and discussion

The structural parameters and energies for all calculated compounds and a few available experimental data are collected in Tables 1–3 and example geometries are shown in

[3] Metal p-contributions were found to be not important for metal-to-ligand bonding an are therefore not listed.

Table 2
Optimised parameters for the $LTcO_3$ compounds

		r(M–O)	r(M–L)	α(O–M–O)	α(L–M–O)	E	ZPE
$HTcO_3$	BP86[a]	1.701	1.661	113.5	105.1	−307.34430	0.03842
	BP86[b]	1.711	1.661	113.9	104.6	−307.27197	0.03793
	MP2[a]	1.727	1.655	110.0	109.0	−306.46931	0.04018
	MP2[b]	1.757	1.677	109.5	109.5	−306.18375	0.04152
TcO_4^-	BP86[a]	1.741		109.5	109.5	−382.14698	0.03598
	MP2[a]	1.763		109.5	109.5	−381.15087	0.03747
	Exp.[c]	1.711					
$FTcO_3$	BP86[a]	1.699	1.861	108.9	110.1	−406.66710	0.03574
	MP2[a]	1.744	1.875	105.6	113.1	−405.67346	0.03722
CH_3TcO_3	BP86[a]	1.705	2.080	112.5	106.2	−346.68765	0.06699
	MP2[a]	1.732	2.053	110.1	108.8	−345.72492	0.06786
CF_3TcO_3	BP86[a]	1.703	2.158	112.9	105.8	−644.51474	0.04480
	MP2[a]	1.729	2.138	109.2	109.8	−643.15445	0.04880
$C_5F_5TcO_3$	BP86[b]	1.716	2.152	2 × 113.1 112.3	2 × 104.7 108.1	−996.37557	0.07192
	MP2[b]	1.770	2.149	2 × 107.7 106.5	2 × 112.4 111.2	−993.65521	0.07793
$C_6F_5TcO_3$	BP86[b]	1.710	2.067	2 × 107.7 106.5	2 × 112.4 111.2	−1034.53278	0.07979
	MP2[b]	1.764	2.086	2 × 111.1 111.2	2 × 107.4 106.7	−1031.70864	0.08597

Distances (r) are given in Å and angles (α) are given in degrees. The electronic total energies (E) and zero point vibrational energies (ZPE) are given in atomic units.
[a] Basis set 1.
[b] Basis set 2.
[c] Ref. [47].

Fig. 1. For the fluorides FMO_3 as well as CH_3ReO_3 and CH_3TcO_3 calculated data are already available. For the other compounds, e.g. the tetroxide anions MO_4^-, $FMnO_3$, $FReO_3$ and CH_3ReO_3, experimental data exists. The calculated M–O bond lengths for the MO_4^- and FMO_3 molecules are in good agreement with the experimentally observed values. The BP86 geometries are closer to the experimental geometries than the MP2 values and MP2 always gives smaller O–M–O bonding angles than BP86. It is well known that MP2 as a single-reference method may not lead to accurate results for transition metal compounds, especially when high oxidation states are involved [34]. The bonding parameters of the HMO_3 molecules show little differences between the two basis sets employed at the BP86 level. At the MP2 level, basis set 2 gives longer bond lengths than basis set 1. The BP86 bonding parameters will be used for further discussion since they are closer to the known experimental values.

CH_3MnO_3 does not have the expected minimum structure at the MP2 level. During optimization, the O–Mn–O bonding angle decreases and the Mn–C bond length elongates until the molecule dissociates. This is in agreement with earlier predictions [13,14] that CH_3MnO_3 is thermodynamically not stable. DFT finds a minimum at the expected structure, but with a rather long Mn–C bond length of 1.98 Å. For perfluorinated cyclopentadienyl compound, $C_5F_5MnO_3$, a minimum structure was found with BP86 as well, but at the MP2 level the Mn–C bond distance again elongates, the O–Mn–O angle gets wider and one oxygen moves close to the C_5F_5 ring, eventually forming a carbon oxygen bond. This shows that $C_5F_5MnO_3$ is thermodynamically not stable. In order to shed some light on this behavior, we calculated the structures of the MO_3 radicals as discussed later (see Table 5 and Fig. 1).

At the BP86 level of theory, all three metal-trioxides have C_{3v} structures with $^2A_1$ ground states, agreeing with earlier calculations for MnO_3 [37] employing the PW91 functional. The O–M–O angles widen from Re to Mn. The SOMO is located at the metal centers for all three atoms. Fig. 2 shows a greater upward extension of the metal centered orbital for the more pyramidal technetium and rhenium compounds, thus allowing a better interaction with the ligands. At the MP2 level MnO_3 moves into the high symmetry D_{3h} arrangement. Here, the orbital containing the radical electron is lower in energy compared to the heavier analogs, and the SOMO shows only small upward extension with significant radical character at the oxygen atoms. Hence, we obtain smaller metal–ligand interactions.

These radical geometries are mirrored in the corresponding organyl compounds. The O–M–O angles increase from Re over Tc to Mn. The Mn–O distances of the perfluorated compounds are around 1.58 Å. The Mn–C distances are 2.035 Å for CF_3MnO_3 and 1.940 Å for $C_6F_5MnO_3$. No crystal structures of manganese compounds with perfluorated ligands have been reported yet. Reported Mn–C distances from crystal structures of η^5 manganocenes

Table 3
Optimised parameters for the $LReO_3$ compounds

		r(M–O)	r(M–L)	α(O–M–O)	α(L–M–O)	E	ZPE
$HReO_3$	BP86[a]	1.723	1.681	113.3	105.3	−304.89560	0.01649
	BP86[b]	1.733	1.680	113.9	104.6	−304.81985	0.01639
	MP2[a]	1.733	1.658	111.4	107.5	−303.94959	0.01659
	MP2[b]	1.764	1.673	111.5	107.4	−303.65325	0.01618
ReO_4^-	BP86[a]	1.760		109.5	109.5	−379.70398	0.01173
	MP2[a]	1.766		109.5	109.5	−378.63429	0.01175
	Exp.[c]	1.739					
$FReO_3$	BP86[a]	1.720	1.874	108.3	110.6	−404.21779	0.01146
	MP2[a]	1.738	1.878	106.7	112.1	403.14397	0.01121
	Exp.[d]	1.692	1.859		109.3		
CH_3ReO_3	BP86[a]	1.726	2.090	112.5	106.3	−344.23974	0.04420
	MP2[a]	1.736	2.060	111.2	107.6	−343.20608	0.04515
	Exp.[e]	1.709	2.060	113.0	106.0		
CF_3ReO_3	P86[a]	1.724	2.171	112.8	106.0	−642.06287	0.02212
	MP2[a]	1.735	2.139	110.8	108.1	−640.62962	0.02273
$C_5F_5ReO_3$	BP86[b]	1.736	2.159	2 × 112.9 112.4	2 × 105.1 107.8	−993.91925	0.05006
	MP2[b]	1.770	2.145	110.3	2 × 108.1 109.6	−991.11649	0.05145
$C_6F_5ReO_3$	BP86[b]	1.737	2.081	2 × 111.5 111.1	2 × 107.6 107.3	−1032.08075	0.05701
	MP2[b]	1.772	2092	2 × 109.4 109.0	2 × 109.6 109.8	−1029.17274	0.05881

Distances (r) are given in Å and angles (α) are given in degrees. The electronic total energies (E) and zero point vibrational energies (ZPE) are given in atomic units.

[a] Basis set 1.
[b] Basis set 2.
[c] Ref. [2].
[d] Refs. [17,49].
[e] Ref. [48].

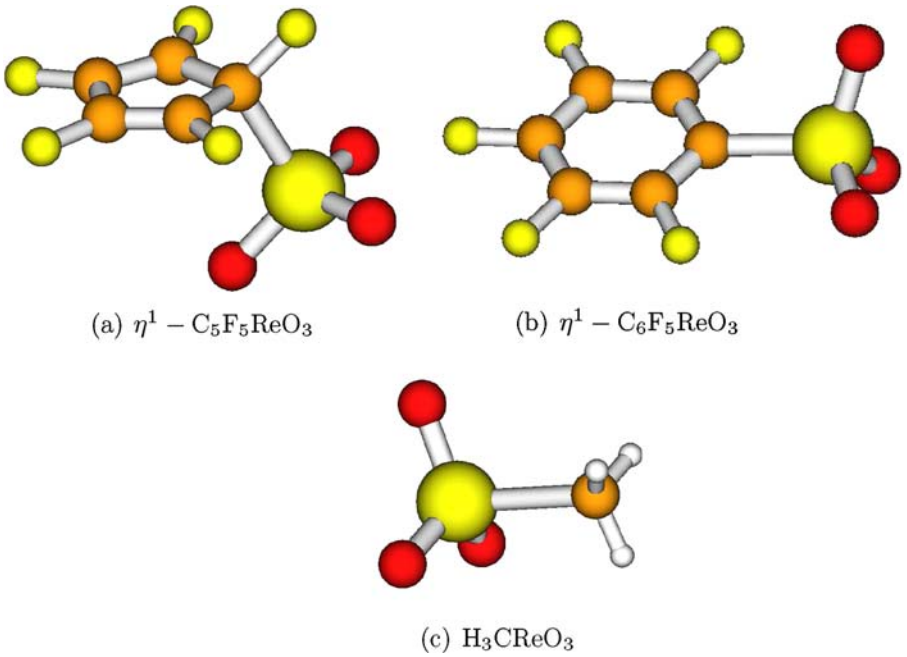


Fig. 1. Structures of calculated perfluorated LMO_3 compounds.

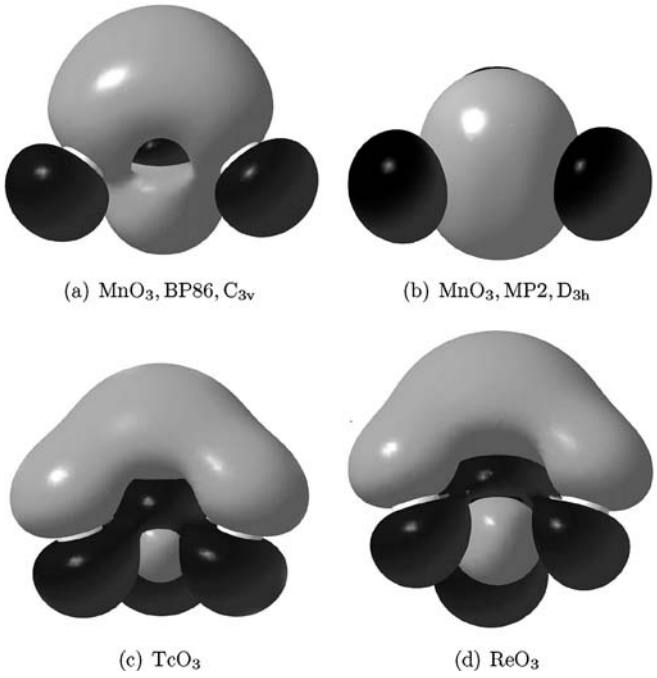


Fig. 2. SOMO representations for MO_3 radicals.

range from 2.09 to 2.45 Å [38]. η^1 Phenyl-manganese compounds have Mn–C bond lengths of 2.055–2.097 Å [39], η^6 phenyl-manganese compounds Mn–C bond lengths range between 2.154 and 2.273 Å [40]. For bonds between manganese and aliphatic carbon atoms we found distances between 1.969 and 2.419 Å [41]. This leads us to the conclusion that both compounds show manganese carbon bonds, in case of the C_6F_5 compound even a stronger bond.

In contrast to the manganese compounds, both the experimentally known CH_3TcO_3 and $C_5F_5TcO_3$ have minimum structures at the BP86 and MP2 levels of theory. The η^1-coordinated $C_5F_5TcO_3$ compound is a true minimum and 12 kcal/mole more stable than the corresponding η^5-coordinated isomer which is a second-order saddle point on the energy hypersurface. As for the rhenium compound, the C_5F_5 compound only shows η^1-coordination. The η^5 coordinated species is only a very shallow minimum lying about 20 kcal/mole higher in energy than the η^1-coordinated global minimum. The experimentally known cyclopentadienyl technetium and rhenium oxides all show η^5 coordination[9] and a gas electron diffraction study of Ru(η^5-C_5F_5)($\eta^5C_5Me_5$) [42] also shows a η^5-coordinated C_5F_5 ring. Tc–C distances in structurally characterized η^5-technetium metallocenes are between 2.26 and 2.33 Å [43], and in (η^1-Cp)Tc(NAr_3) the Tc–C distance is 2.156 Å [44]. The calculated Tc–C bond lengths of 2.158 (CF_3), 2.152 (C_5F_5) and 2.067 (C_6F_5) fit well into the range of structurally characterized technetium compounds. As found for manganese, the C_6F_5 compound has the shortest bond length and promises to be remarkably stable.

As for the perfluorated manganese and technetium compounds the Re-C bond lengths progress from $C_6F_5ReO_3$ (2.081 Å) over $C_5F_5ReO_3$ (2.159 Å) to CF_3ReO_3 (2.171 Å). The Re–C bond lengths of [Re_2(η^5-C_5H_5)(μ-η^1:η^5-C_5H_4)-$(CO)_4$-(2,3,4,6-C_6F_4H)] [45] (2.19(1) Å) and [Re(η^6-C_5-Me_4CH_2)$(CO)_2$ (C_6F_5)][46] (2.20(1) Å) are longer than the calculated values for the C_6F_5 compound, thus indicating a strong rhenium–carbon bond. While no values for rhenium C_5F_5 or CF_3 compounds are available, the Ru–C bond lengths of 2.15–2.20 Å found by gas electron diffraction for Ru(η^5-C_5F_5)($\eta^5C_5Me_5$) [42] indicate that the bond lengths of the CF_3 and C_5F_5 compounds are well in the range of Re–C bonds. The O–Re–O angles of the C_6F_5 compound (111.5° and 111.1°) are smaller than those of the CF_3 compound (112.8 and 110.8) and the C_5F_5 (112.9° and 112.4°). The Re–O bond lengths are constant between 1.724 and 1.737 Å, comparing well with the calculated bond lengths of $FReO_3$ (1.720 Å) and CH_3ReO_3 (1.726 Å). A bond length of 2.16 Å has been obtained by SCF calculations for CF_3ReO_3 [23] comparing surprisingly well with the values obtained from the DFT and MP2 calculations here.

In order to discuss the relative stability of the group 7 trioxo compounds, we decided to calculate the reaction energy of the shown reaction (1):

$$LMO_3 + H_2 \rightarrow HMO_3 + HL \quad (1)$$

with L = O^-, F, CH_3, CF_3, C_5F_5 and C_6F_5 (see Table 4). This reaction should give some insight into the question whether electronegative ligands stabilise the ligand-to-metal bond or not. In addition the tetraoxo anions were taken into account as they are considered to be among the most stable group 7 compounds in the oxidation state +VII.

While the differences between the MP2 and BP86 values are small for the fluoride and methyl compounds, the difference between MP2 and BP86 is up to 24.2 kcal/mol for MnO_4^-. This is due to the well-known MP instabilities that frequently occur in calculations of first row transition

Table 4
The relative stability of LMO_3 compounds to $HMO_3 + H_2$ according to reaction (1) (in kcal/mol)

	Mn			Tc			Re		
	ΔE(BP86)	ΔE(MP2)	$\Delta\Delta E$	ΔE(BP86)	ΔE(MP2)	$\Delta\Delta E$	ΔE(BP86)	ΔE(MP2)	$\Delta\Delta E$
O^-	107.7	83.5	24.2	113.8	125.2	−11.4	118.9	128.5	−9.6
F	4.5	−6.4	10.9	13.1	17.6	−4.5	14.2	13.0	1.2
CH_3	−3.8			−2.9	−0.1	−2.8	−1.8	−0.1	−1.7
CF_3	−7.0	−3.7	−3.3	−9.1	−11.4	2.3	−10.7	−13.0	2.3
C_5F_5	−4.3			−1.1	18.1	−19.2	−0.3	17.3	−17.6
C_6F_5	4.0	15.9	−11.9	1.1	19.6	−18.5	−1.5	13.7	−15.2

Table 5
Optimised parameters for the MO_3 compounds

		r(M–O)	α(O–M–O)	θ	E	ZPE
MnO_3	BP86	1.580	117.6	148.7	−330.19282	0.00884
	MP2	1.565	120.0	180.0	−329.62371	0.02287
TcO_3	BP86	1.706	114.6	135.3	−306.71838	0.02818
	MP2	1.713	110.8	123.4	−305.82460	0.03823
ReO_3	BP86	1.726	114.2	133.8	−304.25757	0.00845
	MP2	1.756	109.9	121.0	−303.29506	0.01153

Distances (r) are given in Å, bond angles (α) and the dihedral angle (θ) are given in degrees. The absolute energies (E) and zero point vibrational energies (ZPE) are given in atomic units. All results in this table were obtained with basis set 1.

metals [35,36]. While the MnO_4^- compounds are favoured by about 100 kcal/mol over the HMO_3 compounds, the energy differences for the other compounds are quite small. While the manganese and technetium fluorides seem to be more favorable or more unfavorable according to the applied method, the rhenium fluoride compound is favoured over $HReO_3$. The methyl compounds are slightly less favoured (by up to 3 kcal/mol) than the HMO_3 compounds. CF_3MO_3 is around 10 kcal/mol less favorable than the hydrogen compound. For C_5F_5 and C_6F_5 alike the BP86 results suggest a stability close to the hydrogen compounds while the MP2 results suggest a higher stability than the hydrogen compound by 13–19 kcal/mol with a maximum for the technetium compound. In summary, the CF_3 compounds are the least stable compounds and the C_6F_5 and sometimes the C_5F_5 compounds have a slightly higher stability than the methyl compounds. An explanation for the low stability of the CF_3 compound might be that while O^-, F^-, C_5F_5 and C_6F_5 are involved in π-bonding and CH_3 is a σ-donor, CF_3 only acts as a σ-acceptor.

To illustrate the above findings a natural bond orbital analysis (NBO) was carried out (see Table 6). The charge of the metal atom obtained from the NBO analysis increases from manganese (0.78–1.02) over technetium (1.47–1.76) to rhenium (1.72–1.79). The metal charge is highest in the fluorides and lowest in the C_5F_5 and C_6F_5 compounds. The charge of the oxygen atoms remains almost constant for all neutral compounds at −0.27 for Mn, −0.44 for Tc and −0.53 for Re. In the methyl and C_6F_5 compounds the carbon bound to the metal atom has a substantial negative charge of −0.70 to −0.97 for CF_3 and −0.30 to −0.50 for C_6F_5. The bonded carbon atom of C_5F_5 is almost neutral. All other carbon ring atoms have positive charges. The population of d-orbitals of the metal atom increases from rhenium over technetium to manganese. As expected the fluorides have the lowest d-electron population on the metals. The s-orbital population seems almost unaffected by the change of ligands. The electron population on manganese is somewhat higher than expected just from considering the electron densities and is probably due to the smaller ionic radius of manganese where the charge of the nucleus acts stronger on the dense inner shell electrons than in technetium and rhenium with their more polarizable electron shell structure.

Table 6
Atomic charges and populations from NBO analyses for the group 7 trioxides (in units of e)

	M	O	F/H	C	$(n-1)d$	ns
MnO_4^-	0.91	−0.48			5.81	0.25
$HMnO_3$	0.78	−0.27	0.04		5.85	0.35
$FMnO_3$	1.02	−0.22	−0.35		5.74	0.23
CH_3MnO_3	0.88	−0.28	0.03	−0.70	5.81	0.30
CF_3MnO_3	0.81	−0.27	0.01	0.87	5.84	0.32
$C_5F_5MnO_3$	0.77	−0.27	−0.28/−0.29	0.31/0.18	5.87	0.30
$C_6F_5MnO_3$	0.77	−0.22	−0.29	0.33/−0.30	5.88	0.31
TcO_4^-	1.62	−0.65			5.12	0.23
$HTcO_3$	1.47	−0.45	−0.10		5.17	0.36
$FTcO_3$	1.76	−0.4	−0.43		5.02	0.21
CH_3TcO_3	1.53	−0.46	−0.15	−0.94	5.26	0.31
CF_3TcO_3	1.49	−0.45	−0.15	0.73	5.17	0.33
$C_5F_5TcO_3$	1.42	0.43	−0.28/−0.31	0.30/0.08	5.22	0.31
$C_6F_5TcO_3$	1.52	−0.43	−0.29	0.33/−0.42	5.14	0.31
ReO_4^{6-}	1.97	−0.74			4.70	0.29
$HReO_3$	1.79	−0.55	−0.13		4.77	0.43
$FReO_3$	2.08	−0.54	−0.46		4.63	0.27
CH_3ReO_3	1.87	−0.56	−0.20	−0.86	4.76	0.37
CF_3ReO_3	1.79	−0.54	−0.18	0.77	4.80	0.40
$C_5F_5ReO_3$	1.72	−0.51	−0.31/−0.28	0.31/0.04	4.83	0.39
$C_6F_5ReO_3$	1.78	−0.50	−0.29	0.33/−0.50	4.80	0.37

4. Conclusion

Group 7 (Mn, Tc, Re) LMO_3 complexes with perfluorated ligands (CF_3, C_5F_5 and C_6F_5) were investigated. While the CF_3 compounds are the least stable of the investigated molecules, the η^1-bonded C_5F_5 and C_6F_5 compounds of technetium and rhenium show a higher stability than the experimentally known methyl trioxo compounds of these metals. Calculations of C_5F_5 as well as for the experimentally unknown CH_3MnO_3 at the MP2 level lead to decomposition of the compounds, thus indicating that these compounds do not exist. The stabilization of C_6F_5 and C_5F_5 compared to CF_3 is due to π-bonding. The data for $C_6F_5MnO_3$ suggest that it is a promising candidate for synthesis and might be the first organyl-manganese trioxide.

Acknowledgements

We are grateful to Prof. Gernot Frenking (Marburg) for useful discussions. We thank the Alexander von Humboldt Foundation, the Auckland University Research Committee and Massey University for supporting this work.

References

[1] W.A. Nugent, J.M. Mayer, Metal–ligand Multiple Bonds, Wiley, New York, 1988.
[2] I.R. Beattie, P.J. Jones, Inorg. Chem. 18 (1979) 2318.
[3] W.A. Herrmann, J.G. Kuchler, W. Wagner, J.K. Felixberger, E. Herdtweck, Angew. Chem. 100 (1988) 420.

[4] W.A. Herrmann, J.G. Kuchler, W. Wagner, J.K. Felixberger, E. Herdtweck, Angew. Chem., Int. Ed. 27 (1988) 394.
[5] W.A. Herrmann, R. Serrano, H. Bock, Angew. Chem., Int. Ed. 23 (1984) 383.
[6] A.H. Klahn-Oliva, D. Sutton, Organometallics 3 (1984) 1313.
[7] F.E. Kühn, W.A. Herrmann, Chemtracts 14 (2001) 59.
[8] D.M. Hoffman, in: G. Wilkinson, F.G.A. Stone, E.W. Abel (Eds.), Comprehensive Organometallic Chemistry II, vol. 6, Pergamon, Oxford, 1995, p. 231.
[9] F.E. Kühn, W.A. Herrmann, Struct. Bond. 97 (2000) 213.
[10] B. Schmidt, J. Prakt. Chem. 339 (1997) 493.
[11] W.A. Herrmann, R. Alberto, P. Kiprof, F. Baumgärtner, Angew. Chem. 102 (1990) 208.
[12] W.A. Herrmann, R. Alberto, P. Kiprof, F. Baumgärtner, Angew. Chem., Int. Ed. 29 (1990) 189 (or *Cp** TeO_3; see notes in this paper).
[13] T. Szyperski, personal communication.
[14] T. Szyperski, P. Schwerdtfeger, Angew. Chem., Int. Ed. 28 (1989) 1228.
[15] B. Kanallakopulus, B. Nuber, K. Raptis, M.L. Ziegler, Angew. Chem., Int. Ed. 28 (1989) 1055.
[16] A.K. Burrell, F.A. Cotton, L.M. Daniels, V. Petriceks, Inorg. Chem. 34 (1995) 4253.
[17] J.F. Lotspeich, A. Javan, A. Engelbrecht, J. Chem. Phys. 31 (1959) 633.
[18] P. Gisdkis, N. Rösch, J. Am. Chem. Soc. 123 (2001) 697.
[19] R.M. Dickson, T. Ziegler, Int. J. Quantum Chem. 58 (1996) 681.
[20] V. Pershina, J. Chem. Phys. 114 (2000) 1441.
[21] S. Kötlmeier, V.A. Nasluzov, W.A. Herrmann, N. Rösch, Organometallics 16 (1997) 1786.
[22] (a) M. de Simone, M. Coreno, J.C. Green, S. McGrady, H. Pritchard, Inorg. Chem. 42 (2003) 1908;
(b) É. Bencze, J. Mink, C. Németh, W.A. Herrmann, B.V. Lokshin, F.E. Kühn, J. Organomet. Chem. 642 (2002) 246;
(c) S. Köstlmeier, O.D. Häberlen, N. Rösch, Organometallics 15 (1996) 1872;
(d) S. Köstlmeier, G. Pacchioni, N. Rösch, J. Organomet. Chem. 514 (1996) 111;
(e) S. Köstlmeier, O.D. Häberlen, N. Rösch, W.A. Herrman, B. Solouki, H. Bock, Organometallics 15 (1996) 1872.
[23] R. Wiest, T. Leininger, G.-H. Jeng, M. Bénard, J. Phys. Chem. 96 (1992) 10800.
[24] C. Mealli, J.A. Lopez, M.J. Calhorda, C.C. Romao, W.A. Herrmann, Inorg. Chem. 33 (1994) 1139.
[25] R.C. Boehm, A. Banerjee, Chem. Phys. 167 (1992) 291.
[26] C. Elschenbroich, A. Salzer, Organometallics, 2nd ed., A Concise Introduction, VCH, 1992.
[27] M.J. Frisch, G.W. Trucks, H.B. Schlegel, G.E. Scuseria, M.A. Robb, J.R. Cheeseman, V.G. Zakrzewski, J.A.M. Jr., R.E. Stratmann, J.C. Burant, S. Dapprich, J.M. Millam, A.D. Daniels, M.C.S.K.N. Kudin, O. Farkas, J. Tomasi, V. Barone, M. Cossi, R. Cammi, B. Mennucci, C. Pomelli, C. Adamo, S. Clifford, J. Ochterski, G.A. Petersson, P.Y. Ayala, Q. Cui, K. Morokuma, D.K. Malick, A.D. Rabuck, K. Raghavachari, J.B. Foresman, J. Cioslowski, J.V. Ortiz, A.G. Baboul, B.B. Stefanov, G. Liu, A. Liashenko, P. Piskorz, I. Komaromi, R. Gomperts, R.L. Martin, D.J. Fox, T. Keith, M.A. Al-Laham, C.Y. Peng, A. Nanayakkara, C. Gonzalez, M. Challacombe, P.M.W. Gill, B. Johnson, W. Chen, M.W. Wong, J.L. Andres, C. Gonzalez, M. Head-Gordon, E.S. Replogle, J.A. Pople, GAUSSIAN98, Revision A.8, Pittsburgh, PA, 1998.
[28] M. Dolg, U. Wedig, H. Stoll, H. Preuss, J. Chem. Phys. 86 (1987) 866.
[29] D. Andrae, U. Häussermann, M. Dolg, H. Stoll, H. Preuss, Theor. Chim. Acta 77 (1990) 123.
[30] T.H. Dunning Jr., J. Chem. Phys. 90 (1989) 1007.
[31] D.E. Woon, T.H. Dunning Jr., J. Chem. Phys. 98 (1993) 1358.
[32] A.E. Reed, L.A. Curtiss, F. Weinhold, Chem. Rev. 88 (1988) 899.
[33] A.E. Reed, R.B. Weinstock, F. Weinhold, J. Chem. Phys. 83 (1985) 735.
[34] M. Seth, F. Cooke, P. Schwerdtfeger, J.-L. Heully, M. Pelissier, J. Chem. Phys. 109 (1998) 3935.
[35] K. Raghavachari, G.W. Trucks, J. Chem. Phys. 91 (1989) 1062.
[36] K. Raghavachari, G.W. Trucks, J. Chem. Phys. 91 (1989) 2457.
[37] G.L. Gutsev, B.K. Rao, P. Jena, X. Li, L.-S. Wang, J. Chem. Phys. 113 (2000) 1473.
[38] R.M. Bellabarba, G.P. Clancy, P.T. Gomes, A.M. Martins, L.H. Rees, M.L.H. Green, J. Organomet. Chem. 640 (2001) 93.
[39] (a) R.J. Morris, G.S. Girolami, Organometallics 6 (1987) 1815;
(b) R.J. McKinney, C.B. Knobler, B.T. Huie, H.D. Kaesz, J. Am. Chem. Soc. 99 (1977) 2988;
(c) R.G. Little, R.J. Doedens, Inorg. Chem. 12 (1973) 844.
[40] (a) J.L. Moler, D.P. Eyman, L.M. Mallis, Inorg. Chem. 31 (1992) 1816;
(b) A. Auffrant, D. Prim, F. Rose-Munch, E. Rose, J. Vaissermann, Organometallics 20 (2001) 3214.
[41] (a) Y.-J. Lee, S.-J. Kim, C.-H. Kang, J. Ko, S.O. Kang, P.J. Caroll, Organometallics 17 (1998) 1109;
(b) V. Riollet, C. Copÿret, J.-M. Basset, L. Rousset, D. Bouchu, L. Grosvalet, M. Perrin, Angew. Chem., Int. Ed. 41 (2002) 3025.
[42] B.F. Johnston, D.W.H. Rankin, H.E. Robertson, R.P. Hughes, J.P. Lomprey, Organometallics 21 (2002) 4840.
[43] (a) J. Bernard, K. Ortner, B. Spingler, H.-J. Pietzsch, R. Alberto, Inorg. Chem. 42 (2003) 1014;
(b) J.E. Joachim, C. Apostolidis, B. Kanellakopulos, D. Meyer, B. Nuber, K. Raptis, J. Rebizant, M.L. Ziegler, J. Organomet. Chem. 492 (1995) 199.
[44] A.K. Burell, J.C. Bryan, Organometallics 11 (1992) 3501.
[45] F. Godoy, C.L. Higgit, A.H. Klahn, B. Oelckers, S. Parsons, R.N. Perutz, J. Chem. Soc., Dalton Trans. (1999) 2039.
[46] A.H. Klahn, B. Oelckers, F. Godoy, M.T. Garland, A. Vega, R.N. Perutz, J. Chem. Soc., Dalton Trans. (1998) 3079.
[47] I. Baptista de Alleluia, J. Burgess, C. Keller, S. Möbius, R.D. Peacock, S. Ruprecht, K. Schwochau, in: H.K. Kugler, C. Keller (Eds.), Gmelin Handbook of Chemistry, Technetium, 8th ed., vol. 2 Suppl., Springer, Berlin, 1983.
[48] W.A. Hermann, P. Kiprof, K. Rypdal, J. Tremmel, R. Blom, R. Alberto, J. Behm, R.W. Albach, H. Bock, B. Solouki, J. Mink, D. Lichtenberger, N.E. Gruhn, J. Am. Chem. Soc. 113 (1991) 6527.
[49] (a) G.J. Palenik, Inorg. Chem. 6 (1967) 503;
(b) C.J. Lock, G. Turner, Acta Crystallogr. B31 (1975) 1764;
(c) G. Meyer, R. Hoppe, Z. Anorg. Allg. Chem. 420 (1976) 40.

Available online at www.sciencedirect.com
ScienceDirect
Polyhedron 26 (2007) 493–507
POLYHEDRON
www.elsevier.com/locate/poly

Novel monomeric barium complexes as volatile precursors for chemical vapour deposition

Matthew R. Hill, Jennifer J. Russell, Nicholas K. Roberts *, Robert N. Lamb

Department of Surface Science and Technology, School of Chemistry, The University of New South Wales, Sydney NSW 2052, Australia

Received 31 March 2006; accepted 24 August 2006
Available online 10 September 2006

Abstract

A new range of barium complexes with single encapsulating ligands have been prepared for use in chemical vapour deposition (CVD). A novel pathway providing an unprecedented sequence of barium carbamates is reported. New dianionic bis β-ketoesterates and their barium, strontium and calcium derivatives were synthesised. High resolution mass spectrometry showed some barium derivatives to be monomeric, and preliminary testing indicated some volatility in these species. Calcium and strontium complexes were found to have nuclearities that varied according to their ionic radii relative to the chain length of the encapsulating ligand.
© 2006 Elsevier Ltd. All rights reserved.

Keywords: Barium; CVD; Precursor; Monomeric; Strontium; Calcium; Volatile

1. Introduction

Barium is important in the microelectronics and high temperature superconductor (HTSC) thin-film industries. Ferroelectric perovskites such as $BaTiO_3$ are key materials in the development of dynamic and non-volatile random-access memories [1–4], and research within the HTSC industry is largely focussed on films of yttrium barium cuprate ($YBa_2Cu_3O_{7-x}$) for the realisation of viable HTSC devices [5–8].

Development of a chemical vapour deposition route to these thin film materials has been hindered by a lack of barium precursors with sufficient volatility and stable vapour pressures. The dearth of suitable complexes arises from the chemistry and coordination proclivities of the Ba^{2+} ion, and in particular from its large size-to-charge ratio. The Ba^{2+} ion is exceptionally large, at 149 pm in diameter, and whilst this size creates useful distortion within a perovskite unit cell, it causes significant problems when making chemical vapour deposition (CVD) precursors. Many barium complexes have high coordination numbers (commonly 8–13), and tend to form oligomeric species via oxo-bridging to satisfy the high coordination number requirements of the large metal ion. Complexes of such high nuclearities are involatile, and their formation must be prevented if a volatile complex is desired. However, the relatively low ionic charge of the metal ion means that there would be insufficient coordination if anionic ligands were used alone. Thus, the synthesis of a ligand that engenders a volatile complex is not simple. This challenge has aroused strong interest over recent years, spawning many varying approaches. Fluorinated complexes have been particularly popular for enhancing the volatility of barium precursors for CVD [9–25]. A significant group of derivatives have been reported, but all are thwarted by the common problem of fluorine contamination in any thin films derived from these complexes [26–29]. As a consequence, volatile non-fluorinated complexes are highly sought after.

In various approaches to non-fluorinated barium CVD precursors, volatility has been imparted by the use of ligands with sterically demanding and/or neutral donor atoms. It has been found that sterically hindered barium derivatives of low coordination number are volatile, but they sublime

* Corresponding author. Tel.: +61 2 9385 5087; fax: +61 2 9385 6141.
E-mail addresses: n.roberts@unsw.edu.au (N.K. Roberts), r.lamb@unsw.edu.au (R.N. Lamb).

0277-5387/$ - see front matter © 2006 Elsevier Ltd. All rights reserved.
doi:10.1016/j.poly.2006.08.032

with significant concomitant thermal decomposition. This occurs regardless of the degree of steric hindrance that has been incorporated into the structure, in an attempt to inhibit the μ-oxo bridging to adjacent metal centres that is thought to initiate the decomposition. The use of sterically hindering components with appended neutral coordinative sites has been more successful in engendering volatile species. These ligands typically have two portions: the anionic component with sterically demanding groups, and a neutral coordinating component that is bound to the anionic component in varying manners, as exemplified in Fig. 1.

Compounds **1** [30] and **2** [31] represent unsuccessful attempts to create monomeric barium complexes. The spacing between the diketonate and oligoether moieties is unsuitable because strained four- or seven-membered rings would be enforced, upon the formation of monomeric species. Consequently the undesirable bridging to adjacent metal centres is actually more stable, and thus preferred. In contrast, compounds **3** [32–35] and **4** [36,37] are volatile complexes, each having two mono-anionic ligands with an appropriate spacing between the diketonate and oligoether components. Although these compounds are volatile, they sublime with substantial thermal decomposition, largely because the two separate ligands do not sufficiently cloak the large metal ion. The work of Studebaker et al. [29] is most significant in this field. They reported the ketoiminate **5** [29,38], where one encapsulating ligand was used to take best advantage of the increased stability afforded by the chelate effect. This increase in ligand sophistication improved the characteristics of prospective barium CVD complexes, but at the same time it increased the synthetic difficulty of preparing more advanced ligand systems.

It was clear to us that dianionic encapsulating ligands should be at the forefront of further research in this area. Exploration of new ligand systems, and the adaptation of earlier work in the attachment of donor chains to β-diketonates were of particular interest.

We report herein the synthesis of a class of encapsulated barium bis-carbamato complexes, and a new group of alkaline earth bis-ketoesterates that show promise for CVD applications.

2. Results and discussion

2.1. Barium carbamato complexes

Complexes of organic carbamates have been successfully applied as precursors to the SSCVD of a number of thin film materials, including MgO [39], ZnO [40], Sb_2O_3 [41], ZnS [42] and CdSe [43]. The synthesis of these complexes is comparatively simple, making the carbamato ligand an attractive proposition for barium CVD precursors. However, carbamates have not been applied as a ligand in barium chemistry, and in fact there have been, to date, no reports of any structurally characterised Ba, Sr, or Ca carbamato complex. A noteworthy observation from the organic carbamate complexes mentioned above was the agency of the trivalent nitrogen atom in providing an extra functionality. This extra branching simplified the assembly of all the requirements of a CVD ligand: the anionic component, the neutral donor polyether chain, and the sterically impeding alkyl group.

The general strategy adopted in the preparation of these complexes, as outlined in Scheme 1, was to prepare oligoether ligands of different chain lengths, terminated by secondary diamines **8** bearing various bulky or coordinating alkyl or aryl 'R' substituents. These amines afforded the complexes **9** through a CO_2 insertion reaction. The simple high yielding synthesis of the bromides **7** [44] at the start led directly to the secondary amines **8** by using the relevant primary amine in large excess [45]; this stratagem bypassed the extra steps of mono-protection, acylation, deacylation and alkylation that are usually employed to produce a mono-alkylated amine. The synthesis of the

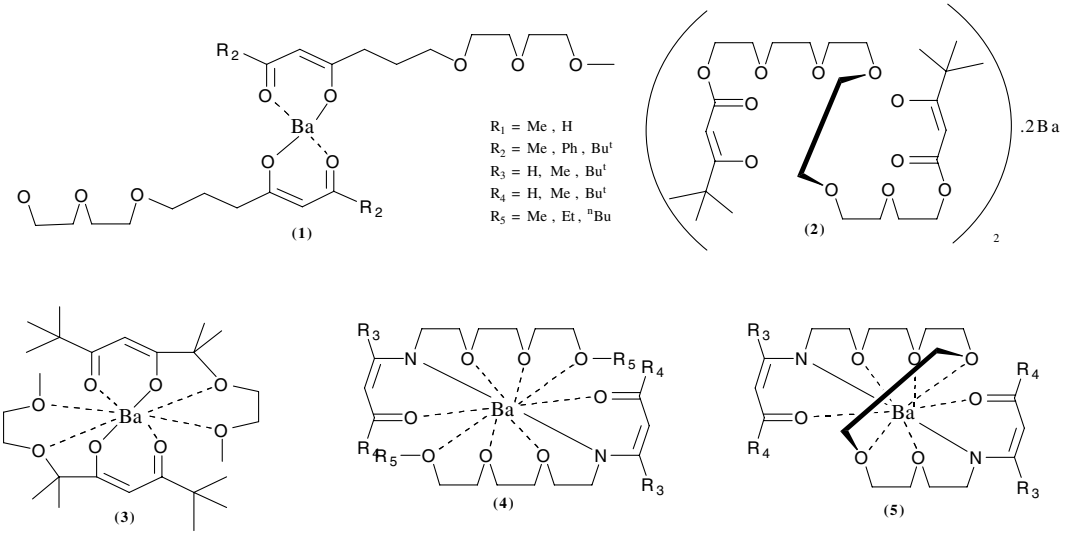
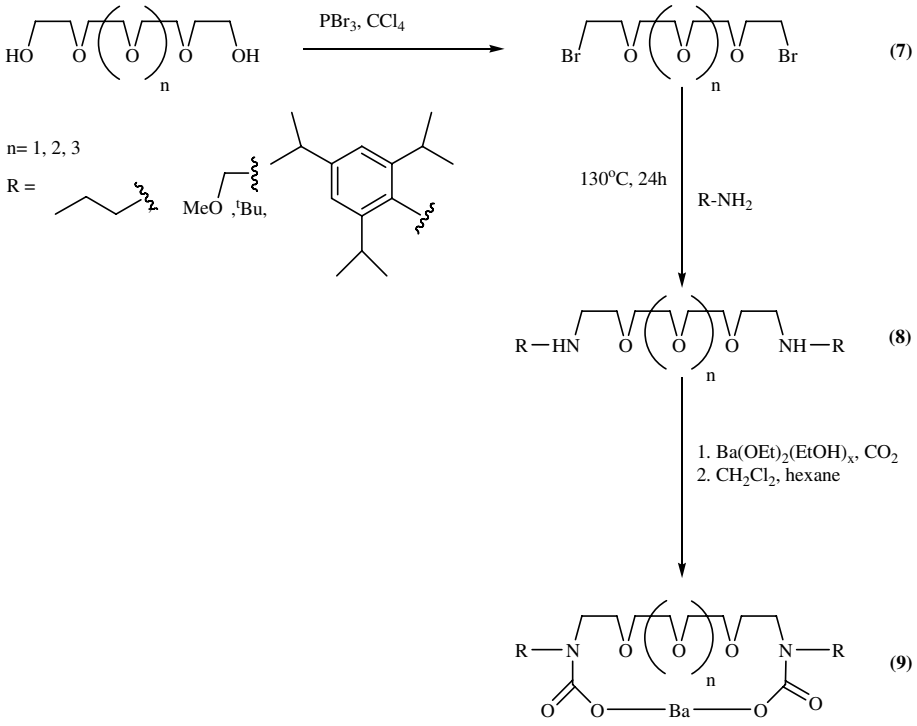


Fig. 1. Barium complexes **1** [30], **2** [31], **3** [32–35], **4** [36,37], and **5** [29,38].



Scheme 1. Synthetic scheme for encapsulating barium carbamates.

barium carbamates **9** proved to be more difficult. Their preparation was circumscribed by the strict reaction conditions necessary to prepare these compounds in preference to decomposition or other unwanted side reactions:

- Anhydrous conditions were needed to promote the formation of carbamates in preference to carbonates.
- Elevated temperatures were avoided as this could have resulted in decarboxylation.
- Commonly used insoluble barium sources (i.e. BaH_2, Ba/NH_3) were not reactive enough.

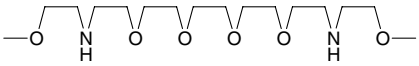
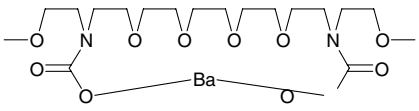
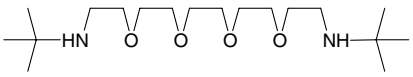
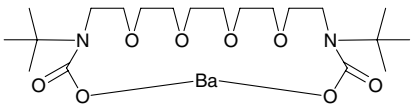
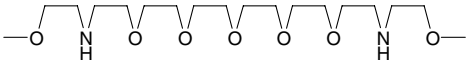
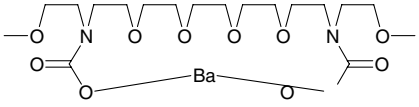
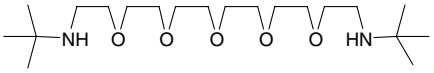
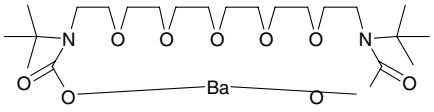
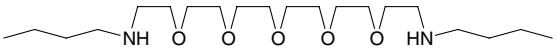
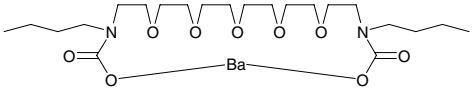
A soluble anhydrous barium source needed to be used, whose ligands would readily detach at room temperature without reacting with the CO_2 that is required to form the desired complexes. We found a reactive alkoxide $Ba(OEt)_2(EtOH)_x$, formed by reacting barium metal with excess dry ethanol, was suitable. The ethoxide ligand readily detached in the presence of the protonated, strongly chelating ligand **8** in CH_2Cl_2 solution, to release EtOH and an excellent yield of the barium carbamato complex **9**, which was isolated by precipitation with hexane.

Using this general method, a broad class of unprecedented encapsulating barium carbamato complexes were synthesised in excellent yields, as shown in Table 1. It was possible to prepare complexes that had varying degrees of steric hindrance and donor chain length. The volatility testing performed on the encapsulating carbamato complexes was disappointing, however, as it clearly revealed that these complexes were unsuitable for CVD. The typical thermogravimetric analysis shown in Fig. 2 indicated that these carbamates began to decompose immediately upon heating, and therefore did not possess sufficient thermal stability to remain intact at the necessary elevated temperatures. It was likely that the complexes were not actually monomeric in nature, but actually an interpenetrating web of carbamato ligands bridging between adjacent metal sites to form polymeric species.

Further reflections on the available coordination modes of the carbamate ligand group offer some insight into the problem. The coordination of a carbamato ligand group to a single barium ion in a mononuclear complex would entail the formation of either a strained four- or seven-membered ring (see Fig. 3), depending on whether the nitrogen atom of the carbamate is or is not coordinated. Furthermore, the carbonyl oxygen must, by default, point outwards, where it could participate in undesirable bridging to a neighbouring complex. Thus, mononuclear coordination of these carbamate ligands is probably unfavourable compared to bridging polymeric coordination. Previous examples of bridged bonding were evident in complexes **1** and **2**, where monomeric chelation would cause ring strain. Dimeric and polymeric species formed in preference, and these were likewise involatile.

Whilst extensive attempts at crystallising the barium carbamato species **9** for use in X-ray crystallography proved ultimately to be unsuccessful, some experimental evidence supported the proposed oligomeric/polymeric arrangement of these complexes. Firstly, the molecular ion was never observed in any mass spectrometric experiments, even under the gentlest of ionisation conditions.

Table 1
Summary of barium carbamato complexes and the ligands from which they were derived

Ligand (yield, identification)	Ba complex (yield, identification)
 (78%, **10**)	 (78%, **11**)
 (69%, **12**)	 (81%, **13**)
 (34%, **14**)	 (85%, **15**)
 (72%, **16**)	 (89%, **17**)
 (70%, **18**)	 (98%, **19**)

Instead, a complicated series of higher m/z ions were generally observed, which we ascribe to the presence of higher nuclearity species. Secondly, although the compounds were soluble in many polar organic solvents, the dissolution was initially very slow, even though the complexes ultimately proved to be highly soluble. Such a slow dissolution, apparently under kinetic control, could arise from the solvent progressively replacing oxo-bridging bonds. Although a painstaking experimental investigation might have revealed the structures of these complexes, we chose to direct our efforts instead to the synthesis of monomeric barium complexes as a potentially more fruitful area.

2.2. Barium β-diketonates

The β-diketonato moiety is the dominant ligand in the quest for volatile barium complexes. The ligand provides sites for the incorporation of sterically demanding groups, and points of attachment for neutral coordinative components. Also, β-diketonates impart good thermal stability to metal complexes. As shown earlier in Fig. 1, there have been some attempts at attaching neutral coordinative groups to these ligands, but these preliminary works have been limited in their scope and success.

One of our early approaches to making an encapsulating barium complex **23** is illustrated in Scheme 2. Whilst the phase transfer reaction afforded the diester **21** in fair yield, quite different conditions were required depending upon the length of the glycol portion. We think this was due to the tendency of the glycol chain to chelate about metal cations, thereby affecting reaction progress [46]. The propensity of the glycol chain to chelate metal atoms may have also been the reason that subsequent attempts to use Claisen condensations to prepare the diketonate **22** proved

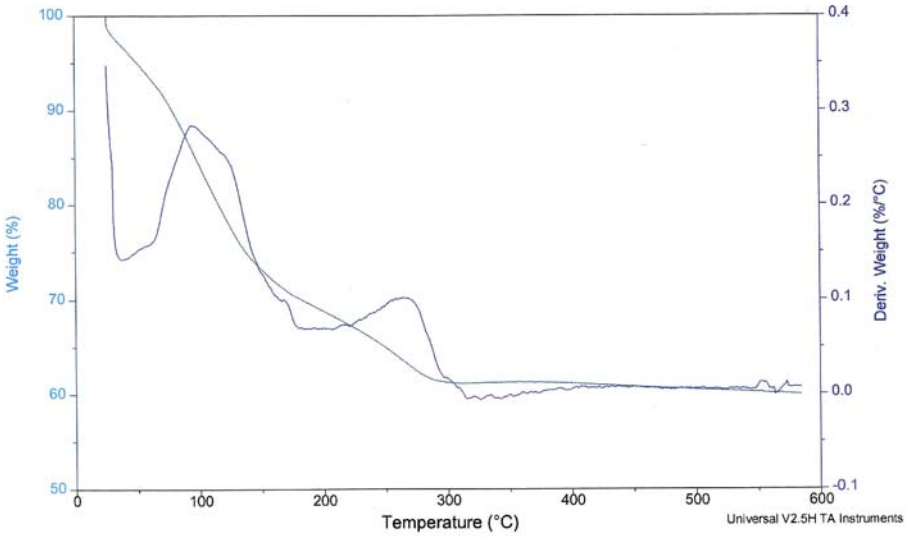


Fig. 2. A typical thermogravimetric analysis of a barium carbamato complex **19**.

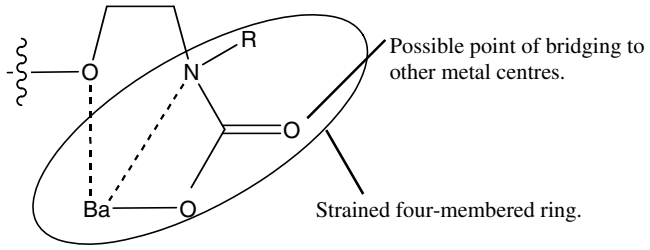
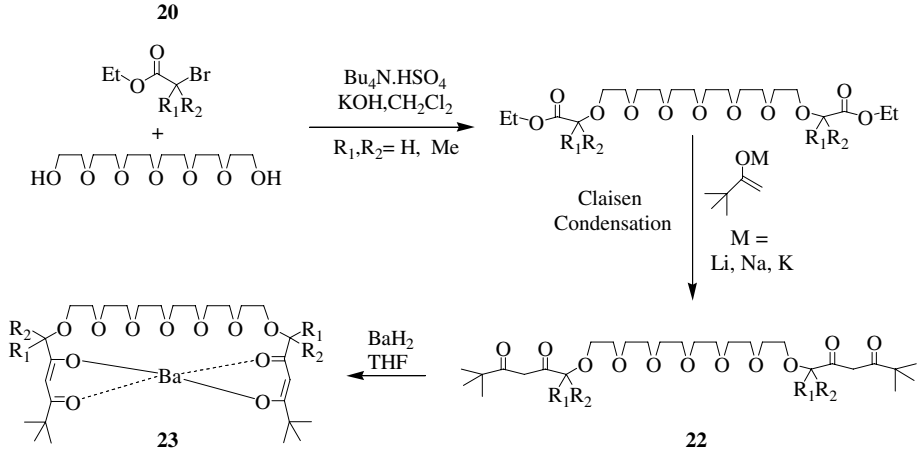


Fig. 3. The structural requirements of a monomeric barium carbamato complex.

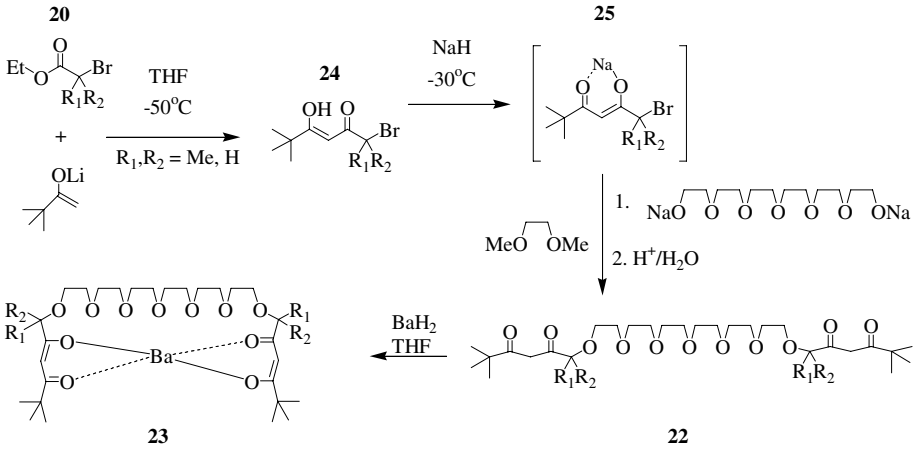
to be unsuccessful, even when a number of conditions and reagents were tried.

A simple means of circumventing the possible problems of hindering glycol chains in the formation of β-diketonates was to prepare the diketonate portion of the ligand before attaching the glycol component. Thus, the Claisen condensation to form the bromodiketone **24** proceeded well (Scheme 3), although care was needed to avoid exposure of some derivatives to light, which promoted bromine cleavage and the decomposition of **24**.

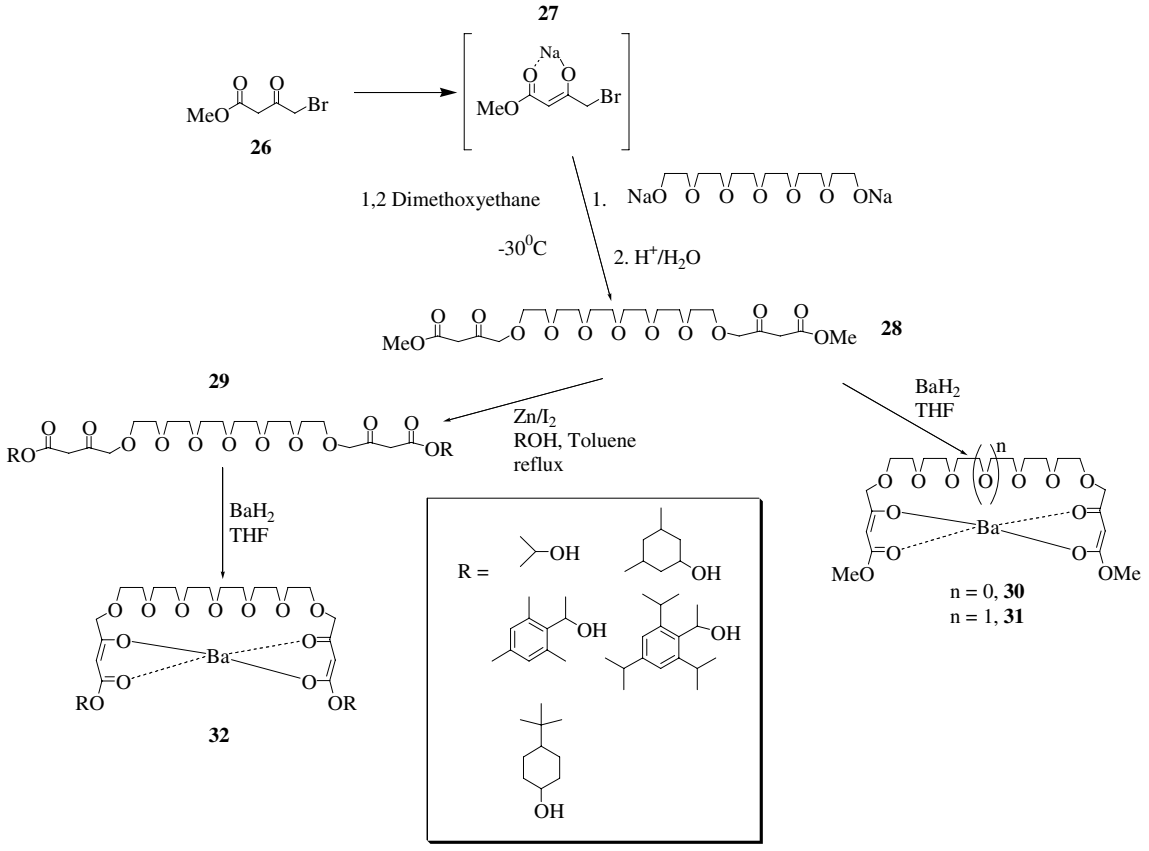
The next step of linking the bromo derivative to the glycol chain, to make **22**, was unsuccessful when we applied standard procedures [47]. Workup of the reaction mixture yielded unreacted glycol chains and self-condensed diketonate moieties. From this result we surmise that the reaction of the sodium chelate **25** with the glycolate salt is hindered by the two R groups α- to the bromine, so that intramolecular condensation of **25** is favoured over reaction with the glycolate. We attempted to attenuate the diketonate reactivity by forming its more covalent lithium salt, whilst boosting the glycolate reactivity by forming its potassium salt – but to no avail. Upon the failure of this approach, we reduced the steric crowding adjacent to the bromine atom, and did obtain successful intermolecular reaction with the glycolate salt. This modification is illustrated in Scheme 4.



Scheme 2. A proposed synthetic route to a diketonate complex of a single dianionic ligand.



Scheme 3. A second synthetic route to encapsulating barium diketonate complexes.

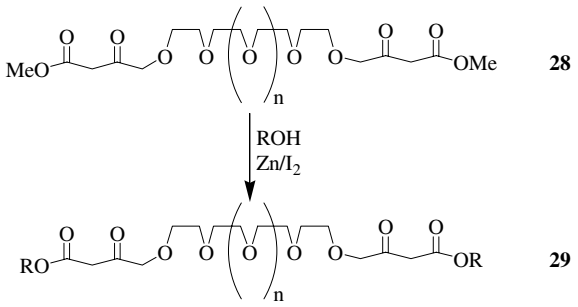


Scheme 4. The successful preparation of chelating diester barium complexes.

The successful synthesis of the dimethyl ester **28** (Scheme 4) has been reported previously [47]. Undoubtedly the resonance effect of the methoxy group helps stabilise the sodium β-diketonate complex **27**. Reactions of homologues of **28** with BaH_2 delivered the barium complexes **30** and **31** in good yields. The monomeric structure of each complex was confirmed by high resolution mass spectrometry. Whilst the ready synthesis of **28** is consistent with our ideas on steric hindrance, the resulting complexes **30** and **31** were not suitable for CVD precursors. They readily cleave off their oligo-ethylene oxide moiety when heated. Such behaviour was predictable, however, as these complexes lack sufficient steric shielding of the metal ion to isolate the barium atoms sufficiently from donor groups on neighbouring complexes.

Therefore, it was necessary to develop a method of introducing a sterically bulky component to the diester ligand. We sought a method of introducing a sterically

bulky group into the diester ligand other than α- to the oligoglycol attachment. The ester group in **28** offered a means of introducing such a group through a transesterification route. Transesterifications proceeded with moderate success in the presence of the Zn/I_2 heterogenous catalytic system. Illustrated below is a summary of these results.



28

29

In Table 2 the limitations of this approach are exposed. No transesterifications were successful in the presence of the longest hexaethylene glycol chain. The difficulty of performing conventional organic reactions on this length of glycol chain has been illustrated by the results outlined in Scheme 3 and 4. Shorter chain lengths produced several hindered species in moderate to good yield, yet attempts to perform transesterifications with desirable *tert*-butyl or fluorinated alcohols were unsuccessful. Also, it was necessary to use benzyl alcohols instead of bulky phenols, as it is known that phenyl alcohols undergo self-condensation reactions under the reaction conditions, to form coumarins [48].

Nevertheless, the successful transesterifications performed represented a novel approach to the synthesis of new prospective ligands for barium and other alkaline earth complexes. The results of attempted complexation reactions are listed in Table 3.

An appraisal of these results allows some conclusions to be drawn. It was not possible to form metal complexes with the bulky aromatic ligands **38** or **39**. Evidently, the sterically bulky components of these ligands were too large to allow effective coordination of a metal atom. The effect of steric bulk was more pronounced than expected, as the barium ion did not complex with any ligand containing groups more bulky than an isopropyl derivatisation; only **34** gave a reasonable yield (65% of **6**) by reaction with BaH_2.

The utility of ligands made by this route for our aim of barium ion complexation was not ideal. The transesterification method failed each time we tried to make the long ligand chain compounds that we thought were needed for stable barium complexation. The hypothesis that stable complexation of alkaline earth cations required a matching of cation size to ligand chain length was tested by comparing the strengths of calcium and strontium complexation with the barium results. In general we found that the short chain length ligands, which failed to complex with barium, did complex with calcium and strontium. Thus, **37** failed to react with barium, but gave the strontium complex **45** in

Table 2
Transesterifications of oligoether diesters

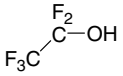
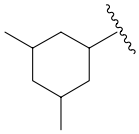
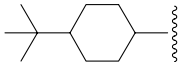
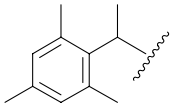
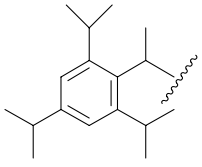
Bulky substituent (R)	Chain length (*n*)	Result/yield (%)	Identification
	1	78	**33**
	2	60	**34**
	3	unsuccessful	
	2	unsuccessful	
	3	unsuccessful	
	2	unsuccessful	
	3	unsuccessful	
	2	unsuccessful	
	3	unsuccessful	
	2	59	**35**
	3	unsuccessful	
	1	75	**36**
	2	47	**37**
	3	unsuccessful	
	2	76	**38**
	3	unsuccessful	
	2	54	**39**
	3	unsuccessful	

Table 3
A summary of metal complexation reactions of oligoethylene oxide ketodiesters **33**–**39**

Ligand	Metal	Result/yield (%)	Product
33	Ca	50	**40**
34	Ca	69	**41**
	Sr	83	**42**
	Ba	65	**6**
35	Sr	unsuccessful	
	Ba	unsuccessful	
36	Ca	68	**43**
37	Ca	72	**44**
	Sr	96	**45**
	Ba	unsuccessful	
38	Sr	unsuccessful	
	Ba	unsuccessful	
39	Sr	unsuccessful	
	Ba	unsuccessful	

96% yield. However, bulky ligands **38** and **39** did not complex to strontium any more then they did to barium.

Synthesis of calcium complexes **40**, **41**, **43** and **44** provided some interesting results. The pentaethylene oxide complexes **41** and **43** were prepared using CaH_2 and were identified as $[LCa_2]^{2+}$ by high resolution mass spectrometry. This highlighted the result of a ligand being greater in length than required to gird the circumference of a single metal ion; an additional metal atom was needed to fulfill the available coordination sites. The shorter chain ligand **33** afforded the complexes **40** and **44**, but freshly prepared $Ca(O^iPr_2)_2$ reagent was required, as CaH_2 or Ca/NH_3 were not reactive enough. Mass spectrometry indicated a stoichiometry of the type Ca_3L_2. The Ca/L stoichiometric ratio was lower as the chain length was decreased.

The thermal properties of the limited accessible barium complexes in this system were measured (Fig. 4). It was notable that these complexes had a far greater thermal stability (ca. 175 °C) than the previously described carbamato derivatives. Above 175 °C the compounds decomposed continuously to residues of varying compositions. The percentage yields of residue were compared to an idealised yield expected if pure BaO had been formed (Table 4).

The pentaethylene oxide methyl ester **30** decomposed to a mass of residue greater than that expected if the material had decomposed to BaO. As decarboxylation of the ester groups on **30** is plausible, the formation of some $BaCO_3$ in the residue could account for the mass excess. In contrast, the longer chain ester complex **31** decomposed to a residue weight corresponding to BaO, so no generality can be drawn from these few results. The most interesting thermogravimetric result was that the isopropyl ester complex **6** gave half the weight of residue expected, as calculated for BaO. Evidently considerable barium was lost in volatile form, either due to volatility of **6** or of an intermediate pyrolysis product. Encouraged by this result we tested **6** under CVD conditions, but we found that it was not volatile enough to deliver sufficient material to the surface of the substrate. In another test the substrate was used cold, to collect a sample of the species delivered in the effluent stream from the hot Knüdsen cell. XPS analysis of the condensate showed that some **6** was present, but the spectra showed a low atomic abundance of barium, indicating significant thermal decomposition had occurred.

Table 4
Residues remaining following thermal decomposition of barium complexes

Complex	Percentage residue of BaO	Observed percentage residue
6	23.2	12.3
30	25.3	31.8
31	23.6	23.1

3. Summary and conclusions

The metal complexation studies reported represent significant advances in making a range of derivatives of barium, strontium and calcium, with some of the characteristics needed for CVD.

A novel synthetic scheme has been devised which afforded a sequence of barium carbamato complexes in relatively few steps, and in good yields. Preliminary characterisation of these complexes showed that they were neither monomeric nor volatile. Thermogravimetric analysis of the carbamato complexes revealed that none of the carbamato derivatives possessed sufficient thermal stability to be volatile, regardless of their structure.

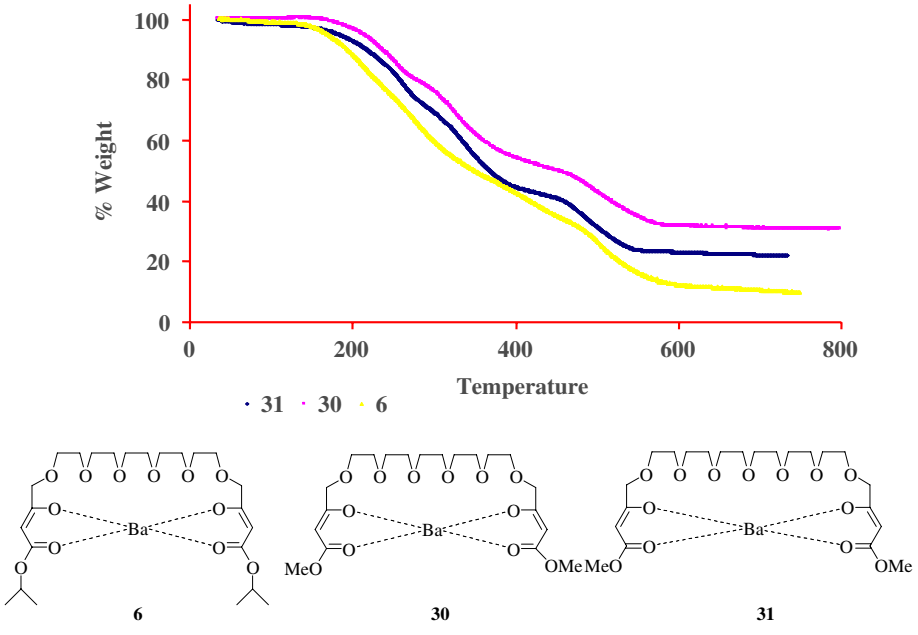


Fig. 4. Thermogravimetric analysis of barium diketonates.

A different approach yielded barium, calcium and strontium complexes of oligoethylene oxide β-ketoesterates. However, the ligands available for metal complexation turned out to be limited by the hindering nature of longer oligo-ethylene oxide components in preparative reactions, and there was in addition limited success in the transesterifications in the presence of long oligo-ethylene oxide chains. Also, of the ligands that could be successfully synthesised, those with highly hindered substituents did not form stable metal complexes. Significantly, high-resolution mass spectrometry of the compounds that could be made revealed that the strontium and barium analogues were monomeric, whereas calcium derivatives of various chain length ligands arranged themselves as either Ca_2L or Ca_3L_2. Repeated attempts to crystallise these complexes indicated that they were most likely non-crystalline in nature. Thermogravimetric analysis of these metal complexes showed they were more thermally stable compared to the class of carbamato complexes we made at first. The isopropyl-substituted barium complex **6** exhibited promising volatility during these analyses. However, the volatility was insufficient for useful barium-containing films to be grown.

4. Experimental

Infrared spectra were recorded as KBr disks and as neat liquids on a Perkin–Elmer 580B spectrometer. ^{1}H NMR and ^{13}C NMR spectra were recorded on a Bruker AC300F spectrometer at 300 MHz. Solvents and reagents were purified by the literature methods. Attempts to record microanalytical data for compounds described within did not give the expected results because ligands containing oligoethylene oxide segments could not be distilled, even at reduced pressures and elevated temperatures, and hence could not be isolated in a sufficient purity. X-ray quality crystals of metal complexes could not be obtained, and hence similar purity problems hindered their elemental analysis. Instead, high resolution mass spectrometry was used to definitively confirm the identity of reported compounds. High resolution mass spectra were obtained by electrospray in positive ion mode with a capillary voltage of 50 V and an ion source temperature of 190 °C. Mass spectra of metal carbamate complexes could not be obtained due to their instability under ionisation. Meaningful data could not be obtained even with the most 'gentle' ionisation techniques including MALDI and electrospray. Ca, Sr and Ba complexes reported are moderately air sensitive, and rapidly hydrolyse when exposed to moist air. BaH_2 was purchased from Aldrich and was used as received.

4.1. 1,14-Dibromo-3,6,9,12-tetraoxatetradecane (*46*)

This compound was prepared by following a procedure previously reported [44,49]. A solution of PBr_3 (12.78 g, 4.70×10^{-2} mol) in CCl_4 (13 mL) was added dropwise to a solution of pentaethylene glycol (15.00 g, 6.30×10^{-2} mol) in CCl_4 (21 mL). The resulting mixture was then refluxed for 2 h. Ice (70 g) was added to the cooled solution. The organic layer was then washed with a saturated solution of $NaHCO_3$ (30 mL), water (30 mL) and dried over $MgSO_4$. Removal of volatiles in vacuo afforded a viscous yellow liquid, **73** (9.20 g, 40%). ^{1}H NMR: ($CDCl_3$) δ (ppm): 3.43 (t, 4H, $2\times CH_2Br$), 3.62 (m, 12H, $3\times OCH_2CH_2O$), 3.77 (t, 4H, $2\times OCH_2CH_2Br$). ^{13}C NMR ($CDCl_3$) δ (ppm): 30.21 ($2\times CH_2Br$), 70.45 (OCH_2CH_2O), 70.56 (OCH_2CH_2O), 71.10 ($3\times OCH_2CH_2O$). These spectra were in good agreement with the literature [44,49].

4.2. 1,17-Dibromo-3,6,9,12,15-pentaoxaheptadecane (*47*)

A similar procedure to that for **46** was employed, using hexaethylene glycol (25.00 g, 8.90×10^{-2} mol) and PBr_3 (18.06 g, 6.7×10^{-2} mol) and delivered **47** as a very viscous pale yellow liquid (21.65 g, 60%). ^{1}H NMR: ($CDCl_3$) δ (ppm): 3.42 (t, 4H, $2\times CH_2Br$), 3.61 (m, 16H, $4\times OCH_2CH_2O$), 3.76 (t, 4H, $2\times OCH_2CH_2Br$). ^{13}C NMR ($CDCl_3$) δ (ppm): 30.24 ($2\times CH_2Br$), 70.43 (OCH_2CH_2O), 70.47 (OCH_2CH_2O), 71.55 ($2\times OCH_2CH_2O$), 71.08 (OCH_2CH_2O). These spectra were in good agreement with the literature.

4.3. 1,17-Di(n-butylamino)-3,6,9,12,15-pentaoxaheptadecane (*18*)

This material was prepared by adaptation of a procedure first described by King et al. [45] To a mixture of powdered NaOH (0.98 g, 2.46×10^{-2} mol) in Et_2O (50 mL) **47** (5.00 g, 1.23×10^{-2} mol) and *n*-butyl amine (17.90 g, 2.45×10^{-1} mol) were added. The resultant mixture was refluxed for 24 h, and left overnight to cool. Precipitated NaBr was filtered off and the filtrate evaporated to dryness. Water was added to the resulting oily residue (20 mL). The aqueous solution was then extracted with dichloromethane for 48 h using a continuous liquid-liquid phase extraction setup. The organic phase was dried and the volatiles removed in vacuo to deliver a pale yellow liquid **18** (3.38 g, 70%). ^{1}H NMR: ($CDCl_3$) δ (ppm): 0.87 (t, 6H, $2\times CH_3CH_2$), 1.31 (hextuplet, 4H, $2\times CH_3CH_2$), 1.43 (p, 4H, $2\times CH_2CH_2CH_3$), 1.71 (br s, 2H, $2\times NH$), 2.57 (t, 4H, $2\times CH_2CH_2CH_2CH_3$), 2.74 (t, 4H, $2\times NHCH_2$), 3.61 (m, 20H, $5\times OCH_2CH_2O$). ^{13}C NMR ($CDCl_3$) δ (ppm): 13.87 ($2\times CH_3CH_2$), 20.35 ($2\times CH_3CH_2$), 32.14 ($2\times CH_2CH_2CH_3$), 49.22 ($2\times CH_2CH_2CH_2CH_3$), 49.54 ($2\times NHCH_2$), 70.21 (OCH_2CH_2O), 70.41 ($2\times OCH_2CH_2O$), 70.48 (OCH_2CH_2O), 70.51 (OCH_2CH_2O). μ_{max}: 1115, 1455, 1654, 2925, 3315, 3521 cm^{-1}. Found, HRMS m/z 415.315367 $(M+Na)^+$. $C_{20}H_{44}N_2O_5Na$ requires 415.314793, $\Delta = 1.38$ ppm.

4.4. 1,17-Di(tert-butylamino)-3,6,9,12-tetraoxatetradecane (*12*)

By using a similar procedure to that for **18** with **46** (2.46 g, 6.76×10^{-3} mol), *tert*-butyl amine (10.00 g,

1.37×10^{-1} mol), powdered NaOH (0.54 g, 1.35×10^{-2} mol) and THF (30 mL), **12** was isolated as a clear orange liquid (1.63 g, 69%). ^{1}H NMR: ($CDCl_3$) δ (ppm): 1.02 (s, 18H, $2 \times (CH_3)_3C$), 1.41 (br s, 2H, $2 \times NH$), 2.65 (t, 4H, $2 \times NHCH_2$) 3.57 (m, 16H, $4 \times OCH_2CH_2O$). ^{13}C NMR ($CDCl_3$) δ (ppm): 28.83 ($2 \times (CH_3)_3C$), 41.86 ($2 \times NHCH_2$), 49.84 ($2 \times (CH_3)_3C$) 70.09 (OCH_2CH_2O), 70.35 (OCH_2CH_2O), 70.45 (OCH_2CH_2O), 71.31 (OCH_2CH_2O). μ_{max}: 1107, 1467, 1639, 2947, 3321, 3546 cm^{-1}. Found, HRMS *m/z* 371.289013 $(M+Na)^+$. $C_{18}H_{40}N_2O_4Na$ requires 371.288578, $\Delta = 1.17$ ppm.

4.5. 1,17-Di(tert-butylamino)-3,6,9,12,15-pentaoxaheptadecane (16)

This compound was prepared in a similar fashion to **18** using **47** (2.76 g, 6.76×10^{-3} mol), *tert*-butyl amine (10.00 g, 1.37×10^{-1} mol), powdered NaOH (0.54 g, 1.35×10^{-2} mol) and THF (30 mL), yielding a **16** as a clear orange liquid (1.91 g, 72%). ^{1}H NMR: ($CDCl_3$) δ (ppm): 1.09 (s, 18H, $2 \times (CH_3)_3C$), 2.73 (t, 4H, $2 \times NHCH_2$) 2.91 (br s, 2H, $2 \times NH$), 3.62 (m, 20H, $5 \times OCH_2CH_2O$). ^{13}C NMR ($CDCl_3$) δ (ppm): 28.65 ($2 \times (CH_3)_3C$), 41.89 ($2 \times NHCH_2$), 50.38 ($2 \times (CH_3)_3C$) 70.04 (OCH_2CH_2O), 70.17 (OCH_2CH_2O), 70.68 (OCH_2CH_2O), 70.97 (OCH_2CH_2O), 72.31 (OCH_2CH_2O). μ_{max}: 1107, 1468, 1643, 2951, 3321, 3535 cm^{-1}. Found, HRMS *m/z* 415.314869 $(M+Na)^+$. $C_{20}H_{44}N_2O_5Na$ requires 415.314793, $\Delta = 0.18$ ppm.

4.6. 1,17-Di(2-methoxyethylamino)-3,6,9,12-tetraoxatetradecane (10)

A mixture of **46** (0.84 g, 2.30×10^{-3} mol), 2-methoxy ethylamine (0.92 g, 4.60×10^{-2} mol) and powdered NaOH (0.18 g, 4.60×10^{-3} mol) in Et_2O (20 mL) were reacted similarly to that for **18** to afford a viscous orange liquid **10** (0.63 g, 78%). ^{1}H NMR: ($CDCl_3$) δ (ppm): 1.93 (br s, 2H, $2 \times NH$), 2.78 (m, 8H, $4 \times NHCH_2$), 3.31 (s, 6H, $2 \times OCH_3$), 3.45 (t, 4H, $2 \times CH_3OCH_2$), 3.71 (m, 16H, $4 \times OCH_2CH_2O$). ^{13}C NMR ($CDCl_3$) δ (ppm): 49.19 ($2 \times NHCH_2$), 49.22 ($2 \times NHCH_2$), 58.68 ($2 \times CH_3O$), 70.29 (OCH_2CH_2O), 70.45 (OCH_2CH_2O), 70.51 (OCH_2CH_2O), 70.59 (OCH_2CH_2O), 72.04 (OCH_2CH_2O). μ_{max}: 1114, 1456, 1656, 2873, 3332, 3568 cm^{-1}. Found, HRMS *m/z* 375.247659 $(M+Na)^+$. $C_{16}H_{36}N_2O_6Na$ requires 375.247107, $\Delta = 1.47$ ppm.

4.7. 1,17-Di(2-methoxyethylamino)-3,6,9,12,15-pentaoxaheptadecane (14)

A procedure analogous to that for **18** using powdered NaOH (0.98 g, 2.46×10^{-2} mol), 2-methoxy ethyl amine (18.39 g, 2.45×10^{-1} mol), **47** (5.00 g, 1.23×10^{-2} mol), and Et_2O (50 mL) afforded **14** as a viscous orange liquid (1.65 g, 34%). ^{1}H NMR: ($CDCl_3$) δ (ppm): 1.91 (br s, 2H, $2 \times NH$), 2.78 (m, 8H, $4 \times NHCH_2$), 3.32 (s, 6H, $2 \times OCH_3$), 3.46 (t, 4H, $2 \times CH_3OCH_2$), 3.62 (m, 20H, $5 \times OCH_2CH_2O$). ^{13}C NMR ($CDCl_3$) δ (ppm): 49.20 ($2 \times OCH_3$), 53.94 ($2 \times NHCH_2$), 58.66 ($2 \times CH_3O$), 70.20 (OCH_2CH_2O), 70.26 (OCH_2CH_2O), 70.42 (OCH_2CH_2O), 70.49 (OCH_2CH_2O), 70.56 (OCH_2CH_2O), 72.02 (OCH_2CH_2O). μ_{max}: 1117, 1456, 1655, 2875, 3329, 3531 cm^{-1}. Found, HRMS *m/z* 419.271333 $(M+Na)^+$. $C_{18}H_{40}N_2O_7Na$ requires 419.273217, $\Delta = 4.49$ ppm.

4.8. 3,6,9,12,15-Pentaoxaheptadecane 1,17-di(n-butylcarbamato) barium (II) (19)

Barium metal (0.25 g, 1.79×10^{-3} mol) was added to dry EtOH (30 mL) under N_2. Over a period of 5 min, the Ba metal dissolved with evolution of H_2. The solvent was then removed with a mechanical vacuum, with the solid being further dried at reduced pressure for an additional 3 h. The white solid was then dissolved in dry dichloromethane (30 mL) and **18** (0.77 g, 1.97×10^{-3} mol) was added. CO_2 was passed over the solution until its uptake was no longer evident. The solvent was then evaporated off and hexane (30 mL) added. The resulting precipitate was filtered off and dried in vacuo to deliver a tan solid **19** (1.18 g, 98%). ^{1}H NMR: ($CDCl_3$) δ (ppm): 0.91 (t, 6H, $2 \times CH_3CH_2$), 1.35 (sextet, 4H, $2 \times CH_3CH_2$), 1.47 (p, 4H, $2 \times CH_2CH_2CH_3$), 2.60 (t, 4H, $2 \times CH_2CH_2CH_2CH_3$), 2.78 (t, 4H, $2 \times NHCH_2$), 3.65 (m, 20H, $5 \times OCH_2CH_2O$). μ_{max}: 1467, 1546, 1651, 2865, 2924, 3412 cm^{-1}.

4.9. 3,6,9,12-Tetraoxatetradecane 1,17-di(2-methoxyethylcarbamato) barium (II) (11)

Use of **10** (0.50 g, 1.42×10^{-3} mol), BaH_2 (0.18 g, 1.28×10^{-3} mol), EtOH (20 mL), dichloromethane (20 mL), hexane (20 mL), and CO_2 in a manner similar to that described for **19** gave **11** as a pale yellow solid (0.57 g, 78%). ^{1}H NMR: ($CDCl_3$) δ (ppm): 1.93 (br s, 2H, $2 \times NH$), 2.78 (m, 8H, $4 \times NHCH_2$), 3.31 (s, 6H, $2 \times OCH_3$), 3.45 (t, 4H, $2 \times CH_3OCH_2$), 3.71 (m, 16H, $4 \times OCH_2CH_2O$). μ_{max}: 1464, 1543, 1644, 2854, 2951, 3455 cm^{-1}.

4.10. 3,6,9,12,15-Pentaoxaheptadecane 1,17-di(2-methoxyethylcarbamato) barium (II) (15)

A synthetic procedure similar to that for **19** delivered from Ba metal (0.49 g, (3.58×10^{-3} mol), EtOH (30 mL), **14** (1.54 g, 3.89×10^{-3} mol), CH_2Cl_2 (30 mL), CO_2 and hexane (30 mL), a pale yellow solid **15** (1.89 g, 85%). ^{1}H NMR: ($CDCl_3$) δ (ppm): 2.80 (m, 8H, $4 \times NHCH_2$), 3.35 (s, 6H, $2 \times OCH_3$), 3.48 (t, 4H, $2 \times CH_3OCH_2$), 3.64 (m, 20H, $5 \times OCH_2CH_2O$). μ_{max}: 1462, 1547, 1643, 2854, 2923, 3426 cm^{-1}.

4.11. 3,6,9,12-Tetraoxatetradecane 1,17-di(tert-butylcarbamato) barium (II) (13)

A procedure similar to **19** using **12** (1.00 g, 2.87×10^{-3} mol), Ba metal (0.36 g, 2.58×10^{-3} mol), EtOH

(30 mL), dichloromethane (30 mL), hexane (30 mL) and CO_2 delivered **13** as a light brown solid (1.17 g, 81%). ^{1}H NMR: ($CDCl_3$) δ (ppm): 1.07 (s, 18H, $2\times(CH_3)_3C$), 2.69 (t, 4H, $2\times NHCH_2$) 3.63 (m, 16H, $4\times OCH_2CH_2O$). μ_{max}: 1098, 1459, 1654, 2935, 3317, 3555 cm^{-1}.

4.12. 3,6,9,12,15-Pentaoxaheptadecane 1,17-di(tert-butylcarbamato) barium (II) (17)

By following a procedure similar to that for **19** using **16** (1.00 g, 2.55×10^{-3} mol), Ba metal (0.36 g, 2.58×10^{-3} mol), EtOH (30 mL), dichloromethane (30 mL), hexane (30 mL) and CO_2 **17** was isolated as a light brown solid (1.40 g, 89%). ^{1}H NMR: ($CDCl_3$) δ (ppm): 1.12 (s, 18H, $2\times(CH_3)_3C$), 2.77 (t, 4H, $2\times NHCH_2$), 3.67 (m, 20H, $5\times OCH_2CH_2O$). μ_{max}: 1113, 1471, 1654, 2935, 3308, 3521 cm^{-1}.

4.13. Bis(methyl)-5,8,11,14,17,20-hexaoxa-3,22-dioxo-tetracosadianoate (48)

This compound was prepared according to Kellogg et al. [47]. To a suspension of 60% NaH in mineral oil (3.23 g, 7.70×10^{-2} mol), washed three times with hexane under N_2, 100 mL of dry 1,2-dimethoxyethane (DME) was added. The solution was cooled to −30 °C and methyl 4-bromo-3-oxobutanoate [50] (15.00 g, 7.70×10^{-2} mol) in DME (50 mL) added dropwise. After stirring for 20 min at −30 °C, a solution of the disodium salt of pentaethylene glycol, made by treatment of the glycol (9.16 g, 3.84×10^{-2} mol) in DME (50 mL) with NaH (3.23 g, 7.70×10^{-2} mol) was introduced dropwise, maintaining the temperature below 0 °C. At the completion of this addition, the resulting mixture was refluxed for 16 h. Workup with dilute HCl (2 M, 50 mL), extraction with CH_2Cl_2 (3×100 mL), drying over $MgSO_4$, followed by evaporation of the solvent delivered **48** as an orange oil (9.30 g, 78%). ^{1}H NMR: (300 MHz, $CDCl_3$) δ (ppm): 3.54 (s, 4H, $2\times C(=O)CH_2C(=O)$), 3.62 (m, 20H, $5\times OCH_2CH_2O$), 3.72 (s, 6H, $2\times OCH_3$), 4.18 (s, 4H, $2\times CH_2OCH_2C(=O)$). ^{13}C NMR (76.6 MHz, $CDCl_3$) δ (ppm): 45.70 ($2\times C(=O)CH_2C(=O)$), 52.13 ($2\times OCH_3$), 70.36 ($5\times OCH_2CH_2O$), 76.07 ($2\times OCH_2C(=O)$), 167.38 ($2\times CH_3OC(=O)$), 201.80 ($2\times CH_2C(=O)$). μ_{max}: 1105, 1724, 2876, 3442 cm^{-1}. Found: HRMS *m/z* 489.195732 $(M+Na)^+$. $C_{20}H_{34}O_{12}Na$ requires 489.194796, $\Delta = 1.90$ ppm.

4.14. Bis(methyl)-5,8,11,14,17,20,23-heptaoxa-3,27-dioxo-hexacosadianoate (49)

By adapting the above procedure, using methyl 4-bromo-3-oxobutanoate (1.87 g, 9.57×10^{-3} mol), NaH (2×0.40 g, $2\times9.57\times10^{-3}$ mol), hexaethylene glycol (1.35 g, 4.79×10^{-3} mol) and DME (120 mL), **49** was isolated as a brown oil (1.14 g, 46%). ^{1}H NMR: (300 MHz, $CDCl_3$) δ (ppm): 3.54 (s, 4H, $2\times C(=O)CH_2C(=O)$), 3.63 (m, 24H, $6\times OCH_2CH_2O$), 3.72 (s, 6H, $2\times OCH_3$), 4.18 (s, 4H, $2\times CH_2OCH_2C(=O)$). ^{13}C NMR (76.6 MHz, $CDCl_3$) δ (ppm): 45.50 ($2\times C(=O)CH_2C(=O)$), 52.22 ($2\times OCH_3$), 70.46 ($6\times OCH_2CH_2O$), 76.16 ($2\times OCH_2C(=O)$), 167.43 ($2\times CH_3OC(=O)$), 201.86 ($2\times CH_2C(=O)$). μ_{max}: 1439, 1747, 2875, 3516 cm^{-1}. Found: HRMS *m/z* 533.224086 $(M+Na)^+$. $C_{22}H_{38}O_{13}Na$ requires 533.221011, $\Delta = 5.80$ ppm.

4.15. Bis(methyl)-5,8,11,14,17,20-hexaoxa-3,22-dioxo-tetracosadianato barium (II) (30)

Metal complexes were prepared under Schlenk conditions. To a solution of **48** (1.00 g, 2.14×10^{-3} mol) in THF (30 mL) was added BaH_2 (0.40 g, 2.85×10^{-3} mol) and the resulting suspension was heated at reflux for 12 h under N_2. Excess BaH_2 was filtered from the brown solution, the solvent was removed in vacuo, followed by the addition of hexane (30 mL). The resulting pale brown precipitate was then filtered off and dried to afford **30** as a tan powder (1.27 g, 98%). ^{1}H NMR: (300 MHz, $CDCl_3$) δ (ppm): 3.28 (s, 6H, $2\times OCH_3$), 3.47 (s, 2H, $2\times C(=O)CHC(=O)$), 3.64 (br s, 20H, $5\times OCH_2CH_2O$), 4.52 (s, 4H, $2\times CH_2OCH_2C(=O)$). ^{13}C NMR (76.6 MHz, $CDCl_3$) δ (ppm): 25.55 ($2\times OCH_3$), (49.39 $2\times(C(=O)-CHC(=O))$), 68.31 ($6\times OCH_2CH_2O$), 74.21 ($2\times CH_2O-CH_2C(=O)$), 170.11 ($2\times CH_3OC(=O)$), 181.68 ($2\times CH_2C(=O)$). μ_{max}: 1478, 1634, 2952, 3433 cm^{-1}. Found: HRMS *m/z* 603.108574 (M^+). $C_{20}H_{32}O_{12}Ba$ requires 603.102438, $\Delta = 10.20$ ppm.

4.16. Bis(methyl)-5,8,11,14,17,20,23-heptaoxa-3,27-dioxo-hexacosadianato barium (II) (31)

A mixture of **49** (2.00 g, 3.91×10^{-3} mol) and BaH_2 (0.70 g, 5.07×10^{-3} mol) in THF (50 mL) was heated at reflux overnight under N_2 and then cooled to room temperature. The resulting suspension was filtered, the solvent removed under vacuum and replaced by hexane (30 mL). A dark orange powder then formed, which was isolated as **31** (2.15 g, 85%). ^{1}H NMR: (300 MHz, $CDCl_3$) δ (ppm): 3.48 (s, 6H, $2\times OCH_3$), 3.61 (br s, 24H, $6\times OCH_2-CH_2O$), 3.65 (s, 2H, $2\times C(=O)CHC(=O)$), 4.35 (s, 4H, $2\times CH_2OCH_2C(=O)$). ^{13}C NMR (76.6 MHz, $CDCl_3$) δ (ppm): 25.48 ($2\times OCH_3$), (49.45 $2\times(C(=O)CHC(=O))$, 70.44 ($6\times OCH_2CH_2O$), 76.53 ($2\times CH_2OCH_2C(=O)$), 170.02 ($2\times CH_3OC(=O)$), 181.91 ($2\times CH_2C(=O)$). μ_{max}: 1107, 1446, 1648, 2921, 3455 cm^{-1}. Found: HRMS *m/z* 647.127995 (M^+). $C_{22}H_{36}O_{13}Ba$ requires 647.128243, $\Delta = -0.40$ ppm.

4.17. Bis(2-propyl)-5,8,11,14,17,20-hexaoxa-3,22-dioxo-tetracosadianoate (34)

This compound was prepared by the successful adaptation of a procedure outlined by Chavan and co-workers [48]. Compound **48** (1.00 g, 1.96×10^{-3} mol) was added to a mixture of zinc powder (0.55 g, 8.5×10^{-3} mol) and

a catalytic quantity of I_2 in isopropanol (30 mL), which was then heated to reflux for a period of 24 h. The resulting mixture was then cooled to room temperature, and dilute HNO_3 (20 mL) was added. The organic layer was separated and the aqueous layer extracted with Et_2O (3×50 mL). The combined organic extracts were dried over $MgSO_4$, filtered, and the solvent removed in vacuo to afford **34** as a yellow oil (1.31 g, 60%). ^{1}H NMR: (300 MHz, $CDCl_3$) δ (ppm): 1.26 (d, 12H, $4 \times CH_3CH$), 3.49 (s, 4H, $2 \times C(=O)CH_2C(=O)$), 3.68 (m, 20H, $5 \times OCH_2CH_2O$), 4.24 (s, 4H, $2 \times CH_2OCH_2C(=O)$), 5.04 (septet, 2H, $2 \times CH_3CH$). ^{13}C NMR (76.6 MHz, $CDCl_3$) δ (ppm): 21.60 ($4 \times CH_3$), 46.10 ($2 \times C(=O)CH_2C(=O)$), 69.00 ($2 \times CH_3CH$)), 70.33 ($5 \times OCH_2CH_2O$), 76.06 ($2 \times OCH_2C(=O)$), 166.49 ($2 \times CH_3OC(=O)$), 201.71 ($2 \times CH_2C(=O)$). μ_{max}: 1109, 1460, 1721, 2951, 3516 cm^{-1}. Found: HRMS m/z 545.256157 $(M+Na)^+$. $C_{24}H_{42}O_{12}Na$ requires 545.256848, $\Delta = -1.20$ ppm.

4.18. Bis(3,5-cyclohexyl)-5,8,11,14,17,20-hexaoxa-3,22-dioxo-tetracosadianoate (35)

Compound **35** was prepared according to the method described for **34**. To a solution of **48** (1.98 g, 4.24×10^{-3} mol) in toluene (10 mL) was slowly added 3,5 dimethylcyclohexanol (1.20 g, 9.32×10^{-3} mol) in toluene (10 mL), followed by zinc powder (0.55 g, 8.48×10^{-3} mol) and a catalytic quantity of I_2. The mixture was heated to reflux overnight. After cooling, 2M HNO_3 (50 mL) was added, and the mixture extracted with CH_2Cl_2 (3×75 mL), the isolated crude mixture was purified using chromatography over silica gel (CH_2Cl_2) to give **35** as a brown oil (1.85 g, 59%). ^{1}H NMR: (300 MHz, $CDCl_3$) δ (ppm): 0.92 (d, 12H, $4 \times CH_3CH$), 1.49 (m, 4H, $2 \times CHCH_2CH$), 1.62 (d, 8H, $4 \times CHCH_2CH$), 1.96 (d, 4H, $4 \times CH_3CH$), 3.48 (s, 4H, $2 \times C(=O)CH_2C(=O)$), 3.63 (m, 20H, $5 \times OCH_2CH_2O$), 4.18 (s, 4H, $2 \times CH_2OCH_2C(=O)$), 4.76 (s, 2H, $2 \times OCH$). ^{13}C NMR (76.6 MHz, $CDCl_3$) δ (ppm): 19.05 ($4 \times CH_3CH$), 30.45 ($4 \times CHCH_3$), 39.61 ($4 \times CHCH_2CH$), 39.93 ($2 \times CHCH_2CH$), 46.12 ($2 \times C(=O)CH_2C(=O)$), 70.48 ($5 \times OCH_2CH_2O$), 74.13 ($2 \times CHO$), 76.19 ($2 \times OCH_2C(=O)$), 166.47 ($2 \times CH_3OC(=O)$), 201.88 ($2 \times CH_2C(=O)$). μ_{max}: 1109, 1460, 1723, 2950, 3440 cm^{-1}. Found: HRMS m/z 681.382761 $(M+Na)^+$. $C_{34}H_{58}O_{12}Na$ requires 681.382598, $\Delta = 0.22$ ppm.

4.19. Bis(4-tert-butylcyclohexyl)-5,8,11,14,17,20-hexaoxa-3,22-dioxo-tetracosadianoate (37)

By following a procedure similar to that for **35**, chromatography over silica gel with light petroleum/ethyl acetate eluent (5:1) afforded 1.50 g of an orange liquid (47%), **37**, from **48** (1.00 g, 4.29×10^{-3} mol), 4-*tert*-butylcyclohexanol (1.34 g, 8.58×10^{-3} mol), Zn powder (0.56 g, 8.58×10^{-3} mol) and a catalytic amount of I_2 in toluene (30 mL). ^{1}H NMR: (300 MHz, $CDCl_3$) δ (ppm): 0.83 (s, 18H, $2 \times C(CH_3)_3$), 1.07 (m, 2H, $2 \times (CH_3)_3CH$), 1.19 (m, 4H, $2 \times CHCH_2CH$), 1.58 (m, 4H, $2 \times CH_2$), 1.77 (m, 2H, $2 \times CH_2$), 2.02 (s, 4H, $2 \times CH_2$), 3.46 (s, 4H, $2 \times C(=O)CH_2C(=O)$), 3.64 (m, 20H, $5 \times OCH_2CH_2O$), 4.11 (s, 2H, $2 \times OCH$), 4.20 (s, 4H, $2 \times CH_2OCH_2C(=O)$). ^{13}C NMR (76.6 MHz, $CDCl_3$) δ (ppm): 26.11 ($2 \times (CH_3)_3CH$), 27.33 ($4 \times (CH_3)_3CH$), 30.35 ($2 \times CH_2$), 31.84 ($2 \times CH_2$), 46.08 ($2 \times CH_2$), 47.34 ($2 \times C(=O)CH_2C(=O)$), 50.68 ($2 \times OCH$), 65.75 ($2 \times CH_2$), 70.90 ($5 \times OCH_2CH_2O$), 72.64 ($2 \times CHO$), 76.23 ($2 \times OCH_2C(=O)$), 166.53 ($2 \times CH_3OC(=O)$), 206.94 ($2 \times CH_2C(=O)$). μ_{max}: 1116, 1460, 1721, 2955, 3431 cm^{-1}. Found: HRMS m/z 737.442976 $(M+Na)^+$. $C_{38}H_{66}O_{12}Na$ requires 737.444649, $\Delta = 2.27$ ppm.

4.20. Bis(1-(1,3,5-trimethylbenzyl)-ethyl)-5,8,11,14,17,20-hexaoxa-3,22-dioxo-tetracosadianoate (38)

The transesterification of **38** was performed according to the method described above. Toluene (30 mL), Zn powder (0.36 g, 5.54×10^{-3} mol), **48** (1.29 g, 2.77×10^{-3} mol) and 1-(2,4,6-trimethylphenyl)-ethanol (1.00 g, 6.09×10^{-3} mol) gave **38** after chromatography over silica gel (1:1 EtOAc/CH_2Cl_2) as a pale brown liquid (1.54 g, 76%). ^{1}H NMR: (300 MHz, $CDCl_3$) δ (ppm): 1.56 (d, 6H, $2 \times CH_3CH$), 2.23 (m, 18H, $6 \times CCH_3$), 3.48 (s, 4H, $2 \times C(=O)CH_2C(=O)$), 3.65 (m, 20H, $5 \times OCH_2CH_2O$), 4.16 (s, 4H, $2 \times CH_2OCH_2C(=O)$), 6.31 (q, 2H, $2 \times CHCH_3$), 6.80 (s, 4H, $4 \times ArH$). ^{13}C NMR (76.6 MHz, $CDCl_3$) δ (ppm): 19.39 ($4 \times ArCH_3$), 20.28 ($2 \times ArCH_3$), 45.84 ($2 \times C(=O)CH_2C(=O)$), 61.62 ($2 \times CHCH_3$), 70.49 ($5 \times OCH_2CH_2O$), 76.13 ($2 \times OCH_2C(=O)$), 129.90 ($4 \times CH$), 133.64 ($4 \times CH_3C$), 135.82 ($2 \times CH_3C$), 137.09 ($2 \times CCH$), 166.18 ($2 \times CH_3OC(=O)$), 201.73 ($2 \times CH_2C(=O)$). μ_{max}: 1109, 1452, 1724, 2874, 3482 cm^{-1}. Found: HRMS m/z 753.383791 $(M+Na)^+$. $C_{40}H_{58}O_{12}Na$ requires 753.382148, $\Delta = 2.18$ ppm.

4.21. Bis(1-(1,3,5-triisopropylbenzyl)-ethyl)-5,8,11,14,17,20-hexaoxa-3,22-dioxo-tetracosadianoate (39)

The use of **48** (0.43 g, 9.14×10^{-4} mol), Zn powder (0.12 g, 1.83×10^{-3} mol), 1-(2,4,6-triisopropylphenyl)-ethanol (0.50 g, 2.01×10^{-3} mol) and a catalytic quantity of iodine in toluene (20 mL) according to the method described above, followed by chromatography over silica gel (1:1 EtOAc/CH_2Cl_2) gave **39** as a dark orange liquid in 54% yield (0.44 g). ^{1}H NMR: (300 MHz, $CDCl_3$) δ (ppm): 1.21 (d, 36H, $2 \times CH_3CH$), 1.65 (d, 6H, $2 \times CHCH_3$), 2.82 (septet, 6H, $6 \times (CH_3)_2CH$), 3.49 (s, 4H, $2 \times C(=O)CH_2C(=O)$), 3.64 (m, 20H, $5 \times OCH_2CH_2O$), 4.18 (s, 4H, $2 \times CH_2OCH_2C(=O)$), 6.56 (q, 2H, $2 \times CHCH_3$), 7.00 (s, 4H, $4 \times ArH$). ^{13}C NMR (76.6 MHz, $CDCl_3$) δ (ppm): 21.98 ($2 \times CHCH_3$), 23.77 ($12 \times CH_3CHAr$), 33.96 ($6 \times CH_3CHAr$), 46.05 ($2 \times C(=O)CH_2C(=O)$), 62.65 ($2 \times CHCH_3$), 69.46 ($5 \times OCH_2CH_2O$), 76.16 ($2 \times OCH_2C(=O)$), 128.22 ($4 \times CH$), 131.50

($4\times CH_3C$), 148.19 ($6\times CH_3C$), 166.38 ($2\times CH_3OC(=O)$), 201.66 ($2\times CH_2C(=O)$). μ_{max}: 1106, 1608, 1651, 1724, 2958, 3501 cm^{-1}. Found: HRMS *m/z* 921.570555 $(M+Na)^+$. $C_{46}H_{73}O_{12}Na$ requires 921.569849, $\Delta =$ 0.80 ppm.

4.22. Bis(2-propyl)-5,8,11,14,17,20-hexaoxa-3,22-dioxo-tetracosadianato barium (II) (**6**)

Barium hydride (0.25 g, 1.76×10^{-3} mol) was added to a solution of **34** (0.80 g, 1.41×10^{-3} mol) in dry THF (70 mL) and the resulting mixture was heated to reflux overnight. Excess BaH_2 was filtered off, and the solvent removed in vacuo. Hexane (30 mL) was added to the residue, causing **6** to precipitate out as a tan powder in 65% yield. ^1H NMR: (300 MHz, $CDCl_3$) δ (ppm): 1.24 (d, 12H, $2\times CH_3CH$), 3.64 (br s, 20H, $5\times OCH_2CH_2O$), 4.63 (s, 2H, $2\times C(=O)CHC(=O)$), 4.94 (s, 4H, $2\times CH_2OCH_2C(=O)$), 5.06 (heptet, 2H, $2\times CH_3CH$). ^{13}C NMR (76.6 MHz, $CDCl_3$) δ (ppm): 21.91 ($4\times CH_3$), 46.23 ($2\times C(=O)CH_2C(=O)$), 68.65 ($2\times CH_3CH$)), 70.48 ($5\times OCH_2CH_2O$), 76.06 ($2\times OCH_2C(=O)$), 166.50 ($2\times CH_3OC(=O)$), 202.10 ($2\times CH_2C(=O)$). μ_{max}: 1450, 1645, 2960, 3440 cm^{-1}. Found: HRMS *m/z* 659.164837 (M^+). $C_{24}H_{40}O_{12}Ba$ requires 659.164596, $\Delta = 0.40$ ppm.

4.23. Bis(methyl)-5,8,11,14,17,20,23-heptaoxa-3,27-dioxo-hexacosadianato strontium (II) (**50**)

This pale yellow solid was isolated in a manner similar to that of **6**, with **49** (0.33 g, 6.46×10^{-4} mol) and $Sr(O^iPr_2)_2$ (0.20, 9.71×10^{-4} mol) being employed as reactants in 30 mL THF (0.35 g, 91%). ^1H NMR: (300 MHz, $CDCl_3$) δ (ppm): 3.48 (s, 6H, $2\times OCH_3$), 3.61 (br s, 24H, $6\times OCH_2CH_2O$), 3.65 (s, 2H, $2\times C(=O)CHC(=O)$), 4.37 (s, 4H, $2\times CH_2OCH_2C(=O)$). ^{13}C NMR (76.6 MHz, $CDCl_3$) δ (ppm): 25.51 ($2\times OCH_3$), 49.45 ($2\times(C(=O)CHC(=O))$), 70.38 ($6\times OCH_2CH_2O$), 76.52 ($2\times CH_2OCH_2C(=O)$), 170.01 ($2\times CH_3OC(=O)$), 184.87 ($2\times CH_2C(=O)$). μ_{max}: 1111, 1438, 1660, 2930, 3423 cm^{-1}. Found, HRMS *m/z* 619.111404 $(M+Na)^+$. $C_{22}H_{36}O_{13}SrNa$ requires 619.110505, $\Delta = 1.4$ ppm.

4.24. Bis(methyl)-5,8,11,14,17,20-hexaoxa-3,22-dioxo-tetracosadianato strontium (II) (**51**)

By adapting the method described for **50**, reaction of $Sr(O^iPr)_2$ (0.30 g, 1.46×10^{-3} mol)) and **48** (0.50 g, 1.07×10^{-3} mol) afforded 0.46 g of **51** (0.45 g, 78%) as a tan solid. ^1H NMR: ($CDCl_3$) δ (ppm): 3.48 (s, 6H, $2\times OCH_3$), 3.63 (br s, 24H, $6\times OCH_2CH_2O$), 3.68 (s, 2H, $2\times C(=O)CHC(=O)$), 4.41 (s, 4H, $2\times CH_2OCH_2C(=O)$). ^{13}C NMR (76.6 MHz, $CDCl_3$) δ (ppm): 25.42 ($2\times OCH_3$), 49.63 ($2\times(C(=O)CHC(=O))$), 70.89 ($6\times OCH_2CH_2O$), 76.69 ($2\times CH_2OCH_2C(=O)$), 168.31 ($2\times CH_3OC(=O)$), 183.45 ($2\times CH_2C(=O)$). μ_{max}: 1103, 1451, 1645, 2932, 3421 cm^{-1}. Found, HRMS *m/z* 553.102597 $(M+H)^+$. $C_{20}H_{33}O_{12}Sr$ requires 553.103765, $\Delta = 2.10$ ppm.

4.25. Bis(2-propyl)-5,8,11,14,17,20-hexaoxa-3,22-dioxo-tetracosadianato strontium (II) (**42**)

This tan solid was prepared from **34** (0.50 g, 8.6×10^{-4} mol), $Sr(O^iPr_2)_2$ (0.25 g, 1.21×10^{-3} mol) and THF (30 mL) in a manner similar to that for other metal complexes described above (0.48 g, 83%). ^1H NMR: (300 MHz, $CDCl_3$) δ (ppm): 1.21 (d, 12H, $2\times CH_3CH$), 3.64 (br s, 20H, $5\times OCH_2CH_2O$), 4.61 (s, 2H, $2\times C(=O)CHC(=O)$), 4.87 (s, 4H, $2\times CH_2OCH_2C(=O)$), 5.12 (heptet, 2H, $2\times CH_3CH$). ^{13}C NMR (76.6 MHz, $CDCl_3$) δ (ppm): 21.86 ($4\times CH_3$), 46.27 ($2\times C(=O)CH_2C(=O)$), 68.91 ($2\times CH_3CH$)), 70.48 ($5\times OCH_2CH_2O$), 76.12 ($2\times OCH_2C(=O)$), 166.93 ($2\times CH_3OC(=O)$), 201.45 ($2\times CH_2C(=O)$). μ_{max}: 1115, 1450, 1654, 2955, 3469 cm^{-1}. Found: HRMS *m/z* 609.165994 (M^+). $C_{24}H_{40}O_{12}Sr$ requires 609.166543, $\Delta = 1.00$ ppm.

4.26. Bis(4-tert-butylcyclohexyl)-5,8,11,14,17,20-hexaoxa-3,22-dioxo-tetracosadianato strontium (II) (**45**)

Reaction of $Sr(O^iPr_2)_2$ (0.30 g, 1.45×10^{-3} mol) and **37** (0.80 g, 1.08×10^{-3} mol) in THF (30 mL) afforded **45** as a pale brown solid (0.83 g, 96%). ^1H NMR: (300 MHz, $CDCl_3$) δ (ppm): 0.85 (s, 18H, $2\times C(CH_3)_3$), 1.11 (m, 2H, $2\times(CH_3)_3CH$), 1.23 (m, 4H, $2\times CHCH_2CH$), 1.51 (m, 4H, $2\times CH_2$), 1.77 (m, 2H, $2\times CH_2$), 2.03 (s, 4H, $2\times CH_2$), 3.67 (m, 20H, $5\times OCH_2CH_2O$), 4.11 (s, 2H, $2\times OCH$), 4.26 (s, 4H, $2\times CH_2OCH_2C(=O)$), 5.09 (s, 2H, $2\times C(=O)CHC(=O)$). ^{13}C NMR (76.6 MHz, $CDCl_3$) δ (ppm): 26.12 ($2\times(CH_3)_3CH$), 27.51 ($4\times(CH_3)_3CH$), 30.35 ($2\times CH_2$), 31.87 ($2\times CH_2$), 46.11 ($2\times CH_2$), 47.39 ($2\times C(=O)CHC(=O)$), 50.68 ($2\times OCH$), 65.83 ($2\times CH_2$), 70.97 ($5\times OCH_2CH_2O$), 72.17 ($2\times CHO$), 76.51 ($2\times OCH_2C(=O)$), 166.51 ($2\times CH_3OC(=O)$), 207.35 ($2\times CH_2C(=O)$). μ_{max}: 1107, 1465, 1721, 2930, 3432 cm^{-1}. Found: HRMS *m/z* 801.343300 $(M+H)^+$. $C_{38}H_{65}O_{12}Sr$ requires 801.354750, $\Delta = 14.00$ ppm.

4.27. Bis(methyl)-5,8,11,14,17,20-hexaoxa-3,22-dioxo-tetracosadianato calcium (II) (**52**)

Compound **52** was isolated as a tan solid from **48** (0.50 g, 1.07×10^{-3} mol), CaH_2 (0.10 g, 2.20×10^{-3} mol) and THF (30 mL) in 78% yield (0.42 g). ^1H NMR: (300 MHz, $CDCl_3$) δ (ppm): 3.31 (s, 6H, $2\times OCH_3$), 3.48 (s, 2H, $2\times C(=O)CHC(=O)$), 3.63 (br s, 20H, $5\times OCH_2CH_2O$), 4.55 (s, 4H, $2\times CH_2OCH_2C(=O)$). ^{13}C NMR (76.6 MHz, $CDCl_3$) δ (ppm): 25.55 ($2\times OCH_3$), 49.45 ($2\times(C(=O)CHC(=O))$), 69.22 ($6\times OCH_2CH_2O$), 74.22 ($2\times CH_2OCH_2C(=O)$), 170.11 ($2\times CH_3OC(=O)$), 183.56 ($2\times CH_2C(=O)$). μ_{max}: 1455, 1621, 2937, 3450 cm^{-1}. Found: HRMS *m/z* 544.113984 $(M+Ca)^+$. $C_{20}H_{32}O_{12}Ca_2$ requires 544.114558, $\Delta = 1.05$ ppm.

4.28. Bis(4-tert-butylcyclohexyl)-5,8,11,14,17,20-hexaoxa-3,22-dioxo-tetracosadianato calcium (II) (**44**)

Compound **44** was isolated from **37** (0.81 g, 1.10×10^{-3} mol), CaH_2 (0.10 g, 2.20×10^{-3} mol) and THF (30 mL). The material was washed twice with heptane to deliver a pale brown solid (0.63 g, 72%). ^{1}H NMR: (300 MHz, $CDCl_3$) δ (ppm): 0.85 (s, 18H, $2\times C(CH_3)_3$), 1.09 (m, 2H, $2\times(CH_3)_3CH$), 1.21 (m, 4H, $2\times CHCH_2CH$), 1.47 (m, 4H, $2\times CH_2$), 1.77 (m, 2H, $2\times CH_2$), 1.99 (s, 4H, $2\times CH_2$), 3.70 (m, 20H, $5\times OCH_2CH_2O$), 4.11 (s, 2H, $2\times OCH$), 4.29 (s, 4H, $2\times CH_2OCH_2C(=O)$), 5.03 (s, 2H, $2\times C(=O)CHC(=O)$). ^{13}C NMR (76.6 MHz, $CDCl_3$) δ (ppm): 26.12 ($2\times(CH_3)_3CH$), 27.49 ($4\times(CH_3)_3CH$), 30.36 ($2\times CH_2$), 31.88 ($2\times CH_2$), 46.12 ($2\times CH_2$), 47.28 ($2\times C(=O)CHC(=O)$), 50.32 ($2\times OCH$), 65.71 ($2\times CH_2$), 71.23 ($5\times OCH_2CH_2O$), 72.17 ($2\times CHO$), 76.49 ($2\times OCH_2C(=O)$), 166.51 ($2\times CH_3OC(=O)$), 203.55 ($2\times CH_2C(=O)$). μ_{max}: 1107, 1455, 1726, 2928, 3451 cm^{-1}. Found: HRMS m/z $(M+Ca)^{2+}$ 396.181644. $C_{38}H_{64}O_{12}Ca_2$ requires 396.181932, $\Delta=-0.80$ ppm.

4.29. Bis(2-propyl)-5,8,11,14,17,20-hexaoxa-3,22-dioxo-tetracosadianato calcium (II) (**41**)

This yellow powder (0.65 g, 77%) was isolated from **34** (0.80 g, 1.5×10^{-3} mol), CaH_2 (0.10 g, 2.34×10^{-3} mol) and THF (70 mL). ^{1}H NMR: ($CDCl_3$) δ (ppm): 1.26 (d, 12H, $2\times CH_3CH$), 3.65 (m, 20H, $10\times OCH_2$), 4.11 (s, 2H, $2\times C(=O)CHC(=O)$), 4.85 (s, 4H, $2\times CH_2OCH_2C(=O)$), 4.98 (heptet, 2H, $2\times CH_3CH$). ^{13}C NMR ($CDCl_3$) δ (ppm): 21.71 ($4\times CH_3$), 47.11 ($2\times C(=O)CH_2C(=O)$), 67.85 ($2\times CH_3CH$)), 69.88 ($5\times OCH_2CH_2O$), 71.84 ($2\times OCH_2C(=O)$), 172.84 ($2\times CH_3OC(=O)$), 202.29 ($2\times CH_2C(=O)$). μ_{max}: 1111, 1467, 1731, 2930, 3449 cm^{-1}. Found, HRMS m/z 300.087342 $(M+Ca)^{2+}$. $C_{24}H_{40}O_{12}Ca_2$ requires 300.088032, $\Delta=-2.30$ ppm.

4.30. Bis-(methyl)-5,8,11,14,17,-pentaoxa-3,19-dioxo-unacosadianoate (**53**)

A similar procedure to that employed for **48** was employed [47], using methyl 4-bromo-3-oxobutanoate (22.10 g, 1.13×10^{-1} mol), tetraethylene glycol (11.02 g, 5.68×10^{-2} mol), 1,2-dimethoxyethane (200 mL) and sodium hydride (5.46 g, 2.26×10^{-1} mol) delivering 15.09 g of a viscous brown liquid (63%). ^{1}H NMR: (300 MHz, $CDCl_3$) δ (ppm): 3.52 (s, 4H, $2\times C(=O)CH_2C(=O)$), 3.62 (m, 16H, $4\times OCH_2CH_2O$), 3.70 (s, 6H, $2\times OCH_3$), 4.16 (s, 4H, $2\times CH_2OCH_2C(=O)$). ^{13}C NMR (76.6 MHz, $CDCl_3$) δ (ppm): 45.48 ($2\times C(=O)CH_2C(=O)$), 52.21 (OCH_3), 70.20 ($4\times OCH_2CH_2O$), 76.11 ($2\times OCH_2C(=O)$), 167.43 ($2\times CH_3OC(=O)$), 201.86 ($2\times CH_2C(=O)$). μ_{max}: 1107, 1710, 2865, 3421 cm^{-1}. Found: HRMS m/z 445.167998 $(M+Na)^+$. $C_{18}H_{30}O_{11}Na$ requires 445.168031, $\Delta=0.10$ ppm.

4.31. Bis(2-propyl)-5,8,11,14,17-pentaoxa-3,19-dioxo-unacosadianoate (**33**)

Zn powder (1.69 g, 2.60×10^{-2} mol), **53** (5.0 g, 1.20×10^{-2} mol), isopropanol (15 mL), I_2 (0.01 g) and toluene (30 mL) were refluxed for three days. A work up procedure similar to that for other transesterifications described above afforded a free flowing orange liquid **33** (4.60 g, 78%). ^{1}H NMR: (300 MHz, $CDCl_3$) δ (ppm): 1.24 (d, 12H, $4\times CH_3CH$), 3.48 (s, 4H, $2\times C(=O)CH_2C(=O)$), 3.63 (m, 16H, $4\times OCH_2CH_2O$), 4.18 (s, 4H, $2\times CH_2OCH_2C(=O)$), 5.05 (septet, 2H, $2\times CH_3CH$). ^{13}C NMR (76.6 MHz, $CDCl_3$) δ (ppm): 21.68 ($4\times CH_3$), 46.08 ($2\times C(=O)CH_2C(=O)$), 67.58 ($2\times CH_3CH$)), 70.51 ($5\times OCH_2CH_2O$), 76.93 ($2\times OCH_2C(=O)$), 166.49 ($2\times CH_3OC(=O)$), 201.93 ($2\times CH_2C(=O)$). μ_{max}: 1115, 1718, 2933, 3543 cm^{-1}. Found: HRMS m/z 501.230143 $(M+Na)^+$. $C_{22}H_{38}O_{11}Na$ requires 501.230635, $\Delta=0.90$ ppm.

4.32. Bis(4-tert-butylcyclohexyl)-5,8,11,14,17-pentaoxa-3,19-dioxo-unacosadianoate (**36**)

A procedure similar to that above using **53** (5.00 g, 1.18×10^{-2} mol), 4-*tert*-butylcyclohexanol (4.06 g. 2.60×10^{-2} mol), Zn powder (1.69 g, 2.60×10^{-2} mol) and a catalytic amount of I_2 in toluene (30 mL), afforded a very thick viscous orange liquid (6.14 g, 75%). ^{1}H NMR: (300 MHz, $CDCl_3$) δ (ppm): 0.84 (s, 18H, $2\times C(CH_3)_3$), 1.17 (m, 2H, $2\times(CH_3)_3CH$), 1.26 (m, 4H, $2\times CHCH_2CH$), 1.78 (m, 4H, $2\times CH_2$), 1.99 (m, 2H, $2\times CH_2$), 2.14 (s, 4H, $2\times CH_2$), 3.45 (s, 4H, $2\times C(=O)CH_2C(=O)$), 3.67 (m, 16H, $4\times OCH_2CH_2O$), 4.11 (s, 2H, $2\times OCH$), 4.20 (s, 4H, $2\times CH_2OCH_2C(=O)$). ^{13}C NMR (76.6 MHz, $CDCl_3$) δ (ppm): 25.29 ($2\times(CH_3)_3CH$), 27.33 ($4\times(CH_3)_3CH$), 30.36 ($2\times CH_2$), 32.40 ($2\times CH_2$), 46.08 ($2\times CH_2$), 47.35 ($2\times C(=O)CH_2C(=O)$), 50.65 ($2\times OCH$), 65.73 ($2\times CH_2$), 70.19 ($4\times OCH_2CH_2O$), 71.01 ($2\times CHO$), 76.49 ($2\times OCH_2C(=O)$), 166.51 ($2\times CH_3OC(=O)$), 201.91 ($2\times CH_2C(=O)$). μ_{max}: 1117, 1463, 1725, 2970, 3451 cm^{-1}. Found: HRMS m/z 693.416948 $(M+Na)^+$. $C_{36}H_{62}O_{11}Na$ requires 693.418426, $\Delta=2.10$ ppm.

4.33. Bis(2-propyl)-5,8,11,14,17-pentaoxa-3,19-dioxo-unacosadianato calcium (II) (**40**)

To a solution of **33** (0.50 g, 1.04×10^{-3} mol) in THF (30 mL), freshly made $Ca(O^iPr)_2$ (0.20 g, 1.26×10^{-3} mol) was added. The resulting mixture was refluxed overnight, filtered, and the product precipitated from hexane (30 mL) to afford **40** as a pale brown solid (0.55 g, 50%). ^{1}H NMR: (300 MHz, $CDCl_3$) δ (ppm): 1.21 (d, 12H, $4\times CH_3CH$), 3.64 (m, 16H, $4\times OCH_2CH_2O$), 4.18 (s, 4H, $2\times CH_2OCH_2C(=O)$), 4.87 (s, 2H, $2\times C(=O)CHC(=O)$), 5.07 (septet, 2H, $2\times CH_3CH$). ^{13}C NMR (76.6 MHz, $CDCl_3$) δ (ppm): 21.73 ($4\times CH_3$), 47.21 ($2\times C(=O)CHC(=O)$), 67.55 ($2\times CH_3CH$), 70.55 ($5\times OCH_2CH_2O$),

76.93 ($2\times OCH_2C(=O)$), 166.49 ($2\times CH_3OC(=O)$), 201.95 ($2\times CH_2C(=O)$). μ_{max}: 1115, 1718, 2951, 3535 cm^{-1}. Found: HRMS *m/z* 536.170747 $(2M+Ca)^{2+}$. $C_{44}H_{72}O_{22}Ca_3$ requires 536.169012, $\Delta = 3.10$ ppm.

4.34. Bis(4-tert-butylcyclohexyl)-5,8,11,14,17-pentaoxa-3,19-dioxo-unacosadianato calcium (II) (**43**)

This compound was prepared in a manner similar to that for **40** using **36** (0.50 g, 7.45×10^{-4} mol), THF (30 mL), $Ca(O^iPr)_2$ (0.15 g, 9.47×10^{-4} mol) to afford **43** as a dark yellow powder (0.53 g, 68%). ^1H NMR: (300 MHz, $CDCl_3$) δ (ppm): 0.84 (s, 18H, $2\times C(CH_3)_3$), 1.15 (m, 2H, $2\times(CH_3)_3CH$), 1.28 (m, 4H, $2\times CHCH_2CH$), 1.78 (m, 4H, $2\times CH_2$), 1.99 (m, 2H, $2\times CH_2$), 2.19 (s, 4H, $2\times CH_2$), 3.49 (s, 2H, $2\times C(=O)CHC(=O)$), 3.71 (m, 16H, $4\times OCH_2CH_2O$), 4.10 (s, 2H, $2\times OCH$), 4.20 (s, 4H, $2\times CH_2OCH_2C(=O)$). ^{13}C NMR (76.6 MHz, $CDCl_3$) δ (ppm): 25.30 ($2\times(CH_3)_3CH$), 27.45 ($4\times(CH_3)_3CH$), 30.50 ($2\times CH_2$), 32.43 ($2\times CH_2$), 46.12 ($2\times CH_2$), 47.50 ($2\times C(=O)CH_2C(=O)$), 50.81 ($2\times OCH$), 65.73 ($2\times CH_2$), 70.21 ($4\times OCH_2CH_2O$), 71.01 ($2\times CHO$), 76.51 ($2\times OCH_2C(=O)$), 166.51 ($2\times CH_3OC(=O)$), 204.37 ($2\times CH_2C(=O)$). μ_{max}: 1111, 1465, 1710, 2965, 3451 cm^{-1}. Found: HRMS *m/z* 728.357415 $(2M+Ca)^{2+}$. $C_{72}H_{120}O_{22}Ca_3$ requires 728.356902, $\Delta = 0.70$ ppm.

References

[1] Y. Akishige, K. Fukano, Jpn. Kokai Tokkyo Koho (2004) 23 (Shimane University, Japan).
[2] W.W. Zhuang, W. Pan, B.D. Ulrich, J.J. Lee, L. Stecker, A. Burmaster, D.R. Evans, S.T. Hsu, M. Tajiri, A. Shimaoka, K. Inoue, T. Naka, N. Awaya, K. Sakiyama, Y. Wang, S.Q. Liu, N.J. Wu, A. Ignatiev, Technical Digest – International Electron Devices Meeting (2002) 193.
[3] H.G. Kwon, Y. Oh, J.W. Park, Y.K. Lee, C.G. Kim, Y. Kim, Mater. Res. Soc. Symp. Proc. 765 (2003) 115.
[4] C.S. Hwang, Surf. Eng. Series 2 (2001) 205.
[5] B.-R. Kim, S.-C. Hwang, H.-G. Lee, H.-S. Shin, Korean J. Chem. Eng. 17 (2000) 524.
[6] S.-W. Yang, Y.-S. Kim, H.-S. Shin, Kongop Hwahak 8 (1997) 589.
[7] Y. Mizushima, I. Hirabayashi, J. Mater. Res. 11 (1996) 2698.
[8] V. Burtman, M. Schieber, I. Brodsky, H. Hermon, Y. Yaroslavsky, J. Cryst. Growth 166 (1996) 832.
[9] D.C. Bradley, M. Hasan, M.B. Hursthouse, M. Motevalli, O.F.Z. Khan, R.G. Pritchard, J.O. Williams, J. Chem. Soc., Chem. Commun. (1992) 575.
[10] D.G. Gilliland, M.L. Hitchman, S.C. Thompson, D.J. Cole-Hamilton, J. Phys. III 2 (1992) 1381.
[11] N. Kuzmina, M. Ryazanov, S. Troyanov, Polyhedron 18 (1999) 2177.
[12] K. Timmer, K.I.M.A. Spee, A. Mackor, H.A. Meinema, A.L. Spek, P. Van der Sluis, Inorg. Chim. Acta 190 (1991) 109.
[13] H.D. Inerowicz, T.M. Chandrasekhar, G. Atkinson, R.L. White, Anal. Chim. Acta 289 (1994) 249.
[14] G. Malandrino, I.L. Fragala, D.A. Neumayer, C.L. Stern, B.J. Hinds, T.J. Marks, J. Mater. Chem. 4 (1994) 1061.
[15] T.J. Marks, J.A. Belot, C.J. Reedy, R.J. McNeely, D.B. Studebaker, D.A. Neumayer, C.L. Stern, J. Alloys Compd. 251 (1997) 243.
[16] J.A. Belot, D.A. Neumayer, C.J. Reedy, D.B. Studebaker, B.J. Hinds, C.L. Stern, T.J. Marks, Chem. Mater. 9 (1997) 1638.
[17] R. Gardiner, D.W. Brown, P.S. Kirlin, A.L. Rheingold, Chem. Mater. 3 (1991) 1053.
[18] D.A. Neumayer, D.B. Studebaker, B.J. Hinds, C.L. Stern, T.J. Marks, Chem. Mater. 6 (1994) 878.
[19] A.R. Teren, J.A. Belot, N.L. Edleman, T.J. Marks, B.W. Wessels, Chem. Vapor Depos. 6 (2000) 175.
[20] V.K. Khamylov, T.S. Pochekutova, B.I. Petrov, S.P. Lukina, G.K. Fukin, S.Y. Khorshev, Y.A. Kurskii, Dokl. Chem. 403 (2005) 132.
[21] N.P. Kuz'mina, I.E. Soboleva, V.A. Ketsko, S.I. Troyanov, Mendeleev Commun. (1999) 87.
[22] L. Huang, S.B. Turnipseed, R.C. Haltiwanger, R.M. Barkley, R.E. Sievers, Inorg. Chem. 33 (1994) 798.
[23] R.E. Sievers, S.B. Turnipseed, L. Huang, A.F. Lagalante, Coord. Chem. Rev. 128 (1993) 285.
[24] M. Motevalli, P. O'Brien, I.M. Watson, Polyhedron 15 (1996) 1865.
[25] W.A. Wojtczak, M.J. Hampden-Smith, E.N. Duesler, Inorg. Chem. 37 (1998) 1781.
[26] Y. Chi, S. Ranjan, T.-Y. Chou, C.-S. Liu, S.-M. Peng, G.-H. Lee, Dalton Trans. (2001) 2462.
[27] Y. Chi, S. Ranjan, P.-W. Chung, H.-Y. Hsieh, S.-M. Peng, G.-H. Lee, Inorg. Chim. Acta 334 (2002) 172.
[28] D.A. Neumayer, J.A. Belot, R.L. Feezel, C. Reedy, C.L. Stern, T.J. Marks, L.M. Liable-Sands, A.L. Rheingold, Inorg. Chem. 37 (1998) 5625.
[29] D.B. Studebaker, D.A. Neumayer, B.J. Hinds, C.L. Stern, T.J. Marks, Inorg. Chem. 39 (2000) 3148.
[30] J.A.P. Nash, S.C. Thompson, D.F. Foster, D.J. Cole-Hamilton, J.C. Barnes, J. Chem. Soc., Dalton Trans. (1995) 269.
[31] S.L. Castro, O. Just, W.S. Rees Jr., Angew. Chem. 39 (2000) 933.
[32] J.H. Lee, W.Y. Yang, S.W. Rhee, D. Kim, J. Phys. IV 11 (2001) Pr3/215.
[33] J.-H. Lee, M.-Y. Park, S.-W. Rhee, J. Vac. Sci. Technol. A 17 (1999) 3115.
[34] J.-H. Lee, S.-W. Rhee, J. Mater. Res. 14 (1999) 3988.
[35] J.-H. Lee, S.-W. Rhee, Electrochem. Solid-State Lett. 2 (1999) 510.
[36] D.L. Schulz, B.J. Hinds, D.A. Neumayer, C.L. Stern, T.J. Marks, Chem. Mater. 5 (1993) 1605.
[37] D.L. Schulz, B.J. Hinds, C.L. Stern, T.J. Marks, Inorg. Chem. 32 (1993) 249.
[38] D.B. Studebaker, Northwestern University, USA. FIELD URL: Northwestern University, 1999, p. 108.
[39] M.R. Hill, A.W. Jones, J.J. Russell, N.K. Roberts, R.N. Lamb, J. Mater. Chem. 14 (2004) 3198.
[40] A.J. Petrella, H. Deng, N.K. Roberts, R.N. Lamb, Chem. Mater. 14 (2002) 4339.
[41] G.A. Horley, M.F. Mahon, K.C. Molloy, P.W. Haycock, C.P. Myers, Inorg. Chem. 41 (2002) 5052.
[42] E.Y.M. Lee, N.H. Tran, J.J. Russell, R.N. Lamb, J. Phys. Chem. B 107 (2003) 5208.
[43] B. Ludolph, M.A. Malik, Chem. Commun. (Cambridge) (1998) 1849.
[44] H.J. Cristau, L. Chiche, F. Fallouh, P. Hullot, G. Renard, H. Christol, New J. Chem. 8 (1984) 191.
[45] A.P. King, C.G. Krespan, J. Org. Chem. 39 (1974) 1315.
[46] V. Wittmann, S. Takayama, K.W. Gong, G. Weitz-Schmidt, C.-H. Wong, J. Org. Chem. 63 (1998) 5137.
[47] R.M. Kellogg, T.J. Van Bergen, H. Van Doren, D. Hedstrand, J. Kooi, W.H. Kruizinga, C.B. Troostwijk, J. Org. Chem. 45 (1980) 2854.
[48] S.P. Chavan, K. Shivasankar, R. Sivappa, R. Kale, Tetrahedron Lett. 43 (2002) 8583.
[49] O.S. Mills, N.J. Mooney, P.M. Robinson, C.I.F. Watt, B.G. Box, J. Chem. Soc., Perkin Trans. 2 (1995) 697.
[50] A. Burger, G.E. Ullyot, J. Org. Chem. 12 (1947) 342.

Available online at www.sciencedirect.com
ScienceDirect
Polyhedron 26 (2007) 508–518
POLYHEDRON
www.elsevier.com/locate/poly

Base catalysed substitution reactions of octahedral cobalt(III) complexes: Mechanism switching by changing the leaving group

W. Gregory Jackson *, Alistair Dickie, Kerrina Wells

School of Physical, Environmental and Mathematical Sciences, Chemistry, UNSW@ADFA, The University of New South Wales, Australian Defence Force Academy, Canberra, ACT 2600, Australia

Received 22 April 2006; accepted 24 August 2006
Available online 3 September 2006

Abstract

The rates of base catalysed hydrolysis of six *asym*-$[Co(dmptacn)X]^{n+}$ and six *asym*-$[Co(dmpmetacn)X]^{n+}$ complexes ($X = Br^-$, NO_3^-, $MeSO_3^-$, $CF_3SO_3^-$, Me_2SO, SO_4^{2-}) have been studied to explore the role of the leaving group and the formal charge on these complex ions in determining the effective site of deprotonation, at one of the four distinct α-CH_2 pyridyl sites or at an NH centre. The work corroborates the new pseudo-aminate mechanism established for the chloro derivatives. Deuterium exchange and proton NMR experiments have shown that the site of deprotonation is leaving group dependent, the first time this long-standing speculative idea has been proven. This work has also shown that the effect of improving the leaving group can override rate limiting deprotonation to the point where NH deprotonation, via the normal S_N1CB mechanism, operates rather than the rate limiting pseudo-aminate mechanism. The steric course of substitution has been determined and the reaction via NH deprotonation, enforced by employing an exceptionally good leaving group such as the triflate ion, has uncovered a non-retentive pathway leading to the previously unknown (and unstable) *sym* isomeric product. The steric course of substitution is shown to be mechanism dependent. For reaction via α-CH_2 deprotonation, which of the two arms is utilised proved quite leaving group dependent, although the specific proton on a particular 'arm' was always the same, consistent with the requirements of this new mechanism.
© 2006 Elsevier Ltd. All rights reserved.

Keywords: Leaving group; Cobalt(III); Inorganic synthesis; Pseudo-aminate mechanism; Base hydrolysis; Pyridylamine ligands

1. Introduction

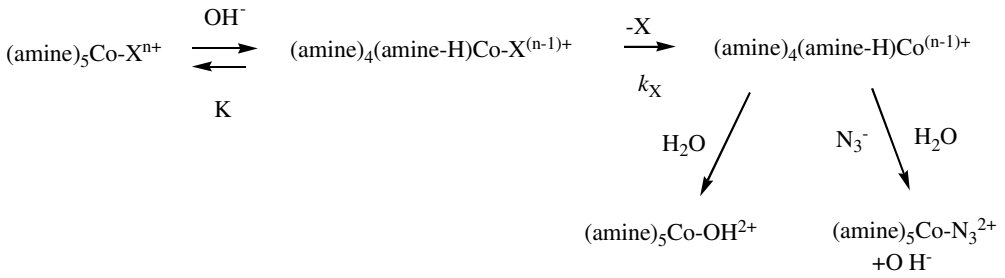
When a $[(amine)_5CoX]^{n+}$ or $[(en)_2ACoX]^{n+}$ species is reacted in aqueous base containing a competing nucleophile such as N_3^-, both hydroxo and azido products are formed [1,2]. The relative amounts, and their stereochemistry, are closely independent of the nature of the leaving group [3–6], consistent with a mechanism that does not involve X at the product determining stage (Scheme 1).

Careful product distribution studies, however, have shown a slight but real dependence on the nature of X (and its charge) [7,8]. This has been interpreted in terms of a very short-lived five coordinate intermediate, in which X remains present in the ionic atmosphere; others believe there are no intermediates [8]. Another explanation is that base hydrolysis proceeds not by NH deprotonation at a single site but rather at multiple sites, in which case the relative rates of the alternative processes depend upon the leaving group X even if genuine pentacoordinate intermediates are involved, and the product distribution will accordingly reveal a leaving group dependence.

One approach to the resolution of this problem has been the design of complexes that bear a single NH centre [3,9]. This led to the examination of the *asym*-$[Co(dmptacn)Cl]^{2+}$ ion [10] and earlier [11] the *asym*-$[Co(dmpmetacn)Cl]^{2+}$ derivative (Figs. 1 and 2). Remarkably, for both ions base catalysed substitution of Cl^- was found to occur via deprotonation at an α-CH_2 centre, even for the dmptacn complex which bears a potentially deprotonatable NH site. Moreover, deprotonation proved to be rate limiting. Since normal base hydrolysis involves the cleavage of the

* Corresponding author.
E-mail address: wgj@adfa.edu.au (W.G. Jackson).

0277-5387/$ - see front matter © 2006 Elsevier Ltd. All rights reserved.
doi:10.1016/j.poly.2006.08.021



Scheme 1. The 'normal' S_N1CB mechanism for base catalysed substitution.

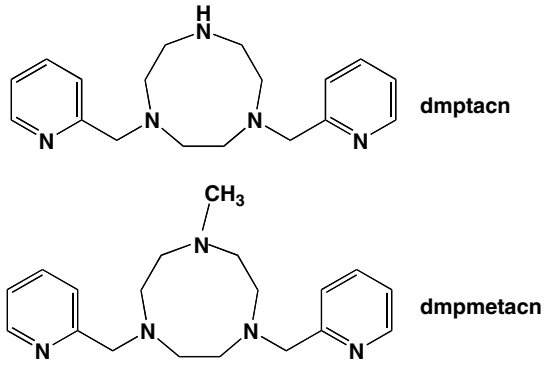


Fig. 1. Ligand structures.

metal-leaving group bond as the rate determining step, it was reasoned that improving the leaving group could force the *asym*-$[Co(dmptacn)X]^{n+}$ complex to base hydrolyse via the normal S_N1CB process, i.e., through deprotonation at NH rather than at the $-CH_2-$ centre.

Herein, we report the base hydrolysis kinetics, proton exchange experiments and product distributions for the reactions of a range of *asym*-$[Co(dmptacn)X]^{n+}$ and *asym*-$[Co(dmpmetacn)X]^{n+}$ complexes ($X = Cl^-$, Br^-, NO_3^-, SO_4^{2-}, Me_2SO, $CH_3SO_3^-$, $CF_3SO_3^-$) to explore the role of the leaving group in controlling the effective site of deprotonation in base catalysed substitution.

2. Experimental

All chemicals were AnalaR or an equivalent grade. Carbon-13 and proton NMR spectra were recorded with a Varian Unity Plus 400 MHz instrument at 20 °C. Solvents used were D_2O with dioxane as the internal reference (^{13}C, δ 69.27 relative to NaDSS), and Me_2SO-d_6 with the central peak of the CD_3 septet as the reference (^{13}C, δ 39.37 relative to $SiMe_4$). Full visible absorption spectra and absorbance–time traces were recorded with a HP8453 diode array vis–UV spectrophotometer thermostated to 25.00 ± 0.05 °C with use of a Lauda RM6 circulating water bath. Cation exchange media used were Dowex 50Wx2 (H^+ form, 200–400 mesh; Biorad) and SP-Sephadex C25 (Na^+ form; Pharmacia). Carbon dioxide free Milli-Q water was used for all physical measurements.

2.1. Complexes

The dmptacn and dmpmetacn complexes were prepared by identical methods as now described for dmptacn. The methyl ligand derivatives tended to be less water soluble. The complexes were characterised by elemental analyses (Table 1S), ^1H (Table 2S) and ^{13}C (Table 3S) NMR, and visible–UV (Table 4S) spectroscopy.

2.1.1. Asym-[Co(dmptacn)Cl](ClO4)2 and asym-[Co(dmptacn)OH2](ClO4)3

These were prepared and characterised as described previously [11]. The chloro complexes were converted to Cl^- salts by ion exchange on Dowex 50WX2 (H^+ form, 200–400 mesh) using a 0.1 M HCl wash, elution with 4 M HCl and rota-evaporation to dryness.

2.1.2. Asym-[Co(dmptacn)OS(CF3)O2](ClO4)2

Asym-[Co(dmptacn)Cl]Cl_2 (5 g) added slowly to neat CF_3SO_3H (25 mL; MMM Co., or Aldrich) was heated on

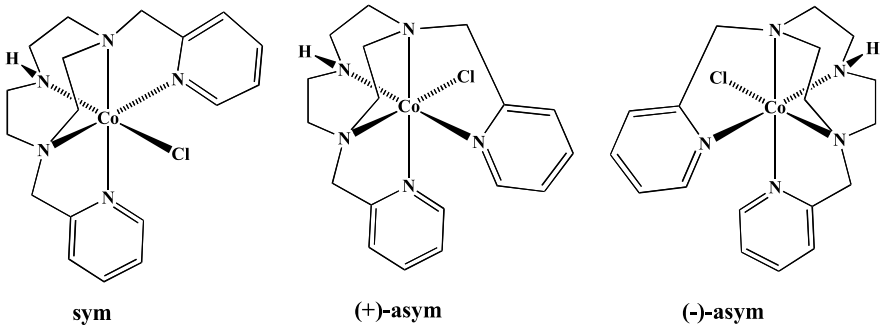


Fig. 2. The two geometric isomers of $[Co(dmptacn)Cl]^{2+}$, showing the enantiomers of the *asym* form.

a steam bath for 2 h while gently purging with dry N_2. The cooled product mixture was slowly poured into ice cold ether (800 mL), while well stirred. The resultant pink–orange solid was collected, washed with ether, dried and recrystallised from a minimum volume of water (ca. 20 °C) by filtering and diluting with a fifth volume of 5 M $HClO_4$ (50:50 ice/72% $HClO_4$). The crystals of *asym*-[Co(dmptacn)$OS(CF_3)O_2$]$(ClO_4)_2$ that deposited rapidly were collected, washed with ethanol and ether, and air dried. Yield: 7.2 g, 95%.

2.1.3. *Asym*-[Co(dmptacn)Br]$(ClO_4)_2$

This was prepared by heating *asym*-[Co(dmptacn)OH_2]$(ClO_4)_3$ (1 g) or *asym*-[Co(dmptacn)$OS(CF_3)O_2$]$(ClO_4)_2$ (1.5 g) in HBr (48%, 15 mL) on a steam bath for 3 h. The product was crystallised directly through the addition of 72% $HClO_4$ (5 mL), and recrystallised to purity from water as described for the triflato complex. Yield: 85%.

2.1.4. *Asym*-[Co(dmptacn)OSO_3H]$ZnCl_4$

Asym-[Co(dmptacn)$OS(CF_3)O_2$]$(ClO_4)_2$ (1.5 g) was reacted at ambient temperature in H_2SO_4 (15 mL, 98%) for 5 days. The crude product was purified by dilution with ice (200 g), absorption on and elution (f M HCl) from Dowex. The first band was the 1 + sulfato species which was crystallised by rotaevaporation of the HCl at <40 °C. It was recrystallised from a minimum volume of water by adding a fifth volume of 2 M 'H_2ZnCl_4' (2 M $ZnCl_2$ in 5 M HCl) and careful addition of iso–propanol. The red-purple crystals were collected, washed with iso–propanol and ether and air dried. Yield: 65%.

2.1.5. *Asym*-[Co(dmptacn)$OSMe_2$]$(ClO_4)_3$

Asym-[Co(dmptacn)$OS(CF_3)O_2$]$(ClO_4)_2$ (1.5 g) was heated for 30 min in Me_2SO (15 mL) at 60 °C and then cooled and poured slowly into ether (300 mL) containing *iso*–propanol (20 mL). The crude pink *asym*-[Co(dmptacn)-$OSMe_2$]$^{3+}$ salt so obtained was recrystallised from water as the perchlorate, as described for the triflato complex. Yield: 90%.

2.1.6. *Asym*-[Co(dmptacn)$OS(CH_3)O_2$]$(ClO_4)_2$

This was prepared and purified as described for the Me_2SO complex but using neat CH_3SO_3H (20 mL; Aldrich) as solvent and a longer reaction time (3 h). Yield: 85%.

2.1.7. *Asym*-[Co(dmptacn)ONO_2]$(ClO_4)_2$

Finely divided *asym*-[Co(dmptacn)Cl]Cl_2 (1 g) was stirred in 5 M HNO_3 (20 mL), which had been saturated with $Hg(NO_3)_2$, for 4 days at ambient temperature. Perchloric acid (5 mL) was added to the resultant suspension, and the mixture chilled for several hours. The collected product was recrystallised from water as described for the triflato complex. Yield: 74%.

2.1.8. d_4-*Asym*-[Co(dmptacn)$OS(CF_3)O_2$]$(ClO_4)_2$

This was synthesised from the perdeuterated chloro complex d_4-*asym*-[Co(dmptacn)Cl]Cl_2 as described for the normal triflato species. There was no H/D exchange observed under the conditions.

2.2. Recovery

All these expensive ligand complexes were recovered after all the physical measurements by ion exchange on Dowex; digestion of the combined eluates (in 3–4 M HCl) in neat triflic acid, after removal of the HCl through rota-evaporation, converted everything cleanly to the triflato complex which was isolated as described above. The deuterated complexes required back exchanging in 1 M NaOH prior to this treatment.

2.3. Buffer solutions

The buffers employed consisted of ethanolamine (0.40 M) solutions that had been partly neutralized (0.1–0.9 equiv.) with HCl, with the ionic strength adjusted to 2.00 M with NaCl. They were diluted 1:1 for use. The pH determinations were performed as described previously [10].

2.4. Hydrolysis kinetics

The kinetics of base hydrolysis were measured in a series of ethanolamine buffers employed previously [11,10,12] and also in NaOH/NaCl ($I = 1.0$ M) at 25.00 ± 0.05 °C. Spectrophotometric data were collected as full spectra (650–300 nm) versus time, in triplicate, and analysed as described previously. Sharp isosbestic points were observed for all reactions. Runs were performed in triplicate and at several pH values, and the results k(obsd)/[OH^-] averaged to provide k_{OH} data. The first order rates of acid hydrolysis were determined spectrophotometrically for the two triflate complexes in 0.1 M CF_3SO_3H by well established methods. Sharp isosbestic points were observed at 395, 440 and 544 nm for the base hydrolysis of *asym*-[Co(dmpmetacn)-$OS(CF_3)O_2$]$^{2+}$, and at 438 and 503 nm for acid hydrolysis. For the *asym*-[Co(dmptacn)$OS(CF_3)O_2$]$^{2+}$ complex in acid hydrolysis, the isosbestic points in acid were similar, at 432 and 504 nm.

2.5. Proton exchange

Samples (0.10 g) of [Co(dmptacn)X]$(ClO_4)_n$ and [Co-(dmpmetacn)X]$(ClO_4)_n$ ($X = CF_3SO_3^-, Me_2SO, CH_3SO_3^-$) were reacted in D_2O/0.1 M NaOD (20 mL) for ca. 3 s at 25 °C using an inverted Y-tube method (thermally pre-equilibrated Co in 10 mL of D_2O in one arm, 10 mL of 0.2 M NaOD in the other) and then rapidly acid quenched with 1 M $HClO_4$ (10 mL). Product (*asym*-[Co(dmptacn)-OH_2]$(ClO_4)_3$ or *asym*-[Co(dmpmetacn)OH_2]$(ClO_4)_3$) and recovered reactant were separated and isolated as described previously [11], and their ^1H and ^{13}C NMR spectra were recorded in Me_2SO-d_6. For several of the complexes the reactant was completely consumed and only the product (*asym–sym*-OH) was isolatable, as the aqua complex

mixture. In some cases the aqua product was converted back to the chloro species in hot HCl (4 h, 90 °C), or more conveniently by solid state anation (125 °C, 1 h) of $[CoL(OH_2)]Cl_3$ obtained directly off the ion exchange column after rotaevaporation of the HCl (L = dmptach or dmpmetacn); control experiments established that there was no H/D exchange under either set of conditions. The materials so obtained were routinely recrystallised from water as the perchlorate salts.

Control experiments were conducted on samples of *asym*-$[CoL(OH_2)](ClO_4)_3$ reacted in D_2O/OD^- for identical time periods.

2.6. Steric course of substitution

This was determined for each reaction by NMR as described previously [10,11]. The product was *asym*-$[Co(dmptacn)OH]^{2+}$ or *asym*-$[Codmpmetacn)OH]^{2+}$ in all cases, except for the reactions of the *asym*-$[Co(dmptacn)ONO_2]^{2+}$, *asym*-$[Co(dmptacn)OSMe_2]^{3+}$ and *asym*-$[Co(dmptacn)O_3SCF_3]^{2+}$ ions which, for the first time, revealed some *sym*-$[Co(dmptacn)OH]^{2+}$ product, Fig. 2,[1] clearly identified in both the ^1H and ^{13}C spectra as the component having exactly half the number of signals that the C_1 *asym* species showed.

3. Results and discussion

3.1. Syntheses

The *asym*-$[Co(dmptacn)X](ClO_4)_n$ and *asym*-$[Co(dmpmetacn)X](ClO_4)_n$ (X = Cl^-, OH_2) complexes have been fully characterised previously, through three X-ray structures and extensive 1D and 2D NMR studies [10,11,13]. There are two possible isomeric forms (Fig. 2) but until now only the *asym* form has been observed. The *asym* isomer is chiral; *asym*-$[Co(dmptacn)Cl]^{2+}$ has been optically resolved [10].

The remaining derivatives reported herein (X = $CF_3SO_3^-$, $CH_3SO_3^-$, NO_3^-, Me_2SO, Br^- and SO_4^{2-}) were synthesised by a range of established methods, with some modifications. The basic starting materials were the triflate complexes, made from the known [10,11] chloro derivatives (Cl^- salts) reacted in hot triflic acid. The isolated triflate complexes, as their triflate salts, were reacted in neat CH_3SO_3H, Me_2SO or H_2SO_4, or concentrated aqueous HBr, to give the corresponding substitution products [14], the last via anation of the first formed aqua complex [15]. The nitrato derivative was made by Hg(II) induced reaction of the chloro or bromo complex in strong NO_3^- media, analogously to the synthesis of related nitrato complexes [14]. Nitrato complexes have also been obtained by the solid state anation of the nitrate salts of the corresponding aqua species [1], or using the Ag^+ induced process for the chloro complex in strong HNO_3 [16].

3.2. Characterisation

All new compounds were analysed satisfactorily (some were hydrates; Table 1S, Supplementary data). The sulfato complexes, from aqueous 'H_2ZnCl_4', crystallised as their protonated forms which is unusual for bound sulfate, and likely reflects the propensity of $ZnCl_4^{2-}$ to selective crystallize 2+ cations. The ^1H and ^{13}C NMR spectra for all complexes (Tables 2S and 3S, Supplementary data) were clean, and indicative of the *asym* (C_1 symmetry) configuration, Fig. 2. There is the expected similarity amongst these spectra, and we note the NH resonance for the dmptacn compounds is quite X dependent. The essential characteristics of these spectra have been discussed in detail previously. The absorption maxima for the Vis–UV spectra are recorded in Table 4S, and again, they show the expected X dependence.

3.3. Acid hydrolysis of asym-$[Co(dmptacn)(OS(CF_3)O_2]^{2+}$ and asym-$[Co(dmpmetacn)(OS(CF_3)O_2)]^{2+}$

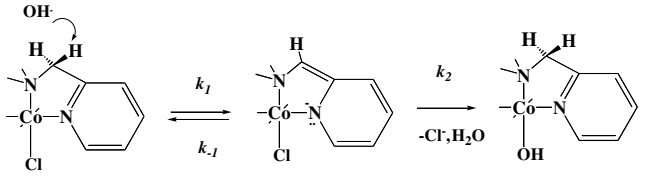
Since the discovery [15,17–20] and widespread use of the triflate ion $CF_3SO_3^-$ as a good leaving group in coordination chemistry, kinetic studies on the slower classic metal ion substitution systems, notably Cr(III), Os(III), Ru(III), Pt(IV), Co(III), Rh(III) and Ir(III), have shown that the metal-O(triflate) bond is acid hydrolysed rapidly, usually on the sec to min half-life time scale at 25 °C, and at a rate which is not especially metal ion dependent for the inert d^3 or d^6 electron configuration [7,15,17,18,21–26]. Many of these studies have involved the pentaammine complexes, $[M(NH_3)_5OS(CF_3)O_2]^{n+}$. The present study presents a quite different picture, with the *asym*-$[Co(dmptacn)OS(CF_3)O_2]^{2+}$ complex hydrolysing with a half-life of 6.9 h; the methyl-ligand derivative is even slower, $t_{1/2}$ 37 h, and clearly these rates are very slow by previously determined standards for a triflato complex. The $[Co(NH_3)_5OS(CF_3)O_2]^{2+}$ ion, for example [27,28], is 1000-fold more reactive than its dmptacn counterpart. As yet, there are no acid hydrolysis data for other leaving groups, within the tacn-derived pentadentate ligand systems, for further comparisons and analysis.

3.4. Base hydrolysis of asym-$[Co(dmpmetacn)X]^{2+}$

All seven dmpmetacn complexes must base hydrolyse by the recently discovered pseudo-aminate mechanism [11] since there are no NH protons available for the normal S_N1CB process. The origin of the base catalysis in these compounds is shown in Scheme 2.

A requirement of this mechanism is proton exchange at one of the four inequivalent α-pyridyl CH_2 protons during the act of base hydrolysis. This was demonstrated for the $[Co(dmpmetacn)Cl]^{2+}$ complex by showing that the

[1] The synthesis, characterization and kinetics of acid and base hydrolysis of the *sym* isomers will be reported separately.



Scheme 2. The pseudo-aminate mechanism for base catalysed substitution.

product for base hydrolysis in D_2O/OD^- had 1.0 D in the α-pyridyl methylenes, and that the *asym*-[Co(dmpmetacn)OD]$^{2+}$ product did not subsequently exchange at the α-CH_2 sites anywhere near rapidly enough to account for this [11]. Moreover, reactant recovered after about one $t_{1/2}$ of base hydrolysis contained negligible D, which showed that, once deprotonated, Cl^- loss was faster than reprotonation in the conjugate base intermediate ($k_2 \gg k_{-1}$; Scheme 2). This was a classic case of rate limiting deprotonation, confirmed by the large kinetic isotope effect observed (k_H/k_D ca. 4.5)

The specific rates of base hydrolysis for the seven *asym*-[Co(dmpmetacn)X]$^{n+}$ (and *asym*-[Co(dmptacn)X]$^{n+}$) complexes are presented in Table 1, along with the corresponding values [27–29] for the classic $[Co(NH_3)_5X]^{n+}$ ions. The simple pentaammine complexes clearly react via NH_3 deprotonation, although whether this is *cis*- or *trans*-X deprotonation is arguable; indeed, the deprotonation site may even be leaving group dependent. The order of reactivity is $CF_3SO_3^- > CH_3SO_3^- > Me_2SO > NO_3^- > Br^- > Cl^- > SO_4^{2-}$. For the dmpmetacn series of complexes, this order is largely retained, although the spread of values is much smaller. There are the 'slower' complexes, X = SO_4^-, Cl^- and Br^-, and the 'faster' reactants, X = NO_3^- and Me_2SO. The 'fastest' are the sulfonates, X = $CH_3SO_3^-$ and $CF_3SO_3^-$, and here there is an anomaly. The simple pentaammine complexes are more reactive, especially for the triflate ions where the rate difference exceeds 5000.

The rate comparison here is compounded by the fact that, in the pentaammine series, the deprotonation site is an NH_3 (*cis* or *trans* to the leaving group) [30,31], whereas for the dmpmetacn complexes, not only is the site of deprotonation different (at an α-pyridyl CH_2 centre), but the proton abstraction step is rate determining [11]. The variation in rate with leaving group therefore reflects the variation in acidity of the –CH_2-centre in question, whereas for the pentaammines, the observed k_{OH} value (=$k_X K$; Scheme 1) reflects both the acidity of the relevant NH_3 and the reactivity (k_X) of the conjugate base generated from it, which in turn is related to the Co–X bond strength for what are undoubtedly [5] dissociative reactions.

Sulfonates are known to enhance the acidity of *cis*-amines [32], and if the deprotonation site is at the *cis* ammine for the $[Co(NH_3)_5X]^{2+}$ complexes, as some believe [33], then this can account for the anomaly noted, with the (unsupported) assumption that the sulfonates do not affect the acidity of the α-pyridyl proton to the same extent. The other component of the anomaly is the Co–OS(CR)O_2 bond strength (R = CH_3 or CF_3). This bond has been regarded as generally weak, compared to that for other leaving groups under comparison, since in the acid hydrolysis reactions, also largely dissociative processes, the sulfonates are hydrolysed rapidly [23,24,27,28]. Consistent with this analysis, the *asym*-[Co(dmpmetacn)OS(CF_3)O_2]$^{2+}$ ion is extraordinarily unreactive in acid hydrolysis, with a $t_{1/2}$ of 37 h, compared to a $t_{1/2}$ of 29 s for [Co(NH_3)$_5$-OS(CF_3)O_2]$^{2+}$. We are, as yet, unsure of the origin of the relative inertness of the triflato complexes of the dmpmetacn and dmptacn ligands.

Table 1
Second-order rate constants (k_{OH}) for the base hydrolysis of *asym*-[Co(dmptacn)X]$^{n+}$, *asym*-[Co(dmpmetacn)X]$^{n+}$ and $[Co(NH_3)_5X]^{n+}$, I = 1.0 M (NaCl or $NaClO_4$), 25 °C

k_{OH} (M^{-1} s^{-1})				
X	dmptacn[a]	dmpmetacn[a]	k_{Me}/k_H	$(NH_3)_5$[b,e,f]
$CF_3SO_3^-$	1260 1135[c]	19.7	0.016	$>10^5$ (27000)
$CH_3SO_3^-$	3.0	6.7	2.25	55 (2000)
Me_2SO-*O*	4.2	16.7	4.0	5.5 (220)
NO_3^-	3.4	4.2	1.2	5.5 (240)
Br^-	0.25	1.6	6.4	1.4 (39)
Cl^-	0.040	0.70	17.5	0.23 (18)
SO_4^{2-}	0.084[d]	1.1[d]	13.1	0.049 (9)

[a] Ethanolamine/HCl/NaCl buffers, I = 1 M, except where noted otherwise.
[b] Data for $[Co(NH_3)_5X]^{n+}$; $NaClO_4$, 1 M.
[c] A.J. Dickie, Honours thesis, UNSW, 1995.
[d] NaOH/NaCl, I = 1 M.
[e] Values for 10^7 k_s are included in parentheses.
[f] Refs. [27–29].

3.5. Base hydrolysis of *asym*-[Co(dmptacn)X]$^{n+}$

The regular S_N1CB mechanism (Scheme 1), for which the deprotonation–reprotonation equilibrium is fast compared to the rate of loss of X from the conjugate base, leads to the rate expression, $k_{OH} = k_X \cdot K$. Note that K *may* be X dependent but k_X certainly is, and a rough guide to the X dependence of k_X values are the acid hydrolysis rates, shown in parenthesis in Table 1. These range from 2×10^{-2} s^{-1} for $CF_3SO_3^-$ to 9×10^{-7} s^{-1} for SO_4^{2-}, a factor of ca. 2×10^4. On the other hand, for a rate limiting deprotonation mechanism (Scheme 2), $k_{OH} = k_1$, where k_1 measures the rate of proton abstraction from an active α-CH_2 site, and this is not anticipated to be strongly X dependent. For the *asym*-[Co(dmptacn)Cl]$^{2+}$ complex, the data suggested that reaction via the NH centre was negligible, perhaps at most 5% (i.e. >20:1 for the alternate reaction pathways). To switch this to, say, >1:20 would require an acceleratory factor of at least 400, for the NH over the CH deprotonation pathway. A change in the leaving group from Cl^- to $CF_3SO_3^-$ (10^4 based on k_s values, 10^6 based on k_{OH} values, Table 1) may have been sufficient to do this, but it was unlikely for any of the other leaving groups.

For the *asym*-[Co(dmptacn)X]$^{n+}$ series of complexes, the leaving group dependence of the k_{OH} values is not too dissimilar to that for the *asym*-[Co(dmpmetacn)X]$^{n+}$ series, with the dmpmetacn complexes being somewhat faster (1.2–18-fold). The glaring exception is the triflate complex of dmptacn, where the rate difference is 500-fold and in the reverse sense. Here clearly is the mechanism switch we were anticipating – from C–H deprotonation to N–H deprotonation. Indeed, the dmptacn triflato ion has close to the reactivity of the pentaammine analogue [21],[2] if one corrects for the intrinsic difference in Co-OS(CF_3)O_2 lability. The dmptacn complex is only 10-fold less reactive in base hydrolysis, but 1000-fold in acid hydrolysis, indicating that the triflate ion greatly enhances the acidity of the NH centre in the dmptacn complex (as it did for the CH centre in the dmpmetacn complex). In this sense the chemistry parallels that for other [32] [Co(pentaamine)OS(CF_3)O_2]$^{2+}$ ions.

3.6. Site of deprotonation

Previously we showed that only one particular CH proton was involved for the base catalysed hydrolysis of *asym*-[Co(dmpmetacn)Cl]$^{2+}$, and through extensive 1D and 2D NMR experiments we identified which was the one [11].

The deuteration experiments can show if the –CH– site of deprotonation varies, as the leaving group is varied, given that in the common *asym*-[Co(dmpmetacn)OH]$^{2+}$ product any differences in the CH_2 ^{1}H and ^{13}C signals would be clearly apparent, and we know [10,11] they are not scrambled amongst themselves in base.

It has been pointed out that the complex loses memory of the proton's origin because deprotonation of either proton in a particular 'arm' leads to the *same* conjugate base species, according to our pseudo-aminate mechanism [11]. Further, because the process is rate limiting, the leaving group is expelled before the conjugate base is reprotonated (Scheme 2). This means that, in OD^-/D_2O, the D can end up in one or other position (or both), irrespective of which proton was originally abstracted. By varying the leaving group this proposition can now be tested experimentally (vide infra).

For the *asym*-[Co(dmptacn)Cl]$^{2+}$ complex the situation was similar [10] except here the loss of Cl^- from the conjugate base was competitive in rate with the rate of reprotonation, leading to a reduced kinetic isotope effect but one nonetheless that was significant, k_H/k_D ca. 2.0. The D-labelling experiments for this system were thus equivocal. However, with improved leaving groups it proved possible to increase the rate of loss of leaving group from the conjugate base to the extent that reprotonation of the conjugate base was not competitive. The reactions could be quenched at much shorter reaction times so that the subsequent exchange in the (same) *asym*-[Co(dmptacn)OH]$^{2+}$ product was no longer an issue. On the other hand, the risk was that reaction via a NH deprotonation is increased since the leaving group is much improved.

We tested four additional dmptacn complexes (X = Br^-, NO_3^-, Me_2SO, $CF_3SO_3^-$), and, as a control, two other dmpmetacn complexes (X = $CH_3SO_3^-$ and $CF_3SO_3^-$), both of which were expected to show the exchange of exactly 1.0 CH proton.

The results of deuteration studies aimed at establishing the site or sites of CH deprotonation are presented in Table 2. The results for the dmpmetacn complexes are:

(i) exactly 1.0 D is incorporated by each of the reactants,
(ii) both CH_2 sites ('arms') can be utilised simultaneously,
(iii) the proportion utilised from these two sites is leaving group dependent,
(iv) the proton which is exchanged in one or other of the 'arms' is exclusively one particular one (i.e. deprotonation is regioselective), and
(v) the protons involved are the same for all leaving groups.

The ^{1}H NMR spectra for the dmpmetacn systems are shown in Figs. 1S and 2S (Supplementary data). For X = $MeSO_3^-$ (Fig. 1S), analysis of the deuterated chloro complex derived from the aqua product reveals a 50:50 distribution of the 1.0 D between the two α-CH_2 sites. For the triflato complex, there is also 1.0 D incorporation, but predominantly at the higher field α-CH_2 site (Fig. 2S). There is an overlap of one of the residual CH protons in each of the AB quartets because of the small upfield isotopic shifts.

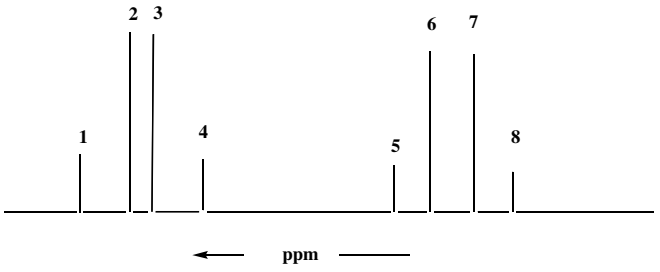
The results for the dmptacn complexes (Table 2) reveal exactly the same trends, although the actual α-CH_2 proton sites involved may be different (they have not all been assigned for the dmptacn complexes). The ^{1}H NMR spectra are shown for the products of base catalysed reaction of the Br^- and Me_2SO complexes in D_2O,OD^- are shown in Figs. 3S and 4S (Supplementary data). The former shows that the higher field α-CH_2 is the preferred deprotonation site (but not exclusively so), that only 1.0 D is incorporated, i.e. there is no reaction via the NH centre, and that the recovered reactant contains no D, confirming rate limiting deprotonation. The product for the reaction of the Me_2SO complex on the other hand has incorporated 0.5 D into each site.

These results show that of all these compounds hydrolyse exclusively by CH deprotonation; it is only the faster of the dmptacn (X = NO_3^- and $CF_3SO_3^-$) complex reactions that involve the NH centre to any extent. This result tends to strengthen the argument [10] for the slowest of them (X = Cl^- and SO_4^{2-}) reacting exclusively via the CH deprotonation route, even though we have not proven this using D labelling studies for these two complexes.

For 'normal' S_N1CB base hydrolysis where acidic amine centres are involved, multiple deprotonation sites can be argued to be a plausible reason for the small but real leaving group dependences of product distributions for

[2] Our experience is that the pentaamminetriflatocobalt(III) complex base hydrolyses much faster than the published data indicate.

Table 2
Fractional deuteration at the four α-CH_2 protons for the product of base catalysed hydrolysis of *asym*-$[Co(dmptacn)X]^{n+}$ and *asym*-$[Co(dmpmetacn)X]^{n+}$



Leaving group	Dmptacn			Dmpmetacn		
	Proton location	%*D*	CHD location	Proton location	%*D*	CHD
Cl^-[a]	C5, C6			C5, C6	100	C8
	C1, C2			C1, C2	0	
	C3, C4			C3, C4	0	
	C7, C8			C7, C8	0	
Br^-	C5, C6	92	C8			
	C1, C2	8	C4			
	C3, C4	0				
	C7, C8	0				
ONO_2^-	C5, C6	60	C8[d]			
	C1, C2	5	C4[d]			
	C3, C4	0				
	C7, C8	0				
$OS(CH_3)O_2^-$				C5, C6	50	C8
				C1, C2	0	
				C3, C4	50	C2
				C7, C8	0	
$OS(CH_3)_2$	C5, C6	50	C8[e]			
	C1, C2	50	C4[e]			
	C3, C4	0				
	C7, C8	0				
$OS(CF_3)O_2^-$	C5, C6	trace[b]	C8	C5, C6	90	C8
	C1, C2	trace[b]	C4	C1, C2	0	
	C3, C4	0		C3, C4	10	C2
	C7, C8	0		C7, C8	0	
OH_2 control	C5, C6	some;	<10%[c]	C5, C6	trace	
	C1, C2	some;	<5%[c]	C1, C2	0	
	C3, C4	0		C3, C4	0	
	C7, C8	0		C7, C8	0	

[a] Reprotonation/deuteration competitive with loss of the Cl^- leaving group.
[b] This is entirely accounted for by the small amount of subsequent exchange in the product hydroxo complex (see[c]). The reaction is entirely via NH deprotonation, and the detectable amount of co-formed *sym*-$[Co(dmptacn)OH]^{2+}$ also appears to be undeuterated at the α-CH_2 sites (refer text).
[d] There is some 35% product which is not deuterated at any of the 4 α-CH_2 protons; this clearly is the NH deprotonation pathway, consistent with the appearance of some *sym*- $[Co(dmptacn)OH]^{2+}$ product together with the predominant *asym*-$[Co(dmptacn)OH]^{2+}$ (refer text).
[e] A trace of *sym*-$[Co(dmptacn)OH]^{2+}$ is also formed here, consistent with a small proportion of reaction via NH deprotonation.

reactants such as *cis*- and *trans*-$[Co(en)_2AX]^{n+}$ (where the *trans*-/*cis*-$[Co(en)_2A(OH)]^{2+}$ ratio defines the product distribution) and $[Co(NH_3)_5X]^{n+}$ ions reacted in H_2O/OH^-/N_3^- (where the $[Co(NH_3)_5N_3]^{2+}$/$[Co(NH_3)_5OH]^{2+}$ ratio defines the product distribution) [4,6]. This idea now has credence, given its clear demonstration for alternative acidic CH centres amongst *asym*-$[Co(dmptacn)X]^{n+}$ complexes (points (ii) and (iii) above), but ironically it is unlikely to be ever proven for simple pentaamine complexes unless examples of rate limiting deprotonation can be found.

Such an opportunity to test the leaving group dependence of the effective site of deprotonation has not presented itself in base hydrolysis studies, and this is the first time that it has been demonstrated.

3.7. D-exchange experiments

To confirm the switch in mechanism from CH to NH deprotonation for the base hydrolysis of the *asym*-$[Co(dmptacn)OS(CF_3)O_2]^{2+}$ complex we needed to show that all four CH_2 protons remained intact in OD^-/D_2O media.

Deuterium can be incorporated into an α-CH_2 site in more than one way. First, base catalysed H/D exchange can occur in the reactant without ligand substitution, such as happens with $[Co(tmptacn)]^{3+}$ [34]. This can mean a $[Co(dmptacn)OH]^{2+}$ product with between 0 and 4 D in the α-CH_2. This prospect can be checked by examining recovered reactant for D content in a partial base hydrolysis experiment. Second, the product hydroxo complex can exchange faster than it is formed, leading to between 1 and 4 D for base hydrolysis via α-CH_2 deprotonation, or between 0 and 4 D for reaction via NH deprotonation. Thirdly, if the rate of reprotonation of the conjugate base is comparable in rate to loss of the leaving group, the hydroxo product will still contain only 1.0 D if the same single site (1 of 4) is involved, but the magnitude of the kinetic isotope effect is reduced, as discussed previously [10]. Finally, if reaction via α-CH_2 deprotonation involves a conjugate base that reprotonates at a very slow rate compared to loss of the leaving group, the product will have exactly 1 D.

Fig. 3 shows the ^1H spectrum for the *asym*-$[Co(dmptacn)OH_2](ClO_4)_3$ complex derived from base hydrolysis of the *asym*-$[Co(dmptacn)ONO_2](ClO_4)_2$ complex in D_2O/OD^-. There is partial deuteration at both sites (much more at **b** than **a**), but less than 1.0 D in total at the methylenes; thus some undeuterated product is apparent, indicating about 35% reaction via the NH centre.

The results for the base hydrolysis of *asym*-$[Co(dmptacn)OS(CF_3)O_2]^{2+}$, the most reactive of all the complexes, are shown in Fig. 4 (and Table 2). The ^1H spectrum is that for regenerated *asym*-$[Co(dmptacn)Cl](ClO_4)_2$ complex, by HCl anation of the base hydrolysis product *asym*-d_n-$[Co(dmptacn)OD]^{2+}$, or solid state anation of *asym*-d_n-$[Co(dmptacn)OH_2]Cl_3$; control experiments showed that

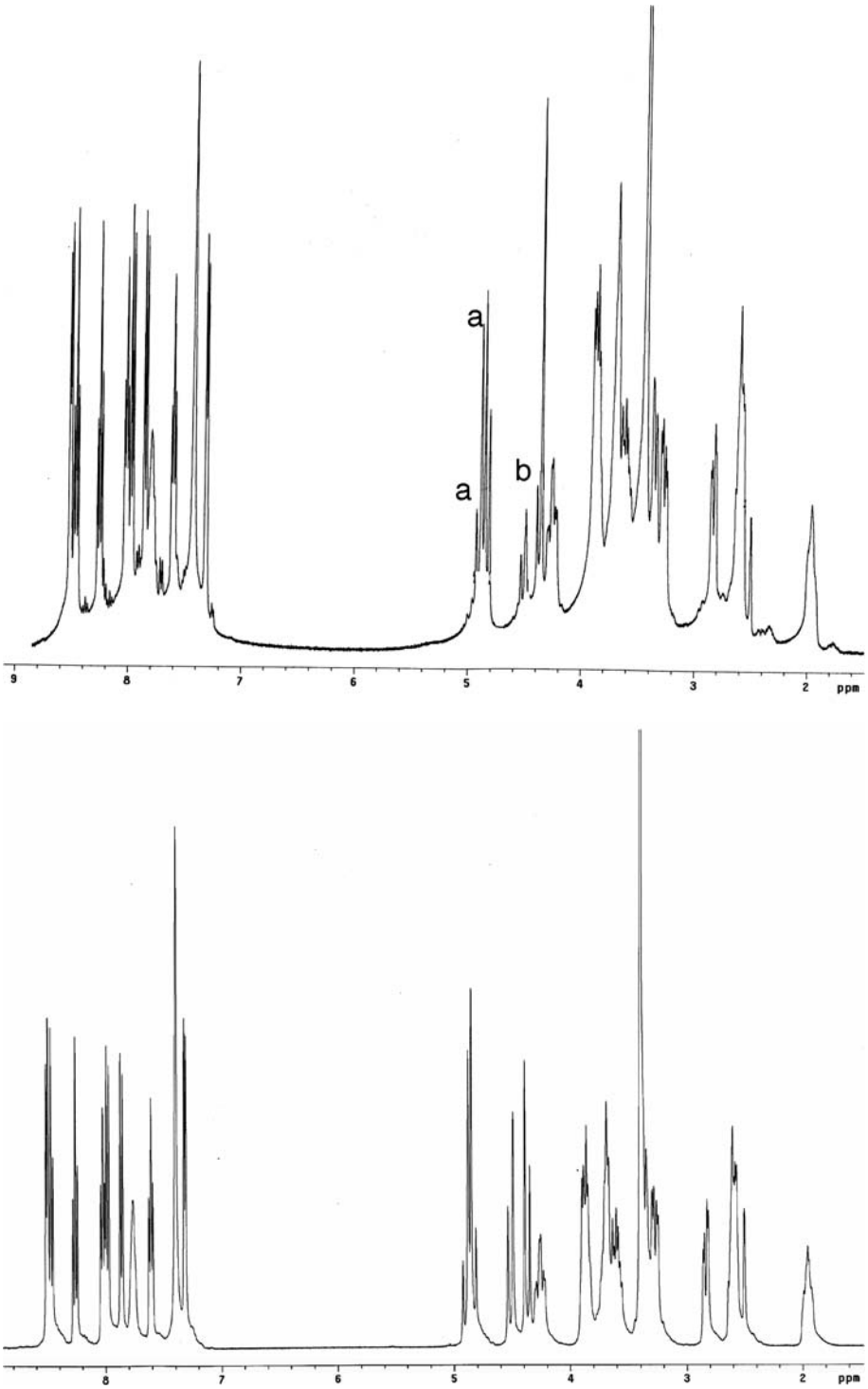


Fig. 3. Top: ^{1}H NMR spectrum of *asym*-[Co(dmptacn)OH_2]$(ClO_4)_3$ in Me_2SO-d_6 derived from the reaction of *asym*-[Co(dmptacn)ONO_2]$(ClO_4)_2$ in D_2O/OD^-: selective deuteration at the lower doublet of the upper α-CH_2 AB quartet (at b) is evident (δ ca. 4.5 ppm), leading to the CHD singlet to the right of b, and there is also a clear evidence of some undeuterated aqua product in this region since there is little deuteration at a. Bottom: the spectrum for authentic *asym*-[Co(dmptacn)OH_2]$(ClO_4)_3$.

these reactions occur without any H/D exchange at either of the –CH_2-sites. The spectrum for the authentic aqua complex is also given. The two sets of AB quartets for the α-pyridyl protons in the ^{1}H spectrum of the OD^-/D^+ cycled material are observed to be unchanged from those for authentic *asym*-[Co(dmptacn)Cl]$(ClO_4)_2$. Further, in the ^{13}C NMR spectrum (not shown) neither C signal, at δ 67.0 and 69.2 ppm, which correspond to the α-CH_2 resonances, is collapsed by D incorporation. It is concluded that the base hydrolysis reaction occurs exclusively via NH deprotonation, i.e., the normal S_N1CB mechanism. Consistent with this result, the rate of base hydrolysis

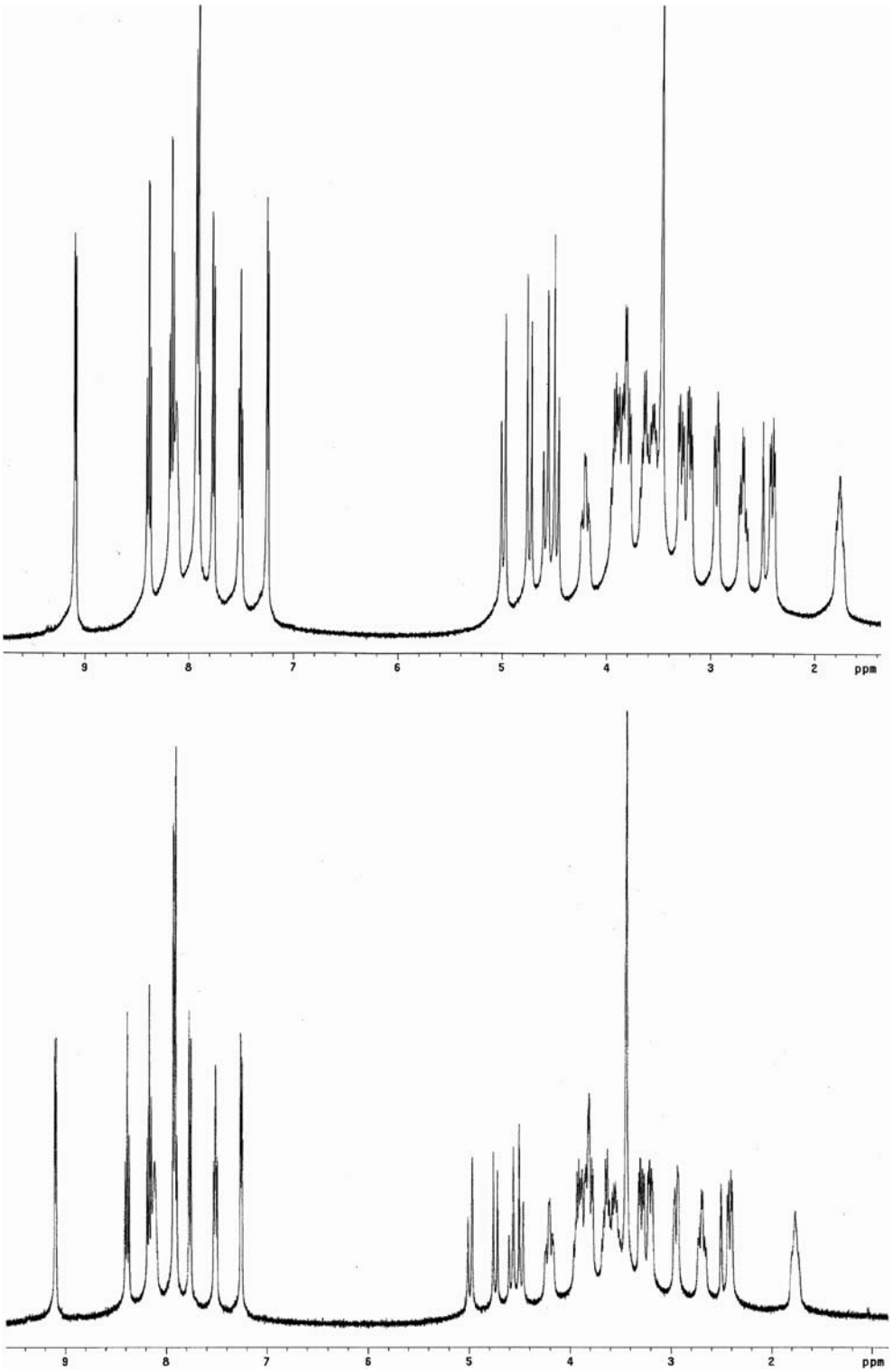


Fig. 4. ^{1}H NMR specta of *asym*-[Co(dmptacn)Cl](ClO$_4$)$_2$ in Me$_2$SO-d_6: Top: recovered from the reaction of *asym*-[Co(dmptacn)OS(CF$_3$)O$_2$](ClO$_4$)$_2$ in D$_2$O/OD$^-$ and Cl$^-$ reanation of the acidified product [Co(dmptacn)OH$_2$]$^{3+}$. Bottom: authentic *asym*-[Co(dmptacn)Cl](ClO$_4$)$_2$. No deuteration at any of the α-CH$_2$ sites (δ 4.5–5 ppm) is apparent.

of h_4-*asym*-[Co(dmptacn)OS(CF$_3$)O$_2$]$^{2+}$ and d_4-*asym*-[Co(dmptacn)OS(CF$_3$)O$_2$]$^{2+}$ measured for one particular buffer were identical, i.e. the kinetic isotope effect is zero (compare the corresponding chloro complexes where the rates differ by 100% [10]).

The reaction scheme involves a potentially reversible CH deprotonation, as believed to be so for the *asym*-[Co(dmptacn)Cl]$^{2+}$ complex, but for the [Co(dmptacn)X]$^{n+}$ species in general any observed rate comparison needs to recognise that the reprotonation reaction (k_{-1}) is common

to all species, while the loss of X from the intermediate $[Co(dmptacn\text{-}H)X]^{(n-1)+}$ ion will be strongly leaving group dependent.

3.8. Steric course of base hydrolysis

The base hydrolysis of the *asym*-$[Co(dmptacn)Cl]^{2+}$ and *asym*-$[Co(dmpmetacn)Cl]^{2+}$ complexes is completely retentive. Similarly, the optically resolved *asym*-$[Co(dmptacn)Cl]^{2+}$ ion involves a negligible loss in activity in a base hydrolysis/HCl anation cycle. Further, the regiospecifically D-labelled *asym*-$[Co(dmpmetacn)Cl]^{2+}$ ion involves no D-site scrambling in base hydrolysis. All these experiments exclude even the transient formation of the *sym* isomer (Fig. 2) en route to hydroxo product.

The base hydrolysis for all the *asym*-$[Co(dmpmetacn)X]^{n+}$ derivatives was also retentive. This fact served to highlight the anomaly now described for the corresponding dmptacn complexes. CH deprotonation is uniformly required for the dmpmetacn complexes, albeit which particular CH site is involved can depend upon the leaving group. The dmptacn complexes can however switch from CH to NH deprotonation, as this work has demonstrated, and we now report that such a switch results in a change of stereochemistry – the product for the base hydrolysis of the triflato complex is an 86:14 mixture of *asym*-/*sym*-OH – the first time a *sym* isomer has been observed in these ligand systems.

The *sym* isomer has been isolated and an independent study of the acid and base hydrolysis of *sym*-$[Co(dmptacn)Cl]^{2+}$ will be described elsewhere. We have been unable to make a *sym*-$[Co(dmpmetacn)X]^{n+}$ derivative as yet because this synthetic route does not work when the NH deprotonation mechanism is blocked through *N*-methylation.

Since we know through the D labelling experiments that the *asym*-$[Co(dmptacn)OS(CF_3)O_2]^{2+}$ complex hydrolyses entirely via NH deprotonation, we took the relative amount of *sym*-OH product in the base hydrolysis reactions of the other *asym*-$[Co(dmptacn)X]^{n+}$ complexes as a measure of what proportion of reaction went via CH deprotonation and what proportion via NH deprotonation. The results showed that only the very reactive triflato complex went via this route, although a little *sym*-OH product was observed for the NO_3^- (5%) and a trace for the Me_2SO complexes; the former translates to 35% reaction via the NH deprotonation route, if the 0% and 14% *sym*-OH product distributions truly characterise the two alternative reaction pathways, and this analysis is in accord with the D-labelling experiments (Table 2).

This important result also shows that the *asym*-$[Co(dmptacn)Cl]^{2+}$ complex does not hydrolyse via any significant NH deprotonation pathway since there is no *sym*-OH product. Some reaction via a NH deprotonation route was one of the two possibilities to account for the reduced kinetic isotope effect observed for this complex; the D labelling experiments [10] were ambiguous and could not resolve this issue.

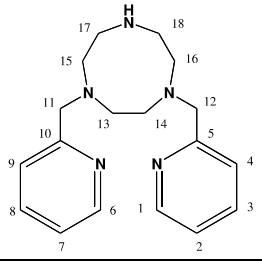
3.9. Isotopic shifts in the ^{13}C NMR spectra

It is now well documented [35] that isotopic substitution of H by D results in readily discernible chemical shift variations in ^{13}C spectra [35]. We have utilised this in following proton exchange by ^{13}C NMR, assigning spectra, and have reported the effect for D substitution at both NH and CH centres [36–38].

Usually the replacement of NH by ND results in an upfield shift of ca.10 Hz at 100 MHz for an α-C centre. The effect is additive, and shifts (smaller) are also discernible for the β-C centre [37].

In the present work, we had occasion to examine these effects in greater detail by recording the ^{13}C NMR spectra for the unequal mixtures of d_4- and h_4-*asym*-$[Co(dmptacn)X]^{n+}$ ions ($X = Cl^-$ and OH_2), Fig. 5S (Supplementary data), and surprisingly observed both positive

Table 3
Isotopic shifts for ^{13}C signals between 1 and 5 bonds from the site of deuteration in the complexes *asym*-$[Co(dmptacn)X](ClO_4)_{2,3}$ ($X = Cl^-$, OH_2) in Me_2SO-d_6



Shifts (ppb) [a]					
Carbon	$^1\Delta$	$^2\Delta$	$^3\Delta$	$^4\Delta$	$^5\Delta$
Chloro complex					
C11, C12	545, 600				
C5, C10		95, 85			
C4, C9			−38, −45		
C1, C6				0, 0[b]	
C3, C8				0, 0[b]	
C2, C7					35, 30
C13, C14			115, 125[c]		
C15, C16			60, 55		
C17, C18		100, 100[e]		0, 0 [b,d]	
Aqua complex					
C11, C12	615, 700				
C5, C10		100, 95			
C4, C9			−40, −50		
C1, C6				0, 0[b]	
C3, C8				0, 0[b]	
C2, C7					35, 30
C13, C14			125, 120[d]		
C15, C16			60, 70		
C17, C18		100, 100[e]		0, 0[b,d]	

[a] Parts per billion. $^1\Delta$, $^2\Delta$ are 1-bond, 2-bond shifts, etc; e.g. for C–N–D it s a 2-bond shift; for this purpose multiple bonds are regarded as one bond. Upfield shifts are defined as positive.

[b] No special resolution techniques applied – ⩽1 Hz shifts would go undetected.

[c] These are compounded $^3\Delta$ and $^4\Delta$ shifts, but largely $^3\Delta$.

[d] Shift for C–D.

[e] Shift for N–D.

and negative shifts, the magnitude of which were not linearly correlated with the type of C nor the location of D substitution. Note that the shifts are for a 2D substitution at an α-CH_2; the numbers would be halved for a 1D substitution.

The shift results are summarised in Table 3. These data are for spectra run at normal rather than enhanced resolution; shifts of $\leqslant$1 Hz would not have been resolved.

A significant result is that the isotopic shifts can be carried across 5 or 6 bonds where the intervening C-backbone is aromatic, and the shifts are of both signs. For the saturated tacn part of the molecules, the shifts are all positive, and rapidly fall off with distance. It is not understood why the C13 and C14 shifts are twice as large as those for C15 and C16 that are also three bonds from the D. Possibly the C13 and C14 shifts are compounded by the 3-bond and 4-bond D substitution, although there is no evidence for a 4-bond shift for either C17 or C18.

Appendix A. Supplementary data

Table 1S, elemental analytical data; Tables 2S and 3S, ^{1}H and ^{13}C NMR data; Table 4S, visible–UV spectral data; Figs. 1S–5S, ^{1}H and ^{13}C NMR spectra. Supplementary data associated with this article can be found, in the online version, at doi:10.1016/j.poly.2006.08.021.

References

[1] D.A. Buckingham, I.I. Olsen, A.M. Sargeson, J. Am. Chem. Soc. 88 (1966) 5443.
[2] D.A. Buckingham, I.I. Olsen, A.M. Sargeson, J. Am. Chem. Soc. 90 (1968) 6654.
[3] W.G. Jackson, Inorg. React. Mech. 4 (2002) 1.
[4] W.G. Jackson, in: I. Bernal (Ed.), The Stereochemistry of Organometallic and Inorganic Compounds, vol. 1, Elsevier, 1986, pp. 255–357.
[5] M.L. Tobe, In A.G. Sykes (Ed.), Advances in Inorganic and Bioinorganic Mechanisms, vol. 2, 1983, pp. 1–94.
[6] W.G. Jackson, A.M. Sargeson, in: P. de Mayo (Ed.), Rearrangements in Ground and Excited States, vol. 2, Academic Press, New York, 1980, pp. 273–378.
[7] N.E. Dixon, W.G. Jackson, W. Marty, A.M. Sargeson, Inorg. Chem. 21 (1982) 688.
[8] N.E. Brasch, D.A. Buckingham, C.R. Clark, K.S. Finnie, Inorg. Chem. 28 (1989) 3386.
[9] Z. Tao, W.G. Jackson, Wuji Huaxue Xuebao 16 (2000) 485.
[10] W.G. Jackson, A.J. Dickie, R. Bhula, J.A. McKeon, L. Spiccia, S.J. Brudenell, D.C.R. Hockless, A.C. Willis, Inorg. Chem. 43 (2004) 6549.
[11] A.J. Dickie, D.C.R. Hockless, A.C. Willis, J.A. McKeon, W.G. Jackson, Inorg. Chem. 42 (2003) 3822.
[12] W.G. Jackson, A.J. Dickie, J.A. McKeon, L. Spiccia, S.J. Brudenell, D.C.R. Hockless, A.C. Willis, Inorg. Chem. 44 (2005) 401.
[13] G.A. McLachlan, S. Brudenell, G.D. Fallon, R.L. Martin, L. Spiccia, E.R.T. Tiekink, J. Chem. Soc., Dalton Trans. (1995) 439.
[14] D.A. Buckingham, I.I. Olsen, A.M. Sargeson, J. Am. Chem. Soc. 89 (1967) 5129.
[15] N.E. Dixon, W.G. Jackson, G.A. Lawrance, A.M. Sargeson, Inorg. Synth. 22 (1983) 103.
[16] D.A. Buckingham, C.R. Clark, W.S. Webley, Inorg. Chem. 30 (1991) 466.
[17] N.E. Dixon, G.A. Lawrance, P.A. Lay, A.M. Sargeson, Inorg. Chem. 22 (1983) 846.
[18] N.E. Dixon, G.A. Lawrance, P.A. Lay, A.M. Sargeson, Inorg. Chem. 23 (1984) 2940.
[19] N.E. Dixon, G.A. Lawrance, P.A. Lay, A.M. Sargeson, H. Taube, Inorg. Synth. 14 (1986) 243.
[20] P.A. Lay, R.H. Magnuson, H. Taube, Inorg. Chem. 28 (1989) 3001.
[21] N.J. Curtis, G.A. Lawrance, P.A. Lay, A.M. Sargeson, Inorg. Chem. 25 (1986) 484.
[22] N.J. Curtis, G.A. Lawrance, A.M. Sargeson, Inorg. Synth. 14 (1986) 277.
[23] G.A. Lawrance, A.M. Sargeson, Inorg. Synth. 24 (1986) 250.
[24] G.A. Lawrance, A.M. Sargeson, Inorg. Synth. 24 (1986) 279.
[25] P.A. Lay, R.H. Magnuson, J. Sen, H. Taube, J. Am. Chem. Soc. 104 (1982) 7658.
[26] P.A. Lay, A.M. Sargeson, Inorg. Synth. 24 (1986) 283.
[27] D.A. Buckingham, P.J. Cresswell, A.M. Sargeson, W.G. Jackson, Inorg. Chem. 20 (1981) 1647.
[28] N.E. Dixon, W.G. Jackson, M.J. Lancaster, G.A. Lawrance, A.M. Sargeson, Inorg. Chem. 20 (1981) 470.
[29] M.L. Tobe, J. Burgess, Inorganic Reaction Mechanisms, Longman, New York, 1999.
[30] F.J. Garrick, Nature 139 (1937) 507.
[31] M. Green, H. Taube, Inorg. Chem. 2 (1963) 948.
[32] P.J. Cresswell, Doctoral thesis, The Australian National University, 1974.
[33] W.G. Jackson, J.A. McKeon, W. Marty, Inorg. React. Mech. 4 (2002) 125.
[34] W.G. Jackson, J.A. McKeon, D.C.R. Hockless, A.C. Willis, Inorg. Chem. 45, in press.
[35] P.E. Hansen, in: G.A. Webb (Ed.), Annual Reports on NMR Spectroscopy, vol. 5, Harcourt Brace, London, 1983, pp. 106–225.
[36] P.M. Angus, W.G. Jackson, Inorg. Chem. 33 (1994) 1569.
[37] W.G. Jackson, Inorg. Chem. 30 (1991) 1570.
[38] P. Comba, W.G. Jackson, W. Marty, L. Zipper, Helv. Chim. Acta 75 (1992) 1147.

Available online at www.sciencedirect.com
ScienceDirect
Polyhedron 26 (2007) 519–523
POLYHEDRON
www.elsevier.com/locate/poly

A new approach to the relationship between bond energy and electronegativity

Derek W. Smith

Department of Chemistry, University of Waikato, Hillcrest Road, Hamilton, New Zealand

Received 10 March 2006; accepted 19 September 2006
Available online 26 September 2006

Abstract

The familiar equation whereby Pauling related heteronuclear bond energies $D_{A–B}$ to the electronegativity difference $\Delta\chi$ ($=|\chi_A - \chi_B|$) and the homonuclear bond energies $D_{A–A}$ and $D_{B–B}$ has been the subject of critical scrutiny for at least half a century. A modification to this equation that combines the concepts of electronegativity and hardness/softness can be rewritten in terms of two quantities x and y, both having absolute significance. Both homo- and heteronuclear bond energies can be rationalised from these new equations. The quantities x are linearly related to Pauling electronegativities, while y appears to be a measure of an atom's intrinsic bonding potential, related to size and availability of valence orbitals.
© 2006 Elsevier Ltd. All rights reserved.

Keywords: Bond energy; Bonding theory; Electronegativity; Hard–soft interactions

1. Introduction

Rationalising the relative strengths of chemical bonds is central to an understanding of chemical reactions. In a singly-bonded diatomic molecule AB, the bond energy is equal to the dissociation energy (distinctions between bond energies and bond enthalpies, and between measurements made at 0 and 298 K, need not concern us). In polyatomic molecules AB_n the experimentally determined bond dissociation energy is often invoked as a measure of bond strength, but the mean bond energy, i.e. the total atomisation energy divided by n, may be more relevant for comparative purposes. Heteronuclear single bond energies $D_{A–B}$ can be related to the homonuclear terms $D_{A–A}$ and $D_{B–B}$ by Pauling's bond energy

$$D_{A–B} = 1/2(D_{A–A} + D_{B–B}) + a(\chi_A - \chi_B)^2 \quad (1)$$

where χ_A and χ_B are the electronegativities of the atoms A and B respectively, and a is equal to 96.5 when all energies are expressed in kJ mol^{-1} (1 eV = 96.5 kJ mol^{-1}). Pauling [1] used Eq. (1) to establish the first scale of electronegativity. Since only relative – not absolute – values can be obtained from Eq. (1), Pauling initially assigned an arbitrary value of zero to hydrogen. In 1934, Mulliken [2] proposed – on sounder theoretical grounds than any of those underlying Eq. (1) – that the electronegativity of an atom was proportional to the arithmetic mean of its ionisation potential and electron affinity (the latter being defined as positive if the electron attachment is exothermic). Mulliken electronegativities are absolute values, and the clear relationship between Pauling and Mulliken electronegativities persuaded Pauling to add 2.05 to his original values, in order to eliminate the intercept on the linear plot between the two sets [1b]. These modified Pauling electronegativities have been treated as having absolute significance in, for example, discussions of electronegativity equalisation [3a] and group electronegativities [3b,4], and are still reproduced in contemporary undergraduate texts. However, it has long been known that Eq. (1) is of limited applicability. It gives poor results for molecules formed by the least electronegative elements, and for fluorides of most metallic elements the calculated bond energies are much too high. As pointed

E-mail address: dw.smith@waikato.ac.nz.

0277-5387/$ - see front matter © 2006 Elsevier Ltd. All rights reserved.
doi:10.1016/j.poly.2006.09.013

out by Pritchard and Skinner [5], Pauling's electronegativities for the elements of Groups 1 and 2 were derived from the heats of formation of crystalline solids such as NaCl(s), and not from the dissociation energies of gaseous molecules like NaCl(g). In Allred's revised Pauling scale [6], values for elements like Na were determined from thermochemical data for crystalline chlorides and bromides. These manoeuvres can be justified on two grounds:

(i) Pauling insisted that the electronegativity of an atom 'represents the attraction of a neutral atom in a stable molecule for electrons' [7]. At room temperature and atmospheric pressure, molecules like NaCl(g) are unstable with respect to polymerisation to form crystalline solids.
(ii) The bonding in fluorides such as NaF(g) is mainly ionic, and their thermochemistry is better treated by Coulombic models; Eq. (1) is applicable for bonds that are predominantly covalent, with a smaller ionic contribution.

In recent years, Eq. (1) has been subjected to increasingly critical scrutiny. It has been argued [8,9] that it is valid only for a limited number of bonds where $\Delta\chi$ (i.e. $|\chi_A - \chi_B|$) is small. The following equation appears to work rather better:

$$D_{A\text{–}B} = 1/2(D_{A\text{–}A} + D_{B\text{–}B}) + a\Delta\chi \quad (2)$$

The use of the geometric mean $(D_{A\text{–}A}D_{B\text{–}B})^{1/2}$ in place of the arithmetic mean is also advantageous, and was preferred by Reddy et al. [8]. Pauling [10] noted that the geometric mean in Eq. (1) had advantages in dealing with, e.g., alkali metal hydrides, but did not use it in constructing his scale. Eq. (2) has the additional attraction that the electronegativity difference $\Delta\chi$ (and hence the electronegativities themselves) can be expressed in units of energy rather than $(\text{energy})^{1/2}$ as implied by Eq. (1) – unless the units of energy are deemed to reside in the constant a. However, it should be noted that Reddy et al. [8] invoked the bond energies of diatomic molecules such as SrCl(g), which are unstable with respect to disproportionation; the dissociation energy of SrCl(g) is rather less the mean bond energy in $SrCl_2$(g) and it can be argued that such molecules are excluded by Pauling's definition [7] from allegiance to Eq. (1). Murphy et al. [9] included in their analysis thermochemical data for molecular species such as the gaseous alkali metal halides and hydrides, which were known not to conform to Eq. (1) and were not invoked in the construction of either the traditional [1b] or revised [6] Pauling scales.

Eq. (1) can be modified [11] to give much better agreement with experimental bond energies using traditional Pauling electronegativities, while obviating a problem with units which troubled Murphy et al. [9]. Moreover, Eq. (1) and its variants have an advantage over Eq. (2) in dealing with metatheses of the type

$$AX + BY \rightarrow AY + BX \quad (3)$$

According to Eq. (2), such a reaction should always be thermoneutral ($\Delta H^o = 0$). But, as noted by Pauling [12], metatheses as in Eq. (3) are usually exothermic if $\chi_A < \chi_B < \chi_X < \chi_Y$. It can readily be predicted from Eq. (1) that for Reaction (3)

$$\Delta H^o = 2a(\chi_B - \chi_A)(\chi_X - \chi_Y) \quad (4)$$

This provides a valuable rationale for many synthetic strategies. For example, the reaction

$$R_3SnCl + R'Li \rightarrow R_3SnR' + LiCl \quad (5)$$

is driven thermodynamically by the highly exothermic enthalpy/free energy of formation of LiCl, where the most and least electronegative elements are brought into combination. The synthetic utility of Grignard reagents and metal hydrides such as $LiAlH_4$ can be similarly rationalised. However, Pearson [13] noted a number of cases where electronegativity considerations predict the wrong sign for ΔH^o. For example, the reaction

$$LiF(g) + CsI(g) \rightarrow LiI(g) + CsF(g) \quad (6)$$

should be exothermic since the least and most electronegative of all the elements – Cs and F respectively – are combined on the right hand side of Eq. (6). But – as was noted by Pearson [13] – the experimental ΔH^o for the reaction ion Eq. (6) is positive: standard thermochemical tabulations [14] lead to a value of $+51.6\ \text{kJ mol}^{-1}$ (Pearson [13], using older thermochemical data, gave $\Delta H^o = +71\ \text{kJ mol}^{-1}$). Pearson [13,15] – noting that cations and anions are respectively acids and bases in the Lewis sense – proposed that the thermochemistry of metathetic reactions is best explained in terms of the affinity of hard acids for hard bases, and of soft acids for soft bases, together with the enmity between hard-soft acid-base pairs. Thus Pauling stressed the attraction of opposites as optimising the strength of a chemical bond, while Pearson advocated 'like goes with like'. In an attempt to resolve this 'Pearson–Pauling paradox' [16], it was proposed [17] that the enthalpy of formation ΔH_f^o of a binary substance A_pB_q could be expressed as

$$-\Delta H_f^o(A_pB_q)/n = a[(x_A - x_B)^2 - (y_A - y_B)^2] \quad (7)$$

where $n = pn_A(=-qn_B)$, n_A and n_B being respectively the oxidation numbers of A and B. The parameter x was deemed to have the same meaning as the Pauling electronegativity χ, while y was tentatively related to the diffuseness of an atom's valence orbitals; a mismatch in y values would tend to weaken the bonding. While y is not a direct measure of hardness/softness, a plot of y against x effects an excellent demarcation between hard and soft acids. Soft acids/bases tend to be large ions formed by atoms of relatively high electronegativity. Eq. (7) permits the rationalisation of other thermochemical data, for example the effectiveness of binary fluorides as fluorinating agents, the thermal stabilities of oxides and the stabilisation of high/low oxidation states by fluorides/iodides respectively. Thus the Pauling and Pearson approaches can be reconciled.

2. An alternative approach

Further development of Eq. (7) permits new insights into the relative strengths of chemical bonds. It is easy – with the same notation as in Eqs. (1) and (2) – to derive Eq. (11) from Eqs. (8)–(10)

$$D_{A\text{–}A} = y_A^2 - x_A^2 \tag{8}$$

$$D_{B\text{–}B} = y_B^2 - x_B^2 \tag{9}$$

$$D_{A\text{–}B} = y_A y_B - x_A x_B \tag{10}$$

$$D_{A\text{–}B} - 1/2(D_{A\text{–}A} + D_{B\text{–}B}) = 1/2[(x_A - x_B)^2 - (y_A - y_B)^2] \tag{11}$$

For a gaseous molecular substance AB_n, the left hand sides of Eqs. (7) and (11) are identical; the right hand sides differ only in the units of x and y. From Eq. (7), only differences in the parameters x and y can be determined by analysis of experimental thermochemical data; x_H was set equal to the Pauling value of 2.1 and y_H was arbitrarily assigned a value of zero [17]. But in Eqs. (8)–(10), the x and y parameters assume an absolute significance, and homonuclear, singly-bonded diatomic molecules as well as heteronuclear AB_n are embraced. A fresh interpretation of bond energies in relation to electronegativity begins to emerge. Experimentally, the strongest homonuclear single bonds are H–H > C–C > B–B > S–S > Cl–Cl. These are all relatively small atoms (with covalent radii <1.05 Å) and of intermediate electronegativity (2.5 ± 0.5 on the traditional Pauling scale). The weakest homonuclear single bonds are formed by atoms of high electronegativity (F–F, O–O) and also by atoms of low electronegativity (Li–Li, etc.). These observations are consistent with Eqs. (8) and (9) if y is related to atomic size – small atoms having large values of y – and if x is close to zero for atoms around the middle of the electronegativity scale. Thus x is not to be identified with an absolute electronegativity; it is an absolute quantity linearly related to electronegativity in the Pauling/Mulliken sense. O and F are to be assigned large, positive values of x, while atoms of low electronegativity have negative values. The weakness of the F–F and O–O bonds is usually attributed in undergraduate texts to repulsion between lone pairs of electrons, although other explanations have been proposed [18,19]. We are dealing with covalent bonds in which pairs of electrons – one from each atom – are shared. It can be argued that x_A represents the balance between the willingness of A to contribute an electron to a shared pair, and its tendency to attract an electron from the other atom, as implied by the Mulliken definition of electronegativity (2). The weakness of the F–F bond is then attributed to the unwillingness of the fluorine atoms to share their unpaired electrons on an equal footing. An atom of low electronegativity such as lithium prefers to give than to receive or share, resulting in a weak Li–Li bond. The strongest homopolar bonds will result where x_A^2 is small (i.e. where x_A is close to zero, as in atoms of intermediate electronegativity) and y_A^2 is large(small atom). The strongest heteropolar bonds will be formed between small atoms where the product $x_A x_B$ is negative, i.e. one atom is of high and the other of low electronegativity. There is no need explicitly to invoke ionic-covalent resonance in these arguments.

2.1. Calculating scales of x and y

We now set out to determine numerical values of x and y from Eqs. (8)–(10), beginning with hydrogen and the halogens which form unequivocally singly bonded diatomic molecules. Regression analysis led to values for the ten x and y parameters for these five elements from the 15 experimental bond energies (taken from Ref. [9]). It was found

Table 1
Values of y and x for main group elements, with Pauling electronegativities χ_P from Eq. (12) and original Pauling values $\chi_P(o)$ from Ref. [1b]

Element	y	x	χ_P	$\chi_P(o)$
H	20.99 ± 0.32	0	2.18	2.1
F	27.55 ± 0.77	24.43 ± 0.91	3.84 ± 0.06	4.0
Cl	20.30 ± 0.67	12.91 ± 1.01	3.06 ± 0.07	3.0
Br	17.08 ± 0.62	9.99 ± 0.99	2.86 ± 0.07	2.8
I	13.49 ± 0.55	4.29 ± 0.95	2.47 ± 0.06	2.5
O	22.02 ± 0.29	18.52 ± 0.39	3.44 ± 0.03	3.5
S	17.00 ± 0.58	4.68 ± 1.02	2.50 ± 0.07	2.5
Se	14.99 ± 0.40	2.78 ± 0.70	2.37 ± 0.05	2.4
Te	13.39 ± 0.39	−0.63 ± 0.60	2.14 ± 0.04	2.1
N	18.63 ± 0.04	13.72 ± 0.07	3.11 ± 0.01	3.0
P	15.05 ± 0.91	−2.96 ± 1.39	1.98 ± 0.09	2.1
As	14.31 ± 0.49	−1.83 ± 0.75	2.06 ± 0.05	2.0
Sb	12.59 ± 0.40	−4.03 ± 0.61	1.91 ± 0.04	1.9
C	19.81 ± 0.02	5.96 ± 0.05	2.59 ± 0.01	2.5
Si	15.43 ± 0.26	−6.90 ± 0.40	1.71 ± 0.03	1.8
Ge	14.09 ± 0.38	−3.64 ± 0.59	1.93 ± 0.04	1.8
Sn	12.39 ± 0.85	−5.75 ± 1.84	1.79 ± 0.13	1.8
B	18.38 ± 0.14	−5.56 ± 0.21	1.80 ± 0.01	2.0

that x_H was equal to $+0.05 \pm 0.86$ (kJ mol^{-1})$^{1/2}$; in order to economise on parameters, x_H was arbitrarily set equal to zero, as in Pauling's original scale [1a]. With the remaining 9 parameters, the 15 experimental bond energies were reproduced with a mean error of 7.0 kJ mol^{-1}. Using the values of x and y thus obtained, the corresponding parameters for B, C, Si, Ge, Sn, N, P, As, Sb, O, S, Se and Te were calculated by regression analysis from experimental bond energies (again from Ref. [9]) for $D_{A–A}$ and $D_{A–X}$ (X = H, F, Cl, Br, I). For some elements, not all of these six values are available. For others, some of the bond energies given in Ref. [9] were not used:

(i) It has been argued [4] that C–F, N–F and O–F bond energies are enhanced by contributions from resonance structures such as $F^-O{=}F^+$; in the language of molecular orbital theory, this arises from interaction between filled π orbitals on the fluorine atoms and empty σ antibonding MOs. These bond energies were therefore rejected in the analysis.
(ii) The value of 235 kJ mol^{-1} quoted [9] for O–Br is evidently the dissociation energy of the BrO radical, and not the mean bond energy in Br_2O.
(iii) The figure of 211.7 kJ mol^{-1} for $D_{Te–Te}$ is too high – it exceeds the atomisation enthalpy of elemental Te by some 15 kJ mol^{-1}.

The $D_{A–A}$ values for A = C, Si, Ge and Sn are usually taken from the atomisation enthalpies of the elemental substances in the diamond-type structure. For the heavier elements at least, these may be enhanced by longer-range interactions; in other words, bands rather than bonds are more appropriate. There is evidence [20] that $D_{Si–Si}$ is about 20 kJ mol^{-1} smaller in silanes than in elemental silicon. Thus $D_{A–A}$ was ignored in the analysis for these elements.

3. Results and discussion

The final values by regression analysis of x and y for Main Group elements (excluding the most electropositive, metallic elements for which Eq. (1) is demonstrably inapplicable, for the reasons already outlined) are collected in Table 1. As illustrated in Fig. 1, there is an excellent linear correlation ($R = 0.989$) between the x parameters and traditional Pauling electronegativities χ_P [12] according to Eq. (12):

$$\chi_P = 2.18 + 0.068x \quad (12)$$

Values of χ_P thus obtained are given in Table 1. It is not to be inferred that x_A is to be identified with the electronegativity of the atom/element A; rather, the x parameters are quantities which can be linearly correlated with electronegativities. The same R value is obtained with Allred's revised Pauling values (6). With Allen's spectroscopic scale [21], the correlation coefficient R is only 0.970. However, the x and χ_P values in Table 1 fulfil some of Allen's criteria [9,21]:

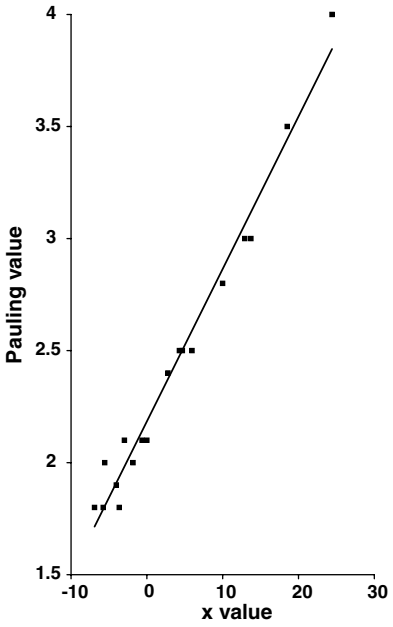


Fig. 1. Plot of x against traditional Pauling electronegativities from Ref. [1b].

(i) Silicon has the lowest x of all the metalloids; tin ought to be lower, but x_{Sn} is poorly determined, on account of the large experimental uncertainty in D(Sn–F).
(ii) We find $x_N > x_{Cl}$, though not within the limits of experimental uncertainty (it has been pointed out [22] that the argument set out in Ref. [9] for the higher electronegativity of N compared with Cl appears to be based on the erroneous proposition that N never exhibits the+5 oxidation state, while Cl(+7) is known).
(iii) The alternation between the second and third element in Group 14 – i.e. $\chi_{Si} < \chi_{Ge}$ – is apparent; this becomes less marked in Group 15 and has disappeared by Group 17.

We now look at trends in the parameter y. I tentatively propose that this measures the intrinsic bonding potential of an atom. It is primarily related to atomic size, and to the suitability in energy and radial extension of its valence orbitals. To some extent these variables parallel electronegativities. However, y_H is smaller than y_O or y_F. This may reflect that fact that hydrogen has only a single valence orbital, 1s, while oxygen and fluorine – even if only σ bonding is considered – can employ both 2s and 2p, and enjoy the benefits of hybridisation. But there is not a steady increase in y_A across the first short period; the discontinuity between C and N, and the abrupt increase between O and F are striking. Similar but less marked discontinuities are observed between Groups 14 and 15, and between Groups 16 and 17 among the heavier elements. An explanation for this behaviour may be found in considerations of exchange energy stabilisation in free atoms [23], which favours the

formation of atoms such as N and O (having more than one unpaired electron in their ground states) and thus lowers N–N and O–O bond energies. For heavier atoms such as I, spin–orbit coupling also affects homopolar bond energies.

4. Conclusions

It is widely believed that the familiar Pauling bond energy equation yields only *differences* in atomic electronegativities, which can be used to rationalise the relative strengths of heteronuclear bonds. The absolute – as opposed to relative – significance of Pauling electronegativities rests upon their linear relationship with Mulliken's values. This paper shows how absolute quantities x related to Pauling electronegativities can be derived from thermochemical data. These, together with the values of the 'intrinsic bonding potential' y, enable the rationalisation of the relative magnitudes of homonuclear as well as heteronuclear bond energies.

It is useful to compare the present treatment with other two-parameter models for the rationalisation of bond strengths. Drago and Wayland [24] separated the strength of the dative bond in a Lewis acid/base adduct into ionic and covalent components. Attempts to construct quantitative scales of hardness/softness focus on the principle that the hard-hard interaction is primarily ionic, while the soft-soft interaction is covalent [25,26]. The model proposed in the present paper differs from these, and from the traditional Pauling treatment, in that no ionic–covalent dichotomy needs to be invoked explicitly. The parameters are related to the atom's capacity to form covalent bonds by electron sharing, and the model is inappropriate for molecules (such as the alkali halides) where the bonding is predominantly ionic.

Obviously a two-parameter model will work better than one with only a single parameter. Is the superior performance of our model merely a statistical artifice, or do the x and y parameters have real meaning that can enrich our understanding of bond energies? The excellent correlation between the x values and Pauling electronegativities – which have largely stood the test of time – can scarcely be fortuitous, and the periodic trends in the y parameter can be rationalized rather well.

References

[1] (a) L. Pauling, J. Am. Chem. Soc. 54 (1932) 3570;
(b) L. Pauling, The Nature of the Chemical Bond, third ed., Cornell University Press, Ithaca, NY, 1960, p. 93.
[2] R.S. Mulliken, J. Chem. Phys. 2 (1934) 782, 3 (1935) 573.
[3] (a) S.G. Bratsch, J. Chem. Educ. 61 (1984) 588;
(b) S.G. Bratsch, J. Chem. Educ. 62 (1985) 101.
[4] (a) D.W. Smith, J. Chem. Soc., Faraday Trans. 94 (1998) 201;
(b) D.W. Smith, J. Organomet. Chem. 585 (1999) 150.
[5] H.O. Pritchard, H.A. Skinner, Chem. Rev. 55 (1955) 745.
[6] A.L. Allred, J. Inorg. Nucl. Chem. 17 (1961) 215.
[7] L. Pauling, Ref. [1b], p. 95.
[8] R.R. Reddy, T.V.R. Rao, R. Viswanath, J. Am. Chem. Soc. 111 (1989) 2914.
[9] L.R. Murphy, T.L. Meek, A.L. Allred, L.C. Allen, J. Phys. Chem. A 104 (2000) 5867.
[10] L. Pauling, Ref. [1b], p. 82.
[11] D.W. Smith, J. Phys. Chem. A 106 (2002) 5951.
[12] L. Pauling, Ref. [1b], p. 103.
[13] R.G. Pearson, Chem. Commun. (1968) 65.
[14] D.D. Wagman, W.H. Evans, V.B. Parker, R.H. Schumm, I. Halow, S.M. Bailey, K.L. Churney, R.L. Nuttall, J. Phys. Chem. Ref. Data 11 (Suppl. No. 2) (1982).
[15] R.G. Pearson, Hard and Soft Acids and Bases, Dowden, Hutchison and Ross, Stroudsburg, PA, 1973.
[16] J.E. Huheey, Inorganic Chemistry, third ed., Harper and Row, New York, 1983, p. 320.
[17] D.W. Smith, J. Chem. Educ. 67 (1990) 911.
[18] P. Politzer, J. Am. Chem. Soc. 91 (1969) 6235.
[19] D.W. Smith, J. Chem. Educ. 77 (2000) 780.
[20] D.W. Smith, J. Chem. Educ. 65 (1988) 414.
[21] L.C. Allen, J. Am. Chem. Soc. 111 (1989) 9003.
[22] D.W. Smith, J. Chem. Educ. 82 (2005) 1202.
[23] D.W. Smith, J. Chem. Educ. 81 (2004) 886.
[24] R.S. Drago, B.B. Wayland, J. Am. Chem. Soc. 87 (1965) 3671.
[25] R.D. Hancock, A.E. Martell, J. Chem. Educ. 73 (1996) 654.
[26] P.W. Ayers, J. Chem. Phys. 123 (2005) 141102.

Available online at www.sciencedirect.com
ScienceDirect
Polyhedron 26 (2007) 524–533
POLYHEDRON
www.elsevier.com/locate/poly

Application of UV–Vis, near-infrared and mid-infrared spectroscopy to the study of Mn-bearing humites

Sara Palmer, B. Jagannadha Reddy, Ray L. Frost *

Inorganic Materials Research Program, School of Physical and Chemical Sciences, Queensland University of Technology, GPO Box 2434, Brisbane Queensland 4001, Australia

Received 17 July 2006; accepted 23 September 2006
Available online 29 September 2006

Abstract

The combination of electronic and vibrational spectra has been applied to correlate the spectral properties, with composition, structure and cation substitutions such as Mn, Fe, Ca and Zn for Mg in humites: norbergite, alleghanyite, leucophoenicite and sonolite with increasing number of silicate layers, 1, 2, 3 and 4. The observation of two broad bands in the visible range, near 550 and 450 nm (18 180 and 22 220 cm^{-1}) and one sharp band around 410 nm (24 390 cm^{-1}) is characteristic of Mn^{2+} in alleghanyite and leucophoenicite. The study of UV–Vis (electronic) spectral features confirms Mn as a major substituent in these two samples. Cation impurities like Zn and Ca as revealed from EDX analysis might be the cause for the absence of Mn-type spectrum in sonolite. The first observation is the near-infrared spectra of all four minerals in the first fundamental overtone OH-stretching mode are different and each mineral is characterized by its NIR spectrum. The feature in the range 7180–6600 cm^{-1} [1393–1515 nm or 1.39–1.52 μm] corresponds to the overtones of OH stretching vibrational modes of the humite groups observed in their IR spectra over the range, 3680–3320 cm^{-1}. The infrared spectra of the hydrous components of OH and SiO_4 groups in the mineral structure act as an aid to distinguish the minerals of the humite mineral group. A band at 541 cm^{-1} is assigned to MnO stretching mode.
© 2006 Elsevier Ltd. All rights reserved.

Keywords: Norbergite; Alleghanyite; Leucophoenicite; Sonolite,UV–Vis, NIR and mid-IR spectroscopy; Electronic spectra of Mn^{2+}; Overtone and combination bands; Layered silicates

1. Introduction

The humite minerals have been studied for almost 100 years [1–9]. Crystal structures were elucidated in the 1960s and 1970s [10–12,10,13–20]. The minerals are structurally analagous to olivine [21]. Much variation in the composition of the minerals is observed due to isomorphic substitution [21]. Many of the minerals contain manganese as the substituent [21–24]. No near-infrared spectroscopic studies of the minerals have been forthcoming. The humite minerals are a group of four homologues that are represented by the general formula nMg_2SiO_4. $Mg(OH,F)_2$ where $n = 1$ for norbergite, $n = 2$ for chondrodite, $n = 3$ for humite and $n = 4$ for clinohumite [25]. The humite group of minerals forms a morphotropic series with the mineral olivine and brucite. The members of this group differ not only by chemistry but by the number of olivine or silicate layers that are present between the brucite layers. There can be either one, two, three or four layers of the silicate layers between each brucite-like sheet. This has the effect of extending the unit cell of the minerals and affecting their symmetries.

The humite minerals are a homologous series of magnesium–ferrous–manganese orthosilicates whose structures are based on hexagonal closest-packed arrays of anions (O,F,OH) with octahedral and tetrahedral cation distributions related to that in forsterite. In humite there are 4 distinct octahedra; M(1)O6 and M(2)O6, like those in olivine, and M(2)O5(F,OH)1 and M(3)O4(F,OH)2, like those in

* Corresponding author. Tel.: +61 7 3864 2407; fax: +61 7 3864 1804.
E-mail address: r.frost@qut.edu.au (R.L. Frost).

0277-5387/$ - see front matter © 2006 Elsevier Ltd. All rights reserved.
doi:10.1016/j.poly.2006.09.038

chondrodite. Ferrous Fe is ordered in equal amounts (approximately 0.1 Fe^{2+}) into the more distorted octahedra with 6 O ligands but avoids the less distorted octahedra with 1 or 2 (F,OH) ligands. In these closely packed orthosilicates, all anions are charge-balanced, and Fe^{2+} prefers the more distorted sites than those with the more polarizable ligands. In Mg/Fe olivines the M(1)O6 octahedron is significantly smaller but slightly more distorted than M(2)O6. A general mineralogy, chemistry and crystal structures of the humite series and Mn-analogues have been well-studied and summarized by Ribbe et al. [17,21,27]. A recent study of the structure of a natural chondrodite by neutron diffraction demonstrated that hydrogen is found to occupy the H1 site. The significance of hydrogen-bonding has been explained in humite structures containing varying amounts of OH, F and Ti [6]. A few spectroscopic studies are made on humite [26,28,29] and iron-rich clinohumites [30]. There are many studies reported on the vibrational modes of olivines by infrared and Raman spectroscopy [10–12,10,13–15].

Humites may contain Mg, Ca, Ti, Mn, Fe and Zn although only Mg, Mn and Ca form end members. These cations are ordered into the octahedral sites which vary in distortion, ligancy, size, and symmetry. A better understanding of the behaviour of cations substitution for Mg in humites is expected to provide a helpful guidance for spectral analysis of Mn-bearing minerals. It is our intention that makes the study of manganese humites and to compare with the Mg bearing humite.

Norbergite, $Mg_3(SiO_4)(OH,F)_2$ is a member of humite group. Humite group minerals possess silicate layers and oxide layers in their structures. The silicate layers and oxide layers have the same structure as olivine and brucite respectively. The Raman spectra of norbergite samples were investigated and explained the dependence of OH Raman bands on temperature and pressure [31]. The magnesium humites (norbergite, chondrodite, humite and clinohumite) have been studied and summarized [32]. Their manganese analogues (alleghanyite, leucophoenicite, sonalite, jerrygibbsite, ribbeite and manganhumite) have received less attention. They are, in general, less common, found in metamorphosed Mn-deposits. Alleghanyite, $Mn_5(SiO_4)(OH)_2$ species crystal structure was reported by Rentzeperis [33], a high Mg alleghanyite from Sterling Hill was described by Petersen et al. [34] and later crystal structure refinement report [35] shows cations in alleghanyite and all other humite group minerals are ordered in octahedral sites accordingly to size criteria, eventhough ligancy (O, OH, F) may be the controlling factor where charge balance and crystal-field effects are involved. Penfield and Warren [36] disclosed originally the mineral, leucophoenicite, $(Mn^{2+})_7(SiO_4)_3(OH)_2$ and its crystal structure solved by Moore [37,38] confirms edge-sharing, half-occupied, silicate tetrahedra and is structurally distinct from the humite group minerals. Later, the study of TEM images of leucophoenicite [39], supports the structure analysis done by Moore's structural report [37]. Sonlitnolite, $Mn_9^{2+}(SiO_4)_4(OH)_2$ was first described by Yoshinaga [40]. from eleven localities in Japan and crystal structure was discussed by Ribbe [32].

The expression of Mn humite minerals, their formula, number of silicate layers and symmetry class are described in Table 1. Previous studies have been based on the chemistry and structural analysis. No spectroscopic studies were included in previous research and this is why we are presenting this work. In this communication, we present the spectroscopic investigations of selected manganese humites (alleghanyite, leucophoenicite, sonalite) and Mg-humite for comparison.

2. Experimental

2.1. Minerals

The minerals used in this work listed in Table 1 were obtained on loan from The South Australian Museum and from the Mineralogical Research Company. The minerals have been analysed by X-ray diffraction for phase identification and by SEM together with electron probe analysis for chemical composition.

2.2. SEM and EDX analysis

For X-ray microanalysis (EDX), samples were embedded in araldite resin and polished with diamond paste on Lamplan 450 polishing cloth using water as a lubricant.

Table 1
Table of Mn-humite and Mg-humite minerals, their formula, number of silicate layers and symmetry class

Mineral name	Origin	Ideal formula	Formula calculated from EDX analysis	Silicate layers	Class
Norbergite	Franklin Limestone Quarry, Franklin, Sussex County, New Jersey	$Mg_3(SiO_4)(OH,F)_2$	$Mg_{2.80}Fe_{0.03}Ca_{0.01}(SiO_4)F_{1.19}(OH)_{0.49}$	1	orthorhombic
Alleghanyite	Hamayokokawa Mine, Tatuno Cho, Nagano Prefecture, Japan	$(Mn^{2+})_5(SiO_4)_2Mg(OH, F,)_2$	$Mn_{11.48}(SiO_4)_2(OH,F)_{3.48}$	2	monoclinic
Leucophoenicite	Parker Shaft, Franklin, Sussex County, New Jersey	$(Mn^{2+})_7(SiO_4)_3(OH)_2$	$Mn_{6.47}Mg_{0.19}Ca_{0.45}(SiO_4)_3(OH)_{2.22}$	3	monoclinic
Sonalite[a]	Franklin Limestone quarry, Franklin, Sussex County, New Jersey	$(Mn^{2+})_9(SiO_4)_4(OH,F)_2$	$Mn_{0.9}{}^{2+}$, $Zn^{2+}0.06$, $Ca_{0.03}{}^{2+}(SiO_4)_4(OH_{0.56}, F_{0.44})$	4	monoclinic

[a] Formula calculated from the data reported by Dunn [24].

Next, the samples were coated with a thin layer of evaporated carbon for conduction and examined in a JEOL 840A analytical SEM (JEOL Ltd., Tokyo, Japan) at 25 kV accelerating voltage. Preliminary analyses of the humite mineral samples were carried out on the FEI Quanta SEM using an EDAX microanalyser (FEI Company, Hillsboro, Oregon, USA), and microanalysis of the clusters of fine crystals was carried out using a full standards quantitative procedure on the JEOL 840 SEM using a Moran Scientific microanalysis system (Tokyo, Japan). Oxygen was not measured directly but calculated using assumed stoichiometries to the other elements analysed.

2.3. UV–Vis spectroscopy

UV–Vis spectrophotometer (Varian Cary 3, Melbourne, Australia), equipped with a Diffuse Reflectance Accessory (DRA) was employed to record the electronic spectra of the samples in the region between 200 and 900 nm (50 000–11 110 cm^{-1}). This technique allows the study of the reflectance spectra of the samples in the powder form. The DRA consists of a 73 mm diameter integrating sphere, featuring an inbuilt high performance photomultiplier. Sample was mounted on coarse filter paper by resuspending the sample and submerging the filter paper into the suspension. Initially a base line was recorded using two pressed polytetrafluoroethylene (PTFE) reference disks. Next, the sample was mounted flat over the sample port and the reflectance spectrum of the sample, relative to the reference disks, was collected by the integrating sphere. By placing the sample flat any specular components of reflectance should be directed out of the DRA entrance port, as the angle of incidence is 0°. The diffuse reflectance measurements were converted into absorption (arbitrary units) using the Kubelka-Munk function. Data manipulation was performed using Microsoft Excel.

2.4. NIR and infrared spectroscopy

NIR spectra were collected on a Nicolet Nexus FT-IR spectrometer with a Nicolet Near-IR Fibreport accessory in diffuse reflectance mode. A white light source was used, with a quartz beam splitter and TEC NIR InGaAs detector. Spectra were obtained from 11 000 to 4000 cm^{-1} (909–2500 nm) by the co-addition of 64 scans at a resolution of 8 cm^{-1}. A mirror velocity of 1.2659 m/s was used. The spectra were transformed using the Kubelka–Munk algorithm ($f(R_\infty) = (1 - R_\infty)^2/2R_\infty$) for comparison with absorption spectra.

Mid-infrared and NIR spectra were obtained using an FT spectrometer (Nicolet Nexus, Madison, Wisconsin, USA) with a ''smart endurance'' single bounce diamond ATR cell. Spectra over the 4000–500 cm^{-1} (2500–20,000 nm) range were obtained by the co-addition of 64 scans with a resolution of 4 cm^{-1} and a mirror velocity of 0.6329 cm/s.

The spectral manipulations of baseline adjustment, smoothing, and normalisation were performed using the Spectracalc software package GRAMS (Galactic Industries Corporation, NH, USA). Band component analysis was carried out using peakfit software (Jandel Scientific, Postfach 4107, D-40688 Erkrath, Germany). Lorentz–Gauss cross product functions were used through out and peak fit analysis undertaken until squared correlation coefficients with R^2 greater than >0.995 were obtained.

3. Results and discussion

3.1. SEM analysis

The EDX quantitative analyses were made on different areas of the samples. and selected one set of EDX spectra of humites studied in this work. The spectra were de-convoluted and calibrated to produce the chemical formula as given in Table 1. The analysis is in harmony with the accepted formula of humites. The data in the table shows Mg is major and Fe as minor impurity in norbergite where as other minerals are rich in manganese with minor inclusions of Mg, Ca, Zn and F. For sonalite, the chemical formula has been calculated from the analytical data reported for manganese humites, including sonalite originating from Franklin, New Jersey [24]. The sonolite mineral from the same origin is used in the present study.

3.2. UV–Vis (electronic) spectroscopy

For a given symmetry, transition metal ion can produce a characteristic absorption spectrum and spectra of minerals may be used to identify ions in unusual oxidation states and the symmetry of co-ordination states. The electronic spectra of iron group ions can be studied in the 200–900 nm region (50 000–11 110 cm^{-1}). The valency of manganese is two in most of the minerals. The ground state for Mn^{2+} (d^5) is ^6S which transforms into $^6A_{1g}$ in crystal field. The excited states of d^5 ions are quartet (^4G, ^4F,^4D,^4P) and doublet (^2I, ^2H,^2G,^2F,^2D,^2P, ^2S) terms. Thus sextet–quartet/sextet–doublet transitions result for d^5 ions and are called spin-forbidden transitions. Usually sextet–quartet transitions are observed and Mn^{2+} ion in octahedral co-ordination gives rise to two broad bands in the range 600–450 nm (16 665–22 220 cm^{-1}) and one sharp band around 400 nm (25 000 cm^{-1}) [41–43]. The study of UV–Vis spectroscopy of humites, reveals the electronic spectra for two samples, alleghanyite and leucophoenicite. It is not surprising to note the absence of a Mn-spectrum in norbergite since Mg is major cation. Whereas in sonolite the contribution by Mn is expected but surprisingly is absent in the spectrum. At least there are two reasons that can be reasonably accounted. The presence of Mn is very low when compared to the other two Mn-bearing humites. The other factor, for the suppression of the spectrum is due to the presence of cations like Zn and Ca. The contribution of cations, like Zn and Ca might be effective for masking

the Mn-type spectrum in sonolite ($Mn_{0.9}^{2+}Zn_{0.06}^{2+}$-$Ca_{0.03}^{2+}(SiO_4)_4(OH_{0.56}F_{0.44})$.

The electronic spectra of the two bivalent Mn-minerals; alleghanyite, $Mn_{11.48}(SiO_4)_2(OH,F)_{3.48}$ and leucophoenicite, $Mn_{6.47}Mg_{0.19}Ca_{0.45}(SiO_4)_3(OH)_{2.22}$ are shown in Fig. 1. The spectra of the two samples look alike but band positions differ only slightly. The observation of two broad bands in the visible range, near 550 and 450 nm (18 180 and 22 220 cm^{-1}) and one very sharp band around 410 nm (24 390 cm^{-1}) are characteristic of Mn^{2+} in these minerals. The first broad feature observed at 549 nm (18 215 cm^{-1}) is attributed to $^6A_{1g}(S) \rightarrow {}^4T_{1g}(G)$ transition and a similar broad band but relatively less intense at 453 nm (22 075 cm^{-1}) is identified as $^6A_{1g}(S) \rightarrow {}^4T_{2g}(G)$ transition. These transitions are shifted for leucophoenicite, at 558 (17 920 cm^{-1}) and 441 nm (22 675 cm^{-1}) with additional shoulder at 435 nm (22 990 cm^{-1}). For Mn-rich mineral, sursasite, bands at 580 nm (17 240 cm^{-1}) and 515 nm (19 420 cm^{-1}) are assigned to $^6A_{1g}(S) \rightarrow {}^4T_{1g}(G)$ and $^6A_{1g}(S) \rightarrow {}^4T_{2g}(G)$ transition respectively [44]. $^4A_{1g}(G)$ and $^4E_{1g}(G)$ states give rise to sharp bands because of these states are independent of crystal-field, *Dq* [45]. The sharp line like bands of alleghanyite in UV region at 413 nm (24 210 cm^{-1}) and 408 nm (24 510 cm^{-1}) are identified as independent crystal-field transitions and are assigned to $^6A_{1g}(S) \rightarrow {}^4A_{1g}(G)$ and $^6A_{1g}(S) \rightarrow {}^4E_{1g}(G)$ transitions respectively. An almost a similar feature is seen for leucophoenicite. These bands are shifted to higher wavenumbers in the UV region. Mn^{2+} in silicate melts and glasses consist of a band at 415 nm (24 095 cm^{-1}) and explained the cause of this band by two transitions, $^6A_{1g}(S) \rightarrow {}^4A_{1g}(G)$ and $^6A_{1g}(S) \rightarrow {}^4E_{1g}(G)$ [46]. The observation of splitting for the UV band at around 410 nm (24 390 cm^{-1}) shows with distinguishable energy may be explained by the distortion of octahedral symmetry of Mn^{2+} ions in both the minerals. The assignment of the Mn^{2+} bands in humites are presented in Table 2 alongwith the bands reported for Mn-bearing silicate [44].The variation in band positions with shifts to higher wavenumbers may be due to the presence of Mg and Ca in these minerals.

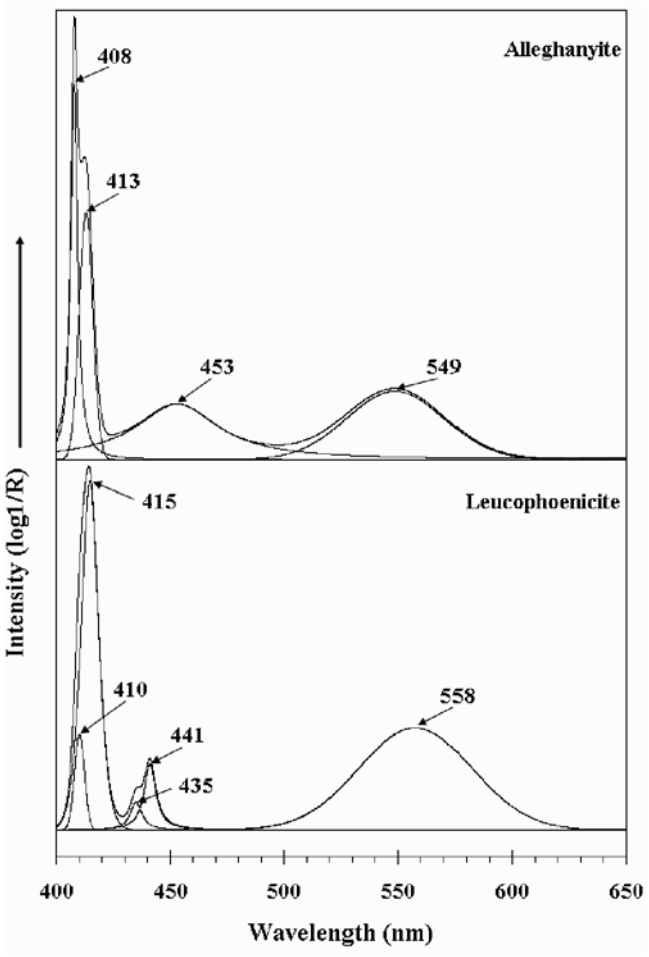


Fig. 1. UV–Vis reflectance spectra of alleghanyite and leucophoenicite in the 400–650 nm region.

3.3. NIR spectroscopy

Near-infrared spectra of Mn-humite mineral group covering a wide range in composition show diagnostic absorption bands related to vibrational processes involving hydroxyl units. Many of these absorption bands are relatively broad and overlapping. However, by the application of spectral analysis methods like continuum removal and derivate analysis permit minerals (under study) to be distinguished. The main spectral differences between the minerals

Table 2
Assignment of Mn^{2+} bands in Mn-humites and a comparison with Mn-silicate sursasite

Transition	Alleghanyite $[Mn_{11.48}(SiO_4)_2(OH,F)_{3.48}]$		Leucophoenicite $[Mn_{6.47}Mg_{0.19}Ca_{0.45}(SiO_4)_3(OH)_{2.22}]$		Sursassite (reported) [44] $[Mn^{2+}Al_3(SiO_4)(Si_2O_7)(OH)_3]$	
	λ (nm)	ν (cm^{-1})	λ (nm)	ν (cm^{-1})	λ (nm)	ν (cm^{-1})
$^6A_{1g}(S) \rightarrow {}^4T_{1g}(G)$	549	18 215	558	17 920	580	17 240
$^6A_{1g}(S) \rightarrow {}^4T_{1g}(G)$					550c	18 180c
$^6A_{1g}(S) \rightarrow {}^4T_{2g}(G)$	453	22 075	441	22 675	515	19 420
$^6A_{1g}(S) \rightarrow {}^4T_{2g}(G)$			435sh	22 990sh		
$^6A_{1g}(S) \rightarrow {}^4A_{1g}(G)$	413	24 210	415	24 095	470	21 280
$^6A_{1g}(S) \rightarrow {}^4E_{1g}(G)$	408	24 510	410	24 390	450c	22 220c

sh—shoulder; c—component.

are illustrated in plots showing major absorption band centres and other spectral feature positions. The observed NIR spectral features may conveniently subdivide into three regions (Figs. 2–4): (a) the first region is the high wavenumber region 7400–6400 cm^{-1} (1351–1562 nm) (1.35–1.56 μm) attributed to the OH-stretching and bending modes (Fig. 2); (b) the 5650–4650 cm^{-1} (1770–2150 nm) (1.77–2.15 μm) region attributed to combination of OH and Si–OH modes shown in Fig. 3 and (c) the 4600–4000 cm^{-1} (2174–2500 nm) (2.17–2.50 μm) region assigned to the combination of the stretching and deformation modes of humite minerals and are related manganese(II) hydroxide and the spectra are shown in Fig. 4.

3.3.1. The 7400–6400 cm^{-1} (1351–1562 nm) (1.35–1.56 μm) spectral region

In this spectral region where the first overtones of the OH-stretching vibrations are shown for norbergite, alleghanyite, leucophoenicite and sonalite in Fig. 2. Norbergite, a single-layered silicate, shows unique spectrum at around 7180 $cm^{-1}$and the spectrum is resolved into one sharp peak at 7180 cm^{-1} (1393 nm) (1.39 μm)and two weak bands at 7165 and 7035 cm^{-1} (1396 and 1422 nm) (1.40 and 1.42 μm). These bands are shifted to lower wavenumbers and appear with distorted modes for the two-layered and three-layered alleghanyite and leucophoenicite minerals respectively. It may also be explained that the possible substitutions of cations of Mn/Zn/Ca/Fe for Mg are responsible for the complexity of bands in their spectra. The spectrum is more complicated for the four-layered sonolite and may be resolved into a series of overlapping bands. The first observation is the spectra of all the four minerals in the region 7400–6400 cm^{-1} (1351–1562 nm) (1.35–1.56 μm) are different and each mineral is characterized by NIR spectrum. Bands from 7180 to 6600 cm^{-1} (1393–1515 nm) (1.39–1.52 μm) correspond to the overtones of OH stretching vibrational modes of the humite groups shown in their IR spectra over the range, 3680–3320 cm^{-1} (Fig. 4). Bands appear as shoulders to the higher wavenumbers of the sharp peak at 7180 cm^{-1} (1393 nm) (1.39 μm) may be attributed to the combination of OH-stretching fundamental and MOH-deformation modes ($2 \times$ OH fundamental + OH deformation) [47]. These spectral features confirm range of compositional variations in humite group minerals. For example, M = Mg in sonalite, the weak shoulders at 7205 cm^{-1}

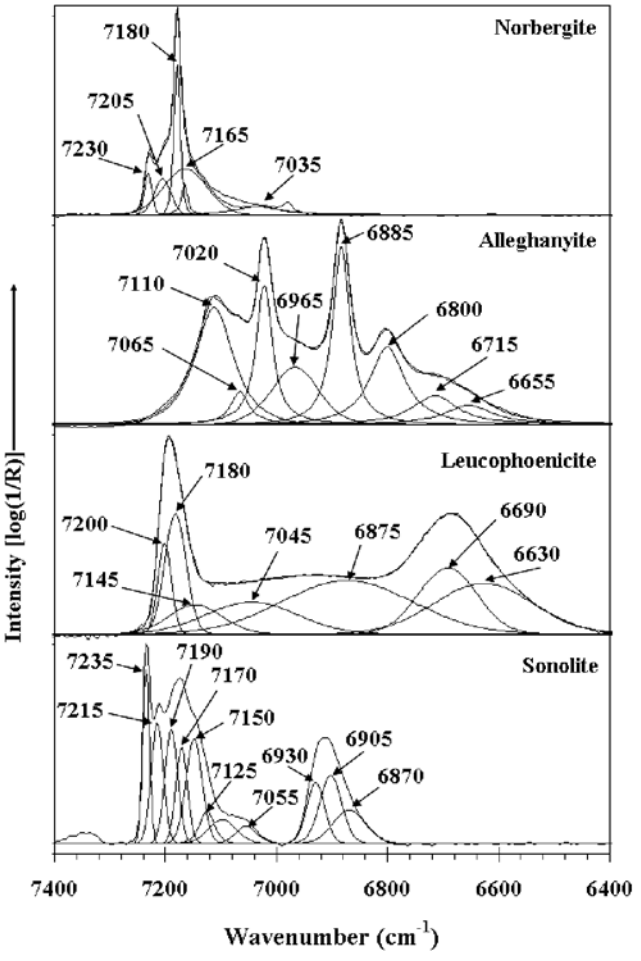


Fig. 2. NIR reflectance spectra of norbergite, alleghanyite, leucophoenicite and sonolite in the 7400–6400 cm^{-1} region.

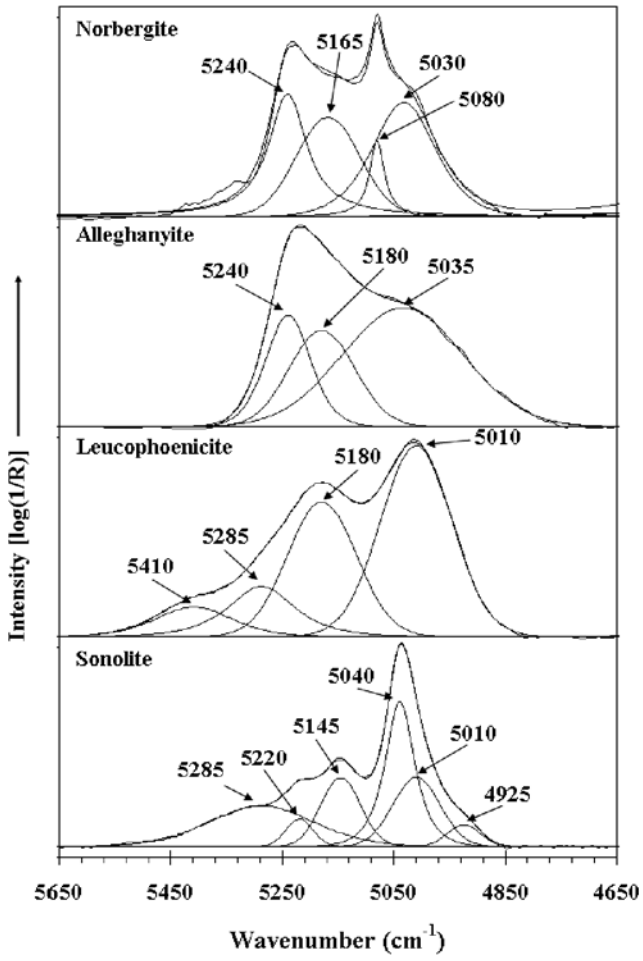


Fig. 3. NIR reflectance spectra of norbergite, alleghanyite, leucophoenicite and sonolite in the 5650–4650 cm^{-1} region.

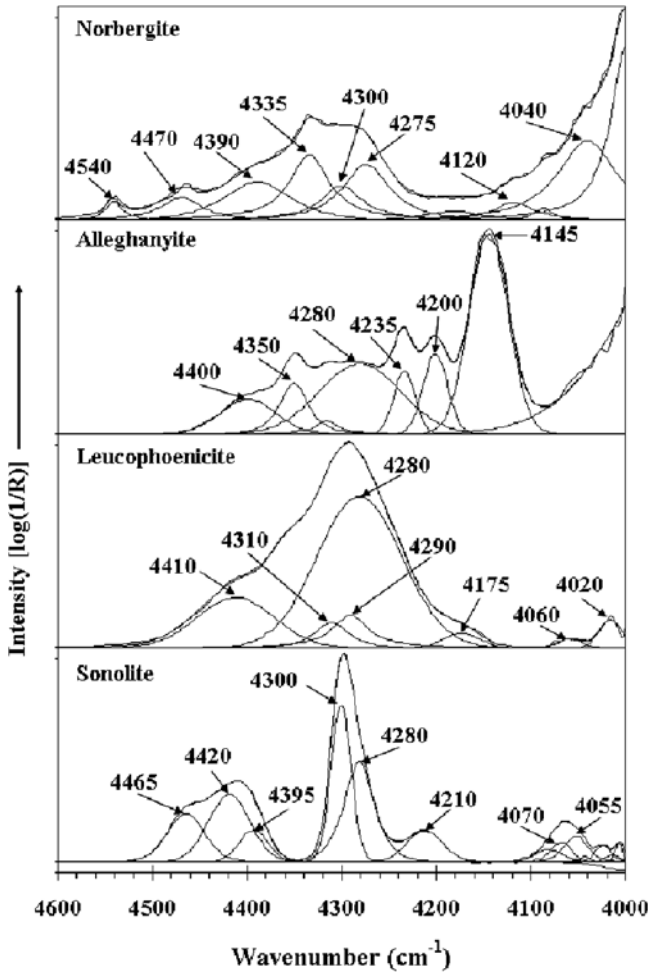


Fig. 4. NIR reflectance spectra of norbergite, alleghanyite, leucophoenicite and sonolite in the 4600–4000 cm^{-1} region.

(1388 nm) (1.39 μm) cm^{-1} might be the result of MgOH. The same band appears with variable band positions and intensity in other minerals. For alleghanyite, leucophoenicite and sonalite 'M' may be Mn/Ca/Zn that causes the change in intensity and positions of bands in the spectrum.

3.3.2. The 5650–4650 cm^{-1} (1770–2150 nm) (1.77–2.15 μm) spectral region

The 5650–4650 cm^{-1} (1770–2150 nm) (1.77–2.15 μm) spectral region (Fig. 3) shows a number of vibrational modes. The broad spectrum centred at 5200 cm^{-1} (1923 nm) (1.92 μm) is a common feature to the spectra of humites. Each spectrum is resolved into three peaks. The most pronounced band registered in all the spectra is near 5030 cm^{-1} (1988 nm) (1.99 μm) is probably due to the combination of OH and Si–OH modes [48]. The observation of the most intense band for Fe-humites at 5200 cm^{-1} (1923 nm) (1.92 μm) has been attributed to the combinational band of OH and Si–OH modes. For norbergite the main bands are located at 5240, 5165 and 5030 cm^{-1} (1908, 1936 and 1988 nm) (1.91, 1.94 and 1.99 μm) and alleghanyite displays almost similar spectrum with a little/minor variation of band positions. The intensity and position of the bands are variable in leucophoenicite and sonalite from one another. The complexity of bands increases with the order of silicate layers in humites. Thus Fig. 3 shows characteristic patterns due to SiO_4 units for single-layered (norbergite), two-layered (alleghanyite), three-layered (leucophoenicite) and four-layered (sonolite) of silicate layers between the brucite layers of humite groups. In particular, the spectrum of four-layered silicate mineral, sonolite shows four individual weak intensity bands at 5285, 5145, 5040 and 5010 cm^{-1} (1892, 1944, 1984 and 1996 nm) (1.89,1.94, 1.98 and 2.00 μm) and three-layered, leucophoenicite at 5410, 5285 and 5180 and 5010 cm^{-1} (1848, 1892, 1931 and 1996 nm) (1.85, 1.89, 1.93 and 2.00 μm) suggest the contribution of weak intensity bands by OH-stretching vibrations of hydroxyl groups.

3.3.3. The 4600–4000 cm^{-1} (2174 to2500 nm) (2.17–2.50 μm) spectral region

This spectral region results from combination of IR fundamental modes observed in the mid-IR range. Fig. 4 shows four main groups of bands at 4540, 4470, 4335, and 4120 cm^{-1} (2203, 2237, 2307 and 2427 nm) (2.20, 2.24, 2.31 and 2.43 μm) for norbergite and a similar series of bands exhibit by Fe-humites. Bands in the range, 4540–4470 cm^{-1} (2203–2237 nm) (2.20–2.24 μm) in humite minerals are the combination of fundamental bands due to Si–OH bonding [49]. The bands around 4500–4300 cm^{-1} (2222–2326 nm) (2.22–2.33 μm) appear due to the combinations of OH-stretching and M–OH bending modes, where M may be Mg, Mn, Al and/or Fe [50]. The observation of combination bands in NIR spectra for tourmalines shows bands at 4529, 4454, 4356 and 4238 cm^{-1} (2208, 2245, 2296 and 2360 nm) (2.21, 2.25, 2.30 and 2.36 μm) [51]. For the humite mineral group, three bands centred at 4300, 4200 and 4100 cm^{-1} (2326, 2381 and 2439 nm) (2.33, 2.38 and 2.44 μm) and same set of bands are displayed by norbergite and alleghanyite with minimal band position differences. Well resolved bands appear in leucophoenicite and sonalite near 4300 cm^{-1} (2326 nm) (2.33 μm) band. OH-bending mode is clearly resolved in humites near 756–724 cm^{-1}. The second band in the range 4300–4200 cm^{-1} (2326–2381 nm) (2.33–2.38 μm) is attributed to MnOH vibrations (combination of OH-stretching and M–OH-bending modes) [50]. The low wavenumber bands near 4100 cm^{-1} (2439 nm) (2.44 μm) may be attributed to (Mg/Ca/Zn)OH units. The shift of combination bands of OH-stretching and M–OH bending modes to lower wavenumbers in humite groups shows compositional variation and possible substitutions of Mn^{2+}, Fe^{2+}, Zn^{2+}, Ca^{2+} for Mg^{2+}.

3.4. Mid-IR spectroscopy

The mid-infrared spectra of the humite minerals are subdivided into three regions according to the observed features in their spectra.

(1) The 3750–3250 cm^{-1} region corresponds to OH-stretching vibrations.
(2) The 1100–500 cm^{-1}region corresponds to the various stretching and bending vibrations of SiO_4 units.

The spectra of OH-stretching region are shown in Fig. 5. The stretching and bending vibrations in the ranges, 1050–800 cm^{-1} and 750–500 cm^{-1} are shown in Fig. 6. The hydrous components of OH and SiO_4 groups in the mineral structure act as an aid to distinguish the humite group minerals by FTIR spectroscopy. This technique is a rapid one and most sensitive to identify the OH and SiO_4 groups in minerals. The spectra of the hydroxyl-stretching region of humites are shown in Fig. 5. Norbergite shows two bands at 3581 and 3572 cm^{-1} whereas the spectrum of alleghanyite shifts to lower wavenumbers with a splitting of the second band and the bands are 3528, 3484, 3495 and 3469 cm^{-1}. The three-layered leucophoenicite spectrum also moved further to a lower region at 3368, 3344, 3322 and 3284 cm^{-1}. The OH region of four-layered becomes complex and more number of bands resolved at 3679, 3642, 3542 and 3465 cm^{-1} for sonolite. The shift to lower

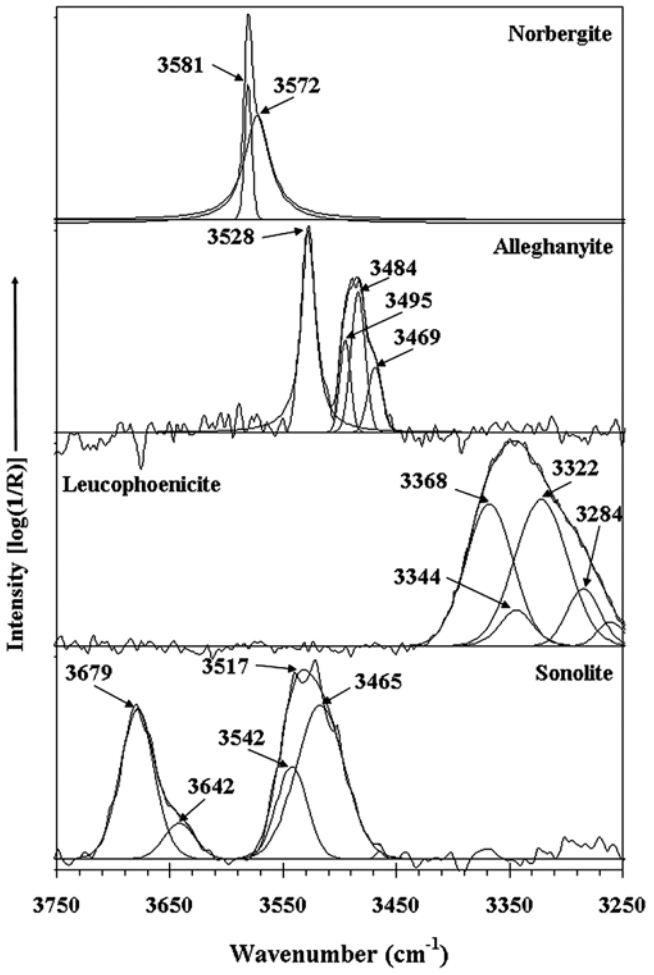


Fig. 5. IR reflectance spectra of norbergite, alleghanyite, leucophoenicite and sonolite in the 3750–3250 cm^{-1} region.

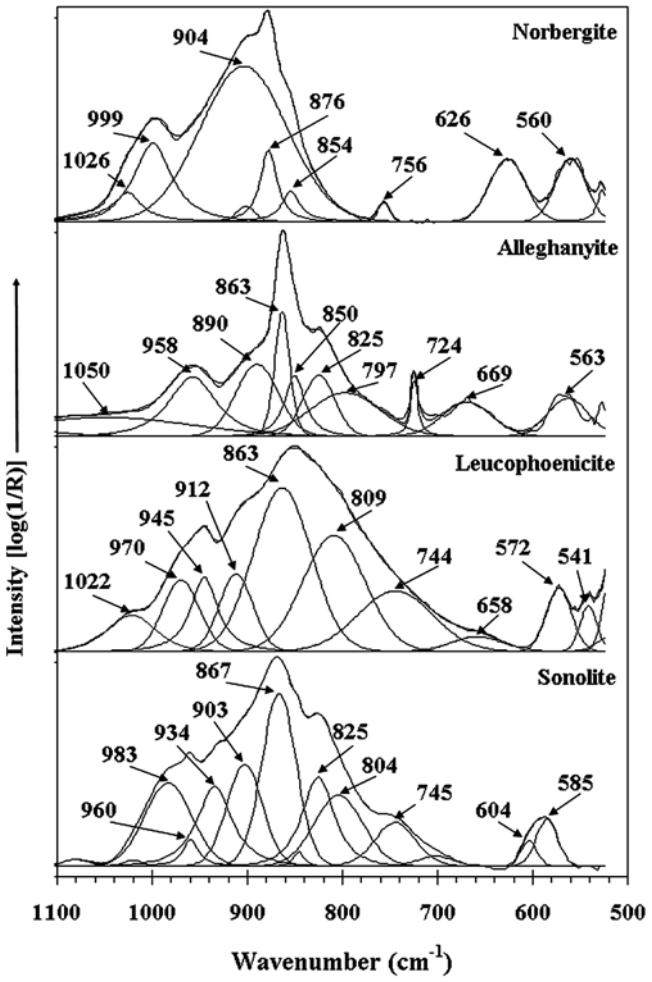


Fig. 6. IR reflectance spectra of norbergite, alleghanyite, leucophoenicite and sonolite in the 1100–500 cm^{-1} region.

energy of the spectrum might be the cause of cations like, Ca and Zn, besides Mn in sonolite. A set of six modes at 3685, 3650, 3571, 3561, 3411 and 3393 cm^{-1} have been reported in the OH fundamental stretching region of chondrodite from Keral Khondalite Belt, India [47]. Analysis of IR spectra of Mg-rich chondrodites having cation impurities like Fe, Ti shows various stretching and bending modes of (Mg–O) and (SiO_4) groups. The assignment of the observed vibrational modes for OH-stretching vibrations and SiO_4 stretching/bending vibrations in IR-spectra of humite minerals is presented in Table 3 and compared with data reported for chondrodites from different localities: (1) chondrodite from Keral Khondalite Belt, India [47], (2) sample originated from Limecrest Quarry, Newton, New Jersey, USA [52] and the mineral from UC, Berkeley, USA [53]. The reason for the difference in band positions of the OH-stretching vibrations is attributed to the strength of the hydrogen bond formed between the OH units of the brucite-like layer and the adjacent olivine layers. It is clear from their spectra (Fig. 5) the complexity of OH spectrum increases with number of silicate layers in humites. However, IR spectroscopy is able to differentiate the mineral group from one, two, three or four-layered of

Table 3
Assignments of the observed IR modes (cm^{-1}) for different humite minerals

Norbergite (Franklin Limestone Quarry, New Jersey) [Present study]	Alleghanyite (Hamayokokawa Mine, Japan) [Present study]	Leucophoenicite (Parker Shaft, New Jersey) [Present study]	Sonalite (Franklin Limestone quarry, New Jersey) [Present study]	Chondrodite (Kerala Khondalite Belt, India) [47]	Chondrodite (Limecrest Quarry, New Jersey, USA) [52]	Chondrodite (UC, Berkeley, USA) [53]	Assignment
			3679	3692	3687	3690	hydroxyl stretch
			3642sh	3674		3662	hydroxyl stretch
3581	3528			3571			hydroxyl stretch
3572	3495			3412	3568	3568	hydroxyl stretch
	3484		3465		3559	3560	hydroxyl stretch
	3469sh						
		3368		3412			hydroxyl stretch
		3344c		3392c			
		3322			3385	3382	hydroxyl stretch
		3284sh					
1026	1050	1022					SiO_4-asymmetric stretch
999	958	970	983	997	987	994	SiO_4-asymmetric stretch
904	890	945	903sh	961	955	955	SiO_4-asymmetric stretch
		912sh					
876	863	863	867	887	891	892	SiO_4-asymmetric stretch
854	850		825	847	850	851	SiO_4-asymmetric stretch
	825	809	804				SiO_4-asymmetric stretch
	797sh						
756	724	744	745	754	761	757	M–OH deformation
				745sh	748sh		
626	669	658	604	613	619	618	SiO_4-asymmetric bend/ MgO_6 motion
560	563	572	585				MO stretching vibrations (M = Fe/Mn/Ca/Zn)
		541		534	541	551	MO stretching vibrations (M = Fe/Mn/Ca/Zn)
				494	489		MOH deformation vibrations (M = Fe/Mn/Ca/Zn)
					440		MOH vibrations (M = Fe/Mn/Ca/Zn)
				420	418		MOH vibrations (M = Fe/Mn/Ca/Zn)
					397		MOH vibrations (M = Fe/Mn/Ca/Zn)

sh—shoulder; c—component.

silicates of humite mineral group, norbergite, alleghanyite, leucophoenicite, sonalite by the main OH bands observed at 3581, 3484 and 3322 cm^{-1} respectively with an exception to 3679 cm^{-1} in sonolite.

There are several investigations published on hydrous magnesium silicates and analyses present for stretching and bending modes of Mg–O and SiO_4 groups in the mid-infrared region [52–55]. Number of modes have been detected in the region 1100–500 cm^{-1} for the various compositions (Fig. 6). All the network modes concerned with SiO_4 stretching modes observed here in the range 1050–800 cm^{-1} are comparable with the modes reported in chondrodites (Table 3). Norbergite, a Mg-humite, gives rise to five mode at 1026, 999, 904, 876 and 854 cm^{-1}. The spectra of all Mn-bearing humites, were observed to have shifted to lower wavenumber. All the samples show a number of peaks on either side of the most intense peak centred near 876 cm^{-1}. The patterns look alike but show bands with varying intensities and band positions. Thus the main SiO_4 stretching mode centred near 876 cm^{-1}(Fig. 6) shows shift to lower wavenumber for Mn-bearing minerals, alleghanyite, leucophoenicite and sonalite. The spectra leucophoenicite and sonalite which are the minerals with three and four-silicate layers respectively show increased in complexity and overlapping bands. The M–OH deformation modes observed near 756 cm^{-1} and two weak bands near 680–500 cm^{-1} are the most probable result of SiO_4 bending vibrations and Mn–O vibrations.

4. Conclusions

The study of UV–Vis spectroscopy of humites, reveals the electronic spectra by two samples, alleghanyite and leucophoenicite. It is of surprise to see the absence of Mn-type spectrum in sonolite, even though the representative chemical formula obtained from EDX analysis shows the presence of manganese in the sample and may be accounted for the impurities like cations of Ca and Zn. The loss of the Mn-spectrum for sonolite, looks as if cation impurities like Ca and Zn are responsible $(Mn_{0.9}{}^{2+}Zn_{0.06}{}^{2+}Ca_{0.03}{}^{2+}(SiO_4)_4(OH_{0.56}F_{0.44}))$.

A pair of sharp bands of alleghanyite and leucophoenicite in UV region at around 410 nm (24 390 cm^{-1}) is identified as due to independent crystal-field transitions of Mn^{2+} ion and are assigned to $^6A_{1g}(S) \rightarrow {}^4A_{1g}(G)$ and $^6A_{1g}(S) \rightarrow {}^4E_{1g}(G)$ transitions. The observation of splitting (300 cm^{-1}) (5 nm) of the UV band shows with distinguishable energy may be explained by the distortion of octahedral symmetry of the Mn-bearing humites. The shift of combinational bands of OH-stretching and M–OH bending modes to lower wavenumbers in humite group minerals shows compositional variation and possible substitutions of Mn^{2+}, Fe^{2+}, Zn^{2+}, Ca^{2+} for Mg^{2+}. The humite mineral group is characterized by two OH-stretching vibrations over the range 3680–3320 cm^{-1}. A series of SiO_4 stretching modes displayed over the range, 1050–800 cm^{-1} symmetrically on either side of an intense peak centred near 876 cm^{-1} and the complexity of SiO_4 stretching and bending spectra increases with the number of silicate layers in Mn-bearing humite minerals.

Acknowledgements

The financial and infra-structure support of the Queensland University of Technology, Inorganic Materials Research Program is gratefully acknowledged. The Australian Research Council (ARC) is thanked for funding the instrumentation. One of the authors, B. Jagannadha Reddy is grateful to the Queensland University of Technology for the award of a Visiting Fellowship.

References

[1] C. Palache, Cambridge Am. J. Sci. 29 (1910) 177.
[2] P. Geijer, Geol. For. Forh. 48 (1926) 84.
[3] W.H. Taylor, J. West, Proc. Roy. Soc. (London) A117 (1927) 517.
[4] E.S. Larsen, Am. Mineral. 13 (1928) 354.
[5] E.S. Larsen, L.H. Bauer, H. Berman, Am. Mineral. 13 (1928) 349.
[6] A.F. Rogers, Am. Mineral. 20 (1935) 25.
[7] K. Rankama, Bull. Commun. Geol. Finlande 123 (1938) 81.
[8] H. Strunz, Z. Kristallogr., Kristallgeomet., Kristallphys., Kristallchem. 99 (1938) 513.
[9] K. Rankama, Am. Mineral. 32 (1947) 146.
[10] N.W. Jones, Am. Mineral. 54 (1969) 309.
[11] R.M. Ganiev, Y.A. Kharitonov, V.V. Ilyukhin, N.V. Belov, Dokl. Akad. Nauk SSSR 188 (1969) 1281.
[12] G.V. Gibbs, P.H. Ribbe, Am. Mineral. 54 (1969) 376.
[13] N.W. Jones, P.H. Ribbe, G.V. Gibbs, Am. Mineral. 54 (1969) 391.
[14] G.V. Gibbs, P.H. Ribbe, C.P. Anderson, Am. Mineral. 55 (1970) 1182.
[15] P.J. Rentzeperis, Z. Kristallogr, Kristallgeomet., Kristallphys., Kristallchem. 132 (1970) 1.
[16] Y.K. Egorov-Tismenko, I.P. Deineko, M.A. Simonov, N.V. Belov, Kristallografiya 16 (1971) 1174.
[17] P.H. Ribbe, G.V. Gibbs, Am. Mineral. 56 (1971) 1153.
[18] P.J. Rentzeperis, Chim. Chron. 1 (1972) 267.
[19] E.L. Belokoneva, M.A. Simonov, N.V. Belov, Kristallografiya 18 (1973) 1275.
[20] K. Robinson, G.V. Gibbs, P.H. Ribbe, Am. Mineral. 58 (1973) 43.
[21] P.H. Ribbe, G.V. Gibbs, N.W. Jones, Mineral. Mag. J. Mineral. Soc. 36 (1876-1968) 966.
[22] W.B. Simmons Jr., D.R. Peacor, E.J. Essene, G.A. Winter, Mineral. Record 12 (1981) 167.
[23] G.A. Winter, E.J. Essene, D.R. Peacor, Am. Mineral. 68 (1983) 951.
[24] P.J. Dunn, Am. Mineral. 70 (1985) 379.
[25] J.W. Anthony, R.A. Bideaux, K.W. Bladh, M.C. Nichols, in: Phosphates, Arsenates and Vanadates, Handbook of Mineralogy, vol. IV, Mineral Data Publishing, Tucson, Arizona, 2003.
[26] B. Wunder, Contrib. Mineral. Petrol. 132 (1998) 111.
[27] P.H. Ribbe, Rev. Miner. 5 (1980) 231.
[28] K.B.N. Sarma, B. Madhusudhana, B.J. Reddy, S. Vedanand, G. Srinivasulu, Solid State Commun. 78 (1991) 751.
[29] K.B.N. Sarma, B.J. Reddy, S.V.J. Lakshman, Proc. Nucl. Phys. Solid State Phys. Sympos. C 24 (1982) 471.
[30] A.N. Platonov, K. Langer, M. Wildner, E.V. Polshin, S.S. Matsyuk, Z. Kristallogr. 216 (2001) 154.
[31] L.G. Liu, C.C. Lin, T.P. Mernagh, Eur. J. Mineral. 11 (1999) 1011.
[32] P.H. Ribbe, Reviews in Mineralogy, vol. 5, Mineralogical Society of America, Washington, DC, 1982, p. 231.

[33] P.J. Rentzeperis, Z. Kristallogr. 132 (1970) 1.
[34] O.V. Petersen, J. Bullhorn, P.J. Dunn, Mineral. Record 15 (1984) 299.
[35] C.A. Francis, Am. Mineral. 70 (1985) 182.
[36] S.L. Penfield, C.H. Warren, Am. J. Sci. 8 (1899) 339.
[37] P.B. Moore, Am. Mineral. 52 (1967) 1226.
[38] P.B. Moore, Am. Mineral. 55 (1970) 1146.
[39] T.J. White, B.G. Hyde, Am. Mineral. 68 (1983) 1009.
[40] M. Yoshinaga, Memoir Faculty of Science, Kyushu University, Series D, Geology, vol. 14, 1963, p. 1.
[41] P.G. Manning, Can. Mineral. 9 (1968) 348.
[42] K.L. Keester, W.B. White, in: Papers and Proc. 5th Gen. Meet., Cambridge, England, Mineral. Soc., London, 1968, p. 22.
[43] D.S. McClure, Chem. Phys. 39 (1963) 2284.
[44] B. Jagannadha Reddy, R.L. Frost, Spectrochim. Acta Part A 65 (2006) 684.
[45] C.J. Ballhausen, Introduction to Ligand Field Theory, Mc-Graw Hill Book Company, New Delhi, 1962.
[46] H. Keppler, Am. Mineral. 77 (1992) 62.
[47] P.S.R. Prasad, L.P. Sarma, Am. Mineral. 89 (2004) 1056.
[48] P. Yu, R.J. Kirkpatrick, B. Poe, P.F. McMillan, X. Cong, J. Am. Ceram. Soc. 82 (1999) 742.
[49] A.K. Kronenberg, Reviews in Mineralogy, vol. 29, Mineralogical Society of America, Washington, DC, 1994, p. 123.
[50] R.N. Clark, T. King, M. Klefwa, G.A. Swayze, N.J. Vergo, Geophys. Res. B95 (1990) 12653.
[51] P.S.R. Prasad, D.S. Sarma, Gondwana Res. 8 (2005) 265.
[52] H. Cynn, A.M. Hofmeister, P.C. Burnley, A. Novrotsky, Phys. Chem. Mineral. 23 (1996) 361.
[53] Q. Williams, Vibrational spectroscopic study of hydrogen in high pressure minerals assemblages, in: Y. Syono, M.M. Manghnani (Eds.), High Pressure Research: Applications to Earth and Planetary Sciences, Terra Publishing Company, Tokyo, 1992, p. 289.
[54] M. Akaogi, S.I. Akimoto, Phys. Chem. Mineral. 13 (1986) 161.
[55] A.M. Hofmeister, H. Cynn, P.C. Burnley, C. Meade, Am. Mineral. 84 (1999) 454.

Available online at www.sciencedirect.com
ScienceDirect
Polyhedron 26 (2007) 535–542
POLYHEDRON
www.elsevier.com/locate/poly

Syntheses and study on nickel and copper complexes with 1,3,5-benzenetricarboxylic acid. Crystal and molecular structure of $[Cu_3(mdpta)_3(btc)](ClO_4)_3 \cdot 4H_2O$

Pavel Kopel [a,*], Jiří Kameníček [a], Václav Petříček [b], Aleš Kurečka [a], Božena Kalinska [c], Jerzy Mrozinski [c]

[a] Department of Inorganic Chemistry, Faculty of Science, Palacký University, Křížkovského 10, CZ-771 47 Olomouc, Czech Republic
[b] Institute of Physics, Academy of Science, Na Slovance 10, CZ-18221 Prague, Czech Republic
[c] Faculty of Chemistry, University of Wroclaw, 14 F. Joliot-Curie, PL-50 383 Wroclaw, Poland

Received 26 May 2006; accepted 4 August 2006
Available online 18 August 2006

Abstract

Nickel and copper complexes containing 1,3,5-benzenetricarboxylic acid, with a combination of selected N-donor ligands and Schiff bases, of the composition $Ni_3(bimz)_6(btc)_2 \cdot 12H_2O$ (**1**), $Ni_3(btz)_9(btc)_2 \cdot 12H_2O$ (**2**), $Ni_2(L_1)(btc) \cdot 7H_2O$ (**3**), $Ni_3(L_2)_2(Hbtc) \cdot 9H_2O$ (**4**), $Ni_2(L_3)(btc) \cdot 4H_2O$ (**5**), $Cu_2(L_4)(btc) \cdot 7H_2O$ (**6**), $[Cu_3(pmdien)_3(btc)](ClO_4)_3 \cdot 6H_2O$ (**7**) and $[Cu_3(mdpta)_3(btc)](ClO_4)_3 \cdot 4H_2O$ (**8**); H_3btc = 1,3,5-benzenetricarboxylic acid, bimz = benzimidazole, btz = 1,2,3-benztriazole, L_1 = 2-[(phenylimino)methyl]phenol, L_2 = *N*,*N*′-bis-(salicylidene)propylenediamine, L_3 = 2-{[(2-nitrophenyl)methylene]amino}phenol, L_4 = 2-[(4-methoxy-phenylimino)methyl]-phenol, pmdien = *N*,*N*,*N*′,*N*″,*N*″-pentamethyldiethylenetriamine, mdpta = *N*,*N*-bis-(3-aminopropyl)methylamine, have been synthesized. The complexes have been studied by elemental analysis, IR, UV–Vis spectroscopies, magnetochemical and conductivity measurements and selected compounds also by thermal analysis. The crystal and molecular structure of complex **8** was solved. The complex is trinuclear with btc^{3-}-bridge. The coordination polyhedron around each copper atom can be described as a distorted square with a $CuON_3$ chromophore formed by one oxygen atom of carboxylate and three nitrogen atoms of mdpta. The magnetic properties of **8** have been studied in the 1.8–300 K temperature range revealing a very weak antiferromagnetic exchange interaction with $J = -0.56\ cm^{-1}$ for $g = 2.13(9)$. The antimicrobial activities against selected strains of bacteria were evaluated. It was found that only complex **5** is able to inhibit the growth of *Staphylococcus* strains.
© 2006 Elsevier Ltd. All rights reserved.

Keywords: Nickel(II); Copper(II); 1,3,5-Benzenetricarboxylic (trimesic) acid complexes; X-ray structure; Magnetic properties

1. Introduction

Transition metal complexes with N-donor ligands bridged by carboxylic acids are studied not only for interesting magnetic and spectral properties, but also as catalysts or nano-materials precursors and for applications in pharmaceutical industry for their potential antibacterial, antiviral and antitumour effects [1–3].

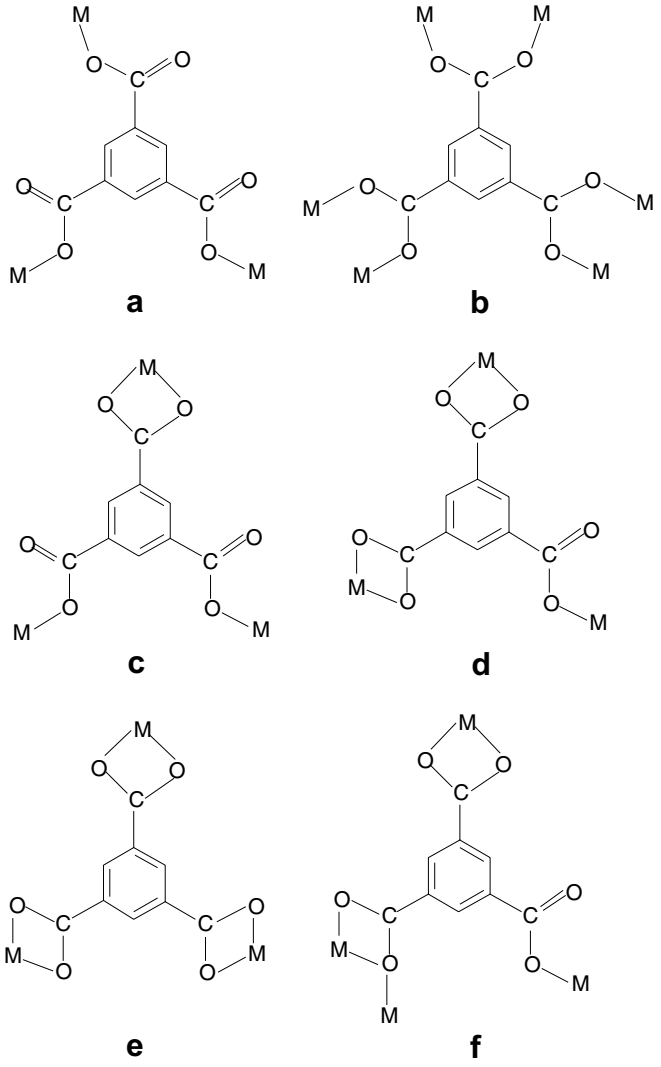
1,3,5-Benzenetricarboxylic acid (trimesic acid) is a tricarboxylic acid with potentially six oxygen donor atoms, which can be coordinated to the central atoms in different coordination modes. Transition metal complexes with the 1,3,5-benzenetricarboxylate anion which is not coordinated to central atom are rather rare [4,5]. Many polynuclear complexes with a btc bridge have been studied and different coordination modes of carboxylato groups have been proved by X-ray analysis: (a) tris-monodentate [6–8]; (b) tris-bidentate [9]; (c) chelating bidentate and bis-monodentate [10]; (d) chelating bis-bidentate and monodentate [11];

* Corresponding author. Tel.: +420 585634354; fax: +420 585225737.
E-mail address: pavel.kopel@upol.cz (P. Kopel).

0277-5387/$ - see front matter © 2006 Elsevier Ltd. All rights reserved.
doi:10.1016/j.poly.2006.08.010

(e) chelating tris-bidentate [12]; chelating/bridging bidentate and monodentate [13] (see Scheme 1). Nickel complexes with btc in combination with tetraaza- and hexaazamacrocyclic ligands, pyridine derivatives or polybasic alcohols, have been prepared and structurally characterized [14–19]. The hydrothermal method has been used for the preparation of Mn, Co and Zn complexes with a $btcH^{2-}$ bridge. The structures consist of double stranded chains of dianions and dimeric units. Magnetic studies showed that a ferromagnetic interaction occurs in Mn and Co complexes [20]. Synthesis and study of copper complexes containing btc bridges and *N*-heterocyclic amines have been reported [21–23]. Comba et al. have prepared a copper complex; X-ray analysis confirmed that the btc^{3-} anion is situated outside the coordination sphere [24].

The aim of our work was the preparation and study of nickel and copper complexes containing a combination of btc^{3-} anion and selected N-donor ligands or Schiff bases in the coordination sphere (the used ligands are depicted in Scheme 2). The ligands were used to block coordination sites of the central atoms and to prevent formation of polymers. We prepared also trinuclear species and solved the X-ray structure of complex **8**. EPR and magnetic study of the complex proved that the benzenetricarboxylate bridge is not suitable for exchange interactions between the central atoms.



Scheme 1. Coordination modes of benzene-1,3,5-tricarboxylic acid (H_3btc).

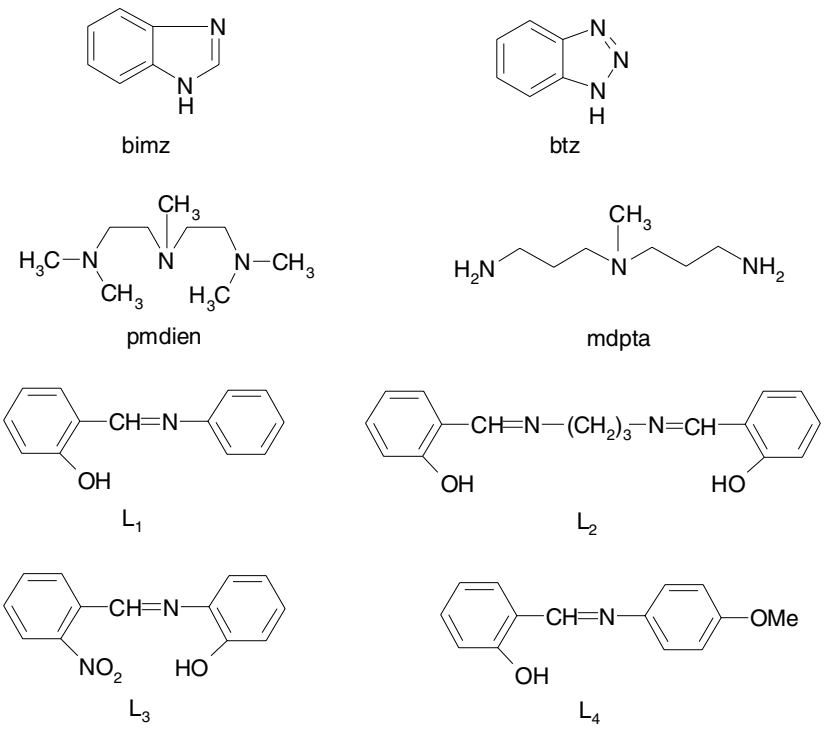
2. Experimental

2.1. Materials and methods

All chemicals and solvents were supplied from Aldrich, Carlo Erba and Lachema (Czech Republic) and were used as received. Compound $Ni(Hbtc) \cdot 12H_2O$ was prepared by the reaction of $NiCO_3 \cdot 2Ni(OH)_2 \cdot 4H_2O$ (6.76 g, 30 mmol) and H_3btc (7.10 g, 20 mmol) in water (50 cm^3). The reaction mixture was refluxed for 5 h. After cooling, a green precipitate was filtered off, washed with water and dried in air. Schiff base L_2 was obtained by condensation of salicylaldehyde (4.18 cm^3, 20 mmol) with 1,3-diaminopropane (1.66 cm^3, 20 mmol) in ethanol (100 cm^3). Na_3btc was prepared by neutralization of H_3btc (2.1 g, 10 mmol) with NaOH (1.2 g, 30 mmol) in water (100 cm^3).

The C, H, N analyses were carried out on an EA 1108 instrument (Fisons). The content of nickel and copper was determined by chelatometric titration on murexid as an indicator. UV–Vis spectra were recorded on an UV–Vis Spectrometer Lambda 35 (Perkin–Elmer) and IR spectra on a FT-IR Spectrometer Spectrum One (Perkin–Elmer) using KBr pellets. The molar conductivity was measured on a Conductivity Meter LF 340 (WTW, Germany). Thermal analysis was performed on an Exstar (Seiko Instruments Inc.). Magnetochemical data at room temperature were obtained by the Faraday method. $Hg[Co(SCN)_4]$ was used as a calibrant. Magnetization measurements at a magnetic field of 0.5 T in the temperature range 1.8–300 K were performed using a Quantum Design SQUID-based MPMSXL-5-type magnetometer. The SQUID magnetometer was calibrated with a palladium rod sample (Materials Research Corporation, measured purity 99.9985%). The superconducting magnet was generally operated at a field strength ranging from 0 to 5 T. Corrections are based on subtracting the sample-holder signal and contribution χ_D estimated from Pascal constants (-401×10^{-6} cm^3 mol^{-1} per trimer). A temperature-independent paramagnetism of 60×10^{-6} cm^3 K mol^{-1} for the copper(II) ion was used. Additional magnetization measurements were made at 2 K in a magnetic field from 0 to 5 T. EPR spectra were recorded at 293 and 77 K on a Bruker ESP 300 spectrometer operating at X-band equipped with an ER 035M Bruker NMR gaussmeter and an HP 5350B Hewlett–Packard microwave frequency counter. The spectrum at 4.2 K was measured with an X-band Radiopan SE/X 2543 Spectrometer.

The antimicrobial activities of the complexes against *Staphylococcus aureus* CCM 3953, *Enterococcus faecalis* CCM 4224, *Escherichia coli* CCM 3954, *Pseudomonas*



Scheme 2. Structural formulas of used ligands.

aeruginosa CCM 3955, *Staphylococcus epidermidis*, *S. aureus* MRSA, *Enterococcus faecium* VRE and *Klebsiella pneumoniae* ESBL were estimated and expressed as minimal inhibitory concentrations MIC ($\mu g\,mL^{-1}$). The bacteria were inoculated into a liquid medium (Mueller–Hinton or Brain Heart Infusion broth). The test complexes were dissolved in DMSO and diluted by water. Solutions with concentrations 100–0.78 $\mu g\,mL^{-1}$ were used for testing. Bacteria were cultured for 24 h at 37 °C; then the growth of microorganisms was observed. When no growth of microorganisms was observed in the medium containing the lowest concentration of test materials, the MIC of the test material was defined at this point of dilution. All compounds were tested two times and results are given as an average of two independent experiments [25].

2.2. Syntheses

2.2.1. $Ni_3(bimz)_6(btc)_2 \cdot 12H_2O$ (**1**)

Bimz (0.47 g, 4 mmol), dissolved in ethanol (96%, 25 cm^3) was added to a suspension of $Ni(Hbtc) \cdot 12H_2O$ (0.48 g, 1 mmol) in water (50 cm^3). The reaction mixture was refluxed for 5 h. After cooling a violet-blue precipitate was filtered off, washed with small amounts of ethanol and dried at room temperature. Yield: 64%.

2.2.2. $Ni_3(btz)_9(btc)_2 \cdot 12H_2O$ (**2**)

A solution of $Ni(ClO_4)_2 \cdot 6H_2O$ (0.37 g, 1 mmol) in water (25 cm^3) was mixed with a solution of Na_3btc (0.1 mol/dm^3, 3.3 cm^3). After addition of btz (0.24 g, 2 mmol) dissolved in hot water (25 cm^3) a violet-blue precipitate was formed. It was filtered off, washed with water and dried at room temperature. Yield: 56%.

2.2.3. $Ni_2(L_1)(btc) \cdot 7H_2O$ (**3**)

$NiCl_2 \cdot 6H_2O$ (0.24 g, 1 mmol) was dissolved in ethanol (25 cm^3). After addition of Schiff base L_1 (0.20 g, 1 mmol) a yellow-green solution was obtained. Triethylamine (0.14 cm^3, 1 mmol) was added and solution color changed to dark green. After addition of a solution of Na_3btc (0.1 mol/dm^3, 3.3 cm^3) a green precipitate was formed. It was filtered off, washed with water and ethanol and dried at room temperature. Yield: 44%.

2.2.4. $Ni_3(L_2)_2(Hbtc) \cdot 9H_2O$ (**4**)

$NiCl_2 \cdot 6H_2O$ (0.23 g, 1 mmol) was dissolved in ethanol (25 cm^3). After addition of a solution of Schiff base L_2 (0.2 mol/dm^3, 5 cm^3), a dark green solution was obtained. Triethylamine (0.14 cm^3) was added and the solution color turned brown-red. After addition of a solution of Na_3btc (0.1 mol/dm^3, 3.3 cm^3) a green precipitate was obtained. It was filtered off, washed with water and ethanol and dried at room temperature. Yield: 71%.

2.2.5. $Ni_2(L_3)(btc) \cdot 4H_2O$ (**5**)

$Ni(ClO_4)_2 \cdot 6H_2O$ (0.37 g, 1 mmol) was dissolved in ethanol (50 cm^3). After addition of Schiff base L_3 (0.49 g, 2 mmol) a brown-yellow solution was obtained. Triethylamine (0.28 cm^3) was added and the solution color turned dark red. After addition of a solution of Na_3btc (0.1 mol/dm^3, 3.3 cm^3) a brown precipitate was formed. It was

filtered off, washed with water and ethanol and dried at room temperature. Yield: 69%.

2.2.6. $Cu_2(L_4)(btc)\cdot 7H_2O$ (6)

$CuCl_2\cdot 2H_2O$ (0.17 g, 1 mmol) was dissolved in methanol (25 cm^3). After addition of Schiff base L_4 (0.23 g, 1 mmol) a brown-yellow solution was obtained. Triethylamine (0.14 cm^3) was added and the solution color turned dark brown. After addition of a solution of Na_3btc (0.1 mol/dm^3, 3.3 cm^3) a brown precipitate was obtained. It was filtered off, washed with water and ethanol and dried at room temperature. Yield: 77%.

2.2.7. $[Cu_3(pmdien)_3(btc)](ClO_4)_3\cdot 6H_2O$ (7)

Pmdien (0.21 cm^3, 1 mmol) was added to a solution of $Cu(ClO_4)_2\cdot 6H_2O$ (0.37 g, 1 mmol) in water (25 cm^3). After addition of Na_3btc solution (0.1 mol/dm^3, 3.3 cm^3), a dark blue precipitate was formed. It was filtered off, washed with ethanol and dried at room temperature. Yield: 56%.

2.2.8. $[Cu_3(mdpta)_3(btc)](ClO_4)_3\cdot 4H_2O$ (8)

Mdpta (0.32 cm^3, 2 mmol) was added to a solution of $Cu(ClO_4)_2\cdot 6H_2O$ (0.74 g, 2 mmol) in ethanol (50 cm^3) After addition of a solution of Na_3btc (0.1 mol/dm^3, 3.3 cm^3), a dark blue solution was obtained. Dark blue crystals were obtained in one week. The crystals were collected on a frit, washed with water and dried at room temperature. Yield: 48%.

2.3. X-ray crystallography

X-ray data were collected using a four circle κ-axis diffractometer Xcalibur™2 (Oxford Diffraction) equipped with a Sapphire2 CCD detector, a monochromator Enhance and a Cryojet cooler system, using Mo Kα radiation at 107 K. The CrysAlis program package (1.171.7 version) was used for data reduction. Details of the structure are discussed in Section 3.2.

3. Results and discussion

3.1. Physical techniques

The results of the elemental analyses and physico-chemical study are listed in Tables 1 and 2. The IR spectra of all the complexes show the characteristic bands of carboxylate groups in the region 1542–1614 cm^{-1} for the $\nu_{as}(COO^-)$ and 1350–1378 cm^{-1} for the $\nu_s(COO^-)$ vibrations. IR spectra of complexes containing Schiff bases (**3**–**6**) exhibit bands at 1614–1618 cm^{-1}, which can be assigned to the ν(C=N) vibrations. In the IR spectra of copper complexes **7** and **8** bands were found at 1096, 618 cm^{-1} and 1091, 624 cm^{-1} for **7** and **8**, which can be assigned to the $\nu_3(ClO_4)$ and $\nu_4(ClO_4)$ vibrations, typical for a non-coordinated perchlorate anion [26].

The nickel complexes have effective magnetic moments in the 2.73–3.72 B.M. range (per one Ni atom). For these complexes we can assume octahedral (**1**, **4**, **5**) or penta-coordinated (**2**, **3**) arrangements of donor atoms around

Table 1
Analytical data

Complex	Found/calc. (%)				
	C	H	N	Cl	Ni, Cu
(**1**) $Ni_3(bimz)_6(btc)_2\cdot 12H_2O$	47.4/47.6	4.2/4.4	11.0/11.1		11.7/11.6
(**2**) $Ni_3(btz)_9(btc)_2\cdot 12H_2O$	46.3/46.0	3.7/4.0	19.7/20.1		9.5/9.4
(**3**) $Ni_2(L_1)(btc)\cdot 7H_2O$	40.5/40.9	4.9/4.2	2.9/2.2		18.1/18.1
(**4**) $Ni_3(L_2)_2(Hbtc)\cdot 9H_2O$	46.9/46.6	5.4/4.9	5.7/5.1		15.7/15.9
(**5**) $Ni_2(L_3)(btc)\cdot 4H_2O$	41.9/41.4	3.9/32	4.9/4.4		18.9/18.4
(**6**) $Cu_2(L_4)(btc)\cdot 7H_2O$	40.2/40.2	4.7/4.3	2.5/2.0		18.3/18.5
(**7**) $[Cu_3(pmdien)_3(btc)](ClO_4)_3\cdot 6H_2O$	32.9/32.7	5.9/6.4	9.4/9.5	7.0/8.0	14.7/14.3
(**8**) $[Cu_3(mdpta)_3(btc)](ClO_4)_3\cdot 4H_2O$	29.9/29.9	5.5/5.7	10.5/10.5	10.1/8.8	16.2/15.8

Table 2
Results of physico-chemical study

Complex	μ_{eff} (B.M.)	UV–Vis	IR (cm^{-1})		
	(per Ni, Cu)	$\times 10^3$ (cm^{-1})	$\nu_{as}(COO^-)$	$\nu_s(COO^-)$	ν(C=N)
(**1**) $Ni_3(bimz)_6(btc)_2\cdot 12H_2O$	3.29	17.5; 28.0	1610	1366	
(**2**) $Ni_3(btz)_9(btc)_2\cdot 12H_2O$	3.60	17.5; 27.1	1612	1371	
(**3**) $Ni_2(L_1)(btc)\cdot 7H_2O$	3.72	15.5; 27.4	1542	1369	1614
(**4**) $Ni_3(L_2)_2(Hbtc)\cdot 9H_2O$	2.73	24.6; 27.5	1546	1365	1614
(**5**) $Ni_2(L_3)(btc)\cdot 4H_2O$	2.89	21.4; 27.7	1567	1378	1614
(**6**) $Cu_2(L_4)(btc)\cdot 7H_2O$	2.07	24.3; 28.1	1552	1358	1618
(**7**) $[Cu_3(pmdien)_3(btc)](ClO_4)_3\cdot 6H_2O$	1.94	15.5; 29.4	1600	1350	
(**8**) $[Cu_3(mdpta)_3(btc)](ClO_4)_3\cdot 4H_2O$	1.90	16.2; 33.7	1614	1372	

the central nickel atom. The large magnetic moments can be due to large orbital contributions expected for trigonal bipyramidal Ni(II) complexes with orbitally degenerate states [27]. If we assume a distorted octahedral arrangement for complexes **1**, **4** and **5**, the bands found in UV–Vis spectra in the 17 500–21 400 cm^{-1} and 22 900–28 000 cm^{-1} region can be assigned to the $^3A_{2g}(F) \rightarrow {}^3T_{1g}(F)$ and $^3A_{2g}(F) \rightarrow {}^3T_{1g}(P)$ transitions, respectively [28]. The UV–Vis bands of complexes **2** (at 15 500, 27 400 cm^{-1}) and **3** (at 17 500, 27 100 cm^{-1}), can be assigned to the $^3E' \rightarrow {}^3E''$ and $^3E' \rightarrow {}^3A_2'$ transitions, respectively, when a trigonal-bipyramidal geometry is suggested [29].

TG curves of the complexes **3**–**5** (not shown) exhibit no plateau that could be assigned to thermally stable intermediates. The thermal decomposition is complete between 425 and 480 °C and the final product is NiO, which was confirmed by powder X-ray diffraction analysis.

The copper complexes exhibit effective magnetic moments in the 1.90–2.07 B.M. range (per one Cu atom). These values are in good agreement with the assumption of one unpaired electron of Cu(II) ion where an orbital contribution also occurs [30]. The UV–Vis absorption spectra of the copper complexes contain bands in the region 15 500–24 300 cm^{-1} and 28 100–33 700 cm^{-1}, belonging probably to d–d and CT transitions. Complex **6** could be polymeric and we can assume an octahedral or pentacoordinated arrangement of the chromophore. In complex **7** we can assume a similar arrangement of donor atoms around the central copper atom as in complex **8** (confirmed by single crystal X-ray analysis).

The complexes are insoluble in most common organic solvents except for complex **7**, which is soluble in dimethylformamide and water. The molar conductivity of complex **7** in dimethylformamide (10^{-3} mol dm^{-3}) is 218.1 S cm^2 mol^{-1}, which is a value typical for 3:1 electrolytes [31]. The perchlorate anions are situated outside the coordination sphere of the central copper atom.

The antimicrobial activities of the complexes were estimated and it was found that only complex **5** exhibits a very small activity against *S. aureus* CCM 3953, *S. epidermidis* and *S. aureus* MRSA for the maximum concentration used (100 μg mL^{-1}). The remaining complexes do not significantly inhibit the growth of the test organisms.

Table 3
Crystal data and structure refinement of $[Cu_3(mdpta)_3(btc)](ClO_4)_3 \cdot 4H_2O$

Chemical formula	$Cu_3C_{30}H_{70}N_3O_{23}Cl_3$ (M = 1203.90)
Temperature (K)	107(2)
Cell setting; space group	monoclinic; $P2_1/n$
Unit cell dimensions	
a (Å)	18.5892(3)
b (Å)	9.7725(3)
c (Å)	26.5520(3)
β (°)	92.315(4)
V (Å^3)	4819.578
Formula units; D_x (Mg m^{-3})	4; 1.659
Crystal form; color	prismatic; blue
Crystal size (mm)	0.4 × 0.4 × 0.2
Data collection	
Diffractometer	Oxford diffraction CCD
Radiation type	Mo Kα
Wavelength (Å)	0.71069
Absorption correction type	none
Absorption coefficient μ (mm^{-1})	1.565
Range of h, k, l	$-27 \leqslant h \leqslant 27$; $-13 \leqslant k \leqslant 11$; $-39 \leqslant l \leqslant 36$
θ Range (°)	2.73–32.17
Reflections measured/unique/observed	47 612/15 453/10 361
Criterion for observed reflections	$I > 3\sigma(I)$
R_{int}	0.0466
Refinement	
Refinement on	F
R, wR	0.0509, 0.0654
S	1.85
Number of parameters	620
Weighting scheme	$w = [\sigma^2(F) + (0.02F)^2]^{-1}$
$(\Delta/s.u.)_{max}$	0.0069
$\Delta\rho_{max}$ (e Å^{-3})/$\Delta\rho_{min}$ (e Å^{-3})	1.58/−1.25
Extinction correction	none
Source of atomic scattering factors	international tables for X-ray crystallography (1992, Vol. C)

3.2. Crystal structure of $[Cu_3(mdpta)_3(btc)](ClO_4)_3 \cdot 4H_2O$ (**8**)

The structure was solved by standard SHELX programs [32,33]. Crystal data and structure refinement is given in Table 3; selected bond and angles are listed in Table 4. It is apparent that the molecule (see Fig. 1) forms a trinuclear

Table 4
Selected bond lengths (Å) and angles (°) of $[Cu_3(mdpta)_3(btc)](ClO_4)_3 \cdot 4H_2O$

Bond lengths	
Cu1–O1	2.058(2)
Cu2–O3	2.009(2)
Cu3–O5	2.012(2)
Cu1–N1	1.971(3)
Cu1–N2	2.046(3)
Cu1–N3	1.957(2)
Cu2–N4	2.010(3)
Cu2–N5	2.037(3)
Cu2–N6	1.989(3)
Cu3–N7	1.987(3)
Cu3–N8	2.024(3)
Cu3–N9	1.960(3)
Bond angles	
O1–Cu1–N3	85.22(9)
O1–Cu1–N1	84.69(9)
N1–Cu1–N2	97.41(10)
N2–Cu1–N3	94.13(10)
O3–Cu2–N4	87.48(9)
O3–Cu2–N6	88.08(9)
N5–Cu2–N6	98.09(10)
N4–Cu2–N5	92.86(10)
O5–Cu3–N7	91.68(10)
O5–Cu3–N9	93.42(12)
N7–Cu3–N8	95.90(11)
N8–Cu3–N9	93.86(13)

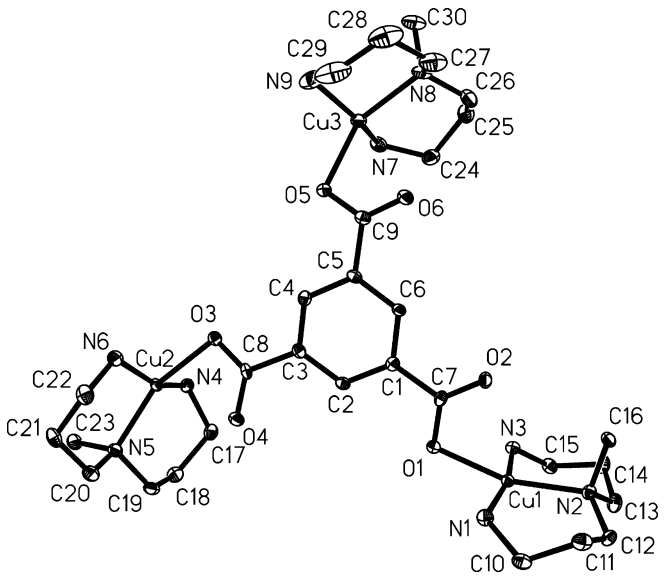


Fig. 1. Molecule of $[Cu_3(mdpta)_3(btc)](ClO_4)_3 \cdot 4H_2O$. Thermal ellipsoids are drawn at 50% probability level. Perchlorate ions and solvating water molecules are omitted for clarity.

copper complex, containing three CuN_3O chromophores connected via a benzene-1,3,5-tricarboxylate bridge. The perchlorate anions and water molecules are out of the coordination sphere. The geometry of the chromophores is square planar (see Table 4), but with a significant tetrahedral distortion. The deviations from ideal CuN_3O planes (in Å) are for O-atoms: from 0.239(2) to −0.375(2); for N-atoms: from 0.081(2) to 0.582(3) and from −0.383(2) to −0.734(2). The dihedral angles between Cu(1)O(1)N(1)N(2)N(3) (**A**), Cu(2)O(3)N(4)N(5)N(6) (**B**) and Cu(3)O(5)N(7)N(8)N(9) (**C**) are: **A**–**B** 106.5(2)°; **A**–**C** 96.5(2)° and **B**–**C** 9.9(3)°.

The subsequent anisotropic refinement converged to a reasonable fit $R_1 = 0.0757$ for observed reflections $I > 3\sigma(I)$. However, Fourier maps in the vicinity of one of the ClO_4^- anions revealed a clear indication of some disorder. Even more convincing was the difference Fourier map in the same area. Another Cl position slightly shifted from the original one has been located. Moreover we could also localize a separate peak having a reasonable distance from that new Cl position. The vector between these two new atoms had the opposite direction with respect to one of original Cl–O bonds. This made it possible to deduce that the second position of ClO_4^- is related to the basic position by a rotation about 180° perpendicular to the original Cl–O bond. The remaining three new oxygen positions could not be localized so clearly because the rotation brings them too close the original ones.

The rigid body option of Jana 2000 has been used to make a final refinement [34]. One molecule with adjustable shape in the two above mentioned positions has been used. Together with the average geometry of ClO_4 we refined also translation and rotation parameters for each position and the site occupancies restricted by the complementary condition. The occupancy of the new position was refined to 0.235(2).

As the next step we have localized five possible positions for water molecules. Three of them were regularly distributed over the available space. Two remaining peaks, located in the vicinity of the disordered ClO_4^-, were not fully occupied and the refined occupancies were in a close relationship with those for the two positions of ClO_4^-. A more detailed analysis of O–O distances showed that the more occupied position of the water molecule makes too short a distances with oxygen atoms from the less occupied ClO_4^- position and vice versa.

Finally, the structure has been completed with the hydrogen atoms except for those belonging to water molecules. The H positions were restrained to keep an ideal geometry during the refinement.

3.3. EPR spectra and magnetic properties of $[Cu_3(mdpta)_3(btc)](ClO_4)_3 \cdot 4H_2O$ (**8**)

The magnetic properties of the trimer were determined over the temperature range 1.8–300 K. Plots of the magnetic susceptibility and reciprocal magnetic susceptibility are given in Fig. 2. The magnetic dependence of the experimental and calculated $\chi_{Cu}T$ in the field (0.5 T) for the trimer (χ_{Cu} is the susceptibility value per one copper center) is shown in Fig. 3.

The Curie–Weiss behavior indicates a linear relation of the reciprocal magnetic susceptibility curve at higher temperatures (100–300 K) with a Curie constant $C = 0.426\ cm^3\ mol^{-1}\ K$ and Weiss-constant, $\theta = -1.74$ K and a small anomaly is observed only at the lowest temperatures. The compound reveals a magnetic behavior which is characteristic of antiferromagnetic spin coupling. The $\chi_{Cu}T$ values decreases gradually with lowering of the temperature, from $0.425\ cm^3\ mol^{-1}\ K$ at 300 K to $0.256\ cm^3\ mol^{-1}\ K$ at 1.8 K, and the effective magnetic moment from 1.85 B.M. at 300 K to 1.43 B.M. at 1.8 K.

The powdered sample of the complex indicates a rhombic deformed square-pyramidal EPR spectrum in

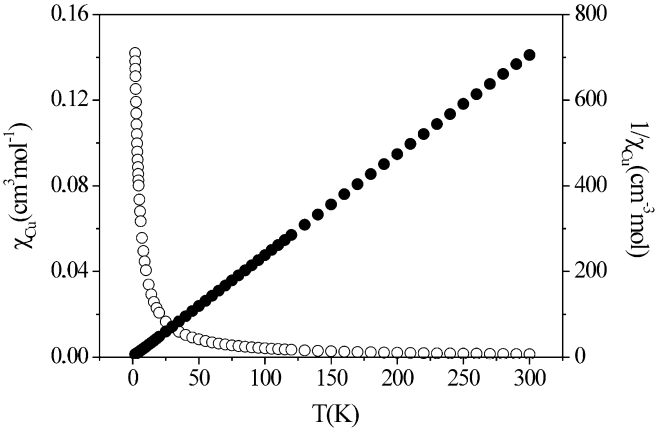


Fig. 2. Plots of the magnetic data χ_{Cu} (○) and $1/\chi_{Cu}$ (●) versus temperature for $[Cu_3(mdpta)_3(btc)](ClO_4)_3 \cdot 4H_2O$.

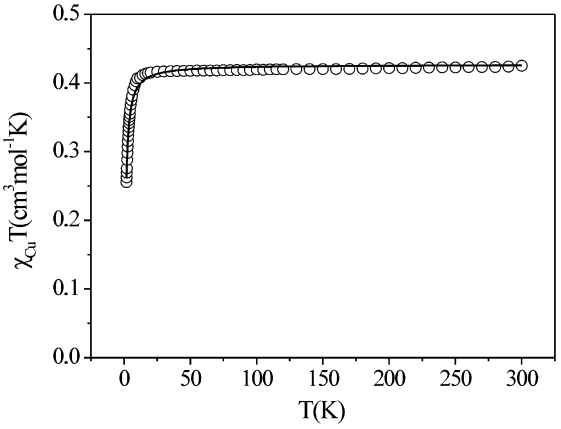


Fig. 3. Plots of the magnetic data $\chi_{Cu}T$ experimental (○) versus temperature for $[Cu_3(mdpta)_3(btc)](ClO_4)_3 \cdot 4H_2O$. Full line represents the calculated curve (see text).

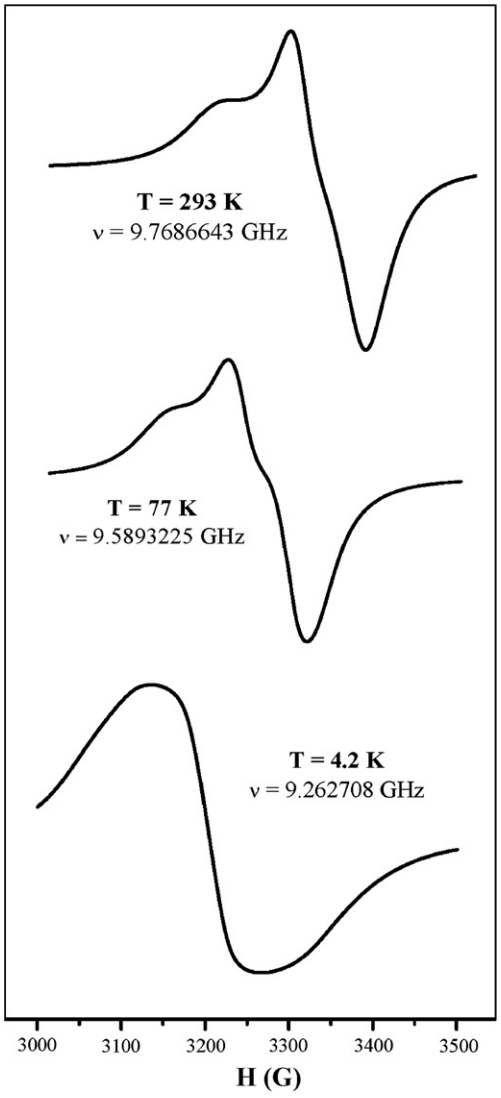


Fig. 4. X-band EPR spectra of a powdered sample of $[Cu_3(mdpta)_3(btc)](ClO_4)_3 \cdot 4H_2O$ at different temperatures.

the higher temperature region (Fig. 4) with spectroscopic splitting factors $g_1 = 2.17_8$, $g_2 = 2.11_8$, $g_3 = 2.07_0$ at 293 K and $g_1 = 2.17_4$, $g_2 = 2.11_9$, $g_3 = 2.06_8$ at 77 K.

At liquid helium temperature (4.2 K), an isotropic EPR signal with a single symmetric line only at $g = 2.06(1)$ with $\delta H_{pp} = 180$ G is observed.

X-ray analysis indicated that the Cu(II) centers form a regular triangle. An isotropic exchange model Hamiltonian of the trimer can be written as follows:

$$\widehat{H} = -2J(\widehat{S}_1\widehat{S}_2 + \widehat{S}_2\widehat{S}_3 + \widehat{S}_1\widehat{S}_3)$$

where $S_i = 1/2$, J is an exchange parameter.

A closed-form solution of the magnetic susceptibility derived from the susceptibility takes the form [35–39]:

$$\chi = \frac{Ng^2\mu_B^2}{4kT}\frac{1 + 5e^{3J/kT}}{1 + e^{3J/kT}}$$

where N, g, β, k and T have their usual meanings and both J and g factors were calculated in the fitting processes. The best least-squares fit (solid lines in Fig. 3) was obtained for the following values: $J = -0.56\ cm^{-1}$, $g = 2.13_9$ and $R = 4.79 \times 10^{-5}$.

$$R = \sqrt{\left\{\sum_{i=1}^{n}\left[(\chi_M^{exp})_i - (\chi_M^{calc.})_i\right]^2 \Big/ (\chi_M^{exp})_i^2\right\} \Big/ \sum_{i=1}^{n} 1 \Big/ (\chi_M^{exp})_i^2}$$

Acknowledgements

This work was supported by the Polish Ministry of Education and Science, Grant No. 1 T09A 124 30. Authors thank Mgr. Jiří Mikulík for collection and reduction of X-ray data, Assoc. Prof. Zdeněk Šindelář for magnetochemical measurements at room temperature, Drs. M. Kolář and K. Doležal for antimicrobial testing and Mr. Jan Wala for powder X-ray data collection.

Appendix A. Supplementary data

Crystallographic data are deposited in Cambridge Crystallographic Data Centre, No. CCDC 601336. Copies of the data can be obtained free of charge on application to CCDC, 12 Union Road, Cambridge CB2 1EZ, UK; fax +44 1223 336 033; e-mail: deposit@ccdc.cam.ac.uk or http://www.ccdc.cam.ac.uk. Supplementary data associated with this article can be found, in the online version, at doi:10.1016/j.poly.2006.08.010.

References

[1] M.O. Keeffe, M. Eddaoudi, H. Li, T. Reineke, O.M. Yaghi, J. Solid State Chem. 3 (2000) 2000.
[2] S. Feng, R. Xu, Acc. Chem. Res. 34 (2001) 239.
[3] G. Ferey, Chem. Mater. 13 (2001) 3084.
[4] X.-J. Yang, B. Wu, W.H. Sun, C. Janiak, Inorg. Chim. Acta 343 (2003) 366.
[5] D. Braga, A. Angeloni, E. Tagliavini, F. Grepioni, J. Chem. Soc., Dalton Trans. (1998) 1961.

[6] M.J. Plater, M.R.J. Foreman, R.A. Howie, J.M.S. Skakle, E. Coronado, C.J. Gomez-Garcia, T. Gelbrich, M.B. Hursthouse, Inorg. Chim. Acta 319 (2001) 159.
[7] G. Wu, X. Shi, Q. Fang, G. Tian, L. Wang, G. Zhu, A.W. Addison, Y. Wei, S. Qiu, Inorg. Chem. Commun. 6 (2003) 402.
[8] X. Li, D. Sun, R. Cao, Y. Sun, Y. Wang, W. Bi, S. Gao, M. Hong, Inorg. Chem. Commun. 6 (2003) 908.
[9] O.M. Yaghi, C.E. Davis, G. Li, H. Li, J. Am. Chem. Soc. 119 (1997) 2861.
[10] O.M. Yaghi, H. Li, T.L. Groy, J. Am. Chem. Soc. 118 (1996) 9096.
[11] M.R.J. Foreman, T. Gelbrich, M.B. Hursthouse, M.J. Plater, Inorg. Chem. Commun. 3 (2000) 234.
[12] C. Daiguebonne, Y. Gérault, F. Le Dret, O. Guillou, K. Boubekeur, J. Alloys Compd. 344 (2002) 179.
[13] M.J. Plater, R.A. Howie, A.J. Roberts, Chem. Commun. (1997) 893.
[14] K.Y. Choi, K.M. Chun, I.H. Suh, Polyhedron 20 (2001) 57.
[15] T.B. Lu, H. Xiang, R.L. Luck, L. Jiang, Z.W. Mao, L.N. Ji, New J. Chem. 26 (2002) 969.
[16] H.J. Choi, M.P. Suh, J. Am. Chem. Soc. 120 (1998) 10622.
[17] C.J. Kepert, T.J. Prior, M.J. Rosseinsky, J. Am. Chem. Soc. 122 (2000) 5158.
[18] T.J. Prior, M.J. Rosseinsky, Inorg. Chem. 42 (2003) 1564.
[19] C.J. Kepert, M.J. Rousseinsky, Chem. Commun. (1998) 31.
[20] M.J. Plater, M.R.S. Foreman, E. Coronado, C.J. Gomez-Garcia, A.M.Z. Slawin, J. Chem. Soc., Dalton. Trans. (1999) 4209.
[21] D. Cheng, M.A. Khan, R.P. Houser, Inorg. Chem. 40 (2001) 6858.
[22] H. Oshio, H. Ichida, J. Phys. Chem. 99 (1995) 3294.
[23] H.S. Huh, D. Min, Y.K. Lee, S.W. Lee, Bull. Korean Chem. Soc. 23 (2002) 619.
[24] P. Comba, Y.D. Lampeka, A.Y. Nazarenko, A.I. Prikhodko, H. Pritzkow, Eur. J. Inorg. Chem. (2002) 1464.
[25] National Committee for Clinical Laboratory Standards. Performance Standards for Antimicrobial Susceptibility Testing. Approved standard–eighth ed., NCCLS document, M2-A8. Wayne, PA, USA, 2003, pp. 1–70.
[26] P. Scholer, A.E. Merbach, Inorg. Chim. Acta 15 (1975) 15.
[27] G. Wilkinson, Comprehensive Coordination Chemistry, Pergamon, Oxford, 1987.
[28] A.B.P. Lever, Inorganic Electronic Spectroscopy, Elsevier, Amsterdam, 1984.
[29] M. Ciampolini, Inorg. Chem. 5 (1966) 35.
[30] E. König, Magnetic Properties of Coordination and Organometallic Transition Metal Compounds, Springer-Verlag, Berlin, 1966.
[31] W.J. Geary, Coord. Chem. Rev. 7 (1971) 81.
[32] G.M. Sheldrick, Acta Crystallogr., Sect. A 46 (1990) 467.
[33] G.M. Sheldrick, SHELXL-97: Program for Crystal Structure Refinement, University of Göttingen, Germany, 1997.
[34] V. Petříček, M. Dušek, Z. Kristallogr. 219 (2004) 692.
[35] B.S. Tsukerblat, B.Y. Kuyarskaya, M.I. Belinski, A.V. Ablov, V.M. Novotvortsev, V.T. Kalinnikov, Theor. Chim. Acta (Berlin) 38 (1975) 131.
[36] M. Inoue, M. Kubo, J. Coord. Chem. 6 (1977) 157.
[37] R.J. Butcher, C.J. O'Connor, E. Sinn, Inorg. Chem. 20 (1981) 537.
[38] J.P. Costes, F. Dahan, J.P. Laurent, Inorg. Chem. 25 (1986) 413.
[39] Y. Nakao, H. Nakamura, W. Mori, T. Sakurai, S. Suzuki, A. Nakahara, Bull. Chem. Soc. Jpn. 59 (1987) 2755.

Available online at www.sciencedirect.com
ScienceDirect
Polyhedron 26 (2007) 543–554
POLYHEDRON
www.elsevier.com/locate/poly

Synthesis and characterization of Cu^{2+}, Ni^{2+} and Zn^{2+} binding capability of some amino- and imidazole hydroxamic acids: Effects of substitution of side chain amino-N for imidazole-N or hydroxamic-N-H for -N-CH_3 on metal complexation

Etelka Farkas [a,*], Dávid Bátka [a], Edit Csapó [a], Péter Buglyó [a], Wolfgang Haase [b], Daniele Sanna [c]

[a] *University of Debrecen, H-4010 Debrecen, Hungary*
[b] *Institut für Physikalische Chemie, Technische Universität, Darmstadt, Germany*
[c] *Istituto C.N.R. di Chimica Biomolecolare, Trav. La Crucca 3, I-07040 Li Punti Sassari, Italy*

Received 11 July 2006; accepted 11 August 2006
Available online 1 September 2006

Abstract

Solution equilibrium studies on Cu(II)-, Ni(II)- and Zn(II)-*N*-Me-β-Alaninehydroxamic acid (*N*-Me-β-Alaha), -*N*-Me-α-alaninehydroxamic acid (*N*-Me-α-Alaha), -Imidazole-4-carbohydroxamic acid (Im-4-Cha), -*N*-Me-imidazole-4-carbohydroxamic acid (*N*-Me-Im-4-Cha) and -Imidazole-4-acetohydroxamic acid (Im-4-Aha) systems have been performed by pH-potentiometry, UV–Vis spectrophotometry, EPR, CD, ESI-MS and ^{1}H NMR methods. According to the results: (i) the amino-N atoms are more basic in *N*-Me-α-Alaha and *N*-Me-β-Alaha than the hydroxamate function, but the trend is just the opposite between the imidazole-N(3) and hydroxamate. (ii) The metal ion anchor is always the hydroxamate part in the amino acid derivatives, while it is always the imidazole-N(3) in the studied imidazolehydroxamic acids. (iii) The three studied *N*-Me derivatives do not form metallacrowns. Only hydroxamate type chelate is formed with *N*-Me-β-Alaha, but with *N*-Me-α-Alaha a new type of coordination mode (via amino-N and hydroxamate-O) also exists. *N*-Me-Im-4-Cha also forms a dinuclear complex, $[M_2L_3]$, with Cu(II) and Ni(II) (but not with Zn(II)). In this complex, one of the three ligands might bridge the two metal ions (five-membered hydroxamate-(O,O) plus five-membered (N_{im}, O_{carb}) bridging bis-chelating mode), while each of the additional two ligands binds to one metal. (iv) The two studied *N*–H derivatives, having dissociable proton on the hydroxamic-N, are able to form metallacrown species. A pentanuclear complex, $[M_5L_4H_{-4}]$, is exclusively formed above pH 4 between Cu(II) and Im-4-Aha. Interestingly, this 12-metallacrown-4 type complex, although together with various mononuclear binding isomers, appears also with Ni(II) and Zn(II). Unfortunately, the complexes of Im-4-Cha are not soluble in water at physiological pH at all.
© 2006 Elsevier Ltd. All rights reserved.

Keywords: Aminohydroxamic acid; Imidazolehydroxamic acid; Cu(II), Ni(II) and Zn(II) complexes; Metalloenzyme inhibitors; Speciation

1. Introduction

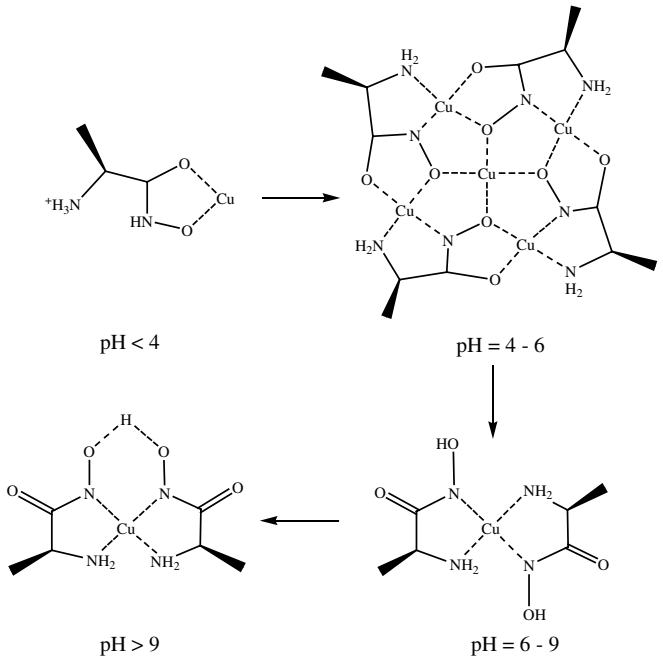
Hydroxamic acids are among the most well studied compounds due to their significance in so many fields [1]. Natural hydroxamate-based compounds, siderophores, play a crucial role in microbial iron(III) storage and transport [1,2]. Hydroxamic acids are also capable for the inhibition of a wide variety of enzymes including matrix metalloproteinases [1–4] or ureases [5,6]. There is no doubt that the inhibitory effect is in correlation with chelation of the catalytic metal center by the hydroxamate function. However, metal complexation of hydroxamic acids depends on many factors, such as the presence of additional potential donor site(s). This is the reason why characterization of the

* Corresponding author. Fax: +36 52 489 667.
E-mail address: efarkas@delfin.klte.hu (E. Farkas).

0277-5387/$ - see front matter © 2006 Elsevier Ltd. All rights reserved.
doi:10.1016/j.poly.2006.08.019

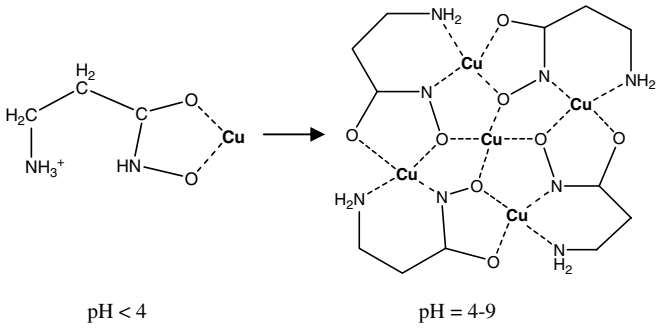
interaction between metal ions and various hydroxamates might provide useful information to understand inhibitory effect of such molecules.

Hydroxamic acid derivatives of natural amino acids have also become into the focus of interest [7–16]. Some of them were prepared to chelate certain trace elements being essential in animal nutrition [12], or as potential metalloenzyme inhibitors [13]. However, the presence of the amino group may cause significant change in the coordination mode compared to that in simple hydroxamic acids. For example, when an amino group is situated in α-position to the hydroxamic moiety (like in α-alaninehydroxamic acid) the coordination to Cu(II) starts via the hydroxamate chelate, but as the pH is increased a metallacrown-type polynuclear species, in which each deprotonated ligand (LH_{-1}) is coordinated in bridging bis-chelating mode, plus one additional metal ion is accommodated in the formed cavity, appears between pH 4 and 6. Although, 15-metallacrown-5 type complexes were synthesized by Pecoraro and co-workers with α-derivatives [8], but in solution 12-metallacrown-4 type was proven by ESI-MS in recent works [10,11]. At pH ca. 6, where the conditional stability of the five-membered (N_{am}, N_{hydr}) chelate overpasses the stability of the five-membered hydroxamate-(O,O), the formation of (N_{am}, N_{hydr}), formation of 4N-coordinated bis-chelated mononuclear species becomes favoured. The four nitrogens remain co-ordinated at pH > 9 too, but, following the deprotonation of one of the coordinated hydroxamate groups, a hydrogen bond is formed between the two ligands [7,10,11]. The suggested bonding modes are the followings:



Although Zn(II) seems to prefer the hydroxamate oxygens somewhat over the nitrogens, a mixed coordination mode in Zn_2L_3 species was also suggested between α-amino acid derivatives and this metal ion [7,14]. Nickel(II) unambiguously prefers the five-membered (N_{am}, N_{hydr}) chelate over the hydroxamate type coordination as it was proved first for the nickel(II)–glycinehydroxamate square planar bis-complex by X-ray investigations [15].

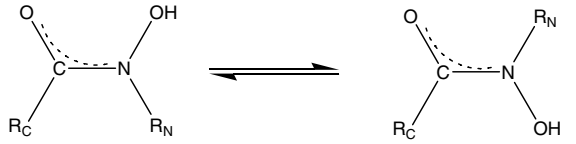
Hydroxamate oxygens of β-alaninehydroxamate start to coordinate to Cu(II) above pH 3, then a pentanuclear 12-metallacrown-4 (shown below) predominates above pH 4 [16].



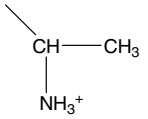
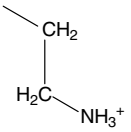
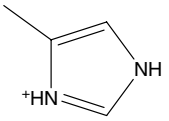
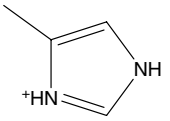
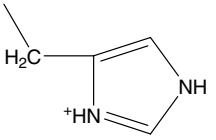
Even a six-membered (N_{am}, N_{hydr}) chelate seems to be more stable than the five-membered hydroxamate (O,O) type one above pH 7 with Ni(II), therefore nitrogen-coordinated planar complex appears in this pH region. Zn(II) prefers hydroxamate type coordination with β-amino acid derivatives [7].

As it is shown above, the coordination behaviour of aminohydroxamic acids is determined highly by the amino-N and hydroxamate-N donors. But what is the situation with *N*-methyl derivatives of aminohydroxamic acids, where coordination via the hydroxamate-N is not possible? Do these derivatives realize only simple hydroxamate type coordination? This is an important question, because chelation of the active-site metal ion by hydroxamate function is thought to be a crucial factor for effective metalloenzyme inhibition by hydroxamate-based molecules [1]. Therefore, the present solution equilibrium study focuses on the complexation between Cu^{2+}, Ni^{2+}, Zn^{2+} ions (these metal ions are often included in the active centres of metalloenzymes) and *N*-methyl derivatives of aminohydroxamic acids, *N*-methyl-L-α-alaninehydroxamic acid (*N*-Me-α-Alaha), *N*-methyl-β-alaninehydroxamic acid (*N*-Me-β-Alaha). Besides, new compounds, imidazole-4-carbohydroxamic acid (Im-4-Cha), *N*-methyl-imidazole-4-carbohydroxamic acid (*N*-Me-Im-4-Cha) or imidazole-4-acetohydroxamic acid (Im-4-Aha), were also studied, in which the highly basic amino-nitrogen is replaced by the less basic imidazole-N donors. These compounds have been synthesized and investigated because of two reasons. Namely, the less basic imidazole donors might provide lower competitive effect to the hydroxamate-type chelation, but, on the other hand, an aromatic imidazole-ring can be involved more easily in non-covalent interactions (such as stacking interactions) than an amino function. Beside pH-potentiometry, UV–Vis, CD, EPR, ^{1}H NMR and ESI-MS measurements

Table 1
Formulae of the studied ligands



(*Z*) (*E*)

Ligands	R_C	R_N
L-*N*-Methyl-α-alaninehydroxamic acid (*N*-Me-α-Alaha)		–CH_3
N-Methyl-β-alaninehydroxamic acid (*N*-Me-β-Alaha)		–CH_3
Imidazole-4-carbohydroxamic acid (Im-4-Cha)		–H
N-Methyl-imidazole-4-carbo-hydroxamic acid (*N*-Me-Im-4-Cha)		–CH_3
Imidazole-4-acetohydroxamic acid (Im-4-Aha)		–H

were carried out in aqueous solution. The formulae of the studied ligands are summarized in Table 1. The results were always compared to the corresponding literature data of L-α-alaninehydroxamic acid (L-α-Alaha) and β-alaninehydroxamic acid (β-Alaha).

2. Experimental

2.1. Synthesis

All chemicals and solvents were of analytical grade and were used without further purification. Imidazole-4-acetic acid hydrochloride, imidazole-4-carboxylic acid was purchased from Aldrich, Z-L-α-alanine from Bachem, diciclohexylcarbodiimide (DCC) from Fluka. Methanol was dried under N_2 using magnesium while dry tetrahydrofurane was made under N_2 using Na wire and benzophenone. L-α-Alaha and β-Alaha were prepared as reported previously [17]. Imidazole-4-carbohydroxamic acid · HCl (Im-4-Cha) and *N*-methylimidazole-4-carbohydroxamic acid · HCl (*N*-Me-Im-4-Cha) were also prepared by using literature methods [18,19].

2.1.1. Z-protected L-α-Alanine methyl esther (*1*)

Z-Alanine (3.0 g, 13.4 mmol) in freshly distilled dry methanol (20 mL) was converted to Z-Ala-methyl esther bubbling dry hydrochloride gas for one hour in ice-bath. Solvent was evaporated in vacuo, affording the pure product as white crystals. Yield: 3.0 g, 97%. TLC: eluent: CH_2Cl_2:MeOH 9:1, R_f: 0.77. ^{1}H NMR (360 MHz, D_2O-DMSO-d^6 mixture): $\delta = 7.53$ (s, 5H, Ar–H), 5.23 (s, 2H, Ar–CH_2), 4.30 (q, 1H, Ala–CH), 3.84 (s, 3H, O–CH_3), 1.48 (d, 3H, Ala-CH_3).

2.1.2. Z protected N-methyl L-α-Alaninehydroxamic acid (*2*)

1 (1.7 g, 7.165 mmol) was reacted with a solution of *N*-methyl hydroxamine (658 mg, 7.88 mmol) in dry methanol (20 mL) and Na-methylate solution (4.15 mL, 3.23 M, 13.40 mmol) at 0 °C. After the reaction mixture was strirred overnight in ice bath, water (4 mL) and 2 M HCl solution was added to neutralize the mixture. Solvent was removed in vacuo and the residual oil was dissolved in water (5 mL). This solution was extracted with ethylacetate (3×15 ml). The organic phase was extracted with 0.2 M NaOH solution (4×50 mL) and the aqueous phase was acidified to pH 2 using 2 M HCl and extracted again with ethylacetate (2×20 mL). After drying on Na_2SO_4, evaporation of the solvent in vacuo yielded a colourless oil. Yield: 430 mg, 24%. TLC: eluent: CH_2Cl_2:MeOH 9:1, R_f: 0.52. ^{1}H NMR (360 MHz, D_2O and DMSO mixture): $\delta = 7.51$ (s, 5H, Ar–H), 5.19 (s, 2H, Ar–CH_2), 4.22 (q, 1H, Ala–CH), 3.32 (s, 3H, N–Me), 1.38 (d, 3H, Ala–CH_3).

2.1.3. N-Methyl-L-α-Alaninehydroxamic acid · HCl (N-Me-α-Alaha) (*3*)

2 (425 mg, 1.68 mmol) was dissolved in dry methanol (10 mL), acidified by using HCl in dry methanol and stirred under H_2 atmosphere for six hours in the presence of palladium charcoal (142 mg 10% Pd). After filtration the solvent was removed in vacuo affording a colourless oil. Yield: 178 mg, 90%. TLC: eluent: CH_2Cl_2:MeOH 9:1, R_f: 0.0, ^{1}H NMR (360 MHz, D_2O): $\delta = 4.58$ (q, 1H, Ala–CH), 3.35 (s, 3H, N–Me), 1.58 (d, 3H, Ala–CH_3). ^{13}C NMR (360 MHz, D_2O): $\delta = 169.57$ (C=O), 47.18 (Ala–CH), 36.17 (N–CH_3), 15.13 (Ala–CH_3).

2.1.4. Z protected N-methyl-O-benzyl-β-alaninehydroxamic acid (*4*)

O-Benzyl-*N*-methyl hydroxylamine hydrochloride (1.75 g, 10.1 mmol) was dissolved in dry methanol (20 mL), chilled, KOH (0.58 g, 10.1 mmol) was added as solid and the mixture was stirred for 15 min under N_2. KCl was filtered out and the solution kept at 0 °C. Z-β-Alanine (1.50 g, 6.73 mmol) was dissolved in dry tetrahydrofurane (40 mL) and chilled. Ethylchloroformiate (0.77 mL, 8.08 mmol) and *N*-methyl morpholine (0.96 ml, 8.75 mmol) were added. After 40 min of stirring at 0 °C the solid was filtered out and the solution dropwise added to the solution of the free hydroxylamine. The reaction

mixture was stirred under N_2 in ice-bath for two hours and for one hour at ambient temperature. The solvent was evaporated in vacuo resulting an oil, which was taken up in ethylacetate (50 mL), washed with the citric acid (0.5 M, 2 × 25 mL), $NaHCO_3$ (0.5 M, 2 × 25 mL) and brine (1 × 25 mL). It was dried on $MgSO_4$ and evaporated to dryness affording a colourless oil. (Yield: 1.0 g, 43%), TLC: eluent: CH_2Cl_2:MeOH 9:1, R_f: 0.85, ^{1}H NMR (360 MHz, D_2O): $\delta = 7.41$ (s, 5H, Ar–H), 5.09 (s, 2H, Ar–CH_2), 3.39 (t, 2H, Ala–CH_2), 3.19 (s, 3H, N–Me), 2.68 (t, 2H, Ala–CH_2).

2.1.5. *N*-Methyl-β-alaninehydroxamic acid · HCl (*N*-Me-β-Alaha) (**5**)

4 (250 mg, 0.73 mmol) was subjected to hydrogenolysis in methanol (10 mL), using palladium charcoal (75 mg, 10% Pd) and HCl solution (1.94 M, 0.65 mL) for four hours. After filtration and evaporation the solution afforded a colourless oil. (Yield: 78 mg, 90%). TLC: eluent: THF:MeOH:H_2O 5:5:1, R_f: 0.25, ^{1}H NMR (360 MHz, D_2O): $\delta = 3.27$ (t, 2H, Ala–CH_2), 3.24 (s, 3H, N–Me), 2.90 (t, 2H, Ala–CH_2), ^{13}C NMR (360 MHz, D_2O): $\delta = 170.28$ (C=O), 35.94 (Ala–CH_2–NH_2), 35.38 (N–CH_3), 28.85 (Ala–CH_2).

2.1.6. Imidazole-4-acetohydroxamic acid · HCl (Im-4-Aha) (**6**)

Imidazole-4-acetic acid hydrochloride (500 mg, 3.08 mmol) and hydroxylamine hydrochloride (630 mg, 9.2 mmol) were dissolved in dry methanol (10 mL) under N_2. At 0 °C dicyclohexylcarbodiimide (DCC) (950 mg, 4.6 mmol) was added. After stirred overnight in ice bath, the reaction mixture was filtered and the residue was evaporated to dryness in vacuo at 40 °C yielding a white foam. It was treated with water (7 mL) and ethanol (8 drops), filtered, washed with a small amount of cold water. The resulting solution was extracted with dichloromethane (6 × 15 mL). The aqueous phase was acidified to pH 2 by using 0.2 M HCl. Solvent was removed in vacuo yielding white crystals, which were recrystallised from ethanol affording white needles. (Yield: 110 mg, 25%). TLC: eluent: CH_2Cl_2:MeOH 9:1, R_f: 0.90. ^{1}H NMR (360 MHz, D_2O): $\delta = 8.66$ (s, 1H, imH^2), 7.38 (1H, imH^5), 3.73 (2H, im-CH_2). ^{13}C NMR (360 MHz, D_2O): $\delta = 167.01$ (C=O), 134.28 (im C^4), 126.01 (im C^2), 117.60 (im C^5), 28.09 (–CH_2–).

2.2. Potentiometric and spectroscopic studies

The exact concentration of the ligand stock solutions was determined by the Gran's method [19]. The Cu(II) and Ni(II) stock solutions were prepared from $CuCl_2$ and $NiCl_2$ (Reanal) dissolved in bi-distilled water. Zn(II) stock solution was made from ZnO (Reanal) dissolved in diluted HCl of known concentration (0.1 M). For the Cu(II), Ni(II) and Zn(II) stock solutions, the exact metal ion concentrations were checked gravimetrically by the use of quinolin-8-olate. The exact concentrations of the ligand stock solutions were determined by pH-potentiometry. The pH-potentiometric and the spectrophotometric measurements were carried out at an ionic strength of 0.2 M (KCl). Temperature was 25.0 ± 0.1 °C. Carbonate-free KOH solution of known concentration (0.2 M) was used as titrant. HCl stock solution was prepared from cc. HCl. The concentration was determined by pH-potentiometric titrations using the Gran's method [20]. Radiometer pHM 84 instrument equipped with Metrohm combined electrode (type 6.0234.110) was used for pH-potentiometric measurements with a Metrohm 715 Dosimat automatic burette. The electrode system was calibrated according to Irving et al. [21] and the pH-metric readings could, therefore, be converted into hydrogen concentration. The water ionization constant (pK_w) determined was 13.76 ± 0.01. All the pH-potentiometric titrations were performed over the pH range of 2–11 or until precipitation occurred. Initial volume of the samples was 3.00–5.00 mL. Ligand concentration was 2–4 mM and metal ion concentration varied in the range of 1–6 mM, the metal to ligand ratios were 1:1, 1:2 and 1:3. The samples were completely deoxygenated by bubbling purified argon for approx. 20 min before the measurements. The equilibrium calculations were performed by the PSEQUAD computer program [22]. A Perkin Elmer Lambda 25 or an Avantes fiber optic spectrophotometer equipped with 10 mm probe head by using 100 ms integration time and an average of 50 spectra were used to record the UV–Vis spectra for the Cu(II) and Ni(II) complexes in the range of 300–800 nm at all metal to ligand ratios studied, in the 1–6 mM metal ion concentration region. CD spectra for L-α-Alaha or L-*N*-Me-α-Alaha and their Cu(II) systems were obtained at 25 °C under a constant flow of nitrogen on a Jasco J-810 spectropolarimeter which was calibrated with an aqueous solution of (1*R*)-(−)-10-camphorsulfonic acid, ammonium salt. Measurements were carried out in water at different pH values, using 1 mm or 1 cm path length cuvettes in the 200–800 nm wavelength region. Spectra represent an average of 8–20 scans. All the solutions were freshly prepared using deionized water. Concentrations of the hydroxamates and their copper(II) complexes used to record CD spectra were 0.004 and 0.002 M, respectively. ^{1}H NMR measurements were made for L-*N*-Me-α-Alaha, *N*-Me-β-Alaha, Im-4-Aha, Im-4-Cha and *N*-Me-Im-4-Cha ligands and for their Zn(II) complexes on Bruker Advance AM 360 by using D_2O as solvent and TSP ((trimethylsilyl)-propionic acid-D4, sodium salt) as standard under the following conditions: metal to ligand ratio was 1:2 in all samples and the analytical concentration of the ligands was 0.005 M. By the study of the dependence of the chemical shifts from pD values between pD 2 and 11 0.1 M NaOD and DCl solutions were used. Magnetic measurements were carried out by using the Evans method [23] on a Bruker Advance II 300 MHz NMR spectrometer. Co-axial NMR tubes were used for the investigations where the inset contained the reference D_2O solution with 2% of *t*-BuOH and in the outer tube had the paramagnetic species dissolved in

D_2O containing 2% of *t*-BuOH. The concentration of the metal ion was 0.003 M at 1:2 metal to ligand ratio. All measurements were carried out without ionic strength. pD values, in range 2–10, were set up with D_2SO_4 or NaOD. Electrospray ionization time-of-flight mass spectrometric (ESI-TOF MS) analysis was made for the Cu(II)-*N*-Me-α-Alaha, -Im-4-Aha and -*N*-Me-Im-4-Cha, for Ni(II)-Im-4-Aha, -Im-4-Cha and -*N*-Me-Im-4-Cha, and Zn(II)-Im-4-aha and -*N*-Me-Im-4-Cha system on a Bruker BIOTOF II ESI-TOF instrument by using 0.006 M ligand concentration at 1:2 metal to ligand ratio at pH 6. The solutions were introduced directly into the ESI source by a syringe pump (Cole-Parmer Ins. Comp. type 74900.) at a flow rate of 2 μL/min. The temperature of drying gas (N_2) was 100 °C. The pressure of the nebulizating gas (N_2) was 30 psi. Voltages applied at the capillary entrance, capillary exit and the first and the second skimmers were −4500, 120, 40 and 30 V, respectively. The spectra were accumulated and recorded by a digitizer at a sampling rate of 2 GHz. The spectrometer was operated at unit mass resolution and was calibrated to sodium trifluoroacetate. Anisotropic X-band EPR spectra of frozen solutions were recorded at 120 K, using a Bruker EMX spectrometer after addition of ethylene glycol to ensure good glass formation. Copper(II) stock solution for EPR measurements were prepared from $CuSO_4 \cdot 5H_2O$ enriched with ^{63}Cu to get better resolution of EPR spectra. Metallic copper (99.3% ^{63}Cu and 0.7% ^{65}Cu) was purchased from JV Isoflex, Moscow, Russia for this purpose and converted into the sulfate.

3. Results and discussion

3.1. Acidity of the ligands

All the ligands studied have two dissociable protons in the totally protonated form (H_2L^+), one at the hydroxamic function, another one at the amino-N or imidazole-N. The dissociation constants have been determined by pH-potentiometric titrations and, together with the previously obtained values for L-α-Alaha and β-Alaha, are summarized in Table 2.

As it is known from the previous results for L-α-Alaha and β-Alaha [24], the two dissociation processes overlap in these two molecules. Consequently, the dissociation constants which can be obtained by pH-potentiometry are macroconstants and cannot be ascribed unambiguously to either of the acidic groups. The dissociation microconstants, characteristic of the acidity of the individual groups, were determined and the values showed that the NH_3^+ group is more acidic than the NHOH group in the α-derivative ($pK_{amino} = 7.48$, $pK_{hydr} = 7.90$), while the acidity sequence is the opposite in the β-Alaha ($pK_{amino} = 8.85$, $pK_{hydr} = 8.47$) [24]. In order to evaluate the acidity trend in the *N*-Me derivatives of these two aminohydroxamic acids, ^1H NMR titrations have been performed in the present work under the conditions given in Section 2. The pD-dependence of the chemical shifts (S.1) clearly demonstrates that the two processes overlap completely in *N*-Me-α-Alaha, but almost quite separated in *N*-Me-β-Alaha. By fitting the curves by the program SCIENTIST [25], the individual constants for the ammonium and hydroxamic functions of *N*-Me-α-Alaha were calculated ($pK_{amino} = 8.63(1)$, $pK_{hydr} = 8.28(1)$). If these values are compared to those for L-α-Alaha, one can conclude that, due to the electronic effect of the methyl substituent[1] and lack of the possibility for hydrogen bond formation, the acidity sequence is just the opposite in the *N*-Me-α-Alaha compared to L-α-Alaha.[2] In β-Alaha the NHOH is already more acidic than the amino group and replacement of *N*-H with *N*-Me makes the hydroxamic group even more acidic. As a result of this, the two dissociation processes of the *N*-Me-β-Alaha are almost separated and the pK_{a1} in Table 2 can be roughly assigned to the deprotonation process of the hydroxamic function, while the pK_{a2} to the dissociation of β-NH_3^+.

For the imidazole derivatives the NMR results suggest that the lower p*K* values in Table 2 belong to the dissociation of the protonated imidazole-N(3), while the higher ones to the hydroxamic functions. On the other hand, because the "side chain" imidazole-N(3) is less isolated in Im-4-Cha than in Im-4-Aha derivatives, the stronger mutual electronic effects result in the more significant increase in the acidities and decrease in p*K* values of the former molecule. Moreover, the exceptionally low pK_{a1} of Im-4-Cha also suggests the existence of hydrogen bond between the imidazole-N and hydroxamic-NH.

Table 2
Dissociation constants (p*K*)[a] of the studied ligands, $t = 25$ °C, $I = 0.2$ M (KCl)

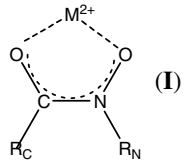
Ligands	pK_{a1}	pK_{a2}
L-α-Alaha	7.34[b]	9.16[b]
N-Me-α-Alaha	7.61(2)	9.25(1)
β-Alaha	8.32[b]	9.59[b]
N-Me-β-Alaha	8.12(1)	9.88(1)
Im-4-Cha	3.76(3)	8.82(1)
N-Me-Im-4-Cha	5.06(3)	8.57(2)
Im-4-Aha	6.17(1)	9.05(2)

[a] Numbers in parenthesis indicated standard deviations.
[b] Ref. [23].

3.2. Metal complexation of the ligands

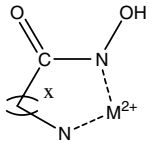
The ligands, shown in Table 1, are able to coordinate to a metal ion by different ways. Possibilities for the formation of chelates are summarized in Scheme 1.

[1] It is known from previous results that the change of *N*-H to *N*-Me substituent results in significant increase in the acidity (decrease of the p*K*) of the hydroxamic function. For example, pK_a for acetohydroxamic acid is 9.27, while for *N*-Me-acetohydroxamic acid is 8.70 [26].
[2] Since D_2O was used in the present work, the values in H_2O can be obtained by correction [27].



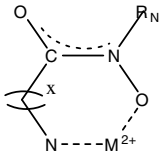
(I)

five-membered
hydroxamate-type chelate
(O,O)



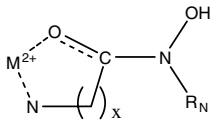
(II)

x = 1 five-membered **($N_{am/im}$, N_{hydr})**
x = 2 six-membered **($N_{am/im}$, N_{hydr})**



(III)

x = 1 six-membered **($N_{am/im}$,O_{hydr})**
x = 2 seven-membered **($N_{am/im}$,O_{hydr})**



(IV)

x = 1 five-membered **($N_{am/im}$,O_{carb})**
x = 2 six-membered **($N_{am/im}$,O_{carb})**

Scheme 1.

Under certain conditions, formation of a chelate, which has the highest conditional stability, is the most favoured. If different chelates have comparable stabilities, mononuclear species with different bonding modes (binding isomers) or oligonuclear complexes (like interesting metallacrowns with amino acid derivatives [8,10,11,16]) can be formed. Structure (**II**) is not possible at all with the *N*-Me derivatives.

3.2.1. Cu(II), Ni(II) and Zn(II) complexes of N-Me-α-Alaha and N-Me-β-Alaha

Although the hydroxamate-type coordination (structure **I**) is the most probable, but, at least theoretically, structure **IV** is also possible with the mono-protonated form of these ligands. In order to obtain somewhat deeper insight into the bonding modes, the stability trends of these two chelates (Structures **I** and **IV**) were evaluated by using model ligands, acetohydroxamic acid (Aha), alanyl-glycine (Ala-Gly) and β-alanyl-glycine (β-AlaGly). Aha was used to model hydroxamate-(O,O) chelation. Assuming that there is no significant difference between the stability of (N_{am}, O_{carb}) chelates formed via terminal amino-N and peptide carbonyl-O donors of the peptides and via amino-N and hydroxamic carbonyl-O donors, the [CuL] complex of Ala-Gly was the model for the five-membered whereas that of β-AlaGly for the six-membered (N_{am}, O_{carb}) chelate. Since the amino-N donor atoms are protonated in the free ligands up to high pH, the metal ions must compete with protons for the binding sites. In such cases, only the pH-dependent conditional constants (K') indicate the metal binding capability of a specific site at a specific pH. To compare the stability of the different type of chelates with each other, the conditional constants for the monochelated metal complexes of the model ligands were calculated. The conditional stability constant can be defined as

$$K' = \beta_{ML}/\alpha_{H_i},$$

where β_{ML} are the corresponding overall stability constants taken from Refs. [26,28] and

$$\alpha_{H_i} = [L]\left(1 + \sum_{i=1}^{n} \beta_{H_iL} \cdot [H^i]\right),$$

where [L] stands for the totally deprotonated form of Aha, AlaGly or β-AlaGly; $n = 1$ for these model ligands and β_{H_iL} is the corresponding protonation constant (in the case of the peptides it is the protonation constant of the amino-N) taken from Refs. [26,28].

The calculated logarithmic K' values for different chelates with copper(II) as a function of pH are shown in Fig. 1.

As Fig. 1 clearly shows, the hydroxamate chelate (structure **I**) is preferred over the structure **IV** (it has the highest

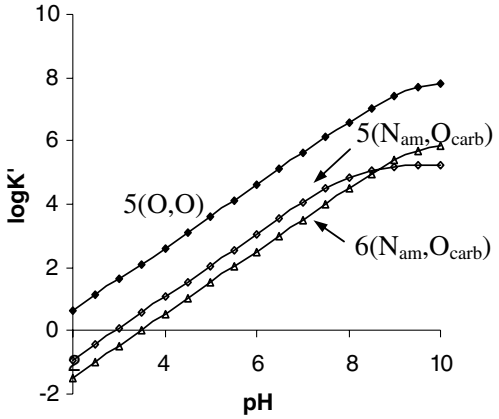


Fig. 1. Calculated pH-dependent logarithmic K' values for five-membered (O,O), five-membered (N_{am}, O_{carb}) and six-membered (N_{am}, O_{carb}) type chelates with copper(II) as a function of pH.

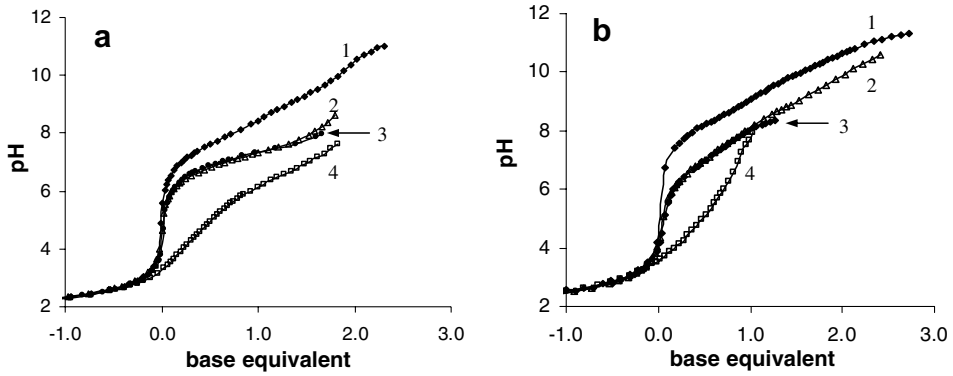


Fig. 2. pH-potentiometric titration curves registered for (a) *N*-Me-α-Alaha (**1**) and for Zn(II)- (**2**), Ni(II)- (**3**), and Cu(II)- (**4**) *N*-Me-α-Alaha systems and for (b) *N*-Me-β-Alaha (**1**) and for Zn(II)- (**2**), Ni(II)- (**3**), and Cu(II)- (**4**) *N*-Me-β-Alaha systems at metal to ligand ratio 1:2, $c_L = 4 \times 10^{-3}$ M.

log K' values) in the whole evaluated pH range. This means that the formation of (N_{am}, O_{carb}) chelate (either five-membered with *N*-Me-α-Alaha or six-membered with *N*-Me-β-Alaha) cannot be expected. Evaluation, made with the other two metal ions led to the same conclusion. Unfortunately, adequate models for the structure **III**, (N_{am}, O_{hydr})-type chelate, which can be formed only with a non-protonated ligand, could not be found.

During the experimental work, first pH-potentiometric titrations for the Cu(II)-, Ni(II)- and Zn(II)-*N*-Me-α-Alaha and -*N*-Me-β-Alaha systems have been performed. Representative titration curves recorded for the free ligands and at 1:2 metal to ligand ratios are shown in Fig. 2.

It is well demonstrated in Fig. 2a and b that these ligands start to interact with Cu(II) below pH 3, but with the other two metals, Ni(II) and Zn(II), only above pH 4. One equivalent of proton is displaced by a Cu(II) or Ni(II) ion from an *N*-Me-β-Alaha molecule before the precipitation starts, while in the presence of Zn(II), the second dissociable proton is released only in the pH-range where the free ligand itself dissociates. Moreover, UV–Vis spectra, recorded for Cu(II)-[3] and also for the Ni(II)-containing samples[4] are very similar to those obtained with acetohydroxamic acid [26]. It means that exclusive hydroxamate-type coordination (structure **I**) occurs with *N*-Me-β-Alaha. Stoichiometry of the complexes and the overall formation constants yielding the best fit of the pH-metric experimental data are given in Table 3. The numerous protonated mono- and bis-chelated complexes of *N*-Me-β-Alaha involve the dissociable proton on the non-coordinated amino group. The species [NiL_2H_{-1}] is most probably a mixed hydroxo complex.

Although, the hydroxamate-type coordination of the mono-protonated *N*-Me-α-Alaha (structure **I**) is assumed

Table 3
Overall stability constants (log β) for the Cu(II), Ni(II) and Zn(II) complexes of *N*-Me-α-Alaha and *N*-Me-β-Alaha, $t = 25$ °C, $I = 0.2$ M (KCl)

Ligand	Species	Cu(II)	Ni(II)	Zn(II)
			log β	
N-Me-α-Alaha	[MLH]	15.16(2)	12.52(2)	12.31(9)
	[ML]	8.86(3)	5.47(3)	5.43(4)
	[MLH_{-1}]		−3.50(6)	
	[ML_2H_2]	28.98(5)		
	[ML_2H]	22.7(4)	17.38(9)	
	[ML_2]	15.77(4)	9.78(4)	9.96(9)
N-Me-β-Alaha	[MLH]	16.71(3)	14.09(3)	14.04(4)
	[ML_2H_2]	31.97(8)	27.60(4)	27.60(4)
	[ML_2H]	23.5(1)	19.39(4)	19.43(6)
	[ML_2]		10.21(4)	10.1(3)
	[ML_2H_{-1}]		−0.11(3)	

(for the stoichiometrries and overall stability constants see Table 3), but the pH-metric experimental results suggest metal ion-induced deprotonation of both dissociable protons,[5] and also the spectroscopic results indicate unambiguously the involvement of the amino-N in the coordination of the non-protonated ligand. To demonstrate this, some UV–Vis spectra and CD spectra recorded for the Cu(II)-*N*-Me-α-Alaha system are presented in Figs. 3 and 4, respectively.

Although, the charge-transfer band with $\lambda_{max} = 380$ nm (Fig. 3) indicates the involvement of the hydroxamate function in the coordination, λ_{max} of the d–d band (see enlarged inset in Fig. 3) decreases continuously and at pH 6.77 (last measured pH before the precipitation) is significantly lower (ca. 620 nm) than the $\lambda_{max} = 650$ nm for the Cu(aceto-hydroxamate)$_2$ complex [26]. If the well-known Sigel–Martin's equation [29] and the parameters determined previously for the various types of donors [25,28] are used for

[3] Charge transfer band, characteristic for the hydroxamate-type interaction appears at ca. 380 nm and the minimum λ_{max} of the d–d band is 650 nm.

[4] One characteristic band at ca. 390 nm and another one at ca. 655 nm, assigned to $^1A_{1g} \rightarrow {}^1A_{2g}$ and $^1A_{1g} \rightarrow {}^1B_{1g}$ transitions, respectively, are reached by pH ca. 7 and remain unchanged until precipitation occurs.

[5] E.g. the dissociation constants (pK_{MLH}), which can be calculated for the MLH = ML + H process from the data of Table 3, are much less (6,30, 7.05, 6.88 for the Cu(II), Ni(II) and Zn(II) complexes, respectively) than pK_{amino} of the free-ligand.

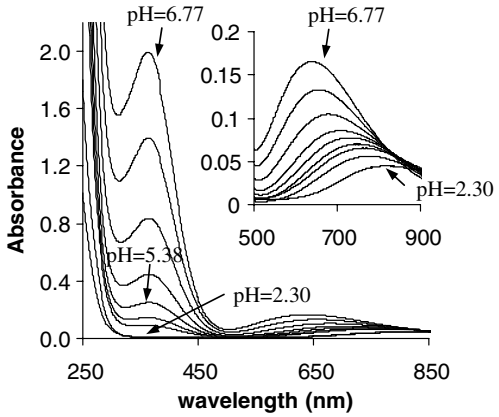


Fig. 3. Representative UV–Vis spectra registered for the Cu(II)-*N*-Me-α-Alaha as a function of pH at 1 to 2 metal to ligand ratio; $c_{Cu(II)} = 6 \times 10^{-3}$ M (inset: enlarged d–d part of the same spectra).

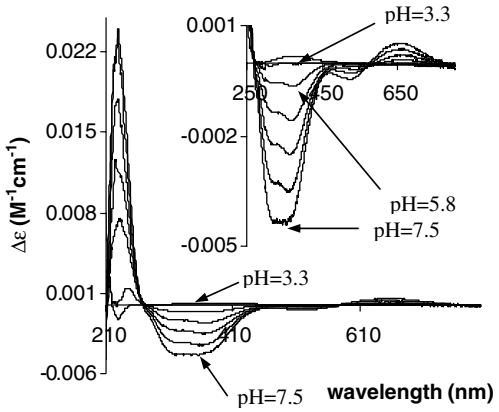


Fig. 4. Representative CD spectra registered for the Cu(II)-*N*-Me-α-Alaha as a function of pH at 1 to 2 metal to ligand ratio; $c_{Cu(II)} = 6 \times 10^{-3}$ M (inset: enlarged CD spectra in the range 250–800 nm).

estimating the absorption maximum, $\lambda_{max} = 620$ nm is obtained when equatorial coordination of three hydroxamate-O and one amino-N donors to a copper(II) ion is assumed.

CD spectra (Fig. 4) exhibit a positive Cotton effect in the 300–400 nm region at pH 3.31 (which is characteristic for hydroxamate type (O,O) coordination of this ligand [13]), but above pH 5 the Cotton effect turns to negative, which indicates a change in the coordination mode. This latter type of spectra can be found in the Cu(II)-L-α-Alaha system in the pH-range, where both nitrogen and oxygen donors are coordinated to the metal ion (see Section 1) [14]. To find whether any polynuclear complex in this pH-range in the Cu(II)-*N*-Me-α-Alaha system is formed, ESI-MS measurements at pH 6 were made but a mononuclear species, $[ML_2H]$, was only found ($m/z = 298$).

Based on the above findings, we can conclude that with a non-protonated *N*-Me-α-Alaha both the five-membered hydroxamate-(O,O) (structure **I**) and six-membered (N_{am}, O_{hydr}) (structure **III**) are formed and the mixed type coordination mode (**I** and **III**) in the bis-complex can be assumed.

3.2.2. Cu(II), Ni(II) and Zn(II) complexes of imidazole derivatives of aminohydroxamic acids, Im-4-Cha, N-Me-Im-4-Cha and Im-4-Aha

An aliphatic amino-N with high basicity in the α- or β-position is replaced by a much less basic, aromatic imidazole-N in the Im-4-Cha and Im-4-Aha derivatives. The effect of this change on the coordination mode(s) has been investigated by pH-potentiometry, UV–Vis, EPR, ^{1}H NMR and ESI MS methods. For the Cu(II)-containing systems magnetic measurements by using the Evans method [23] have also been performed. Out of the recorded pH-metric titration curves only a few examples are shown in Figs. 5a–c.

The titration curves registered before precipitation could be fitted best with the equilibrium models and stability constants shown in Table 4.

Figs. 5a–c clearly show that Cu(II) and Ni(II) are able to displace imidazole-NH even in the case of im-4-Cha where the free ligand itself dissociates already below pH 4 (for pK_a see Table 2). With this ligand, the displacement of imidazole-NH by Zn(II) (which prefers oxygen donors over nitrogen ones) seems questionable in Fig. 5a, but somewhat bigger effect was measured at 1:1 metal to ligand ratio. Also, a small but consequent difference between the chemical shift of the imidazole C(2)-H proton in the absence and presence of Zn(II) ion above pH 3 (see S.2) suggests a week coordination via the imidazole-N(3) of im-4-Cha with Zn(II) too. As a conclusion it may be stated that while the more basic amino-N does not, the less basic imidazole-N behaves as an anchor for Cu(II), Ni(II) or even for Zn(II) and the complex formation often starts at lower pH with imidazole derivatives compared to the amino-N containing counterparts. Most probably, chelate **IV** (which is not formed with the amino derivatives) is formed at the beginning of the interaction between these imidazole-containing ligands and Cu(II), Ni(II) or Zn(II). The first species found in most cases has a stoichiometry of [MLH], in which the proton is at the hydroxamic group. (Stability constant could not be calculated for [ZnLH] complexes of Im-4-Cha and Im-4-Aha.) Beside these similarities obtained with the three ligands, big differences between their metal complexation were also found.

With **Im-4-Cha** precipitation occurred at as low as pH 3 with Cu(II) and at pH 6–7 with Zn(II) and Ni(II) too, therefore a few species could only be detected before precipitation. To clarify the bonding modes, UV–Vis spectra for the Cu(II)- and Ni(II)-containing systems, furthermore EPR and magnetic measurements for the Cu(II)-containing ones have been performed before precipitation occurred. Looking at the visible spectra of the Ni(II) complexes, octahedral geometry is suggested up to pH 6 and continuous blue shift of the λ_{max} assigned to the $^3A_{2g} \rightarrow {}^3T_{1g}$ (655 nm at pH 2 and 605 at pH ca. 6) indicates increasing number of N-donor in the coordination sphere as the pH from 2 to 6 is increased. Taking into account these findings and also those with the analogues amino derivative, L-α-Alaha [8,10,11], first of all N-coordinated mono- and bis-complexes are suggested to form between Im-4-Cha and

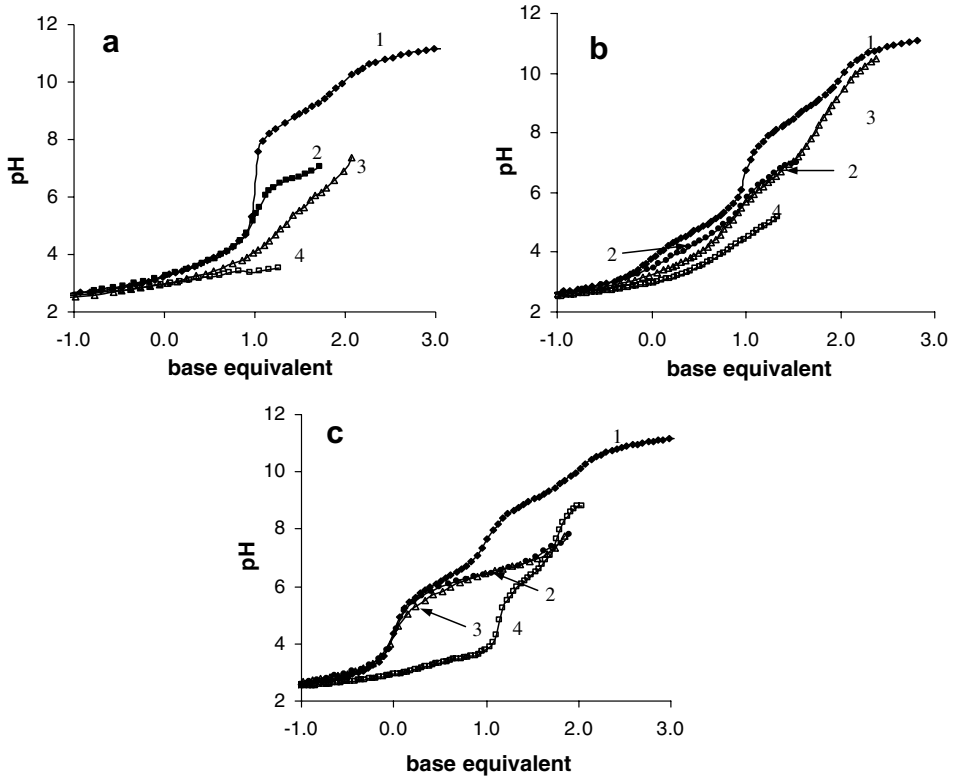


Fig. 5. pH-potentiometric titration curves registered for (a) Im-4-Cha (**1**) and for Zn(II)- (**2**), Ni(II)- (**3**), and Cu(II)- (**4**) Im-4-Cha systems; for (b) *N*-Me-Im-4-Cha (**1**) and for Zn(II)- (**2**), Ni(II)- (**3**), and Cu(II)- (**4**) *N*-Me-Im-4-Cha systems; for (c) Im-4-Aha (**1**) and for Zn(II)- (**2**), Ni(II)- (**3**), and Cu(II)- (**4**) Im-4-Aha systems at metal to ligand ratio 1:2, $c_L = 3 \times 10^{-3}$ M.

Table 4
Overall stability constants ($\log\beta$) for the Cu(II), Ni(II) and Zn(II) complexes of Im-4-Cha, *N*-Me-Im-4-Cha and Im-4-Aha, $t = 25$ °C, $I = 0.2$ M (KCl)

Ligand	Species	Cu(II)	Ni(II)	Zn(II)
			$\log\beta$	
Im-4-Cha	[MLH]	13.16(8)	12.67(2)	
	[ML]		7.24(5)	4.8(1)
	[ML_2]		13.30(5)	
	[$M_6L_5H_{-5}$]	48.4(3)		
N-Me-Im-4-Cha	[MLH]	14.16(7)	13.03(3)	12.55(5)
	[ML]	9.52(1)	6.35(5)	6.34(5)
	[ML_2H_2]	27.14(1)	25.31(4)	24.46(8)
	[ML_2H]	22.66(1)	19.18(5)	18.28(1)
	[ML_2]	16.90(2)	11.54(8)	
	[ML_2H_{-1}]		1.1(2)	
	[ML_3]		15.1(2)	
	[M_2L_3]	29.70(4)		
Im-4-Aha	[MLH]	15.12(3)	12.14(7)	
	[ML]		5.61(5)	5.49(4)
	[ML_2]		10.1(2)	9.8(2)
	[ML_3]		13.7(2)	
	[$M_5L_4H_{-4}$]	46.32(8)	8.8(2)	8.0(2)

Ni(II) below pH 6. Colour of the precipitate appeared just above 6, however, was already yellow, which is characteristic for planar complexes. With Cu(II), EPR results suggest the formation of EPR silent polynuclear complexes where the precipitation occurs. These findings suggest favoured formation of water-insoluble polynuclear species of Im-4-Cha with the studied metal ions. On the analogy of L-α-Alaha (see Section 1), formation of some metallacrown, at least with Cu(II), seems possible. The 91 experimental points registered before the precipitation resulted in slightly better fit (6.1×10^{-3} versus 6.7×10^{-3}) when [$Cu_6L_5H_{-5}$] compared to [$Cu_5L_4H_{-4}$] was involved in the calculation. As a consequence, stability constant for the former species is given in Table 4, but direct proof (including ESI-MS) for exact stoichiometry of the metallacrown species was not obtained.

Im-4-Aha, containing the side-chain imidazole donor in β-position relative to the hydroxamic function, forms somewhat more soluble complexes with Cu(II) and, as a consequence, a wider pH-range could be characterized in solution. All the stability constants calculated by fitting the pH-metric titration curves registered for the three systems before the precipitation are shown in Table 4. The pH-potentiometric results suggest only the formation of a very stable pentanuclear species in a wide pH-range with Cu(II) (see S.3), but much less stable Ni(II)- or Zn(II)-containing species are shown (see Fig. 5c). ESI-MS results obtained at pH 6 are in good agreement with this finding. Predominance of [$Cu_5L_4H_{-4}$]-type species ($\{[Cu_5L_4H_{-4}]H_{-1}\}^+$ with $m/z = 874$; $[Cu_5L_4H_{-4}]^{2+}$ with $m/z = 437$; $\{[Cu_5L_4H_{-4}]Cl\}^+$ with $m/z = 910$) was found.

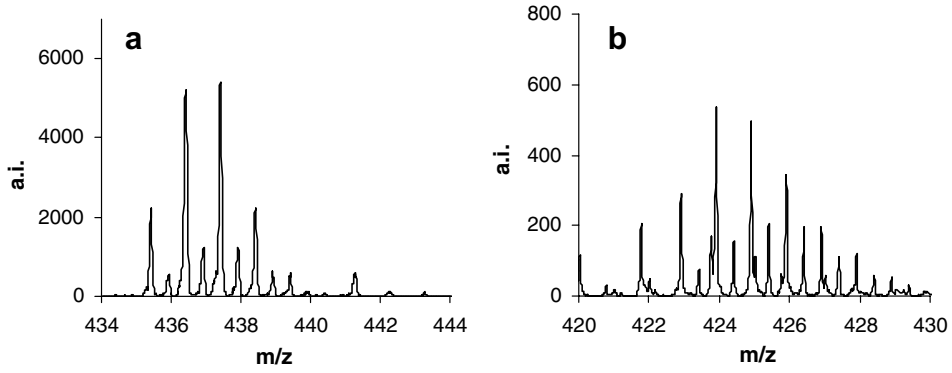
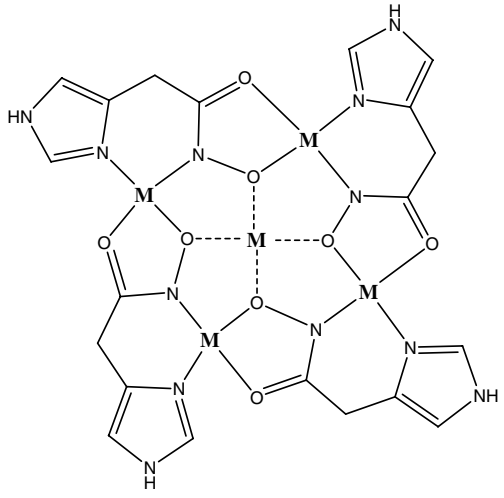


Fig. 6. ESI-MS spectra registered for the (a) Cu(II)-Im-4-Aha, and (b) Ni(II)-Im-4-Aha at pH 6 at 1 to 2 metal to ligand ratio, $c_L = 5 \times 10^{-3}$ M.

Interestingly, the pentanuclear species appears also with Ni(II) and Zn(II). However, because the stability of $[Ni_5L_4H_{-4}]$ and $[Zn_5L_4H_{-4}]$ is lower compared to the copper(II)-containing analogous species, they exist together with various bis- and tris-chelated mononuclear complexes ($[NiL_2H_2]^{2+}$ with $m/z = 170$; $[NiL_2H]^{+}$ with $m/z = 339$; $[NiL_2]K^{+}$ with m/z 377; $[NiL_3H_2]^{+}$ with $m/z = 480$; $[Ni_5L_4H_{-4}]^{2+}$ with $m/z = 424$ and $[ZnL_2H]^{+}$ with $m/z = 345$; $[ZnL_2]K^{+}$ with m/z 383; $[Zn_5L_4H_{-4}]^{2+}$ with $m/z = 438$). Representative parts of the spectra characteristic for the pentanuclear complexes with Cu(II) and Ni(II) are shown in Figs. 6a and b, respectively.

Taking the analogy with the Cu(II) complex of β-Alaha (see Section 1), the following 12-metallocrown-4 type bonding mode is suggested in the pentanuclear complexes with Im-4-Aha (Scheme 2).

***N*-Me-Im-4-Cha**, which is not able to form five-membered (N_{im}, N_{hydr}) chelate, realizes a five-membered (N_{im}, O_{carb}) one (**IV**) at the beginning of the complex formation as detailed above. This is unambiguous for example from the pH-metric results (see Fig. 5b) and it is also suggested for the Zn(II)-containing system by the ^{1}H NMR spectra (Fig. 7).



Scheme 2.

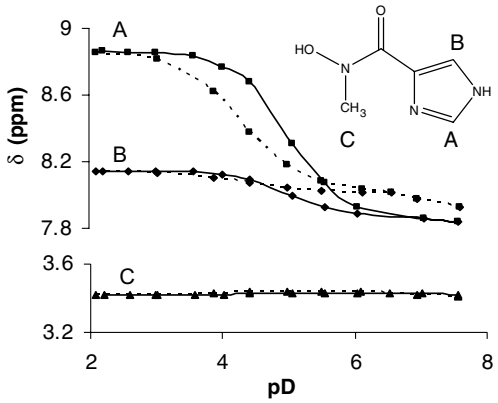


Fig. 7. pD dependence of the ^{1}H NMR chemical shifts recorded for *N*-Me-Im-4-Cha (continuous line) and Zn(II)-*N*-Me-Im-4-Cha (dashed line) system at 1 to 2 metal to ligand ratio, $c_L = 3 \times 10^{-3}$ M (letter A relates C(2)H, B for C(5)H, while C for CH_3 protons).

The chemical shift of the C(2)H proton is assumed to be sensitive to the metal ion coordination via imidazole-N(3), while C(5)H is expected to feel a strong coordination via the hydroxamate function. As it can be seen in Fig. 7 there is interaction with the involvement of imidazole-N(3) already from pD ca. 3, but strong interaction involving hydroxamate starts only at pD ca. 5 (probably after the deprotonation of the hydroxamic group with the formation of structure **III**).[6] In agreement with this result, ESI-MS spectra showed the formation of mononuclear bis-chelated complexes $[ZnL_2H_2]^{2+}$ ($m/z = 173$) and $[ZnL_2H]^{+}$ ($m/z = 345$). Unexpectedly, beside the mononuclear species ($[CuL_2H]^{+}$ with $m/z = 344$; $[CuL_2]K^{+}$ with $m/z = 382$; $[NiL_2H_2]^{2+}$ with $m/z = 170$); ($[NiL_2H]^{+}$ with $m/z = 339$; $[CuL_2]K^{+}$ with $m/z = 377$; $[NiL_3H_2]^{+}$ with $m/z = 480$), dinuclear species $[M_2L_3]^{+}$ (see Fig. 8) appeared (m/z values are 546 and 536 with Cu(II) and Ni(II), respectively).

[6] Structure **III** (instead of **IV**) is suggested, because the significantly more favoured deprotonation of the hydroxamic group from the complexes (pK_{ZnLH} and pK_{ZnL2H2}, which can be calculated from Table 4, are both ca. 6.2) compared to the free ligand ($pK = 8.57$) indicates metal ion induced dissociation of this proton.

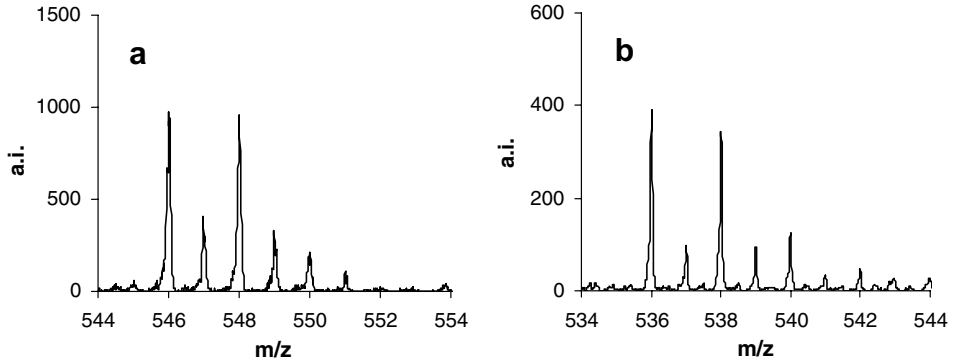


Fig. 8. ESI-MS spectra registered for the (a) Cu(II)-*N*-Me-Im-4-Cha, and (b) Ni(II)-*N*-Me-Im-4-Cha at pH 6 at 1 to 2 metal to ligand ratio, $c_L = 5 \times 10^{-3}$ M.

For Cu(II) this result is also supported by EPR, where the presence of a dimeric species is confirmed by the half field spectra (recorded both for sample with precipitate and filtrate) which shows 7 lines centred at $G \sim 4$ (Fig. 9).

Although stability constants could be calculated for $[Cu_2L_3]$, but the concentration of this species is quite small (see Fig. 10 for the concentration distribution curves). Most probably, the ratio of the dinuclear species is even lower with Ni(II), therefore its stability constant could not be calculated. Neither pH-potentiometric nor ESI-MS results indicated the formation of $[Zn_2L_3]$. Perhaps, the very low stability of the (N_{im}, O_{carb}) chelate compared to the hydroxamate one with Zn(II) causes that the dinuclear species can not be formed with this metal.

One possible structure of $[M_2L_3]$ can be that one of the three ligands binds two metal ions via two joined chelates, while ring stacking between two imidazole rings of the two other coordinating ligands exists (S.4).

All the above results are also supported by magnetic measurements. Magnetic measurements were carried out for the Cu(II)-Im-4-Cha, -*N*-Me-Im-4-Cha and -Im-4-Aha systems. Differences between the chemical shifts of *t*-BuOH in dia- and paramagnetic surroundings as a function of pD are shown in Fig. 11. (Mass magnetic susceptibilities calculated by the Evans's method [22] show completely the same profile, therefore are not shown here.)

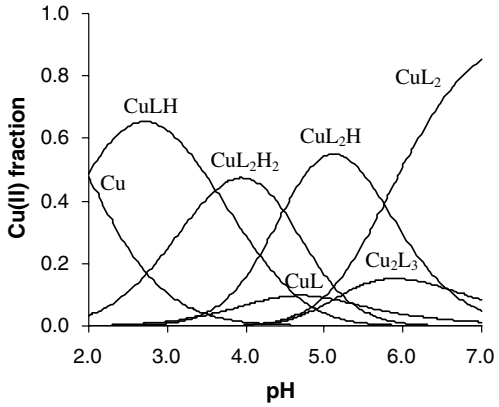


Fig. 10. Concentration distribution curves calculated for Cu(II)-*N*-Me-Im-4-Cha system at 1 to 2 metal to ligand ratio. $c_{ligand} = 4 \times 10^{-3}$ M.

As Fig. 11 reveals the chemical shift differences practically do not show pD dependence in the case of Cu(II)-*N*-Me-Im-4-Cha system, where only mononuclear species are formed (dotted line). Negligible dependence can be seen

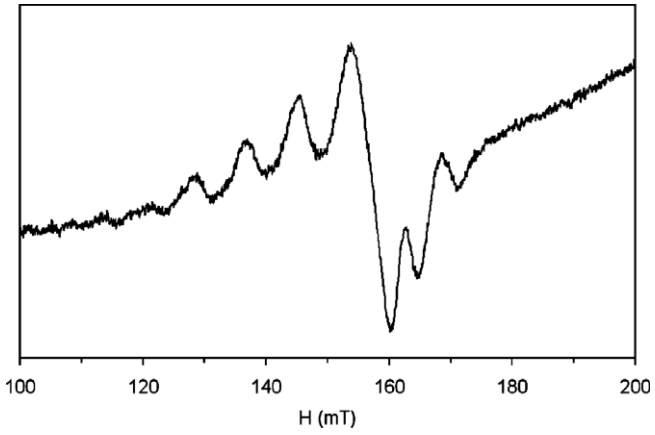


Fig. 9. Half field EPR spectra registered for Cu(II)-*N*-Me-Im-4-Cha system at 1 to 2 metal to ligand ratio, at pH ca. 6. $c_L = 3 \times 10^{-3}$ M, $T = 120$ K.

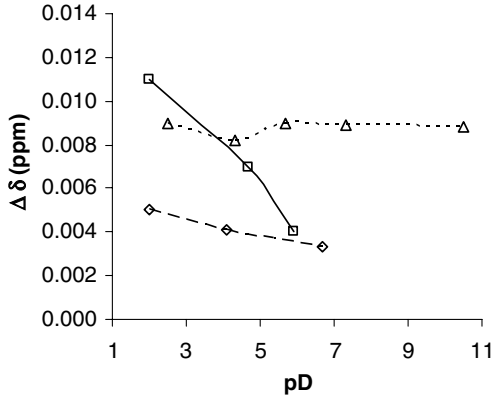


Fig. 11. pD dependence of the differences between the ^{1}H NMR chemical shifts of *t*-BuOH in dia- and paramagnetic surroundings for Cu(II)-*N*-Me-Im-4-Cha (dotted line), Cu(II)-Im-4-Aha (dashed line) and Cu(II)-Im-4-Cha (continuous line) at 1 to 2 metal to ligand ratio. $c_L = 3 \times 10^{-3}$ M.

for Cu(II)-Im-4-Aha (dashed line), but the values are measurably lower compared to that for the former system. This result indicates antiferromagnetic coupling between the copper centres in the latter system, where a metallacrown type polynuclear species with high stability exists. However, a continuous decrease of the $\Delta\delta$ values as a function of pD can be seen with Im-4-Cha (continuous line). This behaviour compared to those of the other two ligands may also led to the conclusion that following the formation of monomeric type complexes at low pD, polymerisation takes place in the Cu(II)-Im-4-Cha system.

4. Conclusion

When solution equilibrium results obtained for H^+, Cu^{2+}, Ni^{2+} and Zn^{2+} complexes of *N*-Me-β-Alaninehydroxamic acid (*N*-Me-β-Alaha), L-*N*-Me-α-Alaninehydroxamic acid (*N*-Me-α-Alaha), Imidazole-4-Carbohydroxamic acid (Im-4-Cha), *N*-Me-Imidazole-4-Carbohydroxamic acid (*N*-Me-Im-4-Cha) and Imidazole-4-Acetohydroxamic acid (Im-4-Aha) are summarized, the following conclusion can be drown: Although, coordination via the hydroxamate chelate is crucial for inhibition of a metalloenzyme (like an MMP or urease) by hydroxamate-based compounds, privilege of the hydroxamate-type (O,O)-coordination may not exist if the amino-N is in chelatable position to the hydroxamate-N in hydroxamic derivatives of α- and β-amino acids. Therefore, *N*-Me-α-Alaha and *N*-Me-β-Alaha have been synthesized and studied, where the hydroxamate-N is not able to coordinate. Only hydroxamate type coordination of *N*-Me-β-Alaha was found with all the three metals, but formation of additional six-membered chelate via the amino-N and hydroxamate-O is suggested parallel to the hydroxamate one in the case of *N*-Me-α-Alaha.

The less basic imidazole-N(3) was found to behave as anchor donor not only to Cu^{2+} and Ni^{2+}, but even to Zn^{2+}, although this latter metal ion prefers oxygen donors over nitrogen ones. By increasing the pH water insoluble polynuclear species have been found to form with Im-4-Cha. A pentanuclear metallacrown is exclusively formed above pH 4 between Cu(II) and Im-4-Aha. The stability of this species with Ni(II) and Zn(II) is significantly lower, and as a consequence, it appears together with various mononuclear bonding isomers in the Ni(II)-Im-4-Aha and Zn(II)-Im-4-Aha systems. Beside the mononuclear species a dinuclear complex, $[M_2L_3]$, was found in the Cu(II)- and Ni(II)-*N*-Me-Im-4-Cha. A possible bonding mode is that one of the three ligands bridges two metal ions, while each of the other two ligands binds to one metal. Stacking interaction between the imidazole rings of the latter two ligands might stabilize this species.

Acknowledgements

This work was supported by the Hungarian Scientific Research Fund (OTKA T 049612 and 046366) and COST D21/01. D.B. thanks for stsm from Debrecen to Darmstadt supported by COST D21 program. P.B. gratefully acknowledges the Hungarian Academy of Sciences for a János Bolyai Research Fellowship. The authors thank Dr. Katalin Osz for her help in the calculation of dissociation microconstants.

Appendix A. Supplementary material

Supplementary data associated with this article can be found, in the online version, at doi:10.1016/j.poly.2006.08.019.

References

[1] E.M.F. Muri, M.J. Nieto, R.D. Sindelar, J.S. Williamson, Curr. Med. Chem. 9 (2002) 1631.
[2] A-M. Albrecht-Gary, A.L. Crumbliss, in: A. Sigel, H. Sigel (Eds.), Metal Ions in Biological Systems, vol. 35, Marcel Dekker, New York, 1998.
[3] A.L. Crumbliss, in: G. Winkelmann (Ed.), Handbook of Microbial Iron Chelates, CRC Press, New York, 1991.
[4] D.T. Puerta, S.M. Cohen, Curr. Top. Med. Chem. 4 (2004) 1551.
[5] S. Benini, W.R. Rypniewski, K.S. Wilson, S. Miletti, S. Ciurli, S. Mangani, J. Biol. Inorg. Chem. 5 (2000) 110.
[6] E.M.F. Muri, H. Mishra, M.A. Avery, J.S. Williamson, Synth. Commun. 33 (2003) 1977.
[7] B. Kurzak, H. Kozłowski, E. Farkas, Coord. Chem. Rev. 114 (1992) 169.
[8] J.J. Bodwin, A.D. Cutland, R.G. Malkani, V.L. Pecoraro, Coord. Chem. Rev. 216–217 (2001) 489.
[9] D. Fournand, J.-L. Pirat, F. Bigey, A. Arnaud, P. Galzy, Inorg. Chim. Acta 353 (1997) 359.
[10] F. Dallavalle, M. Tegoni, Polyhedron 20 (2001) 2697.
[11] M. Careri, F. Dallavalle, M. Tegoni, I. Zagnoni, J. Inorg. Biochem. 93 (2003) 174.
[12] D.A. Brown, A.L. Roche, Inorg. Chem. 22 (1983) 2199.
[13] X. Hu, J. Zhu, S. Srivathsan, D. Pei, Bioorg. Med. Chem. Lett. 14 (2004) 77.
[14] E. Farkas, J. Szöke, T. Kiss, H. Kozłowski, W. Bal, J. Chem. Soc., Dalton Trans. (1989) 2247.
[15] D.A. Brown, A.I. Roche, T.A. Pakkanen, T.T. Pakkanen, K. Smolander, J. Chem. Soc., Chem. Commun. (1982) 676.
[16] B. Kurzak, E. Farkas, T. Glowiak, H. Kozłowski, J. Chem. Soc., Dalton Trans. (1991) 163.
[17] A.H. Blatt, Organic Synthesis, Wiley, New York, 1963.
[18] J.P. Collman, M. Bröring, L. Fu, M. Rapta, R. Schwenninger, J. Org. Chem. 63 (1998) 8084.
[19] T. Kunitake, S. Horie, Bull. Soc. Chem. Japan 48 (1975) 1304.
[20] G. Gran, Acta Chem. Scand. 4 (1950) 559.
[21] H.M. Irving, M.G. Miles, L.D. Pettit, Anal. Chim. Acta 38 (1967) 475.
[22] L. Zékány, I. Nagypál, in: D.L. Leggett (Ed.), Computational Methods for the Determination of Stability Constants, Plenum Press, New York, 1985, p. 291.
[23] D.F. Evans, J. Chem. Soc. (1959) 2003.
[24] E. Farkas, T. Kiss, B. Kurzak, J. Chem. Soc., Perkin Trans. 2 (1990) 1255.
[25] C.L. Perrin, M.A. Fabian, Anal. Chem. 68 (1996) 2127.
[26] E. Farkas, É.A. Enyedy, H. Csóka, J. Inorg. Biochem. 79 (2000) 205.
[27] A. Krezel, W. Bal, J. Inorg. Biochem. 98 (2004) 161.
[28] I. Sóvágó, E. Farkas, Cs. Bertalan, A. Lebkiri, T. Kowalik-Jankowska, H. Kozłowski, J. Inorg. Biochem. 51 (1993) 715.
[29] H. Sigel, R.B. Martin, Chem. Rev. 82 (1982) 385.

Available online at www.sciencedirect.com
ScienceDirect
Polyhedron 26 (2007) 555–562
POLYHEDRON
www.elsevier.com/locate/poly

Synthesis, spectral characterization and photoluminescence properties of cadmium(II) complexes of *N*-[(2-pyridyl)methyliden]-α (or β)-aminonaphthalene (α- or β-NaiPy) and comparison with the complexes of 1-alkyl-2-(naphthyl-α (or β)-azo)imidazole. Single crystal X-ray structure of $[Cd(\beta\text{-NaiPy})_2(ONO_2)_2]$

D. Das, B.G. Chand, J. Dinda, C. Sinha *

Department of Chemistry, Inorganic Chemistry Section, Jadavpur University, Kolkata 700 032, West Bengal, India

Received 4 July 2006; accepted 11 August 2006
Available online 25 August 2006

Abstract

Cadmium(II) complexes of *N*-[(2-pyridyl)methyliden]-α (or β)-aminonaphthalene (α or β-NaiPy) and 1-alkyl-2-(naphthyl-α (or β)-azo)imidazoles (α- or β-NaiR) using Cl^-, ClO_4^- and NO_3^- as anions are spectroscopically characterized. Molar conductance data in nitromethane show that the chloro and nitrite compounds are non-conducting, while the perchlorate complexes are 1:2 electrolytes. The single crystal X-ray structure of $[Cd(N\text{-}\{(2\text{-pyridyl})methyliden\}\text{-}\beta\text{-aminonaphthalene})_2(ONO_2)_2]$ has been determined. The luminescence properties of Cd(II) complexes of α/β-NaiPy are studied and they exhibit ligand centered π–π^* emissions. Naphthylazoimidazoles and their cadmium complexes are non-fluorescent.
© 2006 Elsevier Ltd. All rights reserved.

Keywords: Cadmium(II); Naphthylamine Schiff base; Naphthylazoimidazoles; Crystal structure; Luminescence

1. Introduction

Luminescent metal complexes are a potential field for applications in many areas such as light emitting devices (LEDs), design of optical materials and sensors [1]. Polypyridine complexes of transition and non-transition metals have been extensively used in this field [2–6]. The ligands carry the α-diimine function (–N=C–C=N–). Recent years have witnessed a great deal of interest in the synthesis of new ligands with a diimine group in the framework. The condensation of pyridine-2-carboxaldehyde with aromatic amine has synthesized a Schiff base in which the –N=C– group in the pyridine ring is conjugated with an exocyclic –C=N– group to form a diimine function [7–9]. Schiff bases synthesized from the condensation of naphthyl amines and pyridine-2-carboxaldehyde are scarce [10–12]. The naphthyl group is sterically more crowded, electronically labile and more delocalized than the phenyl group. Thus, the naphthyl substituent in Schiff bases may affect significantly the spectroscopic and photophysical properties of metal complexes compared to the properties of phenyl Schiff bases. In this article we wish to report the synthesis, spectral characterization and luminescence properties of *N*-[(2-pyridyl)methyliden]-α (or β)-aminonaphthalene (α- or β-NaiPy) complexes of Cd(II) using Cl^-, NO_3^- and ClO_4^- as anions. A comparison will be made with the structure and properties of 1-alkyl-2-(naphthylazo)imidazole complexes of Cd(II) under identical environments. Naphthylazoimidazole possesses the azoimine (–N=N–C=N–) chelating function, isoelectronic with the diimine (–N=C–C=N–) unit. A structural confirmation has been carried out for $[Cd(\beta\text{-NaiPy})_2(ONO_2)_2]$ by single crystal X-ray diffraction.

* Corresponding author. Fax: +91 33 24146584.
E-mail address: c_r_sinha@yahoo.com (C. Sinha).

0277-5387/$ - see front matter © 2006 Elsevier Ltd. All rights reserved.
doi:10.1016/j.poly.2006.08.014

2. Experimental

2.1. Materials and measurements

α-Naphthylamine and β-naphthylamine were purchased from Thomas Baker & Co. Pyridine-2-carboxaldehyde was purchased from Lancaster Ltd., England. *N*-[(2-Pyridyl)-methyliden]-α (or β)-aminonaphthalene (α or β-NaiPy) were synthesized by equimolar condensation of pyridine-2-carboxaldehyde and naphthylamine in ethanol following a previously reported procedure [10]. 1-Alkyl-2-(naphthyl-α/β-azo)imidazoles (α/β-NaiR) were synthesized by a published procedure [13]. All other chemicals used were of A.R. quality and were used as received from SRL, India. The solvents were used after drying [14].

UV–Vis spectra were recorded using Lambda 25 Perkin–Elmer spectrophotometers and FT-IR spectra (KBr disc) were obtained from Spectrum RX-1 Perkin–Elmer (4000–450 cm^{-1}) and JASCO model 420 (4000–200 cm^{-1}) spectrophotometers. Microanalyses were collected from a Perkin–Elmer 2400 CHN elemental analyzer. ^1H NMR spectra were recorded on a Bruker 300 MHz FT NMR. Solution electrical conductivity was measured using a Systronics 305 digital conductivity meter. Luminescence properties were measured using a LS-55 Perkin–Elmer fluorescence spectrophotometer at room temperature (298 K) in CH_3CN solution with a 1 cm path length quartz cell.

The fluorescence quantum yield of the α- or β-NaiPy and their cadmium(II) complexes (**5**–**10**) was determined using Coumarin-120 laser dye as a reference with a known ϕ_R of 0.63 in MeCN. The complex and the reference dye were excited at 340 nm, maintaining nearly equal absorbance (~0.1), and the emission spectra were recorded from 350 to 600 nm. The area of the emission spectrum was integrated using the software available in the instrument and the quantum yield is calculated according to the following equation:

$$\phi_S/\phi_R = [A_S/A_R] \times [(Abs)_R/(Abs)_S] \times [\eta_S^2/\eta_R^2]$$

Here, ϕ_S and ϕ_R are the fluorescence quantum yield of the sample and reference, respectively. A_S and A_R are the area under the fluorescence spectra of the sample and the reference respectively, $(Abs)_S$ and $(Abs)_R$ are the respective optical densities of the sample and the reference solution at the wavelength of excitation, and η_S and η_R are the values of the refractive index for the respective solvent used for the sample and reference.

2.2. Preparation of the complexes

2.2.1. Synthesis of di-chloro-N-[((2-pyridyl)methyliden)-α-aminonaphthalene]cadmium(II), Cd(α-NaiPy)Cl_2] (5)

N-[(2-Pyridyl)methyliden)-α-aminonaphthalene] (0.25 g, 1.08 mmol) in MeOH (10 mL) was added dropwise to a methanolic solution (10 mL) of $CdCl_2$ (0.27 g, 1.18 mmol) at room temperature and the resulting mixture was stirred for 3 h. The solution colour turned yellow. The volume was reduced to half of its original volume by slow evaporation in air. Yellow crystals then separated. They were filtered, washed with water, water–MeOH (1:1, v/v). The product was then crystallized by diffusion of a CH_2Cl_2 solution into hexane. The yield was 0.28 g (74%).

Anal. Calc. for $C_{16}H_{12}N_2Cl_2Cd$ (**5**); C, 46.20; H, 2.89; N, 6.74. Found: C, 46.05; H, 2.80; N, 6.85%. UV–Vis spectral data in MeCN (λ_{max} (nm)) 10^{-3} ε ($dm^3\,mol^{-1}\,cm^{-1}$), 410 (0.78), 340 (3.56) (sh), 335 (4.98), 291 (5.91). ^1H NMR ($CDCl_3$), δ, ppm (J, Hz): 7.90 (d, J(HH) = 8.0, 1H, 3-H(Py)), 7.81 (t, J(HH) = 7.0, 2H, 4-,5-H(Py)), 8.45 (d, J(HH) = 8.0, 1H, 6-H(Py)), 8.73 (s, 1H, 7-H(CH=N)), 7.43 (d, J(HH) = 8.0, 1H, 9-H(naphthyl)), 7.32 (m, 1H, 10-H(naphthyl)), 7.39 (m, 4H, 11-H to 14-H(naphthyl)), 7.11 (d, J(HH) = 8.0, 1H, 15-H(naphthyl)). *Anal.* Calc. for $C_{16}H_{12}N_2Cl_2Cd$ (**6**); C, 46.20; H, 2.89; N, 6.74. Found: C, 46.28; H, 2.85; N, 6.68%. UV–Vis spectral data in MeCN (λ_{max} (nm)) 10^{-3} ε ($dm^3\,mol^{-1}\,cm^{-1}$), 418 (0.92), 350 (6.37) (sh), 330 (7.07), 283 (16.86). ^1H NMR ($CDCl_3$), δ, ppm (J, Hz): 7.76 (d, J(HH) = 8.0, 1H, 3-H(Py)), 7.64 (t, J(HH) = 7.0, 2H, 4-,5-H(Py)), 8.42 (d, J(HH) = 8.0, 1H, 6-H(Py)), 8.60 (s, 1H, 7-H(CH=N)), 7.60 (d, J(HH) = 8.0, 1H, 8-H(naphthyl)), 7.52 (d, J(HH) = 7.5, 1H, 10-H(naphthyl)), 7.35 (m, 4H, 11-H to 14-H(naphthyl)), 7.10 (d, J(HH) = 8.0, 1H, 15-H(naphthyl)).

2.2.2. Synthesis of dinitrito-N-[((2-pyridyl)methyliden)-α-aminonaphthalene]cadmium(II), [Cd(α-NaiPy)$_2$(NO_3)$_2$] (7)

N-[(2-Pyridyl)methyliden)-α-aminonaphthalene] (0.25 g, 1.08 mmol) in MeOH (10 mL) was added dropwise to a methanolic solution (10 mL) of $Cd(NO_3)_2 \cdot 4H_2O$ (0.17 g, 0.55 mmol) at room temperature and the resulting mixture was stirred for 3 h. The volume of yellow solution was reduced to half of its original volume by slow evaporation in air. The solution was then kept in a refrigerator, maintaining the temperature at 5 °C. The bright yellow crystalline product was then recrystallized from MeOH–H_2O (1:1, v/v) and dried over $CaCl_2$. The yield was 0.22 g, 64%. [Cd(β-NaiPy)$_2$(NO_3)$_2$] (**8**) was prepared similarly and the yield was 70%.

Anal. Calc. for $C_{32}H_{24}N_6O_6Cd$ (**7**); C, 54.81; H, 3.43; N, 11.99. Found: C, 54.69; H, 3.52; N, 12.09%. UV–Vis spectral data in MeCN (λ_{max} (nm)) 10^{-3} ε ($dm^3\,mol^{-1}\,cm^{-1}$), 436 (1.21), 348 (5.08) (sh), 332 (8.82), 290 (14.94). ^1H NMR ($CDCl_3$), δ, ppm (J, Hz): 7.80 (d, J(HH) = 8.0, 1H, 3-H(Py)), 7.63 (t, J(HH) = 7.0, 2H, 4-,5-H(Py)), 8.40 (d, J(HH) = 8.0, 1H, 6-H(Py)), 8.67 (s, 1H, 7-H(CH=N)), 7.50 (d, J(HH) = 8.0, 1H, 9-H(naphthyl)), 7.41 (m, 1H, 10-H(naphthyl)), 7.30 (m, 4H, 11-H to 14-H(naphthyl)), 7.10 (d, J(HH) = 8.0, 1H, 15-H(naphthyl)). *Anal.* Calc. for $C_{32}H_{24}N_6O_6Cd$ (**8**) C, 54.81; H, 3.43; N, 11.99. Found: C, 54.69; H, 3.52; N, 12.09%. UV–Vis spectral data in MeCN (λ_{max} (nm)) 10^{-3} ε ($dm^3\,mol^{-1}\,cm^{-1}$), 454 (1.47), 340 (5.89)(sh), 334 (14.80), 285 (30.60). ^1H NMR ($CDCl_3$), δ, ppm (J, Hz): 7.76 (d, J(HH) = 8.0, 1H, 3-H(Py)), 7.58 (t, J(HH) = 7.0, 2H, 4-,5-H(Py)), 8.43 (d, J(HH) = 8.0,

1H, 6-H(Py)), 8.60 (s, 1H, 7-H(CH=N)), 7.62 (d, J(HH) = 7.5, 1H, 8-H(naphthyl)), 7.50 (d, J(HH) = 7.5, 1H, 10-H(naphthyl)), 7.32 (m, 4H, 11-H to 14-H(naphthyl)), 7.16 (d, J(HH) = 8.0, 1H, 15-H(naphthyl)).

2.2.3. Synthesis of bis-{N-[((2-pyridyl)methyliden)-α-aminonaphthalene]amine}cadmium(II) perchlorate, [Cd(α-NaiPy)$_2$](ClO$_4$)$_2$ (**9**)

N-[((2-Pyridyl)methyliden)-α-aminonaphthalene] (0.25 g, 1.08 mmol) in MeOH (10 mL) was added dropwise to a methanolic solution (10 mL) of $Cd(ClO_4)_2 \cdot 6H_2O$ (0.23 g, 0.55 mmol) at room temperature and the resulting mixture was stirred for 3 h. The volume of the solution was reduced to half of its original volume by slow evaporation in air. The solution was then kept in a refrigerator, maintaining temperature at 5 °C. The bright yellow crystalline product was then recrystallized from MeOH–H_2O (1:1, v/v) and dried over $CaCl_2$. The yield was 0.24 g, 61%. [Cd(β-NaiPy)$_2$-(ClO$_4$)$_2$] was prepared similarly (yield, 60%).

Anal. Calc. for $C_{32}H_{24}N_4O_8Cl_2Cd$ (**9**); C, 47.29; H, 3.45; N, 6.90. Found: C, 47.35; H, 3.38; N, 7.00%. UV–Vis spectral data in MeCN (λ_{max} (nm)) 10^{-3} ε (dm^3 mol^{-1} cm^{-1}), 416 (1.14), 350 (3.67) (sh), 334 (5.58), 285 (17.955). ^{1}H NMR ($CDCl_3$), δ, ppm (J, Hz): 7.70 (d, J(HH) = 8.0, 1H, 3-H(Py)), 7.62 (t, J(HH) = 7.0, 2H, 4-,5-H(Py)), 8.35 (d, J(HH) = 8.0, 1H, 6-H(Py)), 8.45 (s, 1H, 7-H(CH=N)), 7.46 (d, J(HH) = 8.0, 1H, 9-H(naphthyl)), 7.40 (m, 1H, 10-H(naphthyl)), 7.33 (m, 4H, 11-H to 14-H(naphthyl)), 7.10 (d, J(HH) = 8.0, 1H, 15-H(naphthyl)). *Anal.* Calc. for $C_{32}H_{24}N_4O_8Cl_2Cd$ (**10**); C, 47.29; H, 3.45; N, 6.90. Found: C, 47.38; H, 3.52; N, 7.08%. UV–Vis spectral data in MeCN (λ_{max} (nm)) 10^{-3} ε (dm^3 mol^{-1} cm^{-1}), 430 (1.33), 350 (6.56) (sh), 334 (15.90), 293 (22.90). ^{1}H NMR ($CDCl_3$), δ, ppm (J, Hz): 7.70 (d, J(HH) = 8.0, 1H, 3-H(Py)), 7.59 (t, J(HH) = 7.0, 2H, 4-,5-H(Py)), 8.40 (d, J(HH) = 8.0, 1H, 6-H(Py)), 8.50 (s, 1H, 7-H(CH=N)), 7.60 (d, J(HH) = 8.0, 1H, 8-H(naphthyl)), 7.52 (d, J(HH) = 7.5, 1H, 10-H(naphthyl)), 7.30 (m, 4H, 11-H to 14-H(naphthyl)), 7.12 (d, J(HH) = 8.0, 1H, 15-H(naphthyl)).

2.3. Synthesis of bis-[1-methyl-2-(naphthyl-α-azo)-imidazole]cadmium(II) perchlorate, [Cd(α-NaiMe)$_2$]-(ClO$_4$)$_2$ (**15a**)

1-Methyl-2-(naphthyl-α-azo)imidazole (0.25 g, 1.06 mmol) in MeOH (15 mL) was added dropwise to a methanolic solution (25 mL) of $Cd(ClO_4)_2 \cdot 6H_2O$ (0.50 g, 1.19 mmol) at room temperature and the resulting mixture was stirred for 1 h. The solution was then filtered and kept undisturbed for a week. Orange crystals appeared on the wall of the beaker. The bright crystalline product was then recrystallized by diffusion of a CH_2Cl_2 solution into hexane. The yield was 0.25 g, 60%.

Other compounds were prepared following an identical procedure and isolated in yields of 55–70%.

Anal. Calc. for [Cd(α-NaiMe)Cl$_2$] (**11a**) $C_{14}H_{12}N_4Cl_2Cd$: C, 40.06; H, 2.86; N, 13.35. Found: C, 40.12; H, 2.78; N, 13.47%. UV–Vis spectral data in MeCN (λ_{max} (nm)) 10^{-3} ε (dm^3 mol^{-1} cm^{-1}) 410 (5.80), 338 (4.25), 270 (6.18). ^{1}H NMR ($CDCl_3$), δ, ppm (J, Hz): 7.20 (broad singlet, 1H, 4-H(imidazole)), 6.83 (broad singlet, 1H, 5-H(imidazole)), 8.52 (d, J(HH) = 8.0, 1H, 9-H(naphthyl)), 7.68 (m, 2H, 10,11-H(naphthyl)), 7.41 (m, 2H, 12,13-H(naphthyl)), 7.34 (m, 1H, 14-H(naphthyl)), 7.74 (d, J(HH) = 8.0, 1H, 15-H(naphthyl)), 4.01 (s, 3H, 1-CH_3). *Anal.* Calc. for [Cd(β-NaiMe)Cl$_2$] (**12a**) $C_{14}H_{12}N_4Cl_2Cd$: C, 40.06; H, 2.86; N, 13.35. Found: C, 39.93; H, 2.82; N, 13.43%. UV–Vis spectral data in MeCN (λ_{max} (nm)) 10^{-3} ε (dm^3 mol^{-1} cm^{-1}), 430 (4.20), 333 (6.25), 275 (5.80). ^{1}H NMR ($CDCl_3$), δ, ppm (J, Hz): 7.22 (broad singlet, 1H, 4-H(imidazole)), 6.80 (broad singlet, 1H, 5-H(imidazole)), 8.17 (d, J(HH) = 8.0, 1H, 8-H(naphthyl)), 8.00 (d, J(HH) = 7.5, 10-H(naphthyl)), 7.85 (m, 2H, 11-H(naphthyl)), 7.45 (m, 2H, 12,13-H(naphthyl)), 7.35 (m, 1H, 14-H(naphthyl)), 7.30 (d, J(HH) = 8.0, 1H, 15-H(naphthyl)), 4.08 (s, 3H, 1-CH_3).

Anal. Calc. for Cd(α-NaiEt)Cl$_2$ (**11b**), $C_{15}H_{14}N_4Cl_2Cd$: C, 41.53; H, 3.23; N, 12.92. Found: C, 41.43; H, 3.17; N, 12.77%. UV–Vis spectral data in MeCN (λ_{max} (nm)) 10^{-3} ε (dm^3 mol^{-1} cm^{-1}) 460 (1.80), 411 (2.41), 336 (2.24), 282 (5.20). ^{1}H NMR ($CDCl_3$), δ, ppm (J, Hz): 7.20 (broad singlet, 1H, 4-H(imidazole)), 6.75 (broad singlet, 1H, 5-H(imidazole)), 8.56 (d, J(HH) = 8.0, 1H, 9-H(naphthyl)), 7.73 (m, 2H, 10,11-H(naphthyl)), 7.44 (m, 2H, 12,13-H(naphthyl)), 7.35 (m, 1H, 14-H(naphthyl)), 7.78 (d, J(HH) = 8.0, 1H, 15-H(naphthyl)), 3.80 (quartet, J(HH) = 9.0, 2H, 1-CH_2), 0.86 (t, J(HH) = 7.5, 3H (1-CH_2)–CH_3). *Anal.* Calc. [Cd-(β-NaiEt)Cl$_2$] (**12b**) $C_{15}H_{14}N_4Cl_2Cd$: C, 41.53; H, 3.23; N, 12.92. Found: C, 41.46; H, 3.18; N, 12.98%. UV–Vis spectral data in MeCN (λ_{max} (nm)) 10^{-3} ε (dm^3 mol^{-1} cm^{-1}) 420 (5.15), 395 (10.26), 380 (10.08), 275 (6.80). ^{1}H NMR ($CDCl_3$), δ, ppm (J, Hz): 7.23 (broad singlet, 1H, 4-H(imidazole)), 6.90 (broad singlet, 1H, 5-H(imidazole)), 8.20 (d, J(HH) = 8.0, 1H, 8-H(naphthyl)), 8.00 (d, J(HH) = 7.5, 1H, 10-H(naphthyl)), 7.90 (m, 1H, 11-H(naphthyl)), 7.42 (m, 2H, 12,13-H(naphthyl)), 7.35 (m, 1H, 14-H(naphthyl)), 7.30 (d, J(HH) = 8.0, 1H, 15-H(naphthyl)), 4.50 (quartet, J(HH) = 9.0, 2H, 1-CH_2), 1.10 (t, J(HH) = 7.5, 3H (1-CH_2)–CH_3).

Anal. Calc. for [Cd(α-NaiMe)$_2$](NO$_3$)$_2$ (**13a**); $C_{28}H_{24}N_{10}O_6Cd$: C, 47.43; H, 3.39; N, 19.76. Found: C, 47.51; H, 3.33; N, 19.65%. UV–Vis spectral data in MeCN (λ_{max} (nm)) 10^{-3} ε (dm^3 mol^{-1} cm^{-1}) 467 (5.27), 403 (7.54), 331 (7.93), 269 (9.29). ^{1}H NMR ($CDCl_3$), δ, ppm (J, Hz): 7.24 (broad singlet, 1H, 4-H(imidazole)), 6.80 (broad singlet, 1H, 5-H(imidazole)), 8.45 (d, J(HH) = 8.0, 1H, 9-H(naphthyl)), 7.65 (m, 2H, 10,11-H(naphthyl)), 7.42 (m, 2H, 12,13-H(naphthyl)), 7.32 (m, 1H, 14-H(naphthyl)), 7.72 (d, J(HH) = 8.0, 1H, 15-H(naphthyl)), 3.94 (s, 3H, 1-CH_3). *Anal.* Calc. for [Cd(β-NaiMe)$_2$](NO$_3$)$_2$ (**14a**), $C_{28}H_{24}N_{10}O_6Cd$: C, 47.43; H, 3.39; N, 19.76. Found: C, 47.50; H, 3.35; N, 19.82%. UV–Vis spectral data in MeCN (λ_{max} (nm)) 10^{-3} ε (dm^3 mol^{-1} cm^{-1}), 448 (14.14), 376 (19.60), 287 (15.52). ^{1}H NMR ($CDCl_3$), δ, ppm (J, Hz):

7.20 (broad singlet, 1H, 4-H(imidazole)), 6.80 (broad singlet, 1H, 5-H(imidazole)), 8.16 (d, J(HH) = 8.0, 1H, 8-H(naphthyl)), 7.93 (d, J(HH) = 7.5, 10-H(naphthyl)), 7.86 (m, 2H, 11-H(naphthyl)), 7.45 (m, 2H, 12,13-H(naphthyl)), 7.30 (m, 1H, 14-H(naphthyl)), 7.20 (d, J(HH) = 8.0, 1H, 15-H(naphthyl)), 4.02 (s, 3H, 1-CH_3).

Anal. Calc. for Cd(α-NaiEt)$_2$](NO$_3$)$_2$ (**13b**), $C_{30}H_{28}N_{10}O_6Cd$: C, 48.89; H, 3.80; N, 19.01. Found: C, 48.80; H, 3.74; N, 19.14%. UV–Vis spectral data in MeCN (λ_{max} (nm)) 10^{-3} ε (dm^3 mol^{-1} cm^{-1}) 430 (4.60), 340 (6.20), 270 (7.38). ^{1}H NMR ($CDCl_3$), δ, ppm (J, Hz): 7.15 (broad singlet, 1H, 4-H(imidazole)), 6.82 (broad singlet, 1H, 5-H(imidazole)), 8.52 (d, J(HH) = 8.0, 1H, 9-H(naphthyl)), 7.72 (m, 1H, 10-H(naphthyl)), 7.50 (m, 3H, 11-13-H(naphthyl)), 7.41 (m, 1H, 14-H(naphthyl)), 7.90 (m, 1H, 15-H(naphthyl)), 3.80 (quartet, J(HH) = 9.0, 2H, 1-CH_2), 0.90 (t, J(HH) = 7.5, 3H (1-CH_2)–CH_3). *Anal.* Calc. [Cd(β-NaiEt)$_2$](NO$_3$)$_2$ (**14b**), $C_{30}H_{28}N_{10}O_6Cd$: C, 48.89; H, 3.80; N, 19.01. Found: C, 48.80; H, 3.75 N, 19.08%. UV–Vis spectral data in MeCN (λ_{max} (nm)) 10^{-3} ε (dm^3 mol^{-1} cm^{-1}) 435 (4.80), 340 (4.40), 270 (6.12). ^{1}H NMR ($CDCl_3$), δ, ppm (J, Hz): 7.21 (broad singlet, 1H, 4-H(imidazole)), 6.82 (broad singlet, 1H, 5-H(imidazole)), 8.14 (d, J(HH) = 8.0, 1H, 8-H(naphthyl)), 8.00 (d, J(HH) = 7.5, 1H, 10-H(naphthyl)), 7.92 (m, 1H, 11-H(naphthyl)), 7.42 (m, 2H, 12,13-H(naphthyl)), 7.35 (m, 1H, 14-H(naphthyl)), 7.30 (d, J(HH) = 8.0, 1H, 15-H(naphthyl)), 4.42 (quartet, J(HH) = 7.5, 2H, 1-CH_2), 1.10 (t, J(HH) = 7.5 Hz, 3H (1-CH_2)–CH_3).

Anal. Calc. for [Cd(α-NaiMe)$_2$](ClO$_4$)$_2$ (**15a**), $C_{28}H_{24}N_8O_8Cl_2Cd$: C, 42.89; H, 3.06; N, 14.30. Found: C, 42.77; H, 3.00; N, 14.42%. UV–Vis spectral data in MeCN (λ_{max} (nm)) 10^{-3} ε (dm^3 mol^{-1} cm^{-1}) 466 (11.30), 411 (13.51), 346 (12.05), 270 (12.98). *Anal.* Calc. for [Cd(β-NaiMe)$_2$](ClO$_4$)$_2$ (**16a**), $C_{28}H_{24}N_8O_8Cl_2Cd$: C, 42.89; H, 3.06; N, 14.30. Found: C, 42.84; H, 3.14; N, 14.40%. UV–Vis spectral data in MeCN (λ_{max} (nm)) 10^{-3} ε (dm^3 mol^{-1} cm^{-1}), 443 (5.10), 350 (6.50), 265 (5.40). *Anal.* Calc. for [Cd(α-NaiEt)$_2$](ClO$_4$)$_2$ (**15b**), $C_{30}H_{28}N_8O_8Cl_2Cd$: C, 44.37; H, 3.45; N, 13.80. Found: C, 44.44; H, 3.36; N, 13.71%. UV–Vis spectral data in MeCN (λ_{max} (nm)) 10^{-3} ε (dm^3 mol^{-1} cm^{-1}) 415 (7.89), 392 (6.29), 336 (21.01), 290 (29.12). [Cd(β-NaiEt)$_2$](ClO$_4$)$_2$ (**16b**), $C_{30}H_{28}N_8O_8Cl_2Cd$: C, 44.37; H, 3.45; N, 13.80. Found: C, 44.30; H, 3.52; N, 13.90%. UV–Vis spectral data in MeCN (λ_{max} (nm)) 10^{-3} ε (dm^3 mol^{-1} cm^{-1}) 430 (4.22), 345 (4.17), 266 (6.55). (Because of the sparing solubility of complexes **15** and **16** in $CDCl_3$ we could not run NMR spectra.)

2.4. Crystallographic data collection and refinement of [Cd(β-NaiPy)$_2$(ONO$_2$)$_2$] (**8**)

Crystals were grown by slow evaporation of a methanol solution of the reaction mixture of Cd(NO$_3$)$_2$ and β-NaiPy in 1:1 molar proportion **8**. Crystal parameters and refined data are summarized in Table 1. The data (0.20 × 0.15 × 0.10 mm) were collected in a CCD area detector fine focus sealed tube at 294 K using graphite monochromated (Mo Kα radiation, λ = 0.71073 Å). Unit cell parameters were determined from least-squares refinement of setting angles with 2θ in the range $4.42 \leqslant 2\theta \leqslant 56.60°$. Of 9984 collected data, 3622 with $I > 2\sigma(I)$ were used for structure solution. The hkl ranges are $-39 \leqslant h \leqslant 15$, $-18 \leqslant k \leqslant 20$, $-22 \leqslant l \leqslant 16$. Reflection data were recorded using the ω scan technique. Data were corrected for Lorentz polarization effects and for linear decay. Semi-empirical absorption corrections based on ψ-scans were applied. The structure was solved by the direct method using SHELXS-97 and successive difference Fourier syntheses. All non-hydrogen atoms were refined anisotropically. The hydrogen atoms were fixed geometrically and refined using the riding model. In the final difference Fourier map the residual minima and maxima −0. 237, 0.418 e/Å^3 were evaluated using SHELXL-97. All calculations were carried out using SHELXL-97 [15], ORTEP-32 [16] and PLATON-99 [17] programs.

Table 1
Summarized crystallographic data for [Cd(β-NaiPy)$_2$(ONO$_2$)$_2$] (**8**)

	[Cd(β-NaiPy)$_2$(ONO$_2$)$_2$] (**8**)
Empirical formula	$C_{32}H_{24}N_6O_6Cd$
Formula weight	700.97
Temperature (K)	294(2)
Crystal system	monoclinic
Space group	*C*2/*c*
Crystal size (mm)^3	0.20 × 0.15 × 0.10
Unit cell dimensions	
a (Å)	11.35400(14)
b (Å)	15.5592(18)
c (Å)	16.8936(19)
β (°)	97.683(2)
V (Å)^3	3006.1(6)
Z	4
λ (Å)	0.71073
μ (Mo Kα) (mm^{-1})	0.782
D_{calc} (g cm^{-3})	1.549
Refined parameters	208
Reflections collected	9984
Unique data [$I > 2\sigma(I)$]	3622
R_1[a] [$I > 2\sigma(I)$]	0.0338
wR_2[b]	0.0714
Goodness-of-fit	0.843

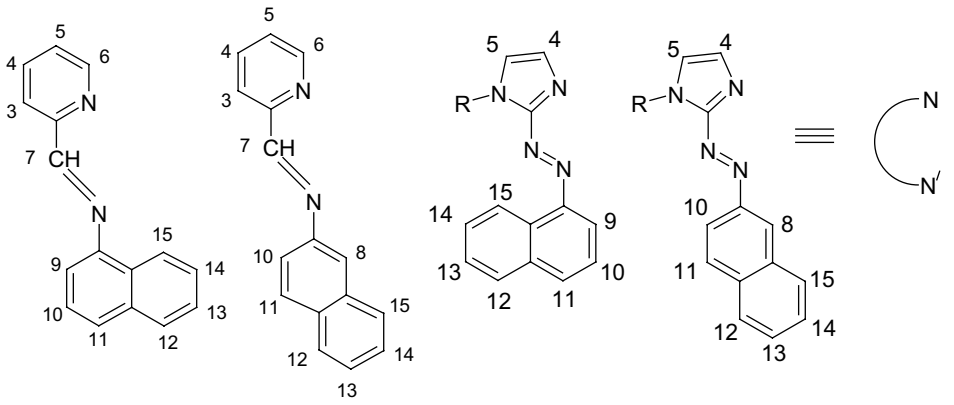
[a] $R_1 = \sum|F_0 - F_c|/\sum F_0$.
[b] $wR_2 = \left[\sum w(F_0^2 - F_c^2)/\sum wF_0^4\right]^{1/2}$, $w = 1/[\sigma^2(F^2) + (0.0424P)^2]$.

3. Results and discussion

3.1. The synthesis and formulation

Two series of *N*,*N*′-chelating ligands are used in this work (Scheme 1) containing azoimine (–N=N–C=N–) and diimine (–N=C–C=N–) functions. *N*-[(2-Pyridyl)-methyliden)-α-aminonaphthalene] (α-NaiPy, **1** and β-NaiPy, **2**) are selected for the diimine system. 1-Alkyl-2-(naphthyl-α/β-azo)imidazoles (α-NaiR, **3** and β-NaiR, **4**; R = Me (**3a**/**4a**), Et (**3b**/**4b**)) belong to the azoimine system.

The complexes were synthesized by reacting a methanol solution of the ligand and different cadmium(II) salts in a



Scheme 1.

1:1 mole ratio for $CdCl_2$ and a 1:2 mole proportion for $Cd(NO_3)_2 \cdot 6H_2O$ or $Cd(ClO_4)_2 \cdot 6H_2O$ (other molar ratios of $CdCl_2$:ligands such as 1:2 or 1:3 also separated complexes of composition identical to the 1:1 mole ratio). Upon slow evaporation of the reaction mixture, yellow to orange crystals were deposited on the wall of the beaker, which were separated by filtration and dried over $CaCl_2$. Microanalytical data support the composition, Cd(α-NaiPy)Cl_2 (**5**)/Cd(β-NaiPy)Cl_2 (**6**), $[Cd(\alpha\text{-NaiPy})_2(ONO_2)_2]$ (**7**)/$[Cd(\beta\text{-NaiPy})_2(ONO_2)_2]$ (**8**), $[Cd(\alpha\text{-NaiPy})_2](ClO_4)_2$ (**9**)/$[Cd(\beta\text{-NaiPy})_2](ClO_4)_2$ (**10**). Molar conductance measurements suggest that the compounds **5**–**8** are non-conducting in nitromethane and support coordinated Cl^- and NO_3^- while **9** and **10** show 1:2 conductivity ($\Lambda_M = 120$–$135\ \Omega^{-1}\ mol^{-1}\ cm^{-1}$). This implies that the complexes **5**, **6** and **9**, **10** are four coordinated while **7** and **8** are six coordinated. Infrared spectra of **7** and **8** exhibit strong stretches at 1420, 1390, 1380 cm^{-1}, which are in agreement with coordinated O–NO_2 [18–20]. $\nu(ClO_4)$ appears in complexes **9** and **10** as a sharp single stretch at *ca.* 1090 and a weak stretch at 625 cm^{-1}. The strong stretches at *ca.* 1610 cm^{-1} in the complexes suggest the presence of ν(C=N) on comparing with reported data [7–9].

The IR stretching frequencies of naphthylazoimidazole–Cd(II) complexes are assigned on comparing with the free ligand data [10]. All the bands have not been assigned and some significant stretching frequencies are set out. The ν(N=N) values are shifted to lower frequency by 10–20 cm^{-1} compared to the free ligand value, which supports coordination of azo-N to Cd(II). Cd(NaiR)Cl_2 (**11, 12**) show two ν(Cd–Cl) at *ca.* 324 and *ca.* 298 cm^{-1}. $\nu(ClO_4)$ of $[Cd(NaiR)_2](ClO_4)_2$ (**15**, **16**) appear at 1082–1091 cm^{-1} with a weak stretch at 624–627 cm^{-1}. $\nu(NO_3)$ of $[Cd(NaiR)_2](NO_3)_2$ (**13**, **14**) appears at 1380–1390 cm^{-1} as a sharp strong stretch which is in agreement with ionic NO_3 nature [13,14]. Molar conductivities of **13**–**16** also support a 1:2 electrolytic nature.

The electronic spectra of the Cd(NaiPy) complexes (**5**–**10**) show a weak absorption at 400–460 nm ($\varepsilon \sim 800$–$1500\ M^{-1}\ cm^{-1}$) along with intense absorptions in the UV region at *ca.* 350 nm and *ca.* 270 nm ($\varepsilon \sim 10^4\ M^{-1}\ cm^{-1}$). These intense transitions may be assigned to intraligand charge transfer (n–π* and π–π*) transitions. The longer wavelength weak transition may be due to a d^{10}(Cd) to π* state of the diimine function (MLCT). The UV–Vis spectra of the Cd-NaiR complexes (**11**–**16**) show weak bands at 410–455 for LMCT and an intense transition below 400 nm which corresponds to intraligand transitions.

The ^1H NMR spectra are recorded in $CDCl_3$ solution for **5**–**8** and **11**–**14**. Data are given in Table 3. The assignment has been made on the basis of spin–spin interactions, and on comparing with the free ligand values [21,22]. Pyridyl-2-(naphthylmethylene)amines exhibit a singlet most downfield which has been assigned to –HC=N–(7H) at 8.75–8.78 ppm. Other signals around 7.7–8.5 ppm refer to pyridine-H (3-H–6-H), and naphthyl signals appear at 7.2–7.6 ppm [10–12]. In the complexes the NMR signals are in general downfield shifted. Of them, the pyridyl protons (3-H to 6-H) are shifted to downfield by >0.5 ppm from that of the free ligand data [6]. The naphthyl protons (8-H to 15-H) remain almost undisturbed.

In the Cd-NaiR complexes (**11**–**16**), the imidazole protons (4-, 5-H) show signals at 7.3–7.4 ppm that are 0.3–0.4 ppm downfield shifted, while the naphthyl protons are insignificantly shifted compared to the free ligand data [21,22].

3.2. Molecular structure of $[Cd(\beta\text{-NaiPy})_2(ONO_2)_2]$ (8)

An ORTEP view of complex **8** is shown in Fig. 1. The Cd center is in a distorted octahedral position surrounded by an N_4O_2 coordination sphere. Each β-NaiPy acts as a diimine type bidentate *N*,*N*′ chelator (*N*,*N*(pyridine); *N*′,*N*(naphthyl)) and NO_3 serves as an O donor ligand. A

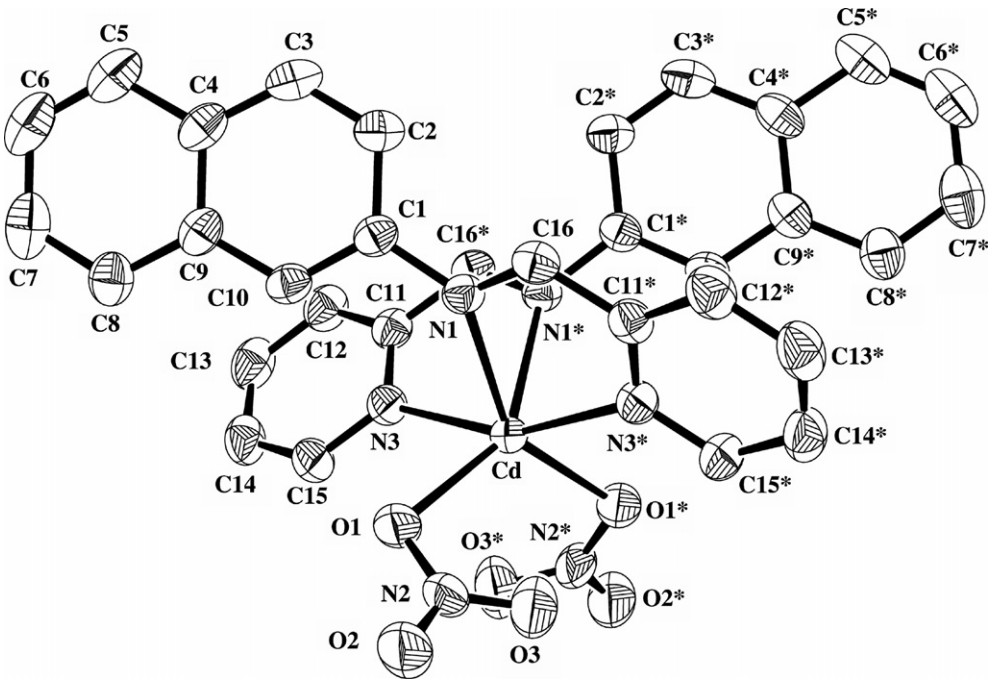


Fig. 1. Molecular structure of $[Cd(\beta\text{-NaiPy})_2(ONO_2)_2]$ (50% probability ellipsoids).

crystallographic 2-fold rotation axis passes through Cd. Bond parameters (Table 2) suggest a longer Cd–N(naphthyl) bond [Cd–N(1) (naphthyl) 2.465(2) Å] than Cd–N(pyridine) bond [Cd–N(3)(pyridine), 2.305(2) Å] and a reasonable chelate angle (N(3)–Cd–N(1), 69.99(7)°). The bond parameters are significantly different from Zn(II) complexes of β-NaiPy. The metric parameters are Zn–N(pyridine) 2.0870(18), Zn–N(naphthyl) 2.2027(17) Å and chelate angle, N(pyridine)–Zn–N(naphthyl) 77.68(7)° in $[Zn(\beta\text{-NaiPy})(N_3)(1,1\text{-}N_3)]_2$ [20], and Zn–N(pyridine) 2.115(9), Zn–N(naphthyl), 2.287(1) Å and N(pyridine)–Zn–N(naphthyl) 94.35(3)° in $[Zn(\beta\text{-NaiPy})_2(ONO_2)_2]$ [23]. $[Ag(\beta\text{-NaiPy})_2](ClO_4)$ shows rather closer metric parameters to Cd(II) than that of the Zn(II) complexes: Ag–N(pyridine), 2.325(3), 2.241(3), Ag–N(naphthyl), 2.318(3), 2.455(3) Å and N(pyridine)–Ag–N(naphthyl), 73.00(9)°, 71.87(10)° [24]. The difference in the structural parameters between Zn(II) and Cd(II) complexes may be explained in view of their position in the periodic table and hence their atom size; Cd(II) > Zn(II). The Cd and Ag are 4d block elements and hence their metric parameters may be comparable. The ligand is planar. The pendant naphthyl ring makes a dihedral angle of 38.32° with the chelated diimine motif. The Cd–O bond distance is 2.3220(19) Å which is expectedly longer than the Zn–O bond length (2.090(2) Å) of the analogous complex, $[Zn(\beta\text{-NaiPy})_2(ONO_2)_2]$ [23]. The angles extended by other donor centers around Cd(II) are in support of a distorted octahedral geometry (Table 2).

Table 2
Selected bond lengths (Å) and bond angles (°) of $[Cd(\beta\text{-NaiPy})_2(ONO_2)_2]$ (**8**)

Bond length		*Bond angle*	
Cd(1)–N(1)	2.465(2)	N(1)–Cd(1)–N(3)[a]	92.43 (7)
Cd(1)–N(3)	2.305(2)	N(1)–Cd(1)–N(3)	69.99(7)
Cd(1)–O(1)	2.3220(19)	N(3)–Cd(1)–O(1)	87.78(7)
C(11)–N(3)	1.332(3)	N(1)–Cd(1)–O(1)[a]	148.54(7)
N(1)–C(16)	1.260(3)	N(3)–Cd(1)–O(1)[a]	102.70(7)
N(2)–O(1)	1.258(3)	O(1)–Cd(1)–O(1)[a]	122.40(11)
N(2)–O(2)	1.219(4)	O(1)–Cd(1)–N(1)	85.13(7)
N(2)–O(3)	1.231(4)	N(1)–Cd(1)–N(1)[a]	74.27(9)
		N(3)–Cd(1)–O(1)[a]	73.66(8)
		O(1)–N(2)–O(2)	120.3(3)
		O(3)–N(2)–O(1)	117.8(3)
		O(3)–N(2)–O(2)	121.9(3)

[a] Symmetry; $-x, y, 1/2 - z$.

An intermolecular hydrogen bond is observed between *m*-H of the Py ring of the chelated ligand of one molecule with the coordinated $O(NO_2)$ of a neighbouring molecule and constitutes a hydrogen bonded 1-D helix along the *c*-axis (Fig. 2) [C(14)–H(14)(A)–O(1)–NO_2(B)]: C(14)–H(14)(A), 0.93 Å, H(14)(A)–O(1)(B), 2.49(3) Å, C(14)(A)–O(1)(B), 3.331(3) Å, ∠(C–H(A)–O(B)), 150.5(5)°. Symmetry: $-x, -y, 1 - z$ where A and B refer to two neighbouring molecules. The packing pattern (Fig. 3) shows C–H–π and π–π interactions. An acceptable C–H–π interaction is observed C(13)–H(13)–Cg(3) (H–Cg(3)): 3.168(7) Å and ∠(C–H–Cg(3)), 118.7(8)° (symmetry: $-1/2 - x, 1/2 - y, 1 - z$) that enhances the strength of the supramolecular chain (Cg(3): C(4), C(5), C(6), C(7), C(8), C(9)). Besides, the π–π interaction, although weak, contributes to enhance the structural rigidity of the molecule. The intramolecular Cg(2)–Cg(2), 4.2798 Å and intermolecular Cg(2)–Cg(3), 4.011, Cg(1)–Cg(2), 4.4201 Å (symmetry: $1/2 - x, 1/2 - y, 1 - z$ for Cg(1); x, y, z for Cg(2); $-x, -y, -z$ for

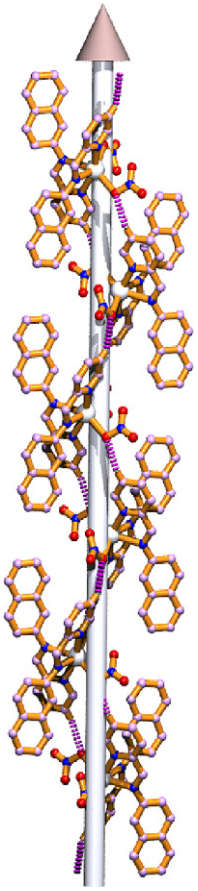


Fig. 2. Helix running along the crystallographic *c*-axis.

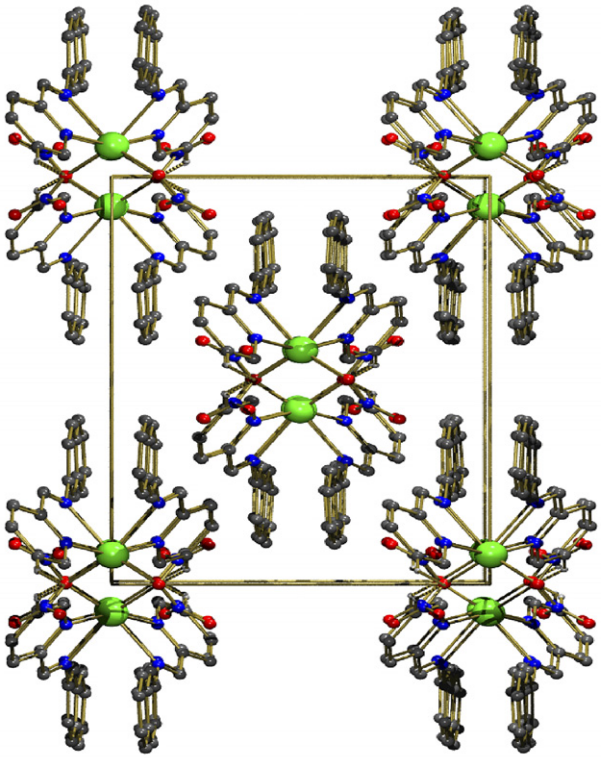


Fig. 3. Unit cell packing view in the *ab* plane.

Cg(3) where Cg(1) is N(3), C(11), C(12), C(13), C(14), C(15); Cg(2) is C(1), C(2), C(3), C(4), C(9), C(10) and Cg(3) is C(4), C(5), C(6), C(7), C(8), C(9)) π–π interactions between pyridyl and naphthyl rings incorporate a robust character to the molecule and lead to the formation of a 3-D supramolecular geometry.

3.3. Photoluminescence properties

No emission originating from metal-centered and MLCT or LMCT excited states are expected for the Cd(II) complexes, since the Cd(II) ion is difficult to oxidize or reduce due to its d^{10} configuration. Thus, the emission observed (Fig. 4 and Table 3) in the complexes is tentatively assigned to the (π–π*) intraligand fluorescence. The luminescence spectra of the ligands in $CHCl_3$ exhibit an emission at 431 (α-NaiPy) and 406 nm (β-NaiPy) at 298 K upon excitation at 330 nm. At 77 K these compounds show an emission at 455 nm (α-NaiPy) and 448 nm (β-NaiPy). Naphthylazoimidazoles (NaiR) are non-luminescent under identical conditions. It is interesting that the Cd(II) complexes show a higher intensity than that of the free ligand value. It has been reported that the metal

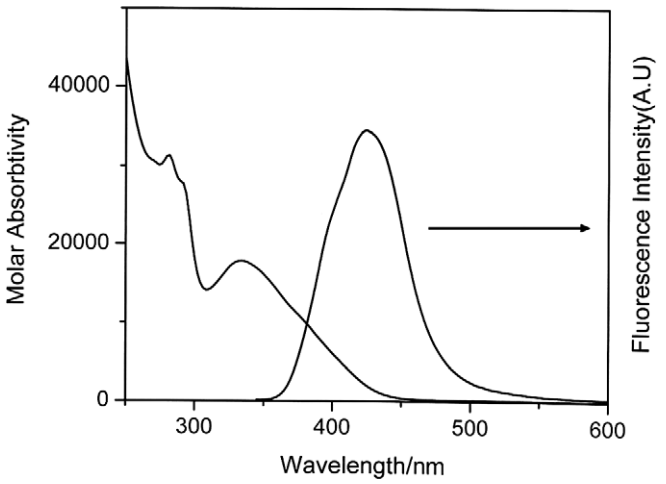


Fig. 4. Absorption and emission spectra of $[Cd(\beta\text{-NaiPy})_2(ClO_4)_2]$ (**10**) in CH_3CN at room temperature (298 K).

Table 3
Absorption (λ_{abs}), emission (λ_{em}) band maxima[a] and quantum yields (ϕ)[b] of Cd(II)–NaiPy complexes (**5**–**10**)

Compound	λ_{abs}/nm	λ_{em}/nm (298 K)	λ_{em}/nm (77 K)	Quantum yield, ϕ
$[Cd(\alpha\text{-NaiPy})Cl_2]$ (**5**)	340	455	480	0.0455
$[Cd(\beta\text{-NaiPy})Cl_2]$ (**6**)	350	447	469	0.0402
$[Cd(\alpha\text{-NaiPy})_2(ONO_2)_2]$ (**7**)	348	450	482	0.0390
$[Cd(\beta\text{-NaiPy})_2(ONO_2)_2]$ (**8**)	340	443	478	0.0348
$[Cd(\alpha\text{-NaiPy})_2](ClO_4)_2$ (**9**)	350	450	480	0.0226
$[Cd(\beta\text{-NaiPy})_2](ClO_4)_2$ (**10**)	350	446	476	0.0187

[a] Solvent: CH_3CN.
[b] Quantum yields are expressed with reference to coumarin-120.

ions can enhance or quench the fluorescence emission of pyridine containing compounds [25–27]. In the absence of metal ions the fluorescence of the ligand is probably quenched by the occurrence of a photoinduced electron transfer (PET) process due to the presence of a lone pair of electrons on the nitrogen atoms. Such a PET process is prevented by the complexation of NaiPy with metal ions; thus the fluorescence intensity may be greatly enhanced by the coordination to Cd(II). The chelation of the ligand increases rigidity and reduces the loss of energy by thermal vibrational decay. At low temperature (77 K) the complexes show a bright greenish-blue emission and have been red shifted by 40–50 nm from the emission in solution at 298 K. This is probably caused by intermolecular interactions in the frozen conditions that effectively decreases the energy gap.

4. Supplementary data

CCDC No. 600511 contains the supplementary crystallographic data for $[Cd(\beta\text{-NaiPy})_2(ONO_2)_2]$. These data can be obtained free of charge via http://www.ccdc.cam.ac.uk/conts/retrieving.html, or from the Cambridge Crystallographic Data Centre, 12 Union Road, Cambridge CB2 1EZ, UK; fax: (+44) 1223 336 033; or e-mail: deposit@ccdc.cam.ac.uk.

Acknowledgements

Financial support from the All India Council of Technical Education (AICTE), New Delhi is gratefully acknowledged. We thank the Single Crystal X-Ray Diffraction Facility Centre, Indian Institute of Technology, Bombay, India for X-ray data collection.

References

[1] J. Shinar (Ed.), Organic Light-Emitting Devices: A Survey, Springer-Verlag, NY, 2004.
[2] K. Kalyansundaram, Coord. Chem. Rev. 46 (1982) 159.
[3] R.-Q. Fan, D.-S. Zhu, Y. Mu, G.-H. Li, Y.-L. Yang, Q. Su, S.-H. Feng, Eur. J. Inorg. Chem. (2004) 4891.
[4] Y.L. Pui, K.K. Cheung, J. Chem. Soc., Dalton Trans. (2000) 3658.
[5] Y. Wang, X.-M. Ouyang, Y.-Z. Li, W.-Y. Sun, Bull. Chem. Soc. Jpn. 76 (2003) 1403.
[6] H.-F. Zhu, L. Li, T. Okamura, W. Zhao, W.-Y. Sun, N. Ueyama, Bull. Chem. Soc. Jpn. 76 (2003) 761.
[7] M. Menon, A. Pramanik, N. Bag, A. Chakravorty, Inorg. Chem. 33 (1994) 403.
[8] M. Menon, A. Pramanik, A. Chakravorty, Inorg. Chem. 34 (1995) 3310.
[9] S. Chowdhury, A.K. Deb, S. Goswami, Polyhedron 13 (1994) 1063.
[10] J. Dinda, C. Sinha, Transition Met. Chem. 28 (2003) 864.
[11] J. Zhang, W. Li, W. Bu, L. Wu, L. Ye, G. Yang, Inorg. Chim. Acta 358 (2005) 964.
[12] L.G. Nickolacheva, C.M. Vogels, R.A. Stefan, H.A. Warwish, S.J. Duffy, R.J. Ireland, A. Decken, R.H. Hudson, S.A. Westcott, Can. J. Chem. 81 (2003) 269.
[13] J. Dinda, P.K. Santra, C. Sinha, L.R. Falvello, J. Organomet. Chem. 629 (2001) 28.
[14] A.I. Vogel, A Text Book of Practical Organic Chemistry, 2nd ed., Longman, London, 1959.
[15] G.M. Sheldrick, SHELXL 97, Program for the Solution of Crystal Structure, University of Gottingen, Germany, 1997.
[16] L.J. Farrugia, J. Appl. Crystallogr. 30 (1997) 565.
[17] A.L. Spek, PLATON, Molecular Geometry Program, University of Utrecht, The Netherlands, 1999.
[18] U. Casellato, P.A. Vigato, Coord. Chem. Rev. 36 (1981) 183.
[19] A.B.P. Lever, E. Mantovani, B.S. Ramaswamy, Can. J. Chem. 49 (1971) 1957.
[20] D. Das, B.G. Chand, K.K. Sarker, J. Dinda, C. Sinha, Polyhedron 25 (2006) 2333.
[21] S. Pal, D. Das, P. Chattopadhyay, C. Sinha, K. Panneerselvam, T.-H. Lu, Polyhedron 19 (2000) 1263.
[22] P. Byabartta, P.K. Santra, T.K. Misra, C. Sinha, C.H.L. Kennard, Polyhedron 20 (2001) 905.
[23] D. Das, J. Dinda, T. Mondal, K.K. Sarker, C. Sinha, J. Indian Chem. Soc. 83 (2006) 83.
[24] D. Das, J. Dinda, T.K. Mondal, C. Sinha, J. Indian Chem. Soc. 83 (2006) 342.
[25] H.F. Zhu, L. Li, T. Okamura, W. Zhao, W.Y. Skn, N. Ueyama, Bull. Chem. Soc. Jpn. 76 (2003) 761.
[26] X.H. Be, H. Liu, M. Du, K.M.C. Wong, V.W.W.W. Yam, Inorg. Chim. Acta 333 (2002) 32.
[27] K.Y. Yu, K.K. Cheung, C.M. Che, J. Chem. Soc., Dalton Trans. (1999) 1581.

Available online at www.sciencedirect.com
ScienceDirect
Polyhedron 26 (2007) 563–571
POLYHEDRON
www.elsevier.com/locate/poly

Immobilization of a copper-Schiff base complex in a Y-zeolite matrix: Preparation, chromogenic behavior and catalytic oxidation

Pratap Kumar Saha [a], Buddhadeb Dutta [a], Sreyashi Jana [a], Rajesh Bera [a], Sandip Saha [a], Ken-ichi Okamoto [b], Subratanath Koner [a,*]

[a] Department of Chemistry, Jadavpur University, Jadavpur, Kolkata 700 032, West Bengal, India
[b] Department of Chemistry, University of Tsukuba, Tsukuba, Ibaraki 305-8571, Japan

Received 11 April 2006; accepted 11 August 2006
Available online 1 September 2006

Abstract

A new zeolite-immobilized hybrid catalyst Cu(MeO-salen)-NaY has been prepared by encapsulating [Cu(MeO-salen)(H_2O)] (**1**) [where MeO-salenH_2 = *N*,*N*′-(ethylene)-bis-(3-methoxysalicylaldimine)] in a NaY zeolite matrix. The hybrid material has been characterized by UV–Vis, IR and EPR spectrometry and by X-ray powder diffraction analysis. The pristine complex [Cu(MeO-salen)(H_2O)] (**1**) has also been synthesized and characterized by all the spectrometric methods mentioned above as well as by single crystal X-ray diffraction analysis. A brilliant color change (green to red) has been observed when the complex [Cu(MeO-salen)(H_2O)] (**1**) is immobilized in the zeolitic matrix. X-ray powder diffraction analysis of Cu(MeO-salen)-NaY reveals that the structural integrity of the mother zeolite in the hybrid material remains intact upon immobilization of the complex. The coordination geometry around the Cu^{II} ion in [Cu(MeO-salen)(H_2O)] is found to be square pyramidal. Spectroscopic studies indicate that coordination geometry of the complex undergoes a significant distortion when it is entrapped in the zeolite cavity. While Cu(MeO-salen)-NaY shows excellent catalytic activity and product selectivity in the hydroxylation of phenol and 1-naphthol, [Cu(MeO-salen)(H_2O)] (**1**) remains virtually catalytically inactive in these reactions.
© 2006 Elsevier Ltd. All rights reserved.

Keywords: Heterogeneous catalysis; Catalytic oxidation; Zeolite; Immobilization; Schiff base

1. Introduction

The ease with which nature performs many of the difficult chemical transformations essential to the life process has long been admired by synthetic chemists. By judicious choice of active sites (in many cases metal complexes) and supports (proteins) nature has built up an impressive array of enzymes that catalyze various reactions such as partial oxidation of unactivated hydrocarbons, electron transfer, etc. in a regio- and stereo-controlled way [1]. In the life process nature selectively generates only that which is necessary in its various activities, producing no undesired waste and side products. In a laboratory, we seldom have such control over reactions. Arguably to attain the success in reproducing life process reactions perfectly in the laboratory is extremely difficult, if not impossible, but mimicking them to a certain extent can increase the efficacy of chemical processes remarkably in comparison to the processes that we follow today. A group of enzymes, for example oxygenase, activate dioxygen to oxidize various kinds of organic substrates into their oxygenates. The metal ions in many of these enzymes act as active centers. Copper, iron and manganese are often found in the active centers in these enzymes [1]. Considerable efforts have been directed to prepare the synthetic mimic of the active center of these unique naturally occurring catalysts to study their catalytic activity in the laboratory [2,3]. Metal complexes of porphyrins, phthalocyanines and Schiff bases that mimic the active center of enzymes have been employed as

* Corresponding author. Fax: +91 33 2414 6584.
E-mail address: snkoner@chemistry.jdvu.ac.in (S. Koner).

0277-5387/$ - see front matter © 2006 Elsevier Ltd. All rights reserved.
doi:10.1016/j.poly.2006.08.018

catalysts in studying many oxidation reactions, but they lose their catalytic activity during the reaction because of the formation of inactive species like μ-oxo dimers or degradation of the complex itself due to oxidation of the ligands. In living systems the protein cavity in which the active center is encapsulated in fact protects the enzymes from undesired dimerization and degradation of ligands. In order to increase the stability and reactivity of synthetic metal complexes they can be encapsulated in a porous matrix [4–7]. Zeolites or molecular sieves structurally resemble enzymes. They are solids with internal networks of linked channels, which open into wider cages or pores. For example, NaY, being a large pore zeolite, has a supercage size of ca. 13 Å. In addition to this it has sodalite cages (diameter ~7 Å). However, the size of the window through which a molecule can enter into the supercage is ca. 8 Å. These cages and/or pores may be used for directing a reaction by immobilizing an active site (usually a metal complex). It is well known that a porous matrix like a zeolite, etc. shows spectacular shape selectivity in catalytic reactions [8]. Heterogenization of a homogeneous catalysts in a porous solid support, in this way, makes the hybrid materials industrially important because the new catalysts: (a) can be easily separated from the reaction mixture and reused with minimum loss of activity; (b) are much more robust than their homogeneous counterparts [9]. The catalysts prepared by immobilizing a metal complex in a porous matrix have shown enhanced catalytic efficacy in comparison to their corresponding homogeneous counterparts [10–12]. Besides, studies on the photochemical and photophysical properties of ruthenium complexes encapsulated in zeolite matrices have been undertaken by several groups [13–15]. It has been found that the photochemical and photophysical properties of neat metal complexes change dramatically upon immobilization in a zeolite matrix. Sykora *et al*. showed that the zeolite immobilized $[Ru(bpy)_n(bpz)_{3-n}]^{2+}$ complex (where bpz is 2,2′-bipyrazine and bpy is 2,2′-bipyridine) can be used to store solar energy by photochemical reactions [13]. Immobilization of certain types of organic compounds in zeolite matrices has demonstrated striking color changes [16]. Recently, organic dye molecules have been immobilized in a zeolite or a molecular sieve to prepare sensors [17,18].

In many metalloenzymes copper(II) ions act as the active center [19–21]. Galactose oxidase is one such mononuclear copper containing enzyme that catalyses stereospecific oxidation of alcoholic or phenolic compounds. The coordination environment of Schiff base complexes of copper(II), for example [Cu(salen)] [salenH_2 = *N*,*N*′-(ethylene)-bis-(salicylaldimine)], mimic the coordination environment of the copper(II) ion of galactose oxidase (Chart 1). Although in recent times attempts have been made to encapsulate copper complexes in a zeolite matrix to mimic this type of enzyme, emphasis has rarely been given to understand the stereo-electronic properties of the copper(II) Schiff base complexes after immobilization [22]. Knowledge regarding the structure of the immobilized

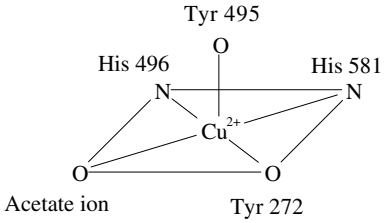


Chart 1.

complex is certainly important to delineate the mechanism of the catalytic reactions and to design new catalysts of this kind. Here we report the synthesis of [Cu(MeO-salen)(H_2O)] (**1**) [MeO-salenH_2 = *N*,*N*′-(ethylene)-bis-(3-methoxy-salicylaldimine)], its X-ray crystal structure, immobilization of complex **1** in a NaY zeolite matrix and the characterization as well as catalytic efficacy in oxidation reactions.

2. Experimental

2.1. Materials

NaY zeolite was procured from Tosoh Corporation, Japan. The ligand, MeO-salenH_2, was prepared from 3-methoxy-salicylaldehyde by condensation with 1,2-ethanediamine following the standard procedure [23,24]. All other chemicals were of AR/GR quality.

2.1.1. Synthesis of [Cu(MeO-salen)(H_2O)] (1)

A solution of $Cu(NO_3)_2 \cdot 3H_2O$ (0.489 g) (2 mmol) in methanol (20 mL) was slowly added to a methanolic solution of MeO-salenH_2 (0.648 g) (2 mmol) with constant stirring. A green precipitate was formed in 30 min on stirring the mixture. The product thus obtained was recrystallized from methanol. X-ray quality green single crystals were obtained on slow evaporation of a methanolic solution of the complex.

2.1.2. Incorporation of copper(II) in NaY

$Cu(NO_3)_2 \cdot 3H_2O$ (4 g), dissolved in 100 ml of H_2O, was stirred continuously for 5 h with NaY (4 g) in suspension. The white zeolite turned blue during the stirring. The solid mass was filtered and washed thoroughly with a copious amount of deionized water and dried under vacuum to give a light blue powder of Cu–NaY. The zeolite thus produced was then used for the immobilization work. Calcination of Cu–NaY was avoided to arrest the migration of copper(II) ions from the vicinity of the supercage.

2.1.3. Immobilization of [Cu(MeO-salen)] in NaY

To prepare Cu(MeO-salen)-NaY, 1 g of Cu–NaY zeolite was mixed with 3 g of MeO-salenH_2 and placed in a closed round-bottom flask containing dry N_2 and heated at 140 °C for an hour with occasional stirring. During heating the mixture turned green. The mixture was then cooled, pulverized and finally subjected to soxhlet extraction with

methanol and acetone. The green solid produced after extraction was then stirred with portions of fresh acetonitrile several times for washing. Interestingly on washing with acetonitrile the green mass transformed to a red solid. This was then collected by filtration and dried in air. This species hereinafter will be designated as Cu(MeO-salen)-NaY.

2.2. X-ray crystallography

2.2.1. Crystal data

$C_{18}H_{20}CuN_2O_5$, $M = 407.91$, orthorhombic space group P_{nma}, $Z = 4$, $a = 9.261(2)$, $b = 24.712(5)$, $c = 7.510(4)$ Å, $V = 1718(1)$ Å^3, $\lambda = 0.71069$ Å, $D_{calc} = 1.576$ gcm^{-3}, $F_{000} = 844$, green block crystal, dimensions = $0.75 \times 0.60 \times 0.23$ mm, $T = 296$ K.

2.2.2. Structure determination

Of the 2402 reflections which were collected on a Rigaku AFC7S diffractometer with graphaite monochromated Mo Kα radiation, 2017 were unique ($R_{int} = 0.010$) with $I > -10.00\sigma(I)$. The structure was solved by direct methods SIR 92 [25]. The non-hydrogen atoms were refined anisotropically and hydrogen atoms were included but not refined. The final cycle of full-matrix least-squares refinement was converged with unweighted and weighted agreement factors of

$$R = \sum \left(F_O^2 - F_C^2\right) \Big/ \sum F_O^2 = 0.099$$

$$R_w = \left[\sum w\left(F_O^2 - F_C^2\right)^2 \Big/ \sum w\left(F_O^2\right)^2\right]^{1/2} = 0.120$$

$$R_1 = \sum \| F_O| - |F_C| \| \Big/ \sum |F_O| = 0.035 \text{ for } I > 2.00(I)$$

2.3. Physical measurements

Infrared and electronic spectra were measured on a Perkin–Elmer 783 and a Hitachi U 3400 spectrophotometer, respectively. EPR spectra were measured on a Varian E-112 spectrometer at room temperature. The X-ray powder diffraction measurements were made on a PW 1730/1710 Philips X ray diffractometer. The copper content of the sample was estimated by a Varian Techtron AA-575ABQ atomic absorption spectrophotometer. The catalytic reaction products were analyzed by a Hewlett–Packard 5880A gas chromatograph equipped with an FID detector. Other measurements were undertaken as reported previously [26].

2.4. Catalytic reactions

The catalytic reactions were undertaken in a glass batch reactor. In a typical reaction 1 g of the substrate was taken in 10 mL of H_2O, 50 mg of the catalyst was added to it and this was equilibrated at a temperature of 45 °C in an oil-bath. 1 mL of a 30% H_2O_2 solution was added to this with continuous stirring. The products were collected at different time intervals and were identified and quantified by GC and verified by GC–MS.

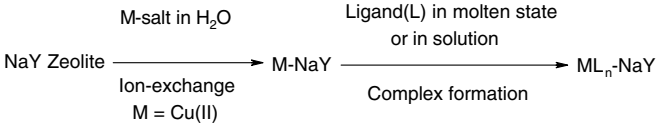
3. Results and discussions

3.1. Preparation and chromotropism

The immobilization of the complex in a zeolite matrix was done by a "ship-in-the-bottle" synthesis technique [6]. The flexible Schiff base ligand (in the molten state) was allowed to react with Cu–NaY (Scheme 1). It is expected that the Cu(MeO-salen) complex will be formed in the supercage as well as on the surface of the Y zeolite. As the complex is neutral only a weak force such as a van der Waals interaction is operative here to catch hold of the complex on the surface of the zeolite. It seems soxhlet extraction with CH_3CN effectively washes the hybrid material but some complex molecules might remain on the surface of the zeolite. Nevertheless complex molecules formed inside the zeolite supercage will be retained after washings. Therefore, it can be postulated that the complex molecules are mostly being physically trapped inside the supercage of the zeolite. A sharp color change (light blue to green) of Cu–NaY was observed on mixing with the molten ligand. On washing (soxhlet) with CH_3CN the green colored crude of Cu(MeO-salen)-NaY catalyst turns to a red powder. Although it is well known that organic molecules often show chromotropism when they are entrapped in a porous matrix [16], such chromotropism of inorganic complexes has rarely been observed when they are immobilized in zeolite matrices [10–12,22]. The total copper content in Cu(MeO-salen)-NaY is given in Table 1. The number of metal complexes formed per supercage of NaY is calculated to be ca. 3. The carbon and nitrogen analysis agrees well with these results.

3.2. X-ray structure of [Cu(MeO-salen)(H_2O)] (1)

An ORTEP [27] diagram of the complex [Cu(MeO-salen)(H_2O)] (**1**) along with the atom numbering scheme



Scheme 1.

Table 1
Elemental analyses for complex **1** and Cu(MeO-salen)-NaY

Species	Copper(II) content (wt%)	Cu-Schiff base concentration (mol/g)
[Cu(MeO-salen)(H_2O)] (**1**)	15.2[a] (15.58[b])	
Cu(MeO-salen)-NaY	1.325[a]	2.1×10^{-4}

[a] AAS.
[b] Calculated.

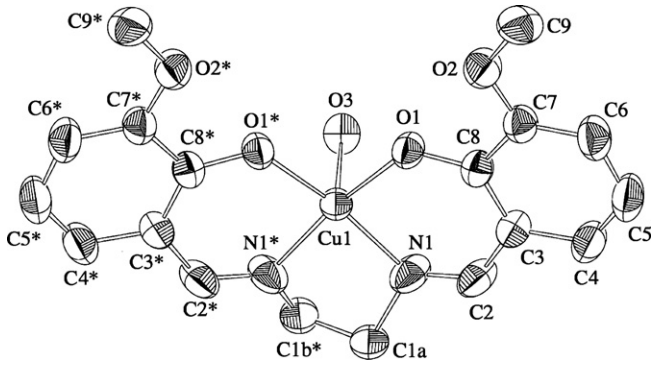


Fig. 1. ORTEP diagram of [Cu(MeO-salen)(H_2O)] (**1**) showing the atom numbering scheme.

Table 2
Selected bond lengths (Å) and angles (°) for complex **1**

Bond lengths (Å)			
Cu–O(1)	1.934(1)	Cu–N(1)	1.959(2)
Cu–O(1*)	1.934(1)	Cu–N(1*)	1.959(2)
Cu–O(3)	2.369(2)		
Bond angles (°)			
O(1)–Cu–O(1*)	90.39(8)	N(1)–Cu–N(1*)	82.7(1)
O(1)–Cu–N(1)	92.24(7)	O(1*)–Cu–N(1)	167.69(8)
O(1)–Cu–N(1*)	167.69(8)	O(1*)–Cu–N(1*)	92.24(7)

is given in the Fig. 1. Selected bond lengths and angles of the complex are listed in Table 2. The coordination geometry around the copper ion is found to be square pyramidal. Two nitrogen atoms of the azomethine groups of the ligand and the two oxygen atoms of the phenoxo groups of the salicylaldehyde occupy the four coordination sites of the copper(II) ion. The fifth coordination site is occupied by the oxygen atom of the aquo ligand present in the complex **1**. Comparison of the ORTEP diagram of complex **1** with the coordination environment of copper in galactose oxidase shows a close resemblance between them. Single crystal X-ray analysis of galactose oxidase (EC 1.1.3.9) reveals that the apical coordination sites of the mononuclear copper (II) moiety in this enzyme are occupied by two nitrogen atoms of histidine moieties (His 581 and His 496) and two oxygen atoms, one from an acetate ion and another one from a tyrosine moiety (Tyr 272), while the axial site is occupied by an oxygen atom of Tyr 495 (Chart 1) [28].

3.3. X-ray powder diffraction

X-ray powder diffraction measurements have been carried out for Cu(MeO-salen)-NaY. Comparison of the XRD pattern of Cu(MeO-salen)-NaY with the standard pattern of NaY shows no appreciable change in peak positions as well as in the relative intensities of the diffraction lines. This indicates that the crystallinity of the zeolitic matrix remained intact upon immobilization of the inorganic complex.

3.4. Thermal analysis

The simultaneous TG-DTA profiles of complex **1** and the catalyst Cu(MeO-salen)-NaY are shown in Figs. 2a and 2b, respectively. The TG curve for complex **1** shows a significant loss of weight in the temperature range 200–350 °C where the corresponding DTA curve shows a broad exothermic peak with a small kink at ca. 276 °C. The exothermic peak indicates the decomposition of the complex moiety (Fig. 2a). The TG curve of Cu(MeO-salen)-NaY shows that the sample starts to lose its weight from a little above the ambient temperature and the curve shows continuous significant weight loss up to ca. 400 °C (Fig. 2b). As the Cu(MeO-salen)-NaY catalyst contains a large amount of loosely bound H_2O molecules in the zeolite cavities, weight loss starts from a very low temperature where virtually no endothermic peak is observed in the corresponding DTA curve. Nevertheless a broad exothermic peak is observed in DTA curve of the catalyst which corresponds well with the decomposition of the copper(II) Schiff base complex present in the catalyst.

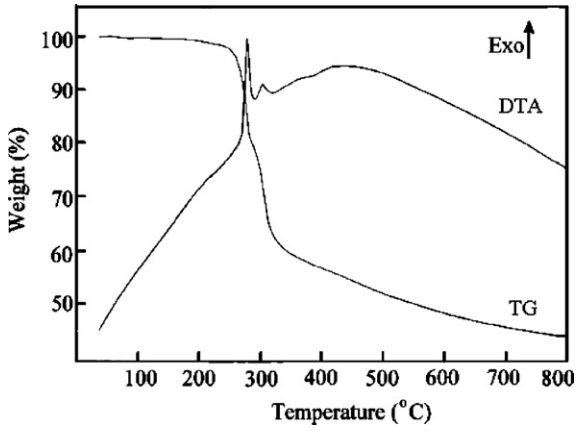


Fig. 2a. TG-DTA profile of [Cu(MeO-salen)(H_2O)] (**1**) [Sample weight: 5.002 mg. Rate of heating: 10 °C/min; Standard: α-Al_2O_3].

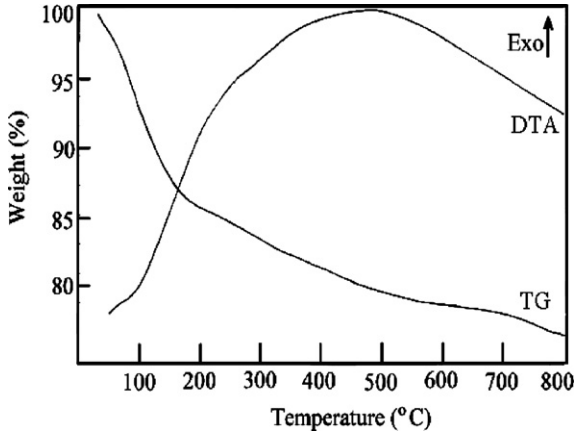


Fig. 2b. TG-DTA profile of Cu(MeO-salen)-NaY catalyst [Sample weight: 10.134 mg. Rate of heating: 10 °C/min; Standard: α-Al_2O_3].

3.5. IR spectroscopy

IR spectral studies of the pristine complex, [Cu(MeO-salen)(H_2O)] and Cu(MeO-salen)-NaY have been undertaken to understand the integrity of the copper(II) Schiff base complex in the zeolite matrix (Fig. 3). Complex **1** shows a sharp band in the range 1630–1650 cm^{-1}, attributable to the azomethine group of the Schiff base ligand [29]. This band in the free ligand appears at frequencies higher by ~10 cm^{-1}. An intense band in the range 1400–1300 cm^{-1} is assigned to the ν(C–O) band of the methoxy group of the ligand [29]. The IR spectrum of Cu(MeO-salen)-NaY shows the presence of all prominent bands for the azomethine group as well as for the C–O vibration of the ligand, appearing in the region 1650–1300 cm^{-1}. As no zeolitic IR band appears in this region of the spectra, except for the band for HOH bending of H_2O at 1650 cm^{-1} that disappears upon careful drying of the catalyst, this may be considered as evidence of the formation of the complexes inside the zeolitic matrix. The vibration bands of the host zeolite obscured the IR bands of the complex in other regions. The IR spectrum of Cu(MeO-salen)-NaY shows an intense band at ca. 1031 cm^{-1} attributable to the asymmetric stretching of the Al–O–Si chain of the zeolite. The symmetric stretching and bending bands of the Al–O–Si framework of the zeolite appear at ca. 732 and 454 cm^{-1}, respectively [30].

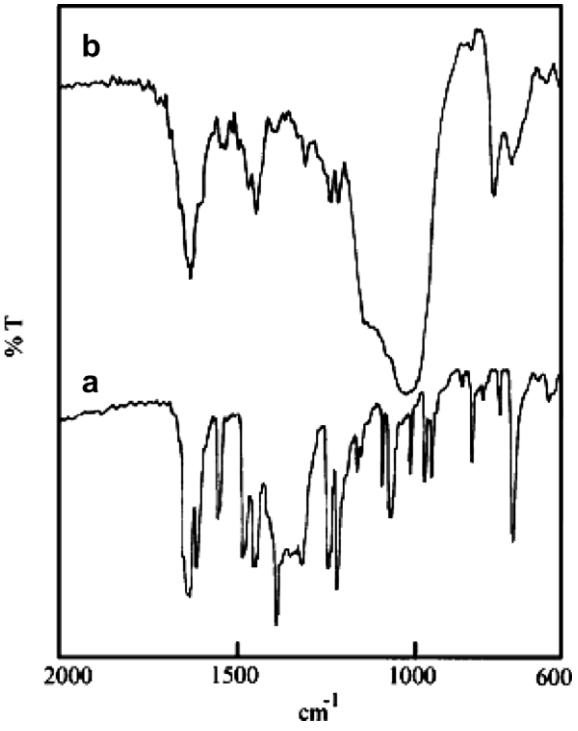


Fig. 3. IR spectra of [Cu(MeO-salen)(H_2O)] (**1**) (a) and Cu(MeO-salen)-NaY catalyst (b).

3.6. UV–Vis spectroscopy

The electronic spectra of the species [Cu(MeO-salen)-(H_2O)] (**1**) and Cu(MeO-salen)-NaY have been measured in the solid state (Fig. 4). The pristine complex, [Cu(MeO-salen)(H_2O)] shows two clear absorption maximum at ca. 17 699 cm^{-1} and 27 397 cm^{-1} whereas the catalyst Cu(MeO-salen)-NaY shows these two peaks at ca. 18 282 cm^{-1} and 27 248 cm^{-1}. All the species show highly intense charge transfer bands in the higher energy region at ca. 35 971 cm^{-1}. The free copper(II) ion has a term symbol ^2D. When the free ion acquires a definite geometry on complex formation the ^2D term splits into several energy states. The splitting of the d-orbitals is related to the stereochemical properties of the complex. It is well established that a Schiff base copper(II) complex with D_{4h} or D_{2h} symmetry can show three/four transitions depending on the metal ligand geometry it acquires on complex formation [31]. The electronic spectrum in the present case is not so well resolved, therefore a D_{4h} symmetry is assumed in all the systems. The transition for $^2B_{1g} \rightarrow {}^2E_g$ (ΔE_{xz}) is expected to be relatively more intense than the other peaks. Gersmann and Swalen assigned the peak maximum observed in the range 18 000–21 000 cm^{-1} to the $^2B_{1g} \rightarrow {}^2B_{2g}$ (ΔE_{xy}) transition and the peak observed in the range 23 100–31 000 cm^{-1} corresponds to the $^2B_{1g} \rightarrow {}^2E_g$ transition for various copper(II) complexes [32]. Lewis et al. also assigned the lower energy band to be due to the $^2B_{1g} \rightarrow {}^2B_{2g}$ transition [33]. The value for the $^2B_{1g} \rightarrow {}^2E_g$ transition could also be estimated from the spin Hamiltonian parameter, which is calculated to be 28 000 cm^{-1}. Therefore it is possible that this higher energy band might sometimes be obscured by the charge transfer band. Indeed in many cases it appears difficult to assign the observed

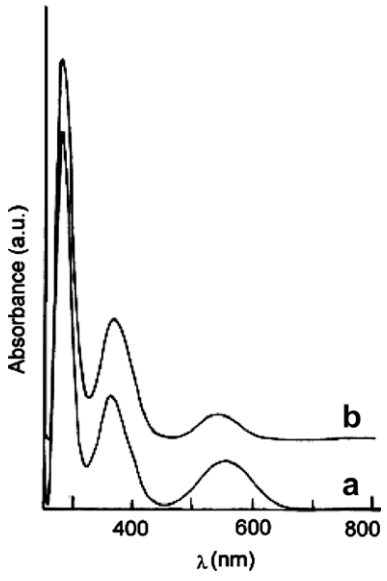


Fig. 4. UV–Vis spectra of [Cu(MeO-salen)(H_2O)] (**1**) (a) and Cu(MeO-salen)-NaY catalyst (b).

peaks to any one of the transitions. In our case two clear excitation bands for $^2B_{1g} \rightarrow {}^2B_{2g}$ (ΔE_{xy}) and $^2B_{1g} \rightarrow {}^2E_g$ (ΔE_{xz}) were observed in the range 18 282–17 699 cm^{-1} and 27 397–27 248 cm^{-1}, respectively. The $^2B_{1g} \rightarrow {}^2B_{2g}$ (ΔE_{xy}) transition is blue shifted on immobilization of the complex in the NaY matrix. The shifting of the $^2B_{1g} \rightarrow {}^2B_{2g}$ band to the higher energy region clearly demonstrates that the in-plane ligand field interaction is becoming stronger on immobilization of the complex in the NaY matrix than in its pristine state.

3.7. EPR studies

The EPR spectra for [Cu(MeO-salen)(H_2O)] (**1**) and Cu(MeO-salen)-NaY have been measured (Fig. 5). Spectral parameters have been calculated using the method of Kneubuhl [34a]. The principal g values calculated using the usual procedure are in agreement with those reported for zeolite immobilized copper Schiff base systems [34b]. It has been observed that for all copper systems $g_\parallel > g_\perp > 2.0023$, suggesting that the unpaired electron occupies the $d_{x^2-y^2}$ orbital, which is characteristic of a tetragonally elongated Cu^{II} system. Hyperfine coupling due to the metal ion, A_{Cu} (for ^{63}Cu, $I = \frac{3}{2}$) was resolved in the case of Cu(MeO-salen)-NaY. These values are given in Table 3. For Cu(MeO-salen)-NaY the $g_\parallel$ and $g_\perp$ values are found to be 2.244 and 2.053, respectively. The $A_\parallel$ value of Cu(MeO-salen)-NaY is calculated to be 145 G from the EPR spectra (Table 3). [Cu(MeO-salen)(H_2O)] also shows an axial EPR spectrum with $g_\parallel$ and $g_\perp$ equal to 2.209 and 2.044 but the hyperfine coupling is not resolved in this case. Immobilization of the complex in the NaY matrix has a significant effect on both the $g_\parallel$ and $g_\perp$ values. The variation in the $g_\parallel$ value on immobilization could be interpreted as being due to the change in the coordination environment around the copper (II) ion. The increase in the $g_\perp$ value could be correlated with distortions from the square planarity of the N_2O_2 chromophore around the copper(II) ion (vide infra).

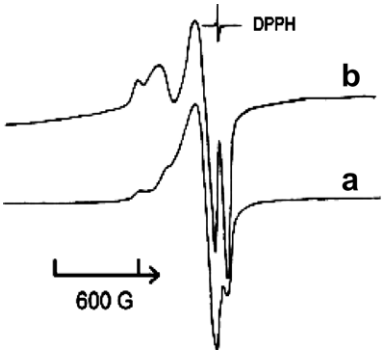


Fig. 5. EPR spectra of [Cu(MeO-salen)(H_2O)] (**1**) (a) and Cu(MeO-salen)-NaY catalyst (b).

Table 3
EPR spectral parameters

Species	$g_\parallel$	$g_\perp$	$A_\parallel$ (Gauss)	$A_\parallel$ ($\times 10^{-4}$ cm^{-1})
[Cu(MeO-salen)(H_2O)] (**1**)	2.209	2.044	200	203
Cu(MeO-salen)-NaY	2.244	2.053	145	159

3.8. Ground-state wave function and bonding parameters

The MO coefficients have been calculated using the ligand field approach adopted by Maki and McGarvey for Schiff base complexes with D_{4h} or D_{2h} symmetry [35,36]. Group theoretical consideration and proper linear combinations of ligand orbitals with the d-orbitals of the copper (II) ion affords the following antibonding wave functions [35,37]:

$$B_{1g} = \alpha d_{x^2-y^2} - \frac{1}{2}\alpha'\left[-\sigma_x^{(1)} + \sigma_y^{(2)} + \sigma_z^{(3)} - \sigma_y^{(4)}\right] \tag{3.1}$$

$$B_{2g} = \beta d_{xy} - \frac{1}{2}\sqrt{(1-\beta^2)}\left[p_y^{(1)} + p_x^{(2)} - p_y^{(3)} - p_x^{(4)}\right] \tag{3.2}$$

$$A_{1g} = \gamma d_{3z^2-r^2} - \frac{1}{2}\sqrt{(1-\gamma^2)}\left[-\sigma_x^{(1)} + \sigma_y^{(2)} + \sigma_z^{(3)} - \sigma_y^{(4)}\right] \tag{3.3}$$

$$E_g \begin{cases} = \delta d_{xz} - \sqrt{(1-\delta^2)}\left(\frac{p_z^{(1)} - p_z^{(3)}}{\sqrt{2}}\right) & \text{(a)} \\ = \delta d_{yz} - \sqrt{(1-\delta^2)}\left(\frac{p_z^{(2)} - p_z^{(4)}}{\sqrt{2}}\right) & \text{(b)} \end{cases} \tag{3.4}$$

Overlap is included only for the B_{1g} state, where α and α' are related:

$$\alpha^2 + \alpha'^2 - 2\alpha\alpha' S = 1 \tag{3.5}$$

Here S is the overlap integral. For Schiff base ligands the value of S is 0.093 [35]. The B_{1g} and A_{1g} states account for the σ bonding to the copper (α and α'). The B_{2g} state represents the in-plane π bonding (β). δ is the coefficient for the MO E_g representing the out-of-plane π bonding and α' is the coefficient for ligand orbitals forming the B_{1g} orbital. Since α, α', β and δ are MO coefficients, their values must be less than or equal to unity. They must be greater than 0.5 otherwise they will have no significance on the degree of covalency in the bonding. The extent of the departure of these coefficients from unity measures the extent of delocalization of the metal electrons due to metal-ligand bonding, hence the extent of covalency. When an unpaired electron is interacting with a magnetic field,the spin Hamiltonian could be expressed as

$$\hat{H} = g_\parallel \beta H_z S_z + g_\perp \beta (H_x S_x + H_y S_y) + A_\parallel S_z I_z + A_\perp (S_x I_x + S_y I_y) \tag{3.6}$$

When the wave function for B_{1g} is applied to the above Hamiltonian, the following EPR spectral parameters can be obtained [35–37]:

$$g_\parallel = 2.0023 - \left(\frac{8\lambda}{\Delta E_{xy}}\right)[\alpha^2\beta^2 - f(\beta)] \tag{3.7}$$

where

$$f(\beta) = \alpha\alpha'\beta S + \frac{1}{2}\alpha\alpha'\beta(1-\beta^2)^{1/2}T(n) \quad (3.8)$$

$$g_\perp = 2.0023 - \left(\frac{2\lambda}{\Delta E_{xz}}\right)[\alpha^2\beta^2 - f(\beta)] \quad (3.9)$$

where

$$f(\beta) = \alpha\alpha'\delta^2 S + \frac{1}{\sqrt{2}}\alpha\alpha'\delta(1-\delta^2)^{1/2}T(n) \quad (3.10)$$

$$A_\parallel = P\left\{\alpha^2\left(\frac{4}{7}+k\right) - 2\lambda\alpha^2\left[\frac{4\beta^2}{\Delta E_{xy}} + \left(\frac{3}{7}\right)\frac{\delta^2}{\Delta E_{xz}}\right]\right\} \quad (3.11)$$

where $P = 2\gamma_{Cu}\beta_e\beta_N\langle d_{x^2-y^2}|r^{-3}|d_{x^2-y^2}\rangle = 0.036\ cm^{-1}$, γ_{Cu} is the magnetogyric ratio, β_e is the Bohr magneton and β_N is the nuclear magneton of ^{63}Cu. The constant k corrects for the Fermi contact term of excited configurations of Cu. The constant $T(n)$ is an integral over the ligand functions and results from the calculation of the matrix elements of the Hamiltonian with the wave functions. Based on these equations, α can be approximately evaluated using the following equation [32]:

$$\alpha^2 = \frac{A_\parallel}{P} + (g_\parallel - 2) + \left(\frac{3}{7}\right)(g_\perp - 2) + 0.04 \quad (3.12)$$

Here, 0.04 approximates the various integrals by an average value.

When π-bonding is present it is necessary to simplify Eqs. (3.7)–(3.10) (unless nuclear and ligand hyperfine structure provide extra data) by ignoring overlap and the small terms in $T(n)$. This leads to expressions previously derived by Stevens [38]:

$$g_\parallel = 2 - \left(\frac{8\lambda\alpha^2\beta^2}{\Delta E_{xy}}\right) \quad (3.13)$$

$$g_\perp = 2 - \left(\frac{2\lambda\alpha^2\delta^2}{\Delta E_{xz}}\right) \quad (3.14)$$

The α values (the d-orbital coefficients for the b_{1g} molecular orbital representing in-plane σ-bonding) were evaluated from Eq. (3.12), whereas the values of α' (the metal d-orbital coefficients for the b_{1g} molecular orbital representing in-plane σ-bonding) were calculated from Eq. (3.5). The values of β (the metal d-orbital coefficients for the b_{2g} molecular orbital representing in-plane π-bonding) were calculated from Eq. (3.13) using the ΔE_{xy} value from electronic spectra whereas δ values were calculated using Eq. (3.14). The MO coefficients were obtained by using the value of $-828\ cm^{-1}$ for λ, the spin–spin coupling constant and $0.036\ cm^{-1}$ for P, dipolar interaction term for a free copper(II) ion (Table 4).

3.9. Catalytic reactions

The oxidation of phenol and 1-naphthol were carried out to test the catalytic efficiency of the prepared catalyst. The results of the reactions are given in Table 5. In both the reactions the hybrid catalyst showed good catalytic activity. It is interesting to note that neither the green species of impure Cu(MeO-salen)-NaY(imp.), nor the Cu-exchanged mother zeolite (Cu–NaY) exhibited any noticeable catalytic activity. The pristine [Cu(MeO-salen)(H_2O)] complex also shows no catalytic activity in solution in the above mentioned oxidation reactions (Table 5). It should be noted that atomic absorption spectroscopic analysis shows copper is not leaching out during oxidation reactions as no copper was detected in the liquid phase of the reaction mixture after completion of the reaction. Hydroxylation of phenol using this catalyst affords two products, viz. catechol and hydroquinone, instead of the three expected products (catechol, hydroquinone and benzoquinone) whereas hydroxylation of 1-naphthol gives selectively only 1,4-naphthoquinone in lieu of three possible products (1,4-naphthoquinone, 1,4-dihydroxy-naphthalene and 1,2-dihydroxy-naphthalene). This clearly demonstrates

Table 4
Electronic d–d transitions and MO coefficients

Species	α^2	α'^2	β^2	ΔE_{xy} (cm^{-1})	δ^2	ΔE_{xz} (cm^{-1})
[Cu(MeO-salen)(H_2O)] (**1**)	0.835	0.250	0.740	17699	0.866	27397
Cu(MeO-salen)-NaY	0.741	0.354	0.897	18282	0.992	27248

Table 5
Catalytic performance of Cu(MeO-salen)-NaY, Cu-NaY and [Cu(MeO-salen)(H_2O)] (**1**)

Catalyst	Reaction time (h)	Conversion (% mass)					
		Phenol			1-Naphthol		
		BQ[a]	CAT[a]	HQ[a]	1,4-NQ[a]	1,4-DHN[a]	1,2-DHN[a]
Cu(MeO-salen)-NaY	3		7.9	4.5	20.5		
	6		11.7	6.2	80.7		
Cu-NaY	6	No detectable activity					
[Cu(MeO-salen)(H_2O)] (**1**)	6	No detectable activity					

[a] BQ, benzoquinone; HQ, hydroquinone, CAT, catachol, 1,4-NQ, 1,4-naphthoquinone, 1,4-DHN, 1,4-dihydroxynaphthalene, and 1,2-DHN, 1,2-dihydroxynaphthalene.

that [Cu(MeO-salen)(H_2O)] on immobilization in a NaY matrix not only shows remarkable catalytic activity in the hydroxylation reactions of phenol and 1-naphthol but also exhibits excellent product selectivity.

4. Conclusion

It is evident from this study that the copper(II) Schiff base complex, [Cu(MeO-salen)(H_2O)] (**1**), which possesses a square pyramidal geometry undergoes a severe distortion in its coordination environment on immobilization in a NaY matrix. The shifting of the $^2B_{1g} \rightarrow {}^2B_{2g}$ band to shorter wavelength in electronic spectra of the catalyst, Cu(MeO-salen)-NaY (red) in comparison to the pristine complex or [Cu(MeO-salen)(H_2O)] (green), indicates that the axial ligand field around the copper(II) ion is weaker in the former [39]. This may be due to loss of the aquo ligand of the complex **1** to give rise to a square planar moiety during entrapment of the complex in the NaY supercage. EPR spectra are in accord with this as the $g_{\|}$ value of the catalyst is higher than that of complex **1** (Table 3) [39,40]. The lower value of the calculated MO coefficient α^2 for the catalyst also suggests that the covalency of the in-plane ligand is increased on immobilization. As a result we observed the chromotropism (color change) in the complex when it is immobilized in the NaY matrix. The concomitant tetrahedral distortion in the CuO_2N_2 chromophoric moiety of the entrapped complex in NaY matrix is also evident as the catalyst shows a higher value of $g_{\perp}$ in comparison to the corresponding value for the complex **1** [41]. In addition the value of MO coefficients β^2 and δ^2, which represents the π-bonding, is higher in the case of catalyst than the pristine complex **1** (Table 4). This indicates that the complex undergoes tetrahedral distortion on entrapment. Interestingly while the pristine complex does not show any catalytic activity towards oxidation reactions, its immobilized variety does. Evidently the copper(II) Schiff base becomes reactive when it suffers distortion. Although more complex and dynamic situations are encountered in metalloproteins, it is tempting to mention that the blue copper protein shows greater reactivity where the active copper(II) site possesses an intermediate coordination environment between square planar and tetrahedral [21]. It is apparent from this study that a square planar copper(II) complex moiety with its two vacant axial positions facilitates nucleophilic attack by the oxidant to enhance the catalytic activity of the hybrid materials in the oxidation reactions. Flexibility of the diamine backbone of Schiff base ligand and fine tuning of the stereoelectronic structure of the complex by introducing different substitutions in the ligand are the crucial factors that govern the reactivity of the Cu^{II} complex.

Acknowledgements

Financial support from the Department of Science and Technology, Government of India, by a Grant (SR/S1/IC-12/2003) (to S.K.) is gratefully acknowledged. P.K.S. and R.B. thank CSIR and B.D. thanks UGC for a research fellowship. We thank SAIF, IIT Madras for EPR spectral measurement (on a chargeable basis).

Appendix A. Supplementary data

Supplementary data are available from The Director, CCDC, 12 Union Road, Cambridge, CB2 1EZ, UK fax: +44 1223 336 033; e-mail: deposit@ccdc.cam.ac.uk or www: http://www.ccdc.cam.ac.uk) on request, quoting the deposition number CCDC 289133 for complex **1**. Supplementary data associated with this article can be found, in the online version, at doi:10.1016/j.poly.2006.08.018.

References

[1] R.W. Hay, Bio-Inorganic Chemistry, Eillis Horwood, Chichester, 1984.
[2] R.A. Sheldon, J.K. Kochi, Metal Catalyzed Oxidations of Organic Compounds, Academic Press, New York, 1981.
[3] T.G. Traylor, A.R. Miksztal, J. Am. Chem. Soc. 111 (1989) 7443, and references therein.
[4] B.M. Weckhuysen, A. Verberckmoes, I.P. Vannijvel, J.A. Pelgrims, P.L. Buskens, P.A. Jacobs, R.A. Schoonheydt, Angew. Chem., Int. Ed. Engl. 34 (1995) 2652.
[5] J.-M. Brégeault, J. Chem. Soc., Dalton Trans. (2003) 3289.
[6] F. Bedioui, Coord. Chem. Rev. 144 (1995) 39, and references therein.
[7] (a) R.F. Parton, I.F.J. Venkelecom, M.J.A. Casselman, C.P. Bezouhanova, J.V. Uytterhoeven, P.A. Jacobs, Nature 370 (1994) 541;
(b) C.-H. Lee, S.-T. Wong, T.-S. Lin, C.-Y. Mou, J. Phys. Chem. B 109 (2005) 775;
(c) R. Ganesan, B. Viswanathan, J. Phys. Chem. B 108 (2004) 7102.
[8] J.E. Huheey, Inorganic Chemistry, Harper Collins Publishers, New York, 1992.
[9] J.M. Thomas, Angew. Chem., Int. Ed. Engl. 38 (1999) 3588.
[10] K. Balkus Jr., M. Eisa, R. Levedo, J. Am. Chem. Soc. 117 (1995) 10753.
[11] I.F.J. Vankelecom, D. Tas, R.F. Parton, V. Van de Vyver, P.A. Jacobs, Angew. Chem., Int. Edit. Engl. 35 (1996) 1346.
[12] S. Koner, Chem. Commun. (1998) 593.
[13] M. Sykora, J.R. Kincaid, Nature 387 (1997) 162.
[14] J.A. Incavo, P.K. Dutta, J. Phys. Chem. 94 (1990) 3075.
[15] M. Sykora, K. Maruszewski, S.M. Treffert-Ziemelis, J.R. Kincaid, J. Am. Chem. Soc. 120 (1998) 3490.
[16] V. Ramamurthy, P. Lakshminarasimhan, C.P. Grey, L.J. Johnston, Chem. Commun. (1998) 2411, and references therein.
[17] J.L. Meinershagen, T. Bein, J. Am. Chem. Soc. 121 (1999) 448.
[18] B. Meier, T. Werner, I. Klimant, O.S. Wolfbeis, Sens. Actuators B 29 (1995) 240.
[19] E.I. Solomon, K.W. Penfield, D.E. Wilcox, Struct. Bonding 53 (1983) 1.
[20] A. Messerschmidt, Struct. Bonding 90 (1998) 37.
[21] A.G. Sykes, Adv. Inorg. Chem. 36 (1991) 377.
[22] S. Deshpande, D. Srinivas, P. Ratnasamy, J. Catal. 188 (1999) 261.
[23] R.H. Holm, G.W. Everett, A. Chakravorty, Prog. Inorg. Chem. 7 (1965) 83.
[24] R.H. Bailes, M. Caovin, J. Am. Chem. Soc. 69 (1947) 1886.
[25] (a) SIR92: A. Altmare, M.C. Burla, M. Camalli, M. Cascarano, C. Giacovazzo, A. Guagliardi, G.J. Polidori, Appl. Crystallogr. 27 (1994) 435;
(b) SHELXS-97: G.M. Sheldrick, A Program for Crystal Structure Determination, University of Göttingen, Germany, 1997;
(c) A.L. Spek, J. Appl. Cryst. 36 (2003) 7.
[26] P.K. Saha, S. Koner, Inorg. Chem. Commun. 7 (2004) 1164.

[27] ORTEP: C.K. Johnson, Report ORNL-5138, Oak Ridge National Laboratory, Oak Ridge, TN, 1976.
[28] N. Ito, S.E.V. Phillips, C. Stevens, Z.B. Ogel, M.J. McPherson, J.N. Keen, K.D.S. Yadav, P.F. Knowles, Nature 350 (1991) 87.
[29] K. Nakamoto, Infrared and Raman Spectra of Inorganic and Coordination Compounds, 4th ed., Wiley Interscience, New York, 1986.
[30] R.M. Barrer, Hydrothermal Chemistry of Zeolite, Academic Press, New York, 1982.
[31] B.J. Hathaway, D.E. Billing, Coord. Chem. Rev. 5 (1970) 143.
[32] H.R. Gersmann, J.D. Swalen, J. Chem. Phys. 36 (1962) 3221.
[33] W.B. Lewis, M. Alei Jr., L.O. Morgan, J. Chem. Phys. 45 (1966) 4003.
[34] (a) F.K. Kneubuhl, J. Chem. Phys. 33 (1960) 1074;
(b) E.F. Murphy, D. Ferri, A. Baiker, S.V. Doorslaer, A. Schweiger, Inorg. Chem. 42 (2003) 2559.
[35] A.H. Maki, B.R. McGarvey, J. Chem. Phys. 29 (1958) 31, and 35.
[36] B.R. McGarvey, J. Phys. Chem. 60 (1956) 71.
[37] R. Neiman, D. Kivelson, J. Chem. Phys. 35 (1961) 149.
[38] K.W.H. Stevens, Proc. Roy. Soc. A 219 (1953) 542.
[39] R.L. Belford, M. Calvin, G. Belford, J. Chem. Phys. 26 (1957) 1165.
[40] H. Yokoi, M. Sai, T. Isobe, Bull. Chem. Soc. Jpn. 42 (1969) 2232.
[41] M.M. Bhadbhade, D. Srinivas, Inorg. Chem. 32 (1993) 5458, and 6122.

Available online at www.sciencedirect.com
ScienceDirect
Polyhedron 26 (2007) 572–580
POLYHEDRON
www.elsevier.com/locate/poly

Synthesis, characterization, DNA interaction and cleavage activity of new mixed ligand copper(II) complexes with heterocyclic bases

M.S. Surendra Babu [a], K. Hussain Reddy [a,*], Pitchika G. Krishna [b]

[a] Department of Chemistry, Sri Krishnadevaraya University, Anantapur, Andhra Pradesh 515003, India
[b] Department of Zoology, Sri Krishnadevaraya University, Anantapur, Andhra Pradesh 515003, India

Received 20 June 2006; accepted 16 August 2006
Available online 9 September 2006

Abstract

Mixed ligand complexes having the formulae $Cu(RPO)_2Py_2$, $Cu(RPO)_2Im_2$ and $Cu(DBO)_2Py_2$ [RPO = resacetophenone oxime, DBO = 2,4-dihydroxybenzophenone oxime, Py = pyridine and Im = imidazole] have been synthesized and characterized by UV–Vis, IR, ESR, cyclic voltammetry and magnetic susceptibility methods. Absorption studies revealed that each of these octahedral complexes is an avid binder of calf thymus DNA. The apparent binding constants for mixed ligand complexes are in order of 10^4–10^5 M^{-1}. Based on the data obtained in the DNA binding studies a partial intercalative mode of binding is suggested for these complexes. The nucleolytic cleavage activity of the adducts was carried out on double stranded pBR322 circular plasmid DNA by using a gel electrophoresis experiment in the presence and absence of oxidant (H_2O_2). All the metal complexes cleaved supercoiled DNA by hydrolytic and oxidative paths. The oxidative path dominates the hydrolytic cleavage. The hydrolytic cleavage of DNA is evidenced from the control experiments showing discernable cleavage inhibition in the presence of the hydroxyl radical inhibitor DMSO or the singlet oxygen quencher azide ion.
© 2006 Elsevier Ltd. All rights reserved.

Keywords: Mixed ligand copper(II) complexes; Oximes; Aromatic bases; CT DNA; Binding interaction; Hydrolytic cleavage

1. Introduction

Oximes are widely recognized ligands [1–5]. Transition metal complexes with O-hydroxy aromatic oximes (e.g. salicylaldoxime (SAO)) have attracted much attention, as they exist as *cis* and *trans* geometrical isomers. Copper complexes are known to assume *trans* structures while cobalt complexes have *cis* structures. We have investigated several cobalt complexes with O-hydroxy carbonyl Schiff bases (tetradentate ligands) containing additional hydroxyl groups [6]. Such additional groups have been exploited to anchor the complexes on a polymer support [7].

Investigation on DNA interactions and cleavage activity of metal complexes with oximes are quite limited [8]. In light of the above and in continuation of our on going research work [9,10] on metal–DNA interactions herein we describe the synthesis characterization, DNA binding and cleavage activity of copper(II) complexes with resacetophenone oxime (2,4-dihydroxyacetophenone oxime) and 2,4-dihydroxybenzophenone oxime and their pyridine and imidazole adducts.

2. Experimental

2.1. Chemical

2,4-Dihydroxybenzophenone and resacetophenone were purchased from Merck, and metals used in the preparation of the complexes are of reagent grade. The solvents used in the synthesis of the ligands and metal complexes were distilled before use. All other chemicals were of AR grade and were used without further purification. Agarose, used in gel

* Corresponding author. Tel.: +91 8554 224347/255752; fax: +91 8554 229043.
E-mail address: Khussainreddy@yahoo.co.in (K.H. Reddy).

0277-5387/$ - see front matter © 2006 Elsevier Ltd. All rights reserved.
doi:10.1016/j.poly.2006.08.026

electrophoresis, was purchased from Sigma–Aldrich, Calf thymus DNA and plasmid pBR322 were purchased from Genie Biolabs, Bangalore, India.

2.2. Instrumentation

The elemental analyses were performed using a Perkin–Elmer 2400 CHNS elemental analyzer. Magnetic moments were determined in the polycrystalline state on a PAR model-155 vibrating sample magnetometer operating at field strength of 2–8 kG. High purity Ni metal (saturation moment 55 emu/g) was used as standard. The molar conductance of the complexes in DMF (10^{-3} M) solution was measured at 28 ± 2 °C with a systronic model 303 direct-reading conductivity bridge. The electronic spectra were recorded in DMF with a Schimadzu UV-160A spectrophotometer. FT-IR spectra were recorded in the range 4000–50 cm^{-1} with a Bruker IFS 66V in KBr and polyethylene medium. ESR spectra were recorded on Varian E-122 X-band spectrophotometers at liquid nitrogen temperature in DMF. The voltammetric measurements were performed on Bio-Analytical Systems (BAS), CV-27 assembly in conjunction with an *X–Y* recorder. Measurements were made on the degassed (N_2 bubbling for 5 min) solution in DMF (10^{-3} M) containing 0.1 M tetraethyl ammonium perchlorate as the supporting electrolyte. The three-electrode system consisted of a glassy carbon (working), platinum (auxiliary) and Ag/AgCl (reference) electrodes. UV–Vis spectra were recorded on a Tech-Comp UV-8500 instrument.

2.3. DNA binding experiments

A solution of CT DNA in 0.5 mM NaCl/5 mM Tris–HCl (pH 7.0) gave a ratio of UV absorbance at 260 and 280 nm, A_{260}/A_{280} of 1.8–1.9, indicating DNA was sufficiently free of protein. A concentrated stock solution of DNA was prepared in 5 mM Tris–HCl/50 mM NaCl in water, pH 7.0 and the concentration of CT DNA were determined by UV absorbance at 260 nm after 1:100 dilutions (in 250 μM in NP). The molar absorption coefficient was taken as 6600 M^{-1} [11]. Stock solutions were stored at 4 °C and were used after no more than four days. Doubly distilled water was used to prepare the buffer solutions. Solution were prepared with the appropriate copper complexes (35 μM of a 1.0 mM solution in DMF), CT DNA (diluted from a 1 mg/ml solution), NaCl (final concentration 50 mM) and Tris–HCl buffer (pH 7.0, final concentration 50 mM) and diluted with H_2O to a total volume of 1 ml. After equilibration (ca. 10 min), the spectra were recorded against an analogous blank solution containing the same concentration of DNA/NaCl and Tris–HCl buffer.

The data were then fitted to Eq. (1) to obtain the intrinsic binding constant, K_b [12]

$$[DNA]/(\varepsilon_a - \varepsilon_f) = [DNA]/(\varepsilon_b - \varepsilon_f) + 1/K_b(\varepsilon_a - \varepsilon_f), \quad (1)$$

where ε_a, ε_f and ε_b are the apparent free and bound metal complex extinction coefficients, respectively. A plot of $[DNA]/(\varepsilon_a - \varepsilon_f)$ versus [DNA] gave a slope of $1/(\varepsilon_b - \varepsilon_f)$ and a *Y*-intercept equal to $1/K_b(\varepsilon_a - \varepsilon_f)$, K_b is the ratio of the slope to the *Y*-intercept.

2.4. Assay of nuclease activity

A DMF solution containing the metal complexes (1 μl of 1 mM) was taken in a clean eppendroff tube and plasmid DNA (1 μl of 0.10 μg/ml) was added. The contents were incubated for 2 h at 37 °C and loaded on 1% agarose gel after mixing 5 μl of loading buffer (0.25% bromophenol blue + 25% xylenecyanol + 30% glycerol sterilized distilled). Electrophoresis was performed at constant voltage (80 V) until the bromophenol blue reached to 3/4 of the gel. Then the gel was stained for 10 min by immersing it in ethidium bromide solution. The gel was then de-stained for 10 min by keeping it in sterile distilled water and the plasmid band was visualized by viewing the gel under a transilluminator and photographed. The efficiency of the DNA cleavage was measured by determining the ability of the complex to form open circular (OC) or nicked circular (NC) DNA from its supercoiled (SC) form by quantitatively estimating the intensities of the bands using the *Vilber Lourmat* (V 99.01) Gel Documentation System. The reactions were carried out under hydrolytic conditions. A control experiment was done in presences of hydroxyl radical scavenger DMSO and singlet oxygen quencher azide ion.

3. Preparation

3.1. Preparation of ligands

Resactophenone oxime (RPO) and 2,4-dihydroxybenzophenone oxime (DBO) ligands were prepared by the reaction of hydroxylammoniumchloride ($NH_2OH \cdot HCl$) with resacetophenone and 2,4-dihydroxybenzophenone, respectively.

Hydroxylammoniumchloride (0.03 mol) and resacetophenone (0.03 mol) were taken in 50% aqueous methanol or 2,4-dihydroxybenzophenone (0.03 mol) in benzene solvent. The resulting mixture was acidified with a few drops of glacial acetic acid and refluxed for 2–3 h. The precipitated compound was filtered, washed with cold water dried under vacuum and recrystallized from aqueous ethanol.

The infra red spectrum of RPO and DBO shows strong and broad bands due to hydrogen-bonded phenolic OH at 2′-position in the region 3000–2800 cm^{-1}. They also exhibit two separate OH bands due to oxime OH at 3237, 3137 cm^{-1} and phenolic OH at 3400, 3350 cm^{-1}, respectively, in addition to >C=N stretching at 1598, 1588 cm^{-1}, respectively. The ^1H NMR spectra of RPO and DBO were recorded in DMSO-d_6 solvent. RPO shows signals at 2.22 (s, 3H), 6.42–7.21 (m, 3H), 9.15 (s, 1H) 10.85 (s, 1H) and 11.79 (s, 1H) assigned to $–CH_3$, $–C_6H_3$,

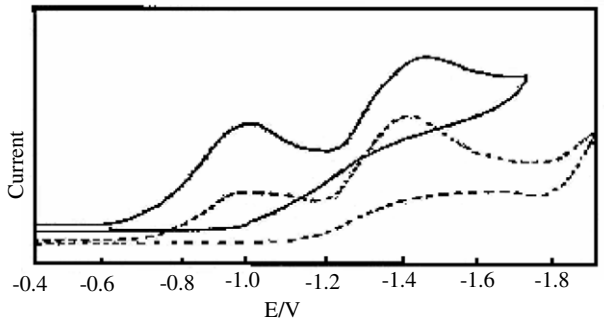


Fig. 1. Cyclicvoltametric profile diagram of RPO (------) and DBO (——).

ortho phenolic OH, *para* phenolic OH and =N–OH (oxime), respectively. Signals corresponding to $-C_6H_3$, $-C_6H_5$, two phenolic OH's and oxime-OH are, respectively, observed in the NMR spectrum of DBO at 6.30–6.45 (m, 3H), 7.22–7.80 (m, 5H), 10.09–10.42 broad (2H) and 12.45 (s, 1H) δ values, respectively. The mass spectrum of RPO shows a molecular ion peak at 167 (m/z) corresponding to its molecular weight. The other important peaks at m/z 150 and 135 are due to loss of –OH and $-CH_3$ from the molecular ion peak. A peak at 121 corresponds to the formation of the $HOC_6H_3NCH_3^+$ ion. The mass spectrum of DBO shows peaks at 229, 213, 183 and 108 corresponding to the molecular ion ($M^{+\cdot}$), $M^{+\cdot}-16$, $HOC_6H_3N–Ph^{+\cdot}$ and  , respectively.

The presence of only cathodic peaks [−1.35 and −1.83 (RPO); −1.42 and −1.87 V (DBO)] in cyclicvoltammograms (Fig. 1) of the ligands suggest an irreversible reduction of the azomethine group. Each peak corresponds to a one electron reduction. A possible mechanism (Scheme 1) is proposed for the reduction of these ligands.

3.2. Synthesis of cuproxime complexes and their pyridine and imidazole adducts

Cuproximes were prepared by mixing copper(II) chloride (4.3 g, 0.025 mol) and oxime [RPO (0.05 mol) or DBO (0.05 mol)] in a 1:2 ratio in 50% aqueous ethanolic medium. The reaction mixture was stirred for 30 min, and the precipitate formed was filtered, washed with hot water and cold methanol. The complexes were dried at 110 °C.

The copper(II) complex (1.5 g) of RPO or DBO was placed in a schlenk tube and dissolved in pyridine (3 ml). The solution was stirred magnetically for 30 min and *n*-hexane (25 ml) was added. After standing for 3–4 days, the dark green product that formed was washed with water and *n*-hexane and dried under reduced pressure over $CaCl_2$.

Cuproxime of RPO (0.01 mol) was placed in a 250-ml round bottom flask. Imidazole (0.05 mol) dissolved in CH_2Cl_2 was added to the contents of the flask. The reaction mixture was refluxed on a water bath for 2 h. On cooling the dark green precipitate that formed was filtered, washed with cold hexane and dried under vacuo over $CaCl_2$.

4. Results and discussion

The present ligands contain two functional groups viz., oxime and phenolic groups (Fig. 2). The ligands and their metal complexes (both the cuproximes and their adducts) are stable at room temperature, are non-hygroscopic, soluble partially in methanol, ethanol and easily soluble in dimethylformamide. The colour, melting point, analytical data, molar conductance and magnetic moment data are summarized in Table 1. Elemental analysis supports the present composition of the complexes. The molar conductivity data suggest that the complexes are non-electrolytes. The magnetic moment values of the complexes indicate the

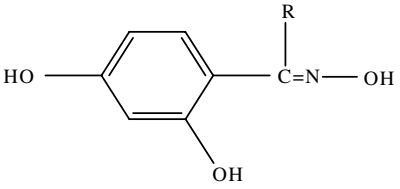
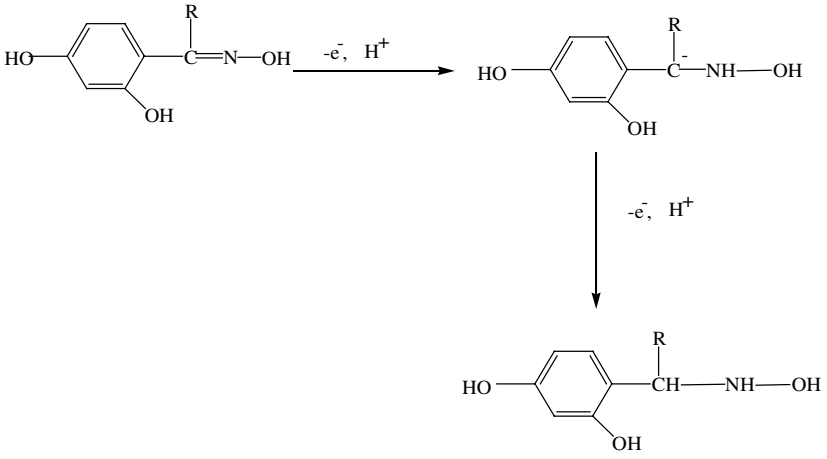


Fig. 2. Structure of ligands; where R = CH_3, RPO; R = C_6H_5, DBO.



Scheme 1. A possible mechanism for reduction of oxime ligands.

Table 1
Physical properties of copper complexes of RPO and DBO and their base adducts

S. no.	Complexes	Colour	Melting point (°C)	Elemental analysis			Molar conductance (Ω^{-1} cm^2 mol^{-1})	μ_{eff} (BM)
				Carbon observed (calulated)	Hydrogen observed (calulated)	Nitrogen observed (calulated)		
I	$Cu(SAO)_2$	green	208–210	50.32 (50.27)	3.38 (3.5)	7.99 (8.12)	5.8	2.18
II	$Cu(RPO)_2$	green	270–275	48.12 (48.31)	4.32 (4.52)	7.12 (7.32)	16.8	2.83
III	$Cu(RPO)_2Py_2$	dark green	193–196	52.15 (52.82)	4.48 (4.82)	8.22 (8.39)	9.0	2.12
IV	$Cu(RPO)_2Im_2$	bluish green	185–188	48.75 (48.94)	4.78 (4.74)	11.74 (12.58)	7.5	2.32
V	$Cu(DBO)_2$	green	224–228	52.17 (52.49)	3.49 (3.52)	4.62 (4.76)	12.2	2.34
VI	$Cu(DBO)_2Py_2$	dark green	215–217	53.48 (53.12)	3.58 (3.49)	7.61 (7.65)	8.5	2.78

presence of one unpaired electron. The copper salicylaldoxime complex [$Cu(SAO)_2$] is used for comparative studies.

The electronic spectral data of the metal complexes are given in Table 2. The spectral data of the complexes are dominated by intense intra-ligand (π–π^*) and charge transfer (CT) bands. The presence of a single d–d band may be attributed to the symmetric nature of the ligand field. In the electronic spectra of the mixed ligand complexes, d–d bands are observed in the high-energy region (Table 2) due to Jahn–Teller distortion observed in octahedral complexes.

The broad band in the IR region 3000–2800 cm^{-1} in RPO and DBO are absent in the corresponding copper chelates suggesting the deprotonation of the 2′-OH phenolic group due to formation of a covalent bond between the copper and phenolic oxygen. Strong bands observed at 1598 and 1588 cm^{-1} assigned to >C=N– stretching vibration in the ligands are shifted to lower frequency in the complexes revealing the participation of the azomethine nitrogen in chelation. The non-ligand bands observed in the far IR spectra of the metal complexes are assigned to ν(M–N) (265, 271 and 289 cm^{-1}) ν(M–O) (576, 589 and 595 cm^{-1}) stretching vibrations. Additional bands observed (1610–1600, 1540–1520, 260–220, 245–230 cm^{-1}) in the IR spectra of the mixed ligand complexes are presumably due to the binding of bases (pyridine/imidazole) to copper via nitrogen donor atoms, preferably in axial positions.

Oxime OH stretching vibrations are observed at a lower frequency in the chelates (3221 and 3128 cm^{-1}), indicating the involvement of oxime OH in strong hydrogen bonding which leads to the formation of a stable 5-membered ring structure. Observance of three evenly distributed bands in the 620–450 cm^{-1} region is characteristic of a *trans*-structure for the complexes [13]. IR spectral data together with electronic and magnetic moment data suggest a *trans* square planar structure for the cuproximes and a *trans* octahedral structure for the mixed ligand copper(II) complexes (Fig. 3a and b).

ESR spectra of all the complexes are recorded in DMF solvent at liquid nitrogen temperature (LNT). The ESR spectra of the copper(II) complexes exhibit a set of four well-resolved peaks in the low field region and a weaker signal in high field region, corresponding to $g_\parallel$ and $g_\perp$, respectively (Fig. 4). The $g_\parallel$ and $g_\perp$ values are 2.245, 2.019 for $Cu(RPO)_2$ and 2.218, 2.015 for $Cu(DBO)_2$, respectively. The trend observed, $g_\parallel > g_\perp > 2.02$, for the present copper complexes is typical of a copper(II) (d^9) ion in axial symmetry with the unpaired electron present in the $d_{x^2-y^2}$ orbital. The $g_\parallel$ value of the parent complexes being less than 2.3 is indicative of significant covalent bonding

Table 2
Electronic spectral data (cm^{-1}) of the copper(II) complexes

Complex	π–π^*	Charge transfer (CT)	d–d
I	35710	28570	14950
II	38460	29850	15625
III	35710	28250	15380
IV	36360	28960	15150
V	37470	29760	16390
VI	36410	27760	15880

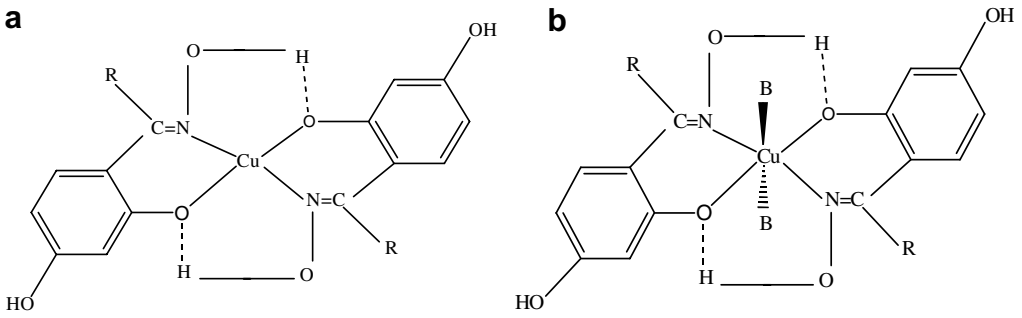


Fig. 3. (a) Structure of copper(II) complexes where R = CH_3, RPO; R = C_6H_5, DBO. (b) Structure of copper(II) adducts where R = CH_3, RPO; R = C_6H_5, DBO; B = pyridine/imidazole.

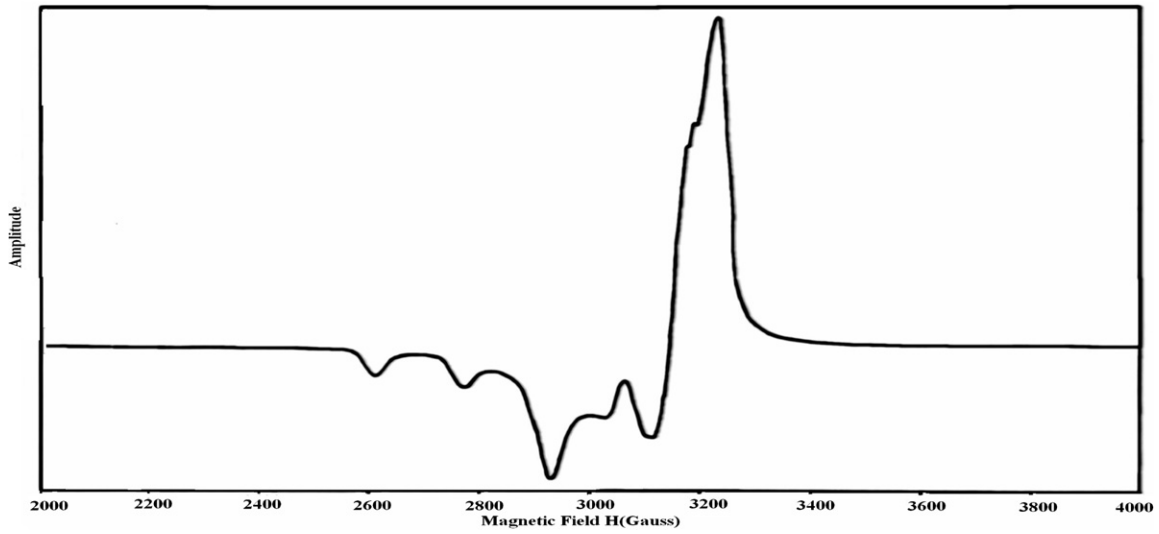


Fig. 4. X-band ESR spectra of the $Cu(RPO)_2Py_2$ complex at liquid nitrogen temperature (LNT) in DMF.

[14,15] in the complexes. The orbital reduction parameters data ($K_{\|} > K_{\perp}$) in Table 3 suggest that the present complexes have out-of-plane π-bonding [16].

Massacesi et al. [17,18] reported $g_{\|}$ values in the range 2.3–2.4 for complexes containing copper–oxygen bonds and 2.2–2.3 for complexes containing copper–nitrogen bonds. The present copper oxime complexes have $g_{\|} = 2.2$–2.4 in conformity with both Cu–O and Cu–N bonds in the cuproximes and their adducts.

The P values for a complex containing N_2O_2 donor atoms fall in the range 0.022–0.029 cm^{-1} [19]. The P values for the mixed ligand complexes are consistent with bonding of copper with nitrogen and oxygen donor atoms [20].

The redox behavior of these complexes has been investigated by cyclic voltammetry at a glassy carbon electrode. Table 4 gives the electrochemical data obtained at a glassy carbon electrode in DMF solution. The cathodic peak current function values were found to be independent of the scan rate. Repeated scans, as well as different scan rates showed that dissociation does not take place. Fig. 5 shows the profile of $Cu(RPO)_2Py_2$ and $Cu(DBO)_2Py_2$ complexes at 50 mV s^{-1} scan rates.

The copper complexes are redox active and show a cyclic voltammetric response in the potential range of 0.35–0.60 V which is assignable to the reduction peak of Cu(II)/Cu(I). All these complexes exhibit quasi-reversible behavior [21] as indicated by the non-equivalent current

Table 3
Spin Hamiltonian and orbital reduction parameters of the copper(II) complexes

Complex	$g_{\|}$	$g_{\perp}$	g_{av}	G	$K_{\|}$	$K_{\perp}$	$A_{\|}$	$A_{\perp}$	A_{av}	α^2	P
II	2.245	2.019	2.094	8.078	0.7657	0.4017	0.0147	0.0075	0.0098	1.5597	0.0261
III	2.346	2.015	2.073	5.264	0.9111	0.7945	0.0279	0.0139	0.0187	0.7532	0.0287
IV	2.354	2.086	2.175	4.202	0.9121	0.7725	0.0214	0.0055	0.0157	0.9758	0.0289
V	2.218	2.015	2.096	10.212	0.8161	0.1615	0.0172	0.0055	0.0094	1.1918	0.0296
VI	2.236	2.069	2.158	5.007	0.8987	0.8028	0.0149	0.0139	0.0143	1.3112	0.0276

Table 4
Cyclic voltammetric data of RPO and DBO copper(II) complexes[a]

Complex	Redox couple	CV cathodic, E_{pc}	CV anodic, E_{pa}	ΔE_p (mV)	$E_{1/2}$	$-i_c/i_a$	$\log K_c$[b]	$-\Delta G^{\circ c}$
I	II/I	0.34	0.59	250	0.47	1.18	178.13	8.12×10^5
II	II/I	0.35	0.60	250	0.47	1.28	133.11	7.72×10^5
III	II/I	0.38	0.55	170	0.45	1.09	195.58	11.35×10^5
IV	II/I	0.36	0.57	210	0.46	1.13	158.33	9.19×10^5
V	II/I	0.38	0.58	200	0.48	1.29	166.25	9.65×10^5
VI	II/I	0.42	0.59	170	0.51	1.04	195.58	11.35×10^5

[a] Recorded in DMF at room temperature with Et_4NClO_4 as supporting electrolyte, glassy carbon as working electrode, Pt wire as auxiliary electrode and Ag/AgCl as reference electrode; scan rate 50 mV s^{-1}.
[b] $\log K_c = 0.434ZF/RT\Delta E_p$.
[c] $\Delta G^{\circ} = -2.303RT\log K_c$.

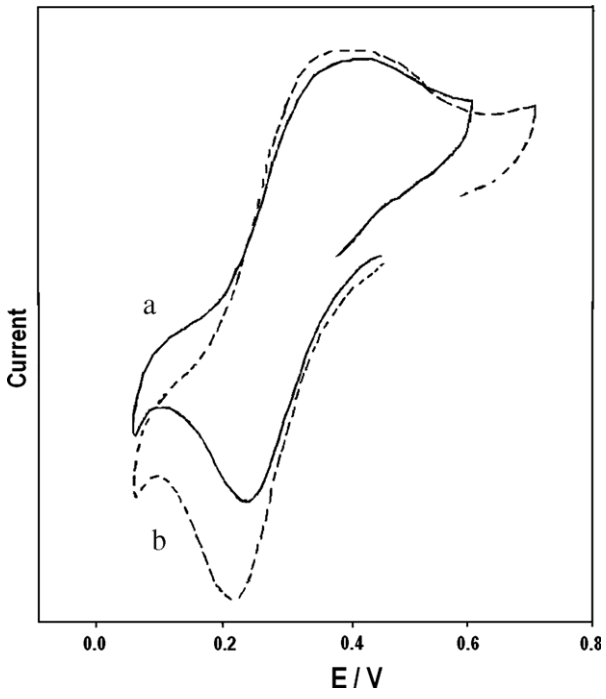


Fig. 5. Cyclic voltametric profile of (a) $Cu(RPO)_2Py_2$ (——); (b) $Cu(DBO)_2Py_2$ (------).

intensity of cathodic and anodic peaks ($i_c/i_a = 0.512$–0.322 V). All complexes have a large separation between the anodic and cathodic peaks (100–250 mV) indicating the quasi-reversible character. The ΔG° values of the mixed ligand complexes are greater than the parent complexes, showing that these complexes are more stable than their parent complexes.

The $E_{1/2}$ values of the adducts and complexes are comparable with other complexes showing nuclease activity [22]. The $E_{1/2}$ values of the parent complexes and mixed ligand complexes are high suggesting that the complexes undergo a more facile redox change which is the requirement for DNA cleavage [23].

4.1. Electronic absorption titrations

The binding interaction of the copper complexes with DNA was monitored by UV–Vis spectroscopy. The absorption spectra of the copper complexes are compared with and without CT DNA. In the UV region spectra, all the copper(II) complexes exhibit an intense absorption band around 280 nm which is attributed to an n–π^* or π–π^* transition. With increasing concentration of CT DNA, the absorption bands of the complexes are affected, resulting in the obvious tendency of hyperchromism or hypochromism with a hypsochromic shift (1–4 nm). The change in absorbance values with increasing amount of CT DNA were used to evaluate the intrinsic binding constant K_b for the present complexes (Table 5).

In the presence of increasing amounts of CT DNA, the UV–Vis absorption of $Cu(RPO)_2$ and $Cu(DBO)_2$ showed

Table 5
Effect of CT DNA on the absorbance bands and binding constant of the copper complexes and adducts

Complex	λ_{max} (nm)		$\Delta\lambda$ (nm)	H (%)	K_b (M^{-1})
	Free	Bound			
I	341	342.5	1.5	−16.6	2.5×10^4
II	276.0	274.5	1.5	−12.8	3.8×10^5
III	275.5	274.2	1.3	+11.8	2.6×10^4
IV	274.5	272.4	2.1	+12.4	2.1×10^5
V	287.1	284.8	2.3	−15.6	9.9×10^5
	357.0	345.2	12.8	−23.2	
VI	291.5	290.2	1.3	+4.8	1.4×10^4
	325.5	324.2	1.3	+0.5	

hypsochromic shifts (λ_{max}: 1.0 ± 0.5 nm) and hypochromism [hypochromicity: 12.8% for Cu(RPO) and 15.4% for Cu(DBO)]. While the mixed ligand complexes showed hypsochromic (λ_{max}: 1.0 ± 0.5 nm) and hyperchromism [hyperchromicity: +11.8%, +12.4% and +4.8%]. The change in hypochromic to hyperchromic shift from parent complex to mixed ligand complexes suggests that the type of binding mode is different (Fig. 6). This may be attributed to a change in structure from square planar (parent) to octahedral nature (adducts). The binding nature in the mixed ligand complexes is significant due to π-stacking or a hydrophobic interaction of the aromatic pyridine or imidazole bases. The binding constants of the parent complexes are sufficiently high, possibly due to their square planar nature [24]. A strong binding constant for II and V compared with I may be attributed to the presence of an extra OH group in complexes II and V, while V has the highest binding constant, which may be due to an increased π-stacking interaction facilitated by the presence of extra phenyl rings [25].

4.2. Nuclease activity

Gel electrophoresis experiments using pBR322 circular plasmid DNA were performed with the ligands and their complexes in the presence and absence of H_2O_2 as an oxidant. At micro-molar concentrations, for 2 h incubation periods, the ligands exhibit no significant cleavage activity in the absence or presence of oxidant (H_2O_2). The nuclease activity is greatly enhanced by the incorporation of copper ion in the respective ligands. The nuclease activity of the complexes was also investigated in the presence of a free radical scavenger, dimethylsulfoxide (DMSO) and a singlet oxygen quencher, azide ion (NaN_3).

From Fig. 7a it is evident that the complexes cleave DNA more efficiently in the presence of an oxidant. This may be attributed to the formation of hydroxyl free radicals. The production of a hydroxyl radical due to the reaction between the metal complex and oxidant may be explained as shown below [26].

$$(L)Cu^{2+} + H_2O_2 \rightarrow (L)Cu^{3+} + OH + OH^{\cdot}$$

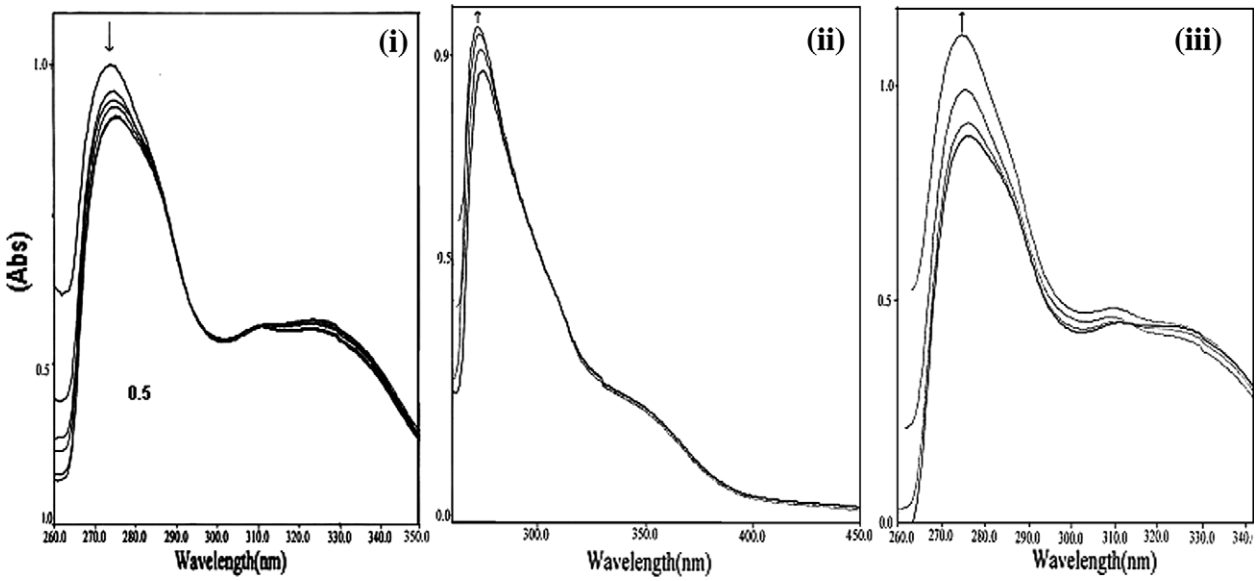


Fig. 6. Variation in absorption spectra of: (i) $Cu(RPO)_2$, (ii) $Cu(RPO)_2Py_2$, and (iii) $Cu(RPO)_2Im_2$ in the absence and presence of increasing amounts of DNA. [CuL] = 35 μM. Arrows show the absorbance changes upon increasing the DNA concentration.

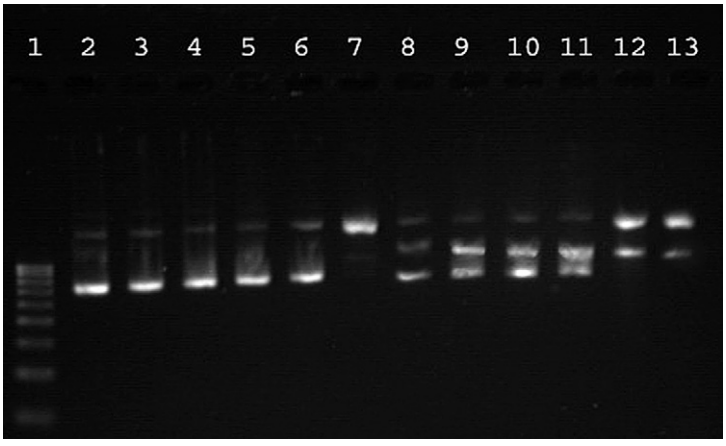


Fig. 7a. Agarose gel (1%) showing the results of electrophoresis of 1 μl of (0.10 μg/ml) pBR 322 plasmid DNA, 2 μl of 0.1 M Tris–HCl (pH 8.0) buffer: 1 μl (1 M) complex in DMF; 10 μl of sterilized distilled water and 2 μl of 9.0 mM H_2O_2 were added, incubation at 37 °C (120 min): Lane 1: Marker; lane 2: DNA (control); lane 3: DNA + H_2O_2 (control); lane 4: DNA + $Cu(RPO)_2$; lane 5: DNA + $Cu(RPO)_2$ + H_2O_2; lane 6: DNA + $[Cu(RPO)_2]Py_2$; lane 7: DNA + $[Cu(RPO)_2]Py_2$ + H_2O_2; lane 8: DNA + $[Cu(RPO)_2]Im_2$; lane 9: DNA + $[Cu(RPO)_2]Im_2$ + H_2O_2; lane 10: DNA + $[Cu(DBO)_2]$; lane 11: DNA + $[Cu(DBO)_2]$ + H_2O_2; lane 12: DNA + $[Cu(DBO)_2]Py_2$; and lane 13: DNA + $[Cu(DBO)_2]Py_2$ + H_2O_2.

Table 6
Selected SC pBR322 DNA cleavage data of copper complexes in Fig. 7a

Lane no.	Reaction condition	Percentage of form I	Percentage of form II	Percentage of form III
2	DNA	92.5	7.5	ND
3	DNA + H_2O_2	92.0	8.0	ND
4	DNA + $Cu(RPO)_2$	79.6	17.1	3.3
5	DNA + $Cu(RPO)_2$ + H_2O_2	69.9	21.9	6.5
6	DNA + $Cu(RPO)_2Py_2$	64.4	34.6	ND
7	DNA + $Cu(RPO)_2Py_2$ + H_2O_2	ND	57.2	39.8
8	DNA + $Cu(RPO)_2Im_2$	51.5	25.2	23.3
9	DNA + $Cu(RPO)_2Im_2$ + H_2O_2	28.5	50.5	21.0
10	DNA + $Cu(DBO)_2$	65.5	21.3	13.2
11	DNA + $Cu(DBO)_2$ + H_2O_2	20.6	45.8	32.4
12	DNA + $Cu(DBO)_2Py_2$	ND	73	27
13	DNA + $Cu(DBO)_2Py_2$ + H_2O_2	ND	51.4	48.6

ND, not detected.

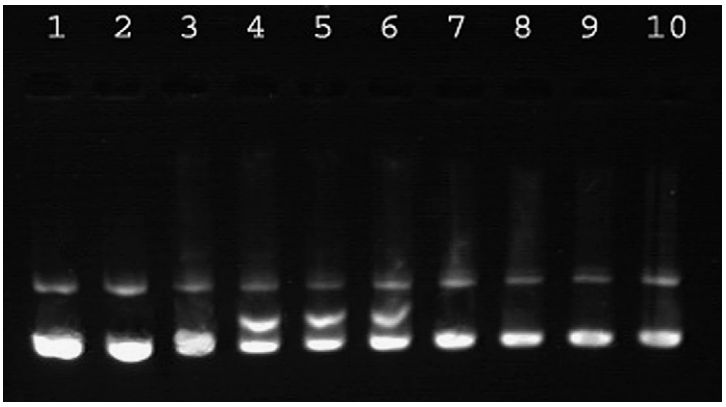


Fig. 7b. Gel electrophoresis diagram for reactions done in the control experiment with an incubation time of 60 min at 37 °C in dark condition with NaN_3 (1 mM) and DMSO (4 μl): Lane 1: DNA; lane 2: DNA + DBO; lane 3: DNA + $CuCl_2$; lane 4: DNA + $[Cu(DBO)_2]Py_2$; lane 5: DNA + $[Cu(DBO)_2]$-Py_2 + DMSO(4 μl); lane 6: DNA + $[Cu(DBO)_2]Py_2$ + NaN_3 (1 mM); lane 7: DNA + RPO; lane 8: DNA + $[Cu(RPO)_2]Py_2$; lane 9: DNA + $[Cu(RPO)_2]$-Py_2 + DMSO(4 μl); and lane 10: DNA + $[Cu(RPO)_2]Py_2$ + NaN_3.

These $OH^{\cdot}$ free radicals participate in the oxidation of the deoxyribose moiety, followed by hydrolytic cleavage of the sugar phosphate backbone [27]. The more pronounced nuclease activity of these adducts in the presence of oxidant as compared to the parent complexes (Fig. 7a, lanes 6–9, 12 and 13) may be due to the increased production of hydroxyl radicals. Even in the absence of oxidant, the mixed ligand complexes exhibit significant DNA cleavage activity when compared to the parent complexes (e.g. lanes 4, 6 and 8). This may be due to the ability of the mixed ligand complexes to associate with DNA, facilitated by aromatic bases (hydrophobic interaction) leading to fair nucleolytic cleavage. From Table 6 it is clear that the percentage of cleavage activity in the presence of oxidant (H_2O_2) follows the order $Cu(RPO)_2Py > Cu(DBO)_2Py > Cu(RPO)_2Im_2$.

The nuclease activity of the complexes has also been investigated in the presence of a free radical scavenger (dimethylsulfoxide) and a singlet oxygen quencher (azide ions). To this end, standard scavengers of reactive oxygen intermediates were included in the electrophoresis process (Fig. 7b). Quantification of the gel afforded the data given in Table 7. Azide (lanes 6 and 10) inhibits to some extent, indicating the involvement of a singlet oxygen in the cleavage activity. The hydroxyl radical scavenger, dimethylsulfoxide (lanes 5 and 9) diminishes the nuclease activity of the compound, which is indicative of the involvement of the hydroxyl radical in the cleavage process. Nuclease activity of the complexes is not completely diminished either in the presence of free radical scavenger or in the presence of singlet oxygen quencher. This means that some DNA is cleaved by other than an oxidative mechanism, possibly by a discernable hydrolytic path.

Table 7
DNA cleavage of pBR 322 by the copper(II)–pyridine adducts (1 mM) in the presence of potential inhibitors (Fig. 7b)

Complex	Percentage of form I	Percentage of form II	Percentage of form III
DNA	87.6	12.4	ND
DBO	85.4	14.6	ND
$CuCl_2$	84.7	15.3	ND
$Cu(DBO)_2Py_2$	52.3	13.4	34.3
$Cu(DBO)_2Py_2$ + DMSO	61.5	7.6	30.9
$Cu(DBO)_2Py_2$ + NaN_3	62.6	14.9	22.5
RPO	80.5	19.5	ND
$Cu(RPO)_2Py_2$	70.7	29.3	ND
$Cu(RPO)_2Py_2$ + DMSO	79.6	20.4	ND
$Cu(RPO)_2Py_2$ + NaN_3	73.8	26.2	ND

ND, not detected.

5. Conclusions

Reports on DNA interactions of copper complexes of polypyridyl and phenanthroline mixed ligand complexes are numerous in the literature, those of interactions of metal oximates and of mixed ligand copper complexes with oximes and aromatic bases have not been investigated so far. In this study, we have attempted to unravel the DNA interactions and cleavage activity of mixed ligand copper complexes. The increase in binding constants of copper complexes II and V compared with the $Cu(SAO)_2$ complex (I) may be due to formation of a strong hydrogen bonding interaction between the coordinated ligands (RPO and DBO). The mixed ligand complex with imidazole appears to be a better DNA binding agent than the corresponding pyridine analogue, possibly due to the additional free nitrogen atom that may facilitate to strengthen the DNA interaction via hydrogen bonding. Since the complexes are found to cleave DNA even in the presences of free radical scavenger (DMSO) and singlet oxygen quencher (NaN_3) these complexes may also be regarded as hydrolytic cleavage agents.

Acknowledgment

Financial support received form the University Grant Commission, New Delhi, India [F12-118/2001] is gratefully acknowledged.

References

[1] (a) M.A. Akbar, S.F. Livingstone, Coord. Chem. Rev. 13 (1974) 101; (b) A. Chakravorthy, Coord. Chem. Rev. 13 (1974) 1.
[2] P.S. Reddy, K.H. Reddy, Polyhedron 19 (2000) 168.
[3] D. Mandal, B.D. Gupta, Organometallics 24 (2005) 1501.
[4] V. Vijaikanth, B.D. Gupta, D. Mandal, S. Shekhar, Organometallics 24 (2005) 4454.
[5] B.D. Gupta, V. Vijaikanth, V. Singh, Organometallics 23 (2004) 2069.
[6] S. Sailaja, M.R. Reddy, K.M. Raju, K.H. Reddy, Indian J. Chem. A 38 (1999) 156.
[7] S. Sailaja, M.R. Reddy, K.M. Raju, K.H. Reddy, Polyhedron 19 (2000) 168.
[8] A. Kumbhar, S. Damle, P. Kulkarni, D. Srinivas, V. Chatur, Indian J. Chem. A 35A (1996) 533.
[9] K.H. Reddy, M.S. Babu, P.S. Babu, S. Dayananda, Indian J. Chem. A 43 (2004) 1233.
[10] K.H. Reddy, P.S. Reddy, P.R. Babu, Transition Met. Chem. 25 (2000) 505.
[11] M.E. Reichmann, S.A. Rice, C.A. Thomas, P. Doty, J. Am. Chem. Soc. 76 (1954) 3047.
[12] A. Wolfe, G.H. Shimer, T. Meehan, Biochemistry 26 (1987) 6392.
[13] M.N. Hughes, W.R. McWhimmie, J. Inorg. Nucl. chem. 28 (1966) 1659.
[14] M.J.M. Campbell, Coord. Chem. Rev. 15 (1975) 277.
[15] L. Sacconi, M. Galimpohni, J. Chem. Soc. (1964) 276.
[16] B.J. Hathaway, Struct. Bond. 14 (1973) 60.
[17] M. Massacesi, D.G. Ponticelli, V.B. Addepalli, V.G. Krishnan, J. Mol. Struct. 48 (1978) 55.
[18] M. Massacesi, D.G. Ponticelli, V.B. Addepalli, V.G. Krishnan, J. Mol. Struct. 51 (1979) 27.
[19] H.R. Gersmann, J.R. Swales, J. Chem. Phys. 36 (1962) 3221.
[20] K.H. Reddy, P.S. Reddy, P.R. Babu, J. Inorg. Biochem. 77 (1999) 169.
[21] A.A. Kumbhar, S.B. Rendye, D.X. West, A.E. Libetra, Transition Met. Chem. 16 (1991) 276.
[22] C.C. Cheng, S.E. Rokita, C.J. Burrows, Angew. Chem., Int. Ed. Engl. 32 (1993) 273.
[23] C.V. Sastri, D. Eswaramoorthy, L. Giribabu, B.G. Maiya, J. Inorg. Biochem. 94 (2003) 138.
[24] L.A. Lipscomb, F.X. Zhou, S.R. Presnell, R.J. Woo, M.E. Peek, R.R. Plaskon, L.D. Williams, Biochemistry 35 (1983) 2818.
[25] J. Liu, H. Zhang, C. Chen, H. Deng, T. Lu, L. Ji, J. Chem. Soc., Dalton Trans. (2003) 114.
[26] K. Yamamoto, S. Kawanishi, J. Biol. Chem. 264 (1984) 15.
[27] P. Merfey, E.R. Robinson, Mutat. Res. 86 (1981) 155.

Available online at www.sciencedirect.com
ScienceDirect
Polyhedron 26 (2007) 581–588
POLYHEDRON
www.elsevier.com/locate/poly

Crystal structure of an unusual bis(fluorous phosphine) ruthenium(III) complex derived from a fluorous Grubbs' catalyst

Rosenildo Corrêa da Costa, Frank Hampel, J.A. Gladysz *

Institut für Organische Chemie, Friedrich-Alexander Universität Erlangen-Nürnberg, Henkestraße 42, 91054 Erlangen, Germany

Received 10 July 2006; accepted 14 August 2006
Available online 26 August 2006

Abstract

Attempted crystallization of $(H_2IMes)RuCl_2(P(CH_2CH_2R_{f8})_3)(=CHPh)$ (H_2IMes = 1,3-dimesityl-4,5-dihydroimidazol-2-ylidene; $R_{f8} = (CF_2)_7CF_3$) in air affords dark red needles of the octahedral ruthenium(III) salt $[H_3IMes]^+$ *trans*-$[RuCl_4(P(CH_2CH_2R_{f8})_3)_2]^-$, which is structurally characterized. Only crystal structures of square planar adducts of fluorous alkylphosphines have been determined to date. The bond lengths and angles associated with the cation and $RuCl_4L_2$ core are similar to those in related compounds. The lattice exhibits fluorous domains unlike those in square planar complexes, and the ponytail conformations are analyzed in detail. The NC*H*N proton of the cation is hydrogen bonded to two chloride ligands of the anion, and the CH_2CH_2 "backside" is directed at two chloride ligands of another anion, leading to non-fluorous channels in the lattice.
© 2006 Elsevier Ltd. All rights reserved.

Keywords: Fluorous; Phosphine; Ruthenium; Crystal structure; Conformation; Helices; Grubbs' catalyst

1. Introduction

With the emergence of fluorous chemistry over the last decade [1], the structures of highly fluorinated sp^3-hybridized segments of atoms have taken on additional significance. Interestingly, in 1997 only two compounds could be located in the Cambridge Crystallographic Database that featured six or more consecutive CF_2 groups [2,3]. Since then, this number has grown appreciably. However, crystalline fluorous molecules still remain somewhat of a rarity. In our research group, all compounds containing R_{fn} segments with $n \geqslant 6$ are structurally characterized as a matter of course ($R_{fn} = (CF_2)_{n-1}CF_3$).

Crystal structures of several metal complexes of fluorous alkylphosphines have been reported [4–6]. Most of these feature square planar metals with two *trans* donor ligands – either fluorous monophosphines [4] or chelating pincer ligands [5]. All exhibit discrete fluorous domains, thereby providing solid state analogies to the commonly observed spontaneous separations of liquid fluorous and organic phases. In this paper, we describe a distinctly new type of fluorous bis(trialkylphosphine) complex, an anionic octahedral ruthenium(III) species, and its crystallographic characterization. The unusual structural and lattice packing properties are analyzed in detail.

2. Results

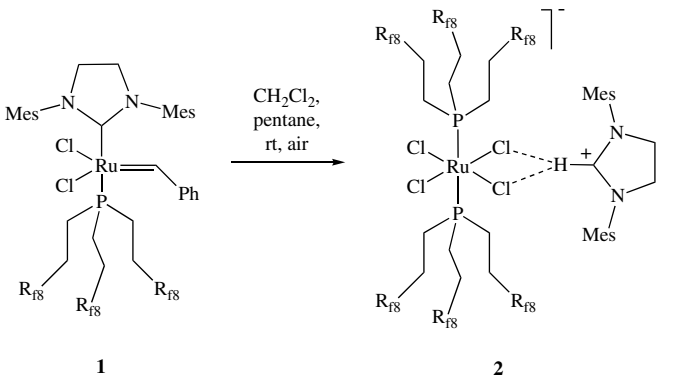
Analogs of Grubbs' second generation catalyst with fluorous trialkylphosphines have recently been reported [7]. A CH_2Cl_2 solution of one of these, $(H_2IMes)RuCl_2(P(CH_2CH_2R_{f8})_3)(=CHPh)$ (**1**; H_2IMes = 1,3-dimesityl-4,5-dihydroimidazol-2-ylidene), was layered with pentane. As shown in Eq. (1), the sample was allowed to slowly concentrate in air. Dark red needles formed, and X-ray data were collected as described in Table 1 and Section 4.

* Corresponding author. Tel.: +49 9131 8522540; fax: +49 9131 8526865.
E-mail address: gladysz@chemie.uni-erlangen.de (J.A. Gladysz).

0277-5387/$ - see front matter © 2006 Elsevier Ltd. All rights reserved.
doi:10.1016/j.poly.2006.08.015

Table 1
Crystallographic data for **2**

Molecular formula	$C_{81}H_{51}Cl_4F_{102}N_2P_2Ru$
Molecular mass	3295.05
Temperature of collection (K)	173(2)
Wavelength (Å)	0.71073
Crystal system	monoclinic
Space group	*C*2/*c*
Unit cell dimensions	
a (Å)	42.1750(9)
b (Å)	11.8440(2)
c (Å)	26.3410(4)
α (°)	90
β (°)	121.1190(11)
γ (°)	90
Volume (Å^3)	11264.4(4)
Z	4
ρ_{calc} (Mg/m^3)	1.943
μ (mm^{-1})	0.477
F(000)	6444
Crystal dimensions (mm)	0.30 × 0.20 × 0.03
Θ Range (°)	2.34–27.48
Range/indices (*h*, *k*, *l*)	−54 to 54; −13 to 15; −34 to 34
Reflections collected	22687
Independent reflections [R_{int}]	12881 [0.0366]
Reflections [$I > 2\sigma(I)$]	8449
Completeness to $\Theta = 27.48°$	99.6%
Maximum and minimum transmission	0.9858 and 0.8702
Refinement method	least-squares on F^2
Data/restraints/parameters	12881/0/868
Goodness-of-fit on F^2	1.011
R Indices [$I > 2\sigma(I)$]	$R_1 = 0.0497$, $wR_2 = 0.1208$
R Indices (all data)	$R_1 = 0.0903$, $wR_2 = 0.1423$
Largest difference in peak/hole (e Å^{-3})	0.799/−0.516



1 **2**

(1)

Refinement gave the unexpected structure depicted in Fig. 1(top). The crystalline material proved to be the salt **2**, with a protonated H_2IMes or dihydroimidazolinium cation, and an octahedral 17-valence-electron ruthenium(III) bis(phosphine) tetrachloride anion. The NC*H*N proton of the $[H_3IMes]^+$ moiety could be located and refined. It was hydrogen bonded to two chloride ligands (*H*–Cl and C–Cl distances, 2.68(5) and 3.455 Å; sum of hydrogen and chlorine van der Waals radii [8], 2.95 Å). The resulting C–H–Ru vector defined a C_2 symmetry axis. The crystal was free of disorder, and the quality of the structure solution was much higher than with many fluorous metal complexes. Key metrical parameters are summarized in Table 2.

The conformations of the $CH_2CH_2R_{f8}$ segments of the symmetry-equivalent phosphine ligands were analyzed. As can be seen in Fig. 1 (bottom), the one starting at C21 (terminating at C30) exhibited an "all-*anti*" conformation, as quantified by the torsion angles summarized in Table 2. The one starting at C11 (terminating at C20) exhibited an initial *anti* CH_2–CH_2–CF_2–CF_2 unit (torsion angle 160.6°), followed by a gauche CH_2–CF_2–CF_2–CF_2 unit (torsion angle 78.8°), and then *anti* CF_2–CF_2–CF_2–CF_2 units (torsion angles 156.3–169.8°). The one starting at C1 also exhibited initial *anti* CH_2–CH_2–CF_2–CF_2 and *gauche* CH_2–CF_2–CF_2–CF_2 units (torsion angles 166.0° and 80.3°), and included a single gauche CF_2–CF_2–CF_2–CF_2 unit (C6–C7–C8–C9; torsion angle 53.3°). These conformations bring two ponytails from one phosphorus in van der Waals contact with one from the other phosphorus, as illustrated in Fig. 2. The van der Waals radius of fluorine is 1.40 (Pauling value)–1.47 Å [8], and the closest intramolecular fluorine–fluorine contact is 2.908 Å (F15A–F24A).

With respect to packing, consider the cation first. As shown in Fig. 3 (top), the CH_2CH_2 "backside" of the dihydroimidazolinium moiety is directed at the two non-hydrogen-bonding chloride ligands of another anion (C–Cl distances 3.706 and 3.744 Å; calculated H–Cl distances, 3.125 and 3.150 Å). This creates non-fluorous channels that propagate throughout the lattice, as illustrated in Fig. 3 (bottom). Two chloride ligands peek out of the fluorous domains in one set of channels (alternating between those that participate in hydrogen bonding and those that do not). The cations emerge from the fluorous regions in another set (alternating between those with the NC*H*N proton pointing up to hydrogen bond to the next anion, and those with the proton pointing down to bond to the anion below). In the fluorous domains, the closest intermolecular fluorine–fluorine contact is 2.681 Å (F14A–F5B).

3. Discussion

3.1. Related ruthenium and imidazolium species

Ruthenium(III) complexes of the general formula Q^+ *trans*-$[RuCl_4L_2]^-$ have been known for some time. One of the first was reported by Stephenson and Wilkinson [9]. They observed that when a red solution of the diamagnetic ruthenium(II) complex $RuCl_2(CO)(pyr)_2$ was allowed to "age" and treated with excess pyridine, the orange paramagnetic ruthenium(III) salt $[pyrH]^+$ *trans*-$[RuCl_4(CO)(pyr)]^-$ could be isolated in 40% yield. Reactions with excesses of phosphines led to species of the formula $[R_3PH]^+$ *trans*-$[RuCl_4(PR_3)_2]^-$ (**Ia**,**b**; Fig. 4). The scope of these reactions was subsequently expanded [10].

Later, imidazolium salts of related complexes with DMSO and imidazole ligands were isolated, as exemplified by **IIa** in Fig. 4 [11]. The crystal structure of **IIa** has not been described, but that of the diamagnetic 18-valence-electron iridium homolog **IIb** has [12,13]. A short contact between one protonated nitrogen of the cation and a

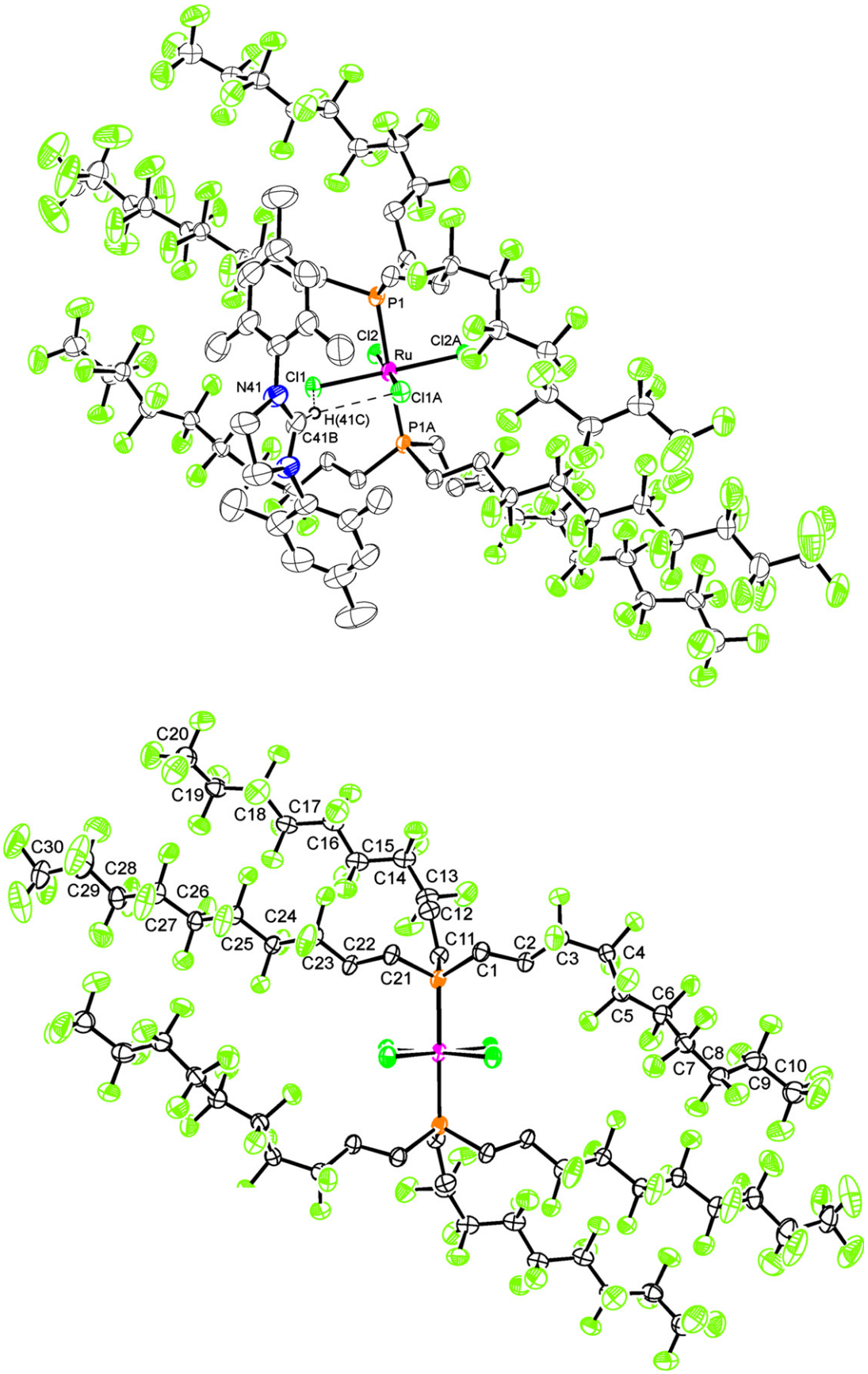


Fig. 1. Molecular structure of **2**: top, full view; bottom, with the cation omitted.

Table 2
Key bond lengths (Å), bond angles (°), and torsion angles (°) for **2**

Ru(1)–Cl(2)	2.3620(8)	P(1)–C(1)	1.828(3)	Cl(1)–H(41C)	2.68(5)
Ru(1)–Cl(1A)	2.3686(8)	P(1)–C(11)	1.832(3)	C(41B)–H(41C)	0.91(6)
Ru(1)–P(1A)	2.3713(9)	P(1)–C(21)	1.834(3)	C(41B)–N(41)	1.308(4)
Cl(2)–Ru(1)–Cl(1A)	178.35(3)	Cl(2)–Ru(1)–P(1A)	88.35(3)	C(11)–P(1)–C(21)	104.01(16)
P(1A)–Ru(1)–P(1)	176.56(4)	Cl(2)–Ru(1)–P(1)	89.21(3)	C(1)–P(1)–Ru(1)	118.52(12)
Cl(2)–Ru(1)–Cl(1)	91.77(3)	Cl(1)–Ru(1)–P(1)	90.68(3)	C(11)–P(1)–Ru(1)	112.18(11)
Cl(2)–Ru(1)–Cl(2A)	89.55(4)	C(1)–P(1)–C(11)	104.33(16)	C(21)–P(1)–Ru(1)	115.93(12)
Cl(1A)–Ru(1)–Cl(1)	86.93(4)	C(1)–P(1)–C(21)	100.06(16)	Ru(1)–Cl(1)–H(41C)	99.2(8)
Cl(1)–Ru(1)–P(1A)	91.82(3)				
P(1)–C(1)–C(2)–C(3)	179.0(2)	P(1)–C(11)–C(12)–C(13)	−174.6(3)	P(1)–C(21)–C(22)–C(23)	−166.5(3)
C(1)–C(2)–C(3)–C(4)	166.0(3)	C(11)–C(12)–C(13)–C(14)	160.6(3)	C(21)–C(22)–C(23)–C(24)	178.0(3)
C(2)–C(3)–C(4)–C(5)	−80.3(4)	C(12)–C(13)–C(14)–C(15)	−78.8(4)	C(22)–C(23)–C(24)–C(25)	−176.8(3)
C(3)–C(4)–C(5)–C(6)	165.4(3)	C(13)–C(14)–C(15)–C(16)	156.3(3)	C(23)–C(24)–C(25)–C(26)	174.3(3)
C(4)–C(5)–C(6)–C(7)	159.2(3)	C(14)–C(15)–C(16)–C(17)	168.7(3)	C(24)–C(25)–C(26)–C(27)	175.4(3)
C(5)–C(6)–C(7)–C(8)	163.3(3)	C(15)–C(16)–C(17)–C(18)	164.3(3)	C(25)–C(26)–C(27)–C(28)	179.9(3)
C(6)–C(7)–C(8)–C(9)	53.3(4)	C(16)–C(17)–C(18)–C(19)	169.8(3)	C(26)–C(27)–C(28)–C(29)	−167.8(4)
C(7)–C(8)–C(9)–C(10)	161.8(3)	C(17)–C(18)–C(19)–C(20)	169.3(3)	C(27)–C(28)–C(29)–C(30)	−164.7(4)
F(3A)–C(3)–C(4)–F(4A)	−81.9(3)	F(5B)–C(5)–C(6)–F(6A)	158.5(3)	F(8A)–C(8)–C(9)–F(9A)	164.5(3)
F(3A)–C(3)–C(4)–F(4B)	35.6(4)	F(5B)–C(5)–C(6)–F(6B)	−83.4(3)	F(8A)–C(8)–C(9)–F(9B)	46.1(4)
F(3B)–C(3)–C(4)–F(4A)	166.4(3)	F(6A)–C(6)–C(7)–F(7A)	−76.6(4)	F(8B)–C(8)–C(9)–F(9A)	−79.1(4)
F(3B)–C(3)–C(4)–F(4B)	−76.1(3)	F(6A)–C(6)–C(7)–F(7B)	166.3(3)	F(8B)–C(8)–C(9)–F(9B)	162.5(3)
F(4A)–C(4)–C(5)–F(5A)	−78.5(3)	F(6B)–C(6)–C(7)–F(7A)	165.0(3)	F(9A)–C(9)–C(10)–F(10A)	70.1(4)
F(4A)–C(4)–C(5)–F(5B)	165.2(2)	F(6B)–C(6)–C(7)–F(7B)	47.9(4)	F(9A)–C(9)–C(10)–F(10B)	50.0(5)
F(4B)–C(4)–C(5)–F(5A)	164.7(3)	F(7A)–C(7)–C(8)–F(8A)	51.2(4)	F(9B)–C(9)–C(10)–F(10A)	46.1(5)
F(4B)–C(4)–C(5)–F(5B)	48.5(3)	F(7A)–C(7)–C(8)–F(8B)	−64.4(3)	F(9B)–C(9)–C(10)–F(10B)	166.2(3)
F(5A)–C(5)–C(6)–F(6A)	42.8(4)	F(7B)–C(7)–C(8)–F(8A)	166.4(3)	F(9A)–C(9)–C(10)–F(10C)	170.5(3)
F(5A)–C(5)–C(6)–F(6B)	160.9(3)	F(7B)–C(7)–C(8)–F(8B)	50.7(4)	F(9B)–C(9)–C(10)–F(10C)	−73.3(4)
F(13A)–C(13)–C(14)–F(14A)	167.4(3)	F(15B)–C(15)–C(16)–F(16A)	−74.9(4)	F(18A)–C(18)–C(19)–F(19A)	51.8(4)
F(13A)–C(13)–C(14)–F(14B)	−76.4(4)	F(15B)–C(15)–C(16)–F(16B)	167.0(3)	F(18A)–C(18)–C(19)–F(19B)	169.8(3)
F(13B)–C(13)–C(14)–F(14A)	−79.9(4)	F(16A)–C(16)–C(17)–F(17A)	46.4(4)	F(18B)–C(18)–C(19)–F(19A)	168.7(3)
F(13B)–C(13)–C(14)–F(14B)	36.3(4)	F(16A)–C(16)–C(17)–F(17B)	164.6(3)	F(18B)–C(18)–C(19)–F(19B)	−73.3(4)
F(14A)–C(14)–C(15)–F(15A)	−86.1(4)	F(16B)–C(16)–C(17)–F(17A)	164.8(3)	F(19A)–C(19)–C(20)–F(20A)	167.0(3)
F(14A)–C(14)–C(15)–F(15B)	157.0(3)	F(16B)–C(16)–C(17)–F(17B))	−77.1(4)	F(19A)–C(19)–C(20)–F(20B)	−71.9(4)
F(14B)–C(14)–C(15)–F(15A)	157.9(3)	F(17A)–C(17)–C(18)–F(18A)	−72.2(4)	F(19B)–C(19)–C(20)–F(20A)	51.0(4)
F(14B)–C(14)–C(15)–F(15B)	41.0(4)	F(17A)–C(17)–C(18)–F(18B)	169.6(3)	F(19B)–C(19)–C(20)–F(20B)	172.1(3)
F(15A)–C(15)–C(16)–F(16A)	168.6(3)	F(17B)–C(17)–C(18)–F(18A)	170.1(3)	F(19A)–C(19)–C(20)–F(20C)	48.4(4)
F(15A)–C(15)–C(16)–F(16B)	50.5(4)	F(17B)–C(17)–C(18)–F(18B)	52.0(4)	F(19B)–C(19)–C(20)–F(20C)	−67.6(4)
F(23A)–C(23)–C(24)–F(24A)	−178.6(3)	F(25B)–C(25)–C(26)–F(26A)	174.5(3)	F(28A)–C(28)–C(29)–F(29A)	−45.3(5)
F(23A)–C(23)–C(24)–F(24B)	−62.5(4)	F(25B)–C(25)–C(26)–F(26B)	−67.7(4)	F(28A)–C(28)–C(29)–F(29B)	−163.3(4)
F(23B)–C(23)–C(24)–F(24A)	66.9(4)	F(26A)–C(26)–C(27)–F(27A)	−62.2(4)	F(28B)–C(28)–C(29)–F(29A)	−161.0(4)
F(23B)–C(23)–C(24)–F(24B)	−176.9(3)	F(26A)–C(26)–C(27)–F(27B)	−179.9(3)	F(28B)–C(28)–C(29)–F(29B)	81.0(5)
F(24A)–C(24)–C(25)–F(25A)	−68.8(3)	F(26B)–C(26)–C(27)–F(27A)	−179.0(3)	F(29A)–C(29)–C(30)–F(30A)	−48.8(6)
F(24A)–C(24)–C(25)–F(25B)	174.1(3)	F(26B)–C(26)–C(27)–F(27B)	63.2(4)	F(29A)–C(29)–C(30)–F(30B)	−166.5(5)
F(24B)–C(24)–C(25)–F(25A)	175.0(3)	F(27A)–C(27)–C(28)–F(28A)	74.4(4)	F(29B)–C(29)–C(30)–F(30A)	67.2(6)
F(24B)–C(24)–C(25)–F(25B)	57.9(4)	F(27A)–C(27)–C(28)–F(28B)	−169.1(3)	F(29B)–C(29)–C(30)–F(30B)	−50.5(6)
F(25A)–C(25)–C(26)–F(26A)	57.6(4)	F(27B)–C(27)–C(28)–F(28A)	−168.9(4)	F(29A)–C(29)–C(30)–F(30C)	71.3(6)
F(25A)–C(25)–C(26)–F(26B)	175.3(3)	F(27B)–C(27)–C(28)–F(28B)	−52.5(4)	F(29B)–C(29)–C(30)–F(30C)	−172.8(5)

chloride ligand was noted (3.21(1) Å). The crystal structure of the analogous ruthenium complex with a thiazole ligand and thiazolium cation, **IIc**, has also been reported [14]. The closest contact between the protonated nitrogen and a chloride ligand in **IIc** is 4.18 Å.

To our knowledge, only two salts with anions of the formulae $[RuCl_4(PR_3)_2]^-$ have been structurally characterized, **Ic** and **Id** (Fig. 4) [15,16]. Both feature polymetallic cations that do not allow the possibility of hydrogen bonding, and were obtained in low yield in the course of exploratory synthetic studies. Despite the lack of hydrogen bonding, these represent the best available structural models for the ruthenium core in **2**. Complex **Ic** exhibits ruthenium–chlorine bond lengths of 2.361(4)–2.367(4) Å, ruthenium–phosphorus bond lengths of 2.372(5) Å, and bond angles between *cis* atoms ranging from 88.2(2)° to 91.8(2)°. The corresponding values for **Id** are 2.350(1)–2.365(1) Å, 2.417(1) Å, and 87.58(5)–94.01(4)°. These compare very closely to the ruthenium–chlorine bond lengths (2.3620(8)–2.3686(8) Å), ruthenium–phosphorus bond lengths (2.3713(9) Å), and bond angles between *cis* atoms (86.93(4)–91.82(3)°) in **2**.

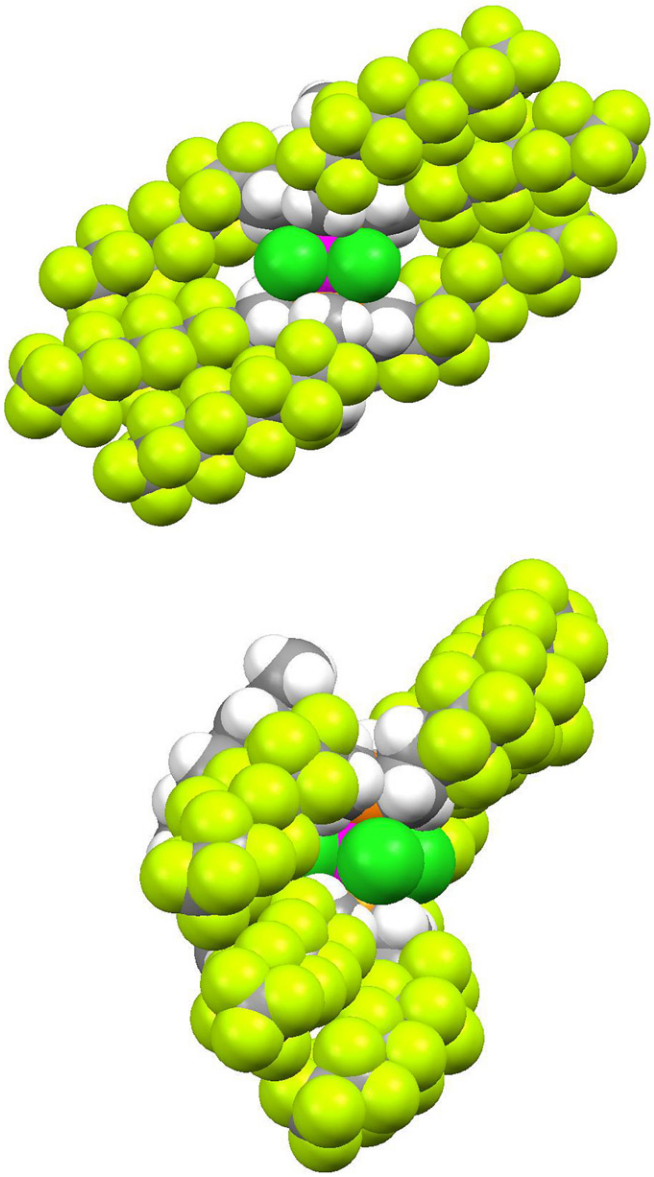
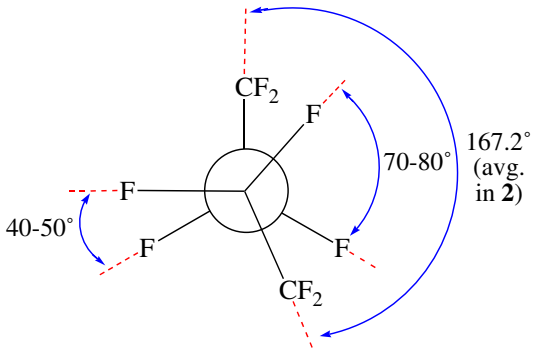


Fig. 2. Space filling representations of **2**: top, from the side of the chloride ligands that do not hydrogen bond to the cation; bottom, top view rotated counter-clockwise about a vertical axis.

There are an enormous number of structurally characterized imidazolium salts that exhibit hydrogen bonding. To our knowledge, no crystal structures containing protonated H_2IMes have been determined. However, there are at least two crystal structures that contain the dehydrogenated analog, protonated IMes [17–19]. One of these exhibits hydrogen bonding between the NC*H*N proton and a phenolate anion [17,18]. Interestingly, a CH=CH proton of the five membered ring interacts with the π cloud of a phenolate anion of a neighboring ion pair. This is reminiscent of the double-faced interaction of the $[H_3IMes]^+$ moiety in Fig. 3 (top). The other structure involves hydrogen bonding to a thiolate ligand of an aluminum-based anion [19]. The C⋯N distances in these compounds (1.330(3)–1.343(2) Å) are slightly longer than in **2** (1.308(4) Å), consistent with delocalization of the nitrogen lone pairs over a more extensive unsaturated framework.

3.2. Conformational and preparative aspects

It is now well-established that the lowest energy (*anti*) conformations of *n*-perfluoroalkanes and perfluoroalkyl groups exhibit C–C–C–C torsion angles somewhat less than those of *n*-alkanes (ca. 166° versus 180°), as illustrated by **III** [20,21]. This relieves certain electrostatically repulsive interactions, and leads to new attractive interactions [21]. Accordingly, the torsion angles of the *anti* CF_2–CF_2–CF_2–CF_2 segments of **2** (Table 2) average 167.2°. This imparts a slight twist, and the twists propagate with the same clockwise or counter-clockwise sense to give helical $(CF_2)_n$ moieties. As expected from **III**, the average torsion angles of the *anti* F–CF_2–CF_2–F segments in **2** (168.1°) are also somewhat less than their counterparts in *n*-alkanes (180°). Furthermore, the torsion angles of the *gauche* F–CF_2–CF_2–F segments generally fall into two regimes, one of ca. 40–50° and the other of ca. 70–80°.



III

As can be seen in Fig. 2, the two ponytails from each phosphorus atom that pack nearly in van der Waals contact exhibit the opposite helical chirality. The third adjacent ponytail, originating from the other phosphorus atom, contains the unique gauche CF_2–CF_2–CF_2–CF_2 segment. Helical relationships between ponytails from different molecules were not examined. Recently, the helical nature of fluorous ponytails has been exploited in supramolecular phenomena [22,23], and shown to persist in solution through VCD measurements [24].

Three square planar complexes containing *trans* fluorous trialkylphosphines have been structurally characterized: *trans*-$RhCl(CO)(P((CH_2)_2R_{f6})_3)_2$ [4a,4b], the iridium analog *trans*-$IrCl(CO)(P((CH_2)_2R_{f6})_3)_2$ [4a], and *trans*-$PtCl_2(P((CH_2)_2R_{f6})_3)_2$ [4e]. In the first two, which are isostructural, four of the ponytails are approximately coplanar, with two extending in an all-*anti* conformation from each phosphorus atom perpendicular to the coordination plane – one above and one below. As shown in Fig. 5 (left stack), the remaining two ponytails extend on a common side of the plane of the other four, and contain *gauche* CH_2–CF_2–

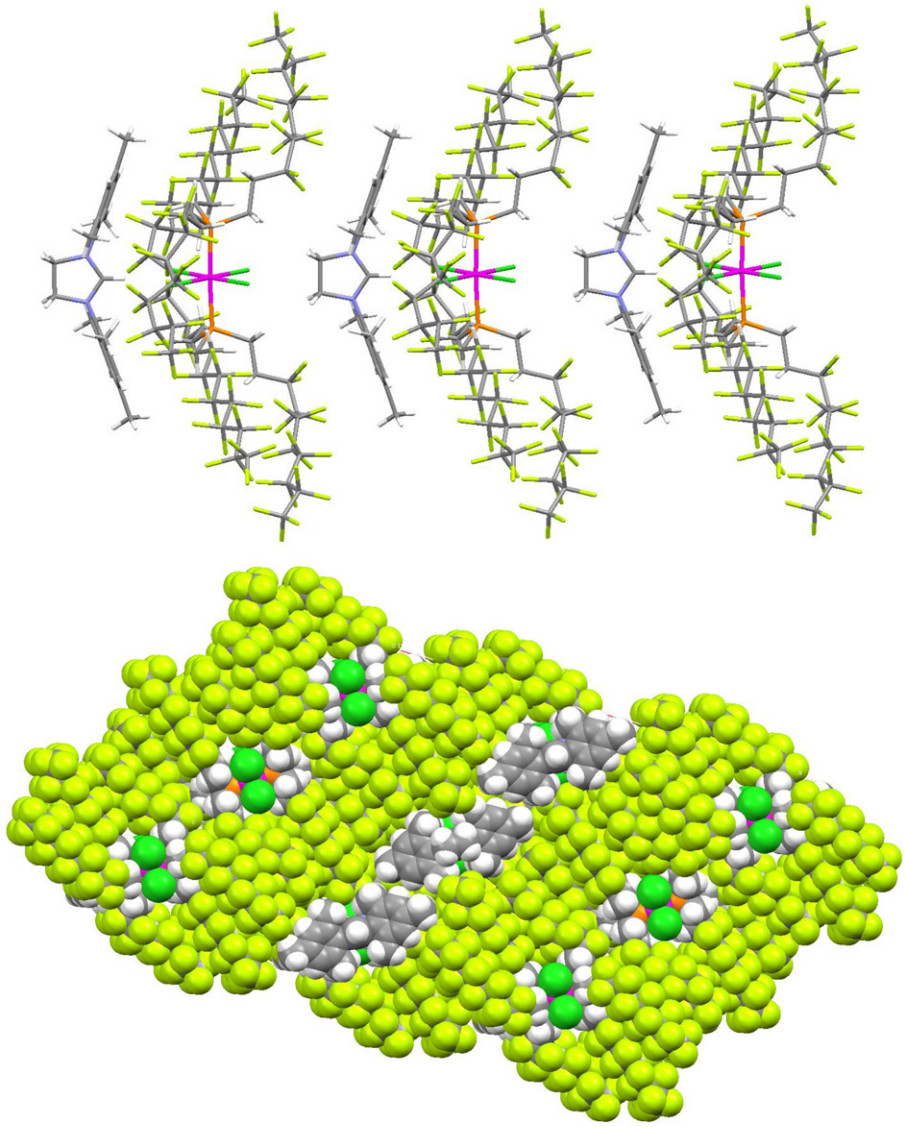
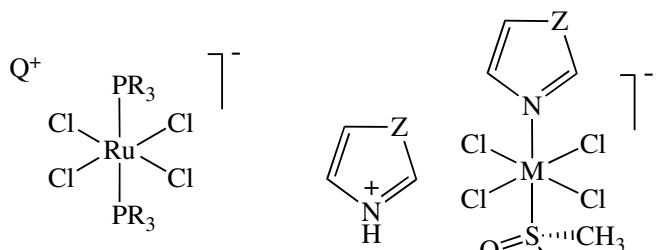


Fig. 3. Packing diagrams for **2**: top, relationship of the cation to the chloride ligands; bottom, fluorous and non-fluorous domains.



I

PR_3 / Q^+ =
a, Et_3P / Et_3PH^+
b, Et_2PhP / Et_2PhPH^+
c, Et_3P / $[Ru_3Cl_6(PEt_3)_6]^+$
d, Ph_3P / $[Ru_6S_8(PPh_3)_6]^+$

II

M / Z =
a, Ru / NH
b, Ir / NH
c, Ru / S

Fig. 4. Other relevant ruthenium(III) tetrachloride complexes.

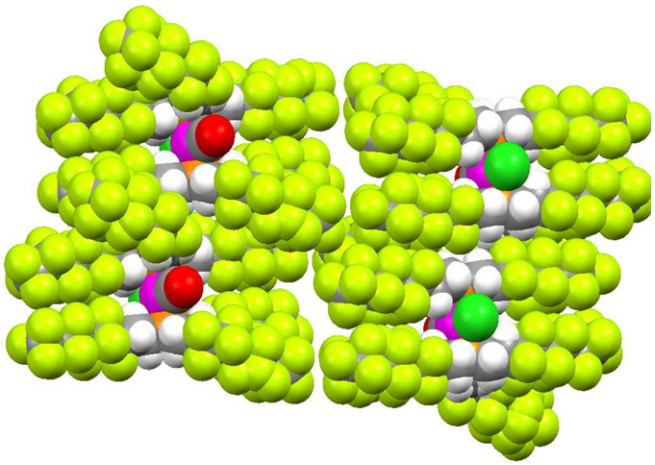


Fig. 5. Packing motif for square-planar complexes of the formula *trans*-$MCl(CO)(P(CH_2)_2R_{f6})_2$ (M = Rh (depicted), Ir). The coordination plane is roughly perpendicular to the plane of the paper.

CF_2–CF_2 linkages. They are splayed in a manner that allows a sandwich-like fit with two comparable chains of a second molecule, leaving a rather flat backside (right stack, Fig. 5). The *anti*/*gauche* sequences within the ponytails of the platinum complex are identical, but the P–M–P conformation differs, resulting in a different packing arrangement.

This study adds to growing number of cases where a small amount of an interesting and unexpected inorganic complex, obtained by serendipity, could be unambiguously characterized due to the ease of modern crystallographic techniques. Perhaps analogous oxidation products will be obtained from other ruthenium(II) metathesis catalysts in the future. Although the syntheses of the ruthenium(III) tetrachloride complexes in Fig. 4 often proceed in modest yields, it is highly probable that an efficient, directed synthesis of **2** or a salt with an alternative cation could be achieved. While this would be beyond the scope of the present work, it should be noted that ruthenium(III) complexes – including several imidazolium salts of *trans*-$[RuCl_4L_2]^-$ anions – have gained prominence as anti-cancer agents [25]. Species such as **2** would have distinctly different phase and redox properties that could be beneficial with respect to physiological transport and the proposed mechanisms of activation [25].

4. Experimental

Crystallography: A CH_2Cl_2 solution of **1** [7] was layered with pentane and kept in air at room temperature. After 4 d, dark red needles were taken to a Nonius KappaCCD diffractometer for data collection as outlined in Table 1. Cell parameters were obtained from 10 frames using a 10° scan and refined with 12225 reflections. Lorentz, polarization and empirical absorption corrections [26] were applied. The space group was determined from systematic absences and subsequent least-squares refinement. The structure was solved by direct methods. The parameters were refined with all data by full-matrix-least-squares on F^2 using SHELXL-97 [27]. Non-hydrogen atoms were refined with anisotropic thermal parameters. The hydrogen atom H41C was located and refined isotropically. Other hydrogen atoms were fixed in idealized positions using a riding model. Scattering factors were taken from the literature [28]. The unanticipated structure **2** exhibited a twofold symmetry axis.

Acknowledgements

We thank the Deutsche Forschungsgemeinschaft (DFG, GL 300/3-3) and Johnson Matthey PMC (precious metal loans) for support.

Appendix A. Supplementary material

CCDC 613200 contains the supplementary crystallographic data for **2**. These data can be obtained free of charge via http://www.ccdc.cam.ac.uk/conts/retrieving.html, or from the Cambridge Crystallographic Data Centre, 12 Union Road, Cambridge CB2 1EZ, UK; fax: +44 1223 336 033; or e-mail: deposit@ccdc.cam.ac.uk. Supplementary data associated with this article can be found, in the online version, at doi:10.1016/j.poly.2006.08.015.

References

[1] J.A. Gladysz, D.P. Curran, I.T. Horváth (Eds.), Handbook of Fluorous Chemistry, Wiley/VCH, Weinheim, 2004.
[2] M.-A. Guillevic, A.M. Arif, I.T. Horváth, J.A. Gladysz, Angew. Chem., Int. Ed. Engl. 36 (1997) 1612.
[3] (a) From Ref. [9] in Ref. [2]: P. Kromm, J.-P. Bideau, M. Cotrait, C. Destrade, H. Nguyen, Acta Crystallogr. C50 (1994) 112;
(b) C.R. Jablonski, Z. Zhou, Can. J. Chem. 70 (1992) 2544.
[4] (a) M.-A. Guillevic, C. Rocaboy, A.M. Arif, I.T. Horváth, J.A. Gladysz, Organometallics 17 (1998) 707;
(b) J. Fawcett, E.G. Hope, R.D.W. Kemmitt, D.R. Paige, D.R. Russell, A.M. Stuart, D.J. Cole-Hamilton, M.J. Payne, J. Chem. Soc., Chem. Commun. (1997) 1127;
(c) C.M. Haar, J. Huang, S.P. Nolan, Organometallics 17 (1998) 5018;
(d) D.C. Smith Jr., E.D. Stevens, S.P. Nolan, Inorg. Chem. 38 (1999) 5277;
(e) R.T. Stibrany, S.M. Gorun, J. Organomet. Chem. 579 (1999) 217.
[5] (a) R. Tuba, V. Tesevic, L.V. Dinh, F. Hampel, J.A. Gladysz, Dalton Trans. (2005) 2275;
(b) C.S. Consorti, F. Hampel, J.A. Gladysz, Inorg. Chim. Acta 359 (2006), in press, doi:10.1016/j.ica.2006.07.092.
[6] (a) Crystal structures of metal complexes of fluorous arylphosphines or phosphites: J. Fawcett, E.G. Hope, R.D.W. Kemmitt, D.R. Paige, D.R. Russel, A.M. Stuart, J. Chem. Soc., Dalton Trans. (1998) 3751;
(b) J. Fawcett, E.G. Hope, D.R. Russel, A.M. Stuart, D.R.W. Wood, Polyhedron 20 (2001) 321;
(c) B. Croxtall, J. Fawcett, E.G. Hope, A.M. Stuart, J. Chem. Soc., Dalton Trans. (2002) 491;
(d) D.J. Adams, D. Gudmunsen, J. Fawcett, E.G. Hope, A.M. Stuart, Tetrahedron 58 (2002) 3827;
(e) E. de Wolf, A.L. Spek, B.W.M. Kuipers, A.P. Philipse, J.D. Meeldijk, P.H.H. Bomans, P.M. Frederik, B.-J. Deelman, G. van Koten, Tetrahedron 58 (2002) 3911.
[7] R.C. da Costa, J.A. Gladysz, Chem. Commun. (2006) 2619.
[8] A. Bondi, J. Phys. Chem. 68 (1964) 441.
[9] T.A. Stephenson, G. Wilkinson, J. Inorg. Nucl. Chem. (1966) 945.
[10] T.A. Stephenson, J. Chem. Soc. (A) (1970) 889.
[11] M. Ravera, S. Baracco, C. Cassino, P. Zanello, D. Osella, Dalton Trans. (2004) 2347, and references cited therein.
[12] L. Messori, G. Marcon, P. Orioli, M. Fontani, P. Zanello, A. Bergamo, G. Sava, P. Mura, J. Inorg. Biochem. 95 (2003) 37.
[13] Crystal structure of sodium salt corresponding to **IIa**: E. Alessio, G. Balducci, A. Lutman, G. Mestroni, M. Calligaris, W.M. Attia, Inorg. Chim. Acta 203 (1993) 205.
[14] P. Mura, M. Camalli, L. Messori, F. Piccioli, P. Zanello, M. Corsini, Inorg. Chem. 43 (2004) 3863.
[15] F.A. Cotton, R.C. Torralba, Inorg. Chem. 30 (1991) 4386.
[16] M. Wunder, A.L. Eckermann, T.B. Rauchfuss, D.Z. Fenske, Anorg. Allg. Chem. 631 (2005) 131.
[17] J.A. Cowan, J.A.C. Clyburne, M.G. Davidson, R.L.W. Harris, J.A.K. Howard, P. Küpper, M.A. Leech, S.P. Richards, Angew. Chem., Int. Ed. 41 (2002) 1432.
[18] J.A. Cowan, J.A.C. Clyburne, M.G. Davidson, R.L.W. Harris, J.A.K. Howard, P. Küpper, M.A. Leech, S.P. Richards, Angew. Chem. 114 (2002) 1490.
[19] V. Jancik, H.W. Roesky, Inorg. Chem. 44 (2005) 5556.

[20] (a) B. Albinsson, J. Michl, J. Phys. Chem. 100 (1996) 3418;
(b) J.D. Dunitz, A. Gavezzotti, W.B. Schweizer, Helv. Chim. Acta 86 (2003) 4073.
[21] S.S. Jang, M. Blanco, W.A. Goddard III, G. Caldwell, R.B. Ross, Macromolecules 36 (2003) 5331.
[22] A. Casnati, R. Liantonio, P. Metrangolo, G. Resnati, R. Ungaro, F. Ugozzoli, Angew. Chem., Int. Ed. 45 (2006) 1915.
[23] A. Casnati, R. Liantonio, P. Metrangolo, G. Resnati, R. Ungaro, F. Ugozzoli, Angew. Chem. 118 (2006) 1949.
[24] K. Monde, N. Miura, M. Hashimoto, T. Taniguchi, T. Inabe, J. Am. Chem. Soc. 128 (2006) 6000.
[25] M.J. Clarke, F. Zhu, D.R. Frasca, Chem. Rev. 99 (1999) 2511.
[26] (a) "Collect" Data Collection Software, Nonius B.V., 1998.;
(b) "Scalepack" Data Processing Software: Z. Otwinowski, W. Minor, in: Methods in Enzymology 1997, 276 (Macromolecular Crystallography, Part A), 307.
[27] G.M. Sheldrick, SHELX-97, Program for Refinement of Crystal Structures, University of Göttingen, 1997.
[28] D.T. Cromer, J.T. Waber, in: J.A. Ibers, W.C. Hamilton (Eds.), International Tables for X-ray Crystallography, Kynoch, Birmingham, England, 1974.

Available online at www.sciencedirect.com
ScienceDirect
Polyhedron 26 (2007) 589–599
POLYHEDRON
www.elsevier.com/locate/poly

Electrostatic forces that determine O,O-*trans* versus O,S-*cis* conformers in the aminated porphyrin complexes of Cd(N-NHCO-2-C_4H_3O-tpp)(OAc) and Cd(N-NHCO-2-C_4H_3S-tpp)(OAc)

Jo-Yu Tung [a,*], Jyh-Horung Chen [b]

[a] *Department of Occupational Safety and Health, Chung Hwai College of Medical Technology, Tainan 713, Taiwan*
[b] *Department of Chemistry, National Chung Hsing University, Taichung 40227, Taiwan*

Received 8 June 2006; accepted 14 August 2006
Available online 19 September 2006

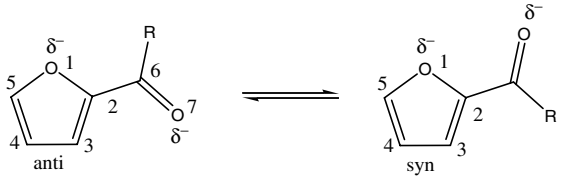
Abstract

Two new diamagnetic, mononuclear and aminated porphyrin complexes of O,O-*trans*-Cd (**3**-*trans*) and O,S-*cis*-Cd (**4**-*cis*) have been synthesized and characterized by ^1H, ^{13}C NMR spectroscopy. The crystal structures of (acetato)(N-2-furancarboxamido-*meso*-tetraphenylporphyrinato)cadmium(II) [Cd(N-NHCO-2-C_4H_3O-tpp)(OAc); **3**-*trans*] and (acetato)(N-2-thiophenecarboxamido-*meso*-tetraphenylporphyrinato)cadmium(II) [Cd(N-NHCO-2-C_4H_3S-tpp)(OAc); **4**-*cis*] were determined. The coordination sphere around Cd^{2+} is a distorted square-based pyramid in which the apical site is occupied by a bidentate chelating OAc^- group for **3**-*trans* and **4**-*cis*. The plane of three pyrrole nitrogen atoms [i.e., N(1), N(2), N(4) for **3**-*trans* and N(1), N(2), N(3) for **4**-*cis*] strongly bonded to Cd^{2+} is adopted as a reference plane 3N. The N(3) and N(4) pyrrole rings bearing the 2-furancarboxamido (Fr) and 2-thiophenecarboxamido groups in **3**-*trans* and **4**-*cis*, respectively, deviate mostly from the 3N plane, thus orienting separately with a dihedral angle of 33.4° and of 31.0°. In **3**-*trans*, Cd^{2+} and N(5) are located on different sides at 1.06 and −1.49 Å from its 3N plane, while in **4**-*cis*, Cd^{2+} and N(5) are also located on different sides at 1.04 and −1.53 Å from its 3N plane. An attractive electrostatic interaction between the Cd^{2+} and $O(4)^-$ atoms in furan stabilizes the O,O-*trans* conformer of **3**. A repulsive electrostatic interaction between Cd^{2+} and $S(1)^+$ destabilizes the O,S-*trans* conformer of **4**. Both of these repulsive and the mutually attractive interactions between $S(1)^+$ and $O(3)^-$ atoms favor the O,S-*cis* rotamer of **4** both in the vapor phase and in low polarity solvents. NOE difference spectroscopy, HMQC and HMBC were employed for the unambiguous assignment of the ^1H and ^{13}C NMR resonances of **3**-*trans* and **4**-*cis* in $CDCl_3$ at 20 and −50 °C.
© 2006 Published by Elsevier Ltd.

Keywords: Cadmium; X-ray diffraction; Electrostatic interaction; O,O-*trans*; O,S-*cis* conformer

1. Introduction

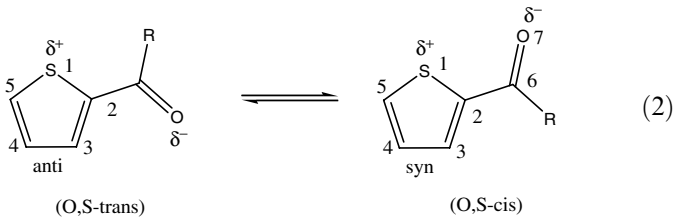
There have been numerous investigations on the rotational equilibrium between the two *anti* and *syn* planar isomers of 2-acyl-furans and -thiophenes (i.e., R = H, CH_3, Et, Pr^i, pentan-3-yl, Bu^t, Cl, F, Bu^tO) [1–6]



(O,O-trans) (O,O-cis) (1)

* Corresponding author. Tel.: +886 6 2674567x815; fax: +886 6 2894028.
E-mail address: joyuting@mail.hwai.edu.tw (J.-Y. Tung).

0277-5387/$ - see front matter © 2006 Published by Elsevier Ltd.
doi:10.1016/j.poly.2006.08.034



(O,S-trans) (O,S-cis) (2)

Group charge density calculations reveal that both oxygen atoms in 2-acyl-furans of the *syn* form, being strongly charged, face increasing repulsive electrostatic interactions (see Eq. (1)). However, in the thiophene carbonyl derivatives, the S atom is positively charged and consequently there is an attractive electrostatic interaction between the S and O atoms in *cis* form (see Eq. (2)) [1]. The major factor determining the stability or instability of the *cis*-isomer is a repulsive electrostatic interaction between the two oxygen atoms for furan carbonyl and an attractive electrostatic interaction between the sulfur and oxygen atoms for the thiophene carbonyl. The O,O-*trans* form has a relatively low dipole moment and is favored in the gas phase or in low polar solvents with dielectric constants (ε) smaller than 5. In a more polar medium, the O,O-*cis* isomer with a higher dipole moment (μ) is favored due to a stronger solute–solvent interaction; as a result the O,O-*cis* form in 2-acyl-furans can be more stable than the O,O-*trans* isomer in solution when the energy difference ΔE ($=E_{syn}-E_{anti}$) is relatively small and $\Delta\mu$ ($=\mu_{syn}-\mu_{anti}$) is large in the gas phase. In the case of the thiophene-2-carbonyl derivative, the more polar O,S-*cis* conformation is found to be more stable in the vapor phase; the *cis* form also predominates in solutions of different polarity; the amount of O,S-*cis* isomer increases slightly with solvent polarity. The energy differences (ΔE) between the rotamers are 4–13 kJ/mol, but the barrier to rotation is ca. 42 kJ/mol [1].

The preparation of *N*-substituted-*N*-aminoporphyrin has been described by three groups [7–11]. In *N*-substituted-*N*-aminoporphyrin, when the H atom of NH_2 is replaced either by the 2-furoncarboxyamino ligand or by the 2-thiophenecarboxyamino group, two new free aminated porphyrins are formed, namely N-2-furancarboxamido-*meso*-tetraphenylporphyrin (N-NHCO-2-C_4H_3-OHtpp; **1**) and N-2-thiophenecarboxamido-*meso*-tetraphenylporphyrin (N-NHCO-2-C_4H_3S-Htpp; **2**) [tpp = dianion of *meso*-tetraphenylporphyrin], which are derivatives of 2-acyl-furans and -thiophenes, respectively. A thorough review of the literature shows that there is no prior report on the metal complexes of **1** and **2**. The lack of previous work on metal complexes of these two ligands prompted us to undertake the synthesis and structural studies of the Cd(II) complexes. Metallation of these aminated porphyrins could lead to mononuclear metal complexes in which the metal is coordinated to four porphyrinic N atoms. Cd(II) is a diamagnetic ion and maintains the d^{10} electron configuration which minimizes intrinsic coordination geometry preferences while favoring coordination by softer ligands. In this paper, we describe the X-ray structural investigation on the metallation of **1** and **2** leading to mononuclear complexes of (acetato)(N-2-furancarboxamido-*meso*-tetraphenylporphyrinato)cadmium(II) [Cd(N-NHCO-2-C_4H_3O-tpp)(OAc); **3**] and (acetato)(N-2-thiophenecarboxamido-*meso*-tetraphenylporphyrinato)cadmium(II) [Cd(N-NHCO-2-C_4H_3S-tpp)(OAc); **4**], respectively. This metallation introduces the metal electrostatic interaction between the Cd(II) atom and the heteroatom of the ring in **3** and **4** as the diamagnetic Cd(II) is just located in the vicinity of the furonylcarboxamido (or thiophenecarboxamido) group in **3** (or **4**). We try to figure out how the metal electrostatic effect influences the O,O-Cd and O,S-Cd conformers of **3** and **4**, respectively. These metal electrostatic effects could be applied to explain the various conformations of thallium(III), bismuth(III) and tin(IV) porphyrin complexes with O,O and O,S rotamers.

2. Experimental

2.1. N-NHCO-2-C_4H_3O-Htpp (1) [9]

A mixture of NaN_3 (1.00 g, 1.54×10^{-2} mol) in distilled water (2 cm^3) and 2-furoyl chloride (2.5 mL, 2.54×10^{-2} mol) was stirred for 30 min. After concentration, the residue was dissolved in CH_2Cl_2 and filtered to remove excess NaN_3 and NaCl. The CH_2Cl_2 layer contained 2-furancarbonyl azide ($C_4H_3OCON_3$). A solution of Zn(tpp) (0.30 g, 1.36×10^{-3} mol) and the above $C_4H_3OCON_3$ in CH_2Cl_2 (100 cm^3) in a stoppered 250 mL Erlenmeyer flask was left for ca. 24 h in the sunlight. To this solution was then added 0.5 N HCl (250 cm^3) with vigorous shaking for 0.5 h. The organic layer, green in color, was separated, solid ammonium carbonate was added to it, and then dried with anhydrous Na_2SO_4. The excess $(NH_4)_2CO_3$ and Na_2SO_4 were removed by filtration. After concentration, the residue was dissolved in a minimum of CH_2Cl_2 and chromatographed on silica gel (50.00 g, 70–230 mesh). The dimensions of the silica gel column were 1.5×17 in. The desired compound was eluted with ethyl acetate (EtOAc)–CH_2Cl_2 [1:9 (v/v)] as a dark purple band on silica gel. Removal of the solvent and recrystallization from CH_2Cl_2–MeOH [1:2 (v/v)] gave the purple solid N-NHCO-2-C_4H_3O-Htpp (**1**) (0.165 g, 2.28×10^{-4} mol, 46.8%), which was again dissolved in CH_2Cl_2 and layered with CH_3OH to get purple crystals for single crystal X-ray analysis. ^{1}H NMR (599.95 MHz, $CDCl_3$, 20 °C): δ 9.12 [d, H_β(10,19), ^3J(H–H) = 4.4 Hz], H_β(a,b) represents two equivalent β-pyrrole protons attached to carbons a and b, respectively; 8.90 [d, H_β(9,20), ^3J(H–H) = 4.8 Hz]; 8.88 [s, H_β(4,5)]; 8.35 [bs, *o*′-H(34,44) and *o*′-H(38,40)], where *o*-H = *ortho* protons; 8.28 [d, *o*-H(26,28), ^3J(H–H) = 6.6 Hz]; 8.19 [d, *o*-H(22,32), ^3J(H–H) = 6.6 Hz]; 8.09 [s, H_β(14,15)]; 7.78–7.82 (m) for *meta* and *para* protons; 5.79 [s, Fr-H_5]; 4.69 [q, Fr-H_4, ^3J(Fr-H_4, Fr-H_5) = 1.8 Hz and ^3J(Fr-H_4, Fr-H_3) = 3.6 Hz]; 1.35 [s, Fr-H_3], where Fr = 2-furancarboxamido. MS (FAB): M^+

724 (calcd for $C_{49}H_{33}N_5O_2$: 724). UV/Vis spectrum, λ (nm) [$\varepsilon \times 10^{-3}$ (M^{-1} cm^{-1})] in CH_2Cl_2: 429 (246.6), 541 (10.2), 582 (10.2), 638 (7.8).

2.2. Preparation of N-NHCO-2-C_4H_3S-Htpp (2) [9]

A mixture of NaN_3 (1.00 g, 1.54×10^{-2} mol) in distilled water (2 cm^3) and 2-thiophenecarbonylchloride (2.5 mL) was stirred for 20 min. After concentration, the residue was dissolved in CH_2Cl_2 and filtered to remove excess NaN_3 and NaCl. The CH_2Cl_2 layer contains 2-thiophenecarbonyl azide ($C_4H_3SCON_3$). A solution of Zn(tpp) (0.27 g, 3.04×10^{-4} mol) and the above $C_4H_3SCON_3$ in CH_2Cl_2 (200 cm^3) in a stoppered 250 mL Erlenmeyer flask was left for ca. 8 h in the sunlight. To this solution was then added 0.5 N HCl (250 cm^3) with vigorous shaking for 0.5 h. The organic layer was separated, solid ammonium carbonate added to it, and then dried with anhydrous Na_2SO_4. The excess $(NH_4)_2CO_3$ and Na_2SO_4 were removed by filtration. After concentration, the residue was dissolved in a minimum of CH_2Cl_2 and chromatographed on silica gel (100.00 g, 70–230 mesh). The dimensions of the silica gel column were 1.5×17 in. The desired compound was eluted with ethyl acetate (EtOAc)–CH_2Cl_2 [1:4 (v/v)] as a dark brown band on silica gel. Removal of the solvent and recrystallization from CH_2Cl_2–MeOH [1:2 (v/v)] gave the purple solid of N-NHCO-2-C_4H_3S-Htpp (**2**) (0.17 g, 2.06×10^{-4} mol, 68%) which was again dissolved in CH_2Cl_2 and layered with CH_3CN to get purple crystals for single crystal X-ray analysis. ^{1}H NMR (599.95 MHz, $CDCl_3$, 20 °C): δ 9.10 [d, H_β(10,19), ^3J(H–H) = 4.2 Hz]; 8.87 [d, H_β(9,20), ^3J(H–H) = 4.2 Hz]; 8.85 [s, H_β(4,5)]; 8.36 [bs, *o*′-H(34,44) and *o*′-H(38,40)], where *o*-H = *ortho* protons; 8.25 [d, *o*-H(22,32), ^3J(H–H) = 7.2 Hz]; 8.16 [d, *o*-H(26,28), ^3J(H–H) = 7.2 Hz]; 8.06 [s, H_β(14,15)]; 7.75–7.80 (m) for *meta* and *para* protons; 5.85 [dd, S-H_5, ^3J(S-H_4, S-H_5) = 5.0 Hz and ^4J(S-H_3, S-H_5) = 1.2 Hz], where S = 2-thiophenecarboxamido; 5.43 [dd, S-H_4, ^3J(S-H_3, S-H_4) = 3.8 Hz and ^3J(S-H_4, S-H_5) = 5.0 Hz]; 3.47 [dd, S-H_3, ^3J(S-H_3, S-H_4) = 3.8 Hz and ^4J(S-H_3, S-H_5) = 1.2 Hz]; −0.35 (s, NH). MS (FAB): M^+ 740 (calcd for $C_{49}H_{33}N_5OS$: 740). UV/Vis spectrum, λ (nm) [$\varepsilon \times 10^{-3}$ (M^{-1} cm^{-1})] in CH_2Cl_2: 430 (278), 541 (21.8), 583 (21.7), 639 (19.4).

2.3. Preparation of Cd(N-NHCO-2-C_4H_3O-tpp)(OAc) (3)

A mixture of N-NHCO-2-C_4H_3O-Htpp (**1**) (76 mg, 0.1 mmol) in CH_2Cl_2 (5 cm^3) and $Cd(OAc)_2 \cdot 2H_2O$ (69 mg, 0.3 mmol) in MeOH (2 cm^3) were refluxed in CH_3CN (20 cm^3) for 3 h. After concentration, the residue was dissolved in CH_2Cl_2 and washed with distilled water to remove excess $Cd(OAc)_2 \cdot 2H_2O$. The CH_2Cl_2 layer was concentrated to dryness affording a blue precipitate, which was recrystallized from toluene–hexane [1:3 (v/v)] yielding a dark blue solid of **3** (51 mg, 0.0548 mmol, 55%). Compound **3** was redissolved in CH_2Cl_2 and layered with toluene to afford blue crystals for single-crystal X-ray analysis. ^{1}H NMR (599.95 MHz, $CDCl_3$, 20 °C): δ 8.89 [s, H_β(2,3)]; 8.76 [d, H_β(14,35), ^3J(H–H) = 4.5 Hz]; 8.73 [d, H_β(13,36), ^3J(H–H) = 4.5 Hz]; 8.61 [s, H_β(24,25)]; 8.62 [d, *o*-H(22,29), ^3J(H–H) = 6.6 Hz]; 8.40 [d, *o*-H(18,33), ^3J(H–H) = 6.6 Hz]; 7.75–7.86 (m, *meta* and *para* protons); 5.72 (s, Fr-H_5); 5.20 (s, Fr-H_4); 4.37 (s, Fr-H_3); 0.17 (s, OAc-Me), −0.99 (s, NH). ^{1}H NMR (599.95 Hz, $CDCl_3$, −50 °C): δ 8.96 [s, H_β(2,3)]; 8.76 [d, H_β(14,35), ^3J(H–H) = 4.2 Hz]; 8.73 [d, H_β(13,36), ^3J(H–H) = 7.8 Hz]; 8.70 [s, H_β(24,25)]; 8.64 [d, *o*-H(22,29), ^3J(H–H) = 7.8 Hz]; 8.48 [d, *o*-H(18,33), ^3J(H–H) = 7.2 Hz]; 8.42 [d, *o*′-H(11,40), ^3J(H–H) = 4.8 Hz]; 8.20 [d, *o*′-H(7,44), ^3J(H–H) = 7.2 Hz]; 7.75–7.91 (m, *meta* and *para* protons); 5.74 (s, Fr-H_5); 5.24 [d, Fr-H_4, ^3J(H–H) = 1.8 Hz]; 4.52 (s, Fr-H_3); 0.18 (s, OAc-Me); −1.12 (s, NH). ^{13}C NMR (150.87 MHz, 20 °C, $CDCl_3$): δ 154.0 [s, C_α(1,4)]; 153.9 [s, C_α(15,34)]; 152.2 [s, C_α(12,37)]; 150.2 [s, C_α(23,26)]; 134.11 [s, C_β(2,3)]; 134.06 [s, C_β(13,36)]; 131.5 [s, C_β(14,35)]; 123.9 [s, C_β(24,25)]; 121.9 [s, C_m(16,17)]; 152.2 [s, Fr–CO]; 141.8 [s, Fr–C_2]; 108.7 [s, Fr–C_3]; 110.2 [s, Fr–C_4]; 143.5 [s, Fr–C_5]; 176.3 [s, OAc-CO]; 18.9 [s, OAc-Me]. MS (FAB): $(M-OAc)^+$ 834 (calcd for $C_{49}H_{31}CdN_5O_2$: 834). UV/Vis spectrum, λ (nm) [$\varepsilon \times 10^{-3}$ (M^{-1} cm^{-1})] in CH_2Cl_2: 442.0 (233.1), 619.1 (17).

2.4. Preparation of Cd(N-NHCO-2-C_4H_3S-tpp)(OAc) (4)

Compound **4** was prepared in the same way as described for **3** in a 52% yield using N-NHCO-2-C_4H_3S-Htpp (**2**). Compound **4** was dissolved in CH_2Cl_2 and layered with toluene to obtain blue crystals for single-crystal X-ray analysis. ^{1}H NMR (599.95 MHz, $CDCl_3$, 20 °C):δ 8.89 [s, H_β(4,5)]; 8.76 [d, H_β(10,19), ^3J(H–H) = 4.2 Hz]; 8.72 [d, H_β(9,20), ^3J(H–H) = 4.2 Hz]; 8.63 [s, H_β(14,15)]; 8.60 [d, *o*-H(38,40), ^3J(H–H) = 7.2 Hz]; 8.40 [d, *o*-H(34,44), ^3J(H–H) = 6.6 Hz]; 7.74–7.86 (m, *meta* and *para* protons); 6.34 [d, S-H_5, ^3J(H–H) = 4.8 Hz]; 5.57 [t, S-H_4, ^3J(H–H) = 4.2 Hz]; 2.99 [d, S-H_3, ^3J(H–H) = 3 Hz]; 0.15 (s, OAc-Me), −1.23 (s, NH). ^{1}H NMR (599.95 MHz, $CDCl_3$, −50 °C): δ 8.95 [s, H_β(4,5)]; 8.75 [d, H_β(10,19), ^3J(H–H) = 3.6 Hz]; 8.71 [s, H_β(14,15)]; 8.70 [d, H_β(9,20), ^3J(H–H) = 3.6 Hz]; 8.61 [d, *o*-H(38,40), ^3J(H–H) = 7.0 Hz]; 8.47 [d, *o*-H(34,44), ^3J(H–H) = 7.0 Hz]; 8.42 [s, *o*′-H(22,32)]; 8.18 [d, *o*′-H(26,28), ^3J(H–H) = 7.2 Hz]; 7.76–7.90 (m, *meta* and *para* protons); 6.42 [d, S-H_5, ^3J(H–H) = 4.8 Hz]; 5.56 [t, S-H_4, ^3J(H–H) = 4.2 Hz]; 2.69 [d, S-H_3, ^3J(H–H) = 3 Hz]; 0.17 (s, OAc-Me), −1.42 (s, NH). ^{13}C NMR (150.87 MHz, 20 °C, $CDCl_3$): δ 154.0 [s, C_α(3,6)]; 149.8 [s, C_α(13,16)]; 152.2 (s) and 153.9 (s) for C_α(1,8) and C_α(11,18); 134.2 [s, C_β(4,5)]; 134.1 [s, C_β(9,20)]; 131.7 [s, C_β(10,19)]; 124.0 [s, C_β(14,15)]; 121.9 [s, C_m]; 155.5 [s, S-CO]; 131.4 [s, S-C_2]; 126.5 [s, S-C_3]; 126.0 [s, S-C_4]; 130.1 [s, S-C_5]; 176.6 [s, OAc-CO]; 18.9 [s, OAc-Me]. MS (FAB): $(M-OAc)^+$ 851 (calcd for $C_{49}H_{32}CdN_5OS$: 851). UV/Vis spectrum, λ (nm) [$\varepsilon \times 10^{-3}$ (M^{-1} cm^{-1})] in CH_2Cl_2: 432.9 (235.9), 543.0 (9.79), 584.0 (11.6), 639.0 (14.3).

2.5. NMR spectroscopy

Proton and ^{13}C NMR spectra were recorded at 599.95 and 150.87 MHz, respectively, on Varian Unity Inova-600 spectrometers locked on deuterated solvent, and referenced to the solvent peak. Proton NMR is relative to CD_2Cl_2 or $CDCl_3$ at $\delta = 5.30$ or 7.24 and ^{13}C NMR to the center line of CD_2Cl_2 or $CDCl_3$ at $\delta = 53.6$ or 77.0. The temperature of the spectrometer probe was calibrated by the shift difference of the methanol resonance in the ^1H NMR spectrum. HMQC (heteronuclear multiple quantum coherence) was used to correlate protons and carbon through one-bond coupling and HMBC (heteronuclear multiple bond coherence) for two- and three-bond proton–carbon coupling. Nuclear Overhauser effect (NOE) difference spectroscopy was employed to determine the ^1H–^1H proximity through space over a distance of up to about 4 Å.

The positive-ion fast atom bombardment mass spectrum (FAB-MS) was obtained in a nitrobenzyl alcohol (NBA) matrix using a JEOL JMS-SX/SX 102A mass spectrometer. UV/Vis spectra were recorded at 20 °C on a HITACHI U-3210 spectrophotometer.

2.6. X-ray crystallography

Table 1 presents the crystal data for $\mathbf{3}\cdot C_6H_5CH_3$ (*trans*) and $\mathbf{4}\cdot CH_2Cl_2$ (*cis*). Measurements were taken on a Bruker AXS SMART-1000 diffractometer using monochromatized Mo Kα radiation ($\lambda = 0.71073$ Å). Empirical absorption corrections were made for **3**-*trans* and **4**-*cis*. The structures were solved by direct methods (SHELXTL-97) [12] and refined by the full-matrix least-squares method. The furan group within **3**-*trans* is disordered with an occupancy factor of 0.6 for O(4)C(51) and 0.4 for O(4′)C(51′). These two atoms [i.e., O(4),C(51)] were refined with isotropic displacement parameters for **3**-*trans*. All non-hydrogen atoms except the above two atoms for **3**-*trans* were refined with anisotropic thermal parameters, whereas all hydrogen atoms were placed in calculated positions and refined with a riding model. Table 2 lists selected bond distances and angles for both $\mathbf{3}\cdot C_6H_5CH_3$ (*trans*) and $\mathbf{4}\cdot CH_2Cl_2$ (*cis*).

Table 1
Crystal structure data for $\mathbf{3}\cdot C_6H_5CH_3$ (*trans*) and $\mathbf{4}\cdot CH_2Cl_2$ (*cis*)

Empirical formula	$C_{58}H_{43}CdN_5O_4$ ($\mathbf{3}\cdot C_6H_5CH_3$ (*trans*))	$C_{52}H_{37}CdCl_2N_5O_3S$ ($\mathbf{4}\cdot CH_2Cl_2$ (*cis*))
Formula weight	986.37	995.23
Space group	*C*2/c	$P\bar{1}$
Crystal system	monoclinic	triclinic
a (Å)	26.0431(16)	8.6025(5)
b (Å)	11.1727(7)	10.2440(6)
c (Å)	31.847(2)	24.8640(13)
α (°)	90	90.616(1)
β (°)	91.995(2)	95.679(1)
γ (°)	90	97.452(1)
V (Å^3)	9260.9(10)	2161.3(2)
Z	8	2
F(000)	3984	1012
D_{calc} (g cm^{-3})	1.403	1.529
μ(Mo Kα) (mm^{-1})	0.527	0.730
S	1.004	1.045
Crystal size (mm)	0.31 × 0.10 × 0.02	0.30 × 0.10 × 0.10
θ (°)	28.35	28.31
T (K)	273(2)	100(2)
Number of reflections measured	11 512	10 677
Number of reflections observed	5680	8390 [$I > 2\sigma(I)$]
R_1[a]	0.0614	0.0551
wR_2[b]	0.1634	0.1321

[a] $R_1 = [\sum\|F_o\| - |F_c\|/\sum|F_o|]$.
[b] $wR_2 = \{\sum[w(F_o^2 - F_c^2)^2]/\sum[w(F_o^2)^2]\}^{1/2}$.

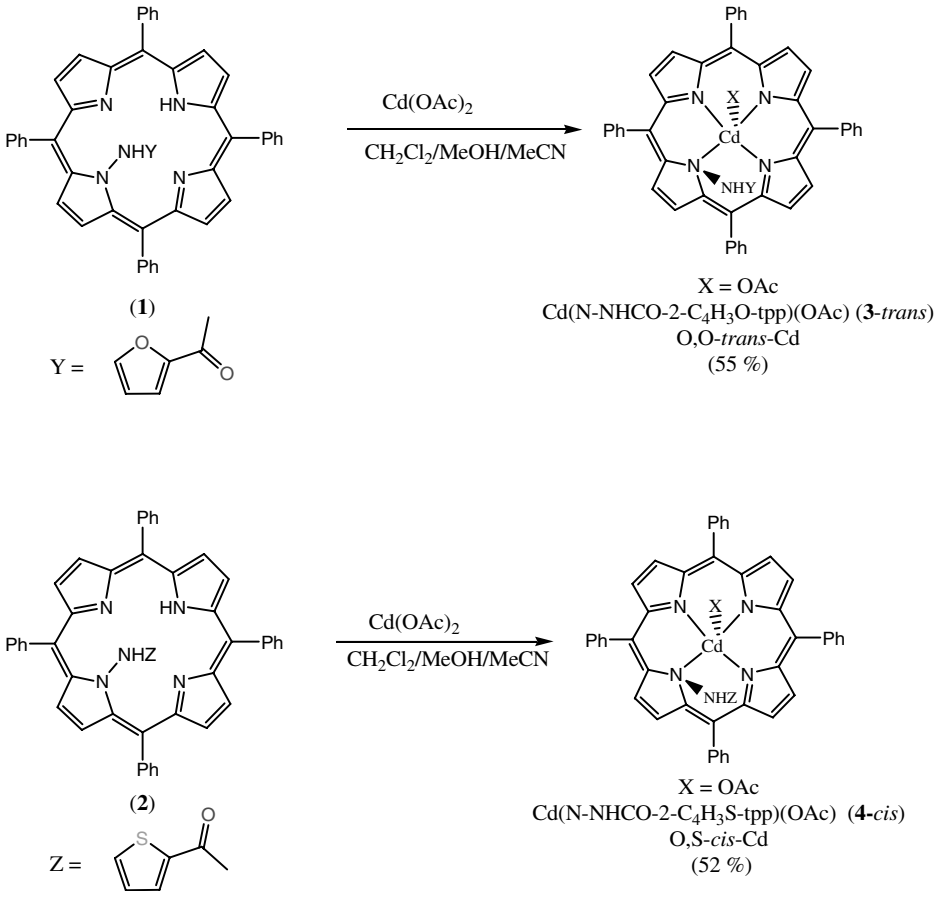
Table 2
Selected bond distances (Å) and angles (°) for compound $\mathbf{3}\cdot C_6H_5CH_3$ (*trans*) and $\mathbf{4}\cdot CH_2Cl_2$ (*cis*)

$\mathbf{3}\cdot C_6H_5CH_3$ (*trans*)			
Bond lengths (Å)			
Cd(1)–N(1)	2.247(4)	Cd(1)–O(1)	2.302(4)
Cd(1)–N(2)	2.296(4)	Cd(1)–O(2)	2.325(4)
Cd(1)···N(3)	2.606(4)	Cd(1)···O(4)	5.098(4)
Cd(1)–N(4)	2.318(4)	Cd(1)···O(3)	5.144(4)
O(3)···O(4)	3.554(4)	O(4)···H(5A)	2.369(4)
Bond angles (°)			
O(1)–Cd(1)–O(2)	56.00(15)	O(2)–Cd(1)–N(1)	156.06(16)
O(1)–Cd(1)–N(1)	100.06(15)	O(2)–Cd(1)–N(2)	109.36(15)
O(1)–Cd(1)–N(2)	117.85(13)	O(2)–Cd(1)–N(4)	108.66(15)
O(1)–Cd(1)–N(4)	116.25(13)	N(2)–Cd(1)–N(4)	124.85(14)
N(1)–Cd(1)–N(2)	80.90(13)	O(4)···H(5A)–N(5)	104.35
N(1)–Cd(1)–N(4)	80.17(13)		
$\mathbf{4}\cdot CH_2Cl_2$ (*cis*)			
Bond lengths (Å)			
Cd(1)–N(1)	2.277(3)	Cd(1)–O(1)	2.289(3)
Cd(1)–N(2)	2.278(3)	Cd(1)–O(2)	2.291(3)
Cd(1)–N(3)	2.303(3)	Cd(1)···O(3)	5.113(3)
Cd(1)···N(4)	2.617(3)	Cd(1)···S(1)	6.798(3)
O(3)···S(1)	2.991(3)		
Bond angles (°)			
O(1)–Cd(1)–O(2)	56.91(11)	O(2)–Cd(1)–N(1)	118.18(11)
O(1)–Cd(1)–N(1)	111.57(11)	O(2)–Cd(1)–N(2)	95.12(11)
O(1)–Cd(1)–N(2)	152.02(11)	O(2)–Cd(1)–N(3)	113.63(11)
O(1)–Cd(1)–N(3)	109.56(11)	N(1)–Cd(1)–N(3)	74.49(10)
N(1)–Cd(1)–N(2)	80.54(11)		
N(1)–Cd(1)–N(3)	125.59(10)		

3. Results and discussion

3.1. Molecular structures of $\mathbf{3}\cdot C_6H_5CH_3$ and $\mathbf{4}\cdot CH_2Cl_2$

Using a d^{10} metal, namely cadmium(II), the new complexes $\mathbf{3}\cdot C_6H_5CH_3$ and $\mathbf{4}\cdot CH_2Cl_2$ were synthesized. The synthetic strategy is outlined in Scheme 1. During the metallation of free bases **1** and **2** with $Cd(OAc)_2$ (Scheme 1), the soft acid Cd^{2+} prefers to retain one OAc^- ligand and coordinate to the N–H proton [i.e., H(2A)] of **1** and **2** to form six-coordinate complexes **3** and **4**. The molecular frameworks are depicted in Fig. 1a for **3** and in Fig. 1b for **4**.



Scheme 1.

The bond distance (Å) of Cd(1)–O(1) is 2.302(4), Cd(1)–O(2) = 2.325(4), and the mean Cd(1)–N(p) = 2.287(4) Å for **3**; for **4**, the values are Cd(1)–O(1) = 2.289(3), Cd(1)–O(2) = 2.291(3) and the mean Cd(1)–N(p) = 2.286(3) Å (Table 2). The cadmium–nitrogen bond distances [Cd(1)–N(1) = 2.247(3), Cd(1)–N(2) = 2.296(4) and Cd(1)–N(4) = 2.318(4) Å of **3**; Cd(1)–N(1) = 2.277(3), Cd(1)–N(2) = 2.278(3) and Cd(1)–N(3) = 2.303(3) Å of **4**] are comparable to those of Cd(1)–N(p) = 2.301(5) Å in Cd(N–NHCO-C_6H_5-tpp)(OAc) [11]. The Cd(1)···N(3) distance of 2.606(4) Å for **3** [or Cd(1)···N(4) distance of 2.617(3) for **4**] is longer than 2.301(5) Å but is significantly shorter than the sum of the van der Waals radii of Cd and N (3.15 Å) [13]. This longer Cd···N(3) contact in **3** [or Cd···N(4) in **4**] may be viewed as a secondary intramolecular interaction. This kind of secondary interaction was earlier observed for both Cd(N-NHCOC_6H_5-tpp)(OAc) with Cd(1)···N(4) = 2.612(5) Å [11] and [Cd(H_3daps)Cl_4]$CH_3CN \cdot 0.25H_2O$ [H_4dap = 2,6-bis(1-salicyloylhydrazonoethyl)pyridine] with Cd···N(6) = 2.74(1) Å [14]. Most chemists seem to consider this secondary interaction between the metal ion and the fourth N as a weak bond in *N*-substituted porphyrin metal complexes. Furthermore, N(1), N(2) and N(4) [or N(1), N(2) and N(3)] are bonded strongly as well as covalently to the Cd atom in **3** [or **4**]. Thus the Cd(II)–2-furancarboxyamido-*meso*-tpp (**3**) and N-2-thiophenecarboxyamido-*meso*-tpp (**4**) structures are quite similar to metal(II) *N*-substituted porphyrin complexes with three strong and one weaker metal–N bond [11,15]. Compound **3** is an O,O-*trans* conformer in the solid phase with a dihedral angle of Ψ [O(3)–C(47)–C(48)–O(4)] = −174.17° and thus we are able to assign it as **3**-*trans*. Compound **4** is an O,S-*cis* conformation (i.e., **4**-*cis*) in the solid phase with Ψ [O(3)–C(47)–C(48)–S(1)] = 1.59°. The geometry around Cd^{2+} is described as a distorted square-based pyramid in which the apical site is occupied by a bidentate chelating OAc^- group in **3**-*trans* and **4**-*cis*. Fig. 2 shows the actual porphyrin skeleton of **3**-*trans* and **4**-*cis*.

We adopt the plane of three strongly bound pyrrole nitrogen atoms [i.e., N(1), N(2) and N(4) for **3**-*trans* and N(1), N(2) and N(3) for **4**-*cis*] as a reference plane, 3N. In **3**-*trans* (or **4**-*cis*), Cd^{2+} and N(5) are located on different sides at 1.06 (or 1.04) and −1.49 Å (or −1.53 Å) from its 3N plane, respectively (Fig. 2). The N(3) and N(4) pyrrole rings bearing the 2-furancarboxamido (Fr) and 2-thiophenecarboxamido groups in **3**-*trans* and **4**-*cis*, respectively, deviate mostly from the 3N plane, thus orienting separately with a dihedral angle of 33.4° and of 31.0°, whereas small angles of 0.7°, 18.5° and 23.7° occur with N(1), N(4) and N(2) pyrrole for **3**-*trans*

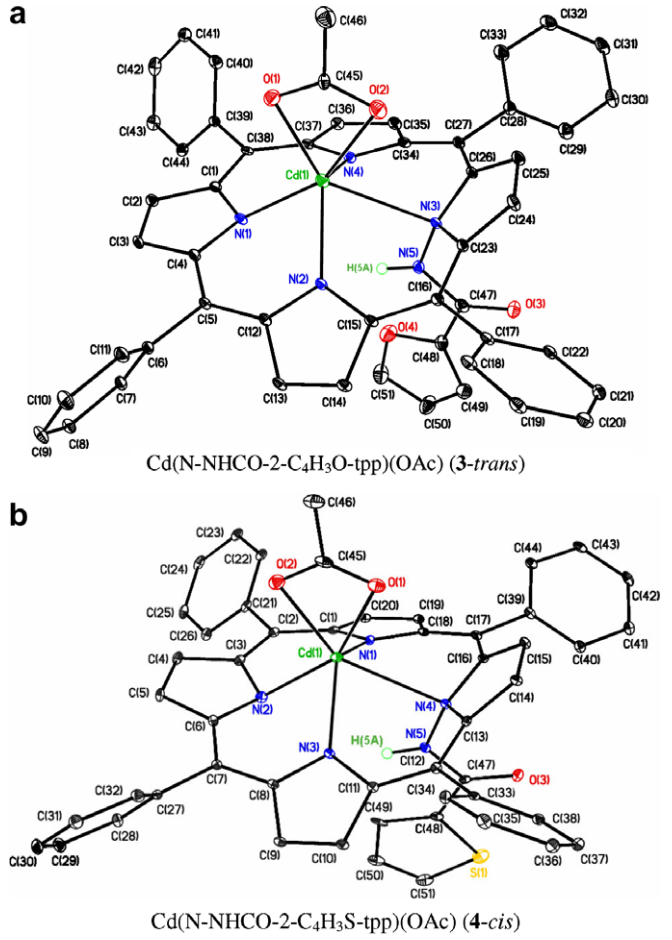


Fig. 1. Molecular configuration and atom-labelling scheme for (a) $3 \cdot C_6H_5CH_3$ (*trans*) and (b) $4 \cdot CH_2Cl_2$ (*cis*), with ellipsoids drawn at 30% probability. Hydrogen atoms, solvent $C_6H_5CH_3$ for $3 \cdot C_6H_5CH_3$ (*trans*) and CH_2Cl_2 for $4 \cdot CH_2Cl_2$ (*cis*) are omitted for clarity.

and the corresponding angles are 18.2°, 23.5° and 17.6° with N(2), N(1) and N(3) pyrrole for **4**-*cis*. In **4**-*cis*, such a large deviation from planarity for the N(4) pyrrole is also reflected by observing a 7.7–10.2 ppm upfield shift of the C_β(C14, C15) at 124.0 ppm compared to 131.7 ppm for C_β(C10, C19), 134.1 ppm for C_β(C9, C20) and 134.2 ppm for C_β(C4, C5). In **3**-*trans*, a similar deviation is also found for N(3) pyrrole by observing a 7.6–10.2 ppm upfield shift of C_β(C24, C25) at 123.9 ppm compared to 134.11 ppm for C_β(C2, C3), 134.06 ppm for C_β(C13, C36) and 131.5 ppm for C_β(C14, C35).

It is noted that the ionic radius for the metal ion increases from 0.82 Å for Zn^{2+} with a coordination number (CN = 5) to 1.09 Å for Cd^{2+} (CN = 6). Because of the larger size of Cd^{2+}, Cd(1), O(2) and O(1) lie 1.06, 2.88 and 3.24 Å, respectively, above the 3N plane in **3**-*trans*, compared to 1.04 Å for Cd(1), 2.92 Å for O(1) and 3.16 Å for O(2) in **4**-*cis* [cf. 0.65 Å for Zn^{2+} in Zn(N-Me-tpp)Cl] (Fig. 2) [16].

The dihedral angles between the mean plane of the skeleton (3N) and the planes of the phenyl groups are 57.6° [C(9)], 32.1° [C(20)], 32° [C(31)] and 56.4° [C(42)] for

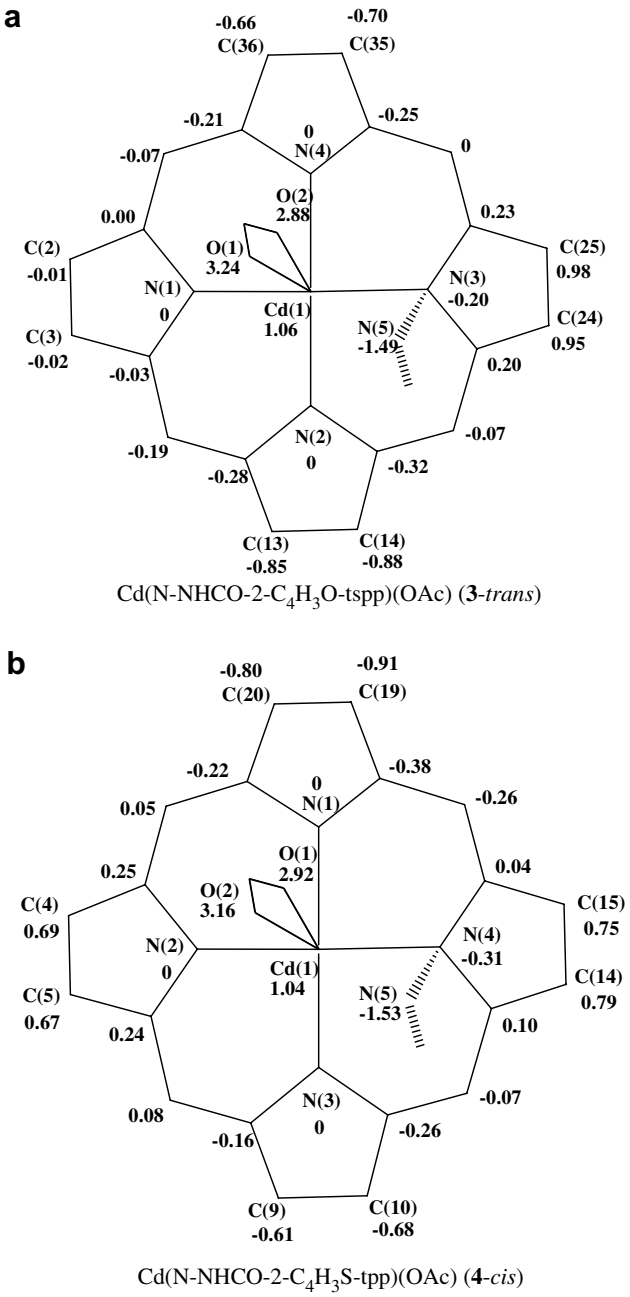


Fig. 2. Diagram of the porphyrinato core ($C_{20}N_4$, Cd, furan, thiophene and OAc) of (a) **3**-*trans* and (b) **4**-*cis*. The values represent the displacement (in Å) of the atoms from the 3N plane [i.e., N(1), N(2), N(4) for **3**-*trans* and N(1)–N(3) for **4**-*cis*].

3-*trans* and the corresponding angles are 44.7°, 42.9°, 34.3° and 35.7° for **4**-*cis*.

3.2. ^1H and ^{13}C NMR spectroscopy data of **3**-trans and **4**-cis in $CDCl_3$

The singlet at −0.35 ppm was assigned to NH protons [i.e., H(2A) and H(5A)] for **2** at 20 °C. Moreover, the signal arising from the NH protons [i.e., H(2A) and H(5A)] of **1** was not observed at 20 °C. At −90 °C, traces of water were

frozen from solution of **1** in CD_2Cl_2. Thus, the frozen water inhibits intermolecular proton exchange between water and NH protons of **1** and allows the observation of a broad singlet for the NH proton at −0.61 ppm ($\Delta\nu_{1/2} = 23$ Hz). Upon metallation, there were no signal of NH (in pyrrole) [i.e., H(1A) for **3** and H(2A) for **4**] for metal porphyrins **3** and **4**. The ^{1}H NMR spectrum of **3** (or **4**) in $CDCl_3$ (Figs. 3 and 4) showed a sharp singlet at $\delta = -0.99$ (or −1.23) ppm ($\Delta\nu_{1/2} = 4$ Hz) for the NH proton at 20 °C. These NMR data for **3** (or **4**) suggest that the NH proton [i.e., H(5A)] bound to N(5) undergoes rapid intermolecular proton exchange with water at 20 °C.

Complexes **3**-*trans* and **4**-*cis* were characterized by ^{1}H (Figs. 3 and 4) and ^{13}C NMR spectra. In solution, the molecule has effective C_s symmetry with a mirror plane running through the N(5)–N(3)–Cd(1)–N(1)–O(1)–O(2) unit for **3**-*trans* or the N(5)–N(4)–Cd(1)–N(2)–O(1)–O(2) unit for **4**-*cis* (Fig. 1). There are four β-pyrrole protons H_β, four β-pyrrole carbons C_β, four α-pyrrole carbons C_α, two different *meso* carbons C_{meso} and two phenyl-C_1 carbons for these two complexes. In **4**-*cis*, the doublet at 8.76 ppm is assigned to $H_\beta(10,19)$ with $^3J(H–H) = 4.2$ Hz, and the other doublet at 8.72 ppm with $^3J(H–H) = 4.2$ Hz is due to $H_\beta(9,20)$ (Fig. 3a). The singlet at 8.89 ppm is assigned to $H_\beta(4,5)$ and the other singlet at 8.63 ppm is due to $H_\beta(14,15)$ (Fig. 3a). In **3**-*trans*, the doublet at 8.76 ppm is due to $H_\beta(14,35)$ with $^3J(H–H) = 4.5$ Hz and the other doublet at 8.73 ppm is due to $H_\beta(13,36)$ with $^3J(H–H) = 4.5$ Hz (Fig. 4a). The singlet at 8.89 ppm is assigned to $H_\beta(2,3)$ and the other singlet at 8.61 ppm is due to $H_\beta(24,25)$ (Fig. 4a).

Fig. 3 depicts the representative ^{1}H spectra for **4**-*cis* in $CDCl_3$ at 20 and −50 °C. At 20 °C, the rotation of the phenyl group along C_1–C_{meso} [C(17)–C(39) or C(12)–C(33)]

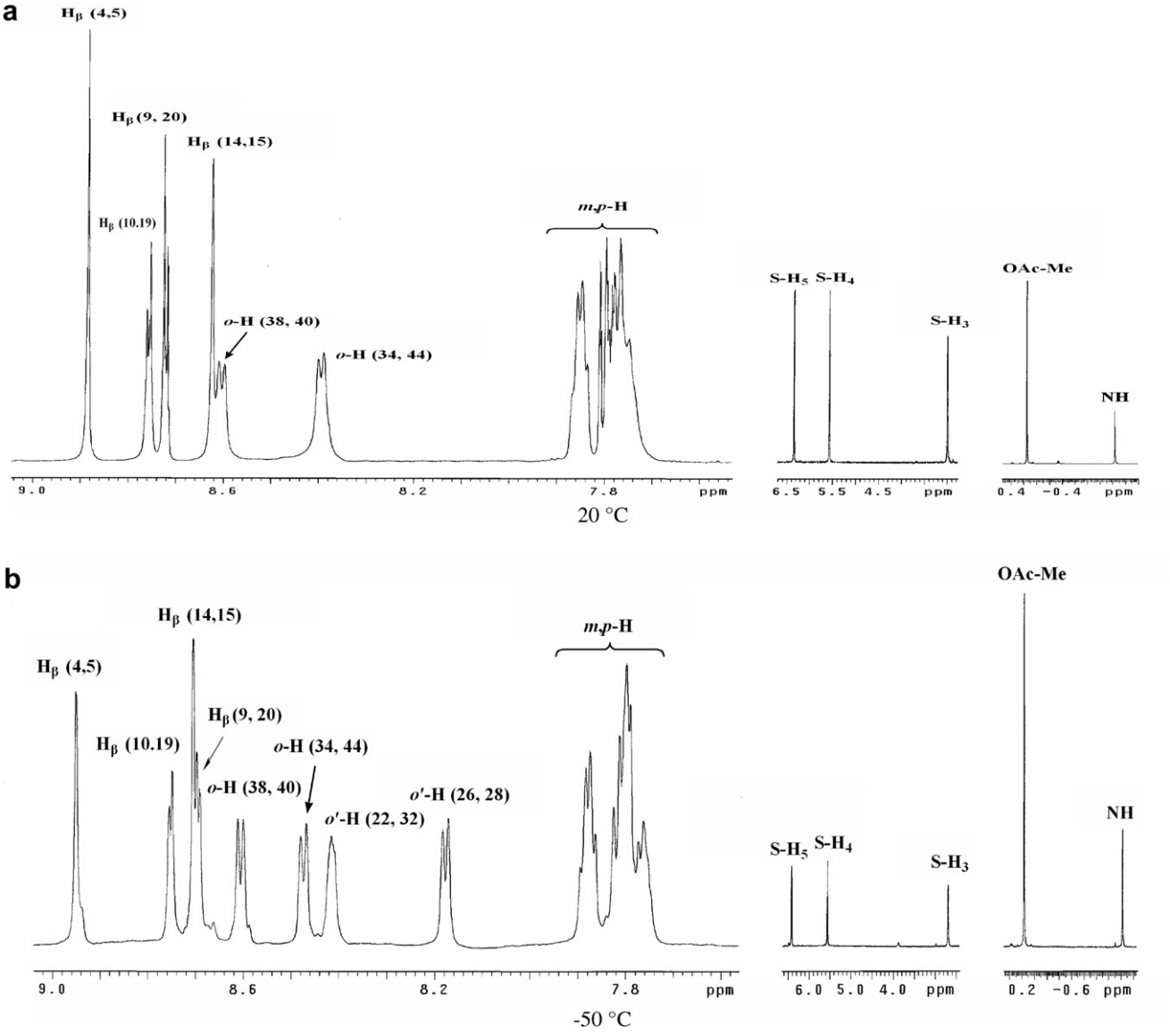


Fig. 3. ^{1}H NMR spectra for **4**-*cis* at 599.95 MHz in $CDCl_3$: (a) 20 °C, (b) −50 °C, where S = 2-thiophenecarboxamido.

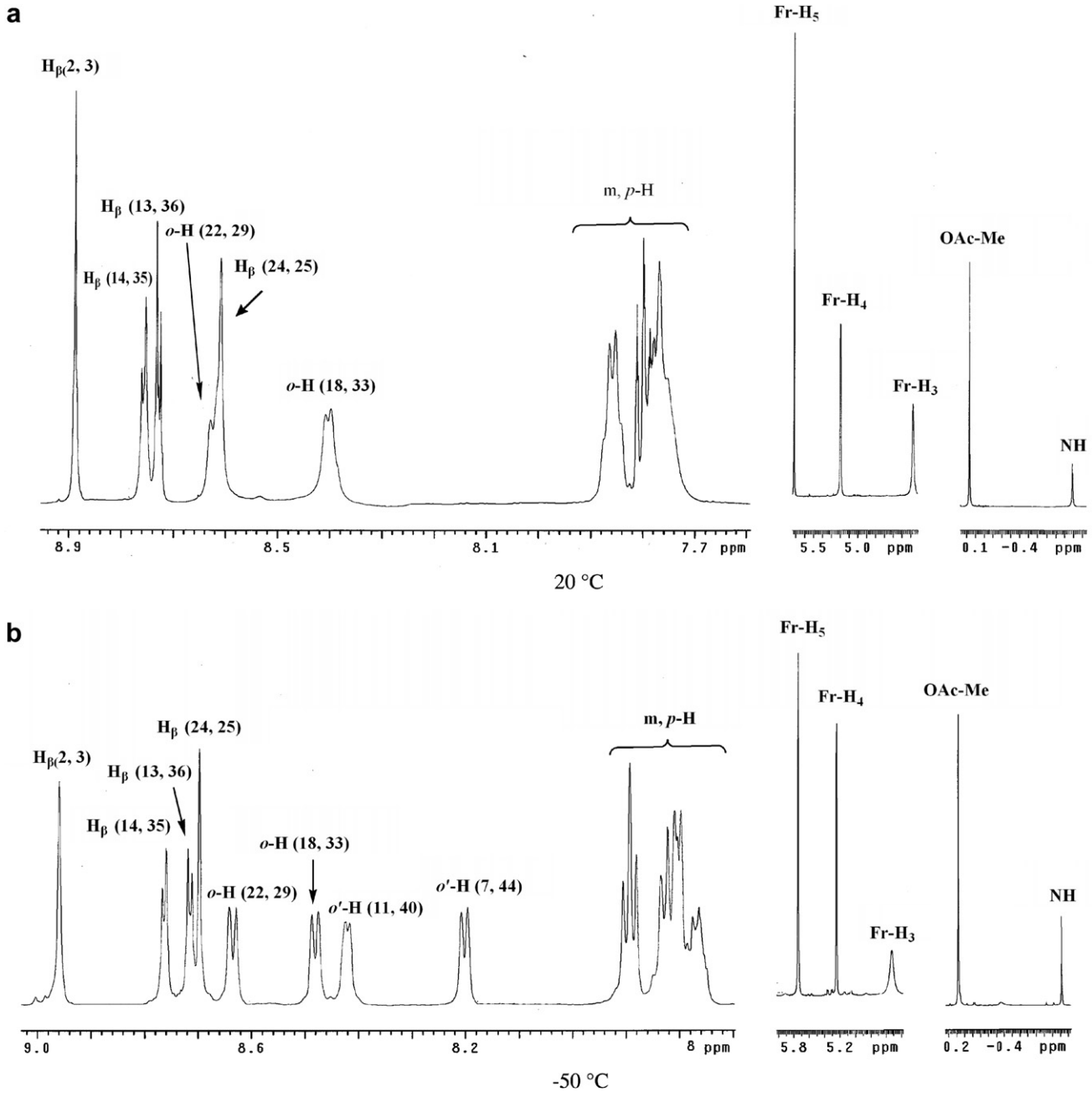
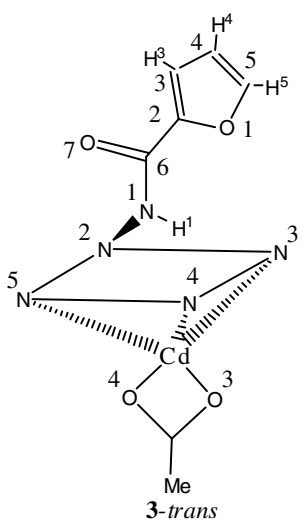


Fig. 4. ^{1}H NMR spectra for **3**-*trans* at 599.95 MHz in $CDCl_3$: (a) 20 °C, (b) −50 °C, where Fr = 2-furancarboxamido.

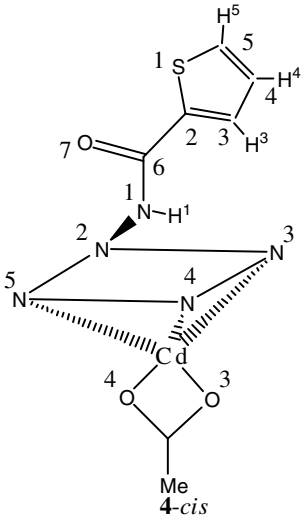
bond is slow. This slow rotation is supported by the two singlets at 8.60 and 8.40 ppm due to *o*-H(38,40) and *o*-H(34,44), respectively (Fig. 3a). Moreover, the rotation of the phenyl group along C(7)–C(27) [or C(2)–C(21)] bond for **4**-*cis* is at the intermediate exchange region. In this intermediate exchange region, the signals are broadened beyond detection. Hence, no signals of *o*′-H(22,32) and *o*′-H(26,28) for **4**-*cis* have been observed at 20 °C (Fig. 3a). At −50 °C, this rotation is extremely slow. Hence, the rate of intramolecular exchange of the *ortho* protons for **4**-*cis* in $CDCl_3$ is also extremely slow. The doublet at 8.61 ppm is assigned to *ortho* protons *o*-H(38,40) with ^3J(H–H) = 7.0 Hz (Fig. 3b). The other doublet at 8.47 ppm is due to *ortho* protons *o*-H(34,44) with ^3J(H–H) = 7.0 Hz. Likewise, the singlet at 8.42 ppm is due to *ortho* proton *o*-H(22,32). The corresponding doublet at 8.18 ppm is due to *o*-H(26,28) with ^3J(H–H) = 7.2 Hz (Fig. 3b). The interpretation of these data were confirmed by the NOE difference spectroscopy for **4**-*cis* in $CDCl_3$ at 20 and −50 °C.

In a similar fashion, the rotation for the phenyl group of **3**-*trans* in $CDCl_3$ at 20 °C along C(27)–C(28) [or C(16)–C(17)] bond is slow and the rotation along C(38)–C(39) [or C(5)–C(6)] is at the intermediate exchange region. Hence, the ^{1}H resonances for the *ortho* protons of **3**-*trans* were observed as two sets of doublets: one doublet at 8.62 ppm is assigned to *ortho* protons *o*-H(22,29) with

Table 3
Group net charges (q) for **3** and **4** by NBO calculations[a]



3-*trans*



4-*cis*

Compound	Conformer	Metal	O^1	S^1	C^2	C^3	C^4	C^5	C^6	O^7	N^1	N^2	N^3	N^4	N^5	O^3	O^4
O,O-Cd	**3**-*trans*	1.674	−0.473		0.227	−0.201	−0.269	0.188	0.635	−0.626	−0.399	−0.324	−0.739	−0.721	−0.727	−0.832	−0.799
O,S-Cd	**4**-*cis*	1.676		0.490	−0.310	−0.168	−0.202	−0.355	0.661	−0.634	−0.415	−0.317	−0.733	−0.719	−0.747	−0.834	−0.803

[a] Group net charges including the attached hydrogen by NBO* calculations.
*E.D. Glendening, A.E. Reed, J.E. Carpenter, F. Weinhold, NBO Version 3.1 in GAUSSIAN-03.

^3J(H–H) = 6.6 Hz and the other doublet at 8.40 ppm is due to *ortho* protons *o*-H(18,33) with ^3J(H–H) = 6.6 Hz (Fig. 4a). Moreover, no signals of *o*′-H(11,40) and *o*′-H(7,44) of **3**-*trans* have been detected at 20 °C (Fig. 4a). However, for *ortho* protons, at −50 °C, the rotation of phenyl group along the C_1–C_{meso} bond in **3**-*trans* is extremely slow, which is evident from the appearance of the four doublets at 8.64 [*o*-H(22,29)], 8.48 [*o*-H(18,33)], 8.42 [*o*′-H(11,40)], and 8.20 [*o*′-H(7,44)] ppm due to four different *ortho* protons of the aromatic ring (Fig. 4b).

Due to the ring current effect, upfield shifts for the ^{1}H resonances of S-H_5, S-H_4 and S-H_3 for **4** with the O,S-*cis* conformer in $CDCl_3$ at −50 °C are $\Delta\delta = -1.21$ [from 7.63 (obtained from 2-acetylthiophene) to 6.42 ppm], −2.13 (from 7.69 to 5.56 ppm) and −4.44 ppm (from 7.13 to 2.69 ppm), respectively (Fig. 3b). Qualitatively, as the distance between the geometrical center (C_t) of the 4N plane and axial protons gets smaller, the shielding effect becomes larger. In **4**-*cis*, the distance for $C_t\cdots$S-H_3, $C_t\cdots$S-H_4 and $C_t\cdots$S-H_5 increases from 3.235, 5.738 to 7.066 Å, individually. As the S-H_3 proton of **4**-*cis* is closer to C_t, the shielding gets larger for this S-H_3. A similar ring current effect is also observed for **3**-*trans*. The occurrence of weak intramolecular hydrogen bonding between one amino hydrogen [H(5A)] and the furan oxygen [O(4)] in O,O-*trans* of **3** is reflected in the long N(5)–H(5A)$\cdots$O(4) (furan) bond distance of 2.358 Å and acute N(5)–H(5A)$\cdots$O(4) (furan) angle of 104.35° (Fig. 1a) [6]. The hydrogen bonding results in a downfield shift of 0.24 ppm for the NH proton which resonances from −1.23 ppm for **4**-*cis* (O,S-*cis*-Cd) to −0.99 ppm for **3**-*trans* (O,O-*trans*-Cd) in $CDCl_3$ at 20 °C (Figs. 3 and 4). This intramolecular H-bonding and electrostatic attraction between $Cd(1)^{2+}$ and $O(4)^-$ restricts the rotation of the furan group along the C(48)–C(47) bond. Thus, as the temperature is increased from −50 °C to 20 °C for **3**-*trans* in $CDCl_3$, Fr-H_3 rotates a degree slightly closer to C_t and a minimum upfield shift of −0.15 ppm was observed for the ^{1}H resonances of Fr-H_3 from 4.52 to 4.37 ppm (Fig. 4).

X-ray diffraction analysis unambiguously confirms that **3**-*trans* and **4**-*cis* have a chelating bidentate OAc^- ligand in the solid phase. Notably, the ring current effects seldom exceed 10 ppm in ^{1}H NMR [17] and 2 ppm in ^{13}C NMR [18]. Hence, the ring current contribution is relatively less important in determining the ^{13}C chemical shifts than proton shifts. The ^{13}C NMR chemical shifts were shown to be a useful tool for diagnosing the nature of acetate ligands, whether unidentate or bidentate in diamagnetic complexes. Unidentate acetate ligands were located at 20.5 ± 0.2 and 168.2 ± 1.7 ppm and bidentate acetate ligands at 18.0 ± 0.7 and 175.2 ± 1.6 ppm [17]. The methyl and carbonyl chemical shifts of the acetate group in **3**-*trans* (or **4**-*cis*) at 20 °C in $CDCl_3$ are separately located at 18.9 (or 18.9) and 176.3 (or 176.6) ppm confirming that the acetate is chelating bidentately and is coordinated to the cadmium atom in **3**-*trans* (or **4**-*cis*) in the solution phase. The difference in chemical shifts for the CO group to be characteristic of either uni- or bidentate acetates are definitely out of the range of the shielding effect of a porphyrin.

NBO group net charges over O(4), O(3) and Cd(1) in **3** (O,O-*trans*-Cd; **3**-*trans*) are −0.473, −0.626 and 1.674, respectively (Table 3). In **3**-*trans*, a weakly repulsive electrostatic interaction between the two oxygen atoms [i,e., $O(3)^-$ and $O(4)^-$] and a strongly attractive electrostatic force between the cadmium [$Cd(1)^{2+}$] and oxygen atom [$O(4)^-$] are two major factors explaining the *trans* conformer of **3** which dominates both in the solid phase and in low polar solvents at low temperature. Group charges for S(1), O(3) and Cd(1) in **4** (O,S-*cis*-Cd; **4**-*cis*) are 0.490, −0.634 and 1.676, respectively (Table 3). In **4**-*cis*, a moderately electrostatic attraction between the sulfur [$S(1)^+$] and oxygen atom [$O(3)^-$] and weakly repulsive electrostatic force between the cadmium [$Cd(1)^{2+}$] and sulfur [$S(1)^+$] are two major factors determining that the *cis* conformer of **4** is favored both in the solid and in low polarity solvents at low temperature.

4. Conclusion

We have investigated two new, diamagnetic and mononuclear cadmium(II) *N*-substituted-*N*-aminoporphyrin complexes **3**-*trans* and **4**-*cis* which exist in O,O-*trans* and O,S-*cis* conformers, respectively, and their X-ray structures have been established. We also demonstrate how the electrostatic repulsive and attractive forces influence the favorable conformers in the case of **3**-*trans* and **4**-*cis*. Both the electrostatic attraction between Cd^{2+} and $O(4)^-$ and the N–H$\cdots$O (furan) H-bond interaction stabilized the O,O-*trans* form of **3**-*trans* in $CDCl_3$ at −50 °C. Both the electrostatic repulsion between Cd^{2+} and $S(1)^+$ and the attractive interaction between $S(1)^+$ and $O(3)^-$ stabilize the O,S-*cis* conformer of **4**.

Acknowledgment

Financial support from the National Science Councils of the ROC under Grant NSC 94-2113-M-005-010 is gratefully acknowledged.

Appendix A. Supplementary material

Fig. S1 shows the molecular structure for O,O-*cis* of **1** at 100(2) K. Fig. S2 shows the molecular structures for O,S-*cis* and O,S-*trans* of **2** at 100(2) K. CCDC 289590 and 289591 contains the supplementary crystallographic data for **3** and **4**. These data can be obtained free of charge via http://www.ccdc.cam.ac.uk/conts/retrieving.html, or from the Cambridge Crystallographic Data Centre, 12 Union Road, Cambridge CB2 1EZ, UK; fax: (+44) 1223-336-033; or e-mail: deposit@ccdc.cam.ac.uk. Supplementary data associated with this article can be found, in the online version, at doi:10.1016/j.poly.2006.08.034.

References

[1] I.S. Han, C.K. Kim, H.J. Jung, I. Lee, Theor. Chim. Acta 93 (1996) 199.
[2] R. Benassi, U. Folli, L. Schenetti, F. Taddei, J. Chem. Soc., Perkin Trans. II (1987) 961.
[3] S.R. Salman, Org. Magn. Reson. 20 (1982) 151.
[4] L. Lunazzi, G. Placucci, C. Chatgilialoglu, D. Macciantelli, J. Chem. Soc., Perkin Trans. II (1984) 819.
[5] D. Casarini, L. Lunazzi, D. Macciantelli, J. Chem. Soc., Perkin Trans. II (1985) 1839.
[6] R. Crespo-Otero, L.A. Montero, G. Rosquete, J.A. Padron-Garcia, R.H. Gonzalez-Jonte, J. Comput. Chem. 25 (2004) 429.
[7] H.J. Callot, Tetrahedron 35 (1979) 1455.
[8] H.J. Callot, J. Fischer, R. Weiss, J. Am. Chem. Soc. 104 (1982) 1272.
[9] H.J. Callot, B. Chevrier, R. Weiss, J. Am. Chem. Soc. 100 (1978) 4733.
[10] K. Ichimura, Bull. Chem. Soc. Jpn. 51 (1978) 1444.
[11] F.A. Yang, J.H. Chen, H.Y. Hsieh, S. Elango, L.P. Hwang, Inorg. Chem. 42 (2003) 4603.
[12] G.M. Sheldrick, SHELXL-97: Program for the Refinement of Crystal Structures from Diffraction Data, University of Göttingen, Göttingen, Germany, 1997.
[13] R.D. Shannon, Acta Crystallogr., Sect. A 32 (1976) 751.
[14] M. Fundo, A. Sousa, M.R. Bermejo, A. Gaorcia-Deibe, A. Sousa-Pedrares, O.L. Hoyos, M. Helliawall, Eur. J. Inorg. Chem. (2002) 703.
[15] M. Ravikanth, T.K. Chandrashekar, Struct. Bond. 82 (1995) 105.
[16] D.K. Lavellee, A.B. Kopelove, O.P. Anderson, J. Am. Chem. Soc. 100 (1978) 3025.
[17] S.J. Lin, T.N. Hong, J.Y. Tung, J.H. Chen, Inorg. Chem. 36 (1997) 3886.
[18] E. Breitmaier, W. Voelter, Carbon-13 NMR Spectroscopy, 3rd ed., VCH, New York, 1990, pp. 110, 116, 117.

Available online at www.sciencedirect.com
ScienceDirect
Polyhedron 26 (2007) 600–606
POLYHEDRON
www.elsevier.com/locate/poly

Osmium-carbonyl complexes of naphthylazoimidazoles. Single crystal X-ray structure of $[Os(H)(CO)(PPh_3)_2(\alpha\text{-NaiEt})](PF_6)$ {α-NaiEt = 1-ethyl-2-(naphthyl-α-azo)imidazole}

T.K. Mondal [a], Joydev Dinda [a], Alexandra M.Z. Slawin [b], J. Derek Woollins [b], C. Sinha [a,*]

[a] Department of Chemistry, Inorganic Chemistry Section, Jadavpur University, Kolkata 700 032, West Bengal, India
[b] Department of Chemistry, University of St. Andrews, St. Andrews, Fife KY16 9ST, UK

Received 18 August 2006; accepted 21 August 2006
Available online 7 September 2006

Abstract

1-Alkyl-2-(naphthyl-α/β-azo)imidazole (α-NaiR **1**; β-NaiR, **2**) react with $[Os(H)(Cl)(CO)(PPh_3)_3]$ in THF and synthesise $[Os(H)(CO)(PPh_3)_2(\alpha/\beta\text{-NaiR})](PF_6)$ (**3**, **4**). The X-ray structure of $[Os(H)(CO)(PPh_3)_2(\alpha\text{-NaiEt})](PF_6)$ (**3c**) shows a distorted octahedral geometry. Other spectroscopic studies (IR, UV–Vis, NMR) support the stereochemistry of the complexes. Addition of Cl_2 in MeCN to **3** or **4** gives $[Os(Cl)(CO)(\alpha/\beta\text{-NaiR})(PPh_3)_2](PF_6)$ (**5**, **6**), which were characterized by spectroscopic studies. The redox properties of the complexes show Os(III)/Os(II), Os(IV)/Os(III) and azo reductions.
© 2006 Elsevier Ltd. All rights reserved.

Keywords: Naphthylazoimidazoles; Hydrido-osmium-carbonyl; X-ray structure; Electrochemistry

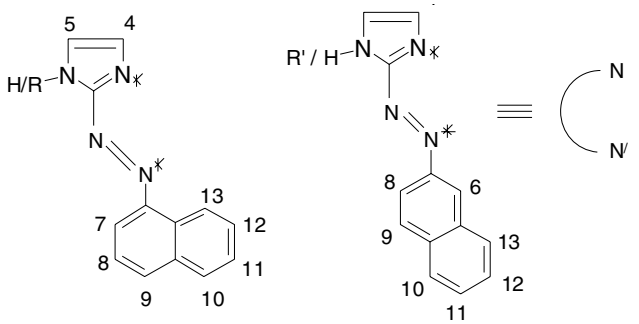
1. Introduction

Polypyridyl complexes of ruthenium and osmium are an active area of current research [1–7]. There are a number of M–polypyridine complexes which bear M–H bonds (M = Ru, Os) [8]. The functional group is the diimine, –N=C–C=N–, and the key feature of these heterocycles is their π-acidity. Recent years have witnessed a great deal of interest in the synthesis of new ligands in the framework of the diimine function (–N=C–C=N–) or the functional modification to design an isoelectronic chelating motif. We have been engaged for the last few years in the design of the azoimine function (–N=C–C=N–) which is a functional modification of the diimine unit. We have synthesized the azoimidazole in the azoimine family [9,10]. Imidazole and its derivatives are chosen because of their chemical and biological ubiquity [11], whilst the azo group enhances the π-acidity and is responsible for photochromism [12], pH—responsive and redox activity of the molecules [3]. It is important to stabilize M–H bonds in the presence of a π-acidic chelating framework in the complexes [13–15].

In this work we have used 1-alkyl-2-(naphthyl-α/β-azo)-imidazoles (α/β-NaiR) as a chelating azoimine function [10,16]. We have synthesized $[Os(H)(CO)(PPh_3)_2(\alpha/\beta\text{-NaiR})]^+$, an osmium-hydrido-carbonyl compound, and the structure has been established by single crystal X-ray diffraction study in one case. The complexes have been reacted with chlorine in acetonitrile. The products, $[Os(Cl)(CO)(PPh_3)_2(\alpha/\beta\text{-NaiR})](ClO_4)$, were characterised by spectroscopic and electrochemical techniques.

* Corresponding author. Fax: +91 033 2413 7121.
E-mail address: c_r_sinha@yahoo.com (C. Sinha).

0277-5387/$ - see front matter © 2006 Elsevier Ltd. All rights reserved.
doi:10.1016/j.poly.2006.08.028



α-NaiR(**1**) β-NaiR(**2**)

H (**a**), Me (**b**), CH_2CH_3 (**c**), CH_2Ph (**d**)

2. Results and discussion

2.1. Synthesis and formulation

The reaction of $[Os(H)(Cl)(CO)(PPh_3)_3]$ and 1-alkyl-2-(naphthyl-α/β-azo)imidazoles (α-NaiR (**1**), β-NaiR (**2**) where R = H (a), Me (b), CH_2CH_3 (c), CH_2Ph (d)) in dry THF under dinitrogen yielded a dark red coloured solution. On evaporation of the solvent to half of its original volume and addition of NH_4PF_6, a dark precipitate appeared after cooling in a deep freezer for overnight. The formulation of the complex, $[Os(H)(CO)(PPh_3)_2(\alpha/\beta\text{-NaiR})](PF_6)$ (**3** for α-NaiR; **4** for β-NaiR) is supported by microanalytical data (see Section 3). Although two geometrical isomers (**3** and **3′** or **4** and **4′**) are possible [CO *trans* to N(azo) or N(imidazole)] we have isolated only one isomer, CO *trans* to N(imidazole) (**3** and **4**). The complexes, **3** and **4**, are diamagnetic and show 1:1 conductivity in acetonitrile solution ($\Lambda_M = 90$–$105\ \Omega^{-1}\ mol^{-1}\ cm^2$). The reaction of α/β-NaiH and $[Os(H)(Cl)(CO)(PPh_3)_3]$ also gave dark coloured crystalline compounds in the presence of NH_4PF_6, but their solubility was too low to carry out any spectral measurements, thus they were not studied further. Reaction of $[Os(H)(CO)(PPh_3)_2(\alpha/\beta\text{-NaiR})](PF_6)$ with Cl_2 in MeCN gave red coloured $[Os(Cl)(CO)(PPh_3)_2(\alpha/\beta\text{-NaiR})](PF_6)$ (**5**, **6**) in high yield (>70%). The hydrido complexes (**3**, **4**) can be regenerated from the chloro complexes (**5**, **6**) by refluxing with $NaBH_4$ in EtOH for 2 h. The formation of hydrido complexes from **5**/**6** has been confirmed by elemental and spectral analysis.

2.2. Molecular structure

The X-ray structure of $[Os(H)(CO)(PPh_3)_2(\alpha\text{-NaiEt})](PF_6)$ (**3c**) is shown in Fig. 1; selected bond parameters are listed in Table 1. The molecule consists of a central Os atom surrounded by six coordination centers and the arrangement is distorted octahedral. The atomic arrangement involves two *trans*-phosphine, a chelated 1-ethyl-2-(naphthyl-α-azo)imidazole (α-NaiEt), hydrido (H^-) and a CO within the OsP_2N_2CH coordination sphere. The H^- is located *trans* to the azo-N coordination. The α-naphthyl ring is inclined at an angle of 46.07(11)° with respect to the chelate ring (Os, N(1), C(2), N(2), N(8)). The *trans*-phosphine angle, P(1)–Ru–P(2) of 167.29 (2)° lies in the range of reported data [17,18]. The steric crowding of phenyl and naphthyl groups may provide this large deviation from the perfect *trans*-angle value. The chelate angle N(1)–Os–N(8) is 74.49(8)°. Other angles about Os define the distorted octahedral geometry.

There is no statistically significant difference in the two Os–N bonds; Os(1)–N(8), [(N8) is azo-N] is 2.1117(19) Å and Os(1)–N(1) (N(1) is imidazole) is 2.109(2) Å. The –N=N– bond length is 1.306(3) Å and is longer than the free ligand azo distance (1.267(3) Å) [16] which is in support of $d\pi(Os) \rightarrow \pi^*(azo)$ charge transmission. The

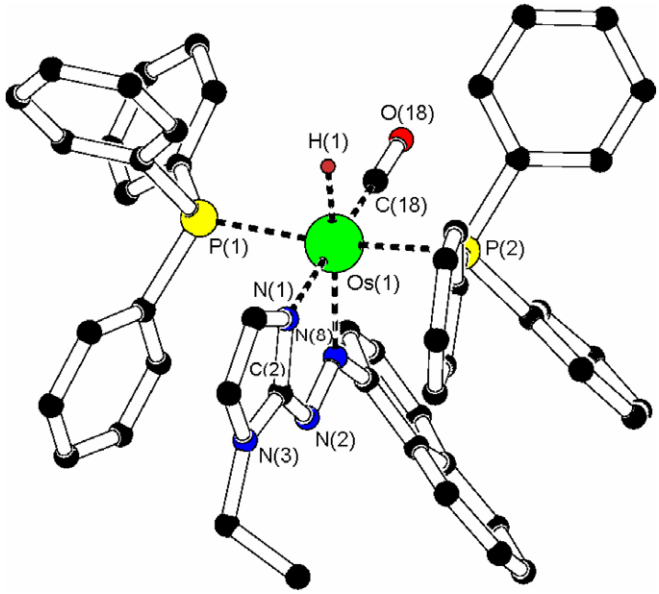


Fig. 1. Single crystal X-ray structure of $[Os(H)(CO)(PPh_3)_2(\alpha\text{-NaiEt})]^+$.

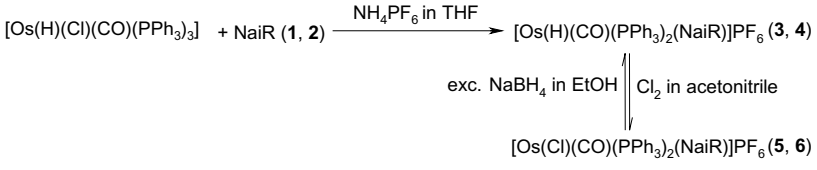


Table 1
Selected bond distances and angles of $[Os(H)(CO)(PPh_3)_2(\alpha\text{-NaiEt})](PF_6)$ (**3b**) along with their esd in parentheses

Distances (Å)		Angles (°)	
Os(1)–C (18)	1.855(3)	N(1)–Os(1)–N(8)	74.49(8)
Os (1)–N(1)	2.109(2)	N(1)–Os(1)–C(18)	177.46(9)
Os (1)–N(8)	2.1117(19)	N(8)–Os (1)–C(18)	103.08(9)
Os (1)–P(1)	2.3916(7)	P(1)–Os(1)–P(2)	167.29(2)
Os(1)–P(2)	2.3670(7)	P(1)–Os(1)–C(18)	95.03(8)
N(2)–N (8)	1.306(3)	P(2)–Os (1)–C(18)	89.17(8)
N(8)–C(8)	1.438(3)	P(1)–Os(1)–N(1)	84.50(6)
N(2)–C(2)	1.362(3)	P(1)–Os (1)–N(8)	94.43(5)
C(18)–O(18)	1.160(3)	P(2)–Os (1)–N(1)	91.82(6)
Os(1)–H(1)	1.600	P(2)–Os(1)–N(8)	96.30(5)
		C(18)–Os(1)–H(1)	88.4(10)
		N(1)–Os(1)–H(1)	94.1(10)
		P(1)–Os(1)–H(1)	85.8(9)
		P(2)–Os(1)–H(1)	82.3(9)
		N(8)–Os(1)–H(1)	168.5(10)

Os–H is *trans* to the Os–N=N-(azo) group. The *trans effect* of the Os–H bond may cause elongation of the –N=N– bond. The *trans* Os–H bond enhances the charge transfer to the N=N function and causes the increase in the N=N distance. The Os–C and C–O bond lengths are 1.855(3) and 1.160(3) Å, respectively. The observed Os–P distances, 2.3916(7), 2.3670 (7) Å, are short in the series of $Os(PPh_3)$ chemistry [17,18].

The intramolecular hydrogen bonding interaction generates a supramolecule. A hydrogen bonded dimer serves as a motif (Fig. 2). An F atom in PF_6^- acts as a bridging agent between two complex units. A bifurcated hydrogen bond [(naph)C(14)–H(14)–F(6)(PF_5)–H(27)–C(27)(PPh_3): C(14)–H(14a), 0.95; H(14a)–F(6), 2.520(2); C(14)–F(6), 3.231(3) Å; ∠C–H–F, 132.0° and C(27)–H(27a), 0.95; H(27a)–F(6), 2.400(1); C(27)–F(6), 3.319(3) Å and ∠C–H–F 163.0°] bridges two molecules and forms a supracyclic dimer. PPh_3 protons form several hydrogen bonding interactions with F–P(F_5) and form a 3-D arrangement.

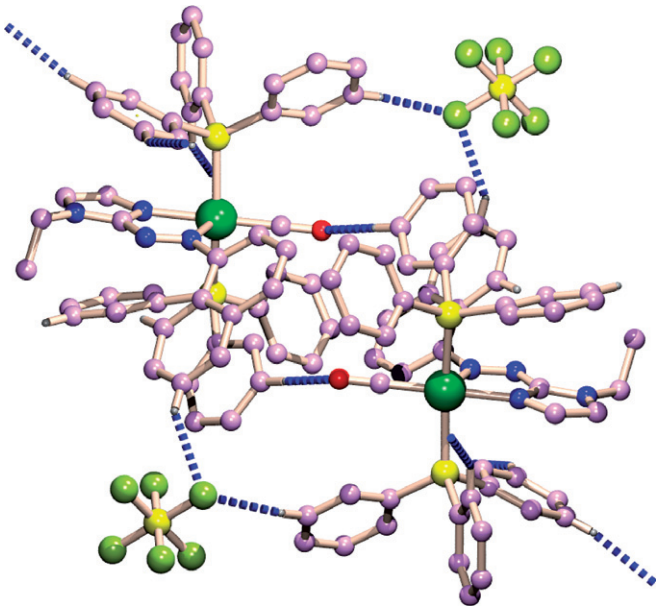


Fig. 2. H-Bonded dimer showing the C–H---F---H–C unit.

2.3. Spectra and bonding

The complexes $[Os(H)(CO)(PPh_3)_2(\alpha/\beta\text{-NaiR})](PF_6)$ (**3**,**4**) show a sharp stretch at 1920–1940 cm^{-1}, which corresponds to ν(CO). The ν(Os–H) band is observed at ca. 2080–2100 cm^{-1}. Other significant vibrations are ν(N=N) and ν(C=N) at 1350–1380 and 1560–1580 cm^{-1}, respectively. The azo stretching is significantly shifted to the lower frequency region compared to the free ligand value (1400–1410 cm^{-1}) [16] and is in support of back donation, $d\pi Os(II) \rightarrow \pi^*$(azo). The single crystal structure determination in one of the complexes also supports a retro-bonding process (vide supra). For the chlorinated complexes (**5**/**6**) ν(CO) is shifted to 1960–1970 cm^{-1} which is higher than the precursor complexes (**3**/**4**). This is corroborated with the absence of σ-donation of Os–H to the Os–CO motif.

The electronic spectra of the complexes **3** and **4** in MeCN show two high intensity transitions at 310–350 and 410–440 nm and these are assigned to ligand-centred charge transfer transitions. An intense broad band at 490–505 nm (Table 2) (Fig. 3), absent in the free ligand, is obviously assigned to a $d\pi(Os) \rightarrow \pi^*$(azoimine) transition [10]. The solution spectra of **5** and **6** show blue shifting by 10–30 nm compared to the hydrido analogues, **3** and **4** respectively.

The ^1H NMR spectra of the complexes are taken in $CDCl_3$ (the proton numbering pattern is shown in Scheme 1) and have been assigned (Table 3) on the basis of spin-spin interactions and on comparison with the free ligand values [10,16]. The X-ray structure determination aids the unambiguous assignment of the protons. The most significant observation is the appearance of a triplet Os–H signal at −9.55 to −9.65 ppm ($^2J_{P-H} = 22$–25 Hz) for $[Os(H)(CO)(PPh_3)_2(\alpha/\beta\text{-NaiR})](PF_6)$. Imidazole protons 4- and 5-H appear as a broad singlet at 7.2–7.3 and 7.0–7.1 ppm, respectively. The singlet nature of the imidazole protons may be due to rapid proton exchange on the NMR time scale. 1-R signals of (α/β)-NaiR in $[Os(H/Cl)(CO)(PPh_3)_2(\alpha/\beta\text{-NaiR})]^+$ appear at their usual position [16]; 1-Me appears as a singlet at 4.10–4.15 ppm; 1-CH_2–CH_3 gives a quartet at 4.45–4.50 ppm, ($J = 8.0$ Hz) and a triplet at 1.5 ppm ($J = 8.0$ Hz) for –CH_2– and –CH_3, respectively; 1-CH_2–(Ph) gives a singlet at 5.65–5.75 ppm. PPh_3 shows multiplets at 7.2–7.4 ppm.

2.4. Electrochemistry

The redox data are summarised in Table 2. $[Os(H)(CO)(PPh_3)_2(\alpha/\beta\text{-NaiR})](PF_6)$ (**3**, **4**) and $[Os(Cl)(CO)(PPh_3)_2(\alpha/\beta\text{-NaiR})](PF_6)$ (**5**, **6**) show two successive redox responses (Fig. 4) in MeCN solution with a Pt-working electrode (+ve to Ag/AgCl) between 0.0 and 1.8 V. The voltammogram is quasireversible in nature as is evident from the peak-to-peak separation data (for a reversible

Table 2
UV–Vis spectral[a] and cyclic voltammetric data[a]

Complex	UV–Vis spectra λ_{max} (nm) ($10^{-3} \in M^{-1} cm^{-1}$)	Cyclic voltammetry		
		E^1_M	E^2_M	Ligand reductions
3b	334(8.46), 410(12.88), 495(5.34)	0.68(160)	1.18(190)	−0.82(160), −1.24[b]
3c	350(5.42), 415(5.98), 500(5.47)	0.58(160)	1.20(170)	−0.88(180), −1.22[b]
3d	332(4.76), 442(5.64), 504(3.94)	0.70(140)	1.32(170)	−0.78(160), −1.32[b]
4b	352(6.25), 421(7.29), 492(8.20)	0.68(130)	1.35(180)	−0.87(160), −1.35[b]
4c	350(3.88), 428(6.19), 496(2.94)	0.60(160)	1.22(170)	−0.85(180), −1.30[b]
4d	328(4.82), 438(6.34), 498(3.26)	0.70(160)	1.22(170)	−0.82(160), −1.35[b]
5b	337(5.48), 458(7.09), 506(5.38)	0.77(130)	1.30(160)	−0.80(150), −1.25[b]
5c	358(5.48), 430(5.94), 534(5.38)	0.68(120)	1.27(170)	−0.74(150), −1.23[b]
5d	336(5.24), 454(4.78), 520(3.86)	0.81(130)	1.40(160)	−0.72(160), −1.20[b]
6b	338(8.22), 425(9.26), 510(6.36)	0.75(130)	1.30(180)	−0.90(180), −1.40[b]
6c	356(3.68), 468(5.07), 512(6.19)	0.78(120)	1.36(180)	−0.77(170), −1.32[b]
6d	336(4.94), 356(5.44), 505(3.44)	0.80(130)	1.36(170)	−0.78(160), −1.37[b]

[a] Solvent MeCN, Pt-disk working electrode, Ag/AgCl reference electrode, Pt wire auxiliary electrode, [*n*-Bu_4N][ClO_4] supporting electrolyte. $E^1_M = 0.5(E_{pa} + E_{pc})$, V for Os(III)/Os(II) couple, E^2_M for Os(IV)/Os(III) couple in unit of V, $\Delta E_p = |E_{pa} - E_{pc}|$, mV; E_{pc} (cathodic-peak-potential), E_{pa} (anodic-peak-potential).
[b] E_{pc} (cathodic-peak-potential).

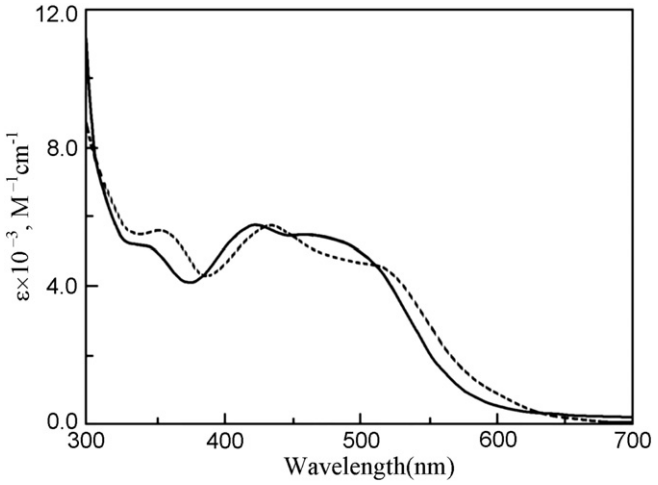


Fig. 3. Absorption spectra of [Os(H)(CO)(PPh_3)$_2$(α-NaiEt)](PF_6)] (**3c**) (—) [Os(Cl)(CO)(PPh_3)$_2$(α-NaiEt)](PF_6)] (**5c**) (- - -) (in acetonitrile).

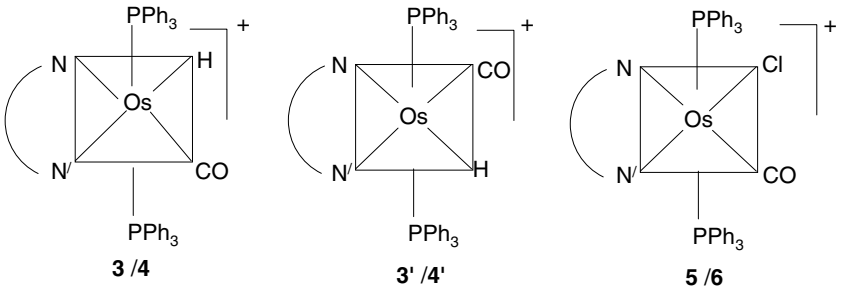
cyclic voltammogram ΔE_p is 60 mV and in the present complexes $\Delta E_p > 120$ mV and is quasi-reversible). The nature of the voltammogram does not change with scan rate (50–250 mV S^{-1}). Os(II) can sequentially exhibit Os(III)/Os(II) and Os(IV)/Os(III) redox processes at positive to Ag/AgCl reference electrode. Thus, two redox couples are referred to metal centred oxidations: Os(III)/Os(II) and Os(IV)/Os(III). Redox couples of [Os(H)(CO)(PPh_3)$_2$(α/β-NaiR)](PF_6) (**3**, **4**) at 0.6–0.70 and 1.1–1.3 V are shifted to 0.7–0.8 and 1.2–1.4 V, respectively, in [Os(Cl)(CO)(PPh_3)$_2$(α/β-NaiR)](PF_6) (**5**, **6**). The effect of the electron withdrawing Cl in the latter complexes may be the reason for this redox shifting.

On scanning to the negative direction (0 to −1.8 V), two redox responses are observed (Fig. 4). First response is quasireversible ($\Delta E_p \geqslant 120$ mV) and the second one appears at <−1.2 V which is irreversible in nature. Ligand reduction of azoimidazole complexes appears at negative potential [16b]. The chelated ligand belongs to the azoimine family and can accommodate two electrons centred at the azo group (–N=N–). On comparing with the literature [13,16,19], the reductive responses may be due to accommodation of electrons in the azo dominated function [–N=N]/[–N⁻–N–]$^-$ and [–N⁻–N]$^-$/[–N–N–]$^{2-}$.

3. Experimental

3.1. Materials

The 1-alkyl-2-(naphthyl-α/β-azo)imidazoles were synthesized following a previously published procedure [16]. [Os(H)(Cl)(CO)(PPh_3)$_3$] was also prepared by a reported method [20]. Imidazole and all other organic chemicals and inorganic salts were available from Sisco Research Lab,



Scheme 1.

Table 3
^{1}H NMR spectral data of the compounds in $CDCl_3$ at 298 K

Complex	4-H[a]	5-H[a]	6-H[a]	7-H[a]	8-H	9-12-H[d]	13-H[b]	N(1)–R	Os–H[c,g]	PPh_3
3b	7.18	7.05		7.68	7.68[c](7.0)	7.55	7.86(7.5)	4.14[f]	−9.63(23.4)	7.25–7.35
3c	7.15	7.06		7.66	7.66[c](7.0)	7.46	7.84(7.0)	4.46(9.0), 1.50(7.5)[e]	−9.59(22.8)	7.20–7.35
3d	7.18	7.09		7.73	7.73[c](7.0)	7.61	7.90(7.0)	5.78[f]	−9.55(24.0)	7.30–7.40
4b	7.16	7.04	7.93		7.59[b](7.5)	7.50	7.80(7.0)	4.09[f]	−9.67(22.0)	7.25–7.35
4c	7.14	7.00	7.89		7.55[b](7.5)	7.43	7.76(7.0)	4.51(9.0), 1.52(7.0)[e]	−9.60(23.6)	7.20–7.30
4d	7.21	7.11	7.98		7.67[b](7.5)	7.56	7.87(7.0)	5.68[f]	−9.56(22.0)	7.25–7.35
5b	7.36	7.21		7.86	7.86[c](7.0)	7.74	7.94(7.0)	4.23[f]		7.30–7.45
5c	7.38	7.23		7.88	7.88[c](7.0)	7.61	7.98(7.0)	4.57(8.5), 1.58(7.5)[e]		7.30–7.40
5d	7.34	7.25		7.90	7.87[c](7.0)	7.82	7.90(7.0)	5.87[f]		7.40–7.52
6b	7.34	7.18	8.05		7.76[b](7.5)	7.62	7.96(7.0)	4.19[f]		7.35–7.45
6c	7.22	7.16	8.02		7.68[b](7.5)	7.57	7.88(7.5)	4.62(9.0), 1.64(8.0)[e]		7.35–7.45
6d	7.41	7.27	8.10		7.84[b](7.5)	7.72	7.97(7.0)	5.76[f]		7.35–7.45

[a] Broad singlet.
[b] Doublet.
[c] Triplet.
[d] Multiplet.
[e] $\delta(-CH_2-CH_3)$ quartet for $-CH_2-$ and triplet for $-CH_3$.
[f] Singlet.
[g] Coupling constant ^2J refers to $^{31}P-^1H$ coupling.

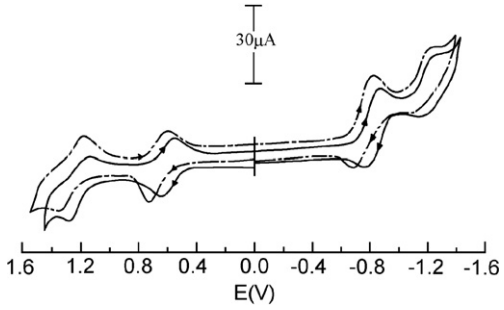


Fig. 4. Cyclic voltammogram of $[Os(H)(CO)(PPh_3)_2(\alpha\text{-NaiEt})](PF_6)$ (**3c**) (—); $[Os(Cl)(CO)(PPh_3)_2(\alpha\text{-NaiEt})](PF_6)$ (**5c**) (– – –) in acetonitrile using a Pt-working electrode and a Ag/AgCl reference electrode.

Mumbai, India. The purification of acetonitrile and preparation of *n*-tetra-butylammonium perchlorate $[n\text{-}Bu_4N][ClO_4]$ for the electrochemical work were done as reported before [9]. Dinitrogen was purified by bubbling through an alkaline pyrogallol solution. All other chemicals and solvents were of reagent grade and were used without further purification. Commercially available SRL silica gel (60–120 mesh) was used for column chromatography.

3.2. Physical measurements

Microanalytical data (C, H, N) were collected on a Perkin–Elmer 2400 CHNS/O elemental analyzer. Spectroscopic data were obtained using the following instruments: UV–Vis spectra, Perkin–Elmer; model Lambda 25. IR spectra (KBr disk, 4000–450 cm^{-1}), Perkin–Elmer; model RX-1. ^{1}H NMR spectra, Bruker (AC) 300 MHz FTNMR spectrometer. Molar conductances were measured using a Systronics conductivity meter 304 model using ca. 10^{-3} M solutions in acetonitrile. Electrochemical measurements were performed using computer-controlled PAR model 250 VersaStat electrochemical instruments with Pt-disk electrodes. All measurements were carried out under a nitrogen environment at 298 K with reference to Ag/AgCl in acetonitrile using $[n\text{-}Bu_4N][ClO_4]$ as the supporting electrolyte. The reported potentials are uncorrected for junction potentials. Magnetic properties were measured using a PAR-155 vibrating sample magnetometer fitted with a Walker scientific magnet. EPR spectra were recorded on a Varian E-109C spectrometer.

3.3. Synthesis of $[Os(H)(CO)(PPh_3)_2(\alpha\text{-NaiMe})](PF_6)$ (*3b*)

To a suspension of $[Os(H)(Cl)(CO)(PPh_3)_3]$ (0.250 g, 0.230 mmol) in dry THF (20 ml) 1-methyl-2-(naphthyl-α-azo)imidazole (α-NaiMe) (0.065 g, 0.28 mmol) was added in the same solvent (10 ml). The solution was stirred and refluxed for 15 h under dinitrogen. The orange red solution turned deep red. It was then cooled and filtered. The filtrate was then evaporated slowly in air to half of its original volume. A THF solution (5 ml) of NH_4PF_6 (0.2 g) was added into this solution and the resulting solution was kept in a deep freezer overnight. A dark precipitate appeared which was filtered, washed with cold THF and then dried in a $CaCl_2$ desiccator in vacuo. Purification was carried out by column chromatography over a silica gel column prepared in benzene. The desired red band was eluted by acetonitrile. It was then evaporated and dried over $CaCl_2$ in vacuo. The yield was 0.16 g (63%).

The other complexes were prepared following an identical procedure. The yield varied between 55% and 65%. Microanalytical data: Calc. (found) for $C_{51}H_{43}N_4OF_6P_3Os$ (**3b**): C, 54.44 (54.35); H, 3.82 (3.76); N, 4.98 (5.11%). For $C_{52}H_{45}N_4OF_6P_3Os$ (**3c**): C, 54.82 (54.95); H, 3.95 (3.88); N, 4.92 (5.01%). For $C_{57}H_{47}N_4OF_6P_3Os$ (**3d**): C, 56.99 (56.89); H, 3.92 (3.86); N, 4.67 (4.63%). For $C_{51}H_{43}N_4OF_6P_3Os$ (**4b**): C, 54.44 (54.39); H, 3.82 (3.78); N, 4.98 (4.94%).

For $C_{52}H_{45}N_4OF_6P_3Os$ (**4c**): C, 54.82 (54.78); H, 3.95 (3.98); N, 4.92 (4.94%). For $C_{57}H_{47}N_4OF_6P_3Os$ (**4d**): C, 56.99 (57.05); H, 3.92 (3.94); N, 4.67 (4.71%).

3.4. Reaction of $[Os(H)(CO)(PPh_3)_2(\alpha/\beta\text{-NaiR})](PF_6)$ (3, 4) with Cl_2 in MeCN

To a MeCN solution of $[Os(H)(CO)(PPh_3)_2(\alpha/\beta\text{-NaiR})](PF_6)$, a few drops of Cl_2 saturated MeCN was added and the resulting solution was stirred. The solution colour changed immediately from red to red-violet. The volume was reduced by slow evaporation and addition of NH_4PF_6 separated out crystalline compounds. A red-violet band was separated by chromatography. The eluent was evaporated to dryness, then the dark mass was water washed and dried over $CaCl_2$. Microanalytical data of the complexes support the composition $[Os(Cl)(CO)(PPh_3)_2(\alpha/\beta\text{-NaiR})](PF_6)$ and conductivity data ($\Lambda_M = 100$–$110\ \Omega^{-1}\ cm^2\ mol^{-1}$) suggests a 1:1 electrolyte.

$$[Os(H)(CO)(PPh_3)_2(\alpha/\beta\text{-NaiR})]^+ \xrightarrow{Cl_2 \text{ in MeCN}} [Os(Cl)(CO)(PPh_3)_2(\alpha/\beta\text{-NaiR})]^+$$

Microanalytical data: Calc. (found) for $C_{51}H_{42}N_4OClF_6P_3Os$ (**7b**): C, 52.83 (52.79); H, 3.62 (3.59); N, 4.83 (4.80%). For $C_{52}H_{44}N_4OClF_6P_3Os$ (**7c**): C, 53.22 (53.24); H, 3.75 (3.76); N, 4.77 (4.78%). For $C_{57}H_{46}N_4OClF_6P_3Os$ (**7d**): C, 55.41 (55.38); H, 3.73 (3.71); N, 4.54 (4.52%). For $C_{51}H_{42}N_4OClF_6P_3Os$ (**8b**): C, 52.83 (52.87%); H, 3.62 (3.64%); N, 4.83 (4.86%). For $C_{52}H_{44}N_4OClF_6P_3Os$ (**8c**): C, 53.22 (53.19); H, 3.75 (3.73); N, 4.77 (4.79). For $C_{57}H_{46}N_4OClF_6P_3Os$ (**8d**): C, 55.41 (55.36); H, 3.73 (3.69); N, 4.54 (4.52%).

3.5. X-ray crystal structure determination

Crystals of $[Os(H)(CO)(PPh_3)_2(\alpha\text{-NaiEt})](PF_6)$ (**3c**) were grown by slow diffusion of a CH_2Cl_2 solution of the complex into hexane. The prismatic red crystal was of dimensions $0.20 \times 0.10 \times 0.10$ mm. Data were collected using a CCD area detector rotating anode radiation source and a confocal optics monochromator of Mo-Kα radiation ($\lambda = 0.71073$ Å) at 93(2) K. Data collections were performed in the 2θ range 3.1–52.74° Absorption corrections were carried out by the multiscan process. Out of a total of 30,568 reflections, 9226 unique data (8451 of $I > 2\sigma(I)$) were used for the structure determination. Data reduction were carried out using Crystalclear 1.3.6 (Rigaku Corporation). The structure solution and refinement were carried out using the programs SHELXS-97 [21] and SHELXL-97 [22]. The structure was solved by direct method and refined by full-matrix least-squares refinement based on F^2. All non-hydrogen atoms were refined anisotropically. The hydridic H atom was fixed at a distance of 1.60 Å from the metal [23]. Crystal parameters and refinement results are summarized in Table 4.

Table 4
Summarised crystallographic data for $[Os(H)(CO)(PPh_3)_2(\alpha\text{-NaiEt})](PF_6)$

Empirical formula	$C_{52}H_{45}F_6N_4OP_3Os$
Formula weight	1139.03
Crystal system	monoclinic
Space group	$P2(1)/n$
a (Å)	12.0841(14)
b (Å)	25.549(3)
c (Å)	15.7643(18)
β (°)	103.684(3)
Size (mm^3)	$0.20 \times 0.10 \times 0.10$
V (Å^3)	4728.8(9)
λ (Å)	0.71073
$\rho_{calc.}$ ($Mg\ m^{-3}$)	1.600
Z	4
T (K)	93(2)
μ Mo-Kα (mm^{-1})	2.865
Total reflection collected	30 568
Unique reflections (R_{int})	9226(0.0287)
Refined parameters	609
Largest differences in peak and hole (e Å^{-3})	2.151 and −0.763
R[a] ($I > 2\sigma(I)$)	0.0235
wR[b]	0.0500
Goodness-of-fit[c]	1.043

[a] $R = \sum|F_o - F_c|/\sum F_o$.
[b] $wR = [\sum w(F_o^2 - F_c^2)/\sum wF_o^4]^{1/2}$ where $w = 1/[\sigma_2(F_o^2) + (0.0183P)^2 + 4.1609P]$, where $P = (F_o^2 + 2F_c^2)/3$.
[c] Goodness-of-fit (GOF) is defined as $[w(F_o^2 - F_c^2)/(n_0 - n_p)]^{1/2}$ where n_0 and n_p denote the number of data and variables, respectively.

4. Conclusion

1-Alkyl-2-(naphthyl-α/β-azo)imidazole (α/β-NaiR, **1** and **2**) has been reacted with $[Os(H)(Cl)(CO)(PPh_3)_3]$ in THF to synthesise $[Os(H)(CO)(PPh_3)_2(\alpha/\beta\text{-NaiR})](PF_6)$ (**3**, **4**). The structure of the complexes has been determined by spectroscopic data (FTIR, UV–Vis, ^{1}H NMR) and redox activity was examined by cyclic voltammetry. Single crystal X-ray diffraction measurement in the case of $[Os(H)(CO)(PPh_3)_2(\alpha\text{-NaiEt})](PF_6)$ confirmed the structure. Cl_2 (in MeCN) addition to the hydrido-Os compounds (**3**, **4**) has synthesized $[Os(Cl)(CO)(PPh_3)_2(\alpha/\beta\text{-NaiR})](PF_6)$ (**5**, **6**).

Acknowledgements

Financial support from the Department of Science and Technology, New Delhi and Jadavpur University Potential for Excellence unit are gratefully acknowledged. One of us (T.K.M.) thanks UGC, New Delhi for a fellowship. We thank Dr. G. Mostafa, Department of Physics, Jadavpur University, Kolkata for his help in the structure solution.

Appendix A. Supplementary material

CCDC 288383 contains the supplementary crystallographic data for **3c**. These data can be obtained free of charge via http://www.ccdc.cam.ac.uk/conts/retrieving.html, or from the Cambridge Crystallographic Data Centre, 12 Union Road, Cambridge CB2 1EZ, UK; fax: (+44)

1223-336-033; or e-mail: deposit@ccdc.cam.ac.uk. Supplementary data associated with this article can be found, in the online version, at doi:10.1016/j.poly. 2006.08.028.

References

[1] (a) E.A. Seddon, K.R. Seddon, The Chemistry of Ruthenium, Elsevier, Amsterdam, 1984;
(b) J. Reedijk, in: G. Wilkinson, J.A. Mcclerverty (Eds.), Comprehensive Coordination Chemistry, Pergamon, Oxford, UK, 1987.

[2] (a) K. Kalyansundaram, Coord. Chem. Rev. 46 (1982) 159;
(b) S. Serroni, S. Campagna, F. Puntoriero, C.D. Pietro, N.D. Mcclenaghan, F. Loisean, Chem. Soc. Rev. 30 (2001) 367.

[3] (a) B.K. Ghosh, A. Chakravorty, Coord. Chem. Rev. 95 (1989) 239;
(b) N. Bag, A. Pramanik, G.K. Lahiri, A. Chakravorty, Inorg. Chem. 31 (1992) 40.

[4] A.C.G. Hotze, H. Kooijman, A.L. Spek, J.G. Haasnoot, J. Reedijk, New J. Chem. 28 (2004) 565.

[5] R.E. Shepherd, Coord. Chem. Rev. 247 (2002) 147.

[6] (a) C. Das, A. Saha, C.-H. Hung, G.-H. Lee, S.-M. Peng, S. Goswami, Inorg. Chem. 42 (2003) 198;
(b) K.N. Mitra, S. Goswami, Proc. Indian Acad. Sci. (Chem. Sci.) 111 (1999) 461.

[7] (a) B.K. Santra, G.K. Lahiri, J. Chem .Soc., Dalton Trans. (1998) 1613;
(b) G.K. Lahiri, S. Bhattacharya, S. Goswami, A. Chakravorty, J. Chem. Soc., Dalton Trans. (1990) 561.

[8] J.G. Hassnoot, W. Hinrichs, O. Weir, J.G. Vos, Inorg. Chem. 25 (1986) 4140.

[9] (a) T.K. Misra, D. Das, C. Sinha, P. Ghosh, C.K. Pal, Inorg. Chem. 37 (1998) 1672;
(b) P. Byabartta, S.k. Jasimuddin, B.K. Ghosh, C. Sinha, A.M.Z. Slawin, J.D. Woollins, New J. Chem. 26 (2002) 1415;
(c) P. Byabartta, J. Dhinda, P.K. Santra, C. Sinha, K. Panneerselvam, F.-L. Liao, T.-H. Lu, J. Chem. Soc., Dalton Trans. (2001) 2825;
(d) S. Pal, T.K. Misra, C. Sinha, A.M.Z. Slawin, J.D. Woollinns, Polyhedron 19 (2000) 1925;
(e) S.K. Jasimuddin, P. Byabartta, G. Mostafa, T.-H. Lu, C. Sinha, Polyhedron 23 (2004) 727;
(f) S.k. Jasimuddin, T. Mathur, G. Mostafa, C. Sinha, Inorg. Chim. Acta 358 (2005) 3601.

[10] (a) J. Dinda, S. Pal, B.K. Ghosh, J. Cheng, F.-L. Liao, T.-H. Lu, C. Sinha, J. Coord. Chem. 55 (2002) 1271;
(b) P. Byabartta, S. Pal, T.K. Misra, C. Sinha, F.-L. Liao, K. Panneerselvam, T.-H. Lu, J. Coord. Chem. 55 (2002) 479.

[11] H. Sigel (Ed.), Metal Ions in Biological System, vol. 13, Marcel Dekker, New York, 1981.

[12] J. Otsuki, K. Suwa, K. Narutaki, C. Sinha, I. Yoshikawa, K. Araki, J. Phys. Chem. A 109 (2005) 8064.

[13] (a) M. Shivakumar, K. Pramanik, P. Ghosh, A. Chakravorty, Chem. Commun. (1998) 2103;
(b) M. Shivakumar, A. Chakravorty, Indian J. Chem. Sect. A 39A (2000) 477;
(c) K. Pramanik, M. Shivakumar, P. Ghosh, A. Chakravorty, Inorg. Chem. 39 (2000) 195.

[14] (a) W. Kaim, Coord. Chem. Rev. 219 (2001) 463;
(b) M. Schwach, H.-D. Hausen, W. Kaim, Inorg. Chem. 38 (1999) 2242;
(c) N. Doslik, T. Sixt, W. Kaim, Angew. Chem., Int. Ed. 37 (1998) 2403.

[15] (a) A. Sanyal, P. Banerjee, G.-H. Lee, S.-M. Peng, C.-H. Hung, S. Goswami, Inorg. Chem. 43 (2004) 7456;
(b) B.A. Goodman, J.B. Raynor, Adv. Inorg. Chem. Radiochem. 13 (1970) 135;
(c) A.L. Balch, R.H. Holm, J. Am. Chem. Soc. 88 (1966) 5201.

[16] (a) J. Dinda, Ph.D. Thesis, The University of Burdwan, Burdwan, India, 2003;
(b) J. Dinda, K. Bag, C. Sinha, G. Mostafa, T.-H. Lu, Polyhedron 22 (2003) 1367;
(c) P. Byabartta, P.K. Santra, T.K. Misra, C. Sinha, C.H.L. Kennard, Polyhedron 20 (2001) 905;
(d) S. Pal, D. Das, P. Chattopadhyay, C. Sinha, K. Panneerselvam, T.-H. Lu, Polyhedron 19 (2000) 1263;
(e) J. Dinda, P.K. Santra, C. Sinha, L.R. Falvello, J. Organomet. Chem. 629 (2001) 28;
(f) J. Dinda, U.S. Ray, G. Mostafa, T.-H. Lu, A. Usman, I. Abdul Razak, S. Chantrapromma, H.-K. Fun, C. Sinha, Polyhedron 22 (2003) 247.

[17] P.K. Santra, C. Sinha, W.J. Sheen, F.-L. Liao, T.-H. Lu, Polyhedron 20 (2001) 599.

[18] K.R. Flower, G.L. Leal, R.G. Pritchard, Inorg. Chem. Commun. 7 (2004) 729.

[19] (a) C.K. Pal, S. Chattopadhyay, C. Sinha, A. Chakravorty, Inorg. Chem. 33 (1994) 6140;
(b) C.K. Pal, S. Chattopadhyay, C. Sinha, A. Chakravorty, Inorg. Chem. 35 (1996) 2442;
(c) C.J. Jonson, R. Chang, J. Chem. Phys. 43 (1965) 3183.

[20] N. Ahmad, J.J. Levison, S.D. Robinson, M.F. Uttley, Inorg. Synth. 15 (1975) 45.

[21] G.M. Sheldrick, SHELXS-97, Program for the Solution of Crystal Structure, University of Gottingen, Germany, 1997.

[22] G.M. Sheldrick, SHELXL-97, Program for the Refinement of Crystal Structure, University of Gottingen, Germany, 1997.

[23] M.A. Green, J.C. Huffmann, K.G. Caulton, J. Organomet. Chem. C78 (1983) 243.

Available online at www.sciencedirect.com
ScienceDirect
Polyhedron 26 (2007) 607–616
POLYHEDRON
www.elsevier.com/locate/poly

Structural and spectral studies of novel Co(III) complexes of N(4)-substituted thiosemicarbazones derived from pyridine-2-carbaldehyde

P.F. Rapheal [a], E. Manoj [a], M.R. Prathapachandra Kurup [a,*], E. Suresh [b]

[a] Department of Applied Chemistry, Cochin University of Science and Technology, Kochi, Kerala 682 022, India
[b] Analytical Sciences Division, Central Salt and Marine Chemicals Research Institute, Bhavnagar, Gujarat 364 002, India

Received 23 June 2006; accepted 16 August 2006
Available online 7 September 2006

Abstract

Seven bis(ligand) Co(III) complexes {$[CoL^1_2]NO_3 \cdot H_2O$ (**1**), $[CoL^1_2]Cl \cdot 2H_2O$ (**2**),$[CoL^1_2]ClO_4$ (**3**), $[CoL^2_2]NO_3$ (**4**), $[CoL^2_2]Cl \cdot 2H_2O$ (**5**), $[CoL^3_2]Br \cdot 2H_2O$ (**6**), $[CoL^3_2]ClO_4 \cdot H_2O$ (**7**)} of three thiosemicarbazone ligands {pyridine-2-carbaldehyde-N(4)-*p*-methoxyphenyl thiosemicarbazone [HL^1], pyridine-2-carbaldehyde-N(4)-2-phenylethyl thiosemicarbazone [HL^2] and pyridine-2-carbaldehyde-N(4)-(methyl),N(4)-(phenyl) thiosemicarbazone [HL^3]} were synthesized and physico-chemically characterized. All complexes are assigned octahedral geometries on the basis of spectral studies. The ligands deprotonate and coordinate by means of pyridine nitrogen, azomethine nitrogen, and thiolate sulfur atoms. The single crystal X-ray structures of HL^3 and two nitrate compounds are discussed. The structural studies corroborate the spectral characterization.
© 2006 Elsevier Ltd. All rights reserved.

Keywords: Thiosemicarbazone; Co(III) complex; Pyridine-2-carbaldehyde; Crystal structure

1. Introduction

Schiff bases and their transition metal complexes are of much interest in inorganic chemistry and have been studied extensively. Thiosemicarbazones and their metal complexes are very promising compounds among Schiff bases, due to their beneficial biological applications [1]. It is known that the biological activity of the thiosemicarbazones varies with the N(4) substituent as well as the ketone or aldehyde from which they are derived [2,3]. There are reports that the presence of alkyl groups at the terminal N(4) position can considerably increase their activity [4]. Domag et al. [5] had reported that thiosemicarbazones possess antitubercular activity and after that many papers on the pharmacology of these compounds appeared, indicating that they have wide inhibitory activity against smallpox [6] and several kinds of tumors [7]. They can also be used as pesticides [8] and fungicides [9–12]. The presence of various donor atoms and ability to change the denticity depending on the reaction conditions and starting reagents make thiosemicarbazones of various aldehydes and ketones a special category among organic ligands [13].

Due to the pronounced antibacterial, antimalarial, antitumor and antileukaemic activity of heterocyclic thiosemicarbazones and their metal complexes, these compounds have been attractive to a large number of research groups in recent years [14–22]. Pyridine-2-carbaldehyde thiosemicarbazone and its substituted derivatives and their metal complexes are important members in this series. A large number of complexes of different metals with the above ligands have been studied and biological activities of some of them have been explored [23,24]. In an earlier paper [25] we have reported the synthesis and crystal structure of one of the three present ligands, namely

* Corresponding author. Tel.: + 91 484 2575804; fax: +91 484 2577595.
E-mail addresses: mrp@cusat.ac.in, mrp_k@yahoo.com (M.R. Prathapachandra Kurup).

0277-5387/$ - see front matter © 2006 Elsevier Ltd. All rights reserved.
doi:10.1016/j.poly.2006.08.029

pyridine-2-carbaldehyde N(4)-phenylethyl thiosemicarbazone (HL^2). Chattopadhyay et al. [26] have reported cobalt(III) complexes of the type $[CoL_2]X$ (X = Cl, SCN and N_3) where L is a deprotonated pyridine-2-carbaldehyde thiosemicarbazone. Here we report the synthesis and characterization of a novel ligand pyridine-2-carbaldehyde N(4)-methyl N(4)-phenyl thiosemicarbazone (HL^3) and the cobalt(III) complexes of three pyridine-2-carbaldehyde based thiosemicarbazones. In order to characterize these compounds unequivocally we report the molecular and crystal structures of HL^3 and two complexes, $[CoL^1_2]NO_3$ and $[CoL^2_2]NO_3$.

2. Experimental

Pyridine-2-carbaldehyde (Aldrich) and *p*-anisidine (Fluka) were used as received. Cobalt(II) nitrate hexahydrate, cobalt(II) chloride hexahydrate, cobalt(II) perchlorate hexahydrate (Merck) were used as supplied. 4-Methyl-4-phenyl-3-thiosemicarbazide was prepared as reported previously [27] and solvents were purified by standard procedures before use. *Caution!* Perchlorate salts of metal complexes with organic ligands are potentially explosive and should be handled with care.

2.1. Synthesis of ligands

The thiosemicarbazone ligands (Scheme 1) were obtained by adopting and modifying a reported procedure of Scovill [27]. The synthesis and crystal structure of HL^2 have been published earlier [25].

2.1.1. Synthesis of HL^1

A solution of 1.00 g (5.52 mmol) of 4-methyl-4-phenyl-3-thiosemicarbazide in 5 ml of MeCN was refluxed with 0.679 g (5.52 mmol) of 4-methoxyaniline (*p*-anisidine) and 0.591 g (5.52 mmol) of pyridine-2-carbaldehyde for 1.5 h. The solution was chilled (overnight) and the crystals that separated were collected and washed well with MeCN. Yield: 58%. The compound was recrystallized from ethanol and dried *in vacuo* over P_4O_{10}.

2.1.2. Synthesis of HL^3

A solution of 1.00 g (5.52 mmol) of 4-methyl-4-phenyl-3-thiosemicarbazide in 5 ml of MeCN was mixed with 0.591 g (5.52 mmol) of pyridine-2-carbaldehyde. The solution was heated at reflux for 1 h, chilled (overnight) and the crystals that separated were collected and washed well with MeCN. Yield: 64%. The compound was recrystallized from ethanol and dried *in vacuo* over P_4O_{10}. Single crystals of XRD quality were obtained by slow evaporation of an ethanol solution of the compound.

All analytical and spectroscopic data of the ligands are in good agreement with the expected values.

2.2. Synthesis of complexes

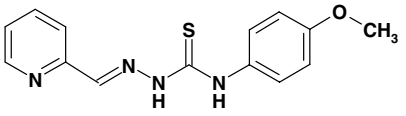
All complexes were prepared by the following general method. To a hot methanolic (20 ml) solution of thiosemicarbazone (0.5 mmol), 0.5 mmol of the cobalt(II) salt dissolved in 10 ml hot methanol was added. The mixture was refluxed for 2 h and allowed to stand for two days at room temperature. The compound formed was filtered, washed with water, methanol and ether. It was then dried *in vacuo* over P_4O_{10}. XRD quality single crystals of **1** and **4** were obtained by the slow evaporation of their methanol solutions.

2.3. Physical measurements

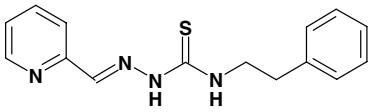
Elemental analyses were carried out using a Vario EL III CHNS analyzer at SAIF, Kochi, India. Infrared spectra were recorded on a Thermo Nicolet, AVATAR 370 DTGS model FT-IR spectrophotometer with KBr pellets and the ATR technique at SAIF, Kochi, India. Electronic spectra were recorded on a Cary 5000 version 1.09 UV–Vis–NIR spectrophotometer using a solution in chloroform.

2.4. X-ray crystallography

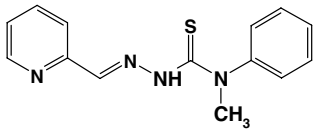
The crystallographic data and structure refinement parameters for the compounds are given in Table 1. The



HL^1



HL^2



HL^3

Scheme 1. The thiosemicarbazones HL^1, HL^2 and HL^3.

Table 1
Crystal refinement parameters of compounds HL^3, $[CoL^1_2]NO_3 \cdot H_2O$ (**1**) and $[CoL^2_2]NO_3$ (**4**)

Parameters	HL^3	$[CoL^1_2]NO_3$ (**1**)	$[CoL^2_2]NO_3$ (**4**)
Empirical formula	$C_{14}H_{14}N_4S$	$C_{28}H_{26}CoN_9O_5S_2$	$C_{30}H_{30}CoN_9O_3S_2$
Formula weight (M)	270.35	691.63	687.68
Temperature (K)	293(2)	293(2)	293(2)
Wavelength (Mo Kα) (Å)	0.71073	0.71073	0.71073
Crystal system	triclinic	triclinic	monoclinic
Space group	$P\bar{1}$	$P\bar{1}$	$P2_1$
Lattice constants			
a (Å)	9.2038(10)	9.849(4)	14.7543(9)
b (Å)	9.6372(11)	13.193(5)	12.0675(18)
c (Å)	9.6497(12)	13.533(6)	27.424(8)
α (°)	63.773(2)	60.879(7)	90.00
β (°)	65.060(2)	79.885(8)	91.109(11)
γ (°)	75.410(2)	86.595(8)	90.00
V (Å^3)	693.94(14)	1511.6(11)	4881.9(17)
Z	2	2	6
ρ_{calc} (Mg m^{-3})	1.294	1.520	1.403
Absorption coefficient, μ (mm^{-1})	0.225	0.761	0.702
F(000)	284	712	2136
Crystal size (mm)	$0.33 \times 0.24 \times 0.18$	$0.24 \times 0.16 \times 0.08$	$0.30 \times 0.25 \times 0.20$
θ Range for data collection (°)	2.36–28.34	1.75–25.00	3.10–25.00
Limiting indices	$-7 \leqslant h \leqslant 11$, $-12 \leqslant k \leqslant 12$, $-12 \leqslant l \leqslant 12$	$-11 \leqslant h \leqslant 11$, $-15 \leqslant k \leqslant 15$, $-16 \leqslant l \leqslant 16$	$-17 \leqslant h \leqslant 15$, $-14 \leqslant k \leqslant 14$, $-32 \leqslant l \leqslant 32$
Reflections collected	4140	10660	20242
Independent reflections (R_{int})	3024 (0.0112)	5240 (0.0752)	15034 (0.0378)
Refinement method	full-matrix least-squares on F^2	full-matrix least-squares on F^2	full-matrix least-squares on F^2
Data/restraints/parameters	3024/0/177	5240/0/408	15034/1/1216
Goodness-of-fit on F^2	1.050	1.034	0.804
Final R indices [$I > 2\sigma(I)$]	$R_1 = 0.0440$, $wR_2 = 0.1214$	$R_1 = 0.0815$, $wR_2 = 0.1724$	$R_1 = 0.0479$, $wR_2 = 0.0733$
R indices (all data)	$R_1 = 0.0516$, $wR_2 = 0.1274$	$R_1 = 0.1322$, $wR_2 = 0.1959$	$R_1 = 0.1134$, $wR_2 = 0.0848$
Largest difference peak and hole (e Å^{-3})	0.251 and −0.197	0.629 and −0.469	0.328 and −0.211

data of HL^3 and **1** were collected using a Bruker Smart Apex CCD diffractometer equipped with graphite-monochromated Mo Kα ($\lambda = 0.71073$ Å) radiation, while compound **4** was diffracted by CrysAlis CCD, Oxford Diffraction Ltd. with graphite-monochromated Mo Kα ($\lambda = 0.71073$ Å) radiation at the National Single Crystal X-ray Diffraction Facility, IIT, Bombay, India. The trial structure was solved using SHELXS-97 [28] and refinement was carried out by full-matrix least-squares on F^2 (SHELXL) [28]. The molecular graphics employed were ORTEP-III [29] and PLATON [30].

3. Results and discussion

The colors and partial elemental analysis data of all the complexes are listed in Table 2. All the complexes are brown in color and soluble in solvents like methanol, ethanol, chloroform and DMF. They are found to be diamagnetic which confirms oxidation to cobalt(III) during the preparation, as has been found previously with heterocyclic N(4)-substituted thiosemicarbazones, and hence corresponds to a d^6 ion in a strong field [31]. The molar conductivities of 10^{-3} M DMF solutions of the complexes indicate

Table 2
Stoichiometries and partial elemental analyses of the complexes

Compounds	Stoichiometries	Anal: Found (Calc.) %				Λ_M[a]
		C	H	N	S	
$[CoL^1_2]NO_3 \cdot H_2O$ (**1**)	$C_{28}H_{26}CoN_9O_5S_2 \cdot H_2O$	47.89 (47.39)	3.85 (3.98)	18.05 (17.76)	9.12 (9.04)	86
$[CoL^1_2]Cl \cdot 2H_2O$ (**2**)	$C_{28}H_{26}CoN_8O_2S_2Cl \cdot 2H_2O$	47.69 (47.97)	4.45 (4.31)	15.97 (15.98)	9.23 (9.15)	78
$[CoL^1_2]ClO_4$ (**3**)	$C_{28}H_{26}CoN_8O_6S_2Cl$	45.89 (46.13)	3.73 (3.59)	15.29 (15.37)	8.79 (8.80)	80
$[CoL^2_2]NO_3$ (**4**)	$C_{30}H_{30}CoN_9O_3S_2$	51.88 (52.40)	4.53 (4.40)	18.36 (18.33)	9.18 (9.33)	92
$[CoL^2_2]Cl \cdot 2H_2O$ (**5**)	$C_{30}H_{30}CoN_8S_2Cl \cdot H_2O$	52.78 (53.05)	4.37 (4.75)	16.21 (16.50)	9.44 (9.75)	67
$[CoL^3_2]Br \cdot 2H_2O$ (**6**)	$C_{28}H_{26}CoN_8S_2Br \cdot 2H_2O$	46.98 (47.13)	4.56 (4.24)	15.75 (15.70)	9.04 (8.99)	89
$[CoL^3_2]ClO_4 \cdot H_2O$ (**7**)	$C_{28}H_{26}CoN_8O_4S_2Cl \cdot H_2O$	46.58 (47.03)	4.06 (3.95)	15.82 (15.67)	9.08 (8.97)	75

[a] Molar conductivity of 10^{-3} M DMF solution, in Ω^{-1} cm^2 mol^{-1}.

that they are 1:1 electrolytes. The partial elemental analysis data and conductance measurement data are consistent with the general formulation of the complexes as $[CoL_2]X$, where X = NO_3, Cl, Br and ClO_4. For the compounds **1**, **5** and **7**, the elemental analysis data matches with the stoichiometry containing one molecule of water of crystallization/lattice water, two molecules in the case of **2** and **6**, whereas no water molecules are present in **3** and **4**. The relevant bond lengths and bond angles of HL^3, $[CoL_2^1]NO_3 \cdot H_2O$ (**1**) and $[CoL_2^2]NO_3$ (**4**) are listed in Table 3. The asymmetric unit of **4** contains three molecules, only one of which is discussed.

3.1. Crystal structure of HL^3

The molecular structure of HL^3, with the atom numbering scheme, is given in Fig. 1. Its existence in the thione form is confirmed by the C=S bond length of 1.6750(14) Å [32]. The molecule exists in the *E* conformation about the N2–N3 bond as evidenced by the C6–N2–N3–C7 dihedral angle of 177.66(16)°. The intramolecular hydrogen bond N3–H1N3···N1 and the intermolecular hydrogen bond C6–H6···N2* facilitate this geometry. The core thiosemicarbazone moiety C6, N2, N3, C7, S1, N4 is in a plane with a maximum deviation of −0.0576(15) Å for the N2 atom and makes an angle of 16.79(8)° with the pyridyl ring. The phenyl ring plane is almost perpendicular {85.38(8)°} to this thiosemicarbazone plane. Relevant C–H···π and Cg···Cg interactions are given in Table 4.

3.2. Crystal structures of $[CoL_2^1]NO_3 \cdot H_2O$ (**1**) and $[CoL_2^2]NO_3$ (**4**)

The molecular structures of **1** and **4** along with the atom numbering schemes are given in Figs. 2 and 3. The metal

Table 3
Selected bond lengths (Å) and bond angles (°) of the compounds[a]

	HL^2	HL^3	$[CoL_2^1]NO_3 \cdot H_2O$ (**1**)	$[CoL_2^2]NO_3$ (**4**)
S(1)–C(7)	1.6849(13)	1.6750(14)	1.747(6)	1.732(6)
S(2)–C(21)			1.730(6)	
S(2)–C(22)				1.776(8)
N(2)–C(6)	1.2837(15)	1.285(2)	1.290(8)	1.305(6)
N(6)–C(20)			1.305(7)	
N(6)–C(21)				1.303(7)
N(2)–N(3)	1.3783(14)	1.3613(17)	1.360(7)	1.336(6)
N(6)–N(7)			1.371(7)	1.333(7)
N(3)–C(7)	1.3587(16)	1.3644(18)	1.321(7)	1.329(6)
N(7)–C(21)			1.330(8)	
N(7)–C(22)				1.292(8)
N(4)–C(7)	1.3401(16)	1.345(2)	1.344(8)	1.324(6)
N(8)–C(21)			1.347(8)	
N(8)–C(22)				1.370(8)
Co(1)–S(1)			2.232(2)	2.2348(17)
Co(1)–S(2)			2.2043(19)	2.2246(17)
Co(1)–N(1)			1.958(5)	1.963(5)
Co(1)–N(5)			1.956(5)	1.973(4)
Co(1)–N(2)			1.876(5)	1.889(4)
Co(1)–N(6)			1.885(5)	1.897(5)
C(6)–N(2)–N(3)	114.37(10)	117.75(13)	118.8(5)	120.3(5)
N(2)–N(3)–C(7)	120.47(10)	120.25(12)	111.6(5)	112.0(5)
N(4)–C(7)–N(3)	116.16(10)	113.87(12)	120.1(5)	116.4(6)
N(3)–C(7)–S(1)	119.25(8)	122.89(12)	123.3(5)	123.8(4)
N(4)–C(7)–S(1)	124.59(9)	123.22(11)	116.6(5)	119.8(5)
N(1)–Co(1)–N(5)			90.8(2)	90.10(18)
N(2)–Co(1)–N(6)			178.1(2)	178.4(2)
S(1)–Co(1)–S(2)			90.73(8)	92.24(7)
S(1)–Co(1)–N(1)			167.97(15)	168.17(16)
S(1)–Co(1)–N(5)			90.76(16)	89.53(13)
S(1)–Co(1)–N(2)			84.99(17)	85.07(16)
S(1)–Co(1)–N(6)			96.01(17)	94.80(15)
N(1)–Co(1)–N(2)			83.0(2)	83.3(2)
N(1)–Co(1)–N(6)			96.0(2)	96.9(2)
N(1)–Co(1)–S(2)			90.10(15)	90.45(14)
N(2)–Co(1)–N(5)			95.2(2)	98.6(2)
N(2)–Co(1)–S(2)			96.41(16)	92.75(13)
S(2)–Co(1)–N(5)			168.41(15)	168.60(17)
S(2)–Co(1)–N(6)			85.23(16)	85.62(19)
N(5)–Co(1)–N(6)			83.2(2)	83.0(2)

[a] Data for HL^2 [25] is taken for comparison.

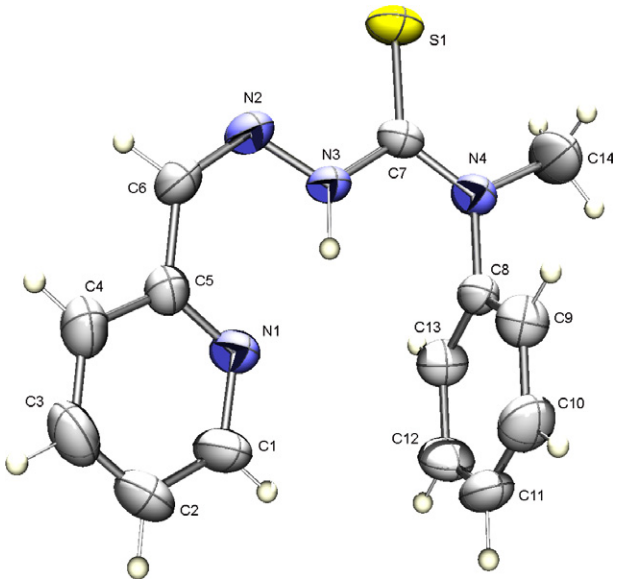


Fig. 1. ORTEP diagram of HL^3 with 50% probability ellipsoids.

Table 4
Interaction parameters of the compound HL^3

π···π interactions			
Cg(I)–Res(I)···Cg(J)	Cg–Cg (Å)	α (°)	β (°)
Cg(1) [1]···Cg(1)[a]	3.6040	0.02	13.54
Equivalent position codes: a = $-x$, $1-y$, $1-z$			
Cg(1) = N1, C1, C2, C3, C4, C5			
CH···π interactions			
X–H(I)–Res(1)···Cg(J)	H···Cg (Å)	X···Cg (Å)	X–H···Cg (°)
C(14)–H(14B) [1]···Cg(2)[a]	2.95	3.7088	137
Equivalent position codes: a = $1-x$, $-y$, $2-z$			
Cg(2) = C(8), C(9), C(10), C(11), C(12), C(13)			

Cg = Centroid, α = dihedral angles between planes I and J, β = angle Cg(1)–Cg(J).

centers in both the complexes possess an octahedral geometry with two deprotonated ligands. The Co(III) ion is coordinated in a *meridional* fashion [33–35] using pairs of *cis* pyridyl nitrogen, *trans* azomethine nitrogen and *cis* thiolate sulfur atoms from two monoanionic ligands. This coordination results in four five membered chelate rings in both complexes. The bond angles suggest a distorted octahedral coordination geometry in both complexes. The dihedral angle formed by the mean planes of the bicyclic chelate systems of each of the ligands is 89.75(13)° in **1** and 83.45(1)° in **4**. In **1**, each bicyclic chelate system, Co1, S1, C7, N3, N2, C6, C5, N1 and Co1, S2, C21, N7, N6, C20, C19, N5, are approximately planar as evidenced by the maximum deviation of −0.057(7) Å for C6 and 0.080(7) Å for C21, respectively. In **4**, the bicyclic chelate system Co1, S1, C7, N3, N2, C6, C5, N1 is approximately planar with a maximum deviation of 0.06297 Å for N1, though its counterpart Co1, S2, C22, N7, N6, C21, C20, N5 show a distortion as evidenced by the maximum deviation of 2.12988 Å for C22. These results suggest the distortion in the octahedral geometry is more in **4** compared to **1**.

On complexation the ligand HL^2 undergoes structural reorientation to coordinate the metal in a NNS manner in **4**. The azomethine nitrogen was in the *E* configuration with both pyridyl nitrogen and sulfur atoms in its metal free form of the ligand, but now is in the *Z* form with both the other donor atoms. The C–S bond length increases to 1.732(6) Å [C7–S1] and 1.776(8) Å [C22–S2] from 1.6849(13) Å in HL^2. The N3–C7 bond length also changes from 1.3587(16) Å to 1.329(6) Å [1.292(8) Å for N7–C22] due to enolization of the ligand for coordination after deprotonation. The Co–S and Co–N bond lengths in both complexes are comparable. The Co–$N_{azomethine}$ bond lengths are shorter compared to Co–$N_{pyridine}$ bond lengths, indicating the greater strength of former bonds compared to the latter.

The molecules of **1** and **4** are packed in a 'face to face' manner within the unit cell, as is evident from Fig. 4 for the case of **1**, a result of diverse hydrogen bonding and C–H···π ring interactions (Tables 5 and 6). The 'face to face' arrangement is along the *b* axis for the case of **1**

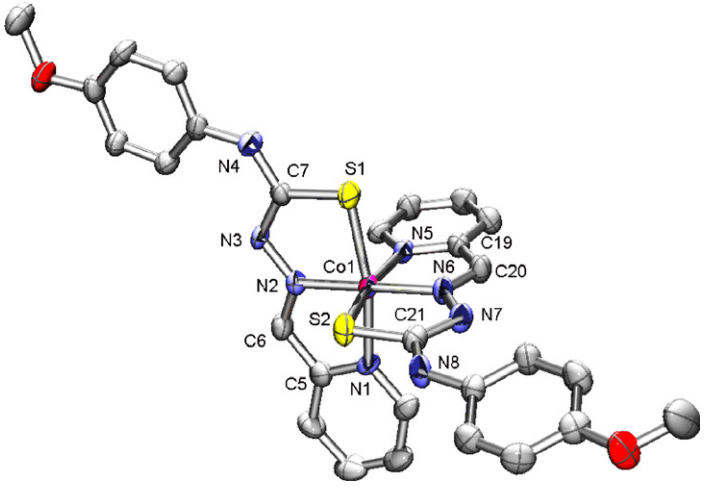


Fig. 2. ORTEP diagram for the compound $[CoL^1_2]NO_3$ (**1**) with 50% probability ellipsoids. Hydrogen atoms and the nitrate ion are omitted for clarity.

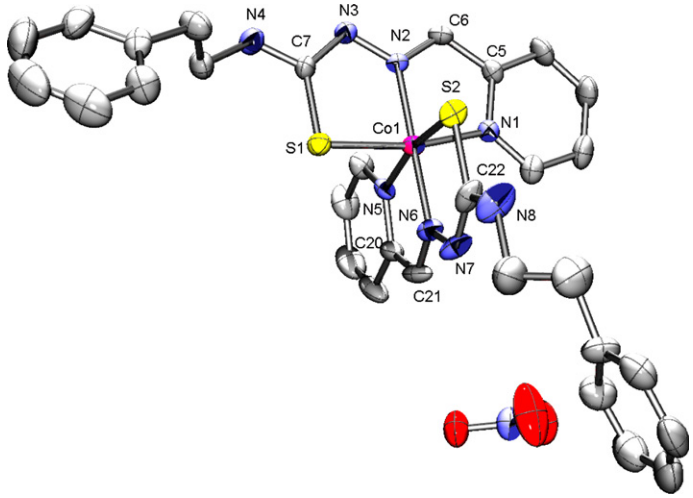


Fig. 3. ORTEP diagram for the compound $[CoL^2_2]NO_3$ (**4**) with 25% probability ellipsoids. Hydrogen atoms are omitted for clarity.

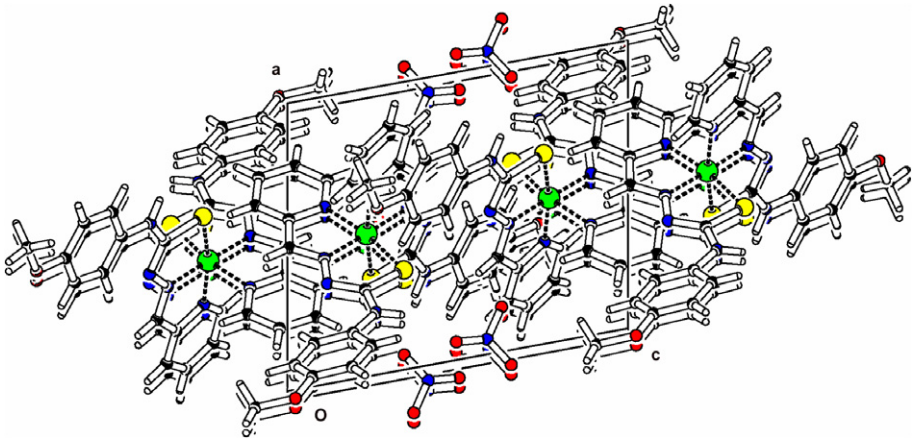


Fig. 4. A view of the molecule $[CoL^1_2]NO_3$ (**1**) along the *b* axis showing face to face packing in the unit cell.

and along the *c* axis for the case of **4** (Fig. 5). Since the latter contains three different molecules in the asymmetric unit, a large number of diverse interactions are present compared to those present in **1**. However, no significant π···π interactions are found in the packing of **4**. The relevant hydrogen bonding interactions of **1** and **4** along with HL^3 are listed in Table 7.

3.3. Infrared spectra

The characteristic IR bands (50–4000 cm^{-1}) for the free ligands (HL^1, HL^2 and HL^3) differ from those of their complexes and provide significant indications regarding the bonding sites of the ligands. IR spectral assignments of the ligands and the complexes are listed in Table 8. A medium band in the range 3129–3158 cm^{-1} in the free ligands due to the $\nu(^2N–H)$ vibration disappears in the spectra of complexes, providing strong evidence for ligand coordination around the cobalt(III) ion in its deprotonated form.

Table 5
Interaction parameters of compound **1**

π···π interaction			
Cg(I)–Res(I)···Cg(J)	Cg–Cg (Å)	α (°)	β (°)
Cg(5) [1]···Cg(7)[a]	3.6973	7.83	29.12
Cg(7) [1]···Cg(5)[a]	3.6973	7.83	22.39
Cg(7) [1]···Cg(7)[b]	3.6339	0.02	18.97

Equivalent position codes: a = 1 − *x*, −*y*, 1 − *z*; b = 1 − *x*, −1 − *y*, 1 − *z*
Cg(5) = N(1), C(1), C(2), C(3), C(4), C(5); Cg(7) = C(8), C(9), C(10), C(11), C(12), C(13)

CH···π interactions			
X–H(I)–Res(1)···Cg(J)	H···Cg (Å)	X···Cg (Å)	X–H···Cg (°)
C(1)–H(1) [1]···Cg(2)[a]	2.81	3.0983	99
C(15)–H(15) [1]···Cg(1)[a]	2.88	3.1389	98
C(15)–H(15) [1]···Cg(3)[a]	2.87	3.1094	96

Equivalent position codes: a = *x*, *y*, *z*
Cg(1) = Co(1), S(1), C(7), N(3), N(2); Cg(2) = Co(1), S(2), C(21), N(7), N(6); Cg(3) = Co(1), N(1), C(5), C(6), N(2)

Cg = Centroid, α = dihedral angles between planes I and J, β = angle Cg(1)–Cg(J).

Table 6
Interaction parameters of compound **4**

CH···π interactions			
X–H(I)–Res(1)···Cg(J)	H···Cg (Å)	X···Cg (Å)	X–H···Cg (°)
C(1)–H(1) [1] → Cg(1)[a]	2.88	3.1630	99
C(1)–H(1) [1] → Cg(4)[a]	2.99	3.2167	96
C(1)–H(1) [1] → Cg(2)[a]	2.93	3.1831	97
C(1)–H(1) [1] → Cg(3)[a]	2.78	3.0836	100
C(2)–H(2) [1] → Cg(15)[a]	2.90	3.4591	120
C(3)–H(3) [1] → Cg(7)[b]	2.61	3.5363	171
C(31)–H(31) [2] → Cg(10)[a]	2.96	3.1897	96
C(31)–H(31) [2] → Cg(12)[a]	2.83	3.1076	99
C(31)–H(31) [2] → Cg(9)[a]	2.88	3.1745	100
C(31)–H(31) [2] → Cg(11)[a]	2.96	3.2015	97
C(32)–H(32) [2] → Cg(7)[b]	2.92	3.4221	115
C(33)–H(33) [2] → Cg(15)[b]	2.58	3.4932	168
C(76)–H(76) [3] → Cg(17)[a]	2.93	3.2103	99
C(76)–H(76) [3] → Cg(19)[a]	2.99	3.2095	95
C(62)–H(62) [3] → Cg(24)[c]	2.79	3.5533	140
C(63)–H(63) [3] → Cg(24)[b]	2.64	3.5568	168
C(61)–H(61) [3] → Cg(18)[a]	2.95	3.2068	97
C(61)–H(61) [3] → Cg(20)[a]	2.84	3.1071	98

Equivalent position codes: a = x, y, z; b = x, $1+y$, z; c = $1-x$, $1/2+y$, $-z$.
Cg(1) = Co1, S1, C7, N3, N2; Cg(2) = Co1, S2, C7, N7, N2; Cg(3) = Co1, N1, C20, C6, N2; Cg(4) = Co1, N1, C5, C6, N2; Cg(7) = C10, C26, C27, C13, C14, C15.

Bands ranging from 1600 to 1350 cm^{-1} suffer significant shifts in the spectra of the complexes, which can be attributed to ν(C=C) and ν(C=N) vibration modes, and their mixing patterns are different from that in the spectra of the ligands. The positive shift of bands corresponding to ν(C=N) in the range 1584–1590 cm^{-1} in the free ligands to 1602–1614 cm^{-1} in the complexes is consistent with the coordination of the azomethine nitrogen to the central Co(III) ion [36,37]. Medium bands at ca. 439–450 cm^{-1} corresponding to ν(Co–N) further support azomethine nitrogen coordination [38,39]. The enolization of the ligands is supported by the increase in ν(N–N) by 58–115 cm^{-1}. The bands in the ranges 1307–1334 and 779–897 cm^{-1} due to ν(C=S) and δ(C=S), respectively, of the free ligands are shifted to lower values, indicating coordination of the thiolate sulfur to the Co(III) ion. The downward shift of the bands in the complexes corresponding to ν(C=S) and δ(C=S) in the free ligands can be attributed to a change of bond order and strong electron delocalization upon chelation [40]. Medium bands in the range at 375–385 cm^{-1} are assignable to ν(Co–S) [41]. A positive shift corresponding to out-of-plane bending vibrations of the pyridine ring in the free ligands (613–622 cm^{-1}) to higher frequencies (617–635 cm^{-1}) in the complexes is confirmative of pyridine nitrogen coordination to the cobalt(III) ion [42]. Medium bands at ca. 255–268 cm^{-1} corresponding to $\nu(Co–N_{pyridyl})$ point towards the coordination of the pyridyl nitrogen to the cobalt(III) ion [43].

The perchlorate complexes **3** and **7** show single broad bands at 1120 and 1123 cm^{-1} and strong bands at 620 and 625 cm^{-1}, indicating the presence of ionic perchlorate [44]. The bands at 1120 and 1123 cm^{-1} are assignable to $\nu_3(ClO_4)$ and unsplit bands at 620 and 625 cm^{-1} assignable to $\nu_4(ClO_4)$. Moreover, no bands assignable to ν_1(930 cm^{-1}) or ν_2(460 cm^{-1}) are observed in their spectra. This, along with unsplit ν_3 and ν_4 bands, show the exclusive presence of a non-coordinated perchlorate group having C_{3v} symmetry and it is supposed to be descended from T_d symmetry due to lattice effects [45].

In the spectra of the complexes **1** and **4** the absence of the combination bands ($\nu_1+\nu_4$) in the region 1700–1800 cm^{-1} rules out the possibility for a coordinated

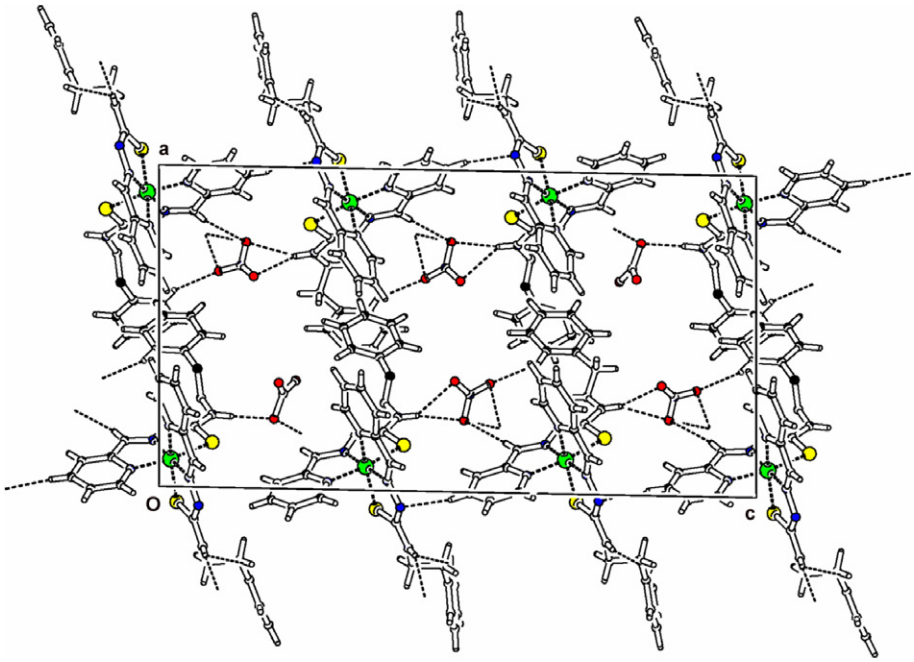


Fig. 5. Unit cell packing of the molecule $[CoL_2^2]NO_3$ (**4**) along the b axis showing hydrogen bonding interactions.

Table 7
H-bonding interactions in the compounds

	Residue	D–H···A	D–H (Å)	H···A (Å)	D···A (Å)	D–H···A (°)
HL^3	1	N3–H1N3···N1[a]	0.88	1.98	2.6768	135
	1	C6–H6···N2[b]	0.93	2.61	3.3540	137
$[CoL^1_2]NO_3 \cdot H_2O$ (**1**)	1	N8–H8A···O3[c]	0.86	2.10	2.922(10)	159
	1	N4–H4A···O4[d]	0.86	2.12	2.964(9)	167
	1	C17–H17···O4[e]	0.93	2.46	3.350(10)	160
	1	C28–H28···S1[f]	0.96	2.86	3.556(10)	131
	1	C18–H18···O1[g]	0.93	2.46	3.221(9)	139
	1	C6–H6···S2[h]	0.93	2.71	3.477(7)	140
	1	C9–H9···N3[a]	0.93	2.24	2.845(10)	122
	1	C23–H23···N7[a]	0.93	2.36	2.929(10)	119
$[CoL^2_2]NO_3$ (**4**)	1	N4–H4N···O5[i]	0.86	2.09	2.9152	160
	1	N8–H8N···O7[a]	0.86	2.16	2.9978	163
	1	N8–H8N···O9[a]	0.86	2.45	3.1914	145
	1	C18–H18···N11[j]	0.93	2.44	3.3499	166
	1	C6–H6···O1[j]	0.93	2.52	3.4235	164
	1	C8–H8A···S1[a]	0.97	2.60	3.0852	111
	1	C8–H8B···N7[a]	0.97	2.40	2.8034	104
	1	C26–H26···O3[j]	0.93	2.58	3.8880	146
	2	N12–H12···O1[k]	0.86	2.25	3.0343	151
	2	N12–H12···O3[k]	0.86	2.41	3.1487	144
	2	N16–H16N···O1[a]	0.86	2.22	3.0474	161
	2	N16–H16N···O2[a]	0.86	2.45	3.1740	143
	2	C48–H48···N19[a]	0.93	2.47	3.3572	160
	2	C51–H51 ···O5[a]	0.93	2.42	3.3256	164
	2	C56–H56···O4[a]	0.93	2.46	3.3890	172
	2	C38–H38A···S3[a]	0.97	2.59	3.0969	112
	3	N20–H20B···O5[a]	0.86	1.99	2.8412	169
	3	N20–H20N···O8[l]	0.86	2.27	3.0763	156
	3	N20–H20N···O9[l]	0.86	2.53	3.2167	137
	3	C86–H86···O8[l]	0.93	2.51	3.4043	161
	3	C63–H63···N3[l]	0.93	2.48	3.3965	167
	3	C66–H66···O9[l]	0.93	2.54	3.4389	161
	3	C68–H68A···S5[a]	0.97	2.68	3.1332	109

D = donor; A = acceptor; equivalent position codes: a = x, y, z; b = $-x, -y, 1-z$; c = $1-x, 1-y, 1-z$; d = $-1+x, -1+y, z$; e = $2-x, 1-y, -z$; f = $-x, 1-y, -z$; g = $x, 1+y, -1+z$; h = $1-x, -y, 1-z$; i = $1+x, y, z$; j = $1-x, -1/2+y, 1-z$; k = $-x, 1/2+y, 1-z$; l = $1-x, 1/2+y, -z$.

Table 8
IR spectral data of the ligands and their complexes (cm^{-1})

Compound	ν(C=N) + ν(N=C)	ν(N–N)	ν/δ(C–S)	py(ip)	py(op)	$\nu(^2$N–H)	$\nu(^4$N–H)	ν(Co–N_{azo})	ν(Co–N_{Py})	ν(Co–S)
HL^1	1584	1024	1334, 837	613	401	3134	3310			
$[CoL^1_2]NO_3 \cdot H_2O$ (**1**)	1604	1137	1315, 827	617	408		3428	446	262	378
$[CoL^1_2]Cl \cdot 2H_2O$ (**2**)	1605	1132	1298, 833	627	410		3402	445	255	383
$[CoL^1_2]ClO_4$ (**3**)	1602	1139	1303, 826	620	412		3419	439	268	385
HL^2	1586	1079	1324, 897	622	406	3129	3374			
$[CoL^2_2]NO_3$ (**4**)	1605	1141	1315, 892	630	416		3405	448	255	375
$[CoL^2_2]Cl \cdot 2H_2O$ (**5**)	1631	1137	1291, 892	630	413		3426	450	258	378
HL^3	1590	1035	1307, 779	614	421	3158				
$[CoL^3_2]Br \cdot 2H_2O$ (**6**)	1603	1137	1292, 770	632	453			443	260	382
$[CoL^3_2]ClO_4 \cdot H_2O$ (**7**)	1603	1137	1292, 764	635	433			440	264	374

nitrato group. The presence of bands at ca. 840 (ν_2), 1384 (ν_3) and 706 cm^{-1} (ν_4) for **1** and bands at 725, 1384 and 842 cm^{-1} for **4** clearly points out the uncoordinated nature of the nitrate group [46]. According to Stefov et al., coordinated water should exhibit bands at 825, 575 and 500 cm^{-1}. The absence of bands in these regions in the spectra of complexes **1**, **2**, **5**, **6** and **7** shows that the water molecules are not coordinated but are present as lattice water [47].

3.4. Electronic spectra

The electronic spectral assignments of the ligands and their complexes are given in Table 9. The electronic spectra of spin paired trivalent cobalt complexes of approximate O_h symmetry have the following assignments of d–d bands: ν_1: $^1T_{1g} \leftarrow {}^1A_{1g}$; ν_2: $^1T_{2g} \leftarrow {}^1A_{1g}$; ν_3: $^3T_{1g} \leftarrow {}^1A_{1g}$; ν_4: $^3T_{2g} \leftarrow {}^1A_{1g}$ [45]. The ν_1 bands are assigned values ~19 646–21 052 cm^{-1} and $\nu_2 \sim 25\,000$ cm^{-1}. The band

Table 9
Electronic spectra (cm^{-1}) of the ligands and their complexes

Compound	$^1T_{1g} \leftarrow {}^1A_{1g}$	$^1T_{2g} \leftarrow {}^1A_{1g}$ + LMCT	$^3T_{2g} \leftarrow {}^1A_{1g}$	$n \rightarrow \pi^*$	$\pi \rightarrow \pi^*$
HL^1				30769	42735
$[CoL^1_2]NO_3 \cdot H_2O$ (**1**)	19701	24708	16548	30982	43206
$[CoL^1_2]Cl \cdot 2H_2O$ (**2**)	19646	24691	16393	30960	43103
$[CoL^1_2]ClO_4$ (**3**)	20107	25008	16804	31206	42986
HL^2				30960	42194
$[CoL^2_2]NO_3$ (**4**)	21052	24519	17793	31347	43859
$[CoL^2_2]Cl \cdot 2H_2O$ (**5**)	20619	25000	17513	29240	41667
HL^3				30948	42796
$[CoL^3_2]Br \cdot 2H_2O$ (**6**)	20576	25063	17953	31408	43212
$[CoL^3_2]ClO_4 \cdot H_2O$ (**7**)	20534	25000	17422	31396	43096

assigned to v_2 is a combination band between it and the more intense $S \rightarrow Co^{III}$ charge-transfer bands. Very weak bands at ~16393–17953 cm^{-1} correspond to spin forbidden $^3T_{2g} \leftarrow {}^1A_{1g}$ transitions. From the spectra it can be concluded that two well separated high energy bands corresponding to spin allowed singlet → singlet transitions have been observed with the occasional presence of low energy spin forbidden bands.

Acknowledgements

P.F. Rapheal and E. Manoj thank the University Grants Commission, New Delhi, India for financial support. M.R.P. Kurup is thankful to the DST, New Delhi, India for financial support.

Appendix A. Supplementary material

Crystallographic data for the structural analysis have been deposited with the Cambridge Crystallographic Data Center. CCDC 605916, 605917 and 605918 contain the supplementary crystallographic data for compounds **1**, HL^3 and **4**. These data can be obtained free of charge via http://www.ccdc.cam.ac.uk/conts/retrieving.html, or from the Cambridge Crystallographic Data Centre, 12 Union Road, Cambridge CB2 1EZ, UK; fax: (+44) 1223-336-033; or e-mail: deposit@ccdc.cam.ac.uk. Supplementary data associated with this article can be found, in the online version, at doi:10.1016/j.poly.2006.08.029.

References

[1] S.B. Padhye, G.B. Kauffman, Coord. Chem. Rev. 63 (1985) 127 and references therein.
[2] D.X. West, S.B. Padhye, P.B. Sonawane, Struct. Bond. 76 (1991) 1.
[3] D.X. West, A.E. Liberta, S.B. Padhye, R.C. Chikate, P.B. Sonawane, A.S. Kumbhar, R.G. Yerande, Coord. Chem. Rev. 123 (1993) 49.
[4] A.E. Liberta, D.X. West, Biometals 5 (1992) 121.
[5] G.D. Domag, R.B. Chenich, F.M. Mietzch, H. Schmidt, Naturwissenschaften 33 (1946) 494.
[6] D.J. Baaer, L.S. Vincent, C.H. Kempe, A.W. Downe, Lancet 2 (1963) 494.
[7] H.G. Petering, H.H. Buskirk, G.E.E. Underwood, Cancer Res. 64 (1964) 367.
[8] C.W. Johnson, J.W. Joyner, R.P. Perry, Antibiot. Chemother. 2 (1952) 636.
[9] B.G. Benns, B.A. Gingras, C.H. Bayley, Appl. Microbiol. 8 (1961) 353.
[10] D.X. West, C.S. Carlson, Transition Met. Chem. 15 (1990) 383.
[11] D.X. West, C.S. Carlson, C.P. Galloway, Transition Met. Chem. 15 (1990) 91.
[12] K. Lichermeister, Z. Naturforsch., Beil B 5 (1950) 79.
[13] N.M. Samus, V.I. Tsapkov, A.P. Gulya, Russ. J. Gen. Chem. 74 (2004) 1428.
[14] E. Bermejo, A. Castineiras, L.M. Fostiak, I.G. Santos, J.K. Swearingen, D.X. West, Polyhedron 23 (2004) 2303.
[15] I.G. Santos, A. Hagenbach, U. Abram, J. Chem. Soc., Dalton Trans. (2004) 677.
[16] H. Beraldo, W.F. Nacif, L.R. Teixeira, J.S. Rebouças, Transition Met. Chem. 27 (2002) 85.
[17] J.P. Scovill, D.L. Klayman, C.F. Franchino, J. Med. Chem. 25 (1982) 1261.
[18] M.S. Bakkar, M.Y. Siddiqi, M.S. Monshi, Synth. React. Inorg. Met-Org. Nano-Met. Chem. 33 (2003) 1157.
[19] F. Yakuphanoglu, A. Balaban, F. Dagdelen, Y. Aydogdu, M. Sekerci, B. Erk, Synth. React. Inorg. Met-Org. Nano-Met. Chem. 32 (2002) 1865.
[20] Ý. Kýzýlcýklý, Y. Mesut, Synth. React. Inorg. Met-Org. Nano-Met. Chem. 33 (2003) 949.
[21] B.S. Garg, M.R.P. Kurup, S.K. Jain, Y.K. Bhoon, Synth. React. Inorg. Met.-Org. Chem. 28 (1998) 415.
[22] A. Sreekanth, M. Joseph, H.-K. Fun, M.R.P. Kurup, Polyhedron 25 (2006) 1408.
[23] A.B. Ablov, N.I. Belichuk, Russ. J. Inorg. Chem. 14 (1969) 93.
[24] R. Raina, T.S. Srivastava, Inorg. Chim. Acta 67 (1982) 83.
[25] H.-K. Fun, S. Chantrapromma, P.F. Rapheal, V. Suni, M.R.P. Kurup, Acta Crystallogr. E 62 (2006) o125.
[26] S.K. Chattopadhyay, M. Hossain, S. Ghosh, A.K. Guha, Transition Met. Chem. 15 (1990) 473.
[27] J.P. Scovill, Phosphorous Sulfur Silicon 60 (1991) 15.
[28] G.M. Sheldrick, SHELXS-97 and SHELXL-97, Bruker AXS Inc., Madison, WI, 1997.
[29] L.J. Farrugia, J. Appl. Crystallogr. 30 (1997) 565.
[30] A.L. Spek, J. Appl. Crystallogr. 36 (2003) 7.
[31] R.P. John, A. Sreekanth, M.R.P. Kurup, S.M. Mobin, Polyhedron 21 (2002) 2515.
[32] L. Latheef, E. Manoj, M.R.P. Kurup, Acta Crystallogr. C 62 (2006) o16.
[33] H.-S. Wang, L. Huang, Z.F. Chen, X.-W. Wang, J. Zhou, S.-M. Shi, H. Liang, K.B. Yu, Acta Crystallogr. E 60 (2004) m354.
[34] S.K. Chattopadhyay, T. Banerjee, P. Roychaudhury, T.C.W. Mak, S. Ghosh, Transition Met. Chem. 22 (1997) 216.
[35] D.X. West, M.A. Lockwood, A. Castineiras, Transition Met. Chem. 22 (1997) 447.
[36] B.S. Garg, M.R.P. Kurup, S.K. Jain, Y.K. Bhoon, Transition Met. Chem. 13 (1988) 309.

[37] M.J.M. Campbell, Coord. Chem. Rev. 17 (1975) 279.
[38] K. Nakamoto, Infrared and Raman Spectra of Coordination Compounds, 3rd ed., Wiley, New York, 1978.
[39] A. Sreekanth, U.L. Kala, C.R. Nayar, M.R.P. Kurup, Polyhedron 23 (2004) 41.
[40] P. Bera, R.J. Butcher, S. Chaudhuri, N. Saha, Polyhedron 21 (2002) 1.
[41] M.B. Ferrari, G.G. Fava, M. Lanfranchi, C. Pelizzi, P. Tarasconi, J. Chem. Soc., Dalton Trans. (1991) 1951.
[42] M.A. Ali, M.T.H. Tarafdar, J. Inorg. Nucl. Chem. 39 (1977) 1785.
[43] B.S. Garg, M.R.P. Kurup, S.K. Jain, Y.K. Bhoon, Transition Met. Chem. 16 (1991) 111.
[44] A.M. Bond, R.L. Martin, Coord. Chem. Rev. 54 (1984) 23.
[45] R. Osterberg, Coord. Chem. Rev. 12 (1974) 309.
[46] D.N. Sathyanarayana, Vibrational Spectroscopy, New Age International, New Delhi, 2004, p. 400.
[47] V. Stefov, V.M. Petrusevski, B. Soptrajanov, J. Mol. Struct. 293 (1993) 97.

Available online at www.sciencedirect.com
ScienceDirect
Polyhedron 26 (2007) 617–625
POLYHEDRON
www.elsevier.com/locate/poly

Synthesis and characterization of new polymeric phthalocyanines substituted with diaza-18-crown-6 macrocycles through ethyleneoxy bridges

Ahmet Bilgin [a,*], Çiğdem Yağcı [a], Ayşegül Mendi [b], Ufuk Yıldız [b]

[a] Department of Science Education, University of Kocaeli, 41380 Kocaeli, Turkey
[b] Department of Chemistry, University of Kocaeli, 41380 Kocaeli, Turkey

Received 18 July 2006; accepted 24 August 2006
Available online 5 September 2006

Abstract

A tetranitrile monomer was synthesized by nucleophilic aromatic substitution of *N*,*N*′-bis(2-hydroxyethyl)-4,13-diaza-18-crown-6 onto 4-nitrophthalonitrile. A series of polymeric metal-free and metallophthalocyanine (M = 2H, Zn, Cu, Co and Ni) polymers was prepared by polymeric tetramerization reaction of the tetranitrile monomer with proper materials. The electrical conductivities of the polymeric phthalocyanines measured as gold sandwiches were found to be $\sim 10^{-9}$–10^{-4} S cm^{-1} in a vacuum and in argon. The extraction ability of the metal-free polymeric phthalocyanine was evaluated in tetrahydrofuran using several alkali metal picrates such as Li^+, Na^+, K^+ and Cs^+. The extraction affinity of the metal-free polymeric phthalocyanine for K^+ was found to be highest in the heterogeneous solid–liquid phase extraction experiments. The disaggregation property of the metal-free polymeric phthalocyanine was investigated with sodium, potassium and ammonium ions and methanol. All the novel compounds were characterized by using elemental analysis, UV–Vis, FT-IR, NMR and MS spectral data and DTA/TG.
© 2006 Elsevier Ltd. All rights reserved.

Keywords: Bisphthalonitrile; Diaza-18-crown-6; Electrical conductivity; Extraction; Polymeric phthalocyanine

1. Introduction

Phthalocyanines have found practical applications in a wide range of high technology fields such as nonlinear optics, photosensitizers, gas sensors, catalysts, liquid crystals, optical data storage, sensitizers for photodynamic therapy of cancer, electrodes in fuel cell, photoelectric conversion materials in solar cells, and laser service substances, among others [1–3]. A great number of remarkable applications of phthalocyanines arise from their unique 18π electron conjugated aromatic cloud, which makes them present high thermal and chemical stability and remarkable photoelectric properties [4].

A combination of a phthalocyanine with a polymer or incorporation of a phthalocyanine into a polymer is a powerful tool for designing materials with interesting properties [5]. Polymeric phthalocyanines were mainly prepared via polycyclotetramerization reactions of bifunctional monomers such as various nitriles [6–21] or tetracarboxylic acid derivatives [22–25] in the presence of metal salts or metals. We have previously synthesized novel phthalocyanines carrying various macrocyclic groups and polymeric phthalocyanines [26].

In the present work, metal-free and metallophthalocyanine polymers which contain ethyleneoxy diaza-18-crown-6 moieties were synthesized and characterized. The electrical conductivities of the polymers as Au/MPc/Au sandwiches in a vacuum and in argon atmosphere were examined. The viscosity properties of all the polymers and alkali

* Corresponding author. Tel.: +90 262 3032438; fax: +90 262 3032403.
E-mail address: abilgin@kou.edu.tr (A. Bilgin).

0277-5387/$ - see front matter © 2006 Elsevier Ltd. All rights reserved.
doi:10.1016/j.poly.2006.08.027

metal extraction ability and disaggregation property of the metal-free polymeric phthalocyanine were investigated.

2. Experimental

2.1. Materials

Phosphorus pentoxide (P_2O_5), 1,8-diazabicyclo[5.4.0]-undec-7-ene (DBU), ethyl alcohol, *n*-pentanol, dimethylformamide (DMF), tetrahydrofuran (THF), chloroform, dichloromethane, petroleum ether, quinoline, sulphuric acid, hydrochloric acid, pyridine, acetone, 1,2-bis(2-iodoethoxy)ethane, sodium iodide, sodium thiosulfate, acetonitrile, sodium carbonate, dioxane, ethylene oxide, methanol, 1,2-(2-aminoethoxy)ethane were received from Merck and used as supplied. Cesium carbonate (Cs_2CO_3) was received from Merck and used after drying in oven at 250 °C for 36 h. All organic solvents were dried and purified as described by Perrin and Armarego [27]. 4-Nitrophthalonitrile was synthesized as described in the literature [28]. 1,10-Diaza-18-crown-6 was synthesized according to the literature [29].

2.2. Measurements

Melting points of the compounds were determined with an electrothermal melting point apparatus and were uncorrected. ^{1}H NMR spectra were recorded on a Varian Mercury Plus 300 MHz spectrometer with $CDCl_3$ as solvent and tetramethylsilane as the internal standard. ^{13}C NMR spectra were recorded on a Varian Mercury Plus 75 MHz spectrometer with $CDCl_3$ as the solvent and tetramethylsilane as the internal standard. Transmission IR spectra of samples were recorded on a FTIR spectrophotometer (Shimadzu FTIR-8201 PC) with the samples in KBr pellets. Optical spectra in the UV–Vis region were recorded with a model Shimadzu 1601 UV–Vis spectrometer using standard cuvettes with a fixed 1 cm pathlength at room temperature. The d.c. conductivity was measured by a Autolab 30 Voltammetry-FRA 2 frequency analyser. The frequency range was of 100 Hz–1 MHz and applied amplitude (rms) was 10 mV. Mass spectra were measured on a Varian MAT 711 and on Micromass Quatro LC/ULTIMA LC-MS MS spectrometers. The elemental analysis of the compounds was determined on a CHNS-932 LECO instrument. The metal contents of the metallophthalocyanine polymers were determined with a Unicam 929 AA spectrophotometer in solutions prepared by decomposition of the metallophthalocyanines in conc. sulfuric acid and conc. nitric acid solution followed by digestion in conc. hydrochloric acid solution and deionize water. Differential thermal analysis (DTA/TG) was performed on a Linseis L81 instrument in air atmosphere with a heating rate of 10 °C/min in a temperature range of 50–750 °C. Intrinsic viscosities of freshly prepared dilute solutions of phthalocyanine polymers were measured in conc. H_2SO_4 at 25 °C by use of an Ubbelohde viscometer.

2.3. Synthesis

2.3.1. Preparation of N,N′-bis(2-hydroxyethyl)-4,13-diaza-18-crown-6 (3)

A mixture of 1,10-diaza-18-crown-6 (3 g, 11.44 mmol) and methanol (20 mL) was charged into a 250-mL three-necked flask on ice-bath. Ethylene oxide (2.7 mL) was cooled to −20 °C and then added dropwise into the reaction flask over a period of 10 min. After adding, ice-bath was changed with oil-bath. The reaction mixture was refluxed first for 4 h with a condenser which was cooled to −20 °C and then 3 more hours with an ordinary condenser under nitrogen atmosphere at 65–70 °C. The reaction was ended and the solvent, methanol, was evaporated. The residue was distilled under vacuum at 200–210 °C (0.10-mm Hg) to yield pale yellow product. Refractive index of the product was 1.4937 at 20 °C. After the product was cooled to −10 °C, some part of the product was precipitated as white crystals. They were mechanically separated from the mother liquor; m.p., 49–51 °C.

Compound **3**: yield, 2.88 g (72%). *Anal.* Calc. for $C_{16}H_{34}N_2O_6$: C, 54.84; H, 9.78; N, 7.99. Found: C, 55.01; H, 9.64; N, 8.12%. IR (KBr): ν_{max} (cm^{-1}): 3327 (s, OH), 2955–2810 (–CH_2–), 1483, 1477, 1442, 1361, 1353, 1255, 1126–1045 (s, CH_2O–), 954, 875. ^{1}H NMR ($CDCl_3$): $\delta = 4.43$ (s, broad, 2H, D_2O exchangeable, OH), 3.69 (q, *J* 7.11 Hz, 4H, NCH_2CH_2OH), 3.53 (s, 8H, –OCH_2CH_2O), 3.29 (t, *J* 6.48 Hz, 8H, NCH_2CH_2O), 2.66 (t, *J* 7.11 Hz, 4H, NCH_2CH_2OH), 2.50 (t, *J* 6.44 Hz, 8H, NCH_2CH_2O). ^{13}C NMR ($CDCl_3$): $\delta = 70.34$ (–OCH_2CH_2O), 66.75 (NCH_2CH_2O), 60.14 (NCH_2CH_2OH), 56.43 (NCH_2CH_2-OH), 54.15 (NCH_2CH_2O). MS (Electron impact, EI), *m*/*z* (%): 369.08 (3.12) $[M + H_2O+1]^+$, 352.22 (1.23) $[M + 2]^+$, 351.25 (1.90) $[M + 1]^+$, 350.25 (1.8) $[M]^+$, 349.11 (1.02) $[M - 1]^+$, 333.31 (1.24) $[M - OH]^+$, 319.36 (100.00) $[M - CH_2OH]^+$, 289.17 (23.36) $[M + 1 - 2CH_2OH]^+$, 275.42 (20.13) $[M + 1 - C_3H_8O_2]^+$, 188.32 (10.29), 176.20 (10.81), 162.45 (25.52), 146.43 (20.73), 132.09 (18.32), 114.28 (35.67), 100.39 (40.56).

2.3.2. Preparation of N,N′-bis (2-oxyethyl-phthalonitrilo)-4,13-diaza-18-crown-6 (5)

A mixture of 4-nitrophthalonitrile (2.47 g, 14.28 mmol) and dry DMF (10 mL) was charged into a 200-mL three-necked flask and stirred at room temperature under nitrogen inert atmosphere. *N*,*N*′-Bis(2-hydroxyethyl)-4,13-diaza-18-crown-6 (2.5 g, 7.14 mmol) was added to the solution and the temperature was increased up to 50 °C. Powdered Cs_2CO_3 (7.12 g, 21.42 mmol) was added to the system in five equal portions at 45 min intervals with efficient stirring and the reaction system was stirred at the same temperature (50 °C) for 7 days. Aliquots were taken and checked periodically for completeness of the reactions and observed by thin layer chromatography (TLC) (8:2 chloroform:methanol). The reaction system was cooled and poured into ice-water and then mixed for 3 h. The mixture was extracted with chloroform (4 × 50 mL) and

organic phase was dried over $MgSO_4$. Chloroform was evaporated and oily brown crude product was obtained. The yield was recrystallized from a mixture of ethanol:diethyl ether (3:1; v/v) and dried again under vacuum over P_2O_5. The final brown solid **5** was soluble in chloroform, DMF, DMSO, pyridine, THF and dichloromethane.

Compound **5**: yield, 3.96 g (92%); m.p., 156 °C. *Anal.* Calc. for $C_{32}H_{38}N_6O_6$: C, 63.77; H, 6.36; N, 13.94. Found: C, 63.94; H, 6.22; N, 13.65%. IR (KBr): ν_{max} (cm^{-1}): 3040 (aromatic =CH), 2920–2865 (aliphatic CH_2), 2230 (C≡N), 1601 (aromatic —C=C—), 1420, 1389, 1260 (Ar–O–C), 1126–1049 (CH_2–O–CH_2), 943 and 881. ^{1}H NMR ($CDCl_3$): $\delta = 7.99$ (d, J 8.00 Hz, 2H, ArH), 7.53 (d, J 8.53 Hz, 2H, ArH), 7.44 (dd, J 9.30 Hz, 2H, ArH), 4.18 (t, J 7.23 Hz, 4H, N–CH_2–CH_2O–Ar), 3.65 (s, 8H, –OCH_2-CH_2O), 3.11 (t, J 6.82 Hz, 8H, NCH_2CH_2O), 2.80 (t, J 7.23 Hz, 4H, NCH_2CH_2O–), 2.55 (t, J 6.82 Hz, 8H, NCH_2CH_2O). ^{13}C NMR ($CDCl_3$): $\delta = 162.92$ (C_4), 135.42 (C_6), 121.95 (C_5), 119.81 (C_3), 117.32 (C_2), 116.48 (C_7), 115.96 (C_8), 110.00 (C_1), 71.39 (C_9), 69.58 (C_{13}), 67.37 (C_{12}), 55.49 (C_{11}), 55.08 (C_{10}). MS, m/z (%): 736.21 (7.17) $[M + Cs + 1]^+$, 603.74 (10.26) $[M + 1]^+$, 602.58 (11.42) $[M]^+$, 527.38 (35.06), 459.25 (12.76) $[M - C_8H_3N_2O]^+$, 445.36 (48.17) $[M - C_9H_5N_2O]^+$, 316.43 (60.21) $[M - C_{16}H_6N_4O_2]^+$, 288.12 (100.00) $[M - C_{18}H_{10}N_4O_2]^+$, 188.16 (21.03), 176.78 (16.54), 143.47 (70.73), 127.82 (38.34), 114.28 (42.23), 100.02 (31.26).

2.3.3. Preparation of metal-free polymeric phthalocyanine (*6*)

A mixture of compound **5** (0.602 g, 1 mmol), *n*-pentanol (5 mL) and 1,8-diazabicyclo[5.4.0]undec-7-ene (DBU) (0.155 g, 1 mmol) was placed in a standard Schlenk tube under nitrogen atmosphere and degassed several times. The temperature was gradually increased up to 90 °C and degassed again with nitrogen. Then the reaction mixture was stirred at 145 °C for 12 h. After the reaction mixture was cooled and decanted, the residue was stirred with methanol:petroleum ether mixture (10 mL, 1/1; v/v). The product **6** was filtered off, washed with DMF, methanol, acetone and diethyl ether and dried in air. The final dark green solid **6** was soluble in H_2SO_4, hot pyridine and poorly soluble in chloroform, dichloromethane and THF.

Compound **6**: yield, 0.43 g; m.p. >300 °C. *Anal.* Calc. for $(C_{128}H_{154}N_{24}O_{24})_n$ (2411.16): C, 63.72; H, 6.43; N, 13.93. Found: C, 63.48; H, 6.65; N, 14.12%. IR (KBr): ν_{max} (cm^{-1}): 3275 (N–H), 3055 (aromatic =CH), 2970–2840 (CH_2), 2223 (C≡N), 1642 (—C=N—), 1598 (aromatic —C=C—), 1469, 1380, 1265 (Ar–O–C), 1130–1040 (CH_2–O–CH_2), 1030, 960, 853, 682 and 530 cm^{-1}. ^{1}H NMR (pyridine-d_5): $\delta = 8.42$–8.18 (m, br, 96H, ArH), 4.34 (t, J 7.15 Hz, 64H, N–CH_2–CH_2O–Ar), 3.54 (s, 128H, –OCH_2-CH_2O), 3.22 (t, J 6.52 Hz, 128H, NCH_2CH_2O), 2.87 (t, J 7.15 Hz, 64H, NCH_2CH_2O–), 2.57 (t, J 6.52 Hz, 128H, NCH_2CH_2O). MS (FAB positive), m/z: 9645.87 $[M + 1]^+$.

2.3.4. Preparation of Zn-containing polymer (*7*)

A mixture of bisphthalonitrile compound **5** (0.602 g, 1 mmol), zinc acetate dihydrate [$Zn(CH_3COO)_2 \cdot 2H_2O$] (0.112 g, 0.5 mmol) and amyl alcohol (5 mL) was put in a flask and the temperature was increased up to 160 °C. DBU (0.08 g, 0.08 mL, 0.5 mmol) was added dropwise with a syringe to the system at the same temperature. The reaction was treated at 160 °C for 12 h under reflux and nitrogen atmosphere. After cooling, 10 mL of methanol–water mixture (1:1, v/v) was added to the system and stirred for 45 min. The crude product was filtered and washed with methanol, DMF, distilled water, petroleum ether and acetone. The final green product **7** was dried under vacuum over P_2O_5 at 100 °C.

Compound **7**: yield, 0.40 g; m.p. >300 °C. *Anal.* Calc. for $(C_{128}H_{156}N_{20}O_{32}Zn)_n$ (2549.05): C, 60.24; H, 6.16; N, 10.98; Zn, 2.56. Found: C, 60.45; H, 6.37; N, 10.69; Zn, 2.67%. IR (KBr): ν_{max} (cm^{-1}): 3390 (imide N–H), 3054 (aromatic =CH), 2990–2789 (CH_2), 1770 (sym. C=O), 1720 (asym. C=O), 1640 (—C=N—), 1598 (aromatic —C=C—), 1485, 1421, 1326, 1254 (Ar–O–C), 1160–1040 (C–O–C), 957, 842 and 650 cm^{-1}.

2.3.5. Preparation of Cu-containing polymer (*8*)

A mixture of bisphthalonitrile compound **5** (0.602 g, 1 mmol), $Cu(CH_3COO)_2 \cdot H_2O$ (0.100 g, 0.5 mmol) and amyl alcohol (3 mL) was put in a flask. The temperature was increased up to 160 °C and degassed three times under nitrogen atmosphere. Then, DBU (0.08 mL, 0.08 g, 0.5 mmol) was added drop by drop with a syringe into the system. The reaction was treated at 160 °C for 12 h under reflux and nitrogen atmosphere. The reaction mixture was cooled, diethyl ether–methanol mixture (5 mL, 1:1) was added and stirred for 1 h. The mixture was filtered and the solid part was washed with distilled water, DMF, ethanol and diethyl ether. The final product **8** was dried under vacuum over P_2O_5 at 100 °C.

Compound **8**: yield, 0.38 g; m.p. >300 °C. *Anal.* Calc. for $(C_{128}H_{156}N_{20}O_{32}Cu)_n$ (2548.05): C, 60.28; H, 6.17; N, 10.98; Cu, 2.49. Found: C, 60.51; H, 6.43; N, 11.17; Cu, 2.26%. IR (KBr): ν_{max} (cm^{-1}): 3360 (imide N–H), 3062 (aromatic =CH), 2980–2853 (CH_2), 1774 (sym. C=O), 1713 (asym. C=O), 1636 (—C=N—), 1601 (aromatic —C=C—), 1493, 1428, 1330, 1262 (Ar–O–C), 1155–1020 (C–O–C), 964, 856 and 590 cm^{-1}.

2.3.6. Preparation of Co-containing polymer (*9*)

A mixture of bisphthalonitrile compound **5** (0.602 g, 1 mmol), dry quinoline (2 mL) and $CoCl_2 \cdot 6H_2O$ (0.120 g, 0.5 mmol) was kept in a flask and degassed three times with nitrogen. The reaction mixture was treated at 220 °C under reflux and nitrogen inert atmosphere. After 24 h of stirring, the reaction mixture was cooled and then diethyl ether (25 mL) was added and then filtered off. The solid part was washed with methanol:diethyl ether mixture (20 mL, 1:1), DMF, hot ethanol, acetone and filtered off. The final product **9** was dried under vacuum over P_2O_5 at 100 °C. The final green product **9** was soluble in H_2SO_4 and poorly soluble in pyridine.

Compound **9**: yield, 0.31 g; m.p. >300 °C. *Anal*. Calc. for $(C_{128}H_{156}N_{20}O_{32}Co)_n$ (2544.05): C, 60.39; H, 6.18; N, 11.00; Co, 2.32. Found: C, 60.17; H, 6.41; N, 11.23; Co, 2.64%. IR (KBr): ν_{max} (cm^{-1}): 3400 (imide N–H), 3048 (aromatic =CH), 2920–2796 (CH_2), 1776 (sym. C=O), 1718 (asym. C=O), 1641 (—C=N—), 1612 (aromatic —C=C—), 1500, 1435, 1323, 1265 (Ar–O–C), 1148–1032 (C–O–C), 972, 870 and 623 cm^{-1}.

2.3.7. Preparation of Ni-containing polymer (*10*)

A mixture of bisphthalonitrile compound **5** (0.602 g, 1 mmol), dry quinoline (1.5 mL) and $NiCl_2 \cdot 6H_2O$ (0.122 g, 0.5 mmol) was charged in a standard Schlenk tube and degassed three times with nitrogen. The temperature was increased up to 220 °C and treated for 24 h under reflux and nitrogen inert atmosphere. The system was cooled to room temperature and methanol:water (10 mL, 1:1; v/v) mixture was added to the system and stirred at room temperature for 1 h. The product was filtered off and washed with DMF, methanol, distilled water, petroleum ether. The final green product **10** was dried under vacuum over P_2O_5 at 100 °C. The product **10** was soluble in H_2SO_4 and poorly soluble in pyridine.

Compound **10**: yield, 0.37 g; m.p. >300 °C. *Anal*. Calc. for $(C_{128}H_{156}N_{20}O_{32}Ni)_n$ (2543.05): C, 60.40; H, 6.18; N, 11.01; Ni, 2.31. Found: C, 60.64; H, 6.06; N, 11.35; Ni, 2.52%. IR (KBr): ν_{max} (cm^{-1}): 3413 (imide N–H), 3043 (aromatic =CH), 2925–2875 (CH_2), 1772 (sym. C=O), 1710 (asym. C=O), 1642 (—C=N—), 1605 (aromatic —C=C—), 1513, 1420, 1325, 1257 (Ar–O–C), 1160–10430 (C–O–C), 974, 846 and 610 cm^{-1}.

2.3.8. The conversion of cyano end groups of the metal-free polymeric phthalocyanine into imido groups (*6a*)

A sample of the metal-free polymeric phthalocyanine (**6**) (150 mg) was dissolved in a minimum volume of H_2SO_4 (96 wt%) at room temperature. After 3–4 h of stirring, the reaction mixture was filtered. The filtrate was poured into excess amount of ice-water mixture. The dark green crude product was washed with distilled water until the washings were neutral. Then the final product **6a** was washed with ethanol and diethyl ether and dried under vacuum over P_2O_5 at 100 °C.

Compound **6a**: yield, 0.12 g; m.p. >300 °C. Elemental analyses (for imide end groups): *Anal*. Calc. for $(C_{128}H_{158}N_{20}O_{32})_n$ $(2487.14)_n$: C, 61.77; H, 6.40; N, 11.26. Found: C, 61.89; H, 6.26; N, 11.54%. IR (KBr): ν_{max} (cm^{-1}): 3385 (imide N–H), 3310 (N–H), 3050 (aromatic =CH), 2980–2852 (CH_2), 1772 (sym. C=O), 1720 (asym. C=O), 1629 (—C=N—), 1596 (aromatic —C=C—), 1508, 1491, 1448, 1324, 1242 (Ar–O–C), 1151–1040 (C–O–C), 975, 940–840, and 543 cm^{-1}.

2.3.9. Metal analysis of the polymeric phthalocyanines

A sample of the metallophthalocyanine polymers (**7**–**10**) (10 mg) was added into concentrated sulfuric acid (2.5 mL) and conc. nitric acid (3.5 mL). The mixture was heated for 2 h at 160 °C in an oil-bath. The solution was firstly digested in conc. HCl acid solution and then diluted with deionize water (500 mL). The determination of metal ions was conducted by atomic absorption measurements.

Table 1
Alkaline metal picrate extractions for **6**[a] under solid/liquid two-phase conditions

Metal ion	Extractability of the metal-free polymeric phthalocyanine (**6**) (%)[b]	λ_{max} (nm) of metal picrate
Li^+	6.01 ± 0.01	362
Na^+	77.17 ± 0.01	356
K^+	94.25 ± 0.01	364
Cs^+	22.16 ± 0.01	354

[a] Temperature 25 ± 1 °C; THF phase (10 mL), [picrate] = 3.0×10^{-3} M; host molecule = 20 mg.
[b] Average and standard deviation for three independent measurements.

2.3.10. Measurement of the alkali metal-binding properties of the polymeric metal-free phthalocyanine

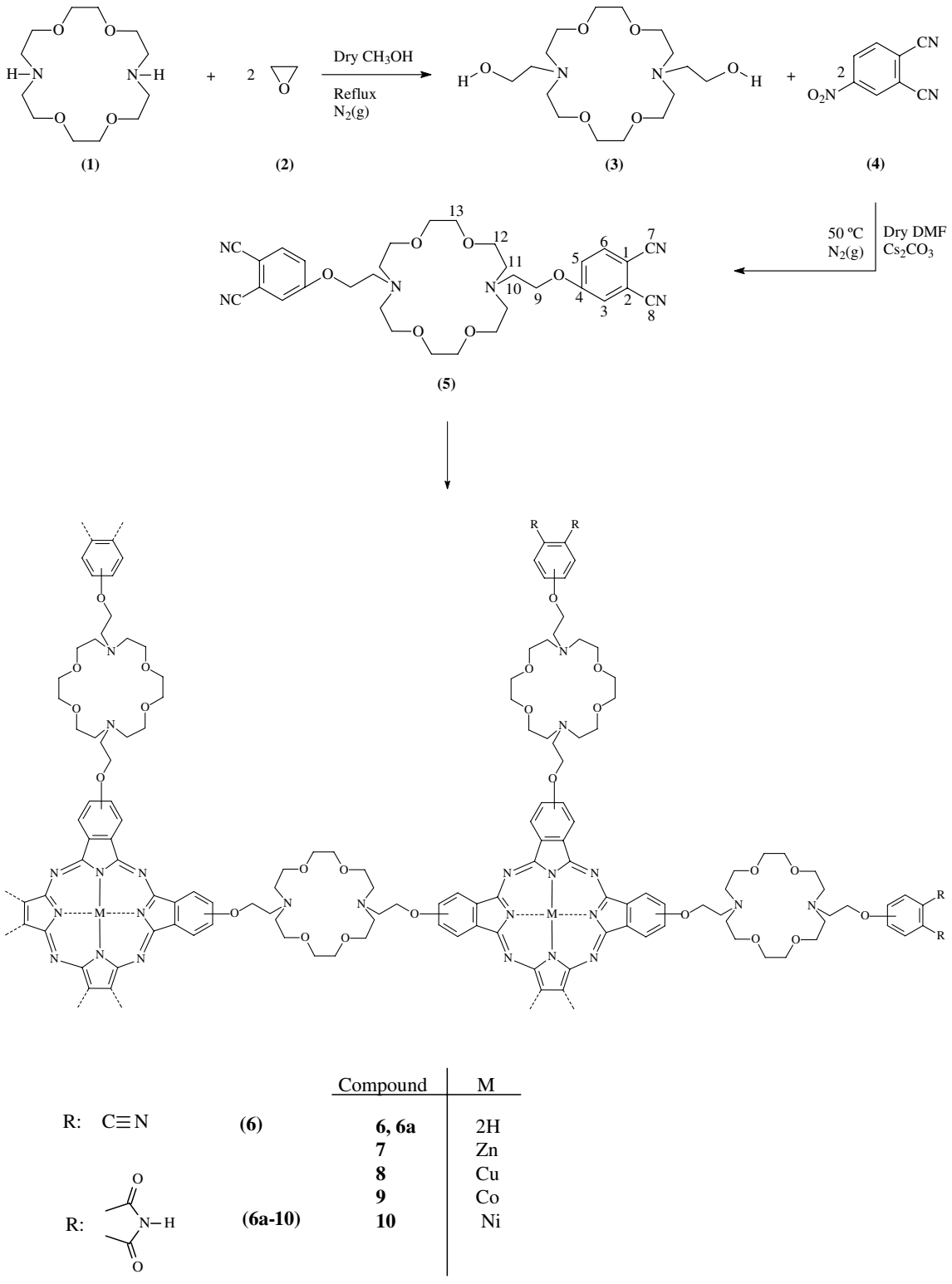
The extraction properties of **6** were investigated under solid–liquid phase condition by using alkali metal picrates (Li^+, Na^+, K^+ and Cs^+) as substrates and measuring by UV–Vis the amounts of picrate in THF phase before and after treatment with polymers in suspension. Suspensions were prepared by mixing 25 mg of the polymeric metal-free phthalocyanine (**6**) and the alkali metal picrate solutions as described in previous article [26g]. The prepared suspensions were put in plastic bottles and shaken vigorously for 24 h at room temperature. Results and experimental conditions are reported in Table 1. In the absence of host **6**, blank experiment, no metal ion picrate extraction was detected. The extractability was determined based on the absorbance of picrate ion in the THF suspensions. The extractability was calculated by using the following equation:

$$E(\%) = [(A_0 - A)/A_0] \times 100$$

where A_0 is the absorbance in the absence of ligand. A denotes the absorbance in THF suspension phase after extraction.

3. Results and discussion

The synthesis of the *N*,*N*′-bis(2-hydroxyethyl)-4,13-diaza-18-crown-6 (**3**) was performed by starting with 4,13-diaza-18-crown-6 (**1**) and ethylene oxide (**2**) in methanol (Scheme 1). The yield (72%) was higher than the known procedure (51%) [29] and the product was partly solid (m.p., 49–51 °C) while it was said to be oily in the literature reference. Elemental analysis and mass spectral data of **3** were satisfactory: 350.25(1.8) $[M]^+$. In ^1H NMR ($CDCl_3$) spectrum of **3**, NH group of compound **1** disappeared as expected. ^1H NMR spectrum of **3** showed new signal at $\delta = 4.43$ (s, broad, 2H, OH) and also the proton-decoupled ^{13}C NMR spectrum of **3** indicates the presence of primary alcohol carbon atoms at $\delta = 60.14$ (NCH_2CH_2OH) and 56.43 (NCH_2CH_2OH), respectively. The IR spectrum of **3** was easily verified with the disappearance of N–H and



Scheme 1. Synthesis of new polymeric phthalocyanine polymers substituted with diaza-18-crown-6 macrocycles through ethyleneoxy bridges.

presence of O–H stretching vibrations at 3327 cm^{-1}. The difference between the IR spectra of **1** and **3** is clear from the absence of characteristic vibrations such as N–H. 4-Nitrophthalonitrile (**4**) was treated with **3** in the presence of Cs_2CO_3in DMF to afford tetranitrile monomer **5** with high yield (92%). Final purification of tetranitrile derivative **5** by recrystallization afforded **5** for which elemental analysis and EI mass spectral data were satisfactory: 602.58 $[M]^+$. In ^1H NMR spectrum of **5**, OH group of compound **3** disappeared as expected. The disappearance of OH and the presence of Ar–O–C at 1260 cm^{-1} and the presence of C≡N functional group at 2230 cm^{-1} in the IR spectrum

of compound **5** confirm the formation of desired compound **5**.

The metal-free phthalocyanine polymer was synthesized by heating mixture of **5**, DBU and amyl alcohol in a Schlenk tube [30]. The transition metal complexes were prepared from the tetracyano compound **5** and the corresponding metal salt in proper solvent (Scheme 1).

The molecular weights of the polymers could not be determined using traditional methods because of their poor solubility in organic solvents, but by comparison of the IR absorption bands of the end groups with those of the bridging groups [15,31]. On the other hand, according to the FAB mass spectra analysis of **6** using the soluble part (~80%) of **6** in pyridine, we can say that **6** is a tetramer molecule. The ^{1}H NMR spectrum of the soluble part of the **6** in pyridine-d_5 displayed broad signals, and the protons of the phthalocyanine core were invisible, even at elevated temperatures. This effect was attributed to strong aggregation of the molecules.

The IR spectra of metal-free **6**, **6a** and metallophthalocynaine polymers (**7**–**10**) are very similar. The significant difference is the presence of ν(N–H) vibrations of the inner phthalocyanine core which are assigned to a weak band at 3275 cm^{-1} in the metal-free molecule. These bands disappear in the spectra of the metallophthalocyanine polymers. These bands are especially beneficial for characterization of metal-free phthalocyanine polymers, as there is little frequency dependence on ring substitution and they are not overlapped by strong tetranitrile monomer absorptions [10]. The end groups of the metal-free phthalocyanine polymer were cyano groups (2223 cm^{-1}) while the end groups of the metallophthalocyanine polymers were imido groups (~1776–1710 cm^{-1}). The existence of imido groups in the case of metallophthalocyanine polymers was attributed to the presence of the moisture during work-up and the hydrated metal salts. There was little shift to longer wavelength numbers in most of the IR bands of the metal complexes with respect to the metal-free analogues [10,32].

The elemental analyses of the metal-free and metallophthalocyanine polymers (**6**, **6a**, **7**–**10**) were satisfactory.

The metal-free (**6**) and metallo polymers (**7**–**10**) gave typical UV–Vis absorptions spectra of phthalocyanines (Table 2). As it can bee seen in Table 2 there is a shoulder at the slightly higher energy sides for all products. The presence of shoulders in the UV–Vis spectra of the all polymers corresponds to the aggregated or non-aggregated species in conc. sulfuric acid. Metal-free phthalocyanine polymer (**6**) decomposes slowly by hydrolysis in conc. H_2SO_4, which is demonstrated by a decrease of the absorption coefficient at longer wavelengths. Metal-containing polymers (**7**–**10**), however, were stable. When going from organic solvents to concentrated H_2SO_4, the long-wave absorption band underwent a significant bathochromic shift, which is due to degradation and weak protonation of the phthalocyanine ring at the *meso* nitrogen atoms. The intensity of these absorptions also decreased. The UV–Vis spectrum of **6** was obtained in pyridine and conc. H_2SO_4. The electronic absorption spectrum of **6** in pyridine at room temperature is shown in Fig. 1. There were the split Q-band as expected and there were two strong bands in the visible region [33]. The split Q-band which is characteristic for metal-free phthalocyanines observed at λ_{max} 706 and 672 nm with a shoulder at 640 nm, indicating the monomeric species; the monomeric species with D_{2h} symmetry shows two intense absorptions at around 700 nm [34,35]. On the other hand, such split Q-band absorptions in pyridine are due to $\pi \Rightarrow \pi^*$ transition of this fully conjugated 18π electron systems [26a]. In the case of a H_2SO_4 solution of **6**, the primary band in the visible region was broadened and shifted to longer wavelength (104 nm). In all cases the intensities in the UV (Soret band transition) and Vis (Q-band transition) were $I_{UV}/I_{Vis} \leqslant 1$ (Table 2). This result indicates the absence of poly(isoindolinine) co-units in all of the polymeric phthalocyanines (**6**–**10**).

Disaggregation of the metal-free polymeric phthalocyanine (**6**), followed by changes in the visible spectra after the addition of methanol, several alkali and NH_4^+ cation, constitute an effective route for characterizing the complexation behavior of the ethyleneoxy diaza-18-crown-6 peripheral substituents. Firstly, we clarified whether methanol has any effect or not on the visible spectrum of **6**. For this purpose, different amounts of methanol were added to the solution of **6** in pyridine. As can be seen in Fig. 1 decreases in the intensities of Q bands were observed in the visible absorption spectrum of **6** with increasing the amounts of methanol. This can be due to the dilution. Then the different concentration of metal salts (e.g. $NaNO_3$, KNO_3, NH_4NO_3) solutions in methanol (1.0×10^{-3} M)

Table 2
Wavelength and relative absorbance intensities of the UV–Vis spectra of the polymeric phthalocyanines

Compound	M	Solvent	λ/nm ($A_{rel.} \times 10^{-1}$)									Ratio[a] UV–Vis
6	2H	pyridine	706 (2.19)	672 (2.24)	640[b] (1.48)	606 (1.48)	389 (2.14)	360 (2.19)	320 (2.40)	301 (2.51)	285 (2.00)	0.91
		H_2SO_4	810 (1.86)	720[b] (1.70)	675 (0.79)	608 (0.60)	392 (1.02)	345 (2.19)	320 (2.40)	274 (2.95)		1.59
7	Zn	H_2SO_4	850 (2.88)	819[b] (2.40)	736 (1.12)	619 (0.26)	458 (2.24)	365 (1.95)	327 (1.51)	297 (1.38)		0.48
8	Cu	H_2SO_4	832 (1.20)	775[b] (0.78)	732 (0.52)	617 (0.19)	430 (0.85)	412 (0.35)	338 (0.69)	304 (1.10)		0.92
9	Co	H_2SO_4	816 (1.74)	755[b] (0.89)	720 (0.55)	663 (0.08)	391 (2.40)	377 (1.45)	326 (2.14)	292 (2.45)		1.41
10	Ni	H_2SO_4	816 (2.51)	758[b] (0.79)	719 (0.52)	639 (0.33)	460 (2.57)	414 (2.24)	378 (2.00)	297 (2.88)		1.14

[a] Intensity ratio of absorption B bands at λ = 274–304 nm and Q bands at λ = 719–850 nm (C = 1.0×10^{-4} g/L in H_2SO_4, 1.0×10^{-3} g/L in pyridine).
[b] Shoulder.

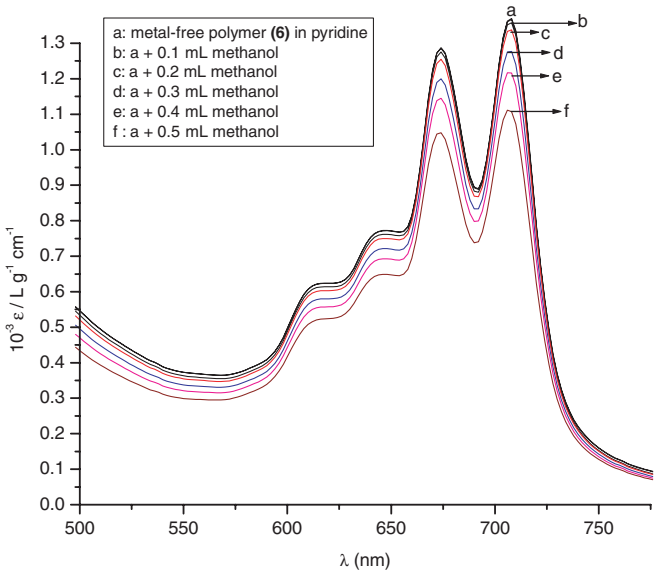


Fig. 1. Changes in the visible spectra of **6** in pyridine (1.0×10^{-3} g/L) after the addition different amounts of methanol.

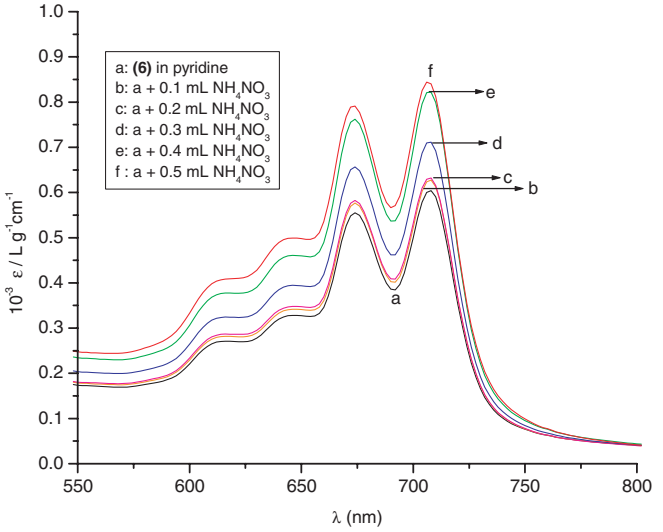


Fig. 2. Changes in the visible spectra of **6** in pyridine (1.0×10^{-3} g/L) after the addition of NH_4NO_3 solutions in methanol (1.0×10^{-3} M).

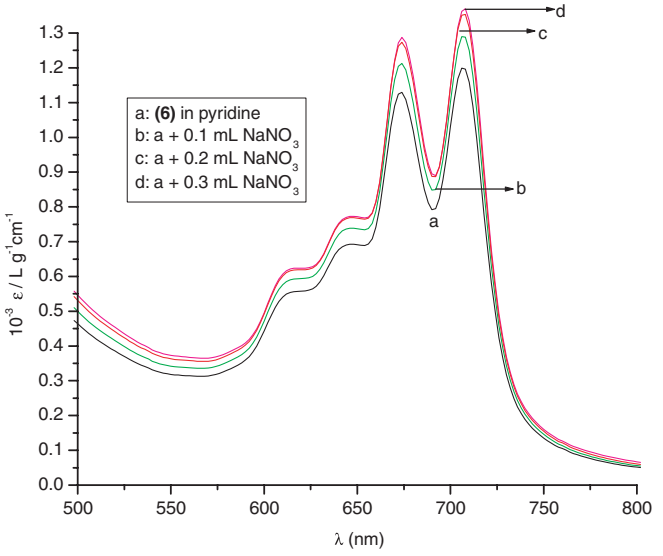


Fig. 3. Changes in the visible spectra of **6** in pyridine (1.0×10^{-3} g/L) after the addition of $NaNO_3$ solutions in methanol (1.0×10^{-3} M).

were added to the solution of the metal-free polymeric phthalocyanine (**6**) in pyridine (1.0×10^{-3} g/L). When we added $NaNO_3$, KNO_3 and NH_4NO_3 solutions to the metal-free polymeric phthalocyanine (**6**) solution caused a dramatic change due to disaggregation in the visible spectrum of **6** even in spite of dilution effect of methanol. This observation can be attributed to the disaggregation of **6** by trapped Na^+, K^+ and NH_4^+ ions in the diaza-18-crown-6 units, the radius cavity of which is harmonious with these ions and there is no intermolecular complexation between the phthalocyanine units [36] (Figs. 2–4).

The intrinsic viscosities of dilute solutions of polymers were measured by means of Ubbelohde viscometer. The intrinsic viscosities of all polymers were similar (Table 3). Fig. 5 shows the viscosities of polymers as a function of polymer concentration, and indicates that viscosities decreased depending on polymer concentration. This behavior can be explained by two effects: (1) degradation of the polymers and (2) weakly protonation of the four bridging nitrogen atoms at the periphery of each phthalocyanine polymer and the nitrogen atoms of the diaza-18-crown-6 units. On the other hand, there were linear decreasing in the case of **7** and **9** while polynomial decreasing in the case of **6**, **8** and **10** (Fig. 5). It can be probably due to lower stability of **6**, **8** and **10** than those of others, **7** and **9**.

The structure of the polymers was an Au/MPc/Au sandwich in the configuration commonly used for the electrical conductivity measurements [37]. To prepare the samples, powdered materials were pressed at a load of 2 tons for 3 min into disk-shaped compacts with a thickness of 0.45–0.60 mm. The d.c. conductivity was measured by a Autolab 30 Voltammetry-FRA 2 frequency analyser. The frequency range was of 100 Hz–1 MHz and applied amplitude (rms) was 10 mV. The electrical conductivities of the polymers were measured in a vacuum and in argon atmosphere. Table 3 shows the d.c. electrical conductivities of polymers **6**, **6a**, **7**–**10**. These values correspond to semi-conductive materials as encountered in number-substituted phthalocyanine derivatives [26g]. The conductivity values obtained under an argon atmosphere were higher than those of under vacuum for all polymers probably due to absorbed oxygen in argon [38].

The thermal stability of the phthalocyanine polymers (**6**–**10**) was determined by thermal analysis. Due to high thermal stability of the phthalocyanine core, cleavage of the substituent macrocycles takes place first and then the main decomposition occurs above 400 °C [39]. But, the crown ether units are not stable at temperatures above 300 °C even under inert conditions [40]. The initial decomposition temperature decreased in the order **7** > **9** > **10** > **8** > **6** (Table 4).

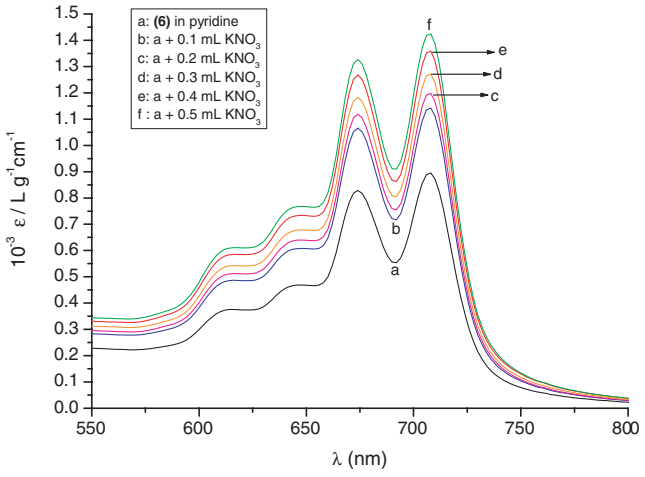


Fig. 4. Changes in the visible spectra of **6** in pyridine (1.0×10^{-3} g/L) after the addition of KNO_3 solutions in methanol (1.0×10^{-3} M).

Table 3
Electrical conductivity and intrinsic viscosities of the polymeric phthalocyanines at room temperature

Compound	M	Conductivity (S cm^{-1})		Pellet thickness (mm)	Intrinsic viscosity, η (H_2SO_4)
		In argon	In vacuum		
6	2H	1.12×10^{-7}	9.76×10^{-8}	0.55	0.75
6a	2H	1.83×10^{-7}	1.01×10^{-7}	0.45	
7	Zn	1.05×10^{-7}	7.48×10^{-8}	0.60	0.67
8	Cu	3.06×10^{-7}	6.28×10^{-7}	0.45	0.89
9	Co	2.70×10^{-8}	8.77×10^{-8}	0.55	0.62
10	Ni	2.88×10^{-4}	1.56×10^{-5}	0.60	0.89

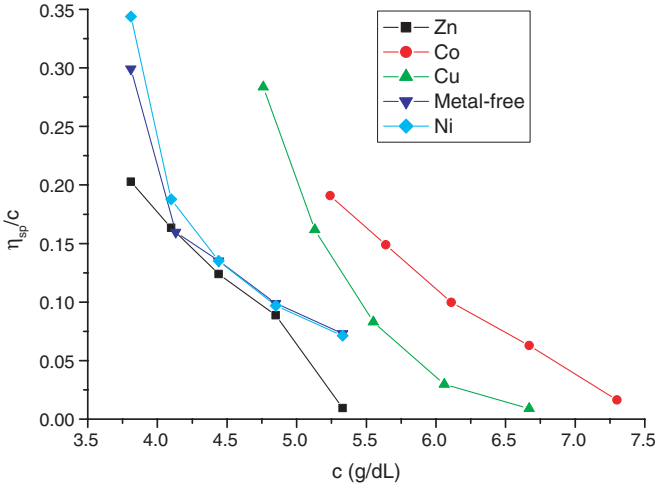


Fig. 5. Intrinsic viscosities of the polymeric phthalocyanines.

Cu-containing polymer **8** was the most rapidly degraded metallophthalocyanine while Zn-, Ni- and Co-containing metallophthalocyanine polymers showed good thermal stability under working conditions.

The alkali metal-binding ability of diaza-18-crown-6 units containing polymers were evaluated. Due to their insolubility, heterogeneous phase extraction of alkali metal picrates from THF solutions to the solid metal-free polymer was investigated. Picrate was used as counter anion for all compounds. The results can be seen in Table 1. Examinations of the data reveal the following results: (a) the tendency of binding alkali picrates goes parallel with the increase in the ionic diameter except for Cs^+ and (b) the highest extraction affinity of **6** was determined as 94.25% for K^+. The extraction affinity of **6** for Li^+, Na^+, K^+, Cs^+ were determined as 6.01%, 77.17%, 94.25% and 22.16%, respectively. The highest extraction affinity in the case of K^+ is probably due to the more compatibility of K^+ with macrocyclic unit than the other ions.

Table 4
Thermal properties of the polymeric phthalocyanines

Compound	M	Initial decomposition temperature in °C	Main decomposition temperature in °C
6	2H	335	475
7	Zn	400	675
8	Cu	350	590
9	Co	360	660
10	Ni	355	625

4. Conclusions

We have presented the synthesis and characterization of polymeric phthalocyanines with diaza-18-crown-6 ethyleneoxy bridges. The metal-free phthalocyanine polymer (**6**) and metallophthalocyanine polymers were prepared using a tetranitrile monomer and proper materials. Zn-, Ni- and Co-containing polymers showed good thermal stability while Cu-containing and the metal-free polymers were the most rapidly degraded. The electrical conductivities of the polymeric phthalocyanines measured as gold sandwiches were found to be 10^{-9}–10^{-4} S cm^{-1} *in vacuo* and argon. The extraction ability of **6** was evaluated in THF by using several alkali metal picrates and the highest extraction affinity was observed for K^+. The intrinsic viscosity of the metal-free polymer and metallophthalocyanine polymers were similar. The metal-free polymeric phthalocyanine (**6**) had a clear disaggregation tendency with the addition of KNO_3, $NaNO_3$ and NH_4NO_3.

Acknowledgements

This study was supported by The Scientific and Technical Research Council of Turkey (TUBITAK), Project Number: TBAG-2453(104T065) (Ankara, Turkey). We are also indebted to Prof. Dr. M. Hanack (University of Tübingen/Germany) and Dr. U. Kadiroglu (University of Kocaeli/Turkey) for assistance with some spectral data.

References

[1] E.M. Maya, E.M. Garcia-Frutos, P. Vazquez, T. Torres, J. Phys. Chem. A 107 (2003) 2110.
[2] C.C. Leznoff, A.B.P. Lever, Phthalocyanines: Properties and Applications, Vols. 1–4, VCH–Wiley, New York, 1989, 1993, 1993, 1996.

[3] N.B. McKeown, Phthalocyanine: Materials Synthesis, Structure and Function, Cambridge University Press, Cambridge, 1998.
[4] X. Du, C. Ma, X. Hou, G. Wang, W. Li, G. Du, Heterocycles 60 (2003) 2535.
[5] M. Hanack, H. Heckmann, R. Polley, in: E. Schaumann (Ed.), Houben-Weyl Methods of Organic Chemistry, 4th ed., Vol. E9d, Georg Thieme Verlag, Stuttgart, 1998, p. 739.
[6] N. Akdemir, E. Ağar, S. Şaşmaz, İ.E. Gümrükçüoğlu, T. Çelebi, Dyes Pigments 69 (2006) 1.
[7] S. Makhseed, N.B. McKeown, K. Msayib, A. Bumajdad, J. Mater. Chem. 15 (2005) 1865.
[8] J. Zhang, X. Liu, H. Wen, M. Xie, X. Cai, Polym. Int. 42 (1997) 363.
[9] A.A. Berlin, A.I. Sherle, Inorg. Macromol. Rev. 1 (1971) 235.
[10] D. Wöhrle, U. Marose, R. Knoop, Makromol. Chem. 186 (1985) 2209.
[11] T. Hara, Y. Ohkatsu, T. Osa, Bull. Chem. Soc. Jpn. 48 (1975) 85.
[12] H. Inoue, Y. Kida, E. Imato, Bull. Chem. Soc. Jpn. 40 (1967) 184.
[13] C.J. Norrel, H.A. Pohl, M. Thomas, K.D. Berlin, J. Polym. Sci., Polym. Phys. Ed. 12 (1974) 913.
[14] W. Hanke, Z. Anorg. Allg. Chem. 347 (1966) 67.
[15] (a) D. Wöhrle, B. Schulte, Makromol. Chem. 189 (1988) 1167; (b) D. Wöhrle, B. Schulte, Makromol. Chem. 189 (1988) 1229.
[16] A.W. Snow, J.R. Griffith, N.P. Marullo, Macromolecules 17 (1984) 1614.
[17] C.S. Marvel, M.M. Martin, J. Am. Chem. Soc. 80 (1958) 6600.
[18] T.M. Keller, J. Polym. Sci., Polym. Lett. Ed. 25 (1987) 2569.
[19] J.A. Hinkley, J. Appl. Polym. Sci. 29 (1984) 3339.
[20] G. Manecke, D. Wöhrle, Makromol. Chem. 102 (1967) 1.
[21] A.G. Gürek, Ö. Bekaroglu, J. Porphyr. Phthalocya. 1 (1997) 227.
[22] B.N. Achar, K.S. Lokesh, J. Organomet. Chem. 689 (2004) 2601.
[23] G. Koß mehl, M. Rohde, Makromol. Chem. 178 (1977) 715.
[24] C.S. Marvel, J.H. Rassweiler, J. Am. Chem. Soc. 80 (1958) 1197.
[25] D.R. Boston, J.C. Bailar, Inorg. Chem. 11 (1972) 1578.
[26] (a) Y. Gök, H. Kantekin, A. Bilgin, D. Mendil, İ. Degirmencioglu, J. Chem. Soc., Chem. Commun. 3 (2001) 285; (b) A. Bilgin, B. Ertem, Y. Gök, Tetrahedron Lett. 44 (2003) 3829; (c) A. Bilgin, Y. Gök, Tetrahedron Lett. 43 (2002) 5343; (d) A. Bilgin, B. Ertem, Y. Gök, Tetrahedron Lett. 44 (2003) 6937; (e) A. Bilgin, B. Ertem, Y. Gök, Polyhedron 24 (2005) 1117; (f) A. Bilgin, B. Ertem, Y. Gök, Supramol. Chem. 17 (2005) 277; (g) A. Bilgin, Ç. Yağcı, U. Yıldız, Macromol. Chem. Phys. 206 (2005) 2257.
[27] D.D. Perrin, W.L.F. Armarego, Purification of Laboratory Chemicals, 2nd ed., Pergamon Press, Oxford, 1989.
[28] G.J. Young, W. Onyebuagu, J. Org. Chem. 55 (1990) 2155.
[29] S. Kulstad, L.A. Malmsten, Acta Chem. Scand. B 33 (1979) 469.
[30] A.W. Snow, J.S. Shirk, R.G.S. Pong, J. Porphyr. Phthalocya. 4 (2000) 518.
[31] F. Chavez, A.D. Sherry, J. Org. Chem. 54 (1989) 2990.
[32] D. Wöhrle, E. Preubner, Makromol. Chem. 186 (1985) 2189.
[33] I. Yılmaz, Ö. Bekaroğlu, Chem. Ber. 129 (1996) 967.
[34] O.E. Sielcken, M.M. van Tilborg, R. Hendricks, W. Drenth, R.J.M. Nolte, J. Am. Chem. Soc. 109 (1987) 4261.
[35] E.A. Cuellar, T.J. Marks, Inorg. Chem. 20 (1981) 3766.
[36] J.M. Lehn, J.P. Savuage, J. Am. Chem. Soc. 97 (1975) 6700.
[37] H. Pagnia, N. Sotnik, Phys. Status Solidi A 108 (1988) 11.
[38] J. Simon, J.J. Andre, in: J.M. Lehn, C.W. Rees (Eds.), Molecular Semiconductors, Springer-Verlag, Berlin, 1985, p. 136.
[39] D. Wöhrle, B. Schulte, Makromol. Chem. 186 (1985) 2229.
[40] V. Ahsen, T. Yilmazer, Ö. Bekaroğlu, Makromol. Chem. 189 (1988) 2533.

Available online at www.sciencedirect.com
ScienceDirect
Polyhedron 26 (2007) 626–630
POLYHEDRON
www.elsevier.com/locate/poly

Supramolecular stabilization of the phosphite-based polyoxomolybdate $[Mo_6(PO_3)(HPO_3)_3O_{18}]^{9-}$

José R. Galán Mascarós *, Carlos Martí-Gastaldo

Instituto de Ciencia Molecular, Universidad de Valencia, Polígono de la Coma, s/n, 46980 Paterna, Spain

Received 27 June 2006; accepted 25 August 2006
Available online 8 September 2006

Abstract

A novel phosphite-based hetero-polyoxomolybdate, $[Mo_6(PO_3)(HPO_3)_3O_{18}]^{9-}$, has been isolated and structurally characterized. The most striking feature of this polyanion is the presence of peripheral phosphite groups linked to the MoO_6 octahedra. In the solid state, this cluster shows strong hydrogen bonding interactions that apparently play a key role in its stabilization and isolation from solution.
© 2006 Elsevier Ltd. All rights reserved.

Keywords: Polyoxometalates; Supramolecular chemistry; Molybdenum; Hydrogen bonding; Phosphite

1. Introduction

Polyoxometalates (POM) are discrete polyanionic fragments of early transition metal oxides, specially vanadium, molybdenum and tungsten, which usually adopt highly symmetrical structural motifs. The introduction of heteroatoms such as P, As, Sb, Se or Bi in polyoxometalates leads to higher versatility in the chemical properties and molecular structures. Although the research on POM chemistry [1–3] began more than hundred years ago, they reached great importance from the second half of the 20th century and up to this date. The great interest of this subject is justified because the large structural variety and tunable chemical and physical properties make POM very attractive candidates which can be used in very different fields such as catalysis [4,5] (homogeneous and heterogeneous), electrochemistry [6], electrochromism [7], conductivity [8], magnetism [9–11] or medicine [12,13] (anti-viral and anti-tumoral agents).

The controlled formation of polyoxometalates, and specially the rational directed synthesis of specific structures presents a major challenge, attending to the large number of factors which must be considered relevant in their synthesis: temperature, molecular ratio M/X, the nature of the solvent, pH value or the nature of the counter ions. In the search for novel structural motifs, some different synthetic strategies from normal solution techniques have successfully been employed, as hydrothermal methods [14,15].

Although their great structural diversity, from the well-known Keggin and Dawson-Wells structures to giant nanosized clusters [16], all polyoxometalates are formed from a relatively low number of highly symmetrical MO_x polyhedrons, usually octahedral or tetrahedral, and in some cases pentacoordinated square-based pyramids, where the corners of the polyhedra are occupied by oxygen atoms. On the contrary, polyoxometalates possessing pyramidal lone electron pair atoms in its structure are quite rare, although some examples have been described with elements such as P^{III}, As^{III}, Sb^{III}, Se^{IV} or Bi^{III} [17–20]. Most of these are coming from the search for aminoacid-bound polyanions, where the pyramidal lone electron pair atom resides in the center of a hexagonal ring of V, Mo or W octahedra, lying slightly above the plane defined by the

* Corresponding author. Present address: Instituto de Ciencia Molecular, Universidad de Valencia, Dr. Moliner 50, E-46100 Burjasot, Spain. Tel.: +34 963544420; fax: +34 963543273.
E-mail address: jose.r.galan@uv.es (J.R. Galán Mascarós).

0277-5387/$ - see front matter © 2006 Elsevier Ltd. All rights reserved.
doi:10.1016/j.poly.2006.08.030

metal atoms, with the three oxygen atoms of the $[H_nX^{III}O_3]^{-3+n}$ $(0 < n < 3)$ unit acting as bridges between the metal centers.

Using the flexibility of the hexameric core of Mo(VI) octahedra, which appears to be a recurrent structural motif in POM chemistry, in this work we report the synthesis and structural characterization of a novel phosphite-based polymolybdate, that exhibits for the first time terminal pyramidal lone electron pair units. Due to this peculiar feature, $[Mo_6(PO_3)(HPO_3)_3O_{18}]^{9-}$ can only be isolated in the presence of strong hydrogen bonding interactions, promoted in this case by ethylendiamine molecules.

2. Experimental

2.1. Synthesis

All reagents were of commercial grade and used without further purification.

$Na(H_2en)_4[Mo_6(PO_3)(HPO_3)_3O_{18}]\cdot 3H_2O$ (**1**) was synthesized as yellow block-like crystals in 40% yield (based on Mo, 1.7 mmol). Two solutions were prepared separately: (A) $Na_2MoO_4\cdot 2H_2O$ (0.4 g; 1.7 mmol) and NH_4VO_3 (0.2 g; 1.7 mmol) in 7 mL of water and (B) $Ni(OAc)_2$ (0.35 g; 1.4 mmol) and ethylenediamine (3 mL) in 3 mL of water. Solution (B) is added to solution (A) and the mixture is stirred for 10 min. After that a 50% (wt%) H_3PO_3 aqueous solution is prepared "in situ" and slowly added, pH of the solution was controlled very carefully, the solution presented violet color and a starting pH value of 11, after the acid addition the solution presented a pH value of 6.6 and its color had turned to dark green. The resulting dark green solution was filtered to remove any solid in solution and was left to stand at room temperature. After several days the block-like pale-yellow crystals of **1** were collected by filtration and separated by hand. The IR spectrum of compound **1** exhibited a pattern of bands at 1621(m), 1520(m), 1455(w), 1327(w), 1088(s), 1031(s), 910(s), 669(m), 592(w), 561(w) and 503(w) cm^{-1} (see Table 1).

2.2. Physical measurements

A yellow plate-like single crystal with dimensions $0.3\times 0.1\times 0.3$ mm was mounted on a glass fiber for indexing and intensity data collection at room temperature on a Siemens SMART KappaCCD diffractometer equipped using graphite-monochromated Mo Kα radiation ($\lambda =$ 0.71073 Å). Direct methods were used to solve the structure and to locate the heavy atoms (SIR-97) [21]. The remaining atoms were found from successive difference maps and refined against F^2 with a full-matrix least-squares algorithm using SHELXL-97 [22]. The final cycle of refinement, including the atomic coordinates, anisotropic thermal parameters (all metal and phosphorus atoms), and isotropic thermal parameters (all oxygen, carbon and nitrogen atoms), converged at $R_1 = 0.0528$ and $wR_2 = 0.1135$. Crystallographic data are summarized in Table 2.

Table 1
Selected bond lengths (Å) for $Na(H_2en)_4[Mo_6(PO_3)(HPO_3)_3O_{18}]\cdot 3H_2O$ (**1**)

Mo1–O7	1.691(7)	Mo5–O5	1.703(7)
Mo1–O1	1.750(7)	Mo5–O11	1.711(7)
Mo1–O18	1.901(6)	Mo5–O16	1.887(7)
Mo1–O13	1.909(7)	Mo5–O17	1.976(6)
Mo1–O22	2.207(7)	Mo5–O26	2.200(7)
Mo1–O19	2.318(6)	Mo5–O21	2.319(6)
Mo2–O8	1.689(7)	Mo6–O12	1.708(7)
Mo2–O2	1.718(7)	Mo6–O6	1.727(7)
Mo2–O14	1.887(7)	Mo6–O17	1.914(6)
Mo2–O13	1.959(6)	Mo6–O18	1.915(6)
Mo2–O23	2.183(7)	Mo6–O27	2.269(7)
Mo2–O19	2.406(6)	Mo6–O21	2.360(6)
Mo3–O9	1.689(7)	P1–O19	1.518(7)
Mo3–O3	1.720(7)	P1–O21	1.523(7)
Mo3–O14	1.906(7)	P1–O20	1.543(7)
Mo3–O15	1.919(6)	P2–O23	1.513(7)
Mo3–O24	2.202(7)	P2–O28	1.525(7)
Mo3–O20	2.352(7)	P2–O22	1.531(7)
Mo4–O10	1.698(8)	P3–O29	1.522(8)
Mo4–O4	1.701(6)	P3–O24	1.538(7)
Mo4–O16	1.915(7)	P3–O25	1.539(7)
Mo4–O15	1.967(7)	P4–O30	1.506(8)
Mo4–O20	2.272(7)	P4–O27	1.538(7)
Mo4–O25	2.294(7)	P4–O26	1.540(7)

Table 2
Crystal data and main refinement parameters for $Na(H_2en)_4[Mo_6(PO_3)(HPO_3)_3O_{18}]\cdot 3H_2O$

Empirical formula	$C_8H_{49}Mo_6N_8NaO_{33}P_4$
Molecular weight	1508.06
Space group	*Cc*
a (Å)	17.9130(4)
b (Å)	18.2850(4)
c (Å)	12.6920(4)
β (°)	97.8040(10)
V (Å^3)	4118.63(2)
Z	4
D_{calc} (g cm^{-3})	2.432
μ (mm^{-1})	2.050
F(000)	2960
Measured reflections	8913
2*θ* Range (°)	3.20–64.90
Unique reflections/R_{int}	8903/0.0217
Reflections with $[I > 2\sigma(I)]$/parameters	7633/550
R (F_o)[a]	0.0528
R_w (F_o^2)[b]	0.1135
Goodness-of-fit	1.024
Maximum/minimum Δ*ρ* (e/Å^3)	1.931/−1.329

[a] $R = \sum(F_o - F_c)/\sum(F_o)$.
[b] $R_w = \{\sum[w(F_o^2 - F_c^2)^2]/\sum[w(F_o^2)^2]\}^{1/2}$; $w = 1/[\sigma^2(F_o^2) + 0.0566P^2 + 31.1568P]$, where $P = (F_o^2 + 2F_c^2)/3$.

3. Results and discussion

$[Mo_6(PO_3)(HPO_3)_3O_{18}]^{9-}$ was obtained in good yield as $Na(H_2en)_4[Mo_6(PO_3)(HPO_3)_3O_{18}]\cdot 3H_2O$ (**1**). It is the main product from the reaction of an aqueous solution of $Na_2MoO_4\cdot 2H_2O$, NH_4VO_3, $Ni(OAc)_2$ and ethylenediamine in the presence of the H_3PO_3 acid with strict control of the pH value during the reaction. Usually, this type of

reactions yield reduced heteropolymolybdates, with the phosphite getting oxidized to phosphate $(PO_4)^{3-}$ [23]. Surprisingly, in the mild conditions we use (room temperature during all the process) the phosphorus atoms maintain its oxidation state in the final compound. We attempted many times to obtain compound **1** in the absence of NH_4VO_3 and $Ni(OAc)_2$, two reagents that do not appear in compound **1**, but we did not succeed in the isolation of this polyanion. Therefore, these reagents must participate somehow in the process. It is difficult to explain their role in the reaction, though. NH_4VO_3 is probably involved in the control of the pH value and the Ni^{2+} ions in the given concentration of free ethylenediamine in solution. It is important to remark that ethylenediamine molecules are crucial in the stabilization of the final structure through hydrogen bond interactions which links the polyanionic clusters leading to the final packing.

The structure of **1** contains $[Mo_6(PO_3)(HPO_3)_3O_{18}]^{9-}$ anions, surrounded by protonated ethylendiamine and solvent molecules. The structure of polyanion (Fig. 1) consists of a six-membered ring of MoO_6 octahedra, which alternate in sharing edges and corners. A central phosphite group is present with its phosphorus atom located slightly above the plane of six molybdenum atoms. The most striking feature of this new polymolybdate resides in the existence of other three terminal phosphite groups on one side of the ring, capping the edge-sharing Mo dimers with two oxygen atoms, with the free oxygen atom from each group perpendicular to the ring, forming a basket-like structure. The lone pair of the central phosphite group also points towards same side of the ring as the peripheral phosphite groups. The octahedral coordination of the Mo atoms is completed with two terminal oxo groups, one equatorial on the plane of the ring, and the other on the opposite side of the ring with respect to the phosphite groups. The polyanion is highly symmetric with a molecular threefold axis running through the central phosphorus atom, perpendicular to the plane defined by the Mo atoms.

The Mo–O distances to the phosphite oxygen atoms (2.402 Å $\leqslant d \geqslant$ 2.186 Å) are larger than the rest of Mo–O distances (1.881 Å $< d <$ 1.986 Å). All phosphorus atoms present the same trigonal pyramid geometry, with all P–O distances in a 0.03 Å range and all O–P–O angles in a 4.06° range. Only the terminal O atoms from the phosphite appear protonated, according to the bond-valence sum calculation [24]. Taking this into account, the overall charge for the polyanion is −9. Therefore, the ethylendiamine molecules must be protonated, for electroneutrality. The presence of one Na atom was revealed by elemental analysis, and its position in the structure was assigned to the only peak surrounded exclusively by O atoms, with no interactions with any ethylendiamine unit.

It is important to state the existence of significant hydrogen bonding interactions in the structure. The strongest ones involve oxygen atoms of the peripheral phosphite groups and hydrogen atoms protonated ethylendiamine cations (Fig. 2). This also dictates the conformation of the ethylendiamine molecules. Two of them present a *cis* conformation. Terminal oxygen O28 is chelated by one ethylendiamine unit, with O···N distances 2.794(13) and 2.791(12) Å to N5 and N6, respectively. Terminal oxygen O29 interact with the other ethylendiamine in *cis*

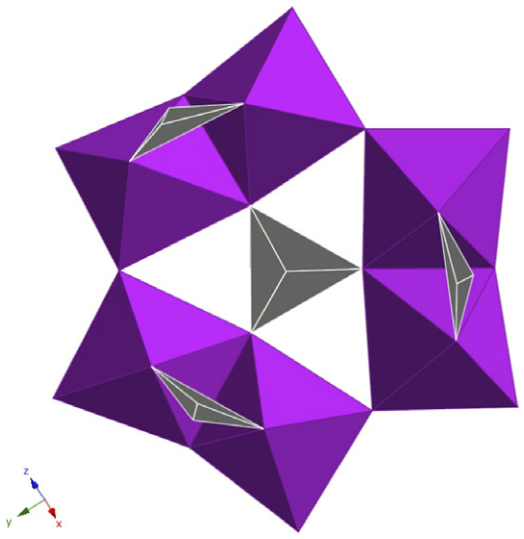


Fig. 1. Polyhedral representation of the polymolybdate anion. The MoO_6 octahedra are shown in violet and the PO_3^{3-} and HPO_3^{2-} groups in grey. (For interpretation of the references to color in this figure legend, the reader is referred to the web version of this article.)

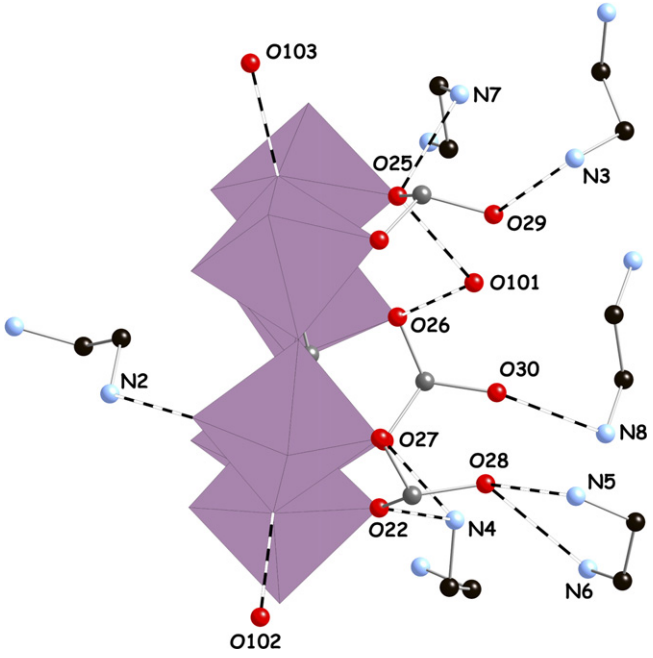


Fig. 2. Representation of the shortest hydrogen bonding interactions (dashed lines) between a $[Mo_6(PO_3)(HPO_3)_3O_{18}]^{9-}$ polyanion and its surroundings in the crystal structure of **1**. The balls represent molybdenum (violet), phosphorus (grey), oxygen (red), nitrogen (blue), carbon (black) (H atoms omitted for the sake of clarity). (For interpretation of the references to color in this figure legend, the reader is referred to the web version of this article.)

(O29···N3 = 2.684(11) Å) that connects to adjacent anions through the N4···O22 and N4···O27 contacts (2.688(11) and 2.742(11) Å, respectively). Terminal oxygen O30 shows a close contact (O30···N8 = 2.691(11) Å) to an ethylendiamine group, that exhibits *trans* configuration. This cation also links to adjacent anions through the slightly longer N7···O7 and N7···25 hydrogen bonds (2.842(12) and 2.869(11) Å, respectively). Finally, the remaining ethylendiamine shows stronger interactions with the opposite side of the anions, for a shortest distance of 2.777(13) Å (O2···N2). The water molecules play also an important role in the H bonding network. Water O101 shows contacts at 2.701(11) and 2.771(12) Å to oxygen atoms from phosphite groups (O26 and O25, respectively). The other two water molecules, on the contrary, bind core oxo groups: O102···O13 = 2.745(12) Å and O103···O15 = 2.754(12) Å. All these contacts, along with many other ones below 2.9 Å, create a complex 3D H-bonding network, showing a layered pseudo-hexagonal packing for the polyanions. Two types of layers can be distinguished running perpendicular to the *a* axes with a repeating pattern ...AB... (Fig. 3).

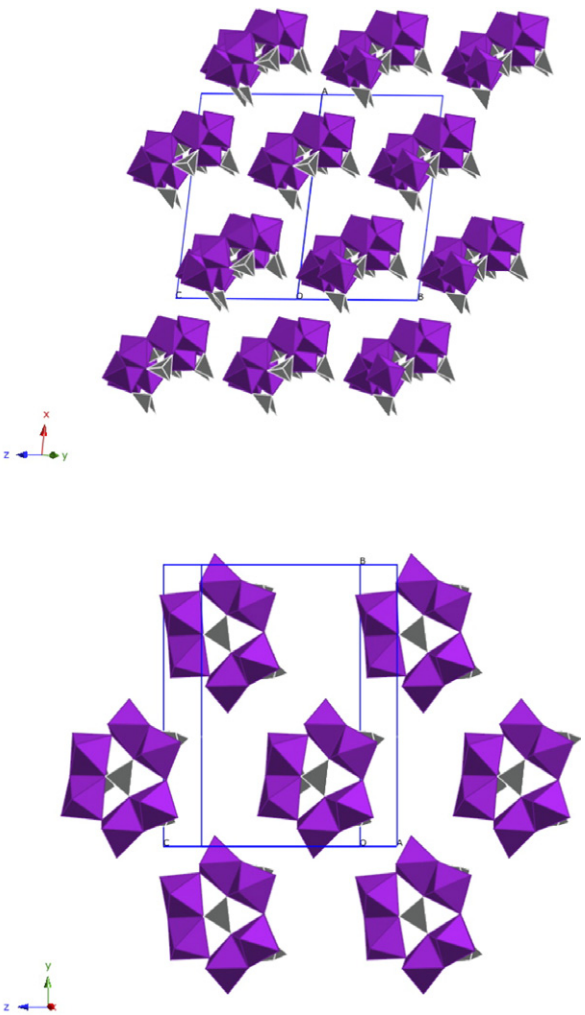


Fig. 3. (Top) View of the anionic layers of $[Mo_6(PO_3)(HPO_3)_3O_{18}]^{9-}$ units and their packing along the *a* axis. (Bottom) View of the pseudo-hexagonal packing on the *bc* plane. The color code is the same as in Fig. 1. (For interpretation of the references to color in this figure legend, the reader is referred to the web version of this article.)

In addition to their influence in determining the crystal structure, the O···N interactions between phosphite and ethylendiamine groups should also favor the stability of this compound in solution, allowing for its crystallization. As mentioned before, this is the first example of a POM with terminal phosphite groups, and the presence of so many, strong and varied interactions of these groups with the surrounding cations evidence that they are an important factor for its stability.

The structure of the $[Mo_6(PO_3)(HPO_3)_3O_{18}]^{9-}$ cluster is reminiscent of other similar structures, with several differences: on one hand, all other structures possess only one central pyramidal lone electron pair unit, with the three capping positions occupied either by carboxylate [17,18], organoarsonate [25,26], or tetrahedral $[X^{VI}O_4]^{2-}$ groups (X = S, Se) [19,20]. In most cases the cluster appears partially reduced, and in all cases the cluster is in its anionic form.

All attempts to dissolve **1** in any common organic or inorganic solvent failed, even in mixtures of them. Acid or basic solutions are able to dissolve the solid, but the cluster does not exist in solution as proven by mass spectroscopy, and cannot be recovered anymore.

4. Conclusions

In this paper we report the synthesis and structural characterization of a novel phosphite based polyoxometalate with formula $[Mo_6(PO_3)(HPO_3)_3O_{18}]^{9-}$. It is important to remark that few POMs with pyramidal lone electron pair atoms in their structure have been previously described and, in addition, **1** is the first example where such trigonal pyramidal polyhedra appear as terminal groups. A strong hydrogen bonded network stabilizes this POM in the solid state. As chemistry interest is moving from molecular to supramolecular organizations, this cluster is a clear example of how supramolecular chemistry can indeed expand the reach of molecular species. The poor solubility of **1** could now be improved by exchange of ethylendiamine by other ligands, able to participate in hydrogen bonded networks to assure its stability. Then, **1** could be used as building block in other reactions, either as ligand towards transition metal cations, or even as a source of hexa-vacant Keggin-type structure $[Mo_6(PO_3)O_{18}]$, by removal of the very labile phosphite groups. Such species would have 12 terminal oxygen atoms, which are strong basic sites susceptible to be attacked by electrophilic species in condensation reactions.

5. Supplementary material

CCDC 609184 contains the supplementary crystallographic data for **1**. These data can be obtained free of

charge via http://www.ccdc.cam.ac.uk/conts/retrieving.html, or from the Cambridge Crystallographic Data Centre, 12 Union Road, Cambridge CB2 1EZ, UK; fax: (+44) 1223-336-033; or e-mail: deposit@ccdc.cam.ac.uk.

Acknowledgements

This work was supported by the Spanish Ministerio de Ciencia y Tecnología (BQU2002-01091) and by the Generalitat Valenciana (GV04A-0077). C.M.-G. thanks the Spanish Ministerio de Educación y Ciencia for a Ph.D. fellowship.

References

[1] M.T. Pope, A. Müller (Eds.), Polyoxometalate Chemistry: From Topology via Self-Assembly to Applications, Kluwer, Dordrecht, 2001.
[2] M.T. Pope, A. Müller (Eds.), Polyoxometalates: From Platonic Solids to Anti Retroviral Activity, Kluwer, Dordrecht, 1994.
[3] J.J. Borrás-Almenar, E. Coronado, A. Müller, M.T. Pope (Eds.), Polyoxometalate Molecular Science, NATO Science Series, Kluwer, Dordrecht, 2001.
[4] Ivan V. Kozhevnikov, Chem. Rev. 98 (1998) 171.
[5] N. Mizuno, M. Misono, Chem. Rev. 98 (1998) 199.
[6] M. Sadakane, E. Steckhan, Chem. Rev. 98 (1998) 219.
[7] T. Yamase, Chem. Rev. 98 (1998) 307.
[8] E. Coronado, C.J. Gómez-García, Chem. Rev. 98 (1998) 273.
[9] A. Müller, F. Peters, M.T. Pope, D. Gatteschi, Chem. Rev. 98 (1998) 239.
[10] A. Müller, E. Krickemeyer, J. Meyer, H. Bögge, F. Peters, W. Plass, E. Diemann, S. Dillinger, F. Nonnenbruch, M. Randerath, C. Menke, Angew. Chem., Int. Ed. Engl. 34 (1995) 2122.
[11] J.M. Clemente-Juan, E. Coronado, J.R. Galán-Mascarós, C.J. Gómez-García, Inorg. Chem. 38 (1999) 55.
[12] J.T. Rhule, C.L. Hill, D.A. Judd, R.F. Schinazi, Chem. Rev. 98 (1998) 327.
[13] C.L. Hill, X. Zhang, Nature 373 (6512) (1995) 324.
[14] A. Muller, H. Reuter, S. Dillinger, Angew. Chem., Int. Ed. Engl. 34 (1995) 2328.
[15] A. Dolbecq, P. Mialane, L. Lisnard, J. Marrot, F. Secheresse, Chem. Eur. J. 9 (2003) 2914.
[16] A. Müller, S.Q.N. Shah, H. Bogge, M. Schmidtmann, Nature 397 (1999) 48.
[17] U. Kortz, M.G. Savelieff, F.Y. Abou Ghali, L.M. Khalil, S.A. Maalouf, D.I. Sinno, Angew. Chem., Int. Ed. 41 (2002) 4070.
[18] U. Kortz, J. Vaissermann, R. Thouvenot, P. Gouzerh, Inorg. Chem. 42 (2003) 1135.
[19] U. Kortz, Inorg. Chem. 39 (2000) 625.
[20] C. Livage, E. Dumas, C. Marchal-Roch, G. Hervé, C.R. Acad. Sci. Paris, Sèrie IIc 3 (2000) 95.
[21] A. Altomare, M.C. Burla, M. Camalli, G.L. Cascarano, G. Giacovazzo, A.G.G. Moliterni, G. Polidori, R. Spagna, J. Appl. Crystallogr. 32 (1999) 115.
[22] G.M. Sheldrick, University of Göttingen, Göttingen, Germany.
[23] X. Ya, Z. Hao-Guo, C. Hu, Y. Xiao-Zeng, Chem. Commun. (1999) 787.
[24] I.D. Brown, D. Altermatt, Acta Crystallogr., Sect. B 41 (1985) 244.
[25] W. Kwak, L.M. Rajkovic, J.K. Stalick, M.T. Pope, C.O. Quicksall, Inorg. Chem. 15 (1976) 2778.
[26] W. Kwak, L.M. Rajkovic, M. T Pope, C.O. Quicksall, K.Y. Matsumoto, Y. Sasaki, J. Am. Chem. Soc. 99 (1977) 6463.

Available online at www.sciencedirect.com
ScienceDirect
Polyhedron 26 (2007) 631–636
POLYHEDRON
www.elsevier.com/locate/poly

Trinuclear Schiff base complexes with uranium(V) and copper(II) or zinc(II) ions

Lionel Salmon, Pierre Thuéry, Michel Ephritikhine *

Service de Chimie Moléculaire, DSM, DRECAM, CNRS URA 331, Laboratoire Claude Fréjacques, Bat. 125, CEA/Saclay, 91191 Gif-sur-Yvette, France

Received 12 June 2006; accepted 23 August 2006
Available online 30 August 2006

Abstract

Treatment of the uranium(IV) complexes $[\{ML^1(py)\}_2U^{IV}]$ (M = Cu, Zn; L^1 = *N*,*N*′-bis(3-hydroxysalicylidene)-1,3-propanediamine) with silver nitrate in pyridine led to the formation of the corresponding cationic uranium(V) species which were found to be thermally unstable and were converted back into the parent U^{IV} complexes; no electron transfer was observed in solution between the U^{IV} and U^V compounds. In the crystals of $[\{ML^1(py)\}_2U^{IV}][\{ML^1(py)\}_2U^V][NO_3]$, the neutral U^{IV} and cationic U^V species are clearly identified by the distinct U–O distances. Similar reaction of $[\{ZnL^2(py)\}_2U^{IV}]$ [L^2 = *N*,*N*′-bis(3-hydroxysalicylidene)-1,4-butanediamine] with $AgNO_3$ gave crystals of $[\{ZnL^2(py)\}U^V\{ZnL^2(py)_2\}][NO_3]$ but the copper counterpart was not isolated. Crystals of $[\{ZnL^1(py)\}_2U^V][OTf]\cdot THF$ ($OTf = OSO_2CF_3$) were obtained fortuitously from the reaction of $[Zn(H_2L^1)]$ and $U(OTf)_3$.
© 2006 Elsevier Ltd. All rights reserved.

Keywords: Uranium(V); Heterotrimetallic complexes; Crystal structure

1. Introduction

We recently reported on the synthesis, crystal structure and magnetic behaviour of a series of trinuclear Schiff base complexes of general formula $[\{ML^i(py)_x\}_2An^{IV}]$ (M = Cu, Zn; An = Th, U) where the central actinide(IV) ion is surrounded by the eight oxygen atoms of two hexadentate bicompartmental Schiff base ligands L which are orthogonal to one another and contain a Cu^{II} or Zn^{II} ion in their inner N_2O_2 cavity [1,2]. We were interested in studying the corresponding uranium(V) derivatives $[\{ML^i(py)_x\}_2U^V]^+$ for two reasons. The synthesis of such complexes is somewhat challenging because of the instability of U^V versus U^{IV} and U^{VI}, but a number of pentavalent uranium compounds with oxygen ligands have been isolated [3–7], since the discovery of the alkoxides $U(OR)_5$ [8]. The isolation of the $[\{ML^i(py)_x\}_2U^V]^+$ complexes, first examples of heteronuclear compounds associating 3d and $5f^1$ ions, would permit to determine the nature of the magnetic interaction between these ions. The presence of a single f electron on the U^V ion could facilitate the elaboration of a general theoretical model to describe the magnetic susceptibility of a 4f or 5f ion which possesses a first-order orbital momentum. Here we present our attempts to synthesize the compounds $[\{ML^i(py)_x\}_2U^V][NO_3]$ [M = Cu or Zn; L^1 = *N*,*N*′-bis(3-hydroxysalicylidene)-R with R = 1,3-propanediamine ($i = 1$) or 1,4-butanediamine ($i = 2$)] by oxidation of the parent uranium(IV) complexes with $AgNO_3$; these reactions afforded crystals of $[\{ML^1(py)\}_2U^{IV}][\{ML^1(py)\}_2U^V][NO_3]\cdot 4py$ (M = Cu, Zn) and $[\{ZnL^2(py)\}U^V\{ZnL^2(py)_2\}][NO_3]\cdot py$ which were characterized by X-ray diffraction analysis. We also describe the crystal structure of $[\{ZnL^1(py)\}_2U^V][OTf]\cdot THF$ ($OTf = OSO_2CF_3$) which was obtained fortuitously from the reaction of $[Zn(H_2L^1)]$ and $U(OTf)_3$. However, the unsuccessful synthesis of the pure $Cu^{II}_2U^V$ compounds precluded the magnetic properties to be investigated.

* Corresponding author. Tel.: +33 1 69 08 64 36; fax: +33 1 69 08 66 40.
E-mail addresses: salmon@drecam.cea.fr (L. Salmon), pierre.thuery@cea.fr (P. Thuéry), ephri@drecam.cea.fr (M. Ephritikhine).

0277-5387/$ - see front matter © 2006 Elsevier Ltd. All rights reserved.
doi:10.1016/j.poly.2006.08.016

2. Results and discussion

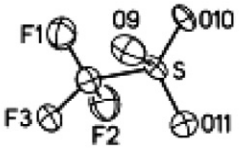
2.1. Synthesis of the complexes

In the presence of one equivalent of $AgNO_3$ in pyridine at 20 °C, $[\{CuL^1(py)\}_2U^{IV}]$ was partially transformed into the uranium(V) derivative $[\{CuL^1(py)\}_2U^{V}][NO_3]$; no electron transfer was detected by NMR spectroscopy between the U^{IV} and U^{V} complexes. Total conversion of U^{IV} into U^{V} required the addition of three equivalents of the silver salt and after usual work-up, $[\{CuL^1(py)\}_2U^{V}][NO_3]$ was isolated as a black powder in 28% yield. While the ^1H NMR spectrum did not show the presence of impurities, the elemental analyses were not satisfactory and attempts to purify the product were unsuccessful. The uranium(V) complex was found to be sensitive to heat, being converted back into the U^{IV} congener. Dark brown crystals of the mixed-valence compound $[\{CuL^1(py)\}_2U^{IV}][\{CuL^1(py)\}_2U^{V}][NO_3]\cdot 4py$ were deposited from a pyridine solution at 80 °C. The synthesis of $[\{ZnL^1(py)\}_2U^{V}][NO_3]$ was easier than that of the copper analogue, not requiring an excess of $AgNO_3$, and this $Zn_2^{II}U^{V}$ complex proved to be stable, up to 80 °C, towards the $U^{V}\rightarrow U^{IV}$ reduction. However, it was not obtained analytically pure; a refluxing pyridine solution of the complex deposited dark brown crystals of $[\{ZnL^1(py)\}_2U^{IV}][\{ZnL^1(py)\}_2U^{V}][NO_3]\cdot 4py$. In contrast, oxidation of $[\{ZnL^2(py)\}_2U^{IV}]$ was totally achieved upon addition of one equivalent of $AgNO_3$ in pyridine, and dark brown crystals of the stable, analytically pure, uranium(V) compound $[\{ZnL^2(py)\}U^{V}\{ZnL^2(py)_2\}][NO_3]\cdot py$ were isolated in 80% yield. Unfortunately, the copper analogue of this $Zn_2^{II}U^{V}$ complex was not obtained in a pure form. As previously noted with uranium(V) amide compounds, the factors, steric and electronic, which determine the stability of the +5 oxidation state of uranium are not well understood [4].

Treatment of $[Zn(H_2L^1)]$ with $U(OTf)_3$ in pyridine afforded a mixture of the dinuclear and trinuclear uranium(IV) complexes $[\{ZnL^1(py)_x\}U^{IV}(OTf)_2]$ and $[\{ZnL^1(py)_x\}_2U^{IV}]$. This result is not surprising since oxidation reactions of trivalent uranium complexes by alcohols and phenols have some precedents [9–11]. Heating the mixture under reflux gave dark yellow crystals of $[Hpy][\{ZnL^1(py)\}_2U^{IV}][OTf]$ together with a few dark brown crystals of $[\{ZnL^1(py)\}_2U^{V}][OTf]\cdot THF$; this latter uranium(V) complex likely resulted from oxidation by adventitious traces of air.

2.2. Crystal structures of the complexes

The crystal structures of the M_2U complexes permit, after the couple of dithiolene compounds $[U(C_8H_8)(dddt)_2]^{n-}$



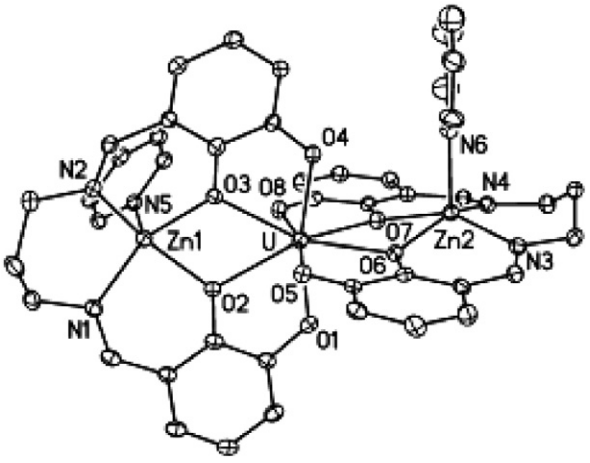


Fig. 2. View of $[\{ZnL^1(py)\}_2U^{V}][OTf]$. The hydrogen atoms are omitted for clarity. Displacement ellipsoids are drawn at the 20% probability level.

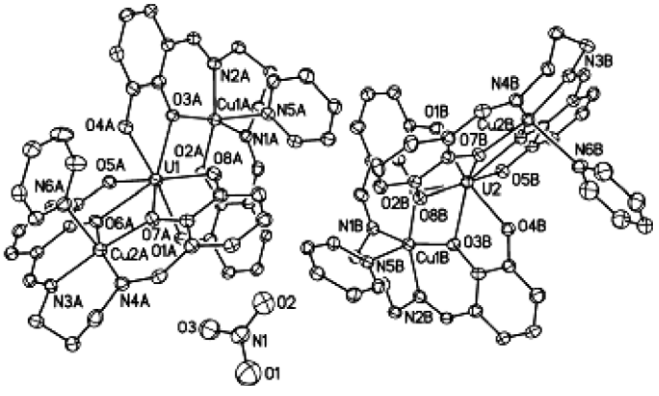


Fig. 1. View of $[\{CuL^1(py)\}_2U^{IV}][\{CuL^1(py)\}_2U^{V}][NO_3]$. The hydrogen atoms are omitted for clarity. Only one position of the disordered pyridine molecule is represented. Displacement ellipsoids are drawn at the 20% probability level.

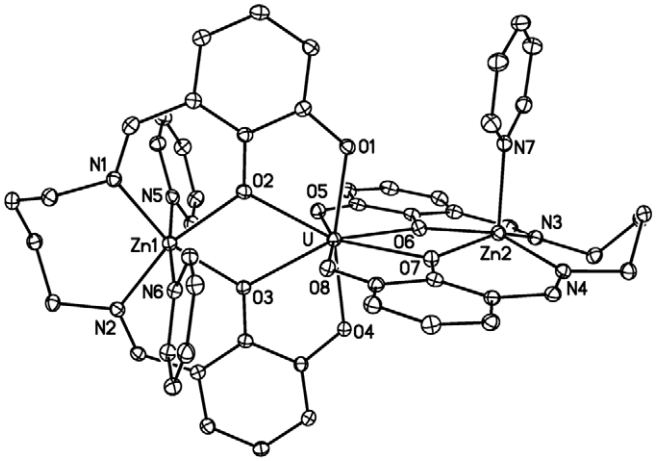


Fig. 3. View of the cation $[\{ZnL^2(py)\}U^{V}\{ZnL^2(py)_2\}]^{+}$. The hydrogen atoms are omitted for clarity. Displacement ellipsoids are drawn at the 20% probability level.

($n = 1$ or 2; dddt = 5,6-dihydro-1,4-dithiin-2,3-dithiolate) [12], a direct comparison of analogous U^{IV} and U^{V} derivatives. All the trinuclear compounds adopt the same structure which has already been described with the series of $[\{ML^{i}(py)_x\}_2An^{IV}]$ complexes. The 3d ions occupy the inner N_2O_2 cavities of the bicompartmental Schiff base ligands and are found in a square-pyramidal or octahedral coordination mode, depending on whether one or two pyridine molecules are attached to them; the uranium atom is inside the dodecahedron defined by the oxygen atoms of the L^{i} ligands, which form two orthogonal trapeza, O1–O2–O3–O4 and O5–O6–O7–O8. Views of $[\{CuL^{1}(py)\}_2U^{IV}]$-$[\{CuL^{1}(py)\}_2U^{V}][NO_3]$, $[\{ZnL^{1}(py)\}_2U^{V}]$ [OTf] and of the cation $[\{ZnL^{2}(py)\}U^{V}\{ZnL^{2}(py)_2\}]^{+}$ are shown in Figs. 1–3, respectively; selected bond lengths and angles are listed in Table 1.

The crystals of $[\{ML^{1}(py)\}_2U^{IV}][\{ML^{1}(py)\}_2U^{V}]$-$[NO_3]\cdot 4py$, isomorphous for M = Zn and Cu, are

Table 1
Selected bond lengths (Å) and angles (°) in the M_2U complexes

	$[\{CuL^{1}(py)\}_2U]_2[NO_3]\cdot 4py$		$[\{ZnL^{1}(py)\}_2U]_2[NO_3]\cdot 4py$		$[\{ZnL^{2}(py)\}U^{V}$-$\{ZnL^{2}(py)_2\}]$ $[NO_3]\cdot py$	$[\{ZnL^{1}(py)\}_2U^{V}]$-$[OTf]\cdot THF$	[Hpy]-$[\{ZnL^{1}(py)\}_2$-$U^{IV}][OTf]$
	$[\{CuL^{1}(py)\}_2U^{IV}]$	$[\{CuL^{1}(py)\}_2U^{V}]^{+}$	$[\{ZnL^{1}(py)\}_2U^{IV}]$	$[\{ZnL^{1}(py)\}_2U^{V}]^{+}$			
U–O1	2.294(7)	2.179(7)	2.317(10)	2.177(9)	2.193(3)	2.199(5)	2.284(3)
U–O2	2.448(7)	2.380(6)	2.432(10)	2.361(8)	2.369(3)	2.403(5)	2.404(3)
U–O3	2.446(6)	2.404(6)	2.417(8)	2.392(8)	2.395(3)	2.369(5)	2.422(3)
U–O4	2.294(7)	2.177(7)	2.314(10)	2.174(9)	2.202(3)	2.173(6)	2.458(3)
U–O5	2.294(7)	2.188(6)	2.296(8)	2.176(9)	2.183(3)	2.212(5)	2.262(3)
U–O6	2.473(7)	2.398(6)	2.446(9)	2.387(8)	2.375(3)	2.386(5)	2.418(3)
U–O7	2.452(7)	2.406(6)	2.422(10)	2.386(8)	2.420(3)	2.369(5)	2.433(3)
U–O8	2.289(7)	2.190(7)	2.315(9)	2.190(9)	2.171(3)	2.193(6)	2.274(3)
⟨U–O⟩	2.37(8)	2.29(11)	2.37(6)	2.28(10)	2.29(10)	2.29(9)	2.37(8)
⟨U–O_b⟩	2.455(11)	2.397(10)	2.429(11)	2.382(12)	2.39(2)	2.382(14)	2.419(10)
⟨U–O_t⟩	2.293(2)	2.184(6)	2.311(8)	2.179(6)	2.187(12)	2.194(14)	2.32(8)
M1–O2	1.944(7)	1.954(6)	2.025(8)	2.040(9)	2.084(3)	2.044(5)	2.006(3)
M1–O3	1.945(7)	1.933(7)	2.030(10)	2.026(9)	2.051(3)	2.038(5)	2.081(3)
M1–N1	1.996(9)	1.985(9)	2.047(14)	2.051(12)	2.074(3)	2.050(7)	2.068(4)
M1–N2	1.976(8)	2.016(8)	2.069(11)	2.080(13)	2.098(4)	2.064(7)	2.040(4)
M1–N5	2.344(9)	2.275(8)	2.110(11)	2.062(12)	2.287(4), 2.256(4)[a]	2.064(7)	2.075(4)
M2–O6	1.951(7)	1.941(6)	1.995(10)	2.021(9)	2.086(3)	2.036(5)	2.033(3)
M2–O7	1.959(7)	1.970(6)	2.052(9)	2.046(8)	2.049(3)	2.046(5)	2.057(3)
M2–N3	2.016(8)	2.007(8)	2.085(12)	2.100(10)	2.064(4)	2.056(7)	2.073(4)
M2–N4	1.999(9)	1.981(8)	2.072(13)	2.030(11)	2.092(4)	2.043(7)	2.052(4)
M2–N6	2.299(9)	2.307(7)	2.063(13)	2.086(12)	2.094(4)[b]	2.067(7)	2.088(4)
⟨M–O⟩	1.950(6)	1.950(14)	2.03(2)	2.033(10)	2.068(18)	2.041(4)	2.04(3)
⟨M–N⟩	1.997(14)	1.997(15)	2.068(14)	2.07(3)	2.082(14)	2.053(8)	2.058(13)
M1···U	3.6365(13)	3.6393(12)	3.6624(19)	3.6987(16)	3.7271(5)	3.7190(10)	3.6567(6)
M2···U	3.6812(13)	3.6533(12)	3.7193(19)	3.7088(16)	3.7594(5)	3.6774(10)	3.7139(5)
O1–U–O4	167.8(3)	167.0(2)	166.3(4)	165.8(3)	165.74(10)	166.8(2)	162.08(11)
O2–U–O3	59.2(2)	58.2(2)	61.0(3)	59.3(3)	61.01(9)	59.11(18)	62.74(11)
O5–U–O8	167.1(3)	167.0(2)	166.7(4)	166.2(3)	166.13(11)	167.2(2)	164.20(12)
O6–U–O7	58.8(2)	58.7(2)	59.8(3)	59.3(3)	59.39(9)	59.72(18)	60.55(11)
N1–M1–N2	99.1(4)	100.4(4)	98.6(5)	98.9(6)	109.27(14)	99.0(3)	96.95(17)
N3–M2–N4	98.0(4)	99.6(3)	97.2(5)	97.6(4)	104.17(14)	99.9(3)	97.10(17)
N1–M1–O2	90.1(3)	91.2(3)	86.7(4)	88.3(4)	88.96(13)	88.9(3)	89.16(15)
N2–M1–O3	92.0(3)	91.4(3)	89.9(5)	89.5(4)	90.37(12)	89.3(2)	88.02(15)
N3–M2–O6	91.3(3)	92.2(3)	88.8(5)	90.1(4)	88.34(13)	89.5(2)	88.89(15)
N4–M2–O7	91.1(3)	91.2(3)	87.9(4)	89.3(4)	89.36(13)	89.2(2)	87.55(15)
O2–M1–O3	76.8(3)	73.6(3)	74.8(4)	70.7(3)	71.58(11)	70.4(2)	75.84(13)
O6–M2–O7	76.4(3)	74.1(3)	73.7(4)	71.0(3)	70.15(11)	70.9(2)	73.44(13)
M1–O2–U	111.3(3)	113.9(3)	110.2(4)	114.2(4)	113.51(12)	113.2(2)	111.71(14)
M1–O3–U	111.3(3)	113.7(3)	110.6(4)	113.4(4)	113.67(12)	114.9(2)	108.36(13)
M2–O6–U	112.1(3)	114.3(3)	113.4(4)	114.3(4)	114.70(12)	112.3(2)	112.84(15)
M2–O7–U	112.6(3)	112.8(3)	112.2(4)	113.4(4)	114.30(12)	112.6(2)	111.32(14)
M1···U···M2	174.70(3)	175.44(3)	171.40(4)	170.12(4)	177.240(11)	168.76(2)	174.259(14)
α_1[c]	10.6(4)	6.8(5)	16.4(4)	13.2(6)	4.2(2)	13.0(3)	10.4(2)
α_2[c]	0.2(3)	3.6(6)	8.6(4)	12.2(6)	10.4(2)	18.3(3)	11.9(2)

[a] Zn1–N6.
[b] Zn2–N7.
[c] α_1 and α_2 are the dihedral angles between the two halves of the M1–O2–O3–U and M2–O6–O7–U bridging cores.

composed of discrete neutral and cationic trinuclear complexes $[\{ML^1(py)\}_2U]^{0,+1}$, nitrate ions and solvent molecules. The attribution of the electronic charge, 0 or +1, and consequently the uranium oxidation state, +4 or +5, to the complexes labelled A and B, respectively, is unambiguous in view of the distinct geometrical parameters; this clear differentiation is in agreement with the absence of electron transfer observed in solution. The bond lengths and angles in the neutral complexes A are essentially the same as those found in the previously reported structures of $[\{CuL^1(py)\}U^{IV}\{CuL^1\}]\cdot py$ and $[\{ZnL^1(py)\}_2U^{IV}]\cdot 2.5py$ [1]. The geometrical parameters in $[Hpy][\{ZnL^1(py)\}_2U^{IV}][OTf]$ are also quite similar, except the U–O4 distance which is larger because of the presence of an hydrogen bond between O4 and the pyridinium cation [N7···O4 2.535(5) Å, N7–H···O4 173°]. However, the U–O distances in the cationic species B are systematically shorter than the corresponding U–O distances in the neutral counterparts A, in agreement with the variation in the radii of the U^{IV} and U^V ions [13]; this shortening is more important for the U–O_t distances between the metal and the terminal oxygen atoms O1, O4, O5 and O8 (ca. 0.11 Å) than for the U–O_b distances between the metal and the bridging oxygen atoms O2, O3, O6 and O7 (ca. 0.05 Å). Moreover, the average U–O, U–O_b and U–O_t distances in complex B of $[\{ZnL^1(py)\}_2U^{IV}][\{ZnL^1(py)\}_2U^V][NO_3]\cdot 4py$ are quite identical to those measured in the uranium(V) cations of $[\{ZnL^1(py)\}_2U^V][OTf]\cdot THF$ and $[\{ZnL^2(py)\}U^V\{ZnL^2(py)_2\}][NO_3]\cdot py$. Comparison of the structure of the latter with that of the uranium(IV) analogue $[\{ZnL^2(py)\}_2U^{IV}]\cdot 2py$ [2] shows the same differences between the U^{IV}–O and U^V–O distances. The coordination geometry of the 3d ions is not significantly affected by changing the oxidation state of uranium in the $[\{ML^i(py)\}_2U]^{0,+1}$ complexes. In particular, the average M–O and M–N distances in complexes A and B of $[\{ML^1(py)\}_2U^{IV}][\{ML^1(py)\}_2U^V][NO_3]$ are identical, with values of 1.950 and 1.997 Å for M = Cu and 2.03 and 2.07 Å for M = Zn, respectively. As observed with the uranium(IV) compounds $[\{ML^i(py)\}_2U^{IV}]$, the length of the diimino chain of L^i has practically no influence on the environment of the U^V ion, while the Zn···U distances slightly increase by ca. 0.04 Å when passing from L^1 to L^2.

3. Experimental

3.1. General

All reactions were carried out under argon (<5 ppm oxygen or water) using standard Schlenk-vessel and vacuum-line techniques or in a glove box. Solvents were dried by standard methods and distilled immediately before use; deuterated pyridine (Eurisotop) was distilled over NaH and stored over 3 Å molecular sieves. The ^1H NMR spectra were recorded on a Bruker DPX 200 instrument and referenced internally using the residual protio solvent resonances relative to tetramethylsilane ($\delta = 0$). Elemental analyses were performed by Analytische Laboratorien at Lindlar (Germany). The complexes $[Zn(H_2L^1)]$, $[\{ML^i(py)_x\}_2U]$ [1,2] and $U(OTf)_3$ [14] were synthesized as previously described.

3.2. Syntheses

3.2.1. Reaction of $[\{CuL^1(py)\}_2U^{IV}]$ and $AgNO_3$

(a) An NMR tube was charged with $[\{CuL^1(py)\}_2U^{IV}]$ (10.0 mg, 0.0087 mmol) and $AgNO_3$ (1.5 mg, 0.0087 mmol) in pyridine-d_5 (0.4 mL). After 1 h at 20 °C, the spectrum indicated that 60% of the uranium(IV) complex were converted into the uranium(V) derivative $[\{CuL^1(py)\}_2U^V][NO_3]$. ^1H NMR spectrum (pyridine-d_5, 23 °C): −12.20 (4H, –CH_2–), 5.65, 10.32 and 25.54 (3 × 4H, aromatic H), 101.20 (8H, NCH_2). Further addition of 2 equiv. of $AgNO_3$ (3.0 mg, 0.0174 mmol) led to the complete formation of the uranium(V) complex. Dark brown crystals of $[\{CuL^1(py)\}_2U^{IV}][\{CuL^1(py)\}_2U^V][NO_3]\cdot 4py$ were obtained after heating the mixture at 80 °C for 5 days. The uranium(IV) complex was the sole species detected in solution after prolonged heating at 110 °C.

(b) A flask was charged with $[\{CuL^1(py)\}_2U^{IV}]$ (80.0 mg, 0.075 mmol) and $AgNO_3$ (38.1 mg, 0.225 mmol) in pyridine (15 mL). After stirring for 2 days at 20 °C, the Ag precipitate was filtered off, the solution was evaporated to dryness, leaving a black powder of $[\{CuL^1(py)\}_2U^V][NO_3]$ which was washed with pyridine (5 mL) and dried under vacuum (25 mg, 28%). The ^1H NMR spectrum does not show the presence of impurities but the elemental analyses suggest contamination with $AgNO_3$. *Anal.* Calc. for $C_{44}H_{38}N_7O_{11}Cu_2U$: C, 43.81; H, 3.15; N, 8.13. Found: C, 39.46; H, 3.18; N, 9.48%.

3.2.2. Reaction of $[\{ZnL^1(py)\}_2U^{IV}]$ and $AgNO_3$

(a) An NMR tube was charged with $[\{ZnL^1(py)\}_2U^{IV}]$ (10.0 mg, 0.0087 mmol) and $AgNO_3$ (1.5 mg, 0.0087 mmol) in pyridine-d_5 (0.4 mL). The spectrum indicated the quantitative formation of $[\{ZnL^1(py)\}_2U^V][NO_3]$. ^1H NMR spectrum (pyridine-d_5, 23 °C): 1.29 (4H, –CH_2–), 3.25 (8H, NCH_2), 5.65 (4H, CH=N), 5.90, 8.36 and 8.66 (3 × 4H, aromatic H). The uranium(V) compound was stable up to 80 °C, but was converted into the U^{IV} congener upon heating at 110 °C. Dark brown crystals of $[\{ZnL^1(py)\}_2U^{IV}][\{ZnL^1(py)\}_2U^V][NO_3]\cdot 4py$ were obtained after heating at 110 °C for 5 days.

(b) A flask was charged with $[\{ZnL^1(py)\}_2U^{IV}]$ (120.0 mg, 0.104 mmol) and $AgNO_3$ (17.8 mg, 0.104 mmol) in pyridine (15 mL). After stirring for 12 h at 20 °C, the Ag precipitate was filtered off, the solution was evaporated to dryness, leaving a black powder of $[\{ZnL^1(py)\}_2U^V][NO_3]$ which was washed with pyridine (5 mL) and dried under vacuum (57 mg, 45%). Satisfactory elemental analyses were not obtained. *Anal.* Calc. for $C_{44}H_{38}N_7O_{11}Zn_2U$: C, 43.68; H, 3.14; N, 8.11. Found: C, 41.38; H, 3.34; N, 9.06%.

3.2.3. Reaction of $[\{ZnL^2(py)\}_2U^{IV}]$ and $AgNO_3$

An NMR tube was charged with $[\{ZnL^2(py)\}_2U^{IV}]$ (10.0 mg, 0.0085 mmol) and $AgNO_3$ (1.5 mg, 0.0085 mmol) in pyridine-d_5 (0.4 mL). The spectrum indicated the quantitative formation of $[\{ZnL^2(py)\}_2U^{V}][NO_3]$. ^{1}H NMR spectrum (pyridine-d_5, 23 °C): 1.27 (8H, –CH_2–), 3.20 (8H, NCH_2), 5.65 (4H, CH=N), 6.05, 8.55 and 8.81 (3 × 4H, aromatic H). Dark brown crystals of $[\{ZnL^2(py)\}U^{V}\{ZnL^2(py)_2\}][NO_3]\cdot py$ were obtained after heating at 60 °C for 5 days (9.0 mg, 80%). The elemental analyses are in agreement with the formula $[\{ZnL^2(py)\}U^{V}\{ZnL^2(py)_2\}][NO_3]$. *Anal.* Calc. for $C_{51}H_{47}N_8O_{11}Zn_2U$: C, 46.51; H, 3.57; N, 8.51. Found: C, 46.38; H, 3.72; N, 8.69%.

3.2.4. Reaction of $[Zn(H_2L^1)]$ and $U(OTf)_3$

An NMR tube was charged with $[Zn(H_2L^1)]$ (5.0 mg, 0.013 mmol) and $U(OTf)_3$ (9.1 mg, 0.013 mmol) in pyridine (0.4 mL). After 30 min at 20 °C, the spectrum showed the formation of the dinuclear $[\{ZnL^1(py)_x\}U^{IV}(OTf)_2]$ and trinuclear $[\{ZnL^1(py)_x\}_2U^{IV}]$ uranium(IV) species in the relative proportions of 50:50. ^{1}H NMR spectrum of $[\{ZnL^1(py)_x\}U^{IV}(OTf)_2]$ (pyridine-d_5, 23 °C): −14.27 (2H, –CH_2–), −10.11 (4H, NCH_2), 21.13, 45.25 and 97.87 (3 × 2H, aromatic H); ^{1}H NMR spectrum of $[\{ZnL^1(py)_x\}_2U^{IV}]$ (pyridine-d_5, 23 °C): −9.45 (4H, –CH_2–), −7.72 (8H, NCH_2), 0.10 (4H, CH=N), 5.44, 14.92, and 24.97 (3 × 4H, aromatic H). Prolonged heating of the solution at 110 °C led to the formation of dark yellow crystals of $[Hpy][\{ZnL^1(py)\}_2U^{IV}][OTf]$ together with few dark brown crystals of $[\{ZnL^1(py)\}_2U^{V}][OTf]\cdot THF$.

3.3. Crystallography

The data were collected at 100(2) K on a Nonius Kappa-CCD area detector diffractometer using graphite-monochromated Mo Kα radiation ($\lambda = 0.71073$ Å). The crystals were introduced into glass capillaries with a protecting "Paratone-N" oil (Hampton Research) coating. The unit cell parameters were determined from 10 frames, then refined on all data. The data (φ-scans) [15] were processed with HKL2000 [16]. The structures were solved by Patterson map interpretation or by direct methods with SHELXS-97 and subsequent Fourier-difference synthesis and refined by full-matrix least-squares on F^2 with SHELXL-97 [17]. Absorption effects were corrected empirically with the program DELABS in PLATON [18]. All non-hydrogen atoms were refined with anisotropic displacement parameters, except when specified below. Special details are as follows.

$[\{CuL^1(py)\}_2U^{IV}][\{CuL^1(py)\}_2U^{V}][NO_3]\cdot 4py$. The pyridine molecule bound to Cu2B is disordered over two positions sharing the nitrogen and *para*-carbon atoms, which have been refined with occupancy parameters constrained to sum to unity. All non-hydrogen atoms were refined with anisotropic displacement parameters, except for those of one badly resolved solvent pyridine molecule, which has been refined with a common isotropic displacement factor for the six atoms. Three pyridine molecules

Table 2
Crystal data and structure refinement details

Compound	$[\{CuL^1(py)\}_2U]_2$-$[NO_3]\cdot 4py$	$[\{ZnL^1(py)\}_2U]_2$-$[NO_3]\cdot 4py$	$[\{ZnL^2(py)\}U$-$\{ZnL^2(py)_2\}][NO_3]\cdot py$	$[\{ZnL^1(py)\}_2U]$-$[OTf]\cdot THF$	$[Hpy][\{ZnL^1(py)\}_2U]$-$[OTf]$
Empirical formula	$C_{108}H_{96}Cu_4N_{17}O_{19}U_2$	$C_{108}H_{96}N_{17}O_{19}U_2Zn_4$	$C_{56}H_{52}N_9O_{11}UZn_2$	$C_{49}H_{46}F_3N_6O_{12}SUZn_2$	$C_{50}H_{44}F_3N_7O_{11}SUZn_2$
Molecular weight (g mol^{-1})	2666.24	2673.56	1395.84	1368.75	1376.75
Crystal system	triclinic	triclinic	monoclinic	monoclinic	orthorhombic
Space group	$P\bar{1}$	$P\bar{1}$	$P2_1/n$	$P2_1/c$	$P2_12_12_1$
a (Å)	15.5551(5)	15.5504(17)	9.8035(2)	15.8582(9)	16.3831(4)
b (Å)	17.0290(6)	16.9840(16)	16.2913(7)	16.8708(10)	17.1920(6)
c (Å)	21.9285(10)	21.816(2)	32.6113(11)	19.3905(8)	17.5034(6)
α (°)	92.421(2)	91.964(6)	90	90	90
β (°)	108.794(2)	108.598(5)	94.771(2)	109.992(3)	90
γ (°)	108.307(2)	108.784(5)	90	90	90
V (Å^3)	5153.7(4)	5109.4(9)	5190.4(3)	4875.1(4)	4930.0(3)
Z	2	2	4	4	4
D_{calc} (g cm^{-3})	1.718	1.738	1.786	1.865	1.855
μ(Mo Kα) (mm^{-1})	4.019	4.161	4.102	4.415	4.365
F(000)	2630	2638	2764	2692	2704
Reflections collected	34313	34848	31886	33127	34074
Independent reflections	17712	17708	9133	9158	9302
Observed reflections $[I > 2\sigma(I)]$	13415	10173	7929	6825	8515
R_{int}	0.054	0.102	0.052	0.081	0.055
Parameters refined	1347	1348	712	667	676
R_1	0.064	0.078	0.032	0.053	0.029
wR_2	0.170	0.191	0.070	0.122	0.057
S	1.060	0.990	1.096	1.059	1.045
$\Delta\rho_{min}$ (e Å^{-3})	−1.46	−1.88	−0.43	−1.71	−0.56
$\Delta\rho_{max}$ (e Å^{-3})	1.24	1.36	0.39	1.33	0.67

have been refined as idealized hexagons and two of them were affected with a 0.5 occupancy parameter in order to retain acceptable displacement factors. Some restraints on displacement parameters were applied for the atoms of the nitrate ion, seemingly affected with unresolved disorder. Some short C···C and H···H contacts involving the badly resolved, partially occupied pyridine molecules indicate the presence of unresolved disorder or the presence of positions which cannot be occupied simultaneously.

$[\{ZnL^{1}(py)\}_2U^{IV}][\{ZnL^{1}(py)\}_2U^{V}][NO_3]\cdot 4py$. This compound is isomorphous with the copper analogue and the same problems arising from disorder are present. All non-hydrogen atoms were refined with anisotropic displacement parameters, except for those of two badly resolved solvent pyridine molecules, which have been refined as idealized hexagons with a common isotropic displacement factor and an occupancy parameter of 0.5 each in order to retain an acceptable value for the displacement factor. Some restraints on displacement parameters were applied for the atoms of the nitrate ion, seemingly affected with unresolved disorder, for some atoms of one of the bridges in the Schiff base B and for some atoms of the pyridine molecules. Some short C···C and H···H contacts involving the badly resolved, partially occupied pyridine molecules indicate the presence of unresolved disorder or the presence of positions which cannot be occupied simultaneously.

$[\{ZnL^{1}(py)\}_2U^{V}][OTf]\cdot THF$. Restraints on displacement parameters were applied for the oxygen and fluorine atoms of the trifluoromethanesulfonate counter-ion and for the atoms of the THF solvent molecule.

$[Hpy][\{ZnL^{1}(py)\}_2U^{IV}][OTf]$. The hydrogen atom bound to the pyridinium nitrogen atom N7 was found on a Fourier-difference map.

The carbon-bound hydrogen atoms were introduced at calculated positions (except for those of the disordered pyridine molecules in $[\{ML^{1}(py)\}_2U^{IV}][\{ML^{1}(py)\}_2U^{V}][NO_3]\cdot 4py$). All hydrogen atoms were treated as riding atoms with an isotropic displacement parameter equal to 1.2 times that of the parent atom. Crystal data and structure refinement details are given in Table 2. The molecular plots were drawn with SHELXTL [19].

4. Supplementary material

Crystallographic data for the structural analysis have been deposited with the Cambridge Crystallographic Data Centre, CCDC Nos. 610524–610528. Copies of this information may be obtained free of charge from The Director, CCDC, 12 Union Road, Cambridge CB2 1EZ, UK (fax: +44 1223 336 033; e-mail: deposit@ccdc.cam.ac.uk or www: http://www.ccdc.cam.ac.uk).

References

[1] L. Salmon, P. Thuéry, E. Rivière, J.J. Girerd, M. Ephritikhine, Dalton Trans. (2003) 2872.
[2] L. Salmon, P. Thuéry, E. Rivière, M. Ephritikhine, Inorg. Chem. 45 (2006) 83.
[3] D.S.J. Arney, C.J. Burns, J. Am. Chem. Soc. 115 (1993) 9840.
[4] C. Boisson, J.C. Berthet, M. Lance, J. Vigner, M. Nierlich, M. Ephritikhine, J. Chem. Soc., Dalton Trans. (1996) 947.
[5] P.C. Leverd, M. Nierlich, Eur. J. Inorg. Chem. (2000) 1733.
[6] P.B. Duval, C.J. Burns, D.L. Clark, D.E. Morris, B.L. Scott, J.D. Thompson, E.L. Werkema, L. Jia, R.A. Andersen, Angew. Chem., Int. Ed. 40 (2001) 3358.
[7] F.A. Cotton, D.O. Marler, W. Schwotzer, Inorg. Chem. 23 (1984) 4211.
[8] R.G. Jones, E. Bindschadler, G. Karmas, G.A. Martin, J.R. Thirtle, F.A. Yoeman, H. Gilman, J. Am. Chem. Soc. 78 (1956) 4289.
[9] S.D. Stults, R.A. Andersen, A. Zalkin, Organometallics 9 (1990) 1623.
[10] L. Karmazin, M. Mazzanti, J. Pécaut, Inorg. Chem. 42 (2003) 5900.
[11] D.L. Clark, A.P. Sattelberger, W.G. Van der Sluys, J.G. Watkin, J. Alloys Compd. 180 (1992) 303.
[12] L. Belkhiri, T. Arliguie, P. Thuéry, M. Fourmigué, A. Boucekkine, M. Ephritikhine, Organometallics 25 (2006) 2782.
[13] R.D. Shannon, Acta Crystallogr., Sect. A 32 (1976) 751.
[14] J.C. Berthet, M. Lance, M. Nierlich, M. Ephritikhine, Eur. J. Inorg. Chem. (1999) 2005.
[15] Kappa-CCD Software, Nonius BV, Delft, 1998.
[16] Z. Otwinowski, W. Minor, Methods Enzymol. 276 (1997) 307.
[17] G.M. Sheldrick, SHELXS-97 and SHELXL-97, University of Göttingen, Göttingen, Germany, 1997.
[18] A.L. Spek, PLATON, University of Utrecht, Utrecht, 2000.
[19] G.M. Sheldrick, SHELXTL, Version 5.1, Bruker AXS Inc., Madison, WI, 1999.

Available online at www.sciencedirect.com
ScienceDirect
Polyhedron 26 (2007) 637–644
POLYHEDRON
www.elsevier.com/locate/poly

Synthesis characterization and X-ray crystal structures of *cis*-1,4-diaminocyclohexane-platinum(II) nucleobase adducts

Shaikh Shamsuddin [a], Mohammad S. Ali [a], Kenton H. Whitmire [b], Abdul R. Khokhar [a,*]

[a] *Department of Experimental Therapeutics, Unit 353, The University of Texas M.D. Anderson Cancer Center, 1515 Holcombe Blvd., Houston, TX 77030, United States*

[b] *Department of Chemistry, MS 60, Rice University, 6100 Main Street, Houston, TX 77005, United States*

Received 21 April 2006; accepted 24 August 2006
Available online 12 September 2006

Abstract

Platinum complexes of the type [Pt(*cis*-1,4-DACH)(L)$_2$]X, where *cis*-1,4-DACH = *cis*-1,4-diaminocyclohexane; L = adenine (ade) (**1**), hypoxanthine (hyp) (**2**), 9-methylguanine (9-megua) (**3**), cytosine (cyt) (**4**), or 1-methylcytosine (1-mecyt) (**5**); and X = SO_4 or Cl_2 groups, were synthesized and characterized by elemental analysis and by ^{1}H, ^{13}C, and ^{195}Pt nuclear magnetic resonance spectroscopy. The crystals of [Pt(*cis*-1,4-DACH)(9-megua)$_2$]SO_4[9-megua-H]$_2SO_4$ (**3**) and [Pt(*cis*-1,4-DACH)(1-mecyt)$_2$]$Cl_2 \cdot 6H_2O$ (**5**) were also subjected to single-crystal X-ray diffraction. The base/PtN4 coordination plane dihedral angles were 74.55° and 85.61° in complex **3** and 78.12° and 81.80° in complex **5**. The platinum had distorted square planar geometry in both complexes; the two adjacent corners were occupied by the two nitrogen atoms of *cis*-1,4-DACH, and the other two corners were occupied by the two N7 atoms of 9-megua in complex **3** and the two N3 atoms of 1-mecyt in complex **5**. The *cis*-1,4-DACH, which has a unique twist-boat configuration, formed a seven-member chelating ring with platinum, which led to considerable strain during bidentate *cis*-1,4-DACH binding. Cations of both complexes **3** and **5** adopted C_2 molecular symmetry. These adducts were the models for the intrastand cross-links that were relevant to the binding of the Pt(II) antitumor drugs to DNA.
© 2006 Elsevier Ltd. All rights reserved.

Keywords: Platinum; *cis*-1,4-Diaminocylohexane; Nucleobase; Adducts; Crystal structures

1. Introduction

Undesirable side effects and acquired drug resistance limit the clinical effectiveness of cisplatin and its second-generation analog carboplatin [1–6]. Consequently, a third-generation of platinum (Pt) complexes have been developed with 1,2-diaminocyclohexane (DACH) [7–14] as its ligand; these complexes exhibit activity against cisplatin-resistant tumors [15–17]. The DACH-Pt analogs ormaplatin [18] and oxaliplatin [19] and the liposome-entrapped *cis*-bis(neodecanoato)(*trans*-1(*R*),2(*R*)-DACH)-Pt(II) have shown promise in clinical trials [20]. In our laboratory, we have expanded on this research by developing a new class of Pt complexes that have *cis*-1,4-DACH as the carrier ligand [21–25].

Substantial evidence has shown that Pt-based antitumor drugs have DNA as their primary target and block DNA replication as their primary mechanism of action [26–28]. The most frequent DNA adduct of cisplatin is the d(GpG) intrastrand N7, N7 crosslink, which accounts for roughly 60% of these adducts [29,30]. The second most abundant DNA adduct of cisplatin is the d(ApG) intrastrand N7, N7 crosslink, which accounts for approximately 20–30% [31]. Another, less frequent adduct involves N3 of cytosine in cytidine-rich DNA regions [32–34]. Hambley et al. reported a [Pt^{II}(hmp)Cl_2] with homopiperazine as the non leaving amine ligand to interact stereospecifically with DNA to form mostly bifunctional interstrand, and substantially intrastrand adduct [35].

* Corresponding author. Tel.: +1 713 792 2837; fax: +1 713 745 1176.
E-mail address: akhokhar@mdanderson.org (A.R. Khokhar).

0277-5387/$ - see front matter © 2006 Elsevier Ltd. All rights reserved.
doi:10.1016/j.poly.2006.08.033

The X-ray structures of all possible cisplatin-bound nucleic acid base adducts have been reported [28–30], providing insight into the structural changes that occur on platination [36–41]. However, little is known about the antitumor Pt complexes containing *cis*-1,4-DACH. *cis*-1,4-DACH exists in three isomeric forms: axial/equatorial (chair), diequatorial (boat), and diaxial (twist-boat) (Fig. 1). Most common is the chair (axial/equatorial) conformation, in which the disposition of the two NH_2 groups is highly unfavorable to chelation. However, in the diaxial (twist-boat) conformation, the molecule can chelate to a metal ion. As shown in our previous studies of the crystal structure of Pt complexes [21–24], *cis*-1,4-DACH assumes the twist-boat conformation in these complexes to facilitate its binding to Pt to form a seven-member chelating ring.

These complexes have shown great clinical promise. The findings that [Pt(*cis*-1,4-DACH)Cl_2] exhibits more in vitro cytotoxicity than either cisplatin or tetraplatin [21] and also has substantial in vivo activity in Pt-DACH-resistant L1210 leukemia cell lines suggest that differences in shape or conformation are important in eliciting the antitumor activity of (*cis*-1,4-DACH)-Pt complexes [24,42]. This marked level of activity also supports the notion that these novel Pt complexes are neither a cisplatin- nor a [Pt(1*R*, 2*R*-DACH)Cl_2]-type analog but rather a system that incorporates properties of both. Although the mechanism underlying the antitumor reactivity has not been established [43], obvious possibilities include the processes of mono- or diadduct formation, recognition and repair, and translation. Hence, *cis*-1,4-DACH-Pt adducts are models for the intrastrand cross-links that are relevant to the binding of Pt antitumor drugs to DNA [44,45].

Here, we report the synthesis and characterization of nucleobase complexes containing *cis*-1,4-DACH-Pt and the crystal structures of [Pt(*cis*-1,4-DACH)(9-methylguanine)$_2$]SO_4[9-methylguanine-H]$_2SO_4$ and [Pt(*cis*-1,4-DACH)(1-methylcytosine)$_2$]$Cl_2 \cdot 6H_2O$ adducts.

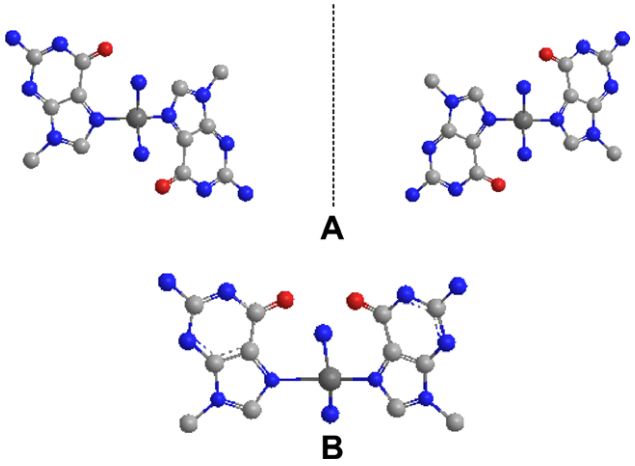


Fig. 1. Structures of [Pt(*cis*-1,4-DACH)$(L)_2$] complexes (from which the cyclohexyl ring has been omitted for clarity) showing the possible relative orientations of the methylguanine ligands. The ligands can be arranged so that they are related by a C_2 axis, which generates an enantiomeric pair (A), or by a mirror plane (B).

2. Experimental

2.1. Chemicals

Adenine (ade), hypoxanthine (hyp), 9-methylguanine (9-megua), cytosine (cyt), and 1-methylcytosine (1-mecyt) were purchased from Aldrich Chemical Co. (Milwaukee, WI). 1,4-DACH in an 80% *cis* and 20% *trans* mixture was purchased from TCI Organics, Portland, OR. K_2PtCl_4 was purchased from Johnson Mathey (Searbrook, NH). Silver nitrate, *N*,*N*-dimethylformamide (DMF), and potassium chloride were purchased from Fisher Scientific Co. (Houston, TX).

2.2. Physical measurements

Elemental analyses were performed by Robertson Microlit Laboratories Inc. (Madison, NJ). ^1H, ^{13}C, and ^{195}Pt nuclear magnetic resonance (NMR) spectra were recorded at 43.055 MHz using a Bruker 300-MHz spectrometer with a 5-mm tunable probe. Chemical shifts were measured relative to an external standard of 2.2 M Na_2PtCl_6 in D_2O at 0.00 ppm.

2.3. Preparation of Pt complexes

[Pt(*cis*-1,4-DACH)(SO_4)] and [Pt(*cis*-1,4-DACH)Cl_2] were synthesized as described previously [22–25].

2.3.1. [Pt(*cis*-1,4-DACH)$(ade)_2$]$SO_4 \cdot 2H_2O$ (**1**)

[Pt(*cis*-1,4-DACH)$(SO_4)H_2O$] (0.42 g; 1.00 mmol) was dissolved in 25 mL of water, after which ade (0.23 g; 1.70 mmol) in 10 mL of water was added. The reaction mixture was stirred at 40 °C for 96 h. The clear, pale yellow solution that formed was filtered, concentrated to 5 ml, and then treated with acetone to induce precipitation. The resultant solid product was washed with cold water and acetone and dried over P_2O_5 under a vacuum. The yield was 67%. *Anal.* Calc.: C, 27.00; H, 3.93; N, 23.62. Found: C, 27.35; H, 3.87; N, 23.91%. ^1H NMR [δ, ppm in D_2O]: C_2H, 8.21; C_8H, 8.29. ^{13}C NMR [δ, ppm in D_2O]: C_2, 152.91; C_4, 154.67; C_5, 115.89; C_6, 150.92; C_8, 143.65. ^{195}Pt NMR: δ −2565 ppm.

2.3.2. [Pt(*cis*-1,4-DACH)$(hyp)_2$]$SO_4 \cdot 2H_2O$ (**2**)

Complex **2** was prepared in the same way as complex **1**. The yield was 75%. *Anal.* Calc.: C, 27.62; H, 3.45; N, 20.14. Found: C, 27.32; H, 3.10; N, 19.87%. ^1H NMR (δ, ppm in D_2O): C_2H, 8.86; C_8H, 8.95. ^{13}C NMR [δ, ppm in DMSO-d_6]: C_2, 154.02; C_4, 156.03; C_5, 116.24; C_6, 145.58; C_8, 141.09. ^{195}Pt NMR: δ −2590 ppm.

2.3.3. [Pt(*cis*-1,4-DACH)$(9\text{-megua})_2$]SO_4-[9-megua-H]$_2SO_4$ (**3**)

Complex **3** was prepared in the same way as complex **1**, but it was further redissolved in a minimum volume of water filtered and kept for slow evaporation at room

temperature. The colorless crystals obtained were filtered, washed with cold water, and dried under a vacuum. The yield was 60%. *Anal*. Calc.: C, 30.96; H, 3.78; N, 26.49. Found: C, 30.89; H, 3.95; N, 26.67%. ^{1}H NMR [δ, ppm in D_2O]: C_8H, 7.87; CH_3, 3.53. ^{13}C NMR [δ, ppm in D_2O]: C_2, 154.87; C_4, 157.46; C_5, 113.53; C_6, 151.65; C_8, 142.42; CH_3, 30.89. ^{195}Pt NMR: δ −2479 ppm.

2.3.4. *[Pt(cis-1,4-DACH)(cyt)$_2$]SO$_4$ · 2H$_2$O (**4**)*

Complex **4** was prepared in the same way as complex **1**. The yield was 72%. *Anal*. Calc.: C, 25.33; H, 4.22; N, 16.89. Found: C, 25.45; H, 4.43; N, 16.91%. ^{1}H NMR [δ, ppm in D_2O]: C_5H, 6.03; C_6H, 7.50. ^{13}C NMR [δ, ppm in D_2O]: C_2, 156.37; C_4, 166.67; C_5, 94.89; C_6, 144.03. ^{195}Pt NMR: δ −2695 ppm.

2.3.5. *[Pt(cis-1,4-DACH)(1-mecyt)$_2$]Cl$_2$ · 6H$_2$O (**5**)*

[Pt^{II}(1,4-DACH)Cl$_2$] (0.38 g; 1.00 mmol) was suspended in 25 mL of water, after which 1-mecyt (0.22 g; 1.76 mmol) in 10 mL of water was added. The reaction mixture was stirred at 40 °C for 48 h. A clear solution was obtained, which was filtered and concentrated to 5 mL under reduced pressure. The solution was then treated with acetone to induce precipitation. The resultant solid product was washed with cold water and acetone and then dried under a vacuum. The product was subsequently redissolved in a minimum volume of water kept for slow evaporation at room temperature. The colorless crystals obtained were filtered, washed with cold water, and dried in a vacuum. The yield was 60%. *Anal*. Calc.: C, 28.83; H, 4.84; N, 16.81. Found: C, 28.78; H, 4.76; N, 16.58%. ^{1}H NMR [δ, ppm in D_2O]: CH_3, 3.43; C_5H, 5.71; C_6H, 7.59. ^{13}C NMR [δ, ppm in D_2O]: C_2, 156.23; C_4, 165.97; C_5, 94.85; C_6, 148.64; CH_3, 38.49. ^{195}Pt NMR: δ −2650 ppm.

2.4. Crystallographic measurements

X-ray crystallographic data were collected with a single-crystal X-ray diffractometer (AFC5S; Rigaku), and data collection and reduction software (TEXSAN *Single Crystal Structure Analysis Software* 5.0; Molecular Structure Corporation, The Woodlands, TX) [46]. Crystals suitable for analysis were mounted on the tip of a glass fiber. Data collection and refinement parameters are summarized in Table 1. The data were corrected for Lorentz and polarization effects and for absorption.

The crystal structures of complexes **3** and **5** were resolved, refined, and plotted directly by using the software contained in the SHELXTL 6.10 program library [47]. For complexes **3** and **5**, the Pt atoms were shown to sit on a

Table 1
Crystallographic data and structure refinement for complexes [Pt(*cis*-1,4-DACH)(9-megua)$_2$]SO$_4$[9-megua-H]$_2$SO$_4$ (**3**) and [Pt(*cis*-1,4-DACH)-(1-mecyt)$_2$]Cl$_2$ · 6H$_2$O (**5**)

Data	**3**	**5**
Empirical formula	$C_{30}H_{44}N_{22}O_{15}PtS_2$	$C_{16}H_{40}N_8O_8PtCl_2$
Formula weight	1210.07	738.55
Temperature (*K*)	223(2)	293(2)
Wavelength (Mo Kα) Å	0.71073	0.71073
Crystal system	monoclinic	monoclinic
Space group	*C*2/*c* (#15)	*C*2/*c* (#15)
Unit cell dimensions		
a (Å)	31.809(6)	25.233(5)
b (Å)	9.427(2)	9.182(2)
c (Å)	19.213(4)	14.222(3)
β (°)	121.21(3)	120.10(3)
Volume (Å^3)	4927.5(17)	2850.7(10)
Z	4	4
D_{calc} (Mg/m^3)	1.631	1.721
μ (mm^{-1})	3.016	5.161
F(000)	2424	1472
Crystal size (mm)	0.50 × 0.40 × 0.40	0.4 × 0.3 × 0.3
θ Range for data collection (°)	2.13–27.41	2.41–27.49
Index ranges	$-37 \leqslant h \leqslant 37$, $-11 \leqslant k \leqslant 11$, $-22 \leqslant l \leqslant 22$,	$-32 \leqslant h \leqslant 32$, $-11 \leqslant k \leqslant 11$, $-18 \leqslant l \leqslant 18$
Number of reflections collected	8863	6702
Independent reflections [R_{int}]	4347 [0.0343]	3282 [0.0345]
Absorption correction	semi-empirical, φ scans	DFABS
Maximum and minimum transmission	0.3784 and 0.3139	1.0 and 0.4087
Refinement method	full-matrix least-squares on F^2	full-matrix least-squares on F^2
Data/restraints/parameters	4347/0/322	3282/0/162
Goodness-of-fit on F^2	1.022	1.214
Final *R* indices [$I > 2\sigma(I)$]	$R_1 = 0.0820$, $wR_2 = 0.2214$	$R_1 = 0.0408$, $wR_2 = 0.1091$
R indices (all data)	$R_1 = 0.1266$, $wR_2 = 0.2530$	$R_1 = 0.0473$, $wR_2 = 0.1116$
Extinction coefficient	0.0067(5)	0.0053(3)
Largest difference in peak and hole (e Å^{-3})	2.009 and −3.387	2.327 and −3.076

crystallographic twofold axis, so that only half of the DACH ring and one of the N-base ligands were unique. In complex **3**, all nonhydrogen atoms were refined with anisotropic displacement parameters, except for the carbon atoms of the *cis*-1,4-DACH ring, which were disordered; this disorder could not be resolved. Because the configurations of the solid-state structures of complexes **3** and **5** are chiral, the possibility that the space group was *Cc* rather than *C*2/*c* was considered for both. For complex **3**, no acceptable solution could be obtained using the Patterson map or direct methods for the space group *Cc*. Attempts to remove the center of symmetry from the *C*2/*c* solution were not successful and gave no refineable solution. For complex **5**, the structure was resolved and refined in *Cc*, but the data obtained did not support anisotropic refinement of all nonhydrogen atoms, some of which were non-positive definite. Additionally, the data for complex **5** indicated that it was a racemic twin. Given these findings, the centrosymmetric space groups were chosen in both cases as the best solutions. Consequently, the bond distances and angles associated with those group as reported here should be viewed with caution. Furthermore, the [Pt(*cis*-1,4-DACH)(9-megua)$_2$]SO_4 complex cocrystallized with [9-megua-H]$_2SO_4$. In addition to two water molecules of solvation, the crystal structure of complex **3** contained additional water molecules that could not be refined satisfactorily. The contribution of the additional water molecules of solvation was taken into account by using the squeeze routine in the PLATON X-ray data refinement software package [48] where a total of 126e was found in the void volume of the crystal. A structural analysis of complex **5** showed the presence of three oxygen atoms attributable to the lattice waters of crystallization, giving an overall formula of six water molecules per Pt complex.

For both complexes **3** and **5** hydrogen atoms were calculated in ideal positions (i.e., riding model), and F^2 was refined using all reflections. The weighted *R* factors (*wR*) and goodness-of-fit determinations were based on F^2. Conventional *R* factors were based on *F*, with *F* set to zero for negative F^2. *R* factors based on F^2 were statistically about twice as large as those based on *F*, and *R* factors based on all data were expected to be even larger. Selected bond distances and angles for complex **3** are shown in Table 2 and for complex **5** in Table 3.

Table 2
Selected bond distances (Å) and bond angles for complex [Pt(*cis*-1,4-DACH)(9-megua)$_2$]SO_4[9-megua-H]$_2SO_4$ (**3**)

Pt(1)–N(7)	2.007(12)
Pt(1)–N(41)	2.028(13)
N(7)–C(8)	1.290(19)
N(7)–Pt(1)–N(7)#1	89.4(6)
N(7)–Pt(1)–N(41)#1	86.6(5)
N(7)#1–Pt(1)–N(41)#1	175.9(5)
N(7)–Pt(1)–N(41)	175.9(5)
N(7)#1–Pt(1)–N(41)	86.6(5)
N(41)#1–Pt(1)–N(41)	97.4(8)
C(8)–N(7)–Pt(1)	126.8(10)
C(5)–N(7)–Pt(1)	128.1(11)
C(41)–N(41)–Pt(1)	124.7(17)

Symmetry transformations used to generate equivalent atoms: #1 $-x$, y, $-z+1/2$.

Table 3
Selected bond distances (Å) and bond angles (°) for complex [Pt(*cis*-1,4-DACH)(1-mecyt)$_2$]$Cl_2 \cdot 6H_2O$ (**5**)

Pt(1)–N(3)	2.041(5)
Pt(1)–N(13)	2.054(5)
N(3)#1–Pt(1)–N(3)	90.9(3)
N(3)#1–Pt(1)–N(13)	176.17(18)
N(3)–Pt(1)–N(13)	85.7(2)
N(3)#1–Pt(1)–N(13)#1	85.7(2)
N(3)–Pt(1)–N(13)#1	176.17(18)
N(13)–Pt(1)–N(13)#1	97.7(3)
C(4)–N(3)–Pt(1)	122.6(4)
C(2)–N(3)–Pt(1)	116.1(4)
C(10)–N(13)–Pt(1)	125.7(4)

Symmetry transformations used to generate equivalent atoms: #1 $-x$, y, $-z+3/2$.

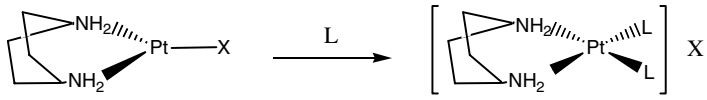
3. Results and discussion

3.1. Characterization of complexes

Scheme 1 shows the synthetic route and structure of the Pt complexes **1**–**5**. These complexes were all characterized by elemental analysis and ^{1}H, ^{13}C, and ^{195}Pt NMR spectroscopy.

The theoretical values obtained from the elemental analyses were in good agreement with the actual findings. The singlets observed in the range of −2565 to −2695 ppm in the ^{195}Pt NMR spectra were assignable to the Pt–N4 system and were similar to those of related square planar Pt(II) complexes that had four nitrogens as donor atoms [49]. In ^{1}H NMR spectra, the peaks corresponding to the C_8H protons of ade, hyp, and 9-megua shifted downfield by 0.2, 0.7, and 0.3 ppm, respectively, in complexes **1**–**3** compared with the corresponding ligands, which indicated the coordination of N7 to the Pt atom. In complexes **4** and **5**, a downfield shift of 0.1 ppm in the C_5H proton peaks of cyt and 1-mecyt compared with the corresponding ligands indicated the coordination of Pt to N3.

The proton-decoupled ^{13}C NMR spectra of purine and pyrimidine bases were obtained from the Integrated Spectral Data Base System for Organic Compounds for comparison with the spectra we obtained. In complexes **1**–**3**, a downfield shift of 3.35–3.71 ppm was observed at C_5 and an upfield shift of 3.18–4.52 ppm at C_8 compared with free ligands, ade, hyp, or 9-megua. In complexes **4** and **5**, an upfield shift of 3.09–3.54 ppm was observed at C_2 and of 1.00–1.20 ppm at C_4 compared with cyt and 1-mecyt. These identical shifts in both substituted and unsubstituted purine and pyrimidine base complexes support the notion that N7 and N3 are binding sites in the purine and pyrimidine bases, respectively. Scheme 1 shows the general structure of complexes **1**–**5**.



L = adenine (ade), hypoxanthine (hyp), 9-methyl guanine (9-megua), cytosine (cyt), 1-methylcytosine (1-mecyt)

X = SO_4, H_2O or 2Cl

Scheme 1.

3.2. X-ray crystal structures

The X-ray crystal structure of complex **3** is shown in Fig. 2a and of complex **5** in Fig. 2b. respectively. Selected bond lengths and bond angles for each compound are given in Tables 2 and 3, respectively. The Pt atom in both complexes had a distorted square planar geometry, with the angles mostly deviating from the expected values of 90° and 180°. A longer bite distance in the chelating ligand (*cis*-1,4-DACH) caused the distortion. The two adjacent corners of the Pt plane were occupied by two nitrogen atoms of the *cis*-1,4-DACH molecule, while the other two positions were occupied by the N7 atoms of two 9-megua moieties in complex **3** and the N3 atoms of two 1-mecyt moieties in complex **5**. *cis*-1,4-DACH, which exists in a unique twist-boat configuration, formed a 7-member chelating ring with the Pt atom.

The N–Pt–N angle in the *cis*-1,4-DACH-Pt region expanded to 97.1° in complex **3** and to 97.8° in complex **5** because of geometric constraints imposed by the ligands. However, the same bond angle in the cisplatin adducts is about 90°, as reported previously for complexes $[Pt(NH_3)_2(9\text{-ethylguanine})_2]SO_4$ (93.2°),[1] $[Pt(NH_3)_2(9\text{-ethylguanine})_2][Pt(CN)_4]$ (87.8°) [49], $[Pt(NH_3)_2(9\text{-ethylguanine})(1\text{-methylcytosine})](ClO_4)_2$ (90.0°) [50], and *cis*-$[Pt(NH_3)_2(9\text{-methyladenine})(9\text{-ethylguanine})](NO_3)_2$ (88.9°) [48]. The expansion of this bond angle was compensated for by contraction of the N(7)–Pt–(N41) and N(3)–Pt–N(13) bond angles to 87° in complex **3** and to 85.7° in complex **5**. The average Pt–N bond lengths of 2.033(8) Å [51] in complexes **3** and **5** were within the range normally observed for cisplatin-nucleobase adducts [48].[1]

The dihedral angles between the purine or pyrimidine ligands and the Pt coordination plane (9-megua 1/Pt–N4 = 74.54° and 9-megua 2/Pt–N4 = 85.61° in complex **3** and 1-mecyt 1/Pt–N4 = 78.12° and 1-mecyt 2/Pt–N4 = 81.80° in complex **5**) were large and prevented any substantial intracomplex base-to-base interaction. In analogous complexes, one of the nucleobase rings forms

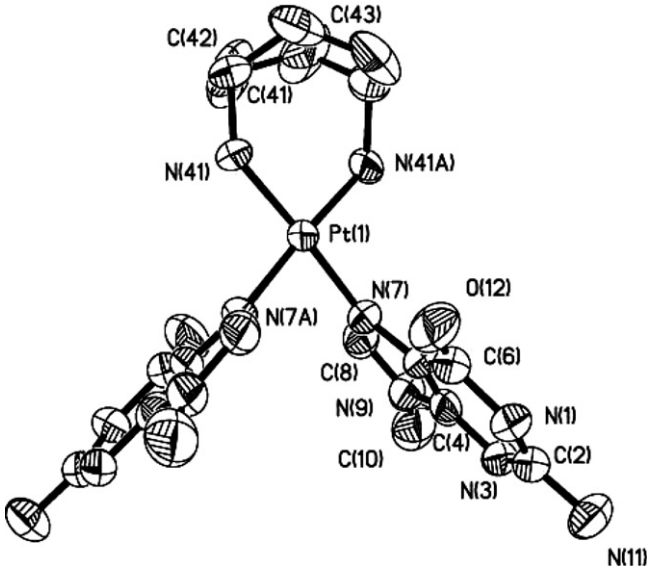


Fig. 2a. ORTEP representation of the structure of complex **3**. [Pt(*cis*-1,4-DACH)(9-megua)$_2$]SO_4[9-megua-H]$_2SO_4$ and hydrogen atom are omitted for clarity.

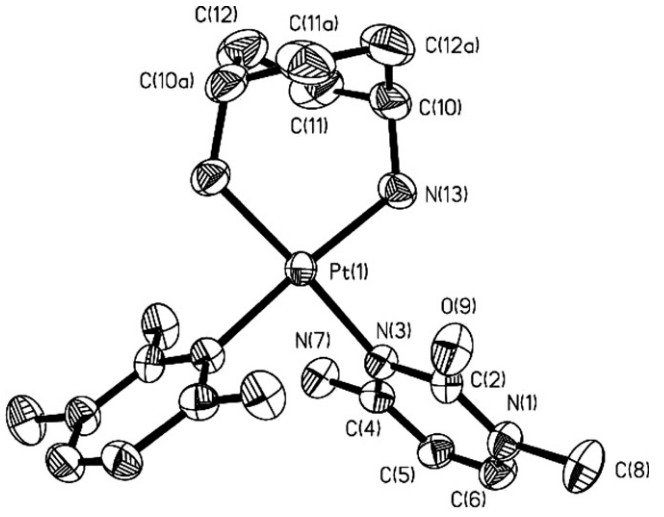


Fig. 2b. ORTEP representation of the structure of complex **5**. [Pt(*cis*-1,4-DACH)(1-mecyt)$_2$]Cl_2 and hydrogen atom are omitted for clarity.

[1] The average values of ESD are calculated via the Scatter formula:

$$\sigma = \left[\sum_{i=1}^{i=N} (d_i - d)^2 \Big/ (N-1)\right]^{1/2}$$

They are thus external estimates of the ESD based on an individual measurement.

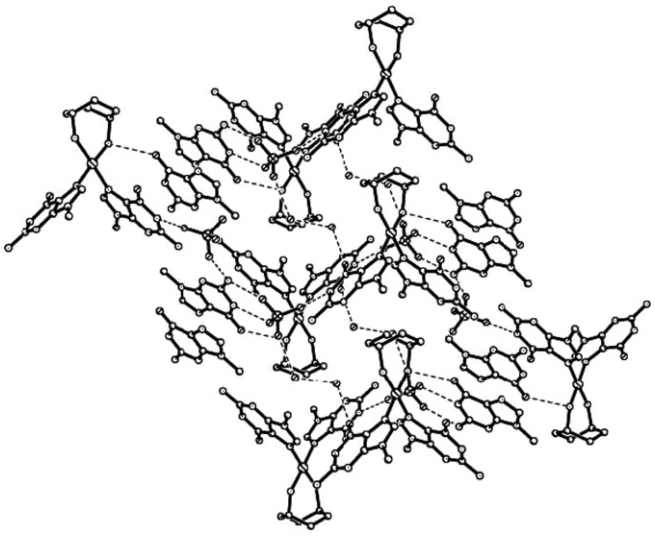


Fig. 3a. A view of the molecular packing of [Pt(*cis*-1,4-DACH)-(9-megua)$_2$]SO_4[9-megua-H]$_2SO_4$.

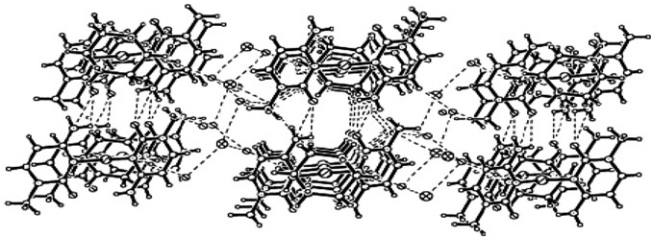


Fig. 3b. A view of the molecular packing of [Pt(*cis*-1,4-DACH)-(1-mecyt)$_2$]Cl_2.

a smaller angle (~50°) with the Pt plane, leading to internal hydrogen bonds [44,45]. Views of the molecular packing of both crystals structures are shown in Fig. 3. In the cations of complexes **3** and **5**, the purine or pyrimidines nucleobases are coordinated to Pt at their N7 and N3 locations, respectively.

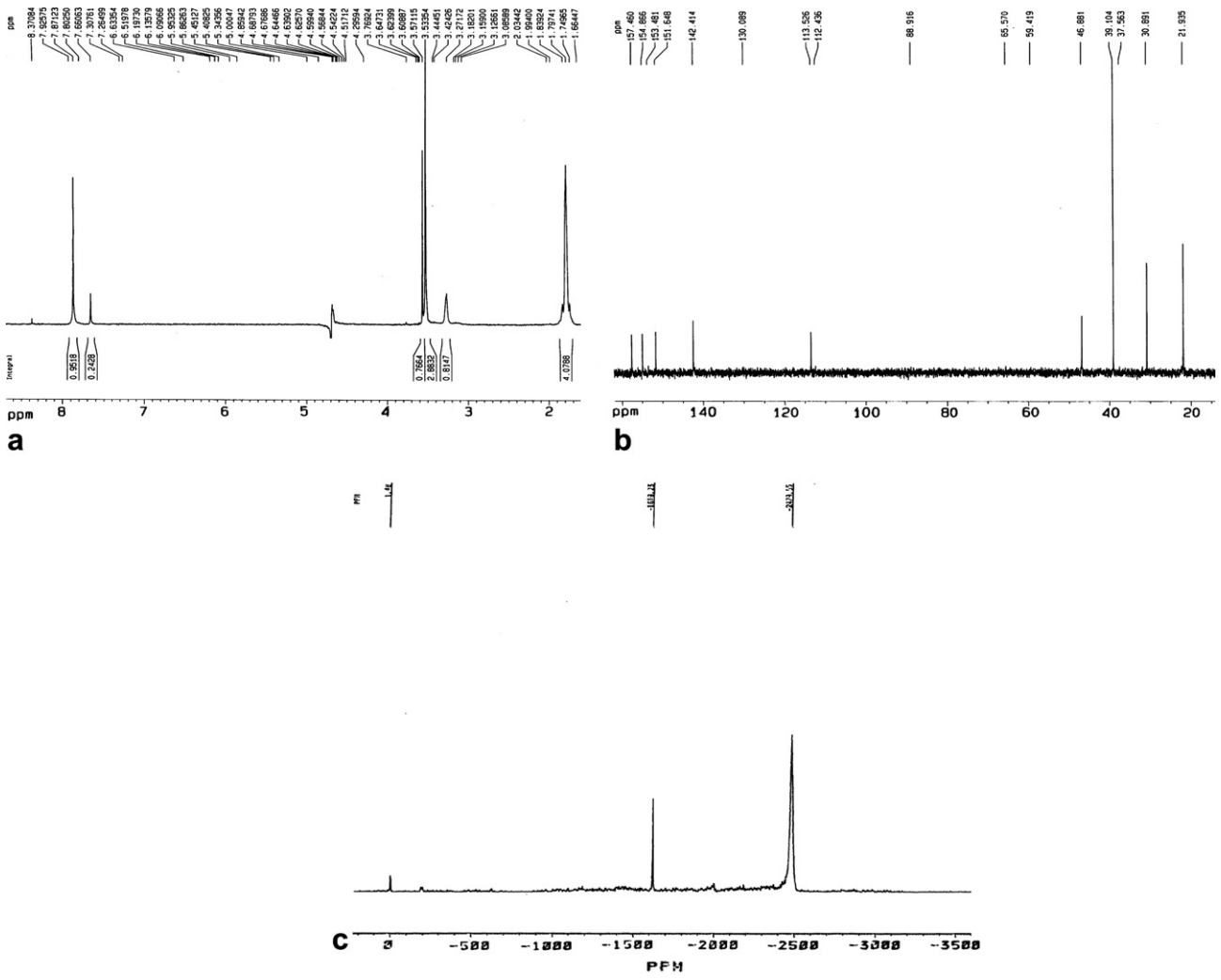


Fig. 4. NMR spectra of [Pt(*cis*-1,4-DACH)(9-megua)$_2$]SO_4[9-megua-H]$_2SO_4$. (a) ^{1}H NMR. (b) ^{13}C NMR. (c) ^{195}Pt NMR.

The starting (*cis*-1,4-DACH)$PtCl_2$ and the planar nucleobase ligands are not chiral because they both contain mirror planes of symmetry. However, when the nucleobase and ligands are attached to Pt, as they are in Fig. 1, they are oriented so that the overall resulting complex has either a C_2 or a mirror symmetry. The latter is not observed in the figure, meaning that the complexes have C_2 symmetry and are thus chiral. Because the reaction methodology began with nonchiral starting materials, the expected product was a racemic mixture of the two enantiomeric forms, as shown in Fig. 1a. The crystallographic determination of such systems can be ambiguous, given that the data often allow for refinement in either a centrosymmetric space group, in which the molecule sits on a crystallographic C_2 axis, or in a noncentrosymmetric space group, in which no crystallographic symmetry is imposed but noncrystallographic C_2 symmetry is still present the molecule. For the determinations of **3** and **5**, both possibilities were considered. The refinements proceeded best in the centrosymmetric space group $C2/c$, which represented racemic mixtures. For complex **3**, refinement could also be performed in the noncentrosymmetric Cc group, but full anisotropic refinement was not possible without some atoms becoming nonpositive definite. The structure of complex **5** could not be resolved in the Cc group. Presumably, in solution, free rotation about the Pt–N bonds occurs so that the isolation of a single enantiomer is not feasible (see Fig. 4).

Different mapping techniques have demonstrated that the reaction product both in vitro and in vivo involves loss of two chloride ions and binding of platinum to the N7 atoms of two adjacent guanines or adjacent adenine/guanine bases [52]. Theses type of interactions inhibit shielding the adduct from nucleotide excision repair, replication, and interfere with transcription by recruting essential transcription factors from their native binding sites [53–57]. It has been shown by NMR and X-ray studies that when cisplatin or *cis*-dichloro-*trans*-diacetato-ammine-cyclohexylamineplatinum(IV) (JM216) binds to adjacent guanine residues on duplex DNA, it distorts the double helix by causing a bend towards the major groove and a widening and flattening of the minor groove [58–62]. Significant differences in the effectiveness of ethylenediamine-platinum and 1,2-diaminocyclohexane-platinum (1,2-DACH-Pt) adducts in inhibiting transformation efficiency in a repair-deficient strain of *Escherichia coli* suggest that carrier ligand effects on resistant cell lines arise from differences in the ability of certain Pt-DNA adducts to inhibit other process, such as replication or transcription [59,60]. In this context a series of Pt(II)- and Pt(IV)-DNA adducts with cisplatin, 1,2-diaminocyclohexane, 1,4-diaminocylohexane, and homopiperazine have been synthesized and structurally and spectroscopically characterized and their different orientation are reported in their crysytal structures [48,49,63–66]. These structural distortions and differences in carrier ligand effect in turn likely affect the ability of the platinum drugs to block DNA replication and transcription [67,68].

4. Conclusions

In our continuous effort to investigate any correlation between anticancer activity and the DNA adduct profile, which may contribute to the understanding mechanism of action of such platinum based anticancer agents, that are structurally and functionally distinct from cisplatin prompted us to report here the synthesis and characterization of Pt(II) diadducts with DNA bases. Additionally, the crystal structures of [Pt(*cis*-1,4-DACH)(9-megua)$_2$]SO_4-[9-megua-H]$_2SO_4$ (**3**) and [Pt(*cis*-1,4-DACH)(1-mecyt)$_2$]-$Cl_2 \cdot 6H_2O$ (**5**) were determined by X-ray crystallography.

Acknowledgement

We thank Dr. Teyeb Ould Ely of the Department of Chemistry at Rice University for technical support.

Appendix A. Supporting material

CCDC 279264 and 279256 contains the supplementary crystallographic data for **3** and **5**. These data can be obtained free of charge via http://www.ccdc.cam.ac.uk/conts/retrieving.html, or from the Cambridge Crystallographic Data Centre, 12 Union Road, Cambridge CB2 1EZ, UK; fax: (+44) 1223 336 033; or e-mail: deposit@ccdc.ac.uk. Supplementary data associated with this article can be found, in the online version, at doi:10.1016/j.poly.2006.08.033.

References

[1] W.B. Pratt, R.W. Ruddon, W.D. Ensminger, J. Maybaum, The Anticancer Drugs, Oxford University Press, New York, NY, 1994, p. 133.
[2] I.H. Krakoff, in: M. Nicolini (Ed.), Platinum and Other Metal Coordination Compounds in Cancer Chemotherapy: Clinical Applications of Platinum Complexes, Martinus Nijhoff, Boston, MA, 1988, p. 351.
[3] P.J. Loehrer Sr., S.D. Williams, L.H. Einhorn, J. Natl. Cancer Inst. 80 (1988) 1373.
[4] P.J. Loehrer, L.H. Einhorn, Ann. Intern. Med. 100 (1984) 704.
[5] A.H. Calvert, S.J. Harland, D.R. Newell, Z.H. Siddik, K.R. Harrap, Cancer Treat. Rev. (Suppl. A) 12 (1985) 51.
[6] B.W. Booth, R.B. Weiss, A.H. Korzun, W.C. Wood, R.W. Carey, L.C. Panasci, Cancer Treat. Rep. 69 (1985) 919.
[7] M.J. Cleare, J.D. Hoeschele, Platinum Metals Rev. 17 (1973) 2.
[8] H. J Ridgway, R.I. Speer, L.M. Hall, D.P. Stewart, A.D. Newman, M. J Hill, J. Clin. Hematol. Oncol. 7 (1977) 220.
[9] R. Perez-Soler, A.R. Khokhar, M.P. Hacker, G. Lopez-Berestein, Cancer Res. 46 (1986) 6269.
[10] M. Noji, K. Suzuki, T. Tashiro, K. Harada, K. Masuda, Y. Kidani, Chem. Pharm. Bull. 35 (1987) 221.
[11] A.R. Khokhar, S. Al-Baker, I.H. Krakoff, R. Perez-Soler, Cancer Chemother. Pharmcol. 23 (1989) 219.
[12] Y. Kidani, Trends Inorg. Chem. 1 (1990) 107.
[13] A.R. Khokhar, S. Albaker, R. Perez-Solar, Anti-Cancer Drugs 3 (1992) 95.
[14] W. Schmidt, S. Chaney, Cancer Res. 53 (1993) 799.
[15] A. Eastman, S. Illenye, Cancer Treat. Rep. 68 (1984) 1189.
[16] J.H. Burchenal, K. Kalaher, K. Dew, L. Lokys, G. Galle, Biochimie 60 (1978) 961.

[17] J.H. Burchenal, K. Kalaher, T. O'Toole, J. Chisholm, Cancer Res. 37 (1977) 3455.
[18] M.C. Christinan, E. Kohn, G. Sarosy, C. Link, P. Davis, D. Adamo, R.B. Weiss, L. Brewster, F. Lombardo, E. Reed, Proc. Am. Soc. Clin. Oncol. (Abstract) 11 (1992) 117.
[19] M.J. Extra, M. Espie, F. Calvo, C. Ferme, L. Mignot, M. Marty, Cancer Chemother. Pharmacol. 25 (1990) 299.
[20] R. Perez-Soler, G. Lopez-Berestein, J. Lautersztain, S. Al-Baker, K. Francis, D. Macias-Kiger, M.N. Raber, A.R. Khokhar, Cancer Res. 50 (1990) 4254.
[21] J.D. Hoeschele, H.D. Showalter, A.J. Kraker, W.L. Elliott, B.J. Roberts, J.W.J. Kampf, Med. Chem. 37 (1994) 2630.
[22] S. Shamsuddin, I. Takahashi, Z.H. Siddik, A.R. Khokhar, Inorg. Biochem. 61 (1996) 291.
[23] S. Shamsuddin, J.W. van Hal, J.L. Stark, K.H. Whitmire, A.R. Khokhar, Inorg. Chem. 36 (1997) 5969.
[24] S. Shamsuddin, C.S. Santillan, J.L. Stark, K.H. Whitmire, Z.H. Siddik, A.R. Khokhar, J. Inorg. Biochem. 71 (1998) 29.
[25] M.S. Ali, A.R. Khokhar, J. Inorg. Biochem. 96 (2003) 452.
[26] J.J. Robert, M.P. Pera Jr., in: S. Neidle, M.J. Waring (Eds.), Molecular Aspects of Anti-Cancer Drug Action, Macmillan, London, 1983, p. 183.
[27] J. Reedijk, A.M.J. Fichtinger-Schepman, A.T. van Oosterom, P. van de Putte, Struct. Bonding 67 (1987) 53.
[28] S.E. Sherman, S.J. Lippard, Chem. Rev. 87 (1987) 1153.
[29] E.R. Jamieson, S.J. Lippard, Chem. Rev. 99 (1999) 2467.
[30] A.M.J. Fichtinger-Schepman, J.L. van der Veer, J.H.J. den Hartog, P.H.M. Lohman, J. Reedijk, Biochemistry 707 (1985) 707.
[31] A. Eastman, Biochemistry 25 (1986) 3912.
[32] L.G. Marzilli, T.J. Kistenmacher, G.L. Eichhorn, L. Gunther, in: T.G. Spiro (Ed.), Metal Ions in Biology, Nucleic Acid–Metal Ion Interaction, vol. 1, Wiley, New York, 1980, p. 179.
[33] J.K. Barton, S.J. Lippard, in: Metal Ions in Biology, Nucleic Acid–Metal Ion Interaction, vol. 1, Wiley, New York, 1980, p. 31.
[34] G.L. Cohen, J.A. Ledner, W.R. Bauer, H.M. Ushay, C. Caravana, S.J. Lippard, J. Am. Chem. Soc. 102 (1980) 2487.
[35] E.C.H. Ling, W.G. Allen, T.W. Hambley, J. Am. Chem. Soc. 116 (1994) 2673.
[36] P.M. Takahara, A.C. Rosenzweig, C.A. Federick, S.J. Lippard, Nature 377 (1995) 649.
[37] P.M. Takahara, C.A. Federic, S.J. Lippard, J. Am. Chem. Soc. 118 (1996) 12309.
[38] A. Gelasco, S.J. Lippart, Biochemistry 37 (1998) 9230.
[39] H.K. Choi, A. Terzis, R.C. Stevens, R. Bau, R. Haugwitz, V.L. Narayanan, M. Wolpert-DeFillippes, Biochem. Biophys. Res. Commun. 156 (1988) 1120.
[40] H.K. Choi, S.K.S. Huang, R. Bau, Biochem. Biophys. Res. Commun. 156 (1988) 1125.
[41] R. Bau, M. Sabat, in: B. Lippert (Ed.), Cisplatin, Verlag Helvitica Chimica Acta, Zürich, Switz, 1999, p. 319.
[42] R.J. Knox, F. Friedlos, D.A. Lydall, J.J. Roberts, Cancer Res. 46 (1986) 1972.
[43] TEXSAN Single Crystal Structure Analysis Software 5.0; Molecular Structure Corporation, The Woodlands, TX, 1990.
[44] G.M. Sheldrick, SHELXTL 6.1, Göttingen, Germany, 2001.
[45] A.L. Speck, PLATON, A Multipurpose Crystallographic Tool, Utrecht University, The Netherlands, 2001.
[46] P.S. Pregosin, Coord. Chem. Rev. 44 (1982) 247.
[47] H. Schollhorn, G. Raudaschl-Sieber, G. Muller, U. Thewalt, B. Lippert, J. Am. Chem. Soc. 107 (1985) 5932.
[48] R. Faggiani, B. Lippert, C.J.L. Lock, R.A. Speranzini, Inorg. Chem. 21 (1982) 3216.
[49] G. Schröder, J. Kozelka, M. Sabat, M.H. Fouchet, R. Beyerle-Pfnür, B. Lippert, Inorg. Chem. 35 (1996) 1647.
[50] B. Lippert, G. Raudaschl, C.J.L. Lock, P. Pilion, Inorg. Chim. Acta 93 (1984) 43.
[51] V. Brabec, J. Kasparkova, Drug Resist. Updat. 5 (2002) 147.
[52] N. Farrell, Y. Qu, Inorg. Chem. 28 (1989) 3416.
[53] W.J. Heiger-Bernays, J.M. Essigmann, S.J. Lippard, Biochemstry 29 (1990) 8461.
[54] K.M. Comess, J.N. Burstyn, J.M. Essigmann, S.J. Lippard, Biochemistry 31 (1992) 3975.
[55] B.D. Zamble, S.J. Lippard, in: B. Lippaert (Ed.), Cisplatin – Chemistry and Biochemistry of a Leading Anticancer Drugs, Verlag Helvitica Chimica Acta, Zurich, Switz, 1999, p. 73.
[56] P. Vichi, F. Coin, J. P Renaud, W. Vermeulen, L.H.J. Hoeijmakers, D. Moras, J.M. Egly, J. Embo 16 (1997) 7444.
[57] B.A. Donahue, M. Augot, S.F. Bellon, D.K. Toney, S.J. Lippard, J.M. Essigmann, Biochemistry 29 (1990) 5872.
[58] A. Vaisman, S.E. Lim, S.M. Patrick, W.C. Copland, D.C. Hinkle, J.J. Terchi, S.G. Chaney, Biochemistry 38 (1999) 11026.
[59] J.D. Page, I. Husain, A. Sancar, S.G. Chaney, Biochemistry 29 (1990) 1016.
[60] G.R. Gibbon, J.D. Page, S.K. Mauldin, S.G. Chaney, Cancer. Res. 50 (1990) 6497.
[61] P.M. Takahara, C.A. Fedrick, S.J. Lippard, J. Am. Chem. Soc. 118 (1996) 12309.
[62] A. Gelasaco, S.J. Lippard, Biochemistry 37 (1998) 9230.
[63] G. Schröder, M. Sabat, I. Baxter, J. Kozelka, B. Lippert, Inorg. Chem. 36 (1997) 490.
[64] M.S. Ali, S.R. Ali-Khan, H. Ojima, I.Y. Guzman, K.H. Whimire, Z.H. Siddik, A.R. Khokhar, J. Inorg. Biochem. 99 (2000) 795.
[65] M.S. Ali, E. Longoria Jr., T.O. Ely, K.H. Whitmire, A.R. Khokhar, Polyhedron 25 (2006) 2065.
[66] M.S. Ali, A.R. Khokhar, J. Inorg. Biochem. 96 (2003) 452.
[67] S.U. Dunham, C.J. Turner, S.J. Lipaard, J. Am. Chem. Soc. 120 (1998) 5395.
[68] E.D. Scheef, S.B. Howell, Proc. Am. Assoc. Cancer Res. 39 (1998) 158.

Available online at www.sciencedirect.com
ScienceDirect
Polyhedron 26 (2007) 645–652
POLYHEDRON
www.elsevier.com/locate/poly

Strictly heterodinuclear compounds containing U^{4+} and Cu^{2+} or Ni^{2+} ions

Lionel Salmon, Pierre Thuéry, Michel Ephritikhine *

Service de Chimie Moléculaire, DSM, DRECAM, CNRS URA 331, Laboratoire Claude Fréjacques, CEA/Saclay, 91191 Gif-sur-Yvette, France

Received 18 July 2006; accepted 25 August 2006
Available online 3 September 2006

Abstract

Treatment of $[M(H_2L^i)]$ with UCl_4 in pyridine led to the formation of the dinuclear complexes $[ML^i(py)UCl_2(py)_2]$ and/or $[Hpy][ML^i(py)UCl_3]$ [L^i = *N*,*N*′-bis(3-hydroxysalicylidene)-R, R = 1,2-phenylenediamine ($i = 1$), R = *trans*-1,2-cyclohexanediamine ($i = 2$), R = 2-amino-benzylamine ($i = 3$), R = 1,3-propanediamine ($i = 4$), R = 2,2-dimethyl-1,3-propanediamine ($i = 5$); M = Cu or Ni]. The crystal structures show that the 3d and 5f ions occupy, respectively, the N_2O_2 and O_4 cavities of the Schiff base ligand, the U^{4+} ion adopting a dodecahedral or pentagonal bipyramidal configuration in the neutral and anionic complexes, respectively.
© 2006 Elsevier Ltd. All rights reserved.

Keywords: Uranium; Copper; Nickel; Schiff base; Dinuclear; X-ray crystal structure

1. Introduction

Polynuclear complexes containing both d- and f-block transition metals attract much attention for their interesting magnetic behaviour [1] and their potential in the development of molecular-based materials with controlled properties [2,3]. Most studies were devoted to copper(II)–gadolinium(III) (3d–4f) complexes in which both ferro- [4–8] and antiferromagnetic [9,10] interactions have been observed. When the lanthanide(III) ion, Ln^{3+}, is different from gadolinium, the presence of a first-order orbital momentum complicates the analysis of the magnetic properties which are governed by both the thermal population of the Stark components of the 4f ion and the 3d–4f interaction. The nature of this interaction could be determined by subtracting the sole contribution of the lanthanide ion, which is reflected by the magnetic behaviour of isostructural derivatives in which the paramagnetic 3d ion, i.e. Cu^{2+}, has been replaced by a diamagnetic ion, i.e. Zn^{2+} [11,12]. In the last past years, the first compounds containing both 3d and 5f ions have been isolated [13–18]. In addition to the challenge of their synthesis, such complexes are attractive for their magnetic properties which, by comparison with those of the 3d–4f derivatives, would reflect the greater spatial extension of the 5f orbitals. We have prepared a series of trinuclear compounds of general formula $[\{ML^i(py)\}_2U]$ (M = Cu, Zn) which differ by the length of the diimino chain of the Schiff base ligand L and whose magnetic properties were found to be dependent on the Cu···U distance [15,16]. With L^6 = *N*,*N*′-bis(3-hydroxysalicylidene)-2-methyl-1,2-propanediamine, we succeeded in isolating the first strictly dinuclear compound of paramagnetic 3d and 5f ions, $[CuL^6(py)U(acac)_2]$, from an equimolar mixture of $[Cu(H_2L^6)]$ and $U(acac)_4$ [17]. This dinuclear compound was the sole to have been obtained pure since the use of the other Schiff base ligands led invariably to the straightforward formation of the Cu_2U complexes. Here we present the crystal structure of new CuU and NiU compounds in this family which were synthesized by using UCl_4 instead of $U(acac)_4$ as the uranium precursor. Unfortunately, attempts to isolate and characterize the ZnU analogues were unsuccessful, precluding any magnetic studies.

* Corresponding author. Fax: +33 1 69 08 66 40.
E-mail addresses: michel.ephritikhine@cea.fr, ephri@drecam.cea.fr (M. Ephritikhine).

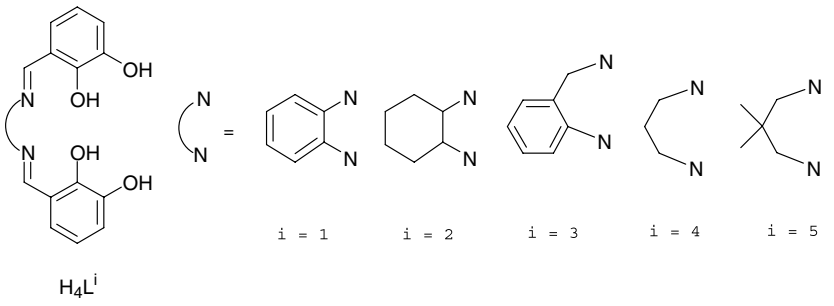
0277-5387/$ - see front matter © 2006 Elsevier Ltd. All rights reserved.
doi:10.1016/j.poly.2006.08.022

2. Results and discussion

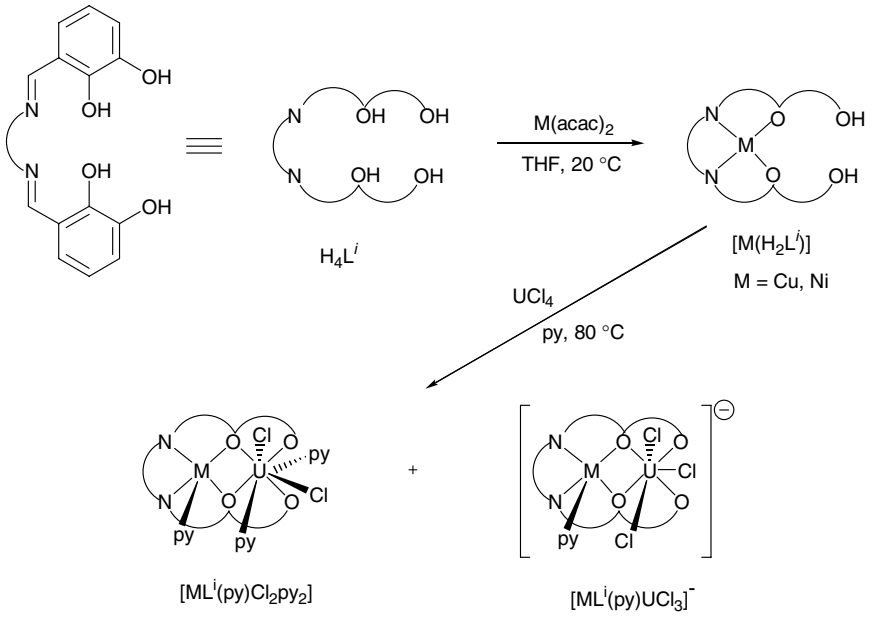
2.1. Synthesis of the complexes

The Schiff bases H_4L^i [L^i = *N*,*N*′-bis(3-hydroxysalicylidene)-R, R = 1,2-phenylenediamine ($i = 1$), R = *trans*-1,2-cyclohexanediamine ($i = 2$), R = 2-amino-benzylamine ($i = 3$), R = 1,3-propanediamine ($i = 4$), R = 2,2-dimethyl-1,3-propanediamine ($i = 5$)] are represented in Scheme 1. Reactions of $[M(H_2L^i)]$ (M = Cu, Ni or Zn) with one equivalent of $U(acac)_4$ in refluxing pyridine afforded directly the trinuclear compounds $[\{ML^i(py)\}_2U]$, without it being possible to isolate the $[ML^i(py)U(acac)_2]$ intermediates [15,16]. Similar treatment of $[M(H_2L^i)]$ (M = Cu, Ni) with UCl_4 in place of $U(acac)_4$ afforded the dinuclear compounds $[ML^i(py)UCl_2(py)_2]$ and/or $[Hpy][ML^i(py)UCl_3]$ (Scheme 2). The synthesis of these complexes is likely favoured by the retention of the chloride ion on the metal centre while reactions with $U(acac)_4$ lead to the irreversible elimination of acacH. The orange microcrystalline powder of $[CuL^1(py)UCl_2(py)_2]$ (**1**) was obtained in 97% yield by treatment of $[Cu(H_2L^1)]$ with UCl_4 in pyridine at 80 °C, while similar reaction of $[Cu(H_2L^2)]$ gave a mixture of green crystals of $[CuL^2(py)UCl_2(py)_2]$ (**2**) and orange crystals of $[Hpy][CuL^2(py)UCl_3]$. Under the same experimental conditions, the anionic compounds $[Hpy][CuL^i(py)UCl_3]$ [$i = 3$ (**3**), 4 (**4**) and 5 (**5**)] were the sole products isolated from $[Cu(H_2L^i)]$, as dark brown ($i = 3$), dark yellow ($i = 4$) and light green ($i = 5$) crystals. Similar reactions of $[Ni(H_2L^i)]$ ($i = 3$, 5) and UCl_4 led to the formation of the anionic complexes $[Hpy]_2[NiL^3(py)_2UCl_3][NiL^3(py)UCl_3]$ (**6**) and $[Hpy][NiL^5(py)UCl_3]$ (**7**).

As mentioned in Section 1, the nature of the Cu–U or Ni–U interaction in these dinuclear compounds can be determined by comparison of their magnetic properties with those of the ZnU analogues. Unfortunately, reactions of $[Zn(H_2L^i)]$ ($i = 2$–5) with UCl_4 gave insoluble powders which could not be fully characterized. Only the products obtained from $[Zn(H_2L^1)]$ were soluble in pyridine but, surprisingly, the ^1H NMR spectra revealed the presence of two compounds with a dissymmetric structure, all the protons of the Schiff base ligands being magnetically unequivalent.



Scheme 1. The H_4L^i Schiff bases.



Scheme 2. Synthesis of the complexes.

Obviously, the ZnU analogue of **1** was not formed and, in the absence of crystallographic analysis, these complexes have not been identified.

2.2. Crystal structures of the complexes

Crystals of **1**·2py, **2**·2py, **3**·1.25py, **4**, **5**·py, **6**·1.5py and **7**·py suitable for X-ray diffraction analysis were obtained by crystallization from pyridine. Views of **1** and **4** are shown in Figs. 1 and 2, respectively, and selected bond lengths and angles are listed in Table 1. The asymmetric unit of **2**·2py contains two independent enantiomer molecules, $[Cu[(R,R)\text{-}L^2](py)UCl_2(py)_2]$ and $[Cu[(S,S)\text{-}L^2](py)\text{-}UCl_2(py)_2]$ (see Section 4.3), and the asymmetric unit of **3**·1.25py contains two identical independent molecules. In all the CuU complexes **1**–**5**, the copper and uranium atoms occupy, respectively, the N_2O_2 and O_4 cavities of the Schiff base ligand and are bridged by the two oxygen atoms O(2) and O(3) of the salicylidene fragments; the Cu^{2+} ions adopt a square pyramidal coordination mode, being displaced from the N_2O_2 base towards the pyridine ligand by 0.20–0.27 Å. In the neutral compounds **1** and **2**, the U^{4+} ion is bound to two chloride ions and two nitrogen atoms of pyridine ligands and is found in a dodecahedral environment defined by the two trapezia O(1)–O(2)–O(3)–O(4) and Cl(1)–N(3)–Cl(2)–N(4) intersecting at an angle of 89.43(9)° in **1** and 89.47(17) and 89.83(17)° in **2**. The anionic complexes **3**, **4** and **5** differ by the displacement of the two pyridine ligands with a chloride ion, and the seven coordinate uranium atom is in a pentagonal bipyramidal configuration with Cl(1) and Cl(3) in apical positions. The charge is compensated with that of a pyridinium ion which is hydrogen bonded to a pyridine nitrogen atom in **3** (in which the pyridinium ions are disordered, Section 4.3) or to one phenoxide oxygen atom in **4** or **5** [N(4)···O(4) 2.828(6) Å, N(4)–H···O(4) 166° in **4**, N(4)···O(1) 2.667(9) Å (pyridinium proton not found) in **5**]. The length of the diimino chain of L^i and the configuration of the U^{4+} ion in complexes **1**–**5** have no major influence on the U–O distances, which average 2.44(3) Å [bridging O(2) and O(3)] and 2.25(3) Å [terminal O(1) and O(4)], and on the O(2)–U–O(3) and O(1)–U–O(4) angles which vary from 59.3(2) to 62.4(3)° and from 164.0(3) to 167.7(2)°, respectively; these values are quite identical to those found in the series of $[\{CuL^i(py)\}_2U]$ compounds. However, as also observed in the trinuclear complexes, the length of the diimino chain of L^i has a marked effect on the coordination of the 3d metal, in particular the N(1)–Cu–N(2) and O(2)–Cu–O(3) angles which are, respectively, ca. 10° smaller and 6° larger in **1** and **2** than in **3**, **4** and **5**. In relation to these variations, the Cu..U distances increase by passing from L^1 and L^2 to L^3, L^4 and L^5, with average values of 3.541(7) and 3.632(15) Å. The mean values of the U–Cl bond lengths, 2.73(2) Å in **1** and **2** and 2.68(2) Å in **3**, **4** and **5**, are among the largest reported in the Cambridge Structural Database (CSD, Version 5.27) [19].

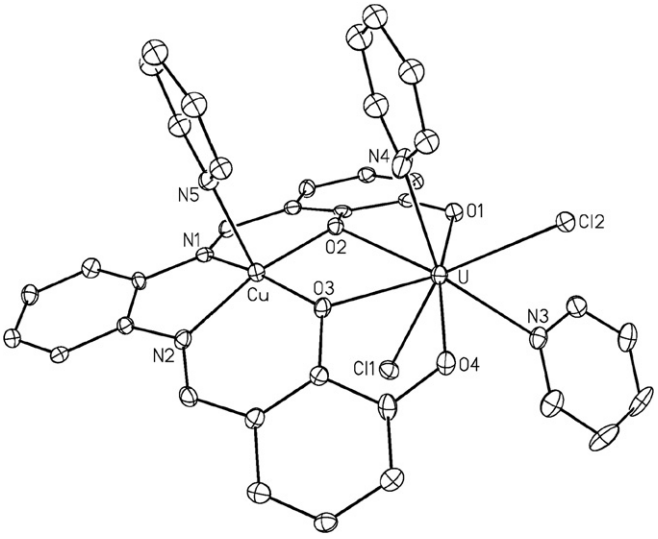


Fig. 1. View of complex **1**. The hydrogen atoms are omitted for clarity. Only the principal component of the disordered pyridine molecules is represented. Displacement ellipsoids are drawn at the 30% probability level.

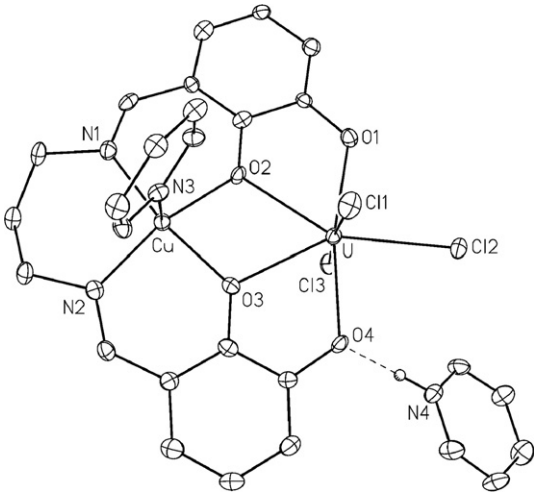


Fig. 2. View of complex **4**. The hydrogen atoms (except the pyridinium one) are omitted for clarity. The hydrogen bond is shown as a dashed line. Displacement ellipsoids are drawn at the 30% probability level.

Crystals of **6**·1.5py contain two different anionic complexes $[NiL^3(py)_2UCl_3]^-$ and $[NiL^3(py)UCl_3]^-$, denoted A and B, respectively. The distinct configurations of the Ni atom, octahedral in A and square pyramidal in B, have no influence on the Ni–O(2,3) and Ni–N(1,2) distances. In fact, the 3d ion in complex A is in the mean plane of the N_2O_2 cavity [distance to the plane 0.026(3) Å] while it is out of this plane in complex B, by 0.364(3) Å; however, the Ni–O and Ni–N distances are not shorter in A than in B because of the enlargement of the N_2O_2 cavity, in relation with the variation of the N–Ni–N and N–Ni–O angles which are larger in A than in B, by ca. 5° and 2°, respectively.

Comparison of the structures of **6** (complex B) and **3**, and of **7** and **5**, which are isomorphous, indicate that the

Table 1
Selected bond lengths (Å) and angle (°) in the dinuclear complexes

	1·2py	**2**·2py[a]	**3**·1.25py[a]	**4**	**5**·py	**6**·1.5py[b]	**7**·py
U–O(1)	2.227(4)	2.247(8)/2.223(9)	2.248(6)/2.234(7)	2.232(4)	2.305(5)	2.278(6)/2.247(6)	2.247(4)
U–O(2)	2.449(4)	2.422(9)/2.490(7)	2.405(7)/2.414(7)	2.407(4)	2.421(5)	2.387(5)/2.398(5)	2.410(4)
U–O(3)	2.491(4)	2.483(8)/2.431(8)	2.423(6)/2.427(7)	2.420(4)	2.412(5)	2.405(5)/2.427(5)	2.409(4)
U–O(4)	2.225(4)	2.219(9)/2.260(8)	2.273(7)/2.240(6)	2.292(4)	2.254(6)	2.274(5)/2.242(6)	2.284(4)
U–Cl(1)	2.7072(15)	2.721(3)/2.709(3)	2.655(3)/2.707(3)	2.6499(14)	2.659(3)	2.698(2)/2.650(2)	2.650(2)
U–Cl(2)	2.7472(15)	2.751(3)/2.746(3)	2.683(3)/2.674(3)	2.6660(15)	2.678(2)	2.719(2)/2.706(2)	2.687(2)
U–Cl(3)			2.706(3)/2.644(3)	2.6921(14)	2.687(2)	2.656(2)/2.714(2)	2.674(2)
U–N(3)	2.595(5)	2.622(11)/2.582(12)					
U–N(4)	2.631(5)	2.614(10)/2.604(10)					
⟨U–O⟩	2.35(12)	2.34(11)/2.35(11)	2.34(8)/2.33(9)	2.34(8)	2.35(7)	2.34(6)/2.33(8)	2.34(7)
⟨U–O_b⟩	2.47(2)	2.45(3)/2.46(3)	2.414(9)/2.421(6)	2.414(6)	2.417(4)	2.396(9)/2.413(15)	2.410(1)
⟨U–O_t⟩	2.226(1)	2.233(14)/2.24(2)	2.261(12)/2.237(3)	2.26(3)	2.28(3)	2.276(2)/2.245(2)	2.27(2)
M–O(2)	1.915(4)	1.930(8)/1.913(8)	1.928(6)/1.945(7)	1.945(4)	1.981(6)	1.988(5)/1.971(6)	1.992(4)
M–O(3)	1.925(4)	1.940(8)/1.933(8)	1.940(7)/1.923(7)	1.964(4)	1.957(6)	1.983(5)/1.991(6)	1.994(5)
M–N(1)	1.947(5)	1.955(9)/1.949(10)	1.967(9)/1.936(8)	1.995(5)	1.995(7)	1.985(7)/2.025(7)	2.010(5)
M–N(2)	1.948(5)	1.941(10)/1.937(10)	1.972(8)/2.007(8)	1.996(5)	1.983(7)	2.022(6)/2.012(7)	2.034(6)
M–N(3)			2.270(8)/2.304(9)	2.261(4)	2.304(7)	2.197(7)/2.026(7)	2.048(6)
M–N(5)	2.275(4)	2.287(10)/2.293(11)					
M···U	3.5451(7)	3.5305(15)/3.5472(15)	3.6152(13)/3.6232(13)	3.6335(7)	3.6545(10)	3.6557(11)/3.6465(11)	3.6707(9)
O(1)–U–O(4)	164.08(15)	164.0(3)/164.8(3)	167.7(2)/167.1(3)	166.77(14)	167.34(19)	168.97(19)/166.82(19)	166.87(16)
O(2)–U–O(3)	61.48(12)	62.4(3)/61.5(3)	59.3(2)/59.3(2)	59.36(13)	59.70(19)	60.09(18)/60.52(19)	60.06(14)
Cl(1)–U–N(4)	142.97(12)	141.8(2)/143.8(2)					
Cl(2)–U–N(3)	72.55(12)	73.5(2)/72.6(2)					
Cl(1)–U–Cl(2)			88.83(10)/94.92(10)	88.44(5)	90.53(9)	86.91(7)/90.43(7)	91.40(10)
Cl(2)–U–Cl(3)			89.62(9)/91.57(9)	87.09(5)	88.98(8)	91.85(7)/91.33(7)	89.32(9)
N(1)–M–N(2)	84.6(2)	85.9(4)/86.0(4)	95.5(4)/96.6(4)	99.7(2)	97.7(3)	100.4(3)/95.2(3)	97.4(2)
N(1)–M–O(2)	94.75(18)	94.7(4)/94.4(4)	91.8(3)/92.6(3)	90.66(18)	91.4(3)	92.1(2)/90.2(3)	90.1(2)
N(2)–M–O(3)	95.17(19)	93.7(4)/94.6(4)	92.8(3)/92.8(3)	91.83(18)	91.8(3)	93.2(2)/91.7(3)	91.1(2)
O(2)–M–O(3)	82.24(16)	82.2(3)/81.7(3)	76.3(3)/76.4(3)	75.37(16)	75.3(2)	74.3(2)/75.7(2)	74.46(17)
M–O(2)–U	108.04(17)	107.9(3)/106.6(3)	112.7(3)/112.0(3)	112.76(17)	111.8(3)	113.1(2)/112.8(2)	112.68(18)
M–O(3)–U	106.08(16)	105.3(3)/108.2(4)	111.4(3)/112.3(3)	111.53(16)	113.1(3)	112.5(2)/110.9(2)	112.64(18)
α[c]	13.5(3)	13.9(5)/12.9(5)	4.6(5)/0.3(3)	8.7(2)	1.1(5)	0.9(1)/3.3(3)	3.6(4)

[a] Values for the two independent molecules.
[b] Values for complexes A and B (see text); Ni–N(4) in complex A 2.236(7) Å.
[c] α is the dihedral angle between the two halves of the MO(2)O(3)U bridging core.

coordination geometry of the U^{4+} ion is quite identical in all the complexes. However, the Ni–O and Ni–N(1,2) distances are larger than the corresponding Cu–O and Cu–N distances, by ca. 0.04 Å, whereas the radius of the Ni^{2+} ion is 0.02 Å smaller than that of Cu^{2+} [20]. The Ni^{2+} ion is more displaced than Cu^{2+} from the N_2O_2 plane, by ca. 0.35 versus 0.25 Å, and the Ni–N(py) distances of 2.026(7) and 2.048(6) Å are much smaller than the average Cu–N(py) distance of 2.29(2) Å. The same variations in the structural parameters of the square pyramidal Ni^{2+} and Cu^{2+} ions were observed in the trinuclear complexes [{NiL^5(py)}$_2$U] and [{CuL^5(py)]U[CuL^5}].

3. Conclusion

The difficulty in obtaining strictly dinuclear CuU and ZnU complexes from reactions of [M(H_2L^i)] (M = Cu, Ni or Zn) with U(acac)$_4$ arises from the straightforward formation of the corresponding trinuclear compounds [{ML^i(py)}$_2$U]. Replacement of U(acac)$_4$ with UCl_4 permitted to prepare CuU and NiU complexes, either as neutral or anionic derivatives [ML^i(py)UCl_2(py)$_2$] and [Hpy][ML^i(py)UCl_3], but the unsuccessful isolation and characterization of the ZnU analogues precluded any studies of the Cu–U or Ni–U exchange interaction.

4. Experimental

4.1. General

All reactions were carried out under argon (<5 ppm oxygen or water) using standard Schlenk-vessel and vacuum-line techniques or in a glove box. Solvents were dried by standard methods and distilled immediately before use; deuterated pyridine (Eurisotop) was distilled over NaH and stored over 3 Å molecular sieves. The ^{1}H NMR spectra were recorded on a Bruker DPX 200 instrument and referenced internally using the residual protio solvent resonances relative to tetramethylsilane (δ 0). Elemental analyses were performed by Analytische Laboratorien at Lindlar (Germany).

The Schiff bases H_4L^i (i = 1–5) were synthesized by published methods [21]. The acac compounds M(acac)$_2$ (Cu, Ni and Zn) (Aldrich) were used without purification; UCl_4

was prepared as previously reported [22]. The complexes $[M(H_2L^i)]$ were synthesized in THF by reaction of H_4L^i with 1 equiv. of $M(acac)_2$.

4.2. Syntheses

The complexes can be divided into two series of general formula $[ML^i(py)UCl_2(py)_2]$ and $[Hpy][ML^i(py)UCl_3]$. One example in each series, **1** and **4**, has been characterized by its elemental analyses; all the complexes or their solvates were characterized by X-ray diffraction analysis.

4.2.1. $[CuL^1(py)UCl_2(py)_2]$ (*1*)

A flask was charged with $[Cu(H_2L^1)]$ (150 mg, 0.37 mmol) and UCl_4 (139 mg, 0.37 mmol) in pyridine (25 mL). The reaction mixture was heated at 80 °C for 12 h; the brown-orange powder of **1** was filtered off, washed with pyridine (20 ml) and dried under vacuum (340 mg, 97%).

The complex could not be characterized by its ^{1}H NMR spectrum because of its insolubility in organic solvents. *Anal.* Calc. for $C_{35}H_{27}N_5O_4Cl_2CuU$: C, 44.05; H, 2.83; N, 7.34. Found: C, 43.89; H, 3.03; N, 7.49%. Crystals of **1**·2py were obtained by heating a suspension of **1** in pyridine at 80 °C.

4.2.2. $[CuL^2(py)UCl_2(py)_2]$ (*2*) and $[Hpy][CuL^2(py)UCl_3]$

An NMR tube was charged with $[Cu(H_2L^2)]$ (6.0 mg, 0.0144 mmol) and UCl_4 (5.5 mg, 0.0144 mmol) in pyridine-d_5 (0.4 mL). Immediately, at 20 °C, a brown powder precipitated and the ^{1}H NMR indicated the presence of two species A and B in the relative proportions of 2:1. The tube was heated at 80 °C and the NMR spectrum showed the presence of both species in relative proportions 1:1. Prolonged heating at 80 °C led to the crystallization of a mixture of light green platelets of $[CuL^2(py)UCl_2(py)_2]\cdot 2py$ (**2**·2py) and orange platelets of $[Hpy][CuL^2(py)UCl_3]$.

^{1}H NMR of species A: 15.35, 18.29 and 41.61 (3×2 H, aromatic H). ^{1}H NMR of species B: 16.57 and 42.79 (4 H + 2 H, aromatic H). Broad signals at −16.1, −12.8, −6.2 and 1.4 are attributed to the protons of the cyclohexyl rings of both compounds; a signal at δ 21.2 can be attributed to the Hpy proton.

4.2.3. $[Hpy][CuL^3(py)UCl_3]$ (*3*)

An NMR tube was charged with $[Cu(H_2L^3)]$ (5.0 mg, 0.0118 mmol) and UCl_4 (4.5 mg, 0.0118 mmol) in pyridine-d_5 (0.4 mL). The tube was heated at 80 °C for 1 d and the spectrum indicated the presence of the sole complex **3**. Prolonged heating at 80 °C led to the crystallization of dark brown platelets of **3**·1.25py.

^{1}H NMR (pyridine-d_5, 23 °C): −16.5, −6.84, 1.32 and 12.29 (4×1 H, Ph of the diimino chain), 17.52 and 18.15 (2×1 H, aromatic H), 23.12 (3 H, aromatic H and pyH), 40.23 (2 H, aromatic H), 106.2 and 107.8 (2×1 H, NCH_2).

4.2.4. $[Hpy][CuL^4(py)UCl_3]$ (*4*)

(a) An NMR tube was charged with $[Cu(H_2L^4)]$ (5.0 mg, 0.0133 mmol) and UCl_4 (5.1 mg, 0.0133 mmol) in pyridine-d_5 (0.4 mL). After heating at 80 °C for 5 d, the spectrum indicated the presence of the sole complex **4** which crystallized as dark yellow platelets.

^{1}H NMR (pyridine-d_5, 23 °C): −25.59 (2 H, CH_2) 10.46, 19.69 and 44.10 (3×2 H, aromatic H), 93.42 and 116.90 (2×2 H, NCH_2).

(b) A flask was charged with $[Cu(H_2L^4)]$ (50 mg, 0.13 mmol) and UCl_4 (50 mg, 0.13 mmol) in pyridine (15 mL). The reaction mixture was heated for 6 h at 80 °C; the brown powder of **4** was filtered off, washed with pyridine (10 mL) and dried under vacuum (55 mg, 47%). *Anal.* Calc. for $C_{27}H_{25}N_4O_4Cl_3CuU$: C, 36.94; H, 2.85; N, 6.39. Found: C, 36.81; H, 3.05; N, 6.59%.

4.2.5. $[Hpy][CuL^5(py)UCl_3]$ (*5*)

An NMR tube was charged with $[Cu(H_2L^5)]$ (5.0 mg, 0.0124 mmol) and UCl_4 (4.7 mg, 0.0124 mmol) in pyridine-d_5 (0.4 mL). The tube was heated at 80 °C for 12 h and the NMR spectrum of the limpid dark brown solution indicated the presence of the sole complex **5**. Prolonged heating at 80 °C led to the crystallization of light green needles of **5**·py.

^{1}H NMR (pyridine-d_5, 23 °C): −10.83 (6 H, Me) 10.34, 19.28 and 43.14 (3×2 H, aromatic H), 110.7 (4 H, NCH_2); a signal at δ 20.02 can be attributed to the Hpy proton.

4.2.6. $[Hpy]_2[NiL^3(py)_2UCl_3][NiL^3(py)UCl_3]$ (*6*)

An NMR tube was charged with $[Ni(H_2L^3)]$ (5.0 mg, 0.0119 mmol) and UCl_4 (4.5 mg, 0.0118 mmol) in pyridine-d_5 (0.4 mL). After 30 min at 20 °C, the spectrum of the red solution showed the formation of **6** as the sole product. Prolonged heating at 80 °C led to the crystallization of orange platelets of **6**·1.5py.

^{1}H NMR (pyridine-d_5, 23 °C): −13.37, −4.59, −0.52 and 13.72 (4×1 H, Ph of the diimino chain), 18.91 and 29.16 (2×2 H, aromatic H), 29.29 (1 H, Hpy), 35.60 and 35.92 (2×1 H, aromatic H), 94.9 (2 H, NCH_2).

4.2.7. $[Hpy][NiL^5(py)UCl_3]$ (*7*)

An NMR tube was charged with $[Ni(H_2L^5)]$ (5.0 mg, 0.0125 mmol) and UCl_4 (4.8 mg, 0.0125 mmol) in pyridine-d_5 (0.4 mL). After 30 min at 20 °C, the spectrum of the dark green solution containing a small quantity of green powder showed the formation of **7** together with another unidentified compound. Light green crystals of **7**·py were deposited after heating at 80 °C for 2 d.

^{1}H NMR (pyridine-d_5, 23 °C): −7.14 (6 H, Me); 12.28, 22.25 and 38.55 (3×2 H, aromatic H), 99.6 (4 H, NCH_2).

4.2.8. Reaction of $[Zn(H_2L^1)]$ and UCl_4

An NMR tube was charged with $[Zn(H_2L^1)]$ (5.0 mg, 0.0122 mmol) and UCl_4 (4.6 mg, 0.0122 mmol) in pyridine-d_5 (0.4 mL). After 30 min at 20 °C, the spectrum of the orange-red solution showed the signals of two

complexes denoted A and B, in relative proportions of 50:50. Complex B was the sole complex in solution after 24 h at 80 °C.

^{1}H NMR (complex A): −35.07, −16.25, −10.80, −7.42, −6.54 and −0.15 (6 × 1 H, Ph of the diimino chain and CH=N), 17.89, 18.76, 21.97, 34.08, 36.06 and 89.77 (6 × 1 H, aromatic H).

^{1}H NMR (complex B): −28.23, −23.50, −15.96 and −10.80 (4 ×1 H, Ph of the diimino chain), −8.78 and −6.23 (2 × 1 H, CH=N), 12.30, 20.81, 25.70, 29.50, 35.53 and 40.62 (6 × 1 H, aromatic H).

4.3. Crystallography

The data were collected at 100(2) K on a Nonius KappaCCD area detector diffractometer [23] using graphite-monochromated Mo Kα radiation (λ 0.71073 Å). The crystals were introduced in glass capillaries with a protecting "Paratone-N" oil (Hampton Research) coating. The unit cell parameters were determined from 10 frames, then refined on all data. A 180° φ-range was scanned with 2° steps during data collection, with a crystal-to-detector distance fixed to 28 or 30 mm. The data were processed with HKL2000 and DELABS [24]. The structures were solved by direct methods with SHELXS-97 and subsequent Fourier-difference synthesis and refined by full-matrix least-squares on F^2 with SHELXL-97 [25]. Absorption effects were corrected empirically with the program HKL2000 DELABS in PLATON [26]. All non-hydrogen atoms were refined with anisotropic displacement parameters, unless specified below. The carbon-bound hydrogen atoms were introduced at calculated positions in all compounds (except for some disordered parts). All hydrogen atoms were treated as riding atoms with an isotropic displacement parameter equal to 1.2 (NH, CH, CH_2) or 1.5 (CH_3) times that of the parent atom. Specific details are as follows:

Compound **1**·2py. Two of the metal-bound pyridine molecules are disordered over two sites, sharing only atom N(4) in the first molecule, and N(5) and the *para* carbon atom in the second. The disordered components were affected with occupancy factors constrained to sum to unity; these factors appeared to be identical (and were then constrained to be so) for the components of the two molecules which are nearly parallel to one another. The disordered carbon atoms were refined isotropically, with some restraints on bond lengths and displacement parameters.

Compound **2**·2py. The space group $P2_1/c$ used for the seemingly isomorphous compound **1**·2py would be correct for most of the structure, in particular for the metal atoms, but it does not permit a good refinement of some parts of the structure such as the pyridine molecules, even with the use of restraints. Moreover, it can be ruled out with reasonable confidence on the basis of systematic extinctions, in spite of the low crystal quality. The solution adopted corresponds to the chiral space group $P2_1$ with two independent molecules in the asymmetric unit, which constitute an enantiomorph pair. The case of non-centrosymmetric racemates was investigated in detail, but that of the even more surprising racemates crystallizing in chiral space groups (i.e. containing only proper symmetry elements) seems to be illustrated by only 17 organic structures in the CSD [27]. In the present case, the presence of a pseudo-inversion centre is found with an 83% fit only by the program ADDSYM [26] and the passage from a centrosymmetric to a chiral space group could be due to the different positions of the coordinated pyridine molecules in the two complexes. Restraints on displacement parameters have been applied for some badly behaving atoms, particularly in the solvent molecules. Crystals of the compound [Hpy][CuL^2(py)UCl_3] were also obtained from the same preparation, but it was only possible to get a rough model of the structure due to the lack of crystals of sufficient quality.

Compound **3**·1.25py. Three pyridine molecules are disordered, one around a symmetry center and the others over two positions which have been refined with occupancy parameters constrained to sum to unity. Several locations for the pyridinium proton (which has not been found) are thus possible. Three pyridine molecules have been refined as idealized hexagons. The disordered carbon atoms have been refined isotropically and restraints have been applied for some badly behaving atoms in the pyridine molecules. Several short contacts indicate that some of the disordered pyridine positions cannot be occupied simultaneously with their equivalent through the symmetry centre.

Compound **4**. The pyridinium hydrogen atom has been found on a Fourier-difference map.

Compounds **5**·py and **7**·py. The pyridinium hydrogen atom was not found in either of these two isomorphous compounds. Restraints on displacement parameters have been applied for five atoms of the pyridine molecules in **7**. The absolute structure was determined, with Flack parameter values of −0.007(7) and −0.003(6) for **5** and **7**, respectively, [28].

Compound **6**·1.5py. Two pyridine molecules are disordered around a symmetry centre, one of them being further disordered over two positions which have been refined with occupancy parameters of 0.5. Several locations for the pyridinium proton (which has not been found) are thus possible, with two short N···N contacts indicating possible hydrogen bonds. Some restraints have been applied for some atoms in the more badly resolved pyridine molecules.

Crystal data and structure refinement parameters are given in Table 2. The molecular plots were drawn with SHELXTL [29].

5. Supplementary material

CCDC No. 614903–614909 contains the supplementary crystallographic data for **1**–**7**. These data can be obtained free of charge via http://www.ccdc.cam.ac.uk, or from the Cambridge Crystallographic Data Centre, 12 Union

Table 2
Crystal data and structure refinement details

	1·2py	**2**·2py	**3**·1.25py	**4**	**5**·py	**6**·1.5py	**7**·py
Chemical formula	$C_{45}H_{37}Cl_2N_7O_4CuU$	$C_{45}H_{43}Cl_2N_7O_4CuU$	$C_{37.25}H_{31.25}Cl_3N_{5.25}O_4CuU$	$C_{27}H_{25}Cl_3N_4O_4CuU$	$C_{34}H_{34}Cl_3N_5O_4CuU$	$C_{41}H_{35}Cl_3N_6O_4NiU$	$C_{34}H_{34}Cl_3N_5O_4NiU$
M (g mol^{-1})	1112.29	1118.33	1024.35	877.43	984.58	1078.84	979.75
Crystal system	monoclinic	monoclinic	triclinic	orthorhombic	orthorhombic	triclinic	orthorhombic
Space group	$P2_1/c$	$P2_1$	$P\bar{1}$	$Pbca$	$Pna2_1$	$P\bar{1}$	$Pna2_1$
a (Å)	15.6919(7)	11.4498(6)	12.9433(5)	9.8277(4)	11.7091(4)	12.8890(10)	11.7070(5)
b (Å)	23.2164(11)	23.8206(13)	17.1945(13)	16.4947(4)	18.3821(9)	17.2459(16)	18.4073(8)
c (Å)	11.4594(3)	15.7660(5)	18.3548(12)	35.0982(15)	16.6790(8)	18.6269(15)	16.7945(8)
α (°)	90	90	68.133(3)	90	90	88.815(4)	90
β (°)	93.029(3)	92.372(3)	74.384(4)	90	90	73.460(5)	90
γ (°)	90	90	84.406(4)	90	90	86.681(5)	90
V (Å^3)	4168.9(3)	4296.4(4)	3651.1(4)	5689.6(4)	3590.0(3)	3962.4(6)	3619.1(3)
Z	4	4	4	8	4	4	4
D_{calc} (g cm^{-3})	1.772	1.729	1.864	2.049	1.822	1.808	1.798
μ (Mo Kα) (mm^{-1})	4.571	4.436	5.280	6.756	5.365	4.810	5.255
F(000)	2172	2196	1982	3352	1908	2104	1904
Total reflections	28239	28427	25288	33332	23890	27203	23608
Independent reflections	7418	14815	12825	5341	6738	13899	6864
Observed reflections $[I > 2\sigma(I)]$	5801	12293	8478	3911	5118	9853	5909
R_{int}	0.083	0.073	0.081	0.096	0.105	0.068	0.071
Parameters	531	1082	883	361	435	1027	435
R_1 (observed data)	0.039	0.051	0.057	0.034	0.042	0.051	0.034
wR_2 (all data)	0.086	0.108	0.138	0.063	0.077	0.112	0.070
S	1.005	1.008	1.015	0.997	1.007	1.011	1.044
$\Delta\rho_{min}$ (e Å^{-3})	−1.10	−1.17	−1.34	−0.77	−0.63	−1.25	−0.92
$\Delta\rho_{max}$ (e Å^{-3})	0.94	0.84	1.42	0.56	0.63	1.50	0.75

Road, Cambridge CB2 1EZ, UK; fax: (+44) 1223-336-033; or deposit@ccdc.cam.ac.uk.

References

[1] A. Bencini, C. Benelli, A. Caneschi, L. Carlin, A. Dei, D. Gatteschi, J. Am. Chem. Soc. 107 (1985) 8128.
[2] R.E.P. Winpenny, Chem. Soc. Rev. 27 (1998) 447.
[3] C. Benelli, D. Gatteschi, Chem. Rev. 102 (2002) 2369.
[4] J.P. Costes, M. Auchel, F. Dahan, V. Peyrou, S. Shova, W. Wernsdorfer, Inorg. Chem. 45 (2006) 1924.
[5] R. Gheorghe, P. Cucos, M. Andruh, J.P. Costes, B. Donnadieu, S. Shova, Chem. Eur. J. 12 (2006) 187.
[6] F. He, M.L. Tong, X.M. Chen, Inorg. Chem. 44 (2005) 8285.
[7] T. Yamaguchi, Y. Sunatsuki, M. Kojima, H. Akashi, M. Tsuchimoto, N. Re, S. Osa, N. Matsumoto, Chem. Commun. (2004) 1048.
[8] J.P. Costes, F. Dahan, G. Novitchi, V. Arion, S. Shova, J. Lipkowski, Eur. J. Inorg. Chem. (2004) 1530.
[9] J.P. Costes, F. Dahan, A. Dupuis, Inorg. Chem. 39 (2000) 169.
[10] J.P. Costes, F. Dahan, A. Dupuis, Inorg. Chem. 39 (2000) 5994.
[11] J.P. Costes, F. Dahan, A. Dupuis, J.P. Laurent, Chem. Eur. J. 4 (1998) 1616.
[12] M.L. Kahn, C. Mathonière, O. Kahn, Inorg. Chem. 38 (1999) 3692.
[13] K.P. Mortl, J.P. Sutter, S. Golhen, L. Ouahab, O. Kahn, Inorg. Chem. 39 (2000) 1626.
[14] T. Le Borgne, E. Rivière, J. Marrot, P. Thuéry, J.J. Girerd, M. Ephritikhine, Chem. Eur. J. 8 (2002) 774.
[15] L. Salmon, P. Thuéry, E. Rivière, J.J. Girerd, M. Ephritikhine, Dalton Trans. (2003) 2872.
[16] L. Salmon, P. Thuéry, E. Rivière, M. Ephritikhine, Inorg. Chem. 45 (2006) 83.
[17] L. Salmon, P. Thuéry, E. Rivière, J.J. Girerd, M. Ephritikhine, Chem. Commun. (2003) 762.
[18] L. Salmon, P. Thuéry, M. Ephritikhine, Polyhedron 22 (2003) 2683.
[19] F.H. Allen, Acta Crystallogr., Sect. B 58 (2002) 380.
[20] R.D. Shannon, Acta Crystallogr., Sect. A 32 (1976) 751.
[21] A. Aguiari, E. Bullita, U. Casellato, P. Guerriero, S. Tamburini, P.A. Vigato, Inorg. Chim. Acta 202 (1992) 157.
[22] J.A. Hermann, J.F. Suttle, Inorg. Synth. 5 (1957) 143.
[23] Kappa-CCD Software, Nonius BV, Delft, The Netherlands, 1998.
[24] Z. Otwinowski, W. Minor, Methods Enzymol. 276 (1997) 307.
[25] G.M. Sheldrick, SHELXS-97 and SHELXL-97, University of Göttingen, Germany, 1997.
[26] A.L. Spek, PLATON, University of Utrecht, The Netherlands, 2000.
[27] B. Dalhus, C.H. Görbitz, Acta Crystallogr., Sect. B 56 (2000) 715.
[28] H.D. Flack, Acta Crystallogr., Sect. A 39 (1983) 876.
[29] G.M. Sheldrick, SHELXTL, Version 5.1, University of Göttingen, Germany, distributed by Bruker AXS, Madison, WI, 1999.

Available online at www.sciencedirect.com
ScienceDirect
Polyhedron 26 (2007) 653–658
POLYHEDRON
www.elsevier.com/locate/poly

Structures and conformations of protonated O_2N_2- and O_2N_3-macrocyclic ligand salts

Lidia Babosa [a], Leonard F. Lindoy [a,b,*], Brian W. Skelton [c], Allan H. White [c]

[a] School of Pharmacy and Molecular Sciences, James Cook University, Townsville, Queensland 4811, Australia
[b] School of Chemistry F11, University of Sydney, Sydney, NSW 2006, Australia
[c] School of Biomedical, Biomolecular and Chemical Sciences, Chemistry M313, University of Western Australia, Crawley 6009, Australia

Received 2 August 2006; accepted 24 August 2006
Available online 3 September 2006

Abstract

Single crystal X-ray structure determinations are described for salts of 5,6,14,15-dibenzo-1,4-dioxa-8,12-diazacyclopentadeca-5,14-diene (L^1) (mono-protonated, as its $F_3CSO_3^-$ ('tfs') salt, and diprotonated, as its nitrate salt) and 5,6,17,18-dibenzo-1,4-dioxa-8,11,15-triazacyclooctadeca-5,17-diene (L^2) (diprotonated, as its tfs salt), defining their protonic hydrogen atom distributions and conformations. In $(L^1H)(tfs)$, an NH group is protonated, the associated hydrogen atoms interacting one within the cation to the other NH group, the other with a tfs oxygen atom. In $(L^1H_2)(NO_3)_2$ (two phases), both NH groups are protonated; in each case, although one NH_2^+ group is oriented so that one of its hydrogen atoms is directed within the ring to the adjacent oxygen atom, there is a competing interaction with a nitrate oxygen atom. All other NH_2^+ hydrogen atoms interact with nitrate oxygen atoms. In $(L^2H_2)(tfs)_2$, the peripheral NH groups are protonated, the protonic hydrogen atoms interacting with tfs anions disposed above and below the macrocycle, making a tight $[(L^2H_2)(tfs)_2]$ cluster.
© 2006 Published by Elsevier Ltd.

Keywords: X-ray; Macrocycles; Protonation; Anion

1. Introduction

A continuing theme in our prior studies has been the design and synthesis of macrocyclic ligands for metal-ion recognition. For example, we have undertaken a number of such studies employing series of mixed-donor macrocycles for which the 15-membered, O_2N_2-system 5,6,14,15-dibenzo-1,4-dioxa-8,12-diazacyclopentadeca-5,14-diene (L^1), and the 17-membered O_2N_3-system, 5,6,17,18-dibenzo-1,4-dioxa-8,11,15-triazacyclooctadeca-5,17-diene (L^2), may be considered to be the parent rings [1,2]. In these studies parameters such as the macrocyclic ring size, its donor atom set, the spacing between donor atoms and the presence of substituents on the nitrogen donor atoms were all varied in a systematic manner while the nature of the interaction with a range of first-row transition and post-transition metal ions was monitored. Such a strategy has resulted in a number of examples of significant metal ion discrimination being observed within the above metal ions series [3–5].

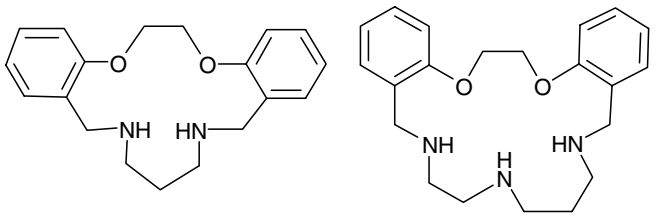
Attempts by us to extend studies of the above type to the trivalent lanthanoid ions were not successful. When we endeavoured to prepare complexes of L^1 and L^2 by reacting them with europium(III) nitrate or trifluoromethanesulfonate (≡ 'triflate' ≡ $F_3CSO_3^-$ ≡ tfs) in ethanol, the crystalline materials isolated were shown by single crystal X-ray studies in three cases to be simply salts of the diversely protonated ligands.

The above behaviour parallels recently reported results [6] describing attempts to form complexes of L^1 with the sodium salts NaX (X = picrate, ClO_4, BF_4, PF_6, SCN,

* Corresponding author. Address: School of Chemistry F11, University of Sydney, Sydney, NSW 2006, Australia. Tel.: +61 2 9351 4400; fax: +61 2 9351 3329.
E-mail address: lindoy@chem.usyd.edu.au (L.F. Lindoy).

0277-5387/$ - see front matter © 2006 Published by Elsevier Ltd.
doi:10.1016/j.poly.2006.08.023

and BPh_4). These studies also resulted in the isolation of metal-free protonated ligand salts of the corresponding anions; the respective products were shown to be mono- and hemi-protonated derivatives containing a diversity of cation···anion interaction types. In view of this, we now wish to augment this record with further structural results for cyclic derivatives of this type, two of which involve diprotonated species. These thus extend the array of forms and types found for such systems, as well as aiding an understanding of the anion binding therein.



L^1 L^2

2. Experimental

The three protonated salts, $(L^1H)(tfs)$, $(L^1H_2)(NO_3)_2$ (two phases) and $(L^2H_2)(tfs)_2$, were obtained on the addition of europium(III) nitrate to a solution of the corresponding free ligand, on a 1:1 millimolar scale, in a few mL of hot ethanol. Colorless crystals of the (europium-free) relevant salts were obtained on allowing the solutions to stand and slowly evaporate at ambient temperature.

2.1. Structure determinations

Initially, unique room-temperature single-counter diffractometer data sets were measured ($2\theta/\theta$ scan mode; monochromatic Mo Kα radiation, $\lambda = 0.7107_3$ Å, $2\theta_{max} = 50°$; T ca. 295 K), yielding N independent data, used without absorption correction in the refinements, N_0 with $I > 3\sigma(I)$ being considered 'observed', refining anisotropic displacement parameter forms for the non-hydrogen atoms, $(x, y, z, U_{iso})_H$ being also refined or constrained at estimates, supported by difference map evidence. The determinations were of indifferent quality and, material for two of the materials having been preserved, redeterminations were undertaken with the advent of a 'low'-temperature CCD facility, full spheres of data being measured (Bruker AXS instrument, ω-scans, $2\theta_{max} = 50°$; T ca. 153 K), $N_{t(otal)}$ reflections being merged (R_{int} cited) after 'empirical'/multi-scan absorption correction (proprietary software), the 'observed' criterion being $F > 4\sigma(F)$. Conventional residuals, R, R_w are cited on $|F|$ at convergence (weights $= (\sigma^2(F) + 0.0004F^2)^{-1}$). Neutral atom complex scattering factors were employed within various versions of the Xtal 3.x program system [7]. Pertinent results are given below and in the figures, the latter showing 20% (295 K), 50% (153 K) probability amplitude displacement ellipsoids for the non-hydrogen atoms, hydrogen atoms having arbitrary radii of 0.1 Å; individual variations in procedure are cited as 'variata'. Full *cif* depositions, which follows a further refinement cycle on F^2, reside with the Cambridge Crystallographic Data Base, CCDC 611987-611990.

2.1.1. Crystal/refinement data

2.1.1.1. $(L^1H)(tfs)$. $C_{20}H_{25}F_3N_2O_5S$, $M = 462.5$, triclinic, space group $P\bar{1}$ (C_i^1, No. 2), $a = 12.485(3)$, $b = 10.365(2)$, $c = 9.275(2)$ Å, $\alpha = 87.03(1)$, $\beta = 69.62(2)$, $\gamma = 89.28(2)°$, $V = 1124$ Å^3. D_c $(Z = 2) = 1.36_7$ g cm^{-3}. $\mu_{mo} = 2.0$ cm^{-1}; specimen: $0.20 \times 0.60 \times 0.25$ mm; $N = 3926$, $N_0 = 2506$; $R = 0.060$, $R_w = 0.065$. $(x, y, z, U_{iso})_H$ refined. Single-counter instrument, T ca. 295 K.

Comment. Displacement parameters were high on the anion components, no disorder being resolvable.

2.1.1.2. $(L^1H_2)(NO_3)_2$. $C_{19}H_{26}N_4O_8$, $M = 438.4$, triclinic, space group $P\bar{1}$.

2.1.1.2.1. Z = 2 form. $a = 12.525(5)$, $b = 10.207(5)$, $c = 9.229(4)$ Å, $\alpha = 68.06(4)$, $\beta = 75.31(3)$, $\gamma = 80.21(4)°$, $V = 1055$ Å^3. $D_c = 1.38_0$ g cm^{-3}. $\mu_{Mo} = 1.1$ cm^{-1}; specimen: $0.08 \times 0.24 \times 0.55$ mm. $N = 3691$, $N_0 = 1489$; $R = 0.073$, $R_w = 0.071$. $(x, y, z, U_{iso})_H$ constrained. Single counter instrument, T ca. 295 K.

2.1.1.2.2. Z = 4 form. $a = 9.067(2)$, $b = 14.774(2)$, $c = 16.018(3)$ Å, $\alpha = 80.233(5)$, $\beta = 80.350(4)$, $\gamma = 87.637(5)°$, $V = 2084$ Å^3. $D_c = 1.39_7$ g cm^{-3}. $\mu_{Mo} = 1.1$ cm^{-1}; specimen: $0.40 \times 0.30 \times 0.05$ mm; 'T'$_{min/max} = 0.88$. $N_t = 42\,995$, $N = 6075$ ($R_{int} = 0.067$), $N_0 = 4512$; $R = 0.064$, $R_w = 0.072$. $(x, y, z, U_{iso})_H$ refined. CCD instrument, T ca. 153 K.

2.1.1.3. $(L^2H_2)(tfs)_2$. $C_{23}H_{31}F_6N_3O_8S_2$, $M = 655.6$. Monoclinic, space group $P2_1/c$ ($C_{2/h}^5$, No. 14), $a = 12.080(4)$, $b = 18.530(6)$, $c = 12.810(4)$ Å, $\beta = 95.758(5)°$, $V = 2853$ Å^3. D_c $(Z = 4) = 1.52_2$ g cm^{-3}. $\mu_{Mo} = 2.8$ cm^{-1}; specimen: $0.19 \times 0.09 \times 0.05$ mm; 'T'$_{min/max} = 0.82$. $N_t = 21\,677$, $N = 4830$ ($R_{int} = 0.10$), $N_0 = 2972$; $R = 0.064$, $R_w = 0.080$. $(x, y, z, U_{iso})_H$ constrained. CCD instrument, T ca. 153 K.

3. Results and discussion

In the recent report [6] mentioned above, the structural characterization of the metal-free products crystallized from methanol solutions of the sodium salts (NaX) and L^1 were described. In these studies ratios of NaX:L^1 of 1:1 were employed for the reactions in the presence of picrate and BPh_4 counterions (=X), yielding for the picrate, $(HL^1)(pic)$, and for BPh_4, $(H_2L_3^1)(BPh_4)_2$. The latter was not structurally characterized but was shown to yield $(HL)(BPh_4)$ on recrystallization from acetonitrile and the structure of this product was obtained. This latter product was also obtained when the synthesis was carried out directly in acetonitrile. For $X = ClO_4$, BF_4, PF_6, SCN, ratios of NaX:L^1 of 1:2 were employed, with the products in these cases having novel $(HL_2^1)X$ stoichiometries.

In the present work, the results of our single crystal X-ray structure determinations are in general consistent

with the above formulations. In our case the crystallization of L^1 or L^2 with europium(III) nitrate or triflate in 1:1 ratio from ethanol yielded unsolvated products of type $(HL^1)(tfs)$, $(H_2L^1)(NO_3)_2$ and $(H_2L^2)(tfs)_2$. All three are metal free and the first two show a generally higher degree of protonation for L^1 (with one exception). This is consistent with the use of the trivalent lanthanoid species, which are more acidic than the group 1 metal ions in solution. A

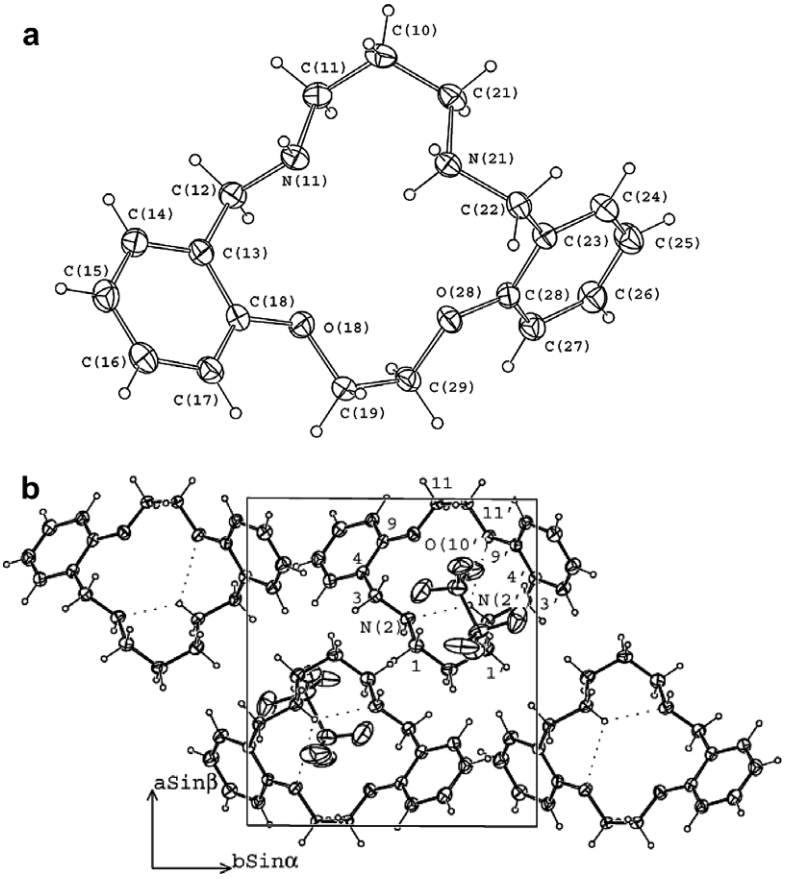


Fig. 1. (a) The $(L^1H)^+$ cation in $(L^1H)(tfs)$. (b) Unit cell contents of $(L^1H)(tfs)$, projected down *c*.

Table 1
$NH_{(2)}\cdots O$ hydrogen-bonding interactions

Atoms	Distance (Å)	Atoms	Distance (Å)
(a) $(L^1H)(tfs)$			
N(21), H(21C)···N(11)	2.876(4), 2.23(2)		
H(21D)···O(13)	2.877(3), 2.04(2)		
(b) $(L^1H_2)(NO_3)_2$ ($P\bar{1}, Z = 2$ phase)			
N(11), H(11C)···O(11^i)	2.848(6), 1.9_6	N(21), H(21C)···O(11)	2.956(10), 2.1_6
H(11D)···O(23)	2.861(7), 2.1_6	H(21D)···O(22^i)	2.916(8), 2.0^*_8
Transformations of the asymmetric unit i: $x, y, z-1$; ii: $1-x, 1-y, 1-z$			
*To O(21^i) are 3.016(10), 2.2_0			
(c) $(L^1H_2)(NO_3)_2$ ($P\bar{1}, Z = 4$ phase)			
N(11), H(11C)···O(11^i)	2.897(3), 2.0_8	N(31), H(31C)···O(42^{iii})	2.803(3), 1.9_0
H(11D)···O(32)	2.813(3), 1.9_1	H(31D)···O(22^{iii})	2.900(3), 2.2_8
N(21), H(21C)···O(23)	2.805(3), 1.8_8	N(41), H(41C)···O(12^{iv})	2.936(3), 2.0_6
H(21D)···O(32^{ii})	2.842(3), 2.0_5	H(41D)···O(42^{iv})	2.884(3), 2.0_8
Transformations of the asymmetric unit i: $x-1, y, z$; ii: $x+1, y, z$; iii: $1-x, 2-y, 1-z$; iv: $2-x, 2-y, 1-z$			
(d) $(L^2H_2)(tfs)_2$			
N(12), H(12C)···O(21)	2.885(5), 1.9_7	N(21), H(21C)···O(13)	2.992(6), 2.2_9
H(12D)···O(13)	2.983(5), 2.1_1	H(21D)···O(11)	2.895(5), 2.1_1
N(10), H(10)···O(22)	3.118(5), 2.3_6		

Table 2
Torsion angles in the $L^1H_{1,2}$ macrocycles (°)

Atoms	$n = 1$[a]	$n = 2$[a]
$n'1$–$n0$–$n1$–N($n1$)	**69.2(4)**; *−52.4(7)*; −51.5(4), −51.0(3)	**−64.2(4)**; *−164.5(2)*; −167.0(2), −160.3(2)
$n0$–$n1$–N($n1$)–$n2$	**179.4(3)**; *−57.1(6)*; −51.8(4), −60.9(3)	**−176.3(2)**; *−164.2(5)*; −168.5(2), −167.6(2)
$n1$–N($n1$)–$n2$–$n3$	**−171.6(2)**; *−179.9(3)*; 177.8(3), −175.9(3)	**−64.8(4)**; *−64.4(6)*; −62.6(3), −63.4(3)
N($n1$)–$n2$–$n3$–$n8$	**−73.1(3)**; *−69.7(6)*; −71.8(3), −68.4(7)	**−71.5(4)**; *91.2(5)*; 88.9(3), 89.2(3)
$n2$–$n3$–$n8$–O($n8$)	**−2.4(4)**; *7.0(7)*; 7.1(4), 5.7(4)	**1.0(5)**; *−0.2(5)*; 2.5(4), −1.0(4)
$n3$–$n8$–O($n8$)–$n9$	**179.5(3)**; *−174.1(5)*; −173.4(2), −175.4(3)	**178.7(3)**; *−176.2(4)*; −173.8(2), −177.9(3)
$n8$–O($n8$)–$n9$–$n'9$	**179.3(2)**; *−154.9(5)*; −159.5(2), −150.2(3)	**−174.5(3)**; *−177.1(4)*; 177.0(2), −177.7(3)
O($n8$)–$n9$–$n'9$–O($n'8$)	**66.0(3)**; *−66.0(6)*; −67.6(3), −64.6(4)	
θ		**65.6(2)**; *49.2(3)*; 52.0(2), 50.4(2)

Carbon atoms are denoted by number only; the three values in each entry are for (**L^{1}H**)(tfs); $(L^1H_2)(NO_3)_2$ ($Z = 2$ form); $(L^1H_2)(NO_3)_2$ ($Z = 4$ form; two cations). θ is the interplanar dihedral angle between the pair of aromatic C_6 ring planes; n' denotes the alternate ligand segment.
[a] In the $Z = 4$ (triclinic) nitrate, for $n = 1$, 2 read $n = 3$, 4.

consequence of the lower ratio of X to protonated ligand in the ClO_4, BF_4, PF_6, SCN arrays, in which, as in all arrays under discussion, the ring NH groups are protonated rather than O, is a propensity toward hydrogen-bonding either within the macrocycle (NH···N or NH···O) or between adjacent macrocycles (NH···N). Despite the differing degree of protonation between the compounds of Ref. [6], the macrocycle conformations of the L^1 arrays are similar throughout, as indicated persuasively by Fig. 10 of this reference.

In the structure of (L^1H)(tfs), (Fig. 1, Tables 1 and 2), one formula unit, devoid of crystallographic symmetry, comprises the asymmetric unit of the structure, containing the only singly protonated cation of the present array of compounds. The macrocycle conformation (Fig. 1, Table 2) is the same as that found in the previous study [6]. Hydrogen-bonding is found from the protonated NH_2^+ (21) grouping, the hydrogen atoms being disposed so that one H(21C) is directed toward the unprotonated N(11) with a longer distance across the ring toward O(28) [N(21), H(21C)···O(28) 3.021(3), 2.5, Å]. The other hydrogen atom, H(21D), interacts with one of the tfs anion oxygen atoms so that an ion-pair is formed.

Remarkably, the specimen defined at low-temperature for $(L^1H_2)(NO_3)_2$ differs from that occurring at room-temperature, the former having two independent formula units devoid of crystallographic symmetry comprising the asymmetric unit of the structure (153 K, $Z = 4$), while the other (295 K, $Z = 2$) has one. Both forms are triclinic, $P\bar{1}$, each with a short axis ca. 9.1 Å; both have overlapping cation strings, running along a in the $Z = 2$ form, and the bc cell diagonal in the $Z = 4$ form. The most immediately obvious difference lies in the disposition of the anions, the two independent nitrate groups lying quasi-parallel to the short cell axis in the $Z = 2$ form, while in the $Z = 4$ form nitrate groups 2, 3 are thus disposed, with nitrate 1 quasi-normal to the axis (Figs. 2 and 3). The macrocycle conformations are similar throughout the three independently defined specimens (Table 2) and different to that of the less heavily protonated forms discussed previously. Within the macrocycle, the conformation of the C_3 string between the pair of nitrogen atoms is now such that the NH···N intra-cation

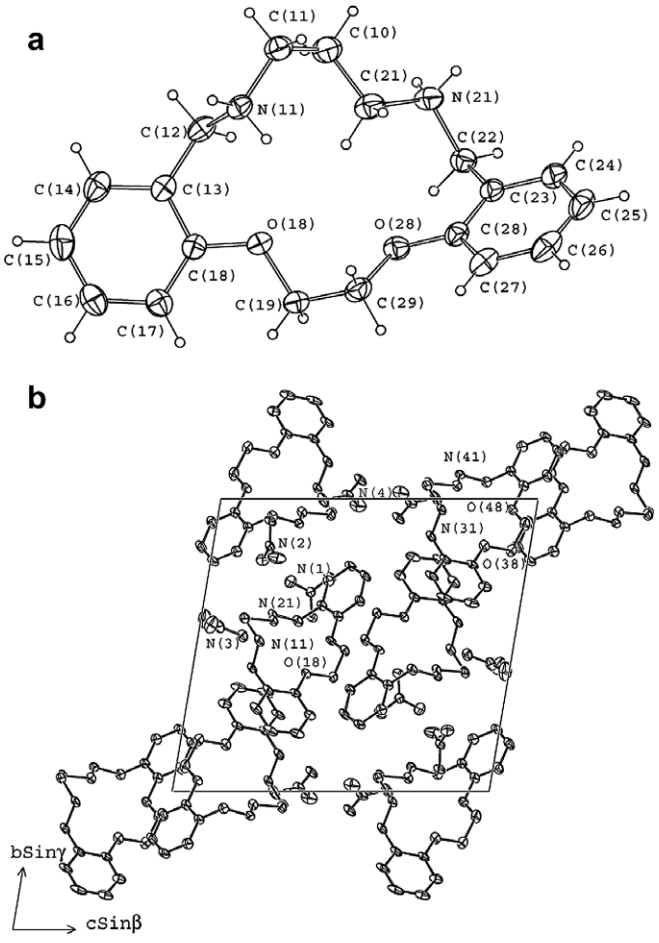


Fig. 2. (a) The $(L^1H_2)^{2+}$ cation in $(L^1H_2)(NO_3)_2$ ($Z = 2$ form). (b) Unit cell contents of $(L^1H_2)(NO_3)_2$ ($Z = 2$ form) projected down a.

interactions found in the mono-protonated forms are no longer feasible. The nitrogen atoms of each ring are oriented so that for each there is still indeed an '*endo*'-NH hydrogen atom, but its proximity to the associated oxygen atom is now appreciably closer. In the $Z = 2$ form, all NH hydrogen atoms interact with the nitrate groups, two of these with nitrate 1 with a pair of such anions related by a simple translation along the short axis, thus generating a strand of alternating anions and cations in that dimension,

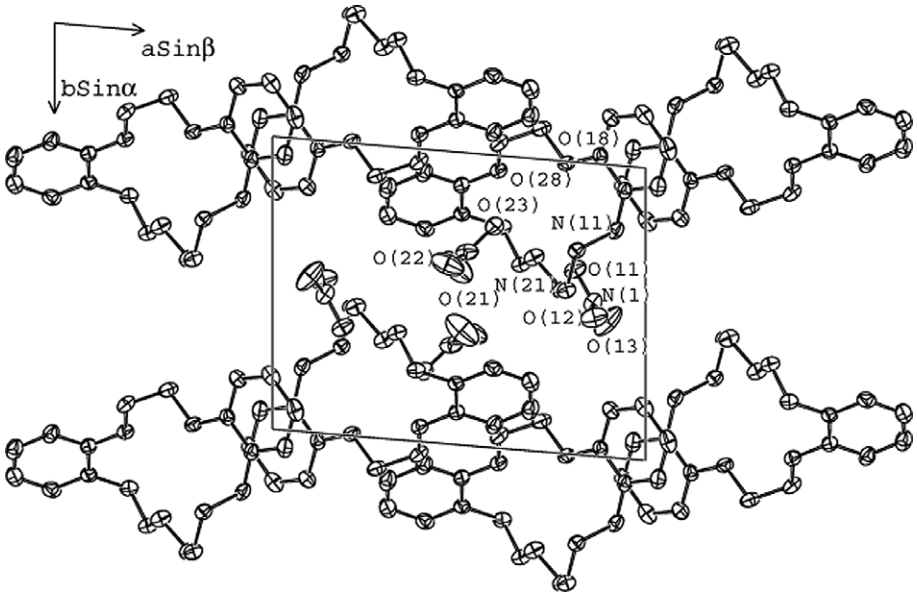


Fig. 3. Unit cell contents of $(L^1H_2)(NO_3)_2$ ($Z = 4$ form), projected down c.

Table 3
Torsion angles $(L^2H_2)(tfs)_2$ (°)

Atoms	Angle	Atoms	Angle
20–N(10)–10–11	−173.0(5)	10–N(10)–20–21	−167.5(5)
N(10)–10–11–12	−65.3(6)		
10–11–12–N(12)	68.4(6)	N(10)–20–21–N(21)	71.5(5)
11–12–N(12)–13	148.2(4)	20–21–N(21)–22	173.4(5)
12–N(12)–13–14	70.4(5)	21–N(21)–22–23	−177.3(4)
N(12)–13–14–19	85.0(5)	N(21)–22–23–28	−79.9(6)
13–14–19–O(19)	−2.9(6)	22–23–28–O(28)	4.9(7)
14–19–O(19)–30	177.8(4)	23–28–O(28)–29	−177.3(5)
19–O(19)–30–29	−179.5(4)	28–O(28)–29–30	−77.2(6)
O(19)–30–29–28	−79.2(5)	θ	69.6(2)

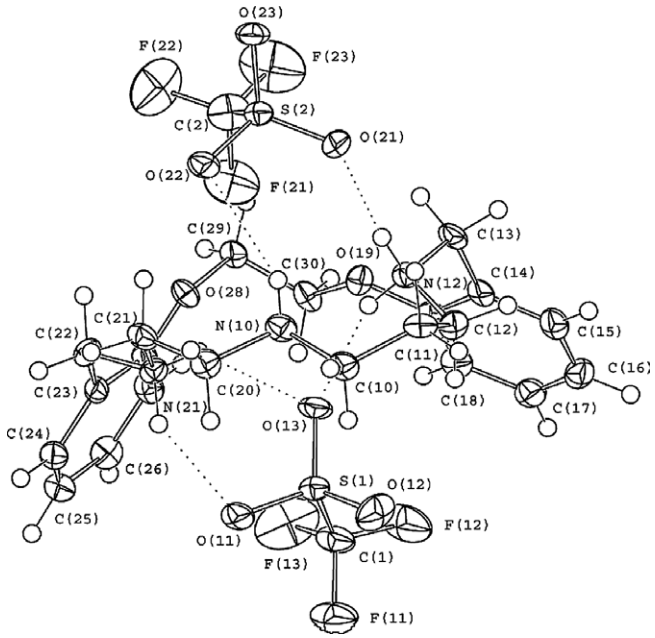


Fig. 4. The $[(L^2H_2)(tfs)_2]$ aggregate.

with similar inversion related interactions with nitrate 2 linking the cations along b, resulting in a two-dimensional web. The dispositions in the $Z = 4$ form are rather similar, nitrates 3 linking cations 1 along a, with nitrates 1, 2 linking in the other dimensions to cations 2, and nitrates 4 linking cations 2 along a.

In $(L^2H_2)(tfs)_2$, the cation is also diprotonated, the protonic hydrogen atoms being associated with the peripheral rather than the central nitrogen atom, which has none of the protonic hydrogen atoms in its near vicinity, similarly true of the macrocycle oxygen atoms; one formula unit, devoid of crystallographic symmetry, comprises the asymmetric unit of the structure. Here the interactions between cation and anion are tight and unambiguously confined within the asymmetric unit, forming a cluster $[(L^2H_2)(tfs)_2]$ with anion 1 approaching to one side of the macrocycle, O(11) interacting with H(21D) and O(13) with H(12D, 21C), and anion 2 from the other side, O(21) interacting with H(12C) and O(22), less strongly, with the central NH hydrogen atom H(10) (Tables 1 and 3, Fig. 4).

4. Concluding remarks

The present results extend the known protonated forms of the O_2N_2-donor macrocycle L^1 as well as providing a comparative structure of a related protonated O_2N_3-donor structure. They also show that under the conditions employed, the affinities of L^1 and L^2 for protons are higher than for europium(III). Further, they provide insight into the modes of anion binding in such macrocyclic species, a topic of much current interest [8,9] with implications for a range of biological, sensing, separation (including ion exchange and solvent extraction) applications.

Acknowledgement

We thank the Australian Research Council for support.

Appendix A. Supplementary data

Supplementary data associated with this article can be found, in the online version, at doi:10.1016/j.poly.2006.08.023.

References

[1] (a) K.R. Adam, L.F. Lindoy, H.C. Lip, J.H. Rea, B.W. Skelton, A.H. White, J. Chem. Soc., Dalton Trans. (1981) 74;
(b) K.R. Adam, A.J. Leong, L.F. Lindoy, H.C. Lip, B.W. Skelton, A.H. White, J. Am. Chem. Soc. 105 (1983) 4645;
(c) D.S. Baldwin, P.A. Duckworth, G.R. Erickson, L.F. Lindoy, M. McPartlin, G.M. Mockler, W.E. Moody, P.A. Tasker, Aust. J. Chem. 40 (1987) 1861;
(d) K.R. Adam, A.J. Leong, L.F. Lindoy, G. Anderegg, J. Chem. Soc., Dalton Trans. (1988) 1733, and references therein;
(e) P.A. Duckworth, L.F. Lindoy, M. McPartlin, P.A. Tasker, Aust. J. Chem. 46 (1993) 1787.

[2] D.S. Baldwin, B.F. Bowden, P.A. Duckworth, L.F. Lindoy, B. McCool, G.V. Meehan, I. Vasilescu, S.B. Wild, Aust. J. Chem. 55 (2002) 597.

[3] K.R. Adam, M. Antolovich, D.S. Baldwin, L.G. Brigden, P.A. Duckworth, L.F. Lindoy, A. Bashall, M. McPartlin, P.A. Tasker, J. Chem. Soc., Dalton Trans. (1992) 1869.

[4] K.R. Adam, D.S. Baldwin, P.A. Duckworth, L.F. Lindoy, M. McPartlin, A. Barshall, H.R. Powell, P.A. Tasker, J. Chem. Soc., Dalton Trans. (1995) 1127.

[5] K.R. Adam, D.S. Baldwin, L.F. Lindoy, G.V. Meehan, I. Vasilescu, G. Wei, Inorg. Chim. Acta 352 (2003) 46.

[6] L. Tušek-Božić, A. Višnjevac, E. Marotta, B. Kojic-Prodić, Polyhedron 24 (2005) 97.

[7] For example S.R. Hall, D.J. du Boulay, R. Olthof-Hazekamp (Eds.), 'The Xtal 3.7 System', University of Western Australia, 2001.

[8] J.L. Sessler, W.-S. Cho, P.A. Gale, Anion Receptor Chemistry, RSC, UK, 2006.

[9] K. Wichmann, B. Antonioli, T. Söhnel, M. Wenzel, K. Gloe, K. Gloe, J.R. Price, L.F. Lindoy, C. Wilson, M. Schröder, Coord. Chem. Rev., in press, doi:10.1016/j.ccr.2006.07.010.

Available online at www.sciencedirect.com
ScienceDirect
Polyhedron 26 (2007) 659–672
POLYHEDRON
www.elsevier.com/locate/poly

Structure, stacking interactions and magnetism of compounds with oxalate-bridged dinuclear $Cu^{II}Cu^{II}$ and $Cu^{II}Nb^{V}$ units

Marijana Jurić [a], Berislav Perić [a], Nevenka Brničević [a,*], Pavica Planinić [a], Damir Pajić [b], Krešo Zadro [b], Gerald Giester [c]

[a] *Ruđer Bošković Institute, Bijenička cesta 54, 10000 Zagreb, Croatia*
[b] *Department of Physics, Faculty of Science, University of Zagreb, Bijenička cesta 32, 10000 Zagreb, Croatia*
[c] *Institut für Mineralogie und Kristallographie, Universität Wien – Geozentrum, Althanstraße 14, 1090 Wien, Austria*

Received 21 July 2006; accepted 25 August 2006
Available online 3 September 2006

Abstract

Two novel compounds of the formulae $[\{Cu(phen)_2\}_2(\mu\text{-}C_2O_4)][Cu(phen)_2(\mu\text{-}C_2O_4)NbO(C_2O_4)_2]_2 \cdot 8H_2O$ (**1**) and $[\{Cu(bpy)_2\}_2(\mu\text{-}C_2O_4)][Cu(bpy)_2(\mu\text{-}C_2O_4)NbO(C_2O_4)_2]_2 \cdot 0.5bpy \cdot 7H_2O$ (**2**) (phen = 1,10-phenanthroline, bpy = 2,2′-bipyridine) have been prepared and characterized by single crystal X-ray diffraction, IR spectroscopy and magnetic susceptibility measurements. The molecular structure of both **1** and **2** consists of a discrete $Cu^{II}Cu^{II}$ oxalate-bridged dinuclear $[\{Cu(L)_2\}_2(\mu\text{-}C_2O_4)]^{2+}$ cation (**A** unit) and two $Cu^{II}Nb^{V}$ oxalate-bridged dinuclear $[Cu(L)_2(\mu\text{-}C_2O_4)NbO(C_2O_4)_2]^{-}$ anions (**B** units) (L = phen, bpy). In **1** a crystallographic inversion centre is located in the middle of the oxalate bridge of the **A** unit, whereas in **2** an analogous inversion centre is missing. In the **A** units the copper(II) atoms adopt a tetragonally elongated octahedral coordination with the equatorial planes being perpendicular to the mean planes of the oxalate bridge and parallel to each other. In both structures, similar one-dimensional motifs are generated through the ligand stacking interactions, with a difference that one free bipyridine molecule, present in **2**, intercalates into one of the motifs. It is shown that the phenanthroline ligand, due to its ability of stacking through the central aromatic ring, causes longer intermolecular Cu···Cu distances than the bipyridine ligand. The magnetic susceptibility measurements (1.8–290 K) show the ferromagnetic exchange interaction between the copper(II) atoms in the **A** units of both compounds, with $J = +5.9\ cm^{-1}$ and $+7.9\ cm^{-1}$ for **1** and **2**, respectively (J – the exchange parameter in the isotropic spin Hamiltonian $\mathbf{H}_{INT} = -J\mathbf{S}_1 \cdot \mathbf{S}_2$).
© 2006 Elsevier Ltd. All rights reserved.

Keywords: Copper–niobium complexes; Dinuclear units; Crystal structures; Oxalate bridges; Ferromagnetic interaction

1. Introduction

The use of tris(oxalato)metallates, $[M^{III}(C_2O_4)_3]^{3-}$ (M^{III} = Cr, Fe, Ru, V), in the synthesis of new homo- or heterometallic oxalate-bridged complex systems is constantly growing. In the reactions of these anions with organic and inorganic cations different structure types resulted ranging from discrete polynuclear metal species [1–3] to polymeric one- (1D) [4,5], two- (2D) [6–13] or three-dimensional (3D) [14–16] assemblies. In these investigations the scientists have been trying to couple two or more paramagnetic metal centres using the oxalate $C_2O_4^{2-}$ anion, due to its ability of exhibiting a bis(bidendate) bridging coordination mode and to mediate the magnetic exchange interaction between metal ions. In general, the magnetic properties of these systems follow their structure types.

Within the discrete molecules ferro- or antiferromagnetic exchange interactions have been found [1–3]. The 1D structure of $[K(18\text{-crown-6})][Mn(H_2O)_2Cr(C_2O_4)_3] \cdot 0.5(18\text{-crown-6})$ (18-crown-6 = $C_{12}H_{24}O_6$) shows the ferromagnetic coupling within the chains as well as between the

* Corresponding author. Tel.: +385 1 456 1189; fax: +385 1 468 0098.
E-mail address: brnicevi@irb.hr (N. Brničević).

0277-5387/$ - see front matter © 2006 Elsevier Ltd. All rights reserved.
doi:10.1016/j.poly.2006.08.024

chains reaching the bulk ferromagnetic ordering below 3.5 K [5]. The long-range magnetic order has been detected for the 2D honeycomb layered structured compound of the composition $A[M^{II}M^{III}(C_2O_4)_3]$ (A = organic monocation; M^{II} = Mn, Fe, Co, Ni, Cu, Zn, V; M^{III} = Cr, Fe, Ru, V). Ferro- or ferrimagnets are formed depending on metal ion, with T_c values in the range 5–14 K for $[M^{II}Cr^{III}(C_2O_4)_3]^-$ [6,8,10], and 13 K for $[Fe^{II}Ru^{III}(C_2O_4)_3]^-$ [11,12]. Compounds $A[V^{II}V^{III}(C_2O_4)_3]$ and $A[V^{II}V^{III}(C_2O_4)_3(H_2O)_2]$ order as ferrimagnets at 11 and 30 K, respectively [13]. A series of compounds $[Fe^{II}Fe^{III}(C_2O_4)_3]^-$ behave as ferrimagnets with T_c in the range 33–48 K [9]. The long-range ferromagnetic order with T_c up to 6.6 K within the 3D structures of tris(oxalato)metallates was found for a series of compounds $[Z^{II}(bpy)_3][ClO_4][M^{II}Cr^{III}(C_2O_4)_3]$ (Z^{II} = Ru, Fe, Co, Ni; M^{II} = Mn, Fe, Co, Ni, Cu, Zn) [16].

In relation to the study with tris(oxalato)metallates we have extended the investigations to the complex oxotris(oxalato)niobate(V) anion, $[NbO(C_2O_4)_3]^{3-}$, investigated earlier in our laboratory [17]. Unexpectedly, in the reaction of this anion with $CuCl_2 \cdot 2H_2O$ and ethanol solution of 1,10-phenanthroline we have isolated $[\{Cu(phen)_2\}_2(\mu\text{-}C_2O_4)][Cu(phen)_2(\mu\text{-}C_2O_4)NbO(C_2O_4)_2]_2 \cdot 8H_2O$ (**1**), and in the reaction with $[Cu(bpy)_3]Cl_2 \cdot 6H_2O$ the compound $[\{Cu(bpy)_2\}_2(\mu\text{-}C_2O_4)][Cu(bpy)_2(\mu\text{-}C_2O_4)NbO(C_2O_4)_2]_2 \cdot 0.5bpy \cdot 7H_2O$ (**2**) has formed. Both compounds contain $Cu^{II}Cu^{II}$ and $Cu^{II}Nb^{V}$ oxalate-bridged dinuclear units with a ferromagnetic spin-exchange interaction within the former.

2. Experimental

2.1. Materials

All reagents used in the syntheses were purchased from commercial sources and applied without further purification. Synthesis of $(NH_4)_3[NbO(C_2O_4)_3] \cdot H_2O$ and $[Cu(bpy)_3]Cl_2 \cdot 6H_2O$ was performed according to the methods in the literature [18–20].

2.2. Synthesis of the complexes

2.2.1. $[\{Cu(phen)_2\}_2(\mu\text{-}C_2O_4)][Cu(phen)_2(\mu\text{-}C_2O_4)NbO(C_2O_4)_2]_2 \cdot 8H_2O$ (*1*)

To an aqueous solution (10 mL) of $(NH_4)_3[NbO(C_2O_4)_3] \cdot H_2O$ (0.106 g, 0.238 mmol) an aqueous solution (5 mL) of $CuCl_2 \cdot 2H_2O$ (0.081 g, 0.477 mmol) and an ethanol solution (5 mL) of phen (0.189 g, 0.953 mmol) were added dropwise by stirring at room temperature. Immediately, the reaction mixture became cloudy forming a blue precipitate, which was removed by filtration. Almost at the same time two kinds of single crystals started to grow up: blue needles of $[Cu(phen)(C_2O_4)H_2O] \cdot H_2O$ [21] and light green polyhedral crystals of **1**. They were separated mechanically. The green crystals of **1** were washed with water and dried in air. The yield was 0.046 g, 17% (based on Nb). *Anal.* Calc. for $C_{110}H_{80}Cu_4Nb_2N_{16}O_{38}$ (M_r = 2673.88): C, 49.41; H, 3.02; N, 8.38. Found: C, 49.72; H, 3.12; N, 8.51%. IR $\tilde{\nu}/cm^{-1}$: 3422 (m, br), 3060 (w), 1735 (w), 1710 (vs), 1692 (vs), 1647 (sh), 1630 (vs), 1585 (m), 1517 (m), 1493 (w), 1453 (w), 1427 (s), 1401 (s), 1362 (s), 1341 (m), 1295 (m), 1250 (m), 1223 (w), 1153 (w), 1142 (w), 1105 (w), 1090 (w), 1035 (w), 1001 (w), 943 (m), 906 (m), 868 (sh), 853 (s), 802 (m), 793 (m), 724 (s), 651 (w), 644 (w), 541 (w), 475 (w), 428 (w), 397 (w), 364 (w), 333 (w).

2.2.2. $[\{Cu(bpy)_2\}_2(\mu\text{-}C_2O_4)][Cu(bpy)_2(\mu\text{-}C_2O_4)NbO(C_2O_4)_2]_2 \cdot 0.5bpy \cdot 7H_2O$ (*2*)

After mixing an aqueous solution (10 mL) of $(NH_4)_3[NbO(C_2O_4)_3] \cdot H_2O$ (0.104 g, 0.234 mmol) and an aqueous solution (10 mL) of $[Cu(bpy)_3]Cl_2 \cdot 6H_2O$ (0.166 g, 0.234 mmol) the resulting blue solution became cloudy and a blue precipitate formed. The reaction mixture was left for 24 h when the precipitate was removed by filtration. The filtrate was allowed to concentrate slowly at ambient conditions. In the period of five days blue polyhedra-like single crystals of **2** were obtained, which were filtered off, washed with water and dried in air. The yield was 0.086 g, 58% (based on Cu). *Anal.* Calc. for $C_{99}H_{82}Cu_4Nb_2N_{17}O_{37}$ (M_r = 2541.80): C, 46.78; H, 3.25; N, 9.37. Found: C, 46.48; H, 3.22; N, 9.34%. IR $\tilde{\nu}/cm^{-1}$: 3425 (m, br), 3074 (w), 1730 (sh), 1711 (vs), 1687 (vs), 1648 (sh), 1631 (s), 1598 (s), 1493 (m), 1474 (m), 1443 (s), 1376 (s), 1316 (m), 1301 (w), 1286 (sh), 1242 (w), 1178 (w), 1160 (w), 1101 (w), 1060 (w), 1045 (w), 1029 (m), 1014 (w), 933 (m), 904 (m), 801 (m), 792 (m), 775 (s), 734 (m), 650 (w), 633 (w), 543 (w), 482 (w), 421 (w), 397 (w), 362 (w), 339 (m).

2.3. Physical measurements

Elemental analyses for C, H and N were carried out using a Perkin–Elmer Model 2400 microanalytical analyser.

Infrared spectra were recorded as KBr pellets on an ABB Bomem FT model MB 102 spectrometer in the 4000–200 cm^{-1} region.

The magnetic data for **1** and **2** were collected on a commercial SQUID magnetometer (MPMS-5, Quantum Design). The measurements were performed in the temperature range 1.8–290 K for the applied magnetic field of 1 T. The field dependence of the magnetic moments was checked up to 5 T and both compounds showed linearity up to more than 1 T; therefore, the susceptibilities analyzed here are field-independent. Prior to any calculation, the measured data were corrected against the sample holder's contribution. Diamagnetic corrections for the constituent atoms were estimated from the Pascal's constants [22] and found to be -1389×10^{-6} cm^3 mol^{-1} (**1**) and -1034×10^{-6} cm^3 mol^{-1} (**2**). The magnetic susceptibilities were also corrected for the temperature-independent paramagnetism (60×10^{-6} cm^3 mol^{-1} per Cu^{II}) [23].

2.4. X-ray crystallographic study

Suitable single crystals of **1** and **2** were selected and mounted on an Enraf-Nonius Kappa CCD diffractometer. All data were collected by graphite monochromated Mo-Kα radiation ($\lambda = 0.71073$ Å) at 200 K. Crystals of dimensions small enough (ca. $0.12 \times 0.1 \times 0.1$ mm) to avoid errors generated by the absorption of the X-rays in the samples were chosen. Data reduction and determination of the unit cell parameters were performed using the DENZO-SCALEPACK program [24].

Both structures were solved and refined by the SHELXS-97 and SHELXL-97 programs [25,26]. The majority of non-hydrogen atoms were found by direct methods and the rest of them were located from subsequent difference Fourier syntheses. All non-hydrogen atoms were refined with anisotropic thermal displacement parameters (ADP) and hydrogen atoms were treated with isotropic thermal displacement parameters. Hydrogen atoms from phenanthroline or bipyridine moieties were placed in the calculated positions and restrained to ride on the atoms to which they were bonded, with $U_{iso}(H) = 1.2U_{eq}(C)$. Starting positions of hydrogen atoms from crystal water molecules were located by the M. Nardelli algorithm [27] implemented in the WINGX program [28]. Later on, the crystal water molecules were treated as rigid groups [O–H distances of 0.84 Å, H–O–H angles of 104°, $U_{iso}(H) = 1.2U_{eq}(O)$], leaving rotations of the molecules to be free. To improve convergence of the last refinement cycles, few additional restraints were added. For compound **2** we found that the O34, C56, C57 and C58 atoms possess somewhat unusual (elongated) ADP parameters. Details on crystallographic structural analyses of compounds **1** and **2** are summarized in Table 1.

Table 1
Crystallographic data for compounds **1** and **2**

	1	**2**
Empirical formula	$C_{110}H_{80}Cu_4Nb_2N_{16}O_{38}$	$C_{99}H_{82}Cu_4Nb_2N_{17}O_{37}$
Formula weight	2673.88	2541.80
Crystal system	triclinic	triclinic
Space group	$P\bar{1}$	$P\bar{1}$
a (Å)	10.9529(2)	15.974(1)
b (Å)	15.4513(2)	16.241(1)
c (Å)	17.3336(3)	21.436(2)
α (°)	101.317(1)	70.23(1)
β (°)	103.525(1)	82.17(1)
γ (°)	108.088(1)	85.22(1)
V (Å^3)	2593.93(7)	5180.5(7)
Z	1	2
D_{calc} (g cm^{-3})	1.712	1.629
μ (cm^{-1})	1.120	1.116
$F(000)$	2708	2578
Θ_{max} (°)	30.48	30.51
Reflections collected	29225	62552
Unique reflections	15591	31506
Observed reflections	9873	22403
Number of parameters	778	1453
R_1 ($I > 2\sigma(I)$), wR_2	0.0479, 0.1291	0.0461, 0.1354
Goodness-of-fit	1.026	1.046
$\Delta\rho_{max}$, $\Delta\rho_{min}$	1.453, −0.822	2.432, −2.520

3. Results and discussion

3.1. Molecular structures

Both compounds **1** and **2** contain one oxalate-bridged $Cu^{II}Cu^{II}$ unit (**A**) and two oxalate-bridged $Cu^{II}Nb^{V}$ units (**B**) (Figs. 1 and 2). In **1**, there is a crystallographic inversion centre in the middle of the oxalate bridge of the **A** unit; in this way, just one half of the **A** unit and only one of the two **B** units are symmetrically independent (Fig. 1). In **2**, the lack of an analogous crystallographic centre of symmetry in the **A** unit, results in crystallographic independency of all atoms, in the **A** unit as well as in both of the **B** units (**B1** and **B2**). Units of the **A** type possess an approximate $2/m$ molecular symmetry in both compounds.

In **1** and **2** the copper(II) atoms (d^9 configuration) are octahedrally coordinated by four nitrogen atoms from the two phenanthroline or bipyridine ligands, respectively, and by two oxygen atoms from the bridging oxalate groups. In addition to the expected trigonal distortion (three bidendate ligands), a tetragonal elongation in the Cu environment is also observed. In the **A** unit of **1**, the O4 and N3 atoms are connected to the Cu1 atom at distances that are in average for 0.29 Å larger than for the other four atoms (Table 2). Thus, Cu1 is located in a tetragonally elongated coordination environment with the four-fold axis roughly matching the Cu1–O4 and Cu1–N3 bonds direction. With respect to the **A** unit of **2**, the Cu1–N2 and Cu1–O3 bond lengths are in average for 0.26 Å larger than the other four [around Cu1] and the Cu2–O5 and Cu2–N6 bond lengths are in average for 0.23 Å larger than the others [around Cu2] (Table 1), confirming a tetragonally elongated coordination of the Cu atoms. Tetragonal elongation of the ligand field is very frequent for copper(II) ions [23] and this is a nice example of the Jahn-Teller effect; the system with an orbitally degenerate ground state (^2E_g, for a perfect octahedral ligand field) spontaneously undergoes a tetragonal distortion reaching the orbitally non-degenerate $^2B_1$ ground state. More precisely, the Cu1 atom in **1** and the Cu1 and Cu2 atoms in **2** are parts of the *cis*-CuN_4O_2 chromophores, which cannot be described in a perfect octahedral symmetry; since, the observed elongations are consequences of a pseudo Jahn-Teller effect [30]. Anyway, these elongations enable us to identify the topology and the type of the atomic Cu orbitals ($d_{x^2-y^2}$ or d_{z^2}) that should be considered as the main parts of the magnetic orbitals, i.e. the orbitals carrying one unpaired electron (spin). In tetragonally elongated environments, $d_{x^2-y^2}$ should be singly occupied [23,30]. The lobes of the $d_{x^2-y^2}$ orbital should be oriented toward the 4 nearest atoms in the coordination environment of Cu atoms. Therefore, the magnetic orbital of the Cu1 atom in **1** should lie in the mean plane of the N1, N2, N4 and O3 atoms and due to the crystallographic centre of symmetry,

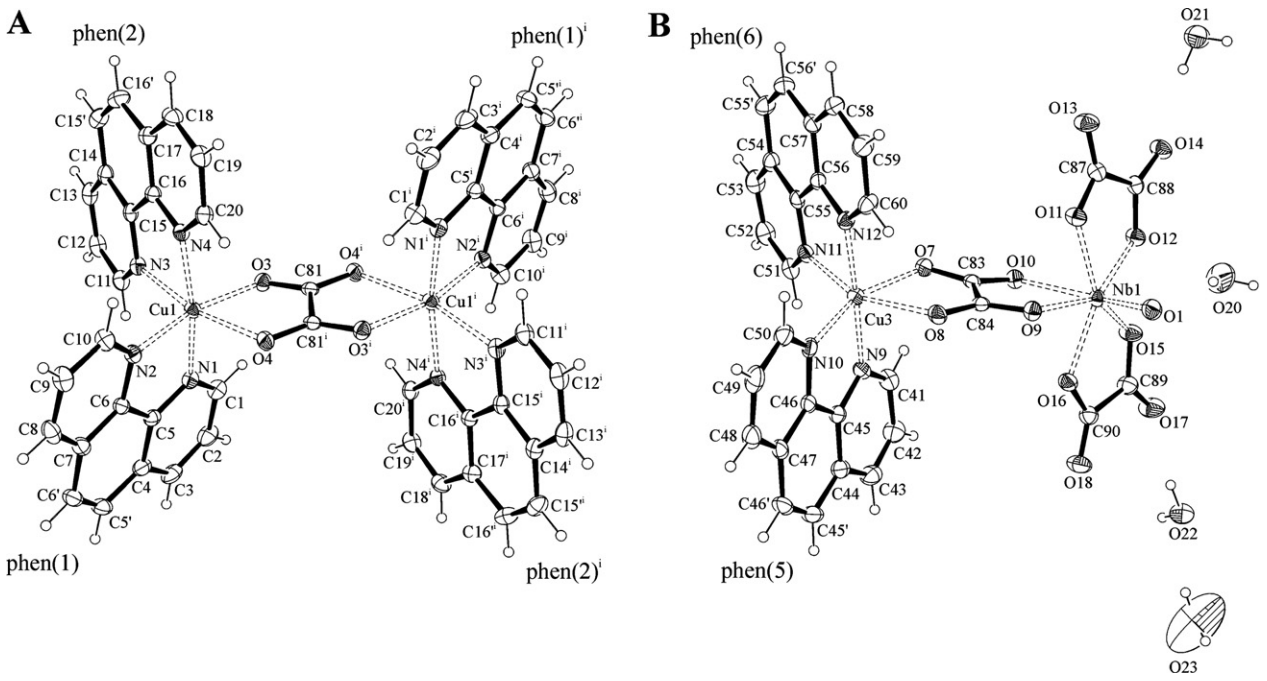


Fig. 1. ORTEP-III drawings [29] of the molecular structure of **1** with atom numbering scheme [symmetry code: (i) $1-x, -y, -z$].

the magnetic orbital of the $Cu1^{i}$ atom should lie in the mean plane of the $N1^{i}$, $N2^{i}$, $N4^{i}$ and $O3^{i}$ atoms [symmetry code: (i) $1-x, -y, -z$]. The magnetic orbitals of Cu1 and $Cu1^{i}$ in the **A** unit are therefore parallel to each other and both of them perpendicular to the plane of the bridging oxalate group. They are also parallel with the planes of phen(1) and phen(1)^{i} and perpendicular to the planes of phen(2) and phen(2)^{i}. The intramolecular distance $Cu1\cdots Cu1^{i}$ in **1** is 5.6193(5) Å. In **2**, the magnetic orbital of the Cu1 atom should lie in the mean plane of the N1, N3, N4 and O4 atoms, while the magnetic orbital of the Cu2 atom should lie in the mean plane of the N5, N7, N8 and O6 atoms. Again, the magnetic orbitals turn out to be parallel to each other and perpendicular to the plane of the bridging oxalate group. They are parallel with the planes of bpy(2) and bpy(4) and perpendicular to the planes of bpy(1) and bpy(3). The intramolecular distance $Cu1\cdots Cu2$ in **2** is 5.6340(7) Å, i.e. only for 0.015 Å larger than the analogous distance in **1**.

In regard to the **B** units, tetragonal elongations of the coordination geometry around the Cu atoms are in both compounds more questionable, because the pairs of the largest bond lengths are not necessarily those that are oppositely oriented (Table 2, Figs. 1 and 2). Anyway, the largest bond length in each particular coordination environment around Cu comprises one of the oxygen atoms from the bridging oxalate group, i.e. O8 (from the **B** unit of **1** and the **B1** unit of **2**) or O20 (from the **B2** unit of **2**). Also, the three shortest bond lengths are always made up by three nitrogen atoms from phenanthroline or bipyridine ligands, i.e. N9, N10 and N12 (from the **B** unit of **1** and the **B1** unit of **2**) and N13, N14 and N16 (from the **B2** unit of **2**). The remaining nitrogen atoms [N11 and N15] are those that are oppositely oriented to the O8 and O20 atoms, respectively, having in average for 0.13 Å larger bond lengths toward the Cu atoms than the three shortest ones. Therefore, it can be still assumed that a tetragonal elongation driven by the Jahn-Teller effect is present in the observed Cu atom environments. The remaining oxygen atoms from the bridging oxalate groups [O7 and O19] are connected to the Cu atoms at comparably large distances (Table 2). If the $d_{x^2-y^2}$ orbital is still the one with the highest energy, it should remain the main part of the magnetic orbitals of the Cu3 and Cu4 magnetic centres. Therefore, in one magnetic centre (Cu3) this orbital should lie in the mean plane of the N9, N10 and N12 atoms and in the other one (Cu4) this orbital should lie in the mean plane of the N13, N14 and N16 atoms. In both cases, the orbitals are perpendicular to the plane of the bridging oxalate groups, parallel with one phenanthroline (bipyridine) ligand [phen(5) or bpy(5) for Cu3 and bpy(7) for Cu4] and perpendicular to the other phenanthroline (bipyridine) ligand [phen(6) or bpy(6) for Cu3 and bpy(8) for Cu4].

The environments of the Nb atoms in the **B** units of **1** and **2** are similar to those previously observed in other compounds containing the $[NbO(C_2O_4)_3]^{3-}$ entities [18,19]. The relevant Nb–O bonds are listed in Table 3. Six oxygen atoms from the three oxalate ligands and one oxo-oxygen atom comprise the coordination number seven around Nb, in distorted pentagonal–bipyramidal geometry, where one of the oxalate groups serves as a bridge between the Nb and Cu atoms. The equatorial plane of the pentagonal bipyramid around Nb1 is defined by the O9, O11, O12, O15 and O16 atoms, whereas a similar plane for Nb2 in **2** is defined by the O21, O23, O24, O27 and O28 atoms. The oxo-oxygen atoms [O1 or O2] are located in the

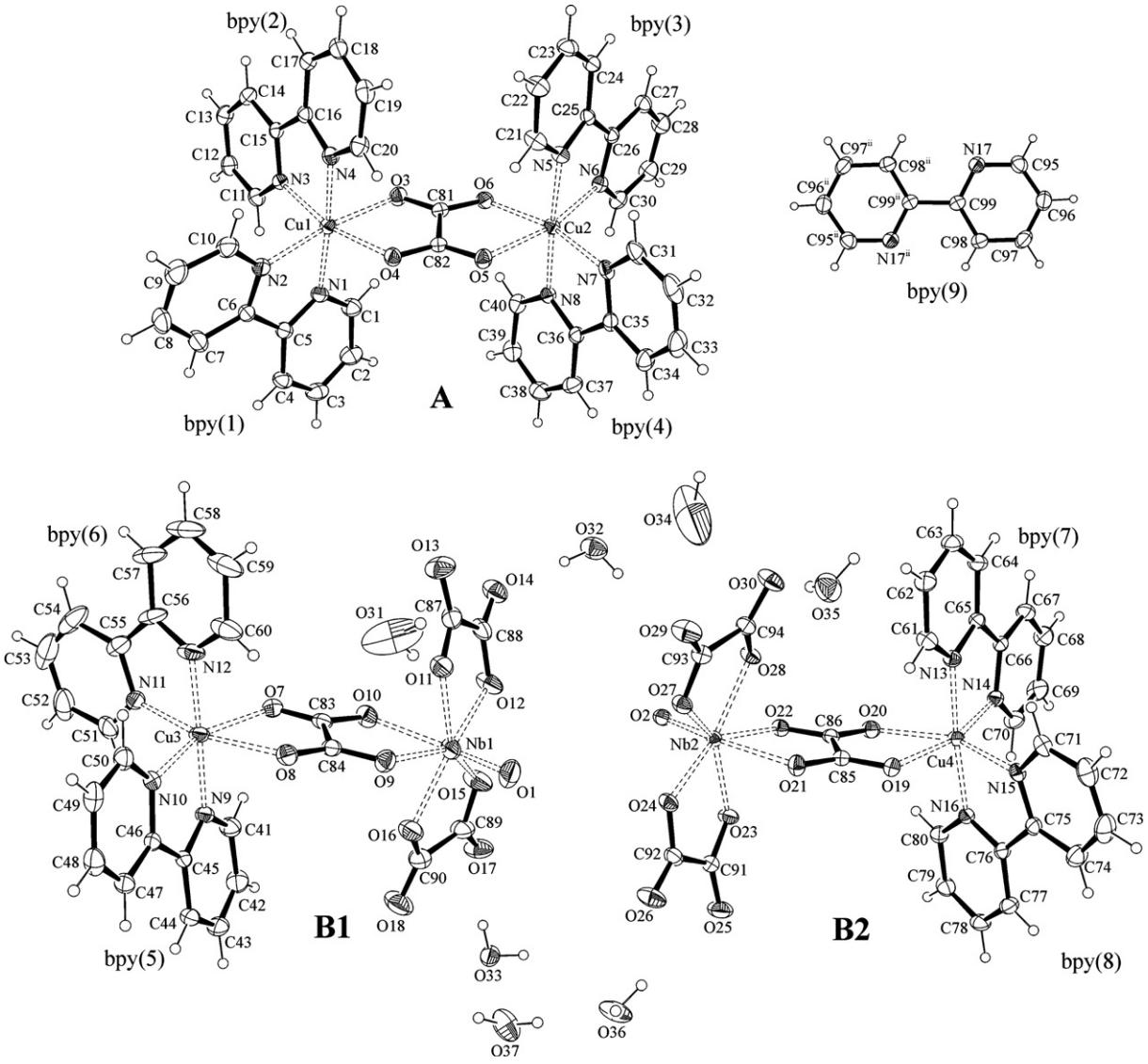


Fig. 2. ORTEP-III drawings [29] of the molecular structure of **2** with atom numbering scheme [symmetry code (ii): $1-x$, $1-y$, $1-z$].

apices of the pentagonal bipyramids and are at the shortest interatomic distances from Nb, confirming a double-bond character of the Nb=O bond. The other apices of the coordination polyhedra around Nb are occupied by the oxygen [O10 or O22] atoms from the bridging oxalate groups. These atoms have the largest Nb–O bond lengths and are just diametrically opposite to the O8 and O20 atoms (inside

Table 2
The Cu–N and Cu–O bond lengths (Å) in compounds **1** and **2**

	1	**2**		**1**	**2**
A units			*B units*		
Cu1–N1	2.010(2)	2.025(2)	Cu3–N9	1.998(2)	1.977(2)
Cu1–N2	2.037(2)	2.212(2)	Cu3–N10	2.099(2)	2.081(2)
Cu1–N3	2.290(2)	2.038(2)	Cu3–N11	2.169(2)	2.142(3)
Cu1–N4	2.015(2)	2.011(2)	Cu3–N12	2.007(2)	1.982(3)
Cu1–O3	2.012(2)	2.350(2)	Cu3–O7	2.153(2)	2.161(2)
Cu1–O4	2.328(2)	2.000(2)	Cu3–O8	2.317(2)	2.377(2)
Cu2–N5		2.016(2)	Cu4–N13		1.993(2)
Cu2–N6		2.196(2)	Cu4–N14		2.083(2)
Cu2–N7		2.060(2)	Cu4–N15		2.156(2)
Cu2–N8		1.992(2)	Cu4–N16		2.004(2)
Cu2–O5		2.316(2)	Cu4–O19		2.154(2)
Cu2–O6		2.050(2)	Cu4–O20		2.348(2)

Table 3
The Nb–O bond lengths (Å) in compounds **1** and **2**

	1	**2**
Nb1–O1	1.697(2)	1.709(3)
Nb1–O9	2.156(2)	2.136(2)
Nb1–O10	2.259(2)	2.255(2)
Nb1–O11	2.155(2)	2.153(2)
Nb1–O12	2.104(2)	2.105(2)
Nb1–O15	2.096(2)	2.094(2)
Nb1–O16	2.116(2)	2.119(2)
Nb2–O2		1.712(2)
Nb2–O21		2.146(2)
Nb2–O22		2.256(2)
Nb2–O23		2.128(2)
Nb2–O24		2.093(2)
Nb2–O27		2.104(2)
Nb2–O28		2.137(2)

the bridging oxalate ligands) that are at the largest distances from the Cu atoms (Figs. 1 and 2, Table 3).

The Nb atoms are in the diamagnetic +5 oxidation state. This is naturally understood from the charge neutrality requirements, but could be also verified by the method of bond-valence parameters given by Brese and O'Keeffe [31]. This method associates the valence of a bond between two atoms, v_{ij}, with the corresponding bond length, d_{ij}, according to the relation:

$$v_{ij} = \exp[(R_{ij} - d_{ij})/0.37] \quad (1)$$

The bond-valence parameter, R_{ij}, should not depend on the structure, but on the type of the atoms connected by a chemical bond only. The sum of all bond valences over the atoms in a coordination polyhedron should be equal to the oxidation state of the central atom. Using a value of 1.911 for R_{ij}, as found for the Nb^{V} and O combination [31], the calculation leads to the bond valence sum of 4.98, 4.96 and 4.94 for Nb1 in **1**, Nb1 in **2** and Nb2 in **2**, respectively. The values corroborate well with the assigned oxidation states of the Nb atoms. Therefore, the dinuclear $Cu^{II}Nb^{V}$ units (**B** units) are the systems containing just one spin (magnetic centre) located on the Cu^{II} atoms.

3.2. Crystal structures

The **A** and **B** units in both **1** and **2** are joined together by specific packing forces into the overall crystal structures. Among the competitive factors, stacking interactions of the aromatic systems seem to have structurally the most significant role. Several types of stacking interactions can be anticipated in both structures: the interactions between two neighbouring **A** units (**A**–**A**), the interactions between two neighbouring **B** units (**B**–**B**) and those appearing between two units of different type (**A**–**B**).

3.2.1. Stacking and C–H···π interactions in *1*

The stacking interactions between the phenanthroline ligands in **1**, classified according to the **A**–**A**, **B**–**B** or **A**–**B** types, and related parameters are listed in Table 4.

The first type (**A**–**A**) involves two phenanthroline ligands [phen(1) and phen(1)^{iii}] mutually related through the centre of symmetry *i* placed in the origin of the unit cell (Fig. 3). Due to this symmetry, the mean planes of the two stacked phenanthroline ligands are parallel ($\Theta = 0$, Table 4) with the distance between them being equal to 3.395(2) Å. However, the distance between their centres of gravity is considerably larger [4.010(2) Å, Table 3], since the ligands are shifted along their mean planes. Actually, the π···π stacking interaction acts between the central aromatic rings of the phenanthroline ligands, and the distance between the centres of gravity of the central rings [3.614(2) Å] is closer to the distance between the mean planes of the two ligands than to the distance between the centres of gravity of the phenanthroline ligands in the whole (Table 4). The existence of two mutually independent crystallographic centres of symmetry, i.e. *i* placed at the origin [connecting two **A** units *via* phen(1)···phen(1)^{iii} interaction] and *i*′ placed in the middle of the **A** unit [coordinates (1/2, 0, 0)] results in a one-dimensional motif extruding along the crystallographic *a* axis (Fig. 3).

The structurally similar stacking interactions connecting the **B** units into another one-dimensional motif are shown in Fig. 4. The interaction phen(5)···phen(5)^{ii} acts through the centre of symmetry *i*″ located at the coordinates (1/2, 1/2, 1/2) and the interaction phen(6)···phen(6)^{iv} connects two units through the centre of symmetry *i*‴ located at the coordinates (0, 1/2, 0). Thus formed one-dimensional motif of the **B** units extrudes in the direction [1, 0, 1]. Again,

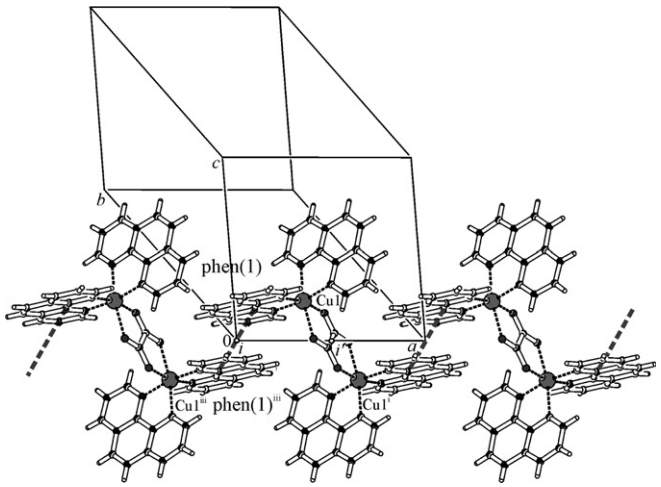


Fig. 3. One-dimensional structural motif in **1** generated by the **A**–**A** type of the phenanthroline stacking interaction (gray dashed lines). Labels and symmetry codes refer to those given in Fig. 1 and Table 4.

Table 4
Stacking interactions with Cu···Cu intermolecular distances in compound **1**

Interaction phen(*i*)··· phen(*j*)	Type	*d* (Å)[a]	Θ (°)[b]	phen(*i*)$_{\perp}$ (Å)[c]	Cu···Cu (Å)[d]
phen(1)···phen(1)^{iii}	**A**–**A**	4.010(2)	0	3.395(2)	8.8147(5)
phen(5)···phen(5)^{ii}	**B**–**B**	4.111(2)	0	3.408(2)	9.2116(5)
phen(6)···phen(6)^{iv}	**B**–**B**	4.076(2)	0	3.501(2)	9.0199(5)
phen(2)···phen(5)	**A**–**B**	5.146(2)	13.30(7)	3.928(2)	7.0091(5)

[a] Distance between the centres of gravity of two phen ligands.
[b] Angle between the mean planes of two phen ligands.
[c] Distance between the centre of gravity of phen(*i*) and the mean plane of phen(*j*).
[d] Distance between two Cu atoms to which phen ligands are coordinated; Symmetry codes: (iii) −*x*, −*y*, −*z*; (ii) 1 − *x*, 1 − *y*, 1 − *z*; (iv) −*x*, 1 − *y*, −*z*.

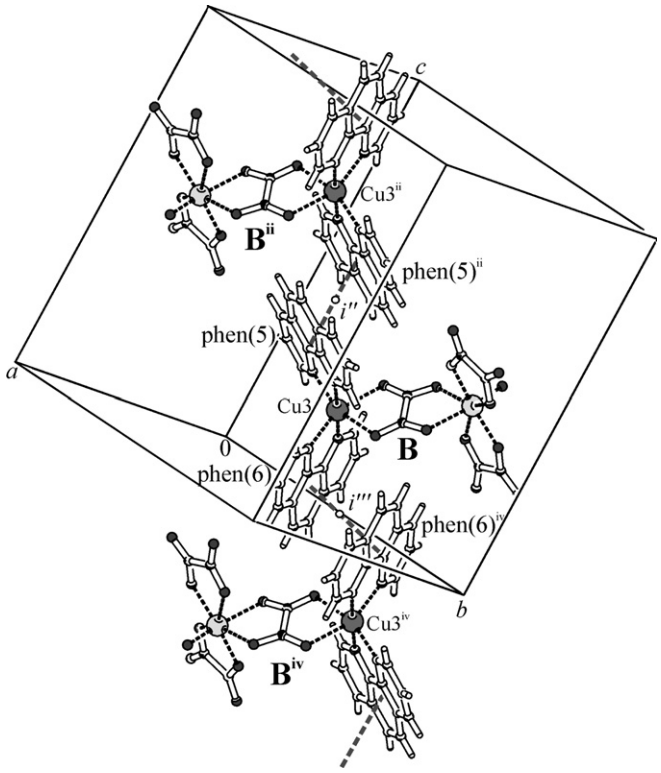


Fig. 4. One-dimensional structural motif in **1** generated by the **B**–**B** type of the phenanthroline stacking interaction (gray dashed lines). Labels and symmetry codes refer to those given in Table 4.

the phenanthroline ligands are mutually shifted in such a way that the central 6-membered aromatic rings are actually located one above another.

In the third type of stacking interactions (**A**–**B**) there is no centre of symmetry between the phenanthroline ligands. This interaction is actually a part of a more complex supramolecular embrace of two phenanthroline ligands from one **A** unit [phen(1) and phen(2)] and two phenanthroline ligands from one **B** unit [phen(5) and phen(6)] (Fig. 5). The phen(2) ligand tends to be parallel with phen(5) (stacking interaction), although the angle between their mean planes is 13.30(7)° (Table 4). The aromatic ring π(4) [N3–C11–C12–C13–C14–C15] from phen(2) is located above the aromatic rings π(8) [C44–C45–C46–C47–C46′–C45′] and π(9) [N10–C46–C47–C48–C49–C50] from phen(5) (Fig. 5). The distances π(4)···π(8) and π(4)···π(9) are 3.706(2) Å and 3.730(2) Å, respectively. These values are smaller than the distance from the centre of gravity of phen(2) to the mean plane of phen(5) (Table 4). In this supramolecular **A**–**B** embrace, three C–H···π interactions: C3–H3···π(11), C49–H49···π(3) and C50–H50···π(2) also appear (Fig. 5). The geometrical parameters for all C–H···π contacts found in the crystal structure are given in Table 5 (using criteria that H···π < 3.4 Å and C–H···π > 100°). The last three interactions listed [C59–H59···π(4)^{v}, C59–H59···π(5)^{v} and C60–H60···π(5)^{v}] actually connect a different **A**–**B** pair, i.e. the **B** unit and one **A**^{v} unit which is translated by one period in the negative direction of the *a* axis [symmetry code: (v) $-1+x, y, z$].

The shortest Cu···Cu intermolecular distance generated by a stacking or C–H···π interaction (Tables 4 and 5) is the one between the Cu1 and Cu3 atoms, having a value of 7.0091(5) Å (**A**–**B** supramolecular embrace, Fig. 5 and Table 4). The next higher value [8.6616(5) Å] is specific for the Cu3···Cu1^{v} contact [**A**–**B** pair in which the **A** unit

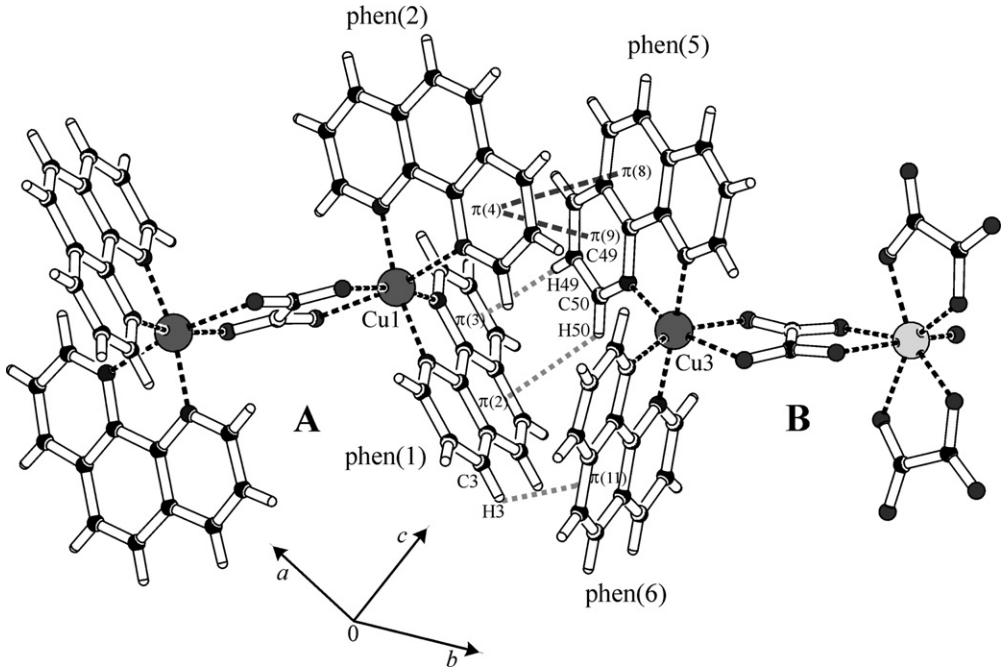


Fig. 5. The **A**–**B** type of supramolecular embrace in **1** made by phenanthroline ligands from two different types of constituents. Three π···π interactions [parts of the phen(2)···phen(5) stacking interaction given in Table 4] are shown by dark dashed gray lines, three C–H···π interactions (first three rows in Table 5) are shown by light dotted gray lines.

Table 5
C–H ···π interactions with Cu···Cu intermolecular distances in compound **1**

Interaction[a]	H ···π (Å)	C ···π (Å)	C–H···π (°)	Cu···Cu (Å)[b]
C3–H3···π(11)	3.198(4)	3.594(4)	107.8(2)	7.0091(5)
C49–H49···π(3)	2.543(4)	3.276(4)	135.9(2)	7.0091(5)
C50–H50···π(2)	3.161(3)	3.793(3)	126.8(2)	7.0091(5)
C59–H59···π(4)^{v}	2.998(4)	3.653(4)	128.6(2)	8.6616(5)
C59–H59···π(5)^{v}	3.121(3)	3.723(3)	124.0(2)	8.6616(5)
C60–H60···π(5)^{v}	2.967(4)	3.658(4)	132.3(2)	8.6616(5)

[a] π(11) = C54–C55′–C56′–C57–C56–C55; π(3) = N2–C6–C7–C8–C9–C10; π(2) = C4–C5–C6–C7–C6′–C5′; π(4) = N3–C11–C12–C13–C14–C15; π(5) = C14–C15–C16–C17–C16′–C15′.
[b] Distance between two Cu atoms to which phen ligands involved in the C–H···π interaction are coordinated; Symmetry code: (v) $-1+x, y, z$.

is translated in the negative direction of the *a* axis], realized through the C–H···π interactions only (Table 5). Therefore, the intermolecular distances between two Cu atoms related through the typical centrosymmetric stacking interactions (Figs. 3 and 4) are just the third, fourth and fifth ones in this range, with the values of 8.8147(5), 9.0199(5) and 9.2116(5) Å, respectively.

3.2.2. Stacking and C–H···π interactions in **2**

The stacking interactions of the bipyridine ligands in **2** are listed in Table 6. Several types of stacking interactions can be distinguished. The first one connecting two **A**-type units actually involves three bipyridine molecules: bpy(1) from an **A** unit, bpy(1)^{ii} from the symmetry-related unit [symmetry code: (ii) $1-x, 1-y, 1-z$] and one free bipyridine molecule [bpy(9)] which intercalates between bpy(1) and bpy(1)^{ii} (Fig. 6). The centre of symmetry of bpy(9) coincides with the crystallographic centre of symmetry *i* located at the position (1/2, 1/2, 1/2). The distance between the centres of gravity of bpy(1) and bpy(9) is 3.710(2) Å, whereas the distance from the centre of gravity of bpy(9) to the mean plane of bpy(1) is 3.346(2) Å. These values are just one half of the values representing the relevant parameters for the bpy(1)···bpy(1)^{ii} pair (Table 6, first row). The angle between the mean planes of bpy(1) and bpy(9) is 5.64(9)°. The second type of stacking interaction connecting the **A** units is realized through the crystallographic centre of symmetry *i*′ located in the vicinity of bpy(3), at the coordinates (1/2, 1, 0) (Table 6, second row). Two independent crystallographic centres of

Table 6
Stacking interactions with Cu···Cu intermolecular distances in compound **2**

Interaction bpy(*i*)··· bpy(*j*)	Type	*d* (Å)[a]	Θ (°)[b]	bpy(*i*)$_{\perp}$ (Å)[c]	Cu···Cu (Å)[d]
bpy(1)···bpy(1)^{iie}	**A**–**A**	7.420(2)	0	6.691(2)	11.003(1)
bpy(3)···bpy(3)^{vi}	**A**–**A**	3.671(2)	0	3.463(2)	7.5887(9)
bpy(5)···bpy(7)^{vii}	**B1**–**B2**	4.090(2)	1.47(8)	3.498(2)	7.9707(9)
bpy(6)···bpy(6)^{viii}	**B1**–**B1**	3.641(3)	0	3.391(3)	7.518(1)
bpy(8)···bpy(8)^{ix}	**B2**–**B2**	3.798(2)	0	3.572(2)	7.6831(8)
bpy(2)···bpy(5)	**A**–**B1**	7.067(2)	3.56(8)	3.433(2)	7.6973(9)
bpy(4)···bpy(7)	**A**–**B2**	6.808(2)	2.72(9)	3.514(2)	7.0632(8)

[a] Distance between the centres of gravity of two bpy ligands.
[b] Angle between the mean planes of two bpy ligands.
[c] Distance between the centre of gravity of bpy(*i*) and the mean plane of bpy(*j*).
[d] Distance between two Cu atoms to which bpy ligands are coordinated.
[e] bpy(9) intercalates between bpy(1) and bpy(1)^{ii}; Symmetry codes: (ii) $1-x, 1-y, 1-z$; (vi) $1-x, 2-y, -z$; (vii) $1+x, -1+y, z$; (viii) $2-x, 1-y, 1-z$; (ix) $-x, 2-y, -z$.

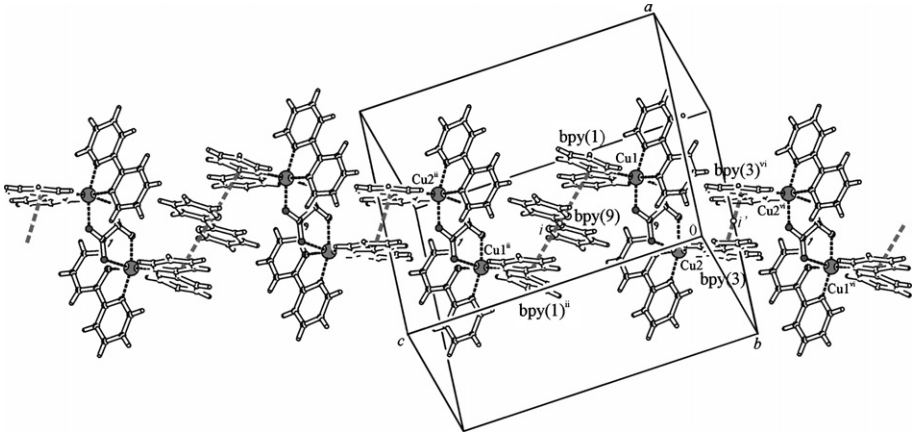


Fig. 6. One-dimensional structural motif in **2** generated by two bipyridine stacking interactions of the **A**–**A** type (gray dashed lines). bpy(9) intercalates between bpy(1) and bpy(1)^{ii}. Labels and symmetry codes refer to those given in Fig. 2 and Table 6.

symmetry generate one-dimensional motif extruding along the crystallographic direction $[0,-1,1]$ (Fig. 6). The motif is very similar to that one encountered for the **A** units in the crystal structure of **1** (Fig. 3), but with an additional free bipyridine molecule intercalating in every other bpy···bpy interaction. Due to this intercalation, a crystallographic centre of symmetry in the middle of the **A** unit can not exist [bpy(3) and bpy(4) are not symmetry related to bpy(1) and bpy(2), respectively], and this causes a lower symmetry of the **A** unit in **2** in comparison with the **A** unit in **1**.

Stacking interactions involving the **B** units in **2** are similar to the corresponding interactions appearing in the crystal structure of **1**. However, a difference arises from the fact that in the structure of **2** two symmetry independent **B** units exist, resulting in three different stacking interactions of the **B**–**B** type, i.e. **B1**–**B2**, **B1**–**B1** and **B2**–**B2** (Table 6). The **B1**–**B2** interaction connects two symmetrically independent **B** units (Table 6, third row). A small angle between the mean planes of the stacked bipyridine ligands and a relatively small difference between the d and bpy(i)$_\perp$ values show that this structural motif is almost centrosymmetric and that the bipyridine molecules on the whole are involved in the **B1**–**B2** stacking interaction. The **B1**–**B1** and **B2**–**B2** stacking interactions are strictly centrosymmetric because they operate across the crystallographic centres of symmetry i'' and i''' [located at the positions $(1,1/2,1/2)$ and $(0,1,0)$, respectively], as well as across the centres of symmetry at their symmetry equivalent positions [in Fig. 7, the i''' centre of symmetry is shown at the position (1, 0, 0)]. These three stacking interactions connect **B1** and **B2** units in a one-dimensional motif which extrudes in the direction $[0,1,1]$ (Fig. 7) and is structurally very similar to that of the **B** units in the crystal structure of **1** (Fig. 3).

The last two stacking interactions from Table 6 (**A**–**B1** and **A**–**B2**) are actually parts of two more complex supramolecular embraces (Fig. 8) and both of them are similar with the **A**–**B** embrace encountered in the crystal structure of **1** (Fig. 5). The **A**–**B1** embrace involves bpy(1) and bpy(2) from the **A** unit and bpy(5) and bpy(6) from the **B1** unit, while the second embrace (**A**–**B2**) involves bpy(3) and bpy(4) from **A** and bpy(7) and bpy(8) from **B2**. Since a centre of symmetry in the middle of the **A** unit can not exist, the **B** units embraced on each side of the **A** unit must be symmetrically independent, as well. Stacking interactions bpy(2)···bpy(5) and bpy(4)···bpy(7) listed in Table 6 do not involve the bipyridine molecules on the whole, but only one of their two pyridyl rings. This is the reason why the differences between the d and bpy(i)$_\perp$ values for this stacking interactions are so large. The π(3) and π(10) rings are stacked in the first interaction [π(3) = N3–C11–C12–C13–C14–C15, π(10) = N10–C46–C47–C48–C49–C50] and the π(7) and π(14) rings are stacked in the second interaction [π(7) = N7–C31–C32–C33–C34–C35, π(14) = N14–C66–C67–C68–C69–C70], as shown in Fig. 8. The distance between the centres of gravity of π(3) and π(10) is 3.973(2) Å, whereas the corresponding distance for π(7) and π(14) is 3.636(2) Å.

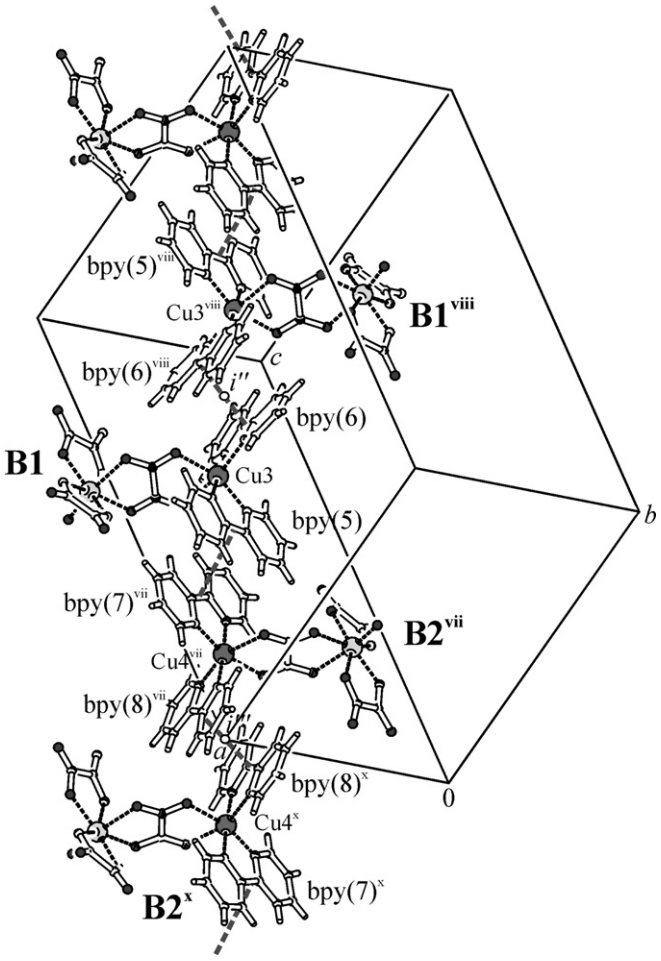


Fig. 7. One-dimensional structural motif in **2**, generated by three bipyridine stacking interactions of the **B**–**B** type (gray dashed lines). Labels and symmetry codes refer to those given in Table 6, except the symmetry code (x): $1-x$, $1-y$, $-z$. The bpy(8)^{vii}···bpy(8)^{x} contact is symmetry equivalent with the bpy(8)···bpy(8)^{ix} contact listed in Table 6.

In Fig. 8, beside mentioned stacking interactions, the three C–H···π interactions involved in the **A**–**B1** and **A**–**B2** supramolecular embraces are also shown. All C–H···π interactions appearing in the structure (with criteria H···π < 3.4 Å and C–H···π > 100°) are listed in Table 7. Comparing C–H···π interactions in **2** with those in **1** (Table 5) it can be observed that interactions involving the C49–H49 and C50–H50 bonds occur in both cases. The **A**–**B1** and **A**–**B2** embraces (Fig. 8) define the intermolecular Cu1···Cu3 and Cu2···Cu4 distances of 7.6973(9) and 7.0632(8) Å, respectively (Tables 6 and 7). Beside mentioned, there is one more C–H···π interaction between the **B2** unit and one **A** unit located one step further along the chain formed by the **A**–**A** stacking interactions shown in Fig. 6. This interaction defines a Cu4···Cu1^{vi} distance of 8.7355(9) Å. The interaction C28–H28···π(4)^{vi} (Table 7, sixth row) actually connects two units of the **A** type [the C28–H28 bond is from the bpy(3) ligand, whereas the

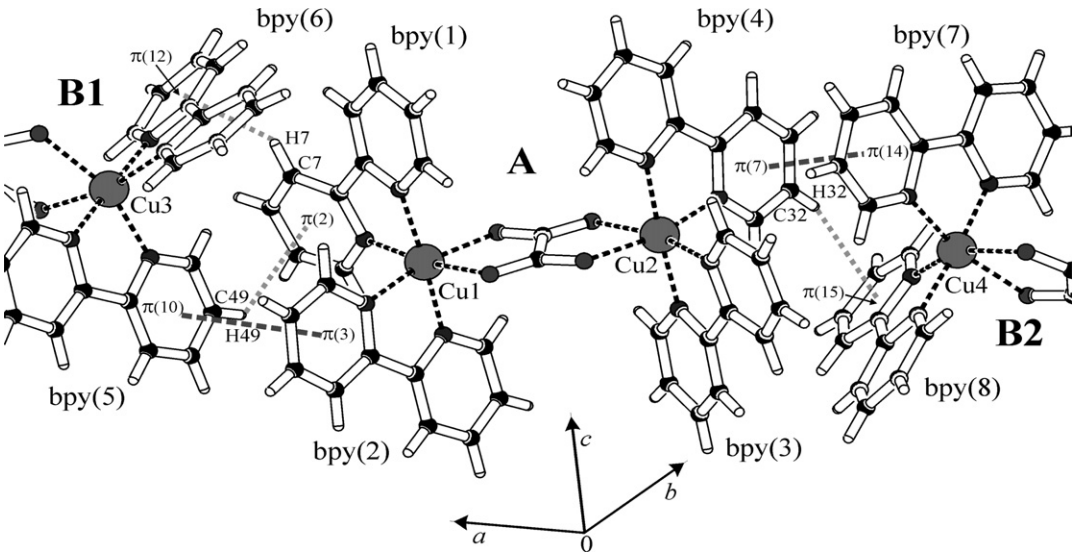


Fig. 8. Two **A**–**B** supramolecular embraces in **2**, made by four bipyridine ligands from two different types of constituents. Two π···π interactions [parts of the bpy(2)···bpy(5) and bpy(4)···bpy(7) stacking interactions given in Table 6] are shown by dark dashed gray lines, while three C–H···π interactions (first three rows in Table 7) are shown by light dotted gray lines.

Table 7
C–H···π interactions with Cu···Cu intermolecular distances in compound **2**

Interaction[a]	H···π (Å)	C···π (Å)	C–H···π (°)	Cu···Cu (Å)[b]
C7–H7···π(12)	2.994(4)	3.748(4)	139.2(2)	7.6973(9)
C49–H49···π(2)	3.238(4)	3.276(4)	135.9(2)	7.6973(9)
C50–H50···π(2)	3.266(4)	3.918(3)	129.0(2)	7.6973(9)
C32–H32···π(15)	2.847(4)	3.670(4)	148.0(2)	7.0632(8)
C79–H79···π(3)^{vi}	3.001(4)	3.671(4)	130.3(2)	8.7355(9)
C28–H28···π(4)^{vi}	2.697(4)	3.586(4)	160.4(2)	9.7606(1)
C97–H97···π(8)^{ii}	3.172(4)	3.886(4)	135.1(2)	

[a] π(12) = N12–C56–C57–C58–C59–C60; π(2) = N2–C6–C7–C8–C9–C10; π(15) = N15–C71–C72–C73–C74–C75; π(3) = N3–C11–C12–C13–C14–C15; π(4) = N4–C16–C17–C18–C19–C20; π(8) = N8–C36–C37–C38–C39–C40.

[b] Distance between two Cu atoms to which phen ligands involved in the C–H···π interaction are coordinated; Symmetry codes: (vi) $1-x, 2-y, -z$; (ii) $1-x, 1-y, 1-z$.

π(4) ring is from the bpy(2) ligand], therefore it superimposes on the one-dimensional stacking motif of the **A** units (Fig. 6). This contact defines the intermolecular Cu2···Cu1^{vi} distance of 9.7606(1) Å. The last C–H···π interaction noted in Table 7 involves the C97–H97 bond from the free bipyridine [bpy(9)] molecule, so the intermolecular Cu···Cu distance is not defined [bpy(9) is not coordinated to any of the Cu atoms]. These last C–H···π interactions given in Table 7 generate longer intermolecular Cu···Cu distances than the **A**–**B1** or **A**–**B2** supramolecular embraces or any of the stacking interactions given in Table 6 [with the exception of the bpy(1)···bpy(1)^{ii} interaction which involves the intercalated bpy(9) molecule]. This is an important difference as compared with the analogous analysis of the Cu···Cu intermolecular distances in **1**.

Taking into consideration the intermolecular Cu···Cu distances generated by the strictly centrosymmetric stacking interactions (first three interactions shown in Table 4 for **1** and the second, fifth and sixth ones in Table 6 for **2**), it can be observed that the corresponding distances are by ca. 1.4 Å longer in **1** than in **2**. This elongation is probably connected with the possibility that the saturation of the π···π stacking interaction with the central aromatic rings exists in phenanthroline, but not in the bipyridine ligands. The additional aromatic rings probably induce a characteristic shift of the neighbouring phenanthroline ligands in the direction of their mean planes, and hence the elongation of the corresponding intermolecular Cu···Cu distance.

3.2.3. Comparison of crystal packing and hydrogen bonds in *1* and *2*

The analyses of stacking interactions in both compounds show two types of one-dimensional infinite structural motifs: the **A**-type (Figs. 3 and 6) and **B**-type arrangements (Figs. 4 and 7). Both types extrude in the different space directions and are sufficient for building up the entire three-dimensional crystalline frameworks. The directions of the **A**-type motifs (as well as the directions of **B**-type) in **1** and **2** are not identical because the unit cells are different (they are chosen to be Niggli reduced cells [32] in both cases). The fact that **2** contain fewer centres of symmetry than **1**, causes the Niggli reduced cells to be different. Nevertheless, the similarity of the unit cells can be observed by comparison of their volumes (Table 1); the volume of the unit cell of **2** is roughly two times larger than that of **1**. Due to two main differences in the packing of mentioned one-dimensional motifs (formed by stacking interactions), some differences in the residual volumes (solvent accessible areas) can be expected. One of the differences is that the structure of **2** hosts one additional free bipyridine molecule (one half per formula unit), and the

other one is that the phenanthroline ligand generates longer intermolecular contacts (as seen through the Cu···Cu distances) than bipyridine. The residual volumes in both structures are occupied by crystal water molecules. Although some of them have similar positions in both structures, the orientations of hydrogen atoms are different. So, the motifs generated by the hydrogen bonds in two structures are not comparable. The relevant parameters for the observed hydrogen bonds in **1** and **2** are listed in Tables 8 and 9, respectively.

3.3. Infrared spectra

The IR spectra of **1** and **2** show characteristic absorption bands of bidentate and bis(bidentate) bridging oxalate groups beside those originating from 1,10-phenanthroline in **1**, and 2,2′-bipyridine in **2**. The absorption bands of weak to medium intensity that occur in the region 3500–3400 cm^{-1} for both complexes, are consistent with the presence of the crystal H_2O molecules. Several strong-intensity absorptions indicate the presence of the bidentate and bis(bidentate) oxalate ligand: ν_{as}(CO) found at 1735, 1710 and 1692 cm^{-1} for **1** and at 1730, 1711 and 1687 cm^{-1} for **2**, ν_s(CO) at 1362 and 1250 cm^{-1} for **1** and at 1376 and 1242 cm^{-1} for **2** as well as δ(OCO) at 793 and 792 cm^{-1} for **1** and **2**, respectively, are consistent with the bidentate oxalate group, whereas ν_{as}(CO) at 1630 and 1631 cm^{-1} for **1** and **2**, respectively, ν_s(CO) at 1295 and 1301 cm^{-1} for **1** and **2**, respectively, beside δ(OCO) found at 802 cm^{-1} for **1** and at 801 cm^{-1} for **2**, are in agreement with the position of corresponding absorptions in oxalate-bridged dinuclear copper(II) complexes [33,34]. Among the other absorption bands in the IR spectra, those located at 943 cm^{-1} and 933 cm^{-1} for **1** and **2**, respectively, are easily recognized as ν(NbO). The relative position of these bands (a higher wave number for **1** than for **2**) is in agreement with the corresponding bond lengths [a shorter Nb=O bond length in **1** (1.1697(2) Å) in comparison to the one in **2** (1.709(3) Å)].

Table 8
Hydrogen-bonding geometry in compound **1**

D–H···A	D–H (Å)	H···A (Å)	D···A (Å)	D–H···A (°)
O20–H201···O12	0.84	2.59	3.191(5)	130
O20–H201···O15	0.84	2.52	3.071(6)	124
O20–H202···O1^{xi}	0.84	2.32	3.091(5)	153
O21–H211···O14	0.84	2.07	2.896(4)	168
O21–H212···O22^{xi}	0.84	2.21	3.000(4)	156
O22–H221···O17	0.84	2.00	2.810(4)	163
O22–H222···O10^{xii}	0.84	2.11	2.918(3)	162
O23–H231···O22	0.84	2.02	2.735(9)	142
O23–H232···O4^{ii}	0.84	1.96	2.766(9)	160

Symmetry codes: (xi) $-x, 2-y, 1-z$; (xii) $1-x, 2-y, 1-z$; (ii) $1-x, 1-y, 1-z$.

Table 9
Hydrogen–bonding geometry in compound **2**

D–H···A	D–H (Å)	H···A (Å)	D···A (Å)	D–H···A (°)
O31–H311···O11	0.84	2.19	2.956(5)	153
O31–H312···O9^{xiii}	0.84	2.47	3.170(7)	141
O32–H321···O14	0.84	2.08	2.196(4)	171
O32–H322···O35^{ii}	0.84	2.02	2.856(4)	177
O33–H331···O17	0.84	1.95	2.785(4)	170
O33–H332···O12^{xiv}	0.84	2.39	3.155(4)	151
O34–H341···O29	0.84	2.23	2.816(7)	127
O34–H342···O18^{xv}	0.84	2.46	2.878(8)	112
O35–H351···O30	0.84	2.21	3.052(4)	176
O35–H352···O33^{xv}	0.84	2.03	2.852(4)	165
O36–H361···O26	0.84	2.06	2.775(4)	143
O36–H362···O5^{ix}	0.84	1.95	2.778(3)	167
O37–H371···O36	0.84	1.99	2.825(4)	176
O37–H372···N17^{ix}	0.84	2.22	2.961(4)	147

Symmetry codes: (xiii) $2-x, -y, 1-z$; (ii) $1-x, 1-y, 1-z$; (xiv) $3-x, -y, 1-z$; (xv) $-2+x, 1+y, z$; (ix) $-x, 2-y, -z$.

3.4. Magnetic properties

The temperature dependences of $\chi_M T$ for **1** and **2** are shown in Fig. 9. The values of $\chi_M T$ for **1** and **2** at temperatures above 120 K are constant with an average of 1.73 and 1.79 $cm^3\,mol^{-1}\,K$ for **1** and **2**, respectively. This corresponds to the effective magnetic moment per molecule $\mu = 3.72\beta$ for **1** and $\mu = 3.78\beta$ for **2**, where β is the Bohr

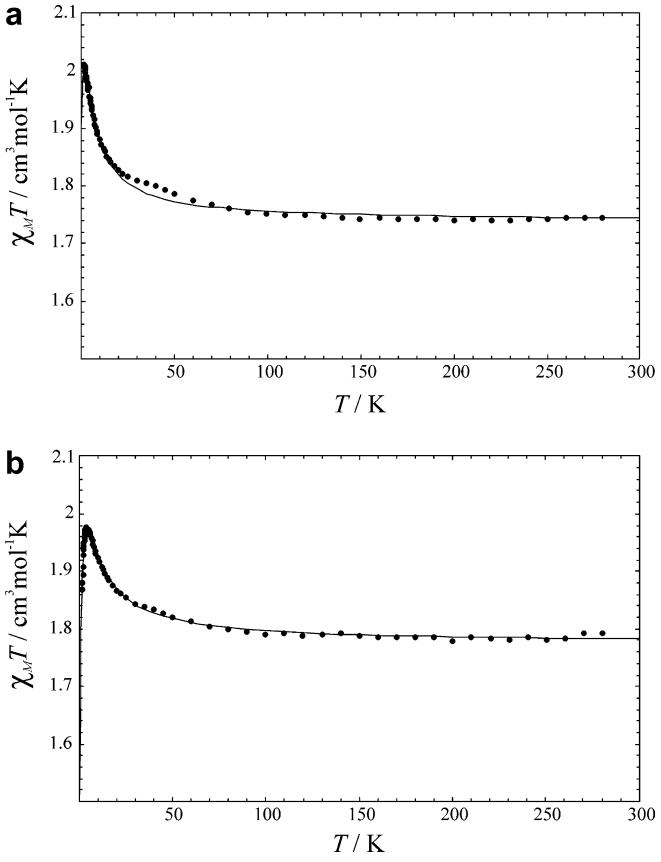


Fig. 9. Temperature dependence of $\chi_M T$ for compounds **1** (a) and **2** (b); the solid lines represent the curves of the best fit.

magneton. Generally, the spin-only value of the magnetic moment for four uncoupled Cu^{II} ions is $\mu = \beta\sqrt{4 \cdot g_{Cu}^2 S_{Cu}(S_{Cu}+1)}$. The measured values correspond to $g = 2.15$ for **1** and $g = 2.17$ for **2**. On cooling the samples below 50 K, the product $\chi_M T$ increases for both compounds, reaching for **1** a maximum value of 2.02 $cm^3\,mol^{-1}K$ at 1.8 K and for **2** a maximum value of 1.98 $cm^3\,mol^{-1}K$ at 5 K, upon what a decrease of $\chi_M T$ for **2** appears. The reciprocal magnetic susceptibility χ^{-1} vs. T plot shows a strong linear dependence above 100 K for both compounds. The Weiss constants ($\Theta = -0.1 \pm 0.1$ for **1** and $\Theta = 0.0 \pm 0.6$ for **2**) point to a negligible long-range order (Θ is determined from high-temperature region, i.e. >120 K). Consequently, the observed magnetic behaviour should be analysed on the molecular level.

Based on the structures, it is reasonable to suppose that magnetic measurements can be explained by the behaviour of a pair of spins $S = 1/2$ coupled *via* the isotropic Heisenberg interaction J [the $Cu^{II}Cu^{II}$ units (**A** type units), $\mathbf{H}_{INT} = -J\boldsymbol{S}_1 \cdot \boldsymbol{S}_2$], and by the uncoupled spins $S = 1/2$ coming from the Cu^{II} ions of the $Cu^{II}Nb^{V}$ units (**B** type units). The Nb^{V} atoms do not contribute to the paramagnetic susceptibility of the compounds as already mentioned. As there are two **B** type units per one **A** type for both structures, the supposed formula for the molar magnetic susceptibility is:

$$\chi' = \chi_{di} + 2\chi_{Curie} \tag{2}$$

wherein the first term is the Bleaney and Bowers expression for the $Cu^{II}Cu^{II}$ dinuclear unit [23]:

$$\chi_{di} = \frac{2Ng^2\beta^2}{kT(3 + e^{-J/kT})} \tag{3}$$

and the second term is a Curie law for $S = 1/2$:

$$\chi_{Curie} = \frac{Ng^2\beta^2}{4kT} \tag{4}$$

A positive interaction parameter J in the first term can explain the observed increase of $\chi_M T$ in the process of cooling. In that case (ferromagnetic interaction) a more populated ground state is the triplet state having a higher spin quantum number S, and hence a higher magnetic moment $\mu_{eff}[\chi T \propto (\mu_{eff})^2]$. A relatively good fit of the susceptibility measurements with the Eq. (2) can be obtained for **1**, but not for **2**, mainly because of the evident decrease of the experimental values for $\chi_M T$ below 5 K (Fig. 9). This decline can be attributed to the additional intermolecular magnetic exchange interaction or to the zero-field splitting on the triplet states of the $Cu^{II}Cu^{II}$ dimer [23]. Zero-field splitting is usually explained in the literature by mutual perturbations caused by lowering of the magnetic centre symmetry and spin–orbit interaction [23]. Because the $Cu^{II}Cu^{II}$ units in both compounds have approximately the same type of molecular symmetry ($C2/m$) there is no reason for the existence of zero-field splitting in one type of compound and not in the other. So, it seems more probable that the observed decrease in the experimental $\chi_M T$ curve for **2** is caused by the weak intermolecular magnetic exchange interactions. Because there are several different intermolecular structural contacts realized by the stacking or C–H$\cdots\pi$ interactions in the crystal structures (Tables 4–7) it is impossible to assign the unique exchange interaction parameter to every particular type of contacts; the final expression for the magnetic susceptibility would become overparameterized. For this reason, the effects of intermolecular magnetic exchange interactions are included in the mean field approximation [35]:

$$\chi = \frac{\chi'}{1 - \frac{zJ'}{Ng^2\beta^2}\chi'} \tag{5}$$

introducing only one parameter (zJ'). The nonlinear fit of the $\chi_M T$ vs. T experimental curves using Eq. (5) gave the following results for the parameters: $J = +5.9(1)$ cm^{-1}, $g = 2.15(1)$, $zJ' = -0.01(1)$ cm^{-1} for **1** and $J = +7.9(2)$ cm^{-1}, $g = 2.17(1)$, $zJ' = -0.10$ (1) cm^{-1} for **2**. The discrepancy factors R, defined as $R = \sum[(\chi_M T)_{obsd.} - (\chi_M T)_{calcd.}]^2 / \sum[(\chi_M T)_{obsd.}]^2$, equal 1.2×10^{-5} and 1.5×10^{-5} for **1** and **2**, respectively. The intermolecular exchange parameter zJ' is antiferromagnetic in both cases: almost zero for **1** and very small for **2**. As shown in the crystal packing analyses, the most frequently observed intermolecular structural motif (between all encountered) is a centrosymmetrical stacking of phenanthroline or bipyridine ligands attached to the neighbouring **A** or **B** units. It is also shown that the intermolecular Cu$\cdots$Cu distances generated by this type of stacking are for ~1.5 Å larger in **1** than in **2**, due to the possibility for stacking of the central aromatic rings in the phenanthroline molecules. This structural difference could be the explanation for the larger zJ' parameter observed for **2** than for **1**. If this assumption is correct, the additional antiferromagnetic exchange interaction should be mediated across the stacked bipyridine ligands. In the literature, there are no much evidences on this kind of mediation of the magnetic exchange interaction. The only exception is the compound [Cu-(acac)(Me_2bpy)-(NCS)] (acac = acetylacetonate; Me_2bpy = 4,4′-dimethyl-2,2′-bipyridine) where the interaction of $J = -0.84$ cm^{-1} was observed [36].

A more reliable parameter that can be extracted from the fitting procedure in the presented magnetochemical analyses of **1** and **2** is the intramolecular magnetic exchange parameter J, the one that couples two Cu^{II} magnetic centres inside the **A** unit into a spin-coupled $Cu^{II}Cu^{II}$ dimer. In both compounds this parameter turns out to be positive, indicating a ferromagnetic interaction between the Cu^{II} ions across the bridging oxalate units. This is not surprising because such behaviour was already encountered in the literature [37] and it corroborates well the theoretical predictions based on DFT calculations [38]. These predictions claim that the ferromagnetic exchange interactions of strength up to 10 cm^{-1} are possible for mutually parallel orientation of the magnetic

orbitals on each Cu^{II} magnetic centre, both perpendicular on the mean plane of the oxalate bridge [38]. The analysis of the molecular geometry of the **A** units in both compounds has shown exactly this kind of orbital topology (see Section 3.1).

4. Conclusion

The oxotris(oxalato)niobate(V) $[NbO(C_2O_4)_3]^{3-}$ ion has been used for the first time as the starting substance for the construction of complex oxalate compounds with oxalate-bridged metal ions. Namely, compounds **1** and **2** contain $Cu^{II}Cu^{II}$ oxalate-bridged $[\{Cu(L)_2\}_2(\mu\text{-}C_2O_4)]^{2+}$ cation (**A** unit) and two $Cu^{II}Nb^{V}$ oxalate-bridged $[Cu(L)_2(\mu\text{-}C_2O_4)NbO(C_2O_4)_2]^{-}$ anions (**B** units). Both substances crystallize in the triclinic space group $P\bar{1}$; in **1** a crystallographic inversion center is located in the middle of the oxalate bridge, in **2** an analogous inversion center is missing. One-dimensional motifs present in both structures have been generated by the ligand stacking interactions. The observed ferromagnetic interaction between copper(II) atoms in the **A** units of both compounds is the consequence of the suitable topology of the magnetic orbitals located on the copper(II) ions.

Acknowledgement

This research was supported by the Ministry of Science, Education and Sports of the Republic of Croatia (Grants Nos. 0098066 and 0119258).

Appendix A. Supplementary data

CCDC-603922 (**1**) and CCDC-603923 (**2**) contain the supplementary crystallographic data for this paper. Copies of this information can be obtained from the Director, CCDC, 12 Union Road, Cambridge CB2 1EZ, UK, fax: +44 1223 336 033, e-mail deposit@ccdc.cam.ac.uk or on the www.ccdc.cam.ac.uk. Supplementary data associated with this article can be found, in the online version, at doi:10.1016/j.poly.2006.08.024.

References

[1] O. Costisor, K. Mereiter, M. Julve, F. Lloret, Y. Journaux, W. Linert, M. Andruh, Inorg. Chim. Acta 324 (2001) 352.
[2] (a) Y. Pei, Y. Journaux, O. Kahn, Inorg. Chem. 28 (1989) 100;
(b) Y.-T. Li, C.-W. Yan, J.-F. Lou, H.-S. Guan, J. Magn. Magn. Mater. 281 (2004) 68;
(c) Y.-T. Li, C.-W. Yan, H.-S. Guan, Transition Met. Chem. 29 (2004) 537;
(d) X.-R. Sun, M.-M. Miao, P. Cheng, D.-Z. Liao, Z.-H. Jiang, G.-L. Wang, Transition Met. Chem. 22 (1997) 302.
[3] M. Jurić, P. Planinić, N. Brničević, D. Milić, D. Matković-Čalogović, D. Pajić, K. Zadro, Eur. J. Inorg. Chem. (2006) 2701.
[4] S. Decurtins, M. Gross, H.W. Schmalle, S. Ferlay, Inorg. Chem. 37 (1998) 2443.
[5] E. Coronado, J.R. Galán-Mascarós, C.J. Gómez-García, C. Martí-Gastaldo, Inorg. Chem. 44 (2005) 6197.
[6] (a) H. Tamaki, Z.J. Zhong, N. Matsumoto, S. Kida, M. Koikawa, N. Achiwa, Y. Hashimoto, H. Ōkawa, J. Am. Chem. Soc. 114 (1992) 6974;
(b) Z.J. Zhong, N. Matsumoto, H. Ōkawa, S. Kida, Chem. Lett. (1990) 87;
(c) M. Ohba, H. Tamaki, N. Matsumoto, H. Ōkawa, S. Kida, Chem. Lett. (1991) 1157.
[7] L.O. Atovmyan, G.V. Shilov, R.N. Lyubovskaya, E.I. Zhilyaeva, N.S. Ovanesyan, S.I. Pirumova, I.G. Gusakovskaya, Y.G. Morozov, JETP Lett. 58 (1993) 766.
[8] S. Decurtins, H.W. Schmalle, H.R. Oswald, A. Linden, J. Ensling, P. Gütlich, A. Hauser, Inorg. Chim. Acta 216 (1994) 65.
[9] C. Mathonière, C.J. Nuttall, S.G. Carling, P. Day, Inorg. Chem. 35 (1996) 1201.
[10] R. Pellaux, H.W. Schmalle, R. Huber, P. Fischer, T. Hauss, B. Ouladdiaf, S. Decurtins, Inorg. Chem. 36 (1997) 2301.
[11] J. Larionova, B. Mombelli, J. Sanchiz, O. Kahn, Inorg. Chem. 37 (1998) 679.
[12] E. Coronado, J.R. Galán-Mascarós, C.J. Gómez-García, J.M. Martínez-Agudo, E. Martínez-Ferrero, J.C. Waerenborgh, M. Almeida, J. Solid State Chem. 159 (2001) 391.
[13] K.S. Min, A.L. Rhinegold, J.S. Miller, Inorg. Chem. 44 (2005) 8433.
[14] S. Decurtins, H.W. Schmalle, P. Schneuwly, H.R. Oswald, Inorg. Chem. 32 (1993) 1888.
[15] (a) S. Decurtins, H.W. Schmalle, P. Schneuwly, J. Ensling, P. Gütlich, J. Am. Chem. Soc. 116 (1994) 9521;
(b) S. Decurtins, H.W. Schmalle, R. Pellaux, P. Schneuwly, A. Hauser, Inorg. Chem. 35 (1996) 1451;
(c) P. Román, C. Guzmán-Miralles, A. Luque, J. Chem. Soc. Dalton Trans. (1996) 3985.
[16] (a) E. Coronado, J.R. Galán-Mascarós, C.J. Gómez-García, J.M. Martínez-Agudo, Inorg. Chem. 40 (2001) 13;
(b) R. Andrés, M. Brissard, M. Gruselle, C. Train, J. Vaissermann, B. Malézieux, J.-P. Jamet, M. Verdaguer, Inorg. Chem. 40 (2001) 4633.
[17] (a) N. Brničević, C. Djordjević, Inorg. Chem. 7 (1968) 1936;
(b) N. Brničević, C. Djordjević, J. Chem. Soc., Dalton Trans. (1974) 165;
(c) N. Brničević, C. Djordjević, J. Less-Common Met. 45 (1976) 45.
[18] M. Šestan, B. Perić, G. Giester, P. Planinić, N. Brničević, Struct. Chem. 16 (2005) 409.
[19] G. Mathern, R. Weiss, Acta Crystallogr., Sect. B 27 (1971) 1610.
[20] F.M. Jaeger, J.A. van Dijk, Z. Anorg. Allg. Chem. 227 (1936) 273.
[21] A.C. Fabretti, G. Franchini, P. Zannini, M. Divaira, Inorg. Chim. Acta 105 (1985) 187.
[22] P.W. Selwood, Magnetochemistry, 2nd edn., Interscience Publishers, Inc., New York, 1956.
[23] O. Kahn, Molecular Magnetism, Wiley-VCH, New York, 1993.
[24] Z. Otwinowski, W. Minor, in: C.W. Carter, R.M. Sweet (Eds.), Methods in Enzymology, Macromolecular Crystallography, part A, vol. 276, Academic Press, London, 1997, p. 307.
[25] M. Sheldrick, SHELXS-97, Program for Crystal Structures Solution, University of Göttingen, Germany, 1997.
[26] M. Sheldrick, SHELXL-97, Program for Crystal Structures Refinement, University of Göttingen, Germany, 1997.
[27] M. Nardelli, J. Appl. Crystallogr. 32 (1999) 563.
[28] L.J. Farrugia, J. Appl. Crystallogr. 32 (1999) 837.
[29] L.J. Farrugia, J. Appl. Crystallogr. 30 (1997) 568.
[30] M.A. Halcrow, Dalton Trans. (2003) 4375.
[31] N.E. Brese, M. O'Keeffe, Acta Crystallogr., Sect. C 47 (1991) 192.
[32] I. Krivy, B. Gruber, Acta Crystallogr., Sect. A 32 (1976) 297.
[33] J. Fujita, A.E. Martell, K. Nakamoto, J. Chem. Phys. 36 (1962) 324.

[34] (a) M.L. Calatayud, I. Castro, J. Sletten, F. Lloret, M. Julve, Inorg. Chim. Acta 300–302 (2000) 846;
(b) A. Gleizes, M. Julve, M. Verdaguer, J.A. Real, J. Faus, X. Solans, J. Chem. Soc., Dalton Trans. (1992) 3209.
[35] R.L. Carlin, A.J. van Duyneveldt, Magnetic Properties of Transition Metal Compounds, Springer-Verlag, New York, 1977.
[36] A.M. Madalan, V.C. Kravtsov, D. Pajić, K. Zadro, Y.A. Simonov, N. Stanica, L. Ouahab, J. Lipkowski, M. Andruh, Inorg. Chim. Acta 357 (2004) 4151.
[37] O. Costisor, M. Brezeanu, Y. Journaux, K. Mereiter, P. Weinberger, W. Linert, Eur. J. Inorg. Chem. (2001) 2061.
[38] J. Cano, P. Alemany, S. Alvarez, M. Verdaguer, E. Ruiz, Chem. Eur. J. 4 (1998) 476.

Available online at www.sciencedirect.com
ScienceDirect
Polyhedron 26 (2007) 673–678
POLYHEDRON
www.elsevier.com/locate/poly

Proton and anion control of framework complexity in copper(II) complex structures derived from 2-(hydroxymethyl)pyridine

Bianca Antonioli [a,b], David J. Bray [b], Jack K. Clegg [b], Katrina A. Jolliffe [c], Kerstin Gloe [a], Karsten Gloe [a,*], Leonard F. Lindoy [b,*]

[a] *Department of Chemistry, Technical University Dresden, 01062 Dresden, Germany*
[b] *Centre for Heavy Metals Research, School of Chemistry, University of Sydney, NSW 2006, Australia*
[c] *School of Chemistry, University of Sydney, NSW 2006, Australia*

Received 20 July 2006; accepted 27 August 2006
Available online 10 September 2006

Abstract

Three copper(II) complexes derived from 2-(hydroxymethyl)pyridine (LH) have been synthesised and a comparative X-ray investigation of their respective crystal structures undertaken. In the absence of added base, LH reacts with copper(II) chloride or nitrate to yield the five-coordinate $[Cu(LH)_2Cl]Cl$ and six-coordinate $[Cu(LH)_2(NO_3)_2]$ species. In the chloro complex the coordination geometry is distorted trigonal bipyramidal, with the pyridyl nitrogens occupying the axial position and two hydroxyl oxygens from the bidentate ligands together with a chloro group occupying the equatorial sites. The structure of the nitrate species, published previously, has been reinvestigated at low temperature in order to specify the weak interactions in the crystal; it contains two molecules of bidentate LH bound *trans* in the equatorial plane while monodentate nitrato ligands occupy the axial sites. In each of these complexes the hydroxyl protons act as hydrogen bond donors, interacting with the non-coordinated chloride anion in $[Cu(LH)_2Cl]Cl$ and the coordinated nitrato groups in $[Cu(LH)_2(NO_3)_2]$ to form bridged, hydrogen-bonded, copper(II)-organic arrays in each case; offset face-to-face π-stacking in the latter produces a two dimensional structure. Further weak CH···Cl, CH···O interactions stabilise both arrangements. The X-ray structure of the complex $[Cu(L)_2]\cdot 4H_2O$ containing the deprotonated ligand is also described. The presence of the latter results in the above hydrogen bonding arrangements being 'switched off' and instead a new two-dimensional network involving bridging tetrameric water clusters hydrogen bound to adjacent ligand hydroxo groups to give extended sheets is generated; offset face-to-face π-stacking occurs between sheets to yield a three dimensional array.
© 2006 Elsevier Ltd. All rights reserved.

Keywords: Copper(II); Crystal structure; Hydrogen bond; Deprotonation; 2-(Hydroxymethyl)pyridine

1. Introduction

The design and synthesis of extended metallo assemblies, particularly those with interesting topologies and/or potential technological applications have received much recent attention [1–3]. As part of these studies, increasing interest has been shown in the weak interactions linking metal complex units in the solid state and such investigations now form a major part of the current activity within the crystal engineering field. In this context, the effect of coordinated ligand protonation/deprotonation on the resulting crystal framework structures has received somewhat less attention, although a number of literature examples do exist [4]. In such systems, it is sometimes possible to 'switch' hydrogen bonding by subtle variation of the pH of the reaction solution used to form the product, resulting in a significant topological change in the framework material isolated.

* Corresponding authors. Tel.: +49 351 4633 4357; fax: +49 351 4633 7287 (K. Gloe); tel.: +61 2 9351 4400; fax: +61 2 9351 3329 (L.F. Lindoy).
E-mail addresses: karsten.gloe@chemie.tu-dresden.de (K. Gloe), lindoy@chem.usyd.edu.au (L.F. Lindoy).

0277-5387/$ - see front matter © 2006 Elsevier Ltd. All rights reserved.
doi:10.1016/j.poly.2006.08.031

In the present study, we have investigated the effect of protonation/deprotonation behaviour on the crystal geometries of three copper(II) complexes generated from 2-(hydroxymethyl)pyridine (LH) under different pH conditions.

Thermodynamic data for the copper(II) complexes of LH have been reported previously [5–11] and detailed IR studies have also been undertaken [12]. Two LH ligands have been well documented to bind in a bidentate fashion to copper(II) to form 5-membered chelate rings via their N,O donor atoms. In the absence of added base, each LH remains protonated forming either a five- or six-coordinate species, depending on the counter anion present. This leaves each alcohol hydrogen free to act as a proton donor [13,14]. In addition to a number of copper(II)/carboxylate derivatives [13], one structure with nitrate as the counter anion [14] has been reported. However, at higher pHs LH is known to deprotonate in the presence of this metal ion to form $[Cu(L)_2]\cdot 4H_2O$, in which two deprotonated ligands (L) bind to the copper in a *trans* square planar arrangement [5–12]. Two further copper(II) structures derived from LH have been reported; the first contains a cubane-like Cu_4O_4 motif with bridging succinate [15] and another has the composition $[Cu(L)(NCS)]_2$ and incorporates a μ-alkoxo bridge [16]. The former structure forms interesting nanoporous 2D sheets which stack via π–π interactions between pyridyl units. We now report a synthetic and X-ray study of the complex structures and crystal arrangements present in three copper(II) complexes derived from 2-(hydroxymethyl)pyridine (LH).

2. Experimental

Reagents and solvents were purchased from commercial sources and were used without further purification. Positive ion electrospray ionisation mass spectra were obtained on a Finnigan LCQ-8 spectrometer with the sample dissolved in methanol/water. Microanalyses were obtained at the Department of Chemistry, TU Dresden.

2.1. Complex synthesis

2.1.1. $[Cu(LH)_2Cl]Cl\cdot H_2O$

$CuCl_2\cdot 2H_2O$ (0.782 g, 4.58 mmol) in ethanol (30 mL) was mixed with 2-(hydroxymethyl)pyridine (1.013 g, 9.28 mmol) in ethanol (20 mL) (indicator paper indicated a pH of ~5). The resulting dark green solution was stirred for 30 min. Green-blue crystals of the title compound were obtained by slow diffusion of ether vapour into the resulting solution over 5 d. A crystal from this crop was used for the X-ray structure determination. The remaining crystals were collected, washed with diethylether then allowed to dry in air. ESI-MS: *m*/*z* 280 $[Cu(L)(LH)]^+$. Yield: 0.952 g (56%). *Anal.* Calc. for $C_{12}H_{16}CuCl_2N_2O_3$: C, 38.87; H, 4.35; N, 7.56. Found: C, 38.62; H, 4.12; N, 7.50%.

2.1.2. $[Cu(LH)_2(NO_3)_2]$

This complex was prepared by a modification of a previously reported synthetic procedure [10]. $Cu(NO_3)_2\cdot 2.5H_2O$ (0.477 g, 2.05 mmol) in ethanol (10 mL) was added to 2-(hydroxymethyl)pyridine (0.448 g, 4.11 mmol) in ethanol (10 mL) (indicator paper indicated a pH of ~5). The resulting dark green solution was stirred for 3 h at 40 °C. Blue crystals of the title compound were obtained by slow diffusion of diethyl ether into the resulting solution over 3 d. A crystal from this crop was used for the X-ray structure determination. The remaining crystals were collected, washed with diethylether then allowed to dry in air. Yield: 0.516 g (62%); ESI-MS: *m*/*z* 280 $[Cu(LH)(L)]^+$; *m*/*z* 343 $[Cu(LH)_2NO_3]^+$. *Anal.* Calc. for $C_{12}H_{14}CuN_4O_8$: C, 35.52; H, 3.48; N, 13.81. Found: C, 35.52; H, 3.34; N, 13.82%.

2.1.3. $[Cu(L)_2]\cdot 4H_2O$

This complex was prepared by a modification of a reported synthesis for a related complex [10]. $CuCl_2\cdot 2H_2O$ (0.393 g, 2.31 mmol) in ethanol (20 mL) was mixed with 2-(hydroxymethyl)pyridine (0.504 g, 4.62 mmol) in ethanol (10 mL). The resulting dark green solution was stirred for 3 h (40 °C) and then adjusted to pH 10 with tetraethylammonium hydroxide. The dark violet solution was allowed to evaporate slowly at ambient temperature over 10 d. Violet crystals formed and one of these was used directly for the X-ray determination. The remainder were washed with diethylether then allowed to dry in air. ESI-MS: *m*/*z* 280 $[Cu(L)(LH)]^+$. Yield: 0.675 g (83%). *Anal.* Calc. for $C_{12}H_{20}CuN_2O_6$: C, 41.01; H, 5.74; N, 7.97. Found: C, 41.05; H, 5.74; N, 8.04%. Substitution of $Cu(NO_3)_2\cdot 2.5H_2O$ or $CuSO_4\cdot 5H_2O$ (in 10 mL of water) in the required stoichiometry for $CuCl_2\cdot 2H_2O$ in this procedure also gave the above product in satisfactory yield in each case.

2.2. X-ray structure determinations

We determined a low temperature X-ray structure of $[Cu(LH)_2(NO_3)_2]$ as part of the present study, but note that it is a redetermination of the reported structure obtained at room temperature [14]. While the results from this and our determination are quite similar, in view of our structure being obtained at low temperature we have included brief details of its determination along with those of the other two (new) structures obtained in the present study.

Data for $[Cu(LH)_2(NO_3)_2]$ were collected at 150(2) K with ω scans to approximately 56° 2θ using a Bruker SMART 1000 diffractometer employing graphite-monochromated Mo Kα radiation generated from a sealed tube (0.71073 Å). For $[Cu(LH)_2Cl]Cl$ and $[Cu(L)_2]\cdot 4H_2O$ data were collected at 150(2) K with φ and ω scans to approximately 66° 2θ using a Bruker-Nonius APEX2-X8-FR591 diffractometer employing graphite-monochromated Mo Kα radiation generated from a rotating anode (0.71073 Å). Data integration and reduction were undertaken with SAINT

and XPREP [17] and subsequent computations were carried out using the WINGX-32 graphical user interface [18]. Structures were solved by direct methods using SIR97 [19]. Multi-scan empirical absorption corrections were applied to data sets using the program SADABS [20]. Data were refined and extended with SHELXL-97 [21]. Non-hydrogen atoms were refined anisotropically. Carbon-bound hydrogen atoms were included in idealised positions and refined using a riding model. Oxygen-bound hydrogen atoms that were structurally evident in the difference Fourier map were included and refined with bond length and angle restraints.

ORTEP depictions of the crystal structures are provided in Figs. 1, 3 and 5. Schematic depictions are given in Figs. 2, 4, 6, 7 and 1S in the ESI†. Hydrogen bonding information is given in Table 1. Where applicable, additional details relating to the X-ray crystal structure refinement are given below and in the ESI† (along with tables of selected bond lengths and angles).

2.3. Crystal structure and refinement data

$$R_1 = \sum ||F_o| - |F_c|| / \sum |F_o| \quad \text{for} \quad F_o > 2\sigma(F_o)$$

$$\text{and} \quad wR_2 = \left\{ \sum [w(F_o^2 - F_c^2)^2] / \sum [w(F_c^2)^2] \right\}^{1/2}$$

where $w = 1/[\sigma^2(F_o^2) + (AP)^2 + BP]$, $P = (F_o^2 + 2F_c^2)/3$ and A and B are listed with the crystal data for each structure.

2.3.1. [Cu(HL)$_2$Cl]Cl

Formula $C_{12}H_{14}Cl_2CuN_2O_2$, $M = 352.69$, monoclinic, space group: $C2/c$(#15), $a = 5.0270(2)$, $b = 24.3050(12)$, $c = 11.3930(4)$ Å, $\beta = 97.489(3)°$, $V = 1380.14(10)$ Å^3, $D_c = 1.697$ g cm^{-3}, $Z = 4$, crystal size 0.229 by 0.049 by 0.028 mm, colour intense blue, habit needle, temperature = 150(2) K, λ(Mo–Kα) = 0.71073 Å, μ(Mo–Kα) = 1.967 mm^{-1}, T(SADABS)$_{min,max} = 0.826$, 0.946, $2\theta_{max} = 67.04$, hkl range −7 to 7, −37 to 37, −17 to 17, $N = 31\,160$, $N_{ind} = 2711$ ($R_{merge} = 0.0853$), $N_{obs} = 1942(I > 2\sigma(I))$, $N_{var} = 91$, residuals: $R_1(F) = 0.0403$, $wR_2(F^2) = 0.0959$, Goodness-of-fit (all) = 1.026, $A = 0.0342$, $B = 2.3008$, $\Delta\rho_{min,max}$: −0.966, 0.494 e$^-$ Å^{-3}.

Table 1
Selected hydrogen-bond geometries in [Cu(LH)$_2$Cl]Cl, [Cu(LH)$_2$(NO$_3$)$_2$], and [Cu(L)$_2$] · 4H$_2$O

D–H	A	H ⋯ A (Å)	D ⋯ A (Å)	D–H ⋯ A (°)
[Cu(LH)$_2$Cl]Cl				
O(1)–H(7)	Cl(2)^{i}	2.17(2)	3.0084(16)	178(2)
[Cu(LH)$_2$(NO$_3$)$_2$]				
O(1)–H(7)	O(3)^{ii}	1.75(2)	2.5484(18)	161(2)
[Cu(L)$_2$] · 4H$_2$O				
O(2)–H(7)	O(1)^{iii}	1.86(3)	2.727(2)	171(3)
O(2)–H(8A)	O(2)^{iv}	1.94(2)	2.724(3)	147(6)
O(2)–H(8B)	O(2)^{ii}	1.98(5)	2.727(3)	140(5)

Symmetry codes: (i) $1 + x, y, z$; (ii) $1 + x, y, z$; (iii) $-x, y, -z$; (iv) $x, 1 - y, z$; (vii) $-x, y, 1 - z$.

2.3.2. [Cu(HL)$_2$(NO$_3$)$_2$]

Formula $C_{12}H_{14}Cu_1N_4O_8$, $M = 405.82$, monoclinic, space group: $P2_1/n$(#14), $a = 7.4421(15)$, $b = 12.233(3)$, $c = 8.4270(17)$ Å, $\beta = 103.779(3)°$, $V = 745.1(3)$ Å^3, $D_c = 1.809$ g cm^{-3}, $Z = 2$, crystal size 0.192 by 0.147 by 0.134 mm, colour pale blue, habit plate, temperature = 150(2) K, λ(Mo–Kα) = 0.71073 Å, μ(Mo–Kα) = 1.521 mm^{-1}, T(SADABS)$_{min,max} = 0.706$, 0.816, $2\theta_{max} = 56.70$, hkl range −9 to 9, −15 to 16, −11 to 10, $N = 7279$, $N_{ind} = 1804$ ($R_{merge} = 0.0277$), $N_{obs} = 1541(I > 2\sigma(I))$, $N_{var} = 118$, residuals: $R_1(F) = 0.0256$, $wR_2(F^2) = 0.0687$, Goodness-of-fit (all) = 1.047, $A = 0.0365$, $B = 0.2713$, $\Delta\rho_{min,max}$: −0.186, 0.377 e$^-$ Å^{-3}.

2.3.3. [Cu(L)$_2$] · 4H$_2$O

Formula $C_{12}H_{20}CuN_2O_6$, $M = 351.84$, monoclinic, space group: $C2/m$(#12), $a = 13.4460(14)$, $b = 7.1130(7)$, $c = 8.2370(7)$ Å, $\beta = 110.674(6)°$, $V = 737.07(12)$ Å^3, $D_c = 1.585$ g cm^{-3}, $Z = 2$, crystal size 0.130 by 0.114 by 0.094 mm, colour purple, habit multiface, temperature = 150(2) K, λ(Mo–Kα) = 0.71073 Å, μ(Mo–Kα) = 1.510 mm^{-1}, T(SADABS)$_{min,max} = 0.789$, 0.868, $2\theta_{max} = 71.00$, hkl range −19 to 19, −10 to 9, −13 to 12, $N = 7562$, $N_{ind} = 1388$ ($R_{merge} = 0.0293$), $N_{obs} = 1242(I > 2\sigma(I))$, $N_{var} = 71$, residuals: $R_1(F) = 0.0373$, $wR_2(F^2) = 0.0844$, Goodness-of-fit (all) = 1.056, $A = 0.0298$, $B = 1.5883$, $\Delta\rho_{min,max}$: −0.661, 0.756 e$^-$ Å^{-3}.

3. Results and discussion

The 2:1 reaction of 2-(hydroxymethyl)pyridine (LH) with copper(II) chloride in ethanol at pH ~5 resulted in a colour change from dark green to blue-green. Slow diffusion of diethyl ether vapour into the resulting solution resulted in the formation of blue crystals of stoichiometry Cu(LH)$_2$Cl$_2$ suitable for X-ray analysis. In accord with related prior work, it was envisaged that ligand LH would remain in its protonated form on coordination at this pH and this was thus found to occur. The resulting structure is presented in Fig. 1.

The copper(II) ion is 5-coordinate and adopts a distorted trigonal bipyramidal geometry with the two pyridyl nitrogen donors occupying the axial positions. Two hydroxyl oxygens and a chloride ligand occupy the equatorial positions; the N(1)–Cu–N(1) and O(1)–Cu–Cl(1) bond angles are 173° and 136°, respectively. The second chloride ion is not coordinated, but is hydrogen bound to two hydroxyl protons belonging to different (adjacent) complex units. This bonding motif is perpetuated throughout the lattice to yield a one-dimensional polymeric structure (Fig. 2). Related 'bound' hydroxy to chloride hydrogen bond interactions also occur in the structures of copper(II) chloride complexes of the related ligands, 2-(2-hydroxyethyl)pyridine and 2,6-bis(hydroxymethyl)pyridine [22–24]. In the present structure, adjacent one-dimensional polymer chains also interact weakly via C–H⋯Cl interactions with the separation between Cl(1) and H(2) being

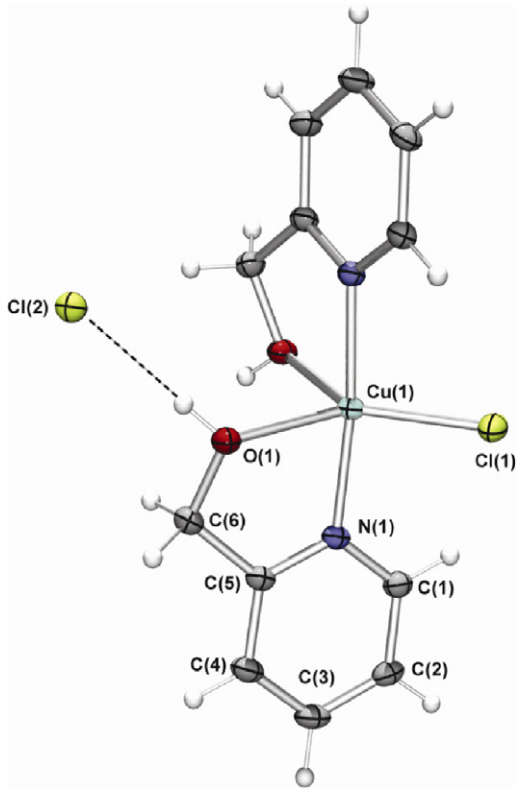


Fig. 1. An ORTEP plot of $[Cu(LH)_2Cl]Cl$ shown with 50% probability ellipsoids. Dashed line indicates a hydrogen bond.

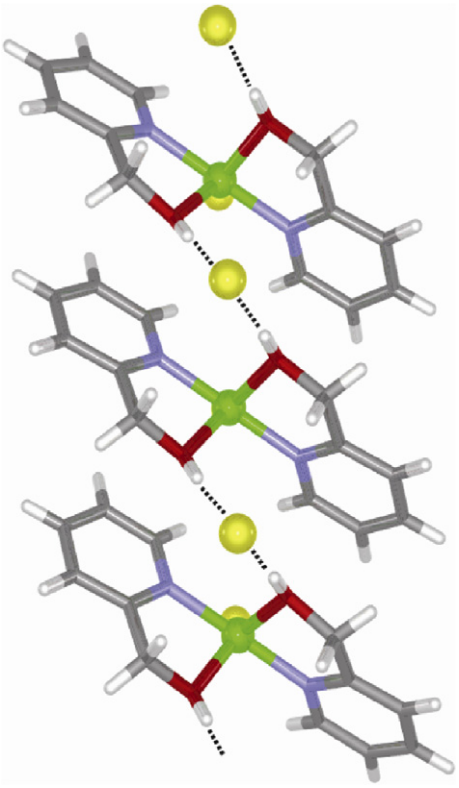


Fig. 2. View of the one-dimensional polymer formed via hydrogen bonding interactions between the hydroxy protons and the chloride anions (projection down the *b*-axis).

2.85 Å. A projection down the *a*-axis showing these interactions is given as Fig. 1S in the ESI. Two C–H to Cl–M distances occur C(1)–H(1)···Cl(1) and C(4)–H(4)···Cl(1) and range between 2.73 and 2.85 Å; both are shorter then the sum of van der Waals radii for hydrogen and chlorine (2.95 Å) [25].

In a similar fashion, the 2:1 reaction of LH with copper(II) nitrate in ethanol (also at pH ~5) resulted in a colour change to blue-green and slow diffusion of diethyl-ether vapour into this solution gave blue crystals of stoichiometry $Cu(LH)_2(NO_3)_2$ suitable for X-ray analysis. In contrast to the structure of the chloride derivative discussed above, the copper(II) ion in this case is octahedral with two nitrate anions occupying the axial positions and the equatorial positions occupied by *trans* bidentate LH ligands. This change in coordination from six to five may reflect the stronger binding of chloride (and hence its ability to donate electron density) over nitrate for latter first row transition metal ions such as copper(II). Again the hydroxyl proton acts as a hydrogen donor, in this case interacting with an oxygen from coordinated nitrate in an adjacent complex such that an infinite one-dimensional polymer is generated (Fig. 4). Similar O–H···O interactions are present in the literature structures of the related species $[Cu(LH)_2(CH_3CHBrCO_2)_2]$ and $[Cu(LH)_2(saccharato)_2]$ [13]. In the present structure pyridyl rings from each one-dimensional polymer chain π–π stack in an offset face to face arrangement with adjacent chains (~3.58 Å) forming an extended two-dimensional structure.

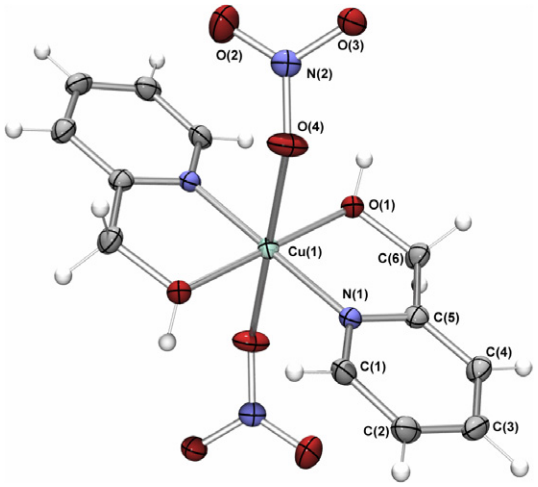


Fig. 3. An ORTEP plot of $[Cu(LH)_2(NO_3)_2]$ shown with 50% probability ellipsoids.

The addition of tetraethylammonium hydroxide to an ethanol solution of either of the above complexes to pH ~10, or indeed adjusting the pH of a solution of LH and copper(II) acetate or sulfate to this value leads to a colour change to deep purple. Slow evaporation of the resulting solution in each case led to the isolation of purple crystals (of identical habit and unit cell) of the previously reported complex $[Cu(L)_2]\cdot 4H_2O$. The X-ray structure of this product is presented in Fig. 5.

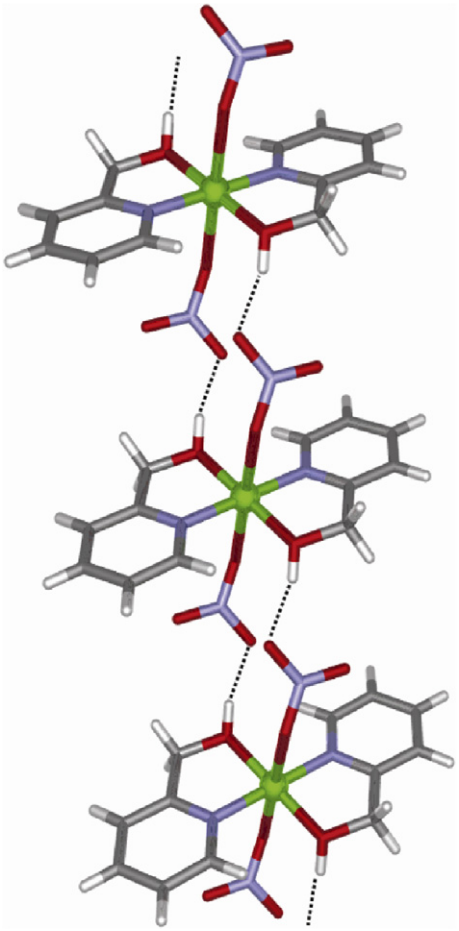


Fig. 4. A segment of the one-dimensional polymer formed by hydrogen bonding interactions in $[Cu(LH)_2(NO_3)_2]$; π-π interactions between chains (not shown) form two-dimensional sheets.

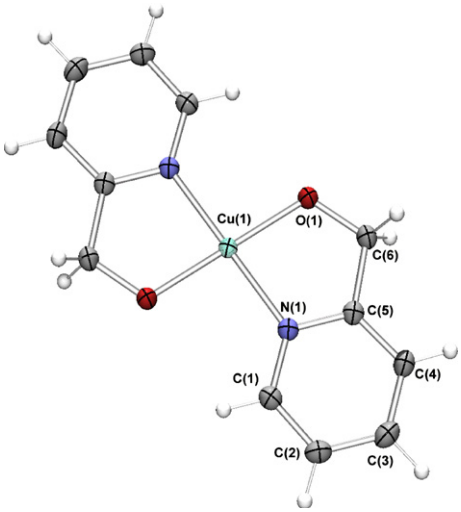


Fig. 5. An ORTEP plot representation of $[Cu(L)_2]\cdot 4H_2O$ shown with 50% probability ellipsoids. Solvent water molecules are omitted for clarity.

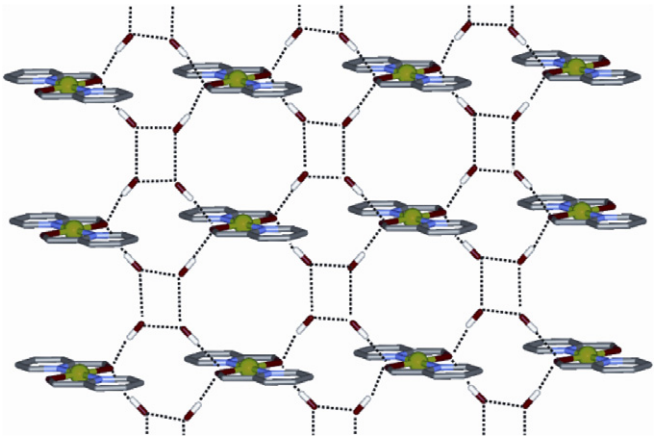


Fig. 6. A schematic representation of a segment of the two-dimensional hydrogen bonded arrangement in $[Cu(L)_2]\cdot 4H_2O$; π–π interactions between sheets (see Fig. 7) result in an infinite three-dimensional network. Hydrogen bonds are indicated by dashed lines.

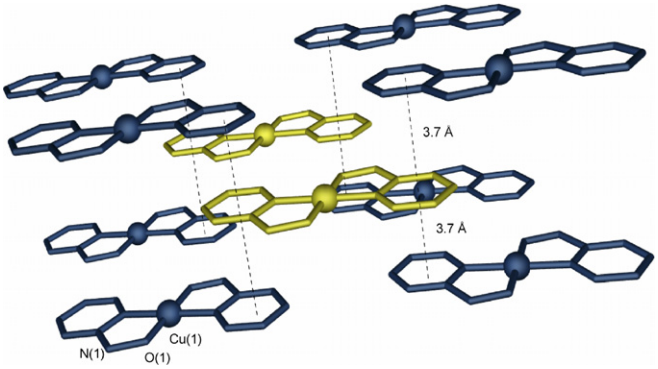


Fig. 7. Offset face-to-face π–π interactions in $[Cu(L)_2]\cdot 4H_2O$. Each of the two-dimensional sheets (blue) interact with adjacent sheets (yellow) via π–π interactions [ring centroid–ring centroid ~3.7 Å] resulting in the formation of an infinite three-dimensional network. (For interpretation of the references to color in this figure legend, the reader is referred to the web version of this article.)

In this case, the structure reveals that $[Cu(L)_2]\cdot 4H_2O$ has a square planar coordination geometry with the deprotonated (bidentate) 2-(hydroxymethyl)pyridine ligands coordinated mutually *trans*. As a consequence, bound oxygen atoms capable of acting as hydrogen bond acceptors have replaced the bound OH hydrogen bond donors in $[Cu(LH)_2Cl]Cl$ and $[Cu(LH)_2(NO_3)_2]$. This results in a change in the simple hydrogen bond patterns observed in the latter complexes to a more complicated arrangement in the former complex (Figs. 6 and 7).

A four-water hydrogen-bonded cluster is present in the structure which acts as a hydrogen bond donor to each of the deprotonated hydroxo atoms in $[Cu(L)_2]\cdot 4H_2O$ to form an infinite one-dimensional tape (see Fig. 6). In the tetrameric water cluster, each water molecule is involved in the formation of three hydrogen bonds, two of which are water–water interactions and one is with a metal complex hydroxo oxygen. Within the cluster, the four oxygen atoms in the tetramer are coplanar and the hydrogen atoms [H(7); H(8a) of O(2)] are at an angle of 32° above and below the ring. The average hydrogen bond distance within the water tetramer is 2.73 Å and is similar to the previously reported calculated value of 2.743 Å for a discrete water

tetramer [26]. Overall, the above water cluster/metal complex-containing tapes are linked via individual complex molecules such that infinite two-dimensional sheets result (Fig. 6).

Each of the two-dimensional sheets depicted in Fig. 6 interact further with adjacent sheets via offset face-to-face π–π interactions (~3.7 Å), resulting in the formation of an infinite three-dimensional network (Fig. 7). Thus, anion substitution in the reaction solution has resulted in a switch from a one-dimensional polymer in the case of $[Cu(LH)_2Cl]Cl$ to a two-dimensional polymer in the case of $[Cu(LH)_2(NO_3)_2]$ and a pH change involving either system results in the formation of the three-dimensional network found in $[Cu(L)_2]\cdot 4H_2O$.

4. Concluding remarks

The present study reports an investigation of the complex structures and crystal arrangements present in three copper(II) complexes derived from 2-(hydroxymethyl)pyridine. The study illustrates the manner by which 'pH switching' of a proton donor to a proton acceptor in the reaction solution used to synthesise the corresponding copper(II) complexes results in significant additional complexity in the resulting crystal network in the latter case.

Acknowledgements

We thank the Australian Research Council and the Deutsche Forschungsgemeinschaft for support. B.A. gratefully acknowledges the Max-Buchner-Stiftung for a research grant and Dr. Catherine Saccavini for assistance.

Appendix A. Supplementary material

CCDC 615290, 615291 and 615292 contain the supplementary crystallographic data for the three crystal structures. These data can be obtained free of charge via http://www.ccdc.cam.ac.uk/conts/retrieving.html, or from the Cambridge Crystallographic Data Centre, 12 Union Road, Cambridge CB2 1EZ, UK; fax: (+44) 1223-336-033; or e-mail: deposit@ccdc.cam.ac.uk. Supplementary data associated with this article giving additional data for the X-ray structures can be found, in the online version, at doi:10.1016/j.poly.2006.08.031.

References

[1] (a) L.F. Lindoy, I.M. Atkinson, Self-assembly in Supramolecular Systems, Royal Society of Chemistry, Cambridge, UK, 2000;
(b) R.M. Yeh, A.V. Davis, K.N. Raymond, in: J.A. McClevety, T.J. Meyer (Eds.), Comprehensive Coordination Chemistry II, vol. 7, Elsevier, Oxford, UK, 2004, p. 327.
[2] (a) C. Janiak, Dalton Trans. (2003) 2781;
(b) O.M. Yaghi, M. O'Keeffe, N.W. Ockwig, H.K. Chae, M. Eddaoudi, J. Kim, Nature 423 (2003) 705;
(c) S. Kitagawa, R. Kitaura, S.-I. Noro, Angew. Chem., Int. Ed. 43 (2004) 2334;
(d) D. Bradshaw, J.B. Claridge, E.J. Cussen, T.J. Prior, M.J. Rosseinsky, Acc. Chem. Res. 38 (2005) 273;
(e) C.J. Kepert, Chem Commun. (2006) 695.
[3] (a) J.K. Clegg, L.F. Lindoy, J.C. McMurtrie, D. Schilter, Dalton Trans. (2005) 857;
(b) J.K. Clegg, L.F. Lindoy, J.C. McMurtrie, D. Schilter, Dalton Trans. (2006) 3114;
(c) J.K. Clegg, K. Gloe, M.J. Hayter, O. Kataeva, L.F. Lindoy, B. Moubaraki, J.C. McMurtrie, K.S. Murray, D. Schilter, Dalton Trans. (2006) 3977.
[4] See, for example M.M. Bishop, L.F. Lindoy, A. Parkin, P. Turner, Dalton Trans. (2005) 2563, and refs. therein.
[5] T.J. Lane, A.J. Kandathil, S.M. Rosalie, Inorg. Chem. 3 (1964) 487.
[6] J. Pinart, C. Petitfaux, J. Faucherre, CR Acad. Sci. Ser. C 281 (1975) 519.
[7] O. Heijiro, Nippon Kagaku Zasshi 86 (1965) 718.
[8] C. Petifaux, Annal. Chim. 8 (1973) 33.
[9] C. Tissier, C. Missegue, J. Chim. Phys. Phys. – Chim. Biologique 65 (1968) 2037.
[10] C. Petitfaux, CR Acad. Sci. Ser C 266 (1968) 465.
[11] Y. Murakami, M. Takagi, Bull. Chem. Soc. Jpn. 38 (1965) 828.
[12] H. Shindo, J.L. Walter, R.J. Hooper, J. Inorg. Nucl. Chem. 27 (1955) 871.
[13] (a) J. Moncol, M. Mudra, P. Lönnecke, M. Koman, M. Melnik, J. Coord. Chem 57 (2004) 1065;
(b) V.T. Yilmaz, S. Guney, O. Andac, W.T.A. Harrison, Polyhedron 21 (2002) 2393;
(c) J. Maroszova, P. Stachova, Z. Vaskova, D. Valigura, M. Koman, Acta Crystallogr. E62 (2006) m109;
(d) N.N. Hoang, F. Valach, M. Dunaj-Jurco, M. Melnik, Acta Crystallogr. C48 (1992) 443.
[14] F. He, D. Liu, Acta Crystallogr. E61 (2005) m1350.
[15] S.G. Ang, B.W. Sun, S. Gao, Inorg. Chem. Commun. 7 (2004) 795.
[16] S.-C. Cheng, H.-H. Wei, Inorg. Chim. Acta 340 (2002) 105.
[17] Bruker, SMART, SAINT and XPREP, Bruker Analytical X-ray Instruments Inc., Madison, Wisconsin, USA, 1995.
[18] L.J. Farrugia, WINGX-32: system of programs for solving, refining and analysing single crystal X-ray diffraction data for small molecules, J. Appl. Cryst. 32 (1999) 837.
[19] A. Altomare, M.C. Burla, M. Camalli, G.L. Cascarano, C. Giocavazzo, A. Guagliardi, A.G.C. Moliterni, G. Polidori, S. Spagna, J. Appl. Cryst. 32 (1999) 115.
[20] G.M. Sheldrick, SADABS: Empirical Absorption and Correction Software, University of Göttingen, Germany, 1999.
[21] G.M. Sheldrick, SHELXL-97: Programs for Crystal Structure Analysis, University of Göttingen, Germany, 1997.
[22] S. Hamamci, V.T. Yilmaz, C. Thöne, Acta Crystallogr. E60 (2004) m159.
[23] S. Winter, W. Seichter, E. Weber, Z. Anorg. Allg. Chem. 630 (2004) 434.
[24] V.T. Yilmaz, S. Hamamci, C. Thöne, J. Coord. Chem. 56 (2003) 787.
[25] A.J. Bondi, J. Chem. Phys. 68 (1964) 441.
[26] S.S. Xantheas, J. Chem. Phys. 102 (1995) 4505.

Available online at www.sciencedirect.com
ScienceDirect
Polyhedron 26 (2007) 679–685
POLYHEDRON
www.elsevier.com/locate/poly

The new type of $[Zr_6(\mu_3\text{-}O)_4(\mu_3\text{-}OH)_4]$ cluster core: Crystal structure and spectral characterization of $[Zr_6O_4(OH)_4(OOCR)_{12}]$ ($R = Bu^t$, $C(CH_3)_2Et$)

P. Piszczek [a,*], A. Radtke [a], A. Grodzicki [a], A. Wojtczak [a], J. Chojnacki [b]

[a] *Faculty of Chemistry, Nicolaus Copernicus University, ul. Gagarina 7, 87-100 Toruń, Poland*
[b] *Chemical Faculty, Gdańsk University of Technology, ul. G. Narutowicza 11/12, 80-952 Gdańsk, Poland*

Received 12 July 2006; accepted 28 August 2006
Available online 3 September 2006

Abstract

Hexanuclear Zr(IV) oxo carboxylate derivatives of the general formula $[Zr_6O_4(OH)_4(OOCR')_{12}]$ ($R' = Bu^t$ (**1**), $C(CH_3)_2Et$ (**2**)) were synthesized from $Zr(OR)_4$ ($R = Pr^i$, $C(CH_3)_2Et$) and appropriate organic acids ($HOOCR'$, $R' = Bu^t$, $C(CH_3)_2Et$) in a molar ratio 1:2. The crystal structures of **1** and **2** were solved in the centrosymmetric $R\bar{3}$ space group. Zirconium atoms form hexanuclear Zr(IV) clusters, linked by 4:4 system of μ_3-oxo/hydoxo bridges and stabilized by *syn–syn* carboxylate groups. Each of the metal ions is surrounded by eight oxygen atoms derived from four μ_3-O; oxo/hydroxo bridges, and four μ-O; carboxylate ones. Analysis of crystallographic and spectroscopic data suggests that four protons migrate between eight oxide bridges of the $[Zr_6O_4(OH)_4(OOCR')_{12}]$ cluster. Thermogravimetric and temperature variable (VT IR) studies have been carried out in order to determine the thermal behaviors of **1** and **2**.
© 2006 Elsevier Ltd. All rights reserved.

Keywords: Zirconium(IV) complexes; Oxo/hydroxo carboxylates; Crystal structure; IR; NMR

1. Introduction

Synthesis and properties of zirconium oxo clusters have been studied extensively in search for the novel type inorganic–organic hybrid polymers [1,2], and precursors of solid-state materials used mainly in sol–gel, but also in chemical vapor deposition methods (CVD) [2–5]. The reaction of $Zr(OR)_4$ with organic acids ($HOOCR'$) yields the multinuclear oxo complexes regardless of the molar ratio employed [6–10]. Kickelbick et al. reported that the reaction of Zr(IV) alkoxides with corresponding organic acids, using the molar ratio 1:4, proceeded with formation of carboxylate derivatives of general formulas $[Zr_6(OH)_4O_4(OMc)_{12}]$ and $[Zr_4O_2(OMc)_{12}]$ [7,8]. In the structure of $[Zr_6(OH)_4O_4(OMc)_{12}]$, zirconium atoms (coordination number 8) form hexanuclear clusters linked by μ_3-oxo and μ_3-hydroxo bridges, which are stabilized by 12 methacrylate ligands. Three of them chelate the Zr(IV) atoms, while the remaining nine carboxylate groups participate in *syn–syn* bridges. The hydrogen atoms of the bridging groups have not been located, however, analysis of Zr–O bond distances and the charge balance indicates the presence of four μ_3-OH groups [6]. A similar type of clusters has also been detected in structures of $[Zr_6(OH)_2O_6(OOCHPh_2)_{10}(phen)_2]$ and also $[Ti_6O_8(\eta^5\text{-}C_5H_5)_6]$ (in this case, the formation of $[Ti(IV)_4Ti(III)_2O_8]$ clusters was postulated) [11,12]. Crystals of other complexes: $[Zr_4O_2(OMc)_{12}]$, $[Zr_6O_2(OPr^i)_{16}(OOC\text{–}C_{10}H_6O)_2]$, $[Zr_6O_2(OMe)_4(OBu^n)_2(OMc)_{14}]$, $[Zr_6O_2(OBu^n)_{10}(OMc)_{10}]$, have been obtained with a 6–15 folds excess of the organic acid ($HOOCR'$, $R' = C_{10}H_6OH$, $CMe{=}CH_2$) [6–8,13]. When Zr/carboxylate ligand ratio was increased from 1:2 to 1:3, as for $[Zr_4O_2(OMc)_{12}]$, the structure of cluster opened up and a distorted butterfly arrangement was formed [6]. The application of sterically varied carboxylic acids

* Corresponding author. Fax: +48 56654 24 77.
E-mail address: piszczek@chem.uni.torun.pl (P. Piszczek).

0277-5387/$ - see front matter © 2006 Elsevier Ltd. All rights reserved.
doi:10.1016/j.poly.2006.08.025

(HOOCR′; R′ = H, CH_3, Pr^i, Bu^t, CH_2Bu^t) in the reaction with zirconium(IV) alkoxides (molar ratio 1:1) leads to the formation of the following products: $[Zr_4O_2(O_2CH)_2(OPr^i)_{10}]$, $[Zr_3O(O_2CCH_3)_5(OPr^i)_5]$, $[Zr_2(OPr^i)_6(O_2CPr^i)_2]_2$, $[Zr_2O(O_2CBu^t)(OPr^i)_7](HOPr^i)_2$, $[Zr_2O(O_2CH_2Bu^t)_2(OPr^i)_6](HOPr^i)$ [9].

A series of multinuclear Ti(IV) oxo carboxylate derivatives with oligomeric ring-shape molecules were synthesized through the reaction of branched acids (HOOCR′, R′ = Bu^t, $C(CH_3)_2Et$) with titanium(IV) alkoxides in a molar ratio 1:2 [14]. Therefore, the aim of the reported research was the synthesis and structural characterization of the novel multinuclear Zr(IV) oxo carboxylate derivatives, obtained in a reaction between $Zr(OR)_4$ (R = Pr^i, $C(CH_3)_2Et$) and HOOCR′ (R′ = Bu^t and $C(CH_3)_2Et$). Thermal behavior of synthesized compounds was studied using thermogravimetric analysis and variable temperature (VT IR) spectroscopy.

2. Results and discussion

Hexanuclear Zr(IV) oxo carboxylate derivatives were prepared in the reaction of the respective zirconium alkoxide ($Zr(OR)_4$, R = Pr^i, $C(CH_3)_2Et$) with the twofold excess of the organic acid (HOOCR′ (R′ = Bu^t, or $C(CH_3)_2Et$)) at room temperature under Ar atmosphere. Considering the literature data [7], the above reaction can be illustrated by the overall equation (1).

$$6Zr(OR')_4 + 20RCOOH \xrightarrow{RT,\ Ar} [Zr_6O_4(OH)_4(OOCR)_{12}] + 8RC(O)OR' + 16R'OH \quad (1)$$

where R′ = Pr^i, $C(CH_3)_2Et$, R = Bu^t, $C(CH_3)_2Et$.

Initially the reaction mixture became turbid, but after 12 h the clear solution was formed. The colorless crystals, suitable for single crystal X-ray studies, were grown by slow evaporation (glovebox, RT) of the solvent after 1 day. Results of elemental analysis suggest the formation of the complex of general formula $[Zr_6O_4(OH)_4(OOCR')_{12}]$ (R′ = Bu^t (**1**), $C(CH_3)_2Et$ (**2**)). The obtained compounds were insoluble in aliphatic and sparingly soluble in aromatic solvents. Although synthesized complexes are relatively stable in the air and not sensitive to the moisture, they were stored at room temperature and under the argon atmosphere during all experiments.

3. X-ray crystallographic structures

Single crystals X-ray analysis revealed that **1** and **2** crystallize in the centrosymmetric $R\bar{3}$ (no. 148) space group for the series of crystals, for which diffraction data were collected at 293 K (Table 1). The structures of these compounds consist of hexanuclear $[Zr_6(\mu_3\text{-}O)_8]^{12+}$ clusters where six equivalent metal ions are arranged in the corners of an octahedron (Fig. 1). Consequently, in all the investigated structures the $[Zr_6(\mu_3\text{-}O)_8]^{12+}$ cluster symmetry was C_{3i}. Since two oxygen atoms (O1) were located on the threefold axis, they were related only by the center of symmetry, and are chemically and structurally identical. The other six oxygen atoms (O2) are related to each other by both the threefold axis and the center, therefore being chemically and structurally equivalent. According to above data, the 2:6 distributions of structurally different oxygen bridges was detected in the cluster as a consequence of the molecular symmetry. That problem is discussed further in the IR spectroscopy section of the paper. The cluster might be constituted by both oxo and hydroxy groups bridging the metal ions. For six Zr^{4+} centers, the electrostatic compensation would require four bridges of each type, besides 12 carboxylate ligands present in the structure. Therefore, the neutral cluster should be built with 4:4 systems of oxo/hydroxy bridges. Contrary to that, the molecular symmetry requirements imposed by the crystal structure allow only 6:2 or 8:0 composition of the bridges. The question of their nature is even more convoluted, since the crystallographic data have shown no trace of any peak that would correspond to the hydrogen atoms belonging to hydroxyl groups. If the cluster is built with eight oxo bridges, the total electric charge of the cluster would be −4, while for eight hydroxyl groups it would be +4.

The crystal structure determination at 293 K did not reveal any additional ions in the crystal lattice that would compensate the non-zero charge of the cluster ion. Considering the previous reports [6] we assumed a mixed architecture with the 4:4 ratio of the O/OH bridges, what has to be consistent with the 6:2 structural constraints on the cluster composition. In this case, the two identical O1 atoms positioned on the threefold axis are related by the center of symmetry and could be either oxo or hydroxy bridges, while the remaining six have to be of identical chemical nature due to the crystallographic symmetry. Only the assumption that four protons migrate between six oxygen (O2) bridging groups permits the explanation of this problem. The oxo/hydroxy ratio within that set is 2:4 in case of two axial oxo bridges, and 4:2 for the axial hydroxyls, respectively. The statistical disorder, imposed by the crystallographic symmetry requirements, would result in 2/3 or 1/3 of hydrogen bound to each of those six bridges. The lack of clear peaks corresponding to the hydrogen atoms of OH groups on the electron density maps indicates their statistical disordering, further supporting the proposed hypothesis. However, no conclusions could be derived for the distribution of two types of oxygen bridges in the studied cluster. In order to improve the quality of crystal structures, the low temperature (at 103 and 123 K) X-ray diffraction studies have been carried out. The cluster architecture and symmetry was identical to that found at 293 K. It is interesting that results of the structure determination were worse than those obtained at room temperature (unpublished results). That may be explained by the observed changes in the stability of crystals with the decrease of the temperature (Fig. 3).

Table 1
Crystallographic data and data collection details

	1	2
Formula sum	$Zr_6O_{32}C_{60}H_{108}$	$Zr_6O_{32}C_{72}H_{132}$
Formula weight	1886	1980
Crystal system	rhombohedral	rhombohedral
Space group	$R\bar{3}$ (no. 148)	$R\bar{3}$ (no. 148)
Unit cell dimensions	$a = 13.498(3)$ Å $\alpha = 107.19(2)°$	$a = 14.064(2)$ Å $\alpha = 107.00(2)°$
Volume (Å^3)	2037.4(8)	2316.7(6)
Z	1	1
Density (calculated) (Mg/m^3)	1.513	1.406
Absorption coefficient (mm^{-1})	0.812	0.715
$F(000)$	948	1012
Crystal size (mm)	$0.10 \times 0.08 \times 0.06$	$0.20 \times 0.17 \times 0.15$
Theta range for data collection (°)	2.93–31.50	2.80–31.33
Index ranges	$-19 \leqslant h \leqslant 18$, $-19 \leqslant k \leqslant 19$, $-19 \leqslant l \leqslant 18$	$-17 \leqslant h \leqslant 19$, $-20 \leqslant k \leqslant 17$, $-20 \leqslant l \leqslant 19$
Reflections collected	19947	23122
Independent reflections	4235	4804
Transmission (maximum/minimum)	0.9529/0.9232	0.9003/0.8701
Refinement method	full-matrix LS	full-matrix LS
Data/restraints/parameters	4235/18/179	4804/16/206
Goodness-of-fit on F^2	1.239	1.143
Final R indices [$I > 2\sigma(I)$]	0.1437	0.0964
R indices (all data)	0.2483	0.1887
Largest difference in peak and hole	1.055 and −1.307	0.611 and −0.528

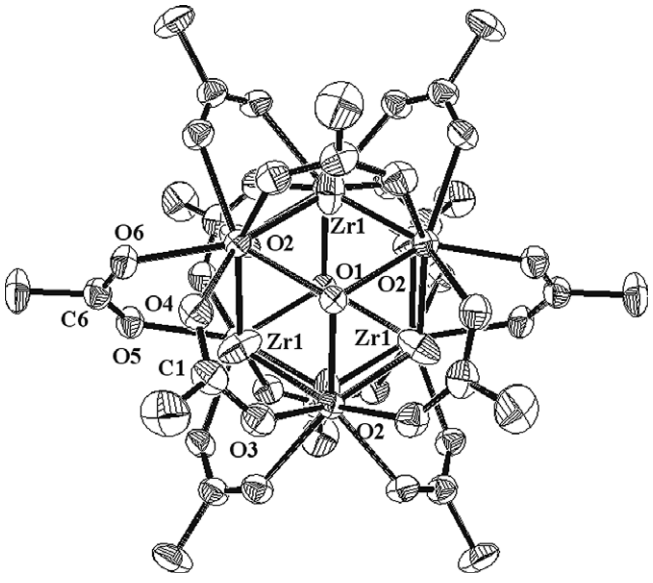


Fig. 1. Perspective view of the $[Zr_6O_4(OH)_4(OOCBu^t)_{12}]$ (**1**) cluster along the threefold axis coinciding with O1–O1′ direction. For clarity, the branched hydrocarbon groups of the carboxylates are not shown.

The distances between atoms within $[Zr_6O_4(OH)_4(OOCR')_{12}]$ cluster and in the coordination sphere of central cation are listed in Table 2. The average Zr1–Zr1 distances within **1** and **2** clusters are 3.510 Å and are similar to the analogous average distances in $[Zr_6(OH)_4O_4(OMc)_{12}]$ cluster [6]. The metal atoms of the octahedron are linked by μ_3-O bridges, which form the $\{Zr_6(\mu_3\text{-}O)_4(\mu_3\text{-}OH)_4\}$ clusters stabilized by twelve *syn–syn* bridges of carboxylate ligands. Each of Zr(IV) ions (coordination number 8) is surrounded by four oxygen atoms of μ_3-O/μ_3-OH bridges and four of carboxylato bridges μ-O(OOC). Oxygen atoms of oxo-bridges show two types of neighborhood: (a) O1 (2×) – where all Zr1–O1 distances are identical, and (b) O2 (4×) – where the narrow differences variation in the length of these bonds are noticed (Table 2). The bridging oxygen atoms are located slightly above each Zr_3 face of that octahedron. In **1** the deviations of the oxygen atoms from the best Zr_3 planes are 0.6807 and 0.6808 Å for O1 and O2 atoms, respectively. In **2**, the analogous deviations are 0.6766 and 0.6695 Å for O1 and O2 atoms, respectively. Trimethylacetate ligands of **1** form the asymmetric bridges, where the length of shorter Zr–O bonds varies in the range 2.202(7)–2.209(7) Å, and longer ones 2.232(7)–2.236(7) Å (C–O distances range 1.254(11)–1.260(12) Å, and 1.277(12)–1.279(11) Å). The presence of two non-equivalent carboxylate groups was also detected in the cluster of **2**. The length of Zr–O and O–C bonds being (a) Zr1–O3 = 2.210(5) Å, C1–O3 1.269(8) Å, and Zr1–O4 2.206(5) Å, C6–O4 1.262(8) Å and (b) Zr1–O5 2.224(5) Å, C6–O5 1.286(8) Å, and Zr1–O6 2.234(5) Å, C6–O6 1.281(8) for the stronger and weaker coordinated μ-OOC bridges, respectively.

Comparison of **1** and **2** crystallographic data with $[Zr_6(OH)_4O_4(OOCMc)_{12}]$ [6] reveled the clear differences in clusters structure, and their packing in the crystal lattice. The assignment of the bridging oxygen atoms to μ_3-O and μ_3-OH groups was possible basing on the analysis of Zr–O distances in $[Zr_6(OH)_4O_4(OOCMc)_{12}]$ (2.060–2.095 Å for μ_3-O, and 2.170–2.410 Å for μ_3-OH [6]). Significant differences in the Zr-(μ-OH) and Zr-(μ-O) bond length were also detected in other type of $[Zr_6(\mu\text{-}O)_n(\mu\text{-}OH)_m]$ cores [15]. Crystallographic data of **1** and **2** exhibited that the length of Zr-(μ_3-O/OH) bonds vary from 2.123(9) to 2.151(8) and from 2.128(5) to 2.138(6) Å, respectively (Table 2). Therefore, the use of criterion mentioned above for identification of μ_3-O and μ_3-OH groups in the structure of studied compounds is difficult. These differences are to small to determine which oxygen atoms may be attributed to oxo or hydroxo groups in the assumed $[Zr\text{-}(\mu_3\text{-}O)_4(\mu_3\text{-}OH)_4]$ core. The centrosymmetric space group and the narrow range of Zr-(μ_3-O/OH) bond length, detected for **1** and **2**, suggest that the migration of protons between oxygen bridges should be assumed. The way of carboxylate ligands association is a next difference between the structure of $[Zr_6(OH)_4O_4(OOCMc)_{12}]$ (chelating and bridging connections [6]) and the structures reported in this paper. The large, branched carboxylate ligands form only *syn–syn* bidendate bridges, stabilizing the $\{Zr\text{-}(\mu_3\text{-}O)\}^{4-}$ clusters. Moreover, their packing in the crystal lattice is different. Kickelbick and Schubert reported that in $[Zr_6(OH)_4O_4(OOCMc)_{12}]$ lattice six clusters are arranged in rings, which form large

Table 2
Selected bond lengths (Å)

$[Zr_6O_4(OH)_4(O_2CR)]$		
Bonds (Å)	R = Bu^t (**1**)	R = C(CH$_3$)$_2$Et (**2**)
ZR1–ZR1^{i}	3.510(2)	3.515(2)
ZR1–ZR1^{ii}	3.506(3)	3.510(1)
ZR1–O1^{iii}	2.133(6)	2.136(4)
ZR1–O2	2.123(9)	2.138(6)
ZR1–O2^{ii}	2.125(9)	2.137(5)
ZR1–O2^{iv}	2.151(8)	2.128(5)
ZR1–O3^{iv}	2.202(7)	2.210(5)
ZR1–O4	2.236(7)	2.206(5)
ZR1–O5	2.232(7)	2.224(5)
ZR1–O6^{i}	2.209(7)	2.234(5)
C1–O3	1.279(11)	1.269(8)
C1–O4	1.254(11)	1.262(8)
C6–O6	1.277(12)	1.286(8)
C6–O5	1.260(12)	1.281(8)

Symmetry codes: (i) y, z, x; (ii) $1-z$, $1-x$, $1-y$; (iii) z, x, y; (iv) $1-y$, $1-z$, $1-x$; (v) $1-x$, $1-y$, $1-z$.

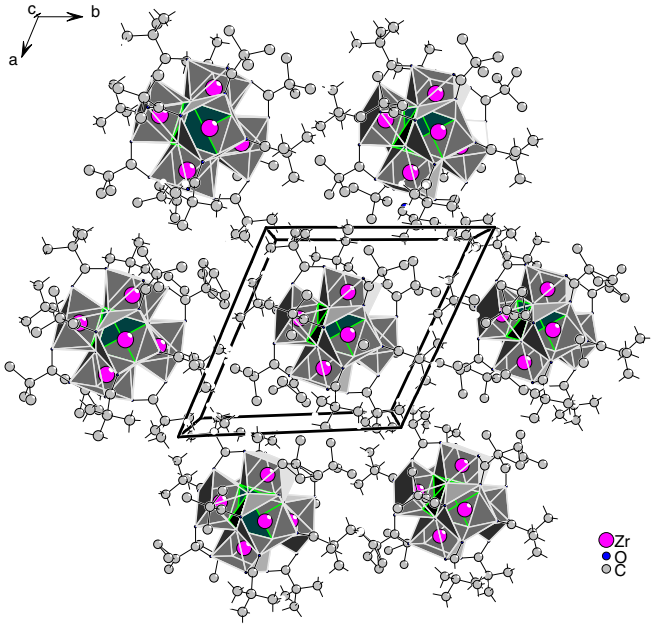


Fig. 2. Packing of the $[Zr_6O_4(OH)_4(OOCBu^t)_{12}]$ (**1**) clusters.

voids parallel to the *c*-axis [6]. The clusters in the structures of **1** and **2** also form rings, but interior of each of them is filled by additional seventh cluster (Fig. 2).

3.1. ^{13}C NMR characterization of Zr(IV) multinuclear oxo carboxylates

Solid-state ^{13}C NMR spectra of **1** and **2** crystalline powders were registered in order to determine the structural differences between the studied compounds (data deposited as a supplementary material). Analysis of these data revealed no significant differences in chemical shifts of methyl, methylene, and quaternary carbon in ^{13}C NMR spectra of studied compounds. Simultaneously, the clear differences were noticed for resonance signals of carbon atoms of coordinated carboxylate groups. The splitting of carboxylate carbon signals were detected in spectra **1** and **2** between 183 and 185 ppm. According to structural data and literature reports [14,16], their chemical shift is characteristic for carbons of bidendate carboxylate groups, which form *syn–syn* bridges. Splitting of these signals suggests the presence of a non-symmetrical carboxylate ligand in $[Zr_6(OH)_4O_4(OOCR')_{12}]$ clusters. Studies of ^{13}C NMR spectra of **1** and **2** in [D$_6$] benzene solutions show clear similarities in the chemical shifts of the resonance signals with their analogues in solid-state spectra (e.g. δ C (COO) $\cong$ 184 ppm in the solid state and $\delta \cong 185$ ppm in solution). This fact shows that $[Zr_6O_4(OH)_4(OOCR')_{12}]$ are stable and their structure does not change even in the solution. Simultaneously, signals from protons of OH or OD groups were not registered.

3.2. Infrared spectroscopy studies

The problems with identification of OH groups caused that cluster structure of **1** and **2** were also characterized by the infrared spectroscopy. IR spectra were recorded between 98 and 350 K, and the wavenumbers of absorption bands with their assignation are listed in Table 3.

Weak bands, which were found at 3672 and 3668 cm^{-1}, in spectra of **1** and **2**, respectively, can be attributed to stretching vibrations (ν(OH)) of bridging OH groups not involved in hydrogen bonds [15,17,18]. No bands corresponding to OH groups forming hydrogen bonds have been found. According to literature reports, the formation of hydrogen bonds results in the shift of the ν(OH) band towards lower wavenumbers, between 3150 and 3550 cm^{-1} [17]. The detection of bands assigned to stretching modes of OH groups (in spectra of **1** and **2**) confirms the presence of hydroxo groups in their structure. Possible effects associated with the protons migration in $[Zr_6O_4(OH)_4(OOCR')_{12}]$ clusters could be visible between 400 and 1000 cm^{-1}. That is the region, where bands corresponding to libration modes of OH groups, stretching vibrations of M-(μ_3-O/OH) bridges, as well as bending and rocking modes of carboxylate groups can be detected [17,19–21]. Analysis of spectra registered at room temperature (RT) exhibited the presence of middle intensity bands at 728 and 724 cm^{-1} for **1** and **2**, respectively. Considering results of previous studies, the frequencies mentioned above were attributed to asymmetric vibrations of the equivalent Zr-(μ_3-O) bridges [21]. In spectra registered at liquid nitrogen temperature (LNT), the splitting of this band was observed (Table 3, Fig. 3b). The proton migration effects caused that in spectra registered at room temperature the splitting of these bands was not observed. Simultaneously, the restrictions of proton migration between oxygen bridges at liquid nitrogen temperature

Table 3
Wavenumbers (cm^{-1}) for the vibrations of carboxylate groups and oxo bridges (Zr–O–Zr) in LNT spectra of $[Zr_6O_4(OH)_4(OOCR')_{12}]$ (where R = Bu^t (**1**), $C(CH_3)_2Et$ (**2**))

Modes	(**1**)		(**2**)	
	Wavenumber (cm^{-1})			
	LNT	RT	LNT	RT
υ (OH)	3676 (w)	3672 (w)	3672 (w)	3667 (w)
$\upsilon(CH_3)$	2957 (m), 2916 (m)	2957 (m), 2925 (m)	2963 (m), 2923 (m)	2965 (m), 2925 (m)
$\upsilon(CH_2)$			2873 (m)	2864 (m)
$\upsilon(CH_3)\upsilon(CH_2)$	2857 (m)	2857 (m)	2853 (m)	2856 (m)
υ_{as}(COO)	1570 (s)	1567 (s)	1566 (s)	1563 (s)
$\delta_{as}(CH_3)$, $\delta(CH_2)$	1485 (s), 1455 (w)	1483 (s)	1480 (s), 1465 (w)	1477 (s), 1452 (w)
υ_s(COO)	1425 (s)	1423 (s)	1417 (m)	1416 (m)
$\delta_s(CH_3)$	1378 (m), 1354 (m)	1377 (m), 1359 (m)	1377 (m), 1355 (m)	1375 (m), 1359 (m)
$\upsilon(C–(CH_3)_3)$, δ(C–C)			1289 (m)	1289 (m)
$\upsilon(C–(CH_3)_3)$, δ(C–C)	1237 (m), 1228 (m)	1226 (m)	1236 (vw), 1209 (m)	1206 (w)
			1186 (w)	1186 (w)
$\rho(CH_3)$	1030 (w)	1029 (w)	1067 (w), 1053 (w)	1065 (w), 1053 (w)
$\rho(CH_3)$	954 (w)	952 (w)	1006 (m)	1007 (m)
υ(C–C)	938 (w)	938 (w)	933 (w)	932 (w)
	818 (w), 805 (w) 788 (w)	816 (w), 805 (w) 788 (w)	813 (w), 805 (w) 799 (w), 766 (w)	800 (w), 768 (w)
υ_{as}(Zr–O–Zr)	729 (m), 718 (w)	728 (m)	725 (m), 717 (w)	724 (m)
δ(OCO)	682 (m)	680 (m)	679 (m)	678 (m)
			633 (m)	632 (m)
ρ(OCO); out of plane	609 (m), 582 (w)	608 (m), 580 (w)	598 (m), 573 (w)	596 (m), 573 (w)
ρ(OCO); in plane	482 (m), 455 (m)	481 (m), 454 (m)	485 (m), 465 (m)	483 (w), 461 (m)
υ(Zr–O), υ(Zr–OH)	427 (m), 420 (m)	419 (m)	457 (m), 417 (m)	455 (m), 419 (m)

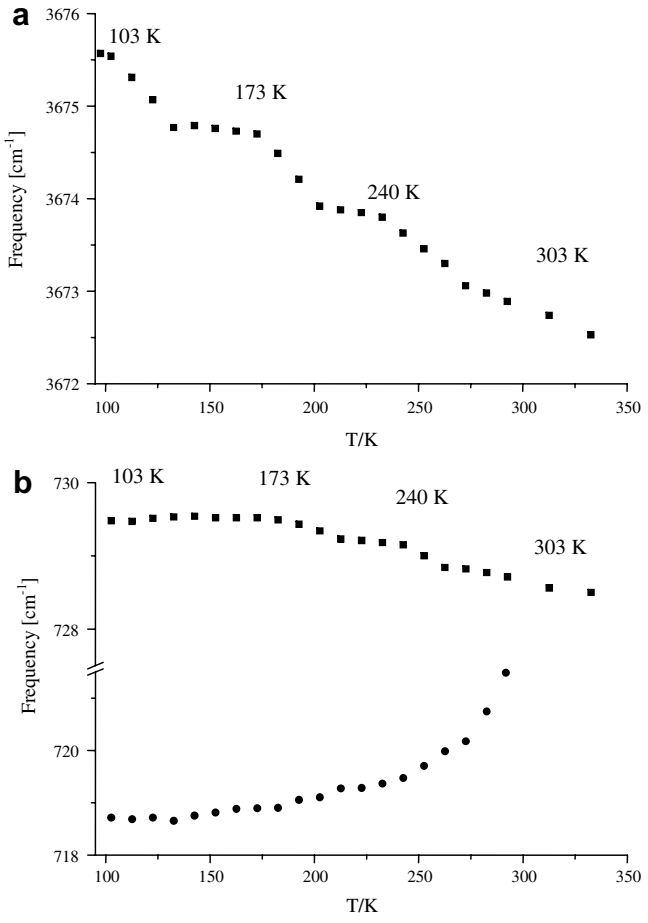


Fig. 3. The temperature dependence of the wavenumber of (a) υ(OH) (3672 cm^{-1}) and (b) υ_{as}(ZrOZr) (728 cm^{-1}) bands of $[Zr_6O_4(OH)_4(OOCBu^t)_{12}]$ (**1**) clusters.

(LNT) and the formation non-equivalent Zr-(μ_3-O/OH) bridges contribute to their splitting. Concluding, the results of IR and X-ray structure determination, give therefore the consistent basis for hypothesis of the proton migration occurring between six oxygen (O2) bridges.

Bands attributed to υ_{as}(COO) and υ_s(COO) vibrations have been detected in IR spectra of **1** and **2** between 1563–1570 cm^{-1} and 1416–1425 cm^{-1} (Table 3). Values of the $\Delta[\upsilon_{as}(COO) - \upsilon_s(COO)]$ parameter, being 147–145 cm^{-1}, are characteristic for bidendate carboxylate groups participating in *syn–syn* bridges [21–23]. Single bands, descended from asymmetric and symmetric vibrations of groups, indicate that all carboxylate groups form equivalent interactions in $[Zr_6O_4(OH)_4(OOCCR)_{12}]$ clusters. The presence of chelating and bridging carboxylate ligands, as in the case of $[Zr_6O_4(OH)_4(OMc)_{12}]$ [6], should result in the significant splitting of these bands. Absorption bands, which were detected between 400 and 700 cm^{-1}, can be attributed to COO bending and rocking vibrations of COO groups (Table 3). Considering previous reports, absorption bands at 650–680 cm^{-1} and 418–480 cm^{-1} were assigned to the bending (δ(OCO)) and rocking (ρ(COO)) vibrations of carboxylate group respectively [21,22]. Data presented in Table 3 show the clear differences in the frequency and splitting of bands descended from OCO bending vibrations. These spectral effects can be explained by the differences in the strength of Zr-(μ-O) carboxylate ligand bonds in the structure of synthesized compounds at low temperatures.

The frequency changes of bands assigned to stretching modes of OH, COO groups, and Zr-(μ_3-O/OH) bridges in spectra registered at RT and LNT indicate the possible

changes in the structure of $[Zr_6O_4(OH)_4(OOCCR)_{12}]$ clusters. These effects were studied using the variable temperature IR (VT IR) spectroscopy. Obtained results have been presented as a dependence between frequency ν(OH) and ν_{as}(Zr(O/OH)Zr) modes versus temperature (Fig. 3). According to these data, the frequency of these vibrations revealed the stepwise changes; first step about 103 K and the other one near 173 and 240 K, respectively. Above effects can be assigned to the phase transitions associated with dynamical changes in the structure **1** and **2** [24,25]. The migration of protons and the rotational disorder of Bu^t or $C(CH_3)_2Et$ groups in the crystal lattice are main factors causing the mentioned changes and explain difficulties in the precise determination of **1** and **2** crystal structure at low temperatures (103 or 123 K).

3.3. Thermal stabilities of studied Zr(IV) carboxylate derivatives

The thermal decomposition pathway of Zr(IV) multinuclear oxo carboxylates was studied using thermogravimetric methods (TGA/DTA) over the temperature range 298–873 K. The thermolysis of **1** proceeds in four endothermic steps, with maxima at 485, 668, 742, and 783 K (data deposited as a supplementary material). The weight loss of 61.0% indicate that decomposition of this compound proceed with complete conversion of this compound to ZrO_2 (calculated weight loss 61.0%) in the whole temperature range. Although **2** form a similar type of the structure as **1**, its thermal decomposition proceeds in two endothermic stages at 493 and 793 K. The sample weight lose (65.0%) indicates the complete conversion of **2** to zirconium oxide (calculated weight loss 64.1). The weak and broad stage which was noticed at 343–473 K can be assigned to the sublimation process. Experiments, with application of the cooling finger of sublimation chamber, exhibited that **2** sublimes between 373 and 453 K. IR spectra of sublimation products proved its occurrence. For **1** that process was not observed. Formation of ZrO_2 as the main decomposition product of **1** and **2** has been confirmed using IR and X-ray diffraction (XRD) methods. Analysis of XRD data proved the formation of ZrO_2 monoclinic form (literature data [26]: 28.18 ($\bar{1}11$), 31.47 (111), 34.15 (002), 34.42 (020), 35.30 (200), 49.30 (022), 50.13 (220); experimental: 28.18 ($\bar{1}11$), 31.46 (111), 34.15 (002), 34.42 (020), 35.30 (200), 49.30 (022), 50.12 (220)). The results of thermogravimetric analysis could be correlated with crystallographic data for **1** and **2**. The structure of **1** is characterized by the strong bridging interactions of carboxylic groups with Zr(IV) cations. Also, one of the Bu^t moieties revealed no rotational disorder and participated in the efficient intra-molecular interactions. Consequently, sublimation of that compound was not observed, while the thermal decomposition starts at 485 K. The cluster of **2** is stable, since its architecture is similar to that found in **1**. The significant rotational disorder of all hydrocarbon moieties results in weaker intra-molecular interactions and sublimation was detected at ~395 K.

4. Conclusions

Two multinuclear zirconium(IV) oxo carboxylates, $[Zr_6O_4(OH)_4(OOCR')_{12}]$ ($R' = Bu^t$ (**1**), $C(CH_3)_2Et$ (**2**)) were prepared in a direct reaction of Zr(IV) alkoxides with the suitable branched organic acids in the molar ratio 1:2, and characterized by elemental analysis, IR, ^{13}C NMR and single crystal X-ray diffraction techniques.

X-ray studies revealed that independently from the kind of Zr(IV) alkoxides ($Zr(OPr^i)_4$ or $Zr(OC(CH_3)_2Et)$ and organic acid used in the synthesis, a similar type of structure is formed. The structures of **1** and **2** consist of centrosymmetric clusters, composed of six zirconium(IV) atoms linked by 4:4 system of μ_3-oxo/hydoxy bridges and stabilized by *syn–syn* carboxylate bridges. Analysis of crystallographic and IR data suggests that four protons migrate between eight of Zr-(μ_3-O) bridges of the $[Zr_6O_4(OH)_4(OOCR')_{12}]$ cluster. The migration effects and the rotational disorder of Bu^t or $C(CH_3)_2Et$ groups in the crystal lattice are the main factors causing the dynamical changes of the structure of**1** and **2**, in the temperature range 98–293 K.

Results of thermal analysis revealed the significant differences in thermal stability of **1** and **2**, although studied compounds form a similar type of the crystallographic structure. In both cases thermolysis of these compounds proceed with their complete conversion to ZrO_2 (monoclinic form).

5. Experimental

5.1. Materials and methods

The studied compounds were synthesized at room temperature under argon atmosphere, using standard Schlenk line and glovebox techniques. $Zr(OR)_4$ ($R = Pr^i$, $C(CH_3)_2Et$) and Bu^tCOOH, $Et(CH_3)_2CCOOH$ (Aldrich) were used as received. The reactions were carried in the mixture of *n*-hexane and Pr^iOH used as a solvent. Both solvents were distilled and stored over the molecular sieves.

Infrared (IR) spectra were recorded on Perkin–Elmer Spectrum 2000 spectrometer within range 400–4000 cm^{-1} with a medium slit width and peak resolution of 4.0 cm^{-1}. The samples of analyzed compounds were studied as a powder dispersed in a KBr pellet. Variable temperature IR spectra were registered between 98 and 353 K using the SPECAC variable temperature cell. Solid-state ^{13}C NMR spectra were registered on Bruker AMX 300. The solution ^{1} and ^{13}C NMR spectra ([D_6]-benzene) were recorded using a 5 mm solution probe on Varian Gemini 200. Thermogravimetric analysis (TGA/DTA) was carried out using SDT 2960 TA Instruments, in nitrogen atmosphere between 298 and 873 K at a ramp rate 3 K^{-1}. X-ray diffraction (XRD) data were collected with a Philips

X'PERT diffractometer; 2Θ ranges 30–80°, Cu Kα radiation and sample spinning (step size – 0.1°, program. res. slit – 0.5, measuring time – 11 s per point).

5.2. Reaction of $Zr(OR)_4$ ($R = Pr^i$, $C(CH_3)_2Et$) with organic acids (RCOOH; $R = Bu^t$ (**1**), $t(CH_3)_2C$ (**2**))

$Zr(OR)_4$ ($R = Pr^i$, $C(CH_3)_2Et$) (1 g of $Zr(OPr^i)_4$ (2.58 mmol) or 1.13 g of $Zr(OC(CH_3)_2Et$ (2.58 mmol)) was added dropwise to a solution of organic acid (0.42 g; 5.16 mmol **1**, and 0.6 g; 5.16 mmol **2**) in the 3 cm^3 of mixture of *n*-hexane and Pr^iOH or $Et(CH_3)_2COH$ (1:1), and stirred for 24 h. Crystals were grown by slow evaporation of the reaction mixture under argon atmosphere (glovebox). The colourless crystals were obtained after 1 day.

5.3. $Zr_6O_8(OOCBu^t)_{12}$ (**1**)

Yield: 61%. The % Zr was gravimetrically determined as ZrO_2. Anal. Calc. for $C_{60}H_{108}O_{32}Zr_6$: C, 38.15; H, 5.75; Zr, 29.0. Found: C, 37.33; H, 6,18; Zr, 28.50%. IR (KBr, cm^{-1}): 1568 (ν_{as}(COO)); 1424 (ν_s(COO)); 729 (ν_{as}(Zr–O–Zr)); 680 (ν_s(Zr–O–Zr)), 607 (δ(OCO)); 481 (ρ(OCO)); ^{13}C NMR (solid-state, δ, ppm) 28.4 ($CH_3(Bu^t)$); 39.7 and 39.9 ($C(Bu^t)$); 183.9 and 184.5 (COO).

5.4. $Zr_6O_8(OOCC(CH_3)_2Et)_{12}$ (**2**)

Yield: 67%. Anal. Calc. for $C_{72}H_{132}O_{32}Zr_6$: C, 42.03; H, 6.42; Zr, 26.6. Found: C, 41.77; H, 6.89; Zr, 25.70%. IR (KBr, cm^{-1}): 1560 and 1566 (ν_{as}(COO)); 1413 (ν_s(COO)); 726 (ν_{as}(Zr–O–Zr); 678 (ν_s(Zr–O–Zr)), 631 and 598 (δ(OCO)); 482 (ρ(OCO)); ^{13}C NMR (solid-state, δ, ppm) 10.0 (CH_3(Et)); 33.1 (CH_2(Et)); 39.7 ($C(Bu^t)$); 43.2 ($CH_3(Bu^t)$); 183.9 and 184.3 (COO).

5.5. X-ray structure data

The diffraction data were collected at 293 K for the single crystals ($0.10 \times 0.08 \times 0.06$ mm **1**, $0.20 \times 0.17 \times 0.15$ mm **2**) using Oxford Diffraction KM4 CCD diffractometer, Mo Kα radiation $\lambda = 0{,}71073$ Å. The reflections have been measured with $\omega - 2\theta$ method. The numerical absorption correction was applied for **1** and **2** (RED167 package of programs, Oxford Diffraction, 2000). Structures of **1** and **2** were solved by the direct methods and refined with full-matrix least-squares procedure on F^2 using SHELX-97 program package [27]. Details of the data collection and structure refinement are presented in Table 1. Crystal data have been deposited with CCDC (deposition numbers CCDC 278496 and 278497 for **1** and **2**, respectively).

Acknowledgement

The authors wish to acknowledge the Polish Committee for Science Research for financial support Grant No. 4T09A 152 23.

Appendix A. Supplementary data

Supplementary data associated with this article can be found, in the online version, at doi:10.1016/j.poly.2006.08.025.

References

[1] U. Schubert, Chem. Mater. 13 (2001) 3487.
[2] U. Schubert, N. Hüsing, A. Lorenz, Chem. Mater. 7 (1995) 2110.
[3] T.C. Rosen, K. Kirschbaum, D.M. Giolando, J. Chem. Soc., Dalton Trans. (2002) 120.
[4] R. Matero, M. Ritala, M. Leskelä, T. Sajavaara, A.C. Jones, J.L. Roberts, Chem. Mater. 16 (2004) 5630.
[5] U. Schubert, J. Chem. Soc., Dalton Trans. (1996) 3343.
[6] G. Kickelbick, U. Schubert, Chem. Ber./Recueil 130 (1997) 473.
[7] G. Kickelbick, U. Schubert, J. Chem. Soc., Dalton Trans. (1999) 1301.
[8] G. Kickelbick, P. Wiede, U. Schubert, Inorg. Chim. Acta 284 (1999) 1.
[9] T.J. Boyle, L.A. Ottley, M.A. Rodriguez, Polyhedron 24 (2005) 1727.
[10] G. Kickelbick, U. Schubert, Eur. J. Inorg. Chem. (1998) 159.
[11] M.Y. Reza, H. Matsushima, M. Koikawa, M. Nakashima, T. Tokii, Polyhedron 18 (1999) 787.
[12] E.A. Arnett, V.M. DePalma, J. Am. Chem. Soc. (1976) 5829.
[13] B. Moraru, S. Gross, G. Kickelbick, G. Trimmel, U. Schubert, Monatsh. Chem. 132 (2001) 993.
[14] P. Piszczek, M. Richert, A. Grodzicki, T. Głowiak, A. Wojtczak, Polyhedron 24 (2005) 663.
[15] G. Bai, H.W. Roesky, J. Li, T. Labahn, F. Cimpoesu, J. Magull, Organometallics 22 (2003) 3034.
[16] B.-H. Ye, X.-Y. Li, I.D. Williams, X.-M. Chen, Inorg. Chem. 41 (2002) 6426.
[17] H.D. Lutz, Structures and Bonding, vol. 82, Springer-Verlag, Berlin, Heidelberg, 1995, p. 85.
[18] M.A. Hasan, M.I. Zaki, L. Pasupulety, J. Mol. Cat. A: Chem. 178 (2002) 125.
[19] M.A. Diaz-Diaz, A. Macias-Gracia, G. Silvero, R. Gordillo, R. Caruso, Ceram. Int. 29 (2003) 471.
[20] G. Von Halden, A. Kirilyuk, D. van Heijnsbergen, B. Sartakov, M.A. Duncan, G. Meijer, Chem. Phys. 262 (2000) 31.
[21] K. Nakamoto, Infrared and Raman Spectra of Inorganic and Coordination Compounds, Part B/V ed., Wiley, New York, 1997, p. 58 and 172.
[22] V. Koleva, D. Stoilova, J. Mol. Struct. 61 (2002) 1.
[23] G.B. Deacon, R.J. Philips, Coord. Chem. Rev. 33 (1980) 227.
[24] A.W. Rakov, Opt. Spectra 10 (1961) 713.
[25] W. Bała, A. Grodzicki, P. Piszczek, M. Wojdyła, A. Bratkowski, M. Szybowicz, T. Runka, M. Drozdowski, J. Mol. Struct. 782 (2006) 177.
[26] B. Bondars, G. Heidemane, J. Grabis, K. Laschke, H. Boysen, J. Schneider, F. Frey, J. Mater. Sci. 30 (1995) 1621.
[27] G.M. Sheldrick, T.M. Schneider, Method Enzymol. 277B (1997) 319.

Available online at www.sciencedirect.com
ScienceDirect
Polyhedron 26 (2007) 686–694
POLYHEDRON
www.elsevier.com/locate/poly

A new trinuclear mixed-valence Co(II)–Co(III) complex stabilized by a bis(salicylidene) based ligand

Suparna Banerjee [a,*], Jiu-Tong Chen [b], Can-Zhong Lu [b]

[a] Department of Chemistry, University College of Science and Technology, University of Calcutta, 92, A.P.C. Road, Kolkata 700 009, India
[b] The State Key Laboratory of Structural Chemistry, Fujian Institute of Research on the Structure of Matter, The Chinese Academy of Sciences, Suzhou, Fujian 350 002, PR China

Received 19 May 2006; accepted 24 August 2006
Available online 19 September 2006

Abstract

The present work deals with a class I mixed valence trinuclear complex $[Co^{II}(\mu\text{-}OAc)_2(\mu\text{-}L)_2Co_2{}^{III}(NCS)_2]$ (**1**) formed by partial aerial oxidation (H_2L = 1,7-bis(2-hydroxyphenyl)-2,6-diazahepta-1,6-diene). The terminal $Co^{III}N_3O_3$ centres exhibit a uniform facial arrangement of both N_3 and O_3 donor sets and the Co^{II} centre is coordinated to six oxygen atoms. Variable temperature magnetic susceptibility measurement reveals that the intermediate Co(II) paramagnetic centre undergoes a very weak spin exchange ($\theta = -6.39$ K, antiferromagnetic) interaction with the two terminal Co(III) diamagnetic centres over the range 300–2 K. A three line EPR spectra at 4 K was characterized with highly anisotropic g tensors and the one line broad spectra at 300 K indicates the strong influence of temperature on the metal spin states, consistent with a high spin Co(II) complex. Two anodic responses appeared at +0.85 ($Co^{2+} \rightarrow Co^{3+}$, reversible) and +1.7 V ($Co^{3+} \rightarrow Co^{4+}$, irreversible) corresponding to one and two electron transfer oxidation respectively. Another reversible signal attributed to $Co^{3+} \rightarrow Co^{2+}$ reduction occurred at −0.5 V, associated with a two electron stoichiometry. Compound **1** reacted with hydrazine to form a square planar orange-red $[Co^{II}(L)]$ species, **2**. Inter conversion between **1** and **2** involves electron exchange coupled with proton transfer.
© 2006 Elsevier Ltd. All rights reserved.

Keywords: Co^{III}–Co^{II}–Co^{III} trinuclear complex; Reaction stoichiometry; Redox behaviour; Magnetic properties; Chemical reduction

1. Introduction

Cobalt complexes based on quadridentate bis(salicylidene) Schiff base ligands, preserve substantial interest relevant to vitamin B_{12} models [1–4] as well as biomimetic catalysts [5–7]. The concerned ligands also draw considerable attention in view of their fascinating μ^2-bridging ability of the phenoxo oxygen atoms affording high nuclearity complexes which could act as promising candidates to offer valuable insight into various natural electron transfer events [8]. High nuclearity coordination complexes thus achieved by this kind of compartmental ligands along with other appropriate coligands provide tractable examples to rationalize magnetic exchange phenomenon [9,10] emerging from temperature dependent interactions between the spin states of individual magnetic centres. Use of bis(salicylidene) ligands with polymethylene spacers of varying flexibility allow us to regulate their electronic and steric demands which of course in association with metal preferences could effectively modulate structural versatility enlightening spin and valence change phenomena.

The unique potentiality of simple ligands has prompted us to synthesize high nuclearity cobalt(II) complexes in the presence of ancillary NCS ligands and to study their electron transfer as well as spin exchange behaviours. Our attempt with 1,7-bis(2-hydroxyphenyl)-2,6-diazahepta-1,6-diene as a representative of the bis(salicylidene) family furnished a novel Co^{III}–Co^{II}–Co^{III} mixed valence octahedral trinuclear species.

* Corresponding author.
E-mail address: suparnaban@rediffmail.com (S. Banerjee).

0277-5387/$ - see front matter © 2006 Elsevier Ltd. All rights reserved.
doi:10.1016/j.poly.2006.08.035

Herein we report the synthesis, spectroscopic characterizations, structure, magnetic properties and redox behaviour of the trimer. We also noted that the trimer undergoes spontaneous chemical reduction.

2. Experimental

2.1. Materials and physical measurements

The ligand H_2L was synthesized by condensation of 1,3-diaminopropane with salicaldehyde in dry methanol following the literature method [11]. All other chemicals were of reagent grade and were used as received. Solvents were dried and distilled prior to use. The IR spectra were recorded on KBr pellets with a Perkin–Elmer RXI FT-IR spectrometer. A Perkin–Elmer 2400 II elemental analyzer was used for microanalysis. FAB mass spectra (matrix, 3-nitrobenzyl alcohol) was done with a JEOL JMS600 spectrometer. Electrochemical measurements were performed under a dinitrogen atmosphere using a PAR model Versastat-2 electrochemical analyzer with a platinum working electrode. The supporting electrolyte was tetraethylammonium perchlorate (TEAP), and the potentials were referenced to the saturated calomel electrode (SCE) without junction correction. X-band EPR spectra in solid and solution states were recorded using a Bruker 300E spectrometer. Variable temperature magnetic susceptibility measurement was performed using a cryogenic S600 SQUID magnetometer.

2.2. Preparation of complexes

2.2.1. Synthesis of $[Co^{II}(\mu\text{-}L)_2(\mu\text{-}OAc)_2Co_2{}^{III}(NCS)_2]\cdot 2CH_3CN$ ($\mathbf{1}\cdot 2CH_3CN$)

To a solution of $Co(OAc)_2\cdot 4H_2O$ (0.05 g, 0.200 mmol) in methanol (25 ml), NH_4SCN (0.01 g, 0.133 mmol) was added and vigorously stirred for 15 min. A yellow solution of the ligand H_2L (0.038 g, 0.133 mmol) in methanol (5 ml) was then added slowly to the metal solution. The resulting brown solution turned green on stirring in air for 3 h. It was then filtered and solvent removal from the filtrate under reduced pressure gave a green residue which was washed twice (10 ml each) with hexane to remove excess ligand, if any. The green mass was dried in vacuum over fused $CaCl_2$, and subsequent recrystallization from acetonitrile solution afforded the crystalline green complex. Yield: 0.062 g (88% based on metal salt). (Anal. Calc. for $C_{44}H_{44}Co_3N_8O_8S_2$: C, 50.10; H, 4.21; N, 10.63. Found: C, 50.16; H, 4.17; N, 10.67%.)

Alternatively, to an orange-red solution of **2** (0.136 g, 0.400 mmol) in 10 ml methanol, a methanolic solution (25 ml) containing $Co(OAc)_2\cdot 4H_2O$ (0.05 g, 0.200 mmol) and NH_4SCN (0.03 g, 0.400 mmol) was added dropwise over a period of 10 min with continuous stirring. The resulting solution turned green on stirring in air for 4 h. It was then filtered and solvent removal from the filtrate under reduced pressure gave a green residue which was washed thrice (10 ml each) with cold water to remove excess of reagents, if any. The green mass was dried in vacuum over conc. H_2SO_4, and subsequent recrystallization from acetonitrile afforded the crystalline green complex. Yield: 0.304 g (72% based on **2**). It has been observed that the reaction time can be considerably reduced to 2 h upon purging dioxygen gas into the reacting solution.

2.2.2. Synthesis of $[Co^{II}L]$ (**2**)

To a green solution of $\mathbf{1}\cdot 2CH_3CN$ (0.300 g, 0.285 mmol) in dichloromethane (60 ml) was added 50% hydrazine hydrate (0.016 g, 0.320 mmol) solution. It was stirred for 45 min at room temperature whereupon the solution gradually turned reddish brown. The resulting solution was stripped of solvent under reduced pressure. The deep brown residue thus obtained was freshly dissolved in dichloromethane (25 ml) and extracted five times with water (50 ml each). On performing subsequent extractions, the colour of the dichloromethane part became intense orange-red in colour. The orange product was then isolated by solvent evaporation and dried in vacuum over fused $CaCl_2$. Yield: 0.158 g (82% based on $\mathbf{1}\cdot 2CH_3CN$). (Anal. Calc. for $C_{17}H_{16}CoN_2O_2$: C, 60.13; H, 4.75; N, 8.26. Found: C, 60.17; H, 4.72; N, 8.32%.)

Alternatively, the concerned ligand H_2L (0.086 g, 0.300 mmol) was dissolved in dry methanol (10 ml), followed by dropwise addition of a methanolic solution (20 ml) containing $Co(OAc)_2\cdot 4H_2O$ (0.038 g, 0.150 mmol) at ambient temperature under stirring. This was continued for 3 h under the passage of dinitrogen gas, which resulted in an orange brown solution. Stripping of solvent furnished an orange brown residue which was washed with *n*-hexane to remove unreacted ligand, if any, and further with cold water to ensure no metal substrate was present. The orange-red complex thus obtained was dissolved dichloromethane and recrystallized by slow evaporation. The product finally was dried over fused $CaCl_2$. Yield: 0.038 g (75% based on metal salt).

2.3. X-ray crystallography

Dark green single crystals of $\mathbf{1}\cdot 2CH_3CN$ were obtained by slow evaporation of solvent from an acetonitrile solution. Data were collected at $T = 130(2)$ K on a Siemens SMART CCD area-detector diffractometer equipped with graphite monochromated Mo Kα radiation ($\lambda = 0.71073$ Å, rotating anode source) in the range $1.64° \leqslant \theta \leqslant 28.29°$. All the data were corrected for Lorentz polarization and absorption using the SADABS [12] routine. The structure was generated by direct methods using SHELXS-97 [13] followed by successive Fourier synthesis and refined by full matrix least squares based on F^2 with SHELXL-97 [14]. Anisotropic displacement parameters were assigned to all non-hydrogen atoms. Hydrogen atoms were inserted at calculated positions; the hydrogen atoms of acetonitrile solvent molecules were not introduced in the model. Significant crystal data are collected in Table 1.

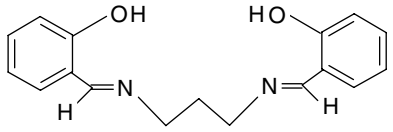
Table 1
Crystal data for complex $\mathbf{1}\cdot 2CH_3CN$

Complex	$\mathbf{1}\cdot 2CH_3CN$
Formula	$C_{44}H_{44}Co_3N_8O_8S_2$
M	1053.78
System	orthorhombic
Space group	*Pna2*(1)
a (Å)	18.740(9)
b (Å	9.630(5)
c (Å)	24.885(13)
α (°)	90.00
β (°)	90.00
γ (°)	90.00
V (Å^3)	4491(4)
Z	4
D (Mg m^{-3})	1.559
T (K)	130(2)
μ (mm^{-1})	1.251
Independent reflections	11 054
R_{int}	0.0550
Collected reflections	32 041
$[I > 2\sigma(I)]$ R_1, wR_2	0.0639, 0.1352

3. Results and discussion

3.1. Synthesis of compounds

Facile condensation of salicylaldehyde and 1,3-diaminopropane in a 2:1 molar ratio respectively, afforded a neutral condensate, 1,7-bis(2-hydroxyphenyl)-2,6-diazahepta-1,6-diene (general abbreviation H_2L, where H atoms are dissociable phenolic hydrogens) which has been employed as a tetradentate chelating ligand in the present work.



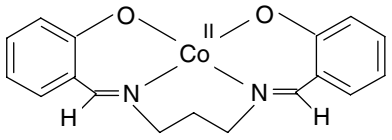
H_2L

In order to synthesize a high nuclearity cobalt-H_2L complex, we reacted 1 mol of H_2L with a 2:2 methanolic mixture of $Co(OAc)_2$ and NH_4SCN, under magnetic stirring at ambient temperature. Subsequent crystallization of the product from acetonitrile solution gave green crystals of the trimeric mixed valence cobalt complex $[Co^{II}(\mu\text{-}OAc)_2(\mu\text{-}L)_2Co_2{}^{III}(NCS)_2]$ (**1**) as authenticated from its X-ray structure determination. In this process the yield of the complex is only ~45%.

We revisited the reaction in search of the concerned oxidizing agent and the appropriate stoichiometries of the metal and ligands to increase the yield of the product. The reaction when carried out under dinitrogen atmosphere only ended up with no formation of the desired product which logically tempted us to believe that atmospheric oxygen acts here as an external oxidant. Subsequently we carried out the reaction (in air) in a 3:2:2 mol ratio of metal, H_2L and NH_4SCN respectively in methanol solution under stirring at ambient conditions. The modified strategy indeed worked excellently and the yield of the product reached even up to 88% after recrystallization from acetonitrile solvent. The stoichiometric equivalents of the ingredients is presented in Eq. (1)

$$3[Co^{II}(OAc)_2] + 2H_2L + 2NH_4SCN + 1/2\,O_2 \rightarrow [Co^{II}(\mu\text{-}OAc)_2(\mu\text{-}L)_2Co_2{}^{III}(NCS)_2] + 2NH_4OAc + 2HOAc + H_2O \quad (1)$$

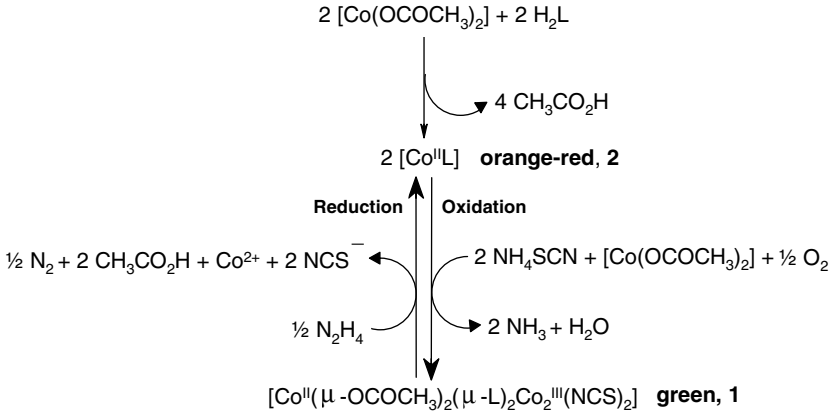
It could be assumed that the reaction was initiated via the formation of a four coordinated mononuclear Co(II) species as the first possible intermediate $[Co^{II}L]$ (**2**) which reacts further with $Co^{II}(OAc)_2$ in the presence of NH_4SCN and ultimately aerial oxidation generates the desired trimer.



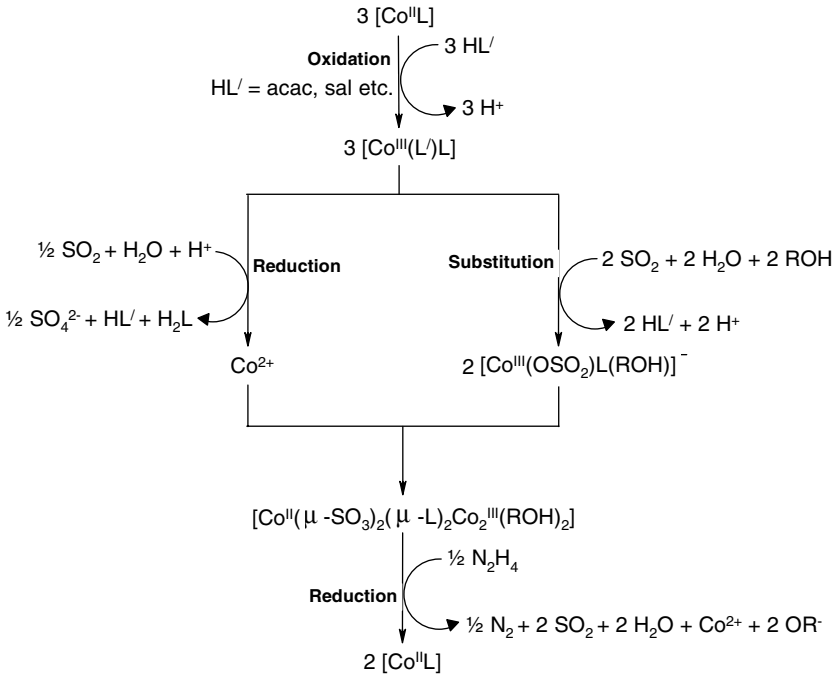
2

To examine the validity of the proposed reaction pathway, we tried to trap the reactive intermediate (**2**), but did not succeed, instead an orange-red coloured complex was isolated by hydrazine reduction of **1**. Potency of N_2H_4 as a reducing agent lies in its unique proton cum electron donor ability involving the reaction $1/2\,N_2H_4 \rightarrow 1/2\,N_2 + 2H^+ + 2e$. Liberated protons cleave the μ^2-OAc linkages of **1** and the Co^{III} centres suffer reduction by consuming the electrons. The outcome of the chemical events is the formation of **2**. Interestingly, the reaction of $[Co^{II}L]$ (**2**) and $Co(OAc)_2$ in a 2:1 mol ratio respectively in methanol in the presence of NH_4SCN (2 mol) afforded the green coloured trimer, **1** (Scheme 1). The reaction has been carried out in air, and under dinitrogen atmosphere the reaction did not occur. Therefore, in the presence of a proton donating agent like ammonium salt, dioxygen from the air is reduced to water via the following reaction, $2NH_4{}^+ + 1/2\,O_2 + 2e \rightarrow 2NH_3 + H_2O$ where the $[Co^{II}L]$ complex acts as a one electron donor and subsequently is oxidized to the complex, $[Co^{II}(\mu\text{-}OAc)_2(\mu\text{-}L)_2Co_2{}^{III}(NCS)_2]$ (**1**).

It is important to note that the only known structurally characterized trimeric mixed valence complex [15] with the H_2L type ligand is $[Co^{II}(\mu\text{-}SO_3)_2(\mu\text{-}L^1)_2Co_2{}^{III}(Pr^nOH)_2]$ (L^1 is a derivative of L where two aldimine protons have been replaced by two methyl groups) and this sulfito bridged trimer was obtained by partial reduction [15] of the corresponding Co^{III} precursor by SO_2 (Scheme 2). Thus both partial oxidation and reduction of Co^{II} and Co^{III} precursors respectively, provide different efficient routes to prepare Co^{III}–Co^{II}–Co^{III} trimers incorporating H_2L/H_2L^1 types of di-Schiff bases.



Scheme 1.



Scheme 2.

3.2. Crystal structure

The asymmetric unit of **1** consists of one neutral $[Co(\mu\text{-}OAc)_2(\mu\text{-}L)_2Co_2(NCS)_2]$ molecule and two acetonitrile solvent molecules. The structure of the complex is depicted in Fig. 1 and selected bond distances and angles are listed in Table 2. The cobalt(III) and cobalt(II) centres are linked by one acetate ion and two phenoxo oxygen atoms of L^{2-}, forming an μ-acetato–bis(μ^2-phenoxo) bridged Co^{III}–Co^{II} motif. Another Co^{III} centre is again bonded with the Co^{III}–Co^{II} motif via a similar bridging segment and generates the Co^{III}–Co^{II}–Co^{III} core.

Co1 has a six-coordinate octahedral geometry in which O1, O2, N4 and N3 atoms of the deprotonated di-Schiff base (L^{2-}) constitute the equatorial plane and N1 and O8 atoms of isothiocyanate and acetate ligands respectively, define the axial direction. The geometry is distorted with an average twist angle of 52.5°. The equatorial plane deviates by only 0.01 Å from the best fit mean plane. One of the two salicyldimine chelate rings (O1, C11, C12, C13, C14, C15, C16, C17 and N3) makes a dihedral angle of 34.5° with the $Co1N_2O_2$ equatorial plane. Likewise, the other salicyldimine ring is inclined by 28.1° with the $Co1N_2O_2$ plane. The trimethylene spacer of L^{2-} adopts a boat configuration with a "V-angle" of 121.1° (180° represents a planar arrangement) [16]. The coordination environment around Co3 is very similar to that of Co1. It (Co3) also sits in a pseudooctahedral environment in which the L^{2-} ligand occupies the equatorial positions (O3, O4, N6 and N5 atoms) and the two apical positions are coordinated by the oxygen atom (O6) of bridging acetate and by an isothiocyanato nitrogen (N2). The average twist angle of the

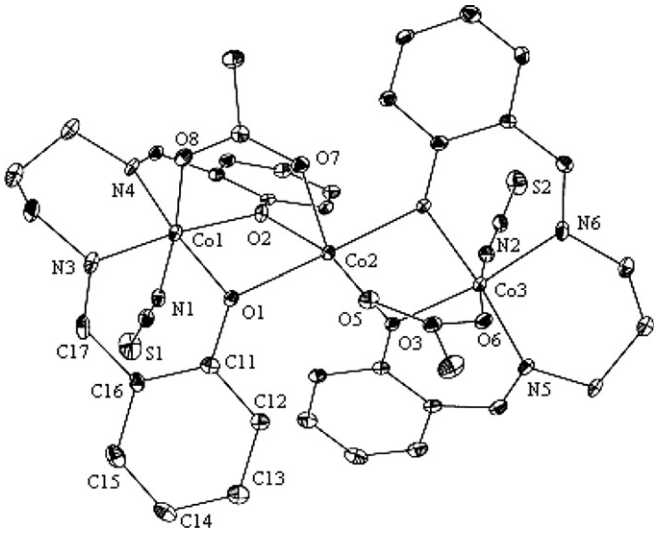


Fig. 1. A perspective view (25% probability thermal ellipsoids) and atom labelling scheme of $[Co(\mu\text{-}OAc)_2(\mu\text{-}L)_2Co_2(NCS)_2]$ (**1**). Hydrogen atoms and solvent molecules are omitted for clarity.

Table 2
Distances (Å) and angles (°) for compound $\mathbf{1}\cdot 2CH_3CN$

Distances			
Co1–O8	1.891(4)	Co2–O1	2.053(4)
Co1–N1	1.892(4)	Co2–O2	2.124(3)
Co1–O2	1.895(3)	Co2–O3	2.137(3)
Co1–O1	1.896(4)	Co3–O6	1.889(4)
Co1–N3	1.916(5)	Co3–N2	1.895(5)
Co1–N4	1.919(5)	Co3–O4	1.896(4)
Co2–O7	2.021(4)	Co3–O3	1.905(3)
Co2–O5	2.033(4)	Co3–N5	1.910(4)
Co2–O4	2.046(3)	Co3–N6	1.923(5)
Angles			
O8–Co1–N1	173.17(17)	O5–Co2–O2	161.52(14)
O8–Co1–O2	91.92(16)	O4–Co2–O2	107.14(14)
N1–Co1–O2	91.63(18)	O1–Co2–O2	72.27(13)
O8–Co1–O1	94.74(16)	O7–Co2–O3	159.15(13)
N1–Co1–O1	91.57(17)	O5–Co2–O3	86.63(14)
O2–Co1–O1	81.06(15)	O4–Co2–O3	72.31(13)
O8–Co1–N3	86.99(18)	O1–Co2–O3	109.17(13)
N1–Co1–N3	90.39(19)	O2–Co2–O3	105.54(13)
O2–Co1–N3	171.08(18)	O6–Co3–N2	173.46(17)
O1–Co1–N3	90.20(18)	O6–Co3–O4	94.35(16)
O8–Co1–N4	85.02(18)	N2–Co3–O4	90.74(18)
N1–Co1–N4	89.02(19)	O6–Co3–O3	91.66(15)
O2–Co1–N4	92.18(17)	N2–Co3–O3	93.19(17)
O1–Co1–N4	173.23(17)	O4–Co3–O3	80.99(15)
N3–Co1–N4	96.54(19)	O6–Co3–N5	86.11(18)
O7–Co2–O5	87.96(15)	N2–Co3–N5	89.3(2)
O7–Co2–O4	87.55(14)	O4–Co3–N5	173.42(17)
O5–Co2–O4	89.63(15)	O3–Co3–N5	92.43(17)
O7–Co2–O1	91.02(14)	O6–Co3–N6	85.70(18)
O5–Co2–O1	90.77(14)	N2–Co3–N6	90.3(2)
O4–Co2–O1	178.49(15)	O4–Co3–N6	89.38(18)
O7–Co2–O2	85.14(14)	O3–Co3–N6	169.80(18)
		N5–Co3–N6	97.2(2)

octahedron is 51.7°. The four donor atoms of L^{2-} describe a satisfactory plane with average mean deviation of 0.02 Å. Two chelated salicyldimine rings make an average dihedral angle of 30.1° with the equatorial $Co_3N_2O_2$ plane. Like Co1, the trimethylene spacer of L^{2-} adopts a boat configuration with a corresponding "V-angle" of 119.5°. A notable feature in the individual CoN_3O_3 environments is a uniform *facial* disposition of both N_3 and O_3 donor sets, maximizing the back-bonding effect. The central Co2 atom is coordinated by phenoxo oxygen atoms (O4 and O1) along the axial direction and the equatorial plane is defined by two acetato (O5 and O7) and two other phenoxo (O2 and O3) oxygen donors. The asymmetric coordination is evident from exclusive *cis* orientations of μ^2-phenoxo oxygen pairs of each of individual L^{2-} ligands and the acetate oxygen donors. In contrast, a *trans* orientation of the μ-sulfito oxygen donors (axially coordinated) around the central Co^{II} atom in the $[Co^{II}(\mu\text{-}SO_3)_2(\mu\text{-}L^1)_2Co_2{}^{III}(Pr^nOH)_2]$ complex [15], is consistent with an inversion symmetry. The $Co2O_6$ octahedral motif is deformed with an average twist angle of 53.3° and the equatorial plane deviates considerably by 0.31 Å from the best fit mean plane.

The average of Co1–O and Co1–N distances are 1.894 Å and 1.909 Å, almost identical to the concerned bond lengths observed for the Co3 atom ($(Co3\text{–}O)_{av} = 1.897$ Å, $(Co3\text{–}N)_{av} = 1.909$ Å). The average bond distance between the central Co2 atom and equatorial oxygen donors (~2.08 Å) is longer than that of the Co2-axial phenoxo oxygen atoms (~2.05 Å), pertinent to ground state distortion. The bond lengths between Co2 and four phenoxo oxygen atoms span the range 2.046–2.137 Å, whereas bond lengths between Co2 and two acetate oxygen atoms lie in the range 2.021–2.033 Å, i.e. on average the Co2–O-(phenoxo) length is ~0.06 Å longer than the Co2–O(acetate) length, attributed to differing bridging modes of the two bridging ligands. All the six Co2–O distances are averaged at 2.059 Å which is significantly longer than the Co(1/3)–O lengths by ca. 0.17 Å, substantiating the fact that the bivalent Co2 atom has a larger radius compared to terminal trivalent cobalt atoms. The Co1···Co2 and Co2···Co3 intra-atomic separations are 3.046(6) and 3.055(5) Å respectively, which could presumably restrict intra-metal spin exchange through mutual interactions. The bridging angles Co1–O1–Co2, Co1–O2–Co2, Co2–O3–Co3 and Co2–O4–Co3 are 100.9°, 98.4°, 98.0° and 101.5°, which indicate non-colinear Co^{III}–O–Co^{II} fragments, not suitable for any significant electronic exchange. This impression has been confirmed by a variable temperature magnetic susceptibility study, discussed later.

3.3. IR spectra

The trimeric mixed valence complex exhibits several distinguishable resonances consistent with the coordination geometry, revealed from structure determination. Vibrationally active acetate ligands display antisymmetric and symmetric stretching vibrations at 1561 and 1410 cm^{-1} respectively. The difference in frequency, Δ ($\nu_{as}(COO^-) - \nu_s(COO^-)$) is 151 cm^{-1} (163 cm^{-1} for free acetate ion), indicating the presence of a deprotonated carboxylate group

coordinated to metal centres in a bridged bidentate fashion [17]. Monodentate N-bound isothiocyanate groups are characterized with an intense signal at 2100 cm^{-1}. The characteristic imine (C=N) stretch of the chelated ligand appears at 1630 cm^{-1} and the red shift of this C=N absorption of about 15 cm^{-1} on going from the free H_2L ligand to the complex suggests a weak π-accepting ability of the coordinated ligand.

3.4. Electrochemistry

Aiming to investigate the electron transfer events of **1**, a cylic voltammetry experiment was performed in acetonitrile solution within the potential range (+2) to (−1) V versus the saturated calomel electrode (SCE) at ambient temperature. The voltammogram of **1** is represented in Fig. 2.

The complex displayed a reversible oxidative response (couple I) at +0.85 V with characteristic anodic (E_{pa}) and cathodic (E_{pc}) peak potentials at +0.89 and +0.81 V respectively. The reversible signal is attributed to the $Co^{2+} \rightarrow Co^{3+}$ oxidation. The ratio of the observed and calculated coulomb accounts for a single electron change ($\mathbf{1} \rightarrow \mathbf{1}^{+}$), obtained from constant potential coulometry at a potential ca. 0.150 V more positive than the $E_{1/2}$ value of the concerned couple which is near to unity (0.97) and confirms one electron oxidation. The relevant electron transfer is represented in Eq. (2)

$$[Co^{III}–Co^{I}–Co^{III}] \rightarrow [Co^{III}–Co^{III}–Co^{III}]^{+} + e \quad (2)$$

The second oxidation reaction (couple II) was commenced at ca. +1.7 V in the anode sweep whereas no response at the counter cathode sweep was observed. The response is assigned to an oxidation of Co(III) to Co(IV) (Eq. (3)). This oxidation is expected to occur at high positive potential due to the relative destabilization of Co^{4+} with respect to Co^{3+} in a N_3O_3 donor environment and electrochemical irreversibility possibly arises from the lability of the Co^{4+} centres on the voltammetric time scale. A two electron stoichiometry of couple II was determined from differential pulse voltammogram (DPV) measurement by direct comparison of the peak height with respect to that of couple I. Irreversibility remains persistent regardless of variable scan rates (0.05–1.0 V s^{-1})

$$[Co^{III}–Co^{III}–Co^{III}]^{+} \rightarrow [Co^{IV}–Co^{III}–Co^{IV}]^{3+} + 2e \quad (3)$$

One of the reviewers suggested that ligand (L^{2-}/NCS^{-}) oxidation might be an alternative event at this potential instead of metal oxidation and the authors need to furnish further evidences (experimental and literature) in support of this assignment.

We did some relevant experiments to re-account the responsible chemical transformation associated with the oxidative response at +1.7 V. Firstly, the monocondensate of salicaldehyde and 1,3-diaminopropane was previously characterized [18] to be redox inactive. Likewise, a voltammetric study of the ligand H_2L in dry acetonitrile solvent over the accessible potential range did not record any signal. Secondly, to verify whether NCS^{-} is redox active, though it is a very remote chance from a theoretical standpoint, we prepared an analogous complex $[Co^{II}(\mu\text{-}OAc)_2(\mu\text{-}L)_2Co_2^{III}(N_3)_2]$ from suitable reagents which expectedly displayed a similar voltammogram (like **1**) attesting the fact that neither of the ancillary ligands (NCS^{-}/N_3^{-}) participate in oxidation. Finally, conclusive evidence in favour of metal oxidation was obtained from a low temperature EPR study of a coulometrically oxidized solution of **1**, performed at a constant potential (+1.85 V). The resulting deep brown solution was silent to EPR and consequently ruled out any possibility of ligand stabilized cationic radical formation via oxidation, which would otherwise respond to EPR with a g value close to the characteristic spin only value (2.002) of a free electron. This observation is in agreement with the electrochemically generated $Co_2^{IV}Co^{III}$ ionic species in which effective spin coupling between the two Co(IV) paramagnets takes place through the intervening diamagnetic Co(III) centre. In addition to the above supportive experimental facts, a literature survey reveals a series of μ^2-acetato-μ^3-oxo based Co(III) trimers [19] undergoing one electron reversible oxidation at ~+1.25 V to mixed valence $[Co_2^{III}Co^{IV}]^{2+}$ species, confirmed by a controlled electrolysis method. Another recently reported Co(IV) complex, $[Co_4O_4(O_2CR)_2(bpy)_4]^{3+}$ is stabilized through a cubane framework [20] supported by acetate groups. Search for stabilizing electronic effects in the authenticated complexes revealed the common presence of a predominantly oxygen rich donor environment around Co(IV) involving bridging oxo ($\mu\text{-}O^{2-}$, σ cum π donor) and bridging acetato ($\mu\text{-}OAc^{-}$, σ donor) moieties along with nitrogenous donors. The structures are characterized with the occurrence of a di(μ^2-oxo)dicobalt motif, a neccessary stabilizing feature. The complex examined in this work bears some resemblance both in terms of structural and electronic aspects to the reported complexes, thereby providing the opportunity to stabilize the $[Co_2^{IV}Co^{III}]^{3+}$ species as happened in practice. On a conspectus of the

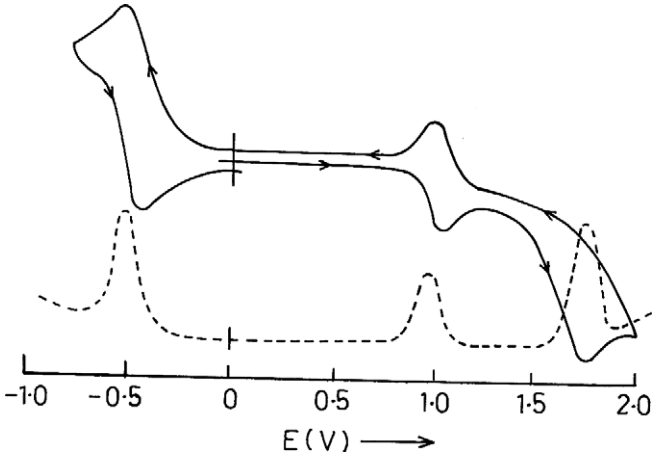


Fig. 2. Cyclic voltammogram of **1** at room temperature in MeCN solvent.

aforecited evidences, the assignment seems to be established.

The reductive response (couple III) occurring at −0.5 V ($\Delta E_p = 90$ mV) is ascribed to a $Co^{3+} \rightarrow Co^{2+}$ transformation. DPV is suggestive of a two electron transfer and the metal valence change associated with couple III is stated in Eq. (4)

$$[Co^{III}–Co^{II}–Co^{III}] + 2e \rightarrow [Co^{II}–Co^{II}–Co^{II}]^2 \quad (4)$$

3.5. Magnetic properties

Magnetic susceptibility of **1** in the polycrystalline state was measured over the temperature range 300–2 K. The magnetic moment at room temperature (300 K) is 5.06μ_B, corresponding to that of a monomeric complex having a cobalt(II) ion in a high spin octahedral environment. The value is higher than the spin only value of high spin cobalt(II) (3.87μ_B; $\mu_S = [4S(S+1)]^{1/2}$; $S = 3/2$) but closer to the value expected for the situation where the contribution of orbital angular momentum [21] is taken into account (5.20μ_B; $\mu_S = [L(L+1) + 4S(S+1)]^{1/2}$; $L = 3$; $S = 3/2$). The observed magnetic moment is in good agreement with the magnetic moment of a non-spin coupled Co(III) ($S = 0$)–Co(II) ($S = 3/2$)–Co(III) ($S = 0$) system, as established from the equation $\mu^2 = \sum \mu_i^2$, where μ_i is the magnetic moment of the individual metal centres of homonuclear polymetallic species [22].

To verify the nature of the spin exchange phenomenon, variable temperature magnetic susceptibility measurement will be of interest indeed. The temperature dependence of the magnetic susceptibility is small as revealed from the linear nature of $1/\chi_M$ versus T graph (Fig. 3), with a correlation constant of 0.999. The data could be fitted to a typical Curie–Weiss model for a $S = 3/2$ system with $\theta = -6.39$ K and $C = 3.24$ cm^3 K mol^{-1}. The magnetic moment remains virtually independent of temperature in the higher temperature range, there being a marginal drop from 5.06μ_B at 300 K to 4.79μ_B at 50 K due to the orbital contribution of the excited E_g states [23]. However, below 50 K, there is a steady decrease in the magnetic moment to a value of 2.76μ_B at 2 K, consistent with significant zero-field splitting leading to an unequal population of the Kramers doublet. Accordingly, it is not unrealistic to assume that the spin exchange interaction (antiferromagnetic) between the variable valence metal atoms is very small and **1** behaves as a high spin monomeric Co(II) species in the solid state throughout the temperature domain.

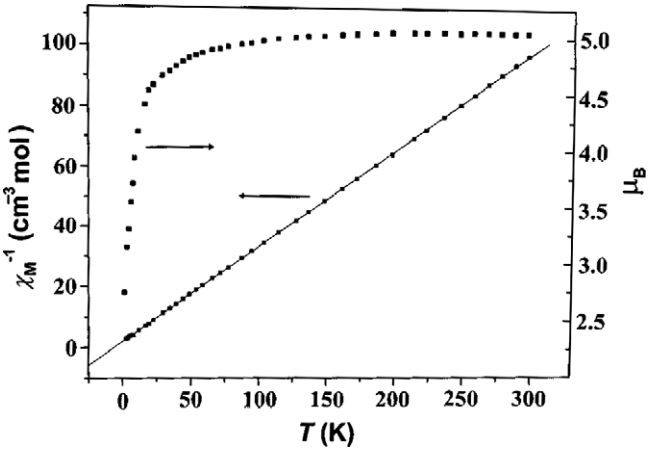


Fig. 3. Variation of χ_M^{-1} with temperature.

3.6. EPR spectra

The X-band EPR spectrum of a polycrystalline powder sample of **1** at 4 K is displayed in Fig. 4. For a $S = 3/2$ spin system (HS Co^{2+}, d^7), the zero field perturbation splits the energy levels into two doublets, $m_s = |\pm 3/2\rangle$ and $|\pm 1/2\rangle$. The nature of the spectrum could be assigned to the transitions between the ground state Kramers doublet with a highly anisotropic g-factor ($g_x = 4.33$, $g_y = 3.27$ and $g_z = 1.99$), which is believed to originate from the involvement of an excited doublet with an effective spin of 3/2 [24]. The spectrum is broad and overlapping in nature at 77 K, thereby eliminating any possibility to resolve the individual g_x and g_y components of the $g_\perp$ absorption. However, the obtained g values are indicative of a weak rhombic distortion, consistent with other high spin Co(II) species. Under axial symmetry the degeneracy of the $^4T_{2g}$ ground state splits into $^4A_{2g}$ and ^4E_g levels and the lower lying term then splits in course of spin–orbit coupling into Kramers doublets, whose zero field splitting energy is larger than the energy of the microwave radiation ($g\beta H$) used for the X-band EPR technique [25]. Owing to the above fact, only the transitions involving the lowest Kramers doublet ($\pm 1/2$) could be expected and indeed has been experimentally found. No hyperfine structure arising from an electron-

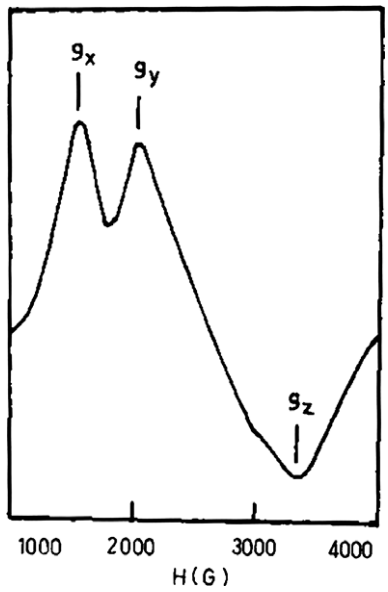


Fig. 4. EPR diagram of complex **1** in the polycrystalline state at 9.1 GHz and 4 K.

nucleus interaction for the ^{59}Co isotope (100% abundance, $I = 7/2$) is observed in the spectrum. The observation corroborates the weak nature of the spin exchange interaction in **1** as otherwise evident from variable temperature magnetic susceptibility measurement ($|\theta| = 6.39$ K). The EPR spectrum in a frozen (4 K) dichloromethane/toluene (2:1) glass also follows a similar pattern ($g_x = 4.29$, $g_y = 3.31$ and $g_z = 2.02$) as observed for a polycrystalline powder sample at 4 K, strongly indicating the retainment of the coordination environment both in solid and solution phases. The powder EPR spectrum recorded at 300 K is fortunately characterized by a single broad line with a centre field g value of 2.60. The single line spectrum could arise from substantial overlapping of the individual g-tensors which could be apparently attributed to considerably fast spin-lattice relaxation processes, thereby significantly reducing the lifetime of the concerned spin doublets [26].

4. Chemical reduction of the trimer: isolation of the product and spectroscopic evidence

The chemically accessible formal potential of the Co^{3+}/Co^{2+} reduction couple of **1** has tempted us to examine the reductive susceptibility and we have successfully used hydrazine hydrate which reduced the trimer in dichloromethane solution furnishing an orange-red complex, characterized with the help of various spectroscopic techniques and magnetic susceptibility measurement. All the results of the spectroscopic investigations confirm the orange-red complex to be a monomeric, square planar, neutral Co(II) species incorporating L^{2-} chelation. The relevant chemical transformation is depicted in Scheme 1 (vide supra).

UV–Vis spectra of **2** in dichloromethane solution exhibits a lowest energy band maximum at 675 nm followed by a moderate intensity absorption at 500 nm. The other characteristic feature of the spectrum occurred at 378 nm and is believed to be associated with a charge transfer process. The remaining band maxima appearing near and below 300 nm are due to the intraligand transitions, very similar with the absorption of the free H_2L ligand. In the IR spectrum, the prominent imine (C=N) stretch of the chelated ligand appeared at 1620 cm^{-1}, red shift of this vibration by 10 cm^{-1} on going from **1** to **2** suggests a better π-accepting ability of the coordinated ligand in the latter complex, which might stem from superior back-donation from low valent metal to $\pi^*_{C=N}$ orbitals. The ligand did not show any O–H stretching band, confirming the deprotonated oxygen (phenoxo) binding to the metal. Disappearance of characteristic vibrational signals of acetate and NCS groups logically lead us to recognize **2** as a cobalt(II) derivative incorporating only L^{2-} coordination. A cyclic voltammetric study of **2** reveals an irreversible one-electron oxidative response in both coordinating (MeCN) and non-coordinating (DCM) solvents, attributed to a $Co^{2+} \rightarrow Co^{3+}$ transformation at +0.80 V versus SCE. The signal appeared at a lower potential compared to the relevant couple in **1** because of superior stabilization of Co^{3+} ($3d^6$) in a square planar coordination. The X-band EPR spectrum in powder at 77 K is characterized with a broad single line signal. Individual g tensors considerably merge into each other and effectively exhibit a g_{av} absorption at 2.51. Powder susceptibility measurement of **2** was done at room temperature and corresponds to a one electron paramagnetic moment of 2.26μ_B. In general magnetic moments of square planar Co(II) complexes fall in the range 2.1–2.9μ_B, owing to a significant orbital contribution to the spin only magnetic moment [27,28]. The composition of **2** was established convincingly from a FAB mass spectrum, with a maximum molecular ion peak at $m/z =$ 339 which is in very good agreement with the calculated mass of 339.26. Very recent structural elucidation of [*N*,*N*′-bis(2-hydroxynaphthylmethylene)-1,3-propanediaminato]cobalt(II) [29] confirms the square planar geometry of **2** beyond doubt.

5. Conclusion

The bis(salicylidene) based schiff base ligand afforded a new Co^{III}–Co^{II}–Co^{III} trinuclear complex via partial aerial oxidation of a Co^{II} precursor. The coordination is completed by bridging acetate and monodentate N-bound isothiocyanate ions. Structure determination reveals a uniform facial disposition of N_3 and O_3 donor atoms around the terminal Co^{III} centres, augmenting the ligand field strength compared to the $Co^{II}O_6$ environment. Variable temperature magnetic susceptibility and EPR studies authenticate **1** as a valence trapped species in both solid and solution phases. Cyclic voltammogram of **1** reveals prominent oxidative and reductive signals ascribed to $Co^{2+} \rightarrow Co^{3+}$, $Co^{3+} \rightarrow Co^{4+}$ and $Co^{3+} \rightarrow Co^{2+}$ transformations and interestingly the latter two processes involve a formal two-electron transfer. Chemical reduction of **1** by hydrazine furnished a square planar $[Co^{II}L]$ species, **2**.

6. Supplementary material

CCDC 243420 contains the supplementary crystallographic data for the structure reported in this paper. These data can be obtained free of charge via http://www.ccdc.cam.ac.uk/conts/retrieving.html, or from the Cambridge Crystallographic Data Centre, 12 Union Road, Cambridge CB2 1EZ, UK; fax: (+44) 1223-336-033; or e-mail: deposit@ccdc.cam.ac.uk.

Acknowledgements

One of the authors (S.B.) is thankful to University Grants Commission (UGC), India; for awarding Research Fellowship (Sanction No. UGC/548/jr. Fellow Sc. 2001/2002). We are sincerely thankful to Dr. Jaydip Gangopadhyay, Department of Chemistry, St. Paul's C. M. College, Kolkata 9, for his help.

References

[1] J.J.R. Frasto da Silva, R.J.P. Williams, The Biological Chemistry of the Elements, Clarendon Press, Oxford, 1997.
[2] L.G. Marzilli, M.F. Summers, N. Bresciani-Pahor, E. Zangrando, J.P. Charland, L. Randaccio, J. Am. Chem. Soc. 107 (1985) 6880.
[3] M.F. Summers, L.G. Marzilli, N. Bresciani-Pahor, L. Randaccio, J. Am. Chem. Soc. 106 (1984) 4478.
[4] M. Calligaris, G. Nardin, L. Randaccio, Coord. Chem. Rev. 7 (1972) 385.
[5] B. Meunier, Biomimetic Oxidations Catalysed by Transition Metals, Imperial College Press, London, 2000.
[6] T. Kuroda-Sowa, M. Lamm, A.L. Rheingold, C. Frommen, W.M. Reitt, M. Nakano, A.L. Maniero, L.C. Brunel, G. Christou, D.N. Hendrickson, Inorg. Chem. 40 (2001) 6469.
[7] A. Nishinaga, T. Yamada, H. Fujisawa, K. Ishizani, H. Ihara, T. Matsura, J. Mol. Catal. 48 (1988) 249.
[8] (a) T. Katsuki, Coord. Chem. Rev. 140 (1995) 189;
(b) L. Canali, D.C. Sherrington, Chem. Soc. Rev. 28 (1999) 85;
(c) E.I. Solomon, T.C. Brunold, M.Z. Davis, J.N. Kemsley, S.K. Lee, N. Lehnert, A.J. Skulan, Y.S. Yang, J. Zhou, Chem. Rev. 100 (2000) 235.
[9] (a) J.A. Bonadies, M.L. Kirk, M. Soolah, D.P. Kessissoglou, W.E. Hatfield, V.L. Pecoraro, Inorg. Chem. 28 (1989) 2037;
(b) B.S. Snyder, G.S. Patterson, A.J. Abrahamson, R.H. Holm, J. Am. Chem. Soc. 111 (1989) 5214.
[10] (a) A.C. Rizzi, C.D. Brondino, R. Calvo, R. Baggio, M.T. Garland, R.E. Rapp, Inorg. Chem. 42 (2003) 4409;
(b) V.G. Makhankova, O.Y. Vassilyeva, V.N. Kokozay, B.W. Skelton, L. Sorace, D. Gatteschi, J. Chem. Soc., Dalton Trans. (2002) 4253;
(c) B. Chiari, A. Cinti, O. Crispu, F. Demartin, A. Pasini, O. Piovesana, J. Chem. Soc., Dalton Trans. (2001) 3611.
[11] M. Hariharan, F.L. Urbach, Inorg. Chem. 8 (1969) 556.
[12] G.M. Sheldrick, SADABS, University of Gottingen, Germany, 1996.
[13] G.M. Sheldrick, SHELXS-97, University of Gottingen, Germany, 1997.
[14] G.M. Sheldrick, SHELXS-97, University of Gottingen, Germany, 1997.
[15] C. Fukuhara, E. Asato, T. Shimoji, K. Katsura, M. Mori, K. Matsumoto, S. Ooi, J. Chem. Soc., Dalton Trans. (1987) 1305.
[16] C.J. Siemer, N. Goswami, P.K. Kahol, M.J. Van Stipdonk, D.M. Eichhorn, Inorg. Chem. 40 (2001) 4081.
[17] K. Nakamoto, Infrared and Raman spectra of inorganic and coordination compounds, Theory and Applications in Inorganic Chemistry, 5th ed., John Willey and Sons, Inc., New York, 1997.
[18] S. Banerjee, M.G.B. Drew, C.Z. Lu, J. Tercero, C. Diaz, A. Ghosh, Eur. J. Inorg. Chem. (2005) 2376.
[19] J.K. Beattie, C.U. Beck, P.A. Lay, A.F. Masters, Inorg. Chem. 42 (2003) 8366.
[20] K. Dimitrou, A.D. Brown, T.E. Concolino, A.L. Rheingold, G. Christou, Chem. Commun. (2001) 1284.
[21] R.S. Drago, Physical Methods in Chemistry, Saunders, Philadelphia, 1997.
[22] A. Gerli, K.S. Hagen, L.G. Marzilli, Inorg. Chem. 30 (1991) 4673.
[23] J.S. Wood, J. Chem. Soc. A. (1969) 1582.
[24] A. Abragam, B. Bleaney, Electron Paramagnetic Resonance of Transition Metal Ions, Clarendon, Oxford, UK, 1970.
[25] A. Abragam, M.H.L. Prycl, Proc. R. Soc. London, Ser. A 206 (1951) 173.
[26] A. Bencini, D. Gatteschi, Esr spectra of metal complexes of the first transition series in low symmetry environments, Transition Metal Chemistry, vol. 8, M. Dekker, New York, 1982, Chapter 1.
[27] J. Chatt, B.L. Shaw, J. Chem. Soc. (1961) 285.
[28] (a) B.N. Figgis, R.S. Nyholm, J. Chem. Soc. (1954) 12;
(b) B.N. Figgis, R.S. Nyholm, J. Chem. Soc. (1959) 338.
[29] Z.L. You, H.L. Zhu, W.S. Liu, Acta Crystallogr. E60 (2004) m654.

Available online at www.sciencedirect.com
ScienceDirect
Polyhedron 26 (2007) 695–707
POLYHEDRON
www.elsevier.com/locate/poly

Synthesis, characterization, and electrochemical, spectroelectrochemical and electrical measurements of novel ball-type four 1,1′-methylenedinaphthalen-2-ol bridged metal-free, zinc(II) and cobalt(II), and metal-free clamshell phthalocyanines

Zafer Odabaş [a], Ahmet Altındal [b], Ali Rıza Özkaya [a], Mustafa Bulut [a], Bekir Salih [c], Özer Bekaroğlu [a,*]

[a] Department of Chemistry, Marmara University, Faculty of Science and Letters, 34722 Göztepe, Istanbul, Turkey
[b] Department of Physics, Marmara University, Faculty of Science and Letters, 34722 Göztepe, Istanbul, Turkey
[c] Department of Chemistry, Hacettepe University, 06532 Ankara, Turkey

Received 3 August 2006; accepted 30 August 2006
Available online 22 September 2006

Abstract

The new ball-type bisphthalocyanines [metal-free **6**, Zn(II) **7** and Co(II) **8**] were synthesized from the corresponding 4,4′-[1,1′-methylenebis(naphthalene-2,1-diyl)]bis(oxy)di-phthalonitrile **4**, which can be obtained from the reaction of 4-nitrophthalonitrile (**2**) with 1,1′-methylenedinaphthalen-2-ol **3**. A novel clamshell type bisphthalocyanine **5** was synthesized from compound **4** and 4,5-bis(hexylthio)phthalonitrile **1**. The novel compounds have been characterized by elemental analysis, UV/Vis, IR, ^{1}H NMR and MALDI-TOF Mass spectroscopies. The electrochemical and spectroelectrochemical measurements showed the formation of various mixed-valence oxidation and reduction species, due to the strong intramolecular interactions between the two phthalocyanine rings, especially in the ball-type phthalocyanines. The conduction properties of the compounds have been examined by d.c. and impedance spectroscopy measurements as function of temperature and frequency. D.c. conductivity, measured between 290 and 480 K, is thermally activated with the activation energy ranging between 0.62 and 0.84 eV. The a.c. results gave a power law behaviour, $\sigma_{a.c.} = A(T)\omega^s$, in which the frequency exponent s decreases with temperature for **6**, **7** and **8**. The bulk resistance of the samples was derived from complex impedance spectra. It was found that the bulk resistance shows a typical negative temperature coefficient of resistance, decreasing with a rise in temperature, like that of a semiconductor.
© 2006 Elsevier Ltd. All rights reserved.

Keywords: Ball type; Clamshell; Bisphthalocyanine; Synthesis; Spectroelectrochemistry; Impedance spectroscopy

1. Introduction

Phthalocyanines (Pcs) have been the subject of great interest in areas such as semiconductors, chemical sensors, liquid crystals, molecular metals, catalysis, electrochromism and non-linear optics [1,2]. While the parent molecules have a number of useful properties, considerable effort has focused on the design of novel structures which may show improved or novel characteristics. In this respect, the attention of investigators has been attracted to binuclear Pcs linked by various kinds of bridges, i.e., lanthanoid and actinoid sandwich dimmers [3–6], covalently linked cofacial dimmers [7–9], planar homo- and

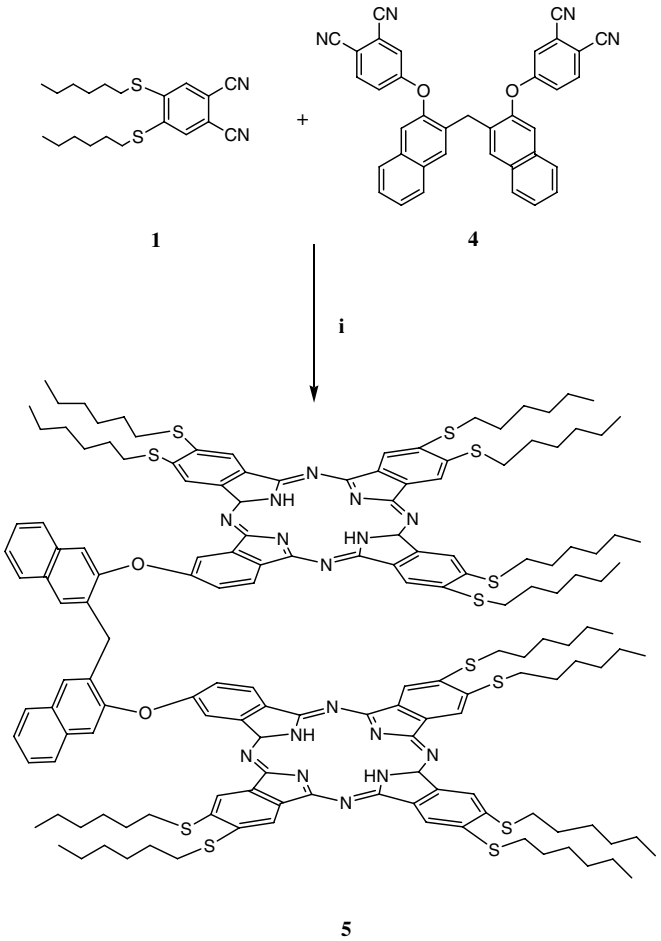
* Corresponding author. Present address: Bilim Sokak, Kardesler Apt., No. 6/9, Erenköy, Istanbul, Turkey. Tel.: +90 216 359 01 30; fax: +90 216 386 08 24.
E-mail address: obekaroglu@marmara.edu.tr (Ö. Bekaroğlu).

0277-5387/$ - see front matter © 2006 Elsevier Ltd. All rights reserved.
doi:10.1016/j.poly.2006.08.039

hetero-dimers sharing a common aromatic ring or linked by other units [10–14] and linear dimers linked by flexible alkyl chains [15,16]. A strong interaction between the halves of the molecule was usually detected in electronic absorption spectra and by electrochemistry. Due to intermolecular and/or intramolecular interactions between the Pc rings, the Q bands were usually much broader than in the monomers, or split. Moreover, since the redox couples observed in monomeric species may split into two couples, the spectra of mixed-valence species have been recorded. It was suggested that electron cloud overlap is important for strong interactions.

We have reported recently on the synthesis, characterization and electrical, electrochemical and gas sensing properties of a novel sandwich dilutetium tetra Pc [17–19], a cyclic borazine derivative containing three phthalocyaninato Zn(II) macrocycles [20] and a ball-type four *t*-butylcalix[4]arene bridged binuclear Zn(II) Pc [21]. These novel compounds showed interesting electrical, electrochemical and/or electrochromic properties.

Many Pc dimers and multimers, having various kinds of linkage, have been reported to date. These dimers and multimers, especially those with rigid cofacial configurations, usually show spectroscopic, electrochemical and electrical properties which differ significantly from the parent monomers. Although the first synthesis of ball-type binuclear Pcs has been reported by Zefirov's group [22], no detailed study on the electrochemistry, spectroelectrochemistry and electrical properties of this type of Pcs has yet been carried out. In this paper, we present the first detailed study on the preparation, characterization, spectroelectrochemical and electrical properties of some new metal-free and metallophthalocyanines of the clamshell or ball type (Schemes 1 and 2).



Scheme 1. (i) Li, pentan-1-ol, N_2, 180 °C.

2. Experimental

The starting materials **1** and **2** were synthesized by the methods described previously in the literature [23]. Compound **3** was used as supplied commercially. IR spectra were recorded on a Shimadzu FTIR-8300 spectrophotometer as KBr pellets. Electronic spectra were recorded on a Shimadzu UV-1601 spectrophotometer. Elemental analyses were performed by the Instrumental Analysis Laboratory of Tubitak – Ankara. ^{1}H NMR spectra were recorded in *d*-chloroform, *d*-dimethylsulfoxide and *d*-acetone with a Mercury-Vx 400 MHz instrument. Mass spectra were acquired in linear and reflectron modes with an average of 50 and 100 shots on a Voyager-DE™ PRO MALDI-TOF mass spectrometer (Applied Biosystems, USA) equipped with a nitrogen UV-Laser operating at 337 nm.

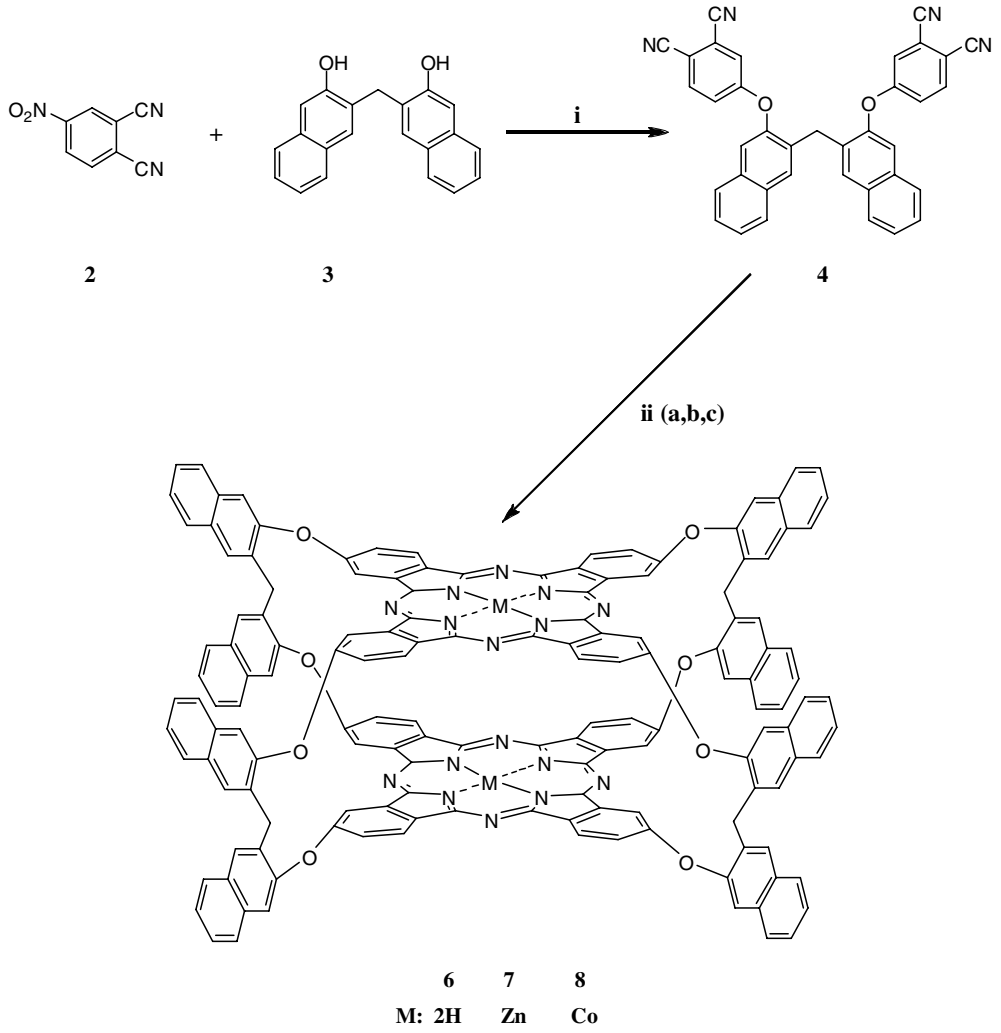
2.1. Synthesis

2.1.1. 4,4′-[1,1′-Methylenebis (naphthalene-2,1-diyl)]-bis(oxy)diphthalonitrile (**4**)

A mixture of **3** (0.60 g, 2 mmol) and **2** (0.69 g, 4 mmol) in 20 mL dimethylsulfoxide (DMSO) was stirred at room temperature under argon. K_2CO_3 (0.828 g, 6 mmol) was added into the mixture over a period of 2 h. After stirring the reaction mixture for a further 24 h, the undissolved salt was removed by filtration. The reaction mixture was poured into water (100 mL) and stirred. The precipitate was filtered and washed with water. The residue was chromatographed by silica gel and eluted with CH_2Cl_2 (DCM). Yield; 1.0 g (91%). Compound **4** is soluble in chloroform, tetrahydrofuran (THF) and acetone. Mp: 268 °C. *Anal.* Calc. for $C_{37}H_{22}N_4O_2$: C, 80.13; H, 4.00; N, 10.10. Found: C, 79.93; H, 3.92; N, 9.95%; IR (KBr pellet) ν, cm^{-1}: 3074 (Ar–H), 2231 (C≡N), 1566–1587 (C=C), 1245–1282 (Ar–O–Ar); ^{1}H NMR (*d*-acetone) δ 8.32 (d, $J = 8.19$ Hz, 2H), 7.92 (d, $J = 8.58$ Hz, 2H), 7.82 (d, $J = 2.34$ Hz, 2H), 7.70 (d, $J = 8.58$ Hz, 2H), 7.56 (m, 4H), 7.10 (brs, 2H), 6.92 (d, $J = 2.34$ Hz, 2H), 6.86 (dd, $J = 8.78$ Hz, $J = 2.34$ Hz, 2H), 4.95 (s, 2H) ppm.

2.1.2. [8,8′-Bis-2,2′(9′,10′,16′,17′,23′,24′-hexylthiophthalocyaninyl)methylendioxynaphthalene] (**5**)

A mixture of compound **1** (1.08 g, 3 mmol) and compound **4** (0.276 g, 0.5 mmol) in 1.5 mL of dry amyl



Scheme 2. (i) K_2CO_3, DMSO; (ii) a: Li, pentan-1-ol, N_2, 170 °C; b: $Zn(CH_3COO)_2 \cdot 2H_2O$, 280 °C; c: $Co(CH_3COO)_2 \cdot 4H_2O$, 280 °C.

alcohol was heated in a sealed tube at 80 °C under N_2. After addition of elemental lithium (0.030 g, 4.32 mmol) the reaction mixture was stirred at 180 °C for 6 h. After cooling to room temperature, the dark green mixture was diluted with methanol (10 mL) to precipitate the product and it was filtered. After having been washed successively with hot water, hot ethanol (3×20 mL), and then hot methanol (3×20 mL) to remove the unreacted organic materials, it was dried *in vacuo* (60 °C). The crude product was purified by column chromatography with silica gel, eluting with chloroform. Yield: 204 mg (15%). This compound is soluble in chloroform, DCM, THF and dimethylformamide (DMF). Mp > 350 °C. *Anal.* Calc. for $C_{157}H_{192}N_{16}O_2S_{12}$: C, 69.32; H, 7.11; N, 8.24; S, 14.15. Found: C, 69.03; H, 7.31; N, 8.53; S, 13.95%. MS (MALDI-TOF): *m/z* 2721 $[M+H]^+$, IR (KBr pellet) *ν*, cm^{-1}: 3357 (–NH), 3060 (arom.-CH), 2925–2858 (aliph.-CH_2), 1651–1591 (C=C), 1232 (Ar–O–Ar); UV–Vis (CH_2Cl_2), nm (log ε): 730 (5.149), 690 (5.406), 645 (5.470), 330 (5.733); ^1H NMR (*d*-chloroform): δ, ppm 8.21–7.1 (m, 30H, arom.), 3.79–3.75 (m, 2H, Ar–CH_2), 2.90–2.95 (m, 120H, aliph.-CH_2), 1.63 (m, 36H, –CH_3).

2.1.3. [8,8′-Tetrakis-bis-(2′,10′,16′,24′-phthalocyaninyl) methylendioxynaphthalene] (6)

A suspension of compound **4** (0552 g, 1 mmol) in 1.5 mL of dry amyl alcohol was heated in a sealed tube at 80 °C under N_2. After addition of elemental lithium (0.035 g, 5.043 mmol) to the reaction mixture, a dark green colour appeared in 15 min. The reaction mixture was stirred at 170 °C for 8 h. After cooling to room temperature, methanol (20 mL) was added to precipitate the product, which was then filtered. The residue was washed successively with first hot water then with hot methanol and diethyl ether before drying it *in vacuo* (70 °C). The residue was coarsely fractionated on a silica gel column eluting with chloroform and a gradient of chloroform-methanol up to 5% methanol. Yield: 55 mg (10%). This compound is soluble in THF, DMF. Mp > 350 °C. *Anal.* Calc. for $C_{148}H_{84}N_{16}O_8$: C, 80.28; H, 3.82; N, 10.12. Found: C, 80.07; H, 3.65; N, 10.05%; MS (MALDI-TOF): *m/z* 2215

$[M+H]^+$, IR (KBr pellet) ν, cm^{-1}: 3321 (>NH), 3059 (arom.-CH), 2941 (aliph.-CH_2), 1655–1589 (C=C), 1383–1229 (Ar–O–Ar); UV–Vis (DMSO), nm ($\log\varepsilon$): 710 (5.174), 680 (5.336), 630 (5.398), 325 (5.693); ^1H NMR (*d*-chloroform): δ, ppm 8.18–6.80 (m, 72H, arom.), 4.80 (m, 8H, Ar–CH_2).

2.1.4. [8,8′-Tetrakis-bis-(2′,10′,16′,24′-phthalocyaninato-dizinc(II))methylendioxynaphthalene] (7)

A mixture of compound **4** (0552 g, 1 mmol) and $Zn(OAc)_2\cdot 2H_2O$ (0.200 g, 1.2 mmol) was powdered in a quartz crucible and heated in a sealed glass tube for 3 min under a dry N_2 atmosphere at 280 °C. After cooling to room temperature, 5 mL of DMF was added to the residue to dissolve the product. The reaction mixture was precipitated by adding water. The precipitate was filtered, multiply washed first with hot water and then with hot ethanol in order to eliminate the unreacted starting materials, and dried *in vacuo*. Then, the crude product was washed with methanol, ethanol, acetonitrile and acetone for 12 h respectively in a soxhlet apparatus. The residue was coarsely fractionated on a silica gel column eluting with chloroform and a gradient of chloroform–THF up to 100% THF. Yield: 57 mg (9.75%). This compound is soluble in chloroform, DCM, THF, DMF and DMSO Mp > 350 °C. *Anal.* Calc. for $C_{148}H_{80}N_{16}O_8Zn_2$: C, 75.93; H, 3.44; N, 9.57. Found: C, 75.82; H, 3.24; N, 9.65%; MS (MALDI-TOF): *m*/*z* 2337 $[M+H]^+$, 2355 $[M+H_2O+H]^+$, IR (KBr pellet) ν, cm^{-1}: 3059 (arom.-CH), 2925 (aliph.-CH_2), 1655–1591 (C=C), 1232 (Ar–O–Ar); UV–Vis (CH_2Cl_2), nm ($\log\varepsilon$): 730 (5.545), 700 (5.488), 635 (5.100), 375 (5.362), 325 (5.510); ^1H NMR (*d*-chloroform): δ, ppm 8.25–6.50 (m, 72H, arom.), 4.80–4.70 (m, 8H, Ar–CH_2).

2.1.5. [8,8′-Tetrakis-bis-(2′,10′,16′,24′-phthalocyaninato-dicobalt(II))methylendioxynaphthalene] (8)

A mixture of compound **4** (0.200 g, 0.337 mmol) and $Co(OAc)_2\cdot 4H_2O$ (0.130 g, 0.522 mmol) was powdered in a quartz crucible and heated in a sealed glass tube for 5 min under a dry N_2 atmosphere at 280 °C. After cooling to room temperature, a blue-green reaction product was obtained, isolated and purified using the same procedure as explained above for **7**. Yield: 45 mg (7.75%). This compound is soluble in chloroform, DCM, THF, DMF and DMSO. Mp > 350 °C. *Anal.* Calc. for $C_{148}H_{80}N_{16}O_8Co_2$: C, 76.35; H, 3.46; N, 9.63. Found: C, 76.3; H, 3.51; N, 9.61%; MS (MALDI-TOF): *m*/*z* 2327 $[M+H]^+$, IR (KBr pellet) ν, cm^{-1}: 3063 (arom.-CH), 2934 (aliph.-CH_2), 1653–1591 (C=C), 1275–1232 (Ar–O–Ar); UV–Vis (CH_2Cl_2), nm ($\log\varepsilon$): 690 (5.632), 627 (5.033), 343 (5.556).

2.2. Electrochemical and spectroelectrochemical measurements

The cyclic voltammetry (CV) and controlled potential coulometry (CPC) measurements were carried out with a Princeton Applied Research Model VersaStat II potentiostat/galvanostat controlled by an external PC and utilizing a three-electrode configuration at 25 °C. The working electrode was a Pt plate with a surface area of 0.10 cm^2. The surface of the working electrode was polished with a H_2O suspension of Al_2O_3 before each run. The last polishing was done with a particle size of 50 nm. A Pt wire served as the counter electrode. A saturated calomel electrode (SCE) was employed as the reference electrode separated from the bulk of the solution by a double bridge. The ferrocene/ferrocenium couple (Fc/Fc^+) was also used as an internal standard. Electrochemical grade tetrabutylammonium perchlorate (TBAP) in extra pure DMSO and DCM was employed as the supporting electrolyte at a concentration of 0.10 mol dm^{-3}. High purity N_2 was used for deoxygenating the solution for at least 20 min prior to each run and to maintain a nitrogen blanket during the measurements. For CPC studies, a Pt gauze working electrode (10.5 cm^2 surface area), Pt wire counter electrode separated by a glass bridge and SCE as a reference electrode were used. The spectroelectrochemical measurements were carried out by an Agilent Model 8453 diode array spectrophotometer equipped with a potentiostat/galvanostat and utilizing a three-electrode configuration of a thin layer quartz spectroelectrochemical cell at 25 °C. The working electrode was a transparent Pt gauze. A Pt wire counter electrode separated by a glass bridge and a SCE reference electrode separated from the bulk of the solution by a double bridge were used.

2.3. Electrical conductivity and impedance measurements

For the electrical characterization, conductivity and impedance measurements, ten-finger interdigital gold electrodes with 50 μm gap were deposited photolithographically on pre-cleaned corning glass substrate. Prior to the vacuum evaporation, the glass substrates were thoroughly cleaned ultrasonically. Thin films of the compounds were obtained by spin-coating chloroform solutions of the products over the electrode arrays to obtain devices suitable for d.c. conductivity and impedance measurements. The materials were dissolved in extra pure grade chloroform at concentrations of $\sim 5\times 10^{-4}$ M for all the compounds. Fifty microlitres of such solutions were added with a glass pipette onto the IDT structure held onto spinner (Speciality Coatings Systems Inc., Model P6700 Series). The substrate spun at 200 rpm for 10 s and the solvent evaporated during this period, producing a homogeneous film of the phthalocyanine derivatives. The substrate temperature was kept constant at 293 K during deposition of the materials over the electrodes. Current–voltage (*I*–*V*) measurements were performed in a vacuum of 10^{-3} mbar between 290 and 480 K by using a Keithley 617 electrometer. Dc conductivity values were calculated from the measured current–voltage (*I*–*V*) characteristics by using the relation $\sigma_{d.c.} = [I\cdot d/V(2n-1)l\cdot h]$, where I is the measured current, V is the bias voltage, d is the electrode spacing, n is the number of electrode finger pairs, l is the overlap length of the electrode

fingers and *h* is the thickness of the electrodes. A.c. conductivity and low signal impedance spectra measurements were carried out with a Keithley 3330 LCZ meter in the frequency range 40 Hz to 100 kHz in the temperature range 290–480 K. During the measurement the temperature of the sample was controlled with a Leybold LTC 60 temperature controller. The conductivity data were recorded using an IEEE 488 data acquisition system incorporated to a personal computer.

3. Results and discussion

3.1. Synthesis

The synthesis of bisphthalodinitriles is based on the reaction of diols with an excess of compound **2** (DMF or DMSO in the presence of K_2CO_3 as a base, at 20 °C for 60–96 h) [24,25]. Our key starting material is compound **4** which can be obtained via the reaction of compound **2** and **3**, in dry DMSO in the presence of K_2CO_3, in a yield 91%. The metal-free clamshell-type Pc, **5** was also obtained by the reaction of compound **4** with **1** using the statistically mixed condensation method in dry *n*-penthanol and in the presence of lithium as a catalyst (Scheme 1).

A new ball-type metal-free Pc **6** was prepared by the reaction of compound **4** with lithium in dry *n*-penthanol. Compound **4** was also tetramerized to ball-type **7** and **8** (Scheme 2).

Elemental analysis, IR, ^{1}H NMR, MASS and UV/Vis spectra confirmed the proposed structures of the compounds. A diagnostic feature of Pc formation from compound **4** was the disappearance of the sharp intense CN vibration band at 2231 cm^{-1} in IR spectrum. The spectra of compounds **4**–**8** showed Ar–O–Ar peaks at 1225–1285 cm^{-1}, C=C (in phenyl and naphthalene rings) peaks at 1560–1655 cm^{-1}, aromatic CH peaks at 3060–3070 cm^{-1} and aliphatic CH_2 and CH_3 peaks at 2860–2945 cm^{-1}. The weak band around 3320–3360 cm^{-1} for **5** and **6** can be attributed to the N–H stretching frequency of the metal-free inner core.

The UV–Vis spectra of **5** in DCM and **6**, **7** and **8** in DMSO showed characteristic absorptions between 627 and 730 nm in the Q-band region (Table 1). The Q band observed for the compounds was attributed to the $\pi \rightarrow \pi^*$ transition from the highest occupied molecular orbital (HOMO) to the lowest unoccupied molecular orbital (LUMO) of the Pc ring. The other bands (B) in the UV region at 325–375 nm were observed due to the transitions from the deeper π levels to the LUMO. The spectra of **5** and **6** involved a double Q band, which is quite typical for metal-free Pc. The characteristic double Q band for each metal-free Pc was barely evident even at 10^{-7} mol dm^{-3} concentration. The Q band S_1 emission is still observed but with an unusually broad spectrum [26–29]. In addition, a third band at the blue side of the double Q band for each metal-free complex was observed. These bands, in addition to the broadness of the spectra, are indicative of intramolecular coupling between the Pc rings in these complexes. The compounds **7** and **8** show characteristic absorptions around 600 and 730 nm in the Q band region. As expected, well splitting of the Q band in the spectrum of $[ZnPc]_2$, **7**, was observed. This can be attributed to strong intramolecular interactions between the Pc rings, probably due to the ball-type cofacial structure. Although the Q band in the spectrum of **8** is not split, a well-defined absorption at 627 nm can be attributed to intramolecular interactions.

Table 1
UV–Vis data for the phthalocyanines

Compound	λ/nm ($\log\varepsilon$/dm^3 mol^{-1} cm^{-1})
5[a]	730 (5.149), 690 (5.406), 645 (5.470), 330 (5.733)
6[b]	710 (5.174), 680 (5.336), 630 (5.398), 325 (5.693)
7[b]	730 (5.545), 700 (5.488), 635 (5.100), 375 (5.362), 325 (5.510)
8[b]	690 (5.632), 627 (5.033), 343 (5.556)

[a] In DCM.
[b] In DMSO.

The ^{1}H NMR spectra were also in good correlation with the structure of the synthesized compounds. In the ^{1}H NMR spectrum of compound **4**, which was taken in *d*-acetone, the phenyl protons appeared at 7.92 ppm (d), 7.82 ppm (d) and 6.86 ppm (dd), naphthalene protons at 8.32 ppm (d), 7.70 ppm (d), 7.56 ppm (m), 7.10 ppm (brs) and 6.92 ppm (d) and CH_2 protons at 4.95 ppm (s). In the ^{1}H NMR spectra of **5**, **6** and **7**, which were taken in *d*-chloroform, the aromatic protons appeared at 8.25–6.45 ppm (m) and Ar–CH_2 peaks at 4.80–4.70 ppm (m). In addition, in the ^{1}H NMR spectrum of **5**, the –CH_3 protons at the end of the chain appeared at 1.65 ppm and aliphatic –CH_2– protons at 2.90–2.95 ppm. In the ^{1}H NMR spectra of **5** and **6**, NH protons could not be observed, probably due to the broad nature of these peaks in the presence of intense resonances of the Pc ring [30].

A 3,5-dinitrobenzoic acid (DNB) MALDI matrix was used and prepared in chloroform at a concentration of 20 mg/mL for **5** and α-cyano-4-hydroxycinnamic acid was prepared in chloroform at a concentration of 20 mg/mL for **6**. MALDI samples were prepared by mixing sample solutions (4 mg/mL) with the matrix solution (1:10 v/v) in a 0.5 mL eppendorf® microtube. Finally 1 μL of this mixture was deposited on the sample plate, dried at room temperature and then analyzed. The protonated molecular ion peak of the ligand was observed at 2721 Da together with some fragment ion peaks. The mass difference between these peaks corresponding to 84 Da mass resulted from cyclohexane elimination from the ligand at the side groups.

In the MALDI-MS spectrum of **6**, beside the cyclohexane elimination, two main fragment ions were observed at 1491 and 1226 Da mass, resulting from breakage of the bond between the oxygen and aromatic ring which exist in the core of the ligand.

For compound **6**, a protonated molecular ion peak was observed at 2215 Da. This value exactly overlaps with the mass of **6** calculated theoretically from its elemental composition. Beside the protonated molecular ion peak of the complex, two other intense and one low intensity peaks were observed with 282 Da mass differences from each other and the protonated molecular ion peak. These peak masses indicate a fragmentation resulting from the protonated molecular ion of the complex with a 282 Da mass loss from both sides of the complex. This fragment indicates that the leaving group could be $C_{21}H_{14}O$, which exists as an end group in the chemical structure of **6**.

3-Indole acrylic acid (IAA) MALDI matrix was used and prepared in chloroform at a concentration of 20 mg/mL for **7**. The peak group representing the protonated molecular ion of the complex was observed starting with 2330 Da mass and finishing with 2338 Da, following each other by 1 Da mass differences. This type of mass distribution results from the isotopic mass distribution of carbon (mainly ^{13}C) and the isotopes of zinc in the metal complex. These peaks resulted from water adduct, side chain eliminations (oxygen leaving). This indicated that the complex was more stable under the MALDI matrix conditions and also under the laser energy.

2,5-Dihydroxybenzoic acid (DHB) MALDI matrix was used and prepared in chloroform at a concentration of 20 mg/mL for **8**. The positive ion MALDI-MS spectrum of **8** ($C_{148}H_{80}N_{16}O_8Co_2$) is given in Fig. 1. The peak group representing the protonated molecular ion of **8** was observed starting with 2325 Da mass and finishing with 2330 Da, following each other by 1 Da mass differences, as in **7**, from the isotropic mass distribution.

3.2. Electrochemistry and spectroelectrochemistry

The redox properties of the complexes were examined by cyclic and differential pulse voltammetry, and CPC in DMSO/TBAP or DCM/TBAP. A summary of the relevant electrochemical data is given in Table 2. Typical cyclic and differential pulse voltammograms for **8** are shown in Fig. 2. The CPC studies showed that all the redox processes for the complexes, except the reduction couples of **5**, involve

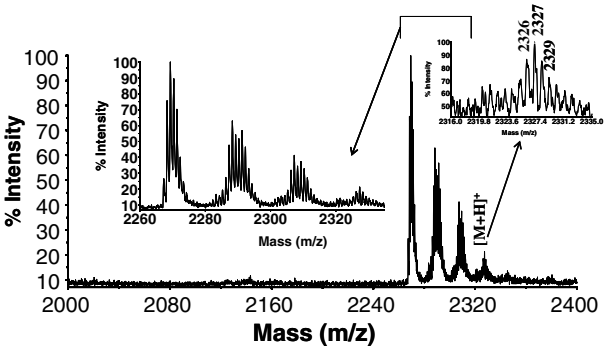


Fig. 1. Mass spectra of **8** (reflectron).

Table 2
The electrochemical data for **5** in DCM, and for **6**, **7** and **8** in DMSO[a]

Complex	Redox processes	$E_{1/2}$ (*V*)	ΔE_p (*V*)	ΔE (*V*)	ΔE_s (*V*)
5	$[H_2Pc(-1)]_2^{2+}/[H_2Pc(-2)\cdot H_2Pc(-1)]^+$	1.14	0.06		0.32
	$[H_2Pc(-2)\cdot H_2Pc(-1)]^+/[H_2Pc(-2)]_2$	0.82	0.06	1.54	
	$[H_2Pc(-2)]_2/[H_2Pc(-3)]_2^{2-}$	−0.72	0.05		
	$[H_2Pc(-3)]_2^{2-}/[H_2Pc(-4)]_2^{4-}$	−0.90	0.06		
	$[H_2Pc(-4)]_2^{4-}/[H_2Pc(-5)]_2^{6-}$	−1.76	0.04		
6	$[H_2Pc(-1)]_2^{2+}/[H_2Pc(-2)\cdot H_2Pc(-1)]^+$	0.79	0.06		0.40
	$[H_2Pc(-2)\cdot H_2Pc(-1)]^+/[H_2Pc(-2)]_2$	0.39	0.06	1.06	
	$[H_2Pc(-2)]_2/[H_2Pc(-2)\cdot H_2Pc(-3)]^-$	−0.67	0.14		0.33
	$[H_2Pc(-2)\cdot H_2Pc(-3)]^-/[H_2Pc(-3)]_2^{2-}$	−1.00	0.14		
	$[H_2Pc(-3)]_2^{2-}/[H_2Pc(-3)\cdot H_2Pc(-4)]^{3-}$	−1.36	0.12		0.31
	$[H_2Pc(-3)\cdot H_2Pc(-4)]^{3-}/[H_2Pc(-4)]_2^{4-}$	−1.67	0.08		
7	$[Zn(II)Pc(-2)\cdot Zn(II)Pc(-1)]^+/[Zn(II)Pc(-2)]_2$	0.53	0.10	1.31	
	$[Zn(II)Pc(-2)]_2/[Zn(II)Pc(-2)\cdot Zn(II)Pc(-3)]^-$	−0.78	0.32		0.43
	$[Zn(II)Pc(-2)\cdot Zn(II)Pc(-3)]^-/[Zn(II)Pc(-3)]_2^{2-}$	−1.21	0.34		
	$[Zn(II)Pc(-3)]_2^{2-}/[Zn(II)Pc(-3)\cdot Pc(-4)]^{3-}$	−1.46	0.20		0.24
	$[Zn(II)Pc(-3)\cdot Zn(II)Pc(-4)]^{3-}/[Zn(II)Pc(-4)]_2^{4-}$	−1.70	0.24		
8	$[Co(II)Pc(-2)\cdot Co(III)Pc(-2)]^+/[Co(II)Pc(-2)]_2$	0.46	0.14	0.79	
	$[Co(II)Pc(-2)]_2/[Co(II)Pc(-2)\cdot Co(I)Pc(-2)]^-$	−0.33	0.14		0.44
	$[Co(II)Pc(-2)\cdot Co(I)Pc(-2)]^-/[Co(I)Pc(-2)]_2^{2-}$	−0.77	0.34		
	$[Co(I)Pc(-2)]_2^{2-}/[Co(I)Pc(-2)\cdot Co(I)Pc(-3)]^{3-}$	−1.35	0.10		0.23
	$[Co(I)Pc(-2)\cdot Co(I)Pc(-3)]^{3-}/[Co(I)Pc(-3)]_2^{4-}$	−1.58	0.12		

[a] Potentials are reported with respect to the SCE. Half-wave potentials in DCM *vs.* Fc/Fc^+ couple correspond approximately with the above **5** data minus 0.45 V. Half-wave potentials in DMSO *vs.* Fc/Fc^+ couple correspond approximately with the above **6**, **7** and **8** data minus 0.50 V. $E_{1/2}$ values were measured by cyclic voltammetry [$E_{1/2} = (E_{pa} + E_{pc})/2$] or differential pulse voltammetry. The peak separation values ($\Delta E_p = E_{pa} - E_{pc}$) are reported at 0.100 V s^{-1}. ΔE is the potential difference between the first oxidation and first reduction potentials. It represents the HOMO–LUMO gap for **5**, **6** and **7**, but the charge transfer transition for **8** involving redox-active metal centers. ΔE_s indicates mixed-valence splitting energy for the relevant split redox couples.

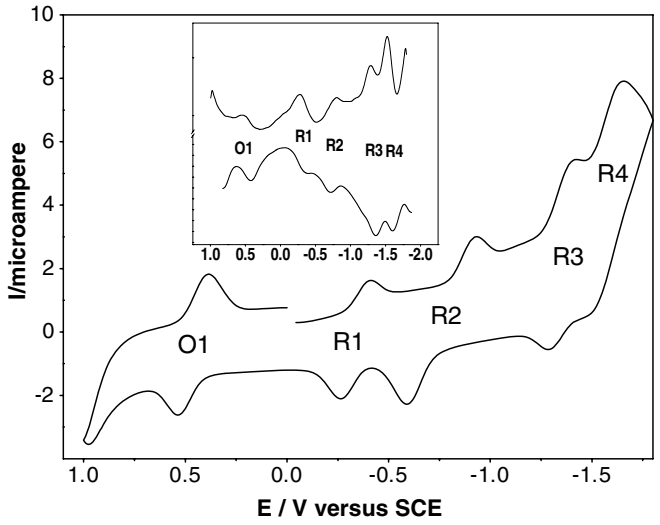


Fig. 2. Cyclic and differential pulse voltammograms of **8** at 0.100 V s^{-1} in DMSO/TBAP solution.

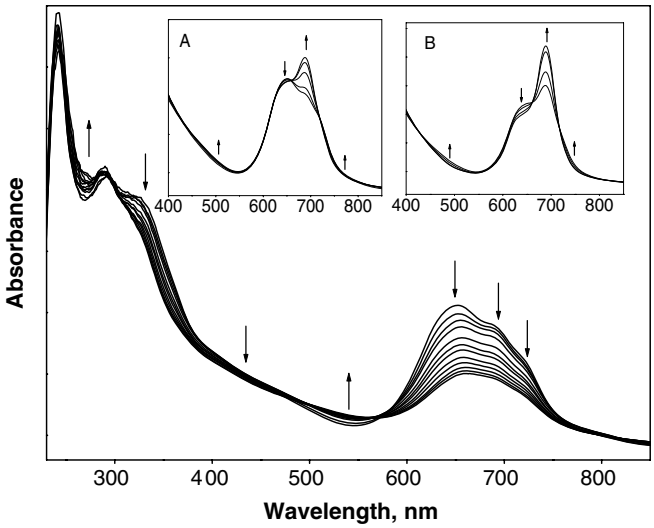


Fig. 3. UV–Vis spectra of **5** and spectral changes during its first oxidation, first reduction (inset A) and second reduction (inset B) in DCM/TBAP solution.

the transfer of one electron. The number of electrons transferred in each reduction process of **5** was found to be two. The spectroelectrochemical properties were also examined by recording the UV–Vis spectral changes during the stepwise reductions and oxidations of the complexes.

The CV of **5** gave two one-electron quasi-reversible oxidation couples and three two-electron quasi-reversible reduction couples within the potential limits of the DCM/TBAP medium. The two one-electron oxidation couples may be attributed to the stepwise oxidation of the two Pc rings in **5**, and thus to the formation of mixed valence $[H_2Pc(-2) \cdot H_2Pc(-1)]^{+}$ species in the first step and doubly oxidized $[H_2Pc(-1)]_2^{2+}$ species in the second step, probably due to intramolecular cofacial electronic coupling between the two Pc rings. No splitting was observed in the two-electron reduction processes. Thus, there is no stabilization of the mixed-valence anion radical species. The involvement of two electrons in each reduction process of **5** should suggest that the two Pc rings are reduced simultaneously. This may be due to uncoupling of cofacial conformations prior to or/and simultaneously with the first reduction process. In that case, the coupling between the halves of the molecule is not important enough to cause the splitting of the reduction processes. This type of electrochemical behaviour was observed previously for a clamshell-type binuclear Pc, permitting only the observation of mixed-valence ring-oxidized species [31]. In order to provide additional support for the assignment of the redox processes, spectroelectrochemical measurements were also carried out. The UV–Vis spectra of the original **5** and the spectral changes recorded during its first oxidation, first reduction and second reduction in DCM/TBAP are shown in Fig. 3. The spectrum of **5** is considerably broad with three Q band absorptions at 645, 689 and 728 nm. We should note that the splitting of the Q band into three bands were more noticeable in the absence of TBAP. The presence of TBAP in spectroelectrochemical measurements caused a decrease in the absorption ratio of 645 nm/689 nm. TBAP probably causes a decrease in the intramolecular coupling between the Pc rings, due to possible changes in the cofacial clamshell conformation, as reported previously [31]. However, the spectrum recorded in DCM/TBAP was highly similar in the maximum absorption values to that in DCM, with just small differences. In dimeric Pcs, intramolecular coupling between the rings causes a band at the red side of the characteristic Q band, at around 630 nm. Thus, the band at 645 nm in the broad spectrum of metal-free Pc **5** may be attributed to the cofacial intramolecular coupling. Furthermore, there was an increase in the absorption at 689 nm while the absorption at around 645 nm decreases during the stepwise controlled potential electrolyis of a solution of **5** at potentials slightly more negative than the first and second reduction potentials (insets A and B in Fig. 3). This presumably arises from the decrease in intramolecular coupling, as a result of the repulsion between the negatively charged Pc rings. Upon the third reduction, in contrast to the first and second reductions, there was a decrease in absorption of all the bands. This may be due to decomposition of the doubly reduced species under the conditions of electrolysis at a considerably negative constant potential. Upon the first oxidation, the absorption of all the three bands at the Q band region decreased. However, the absorption in some regions below 576 nm increased, and well-defined isosbestic points were obtained at 315, 456 and 576 nm. The spectrum obtained after the first oxidation was still broad at the Q band region. This is characteristic for ring-oxidized mixed-valence species [31]. The broadness may suggest that intramolecular coupling between the Pc rings is still remarkable after the first oxidation. The second oxidation to the fully oxidized $[H_2Pc(-1)]_2^{2+}$ species occurs at

considerably positive potentials. Unfortunately, probably for this reason, well-defined spectral changes for the second oxidation could not be obtained.

The metal-free ball-type complex, **6** displayed four one-electron quasi-reversible reduction couples and two one-electron reversible oxidation couples (Table 2). The stepwise one-electron processes imply the existence of mixed-valence first- and second-reduced, and first-oxidized species. The half-wave potentials of these processes and the relevant electrochemical data are given in Table 2. All the redox processes for **5** and **6** are ligand-based since these complexes are metal-free. The voltammetric behaviour of the ball-type **6** is remarkably different from the clamshell-type **5**, especially on the reduction side. In contrast to **5**, the formation of stable mixed-valence first- and second-reduced species is observed for **6**, in addition to the formation of mixed-valence first-oxidized species, as a result of the splitting of the Pc(-2)/Pc(-3) and Pc(-3)/Pc(-4) redox couples. It may be concluded that the binding of two Pc rings at two sides in the ball-type **6** causes stronger intramolecular cofacial coupling, compared to the clamshell-type **5**. Moreover, the first oxidation of **6** occurs at a potential 400 mV less positive with respect to that of **5**, while the first reductions of the complexes occur at relatively approximate potentials. The difference between the first oxidation and the first reduction potentials in these complexes corresponds to the HOMO–LUMO gap. As a result, the HOMO–LUMO transition is remarkably narrower for **6** (1.54 V for **5** and 1.06 V for **6**). This should be also due to the strong electronic coupling and the splitting of molecular orbitals. The UV–Vis spectra of the original **6** and the well-defined spectral changes during its stepwise controlled potential electrolysis for reduction and oxidation couples provided additional support for these comments. Fig. 4 shows the UV–Vis spectra of the original **6** and typical well-defined spectral changes during its first reduction, first oxidation and second oxidation. The UV–Vis spectrum of the original **6** gave a split Q band with two strong absorptions at 630 and 680 nm, and a shoulder at 710 nm. In this spectrum, in addition to the clear splitting into three bands, the absorption at 630 nm, corresponding to the intramolecular coupling in binuclear Pcs is remarkably higher than those at 680 and 710 nm. During the first reduction process, the general spectral change is the decrease in the absorption ratio of $A(630)/A(680)$. This behaviour may be attributed to the decrease in coupling, due to the negative charge of Pc rings and thus to the repulsion forces. However, in contrast to **5**, the coupling is still not negligible since the absorption band at around 630 nm has a considerable value (Fig. 4). Furthermore, it was observed that the absorption band at around 630 nm was still a remarkable value compared to that at 680 nm, even after the third reduction process. Upon the first oxidation of **6**, the absorption at 680 nm increases while a slight decrease in absorption at 630 nm is observed (inset A in Fig. 4). After the second oxidation, the peak at 630 nm peak is still higher than the peak at 680 nm (inset B in Fig. 4). This may be due to the delocalization of the positive charge on the whole molecule.

The CV of the ball-type $[ZnPc]_2$ **7** displayed quasi-reversible four one-electron reduction and a one-electron oxidation processes (Table 2). These redox processes should also be associated with the presence of mixed-valence first- and second-reduced, and first-oxidized species. Fig. 5 shows the UV–Vis spectra of the original complex **7** and the spectral changes during the first, second (inset A) and third (inset B) reductions in DMSO/TBAP. The well-split Q band and the presence of a shoulder at 635 nm in the spectra of the original complex indicate strong intramolecular coupling between the two Pc rings. During the first reduction, the absorption at 700 nm increases with a blue shift to 686 nm, and a sharp decrease in the absorption at

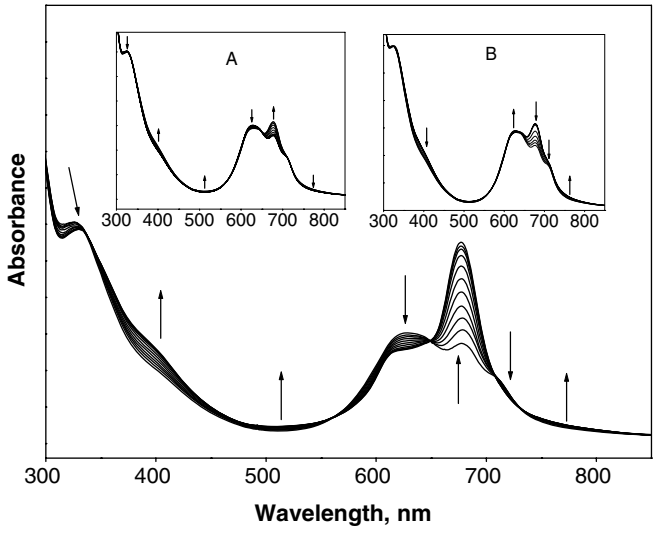


Fig. 4. UV–Vis spectra of **6** and spectral changes during its first reduction, first oxidation (inset A) and second oxidation (inset B) in DMSO/TBAP solution.

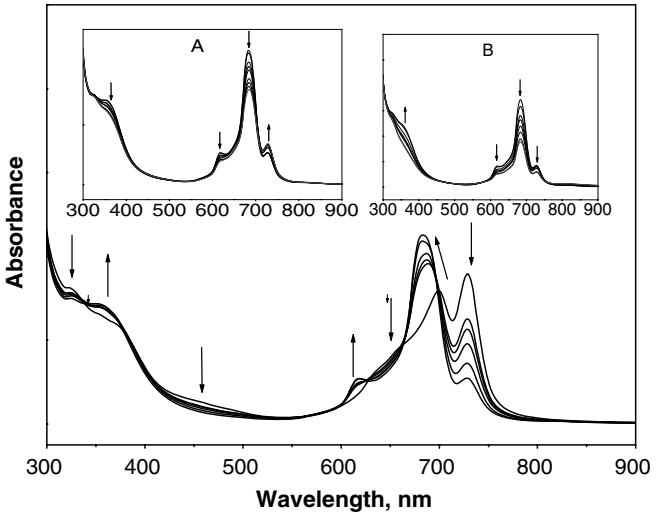


Fig. 5. UV–Vis spectra of **7** and spectral changes during its first, second (inset A) and third reduction (inset B) in DMSO/TBAP solution.

730 nm without any shift is observed. In the meantime, the absorption of the shoulder at 635 nm decreases and a sharp peak at 620 nm appears, indicating the decrease in coupling. These spectral changes with the changes around the soret band are associated with well-defined isosbestic points at 700, 664, 627, 582, 375 and 340 nm. During the second reduction process, there was a decrease in the absorption of the peaks at 355, 686 and 620 nm, and an increase in the absorption of the peak at 730 nm (inset A in Fig. 5). Upon the third reduction, the absorption of the B band at around 360 nm increases while the absorption of the other peaks around the Q band decreases (inset B in Fig. 5). In contrast to **6**, after the reduction processes, the absorption at around 630 nm was considerably lower compared to the absorption at 686 nm, indicating negligible coupling for the reduced species. This may be due to the relatively higher repulsion forces and the increase in the distance between the two Pc rings during the reduction processes. Upon the first oxidation, similar spectral changes with those of the first reduction were observed with the formation of slightly different isosbestic points.

Compound **8** also displayed four quasi-reversible one-electron reduction and a one-electron oxidation processes in DMSO/TBAP (Fig. 2 and Table 2). However, the nature of these redox processes should be different, compared to those of **6** and **7**. It is clear from the previous studies that the Co(II) metal center is redox-active in metallo Pcs [32]. In addition, its redox behaviour strongly depends on the presence or absence of coordinating solvent or supporting electrolyte ions. Previous reports on the electrochemistry of Co(II) Pcs clearly suggested that both the first reduction and first oxidation processes in these complexes are metal-based in polar coordinating solvents such as DMSO and DMF. Since compound **8** is a binuclear cofacial complex, and thus involves two Co(II) centers, the oxidation and the first two reductions probably correspond to $[Co(II)Pc(-2)\cdot Co(III)Pc(-2)]^{+}/[Co(II)Pc(-2)]_2$, $[Co(II)Pc(-2)]_2/[Co(II)Pc(-2)\cdot Co(I)Pc(-2)]^{-}$ and $[Co(II)Pc(-2)\cdot Co(I)Pc(-2)]^{-}/[Co(I)Pc(-2)]_2^{2-}$ redox processes, respectively. On the other hand, the third and fourth reductions should be related to the splitting of the Pc(-2)/Pc(-3) couple, and thus is ligand-based, corresponding to $[Co(I)Pc(-2)]_2^{2-}/[Co(I)Pc(-2)\cdot Co(I)Pc(-3)]^{3-}$ and $[Co(I)Pc(-2)\cdot Co(I)Pc(-3)]^{3-}/[Co(I)Pc(-3)]_2^{4-}$ redox processes, respectively. In contrast to the data in this study and in the articles about Nap- and Ant[CoTRNPc]$_2$ [33,34], it was reported previously that neither the Co(II)/Co(III) nor Co(II)/Co(I) redox couples are split in a coordinating solvent such as DMF or DMSO for some planar and cofacial binuclear Co(II) Pcs [35,36]. The different behaviour was assigned to insufficient intramolecular coupling for splitting, rearrangement to a less coupled conformation prior to electron transfer and/or axial coordination of solvent molecules to the cobalt atoms, which may be sterically hindered in the cofacial complexes. The splits observed in this study may be attributed to the interactions between the two cobalt centers, which are probably held in close proximity by the cofacial ligand geometry, resulting in overlap of their d_{z^2} orbitals along the cobalt–cobalt axis. The UV–Vis spectrum of original **8** and the spectral changes during its reduction and oxidation processes are given in Fig. 6. Surprisingly, the spectra of **7** and **8** are different. In contrast to **7**, the Q band in the spectrum of **8** is not split. This may result from the difference in coordinative properties in axial positions of the metal centers in **7** and **8**. Another alternative or additional reason for the difference may be less intramolecular coupling in **8** compared to **7**. However, complex **8** displays a peak as a shoulder at 627 nm, indicating the presence of intramolecular coupling. The spectroelectrochemical measurements in solution have a vital importance in confirming the assignment of the redox processes in the Pcs, especially in cobalt Pcs. Upon first reduction (Fig. 6a), the formation of Co(I) species is indicated by the appearance of a new absorption at 488 nm, associated with a metal-to-ligand charge transfer (MLCT) from Co(I) to the Pc ring [37,38]. During the second reduction, the absorption of the newly formed MLCT peak continues increasing while the Q band absorption at 690 nm decreases (Fig. 6b). In the meantime, a shoulder at the red side of the main peak at 690 nm appears. Therefore, the spectrum of the mixed-valence Co(II)/Co(I) species obtained during the first reduction is different from that of the fully reduced Co(I)/Co(I) species obtained during the second reduction. The Co(II)/Co(I) mixed-valence species has a much weaker MLCT band. This implies that the added first electron may be delocalized over the extended ring system. This type of behaviour was observed previously for the (-1)-bridged binuclear [CoTRNPc]$_2$ [35]. Upon the third reduction, the MLCT peak at 488 nm decreases, in contrast to the first and second reduction processes (Fig. 6c). This is probably due to the ring reduction and formation of mixed-valence ring-reduced species. The formation of mixed-valence Co(II)/Co(III) species is indicated by the appearance of a new absorption at 485 nm, associated with MLCT from Co(III) to the Pc ring (Fig. 6d). The shift in the Q band absorption from 690 nm to 697 nm also provides additional support for a metal-based first oxidation. The spectrum of the mixed-valence Co(II)/Co(III) species is different from that of classical $[Co(III)Pc(-2)]^{+}$ cation radical species. Generally, a new peak at around 480 nm does not appear during the first oxidation of mono Pcs [39].

The mixed-valence splitting values for the various redox couples of metal-free clamshell-type **5** and ball-type **6**, **7** and **8** are within the range of 0.23–0.44 V, indicating the existence of various stable mixed-valence species. The Pc(-1)/Pc(-2) mixed-valence species of **6** appears to be more stable than that of **5**. This should arise from the ball-type rigid structure of **5**, leading to strong intramolecular cofacial interactions. It appears that for the ball-type **7**, Pc(-2)/Pc(-3) mixed-valence species are much more stable than the Pc(-3)/Pc(-4) mixed-valence species. Similarly, Co(II)/Co(I)

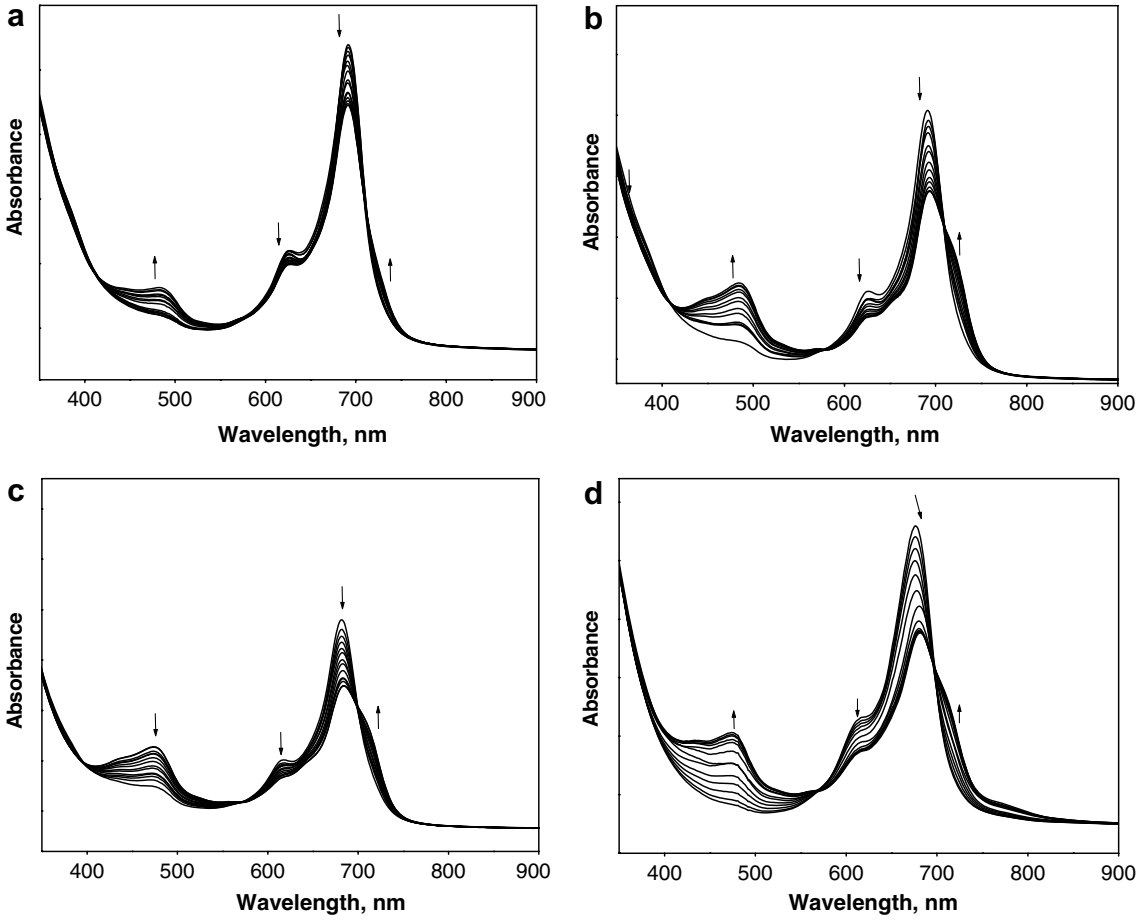


Fig. 6. UV–Vis spectra of **8** and spectral changes during its redox processes in DMSO/TBAP solution: (a) The first reduction; (b) the second reduction; (c) the third reduction; (d) the first oxidation.

mixed-valence species of ball-type **8** are more stable than its Pc(-2)/Pc(-3) mixed-valence species.

3.3. Electrical conductivity and impedance spectroscopy

To obtain valuable information on the processes taking place in the film of the compounds, the temperature dependence of the d.c. electrical conductivity was examined. A conduction mechanism frequently observed in Pc thin film is thermally activated conduction. The value of the thermal energy of electrical conduction, E_A, calculated from the curves $\ln \sigma_{d.c.} = f(1/T)$, ranged between 0.38. and 0.91 eV. The calculations were made by taking into account the expression;

$$\sigma_{d.c.} = \sigma_0 \exp(-E_A/kT) \quad (1)$$

where E_A is the thermal activation energy of the electrical conduction, T is temperature, k is Boltzmann's constant and σ_0 is a parameter depending on the semiconductor nature. The linear dependence in the Arrehenius plot suggests the presence of only one conduction mechanism, assuming that the dominant levels are the conduction and valence bands in the temperature range of 290–480 K for the films of the compounds. Among the ball type compounds investigated, the metal-free Pc of ball type, **6**, showed the lowest electrical conductivity, especially at high temperature. It should be noticed that the d.c. conductivity of compounds **7** and **8** are nearly of the same order, even at high temperatures. It is well established that the electrical conductivities of phthalocyaninato and related compounds depend very much upon the central metal atom, the nature of substituent groups, overlap of the π-electron systems between the pc molecules and the stacking arrangement of the molecules. The lowest conductivity for compound **6** suggests that the central metal atom does play a dominant role in charge transfer of the ball type Pc thin film. The higher conductivity of **7** and **8** can be attributed to the decrease of the separation distance between the Pc macrocycles, because of the inserted metal atom. A comparison of the d.c. conductivities of metal-free Pc of clamshell type, **5**, and metal-free Pc of ball type, **6**, indicates that **5** has a higher conductivity than **6** for all temperatures. The higher conductivity of **5** can be expected here due to the differences in the stacking arrangement of the Pc molecules. This difference in arrangement may result in altering the interaction of the π-electron systems between the different molecules, which may affect the electrical conductivity of the Pc.

The electrical behaviour of the materials is often characterized in terms of complex impedance spectra. The impedance spectroscopy technique is based on analyzing the a.c. response of a system to a sinusoidal excitation and subsequent measurements of impedance as function of the frequency of sinusoidal excitation. The analysis of the impedance data may allow an estimation of the values of circuit elements which are directly related to the material properties, e.g, the bulk resistance, the grain boundary resistance, the double-layer capacitance, etc. Fig. 7a shows the measured complex impedance spectra (Cole–Cole plot) of the compounds recorded in the frequency range 40–100 kHz at room temperature. The room temperature impedance spectra of the compounds are characterized by the appearance of semicircular shaped arcs. It was observed that temperature has a strong effect on the impedance spectra of the compounds. As temperature rises, the semicircular arcs transform into full semicircles. Fig. 7b shows the impedance spectra of the compounds at 430 K. A simple semicircle in the Cole–Cole plot is considered to result when the electrical processes in the materials arise basically due to the contribution from the bulk material. In the simple semicircle case, the measured impedance data can be modelled as an equivalent electrical circuit comprising of a capacitor, C, in parallel with a resistor, R_1, in series with another resistor, R_2. The series resistance in the equivalent circuit represent the ohmic losses in the experimental set-up and electrode sheet resistance. The parallel resistance is the bulk resistance of the coating material. The values of R_1 and R_2 can be obtained from the intercept of the spectrum on the real axis at low and high frequencies, respectively. The values of bulk resistance for all the compounds have been estimated from the complex impedance spectra as a function of temperature. A monotonic decrease in R_1 was observed with the rise in temperature. This observation suggest that the increase of temperature lowers the barrier for charge transport.

The frequency dependence of conductivity can also give information about the conduction mechanism in the film. It is known that [40] when the localized states are randomly distributed, the a.c. conductivity depends on frequency as

$$\sigma_{ac} \propto \omega^s \tag{2}$$

where ω is the angular frequency, and the frequency exponent, s, is a material dependent constant. When the conductivity of the compounds is measured by using the a.c. technique, the trend observed is essentially the same found for d.c. conductivities: **5** > **7** > **8** > **6**. These results for ac conductivity are in agreement with the observed d.c. conductivity. Fig. 8 shows the measured a.c. conductivity of the compounds in the frequency range, 40–10^5 Hz at 355 K. A similar frequency dependence is also observed for other temperatures. Fig. 8 indicates that the a.c. conductivity obeys the relation $\sigma_{ac} = A\omega^s$, where A is a constant. Many mechanisms can be operative for charge transport in Pc compounds. Different conduction mechanisms can lead to ω^s type of behaviour for a.c. conductivity, but it is not easy to decide which mechanisms are responsible for the observed conduction. The variation of the exponent s with temperature gives information about the conduction mechanism. The values of the frequency exponent s, estimated from the slopes of the curves in Fig. 8, were found to be less than unity for all the compounds, which is consistent with the general behaviour of Pc films [41]. The exponent s calculated from the slopes

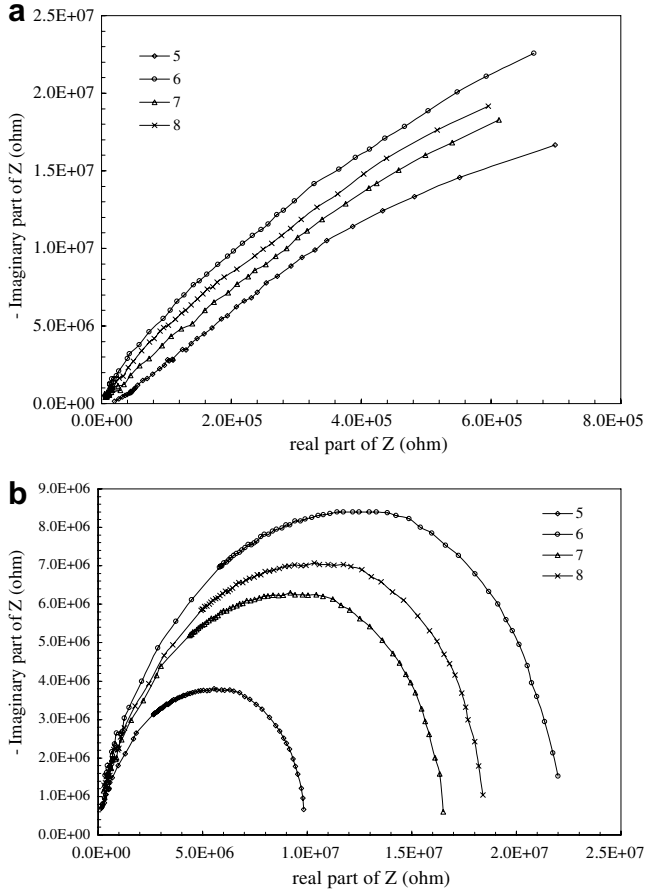


Fig. 7. Impedance spectra of the compounds (a) at room temperature (b) 430 K.

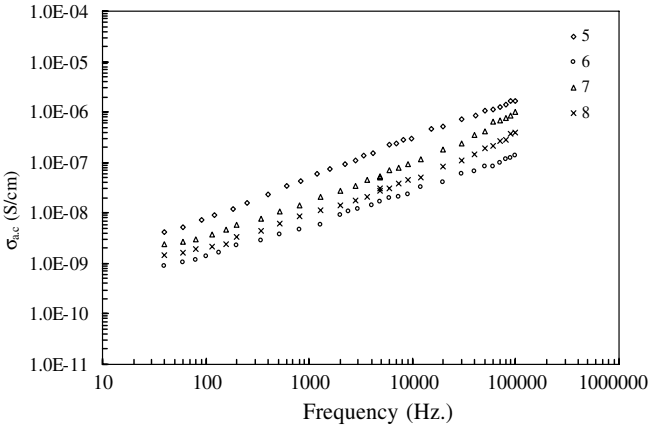


Fig. 8. The frequency dependence of the a.c. conductivity of films of the compounds at 355 K.

of Fig. 8 is temperature dependent and decreases with increasing temperature for the compounds **6**, **7** and **8**. A temperature independent frequency exponent *s*, with a value of ~0.78, was observed for **5**. It is observed that the values of *s* lie in the range 0.76–0.82. The observed behaviour of *s* for **5** allows the conclusion that the Quantum Mechanical Tunelling model (QMT) is a possible conduction mechanism. According to this model the conduction occurs by means of thermally assisted QMT. The QMT model predicts a temperature independent *s* with a constant value around 0.8, which is given by

$$s = 1 - \frac{4}{\ln(\omega\tau_0)} \tag{3}$$

where ω is the angular frequency and τ_0 the characteristic relaxation time of the carrier

The temperature independent frequency exponent *s* for **5** is consistent with the prediction of the QMT model. It was also observed that *s* is definitely a function of temperature for compounds **6**, **7** and **8**, and shows a general tendency to increase with decreasing temperature. The decrease in *s* with temperature cannot be explained by the QMT model. In the case of compounds **6**, **7** and **8** a hopping conduction process, which was developed by Eliot [42], is applicable. According to this model, a charge carriers hops between sites over the potential barrier separating them, rather than tunnelling through the barrier. The expression for conductivity in this model [43] is given by

$$\sigma_{ac}(\omega) = \frac{\pi^2 N^2 \varepsilon}{24}\left(\frac{8q^2}{\varepsilon W_{OB}}\right)^6 \frac{\omega^s}{\tau_0^\beta} \tag{4}$$

where ε is the dielectric constant, W_{OB} the optical band gap, τ_0 a characteristic relaxation time, *q* electronic charge, and *N* is the spatial density of defect states. The frequency exponent *s* for this model is evaluated as

$$s = 1 - \beta = 1 - 6k_B T/W_{OB} \tag{5}$$

where k_B is Boltzmann's constant. Therefore, according to the Correlated Barrier Hopping (CBH) model, *s* should be temperature dependent. A comparison of the experimentally determined *s* values with the prediction of the CBH model suggest that the dependence of the exponent *s* on temperature is in agreement with the prediction of the CBH model for compounds **6**, **7** and **8**.

Acknowledgements

This work was supported partly by the Turkish Academy of Sciences (TUBA), The Research Fund of Marmara University (SCIENCE-107/020603) and Scientific and Technical Research Council of Turkey (TUBITAK) [TBAG-HD/50 (105T262)].

References

[1] C.C. Leznoff, A.B.P. Lever (Eds.), Phthalocyanines – Properties and Applications, vols. 1–4, New York, 1989, 1992, 1993 and 1996.
[2] N.B. McKeown, Phthalocyanines Materials – Synthesis, Structure and Functions, Cambridge University Press, Cambridge, 1998.
[3] Ş. Merey, Ö. Bekaroğlu, J. Chem. Soc. (1999) 4503.
[4] K.M. Kadish, T. Nakanishi, A. Gürek, V. Ahsen, İ. Yılmaz, T. Nakanishi, J. Phys. Chem. 105 (2001) 9817.
[5] N. Koike, H. Uekusa, Y. Ohashi, C. Harnoode, F. Kitamura, T. Ohsaka, K. Tokuda, Inorg. Chem. 35 (1996) 5798.
[6] J. Jiang, D.P. Arnold, H. Yu, Polyhedron 18 (1999) 2129.
[7] (a) C.C. Leznoff, H. Lam, W.A. Nevin, N. Kobayashi, P. Janda, A.B.P. Lever, Angew. Chem., Int. Engl. 26 (1987) 1021; (b) H. Lam, S.M. Marcuccio, P.I. Svirskaya, S. Greenberg, C.C. Leznoff, R.L. Cerny, Can. J. Chem. 67 (1989) 1087.
[8] N. Kobayashi, Y. Yanagisawa, T. Osa, H. Lam, C.C. Leznoff, Anal. Chem. 6 (1990) 813.
[9] N. Kobayashi, H. Lam, W.A. Nevin, P. Janda, C.C. Leznoff, A.B.P. Lever, Inorg. Chem. 29 (1990) 3415.
[10] N. Kobayashi, H. Lam, W.A. Nevin, P. Janda, C.C. Leznoff, T. Koyama, A. Monden, H. Shirai, J. Am. Chem. Soc. 116 (1994) 879.
[11] N. Kobayashi, M. Numao, R. Kondo, S. Nakajima, T. Osa, Inorg. Chem. 30 (1991) 2241.
[12] N. Kobayashi, J. Chem. Soc., Chem. Commun. (1991) 1203.
[13] N. Kobayashi, Y. Higashi, T. Osa, Chem. Lett. (1994) 1813.
[14] E.M. Garcia-Frutos, F. Fernandez-Lazaro, E.M. Maya, P. Vazquez, T. Torres, J. Org. Chem. 65 (2000) 6841.
[15] S. Vigh, H. Lam, P. Janda, A.B. P Lever, C.C. Leznoff, R.L. Cerny, Can. J. Chem. 69 (1991) 1457.
[16] (a) E.M. Maya, P. Vazquez, T. Torres, Chem. Eur. J. 5 (1999) 2004; (b) K.H. Schweikart, M. Hanack, Eur. J. Org. Chem. (2000) 2551; (c) E.M. Maya, P. Vazquez, T. Torres, L. Gobbi, F. Diedrich, S. Pyo, L. Echegoyen, J. Org. Chem. 65 (2000) 823.
[17] Ş. Abdurrahmanoğlu, A. Altındal, A.R. Özkaya, M. Bulut, Ö. Bekaroğl, Chem. Commun. (2004) 2096.
[18] A. Altındal, Ş. Abdurrahmanoğlu, M. Bulut, Ö. Bekaroğlu, Synth. Met. 150 (2005) 181.
[19] Ş. Abdurrahmanoğlu, A.R. Özkaya, M. Bulut, Ö. Bekaroğlu, J. Chem. Soc., Dalton Trans. (2004) 4022.
[20] M. Özer, A. Altındal, A.R. Özkaya, M. Bulut, Ö. Bekaroğlu, Synth. Met. 155 (2005) 222.
[21] T. Ceyhan, A. Altındal, A.R. Özkaya, M.K. Erbil, B. Salih, Ö. Bekaroğlu, Chem. Commun. (2006) 320.
[22] A.Y. Tolbin, A.V. Ivanov, L.G. Tomilova, N.S. Zefirov, J. Porphyrins Phthalocyanines 7 (2003) 162.
[23] J.G. Young, W. Onyebuago, J. Org. Chem. 55 (1990) 2155.
[24] C.C. Leznoff, S.M. Marcuccio, S. Greenberg, A.B.P. Lever, K.B. Tomer, Can. J. Chem. (1965) 623.
[25] C.C. Leznoff, D.M. Drew, Can. J. Chem. 74 (1966) 307.
[26] C.C. Leznoff, H. Lam, S.M. Marcuccio, W.A. Nevin, P. Janda, N. Kobayashi, A.B.P. Lever, J. Chem. Soc., Chem. Commun. (1987) 699.
[27] E.S. Dosworth, A.B.P. Lever, P. Seymour, C.C. Leznoff, J. Phys. Chem. (1985) 5698.
[28] A.B.P. Lever, Adv. Inorg. Chem. Radiochem. 7 (1965) 27.
[29] P.C. Minor, M. Gouterman, A.B.P. Lever, Inorg. Chem. 24 (1985) 1894.
[30] P. Matlaba, T. Nyokong, Polyhedron 21 (2002) 2463.
[31] V. Manivannan, W.A. Nevin, C.C. Leznoff, A.B.P. Lever, J. Coord. Chem. 19 (1988) 139.
[32] A.B.P. Lever, E.R. Milaeva, G. Speier, in: C.C. Leznoff, A.B.P. Lever (Eds.), Phthalocyanines: Properties and Applications, vol. 3, VCH, New York, 1993, p. 1.
[33] C.C. Leznoff, H. Lam, W.A. Nevin, N. Kobayashi, P. Janda, A.B.P. Lever, Angew. Chem., Int. Ed. 26 (1987) 1021.
[34] N. Kobayashi, H. Lam, W.A. Nevin, P. Janda, C.C. Leznoff, A.B.P. Lever, Inorg. Chem. 29 (1990) 3415.
[35] N. Kobayashi, H. Lam, W.A. Nevin, P. Janda, C.C. Leznoff, T. Koyama, A. Monden, H. Shirai, J. Am. Chem. Soc. 116 (1994) 879.

[36] W.A. Nevin, M.R. Hempstead, W. Liu, C.C. Leznoff, A.B.P. Lever, Inorg. Chem. 26 (1987) 570.
[37] W.A. Nevin, W. Liu, S. Greenberg, M.R. Hempstead, S.M. Marcuccio, M. Melnik, C.C. Leznoff, A.B.P. Lever, Inorg. Chem. 26 (1987) 891.
[38] M.J. Stillman, A.J. Thompson, J. Chem. Soc., Faraday Trans. 2 70 (1974) 790.
[39] B. Abboola, K.I. Ozoemena, T. Nyokong, Electrochim. Acta 51 (2006) 4379.
[40] M. Pollak, T.H. Geballe, Phys. Rev. 122 (1961) 1743.
[41] T. Ceyhan, A. Altındal, M.K. Erbil, Ö. Bekaroğlu, Polyhedron 25 (2006) 737.
[42] S.R. Elliot, Adv. Phys. 36 (1987) 135.
[43] A.R. Long, Adv. Phys. 31 (1982) 553.

Available online at www.sciencedirect.com
ScienceDirect
Polyhedron 26 (2007) 708–718
POLYHEDRON
www.elsevier.com/locate/poly

Synthesis and solid-state structural characterisation of Pt(II,IV) bromide complexes containing bidentate organothiomethylpyridine heteroleptic ligands

Roderick C. Jones [a], Brian W. Skelton [b], Vicki-Anne Tolhurst [a,*], Allan H. White [b], Adele J. Wilson [a], Allan J. Canty [a,*]

[a] School of Chemistry, University of Tasmania, Private Bag 75, Hobart, TAS 7001, Australia
[b] Chemistry M313, University of Western Australia, Crawley, WA 6009, Australia

Received 24 July 2006; accepted 1 September 2006
Available online 5 September 2006

Abstract

A convenient synthetic method for the preparation of organothiomethylpyridine ligands 2-($RSCH_2$)C_5H_4N (R = Ph ($\mathbf{L}^1$), Me ($\mathbf{L}^2$)), 2-MeS–6-Me-C_5H_3N ($\mathbf{L}^3$), and 2-MeS–4-Me-C_5H_3N ($\mathbf{L}^4$) via the initial lithiation of substituted 2-picolines followed by the nucleophilic reaction with a diorganyldisulfide is described. The complexes [$PtBr_2$L] (L = $\mathbf{L}^1$–$\mathbf{L}^4$) have been prepared in good to high yields as yellow solids with low solubility in organic solvents. The solid state structures of the complexes have been determined, showing the spatial arrangement of the complexes to depend significantly upon varying substituents within the ligand. The complexes undergo oxidation by bromine to form the tetravalent complexes [$PtBr_4$(L)] (L = $\mathbf{L}^1$–$\mathbf{L}^4$). The solid state structures of [$PtBr_4$($\mathbf{L}^2$)] and [$PtBr_4$($\mathbf{L}_4$)] have been determined, and shown to be monomeric with the ligand chelating the platinum centre.
© 2006 Elsevier Ltd. All rights reserved.

Keywords: Platinum; Mixed donor ligands; Pyridine; Thioether; X-ray crystal structures

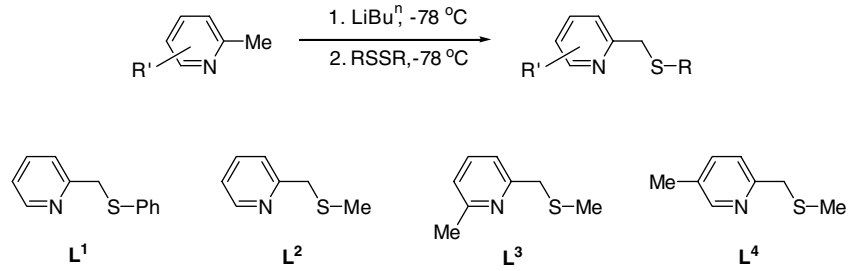
1. Introduction

The coordination chemistry of platinum(II) containing thio-, seleno- and telluroether ligands has been well established [1–3]. In contrast, reported platinum(IV) complexes containing N– and S– (or Se–) donor ligands are fewer [4–9]. Pyridylthioether ligands are a class of simple and fundamental heteroleptic ligands [10], and we have recently prepared a number of Pt(II) and Pd(II) chloride complexes, including Pd(II) complexes that facilitate Heck catalysis, containing the mixed donor ligands 2-($RECH_2$)C_5H_4N (RE = MeS, PhS, MeSe) and investigated their behaviour in solution using DFT calculations [11]. Comparison of the solid state structures of [MCl_2{2-($PhSCH_2$)C_5H_4N}] (M = Pd, Pt) and results from theoretical studies of solution processes indicate that the Pt–S bond is stronger than Pd–S, consistent with the softer Lewis acidity of platinum compared with palladium. Similar trends in bond distances in isomorphous structures of palladium and platinum complexes containing homoleptic and heteroleptic ligands have been observed and theoretical calculations have been performed [12–16].

There are several known methods for preparing thioether–pyridine heteroleptic ligand systems [17–25]. Reported methods of synthesis tend to be specific for the individual target molecule. However, an early report of the isolation of 2-($PhSCH_2$)-3-Me-C_5H_3N on reaction of 2,3-$Me_2C_5H_3N$ with $LiBu^n$ and PhSSPh [20] indicates the potential for development of a simple generic method. Herein, we describe the application of this method for the preparation of previously reported ligands $\mathbf{L}^1$–$\mathbf{L}^3$ [17,20,25] and the new ligand $\mathbf{L}^4$, that illustrates versatility

* Corresponding authors. Tel.: +61 3 6226 2162; fax: +61 3 6226 2858.
E-mail addresses: vicki-anne.gardiner@industry.gov.au (V.-A. Tolhurst), Allan.Canty@utas.edu.au (A.J. Canty).

0277-5387/$ - see front matter © 2006 Elsevier Ltd. All rights reserved.
doi:10.1016/j.poly.2006.09.001



Scheme 1. Synthesis of substituted pyridyl thioether ligands, $\mathbf{L}^1$–$\mathbf{L}^4$.

in the range of substitution on the pyridyl ring and in the thioether group (Scheme 1). The synthesis and characterisation of Pt(II,IV) bromide complexes of ligands $\mathbf{L}^1$–$\mathbf{L}^4$ are described, allowing a systematic investigation into the effects of ligand, in particular the effect of adding a methyl group to the pyridyl ring in the 6-position, using single crystal X-ray diffraction studies.

2. Experimental

2.1. Materials and methods

All reactions were performed under argon gas using standard Schlenk techniques. Platinum(II) chloride was obtained as a loan from Johnson Matthey and was used without purification. All solvents were degassed prior to use. Infra-red spectra were recorded as KBr pressed discs on a Bruker IF55 Infra-red Spectrometer. Mass spectra of the complexes were recorded on a Kratos Analytical Concept ISQ mass spectrometer. ^{1}H and ^{13}C{^{1}H} NMR spectra were recorded on a Varian Mercury Plus NMR spectrometer operating at 299.9 and 75.4 MHz in deuterated dimethylsulfoxide or deuterated chloroform and referenced to the residual resonances of the solvent (δ 2.33 and 7.25 ppm (^{1}H), respectively, 77.0 ppm (^{13}C{^{1}H} in $CDCl_3$)). Microanalyses (C, H, N, S) were determined by The Microanalysis Service, Central Science Laboratory, University of Tasmania.

2.2. Syntheses of ligands $\mathbf{L}^1$–$\mathbf{L}^4$

2.2.1. 2-(Phenylthiomethyl)pyridine ($\mathbf{L}^1$)

A solution of LiBu^n (6.00 mL of a 1.6 M hexane solution) was added dropwise to a stirred solution of 2-picoline (1.0 mL, 10.1 mmol) in Et_2O (25 mL) at −78 °C. The reaction was allowed to warm to ambient temperature, after which it was added dropwise to a stirred solution of diphenyl disulphide (2.36 g, 10.8 mmol) in THF (35 mL) at −78 °C. The solution was allowed to warm to room temperature and stirred for 12 h. Water was then added and the aqueous layer extracted with Et_2O (3 × 30 mL). The organic phase was dried (Na_2SO_4), and the solvent removed in a vacuum resulting in an oil. The product was purified by passing through a silica plug (5% Et_2O in petroleum spirit (b.p. 40–60 °C)) to give a yellow oil (0.96 g, 47%). *Anal.* Calc. for $C_{12}H_{11}NS$: C, 71.60; H, 5.51; N, 6.96; S, 15.93. Found: C, 71.86; H, 5.31; N, 6.85; S, 15.79%. ^{1}H NMR (299.9 MHz, $CDCl_3$, 25 °C) δ 8.54 (d, $^3J = 4.8$ Hz, 1H, H_6), 7.59 (“dt”, $^3J = 7.8$, 1.5 Hz, 1H, H_4), 7.32 (m, 2H, H_3,H_{2b}), 7.24 (t, $^3J = 7.2$ Hz, 1H, H_{2c}), 7.16 (m, 2H, H_5, H_{2d}), 4.27 (s, 2H, CH_2); ^{13}C{^{1}H} NMR (75.4 MHz, 20 °C, $CDCl_3$) δ 157.9 (C_2), 149.5 (C_6), 137.0 (C_4), 136.0 (C_{2a}), 129.9 (C_{2b}), 127.7 (C_{2c}), 126.6 (C_{2d}), 123.2 (C_3), 122.3 (C_5), 40.7 (CH_2). EI *m/z* 201 $[M]^+$, [$^{12}C_{12}$ $H_{11}$$^{14}N$$^{32}S_{201}$], 186 $[M - Me]^+$ [$^{12}C_{11}H_8$$^{14}N$$^{32}S_{186}$], 168 $[M - SH]^+$ [$^{12}C_{12}H_{10}$$^{14}N_{168}$], 92 $[M - SPh]^+$ [$^{12}C_6H_6$$^{14}N_{92}$].

2.2.2. 2-(Methylthiomethyl)pyridine ($\mathbf{L}^2$)

The procedure used was as for $\mathbf{L}^1$, except that after drying of the Et_2O extract and removal of solvent, to give a pale yellow oil (85%). The product was used without further purification. *Anal.* Calc. for C_7H_9NS: C, 60.39; H, 6.52; N, 10.06; S, 23.03. Found: C, 60.35; H, 6.35; N, 10.18; S, 22.92%. ^{1}H NMR (299.9 MHz, $CDCl_3$, 25 °C) δ 8.51 (d, $^3J = 4.2$ Hz, 1H, H_6), 7.66 (“dt”, $^3J = 7.8$, 1.8 Hz, 1H, H_4), 7.35 (d, $^3J = 7.8$ Hz, 1H, H_3), 7.16 (ddd, $^3J = 4.2$, 1.5, 0.9 Hz, 1H, H_5) 3.79 (s, 2H, CH_2), 2.04 (s, 3H, CH_3); ^{13}C{^{1}H} NMR (75.4 MHz, 20 °C, $CDCl_3$) δ 158.7 (C_2), 149.2 (C_6), 137.2 (C_4), 123.4 (C_3), 122.2 (C_5), 40.1 (CH_2), 15.4 (CH_3). EI *m/z* 139 $[M]^+$, [$^{12}C_7$-$H_9$$^{14}N$$^{32}S_{139}$].

2.2.3. 2-(Methylthiomethyl)-6-methylpyridine ($\mathbf{L}^3$)

The procedure used was as for $\mathbf{L}^2$ using 2,6 lutidine (68%). The product was used without further purification. *Anal.* Calc. for $C_8H_{11}NS$: C, 62.70; H, 7.24; N, 9.14; S, 20.92. Found: C, 62.56; H, 7.38; N, 8.98; S, 20.61%. ^{1}H NMR (299.9 MHz, $CDCl_3$, 25 °C) δ: 7.53 (“t”, $^3J = 7.8$ Hz, 1H, H_4), 7.15 (d,$^3J = 7.8$, 1H, H_3), 7.01 (d, $^3J = 7.8$ Hz, 1H, H_5), 3.76 (s, 2H, CH_2), 2.53 (s, 3H, C_6–CH_3), 2.04 (s, 3H, S–CH_3); ^{13}C{^{1}H} NMR (75.4 MHz, 20 °C, $CDCl_3$) δ 158.0 (C_6), 157.9 (C_2), 137.3 (C_4), 121.8 (C_5), 120.2 (C_3), 40.2 (CH_2), 24.6 (C_6–CH_3), 15.4 (S–CH_3). LSIMS (*m/z*) 152 $(M - H)^+$ [$^{12}C_8H_{11}$$^{14}N$$^{32}S_{152}$].

2.2.4. 2-(Methylthiomethyl)-4-methyl pyridine ($\mathbf{L}^4$)

The procedure used was as for $\mathbf{L}^2$ using 2,4-lutidine (87%). The product was used without further purification. *Anal.* Calc. for $C_8H_{11}NS$: C, 62.70; H, 7.24; N, 9.14; S,

20.92. Found: C, 62.75; H, 7.24; N, 9.26; S, 20.68%. ^{1}H NMR (299.9 MHz, $CDCl_3$, 25 °C) δ 8.36 (d, $^3J = 5.1$ Hz, 1H, H_6), 7.18 (s, 1H, H_3), 6.98 (d, $^3J = 4.8$ Hz, 1H, H_5), 3.75 (s, 2H, CH_2), 2.33 (s, 3H, C_4–CH_3), 2.04 (s, 3H, S–CH_3); ^{13}C{^{1}H} NMR (75.4 MHz, 20 °C, $CDCl_3$): δ 158.5 (C_2), 149.0 (C_6), 148.3 (C_4), 124.1 (C_3), 123.2 (C_5), 40.1 (CH_2), 21.3 (C_4–CH_3), 15.4 (S–CH_3). LSIMS (*m*/*z*) 152 $(M - H)^+$ [$^{12}C_8H_{11}{}^{14}N^{32}S_{152}$].

2.3. Syntheses of complexes [$PtBr_2L$] ($L = \mathbf{L}^1$ (**1**), $\mathbf{L}^2$ (**2**), $\mathbf{L}^3$ (**3**), $\mathbf{L}^4$ (**4**))

Sodium bromide (0.827 mmol) and $PtCl_2$ (0.376 mmol) were refluxed in MeCN (30 mL) for 24 h. The light brown solution was filtered and the appropriate ligand (0.381 mmol) was added. The mixture was allowed to stir at room temperature (16 h). The MeCN volume was reduced in a vacuum (ca. 1 mL) and Et_2O added to afford an off-white precipitate. The solid was collected and washed with Et_2O, yielding the desired compound.

[$PtBr_2(\mathbf{L}^1)$] (**1**) (69%). *Anal.* Calc. for $C_{12}H_{11}Br_2NPtS$: C, 25.91; H, 1.99; N, 2.52. Found: C, 25.50; H, 1.83; N, 2.26%. ^{1}H NMR (299.9 MHz, DMSO-d_6, 25 °C) δ: 9.69 (m, 1H, C_5H_4N), 8.15 (m, 1H, C_5H_4N), 7.84 (m, 1H, C_5H_4N), 7.75 (m, 2H, C_6H_5), 7.44 (m, 3H, C_6H_5), 5.23, 4.84 (m, 2H, CH_2). IR (KBr, cm^{-1}): 3114(w), 3085(w), 3056(w), 2968(w), 2942(s), 1892(m), 1605(m), 1476(s), 1446(s), 1394(m), 1312(w), 1268(w), 1160(w), 1111(w), 1063(w), 1021(w), 966(w), 895(w), 756(vs), 685(m), 483(m), 438(w). LSIMS (*m*/*z*): 476 ([$^{195}Pt^{80}BrC_{11}H_{12}NS$]$^+$ 476).

[$PtBr_2(\mathbf{L}^2)$] (**2**) (87%). *Anal.* Calc. for $C_7H_9Br_2NPtS$: C, 17.02; H, 1.84; N, 2.84; S, 6.49. Found: C, 17.20; H, 2.00; N, 2.85; S, 6.07%. ^{1}H NMR (299.9 MHz, DMSO-d_6, 25 °C) δ: 9.59 (m, 1H, C_5H_4N), 8.18 (m, 1H, C_5H_4N), 7.87 (m, 1H, C_5H_4N), 7.55 (m, 1H, C_5H_4N), 4.80, 4.50 (m, 2H, CH_2), 2.47 (s, $J_{Pt-H} = 18$ Hz, 3H, CH_3). IR (KBr, cm^{-1}): 3080(w), 2992(w), 1955(s), 2898(s), 1610(s), 1474(s), 1447(m), 1423(m), 1395(m), 1318(m), 1271(m), 1166(s), 1111(w), 1062(w), 993(m), 974(m), 898(w), 862(w) 827(w), 770(vs), 709(w), 473(w), 434(w). LSIMS (*m*/*z*): 414 ([$^{195}Pt^{80}BrC_7H_9NS$]$^+$ 414).

[$PtBr_2(\mathbf{L}^3)$] (**3**) (75%). *Anal.* Calc. for $C_8H_{11}Br_2NPtS$: C, 18.91; H, 2.18; N, 2.76. Found: C, 18.88; H, 2.24; N, 6.03%. ^{1}H NMR (299.9 MHz, DMSO-d_6, 25 °C) δ: 7.62 (m, 1H, C_5H_3N), 7.17 (m, 1H, C_5H_3N), 7.10 (m, 1H, C_5H_3N), 4.77 (s, br, 2H, CH_2), 2.49 (s, 3H, CH_3), 2.41 (s, 3H, CH_3). IR (KBr, cm^{-1}) 2994(w), 2958(m), 2907(s), 1606(m), 1568(w), 1465(s), 1412(m), 1315(m), 1263(w), 1170(m), 1140(w), 1110(w), 970(m), 877(w), 796(s). LSIMS (*m*/*z*): 531 ([$^{195}Pt^{80}Br_2C_8H_{11}NS$+Na]$^+$ 531).

[$PtBr_2(\mathbf{L}^4)$] (**4**) (81%). *Anal.* Calc. for $C_8H_{11}Br_2NPtS$: C, 18.91; H, 2.18; N, 2.76. Found: C, 18.94; H, 2.32; N, 2.73%. ^{1}H NMR (299.9 MHz, DMSO-d_6, 25 °C) δ: 9.39 (m, 1H, C_5H_3N), 7.72 (m, 1H, C_5H_3N), 7.38 (m, 1H, C_5H_3N), 4.75, 4.43 (m, 2H, CH_2), 2.43 (s, $J_{Pt-H} = 18.0$ Hz, 3H, CH_3), 2.32 (s, 3H, CH_3). IR (KBr, cm^{-1}): 2987(w), 2951(m), 2900(m), 1623(s), 1482(m), 1451(m), 1423(w), 1391(w), 1373(w), 1312(w), 1279(w), 1176(w), 1154(w), 1033(m), 977(m), 897(w), 823(m), 436(w). LSIMS (*m*/*z*): 531 ([$^{195}Pt^{80}Br_2C_8H_{11}NS$+Na]$^+$ 531).

2.4. Synthesis of complexes [$PtBr_4L$] ($L = \mathbf{L}^1$ (**5**), $\mathbf{L}^2$ (**6**), $\mathbf{L}^3$ (**7**), $\mathbf{L}^4$ (**8**))

A solution of [$PtBr_2(\mathbf{L}^1)$] (50 mg, 0.101 mmol) in MeCN (3 mL) was added to a concentrated solution of Br_2 in CCl_4 (1 mL). The red solution was allowed to stir at room temperature for 25 min, Et_2O was added to the red solution to afford an orange precipitate which was then isolated and washed with Et_2O to give **5** (44 mg, 67%). *Anal.* Calc. for $C_{12}H_{11}Br_4NPtS$: C, 20.13; H, 1.55; N, 1.96; S, 4.48. Found: C. 20.21; H. 1.74; N. 2.01; S. 4.37%. ^{1}H NMR (299.9 MHz, DMSO-d_6, 25 °C) δ: 9.30–9.42 (m, 1H, C_5H_3N), 8.29–8.35 (m, 1H, C_5H_3N), 8.22–8.24 (m, 1H, C_5H_3N), 7.81–7.86 (m, 1H, C_5H_3N), 7.48–7.64 (m, 5H, C_6H_5), 5.64 (m, 2H, CH_2). IR (KBr, cm^{-1}): 3110(w), 3035(w), 1915(m), 2857(w), 1604(m), 1558(m), 1483(m), 1440(s), 1388(m), 1311(w), 1270(w), 1247(w), 1158(w), 1110(w), 1064(w), 1035(w), 896(w), 867(w), 821(w), 763(s), 750(vs), 677(m), 482(w), 419(w).

2.4.1. [$PtBr_4(\mathbf{L}^2)$] (**6**)

The procedure used was as for [$PtBr_4(\mathbf{L}^1)$] using $\mathbf{L}^2$ (70%). *Anal.* Calc. for $C_7H_9Br_4NPtS$: C, 12.86; H, 1.39; N, 2.14; S, 4.90. Found: C, 12.68; H, 1.40; N, 2.19; S, 4.20%. ^{1}H NMR (299.9 MHz, DMSO-d_6, 25 °C) δ: 9.40 (m, 1H, C_5H_4N), 8.23 (m, 1H, C_5H_4N), 7.99 (m, 1H, C_5H_4N), 7.81 (m, 1H, C_5H_4N), 5.21, 5.02 (AB spin system, 2H, CH_2), 2.69 (s, $J_{Pt-H} = 18.3$ Hz, 3H, CH_3). IR (KBr, cm^{-1}) 3109(w), 3068(w), 3028(w), 3004(w), 2956(s), 2897(s), 1652(m), 1602(s), 1558(m), 1474(s), 1398(s), 1385(s), 1316(w), 276(m), 1243(w), 1165(w), 1110(m), 1060(w), 1033(w), 959(m), 895(w), 866(w), 825(m), 775(vs), 754(m), 692 (w), 657(w), 483(w), 436(w).

2.4.2. [$PtBr_4(\mathbf{L}^3)$] (**7**)

The procedure used was as for [$PtBr_4(\mathbf{L}^1)$] using $\mathbf{L}^3$ (75%). *Anal.* Calc. for $C_8H_{11}Br_4NPtS$: C, 14.39; H, 1.66; N, 2.10; S, 4.80. Found: C, 14.20; H, 1.67; N, 2.16; S, 4.23%. ^{1}H NMR (299.9 MHz, DMSO-d_6, 25 °C) δ: 8.41 (m, 1H, C_5H_4N), 7.79 (m, 2H, C_5H_4N), 5.50 (s, broad, 2H, CH_2), 2.70 (s, $J_{Pt-H} = 18.1$ Hz, 3H, CH_3), 2.04 (s, 3H, CH_3). IR (KBr, cm^{-1}): 2957(s), 2910(m), 1616(s), 1481(w), 1394(m), 1311(w), 1269(s), 1032(m), 980(w), 956(m), 829(m), 563(w), 443(w).

2.4.3. [$PtBr_4(\mathbf{L}^4)$] (**8**)

The procedure used was as for [$PtBr_4(\mathbf{L}^1)$] using $\mathbf{L}^4$ (73%). *Anal.* Calc. for $C_8H_{11}Br_4NPtS$: C, 14.39; H, 1.66; N 2.10. Found: C, 14.87; H, 1.84; N, 2.17%. ^{1}H NMR (299.9 MHz, DMSO-d_6, 25 °C) δ: 9.20 (m, 1H, C_5H_4N), 7.84 (m, 1H, C_5H_4N), 7.63 (m, 1H, C_5H_4N), 5.12, 4.93 (AB spin system, 2H, CH_2), 2.69 (s, $J_{Pt-H} = 18.0$ Hz, 3H, CH_3), 2.51 (s, 3H, CH_3). IR (KBr, cm^{-1}): 2959(m),

2903(m), 1597(m), 1571(m), 1459(s), 1433(m), 1398(s), 1367(s), 1316(m), 1297(w), 1202(w), 1171(m), 1118(m), 1038(m), 970(s), 852(w), 779(s).

2.5. X-ray crystallographic studies

Suitable crystals for X-ray diffraction studies of $[PtBr_2L]$ ($L = \mathbf{L}^1$ (**1**), $\mathbf{L}^2$ (**2**), $\mathbf{L}^3$ (**3**), $\mathbf{L}^4$ (**4**)) and $[PtBr_4(\mathbf{L}^2)]$ were grown from $MeNO_2/Et_2O$ (vapour diffusion). Full spheres of CCD area-detector diffractometer data for all complexes were measured (Bruker AXS, ω-scans, monochromatic Mo Kα radiation, $\lambda = 0.7107_3$ Å, T ca. 153 K), N_{total} reflections merging to N unique (R_{int} cited) after 'empirical'/multiscan absorption correction (proprietary software), N_o with $F > 4\sigma(F)$ being considered "observed" and used in the full matrix least squares refinements. $(x, y, z, U_{iso})_H$ were refined for **2a** only, constrained in the remainder. Neutral atom complex scattering factors were employed within the context of the XTAL 3.7 program system [26]. Pertinent results are given above and in the tables and figures, the latter showing 50% probability amplitude displacement envelopes for the non-hydrogen atoms, hydrogen atoms having arbitrary radii of 0.1 Å.

3. Results and discussion

3.1. Synthesis of ligands

Lithiation of the α-carbon of a substituted pyridine using $LiBu^n$ affords the carbanion which then undergoes a nucleophilic substitution reaction with an appropriate diorganyl disulfide to afford the desired heteroleptic substituted pyridyl thioether compounds, $\mathbf{L}^1$–$\mathbf{L}^4$, in 47–87% yield (Scheme 1). This is a relatively simple and efficient "one-pot" synthesis, suitable for both MeSSMe and PhSSPh. The ligands, including the new ligand $\mathbf{L}^4$, were characterised using ^1H and $^{13}C\{^1H\}$ NMR spectroscopy, EI mass spectrometry, and elemental analysis.

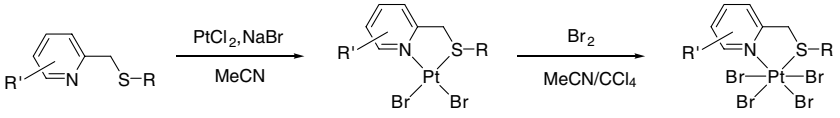
The room temperature ^1H NMR spectra of the methylthioether ligands, $\mathbf{L}^3$ and $\mathbf{L}^4$, are as expected and show no obvious trends upon substitution of the pyridyl ring compared with the spectrum of $\mathbf{L}^2$. The aromatic protons are observed as resonances between 6.98 and 8.36 ppm; methylene protons can be seen as a sharp singlet at 3.79 and 3.75 ppm for $\mathbf{L}^3$ and $\mathbf{L}^4$, respectively. The SMe moiety is observed as a singlet at 2.04 ppm for $\mathbf{L}^3$ and $\mathbf{L}^4$, respectively, while the second singlet, observed at 3.79 and 2.33 ppm, corresponds to the methyl substituent on the pyridyl ring at the 6- and 4-position, respectively.

The $^{13}C\{^1H\}$ NMR spectra of $\mathbf{L}^3$ and $\mathbf{L}^4$ exhibit resonances in the range of 158.5–120.2 ppm for the aromatic carbon atoms. The methylene carbons are observed at 40.2 and 40.1 ppm, while the resonance corresponding to the methyl substituent of the sulfur is observed at 15.4 ppm for both ligands. Another signal corresponding to the methyl substituent on the pyridyl ring occurs at 24.6 ppm and 21.3 ppm for $\mathbf{L}^3$ and $\mathbf{L}^4$, respectively.

3.2. Synthesis of $[PtBr_2L]$ and $[PtBr_4L]$ complexes

Treatment of $PtBr_2$ (formed in situ from $PtCl_2$ and NaBr) with a slight excess of **L** in MeCN afforded the complexes $[PtBr_2L]$ ($L = \mathbf{L}^1$ (**1**), $\mathbf{L}^2$ (**2**), $\mathbf{L}^3$ (**3**),$\mathbf{L}^4$ (**4**)) as pale yellow solids in 69–87% yield (Scheme 2). The compounds are stable to air and moisture and have limited solubility in organic solvents. LSI mass spectra of the complexes exhibit an ion, corresponding to $[M + Na]^+$, where the sodium atom entered the matrix from slight contamination of starting material. The mass spectrum of $[PtBr_2\mathbf{L}^1]$ exhibits an additional ion at m/z 553, corresponding to the ion $[M - Br+L]^+$. The $[PtBr_4L]$ complexes ($L = \mathbf{L}^1$ (**5**), $\mathbf{L}^2$ (**6**), $\mathbf{L}^3$ (**7**), $\mathbf{L}^4$ (**8**)) were prepared in good yield (67–75%) by treatment of $[PtBr_2L]$ in MeCN with a solution of Br_2/CCl_4 at room temperature for 30 min (Scheme 1). The complexes are air stable orange powders, with very limited solubility, thus making characterisation difficult.

The ^1H NMR spectra for all complexes exhibit a second-order spectrum with an AB spin system for the methylene protons between 5.64 and 4.43 ppm. Resonances corresponding to the pyridyl protons are observed as various multiplets between 9.69 and 7.10 ppm. The methyl protons in **2**–**4** are observed as singlets between 2.49 and 2.32 ppm which are further downfield than those of the analogous chloride complexes because of the increased *trans*-effect of the bromide ligand. Variable temperature ^1H NMR studies of $[PtBr_2\mathbf{L}^2]$ were used to investigate the effect of changing halide ligands on the *E*-inversion process. The coalescence temperature of the methylene protons in $[PtBr_2\mathbf{L}^2]$ (150 °C) is slightly lower than that for the analogous $[PtCl_2\mathbf{L}^2]$ complex (157 °C) [11], and has previously been observed for platinum halide complexes containing dithioether ligands, being explained in terms of the increased *trans*-influence of the heavier halide [27]. The ^1H NMR spectra of the Pt(IV) complexes **5**–**8** were similar



Scheme 2. Synthesis of $[PtBr_2L]$ (**1**–**4**) and $[PtBr_4L]$ (**5**–**8**) complexes.

to those of the Pt(II) complexes in that a second-order AB spin coupling pattern was observed for the methylene protons of the ligand. All other features of the spectra were as expected with aromatic protons observed in the typical region, and the methyl protons of complexes **6**, **3** and **4** being observed as singlets between 2.70 and 2.04 ppm.

*3.3. Structures of [$PtBr_2(L^1)$] (**1**), [$PtBr_2(L^2)$] (**2**), [$PtBr_2(L^3)$] (**3**), [$PtBr_2(L^4)$] (**4**), [$PtBr_4(L^2)$] (**6**), and [$PtBr_4(L^4)$] (8)*

All of the Pt(II) complexes (Figs. 1–8, and Tables 1 and 2) crystallise with the asymmetric unit comprised of a monomeric species with distorted square planar geometry for platinum. The Pt–S bond distances in all the [$PtBr_2L$] complexes (2.238(2)–2.250(3) Å) are comparable to those observed in [$PtBr_2(PhS(CH_2)_2SPh)$] (2.249(3), 2.248(3) Å) [28]. Similarly, the Pt–N bond distances (2.033(6)–2.058(4) Å) are comparable to those found in complexes such as [$PtBr_2(Me_2$-phen)] (Me_2-phen = 2,9-dimethyl-1,10-phenanthroline) (2.049(7), 2.058(9) Å) [29]. The Pt–Br bond distances in the complexes [$PtBr_2L$] range from 2.4220(9) to 2.4630(9) Å and are typical, with the shortest bond associated with the bromine atom *trans* to the pyridyl nitrogen and the longest associated with the bromine atom *trans* to the sulfur atom, the latter values also comparable with those of [$PtBr_2(PhS(CH_2)_2SPh)$] (2.430(1), 2.434(1)) [28].

The effect of changing the halide from Cl to Br in the coordination sphere about the platinum can be seen by comparing the structures of the analogous complexes [$PtCl_2(L^1)$] and [$PtBr_2(L^1)$] [11] (see also Table 2). Increases in Pt–S and Pt–N bond distances in [$PtBr_2(L^1)$] (2.2423(11) and 2.058(4) Å, respectively), compared to those of the complex [$PtCl_2(L^1)$] (2.235(1) and 2.034(3) Å, respectively), are consistent with the increased *trans*-influence of the bromide ligand. The strain of the two complexes appears comparable, with the puckering of the five-membered chelate

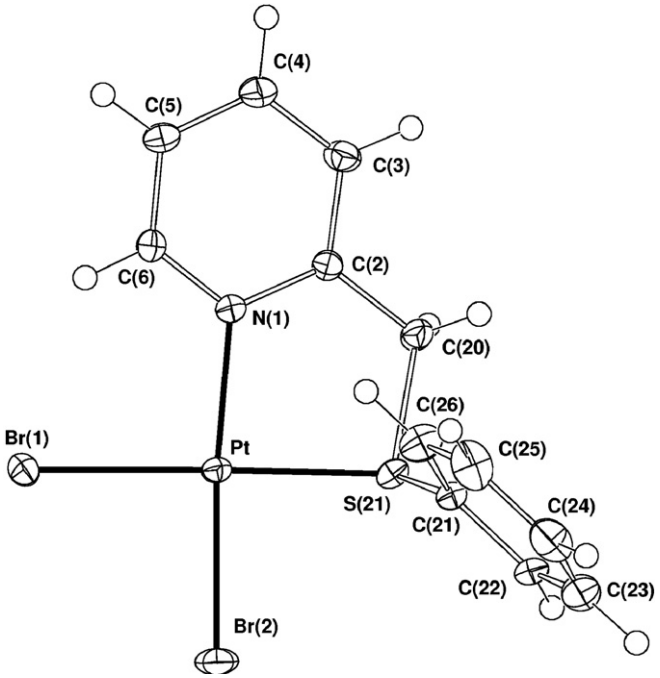


Fig. 1. Molecular projection of [$PtBr_2(L^1)$] (**1**).

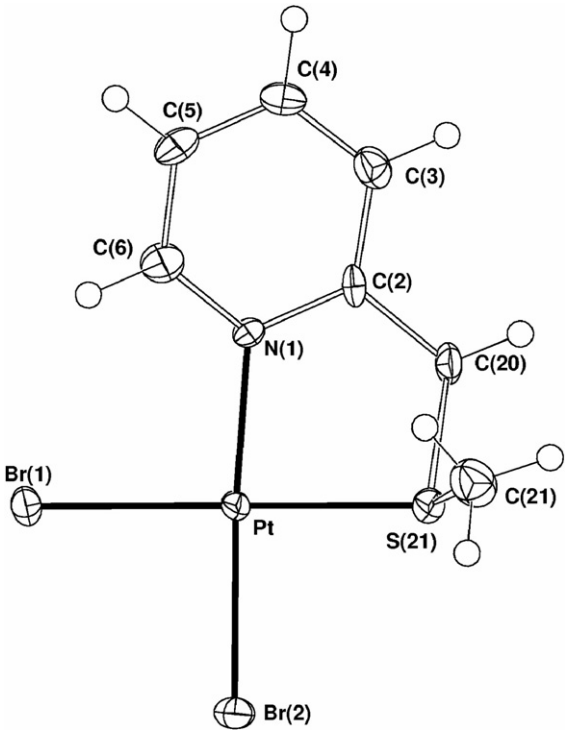


Fig. 2. Molecular projection of [$PtBr_2(L^2)$] (**2**).

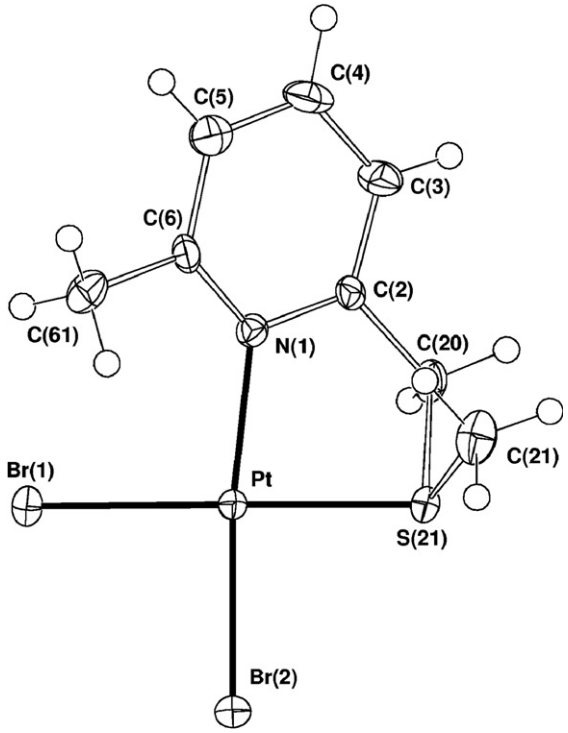


Fig. 3. Molecular projection of [$PtBr_2(L^3)$] (**3**).

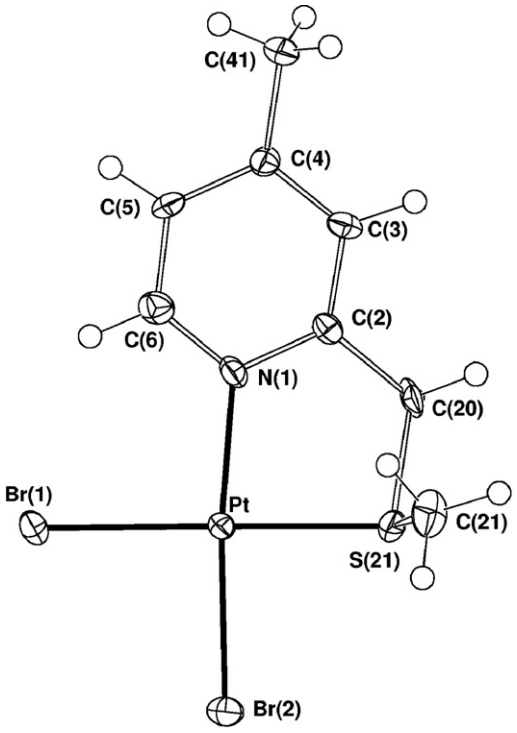


Fig. 4. Molecular projection of $[PtBr_2(L^4)]$ (**4**).

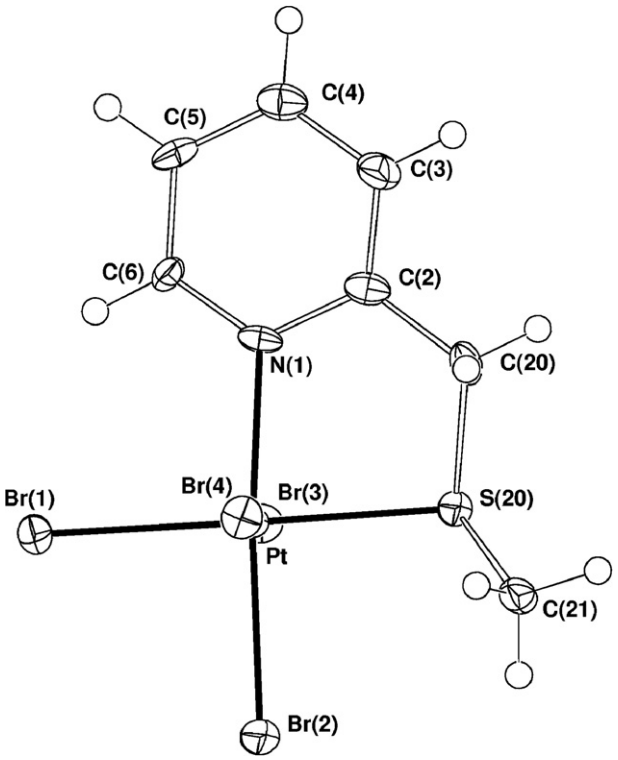


Fig. 6. Molecular projection of $[PtBr_4(L^2)]$ (**6**).

rings being similar, as are the associated atom deviations from the C_5N plane (the coordination plane in most cases is somewhat puckered). Changes in the Pt–S and Pt–N bond distances are negligible, despite the variation in *trans*-influence of the bromide atoms.

Variation of the thioether substituent from Ph to Me has little to no effect on bond lengths within the coordination environment of the platinum, but there are subtle effects on the bond angles and strain within the molecule. These are evident in the parameters of Table 2, where data for the present compounds is marshalled comparatively with other relevant data from the literature. The slightly more acute 'bite' angle of the methylthioether complex, **2** (Fig. 2), compared to the phenylthioether complex, **1**, is accompanied by an increase in the strain of the chelate ring, most evident in the differences in associated torsion angles (Table 2). The decrease in the bite angle in complex **2** (85.8(2)°) is offset by a relaxation of all other bond angles about the platinum except the Br(1)–Pt–Br(1) angle which is slightly more acute for the methylthioether complex (89.57(3)°; cf. 90.06(2)° for complexes **2** and **1**, respectively).

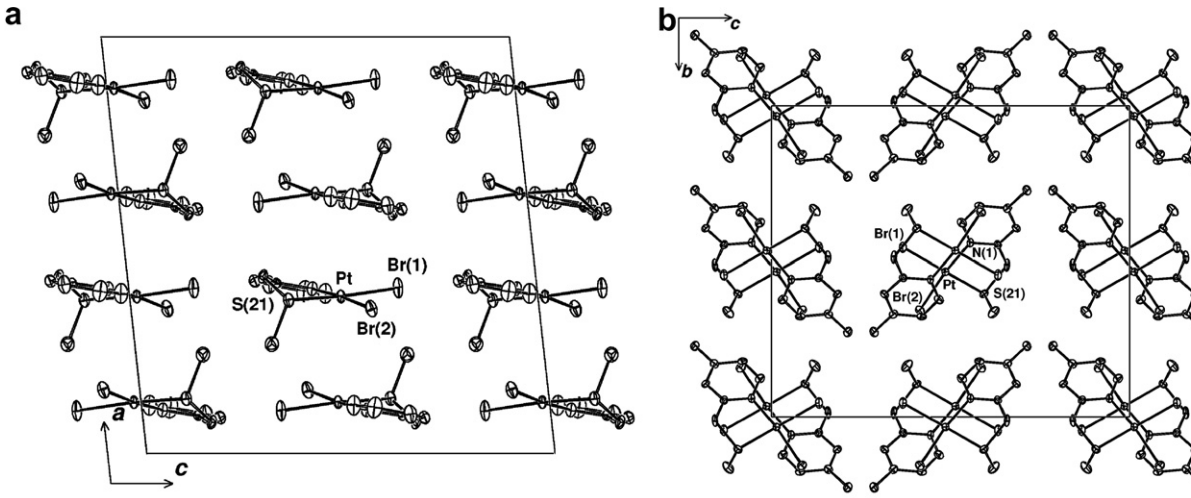


Fig. 5. (a,b). Unit cell contents of **2** and **4**, projected down *b* and *a*, respectively. (The closest Pt···Pt contacts in these structures are 4.2234(7), 3.7364(6) Å, respectively.)

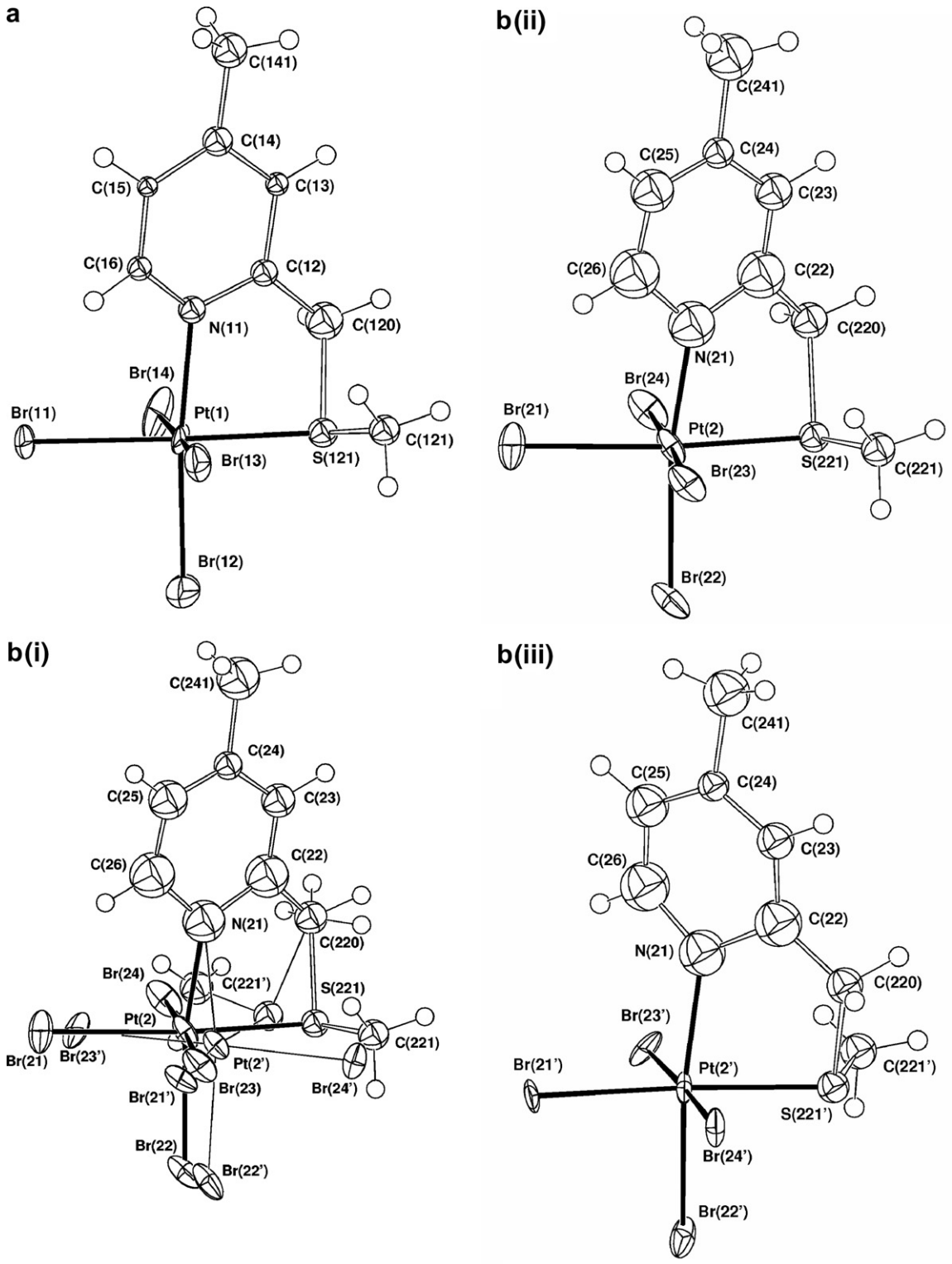


Fig. 7. Molecular projections of $[PtBr_4(\mathbf{L}^4)]$ (**8**). (a) Molecule 1. (b) Molecule 2: (i) the disordered composite and (ii, iii) the two deconvoluted components.

The addition of a methyl moiety at the 6-position of the pyridyl ring dramatically changes the overall shape of the molecule from that of the complex containing the unsubstituted ligand, the effects paralleling that previously observed in the counterpart *t*-butyl substituted palladium(II) chloride analogues (Table 2) [30]. This is most strongly evidenced in the changes in torsion angles in the chelate ring which in turn bring about a dramatic twist in the MX_2 array relative to the pyridine plane (Table 2). There is a lengthening of the Pt–N bond distance in **3** compared to that in **2** (2.055(7), 2.034(7) Å, respectively), associated with an increase in the Br(1)–Pt–N(1) bond angle

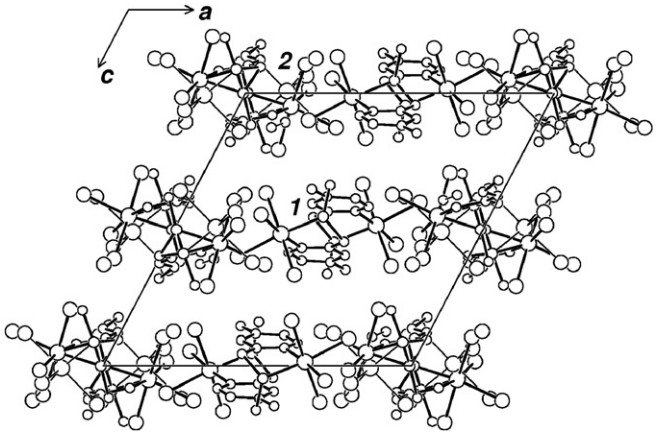


Fig. 8. Unit cell contents of $[PtBr_4(\mathbf{L}^4)]$ (**8**), projected down *b*.

(96.7(2), 94.5(2)°, respectively) because of steric interactions between the 6-methyl substituent of the pyridyl ring and the *cis* bromine atom. A concomitant of the lengthened Pt–N bond is a decrease in the bite angle of the ligand (83.7(2)° (**3**), 85.8(2)° (**2**)). When the substitution of the ligand occurs at the 4-position of the pyridyl ring, the overall shape of the complex (**4**, Fig. 4) resembles that of **2** where the ligand is unsubstituted, suggesting that the change in the structure of **3** is due mostly to the increased steric strain brought on by the addition of the methyl substituent at the 6-position rather than electronic differences in the complexes. Interesting stackings of the planar components of the molecules are observed (Fig. 5).

The Pt(IV) complex $[PtBr_4(\mathbf{L}^2)]$ (**6**) crystallises in the orthorhombic space group $Pna2_1$ with the asymmetric unit comprised of a monomeric species containing distorted octahedral geometry (Fig. 6). Bond distances and angles are listed in Table 3. The Pt–N bond distance of $[PtBr_4(\mathbf{L}^1)]$ (2.101(10) Å) is also shorter than that in $[PtBrMe_3$(2,6-bis(*p*-tolylthiomethyl)pyridine)] (2.311(6) Å) [4], and again can be attributed to the different *trans*-influence that the methyl group has on the nitrogen centre compared to the bromide atom. The five-membered chelate ring in $[PtBr_4(\mathbf{L}^2)]$ is significantly more puckered than observed in the structure of $[PtBr_2(\mathbf{L}^2)]$, with the sulfur atom out of the Pt–N(1)–C(2)–C(21) plane (χ^2 19) by 0.68(2) Å, which may be attributed to the increased steric hindrance between the lone pair of electrons on the sulfur atom with the bromine atoms due to the increased coordination number of the platinum. The large ring puckering is reflected in the larger than ideal Br(4)–Pt–S(21) bond angle (93.99(9)°) and the smaller than ideal Br(3)–Pt–S(21) bond angle (86.49(9)°). The ligand bite angle (N(1)–Pt–S(21)) at 83.6(3)° is significantly smaller than that seen in the $[PtBr_2(\mathbf{L}^2)]$ complex (85.8(2)°) but is consistent with the lengthening of the Pt–N and Pt–S bonds associated with the higher coordination number. The Pt–S bond distance in $[PtBr_4(\mathbf{L}^2)]$ (2.329(3) Å) is longer than in $[PtBr_2(\mathbf{L}^2)]$, consistent with an increase in the coordination number of the platinum. However, it is also shorter relative to the Pt–S bond distances of $[PtBrMe_3(Me_2N(CH_2)_2SC_6H_4$-Me-4)] (2.437(3) Å) [8] and $[PtBrMe_3$(2,6-bis(*p*-tolylthiomethyl)pyridine)] (2.419(4) Å)[4] which can be attributed to the difference in *trans* influence of the methyl compared to the bromide group.

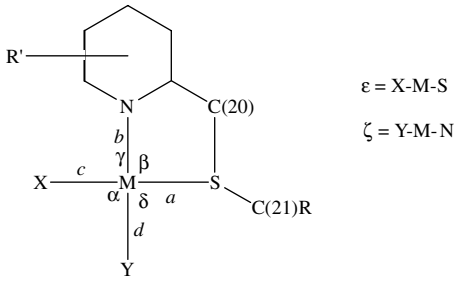
Crystals of $[PtBr_4(\mathbf{L}^4)]$ (**8**) were small and data of an unsatisfactory quality, with, further, a disordered model resulting in an inferior determination, replicated in a later study on an instrument of more recent manufacture and

Table 1
Crystallographic data of $[PtBr_2(\mathbf{L}^1)]$ (**1**), $[PtBr_2(\mathbf{L}^2)]$ (**2**), $[PtBr_2(\mathbf{L}^3)]$ (**3**), $[PtBr_2(\mathbf{L}^4)]$ (**4**), $[PtBr_4(\mathbf{L}^2)]$ (**6**), and $[PtBr_4(\mathbf{L}^4)]$ (**8**)

Complex	$[PtBr_2(\mathbf{L}^1)]$ (**1**)	$[PtBr_2(\mathbf{L}^2)]$ (**2**)	$[PtBr_2(\mathbf{L}^3)]$ (**3**)	$[PtBr_2(\mathbf{L}^4)]$ (**4**)	$[PtBr_4(\mathbf{L}^2)]$ (**6**)[a]	$[PtBr_4(\mathbf{L}^4)]$ (**8**)
Formula	$C_{12}H_{11}NSPtBr_2$	$C_7H_9NBr_2PtS$	$C_8H_{11}NBr_2PtS$	$C_8H_{11}NBr_2PtS$	$C_7H_9NSPtBr_4$	$C_8H_{11}NSPtBr_4$
M	556.18	494.11	508.14	508.14	653.92	667.94
Crystal system	monoclinic	monoclinic	monoclinic	orthorhombic	orthorhombic	monoclinic
Space group	$P2_1/n$	$C2/c$	$P2_1/n$	*Pbca*	$Pna2_1$	$P2_1/c$
Unit cell dimensions						
a (Å)	9.334(1)	15.888(2)	8.3219(8)	8.687(1)	14.273(2)	15.018(6)
b (Å)	13.109(2)	8.947(1)	8.5534(8)	15.229(2)	9.179(2)	13.998(6)
c (Å)	11.307(1)	15.482(2)	16.421(2)	17.555(2)	9.800(2)	14.994(6)
β (°)	95.442(3)	96.279(3)	97.501(2)			117.530(7)
U (Å^3)	1377.3(5)	2187.5(8)	1158.8(3)	2322.3(8)	1283.9(6)	2795(3)
D_{calc} (g cm^{-3})	2.682	3.000	2.912	2.906	3.382	3.174
Z	4	8	4	8	4	8
μ (mm^{-1})	16.1	20.3	19.1	19.1	23.5	21.6
Specimen (mm)	0.10 × 0.10 × 0.09	0.08 × 0.06 × 0.04	0.16 × 0.07 × 0.03	0.17 × 0.06 × 0.04	0.35 × 0.12 × 0.04	0.18 × 0.06 × 0.02
$T_{min/max}$	0.53	0.44	0.47	0.42	0.34	0.39
$2\theta_{max}$ (°)	75	60	75	60	75	50
N_t	27022	21282	23212	41083	24621	20651
$N(R_{int})$	7220(0.057)	3148(0.087)	4090(0.061)	3338(0.048)	3465(0.094)	4903(0.17)
N_o	5467	2518	3244	2712	2877	3141
R	0.038	0.037	0.042	0.030	0.046	0.105
R_w	0.043	0.077	0.095	0.071	0.061	0.14
GOOF	1.09	1.30	1.18	1.19	1.11	0.92

[a] χ_{abs} 0.00(2).

Table 2
Selected bond angles and distances for $[PtBr_2\mathbf{L}^n]$ ($n = 1$(**1**), 2(**2**), 3(**3**), **4**(4)) and related $[MX_2L]$ species



M	Pd				Pt					
R	Me	^{t}Bu	^{t}Bu	Ph	Ph	Ph	Ph	Me	Me	Ph
R′	H	H	6-Me	H	H	H	H	6-Me	5-Me	H
X	Cl	Cl	Cl	Cl	Cl	Br	Br	Br	Br	Cl
Y	Me	Me	Me	Cl	Cl	Br	Br	Br	Br	COMe
Ref. (cpd)	(2 mols.) [31]	[30]	[30]	[11]	[11]	(**1**)[a]	(**2**)[a]	(**3**)[a]	(**4**)[a]	[32]
Distances (Å)										
a	2.257(5), 2.255(6)	2.259(1)	2.268(2)	2.2540(5)	2.235(1)	2.2423(11)	2.250(2)	2.248(2)	2.238(2)	2.257(2)
b	2.16(1), 2.17(1)	2.162(5)	2.229(4)	2.045(1)	2.034(3)	2.058(4)	2.034(7)	2.055(7)	2.033(6)	2.190(5)
c	2.315(6), 2.340(6)	2.347(1)	2.336(2)	2.3162(5)	2.316(1)	2.4504(5)	2.4512(9)	2.4630(9)	2.4597(8)	2.320(2)
d	2.01(1), 2.00(1)	2.035(7)	2.048(5)	2.2887(6)	2.296(1)	2.4307(6)	2.4243(10)	2.4220(9)	2.4322(9)	1.997(6)
Angles (°)										
α	91.6(6), 90.7(6)	89.3(2)	87.6(2)	90.90(2)	89.79(4)	90.06(2)	89.57(3)	89.77(3)	90.70(3)	89.6(2)
β	84.1(4), 83.8(4)	84.8(1)	82.8(1)	86.32(3)	86.6(1)	86.7(1)	85.8(2)	83.7(2)	85.5(2)	83.2(1)
γ	95.3(4), 95.7(4)	95.3(1)	99.4(1)	94.50(3)	94.2(1)	94.9(1)	94.5(2)	96.7(2)	95.1(2)	94.5(1)
δ	88.8(6), 89.6(6)	90.7(2)	89.9(2)	88.74(1)	89.70(4)	88.73(3)	90.37(6)	89.95(6)	88.81(5)	92.8(2)
ε	177.6(2), 176.2(2)	178.8(1)	168.4(1)	174.40(1)	175.15(3)	174.20(3)	175.87(6)	166.91(6)	179.10(5)	176.15(6)
ζ	172.3(7), 173.2(7)	174.9(2)	172.7(2)	172.95(3)	174.73(9)	173.7(1)	175.5(2)	173.5(2)	173.2(2)	175.2(2)
Torsion angles (°) (carbon atoms are denoted by number only) (presented in a common chirality)										
N–M–S–21	84.3(7), 83.1(7)	90.7(2)	76.7(2)	93.12(6)	92.5(2)	94.8(2)	80.0(4)	62.0(5)	82.6(4)	81.3(3)
2–20–S–21	−75(1), −74(1)	−87.0(4)	−72.3(4)	−91.3(1)	−91.1(3)	−93.3(3)	−75.4(6)	−62.3(7)	−75.5(6)	−74.5(5)
N–M–S–20	−19.2(6), −19.3(6)	−17.0(2)	−33.4(2)	−14.50(5)	−15.5(2)	−13.9(2)	−22.2(4)	−37.9(4)	−20.6(3)	−23.8(3)
M–S–20–2	32(1), 30(1)	25.5(4)	44.2(4)	20.1(1)	21.4(3)	19.4(3)	33.1(6)	47.5(6)	32.1(5)	37.0(5)
S–20–2–N	−31(2), −29(2)	−21.5(5)	−29.4(6)	−16.9(2)	−18.0(5)	−16.6(5)	−31.4(9)	−33.9(10)	−31.1(8)	−33.9(7)
20–2–N–M	13(2), 10(2)	4.1(5)	−4.7(6)	2.7(2)	3.1(5)	3.2(5)	10.3(9)	−3.1(10)	11.6(9)	10.9(8)
2–N–M–S	7.1(9), 9(1)	10.2(3)	27.1(4)	9.12(9)	9.6(3)	8.3(3)	10.4(6)	29.3(6)	8.6(5)	11.4(5)
Atom deviations from the C_5N plane (δÅ) (C(21) as datum)										
δM	0.25(2), 0.13(2)	0.059(9)	−0.089(9)	0.001(2)	−0.005(6)	−0.007(6)	0.20(1)	0.08(1)	0.27(1)	0.27(1)
δX	−0.08(3), −0.16(3)	−0.34(1)	−1.58(1)	−0.621(3)	−0.627(8)	−0.644(9)	−0.54(2)	−1.64(2)	−0.21(1)	−0.36(1)
δY	0.65(4), 0.35(4)	0.07(2)	−0.06(2)	0.243(3)	0.181(10)	0.22(1)	0.57(3)	0.39(2)	0.77(2)	0.63(2)
δC(20)	−0.10(3), −0.10(3)	−0.05(1)	0.123(9)	−0.029(2)	−0.028(7)	−0.033(8)	−0.08(2)	0.18(1)	−0.12(1)	−0.12(1)
δS	0.66(3), 0.55(3)	0.49(1)	0.984(9)	0.394(2)	0.415(7)	0.365(8)	0.72(2)	1.25(1)	0.67(1)	0.76(1)
δC(21)	2.40(3), 2.33(3)	2.34(1)	2.79(1)	2.151(3)	2.177(8)	2.127(9)	2.44(2)	2.76(1)	2.43(1)	2.47(1)

[a] This work.

Table 3
Selected bond distances and angles for $[PtBr_4L]$ ($L = L^2$(**6**), L^4(**8**))

	$[PtBr_4(L^2)]$ (**6**)	$[PtBr_4(L^4)]$ (**8**)	
		Molecule 1	Molecule 2 (2 cpts.)
Bond distances (Å)			
Pt–Br(1)	2.490(2)	2.469(5)	2.49(1), 2.45(2)
Pt–Br(2)	2.445(1)	2.431(5)	2.46(1), 2.43(2)
Pt–Br(3)	2.468(1)	2.467(4)	2.47(1), 2.47(1)
Pt–Br(4)	2.473(1)	2.448(4)	2.45(1), 2.47(1)
Pt–N(1)	2.10(1)	2.08(3)	2.03(4), 2.13(4)
Pt–S(21)	2.329(3)	2.301(11)	2.28(2), 2.34(3)
Bond angles (°)			
Br(1)–Pt–Br(2)	88.93(5)	91.1(2)	91.7(4), 90.3(7)
Br(1)–Pt–Br(3)	88.66(5)	89.4(1)	89.2(4), 90.0(5)
Br(1)–Pt–Br(4)	90.84(5)	88.6(2)	88.1(3), 87.4(4)
Br(1)–Pt–N(1)	95.7(5)	94.8(9)	97(1), 100(1)
Br(1)–Pt–S(21)	177.25(8)	173.5(2)	172.3(5), 171.9(6)
Br(2)–Pt–Br(3)	91.45(8)	91.1(1)	90.4(4), 88.8(5)
Br(2)–Pt–Br(4)	89.49(5)	89.4(2)	89.4(4), 91.1(4)
Br(2)–Pt–N(1)	175.3(7)	174.1(9)	169.7(9), 164(1)
Br(2)–Pt–S(21)	91.71(9)	89.3(3)	90.7(5), 89.1(8)
Br(3)–Pt–Br(4)	178.93(6)	177.9(2)	177.3(3), 177.4(6)
Br(3)–Pt–N(1)	88.9(3)	88.7(6)	83(1), 79(1)
Br(3)–Pt–S(21)	93.99(9)	97.0(2)	98.1(5), 98.1(6)
Br(4)–Pt–N(1)	90.2(3)	91.0(6)	97(1), 101.2(9)
Br(4)–Pt–S(21)	86.49(9)	85.0(2)	84.6(5), 84.5(6)
N(1)–Pt–S(21)	83.6(3)	84.9(9)	82(1), 82(1)
Torsion angles (°)			
S(21)–Pt–N(1)–C(2)	−12.2(8)	13(2)	26(3), −38(3)
Pt–N(1)–C(2)–C(20)	−9.4(1)	11(4)	−2(4), 23(4)
N(1)–C(2)–C(20)–S(21)	32.8(15)	−35(4)	−32(4), 12(5)
C(2)–C(20)–S(21)–Pt	−35.3(1)	37(3)	45(3), −35(7)
C(20)–S(21)–Pt–N(1)	23.7(5)	−26(1)	−33(2), 32(1)
C(21)–S(21)–Pt–N(1)	128.6(6)	79(1)	78(3), −72(5)
Out-of-plane deviations (Å)			
$\delta Pt(C_5N)$	0.14(2)	0.10(4)	0.05(6), −0.75(6)

at a lower temperature. Two independent molecules, devoid of crystallographic symmetry comprise the asymmetric unit of the structure. One is ordered, refining unproblematically, albeit with isotropic displacement parameter forms for S, C, N. The other comprises a pair of disordered superimposed components (Fig. 7), the disorder resolvable in all atoms except MeC_5H_3NC, occupancies refining to 0.605(9) and complement. The disorder is a consequence of co-crystallisation at site 2 of molecules differing in the orientation of the S–Me group. Although the geometries are imprecise, with the chelate rings of similar conformations in molecules 1 and the two components of molecule 2 (one component of the latter being of opposite chirality) (Table 2), it is interesting to find that the chelate ring conformation is somewhat different to that found in $[PtBr_4(L^2)]$ (**6**), best appreciated by observation of the pendant S–Me disposition. Disorder is not resolved in the aromatic ring of molecule 2, although its displacement parameters are high, perhaps because of the constraint of parallel packing of the aromatic planes in the lattice (Fig. 8), their being some tendency for the molecules to be disposed in sheets.

4. Conclusions

A relatively simple generic synthetic method has been developed for the preparation of substituted pyridyl thioether ligands, one of the most fundamental heteroleptic ligand systems. The solid-state structures of a number of $PtBr_2L$ complexes containing pyridyl thioether ligands were elucidated. The deviation from ideal square planar geometry is influenced by the substitution of a methyl group at the 6-position of the pyridyl ring. The electronic effects of the methyl group have minimal effect on the structure. Variation of the thioether substituent from Ph to Me has little to no effect on bond lengths within the coordination environment of the platinum, but there are subtle effects on the bond angles and strain, with the square planar geometry becoming less tetrahedrally distorted and the distance between the sulfur atom and the chelate ring becoming greater in the thiomethyl complex $[PtBr_2(L^2)]$. It is hoped that such investigations into the effect of ligand variation on the structure of the compounds will help to understand what characteristics influence their catalytic activity.

Acknowledgements

We thank the Australian Research Council for funding this project (V.-A.T. is an ARC APD Fellow). We also thank Johnson-Matthey for the generous loan of $PtCl_2$.

Appendix A. Supplementary material

CCDC Nos. 258137, 258138, 258139, 258140, 258141 and 615111 contain the supplementary crystallographic data for this paper. These data can be obtained free of charge at www.ccdc.cam.ac.uk/conts/retrieving.html, or from the Cambridge Crystallographic Data Centre, 12 Union Road, Cambridge CB2 1EZ, UK; fax: (+44) 1223-336-033; or e-mail: deposit@ccdc.cam.ac.uk. Supplementary data associated with this article can be found, in the online version, at doi:10.1016/j.poly.2006.09.001.

References

[1] S.G. Murray, F.R. Hartley, Chem. Rev. 81 (1981) 365.
[2] E.G. Hope, W. Levason, Coord. Chem. Rev. 122 (1993) 109.
[3] W. Levason, S.D. Orchard, G. Reid, Coord. Chem. Rev. 225 (2002) 159.
[4] E.W. Abel, P.J. Heard, K.G. Orrell, M.B. Hursthouse, M.A. Mazid, J. Chem. Soc., Dalton Trans. (1993) 3795.
[5] B. Pitteri, G. Marangoni, L. Cattalini, T. Bobbo, J. Chem. Soc., Dalton Trans. (1995) 3953.
[6] S. Chattopadhyay, C. Sinha, P. Basu, A. Chakravorty, Organometallics 10 (1991) 1135.
[7] P.J. Heard, D.A. Tocher, J. Organomet. Chem. 549 (1997) 295.
[8] V.K. Jain, S. Chaudhury, R. Bohra, Polyhedron 12 (1993) 2377.
[9] A. Knödler, W. Kaim, V.K. Jain, S. Záliš, J. Organomet. Chem. 655 (2002) 218.
[10] L. Canovese, G. Chessa, F. Visentin, P. Uguagliati, Coord. Chem. Rev. 248 (2004) 945.
[11] R.C. Jones, R.L. Madden, B.W. Skelton, V.–A. Tolhurst, A.H. White, A.J. Wilson, A. Williams, B.F. Yates, Eur. J. Inorg. Chem. (2005) 1048.
[12] J.M. Wisner, T.J. Bartczak, J.A. Ibers, J.J. Low, W.A. Goddard III, J. Am. Chem. Soc. 108 (1986) 347.
[13] J.M. Wisner, T.J. Bartczak, J.A. Ibers, Organometallics 5 (1986) 2044, and references therein.
[14] W. Kläui, M. Glaum, T. Wagner, M.A. Bennett, J. Organomet. Chem. 472 (1994) 355.
[15] R.E. Marsh, W.P. Schaefer, D.K. Lyon, J.A. Labinger, J.E. Bercaw, Acta Crystallogr., Sect. C 48 (1992) 1603.
[16] A.J. Canty, A. Dedieu, H. Jin, A. Milet, B.W. Skelton, S. Trofimenko, A.H. White, Inorg. Chim. Acta 287 (1999) 27.
[17] K. Kahmann, H. Sigel, H. Erlenmeyer, Helv. Chim. Acta 47 (1964) 1754.
[18] L. Bauer, L.A. Gardella, J. Org. Chem. 28 (1963) 1323.
[19] E.W. Ainscough, E.N. Baker, A.M. Brodie, N.G. Larsen, K.L. Brown, J. Chem. Soc., Dalton Trans. (1981) 1746.
[20] E. Ghera, Y. Ben-David, H. Rapoport, J. Org. Chem. 48 (1983) 774.
[21] B.M. Trost, R. Braslau, J. Org. Chem. 53 (1988) 532.
[22] L. Canovese, F. Visentin, P. Uguagliati, G. Chessa, A. Pesce, J. Organomet. Chem. 566 (1998) 61.
[23] L. Canovese, F. Visentin, P. Uguagliati, G. Chessa, V. Lucchini, G. Bandoli, Inorg. Chim. Acta 275 (1998) 385.
[24] H.L. Holland, C.D. Turner, P.R. Andreana, D. Nguyen, Can. J. Chem. 77 (1999) 463.
[25] L. Canovese, G. Chessa, C. Santo, F. Visentin, P. Uguagliati, Inorg. Chim. Acta 346 (2003) 158.
[26] S.R. Hall, D.J. du Boulay, R. Olthof-Hazekamp (Eds.), The XTAL 3.7 System, University of Western Australia, 2000.
[27] F.R. Hartley, S.G. Murray, W. Levason, H.E. Soutter, C.A. McAuliffe, Inorg. Chim. Acta 35 (1979) 265.
[28] G. Marangoni, B. Pitteri, V. Bertolasi, P. Gilli, Inorg. Chim. Acta 234 (1995) 173.
[29] R.J.H. Clark, F.P. Fanizzi, G. Natile, C. Pacifico, C.G. van Rooyen, D.A. Tocher, Inorg. Chim. Acta 235 (1995) 205.
[30] L. Canovese, F. Visentin, G. Chessa, F. Visentin, G. Chessa, P. Uguagliati, G. Bandoli, Organometallics 19 (2000) 461.
[31] Canovese et al., J. Organomet. Chem. 650 (2002) 43.
[32] Gosavi et al., Inorg. Chim. Acta 357 (2004) 1781.

Available online at www.sciencedirect.com
ScienceDirect
Polyhedron 26 (2007) 719–724
POLYHEDRON
www.elsevier.com/locate/poly

Synthesis and crystal structure of four Pd(II) complexes containing *nido* or *closo* carborane diphosphine ligands

J.-M. Dou *, D.-P. Zhang, D.-C. Li, D.-Q. Wang

Department of Chemistry, Liaocheng University, Liaocheng 252059, PR China

Received 21 July 2006; accepted 31 August 2006
Available online 22 September 2006

Abstract

Three Pd(II) complexes $[Pd_2(\mu\text{-}Cl)_2\{7,8\text{-}(PPh_2)_2\text{-}7,8\text{-}C_2B_9H_{10}\}_2]\cdot 0.25CH_2Cl_2$ (**1**), $[Pd\{7,8\text{-}(PPh_2)_2\text{-}7,8\text{-}C_2B_9H_{10}\}_2]\cdot 4CHCl_3$ (**2**) and $[PdCl_2(1,2\text{-}(PPh_2)_2\text{-}1,2\text{-}C_2B_{10}H_{10})]$ (**3**) have been synthesized by the reactions of $1,2\text{-}(PPh_2)_2\text{-}1,2\text{-}C_2B_{10}H_{10}$ with $PdCl_2$ in acetonitrile, cyanophenyl and dichloromethane, respectively. A fourth complex, $[PdI_2(1,2\text{-}(PPh_2)_2\text{-}1,2\text{-}C_2B_{10}H_{10})]$ (**4**), was obtained by a ligand exchange reaction through the substitution of the Cl^- of complex **3** with I^-. All four complexes have been characterized by elemental analysis, FT-IR, ^1H and ^{13}C NMR spectroscopy and X-ray structure determination. Single crystal X-ray determination showed that the carborane cage, *nido* for **1**, **2** and *closo* for **3**, **4**, was coordinated bidentately to the Pd atom through the two P atoms, and the geometry at the Pd atom was square-planar in all the complexes.
© 2006 Elsevier Ltd. All rights reserved.

Keywords: Synthesis and crystal structure; Pd(II) complexes; $1,2\text{-}(PPh_2)_2\text{-}1,2\text{-}C_2B_{10}H_{10}$; $[7,8\text{-}(PPh_2)_2\text{-}7,8\text{-}C_2B_9H_{10}]^-$

1. Introduction

Bidentate ligands have played an important role in the development of catalytic applications of metal organic complexes [1]. Two of the fundamentals for these catalysts are that two *cis*positions of the metal center are available to perform the reaction, and bidentate phosphines have already been demonstrated to be very convenient for this sort of catalysis [2]. The influence of substitution at the cluster carbon atoms in *o*-carborane by electron rich element phosphorus has been of interest to us. Among of the derivatives of *o*-carborane, the *closo* diphosphine $1,2\text{-}(PPh_2)_2\text{-}1,2\text{-}C_2B_{10}H_{10}$ and the *nido* $[7,8\text{-}(PPh_2)_2\text{-}7,8\text{-}C_2B_9H_{10}]^-$ anion degraded from the *closo* species are two typical bidentate phosphine ligands [3,4]. Because the two phosphorus atoms bonded to the two adjacent carbon atoms of the *o*-carborane are fixed by the geometry of the carborane skeleton in an eclipsed conformation at *cis* positions, a stable complex can be formed through a five-membered chelating ring between the ligand and a metal atom. Several Pd(II) complexes with *closo* or *nido* carborane diphosphine ligands, such as $[PdCl_2(1,2\text{-}(PPh_2)_2\text{-}1,2\text{-}C_2B_{10}H_{10})]\cdot CH_2Cl_2$ [5], $[PdClMe(1,2\text{-}(PPh_2)_2\text{-}1,2\text{-}C_2B_{10}H_{10})]\cdot CH_2Cl_2$ [6], $[PdBr_{1.133}Cl_{0.867}(1,2\text{-}(PPh_2)_2\text{-}1,2\text{-}C_2B_{10}H_{10})]\cdot CH_2Cl_2$, $[PdBr_2(1,2\text{-}(PPh_2)_2\text{-}1,2\text{-}C_2B_{10}H_{10})]\cdot CH_2Cl_2$ and $[PdBrCl_{0.541}Me_{0.459}(1,2\text{-}(PPh_2)_2\text{-}1,2\text{-}C_2B_{10}H_{10})]\cdot CHCl_3$ [7], where the structures have been characterized by X-ray diffraction, have been reported. Considering the importance of Pd as a metal in catalysis, we are also interested in this kind of complex and reported a Pd(II) complex with the formula $[PdCl(PPh_3)\{7,8\text{-}(PPh_2)_2\text{-}7,8\text{-}C_2B_9H_{10}\}]\cdot 1.25CH_2Cl_2$ [8]. Recently, we investigated the reactions of the *closo* diphosphine ligand with $PdCl_2$ in three different solvents and obtained three Pd(II) complexes with the formula $[Pd_2(\mu\text{-}Cl)_2\{7,8\text{-}(PPh_2)_2\text{-}7,8\text{-}C_2B_9H_{10}\}_2]\cdot 0.25CH_2Cl_2$ (**1**), $[Pd\{7,8\text{-}(PPh_2)_2\text{-}7,8\text{-}C_2B_9H_{10}\}_2]\cdot 4CHCl_3$ (**2**) and $[PdCl_2(1,2\text{-}(PPh_2)_2\text{-}1,2\text{-}C_2B_{10}H_{10})]$ (**3**). By using a ligand exchange reaction, we have also obtained the complex $[PdI_2(1,2\text{-}(PPh_2)_2\text{-}1,2\text{-}C_2B_{10}H_{10})]$ (**4**). All the complexes were characterized by elemental analysis, FT-IR, ^1H and ^{13}C NMR spectroscopy and X-ray structure determination.

* Corresponding author. Tel.: +86 635 8239069.
E-mail address: jmdou@lctu.edu.cn (J.-M. Dou).

0277-5387/$ - see front matter © 2006 Elsevier Ltd. All rights reserved.
doi:10.1016/j.poly.2006.08.038

2. Experimental

2.1. Reagents and techniques

All the reactions were carried out under an atmosphere of dry, oxygen-free dinitrogen. Some subsequent manipulations were performed in the air. Solvents were dried with suitable drying agents, distilled under dinitrogen and deoxygenated prior to use. 1,2-$(PPh_2)_2$-1,2-$C_2B_{10}H_{10}$ was prepared according to the literature procedure [3]. All chemicals were purchased and used as received. Infrared spectra were recorded in the range 400–4000 cm^{-1} from KBr pellets on a Nicolet-460 FT-IR spectrophotometer. Elemental analysis (C, H) was carried out with a Perkin–Elemer 2400 II elemental analyzer. The ^1H and ^{13}C NMR were recorded on a Varian Mercury 400 spectrometer in $CDCl_3$ solution with tetramethylsilane (TMS) as an internal standard at 400.15 and 100.63 MHz, respectively. The ^{13}C spectra are broadband proton decoupled. The chemical shifts are reported in parts per million with respect to the references and are stated relative to external TMS for ^1H and ^{13}C NMR.

2.2. Synthetic procedures

2.2.1. Preparation of $[Pd_2(\mu\text{-}Cl)_2\{7,8\text{-}(PPh_2)_2\text{-}7,8\text{-}C_2B_9H_{10}\}_2]\cdot 0.25CH_2Cl_2$ (1)

$PdCl_2$ (18.8 mg, 0.10 mmol) and 1,2-$(PPh_2)_2$-1,2-$C_2B_{10}H_{10}$ (51.2 mg, 0.10 mmol) were added to 10 ml acetonitrile and the mixture was refluxed for 6 h under the protection of dry N_2. The yellow solid that formed was filtered off, washed with acetonitrile, and dried in vacuum (26.4 mg, 41.0%). M.p. 278–279 °C. A crystal suitable for X-ray diffraction was obtained from a dichloromethane–*n*-hexane solution. FT-IR ν_{KBr} (cm^{-1}): 3052 m, 2540 m, 1435 m, 1098 m, 741 m. ^1H NMR (400.15 MHz, $CDCl_3$): −2.1 ppm (2H, B–H–B); ^{13}C NMR (100.63 MHz, $CDCl_3$): 124–131 ppm (48C), 76.5 ppm (4C). *Anal.* Calc. for $C_{52.25}H_{60.5}B_{18}Cl_{2.50}P_4Pd_2$: C, 47.96; H, 4.66; Found: C, 47.82; H, 4.71%.

2.2.2. Preparation of $[Pd\{7,8\text{-}(PPh_2)_2\text{-}7,8\text{-}C_2B_9H_{10}\}_2]\cdot 4CHCl_3$ (2)

$PdCl_2$ (18.8 mg, 0.10 mmol) was added to a solution of 1,2-$(PPh_2)_2$-1,2-$C_2B_{10}H_{10}$ (102.4 mg, 0.20 mmol) in 10 ml cyanophenyl and stirred for 10 h under the protection of dry N_2. The yellow solid that formed was filtered off, and dried in vacuum (42.7 mg, 38.5%). M.p. 236–237 °C. A crystal for X-ray diffraction was grown from a chloroform solution layered with ether. FT-IR ν_{KBr} (cm^{-1}): 3042 m, 2560 m, 1423 m, 1108 m, 735 m. ^1H NMR (400.15 MHz, $CDCl_3$): −2.13 ppm (2H, B–H–B); ^{13}C NMR (100.63 MHz, $CDCl_3$): 125–132 ppm (48C), 77.1 ppm (4C). *Anal.* Calc. for $C_{56}H_{64}B_{18}Cl_{12}P_4Pd$: C, 42.37; H, 4.06; Found: C, 42.30; H, 4.00%.

2.2.3. Preparation of $[PdCl_2(1,2\text{-}(PPh_2)_2\text{-}1,2\text{-}C_2B_{10}H_{10})]$ (3)

$PdCl_2$ (18.8 mg, 0.10 mmol) was added to a solution of 1,2-$(PPh_2)_2$-1,2-$C_2B_{10}H_{10}$ (51.2 mg, 0.10 mmol) in 10 ml dichloromethane. The mixture was refluxed for 3 h under the protection of dry N_2, and concentrated to 5 ml, and then 20ml *n*-hexane was added to precipitate the solid. Yield: 53.8 mg, 78.0%. M.p. 291–292 °C. A crystal suitable for X-ray diffraction was obtained from a CH_2Cl_2 solution after partial evaporation the solvent. FT-IR ν_{KBr} (cm^{-1}): 3000 m, 2600 m, 1433 m, 1080 m, 755 m. ^1H NMR (400.15 MHz, $CDCl_3$): 7.2–7.6 ppm (20H); ^{13}C NMR (100.63 MHz, $CDCl_3$): 124–132 ppm (24C), 76.3 ppm (2C). *Anal.* Calc. for $C_{26}H_{30}B_{10}Cl_2P_2Pd$: C, 45.26; H, 4.38; Found: C, 45.40; H, 4.32%.

2.2.4. Preparation of $[PdI_2(1,2\text{-}(PPh_2)_2\text{-}1,2\text{-}C_2B_{10}H_{10})]$ (4)

KI (1.0 mmol, 166 mg) was added to the dichloromethane solution obtained from the preparation of complex **3**. The suspension was refluxed for 5 h under the protection of dry N_2, and then filtered. The yellow filtrate was concentrated to 5 ml, and 20 ml *n*-hexane was added to precipitate the solid. Yield 43.2 mg, 49.5%. M.p. 261–262 °C. A crystal suitable for X-ray diffraction was obtained from a dichloromethane–*n*-hexane solution. FT-IR ν_{KBr} (cm^{-1}): 3030 m, 2590 m, 1445 m, 1090 m, 727 m. ^1H NMR (400.15 MHz, $CDCl_3$): 7.2–7.6 ppm (20H); ^{13}C NMR (100.63 MHz, $CDCl_3$): 125–133 ppm (24C), 77.3 ppm (2C). *Anal.* Calc. for $C_{26}H_{30}B_{10}I_2P_2Pd$: C, 35.78; H, 3.47; Found: C, 35.60; H, 3.38%.

2.3. X-ray crystallography data collection and processing

The collection of crystallographic data for the four complexes was carried out on a Bruker Smart-1000 CCD diffractometer, using graphite-monochromatized Mo-Kα radiation ($\lambda = 0.71073$ Å) at 298(2) K. The structures were solved by direct method and expanded using Fourier difference techniques with the SHELXTL-97 program package [9]. The solvent CH_2Cl_2 in complex **1** was disordered and partially occupied atoms were refined with isotropic displacement parameters, whilst the remaining non-hydrogen atoms were refined anisotropically by full-matrix least-squares calculations on F^2. All the H atoms were located in a difference Fourier map and thereafter refined isotropically, except the bridge H atoms of the *nido* carborane skeleton. These bridge H atoms were refined isotropically with fixed *U* values. Details of the crystal parameters, data collection and refinement are summarized in Table 1.

3. Results and discussion

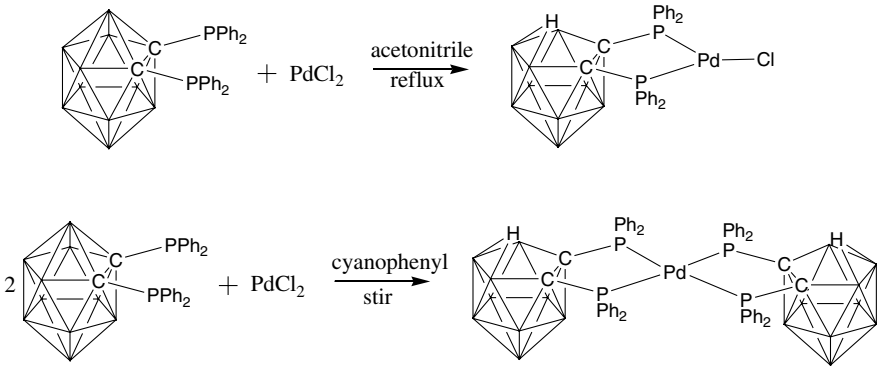
3.1. Synthesis

The metal driven degradation of the *closo* carborane diphosphine 1,2-$(PPh_2)_2$-1,2-$C_2B_{10}H_{10}$ with C–P retention

Table 1
Details of the crystal parameters, data collection and refinement for complexes **1**, **2**, **3** and **4**

Crystal data	**1**	**2**	**3**	**4**
Empirical formula	$C_{52.25}H_{60.5}B_{18}Cl_{2.50}P_4Pd_2$	$C_{56}H_{64}B_{18}Cl_{12}P_4Pd$	$C_{26}H_{30}B_{10}Cl_2P_2Pd$	$C_{26}H_{30}B_{10}I_2P_2Pd$
Formula weight	1308.39	1587.33	689.84	872.74
Temperature (K)	298(2)	298(2)	298(2)	298(2)
Wavelength (Å)	0.71073	0.71073	0.71073	0.71073
Crystal system	monoclinic	monoclinic	triclinic	monoclinic
Space group	*C*2/*c*	*P*2(1)/*c*	$P\bar{1}$	*P*2(1)/*n*
a (Å)	28.384(12)	22.321(9)	8.4846(15)	12.003(3)
b (Å)	16.575(7)	16.465(6)	11.0660(19)	18.202(4)
c (Å)	21.392(9)	19.922(8)	17.148(3)	14.631(3)
α (°)	90	90	89.031(2)	90
β (°)	128.635(5)	94.096(7)	85.447(2)	95.759(4)
γ (°)	90	90	75.456(2)	90
V (Å^3)	7862(6)	7303(5)	1553.5(5)	3180.4
Z	4	4	2	4
Absorption coefficient (mm^{-1})	0.652	0.818	0.891	2.644
D (Mg m^{-3})	1.105	1.444	1.475	1.823
F(000)	2634	3200	692	1672
Crystal size (mm)	$0.39 \times 0.38 \times 0.34$	$0.35 \times 0.33 \times 0.31$	$0.48 \times 0.33 \times 0.21$	$0.33 \times 0.31 \times 0.29$
Theta range (°)	2.29–25.01	1.81–25.01	1.90–25.01	2.09–25.01
Limiting indices	$-31 \leqslant h \leqslant 33$	$-26 \leqslant h \leqslant 24$	$-7 \leqslant h \leqslant 10$	$-14 \leqslant h \leqslant 13$
	$-19 \leqslant k \leqslant 19$	$-16 \leqslant k \leqslant 19$	$-13 \leqslant k \leqslant 12$	$-21 \leqslant k \leqslant 17$
	$-25 \leqslant l \leqslant 19$	$-22 \leqslant l \leqslant 23$	$-19 \leqslant l \leqslant 20$	$-12 \leqslant l \leqslant 17$
Independent reflection	6643	12664	5400	5558
Max. and min. transmission	0.8088 and 0.7851	0.7855 and 0.7627	0.8350 and 0.6744	0.5144 and 0.4757
Goodness-of-fit on F^2	1.006	1.017	1.005	1.000
$R[I > 2\sigma(I)]$	$R_1 = 0.0707$	$R_1 = 0.0707$	$R_1 = 0.0362$	$R_1 = 0.0416$
	$wR_2 = 0.1591$	$wR_2 = 0.1726$	$wR_2 = 0.0861$	$wR_2 = 0.1186$
R (all data)	$R_1 = 0.2072$	$R_1 = 0.1543$	$R_1 = 0.0529$	$R_1 = 0.0500$
	$wR_2 = 0.2128$	$wR_2 = 0.2372$	$wR_2 = 0.0978$	$wR_2 = 0.1265$
Largest difference in peak and hole ($\times 10^2$ e Å^{-3})	1.125 and −0.609	1.106 and −0.850	0.545 and −0.311	1.162 and −1.320

was first disclosed by Teixidor's group in 1993 [4]. Based on the result, much research work has been done relevant to this area by this group [10–13], and many complexes containing the *nido*-[7,8-$(PPh_2)_2$-7,8-$C_2B_9H_{10}$]$^-$ anion, such as Ru [14], Rh [15], Au [16,17], Ag [18] and Ni, Pd and Pt [8], have been reported. By treatment of $PdCl_2$ with the *closo* diphosphine ligand 1,2-$(PPh_2)_2$-1,2-$C_2B_{10}H_{10}$ in a molar ratio 1:1 in acetonitrile under refluxing conditions, we obtained a binuclear Pd complex with the formula [Pd_2-(μ-Cl)$_2${7,8-$(PPh_2)_2$-7,8-$C_2B_9H_{10}$}$_2$]$\cdot$ 0.25CH_2Cl_2 (**1**), in which the *closo* structure of the carborane skeleton was also degraded. When the $PdCl_2$:carborane diphosphine ligand ratio was changed to 1:2 with the conditions otherwise the same, the same product was obtained, indicating that the ratio of the reactants has no influence on the result of this reaction. However, when the reaction was carried out with the starting material $PdCl_2$ and 1,2-$(PPh_2)_2$-1,2-$C_2B_{10}H_{10}$ with a molar ratio 1:2 in cyanophenyl, the complex [Pd{7,8-$(PPh_2)_2$-7,8-$C_2B_9H_{10}$}$_2$]$\cdot$ 4$CHCl_3$ (**2**) was obtained, in which the two Cl ions of the initial $PdCl_2$ were substituted by the *nido* carborane diphosphine anion [7,8-$(PPh_2)_2$-7,8-$C_2B_9H_{10}$]$^-$. The reactions are shown in Scheme 1. From these results, it seemed that the solvent could play an important role in the formation process of the complexes.



Scheme 1. The reactions for the preparation of complexes **1** and **2**.

In strong nucleophilic solvents, such as ethanol [8], acetonitrile and cyanophenyl, the *closo* carborane skeleton could be degraded in the reactions of Pd compounds with the *closo* ligand. However, in mild nucleophilic solvents, for example dichloromethane, the *closo* structure of the carborane could be preserved [6,7]. The complex $[PdCl_2(1,2\text{-}(PPh_2)_2\text{-}1,2\text{-}C_2B_{10}H_{10})]\cdot CH_2Cl_2$ could be obtained by the reactions of the *closo* ligand with $[PdCl_2(cod)]$ in CH_2Cl_2 or $[PdCl_2(PhCN)_2]$ in toluene [5]. Here, we revised the method for the preparation of this complex. By using $PdCl_2$ as the initial material to react with the *closo* ligand in dichloromethane under refluxing conditions, we also obtained this complex. This result further confirmed the conclusion that a mild nucleophilic solvent could avoid the degradation of the *closo* diphosphine ligand. The corresponding PdI_2 complex $[PdI_2(1,2\text{-}(PPh_2)_2\text{-}1,2\text{-}C_2B_{10}H_{10})]$ (**4**) was obtained through the substitution of Cl^- in $[PdCl_2(1,2\text{-}(PPh_2)_2\text{-}1,2\text{-}C_2B_{10}H_{10})]$ with I^- under refluxing conditions in CH_2Cl_2 after several hours. The bromide derivative could also be afforded by this type of ligand exchange reaction, although the process was more difficult than that for the preparation of complex **4** (refluxing for 8 days) [7].

3.2. Spectral characterization

All the complexes were characterized by FT-IR, ^1H and ^{13}C NMR spectroscopy. The IR spectra of these complexes were very similar to each other and exhibited absorptions characteristic of terminal B–H vibrations at about 2540–2600 cm^{-1}in the four complexes, which are in the normal range for B–H vibrations of 2625–2450 cm^{-1} [19]. The absorptions at 3052, 3042, 3000 and 3030 cm^{-1} might be attributed to the ν_{C-H} stretching vibration of the benzene rings. Several peaks were found from 1695 to 1410 cm^{-1}, which might be assigned to $\nu_{C=C}$ stretching vibrations. The peak at ca. 1400 cm^{-1} was the in-plane deformation mode of the benzene ring, and the peak at ca. 1100 cm^{-1} was the absorption of $\nu_{C(phenyl)-P}$, which was a little shifted in keeping with phosphorus coordination to the carborane moiety. The absorption at approximately 740 cm^{-1} showed the existence of cage deformation. The ^1H NMR spectra (400.15 MHz) of these complexes displayed a complex pattern of resonances at about 7.1–7.6 ppm which could be attributed to the phenyl-H of the PPh_2 groups. A resonance at ca. −2.1 ppm is the bridge H atom of B–H–B [4]. In the ^{13}C NMR spectra (100.63 MHz), a resonance at ca. $\delta = 130$ ppm could be assigned to the benzene ring C atoms, and a resonance at ca. $\delta = 77$ could be assigned to the carbon atom of carborane cage (Cc) [20].

3.3. Crystallographic data of the complexes

Crystal structures of the four complexes are shown in Figs. 1–4, respectively. Selected bond lengths and angles are given in Table 2. Complex **1** crystallizes in the monoclinic space group *C*2/*c*, containing four formula units in the unit cell and the disordered solvent CH_2Cl_2. The molecular structure of complex**1** is symmetrical and the symmetry transformations used to generate equivalent atoms are $-x+1/2,\ -y+3/2,\ -z+2$. Two Cl atoms bridge the two same Pd[7,8-$(PPh_2)_2$-7,8-$C_2B_9H_{10}$] units. The dihedral angel between central plane formed by the $[Pd_2Cl_2]$ unit and the side P(1)Pd(1)P(2) plane is only 3.3°, indicating that these two planes are almost parallel to each other. The Pd–Cl distance, 2.394(3) Å, is almost equal to the bond length of 2.405(5) Å in $[Pd_2(\mu\text{-}Cl)_2\{7,8\text{-}(P^iPr_2)_2\text{-}7,8\text{-}C_2B_9H_{10}\}_2]$ [12], but slightly longer than the average distance of 2.338(2) Å in $[PdCl(PPh_3)\{7,8\text{-}(PPh_2)_2\text{-}7,8\text{-}C_2B_9H_{10}\}]\cdot 1.25\ CH_2Cl_2$ [8]. The two Pd–P bonds (2.233(2) and 2.236(2) Å) and the P–Pd–P angle (85.23(8)°) are all consistent with the average values 2.238 Å and 87.0(1)° in $[Pd_2(\mu\text{-}Cl)_2\{7,8\text{-}(P^iPr_2)_2\text{-}7,8\text{-}C_2B_9H_{10}\}_2]$. The average distances of P–Cc, 1.817 Å, and

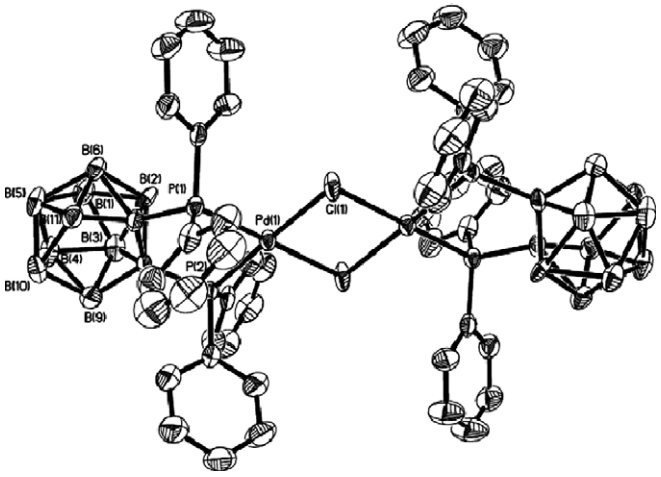


Fig. 1. Perspective view of complex unit of **1**. The H atoms are omitted for clarity.

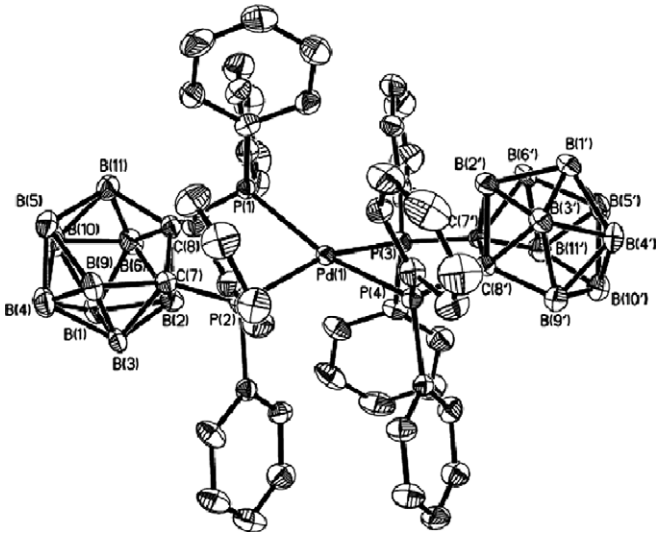


Fig. 2. Perspective view of complex unit of **2**. The H atoms are omitted for clarity.

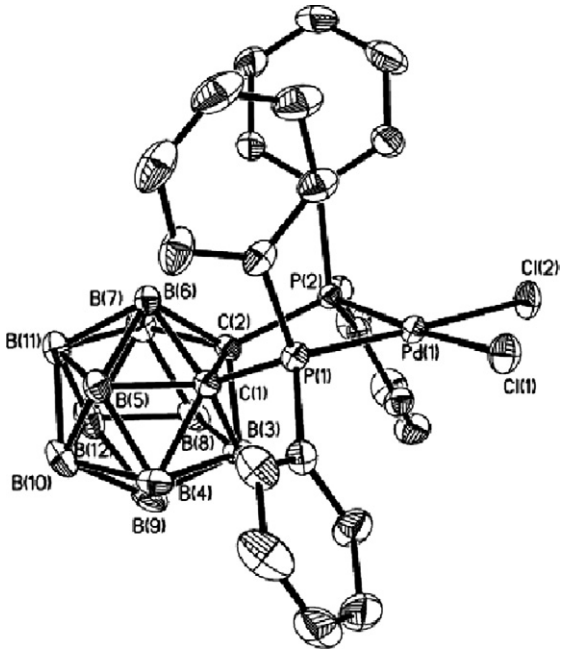


Fig. 3. The crystal structure of complex **3**. The H atoms are omitted for clarity.

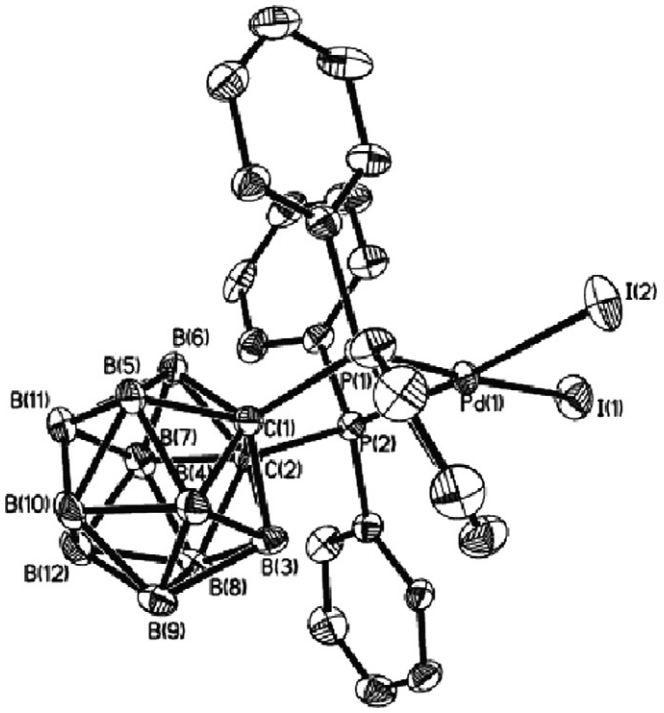


Fig. 4. The crystal structure of complex **4**. The H atoms are omitted for clarity.

Cc–Cc, 1.556(13) Å, are slightly shorter than the corresponding distances, 1.87 and 1.61(2) Å, in $[NMe_4]$-[7,8-$(PPh_2)_2$-7,8-$C_2B_9H_{10}$] · CH_3CH_2OH [10], implying that coordination of the ligand to the Pd atom has an influence on these bond lengths.

Complex **2** also contains four formula units in the unit cell and the solvent $CHCl_3$, and crystallizes in the monoclinic space group *P*2(1)/*c*. The central Pd atom is coordinated to four P atoms coming from two *nido* carborane diphosphine anions [7,8-$(PPh_2)_2$-7,8-$C_2B_9H_{10}]^-$. The geometry at the Pd atom is seriously distorted square-planar with a mean deviation from the P(1)P(2)P(3)P(4)Pd(1) plane of 0.3141 Å, and the angles around Pd (Table 2) deviate much from the values for a regular square-planar coordination mode. The distances of the four Pd–P bonds are almost equal to each other, and the average value of 2.362 Å is obviously longer than those in complex **1**, which can be attributed to the steric effect of the two ligands. The angles of P(1)–Pd(1)–P(2), 82.63(7)°, and P(3)–Pd(1)–P(4), 82.86(7)°, are slightly smaller than the value of 85.23(8)° in $[Pd_2(\mu\text{-}Cl)_2\{7,8\text{-}(P^iPr_2)_2\text{-}7,8\text{-}C_2B_9H_{10}\}_2]$. As for the other parameters in complex **2**, such as the distances of P–Cc and Cc–Cc as listed in Table 2, no noticeable differences have been found on comparison to those in complex **1**.

Table 2
Selected bond lengths (Å) and angles (°) for complexes **1**, **2**, **3** and **4**

1		**2**			**3** (X=Cl)	**4** (X=I)
Pd(1)–P(1)	2.233(2)	Pd(1)–P(1)	2.359(2)	Pd(1)–P(1)	2.239(1)	2.262(14)
Pd(1)–P(2)	2.236(2)	Pd(1)–P(2)	2.362(2)	Pd(1)–P(2)	2.239(1)	2.262(14)
Pd(1)–Cl(1)	2.394(3)	Pd(1)–P(3)	2.359(2)	Pd(1)–X(1)	2.333(1)	2.622(7)
Pd(1)–Cl(1)#1	2.395(2)	Pd(1)–P(4)	2.368(2)	Pd(1)–X(2)	2.330(1)	2.614(7)
P(1)–C(7)	1.814(9)	P(1)–C(7)	1.824(8)	P(1)–C(1)	1.873(4)	1.883(5)
P(2)–C(8)	1.819(9)	P(2)–C(8)	1.833(8)	P(2)–C(2)	1.883(3)	1.885(5)
C(7)–C(8)	1.556(13)	P(3)–C(7′)	1.817(8)	C(1)–C(2)	1.677(5)	1.687(7)
P(1)–Pd(1)–P(2)	85.23(8)	P(4)–C(8′)	1.832(8)	P(2)–Pd(1)–P(1)	89.73(4)	91.37(5)
P(1)–Pd(1)–Cl(1)	94.16(8)	C(7)–C(8)	1.556(11)	P(2)–Pd(1)–X(2)	174.09(4)	175.39(4)
Cl(1)–Pd(1)–Cl(1)#1	85.18(8)	P(1)–Pd(1)–P(4)	160.55(7)	P(1)–Pd(1)–X(2)	88.44(4)	87.77(4)
P(2)–Pd(1)–Cl(1)#1	95.33(8)	P(1)–Pd(1)–P(3)	103.93(7)	P(2)–Pd(1)–X(1)	89.77(4)	88.88(4)
P(2)–Pd(1)–Cl(1)	177.3(11)	P(1)–Pd(1)–P(2)	82.63(7)	P(1)–Pd(1)–X(1)	178.75(4)	176.97(4)
P(1)–Pd(1)–Cl(1)#1	177.8(11)	P(3)–Pd(1)–P(4)	82.86(7)	X(2)–Pd(1)–X(1)	91.94(4)	91.74(2)
C(7)–P(1)–Pd(1)	111.3(3)	P(2)–Pd(1)–P(4)	96.99(7)	C(1)–P(1)–Pd(1)	108.0(10)	108.1(2)
C(8)–P(2)–Pd(1)	110.9(3)	P(3)–Pd(1)–P(2)	160.52(7)	C(2)–P(2)–Pd(1)	108.1(11)	107.6(2)
C(7)–C(8)–P(2)	114.2(6)	C(7)–C(8)–P(2)	116.2(5)	C(2)–C(1)–P(1)	113.1(2)	113.8(3)
C(8)–C(7)–P(1)	113.5(5)	C(8)–C(7)–P(1)	114.2(5)	C(1)–C(2)–P(2)	113.3(2)	114.8(3)

Symmetry transformations used to generate equivalent atoms for complex **1**: $-x+1/2$, $-y+3/2$, $-z+2$.

As for complex **4**, the Pd atom is also four coordinate, in which two positions are occupied by the *closo* carborane diphosphine 1,2-$(PPh_2)_2$-1,2-$C_2B_{10}H_{10}$, and the other two come from two I atoms in *cis* positions, fulfilling the slightly distorted square-planar coordination. The mean derivation from the P(1)P(2)Pd(1)I(1)I(2) plane is only 0.0258 Å. The two I–Pd bond lengths are 2.622(7) and 2.614(7) Å, which are comparable to the analogous distances of 2.6649(8) and 2.6446(10) Å in [PdI_2(dppe)] [21]. The I–Pd–I angle of 91.74(2)° is almost equal to Cl–Pd–Cl angle of 91.94(4)° in complex **3**. Other bond lengths and angles in the coordination sphere of [PdI_2(1,2-$(PPh_2)_2$-1,2-$C_2B_{10}H_{10}$)] agree well with the corresponding values in [$PdCl_2$(1,2-$(PPh_2)_2$-1,2-$C_2B_{10}H_{10}$)]·CH_2Cl_2 [5]. Comparison of the configuration of the *closo* carborane diphosphine ligand in complex **4** with that in the free 1,2-$(PPh_2)_2$-1,2-$C_2B_{10}H_{10}$ ligand reveals differences. In the free ligand the P(1)–C(1)–C(2)–P(2) torsion angle is 10.6(3)° [22], while this angle in complex **4** is only 0.6(5)°. This data indicates that coordination of the ligand to Pd(II) alters the symmetry of the ligand. On comparison to that in the free *closo* ligand, the symmetry of the ligand in the complex **4** closely approaches C_{2v}.

4. Conclusions

In this paper we have reported four Pd(II) complexes containing *closo* or *nido* carborane diphosphine ligands, which were obtained by the reactions of the *closo* ligand 1,2-$(PPh_2)_2$-1,2-$C_2B_{10}H_{10}$ with $PdCl_2$ in different solvents or by a ligand exchange reaction. The results indicate that the solvent plays an important role in these reactions, both for the degradation of the *closo* carborane skeleton and for the formation process of the complexes.

5. Supplementary material

CCDC 608198, 608199, 608201, 608200, contain the supplementary crystallographic data for **1**, **2**, **3** and **4**. These data can be obtained free of charge via http://www.ccdc.cam.ac.uk/conts/retrieving.html, or from the Cambridge Crystallographic Data Centre, 12 Union Road, Cambridge CB2 1EZ, UK; fax: (+44) 1223-336-033; or e-mail: deposit@ccdc.cam.ac.uk.

Acknowledgements

This work was supported by the National Natural Science Foundation of P. R. China (project no. 20371025) and Open Research Fund Program of Key Laboratory of Marine Drugs (Ocean University of China).

References

[1] (a) K. Issleib, D. Muller, Chem. Ber. 92 (1959) 3175;
(b) P.W.N.M. van Leeuwen, P.C.J. Kamer, J.N.H. Reek, P. Dierkes, Chem. Rev. 100 (2000) 2741.
[2] J.S. Kim, J.H. Pawlow, L.M. Wojcinski II, S. Murtuza, S. Kacker, A. Sen, J. Am. Chem. Soc. 120 (1998) 1932.
[3] R.P. Alexander, H. Schroeder, Inorg. Chem. 2 (1963) 1107.
[4] F. Teixidor, C. Viñas, M.M. Abad, M. Lopez, J. Casabó, Organometallics 12 (1993) 3766.
[5] S. Paavola, R. Kivekäs, F. Teixidor, C. Viñas, J. Organomet. Chem. 606 (2000) 183.
[6] S. Paavola, F. Teixidor, C. Viñas, R. Kivekäs, J. Organomet. Chem. 645 (2002) 39.
[7] S. Paavola, F. Teixidor, C. Viñas, R. Kivekäs, J. Organomet. Chem. 657 (2002) 187.
[8] D.P. Zhang, J.M. Dou, D.C. Li, D.Q. Wang, Inorg. Chim. Acta 359 (2006) 4243.
[9] G.M. Sheldrick, SHELXTL 5.10 for Windows NT: Structure Determination Software Programs, Bruker Analytical X-ray Systems, Madison, WI, 1997.
[10] F. Teixidor, C. Viñas, M.M. Abad, R. Nuñez, R. Kivekäs, R. Sillanpää, J. Organomet. Chem. 503 (1995) 193.
[11] F. Teixidor, C. Viñas, M.M. Abad, R. Kivekäs, R. Sillanpää, J. Organomet. Chem. 509 (1996) 139.
[12] C. Viñas, M.M. Abad, F. Teixidor, R. Sillanpaa, R. Kivekas, J. Organomet. Chem. 555 (1998) 17.
[13] F. Simal, S. Sebille, A. Demonceau, A.F. Noels, R. Nunez, M.M. Abad, F. Teixidor, C. Viñas, Tetrahedron Lett. 41 (2000) 5347.
[14] R. Nunez, C. Viñas, F. Teixidor, M.M. Abad, Appl. Orgmet. Chem. 17 (2003) 509.
[15] F. Teixidor, C. Viñas, M.M. Abad, C. Whitaker, J. Rius, Organometallics 15 (1996) 3154.
[16] (a) C. Gimeno, P.G. Jones, A. Laguna, Inorg. Chem. 35 (1996) 1361;
(b) O. Crespo, M.C. Gimeno, P.G. Jones, A. Laguna, M.D. Villacampa, Angew. Chem., Int. Ed. Engl. 36 (1997) 993;
(c) M.J. Calhorda, O. Crespo, M.C. Gimeno, P.G. Jones, A. Laguna, J.M. López-de-Luzuriaga, J.L. Perez, M.A. Ramón, L.F. Veiros, Inorg. Chem. 39 (2000) 4280.
[17] D.P. Zhang, J.M. Dou, D.C. Li, D.Q. Wang, J. Coord. Chem., in press.
[18] O. Crespo, M.C. Gimeno, P.G. Jones, A. Laguna, J. Chem. Soc., Dalton Trans. (1996) 4583.
[19] (a) N. Kazuo, Infrared and Raman Spectra of Inorganic and Coordination Compounds (Translated by D.R. Huang, R.Q. Wang), Chemical Industry Press, Beijing, 1986, p. 175;
(b) J.E. Crook, N.N. Greenwood, J.D. Kennedy, J. Chem. Soc., Dalton. Trans. (1972) 171.
[20] V.P. Balema, M. Pink, J. Sieler, E. Hey-Hawkins, L. Hennig, Polyhedron 17 (1998) 2087.
[21] W. Oberhauser, C. Bachmann, T. Stampfl, R. Haid, P. Bruggeller, Polyhedron 16 (1997) 2867.
[22] D.P. Zhang, J.M. Dou, D.C. Li, D.Q. Wang, Acta. Crystallogr. Sect. E 62 (2006) 418.

Available online at www.sciencedirect.com
ScienceDirect
Polyhedron 26 (2007) 725–735
POLYHEDRON
www.elsevier.com/locate/poly

Three new dinuclear bis-μ-azido-bridged Cu(II) compounds with di-2-pyridylamine as a ligand: Syntheses, X-ray structure and magnetic measurements

Sujittra Youngme [a,*], Thidarat Chotkhun [a], Somying Leelasubcharoen [a], Narongsak Chaichit [b], Chaveng Pakawatchai [c], Gerard A. van Albada [d], Jan Reedijk [d]

[a] Department of Chemistry, Faculty of Science, Khon Kaen University, Khon Kaen 40002, Thailand
[b] Department of Physics, Faculty of Science and Technology, Thammasat University Rangsit, Pathumthani 12121, Thailand
[c] Department of Chemistry, Faculty of Science, Prince of Songkla University, Hatyai, Songkla 90112, Thailand
[d] Leiden Institute of Chemistry, Gorlaeus Laboratories, Leiden University, P.O. Box 9502, 2300 RA Leiden, The Netherlands

Received 3 August 2006; accepted 1 September 2006
Available online 1 October 2006

Abstract

Three new dinuclear copper(II) compounds: $[Cu_2(dpyam)_2(\mu_{1,1}\text{-}N_3)_2(O_2CH)_2]$ (**1**), $[Cu_2(dpyam)_2(\mu_{1,1}\text{-}N_3)_2(O_2CCH_3)_2]$ (**2**) and $[Cu_2(dpyam)_2(\mu_{1,1}\text{-}N_3)_2(O_2CCH_2CH_3)_2]$ (**3**) have been synthesized and characterized crystallographically and spectroscopically. Compounds **1**, **2** and **3** consist of a dinuclear unit in which both Cu(II) ions are connected through two end-on azido bridges providing a distorted square pyramidal geometry with a CuN_4O chromophore. The Cu···Cu separations are 3.195, 3.200 and 3.247 Å for compounds **1**, **2** and **3**, respectively. The magnetic properties have been measured in the range from 5 to 300 K and correlated with the molecular structures. All three compounds show a medium to weak ferromagnetic exchange interactions between the Cu(II) ions dominated by the bridging azido ligands, with a singlet-triplet splitting (J) of 63.3, 63.8 and 5.1 cm^{-1}, for compounds **1**, **2** and **3**, respectively. A large zero-field splitting of about 0.4 cm^{-1} is observed in the EPR for compounds **1** and **2**.
© 2006 Elsevier Ltd. All rights reserved.

Keywords: Copper(II); Crystal structure; Azido-bridged; EPR; Magnetism

1. Introduction

Recently, the synthesis of pseudohalide bridged compounds, N_3^-, NCS^-, NCO^-, continue being the great interest subject, and intensive investigations have taken place as a result of their diverse structures and applications in magnetic materials [1]. The use of a variety of different bridging ligand has afforded an interesting array of molecular systems with a new architecture. Therefore, it is essential to choose appropriate bridges to rationally design magnetic systems with desirable property [2]. Among them, the azide anion has received the major attention owing to its versatility as a ligand and the wide variety of magnetic behaviours [1–20]. The magnetic characters of the azido-bridged compounds are readily predicted in view of its binding pattern: the most common bridging modes of azide are the end-on ($\mu_{1,1}$-N_3, EO) [2–4,9,10] and the end-to-end ($\mu_{1,3}$-N_3, EE) fashions [2,4–8], which generally lead to ferromagnetic and antiferromagnetic interactions, respectively. However, the end-on bridging does result in antiferromagnetism; the critical angle for accidental orthogonality is ≈108.5°, when the bridging angle exceeds a critical value [11–14]. This correlation is valid only for basal–basal coordination, sometimes also applied to basal–apical coordination mode, which may lead to confusion [1d]. In the basal–apical type of compounds, usually the coupling is very small as the magnetic orbital describing the single electron is mainly of a $d_{x^2-y^2}$ type lying in the basal plane of the

* Corresponding author. Fax: +66 43 202 373.
E-mail address: sujittra@kku.ac.th (S. Youngme).

0277-5387/$ - see front matter © 2006 Elsevier Ltd. All rights reserved.
doi:10.1016/j.poly.2006.09.073

metal center and has only a small contribution on the axis perpendicular to the basal plane [15]. The magnetic behaviour for three compounds having doubly bridged azido ligands, in the basal–basal mode for compounds **1** and **2** and in the basal–apical mode for compound **3**, predicts a medium (compounds **1** and **2**) to a weak (compound **3**) ferromagnetic coupling [1]. Based on structural considerations, the end-on bridge is responsible for a ferromagnetic route.

In this study, the synthesis, X-ray crystal structures, spectroscopic and magnetic properties of three dinuclear copper(II) compounds, $[Cu_2(dpyam)_2(\mu_{1,1}\text{-}N_3)_2(O_2CH)_2]$ (**1**), $[Cu_2(dpyam)_2(\mu_{1,1}\text{-}N_3)_2(O_2CCH_3)_2]$ (**2**) and $[Cu_2(dpyam)_2(\mu_{1,1}\text{-}N_3)_2(O_2CCH_2CH_3)_2]$ (**3**) (dpyam = di-2-pyridylamine), all containing bridging azide anions, are reported.

2. Experimental

2.1. Materials and measurements

The di-2-dipyridylamine was purchased as commercial chemicals from Aldrich. All reagents are commercial grade materials and were used without further purification. Elemental analyses (C, H, N) were determined on a Perkin–Elmer PE 2400 CHNS/O Analyzer.

IR spectra were recorded on a Perkin–Elmer Spectrum One FT-IR spectrophotometer as KBr disc in the 4000–450 cm^{-1} spectral range. Solid-state (diffuse reflectance) electronic spectra were measured as polycrystalline samples on a Perkin–Elmer Lambda2S spectrophotometer. The X-band powder EPR spectra were obtained on polycrystalline samples at room temperature and 77 K with a JEOL RE2X electron spin resonance spectrometer. Magnetic susceptibility measurements (5–300 K) were carried out using a Quantum design MPMS-5S SQUID magnetometer (measurements carried out at 0.1 mT). Data were corrected for magnetization of the sample holder and for diamagnetic contributions, which were estimated from the Pascal constants.

Caution: Azido complexes of transition metal ions containing organic ligands are potentially explosive. Only a small amount of material should be prepared and handled with care.

2.2. Syntheses

2.2.1. $[Cu_2(dpyam)_2(\mu_{1,1}\text{-}N_3)_2(O_2CH)_2]$ (1)

The ligand dpyam (0.17 g, 1 mmol), dissolved in methanol/DMF (20/5 ml) and a solid of $Cu(O_2CH)_2 \cdot nH_2O$ (0.31 g, 2 mmol) were mixed together, followed by addition of an aqueous solution of NaN_3 (0.065 g, 1 mmol, in 2 ml) with continuous stirring. The green solution was slowly evaporated at room temperature until brownish crystals of **1** separated. Yield ca. 80%. *Anal*. Calc. for $C_{22}H_{20}Cu_2N_{12}O_4$: C, 41.06; H, 3.13; N, 26.12. Found: C, 40.90; H, 2.96; N, 26.32%.

2.2.2. $[Cu_2(dpyam)_2(\mu_{1,1}\text{-}N_3)_2(O_2CCH_3)_2]$ (2)

Compound **2** synthesized from $Cu(O_2CCH_3)_2 \cdot nH_2O$ (0.364 g, 2 mmol) and NaN_3 (0.650 g, 1 mmol) in a similar procedure as **1**. The green solution was slowly evaporated at room temperature until brownish-green crystals of **2** separated. Yield ca. 70%. *Anal*. Calc. for $C_{24}H_{24}Cu_2N_{12}O_4$: C, 42.92; H, 3.60; N, 25.02. Found: C, 42.60; H,3.36; N, 25.32%.

2.2.3. $[Cu_2(dpyam)_2(\mu_{1,1}\text{-}N_3)_2(O_2CCH_2CH_3)_2]$ (3)

Compound **3** synthesized from $Cu(OH)_2$ (0.195 g, 2 mmol), $NaO_2CCH_2CH_3$ (0.192 g, 2 mmol) and NaN_3 (0.650 g, 1 mmol) in a similar procedure as **1**. The resulting green solution was allowed to stand at room temperature. Green crystals appeared. Yield ca. 70%. *Anal*. Calc. for $C_{26}H_{28}Cu_2N_{12}O_4$: C, 44.63; H, 4.03; N, 24.02. Found: C, 44.89; H, 3.90; N, 24.00%.

2.3. Crystallography

The X-ray single-crystal data for the three compounds were collected at 273 K for compounds **1**, **2** and at 293 K for **3**, respectively, on a 1 K Bruker SMART CCD area-detector diffractometer using graphite monochromated Mo Kα radiation ($\lambda = 0.71073$ Å) at a detector distance of 4.5 cm and swing angle of $-30°$. A hemisphere of the reciprocal space was covered by combination of three sets of exposures; each set had a different ϕ angle (0°, 88°, 180°) and each exposure of 40 s covered 0.3° in ω. Data reduction and cell refinements were performed using the program SAINT [21]. An empirical absorption correction by using the SADABS [22] program was applied, which resulted in transmission coefficients ranging from 0.741 to 1.000 for compound **1**, 0.608 to 1.000 for compound **2** and 0.818 to 1.000 for compound **3**. The structures were solved by direct methods and refined by full matrix least-squares method on $(F_{obs})^2$ with anisotropic thermal parameters for all non-hydrogen atoms using the SHELXTL-PC V 6.12 software package [23]. All hydrogen atoms were located in a difference Fourier map and refined isotropically, except H atoms of acetate (compound **2**) and propionate anions (compound **3**) which were fixed geometrically with the HFIX utility. The molecular graphics were created by using SHELXTL-PC [23] package. The crystal and refinement details for three compounds are listed in Table 1.

3. Results and discussion

3.1. Crystal structure of $[Cu_2(dpyam)_2(\mu_{1,1}\text{-}N_3)_2(O_2CH)_2]$ (1)

The structure of compound **1** consists of neutral dinuclear entities. Each of them results from the pairing of two mononuclear units related via an inversion centre. A view of the dinuclear species is given in Fig. 1. Relevant bond distances and angles are reported in Table 2. Each copper(II) ion has a markedly distorted square pyramidal

Table 1
Crystal and refinement data for compounds **1**, **2** and **3**

Compound	**1**	**2**	**3**
Molecular formula	$C_{22}H_{20}Cu_2N_{12}O_4$	$C_{24}H_{24}Cu_2N_{12}O_4$	$C_{26}H_{28}Cu_2N_{12}O_4$
Molecular weight	643.58	671.63	699.68
T (K)	273(2)	273(2)	293(2)
Crystal system	monoclinic	orthorhombic	monoclinic
Space group	$P2(1)/n$	$Pbca$	$P2(1)/c$
a (Å)	7.6120(1)	11.6453(4)	7.3022(4)
b (Å)	16.4007(1)	14.2258(5)	9.7478(6)
c (Å)	10.5104(1)	16.4774(6)	20.915(1)
β (°)	103.674(1)	90.00	90.874(1)
V (Å^3)	1274.95(2)	2729.7(2)	1488.5(2)
Z	2	4	2
D_c (g cm^3)	1.676	1.634	1.561
μ (mm^{-1})	1.724	1.614	1.484
$F(000)$	652	1368	716
Crystal size (mm)	$0.22 \times 0.27 \times 0.40$	$0.35 \times 0.50 \times 0.70$	$0.32 \times 0.23 \times 0.14$
Number of reflection collected	9275	18801	12733
Number of unique reflections [R_{int}]	3637 [0.0220]	4013 [0.0593]	3583 [0.0197]
Data/restraints/parameter	3637/0/221	4013/0/227	3580/0/255
Goodness-of-fit	1.108	1.072	1.073
Final R indices [$I > 2\sigma(I)$]	$R_1 = 0.033$, $wR_2 = 0.076$	$R_1 = 0.036$, $wR_2 = 0.098$	$R_1 = 0.028$, $wR_2 = 0.079$
R indices (all data)	$R_1 = 0.043$, $wR_2 = 0.080$	$R_1 = 0.051$, $wR_2 = 0.106$	$R_1 = 0.031$, $wR_2 = 0.082$
Largest difference in peak and hole (e Å^3)	0.42 and −0.41	0.66 and −0.88	0.32 and −0.38

$R = \sum \|F_o| - |F_c\| / \sum |F_o|$, $R_w = [\sum w\{|F_o| - |F_c|\}^2 / \sum w|F_o^2|^2]^{1/2}$.

geometry with a high τ value of 0.38. The structure index is defined as $\tau = (\beta - \alpha)/60$, where β and α are the largest coordination angles, $\tau = 0$ for square pyramidal (SP) and $\tau = 1$ for trigonal bipyramidal (TBP) geometry [24,25], of the CuN_4O chromophore, with two nitrogen atoms of the two bridging azide ligands (Cu–N distances 1.991(1), 2.143(1) Å), a nitrogen of the dpyam ligand (Cu–N distance 1.988(1) Å) and an oxygen atom of the formato ligand (Cu–O distance 2.014(1) Å) forming the basal plane. The axial site of each copper(II) atom is occupied by another nitrogen atom of the dpyam ligand (Cu–N distance 2.129(1) Å) which is slightly shorter than the equatorial bond, Cu(1)–N(4), indicating an unusual square pyramidal geometry found in compound **1**. The copper(II) atoms of the compound are linked through a double azido bridges in an end-on bridging mode from the equatorial position of one copper chromophore to the equatorial position of the other one. The tetrahedral twist of the square base

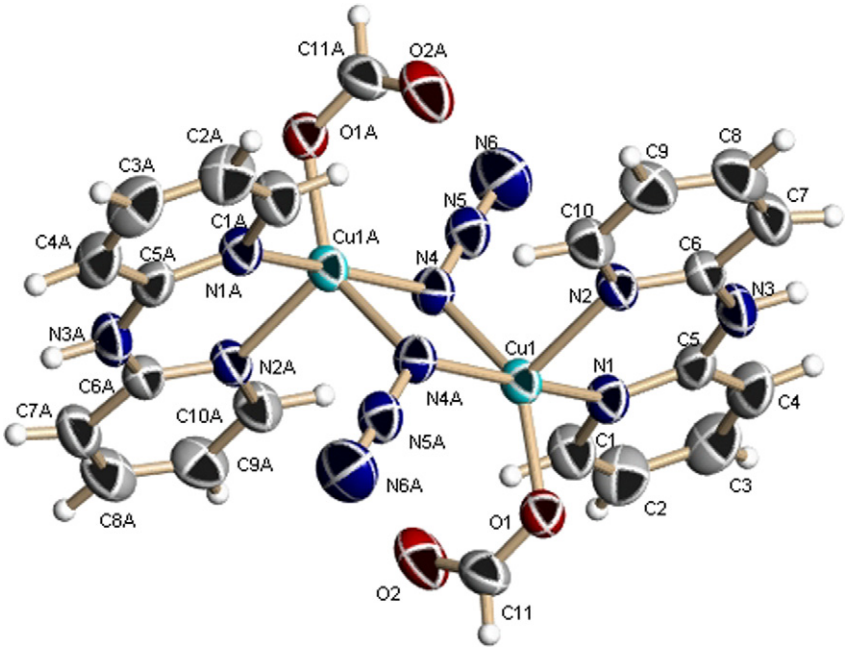


Fig. 1. ORTEP 50% probability plot of $[Cu_2(dpyam)_2(\mu_{1,1}\text{-}N_3)_2(O_2CH)_2]$ (**1**).

Table 2
Selected bond lengths (Å) and angles (°) of $[Cu_2(dpyam)_2(\mu_{1,1}\text{-}N_3)_2(O_2CH)_2]$ (**1**)

Cu(1)–N(1)	1.988(2)	Cu(1)–O(1)	2.014(2)
Cu(1)–N(2)	2.129(2)	Cu(1)–N(4)A	1.991(2)
Cu(1)–N(4)	2.143(2)	Cu(1)–Cu(1)A	3.193(3)
Cu(1)–O(2)	2.945(1)	N(5)–N(6)	1.139(3)
N(4)–N(5)	1.209(2)		
N(1)–Cu(1)–N(4)A	168.9(1)	N(1)–Cu(1)–N(4)	91.1(1)
N(4)A–Cu(1)–O(1)	93.5(1)	N(1)A–Cu(1)–N(4)	78.9(1)
N(4)A–Cu(1)–N(2)	96.6(1)	N(2)–Cu(1)–N(4)	102.9(1)
N(1)–Cu(1)–O(1)	92.1(1)	N(1)–Cu(1)–N(2)	90.3(1)
O(1)–Cu(1)–N(4)	146.1(1)	Cu(1)–N(4)– Cu(1)A	101.1(1)
O(1)–Cu(1)–N(2)	110.8(1)	O(2)–Cu(1)–N(2)	159.4(1)
N(6)–N(5)–N(4)	178.7(2)		

Hydrogen bonds	D–H	H···A	D···A	D–H···A
N(3)–H(5)···O(2) [1/2 − *x*, 1/2 + *y*, 1/2 − *z*]	0.91	1.92	2.829(7)	175

defined by a dihedral angle between the CuN_2 and CuNO planes is at a quite high value of 34.0° and consequently, the copper atom is displaced 0.36 Å from its individual plane. The Cu···Cu separation is 3.195 Å, while the Cu–N_{azido}–Cu bridging angle is 101.1(1)°, which is an usual angle of azide bridges in most metal compounds [26–28]. The dpyam ligand is slightly folded, as the value of the dihedral angle between the planar pyridine rings is 4.9°. An oxygen atom of the formato ligand is at a distance of 2.945(1) Å from the copper(II) atom, which is slightly too long to be considered as a semi-coordination bond.

The crystal lattice is stabilized by hydrogen bonding between the amine N and an oxygen atom of neighboring formato group with a N···O contact of 2.829(7) Å leading to the formation of the 2D network. Details of the hydrogen bonding are listed in Table 2.

3.2. Crystal structure $[Cu_2(dpyam)_2(\mu_{1,1}\text{-}N_3)_2(O_2CCH_3)_2]$ (**2**)

The structure of **2** (Fig. 2) consists of a dinuclear unit $[Cu_2(dpyam)_2(\mu_{1,1}\text{-}N_3)_2(O_2CCH_3)_2]$ in which the copper(II)

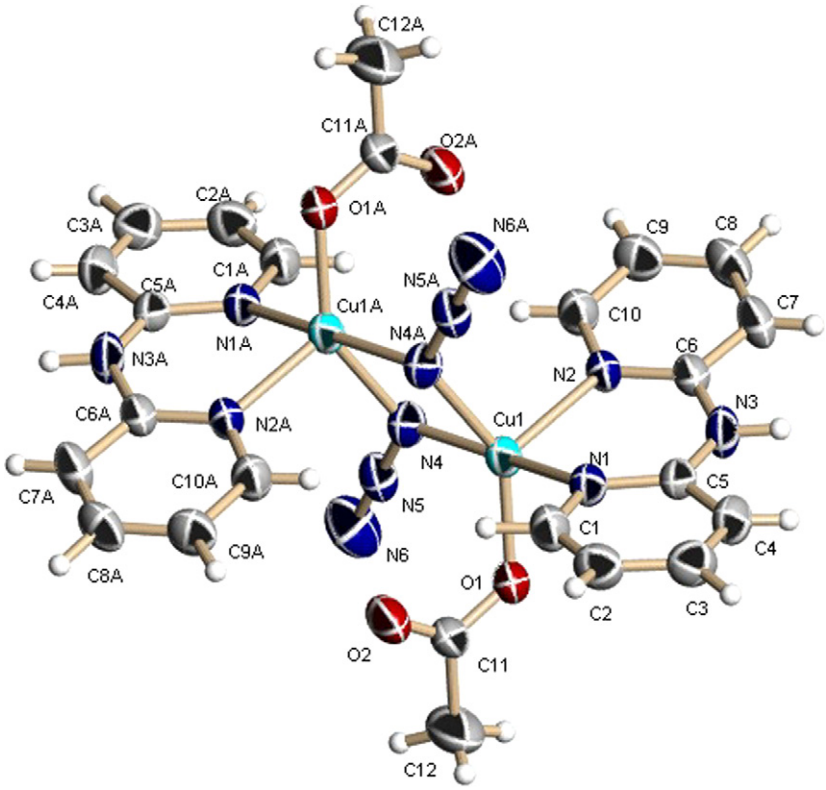


Fig. 2. ORTEP 50% probability plot of $[Cu_2(dpyam)_2(\mu_{1,1}\text{-}N_3)_2(O_2CCH_3)_2]$ (**2**).

Table 3
Selected bond lengths (Å) and angles (°) of $[Cu_2(dpyam)_2(\mu_{1,1}\text{-}N_3)_2(O_2CCH_3)_2]$ (**2**)

Cu(1)–N(1)	1.987(2)	Cu(1)–O(1)	1.967(2)
Cu(1)–N(2)	2.120(2)	Cu(1)–N(4)A	2.143(2)
Cu(1)–N(4)	1.997(2)	Cu(1)–Cu(1)A	3.200(1)
Cu(1)–O(2)	2.997(2)	N(5)–N(6)	1.141(3)
N(4)–N(5)	1.206(2)		
N(1)–Cu(1)–N(4)A	94.1(1)	N(1)–Cu(1)–N(4)	172.2(1)
N(4)A–Cu(1)–O(1)	143.3(1)	N(4)–Cu(1)–N(4)A	78.8(1)
N(4)A–Cu(1)–N(2)	103.3(1)	N(2)–Cu(1)–N(4)	95.7(1)
N(1)–Cu(1)–O(1)	90.8(1)	N(1)–Cu(1)–N(2)	89.2(1)
O(1)–Cu(1)–N(4)	93.0(1)	Cu(1)–N(4)–Cu(1)A	101.2(1)
O(1)–Cu(1)–N(2)	113.2(1)	N(5)–N(4)–Cu(1)A	125.7(1)
N(6)–N(5)–N(4)	179.0(2)	N(5)–N(4)–Cu(1)	122.4(2)

Hydrogen bonds	D–H	H···A	D···A	D–H···A
N(3)–H(5)···O(2) [1/2 − *x*, 1/2 + *y*, 1/2 − *z*]	0.86	2.01	2.864(8)	173

atoms are bridged by two azido ions in an end-on fashion. Each of them results from the pairing of two mononuclear units related via an inversion centre. Relevant bond distances and angles are reported in Table 3.

The five-coordinate CuN_4O chromophore around the copper(II) ion consists of two nitrogen atoms of two bridging azide ligands (Cu–N distances 1.997(2), 2.143(2) Å), two nitrogen atoms of a dpyam ligand (Cu–N distances 1.987(2), 2.120(2) Å) and an oxygen atom of an acetato ligand (Cu–O distance 1.967(2) Å). The largest basal angles angle are 172.1(1)° and 143.3(1)°, the distortion parameter τ in this case is 0.48, so the geometry can be described as an extremely distorted square pyramidal geometry with the axial site Cu(1)–N(2), both copper(II) ions of the compound are linked through a double azido bridges in an end-on bridging mode from the equatorial position of one copper chromophore to the equatorial position of the other one. The tetrahedral twist of the square base defined by a dihedral angle between the CuN_2 and CuNO planes is at a high value of 36.0° and consequently, the copper atom is displaced 0.36 Å from its individual plane. The Cu···Cu separation is 3.200(1) Å, while the Cu–N_{azido}–Cu bridging angle is 101.2(1)°. An oxygen atom of the acetato ligand is at a distance of 2.997(2) Å from the copper(II) atom, which is also too long to be considered as a semi-coordination bond. The crystal lattice is stabilized by hydrogen bonding between the amine N and an oxygen atom of neighboring formato group with a N···O contact of 2.864(9) Å leading to the formation of the 2D network. Details of the hydrogen bonding are listed in Table 3.

3.3. Crystal structure of $[Cu_2(dpyam)_2(\mu_{1,1}\text{-}N_3)_2(O_2CCH_2CH_3)_2]$ (3)

Compound **3** is made up of one-half $[Cu(dpyam)(\mu_{1,1}\text{-}N_3)(O_2CCH_2CH_3)]^+$ moiety, which the other half being symmetry related via a centre of symmetry. This unit depicted in Fig. 3. Selected bond distances and angles are reported in Table 4. Each copper(II) ion is five coordinated in the form of distorted square pyramidal geometry ($\tau = 0.30$) of the CuN_4O chromophore (see Fig. 4c). The square base comprises two nitrogen atoms of the dpyam ligand (Cu–N distances 2.011(1), 1.999(1) Å), an oxygen atom of the propionato ligand (Cu–O distance 1.960(1) Å) and a nitrogen atom of the azido ligand (Cu–N distance 2.006(1) Å), with a tetrahedral twist between the CuN_2 and CuNO planes of 21.0°. The coordination of the apical position is formed by a nitrogen atom from another azido anion (Cu–N distance 2.348(1) Å). Both copper(II) atoms of the compound are linked through a double azido bridge in an end-on bridging mode from the equatorial position of one copper chromophore to the axial position of the other one. Both square bases are parallel in a partial face-to-face manner. The copper atom is displaced 0.16 Å from the square plane. The Cu···Cu separation is 3.247 Å, while the Cu–N_{azido}–Cu bridging angle is 96.2(1)°. The dpyam ligand is non-planar, a dihedral angle of 17.3° occurs between the individual pyridine rings and the dpyam bite angle is 89.2(1)°. An oxygen atom of the propionato ligand is at a distance of 2.848(1) Å from the copper(II) atom, which is too long to be considered as a semi-coordination bond. The hydrogen bonding involving the amine N and an oxygen atom of acetato group with a N···O contact of 2.796(7) Å. leads to the formation of the 2D network. Details of the hydrogen bonding are listed in Table 4.

3.4. Spectral characterization

3.4.1. Electronic and IR spectra

The IR spectra show an intense absorption peak at 2062, 2060 and 2047 cm^{-1} for compounds **1**, **2** and **3**, respectively, which can be assigned to the $\nu_{as}(N_3)$ stretching vibration of the azide ligand in the end-on coordination mode. The strong bands at 1581, 1340 cm^{-1} for **1**, 1567 and 1402 cm^{-1} for **2** and 1555, 1426 cm^{-1} for **3** are assigned to the $\nu_{as}(COO^-)$ and $\nu_s(COO^-)$ modes of the carboxylate group within a dinuclear species.

The electronic diffuse reflectance spectrum of **3** shows an asymmetric broad band at 14 890 cm^{-1} and low-energy

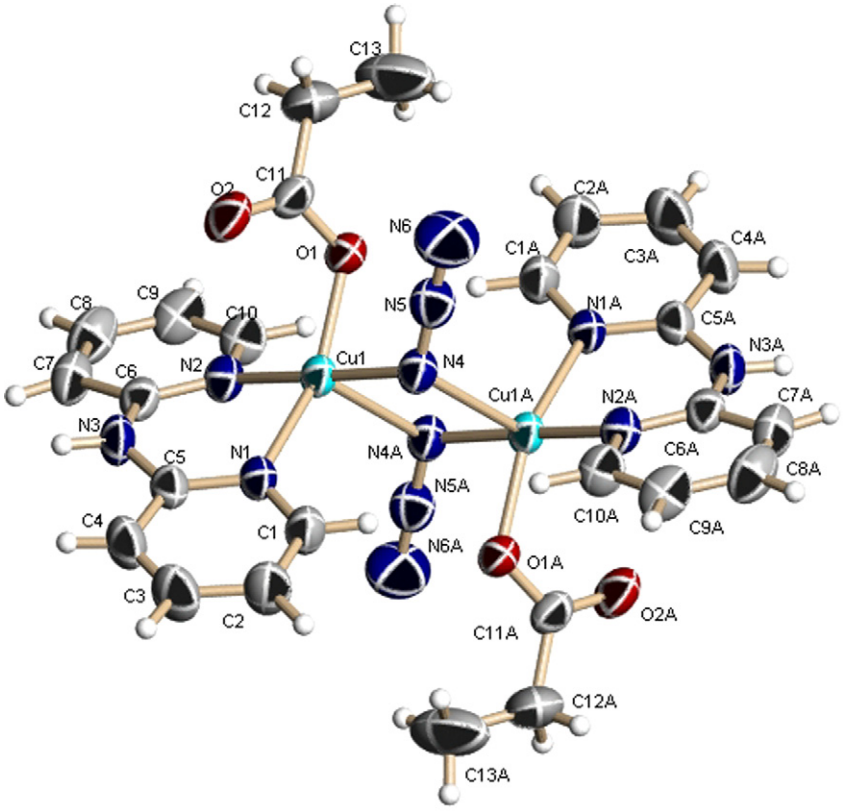


Fig. 3. ORTEP 50% probability plot of $[Cu_2(dpyam)_2(\mu_{1,1}\text{-}N_3)_2(O_2CCH_2CH_3)_2]$ (**3**).

Table 4
Selected bond lengths (Å) and angles (°) of $[Cu_2(dpyam)_2(\mu_{1,1}\text{-}N_3)_2(O_2CCH_2CH_3)_2]$ (**3**)

Cu(1)–N(1)	2.011(1)	Cu(1)–O(1)	1.960(1)
Cu(1)–N(2)	1.999(1)	Cu(1)–N(4)A	2.348(1)
Cu(1)–N(4)	2.006(1)	Cu(1)–Cu(1)A	3.247(2)
Cu(1)–O(2)	2.848(1)	N(5)–N(6)	1.144(2)
N(4)–N(5)	1.201(2)		
N(1)–Cu(1)–N(4)A	106.6(1)	N(1)–Cu(1)–N(4)	93.5(1)
N(4)A–Cu(1)–O(1)	94.4(1)	N(2)–Cu(1)–N(4)	177.1(1)
N(4)A–Cu(1)–N(2)	94.2(1)	N(1)–Cu(1)–N(2)	89.2(1)
N(1)–Cu(1)–O(1)	159.0(1)	Cu(1)–N(4)– Cu(1)A	96.2(1)
O(1)–Cu(1)–N(4)	88.8(1)	O(1)–Cu(1)–N(2)	89.2(1)
N(5)–N(4)–Cu(1)	119.7(1)	N(5)–N(4)A–Cu(1)	120.0(1)
O(2)–Cu(1)–N(4)A	144.7(1)	N(6)–N(5)–N(4)	177.9(2)

Hydrogen bonds	D–H	H···A	D···A	D–H···A
N(3)–H(5)···O(2) [1/2 − x, 1/2 + y, 1/2 − z]	0.86	1.93	2.796(7)	177

shoulder at 11 580 cm^{-1}. This feature is consistent with the distorted square pyramidal geometry and the d_{z^2}, d_{xz}, $d_{yz} \rightarrow d_{x^2-y^2}$ and $d_{xy} \rightarrow d_{x^2-y^2}$ transitions, respectively. Incase of compounds **1** and **2**, the spectrum shows two bands with nearly equal intensity at 12 980 and 9660 cm^{-1} (for compound **1**) and 12 580 and 9690 cm^{-1} (for compound **2**). The unusual apparent at low frequencies in **1** and **2** arises due to large tetrahedral twist of the square base and a shorter axial bond distance as compared to those of **3**. However, both bands of **1** and **2** are assigned to be the $d_{xy}, d_{yz}, d_{xz} \rightarrow d_{x^2-y^2}$ and $d_{z^2} \rightarrow d_{x^2-y^2}$ transitions [29].

3.4.2. EPR and magnetic properties

The EPR spectra of compounds **1** and **2** were recorded as a polycrystalline powder at RT and 77 K from 0 to 800 mT at X-band frequency ($h\nu = 0.325$ cm^{-1}).

The observed EPR spectrum of compound **1** and **2** reveals typical triplet spectra with a zero-field splitting parameter $D < h\nu$. The spectra are almost identical for both

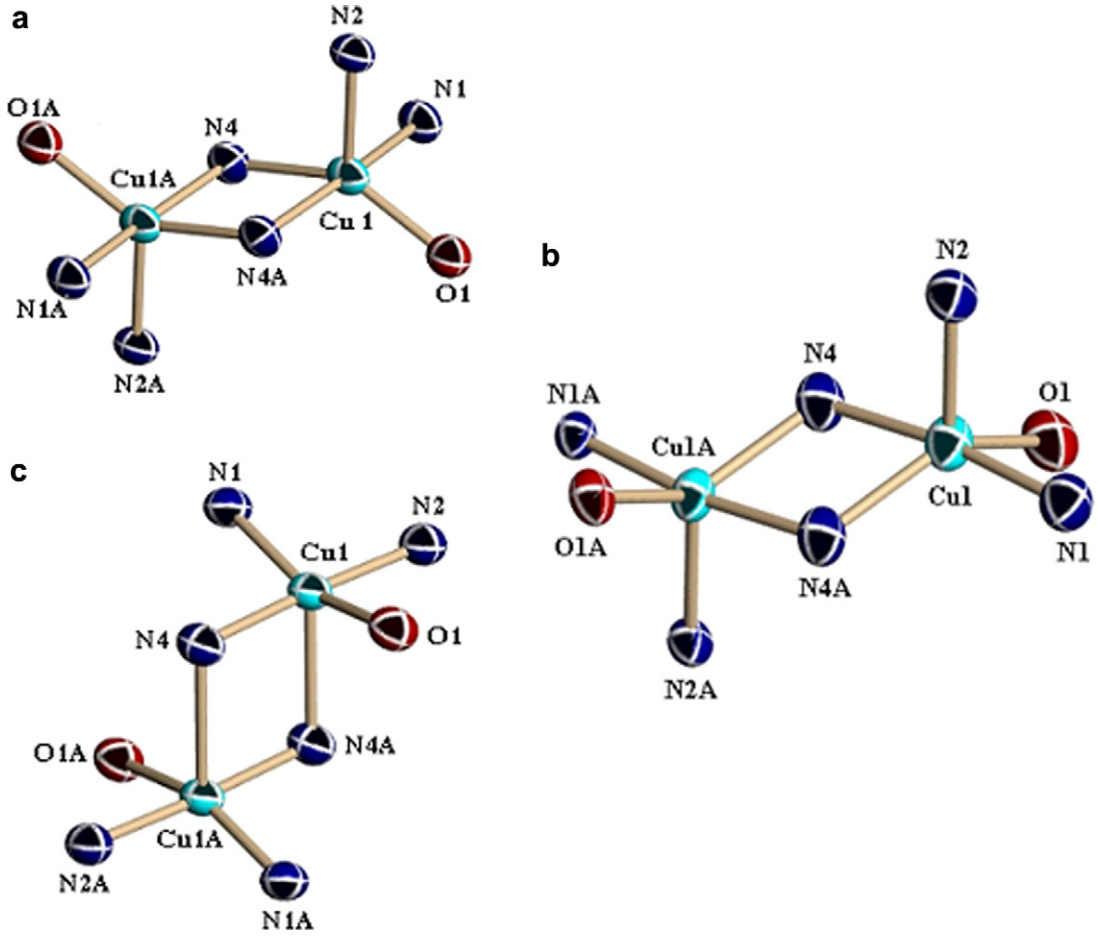


Fig. 4. The chromophore of (a) $[Cu_2(dpyam)_2(\mu_{1,1}\text{-}N_3)_2(O_2CH)_2]$ (**1**), (b) $[Cu_2(dpyam)_2(\mu_{1,1}\text{-}N_3)_2(O_2CCH_3)_2]$ (**2**) and (c) $[Cu_2(dpyam)_2(\mu_{1,1}\text{-}N_3)_2\text{-}(O_2CCH_2CH_3)_2]$ (**3**).

compounds and hardly no change is observed at RT and 77 K. Two representative EPR spectra are given as Fig. 5 (compound **1** at RT) and Fig. 6 (compound **3** at RT). Others are given as supplementary material. Compound **1** shows very broad absorptions (at RT) at 110, 250 and 460 mT (110, 275 and 490 mT for compound **2**), which are too broad for assignment and/or simulation. A rough estimate for the zero-field splitting is 0.4 cm^{-1}. The sharp weak absorptions at around 320 mT are from monomeric impurity.

The EPR spectrum of compound **3** was recorded at RT and 77 K from 220 to 420 mT, and both show an axial $S = 1/2$ spectrum with a $g_\perp$ of 2.09 and unresolved $g_\parallel$ of 2.26. These values are in agreement with a $d_{x^2-y^2}$ ground state [29].

At RT a very weak half-field signal is observed at 160 mT, typical for dinuclear species. However, at 77 K this signal is not observed. The observed EPR spectra are in agreement with the magnetic behaviour of the three compounds (vide infra).

The magnetic susceptibility of all three compounds has been measured from 5 to 300 K. The magnetic properties of the compounds are depicted in Figs. 7–9, for compounds **1**–**3**, respectively, in the form of μ_{eff} versus T plots for one copper(II) ion. Compounds **1** and **2** show a very similar magnetic behaviour. At 300 K the μ_{eff} is 1.89 μ_B per copper ion for compound **1** (1.84 μ_B, for **2**), which is somewhat

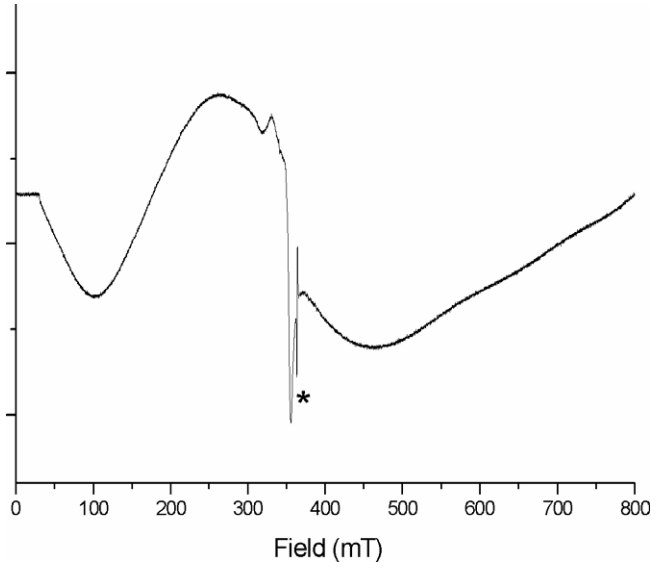


Fig. 5. EPR spectrum of compound **1** at RT (the starred peak is the internal reference, DPPH).

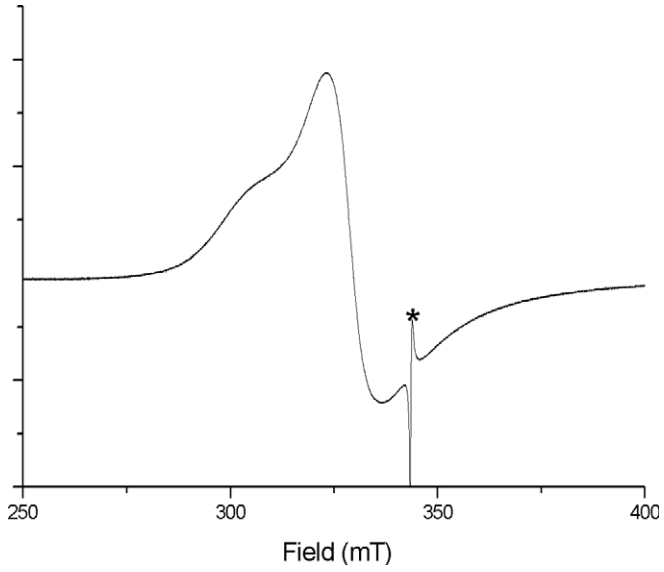


Fig. 6. EPR spectrum of compound **3** at RT (the starred peak is the internal reference, DPPH).

above the spin-only value for a single uncoupled spin $S = 1/2$ copper(II) centre. Upon cooling it raises gradually to reach 2.02 and 2.04 μ_B, at around 25 K, for compounds **1** and **2**, respectively. This behaviour is typical for medium to strong ferromagnetically coupled copper(II) dinuclear compound. Below that temperature, μ_{eff} then diminishes till a value around 1.92 μ_B for compound **1** (2.00 μ_B for **2**) at 5 K, which may originate from intermolecular antiferromagnetic interactions, or from the paramagnetic impurities present in the samples (vide infra).

The magnetic properties of compound **3** differ from that of compounds **1** and **2**. At 300 K the μ_{eff} is 1.74 μ_B per copper ion for compound **3**, which is about the spin-only value calculated for an uncoupled spin $S = 1/2$ copper(II) centre. Upon cooling, this value stays almost constant till about 50 K, where it increases gradually to reach 1.86 μ_B, at

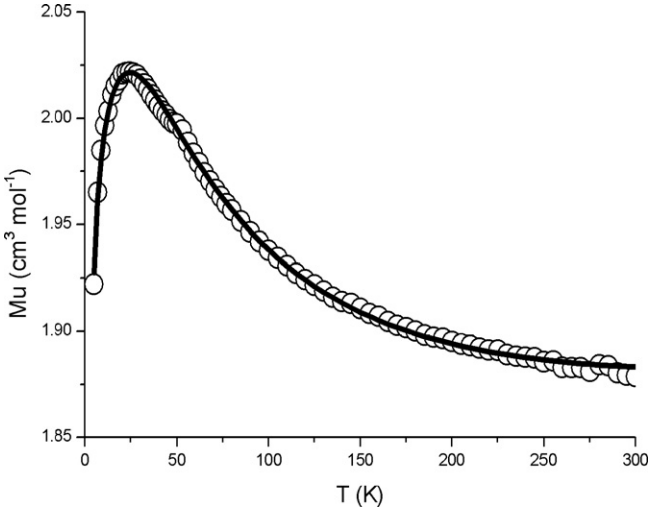


Fig. 7. A plot of the temperature dependence of μ_{eff} vs. T per Cu(II) ion for compound **1**. The solid line represents the calculated curve (see text).

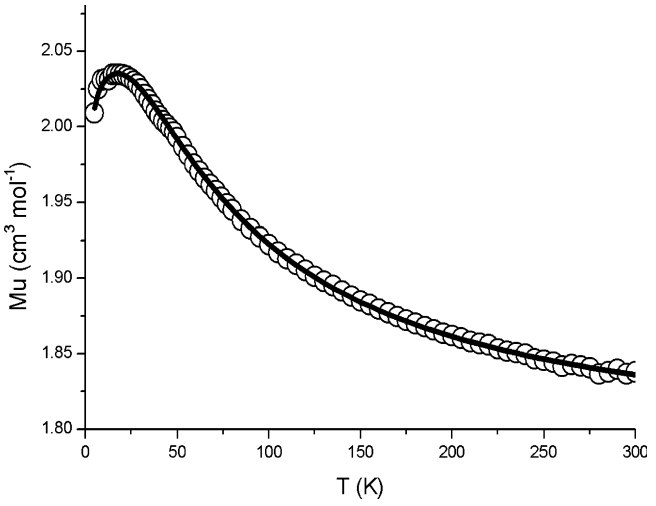


Fig. 8. A plot of the temperature dependence of μ_{eff} vs. T per Cu(II) ion for compound **2**. The solid line represents the calculated curve (see text).

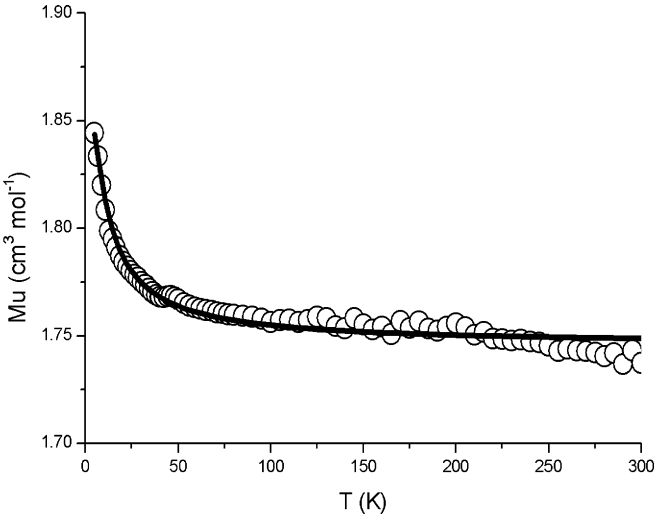


Fig. 9. A plot of the temperature dependence of μ_{eff} vs. T per Cu(II) ion for compound **3**. The solid line represents the calculated curve (see text).

5 K (see Fig. 8). This magnetic behaviour is typical for very weak ferromagnetically coupled copper(II) ions in a dinuclear compound.

The theoretical expression for the magnetic susceptibility for two interacting $S = 1/2$ centers, based on the general Hamiltonian [30] is: $H_{ex} = -JS_1S_2$, in which the exchange parameter J, is negative for antiferromagnetic and positive for ferromagnetic interaction. The magnetic data were fitted to the equation given in the literature for dinuclear copper compounds ([30], p. 132):

$$\chi_m = (2Ng^2\beta^2)[kT - (2zJ'/(3 + \exp(-J/kT)))]^{-1} \times [3 + \exp(-J/kT)]^{-1}(1 - p) + \chi_p p + \mathrm{TIP},$$

in which N, g, β, k and T have their usual meanings.

The parameter p denotes the fraction of paramagnetic impurity in the sample and zJ' refers to the interaction between neighbouring dinuclear identities. A temperature

Table 5
Selected magneto-structural data for double end-on azido-bridged dinuclear Cu(II) compounds

Compound[a]	Chromophore mode[b]	Configuration	Geometry[c]	τ	Cu–N_a (Å)[d]	Cu–N_b (Å)[e]	θ (°)[f]	Cu–Cu (Å)	J (cm^{-1})	Reference
$[Cu_2(dpyam)_2(\mu_{1,1}\text{-}N_3)_2(O_2CH)_2]$ (**1**)	CuN_3ON'	eq–eq	Spy.	0.38	1.991, 2.143		101.1	3.19	+63.3	this work
$[Cu_2(dpyam)_2(\mu_{1,1}\text{-}N_3)_2(O_2CCH_3)_2]$ (**2**)	CuN_4O	eq–eq	Spy.	0.48	1.997, 2.142		101.2	3.20	+63.8	this work
$[Cu_2(N_3)_2(4\text{-Etpy})_4(NO_3)_2]$ (**13**)	CuN_2OO'	eq–eq	Oct.		1.996, 2.004		98.2	3.02	+230.1	[15]
$[Cu_2(N_3)_2(3\text{-ampy})_4\ (NO_3)_2]\cdot C_2H_5OH$ (**14**)	CuN_2O_2	eq–eq	Oct.		2.000, 2.006		97.5	3.01	+223.2	[15]
$[Cu_2(dpyam)_2(\mu_{1,1}\text{-}N_3)_2(O_2CCH_2CH_3)_2]$ (**3**)	CuN_3ON'	ax–eq	Spy.	0.30	2.003	2.348	96.2	3.25	+5.1	this work
$[Cu(terpy)(N_3)(H_2O)]_2(PF_6)_2$ (**4**)	CuN_4ON'	ax–eq	Oct.		1.927	2.851	95.7	3.60	−2.9	[9]
$[Cu(bipy)(N_3)_2]_n$ (**5**)	CuN_4N'	ax–eq	Spy.	0.06	1.961	2.684	96.8	3.51	−2.7	[34]
$[Cu(dpp)(N_3)_2]_n$ (**6**)	CuN_4N'	ax–eq	Spy.	0.12	1.953	2.744	96.9	3.57	−2.3	[31]
$[Cu(aepi)(N_3)_2]_2$ (**7**)	CuN_4N'	ax–eq	Spy.	0.15	2.016	2.381	98.8	3.35	−3.1	[2]
$[Cu_2L_2(N_3)_2]$ (**8**)	CuN_3ON'	ax–eq	Spy.	0.18	2.019	2.551	86.9	3.17	+24	[32]
$[\{Cu(terpy)(N_3)\}_2](PF_6)_2$ (**9**)	CuN_4N'	ax–eq	Spy.		1.954	2.469	96.3	3.31	−0.5	[9]
$[Cu(L^1)(N_3)]_2$ (**10**)	CuN_3ON'	ax–eq	Spy.	0.02	2.039	2.440	90.5	3.19	−1.8	[33]
$[Cu(L^2)(N_3)]_2$ (**11**)	CuN_3ON'	ax–eq	Spy.	0.17	2.020	2.546	86.8	3.16	−3.1	[33]
$[Cu(L^3)(N_3)]_2$ (**12**)	CuN_3ON'	ax–eq	Spy.	0.26	2.060	2.475	93.6	3.32	+2.9	[33]

[a] Abbreviations: L = 7-amino-4-methyl-5-aza-3-hepten-2-onato (1-); L^1 = *N*-(3-aminopropyl)salicylaldimine; L^2 = 7-amino-4-methyl-5-azahept-3-en-2-one; L^3 = 8-amino-4-methyl-5-azaoct-3-en-2-one; me_2tn = 2,2-dimethylpropane-1,3-diamine; bipy = 2,2′-bipyridine; terpy = 2,2′:6′2″-terpyridine; dien = diethylenetriamine; aepi = 1-(2-aminoethyl)piperidin; dpp = 2,3-bis(2-pyridyl)pyrazine; 4-Etpy = 4-ethylpyridine; 3-ampy = 3-aminopyridine; dpa = di-2-pyridylamine.

[b] eq = equatorial, ax = axial.

[c] Spy. = square pyramidal, TBP = trigonal bipyramidal, Oct. = octahedral.

[d] The basal Cu–$N_{(azido)}$ bond length.

[e] The apical Cu–$N_{(azido)}$ bond length.

[f] The angle at Cu–$N_{(azido)}$–M.

independent paramagnetism (TIP) was also considered and fixed at 60×10^{-6} per copper ion. The fit was accomplished by minimisation of $R = \sum(\chi_m \cdot T_{calc} - \chi_m \cdot T_{obs})^2/(\chi_m \cdot T_{obs})^2$ by least-squares procedure. The best fit was obtained for compound **1** with the following values: $J = 63.3\ cm^{-1}$, $g = 2.06$, $zJ' = -3.3\ cm^{-1}$, $p = 0.04$, with a final R of 2.0×10^{-4} (see solid line in Fig. 7). For compound **2** these values are $J = 63.8\ cm^{-1}$, $g = 2.05$, $zJ' = -0.8\ cm^{-1}$, $p = 0.01$, with a final R of 9.0×10^{-5} (see solid line in Fig. 8). For compound **3** these values are $J = 5.1\ cm^{-1}$, $g = 2.02$, $zJ' = -2.2\ cm^{-1}$, $p = 0.06$, with a final R of 1.5×10^{-3} (see solid line in Fig. 9). These values are in agreement with the structural results (see Section 4).

3.4.3. Comparison of structures and magnetic properties

The compounds together with a number of related dinuclear copper(II)-azido compounds are listed in Table 5 in which two copper(II) atoms are bridged through two bridging azide anions with the basal–basal coordination; $[Cu_2(N_3)_2(4\text{-Etpy})_4(NO_3)_2]$ (**13**) and $[Cu_2(N_3)_2(3\text{-mpy})_4(NO_3)_2] \cdot C_2H_5OH$ (**14**) [15], and basal–apical mode; $[Cu(terpy)(N_3)(H_2O)]_2(PF_6)_2$ (**4**) and $[\{Cu(terpy)(N_3)\}_2](PF_6)_2$ (**9**) [9], $[Cu(bipy)(N_3)_2]_n$ (**5**) ($s = 0.06$) [34], $[Cu(dpp)(N_3)_2]_n$ (**6**) ($s = 0.12$) [31], $[Cu(aepi)(N_3)_2]_2$ (**7**) ($s = 0.15$) [2], $[L_2(N_3)_2Cu_2]$ (**8**) ($s = 0.18$) [33], $[Cu(L^1)(N_3)]_2$ (**10**) ($s = 0.02$), $[Cu(L^2)(N_3)]_2$ (**11**) ($s = 0.17$) and $[Cu(L^3)(N_3)]_2$ (**12**) ($s = 0.26$) [33]. For compounds with the basal–basal coordination, **13** and **14** are strong ferromagnetic with the high J values of 230.1 and 223.2 cm^{-1}, corresponding to the small θ angles of 98.2° and 97.5°, respectively (<108.5°) [11–14]. The present compounds **1** and **2** which involve the larger θ angles, 101.1° and 101.2°, respectively (<108.5°) reasonably provide a weaker ferromagnetic coupling. In addition, the marked distortion in Cu(II) geometry of both compounds may also be responsible for the lower J values of **1** and **2**, lower than expected, leading to a medium strong ferromagnetic interaction. In the case of basal–apical bridging fashion as in other remaining compounds in Table 5 including the present compound **3**, θ is not the determining factor of magnetic nature [15]. Their magnetic properties are weak ferromagnetic, compounds **3**, **8** and **12**, or weak antiferromagnetic interaction, compounds **4**–**7** and **9**–**11**. In these compounds the bridges connect an equatorial site with a high spin density to an apical site which has a weak spin density explaining the weak interaction observed.

4. Conclusion

In this paper we have presented the synthesis and magnetic study of three new azido-bridged copper(II) compounds with dpyam. The coordination geometry around each copper(II) ion is distorted square pyramidal for all three compounds. The azide ions in the compounds bridge two copper centers through one nitrogen atom (end-on bridging mode). Both azido bridges in compounds **1** and **2** involve the basal–basal coordination while each bridging N atom in compound **3** occupies an equatorial position on Cu1 and an axial position on Cu1A. The strong magnetic interaction requires good σ orientation of magnetic orbitals and superexchange properties of bridging ligand. In the basal–basal type of compounds **1** and **2**, the magnetic orbital is $d_{x^2-y^2}$ for copper center directed toward the bridging azido ligand corresponding to a medium strong ferromagnetic interaction, but a reduction of the ferromagnetic contribution will be observed when the geometry becomes distorted. The overlap of the orbitals thus becomes weaker and also such interaction becomes weaker. For compound **3**, the coupling is very small as the magnetic orbital of a $d_{x^2-y^2}$ type lying in the basal plane of the copper center and has only a small contribution on the axis perpendicular to the basal plane. All three compounds display a dominant ferromagnetic behaviour, but the magnitude of the exchange interaction is much smaller in the case of **3**.

Acknowledgements

The authors are very grateful to The Thailand Research Fund (Grant Nos. RTA 4880008 and BRG 4980007) and the Higher Education Development Project: Postgraduate Education and Research Program in Chemistry, Thailand for financial support. The work described in the present paper has also been supported by the Leiden University Study group WFMO (Werkgroep Fundamenteel Materialen Onderzoek). Support of the NRSC Catalysis (Research School Combination of HRSMC and NIOK) is kindly acknowledged.

Appendix A. Supplementary material

CCDC 616469, 616470 and 616471 contain the supplementary crystallographic data for **1**, **2** and **3**. These data can be obtained free of charge via http://www.ccdc.cam.ac.uk/conts/retrieving.html, or from the Cambridge Crystallographic Data Centre, 12 Union Road, Cambridge CB2 1EZ, UK; fax: (+44) 1223-336-033; or e-mail: deposit @ccdc.cam.ac.uk. Supplementary data associated with this article can be found, in the online version, at doi:10.1016/j.poly.2006.09.073.

References

[1] (a) M. Julve, M. Verdaguer, G. De Munno, J.A. Real, G. Bruno, Inorg. Chem. 32 (1993) 795;
(b) R. Vicente, A. Escuer, E. Penalba, X. Solans, M. Font-Bardia, Inorg. Chim. Acta 255 (1997) 7;
(c) A. Escuer, R. Vicente, J. Ribas, M.S. El Fallah, X. Solans, Inorg. Chim. Acta 216 (1994) 5;
(d) L.K. Thompson, S.S. Tandon, Comments Inorg. Chem. 18 (1996) 125.
[2] Y.S. You, C.S. Hong, K.M. Kim, Polyhedron 24 (2005) 249.
[3] M.G. Barandika, R. Cortes, L. Lezama, M.K. Urtiaga, M.I. Arriortua, T. Rojo, J. Chem. Soc., Dalton Trans. (1999) 2971.
[4] J. Comarmond, P. Plumere, J.-M. Lehn, Y. Agnus, R. Louis, R. Weiss, O. Kahn, I. Morgenstern-Badarau, J. Am. Chem. Soc. 104 (1982) 6330.

[5] A. Escuer, I. Castro, F. Mautner, M.S. El Fallah, R. Vicente, Inorg. Chem. 36 (1997) 4633.
[6] A. Escuer, R. Vicente, M.S. El Fallah, X. Solans, M. Font-Bardia, Inorg. Chim. Acta 278 (1998) 43.
[7] T.K. Maji, P.S. Mukherjee, G. Mostafa, T. Mallah, J. Cano-Boquera, N.R. Chaudhuri, Chem. Commun. (2001) 1012.
[8] P. Chaudhuri, K. Oder, K. Wieghardt, B. Nuber, J. Weiss, Inorg. Chem. 25 (1986) 2818.
[9] (a) R. Cortés, M.K. Urtiaga, L. Lezama, J.I.R. Larramendi, M.I. Arriortua, T. Rojo, J. Chem. Soc., Dalton (1993) 3685;
(b) M.I. Arriortua, M.K. Urtiaga, M. Insausti, J.L. Mesa, T. Rojo, Polyhedron 10 (1991) 2451.
[10] (a) M.A.S. Goher, F.A. Mautner, Polyhedron 15 (1996) 5;
(b) F.A. Mautner, M.A.S. Goher, Polyhedron 15 (1996) 1133;
(c) M.A.S. Goher, T.C. Mak, Inorg. Chim. Acta 85 (1984) 117;
(d) M.I. Arriortua, M.K. Urtiaga, M. Insausti, J.L. Mesa, T. Rojo, Polyhedron 10 (1991) 2451;
(e) F.A. Mautner, M.A.S. Goher, Polyhedron 12 (1993) 2823;
(f) M.A.S. Goher, N.A. Al-Salem, F.A. Mautner, Polyhedron 15 (1996) 4513.
[11] L.K. Thompson, S.S. Tandon, M.E. Manuel, Inorg. Chem. 34 (1995) 2356.
[12] E. Ruiz, J. Cano, S. Alvarez, P. Alemany, J. Am. Chem. Soc. 120 (1998) 11122.
[13] S.S. Tandon, L.K. Thompson, M.E. Manuel, J.N. Bridson, Inorg. Chem. 33 (1994) 5555.
[14] C. Adamo, V. Baron, A. Bencini, F. Totti, I. Ciofini, Inorg. Chem. 38 (1999) 1996.
[15] A. Escuer, M.A.S. Goher, F.A. Mautner, R. Vicente, Inorg. Chem. 39 (2000) 2107.
[16] A. Escuer, R. Vicente, M.S. El Fallah, X. Solans, M. Font-Bardia, Inorg. Chim. Acta 247 (1996) 85.
[17] A. Escuer, R. Vicente, J. Ribas, X. Solans, Inorg. Chem. 34 (1995) 1793.
[18] O. Kahn, S. Sicorav, J. Gouteron, S. Jeannin, Y. Jeannin, Inorg. Chem. 22 (1983) 2877.
[19] M.-F. Charlot, O. Kahn, M. Chaillet, C. Larrieu, J. Am. Chem. Soc. 108 (1986) 2574.
[20] (a) M.A.S. Goher, Rev. Inorg. Chem. 7 (1985) 299;
(b) O. Kahn, Comments Inorg. Chem. 3 (1984) 104;
(c) O. Kahn, M.L. Boillot, in: K.D. Karlin, J. Zubieta (Eds.), Biological and Inorganic Aspects of Copper Coordination Chemistry, vol. 2, Adenine, New York, 1985, p. 187.
[21] Siemens SAINT 1996, Version4 Software Reference Manual, Siemens Analytical X-Ray Systems, Inc., Madison, WI, USA.
[22] G.M. Sheldrick, SADABS, Program for Empirical Absorption correction of Area Dectector Data, University of Göttingen, Göttingen, Germany, 1996.
[23] Bruker XSHELL 1999, Version 6.12 Reference Manual, Bruker AXS, Inc., Madison, WI, USA.
[24] A.W. Addison, T.N. Rao, J. Reedijk, J. van Rijn, G.C. Verschoor, J. Chem. Soc., Dalton Trans. (1984) 1349.
[25] M. Brophy, G. Murphy, C. O'Sullivan, B. Hathaway, B. Murphy, Polyhedron 18 (1999) 611.
[26] A.M. Golub, H. Kohler, V.V. Skopenko (Eds.), Chemistry of Pseudohalides, Elsevier, Amsterdam, 1986.
[27] J. Ribas, A. Escuer, M. Monfort, R. Vicente, R. Cortes, L. Lezama, T. Rojo, Coord. Chem. Rev. 193 (1999) 1027.
[28] T.K. Karmakar, S.K. Chandra, J. Ribas, G. Mostafa, T.-H. Lu, B.K. Ghosh, Chem. Commun. (2002) 2364, and references therein.
[29] B.J. Hathaway, in: G. Wilkinson, R.D. Gill, J.A. McCleverty (Eds.), Comprehensive Coordination Chemistry, vol. 5, Pergamon Press, Oxford, 1987.
[30] O. Kahn, Molecular Magnetism, VCH Publishers, New York, 1993.
[31] H. Grove, M. Julve, F. Lloret, P.E. Kruger, K.W. Törnoos, J. Sletten, Inorg. Chim. Acta 325 (2001) 115.
[32] J.P. Costes, F. Dahan, J. Ruiz, J.P. Laurent, Inorg. Chim. Acta 239 (1995) 53.
[33] M.S. Ray, A. Ghosh, R. Bhattacharya, G. Mukhopadhyay, M.G.B. Drew, J. Ribas, J. Chem. Soc., Dalton Trans. (2004) 252.
[34] G. De Munno, M.G. Lombardi, M. Julve, F. Lloret, J. Faus, Inorg. Chim. Acta 282 (1998) 82.

Available online at www.sciencedirect.com
ScienceDirect
Polyhedron 26 (2007) 736–740
POLYHEDRON
www.elsevier.com/locate/poly

Synthesis, X-ray crystal structure and magnetic study of the 1D $\{[Cu(N,N\text{-diethyl-1,2-ethanediamine})(\mu_{1,5}\text{-dca})(dca)]\}_n$ complex

Dasarath Mal [a], Chandan Adhikary [a], Eva Rentschler [b], Yoshitaro Miyashita [c], Ken-Ichi Okamoto [c], Subratanath Koner [a,*]

[a] *Department of Chemistry, Jadavpur University, Kolkata 700 032, India*
[b] *Institut für Anorganische Chemie und Analytische Chemie, Johannes Gutenberg Universität, Staudingerweg, 55099 Mainz, Germany*
[c] *Department of Chemistry, University of Tsukuba, Tsukuba, Ibaraki 305-8571, Japan*

Received 9 June 2006; accepted 25 August 2006
Available online 23 September 2006

Abstract

A new complex, $\{[CuL(\mu_{1,5}\text{-dca})(dca)]\}_n$ (**1**), has been synthesized from the reaction of $Cu(NO_3)_2 \cdot 3H_2O$, *N*,*N*-diethyl-1,2-ethanediamine (L) and sodium dicyanamide (Nadca) in aqueous medium. Single crystal X-ray analysis reveals that the complex has a 1D infinite zigzag chain structure in which copper(II) ions are bridged by single dicyanamide ligands in an end-to-end fashion. The chains propagate parallel to the crystallographic *b*-axis and they are stacked one upon another along the *c*-axis. The coordination environment of the copper(II) centers are distorted square-pyramidal. Of the four coordination sites of the basal plane of the square-pyramid, two are occupied by the nitrogen atoms of the diamine and the remaining two sites are occupied by the terminal nitrogen atoms of the bridging dca groups. One terminal nitrogen atom of a monodentate dca group occupies the apical position of the coordinated polyhedra. [CuL(dca)] units are then connected to each other through a $\mu_{1,5}$-dca bridge to form 1D chains. The variable temperature magnetic susceptibility measurements evidenced weakly antiferromagnetic interactions ($J = -0.35\ cm^{-1}$) in $\{[CuL(\mu_{1,5}\text{-dca})(dca)]\}_n$ (**1**).
© 2006 Elsevier Ltd. All rights reserved.

Keywords: Dicyanamide; Copper diamine complex; 1D chain; Antiferromagnetic; X-ray crystal structure

1. Introduction

Pseuohalide bridged transition metal containing coordination polymers have long been studied for their interesting magnetic properties [1,2]. Recently, the larger pseudohalide ligand dicyanamide $[N(CN)_2]^-$ (dca) has attracted a lot of attention due to the discovery of long-range magnetic ordering in the 3D systems α-$M(dca)_2$, M = Cr, Mn, Fe, Co, Ni, Cu [3–5]. In this context, variability of the coordination modes of the dca ligand is particularly interesting, which allows the preparation of compounds with various kinds of architectures: mononuclear, polynuclear, as well as 1D, 2D and 3D networks [6]. The copper(II) ion often adopts a five-coordinated structure due to plasticity of its coordination geometry. Quite a few 1D compounds have been reported in which pseudohalogens connect adjacent metal ions along the chain due to the flexibility in the coordinating ability of the copper(II) ions [1,7,8]. 1D chain compounds, $\{[CuL1(\mu_{1,5}\text{-dca})(dca)]\}_n$ with L1 = 2,2′-bipyridine or 2,2′-bipyridylamine have been reported where copper(II) ions are bridged by a single $\mu_{1,5}$-dca group [9–11]. While a weak antiferromagnetic coupling between copper(II) centers has been observed for the complexes with 2,2′-bipyridine, no significant magnetic coupling was observed in $\{[Cu(2,2'\text{-bipyridylamine})(\mu_{1,5}\text{-dca})(dca)]\}_n$. Magnetic interactions through dca bridges are generally weak but their nature, *i.e.* ferromagnetic or antiferromagnetic cannot

* Corresponding author. Tel.: +91 33 2414 6666x2505; fax: +91 33 2414 6584.
E-mail address: snkoner@chemistry.jdvu.ac.in (S. Koner).

0277-5387/$ - see front matter © 2006 Elsevier Ltd. All rights reserved.
doi:10.1016/j.poly.2006.08.037

be easily predicted due to the need of successful theoretical models to analyze the magneto-structural correlations of these systems which thus deserve more studies. As a result, studies on dca bridged compounds have received intense attention in recent times [6,12–14]. Particularly, 1D chain compounds with a linear or zigzag geometry are of current interest in magnetochemistry and condensed matter physics due to the possibility of generating Haldane gap type systems and single chain magnets [15–17].

In the present study, we report the synthesis, X-ray crystal structure and magnetic study of a new 1D infinite chain compound $\{[CuL(\mu_{1,5}\text{-dca})(dca)]\}_n$ ([L = *N*,*N*,-diethyl-1,2-ethanediamine)] (**1**).

2. Experimental

2.1. General

Copper(II) nitrate trihydrate (Aldrich) and sodium dicyanamide (Aldrich) were used without further purification. All other chemicals used were of AR grade. The instruments used for measurements were reported earlier [18].

2.2. Synthesis of $\{[CuL(\mu_{1,5}\text{-dca})(dca)]\}_n$ (1)

$Cu(NO_3)_2 \cdot 3H_2O$ (0.25 mmol, 60 mg) and *N*,*N*-diethyl-1,2-ethanediamine (0.25 mmol, 27 mg) were dissolved together in 10 ml of water, which produced immediately a blue colored solution. To this, an aqueous solution of dca (0.5 mmol, 44 mg) was added with stirring. The resulting solution was then filtered and allowed to evaporate slowly at room temperature. Deep blue rhomboid crystals of complex (**1**) appeared in 10 days. The crystals were filtered, washed with water and dried in air (Yield 85%). *Anal*. Calc. for $C_{20}H_{32}Cu_2N_{16}$: C, 38.5; H, 5.1; N, 35.9. Found: C, 38.2; H, 4.7; N, 35.3%. IR spectra (KBr): ν_s(C≡N), 2140; ν_{as}(C≡N), 2220; ν_s(C≡N) + ν_{as}(C≡N), 2260; ν_{as}(C—N), 1380 cm^{-1}.

2.3. X-ray crystallography

2.3.1. Crystal data

$C_{10}H_{16}N_8Cu$, $M =$ 311.84, monoclinic, space group $P2_1/n$, $a = 7.3479(2)$, $b = 12.2358(4)$, $c = 32.6615(11)$ Å, $\beta = 91.1491(5)°$, $V = 2935.92(16)$ Å^3, $Z = 8$, $D_{calc} = 1.411$ g cm^{-3}, $F_{000} = 1288$, $\mu = 1.489$ mm^{-1}, green block crystal, dimensions = 0.35 × 0.35 × 0.10 mm, $T = 296.1$ K.

2.3.2. X-ray single crystal structure determination of (1)

A rectangular blue single crystal of complex (**1**) was selected for collecting X-ray data. All measurements were made on a Rigaku AFC7 diffractometer using graphite monochromated Mo Kα radiation ($\lambda = 0.71070$ Å) equipped with a Rigaku Mercury CCD detector. Of the 22 392 reflections that were collected, 12 388 ($R_{int} = 0.030$) were unique. The collected intensity data were corrected for Lorentz and polarization effects and an empirical absorption correction was also employed. Data were collected and processed using the CRYSTALCLEAR (Rigaku) program [19]. The structures were solved by direct methods (SIR 97) [20] and expanded using Fourier techniques. Some non-hydrogen atoms were refined anisotropically, while the rest were refined isotropically. Hydrogen atoms were refined using the riding model. The final cycle of full-matrix least-squares refinement was converged with unweighted and weighted agreement factors of 0.0568 and 0.2098, respectively. All calculations were carried out using CRYSTALSTRUCTURE [21], CRYSTALS [22] and PLATON [23]. The molecular graphics software used were ORTEP III [24] and MERCURY [25].

3. Results and discussion

3.1. X-ray structure of complex (1)

The ORTEP diagram of the asymmetric unit of (**1**) with the atom numbering scheme is shown in Fig. 1. Selected bond lengths and angles of complex (**1**) are listed in Table 1. The geometry around the copper centers could be described as distorted square-pyramidal with the basal planes defined by two nitrogen atoms of coordinated diamine and two terminal nitrogen atoms of the bridging dca ligand (N1, N2, N11, N14 for Cu1; N6, N7, N13, $N16^i$ for Cu2), while the coordinated nitrogen atoms of the monodentate dca ligand occupy the apical positions (N3 and N8) (symmetry operation i = $x, y - 1, z$). The crystal structure of complex (**1**) is characterized by [CuL($\mu_{1,5}$-dca)(dca)] units linked into 1D polymeric chains where one dca anion connects the copper(II)ion of the symmetry related unit in an end-to-end bridging mode. The chains propagate parallel to the crystallographic *b*-axis while they are stacked one upon another along the crystallographic *c*-axis (Fig. 2). The chains are connected with each other through strong H-bonds between amine hydrogen and terminal nitrogen atoms of the monodentate dca ligand (*vide infra*). The $\{N(CN)_2\}^-$ ligands present in complex (**1**) are bent around the amide nitrogen atom through an angle *ca.* 124°. The trigonality index τ (=$(\phi_1 - \phi_2)/60$, where ϕ_1, ϕ_2 are the two largest L–M–L angles of the coordination sphere) has been calculated for the penta-coordinated copper sites [26]. The τ values are found to be 0.46 and 0.35 for Cu1 and Cu2, respectively, confirming the square-pyramidal character of both the copper sites ($\tau = 0$ infers a perfect square-pyramid, and a $\tau = 1$, a perfect trigonal bipyramid). This is also apparent in the large variation of the basal N–Cu–N (*trans*) angles (176.1–148.4° for Cu1, 173.2–152.4° for Cu2). The Cu–N (basal) bond distances in complex (**1**), ranging between 1.971(4)–2.202(6) Å for Cu1 and 1.975(5)–2.121(4) Å for Cu2 (Table 1), are consistent with the corresponding values reported for analogous copper(II) systems [27,28]. The shortening of the Cu–N basal bond lengths in comparison to the Cu–N(apical) lengths [1.955(6)–2.185(5)] Å is a result of the Jahn–Teller

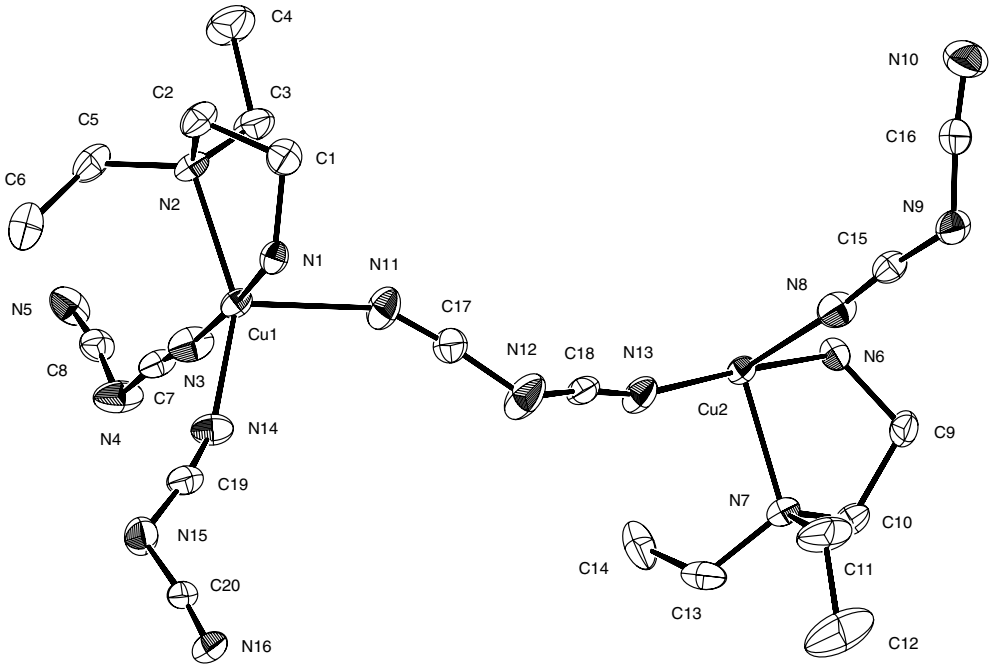


Fig. 1. ORTEP diagram of complex (**1**) showing the atom numbering scheme.

Table 1
Selected bond distances (Å) and bond angles (°) for complex (**1**)

Bond lengths (Å)			
Cu(1)–N(1)	1.971(4)	Cu(2)–N(13)	1.975(5)
Cu(1)–N(2)	2.092(4)	Cu(2)–N(16)^{i}	2.007(5)
Cu(1)–N(3)	1.955(6)	N(2)–C(3)	1.488(9)
Cu(1)–N(11)	2.202(6)	N(4)–C(7)	1.290(9)
Cu(1)–N(14)	2.015(5)	C(1)–C(2)	1.522(9)
Cu(2)–N(6)	1.978(4)	C(11)–C(12)	1.457(18)
Cu(2)–N(7)	2.121(4)	N(1)–C(1)	1.451(8)
Cu(2)–N(8)	2.185(5)	N(2)–C(2)	1.483(8)
Bond angles (°)			
N(1)–Cu(1)–N(2)	84.56(19)	N(6)–Cu(2)–N(13)	173.2(2)
N(1)–Cu(1)–N(3)	176.1(2)	N(16)^{i}–Cu(2)–N(6)	88.3(2)
N(1)–Cu(1)–N(11)	90.1(2)	N(7)–Cu(2)–N(8)	102.7(2)
N(1)–Cu(1)–N(14)	89.2(2)	N(7)–Cu(2)–N(13)	93.0(2)
N(2)–Cu(1)–N(3)	92.7(2)	N(7)–Cu(2)–N(16)^{i}	152.4(2)
N(2)–Cu(1)–N(11)	106.5(2)	N(8)–Cu(2)–N(13)	95.7(2)
N(2)–Cu(1)–N(14)	148.4(2)	N(8)–Cu(2)–N(16)^{i}	88.3(2)
N(3)–Cu(1)–N(11)	93.4(2)	N(13)–Cu(2)–N(16)^{i}	91.1(2)
N(3)–Cu(1)–N(14)	91.7(2)	N(6)–Cu(2)–N(7)	84.47(19)
N(11)–Cu(1)–N(14)	104.5(2)	Cu(1)–N(2)–C(3)	105.9(3)
Cu(1)–N(1)–C(1)	109.0(3)	N(6)–Cu(2)–N(8)	91.0(2)

Symmetry operation i = $x, -1 + y, z$.

effect for the d^9 configuration of the Cu^{II} ion in a square-pyramidal environment. The Cu···Cu distances in complex (**1**) were *ca.* 8.054–8.314 Å which are rather long to have effective magnetic coupling.

Fig. 2 shows H-bonded infinite 1D zigzag chains of $\{[CuL(\mu_{1,5}\text{-dca})(dca)]\}_n$ (**1**) that extend along the crystallographic *b*-axis. Intermolecular N–H···N hydrogen bonds, N1···N5^{ii} 2.982(16) Å, H1···N5^{ii} 2.050 Å, N1–H1···N5^{ii}

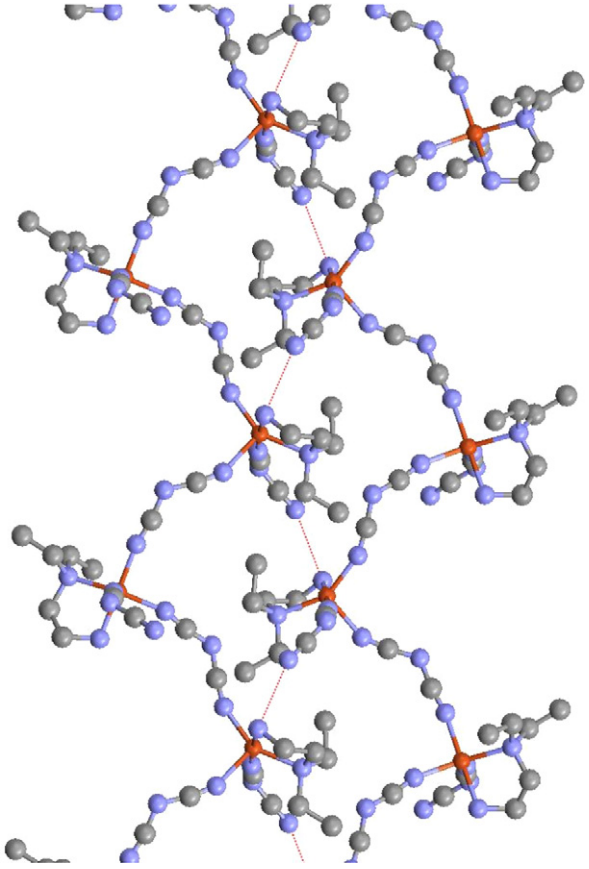


Fig. 2. Diagram showing stacking of 1D chains of complex (**1**). Red dotted lines denote the H-bonding as discussed in the text. (For interpretation of the references to color in this figure legend, the reader is referred to the web version of this article.)

166.24° interlink the chains via the amine hydrogen and terminal nitrogen atoms of the monodentate dca ligands (symmetry operation ii = $1/2 - x, 1/2 + y, 1/2 - z$).

3.2. Magnetic study

The temperature dependence of the molar magnetic susceptibility, χ_M, for complex (**1**) in the 2–290 K temperature range was measured with a superconducting quantum interference device (SQUID) magnetometer, under magnetic fields of 1 T and it is shown in Fig. 3. The $\chi_M T$ value (per Cu^{2+} ion), 0.44 $cm^3\ mol^{-1}$ K, at 290 K for complex (**1**) is slightly higher than the expected value for an isolated magnetically uncoupled copper(II) ion ($\chi_M T = 0.37$ $cm^3\ mol^{-1}$ K for $g = 2.0$). Upon cooling the $\chi_M T$ value of complex (**1**) remains almost unchanged until *ca.* 40 K, and then decreases rapidly to reach 0.38 $cm^3\ mol^{-1}$ K at around 2 K, which clearly indicates that the magnetic interaction between the copper(II) ions is antiferromagnetic.

In order to explain the magnetic properties of complex (**1**), a simple case of an isotropic infinite chain model that is provided by an array of equally spaced copper(II) ions bridged through $\mu_{1,5}$-dca ligands with $S = 1/2$ local spins has been considered. The spin Hamiltonian of such a system can be written as $H = -J \sum \hat{S}_{Ai} \cdot \hat{S}_{Ai+1}$. For an infinite 1D chain system no analytical method is available to determine the energies of low-lying states and magnetic susceptibility. However, a numerical expression that may be used to fit the magnetic susceptibility data is given by Estes et al. [29]:

$$\chi_M = \frac{Ng^2\beta^2}{kT} \frac{0.25 + 0.074975x + 0.075235x^2}{1.0 + 0.9931x + 0.172135x^2 + 0.757825x^3} \quad (1)$$

where $x = |J|/kT$. Fitting of the magnetic susceptibility data with Eq. (1) yielded the parameter values $J = -0.35(0.04)$ cm^{-1}, $g = 2.2(0.1)$, with an agreement factor $R = 1.8 \times 10^{-8}$. Fig. 3 shows the result of this fit. As can be seen in Fig. 3, the χ_M versus T curve does not go through a rounded maximum for complex (**1**), a feature which is usually observed for a bulk antiferromagnetic systems. This indicates the complex $\{[Cu_2L_2(\mu_{1,5}\text{-dca})_2(dca)_2]\}_n$ (**1**) does not show any long-range ordering up to 2 K. T_{max}, the temperature at which χ_M becomes a maximum could be calculated for a bulk antiferromagnetic system using Bonner and Fisher's equation [30], $kT_{max}/|J| = 0.641$. T_{max} in the case of complex (**1**) is found to be 0.57 K. Hence, we did not reach a low enough temperature to observe a folded-knee type χ_M versus T plot for complex (**1**). The magnetic interaction for single end-to-end dicyanamido zigzag 1D chain compounds *viz.* $\{[Cu(2,2'\text{-bipyridine})(\mu_{1,5}\text{-dca})(dca)]\}_n$ ($J = -0.10$ cm^{-1}) and $\{[Cu(pyim)(\mu_{1,5}\text{-dca})(H_2O)]\}_n$ ($J = -0.35$ cm^{-1}) [pyim = 2-(2-pyridyl)-imidazole] is antiferromagnetic [9–11]. However, the magnetic interaction in linear 1D chains of an octahedral copper(II) complex bridged by tricyanomethanide is reported to be ferromagnetic [31].

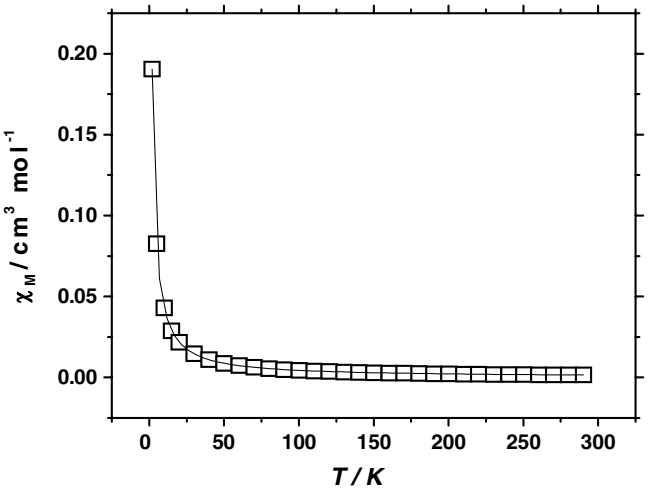


Fig. 3. χ_M vs. T (□) plot for complex (**1**). Solid lines represent the best fit of the data with the model described in the text.

4. Conclusion

Summarizing the above discussion we can conclude that we have synthesized a new 1D infinite zigzag chain compound, $\{[CuL(\mu_{1,5}\text{-dca})(dca)]\}_n$. The magnetic measurement shows that the coupling between copper(II) ions is antiferromagnetic. Dicynamide in this case also is found to be a weak antiferromagnetic coupler as reported earlier [9–11,32]. The result is, however, not inconsistent with the theoretical prediction based on extended Hückel calculations [33].

5. Supplementary materials

CCDC 609951 contains the supplementary crystallographic data for (**1**). These data can be obtained free of charge via http://www.ccdc.cam.ac.uk/conts/retrieving.html, or from the Cambridge Crystallographic Data Centre, 12 Union Road, Cambridge, CB2 1EZ, UK; fax: (+44) 1223-336-033; or e-mail: deposit@ccdc.cam.ac.uk.

Acknowledgements

The work was financially supported by the CSIR, New Delhi, by a grant (01/(1972)/05/EMR II) to S.K. We acknowledge the help rendered by SAIF, CDRI, Lucknow, for elemental analyses (on chargeable basis).

References

[1] (a) J. Ribas, A. Escuer, M. Monfort, R. Vicente, R. Cortés, L. Lezama, T. Rojo, Coord. Chem. Rev. 193–195 (1999) 1027;
(b) J.L. Manson, A.M. Arif, J.S. Miller, Chem. Commun. (1999) 1479.
[2] (a) O. Kahn, Molecular Magnetism, VCH, New York, 1993;
(b) O. Kahn, Comments Condens. Mater. Phys. 17 (1994) 39;
(c) J.R. Long, in: P. Yang (Ed.), Chemistry of Nanostructured Materials, World Scientific, Hong Kong, 2003.
[3] (a) S.R. Batten, P. Jensen, B. Moubaraki, K.S. Murray, R. Robson, Chem. Commun. (1998) 439;

(b) M.R. Pederson, A.Y. Liu, T. Baruah, E.Z. Kurmaev, A. Moewes, S. Chiuzbian, M. Neumann, K.L. Stevenson, D. Ederer, Phys. Rev. B 66 (2002) 014446.
[4] M. Kurmoo, C.J. Kepert, New J. Chem. 22 (1998) 1515.
[5] J.L. Manson, C.R. Kmety, Q.-Z. Huang, J.W. Lynn, G.M. Bendele, S. Pagola, P.W. Stephens, L.M. Liable-Sands, A.L. Rheingold, A.J. Epstein, J.S. Miller, Chem. Mater. 10 (1998) 2552.
[6] S.R. Batten, K.S. Murray, Coord. Chem. Rev. 246 (2003) 103.
[7] S. Saha, S. Koner, J.-P. Tuchagues, A.K. Boudalis, K.-I. Okamoto, S. Banerjee, D. Mal, Inorg. Chem. 44 (2005) 6379 and references therein.
[8] L. Zhang, L.-F. Tang, Z.-H. Wang, M. Du, M. Julve, F. Lloret, J.-T. Wang, Inorg. Chem. 40 (2001) 3619.
[9] B. Vangdal, J. Carranza, F. Lloret, M. Julve, J. Sletten, J. Chem. Soc., Dalton Trans. (2002) 566.
[10] I. Potocnak, M. Burcak, C. Wagner, L. Jagar, Acta Crystallogr. C 58 (2002) m327.
[11] J. Carranza, C. Brennan, J. Sletten, F. Lloret, M. Julve, J. Chem. Soc., Dalton Trans. (2002) 3164.
[12] L.F. Jones, L. O'Dea, D.A. Offermann, P. Jensen, B. Moubaraki, K.S. Murray, Polyhedron 25 (2006) 360.
[13] J.A. Schlueter, J.L. Manson, U. Geiser, Inorg. Chem. 44 (2005) 3194.
[14] J.L. Manson, Q. Huang, J.W. Lynn, H.-J. Kou, M.-H. Whangbo, R. Batman, T. Otsuka, N. Wada, D.N. Argyriou, J.S. Miller, J. Am. Chem. Soc. 123 (2001) 162.
[15] J.-P. Renard, L.-P. Regnault, M. Verdaguer, in: Magnetism: Molecules and Materials, Wiley–VCH, Weinheim, 2001, pp. 49.
[16] A. Caneschi, D. Gatteschi, N. Lalioti, C. Sangregorio, R. Sessoli, G. Venturi, A. Vindigni, A. Rettori, M.G. Pini, M.A. Novak, Angew. Chem., Int. Ed. 40 (2001) 1760.
[17] T. Kajiwara, M. Nakano, Y. Kaneko, S. Takaishi, T. Ito, M. Yamashita, A. Igashira-Kamiyama, H. Nojiri, Y. Ono, N. Kojima, J. Am. Chem. Soc. 127 (2005) 10151.
[18] S. Koner, S. Saha, K. Okamato, J.-P. Tuchagues, Inorg. Chem. 42 (2003) 4668.
[19] (a) CRYSTALCLEAR: CRYSTALCLEAR Software User's Guide, Molecular Structure Corporation, 1999;
(b) J.W. Plugrath, Acta Crystallogr. D 55 (1999) 1718.
[20] SIR97: A. Altomare, M. Burla, M. Camalli, G. Cascarano, C. Giacovazzo, A. Guagliardi, A. Moliterni, G. Polidori, R. Spagna, J. Appl. Cryst. 32 (1999) 115.
[21] CRYSTAL STRUCTURE 3.5.1: Crystal Structure Analysis Package, Rigaku and Rigaku/MSC (2000–2003), 9009 New Trails Dr. The Woodlands, TX, USA.
[22] D.J. Watkin, C.K. Prout, J.R. Carruthers, P.W. Betteridge, CRYSTALS issue 10, Chemical Crystallography Laboratory, Oxford, UK, 1996.
[23] A.L. Spek, J. Appl. Cryst. 36 (2003) 7.
[24] M.N. Burnett, C.K. Jonnson, ORTEP III, Report ORNL-6895, Oak Ridge National Laboratory, Tennessee, USA, 1996.
[25] I.J. Bruno, J.C. Cole, P.R. Edgington, N.K. Kessler, C.F. Macrwe, P. Maccabe, J. Pearson, R. Taylor, Acta Crystallogr. B58 (2002) 389.
[26] (a) B.J. Hathaway, Struct. Bond. 14 (1973) 49;
(b) A.W. Addison, T. Nageswara, J. Reedijk, J. van Rijn, G.C. Verchoor, J. Chem. Soc., Dalton Trans. (1984) 1349.
[27] J.H. Aiu, Z.R. Liao, X.G. Meng, L. Zhu, Z.M. Wang, K.B. Yu, Polyhedron 24 (2005) 1617.
[28] B. Zhang, H.Z. Kou, Y. He, H.G. Wang, A.L. Cui, Acta Crystallogr. C 60 (2005) m341.
[29] W.E. Estes, D.P. Gavel, W.E. Hatfield, D. Hodgson, Inorg. Chem. 17 (1978) 1415.
[30] J.C. Bonner, M.E. Fisher, Phys. Rev. A 135 (1964) 640.
[31] J. Kozisek, M. Hvastijova, J. Kohout, J. Mrozinski, H. Kohler, J. Chem. Soc., Dalton Trans. (1991) 1773.
[32] (a) J. Carranza, J. Sletten, F. Lloret, M. Julve, Inorg. Chim. Acta 357 (2004) 3304;
(b) J. Luo, M. Hong, J. Weng, Y. Zhao, R. Cao, Inorg. Chim. Acta 329 (2002) 59.
[33] A. Escuer, F.A. Mautner, N. Sanz, R. Vicente, Inorg. Chem. 39 (2000) 1668.

Available online at www.sciencedirect.com
ScienceDirect
Polyhedron 26 (2007) 741–747
POLYHEDRON
www.elsevier.com/locate/poly

Metal–radical complexes $[M(NITm\text{-}Py)_2(N_3)_2(DMSO)_2]$ [M = Cu(II), Ni(II), Co(II)]: Syntheses, crystal structures and magnetic properties

Yun-He Xu, Xiao-Ni Qu, Hai-Bin Song, Li-Cun Li *, Zong-Hui Jiang, Dai-Zheng Liao

Department of Chemistry, Nankai University, Weijing Road 94, Nankai District, Tianjin 300071, PR China

Received 3 August 2006; accepted 25 August 2006
Available online 19 September 2006

Abstract

Three new metal–radical complexes of the formula $[M(NITm\text{-}Py)_2(N_3)_2(DMSO)_2]$ [M = Cu(II) **1**, Ni(II) **2**, Co(II) **3**; NITmPy = 2-(3′-pyridyl)-4,4,5,5-tetramethylimidazoline-1-oxyl-3-oxide] were synthesized and characterized structurally as well as magnetically. Three complexes are three-spin complexes in which two NITmPy radical ligands are coordinated to the metal ion through the nitrogen atoms of the pyridyl rings. The magnetic behaviors of the three complexes are investigated. Complexes **1** and **2** show ferromagnetic interactions while antiferromagnetic coupling is predominant for complex **3**. The magnetic properties are analyzed in connection with their structures and the magnetic exchange mechanism is discussed.
© 2006 Elsevier Ltd. All rights reserved.

Keywords: Nitronyl nitroxide radical; Crystal structure; Magnetic properties; Complexes

1. Introduction

In the field of molecular-based magnetic materials, the coordination of paramagnetic metal ions with organic radical molecules has become a very promising strategy. By employment of this strategy, a large number of metal–radical complexes with various structures have been synthesized and magnetically characterized [1–5]. Some of these complexes show spontaneous magnetization with T_c up to 46 K [6].

It has been a pursuing goal to obtain new bulk molecular-based magnets with a high critical temperature and this has been directed in the preparation of 2D and even 3D metal–radical complexes [7–9]. However, recently some intense interesting discrete molecules have been prepared by using the metal–radical approach. Rey et al. have reported that the reaction of $Cu(hfac)_2$ with nitronyl nitroxide leads to a molecular cluster exhibiting a molecular spin transition [10]; Koga and coworkers have obtained cobalt(II) complexes with *N*-*tert*-butylnitroxides showing interesting magnetic relaxation behavior in frozen solution [11]. On the other hand, discrete metal–radical complexes with a definite geometry are good candidates for the fundamental studies of magneto-structural correlations, especially how the structural factors affect the metal–radical interactions. Such investigation is necessary not only for understanding the magnetic exchange mechanism between the metal and organic radical but also for guiding the design of new organic radical ligands for the development of novel molecular magnetic materials [12]. With this in mind, here we report three new coordination complexes involving nitronyl nitroxide ligands and azide, namely, $[M(NITmPy)_2(N_3)_2(DMSO)_2]$ [M = Cu(II), Ni(II), Co(II); NITmPy = 2-(3′-pyridyl)-4,4,5,5-tetramethylimidazoline-1-oxyl-3-oxide].

* Corresponding author.
E-mail address: llicun@nankai.edu.cn (L.-C. Li).

0277-5387/$ - see front matter © 2006 Elsevier Ltd. All rights reserved.
doi:10.1016/j.poly.2006.08.036

2. Experimental

2.1. General

All reagents were purchased from commercial sources and were used as received. 2-(3′-Pyridyl)-4,4,5,5-tetramethylimidazoline-1-oxyl-3-oxide (NITmPy) was prepared by the literature method [13]. Elemental analyses for C, H and N were carried out with a Perkin–Elmer 240 elemental analyzer. The infrared spectra were recorded in KBr pellets in the range 4000–400 cm^{-1} on a Bruker Tensor 27 IR spectrometer. Variable-temperature magnetic susceptibilities were measured on a MPMS XL-7 SQUID magnetometer. Diamagnetic corrections were made with Pascal's constants for all the constituent atoms.

2.2. Synthesis

$[Cu(NITmPy)_2(N_3)_2(DMSO)_2]$ (**1**): A methanol solution (10 mL) of NaN_3 (0.026 g, 0.4 mmol) was added to a methanol solution (20 mL) of $Cu(NO_3)_2 \cdot 3H_2O$ (0.0483 g, 0.2 mmol) and NITmPy (0.0936 g, 0.4 mmol). After the resulting blue solution was stirred for 2 h, 5 mL of DMSO was added. Further stirring for another 1h gave rise to a blue solution. Dark blue single crystals suitable for X-ray analysis were obtained by slow evaporation at room temperature after two weeks. Yield 0.100 g (67%). *Anal.* Calc. for $C_{28}H_{44}N_{12}CuO_6S_2$: C, 43.50; H, 5.70; N, 21.75. Found: C, 42.86; H, 5.76; N, 21.43%. IR data (KBr, cm^{-1}): $\nu = 2040$ (s), 1600 (m), 1397 (s), 1320 (s).

$[Ni(NITmPy)_2(N_3)_2(DMSO)_2]$ (**2**): This complex was prepared by a procedure similar to that for **1**, using $Ni(NO_3)_2 \cdot 6H_2O$ instead of $Cu(NO_3)_2 \cdot 3H_2O$. Yield 0.076 g (50%). *Anal.* Calc. for $C_{28}H_{44}N_{12}NiO_6S_2$: C, 43.77; H, 5.73; N, 21.89. Found: C, 44.40; H, 5.52; N, 20.89%. IR data (KBr, cm^{-1}): $\nu = 2042$ (s), 1605 (m), 1370 (s), 1323 (s).

$[Co(NITmPy)_2(N_3)_2(DMSO)_2]$ (**3**): This complex was prepared by a procedure similar to that for **1**, using $Co(CH_3COO)_2 \cdot 4H_2O$ instead of $Cu(NO_3)_2 \cdot 3H_2O$. Yield 0.046 g (30%). *Anal.* Calc. for $C_{28}H_{44}N_{12}CoO_6S_2$: C, 43.76; H, 5.73; N, 21.88. Found: C, 43.91; H, 5.65; N, 21.11%. IR data (KBr, cm^{-1}): $\nu = 2041$ (s), 1610 (m), 1375 (s), 1325 (s).

2.3. X-ray crystallographic study

Single crystal X-ray diffraction data for complexes **1** and **3** were collected on a Bruker SMART 1000 CCD diffractometer employing graphite-monochromated Mo Kα radiation ($\lambda = 0.71073$ Å), while those of complex **2** were collected using a Bruker SMART APEXII CCD diffractometer with graphite-monochromated Mo Kα radiation ($\lambda = 0.71073$ Å). The structures were solved by direct methods and refined by full matrix least-squares on F^2 using SHELXS 97 [14] and SHELXL 97 [15] programs, respectively. Non-hydrogen atoms were refined anisotropically and hydrogen atoms were placed in calculated positions and refined isotropically using a riding model. The crystallographic data for complexes **1**–**3** are listed in Table 1, and selected bond lengths and angles are listed in Table 2.

Table 1
Crystallographic data for complexes **1**–**3**

Complex	**1**	**2**	**3**
Empirical formula	$C_{28}H_{44}N_{12}CuO_6S_2$	$C_{28}H_{44}N_{12}NiO_6S_2$	$C_{28}H_{44}N_{12}CoO_6S_2$
Formula weight	772.41	767.58	767.80
Crystal system	triclinic	triclinic	triclinic
Space group	$P\bar{1}$	$P\bar{1}$	$P\bar{1}$
a (Å)	7.256(3)	7.2943(15)	7.2848(14)
b (Å)	10.411(4)	10.154(2)	10.2105(19)
c (Å)	12.351(4)	12.626(3)	12.662(2)
α (°)	96.707(6)	99.127(3)	98.782(3)
β (°)	103.566(6)	103.555(3)	103.140(3)
γ (°)	92.224(6)	93.262(3)	93.590(3)
V (Å^3)	898.7(6)	893.3(3)	901.8(3)
Z	1	1	1
ρ_{calcd} (g/cm^3)	1.427	1.427	1.414
μ (mm^{-1})	0.782	0.718	0.649
$F(000)$	405	404	403
θ Range (°)	1.71–25.01	2.04–25.02	2.03–26.38
Limiting indices	$-8 \leqslant h \leqslant 8$, $-12 \leqslant k \leqslant 12$, $-7 \leqslant l \leqslant 14$	$-8 \leqslant h \leqslant 8$, $-12 \leqslant k \leqslant 11$, $-15 \leqslant l \leqslant 13$	$-9 \leqslant h \leqslant 8$, $-12 \leqslant k \leqslant 8$, $-12 \leqslant l \leqslant 15$
Reflections collected	4589	4882	5103
Independent reflections [R(int)]	3152 [0.0158]	3121 [0.0163]	3617 [0.0136]
Data/restraints/parameters	3152/0/229	3121/0/229	3617/0/229
Goodness-of-fit on F^2	1.029	1.050	1.026
Final R indices [$I > 2\sigma(I)$]	$wR_1 = 0.0327$, $wR_2 = 0.0798$	$wR_1 = 0.0339$, $wR_2 = 0.0845$	$wR_1 = 0.0349$, $wR_2 = 0.0912$
R indices (all data)	$wR_1 = 0.0427$, $wR_2 = 0.0863$	$wR_1 = 0.0470$, $wR_2 = 0.0888$	$wR_1 = 0.0461$, $wR_2 = 0.0991$
Largest difference peak and hole (e Å^{-3})	0.347 and −0.310	0.266 and −0.281	0.392 and −0.327

Table 2
Selected bond lengths (Å) and angles (°) for complexes **1**, **2** and **3**

Complex ***1***			
Cu(1)–N(4)	1.997(2)	Cu(1)–O(3)	2.454
Cu(1)–N(1)	2.040(2)	O(2)–N(3)	1.277(2)
O(1)–N(2)	1.278(3)		
N(4)–Cu(1)–N(1)	88.31(8)	O(3)–S(1)–C(14)	105.2(1)
O(1)–N(2)–C(6)	126.8(2)	O(1)–N(2)–C(7)	121.1(2)
C(6)–N(2)–C(7)	112.0(2)	O(2)–N(3)–C(6)	126.3(2)
O(2)–N(3)–C(10)	122.4(2)	C(6)–N(3)–C(10)	111.0(2)
O(3)–S(1)–C(13)	107.2(1)	C(1)–N(1)–C(5)	117.8(2)
Complex ***2***			
Ni(1)–N(4)	2.067(2)	Ni(1)–O(3)	2.103(2)
Ni(1)–N(1)	2.103(2)	O(1)–N(2)	1.275(2)
O(2)–N(3)	1.271(3)		
N(4)–Ni(1)–O(3)	84.33(8)	N(4A)–Ni(1)–N(1)	92.06(9)
N(4)–Ni(1)–N(1)	87.94(9)	O(3)–Ni(1)–N(1)	88.67(7)
O(1)–N(2)–C(6)	126.8(2)	O(1)–N(2)–C(10)	122.3(2)
C(6)–N(2)–C(10)	110.7(2)	O(2)–N(3)–C(6)	127.0(2)
O(2)–N(3)–C(7)	121.4(2)	C(6)–N(3)–C(7)	111.6(2)
Complex ***3***			
Co(1)–N(4)	2.084(2)	Co(1)–O(3)	2.140(2)
Co(1)–N(1)	2.159(2)	O(1)–N(2)	1.277(2)
O(2)–N(3)	1.271(3)		
N(4)–Co(1)–O(3)	84.94(8)	N(4B)–Co(1)–N(1)	91.73(8)
N(4)–Co(1)–N(1)	88.27(8)	O(3B)–Co(1)–N(1)	91.79(7)
O(1)–N(2)–C(6)	126.4(2)	O(1)–N(2)–C(7)	122.6(2)
C(6)–N(2)–C(7)	110.7(2)	O(2)–N(3)–C(6)	127.2(2)
O(2)–N(3)–C(10)	121.6(2)	C(6)–N(3)–C(10)	111.2(2)

Symmetry transformations used to generate equivalent atoms: (A) $-x+1$, $-y$, $-z$; (B) $-x$, $-y+1$, $-z$.

3. Results and discussion

3.1. Description of the crystal structures

3.1.1. *[Cu(NITmPy)$_2$(N$_3$)$_2$(DMSO)$_2$] (**1**)*

An ORTEP drawing of **1** is shown in Fig. 1. The whole molecule is centrosymmetric and two paramagnetic radical ligands NITmPy are *trans*-coordinated to the copper(II) ion. The copper(II) ion is located in a 4 + 2 coordination environment in which the basal plane is formed by two nitrogen atoms (N(1), N(1A)) from the pyridyl rings of the NITmPy ligands with a Cu–N bond length of 2.040(2) Å and another two nitrogen atoms (N(4), N(4A)) from two azido ligands with a Cu–N bond length of 1.997(2) Å. The apical positions are occupied by two oxygen atoms (O(3), O(3A)) from two DMSO molecules with a Cu–O bond distance of 2.454 Å, which is significantly longer than the basal distances. The dihedral angle between the pyridyl ring and nitroxide group (O(1)–N(2)–C(6)–N(3)–O(2)) is 28.6°. The shortest contact between nitroxide groups is 4.044 Å. It should be noted that the closest contact is observed between the oxygen atom (O(2)) of the nitroxide group and the carbon atom (C′(3)) belonging to an adjacent molecule (O(2)–C′(3) = 3.357 Å) (shown in Fig. 2).

3.1.2. *[Ni(NITmPy)$_2$(N$_3$)$_2$(DMSO)$_2$] (**2**) and [Co(NITmPy)$_2$(N$_3$)$_2$(DMSO)$_2$] (**3**)*

Complexes **2** and **3** are isostructural and an ORTEP drawing of the molecular structure with the atomic labelling is shown in Fig. 3. The metal ion is located on an inversion center and adopts a distorted octahedral geometry. It is bound to two nitrogen atoms from the pyridyl rings of radical ligands and two oxygen atoms from DMSO molecules in the basal plane in addition to two azide ligands occupying the apical positions. The metal–N(pyridyl) bond distances are 2.103(2) and 2.159(2) Å for **2** and **3**, respectively, and the metal–O(DMSO) bond distances are 2.103(2) for **2** and 2.140(2) Å for **3**, whereas the metal–N(azido) bond distances are 2.067(2) and 2.084(2) Å for **2** and **3**, respectively, which are shorter than those of the basal plane. Thus, contrary to complex **1**, the metal ions of complexes **2** and **3** are in an axially compressed octahedral geometry. The dihedral angles between the pyridyl rings and NO–C–NO moieties are 27.5° and 28.2° for **2** and **3**, respectively. The shortest contacts between nitroxide groups are 4.102 and 4.144 Å for **2** and **3**, respectively. Similarly, the observed closest contacts between the oxygen atom of the nitroxide group and the carbon atom of an adjacent molecule are 3.395 and 3.380 Å for complexes **2** and **3**, respectively.

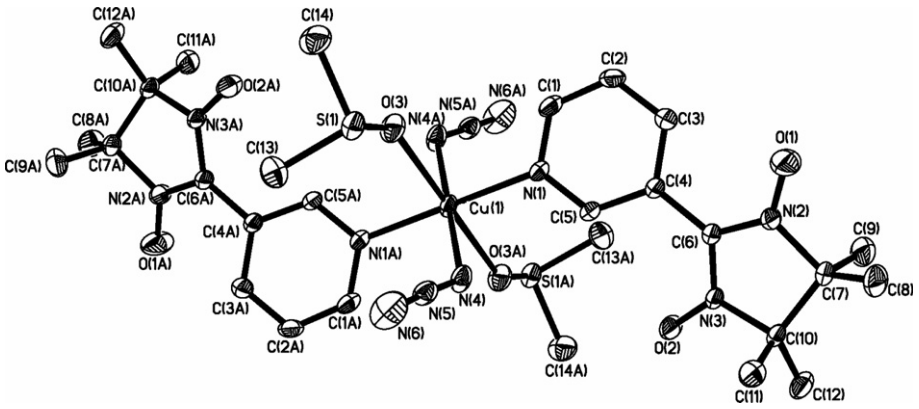


Fig. 1. An ORTEP drawing of [Cu(NITmPy)$_2$(N$_3$)$_2$(DMSO)$_2$] with atom-labelling and 30% thermal ellipsoids.

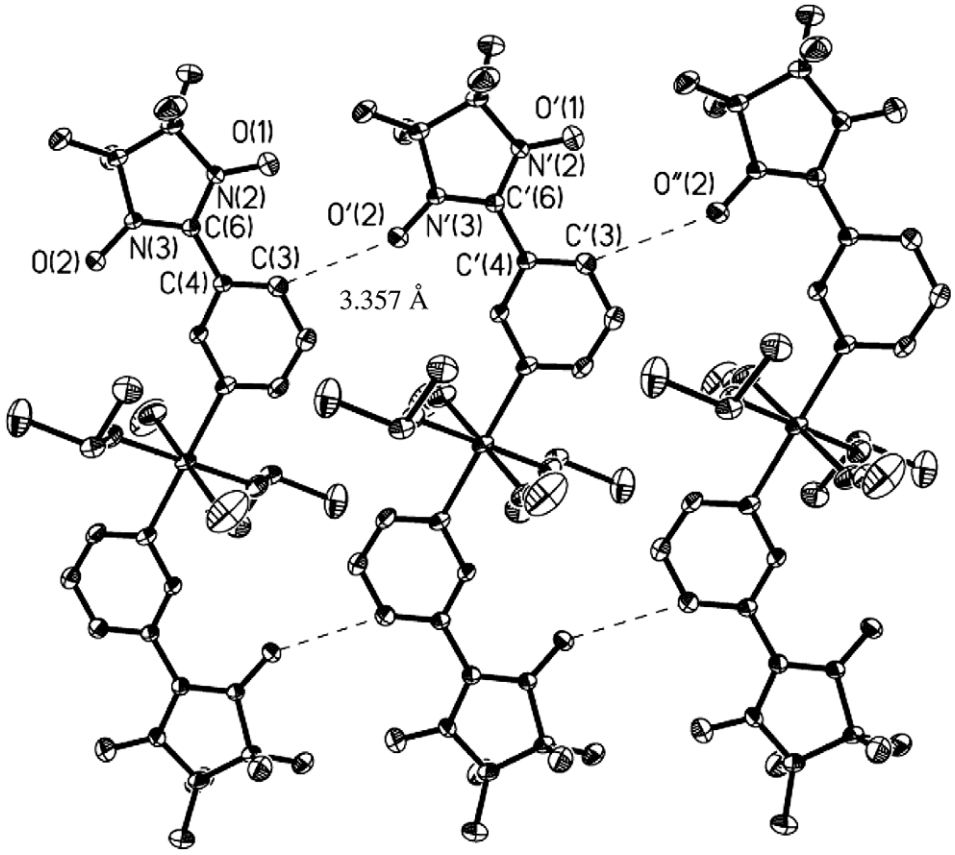


Fig. 2. The closest contact in $[Cu(NITmPy)_2(N_3)_2(DMSO)_2]$ showing exchange coupling through the NO···C pathway.

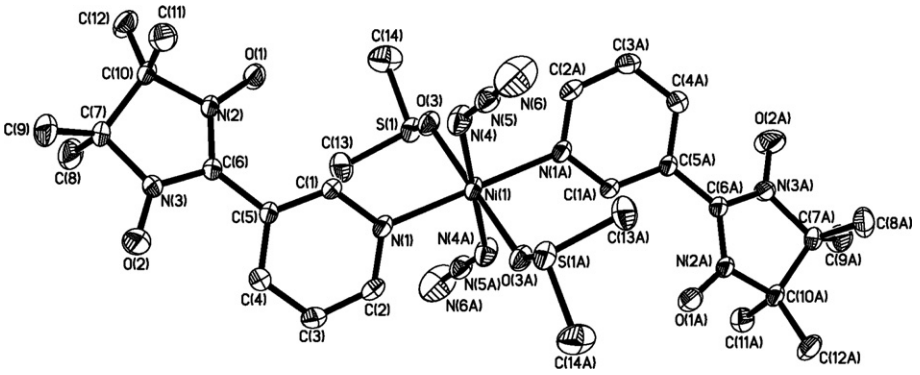


Fig. 3. An ORTEP drawing of $[Ni(NITmPy)_2(N_3)_2(DMSO)_2]$ with atom-labelling and 30% thermal ellipsoids.

3.2. Magnetic properties and discussion

The temperature dependence of the magnetic susceptibilities for the three complexes was measured in the temperature range 1.8–300 K with an applied field of 2000 G. Fig. 4 shows the variation of the molar magnetic susceptibility in terms of the reciprocal of χ_M and μ_{eff} for complex **1**. The value of the effective magnetic moment μ_{eff} is 2.91 μ_B at 300 K, close to the spin-only value (3.0 μ_B) expected for three uncorrelated $S = 1/2$ spins with $g = 2.00$. As the temperature is lowered, the μ_{eff} value gradually increases and reaches a maximum of 3.41 μ_B at 7.0 K, then it decreases quickly. The variation of χ_M with temperature obeys the Curie–Weiss law as there is linear relationship between $1/\chi_M$ and T. The corresponding Curie constant (C) and Weiss constant (Θ) are found to be 1.08 $cm^3\,K\,mol^{-1}$ and 4.31 K. These results are characteristic of a system with a ferromagnetic interaction. Previous experimental and theoretical results have showed that the nitronyl nitroxide group of the radical has a large positive spin density, while large negative spin density is located on the sp^2 carbon atom bridging two NO groups, and there is weak alternative delocalization on the pyridyl ring [16,17]. This will lead to magnetic coupling between the metal ion and the

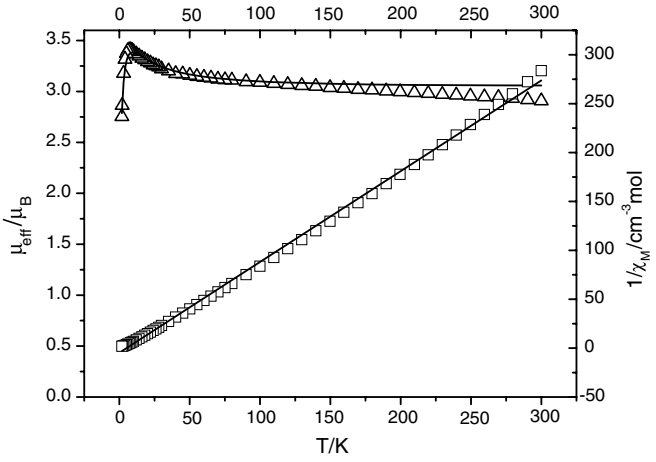


Fig. 4. Plot of $1/\chi_M$ (□) and μ_{eff} (△) vs. T for complex **1**. The solid line corresponds to the best theoretical fits.

NITmPy radical through the pyridyl ring, and NITmPy radical ligands through space. For complex **1**, according to the crystal structure, there are mainly three kinds of magnetic interactions, namely: (i) Cu(II) interacting with the coordinated NITmPy radical; (ii) magnetic coupling between neighboring NITmPy radicals through the NO···C pathway (3.357 Å); (iii) interaction between neighboring NO groups of NITmPy radicals through space (4.044 Å). The magnetic coupling between neighboring NO groups should be a weak antiferromagnetic interaction due to a rather large separation (4.044 Å) [18–20]. The magnetic interaction between neighboring NITmPy radicals through the NO···C pathway should be a weak ferromagnetic interaction because the closest contact involves the oxygen atom (O(2)) of an uncoordinated NO group which carries a large positive spin density and the carbon atom (C′(3)) of the adjacent NITmPy radical that carries a small negative spin density (O(2)···C′(3) = 3.357 Å) and these two atoms carrying opposite signs of the spin density alternate leading to ↑N″(3)–O″(2)↑···↓C′(3)–↑C′(4)–↓C′(6)–↑N′(3)–↑O′(2)···↓C(3), which matches McConnell's criteria [21]. The last two kinds of magnetic interactions should dominate at low temperature. Consequently, the experimental data was fitted to Eq. (1), derived from the spin Hamiltonian $\widehat{H} = -2J\sum(\widehat{S}_{Cu}\widehat{S}_R + \widehat{S}_{Cu}\widehat{S}_R)$. Considering the magnetic behavior at low temperature, the mean-field approximation, zJ', was introduced.

$$\chi_{tri} = \frac{N\beta^2}{4kT}\frac{g_3^2 + g_2^2\exp(-2J/kT) + 10g_1^2\exp(J/kT)}{1 + \exp(-2J/kT) + 2\exp(J/kT)} \quad (1)$$

$$\chi_M = \chi_{tri}/[1 - \chi_{tri}(2zJ'/Ng^2\beta^2)]$$

with

$$g_1 = (2g_{rad} + g_{Cu})/3$$

$$g_2 = (4g_{rad} - g_{Cu})/3$$

$$g_3 = g_{Cu}$$

The best fitting leads to $J = 7.43\ cm^{-1}$, $zJ' = -0.47\ cm^{-1}$, $g_{Cu} = 2.02$, $g_{rad} = 2.0$ (fixed), and $R = 1.13\times10^{-3}$ (R value is defined as $\sum[(\chi_M)_{obs} - (\chi_M)_{calc}]^2/\sum[(\chi_M)_{obs}]^2$). The fitting results indicate the magnetic interaction between copper(II) and the coordinated NITmPy radical is a ferromagnetic interaction.

The magnetic susceptibility data of complex **2** in form of $1/\chi_M$ and μ_{eff} versus T plots are given in Fig. 5. At room temperature, the μ_{eff} value is 3.92 μ_B, which is slightly higher than the expected value (3.79 μ_B) for isolated $S_{Ni} = 1$ and two $S_{rad} = 1/2$ spins. This value smoothly increases upon cooling and reaches a maximum of 4.37 μ_B at 8.0 K, and then decrease rapidly to 1.8 K. The magnetic susceptibility data follows the Curie–Weiss law with $C = 1.92\ cm^3\ K\ mol^{-1}$ and $\Theta = 2.85$ K. The results suggest a ferromagnetic interaction between the nickel(II) ion and NITmPy radical. Based on the crystal structure, the present magnetic system is similar to that of complex **1**. The magnetic interactions between neighboring NO groups of NITmPy radicals through space (4.102 Å) lead to weak antiferromagnetic interactions and the magnetic coupling between neighboring NITmPy radicals through the NO···C pathway (3.395 Å) results in weak ferromagnetic interactions. Therefore, the magnetic behavior of complex **2** can be explained by a theoretical expression (2) deduced from the spin Hamiltonian $\widehat{H} = -2J\sum(\widehat{S}_{Ni}\widehat{S}_R + \widehat{S}_{Ni}\widehat{S}_R)$, where J represents the magnetic interaction between the Ni(II) ion and the coordinated NITmPy radical. The weak antiferro- and ferromagnetic interactions and the zero field splitting of the nickel(II) ion were considered in the mean-field approximation as zJ'.

$$\chi_M = \frac{N\beta^2}{2kT}\frac{(g_{Ni} + g_R)^2(5 + e^{-4x}) + 4g_{Ni}^2e^{-2x}}{5 + 3e^{-4x} + e^{-6x} + 3e^{-2x}} \quad (2)$$

$$\chi_{total} = \chi_M/[1 - \chi_M(2zJ'/Ng^2\beta^2)]$$

The best fit to the experimental magnetic data gives following parameters: $g_{Ni} = 2.12$, $g_{rad} = 2.0$ (fixed), $J = 3.61\ cm^{-1}$, $zJ' = -0.31\ cm^{-1}$, $R = 1.0\times10^{-2}$. The fitting results show the nickel(II) ion is ferromagnetically coupled with the NITmPy radical ligand.

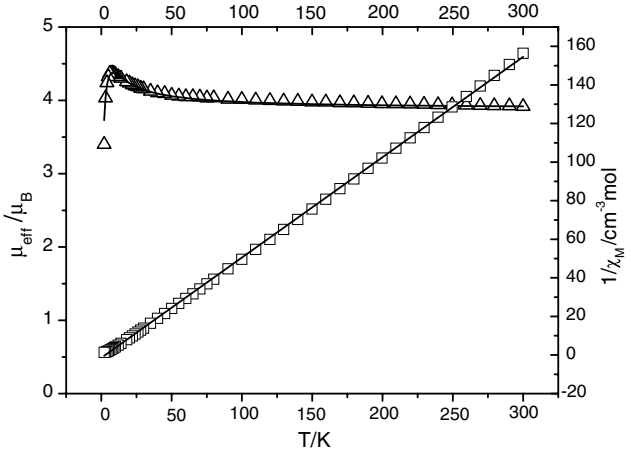


Fig. 5. Plot of $1/\chi_M$ (□) and μ_{eff} (△) vs. T for complex **2**. The solid line represents the best theoretical fits.

The magnetic behavior of complex **3** is shown in Fig. 6. The value of the μ_{eff} at 300 K is 5.57 μ_B, which is obviously larger than that expected for non-interacting $S_{Co} = 3/2$ and two $S_{rad} = 1/2$ spins (4.58 μ_B), indicating an unquenched orbital contribution. It can be seen that, with decreasing temperature, the μ_{eff} value continuously decreases to reach a minimum of 4.83 μ_B at 16.0 K and then it slightly increases to reach a small peak with a value of 4.87 μ_B at 6.0 K and finally decreases down to 4.39 μ_B at 1.8 K. Above 45 K, the magnetic data can be fitted to the Curie–Weiss law with $C = 4.09\ \mathrm{cm^3\ K\ mol^{-1}}$ and $\Theta = -15.68$ K. The results imply there exist an antiferromagnetic interaction between the cobalt(II) ion and NITmPy radical. Using Eq. (3) [22] with $g_{rad} = 2.0$, this leads to $g_{Co} = 2.67$, which is a reasonable value for octahedral high-spin cobalt(II) complexes [23].

$$C = \frac{N\beta^2}{3k}[2g_{rad}^2 S_{rad}(S_{rad}+1) + g_{Co}^2 S_{Co}(S_{Co}+1)] \quad (3)$$

Similarly, there exist weak antiferromagnetic interactions between neighboring NO groups of NITmPy radicals through space (4.144 Å) and ferromagnetic coupling between neighboring NITmPy radicals through the NO···C pathway (3.380 Å). The latter can be confirmed by an observed small peak at lower temperature in the plot of μ_{eff} versus T. The strict analysis of magnetic data for cobalt(II) complexes need to consider the effects of spin-orbit coupling and zero-field splitting. Moreover, at low temperature, the octahedral cobalt(II) energy levels become largely depopulated, until eventually a single Kramer doublet is occupied. Therefore it is very difficult to find an elaborate model incorporating all of these to fit the magnetic data at low temperature. However, according to Sinn [24], the higher temperature magnetic data (above 70 K) may be approximately interpreted by the isotropic spin Hamiltonian. Thus the magnetic data above 70 K can be analyzed with Eq. (4) derived from the Hamiltonian $\widehat{H} = -2J\sum(\widehat{S}_{Co}\widehat{S}_R + \widehat{S}_{Co}\widehat{S}_R)$, where J represents the magnetic interaction between the Co(II) ion and the coordinated NITmPy radical. The expression of the magnetic susceptibility is given below:

$$\chi_M = \frac{N\beta^2}{4kT} \times \frac{35g_1^2 + 10g_2^2\exp(-5x) + g_3^2\exp(-8x) + 10g_4^2\exp(-3x)}{3 + 2\exp(-5x) + \exp(-8x) + 2\exp(-3x)} \quad (4)$$

with $\chi = J/kT$, $g_1 = (3g_{Co} + 2g_R)/5$, $g_2 = (11g_{Co} + 4g_R)/15$, $g_3 = (5g_{Co} - 2g_R)/3$, $g_4 = g_{Co}$.

The best fit for the magnetic data (70–300 K) leads to $g_{Co} = 2.66$, $g_{rad} = 2.0$ (fixed), $J = -6.18\ \mathrm{cm^{-1}}$, $R = 1.0 \times 10^{-4}$. The fitting results show that the exchange coupling between the Co(II) ion and NITmPy radical is weakly antiferromagnetic.

The magnetic studies of the three complexes show that the copper(II) and nickel(II) ions are ferromagnetically coupled with the coordinated NITmPy radical ligands while an antiferromagnetic interaction is observed between the cobalt(II) ion and NITmPy radial ligand. This may be understood by a spin polarization mechanism [16,17,21,25–28] or the orbital symmetry [29,30]. According to spin polarization analysis (Scheme 1), the ferromagnetic interactions between the metal and radical in complexes **1** and **2** are anticipated. This is just in agreement with the above fitting results on basis of the experimental magnetic data. For complex **3**, the spin polarization mechanism cannot explain its magnetic behavior. However, based on the orbital symmetry, the cobalt(II) ion of complex **3** has two magnetic orbitals with σ symmetry ($d_{x^2-y^2}, d_{z^2}$), which are orthogonal to the magnetic orbital (π^*) of the radical, leading to a ferromagnetic interaction, and one magnetic orbital with π symmetry (either of d_{xy}, d_{xz}, d_{yz}) that will be able to overlap with the magnetic orbital of the radical leading to antiferromagnetic coupling. The observed antiferromagnetic coupling in complex **3** can be attributed to the good overlap of the magnetic orbitals which is capable of overcoming the ferromagnetic component. The observed weak magnetic coupling between the metal ion and NITmPy radical is consistent with the reported magnetic exchange [31–34] of pyridine substituted nitroxide–metal complexes due to the small spin density on the nitrogen atom.

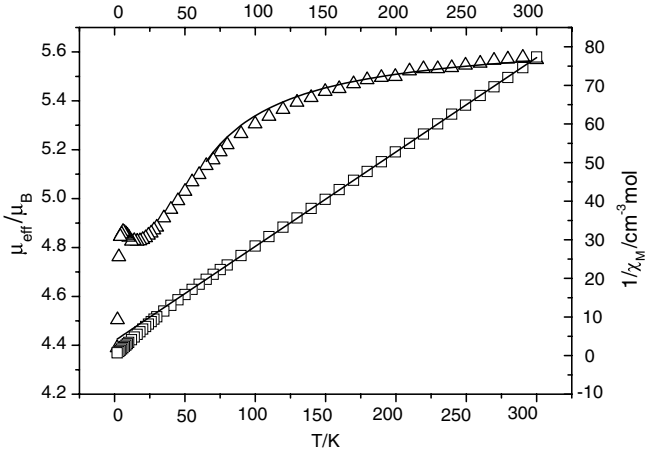
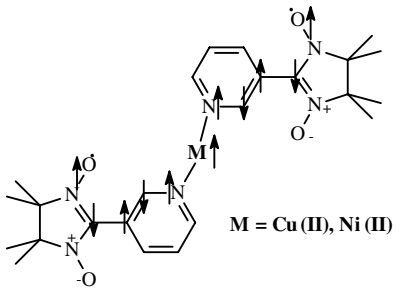


Fig. 6. Plot of $1/\chi_M$ (□) and μ_{eff} (△) vs. T for complex **3**. The solid line represents the best theoretical fits (70–300 K).



Scheme 1. Spin polarization mechanism for intramolecular ferromagnetic coupling in complexes **1** and **2**.

4. Conclusion

We have successfully obtained three new metal–radical complexes **1**–**3** of the formula $[M(NITmPy)_2(N_3)_2(DMSO)_2]$ [M = Cu(II), Ni(II), Co(II)]. For the three complexes, the crystal structural analyses indicate that two NITmPy radical ligands are coordinated to the metal ions via the nitrogen atoms of the pyridyl rings to afford the three-spin complexes. Ferromagnetic interactions are observed in complexes **1** and **2**, whereas an antiferromagnetic interaction dominates in complex **3**. A spin polarization mechanism and orbital symmetry are used to explain the magnetic coupling for complexes **1** and **2**, and **3**, respectively.

5. Supplementary material

CCDC 612405, 612406 and 612407 contains the supplementary crystallographic data for **1**, **3** and **2**. These data can be obtained free of charge via http://www.ccdc.cam.ac.uk/conts/retrieving.html, or from the Cambridge Crystallographic Data Centre, 12 Union Road, Cambridge CB2 1EZ, UK; fax: (+44) 1223-336-033; or e-mail: deposit@ccdc.cam.ac.uk.

Acknowledgement

This work was supported by the National Science Foundation of China (Nos. 20471032, 20331010).

References

[1] O. Kahn, Molecular Magnetism, VCH, New York, 1993.
[2] A. Caneschi, D. Gatteschi, P. Rey, Prog. Inorg. Chem. 39 (1991) 331.
[3] H. Iwamura, K. Inoue, T. Hayamizu, Pure Appl. Chem. 68 (1996) 243.
[4] P.M. Lahti (Ed.), Magnetic Properties of Organic materials, Marcel Dekker, New York, 1999.
[5] A. Caneschi, D. Gatteschi, R. Sessoli, P. Rey, Acc. Chem. Res. 22 (1989) 392.
[6] K. Inoue, T. Hayamizu, H. Iwamura, D. Hashizume, Y. Ohashi, J. Am. Chem. Soc. 118 (1996) 1803.
[7] K. Fegy, D. Luneau, T. Ohm, C. Paulsen, P. Rey, Angew. Chem. Int. Ed. 37 (1998) 1270.
[8] K. Fegy, D. Luneau, E. Belorizky, M. Novac, J.-L. Tholence, C. Paulsen, T. Ohm, C. Paulsen, P. Rey, Inorg. Chem. 37 (1998) 4524.
[9] F. Mathever, D. Luneau, J. Am. Chem. Soc. 123 (2001) 7465.
[10] F. Lanfranc de Panthou, E. Belorizky, R. Calemzuk, D. Luneau, C. Marcenat, E. Ressouche, P. Thurek, P. Rey, J. Am. Chem. Soc. 117 (1995) 11247.
[11] S. Kanegawa, S. Karasawa, M. Nakano, N. Koga, Chem. Commun. (2004) 1750.
[12] R.D. Willet, D. Gatteschi, O. Kahn (Eds.), Magneto-structural Correlations in Exchange Coupled Systems, NATO ASI Series C140, D. Reidel, Dordrecht, The Netherlands, 1985.
[13] M.S. Davis, K. Morokuma, R.W. Kreilick, J. Am. Chem. Soc. 94 (1972) 5588.
[14] G.M. Sheldrick, SHELXS-97, Program for the Solution of Crystal Structure, University of Göttingen, Göttingen, Germany, 1997.
[15] G.M. Sheldrick, SHELXL-97, Program for the Refinement of Crystal Structure, University of Göttingen, Göttingen, Germany, 1997.
[16] A. Zheludev, V. Barone, M. Bonnet, B. Delley, A. Rand, E. Ressouche, P. Rey, R. Subra, J. Schweizer, J. Am. Chem. Soc. 116 (1994) 2019.
[17] K. Yamaguchi, M. Okumura, M. Nakano, Chem. Phys. Lett. 191 (1992) 237.
[18] A. Caneschi, F. Ferraro, D. Gatteschi, P. Rey, R. Sessoli, Inorg. Chem. 29 (1990) 1756.
[19] A. Caneschi, D. Gatteschi, J. Laugier, P. Rey, R. Sessoli, Inorg. Chem. 27 (1988) 1553.
[20] A. Caneschi, F. Ferraro, D. Gatteschi, P. Rey, R. Sessoli, Inorg. Chem. 29 (1990) 4217.
[21] H.M. McConnell, J. Chem. Phys. 39 (1963) 1910.
[22] L.M. Field, M.C. Moron, P.M. Lahti, F. Palacio, A. Paduan-Filho, N.F. Oliveira Jr., Inorg. Chem. 45 (2006) 2562.
[23] R.L. Carlin, Magnetochemistry, Springer, Berlin, Germany, 1986, pp. 65–66.
[24] E. Sinn Coord, Chem. Rev. 5 (1970) 313.
[25] Y. Ishimura, K. Inoue, N. Koga, H. Iwamura, Chem. Lett. (1994) 1693.
[26] M. Kitano, Y. Ishimura, K. Inoue, N. Koga, H. Iwamura, Inorg. Chem. 33 (1994) 6012.
[27] L.M. Field, P.M. Lahti, F. Palacio, A. Paduan-Fiho, J. Am. Chem. Soc. 125 (2003) 10110.
[28] H.-H. Lin, H.-H. Wei, G.-H. Lee, Y. Wang, Polyhedron 20 (2001) 3057.
[29] D. Luneau, P. Rey, J. Laugier, P. Fries, A. Caneschi, D. Gatteschi, R. Sessoli, J. Am. Chem. Soc. 113 (1991) 1245.
[30] Z.-N. Chen, J. Qiu, J.-M. Gu, M.-F. Wu, W.-X. Tang, Inorg. Chim. Acta 233 (1995) 131.
[31] I. Dasna, S. Golhen, L. Ouahab, N. Daro, J.-P. Sutter, New J. Chem. 25 (2001) 1572.
[32] I. Dasna, S. Golhen, L. Ouahab, M. Fettouhi, O. Pena, N. Daro, J.-P. Sutter, Inorg. Chim. Acta 326 (2001) 37.
[33] H.-M. Wang, Z.-L. Liu, C.-M. Liu, D.-Q. Zhang, Z.-L. Lu, H. Geng, Z.-G. Shuai, D.-B. Zhu, Inorg. Chem. 43 (2004) 4091.
[34] M. Fettouhi, M. Khaled, A. Waheed, S. Golhen, L. Ouahab, J.-P. Sutter, O. Kahn, Inorg. Chem. 38 (1999) 3967.

Available online at www.sciencedirect.com
ScienceDirect
Polyhedron 26 (2007) 749–756
POLYHEDRON
www.elsevier.com/locate/poly

Synthesis, spectral characterization and structural investigation on some 4-aminoantipyrine containing Schiff base Cu(II) complexes and their molecular association

P. Mosae Selvakumar, E. Suresh *, P.S. Subramanian *

Analytical Science Division, Central Salt and Marine Chemicals Research Institute (CSIR), Gijubhai Badhegha Marg, Bhavnagar, Gujarat 364 002, India

Received 1 August 2006; accepted 4 September 2006
Available online 22 September 2006

Abstract

Compounds $[Cu(L_1)_2]$ (**1**) and $[Cu(L_2)_2]$ (**2**), where L_1 and L_2 are Schiff base ligands of 4-aminoantipyrine and substituted salicylaldehydes, were synthesized and characterized using various spectroscopic techniques such as elemental analysis, UV–Vis, IR, and NMR. The single crystal X-ray structures for L_1, L_2, and their corresponding Cu(II) complexes assembled in a 1:2 metal to ligand ratio were analyzed for their various weak H-bonding and dimeric association. The structural analysis of compounds **1** and **2**, being the first crystal structures in this series, deserves special attention to help further the understanding in this area of structure–reactivity correlation studies. Further these compounds, composed of very similar chemical composition with a small difference in the substituent on the salicylaldehyde moiety, influenced through various weak inter- and intramolecular H-bonding and C–H$\cdots\pi$ interactions, rearrange the geometry around Cu(II) from a tetrahedrally distorted square planar geometry in $[Cu(L_1)_2]$ (**1**) to square planar in $[Cu(L_2)_2]$ (**2**). Steric strain imposed by the methyl substitution on the 4-aminoantipyrine moiety of the Schiff base ligand, causing this small change of the Cu(II) geometry, along with various weak interactions is analyzed in detail.
© 2006 Elsevier Ltd. All rights reserved.

Keywords: Copper (II) complex; Crystal structure; Schiff base; Antipyrine

1. Introduction

Schiff bases of 4-aminoantipyrine and its complexes are known for their variety of applications in the area of catalysis [1,2], clinical applications [3], and pharmacology [4]. New kinds of chemo-therapeutic agents containing Schiff bases have gained significant attention among biochemists [1] and of those aminopyrines are commonly administered intravenously to detect liver disease [3] in clinical treatment. Hence a systematic understanding on the structure–reactivity correlation has warranted synthesis and characterization of a variety of Schiff base complexes containing different 2-hydroxy aromatic moieties such as furan-2-aldehyde, thiophene-2-aldehyde [4], and pyrrole-2-carboxaldehyde [5], etc. Thus there are a number of reports on compounds based on aminopyridine Schiff bases, though accounts of their crystal structures are limited. The salicylaldehyde based SAAP [6] and pyrrole based HPAP [5] Schiff base ligands and their Cu(II) [7] and lanthanum (Pr, Nd, Gd, Dy, Y, U) complexes [8,9] have been reported already. Although there are many compounds in the literature, our search on the CCDC shows no crystal structure has been reported so far and the structures of those entire complexes are elucidated only with spectroscopic evidence. With this in view, the present report accounts for the synthesis of two antipyrine Schiff base ligands L_1 and L_2 (Fig. 1) and their Cu(II) complexes $[Cu(L_1)_2]$ (**1**), and $[Cu(L_2)_2]$ (**2**), with a special impetus on their structural investigations. Further, the structural

* Corresponding authors. Tel.: +91 278 2567760; fax: +91 278 2566970 (P.S. Subramanian).
E-mail addresses: esuresh@csmcri.org (E. Suresh), siva140@yahoo.co.in (P.S. Subramanian).

0277-5387/$ - see front matter © 2006 Elsevier Ltd. All rights reserved.
doi:10.1016/j.poly.2006.09.004

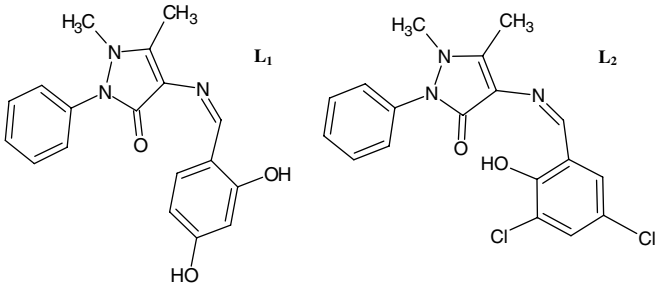


Fig. 1. Schiff base ligand system L_1 and L_2.

analysis in the present report explores that the weak interactions introduced by varying the substitution on the salicylaldehyde unit, modify the Cu(II) geometry from a tetrahedrally distorted square planar to a distorted square planar geometry.

2. Experimental

2.1. Materials

$Cu(CH_3COO)_2 \cdot H_2O$, 4-aminoantipyrine, 2,4-dihydroxybenzaldehyde, and 3,5-dichlorosalicylaldehydes were purchased from Aldrich & Co. All these chemicals were used as received without any further purification.

2.2. Synthesis

2.2.1. Preparation of the ligands: $L_1 \cdot MeOH$

A 1:1 equimolar methanolic solution of 4-aminoantipyrine (0.406 gm, 0.001 mol) and 2,4-dihydroxybenzaldehyde (0.276 gm, 0.001 mol) were mixed and gently heated for 2 h with constant stirring. The characteristic yellow precipitate obtained by Schiff base condensation was filtered out and kept for crystallization, dissolving in methanol. Fine yellow crystals obtained upon slow evaporation at room temperature were characterized, including single crystal X-ray diffraction. L_1: 4-{[(1*Z*)-(2,4-dihydroxyphenyl)methylene]-amino}-1,5-dimethyl-2-phenyl-1,2-dihydro-3*H*-pyrazol-3-one. NMR data (δ, *Methanol-d_4*): 13.55 (br s, –OH, 1H), 9.63 (s, CH=N, 1H), 7.56–7.20 (m, Ar phenyl, 5H), 6.40–6.31 (m, Ar, 3H), 3.14 (s, N–CH_3, 3H), 2.35 (s, C–CH_3, 3H). IR data (KBr, cm^{-1}): 3500–2900 (weak, br), 1615 (st, intense), 1586 (s, br). UV–Vis [CH_3CN, λ_{max}, nm, (ε, M^{-1}, cm^{-1})], 336 (3030), 422 (2840). ES [MSI] Calc for $C_{19}H_{21}N_3O_4$ (m/z+H^+) = 323.34. Found = 324.26. *Anal.* Calc. for $C_{19}H_{21}N_3O_4$: C, 64.21; H, 5.95; N, 11.82. Found: C, 63.86; H, 5.56; N, 12.25%.

2.2.2. Synthesis of L_2

4-{[(1*Z*)-(3,5-dichloro-2-hydroxyphenyl)methylene]amino}-1,5-dimethyl-2-phenyl-1,2-dihydro-3*H*-pyrazol-3-one. The above synthetic procedure was repeated for L_2 appropriately adapting 3,5-dichlorosalicylaldehyde in place of 2,4-dihydroxybenzaldehyde. NMR data (δ, $CDCl_3$): 14.3 (br s, OH, 1H), 9.75 (s, CH=N, 1H), 7.55-7.26 (m, Ar 7H), 3.23 (s, N-CH_3,3H), 2.45 (s, C–CH_3,3H). IR data (KBr, cm^{-1}) 3639–2593 (br), 1665 (sharp, st), 1589 (sharp, st). UV–Vis [CH_3CN, λ_{max}, nm, (ε, M^{-1}, cm^{-1})], 345 (3000), 380 (2800). ES [MSI] Calc for $C_{18}H_{15}Cl_2N_3O_2$ (m/z) = 375.05; Found = (m/z+H^+) = 376.25; (m/z+Na^+) = 398.24. *Anal.* Calc. for $C_{18}H_{15}Cl_2N_3O_2$; C, 57.46; H, 4.02; N, 11.17. Found: C, 57.5; H, 3.95; N, 11.0%.

2.2.3. Preparation of complexes $[Cu(L_1)_2]$ (**1**), and $[Cu(L_2)_2]$ (**2**)

The Schiff base ligand L_1 (0.071 gm, 0.002 mmol), dissolved in chloroform, was mixed with an ethanolic solution of $[Cu(CH_3COO)_2] \cdot H_2O$ (0.199 gm, 0.001 mmol) and allowed to stir continuously. The immediate color change from green to dark red indicates complexation. Upon slow evaporation at room temperature, the dark red crystals were obtained in 48 h. $[Cu(L_1)_2]$ (**1**): UV–Vis [CH_3CN, λ_{max}, nm, (ε, M^{-1}, cm^{-1})], 364 (1980), 509 (80). ES [MSI] Calc for $CuC_{36}H_{30}N_6O_6$ (m/z+H^+) = 708.18. Found = 708.30. *Anal.* Calc. for $CuC_{36}H_{30}N_6O_6$: C, 61.05; H, 4.55; N, 11.88. Found: C, 61.5; H, 4.48; N, 11.36%. $[Cu(L_2)_2]$ (**2**): The above procedure was repeated for **2** adapted for L_2 with a 1:2 $Cu(CH_3COO) \cdot H_2O$: L_2 ratio. UV–Vis [CH_3CN, λ_{max}, nm, (ε, M^{-1}, cm^{-1})], 359 (6970), 427 (1300), 531 (300). ES [MSI] Calc for $CuC_{36}H_{28}Cl_4N_6O_4$ (m/z+H^+) = 814.02. Found = 814.02. *Anal.* Calc. for $CuC_{36}H_{28}Cl_4N_6O_4$: C, 53.11; H, 3.46; N, 10.32. Found: C, 52.99; H, 3.97; N, 10.20%.

2.3. Physical measurements

Microanalysis of the complexes was done using a Perkin–Elmer PE 2400 series II CHNS/O elemental analyzer. IR spectra were recorded using KBr pellets (1% w/w) on a Perkin–Elmer Spectrum GX FT-IR spectrophotometer. Electronic spectra were recorded on a Schimadzu UV 3101PC spectrophotometer. Mass analyses were performed using electron spray ionization (ESI) technique on a Waters Q Tof-micro mass spectrometer. ^1H NMR spectra were recorded on a Bruker Avance DPX 200 FT-NMR spectrometer. Chemical shifts for proton resonances are reported in ppm (δ) relative to tetramethylesilane.

2.4. X-ray crystallography

A summary of the crystallographic data and details of data collection for L_1, L_2 and **1**, **2** are given in Table 1. Selected bond distances and bond angles for compounds **1** and **2** are given in Table 2. In each case, a crystal of suitable size was selected from the mother liquor and immersed in partone oil, then mounted on the tip of a glass fiber and cemented using epoxy resin. Intensity data for all three crystals were collected using Mo Kα (λ = 0.71073 Å) radiation on a Bruker SMART APEX diffractometer equipped with a CCD area detector. The data integration and reduction were processed with SAINT [10] software. An empirical

Table 1
Summary of crystallographic data for the compounds

Code	L_1	L_2	1	2
Chemical formula	$C_{19}H_{21}N_3O_4$	$C_{18}H_{15}Cl_2N_3O_2$	$C_{36}H_{32}Cu_1N_6O_6$	$C_{18}H_{14}Cl_2Cu_{0.50}N_3O_2$
Formula weight	355.39	376.23	708.22	406.99
a (Å)	13.9443(16)	7.0141(8)	10.2073(16)	23.197(2)
b (Å)	6.8950(8)	8.0449(9)	12.1721(19)	6.7034(6)
c (Å)	19.390(2)	30.487(3)	13.776(2)	22.443(2)
α (°)	90.0	90	74.189(3)	90
β (°)	109.953(2)	90.972(2)	74.273(3)	90.918(3)
γ (°)	90	90	80.569(3)	90
Z	4	4	2	8
V (Å^3)	1752.4(3)	1720.1(3)	1577.7(4)	3489.4(6)
Crystal system	monoclinic	monoclinic	triclinic	monoclinic
Space group	$P2_1/c$	$P2_1/n$	$P\bar{1}$	$C2/c$
Radiation used, λ (Å)	0.71073	0.71073	0.71073	0.71073
$\rho_{calc.}$ (g cm^{-3})	1.347	1.453	1.491	1.549
Absolute coefficient, μ (mm^{-1})	0.096	0.394	0.751	0.983
Temperature (K)	100	293	293	293
R_1 on $[(F_o^2)]$[a]	0.0534	0.0482	0.0621	0.0382
wR_2 on (F_o^2)[b]	0.1285	0.1237	0.1526	0.0954

[a] $R = \sum \|F_o| - |F_c\| / \sum |F_o|$.

[b] $R_w = [Sw(F_o^2 - F_c^2)^2]/S[w(F_o^2)^2]^{1/2}$; $w = 1/\sigma(F_o)^2$.

Table 2
Selected bond distances (Å) and angles (°) for complexes **1** and **2** with estimated standard deviations in the parenthesis

	1	2
Bond length (Å)		
Cu(1)–O(3)	1.887(3)	
Cu(1)–O(2)		1.8878(14)
Cu(1)–O(2)#1		1.8878(14)
Cu(1)–O(6)	1.924(3)	
Cu(1)–N(6)	1.953(3)	
Cu(1)–N(3)	1.967(3)	1.9567(17)
Cu(1)–N(3)#1		1.9567(17)
Bond angle (°)		
O(3)–Cu(1)–O(6)	91.78(12)	
O(3)–Cu(1)–N(6)	145.30(13)	
O(6)–Cu(1)–N(6)	94.07(13)	
O(3)–Cu(1)–N(3)	95.95(13)	
O(6)–Cu(1)–N(3)	143.74(13)	
N(6)–Cu(1)–N(3)	99.23(13)	
O(2)#1–Cu(1)–O(2)		154.31(9)
O(2)#1–Cu(1)–N(3)#1		90.75(6)
O(2)–Cu(1)–N(3)#1		93.63(6)
O(2)#1–Cu(1)–N(3)		93.63(6)
O(2)–Cu(1)–N(3)		90.75(6)
N(3)#1–Cu(1)–N(3)		160.18(10)

absorption correction was applied to the collected reflections using SADABS [11]. The structures were solved by direct methods using SHELXTL [11b] and were refined on F^2 by the full-matrix least-squares technique using the SHELXL-97 [12] package. Graphics are generated using ORTEP. Packing and H-bonding diagrams are generated by PLATON [13] and MERCURY [116]. In all the four compounds, non-hydrogen atoms were refined anisotropically until convergence was reached and hydrogen atoms attached to all carbon atoms were geometrically fixed using the program SHELXTL.

3. Results and discussion

3.1. Spectral investigation

The Schiff base ligands L_1 and L_2 are yellow in color and are soluble in almost all organic solvents, such as methanol, acetonitrile, chloroform, acetone, DMF and DMSO, and the corresponding metal complexes $[Cu(L_1)_2]$ (**1**) and $[Cu(L_2)_2]$ (**2**) obtained with a 1:2 metal ligand ratio are found to be dark red in color. The electronic spectra for both these ligands behave very similarly and show two characteristic bands at 336–360 nm and 420 nm representing intra ligand charge transfer transitions. The corresponding metal complexes **1** and **2** exhibit a characteristic d-d band at 500–530 nm with a broad spectral feature. While the position of λ_{max} is attributable to the square planar geometry, the broadness of the spectral pattern can be attributed to the degree of distortion in the geometry. The three characteristic IR signals for L_1 and L_2, corresponding to (i) OH; (ii) C=O, C=N; (iii) phenolate oxygen C···O, were analyzed. The broad IR signal centered at 3430 cm^{-1} obtained for both the free ligands L_1 and L_2 can be ascribed to the OH functional groups. The compounds **1** and **2** show sharp and intense peaks in the range of 1572–1589 cm^{-1} and 1616–1665 cm^{-1} which can be attributed to $\nu_{CH=N}$ and $\nu_{C=O}$ stretching modes respectively. The characteristic peak at 9.6–9.75 δ in the ^{1}H NMR spectrum further confirms the azomethine CH=N condensation. The disappearance of the OH peak and the significant shift in the $\nu_{C=N}$ stretching frequency in **1** and **2**, with respect to the corresponding free ligands, indicate the complexation with the Cu(II) center. The shift in the azomethine peak by 10–15 cm^{-1} in the IR spectra indicates its involvement in coordination. The IR signal observed at

1616–1665 cm^{-1}, representing the C=O group attached to the antiypyrine five-membered ring remains unchanged in compounds **1** and **2** with respect to the free ligands, symbolizing that it is not involved in the coordination.

3.2. Crystal structure and molecular association

3.2.1. Structure of L_1

The Schiff base ligand L_1 crystallizes in the monoclinic space group $P2_1/c$, along with methanol as a solvent of crystallization. Fig. 2a–c represents the ORTEP diagram for L_1, its dimeric association and the intermolecular C–H···N interaction through molecular pairs along the *c*-axis, respectively. The *meta*-dihydroxy substituted salicylyl phenyl ring C11–C16 is almost in the same plane (mean plane deviation 12.89°), while the phenyl ring C1–C6 of the antipyrine moiety is tilted by 49.67° with respect to the central five-membered ring. The mode of molecular packing influenced through the mode of H-bonding is dictated by variation in the substitutions on the salicyl phenyl ring.

As depicted in Fig. 2b, the molecules are oriented in such a way that the C18 methyl group of the antipyrine ring is aligned towards the azomethine N3, making strong intermolecular C–H···N interactions forming molecular pairs along the *c*-axis [C(18)–H(18A)···N(3); H(18A)···N(3) = 2.58 Å C(18)···N(3) = 3.536(2) Å, ∠C(18)–H(18A)···N(3) = 171°, symmetry code: $1-x, -1/2+y, 1/2-z$]. H18C from the same methyl group is involved in an intermolecular C–H···O interaction with the exocyclic ketonic oxygen of the antipyrine ring along the *b*-axis [C(18)–H(18C)···O(1); H(18C)···O(1) = 2.41 Å, C(18)···O(1) = 3.358(2) Å, ∠C(18)–H(18C)···O(1) = 167° symmetry code: $x, -1+y, z$] which is well within the range in the review articles reported by Steiner [15a] and Nangia [15b]. In addition to the C–H···N interaction, the lattice methanolic OH acts as both donor and acceptor through O–H···O hydrogen bonding with the molecular pairs (Fig. 2b) of the L_1 moiety from either side creating a layered hydrogen bonded motif. The O–H···O hydrogen bonding parameters, with the symmetry code, between the lattice methanol with ketonic oxygen O1 of the antipyrine ring and the phenolic hydrogen H2A of the ligand moiety are as follows: O(4)–H(4A)···O(1); H(4A)···O(1) = 1.86 Å; O(4)···O(1) = 2.671(2) Å, ∠O(4)–H(4A)···O = 171°, symmetry code: $1-x, -1/2+y, 3/2-z$ and O(2)–H(2A)···O(4):H(2A)···O(4) = 1.85 Å, O(2)···O(4) = 2.665(2) Å, ∠O(2)–H(2A)···O(4) = 171°, symmetry code: $x, 5/2-y, -1/2+z$. In addition to this intermolecular hydrogen bonding, intramolecular O–H···N and C–H···O interactions also exist for the stabilization of the ligand moiety, incorporating the methanol molecule in the crystal lattice (Fig. 2c).

3.2.2. Structure of L_2

Ligand L_2 crystallizes in monoclinic space group $P2_1/n$ with four molecules in the unit cell. Fig. 3a and b represents the ORTEP diagram and their dimeric association of L_2. In L_2, the *ortho* and *para* positions of the phenyl ring, with respect to the OH group, are substituted by Cl1 and Cl2 respectively. The dichloro substituted "sal" phenyl ring (C11–C16) is in the same plane, while the phenyl ring C1–C6 of the antipyrine moiety is tilted by 36.64° with respect to the central five-membered ring. The tilt of the phenyl group (C1–C6) with respect to central five-membered ring can be attributed to various molecular interactions involved in the packing pattern.

The molecules are packed along the *ac*-plane with a slight offset in adjacent layers to make an effective dimeric

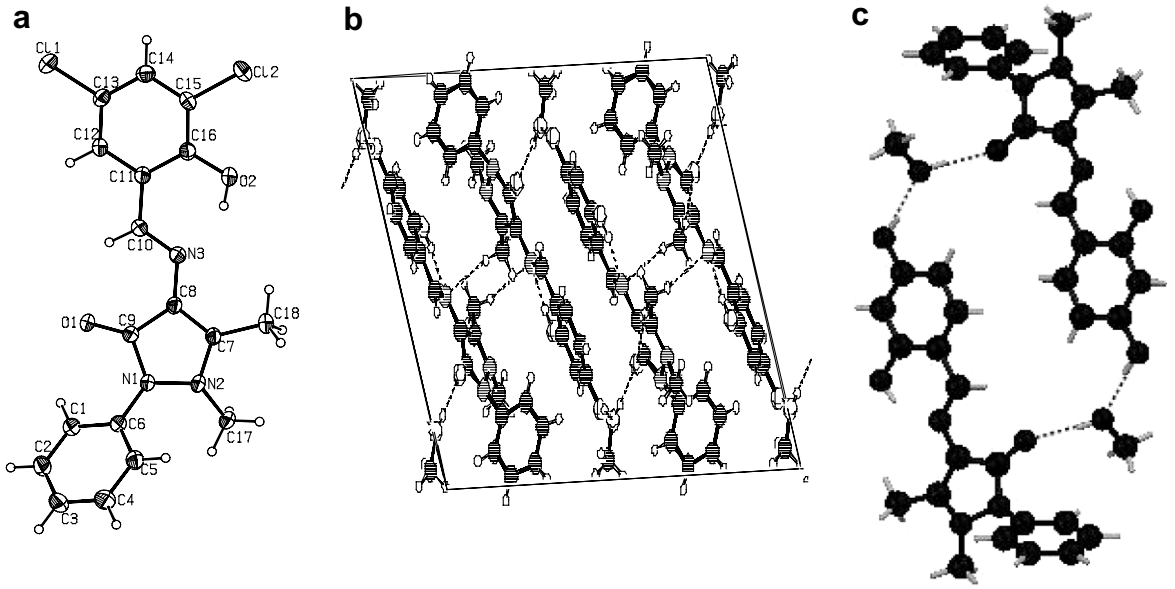


Fig. 2. (a) ORTEP diagram with the atom numbering for L_1, (b) intermolecular CH···N interaction mediated molecular pairs and (c) dimeric association through methanol.

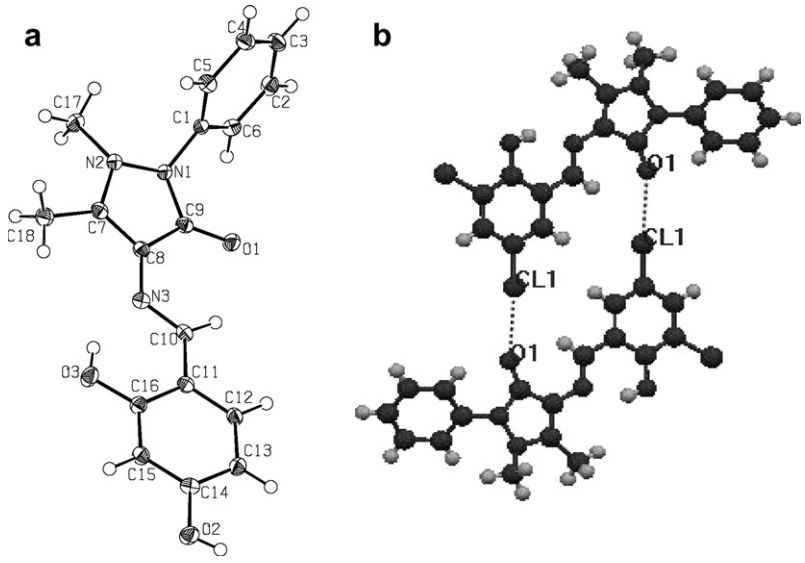


Fig. 3. (a) ORTEP diagram with the atom numbering for L_2 and (b) dimeric association of L_2.

association via a C=O···Cl interaction. The close up view of the dimeric association via the C=O···Cl interaction between a centro-symmetric pair is shown in Fig. 3b. Thus, Cl1 attached to the "sal" phenyl ring makes contact with the exocyclic ketonic oxygen O1 of the five-membered antipyrine ring with an O···Cl distance of 3.010 Å and angle ∠C=O···Cl of 158.12°, which is well within the range reported earlier [15c]. The observed O···Cl distance (3.010 Å) is shorter than the sum of the Van der Waals radii for Cl and O (3.2 Å) and this short contact is due to the partial positive and negative charge residing on Cl1 and O1 respectively. Further, the O···Cl short contacts observed in pentachloronitrobenzene by Tanaka et al. [15d] and 2-chloro-4,6-dinitrophenol by Andersen et al. [15e] also support a similar mode of interaction with partial negative and positive charges between the O and Cl atoms at a distance 3.01 Å and 3.054 Å, respectively. Intramolecular O–H···N H-bonding between the phenolic hydrogen H2 and N3 (O(2)–H(2)···N(3):H(2)···N(3) = 1.87 Å; O(2)···N(3) = 2.597(2) Å; ∠O(2)–H(2)···N(3) = 148°) and a C–H···O interaction (C(10)–H(10)···O(1):H(10)···O(1) = 2.28 Å; C(10)···O(1) = 2.972(3) Å and C(10)–H(10)···O(1) = 130°) between H10 and the exocyclic ketonic oxygen O1 of the five-membered ring are also observed, and these intramolecular H-bonding interactions have an effect on the conformation of the molecule, including the tilt of the phenyl ring with respect to the five-membered ring.

3.2.3. Structure of $[Cu(L_1)_2]$ (1)

An ORTEP view of the neutral Cu(II) complex, **1** with the atom numbering scheme is shown in Fig. 4. The metal center possesses a tetrahedrally distorted square planar geometry with N2O2 donor atoms coordinating from two different Schiff base ligands L_1. Even though the ligand is tridentate in nature, it binds the Cu(II) ion, in a bidentate fashion through the deprotonated phenolic oxygen of the phenyl ring and nitrogen of the azomethine group, leaving

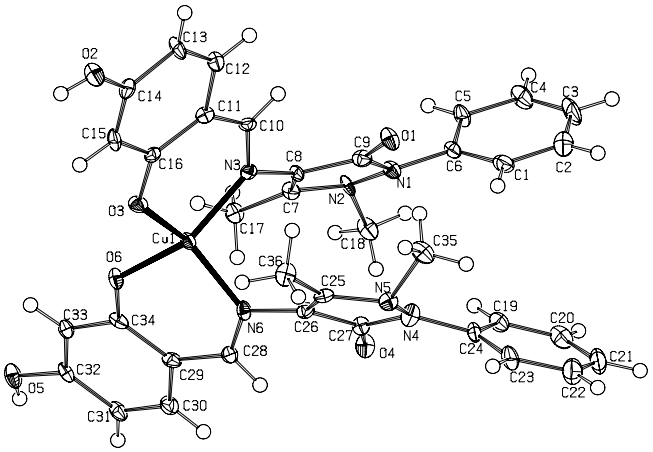


Fig. 4. ORTEP diagram of *1* with the atom numbering scheme.

the antipyrine exocyclic ketonic oxygen O4 and O1 free. The steric strain imposed by the methyl substitution on the antipyrine moiety restricts the ligand towards bidentate coordination from its tridentate nature. The Cu–N distances (Cu1–N3 = 1.967(3) Å; Cu1–N6 = 1.953(3) Å) and Cu–O distances (Cu1–O3 = 1.887(3) Å; Cu1–O6 = 1.924(3) Å) are well within the range reported for related Schiff base complexes of Cu(salen) [16,17]. The *cis* angles subtended by the six-membered chelate ring with Cu(II) from each ligand [O3–Cu1–N3 = 95.95(13)°, O6–Cu1–N6 = 94.07(13)°, N6–Cu1–N3 = 99.23(13)°, O3–Cu1–O6 = 91.78(12)°] deviate only marginally from the ideal square planar value. However, the trans angles [N6–Cu1–O3 = 145.30(13)° and O6–Cu1–N3 = 143.74(13)°] at the Cu(II) center deviate significantly from an ideal square planar geometry, indicating a tetrahedral bias to the Cu(II) coordination. This may be due to the steric constraints imposed by the methyl groups attached to the five-membered antipyrine ring towards the right approach of

the ligand moiety for metal coordination. This is further strengthened by the mean plane involving the "sal" units from different ligands, which are twisted relative to each other by approximately 58.09° and make angles of 28.86° (C11–C16 and O3) and 37.89° (C29–C34 and O6) with respect to the N2O2 mean plane. The N and O atoms show considerable deviation from the mean plane involving N2O2; *trans* N and O from a different ligand moiety (N3 and O6) are displaced in the downward direction (−0.540 Å and −0.625 Å) while N6 and O3 are in the opposite direction (0.494 Å and 0.540 Å) with Cu(II) contained well within the coordination plane (0.015 Å). It is pertinent to note that such distortions in the Cu(II) geometry of blue copper proteins [18–20] and Cu(salen) [21,22] complexes with tetrahedrally distorted square planar geometry are reported to deserve importance in view of catalytic activity.

The packing diagram viewed down the *a*-axis with various H-bonding interactions in **1** is depicted in Fig. 5. The molecules are aligned as layers along the *b*-axis by strong intermolecular O–H···O interactions, between adjacent molecules via the phenolic hydrogen H5 (from O5) of each coordinated ligand moiety with the ketonic oxygen O1 of the five-membered antipyrine moiety. These hydrogen bonded layers are further cross linked along the *c*-axis generating the bilayer by another intermolecular O–H···O H-bonding between the phenolic hydrogen H2 of the second ligand with the coordinated "sal" oxygen O2 [O(2)–H(2)···O(6):H(2)···O(6) = 1.97 Å, O(2)···O(6) = 2.701(4) Å, ∠O(2)–H(2)···O(6) = 147°]. Intermolecular C–H···O interactions between the bilayers creates a two dimensional H-bonded network in the *bc*-plane [C(17)–H(17A)···O(3):H(17A)···O(3) = 2.51 Å, C(17)···O(3) = 3.323(5) Å, ∠C(17)–H(17A)···O(3) = 142° and C(22)–H(22)···O(2):H(22)···O(2) = 2.43 Å, C(22)···O(2) = 3.340(6) Å,∠C(22)–H(22)···O(2) = 167°]. In addition to the above mentioned intermolecular H-bonding, intramolecular C–H···O H-bonding also exist between the methyl hydrogens H18A and H35A from different ligands with the ketonic oxygens O4 and O1 respectively (C(18)–H(18A)···O(4):H(18A)···O(4) = 2.49 Å; C18···O(4) = 3.364(6), ∠C(18)–H(18A)···O(4) = 151° and C(35)–H(35A)···O(1):H(35A)···O(1) = 2.31 Å, C(35)···O(1) = 3.242(6) Å and ∠C(35)–H(35A)···O(1) = 162°). Thus, the ketonic oxygen O1 and O4 from the two different ligand moieties may be orienting the preferential hydrogen bonding mode rather than coordination with the metal center to impose a tetrahedrally distorted square pyramidal geometry around the Cu(II) center.

3.2.4. Structure of $[Cu(L_2)_2]$ (2)

Compound **2** crystallizes in the centrosymmetric space group $C_{2/c}$ with Cu(II) sitting on a twofold axis. An ORTEP view of the neutral Cu(II) complex with the atom numbering scheme is shown in Fig. 6. The metal center possesses a distorted square planar geometry with N2O2 donor atoms coordinating from two different Schiff base ligands. The Cu(II) ion occupies a special position and coordinates with two symmetry related ligand moieties in a bidentate fashion through the deprotonated phenolic oxygen and nitrogen of the azomethine group, leaving the antipyrine exocyclic ketonic oxygen free. The Cu–N distance (Cu1–N3 = 1.9567(17) Å) and Cu–O distance (Cu1–O2 = 1.8878(14) Å) are well within the range reported for related Schiff base complexes [16,17]. The *cis* angles subtended by the six-membered chelate ring with Cu(II) from each ligand [O2–Cu1–N3 = 90.75(6)°, O(2)a–Cu(1)–N(3) = 93.63(6)°] are within the close range of an ideal square planar value, while the *trans* angles [O(2)a–Cu(1)–O(2) = 154.31(9)° and N(3)a–Cu(1)–N(3) = 160.18(10)°] at the Cu(II) center deviate from square planar geometry, indicating a distorted square planar geometry for the Cu(II) coordination. This can be attributed to the six-membered metal-chelate ring formation by the ligand moiety around Cu(II) and the ligand steric constraints imposed by the methyl groups attached to the five-membered antipyrine ring towards the closer approach for metal coordination. The mean

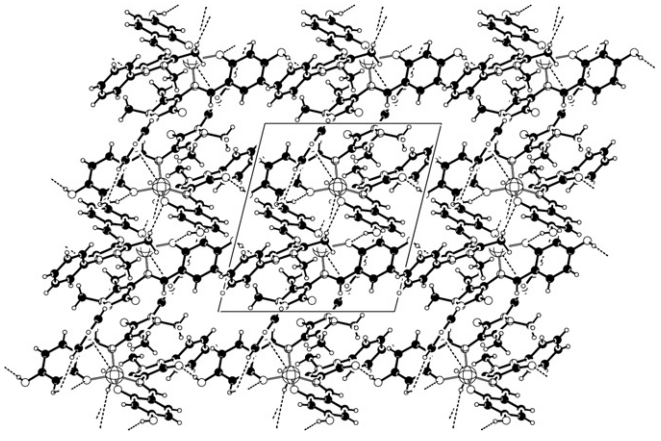


Fig. 5. Packing diagram of **1** viewed down the *a*-axis with various H-bonding interactions.

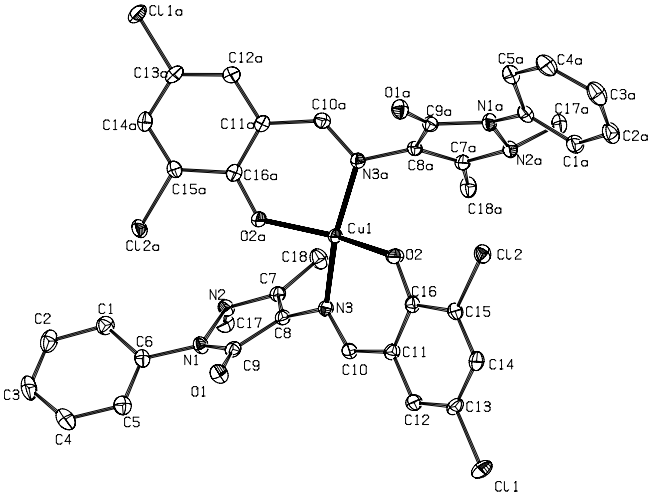


Fig. 6. ORTEP diagram of **2** with the atom numbering scheme. (Hydrogen atoms are omitted for clarity.)

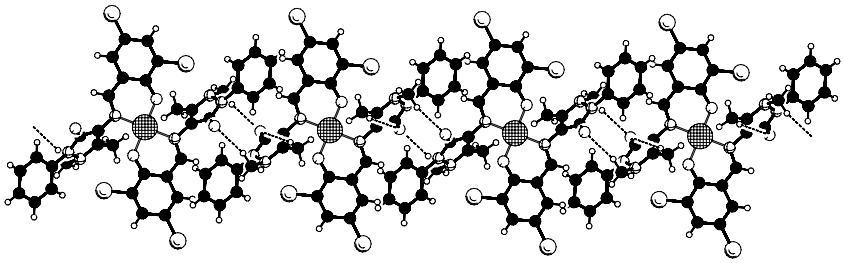


Fig. 7. Packing diagram of **2** viewed down the *b*-axis showing the hydrogen bonding interactions.

plane involving the "sal" units of symmetry related ligands are twisted relative to each other by 34.43° and make a 17.15° angle (angle of C11–C16 and O2) with respect to the N2O2 mean plane, which is comparatively less in **2** indicating much less distortion from the square planar geometry. The Cu(II) atom is contained well in the square base, the *trans* oxygens and *trans* nitrogens coordinated to it from the twofold related ligands are displaced by 0.729° and 1.789° respectively in opposite directions.

A packing diagram of compound **2** viewed down the *b*-axis with hydrogen bonding interactions is shown in Fig. 7. As depicted in the packing, the molecules are arranged in layers along the *c*-axis. The aligned adjacent molecules within the layers are bridged via intermolecular C–H···O hydrogen bonding between the methyl hydrogens H17C and H18C of the five-membered antipyrine ring with the exocyclic ketonic oxygen O1 from either side of the symmetry allied ligand moiety. Details pertinent to the hydrogen bonding interactions and symmetry code are: C(17)–H(17C)···O(1):H(17C)···O(1) = 2.38 Å; C(17)···O(1) = 3.303(3) Å; ∠C(17)–H(17C)···O(1) = 160°, symmetry code: $-x$, $1-y$, $-z$ and C(18)–H(18C)···O(1):H(18C)···O(1) = 2.57 Å; C(18)···O(1) = 3.502(3); ∠C(18)–H(18C)···O(1) = 163°, symmetry code; x, $1+y$, z. The layers along the *c*-axis are also involved in weak C–H···π interactions [23] between the antipyrine phenyl ring and azomethane hydrogen H10, showing the effective closer approach and orientation of the neighboring molecules. Pertinent C–H···π interactions with the symmetry code are C10–H10···Cg1:H10···Cg1 = 2.94 Å, C10···Cg1 = 3.609(2) Å and ∠C10–H10···Cg1 = 130°, symmetry code = $-x$, $1-y$, $-z$, where Cg1 is the centroid of the phenyl ring (C1–C6). In the crystal structures of 5-dimethylnaphthalene [23b] and Resorcinol [23c] the observed CH···π distances range from 2.87 Å to 2.99 Å and 2.77 Å to 2.92 Å which are comparable with the present report for a weak C–H···π contact.

4. Conclusion

In conclusion, we have synthesized two important antipyrine Schiff base ligands and their Cu(II) complexes. The single crystal X-ray structures of **1** and **2**, being the first in the series of this type of compound, illustrate that the mode of weak H-bonding interactions and steric effect imposed by the methyl group has a profound influence on the Cu(II) geometry in **1** and **2**, rearranging from tetrahedrally distorted square planar geometry into distorted square planar.

Acknowledgements

The authors greatly acknowledge Dr. P.K. Ghosh Director of the Central Salt and Marine Chemicals Research Institute for his keen interest and encouragements. The authors P.S. and M.S. acknowledge DST, New Delhi, for the financial support

Appendix A. Supplementary material

CCDC 614053, 614054, 614055 and 614056 contain the supplementary crystallographic data for this paper. These data can be obtained free of charge via http://www.ccdc.cam.ac.uk/conts/retrieving.html, or from the Cambridge Crystallographic Data Centre, 12 Union Road, Cambridge CB2 1EZ, UK; fax: (+44) 1223-336-033; or e-mail: deposit @ccdc.cam.ac.uk. Supplementary data associated with this article can be found, in the online version, at doi:10.1016/j.poly.2006.09.004.

References

[1] K. Bernardo, S. Leppard, A. Robert, G. Commenges, F. Dehan, B. Meunier, Inorg. Chem. 35 (1996) 387.
[2] T. Punniyamurthy, S.J.S. Kalra, J. Iqbal, Tetrahedron Lett. 36 (1995) 8497.
[3] D. Chiaramonte, J.M. Steiner, J.D. Broussard, K. Baer, S. Gumminger, E.M. Moeller, D.A. Williams, R. Shumway, Can. J. Vet. Res. 67 (2003) 183.
[4] (a) A.M. Farghaly, A. Hozza, Pharmazie 35 (1980) 596;
(b) T. Hitoshi, N. Tamao, A. Hideyuki, F. Manabu, M. Takayuki, Polyhedron 16 (1997) 3787.
[5] Kamal.Z. Ismail, Transition Met. Chem. 25 (2000) 522.
[6] A. El-Dissouky, A.K. Shehata, G. El-Mahadey, Polyhedron 16 (1997) 1247.
[7] N. Raman, A. Kulandaisamy, C. Thangaraja, Transition Met. Chem. 29 (2004) 129.
[8] G. Shankar, R.R. Premkumar, S.K. Ramalingam, Polyhedron 5 (1986) 991.
[9] T. Radhakrishnana, P.T. Joseph, C.P. Prabhakaran, J. Inorg. Nucl. Chem. 38 (1976) 2212.
[10] G.M. Sheldrick, SAINT, 5.1 ed., Siemens Industrial Automation Inc., Madison, WI, 1995.
[11] (a) SADABS, Empirical Absorption Correction Program, University of Göttingen, Göttingen, Germany, 1997;
(b) G.M. Sheldrick, SHELXTL Reference Manual: Version 5.1, Bruker AXS, Madison, WI, 1997.

[12] G.M. Sheldrick, SHELXL-97: Program for Crystal Structure Refinement, University of Göttingen, Göttingen, Germany, 1997.
[13] A.L. Spek, PLATON-97, University of Utrecht, Utrecht, The Netherlands, 1997.
[14] Mercury 1.3 Supplied with Cambridge Structural Database; CCDC: Cambridge, UK, 2003–2004.
[15] (a) T. Steiner, Angew. Chem., Int. Ed. 41 (2002) 48;
(b) A. Nangia, Cryst. Eng. Commun. 4 (17) (2002) 93;
(c) P.N. Moorthy, P. Venkatakrishnan, P. Mal, S. Dixit, P. Venugopalan, Cryst. Growth Des. 3 (2003) 581;
(d) I. Tanaka, F. Iwasaki, A. Aihara, Acta Crystallogr., Sect. B 30 (1974) 1546;
(e) E.K. Andersen, I.G.K. Andersen, Acta Crystallogr., Sect. B 31 (1975) 387.
[16] M.M. Bhadbhade, D. Srinivas, Inorg. Chem. 32 (1993) 6122.
[17] P.S. Subramanian, E. Suresh, P. Dastidar, Polyhedron 23 (2004) 2515.
[18] (a) A. Messerschmidt, Struct. Bond. 90 (1998) 37;
(b) E.I. Solomon, K.W. Penfield, D.E. Wilcox, Struct. Bond. 53 (1983) 1.
[19] A. Messerschmidt, Adv. Inorg. Chem. 40 (1994) 121.
[20] A.G. Sykes, Adv. Inorg. Chem. 36 (1991) 377.
[21] C.R. Jacob, S.P. Varkey, P. Ratnasamy, Micropor. Mesopor. Mater. 22 (1998) 465.
[22] C.R. Jacob, S.P. Varkey, P. Ratnasamy, Appl. Catal. A 168 (1998) 353.
[23] (a) Y. Umezawua, S.T. Sudoyama, K. Honda, J. Uzawa, M. Nishio, Bull. Chem. Soc. Jpn. 71 (1998) 1207;
(b) A.C. Hazell, R.G. Hazell, L. Norskov-Lauristein, C.E. Briant, D.W. Jones, Acta Crystallogr., Sect. C 42C (1986) 690;
(c) G.E. Bacon, R.J. Jude, Z. Kristallogr. 138 (1973) 19.

Available online at www.sciencedirect.com
ScienceDirect
Polyhedron 26 (2007) 757–762
POLYHEDRON
www.elsevier.com/locate/poly

Synthesis, characterization and superoxide dismutase activity of some octahedral nickel(II) complexes

R.N. Patel *, Nripendra Singh, V.L.N. Gundla

Department of Chemistry, A.P.S. University, Rewa, M.P. 486 003, India

Received 29 August 2006; accepted 4 September 2006
Available online 29 September 2006

Abstract

Four new mixed ligand nickel(II) complexes viz., $[Ni(tren)(phen)](ClO_4)_2$ (**1**), $[Ni(tren)(bipy)](ClO_4)_2$ (**2**), $[Ni(SAA)(PMDT)]\cdot 2H_2O$ (**3**) and [Ni(SAA)(TPTZ)] (**4**) (tren = tris(2-aminoethylamine), phen = 1,10-phenanthroline, bipy = 2,2′-bipyridine, SAA = salicylidene anthranilic acid, PMDT = *N*,*N*,*N*′,*N*″,*N*″-pentamethyldiethylenetriamine, TPTZ = 2,4,6-tri(2-pyridyl)-1,3,5-triazine) have been synthesized and characterized by means of elemental analysis, spectroscopic, magnetic susceptibility and cyclic voltammetric measurements. Single crystal X-ray analysis of $[Ni(tren)(phen)](ClO_4)_2$ (**1**) and $[Ni(SAA)(PMDT)]\cdot 2H_2O$ (**3**) has revealed the presence of a distorted octahedral geometry. Superoxide dismutase activity of these complexes has also been measured.
© 2006 Elsevier Ltd. All rights reserved.

Keywords: Mixed ligand nickel(II) complexes; Magnetic susceptibility; Single crystal X-ray analysis; Superoxide dismutase activity

1. Introduction

Recently, Ni-containing superoxide dismutase (NiSOD) was isolated from several *Streptomyces* species [1]. The enzymatic activity of NiSOD [2] however is on the same high level as that of Cu–ZnSOD at about $10^9\ M^{-1}\ S^{-1}$ per metal center. The superoxide radical (O_2^-) is an inevitable byproduct of aerobic metabolism which if not eliminated may cause significant cellular damage; consequently, the superoxide radical has been implicated in numerous medical disorders [3]. To avoid such harmful consequences, all oxygen metabolizing organisms possess metalloenzymes known as superoxide dismutases (SODs). SODs are dedicated to keep the concentration of O_2^- in controlled low limits thus protecting biological molecules from oxidative damage. These SODs disproportionate the toxic O_2^- radical to molecular oxygen and hydrogen peroxide [4]. All SODs employ the two-step ping-pong mechanism shown in Eqs. (1) and (2), where M is a redox active metal center capable of both oxidizing and reducing superoxide

$$M^{ox} + O_2^- \rightarrow M^{red} + O_2 \quad (1)$$

$$M^{red} + O_2 + 2H^+ \rightarrow M^{ox} + H_2O_2 \quad (2)$$

X-ray crystallographic studies [5] of NiSODs from *Streptomyces* species have illustrated the nature of the enzyme active site. In both structures, the square pyramidal coordination geometry exhibited by the Ni center in the oxidized form ($NiSOD_{ox}$) is converted to a square-planar geometry in the reduced state ($NiSOD_{red}$), as the axial imidazole group derived from the His1 residue dissociates upon metal ion reduction. The four equatorial ligands include two thiolates from Cys2 and Cys6 in a *cis* arrangement, the deprotonated amide of the Cys2 backbone, and the N-terminal $-NH_2$ group of His1.

The preparation and study of structural models can lead to the understanding of fundamental mechanistic aspects of the enzyme as well as to the development of structure–activity relationships.

In the continuation of our work [6] on polyamines, polypyridyl and salicylideneanthranilic acid containing complexes, here we report the synthesis and characterization of new mixed ligand nickel(II) complexes viz., $[Ni(tren)(phen)](ClO_4)_2$ (**1**), $[Ni(tren)(bipy)](ClO_4)_2$ (**2**),

* Corresponding author. Tel.: +91 7662 231373; fax: +91 7662 230819.
E-mail address: rnp64@yahoo.co.uk (R.N. Patel).

0277-5387/$ - see front matter © 2006 Elsevier Ltd. All rights reserved.
doi:10.1016/j.poly.2006.09.041

[Ni(SAA)(PMDT)]·$2H_2O$ (**3**) and [Ni(SAA)(TPTZ)] (**4**). Single crystal X-ray analysis of **1** and **3**, spectral, redox properties and superoxide dismutase activity of these complexes have also been described.

2. Experimental

2.1. Materials and methods

$Ni(ClO_4)_2 \cdot 6H_2O$, *N*,*N*,*N*′,*N*″,*N*″-pentamethyldiethylenetriamine (PMDT), 2,4,6-tri(2-pyridyl)-1,3,5-triazine (TPTZ) (Aldrich Chemicals), $NiCl_2 \cdot 6H_2O$, 1,10-phenanthroline, 2,2′-bipyridine, methanol, acetonitrile (S.D. Fine Chemicals) and tetrabutylammonium perchlorate (Acros Chemicals) were used as purchased. The Schiff base (SAA) was prepared as described in our earlier publication [6f]. Elemental analyses were performed on an Elementar Vario EL III, Carlo Erba 1108 elemental analyzer. FAB mass spectra were recorded on a JEOL SX 102/DA 6000 mass spectrometer using xenon (6 kV, 10 mA) as the FAB gas. The magnetic susceptibility data were recorded on a Gouy balance at room temperature using mercury(II) tetrathiocyanato cobaltate(II) ($\chi_g = 16.44 \times 10^{-6}$ cgs unit) as the calibrant. The effective magnetic moment was calculated per Ni(II) atom from the equation $\mu_{eff} = 2.83\sqrt{\chi_M T}$ B.M., where χ_M is the molar magnetic susceptibility corrected for diamagnetism of the constituent atoms [7]. UV–Vis spectra were recorded on a Shimadzu UV–Vis 160 spectrophotometer in quartz cells. A BAS-100 Epsilon electrochemical analyzer was used for the cyclic voltammetric experiment in DMSO solution of the complex containing tetrabutylammonium perchlorate (TBAP) as the supporting electrolyte. The three electrodes measurement was carried out at 298 K under nitrogen atmosphere with a platinum working electrode, a platinum wire auxiliary electrode and a silver/silver chloride reference electrode (Ag/AgCl). The SOD activities were evaluated using alkaline DMSO as a source of superoxide radicals (O_2^-) and nitro blue tetrazolium chloride (NBT) as a scavanger [6f,6d].

2.2. Synthesis of the complexes

2.2.1. Preparation of [Ni(tren)(phen)]$(ClO_4)_2$ (1) and [Ni(tren)(bipy)]$(ClO_4)_2$ (2)

To a MeOH solution (10 mL) of $Ni(ClO_4)_2 \cdot 6H_2O$ (1.0 mmol, 0.365 g) a MeOH solution (10 mL) of tren (1.0 mmol, 0.146 g) was added with stirring for 10 min. To the above reaction mixture, a MeOH solution (10 mL) of phen (1.0 mmol, 0.198 g) was added and the stirring was continued for 30 min at 25 °C. After completion of the reaction, the precipitate thus formed was collected by filtration and was dissolved in MeOH:MeCN (1:1 v/v) for recrystallization. After two days of slow evaporation light pink crystals were collected and washed with MeOH . These were dried in air at room temperature and stored in $CaCl_2$ desiccator. Yield, 70%. *Anal.* Calc. for $C_{18}H_{26}N_6NiCl_2O_8$ (**1**): C, 37.03; H, 4.45; N, 14.40. Found: C, 37.55; H, 5.00; N, 14.35%. FAB Mass found: 383. Calc.: 385.17. Complex **2** was synthesized as described above by employing bipy (1.0 mmol, 0.156 g) in place of phen. Yield, 75%. *Anal.* Calc. for $C_{16}H_{26}N_6NiCl_2O_8$ (**2**): C, 34.33; H, 4.65; N, 15.02. Found: C, 34.23; H, 4.50; N, 15.42%. FAB Mass found: 360. Calc.: 361.14.

2.2.2. Synthesis of [Ni(SAA)(PMDT)]·$2H_2O$ (3) and [Ni(SAA)(TPTZ)] (4)

To a MeOH solution (10 mL) of $NiCl_2 \cdot 6H_2O$ (1.0 mmol, 0.237 g), a MeOH solution (10 mL) of the potassium salt of SAA (1.0 mmol, 0.241 g) was added with stirring for 10 min. To the above reaction mixture, a MeOH solution (10 mL) of PMDT (1.0 mmol, 0.173 g) was added and the stirring was continued for 30 min at 25 °C. After completion of the reaction, the dark red reaction mixture was filtered to remove any solid impurities and left for slow evaporation. After two days of slow evaporation dark red crystals were collected and washed with MeOH. These were dried in air at room temperature and stored in $CaCl_2$ desiccator. Yield, 70%. *Anal.* Calc. for $C_{23}H_{38}N_4O_5Ni$ (**3**): C, 58.31; H, 7.18; N, 11.83. Found: C, 57.61; H, 7.56; N, 11.58%. FAB Mass found: 473. Calc.: 473.27. Complex **4** was synthesized as described above by employing TPTZ (1.0 mmol) in place of PMDT. Yield, 75%. *Anal.* Calc. for $C_{32}H_{23}N_7O_3Ni$ (**4**): C, 62.71; H, 3.75; N, 16.00. Found: C, 61.12; H, 4.19; N, 15.54%. FAB Mass found: 611. Calc.: 612.31.

Caution! Perchlorate salts of metal complexes are potentially explosive and should be handled with great care.

2.3. X-ray crystallography

Crystals suitable for single crystal X-ray analysis for the complexes [Ni(tren)(phen)]$(ClO_4)_2$ (**1**) and [Ni(SAA)(PMDT)]·$2H_2O$ (**3**) were grown by slow evaporation of the reaction mixture at room temperature. The single crystals of **1** and **3** were mounted on a glass fiber and used for data collection (Table 1). Crystal data were collected on an Enraf-Nonius $MACH_3$ diffractometer using graphite monochromatized Mo Kα radiation ($\lambda = 0.71073$ Å). The crystal orientation, cell refinement and intensity measurements were made using the program CAD-4PC performing ψ-scan measurements. The structures were solved by direct methods using the program SHELXS-97 [8] and refined by full-matrix least-squares techniques against F^2 using SHELXL-97 [9]. All non-hydrogen atoms were refined anisotropically. All the hydrogen atoms were geometrically fixed and allowed to refine using a riding model.

3. Results and discussion

3.1. Synthesis

All the present mixed ligand nickel(II) complexes have been synthesized by the following sequential routes:

For complexes **1** and **2**

Table 1
Crystal data and structure refinement for complexes $[Ni(tren)(phen)](ClO_4)_2$ (**1**) and $[Ni(SAA)(PMDT)]\cdot 2H_2O$ (**3**)

Empirical formula	$C_{18}H_{26}Cl_2N_6NiO_8$ (**1**)	$C_{23}H_{35}N_4NiO_5$ (**3**)
Formula weight	584.06	506.26
Temperature (K)	293(2)	293(2)
Wavelength (Å)	0.71073	0.71073
Crystal system	orthorhombic	triclinic
Space group	*Pbca*	$P\bar{1}$
Unit cell dimensions		
a (Å)	12.7139(9)	9.2930(9)
b (Å)	14.5544(7)	11.5830(8)
c (Å)	26.668(6)	12.3700(8)
α (°)	90	88.661(6)
β (°)	90	71.503(6)
γ (°)	90	82.416(7)
Volume (Å^3)	4934.8(11)	1251.44(17)
Z	8	2
D_{calc} (Mg/m^3)	1.572	1.344
Absorption coefficient (mm^{-1})	1.05805	0.815
F(000)	2416	538
Crystal size (mm)	$0.20\times0.15\times0.10$	$0.35\times0.30\times0.30$
θ Range for data collection (°)	3.06–25.00	1.74–24.96
Limiting indices	$-15\leqslant h\leqslant 15$, $-17\leqslant k\leqslant 17$, $-31\leqslant l\leqslant 31$	$-11\leqslant h\leqslant 0$, $-13\leqslant k\leqslant 13$, $-14\leqslant l\leqslant 13$
Reflections collected/unique [R_{int}]	47070/4328 [0.0272]	4662/4366 [0.0194]
Completeness to θ=	25.00, 99.8%	24.96, 99.6%
Absorption correction	analytical	ψ-scan
Maximum and minimum transmission	0.84188 and 0.73607	0.7922 and 0.7636
Refinement method	full-matrix least-squares on F^2	full-matrix least-squares on F^2
Data/restraints/parameters	4328/114/396	4366/0/310
Goodness-of-fit on F^2	1.112	1.037
Final R indices [$I>2\sigma(I)$]	$R_1=0.0366$, $wR_2=0.1057$	$R_1=0.0518$, $wR_2=0.1332$
R indices (all data)	$R_1=0.0566$, $wR_2=0.1128$	$R_1=0.0877$, $wR_2=0.1479$
Largest difference in peak and hole (e Å^{-3})	0.384 and −0.207	1.302 and −0.553

$$Ni^{2+} + A \rightarrow [Ni(A)(H_2O)_n]^{2+} \quad (3)$$

$$[Ni(A)(H_2O)_n]^{2+} + B \rightarrow [Ni(A)(B)]^{2+} \quad (4)$$

A = tren, B = bipy/phen

For complexes **3** and **4**

$$Ni^{2+} + C \xrightarrow{\text{Basic Medium}} [Ni(C)(H_2O)_n] \quad (5)$$

$$[Ni(C)(H_2O)_n] + D \rightarrow [Ni(C)(D)] \quad (6)$$

C = SAA, D = PMDT/TPTZ

The target complexes were prepared in a good yield. These complexes were characterized by microanalysis and further characterized by FAB^+ mass spectrometry.

3.2. Crystal structures

Complexes **1** and **3** have been characterized by the single crystal X-ray diffraction technique. The ORTEP views of the complexes are shown in Figs. 1 and 2. Crystallographic data (Table 1), selected bond angles and distances are given in Tables 2 and 3. Complex **1** crystallizes in the orthorhombic system. The structure of **1** was solved in *Pbca* space group, whereas **3** crystallizes in the triclinic $P\bar{1}$ space group. The coordination geometries of complexes **1** and **3** are distorted octahedral. Significant deviation from 90° of the bond angles involving the chelation is observed (Tables 2 and 3). In complex **1** one tetradentate ligand (tren) and

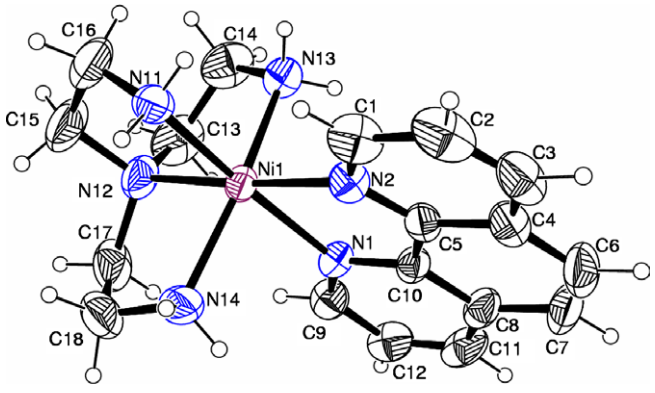


Fig. 1. ORTEP diagram of the complex $[Ni(tren)(phen)]^{2+}$ (**1**).

one bidentate ligand (phen) are coordinated with the nickel(II) center. The coordination sites in the complexes are the tetradentate tris(2-aminoethylamine) group Ni–N(11) = 2.113(2) Å, Ni–N(12) = 2.105(3) Å, Ni–N(13) = 2.129(2) Å, Ni–N(14) = 2.102(3) Å and heterocyclic N of the phen Ni–N(1) = 2.187(2) Å and Ni–N(2) = 2.083(2) Å. Individual, mean bond distances and angles within the coordination polyhedron compare well with those found in other octahedral complexes of Ni(II) involving N-donor atoms [10]. The coordination geometry is distorted from octahedral as ascertained by the observed τ value of 0.059 (the structural index is defined as $\tau=(\beta-\alpha)/60$

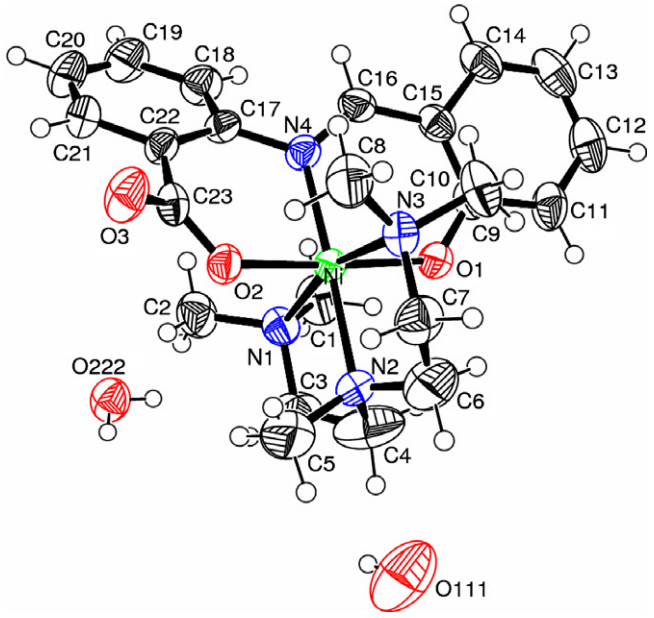


Fig. 2. ORTEP diagram of the complex $[Ni(SAA)(PMDT)]\cdot 2H_2O$ (**3**).

Table 2
Selected bond lengths (Å) and angles (°) for $[Ni(tren)(phen)](ClO_4)_2$ (**1**)

Ni(1)–N(2)	2.083(2)	N(12)–C(13)	1.476(6)
Ni(1)–N(14)	2.102(3)	N(12)–C(17)	1.487(5)
Ni(1)–N(12)	2.105(3)	N(12)–C(15)	1.513(5)
Ni(1)–N(11)	2.113(2)	N(13)–C(14)	1.471(4)
Ni(1)–N(13)	2.129(2)	N(14)–C(18)	1.478(6)
Ni(1)–N(1)	2.187(2)	C(5)–C(10)	1.434(4)
N(1)–C(10)	1.362(3)	C(13)–C(14)	1.503(6)
N(2)–C(5)	1.349(4)	C(17)–C(18)	1.496(7)
N(11)–C(16)	1.453(5)		
N(2)–Ni(1)–N(14)	99.62(12)	N(12)–Ni(1)–N(1)	104.15(10)
N(2)–Ni(1)–N(12)	176.47(11)	N(11)–Ni(1)–N(1)	172.93(10)
N(14)–Ni(1)–N(12)	83.22(13)	N(13)–Ni(1)–N(1)	88.30(9)
C(10)–N(1)–Ni(1)	111.55(18)	C(10)–N(1)–Ni(1)	111.55(18)
N(2)–Ni(1)–N(11)	94.78(11)	C(1)–N(2)–Ni(1)	127.0(2)
N(14)–Ni(1)–N(11)	93.88(11)	C(5)–N(2)–Ni(1)	114.58(18)
N(12)–Ni(1)–N(11)	82.90(12)	C(16)–N(11)–Ni(1)	108.0(2)
N(2)–Ni(1)–N(13)	95.76(9)	C(13)–N(12)–Ni(1)	105.3(2)
N(14)–Ni(1)–N(13)	162.40(12)	C(17)–N(12)–Ni(1)	105.6(2)
N(12)–Ni(1)–N(13)	81.76(12)	C(15)–N(12)–Ni(1)	108.2(2)
N(11)–Ni(1)–N(13)	93.30(10)	C(14)–N(13)–Ni(1)	111.5(2)
N(2)–Ni(1)–N(1)	78.21(9)	C(18)–N(14)–Ni(1)	109.8(3)
N(14)–Ni(1)–N(1)	86.53(10)		

where α and β are the largest coordination angles, β = N(2)–Ni(1)–N(12) 176.5° and α = N(11)–Ni(1)–N(1) 172.9°), such a type of octahedral geometry was observed in similar Ni(II) complexes ($\tau = 0.07$) [11].

In complex **3**, the crystal structure consists of a mononuclear neutral moiety with two water molecules. The coordination sites in complex **3** are the tridentate PMDT group Ni–N(1) = 2.211(3) Å, Ni–N(2) = 2.130(3) Å, Ni–N(3) = 2.327(3) Å and tridentate Schiff base (SAA) containing ONO donors Ni–O(1) = 1.996(3) Å, Ni–N(4) = 2.058(3) Å, Ni–O(2) = 2.015(3) Å. The geometry of the $Ni^{II}N_4O_2$ coordination polyhedron is appreciably elongated and minimally distorted octahedral as ascertained by the observed τ value of 0.06 (β = N(4)–Ni–N(2) 177.27° and α = O(1)–Ni–O(2) 173.41°). The nickel–nitrogen and nickel–oxygen lengths for the octahedral $[Ni(SAA)(PMDT)]\cdot 2H_2O$ (**3**) are comparable to that found in similar types of nickel(II) octahedral complexes [12].

Table 3
Selected bond lengths (Å) and angles (°) for $[Ni(PMDT)(SAA)]\cdot 2H_2O$ (**3**)

Ni–O(1)	1.996(3)	N(4)–C(16)	1.309(5)
Ni–O(2)	2.015(3)	N(4)–C(17)	1.425(5)
Ni–N(4)	2.058(3)	C(3)–C(4)	1.563(9)
Ni–N(2)	2.130(3)	C(6)–C(7)	1.526(8)
Ni–N(1)	2.211(3)	C(10)–O(1)	1.292(5)
Ni–N(3)	2.327(3)	C(10)–C(15)	1.420(6)
N(1)–C(3)	1.476(6)	C(15)–C(16)	1.425(6)
N(2)–C(4)	1.442(7)	C(17)–C(22)	1.405(6)
N(2)–C(6)	1.451(7)	C(22)–C(23)	1.504(6)
N(3)–C(7)	1.476(6)	C(23)–O(2)	1.271(5)
O(1)–Ni–O(2)	173.41(12)	C(2)–N(1)–Ni	113.9(3)
O(1)–Ni–N(4)	90.31(12)	C(1)–N(1)–Ni	110.8(3)
O(2)–Ni–N(4)	89.51(12)	C(3)–N(1)–Ni	105.9(3)
O(1)–Ni–N(2)	90.35(12)	C(4)–N(2)–Ni	103.8(3)
O(2)–Ni–N(2)	90.14(12)	C(6)–N(2)–Ni	105.3(3)
N(4)–Ni–N(2)	177.27(14)	C(5)–N(2)–Ni	117.1(3)
O(1)–Ni–N(1)	90.06(12)	C(9)–N(3)–Ni	113.5(3)
O(2)–Ni–N(1)	96.52(12)	C(8)–N(3)–Ni	113.4(3)
N(4)–Ni–N(1)	94.89(13)	C(7)–N(3)–Ni	103.6(3)
N(2)–Ni–N(1)	82.46(13)	C(16)–N(4)–Ni	122.7(3)
O(1)–Ni–N(3)	87.68(12)	C(17)–N(4)–Ni	120.8(2)
O(2)–Ni–N(3)	85.90(11)	N(2)–Ni–N(3)	80.97(13)
N(4)–Ni–N(3)	101.70(13)	N(1)–Ni–N(3)	163.26(12)

3.3. Magnetic measurements

The magnetic susceptibility measurements in the solid state show that the present complexes are paramagnetic at room temperature. The observed magnetic moments of these complexes are in the range expected for spin-free d^8 systems. The observed magnetic moment values of $[Ni(tren)(phen)](ClO_4)_2$ (**1**), $[Ni(tren)(bipy)](ClO_4)_2$ (**2**), $[Ni(SAA)(PMDT)]\cdot 2H_2O$ (**3**) and [Ni(SAA)(TPTZ)] (**4**) are 3.05, 2.95, 3.22 and 3.25 B.M., respectively. The magnetic moment values (μ_{eff}) lie within the range normally found for other nickel(II) complexes [13].

3.4. Ligand field spectra

The room temperature ligand field spectra (electronic spectra) of these complexes have been recorded in 100% DMSO solution. One representative ligand field spectra is shown in Fig. 3 and band positions are presented in Table 4. These complexes, very similar to one another, show three strong absorptions ($^3A_{2g} \rightarrow {}^3T_{2g}$, $^3A_{2g} \rightarrow {}^3T_{1g}(F)$, $^3A_{2g} \rightarrow {}^3T_{1g}(P)$) and one weak absorption, characteristic of regular octahedral nickel(II) complexes [14]. Experimental absorption maxima corresponding to these three transitions are given in Table 4. Although the presence of distortions ($^3A_{2g} \rightarrow {}^3T_{2g}$, $^3A_{2g} \rightarrow {}^3T_{1g}(F)$, $^3A_{2g} \rightarrow {}^3T_{1g}(P)$) from the ideal octahedral geometry about the Ni atoms is demonstrated by the structural results (X-ray data).

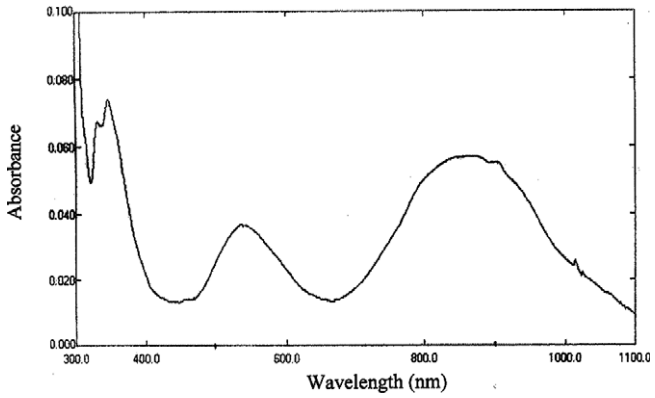


Fig. 3. The UV–Vis spectrum ($0.003\ mol^{-1}\ dm^{-3}$) of [Ni(SAA)-(PMDT)]·$2H_2O$ (**3**) in DMSO.

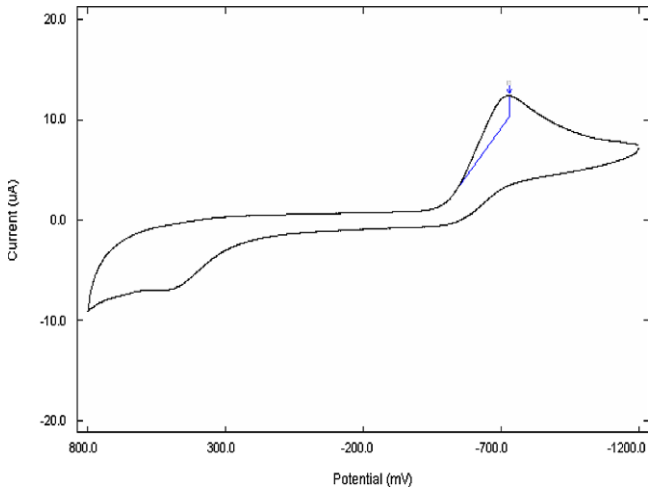


Fig. 4. Cyclic voltammogram ($0.003\ mol^{-1}\ dm^{-3}$) of [Ni(tren)(phen)]·$2H_2O$ (**1**) in DMSO (0.1 M TBAP as supporting electrolyte, scan rate: 500 mV/s).

However, band shapes and positions (assigned on the basis of O_h symmetry) and the ligand field parameter Dq ($3A_{2g} \rightarrow 3T_{2g}$, lowest energy transition) and B (Racah parameter) values, calculated according to the averaged environment rules, are in the range found for octahedrally coordinated nickel(II) ions [15].

3.5. Electrochemistry

Cyclic voltammetry of the present complexes was recorded in DMSO with TBAP as a supporting electrolyte. A representative voltammogram is shown in Fig. 4. The redox processes assigned as Ni(II)/Ni(I) couples are fully irreversible. The voltammograms of these complexes consist of two well-separated peaks, one cathodic potential (E_{pc}) and one anodic potential (E_{pa}). In these complexes reduction waves are observed at more negative potentials. Such type of electrochemistry for six-coordinate nickel(II) complexes is reported by Patra and Mukherjee [16]. The redox potential values for the nickel(II) complexes are presented in Table 5. The pertinent redox couples are represented in the following electron transfer series (Eq. (7)).

$$Ni^{II} \underset{+e^-}{\overset{e^-}{\rightleftharpoons}} Ni^{I} \qquad (7)$$

Table 5
CV Results (in V) for the Ni(II) complexes in different media[a]

Complex	E_{pc} (V)	E_{pa} (V)
[Ni(tren)(phen)]$(ClO_4)_2$ (**1**)	−0.72	0.47
[Ni(tren)(bipy)]$(ClO_4)_2$ (**2**)	−0.78	0.45
[Ni(dien)$(ImH)_3$]$(ClO_4)_2$ (**3**)	−0.75	0.43
[Ni(SAA)(TPTZ)] (**4**)	−0.76	0.45

[a] Reference electrode: Ag/AgCl. Auxiliary electrode: platinum wire. Working electrode: platinum.

3.6. SOD activity

The superoxide dismutase activities for the present complexes have been measured. These complexes exhibit significant catalytic activity towards the dismutation of superoxide anions. Superoxide was enzymatically supplied from alkaline DMSO and SOD activity was evaluated by the NBT assay [6d,6f] following the reduction of NBT to MF^+ kinetically at 560 nm. The concentration causing 50% inhibition of NBT reduction is called IC_{50}. The observed IC_{50} values of the present complexes are comparable with the earlier reported values for copper(II) complexes [6c]. The catalytic activity of NiSOD [2], however, is on the same high level as that of Cu, ZnSOD at about $10^9\ M^{-1}\ s^{-1}$ per metal center. [Ni(tren)(phen)]$(ClO_4)_2$ (**1**) shows highest SOD activity ($IC_{50} = 40\ \mu mol\ dm^{-3}$) where

Table 4
Absorption maxima, Dq, β, B and $\beta°$ of the octahedral Ni(II) complexes (ν_{max} in cm^{-1})

Complex	$^3A_{2g} \rightarrow {}^3T_{2g}$ (ν_1)	$^3A_{2g} \rightarrow {}^3T_{1g}$(F) ($\nu_2$)	$^3A_{2g} \rightarrow {}^3T_{1g}$(P) ($\nu_3$)	ν_2/ν_1	Dq	β	B	$\beta°$
[Ni(tren)(phen)]$(ClO_4)_2$ (**1**)	11170	19050	24400	1.70	1117	0.64	663	36
[Ni(tren)(bipy)]$(ClO_4)_2$ (**2**)	11100	19000	24500	1.71	1110	0.66	680	34
[Ni(SAA)(PMDT)]$(ClO_4)_2$ (**3**)	11630	18690	29400	1.60	1163	0.85	880	15
[Ni(SAA)(TPTZ)] (**4**)	11580	18570	29700	1.60	1158	0.87	902	13

$15B = (\nu_2 + \nu_3) = -3\nu_1$; $\beta = B/Bo$ [Bo (free ion) = 1030]; $\beta° = (1 - \beta) \times 100$.

as [Ni(SAA)(TPTZ)] (**4**) shows lowest SOD activity ($IC_{50} = 58$ μmol dm^{-3}) and the remaining complexes show intermediate values i.e., [Ni(tren)(bipy)]$(ClO_4)_2$ (**2**) shows an IC_{50} value of 48 μmol dm^{-3} and [Ni(SAA)(PMDT)]·$2H_2O$ (**3**) shows an IC_{50} value of 43 μmol dm^{-3}.

4. Conclusion

In this paper, we have described the synthesis and characterization of four new mononuclear nickel(II) complexes [Ni(tren)(phen)]$(ClO_4)_2$ (**1**) [Ni(tren)(bipy)]$(ClO_4)_2$ (**2**), [Ni(SAA)(PMDT)]·$2H_2O$ (**3**) and [Ni(SAA)(TPTZ) (**4**). Complexes **1** and **3** were structurally characterized by single crystal X-ray analysis. Magnetic moment values and spectral data of these complexes have shown a paramagnetic nature of the nickel(II) centre. Superoxide dismutase activity of these complexes was also measured and discussed.

5. Supplementary material

CCDC 298991 and 298970 contain the supplementary crystallographic data for [Ni(tren)(phen)]$(ClO_4)_2$ (**1**) and [Ni(SAA)(PMDT)]·$2H_2O$ (**3**). These data can be obtained free of charge via http://www.ccdc.cam.ac.uk/conts/retrieving.html, or from the Cambridge Crystallographic Data Centre, 12 Union Road, Cambridge CB2 1EZ, UK; fax: (+44) 1223-336-033; or e-mail: deposit@ccdc.cam.ac. uk.

Acknowledgments

Our grateful thanks are due to the National Diffraction Facility, X-ray Division and RSIC (SAIF), IIT Mumbai for single crystal data collection and e.p.r. measurements, respectively. The Head RSIC, Central Drug Research Institute, Lucknow is also thankfully acknowledged for providing analytical and spectral facilities. Financial assistance from UGC [Scheme No.F.30-76/2004(SR)] New Delhi is also thankfully acknowledged.

References

[1] (a) M.E. Stroupe, M. DiDonato, J.A. Tainer, in: A. Messerschmidt, R. Huber, T. Poulos, K. Wieghardt (Eds.), Handbook of Metalloproteins, Wiley, England, 2001;
(b) H.D. Youn et al., Arch. Biochem. Biophys. 334 (1996) 341.
[2] H.D. Youn, E.J. Kim, J.H. Roe, Y.C. Hah, S.O. Kang, Biochem. J. 318 (1996) 889.
[3] (a) J.M. McCord, Superoxide Dismutase 349 (2002) 331;
(b) W. Bayer, J. Imlay, I. Fridovich, Prog. Nucleic Acid Res. Mol. Biol. 40 (1991) 221;
(c) D.C. Wallace, Science 256 (1992) 628;
(d) C.C. Winterbourn, Free Radic. Biol. Med. 14 (1993) 85;
(e) B. Halliwell, in: J.S. Valentine, C.S. Foote, A. Greenberg, J.F. Liebman (Eds.), Active Oxygen in Biochemistry, Blackie Academic and Professional, New York, 1995, p. 313.
[4] (a) I. Fridovich, Annu. Rev. Biochem. 64 (1995) 97;
(b) A.F. Miller, Comments Mol. Cell. Biophs. 9 (1997) 1;
(c) J.S. Valentine, D.L. Wertz, T.J. Lyons, L. Liou, J.J. Goto, E.B. Gralla, Curr. Opin. Chem. Biol. 2 (1998) 253;
(d) A.F. Miller, Curr. Opin. Chem. Biol. 8 (2004) 162.
[5] (a) D.P. Barondeau, C.J. Kassmann, C.K. Bruns, J.A. Tainer, E.D. Getzoff, Biochemsitry 43 (2004) 8038;
(b) J. Wuerges, J.W. Lee, Y.I. Yim, H.S. Yim, S.O. Kang, K.D. Carugo, Proc. Natl. Acad. Sci. USA 101 (2004) 8569.
[6] (a) R.N. Patel, N. Singh, K.K. Shukla, U.K. Chauhan, J. Niclós-Gutiérrez, A. Castiñeiras, Inorg. Chim. Acta 357 (2004) 2469;
(b) R.N. Patel, N. Singh, K.K. Shukla, V.L.N. Gundla, U.K. Chauhan, J. Inorg. Biochem. 99 (2005) 651;
(c) R.N. Patel, N. Singh, K.K. Shukla, V.L.N. Gundla, U.K. Chauhan, Spectrochim. Acta A 63 (2006) 21;
(d) R.N. Patel, N. Singh, K.K. Shukla, U.K. Chauhan, Spectrochim. Acta A 61 (2005) 287;
(e) R.N. Patel, N. Singh, V.L.N. Gundla, Indian J. Chem. 45A (2006) 614;
(f) R.N. Patel, N. Singh, V.L.N. Gundla, Polyhedron (in press);
(g) R.N. Patel, N. Singh, K.K. Shukla, J. Niclös-Gutiérrez, A. Castiñeiras, V.G. Vaidyanathan, B.V. Nair, Spectrochim. Acta A 62 (2005) 261.
[7] E. König, Magnetic Properties of Coordination, Organometallic, Transition Metal Compounds, Springer, Berlin, 1966, p. 1.
[8] G.M. Sheldrick, Acta Crystallogr., Sect. A 46 (1990) 467.
[9] G.M. Sheldrick, SHELXL-97. Program for the Refinement of Crystal Structures, University of Goettingen, Germany, 1997.
[10] (a) K.A. Fraser, M.M. Harding, J. Chem. Soc., Dalton Trans. (1967) 415;
(b) T. Sakurai, H. Iwasaki, T. Katano, Y. Nakahashi, Acta Crystallogr., Sect. B 34 (1978) 660;
(c) M.M. Morelock, M.L. Good, L.M. Trefonas, D. Karraker, L. Maleki, H.R. Eichelkerger, R. Magesti, J. Dodge, J. Am. Chem. Soc. 101 (1979) 4858.
[11] L.P. Battaglia, A.B. Corradi, L. Antolini, G. Marcotrigiano, L. Menabue, G.C. Pellacani, J. Am. Chem. Soc. 104 (1982) 2407.
[12] E. Colacio, M. Ghazi, R. Kivekas, M. Klinga, F. Llorel, J.M. Moreno, Inorg. Chem. 39 (2000) 2770.
[13] (a) C. Alarcon-Payer, T. Pivetta, D. Choqusillo-Lazarto, J.M. Gonzalez-Perez, G. Crisponi, A. Castiñeiras, J. Niclós-Gutiérrez, Inorg. Chem. Commun. 7 (2004) 1277;
(b) M.M. da Mota, J. Rodgers, S.M. Nelson, J. Chem. Soc. A (1969) 2036.
[14] R.S. Drago, D.W. Meek, M.D. Joesten, L. Laroche, Inorg. Chem. 2 (1963) 124.
[15] (a) C. Cairns, S.G. McFall, S.M. Nelson, M.G.B. Drew, J. Chem. Soc., Dalton Trans (1979) 446;
(b) G.R. Brubaker, D.H. Bush, Inorg. Chem. 5 (1996) 2110;
(c) S.T. Chow, C.A. McAuliffe, Prog. Inrog. Chem. 19 (1975) 51.
[16] A.K. Patra, R. Mukherjee, Inorg. Chem. 38 (1999) 1388.

Available online at www.sciencedirect.com
ScienceDirect
Polyhedron 26 (2007) 763–772
POLYHEDRON
www.elsevier.com/locate/poly

Interaction of Fe(III) with herbicide-carboxylato ligands – Di-, tri- and tetra-nuclear compounds: Structure and magnetic behavior

Catherine Dendrinou-Samara [a], Sotiris Katsamakas [a], Catherine Raptopoulou [b], Aris Terzis [b], Vassilis Tangoulis [c,*], Dimitris P. Kessissoglou [a,*]

[a] *Department of General and Inorganic Chemistry, Aristotle University of Thessaloniki, Thessaloniki, 54124, Greece*
[b] *NCSR "Demokritos", Institute of Materials Science, 15310 Aghia Paraskevi Attikis, Greece*
[c] *Department of Materials Science, University of Patras, Patras 26500, Greece*

Received 22 June 2006; accepted 4 September 2006
Available online 19 September 2006

Abstract

The iron complexes with the phenoxyalkanoic acids 3,4-D, 2,3-D and 2,4,5-T in the presence or not of a nitrogen donor heterocyclic ligand, phen, were prepared and characterized. Interaction of Fe(III) with phenoxyalkanoic acids and phen leads to dinuclear neutral complexes while the absence of phen favours trinuclear cationic or tetranuclear neutral forms. The crystal structure of hexakis(2,3-dichlorophenoxyacetato)tris(methanol)oxotri-iron(III) chloride–methanol(1/3), $[Fe_3O(2,3\text{-}D)_6(MeOH)_3]Cl \cdot 3MeOH$ (**2**), and tetrakis(dimethyl-sulfoxide)octakis(2,4,5-trichlorophenoxyacetato)dioxotetra-iron(III) methanol(1/2)–water(1/1)–dimethylsulfoxide(1/0.8), $\{[Fe_4O_2(2,4,5\text{-}T)_8(dmso)_4] \cdot 2MeOH \cdot H_2O \cdot 0.8dmso\}$ (**3**), have been determined and refined by least-squares methods using three-dimensional Mo Kα data.

Magnetic data of the trimer show antiferromagnetic interaction. The ground state of the system is $S = 1/2$ with a small percentage of $S = 5/2$ paramagnetic impurity $\rho = 0.7\%$. For the tetramer, the magnetic data suggest antiferromagnetically coupled system with $S = 0$ ground state, while for the dimer, $\{[Fe_2OCl_2(3,4\text{-}D)_2(phen)_2] \cdot H_2O \cdot 3.5MeOH\}$ a very strong antiferromagnetic exchange interaction between the two ions has been observed. The fitting results give an exchange interaction of $J = 254.1\ cm^{-1}$, with $S = 0$ ground state with a small amount of paramagnetic $S = 5/2$ impurity ($\rho = 0.3\%$).
© 2006 Elsevier Ltd. All rights reserved.

Keywords: Phenoxyalkanoic acids; Trinuclear iron(III) complexes; Tetranuclear iron(III) complexes; Magnetic behavior

1. Introduction

In the bioinorganic area, iron hydroxo- and oxo-bridged dinuclear complexes represent synthetic models of the active sites of various non-heme iron proteins [1–10]. Dinuclear Fe(III) complexes are known in neutral and cationic form [11–14]. Binuclear compounds have been isolated in the presence of chelating nitrogen donor ligands. This class of compounds can be characterized by the presence of [Fe_2-(μ-O)] core while carboxylato groups can also bridge the two metal ions e.g. $[Fe_2O(O_2CMe)_2Cl_2(bpy)_2]$ [11], $[Fe_2O(O_2CCH_2Cl)_2(H_2O)(bpy)_2](NO_3)_2$ [12], $[Fe_2O(O_2CCF_3)_2(Me_2bpy)_4](ClO_4)_2$ [13], $[Fe_2O(O_2CPh)_2(phen)_4]Cl_2$ [14].

Oxo-centered, carboxylate-bridged trinuclear iron complexes [15–18] having the [Fe_3-(μ-O)] core have been characterized in mixed valence $Fe(III)_2Fe(II)$ neutral [17] or homovalence $Fe(III)_3$ mono-cationic clusters with the general formula $[Fe_3O(O_2CR)_6(solvent)_3](X)_{0\text{ or }1}$ [16]. The triangular oxo centered structure was confirmed in 1965 and since then attention has focused on various properties in the solid state. The monocationic complexes which contain three high-spin iron(III) centers, were some of the first metal clusters to which interesting magnetic exchange behavior were observed, e.g. spin frustration, while the

* Corresponding authors. Tel.: +302310997723; fax: +302310997738 (D.P. Kessissoglou).
E-mail address: kessisog@chem.auth.gr (D.P. Kessissoglou).

0277-5387/$ - see front matter © 2006 Elsevier Ltd. All rights reserved.
doi:10.1016/j.poly.2006.09.002

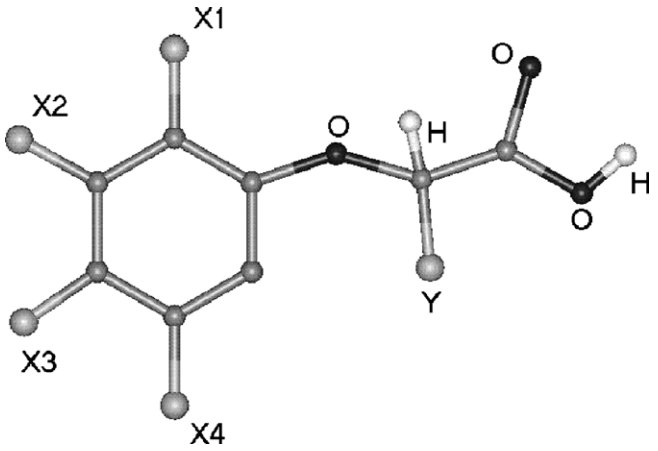
neutral complexes display intriguing temperature-dependent mixed-valence behavior and have been examined by many physical techniques.

The tetranuclear oxide-bridged carboxylate compounds includes three types of butterfly motif [19–23], the "bent" with the pyramidal μ_3-O ions on the same side or on the opposite sides of the fused Fe_3 planes [22–27] or "planar" [28–30] while examples having the rectangular core have also been reported [31]. In this class of compounds cationic e.g. $[Fe_4(OHO)(OH)_2(O_2CMe)_4(phen)_4](ClO_4)_3$, $[Fe_4O_2(O_2CPh)_7(phen)_2](ClO_4)$ [31], $[Fe_4O_2(O_2CMe)_7(bpy)_2]X$ {X = ClO_4 [19], Cl [20]}, $[Fe_4O_2(O_2CEt)_7(bpy)_2]X$ {X = ClO_4 [21], PF_6 [22]}, neutral e.g. $[Fe_4O_2(O_2CPh)_8(phen)_2]$ [31], $[Fe_4O_2Cl_2(O_2CMe)_6(bpy)_2]$ [23], or anionic $[NBu_4^n][Fe_4O_2(O_2CMe)_7(bpy)_2]$ [23] homovalence Fe(III) clusters have been reported. The formation of trinuclear or tetranuclear compounds is absolutely dependent of the solvent used. The use of methanol leads to the formation of the trinuclear species while from dmso or dmf solvents the tetranuclear compounds have been isolated.

The magnetic study of di-, tri- or tetranuclear Fe(III) clusters have shown that the presence of $Fe(III)_x$-O core leads to antiferromagnetically coupled behavior and/or the presence of spin frustration effects [32–42].

Our interest is focused on the interaction of metal ion with carboxylato ligands. We have initiated studies on the co-ordination chemistry of herbicide carboxylate agents with Cu(II), Mn(II), Mn(III), Ni(II) and d^{10} ions in an attempt to examine their mode of binding and possible biological relevance. Phenoxyalkanoic acids interact with metal ions to form complexes which have been shown to have diverse stereochemistries and biological interest [43–47].

In this paper, we report the synthesis, characterization and the magnetic behavior of binuclear, trinuclear and tetranuclear Fe(III) carboxylato compounds with the commercial auxin herbicides, 2,3-D = 2,3-dichlorophenoxy-acetic acid, 3,4-D = 3,4-dichlorophenoxy-acetic acid and 2,4,5-T = 2,4,5-trichlorophenoxy-acetic acid (Scheme 1) in the presence or not of phen = 1,10-phenanthroline.



Scheme 1. General formula of alkanoate ligands used. 2,4,5-T: X_1 = Cl, X_2 = H, X_3 = Cl, X_4 = Cl, Y = H. 3,4-D: X_1 = H, X_2 = Cl, X_3 = Cl, X_4 = H, Y = H. 2,3-D: X_1 = Cl, X_2 = Cl, X_3 = H, X_4 = H, Y = H.

We also report the molecular and the crystal structures of hexakis(2,3-dichloro-phenoxyacetato)tris(methanol)oxotri-iron(III)Chloride–methanol(1/3), $[Fe_3O(2,3\text{-}D)_6(MeOH)_3]Cl \cdot 3MeOH$ (**2**), and tetrakis(dimethyl-sulfoxide)octakis(2,4,5-trichloro-phenoxyacetato)dioxotetra-iron(III) methanol(1/2)–water(1/1)–dimethylsulfoxide(1/0.8), $\{[Fe_4O_2(2,4,5\text{-}T)_8(dmso)_4] \cdot 2MeOH \cdot H_2O \cdot 0.8dmso\}$ (**3**).

2. Experimental

2.1. Reagents and techniques

The chemicals for the synthesis of the compounds were used as purchased. Acetonitrile (CH_3CN) was distilled from calcium hydride (CaH_2) and CH_3OH from magnesium (Mg) and was stored over 3 Å molecular sieves. Diethyl ether, anhydrous grade, dimethylformamide = dmf and dimethylsulfoxide = dmso were used without any further purification. 3,4-D, 2,3-D, 2,4,5-T, phen and $FeCl_3 \cdot 6H_2O$ were purchased from Aldrich Co. All chemicals and solvents were reagent grade.

Infrared spectra (200–4000 cm^{-1}) were recorded on a Perkin–Elmer FT-IR 1650 spectrometer with samples prepared as KBr pellets. UV–Vis spectra were recorded on a Shimadzu-160A dual beam spectrophotometer. Room temperature magnetic measurements were carried out by Faraday's method using mercury tetrathiocyanatocobaltate(II) as a calibrant. Variable-temperature magnetic susceptibility measurements were carried out on powdered samples in the 3–300 K temperature range, using a Quantum Design SQUID susceptometer in a 0.1 kG and 1.0 kG applied magnetic field. Magnetization measurements were carried out at different temperatures in the range 1.8–6 K and in the field range 0–5 T. C, H and N elemental analysis were performed on a Perkin–Elmer 240B elemental analyzer, Fe was determined by atomic absorption spectroscopy on a Perkin–Elmer 1100B spectrophotometer. Electric conductance measurements were carried out with a WTW model LF 530 conductivity outfit and a type C cell, which had a cell constant of 0.996. This represents a mean value calibrated at 25 °C with potassium chloride. All temperatures were controlled with an accuracy of ±0.1 °C using a Haake thermoelectric circulating system.

2.2. Synthetic procedures

2.2.1. Synthesis of the dichlorobis[(3,4-dichlorophenoxy)acetato]bis(1,10-phenanthroline)-oxodiiron(III) $\{[Fe_2OCl_2(3,4\text{-}D)_2(phen)_2] \cdot H_2O \cdot 3.5MeOH\}$ (**1**)

3,4-D (2.22 g, 10 mmol) was dissolved in CH_3OH (20 cm^3) and NaOH (0.40 g, 10 mmol) was added. After 30 min stirring $FeCl_3 \cdot 6H_2O$ (2.7 g, 10 mmol) in CH_3OH (15 cm^3) and phen (1.80 g, 10 mmol) in CH_3OH (10 cm^3) were added drop wise. The reaction mixture was refluxed for 1 h. The red-green solution was reduced in volume and left for slow evaporation. Small green crystals of

{[Fe_2OCl_2(3,4-D)$_2$(phen)$_2$]·H_2O·3.5MeOH} (**1**) suitable for X-ray structure determination were deposited in a week. Yield 45%. (Fw = 1127.19). *Anal*. Calc. for $C_{43.50}H_{40}Cl_6Fe_2N_4O_{11.50}$ requires: C, 46.35; H, 3.55; N, 4.97; Fe 9.91. Found: C, 46.40; H, 3.35; N, 4.95; Fe 9.87%. IR: ν_{max}/cm^{-1} ν_{phen}(C=N):1649(vs); $\nu_{as}(CO_2)$: 1610, 1580(vs); $\nu_{sym}(CO_2)$:1426 (vs) (KBr pellet); UV–Vis: λ(nm)(ε, $dm^3\,mol^{-1}\,cm^{-1}$), dmso solution: 650(63); 530(100); 480(2450).

2.2.2. Hexakis(2,3-dichloro-phenoxyacetato)-tris(methanol)oxotri-iron(III) Chloride-methanol (1/3), [Fe_3O(2,3-D)$_6$(MeOH)$_3$]Cl·3MeOH (2)

2,3-D (2.22 g, 10 mmol) was dissolved in CH_3OH (15 cm^3) and NaOH (0.4 g, 10 mmol) was added. After 30 min stirring $FeCl_3\cdot 6H_2O$ (1.35 g, 5 mmol) in CH_3OH (10 cm^3) were added drop wise. The orange-yellow solution was reduced in volume and left for slow evaporation. Orange-yellow crystals of [Fe_3O(2,3-D)$_6$(MeOH)$_3$]Cl·3MeOH (**2**) suitable for X-ray structure determination were deposited in a week. Yield 30%. (Fw = 1731.37). *Anal*. Calc. for $C_{54}H_{54}Cl_{13}Fe_3O_{25}$ requires: C, 37.46; H, 3.12; Fe, 9.67. Found: C, 37.50; H, 3.08; Fe, 9.59%. IR: ν_{max}/cm^{-1} $\nu_{as}(CO_2)$: 1626, 1578(vs); $\nu_{sym}(CO_2)$:1425 (s) (KBr pellet).

2.2.3. Synthesis of the tetrakis(dimethyl-sulfoxide)-octakis(2,4,5-trichloro-phenoxyacetato) dioxotetrairon(III) methanol(1/2)-water(1/1)- dimethylsulfoxide(1/0.8), {[Fe_4O_2(2,4,5-T)$_8$(dmso)$_4$]·2MeOH·H_2O·0.8dmso} (3)

2,4,5-T (2.25 g, 10 mmol) was dissolved in CH_3OH/dmso 4:1 (20 cm^3) and NaOH (0.4 g, 10 mmol) was added. After 30 min stirring $FeCl_3\cdot 6H_2O$ (1.35 g, 5 mmol) in CH_3OH/dmso 1:1 (15 cm^3) was added drop wise. The reaction mixture was stirred for 1 h and reduced in volume under vacuum and left for slow evaporation. Red-brown crystals of {[Fe_4O_2(2,4,5-T)$_8$(dmso)$_4$]·2MeOH·H_2O·0.8dmso} (**3**), suitable for X-ray structure determination were deposited in a week. Yield 40%. (Fw = 2748.22). *Anal*. Calc. for $C_{75.6}H_{70.8}Cl_{24}Fe_4O_{33.8}S_{4.8}$ requires: C, 33.04; H, 2.57; Fe, 8.12. Found: C, 33.14; H, 2.46; Fe, 8.26%. IR: ν_{max}/cm^{-1} $\nu_{as}(CO_2)$: 1628(s), 1614(vs), 1591(vs); $\nu_{sym}(CO_2)$: 1422(vs) (KBr pellet); UV–Vis: λ(nm)(ε, $dm^3\,mol^{-1}\,cm^{-1}$), dmso solution: 553(95); 468(150).

2.3. X-ray crystallography data and processing

An orange-yellow parallelepiped crystal of [Fe_3O(2,3-D)$_6$(MeOH)$_3$]Cl·3MeOH (**2**) with approximate dimensions $0.10\times0.20\times0.50$ mm, and an red-brown one of {[Fe_4O_2(2,4,5-T)$_8$(dmso)$_4$]·2MeOH·H_2O·0.8dmso} (**3**), with approximate dimensions $0.20\times0.30\times0.50$ mm were mounted in air. Diffraction measurements were made on a Crystal Logic Dual Goniometer diffractometer using graphite monochromated Mo radiation. Crystal data and parameters for data collection are reported in Table 1. Unit cell dimensions were determined and refined by using the angular settings of 25 automatically centered reflections in the range $11° < 2\theta < 23°$ for **2** and **3**. Intensity data were recorded using θ–2θ scan. Three standard reflections monitored every 97 reflections, showed <3.0% intensity fluctuation and no decay. Lorentz, polarization and ψ-scan absorption correction were applied using Crystal Logic software. Scattering Factors were taken from the International Tables for X-ray Crystallography [48]. The structures of **2** and **3** were solved by Direct methods using the programs SHELXS-86 [49], and refined by full-matrix least-squares techniques on F^2 with SHELXL-97 [50].

Table 1
Summary of crystal, intensity collection and refinement data

	2	**3**
Empirical formula	$C_{54}H_{54}Cl_{13}Fe_3O_{25}$	$C_{75.6}H_{70.8}Cl_{24}Fe_4O_{33.8}S_{4.8}$
Formula weight	1731.37	2748.22
Temperature (K)	298	298K
Crystal system	triclinic	monoclinic
Space group	$P\bar{1}$	$C2/c$
a (Å)	15.88(1)	19.450(10)
b (Å)	14.94(1)	22.960(10)
c (Å)	15.78(1)	27.39(2)
α (°)	79.05(3)	90
β (°)	81.22(3)	103.55(2)
γ (°)	77.40(3)	90
Volume (Å^3)	3562.4(5)	11891(12)
Z	2	4
D_{calc} (Mg/m^3)	1.614	1.535
Absorption coefficient (mm^{-1})	1.165	1.171
F(000)	1754	5534
θ Range for data collection (°)	1.74–22.76	2.25–25.00
Index ranges	$-17\leqslant h\leqslant 17$, $-15\leqslant k\leqslant 16$, $0\leqslant l\leqslant 17$	$-14\leqslant h\leqslant 0$, $-27\leqslant k\leqslant 0$, $-28\leqslant l\leqslant 29$
Goodness-of-fit on F^2	1.086	1.017
Final R indices [$I>2\sigma(I)$]	$R_1 = 0.0593$, $wR_2 = 0.1713$[a]	$R_1 = 0.0951$, $wR_2 = 0.2395$[b]

[a] For 7334 reflections with $I>2\sigma(I)$.
[b] For 3545 reflections with $I>2\sigma(I)$.

Further crystallographic details for **2**: $2\theta = 45.5°$, scan speed 2.0°/min, scan range $2.3 + x\alpha_1\alpha_2$ separation, reflections collected/unique = 10015/9603 [$R_{int} = 0.0466$], 882 parameters refined, R_1/wR_2 (for all data) = 0.0806/0.1713, $[\Delta\rho]_{max}/[\Delta\rho]_{min} = 1.029$ and -0.669, $[\Delta/\sigma]_{max} = 0.003$. All hydrogen atoms were introduced at calculated positions as riding on bonded atoms. All non-H atoms were refined anisotropically, including the solving methanols for which no-H atoms were included in the refinement. Further crystallographic details for **3**: $2\theta = 50°$, scan speed 6.0°/min, scan range $1.6 + \alpha_1\alpha_2$ separation, reflections collected/unique/used = 6946/6661 ($R_{int} = 0.0557$)/6661, 648 parameters refined, R_1/wR_2 (for all data) = 0.1762/0.3119, $[\Delta\rho]_{max}/[\Delta\rho]_{min} = 0.937/-0.505$ e/Å^3, $[\Delta/\sigma]_{max} = 0.006$. All hydrogen atoms were introduced at calculated positions as riding on bonded atoms. All non-H atoms were refined anisotropically, except for the solvent molecules which were refined isotropically.

3. Results and discussion

3.1. Synthesis of the complexes

(a) The synthesis of the binuclear complex has been achieved via the reaction of $FeCl_3 \cdot 6H_2O$ with the sodium salt of the ligand in the presence of phen. The reaction involves deprotonation of the ligand using NaOH or CH_3ONa as base, e.g.,

$$C_6H_3Cl_2\text{-}OCH_2COOH + CH_3ONa \rightarrow C_6H_3Cl_2\text{-}OCH_2COONa + CH_3OH$$

$$2C_6H_3Cl_2\text{-}OCH_2COONa + 2FeCl_3 + 2NaOH + 2phen \rightarrow [Fe_2OCl_2(C_6H_3Cl_2\text{-}OCH_2COO)_2(phen)_2] + 4NaCl + H_2O$$

The complex is green crystalline solid soluble in dmf, dmso.

(b) The synthesis of the trinuclear complex has been achieved via one step reaction of $FeCl_3 \cdot 6H_2O$, NaOH, and 2,3-D that results in the formation of the cationic complex,

$$6C_6H_3Cl_2\text{-}OCH_2COOH + 8NaOH + 3FeCl_3 \rightarrow [Fe_3O(C_6H_3Cl_2\text{-}OCH_2COO)_6(MeOH)_3]Cl + 8NaCl + 7H_2O$$

The complex is orange-yellow crystalline solid soluble in dmf, dmso.

(c) The synthesis of the tetranuclear complex has been achieved via the reaction of $FeCl_3 \cdot 6H_2O$ with the sodium salt of the ligand in CH_3OH/dmso. The reaction involves deprotonation of the ligand using NaOH or CH_3ONa as base, e.g.,

$$C_6H_2Cl_3\text{-}OCH_2COOH + CH_3ONa \rightarrow C_6H_2Cl_3\text{-}OCH_2COONa + CH_3OH$$

$$8C_6H_2Cl_3\text{-}OCH_2COONa + 4FeCl_3 + 4\ NaOH \rightarrow [Fe_4O_2(2,4,5\text{-}T)_8(dmso)_4] + 12NaCl + 2H_2O$$

The complex is red-brown crystalline solid soluble in dmf, dmso.

3.2. IR spectroscopy

IR spectroscopy was used as an additional technique to distinguish the structural similarities of the compounds with the same nuclearity as well as the coordination mode of the carboxylato ligands. The overall patterns of all compounds of the same number of metal ions, bi-, tri- and tetra-Fe(III) ions are almost identical supporting analogous structure. Bands of phen in the 1650–1600 cm^{-1}, attributed to ring stretching vibrations, shift to higher frequencies upon chelation in binuclear compounds. Similar shifts occur for the bands between 1250 and 1100 cm^{-1}, while those between 1050 and 700 cm^{-1} shift to lower frequencies with splitting of the band at ~850 cm^{-1} (an out-of-plane C–H deformation).The very strong bands at 1610 and 1580 (**1**), 1624 and 1575 (**2**) and 1614 and 1591 cm^{-1} (**3**) are assigned to the ν_{as}(COO) bidendate mode and the strong bands at 1426 (**1**), 1425 (**2**) and 1422 cm^{-1} (**3**) are assigned to the ν_s(COO) bidentate mode of the carboxylate ligands, respectively. The existence of two types of carboxylato ligands (monodentate, bidentate bridge) in tetranuclear compound **(3)** is reflected in its IR spectrum by the appearance of two ν_{as}(COO) bands at 1628 (monodentate) and 1614 and 1591 cm^{-1}(bidentate bridge); the two ν_s(COO) bands most probably coincide at 1422 cm^{-1}

3.2.1. Description of the structure $[Fe_3O(2,3\text{-}D)_6(MeOH)_3]Cl \cdot 3MeOH$ (2)

Complex **2** crystallizes in the triclinic space group $P\bar{1}$. A structural diagram of the complex appears in Fig. 1. Selected bond distances and angles are given in Table 2.

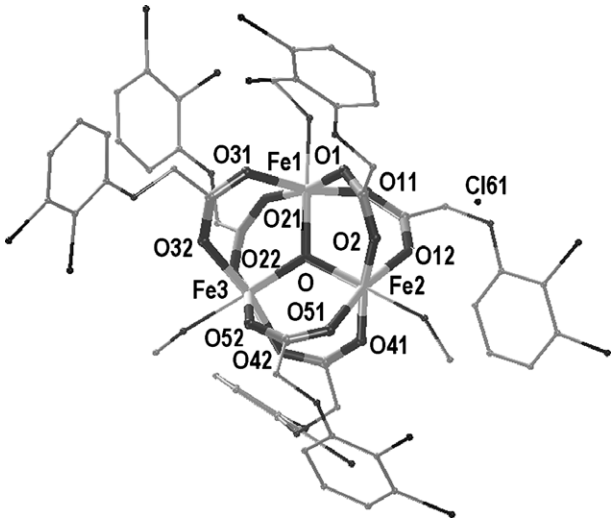


Fig. 1. A diagram of the structure of $[Fe_3O(2,3\text{-}D)_6(MeOH)_3]Cl \cdot 3MeOH$ (**2**).

Table 2
Selected bond distances (Å) and angles for complex **2**

Bond distances (Å)			
Fe(1)–O	1.914(4)	Fe(2)–O(12)	2.026(4)
Fe(1)–O(31)	2.002(4)	Fe(2)–O(51)	2.030(4)
Fe(1)–O(11)	2.006(4)	Fe(2)–OM2	2.046(4)
Fe(1)–O(21)	2.016(4)	Fe(3)–O	1.895(4)
Fe(1)–O(1)	2.022(4)	Fe(3)–O(52)	1.999(4)
Fe(1)–OM1	2.055(4)	Fe(3)–O(22)	2.022(4)
Fe(2)–O	1.917(4)	Fe(3)–O(42)	2.039(4)
Fe(2)–O(41)	2.001(4)	Fe(3)–O(32)	2.039(4)
Fe(2)–O(2)	2.008(4)	Fe(3)–OM3	2.094(4)
Bond angles (°)			
Fe(1)–Fe(3)–Fe(2)	60.08	Fe(2)–Fe(1)–Fe(3)	60.16
Fe(1)–Fe(2)–Fe(3)	59.76	Fe(1)–O–Fe(2)	119.4(2)
Fe(3)–O–Fe(1)	120.0(2)	Fe(3)–O–Fe(2)	120.6(2)
Separations			
Fe(1)...Fe(2)	3.309	Fe(1)...Cl	6.041
Fe(2)...Fe(3)	3.311	Fe(2)...Cl	7.422
Fe(3)...Fe(1)	3.298	Fe(3)...Cl	8.709

The compound is a Fe_3O description. It carries a positive charge. The Fe(1)–O = 1.914(4) Å and Fe(2)–O = 1.917(4) Å distances are almost the same, but the Fe(3)–O = 1.895(4) Å distance is slightly shorter . Again comparing the Fe–O (MeOH) distances, we can see that the bond lengths of Fe(1)–OM1 = 2.055(4) and Fe(2)–OM2 = 2.046(4) are very close, while the Fe(3)–OM3 distance of 2.094(4) Å is obviously longer than the former two. The triangle composed of the Fe(1), Fe(2) and Fe(3) atoms is very close to an equilateral triangle, with Fe(1)...Fe(2) Fe(2)...Fe(3) and Fe(3)...Fe(1) distances of 3.309 Å, 3.311 Å and 3.298 Å, respectively. The Fe(1)–Fe(3)–Fe(2), Fe(2)–Fe(1)–Fe(3) and Fe(1)–Fe(2)–Fe(3) angles are 60.08°, 60.16° and 59.76°, respectively. The central oxygen atom O lies on the Fe(1)Fe(2)Fe(3) plane (0.009 Å). The Fe(III) coordination geometry is slightly distorted octahedron with a terminal methanol oxygen atom, an oxygen atom in the center of the triangle and any other four oxygen atoms from the bridging carboxylate groups completing the coordination to each metal atom.

3.2.2. Description of the structure $[Fe_4O_2(2,4,5\text{-}T)_8(dmso)_4]\cdot 2MeOH\cdot H_2O\cdot 0.8dmso$ (3)

Complex **3** crystallizes in the monoclinic space group $C2/c$ and displays crystallographically imposed C_2 symmetry. A structural diagram of the complex appears in Fig. 2. Selected bond distances and angles are given in Table 3.

The tetranuclear molecule contains a $[Fe_4(\mu_3\text{-}O)_2]^{8+}$ core comprising four Fe(III) ions with a "butterfly" disposition and a μ_3-O^{2-} ion bridging each Fe_3 "wing". Ions Fe(1) and Fe(1′) $[1-x, y, 1.5-z]$ occupy the "hinge" or "body" sites, and Fe(2) and Fe(2′) $[1-x, y, 1.5-z]$ occupy the "wing-tip" sites. Both oxide ions, O and O $[1-x, y, 1.5-z]$, lie slightly out of their respective Fe_3 planes by 0.30 Å with sum of angles of 352.25°. The dihedral angle between the two Fe_3 planes is 158.34°. Thus, the core can be considered as two edge-sharing Fe_3 triangular units with the oxygen atoms out of their Fe_3 planes. Peripheral ligation is provided by eight RCO_2^- groups. The body/wing-tip Fe_2 pairs are bridged by six μ_2-carboxylate groups in syn–syn modes, while two monodentate carboxylate ligands, are coordinated to each of the two body metal ions Fe(1) and Fe(1′).

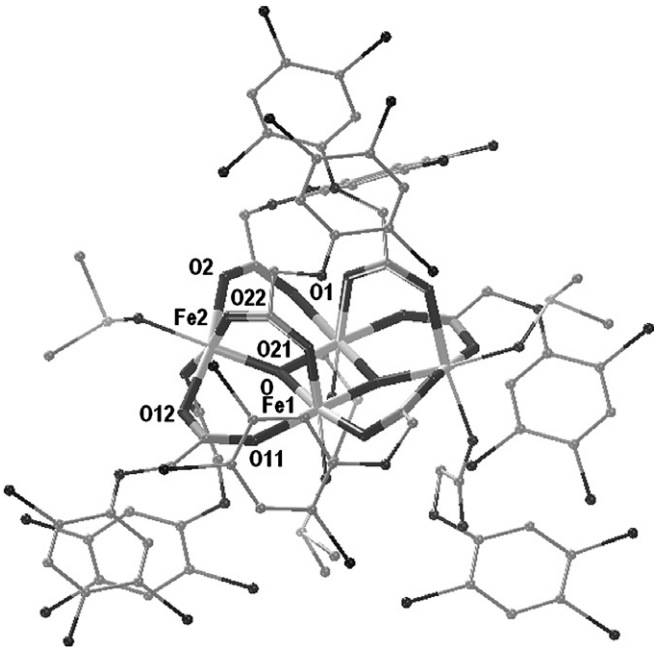


Fig. 2. A diagram of the structure of $[Fe_4O_2(2,4,5\text{-}T)_8(dmso)_4]\cdot 2MeOH\cdot H_2O\cdot 0.8dmso$ (**3**).

Table 3
Selected bond distances (Å) and angles for complex **3**

Bond distances (Å)			
Fe(1)–O	1.917(9)	Fe(2)–O	1.875(8)
Fe(1′)–O	1.919(10)	Fe(2)–O(31)	1.988(9)
Fe(1)–O(41)	2.015(9)	Fe(2)–O(2)	2.009(12)
Fe(1)–O(1)	2.023(9)	Fe(2)–O(51)	2.030(8)
Fe(1)–O(21)	2.039(9)	Fe(2)–O(22)	2.054(9)
Fe(1)–O(11)	2.059(10)	Fe(2)–O(12)	2.084(11)
Bond distances (°)			
O–Fe(1)–O	82.0(4)	O–Fe(2)–O(51)	176.5(4)
O–Fe(1)–O(1′)	170.8(4)	O(31)–Fe(2)–O(22)	172.4(4)
O(41)–Fe(1)–O(21)	168.2(4)	O(2)–Fe(2)–O(12)	168.0(4)
O–Fe(1)–O(11)	175.6(4)	Fe(2)–O–Fe(1′)	124.9(5)
Fe(1)–O–Fe(1′)	97.9(4)	Fe(2)–O–Fe(1)	129.4(5)
Separations			
Fe(1)...Fe(2)	3.363	Fe(1)...Fe(1′)	2.893(5)
Fe(1)...Fe(2′)	3.431	Fe(2)...Fe(2′)	6.038

The metal ions are octahedrally coordinated, their chromophores being FeO_6. The Fe...Fe separations fall into two types. The body/body separation, Fe(1)...Fe(1′), is short (2.893 Å) because these metal ions are bridged by two oxides. The wing-tip/body Fe...Fe separations can be distinguished into two types, those bridged by one (Fe(l)–Fe(2), 3.431 Å) and those bridged by two carboxylate groups (Fe(1)...Fe(2), 3.363 Å). Finally, the wing-tip/wing-tip separation (Fe(2)...Fe(2′), 6.038 Å) is the longest as expected. The "body"-Fe to μ_3-*O* distances are actually the same 1.918 Å and 1.919 Å, whereas the "wing-tip"-Fe to μ_3-*O* distance is slightly shorter 1.874 Å. This symmetry is also reflected in the bond angles at the triply bonding oxide atoms: the Fe(1)–O–Fe(1′) and Fe(2)–O–Fe(2′) angles (97.84° and 82.02°, respectively) are much smaller than the other Fe(1)–O–Fe(2) angles (124.93° and 129.48°). Compound **3** belongs in the family of structurally characterized tetranuclear Fe(III) clusters containing the "butterfly"-type $[Fe_4\mu_3\text{-}O_2]^{8+}$ core [22–31] and the third example having only carboxylato ligands [31]. Comparison of the structural parameters of **3** and those of the other members of the Fe(III) "butterfly" family, shows a noticeable structural difference of the body core that shows an idealized rhombic geometry.

The bridging ligands are bound to two Fe(III) metal ions in a symmetric fashion [Fe(1)–O(1) = 2.022(4) Å, Fe(2)–O(2) = 2.008(4) Å, O(1)–C(1) = 1.281(18) Å, O(2)–C(1) = 1.250(19) Å, Fe(1)–O(11) = 2.059(10) Å, Fe(2)–

O(12) = 2.084(11) Å, O(11)–C(11) = 1.267(15) Å, O(12)–C(11) = 1.273(19) Å]. Each unidentate carboxylato ligand is bound to Fe(III) ion through O(31) in a distance of Fe(2)–O(31) = 1.988(9) Å while the uncoordinated carboxylato oxygen [O(32)–C(31) = 1.25(2) Å] is H-bonded to the water molecule of crystallization [O(32)...Ow(1) = 2.780 Å].

3.3. Magnetic measurements

3.3.1. Magnetic study of the Fe3 system

The temperature dependence of the molar magnetic susceptibility of complex $[Fe_3O(2,3\text{-}D)_6(MeOH)_3]Cl \cdot 3MeOH$ (**2**), in the form of $\chi_M T$, is shown in Fig. 3.

The product $\chi_M T$ (4.5 emu mol^{-1} K at 300 K) decreases steadily with decreasing temperature, reaching the value of 0.66 emu mol^{-1} K at 1.75 K. The room-temperature $\chi_M T$ product is appreciably lower than expected for three uncoupled $S = 5/2$ spins (13.1 emu mol^{-1} K) and clearly reveals the antiferromagnetic behavior of the complex **2** while the low-temperature $\chi_M T$ data does not extrapolate to zero as temperature approaches 0 K as expected for odd-number of interacting half-integer spins. In order to investigate the magnetic behavior of the trinuclear system, a spin-only Heisenberg–Dirac–van Vleck (HDvV) Hamiltonian formalism was used and a C_{2v} point-group symmetry was assumed for the system (Scheme 2).

$$H = J_1(S_1 \cdot S_2 + S_1 \cdot S_3) + J_2(S_2 \cdot S_3) \quad (1)$$

The energies of the spin states as functions of the exchange integrals J_1 and J_2 were derived by using the Kambe [52] vector-coupling approach,

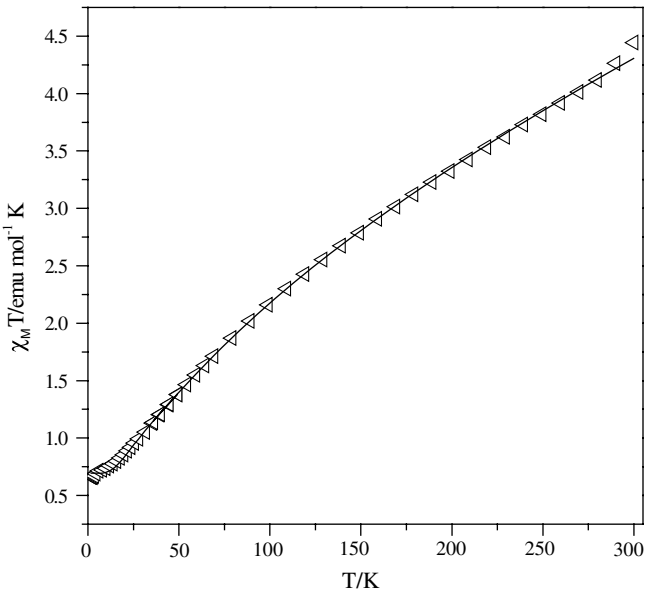
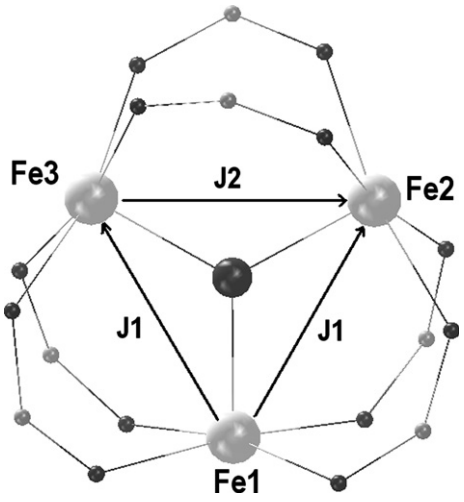


Fig. 3. The temperature dependence of the molar magnetic susceptibility of complex **2**, in the form of $\chi_M T$ vs. T is represented with the open triangles while the solid line represents the best theoretical fit. See text for details.



Scheme 2. Magnetic interactions of **2**.

$$\frac{2E(S_T, S_{23})}{J_2} = \alpha S_T(S_T + 1) + (1 - \alpha)S_{23}(S_{23} + 1) \quad (2)$$

where $S_{23} = S_2 + S_3$ and $S_T = S_1 + S_{23}$ and $\alpha = J_1/J_2$.

Although the point-group symmetry of our system is C_{3v}, no satisfactory fitting was obtained by assuming $J_1 = J_2 = J$. This happens because of the topology of the magnetic ions (an ideal equilateral triangle) which leads to non-preferred spin vector alignment (when the exchange interactions are antiferromagnetic). Having in mind that the interactions are antiferromagnetic, the energy of the spin states depends on S_{23} and in our case the term J_1/J_2 for some *discrete* values could lead to accidental degeneracy and other interesting phenomena of spin frustration. Fig. 4 displays (a) the dependence of the term $\alpha = J_1/J_2$ with the low lying energy levels of the trinuclear system and (b) the case of spin frustration for the value of $\alpha = 0.27$ and 0.57 where the energy levels, in the form of (S_T, S_{23}), (5/2, 0)–(3/2, 1) and (3/2, 1)–(1/2, 2), respectively are accidentally degenerate (FR points). When $\alpha = 1$, the energy of the spin states does not depend on the intermediate spin S_{23} and the ground state is given by two degenerate spin doublets, arising from $S_{23} = 2$ and $S_{23} = 3$. The ground state of the system is (a) $S = 5/2$ for $0 < \alpha < 0.27$; (b) $S = 3/2$ for values $0.27 < a < 0.57$, (c) $S = 1/2$ for values $a > 0.57$, while only the value of the intermediate spin quantum number S_{23} changes for $a > 1$ (Fig. 4).

A fit to the data of Fig. 3 gives $J_1 = 49.5$ cm^{-1}, $J_2 = 66.3$ cm^{-1} ($\alpha = 0.75$), and $g = 2.0$ fixed, with a small percentage of $S = 5/2$ paramagnetic impurity $\rho = 0.7\%$. According to the obtained ratio-parameter, α, a vertical solid line was drawn in Fig. 4 where its cross-sections with the energy levels show the low-lying energy spectrum of the system. For clarification reasons a second graph in Fig. 4 shows the energy difference of the low lying energy states of the system according to the fitting results.

Applying the term $D(S_z^2 - 1)$ to the above magnetic model resulted in no net improvement of the quality of the fit. The value of $D = 0.2$ cm^{-1} was obtained but reveals

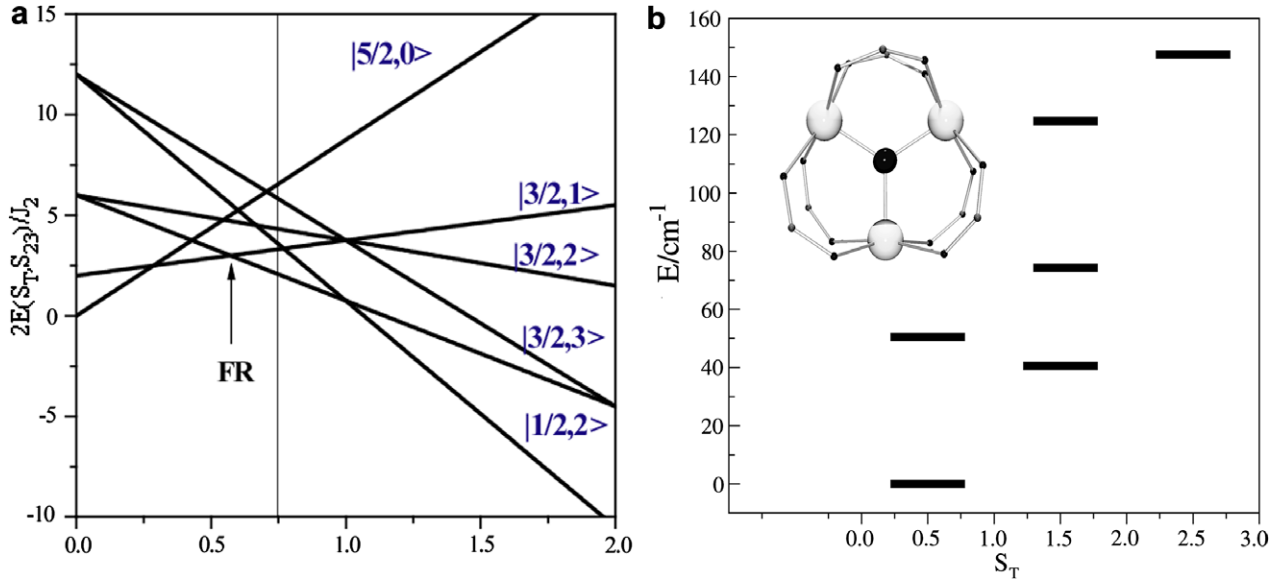


Fig. 4. (a) Dependence of some selective energy levels on the parameter $\alpha = J_1/J_2$; (b) the energy difference of the low lying energy states of the system according to the fitting results (see text for details).

that it does not play an important role in the magnetic behavior of the system in the low-temperature range.

An alternative explanation for the magnetic behavior of complex **2a** retaining its idealized trigonal symmetry in the presence of non-Heisenberg exchange contributions [53–55] is given at the supporting information (Figure 1S).

3.3.2. Magnetic study of the Fe4 system

The room-temperature value of the susceptibility data in the form of $\chi_M T$ is 3.2 emu mol^{-1} K lower than the value expected for four uncoupled 5/2 spins. The values of $\chi_M T$ decrease monotonically with decreasing temperature until a plateau of 0.3 emu mol^{-1} K in the temperature range 17–1.8 K; the residual $\chi_M T$ value is due to a percentage of paramagnetic impurity (Fig. 5).

The data suggest antiferromagnetically coupled system with $S = 0$ ground state. For this complex a total of five exchange parameters J_{ij} are required to cover each possible pairwise exchange interaction between Fe^{III} atoms *i* and *j*; a sixth parameter J_{34} (the numbering scheme is the same as that shown in Scheme 3 is assumed to be zero, given the large distance involved (Fe(3)–Fe(4)) 6.038 Å). However, the main exchange interaction pathway will be via the μ_3-O^{2-} bridges, not the alkanoate bridges, so that from the magnetism viewpoint, the core symmetry is reduced and only three J values are required, $J_{13} = J_{24} = J_{wb}$, $J_{23} = J_{14} = J^*_{wb}$, and $J_{12} = J_{bb}$, where b = body and w = wing-tip. In fact, consideration of the Fe–O and Fe–O–Fe distances and angles in (Table 3) shows that the almost same pyramidality of O(1) and O(2) has a minor influence on these structural parameters and a 2J model appropriate for C_{2V} symmetry, i.e., $J_{wb} = J^*_{wb}$, thus does not appear unreasonable. The Hamiltonian formalism given in Eq. (3) was used to fit the data taking into account a small percentage of $S = 5/2$ paramagnetic impurity (ρ).

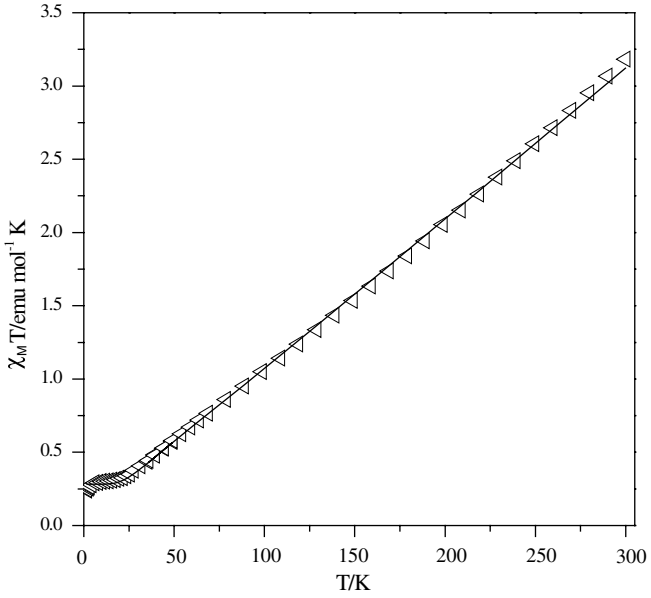
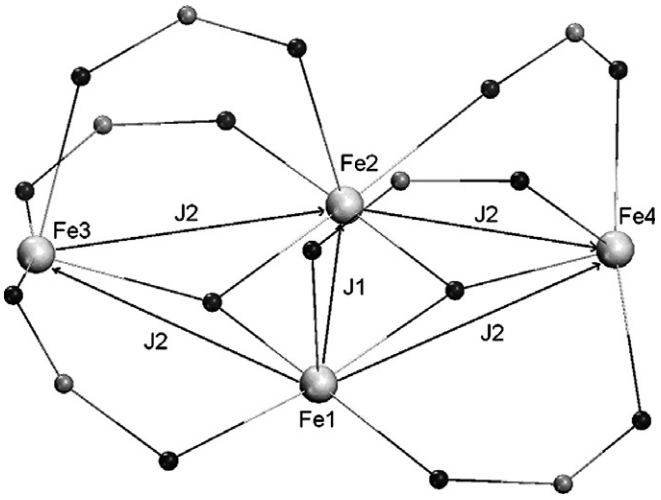


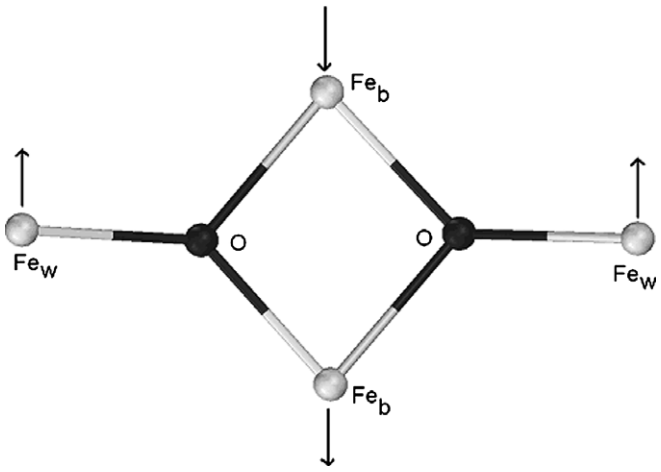
Fig. 5. The temperature dependence of the molar magnetic susceptibility of complex **3**, in the form of $\chi_M T$ vs. T is represented with the open triangles while the solid line represents the best theoretical fit. See text for details.

$$H = J_{bb}(S_1 \cdot S_2) + J_{wb}[(S_1 + S_2)(S_3 + S_4)] \quad (3)$$

The obtained fitting parameters are $J_{bb} = 5.6\ cm^{-1}$, $J_{wb} = 69.7\ cm^{-1}$, $g = 2.0$, and $\rho = 1\%$. The energy difference between the $S = 0$ ground state and the first excited $S = 1$ state is 69 cm^{-1}. An error-surface plot for the fitting shows that while the value of J_{wb} is well determined by the fitting procedure, the value of J_{bb} is not; since J_{wb} is so much stronger than J_{bb} and since there are four J_{wb} interactions and only one J_{bb}, the spin-manifold energies are primarily determined by J_{wb}, making the precise value of



Scheme 3. Magnetic interactions of **3**.



Scheme 4. The spin alignments in **3**.

J_{bb} indeterminate. Thus, a large range of J_{bb} values give essentially equally good fits of the data, although the quoted J_{bb} values give the lowest fitting error. Tetranuclear butterfly iron(III) complexes, and related [30–33] species, are regarded as examples exhibiting spin frustration [34–40]. The strong antiferromagnetic J_{wb} interactions frustrate the weaker J_{bb} interaction leading to the $S = 0$ ground state via the spin alignments shown pictorially in Scheme 4; i.e., the Fe_b spins are parallel in the ground state even though the J_{bb} parameter is most likely negative (antiferromagnetic) [41,42].

A further verification for the amount of paramagnetic impurity is given at the supporting information (figure 2S).

3.3.3. Magnetic study of the Fe2 system

A diagram of the complex $[Fe_2OCl_2(3,4\text{-}D)_2(phen)_2] \cdot H_2O \cdot 3.5MeOH$ (**1**) appears in Fig. 6. Due to low quality of the crystal the structural features[1] of the compound **1** will be used as supporting information in order to define the overall magnetic behavior of the dimmer. Two bidentate alkanoato ligands in *syn–syn* mode and a $\mu\text{-}O^{2-}$ group form bridges between iron atoms separated by 3.159 Å. The distorted octahedral geometry around each Fe(III) is completed with one chelating phen ligand and a chloride ion. The Fe(III)–O–Fe(III) angle of 122.55° and Fe(III)...Fe(III) separation fall in the range 120–124° and 3.090–3.160 Å reported for analogous compounds [11]. The structure is similar with that reported by Vincet et al. [51] while the dinuclear core has been observed in a series of Fe(III) cationic units [11–14].

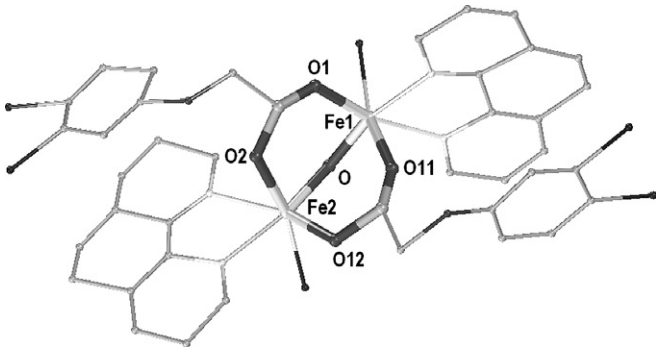


Fig. 6. The dimeric molecule of $\{[Fe_2OCl_2(3,4\text{-}D)_2(phen)_2] \cdot H_2O \cdot 3.5MeOH\}$ (**1**).

The room-temperature value of the susceptibility data in the form of $\chi_M T$ is 0.6 emu mol^{-1} K extremely lower than the value expected for two uncoupled 5/2 spins, which

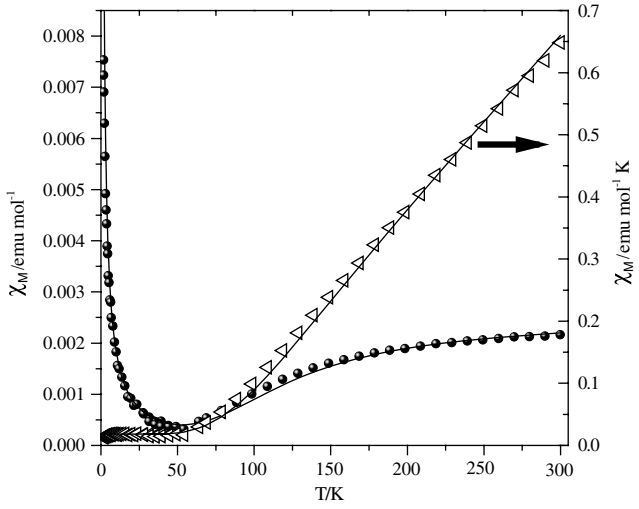


Fig. 7. The temperature dependence of the molar magnetic susceptibility of complex **1**, in the form of $\chi_M T$ vs. T (open triangles) and χ_M vs. T (solid cycles) is represented with the open triangles while the solid lines represents the best theoretical fit. See text for details.

[1] Empirical formula: $C_{43.50}H_{40}Cl_6Fe_2N_4O_{11.50}$; Fw: 1127.19; $T = 298$ K; Crystal sys.: monoclinic; space group: $P2_1/c$; $a = 15.03(4)$ Å; $b = 23.40(6)$ Å; $c = 18.02(4)$ Å; $\alpha = 90.00°$; $\beta = 120.66(5)°$; $\gamma = 90.00°$; $V = 5452(24)$ Å^3; $Z = 4$; D_{calc}: 1.373 Mg/m^3; Final R indices $[I > 2\sigma(I)]$: $R_1 = 0.1788$, $wR_2 = 0.3888$; R-factors based on F^2 are statistically about twice as large as those based on F, and R-factors based on all data will be even larger.

reveals the very strong antiferromagnetic exchange interaction between the two ions (Fig. 7).

The values of $\chi_M T$ decrease monotonically with decreasing temperature until a plateau of 0.02 emu mol^{-1} K in the temperature range 53–1.8 K; the residual $\chi_M T$ value is due to a percentage of paramagnetic impurity which is better shown in the χ_M data (also shown in the same figure) as a curie tail. The fitting results (solid lines in the same figure) gave an exchange interaction $J = 254.1$ cm^{-1} with a small amount of paramagnetic $S = 5/2$ impurity ($\rho = 0.3\%$).

A further verification for the amount of paramagnetic impurity comes from the plot of the reduced magnetization $M/N\mu_B$ vs the external magnetic field at 2 and 4 K (Figure 3S). The nonzero magnetization, although the ground state is $S = 0$, is in accordance with the small percentage of paramagnetic impurity found in the susceptibility data.

4. Conclusion

The structural characterization of bi-, tri- and tetranuclear Fe(III) complexes confirms the ability of alkanoato ligands to give a variety of multinuclear complexes. The formation of binuclear compounds is driven by the presence of chelating phen neutral ligands while the formation of trinuclear or tetranuclear compounds is absolutely dependent of the solvent used. The use of methanol leads to the formation of the trinuclear species while from dmso or dmf solvents the tetranuclear compounds have been isolated. The magnetic behavior of all nuclearities show antiferromagnetic exchange interaction with the ground state of the binuclear and tetranuclear compounds $S = 0$ and for the trinuclear one $S = 1/2$.

Acknowledgements

The Project is co-funded by the European Social Fund & National Resources-EPEAEK II-Archimidis I 2003/21. V.T. would like to thank Nicola Lima and the Department of Chemistry, Florence, Italy, for the magnetic measurements.

Appendix A. Supplementary material

CCDC 284186 and 284185 contain the supplementary crystallographic data for **2** and **3**. These data can be obtained free of charge via http://www.ccdc.cam.ac.uk/conts/retrieving.html, or from the Cambridge Crystallographic Data Centre, 12 Union Road, Cambridge CB2 1EZ, UK; fax: (+44) 1223-336-033; or e-mail: deposit@ccdc.cam.ac.uk. Supplementary data associated with this article can be found, in the online version, at doi:10.1016/j.poly.2006.09.002.

References

[1] D.M. Kurtz Jr., J. Biol. Inorg. Chem. 2 (1997) 159.
[2] M.A.J. Homes, R.E. Stenkamp, J. Mol. Biol. 220 (1991) 723.
[3] L. Que Jr., J. Chem. Soc. Dalton Trans. (1997) 3933.
[4] D.T. Logan, X.-D. Su, A. Aberg, K. Regnström, J. Hajdu, H. Eklund, P. Nordlund, Structure 4 (1996) 1053.
[5] A.C. Rosenzweig, P. Nordlund, P.M. Takahara, C.A. Frederick, Chem. Biol. 2 (1995) 409.
[6] J.B. Vincent, G.-L. Olivier-Lilley, B.A. Averill, Chem. Rev. 90 (1990) 1447.
[7] L. Que Jr., Chem. Rev. 96 (1996) 2607.
[8] G.A. Clegg, J.E. Fitton, P.M. Harrison, A. Treffry, Prog. Biophys. Mol. Biol. 36 (1980) 53.
[9] E.C. Theil, Annu. Rev. Biochem. 56 (1987) 289.
[10] P.M. Harrison, P. Arosio, Biochim. Biophys. Acta 1275 (1996) 161.
[11] A.K. Boudalis, C.P. Raptopoulou, A. Terzis, S.P. Perlepes, Polyhedron 23 (2004) 1271.
[12] K.L. Taft, A. Maschelein, S. Liu, S.J. Lippard, D. Garfinkel-Shweky, A. Bino, Inorg. Chim. Acta 198 (1992) 627.
[13] S. Ménage, J.-M. Vincent, C. Lambeaux, G. Chottard, A. Grand, M. Fontecave, Inorg. Chem. 32 (1993) 4713.
[14] J. Li, J. Zou, M. Wu, Z. Xu, X. You, T.C.W. Mak, Polyhedron 14 (1995) 3519.
[15] A.K. Powell, S.L. Heath, D. Gatteschi, L. Pardi, R. Sessoli, G. Spina, F.D. Giallo, F. Pieralli, J. Am. Chem. Soc. 117 (1995) 2491.
[16] S.M. Oh, D.N. Hendrickson, K.L. Hasset, R.E. Davis, J. Am. Chem. Soc. 107 (1985) 8009.
[17] C.T. Dziobkowski, J.T. Wrobleski, D.B. Brown, Inorg. Chem. 20 (1981) 679.
[18] A.M. Bond, R.J.H. Clark, D.G. Humphrey, P. Panayiotopoulos, B.W. Skelton, A.H. White, J. Chem. Soc., Dalton Trans. (1998) 1845.
[19] J.K. McCusker, J.B. Vincent, E.A. Schmitt, M.L. Mino, K. Shin, D.K. Coggin, P.M. Hagen, J.C. Huffman, G. Christou, D.N. Hendrickson, J. Am. Chem. Soc. 113 (1991) 3012.
[20] R.A. Stukan, V.I. Ponomarev, V.P. Nifontov, K.I. Turte, L.O. Atovmyan, J. Struct. Chem. 26 (1985) 197.
[21] D.L. Jameson, C.-L. Xie, D.N. Hendrickson, J.A. Potenza, H.J. Schugar, J. Am. Chem. Soc. 109 (1987) 740.
[22] B. Yan, Z.-D. Chen, Inorg. Chem. Commun. 4 (2001) 138.
[23] M.W. Wemple, D.K. Coggin, J.B. Vincent, J.K. McCusker, W.E. Streib, J.C. Huffman, D.N. Hendrickson, G. Christou, J. Chem. Soc., Dalton Trans. (1998) 719.
[24] W.H. Armstrong, M.E. Roth, S.J. Lippard, J. Am. Chem. Soc. 109 (1987) 6318.
[25] P. Chaudhuri, M. Winter, P. Fleischhauer, W. Haase, U. Florke, H.-J. Haupt, Inorg. Chim. Acta 212 (1993) 241.
[26] L. Wu, P. Pressprich, P. Coppens, M.J. DeMarco, Acta Crystallogr., Sect. C 49 (1993) 1255.
[27] R.A. Reynolds, W.R. Dunham, D.C. Coucouvanis, Inorg. Chem. 37 (1998) 1232.
[28] V.I. Ponomarev, L.O. Atovmyan, S.A. Bobkova, K.I. Turte, Dokl. Akad. Nauk. SSSR 274 (1984) 368.
[29] S.M. Gorun, S.J. Lippard, Inorg. Chem. 27 (1988) 149.
[30] R. Celenligil-Cetin, R.J. Staples, P. Stavropoulos, Inorg. Chem. 39 (2000) 5838.
[31] A.K. Boudalis, N. Lalioti, G.A. Spyroulias, C.P. Raptopoulou, A. Terzis, A. Bousseksou, V. Tangoulis, J-P. Tuchagues, S.P. Perlepes, Inorg. Chem. 41 (2002) 6474.
[32] W.H. Armstrong, M.E. Roth, S.J. Lippard, J. Am. Chem. Soc. 109 (1987) 6318.
[33] P. Chaudhuri, M. Winter, P. Fleischhauer, W. Haase, U. Florke, H.-J. Haupt, Inorg. Chim. Acta 212 (1993) 241.
[34] J.K. McCusker, J.B. Vincent, E.A. Schmitt, M.L. Mino, K. Shin, D.K. Coggin, P.M. Hagen, J.C. Huffman, G. Christou, D.N. Hendrickson, J. Am. Chem. Soc. 113 (1991) 3012.
[35] D. Gatteschi, A. Caneschi, R. Sessoli, A. Cornia, Chem. Soc. Rev. 25 (1996) 101.
[36] R.E.P. Winpenny, Chem. Soc. Rev. (1998) 447.
[37] C. Benelli, S. Parsons, G.A. Solan, R.E.P. Winpenny, Angew. Chem., Int. Ed. Engl. 35 (1996) 1825.

[38] E.K. Brechin, M.J. Knapp, J.C. Huffman, D.N. Hendrickson, G. Christou, Inorg. Chim. Acta 297 (2000) 389.
[39] E.J. Seddon, J. Yoo, K. Folting, J.C. Huffman, D.N. Hendrickson, G. Christou, J. Chem. Soc., Dalton Trans. (2000) 3640.
[40] P. Ammala, J.D. Cashion, C.M. Kepert, B. Moubaraki, K.S. Murray, L. Spiccia, B.O. West, Angew. Chem., Int. Ed. 39 (2000) 1688.
[41] B. Yan, Z.-D. Chen, Inorg. Chem. Commun. 4 (2001) 138.
[42] E.J. Seddon, J.C. Huffman, G. Christou, J. Chem. Soc., Dalton Trans. (2000) 4446.
[43] C. Dendrinou-Samara, L. Alevizopoulou, L. Iordanidis, E. Samaras, D.P. Kessissoglou, J. Inorg. Biochem. 89 (2002) 89.
[44] C. Dendrinou-Samara, G. Psomas, K. Christophorou, V. Tangoulis, V.P. Raptopoulou, A. Terzis, D.P. Kessissoglou, J. Chem. Soc., Dalton Trans. (1996) 3737.
[45] G. Psomas, C. Dendrinou-Samara, P. Philippakopoulos, V. Tangoulis, C.P. Raptopoulou, H. Samaras, D.P. Kessissoglou, Inorg. Chim. Acta 272 (1998) 24.
[46] C. Dendrinou-Samara, G. Tsotsou, C.P. Raptopoulou, A. Kortsaris, D. Kyriakidis, D.P. Kessissoglou, J. Inorg. Biochem. 71 (1998) 171.
[47] (a) G. Psomas, C.P. Raptopoulou, L. Iordanidis, C. Dendrinou-Samara, V. Tangoulis, D.P. Kessissoglou, Inorg. Chem. 39 (2000) 3042;
(b) A. Dimitrakopoulou, C. Dendrinou-Samara, A.A. Pantazaki, C. Raptopoulou, A. Terzis, E. Samaras, D.P. Kessissoglou, Inorg. Chim. Acta, in press.
[48] G.M. Sheldrick, SADABS, University of Göttingen, Germany.
[49] G.M. Sheldrick, SHELXS-86: Structure Solving Program, University of Göttingen, Germany, 1986.
[50] G.M. Sheldrick, SHELXL-97: Crystal Structure Refinement Program, University of Göttingen, Germany, 1997.
[51] J.B. Vincent, J.C. Huffman, G. Christou, Q. Li, M.A. Nanny, D.N. Hendrickson, R.H. Fong, R.H. Fish, J. Am. Chem. Soc. 110 (1988) 6898.
[52] K. Kambe, J. Phys. Soc. Jpn. 5 (1950) 48.
[53] G. Laughlan, A.I.H. Murchie, D.G. Norman, M.H. Moore, P.C.E. Moody, D.M.J. Lilley, B. Luisi, Science 265 (1994) 520.
[54] S.M. Gorun, S.J. Lippard, Inorg. Chem. 30 (1991) 1625.
[55] P.N. Turowski, W.H. Armstrong, M. E Roth, S.J. Lippard, J. Am. Chem. Soc. 112 (1990) 681.

Available online at www.sciencedirect.com
ScienceDirect
Polyhedron 26 (2007) 773–781
POLYHEDRON
www.elsevier.com/locate/poly

Synthesis and structural studies on di-oxovanadium(V) complexes of *N*(4)-substituted pyrazole based thiosemicarbazones

Arijit Hazra [a], Anil Kumar Barik [b], Sachindranath Pal [c], Samik Gupta [a], Somnath Roy [a], Ray J. Butcher [d], Shie-Ming Peng [e], G.H. Lee [e], Susanta Kumar Kar [a,*]

[a] *Department of Chemistry, University College of Science, 92, Acharya Prafulla Chandra Road, Calcutta 700 009, West Bengal, India*
[b] *Department of Chemistry, St. Paul's C.M. College, 33/1, Raja Rammohan Roy Sarani, Calcutta 700 009, India*
[c] *Department of Chemistry, Sree Chaitanya College, Habra, North 24 Parganas, West Bengal, India*
[d] *Department of Chemistry, Howard University, 2400 Sixth Street, N.W., Washington, DC 200 59, USA*
[e] *Department of Chemistry, National Taiwan University, Taipei 106, Taiwan, ROC*

Received 9 August 2006; accepted 5 September 2006
Available online 22 September 2006

Abstract

Three mononuclear *cis*-dioxovanadium(V) complexes of tridentate thiosemicarbazones derived from 5-methyl-3-formylpyrazole (MPA) and *N*(4)-methyl/ethyl/dimethyl thiosemicarbazide have been synthesized and characterized. Single crystal X-ray analyses were performed with $[VO_2L^1]$ (**1**), $[VO_2L^2]$ (**2**) and $[VO_2L^3]$ (**3**), where L^1, L^2 and L^3 denote the [1 + 1] thiosemicarbazone mono-anions derived from MPA and *N*(4)-substituted methyl/ethyl/dimethyl thiosemicarbazide respectively. In all the complexes the vanadium atom is in a distorted square pyramidal geometry with a N_2SO_2 chromophore. The interesting finding in the work is that in complexes **1** and **2**, the thioimine nitrogen unusually participates in coordination whereas in **3** it is the azomethine nitrogen (quite usual) which is involved in the coordination process.
© 2006 Elsevier Ltd. All rights reserved.

Keywords: Vanadium(V); Spectral properties; Crystal structure; Co-crystals; 5-Methyl-3-formyl-*N*(4)-methyl/ethyl/dimethyl thiosemicarbazones

1. Introduction

The coordination chemistry of vanadium is of great current interest because of the discovery of its presence in abiotic as well as biotic systems. The element is present in some sea squirts [1,2]; mushrooms [3,4] and vanadium containing enzymes such as nitrogenase [5] and haloperoxidases [6], etc. Vanadium(V) complexes are known as potent inhibitors of various enzymes. Another important impetus to the coordination chemistry of vanadium in the context of medical applications has arisen from the ability of vanadium complexes to promote the insulin mimetic activity in pathophysiological state of diabetes mellitus in humans [7–10]. This biological and catalytic relevance of vanadium has prompted the synthesis of numerous model vanadium compounds containing O, N donor ligands, whose spectroscopic, magnetic and redox properties have been widely investigated [11–21]. Some other vanadium complexes of O, N donor ligands have been reported in recent times [22]. Although a volume of work has enriched the vanadium chemistry dealing with heterocyclic thiosemicarbazones [23], up until now, little research has centered on vanadium chemistry with thiosemicarbazones having pyrazole as the heterocyclic part. Therefore, considering the broad spectrum of potentially useful biological implications and the catalytic activity of the metal ion complexes with 5-methyl-3-formyl pyrazole thiosemicarbazones, this communication reports the synthesis, spectroscopic and

* Corresponding author. Tel.: +91 33 24322936; fax: +91 33 23519755.
E-mail address: skkar_cu@yahoo.co.in (S.K. Kar).

0277-5387/$ - see front matter © 2006 Elsevier Ltd. All rights reserved.
doi:10.1016/j.poly.2006.09.005

X-ray crystallographic characterization of three dioxovanadium(V) complexes with 5-methyl-3-formylpyrazole-*N*(4)-methyl/ethyl/dimethyl thiosemicarbazones HL^1, HL^2 and HL^3 respectively. We have reported earlier the synthesis and coordinating behaviour of HL^1 towards the Ni(II) ion [24]. As an extension of the work, we have used the same ligand (HL^1) along with two other similar ligands to study dioxovanadium chemistry in a NNS donor environment. In our previous work [24], we have noticed that the tridentate ligand, HL^1 out of two neighbouring nitrogen atoms – the azomethine and the thioimine – utilizes the azomethine one as one of the donor sites. This common observation is also extensively reported by other authors [23,25] engaged in studies on the coordination behaviour of heterocyclic thiosemicarbazone ligands towards transition metal ions. The peculiarity of this work is that instead of the azomethine nitrogen the unexpected thioimine nitrogen exhibits coordination in HL^1 and HL^2, whereas HL^3 behaves as usual utilizing its azomethine nitrogen as one of the donor atoms. This is quite a novel observation.

2. Experimental

2.1. Reagents and starting materials

Solvents and reagents were obtained from commercial sources and used without further purification unless otherwise stated. *N*(4)-Methyl-3-thiosemicarbazide; *N*(4)-ethyl-3-thiosemicarbazide; *N*(4)-dimethyl-3-thiosemicarbazide were purchased from Aldrich Chemicals, USA. Ethanol was purified using the established method [26].

2.2. Preparation of the ligands HL^1, HL^2, HL^3

All three ligands were synthesized following the same method as reported earlier for HL^1 [24]. *N*(4)-Ethyl-3-thiosemicarbazide and *N*(4)-dimethyl-3-thiosemicarbazide were used instead of *N*(4)-methyl-3-thiosemicarbazide for HL^2 and HL^3 respectively.

HL^1: Yield: ~70%; mp: 201 °C; CHN: (Found: C, 43.54; H, 5.82; N, 34.69%. Calculated for $C_7H_{11}N_5S$: C, 42.63; H, 5.59; N, 35.53); ν_{max}/cm^{-1} 3300, 3190, 1620, 1565, 1040, 865; ^1H NMR δ (d_6-DMSO) 2.26 (3H, s), 2.85 (3H, d), 6.34 (1H, s), 7.95 (1H, s), 8.50 (1H, s), 11.32 (1H, s); $m/z = 197$ (M^+, 100%).

HL^2: Yield: ~67%; mp: 194 °C; CHN: (Found: C, 46.55; H, 5.97; N, 32.86%. Calculated for $C_8H_{13}N_5S$: C, 45.49; H, 6.16; N, 33.17) ν_{max}/cm^{-1} 3300–3210, 1622, 1538, 1027, 837; ^1H NMR δ (d_6-DMSO) 1.06 (3H, t), 2.20 (3H, s), 3.21 (2H, m), 6.33 (1H, s), 7.61 (1H, s), 11.28 (1H, s); $m/z = 211$ (M^+, 53%).

HL^3: Yield: ~69%; mp: 194 °C; CHN: (Found: C, 46.55; H, 5.97; N, 32.86%. Calculated for $C_8H_{13}N_5S$: C, 45.49; H, 6.16; N, 33.17). ν_{max}/cm^{-1} 3300–3200, 1611, 1024, 865; ^1H NMR δ (d_6-DMSO) 2.25 (3H, s), 3.08 (6H, s), 6.24 (1H, s), 8.06 (1H, s), 10.79 (1H, s); $m/z = 211$ (M^+, 82%).

2.3. Preparation of the complexes

2.3.1. Preparation of complex *1*

To a solution of HL^1 (0.447 g, 2.27 mmol) in hot purified ethanol (15 cm^3) was added $VO(acac)_2$ (0.601 g, 2.27 mmol). The green mixture was refluxed for 3 h at water bath temperature, within which time the mixture turned greenish yellow. This mixture was kept at room temperature for slow evaporation. The yellow crystals so formed were filtered off after 72 h, washed with ethanol:water (1:1 v/v) and dried over anhydrous $CaCl_2$. Yield ca. 76%. Yellow crystals of complex **1**, suitable for X-ray diffraction studies were grown by slow evaporation of an ethanolic solution at room temperature.

2.3.2. Preparation of the complexes *2* and *3*

These two complexes were prepared using a similar method as described for **1** employing HL^2 and HL^3 as the ligand respectively. Yields ca. 72% (for **2**) and ca. 69% (for **3**). Pale yellow crystals of **2** and deep orange crystals of **3** suitable for X-ray crystallographic studies were isolated by slow evaporation of an ethanolic solution of the complexes at room temperature.

2.4. Physical measurements

Carbon, hydrogen and nitrogen contents of the ligands HL^1, HL^2 and HL^3 and of the V(V) complexes were determined with a Perkin–Elmer CHNS/O analyzer 2400 at IACS, Kolkata. The molar conductance values of the complexes were measured in DMF solution with a Systronic Model 304 digital conductivity meter. The electronic spectra of the complexes in acetonitrile solution and the diffuse reflectance spectra of the complexes were recorded on a Hitachi model U-3501 spectrophotometer. IR spectra were recorded on a Perkin–Elmer model 883 infrared spectrophotometer. ^1H NMR spectra of the aldehyde and the ligands were recorded in d_6-DMSO with a Bruker AM 300 L (300 MHz) superconducting FTNMR. Mass spectra of the ligands were done with JEOLJMS-AX 500 mass spectrometer. Cyclic voltammetry was carried out using Sycopel model AEW2 1820 F/S instrument. The measurements were performed at 300 K in acetonitrile solution containing 0.2 M TEAP as the supporting electrolyte and 10^{-3}–10^{-4} M of the V(V) complexes, deoxygenated by bubbling with nitrogen. The working, counter and reference electrodes used were a platinum wire, a platinum coil and an SCE.

2.5. Crystallographic measurements

A summary of crystallographic data is given in Table 1. Complete tabulations of crystallographic data, bond lengths and angles, atomic coordinates, thermal parameters and completely labelled ball and stick diagrams are available as supporting information. Data were obtained using a Bruker SMART diffractometer at 293(2) K (for **1**), 93(2) K (for **2**) and 295(2) K (for **3**). Unit cell dimensions

Table 1
Experimental data for the crystallographic analysis

	1	2	3
Empirical formula	$C_7H_{10}N_5O_2SV$	$C_8H_{12}N_5O_2SV$	$C_8H_{12}N_5O_2SV$
Formula weight	279.21	293.24	293.23
Crystal system	monoclinic	triclinic	monoclinic
Space group	$P2(1)/c$ (no. 14)	$P1$ (no. 2)	$P2(1)/c$
Unit cell dimensions			
a (Å)	7.0455(6)	7.8195(9)	13.2257(9)
b (Å)	11.1341(11)	11.9824(14)	12.6042(9)
c (Å)	14.1478(14)	14.2299(17)	7.2882(5)
α (°)	90	114.102(2)	90
β (°)	93.785(2)	101.293(2)	92.031(2)
γ (°)	90	94.933(2)	90
Z	4	4	4
Volume (Å)^3	1107.41(18)	1172.8(2)	1214.18(15)
Temperature (K)	293(2)	93(2)	295(2)
Wavelength (Å)	Mo Kα 0.71073	Mo Kα 0.71073	Mo Kα 0.71073
Crystal size (mm^3)	$0.55 \times 0.15 \times 0.12$	$0.55 \times 0.45 \times 0.25$	$0.25 \times 0.07 \times 0.05$
Absorption coefficient (mm^{-1})	1.077	1.021	0.987
$F(000)$	568	600	600
ρ (observed), ρ (calculated) (g/cm^3)	0.000, 1.675	0.000, 1.661	0.000, 1.604
Reflections collected	2064	5153	10008
Goodness-of-fit on F^2	1.026	1.032	1.155
Final R indices ($I > 2\sigma(I)$)	0.0394	0.0294	$R_1 = 0.0669$, $R_2 = 0.1502$
R indices (all data)	0.0584	0.0324	$R_1 = 0.0830$, $wR_2 = 0.1591$
R, wR, S	0.0394, 0.1024, 1.03	0.0294, 0.0770, 1.03	0.0669, 0.1591, 1.15

were refined by use of the settings of 25 accurately determined reflections, widely separated in reciprocal space. Intensities were measured by ω-scans. A total of 2064 reflections for **1**, 5153 reflections for **2** and 10008 reflections for **3** were collected. The data were averaged ($R_{int} = 0.031\%$ for complex **1**, $R_{int} = 0.0\%$ for complex **2** and $R_{int} = 0.0454\%$ for complex **3**). The structures were solved by direct methods and subsequent Fourier syntheses were used to determine the remaining non-hydrogen atomic positions.

Intensities were collected for Lorentz and polarization effects, and empirical absorption corrections were applied based on a set of ψ-scans. Calculations for **1** and **2** were carried out using Bruker SHELXTL and Bruker SAINT for **3** (data reduction), SHELXL-97 (absorption correction, structure solution or refinement and molecular graphics). The structures were solved using direct methods and refined on F^2 using full matrix least squares techniques with anisotropic displacement factors for all non-hydrogen atoms. Positions of the hydrogen atoms were calculated from the geometry of the molecular skeleton and their thermal displacement parameters were refined isotropically on a group-wise basis. Selected bond lengths and angles are reported in Table 3. H-Bonding distances and angles are shown in Tables 3a and b.

3. Results and discussion

3.1. Characterization of the ligands HL^1, HL^2 and HL^3

The elemental analyses (C, H and N) and IR spectral data [characteristic bands (cm^{-1}) at 3300–3260 (ν_{NH}), 1575 ($\nu_{CH=N}$), 1095 (ν_{N-Pz}), 1000 ($\nu_{C=S}$)] are in good agreement with the structures in Fig. 1. The absence of any band in the 2600–2200 cm^{-1} region of the IR spectra of the free ligands suggests the absence of any thiol tautomer in the solid state [27,28].

3.2. ^1H NMR spectra of the ligands

The ^{1}H NMR spectra (δ_H ppm) in d_6-DMSO at 300 MHz of the ligand HL^1, HL^2 and HL^3 give singlets at δ 2.26 (3H), δ 2.20 (3H) and δ 2.25 (3H) assignable to C_5–CH_3 (ring pz) and singlets at δ 6.34 (1H), δ 6.33 (1H) and δ 6.24 (1H) due to C_4–H (ring pz) respectively. A narrow split doublet at δ 2.85 ($J = 6$ Hz, 3H) for HL^1 is ascribed to the terminal N–CH_3; a narrow-split multiplet at δ 3.21 (2H) and triplet at δ 1.06 ($J = 6.5$ Hz, 3H) for HL^2 are ascribed to terminal NCH_2CH$_3$ and NCH$_2$CH_3 respectively and a singlet at δ 3.08 (6H) for HL^3 is ascribed

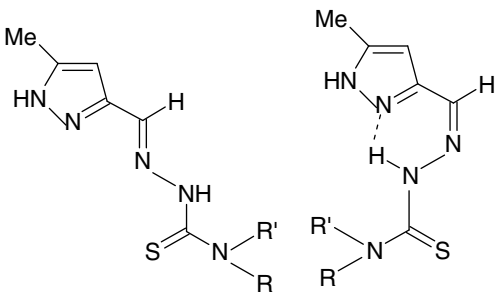


Fig. 1. Structure of the ligands: R = Me, R′ = H in HL^1; R = Et, R′ = H in HL^2; R = Me, R′ = Me in HL^3.

to terminal $N(CH_3)_2$. A slightly broad singlet at δ 7.95 (1H) for HL^1, at δ 7.61 (1H) for HL^2 and a singlet at δ 8.06 (1H) for HL^3 are ascribed to the azomethine proton of the ligand. A singlet at δ 11.32 (1H) for HL^1, at δ 11.28 (1H) for HL^2 and at δ 10.79 (1H) for HL^3 confirm the presence of azomethine NH in all three ligands.

3.3. Characterization of the complex species

The V(V) complexes have been prepared employing a V(IV) starting material such as $VO(acac)_2$. Molecular dioxygen from air serves as the oxidant during the course of the reaction. All the complexes gave satisfactory C, H, N analyses (Table 2) and are diamagnetic in nature. The molar conductance values of the complexes in DMF classify them as non-electrolytes [29].

3.3.1. IR spectra of the complexes

A comparative study of the IR spectral data of the reported complexes with those of the uncomplexed ligand gives meaningful information regarding bonding sites of the ligand molecules. The IR spectra of the complexes show a broad band spanning in the 3400–2900 cm^{-1} region, probably arising from the H-bonding between one of the V=O groups with one pyrazole N atom. The IR band appearing at 1573 cm^{-1} in the free ligand HL^1, HL^2, HL^3 spectra (CH=N) has been observed to shift towards a lower wavenumber by 25–30 cm^{-1} in the IR spectra of **1**, 15–20 cm^{-1} for **2** and by 35–40 cm^{-1} for **3**, due to involvement of the azomethine nitrogen [30] in bonding. In addition, a strong two-band pattern in the 960–840 cm^{-1} region is the signature of the *cis*-dioxovanadium(V) moiety [31] which may be assigned to symmetric and asymmetric ν(O=V=O) vibrations of the *cis*-VO_2 group [32].

An intense strong band at ca. 850 cm^{-1} characteristic for $\nu_{C=S}$ in all three ligands are found to suffer downfield shifts (ca. 80–100 cm^{-1}) after complexation in all the complexes. This indicates that the sulfur atom of the C=S in its deprotonated thiol form functions as the coordination site [30].

3.3.2. Solution spectra of the complexes

A DMF solution of the complexes record spectral data around 34364 cm^{-1} for **1**, 34350 cm^{-1} for **2** and two bands, one around 33350 cm^{-1} and the other around 24250 cm^{-1}, for **3**. Thus for all the complexes, the intense absorption band around 34000 cm^{-1} corresponds to an intraligand transition whereas the additional band for **3** around 24250 cm^{-1} is assignable to a L–V (dπ) LMCT band [33].

3.3.3. ^1H NMR spectra of the Complexes

The ^1H NMR spectral data (δ ppm) of **1**–**3** in d_6-DMSO at 300 MHz give singlets at δ 2.32 (3H), 2.32 (3H) and δ 2.30 (3H) assignable to C_5–CH_3 (Ring Pz) and singlets at δ 6.66 (1H), δ 6.66 (1H) and δ 6.63 (1H) ascribed to C_4–*H* (Ring Pz) respectively. A narrow split doublet at δ 2.95 ($J = 6$ Hz, 3H) for **1** is ascribed to the terminal NCH_3, a narrow split multiplet at δ 3.43 (2H) and triplet at δ 1.18 ($J = 6.5$ Hz, 3H) for **2** are ascribed to terminal NCH_2CH_3 and NCH_2CH_3 respectively, a narrow split singlet at δ 3.26 (6H) for **3** is ascribed to the terminal $N(CH_3)_2$. A slightly broad singlet at δ 8.15 (1H) in **1**, at δ 7.73 (1H) in **2** and appearance of a singlet at δ 8.46 (1H) in **3** is ascribed to the azomethine proton. Thus although the azomethine CH proton appears downfield (compared to the corresponding free ligand) in all the complexes, that in **3** undergoes the maximum downfield shift. This indicates that in **3** the CH azomethine proton, being nearby to the azomethine nitrogen donor center, feels maximum reduction in electron density. In **1** and **2** the azomethine CH proton is quite far from the thioimine nitrogen donor center and hence causes less reduction in electron density around CH. The absence of a singlet around δ 11.3 in **1**, δ 11.1 in **2** and δ 10.8 in **3** confirms the enethiolization process prior to complexation followed by deprotonation during complexation. This is also evident from the X-ray crystal structure studies.

3.3.4. Electrochemistry

Cyclic voltammograms of **1** and **3** were measured in acetonitrile within the potential window +0.20 to −1.5 V. The complexes display irreversible single step one electron responses around −0.78 V vs. SCE corresponding to V(V)/V(IV) reduction. The electrochemical study of **2** could not be performed because of its very poor solubility in the said solvent.

3.3.5. Structure description

The molecular structures of **1**–**3**, including the atom labelling, are shown in Fig. 3a–c respectively (atom labels of **2** appear in lower case in Fig. 3b). Their selected bond lengths and angles are given in Table 3a and b. The $[VO_2L^x]$, $x = 1$–3 unit of the complexes is neutral and mononuclear. In each complex, the unit cell comprises of four molecules. The V atom in each complex is coordinated

Table 2
Analytical data and pertinent physico-chemical properties of the complexes

Complex	Colour	%C	%H	%N	$\Lambda_M\ \Omega^{-1}\ cm^2\ mol^{-1}$ (in DMF)
$[VO_2L^1]$	pale yellow	30.08(30.11)	3.58(3.59)	25.07(25.09)	31
$[VO_2L^2]$	yellow	32.76(33.01)	4.09(4.15)	23.89(24.25)	35
$[VO_2L^3]$	yellow	32.76(33.01)	4.09(4.15)	23.89(24.25)	34

Elemental analyses found (calc.).

to two nitrogen atoms, one thiolato sulfur and two terminal oxo groups. Out of the two nitrogen donor atoms, the pyrazolyl nitrogen is common in all the cases. The other nitrogen is the thioimine (N1 for **1**, N2A/2B for **2**) and the azomethine (N3 for **3**) one.

The thiosemicarbazone molecule functions as singly deprotonated tridentate ligand. The deprotonation is accompanied by tautomerization to the iminothiolate form. The coordination geometry around the V atom in all the three complexes is best described as square pyramidal with a slight distortion towards a trigonal bipyramidal geometry. The Schiff base ligand is coordinated meridionally, occupying the three equatorial positions. The remaining equatorial position is occupied by one of the two oxo groups (O2). The apical position is satisfied by another oxo group (O1). The τ parameters of the complexes (0.20 for **1**, 0.18 for **2** (unit-A), 0.26 for **2** (unit-B) and 0.14 for **3**) also support their square pyramidal geometry. [34,35] The maximum distortion toward trigonal bipyramidal geometry occurs in **2** (unit-B). All the bond angles comprising the adjacent donor atoms in the basal plane and V as well as any one donor atom, V and O1 i.e., O_1VO_2, SVO_1, N_1VO_1 (for **1**, **2**), N_2VO_1 (for **3**), N_3VO_1 (for **1**, **3**) and N_2VO_1 (for **2**) are increased from the ideal value of 90° (Table 3b) because of the shifting of the V-atom from the square plane toward the apical oxygen (O1). The V-atom is shifted from the square plane upward through a distance of 0.560 Å in **1**, 0.569 Å in **2** (unit-A), 0.568 Å in **2** (unit-B) and 0.559 Å in **3**.

The average V=O distances 1.623 Å in **1**, 1.632 Å in **2** and 1.614 Å in **3**, being slightly longer than the normal V=O double bond length of 1.595 Å, indicate that the oxygens are involved in weak hydrogen bonding interactions [36]. The V–N(1) and V–N(3) distances 2.055 and 2.048 Å in **1**, V–N(2A) and V–N(1A) distances 2.071 and 2.050 Å in **2**, V–N(3) and V–N(2) distances 2.184 and 2.043 Å in **3** are in accordance with literature values for V–N distances [36,37].

The asymmetric unit in **2** contains two independent molecules; however, there are conformational differences between them. The vanadium atoms, being separated by a distance of 5.515 Å in the two units A and B, are

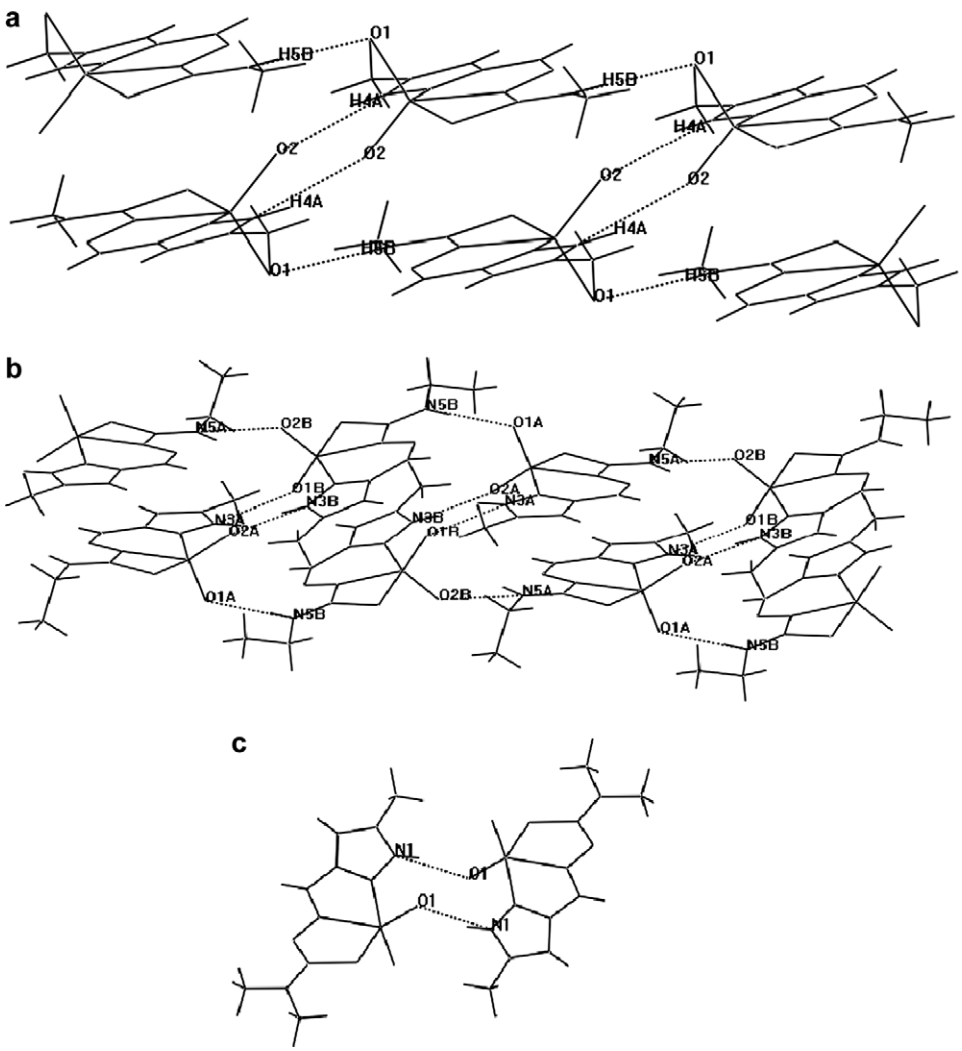


Fig. 2. (a) H-bonding in **1**; (b) H-bonding in **2**; (c) H-bonding in **3**.

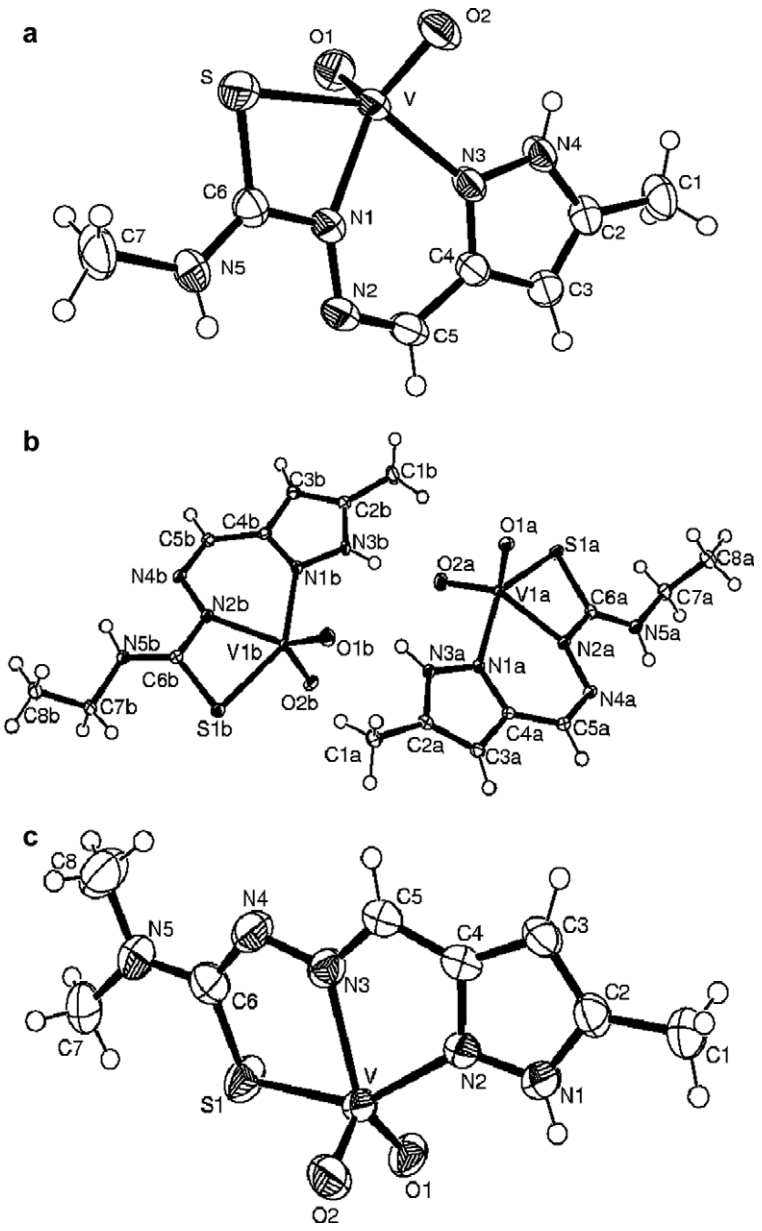


Fig. 3. (a) Molecular structure and atom-numbering scheme for **1** with thermal ellipsoids drawn at the 50% probability level; (b) molecular structure and atom-numbering scheme for **2** with thermal ellipsoids drawn at the 50% probability level. Two equivalent molecules in the asymmetric units, A and B are shown; (c) molecular structure and atom-numbering scheme for **3** with thermal ellipsoids drawn at the 50% probability level.

deviated downward by 0.315 Å and upward by 0.240 Å from the mean plane forming a skew conformation at C1B and C8B and eclipsed at C1A and C7A. The units A and B are joined by weak intermolecular hydrogen bonding.

In case of **1**, C1, C2, C3, C4, N3, N4, C5, N2, N1, C6, S are roughly in the same plane (with a maximal deviation of 0.063 Å) with the vanadium atom shifted by 0.317 Å out of that plane towards O1 [32]. Due to that latter deviation the conformation of the six-membered chelate ring containing V, N3 C4, C5, N2 and N1 atoms is concluded to be an envelope at V. Cremer and Pople [38] puckering analysis shows that the four membered chelate ring containing V, N1, C6 and S atoms also adopts an envelope conformation, but in that case on C6 (with a deviation of 0.111 Å) from the mean plane containing V, S and N1 atoms.

In the case of **2**, C1A/1B, C2A/2B, C3A/3B, C4A/4B, N1A/1B, N3A/3B, C5A/5B, N4A/4B, N2A/2B, C6A/6B and S1A/1B [A for unit-A and B for unit-B] are roughly in the same plane [with a maximal deviation of 0.059 Å for unit-A and 0.056 Å for unit-B]. The vanadium atom is shifted upward by 0.315 Å [for unit-A]/downward by 0.242 Å [for unit-B] out of that plane towards O1A (for unit-A)/O2B (for unit-B). Thus the six-membered chelate ring encompassing V1A/1B, N1A/1B, C4A/4B, C5A/5B, N4A/4B and N2A/2B atoms is enveloped at the vanadium center in each case. Cremer and Pople [38] puckering analysis shows that the four membered chelate ring containing

Table 3
Selected bond lengths (Å) and angles (°), with esds in parentheses

1	(Å)	**2**	(Å)	**3**	(Å)
*(a) Selected bond lengths for **1**, **2** and **3***					
V–S	2.4436(8)	V1A–N1A	2.0501(16)	V–S1	2.3566(14)
V–O1	1.6185(19)	V1A–N2A	2.0712(14)	V–O1	1.629(3)
V–O2	1.627(2)	V1A–S1A	2.4368(6)	V–O2	1.599(3)
V–N1	2.055(2)	V1A–O1A	1.6289(14)	V–N2	2.043(3)
V–N3	2.048(2)	V1A–O2A	1.6352(12)	V–N3	2.184(4)
N3–N4	1.360(3)	V1B–N2B	2.0712(13)	N3–N4	1.357(6)
		V1B–N1B	2.0372(16)		
		V1B–O2B	1.6286(13)		
		V1B–O1B	1.6316(12)		
		V1B–S1B	2.4400(6)		
		N1A–N3A	1.3563(18)		
*(b) Selected bond angles (°) for **1**, **2** and **3***					
O1–V–S	100.28(7)	S1A–V1A–O1A	101.87(5)	N3–V–S1	76.19(10)
O2–V–S	101.45(8)	S1A–V1A–O2A	100.08(5)	O2–V–O1	109.32(16)
O1–V–O2	109.98(10)	S1A–V1A–N1A	144.28(4)	N2–V–O2	101.19(14)
O1–V–N1	116.96(9)	S1A–V1A–N2A	67.42(4)	O1–V–N2	97.12(14)
O1–V–N3	102.47(9)	O1A–V1A–O2A	109.23(6)	N2–V–N3	73.14(14)
V–N3–N4	122.82(16)	O1A–V1A–N1A	102.44(6)	V–N3–N4	125.30(3)
N1–V–N3	78.74(8)	O1A–V1A–N2A	117.04(6)	O2–V–N3	112.68(14)
N1–V–S	67.27(6)	O2A–V1A–N1A	96.16(6)	O2–V–S1	103.52(14)
N3–V–S	144.98(6)	O2A–V1A–N2A	133.55(6)	O1–V–N3	137.95(13)
N1–V–O2	132.90(10)	N1A–V1A–N2A	78.31(6)	O1–V–S1	96.12(10)
N3–V–O2	95.37(9)	S1B–V1B–O1B	100.37(5)	N2–V–S1	146.17(10)
		S1B–V1B–O2B	101.58(5)		
		S1B–V1B–N1B	145.92(4)		
		S1B–V1B–N2B	67.42(4)		
		O1B–V1B–O2B	109.08(6)		
		O1B–V1B–N1B	97.01(6)		
		O1B–V1B–N2B	130.44(6)		
		O2B–V1B–N1B	100.07(6)		
		O2B–V1B–N2B	120.32(6)		
		N1B–V1B–N2B	78.97(6)		

V1A/1B, N2A/2B, C6A/6B and S1A/1B (unit-A and B) also looks like an envelope on C6 (A and B) with a deviation of 0.067 Å (for unit-A)/0.021 Å (for unit-B) from the mean plane containing the V1A/1B, S1A/1B and N2A/2B atoms.

In the case of **3**, C1, C2, C3, C4, N1, N2, C5, N3, N4, C6 and S1 are roughly in the same plane (with a maximal deviation of 0.200 Å) with the vanadium atom shifted by 0.354 Å out of that plane towards O2. Because of this deviation, the conformation of the five-membered chelate ring containing V, C4, C5, N3 and N2 atoms is proposed to be an envelope at V. The other five membered chelate ring containing V, N3, N4, C6 and S1 atoms is also in an envelope conformation on C6 (with a deviation of 0.204 Å) from the mean plane containing the V, N3, N4 and S1 atoms.

Complex **1** is stabilized through a network of weak H-bond interactions (Fig. 2a). The details are presented in Table 4. The H-bond distances between N3B and O2A [2.708 Å] and O1B and N3A [2.748 Å] support a weakly H-bonded structure in **2** (Fig. 2b, Table 4). Similarly the H-bond distance between N1 and O1 in **3** is 2.77 Å, which also indicates the presence of weak H-bonding (Fig. 2c, Table 4).

Table 4
Details of hydrogen bond distances (Å) and angles (°)

Complex	D–H···A	*d* (D–H)	*d* (H···A)	*d* (D···A)	∠(DHA)
1	N4–H4A···O2	0.8500	1.97	2.760(3)	151
	N5–H5B···O1	0.8600	2.16	2.980(3)	161
	N3A–H3AB···O1B	0.8800	2.00	2.7477(18)	141
	N5A–H5AB···N4A	0.8800	2.36	2.687(2)	102
	N5A–H5AB···O2B	0.8800	2.11	2.837(2)	140
2	N3B–H3BB···O2A	0.8800	1.84	2.7080(18)	170
	N5B–H5BB···N4B	0.8800	2.41	2.705(2)	100
	N5B–H5BB···O1A	0.8800	2.12	2.972(2)	163
3	N1–H1A···O1	0.8600	1.90	2.7722(4)	160

4. Conclusion

We have prepared three V(V) complexes employing *N*(4)-mono/disubstituted pyrazole derived thiosemicarbazone ligands. In the case of *N*(4)-monosubstituted (HL^1 and HL^2) ligands, the unexpected thioimine nitrogen and not the expected azomethine nitrogen functions as one of the donor sites, whereas for the *N*(4)-disubstituted ligand (HL^3), the expected azomethine nitrogen acts as the donor site. The coordinating behaviour of similar types of *N*(4)-substituted aldehydo thiosemicarbazone ligands so far reported, in general, establishes that it is the azomethine nitrogen which functions as one of the donor sites toward transition metal ions. This peculiar coordinating behaviour of the thioimine nitrogen is unique for these *N*(4)-monosubstituted pyrazole derived ligands toward V only.

Acknowledgement

One of the authors A.H thanks CSIR, India for awarding a JRF and S.K thanks for financial assistance.

Appendix A. Supplementary material

CCDC 617225, 617226 and 617227 contain the supplementary crystallographic data for **1**, **2** and **3**. These data can be obtained free of charge via htpp://www.ccdc.cam.ac.uk/conts/retrieving.html, or from the Cambridge Crystallographic Data Centre, 12 Union Road, Cambridge CB2 1EZ, UK; fax: +44 1223-336-033; or e-mail: deposit@ccdc.cam.ac.uk. Supplementary data associated with this article can be found, in the online version, at doi:10.1016/j.poly.2006.09.005.

References

[1] P. Frank, R.M.K. Carlson, E.J. Carlson, K.O.J. Hodgson, Inorg. Biochem. 94 (2003) 59–71.
[2] P. Frank, R.M.K. Carlson, E.J. Carlson, K.O. Hodgson, Coord. Chem. Rev. 237 (2003) 31–39.
[3] R.E. Berry, E.M. Armstrong, R.L. Beddoes, D. Collison, S.N. Ertok, M. Helliwell, C.D. Gamer, Angew. Chem., Int. Ed. 38 (1999) 795–797.
[4] (a) K. Kanamori, Coord. Chem. Rev. 237 (2003) 147–161;
(b) D. Rehder, Inorg. Chem. Commun. 6 (2003) 604–617.
[5] R.R. Eady, Coord. Chem. Rev. 237 (2003) 23–30, and references cited therein.
[6] (a) M. Weyand, H.J. Heeht, M. Kiess, M.F. Liaud, H. Vilter, D.J. Schomburg, Mol. Biol. 293 (1999) 595–611;
(b) J.N. Carter-Franklin, J.D. Parrish, R.A. Tehirret-Guth, R.D. Little, A. Butler, J. Am. Chem. Soc. 125 (2003) 3688–3689;
(c) D. Rehder, G. Santoni, G.M. Licini, C. Schulzke, B. Meier, Coord. Chem. Rev. 237 (2003) 53–63.
[7] (a) R.M. Brand, F.G. Hamel, Int. J. Pharm. 183 (1999) 117–123;
(b) P.G. Drake, B.I. Posner, Mol. Cell Biochem. 182 (1998) 79–89;
(c) P.G. Drake, A.P. Bevan, J.W. Burgess, J.J. Bergeron, B.I. Posner, Endocrinology 137 (1996) 4960–4968.
[8] (a) J.W. Eriksson, P. Lönnroth, B.I. Posner, A. Shaver, C. Wesslau, U.P. Smith, Diabetologia 39 (1996) 235–242;
(b) P.J. Stankiewicz, A.S. Tracey, in: H. Sigel, A. Sigel (Eds.), In Metal Ions in Biological Systems: Stimulation of Enzyme Activity by Oxovanadium Complexes, vol. 31, Marcel Dekker, New York, 1995, pp. 249–285 (Chapter 8).
[9] (a) P. Zimmet, K.G.M.M. Alberti, J. Shaw, Nature 414 (2001) 782–787;
(b) D.E. Möller, Nature 414 (2001) 821–827.
[10] (a) H. Sakurai, Y. Kojima, Y. Yoshikawa, K. Kawabc, H. Yasui, Coord. Chem. Rev. 226 (2002) 187–198;
(b) T. Sasagawa, Y. Yoshikawa, K. Kawabc, H. Sakurai, Y. Kojima, J. Inorg. Biochem. 88 (2002) 108–112;
(c) K. Kanamori, K. Nishida, N. Miyata, K. Okamoto, Y. Miyoshi, A. Tamura, H.J. Sakurai, Inorg. Biochem. 6 (2001) 649–656;
(d) M. Melchior, S.J. Rettig, B.D. Liboiron, K.H. Thompson, V.G. Yuen, J.H. McNeill, C. Orgiv, Inorg. Chem. 40 (2001) 4686–4690.
[11] G.J. Colpas, B.J. Hamstra, J.W. Kampf, V.L. Pecoraro, J. Am. Chem. Soc. 118 (1996) 3469.
[12] A.D. Keramidas, A.B. Papaioannou, A. Vlahos, T.A. Kabanos, G. Bonas, A. Makriyannis, C.P. Rapropoulou, A. Terzis, Inorg. Chem. 118 (1996) 3469.
[13] K.K. Nanda, S. Mohanta, S. Ghosh, M. Mukherjee, M. Helliwell, K. Nag, Inorg. Chem. 34 (1995) 2861.
[14] C.R. Cornman, E.P. Zovinka, Y.D. Boyajian, K.M. Geiser-Bush, P.D. Boyle, P. Singh, Inorg. Chem. 34 (1995) 4213.
[15] C.J. Carrano, M. Mohan, S.M. Holmes, R. de la Rosa, A. Butler, J.M. Charnock, C.D. Garner, Inorg. Chem. 33 (1994) 646.
[16] D.C. Crans, P.K. Shin, J. Am. Chem. Soc. 116 (1994) 1305.
[17] E.M. Armstrong, R.L. Beddoes, L.J. Calviou, J.M. Charnock, D. Collison, N. Ertok, J.H. Naismith, C.D. Garner, J. Am. Chem. Soc. 115 (1993) 807.
[18] M.J. Clague, N.L. Keder, A. Butler, Inorg. Chem. 32 (1993) 4754.
[19] V. Vergopoulos, W. Priebsch, M. Fritzsche, D. Rehder, Inorg. Chem. 32 (1844) 1844.
[20] C.R. Cornman, J. Kampf, M.S. Lah, V.L. Pecoraro, Inorg. Chem. 31 (1992) 2035.
[21] A.R. Bulls, C.G. Pippin, F.E. Hahn, K.N. Raymond, J. Am. Chem. Soc. 112 (1990) 2627.
[22] (a) M. Sutradhar, G. Mukherjee, M.G.B. Drew, S. Ghosh, Inorg. Chem. 45 (2006) 5150;
(b) Y. Miyazaki, S. Matsuoka, Y. Miura, H. Sakashita, K. Yoshimura, Polyhedron 24 (2005) 985;
(c) A. Sarkar, S. Pal, Polyhedron 25 (2006) 1689.
[23] (a) M.S. Shongwe, H.N.R. Al-Kharousi, H. Adams, M.J. Morris, E. Bill, Inorg. Chem. 45 (2006) 1103;
(b) M.R. Maurya, A. Kumar, M. Abid, A. Azam, Inorg. Chem. Acta 359 (2006) 2439.
[24] A.K. Barik, S. Paul, R.J. Butcher, J.C. Bryan, S.K. Kar, Polyhedron 18 (1999) 571.
[25] (a) L. Papathanasis, M.A. Demertzis, P.N. Yadav, D. Kovala-Demertzi, C. Prentjas, A. Castiñeiras, S. Skoulika, D.X. West, Inorg. Chim. Acta 357 (2004) 4113;
(b) D.X. West, S.B. Padhye, P.B. Sonawane, Struct. Bonding 76 (1991) 1;
(c) D.X. West, A.E. Liberta, S.B. Padhye, R.C. Chikate, P.B. Sonawane, A.S. Kumbhar, R.G. Yerande, Coord. Chem. Rev. 123 (1993) 49.
[26] D.D. Perrin, W.L.F. Armarego, D.R. Perrin, Purification of Laboratory Chemicals, second ed., Pergamon Press, Oxford, 1980.
[27] M. Akbar Ali, M.T.H. Tarafdar, J. Inorg. Nucl. Chem. 39 (1977) 1785.
[28] M.M. Mostafa, A El. Hammid, M. Shallaby, A.A. El-Asmy, Transit. Met. Chem. 6 (1981) 303.
[29] W.J. Geary, Coord. Chem. Rev. 7 (1971) 81.
[30] S.K. Chattopadhyay, D. Chattopadhyay, J. Banerjee, R. Kuroda, S. Ghosh, Polyhedron 16 (1997) 1925.
[31] S. Samanta, D. Ghosh, S. Mukhopadhyay, A. Endo, Timothy J.R. Weakley, M. Chaudhury, Inorg. Chem. 42 (2003) 1508.
[32] E. Kwiatkowski, G. Romanowski, W. Nowicki, M. Kwiatkowski, K. Suwinska, Polyhedron 22 (2003) 1009.

[33] R. Dinda, P. Sengupta, S. Ghosh, T.C.W. Mak, Inorg. Chem. 47 (2002) 1684, and references cited therein.
[34] E.L. Muetterties, L.J. Guggenberger, J. Am. Chem. Soc. 96 (1974) 1748.
[35] A.W. Addison, T.N. Rao, J. Reedijk, J. Rijn, G.C. van Verschoor, J. Chem. Soc., Dalton Trans. (1984) 1349.
[36] H. Schmidt, M. Bashirpoor, D. Rehder, J. Chem. Soc., Dalton Trans. (1996) 3865.
[37] G. Asgedom, A. Sreedhara, J. Kivikoski, E. Kolehmainen, C.P. Rao, J. Chem. Soc., Dalton Trans. (1996) 93.
[38] D. Cremer, J.A. Pople, J. Am. Chem. Soc. 97 (1995) 1354.

Available online at www.sciencedirect.com
ScienceDirect
Polyhedron 26 (2007) 782–790
POLYHEDRON
www.elsevier.com/locate/poly

Synthesis and characterization of two new coordination supramolecular structures from a versatile unsymmetric 5-(4-pyridyl)-1,3,4-oxadiazole-2-thione (Hpot) ligand

Yong-Tao Wang *, Gui-Mei Tang, Wan-Yong Ma, Wen-Zhu Wan

Department of Chemical Engineering, Shandong Institute of Light Industry, Jinan 250100, China

Received 30 June 2006; accepted 5 September 2006
Available online 23 September 2006

Abstract

Two new inorganic–organic coordination networks based on a versatile and unsymmetric building block 5-(4-pyridyl)-1,3,4-oxadiazole-2-thione (Hpot) and inorganic Co^{II} and Cd^{II} salts have been synthesized in mixed solvent media and structurally characterized by single-crystal X-ray diffraction analysis. Crystal Hpot (**1**) was obtained from methanol solution. Reaction of $Co(NO_3)_2 \cdot 6H_2O$ with Hpot afforded a neutral two-dimensional (2-D) porous coordination polymer $\{[Co(pot)_2] \cdot 6H_2O\}_n$ (**2**) with a (4,4) network, which shows a 3-D supramolecular network through O–H···O weak interactions. While substituting the transition metal ions used in **2** with $Cd(NO_3)_2 \cdot 6H_2O$, a neutral 2-D coordination polymer $[Cd_2(pot)_4]_n$ (**3**) with a (6,3) network which further extended to a 3-D supramolecular structure through versatile hydrogen bonds C–H···X (X = O, N and S) was obtained. It is remarkable that the building block "pot" anion exhibits versatile coordination modes in complexes **2** and **3**. These results indicate that the versatile nature of this rigid unsymmetric ligand, together with the coordination preferences of the metal centers, plays a critical role in construction of novel coordination polymers. The properties of gas absorption, magnetism and luminescence of **2** and **3** have been investigated and discussed in detail.
© 2006 Elsevier Ltd. All rights reserved.

Keywords: Coordination complexes; Gas adsorption; Magnetism; Luminescence; Unsymmetric ligand; 5-(4-Pyridyl)-1,3,4-oxadiazole-2-thione; 5-(4-Pyridyl)-1,3,4-oxadiazole-2-thiol

1. Introduction

In recent decades, the construction of metal–organic coordination architectures has witnessed tremendous growth because of their intriguing structures and potential properties [1–4]. Most efforts have focused on using symmetric ligands (e.g., 4,4′-bipyridine and their analogues) [5,6]. However, the use of unsymmetrical ligands is still rare, though a few unsymmetrical ligands have been reported, for example, 2,3′-bipyridine, 2,4′-bipyridine and 3,4′-bipyridine and their analogues [7]. In this respect, our research has focused on designing new unsymmetrically bridging ligands and investigating their self-assemblies with metal centers. The adoption of unsymmetrically bridging ligands is expected to lead to a broader palette of coordination polymers that can be achieved with symmetric ligands. It is anticipated that unsymmetrical ligands can be assembled around metal centers in diverse arrangements, consequently resulting in unprecedented structural features and novel properties.

In our attempt to investigate the design and control of the self-assemblies of metal–organic frameworks (MOFs), we have successfully developed and constructed the intriguing MOFs based on the unsymmetric rigid or flexible ligands [8]. In this work, we synthesized a new unsymmetric rigid bridging ligand 5-(4-pyridyl)-1,3,4-oxadiazole-2-thione (Hpot), which probably results in the versatile structure of supermolecules or coordination polymers and their desired properties. It has characteristics based on the fol-

* Corresponding author. Tel./fax: +86 531 82350869.
E-mail address: ceswyt@sohu.com (Y.-T. Wang).

0277-5387/$ - see front matter © 2006 Elsevier Ltd. All rights reserved.
doi:10.1016/j.poly.2006.09.008

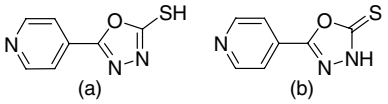


Chart 1. Configuration of Hpot ligand.

lowing advantages: (i) it has two possible configurations (*thione* and *thiol*, see Chart 1), which possesses versatile modes that will lead to novel topological architectures; (ii) it has three potential binding sites. An oxadiazole containing sulfide group exhibiting a variety of coordination modes usually makes the ligand anionic and the framework neutral which gives higher thermal stabilities. The sulfide group generally prefers to coordinate to a soft metal such as Cd(II) [8b]. Meanwhile, the free sulfide groups in the complexes often act as chemical interaction sites, which is attractive for developing new catalytic systems (for example, the moiety can catalyse the transfer of oxygen atoms to produce hydroxy groups) [9]. A pyridyl-type group that is able to satisfactorily complete the coordination sphere of the metal center usually leads to the formation of novel coordination polymers [10]; (iii) it has a strong capability of forming hydrogen bonding interactions that play an important role in the assembly of supramolecular compounds. To the best of our knowledge, this unsymmetric multifunctional building block containing a sulfide group and oxadiazole anion mode is first developed in the process of self-assembly of coordination polymers and supramolecular compounds. Herein, we report the synthesis, characterization and structures of two novel metal complexes with the "pot" ligand, $\{[Co(pot)_2]\cdot 6H_2O\}_n$ (**2**) and $[Cd_2(pot)_4]_n$ (**3**), in which versatile coordination modes of pot were observed. Additionally, the properties of gas adsorption, magnetism and fluorescence for complexes **2** and **3** have also been observed.

2. Experimental

2.1. Materials and physical measurements

The reagents and solvents employed were commercially available and used as received without further purification. The C, H and N microanalyses were carried out with a Perkin–Elmer 240 elemental analyzer. The FT-IR spectra were recorded from KBr pellets in the range 4000-400 cm^{-1} on a Bruker spectrometer. ^1H NMR spectra were recorded on a Bruker ARX-300 NMR spectrometer at 300.132 MHz using DMSO-d_6 as the solvent at room temperature; the DMSO-d_6 signal was used to lock the field and all chemical shifts are given relative to tetramethylsilane (TMS). Thermogravimetric analysis (TGA) data were collected with a Perkin–Elmer TGS-2 analyzer in a N_2 flow at a heating rate of 20 °C min^{-1}. The emission/excitation spectra were recorded on an Edinburgh FLS920 spectrometer equipped with a continuous Xe900 xenon lamp and an nF900 nanosecond flash lamp. The variable-temperature magnetic susceptibilities were measured on a Quantum Design SQUID susceptometer operating at a magnetic field of 0.1 T between 2 and 300 K. The diamagnetic corrections were evaluated from Pascal's constants for all the constituent atoms. Magnetization measurements were carried out at low temperature (2 K) in a 0–5 T range. Gas adsorption measurements were carried out with a Micromeritics ASAP 2010 surface area and porosimetry system. The gas adsorption tests of the desolvate **1** were obtained from the N_2 gas adsorption at 77 K with a volumetric adsorption apparatus. After **2** (712.6 mg) was placed at 80 °C under vacuum for 40 h, the sample had a weight loss of 19.2% ($6H_2O$) for **2**, in agreement with the TGA results.

2.2. Synthesis of the ligand 5-(4-pyridyl)-1,3,4-oxadiazole-2-thione (Hpot, 1)

The ligand Hpot was obtained by the modified literature method [11]. Yield: 78%. Mp: 272 °C. ^1H NMR (300 MHz, DMSO-d_6): $\delta = 8.8$ (d, 2H), 7.8 (d, 2H), 3.4 (br, 1H). IR (KBr, cm^{-1}): ν 3434 (br), 3087 (w), 3032 (m), 2401 (br), 1841 (br), 1596 (s), 1553 (m), 1493 (w), 1420 (w), 1365 (s), 1330 (m), 1309 (w), 1234 (m), 1200 (s), 1149 (s), 1084 (m), 1073 (w), 1051 (s), 1007 (s), 892 (m), 829 (s), 722 (m), 692 (m), 556 (s), 514 (m). ESI-MS (ESITOF N_2): m/z 180 (M+1). *Anal.* Calc. for $C_7H_5N_3OS$: C, 46.92; H, 2.81; N, 23.45. Found: C, 46.80; H, 2.80; N, 23.52%.

2.3. Synthesis of $\{[Co(pot)_2]\cdot 6H_2O\}_n$ (2)

To a solution of Hpot (34 mg, 0.2 mmol) in DMF (10 mL) was added a dilute aqueous solution of NaOH (0.1 M, 2 mL) with stirring to adjust the pH value of the mixture to ca. 7. Then, a water solution (5 mL) of $Co(NO_3)_2\cdot 6H_2O$ (29 mg, 0.1 mmol) was added slowly to the above solution under refluxing conditions for ca. 10 min. The resultant orange solution was filtered after cooling to room temperature. Block purple single-crystals suitable for X-ray diffraction were obtained by slow evaporation of the solvents within one week in 75% yield. *Anal.* Calc. for $C_{14}H_{24}CoN_6O_{10}S_2$: C, 30.06; H, 4.32; N, 15.02. Found: C, 29.95; H, 4.31; N, 15.07%. IR (cm^{-1}): 3408 (br) (ν_{O-H} for H_2O), 1534 (m), 1490 (s), 1424 (s) (skeletal vibrations for pyridyl ring), 1590 (s), 1549 (m), 1200 (s), 1051 (s) (skeletal vibrations for oxadiazole ring).

2.4. $[Cd_2(\mu_2\text{-}pot)_2(\mu_3\text{-}pot)_2]_n$ (3)

Hpot (35 mg, 0.2 mmol) was dissolved in DMF (20 mL). To the above solution was added a dilute aqueous solution of NaOH (0.1 M, 2 mL). A solution of $Cd(NO_3)_2\cdot 6H_2O$ (31 mg, 0.1 mmol) was added to the mixture and a large amount of yellow precipitate formed immediately. The slurry mixture was further vigorously stirred under heating for ca. 30 min, and then filtered after cooling to room temperature. The yellow powdered product was collected and washed with anhydrous methanol. The light-yellow filtrate

was allowed to stand at room temperature, and yellow block single-crystals suitable for X-ray diffraction were obtained by evaporation of the solvents within two weeks. Total yield: 75%. *Anal.* Calc. for $C_{28}H_{16}Cd_2N_{12}O_4S_4$: C, 35.87; H, 1.72; N, 17.93. Found: C, 35.74; H, 1.71; N, 18.00%. IR (cm^{-1}): 1536 (m), 1487 (s), 1425 (s) (skeletal vibrations for pyridyl ring), 1582 (s), 1550 (m), 1185 (s), 1040 (s) (skeletal vibrations for oxadiazole ring).

2.5. X-ray crystallography

Single-crystal X-ray diffraction measurements of **1**–**3** ($0.29 \times 0.09 \times 0.07$ mm, $0.43 \times 0.25 \times 0.24$ mm and $0.25 \times 0.25 \times 0.22$ mm for **1**, **2** and **3**, respectively) were carried out with a Bruker Smart APXII CCD diffractometer equipped with a graphite crystal monochromator situated in the incident beam for data collection at 293(2) K. Data collections were performed with Mo Kα radiation ($\lambda = 0.71073$ Å) by the ω-scan mode. No evidence was found for crystal decay during the data collection of complexes **1**–**3**. All the measured independent reflections were used in the structural analysis, and semi-empirical absorption corrections were applied using the SADABS program. The program SAINT [12] was used for integration of the diffraction profiles. All the structures were solved by direct methods using the SHELXS program of the SHELXTL package and refined with SHELXL [13]. Metal atoms were located from the *E*-maps and other non-hydrogen atoms were located in successive difference Fourier syntheses. The final refinement was performed by full-matrix least-squares methods with anisotropic thermal parameters for all the non-hydrogen atoms on F^2. All the hydrogen atoms were first found in difference electron density maps, and then placed in the calculated sites and included in the final refinement in the riding model approximation with displacement parameters derived from the parent atoms to which they were bonded. A summary of the crystallographic data and structure refinements are listed in Table 1.

Table 1
Crystallographic data and structure refinements for **1**–**3**

Compound	**1**	**2**	**3**
Chemical formula	$C_7H_5N_3OS$	$C_{14}H_{24}CoN_6O_{10}S_2$	$C_{28}H_{16}Cd_2N_{12}O_4S_4$
Formula weight	179.21	559.44	937.57
T (K)	293	293	293
λ (Mo Kα) (Å)	0.71073	0.71073	0.71073
Crystal system	monoclinic	monoclinic	triclinic
Space group	$P2_1/n$	$P2_1/n$	$P\bar{1}$
a (Å)	4.869(1)	9.008(1)	9.895 (1)
b (Å)	13.890(3)	12.697 (1)	10.416(1)
c (Å)	11.811(2)	11.256(1)	16.092(2)
α (°)	90	90	94.363(2)
β (°)	97.998(4)	103.031(2)	103.852(2)
γ (°)	90	90	90.173(2)
V (Å^3)	791.0(3)	1254.3(2)	1605.2(4)
Z	4	2	2
μ (Mo Kα) (mm^{-1})	0.357	0.908	1.643
ρ (g cm^{-3})	1.505	1.481	1.940
Goodness-of-fit	1.080	1.079	1.001
R_1[a] [$I > 2\sigma(I)$]	0.0454	0.0665	0.0524
wR_2[b] (all data)	0.1177	0.2413	0.1659

[a] $R_1 = \sum\|F_o| - |F_c\|/\sum|F_o|$.
[b] $wR_2 = [\sum[w(F_o^2 - F_c^2)^2]/\sum[w(F_o^2)^2]]^{1/2}$.

3. Results and discussion

3.1. Preparation of compounds 2 and 3

Compounds **2** and **3** were obtained as neutral molecular complexes in the water system by the combination of Hpot with cobalt and cadmium salts, respectively. Compound **2** could also be isolated according to the same synthetic procedure, but using $CoSO_4$ or $Co(OAc)_2$ as the source of cobalt (confirmed by X-ray diffraction, IR spectra and elemental analyses). A similar case was also observed for the Cd^{II} complex, which indicates that the final products are independent of the counter-anions of the metal salts. Complexes **2** and **3** have 2:1 ligand:metal compositions. Indeed, in these specific self-assembly processes, the products do not depend on the ligand-to-metal ratio (the results were confirmed by X-ray diffraction, IR spectra and elemental analyses). However, increasing the metal-to-ligand ratio results in a somewhat higher yield and crystal quality. Complexes **2** and **3** are air stable and can retain their structural integrity at room temperature for a considerable length of time. Furthermore, the building block "pot" adopts versatile coordination modes in these complexes, which is discussed in detail below.

3.2. Description of 1

Single X-ray analysis of compound **1** reveals that there is one molecule of Hpot in the asymmetric unit (Fig. 1a). The pyridyl and oxadiazole groups are almost co-planar. A pair of Hpot ligands, each using the oxadiazole and pyridyl nitrogen atoms, forms one donor and accept hydrogen bond (N(3)–H(3)···N(1) 2.732(2) Å) in the head–tail form, resulting in one-dimensional hydrogen-bonded chains [14,15]. Between the adjacent hydrogen-bonded chains, each Hpot molecule further forms two donor–acceptor hydrogen bonds (C(5)–H(5)···S(1) 3.852(1) Å) with the thione sulfur of an adjacent oxadiazole ring to another pyridyl ring, resulting in a two-dimensional hydrogen bonded layer along the (0 1 1) plane. These chains align parallel but right about to each other to form a nearly planar supramolecular layer. Two types of hydrogen-bonded patterns A–D, notated as $R_2^2(16)$ and $R_6^6(30)$, are observed in this 2-D array (Fig. 1b). The layers are further extended into a three-dimensional supramolecular array via offset π–π aromatic stacking interactions with a face-to-face distance of ca. 3.54 Å between oxadiazole and pyridyl rings (see Fig. S1).

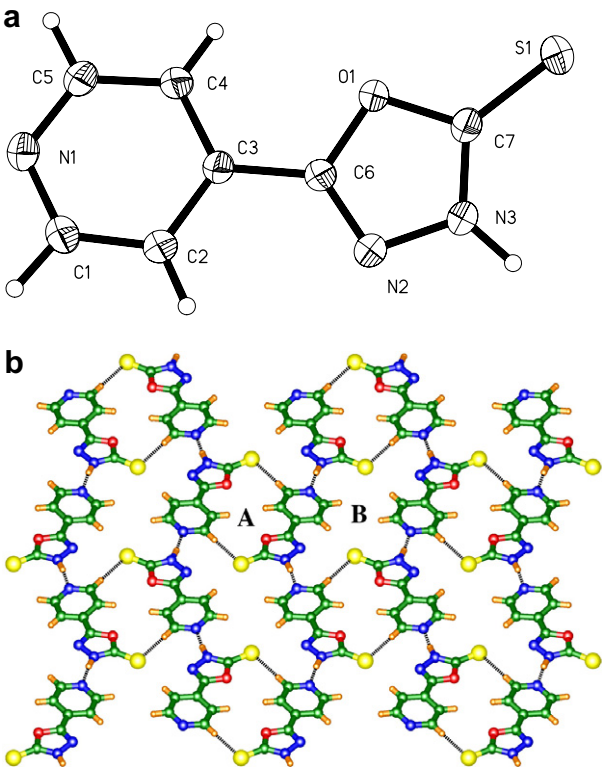
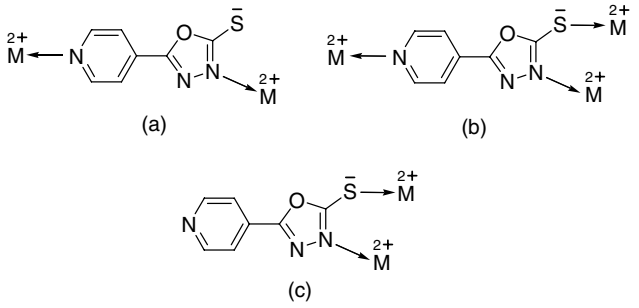


Fig. 1. (a) View of the structure of the free ligand Hpot **1**. (b) 2-D supramolecular network extended by hydrogen bonds along the (0 1 1) plane in **1**. The black dashed-lines stand for hydrogen bonds.

3.3. Description of the crystal structure of $\{[Co(pot)_2(H_2O)_2]\cdot 6H_2O\}_n$ (**2**)

Single X-ray analysis reveals that complex **2** possesses a two-dimensional (2-D) framework constructed of Co(II) centers and "pot" ligands. It is very interesting that the "pot" ligands adopt a μ_2 bridging mode (nitrogen atoms from the pyridyl and oxadiazole groups) in this case, as shown in Scheme 1a. The local coordination environment around the cobalt(II) ion (Fig. 2a) shows that the cobalt sits on a center of symmetry, and each six-coordinate cobalt center is in a perfect octahedron formed by two identical oxadiazole groups (Co(1)–N(1) = 2.158(2) Å) and two pyridine nitrogen atoms (Co(1)–N(3) =



Scheme 1. Coordination modes of ligand "pot" anion.

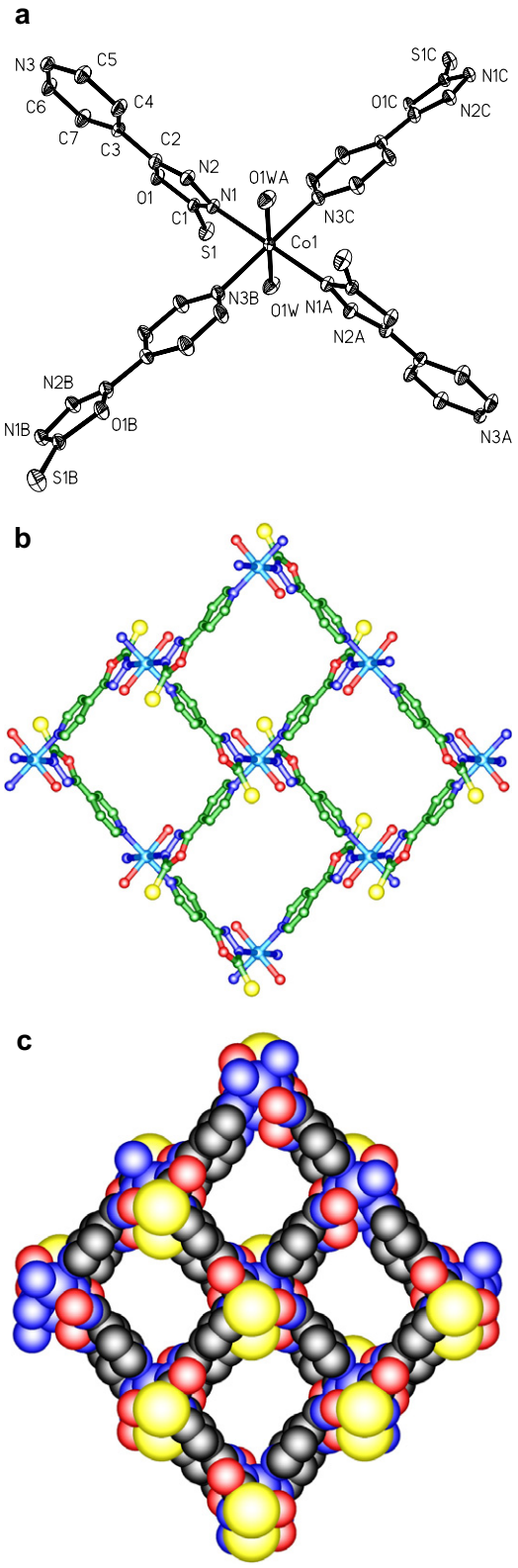


Fig. 2. (a) Local coordination environment around the metal atom for **2** (hydrogen atoms are omitted for clarity). (b) The rhombic grid structure along the *a*-axis for **2**. (c) Space-filling views of the *bc*-plane for **2**. The rhombic grids have the same dimensions with a side length of 10.183 Å and a diagonal measurement of about 12.697 × 15.924 Å (guest water molecules are omitted for clarity).

2.175(3) Å). In addition, two water molecules (Co(1)–O(1w) = 2.101(2) Å) occupy axial positions of the octahedron (see Table 2). Each "pot" ligand in **2** alternately employs its oxadiazole nitrogen atom and pyridine nitrogen atom to coordinate to two cobalt ions, and each cobalt center connects four "pot" ligands. Thus, four cobalt ions and four "pot" ligands form a coplanar tetragon with a side length of 10.183 Å and a diagonal measurement of about 12.697 × 15.924 Å, based on the metal–metal distances. The four cobalt ions lie in the same plane; each subtended "pot" ligand stands up or down the plane. The coplanar shape of the tetragon is understandable, because the "pot" ligand has a rigid linear structure. Such a macrocyclic tetragon (the internal angles of each tetragon are 102.86° and 77.14°) is further extended through the "pot" ligand and metal ions into a 2-D (4,4) neutral network with rhombic grids (Fig. 2b). It is noteworthy that all the cobalt ions in the 2-D frameworks are located in the same plane (see Fig. S2).

Table 2
Selected bond lengths (Å) and angles (°) for compounds **1**–**3**

Compound ***1***			
S(1)–C(7)	1.641(2)	N(2)–N(3)	1.375(2)
O(1)–C(6)	1.372(2)	N(2)–C(6)	1.278(2)
O(1)–C(7)	1.379(2)	N(3)–C(7)	1.328(2)
N(1)–C(1)	1.334(3)	N(3)–H(3)	0.95(3)
N(1)–C(5)	1.334(3)		
C(6)–O(1)–C(7)	105. 6(1)	O(1)–C(6)–N(2)	113.0(2)
C(1)–N(1)–C(5)	117.8(2)	O(1)–C(7)–N(3)	104.9(2)
N(3)–N(2)–C(6)	103.9(1)	S(1)–C(7)–O(1)	124.1(1)
N(2)–N(3)–C(7)	112.6(2)	S(1)–C(7)–N(3)	131.0(2)
Compound ***2***^{i}			
Co(1)–O(1W)	2.101(2)	Co(1)–N(3)^{b}	2.175(3)
Co(1)–N(1)	2.158(2)		
O(1W)^{a}	180.0(1)	O(1W)^{a}–Co(1)–N(3)^{b}	91.4(1)
O(1W)–Co(1)–N(1)	90.9(1)	N(1)–Co(1)–N(3)^{b}	88.5(1)
N(1)–Co(1)–N(1)^{a}	180.0(1)	N(3)^{b}–Co(1)–N(3)^{c}	180.0(1)
Compound ***3***^{ii}			
Cd(1)–N(6)^{a}	2.196(4)	Cd(2)–N(10)	2.206(5)
Cd(1)–N(4)	2.290(5)	Cd(2)–N(12)^{a}	2.286(4)
Cd(1)–N(1)	2.379(5)	Cd(2)–N(7)^{c}	2.368(5)
Cd(1)–S(3)	2.530(2)	Cd(2)–S(1)	2.523(2)
Cd(1)–S(4)^{b}	2.826(2)	Cd(2)–S(2)^{a}	2.808(2)
N(6)^{a}–Cd(1)–N(4)	134.9(2)	N(10)–Cd(2)–N(12)^{a}	136.6(2)
N(6)^{a}–Cd(1)–N(1)	96.2(2)	N(10)–Cd(2)–N(7)^{c}	95.4(2)
N(4)–Cd(1)–N(1)	82.3(2)	N(12)^{a}–Cd(2)–N(7)^{c}	81.9(2)
N(6)^{a}–Cd(1)–S(3)	123.2(1)	N(10)–Cd(2)–S(1)	123.1(1)
N(4)–Cd(1)–S(3)	101.7(1)	N(12)^{a}–Cd(2)–S(1)	100.2(1)
N(1)–Cd(1)–S(3)	93.8(1)	N(7)^{c}–Cd(2)–S(1)	97.1(1)
N(6)^{a}–Cd(1)–S(4)^{b}	82.6(1)	N(10)–Cd(2)–S(2)^{a}	81.2(1)
N(4)–Cd(1)–S(4)^{b}	93.0(1)	N(12)^{a}–Cd(2)–S(2)^{a}	93.3(1)
N(1)–Cd(1)–S(4)^{b}	172.1(1)	N(7)^{c}–Cd(2)–S(2)^{a}	168.9(1)
S(3)–Cd(1)–S(4)^{b}	93.31(5)	S(1)–Cd(2)–S(2)^{a}	93.7(0)

[i]Symmetry code for **2**: a, $-x$, $-y+2$, $-z+1$; b, $-x+1/2$, $y-1/2$, $-z+1/2$; c, $x-1/2$, $-y+5/2$, $z+1/2$.
[ii]Symmetry code for **3**: a, x, $y+1$, z; b, $x+1$, y, z; c, $x-1$, y, z.

The most intriguing feature of the structure for **2** is that there is no interpenetration between adjacent layers. These layers are stacked along the *a*-axis with an ABAB sequence, offset by approximately $0.25(b+c)$ along the *bc*-plane so that large channels are created with a square cross-section of ca. 7 Å × 7 Å, as illustrated in Fig. 2c. The stacking separation between two adjacent sheets is ca. 6.37 Å, and the shortest intersheet Co···Co distance is 9.008 Å. The disordered water molecules (6 per formula unit) are incorporated in the channels and the interlayer regions, which yield a variety of hydrogen bonds, and in turn enhance the stability of the apertures [16]. The crystal structure of **2** is similar to previous works that do not have interpenetrations between adjacent layers and can provide large void spaces to accommodate solvent molecules or ions [17,18], but it is very different from those with diverse interpenetrations filling the void space [19–22]. An analysis of the voids of **2** shows 37.7% of the space empties after the removal of these solvents.

3.4. $[Cd_2(\mu_2\text{-}pot)_2(\mu_3\text{-}pot)_2]_n$ (**3**)

The polymeric structure of **3** was revealed by X-ray single-crystal structure determination and has a neutral 2-D network structure. There are two cadmium ions and four distinct "pot" ligands in each asymmetric unit. In the structure of **3**, the Cd(1)^{II} center coordinates to two nitrogen atoms of oxadiazole groups from two distinct "pot" ligands, two sulfur atoms of oxadiazole groups from two different "pot" ligands, and one pyridyl nitrogen donor, as shown in Fig. 3a. The local coordination geometry around the Cd(1)^{II} atom can be best described as a greatly distorted trigonal bipyramid, in which one nitrogen atom and one sulfur atom from two distinct oxadiazole groups occupy the axial positions (Cd(1)–N_{oz} = 2.379(5) Å, Cd(1)–S(3) = 2.826(2) Å) (see Table 2). The Cd1^{II} center lies approximately in the trigonal least-squares plane defined by N(4)–S(3)–N(6)^{i} (i = x, $y+1$, z) with a deviation of 0.318 Å. Two nitrogen atoms and one sulfur atom are in the equatorial plane (Cd(1)–N(6A) = 2.196(4) Å; Cd(1)–N(4) = 2.290(5) Å; Cd(1)–S(3) = 2.5295(15) Å). In the equatorial plane, the bond angles of N_{py}–Cd(1)–S(3), N_{oz}–Cd(1)–S(3) and N_{py}–Cd(1)–N_{oz} are 101.74(14)°, 123.23(13)° and 134.94(18)°, respectively. Similarly, the coordination geometry of the Cd(2)^{II} metal ion is also a greatly distorted trigonal bipyramid (Fig. 3a), in which the axial positions are occupied by one nitrogen atom and one sulfur atom from two different oxadiazole groups. The Cd(2)^{II} center deviates by ca. 0.336 Å from the base plane defined by N(12)^{i}–S(1)–N(10) (i = $x+1$, y, z), which is slight larger than that of Cd(1)^{II}. In the equatorial plane, the bond lengths of Cd(2)–N_{oz}, Cd(2)–N_{py} and Cd(2)–S, and the bond angles of N_{py}–Cd(2)–S(1), N_{oz}–Cd(2)–S(1) and N_{py}–Cd(2)–N_{oz} are almost equal to that of Cd1, respectively. That is, it is noteworthy that there are two kinds of bridging modes of "pot" ligands in **3**, in which one kind of "pot" ligand shows N atoms and S atoms from

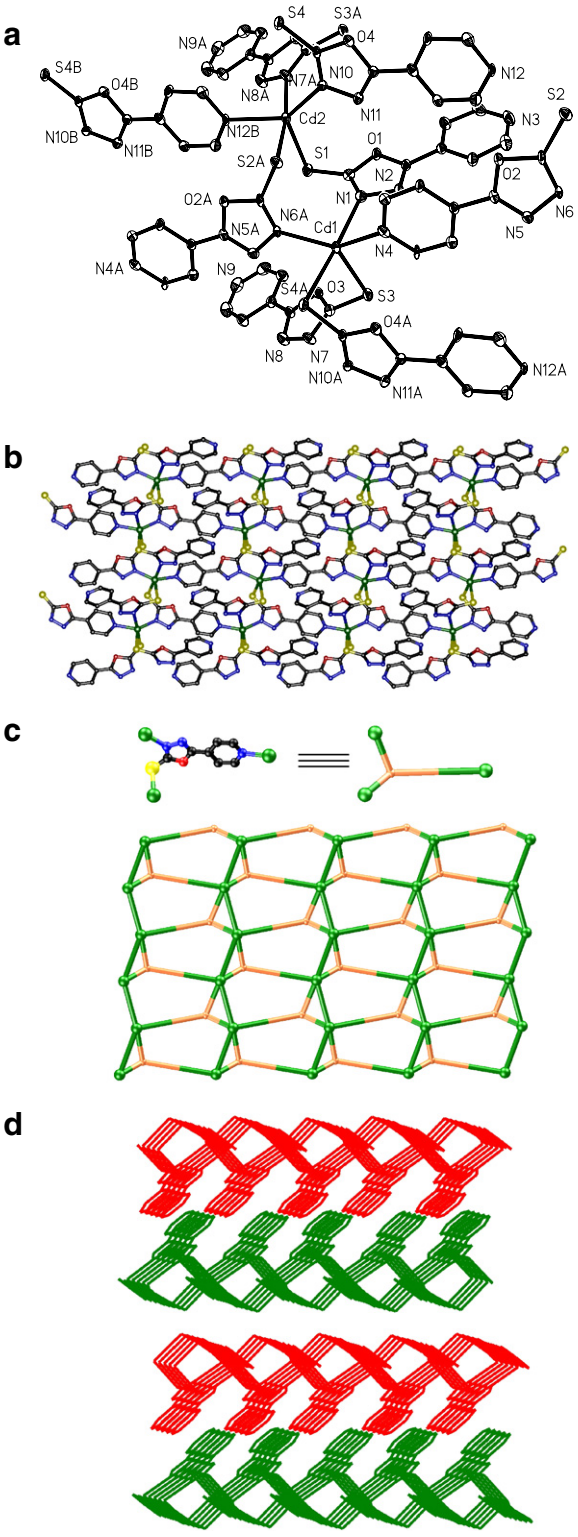


Fig. 3. (a) Local coordination environment around the metal atom for **3** (hydrogen atoms are omitted for clarity). (b) 2-D coordination network along the *c*-axis (hydrogen atoms are omitted for clarity). (c) The simplified 2-D (6,3) network (orange spheres: 3-connected ligand mode). (d) The stacking paragraph in A(−A)A(−A) along the *b*-axis (hydrogen atoms are omitted for clarity).

oxadiazole groups bridging two cadmium ions, that is a 2-connect ligand (Scheme 1c); the another kind of "pot" ligand shows not only N atoms and S atoms from oxadiazole groups coordinating to two Cd^{II} ions, but also N atoms from pyridine groups bridging a third cadmium ion, that is a 3-connect ligand (Scheme 1b). Thus, two "pot" ligands and three Cd(II) ions form a triangle with three side lengths of 5.195 Å, 10.415 Å and 10.094 Å based on the metal–metal distances. The triangle is further extended to a 2-D (6,3) framework with adjacent triagons through sharing Cd(II) ions and "pot" ligands (Fig. 3b and c).

Analysis of the crystal packing of **3** indicates that these 2-D coordinated sheets are closely stacked along the *a*-axis with an A(−A)A(−A) sequence, offset by approximately 0.5 $(y + z)$ along the (0 1 1) plane, as depicted in Fig. 3d. Such a closed packing mode leaves no free space to accommodate guest molecules. The shortest inter-sheet Cd···Cd separation is 6.666(2) Å. As shown in Table 3, there are some hydrogen bonding interactions, H···X (X = O, N and S) separations are in the 2.53–2.84 Å range with C···X (X = O, N and S) distances in the region of 2.892–3.781 Å, and the range of bond angles is between 167° and 171°, being in the normal range of such interactions [15]. These different kinds of hydrogen bonding C–H···X (X = O, or N, or S) weak interactions extend these 2-D layers into a 3-D supermolecular pattern, and in turn further stabilize the 3-D supramolecular packing (see Fig. S3).

3.4.1. Thermogravimetric analysis

To investigate the high thermal stability of the coordination complexes, thermogravimetric analyses (TGA) were conducted to determine the thermal stability of complexes **2** and **3**. TGA of complexes **2** and **3** was performed under a flow of nitrogen gas from room temperature to 700 °C at a heating rate of 20 °C min^{-1}. For **2**, the first weight loss of 19.20% (calcd: 19.30%) from 50 to 120 °C corresponds to the loss of six lattice water molecules per formula unit. Subsequently, the second weight loss of 6.51% (calcd: 6.43%) from 120 to 175 °C corresponds to the loss of two coordinated water molecules per formula unit. The final weight 74.11% (calcd: 74.27%) corresponds to a framework of $[Co(pot)_2]$. Decomposition of the complex begins at 205 °C and ends at 410 °C. The final decomposed product hardly loses any weight upon further heating from 410 to 700 °C. For **3**, a weight loss is not obviously observed in the temperature range 125–170 °C. Subsequently, a slight weight loss occurs in the range 170–210 °C. Decomposition of the complex begins at 210 °C and ends at 420 °C. The final decomposed product hardly loses any weight upon further heating from 420 to 700 °C.

Table 3
Hydrogen bond geometries in the crystal structure of **3**

Complex	D–H···A	D···A (Å)	H···A (Å)	∠D–H···A (°)
3[i]	C(7)–H(7A)–N(9)[a]	3.509(9)	2.59	171
	C(18)–H(18A)–N(3)[b]	3.511(1)	2.59	170
	C(28)–H(28)–S(2)[c]	3.781(7)	2.84	167

[i]Symmetry codes for **3**: a, $-x$, $1 - y$, $1 - z$; b, $-x$, $-y$, $1 - z$; c, $-1 - x$, $-1 - y$, $-z$.

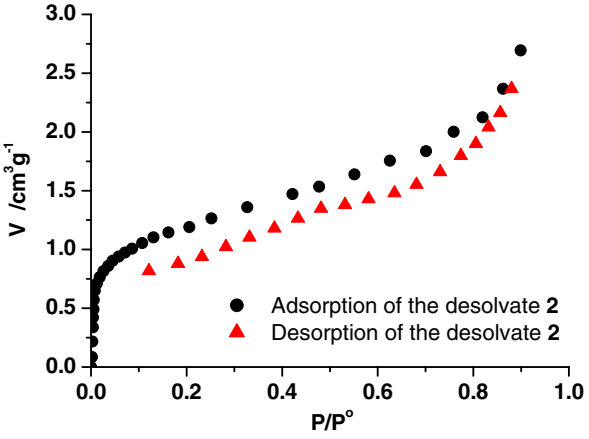


Fig. 4. Gas adsorption isotherms for the anhydrous **2** (the circle stand for the adsorption of the desolvate **2**; the triangle does the desorption of the desolvate **2**).

3.4.2. Gas adsorption isotherm

In view of the microporosity of the complex, the porous compound **2** with channels is investigated for gas adsorption measurements. The gas adsorption isotherms for desolvate **2** were at low levels (1.01 mL/g) with $0.1P_0$ (P_0 = saturation pressure), but were at much higher levels (2.40 mL/g) with $0.9P_0$ (Fig. 4). The pore size distributions of desolvate **2** were calculated and the data were fitted to a Horvath–Kawazoe differential pore volume (HK) plot [23]. The HK plot showed one peak at about 8.2 Å for the desolvate **2**, which agrees with the results of X-ray analysis, and the deviations compared with the crystal structural results should be ascribed to the irregular shapes of the channels [24].

3.4.3. Magnetism property

The magnetic property of complex **2** in the form of $\chi_M T$ versus T plots (χ_M is the molar magnetic susceptibility for one Co^{II} ion) and $M/N\beta$ versus H at 2 K (inset) are shown in Fig. 5. $\chi_M T$ values at 300 K are 3.20 $cm^3\ mol^{-1}$ K for **2**, which are larger than that expected for the spin-only case ($\chi_M T = 1.87\ cm^3\ mol^{-1}$ K, $S = 3/2$), indicating that an important orbital contribution is involved. The $\chi_M T$ values continuously decrease from room temperature to 0.90 $cm^3\ mol^{-1}$ K at 2 K for **2**. The reduced molar magnetization ($M/N\beta$) per Co^{II} tends to $2.3N\beta$ for **2**. The Co···Co distance in complex **2** is 10.183 Å, and the torsion angle between the pyridyl ring and oxadiazole is 5.98°, which avoids any delocalized π-pathway between the Co^{II} ions. As a consequence of these structural features, possible magnetic pathways in **2** are almost non-existent, and thus the magnetic coupling must be almost nil. A quantitative interpretation of the magnetic data are not straightforward because of the orbital degeneracy of octahedral Co^{II}. As indicated by Antolini et al. [25], in non-coupled Co^{II} complexes, the small temperature dependence of down to ca. 100 K rules out any possibility of relevant antiferromagnetic interactions which might in principle also reduce the room-temperature effective magnetic moment. The observed decrease of $\chi_M T$ at lower temperatures can be attributed to the thermal depopulation of the excited Kramer's doublets originated by spin-orbit and low symmetry splitting of $^4T_{1g}$ of the Co^{II} ion.

3.4.4. Fluorescent property

The fluorescence properties and potential applications as light-emitting diodes (LEDs) of aromatic organic molecules, organic polymers and MOFs have been investigated [26]. Construction of MOFs by the judicious choice of building blocks and metal ions can be an efficient method for obtaining new electroluminescent materials, due to the higher thermal stability of MOFs and the ability to alter the emission wavelength of organic materials [27]. The luminescent properties of the free ligand Hpot and its metal complex **3** have been investigated in the solid state. In their solid-state spectra, Hpot exhibits one emission maximum at 346 nm and complex **3** shows one emission peak that is red-shifted to 492 nm (Fig. 6); however, enhancement of fluorescence intensity was not observed. In a word, the emission color of free Hpot is significantly

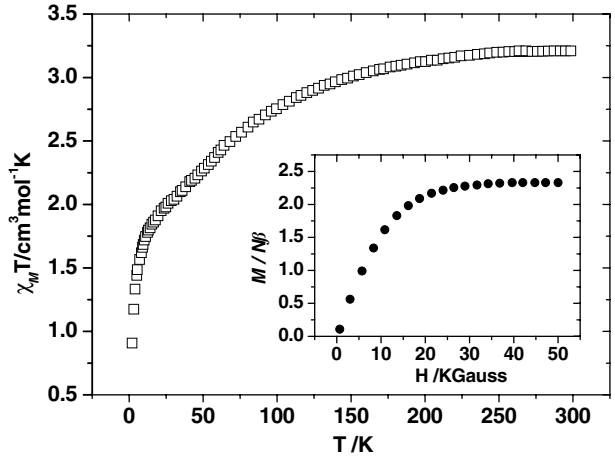


Fig. 5. Plots of the temperature dependence of $\chi_M T$ for **2**. Inset: plot of the reduced magnetization ($M/N\beta$) vs. H at 2 K for **2**.

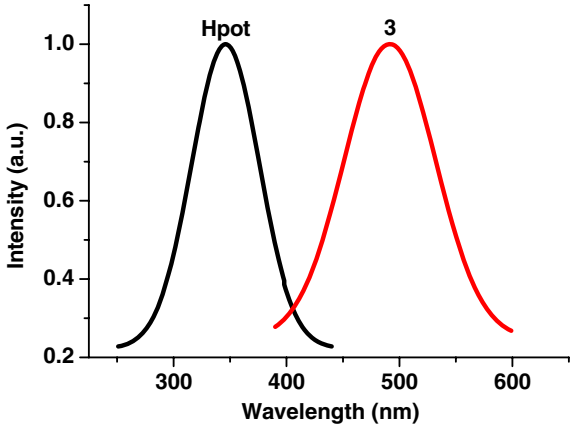


Fig. 6. Photoinduced emission spectra of Hpot and complex **3** in the solid state at room temperature.

affected by its incorporation into the complexes containing metal ions.

4. Conclusions

Two novel 2-D inorganic–organic coordination networks were generated from the multidentate organic ligand 5-(4-pyridyl)-1,3,4-oxadiazole-2-thione (Hpot) and inorganic Co^{II} and Cd^{II} salts. This work demonstrates that the rigid and unsymmetric "pot" anion is capable of coordinating to metal centers with N_{py}, N_{oz} or S donors groups and exhibits versatile coordination modes, which plays a very important role in the properties of these new materials. We are currently extending this result by preparing other new multifunctional ligands of this type with different coordination groups. It is anticipated that this new type of organic ligand will result in a variety of coordination polymers or supramolecules with unique structural features and interesting properties.

Acknowledgements

This work was financially supported by the Starting Funding of Shandong Institute of Light Industry (to Dr. Y.-T. Wang). We are indebted to Prof. X.-M. Chen at Sun Yat-Sen University for his help.

Appendix A. Supplementary material

Additional figures and X-ray crystallographic data in CIF format. CCDC 259468, 267658 and 267660 contain the supplementary crystallographic data for **1**, **2** and **3**. These data can be obtained free of charge via http://www.ccdc.cam.ac.uk/conts/retrieving.html, or from the Cambridge Crystallographic Data Centre, 12 Union Road, Cambridge CB2 1EZ, UK; fax: (+44) 1223-336-033; or e-mail: deposit@ccdc.cam.ac.uk. Supplementary data associated with this article can be found, in the online version. Supplementary data associated with this article can be found, in the online version, at doi:10.1016/j.poly.2006.09.008.

References

[1] (a) For examples: N.W. Ockwig, O. Delgado-Friedrichs, M. O'Keeffe, O.M. Yaghi, Acc. Chem. Res. 38 (2005) 176;
(b) B. Kesanli, W. Lin, Coord. Chem. Rev. 246 (2003) 305;
(c) D. Braga, F. Grepioni, G.R. Desiraju, Chem. Rev. 98 (1998) 1375;
(d) H. Miyasaka, N. Matsumoto, H. Okawa, N. Re, E. Gallo, C. Floriani, J. Am. Chem. Soc. 118 (1996) 981;
(e) H. Kobayashi, H. Tomita, T. Naito, A. Kobayashi, F. Sakai, T. Watanabe, P. Cassoux, J. Am. Chem. Soc. 118 (1996) 368.

[2] (a) For examples: S.R. Seidel, P.J. Stang, Acc. Chem. Res. 35 (2002) 972;
(b) N.L. Rosi, J. Kim, M. Eddaoudi, B. Chen, M. O'Keeffe, O.M. Yaghi, J. Am. Chem. Soc. 127 (2005) 1504;
(c) O. Sato, T. Iyoda, A. Fujishima, K. Hashimoto, Science 271 (1996) 49;
(d) M.J. Zaworotko, Angew. Chem., Int. Ed. 39 (2000) 3052;
(e) G.B. Gardner, D. Venkataraman, J.S. Moore, S. Lee, Nature 374 (1995) 792;
(f) H.Z. Kou, S. Gao, J. Zhang, G.H. Wen, G. Su, R.K. Zheng, X.X. Zhang, J. Am. Chem. Soc. 123 (2001) 11809.

[3] (a) For examples: A.J. Blake, N.R. Champness, P. Hubberstey, W.S. Li, M.A. Withersby, M. Schröder, Coord. Chem. Rev. 183 (1999) 117;
(b) S.S.Y. Chui, S.M.F. Lo, J.P.H. Charmant, A.G. Orpen, I.D. Williams, Science 283 (1999) 1148;
(c) S.R. Batten, R. Robson, Angew. Chem., Int. Ed. 37 (1998) 1460;
(d) N.J. Melcer, G.D. Enright, J.A. Ripmeester, G.K.H. Shimizu, Inorg. Chem. 40 (2001) 4641;
(e) R. Cao, D.F. Sun, Y.C. Liang, M.C. Hong, K. Tatsumi, Q. Shi, Inorg. Chem. 41 (2002) 2087;
(f) M.L. Tong, Y.M. Wu, J. Ru, X.M. Chen, H.C. Chang, S. Kitagawa, Inorg. Chem. 41 (2002) 4846;
(g) C.-D. Wu, W.-B. Lin, Angew. Chem., Int. Ed. 44 (2005) 1958.

[4] (a) For examples: C.-D. Wu, A. Hu, L. Zhang, W. Lin, J. Am. Chem. Soc. 127 (2005) 8940;
(b) J.S. Seo, D. Whang, H. Lee, S.I. Jun, J. Oh, Y.J. Jeon, K. Kimoon, Nature 404 (2000) 982;
(c) O.R. Evans, W.B. Lin, Acc. Chem. Res. 35 (2002) 511;
(d) Q. Ye, Y.-H. Li, Y.-M. Song, X.-F. Huang, R.-G. Xiong, Z. Xue, Inorg. Chem. 44 (2005) 3618.

[5] (a) F. Robinson, M.J. Zaworotko, J. Chem. Soc., Chem. Commun. (1995) 2413;
(b) D. Hagrman, C. Zubieta, D.J. Rose, J. Zubieta, R.C. Haushalter, Angew. Chem., Int. Ed. 36 (1997) 873;
(c) J. Lu, G. Crisci, T. Niu, A.J. Jacobson, Inorg. Chem. 36 (1997) 5140;
(d) M. Kondo, T. Yoshitomi, K. Seki, H. Matsuzaka, S. Kitagawa, Angew. Chem., Int. Ed. 36 (1997) 1725.

[6] (a) N.G. Pschirer, D.M. Ciurtin, M.D. Smith, U.H.F. Bunz, H.-C. zurLoye, Angew. Chem., Int. Ed. 41 (2002) 583;
(b) K. Biradha, Y. Hongo, M. Fujita, Angew. Chem., Int. Ed. 39 (2000) 3843;
(c) D. Hagrman, R.P. Hammond, R. Haushalter, J. Zubieta, Chem. Mater. 10 (1998) 2091;
(d) Z. Huang, H.-B. Song, M. Du, S.-T. Chen, X.-H. Bu, Inorg. Chem. 43 (2004) 931;
(e) Y.-B. Dong, J.-Y. Cheng, R.-Q. Huang, Inorg. Chem. 42 (2003) 5699.

[7] (a) Y.-P. Ren, X.-J. Kong, L.-S. Long, R.-B. Huang, L.-S. Zheng, Cryst. Growth Des. 6 (2006) 572;
(b) C.-M. Liu, D.-Q. Zhang, D.-B. Zhu, Cryst. Growth Des. 6 (2006) 524;
(c) K. Uemura, S. Kitagawa, M. Kondo, K. Fukui, R. Kitaura, H.-C. Chang, T. Mizutani, Chem. Eur. J. 8 (2002) 3587;
(d) K. Uemura, S. Kitagawa, K. Fukui, K. Saito, J. Am. Chem. Soc. 126 (2004) 3817;
(e) A.N. Khlobystov, M.T. Brett, A.J. Blake, N.R. Champness, P.M.W. Gill, D.P. O'Neill, S.J. Teat, C. Wilson, M.J. Schröder, Am. Chem. Soc. 125 (2003) 6753;
(f) I.S. Lee, D.M. Shin, Y.K. Chung, Chem.-Eur. J. 10 (2004) 3158;
(g) D.A. Beauchamp, S.J. Loeb, Chem. Commun. (2002) 2484.

[8] (a) Y.-T. Wang, M.-L. Tong, H.-H. Fan, H.-Z. Wang, X.-M. Chen, J. Chem. Soc., Dalton Trans. (2005) 424;
(b) Y.-T. Wang, H.-H. Fan, H.-Z. Wang, X.-M. Chen, J. Mol. Struct. 740 (2005) 61;
(c) Y.-T. Wang, H.-H. Fan, H.-Z. Wang, X.-M. Chen, Inorg. Chem. 44 (2005) 4148;
(d) Y.-T. Wang, G.-M. Tang, Y. Wu, X.-Y. Qin, D.-W. Qin, J. Mol. Struct. (2006) in press, doi:10.1016/j.molstruc.2006.07.021.

[9] M. Kondo, M. Miyazawa, Y. Irie, R. Shinagawa, T. Horiba, A. Nakamura, T. Naito, K. Maeda, S. Utsuno, F. Uchida, Chem. Commun. (2002) 2156.

[10] S.A. Barnett, N.R. Champness, Coord. Chem. Rev. 246 (2003) 145.
[11] R.W. Young, K.H. Wood, J. Am. Chem. Soc. 77 (1955) 400.
[12] Bruker AXS, SAINT: Software Reference Manual, Madison, WI, 2000.
[13] G.M. Sheldrick, SHELXTL NT Version 6.10: Program for Solution and Refinement of Crystal Structures, University of Göttingen, Göttingen, Germany, 2000.
[14] The graph set topological terminology for the analysis of hydrogen bonded network patterns is described in: M.C. Etter, Acc. Chem. Res. 23 (1990) 120.
[15] G.R. Desiraju, T. Steiner, The Weak Hydrogen Bond in Structural Chemistry and Biology, Oxford University Press, Oxford, 1999.
[16] (a) H. Li, M. Eddaoudi, T.L. Groy, O.M. Yaghi, J. Am. Chem. Soc. 120 (1998) 8571;
(b) K. Endo, T. Koike, T. Sawaki, O. Hayashida, H. Masuda, Y. Aoyama, J. Am. Chem. Soc. 119 (1997) 4117.
[17] (a) M.A. Withersby, A.J. Blake, N.R. Champness, P. Hubberstey, W.S. Li, M. Schröder, Angew. Chem., Int. Ed. 36 (1997) 2327;
(b) L.R. MacGillivray, R.H. Groeneman, J.L. Atwood, J. Am. Chem. Soc. 120 (1998) 2676.
[18] O.M. Yaghi, H.L. Li, T.L. Groy, Inorg. Chem. 36 (1997) 4292.
[19] (a) S.R. Batten, R. Robson, Angew. Chem., Int. Ed. 37 (1998) 1461;
(b) A.J. Blake, N.R. Champness, S.S.M. Chung, W.S. Li, M. Schröder, Chem. Commun. (1997) 1005;
(c) K.A. Hirsch, S.R. Wilson, J.S. Moore, Chem.-Eur. J. 3 (1997) 765.
[20] H. Gudbjartson, K. Biradha, K.M. Poirier, M.J. Zaworotko, J. Am. Chem. Soc. 121 (1999) 2599.
[21] (a) M. Kondon, T. Yoshitomi, K. Seki, H. Matsuzaka, S. Kitagawa, Angew. Chem., Int. Ed. 36 (1997) 1725;
(b) M. Fujita, Y.J. Kwon, O. Sasaki, K. Yamaguchi, K. Ogura, J. Am. Chem. Soc. 117 (1995) 7287.
[22] (a) K. Biradha, K.V. Domasevitch, B. Moulton, C. Seward, M.J. Zaworotko, Chem. Commun. (1999) 1327;
(b) L. Carlucci, G. Ciani, D.M. Proserpio, A. Sironi, J. Chem. Soc., Dalton Trans. (1997) 1801.
[23] G. Horvath, K. Kawazoe, J. Chem. Eng. Jpn. 16 (1983) 470.
[24] S.-I. Noro, S. Kitagawa, M. Kondo, K. Seki, Angew. Chem., Int. Ed. 39 (2000) 2081.
[25] L. Antolini, A.C. Fabretti, D. Gatteschi, A. Giusti, R. Sessoli, Inorg. Chem. 30 (1991) 4858.
[26] U.H.F. Bunz, Chem. Rev. 100 (2000) 1605.
[27] F. Würthner, A. Sautter, Chem. Commun. (2000) 445.

Available online at www.sciencedirect.com
ScienceDirect
Polyhedron 26 (2007) 791–796
POLYHEDRON
www.elsevier.com/locate/poly

Synthesis and characterization of a monomeric and a dihydroxo-bridged dimeric complexes of iron(III) with α-benzoinoxime

Attia S. Attia *, M.F. El-Shahat

Chemistry Department, Faculty of Science, Ain Shams University, Abbasia, Cairo, Egypt

Received 14 August 2006; accepted 6 September 2006
Available online 27 September 2006

Abstract

The reaction of α-benzoinoxime, H_2BNO with $FeCl_3$ in the presence of Et_3N as a base gives the mononuclear Fe(III) complex, $Fe(HBNO)_3$ (**1**). Treatment of **1** with a methanolic solution of KOH at room temperature leads to a dinuclear Fe(III)–Fe(III) complex, $[Fe(HBNO)_2OH]_2$ (**2**). The complexes were initially characterized on the basis of their elemental, mass and thermal analyses. The IR studies were useful in assigning the coordination mode of the benzoinoxime ligand to the iron metal. In addition, the presence of a hydroxo-bridge in the dimeric complex **2** is inferred from the IR spectral studies. Room-temperature Mössbauer studies indicated octahedral, high-spin iron(III). Variable-temperature magnetic susceptibility measurements supported the existence of the μ-dihydroxo-bridging structure core, $Fe^{III}(\mu\text{-}OH)_2Fe^{III}$ in the dinuclear complex **2**. Theoretical modelling of the magnetic data indicated a weak antiferromagnetic spin exchange between the iron(III) centers ($J = -8.35\ cm^{-1}$, $g = 2.01$, $\rho = 0.02$ and $TIP = 1.7 \times 10^{-4}\ cm^3\ mol^{-1}$ for $H = -2JS_1 \cdot S_2$). The electronic spectra of the complexes revealed two bands due to d–d transitions and one band assignable to an oxygen (p_π) → Fe($d_{\pi*}$) LMCT transition observed in each complex. An additional charge-transfer transition, assignable to μ-hydroxo(p_π) → Fe($d_{\pi*}$), was observed for the dimeric complex **2**. The structural and vibrational behaviors of these complexes have been elucidated with quantum mechanical methods.
© 2006 Elsevier Ltd. All rights reserved.

Keywords: Iron complexes; Benzoinoxime; Dimer; Dihydroxo bridge; Magnetic studies; Exchange coupling; Semi-empirical calculations

1. Introduction

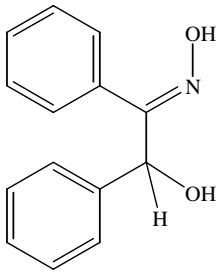
The importance of iron as an essential element can be estimated by the wide range of iron proteins and enzymes playing different roles in biological systems. Proteins containing non-heme iron centers are widely spread in nature. They perform a broad range of functions, especially activating dioxygen for the oxidation of various substrates [1]. Dinuclear iron complexes in particular have biological relevance since they give valuable information about the binding mode of dioxygen to the iron sites of proteins involved in its transport and activation. They provide structural models for dinuclear sites in several proteins involved in oxygen storage of hemerythrin and oxygen activation of methanemonooxygenase [2–4]. Efforts to model these proteins have simulated the study of complexes containing Fe(μ-O)$_2$Fe and Fe(μ-OH)$_2$Fe cores [5–7]. In addition, these systems were treated as models for understanding the magnitude of exchange coupling interactions between the two iron centers and its relation to geometrical parameters [8]. Studies of some diiron complexes have shown that the oxo-bridge is responsible for strong antiferromagnetic coupling ($-50 > J > -200\ cm^{-1}$) and those complexes with hydroxo, alkoxo, phenoxo-bridges are weakly coupled ($0 > J > -30\ cm^{-1}$) [6,8–10].

We reported previously the synthesis and characterization of dinuclear chromium and molybdenum complexes containing oxo and hydroxo-bridged ligands [11,12]. In the present work, we describe the preparation and characterization of two new iron(III) complexes of the

* Corresponding author. Tel.: +20 2 6717 839.
E-mail address: attiasattia@hotmail.com (A.S. Attia).

0277-5387/$ - see front matter © 2006 Elsevier Ltd. All rights reserved.
doi:10.1016/j.poly.2006.09.029

α-benzoinoxime ligand. The coordination properties of the complexes were studied using FTIR, electronic and Mössbauer techniques. A magneto-structural correlation has been studied by variable-temperature magnetic susceptibility and theoretical modelling of the magnetic data. Semi-empirical theoretical calculations (MM+ and parameterized PM3) have been used to predict the most favored geometry for each complex.



α-benzoinoxime ligand (H_2BNO)

2. Experimental

Ferric chloride, $FeCl_3 \cdot 6H_2O$, and α-benzoinoxime, H_2BNO, were used as purchased from Aldrich chemical Co. Inc. Solvents were dried according to standard procedures.

Variable-temperature (10–300 K) magnetic susceptibility measurements were obtained with an Oxford Faraday magnetometer. Mössbauer measurements were carried out on a multichannel analyzer in constant acceleration mode. ^{57}Co in a Rh matrix (20 mc) was used as a radioactive source and was held at room temperature. The isomer shift was expressed relative to an iron metal absorber. Infrared spectra (4000–400 cm^{-1}) were recorded as KBr pellets on a Thermo Nicolet Nexus 670 FTIR spectrometer. The thermal analyses (TGA–DTA) were carried out under nitrogen with a heating rate of 10 °C/min using a Perkin–Elmer thermal analyzer. The electronic absorption spectra (190–1100 nm) were measured on a Cary 50 spectrophotometer. Samples were run on 10^{-4} M solutions in DMSO. Elemental analyses were performed using a Perkin–Elmer 2400 CHN elemental analyzer. The semi-empirical calculations in this study have been carried out using the Hyperchem 6.01 program package [13]. The Polak–Ribiere version of the conjugate gradient method was used in all energy minimization calculations with a coverage criterion less than 0.001 kcal mol^{-1} $Å^{-1}$. First and separately the benzoinoxime ligand was optimized and the results obtained have been applied for the oxime ligand in each calculation thereafter. The values of Fe–O and Fe–N bond lengths and Fe–O–Fe bond angle in the literatures were used as the starting inputs [6,14–17]. Initial optimization of different geometries of the complexes was performed with molecular mechanics (MM+). The geometry was further refined using parameterized PM3 method. Available parameters for Fe metal were implemented in the PM3 semi-empirical method [18]. The parameterized PM3 was used for the geometry optimization of the complexes under study. Theoretical harmonic vibrational frequencies are related to the experimental fundamentals by the optimum scaling factor λ, determined through a least-squares procedure, given by $\lambda = \sum_i^{all} \omega_i^{theor} \nu_i^{expt} / \sum_i^{all} (\omega_i^{theor})^2$, where ω_i^{theor} and ν_i^{expt} are the ith theoretical harmonic and ith experimental fundamental frequencies (in cm^{-1}) [19]. The molecular root mean square error (rms) was calculated by the square root of the sum over all the modes of Δ_{min} given in Ref. [19], where Δ_{min} is the minimized residual for each mode.

2.1. Synthesis of tris(benzoinoximato)iron(III), $Fe(HBNO)_3$ (1)

A solution of triethylamine (0.2 mL) in ethanol (5 mL) was added dropwise to an ethanolic solution (30 mL) of α-benzoinoxime, H_2BNO (0.38 g, 1.67 mmol) with stirring at room temperature. To the resulting solution, was added an ethanolic solution (10 mL) of $FeCl_3 \cdot 6H_2O$ (0.15 g, 0.55 mmol) and the mixture was heated at 70 °C for 18 h. The purple residue was separated from the reaction medium and then washed with cold absolute ethanol and dried. The residue was dissolved in dichloromethane. Chromatographic separation on a neutral Al_2O_3 column eluted with CH_2Cl_2–ether (90:10% v/v) gave $Fe(HBNO)_3$ as a purple band. Purple microcrystals of the complex were obtained by slow evaporation of the solvent with a flow of argon. The crystals were dried in a vacuum overnight. The product was obtained in 0.35 g (87%) yield.

Anal. Calc. for $C_{42}H_{36}FeN_3O_6$ (MW = 734.62): C, 68.67; H, 4.94; N, 5.72. Found: C, 68.50; H, 5.10; N, 5.77%. TGA, % weight loss (temp. °C): 61.22 (75–210), 23.26 (213–436).

2.2. Synthesis of μ-dihydroxobis{bis(benzoinoximato)-iron(III)}, $[Fe(HBNO)_2(\mu\text{-}OH)]_2$ (2)

To a solution of $Fe(HBNO)_3$ (0.5 g, 0.68 mmol) in 10 mL CH_3CN was added 5 mL CH_3OH solution of KOH (0.04 g, 0.71 mmol), and the mixture was stirred for 36 h. The color of the solution turned red and was dried in vacuum. The residue was washed with hot ethanol (95%) to remove KHBNO. Then the residue was redissolved in CH_2Cl_2 and subjected to chromatography on silica gel column with CH_2Cl_2–ether (80:20% v/v). The red band was eluted and collected. A dark red solid was obtained from the eluent by slow evaporation of the solvent with a flow of argon. The solid product was dried in a vacuum overnight. The product as a red solid was obtained in 64% (0.23 g) yield.

Anal. Calc. for $C_{56}H_{50}Fe_2N_4O_{10}$ (MW = 1050.74): C, 64.01; H, 4.80; N, 5.33. Found: C, 63.92; H, 4.77; N, 5.29%. TGA, % weight loss (temp. °C): 46.41 (61–152), 29.27 (154–326), 10.50 (328–480).

3. Results and discussion

The stoichiometric reaction between α-benzoinoxime, H_2BNO and $FeCl_3$ in the presence of triethylamine as a base has yielded the monomeric complex $Fe(HBNO)_3$ (**1**). Addition of OH^- to complex **1** at room temperature afforded the dimeric product **2**. Chromatographic analyses of both complexes have indicated one isomeric form for each complex.

The complexes were initially characterized on the basis of their elemental analyses, mass spectra and thermal analyses (TGA, DTA). The parent ion peak (*m*/*z*) was observed in the mass spectra at 734 and 1051 for complexes **1** and **2**, respectively. The thermal analyses (TGA, DTA) of complex **1** showed a weight loss of 61.22% in the temperature range 75–210 °C, corresponding to the loss of two molecules of benzoinoxime ligand. The mass loss of 23.26% in the temperature range 213–436 °C, corresponds to two phenyl groups and one OH of the third benzoinoxime ligand. For the dimeric complex **2**, three endothermic peaks were observed. The mass loss of 46.41% in the temperature range 61–152 °C corresponds to two benzoinoxime ligands and two OH groups. The other weight losses of 29.27% and 10.50% in the temperature ranges 154–326 and 328–480°C, respectively, are due to gradual decomposition of the organic fragments of the other benzoinoxime ligands.

The primary ligand, α-benzoinoxime, showed characteristic IR bands at 3326, 1670 and 950 cm^{-1} due to the OH, C=N and N–O stretching vibrations of the oxime group. These bands are observed for complex **1** at 3421 (OH), 1625 (C=N), 1089 and 1024 cm^{-1} (N–O). The C=N stretching vibration has shifted by 45 cm^{-1} to lower frequency. In contrast, the bands corresponding to OH and N–O stretches have shifted to higher frequencies with respect to the parent ligand. Such behavior is evidently indicates that the α-benzoinoxime ligands coordinate to the iron metal through the nitrogen atom of the oxime group [11,20]. The presence of two bands for the N–O stretching vibration indicates different types of N–O groups [21,22]. Consequently, the peaks at 1089 and 1024 cm^{-1} are assigned to free N–O and hydrogen-bonded N–O, respectively.

The infrared spectrum of complex **2** revealed two strong absorptions at 968 and 913 cm^{-1} that are not present in the spectrum of the monomeric complex $Fe(HBNO)_3$. In addition, no band between 800 and 850 cm^{-1} attributable to an oxo bridged structural unit is observed in the IR spectrum of the dimeric complex $[Fe(HBNO)_2OH]_2$ [5,10,23]. Furthermore, the similarity in the absorption peaks due to coordinated benzoinoxime ligand in both the monomeric and the dimeric complexes rules against any type of benzoinoximate bridging in the dimer. Therefore, the bands at 968 and 913 cm^{-1} in the $[Fe(HBNO)_2OH]_2$ dimer are assigned to a vibrational mode associated with the $Fe_2(OH)_2^{4+}$ structural unit. Consistent with this assignment, the infrared spectra of $[Fe(pic)_2OH]_2$ and $[Cr(HBNO)(BNIM)OH]_2$ showed bands due to $Fe_2(OH)_2^{4+}$ and $Cr_2(OH)_2^{4+}$ at 950 and 970 cm^{-1}, respectively [10,12]. Similarly to the monomeric complex **1**, a peak due to stretching vibration of oxime OH is observed at 3422 cm^{-1} for the dimeric complex. An additional peak was observed at 3599 cm^{-1} which is assigned to the

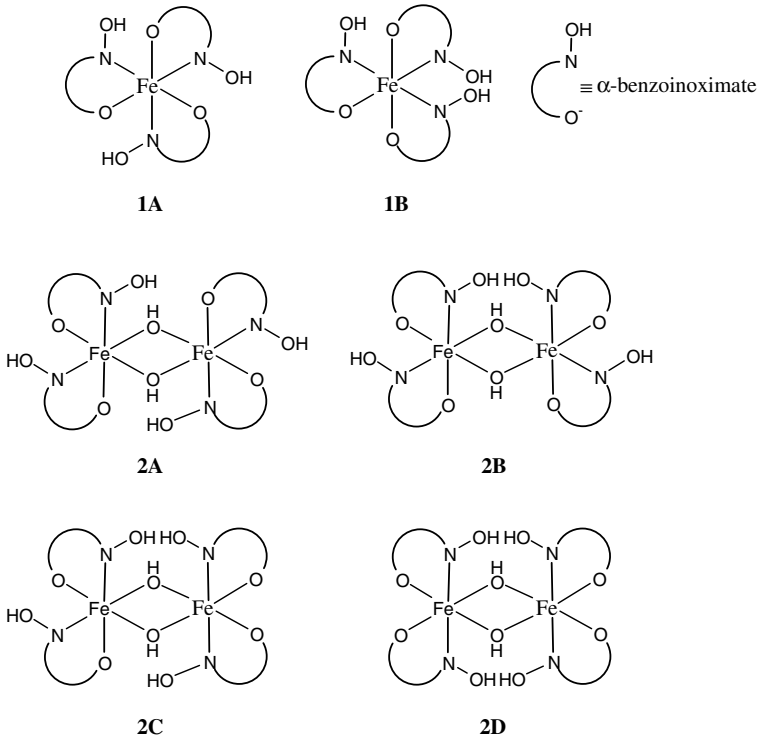


Fig. 1. Chemical structures for complexes **1** and **2** used for semi-empirical calculations.

bridging OH stretch. Finally, bands indicative of two types of N–O groups were observed at 1117 and 1080 cm^{-1} (free N–O) and at 1052 and 1024 cm^{-1} (hydrogen-bonded N–O). Usually, oxime complexes show two N–O bands in the range 1190–1260 and 1071–1110 cm^{-1} for strongly hydrogen-bonded species, whilst in free and weakly hydrogen-bonded species the N–O absorption occurs at ca. 1150 and 1020 cm^{-1} [21,22,24].

The monomeric complex **1** is expected to have two geometrical isomers; facial **1A** and meridional **1B** (Fig. 1), but only one isomer is obtained as indicated by the chromatographic analysis. Now the question is whether the $Fe(HBNO)_3$ has a facial or meridional configuration. Also, the dimeric complex **2**, is expected to adopt one of four geometrical isomers; **2A**, **2B**, **2C** or **2D** (Fig. 1). The spectroscopic techniques gave no information about the geometry of the complex. Hence, it was considered worthwhile to model the complexes using molecular mechanics MM+ and PM3 calculations, especially with the lack of structural analysis due to the poor quality of the crystals obtained.

The PM3 calculated results for each structure are summarized in Table 1. It can be seen that for the $Fe(HBNO)_3$ complex, the facial geometry **1A** is more stable than the meridional one **1B** by 3.8 kcal/mol. These results are in agreement with the structure of the $Co(BMO)_3$ complex, whose structure is characterized with a facial configuration by X-ray diffraction analysis [25]. For the dimeric complex **2**, the energy calculated for **2A** is more stable than those for the other configurations.

The most favored structures for the monomeric and dimeric iron(III) complexes based on semi-empirical PM3 geometry optimization are shown in Fig. 2. In both structures, the benzoinoxime ligand is coordinated to Fe(III) with the oxime nitrogen atom and the deprotonated alcoholic oxygen atom.

The observed and calculated vibrational frequencies for configurations **1A** and **2A** are compared in Table 2. The optimized scale factors determined for **1A** and **2A** are 0.998407 and 0.997745, respectively. The calculated harmonic vibrational frequencies compare well with fundamental experimental frequencies. The calculated root mean square error (rms) per molecule is 70.8 and 64.4 cm^{-1} for **1A** and **2A**, respectively. The rms values compare very well with those reported for vibrational frequency calculations using MP2-fc/631G(d) (rms = 63) and MP2-fc/631G(d,p) (rms = 61) [15].

The magnetic susceptibility data measured for $Fe(HBNO)_3$ revealed a magnetic moment of 5.86 B.M. at 300 K, which is close to the spin-only value (5.92) of high-spin Fe(III). The magnetic moment showed no significant temperature-dependence over the temperature range 300–10 K. Such behavior is indicative of a monomeric, octahedral high-spin Fe(III) complex [23].

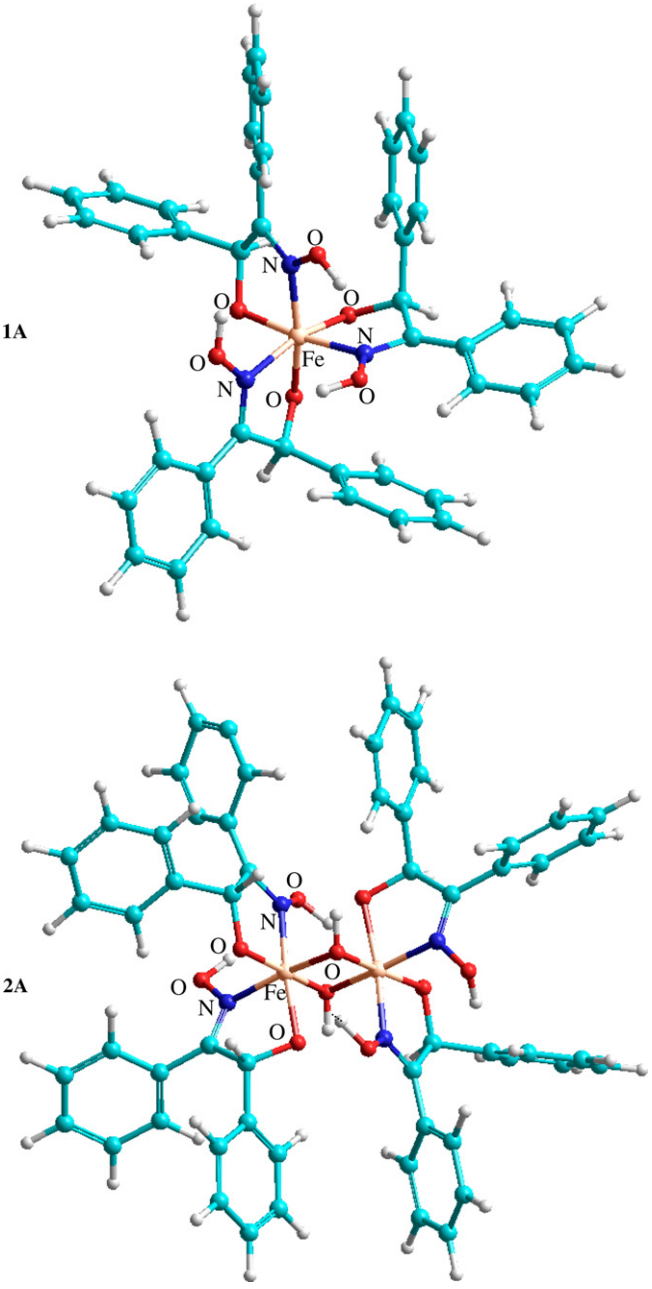


Fig. 2. The most stable geometries for the $Fe(HBNO)_3$ complex (**1A**) and the $[Fe(HBNO)_2OH]_2$ complex (**2A**).

Table 1
Calculated results for each structure of the monomeric complex **1** (**1A** and **1B**) and of the dimeric complex **2** (**2A**, **2B**, **2C** and **2D**)

Calculation results[a,b] (kcal/mol)	1A	1B	2A	2B	2C	2D
Total energy	−191659.1	−191655.3	−278205.7	−278149.9	−278201.5	−278201.1
Heat of formation	−284.63	−280.83	−802.07	−746.25	−797.84	−797.45

[a] Total charge = 0 for all complexes.
[b] The metal in all complexes is high-spin Fe(III).

Table 2
Characteristic calculated and observed vibrational frequencies (cm^{-1}) for conformations **1A** and **2A**

1A		**2A**		Assignment
Calculated	Observed	Calculated	Observed	
		3596	3599	ν(O–H) bridge
3437	3421	3433	3422	ν(O–H) oxime
3064	3063	3083	3061	ν(C–H) aromatic
3029	3019	3029	3024	
2952	2932	2926	2922	ν(C–H) aliphatic
2815	2859	2877	2870	
1645	1625	1619	1629	ν(C=N)
1598	1607	1596	1607	ν(C=C) + ring deformation
		1108	1117	ν(N–O)
1086	1089	1076	1080	
		1048	1050	
1020	1024	1011	1024	
		941	968	ν(Fe–OH–Fe)
		910	913	
481	496	480	496	ν(M–O)
441	448	443		ν(M–N)

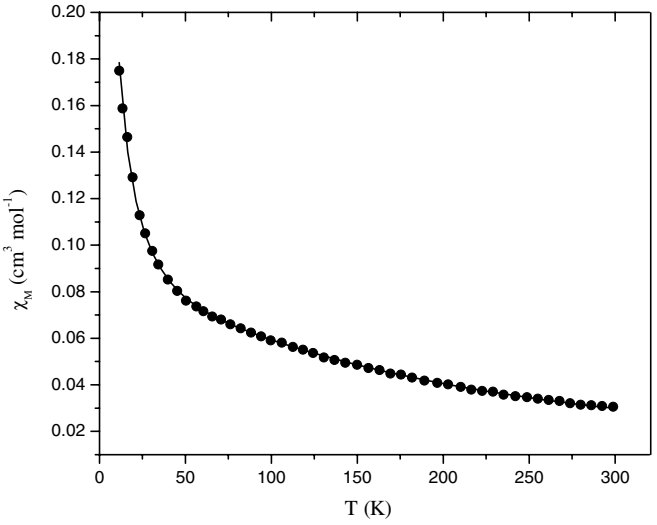


Fig. 3. Temperature dependence of the molar paramagnetic susceptibility, χ_m, curve for $[Fe(HMNO)_2OH]_2$. The solid line represent the least-squares fit of the data to the theoretical equation given in the text.

Magnetic susceptibility data for $[Fe(HBNO)_2OH]_2$ indicate a weak intramolecular antiferromagnetic spin exchange interaction. Both the magnitude and temperature dependence of the magnetic susceptibility typify the behavior of an $S_1 = S_2 = 5/2$ dimer [26]. The effective magnetic moment drops from 8.55 B.M. per molecule at ~300 K to 4.01 B.M. at ~11 K. The data were analyzed with the spin–spin interaction model based on the exchange Hamiltonian($\hat{H} = -2J\hat{S}_1 \cdot \hat{S}_2$). The molar paramagnetic susceptibility of an $S_1 = S_2 = 5/2$ exchange coupled Fe(III)–Fe(III) dimer is given by the following equation [27,28]:

$$\chi_M = \frac{2N\beta^2 g^2}{kT}\left[\frac{\chi'}{\chi''}\right](1-\rho) + \frac{2.19g^2}{T}\rho + \mathrm{TIP}$$
$$\chi' = [(55 + 30\exp(-10J/kT) + 14\exp(-18J/kT) + 5\exp(-24J/kT) + \exp(-28J/kT)]$$
$$\chi'' = [11 + 9\exp(-10J/kT) + 7\exp(-18J/kT) + 5\exp(-24J/kT) + 3\exp(-28J/kT) + \exp(-30J/kT)] \quad (1)$$

where, ρ gauges the amount of magnetically dilute ferric impurities and the other terms have their usual meanings. A non-linear least-squares fit to 51 experimental data points yielded $J = -8.35 \pm 0.2\ cm^{-1}$, $g = 2.01 \pm 0.02$, $\rho = 0.02 \pm 0.01$ and $\mathrm{TIP} = 1.7 \times 10^{-4} \pm 0.02\ cm^3\ mol^{-1}$ with $R = 8.29 \times 10^{-4}$. The fit is illustrated in Fig. 3. The value of the coupling constant J is in good agreement with the values reported for other dihydroxo-bridged Fe(III) dimers [6,10,29]. They exhibited coupling constants in the range of -7 to $-11\ cm^{-1}$. In contrast, oxo-bridged Fe(III) dimers are invariably characterized by a coupling constant near $-100\ cm^{-1}$ [30].

The Mössbauer spectrum of the dimeric complex **2** at 298 K is shown in Fig. 4. The spectrum consists of a single symmetric quadrupole doublet with $\Delta E_Q = 0.87$ mm/s and $\delta = 0.43$ mm/s. The values of the quadrupole splitting, ΔE_Q, and the isomer shift, δ, are consistent with the formulation of a complex containing high-spin Fe(III) and are similar to the Mössbauer parameters reported for number of dihydroxo-bridged diiron(III) dimers [30–32].

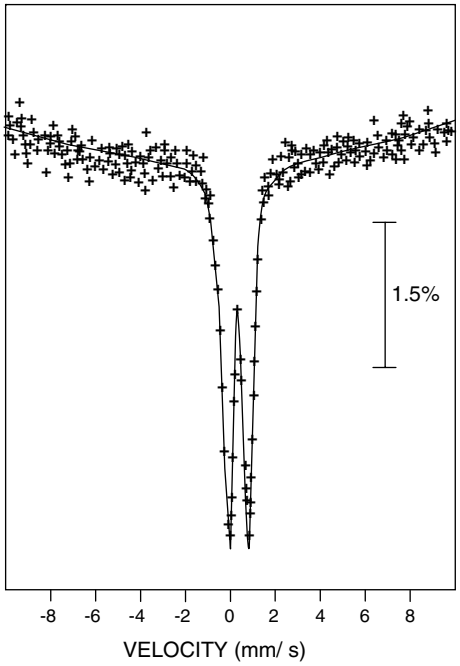


Fig. 4. Room-temperature Mössbauer spectrum of $[Fe(HMNO)_2OH]_2$.

The electronic absorption spectra recorded for the two complexes and the parent ligand as well in DMSO solution over the range 190–1100 nm are summarized in Table 3. The parent ligand displayed two absorptions at 284 and 405 nm corresponding, respectively, to the intraligand π–π^* and n–π^* transitions. The electronic spectra of the Fe(III) complexes are characterized by a band that can

Table 3
The electronic absorption data for α-benzoinoxime and its iron(III) complexes recorded in DMSO

Compound	λ, nm ($\log\varepsilon$)
H_2BNO	284 (2.7), 405[a] (1.5)
$Fe(HBNO)_3$	305 (4.1), 480[a] (3.3), 609 (1.2), 794 (1.0)
$[Fe(HBNO)_2OH]_2$	304 (3.9), 496[a] (3.4), 563 (3.2) 825 (1.1), 935 (1.2)

[a] Shoulder.

be assigned to a ligand-based π–π^* transition, which is normally the most intense band in the higher energy region of the spectra. Both complexes displayed a band that can be assigned to a charge-transfer transition from p_π orbitals of the oxime alcoholic oxygen atom to the half-filled $d_{\pi*}$ orbitals of the Fe(III) metal [32,33]. This band is observed at 480 nm for monomeric complex **1**, and at 496 nm for dimeric complex **2**. The red shift of this charge-transfer band for the dimeric complex with respect to the monomeric complex may explain the colors of the DMSO solutions of the two complexes (solutions of complexes **1** and **2** have purple and red colors, respectively). Two low-energy transitions ($\log\varepsilon \leqslant 1.2$) were observed in the spectra of both complexes and most probably are due to spin-forbidden d–d transitions. They have been assigned to the $^6A_1 \rightarrow {}^4T_1$ and $^6A_1 \rightarrow {}^4T_2$ transitions of high-spin Fe(III) [34]. The dominant feature of the spectrum of the dimeric complex **2** is an intense transition observed at 563 nm ($\log\varepsilon = 3.2$), which is absent in the spectra of both the monomeric complex and the parent ligand itself. This transition can be assigned to a charge-transfer transition from p_π orbitals of the hydroxo-bridged oxygen atom to $d_{\pi*}$ orbitals of the Fe(III) metal. Consistence with this assignment, a similar transition was observed for number of dihydroxo-bridged Fe(III) complexes [32,35].

References

[1] L. Que Jr., R.Y. Ho, Chem. Rev. 96 (1996) 2607.
[2] M.J. Kendrick, M.T. May, M.J. Plishka, K.D. Robinson, Metals in Biological Systems, Ellis Horwood Limited, 1992, p. 87..
[3] S. Sheriff, W.A. Hendrickson, J.L. Smith, J. Mol. Biol. 179 (1987) 273.
[4] R.E. Stenkamp, L.C. Sieker, L.H. Jesen, J. Am. Chem. Soc. 116 (1994) 618.
[5] B.J. Kennedy, K.S. Murray, P.R. Zwack, H. Homborg, W. Kalz, Inorg. Chem. 24 (1985) 3302.
[6] L. Borer, L. Thalken, C. Cecarelli, M. Glick, J.H. Zhang, W.M. Reiff, Inorg. Chem. 22 (1983) 1719.
[7] Y. Zang, Y. Dong, L. Que Jr., J. Am. Chem. Soc. 117 (1995) 1169.
[8] S.M. Gorun, S.J. Lippard, Inorg. Chem. 30 (1991) 1625.
[9] H. Weihe, H.U. Gudel, J. Am. Chem. Soc. 119 (1997) 6539.
[10] H.J. Schugar, G.R. Rossman, H.B. Gray, J. Am. Chem. Soc. 91 (1969) 4564.
[11] A.S. Attia, S.F. El-Mashtoly, M.F. El-Shahat, Polyhedron 22 (2003) 895.
[12] A.S. Attia, S.F. El-Mashtouly, M.F. El-Shahat, Synth. React. Inorg. Met.-Org. Chem. 32 (2002) 509.
[13] Hyberchem 6.01, Hybercube Inc., 2000.
[14] A.S. Attia, B.J. Conklin, C.W. Lange, C.G. Pierpont, Inorg. Chem. 35 (1996) 1033.
[15] K. Kovacs, A.A. Kamnev, J. Mink, C. Nemeth, E. Kuzmann, T. Megyes, T. Grosz, H. Schweiger, A. Vertes, Struct. Chem. 17 (2006) 105.
[16] M. Gerloch, E.D. McKenzie, A.D.C. Towel, J. Chem. Soc. A (1969) 2850.
[17] J.D. Walker, R. Poli, Inorg. Chem. 29 (1990) 756.
[18] M. Mohr, J.P. McNamara, H. Wang, S.A. Rajeev, J. Ge, C.A. Morgado, I.H. Hillier, Faraday Discuss. 124 (2003) 413.
[19] A.P. Scott, L. Radom, J. Phys. Chem. 100 (1996) 6502.
[20] N.S. Biradar, V.B. Mahale, V.H. Kulkarni, J. Inorg. Nucl. Chem. 35 (1973) 2656.
[21] R. Blinc, D. Hadzi, J. Chem. Soc. (1958) 4536.
[22] A. Bignotto, G. Costa, V. Galasso, G. DeAlti, Spectrochim. Acta A26 (1970) 1939.
[23] C.S. Wu, G.R. Rossman, H.B. Gray, G.S. Hammond, H.J. Schugar, Inorg. Chem. 11 (1972) 990.
[24] A.R. Middleton, J.R. Thornback, G. Wilkinson, J. Chem. Soc., Dalton Trans. (1980) 174.
[25] P.S. Reddy, K.H. Reddy, Polyhedron 19 (2000) 1687.
[26] S.A. Cotton, Coord. Chem. Rev. 8 (1972) 185.
[27] W. Wojciechowski, Inorg. Chim. Acta 1 (1967) 319.
[28] C.J. Connor, Prog. Inorg. Chem. 29 (1982) 203.
[29] J.A. Thich, C.C. Ou, D. Powers, B. Vasiliou, D. Mastropaolo, J.A. Potenza, H.J. Schugar, J. Am. Chem. Soc. 98 (1976) 1425.
[30] K.S. Murray, Coord. Chem. Rev. 12 (1974) 1.
[31] J.A. Bertrand, J.L. Breece, A.R. Kalyanaraman, G.J. Long, W.A. Baker, J. Am. Chem. Soc. 92 (1970) 5233.
[32] L. Borer, L. Thalken, J.H. Zhang, W.M. Reiff, Inorg. Chem. 22 (1983) 3174.
[33] B.P. Gaber, V. Miskowski, T.G. Spiro, J. Am. Chem. Soc. 96 (1974) 6868.
[34] T.S. Piper, R.L. Carlin, Inorg. Chem. 2 (1963) 260.
[35] L. Lopes, J. DeLaat, B. Legube, Inorg. Chem. 41 (2002) 2505.

Available online at www.sciencedirect.com
ScienceDirect
Polyhedron 26 (2007) 797–802
POLYHEDRON
www.elsevier.com/locate/poly

The preparation, crystal structure and electrochemistry of (5*Z*,5′*Z*)-2,2′-(alkane-α,ω-diylsulfanyldiyl)bis(5-(3-pyridylmethylene)-3,5-dihydro-4*H*-imidazol-4-ones) and their complexes with cobalt(II) chloride

Elena K. Beloglazkina *, Alexander G. Majouga, Renata B. Romashkina, Anna A. Moiseeva, Nikolai V. Zyk

Department of Chemistry, Moscow State University, 119992 Moscow, Russia

Received 16 June 2006; accepted 6 September 2006
Available online 26 September 2006

Abstract

A series of S-alkylated derivatives of 2-thiohydantoins, containing two 5-(3-pyridylmethylene)-3,5-dihydro-4*H*-imiazole-4-one fragments joined by polymethylene bridges with different numbers of carbon atoms, was synthesized. The title (5*Z*,5′*Z*)-2,2′-(alkane-α,ω-diylsulfanyldiyl)bis(5-(3-pyridylmethylene)-3,5-dihydro-4*H*-imidazol-4-ones) (**L**) were obtained by alkylation of 5-(3-pyridylmethylene)-3-phenyl-2-thiohydantoine by 1,2-dibromoethane, 1,6-dibromohexane or 1,10-dibromodecane in DMF in the presence of potassium carbonate. The complexes of ligands **L** with $CoCl_2 \cdot 6H_2O$ have been synthesized. It is shown that, regardless of the **L**:$CoCl_2$ ratio, complexes with **L**$CoCl_2$ composition are obtained in all cases. The structure of the cobalt(II) chloride complex with (5*Z*,5′*Z*)-2,2′-(ethane-1,2-diyldisulfanyldiyl)bis(5-(3-pyridylmethylene)-3-phenyl-3,5-dihydro-4*H*-imidazol-4-one) was determined by means of the RSA method. The cobalt atom in this complex has a tetrahedral ligand environment and it is coordinated by two chloride anions and two nitrogen atoms of pyridine fragments, forming a 19-membered metallocycle. Electrochemical investigations of the synthesized ligands and complexes have been made by CVA and RDE methods. It is established that the first stage of reduction for the complexes takes place on the metal, whereas the first stage of oxidation takes place on the coordinated chloride-anions.
© 2006 Elsevier Ltd. All rights reserved.

Keywords: N-ligands; Complexes; Cobalt; Molecular structure; Electrochemistry

1. Introduction

Recently we have reported the synthesis and structural and electrochemical investigation for a series of 2-alkylthio-(5-pyridylmethylene)-3,5-dihydro-4*H*-imidazol-4-ones [1,2] and (5*Z*,5′*Z*)-2,2′-(alkane-α,ω-diyldisulfanyldiyl)bis-(5-(α-pyridylmethylene)-3,5-dihydro-4*H*-imidazol-4-one) [3] complexes with $CoCl_2$. Some of these complexes demonstrated the capability to react reversibly with molecular oxygen [2] and to catalyze the alkene epoxidation reactions [2,4].

In this work we describe the synthesis of 4H-imidazol-4-one derivatives **1**–**3**, which contain two 5-(β-pyridylmethylene)-3,5-dihydro-4*H*-imidazol-4-one fragments, joined by polymethylene bridges with different numbers of carbon atoms, and the results of their reactions with cobalt(II) chloride.

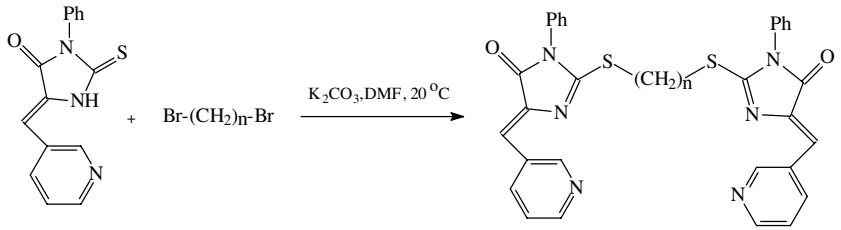
2. Result and discussion

2.1. Synthesis of the ligands and their complexes

Compounds **1**–**3** were obtained by 5-(3-pyridylmethylene)-3-phenyl-2-thiohydantoine alkylation by different α,ω-dibromoalkanes in DMF:

* Corresponding author.
E-mail address: bel@org.chem.msu.ru (E.K. Beloglazkina).

0277-5387/$ - see front matter © 2006 Elsevier Ltd. All rights reserved.
doi:10.1016/j.poly.2006.09.012

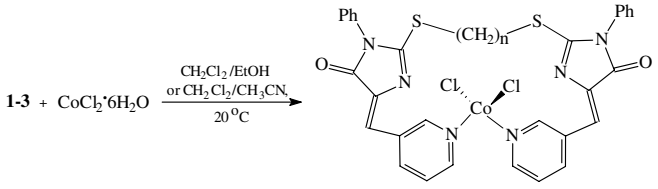


1, n = 2 (68%)
2, n = 6 (80%)
3, n = 8 (72%)

Based on the literature data, S-alkylated derivatives of 2-thiohydantoins are capable of forming coordination compounds in the reactions with transition metal salts, in which the metal ions coordinate with either or both nitrogen and sulfur atoms [5–12].

To obtain the target coordination compounds the method of slow diffusion of a ligand (**1**–**3**) solution in CH_2Cl_2 into a $CoCl_2 \cdot 6H_2O$ solution in EtOH or CH_3CN was used.

Complexes with composition 1:1 ($\mathbf{L} \cdot CoCl_2$) or 2:1 [$\mathbf{L} \cdot (CoCl_2)_2$] *a priori* would be expected as a result of $CoCl_2$ interaction with the examined ligands **1**–**3** (the collective designation "**L**" will be used below). Nevertheless, regardless of the **L**:$CoCl_2$ ratio, complexes **4**–**6** with $\mathbf{L}CoCl_2$ composition were obtained in all cases (according to elemental analysis and RSA data, complexes also contain additional solvents molecules). All the complexes are poorly soluble in EtOH and CH_3CN, but reasonably soluble in DMF and DMSO:



4, n = 2 (97%)
5, n = 6 (95%)
6, n = 10 (90%)

IR spectra of complexes **4**–**6** show C=O, C=N and C=C group absorption bands at 1730–1640 cm^{-1}, a shifted to lower frequencies when compared to the initial ligands.

In the electronic spectra of ligands **1**–**3** there are only the adsorptions bands in the UV-region due to π–π^* and n–π^* transitions. The spectrum of $CoCl_2 \cdot 6H_2O$, having the metal ion in an octahedral ligand environment, involves three bands of d–d transitions with moderate intensity in visible region (at 500–700 nm) (Table 1). UV–Vis spectra of the complexes **4**–**6** are characterized by lowering of the ligand bands intensities in the UV region, and a shift of the d–d transition bands in the visible region and a decrease of their intensity compared to $CoCl_2 \cdot 6H_2O$ (see Table 1 and Fig. 1). Such spectra are conformed to a tetrahedral coordination environment of the Co(II) ions. All the complexes have very similar electronic spectra, which permit the assumption that their structures are analogous. The tetrahedral configuration of the metal ion in the case of complex **2** was confirmed by RSA data.

Table 1
The UV–Vis spectroscopy data for $CoCl_2 \cdot 6H_2O$ and compounds **1**–**6** (CH_3CN, 4×10^{-2} M)

Compound	λ, nm (10^{-4} ε, l mol^{-1} cm^{-1})
$CoCl_2 \cdot 6H_2O$	570 (0.33), 613 (0.32), 680 (0.35)
1	272 (4.79), 364 (5.08)
2	271 (4.69), 361 (4.97)
3	275 (4.85), 364 (5.15)
4	224 (0.69), 359 (0.09), 589 (0.06), 678 (0.09)
5	276 (0.74), 380 (0.09), 560 (0.05), 660 (0.09)
6	259 (0.77), 379 (0.07), 584 (0.08), 675 (0.10)

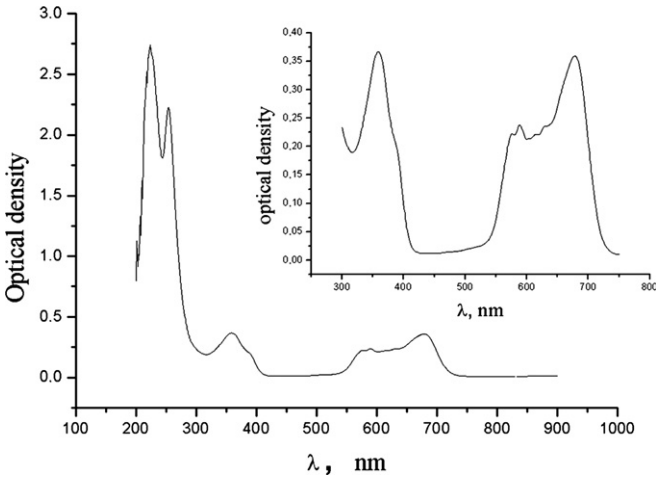


Fig. 1. UV–Vis spectrum of **4** (CH_3CN, 4×10^{-2} M).

2.2. Molecular and crystal structure of *4*

The structure of complex **4** was established by X-ray diffraction. The molecular structure of complex **2**, together with the atom numbering scheme and the selected geometric parameters, is shown in Fig. 2. Crystals available for structural investigation were made by slow diffusion of an ethanolic solution of $CoCl_2 \cdot 6H_2O$ to the solution of ligand **1** in CH_2Cl_2. Crystallographic data and structure

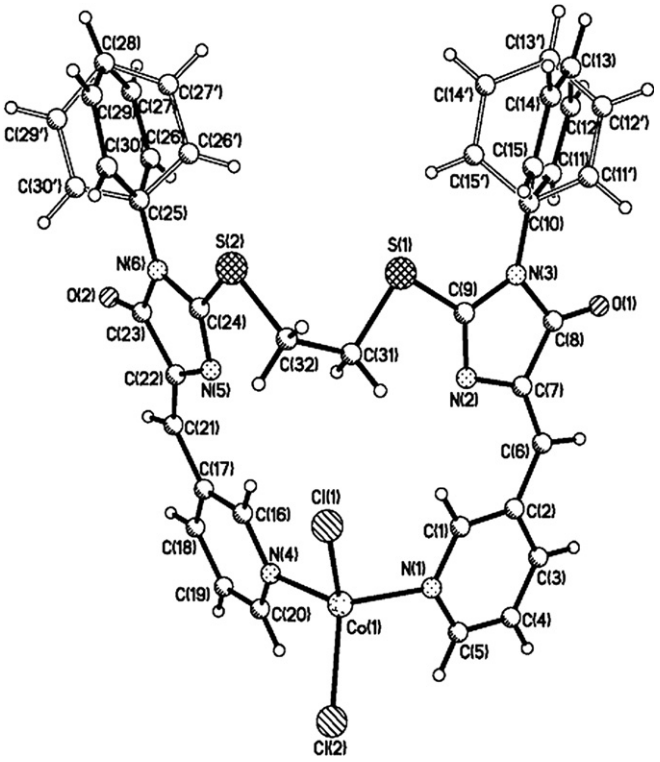


Fig. 2. Molecular structure of **4**. Thermal ellipsoids are given at the 50% probability level.

refinement details are given in Table 2; selected bond lengths and angles – in Table 3. The coordination geometry of the cobalt(II) atom represents a distorted tetrahedron. The metal atom is surrounded by two chloride anions and two nitrogen atoms of pyridine fragments forming a 19-membered metallocycle. This is the first example of a structurally characterized cobalt complex in which a bidentate organic ligand forms such chelate ring upon coordination. The imidazolone and phenyl rings in the ligand fragment are planar and practically coplanar. The phenyl rings in the organic ligand fragment are disordered (see Fig. 2). The two-carbon bridge between the sulfur atoms is orientated to the coordinated cobalt atom; this fact perhaps may be explained by the absence of any repulsion between the phenyl rings at N(3) [N(6)] and H_2C–S-groups in this case.

In the crystal structure of complex **4** additional molecules of methylene chloride and ethanol are present (Fig. 3). The disordered solvate CH_2Cl_2 and EtOH molecules occupy vacancies along the *a*-axis of the crystal.

2.3. Electrochemistry

Compounds **1**–**6** were studied by cyclic voltammetry (CV) and rotating disk electrode (RDE) voltammetry on a glassy-carbon (GC), Pt, and, in some cases, Au electrodes in DMF solutions in the presence of 0.05 M Bu_4NClO_4 as the supporting electrolyte. The electrochemical oxidation and reduction potentials are given in Table 4.

Table 2
Crystal data and structure refinement for **4**

Empirical formula	$C_{33.67}H_{28}Cl_4CoN_6O_{2.33}S_2$
Formula weight	818.47
Temperature (K)	100(2)
Wavelength (Å)	0.71073
Crystal size (mm)	$0.50 \times 0.10 \times 0.03$
Crystal system	triclinic
Space group	$P\bar{1}$
Unit cell dimensions	
a (Å)	4.9445(10)
b (Å)	16.279(3)
c (Å)	23.006(5)
α (°)	72.733(4)
β (°)	84.955(4)
γ (°)	82.968(4)
Volume (Å^3)	1752.4(6)
Z	2
Calculated density (Mg/m^3)	1.551
Absorption coefficient (mm^{-1})	0.957
F(000)	835
θ Range (°)	1.86–26.41
Limiting indices	$-6 \leqslant h \leqslant 6$, $-20 \leqslant k \leqslant 20$, $-28 \leqslant l \leqslant 28$
Reflections collected/independent (R_{int})	17075/7113 (0.1383)
Completeness to $\theta = 26.41$	99.0%
Absorption collection	semi-empirical from equivalents
Refinement method	full-matrix least-squares on F^2
Maximum and minimum transmission	0.971 and 0.766
Data/restraints/parameters	7113/5/461
Goodness-on-fit on F^2	0.973
Final *R* indices [$I > 2\sigma(I)$]	$R_1 = 0.0708$, $wR_2 = 0.1364$
R indices (all data)	$R_1 = 0.1684$, $wR_2 = 0.1646$
Largest difference in peak and hole (e Å^{-3})	0.954 and −0.669

Table 3
Selected bond lengths (Å) and angles (°) for **4**

Bond lengths	*d* (Å)	Bond angles	ω (°)
Co(1)–N(1)	2.039(5)	N(1)–Co(1)–N(4)	111.64(19)
Co(1)–N(4)	2.047(5)	N(1)–Co(1)–Cl(1)	105.80(15)
Co(1)–Cl(1)	2.2300(18)	N(4)–Co(1)–Cl(1)	101.87(15)
Co(1)–Cl(2)	2.2577(18)	N(1)–Co(1)–Cl(2)	104.37(15)
S(1)–C(9)	1.738(6)	N(4)–Co(1)–Cl(2)	106.47(15)
S(1)–C(31)	1.829(6)	Cl(1)–Co(1)–Cl(2)	126.57(7)
S(2)–C(24)	1.732(6)	C(9)–S(1)–C(31)	96.2(3)
S(2)–C(32)	1.795(6)	C(24)–S(2)–C(32)	100.9(3)
N(2)–C(9)	1.292(7)	C(5)–N(1)–C(1)	118.6(5)
N(2)–C(7)	1.408(7)	C(5)–N(1)–Co(1)	121.2(4)
N(5)–C(24)	1.292(7)	C(1)–N(1)–Co(1)	119.5(4)
N(5)–C(22)	1.413(7)	C(9)–N(2)–C(7)	105.9(5)

Ligands **1–3** are apparently oxidized primarily at the sulfur-containing fragment, and reduced at the O=C–C=C system, analogous of 2-methylthio-5-(pyridylmethylene)-dihydro-4*H*-imidazol-4-ones [2].

All complexes **4–6** are oxidized at less positive potentials compared to the corresponding ligands (see Figs. 4 and 5). Its first oxidation peaks at ~1.2 V presumably correspond to oxidation of Cl^- anions. The second oxidation peaks are due to oxidation of the organic ligand fragment. Anodic oxidation on a rotating disk electrode gives two-electron

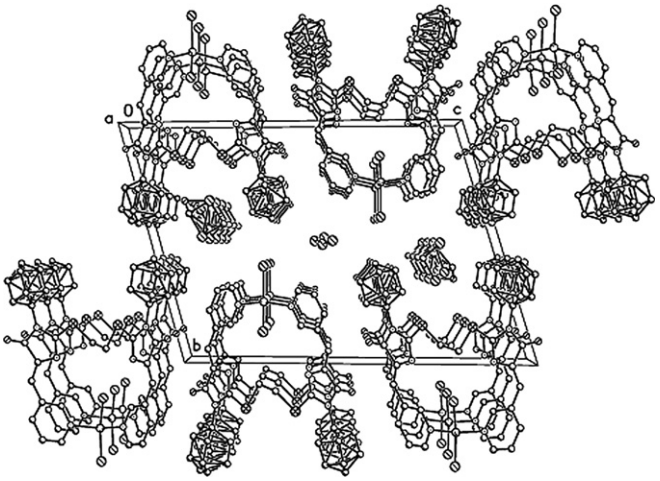


Fig. 3. The fragment of the crystal packing along the *a*-axis of the crystal (hydrogen atoms are omitted for clarity).

Table 4
Electrochemical reduction potentials (E^{Red}) and oxidation potentials (E^{Ox}) of the ligands **1**–**3** and their complexes measured relative to Ag|AgCl|KCl(satd.) by CV (E_p is the peak potential) and RDE ($E_{1/2}$ is the half-wave potential) methods at a glassy-carbon electrode

Compound	E_p^{Red}	$E_{1/2}^{Red}$	E_p^{Ox}	$E_{1/2}^{Ox}$
Ligand **1**	−1.22	−1.18 (2)	1.57	1.52 (2)
	−1.86	−1.93 (1.75)		
	−2.14[b]; −2.29[b]			
	−2.74			
Complex **4**	−1.20/0.02[a]	−1.08	1.18	1.20 (2)
		−2.04 (0.8)	1.52	1.50 (1.7)
Ligand **2**	−1.24	−1.20 (2)	0.96	
	−1.92	−1.95 (1.7)	1.56[c]	
	−2.16[b]			
Complex **5**	−1.25/0.03[a]	−0.88	1.28	1.27 (2)
			1.54	1.53 (1.6)
Ligand **3**	−1.28	−1.22 (2)	1.52	
	−1.98	−1.94 (1.6)		
Complex **6**	−1.25/0.04[d]	−1.08 (2.8)	1.22	1.19 (2)
		−1.83 (5.4)	1.52	

Experimental conditions: DMF, 0.05 M Bu_4NClO_4; CV, 200 mV s^{-1}; RDE, 20 mV s^{-1}; 2800 min^{-1}. The number of electrons transferred in the step, which was determined on a rotating disk electrode by comparing with the one-electron oxidation wave of ferrocene, is given in parentheses.

[a] Peak is not detected without electrolysis at 1.25–1.30 V.

[b] Low-intensity peak.

[c] Peak is better observable on Au electrode.

[d] The reverse peak corresponding to desorption of Co^0 increases with accumulation at the potential of the first reduction wave.

waves for the first stage of oxidation and the one-electron waves for the second stage.

In the cathodic region, the two-electron reduction peaks for complexes **4**–**6** are near to the first peaks of the free ligands reduction, but with an anodic dissolution peak of Co^0 in the reverse scan of the CV curve at 0.02–0.04 V (Fig. 5). The intensity of the latter peak increases −1.30 V. This fact means that the initial stage of reduction occurs "to the metal ions", and independently to either

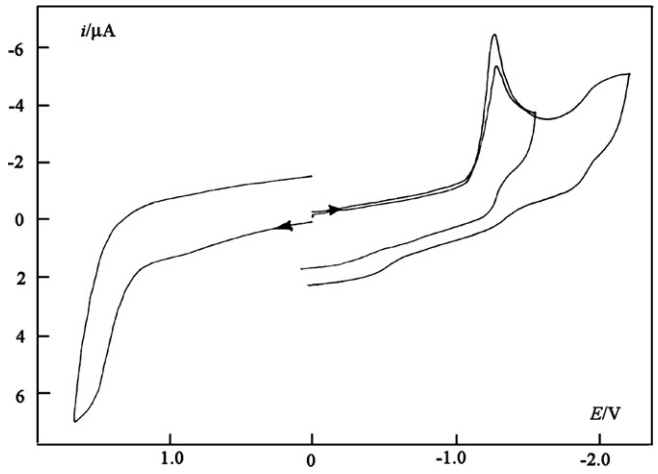


Fig. 4. Cyclic voltammogram of ligand **4** (DMF, 0.05 M Bu_4NClO_4, 10^{-3} M).

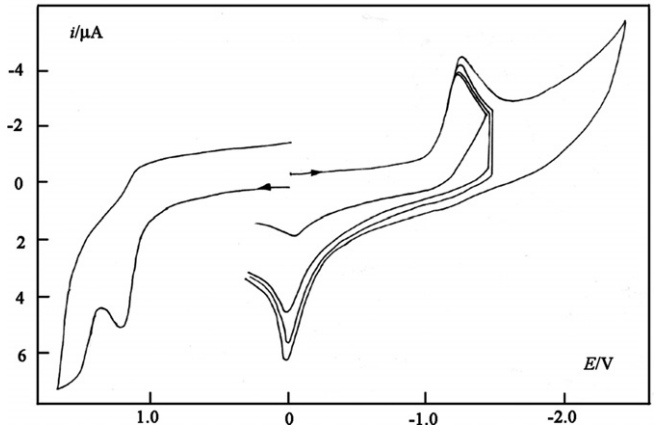


Fig. 5. Cyclic voltammogram of complex **6** (DMF, 0.05 M Bu_4NClO_4, 5×10^{-4} M).

coordinated metal atoms. Note, that the reduced forms of the complexes with a shorter polymethylene bridge between sulfur atoms are more stable than complex **6**, containing the $S(CH_2)_{10}S$-fragment: for the last compound an anodic dissolution peak of Co^0 is observed on the first scan of the CVA curve, whereas for complexes **4** and **5** the said peak is displayed with a marked intensity only under electrolysis at a potential of −1.25 V.

Hereby, complexes **4**–**6** undergo a two-electron reduction "at the metal" in the first step, accompanied by deposition of metallic cobalt on the electrode surface, and are oxidized first at coordinated chloride anions. Both oxidation and reduction first stages are two-electron irreversible processes.

3. Experimental

The starting 2-thioxo-3-phenyl-5-(3-pyridylmethylene)-imidazol-4-one was synthesized from phenyl isothiocyanate, glycine and 3-pyridine carboxaldehyde according to [13].

NMR spectra were registered on a Varian-XR-400 recorder (400 MHz for ^{1}H and 100 MHz for ^{13}C). IR spectra were obtained in Nujol on an IR200 (ThermoNicolet, USA) IR-spectrometer; UV–Vis spectra on a Perkin–Elmer λ-25 spectrometer.

Electrochemical studies were carried out on a PI-50-1.1 potentiostat. Glassy-carbon (2 mm in diameter), Pt (3 mm), or Au (1 mm) disks were used as the working electrodes; a 0.05 M Bu_4NClO_4 solution in DMF served as the supporting electrolyte; Ag/AgCl/KCl(satd.) was used as the reference electrode. All measurements were carried out under argon; the samples were dissolved in the pre-deaerated solvent. Dimethylformamide (high-purity grade) was purified by successive refluxing and vacuum distillation over anhydrous $CuSO_4$ and P_2O_5.

3.1. (5Z,5′Z)-2,2′-(Alkane-α,ω-diyldisylfanyldiyl)bis-(5-(3-pyridylmethylene)-3,5-dihydro-4H-imidazol-4-ones) (typical procedure)

α,ω-Dibromoalkane (0.05 mol) was added to a stirred mixture of 2-thioxo-3-phenyl-5-((*Z*)-3-pyridylmethylene)-2-imidazol-4-one (0.1 mol) and dried K_2CO_3 (0.15 mol) in 50 ml of DMF. The resulted mixture was stirred for 2 h at room temperature, then 50 ml of water was added. The formed precipitate was collected, washed with diethyl ether and recrystallized from ethyl acetate.

*3.1.1. (5Z,5′Z)-2,2′-(Ethane-1,2-diyldisylfanyldiyl)bis-(5-(3-pyridylmethylene)-3,5-dihydro-4H-imidazol-4-one) (**1**)*

M.p. 249 °C. ^{1}H NMR (δ/ppm): 9.20 (d, $J = 1.8$, 1H, H_α–Py), 8.52 (d, $J = 4.9$, 1H, $H_{\alpha'}$–Py), 8.50 (d, $J = 8$, 1H, H_γ–Py), 7.41 (m, 6H, $H_{\beta'}$–Py, Ph), 6.96 (s, 1H, CH=C), 3.86 (s, 2H, CH_2). ^{13}C NMR (δ/ppm): 168.0 (C=O), 164.8 (C=N), 152.9 ($C(H)_{Py}$), 150.0 ($C(H)_{Py}$), 140.0 (C_{Py}), 139.3 ($C(H)_{Py}$), 131.4 (C_{Ph}), 130.7, 129.4 (2C, $C(H)_{Ar}$), 129.0, 127.1 (2C, $C(H)_{Ar}$), 123.8 ($C(H)_{Ar}$), 120.7 (HC=), 30.4 (CH_2S). IR (cm^{-1}): 1730 (C=O), 1670 (C=N), 1640 (C=C), 1508, 1470, 1380, 1248, 1220, 1170. *Anal.* Calc. for $C_{32}H_{24}N_6S_2O_2$: C, 65.29; H, 4.11; N, 14.28. Found: C, 65.89; H, 3.75; N, 14.59%.

*3.1.2. (5Z,5′Z)-2,2′-(Hexane-1,6-diyldisylfanyldiyl)bis-(5-(3-pyridylmethylene)-3,5-dihydro-4H-imidazol-4-one) (**2**)*

M.p. 235 °C. ^{1}H NMR (δ/ppm): 9.31 (d, $J = 2.0$, 1H, H_α–Py), 8.56 (d, $J = 1.8$, 1H, $H_{\alpha'}$–Py), 8.52 (d, $J = 6.5$, 1H, H_γ–Py), 7.41 (m, 6H, $H_{\beta'}$–Py, Ph), 6.95 (s, 1H, CH=C), 3.35 (t, $J = 3.0$, 2H, CH_2), 1.89 (m, 2H, CH_2), 1,58 (m, 4H, CH_2–CH_2). ^{13}C NMR (δ/ppm): 168.8 (C=O), 166.1 (C=N), 152.8 ($C(H)_{Py}$), 150.5 ($C(H)_{Py}$), 140.0 (C_{Py}), 138.2 ($C(H)_{Py}$), 132.3 (C_{Ph}), 130.7, 130.0 (2C, $C(H)_{Ar}$), 129.2, 127.8 (2C, $C(H)_{Ar}$), 127.9 ($C(H)_{Ar}$), 121.0 (HC=), 31.9 (CH_2S), 28.8 (CH_2), 28.2 (CH_2). IR (cm^{-1}): 1730 (C=O), 1670 (C=N), 1645 (C=C), 1495, 1470, 1380, 1248, 1225, 1170. *Anal.* Calc. for $C_{36}H_{32}N_6S_2O_2$: C, 67.06; H, 5.00; N, 13.03%. Found: C, 67.45; H, 4.52; N, 13.36%.

*3.1.3. (5Z,5′Z)-2,2′-(Decane-1,10-diyldisylfanyldiyl)bis-(5-(3-pyridylmethylene)-3,5-dihydro-4H-imidazol-4-one) (**3**)*

M.p. 162 °C. ^{1}H NMR (δ/ppm): 9.19 (c, 1H, H_α–Py), 8.58 (m, 2H, $H_{\alpha'}$–Py + $H_{\gamma'}$–Py), 7.42 (m, 6H, $H_{\beta'}$–Py, Ph), 6.97 (c, 1H, CH=C), 3.32 (t, $J = 3.2$, 2H, CH_2), 1.68 (m, 2H, CH_2), 1.47 (m, 2H, CH_2), 1.31 (m, 4H, CH_2–CH_2). ^{13}C NMR (δ/ppm): 168.7 (C=O), 165.8 (C=N), 152.7 ($C(H)_{Py}$), 150.9 ($C(H)_{Py}$), 138.0 (C_{Py}), 137.2 ($C(H)_{Py}$), 132.3 (C_{Ph}), 130.1, 128.5 (2C, $C(H)_{Ar}$), 129.0, 127.5 (2C, $C(H)_{Ar}$), 129.1 ($C(H)_{Ar}$), 120.4 (HC=), 31.2 (CH_2S), 28.6 (CH_2), 28.1 (CH_2), 27.0 (CH_2), 25.2 (CH_2). IR (cm^{-1}): 1730 (C=O), 1670 (C=N), 1645 (C=C), 1498, 1470, 1376, 1250, 1225, 1167. *Anal.* Calc. for $C_{40}H_{40}N_6S_2O_2$: C, 68.54; H, 5.75; N, 11.99%. Found: C, 68.89; H, 5.48; N, 11.29%.

*3.2. Synthesis of coordination compounds from ligands **1** to **3** and $CoCl_2$ (typical procedure)*

To a solution of 0.068 mmol of ligand **1**, **2** or **3** in CH_2Cl_2 (placed in a glass tube with approximately 1 cm diameter) pure CH_3CN or EtOH (2 ml) was slowly added, in order to form a diphasic system. Then a solution of 0.068 mmol $CoCl_2 \cdot 6H_2O$ in 2–3 ml of CH_3CN or EtOH was added down the tube side, without mixing the ligand and salt solutions. Thereafter the tube was covered and kept for crystal solid precipitation. The solid was filtered and dried in air. All elemental analysis and melting points are given for the complexes obtained from the CH_3CN/CH_2Cl_2 mixture.

*3.2.1. [(5Z,5′Z)-2,2′-(Ethane-1,2-diyldisylfanyldiyl)bis-(5-(3-pyridylmethylene)-3,5-dihydro-4H-imidazol-4-one)]-cobalt(II) dichloride (**4**)*

Blue crystals. M.p. > 340 °C. IR (cm^{-1}): 1725 (C=O), 1640 (C=N), 1600 (C=C), 1500, 1470, 1250, 1225, 1165. *Anal.* Calc. for $C_{32}H_{24}N_6S_2O_2 \cdot CoCl_2 \cdot CH_2Cl_2$: C, 49.33; H, 3.26; N, 10.46. Found: C, 49.99; H, 2.77; N, 10.00%.

*3.2.2. [(5Z,5′Z)-2,2′-(Hexane-1,6-diyldisylfanyldiyl)bis-(5-(3-pyridylmethylene)-3,5-dihydro-4H-imidazol-4-one)]-cobalt(II) dichloride (**5**)*

Greenish-blue powder. M.p. 265 °C. IR (cm^{-1}): 1726 (C=O), 1645 (C=N), 1600 (C=C), 1500, 1465, 1250, 1220, 1175. *Anal.* Calc. for $C_{36}H_{32}N_6S_2O_2 \cdot CoCl_2 \cdot 4CH_2Cl_2$: C, 43.11; H, 3.52; N, 7.54. Found: C, 42.84; H, 3.83; N, 7.98%.

*3.2.3. [(5Z,5′Z)-2,2′-(Decane-1,10-diyldisylfanyldiyl)bis-(5-(3-pyridylmethylene)-3,5-dihydro-4H-imidazol-4-one)]-cobalt(II) dichloride (**6**)*

Green-blue powder. M.p. 190 °C. IR (cm^{-1}): 1725 (C=O), 1645 (C=N), 1600 (C=C), 1505, 1470, 1255, 1220, 1170. *Anal.* Calc. for $C_{40}H_{40}N_6S_2O_2 \cdot CoCl_2 \cdot CH_2Cl_2$: C, 53.78; H, 4.62; N, 9.18. Found: C, 54.67; H, 4.63; N, 9.62%.

Acknowledgement

This work was supported by RFBR (Project No. 04-03-32845).

Appendix A. Supplementary material

CCDC 611164 contains the supplementary crystallographic data for this paper. These data can be obtained free of charge via http://www.ccdc.cam.ac.uk/conts/retrieving.html, or from the Cambridge Crystallographic Data Centre, 12 Union Road, Cambridge CB2 1EZ, UK; fax: (+44) 1223-336-033; or e-mail: deposit@ccdc.cam.ac.uk. Supplementary data associated with this article can be found, in the online version, at doi:10.1016/j.poly.2006.09.012.

References

[1] S.Z. Vatsadze, A.A. Moiseeva, K.P. Butin, N.V. Zyk, Mendeleev Commun. 14 (2004) 115.
[2] E.K. Beloglazkina, S.Z. Vatsadze, A.G. Majouga, N.A. Frolova, R.B. Romashkina, N.V. Zyk, A.A. Moiseeva, K.P. Butin, Russ. Chem. Bull. (Int. Ed.) 54 (2005) 2771.
[3] A.G. Majouga, E.K. Beloglazkina, I.V. Yudin, N.V. Zyk, A.A. Moiseeva, K.P. Butin, Russ. Chem. Bull. (Int. Ed.) 54 (2005) 2163.
[4] E.K. Beloglazkina, A.G. Majouga, R.B. Romashkina, N.V. Zyk, Tetrahedron Lett. 47 (2006) 2957.
[5] R.S. Srivastava, R.R. Srivastava, H.N. Bhargava, Soc. Chim. Fr. 128 (1991) 671.
[6] D. Kushev, G. Gorneva, V. Enchev, E. Naydenova, J. Popova, S. Taxirov, L. Maneva, K. Grancharov, N. Spassovska, J. Inorg. Biochem. 89 (2002) 203.
[7] M. Choudhry, A. Burrows, M. Mingos, J. White, D. Williams, J. Chem. Soc., Chem. Commun. (1995) 1521.
[8] M. Chowdhry, M. Mingos, A. White, D. Williams, Chem. Commun. (1996) 899.
[9] J. Casas, A. Castineiras, N. Playa, A. Sanchez, J. Sordo, J. Varela, E. Vazquez-Lopez, Polyhedron 18 (1999) 3653.
[10] J. Casas, E. Castellano, A. Masias, N. Playa, A. Sanchez, J. Sordo, J. Varela, E. Vazquez-Lopez, Polyhedron 20 (2001) 1845.
[11] P. Molina, A. Tarrada, D. Curiel, C. Ramirez de Arellano, Tetrahedron 55 (1999) 1417.
[12] M. Arca, F. Demartin, F. Devillanova, A. Garau, F. Isaia, V. Lippolis, G. Verani, Inorg. Chem. 37 (1998) 4164.
[13] A.G. Majouga, E.K. Beloglazkina, S.Z. Vatsadze, N.A. Frolova, N.V. Zyk, Russ. Chem. Bull. 53 (2004) 2850.

Available online at www.sciencedirect.com
ScienceDirect
Polyhedron 26 (2007) 803–810
POLYHEDRON
www.elsevier.com/locate/poly

X-ray structure and multinuclear NMR studies of platinum(II) complexes with 5-methyl-1,2,4-triazolo[1,5-*a*]pyrimidin-7(4*H*)-one

Iwona Łakomska [a,*], Andrzej Wojtczak [a], Jerzy Sitkowski [b,c], Lech Kozerski [b], Edward Szłyk [a]

[a] *Department of Chemistry, Nicholas Copernicus University, Gagarina 7, 87-100 Toruń, Poland*
[b] *National Institute of Public Health, Chełmska 30/34, 00-725 Warsaw, Poland*
[c] *Institute of Organic Chemistry, Polish Academy of Sciences, Kasprzaka 44/52, 01-224 Warsaw, Poland*

Received 25 May 2006; accepted 7 September 2006
Available online 26 September 2006

Abstract

New dichloride platinum(II) complexes with 5-methyl-1,2,4-triazolo[1,5-*a*]pyrimidin-7(4*H*)-one (HmtpO) have been synthesized and characterized by thermal analysis, infrared and ^{1}H, ^{13}C, ^{15}N, ^{195}Pt NMR spectroscopy. X-ray crystal structures of *cis*-$PtCl_2(NH_3)$-(HmtpO) (**1**) and *cis*-$PtCl_2(HmtpO)_2 \cdot 4H_2O$ (**2b**) were determined to $R = 0.0332$ and $R = 0.0802$, respectively. In both complexes the Pt(II) ions have a square-planar geometry with two adjacent corners being occupied by two nitrogens of HmtpO molecules for **2b** or NH_3 and HmtpO molecules for **1**, whereas the remaining adjacent corners are occupied by two chloride anions. Spectroscopic data confirm the square planar geometry with N(3) bonded HmtpO, S-bonded dimethylsulfoxide and two *trans* chloride anions for *trans*-$PtCl_2(dmso) \cdot 4H_2O$ (**3**).
© 2006 Elsevier Ltd. All rights reserved.

Keywords: Platinum complex; 1,2,4-Triazolo[1,5-*a*]pyrimidine derivative; Dimethylsulfoxide; Multinuclear NMR; X-ray structure

1. Introduction

Cisplatin is one of the most commonly used anticancer drugs in the treatment of testicular, ovarian, bladder and head and neck cancer [1,2]. Despite the great success of treating certain kinds of cancer there are several side-effects, and both intrinsic and acquired resistance limit the organotropic profile of the drug [3].

There is a continuing interest in development of new platinum complexes, which are less toxic and have a broader activity spectrum. Variation in the nature of the amine can have a significant effect on the activity and toxicity of these complexes. Several platinum complexes with N-heterocyclic ligands, such as imidazole, thiazole, pyridine and purine derivatives, have been reported [4–7].

Triazolopyrimidine derivatives revealed structures similar to purine, differing from it by the presence of a pyrimidine nitrogen atom in a bridgehead position, and the lack of the acidic H-proton in the five-membered ring [8,9]. Triazolopyrimidine derivatives display a great versatility in their interaction with metal ions, because they can bind metal ions through different sites. Reported studies of triazolopyrimidine complexes display an appreciable variability in their molecular structure. There are examples of mono-, di- and multinuclear structures, which exhibited the central ion and inorganic anions influence on the complex's geometry [10–15]. Nevertheless, when triazolopyrimidines act monodentately to the platinum(II) ion, the preferred binding position appears to be N(3) [12,14]. Mononuclear platinum(II) species such as: *cis*-$PtCl_2$-$(HmtpO)_2 \cdot 2H_2O$ [13], *cis*-$[Pt(HmtpO)_2(NH_3)_2](NO_3)_2 \cdot 2H_2O$ [10] and *trans*-$PtCl_2(dmso)(dmtp)$ [14] revealed N(3) coordinated heterocycles. Polymeric compounds are usually obtained due to N(1) and N(3) coordination [16],

* Corresponding author. Fax: +48 56 654 2477.
E-mail address: dziubek@umk.pl (I. Łakomska).

0277-5387/$ - see front matter © 2006 Elsevier Ltd. All rights reserved.
doi:10.1016/j.poly.2006.09.010

whereas dimers with eight-member rings are formed for the N(3), N(4) bridging mode [10]. The exceptions were complexes with 4,5,6,7-tetrahydro-5,7-dioxo-1,2,4-triazolo[1,5-*a*]pyrimidine (H_2tpO_2), where the bidentate ligands were linked through the exocyclic oxygen O(7) and endocyclic nitrogen N(1) [17].

It was recently demonstrated that the coordination compounds with 1,2,4-triazolo[1,5-*a*]pyrimidine revealed biological activity [13,18–21]. Some transition metal complexes with triazolopyrimidines significantly inhibited in vitro cell growth of the epimastigote [19] and Gram(+) and Gram(−) bacteria. The antitumor activity studies (in vitro) of *cis* platinum(II) compounds with the triazolopyrimidine ligands, 5-methyl-1,2,4-triazolo[1,5-*a*]pyrimidin- 7(4*H*)-one (HmtpO) [13], 5,7-diterbutyl-1,2,4-triazolo[1,5-*a*]pyrimidine (dbtp) [20] and 5,7-diphenyl-1,2,4-triazolo[1,5-*a*]pyrimidine (dptp) [20], indicate a moderate antiproliferative activity against the cells of rectal, breast and bladder cancer.

Following this research line, we have tried to synthesize new platinum(II) compounds, which will reveal activity similar to cisplatin, but have an additional functional group, where they could be linked to carrier substances. Therefore, for our studies we have chosen 5-methyl-1,2,4-triazolo[1,5-*a*]pyrimidin-7(4*H*)-one, with a structure similar to the purine ring existing in DNA, as a ligand for platinum(II). In this paper, we present the results on the synthesis and molecular structure characterization of the novel compounds: *cis*-$PtCl_2$(HmtpO)(NH_3) (**1**), *cis*-$PtCl_2(HmtpO)_2 \cdot H_2O$ (**2a**) and *trans*-$PtCl_2$(HmtpO)(dmso) $\cdot 4H_2O$ (**3**).

2. Experimental

2.1. Materials

Dipotassium tetrachloroplatinum(II), 5-methyl-*s*-triazolo[1,5-*a*]pyrimidine-7-ol (98%), potassium hexafluorophosphate (98%), tetraethylammonium chloride hydrate and tetraphenylphosphonium chloride (98%) were purchased from Aldrich, whereas the inorganic salts and organic solvents of analytical grade were from POCh Gliwice (Poland).

2.2. Instrumentation

The content of C, H, N was determined by elemental semi-microanalysis, Pt spectrophotometrically as H_2PtCl_6 on a Specord M40 Carl Zeiss Jena ($\lambda = 400$ nm). Thermogravimetric analyses were performed with a SDT-2960 TA Instrument (samples – 5 mg, heating range 25–1000 °C, heating rate 3.5 deg/min, N_2 atmosphere). IR spectra were measured with a Perkin–Elmer Spectrum-2000 FT-IR spectrometer, using KBr (400–4000 cm^{-1}) and polyethylene discs (100–400 cm^{-1}). The $^1H\{^{13}C\}$ HSQC, $^1H\{^{13}C\}$ HMBC and $^1H\{^{15}N\}$ HMQC spectra were performed with a Varian INOVA-500 NMR spectrometer equipped with an inverse Nalorac Z-gradient shielded probe. The solvent was dmso-d_6, the concentrations of the saturated solutions were ca. 0.01–0.05 M and the temperature was 298 K. The reference standard was TMS for ^1H and ^{13}C, CH_3NO_2 (external) for ^{15}N and K_2PtCl_6 (external) for ^{195}Pt.

The ^{13}C CPMAS spectra were performed with a Bruker AMX 300 MHz spectrometer using a Bruker MAS-VTN500SB BL4 probe head and 4 mm zirconia rotors, at 296 K.

2.3. Preparation of the platinum(II) complexes

Cis-$PtCl_2(dmso)_2$ [22] and $K[PtCl_3(NH_3)]$ [23] were prepared from K_2PtCl_4 by the known method.

Cis-$PtCl_2(NH_3)$(HmtpO) (**1**): To a solution of $K[PtCl_3(NH_3)]$ (0.050 g, 0.13 mmol) in 10 cm^3 of water, a solution of HmtpO (0.0210 g, 0.13 mmol) in 5 cm^3 of 1 M HCl was added. Reaction mixture was stirred at room temperature for 12 h. The yellow precipitate was filtered, washed with water, acetone, diethyl ether and dried in vacuum. Yield 0.0270 g (48%). *Anal.* Calc. for $C_6H_9Cl_2N_5OPt$: Pt, 45.0; C, 16.6; N, 16.2; H, 2.1. Found: Pt, 44.6; C, 16.7; N, 16.0; H, 1.8%.

Cis-$PtCl_2(HmtpO)_2 \cdot H_2O$ (**2a**): A suspension of K_2PtCl_4 (0.100 g; 0.26 mmol) in 5 cm^3 of water was treated with HmtpO (0.0798 g; 0.53 mmol) in 8 cm^3 of 1 M HCl and the reaction mixture stirred at room temperature for 48 h. The yellow precipitate was filtered, washed with water, acetone, diethyl ether and dried in vacuum. Yield 0.0456 g (30%). *Anal.* Calc. for $C_{12}H_{14}Cl_2N_8O_3Pt$: Pt, 33.4; C, 24.7; N, 19.2; H, 2.4. Found: Pt, 33.0; C, 24.3; N, 19.1; H, 2.6%. The thermal analysis confirmed detachment of water molecule (95–140 °C, weight calc. 3.35%, exp. 3.65%). Further decomposition proceeds in several endothermal stages and leads to metallic platinum above 885 °C. By slow crystallization of **2a** from a mixture of HCl and water (1:3 v/v), single crystals of **2b** suitable for X-ray structure analysis were obtained.

Trans-$PtCl_2(dmso) \cdot 4H_2O$ (**3**): A solution of HmtpO (0.036 g; 0.23 mmol) in 5 cm^3 of 1 M HCl was dropped to a solution of *cis*-$PtCl_2(dmso)_2$ (0.100 g, 0.23 mmol) in 10 cm^3 water–ethanol mixture. The reaction mixture was stirred at room temperature for 24 h. The filtrate was left for crystallization and after 3 days a yellow precipitate was filtered off, washed with ethanol, acetone, diethyl ether and dried in vacuum. Yield 0.0443 g (34%). *Anal.* Calc. for $C_8H_{20}Cl_2N_4O_6SPt$: Pt, 34.4; C, 17.0; N, 9.9; H, 3.6. Found: Pt, 34.1; C, 17.1; N, 9.4; H, 3.9%. The content of solvated water molecules in **3** has been confirmed by thermogravimetric analyses. The first endothermic step in the range 83–272 °C corresponds to the mass loss in the TG curves which can be correlated with detachment of 4 water molecules and dimethylsulfoxide (calc. 26.38%, exp. 26.87%). The next endothermic processes (275–820 °C) can be related to decomposition of **3** leaving platinum as a final product.

2.4. X-ray structure determination

Pale yellow crystals of *cis*-$PtCl_2(NH_3)$(HmtpO) (**1**) and *cis*-$PtCl_2(HmtpO)_2 \cdot 4H_2O$ (**2b**) were obtained by slow evaporation from a mixture of HCl and water. Complex **1** crystallized in monoclinic space group $P2_1/c$, whereas complex **2b** crystallized in the triclinic $P\bar{1}$ space group. The X-ray data for **1** and **2b** were collected at 293(2) K with an Oxford Sapphire CCD diffractometer, using Mo Kα radiation ($\lambda = 0.71073$ Å) and the ω–2θ method. The shape-based numerical absorption correction was applied with minimum and maximum transmissions of 0.04914 and 0.39687 for **1** and 0.17132 and 0.55792 for **2b**. The structure was solved by Patterson methods and refined with the full-matrix least-squares method on F2 with the use of the SHELX-97 program package [24]. The data collection and refinement processes are summarized in Table 1. The residual peaks tabulated for **2b** are positioned 1.16 Å from Cl(1) and 0.86 Å from Pt(1), respectively, therefore not indicating any missing atoms. The fractional coordinates of **1**, **2b** and selected bond lengths and angles are presented in Table 4.

Table 1
Crystal data and structure refinement for **1** and **2b**

Identification code	*cis*-$PtCl_2(NH_3)$-(HmtpO) (**1**)	*cis*-$PtCl_2(HmtpO)_2 \cdot 4H_2O$ (**2b**)
Empirical formula	$C_6H_9Cl_2N_5OPt$	$C_{12}H_{20}Cl_2N_8O_6Pt$
Formula weight	435.15	638.4
Temperature (K)	293(2)	293(2)
Wavelength (Å)	0.71073	0.71073
Crystal system	monoclinic	triclinic
Space group	$P2(1)/c$	$P\bar{1}$
Unit cell dimensions		
a (Å)	9.718(2)	7.121(1)
b (Å)	11.417(2)	10.681(1)
c (Å)	11.138(2)	14.817(2)
α (°)		75.08(1)
β (°)	114.27(3)	76.33(1)
γ (°)		71.64(1)
Volume (Å^3)	1126.5(4)	1018.6(2)
Z	4	2
Calculated density (Mg/m^3)	2.560	2.081
Absorption coefficient (mm^{-1})	12.911	7.198
F(000)	804	616
Crystal size (mm)	$0.40 \times 0.18 \times 0.10$	$0.38 \times 0.28 \times 0.23$
Theta range for data collection (°)	2.68–31.17	2.73–31.18
Index ranges	$-12 \leqslant h \leqslant 13$, $-16 \leqslant k \leqslant 16$, $-15 \leqslant l \leqslant 14$	$-10 \leqslant h \leqslant 9$, $-15 \leqslant k \leqslant 15$, $-21 \leqslant l \leqslant 18$
Reflections collected/ unique [R_{int}]	10821/3403 [0.0524]	10043/5940 [0.1559]
Data/restraints/parameters	3403/0/138	5940/0/264
Goodness-of-fit on F^2	1.095	1.089
Final R indices [$I > 2\sigma(I)$]	$R_1 = 0.0332$, $wR_2 = 0.0796$	$R_1 = 0.0802$, $wR_2 = 0.2228$
R indices (all data)	$R_1 = 0.0388$, $wR_2 = 0.0829$	$R_1 = 0.0863$, $wR_2 = 0.2284$
Largest difference peak and hole (e Å^{-3})	3.299 and −2.074	5.759 and −4.496

2.5. Cytotoxic activity

The antiproliferative activity in vitro against HCV29T (bladder cancer) and T47D (breast cancer) cell lines were performed by using the SRB test as described [20].

3. Results and discussion

3.1. NMR spectroscopy

We have measured ^{1}H, ^{13}C and ^{15}N NMR spectra for **1**, **2a** in solution but not for **3** due to the low solubility of this complex in dmso-d_6 and another solvents. The ^{1}H NMR chemical shifts of the studied complexes are listed in Table 2. The spectra exhibit a singlet at 2.41 (**1**), 2.40 (**2a**) and 2.31 ppm (**3**) for the methyl group and singlets from H(2), H(6) (5.99–8.61 ppm) and H(4) (13.55–13.66 ppm) (Table 2). All signals from H(2), H(6) and H(4) are shifted towards lower fields due to coordination of the triazolopyrimidine ligand. This effect being more expressed for H(2) (0.27–0.44 ppm) and H(4) (0.36–0.44 ppm) than H(6) (0.17–0.26 ppm) (Table 2), suggests slightly stronger deshielding of H(2) and H(4). Therefore the monodentate coordination of HmtpO via N(3) can be proposed, because in the case of the bridging mode (N(3), N(4)), the coordination shifts were bigger (ca. 0.88 ppm) [25]. Additionally, the ^{1}H NMR spectrum of **1** exhibited a broad signal for the NH_3 protons ($\delta =$ 4.06 ppm), which confirms its coordination [26–29].

Coordination sites of the heterocyclic ring were determined by ^{1}H{^{15}N} HMQC spectra of the complexes. In

Table 2
^{1}H and ^{13}C NMR chemical shifts (δ) of the ligand HmtpO and its platinum(II) complexes

Compound	H(6)	H(2)	H(4)	C(2)	C(3a)	C(5)	C(6)	C(7)
HmtpO (in dmso-d_6)	5.82	8.17	13.19	151.7	150.5	151.5	98.0	155.8
(**1**) *cis*-$PtCl_2(NH_3)$(HmtpO)	6.02 (+0.20)	8.44 (+0.27)	13.66 (+0.47)	150.6 (−1.1)	149.8 (−0.7)	153.1 (+1.6)	99.8 (+1.8)	154.5 (−1.3)
(**2a**) *cis*-$PtCl_2(HmtpO)_2 \cdot H_2O$	5.99 (+0.17)	8.61 (+0.44)	13.64 (+0.45)	149.9 (−1.8)	149.5 (−1.0)	152.7 (+1.5)	100.2 (+2.2)	154.4 (−1.4)
(**3**) *trans*-$PtCl_2$(dmso)(HmtpO) $\cdot 4H_2O$	6.08 (+0.26)	8.55 (+0.38)	13.55 (+0.36)	148.3[a] (−1.9)	[b]	153.4[a](+0.7)	101.7[a] (+6.5)	155.9[a] (−1.9)
HmtpO (in the solid state)				150.2	[b]	152.7	95.2	157.8

[a] Data from ^{13}C CPMAS NMR.
[b] The signal was not observed in the spectrum.

the ^{15}N NMR spectra four resonances at: −112.7, −257.3, −251.3, −157.8 for **1** and: −112.1, −257.8, −253.5, −157.9 ppm for **2a** were detected (Fig. 1, Table 3). In comparison to the free ligand spectrum, the shielding effect of N(1), N(3) and N(8) in the complexes is evident, while the biggest coordination shift was observed for N(3) (Δ_{coord} = 91–92 ppm) (Table 3). The strong shielding effect of N(3) is an unambiguous result of N(3) coordination in solution.

^{13}C NMR spectra of **1** and **2a** were recorded, while for **3** no peaks were detectable, due to the low solubility of the latter complex. The signals were assigned by a heterocorrelation ^{1}H–^{13}C technique and data are listed in Table 2. The coordination effect has an impact on C(2) and C(3a) signals which are shielded by 0.7–1.9 ppm in relation to free HmtpO, while C(5) and C(6) resonances are detected 0.7–6.5 ppm towards the low field (Table 2) which can be explained by the deshielding effect of the metal due to coordination via N(3).

A spectrum for complex **3** was measured in the solid phase and data are listed in Table 2. It should be noted that this is the first report of a ^{13}C CPMAS spectrum of HmtpO and one of its platinum(II) complexes. The spectrum presents a similar pattern of coordination shifts as observed in solution (Table 2), which indicates HmptO coordination via N(3). However, the coordination shift of the C(6) signal is larger (maximum 6.5 ppm).

^{195}Pt NMR spectra of **1** and **2a** were measured in dmso-d_6 and data are listed in Table 3. The signals of the *cis*-dichloro complexes were observed at −2089 (**2a**) and −2116 (**1**). These values are at lower field than those

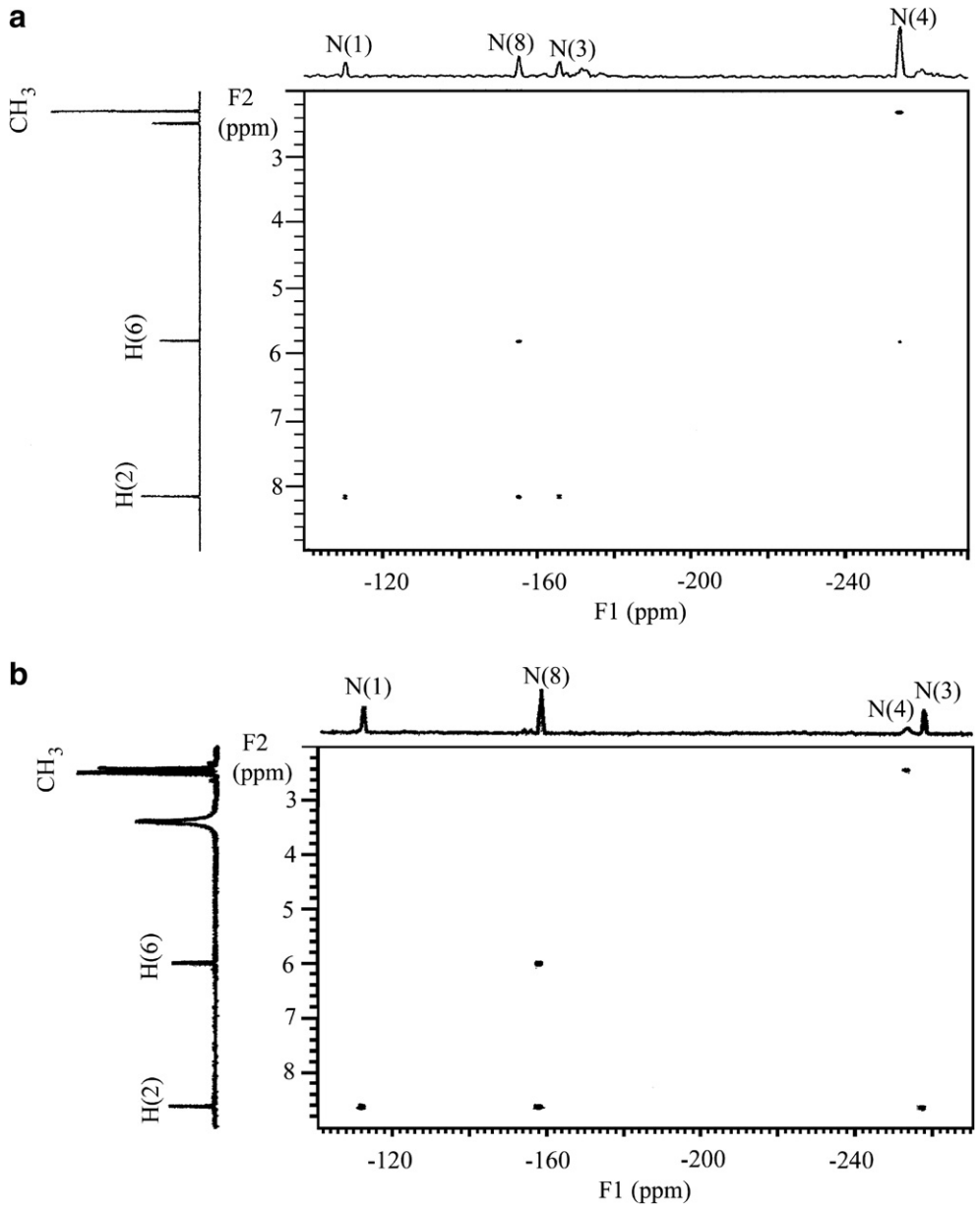


Fig. 1. $^{1}H\{^{15}N\}$ NMR spectra of (a) HmptO; (b) *cis*-$[PtCl_2(HmtpO)_2]\cdot H_2O$ (**1**).

Table 3
^{15}N NMR and ^{195}Pt chemical shifts (δ) of the platinum(II) complexes in dmso-d_6

Compound	N(1)	N(3)	N(4)	N(8)	Pt[a]
HmtpO	−110.8	−165.7	−252.7	−155.3	
(**1**) *cis*-$PtCl_2$(HmtpO)(NH_3)	−112.7 (−1.9)	−257.3 (−91.6)	−251.3 (+1.4)	−157.8 (−2.5)	−2116 (−492)
(**2a**) *cis*-$PtCl_2(HmtpO)_2 \cdot H_2O$	−112.1 (−1.3)	−257.8 (−92.1)	−253.5 (+0.8)	−157.9 (−2.6)	−2089 (−465)

[a] The ^{195}Pt NMR values in parentheses exhibit the chemical shift related to K_2PtCl_4 ($\delta = -1624$ ppm).

reported in the literature for complexes containing amines. This chemical shift range was also observed for other PtN_2Cl_2 chromophore systems [30–32]. In case of Pt(II) complexes containing amines the chemical shifts of ^{195}Pt were noted at: −2188 ppm (Me_2NH), −2224 ppm (*i*-$PrNH_2$), −2104 ppm (NH_3), −2184 ppm (1-adamantanamine), −2235 ppm (cyclobutyloamine) (in dmf-d_7) [33], whereas for *cis*-pyridine derivatives the chemical shifts were between −1998––2021 ppm (in $CDCl_3$) [34]. However, the resonances for the complexes with triazolopyrimidine derivatives are observed at lower field than those reported in the literature for complexes containing aromatic amines. The low field shift of ^{195}Pt signals can be related to a smaller σ electron donation effect in triazolopyrimidine ligands than in aliphatic amines complexes. This phenomenon can cause a reduction of electron density on the Pt(II) nuclei, resulting in its deshielding and larger ^{195}Pt signal coordination shift.

3.2. IR spectra

Absorption bands of ν(C=O) stretching vibrations at 1724 (**1**), 1709 (**2a**), 1714 cm^{-1} (**3**) upon coordination were shifted towards higher frequencies (max. 23 cm^{-1}). In addition, the two most characteristic bands of pyrimidine and imidazole ring skeleton vibrations after coordination appeared at higher frequencies by 18–30 cm^{-1} and 11–19 cm^{-1}, respectively. A similar effect has been already found for other complexes with N(3) coordinated triazolopyrimidine derivatives [13,14,20].

Table 4
Selected bond lengths (Å) and angles (°) for *cis*-$PtCl_2(NH_3)$(HmtpO) (**1**) and *cis*-$PtCl_2(HmtpO)_2 \cdot 4H_2O$ (**2b**)

Bond/angle	**1**	**2b** Ligand I	**2b** Ligand II
Pt(1)–N(3)	2.022(4)	2.059(8)	2.052(9)
Pt(1)–N(21)	2.029(5)		
Pt(1)–Cl(1)	2.2667(15)	2.276(3)	
Pt(1)–Cl(2)	2.2971(16)	2.290(3)	
C(2)–N(3)	1.355(7)	1.355(14)	1.350(13)
N(3)–C(3A)	1.323(6)	1.293(13)	1.286(12)
N(3)–Pt(1)–N(21)	91.7(2)	92.2(3)	
N(3)–Pt(1)–Cl(1)	176.13(13)	178.9(2)	87.6(2)
N(21)–Pt(1)–Cl(1)	87.30(16)		
N(3)–Pt(1)–Cl(2)	89.57(14)	87.8(3)	179.3(2)
N(21)–Pt(1)–Cl(2)	177.49(16)		
Cl(1)–Pt(1)–Cl(2)	91.60(7)	92.30(14)	
C(3A)–N(3)–Pt(1)	129.7(3)	124.3(8)	127.7(7)
C(2)–N(3)–Pt(1)	125.6(3)	126.8(8)	124.9(7)

In the spectrum of **3**, two new intensive absorption bands were detected at 1135 and 1024 cm^{-1}, which can be assigned to ρ_{CH3} rocking vibrations and ν_{SO} stretching vibration, respectively [22,35]. Similar bands were noted in the spectra of *trans*- and *cis*-$PtCl_2$(thiazole)(dmso) where S-bonded dmso was postulated (1150 and 1140 cm^{-1}, respectively) [29,36]. Recently, we have found a ν_{SO} band in the spectra of *trans*-$PtCl_2$(dmso)L complexes (L = 1,2,4-triazolo[1,5-*a*]pyrimidine or its 5,7-disubstituted derivatives), at similar frequencies (1142–1147 cm^{-1}) [14].

From group theory calculations, for a C_{2v} coordination sphere geometry ($PtCl_2N_2$) two of each stretching vibrations of Pt–Cl and Pt–N should of A_1 and B_1 type, all active in IR spectra. Far-IR spectra of complexes **1**–**3** exhibit one broad band of medium intensity, which can be assigned to Pt–Cl vibrations (A_1) (332–342 cm^{-1}). In the spectra of **1** and **2a** the second band appeared as a shoulder, due to coincidence with the ligand normal oscillations. However, the frequencies of the ν(Pt–Cl) bands in the spectra of the studied complexes were in the range characteristic for the *cis* geometry. In the case of platinum(II) complexes with HmtpO one broad band was reported at 330 cm^{-1} [13]. Similar complexes with 1-(2-aminophenyl)isoquinoline derivatives exhibit the band in the range 328–335 cm^{-1} [7], whereas those with substituted benzimidazole derivatives between 337 and 312 cm^{-1}, which is consistent with the values reported in this work [37].

3.3. Crystal structure of *cis*-$PtCl_2(NH_3)$(HmtpO) (**1**)

The crystal structure of **1** is formed by *cis*-$PtCl_2(NH_3)$-(HmtpO) units. The atom numbering scheme of **1** is shown in Fig. 2.

The coordination sphere of **1** is formed by the ammine and HmtpO ligand bonded in *cis* positions and two chloro ligands. The rms deviation of the atoms from the best PtN_2Cl_2 plane is 0.05 Å. The HmtpO ligand is coordinated via the N(3) atom, the Pt–N distance being 2.022(4) Å. The ammonia N(21) atom forms a 2.029(5) Å bond to platinum(II). The chloro ligands form Pt–Cl(1) and Pt–Cl(2) bonds of 2.267(2) and 2.297(2) Å, respectively, as expected for such bonds. The slight elongation of Pt–Cl2 might result from the *trans* influence of the ammine ligand and the steric effect of the HmtpO ligand being stronger than that of the ammine ligand. That conclusion is supported by the observed value of the N(3)–Pt(1)–Cl(2) angle 89.6(1)°, slightly larger than that of 87.3(2)° found for N(21)–Pt(1)–Cl(1).

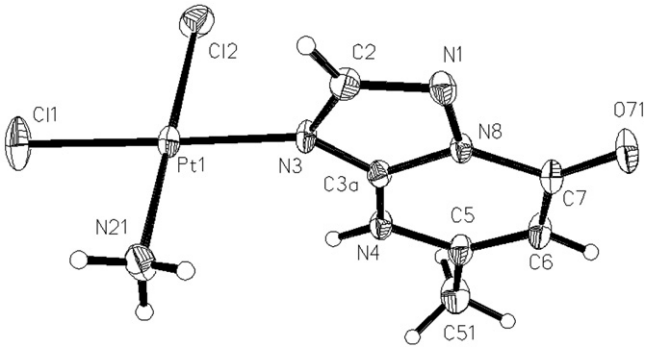


Fig. 2. Molecular structure of compound **1** as determined from X-ray diffraction data.

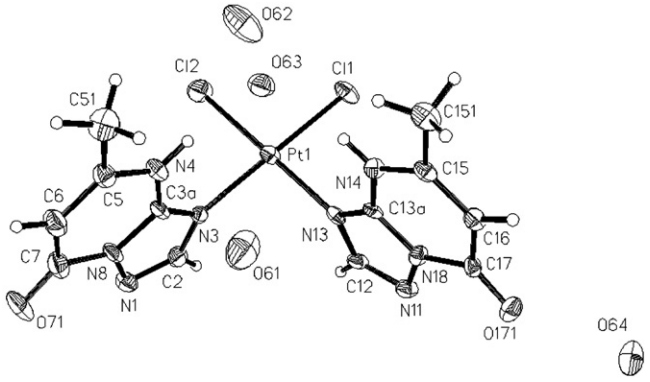


Fig. 3. Molecular structure of compound **2b** as determined from X-ray diffraction data.

The HmtpO ligand is planar, the rms deviation of the atoms from the best plane is 0.0127 Å. However, there is a slight bend of the ring system along the N(8)–C(3a) bond, the angle between the triazole ring and pyrimidine ring planes being 1.1(4)°. The HmtpO ring system is almost perpendicular to the PtN_2Cl_2 plane, the dihedral angle being 88.97°.

The intermolecular interactions in the crystal lattice include a network of hydrogen bonds formed by all donor N–H groups of the ligands. The ammine ligand N(21) forms H-bonds to Cl(2) $[-x+1, y+1/2, -z+3/2]$, O(71) $[x+1, y, z]$ and Cl(1) $[x, -y+1/2, z+1/2]$ atoms (N···Cl/O distances of 3.430, 3.103 and 3.244 Å, respectively). N(1)–H participates in the 2.904 Å contact with N(4) $[x, -y+1/2, z+1/2]$. The C(2)–H and C(6)–H groups form almost linear interactions to chloride ions, C(2)···Cl(2) $[1-x, -y, 2-z]$ and C(6)–H(6A)···Cl(2) $[-x, 0.5+y, 1.5-z]$ being 3.579(6) and 3.551(6) Å, respectively. The corresponding H(2A)···Cl(2) and H(6A)···Cl(2) distances are 2.67 and 2.64 Å, while the C(2)–H(2A)···Cl(2) and C(6)–H(6A)···Cl(2) angles are 165.9° and 167.5°, respectively. Such C–H···Cl interactions have been reported for other complexes of 1,2,4-triazolo-[1,5-*a*]pyrimidines [14] and indicate the significant polarization of these C–H bonds.

3.4. Crystal structure of *cis*-$PtCl_2(HmtpO)_2 \cdot 4H_2O$ (**2b**)

Cis-$PtCl_2(HmtpO)_2 \cdot 4H_2O$ molecules form the crystal structure of **2b**. The atom numbering scheme is shown in Fig. 3.

The structure of the new form of *cis*-$[PtCl_2(HmtpO)_2] \cdot 4H_2O$ (**2b**) was solved in the triclinic $P\bar{1}$ space group. A similar X-ray structure of $[PtCl_2(HmtpO)_2]$ dihydrate was solved in the monoclinic $P2_1/c$ space group with poor diffraction data [13]. However, the authors reported problems with the refinement of the second HmtpO ligand and explained the poor data quality by crystal dehydration during the experiment. Analysis of that paper revealed that one of the HmtpO ligands had a significant disorder, which resulted in its isotropic refinement and large values of the reported atomic displacement parameters, being 5 times the average value for the other HmtpO ligand. Also, authors commented that the poor quality data did not allowed any discussion of the ligand geometry [13]. Therefore, we decided to re-determine the structure of **2b** because of its biological significance and compare it with the structure of **1**. The crystal of **2b** was taken out from the solution and immediately mounted on the diffractometer for a fast experiment with the CCD detector. The reported structure contains four independent water molecules, two of which reveal slightly larger atomic displacement parameters than the other two. That might indicate the ability of the crystal to partially dehydrate and also a possible change of the lattice symmetry. However, the analysis of the experiment does not reveal the possible choice of the monoclinic cell corresponding to the dihydrated complex [13]. Furthermore, the quality of the new triclinic form of the hydrated *cis*-$[PtCl_2(HmtpO)_2] \cdot 4H_2O$ structure (**2b**) reported here is much better than that of the monoclinic form determined by the other authors [13]. Partial dehydration would be consistent with the difficulties of getting high quality diffraction data, we tried several crystals (with relatively high R_{int}), as reported by the other group [13].

Similar to the lower quality complex structure, the coordination sphere is formed by two *cis* chloride ions and two HmtpO ligands bonded to the Pt atom via N(3) atoms [13]. The Pt(1)–Cl(1) and Pt(1)–Cl(2) distances observed in **2b** are 2.276(3) and 2.290(3) Å, respectively and are similar to the analogous distances in complex **1**. The Pt(1)–N(3) and Pt(1)–N(13) distances are 2.059(8) and 2.052(9) Å, respectively and are slightly longer than those found in **1**. The HmtpO ligands are oriented in the same way with respect to the chloride ligands (Fig. 3). Such a position results from the pair of H-bonds formed by the N(4)–H groups to water O(63).

The HmtpO ligands are planar, the rms deviation of the atoms from the best plane is 0.013 and 0.019 Å for the N(1)–N(8) and N(11)–N(18) ligands, respectively. The dihedral angle between the best planes of these two ligands is 70.3(2)°. The corresponding value reported for the

Table 5
Structural differences between mononuclear Pt(II) complexes with triazolopyrimidines

Compounds	Bond distances (Å)		Angles (°)		Ref.
	Pt–N(3)	Pt–Cl	L–Pt–N(3)	Pt–N(3)–C(3A)	
cis-$PtCl_2(HmtpO)_2 \cdot 2H_2O$	2.00(2) 1.98(2)	2.278 (6) 2.274(8)	91.7(4) 89.7(7) 178.5(6) 177.3(4)	129(1) 130(2)	[13]
cis-$[Pt(NH_3)_2(HmtpO)_2](NO_3)_2 \cdot 2H_2O$	2.018(8) 2.012(8)		88.0(3) 90.9(3) 90.6(3) 90.7(3) 176.6(3) 176.3(3)	127.0(6) 129.5(7)	[25]
trans-$PtCl_2$(dmtp)(dmso)	2.048(5)	2.295(2) 2.303(2)	87.63(15) 89.2(2) 176.9(2)	[a]	[14]

[a] Data unavailable.

monoclinic form [13] was 79.8°, and has been strongly affected by the reported HmtpO ring disorder. The dihedral angles formed between the coordination PtN_2Cl_2 plane and HmtpO ring systems are 82.0(2) and 73.4(2)° for N(1)–N(8) and N(11)–N(18) ligands, respectively. The bend of the HmtpO ring system along the N(8)–C(3a) bond is similar to that detected in **1**. The dihedral angle between the triazole ring and pyrimidine ring planes are 1.2(8) and 2.2(6)° for N(1)–N(8) and N(11)–N(18) ring systems.

The intermolecular interactions include the network of H-bonds formed by N(1)–H(1A)···O(64) $[-x-1,-y,-z+1]$, N(4)–H(4A)···O(63) and N(14)–H(14A)···O(63), the corresponding N···O distances being 3.025(2), 2.788(2) and 2.854(2) Å. The water molecules also interact with other waters and chloride ions, although lack of hydrogen atoms in the model does not allow a discussion of the details of those interactions. One C–H···Cl interaction was found, that is analogous to those described for **1**. That is C(12)–H(12A)···Cl(1) $[-x,-y,1-z]$ with a C···Cl distance of 3.693(11) Å and C–H···Cl angle of 173.2°. The series of stacking interactions between the ring systems of the neighboring molecules complete the packing interactions.

Table 5 presents the main structural differences between known mononuclear Pt(II) complexes with triazolopyrimidines. Careful interpretation has shown that the Pt–N and Pt–Cl distances are not significantly different, but the Pt–N bond seems slightly longer when it is in a *trans* position to the chloro ligands. These results indicate that the *trans* influence of the chloro and triazolopyrimidine ligands is very similar and it might be greater for chloro ligands. However, more X-ray data are needed to determine with a bigger probability that the *trans* impact of the chloro ligands is larger than the influence of the heterocyclic ligands.

3.5. Cytotoxic activity

Many transition metals complexes with triazolopyrimidines show significant antitumor activity [13,20]. We have observed high activity of similar platinum(II) complexes with analogs of HmtpO (e.g 5,7-diphenyl-1,2,4-triazolo[1,5-*a*]pyrimidine (dptp) and 5,7-diterbutyl-1,2,4-triazolo[1,5-*a*]pyrimidine (dbtp) [20]). The in vitro antiproliferative activity of the studied platinum compounds **1**, **2a** was determined against two human cell lines: T47D (breast cancer) and HCV29T (bladder cancer). However, the obtained results indicate that studied platinum complexes are not cytotoxic in the concentration range 0.1–100 μg/ml.

4. Conclusion

The molecular structure and antiproliferative activity in vitro of mononuclear platinum(II) complexes with HmtpO were studied. The observed coordination mode via N(3) may be regarded as representative for triazolopyrimidines and analogous to N(9) complexation in purine. The crystal structures of **1**, **2b** indicate that the Pt(II) ion has a square planar geometry with N(3) bonded HmtpO, N-bonded second ligand (NH_3 (**1**) and HmtpO (**2b**)) and two *cis* chloride anions.

The results of the human cancer cell lines treatment with the new platinum(II) complexes confirm lower cytotoxicity of these compounds than cisplatinum in the concentration range 0.1–100 μg/ml.

5. Supplementary material

CCDC 276404 and 276405 contain the supplementary crystallographic data for **1** and **2b**. These data can be obtained free of charge via http://www.ccdc.cam.ac.uk/conts/retrieving.html, or from the Cambridge Crystallographic Data Centre, 12 Union Road, Cambridge CB2 1EZ, UK; fax: (+44) 1223-336-033; or e-mail: deposit@ccdc.cam.ac.uk.

Acknowledgment

Financial support from Polish Committee for Scientific Research (KBN) Grant No 4 T09A 11623 is gratefully acknowledged.

References

[1] P.J. O'Dwyer, J.P. Stevenson, S.W. Johnson, in: B. Lippert (Ed.), Cisplatin in Chemistry and Biochemistry of a Leading Anticancer Drug, Wiley-VCH, Weinheim, 1999, p. 31.
[2] J. Reedijk, Chem. Rev. 99 (1999) 2499.
[3] E.R. Jamiesion, S.J. Lippard, Chem. Rev. 99 (1999) 2467.
[4] L.R. Kelland, in: B. Lippert (Ed.), Cisplatin in Chemistry and Biochemistry of a Leading Anticancer Drug, Wiley-VCH, Weinheim, 1999, p. 498.
[5] K.A. Skov, H. Adomat, M. Doedee, M. Farrell, Anti-Cancer Drug Des. 9 (1994) 103.

[6] N. Farrell, T.B.T. Ha, J.P. Souchard, F.L. Wimmer, S. Cros, N.P. Johnson, J. Med. Chem. 32 (1989) 2240.
[7] F. von Nussbaum, B. Miller, S. Wild, Ch.S. Hilger, S. Schumann, H. Zorbas, W. Beck, W. Steglich, J. Med. Chem. 42 (1999) 3478.
[8] G. Fischer, Z. Chem. 30 (1990) 305.
[9] G. Fischer, Adv. Het. Chem. 57 (1993) 81.
[10] J.A.R. Navarro, M.A. Romero, J.M. Salas, M. Quirós, E.R.T. Tiekink, Inorg. Chem. 36 (1997) 4988.
[11] M.A. Haj, M. Quiros, J.M. Salas, R. Fure, Inorg. Chem. Commun. 4 (2001) 254.
[12] A.H. Velders, F. Ugozzoli, M. Biagini-Cingi, A.M. Montti-Lanfredi, J.G. Haasnoot, J. Reedijk, Eur. J. Inorg. Chem. 2 (1999) 213.
[13] J.A.R. Navarro, J.M. Salas, M.A. Romero, R. Vilaplana, F. Gonzáles-Vilchez, R. Faure, J. Med. Chem. 41 (1998) 332.
[14] E. Szłyk, I. Łakomska, A. Surdykowski, T. Głowiak, L. Pazderski, J. Sitkowski, L. Kozerski, Inorg. Chim. Acta 333 (2002) 93.
[15] K. Akdi, R.A. Vilaplana, S. Kamah, J.A.R. Navarro, J.M. Salas, F. Gonzalez-Vilchez, J. Inorg. Biochem. 90 (2002) 51.
[16] J.A.R. Navarro, M.A. Romero, J.M. Salas, R. Faure, X. Solans, J. Chem. Soc., Dalton Trans. 6 (1997) 1001.
[17] S. Orihuela, M.P. Sanchez, M. Quiros, D. Martin, R. Faure, Polyhedron 17 (1998) 2477.
[18] F. Luque, C. Fernández-Ramos, E. Entrala, M.J. Rosales, M.C. Salas, J. Navarro, M. Sánchez-Moreno, Toxicol. in Vitro 14 (2000) 487.
[19] F. Luque, C. Fernández-Ramos, E. Entrala, M.J. Rosales, J.A. Navarro, M.A. Romero, J.M. Salas, M. Sánchez-Moreno, Comp. Biochem. Physiol. C 126 (2000) 39.
[20] I. Łakomska, E. Szłyk, J. Sitkowski, L. Kozerski, J. Wietrzyk, M. Pełczyńska, A. Nasulewicz, A. Opolski, J. Inorg. Biochem. 98 (2004) 167.
[21] M.A. Romero, J.M. Salas, M. Quiros, D.J. Williams, J. Molina, Transition Met. Chem. 18 (1993) 595.
[22] J.H. Price, A.S. Williamson, R.S. Schramm, B.B. Wayland, Inorg. Chem. 11 (1972) 1280.
[23] E.G. Tolman, W. Brüning, J. Reedijk, A.S. Spek, N. Veldman, Inorg. Chem. 36 (1997) 854.
[24] G.M. Sheldrick, T.M. Schneider, Methods Enzymol. B 277 (1997) 319.
[25] J.A.R. Navarro, M.A. Romero, J.M. Salas, M. Quiros, Inorg. Chem. 36 (1997) 3277.
[26] M. van Beusichem, N. Farrell, Inorg. Chem. 31 (1992) 634.
[27] G. Annibale, M. Bonivento, L. Cattalini, M.L. Tobe, J. Chem. Soc., Dalton Trans. 24 (1992) 3433.
[28] C. Sacht, M.S. Datt, S. Otto, A. Roodt, J. Chem. Soc., Dalton Trans. 5 (2000) 727.
[29] O. Clement, A.W. Roszak, E. Buncel, Inorg. Chim. Acta 253 (1996) 53.
[30] P.S. Pregosin, Coord. Chem. Rev. 44 (1982) 247.
[31] P.S. Pregosin, Transitions Metal Nuclear Magnetic Resonance, Elsevier, Amsterdam, 1991, p. 217.
[32] F.D. Rochon, A. Morneau, Magn. Res. Chem. 29 (1991) 120.
[33] F.D. Rochon, M. Doyon, I.S. Butler, Inorg. Chem. 32 (1993) 2717.
[34] Ch. Tessier, F.D. Rochon, Inorg. Chim. Acta 295 (1999) 25.
[35] F.A. Cotton, R. Francis, W.D. Horrocks, J. Chem. Soc. 64 (1960) 1534.
[36] A. Corina, A.C. Fabretti, M. Bonivent, L. Cattalini, Inorg. Chim. Acta 255 (1997) 405.
[37] F. Gümüş, I. Pamuk, T. Özden, S. Yildiz, N. Diril, E. Öksüzoğlu, S. Gür, A. Özkul, J. Inorg. Biochem. 94 (2003) 255.

Available online at www.sciencedirect.com
ScienceDirect
Polyhedron 26 (2007) 811–817
POLYHEDRON
www.elsevier.com/locate/poly

Nickel(II) complexes of oligopeptides containing aspartyl and glutamyl residues. Potentiometric and spectroscopic studies

Csilla Kállay, Imre Sóvágó, Katalin Várnagy *

Department of Inorganic and Analytical Chemistry, University of Debrecen, H-4010 Debrecen, Hungary

Received 16 August 2006; accepted 8 September 2006
Available online 26 September 2006

Abstract

Nickel(II) complexes of di-, tri- and tetra-peptides built up from Asp and/or Glu residues have been studied by potentiometric, UV–Vis and circular dichroism spectroscopic methods. The stoichiometry of the complexes are the same as in the case of common oligopeptides, but the presence of the side chain carboxylate groups results in differences in their stabilities and coordination modes. The presence of the β-carboxylate groups increases the metal binding affinity of the peptides in all cases. This is due to the coordination of the first, second and third aspartic acid residue in the case of the NiL, $NiH_{-1}L$ and $NiH_{-2}L$ complexes, respectively. The high negative charge of Asp_4 suppresses the metal ion coordination of the third amide function, therefore the $NiH_{-3}L$ complex does not form with this tetrapeptide. In the case of peptides containing glutamic acid, no stability enhancement appears because there is only a weak interaction between the nickel(II) ion and the γ-carboxylate group, which is not able to compensate the disfavoured effect of the increasing negative charge of the complexes.
© 2006 Elsevier Ltd. All rights reserved.

Keywords: Aspartic acid; Glutamic acid; Peptides; Nickel(II); Stability constants

1. Introduction

Nickel is an essential element for many bacteria, plants and probably plays role in the metabolism of higher organisms. Although a deficiency disease for nickel in humans has not been identified, there is substantial evidence for the essential status of nickel [1]. On the other hand, nickel(II) ion is one the most frequent causes of allergic contact dermatitis (ACD) [2]. Dermatitis may be persistent in certain occupations and can result in sick leave or even an inability to work [3]. The initial step of antigen formation in ACD is commonly considered to be a covalent binding of an electrophilic hapten with the nucleophilic residue of proteins or other molecules in the skin [4]. Nickel ions have been shown to dissolve in sweat [5], and in contrast to classical haptens, metal ions do not form stable covalent protein modifications. They are rather known to produce geometrically highly defined coordination complexes with four or six donor atoms such as nitrogen or oxygen in amino acid side chains of appropriate proteins or peptides. Formation of these complexes is reversible and allows the exchange of the allergenic metal ions between different acceptor sites [6,7]. The most common oxygen donor groups in the side chain are the carboxylate groups of aspartic or glutamic acid residues, moreover the aspartic acid residue is part of the active site of biologically significant substances, such as thymopoietin, fibrinopeptide A, angiotensin II, Cu,Zn-superoxide dismutase and transketolase enzymes. Studies of tri-, tetra- and penta-peptides mimicking the active site of these biomolecules demonstrated the important role of the side chain carboxylate groups [8–16].

In our previous paper [17], equilibrium and spectroscopic results on the copper(II) complexes of di-, tri- and tetra-peptides built up from Asp and/or Glu residues

* Corresponding author. Tel.: +36 52512900; fax: +36 52489667.
E-mail address: varnagy@tigris.unideb.hu (K. Várnagy).

0277-5387/$ - see front matter © 2006 Elsevier Ltd. All rights reserved.
doi:10.1016/j.poly.2006.09.014

were studied. In accordance with expectations, it was found that the presence of two to five carboxylate functions generally results in enhanced metal binding ability of the ligands and it is especially true for the oligopeptides of aspartic acid. The presence of N-terminal aspartic acid enhances the stability of CuL with a β-alanine-like (NH_2,β-COO^-) coordination mode. In the case of AspAsp (Asp_2) and AspAspAsp (Asp_3) the (NH_2,N^-,β-COO^-) and (NH_2,N^-,N^-,β-COO^-) coordination modes will be favoured, which contain (5,6) and (5,5,6)-joined chelate ring systems, respectively. The outstanding stability of the latter binding mode and the high negative charge of the corresponding species suppress metal ion coordination of the third amide function of AspAsp-AspAsp (Asp_4).

Less data on the nickel(II) complexes of aspartic acid containing peptides is available. The results obtained from studies on nickel(II) complexes of tri- and tetra-peptide segments of thymopoietin (ArgLysAspVal, ArgLysAsp and ArgLys(Arg)Asp) [9] as well as Asp-AspAsp and a series of tetra-peptides containing one or two Asp or one Glu residue [18] were reported. These results reveal that similarly to copper(II) complexes, the β-carboxylate group of the Asp residue enhances the stability of the complexes, especially for peptides containing Asp on the N-termini. These ligands are coordinated tridentately to nickel(II) ions resulting in formation of octahedral NiL complexes at a lower pH range and NiL_2 for excess of ligands. The formation of the $NiH_{-1}L$ complex is considerable only for tetra-peptides containing the Asp residue in the second position. In other cases its amount is not significant or it is not detectable because of the cooperative deprotonation of the amide nitrogens. The cooperativity is especially high for tri- or tetra-peptides containing Asp in the third position. The formation of a stable $NiH_{-2}L$ complex with (NH_2,N^-,N^-,β-COO^-) coordination hinders the deprotonation of the third amide. The appearance of $NiH_{-3}L$ was not observed in the nickel(II)–thymopoietin segments systems [9], although its formation is supposed above pH 9 (about 0.5 log unit higher pH compared to the nickel(II)–tetraalanine [11] system) for the tetra-peptides containing one or two aspartic residues [18]. The presence of a side chain carboxylate group of glutamic acid, however, has a much smaller effect on the complex formation processes; they are very similar to those of tetraalanine.

In this paper we report the results obtained from the systematic investigations of nickel(II)-complexes of di-, tri- and tetra-peptides containing two or more aspartic and/or glutamic acids (Asp_2, Glu_2, AspGlu, GluAsp, Asp_3, Glu_3, Asp_4) by potentiometric, UV–Vis and circular dichroism (CD) spectroscopic techniques. Our goal was to study the influence of β- and γ-carboxylate groups as well as the effect of increased negative charge of the ligands on the complex formation processes of nickel(II)–ligand systems.

2. Experimental

2.1. Materials

The peptides AspGlu, GluAsp, Asp_2, Glu_2, Asp_3, Glu_3, Asp_4 and Ala_3 were purchased from Bachem and their purities checked by TLC (thin layer chromatography) and HPLC (high performance liquid chromatography) methods. Concentrations of the peptide stock solutions were determined by potentiometric titrations. A stock solution of nickel(II) chloride was prepared from analytical grade reagents and the concentration was checked gravimetrically *via* the precipitation of the oxinate.

2.2. Potentiometric studies

The pH-potentiometric titrations in the pH range 2.5–11.5 were performed on 3 cm^3 samples in the concentration range 2×10^{-3}–8×10^{-3} mol dm^{-3} at metal ion to ligand ratios ranging between 1:3 and 2:1. The measurements were made with a MOLSPIN pH meter equipped with a 6.0234.100 combined electrode (Metrohm) and a MOL-ACS microburette controlled by a computer.

The titrations were performed with a carbonate free stock solution of potassium hydroxide of known concentration. During the titration argon was bubbled through the samples to ensure the absence of oxygen and carbon dioxide, and to stir the solutions. All pH-potentiometric measurements were carried out at a constant ionic strength of 0.2 M KCl and at a constant temperature (298 K). The number of experimental points reached around 50–70 data (cm^3 – pH) for each titration curve. The pH readings were converted into hydrogen ion concentration as described earlier [19]. Protonation constants of the ligands and the overall stability constants ($\log\beta_{pqr}$) of the complexes were calculated by means of general computational programs, PSEQUAD [20] and SUPERQUAD [21], using Eqs. (1) and (2).

$$pM + qH + rL \rightleftharpoons M_pH_qL_r \quad (1)$$

$$\beta_{pqr} = \frac{[M_pH_qL_r]}{[M]^p[H]^q[L]^r} \quad (2)$$

2.3. Spectroscopic measurements

UV–Vis spectra of the nickel(II) complexes were recorded on a Hewlett Packard HP 8453 diode array and on a Perkin–Elmer Lambda 25 double beam spectrophotometer in the same concentration range as used for pH-potentiometry.

CD spectra of the nickel(II) complexes were recorded on a JASCO J-81 spectropolarimeter using 1 or 10 mm cells in the 200–800 nm range in the same concentration range as used for potentiometry. CD spectra of the individual species were calculated by the same general program

(PSEQUAD) as used for the evaluation of potentiometric measurements.

3. Results and discussion

3.1. Acid–base properties of the ligands

All the ligands contain one amino and two to five carboxylate donor functions. The pK values of the ligands [17] and the stability constants of the corresponding nickel(II) complexes are collected in Tables 1 and 2. The complexes with the same stoichiometry have different charges; therefore the charges are not shown.

The highest pK values belong to the protonation equilibria of the terminal amino groups, while the lowest and intermediate values correspond to the protonation of the terminal and side chain carboxylate donor functions, respectively [17].

3.2. Nickel(II) complexes of the dipeptides

It can be seen from Tables 1 and 2 that mostly 1:1 complexes are formed, some bis(ligand) complexes exist only with the dipeptides. The stoichiometry of the complexes formed in the Ni(II)–Asp_2 and Ni(II)–Gly_2 systems is the same, the only difference is the formation of the protonated NiLH species in the first case. The coordination modes of the complexes, however, are different. The NiL and NiL_2 complexes of Gly_2 contain (NH_2,CO) coordination modes in 5-membered chelates, while Asp_2 is able to coordinate as a tridentate ligand in the same complexes. The β-carboxylate group of the first Asp residue can be involved in the coordination beside the amino and carbonyl functions both in the NiL and NiL_2 complexes, resulting in the higher stability of these complexes for Asp_2. The visible absorption spectra support the octahedral geometry showing three absorption maxima at 380, 630, 1050 and at 370, 610, 980 nm for the NiL and NiL_2 complexes of Asp_2, respectively.

The amino acid like coordination favours the deprotonation of the amino nitrogen, therefore these complexes form not only in higher concentrations, but also at lower pH (see Fig. 1). A similar effect of the aspartic acid residue on the N-termini was observed for tetra-peptides AspAlaAlaAla, AspAlaAlaAsp [18] and AspArgValTyr [12]. The higher stability of [NiL] complexes is reflected in the higher values of $\log\beta[\mathrm{NiL}] - \mathrm{p}K_{\mathrm{amino}}$ compared to other dipeptides, on the other hand the higher $\log(K_1/K_2)$ (Table 1) values of AspAsp and AspGlu also support the enhancement of stability of the mono(ligand) complexes, hindering the coordination of a second ligand to form bis(ligand) complexes.

An increase of pH results in the formation of the species $NiH_{-1}L$ above pH 8. The coordination mode is (NH_2,N^-,COO^-) in both cases, but in the case of Asp_2 beside or instead of the C-terminal carboxylate group, the β-carboxylate group of the second aspartic acid residue can be coordinated, increasing the stability of the complex. On the other hand, the amino acid like coordination in the NiL complex hinders the deprotonation of the amide nitrogen. These two effects probably compensate each other, thus there is no difference in the pK_1(amide) values of the two ligands Asp_2 and Gly_2. However, the deprotonation of amide nitrogens in the bis(ligand) complexes of Asp_2 is shifted to a higher pH range (see pK(NiL_2/$NiH_{-1}L_2$) and pK($NiH_{-1}L_2$/$NiH_{-2}L_2$) values in Table 1).

Table 1
Protonation [17] and stability constants ($\log\beta_{pqr}$) of the nickel(II) complexes of dipeptides containing Asp and/or Glu residues ($T = 298$ K; $I = 0.2$ M KCl)

	AspAsp	GluGlu	AspGlu	GluAsp	GlyGly [22]
HL	8.11	8.05	8.03	8.10	8.13
H_2L	12.50	12.62	12.49	12.65	11.30
H_3L	15.87	17.19	15.92	16.48	
H_4L	18.45	20.10	18.59	19.32	
pK_1	2.58	2.91	2.67	2.84	3.17
pK_2	3.37	3.88	3.43	3.83	8.13
pK_3	4.39	4.57	4.46	4.55	
pK_4	8.11	8.05	8.03	8.10	
NiHL	10.08(1)		10.09(4)	9.85(8)	
NiL	5.58(1)	3.82(1)	5.49(1)	4.11(3)	3.96
$NiH_{-1}L$	−3.26(1)	−4.98(2)	−4.01(4)	−4.16(2)	−4.91
NiL_2	9.12(2)	6.03(12)	9.15(3)		7.16
$NiH_{-1}L_2$	−1.21(9)				−2.51
$NiH_{-2}L_2$	−11.95(2)			−12.56(4)	−11.99
pK_1(amide)	8.84	8.80	9.50	8.27	8.87
pK(NiL_2/$NiH_{-1}L_2$)	10.33				9.67
pK($NiH_{-1}L_2$/$NiH_{-2}L_2$)	10.74				9.48
$\lg K_1/K_2$(NiL_2)	2.04	1.61	1.83		0.76
$\lg K_1/K_2$($NiH_{-2}L_2$)	5.43				2.17
$\lg\beta$(NiL) − pK_{amino}	−2.53	−4.23	−2.50	−4.01	−4.17

Table 2
Protonation [17] and stability constants ($\log\beta_{pqr}$) of the nickel(II) complexes of tri- and tetra-peptides ($T = 298$ K; $I = 0.2$ M KCl)

	Asp_3	Glu_3	Asp_4	Gly_3 [22]	Gly_4 [23]	Ala_4 [11]
HL	8.06	8.02	8.15	7.93	7.97	8.13
H_2L	12.84	13.00	13.16	11.25	11.15	11.65
H_3L	16.76	17.29	17.55			
H_4L	20.01	21.14	21.41			
H_5L	22.54	24.18	24.66			
H_6L			27.35			
pK_1	2.53	3.04	2.69	3.32	3.18	3.52
pK_2	3.25	3.85	3.25	7.93	7.97	8.13
pK_3	3.92	4.29	3.86			
pK_4	4.78	4.98	4.39			
pK_5	8.06	8.02	5.01			
pK_6			8.15			
NiH_2L			15.23(6)			
NiHL	10.13(10)		10.84(3)			
NiL	5.29(3)	3.42(3)	5.69(2)	3.75	3.65	3.06
$NiH_{-1}L$	−2.92(4)	−4.70(4)	−2.63(3)	−5.45	−4.45	−4.97
$NiH_{-2}L$	−11.87(4)	−12.31(2)	−10.79(2)	−12.85		
$NiH_{-3}L$					−20.90	−21.29
NiL_2				6.77		
pK_1(amide)	8.21	8.12	8.32	9.20	8.10	8.03
pK_2(amide)	8.95	7.61	8.16	7.40	8.23	8.16
pK_3(amide)					8.23	8.16
$\lg K_1/K_2(NiL_2)$				0.73		
$\lg\beta(NiL) - pK_{amino}$	−2.77	−4.60	−2.46	−4.18	−4.32	−5.07

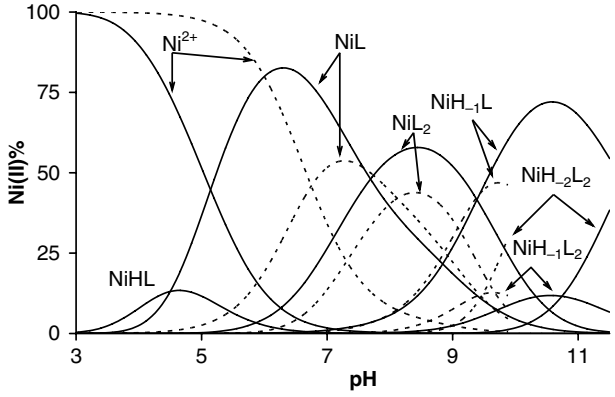


Fig. 1. Species distribution of the complexes formed in the nickel(II)–Asp_2 system (solid line; $c_{Ni(II)} = 2\times10^{-3}$ M. $c_L = 4\times10^{-3}$ M) as a function of pH. Dotted lines are for complexes with Gly_2 ($c_{Ni(II)} = 2\times10^{-3}$ M. $c_L = 4\times10^{-3}$ M).

Among these dipeptides, the complex formation of Glu_2 is the simplest. Only NiL, $NiH_{-1}L$ and NiL_2 complexes are formed, which is followed by precipitation above pH 9. The coordination mode is similar to Gly_2 complexes ((NH_2,CO), (NH_2,N^-,COO^-) and $2(NH_2,CO)$, respectively) but their stabilities are lower. This suggests that γ-carboxylate groups of Glu residues are not included in the complex formation, and the increased negative charge of the ligands even disfavours complex formation. As a consequence the deprotonation of the amide nitrogen for the NiL complex of Glu_2 occurs at a similar pH as in the case of Gly_2. The charges of the complexes $NiH_{-1}L_2$ and $NiH_{-2}L_2$ of Glu_2 would be −5 and −6, respectively, and there are no other factors to compensate this unfavourable effect. Therefore these complexes are not formed in the Ni(II)–Glu_2 system and precipitation occurs at a lower pH than in the case of Gly_2.

The metal binding affinity of AspGlu and GluAsp is between Asp_2 and Glu_2. It is well demonstrated in Fig. 2, where the metal binding ability of the four dipeptides built up from Asp and/or Glu residues is compared to that of Gly_2. We calculated the theoretical distribution of nickel(II) ions between Gly_2 and XaaYaa dipeptide

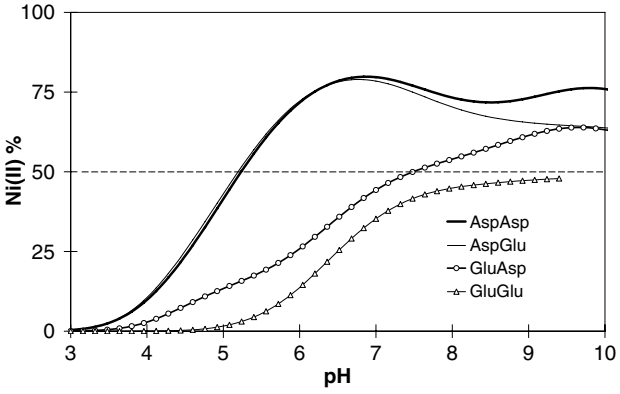


Fig. 2. The total amount of dipeptide complexes formed in the ternary systems containing Ni(II)–Gly_2 and one of the dipeptides of Asp_2, AspGlu, GluAsp and Glu_2 as a function of pH ($c_{Ni(II)} = c_{GlyGly} = c_B = 4.0\times10^{-3}$ M).

(Xaa = Asp or Glu, Yaa = Asp or Glu) and the total amount of complexes of XaaYaa dipeptides is depicted in Fig. 2. This figure unambiguously shows, that the stability enhancement for the species NiL (pH = 4–8.5) is highest and is almost the same for Asp_2 and AspGlu, which comes from the formation of the (NH_2,β-COO^-)-chelate at the N-terminus, as was discussed above. On the other hand, the high stability of (NH_2,N^-,β-COO^-) coordinated $NiH_{-1}L$ complexes resulted in the increase of the total amount of complexes of AspAsp and GluAsp at higher pH (pH = 8.5–10) because of the presence of aspartic acid residues on the C-termini. As a consequence, the metal binding affinity of AspGlu is similar to Asp_2 in the pH range 4–8.5, and decreases following the deprotonation of the amide nitrogen. The metal binding affinity of GluAsp is rather low in the acidic pH range, but increases with the deprotonation of the amide nitrogen, which could be promoted by the binding of the β-carboxylate group of the C-terminal Asp residue.

3.3. Nickel(II) complexes of Asp_3, Glu_3 and Asp_4

Complex formation of Asp_3 and Glu_3 is compared in Fig. 3. It can be seen that Asp_3 is a more effective metal binding ligand. Asp_3 is able to bind to nickel(II) below pH 4, resulting in the formation of the NiHL complex, in which one of the carboxylate groups is protonated. In the case of Glu_3, however, the complex formation processes start only above pH 5. It is clear from Table 2 that only 1:1 complexes are considered as the major species both in equimolar solution and in the presence of a slight excess of ligand. In contrast to earlier data [18] the formation of bis(ligand) complexes was not detected in these cases. These results can be explained by the high negative charge and the size of the ligands, which disfavours the bis(ligand) complex formation (the charge of the NiL_2 complex would be −6 for Asp_3, Glu_3 and −8 for Asp_4).

The fact that in the Ni(II)–Asp_3 system around physiological pH range 80% of the metal ion is bound in the species NiL, shows the enhanced stability of this complex. In the case of Glu_3 there is (NH_2,CO) coordination, while for Asp_3 (NH_2,β-COO^-) coordination is suggested. The latter "β-alanine" like coordination has a remarkable stabilizing effect. However, this coordination mode is not able to hinder the deprotonation of the first amide nitrogen, because the coordination of the second Asp residue is favoured. At the same time, the deprotonation of the second amide nitrogen is suppressed in the case of Asp_3. This process occurs at pH 8 in the Ni(II)–Glu_3 system and pH 9 in the Ni(II)–Asp_3 system. In the first case the species $NiH_{-1}L$ form only in a very low concentration, which indicates that the deprotonation and coordination of the amide nitrogens take place almost cooperatively. This is reflected in the pK_1(amide) and pK_2(amide) values too, which are similar to those of Gly_3 and Gly_4. However, the deprotonation of the two amide functions of Asp_3 takes place in well-separated processes. In this case the formation of $NiH_{-1}L$ is favoured owing to the coordination of the second β-carboxylate group and shifts the formation of the species $NiH_{-2}L$ to higher pH than in the Ni(II)–Glu_3 system. These findings are in good agreement with the earlier published data on similar peptide complexes [18].

It can be seen in Fig. 4, that the complex formation processes of Asp_4 are very similar to those of Asp_3. One more protonated species, NiH_2L, is also formed with this ligand, but all the others are the same regarding either their stoichiometries or coordination modes.

The deprotonation of the first and second amide functions of Asp_4 are less separated than those of Asp_3. Similar to the Cu(II) containing systems [17], the stabilizing role of the binding of β-carboxylate functions are lower because of the size of the ligand. Namely Asp_4 has altogether five carboxylate functions and four of them are present as non-coordinating side chains, loosening the binding strength in the $NiH_{-1}L$ species. Another important feature of the complex formation processes between Ni(II) and Asp_4 comes from the lack of deprotonation and coordination of the third amide function similarly to the Cu(II)–Asp_4 system. However, a notable difference between the copper(II) and nickel(II) containing systems can be concluded

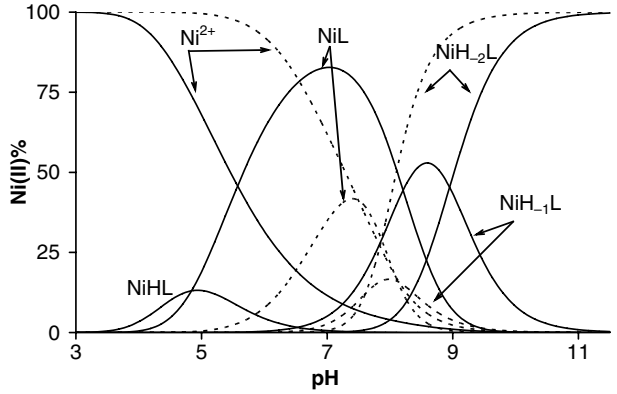


Fig. 3. Species distribution of the complexes formed in the nickel(II)–Asp_3 system (solid line; $c_{Ni(II)} = c_L = 4 \times 10^{-3}$ M) and in the nickel(II)–Glu_3 system (dotted line; $c_{Ni(II)} = c_L = 4 \times 10^{-3}$ M) as a function of pH.

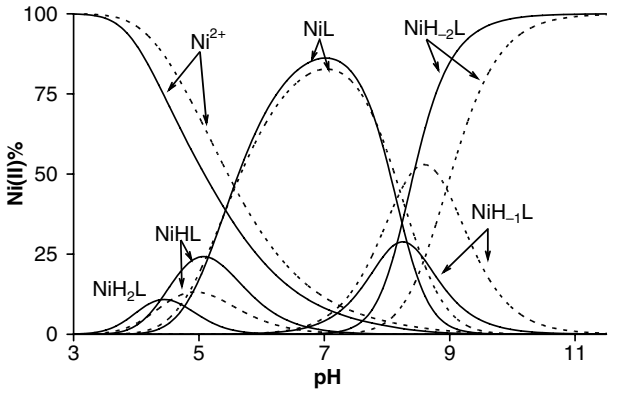


Fig. 4. Species distribution of the complexes formed in the nickel(II)–Asp_4 system (solid line; $c_{Ni(II)} = c_L = 4 \times 10^{-3}$ M) as a function of pH. Dotted lines are for complexes with Asp_3 ($c_{Ni(II)} = c_L = 4 \times 10^{-3}$ M).

from the literature data. In the case of Cu(II), all the tetra- and penta-peptides containing an aspartyl residue in the third position behave like tripeptides, the β-carboxylate group occupies the fourth coordination site of the metal ion and prevents the binding of the subsequent amino acid residues [8–10,24]. On the other hand, this was not observed for the Ni(II)-complexes of AlaAspAspAla, AlaAspAlaAsp and AlaAlaAspAsp. The deprotonation and coordination of the third amide function of these tetra-peptides, containing one or two aspartic acid residues take place, but at higher pH than in the case of Gly_4 [23] or Ala_4. The pK_3 values are 8.29 for AlaAlaAspAla and 9.65–9.70 for the peptides containing two aspartic acid residues [18]. These data demonstrate that the presence of a single aspartic acid in the second or/and third position is not able to prevent the deprotonation of the amide nitrogen and formation of $NiH_{-3}L$ species. On the other hand, the more aspartic acid residues present in the tetra-peptides the higher is the pK_3(amide). This means that the increasing negative charge of the ligand also disfavours the complex formation and $NiH_{-3}L$ does not form in the Ni(II)–Asp_4 system.

In acidic and neutral solution, similarly to the dipeptides, these ligands form octahedral complexes. However, the formation of the $NiH_{-2}L$ complexes is accompanied by significant changes in the visible absorption and CD spectra. The spectral parameters of $NiH_{-2}L$ species are collected in Table 3, and they indicate the square planar geometry of these Ni(II) complexes.

It is clear that the spectra of Asp_3 and Asp_4 are similar to each other, but they are completely different from those of Glu_3, Gly_3 or Ala_3. These similarities and differences can be best explained by the similarities and differences in the binding modes of the ligands. Namely, in the case of Glu_3 only the (NH_2,N^-,N^-,α-COO^-)-coordination mode can exists in the form of (5,5,5)-membered joined chelate rings, similarly to Gly_3. For Asp_4 the donor atoms are the same, but the C-terminal carboxylate could be replaced by the β-carboxylate residue in the form of a (5,5,6)-membered chelate. This results in the difference of CD extrema for the N^-(amide)–Ni(II) charge transfer transition and for the d–d transition both in the CD and visible absorption spectra. The similarity of the spectra of Asp_3 and Asp_4 reflects that for Asp_3 the (NH_2,N^-,N^-,β-COO^-)-coordination mode is preferred over the common "tripeptide like" coordination mode of $NiH_{-2}L$ complexes.

Table 3
Visible and CD spectral parameters of the $NiH_{-2}L$ complexes

Ligand	Vis $\lambda_{max}(\varepsilon)$ [nm(M^{-1} cm^{-1})]	CD $\lambda_{max}(\Delta\varepsilon)$ [nm(M^{-1} cm^{-1})]	
		$N^- \rightarrow$ Ni(II)	d–d
Asp_3	440(265)	232(−5.08)	492(−2.60) 422(+0.88)
Asp_4	438(229)	234(−12.19)	499(−2.10) 426(+1.55)
Glu_3	428(102)	249(+7.34)	474(−3.43)
Gly_3 [22]	427(197)		
Ala_3		248(+4.21)	473(−2.33)

4. Conclusion

The potentiometric and spectroscopic data obtained for nickel(II) complexes of di-, tri- and tetra-peptides containing two to four aspartic and/or glutamic acid residues reveal that side chain carboxylate functions have a significant impact on the complex formation processes of peptides. On the one hand the coordination of the β-carboxylate group enhances the stability of complexes and on the other hand the increase of negative charge of the ligands hinders, and moreover prevents, the formation of complexes characteristic of the nickel(II) common oligopeptide systems.

The presence of N-terminal aspartic acid enhances the stability of NiL complexes in all cases, and the tridentate binding of ligands results in complex formation processes at a lower pH range. The formation of bis(ligand) complexes is also significant for dipeptides (especially Asp_2, AspGlu), but in the case of larger tri- and tetra-peptides the existence of bis(ligand) complexes was not detected because of their high negative charges.

Aspartic acid in the second position stabilizes the $NiH_{-1}L$ complexes and the binding of the (NH_2,N^-,β-COO^-) donor set can be supposed. The presence of aspartic acid in the third position, however, promotes the deprotonation of the second amide nitrogen and formation of $NiH_{-2}L$ complexes. As a consequence, in the case of the ligands built up from aspartic acids alone, the effect of aspartic acid in the first, second and third position may compensate each other. It means that the deprotonation of the first amide nitrogen of Asp_2 takes place around the same pH as that of Glu_2 or Gly_2, and it is different from either AspGlu or GluAsp. Similarly, for Asp_3, the deprotonation of amide nitrogens occurs in well-separated steps, in contrast to Glu_3 and Gly_3 [22] or AlaAlaAspAla and AlaAspAspAla [18], where these processes are cooperative. In the case of Asp_4 the effect of the first aspartic acid is expressed in the enhanced stability of NiL complexes, but the second and third aspartic acid have smaller impact on the deprotonation processes of the amide nitrogens; the pK(amide) values are much closer to those of Gly_4 [23] or Ala_4 [11]. These latter facts are probably caused by an increase of negative charge of the ligand.

The high negative charge of the ligands influences above all the complex formation processes of tri- and tetra-peptides. These effects are as follows:

(i) Bis(ligand) complexes do not form in the case of Asp_3, Glu_3 and Asp_4 in contrast to Gly_3 and AspAlaAlaAla.
(ii) The stabilizing effect of the side chain carboxylate group is smaller for $NiH_{-1}L$ and $NiLH_{-2}$ complexes of Asp_4.

(iii) The deprotonation of the third amide nitrogen cannot be observed in the case of Asp_4, in contrast to Gly_4 and Ala_4 or tetra-peptides containing one or two aspartic acid.

Acknowledgement

This work was supported by the Hungarian Scientific Research Fund (Hungary, OTKA T048352, T042722).

References

[1] R.P. Hausinger, Biochemistry of Nickel, vol. 12, Plenum Press, New York, 1993.
[2] C. Lidén, J.E. Wahlberg, Acta Derm. Venereol. (Stockh.) 74 (1994) 341.
[3] T. Menné, E. Nieboer, Endeavour 13 (1989) 117.
[4] R.L. Baer, The mechanism of allergic contact hypersensitivity, in: A.A. Fisher (Ed.), Contact Dermatitis, Lea and Febiger, Philadelphia, 1986, p. 1.
[5] T. Menné, Ann. Clin. Lab. Sci. 26 (1996) 133.
[6] Y. Zhang, D.E. Wilcox, J. Biol. Inorg. Chem. 7 (2002) 327.
[7] H.-J. Thierse, K. Gamerdinger, C. Junkes, N. Guerreiro, H.U. Weltzien, Toxicology 209 (2005) 101.
[8] I. Sóvágó, T. Kiss, A. Gergely, Inorg. Chim. Acta 93 (1984) L53.
[9] I. Sóvágó, B. Radomska, I. Schőn, O. Nyéki, Polyhedron 9 (1990) 825.
[10] I. Sóvágó, C. Bertalan, L. Göbl, I. Schőn, O. Nyéki, J. Inorg. Biochem. 55 (1994) 67.
[11] B. Decock Le-Reverand, L. Andrianarijaona, C. Livera, L.D. Pettit, I. Steel, H. Kozlowski, J. Chem. Soc., Dalton Trans. (1986) 2221.
[12] B. Decock Le-Reverand, F. Liman, C. Livera, L.D. Pettit, S.I. Pyburn, H. Kozlowski, J. Chem. Soc., Dalton Trans. (1988) 887.
[13] J.-F. Galey, H. Kozlowski, L.D. Pettit, J. Inorg. Biochem. 44 (1991) 149.
[14] L.D. Pettit, S. Pyburn, H. Kozlowski, B. Decock Le-Reverand, F. Liman, J. Chem. Soc., Dalton Trans. (1989) 1471.
[15] B. Bóka, A. Myari, I. Sóvágó, N. Hadjiliadis, J. Inorg. Biochem. 98 (2004) 113.
[16] G. Malandrinos, M. Louloudi, Y. Deliginannakis, N. Hadjiliadis, Inorg. Chem. 40 (2001) 4588.
[17] C. Kállay, K. Várnagy, G. Micera, D. Sanna, I. Sóvágó, J. Inorg. Biochem. 99 (2005) 1514.
[18] H. Kozlowski, A. Lebkiri, Ch.O. Onindo, L.D. Pettit, J.-F. Galey, Polyhedron 14 (1995) 211.
[19] H. Irving, G. Miles, L.D. Pettit, Anal. Chim. Acta 38 (1967) 475.
[20] L. Zékány, I. Nagypál, in: D. Leggett (Ed.), Computational Methods for the Determination of Formation Constants, Plenum Press, New York, 1985, p. 291.
[21] P. Gans, A. Sabatini, A. Vacca, J. Chem. Soc., Dalton Trans. (1985) 1195.
[22] Cs.G. Ágoston, Zs. Miskolczy, Z. Nagy, I. Sóvágó, Polyhedron 22 (2003) 2607.
[23] R.B. Martin, M. Chamberlin, J.T. Edsall, J. Am. Chem. Soc. 82 (1960) 495.
[24] T. Kowalik-Jankowska, M. Jasionowski, L. Lankiewicz, J. Inorg. Biochem. 76 (1999) 63.

Available online at www.sciencedirect.com
ScienceDirect
Polyhedron 26 (2007) 818–828
POLYHEDRON
www.elsevier.com/locate/poly

Copper(II) complexes of *N*(4)-substituted thiosemicarbazones derived from pyridine-2-carbaldehyde: Crystal structure of a binuclear complex

P.F. Rapheal, E. Manoj, M.R. Prathapachandra Kurup *

Department of Applied Chemistry, Cochin University of Science and Technology, Kochi, Kerala 682 022, India

Received 19 July 2006; accepted 11 September 2006
Available online 10 October 2006

Abstract

Ten copper(II) complexes {$[CuL^1Cl]$ (**1**), $[CuL^1NO_3]_2$ (**2**), $[CuL^1N_3]_2 \cdot 2/3H_2O$ (**3**), $[CuL^1]_2(ClO_4)_2 \cdot 2H_2O$ (**4**), $[CuL^2Cl]_2$ (**5**), $[CuL^2N_3]$ (**6**), $[Cu(HL^2)SO_4]_2 \cdot 4H_2O$ (**7**), $[Cu(HL^2)_2](ClO_4)_2 \cdot 1/2EtOH$ (**8**), $[CuL^3Cl]_2$ (**9**), $[CuL^3NCS] \cdot 1/2H_2O$ (**10**)} of three NNS donor thiosemicarbazone ligands {pyridine-2-carbaldehyde-*N*(4)-*p*-methoxyphenyl thiosemicarbazone [HL^1], pyridine-2-carbaldehyde-*N*(4)-2-phenethyl thiosemicarbazone [HL^2] and pyridine-2-carbaldehyde *N*(4)-(methyl), *N*(4)-(phenyl) thiosemicarbazone [HL^3]} were synthesized and physico-chemically characterized. The crystal structure of compound **9** has been determined by X-ray diffraction studies and is found that the dimer consists of two square pyramidal Cu(II) centers linked by two chlorine atoms.
© 2006 Elsevier Ltd. All rights reserved.

Keywords: Thiosemicarbazone; Cu(II) complex; Pyridine-2-carbaldehyde; Crystal structure

1. Introduction

The coordination chemistry involving heterocyclic thiosemicarbazones has been interesting research area in the last 30 years because of their well-documented biological activities. Thiosemicarbazone derivatives have considerable antibacterial, antimalarial, antiviral and antitumor activities [1]. Complexation of such thiosemicarbazone ligands with metal ions has been found to produce synergistic effects on the antiproliferative activities of the parent ligands [2]. It has been reported that copper(II) complexes of heterocyclic *N*(4)-substituted thiosemicarbazones exercise bio-activity through a mechanism involving either inhibition of the enzyme ribonucleotide reductase, or creation of lesions in DNA strands. Studies have also shown that, for these ligands, nature of substitution on the terminal N(4) atom is crucial for the antifungal activity [3].

Pyridine-2-carbaldehyde thiosemicarbazone was the first α-(*N*)-heterocyclic carboxaldehyde thiosemicarbazone, reported to have carcinostatic effects [4]. This thiosemicarbazone ligand coordinates to the metal ions in both the anionic (L^-) and neutral (HL) forms. The anionic L^- form is usually present in $[CuLX]_2$ dimers in which, the metal centers can either be bridged through the thiolate sulfur or the non-thiosemicarbazone co-ligand X (X = Cl, N_3, NCS, etc.) [5]. It is reported that the formation of complexes with S-bridge or X-bridge depends on the nature of the non-thiosemicarbazone ligands. However, the actual underlying reasons for the formation of S- over X-bridged systems are not clear to date [6]. On the basis of these findings, the present communication reports on the optimal conditions for synthesis of ten copper(II) complexes with three ligands, viz., pyridine-2-carbaldehyde *N*(4)-paramethoxyphenyl thiosemicarbazone (HL^1), pyridine-2-carbaldehyde *N*(4)-phenethyl thiosemicarbazone (HL^2) and pyridine-2-carbaldehyde *N*(4)-methyl *N*(4)-phenyl thiosemicarbazone (HL^3) and their characterization

* Corresponding author. Tel.: +91 484 2575804; fax: +91 484 2577595.
E-mail address: mrp@cusat.ac.in (M.R. Prathapachandra Kurup).

0277-5387/$ - see front matter © 2006 Elsevier Ltd. All rights reserved.
doi:10.1016/j.poly.2006.09.091

by physicochemical methods, together with X-ray crystal structure of one of the copper compounds, viz. $[CuL^3Cl]_2$.

2. Experimental

2.1. Materials

Pyridine-2-carbaldehyde (Aldrich), 2-phenylethylamine (Fluka) and *p*-anisidine (Fluka) were used as received. The metal salts copper(II) nitrate trihydrate, copper(II) chloride dihydrate, copper(II) acetate monohydrate, copper(II) perchlorate hexahydrate, copper(II) sulphate pentahydrate, sodium azide and potassium thiocyanate (Merck) were used as supplied. 4-Methyl-4-phenyl-3-thiosemicarbazide was prepared as reported previously [7] and solvents were purified by standard procedures before use. *Caution!* Azide and perchlorate complexes of metals with organic ligands are potentially explosive and should be handled with care.

2.2. Synthesis of ligands

The thiosemicarbazones were obtained by adopting and modifying a reported procedure of Scovill et al. [7]. The synthesis and crystal structure of HL^1 have been published earlier [8]. The structure of the three ligands are given in Scheme 1.

2.2.1. Synthesis of HL^1 and HL^3

HL^1 was synthesized by refluxing a solution of 1.00 g (5.52 mmol) of 4-methyl-4-phenyl-3-thiosemicarbazide in 5 ml of MeCN with 0.679 g (5.52 mmol) of 4-methoxyaniline (*p*-anisidine) and 0.591 g (5.52 mmol) of pyridine-2-carbaldehyde for 1.5 h. HL^3 was synthesized by a similar procedure without the addition of an amine. The solutions were chilled (overnight) and the crystals that formed were collected and washed well with MeCN. The compounds were recrystallized from ethanol and dried *in vacuo* over P_4O_{10}.

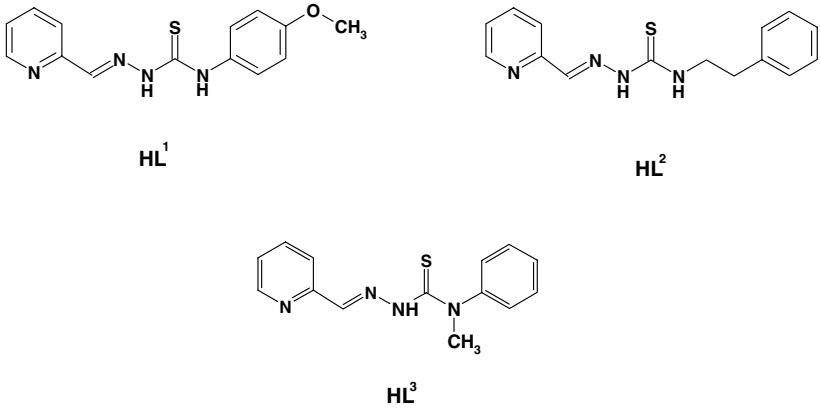
We have reported the syntheses of ligands HL^1 and HL^3 along with the crystal structure of HL^3 recently [9].

2.3. Synthesis of complexes

Refluxing/stirring of alcoholic solution of the ligand with the alcoholic/ aqueous alcoholic solution of the corresponding copper salt yielded the compounds **1**, **2**, **4**, **5**, **7**, **8** and **9** whereas compounds **3**, **6** and **10** were prepared by the metathetical displacement of acetate ion by azide and thiocyanate ion, respectively. Complexes **1**, **5** and **9** were synthesized by refluxing (1 h) 1.5 mmols each of the respective ligands dissolved in 20 ml hot ethanol with 1 mmol of $CuCl_2 \cdot 2H_2O$. In a similar method, complexes **4** and **8** were synthesized by using respective ligands and $Cu(ClO_4)_2 \cdot 6H_2O$ whereas complex **2** was obtained by stirring a hot solution of HL^1 (1.5 mmol) in ethanol (20 ml) with $Cu(NO_3)_2 \cdot 3H_2O$ (1.5 mmol). For the synthesis of **3**, **6** and **10**, the acetate complexes were first prepared by refluxing (15 min) 1.5 mmols each of the respective ligands dissolved in 20 ml hot ethanol with 1.5 mmol of $Cu(OAc)_2 \cdot H_2O$ and the acetate ion was then displaced by azide ion (**3**, **6**) and thiocyanate ion (**10**) by using NaN_3 and KCNS, respectively. The complex **7** was prepared by refluxing (4 h) a mixture of HL^2 (1.5 mmol) and $CuSO_4 \cdot 5H_2O$ (1.5 mmol) in a mixture of ethanol (20 ml) and water (20 ml). Upon evaporation of the solvent, the complexes were precipitated as green or brown solids. The complexes formed were filtered, washed with water, ethanol and ether and dried *in vacuo* over P_4O_{10}.

2.4. Physical measurements

Elemental analyses of the ligand and the complexes were done on a Heracus elemental analyzer at CDRI, Lucknow, India, and on a Vario EL III CHNS analyzer at SAIF, Kochi, India. The IR spectra were recorded on a Thermo Nicolet AVATAR 370 DTGS model FT-IR Spectrophotometer with KBr pellets at SAIF, Kochi. Electronic spectra were recorded on a Cary 5000, version 1.09 UV–Vis–NIR Spectrophotometer from a solution in $CHCl_3$. The EPR spectra of the complexes were recorded on a Varian E-112 Spectrometer using TCNE as the standard at SAIF, IIT, Bombay, India. The magnetic susceptibility



Scheme 1. The thiosemicarbazones HL^1, HL^2 and HL^3.

measurements were carried out at the Indian Institute of Technology, Roorkee, India, at room temperature in the polycrystalline state on a PAR model 155 Vibrating sample magnetometer at 5 kOe field strength. The molar conductances of the complexes in dimethylformamide solutions (10^{-3} M) at room temperature were measured using a direct reading conductivity meter.

2.5. X-ray crystallography

Single crystals of compound **9** of X-ray diffraction quality were grown from its methanol solution by slow evaporation at room temperature in air. The crystallographic data and structure refinement parameters are given in Table 1. The data were collected using a CrysAlis CCD, Oxford Diffraction Ltd., version 1.171.29.2 with graphite monochromated Mo Kα ($\lambda = 0.71073$ Å) radiation on a triclinic single crystal of dimension $0.25 \times 0.20 \times 0.20$ mm with $P\bar{1}$ symmetry at the National Single Crystal X-ray Diffraction Facility, IIT, Bombay, India. The unit cell dimensions and intensity data were measured at 293 K. Empirical absorption correction was done using spherical harmonics, implemented in SCALE3 ABSPACK scaling algorithm. The trial structure was solved using SHELXS-97 [10] and refinement was carried out by full-matrix least squares on F^2 (SHELXL) [10]. Molecular graphics employed were ORTEP-III [11] and PLATON [12].

Table 1
Crystal refinement parameters of compound **9**

Parameters	$[CuL^3Cl]_2$ (**9**)
Empirical formula	$C_{28}H_{26}Cl_2Cu_2N_8S_2$
Formula weight (M)	736.71
Temperature (T) K	293(2)
Wavelength (Mo Kα) (Å)	0.71073
Crystal system	triclinic
Space group	$P\bar{1}$
Lattice constants	
a (Å)	9.2246(18)
b (Å)	9.468(3)
c (Å)	10.714(3)
α (°)	69.41(2)
β (°)	83.157(17)
γ (°)	59.45(2)
V (Å^3)	752.3(3)
Z	1
(ρ_{calc}) (Mg m^{-3})	1.626
Absorption coefficient, μ (mm^{-1})	1.765
F(000)	374
Crystal size (mm)	$0.25 \times 0.20 \times 0.20$
θ Range for data collection (°)	3.16–30.14
Limiting indices	$-13 \leqslant h \leqslant 13$, $-13 \leqslant k \leqslant 13$, $-15 \leqslant l \leqslant 15$
Reflections collected	10909
Independent reflections (R_{int})	4439 (0.0185)
Refinement method	full-matrix least-squares on F^2
Data/restraints/parameters	4439/0/190
Goodness-of-fit on F^2	0.987
Final R indices [$I > 2\sigma(I)$]	$R_1 = 0.0274$, $wR_2 = 0.0708$
R indices (all data)	$R_1 = 0.0428$, $wR_2 = 0.0743$
Largest difference peak and hole (e Å^{-3})	0.410 and −0.215

3. Results and discussion

In all the compounds except **7** and **8** the thiosemicarbazones deprotonate and chelate in thiolate form as evidenced by the IR spectra. The elemental analyses suggest the general empirical formula [CuLX] where X = Cl, NO_3, N_3, ClO_4 and NCS for complexes except **7** and **8**, but the complex **7** turned out to be $[Cu(HL)SO_4]$ and complex **8** to be $[Cu(HL)_2](ClO_4)_2$ with the perchlorate ion out of the coordination sphere. The complexes are appreciably soluble in methanol, ethanol, DMF and DMSO.

The colors, partial elemental analyses, molar conductivities and magnetic susceptibilities of the metal complexes are shown in Table 2. The green and brown colors are common to complexes involving thiosemicarbazone coordination due to the sulfur-to-metal charge-transfer bands, which dominate their visible spectra [13]. The molar conductivity values of the compounds **1**, **2**, **3**, **5**, **6**, **7**, **9** and **10** in 10^{-3} M solution in DMF show that they are non-conductors [14] indicating that the anion and the ligand are coordinated to the central copper(II). But the molar conductivity values of compounds **4** and **8** suggest that they are 2:1 electrolytes. The magnetic susceptibilities at room temperature per copper atom of the complexes except **6**, **8** and **10** suggest interaction between metal centers [15].

3.1. Crystal structure of $[CuL^3Cl]_2$ (9)

The molecular structure of the compound **9** along with atom numbering scheme are given in Fig. 1. The asymmetric unit is formed by one half of the molecule and the other half is related by a center of inversion in the Cu(1)–Cl(1)–Cu(1a)–Cl(1a) ring. The coordination geometry at each Cu(II) is square pyramidal. The ligand HL^3 coordinates the metal in a tridentate manner through its pyridyl nitrogen, azomethine nitrogen and thiolate sulfur, after enolization and deprotonation, to form the basal plane along with one chlorine atom. The basal chlorine atom takes the axial position of the adjacent monomer like its counterpart to result in two distorted square pyramids. The Cu–Cu separation is found to be 3.5330(11) Å. The τ value [16] of 0.139 at metal centers indicates slight distortion from perfect square pyramidal geometry. Thus, the two metal centers are bridged via chlorine atoms resulting in the formation of four five membered rings in which one copper atom is shared by two fused rings. A four membered ring involving the copper atoms and the chlorine atoms is also formed. The five membered ring Cu(1), N(1), C(5), C(6), N(2) is approximately planar with a maximum deviation of 0.0135(18) Å for C5, but Cu(1), N(2), N(3), C(7), S(1) ring is slightly distorted as evidenced by the maximum deviation of 0.1349(18) Å for C7; likewise for their counterpart rings. The four membered ring Cl(1), Cu(1), Cl(1a), Cu(1a) makes an angle of 83.62(3)° with the mean plane of bicyclic

Table 2
Colors, partial elemental analyses, magnetic susceptibilities and molar conductivities of the complexes

Compound	Color	Found (Calc.)%				μ (BM)	Λ_M[a]
		C	H	N	S		
$[CuL^1Cl]$ (**1**)	Brown	43.65(43.75)	3.48(3.41)	14.32(14.58)	8.20(8.34)	1.54	5
$[CuL^1NO_3]_2$ (**2**)	Green	41.12(40.92)	3.17(3.19)	16.97(17.04)	16.97(17.04)	1.14	51
$[CuL^1N_3]_2 \cdot 2/3H_2O$ (**3**)	Brown	42.36(42.36)	3.18(3.47)	24.83(24.70)	8.10 (8.08)	1.39	18
$[CuL^1]_2(ClO_4)_2 \cdot 2H_2O$ (**4**)	Brown	35.85 (36.06)	3.31(3.24)	11.84(12.01)	6.76 (6.88)	0.86	160
$[CuL^2Cl]_2$ (**5**)	Green	47.54(47.12)	4.01(3.95)	14.88(14.65)	8.35 (8.39)	0.99	6
$[CuL^2N_3]$ (**6**)	Brown	46.43(46.32)	3.63(3.89)	25.08(25.21)	8.14(8.24)	2.14	51
$[Cu(HL^2)\ SO_4]_2 \cdot 4H_2O$ (**7**)	Green	37.78(37.53)	4.06(4.20)	11.42 (11.67)	13.01(13.36)	1.41	48
$[Cu(HL^2)_2]\ (ClO_4)_2 \cdot 1/2EtOH$ (**8**)	Green	43.73(43.81)	4.17(4.37)	13.17(12.77)	7.00(7.31)	1.74	132
$[CuL^3Cl]_2$ (**9**)	Green	45.17(45.65)	3.48(3.56)	15.26(15.21)	8.75(8.71)	1.52	7
$[CuL^3NCS] \cdot 1/2H_2O$ (**10**)	Green	44.94 (45.04)	3.13(3.53)	17.4 (17.51)	15.50(16.03)	1.74	11

[a] Molar conductivity of 10^{-3} M DMF solution, in Ω^{-1} cm^2 mol^{-1}.

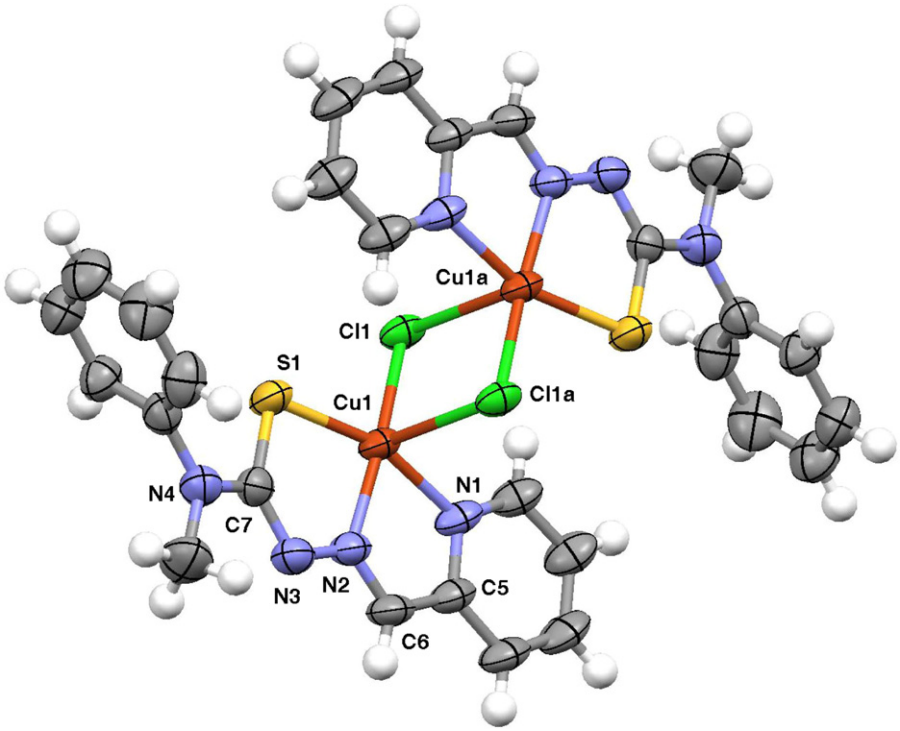


Fig. 1. ORTEP diagram of $[CuL^3Cl]_2$ (**9**) in 50% probability ellipsoids.

chelate system N(1), C(5), C(6), N(2), N(3), C(7), S(1), Cu(1) which is slightly distorted from planarity with a maximum deviation of −0.1979(18) Å for C5. Relevant bond lengths and angles are featured in Table 3. The bridging chlorine atoms are positioned at distances of 2.2587(7) Å for Cl(1) and 2.7245(12) Å for Cl(1a) and make an angle of 90.20(3)° at each metal centers and are in agreement with previous reports [17,18]. The Cu–$N_{azomethine}$ bond length [1.9784(14) Å] is lesser by 0.0541(19) Å compared to Cu–$N_{pyridine}$, indicates the strength of former bond than the latter [18,19].

The ligand HL^3 suffers a structural reorientation upon complexation. The N3 and C5 atoms were in *Z* configuration about the azomethine bond in its metal free form of ligand, is now in *E* form to coordinate the metal as NNS donor ligand. Coordination lengthens the thiosemicarbazone moiety's C(7)–S(1) bond length by 0.0645(22) Å and shortens N(3)–C(7) by 0.0384(18) Å, suggesting deprotonation after enolization. A comparison of the changes in bond lengths and angles are given in Table 3.

The molecules are packed along the *a*-axis directed by the C3–H3···Cl1 intermolecular hydrogen bonding interaction (Table 4). This intermolecular hydrogen bond links the molecules to form one-dimensional polymeric chains (Fig. 2). The aromatic π···π stacking interactions between pyridyl rings (symmetry code: $2 - x$, $1 - y$, $1 - z$ and a Cg–Cg distance of 3.8896 Å) reinforces crystal structure cohesion in molecular packing in the crystal lattice.

Table 3
Selected bond lengths (Å) and bond angles (°) of HL^3 and $[CuL^3Cl]_2$ (**9**)

	HL^3	$[CuL^3Cl]_2$ (**9**)
S(1)–C(7)	1.6750(14)	1.7395(18)
N(2)–C(6)	1.285(2)	1.287(2)
N(2)– N(3)	1.3613(17)	1.352(2)
N(3)–C(7)	1.3644(18)	1.326(2)
N(4)–C(7)	1.345(2)	1.352(2)
Cu(1)–S(1)		2.2481(6)
Cu(1)–N(1)		2.0325(14)
Cu(1)–N(2)		1.9784(14)
Cu(1)–Cl(1)		2.2587(7)
Cu(1)–Cl(1a)		2.7245(12)
C(6)–N(2)–N(3)	117.75(13)	121.34(14)
N(2)–N(3)–C(7)	120.25(12)	111.73(13)
N(4)–C(7)–N(3)	113.87(12)	116.42(15)
N(3)–C(7)–S(1)	122.89(12)	124.89(14)
N(4)–C(7)–S(1)	123.22(11)	118.69(13)
S(1)–Cu(1)–N(1)		162.41(5)
N(1)–Cu(1)–N(2)		80.52(6)
S(1)–Cu(1)–N(2)		83.78(5)
N(1)–Cu(1)–Cl(1)		96.93(5)
N(2)–Cu(1)–Cl(1)		170.75(4)
S(1)–Cu(1)–Cl(1)		97.32(2)
N(1)–Cu(1)–Cl(1a)		90.46(5)
N(2)–Cu(1)–Cl(1a)		98.68(5)
S(1)–Cu(1)–Cl(1a)		99.74(3)
Cl(1)–Cu(1)–Cl(1a)		90.20(3)

Table 4
H-bonding interactions in compound **9**

D–H···A	D–H (°)	H···A (°)	D···A (°)	D–H···A (Å)
C(1)–H(1)···Cl(1)[a]	0.93	2.81	3.3611	119
C(3)–H(3)···Cl(1)[b]	0.93	2.76	3.5754	148

D, donor, A, acceptor, equivalent position codes.
[a] *x*, *y*, *z*.
[b] 1+ *x*, *y*, *z*.

3.2. Infrared spectra

The IR bands most useful for the determination of the mode of coordination are presented in Table 5. The far IR assignments are shown in Table 6. The strong bands at 3310 and 3374 cm^{-1} in the spectra of HL^1 and HL^2 have been assigned to $\nu(^4N–H)$. In the complexes these bands shift to both higher and lower energies, suggesting differences in hydrogen bonding of N(4)H between the uncomplexed and complexed thiosemicarbazone [20]. A medium band in the range 3129–3158 cm^{-1} in the free ligands due to $\nu(^2N–H)$ vibration disappears in the spectra of complexes except **7** and **8**, providing a strong evidence for the ligand coordination around copper(II) ion in the deprotonated form. In the spectra of **7** and **8**, $\nu(^2N–H)$ bands appear at 3219 and 3206 cm^{-1}, respectively, but ν(S–H) band at 2570 cm^{-1} is absent showing that the ligand is in the thione form in these complexes [21]. The intense bands at 1584, 1586 and 1590 cm^{-1} in the spectra of HL^1, HL^2, and HL^3, respectively have been assigned to ν(C=N) of the thiosemicarbazone moiety. These bands are shifted to lower energies in the spectra of the complexes (1553–1573 cm^{-1}), indicating azomethine nitrogen coordination [22]. The presence of bands in the 402–415 cm^{-1} range is assigned to $\nu(Cu–N_{azomethine})$ agree well with previous studies of metal complexes of 2-formylpyridine *N*(4)-substituted thiosemicarbazones [23]. Strong bands found at 1024–1079 cm^{-1} in the ligands are assigned to the ν(N–N) band of the thiosemicarbazone. The increase in the frequency of this band in the spectra of complexes is due to the increase in the bond strength, again confirming the coordination via the azomethine nitrogen [24]. For the complexes containing the anionic ligands, a second band due to ν(N=C) is often resolved, but a number of complexes show only a single, broad band for both ν(C=N) and ν(N=C) modes [25]. The complexes **1**, **2**, **3**, **4**, **5**, **6**, **9** and **10** show bands corresponding to ν(N=C) in the range 1588–1615 $cm^{-1}$where as these bands are not present in the spectra of the complexes **7** and **8**.

The two bands appearing at the frequencies 1334, 1324 and 1307 cm^{-1} [ν(CS) + ν(CN)] and 837, 897 and 779 cm^{-1} (thioamide IV band), respectively, in the spectra of HL^1, HL^2, and HL^3 have been shifted to lower frequencies in the ranges 1289–1367 and 773–897 cm^{-1}, respectively indicating coordination of the thione/thiolato sulfur [26]. The presence of new bands in the range 323–344 cm^{-1} which is assignable to ν(Cu–S) is another indication of sulfur coordination which is found to be consistent with earlier reports [27]. Coordination of the pyridine nitrogen is indicated by a positive shift of the in-plane ring deformation band at 613, 622 and 614 cm^{-1} in the spectra of HL^1, HL^2, and HL^3 to 617–646 cm^{-1} in the spectra of the complexes. Out-of-plane ring deformation bands at 401, 406, and 421 cm^{-1} in the spectra of HL^1, HL^2 and HL^3 are also shifted to higher frequencies [28]. Pyridine nitrogen coordination is further proved by strong bands observed in the region 262–313 cm^{-1} assignable to ν(Cu–N) of pyridine ring as suggested by Clark and Williams [29]. Based on the above spectral evidences, it is confirmed that the ligands HL^1, HL^2, and HL^3 are tridentate, coordinating via the azomethine nitrogen, the pyridyl nitrogen and thione/thiolate sulfur.

The chloro complex **1** shows ν(Cu–Cl) band at 304 cm^{-1}, which is similar to its assignment for terminal chloro ligands in other thiosemicarbazone complexes [30]. In the chloro complexes **5** and **9**, the strong bands observed at 329 and 315 cm^{-1} together with bands at 162 and 164 cm^{-1} have been assigned to the ν(Cu–Cl) in a bridging mode [18]. The crystal structure of **9** confirms the presence of two bridging chlorine atoms.

The nitrato complex **2** has two strong bands at 1287 and 1412 cm^{-1} with a separation of 125 cm^{-1} corresponding to ν_1 and ν_4 and a medium band at 1016 cm^{-1} corresponding to ν_2 of the nitrato group indicating the presence of a terminal monodentate nitrato group [31]. The $\nu_1 + \nu_4$combination bands considered as diagnostic for the monocordinated nitrato group are observed at 1734 and

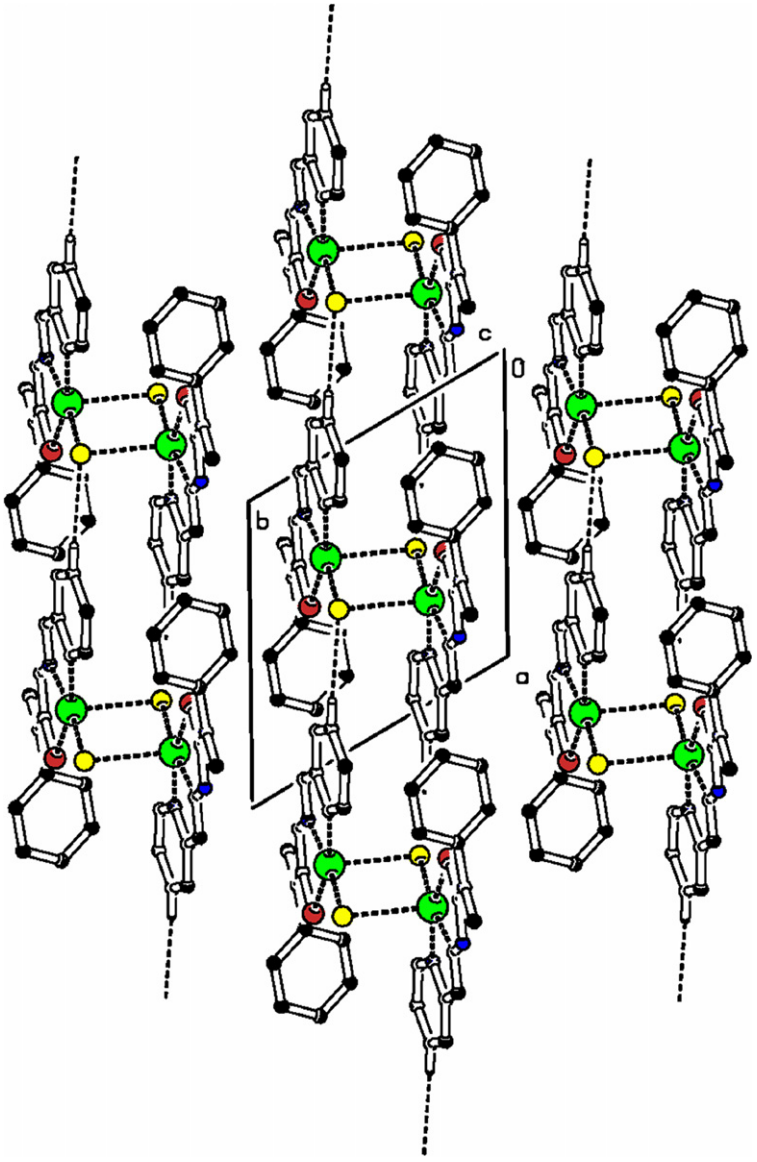


Fig. 2. A view of the unit cell packing of the molecule (**9**) showing hydrogen bonding interactions producing polymeric chains.

Table 5
Infrared spectra (cm^{-1}) of *N*(4)-substituted thiosemicarbazones and their copper complexes

Compounds	*v*C=N	*v*N=C	*v*N–N	*v*/*δ*C–S	py(ip)	py(op)	v^2N–H	v^4N–H
HL^1	1584		1024	1334,837	613	401	3134	3310
$[CuL^1Cl]$ (**1**)	1558	1596	1133	1307,826	646	409		3340
$[CuL^1NO_3]_2$ (**2**)	1564	1597	1135	1308,830	617	417		3321
$[CuL^1N_3]_2 \cdot 2/3H_2O$ (**3**)	1561	1606	1135	1301, 829	617	413		3251
$[CuL^1]_2(ClO_4)_2 \cdot 2H_2O$ (**4**)	1560	1609	1121	1300,837	636	409		3286
HL^2	1586		1079	1324,897	622	406	3129	3374
$[CuL^2Cl]_2$(**5**)	1560	1588	1138	1335,889	628	414		3443
$[CuL^2N_3]$ (**6**)	1573	1592	1083	1313,867	626	412		3446
$[Cu(HL^2)SO_4]_2 \cdot 4H_2O$ (**7**)	1560		1165	1361,890	618	412	3219	3403
$[Cu(HL^2)_2](ClO_4)_2 \cdot 1/2EtOH$ (**8**)	1565		1139	1367, 886	635	419	3206	3330
HL^3	1590		1035	1307, 779	614	421	3158	
$[CuL^3Cl]_2$ (**9**)	1553	1615	1138	1289, 775	636	449		
$[CuL^3NCS] \cdot 1/2H_2O$ (**10**)	1558	1607	1140	1291, 773	631	453		

1749 cm^{-1}. v_3, v_5 and v_6 are observed at 743, 712 and 803 cm^{-1}, respectively [32]. Besides, in the far IR spectrum of the complex, the band observed at 255 cm^{-1} can be assigned to $v(Cu–ONO_2)$ consistent with the bands at 253–280 cm^{-1} reported earlier for $v(Cu–ONO_2)$ in metal complexes [33].

Table 6
Far infrared spectra (cm^{-1}) of the copper complexes

Compound	νCu–$N_{azo.}$	νCu–N_{py}	νCu–S	νCu–Cl	νCu–N_{azido}	νCu–$N_{(NCS)}$	νCu–$O_{nitrato}$
$[CuL^1Cl]$ (**1**)	415	250	325	304			
$[CuL^1NO_3]_2$ (**2**)	415	313	323				255
$[CuL^1N_3]_2 \cdot 2/3H_2O$ (**3**)	407	272	332		429		
$[CuL^1]_2(ClO_4)_2 \cdot 2H_2O$ (**4**)	412	271	325				
$[CuL^2Cl]_2$ (**5**)	415	275	344	329 162			
$[CuL^2N_3]$ (**6**)	402	262	338		435		
$[Cu(HL^2)SO_4]_2 \cdot 4H_2O$ (**7**)	415	280	324				
$[Cu(HL^2)_2](ClO_4)_2 \cdot 1/2EtOH$ (**8**)	414	276	325				
$[CuL^3Cl]_2$ (**9**)	413	297	325	315 164			
$[CuL^3NCS] \cdot 1/2H_2O$ (**10**)	413	297	325			314	

The azido complexes **3** and **6** show sharp bands at 2056 and 2038 cm^{-1} and strong bands at 1243 and 1356 cm^{-1}, respectively. These are assigned to ν_a and ν_s of the coordinated azido group. The broad bands observed at 647 cm^{-1} for both complexes are assigned to δ(N–N–N). ν(Cu–N_{azido}) bands are observed at 446 and 435 cm^{-1}, respectively, for **3** and **6**.

The perchlorate complexes **4** and **8** show single broad bands at 1121 cm^{-1} and strong bands at 626 and 624 cm^{-1}, indicating the presence of ionic perchlorate. The bands at 1121 cm^{-1} are assignable to $\nu_3(ClO_4)$ and the unsplit bands at 626 and 624 cm^{-1} assignable to $\nu_4(ClO_4)$. In the spectrum of the compound **4**, a medium band at 926 cm^{-1} may be due to $\nu_1(ClO_4)$ suggesting that ionic perchlorate is distorted from tetrahedral symmetry due to lattice effects or hydrogen bonding by the NH functions of the coordinated ligand [34]. However, no band assignable to $\nu_1(ClO_4)$ is observable in the spectrum of compound **8**. This along with unsplit ν_3 and ν_4 bands show exclusive presence of non-coordinated perchlorate group.

For the sulfato complex **7**, strong bands at 1116 and 1028 cm^{-1} are assignable to ν_3 of the mono coordinated sulfato group. Medium bands at 939 cm^{-1} (ν_1) and 644 cm^{-1} (ν_4) further confirm the unidentate behaviour of sulfato group [31].

Thiocyanato complex **10** exhibits a strong and sharp band at 2079 cm^{-1}, a weak band at 773 cm^{-1} and another weak band at 484 cm^{-1} which can be attributed to ν(CN), ν(CS) and δ(NCS), respectively. These values are typical for N-bonded thiocyanate complexes. A medium band at 325 cm^{-1} corresponds to ν(Cu–$N_{thiocyanato}$) vibrations which is in agreement with the reported values [35].

3.3. Electronic spectra

The electronic absorption spectra are often very helpful in the evaluation of results furnished by other methods of structural investigation. The tentative assignments of the significant electronic spectral bands of ligands and their copper(II) complexes are presented in Table 7. The electronic spectra in $CHCl_3$ solution of HL^1, HL^2 and HL^3 show the following intraligand absorption maxima: for HL^1, two bands corresponding to $\pi \rightarrow \pi^*$ of the pyridyl ring, benzene ring and imine function of the thiosemicarbazone moiety are observed at 42 730 and 38 760 cm^{-1}; the $n \rightarrow \pi^*$ transitions of the pyridyl ring and imine function of the thiosemicarbazone moiety are observed at 30 770 cm^{-1}; for HL^2, these bands are observed at 42 190, 36 630 and 30 960 cm^{-1}, respectively, and for HL^3 they are observed at 43 290, 38 610 and 30 840 cm^{-1} [36]. The

Table 7
Electronic spectra (cm^{-1}) of *N*(4)-substituted thiosemicarbazones and their copper complexes

Compound	$\pi \rightarrow \pi^*$	$n \rightarrow \pi^*$	CT	d–d
HL^1	42 730, 38 760	30 770		
$[CuL^1Cl]$ (**1**)	41 840, 36 230	31 150	22 990, 27 700	16 420
$[CuL^1NO_3]_2$ (**2**)	42 190, 37 490	35 460	23 150, 27 850	14 880
$[CuL^1N_3]_2 \cdot 2/3H_2O$ (**3**)	42 020, 37 050	34 280	23 510	16 190
$[CuL^1]_2(ClO_4)_2 \cdot 2H_2O$ (**4**)	41 670, 37 880		24 040	15 290
HL^2	42 190, 36 630	30 960		
$[CuL^2Cl]_2$ (**5**)	42 190, 38 610	33 000	23 420, 29 150	16 230
$[CuL^2N_3]$ (**6**)	42 120, 38 790	33 210	23 310	16 270
$[Cu(HL^2)SO_4]_2 \cdot 4H_2O$ (**7**)	41 840	33 110	23 870, 28 980	16 080
$[Cu(HL^2)_2](ClO_4)_2 \cdot 1/2EtOH$ (**8**)	42 190, 38 760	32 570	22 880	16 780
HL^3	43 290, 38 610	30 842		
$[CuL^3Cl]_2$ (**9**)	42 190, 38 760	32 470	23 200	16 370
$[CuL^3NCS] \cdot 1/2H_2O$ (**10**)	42 270, 38 620	31 440	23 760	16 150

$\pi \rightarrow \pi^*$ transitions are not significantly altered on complex formation. In the spectra of the complexes in chloroform solutions the $n \rightarrow \pi^*$ transitions associated with the pyridine ring observed above 30 000 cm^{-1} in the spectra of the thiosemicarbazones are shifted to higher energies, the blue shift indicating coordination *via* the pyridyl nitrogen [17]. Strong bands in the range 22 880–24 040 cm^{-1} observed in the spectra of all Cu(II) complexes are assigned to $S \rightarrow Cu$ and $py \rightarrow Cu$ charge-transfer bands [26]. For the chloro complexes **1** and **5**, the $Cl \rightarrow Cu(II)$ charge transfer bands are found at 27 700 and 29 150 cm^{-1}, respectively, and band at 27 850 cm^{-1} in the spectrum of nitrato complex (**2**) is attributable to nitrato $O \rightarrow Cu(II)$ ligand to metal charge transfer transition [37].

The spectra of the complexes **1**, **3**, **5**, **6**, **7**, **9** (Fig. 3) and **10** exhibit weak d–d bands centered around 16 000 cm^{-1}, that of **2** and **4** are at *ca.* 15 000 cm^{-1}. For a square planar complex with $d_{x^2-y^2}$ ground state, three transitions are possible $d_{x^2-y^2} \rightarrow d_{z^2}$, $d_{x^2-y^2} \rightarrow d_{xy}$ and $d_{x^2-y^2} \rightarrow d_{xz}, d_{yz}$ ($^2A_{1g} \leftarrow {}^2B_{1g}$, $^2B_{2g} \leftarrow {}^2B_{1g}$ and $^2E_g \leftarrow {}^2B_{1g}$) and square pyramidal complexes have the $d_{x^2-y^2} \rightarrow d_{xz}, d_{yz}$ and $d_{x^2-y^2} \rightarrow d_{z^2}$ transitions [38–40]. Since the four d orbitals lie very close together, each transition cannot be distinguished by their energy and hence it is very difficult to resolve the bands into separate components. The broad band observed at 16 780 cm^{-1} in the electronic spectrum of the complex **8** is assigned to $^2E_g \leftarrow {}^2T_{2g}$ transition [41,42]. However, results obtained from electronic spectra do not permit a structural diagnosis free of uncertainty.

3.4. EPR spectra

The copper(II) ion, with a d^9 configuration, has an effective spin of $S = 1/2$ and is associated with a spin angular momentum, $m_s = \pm 1/2$, leading to a doubly degenerate spin state in the absence of a magnetic field. In a magnetic field the degeneracy is lifted between these states and the energy difference between them is given by $E = h\nu = g\beta H$, where h is Planck's constant, ν is the microwave frequency for transition from $m_s = +1/2$ to $m_s = -1/2$, g is the Lande splitting factor (equal to 2.0023 for a free electron), β is the Bohr magneton and H is the magnetic field. For the case of a $3d^9$ copper(II) ion, the appropriate spin Hamiltonian assuming a B_{1g} ground state is given by

$$\widehat{H} = \beta[g_{\|}H_zS_z + g_{\perp}(H_xS_x + H_yS_y)] + A_{\|}I_zS_z + A_{\perp}(I_xS_x + I_yS_y)$$

The EPR spectra of the complexes in the polycrystalline state at 298 K, in solution at 298 and 77 K were recorded in the X band, using 100 kHz field modulation and the g factors were quoted relative to the standard marker TCNE ($g = 2.00277$). EPR spectral assignments of the copper(II) complexes along with the spin Hamiltonian and orbital reduction parameters are given in Table 8.

The EPR spectra of compounds **8** and **10** in the polycrystalline state (298 K) show only one broad signal at 2.0762 and 2.0765, respectively, due to dipolar broadening and enhanced spin lattice relaxation. The spectra of the compounds **2**, **3**, **4**, **5**, **6**, **7** and **9** show typical axial behavior with slightly different $g_{\|}$ and $g_{\perp}$ values. The spectrum of compound **1** gives three g values *viz.* g_1, g_2 and g_3 which indicate rhombic distortion in its geometry. The geometric parameter G, which is a measure of the exchange interaction between the copper centers in the polycrystalline compound, is calculated using the equation: $G = (g_{\|} - 2.0023)/(g_{\perp} - 2.0023)$ for axial spectra and for rhombic spectra, $G = (g_3 - 2)/(g_{\perp} - 2)$ and $g_{\perp} = (g_1 + g_2)/2$. If $G > 4$, exchange interaction is negligible and if it is less than 4, considerable exchange interaction is indicated in the solid complex [43]. In all the copper(II) complexes $g_{\|} > g_{\perp} > 2.0023$ and G value within the range 2.08–4.49 are consistent with a $d_{x^2-y^2}$ ground state [44]. The solution spectra of complexes were recorded in DMF at 298 K. They are isotropic in nature with well-resolved four hyperfine lines (Fig. 4). The hyperfine splitting is due to the interaction of the electron spin with the copper nuclear spin (^{63,65}Cu, $I = 3/2$). The spectra of all the complexes in DMF at 77 K are axial with four copper hyperfine lines in both the parallel and perpendicular regions (Fig. 5). In addition the spectra of some of the complexes show five nitrogen superhyperfine lines in the high field component. For the spectra of all the complexes in frozen DMF the $g_{\|} > g_{\perp}$ values rules out the possibility of trigonal bipyramidal structures for which $g_{\perp} > g_{\|}$ is expected. The binuclear nature of **2**, **3**, **4**, **7** and **9** was confirmed by the presence of half-field signals ($\Delta M_s = \pm 2$) at *ca.* 1600 G (Fig. 6). However, for **5**, the half-field signal at *ca.* 1600 G is not well resolved. The EPR parameters $g_{\|}$, $g_{\perp}$, g_{av}, $A_{\|}$(Cu) and $A_{\perp}$(Cu) and the energies of d–d transition were used to evaluate the bonding parameters α^2, β^2 and γ^2, which may be regarded as measures of the covalency of the in-plane σ bonds, in-plane π bonds, and out-of-plane π bonds, respectively. The value of in plane sigma bonding parameter α^2 was estimated from the following expression:

$$\alpha^2 = -A_{\|}/0.036 + (g_{\|} - 2.0023) + 3/7(g_{\perp} - 2.0023) + 0.04$$

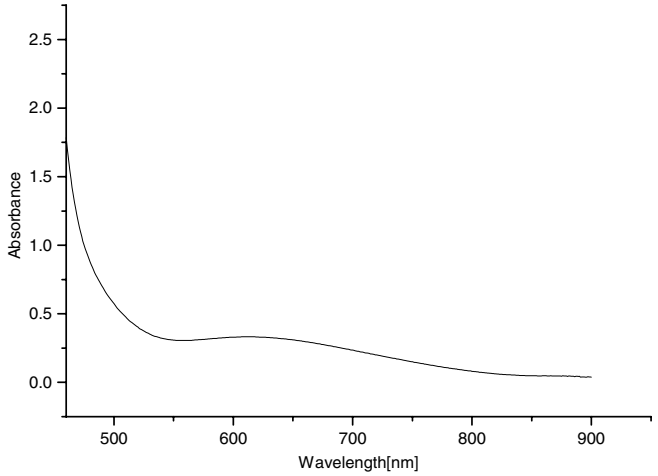


Fig. 3. Electronic spectrum of compound **9** in $CHCl_3$.

Table 8
EPR Spectral parameters of the copper(II) complexes

	1	2	3	4	5	6	7	8	9	10
Polycrystalline (298 K)										
$g_{\parallel}$	2.1167(g_3)	2.1769	2.1349	2.1931	2.1661	2.1635	2.1806		2.1842	
$g_{\perp}$	2.0341(g_1) 2.0746(g_2)	2.0585	2.0471	2.0501	2.0388	2.0423	2.0879		2.0533	
g_{iso} or g_{av}		2.0979	2.0764	2.0978	2.0812	2.0827	2.1188	2.0762	2.0969	2.0765
DMF (298 K)										
g_{iso}	2.081	2.0955	2.0809	2.0955	2.081	2.0809	2.0955	2.0955	2.081	2.0955
A_{iso}	95.53	88.05	92.29	88.05	95.53	92.29	88.05	88.86	95.53	88.86
DMF (77 K)										
$g_{\parallel}$	2.1607	2.1787	2.1544	2.1787	2.1625	2.1563	2.1824	2.1697	2.1609	2.1679
$g_{\perp}$	2.0566	2.0585	2.0487	2.0533	2.0533	2.0504	2.0664	2.0469	2.0518	2.0549
$A_{\parallel}$ (Cu)[a]	186.6	195	187.75	194.9	188.5	187.92	191.9	192.5	186.63	193.99
G	2.19	3.11	2.96	3.99	4.49	4.03	2.08	3.75	3.57	3.15
α^2	0.7400	0.7822	0.7335	0.7797	0.7457	0.7366	0.7785	0.7611	0.7382	0.7670
β^2	0.8468	0.8048	0.8311	0.8184	0.8392	0.8351	0.8493	0.8556	0.8481	0.8283
γ^2	0.9916	0.9085	0.9182	0.8801	0.9479	0.9363	0.9730	0.8833	0.9476	0.9336
K	0.4184	0.4053	0.4067	0.4122	0.4203	0.4069	0.4089	0.3884	0.4141	0.4070
$K_{\parallel}$	0.6266	0.6295	0.6096	0.6381	0.6258	0.6151	0.6612	0.6512	0.6261	0.6353
$K_{\perp}$	0.7338	0.7106	0.6735	0.6862	0.7069	0.6897	0.7575	0.6723	0.6995	0.7161
P	0.0231	0.0251	0.0229	0.0242	0.0233	0.0207	0.0237	0.0241	0.0229	0.0239

[a] A values are given in 10^{-4} cm^{-1}.



Fig. 4. EPR spectrum of **8** in DMF solution at 298 K.

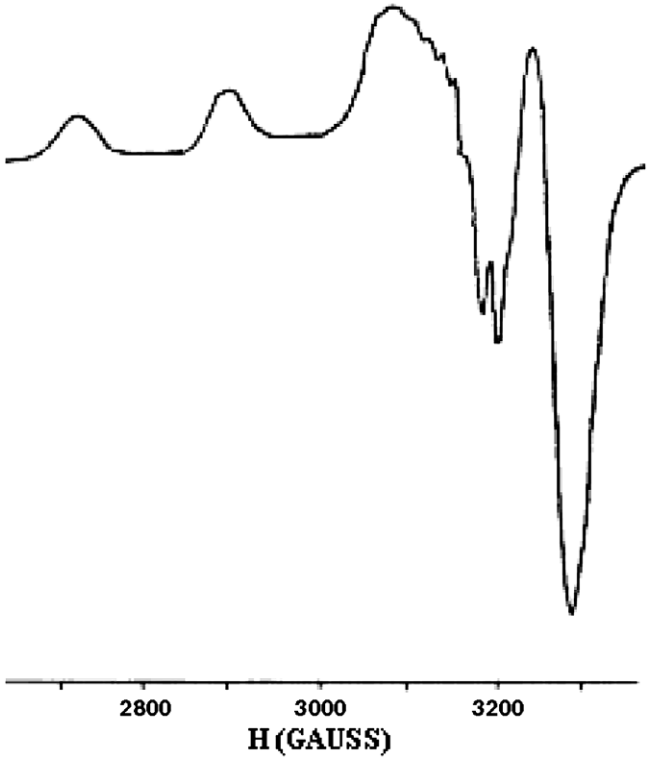


Fig. 5. EPR spectrum of **5** in DMF solution at 77 K.

The orbital reduction factors $K_{\parallel} = \alpha^2\ \beta^2$ and $K_{\perp} = \alpha^2\gamma^2$ were calculated using the following expressions [18]:

$$K_{\parallel}^2 = (g_{\parallel} - 2.0023)\Delta E(\mathrm{d}_{xy} - \mathrm{d}_{x^2-y^2})/8\lambda_0$$

$$K_{\perp}^2 = (g_{\perp} - 2.0023)\Delta E(_{\mathrm{d}_{xz,yz}} - \mathrm{d}_{x^2-y^2})/2\lambda_0$$

where λ_0 is the spin orbit coupling constant and has the value -828 cm^{-1} for a copper(II) d^9 system.

According to Hathaway [45], $K_{\parallel} = K_{\perp} = 0.77$ for pure σ bonding and $K_{\parallel} < K_{\perp}$ for in-plane π bonding, while for out-of-plane π bonding $K_{\parallel} > K_{\perp}$. In all the copper(II) complexes, it is observed that $K_{\parallel} < K_{\perp}$ which indicates the presence of significant in-plane π bonding. Furthermore, α^2, β^2 and γ^2 have values less than 1 which is expected

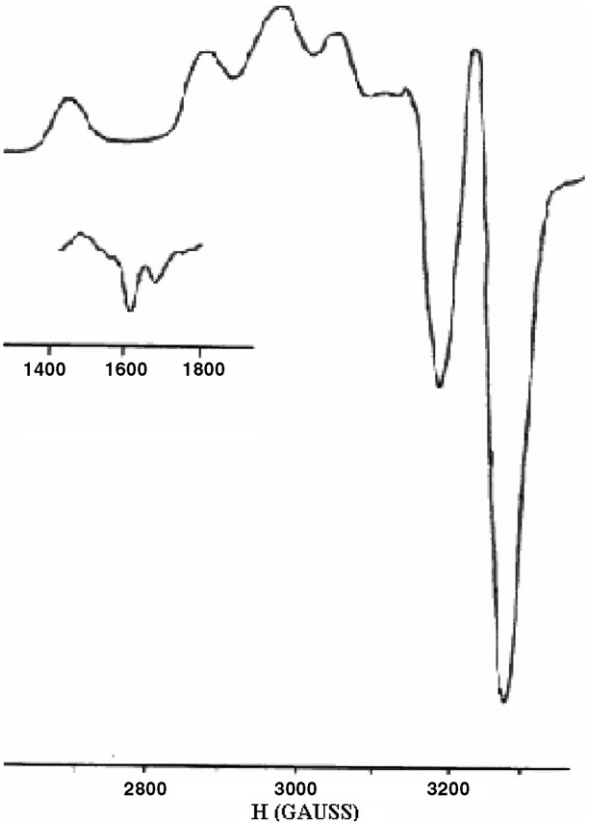


Fig. 6. EPR spectrum of **2** in DMF solution at 77 K.

for 100% ionic character of the bonds and become smaller with increasing covalent bonding. The evaluated values of α^2, β^2 and γ^2 of the complexes are consistent with both strong in plane σ and in plane π bonding. The $g_{\|}$ values are nearly the same for all the complexes indicating that the bonding is dominated by the thiosemicarbazone moiety.

The fact that the $g_3/g_{\|}$ values are less than 2.3 is an indication of significant covalent bonding in these complexes [46]. The Fermi contact hyperfine interaction term K may be obtained from [47]:

$$K = A_{iso}/P\beta^2 + (g_{av} - 2.0023)/\beta^2$$

where P is the free ion dipolar term and its value is 0.036. K is a dimensionless quantity, which is a measure of the contribution of s electrons to the hyperfine interaction. The K values obtained for all the complexes are in agreement with those estimated by Assour [48] and Abragam and Pryce [49].

Acknowledgements

P.F. Rapheal and E. Manoj thank the University Grants Commission, New Delhi, India, for financial support. M.R.P. Kurup is thankful to the CSIR and DST, New Delhi, India, for financial support. We are thankful to National Single Crystal X-ray Diffraction Facility, IIT, Bombay, India for providing XRD data.

Appendix A. Supplementary material

CCDC 613495 contains the supplementary crystallographic data for **9**. These data can be obtained free of charge via http://www.ccdc.cam.ac.uk/conts/retrieving.html, or from the Cambridge Crystallographic Data Centre, 12 Union Road, Cambridge CB2 1EZ, UK; fax: (+44) 1223-336-033; or e-mail: deposit@ccdc.cam.ac.uk. Supplementary data associated with this article can be found, in the online version, at doi:10.1016/j.poly.2006.09.091.

References

[1] A.E. Liberta, D.X. West, Biometals 5 (1992) 121.
[2] Z. Afrasiabi, E. Sinn, J. Chen, Y. Ma, A.L. Rheingold, L.N. Zakharov, N. Rath, S. Padhye, Inorg. Chim. Acta 357 (2004) 271.
[3] D.X. West, A.E. Liberta, S.B. Padhye, R. C Chikate, P.B. Sonawane, A.S. Kumbhar, R.G. Yerande, Coord. Chem. Rev. 123 (1993) 49.
[4] A.C. Sartorelli, K.C. Agrawal, A.S. Tsiftsoglou, A.C. Moore, Adv. Enzyme Regul. 15 (1977) 117.
[5] J.G. Tojal, L. Lezama, J.L. Pizarro, M. Insausti, M.I. Arriortua, T. Rojo, Polyhedron 18 (1999) 3703.
[6] P.G. Saiz, J.G. Tojal, A. Mendia, B. Donnadieu, L. Lezama, J.L. Pizarro, M.I. Arriortua, T. Rojo, Eur. J. Inorg. Chem. 518 (2003) 527.
[7] J.P. Scovill, D.L. Klayman, C.F. Franchino, J. Med. Chem. 25 (1982) 1261.
[8] H.-K. Fun, S. Chantrapromma, P.F. Rapheal, V. Suni, M.R.P. Kurup, Acta Crystallogr. E62 (2006) o125.
[9] P.F. Rapheal, E. Manoj, M.R.P. Kurup, E. Suresh, Polyhedron, (2006), doi:10.1016/j.poly.2006.08.029.
[10] G.M. Sheldrick, SHELXS97 and SHELXL97, Bruker AXS Inc., Madison, Wisconsin, USA, 1997.
[11] L.J. Farrugia, J. Appl. Cryst. 30 (1997) 565.
[12] A.L. Spek, J. Appl. Cryst. 36 (2003) 7.
[13] D.X. West, J.S. Ives, G.A. Bain, A.E. Liberta, J. Valdes-Martinez, K.H. Ebert, S. H-Ortega, Polyhedron 16 (1997) 1895.
[14] W.J. Geary, Coord. Chem. Rev. 7 (1971) 81.
[15] V. Philip, V. Suni, M.R.P. Kurup, M. Nethaji, Polyhedron 25 (2006) 1931.
[16] C.R. Cornman, K.M. Geiser-Bush, S.P. Rowley, P.D. Boyle, Inorg. Chem. 36 (1997) 6401.
[17] A. Sreekanth, M.R.P. Kurup, Polyhedron 22 (2003) 3321.
[18] M. Joseph, M. Kuriakose, M.R.P. Kurup, E. Suresh, A. Kishore, S.G. Bhat, Polyhedron 25 (2006) 61.
[19] V. Philip, V. Suni, M.R.P. Kurup, M. Nethaji, Polyhedron 24 (2005) 1133.
[20] N.S. Youssef, K.H. Hegab, Synth. React. Inorg. Met–Org. Nano-Met. Chem. 35 (2005) 391.
[21] Y.-P. Tian, W.-T. Yu, C.-Y. Zhao, M.-H. Jiang, Z.-G. Cai, H.-K. Fun, Polyhedron 21 (2002) 1219.
[22] R.P. John, A. Sreekanth, M.R.P. Kurup, A. Usman, I.A. Razak, H.-K. Fun, Spectrochim. Acta 59A (2003) 1349.
[23] D.X. West, N.M. Kozub, Transition Met. Chem. 21 (1996) 52.
[24] M. Joseph, V. Suni, M.R.P. Kurup, M. Nethaji, A. Kishore, S.G. Bhat, Polyhedron 23 (2004) 3069.
[25] A. Sreekanth, H.-K. Fun, M.R.P. Kurup, J. Mol. Struct. 737 (2005) 61.
[26] R.P. John, A. Sreekanth, M.R.P. Kurup, S.M. Mobin, Polyhedron 21 (2002) 2515.
[27] K.H. Reddy, M.R. Reddy, K.M. Raju, Ind. J. Chem. 38A (1999) 299.
[28] B.S. Garg, M.R.P. Kurup, S.K. Jain, Y.K. Bhoon, Transition Met. Chem. 16 (1991) 111.
[29] R.J. Clark, C.S. Williams, Inorg. Chem. 4 (1965) 350.

[30] M.B. Ferrari, G.G. Fara, M. Lafranchi, C. Pelizzi, M. Tarasconi, Inorg. Chim. Acta 181 (1991) 253.
[31] K. Nakamoto, Infrared and Raman Spectra of Inorganic and Coordination Compounds, 5th ed., Wiley-Interscience, New York, 1997, pp. 86.
[32] D.N. Sathyanarayana, Vibrational Spectroscopy, New Age International, New Delhi, 2004, pp. 400.
[33] S .K. Jain, B.S. Garg, Y.K. Bhoon, Spectrochim. Acta 42A (1986) 701.
[34] A.M. Bond, R.L. Martin, Coord. Chem. Rev. 54 (1984) 23.
[35] E.W. Ainscough, A.M. Brodie, J.D. Ranford, J.M. Waters, Dalton Trans. 23 (1991) 2125.
[36] A. Sreekanth, S. Sivakumar, M.R.P. Kurup, J. Mol. Struct. 655 (2003) 47.
[37] P. Bindu, M.R.P. Kurup, T.R. Satyakeerty, Polyhedron 18 (1999) 321.
[38] R.P. John, A. Sreekanth, V. Rajakannan, T.A. Ajith, M.R.P. Kurup, Polyhedron 23 (2004) 2549.
[39] A.B.P. Lever, Inorganic Electronic Spectroscopy, 2nd ed., Elsevier, Amsterdam, 1984.
[40] B.J. Hathaway, A.A.G. Tomlinson, Coord. Chem. Rev. 5 (1970) 24.
[41] N. Raman, S. Ravichandran, C. Thangaraja, J. Chem. Sci. 116 (2004) 215.
[42] S.E. Livingstone, J.E. Oluka, Transition Met. Chem. 2 (1977) 190.
[43] B.J. Hathaway, D.E. Billing, Coord. Chem. Rev. 5 (1970) 1949.
[44] M.J. Bew, B.J. Hathaway, R.R. Faraday, J. Chem. Soc., Dalton Trans. (1972) 1229.
[45] B.J. Hathaway, in: G. Wilkinson, R.D. Gillard, J.A. McCleverty (Eds.), Comprehensive Coordination Chemistry, vol. 5, Pergamon, Oxford, 1987.
[46] J.R. Wasson, C. Trapp, J. Phys. Chem. 73 (1969) 3763.
[47] L.S. Lund, J.B. Raynor, J. Chem. Soc., Dalton Trans. (1975) 1389.
[48] M. Assour, J. Chem. Phys. 43 (1965) 2477.
[49] A. Abragam, M.H.L. Pryce, Proc. R. Soc. London, Sect. A 206 (1961) 164.

Available online at www.sciencedirect.com
ScienceDirect
Polyhedron 26 (2007) 829–836
POLYHEDRON
www.elsevier.com/locate/poly

Spectral and structural studies of mono- and binuclear copper(II) complexes of salicylaldehyde N(4)-substituted thiosemicarbazones

E.B. Seena, Maliyeckal R. Prathapachandra Kurup *

Department of Applied Chemistry, Cochin University of Science and Technology, Kochi 682022, Kerala, India

Received 27 February 2006; accepted 8 September 2006
Available online 29 September 2006

Abstract

Three copper(II) complexes of salicylaldehyde N(4)-phenyl thiosemicarbazone (H_2L^1) and two copper(II) complexes of N(4)-cyclohexyl thiosemicarbazone (H_2L^2) have been synthesized and characterized by different physicochemical techniques like magnetic studies and electronic, infrared and EPR spectral studies. The complexes $[(CuL^1)_2] \cdot \frac{1}{2}H_2O$ (**1**) and $[(CuL^2)_2]$ (**4**) having dimeric structure. The thiosemicarbazones bind to the metal as dianionic ONS donor ligand in all the complexes, except in the complex $[Cu(HL^1)_2] \cdot H_2O$ (**2**). In complex **2**, the ligand moieties are coordinated as monoanionic (HL^-) ones. Two of the complexes $[CuL^1dmbipy] \cdot H_2O$ (**3**) and $[CuL^2dmbipy]$ (**5**) have been found to possess the stoichiometry [CuLB], where B = 4,4′-dimethyl-2,2′-bipyridine (dmbipy). The coordination geometry around copper(II) in **5** is trigonal bipyramidal distorted square based pyramidal (TBDSBP), as obtained by X-ray diffraction studies.
© 2006 Elsevier Ltd. All rights reserved.

Keywords: Salicylaldehyde; Phenyl thiosemicarbazide; Cyclohexyl thiosemicarbazide; Copper(II) complexes; 4,4′-Dimethyl 2,2′-bipyridine; X-ray crystallography

1. Introduction

Thiosemicarbazones of aromatic *o*-hydroxyaldehydes and ketones have recently attracted considerable attention because of their potential biological properties. These aromatic thiosemicarbazones most often coordinate as the dianion on deprotonation of the ring hydroxyl group and loss of the N(2) hydrogen of the thiosemicarbazone moiety to form mononuclear as well as binuclear metal complexes. Such types of tridentate ONS donor thiosemicarbazones and their copper complexes have been studied in recent years owing to their pharmacological interest [1]. Spectral and structural studies of a series of biologically active heterocyclic base adducts of copper(II) complexes of salicylaldehyde N(4)-substituted thiosemicarbazones have been reported [2]. Similarly, the binuclear copper(II) complexes of N(4)-substituted thiosemicarbazones have also been investigated recently [3,4]. Here, we also report the synthesis, spectral, structural and EPR studies of some mono- and bi-nuclear complexes of two salicylaldehyde N(4)-substituted thiosemicarbazones.

2. Experimental

2.1. Materials

All compounds used for the synthesis of the thiosemicarbazone ligands were purified by standard methods and solvents were purified by distillation. 4,4′-Dimethyl-2,2′-bipyridine (dmbipy) (Sigma Aldrich) and $Cu(OAc)_2 \cdot H_2O$ (Fluka) were used as received.

* Corresponding author. Tel.: +91 484 2575804; fax: +91 484 2577595.
E-mail addresses: mrp@cusat.ac.in, mrp_k@yahoo.com (M.R.P. Kurup).

0277-5387/$ - see front matter © 2006 Elsevier Ltd. All rights reserved.
doi:10.1016/j.poly.2006.09.040

2.2. Synthesis of the ligands and their copper(II) complexes

Salicylaldehyde N(4)-phenyl and N(4)-cyclohexyl thiosemicarbazones (H_2L^1 and H_2L^2, respectively) were synthesized by the earlier reported method [2,5] (Fig. 1).

2.2.1. $[(CuL^1)_2]\cdot\frac{1}{2}H_2O$ (**1**)

This complex was synthesized by refluxing an ethanolic solution of H_2L^1 (1 mmol, 0.271 g) with an aqueous solution of $Cu(OAc)_2\cdot H_2O$ (1 mmol, 0.1996 g) for 4 h. The complex formed was filtered, washed with ethanol and finally with ether and dried over P_4O_{10} in vacuo.

2.2.2. $[Cu(HL^1)_2]\cdot H_2O$ (**2**)

This complex was synthesized by refluxing an ethanolic solution of H_2L^1 (2 mmol, 0.542 g) with an aqueous solution of $Cu(OAc)_2\cdot H_2O$ (1 mmol, 0.1996 g) for 4 h. The complex formed was filtered, washed with ethanol and finally with ether and dried over P_4O_{10} in vacuo.

2.2.3. $[CuL^1dmbipy]\cdot H_2O$ (**3**)

This complex was synthesized by refluxing an ethanolic solution of H_2L^1 (1 mmol, 0.271 g) and heterocyclic base dmbipy (1 mmol, 0.184 g) with an aqueous solution of $Cu(OAc)_2\cdot H_2O$ (1 mmol, 0.1996 g) for 4 h. The complex formed was filtered, washed with ethanol and finally with ether and dried over P_4O_{10} in vacuo.

2.2.4. $[(CuL^2)_2]$ (**4**)

This complex was prepared by a similar method of the complex **1** by using H_2L^2.

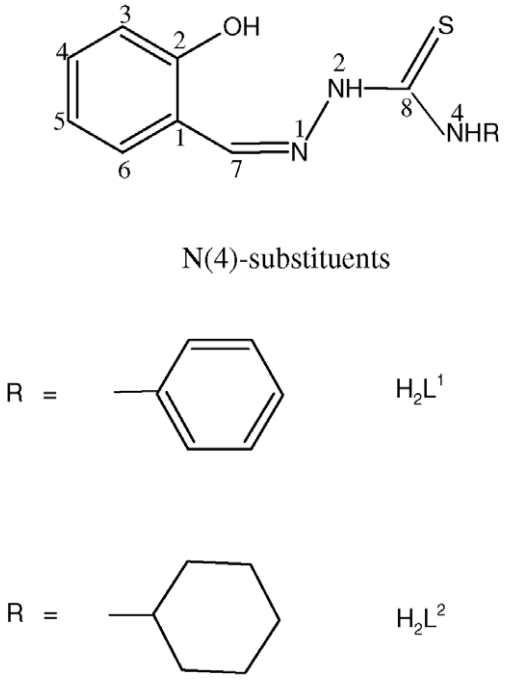


Fig. 1. Formulae of thiosemicarbazone ligands.

2.2.5. $[CuL^2dmbipy]$ (**5**)

The complex **5** was prepared by a similar method of the complex **3** by using H_2L^2.

2.3. Physical measurements

Elemental analyses were performed on a Vario ELIII elemental analyzer at SAIF, Cochin University of Science and Technology, Kochi 22, India. Magnetic susceptibility measurements were performed on a Vibrating Sample Magnetometer using $Hg[Co(SCN)_4]$ as a calibrant. Diamagnetic corrections for various atoms and structural units were computed from Pascal's constants. The FT-IR spectra were recorded on a Thermo Nicolet AVATAR 370 DTGS FTIR spectrometer using KBr pellets in the range 4000–400 cm^{-1} at SAIF, Cochin University of Science and Technology, Kochi 22, India and far IR spectra were recorded in the range 500–50 cm^{-1} on a Nicolet Magna 550 FT-IR spectrophotometer using polyethylene pellets at SAIF, IIT, Bombay, India. Electronic spectra of the ligands and the complexes were recorded on a GENESYS™ 10 Series spectrophotometers in DMF solvent. The EPR spectra were recorded on a Varian E-112 spectrometer using TCNE as the standard at SAIF, IIT, Bombay, India.

2.4. X-ray crystallography

A dark green crystal of the compound **5** having approximate dimensions $0.35\times0.30\times0.30$ mm was sealed in a

Table 1
Crystal data and structure refinement parameters for $[CuL^2dmbipy]$

Empirical formula	$C_{26}H_{29}CuN_5OS$
Formula weight	523.14
Temperature (K)	293(2)
Wavelength (Å)	0.71073
Crystal system	monoclinic
Space group	*C*2/*c*
Unit cell dimensions	
a (Å)	25.6690(19)
b (Å)	14.4860(8)
c (Å)	15.6400(10)
α (°)	90
β (°)	95.678(6)
γ (°)	90
Volume ($Å^3$)	5787.1(7)
Z	8
D_{calc} (Mg/m^3)	1.201
Absorption coefficient (mm^{-1})	0.851
F(000)	2184
Crystal size (mm)	$0.35\times0.30\times0.30$
θ Range for data collection (°)	2.03–24.98
Index ranges	$0\leqslant h\leqslant30$, $0\leqslant k\leqslant17$, $-18\leqslant l\leqslant18$
Reflections collected	5160
Independent reflections [R_{int}]	5041 [0.0361]
Refinement method	full-matrix least-squares on F^2
Data/restraints/parameters	5041/0/313
Goodness-of-fit on F^2	0.981
Final *R* indices [$I>2\sigma(I)$]	$R_1=0.0586$, $wR_2=0.1291$
R indices (all data)	$R_1=0.1830$, $wR_2=0.1619$
Largest difference in peak and hole (e A^{-3})	0.401 and −0.320

glass capillary. The X-ray diffraction data were measured at room temperature (293 K), data acquisition and cell refinement were done using the Argus (Nonius, MACH3 software) [6]. The Maxus software package (Nonius) was used for data reduction [7]. The structure was solved by direct methods and full-matrix least-squares refinement using SHELX 97 [8] package. The positions of all the non-hydrogen atoms were included in the full-matrix least-squares refinement using SHELX 97 program and all the hydrogen atoms were fixed in calculated positions. There were two potentially solvent accessible areas that can be spotted by PLATON [9]. However, we could not figure out any chemically reasonable solvent molecules in the void. Hence program SQUEEZE had been applied and the new file formed has been without solvent molecule. The structure of the compound **5** was plotted using the program DIAMOND Version 3.0 [10]. The final refinement cycle was based on all 5041 independent reflections and 313 variables, the $R_1 = 0.0586$, $wR_2 = 0.1291$. The crystallographic data and structure refinement parameters for the complex at 293 K are given in Table 1.

3. Results and discussion

3.1. Synthesis of the complexes

The complexes **1** and **4** were readily formed by refluxing ethanolic solutions of their respective ligand and $Cu(OAc)_2 \cdot H_2O$ in 1:1 ratio. The complex **2** was formed by using the ligand H_2L^1 and $Cu(OAc)_2 \cdot H_2O$ in 1:2 ratio. The complexes **3** and **5** were prepared by adding their respective ligands, metal salt and polypyridyl base 4,4′-dimethyl 2,2′-bipyridine (dmbipy) in 1:1:1 ratio. After double deprotonation, thiosemicarbazones coordinate as tridentate ligands in the thiolate form (L^{2-}) in all the complexes, except in complex **2**. In complex **2**, it is coordinated as monoanionic (HL^-) form. The elemental analyses of the complexes are in agreement with the general formula $[(ML)_2]$ (for complexes **1** and **4**); $[M(HL)_2]$ (for complex **2**) and [MLB] (for the complexes **3** and **5**) (Table 2). An X-ray quality single crystal of the compound **5** was obtained by slow evaporation of its ethanol solution over a period of 7 days.

Magnetic moments of the complexes were calculated from magnetic susceptibility measurements. The complexes **2**, **3** and **5** exhibit magnetic moments in the range 1.5–1.9 BM, which are close to the spin-only value. The magnetic moments of the complexes **1** and **4** at room temperature were found to be at ca. 1.25 BM. This low magnetic moments may arise due to the antiferromagnetic spin-spin interaction between the neighboring Cu(II) centers [11].

3.2. X-ray diffraction studies of the compound [CuL^2dmbipy]

The molecular structure of the compound **5** along with atom numbering scheme is given in Fig. 2 and selected bond lengths and bond angles are summarized in Table 3. Compound **5** crystallizes in the monoclinic space group $C2/c$. The copper atom in [CuL^2dmbipy] (**5**) is coordinated by phenolato oxygen, O(1), azomethine nitrogen, N(1), thiolato sulfur, S(1), of the thiosemicarbazone and the pyridine nitrogen, N(4) and N(5) of bipyridine derivative and is having an approximately trigonal bipyramidal geometry in which the equatorial positions are occupied by S(1), O(1) and N(5) and the axial positions by N(1) and N(4) [Cu(1)–N(1), 1.951(4) Å, Cu(1)–N(4), 2.016(4) Å] with the N(1)–Cu(1)–N(4) angle of 177.94(16)° being close to the 'ideal' value of 180° which is usual for such systems. In a five-coordinate system, the angular structural parameter (τ) is

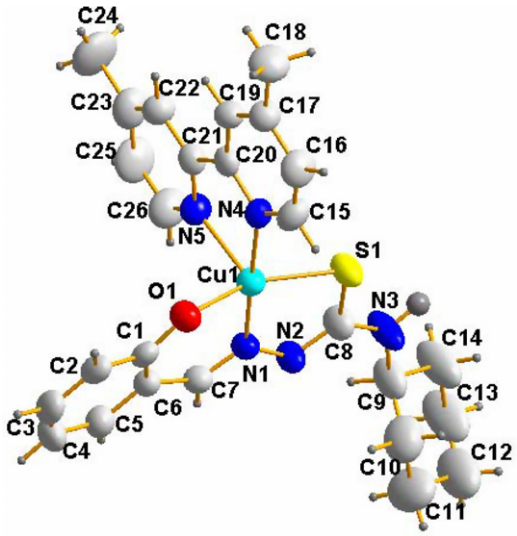


Fig. 2. Structure and labelling scheme for [CuL^2dmbipy].

Table 2
Analytical data of the ligands and their Cu(II) complexes

Compound	Colour	μ_{eff} (BM)	Calculated (found) %		
			C	H	N
H_2L^1	yellow		61.97(62.21)	4.83(5.13)	15.49(15.50)
$[(CuL^1)_2] \cdot \frac{1}{2}H_2O$ (**1**)	brown	1.24	49.84(49.80)	3.44(3.32)	12.46(13.03)
$[Cu(HL^1)_2] \cdot H_2O$ (**2**)	brown	1.51	54.05(54.54)	4.21(4.20)	13.51(13.50)
$[CuL^1dmbipy] \cdot H_2O$ (**3**)	green	1.72	58.36(58.08)	4.71(4.79)	13.09(12.98)
H_2L^2	white		59.65(59.48)	6.97(7.06)	14.91(14.95)
$[(CuL^2)_2]$ (**4**)	brown	1.25	49.61(49.43)	5.06(5.23)	12.40(12.22)
$[CuL^2dmbipy]$ (**5**)	green	1.82	59.69(60.57)	5.59(6.12)	13.39(12.72)

Table 3
Selected bond lengths (Å) and bond angles (°) for [CuL^{2}dmbipy]

Bond lengths			
Cu(1)–N(1)	1.951(4)	C(3)–C(4)	1.372(8)
Cu(1)–S(1)	2.272(15)	O(1)–C(1)	1.301(6)
Cu(1)–N(4)	2.016(4)	N(1)–N(2)	1.387(5)
Cu(1)–O(1)	1.965(3)	N(4)–C(15)	1.330(7)
N(3)–C(8)	1.343(7)	N(5)–C(26)	1.315(8)
C(1)–C(2)	1.404(7)	C(2)–C(3)	1.381(8)
C(4)–C(5)	1.372(8)	S(1)–C(8)	1.732(6)
Cu(1)–N(5)	2.226(5)	C(5)–C(6)	1.396(7)
N(1)–C(7)	1.291(6)	N(2)–C(8)	1.325(6)
N(3)–C(9)	1.467(7)	N(4)–C(20)	1.366(6)
N(5)–C(21)	1.352(6)	C(1)–C(6)	1.429(7)
Bond angles			
N(1)–Cu(1)–O(1)	92.28(16)	O(1)–Cu(1)–N(4)	89.94(15)
O(1)–Cu(1)–N(5)	96.36(16)	N(1)–Cu(1)–S(1)	84.88(13)
N(4)–Cu(1)–S(1)	93.41(12)	C(8)–S(1)–Cu(1)	94.53(19)
C(7)–N(1)–N(2)	113.5(4)	N(2)–N(1)–Cu(1)	122.3(3)
C(8)–N(3)–C(9)	124.2(5)	C(15)–N(4)–Cu(1)	124.5(4)
C(26)–N(5)–C(21)	117.5(5)	C(21)–N(5)–Cu(1)	112.5(4)
O(1)–C(1)–C(6)	124.0(5)	C(3)–C(2)–C(1)	122.2(6)
C(1)–C(6)–C(7)	122.9(5)	N(2)–C(8)–S(1)	125.6(4)
N(3)–C(9)–C(14)	109.9(5)	N(1)–Cu(1)–N(4)	177.94(16)
N(1)–Cu(1)–N(5)	102.14(18)	N(4)–Cu(1)–N(5)	77.23(18)
O(1)–Cu(1)–S(1)	156.71(12)	N(5)–Cu(1)–S(1)	106.84(12)
C(1)–O(1)–Cu(1)	125.6(3)	C(7)–N(1)–Cu(1)	124.0(4)
C(8)–N(2)–N(1)	112.2(4)	C(15)–N(4)–C(20)	116.4(4)
C(20)–N(4)–Cu(1)	119.1(4)	C(26)–N(5)–Cu(1)	130.1(4)
O(1)–C(1)–C(2)	119.6(5)	C(2)–C(1)–C(6)	116.4(5)
C(5)–C(6)–C(7)	117.6(5)	N(1)–C(7)–C(6)	126.3(5)
N(3)–C(8)–S(1)	117.4(4)	N(3)–C(9)–C(10)	111.1(6)

used to propose an index of trigonality. The value of τ is defined by an equation represented by $\tau = (\beta - \alpha)/60$, where β is the greatest basal angle and α is the second greatest angle; τ is 0 for rectangular pyramidal forms and 1 for trigonal bipyramidal forms [12,13]. However, in the case of the five-coordinate system, the structure varies from near regular trigonal bipyramidal (RTB) to near square based pyramidal (SBP). The value of τ for the compound **5** is 0.35, indicates that the coordination geometry around Cu(II) is best described as trigonal bipyramidal distorted square based pyramidal (TBDSBP) [14] with copper displaced 0.2174 Å above the N(1), N(4), S(1) and O(1) coordination plane and towards the elongated apical N(5) atom, at a larger distance of 2.226(5) Å. This value is larger than the normal Cu–N bond lengths reported [15,16]. One of the reasons for the deviation from an ideal stereochemistry is the restricted bite angle imposed by both the L^{2-} and dmbipy ligands. The bite angle around the metal viz, N(4)–Cu(1)–N(5) of 77.23(18)° may be considered normal, when compared with an average value of 77° cited in the literature [17–19]. The O(1)–Cu(1)–N(5) bond angle, 96.36(16), and S(1)–Cu(1)–N(5) bond angle, 106.84(12), indicate a slight tilting of the axial Cu(1)–N(5) bond in the direction of the O(1)–Cu(1) bond and away from S(1)–Cu(1) bond. The dihedral angle formed by the least square plane Cg(4) and Cg(5) is 6.13° for the compound **5**. Ring puckering analyses and least-square plane calculations show that the Cg(3) ring comprising of atoms Cu(1), O(1), C(1), C(6), C(7) and N(1) adopts a screw-boat conformation and Cg(7) ring comprising of atoms C(9), C(10), C(11), C(12), C(13) and C(14) adopts a chair conformation.

Fig. 3 shows the contents of the unit cell along the *b* axis. The assemblage of molecules in the respective manner in the unit cell is resulted by the H bonding, π–π and CH–π interactions as depicted in Table 4. The centroid Cg(4) is involved in π–π interaction with pyridyl ring of the neighboring unit at the distance of 3.7197 Å, the CH–π interactions of the rings Cg(6) and Cg(1) with the neighboring molecules and also intermolecular hydrogen bonding interactions between N(3)–H(3N) and S(1) contribute stability to the unit cell packing.

3.3. IR and electronic spectra

The infrared spectral data of the complexes **1**–**5** are presented in Table 5 with their tentative assignments. On coordination of azomethine nitrogen, ν(C=N) shifts to lower wavenumbers by 10–20 cm^{-1}, as the band shifts from 1613 cm^{-1} in the uncomplexed thiosemicarbazone spectrum to ca. 1596 cm^{-1} in the spectra of the complexes. In all the five Cu(II) complexes, another strong band is found at ca. 1530–1555 cm^{-1}, which may be due to the newly formed ν(N=C) bond, resulting from enolization of the principal thiosemicarbazone ligand. Coordination of azomethine nitrogen is confirmed with the presence of new bands in the range 420–470 cm^{-1}, assignable to ν(Cu–N) for these complexes. For complexes **1**–**5**, ν(Cu–N) bands are at ca. 427 cm^{-1}. The ν(N–N) of the thiosemicarbazones H_2L^1 and H_2L^2 are found at 1149 and 1111 cm^{-1} respectively. The increase in the frequency of this band in the spectra of the complexes, due to the increase in the bond strength, again confirms the coordination *via* the azomethine nitrogen [20]. The decrease in the stretching frequency of C–S bond from ca. 865 cm^{-1} in the thiosemicarbazones by 50–70 cm^{-1} upon complexation indicates coordination *via* its thiolate sulfur. The presence of a new band in the 320–340 cm^{-1} range assignable to ν(Cu–S), is another indication of the involvement of sulfur coordination. In all the five complexes, except in the complex **2**, phenolic oxygen coordinated to copper by loss of the OH proton. A new band in the range 380–395 cm^{-1} in the spectra of the complexes **3** and **5** are assignable to ν(Cu–O). The IR spectra of the complexes **3** and **5** display bands characteristic of coordinated heterocyclic base [21].

The electronic spectra of the complexes in DMF solution are presented in Table 6. Each thiosemicarbazone and its copper(II) complexes have a ring $\pi \rightarrow \pi^*$ bands in the range 32 000–38 000 cm^{-1} and $n \rightarrow \pi^*$ bands in the range 28 000–32 000 cm^{-1}. Two ligand to metal charge transfer bands are found in 24 000–28 000 cm^{-1} range. In accordance with studies of previous copper(II) thiosemicarbazone complexes [22,23], the higher energy bands in the range 26 000–27 000 cm^{-1} is assigned to $S \rightarrow Cu^{II}$ transitions. The bands in the

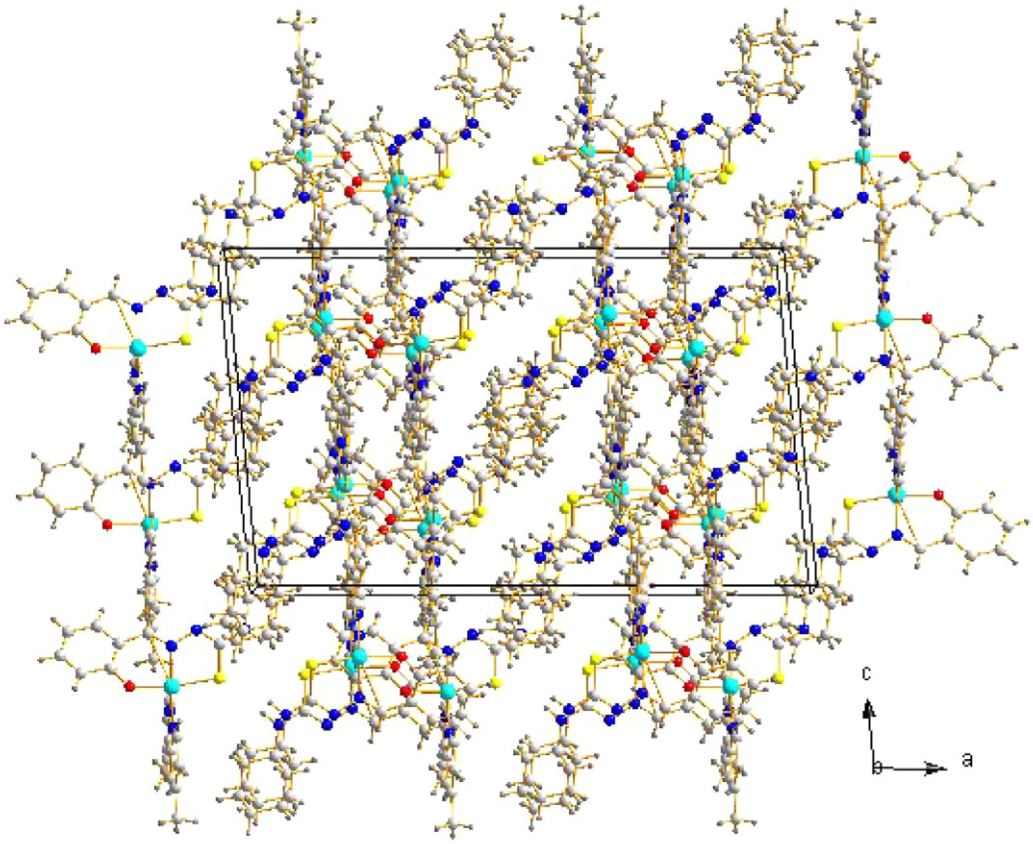


Fig. 3. Unit cell packing diagram of the complex [CuL^2dmbipy] viewed along the *b* axis.

Table 4
Interaction parameters of the compound [CuL^2dmbipy]

Cg(I)–Res(1)–Cg(J)	Cg–Cg (Å)	α (°)	β (°)
π–π interactions			
Cg(4) [1] → Cg(5)[a]	3.7197	6.13	22.51
Cg(5) [1] → Cg(4)[a]	3.7197	6.13	21.67
XH(I)–Cg(J)	H···Cg (Å)	X–H···Cg (°)	X···Cg (Å)
CH–π interactions			
C(18)–H(18)[1] → Cg(6)[b]	2.90	176	3.8605
C(18)–H(18) [1] → Cg(1)[c]	2.96	138	3.7250
C(25)–H(25) [1] → Cg(6)[d]	2.97	165	3.8788

D–H–A	D–H	H–A	D–A	D–H–A
H bonding				
N(3)–H(3N)–S(1)	0.94	2.62	3.5310	165

Equivalent position codes: a = 1/2 − *x*, 1/2 − *y*, −*z*. Cg(4) = N(4), C(15), C(16), C(17), C(19), C(20); Cg(5) = N(5), C(21), C(22), C(23), C(25), C(26).
Equivalent position codes: b = 1/2 − *x*, 1/2 − *y*, −*z*; c = *x*, 1 − *y*, −1/2 + *z*; d = 1/2 − *x*, − 1/2 + *y*, 1/2 − *z*.
D, donor; A, acceptor; Cg, centroid, α, dihedral angles between planes I and J, β = angle Cg(1)–Cg(J).

24 000–25 000 cm^{-1} range are assignable to phenoxy O → Cu^{II} transitions [24]. Each complex has a d–d combination band in the range 14 000–16 000 cm^{-1}, which appears as a weak shoulder on the intraligand and charge transfer bands.

3.4. EPR spectra

The EPR parameters obtained for the compounds in the polycrystalline state at 298 K and in DMF solution at 77 K are presented in Tables 7 and 8.

The EPR spectra of compounds **1**–**5** in the polycrystalline state at room temperature shows different types of geometrical species. The compounds **1**, **3** and **4** show isotropic spectra with only one broad signal at $g = 2.059$, 2.070 and 2.129, respectively. Spectrum of compound **2** gives three *g* values indicating rhombic distortion in its geometry. The values g_1 and g_2 are very close to each other in compound **2**, which means that the rhombic distortion is very small. The spectrum of the compound **5** shows a typical axial one with well-defined $g_\parallel$ and $g_\perp$ values at 2.195 and 2.063, respectively. The geometric parameter *G*, which is a measure of the exchange interaction between the copper centers in the polycrystalline compound, is calculated using the equation: $G = (g_\parallel - 2.0023)/(g_\perp - 2.0023)$ for axial spectra and for rhombic spectra $G = (g_3 - 2.0023)/(g_\perp - 2.0023)$, where $g_\perp = (g_1 + g_2)/2$. If $G < 4.0$ considerable exchange interaction is indicated in the solid complex [25,26]. The *G* value for the compounds **2** and **5** in polycrystalline state at 298 K are 3.55 and 3.17, respectively. In all the copper(II) complexes $g_\parallel > g_\perp > 2.0023$ and *G* values within the range 2.5–4.0 are consistent with a $d_{x^2-y^2}$ ground state.

Table 5
IR spectral assignments for ligands and their Cu(II) complexes

Compound	ν(C=N)	ν(N=C)	ν(N–N)	ν(Cu–N)	ν/δ (C=S)	ν(C–O)	Bands due to heterocyclic base
H_2L^1	1613		1149		1328, 874	1255	
$[(CuL^1)_2]\cdot\frac{1}{2}H_2O$ (**1**)	1594	1555	1153	428	1314, 843	1201	
$[Cu(HL^1)_2]\cdot H_2O$ (**2**)	1599	1540	1153	431	1314, 750	1201	
$[CuL^1dmbipy]\cdot H_2O$ (**3**)	1596	1537	1150	420	1313, 828	1247	1434, 753, 697
H_2L^2	1614		1111		1328, 856	1263	
$[(CuL^2)_2]$ (**4**)	1594	1546	1149	421	1272, 818	1196	
$[CuL^2dmbipy]$ (**5**)	1596	1530	1146	439	1313, 823	1233	1476, 753, 627

Table 6
Electronic spectral assignments for the ligands and their Cu(II) complexes

Compound	π–π^*	n–π^*	LMCT	d–d
H_2L^1	32250	29060		
$[(CuL^1)_2]\cdot\frac{1}{2}H_2O$ (**1**)	33110	31055	27240, 26240	15520
$[Cu(HL^1)_2]\cdot H_2O$ (**2**)	33780	30950, 30300	25970	15640
$[CuL^1dmbipy]\cdot H_2O$ (**3**)	37730, 35080	30950, 30120	25380, 24690	14160
H_2L^2	32150	28730		
$[(CuL^2)_2]$ (**4**)	33000	31250	26310, 24630	16180
$[CuL^2dmbipy]$ (**5**)	34010	31050, 30120	25900, 25120	15430

Table 7
EPR spectral assignments for Cu(II) complexes in polycrystalline state at (298 K) and solution at (77 K)

Compound	Polycrystalline state (298 K)	DMF solution (77 K)					
		$g_\parallel$	$g_\perp$	g_{av}	$A_\parallel$[a]	$A_\perp$[a]	A_{av}[a]
$[(CuL^1)_2]\cdot\frac{1}{2}H_2O$ (**1**)	2.059 (g_{iso})	2.195	2.053	2.100	184.5	19.1	71.9
$[Cu(HL^1)_2]\cdot H_2O$ (**2**)	2.030/2.040/2.120 ($g_1/g_2/g_3$)	2.191	2.053	2.099	184.1	14.4	68.6
$[CuL^1dmbipy]\cdot H_2O$ (**3**)	2.070 (g_{iso})	2.169	2.063	2.098	189.0		
$[(CuL^2)_2]$ (**4**)	2.129 (g_{iso})	2.177	2.045	2.089	182.3	14.3	68.1
$[CuL^2dmbipy]$ (**5**)	2.195/2.063 ($g_\parallel/g_\perp$)	2.167	2.056	2.093	190.5		

[a] Expressed in units of cm^{-1} multiplied by a factor of 10^{-4}.

Table 8
EPR bonding parameters for compounds **1**–**5**

Compound	DMF solution (77 K)									
	G (77 K)	α^2	β^2	γ^2	K	$K_\parallel$	$K_\perp$	f[a]	P	R[b]
$[(CuL^1)_2]\cdot\frac{1}{2}H_2O$ (**1**)	3.66	0.76	0.88	0.89	0.33	0.67	0.68	119.01	0.0235	
$[Cu(HL^1)_2]\cdot H_2O$ (**2**)	3.59	0.76	0.86	0.90	0.33	0.66	0.69	119	0.0240	0.125
$[CuL^1dmbipy]\cdot H_2O$ (**3**)	2.69	0.75	0.78	0.94		0.59	0.71	114.8		
$[(CuL^2)_2]$ (**4**)	3.89	0.73	0.87	0.86	0.31	0.65	0.64	119.4	0.0236	
$[CuL^2dmbipy]$ (**5**)	2.98	0.75	0.81	0.93		0.61	0.70	114		

[a] Expressed in units of (cm).
[b] Parameter $R = (g_2 - g_1)/(g_3 - g_2)$.

The parameter R {R=$(g_2 - g_1)/(g_3 - g_2)$ for rhombic systems} calculated for the compound **2** is 0.125, i.e., $R < 1$, indicating a $d_{x^2-y^2}$ ground state of the copper(II) ion [27,28]. From the g value of a transition metal complex, we can obtain very important information about the structure of the complex.

The EPR spectra of all the compounds in frozen DMF solution at 77 K are axial. Moreover, they show well defined four hyperfine lines in the parallel region corresponding to the electron spin–nuclear spin interaction ($^{63,65}Cu$, $I = 3/2$). The fourth copper hyperfine line is expected to overlap with the high field component ($g_\perp$). However, the half field signal corresponding to the dimer was not observed for the compounds **1** and **4**. In all these compounds, $g_\parallel > g_\perp > 2$, corresponding to the presence of an unpaired electron in the $d_{x^2-y^2}$ orbital [29,30]. For a Cu(II) complex, $g_\parallel$ is a parameter sensitive enough to indicate covalence. For a covalent complex, $g_\parallel < 2.3$. Here also,

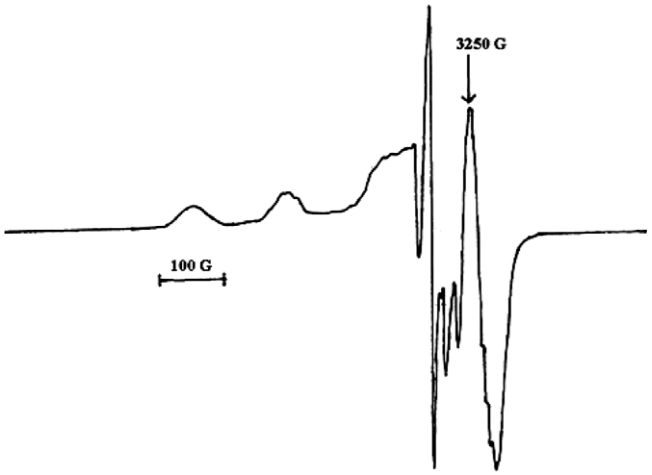


Fig. 4. EPR spectra of the compound **4** in DMF solution (at 77 K).

all the five complexes are covalent in nature. In solution at 77 K, $g_{\|}$ values (2.16–2.19) are almost the same for all the compounds, which indicate similar bonding nature in all of them [31]. In compound **4**, well resolved spectra with four copper hyperfine lines and three superhyperfine lines due to the azomethine nitrogen are observed in DMF (Fig. 4).

The EPR parameters $g_{\|}$, $g_{\perp}$, g_{av}, $A_{\|}$(Cu) and $A_{\perp}$(Cu) and energies of d–d transitions were used to evaluate the bonding parameters α^2, β^2 and γ^2, which may be regarded as measures of covalency of the in-plane σ bonds, in-plane π bonds and out-of-plane π bonds, respectively [32].

The value of in-plane σ bonding parameter α^2 was estimated from the expression [33,34],

$$\alpha^2 = -A_{\|}/0.036 + (g_{\|} - 2.00277) + 3/7(g_{\perp} - 2.00277) + 0.04$$

The following simplified expressions were used to calculate the bonding parameters [35,36]:

$$K_{\|}^2 = (g_{\|} - 2.00277)E_{d\text{–}d}/8\lambda_0$$

$$K_{\perp}^2 = (g_{\perp} - 2.00277)E_{d\text{–}d}/2\lambda_0$$

where $K_{\|} = \alpha^2\beta^2$ and $K_{\perp} = \alpha^2\gamma^2$, $K_{\|}$ and $K_{\perp}$ are orbital reduction factors and λ_0 represents the one electron spin–orbit coupling constant which equals $-828\ cm^{-1}$.

Hathaway [37] pointed out that, for pure σ bonding, $K_{\|} \approx K_{\perp} \approx 0.77$, and for in-plane π bonding, $K_{\|} < K_{\perp}$; while for out-of-plane π bonding $K_{\perp} < K_{\|}$. In all the complexes it is observed that $K_{\|} < K_{\perp}$which indicates the presence of significant in-plane π bonding. The values of the bonding parameters α^2, β^2 and $\gamma^2 < 1.0$ (value of 1.0 for 100% ionic character) indicate significant in-plane π bonding and in-plane σ bonding.

The Fermi contact hyperfine interaction term K may be obtained from [38]

$$K = A_{iso}/P\beta^2 + (g_{av} - 2.00277)/\beta^2$$

where P is the free ion dipolar term and its, value is 0.036. K is a dimensionless quantity, which is a measure of the contribution of s electrons to the hyperfine interaction and is generally found to have a value of 0.30. The K values obtained for all the complexes are in good agreement with those estimated by Assour [39] and Abragam and Pryce [40]. The empirical factor $f = g_{\|}/A_{\|}$ (cm^{-1}), is an index of tetrahedral distortion. In all the five compounds, f falls in the range 114–119 cm corresponding to a copper(II) center with medium distortion [41].

Acknowledgements

The authors are indebted to SAIF, Cochin University of Science and Technology, Kochi, Kerala, India for elemental analyses and IR spectral analysis. We are thankful to National Single Crystal X-ray diffraction Facility, IIT, Bombay, India for providing single crystal XRD results. The financial support by DST, New Delhi, India (No. SR/SI/IC-31/2002) is gratefully acknowledged.

Appendix A. Supplementary material

CCDC 279223 contains the supplementary crystallographic data for **5**. These data can be obtained free of charge via http://www.ccdc.cam.ac.uk/conts/retrieving.html, or from the Cambridge Crystallographic Data Centre, 12 Union Road, Cambridge CB2 1EZ, UK; fax: (+44) 1223-336-033; or e-mail: deposit@ccdc.cam.ac.uk. Supplementary data associated with this article can be found, in the online version, at doi:10.1016/j.poly.2006.09.040.

References

[1] D.X. West, S.B. Padhye, P.S. Sonawane, Struct Bonding 76 (1991) 1.
[2] P. Bindu, M.R.P. Kurup, T.R. Satyakeerty, Polyhedron 18 (1999) 321.
[3] D.X. West, Y. Yang, T.L. Klein, K.I. Goldberg, A.E. Liberta, Polyhedron 14 (1995) 1681.
[4] D.X. West, Transition Met Chem. 22 (1997) 180.
[5] P. Bindu, M.R.P. Kurup, Trans. Met Chem. 22 (1997) 578.
[6] Nonius, MACH3 software, B.V. Nonius, Delft, The Netherlands, 1997.
[7] G.M. Sheldrick, Acta Crystallogr., Sect. A 46 (1990) 467.
[8] G.M. Sheldrick, SHELXL 97 and SHELXS 97, University of Gottingen, Germany, 1997.
[9] A.L. Spek, ORTEP-III and PLATON, a Multipurpose Crystallographic Tool, Utrecht University, Utrecht, The Netherlands, 1999.
[10] K. Brandenburg, DIAMOND Version 3.0, 1997–2004, Crystal Impact GbR, Bonn, Germany.
[11] B.N. Figgis, Introduction to Ligand fields, Wiley, New Delhi, 1976.
[12] A.W. Addison, T.N. Rao, J. Reedijk, J. Van Rijn, G.C. Verschoor, J. Chem. Soc., Dalton Trans. (1984) 1349.
[13] G. Murphy, C.O. Sullivan, B. Murphy, B. Hathaway, Inorg. Chem. 37 (1998) 240.
[14] M. Vaidyanathan, R. Balamurugan, U. Sivagnanam, M. Palaniandavar, J. Chem. Soc., Dalton Trans. (2001) 3498.
[15] P.C. Chieh, G.J. Palenik, Inorg. Chem. 11 (1972) 816.
[16] F. Clifford, E. Counihan, W. Fitzgerald, K. Seff, C. Simmons, S. Tyagi, B. Hathaway, J. Chem. Soc., Chem. Commun. (1982) 196.
[17] C.B. Castellani, G. Gatti, R. Millini, Inorg. Chem. 23 (1983) 4004.
[18] N.J. Ray, B.J. Hathaway, Acta Crystallogr., Sect. B 34 (1978) 3224.
[19] G. Druhan, B.J. Hathaway, Acta Crystallogr., Sect. B 35 (1979) 344.

[20] B.S. Garg, M.R.P. Kurup, S.K. Jain, Y.K. Bhoon, Trans. Met Chem. 13 (1988) 309.
[21] P.B. Sreeja, M.R.P. Kurup, Spectrochim. Acta A 61 (2004) 331.
[22] M. Mikuriya, H. Okawa, S. Kida, Inorg. Chim. Acta 34 (1979) 13.
[23] E.W. Ainscough, A.M. Brodie, N.G. Larsen, Inorg. Chim. Acta 60 (1982) 25.
[24] M. Mikuriya, H. Okawa, S. Kida, Bull. Chem. Soc. Jpn. 53 (1980) 3717.
[25] M. Joseph, M. Kuriakose, M.R.P. Kurup, E. Suresh, A. Kishore, S.G. Bhat, Polyhedron 25 (2006) 61.
[26] I.M. Proctor, B.J. Hathaway, P. Nicholis, J. Chem. Soc. (1968) 1678.
[27] S.S. Kandil, A. El-Dissouky, G.Y. Ali, J. Coord. Chem. 57 (2004) 105.
[28] M.F. El-Shazly, A. El-Dissouky, T.M. Salem, M.M. Osman, Inorg. Chim. Acta 40 (1980) 1.
[29] A. Sreekanth, M.R.P. Kurup, Polyhedron 22 (2003) 3321.
[30] M.J. Bew, B.J. Hathaway, R.R. Faraday, J. Chem. Soc., Dalton Trans. (1972) 1229.
[31] M. Joseph, V. Suni, M.R.P. Kurup, M. Nethaji, A. Kishore, S.G. Bhat, Polyhedron 23 (2004) 3069.
[32] A.H. Maki, B.R. McGarvey, J. Chem. Phys. 29 (1958) 31.
[33] A.H. Maki, B.R. McGarvey, J. Chem. Phys. 29 (1958) 35.
[34] D. Kivelson, R. Neiman, J. Chem. Soc., Dalton Trans. 35 (1961) 149.
[35] B.N. Figgis, Introduction to Ligand Fields, Interscience, New York, 1966, p. 295.
[36] V. Philip, V. Suni, M.R.P. Kurup, M. Nethaji, Polyhedron 24 (2005) 1133.
[37] B.J. Hathaway, Structure and Bonding, Springer Verlag, Heidelberg, 1973, p. 60.
[38] R.S. Nicholson, Anal. Chem. 37 (1965) 1351.
[39] M. Assour, J. Chem. Phys. 43 (1965) 2477.
[40] A. Abragam, M.H.L. Pryce, Proc. R. Soc. London A 206 (1961) 164.
[41] R.P. John, A. Sreekanth, V. Rajakannan, T.A. Ajith, M.R.P. Kurup, Polyhedron 23 (2004) 2549.

Available online at www.sciencedirect.com
ScienceDirect
Polyhedron 26 (2007) 837–844
POLYHEDRON
www.elsevier.com/locate/poly

$^{2,3}J$(P,X) [X = H, C] coupling constants dependency on the ring size, hybridization and substituents in new diazaphospholes and diazaphosphorinanes, NMR and X-ray crystallography studies

Khodayar Gholivand *, Mehrdad Pourayoubi, Zahra Shariatinia

Department of Chemistry, Tarbiat Modares University, P.O. Box 14115-175, Tehran, Iran

Received 20 June 2006; accepted 14 September 2006
Available online 10 October 2006

Abstract

New diazaphospholes and diazaphosphorinanes (**1**–**12**) were synthesized and characterized by ^{1}H, ^{13}C, ^{31}P NMR, mass and IR spectroscopy and elemental analysis. The factors which affect the $^{2,3}J$(P,X) (X=H, C) coupling constants in compounds **1**–**12** were considered. The ring size and the hybridization are parameters which change the ^{2}J(PNH) coupling constant in the sequence benzodiazaphospholes > diazaphospholes > diazaphosphorinanes. Also, attention was paid to exocyclic substituent effects. Asymmetric diazaphospholes **5**–**8** indicate two different $^{2}J(P,C)_{aliphatic}$ values, and the more deshielded carbon atom has a higher coupling constant. The crystal structures of compounds **7** and **10**–**12** were determined by X-ray crystallography. Hydrogen bonds produce a 2D framework for compound **10**, which is composed of two symmetrically independent molecules. Compounds **7**, **11** and **12** exist as a polymeric chain, 2D framework and centrosymmetric dimer, respectively, which are made by hydrogen bonds.
© 2006 Elsevier Ltd. All rights reserved.

Keywords: Diazaphospholes; Diazaphosphorinanes; NMR; X-ray crystallography

1. Introduction

Diazaphospholes and diazaphosphorinanes are considered as important compounds due to their great applications in chemistry and medicine [1,2]. So far, a few structures [3,4] and coupling constant assignments of these compounds have been reported [3]. Stereochemistry, P–C coupling constants in 1,3,2-benzodiazaphospholes [5] and 2-oxo-, 2-thio-diazaphosphorinanes have been presented [6]. Phosphorus–hydrogen coupling constants in some diazaphospholes with three coordinated phosphorus atoms were studied [7]. To further investigate this area, the new diazaphospholes and diazaphosphorinanes **1**–**12** were synthesized and characterized to find effective parameters for $^{2,3}J$(P,X) coupling constants (X = H, C).

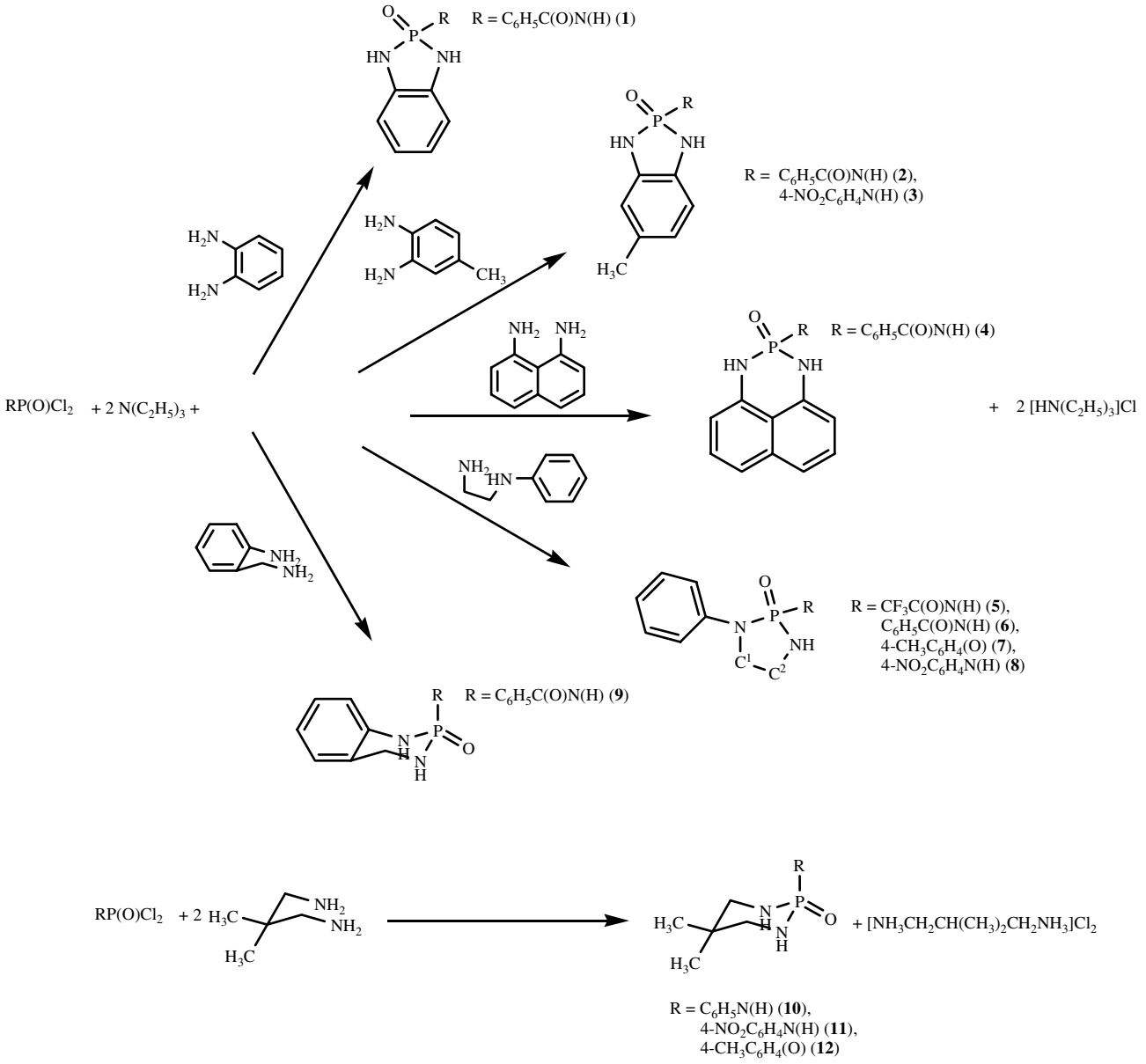
2. Experimental

2.1. Spectroscopic measurements

NMR spectra of compounds **1**–**12** were obtained from their prepared solutions, which must be fresh. ^{1}H and ^{13}C NMR spectra were recorded on a Bruker (Avance DRS) 500 spectrometer. ^{1}H and ^{13}C, and ^{31}P chemical shifts were determined relative to tetramethylsilane (TMS) and 85% H_3PO_4 as external standards, respectively, and HSQC ^{1}H–^{15}N spectra to external TMS and CH_3–NO_2 standards. Infrared (IR) spectra were recorded on a Shimadzu model IR-60 spectrometer. Elemental analysis was performed using a Heraeus CHN-O-RAPID apparatus. High-resolution Mass spectra were obtained with a Shimadzu model QP-1100EX spectrometer (EI, 20 eV).

* Corresponding author. Tel.: +98 21 88011001 4422; fax: +98 21 88006544.
E-mail address: gholi_kh@modares.ac.ir (K. Gholivand).

0277-5387/$ - see front matter © 2006 Elsevier Ltd. All rights reserved.
doi:10.1016/j.poly.2006.09.092



Scheme 1. The preparation of compounds **1**–**12**.

2.2. Syntheses

Syntheses of compounds **1**–**12** were performed by the reaction of *N*-benzoyl- [8], *N*-trifluoroacetyl- [9], *N*-phenyl- [10] and *N*-4-nitrophenyl- [11] phosphoramidic dichloride and (4-tolyl)-dichlorophosphate [12] with the corresponding amines in the presence of an HCl scavenger (triethylamine or an excess amount of the corresponding diamine).

2.3. X-ray measurements

X-ray data were collected on a Bruker SMART 1000 CCD single crystal diffractometer. Routine Lorentz and polarization corrections were applied and an absorption correction was performed using the SADABS program [13]. The structures were refined with SHELXL-97 [14] by full-matrix least-squares on F^2.

3. Results and discussion

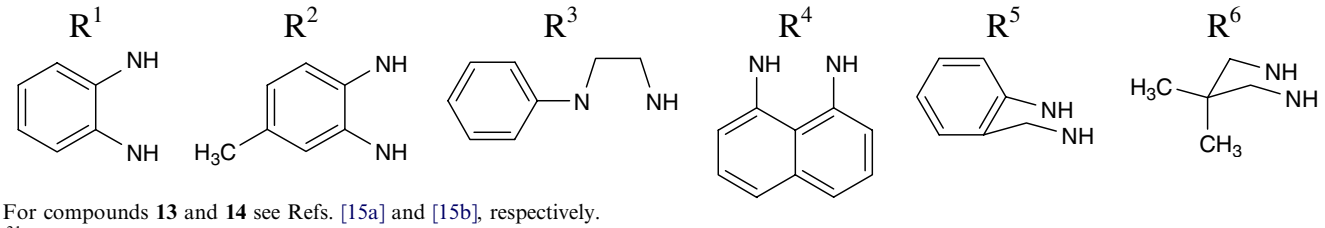
3.1. NMR study

Several new diazaphospholes and diazaphosphorinanes **1**–**12** (Scheme 1) were synthesized to study effective parameters for $^{2,3}J$(P,X) coupling constants (X = H, C).

The effect of ring size on ^2J(PNH): Although the variation of the ^2J(PNH) coupling constant in acyclic phosphoramidates has been considered (in the range of 4–12 Hz) [15–17], less attention has been paid to diazaphospholes and diazaphosphorinanes. The ^{1}H NMR spectrum of

Table 1
^{31}P chemical shifts (ppm) and $^{2}J(PNH)$ (Hz) in compounds **1**–**14**

No.	Compound	$^{2}J(PNH)_{endocyclic}$	$^{2}J(PNH)_{exocyclic}$	δ (^{31}P)
1	$C_6H_5C(O)N(H)P(O)R^1$	17.9	8.4	13.2
2	$C_6H_5C(O)N(H)P(O)R^2$	17.8,18.0	6.5	13.7
3	$4\text{-}NO_2C_6H_4N(H)P(O)R^2$	17.1, 17.2	8.1	12.2
4	$C_6H_5C(O)N(H)P(O)R^4$	5.0	9.4	−10.6
5	$CF_3C(O)N(H)P(O)R^3$	15.3	b	12.8
6	$C_6H_5C(O)N(H)P(O)R^3$	14.8	6.7	14.2
7	$4\text{-}CH_3\text{–}C_6H_4OP(O)R^3$	13.9		18.6
8	$4\text{-}NO_2\text{–}C_6H_4N(H)P(O)R^3$	13.1	6.5	14.9
9	$C_6H_5C(O)N(H)P(O)R^5$	4.6, 5.7	4.9	0.2
10	$C_6H_5N(H)P(O)R^6$	5.0	b	5.0
11	$4\text{-}NO_2\text{–}C_6H_4N(H)P(O)R^6$	5.4	10.3	4.0
12	$4\text{-}CH_3\text{–}C_6H_4OP(O)R^6$	5.2		7.6
13[a]	$C_6H_5OP(O)R^1$	15.0		
14[b]	$ClP(O)R^2$	11.2 and 11.3		1.2



[a,b] For compounds **13** and **14** see Refs. [15a] and [15b], respectively.
[a] ^{31}P chemical shift was not reported in Ref. [15a].

compound **1** shows a doublet at 8.58 ppm with a high value $^{2}J(PNH)$ coupling constant (17.9 Hz) for two equivalent NH protons and a doublet at 9.96 ppm with $^{2}J(PNH) = 8.4$ Hz for the amidic proton. Also, in diazaphospholes **2** and **3**, the two non-equivalent NH protons (of the ring) indicate two high value $^{2}J(PNH)$ coupling constants, Table 1. Compound **4** shows a drastically reduction ($^{2}J(PNH) = 5.0$ Hz) on increasing the ring size (from five to six). ^{1}H NMR spectra of diazaphospholes **5**–**8** show $^{2}J(PNH)$ values in the range 13.1–15.3 Hz, which are reduced in comparison with compounds **1**–**3**. A further reduction was obtained by increasing the ring size in cyclic aliphatic compounds **10**–**12**, Table 1. A major part of the observed changes more likely results from conformational averaging of the orientation of bond vectors in the six-member rings when compared with the more fixed orientation of bond vectors in the five-member rings.

The effect of hybridization on $^{2}J(PNH)$: In compounds **1**–**3** the endocyclic nitrogen atoms of the NH groups are bonded to the carbon atoms with sp^2 hybridization in five-membered rings, but in compounds **5**–**8** they are bonded to sp^3 carbon atoms. $^{2}J(PNH)$ in compounds **5**–**8** are lower than those of compounds **1**–**3**. In molecule **9**, possessing two various NH groups, one of the two NH protons is bonded to a $C(sp^2)$ atom and the other to $C(sp^3)$ in a six-membered ring. The ^{1}H NMR spectrum shows two different coupling constants, $^{2}J(PNH) = 5.7$ Hz (sp^2) and $^{2}J(PNH) = 4.6$ Hz (sp^3).

The effect of the substituent on $^{2}J(PNH)$: A comparison of the benzodiazaphospholes **1**–**3**, **13** and **14** indicates a substituent effect (of the exocyclic group) on $^{2}J(PN_{endocyclic}H)$, in the range of 18.0 Hz (for **1** with a $C_6H_5C(O)NH$ moiety) to 11.2 Hz (for **14** with a Cl substituent), Table 1. Furthermore, in diazaphospholes **5**–**8**, the highest value of $^{2}J(PNH)$ is observed for compound **5** with a $CF_3C(O)N(H)$ electronegative moiety.

$^{3}J(PNCH)$ coupling constants: In the asymmetric diazaphospholes **5**–**8**, four H atoms of the $–CH_2CH_2–$ moiety appear at different chemical shifts with various $^{3}J(PNCH)_{aliphatic}$ coupling constants. Two benzylic protons of diazaphosphorinane **9** are diastereotopic and have different $^{3}J(PNCH)$ coupling constants depending on the dihedral angles with the P atom. ^{1}H NMR spectra of

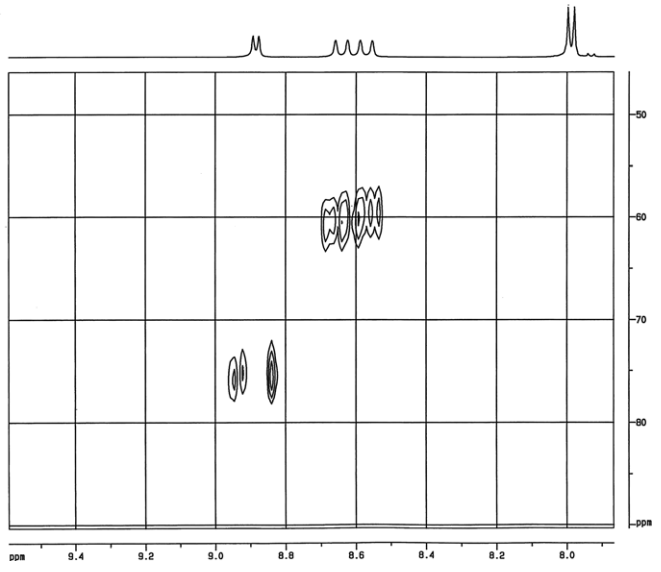
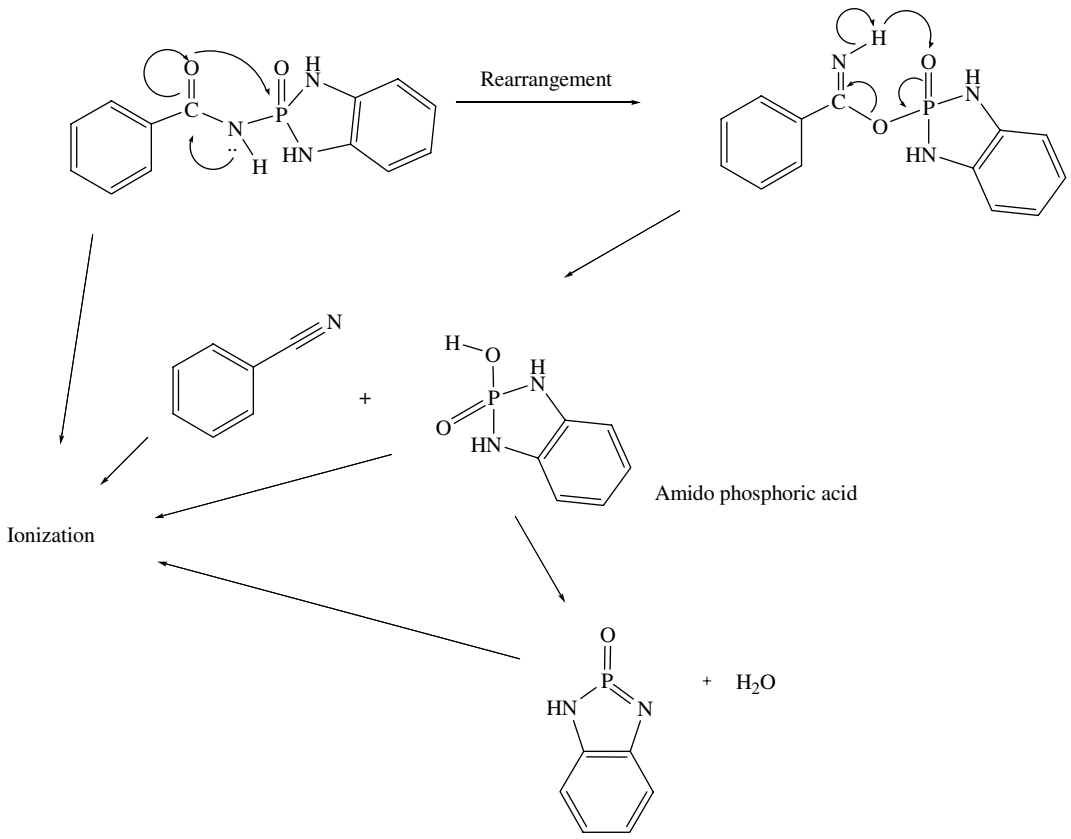


Fig. 1. 2D HSQC ^{1}H–^{15}N spectrum for compound **3**.



Scheme 2. Fragmentation pathway in the mass spectrum of compound **1**.

Table 2
The intensities of $C_6H_5CN^+$ ($m/z = 103$) and other fragments in mass spectra of compounds **1**, **2**, **4**, **6** and **9** (the numbers in parentheses are intensities of these fragments)

Compound	$C_6H_5CN^+$	Amidophosphoric acid	Amidophosphoric acid–H_2O
1	69	170(100)	152(59)
2	100	184(14)	166(2)
4	100	220(65)	202(45)
6	100	184(9)	166(3)
9	100	198(55)	180(21)

compounds **10**–**12** show two different signals for H_{axial} and $H_{equatorial}$. The torsion angles of P–N–C–H_{axial} and P–N–C–$H_{equatorial}$ are about ±70° and ±170°, respectively, obtained from X-ray crystallography. Considering the Karplus equation [18], the values 24.8, 25.1 and 26.7 Hz are related to $^3J(PNCH_{equatorial})$ values in **10**–**12**. These values are larger than $^3J(PNCH)$ values for acyclic phosphoramidates [15–17]. For H_{axial}, the coupling with the P atom was not observed.

Ring size influence on $^2J(P,C)_{aromatic}$: Similar to the $^2J(PNH)$ value, high values for $^2J(P,C)_{aromatic}$ were observed for diazaphospholes **1**–**3** (about 14.0 Hz) which are larger than the values of acyclic phosphoramidates [19].

Deshielded carbon atoms and $^2J(P,C)$: In compounds **5**–**8**, two different signals (and two different $^2J(P,C)$ values) appear for the aliphatic carbon atoms (C^1 and C^2, Scheme 1) and the deshielded C^1 atoms show high values for $^2J(P,C)$ due to the effect of the phenyl ring.

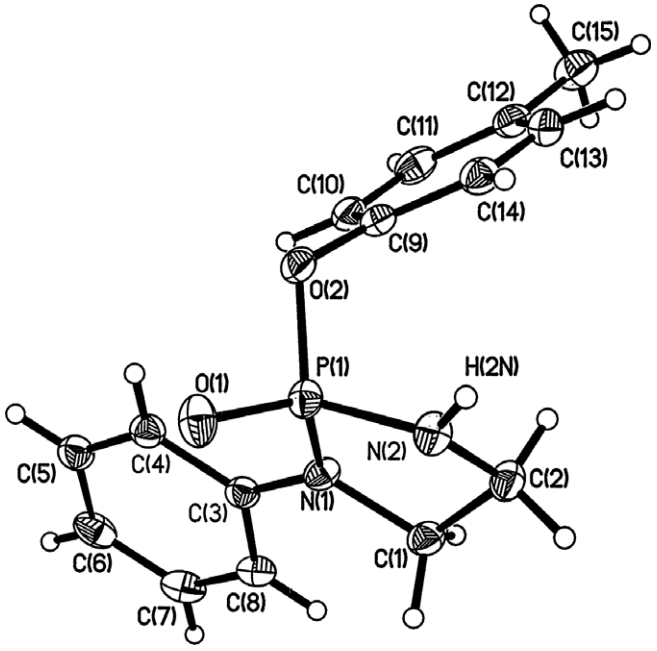


Fig. 2. Molecular structure and atom-labelling scheme for compound **7**, $(4\text{-}CH_3\text{-}C_6H_4O)P(O)[NHCH_2CH_2N(C_6H_5)]$ (50% probability ellipsoids).

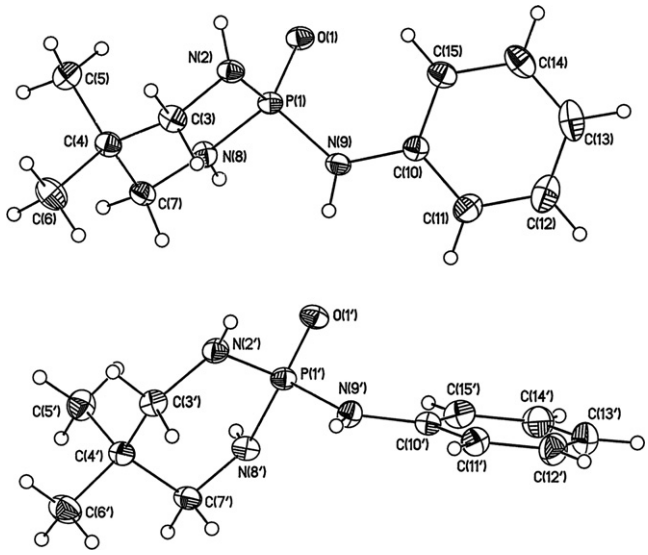


Fig. 3. Molecular structure and atom-labelling scheme for compound **10**, $C_6H_5N(H)P(O)[NHCH_2C(CH_3)_2CH_2NH]$ (50% probability ellipsoids).

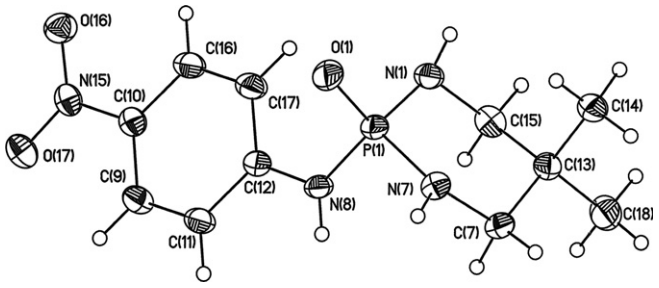


Fig. 4. Molecular structure and atom-labelling scheme for compound **11**, $4\text{-}NO_2\text{-}C_6H_4N(H)P(O)[NHCH_2C(CH_3)_2CH_2NH]$ (50% probability ellipsoids).

Substituent effect on $^2J(P,C)$: In compounds **5**–**8**, both $^2J(P,C^1)$ and $^2J(PNH)$ coupling constants vary with different substituents in the following order: $CF_3C(O)N(H) > C_6H_5C(O)N(H) > 4\text{-}CH_3C_6H_4\text{–}O > 4\text{-}NO_2\text{-}C_6H_4NH$. Similarly, the highest value of $^2J(P,C^2)$ was revealed for compound **5** with the $CF_3C(O)N(H)$ substituent. $^2J(P,C^2)$ values were observed in the sequence $CF_3C(O)N(H) > C_6H_5C(O)N(H) > 4\text{-}NO_2\text{–}C_6H_4NH > 4\text{-}CH_3C_6H_4\text{–}O$.

Table 3
Crystallographic data for compounds **7** and **10**–**12**

	7	**10**	**11**	**12**
Empirical formula	$C_{15}H_{17}N_2O_2P$	$C_{11}H_{18}N_3OP$	$C_{11}H_{17}N_4O_3P$	$C_{12}H_{19}N_2O_2P$
Formula weight	288.28	239.25	284.26	254.26
Temperature (K)	120(2)	120(2)	120(2)	120(2)
Wavelength (Å)	0.71073	0.71073	0.71073	0.71073
Crystal system, space group	orthorhombic, *Pna*2(1)	monoclinic, $P2_1/c$	monoclinic, $P2_1/c$	monoclinic, $P2_1/c$
Unit cell dimensions				
a (Å)	15.348(4)	10.853(3)	14.084(3)	11.8400(11)
b (Å)	13.981(3)	9.139(3)	9.6692(18)	8.9365(8)
c (Å)	6.6695(16)	25.091(7)	9.8710(19)	12.7536(12)
α (°)	90.0	90.0	90.0	90.0
β (°)	90.0	98.274(6)	92.759(4)	104.122(2)
γ (°)	90.0	90.0	90.0	90.0
V (Å^3)	1431.1(6)	2462.8(11)	1342.6(4)	1308.7(2)
Z, calculated density (Mg m^{-3})	4, 1.338	8, 1.291	4, 1.406	4, 1.291
Absorption coefficient (mm^{-1})	0.195	0.208	0.215	0.203
F(000)	608	1024	600	544
Crystal size (mm^3)	$0.50 \times 0.35 \times 0.25$	$0.35 \times 0.29 \times 0.21$	$0.32 \times 0.29 \times 0.21$	$0.4 \times 0.3 \times 0.08$
θ Range for data collection (°)	1.97–27.50	1.90–30.01	2.56–30.06	2.81–30.05
Limiting indices	$-19 \leqslant h \leqslant 19$, $-18 \leqslant k \leqslant 18$, $-8 \leqslant l \leqslant 8$	$-15 \leqslant h \leqslant 15$, $-12 \leqslant k \leqslant 11$, $-35 \leqslant l \leqslant 34$	$-19 \leqslant h \leqslant 19$, $-13 \leqslant k \leqslant 12$, $-13 \leqslant l \leqslant 13$	$-14 \leqslant h \leqslant 16$, $-12 \leqslant k \leqslant 11$, $-17 \leqslant l \leqslant 17$
Reflections collected/unique [R_{int}]	9981/2943 [0.0299]	22982/7118 [0.0485]	15405/3901 [0.0332]	9946/3746 [0.0270]
Completeness to θ (%)	(27.50°) 93.7	(30.01°) 99.1	(30.06°) 99.0	(30.05°) 97.9
Absorption correction	semi-empirical from equivalents	semi-empirical from equivalents	semi-empirical from equivalents	semi-empirical from equivalents
Refinement method	full-matrix least-squares on F^2	full-matrix least-squares on F^2	full-matrix least-squares on F^2	full-matrix least-squares on F^2
Data/restraints/parameters	2943/1/181	7118/0/317	3901/0/174	3746/0 /154
Goodness-of-fit on F^2	1.035	1.040	1.009	1.002
Final R indices	$R_1 = 0.0388$, $wR_2 = 0.0821$	$R_1 = 0.0559$, $wR_2 = 0.1278$	$R_1 = 0.0546$, $wR_2 = 0.1237$	$R_1 = 0.0482$, $wR_2 = 0.1141$
R indices (all data)	$R_1 = 0.0495$, $wR_2 = 0.0858$	$R_1 = 0.0700$, $wR_2 = 0.1342$	$R_1 = 0.0697$, $wR_2 = 0.1301$	$R_1 = 0.0536$, $wR_2 = 0.1175$
Absolute structure parameter	0.09(9)			
Maximum and minimum transmission	0.928 and 0.741	0.862203 and 0.600168	0.801651 and 0.679937	0.984 and 0.923
Largest difference in peak and hole (e Å^{-3})	0.359 and −0.189	0.659 and −0.405	0.512 and −0.376	0.384 and −0.337

Table 4
Selected bond lengths (Å) and angles (°) for compounds **7** and **10**–**12**

7		**10**		**11**		**12**	
P(1)–O(1)	1.4724(17)	P(1)–O(1)	1.4883(13)	P(1)–O(1)	1.4730(14)	P(1)–O(1)	1.4737(10)
P(1)–O(2)	1.6140(15)	P(1)–N(2)	1.6512(15)	P(1)–N(1)	1.6386(17)	P(1)–N(1)	1.6191(12)
P(1)–N(1)	1.6718(16)	P(1)–N(9)	1.6522(16)	P(1)–N(7)	1.6325(16)	P(1)–O(2)	1.6226(10)
P(1)–N(2)	1.6142(19)	P(1′)–O(1′)	1.4862(13)	P(1)–N(8)	1.6708(15)	P(1)–N(2)	1.6275(13)
O(2)–C(9)	1.399(3)	P(1′)–N(9′)	1.6537(16)	O(16)–N(15)	1.245(2)	O(2)–C(6)	1.4103(17)
N(1)–P(1)–N(2)	95.82(9)	O(1)–P(1)–N(2)	109.69(8)	O(1)–P(1)–N(1)	112.06(8)	O(1)–P(1)–N(1)	115.28(6)
O(1)–P(1)–O(2)	105.25(9)	O(1)–P(1)–N(9)	111.37(8)	O(1)–P(1)–N(7)	114.60(9)	O(1)–P(1)–O(2)	111.65(6)
O(1)–P(1)–N(1)	118.69(9)	N(2)–P(1)–N(9)	110.11(8)	O(1)–P(1)–N(8)	113.35(8)	N(1)–P(1)–O(2)	104.39(6)
O(2)–P(1)–N(1)	106.89(8)	O(1′)–P(1′)–N(2′)	114.93(8)	N(1)–P(1)–N(7)	105.41(8)	O(1)–P(1)–N(2)	114.92(6)
P(1)–O(2)–C(9)	121.92(12)	O(1′)–P(1′)–N(8′)	109.74(8)	N(1)–P(1)–N(8)	105.16(8)	N(1)–P(1)–N(2)	106.41(6)
P(1)–N(1)–C(3)	125.65(14)	N(8′)–P(1′)–N(2′)	105.62(8)	N(7)–P(1)–N(8)	105.45(8)	O(2)–P(1)–N(2)	102.95(6)
P(1)–N(1)–C(1)	111.23(13)	O(1′)–P(1′)–N(9′)	111.52(8)	P(1)–N(8)–C(12)	126.54(12)	C(6)–O(2)–P(1)	118.56(8)
P(1)–N(2)–C(2)	111.80(14)	N(2′)–P(1′)–N(9′)	104.51(8)	P(1)–N(7)–C(7)	119.74(13)	C(1)–N(1)–P(1)	117.89(9)

$^{2,3}J(P,C)_{aliphatic}$: In compounds **10**–**12**, $^{3}J(P,C)_{aliphatic} > {}^{2}J(P,C)_{aliphatic}$. Also, $^{2}J(P,C)_{aliphatic}$ in compound **7** is greater than that of compound **12**, due to the ring size effect.

^{31}P NMR study: In diazaphospholes with a five-membered ring heterocycle, the P atoms are more deshielded than those of diazaphosphorinanes with a six-membered ring (Table 1). By considering the high value coupling constants in diazaphospholes, it seems that the deshielded phosphorus atoms in diazaphospholes have a significant interaction with the H atoms.

2D HSQC ^{1}H–^{15}N: The 2D HSQC ^{1}H–^{15}N spectrum for **3** (Fig. 1) indicates the endocyclic N atoms are observed at 59.4 and 60.1 ppm, and NO_2 and NH nitrogen atoms in the 4-$NO_2C_6H_4NH$ moiety are at 75.0 and 75.2 ppm. The spectra of compounds **10**–**12** showed that the aliphatic N atoms appear upfield (at about 20 ppm) and the aromatic N atoms of C_6H_5NH and 4-$NO_2C_6H_4NH$ groups (in **10**, **11**) are downfield (at 61.4 and 75.4 ppm, respectively).

4. Mass spectroscopy investigation

Mass spectra of compounds with the general formula $C_6H_5C(O)N(H)P(O)R$ (**1**, **2**, **4**, **6** and **9**) show a fragment ion at $m/z = 103$, which in compounds **2**, **4**, **6** and **9** are base peaks, and is assigned to $PhCN^+$. In earlier work, Lapidot and Samuel reported on the pyrolysis of *N*-benzoyl phosphoramidates that led to PhCN and the related amidophosphoric acids [20]. Mass spectra of these compounds also show the presence of related amidophosphoric acid cations, with high intensity. In compound **1**, the cation $\overline{(P(O)(OH)(2\text{-}NH\text{-}C_6H_4\text{-}NH)^+)}$ is the base peak. It is assumed that the fragmentation pathway contains P–N cleavage and P–O formation and then the rearranged molecule is cleaved in a pseudo McLafferty mechanism to PhCN and the related amidophosphoric acid cations, see Scheme 2 for compound **1**. The m/z values and the intensities of the amidophosphoric acid fragments of these compounds are given in Table 2. In the next step, a water molecule is removed from the amidophosphoric acid.

4.1. X-ray crystallography

Single crystals of **7** were obtained from a mixture of methanol/acetonitrile and those of **10**–**12** from a mixture of methanol/n-heptane, at room temperature. The structures of these compounds are shown in Figs. 2–5, respectively. Crystallographic data and structure refinement parameters are listed in Table 3 and selected bond lengths and angles are presented in Table 4. The hydrogen bonding data are given in Table 5.

The nitrogen atom environments in the structure of **7** are nearly planar. The sum of the surrounding angles around N(1) and N(2) are slightly lower than sp^2 angles, 358.38° and 356.31°, respectively. P–N bonds in this molecule are smaller than a P–N single bond (1.77 Å) [21]; also, $P–N_{aliphatic}$ (1.614 Å) is stronger than $P–N_{aromatic}$ (1.672 Å). The angle P(1)–O(2)–C(9) is 121.92(12)° (sp^2 angle). Compound **10** exists as two independent molecules (**10** and **10′**) in the crystal lattice. The endocyclic nitrogen atoms in compounds **10**–**12** are distorted from planarity. The deviations from planarity in these structures are larger than that of diazaphosphole **7** and previously reported phodsphoramidates [19,22]. The sum of the angles around the endocyclic N atoms in compounds **10**–**12** (that are in the range of 352.76°–338.59°) are lower than those of diazaphosphole **7**. The exocyclic nitrogen atoms of aniline and nitroaniline groups are relatively planar. P–N bonds in these molecules are in the range 1.6708(15)–1.6192(12) Å (smaller than a P–N single bond). The P=O bond lengths in these molecules are slightly longer than the PO double bond length (1.45 Å) [21]. This bond is in an equatorial position. The equatorial preference for the P=O bond was previously observed by Bentrude [23] and was attributed to the overlap of the endocyclic nitrogen p-orbital with the P–N(exocyclic) anti-bonding orbital.

Hydrogen bonds: Compound **7** forms an infinite zigzag chain via an intermolecular –P=O…H–N– hydrogen bond. In diazaphosphorinane **10**, each independent molecule is connected to its symmetrically similar molecule via two equal –P=O…H–N– hydrogen bonds and produces a centrosymmetric dimer in the crystal lattice, P(1)–

Table 5
Hydrogen bonds D–H...A for compounds **7** and **10**–**12**

Compound	D–H...A	*d*(D–H)	*d*(H..A)	∠DHA	*d*(D..A)
7	N2–H2N...O1 [$-x, -y+1, z-1/2$]	0.936	1.916	170.42	2.843
10	N8–H8N′... O1′ [$-x, -y+1, -z$]	0.811	2.139	170.98	2.943
	N2–H2N...O1 [$-x+1, -y, -z$]	0.888	2.078	167.51	2.950
	N8–H8N...N8′ [$-x, -y+1, -z$]	0.840	2.441	156.90	3.231
	N9′–H9N′...O1 [$x, y+1, z$]	0.881	1.960	175.93	2.839
	N9–H9N...O1′	0.829	2.020	174.80	2.846
	N2′–H2N′...N2 [$-x+1, -y+1, -z$]	0.828	2.479	159.81	3.269
11	N8–H8N...O1 [$-x, -y+1/2, -z+1/2$]	0.806(2)	2.033(4)	165.57(1)	2.820(4)
	N1–H1N...O16 [$-x+1, -y, -z+1$]	0.854(2)	2.316(4)	161.97(1)	2.139(4)
	N7–H7N...O16 [$-x+1, -y+1/2, -z+3/2$]	0.876(2)	2.279(4)	145.14(1)	3.039(4)
12	N1–H1N...O1 [$-x+1, -y+2, -z$]	0.86	1.99	176	2.841(2)
	N2–H2N...O2 [$-x+1, -y+1, -z$]	0.78	2.46	156	3.183(2)

O(1)...H(2N)–N(2) and P(1′)–O(1′)...H(8N′)–N(8′) hydrogen bonds in **10** and **10**′. These dimeric aggregates are connected to each other to form a 2D polymer. Each dimer of **10** is connected to two dimers of **10**′ by two equal P(1)–O(1)...H(9N′)–N(9′) H-bonds and then connected to the two other dimers of **10**′ by two other equal P(1′)–O(1′)...H(9N)–N(9) H-bonds. Therefore, one dimer of **10** is placed between four dimers of **10**′ and vice versa, Fig. 6. Furthermore two weak P(1′)–N(8′)...H(8N)–N(8) and P(1)–N(2)...H(2N′)–N(2′) H-bonds are produced in the packing. Compound **11** exists as a two dimensional polymer in the crystal lattice via –P=O...H–N– and –N–O...H–N– hydrogen bonds. Compound **12** forms centrosymmetric dimers via two equal P(1)–O(1)...H(1N)–N(1) hydrogen bonds and these dimers are connected via a weak H-bonds, P(1)–O(2)...H(2N)–N(2).

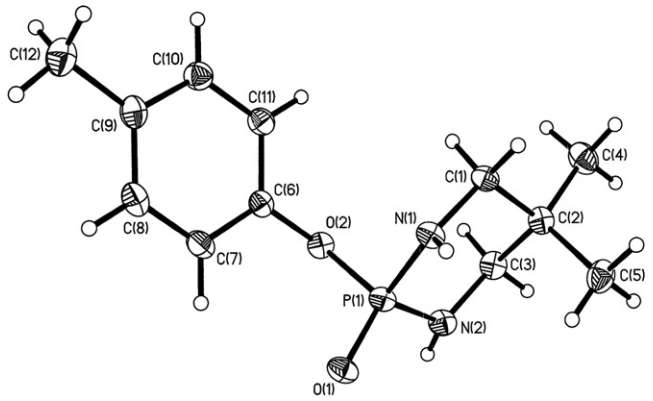


Fig. 5. Molecular structure and atom-labelling scheme for compound **12**, 4-CH_3-$C_6H_4OP(O)[NHCH_2C(CH_3)_2CH_2NH]$ (50% probability ellipsoids).

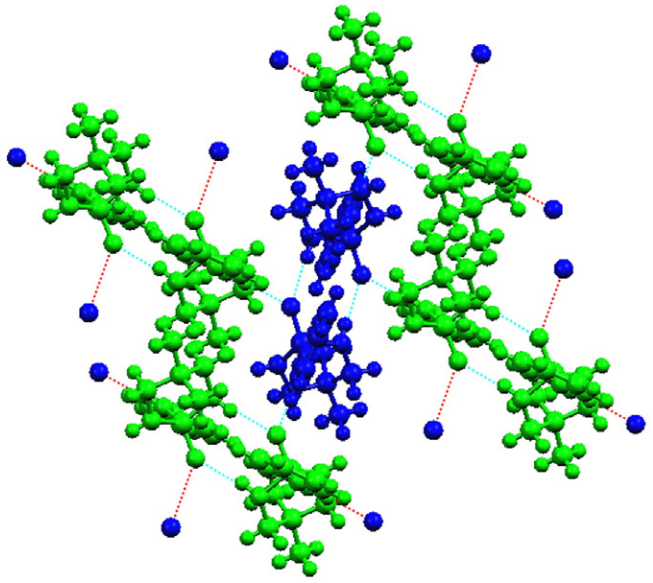


Fig. 6. Each dimer of **10**′ is placed between four dimers of **10**.

Acknowledgement

Support of this work by Tarbiat Modares University is gratefully acknowledged.

Appendix A. Supplementary material

CCDC 247599, 247080, 247082 and 247081 contain the supplementary crystallographic data for **7** ($C_{15}H_{17}N_2O_2P_1$), **10** ($C_{11}H_{18}N_3OP$), **11** ($C_{11}H_{17}N_4O_3P$) and **12** ($C_{12}H_{19}N_2O_2P$). These data can be obtained free of charge via http://www.ccdc.cam.ac.uk/conts/retrieving.html, or from the Cambridge Crystallographic Data Centre, 12 Union Road, Cambridge CB2 1EZ, UK; fax: (+44) 1223-336-033; or e-mail: deposit@ccdc.cam.ac.uk. Spectroscopic data of compounds **1**–**12** can be obtained as supplementary material. Supplementary data associated with this article can be found, in the online version, at doi:10.1016/j.poly.2006.09.092.

References

[1] (a) Z. Li, J. Han, Y. Jiang, P. Browne, R.J. Knox, L. Hu, Bioinorg. Med. Chem. 11 (2003) 4171;
(b) R.F. Borch, G.W. Canute, J. Med. Chem. 34 (1991) 3044.

[2] S. Bauermeister, A.M. Modro, T.A. Modro, Tetrahedron Lett. 30 (1989) 2141.
[3] K. Gholivand, Z. Shariatinia, M. Pourayoubi, S. Farshadian, Z. Naturforsch. B 60 (2005) 1021.
[4] K. Gholivand, M. Pourayoubi, S. Farshadian, S. Molani, Z. Shariatinia, Anal. Sci. 21 (2005) 55.
[5] W.B. Jennings, D. Randall, S.D. Worley, H. Hargis, J .Chem. Soc., Perkin II (1981) 1411.
[6] J.M.A. Al-Rawi, G.Q. Behnam, N. Ayed, R. Kraemer, Magn. Reson. Chem. 23 (1985) 728.
[7] B. Wrackmeyer, E. Kupce, A. Schmidpeter, Magn. Reson. Chem. 29 (1991) 1045.
[8] A.V. Kirsanov, R. Makitra, J. Gen. Chem. 26 (1956) 907.
[9] P.M. Narula, C.S. Day, B.A. Powers, M.A. Odian, A. Lachgar, W.T. Pennington, R.E. Noftle, Polyhedron 18 (1999) 1751.
[10] L.A. Cates, T.L. Lemke, J. Pharm. Sci. 63 (1974) 1736 (Coll. Pharm., Univ. Houston, Houston, TX).
[11] O. Johnson, M. Murray, G. Woodward, J. Chem. Soc., Dalton Trans. (1989) 821.
[12] H. Tolkimth, Ann. N.Y. Acad. Sci. 79 (Art. 7) (1959) 189 (Dow Chem. Co., Midland, MI).
[13] G.M. Sheldrick, SADABS v. 2.01, Bruker/Siemens Area Detector Absorption Correction Program, Bruker AXS, Madison, WI, USA, 1998.
[14] G.M. Sheldrick, SHELEX v. 5.10, Structure Determination Software Suite, Bruker AXS, Madison, WI, USA, 1998.
[15] (a) M.L. Nielsen, J.V. Pustinger, J. Phys. Chem. 68 (1964) 152;
(b) K. Gholivand, S. Ghadimi, H. Naderimanesh, A. Forouzanfar, Magn. Reson. Chem. 39 (2001) 684.
[16] K. Gholivand, Z. Shariatinia, M. Pourayoubi, Z. Anorg. Allg. Chem. 631 (2005) 961.
[17] K. Gholivand, M. Pourayoubi, Z. Shariatinia, H. Mostaanzadeh, Polyhedron 24 (2005) 655.
[18] H.-O. Kalinowski, S. Berger, S. Braun, Carbon-13 NMR Spectroscopy, Wiley, 1991, pp. 527–538 and 593.
[19] G.J. Bullen, F.S. Stephens, R.J. Wade, J. Chem. Soc. A (1969) 1804.
[20] A. Lapidot, D. Samuel, J. Chem. Soc. (1962) 2110.
[21] D.E.C. Corbridge, Phosphorus, an Outline of its Chemistry, Biochemistry and Technology, fifth ed., Elsevier, The Netherlands, 1995.
[22] K. Gholivand, Z. Shariatinia, M. Pourayoubi, Polyhedron 25 (2006) 711.
[23] W.G. Bentrude, W.N. Setzer, M. Khan, A.E. Sopchik, E. Ramli, J. Org. Chem. 56 (1991) 6127.

Available online at www.sciencedirect.com
ScienceDirect
Polyhedron 26 (2007) 845–850
POLYHEDRON
www.elsevier.com/locate/poly

Structural and spectroscopic investigations of the Eu^{III}–CDTA system

Rafał Janicki, Anna Mondry, Przemysław Starynowicz *

Wydział Chemii, Uniwersytet Wrocławski, ul. F. Joliot-Curie 14, 50-383 Wrocław, Poland

Received 20 July 2006; accepted 14 September 2006
Available online 27 September 2006

Abstract

Two crystal structures of Eu^{III} complexes with CDTA (*trans*-1,2-diaminocyclohexane-*N*,*N*,*N*′,*N*′-tetraacetate), $[C(NH_2)_3]_3[Eu_2(CDTA)_2(H_2O)_2]ClO_4 \cdot 7H_2O$ (**I**) and $[C(NH_2)_3][Eu(CDTA)(H_2O)] \cdot 2.375H_2O$ (**II**), are presented. Both structures are polymeric and the central metal ions are eight-coordinate. The first coordination sphere of each Eu^{III} cation contains five carboxylate oxygen atoms, two nitrogen ones and a water molecule. For **I**, as well as for water solutions of the Eu^{III}–CDTA complex at various pH values, the spectroscopic (UV–Vis) properties were investigated.
© 2006 Elsevier Ltd. All rights reserved.

Keywords: Europium(III); CDTA; Structure; UV–Vis spectroscopy

1. Introduction

Lanthanide polyaminopolycarboxylate chelates play an important role both in fundamental investigations and in several areas of practical applications. They are used, among others, as shift reagents in NMR spectroscopy [1], contrast agents in MRI imaging [2], structural probes [3] and luminescent tags in immunoassays [4]. This family of compounds has been epitomized by complexes of Ln^{III} with the ethylenediaminetetraacetate (EDTA) anion, which have been extensively studied both in solution e.g. [5] and in the solid state e.g. [6] and now may serve as a kind of standard when the structure, spectroscopic and/or thermodynamic properties of lanthanide polyaminopolycarboxylates are discussed. It is therefore of interest to find how the properties are altered when the $EDTA^{4-}$ skeleton is modified. In this work we present a study of two Eu^{III} complexes with such a ligand, i.e. *trans*-1,2-diaminocyclohexane-*N*,*N*,*N*′,*N*′-tetraacetate (CDTA). The investigations of Ln^{III}–CDTA complexes carried out so far have been focused to a great part on their properties in aqueous solutions and included thermodynamic as well as spectroscopic aspects. Their stability constants are higher by an order or two of magnitude, depending on the lanthanide, than those of the EDTA complexes [7], and generally saying, they are thermodynamically stable [8]. The spectroscopic studies have revealed that in solutions of Eu^{III}–CDTA complexes an equilibrium exists between two different species, nine- and eight-coordinate, the dissimilarity between them consisting of a different number of coordinated water molecules (three or two) [9]. The average number of these molecules has been found to be 2.3–2.6 and is a little lower than that found in water solutions of the EDTA complexes (2.6–2.8) [5f,5h].

Because of difficulties connected with growing of monocrystals of adequate quality, structural data for Ln^{III}–CDTA complexes are scarce. To the best of the authors' knowledge only three crystal structures of these complexes have been published. Two of them, $NH_4[Ln(CDTA)(H_2O)_2] \cdot 4.5H_2O$ ($Ln = Gd^{III}$, Ho^{III}), are monomeric and isostructural [10,11] whereas in the third one, $Na[Eu(CDTA)(H_2O)] \cdot 4H_2O$ [12], dimeric anions of $[Eu(CDTA)–\mu\text{-}(H_2O)_2–Eu(CDTA)]^{2-}$ are formed. For the last system luminescence properties were also reported. In all these complexes the Ln^{III} ions are eight-coordinate.

In the crystal, the coordination surrounding of Ln^{III} ion is unambiguously defined, therefore the spectra of the

* Corresponding author.
E-mail address: psta@wchuwr.chem.uni.wroc.pl (P. Starynowicz).

0277-5387/$ - see front matter © 2006 Elsevier Ltd. All rights reserved.
doi:10.1016/j.poly.2006.09.031

crystals may be a good starting point for interpretation of spectral data of solution systems. The paucity of such data has motivated us to attempt the preparation of Eu^{III}–CDTA complexes in the crystalline state, to study their crystal structures and spectroscopic properties and to compare the latter with the analogous properties of Eu^{III}–CDTA complexes in solution.

2. Experimental

2.1. Materials

Solutions for spectroscopic measurements: A stock solution of europium chloride was prepared by dissolving Eu_2O_3 (99.99%; Standford materials) in 2 mol dm^{-3} hydrochloric acid. The Eu^{III} ion concentration was determined complexometrically using xylenol orange as an indicator. The stock solution of H_4CDTA (98%; Lancaster) was prepared by half-neutralization with NaOH. The pH of the 1:1.1 Eu^{III}–CDTA solutions was adjusted by a carbonate-free NaOH water solution.

Crystal preparations: An aqueous solution of equimolar quantities of europium perchlorate and H_4CDTA was heated at ca. 80 °C. Next, solid $[C(NH_2)_3]_2CO_3$ was added until the pH value was 5. Large colourless crystals of $[C(NH_2)_3]_3[Eu_2(CDTA)_2(H_2O)_2]ClO_4 \cdot 7H_2O$ (**I**) were formed during slow evaporation. The other crystals, $[C(NH_2)_3][Eu(CDTA)(H_2O)] \cdot 2.375H_2O$ (**II**), were obtained as follows: a suspension of Eu_2O_3 and H_4CDTA was heated at ca. 80 °C. After dissolution of the substrates, the solution was alkalized with $[C(NH_2)_3]_2CO_3$ to a final pH value of 3, and left for crystallization.

2.2. X-ray study

Appropriate crystals were cut from larger ones and mounted on a Kuma KM4 diffractometer equipped with a CCD counter. The collected data were corrected for polarization, Lorentz and absorption, the last calculated from the crystal habit captured from photo scans. Both crystals turned out to be twinned. The twinning of crystal **I** was pseudo-merohedral; this was brought about by the fact that the unit cells spanned by vectors **a**, **b**, **c**, and **a**, **a**–**b**, **a**–**c** have very similar lattice constants. The fraction of the first twin component found from the refinement was 0.676(1). The twinning matrix in **II** was (−1/2 −1/2 0/ −3/2 1/2 0/ −1/2 1/2 −1) with the result that only reflections with $h + k$ even overlapped. The structure of **I** was solved and refined against all reflections, while that of **II** was solved using one twin component and refined against both. The positions of Eu were found from Patterson maps, the rest of the non-H atoms from difference Fourier

Table 1
Crystal data and structure refinement for both crystals

Crystal	**I**	**II**
Empirical formula	$C_{31}H_{72}ClEu_2N_{13}O_{29}$	$C_{15}H_{30.25}EuN_5O_{11.38}$
Formula weight	1430.39	614.65
Temperature (K)	100(2)	100(2)
Wavelength (Å)	0.71073	0.71073
Crystal system, space group	triclinic, $P\bar{1}$	triclinic, $P\bar{1}$
Unit cell dimensions		
a (Å)	10.652(8)	12.09(9)
b (Å)	16.075(13)	18.83(2)
c (Å)	17.943(14)	23.328(15)
α (°)	69.31(7)	66.82(14)
β (°)	73.24(7)	77.15(12)
γ (°)	70.86(7)	77.47(12)
Volume ($Å^3$)	2663(4)	4712(36)
Z, Calculated density (Mg/m^3)	2, 1.784	8, 1.733
Absorption coefficient (mm^{-1})	2.484	2.727
$F(000)$	1448	2474
Crystal size (mm)	$0.27 \times 0.20 \times 0.15$	$0.27 \times 0.18 \times 0.11$
Theta range for data collection (°)	3.03–28.43	2.25–29.07
Index ranges	$-9 \leqslant h \leqslant 14$, $-21 \leqslant k \leqslant 21$, $-23 \leqslant l \leqslant 23$	$-15 \leqslant h \leqslant 16$, $-25 \leqslant k \leqslant 23$, $-31 \leqslant l \leqslant 31$
Reflections collected/unique (R_{int})	18 077/11 545 (0.0341)	25 498/25 498
Completeness to 2θ	86.0%	69.1%
Absorption correction	analytical, from the shape	analytical, from the crystal shape
Maximum and minimum transmission	0.710 and 0.520	0.768 and 0.529
Refinement method	full-matrix least-squares on F^2	full-matrix least-squares on F^2
Data/restraints/parameters	11 545/0/686	25 498/0/1176
Goodness-of-fit on F^2	1.063	0.998
Final R indices $[I > 2\sigma(I)]$	$R(F) = 0.0434$, $Rw(F^2) = 0.1031$	$R(F) = 0.0790$, $Rw(F^2) = 0.1403$
R indices (all data)	$R(F) = 0.0484$, $Rw(F^2) = 0.1059$	$R(F) = 0.1388$, $Rw(F^2) = 0.1620$
Largest differences in peak and hole (e $Å^{-3}$)	2.654 and −2.604	1.800 and −1.616

maps. The positions of the C- and N-bonded hydrogen atoms were calculated geometrically. The refinement was full-matrix with all ordered non-H atoms anisotropic. The oxygen atoms from disordered water molecules (in **II**) were refined isotropically and C- and N-bonded H atoms were constrained to 1.2 times the factors of the relevant C atoms. Because of twinning and partial overlapping of some reflections the precision of the structure determination of **II** unfortunately deteriorated. Our several attempts to find an untwinned sample failed and therefore we decided to solve and refine the structure against the twin data. The large volume of the asymmetric part seems upsetting. However we could not find a cell with smaller volume and herein we present the best model of twinning and the crystal structure which we have been able to find. Both structures were solved and refined by SHELXS97 [13] and SHELXL97 [14], respectively, and the program DIAMOND [15] was used for the molecular graphics. The data concerning the crystal parameters, data collection and refinement details are presented in Table 1.

3. Spectroscopy

3.1. UV–Vis measurements

Electronic absorption spectra were recorded on a Cary 500 UV–VIS–near-IR spectrophotometer. The solutions were measured at room temperature. Only spectra of **I** were recorded because we could not obtain a good sample of **II**. The absorption spectra of **I** were measured at 293 and 30 K (in an Oxford CF 1204 continuous flow helium cryostat). The oscillator strengths (P) were determined using the equation:

$$P = 4.32 \times 10^{-9}(cd)^{-1} \int A(\sigma)\,\mathrm{d}\sigma$$

where c is the concentration of the Eu^{III} ion in M, d is the length of the optical way in cm and $A(\sigma)$ is the absorbance as the function of the wavenumber in cm^{-1}. The P values were not corrected for the population of the $^7F_1$ state at room temperature. Corrected emission spectra were measured on a SLM Aminco 500 spectrofluorometer at 293 and 77 K. For luminescence, the Eu^{III} ion was excited with a wavelength of 394 nm.

4. Results and discussion

4.1. Structure

Both structures are built up from polymeric complex chains, guanidinium cations, water of crystallization (partially disordered in **II**), and, in the case of **I**, also perchlorate anions. The polymeric chains are composed of europium cations, *trans*-1,2-diaminocyclohexane-*N*,*N*,*N*′,*N*′-tetraacetate (CDTA) anions and water molecules coordinated to europium. Each polymer unit (mer) contains a Eu^{III} cation and a CDTA anion which is coordinated to the metal through its four carboxylate oxygen atoms and two nitrogen atoms, filling thus six coordinate sites. The seventh site is occupied by a water molecule. Apart from that each mer donates one of its carboxylate oxygen atoms to the first coordination sphere of an Eu^{III} ion in a neighbouring mer (accepting at the same time an analogous O atom from the other neighbour). In this way infinite polymeric chains are formed and the europium cations are eight-coordinate. In **I** there are two symmetry independent Eu sites, and accordingly two different mers. In **II** the number of symmetry independent Eu sites is 4. Nevertheless, superimposition of all six mers (Fig. 1) shows that their conformations are very similar, the difference being only in small variations of bond lengths and angles. The Eu–O and Eu–N distances (see Table 2) are similar to those found in the europium dimeric complex with CDTA, $Na[Eu(CDTA)H_2O]\cdot 4H_2O$ [12], however the Eu–OH_2 bond distances are significantly longer in the present structures. The Eu–OH_2 average distances are 0.125 Å (compound **I**) and 0.103 Å (compound **II**) longer than in the quoted dimer. These variations may be caused by different modes of interaction of guanidinium and sodium cations with the CDTA moiety, because these cations induce different hydrogen bond networks. In both presented structures the shortest bonds are those involving carboxylate O atoms, the Eu–OH_2 ones are longer, and the

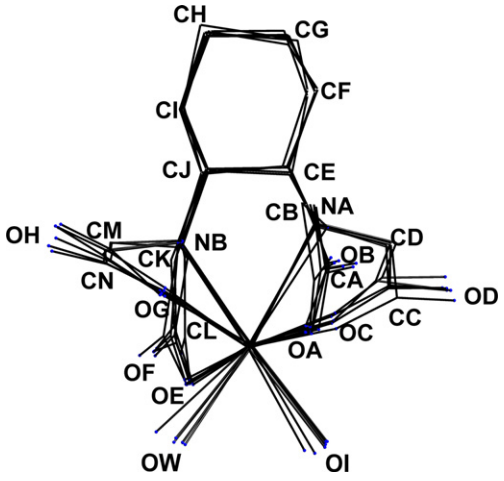


Fig. 1. Superimposed Eu coordination environments in **I** and **II**. The shortened atomic labels stand: OA for O1 and O11 in **I**, O13, O23, O31, O41 in **II**; OB–O2, O12 (**I**), O14, O24, O32, O42 (**II**); OC–O4, O14 (**I**), O11, O21, O33, O43 (**II**); OD–O3, O13 (**I**), O12, O22, O34, O44 (**II**); OE–O7, O16 (**I**), O17, O27, O37, O47 (**II**); OF–O8, O15 (**I**), O18, O28, O38, O48 (**II**); OG–O5, O17 (**I**), O15, O25, O35, O45 (**II**); OH–O6, O18 (**I**), O16, O26, O36, O46 (**II**); OI–O8, O15^{i} (**I**), O48^{j}, O18, O28, O38 (**II**); OW–OW1, OW2 (**I**), OW1, OW2, OW3, OW4 (**II**); NA–N12, N21 (**I**), N11, N21, N31, N41 (**II**); NB–N11, N22 (**I**), N12, N22, N32, N42 (**II**); CA–C1, C21 (**I**), C13, C33, C51, C71 (**II**); CB–C2, C22 (**I**), C14, C34, C52, C72 (**II**); CC–C4, C24 (**I**), C11, C31, C53, C73 (**II**); CD–C3, C23 (**I**), C12, C32, C54, C74 (**II**); CE–C5, C25 (**I**), C15, C35, C55, C75 (**II**); CF–C10, C30 (**I**), C16, C36, C56, C76 (**II**); CG–C9, C29 (**I**), C17, C37, C57, C77 (**II**); CH–C8, C28 (**I**), C18, C38, C58, C78 (**II**); CI–C7, C27 (**I**), C19, C39, C59, C79 (**II**); CJ–C6, C26 (**I**), C20, c40, C60, C80 (**II**); CK–C11, C33 (**I**), C24, C44, C64, C84 (**II**); CL–C12, C34 (**I**), C23, C43, C63, C83 (**II**); CM–C13, C31 (**I**), C22, C42, C62, C82 (**II**); CN–C14, C32 (**I**), C21, C41, C61, C81 (**II**).

Table 2
The Eu–O,N distances in **I** and **II** (Å)

I		**II**	
Eu(1)–O(1)	2.314(6)	Eu(1)–O(48^{j})	2.327(8)
Eu(1)–O(15^{i})	2.339(5)	Eu(1)–O(17)	2.353(9)
Eu(1)–O(7)	2.343(6)	Eu(1)–O(13)	2.374(7)
Eu(1)–O(4)	2.362(6)	Eu(1)–O(15)	2.387(8)
Eu(1)–O(5)	2.364(5)	Eu(1)–O(11)	2.398(11)
Eu(1)–OW1	2.469(6)	Eu(1)–OW1	2.464(16)
Eu(1)–N(11)	2.615(6)	Eu(1)–N(12)	2.602(8)
Eu(1)–N(12)	2.626(6)	Eu(1)–N(11)	2.613(19)
Eu(2)–O(8)	2.311(6)	Eu(2)–O(18)	2.317(13)
Eu(2)–O(11)	2.364(5)	Eu(2)–O(23)	2.354(8)
Eu(2)–O(14)	2.363(5)	Eu(2)–O(27)	2.356(7)
Eu(2)–O(17)	2.369(5)	Eu(2)–O(25)	2.378(8)
Eu(2)–O(16)	2.407(5)	Eu(2)–O(21)	2.387(8)
Eu(2)–OW2	2.458(6)	Eu(2)–OW2	2.429(12)
Eu(2)–N(21)	2.597(6)	Eu(2)–N(21)	2.607(11)
Eu(2)–N(22)	2.604(6)	Eu(2)–N(22)	2.608(19)
		Eu(3)–O(28)	2.301(9)
		Eu(3)–O(31)	2.341(10)
		Eu(3)–O(37)	2.350(11)
		Eu(3)–O(35)	2.395(7)
		Eu(3)–O(33)	2.415(10)
		Eu(3)–OW3	2.429(15)
		Eu(3)–N(31)	2.596(19)
		Eu(3)–N(32)	2.667(9)
		Eu(4)–O(38)	2.297(12)
		Eu(4)–O(45)	2.370(8)
		Eu(4)–O(43)	2.374(10)
		Eu(4)–O(41)	2.375(9)
		Eu(4)–O(47)	2.388(7)
		Eu(4)–OW4	2.444(12)
		Eu(4)–N(42)	2.595(17)
		Eu(4)–N(41)	2.642(14)

Symmetry transformations used to generate equivalent atoms: $^{i}-x-1, y, z$; $^{j}-x+1, y-1, z$.

Eu–N ones are the longest. As far as the conformation of the ligand is concerned, two subsets of methylenecarboxylate groups may be discerned. In each CDTA ligand two such groups are almost parallel. In **II** the angles between the least-squares fitted planes of such planes (namely C13 and C23, C33 and C43, C51 and C63, C71 and C83; the methylenecarboxylate groups are labelled after their central C atoms) are in the range 0.6–10.0°. In **I** the relevant angles differ more: the planes of the groups C1 and C12 are mutually twisted by 21.0°, whereas the groups C21 and C34 are twisted by only 4.5°. The other pairs are twisted by 54.9° and 59.7° in **I**, and 60.1–70.5° in **II**. Apart from that it may be noticed that the C–O bonds are generally longer when the O atom is coordinated to Eu, although the difference between the C–O lengths with O atoms coordinated and uncoordinated falls often within the range of experimental error. The approximate symmetry of all Eu first coordination spheres in both structures is C_2 (after neglecting the difference between the water and the bridging carboxylate O atoms); the axis passes through the center of the cyclohexyl ring, Eu and the bisector of the relevant water–Eu–bridging O atom angle. It is noteworthy that in the presented crystals the CDTA ligand behaves in a way

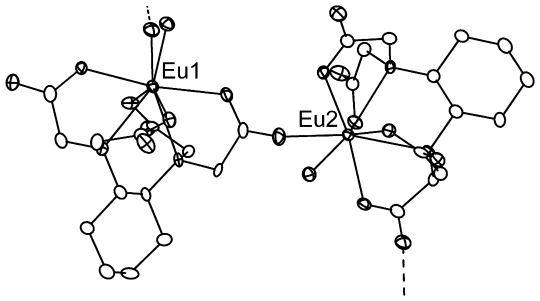


Fig. 2. A fragment of the polymeric chain in **I**.

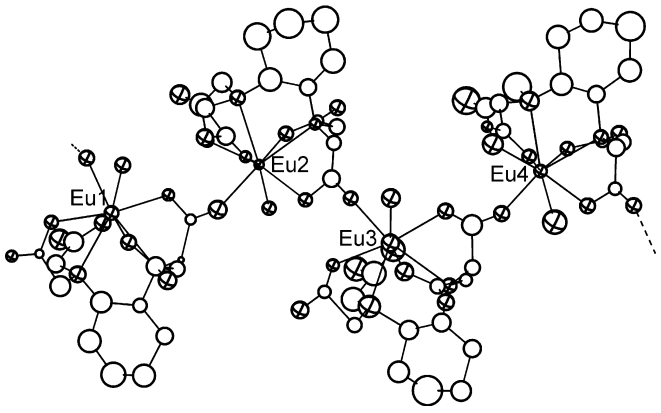


Fig. 3. A fragment of the polymeric chain in **II**.

different to that of its analogue, i.e. ethylenediaminetetraacetate (EDTA). The Eu^{III}–EDTA complexes are monomeric, and the europium cation is nine-coordinate [6d,6e,6f], contrary to the polymeric structures with eight-coordinate Eu ions in the present structures. Fragments of the polymeric complex chains are presented in Figs. 2 and 3.

5. Spectroscopic results

For the $^{7}F_0 \rightarrow {}^{5}D_0$ transition in **I** we were able to observe one peak at 17245 cm^{-1} at room temperature while at 30 K two components at 17241 and 17234 cm^{-1} appeared. The ground ($^{7}F_0$) and emitting ($^{5}D_0$) states of the europium ion are non-degenerate, therefore the number of peaks observed in the range 578–582 nm indicates the number of various chemical surroundings of the Eu^{III} ion. Accordingly we may assume existence of two different europium sites at 30 K and of one site at room temperature. In the absorption spectrum of a related compound, $[C(NH_2)_3][Eu(EDTA)(H_2O)_3]$, only one $^{7}F_0 \rightarrow {}^{5}D_0$ peak was observed at a very similar energy, 17252 cm^{-1} at room temperature [16] and 17243 cm^{-1} at 77 K. Also in the $^{7}F_0 \rightarrow {}^{5}D_1$ and $^{7}F_0 \rightarrow {}^{5}D_2$ transitions the number of components in the spectrum recorded at 77 K is greater than that found in the spectrum taken at 293 K. For the low local symmetry of the Eu^{III} ion in each symmetry independent site the number of the components should be 3 and 5, respectively. At room temperature the number of crystal

field levels in the absorption spectrum for $^7F_0 \rightarrow {}^5D_1$ and $^7F_0 \rightarrow {}^5D_2$ are actually 3 and 5, whereas in the low temperature (30 K) transitions 5 and 7 crystal field components in the range 19 050–19 120 and 21 390–21 550 cm^{-1}, respectively, may be seen (Fig. 4). This may suggest that between 293 and 100 K (taking into account the structural data reported above) a phase transition occurs. The oscillator strengths found in **I** at 293 and 30 K are presented in Table 3. Inspection of these data reveals somewhat anomalous behaviour of these quantities. Namely, the intensities of all the presented transitions increase on lowering the temperature. Such a change might be attributed to a phase transition in the case of $^7F_0 \rightarrow {}^5D_0$ and $^7F_0 \rightarrow {}^5D_2$. The most surprising thing is, however, the anomalous growth of the intensity of the $^7F_0 \rightarrow {}^5D_1$ transition, which is more than twice as intense as theoretically predicted [17]. Such an increase cannot be explained by thermal population of the $^7F_1$ state, which would account only for the loss of approximately 20 % of the intensity at room temperature. The reasons for this phenomenon are unclear, and perhaps need more detailed investigations, which however lie outside the scope of the present paper.

The splitting of the bands may also be observed in emission spectra at 77 K. At room temperature the transition $^5D_0 \rightarrow {}^7F_0$ was unsplit, whereas the $^5D_0 \rightarrow {}^7F_1$ and $^5D_0 \rightarrow {}^7F_2$ transitions had 3 and 4 discernible components. At 77 K the number of observed components was 2 for $^5D_0 \rightarrow {}^7F_0$, 6 for $^5D_0 \rightarrow {}^7F_1$ and 7 for $^5D_0 \rightarrow {}^7F_2$.

The results presented above may serve as a background for the interpretation of the spectroscopic properties of water solutions of the Eu^{III}–CDTA system. These properties remain essentially the same in the pH range between 3.5 and 9. The most significant changes in the absorption spectra are observed above pH 10. In Fig. 4 the absorption spectra of Eu^{III}–CDTA solutions at pH 7.40 and 11.0 have been juxtaposed. For both solutions two maxima at 17 250 and 17 239 cm^{-1} may be observed for the $^7F_0 \rightarrow {}^5D_0$ transition, which confirms the equilibrium of nine- and eight-coordinate isomers, as was previously reported at pH = 6.0 [9]. These values are similar both to the maximum found in the crystal at room temperature and to the analogous maxima found in solutions of the Eu^{III}–EDTA complex (17 254 and 17 240 cm^{-1}) [16]. There is another similarity that perhaps should be mentioned. Namely, the most intense crystal field components in the $^7F_0 \rightarrow {}^5D_2$ transition in both solutions very closely match the analogous components in the spectrum of **I** at room temperature.

Table 3
Oscillator strength values (P) of the Eu^{III} complexes with CDTA

Complex	$^7F_0 \rightarrow {}^5D_0$ $P \times 10^8$	$^7F_0 \rightarrow {}^5D_1$ $P \times 10^8$	$^7F_0 \rightarrow {}^5D_2$ $P \times 10^8$
Eu–CDTA pH 5.26	1.20	1.61	5.90
Eu–CDTA pH 7.40	1.25	1.62	5.34
Eu–CDTA pH 9.16	1.18	1.52	6.20
Eu–CDTA pH 11.0	0.59	1.50	11.4
Crystal $T = 293$ K	0.50	1.44	3.35
Crystal $T = 30$ K	1.38	3.20	11.0

The most remarkable changes may be observed in the values of the oscillator strengths (Table 3). The P value of the transition $^7F_0 \rightarrow {}^5D_0$ remains practically constant up to approximately pH = 9 and then decreases by about half, reaching a value very similar to that calculated for **I**

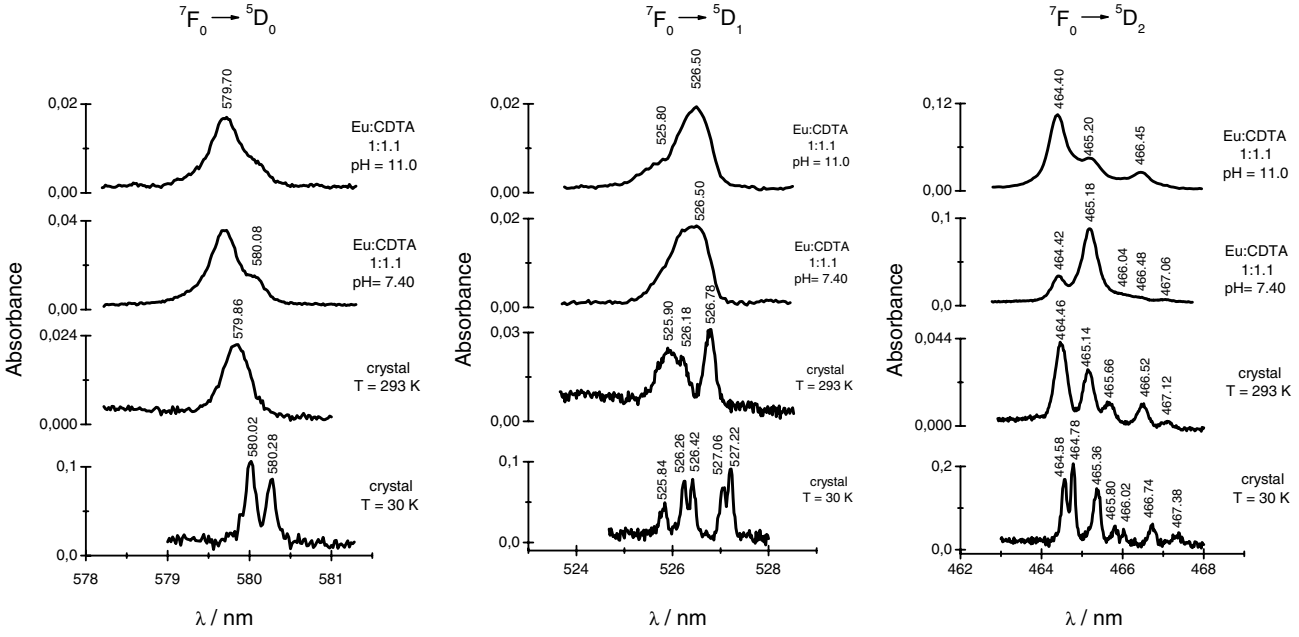


Fig. 4. Absorption spectra of the $^7F_0 \rightarrow {}^5D_{0,1,2}$ transitions of Eu^{III} complexes with CDTA in solution: $c_{Eu} = 44.1$ mM, $d = 5$ cm and in the monocrystal $c_{Eu} = 2.49$ M, $d = 0.102$ cm.

at room temperature. The magnetic-dipole allowed transition $^7F_0 \rightarrow {}^5D_1$ in the solutions and in **I** at 293 K is constant with the *P* value close to the theoretical value [17]. The intensity of the hypersensitive $^7F_0 \rightarrow {}^5D_2$ transition is, out of the three presented ones, the most affected by changes in the europium ion first coordination sphere. The oscillator strength of this band, like that of $^7F_0 \rightarrow {}^5D_0$, does not change essentially up to pH ≈ 9, and then, contrary to the latter transition, doubles at pH = 11. These changes may reflect the alterations within the first coordination sphere of the Eu^{III} ion, consisting of partial substitution of coordinated water molecules by hydroxy anions [5c,5d] and/or formation of a polymeric species [18]. The *P* values for the solutions are greater than in **I** at 293 K, because of molecular dynamics around the metal ion in solutions.

6. Conclusions

The presented results suggest that the CDTA anion behaves in a somewhat different way in comparison to EDTA as far as the structural aspects are concerned. Namely CDTA shows a more pronounced tendency to form polymeric structures with lanthanides. Apart from that the coordination numbers of all Eu^{III}–CDTA complexes are eight while in all known crystal structures of Eu^{III}–EDTA systems the Eu^{III} ion is nine-coordinate. The spectroscopic properties of the presented Eu^{III}–CDTA systems in water solutions rather closely resemble those of related Eu^{III}–EDTA ones. For instance for Eu^{III} complexes with both ligands the $^7F_0 \rightarrow {}^5D_{0,1,2}$ transitions lie at very similar energies. The $[Eu(CDTA)(H_2O)_{3\ or\ 2}]^-$ species remain stable up to pH ≈ 9, then partial hydrolysis and/or polymerization take place. The spectra of $[C(NH_2)_3]_3[Eu_2(CDTA)_2(H_2O)_2]ClO_4 \cdot 7H_2O$ at various temperatures reveal a phase transition in the crystal.

Acknowledgements

The authors would like to thank Ing. Halina Trelińska-Nowak for the spectroscopic measurements and Dr. Andrzej Kochel for help in the X-ray data collection.

Appendix A. Supplementary material

CCDC 615028 and 615027 contain the supplementary crystallographic data for **I** and **II**. These data can be obtained free of charge via http://www.ccdc.cam.ac.uk/conts/retrieving.html, or from the Cambridge Crystallographic Data Centre, 12 Union Road, Cambridge CB2 1EZ, UK; fax: (+44) 1223-336-033; or e-mail: deposit@ccdc.cam.ac.uk.

References

[1] (a) A.D. Sherry, C.F.G.C. Geraldes, in: J.-C.G. Bünzli, G.R. Choppin (Eds.), Lanthanide Probes in Life, Chemical and Earth Sciences. Theory and Practice, Elsevier, Amsterdam, 1989, pp. 93–124;
(b) J.A. Peters, J. Huskens, D.J. Raber, Prog. Nucl. Magn. Reson. Spectrum 28 (1996) 283.
[2] (a) S. Aime, M. Botta, M. Fasano, E. Terreno, Chem. Soc. Rev. 27 (1998) 19;
(b) P. Caravan, J.J. Ellison, T.J. McMurry, R.B. Lauffer, Chem. Rev. 99 (1999) 2293.
[3] C.H. Evans, in: E. Frieden (Ed.), Biochemistry of Lanthanides, Plenum Press, New York, 1990.
[4] (a) J.-C.G. Bünzli, in: J.-C.G. Bünzli, G.R. Choppin (Eds.), Lanthanide Probes in Life, Chemical and Earth Sciences. Theory and Practice, Elsevier, Amsterdam, 1989, p. 219;
(b) I. Hemmilä, V. Laitala, J. Fluoresc. 15 (2005) 529.
[5] (a) G. Geier, C.K. Jørgensen, Chem. Phys. Lett. 9 (1971) 263;
(b) N.A. Kostromina, N.N. Tananaeva, Zh. Neorg. Khim. 16 (1971) 256;
(c) K. Bukietyńska, A. Mondry, Inorg. Chim. Acta 110 (1985) 1;
(d) K. Bukietyńska, A. Mondry, Inorg. Chim. Acta 130 (1987) 145;
(e) J. Dexpert-Ghys, J. Halwani, B. Piriou, Inorg. Chim. Acta 139 (1987) 303;
(f) H.G. Brittain, G.R. Choppin, P.P. Barthelemy, J. Coord. Chem. 26 (1992) 143;
(g) M. Latva, J. Kankare, K. Haapakka, J. Coord. Chem. 38 (1996) 85;
(h) T. Kimura, Y. Kato, J. Alloys Comp. 275-277 (1998) 806.
[6] (a) J.L. Hoard, B. Lee, M.D. Lind, J. Am. Chem. Soc. 87 (1965) 1612;
(b) J.L. Hoard, E. Willstadter, J. Silverton, J. Am. Chem. Soc. 87 (1965) 1611;
(c) H.Y.D. Ke, E.R. Birnbaum, J. Luminen. 63 (1995) 9;
(d) K. Nakamura, T. Kurisaki, H. Wakita, T. Yamaguchi, Acta Crystallogr. C51 (1995) 1559;
(e) J. Wang, X.D. Zhang, W.G. Jia, Y. Zhang, Z.R. Liu, Koord. Khim. 30 (2004) 141;
(f) J. Wang, X.D. Zhang, Y. Zhang, Y. Wang, X.Y. Liu, Z.R. Liu, Koord. Khim. 30 (2004) 901.
[7] (a) T.F. Gritmon, M.P. Goedken, G.R. Choppin, J. Inorg. Nucl. Chem. 39 (1977) 2021;
(b) S.L. Wu, W.DeW. Horrocks Jr., J. Chem. Soc., Dalton Trans. (1997) 1497.
[8] T.F. Gritmon, M.P. Goedken, G.R. Choppin, J. Inorg. Nucl. Chem. 39 (1977) 2025.
[9] N. Graeppi, D.H. Powell, G. Laurenczy, L. Zékány, A.E. Merbach, Inorg. Chim. Acta 235 (1995) 311.
[10] J. Wang, X.D. Zhang, W.G. Jia, H.F. Li, X. Ling, Huaxue Xuebao (Chin.) (Acta Chim. Sinica) 60 (2002) 1452.
[11] J. Wang, Z.R. Liu, X.D. Zhang, W.G. Jia, Gaodeng Xuexiao Huaxue Xuebao (Chin.) (Chem. J. Chin. Uni.) 23 (2002) 2052.
[12] J.-G. Kang, S.-K. Yoon, Y. Sohn, J.-G. Kim, Y.-D. Kim, I.-H. Suh, J. Chem. Soc., Dalton Trans. (1999) 1467.
[13] G.M. Sheldrick, SHELXS-97. Program for structure solution, University of Göttingen, 1997.
[14] G.M. Sheldrick, SHELXL-97. Program for structure refinement, University of Göttingen, 1997.
[15] DIAMOND–Visual Crystal Structure Information System, CRYSTAL IMPACT, Postfach 1251, D-53002 Bonn, Germany.
[16] A. Mondry, R. Janicki, Dalton Trans. (2006) 4702.
[17] W.T. Carnall, T.R. Fields, K. Rajnak, J. Chem. Phys. 49 (1968) 4412.
[18] L. Spaulding, H.G. Brittain, Inorg. Chem. 22 (1983) 3486.

Available online at www.sciencedirect.com
ScienceDirect
Polyhedron 26 (2007) 851–861
POLYHEDRON
www.elsevier.com/locate/poly

Palladium complexes of multidentate pyrazolylmethyl pyridine ligands: Synthesis, structures and phenylacetylene polymerization

Stephen O. Ojwach [a], Ilia A. Guzei [b], James Darkwa [a,*], Selwyn F. Mapolie [c]

[a] Department of Chemistry, University of Johannesburg, Auckland Park Kingsway Campus, Auckland Park 2006, South Africa
[b] Department of Chemistry, University of Wisconsin-Madison, 1101 University Avenue, Madison, WI 53706, USA
[c] Department of Chemistry, University of the Western Cape, Private Bag X17, Bellville 7535, South Africa

Received 7 August 2006; accepted 14 September 2006
Available online 22 September 2006

Abstract

The compounds, 2,6-bis(3,5-dimethylpyrazol-1-ylmethyl)pyridine ($_{Me}$NNN) (**L1**) and 2,6-bis(3,5-ditertbutylpyrazol-1-ylmethyl)pyridine ($_{tBu}$NNN) (**L2**), react with either $[Pd(NCMe)_2Cl_2]$ or [Pd(COD)ClMe] to form the mononuclear palladium complexes $[Pd(_{Me}NNN)Cl_2]$ (**1**), [Pd($_{Me}$NNN)ClMe] (**2**), $[Pd(_{tBu}NNN)Cl_2]$ (**3**) and [Pd($_{tBu}$NNN)ClMe] (**4**). Reactions of **1**, **2** and **4** with the halide abstractor, $NaBAr_4$ (Ar = 3,5-$(CF_3)_2C_6H_3$), led to the formation of stable tridentate cationic species $[Pd(_{Me}NNN)Cl]^+$(**5**), $[Pd(_{Me}NNN)Me]^+$ (**6**) and $[Pd(_{tBu}NNN)Cl]^+$ (**7**) respectively. The analogous carbonyl linker cationic species $[Pd\{(3,5\text{-}Me_2pz\text{-}CO)_2\text{-}py\}Cl]^+$ (**9**) and $[Pd\{(3,5\text{-}^tBu_2pz\text{-}CO)_2\text{-}py\}Cl]^+$ (**10**), prepared by halide abstraction of the neutral complexes $[Pd\{(3,5\text{-}Me_2pz\text{-}CO)_2\text{-}py\}Cl_2]$ and $[Pd\{(3,5\text{-}^tBu_2pz\text{-}CO)_2\text{-}py\}Cl_2]$ by $NaBAr_4$, were however less stable with $t_{1/2}$ of 14 and 2 days respectively. Attempts to crystallize **1** and **3** from the mother liquor resulted in the isolation of the salts $[Pd(_{Me}NNN)Cl]_2[Pd_2Cl_6]$ (**11**) and $[Pd(_{tBu}NNN)Cl]_2[Pd_2Cl_6]$ (**12**). Although when complexes **1**–**4** were reacted with modified methylaluminoxane (MMAO) or $NaBAr_4$, no active catalysts for ethylene oligomerization or polymerization were formed, activation with silver triflate (AgOTf) produced active catalysts that oligomerized and polymerized phenylacetylene to a mixture of *cis-transoidal* and *trans-cisoidal* polyphenylacetylene.
© 2006 Elsevier Ltd. All rights reserved.

Keywords: (Pyrazolylmethyl)pyridine; Bidentate palladium complexes; Tridentate ligand coordination; Cationic palladium complexes; Phenylacetylene; Polymerization

1. Introduction

Multidentate nitrogen based ligands, such as 2,6-bis(organylimino)pyridine and 2,6-bis(pyrazol-1-ylmethyl)-pyridine late transition metal complexes, are good catalysts for the oligomerization and polymerization of olefins [1]. Other nitrogen based ligands such as bidentate α-diimine are also known to form cationic Ni and Pd complexes that polymerize or oligomerize olefins depending on the steric bulk of the ligand backbone [2]. These cationic α-diimine Ni and Pd complexes are often prepared by direct halide abstraction using silver or alkali metal salts of a very weakly coordinating or non-coordinating counter ion. It has been established that the presence of strongly coordinating ligands compete with the monomer for the vacant coordination site in the active catalyst [3]. It is therefore essential to have a weakly coordinating ligand that would not compete with the incoming monomer for the vacant site of the metal and yet would protect the metal in the absence of the substrate.

Recently we have used 2,6-bis(pyrazol-1-ylcarbonyl)pyridine palladium dichloride complexes as catalyst precursors for ethylene polymerization [4]. The ligands in these precursors are potentially tridentate but only coordinate in a bidentate mode through one pyrazolyl and the pyridine nitrogen atoms leaving the second pyrazolyl unit uncoordinated.

* Corresponding author. Tel.: +27 11 489 2838; fax: +27 11 489 2819.
E-mail address: jdarkwa@uj.ac.za (J. Darkwa).

0277-5387/$ - see front matter © 2006 Elsevier Ltd. All rights reserved.
doi:10.1016/j.poly.2006.09.007

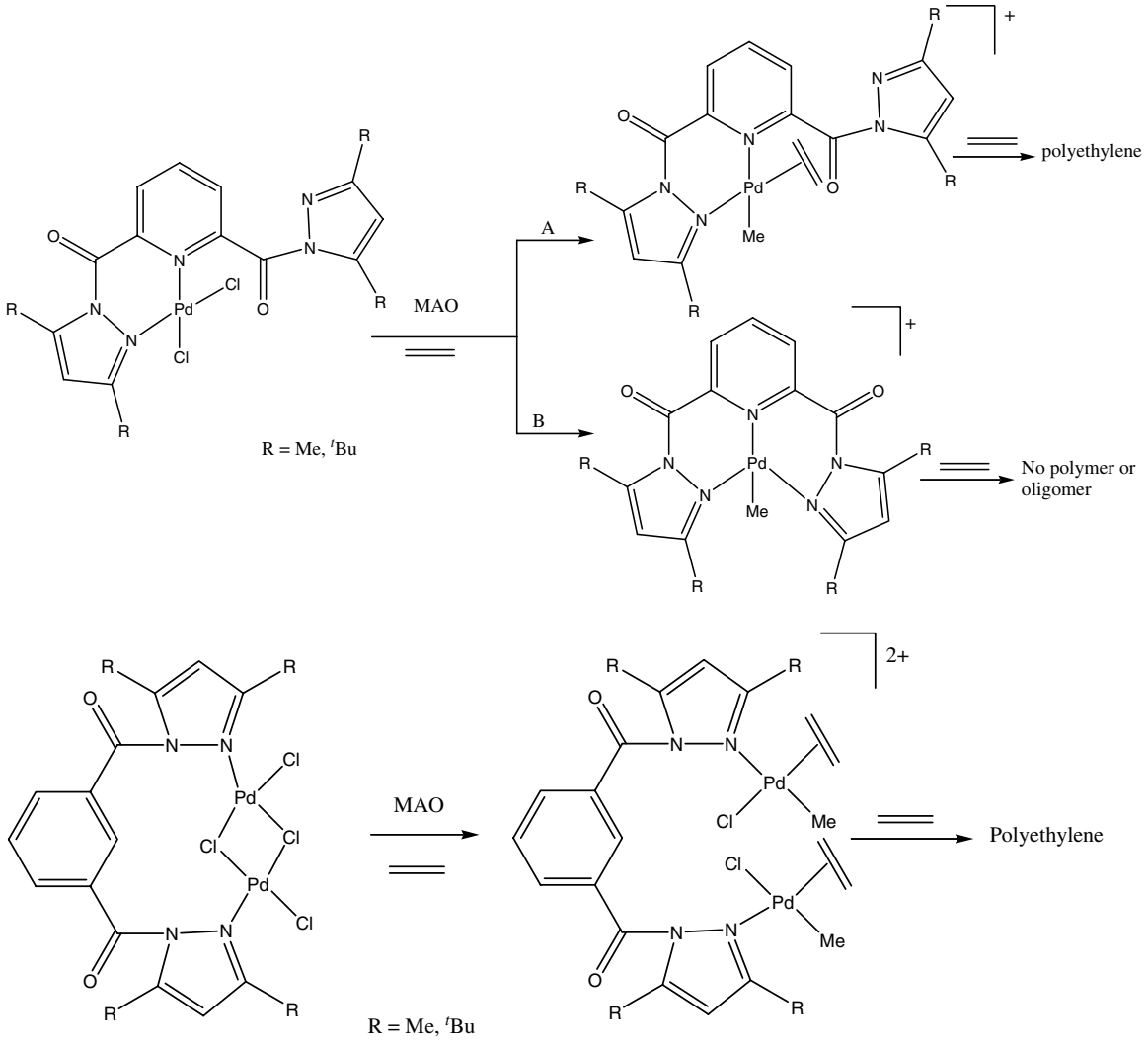
When the complexes are reacted with methylaluminoxane (MAO) as co-catalysts, they form active catalysts for the polymerization of ethylene to give high density polyethylene (HDPE) [4]. However, the expected activity in comparison with our previous catalysts generated from 1,3-bis(pyrazol-1-yl)benzene [5a] is considerably lower, possibly due to the potential of 2,6-bis(pyrazol-1-ylcarbonyl)pyridine to bind in a tridentate coordination mode upon removal of a chloride (Scheme 1). This is likely to result in the ethylene monomer competing with the second pyrazolyl unit in coordinating to the vacant site on the metal in the catalyst (Scheme 1, route B).

The stability of the carbonyl linker catalysts was also found to be lower than the bis(pyrazole)palladium(II) catalysts [5b] and in an attempt to produce more stable catalysts we have replaced the carbonyl linker with a methylene group. Some of the chemistry of 2,6-bis(pyrazol-1-ylmethyl)pyridine have earlier been explored by Steel et al. [6] and others [7]. In a report by Steel et al. [6a] a palladium dichloride complex with this ligand system was formulated as a trinuclear complex with three ligand units. We found 2,6-bis(pyrazol-1-ylmethyl)pyridine to complex with palladium dichloride fragments in a bidentate fashion; bonding through one pyrazolyl nitrogen and the pyridine nitrogen, with the second pyrazolyl unit uncoordinated. The latter coordinates to the palladium metal upon chloride abstraction. These findings and attempts to use the palladium complexes as ethylene and phenylacetylene polymerization catalysts are described in this paper.

2. Experimental

2.1. Materials and instrumentation

Synthetic and ^{1}H NMR experimental manipulations were performed under a nitrogen atmosphere using standard Schlenk techniques and glove box. All solvents were of analytical grade and were dried and distilled prior to use. Toluene and dichloromethane were dried and distilled from sodium/benzophenone and P_2O_5 respectively.



Scheme 1.

2,6-Bis(chloromethyl)pyridine, tetrabutylammonium bromide, silver triflate and phenylacetylene (98%) were obtained from Sigma–Aldrich and used as received. $NaBAr_4$ ($Ar = 3,5\text{-}(CF_3)_2C_6H_3$) was obtained from Boulder Scientific and used as received. The starting materials 3,5-ditertbutylpyrazole [8], [Pd(COD)MeCl] [9,10] and 2,6-bis(3,5-dim-ethylpyrazol-1-ylmethyl)pyridine (**L1**) [6a] were synthesized following the literature procedures. The NMR spectra were recorded on a Varian Gemini 2000 instrument (^1H at 200 MHz and ^{13}C at 50.1 MHz) at room temperature. The chemical shifts are reported in δ (ppm) and referenced to the residual $CHCl_3$ in the NMR solvent. Coupling constants are measured in Hertz (Hz). Elemental analyses were performed by the micro analytical laboratory at the University of Cape Town, South Africa, as a service. Polymer molecular weights were determined by gel permeation chromatography on a Waters 600E instrument equipped with a Waters differential refractometer detector (THF, at 30 °C, rate = 1.0 mL/min) and PL–MIXED-C…™ columns, using polystyrene standards.

2.2. Synthesis of ligands and palladium complexes

2.2.1. 2,6-{(3,5-^{t}Bu$_2$pzCH$_2$)$_2$py} (*L2*)

A mixture of 2,6-bis(bromomethyl)pyridine (1.00 g, 3.79 mmol) and 3,5-di-*tert*-butylpyrazole (1.36 g, 7.58 mmol) in benzene (40 mL), 40% aqueous NaOH (12 mL) and 40% aqueous tetrabutylammonium bromide (10 drops) was refluxed for 18 h. The organic layer was then separated, and evaporated *in vacuo*. The crude product was washed with water (40 mL) to afford an analytically pure compound **L2** as a white solid. Yield = 1.38 g (75%). ^1H NMR ($CDCl_3$): δ 1.23 (18H, s, ^{t}Bu, pz); 1.31 (18H, s, ^{t}Bu, pz); 5.55 (4H, s, CH_2); 5.93 (2H, s, 4H-pz); 6.32 (2H, d, 3,5H-py, $^3J_{HH} = 8.0$); 7.46 (1H, t, 4H-py, $^3J_{HH} = 8.0$). *Anal.* Calc. for $C_{29}H_{45}N_5$: C, 75.16; H, 9.72; N, 15.12. Found: C, 75.01; H, 9.55; N, 15.43%.

2.2.2. [Pd($_{Me}$ÑÑN)Cl$_2$] (*1*)

To a solution of **L1** (0.11 g, 0.39 mmol) in CH_2Cl_2 (20 mL) was added $[Pd(NCMe)_2Cl_2]$ (0.10 g, 0.39 mmol). The pink solution was stirred for 12 h and the product precipitated by addition of hexane (20 mL) to give a pink solid. Yield = 0.10 g (56%). ^1H NMR ($CDCl_3$): δ 2.45 (6H, s, CH_3, pz); 2.51 (6H, s, CH_3, pz); 5.85 (2H, d, CH_2, $^2J_{HH} = 15.2$); 5.93 (1H, s, 4H-pz); 6.17 (2H, d, CH_2, $^2J_{HH} = 15.0$); 6.28 (1H, s, 4H-pz); 8.11 (2H, d, 3,5H-py, $^3J_{HH} = 8.4$); 8.26 (1H, t, 4H-py, $^3J_{HH} = 8.4$). *Anal.* Calc. for $C_{17}H_{21}N_5PdCl_2$: C, 43.22; H, 4.44; N, 14.83. Found: C, 43.31; H, 4.10; N, 14.91%.

2.2.3. [Pd($_{Me}$ÑÑN)MeCl] (*2*)

To a solution of **L1** (0.30 g, 1.07 mmol) in Et_2O (20 mL) was added a solution [Pd(COD)ClMe] (0.27 g, 1.07 mmol) in Et_2O (20 mL). A light yellow precipitate was formed immediately. The mixture was stirred for 3 h, filtered and the material isolated recrystallized from CH_2Cl_2–hexane to give a light yellow solid. Yield = 0.31 g (68%). ^1H NMR ($CDCl_3$): δ 0.97 (3H, s, CH_3,Pd–Me); 2.34 (6H, s, CH_3, pz); 2.49 (6H, s, CH_3, pz); 5.68 (2H, d, CH_2, $^2J_{HH} = 15.4$); 5.74 (d, 2H, CH_2, $^2J_{HH} = 15.4$); 5.91 (2H, s, 4H-pz); 8.08 (1H, t, 4H-py, $^3J_{HH} = 8.4$); 8.15 (2H, d, 3,5H-py, $^3J_{HH} = 8.2$). ^{13}C NMR ($CDCl_3$): δ −7.4; 12.3; 14.9; 52.6; 108.2; 125.3; 141.7; 143.2; 151.8; 152.0. *Anal.* Calc. for $C_{18}H_{24}N_5PdCl \cdot CH_2Cl_2$: C, 42.53; H, 4.85; N, 13.06. Found: C, 42.31; H, 4.77; N, 11.64%.

2.2.4. [Pd($_{tBu}$ÑÑN)Cl$_2$] (*3*)

To a solution of $[Pd(NCMe)Cl_2]$ (0.20 g, 0.78 mmol) in CH_2Cl_2 (20 mL) was added **L2** (0.36 g, 0.78 mmol). The clear orange solution was stirred for 24 h after which an equal volume of hexane was added and kept at −4 °C to afford compound **3** as a yellow solid. Single crystals suitable for X-ray analysis were obtained by slow evaporation of $CDCl_3$ used as ^1H NMR solvent. Yield = 0.35 g (71%). ^1H NMR ($CDCl_3$): δ 1.27 (9H, s, ^{t}Bu, pz); 1.34 (9H, s, ^{t}Bu, pz); 1.41 (9H, s, ^{t}Bu, pz); 1.75 (9H, s, ^{t}Bu, pz); 5.72 (1H, d, CH_2, $^2J_{HH} = 18.6$); 5.78 (1H, d, CH_2, $^2J_{HH} = 15.4$); 5.92 (1H, s, 4H-pz); 5.97 (1H, s, 4H-pz); 6.23 (1H, d, CH_2, $^2J_{HH} = 15.6$); 7.01 (1H, d, CH_2, $^2J_{HH} = 19.0$); 7.44 (2H, d, 3,5H-py, $^3J_{HH} = 8.0$); 7.69 (1H, t, 4H-py, $^3J_{HH} = 8.0$). ^{13}C NMR ($CDCl_3$): δ 30.1; 30.2; 30.6; 31.1; 31.4; 31.8; 32.0; 33.0; 56.4; 56.7; 100.8; 104.3; 122.9; 124.0; 140.4; 153.2; 154.0; 155.2; 162.0; 164.3; 164.6. *Anal.* Calc. for $C_{29}H_{45}N_5PdCl_2 \cdot 0.5CH_2Cl_2$: C, 52.33; H, 6.59; N, 10.17. Found: C, 52.72; H, 7.08; N, 10.26%.

2.2.5. [Pd($_{tBu}$ÑÑN)MeCl] (*4*)

Compound **4** was prepared according to the procedure for **2** using **L2** (0.21 g, 0.45 mmol) and [Pd(COD)MeCl] (0.12 g, 0.45 mmol). Yield = 0.17 g (60%). ^1H NMR ($CDCl_3$): δ 1.03 (3H, s, CH_3, Pd–Me); 1.23 (9H, s, ^{t}Bu, pz); 1.35 (9H, s, ^{t}Bu, pz); 1.41 (9H, s, ^{t}Bu, pz); 1.61 (9H, s, ^{t}Bu, pz); 5.35 (1H, d, CH_2, $^2J_{HH} = 18.6$); 5.53 (1H, d, CH_2, $^2J_{HH} = 15.0$); 5.93 (1H, s, 4H-pz); 5.95 (1H, s, 4H-pz); 6.11 (1H, d, $CH_2{}^2J_{HH} = 15.4$); 6.87 (1H, d, CH_2, $^2J_{HH} = 19.2$); 7. 21 (2H, d, 3,5H-py, $^3J_{HH} = 8.0$); 7.69 (1H, t, 4H-py, $^3J_{HH} = 8.0$). ^{13}C NMR ($CDCl_3$): δ 30.1; 30.4; 30.6; 31.1; 31.5; 32.6; 55.7; 100.3; 103.8; 121.8; 122.2; 138.5; 152.8; 153.7; 162.1. *Anal.* Calc. for $C_{30}H_{48}N_5PdCl$: C, 58.06; H, 7.80; N, 11.28. Found: C, 58.10; H, 8.32; N, 10.13%.

The synthesis of **6** and **7** are described as examples of how the cationic complexes were prepared.

2.2.6. [Pd($_{Me}$ÑÑN)Me]BAr$_4$ (*6*)

To a solution of **2** (0.05 g, 0.11 mmol) in CH_2Cl_2 (10 mL) was added a solution of $NaBAr_4$ (0.10 g, 0.11 mmol) in CH_2Cl_2 (10 mL) and stirred for 10 min. The resultant mixture containing Pd black was filtered over Celite to give a clear solution. Hexane (20 mL) was added to the filtrate and kept at −4 °C to afford colourless single crystals suitable for X-ray analysis. Yield = 0.15 g (30%). ^1H NMR ($CDCl_3$): δ 1.09 (s, 3H, CH_3, Pd–Me); 2.30

(6H, s, CH_3, pz); 2.35 (6H, s, CH_3, pz); 5.14 (2H, d, CH_2, $^2J_{HH} = 15.0$); 5.70 (2H, d, CH_2, $^2J_{HH} = 15.0$); 5.95 (2H, s, 4H-pz); 7.22 (2H, d, 3,5H-py, $^3J_{HH} = 8.0$). 7.55 (1H, t, 4H-py, $^3J_{HH} = 8.2$); 7.49 (4H, s, H_p, BAr_4); 7.68 (8H, s, H_o, BAr_4). *Anal.* Calc. for $C_{50}H_{36}BF_{24}N_5Pd$: C, 46.92; H, 2.73; N, 5.47. Found: C, 47.45; H, 2.48; N, 5.48%.

2.2.7. $[(_{tBu}\hat{N}\hat{N}N)PdCl]BAr_4$ (7)

This compound was synthesized according to the procedure described for **6** using **3** (0.09 g, 0.13 mmol) and $NaBAr_4$ (0.12 g, 0.13 mmol) which gave **7** as a crystalline orange solid. Yield = 0.11 g (58%). ^{1}H NMR ($CDCl_3$): δ 1.43 (18H, s, ^{t}Bu, pz); 1.52 (18H, s, ^{t}Bu, pz); 5.68 (2H, d, CH_2, $^2J_{HH} = 15.2$); 6.08 (2H, s, 4H-pz); 6.21 (2H, d, CH_2, $^2J_{HH} = 15.2$); 7.27 (2H, d, 3,5H-py, $^3J_{HH} = 8.0$); 7.50 (1H, t, 4H-py, $^3J_{HH} = 8.0$); 7.49 (4H, s, H_p, BAr_4); 7.68 (8H, s, H_o, BAr_4). *Anal.* Calc. for $C_{59}H_{57}BF_{24}N_5PdCl$: C, 49.05; H, 3.98; N, 4.85. Found: C, 49.51; H, 4.00; N, 4.97%.

2.3. Phenylacetylene oligomerization and polymerization

In a typical experiment, a solution of AgOTf (0.05 g, 0.2 mmol) in a 20 mL mixture of CH_2Cl_2 and MeCN (1:1) was added to a complex solution of **1** (0.05 g, 0.1 mmol) in CH_2Cl_2 (20 mL). A white precipitate of AgCl formed immediately, the mixture was stirred for 5 min and filtered to give a yellow solution of the active catalyst. To this solution was added 50 equiv. of phenylacetylene monomer (0.64 mL, 5 mmol). The yellow solution gradually turned dark red and was stirred for a further 1 h. After the reaction period, the solution was evaporated to dryness to afford a dark brown crude product, which was dissolved in minimum amount of CH_2Cl_2 and the polymer precipitated from methanol (40 mL). This was dried and weighed to obtain the percent polymer. The methanol solution was allowed to evaporate to dryness to obtain the oligomer fractions. Both the oligomers and polymers were characterized by of ^{1}H NMR spectroscopy and gel permeation chromatography.

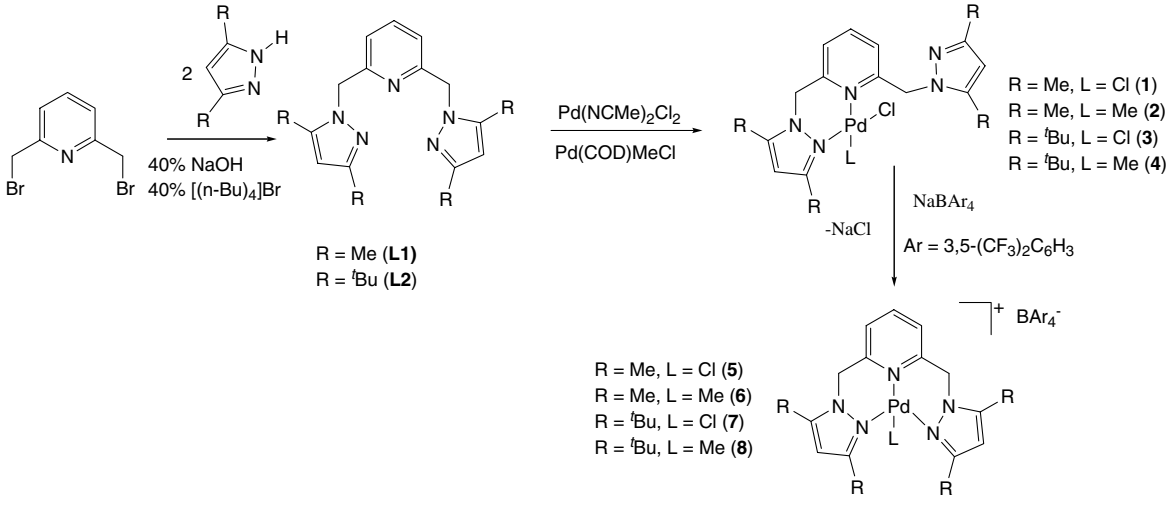
2.4. X-ray crystallography

Crystal evaluation and data collection for **3**, **5**, **6**, **11** and **12** were performed on a Bruker CCD-1000 diffractometer with Mo Kα ($\lambda = 0.71073$ Å) radiation and the diffractometer to crystal distance of 4.9 cm. The initial cell constants were obtained from three series of ω scans at different starting angles. The reflections were successfully indexed by an automated indexing routine built in the SMART program. The absorption correction was based on fitting a function to the empirical transmission surface as sampled by multiple equivalent measurements [11]. The structures were solved by direct methods and refined by least-squares techniques using SHELXTL program [11]. All non-hydrogen atoms were refined with anisotropic displacement coefficients. All hydrogen atoms were included in the structure factor calculation at idealized positions and were allowed to ride on the neighbouring atoms with relative isotropic displacement coefficients.

3. Results and discussion

3.1. Synthesis of bis(pyrazol-1-ylmethyl)pyridine palladium complexes

Compound 2,6-bis(3,5-ditertbutylpyrazol-1-ylmethyl)-pyridine ($_{tBu}\hat{N}\hat{N}N$) (**L2**) was prepared in good yields (75%) via phase transfer catalyzed alkylation of 3,5-ditertbutylpyrazole and 2,6-bis(bromomethyl)pyridine following the literature procedure [6a] described for the synthesis of 2,6-bis(3,5-dimethylpyrazol-1-ylmethyl)pyridine ($_{Me}\hat{N}\hat{N}N$) (**L1**). Compounds **L1** and **L2** reacted with either $[Pd(NCMe)_2Cl_2]$or [Pd(COD)ClMe] to produce the corresponding complexes **1**–**4** in moderate to good yields (Scheme 2).



Scheme 2.

The ^{1}H NMR spectra of **L1** and **L2** gave signature peaks of the four CH_2 linker protons as singlets at 5.28 and 5.55 ppm respectively and typical peaks of methyl and tertbutyl at 2.25 and 2.51 ppm and 1.21 and 1.31 ppm respectively. These peaks were diagnostic in the next step to confirm that complexation of the ligands with the palladium salts had occurred. On complexation of **L1** and **L2**, the CH_2 linker protons appeared as AB quartets. In complexes **1** and **2** these signals are between 5.68–6.17 ppm (**L1** singlet, 5.28 ppm) confirming the presence of diastereotopic protons in axial and equatorial positions. This inequality arises from different chair and boat conformations that depict the existence of restricted rotations in the complexes hence the protons could be subjected to different contributions from the ring currents from the pyrazole or pyridine groups on the NMR time scale. A similar spectrum has been reported for the related Cu complex, $[Cu\{(Me_2pz\text{-}CH_2)_2py\}(PPh_3)]ClO_4$, [7a] in which the CH_2 linker protons were observed as AB quartets at 4.75 and 5.25 ppm.

In complexes **3** and **4**, the CH_2 linker protons appeared as four distinct AB quartets with geminal coupling constants ranging from 15.4 to 19.2 Hz. This highlights the increased restricted rotation in **3** and **4** arising from the more sterically demanding ditertbutyl groups. The large peak separation of the signals ($\Delta\delta = 1.38$ ppm), however, is rather unusual. A smaller peak separation between the CH_2 linker protons ($\Delta\delta = 0.70$ ppm) of the related Ru complex of **L1**, $[Ru\{(\eta^6\text{-}C_6H_6)(Me_2pz\text{-}CH_2)_2py\}]PF_6$, [12] has been reported. Recently Cavell and co-workers reported even a smaller peak separation ($\Delta\delta = 0.07$ ppm) for geminal coupling of the bridging methylene protons of $[Pd(_{t\mathrm{Bu}}\hat{C}\hat{N}C)Me]BF_4$; a feature attributed to the slow inversion of the complex [13]. In contrast to our results, Cavell and co-workers found that in the chloro analogue, $[Pd(_{t\mathrm{Bu}}\hat{C}\hat{N}C)Cl]BF_4$, the methylene protons appear as a singlet at 5.69 ppm probably as a consequence of the lower *trans* effect of the Cl^-, which reduces the $Pd\text{–}N_{(py)}$ bond length and gives the ligand backbone greater ability to undergo unhindered rotation [13]. The ^{1}H NMR spectra of **3** and **4** could be used to diagnose the bidentate bonding mode of compound **L2** in these complexes. For example in **3** one set of peaks at 1.41 and 1.75 ppm for tertbutyl protons and 5.92 ppm for the pyrazolyl ring proton were assigned to the bound pyrazolyl unit while peaks at 1.27 and 1.34 and 5.97 ppm were due to the 'dangling' pyrazolyl unit. This assignment is consistent with the solid state structure of **3** (*vide infra*). Similar spectra have been reported for compounds $[Ru\{(\eta^6\text{-}C_6H_6)(Me_2pz\text{-}CH_2)_2py\}]PF_6$ [12] and $[Pd\{(3,5\text{-}{}^tBu_2pz\text{-}CO)_2py\}Cl_2]$ [4].

3.2. Reactions of complexes *1–4* with $NaBAr_4$

In attempts to generate catalysts for the oligomerization or polymerization of ethylene, 8 mg of complexes **2** and **4** were reacted with either stoichiometric equivalent of $NaBAr_4$ or 1000-fold excess of modified methylaluminoxane (MMAO) in the presence of excess ethylene. We did not observe the formation of oligomers or polymers of ethylene as expected. In subsequent experiments performed on a preparative scale (Scheme 2), ^{1}H NMR spectroscopic analyses suggested the formation of cationic species in which the ligands bind in a tridentate fashion upon chloride abstraction. These cationic species, $[Pd(_{\mathrm{Me}}\hat{N}\hat{N}N)Cl]^+$ (**5**), $[Pd(_{\mathrm{Me}}\hat{N}\hat{N}N)Me]^+$ (**6**) and $[Pd(_{t\mathrm{Bu}}\hat{N}\hat{N}N)Cl]^+$ (**7**), were isolated as BAr_4^- salts and the structures of **5** and **6** (Figs. 2 and 3 respectively) confirmed the tridentate ligand coordination deduced from the spectroscopic data.

Recently we reported that $[Pd\{(3,5\text{-}Me_2pz\text{-}CO)_2py\}Cl_2]$ and $[Pd\{(3,5\text{-}{}^tBu_2pz\text{-}CO)_2py\}Cl_2]$ can be activated with methylaluminoxane (MAO) as co-catalyst to catalyze the polymerization of ethylene [4]. The inability of the cationic species generated from **2** and **4** to promote ethylene polymerization can be attributed to the strong coordination of the 'dangling' arm of the pyrazolyl unit in **2** and **4**, which blocks the vacant coordination site created upon chloride abstraction from the metal centre necessary for the coordination of the ethylene monomer. In the carbonyl linker analogues used to catalyze the polymerization of ethylene [4], it is likely that upon activation with MAO, similar tridentate cationic species are formed but under a high ethylene pressure, one of the coordinated pyrazolyl units dissociates from the Pd centre to allow the ethylene to coordinate and undergo subsequent insertion to form polyethylene (Scheme 1, route A). This behaviour is necessitated by the weaker binding ability of the pyrazolyl units in the carbonyl linker analogues. However, even when **6** and **7** were subjected to ethylene pressures up to 50 atm, there was no formation of polyethylene; an observation which highlights the strength of the $Pd\text{–}N_{(pz)}$ bonds in **6** and **7** relative to the binding affinity of the ethylene monomer.

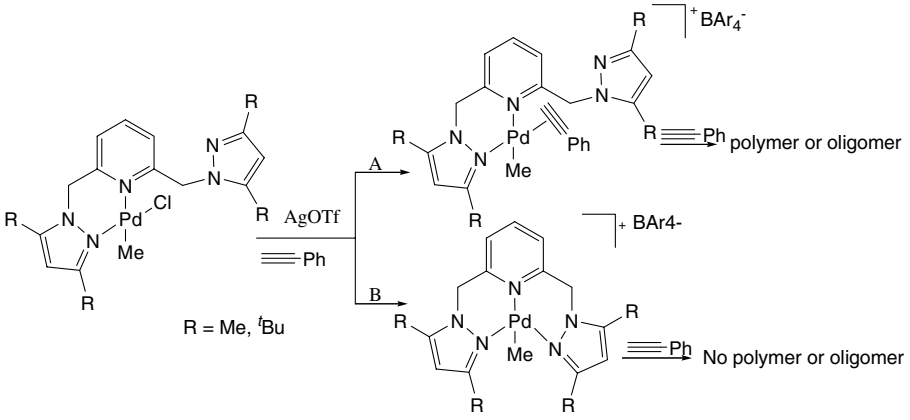
3.3. Oligomerization and polymerization of phenylacetylene

The binding affinity of the monomer is important since in experiments using phenylacetylene instead of ethylene, we did observe the formation of oligomers and polymers of phenylacetylene (Table 1). The active catalysts were generated by reacting complexes **1–4** with AgOTf as halide abstractor in a mixture of CH_2Cl_2 and MeCN (3:1). The ability of catalysts generated from **1** to **4** to oligomerize and polymerize phenylacetylene therefore highlights the significance of the reactivity and the binding affinity of the incoming monomer in displacing or competing with one of the $Pd\text{–}N_{(pz)}$ bonds prior to coordination to the metal centre (Scheme 3, route A). However, the low percentage conversions observed for catalysts **1–4** (36–55%) compared to 90% conversion [10] obtained for the carbonyl linker and bis(pyrazole)palladium(II) complexes under similar conditions suggests the possibility of a competing deactivation pathway. This could arise from the formation of the inactive cationic tridentate species (Scheme 3, route B) which blocks monomer coordination. This argument

Table 1
Phenylacetylene oligomerization and polymerization data[a]

Entry	Catalyst	% Conversion[b]	M_w[c]	M_n[c]	M_w/M_n[c]	% *cis*[d]
1	**1**	51	2552	1575	1.62	44
2	**2**	47	3444	1893	1.82	80
3	**3**	36	2303	1466	1.57	56
4	**4**	38	2062	1350	1.52	74
5	**1**[e]	35	2716	1697	1.72	
6	**1**[f]	55	2230 (620)	1523 (619)	1.48 (1.00)	
7	**2**[g]	47	3613 (684)	2187 (678)	1.65 (1.01)	
8	**2**[h]	12	860	797	1.01	

[a] Conditions: Time = 60 min unless stated otherwise; amount of monomer = 0.64 mL; solvent: CH_2Cl_2:MeCN (40 mL); 3:1, temp = 25 °C; [Pd] = 1.0×10^{-3} mol; phenylacetyelene:[Pd] = 50:1.
[b] Determined by the total mass of the crude product as a percentage of monomer used.
[c] Determined by room temperature GPC using polystyrene standards.
[d] Determined by ^{1}H NMR analysis: *cis* % = $[A_{5.82}/(A_{total}/6)] \times 100$ or *cis* % $A_{5.82} \times 10^4/A_{total} \cdot 16.66$ ($A_{5.82}$ is the integrated peak area of the vinyl proton in the *cis* isomer and A_{total} is the total integrated peak area of the polymer spectrum).
[e] Time = 30 min.
[f] Time = 120 min.
[g] Crude product (mixture of oligomer and polymer).
[h] Oligomer fraction.



Scheme 3.

also supports the slow initiation process observed with systems **1**–**4** as opposed to rapid initiation observed with simple pyrazole and carbonyl linker pyrazolyl palladium complexes [14].

Generally catalysts **1** and **2** bearing methyl substituents on the pyrazolyl ligand showed higher activity than the tertbutyl analogues **3** and **4** (Table 1, entries 1–4). It is likely that the bulkier tertbutyl group hinders monomer coordination resulting in low product yields. We have examined the structurally characterized complexes **3**, **5**, **6**, **11** and **12** from the point of view of the ligand solid angles expressed in percentage of the metal coordination sphere shielded by each ligand. Such an approach provides a quantitative measure of the steric bulk of the ligands [15]. The tridentate ligands in **5**, **6** and **11** shield on average 59.6(10)% of the palladium coordination sphere. The κ^3-($_{t\text{Bu}}\hat{\text{N}}\hat{\text{N}}\hat{\text{N}}$) ligand in **12** shields an enormous 70.1% of the central metal, and the difference of over 10% from its methyl analogue is very significant in terms of dynamic behaviour. As a reference, even ca. 1% changes in the value of a ligand solid angle can affect the ligand's coordination mode [16]. However, it is interesting to note the size of the κ^2-($_{t\text{Bu}}\hat{\text{N}}\hat{\text{N}}\text{N}$) ligand in **3**; the shielding percentage of this ligand is only 51.0%, and thus the flexibility of ($_{t\text{Bu}}\hat{\text{N}}\hat{\text{N}}\text{N}$) can play a major role in the kinetics of the system. Time dependent polymerization experiments with catalyst **1** (Table 1, entries 1, 5 and 6) showed little variation in the percent conversion of monomer after 60 min. This is a typical feature involving catalyst decomposition with time [17] and in our case would suggest active catalysts forming tridentate species via route B in Scheme 3.

The stereochemistry of the polymers was determined by ^{1}H NMR spectroscopy. A typical ^{1}H NMR spectrum of polymers obtained showed a sharp singlet at 5.85 ppm for the vinylic protons, and broad singlets at 6.65 and 6.91 ppm corresponding to the phenyl *ortho* and *meta* protons respectively. From the ^{1}H NMR data, it is evident that all the polymers were a mixture of *cis-transoidal* and

trans-cisoidal [18] with the percentage *cis* content ranging from 44 to 80 (Table 1, entries 1–4). The *cis* and *trans* content of the polyphenylacetylene formed were established by the NMR method reported by Perec et al. [18a] and the formula to calculate the *cis* and *trans* content of the polymer is included as a footnote in Table 1. However, there was no clear dependence of the polymer stereochemistry with respect to catalyst structure.

GPC analysis showed the presence of both oligomers ($M_w = 620$–860) and low molecular weight polymers ($M_w = 2062$–3444) (Table 1, entries 1–4, 7 and 9). For example analysis of the crude products from catalysts **2** (Table 1, entry 7) gave a bimodal distribution GPC trace corresponding to oligomers of average M_w of 684 and polymers of average M_w of 3613. Upon purification of this product, the oligomers (methanol soluble fraction) and polymers (methanol insoluble) gave average M_w of 860 and 3444 respectively.

Table 2
Selected ^{1}H NMR signals and half lives ($t_{1/2}$) of the cationic complexes **5**–**10** in $CDCl_3$

Compound	^{1}H NMR ($CDCl_3$, ppm)				$t_{1/2}$ (days)
	CH_2	4H-pz	$_R$pz (R = Me or ^{t}Bu)	4H-py	
5	5.25, 5.95	5.99	2.35, 2.57	7.27	>30
6	5.14, 5.70	5.95	2.30, 2.35	7.55	>30
7	5.74, 6.31	6.07	1.41, 1.66	7.40	>30
8	5.68, 6.21	6.08	1.41, 1.52	7.50	>30
9		6.38	2.57, 2.67	8.04	14
10		6.57	1.17, 1.76	8.01	2

3.4. Stability of cationic and neutral species of *1–4*

Following the attempts to establish the ability of **2** and **4** to produce active catalysts for ethylene polymerization as described above, we investigated the stability of the cationic species with CH_2 and CO linkers using complexes **1**–**4**, [Pd{(3,5-Me_2pz-CO)$_2$py}Cl_2] and [Pd{(3,5-^{t}Bu$_2$pz-CO)$_2$py}Cl_2]. In a typical experiment, **1** (6 mg, 0.012 mmol) and $NaBAr_4$ (12 mg, 0.012 mmol) were placed in a J-Young NMR tube and about 0.4 mL $CDCl_3$ added and the reaction followed by ^{1}H NMR spectroscopy. In all cases the cationic species of **1**–**4** were formed within 10 min but reactions of the CO linker analogues took up to 4 h to go to completion. The stability of the cationic species [Pd($_{Me}$ÑÑN)Cl]$^+$ (**5**), [Pd($_{Me}$ÑÑN)Me]$^+$ (**6**), [Pd($_{tBu}$ÑÑN)Cl]$^+$ (**7**), [Pd($_{tBu}$ÑÑN)Me]$^+$ (**8**), [Pd{(3,5-Me_2pz-CO)$_2$py}Cl]$^+$ (**9**) and [Pd{(3,5-^{t}Bu$_2$pz-CO)$_2$py}Cl]$^+$ (**10**) also varied. By using the proton peaks of the BAr_4^- counter ion in these salts as internal standard, we established that species **5**–**8** were stable for 30 days without any signs of decomposition while the carbonyl linker counterparts, **9** and **10**, had $t_{1/2}$ of 14 and 2 days respectively (Table 2). The low stability of **9** and **10** may arise from the effect of the carbonyl group in reducing the donor ability of the pyrazolyl nitrogen atoms in **9** and **10** compared to the cations with methylene linkers, **5**–**8**. The stability of the cationic species **5**–**8** might explain why reactions of **1**–**4** with either MMAO or $NaBAr_4$ did not result in the production of active ethylene polymerization catalysts.

Another interesting observation made during attempts to grow crystals of complexes **1**–**4** is that the species that crystallized depended on the procedure used. Attempts to

Table 3
Crystal data and structure refinement parameters for compounds **3**, **5**, **6**, **11** and **12**

Parameter	**3**	**5**	**6**	**11**	**12**
Formula	$C_{31}H_{47}Cl_8N_5Pd$	$C_{50}H_{35}BCl_3F_{24}N_5Pd$	$C_{50}H_{36}BF_{24}N_5Pd$	$C_{38}H_{46}Cl_{20}N_{10}Pd_4$	$C_{64}H_{102}Cl_{20}N_{10}Pd_4$
Fw	879.74	1385.39	1280.05	1777.45	2146.16
Temperature (K)	100(2)	100(2)	100(2)	100(2)	100(2)
Wavelength (Å)	0.71073	0.71073	0.71073	0.71073	0.71073
Cryst system	triclinic	monoclinic	monoclinic	triclinic	triclinic
Space group	$P\bar{1}$	$P2_1/n$	$P2_1/n$	$P\bar{1}$	$P\bar{1}$
A (Å)	10.7180(15)	15.498(2)	10.8623(16)	9.6999(17)	10.0902(10)
B (Å)	12.6687(19)	9.2217(12)	17.848(3)	9.7901(17)	14.1549(14)
C (Å)	15.490(2)	38.010(5)	26.862(4)	17.018(3)	15.7395(15)
α (°)	87.557(3)	90	90	87.410(3)	88.201(2)
β (°)	70.102(2)	100.563(2)	96.444(2)	89.354(3)	85.368(2)
γ (°)	81.527(3)	90	90	64.335(3)	77.909(2)
Volume (Å^3)	1956.05(4)	5340.5(12)	5174.7(13)	1455.1(4)	2190.7(4)
Z	2	4	4	1	1
$D_{calc.}$ (Mg/m^3)	1.494	1.723	1.643	2.028	1.627
Absorption coefficient (mm^{-1})	1.050	0.624	0.487	2.176	1.461
F(000)	900	2752	2552	868	1080
Final *R* indices (R_1)	0.0509	0.0640	0.0409	0.0626	0.0355
Reflections collected	9611	41 777	42 250	16 921	13 905
Completeness to theta (%)	95.2	99.6	99.8	92.8	89.3
Goodness-of-fit on F^2	1.030	1.067	1.097	0.977	1.036
Largest difference peak and hole (e Å^{-3})	1.220 and −0.600	3.243 and −1.802	1.353 and −1.309	1.275 and −1.660	0.835 and −0.636

grow crystals of **1** and **3** directly from the mother liquor (reaction mixture) gave crystals of tridentately bound cationic species with $[Pd_2Cl_6]^{2-}$ as counter ion (**11** and **12**) within 7 days. On the other hand, when **3** was precipitated out initially from the reaction mixture and subsequently re-dissolved in CH_2Cl_2, crystals of **3** were obtained. Crystals of **3** were dissolved in $CDCl_3$ and monitored for 21 days by ^1H NMR but showed no signs of forming the cationic species **12**. It is not clear what causes the formation of **11** and **12** from the reaction mixture which does not occur when **1** and **3** are first isolated and re-dissolved in CH_2Cl_2. However, both **11** and **12** crystallized with solvent molecules and rapidly lost solvent when crystals were removed from the mother liquor and became insoluble. It was therefore difficult to further characterize these materials.

3.5. Molecular structure determination by single crystal X-ray crystallography

Single crystals suitable for X-ray analysis of complexes **3** and **5** were grown by slow evaporation of the dichloromethane solvent at room temperature while crystals of **6** were grown by slow diffusion of hexane into dichloromethane at −4 °C. In other attempts to obtain crystals of **1** and **3**, cationic tridentate palladium complexes $2[(_{Me}\hat{N}\hat{N}\hat{N})PdCl]^+$ (**11**) and $2[(_{tBu}\hat{N}\hat{N}\hat{N})PdCl]^+$ (**12**) with $[Pd_2Cl_6]^{2-}$ counter ions were obtained as described earlier.

Crystallographic data for **3**, **5**, **6**, **11** and **12** are presented in Table 3, while selected bond lengths and angles are given in Table 4. Solid state structures of **3**, **5**, **6**, **11** and **12** are shown in Figs. 1–5 respectively. The five palladium complexes contain the central metal in a slightly distorted

Table 4
Selected bond lengths (Å) and bond angles (°) for **3**, **5**, **6**, **11** and **12**

	3 X = Cl(2)	**5** X = Cl(1)	**6** X = C(1)	**11** X = Cl(1)	**12** X = Cl(1)
Bond lengths					
Pd(1)–N(1)	2.026(3)	2.007(4)	2.028(2)	2.011(5)	2.029(2)
Pd(1)–N(3)	2.042(3)	2.031(4)	2.128(2)	2.010(5)	1.9925(19)
Pd(1)–N(5)		2.023(4)	2.043(2)	2.012(5)	2.028(2)
Pd(1)–X	2.3125(5)	2.2803(13)	2.029(3)	2.2838(18)	2.2872(6)
N(1)–N(2)	1.371(4)	1.366(6)	1.369(3)	1.381(7)	1.381(3)
N(4)–N(5)	1.371(4)	1.367(6)	1.370(3)	1.356(7)	1.378(3)
Bond angles					
N(1)–Pd(1)–N(3)	84.00(13)	87.39(17)	86.07(9)	88.81(2)	84.87(10)
N(3)–Pd(1)–X	173.92(10)	177.63(12)	175.95(11)	175.1(1)	178.69(6)
N(1)–Pd(1)–X	94.36(10)	91.07(12)	93.73(15)	92.13(11)	94.59(9)
N(1)–Pd(1)–N(5)		175.85(17)	172.90(9)	175.1(2)	170.77(8)
N(3)–Pd(1)–N(5)		88.57(17)	88.03(9)	86.9(2)	85.94(8)

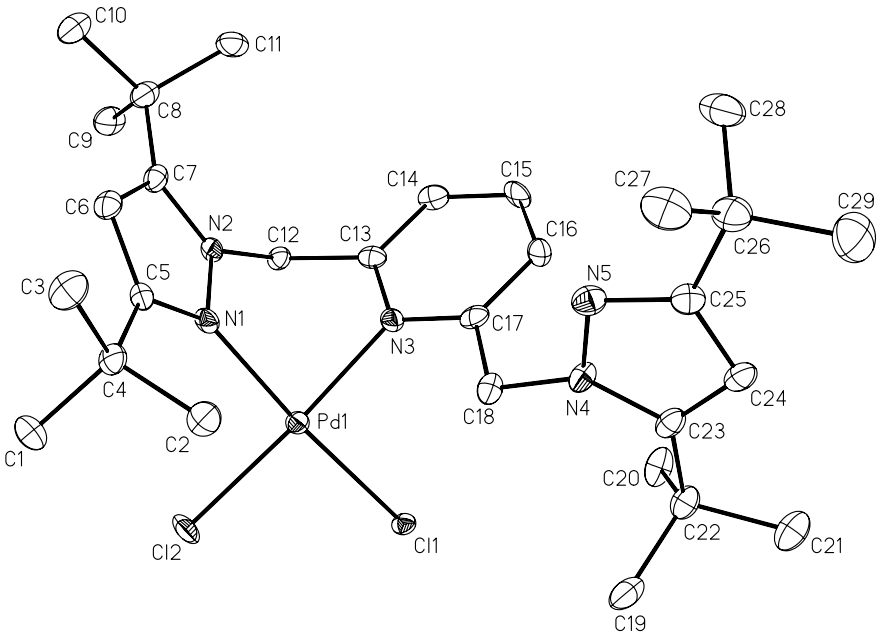


Fig. 1. Molecular structure of complex **3** shown with 50% probability ellipsoids. The hydrogen atoms are omitted for clarity.

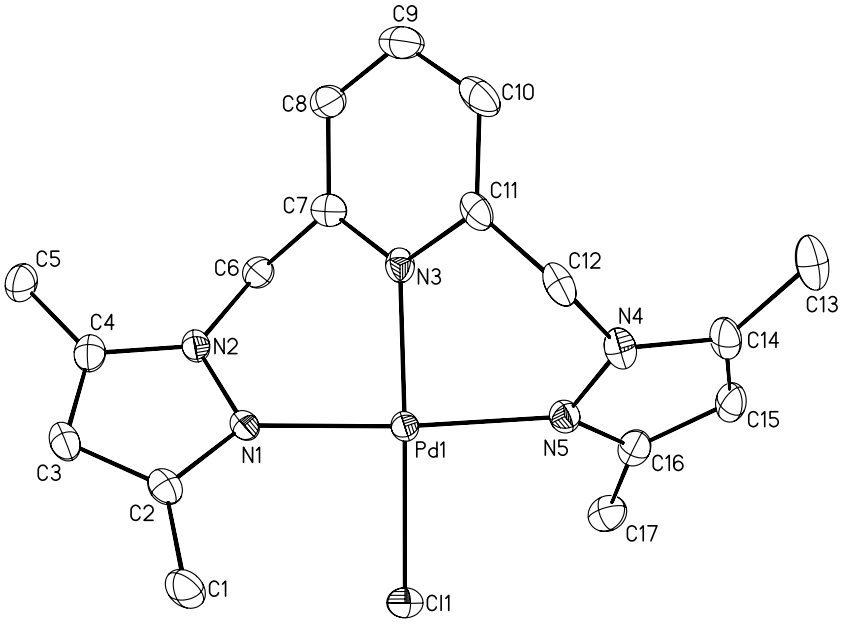


Fig. 2. Molecular structure of cation of **5** shown with 50% probability ellipsoids. The boron counter ion and hydrogen atoms are omitted for clarity.

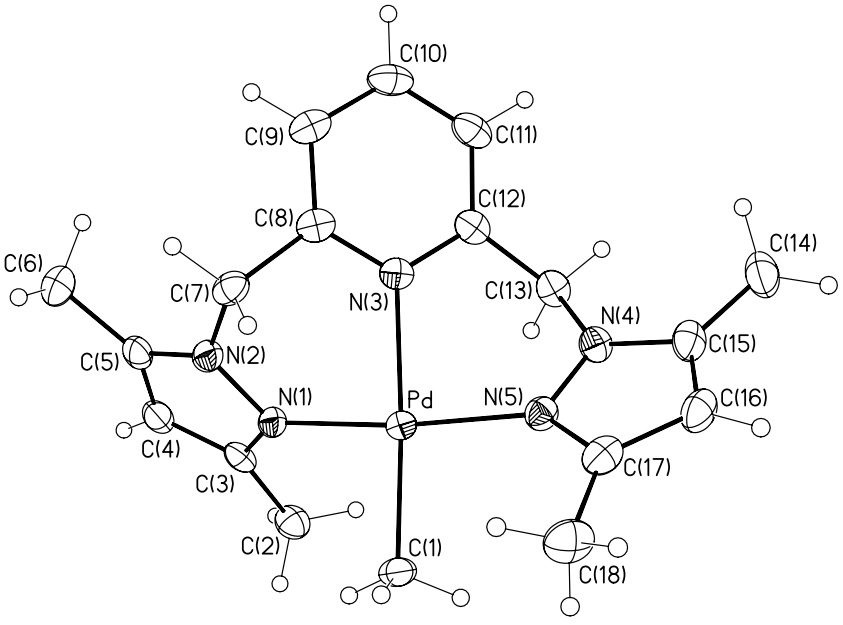


Fig. 3. Molecular structure of cation of **6** shown with 50% probability ellipsoids. The boron counter ion is omitted for clarity.

square planar geometry. In the structure of **3** (Fig. 1) the nitrogen atom, N5, of the free pyrazolyl unit is directed away from the palladium metal. It is therefore evident that the rotation about the CH_2 linker in the κ^2-2,6-{(3,5-^{t}Bu$_2$pzCH$_2$)$_2$py} ligand yields a κ^3-2,6-{(3,5-^{t}Bu$_2$pzCH$_2$)$_2$py} ligand in the cationic species **12** (Fig. 5). The $[Pd_2Cl_6]^{2-}$ in the structures of **11** and **12** occupies a crystallographic inversion centre with the two cationic palladium complexes residing on each side of the anion. The spatial arrangement of the cationic palladium moieties in **11** and **12** is such that the Pd–Cl bonds of the cationic complexes are facing away from the central $[Pd_2Cl_6]^{2-}$ unit.

The average bond lengths of the Pd–$N_{(pz)}$ of 2.026(3), 2.015(11), 2.026(11), 2.012(5) and 2.029(2) Å of complexes **3**, **5**, **6**, **11** and **12** respectively are all slightly shorter than the average Pd–N(pz) bond length of 2.06(9) Å obtained by averaging 607 bonds in 229 relevant complexes reported to the Cambridge Structural Database (CSD) [19] but the difference is not statistically significant because of the high uncertainties for the average Pd–$N_{(pz)}$ bond length of 2.06(9) Å.

The average Pd–N(pz) distance of 2.015(11) Å in **5** is somewhat shorter than that in **6** (2.036(11) Å), however the difference is not statistically significant. On the other

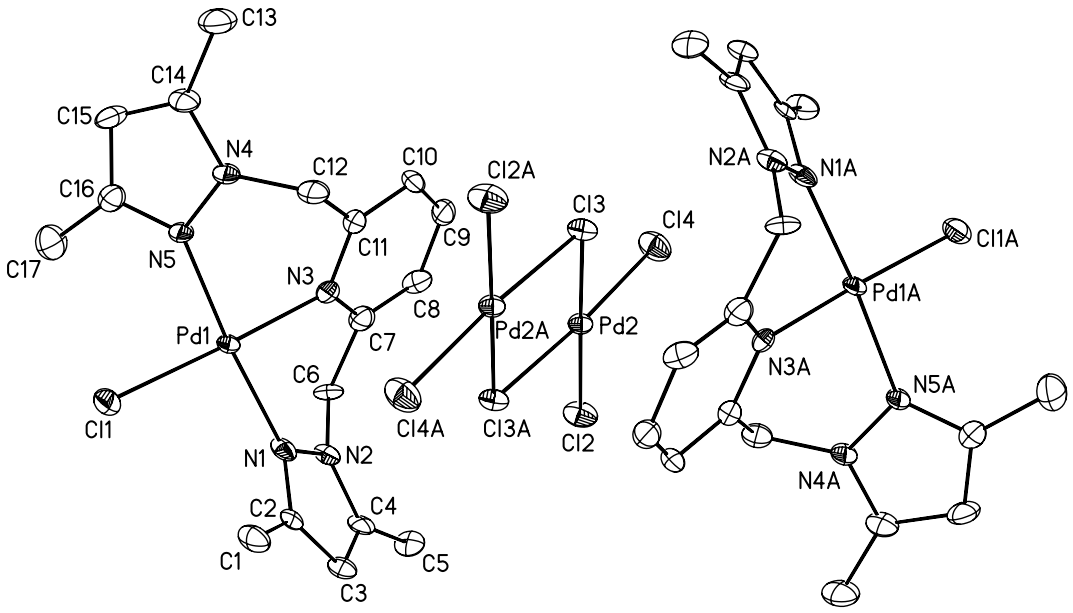


Fig. 4. Molecular structure of compound **11** shown with 50% probability ellipsoids. The hydrogen atoms are omitted for clarity.

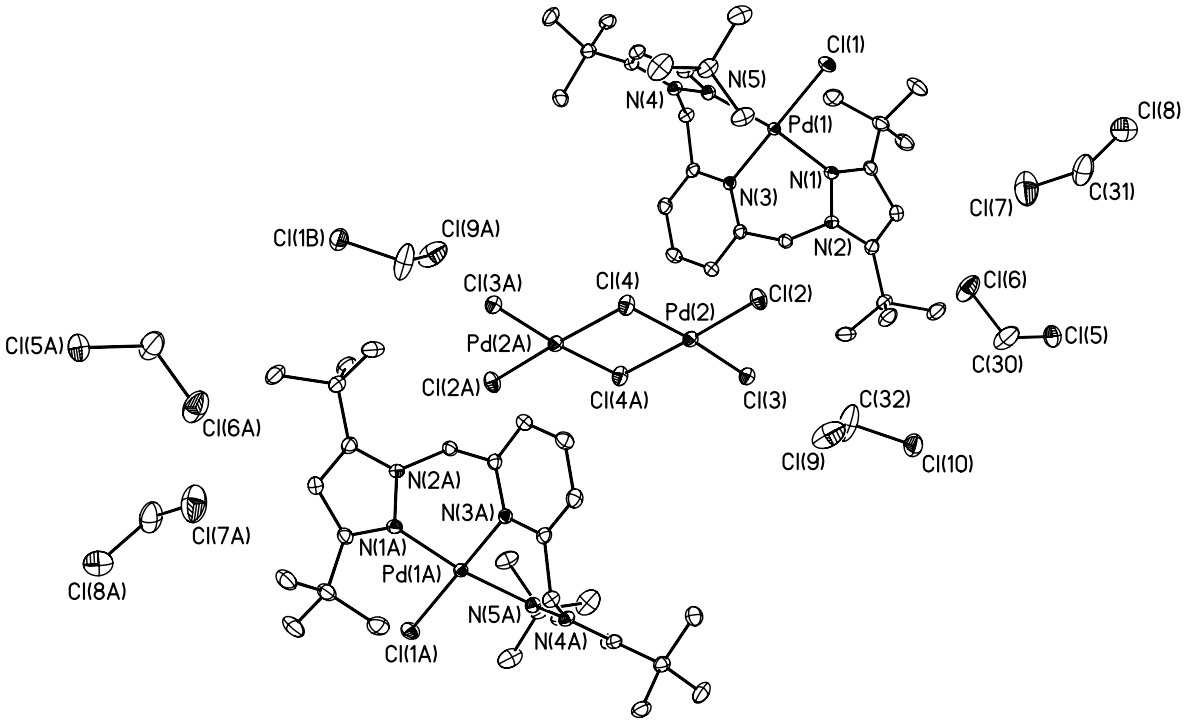


Fig. 5. Solid state structure of solvated complex **12** shown with 50% probability ellipsoids. The hydrogen atoms are omitted for clarity.

hand, the Pd–N(py) distance in **6** is substantially longer than those in **5**, **11** and **12**, and that is attributed to the high *trans* influence of the methyl group as compared to the chloro ligand. A shorter Pd–N(py) bond length 2.128(2) Å for **6** and 2.031(4) Å for **5**. A shorter Pd–$N_{(py)}$ bond length of 2.036(3) Å has been recently reported for the chloro complex, [Pd(ĈN̂C)Cl]BF_4 compared to 2.116(3) Å of the methyl analogue, [Pd(ĈN̂C)Me]BF_4 [20]. The average bond length of Pd–$N_{(py)}$ of 2.028(2) Å and Pd–C of 2.044(1) Å of **6** are significantly shorter than those reported for the carbene methylene bridged cationic Pd complex [Pd(ĈN̂C)Me]BF_4 of 2.0154(9) and 2.044(1) Å respectively [20]. The Pd–Cl bond distances of 2.3125(5) Å (**3**), 2.2803(13) Å (**5**), 2.2838(18) Å (**11**) and 2.2872(6) Å (**12**) in the mononuclear complexes agree well with the average bond distances of 2.33(5) Å determined by averaging 2055 Pd–Cl bonds in 1268 relevant complexes reported to the CSD [19]. Interestingly, the average Pd–$N_{(pz)}$ bond distances of 2.026(3) Å (**3**) and 2.029(2) Å (**12**) and Pd–Cl bond distances of 2.3125(5) Å (**3**) and

2.2872(6) Å (**12**) are statistically similar even though the Pd metal in **12** is more electrophilic and is expected to have shorter bond distances. Surprisingly, the longer $Pd–N_{(pz)}$ distance of 2.012(5) Å is observed for **11** than for **12** (2.028(2) Å) that contains a bulkier tridentate ligand.

4. Conclusions

The potentially tridentate bis(pyrazolylmethyl)pyridine compounds form monometallic palladium complexes with one uncoordinated pyrazolyl unit when complexed with either $[PdCl_2(NCMe)_2]$ or [Pd(COD)MeCl]. Coordination of the dangling pyrazolyl unit upon chloride abstraction in an attempt to generate catalysts for ethylene oligomerization or polymerization results in the formation of inactive cationic tridentate species. The same palladium complexes however, do form catalysts that catalyze the oligomerization and polymerization of the more reactive phenylacetylene producing a mixture of oligomers and low molecular weight polyphenylacetylene. Competitive coordination of phenylacetylene and the second pyrazolyl unit to the Pd metal centre appears to control the catalysis process. The polydentate ligands were also characterized with the use of the ligand solid angles.

Acknowledgement

Funding for this project was provided by National Research Foundation, Department of Science and Technology, Centre of Excellence in Catalysis (NRF-DST, c*change) South Africa.

Appendix A. Supplementary material

CCDC 605039, 606395, 604750, 604751, and 604749 contains the supplementary crystallographic data for **3**, **5**, **6**, **11**, and **12**. These data can be obtained free of charge via http://www.ccdc.cam.ac.uk/conts/retrieving.html, or from the Cambridge Crystallographic Data Centre, 12 Union Road, Cambridge CB2 1EZ, UK; fax: (+44) 1223-336-033; or e-mail: deposit@ccdc.cam.ac.uk. Supplementary data associated with this article can be found, in the online version, at doi:10.1016/j.poly.2006.09.007.

References

[1] (a) S. Ittel, M. Brookhart, L.K. Johnson, Chem. Rev. 100 (2000) 1169;
(b) S. Mecking, Coord. Chem. Rev. 203 (2000) 325;
(c) V.C. Gibson, S.K. Spitzmesser, Chem. Rev. 103 (2003) 283;
(d) C. Bianchini, G. Giambastiani, I.G. Rios, G. Mantovani, A. Meli, A.M. Segarra, Coord. Chem. Rev. 250 (2006) 1391.
[2] (a) C.M. Killian, L.K. Johnson, M. Brookhart, Organometallics 16 (1997) 2005;
(b) S.A. Srejda, L.K. Johnson, M. Brookhart, J. Am. Chem. Soc. 121 (1999) 10634.
[3] (a) L.K. Johnson, C.M. Killian, M. Brookhart, J. Am. Chem. Soc. 117 (1995) 6414;
(b) S. Mecking, L.K. Johnson, M. Brookhart, J. Am. Chem. Soc. 118 (1996) 267;
(c) P.K. Byers, A.J. Canty, B.W. Skelton, A.H. White, J. Organomet. Chem. 393 (1990) 299.
[4] M.S. Mohlala, I.A. Guzei, J. Darkwa, S.F. Mapolie, J. Mol. Catal. A: Chem. 241 (2005) 93.
[5] (a) I.A. Guzei, K. Li, G.A. Bikzhanova, J. Darkwa, S.F. Mapolie, Dalton Trans. 715 (2003);
(b) K. Li, I.A. Guzei, J. Darkwa, S.F. Mapolie, J. Organomet. Chem. 660 (2002) 108.
[6] (a) A.A. Watson, D.A. House, P.J. Steel, Inorg. Chim. Acta 130 (1987) 167;
(b) D.A. House, P.J. Steel, A.A. Watson, Aus. J. Chem. 48 (1995) 1549.
[7] (a) S. Mahapatra, R.N. Mukherjee, J. Chem. Soc., Dalton Trans. (1991) 2911;
(b) N. Gupta, S. Mukherjee, S. Mahapatra, M. Ray, R.N. Mukherjee, Inorg. Chem. 31 (1992) 139;
(c) A.R. Karam, E.L. Catari, F.L. Linares, G. Agrifoglio, C.L. Albano, A.D. Barrios, T.E. Lehmann, S.V. Pekerar, L.A. Albornoz, R. Atencio, T. Gonzalez, H.B. Ortega, P. Joskowics, Appl. Catal. A: Gen. 280 (2005) 165.
[8] J. Elguero, E.J.R. Jacquier, Bull. Soc. Chim. Fr. 2 (1968) 707.
[9] D. Drew, J.R. Doyle, Inorg. Synth. 13 (1972) 47.
[10] E. Rule, I.M. Han, C.J. Elsevier, K. Vrieze, P.W.N.M. Van Leeuwen, C.F. Roobeek, M.C. Zoutberg, Y.F. Wand, C.H. Stam, Inorg. Chim. Acta 169 (1990) 5.
[11] Bruker-AXS SADABS V.2.05, SAINT V.6.22, SHELXTL V.6.10 & SMART 5.622 Software Reference Manuals. Bruker-AXS, Madison, WI, USA, 2000–2004.
[12] Z. Shirin, R. Mukherjee, J.F. Richardson, R.M. Buchanan, J. Chem. Soc., Dalton Trans. (1994) 465.
[13] D.J. Nielsen, K.J. Cavell, B.W. Skelton, A.H. White, Inorg. Chim. Acta 359 (2006) 1855.
[14] K. Li, M.S. Mohlala, T.V. Segapelo, P.M. Shumbula, I.A. Guzei, J. Darkwa, unpublished results.
[15] I.A. Guzei, M. Wendt, Dalton Trans. (2006) 3991.
[16] G.K. Fukin, I.A. Guzei, E.V. Baranov, J. Coord. Chem., in press.
[17] Y. Chen, R. Chen, C. Qian, X. Dong, J. Sun, Organometallics 22 (2003) 4312.
[18] (a) C.I. Simionescu, V. Percec, S.J. Dumetrescu, Polym. Chem. Ed. 15 (1977) 2497;
(b) A.Forlani, S. Liccocia, M.V. Russo, J. Polym. Sci. A: Polym. Chem. 24 (1986) 991.
[19] F.H. Allen, Acta Crystallogr., Sect. B 58 (2002) 380.
[20] D.J. Nielsen, K.J. Cavell, B.W. Skelton, A.H. White, Inorg. Chim. Acta 327 (2002) 116.

this work were obtained by anodic oxidation of the metals in ethanol in the presence of LiCl as a conductive additive according to [8]. Rhenium oxide was prepared by direct oxidation of a powder of rhenium metal in a flow of dry oxygen gas at 460–480 °C. The resulting bright yellow crystals were collected under dry oxygen and sealed and stored in evacuated glass ampoules. IR spectra were registered for nujol mulls on a Perkin–Elmer Spectrum 100 instrument. ^{1}H and ^{13}C NMR spectra were registered for $CHCl_3$ solutions on a Bruker 400 MHz instrument at 300 K. Microanalysis studies of all samples have been carried out at the laboratory of Organic Analysis of the Moscow State Academy of Fine Chemical Technology using a Heraeus CHN-O-RAPID instrument (standard deviations: C ±0.3%, H ±0.1%).

2.1. $Nb_4O_2(OEt)_{14}(ReO_4)_2$ (1)

$Nb_2(OEt)_{10}$ (0.4398 g) was dissolved in 5 ml toluene. Rhenium (VII) oxide (0.5063 g) was added to the obtained solution, which immediately changed color from light yellowish to light brown. The mixture was stirred until complete dissolution of Re_2O_7 for 20–30 min at room temperature. The obtained solution was quickly warmed to 60 °C and subjected to a short reflux. The solution turned reddish brown and the formation of colorless crystals could be observed. The reaction vessel was cooled to room temperature and left for crystallization overnight. The mother liquor was then removed by decantation and the practically colorless crystals were dried in vacuum. Yield: 0.8296 g (83%). *Anal.* Calc. for $H_{70}C_{28}O_{24}Nb_4Re_2$: C, 19.81; H, 4.30. Found: C, 21.91; H, 4.59%. IR, ν/cm^{-1}: 1277 s br, 1099 m, 1068 m, 1020 sh, 932 st, 892 sh, 878 m, 814 st, 536 m br, 478 sm br. ^{1}H NMR, δ, ppm (interpretation): 4.93 poorly resolved quadruplet (2H, CH_2, OEt-group in *trans*-position to the μ-O-ligand), 4.69 poorly resolved quadruplet (4H, CH_2, OEt-group in *trans*-position to the μ-OEt-ligand), 4.64 well resolved quadruplet (2H, CH_2, OEt-group in *trans*-position to the μ-OEt-ligand, $J = 5.6$ Hz), 4.55 poorly resolved quadruplet (2H, CH_2, OEt-group in *trans*-position to the μ-OEt-ligand), 4.43 poorly resolved quadruplet (4H, CH_2, μ-OEt-ligand), 1.38 poorly resolved triplet (9H, CH_3), 1.29 poorly resolved triplet (6H, CH_3), 1.22 poorly resolved triplet (3H, CH_3), 1.20 poorly resolved triplet (3H, CH_3). MS, *m*/*z* (%), interpretation: 271(100), $Nb(OEt)_4^+$, 265 (67.3), $ReO(OEt)(OH)^+$, 229 (43.4), $Nb(OEt)_2(OH)(OCH_3)^+$, 169 (17.7), $NbO(OEt)(OH)^+$. In an analogous synthesis the crystallization was also carried out at −15 °C yielding the product **1a**.

2.2. $Ta_4O_2(OEt)_{14}(ReO_4)_2$ (2)

A procedure analogous to that for compound **1** was applied, using $Ta_2(OEt)_{10}$ (1.7483 g) and Re_2O_7 (0.5292 g). Yield: 2.0302 g (86%). *Anal.* Calc. for $H_{70}C_{28}O_{24}Ta_4Re_2$: C, 16.28; H, 3.58. Found: C, 17.82; H, 3.74%. IR, ν/cm^{-1}: 1304 sm, 1108 m br, 1076 m, 1018 sm br, 936 m, 892 sh, 876 m, 810 st br, 668 sm, 527 m br, 479 sm br. ^{1}H NMR, δ, ppm (interpretation): 4.83 (2H, CH_2, OEt-group), 4.68 (2H, CH_2, OEt-group), 4.61 (4H, CH_2, OEt-group), 4.58 (4H, CH_2, OEt-group), 4.32 (2H, CH_2, OEt-group), 1.38 and 1.25 (21H in total, CH_3), all signals were poorly resolved. ^{13}C NMR, δ, ppm (interpretation): 72.94, 71.19 higher intensity, 70.89, 70.57, 70.25, 69.90, 69.41 (*C*H_2, OEt-group), 19.05, 18.94, 18.70, 18.55, 18.45, 18.05, 17.80 (*C*H_3, OEt-group). MS, *m*/*z* (%), interpretation: 361 (100), $Ta(OEt)_4^+$, 265 (64.7), $ReO(OEt)(OH)^+$, 219 (16.2), ReO_2^+. In an analogous synthesis the crystallization was also carried out at −15 °C yielding the product **2a**.

2.3. Crystallography

The data collection has been carried out at room temperature using a Bruker SMART CCD 1 K diffractometer at the Department of Chemistry, SLU and at $T = 100$ K using an Excalibur with sapphire-3 CCD detector (Oxford Diffraction Ltd.) at the Department of Structural Chemistry, Stockholm University (Mo Kα radiation, graphite-monochromator) for the experimental details see Table 1. The structures were solved by direct methods. Metal atom coordinates were located in the initial solution and all the other non-hydrogen atoms in the subsequent difference Fourier syntheses. All non-hydrogen atoms were refined by full-matrix techniques, first in isotropic and then in anisotropic approximation. The coordinates of the hydrogen atoms were calculated geometrically and introduced in the final refinement in isotropic approximation using a riding model. All calculations were performed using SHELXTL-NT program package [9] on a personal computer.

3. Results and discussion

The molecular structures of $Nb_4O_2(OEt)_{14}(ReO_4)_2$ (**1**) and $Ta_4O_2(OEt)_{14}(ReO_4)_2$ (**2** and **2a**) are very close to each other (see Fig. 1, Tables 1 and 2). Each of them contains a practically rectangular M(V)$_4$ core, where M(V) = Nb or Ta. Each M(V) atom is octahedrally coordinated. The octahedra along one pair of the edges in the rectangle share an edge, a pair of OEt-ligands. The thus defined pairs of octahedra are connected to each other via almost ideally linear oxo-bridges, defined by O(9) atoms (Ta(1A)–O(9)–Ta(2) 175.7(9)° and Ta(1A)–O(9)–Ta(2) 178.2(6)° in **2** and **2a**, respectively). The perrhenate ligands are attached to the rectangle in a centrosymmetric manner, i.e. to the Ta atoms defining one of its diagonals. The coordination of each of these atoms is completed by two terminal alkoxide ligands. The other two tantalum atoms bear three terminal alkoxide ligands each.

Both alkoxide and oxo-ligands are efficient π-donors, which leads to the increase of the bond order in the terminal M=O and M–O(R) fragments and asymmetric bonding for the bridging ligands. The normal bond length for

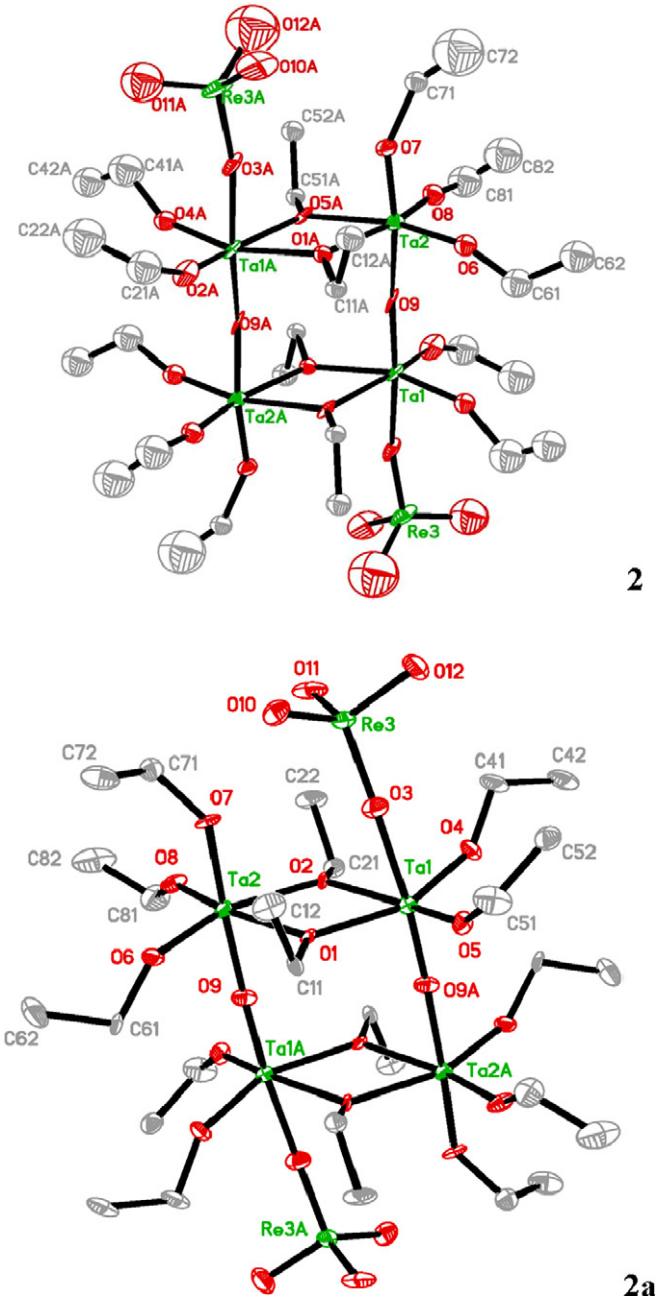


Fig. 1. Molecular structures of the **2** and **2a** samples of $Ta_4O_2(OEt)_{14}(ReO_4)_2$. The thermal ellipsoids are provided with 10% probability.

ordinary metal–oxygen bonds can be estimated from the sum of the covalent radii for the corresponding atoms, $r_c(O) = 0.66$ Å; $r_c(Re) = 1.37$ Å; $r_c(Ta) = 1.43$ Å; $r_c(Nb) = 1.43$ Å. This gives $r_c(M) + r_c(O)$ of 2.03–2.09 Å for Re, Nb and Ta. The analysis of the bond lengths (see Table 2) indicates double bonding for all the Re=O fragments with a slightly longer Re–μ-O(3) bond (1.738(18) and 1.753(9) Å in **2** and **2a**, respectively) compared to truly terminal Re–O bonds (1.55(6)–1.66(8) Å in **2** and 1.677(11)–1.695(11) Å in **2a**). The Ta–O and Nb–O bonds opposite the M(V)–O-Re bridges are in their turn considerably elongated (2.237(13), 2.118(18) and 2.175(9) Å in **1**, **2** and **2a**, respectively). The

Table 1
Crystal data and the diffraction experiments details for compounds **1**, **2** and **2a**

Compound	**1**	**2**	**2a**
Chemical composition	$C_{28}H_{70}O_{24}Nb_4Re_2$	$C_{28}H_{70}O_{24}Ta_4Re_2$	$C_{28}H_{70}O_{24}Ta_4Re_2$
Formula weight	1534.88	1887.04	1887.04
Crystal system	monoclinic	monoclinic	monoclinic
Space group	$P2_1/n$	$P2_1/n$	$P2_1/n$
μ (mm^{-1})	5.505	12.978	13.772
R_1	0.0707	0.0675	0.0712
wR_2	0.2002	0.1513	0.1807
a (Å)	13.175(5)	13.227(5)	12.7741(11)
b (Å)	13.532(2)	13.453(6)	13.2245(9)
c (Å)	14.951(5)	14.982(7)	14.8551(14)
α (°)	90	90	90
β (°)	99.967(18)	100.408(10)	100.58(8)
γ (°)	90	90	90
V ($Å^3$)	2625.2(14)	2622.0(19)	2470.9(4)
T (K)	295(2)	295(2)	100(2)
Z	2	2	2
Number of independent reflections (R_{int})	2808 (0.0480)	2806 (0.1303)	6864 (0.0827)
Number of observed reflections [$I > 2\sigma(I)$]	1766	1570	4309

bonds of the M(V) atoms to the μ-O(9) oxo-bridging atoms are also asymmetric. The part M(1)–μ-O(9), situated in a *trans*-position to the elongated bond of the perrhenate ligand, is considerably shorter than the other part of the bridge M(2)–μ-O(9) (1.858(17) and 1.833(9) Å compared to 1.967(17) and 2.038(9) Å, respectively). Generally the bond lengths distribution can be rationalized with respect to the multiplicity of the M–O bonds (decreasing π-contribution) in the series:

$$r(\text{Re–O})\text{term} < r(\text{Re–O})\mu < r(\text{Ta–OR})\text{term} < r(\text{Ta–O})\mu < r(\text{Ta–OR})\mu < r(\text{Ta–O–Re})\mu$$

It is interesting to compare the bonding parameters in the structures of the ethoxide derivatives with those in the structures of their methoxide analogs (see Table 3). It can clearly be seen that the lengths of all M–O bonds in the structures of $M^V_4O_2(OMe)_{14}(ReO_4)_2$ are noticeably shorter than those in the structures of $M^V_4O_2(OEt)_{14}(ReO_4)_2$. The reason for this difference lies most probably in the much higher density of packing in the structures of the methoxides, resulting in closer intermolecular contacts and contraction of the M–O distances.

The density of packing also constitutes a major difference between the structure of the forms of $Ta_4O_2(OEt)_{14}(ReO_4)_2$ isolated at different temperatures (compounds **2** and **2a**). In this latter case the bond lengths appear very similar and the strong decrease in the cell volume results from the general contraction in the M–O–C and O–C–C bond angles. The packing conserves the same motive and the low-temperature structure (isolated from the sample

Table 2
Selected bond lengths in the structures of $Ta_4O_2(OEt)_{14}(ReO_4)_2$

Compound **2**		Compound **2a**	
Ta(1)–O(4) (term. eq. OEt)	1.859(9)	Ta(1)–O(2) (term. eq. OEt)	1.85(2)
Ta(1)–O(5) (term. eq. OEt)	1.864(8)	Ta(1)–O(4) (term. eq. OEt)	1.86(2)
Ta(1)–O(1) (μ-OEt)	2.071(9)	Ta(1)–O(1) (μ-OEt)	2.061(17)
Ta(1)–O(2) (μ-OEt)	2.094(8)	Ta(1)–O(5) (μ-OEt)	2.062(16)
Ta(1)–O(9A) (Ta–μ-O–Ta)	1.833(9)	Ta(1)–O(9) (Ta–μ-O–Ta)	1.858(17)
Ta(1)–O(3) (Ta–μ-O–Re)	2.175(9)	Ta(1)–O(3) (Ta–μ-O–Re)	2.118(18)
Ta(2)–O(6) (term. eq. OEt)	1.852(9)	Ta(2)–O(6) (term. eq. OEt)	1.87(2)
Ta(2)–O(8) (term. eq. OEt)	1.872(9)	Ta(2)–O(8) (term. eq. OEt)	1.87(2)
Ta(2)–O(7) (term. eq. OEt)	1.902(8)	Ta(2)–O(7) (term. eq. OEt)	1.857(17)
Ta(2)–O(9) (Ta–μ-O–Ta)	2.038(9)	Ta(2)–O(9) (Ta–μ-O–Ta)	1.967(17)
Ta(2)–O(2) (μ-OEt)	2.076(9)	Ta(2)–O(1) (μ-OEt)	2.077(15)
Ta(2)–O(1) (μ-OEt)	2.113(8)	Ta(2)–O(5) (μ-OEt)	2.087(15)
Re(3)–O(3) (Ta–μ-O–Re)	1.753(9)	Re(3)–O(3) (Ta–μ-O–Re)	1.738(18)
Re(3)–O(10) (term. O)	1.677(11)	Re(3)–O(10) (term. O)	1.58(3)
Re(3)–O(12) (term. O)	1.677(12)	Re(3)–O(11) (term. O)	1.55(6)
Re(3)–O(11) (term. O)	1.695(11)	Re(3)–O(12) (term. O)	1.66(8)

Table 3
Comparison of the metal–oxygen bond lengths in the room temperature structures of $Ta_4O_2(OEt)_{14}(ReO_4)_2$ (**2**) and $Ta_4O_2(OMe)_{14}(ReO_4)_2$

Bond	Bond length (Å)	
	$Ta_4O_2(OEt)_{14}(ReO_4)_2$[a]	$Ta_4O_2(OMe)_{14}(ReO_4)_2$[b]
Ta–O (term. eq. OEt)	1.85–1.87	1.82–1.86
Ta–O (term. ax. OEt)	1.86–1.90	1.77
Ta–O (μ-OEt)	2.06–2.11	2.03–2.11
Ta–O (Ta–μ-O–Ta)	1.83–2.04	1.77–2.02
Ta–O (Ta–μ-O–Re)	2.12–2.18	2.24
Re–O (Ta–μ-O–Re)	1.74–1.75	1.65
Re–O (term. O)	1.55–1.68	1.44–1.70

[a] This work.
[b] Literature data [8].

crystallized at −15 °C and where the data collection has been carried out at −120 °C) cannot be, in direct crystallographic meaning, considered as a different modification. It should be noted, however, that when the crystals isolated at −15 °C are transferred to room temperature for selection of a crystal for X-ray study, they "explode" under the paraffin oil. This indicates high steric tension and occurs most probably because these crystals have a complex domain structure. The quick warming up of the domains situated closer to the surface leads evidently to their quicker expansion than those inside the volume of the crystal, which makes them shrink on the contact surface and leave the crystal with a convection stream. We have noticed this phenomenon in a number of cases, where a strong dependence of the cell volume on temperature was observed, both in the presence and in the absence of true phase transitions.

Compounds **1** and **2** are soluble in hydrocarbon solvents at room temperature (about 5 wt%) and according to the NMR spectra appear to conserve their molecular geometry in solution. Both ^1H and ^{13}C spectra show the presence of the different structural functions for the ethoxide ligands present in molecules of **1** and **2**. The well-resolved ^{13}C spectrum in the methyl carbon region displays a separate signal for each alkoxide group. Their solutions are stable in time: the spectra remain unchanged and no coloration and/or precipitation can be observed for the solutions in either hexane or toluene at this concentration. This makes them attractive precursors for the deposition of rhenium oxide catalysts on different substrates using sol–gel technology.

It should be mentioned that the oxoalkoxides $M^V_4O_2(OEt)_{14}(ReO_4)_2$ are the only family of alkoxide perrhenates that can be isolated for the ethoxide derivatives. No non-oxo alkoxide perrhenate species could be isolated in this case in contrast to the methoxides, where the non-oxo $M^V_2(OMe)_8(ReO_4)_2$ complexes were formed at low temperatures. This difference is caused evidently by easier oxidation of ethanol resulting in release of water and formation of oxospecies. Crystallization of $M^V_4O_2(OEt)_{14}(ReO_4)_2$ occurs even on cooling the reaction mixture, but the gentle warming described in the provided experimental procedures offers higher yields of them.

4. Conclusions

Reproducibly soluble and solution stable oxo-alkoxo-perrhenate derivatives of niobium and tantalum, $M^V_4O_2(OEt)_{14}(ReO_4)_2$, can be obtained in high yields by the interaction of $M^V(OEt)_5$ with rhenium heptoxide. The isolation of crystals of these compounds has to be carried out at room temperature because of the strong temperature dependence of the unit cell volume, making crystals isolated in the cold transform into a powder on heating to room temperature.

Acknowledgments

The authors express their gratitude to Lars Eriksson, Department of Structural Chemistry, Stockholm University for the assistance with data collection on compound **2a** and to the Swedish Research Council, the Royal Swedish Academy of Sciences (KVA) and Russian Foundation

for Basic Research (RFBR Project No. 06-03-32444) for financial support.

Appendix A. Supplementary material

CCDC 617392, 617393 and 617394 contain the supplementary crystallographic data for **1**, **2** and **2a**. These data can be obtained free of charge via http://www.ccdc.cam.ac.uk/conts/retrieving.html, or from the Cambridge Crystallographic Data Centre, 12 Union Road, Cambridge CB2 1EZ, UK; fax: (+44) 1223-336-033; or e-mail: deposit @ccdc.cam.ac.uk. Supplementary data associated with this article can be found, in the online version, at doi:10.1016/j.poly.2006.09.088.

References

[1] M.A. Aegerter, Solar Energy Mater. 68 (2001) 401.
[2] D. Bayot, B. Tinant, M. Devillers, Inorg. Chem. 44 (2005) 1554.
[3] T. Kusakari, T. Sasaki, Y. Iwasawa, Chem. Commun. (2004) 992.
[4] C.B. Rodella, J.A.M. Calvacante, R. Buffon, Appl. Catal. A 274 (2004) 213.
[5] T. Oikawa, T. Ookoshi, T. Tanaka, T. Yamamoto, M. Onaka, Micropor. Mesopor. Mater. 74 (2004) 93.
[6] V.G. Kessler, Chem. Commun. (2003) 1213.
[7] P. Scheglov, G.A. Seisenbaeva, D.V. Drobot, V.G. Kessler, Chem. Mater. 14 (2002) 2378.
[8] G.A. Seisenbaeva, A.V. Shevelkov, L. Kloo, S. Gohil, J. Tegenfeldt, V.G. Kessler, J. Chem. Soc., Dalton Trans. (2001) 2762.
[9] Bruker SHELXTL-NT Reference Manual, 1998.

resonances of the methylene protons of the [S_2CNEt_2] ligand of complex **3** appear as two sets of quartets at 4.03 and 3.72 ppm. A triplet at 1.27 ppm, assignable to the methyl protons of the [S_2CNEt_2] ligand, was also observed. Protons corresponding to the cyclopentadienyl ligand also appear at 4.74 ppm while the PPh_3 peaks are observed as a bunch in the aromatic region. The IR spectrum taken in KBr showed a strong peak at 1491 cm^{-1}, unambiguously assignable to the ν_{CN} vibration of [S_2CNEt_2] [7]. We also observed bands at 2277 cm^{-1} and 1084 cm^{-1} assignable to ν_{CN} of coordinated CH_3CN and ν_{BF} of BF_4^-. We have employed this synthetic strategy hoping that the *in situ* generated complex [$CpOs(PPh_3)_2(CH_3CN)$]BF_4 (**2 · BF$_4$**) would easily give **3** or the chelate complex [$CpOs(PPh_3)_2(\kappa^2\text{-}S_2CNEt_2)$]. Unfortunately, we never obtain the latter compound, and to our surprise attempts to separate **2 · BF$_4$** and **3** proved to be futile owing to the similar solubility of these two complexes.

Then, we attempted to synthesize **3** from [$CpOs(PPh_3)_2(CH_3CN)$]BF_4 (**2 · BF$_4$**) and $Na \cdot S_2CNEt_2$ in refluxing methanol (Scheme 1). The formation of **3** may be gauged by the appearance of white precipitate after about one hour of refluxing. But to our surprise, a ^1H NMR spectrum taken in $CDCl_3$ of this crude product still showed the presence of **2 · BF$_4$**. Fortunately, after many attempts, we were able to get single crystals from this crude product by slow diffusion of hexane into an acetone solution of this mixture; very pale yellow crystals were obtained after one week leaving an oily blackish-yellow residue on the wall of the crystallization tube and the ^1H NMR spectrum revealed that this is a decomposed material. The ^1H NMR, $^{13}P\{^1H\}$ NMR, IR, elemental analysis as well as the X-ray crystallographic analysis of these crystals has revealed that this compound is the starting [$CpOs(PPh_3)_2(CH_3CN)$]BF_4 (**2 · BF$_4$**). However, as no report of the structural data of this compound is available in the literature, we have reported this structure here. The ORTEP diagram is shown in Fig. 1. For the final attempt, we tried the reaction starting from a new complex [$CpOs(PPh_3)_2(DMSO)$]BF_4 (**4 · BF$_4$**), however this compound does not seem to undergo the anticipated substitution reaction in the present experimental conditions. The complex [$CpOs(PPh_3)_2(DMSO)$]BF_4 (**4 · BF$_4$**) was prepared by the reaction of [$CpOs(PPh_3)_2Br$] with an excess of DMSO in methanol. The compound is isolated as a very pale yellow hydroscopic powder. It was characterized with the help of IR, ^1H and $^{13}P\{^1H\}$ spectroscopy. The IR spectrum showed a band at 1023 cm^{-1}, assignable to S-bound DMSO [8].

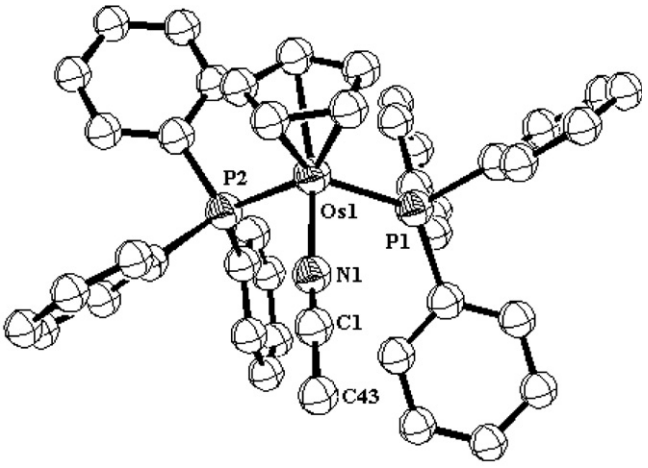
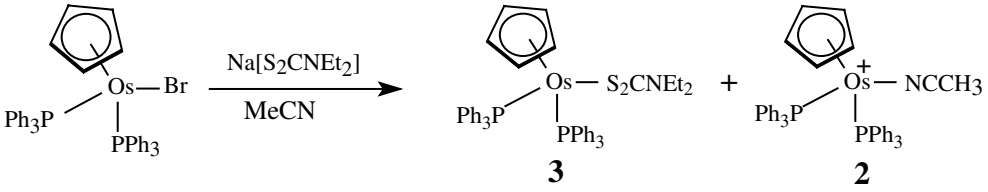


Fig. 1. Molecular structure of [$CpOs(PPh_3)_2(MeCN)$]BF_4 (**2 · BF$_4$**) with BF_4^- and all the hydrogens atoms omitted for clarity.

The ^1H NMR spectrum showed a resonance of the methyl group of the coordinated DMSO at 3.53 and 3.43 ppm. The $^{13}P\{^1H\}$ NMR showed a singlet at −2.67 ppm, suggesting a similar environment of both P atoms of the PPh_3 ligands. Thus, all our attempts to isolate the pure [$CpOs(PPh_3)_2(\kappa^1\text{-}S_2CNEt_2)$] (**3**) were unsuccessful.

In the complex [$CpOs(PPh_3)_2(CH_3CN)$]BF_4 (**2 · BF$_4$**), the osmium(II) centre adopts a pseudo-octahedral coordination geometry with an almost linear Os1–N1–C1 (171.16°) moiety occupying one site. The bond lengths N1–C1 (1.132(6) Å) and C1–C43 (1.455(8) Å) are in very close agreement with those reported for [$CpRu(CH_3CN)_3$]BF_4 where $N\text{–}C_{av} = 1.131$ Å and $C\text{–}C_{av} = 1.445$ Å [9]. The other coordination sites are occupied by a pentahapto-bound cyclopentadienyl ligand and two triphenylphosphines. The Os–P1 and Os–P2 bond lengths [2.328 Å and 2.343 Å respectively] are comparable with those found in [$CpOs(=C=C=CPh_2)(PPh_3)_2$][$PF_6$] [10] and [$CpOs(PPh_3)_2(OSO_2CF_3)$] [11].

We have extended our work to a closely related system, the reaction of [$CpRu(PPh_3)_2Cl$] or [$CpRu(PPh_3)_2(CH_3CN)$]BF_4 with $Na.S_2CNEt_2$ leads to the formation of an orange colored complex that is soluble in almost all common solvents, even in hexane. The IR spectrum showed a strong ν_{CN} peak at 1483 cm^{-1}. The ^1H NMR spectrum showed the resonance of the cyclopentadienyl ligand at 6.22 ppm, a bunch of peaks corresponding to methylene proton in the range of 3.76–4.42 ppm and a triplet at 1.28 ppm. Thus, IR and ^1H NMR data clearly suggested the formation of the expected well-known bidentate



Scheme 1.

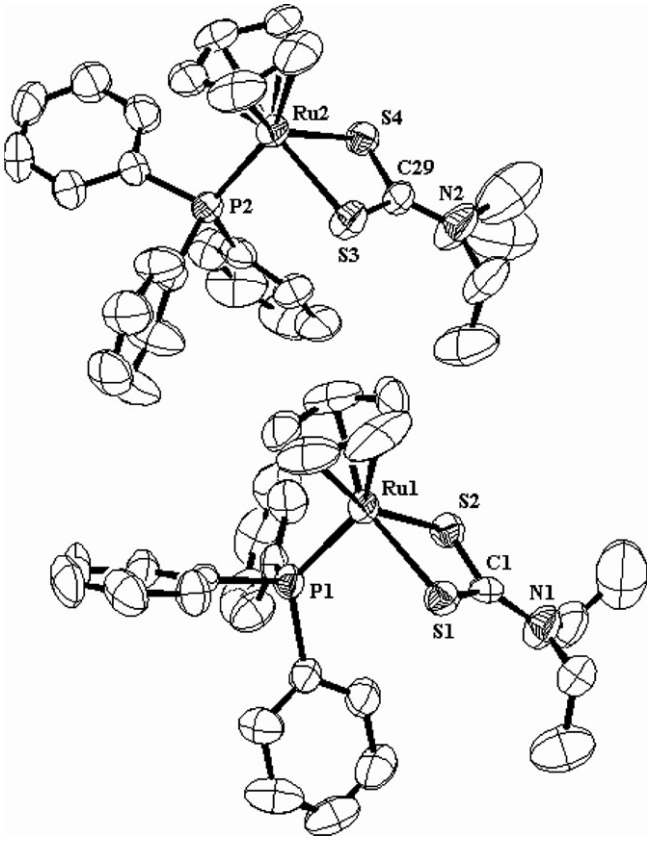


Fig. 2. Molecular structure of $[CpRu(PPh_3)_2(\kappa^2\text{-}S_2CNEt_2)]$ (**5**) with all the hydrogen omitted for clarity.

diethylthiocarbamato complex $[CpRu(PPh_3)(\kappa^2\text{-}S_2CNEt_2)]$ (**5**), the X-ray crystal structure determination also confirmed these spectroscopic evidences and has revealed that the compound contain two independent, discrete molecules (Fig. 2). The molecules are structurally identical except in the orientation of the ethyl group of the $[S_2CNEt_2]$ ligand. The metrical bonding parameters are comparable to those found in the analogous complexes $[CpRu(PPh_3)(S_2CNMe_2)]$ [12] and $[CpRu(PPh_3)(S_2CNPr_2)]$ [13].

3. Experimental

All solvents were dried and purified by standard procedures. ^1H and $^{13}P\{^1H\}$ NMR spectra were recorded on a Bruker 300 MHz spectrometer using Me_4Si and H_2PO_4 (85%) respectively as internal standards. IR spectra were recorded using a Nicolet Impact Spectrophotometer. $Na \cdot S_2CNEt_2 \cdot 3H_2O$ was obtained from a commercial source and was used as received. $[CpOs(PPh_3)_2Br]$ [14], $[CpOs(PPh_3)_2(MeCN)]BF_4$ (**2 · BF$_4$**) [6], $[CpRu(PPh_3)_2X]$, (X = Cl, MeCN) [15] were prepared according to literature procedures.

3.1. Synthesis of $[CpOs(PPh_3)_2(\kappa^1\text{-}S_2CNEt_2)]$ (3)

A mixture of $[CpOs(PPh_3)_2(MeCN)]BF_4$ (**2 · BF$_4$**) (0.05 g, 0.055 mmol) and $Na \cdot S_2CNEt_2 \cdot 3H_2O$ (0.013 g, 0.055 mmol) in 10 mL methanol was refluxed for 10 h, whereby the color of the solution changed to bright yellow with some whitish materials settling down at the bottom of the flask. The solvent was removed *in vacuo* and the residue was extracted with CH_2Cl_2 and filtered through a short silica gel column. Subsequent concentration and addition of excess hexane yielded a pale yellow powder containing a mixture of **3** and **2 · BF$_4$**. Yield: 0.038 g. ^1H NMR ($CDCl_3$, δ): 7.67–7.20 (m, 30H, Ph), 4.74 (s, 5H, Cp), 4.03 (qr, 2H, 7 Hz, CH_2), 3.72 (qr, 2H, 7 Hz, CH_2), 1.27 (t, 6H, CH_3). $^{13}P\{^1H\}$ NMR}: −1.53 (s). IR (KBr, cm^{-1}): 1491 (w), 1433 (ms), 1084 (ν_{BF}, s), 1055 (s), 750 (m), 697 (s).

3.2. Synthesis of $[CpOs(PPh_3)_2(DMSO)]BF_4$ (4 · BF$_4$)

A mixture of $[CpOs(PPh_3)_2Br]$ (0.1 g, 0.117 mmol) and dimethylsulfoxide (1 mL, 0.055 mmol) in methanol (30 mL) was refluxed for 3 h, whereby the color of the solution changed to very pale transparent yellow. The solvent was removed in vacuo and the residue was extracted with CH_2Cl_2 and loaded onto a short alumina column. The compound was eluted with methanol. Concentration of this methanol solution and addition of diethylether with vigorous shaking gave the very pale yellow solid of **4 · BF$_4$**. ^1H NMR ($CDCl_3$, δ): 7.49–7.14 (m, 30H, Ph), 5.47 (s, 5H, Cp), 3.53 (s, 3H, CH_3), 3.43 (s, 3H, CH_3). $^{13}P\{^1H\}$ NMR}: −2.67 (s). IR (KBr, cm^{-1}):1023 (ν_{SO}), 1089 (ν_{BF}).

3.3. Synthesis of $[CpRu(PPh_3)_2(\kappa^2\text{-}S_2CNEt_2)]$ (5)

A mixture of $[CpRu(PPh_3)_2(MeCN)]BF_4$ (0.05 g, 0.061 mmol) or $[CpRu(PPh_3)_2Cl]$ (0.044 g, 0.061 mmol) and $Na \cdot S_2CNEt_2 \cdot 3H_2O$ (0.014 g, 0.061 mmol) in methanol (10 mL) was refluxed for 8 h, then the solvent was removed *in vacuo* and the residue was extracted with CH_2Cl_2 and filtered through a short silica gel column. CH_2Cl_2 was removed *in vacuo* and the residue was extracted with hexane, which on standing overnight yielded orange crystals of **5**. Yield: 0.040 g, 59%. ^1H NMR ($CDCl_3$, δ): 7.67–7.31 (m, 30H, Ph), 6.22 (s, 5H, Cp), 4.53–3.42 (m, 12H, CH_2), 1.24 (t, 3H, 7.3 Hz, CH_3).$^{13}P\{^1H\}$ NMR}: 19.6 (s). IR (KBr, cm^{-1}): 1483 (ν_{CN}, s), 1457 (w), 1429(s), 1271 (s), 1214(w), 1141(m), 1089 (s), 748 (m), 696(s).

4. X-ray data collection and solution

Suitable single crystals for X-ray analysis of complex **2 · BF$_4$** were grown by slow diffusion of hexane into a concentrated acetone solution and **5** were grown by slow evaporation of a hexane/dichloromethane solution (1:2 v/v). A summary of the single-crystal X-ray structure analyses are shown in Table 1, and selected bond lengths and bond angles are presented in Tables 2 and 3 respectively. The X-ray intensity data were measured on a Bruker SMART APEX CCD area detector system equipped with a graphite monochromator and a Mo Kα fine-focus sealed tube

Table 1
Crystal data summary and structure refinement for complexes **2 · BF$_4$** and **5**

Empirical formula	$C_{43}H_{38}BF_4NOsP_2$	$C_{56}H_{60}N_2P_2Ru_2S_4$
Formula weight	907.69	1153.38
Temperature (K)	298(2)	298(2)
Wavelength (Å)	0.71073	0.71069
Crystal system	monoclinic	monoclinic
Space group	*P*2(1)/*c*	*P*2(1)/*c*
Unit cell dimensions		
a (Å)	10.2948(13)	27.226(5)
b (Å)	17.080(2)	10.4000(18)
c (Å)	21.840(3)	19.566(3)
β (°)	90.310(2)	101.174(3)
Volume (Å^3)	3840.1(9)	5435.0(16)
Z,	4	4
D_{calc} (Mg/m^3)	1.565	1.410
F(000)	1788	2368
Absorption coefficient (mm^{-1})	3.455	0.806
Crystal size (mm)	0.45 × 0.20 × 0.10	0.13 × 0.20 × 0.44
θ Range for data collection (°)	1.51–28.29	0.76–28.41
Limiting indices	$-13 \leqslant h \leqslant 10$, $-22 \leqslant k \leqslant 17$, $-29 \leqslant l \leqslant 28$	$-29 \leqslant h \leqslant 36$, $-13 \leqslant k \leqslant 13$, $-26 \leqslant l \leqslant 17$
Reflections collected	25027	33187
Independent reflections (R_{int})	9272(0.0364)	12842(0.0737)
Refinement method	full-matrix least-squares on F^2	full-matrix least-squares on F^2
Data/restraints/parameters	9272/0/469	7619/0/406
Goodness-of-fit on F^2	1.050	1.014
Final R_1	0.0370	0.0813
Final wR_2	0.0837	0.1905
Largest difference in peak and hole (e$^-$/Å^3)	0.886 and −0.644	0.99 and −0.815

Table 2
Selected bond lengths and angles for the compound [CpOs(PPh$_3$)$_2$(CH$_3$CN)]BF$_4$ (**2 · BF$_4$**)

Bond lengths (Å)		Bond angle (°)	
C1–N1	1.132(6)	Os1–N1–C1	171.1(4)
C1–C43	1.455(8)	N1–C1–C43	179.4(9)
Os1–N1	2.026(3)	N1–Os1–P1	98.76(10)
Os1–P1	2.328(10)	N1–Os1–P2	91.76(11)
Os1–P2	2.348(10)	P1–Os1–P2	100.87(3)

Table 3
Selected bond lengths and angles for the compound [CpRu(PPh$_3$)$_2$-(κ^2- S$_2$CNEt$_2$)] (**5**)

Bond lengths (Å)		Bond angle (°)	
C1–N1	1.344(8)	N1–C1–S1	125.2(5)
C1–S1	1.702(7)	N1–C1–S2	123.7(5)
C1–S2	1.717(7)	S1–C1–S2	110.9(4)
Ru1–S1	2.4007(18)	S1–Ru1–S2	71.61(6)
Ru1–S2	2.4133(18)	P1–Ru1–S2	90.11(6)
P1–Ru1	2.2818(19)	P1–Ru1–S1	94.88(6)
C29–N2	1.320(9)	C1–S1–Ru1	89.1(2)
C29–S4	1.699(7)	S4–Ru2–S3	72.07(7)
C29–S3	1.718(7)	C29–S4–Ru2	88.6(2)
Ru2–S3	2.3982(19)	C29–S3–Ru2	87.9(2)
Ru2–S4	2.3921(19)	P2–Ru2–S4	95.44(7)
P2–Ru2	2.2892(19)	N2–C29–S4	125.5(6)
		S4–C29–S3	111.1(4)
		N2–C29–S3	123.4(6)

($\lambda = 0.71073$ Å) operated at 1600 W power (50 kV, 32 mA). The detector was placed at a distance of 5.8 cm from the crystal. A total of 1850 frames were collected with a scan width of 0.3° in ω and the frames were integrated with the Bruker SAINT software package using a narrow-frame integration algorithm. Data were corrected for absorption effects using the multiscan technique (SADABS) [16]. The structures were solved and refined using the Bruker SHELXTL (Version 6.1) software package [17].

Acknowledgements

R.L. thanks the Council of Scientific and Industrial Research, India for SRF fellowship and H.P.Y. thanks NSF grant CHE-0131112 for the X-ray facility.

Appendix A. Supplementary material

CCDC numbers 281619 and 604139 contain the supplementary crystallographic data for **2 · BF$_4$** and **5**. These data can be obtained free of charge via http://www.ccdc.cam.ac.uk/conts/retrieving.html, or from the Cambridge Crystallographic Data Centre, 12 Union Road, Cambridge CB2 1EZ, UK; fax: (+44) 1223-336-033; or e-mail: deposit@ccdc.cam.ac.uk. Supplementary data associated with this article can be found, in the online version, at doi:10.1016/j.poly.2006.09.042.

References

[1] G. Hogarth, Prog. Inorg. Chem. 53 (2005) 71.
[2] J.V. Dubrawski, R.D. Feltham, Inorg. Chem. 19 (1980) 355.
[3] I.R. Baird, B.R. Cameron, R.T. Skerlj, Inorg. Chim. Acta 353 (2003) 107.
[4] (a) M.A. Bennett, K. Khan, E. Wenger, in: G. Wilkinson, F.G.A. Stone, E.W. Abel (Eds.), Comprehensive Organometallic Chemistry II, second ed., vol. 7, Elsevier, Oxford, 1995, p. 513 (Chapter 8); (b) S.G. Davies, J.P. McNally, A.J. Smallridge, Adv. Organomet. Chem. 30 (1991) 1.
[5] T. Wilczewski, J. Organomet. Chem. 224 (1982) C1.
[6] R. Lalrempuia, P.J. Carroll, M.R. Kollipara, Polyhedron 22 (2003) 1391.
[7] (a) F.A. Cotton, J.A. McCleverty, Inorg. Chem. 3 (1964) 1398; (b) C. O'Connor, J.D. Gilbert, G. Wilkinson, J. Chem. Soc. A. 84 (1969).
[8] (a) A.M. Khenkin, L.J.W. Shimon, R. Neumann, Inorg. Chem. 42 (2003) 3331; (b) N.V. Mockus, J.L. Petersen, J.J. Rack, Inorg. Chem. 45 (2006) 8.
[9] W. Luginbühl, P. Zbinden, P.A. Pittet, T. Armbruster, H. Beat Bürgi, A.E. Merbach, A. Ludi, Inorg. Chem. 30 (1991) 2350.
[10] R. Lalrempuia, H. Yennawar, Y.A. Mozharivskyj, M.R. Kollipara, J. Organomet. Chem. 689 (2004) 539.
[11] P.W. Wanandi, T. Don Tilley, Organometallics 16 (1997) 4299.
[12] G. Hogarth, S. Faulkner, Inorg. Chim. Acta 359 (2006) 1018.
[13] W. Cordes, M. Draganjac, Acta Crystallogr., Sect. C. 44 (1988) 363.
[14] M.I. Bruce, P.J. Low, B.W. Skelton, E.R.T. Tiekink, A. Werth, A.H. White, Aust. J. Chem. 48 (1995) 1887.
[15] M.I. Bruce, N.J. Windsor, Aust. J. Chem. 30 (1977) 1601.
[16] Bruker Analytical X-ray Systems, Madison, USA, 2002.
[17] G. Sheldrick, SHELXL-93, Program for Crystal Structure Refinement, Institüt für Anorganische Chemie der Universität, Göttingen, Germany, 1993.

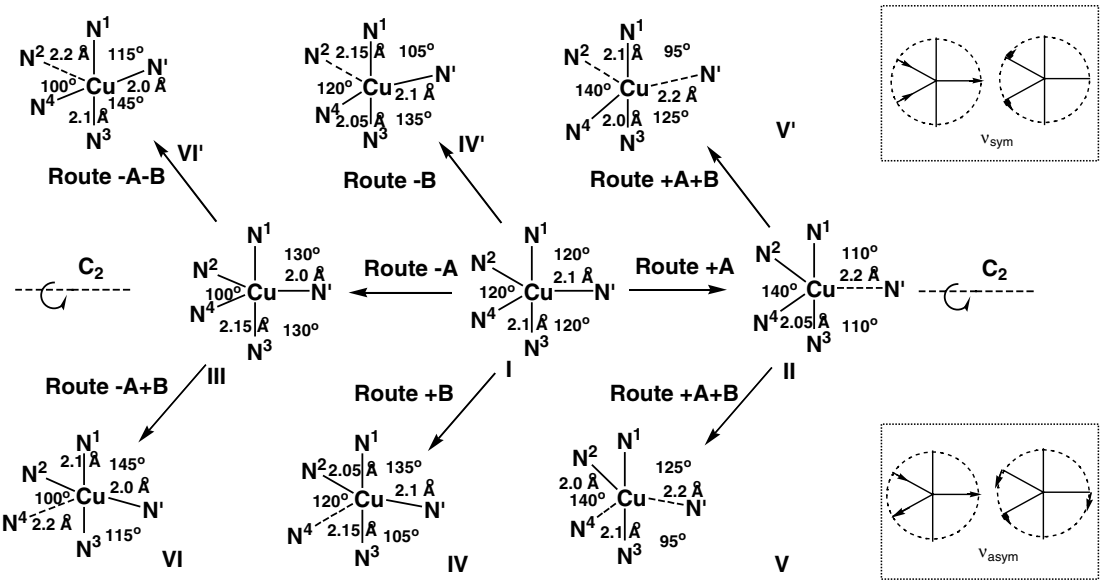


Fig. 1. The forms of distortion of the RTB CuN_4N' chromophore involving the $\pm A$, $\pm B$ and $\pm A$ $\pm B$ routes.

by soft modes of vibration of the more regular stereochemistries. Hence, the concept of a structural pathway [3–5], Fig. 1, for [Cu(chelate)$_2$X][Y] type complexes has been developed.

In 1984, Addison, Reedijk and co-workers introduced a very useful parameter, τ, which provides a measure of the degree of square-based pyramidal (SBP) versus trigonal bipyramidal (TBP) geometry adopted by five-coordinate Cu(II) complexes [6]. This parameter provides a convenient tool for comparing structures of similar five-coordinate Cu(II) complexes. The parameter τ is defined as $(\beta - \alpha)/60$, where β and α are the largest coordination angles, and its value varies from 0 (in regular SBP) to 1 (in regular TBP). The molecular structures of five-coordinate copper(II) complexes range extensively from regular trigonal bipyramidal (RTBP, D_{3h}) to regular square based pyramidal (RSBP, C_{4v}) with most complexes falling between these two stereochemistries [7], somewhere along the classical Berry pathway [6,8]. This feature can be useful in probing the relationships between structural correlations and the respective structural pathway involving vibronic type coupling.

In the majority of [Cu(chelate)$_2$X][Y] complexes the differences in stereochemistry may be associated with the differences in the ligands present i.e. chelate = 2,2′-bipyridine (bipy), 1,10-phenanthroline (phen) and di-2-pyridylamine (dpyam) and X = Cl^-, Br^-, I^- or H_2O, respectively. A number of structural pathways of various copper(II) five-coordinate series, [Cu(bipy)$_2$X][Y] and [Cu(phen)$_2$X][Y] have now been reported in the literature [3,9]. These systems represent various types of structural pathways and such structural correlations have been found to be consistent with spectroscopic data involving EPR and electronic reflectance spectra. However, structural studies and structural correlations involving five-coordinate complexes containing the more flexible dpyam ligand and a pseudohalide, such as NCO^- have not been reported to date in the literature. Moreover, the square pyramidal geometry in new dpyam complexes is inherently different than previously reported five-coordinate square pyramidal geometries involving copper(II) and other chelate ligands [3,9]. The axial position of the square pyramid in this complex series is the occupied by dpyam nitrogen which is different from those of the bipy and phen series to which the halide or H_2O is occupied. Hence, it is of interest to look at potential structural correlations and investigate the existence of a potential structural pathway for the series of five-coordinate copper(II) complexes of the type, [Cu(dpyam)$_2$(NCO)][Y].

2. Experimental

2.1. General

The ligand, di-2-pyridylamine and all reagents are commercial grade materials and were used without further purification. IR spectra were recorded on a Perkin–Elmer Spectrum One FT-IR spectrophotometer as KBr disc in the 450–4000 cm^{-1} spectral range. Solid-state (diffuse reflectance) electronic spectra were measured as polycrystalline samples on a Perkin–Elmer Lambda 2S spectrometer, over the range 8000–18 000 cm^{-1}. X-band electron paramagnetic resonance (EPR) measurements were performed at room temperature on a JEOL RE2X spectrometer, using DPPH ($g = 2.0036$) as a standard. Higher EPR frequencies were employed in experiments conducted at 77 K: K-band (~27 GHz), V-band (~54 GHz) and W-band (~100 GHz). In this case a transmission single-pass home-made spectrometer based on a superconducting magnet was used [10]. Elemental analyses (C, H, N) were determined on a Perkin–Elmer PE2400 CHNS/O.

[Cu(dpyam)$_2$(NCO)](Br) (**1**): A warm solution of di-2-pyridylamine (0.171 g, 1.0 mmol) in methanol (15 cm^3) was added to a hot aqueous solution (15 cm^3) of $CuBr_2$ (0.071 g, 0.5 mmol). Solid KNCO (0.162 g, 2.0 mmol) was then added to the reaction mixture. The solution was allowed to evaporate at room temperature in air. Dark green needle-like crystals of **1** deposited after three days. The crystals were filtered off, washed with mother liquor and air-dried. Yield: ca. 95%. *Anal*. Calc. for $C_{21}H_{18}N_7CuOBr$: C, 47.78; H, 3.44; N, 18.57. Found: C, 47.84; H, 3.35; N, 18.70%.

[Cu(dpyam)$_2$(NCO)](CF$_3$SO$_3$) (**2**): A warm solution of di-2-pyridylamine (0.171 g, 1.0 mmol) in methanol (15 cm^3) was added to a hot aqueous solution (15 cm^3) of $Cu(CF_3SO_3)_2$ (0.181 g, 0.5 mmol). An aqueous solution (20 cm^3) of KNCO (0.162 g, 2.0 mmol) was then added. The green solution was slowly evaporated at room temperature. After several days, dark green needle-like crystals of **2** formed. The crystals were filtered off, washed with mother liquor and air-dried. Yield: ca. 60%. *Anal*. Calc. for $C_{22}H_{18}N_7CuO_4F_3S$: C, 44.26; H, 3.03; N, 16.42. Found: C, 43.98; H, 2.98; N, 16.29%.

[Cu(dpyam)$_2$(NCO)](BF$_4$) · dpyam (**3**): A warm solution of di-2-pyridylamine (0.171 g, 1.0 mmol) in methanol (15 cm^3) was added to a hot aqueous solution (15 cm^3) of $Cu(BF_4)_2 \cdot nH_2O$ (0.118 g, 0.5 mmol). An aqueous solution (10 cm^3) of KNCO (0.081 g, 1.0 mmol) was then added to the reaction mixture. The green solution was slowly evaporated at room temperature. Green needle-like crystals of **3** deposited after several days. The crystals were filtered off, washed with mother liquor and air-dried. Yield: ca. 75%. *Anal*. Calc. for $C_{31}H_{27}N_{10}CuOBF_4$: C, 52.74; H, 3.85; N, 19.84. Found: C, 53.08; H, 4.00; N, 19.67%.

[Cu(dpyam)$_2$(NCO)](Cl) · 4H$_2$O (**4**): A warm solution of di-2-pyridylamine (0.171 g, 1.0 mmol) in methanol (15 cm^3) was added to a boiling aqueous solution (15 cm^3) of $CuCl_2 \cdot 2H_2O$ (0.085 g, 0.5 mmol). KNCO (0.041 g, 0.5 mmol) was then added to the reaction mixture. The green solution was slowly evaporated at room temperature. After two weeks, green needle-like crystals of **4** formed. The crystals were filtered off, washed with mother liquor and air-dried. Yield: ca. 78%. *Anal*. Calc. for $C_{21}H_{26}N_7CuO_5Cl$: C, 45.41; H, 4.71; N, 17.65. Found: C, 45.28; H, 4.57; N, 17.67%.

[Cu(dpyam)$_2$(NCO)](NO$_3$) (**5**): A warm solution of di-2-pyridylamine (0.171 g, 1.00 mmol) in methanol (15 cm^3) was added to a hot aqueous solution (10 cm^3) of $Cu(NO_3)_2 \cdot 3H_2O$ (0.121 g, 0.5 mmol). Solid KNCO (0.081 g, 1.0 mmol) was then added. The green solution was slowly evaporated at room temperature. After several days dark green-like rod-shaped crystals of **5** formed. The crystals were filtered off, washed with mother liquor and air-dried. Yield: ca. 88%. *Anal*. Calc. for $C_{21}H_{18}N_8CuO_4$: C, 52.80; H, 3.32; N, 20.05. Found: C, 52.56; H, 3.24; N, 20.17%.

[Cu(dpyam)$_2$(NCO)](PF$_6$) (**6**): A warm solution of di-2-pyridylamine (0.17 g, 1.00 mmol) in methanol (15 cm^3) was added to a hot aqueous solution (10 cm^3) containing $Cu(CH_3COO)_2 \cdot nH_2O$ (0.091 g, 0.5 mmol) and KNCO (0.081 g, 1.0 mmol). An aqueous solution (15 cm^3) of KPF_6 (0.184 g, 1.0 mmol) was then added. The green solution was slowly evaporated at room temperature. After several days, green rod-shaped crystals of **6** formed. The crystals were filtered off, washed with mother liquor and air-dried. Yield: ca. 90%. *Anal*. Calc. for $C_{21}H_{18}N_7CuOPF_6$: C, 45.83; H, 2.88; N, 15.59. Found: C, 45.65; H, 2.77; N, 15.46%.

[Cu(dpyam)$_2$(NCO)](ClO$_4$) (**7**): A warm solution of di-2-pyridylamine (0.171 g, 1.0 mmol) in methanol (15 cm^3) was added to a hot aqueous solution (10 cm^3) of $Cu(ClO_4)_2 \cdot nH_2O$ (0.185 g, 0.5 mmol). An aqueous solution (15 cm^3) of KNCO (0.081 g, 1.0 mmol) was then added. The dark green solution was slowly evaporated at room temperature. After a week, dark green needle-like crystals of **7** formed. The crystals were filtered off, washed with mother liquor and air-dried. Yield: ca. 75%. *Anal*. Calc. for $C_{21}H_{18}N_7CuO_5Cl$: C, 49.41; H, 3.11; N, 16.80. Found: C, 49.58; H, 2.99; N, 16.68%. *Caution*: perchlorates are explosive!

[Cu(dpyam)$_2$(NCO)](BPh$_4$) (**8**): A warm solution of di-2-pyridylamine (0.171 g, 1.0 mmol) in methanol (15 cm^3) was added to a hot aqueous solution (10 cm^3) of $Cu(CH_3COO)_2 \cdot nH_2O$ (0.091 g, 0.5 mmol). Solid KNCO (0.081 g, 1.00 mmol) and solid of $NaBPh_4$ (0.342 g, 1.0 mmol) were then added to the reaction mixture. The green solution was slowly evaporated at room temperature. After two weeks, green rod-shaped crystals of **8** formed. The crystals were filtered off, washed with mother liquor and air-dried. Yield: ca. 80%. *Anal*. Calc. for $C_{45}H_{38}N_7CuOB$: C, 70.45; H, 4.99; N, 12.78. Found: C, 70.47; H, 5.00; N, 13.01%.

2.2. Crystallography

The X-ray single-crystal data of complexes **1**–**3** and **5**–**8** were collected at 293 K on a 4 K Bruker SMART CCD area-detector diffractometer rotating anode, graphite monochromated Mo Kα radiation ($\lambda = 0.71073$ Å) using the SMART program [11]. Data reduction and cell refinements were performed using the program SAINT [12]. An empirical absorption correction was applied using the SADABS [13] program, which resulted in transmission coefficients ranging from 0.854 to 1.000 for **1**, 0.402 to 1.000 for **2**, 0.774 to 1.000 for **3**, 0.811 to 1.000 for **5**, 0.890 to 1.000 for **6**, 0.834 to 1.000 for **7** and 0.898 to 1.000 for **8**. The unit-cell parameters of complex **4** were determined and the intensity data collected on an Enraf-Nonius MACH3 diffractometer with Mo Kα radiation ($\lambda = 0.70183$ Å) at 298 K. An absorption correction was performed using the ψ-scan program, which resulted in transmission coefficients ranging from 0.904 to 1.000.

All eight structures were solved by direct methods and refined by full-matrix least-squares method on $(F_{obs})^2$ with

anisotropic thermal parameters for all nonhydrogen atoms using the SHELXTL-PC V 6.12 [14] software package. All hydrogen atoms in **1**–**8** were located by difference synthesis and refined isotropically, except the hydrogen atoms of the water molecules in **4**, which we were unable to locate and not fix. The molecular graphics were created using SHELXTL-PC. The O atom in isocyanato group of **2** and **3** showed disorder; the occupancies of the disordered positions were initially refined and later fixed at 0.5 and 0.5 for **2** and 0.7 and 0.3 for **3**. The F and O atoms of the trifluoromethanesulfonate group of **2** showed disorder; the occupancies of the disordered positions were initially refined and later fixed at 0.5 and 0.5, respectively. The F atoms of the tetrafluoroborate group of **3** and hexafluorophosphate group of **6** also showed disorder. They were divided into two sets with occupancies of 0.5 and 0.5. The O atoms of the perchlorate group of **7** showed disorder; the occupancies of the disordered positions were initially refined and later fixed at 0.5 and 0.5, respectively. The crystal and refinement details for complexes **1**–**8** are listed in Table 1. Selected bond lengths and bond angles are given in Table 2. Fig. 2 shows a representative molecular structure for the $[Cu(dpyam)_2(NCO)]^+$ cation, the atomic numbering scheme and the angle notation used.

3. Results and discussion

3.1. Crystal structures

The asymmetric unit of complexes **1**–**8** involves a $[Cu(dpyam)_2(NCO)]^+$ cation and Br^-, $CF_3SO_3^-$, $BF_4^-\cdot$ dpyam, $Cl^-\cdot 4H_2O$, NO_3^-, PF_6^-, ClO_4^- and BPh_4^- anions, respectively in the lattice. In addition, **3** and **4** involve one dpyam molecule and four water molecules in the unit cell, respectively. None of the anions or water molecules is close enough (<3.0 Å) to be considered even weakly semi-coordinated to the copper(II) cation [15]. The structure of the cations all involve a five-coordinate CuN_4N' chromophore, with a square pyramidal stereochemistry having a trigonal bipyramidal distorted square based pyramidal stereochemistry (TBDSBP) in **1**–**5**, an intermediate five-coordinate stereochemistry for **6** and **7**, and a square based pyramidal distortion (SBPDTB) for **8**. All eight complexes are further examples of distortion isomers of the $[Cu(dpyam)_2(NCO)]^+$ cation, whose stereochemistries are related by the structural pathways of Fig. 1. No attempt will be made to describe the individual structures of complexes **1**–**8**, Table 2, but scatter-plot analysis will be used to compare their structures with that of $[Cu(dpyam)_2(NCO)](SO_4)_{0.5}\cdot dpyam\cdot 0.5H_2O$ (**9**) the only other complex of known crystal structure [16]. Table 2 summarises the selected bond lengths and angles of all eight complexes, sequenced in order of their τ values, where $\tau = (\alpha_8 - \alpha_1)/60$ [6], and Table S1 summarises the maximum, minimum, difference (Δ) and average bond length and bond angle values for the series of nine $[Cu(dpyam)_2(NCO)][Y]$ complexes. Table S3 gives the sums of the in-plane bond angles, and bond distances, Cu–N(2), Cu–N(4) and Cu–N′, respectively.

3.2. The $[Cu(dpyam)_2(NCO)][Y]$ data

The structures of the nine five-coordinate CuN_4N' chromophores vary from TBP to near SBP, reflected in a range of τ values of 0.76–0.09, $\Delta\tau = 0.67$. This is a substantial variation in τ, the largest seen to date for the cation distortion isomers of the $[Cu(dpyam)_2X][Y]$ series of complexes [17]. None of the complexes has a near RTB (regular trigonal bipyramidal) stereochemistry or lies on a twofold axis of symmetry. Six complexes (**1**–**5** and **9**) have τ values in the more limited range of 0.09 to 0.31 and their stereochemistries are best described as TBDSBP. Complexes **6** and **7** have τ values of 0.53 and 0.54 and their stereochemistries are best described as intermediate five coordinate. Complex **8** has a τ value of 0.76 and its stereochemistry is best described as SBPDTB.

Relative to a RTB stereochemistry, the out-of-plane distances, Table 2, show only small differences, Table S1, with ΔCu–N(1) = 0.030 Å and ΔCu–N(3) = 0.044 Å. The largest variations in bond lengths are present in the equatorial bond distances Cu–N(4), Cu–N′ and Cu–N(2), respectively. The Cu–N(4) distances show the largest variation ranging from 2.089(1) to 2.283(3) Å, with $\Delta = 0.194$ Å and with an average value = 2.182(3) Å. The Cu–N(2) distances vary from 2.014(10) to 2.074(2) Å, with $\Delta = 0.060$ Å and with a mean value = 2.044(2) Å. The Cu–N′ distances range from 1.903(3) to 1.984(1) Å, with $\Delta = 0.081$ Å and with an average value = 1.947(1) Å. The average of the in-plane Cu–N(2,4,N′) distances, 2.057(2) Å, is greater than the average of the axial Cu–N(1,3) distances, 2.015(1) Å, by 0.042 Å, consistent with a TB stereochemistry and slightly lesser than the difference of 0.1 Å normally observed [18]. The out-of-plane bond angles, Table 2, show only small differences, Table S1, with $\Delta\alpha_{4-7}$ and $\Delta\alpha_{8-10}$ ranging from 3.6° to 6.5° and 6.2–15.4°, respectively. The α_1 in-plane angles show the largest variation ranging from 124.7(2)° to 167.1(1)°, with $\Delta = 42.4°$ and with a mean value = 151.8(1)°. The α_2 angles show the smallest variation ranging from 98.8(2)° to 119.4(1)°, with $\Delta = 20.6°$ and average = 108.4(1)°. The α_3 angles vary from 93.7(1)° to 115.9(1)°, with $\Delta = 22.6°$ and with an average value = 99.3(1)°. From Table 2 it is noticeable that within the range of τ values of 0.76–0.09, there is slight gap of 0.22 in τ value between the value of 0.54 for **7** to the next value of 0.76 for **8**. This gap corresponds with a change in the ratio of the α_9 and α_{10} angles, for τ values >0.54, $\alpha_9 > \alpha_{10}$, but for τ values <0.54, $\alpha_9 < \alpha_{10}$. These relatives have been used to suggest a structural pathway from a regular trigonal bipyramidal to a distorted square-based pyramidal stereochemistry and suggest that, **1**–**9** form a point in a more extensive structural pathway for the CuN_4N' chromophore.

Table 1
Crystallographic and structure refinement data for eight [Cu(dpyam)$_2$(NCO)][Y] complexes

	1	**2**	**3**	**4**	**5**	**6**	**7**	**8**
Formula	$C_{21}H_{18}N_7CuOBr$	$C_{22}H_{18}N_7CuO_4F_3S$	$C_{31}H_{27}N_{10}CuOBF_4$	$C_{21}H_{26}N_7CuO_5Cl$	$C_{21}H_{18}N_8CuO_4$	$C_{21}H_{18}N_7CuOPF_6$	$C_{21}H_{18}N_7CuO_5Cl$	$C_{45}H_{38}N_7CuOB$
M	527.87	597.03	705.98	555.48	509.97	592.93	547.38	767.22
Crystal system	monoclinic	orthorhombic	monoclinic	monoclinic	monoclinic	monoclinic	monoclinic	monoclinic
Space group	$P2_1/n$	$Pbca$	$P2_1/n$	$P2_1$/c	$P2_1/n$	$P2_1/n$	$P2_1/n$	$P2_1/n$
a (Å)	10.9720(1)	15.8752(2)	19.9263(6)	7.1030(3)	11.0911(2)	8.3080(1)	8.1782(6)	13.2229(1)
b (Å)	16.5463(1)	16.7884(2)	7.6268(3)	27.9710(2)	16.323(3)	20.2070(3)	20.1466(1)	9.7836(7)
c (Å)	12.0719(1)	18.6085(3)	22.7070(9)	12.6930(8)	11.8435(2)	14.0520(2)	13.9620(9)	29.805(2)
α (°)	90	90	90	90	90	90	90	90
β (°)	98.492(2)	90	112.410(1)	96.899(3)	99.934	91.061(3)	91.8200(1)	101.8880(1)
γ (°)	90	90	90	90	90	90	90	90
V (Å)^3	2167.6(3)	4959.5(1)	3190.3(2)	2503.6(2)	2112.1(6)	2358.6(6)	2299.3(3)	3773.1(5)
Z	4	8	4	4	4	4	4	4
D_c (g cm^3)	1.618	1.599	1.470	1.452	1604	1670	1581	1351
μ (mm^{-1})	2879	1.032	0.752	1.024	1.083	1.072	1.115	0.625
F(000)	1060	2424	1444	1116	1044	1196	1116	1596
Crystal size (mm)	$0.20 \times 0.16 \times 0.04$	$0.38 \times 0.28 \times 0.25$	$0.25 \times 0.15 \times 0.10$	$0.43 \times 0.20 \times 0.18$	$0.15 \times 0.12 \times 0.06$	$0.26\times 0.08 \times 0.06$	$0.16\times 0.13 \times 0.08$	$0.39 \times 0.19 \times 0.13$
Number of reflection collected	18832	33809	22102	8129	11204	20607	14511	32358
Number of unique reflections (R_{int})	5169 (0.0542)	7225 (0.0384)	9087 (0.0804)	3869 (0.0394)	3846 (0.0478)	5657 (0.0572)	5436 (0.0381)	9035 (0.0284)
Data/restraints/parameter	5169/0/352	7225/0/422	9087/0/582	3869/0/389	3846/0/380	5657/0/461	5436/0/396	9035/0/648
Goodness-of-fit	1.030	1.027	1.010	1.105	1.018	1.029	1.035	1.054
Final R indices [$I > 2\sigma$(I)]	$R_1 = 0.0514$, $wR_2 = 0.1023$	$R_1 = 0.0587$, $wR_2 = 0.1493$	$R_1 = 0.0789$, $wR_2 = 0.1010$	$R_1 = 0.0472$, $wR_2 = 0.1318$	$R_1 = 0.0405$, $wR_2 = 0.0884$	$R_1 = 0.0541$, $wR_2 = 0.1065$	$R_1 = 0.0649$, $wR_2 = 0.1611$	$R_1 = 0.0471$, $wR_2 = 0.1117$
R indices (all data)	$R_1 = 0.0898$, $wR_2 = 0.1151$	$R_1 = 0.0827$, $wR_2 = 0.1662$	$R_1 = 0.2606$, $wR_2 = 0.1453$	$R_1 = 0.0768$, $wR_2 = 0.1655$	$R_1 = 0.0583$, $wR_2 = 0.095$	$R_1 = 0.0944$, $wR_2 = 0.1197$	$R_1 = 0.0966$, $wR_2 = 0.1790$	$R_1 = 0.0636$, $wR_2 = 0.1201$
Largest differential peak and hole (e Å^3)	0.489, −0.481	0.728, −0.674	0.208, −0.223	0.515, −0.583	0.362, −0308	0.317, −0.371	0.799, −0.452	0.349, −0.395

Table 2
Selected bond lengths (Å) and angles (°) for the [Cu(dpyam)$_2$(NCO)][Y]

	Y								
	Br^- (**1**)	$CF_3SO_3^-$ (**2**)	BF_4^- · dpyam (**3**)	$Cl^- \cdot 4H_2O$ (**4**)	NO_3^- (**5**)	$(SO_4)_{0.5}^{2-}$ · dpyam · $0.5H_2O$ (**9**[11])	PF_6^- (**6**)	ClO_4^- (**7**)	BPh_4^- (**8**)
Cu–N′	1.945(3)	1.949(3)	1.933(4)	1.955(5)	1.950(3)	1.903(13)	1.949(3)	1.952(4)	1.984(1)
Cu–N(1)	2.030(3)	2.029(3)	2.000(4)	2.008(3)	2.008(2)	2.028(10)	2.008(2)	2.002(3)	2.017(1)
Cu–N(3)	2.045(3)	2.025(3)	2.001(3)	2.012(3)	2.008(3)	2.012(10)	2.013(2)	2.013(3)	2.018(1)
Cu–N(2)	2.021(3)	2.047(2)	2.025(3)	2.016(4)	2.043(2)	2.014(10)	2.074(2)	2.068(3)	2.072(1)
Cu–N(4)	2.283(3)	2.245(3)	2.157(4)	2.181(3)	2.185(2)	2.162(10)	2.169(3)	2.167(3)	2.089(1)
α_1	167.1(1)	159.4(1)	156.2(1)	157.9(1)	157.3(1)	154.7(5)	144.6(1)	144.1(2)	124.7(2)
α_2	98.8(2)	102.8(2)	104.4(1)	104.0(1)	109.1(1)	104.6(5)	116.9(1)	115.6(1)	119.4(1)
α_3	94.1(2)	97.8(1)	99.3(1)	98.1(1)	93.7(1)	100.7(5)	98.5(1)	100.2(1)	115.9(1)
α_4	92.7(1)	94.2(2)	90.4(1)	89.4(1)	92.5(1)	90.1(5)	89.6(1)	89.6(1)	94.9(1)
α_5	92.4(1)	92.4(1)	87.8(1)	88.3(1)	91.8(1)	90.0(5)	88.0(2)	87.4(1)	94.7(1)
α_6	86.2(1)	86.2(1)	87.5(1)	86.6(1)	86.4(1)	85.5(4)	87.7(1)	88.3(1)	89.1(1)
α_7	82.2(1)	85.3(1)	88.7(1)	86.0(1)	86.1(1)	85.9(5)	87.2(2)	87.7(1)	88.5(1)
α_8	172.8(1)	173.1(1)	170.0(2)	173.7(1)	175.3(1)	173.0(5)	176.2(1)	176.2(1)	170.3(2)
α_9	89.9(1)	88.3(1)	90.2(1)	93.3(1)	88.9(1)	91.5(4)	92.6(1)	92.7(1)	86.2(1)
α_{10}	92.0(1)	91.3(1)	101.3(1)	100.3(1)	94.2(1)	100.9(5)	96.5(1)	95.7(1)	85.9(1)
τ	0.09	0.23	0.23	0.26	0.30	0.31	0.53	0.54	0.76

3.3. Scatter-plot analysis for the [Cu(dpyam)$_2$(NCO)][Y] series of complexes

This section presents the data for the [Cu(dpyam)$_2$-(NCO)][Y] series of complexes, Table 2, using scatter-plot analysis. The scatter plots (Fig. 3) discussed are as follows: (a) τ versus Cu–N(4), (b) α_3 versus α_1, (c) α_3 versus Cu–N′ and (d) Cu–N(2) versus Cu–N(4). An overview of the range of stereochemistries is provided by the plot of τ versus Cu–N(4). However, as τ involves two simultaneous angle changes, it will not be used further. A number of suggested extreme data points, Table S2, are included in the plots, with the geometry of the extreme seesaw stereochemistry illustrated in Fig. S1. The nine data points in Fig. 3(a) vary from trigonal bipyramidal, TB, to near regular square-based pyramidal, RSBP, with the τ values decreasing from 0.76 to 0.09, respectively as the Cu–N(4) distances increase from 2.089(1) to 2.283(3) Å. The data points show a broad *inverse* trend, and clearly do not cluster around the RTB geometrical point. This plot provides an overview of the observed stereochemistries of the [Cu(dpyam)$_2$(NCO)][Y] series of complexes. There is one data point, **1**, at near SBP with $\tau = 0.09$, but there are no data points at RTB ($\tau = 1.0$). Five of the nine data points have τ values in the range 0.23–0.31 with stereochemistries best described as TBDSBP. Two data points **6** and **7** lie on the main correlation trend-line containing the RTB and RSBP data points. Two data points, **4** and **8** lie on a parallel correlation, with the remaining one data point, **9** lying nearby. Data points **1** and **2** lie off the RTB → RSBP trendline, due to their slightly long Cu–N(4) bond distances, which are ≈0.1 Å greater than expected [16].

The data points in Fig. 3(b) show the α_3 values decreasing from 115.9(1)° to 94.1(2)° as the α_1 values concomitantly increase from 124.7(2)° to 167.1(1)°. All eight data points have α_1 values >120° and α_3 values <120°, Table 2. Eight data points are found in the $-A + B$ section of the graph. The exception is data point, **1**, which lies close to the RSBP reference point. It is noticeable that within the α_1 and α_3 data set, point **1** has greater α_1 and α_3 values compared to those of a RSBP stereochemistry. There is no data points, which lies on the RTB → RSBP ($-A + B$) distortion pathway. Four data points, **2**, **3**, **4** and **9**, and the SBP data point, show an *inverse* trend, with each of these data points having α_2 105 ± 2°. The remaining data points, **8**, **7** and **5**, lie on two possible parallel correlations (---) displaying α_2 values of 120 ± 2°, 115 ± 2° and 110 ± 1°, respectively. This series of three possible parallel correlations have the same gradients. The data points show a SBP distortion, but only the correlation containing the data points corresponding to an α_2 value of 105° can end up at RSBP. For each parallel correlation, the α_2 values remain constant, therefore $\Delta\alpha_1\uparrow \approx \Delta\alpha_3\downarrow$ as $\alpha_1 + \alpha_2 + \alpha_3 = 360°$, Table S3, and possibly suggesting the occurrence of preferred or magic angles [19]. The % $-A$ and % $+B$ distortion values calculated from the in-plane α_1 and α_3 bond angle data of Fig. 3(b) are given in Table 3.

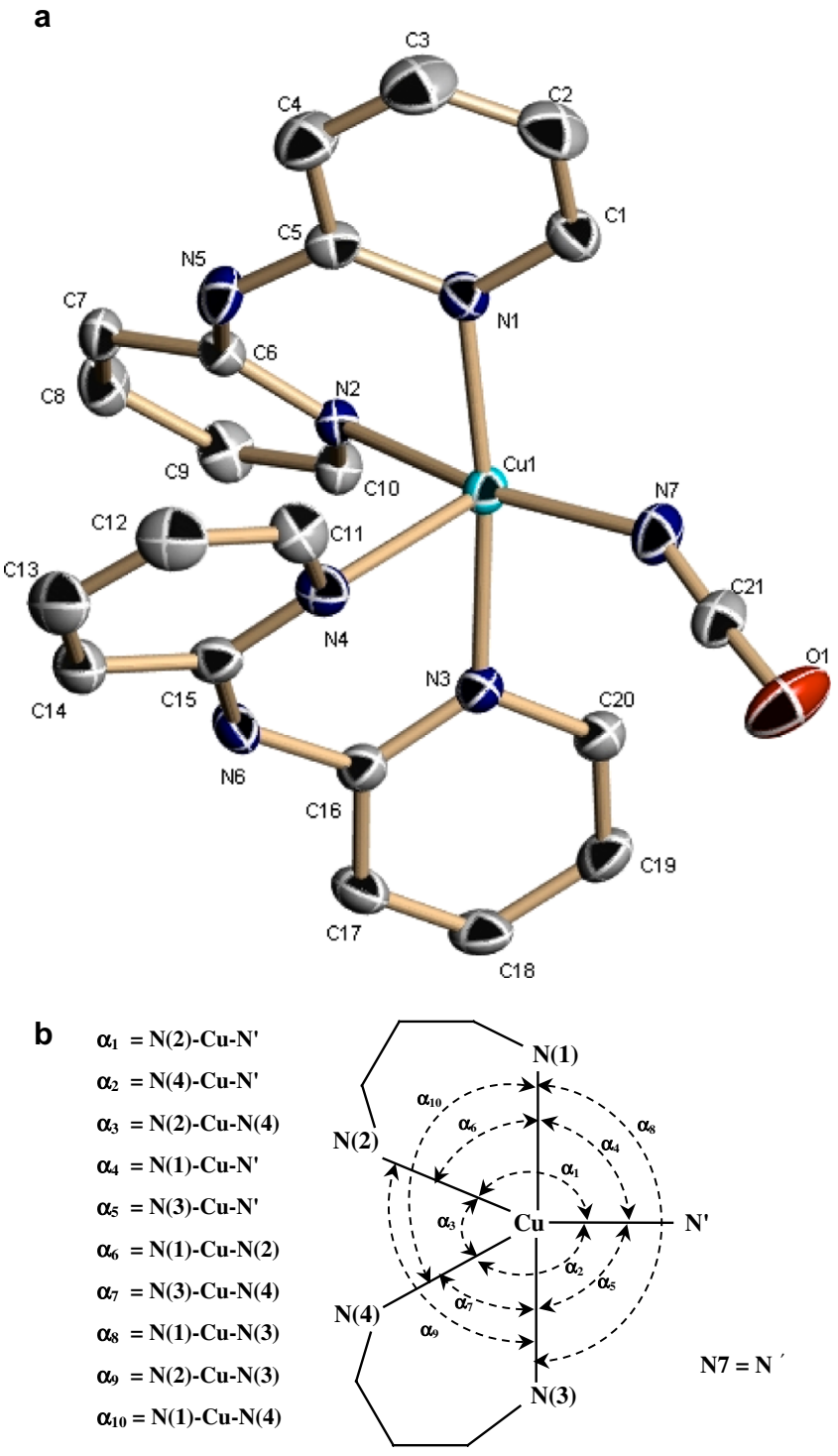


Fig. 2. (a) The molecular structure of the $[Cu(dpyam)_2(NCO)]^+$ cation of complex **1**, (b) the atom numbering scheme and α_n notation for the CuN_4N' chromophore.

The nine data points in Fig. 3(c) show the α_3 values decreasing from 115.9(1)° to 94.1(2)°, $\Delta\alpha_3 = 21.8°$ as the Cu–N′ distances decrease from 1.984(1) to 1.903(13) Å, ΔCu–N′ = 0.081Å. All data points have α_3 values <120° and Cu–N′ distances <2.092 Å, suggesting $-A$ route distortion. Data point, **8** lies well off the $-A \rightarrow$ RTB $\rightarrow +A$ pathway, with Cu–N′ distances significantly shorter, ≈0.08 Å, than predicted from its corresponding α_3 values, while data points **1**–**7** also seem to have slightly shorter Cu–N′ distances, ≈0.05 Å, than expected from their corresponding α_3 values. There are no data points connecting the RTB data point to the extreme 'see saw' data point (the $-A$ route distortion, SSDTB in Fig. S1) There are two possible higher parallel trend lines involving one data point **8**, and two data

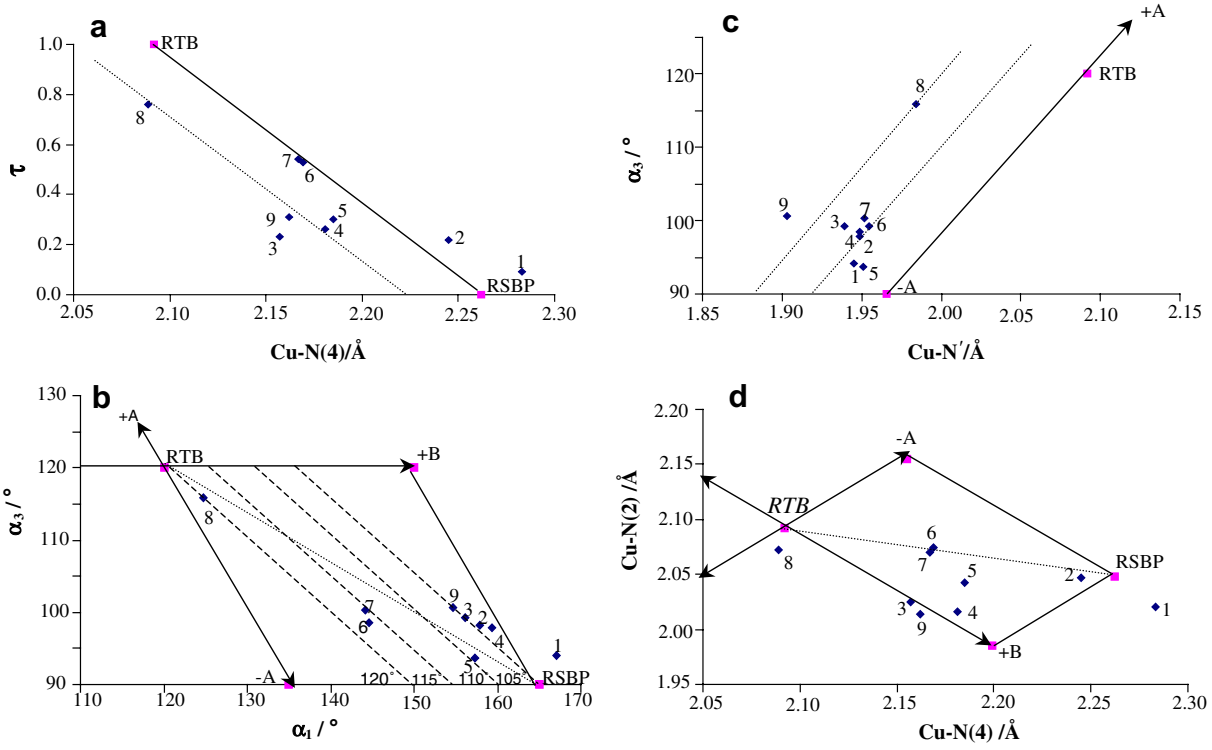


Fig. 3. Standard scatter plots for the [Cu(dpyam)(NCO)][Y] complexes.

points, **2** and **6** with **1**, **3**, **4**, **5** and **7** lying close by. These linear correlations do not have enough data points to be convincing. However, it is significant that the three correlations involve approximately equal separations between the lines of either ≈11° in the α_3 values or of ≈0.040 Å in the Cu–N′ distances. If the data of Fig. 3(c) are related to those of Fig. 1, then both the α_3 angles and the Cu–N′ distances correspond to a pure $-A$ route distortion of the RTB stereochemistry. In practice, the α_1 and α_2 angles are not even approximately equal, varying from $\Delta(\alpha_1 - \alpha_2) = 5.3$–$68.3°$, Table 2. The extreme $-A$ route distortion is clearly five-coordinate, with three short bonds,

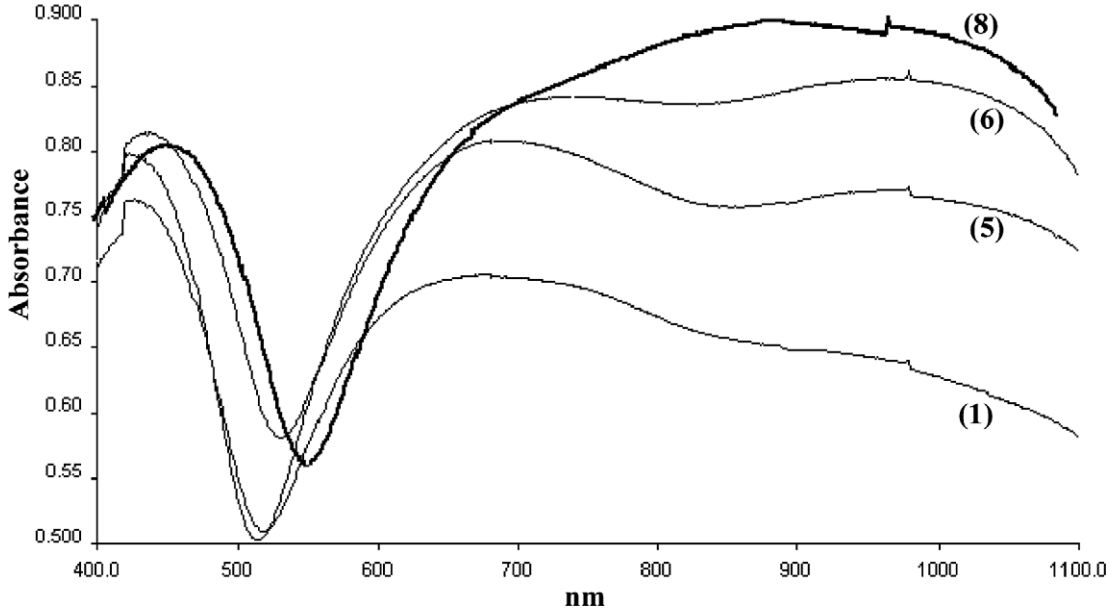


Fig. 4. Electronic reflectance spectra of representative $[Cu(dpyam)_2(NCO)][Y]$ complexes with different τ values: $\tau = 0.09$ for (**1**), 0.30 for (**5**), 0.53 for (**6**) and 0.76 for (**8**).

Table 3
The % $-A$ and % $+B$ route distortion values of the complexes calculated using the in-plane angle data of Fig. 3(b)

	Complex							
	1	**2**	**3**	**4**	**5**	**9**	**6**	**7**	**8**
% $-A$		82.0	77.3	81.2	97.9	71.7	80.0	73.2	15.3
% $+B$		94.4	85.8	89.6	80.7	83.0	46.1	47.2	8.8

Cu–N(1) = Cu–N(3) ≈ 2.0 Å, Cu–N′ ≈ 1.95 Å, and two longer bonds, Cu–N(2) = Cu–N(4) ≈ 2.15 Å, with in-plane angles of $\alpha_1 = \alpha_2 = 135°$ and $\alpha_3 = 90°$.

The data points in Fig. 3(d) show the Cu–N(2) distances decreasing from 2.074(2) to 2.014(10) Å, while the Cu–N(4) distances increase from 2.089(1) to 2.283(3) Å. Five data points, **2**, **4**–**7** are observed in the $-A + B$ quadrant of the graph, with points **1**, **3**, **8** and **9** lying outside this quadrant. There are no data points on the RTB $\rightarrow \pm A$ trendline, but there is one data point, **3** which lies directly on the RTB $\rightarrow +$ B route pathway. There are two data points **6** and **7** which also lie precisely on the RTB $\rightarrow$ RSBP ($-A + B$) pathway, with data point **2**, lying close by. Table 4 shows the % $-A$ and % $+B$ distortion values of the complexes calculated using the in-plane Cu–N(2) and Cu–N(4) distance data. The values are closely comparable to those in Table 3 using the corresponding in-plane bond angle data. In general, Tables 3 and 4 show a large % $-A$ and a large % $+B$ distortion. Data point **8** is exceptional because it shows a few % $-A$ and % $+B$ distortion values.

3.4. General conclusions and comparison of the [Cu(dpyam)$_2$(NCO)][Y] series with other [Cu(chelate)$_2$(X)][Y] series of complexes

The information obtained from the scatter-plot analysis of this series of nine [Cu(dpyam)$_2$(NCO)][Y] complexes can be summarised as follows:

(1) The distribution of the data points is not random, with respect to the RTB and RSBP data points. They involve a significant spread of 42° and 0.19 Å, Table S1.
(2) The τ plot is consistent with a SBP distortion of the RTB CuN_4N' chromophore, but with neither the RTB or RSBP structures present. Data point, **1**, has extreme to near RSBP geometry with a τ value of 0.09. Five complexes have τ values in the range of 0.23–0.31. Data points, **6** and **7**, have an intermediate τ values of 0.53 and 0.54, respectively. Data point, **8**, has an exceptional τ value of 0.76, which equates with an unusual SBPDTB stereochemistry for a [Cu(dpyam)$_2$(NCO)][Y] complex.
(3) The plot of α_3 versus α_1 shows data points lying on parallel correlations, with fixed α_2 values of $120 \pm 5°$, 10° or 15°, suggesting the existence of preferred or magic angles, consistent with $\alpha_1 + \alpha_2 + \alpha_3 = 360°$, Table S3.
(4) The ±A and ±B axes of Fig. 1 can be superimposed on the plots. All data points lie in the $-A + B$ section of the graphs except data point **1** which lies close to the RSBP stereochemistry. Tables 3 and 4 show the % $-A$ and % $+B$ distortion values of the complexes calculated from the in-plane angle and distance data and show large % values of both $-A$ and $+B$ distortion.
(5) The five-coordinate structures of the dpyam series are comparable to the five-coordinate copper(II) complexes [Cu(chelate)$_2$(X)][Y] when chelate = bipy and phen and X = Cl^-, Br^-, I^- and H_2O. Those of the bipy and phen families also show distortions ranging from RTB to RSBP, but differ in two aspects. First, almost all the τ values in the corresponding bipy and phen complexes range between intermediate to near RTB, [Cu(phen)$_2$Cl][Y] [9a] (0.56–0.81), [Cu(phen)$_2$Br][Y] [9b] (0.72–0.95), [Cu(phen)$_2$I][Y] [9b] (0.84–1.06), [Cu(bipy)$_2$Cl][Y] [3,9d] (0.53–1.00), [Cu(bipy)$_2$Br][Y] [9b,9d] (0.49–0.91), [Cu(bipy)$_2$I][Y] [9b] (0.80–0.90) and [Cu(chelate)$_2$(OH$_2$)][Y]$_2$ [9c] (0.53–0.89), which differ significantly from the dpyam series of complexes where most τ values = 0.09–0.54 due to the more flexible dpyam ligand. Secondly, the distortion structural pathway in the dpyam series involves a $-A + B$ route (Fig. 1), which is different from that of the higher symmetry with twofold axis of [Cu(chelate)$_2$(OH$_2$)][Y]$_2$ series which involves, a unique ±A route.

The stereochemistries of the [Cu(chelate)$_2$(OH$_2$)][Y]$_2$ complexes differ from that of the dpyam complexes in having a crystallographic twofold axis of symmetry and hence are best described as having a pure $\pm A$ route distortion, which involves the pure ν_{sym}^{str} and ν_{sym}^{bend} modes of vibration. The [Cu(dpyam)$_2$(NCO)][Y] complexes in contrast, with their slight contraction along the Cu–N′ distance (opposite α_3), their non-equivalence of the α_1 and α_2 angles without a

Table 4
The % $-A$ and % $+B$ route distortion values of the complexes calculated using the in-plane distance data of Fig. 3(d)

	Complex							
	1	**2**	**3**	**4**	**5**	**9**	**6**	**7**	**8**
% $-A$		82.5		7.9	28.6		46.0	38.1	
% $+B$		91.8	60.9	76.8	66.5	69.3	45.9	44.0	8.4

twofold axis of symmetry are considered to involve a $-A + B$ route distortion with the obvious domination of $+B$ over $-A$, involving all the four modes of vibration ν_{sym}^{str}, ν_{sym}^{bend}, ν_{asym}^{str} and ν_{asym}^{bend}, namely the molecular structure **VI** of Fig. 1. Alternatively, the precise coordination geometry displayed may be interpreted [9b] as an effect of vibronic coupling of a linear combination of the nuclear modes of vibrations ν_{sym}, a symmetric C_2 mode, and ν_{asym}, an asymmetric non-C_2 mode, of the CuN_4N' chromophore.

3.5. IR, electronic properties and EPR of the [Cu(dpyam)$_2$(NCO)][Y] complexes

The infrared spectra display a strong band at 2214 and 2180 cm^{-1} for **1**, 2214 cm^{-1} for **2**, 2209 cm^{-1} for **3**, 2220 cm^{-1} for **4**, 2219 and 2202 cm^{-1} for **5**, 2222 cm^{-1} for **6**, 2214 cm^{-1} for **7** and 2218 cm^{-1} for **8**, which can be assigned to the ν_{asym}(NCO) absorption band. The spectrum of **2** also displays a broad and intense band at approximately 1280–1040 cm^{-1}, consistent with the characteristic peak $\nu_4(SO_3)$ of $CF_3SO_3^-$ anion. The spectrum of **3** displays a broad and intense band at approximately 1074–1014 cm^{-1}, consistent with the characteristic peak of BF_4^- anion. The spectrum of **5** displays an intense band at approximately 1384 and 1307 cm^{-1}, consistent with the characteristic peak of ν_{as}(NO) and ν_s(NO) of NO_3^- anion. The spectrum of **6** displays a broad and intense band at approximately 845–837 cm^{-1}, consistent with the characteristic peak of PF_6^- anion. The spectrum of **7** displays a broad and intense band at approximately 1166–1076 cm^{-1}, consistent with the characteristic peak of ClO_4^- anion.

The polycrystalline electronic reflectance spectra of complexes **1**, **5**, **6** and **8** are represented in Fig. 4. For **8** a single d → d transition occurs at 11 420 cm^{-1} (876 nm), with some evidence of an unresolved high-energy shoulder at 12 880 cm^{-1} (776 nm), consistent with near TB stereochemistry ($\tau = 0.76$). The one-electron ground-state configuration is $d_{z^2} > d_{xy} \approx d_{x^2-y^2} > d_{xz} \approx d_{yz}$. The principal absorption may be assigned as a $d_{x^2-y^2} \rightarrow d_{z^2}$ transition, with the low-energy assigned as a $d_{xz} \approx d_{yz} \rightarrow d_{z^2}$ transition. The electronic spectrum of **8** is comparable to those of complexes with similar Cu(II) environment [Cu(phen)$_2$Cl][Y], Y = $BF_4 \cdot 0.5H_2O$, PF_6 and ClO_4 [9a], [Cu(phen)$_2$Br][Y], Y = Br · H_2O, ClO_4 and PF_6 [9b]. The spectra of **6** and **7**, $\tau = 0.53$ and 0.54, respectively, both having an intermediate stereochemistry between RTB and RSBP, involve two clearly resolved peaks at 10 330 cm^{-1} (968 nm) and 13 870 cm^{-1} (721 nm) for **6** and 10 350 (966 nm) and 13 800 cm^{-1} (725 nm) for **7**, with the lower-energy peak showing a slightly greater intensity, consistent with the intermediate five-coordinate geometry. The one-electron ground-state configuration is $d_{x^2-y^2} > d_{z^2} > d_{xy} > d_{xz} \approx d_{yz}$. The transitions may be assigned as the $d_{z^2} \rightarrow d_{x^2-y^2}$ transition for the low-energy peak and the $d_{xz} \approx d_{yz} \rightarrow d_{x^2-y^2}$ transition for the high-energy peak. The electronic spectra of **6** and **7** are comparable to those of complex with similar environment [Cu(phen)$_2$Cl][CF_3SO_3] · H_2O [9a]. Complexes **1**–**5**, $\tau = 0.09$–0.31, which have a TBDSBP stereochemistry, involve high-energy, high-intensity peak at 14 510 cm^{-1} (689 nm), 14 420 cm^{-1} (694 nm), 14 240 cm^{-1} (702 nm), 14 200 cm^{-1} (704 nm) and 13 930 cm^{-1} (718 nm), respectively, with low-energy, low-intensity shoulder at 10 150 cm^{-1} (985 nm), 10 180 cm^{-1} (982 nm), 10 220 cm^{-1} (978 nm), 10 350 cm^{-1} (966 nm) and 10 270 cm^{-1} (974 nm), respectively. The one-electron ground state configuration is $d_{x^2-y^2} > d_{z^2} > d_{xy} > d_{xz} \approx d_{yz}$. The transitions may be assigned as the $d_{z^2} \rightarrow d_{x^2-y^2}$ transition for the low-energy shoulder and the $d_{xz} \approx d_{yz} \rightarrow d_{x^2-y^2}$ transition for the high-energy peak. The electronic spectra of **1**–**5** are comparable to those of complexes with similar environment [Cu(phen)$_2$Cl][BPh_4] [9a] and [Cu(phen)$_2$Br][BPh_4] [9b].

The corresponding spectro-structural correlation plots (Fig. S2) reveal that ΔE values increase with increasing τ values for the low-energy peak and the reverse result has been found for the higher-energy peaks. It is evident from Fig. S3, that the basal angles themselves correlate very well with the ΔE values. This plot clearly indicates that a linear correlation between τ and the ΔE values exists in the set of **1**–**8** where α and β have been defined consistently.

The polycrystalline X-band EPR spectrum at room temperature of complexes **1**–**8** is isotropic (Table 5), yielding no information in relation to the electronic ground state. Low-temperature (77 K) EPR spectra were performed at higher frequencies (K-band and V-band) than X-band, both on polycrystalline samples, and DMSO solutions, in

Table 5
Consensus *g*-values for all 8 complexes from EPR

	Complex							
	1	**2**	**3**	**4**	**5**	**6**	**7**	**8**
X-band								
g_i (RT)	2.1515	2.1576	2.1157	2.1154	2.1084	2.0982	2.1079	2.1324
K and V-band[a]								
g_x	2.05	2.04	2.05	2.030	2.03	2.05	2.04	2.185
g_y	2.05	2.10	2.08	2.075	2.09	2.13	2.08	2.185
g_z	2.27	2.17	2.28	2.245	2.17	2.20	2.24	2.005

[a] Estimated error: ±0.01 for samples 4 and 8, ±0.02 for all others.

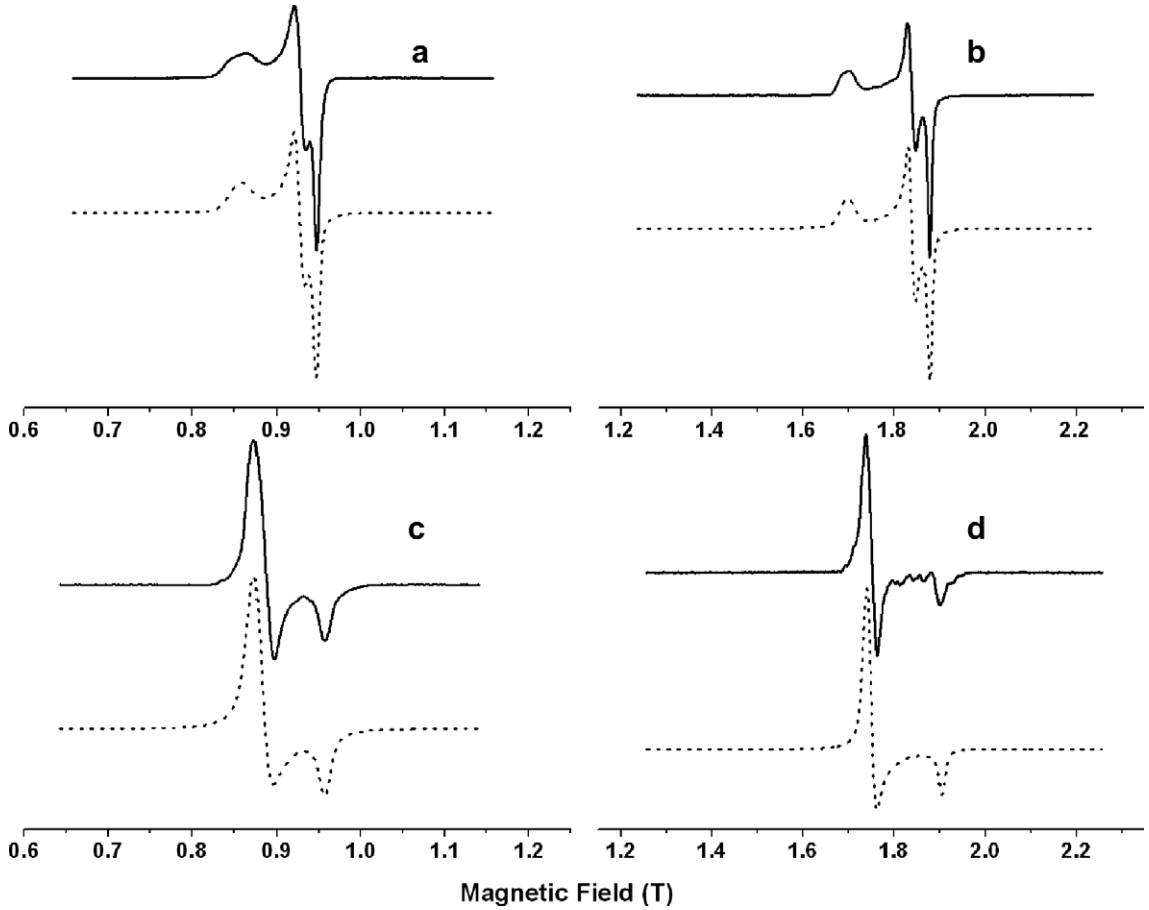


Fig. 5. Experimental (solid line) and simulated (dash line) EPR spectra of complex **4** (a and b) and complex **8** (c and d) at K-band (26.8 GHz, left side) and V-band (53.6 GHz, right side). Simulation parameters: (a) $g_x = 2.022$, $g_y = 2.067$, $g_z = 2.235$; (b) $g_x = 2.037$, $g_y = 2.082$, $g_z = 2.255$; (c) $g_\perp = 2.185$, $g_\parallel = 2.005$; (d) $g_\perp = 2.193$, $g_\parallel = 2.010$. Temperature: 77 K; magnetic field sweep rate: 2 mT/s; magnetic field modulation: frequency 40 kHz, amplitude 1 mT.

order to increase the *g*-value resolution, and possibly also resolve hyperfine structure. Indeed, Q-band (34 GHz) spectra of frozen DMSO solutions showed nicely resolved parallel and perpendicular g components, with a hyperfine structure due to the nuclear $I = 3/2$ spin characteristic for Cu^{2+} observed on top of the parallel component (not shown), this was expected to study the correlation between the five-coordinate geometries and the hyperfine splitting ($A_\parallel$ values). However, an analysis of the solution spectra revealed that the complexes under study are decomposed, or otherwise altered in these conditions. These studies were consequently abandoned. Instead, EPR on polycrystalline samples at K-band (27 GHz) and V-band (54 GHz) was successful in fully resolving *g*-values. Fig. 5 shows spectra of **4** and **8** at both frequencies, accompanied by powder simulations using *g*-values as in Table 5. Table 5 also presents *g*-values for the remaining complexes under study. The EPR spectra of complexes **1**–**7** are in rhombic type [4,7] and three *g*-factors are obtained as in Table 5, with the lowest *g*-values > 2.0 which is consistent with the $d_{x^2-y^2}$ ground state, while the EPR spectrum of complex **8** is axial with $g_\perp = 2.185$ and $g_\parallel = 2.005$, consistent with a d_{z^2} ground state for the approximately trigonal bipyramidal stereochemistry of the CuN_4N' chromophore present, $g_\perp \gg g_\parallel > 2.0$.

4. Conclusions

The present report describes the preparation, crystal structure determination, spectroscopic properties and structural pathway of the five-coordinate copper(II) complexes with pseudohalide ligand, NCO^-. The structure of the $[Cu(dpyam)_2(NCO)]^+$ cations all involve a five-coordinate CuN_4N' chromophore with TBDSBP in **1**–**5** and **9** ($\tau = 0.09$–0.31, respectively). Complexes **6** and **7** exhibit an intermediate five-coordinate, slightly distorted toward TBP ($\tau = 0.53$ and 0.54, respectively). The complex **8** shows SBPDTB with a τ value of 0.76. The detailed structure of a five-coordinate copper(II) complex is dependent upon the type of counter anion in the lattice, due to the 'Plasticity Effect', showing how the same complex in different crystal modifications, can have slightly different structures. In the present work the 'Plasticity Effect' has been considerably extended by reference to cation distortion isomers, in which the structures of a given cation is modified in the presence of different counter anions. The relatively small structural

differences produced have been correlated to suggest the existence of a continuous 'Structural Pathway', connecting the extreme structures, with the individual structures linked by a soft mode of vibration. All data points are found in the $-A + B$ section of the graph, except a data point **1**, which is closed to RSBP. It is noticeable that the α_1 and α_3 of **1** are greater than the usual values of α_1 and α_3 usually found for RSBP complexes, leading to this deviation. Moreover, this structure is the most extreme RSBP known of five-coordinate with dpyam ligand.

Acknowledgements

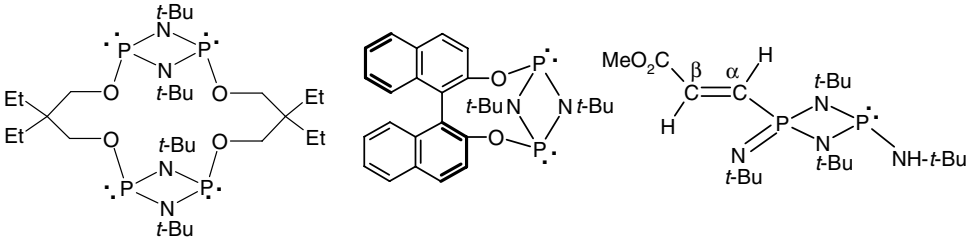
The authors gratefully acknowledge The Thailand Research Fund (Grant Nos. RTA 4880008 and BRG 4980007) and the Higher Education Development Project: Postgraduate Education and Research Program in Chemistry, Thailand, for financial support. The authors are very grateful to Prof. Jan Reedijk and Gerard A. van Albada (Leiden University, The Netherland) for X-band EPR measurement at room temperature.

Appendix A. Supplementary material

CCDC numbers 295201, 295202, 295203, 295204, 295205, 295206, 295207 and 295208 contain the supplementary crystallographic data for **1**, **2**, **3**, **4**, **5**, **6**, **7** and **8**. These data can be obtained free of charge via http://www.ccdc.cam.ac.uk/conts/retrieving.html, or from the Cambridge Crystallographic Data Centre, 12 Union Road, Cambridge CB2 1EZ, UK; fax: (+44) 1223-336-033; or e-mail: deposit@ccdc.cam.ac.uk. Supplementary data associated with this article can be found, in the online version, at doi:10.1016/j.poly.2006.09.027.

References

[1] (a) H.A. Jahn, E. Teller, Proc. R. Soc. London 161 (1937) 220;
(b) I.B. Bersuker, Chem. Rev. (2001) 1067.
[2] J. Gaăzo, I.B. Bersuker, J. Garaj, M. Kabešová, J. Kohout, H. Langfelderová, M. Melnik, M. Serator, F. Valach, Coord. Chem. Rev. 19 (1976) 253.
[3] P. Nagle, E. O'Sullivan, B.J. Hathaway, E.J. Muller, J. Chem. Soc., Dalton Trans. (1990) 3399.
[4] B.J. Hathaway, Struct. Bonding (Berlin) 57 (1984) 55.
[5] (a) H. Burgi, J.D. Dunitz, Acc. Chem. Res. 16 (1983) 153;
(b) J.D. Dunitz, X-ray Analysis and Structure of Organic Molecules, Cornell University Press, London, 1979 (Chapter 7).
[6] A.W. Addison, T.N. Rao, J. Reedijk, J. van Rijn, G.C. Verschoor, J. Chem. Soc., Dalton Trans. (1984) 1349.
[7] (a) B.J. Hathaway, D.E. Billing, Coord. Chem. Rev. 5 (1970) 143;
(b) D. Reinen, C. Friebel, Inorg. Chem. 23 (1984) 791.
[8] A.W. Addison, T.N. Rao, E. Sinn, Inorg. Chem. 23 (1984) 1957.
[9] (a) G. Murphy, P. Nagle, B. Murphy, B.J. Hathaway, J. Chem. Soc., Dalton Trans. (1997) 2645;
(b) G. Murphy, C. O'Sullivan, B. Murphy, B. Hathaway, Inorg. Chem. 37 (1998) 240;
(c) G. Murphy, C. Murphy, B. Murphy, B.J. Hathaway, J. Chem. Soc., Dalton Trans. (1997) 2653;
(d) C. O' Sullivan, G. Murphy, B. Murphy, B.J. Hathaway, J. Chem. Soc., Dalton Trans. (1999) 1835;
(e) B. Murphy, B. Hathaway, Coord. Chem. Rev. 243 (2003) 237.
[10] A.K. Hassan, L.A. Pardi, J. Krzystek, A. Sienkiewicz, P. Goy, M. Rohrer, L.C. Brunel, J. Magn. Reson. 142 (2000) 300.
[11] Bruker, SMART (Version 5.6), Bruker AXS Inc., Madison, WI, USA, 2000.
[12] Siemens, SAINT, Version 4 Software Reference Manual, Siemens Analytical X-Ray Systems, Inc., Madison, WI, USA, 1996.
[13] G.M. Sheldrick, SADABS, Program for Empirical Absorption correction of Area Detector Data, University of Göttingen, Göttingen, Germany, 1996.
[14] Siemens, SHELXTL. 1997, Version 6.12 Reference Manual, Siemens Analytical X-Ray Systems, Inc., Madison, WI, USA, 1997.
[15] I.M. Procter, B.J. Hathaway, P. Nicholls, J. Chem. Soc. A (1968) 1678.
[16] P. Akhter, B. Hathaway, Acta Crystallogr., Sect. C 47 (1991) 86.
[17] (a) S. Youngme, N. Chaichit, C. Pakawatchai, S. Booncoon, Polyhedron 21 (2002) 1279;
(b) A. Camus, A. Facchinetti, N. Marsich, A.M.M. Lanfredi, F. Ugozzoli, Inorg. Chim. Acta 290 (1999) 180;
(c) W.P. Jensen, R.A. Jacobson, Inorg. Chim. Acta 49 (1981) 199;
(d) J.E. Johnson, R.A. Jacobson, J. Chem. Soc., Dalton Trans. (1973) 580;
(e) R.A. Jacobson, W.P. Jensen, Inorg. Chim. Acta 114 (1986) L9;
(f) J. Sletten, K. Svardal, A. Sørensen, Acta Chem. Scand. 47 (1993) 1091.
[18] F. Huq, A.C. Shapski, J. Chem. Soc. A (1971) 1927.
[19] (a) B. Murphy, M. Aljabri, M. Light, M.B. Hursthouse, Trans. Met. Chem. 29 (2004) 394;
(b) B. Murphy, G. Roberts, S. Tyagi, B.J. Hathaway, J. Mol. Struct. 698 (2004) 25;
(c) B. Murphy, B.J. Hathaway, J. Coord. Chem. 56 (2003) 493;
(d) B. Murphy, M. Aljabri, M. Light, M.B. Hursthouse, J. Chem. Cryst. 33 (2003) 195.



3 (from ref. 13) **4** (from ref. 14) **5** (from ref. 15)

6 (from ref. 16) **7** (from ref. 17) **8** (from ref. 18)

(N-connected complex) (Dimeric via Hydrogen bonding)

Chart 1.

In our investigations on organophosphonates [28–31], we were interested in a polymerizable phosphorus based system with alkene/alkyne substituents at two ends that would ultimately lead to polymer-terminated phosphonic acids as the end products. For this purpose, we realized that the easily synthesized and inexpensive precursor *cis*-$[ClP(\mu\text{-}N\text{-}t\text{-}Bu)]_2$ (**1**) with two reactive P–Cl ends is an attractive precursor. In this paper, we report that the products of *cis*-**1** with various propargylic alcohols undergo facile rearrangement to lead to bis-allenes incorporated into a cyclic $[NP]_2$ skeleton. We also describe the first examples of the *cis*- and the *trans*-allenic cyclophosph(V)azane [or bis-(allenyl)phosphoramidates] isomers bearing the same substituents that are characterized by X-ray crystallography. The resulting compounds, we believe, are useful precursors for polymerization reactions. In order to probe this reaction further, the reaction of **1** with the Baylis–Hillman alcohol $PhCH(OH)C(CO_2Me)=CH_2$ [32] is also examined and the results are compared with those utilizing propargylic alcohols.

2. Experimental

Chemicals were procured from Aldrich or local manufacturers; they were purified when required according to standard procedures [33]. All reactions, unless stated otherwise, were performed in a dry nitrogen atmosphere. ^1H, ^{13}C and $^{31}P\{H\}$ NMR spectra were recorded using a 200 or a 400 MHz spectrometer in $CDCl_3$ (unless stated otherwise) with shifts referenced to $SiMe_4$ ($\delta = 0$) or 85% H_3PO_4 ($\delta = 0$). Infrared spectra were recorded on a JASCO FT/IR 5300 FT-IR spectrometer. Melting points were determined by using a local hot-stage melting point apparatus and are uncorrected. Microanalyses were performed using a Thermo Finnigan EA1112 analyzer.

The precursor $[ClP(\mu\text{-}N\text{-}t\text{-}Bu)]_2$ (**1**) was prepared using a literature procedure [34].

2.1. Synthesis of allenylphosphoramidates $[RR'C{=}C{=}CHP(O)(\mu\text{-}N\text{-}t\text{-}Bu)]_2$ (9–11)

2.1.1. General procedure

To a solution of **1** (2.04 g, 7.4 mmol) in dry THF (30 mL) was added triethylamine (1.49 g, 14.8 mmol) at 0 °C, the mixture stirred for 5 min and then the required substituted propargyl alcohol $HC{\equiv}CCR'R''(OH)$ (14.8 mmol) was added at 0 °C. The reaction mixture was stirred for 3 h at room temperature and the formed triethylamine hydrochloride was filtered off. The filtrate was heated under reflux for 15–18 h and the solvent removed *in vacuo*. Compound **9** was purified by crystallization from THF. The geometrical isomers of **10** or **11** were separated using column chromatography (15% ethyl acetate in hexane).

2.1.2. *cis*-$[H_2C{=}C{=}CHP(O)(\mu\text{-}N\text{-}t\text{-}Bu)]_2$ (9)

Yield: 1.76 g (75%). Mp: 159–161 °C. IR (KBr, cm^{-1}): 3059, 2971, 1962, 1937, 1464, 1370, 1256, 1086. ^1H NMR (400 MHz, $CDCl_3$): δ 1.48 (s, 18H, *t*-Bu–*H*), 5.09–5.14 (m, 4H, C=CH_2), 5.45–5.50 (m, 2H, PC*H*). ^{13}C NMR (50 MHz, $CDCl_3$): δ 30.9 (s, $C(CH_3)_3$), 55.5 (s, $C(CH_3)_3$), 76.8 (d, $^3J \sim 8.5$ Hz, C=*C*H_2), 85.0 (dd, $^1J(P\text{–}C) \sim 161.9$ Hz, $^3J(P\text{–}C) = 6.1$ Hz P*C*), 215.9 (s, PC=*C*). ^{31}P NMR (160 MHz, $CDCl_3$): δ 2.5. *Anal.* Calc. for $C_{14}H_{24}N_2O_2P_2$: C, 53.5; H, 7.7; N, 8.9. Found: C, 53.7; H, 7.7; N, 8.9. X-ray structural analysis was performed for this sample.

Analogous reaction of **1** with the alcohols $HC{\equiv}CCH(Me)(OH)$ and $HC{\equiv}CC(Ph)(Me)(OH)$ also gave essentially a single product ascribable to the *cis*-isomer

in each case [δ(P) 3.1 and 2.4 respectively] but we did not make attempts to isolate them.

*2.1.3. cis-[Me_2C=C=CHP(O)(μ-N-t-Bu)]$_2$ (**10a**)*

Yield: 1.65 g (60%). Mp: 160–164 °C. IR (KBr, cm^{-1}): 2971, 1960, 1750, 1373, 1260, 1225, 1088. ^{1}H NMR (400 MHz, $CDCl_3$): δ 1.43 and 1.44 (2s, 18H, *t*-Bu–*H*), 1.78 (m, 12H, C=C(CH_3)$_2$), 5.25 (br m, 2H, PC*H*). ^{13}C NMR (50 MHz, $CDCl_3$): δ 18.8 (s, C=C(*C*H$_3$)$_2$), 31.1 (s, NC(*C*H$_3$)$_3$), 55.2 (s, N*C*(CH$_3$)$_3$), 83.5 (dd, ^1J(P–C) $\sim$ 163.8 Hz, ^3J(P–C) = 7.3 Hz P*C*), 97.8 (dd $\rightarrow$ t, $^{3,5}J \sim 8.5$ Hz, C=*C*Me$_2$), 211.8 (s, PC=*C*). ^{31}P NMR (160 MHz, $CDCl_3$): δ 4.9. *Anal.* Calc. for $C_{18}H_{32}N_2O_2P_2$: C, 58.4; H, 8.7; N, 7.6. Found: C, 58.4; H, 8.7; N, 7.6. X-ray structural analysis was performed for this sample.

*2.1.4. trans-[Me_2C=C=CHP(O)(μ-N-t-Bu)]$_2$ (**10b**)*

Yield: 0.41 g (15%). Mp: 212–216 °C. IR (KBr, cm^{-1}): 2971, 1958, 1474, 1354, 1262, 1082, 912. ^{1}H NMR (400 MHz, $CDCl_3$): δ 1.39, 1.41 and 1.44 (3s, 18H, *t*-Bu–*H*), 1.77–1.80 (m, 12H, C=C(CH_3)$_2$), 5.46 (br, 2H, PC*H*). ^{13}C NMR (50 MHz, $CDCl_3$): δ 18.8 (s, C=C(*C*H$_3$)$_3$), 30.9 and 32.0 (2s in 2:1 ratio, NC(*C*H$_3$)$_3$), 54.8 (s, N*C*(CH$_3$)$_3$), 85.5 (d, ^1J(P–C) = 156.5 Hz, P*C*), 98.0 (s, C=*C*Me$_2$), 212.5 (s, PC=*C*). ^{31}P NMR (160 MHz, $CDCl_3$): δ 9.2. *Anal.* Calc. for $C_{18}H_{32}N_2O_2P_2$: C, 58.4; H, 8.7; N, 7.6. Found: C, 58.3; H, 8.7; N, 7.8. X-ray structural analysis was performed for this sample.

*2.1.5. cis-[(Me)(Et)C=C=CHP(O)(μ-N-t -Bu)]$_2$ (**11a**)*

Yield: 1.17 g (40%). Mp: 148–152 °C. IR (KBr, cm^{-1}): 2967, 1958, 1458, 1368, 1260, 1225. ^{1}H NMR (400 MHz, $CDCl_3$): δ 1.07 (t, 6H, ^3J(H–H) $\sim$ 7.3 Hz, CH$_2$CH_3) 1.45 (s, 18H, *t*-Bu–*H*), 1.76–1.79 (m, 6H, C=CH_3), 2.08 (br m, 4H, CH_2CH$_3$), 5.29 (br, 2H, PC*H*). ^{13}C NMR (50 MHz, $CDCl_3$): δ 12.0 (s, CH$_2$*C*H$_3$), 17.3 (s, *C*H$_2$CH$_3$), 26.4 (s, C=*C*H$_3$), 31.1 (s, NC(*C*H$_3$)$_3$), 55.2 (s, N*C*(CH$_3$)$_3$), 85.2 (dd, ^1J(P–C) $\sim$ 162.6 Hz, ^3J(P–C) = 7.3 Hz, P*C*), 104.1 (d, $J \sim 8.5$ Hz, C=*C*(Me)(Et)), 211.8 (s, PC=*C*). ^{31}P NMR (160 MHz, $CDCl_3$): δ 4.6. *Anal.* Calc. for $C_{20}H_{36}N_2O_2P_2$: C, 60.3; H, 9.1; N, 7.0. Found: C, 60.3; H, 9.1; N, 7.2.

*2.1.6. trans-[(Me)(Et)C=C=CHP(O)(μ-N-t-Bu)]$_2$ (**11b**)*

This was crystallized from dichloromethane. Yield: 0.44 g (15%). Mp: 198–200 °C. IR (KBr, cm^{-1}): 2969, 1950, 1456, 1368, 1262, 1235. ^{1}H NMR (400 MHz, $CDCl_3$): δ 1.09 (t, 6H, ^3J(H–H) $\sim$ 7.3 Hz, CH$_2$CH_3) 1.43 (s, 18H, *t*-Bu–*H*), 1.80 (s, 6H, C=CH_3), 2.12 (br m, 4H, CH_2CH$_3$), 5.58 (br, 2H, PC*H*). ^{13}C NMR (50 MHz, $CDCl_3$): δ 12.1 (s, CH$_2$*C*H$_3$), 17.2 (s, *C*H$_2$CH$_3$), 26.4 (s, C=*C*H$_3$), 30.9 (br s, NC(*C*H$_3$)$_3$), 53.4 and 54.7 (2s, N*C*(CH$_3$)$_3$), 87.1 (d, ^1J(P–C) = 157.7 Hz, P*C*), 104.1 (s, C=*C*(Me)(Et)), 212.1 (s, PC=*C*). ^{31}P NMR (160 MHz, $CDCl_3$): δ 9.0. *Anal.* Calc. for $C_{20}H_{36}N_2O_2P_2$: C, 60.3; H, 9.1; N, 7.0. Found: C, 60.3; H, 9.2; N, 7.0.

2.1.7. [((Ph)HC=C(CO_2Me)-CH_2)(O)P-μ-N-t-Bu]$_2$ · H_2O (13 · H_2O)

This compound was prepared by treating **1** (2.20 g, 8 mmol) in dry THF (30 mL) with the Baylis–Hillman alcohol PhCH(OH)C(CO_2Me)=CH_2 (3.08 g, 16 mmol) in the presence of Et_3N (1.70 g, 16.8 mmol) at 0 °C. The reaction mixture was stirred for 5 h at room temperature and the formed triethylamine hydrochloride was filtered off. The solvent was removed *in vacuo* and the reaction mixture heated at 150 °C for 20 min to afford **13** in quantitative yields [^{31}P NMR]; it was purified by passing through a short silica-gel column (eluent: hexane–ethyl acetate). Crystallization (dichloromethane + hexane) in open air led to **13** · H_2O. Yield: 4.70 g (quantitative). Mp: 117–119 °C. IR (KBr, cm^{-1}): 2973, 1701, 1451, 1372, 1267, 1065. ^{1}H NMR (400 MHz, $CDCl_3$): δ 1.29, 1.30 (2s, 18H, *t*-Bu–*H*), 3.64 (d, 4H, ^2J(P–H) = 18.0 Hz, PCH_2), 3.85, 3.86 (2s, 6H, 2OCH_3), 7.36–7.80 (m, 12H, 2C=C*H* + Ar–*H*). This sample showed a peak at $\delta \sim 1.67$ (close to water of $CDCl_3$) in addition to the other peaks. ^{13}C NMR (100 MHz, $CDCl_3$): 30.8, 30.8$_8$ and 30.9$_2$ (3s, NC(*C*H$_3$)$_3$), 32.8 (dd, ^1J(P–C) = 108.4 Hz, ^3J(P–C) = 6.6 Hz, P*C*), 52.4 (s, COO*C*H$_3$), 56.1 (s, N*C*(CH$_3$)$_3$), 124.8 (d, ^2J(P–C) = 11.6 Hz, PC*C*), 128.7, 129.1, 129.6, 134.8 (Ar*C*), 141.3 (d, ^3J(P–C) = 12.1 Hz, C=*C*(Ph)), 168.2 (s, *C*OOCH$_3$). ^{31}P NMR (160 MHz, $CDCl_3$): δ 20.8. *Anal.* Calc. for $C_{30}H_{42}N_2O_7P_2$: C, 59.6; H, 7.0; N, 4.6. Found: C, 59.6; H, 7.0; N, 4.6. X-ray structural analysis was performed on this sample.

2.2. X-ray crystallography

Single crystal X-ray data were collected on an Enraf-Nonius MACH3 or on a Bruker AXS-SMART diffractometer, using Mo Kα ($\lambda = 0.71073$ Å) radiation. The structures were solved by direct methods and refined by full-matrix least squares method using standard procedures [35]. All non-hydrogen atoms were refined anisotropically; hydrogen atoms were fixed by geometry using a riding model except for the solvent molecules. The terminal carbon atoms of the *t*-butyl groups showed higher thermals than the N–C carbon in these systems. Crystallographic data as .CIF files are deposited (CCDC Nos. 618526–618529).

2.2.1. Crystal data

Compound **9**: $C_{14}H_{24}N_2O_2P_2$, $M = 314.29$, orthorhombic, space group *Pnca*, $a = 11.556(2)$, $b = 17.406(4)$, $c = 18.298(4)$ Å, $V = 3680.5(13)$ Å^3, $Z = 8$, $\mu = 0.239$ mm^{-1}, data/restraints/parameters: 3240/0/203, R indices ($I > 2\sigma(I)$): $R_1 = 0.0493$, wR_2 (all data) = 0.1528.

Compound **10a**: $C_{18}H_{32}N_2O_2P_2$, $M =$ 370.40, monoclinic, space group $P2_1/c$, $a = 10.1983(13)$, $b = 10.8569(14)$, $c = 21.244(3)$ Å, $\beta = 100.984(2)$, $V = 2309.1(5)$ Å^3, $Z = 4$, $\mu = 0.199$ mm^{-1}, data/restraints/parameters: 4058/0/227, R indices ($I > 2\sigma(I)$): $R_1 = 0.0618$, wR_2 (all data) = 0.2020.

Compound **10b**: $C_{18}H_{32}N_2O_2P_2$, $M = 370.40$, triclinic, space group $P\bar{1}$, $a = 7.5400(15)$, $b = 8.9400(18)$, $c = 9.4900(19)$ Å, $\alpha = 62.84(3)°$, $\beta = 74.57(3)°$, $\gamma = 89.33(3)°$, $V = 544.1(3)$ Å^3, $Z = 1$, $\mu = 0.212$ mm^{-1}, data/restraints/parameters: 1922/0/114, R indices ($I > 2\sigma(I)$): $R_1 = 0.0652$, wR_2 (all data) = 0.1922.

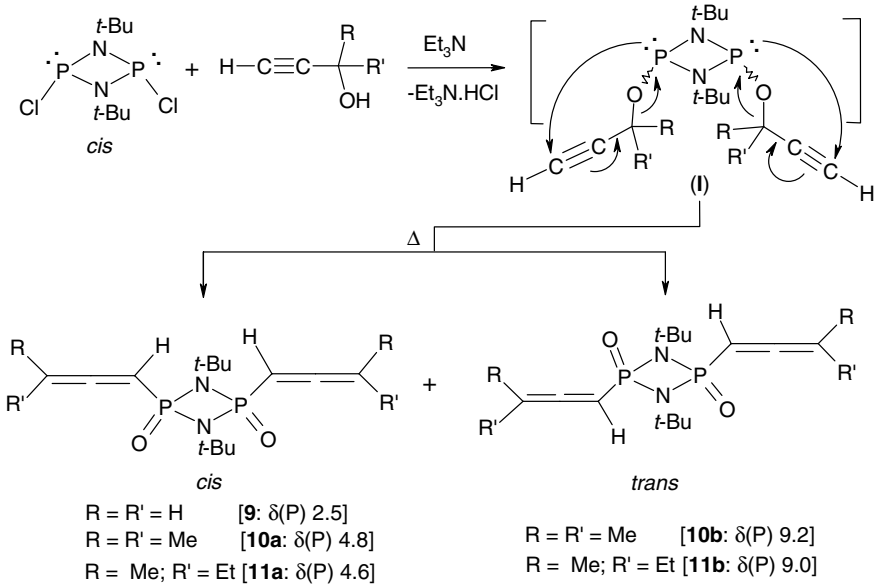
Compound **13** · H_2O: $C_{30}H_{42}N_2O_7P_2$, $M = 604.60$, triclinic, space group $P\bar{1}$, $a = 8.786(2)$, $b = 12.570(3)$, $c = 15.540(3)$ Å, $\alpha = 95.41(3)°$, $\beta = 97.33(3)°$, $\gamma = 107.32(3)°$, $V = 1609.1(6)$ Å^3, $Z = 2$, $\mu = 0.181$ mm^{-1}, data/restraints/parameters: 5667/3/403, R indices ($I > 2\sigma(I)$): $R_1 = 0.0591$, wR_2 (all data) = 0.1630.

3. Results and discussion

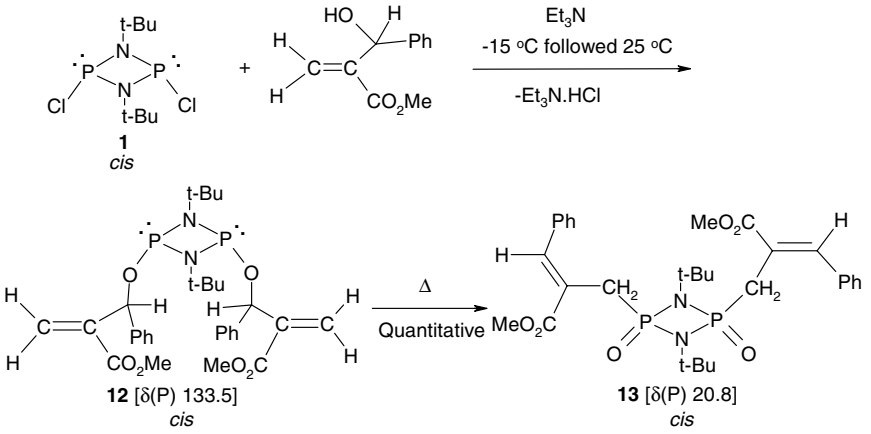
3.1. Synthesis, spectra and mode of formation

Compounds **9**, **10a**,**b** and **11a**,**b** are synthesized by treating *cis*-[ClP(μ-*N*-*t*-Bu)]$_2$ (**1**) with the corresponding propargylic alcohol in the presence of triethylamine as shown in Scheme 1. The initially formed (alkoxy)cyclodi*phosph(III)*azanes **I** undergo thermal rearrangement to give rise to the (allenyl)cyclodi*phosph(V)*azane products. The reaction using the unsubstituted propargylic alcohol HC≡CCH$_2$OH gives essentially the *cis*-isomer **9** and only traces of the *trans*-isomer. In contrast, substituted propargyl alcohols HC≡CC(Me)(R)OH (R = Me, Et) afforded both *cis*- and *trans*-isomeric products **10a**,**b** and**11a**,**b** in decent yields. These two isomers are readily distinguishable by their ^{31}P NMR chemical shifts with the *trans*-isomer appearing downfield by ~4.5 ppm. Although this feature is similar to that of P(III) derivatives ($\Delta\delta \sim 52$ ppm) [16], the $\Delta\delta$ values between the two isomers are smaller for **10a**,**b** and **11a**,**b**. The ^{13}C NMR spectra show a characteristic doublet ($^1J = 156$–164 Hz) for the P–C carbon at δ 84–87. The signal for the *trans*-isomer appears at lower field with a lower ^1J(P–C) value compared to the *cis*-isomer. The IR stretch for the allenic moiety appears at 1950–1960 cm^{-1} with that for the *trans*-isomer appearing at slightly lower wave number.

Since the starting material **1** has a *cis*-disposition of the two P–Cl groups, one may expect the reaction to lead to only *cis*-isomer of the P(III) alkoxide **I** as long as the phosphazane ring remains intact during the reaction. Although, as briefly pointed out in the Introduction, this may not be the case when lithium or sodium alkoxides/aryloxides are used, it is more likely when alcohol/triethylamine system is used [5]. If only *cis*-P(III) alkoxide is formed, it may be expected that rearrangement to the allenyl phosphoramidates **9**–**11** leads only to the corresponding *cis*-isomer. We made an attempt to identify the P(III) intermediate **I** in the case of **10a**,**b** by performing the reaction at −15 °C (ca. ~1 h) in THF and recording the ^{31}P NMR spectrum immediately (<1 h). However, the reaction mixture showed essentially the P(V) products **10a**,**b**, indicating that the rearrangement is very facile under these conditions. Even the partially rearranged products with P(III)–*N*–P(V) system were not observed. The *cis*-compound **10a** was stable up to 180 °C/2 h and no perceptible conversion to the *trans*-form was noticed [^{31}P NMR]. Also, the *trans*-P(V) compound **10b** did not appear to convert to the *cis*-form upon heating. Thus, once formed, **10a** and **10b** do not isomerize. We also tried to see if use of the lithium salt of the corresponding propargyl alcohol could increase the yield of the *trans*-isomer **10b**. Although the reaction mixture showed more of the *trans*-product, there were many other peaks that hampered a complete analysis. Preliminary theoretical calculations (using coordinates from X-ray structure and optimizing the geometry) done at B3LYP/6-31G** level suggest that the *cis*-isomer **10a** is



Scheme 1.

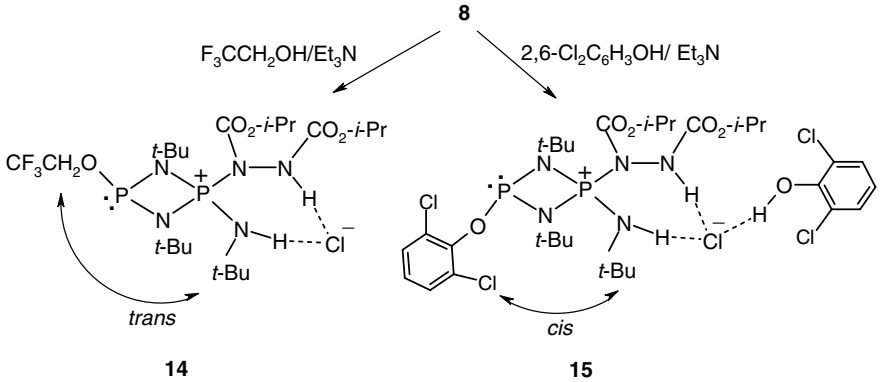


Scheme 2.

marginally more stable than the *trans*-isomer **10b** by ~6.5 kJmol^{-1} in the gas phase.

Since it is known that allyloxy products of P(III) derivatives also can rearrange to their respective P(V) phosphonates [28,36], we wanted to check the feasibility of identifying the intermediates in these cases for comparison. Thus we treated the Baylis–Hillman alcohol (a substituted allyl alcohol) $PhCH(OH)C(CO_2Me)=CH_2$ with $[ClP(\mu\text{-}N\text{-}t\text{-}Bu)]_2$ (**1**) (Scheme 2). In this case, we could observe mainly the *cis*-alkoxy P(III) product **12** *prior to rearrangement* by ^{31}P NMR [δ(P) 133.5]. The assignment of a *cis*-structure to **12** is based upon comparison of its δ(P) value with those available in the literature for other compounds [5,16]. The same mixture after a day at 25 °C showed a complete absence of **12** and the peak corresponding to **13** started developing [δ(P) 20.8]. Upon heating the original reaction mixture at 150 °C for 20 min, only the *cis*-isomer **13** is formed quantitatively. Interestingly, in the initial reaction mixture, there is a P(V) product exhibiting two close peaks at δ(P) 24.3 and 24.4 ascribable to the *trans*-isomer of **13** (further isomerism is possible at the site of the C=C bond which may be the reason for two peaks with close δ(P) values). Another peak at $\delta \sim 101.6$ is unassigned. None of these intermediates is seen after heating the original reaction mixture at 150 °C.

As regards *cis–trans*-isomerism in other types of cyclodiphosph(V)azanes, X-ray structures of *cis*- and *trans*-$[RNHP(S)NR]_2$ are reported but both the isomers with the same R group are not seen [21]. In these cases, the reaction chemistry is different and the compounds were obtained by sulfur-oxidation of the respective aminocyclodiphosph(III)azanes. In the reaction of compound **8** with 2,2,2-trifluoroethanol and 2,6-dichlorophenol in the presence of Et_3N, we have previously reported that the P(III)–*N*–P(V) products obtained have different stereochemistry [20,37]. While the former gave *trans*-product **14**, the latter afforded the *cis*-product **15**. This feature reveals that the incoming nucleophile also has a role to play in determining the geometry of the final products. The reactive site in these cases is the same P(III)–Cl bond in **8** which is *cis* to the P=N(*t*-Bu) group at the other phosphorus. Based on these observations and the fact that we did not observe the isomerization of pure *cis* (**10a**) or *trans* (**10b**) allenyl compounds, we think that the formation of *cis*- and *trans*-isomeric pairs **10a**,**b** and **11a**,**b** takes place via thermal rearrangement of *cis*- and *trans*-P(III) alkoxy products of type **I**. In the formation of **13** that contains sterically more demanding substituents, however, it is possible that the rearranged P(V) *trans*-product/s [δ(P) 24.3, 24.4] isomerize to the *cis*-form [δ(P) 20.8]. This proposition needs further confirmation since there is also a possibility of monomer (phosphazene)-dimer (diphosphazane) equilibrium in these systems [38]:



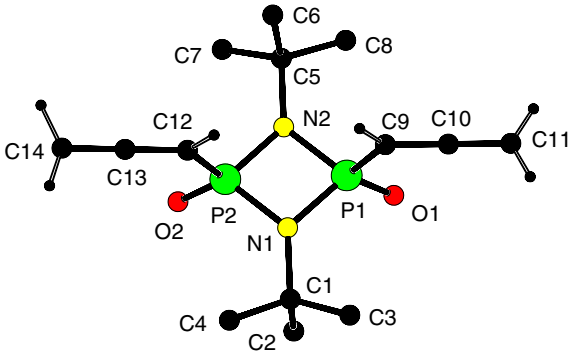


Fig. 1. Molecular structure of **9**.

3.2. X-ray structures of *9*, *10a,b* and *13* · H_2O

The molecular structures of **9**, **10a** and **10b** are shown in Figs. 1 and 2. Selected geometrical parameters are given in Table 1. Since phosphorus atoms are chemically equivalent, the endocyclic P–N distances to a particular phosphorus atom are nearly equal. These P–N distances [1.660–1.680 Å] are clearly shorter than those found for several other cyclodiphosph(III)azanes (1.71–1.74 Å) [39] or the apical P–N bonds in pentacoordinate phosphoranes [40]. Although the allenic C=C bonds in **9** appear to be slightly shorter than those found in **10a**,**b**, the variations are within the three times the esd's and hence a definite conclusion cannot be given. The P–C bond distance in all the three compounds is in the expected range [41]. The ring nitrogen atoms are essentially planar with the sum of the bond angles at nitrogen in the range 356–360°. This feature is unlike that in the P(III) compound $Et_2C[CH_2OP(\mu\text{-}N\text{-}t\text{-}Bu)_2PNH\text{-}t\text{-}Bu]_2$ wherein the ring nitrogen atoms are non-planar [$\sum N = 347–348°$] [39]. The $[NP]_2$ rings in all the three compounds are essentially planar with the maximum deviation of 0.02 Å found for **10a**.

The *cis*-stereochemistry in **13** · H_2O is also clearly revealed by X-ray crystallography (Fig. 3). The P–N distances are similar to those observed in **9** and **10a**,**b**, but the P–C bonds (mean 1.815 Å) are slightly longer. The $[NP]_2$ ring is slightly distorted with the mean deviation of the fitted atoms from the mean plane of the ring being ~0.03 Å. The ring nitrogen atoms are more pyramidal [$\sum N(1) = 358.3°$; $\sum N(2) = 352.2°$] than those in **9** and **10a**,**b**. The solvate water molecule is hydrogen bonded to the phosphoryl oxygen atoms, but since this was not the

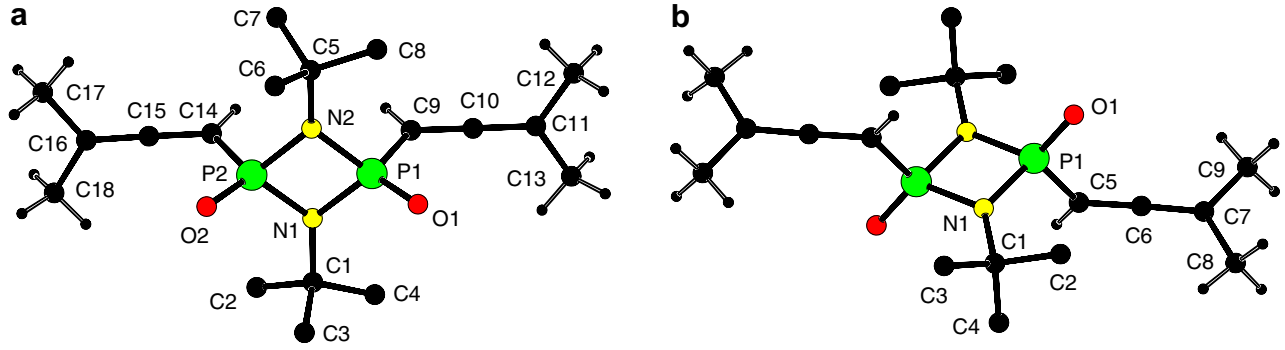


Fig. 2. Molecular structures of (a) **10a** and (b) **10b**.

Table 1
Selected bond lengths (Å) and bond angles (°) for **9** and **10a**,**b** with esd's

Compound **2**		Compound **10a**		Compound **10b**	
P(1)–N(1)	1.675(2)	P(1)–N(1)	1.678(3)	P(1)–N(1)	1.674(3)
P(1)–N(2)	1.677(2)	P(1)–N(2)	1.673(3)	P(1)–N(1′)	1.668(3)
P(2)–N(1)	1.672(2)	P(2)–N(1)	1.683(3)	P(1)–C(5)	1.768(4)
P(2)–N(2)	1.659(2)	P(2)–N(2)	1.678(3)	C(5)–C(6)	1.294(5)
P(1)–C(9)	1.775(2)	P(1)–C(9)	1.764(4)	C(6)–C(7)	1.304(5)
P(2)–C(12)	1.778(2)	P(2)–C(14)	1.768(4)		
C(9)–C(10)	1.293(3)	C(9)–C(10)	1.290(5)		
C(10)–C(11)	1.283(3)	C(10)–C(11)	1.308(5)		
C(12)–C(13)	1.286(3)	C(14)–C(15)	1.303(5)		
C(13)–C(14)	1.297(4)	C(15)–C(16)	1.302(5)		
N(1)–P(1)–N(2)	83.8(1)	N(1)–P(1)–N(2)	84.4(3)	N(1)–P(1)–N(1′)	83.8(2)
N(1)–P(2)–N(2)	84.48(9)	N(1)–P(2)–N(2)	84.1(2)	P(1)–N(1)–P(1′)	96.2(2)
P(1)–N(1)–P(2)	95.6(1)	P(1)–N(1)–P(2)	95.5(2)		
P(1)–N(2)–P(2)	96.1(1)	P(1)–N(2)–P(2)	95.9(2)		

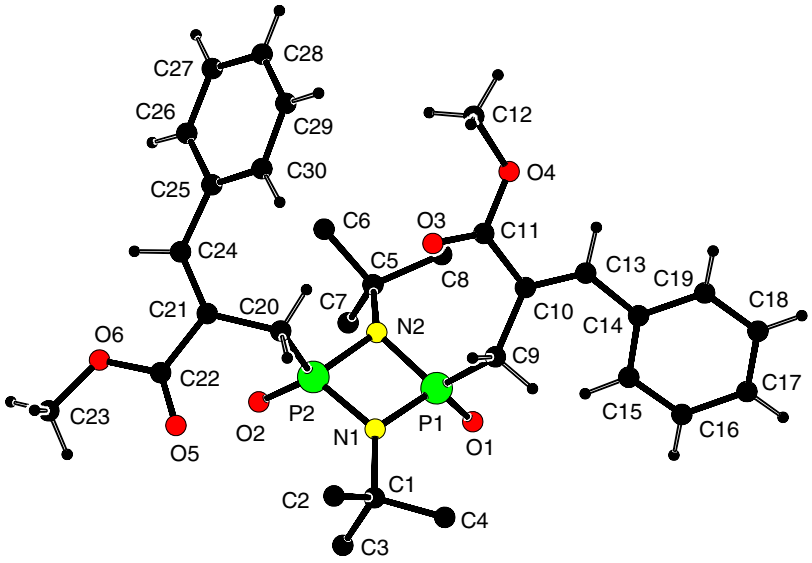


Fig. 3. Molecular structure of **13** · H_2O; solvate water and *t*-butyl hydrogen atoms are not shown. Selected bond parameters: P(1)–N(1) 1.670(2), P(1)–N(2) 1.666(2), P(1)–C(9) 1.817(3), P(2)–N(1) 1.676(2), P(2)–N(2) 1.690(2), P(2)–C(20) 1.814(3) Å; N(2)–P(1)–N(1) 85.10(12), N(1)–P(2)–N(2) 84.18(11), P(1)–N(1)–P(2) 95.37(13), P(1)–N(2)–P(2) 94.99(12)°.

interest in the present study, we have not probed this aspect further.[1]

4. Summary and outlook

What we have shown here is that both the *cis*- and *trans*-forms of allenylphosphoramidates based on a cyclodiphosph(V)azane skeleton can be readily obtained by treating the well-known precursor $[ClP(\mu\text{-}N\text{-}t\text{-}Bu)]_2$ (**1**) with substituted propagylic alcohols in the presence of triethylamine. Although the precursor **1** has a *cis*-geometry, both the *cis* and *trans* rearranged products are obtained in many cases. X-ray structural characterization for both the isomers from a single system has been achieved for the first time. These compounds, by means of the allenyl residues at two ends, have the potential to be used for further reactions including polymerization. The derivative **13** could also be a good substrate for the Horner–Wadsworth–Emmons reaction [36].

Acknowledgements

We thank the Council of Scientific and Industrial research (CSIR, New Delhi) for financial support. N.N.B.K. also thanks CSIR for a fellowship. The National Single Crystal Diffractometer Facility at the University of Hyderabad funded by DST (New Delhi) as well as CAS and UPE programmes of the UGC are also gratefully acknowledged.

Appendix A. Supplementary material

CCDC 618526, 618527, 618528 and 618529 contain the supplementary crystallographic data for this paper. These data can be obtained free of charge via http://www.ccdc.cam.ac.uk/conts/retrieving.html, or from the Cambridge Crystallographic Data Centre, 12 Union Road, Cambridge CB2 1EZ, UK; fax: (+44) 1223-336-033; or e-mail: deposit@ccdc.cam.ac.uk. Supplementary data associated with this article can be found, in the online version, at doi:10.1016/j.poly.2006.09.009

References

[1] R. Keat, Top. Curr. Chem. 102 (1982) 84.
[2] L. Stahl, Coord. Chem. Rev. 210 (2000) 203.
[3] G.G. Briand, T. Chivers, M. Krahn, Coord. Chem. Rev. 233–234 (2002) 237.
[4] S.S. Kumaravel, S.S. Krishnamurthy, T.S. Cameron, A. Linden, Inorg. Chem. 27 (1988) 4546, and references cited therein.
[5] M. Vijjulatha, K.C. Kumara Swamy, J.J. Vittal, L.L. Koh, Polyhedron 18 (1999) 2249.
[6] M. Vijjulatha, S. Kumaraswamy, K.C. Kumara Swamy, U. Engelhardt, Polyhedron 18 (1999) 2557.
[7] G.R. Lief, C.J. Carrow, L. Stahl, R.J. Staples, Chem. Commun. (2001) 1562.
[8] G.G. Briand, T. Chivers, M. Parvez, G. Schatte, Inorg. Chem. 42 (2003) 525.
[9] F. Garcia, J.M. Goodman, R.A. Kowenicki, M. McPartlin, L. Riera, M.A. Silva, A. Wirsing, D.S. Wright, Dalton Trans. (2005) 1764.
[10] F. Dodds, F. García, R.A. Kowenicki, M. McPartlin, A. Steiner, D.S. Wright, Chem. Commun. (2005) 3733.

[1] In the structure, two water molecules with half occupancy at each site per molecule of the phosphazane are present. Overall, there is only one water molecule per cyclodiphosphazane. The relevant hydrogen bond parameters are (D–H···A; Å, Å, Å, °): O(7)–H(7D)···O(1′) 0.77(8), 2.26(9), 2.981(7), O(7)–H(7E)···O(1″) 0.90(9), 2.12(10), 2.986(7), 162(8); 156(8); O(8)–H(8D)···O(2‴) −0.98(4), 2.11(4), 3.078(7), 170(10); O(8)–H(8E)···O(7) 1.17(4), 1.86(7), 2.939(9), 151(8). Symmetry equivalents: (′) $1-x$, $1-y$, $-z$; (″) x, $1+y$, z; (‴) $1+x$, $1+y$, z]. Since at each location, only half water molecule is present, the hydrogen bond distances may not mean much.

[11] F. Dodds, F. García, R.A. Kowenicki, M. McPartlin, L. Riera, A. Steiner, D.S. Wright, Chem. Commun. (2005) 5041, and references cited therein.
[12] P. Kommana, K.C. Kumara Swamy, Inorg. Chem. 39 (2000) 4384.
[13] P. Kommana, K.V.P. Pavan Kumar, K.C. Kumara Swamy, Indian J. Chem. 42A (2003) 2371.
[14] Manab Chakravarty, P. Kommana, K.C. Kumara Swamy, Chem. Commun. (2005) 5396.
[15] N.N. Bhuvan Kumar, Manab Chakravarty, K.C. Kumara Swamy, New J. Chem. (2006) 0000.
[16] V.S. Reddy, S.S. Krishnamurthy, M. Nethaji, J. Chem. Soc., Dalton Trans. (1994) 2661, and references cited therein.
[17] P. Chandrasekaran, J.T. Mague, M.S. Balakrishna, Inorg. Chem. 44 (2005) 7925.
[18] P. Chandrasekaran, J.T. Mague, M.S. Balakrishna, Inorg. Chem. 45 (2006) 6678.
[19] L. Grocholl, L. Stahl, R.J. Staples, Chem. Commun. (1997) 1465.
[20] N. Satish Kumar, K. Praveen Kumar, K.V.P. Pavan Kumar, P. Kommana, J.J. Vittal, K.C. Kumara Swamy, J. Org. Chem. 69 (2004) 1881.
[21] T.G. Hill, R.C. Haltiwanger, M.L. Thompson, S.A. Katz, A.D. Norman, Inorg. Chem. 33 (1994) 1770.
[22] V.S. Reddy, S.S. Krishnamurthy, M. Nethaji, J. Organomet. Chem. 438 (1992) 99.
[23] S.S. Kumaravel, S.S. Krishnamurthy, B.R. Vincent, T.S. Cameron, Z. Naturforsch. 41B (1986) 1067.
[24] A.D. Woods, M. McPartlin, Dalton Trans. (2004) 90.
[25] W.A. Kamil, M.R. Bond, J.M. Shreeve, Inorg. Chem. 26 (1987) 2015.
[26] L. Manojlvoic-Muir, K.W. Muir, J. Chem. Soc., Dalton Trans. (1974) 2395 [X-ray structure of $\{Cl(O)P(\mu\text{-}N\text{-}t\text{-}Bu)\}_2$].
[27] N. Dastagiri, A.J. Elias, A. Vij, J. Chem. Soc., Dalton Trans. (1997) 2167.
[28] K. Senthil Kumar, K.C. Kumara Swamy, J. Organomet. Chem. 637–639 (2001) 616.
[29] Manab Chakravarty, B. Srinivas, C. Muthiah, K.C. Kumara Swamy, Synthesis (2003) 2368.
[30] K.C. Kumara Swamy, S. Kumaraswamy, K. Senthil Kumar, C. Muthiah, Tetrahedron Lett. 46 (2005) 3347, and references cited therein.
[31] Manab Chakravarty, K.C. Kumara Swamy, J. Org. Chem., in press.
[32] D. Basavaiah, A.J. Rao, T. Satyanarayana, Chem. Rev. 103 (2003) 811.
[33] D.D. Perrin, W.L.F. Armarego, D.R. Perrin, Purification of Laboratory Chemicals, Pergamon, Oxford, UK, 1986.
[34] A.R. Davis, A.T. Dronsfield, R.N. Hazeldine, D.R. Taylor, J. Chem. Soc., Perkin Trans. 1 (1973) 379.
[35] (a) G.M. Sheldrick, SHELX-97—A Program for Crystal Structure Solution and Refinement, University of Göttingen, 1997;
(b) G.M. Sheldrick, SADABS, Siemens Area Detector Absorption Correction, University of Göttingen, Germany, 1996;
(c) G.M. Sheldrick, SHELXTL NT Crystal Structure Analysis Package, version 5.10, Bruker AXS, Analytical X-ray System, WI, USA, 1999.
[36] See, for example: C. Muthiah, K. Senthil Kumar, J.J. Vittal, K.C. Kumara Swamy, Synlett (2002) 1787.
[37] K.C. Kumara Swamy, K. Praveen Kumar, N.N. Bhuvan Kumar, J. Org. Chem. 71 (2006) 1002.
[38] N. Burford, C.A. Dyker, A.D. Phillips, H.A. Spinney, A. Decken, R. McDonald, P.J. Ragogna, A.L. Rheingold, Inorg. Chem. 43 (2004) 7502.
[39] P. Kommana, J.J. Vittal, K.C. Kumara Swamy, Polyhedron 22 (2003) 843, and references cited therein.
[40] P. Kommana, S. Kumaraswamy, J.J. Vittal, K.C. Kumara Swamy, Inorg. Chem. 41 (2002) 2356.
[41] (a) W.-M. Xu, X.-R. Hu, J.-M. Chu, Acta Crystallogr., Sect. E 60 (2004) o2214;
(b) C.M. Angelov, D.A. Mazzuca, J.P. van den Heever, R. McDonald, A.J.B. McEwen, J.R. Mercer, Acta Crystallogr., Sect. E 58 (2002) o399.

second- and third-order nonlinear optical properties in solution, high thermal stability, mesogenic behavior, Langmuir–Blodgett film formation, semiconducting properties, etc. [28–33].

There are three principal synthetic strategies for preparing unsymmetrical phthalocyanines made up of two different phthalonitrile units in 3:1 ratio: the statistical condensation route, the polymer support route and the subphthalocyanine route [34–37]. The most common method is the statistical condensation of two differently substituted dinitriles or diiminoisoindolines followed by chromatographic separation of the resulting mixture [38–40].

In contrast to their tetra-crowned analogs, unsymmetrical crown-ether phthalocyanine derivatives have been the subject of only few studies [41–45]. Mono-functional phthalocyanines with only one reactive functional group such as one nitro, sulfo, amino, hydroxyl or carboxyl group is important intermediate for the synthesis of many new mononuclear, binuclear and polynuclear phthalocyanines [46–48].

The electrochemistry of these complexes has attracted increasing attention to settle their usage in various areas such as photosensitization, gas sensor, catalysis, photovoltaic cell, and electrochromic display. These fundamental usages of the complexes are arisen from their superior electron transfer capacities [1,49–55]. The electron transfer abilities of phthalocyanines depend on the kind and the number of the substituents and are due to the interaction between the phthalocyanine ring and the metal center which is influenced by the conjugated π-electron current of the phthalocyanine ring. Determination of electron transfer properties of a compound is a primary activity for the technological application of the materials. An electrochemical reaction involves not only electron charge transfer, but also involves various processes such as adsorption of electroactive species on the electrode, aggregation of the species, and the contribution of coupled chemical reactions. Especially particular electrochemical processes are accurately required in the development of functional materials [56–58].

In the present paper, the preparation, characterization and spectral properties of unsymmetrical metallophthalocyanines with three crown-ether units and one nitro side group are described. Electrochemical analysis of CuPc was also carried out by cyclic voltammetry techniques and differential pulse voltammetry.

2. Experimental

IR spectra were recorded on a Perkin Elmer Spectrum One FT-IR (ATR sampling accessory) spectrophotometer, electronic spectra on a Unicam UV2 spectrophotometer. ^{1}H NMR spectra were recorded on a Bruker 250 MHz spectrometer using TMS as internal reference. Mass spectra were performed on Ultima Fourier transform and Varian 711 mass spectrometer. All reagents and solvents were dried and purified as described by Perrin and Armarego [59]. The homogeneity of the products was tested in each step by TLC. 4-Nitrophthalonitrile (**1**) [60] and 1-{[(benzo-15-crown-5)-4′-yl]oxy}phthalonitrile (**2**) [27] were synthesized according to published methods, by a multistep reaction sequence.

All electrochemical techniques were carried out with a Princeton Applied Research Model Versastat II potentiostat/galvanostat controlled by an external PC utilizing a three-electrode configuration at 25 °C. The working electrode was a Pt plate with an area of 0.10 cm^2. The surface of the working electrode was polished with a H_2O suspension of Al_2O_3 before each run. The last polishing was done with a particle size of 50 nm. A Pt wire served as the counter electrode. A saturated calomel electrode (SCE) was employed as the reference electrode and separated from the bulk of the solution by a double bridge containing saturated KCl adjacent to SCE and solvent and carrier adjacent to the solution. Ferrocene/ferrocenium internal reference electrode was used and all potential were given with respect to Fc/Fc^+ couple. Electrochemical grade tetrabutylammoniumperchlorate (*TBAP*) in extra pure *DCM* was employed as the supporting electrolyte at a concentration of 0.1 mol dm^{-3}. High purity N_2 was used for deaeration and to maintain a nitrogen blanket for at least 15 min prior to each run. For CPC studies, a Pt gauze working electrode (10.5 cm^2 surface areas) and a Pt wire counter electrode separated with a double bridge were used.

2.1. 2-Nitro-9,16,23-tri{[(benzo-15-crown-5)-4′-yl]oxy}-phthalocyaninatozinc(II) (3)

A mixture of 0.084 g of **1** (0.48 mmol), 0.59 g of **2** (1.44 mmol), 0.09 g of anhydrous $Zn(CH_3COO)_2$ (0.48 mmol), and 1.5 ml of anhydrous DMF was mixed in a glass tube which was sealed under nitrogen and heated and stirred at 145 °C for 18 h. The dark green mixture was cooled to room temperature and diluted with methanol until the crude product precipitated. The precipitate was filtered off and washed several times with hot ethanol and methanol to remove the by products. The resulting dark colored residue was purified by column chromatography on alumina with $CHCl_3$ as an eluent to give the first fraction of symmetrical crown-ether substituted phthalocyanine and the second fraction consisting largely of **3**. The crude unsymmetrical product was further purified by column chromatography on alumina with $CHCl_3$/MeOH (6:1) as an eluent to give pure product. Yield: 0.10 g, 15%. *Anal.* Calc. for $C_{74}H_{69}N_9O_{20}Zn$: C, 60.47; H, 4.73; N, 8.58. Found: C, 60.21; H, 4.69; N, 8.45%; m.p. > 200 °C. IR, ν (cm^{-1}): 2952–2868 (CH aliph.), 1598, 1505, 1334, 1255–1217(Ar–O–C), 1119–1081(C–O–C), 988, 934, 848 cm^{-1}; ^{1}H NMR ($CDCl_3$): δ: 7.71–7.67 (m, 3H, Ar–H), 7.53–7.49 (m, 9H, Ar–H), 6.82–6.38 (m, 9H, Ar–H), 4.26–3.75 (m, 48H, O–CH_2); UV–Vis λ_{max} (nm) (log ε) in $CHCl_3$: 377 (4.59), 675 (4.87), 696 (4.82).

2.2. 2-Nitro-9,16,23-tri{[(benzo-15-crown-5)-4′-yl]oxy}-phthalocyaninatocupper(II) (4)

A mixture of 0.112 g of **1** (0.64 mmol), 0.79 g of **2** (1.92 mmol), 0.104 g of anhydrous $CuCl_2$ (0.64 mmol), and 2 ml of anhydrous DMF was mixed in a glass tube which was sealed under nitrogen and heated and stirred at 150 °C for 24 h. The dark green mixture was cooled to room temperature and then methanol was added in order to precipitate the product. The residue was filtered off and then washed several times with hot ethanol. The green precipitate was chromatographed on alumina, fist using $CHCl_3$ as eluent to yield the symmetrical phthalocyanine and the desired product was finally collected by elution with $CHCl_3/CH_3OH$ (6:1). Yield: 0.20 g, 22%. *Anal.* Calc. for $C_{74}H_{69}N_9O_{20}Cu$: C, 60.55; H, 4.74; N, 8.59. Found: C, 60.32; H, 4.67; N, 8.28%; m.p. > 200 °C. IR, ν (cm^{-1}): 2926–2862 (CH aliph.), 1725, 1599, 1504, 1454, 1258–1217 (Ar–O–C), 1117–1070 (C–O–C), 986, 939, 826 cm^{-1}; MS(FAB) m/z: 1467 $[M]^+$; UV–Vis λ_{max} (nm) ($\log\varepsilon$) in $CHCl_3$: 338 (4.81), 627 (4.82), 679 (4.83).

2.3. 2-Nitro-9,16,23-tri{[(benzo-15-crown-5)-4′-yl]oxy}-phthalocyaninatocobalt(II) (5)

A mixture of 0.084 g of **1** (0.48 mmol), 0.59 g of **2** (1.44 mmol), 0.066 g of anhydrous $CoCl_2$ (0.48 mmol), and 2 ml of anhydrous DMF was heated and stirred at 140 °C in a sealed glass tube for 32 h under nitrogen. After cooling to room temperature, blue–green suspension was treated with H_2O: methanol (1:1) and centrifuged. The precipitate was washed several times with methanol and dried. The product was isolated on alumina column first with $CHCl_3$ and then with $CHCl_3/CH_3OH$ (6:1) as eluent. Yield: 0.07 g, 10%. *Anal.* Calc. for $C_{74}H_{69}N_9O_{20}Co$: C, 60.74; H, 4.75; N, 8.61. Found: C, 60.43; H, 4.71; N, 8.46%; m.p. > 200 °C. IR, ν (cm^{-1}): 2936–2865 (CH aliph.), 1722, 1597, 1502, 1451, 1267–1218 (Ar–O–C), 1120–1095 (C–O–C), 985, 935, 824 cm^{-1}; MS(FAB) m/z: 1463 $[M]^+$; UV–Vis λ_{max} (nm) ($\log\varepsilon$) in $CHCl_3$: 338 (4.62), 630 (4.26), 678 (4.87).

2.4. 2-Nitro-9,16,23-tri{[(benzo-15-crown-5)-4′-yl]oxy}-phthalocyaninatonickel(II) (6)

A mixture of 0.084 g of **1** (0.48 mmol), 0.59 g of **2** (1.44 mmol), 0.061 g of anhydrous $NiCl_2$ (0.48 mmol), and 1.5 ml of anhydrous DMF was mixed in a glass tube which was sealed under nitrogen and heated and stirred at 155 °C for 30 h. The dark green mixture was cooled to room temperature and diluted with methanol until the crude product precipitated. The precipitate was filtered off and washed several times with hot ethanol and methanol to remove unreacted materials. The green product was isolated on alumina column first with $CHCl_3$ and then with $CHCl_3$/MeOH (6:1) as eluent. Yield: 0.04 g, 6%. *Anal.* Calc. for $C_{74}H_{69}N_9O_{20}Ni$: C, 60.75; H, 4.75; N, 8.62. Found: C, 60.39; H, 4.61; N, 8.32%; m.p. > 200 °C. IR, ν (cm^{-1}): 2918–2849 (CH aliph.), 1733, 1599, 1505, 1454, 1258–1218 (Ar–O–C), 1121–1085 (C–O–C), 988, 937, 827 cm^{-1}; ^1H NMR ($CDCl_3$): δ: 7.68–7.64 (m, 3H, Ar–H), 7.51–7.45 (m, 9H, Ar–H), 6.79–6.35 (m, 9H, Ar–H), 4.25–3.73 (m, 48H, O–CH_2); UV–Vis λ_{max} (nm) ($\log\varepsilon$) in $CHCl_3$: 338 (4.56), 624 (4.22), 675 (4.92).

3. Results and discussion

3.1. Synthesis and characterization

Scheme 1 shows the synthesis of the target unsymmetrical phthalocyanines **3**–**6**. The study was based on mixed-condensations involving a 4-nitrophthalonitrile (**1**) and 1-{[(benzo-15-crown-5)-4′-yl]-oxy} phthalonitrile (**2**). Compound **2** was obtained by the base-catalyzed nucleophilic aromatic nitro displacement of 4-nitrophthalonitrile with 4′-hydroxybenzo-15-crown-5 [27]. The reaction was carried out in a single step synthesis by using the K_2CO_3 as the nitro-displacing base at 30 °C in dry DMF under N_2 atmosphere.

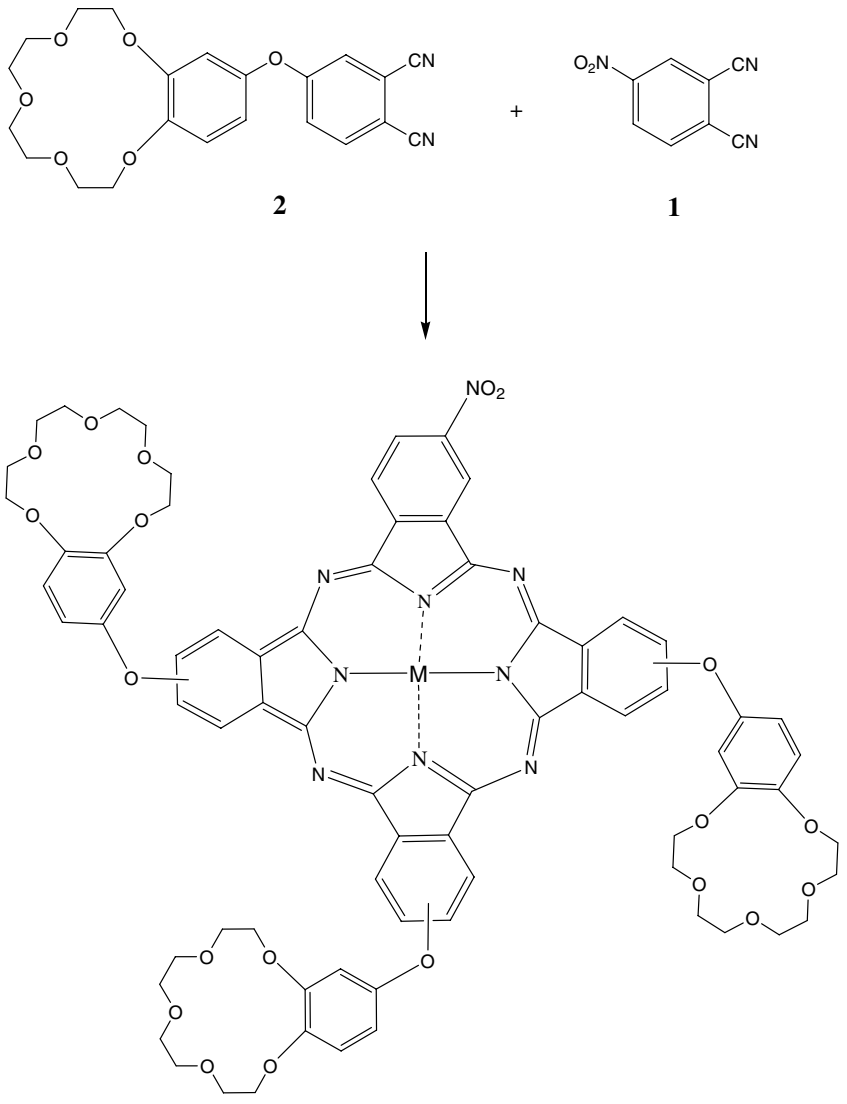
Statistical considerations predict that two phthalonitriles A and B, if of the same reactivity, when reacted together in the ratio 3:1 will give a mixture of the symmetric Pc (AAAA), and the desired 3:1 Pc (AAAB) and other cross-condensation products [34,61].

In this work, the phthalocyanines were synthesized by co-cyclotetramerization of three equivalents of **2** and one equivalent of **1** in the presence of the anhydrous metal salts $Zn(CH_3COO)_2$, $CuCl_2$, $CoCl_2$, or $NiCl_2$ in anhydrous DMF. Different molar ratios were used in order to increase the yield of the aimed unsymmetrically substituted phthalocyanines **3**–**6**. However, a 3:1 ratio of the two precursors was found to be the most suitable for dinitriles **1** and **2**.

In work-up procedure after tetramerization reaction between **1** and **2**, the crude products were chromatographed over alumina using $CHCl_3$ as eluent. In all cases the first fraction proved to be the totally symmetrical crown-ether substituted phthalocyanines identified TLC by comparison with authentic samples [27]. The second fraction still contained traces of the symmetrical phthalocyanine together with the products **3**–**6**. This mixture was re-chromatographed using $CHCl_3/CH_3OH$ (6:1) as eluent. The first fraction in this second separation process was still the symmetrical phthalocyanine derivative and it was discarded. The subsequent fraction was identified as the required 3:1 phthalocyanine derivative in **3**–**6**.

The novel compounds were characterized by IR, NMR, Mass, and UV–Vis spectral data together with elemental analysis. Spectral investigations and the results are in accord with the proposed structures.

In the IR spectrum of **3**–**6** the vibrations of the crown ether moieties kept their places, but as expected, the C≡N stretching vibrations of the starting materials **1** and **2** disappeared after phthalocyanine formation. This



	3	4	5	6
M	Zn^{2+}	Cu^{2+}	Co^{2+}	Ni^{2+}

Scheme 1. Synthesis of the unsymmetrical phthalocyanines **3**–**6**.

spectrum exhibits characteristic frequencies at around 2952–2868 (C–H), 1255–1217 (Ar–O–C) and 1119–1081 (C–O–C) cm^{-1}. In the ^1H NMR spectrum of **3**, the aromatic protons of the phthalocyanine core appear at around 7.71–7.49 ppm while those of crown ether moiety appear at 6.82–6.38 ppm. The ether protons of the crown ether group are observed between 4.26 and 3.75 ppm. The IR spectra of **3**–**6** and ^1H NMR spectra of **3** and **6** are very similar.

In addition, the assignment of the product to a 3:1 combination of the reactant was made on the basis of elemental analysis and mass spectral data results confirming the proposed structures. The molecular ion peaks at 1467 and 1463 were obtained by FAB-MS for **4** and **5**.

The electronic spectra of all phthalocyanine derivatives exhibit two main bands a Soret or B band (π–π^*) between 300 and 400 nm and another around 600–700 nm denoted the Q band (π–π^*). The symmetric phthalocyanines with four benzo-15-crown-5 units through oxy-bridges have similar electronic spectra with intense single band for both the Q and B band. In contrast, the electronic spectra on unsymmetrical phthalocyanines **3**–**6**, with three crown ether units and nitro group, clearly show a splitting of the Q band (Fig. 1) [44,46,62–64]. The electronic absorption spectra of **3**–**6** exhibit a split Q band at 675 and 696; 627 and 679; 630 and 678; and 624 and 675 nm, respectively. These differences are consequence of unsymmetry in these molecules which can be described by Gauterman's four-orbital model for the optical spectra of porphyrins and porphyrazines [65].

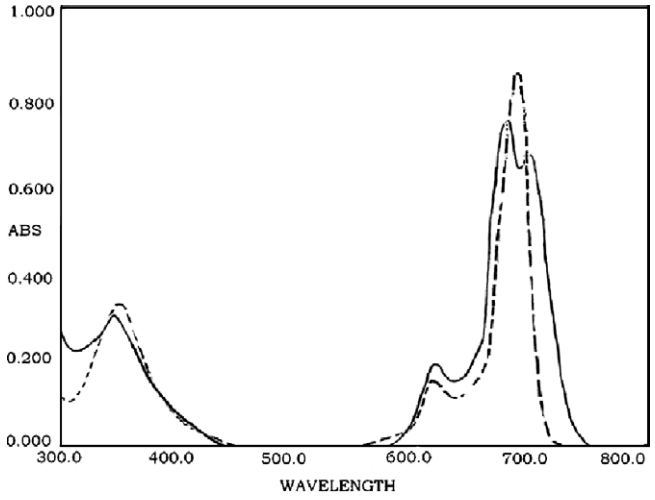


Fig. 1. UV–Vis spectra of symmetrically substituted zinc phthalocyanine with four benzo-15-crown-5 (– – – –) and, the unsymmetrical zinc phthalocyanine **3** (—-) in chloroform solution.

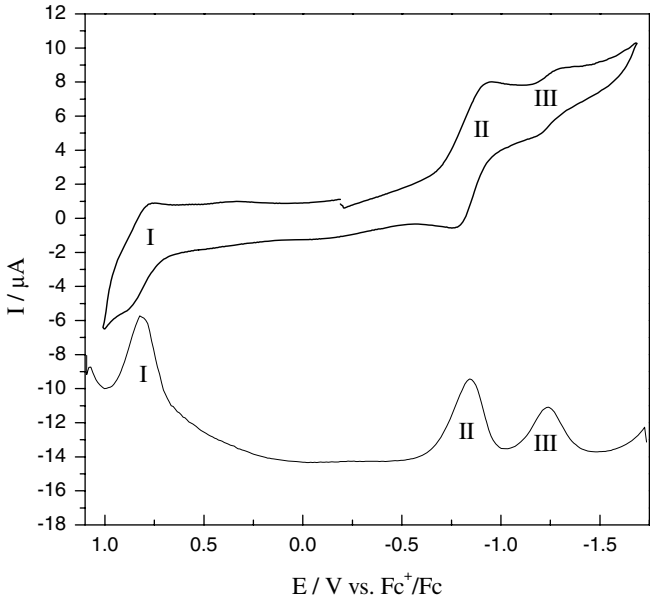


Fig. 2. Cyclic and differential pulse voltammograms of 5.0×10^{-4} mol dm^{-3} of **4** in 0.1 mol dm^{-3} TBAP/DCM electrolyte system at 0.100 mV s^{-1} scan rate.

3.2. Electrochemical measurements

Electrochemical properties of **4** were studied by cyclic voltammetry (CV) and differential pulse voltammetry (DPV) at different scan rates. The CVs of the complex shown in Fig. 1 display two reduction processes at −0.857 and −1.245 V during the cathodic scan and one oxidation process at 0.815 V during the anodic scan vs. Fc/Fc^+ at 0.100 Vs^{-1} scan rate with in the available potential range of TBAP/DCM solvent system. DPVs support the redox processes recorded with CV. The reduction and oxidation behavior of metallophthalocyanine derivatives is due to the interaction between the phthalocyanine ring and the central metal ions. If the transition metal ion concerned has no accessible d orbital levels lying within the $1a_{1u}$ (HOMO)-$1e_g$ (LUMO) gap of a phthalocyanine species, then its redox chemistry will appear very like that of redox inactive metallophthalocyanines. The copper group behaves in this fashion, with the Cu(II) central ion being unchanged as the CuPc unit is either oxidized or reduced [1,56–58]. These studies clearly point out that all of these processes could be ascribed to the phthalocyanine ring electron transfer reactions. According to these studies the redox processes of **4** recorded in this study are as shown in the following equation:

$$[\mathrm{Cu(II)Pc}(-1)]^{+} \underset{0.815\ \mathrm{V}}{\overset{e^-}{\Longleftrightarrow}} [\mathrm{Cu(II)Pc}(-2)] \underset{-0.857\ \mathrm{V}}{\overset{e^-}{\Longleftrightarrow}} [\mathrm{Cu(II)Pc}(-3)]^{1-} \underset{-1.245\ \mathrm{V}}{\overset{e^-}{\Longleftrightarrow}} [\mathrm{Cu(II)Pc}(-4)]^{2-} \quad (1)$$

The voltammogram of **4** carrying three benzo-15-crown-5 units and one nitro is compared with the voltammogram of ZnPc carrying four benzo-15-crown-5 units, studied in our previous study [27]. The results clearly show that substitution of the electron withdrawing nitro group instead of one of the four benzo-15-crown-5 units shifts the electrochemical processes approximately 200 mV to the positive potentials. All redox couples labeled as I, II, and III in Fig. 2 show quasi-reversible peak character which have ΔE_p of 96, 115, and 90 mV at 0.100 Vs^{-1} scan rate and increases with increasing scan rates. Constant values of $I_p/v^{1/2}$ suggest diffusion-controlled electron transfer mechanism for all redox processes. The ratios of I_{pc}/I_{pa} for all processes are approximately unity and do not considerably vary with the scan rates, supporting diffusion-controlled mass transfer mechanism of the complex. The peak-to-peak separation of the processes II and III (388 mV) is generally common for metallophthalocyanines containing electrochemically inactive metal center. The difference between the average value of the half-wave potentials of the first reduction (−0.857 V) and first oxidation (0.815 V) gives the measure of gap (1.672 V) between the HOMO and LUMO for the complex, characterizing the phthalocyanines carrying electrochemically inactive metal center [1,27,40,56–58,66–68]. In conclusion, cyclic voltammetric and differential pulse measurements showed that **4** give three ligand-centered redox processes indicating quasi-reversible peak behaviors. Peak-to-peak separation and HOMO–LUMO gap of the complex are in harmony with the common phthalocyanine complexes.

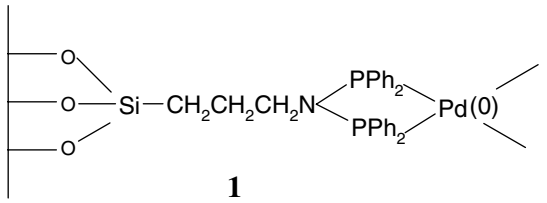
Acknowledgement

This work was supported by the Research Fund of the Technical University of Istanbul and State Planning Organization (DPT).

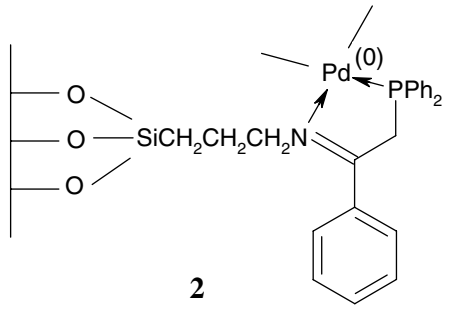
References

[1] C.C. Leznoff, A.B.P. Lever (Eds.), Phthalocyanines Properties and Applications, vol. 1–4, VCH, Weinheim, 1989–1996.

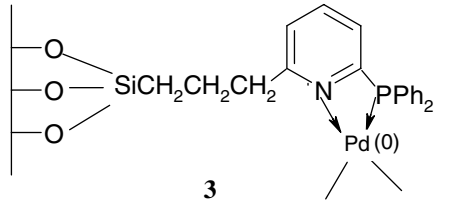
[2] N.B. McKeown (Ed.), Phthalocyanines Materials, Cambridge University Press, Cambridge, 1998.
[3] I. Scalise, E.N. Durantimi, Bioorg. Med. Chem. 13 (2005) 3037.
[4] K. Sakamoto, T. Kato, E.O. Okumura, M. Watanabe, M.J. Cook, Dyes Pigments 64 (2005) 63.
[5] M.I. Newton, T.K.H. Starke, M.R. Willis, G. Mchale, Sens. Actuat. B 67 (2003) 307.
[6] N. Kobayashi, W.A. Nevin, Appl. Organomet. Chem. 10 (1996) 579.
[7] D. Wöhrle, J. Gitzel, G. Krawczyk, E. Tsuchida, H. Ohno, T. Nishisaka, J. Macromol. Sci. Chem. A 25 (1998) 1227.
[8] M. Hanack, M. Lang, Adv. Mater. 6 (1994) 819.
[9] C.J. Pedersen, J. Am. Chem. Soc. 89 (1967) 7017.
[10] S. Patai (Ed.), The Chemistry of Ethers, Crown Ethers, Hydroxy Groups and Their Sulphur Analogues, John Wiley and Sons, Chichester, 1980.
[11] S.R. Cooper (Ed.), Crown Compounds: Toward Future Applications, VCH, New York, 1992, pp. 1–324.
[12] E. Hamuryudan, Ş. Merey, Z.A. Bayır, Dyes Pigments 59 (2003) 263.
[13] A.N. Cammidge, G. Berber, I. Chambrier, P.W. Hough, M.J. Cook, Tetrahedron 61 (2005) 4067.
[14] Ö. Bekaroğlu, Appl. Organomet. Chem. 10 (1996) 605.
[15] E. Hamuryudan, Ö. Bekaroğlu, J. Chem. Res. (S) (1993) 460.
[16] M. Hanack, D. Meng, A. Beck, M. Sommerauer, L.R. Subramanian, J. Chem. Soc. Chem. Commun. (1993) 58.
[17] E. Hamuryudan, Z.A. Bayır, Ö. Bekaroğlu, Dyes Pigments 43 (1999) 77.
[18] M. Koçak, A. Cihan, A.İ. Okur, A. Gül, Ö. Bekaroğlu, Dyes Pigments 45 (2000) 9.
[19] Y. Gök, H. Kantekin, İ. Değirmencioğlu, Supramol. Chem. 15 (2003) 335.
[20] M. Kandaz, M.N.U. Yaraşır, A. Koca, Ö. Bekaroğlu, Polyhedron 21 (2002) 255.
[21] Y. Arslanoğlu, A.M. Sevim, E. Hamuryudan, A. Gül, Dyes Pigments 68 (2006) 129.
[22] J. Simon, M.K. Engel, C. Soulie, New J. Chem. 16 (1992) 287.
[23] A.R. Koray, V. Ahsen, Ö. Bekaroğlu, J. Chem. Soc. Commun. (1986) 932.
[24] N. Kobayashi, Y. Nishiyama, J. Chem. Soc. Chem. Commun. (1986) 1462.
[25] R. Hendriks, O.E. Sielcken, W. Dreath, R.J.M. Nolte, J. Chem. Soc. Chem. Commun. (1986) 1464.
[26] H. Engelkamp, R.J.M. Nolte, J. Porphyr. Phthalocya. 4 (2000) 454.
[27] E. Hamuryudan, Dyes Pigments 68 (2006) 151.
[28] M.J. Cook, Chem. Record. 2 (2002) 225.
[29] G. Rojo, F. Agullo-Lopez, B. Cabezon, T. Torres, S. Brasselet, I. Ledoux, J. Zyss, J. Phys. Chem. B 104 (2000) 4295.
[30] V. Stefani, B. Cabezon, E.L.G. Denardin, D. Samios, T. Torres, J. Mater. Chem. 10 (2000) 2187.
[31] G.J. Clarkson, N.B. McKeown, K.E. Treacher, J. Chem. Soc. Perkin Trans. I 14 (1995) 1817.
[32] R.H. Poynter, M.J. Cook, M.A. Chesters, D.A. Slater, J. McMurdo, K. Welford, Thin Solid Film (1994) 243.
[33] F. Armand, B. Cabezon, M.V. Martinez-Diaz, A. Ruaudel-Teixier, T. Torres, J. Mater. Chem. 7 (1997) 1741.
[34] G. de la Torre, C.G. Claessens, T. Torres, Eur. J. Org. Chem. (2000) 2821.
[35] C.C. Leznoff, T.W. Hall, Tetrahedron Lett. 23 (1982) 3023.
[36] N. Kobayashi, R. Kondo, S.I. Nakajima, T. Osa, J. Am. Chem. Soc. 112 (1990) 9640.
[37] S. Gürsoy, Z.A. Bayır, E. Hamuryudan, Ö. Bekaroğlu, Monatsh. Chem. 131 (2000) 287.
[38] Z.A. Bayır, Ş. Merey, E. Hamuryudan, Monatsh. Chem. 134 (2003) 1027.
[39] N. Korkmaz, E. Hamuryudan, Monatsh. Chem. 135 (2004) 513.
[40] A. Kalkan, A. Koca, Z.A. Bayır, Polyhedron 23 (2004) 3155.
[41] B. Cabezon, E. Quesada, S. Esperanza, T. Torres, Eur. J. Org. Chem. (2000) 2767.
[42] S.J. Lange, J.W. Sibert, A.G.M. Barrett, B.M. Hoffman, Tetrahedron 56 (2000) 7371.
[43] D. Pernin, K. Haberroth, J. Simon, J. Chem. Soc. Perkin Trans. I (1997) 1265.
[44] N. Kobayashi, M. Togashi, T. Osa, K. Ishii, S. Yamauchi, H. Hino, J. Am. Chem. Soc. 118 (1996) 1073.
[45] E. Musluoğlu, A. Gürek, V. Ahsen, A. Gül, Ö. Bekaroğlu, Chem. Ber. 125 (1992) 2337.
[46] M. Tian, T. Wada, H. Sasabe, Dyes Pigments 52 (2002) 1.
[47] A. Hirth, A.K. Sobbi, D. Wöhrle, J. Porphyr. Phthalocya. 1 (1997) 275.
[48] A. Sastre, T. Torres, M. Hanack, Tetrahedron Lett. 36 (1995) 8501.
[49] K.M. Kadish, G. Moninot, Y. Hu, D. Dubois, A. Ibnlfassi, J.M. Barbe, R. Guilard, J. Am. Chem. Soc. 115 (1993) 8153.
[50] P.M.S. Monk, R.J. Mortimer, D.R. Rosseinsky, Electrochromism: Fundamentals and Applications, VCH Publishers, Weinheim, 1995.
[51] K. Kasuga, M. Tsutsui, Coord. Chem. Rev. 32 (1980) 67.
[52] J.D. Wright, Prog. Surf. Sci. 31 (1989) 1.
[53] J. Simon, P. Bassoul (Eds.), Design of Molecular Materials – Supramolecular Engineering, Wiley and Sons, Chichester, UK, 2000.
[54] D. Wöhrle, D. Meissner, Adv. Mater. 3 (1991) 129.
[55] K.M. Kadish, K.M. Smith, R. Guilard (Eds.), The Porphyrine Handbook, Academic Press, Burlington, MA, 2000.
[56] A.R. Özkaya, E. Hamuryudan, Z.A. Bayir, Ö. Bekaroğlu, J. Porphyr. Phthalocya. 7 (2000) 689.
[57] A.B.P. Lever, S. Liccocia, P. Minor, B.S. Ramaswamy, S.R. Pickens, K. Magnell, J. Am. Chem. Soc. 103 (1981) 6800.
[58] A.B.P. Lever, P.C. Minor, Inorg. Chem. 20 (1980) 4015.
[59] D.D. Perrin, W.L.F. Armarego, Purification of Laboratory Chemicals, second ed., Pergamon, Oxford, 1980.
[60] J.G. Young, W.J. Onyebuagu, Org. Chem. 55 (1990) 2155.
[61] J.V. Bacboord, M.J. Cook, E. Hamuryudan, J. Porphyr. Phthalocya. 4 (2000) 1520.
[62] T.F. Baumann, M.S. Nasir, J.W. Sibert, A.J.P. White, M.M. Olmstead, D.J. Williams, A.G.M. Barrett, B.M. Hoffman, J. Am. Chem. Soc. 118 (1996) 10479.
[63] A.G. Cabello, P. Vasquez, T. Torres, J. Organomet. Chem. 637 (2001) 751.
[64] A. Gonzalez, P. Vazquez, T. Torres, Tetrahedron Lett. 40 (1999) 3263.
[65] M. Gouterman, in: D. Dolphin (Ed.), The Porphyrins, vol. III, Academic Press, New York, 1978, pp. 1–165.
[66] A.B.P. Lever, Adv. Inorg. Chem. Radiochem. 7 (1965) 27.
[67] A. Koca, M.K. Şener, M.B. Koçak, A. Gül, Trans. Met. Chem. 30 (2005) 399.
[68] A. Koca, H.A. Dinçer, M.B. Koçak, A. Gül, Russ. J. Electrochem. 42 (2006) 31.



1

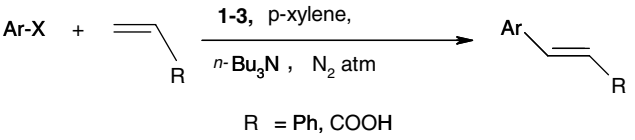


2



3

Probably the bidentate nature of the three ligands in systems **1**–**3** and the bigger bite in the case of **1** than diphenylphosphinomethane (dppm) are responsible for the enhanced stability. The good reactivity in the case of **1** and **3** originates from the formation of four membered chelate rings



(1)

The results of these investigations are given in this paper.

2. Experimental

The C and H analyses were carried out with a Perkin–Elmer elemental analyzer 240 C. The ^{1}H and $^{13}C\{^{1}H\}$ NMR spectra were recorded on a Bruker Spectrospin DPX-300 NMR spectrometer at 300.13 and 75.47 MHz, respectively. ^{13}C CPMAS spectra were recorded on a Bruker DSX-300 NMR spectrometer at 75.47 MHz. A flame atomic absorption spectrometer (FAAS) of the Perkin–Elmer Instruments, Shelton, USA, model Analyst 100 equipped with an air–acetylene flame was used for Pd determination.

2.1. Synthesis of aminopropyl silica gel (APSG)

Silica gel was boiled with 5 N HCl for 8 h, filtered, washed with water until free from acid, dried at 110 °C for 12 h and degassed with nitrogen at 100 °C under *vacuo*. The resulting activated silica gel (10.0 g) was mixed with (3-aminopropyl)triethoxysilane (20.0 cm^3) in 150 ml of dry *p*-xylene under dry dinitrogen atmosphere. The mixture was refluxed for 72 h, after which the resulting aminopropyl silica gel (APSG) was filtered. It was washed successively with *p*-xylene (4×50 cm^3), ethanol (4×50 cm^3) and acetone (3×50 cm^3). The APSG was dried in *vacuo* at 80–100 °C and stored under inert conditions. N, 4.42%. IR (KBr cm^{-1}) 3463 (NH stretching), 1644 (CH_2), 1588 (NH bending); ^{13}C CP-MAS NMR (δ, ppm): 10.2 (Si–CH_2), 25.1 (CH_2), 47.5 (N–CH_2).

2.2. Deactivation of unreacted silanol groups of silica gel

Aminopropyl silica gel (APSG) (1.0 g) was mixed with dichlorodimethylsilane (2 cm^3) in dry diethylether (20 cm^3) and the mixture was stirred under an inert atmosphere for 1 h. Deactivated APSG was filtered, washed with degassed (with N_2) ether (5×10 cm^3), dried in *vacuo* and stored under inert conditions.

2.3. Reaction of deactivated APSG with PPh_2Cl

A mixture of deactivated APSG (1.0 g) and chlorodiphenylphosphine (1.64 cm^3) was refluxed in dry benzene under nitrogen atmosphere in presence of triethylamine (0.06 cm^3) for 48 h. Silica gel functionalized with Ph_2PNPPh_2 groups (PNPSG) was filtered, washed successively with ethanol (5×30 cm^3) and acetone (5×30 cm^3), dried under *vacuo* and stored in an inert atmosphere. Analysis: C, 9.85, H, 1.74, N, 1.27%. IR (KBr, cm^{-1}): 1437 and 1484 (CH_2), 2900–3075 (CH aromatic). ^{13}C CP-MAS NMR, δ (ppm): 10.2 (Si–CH_2), 25.1(CH_2), 47.5 (N–CH_2) 132.7 (Ar–C, PPh_2).

2.4. Synthesis of *1*

One gram of PNPSG was mixed with $PdCl_2$ (0.52 g), dissolved in acetone (30 cm^3) and the mixture was refluxed for 48 h under nitrogen atmosphere to give red-brown PNPSG complexed with Pd(II). It was filtered, washed with degassed acetone (3×10 cm^3) and dried under vacuum. PNPSG loaded with Pd(II) was treated with hydrazine hydrate (1.5 g), then dissolved in ethanol (30 cm^3) at 30 °C under nitrogen atmosphere. The resulting product (PNPSG loaded with Pd(0)), reddish in colour, was filtered and washed with degassed (with nitrogen) ethanol (4×30 cm^{-3}) and diethylether (2×30 cm^{-3}), and dried under *vacuo*. It was stored under an inert atmosphere. To determine the Pd content of PNPSG loaded with Pd(0) (**1**), it was treated successively with 20 cm^3 mixture of concentrated HNO_3 and HCl (1:3) and $HClO_4$ (10 cm^3), and filtered. The filtrate was diluted to 50 cm^3 with distilled water and subjected to FAAS determination using a precalibrated instrument. Pd content = 141 μmol g^{-1}.

2.5. Synthesis of **2**

Deactivated APSG (2.0 g) was mixed with 2-(1,1-diphenylphosphino)-1-phenyl-1-ethanone (1.18 g, 3.9 mmol) in dry ethanol (30 cm^3) and the mixture was stirred under nitrogen atmosphere for 48 h. The modified silica gel was filtered, washed successively with degassed (with nitrogen) ethanol (5×30 cm^3) followed by acetone (5×30 cm^3), dried under vacuum and stored in an inert atmosphere. Analysis: C, 9.70; H, 1.79; N, 1.72%. IR (KBr, cm^{-1}): 1460 (deformation mode of CH_2 of the *n*-propyl chain), 1546–1639 (skeleton vibrations of the ring), 1845 (C=N stretching) 2784–2933 cm^{-1} (CH_2 stretching), 3023–3128 (CH stretching of the aromatic ring). ^{13}C CP-MAS NMR (δ, ppm): 9.8 (Si–CH_2), 22.0 (CH_2), 42.5 (N–CH_2), 127.8 (Ar–C), 160.0 (C=N).

The silica gel loaded with 2-(1,1-diphenylphosphino)-1-phenyl-1-ethanone (1.0 g) was mixed with $PdCl_2$ (0.30 g, 1.69 mmol) dissolved in acetone (30 cm^3) and the mixture was refluxed for 48 h under nitrogen atmosphere to give red-brown Pd(II) immobilized silica gel. It was filtered, washed with degassed acetone (3×10 cm^3) and dried under vacuum. Pd(II) immobilized gel was treated with hydrazine hydrate (1.5 g) dissolved in ethanol (30 cm^3) at 30 °C under nitrogen atmosphere. The resulting red-brown Pd(0) immobilized gel (**2**) was filtered and washed with degassed (with nitrogen) ethanol (4×30 cm^3) and diethylether (2×30 cm^3), and dried under *vacuo*. It was stored under an inert atmosphere. ^{13}C CP MAS (δ, ppm) 18.3 (Si–CH_2), 28.5 (CH_2), 39.3 (N–CH_2), 126.4 (Ar–C). The Pd content loaded on **2** was determined by FAAS, as described in the case of **1**. Pd content = 156 μmol g^{-1}.

2.6. Synthesis of 2-diphenylphosphinopyridine immobilized silica gel and **3**

2-Diphenylphosphinopyridine (2.75 g, 10.45 mmol) was reacted with *n*-BuLi–LiDMAE (DMAE = dimethylaminoethoxide) under nitrogen atmosphere. (3-Chloropropyl)triethoxysilane (2.07 g, 10.45 mmol) was added dropwise to the mixture at −78 °C and the mixture was allowed to come to room temperature overnight. The THF was evaporated on a rotary evaporator and deoxygenated dichloromethane (30 cm^3) was added to extract the compound. The dichloromethane layer was filtered through celite and evaporated on a rotary evaporator to get 2-(1,1-diphenylphosphino)-6-[3-(1,1,1-triethoxysilyl)propyl]pyridine as a colourless oil to which activated silica gel (2.0 g) in dry *p*-xylene was added, and the mixture was refluxed under nitrogen atmosphere for 48 h. The modified silca gel was filtered, washed successively with ethanol (5×30 cm^3) and acetone (5×30 cm^3), dried under vacuum and stored in an inert atmosphere. Analysis: C, 9.66; H, 2.80; N, 1.76%. IR (KBr, cm^{-1}): 3000–3220 (CH stretching of the aromatic ring), 2850–2950 (aliphatic CH stretching), 1510–1646 (skeleton vibrations involving C–C stretching within the ring), 1420, 1485 (deformation of CH_2 of the *n*-Pr chain), 695–803 (out of plane pyridine ring bending), 1150 (P–C_6H_5 stretching vibrations).

To cap unreacted –SiOH groups, ligand anchored silica gel (1.0 g), was mixed with dichlorodimethylsilane (2 cm^3) in dry diethylether (20 cm^3), and the mixture was stirred under an inert atmosphere for 1 h. The resulting products were filtered, washed with degassed (with nitrogen) diethylether (5×10 cm^3), dried in *vacuo* and stored under inert conditions.

One gram of the ligand anchored silica gel, after capping, was mixed with $PdCl_2$ (0.30 g, 1.69 mmol), dissolved in acetone (30 cm^3) and the mixture was refluxed for 48 h under nitrogen atmosphere to give red-brown Pd(II) immobilized gel. It was filtered, washed with degassed acetone (3×10 cm^3) and dried under vacuum. Pd(II) immobilized gel was treated with hydrazine hydrate (1.5 g) dissolved in ethanol (30 cm^3) at 30 °C under nitrogen atmosphere. The resulting Pd(0) immobilized gel (**3**), red brown in colour, was filtered and washed with degassed (with nitrogen) ethanol (4×30 cm^3) and diethylether (2×30 cm^3) and dried under *vacuo*. It was stored under an inert atmosphere. ^{13}C CP-MAS NMR (δ, ppm) 10.1 (Si–CH_2) 26.0 (CH_2), 64.4 (N–CH_2), 120.0 (phenyl carbon), 132.0 (pyridine carbon). The Pd content loaded on **3** was determined by FAAS, as described in the case of **1**. Pd content = 132 μmol g^{-1}.

2.7. Synthesis of (*E*)-3-(4-chlorophenyl)acrylic acid (**4**)

A mixture of acrylic acid (0.20 g, 2.75 mmol), *p*-chloroiodobenzene (0.70 g, 2.50 mmol), tri(*n*-butyl)amine (1.0 g, 5.5 mmol), *p*-xylene (2.0 cm^{-3}) and each of the catalysts **1**–**3** (37.5 mg) was stirred under nitrogen atmosphere in an oil bath at 110 °C for 8 h. The reaction was monitored by TLC. After completion of the reaction, the mixture was cooled to room temperature. The catalyst was filtered and washed with chloroform (3×10 cm^3) followed by acetone (3×10 cm^3) to remove the reagents from it, dried in *vacuo* and stored under inert conditions for re-use. The filtrate was mixed with $NaHCO_3$ (0.50 g) and water (30 cm^3). The mixture was stirred for 1 h at room temperature. The aqueous phase was separated and acidified with 5 N HCl. After cooling to 0 °C, the solid precipitate was filtered, washed with water and air dried to give (*E*)-3-(4-chlorophenyl)acrylic acid. Mp 250–251 °C; *Anal*. Calc. for $C_9H_7ClO_2$: C, 59.17, H, 3.83. Found: C, 59.12, H, 3.82%. ^1H NMR (DMSO-d_6, 25 °C): δ (vs TMS): 6.52–6.58 (d, IH, CH–COOH), 7.46–7.49 (d, 2H, Ar–H *o* to Cl), 7.55–7.60 (d, 1H, CH Ar–CH), 7.71–7.74 (d, 2H, Ar–H *m* to Cl); ^{13}C {^1H} NMR (DMSO-d_6, 25 °C): δ (vs TMS) 120.1 (CH–COOH), 128.1 (Ar–C *m* to Cl), 130.87 (Ar–C *o* to Cl), 133.2 (Ar–C *p* to Cl), 134.7 (Ar–C–Cl), 142.5 (Ar–CH), 167.4 (C=O).

2.8. Synthesis of (*E*)-3-(4-nitrophenyl)acrylic acid (**5**)

A mixture of acrylic acid (0.20 g, 2.75 mmol), *p*-iodonitrobenzene (0.62 g, 2.50 mmol)/*p*-bromonitrobenzene

(0.50 g 2.5 mmol) (10 mol% of PPh_3 was also added in the case of *p*-bromonitrobenzene) and tri-(*n*-butyl)amine (1.0 g, 5.5 mmol) in *p*-xylene (2.0 cm^3) was made. After adding one of the catalysts **1**–**3** (37.5 mg), the mixture was stirred under nitrogen atmosphere in an oil bath at 110 °C (140 °C for *p*-bromonitrobenzene) for 8 h. The reaction was monitored with TLC. After completion of the reaction, the mixture was cooled to room temperature. The catalyst was filtered and washed with chloroform (3×10 cm^3) followed by acetone (3×10 cm^3) to remove the reagents from it, dried in *vacuo* and stored under inert conditions for re-use. The filtrate was mixed with $NaHCO_3$ (0.50 g) and water (30 cm^3). The mixture was stirred for 1 h at room temperature. The aqueous phase was separated and acidified with 5 N HCl. After cooling to 0 °C, the solid precipitate was filtered, washed with water and air dried to give (*E*)-3-(4-nitrophenyl)acrylic acid. Mp 286–287 °C; *Anal*. Calc. for $C_9H_7NO_4$: C, 55.95; H, 3.62. Found: C, 55.89; H, 3.61%. ^1H NMR (DMSO-d_6, 25 °C): δ (vs TMS) 6.71–6.76 (d, 1H, CH–COOH), 7.66–7.71 (d, 1H, CH Ar–CH), 7.95–7.98 (d, 2H, Ar–H *o* to NO_2), 8.21–8.24 (d, 2H, Ar–H *m* to NO_2); ^{13}C NMR (DMSO-d_6, 25 °C): δ (vs TMS) 123.6 (CH), 123.9 (Ar–CH, *o* to NO_2), 130.3 (Ar–CH, *m* to NO_2) 140.7 (Ar–CH *p* to NO_2), 141.3 (Ar–CH), 147.9 (Ar–C–NO_2), 167.0 (C=O).

2.9. Synthesis of (*E*)-1-(4-chlorophenyl)-2-phenylethene (**6**)

A mixture of styrene (0.28 g, 2.75 mmol), *p*-chloroiodobenzene (0.70 g, 2.5 mmol), *n*-Bu_3N (0.54 g, 3.0 mmol) made in *p*-xylene (2.0 cm^3) and Pd(0) catalyst **1**–**3** (37.5 mg) was stirred under nitrogen atmosphere in an oil bath at 110 °C for 8 h. Thereafter the mixture was cooled to room temperature and stirred with chloroform (40 cm^3). The catalyst was filtered, washed with chloroform (3×10 cm^3) followed by acetone (3×10 cm^3), dried in *vacuo* and stored under inert atmosphere for re-use. The filtrate was washed with 5 N HCl (2×15 cm^3), water (2×20 cm^3), brine (2×10 cm^3), and then dried over Na_2SO_4. The crude product obtained after the evaporation of the solvent on a rotary evaporator of this filtrate was purified through a silica gel column using hexane–ethylacetate mixture (9:1). The solid product thus obtained was recrystallized from ethanol to get pure (*E*)-1-(4-chlorophenyl)-2-phenylethene. Mp 129 °C; *Anal*. Calc. for $C_{14}H_{11}Cl$: C, 78.32; H, 5.12. Found: C, 78.12; H, 5.10%. ^1H NMR ($CDCl_3$, 25 °C): δ (vs TMS): 7.06 (s, 2H, CH=CH), 7.25–7.51 (m, 9H, Ar–H); ^{13}C NMR ($CDCl_3$, 25 °C): δ (vs TMS) 126.5 (Ar–CH), 127.3 (Ar–C *o* to CH=CH), 127.6 (Cl–Ar–CH), 127.8 (Ar–C *p* to CH=CH), 128.7 (Ar–C *m* to CH=CH), (Ar–C *m* to Cl), 129.2 (Ar–C *o* to Cl), 133.1 (Ar–C–Cl), 135.8 (Ar–C *p* to Cl), 136.9 (Ar–C–CH=CH).

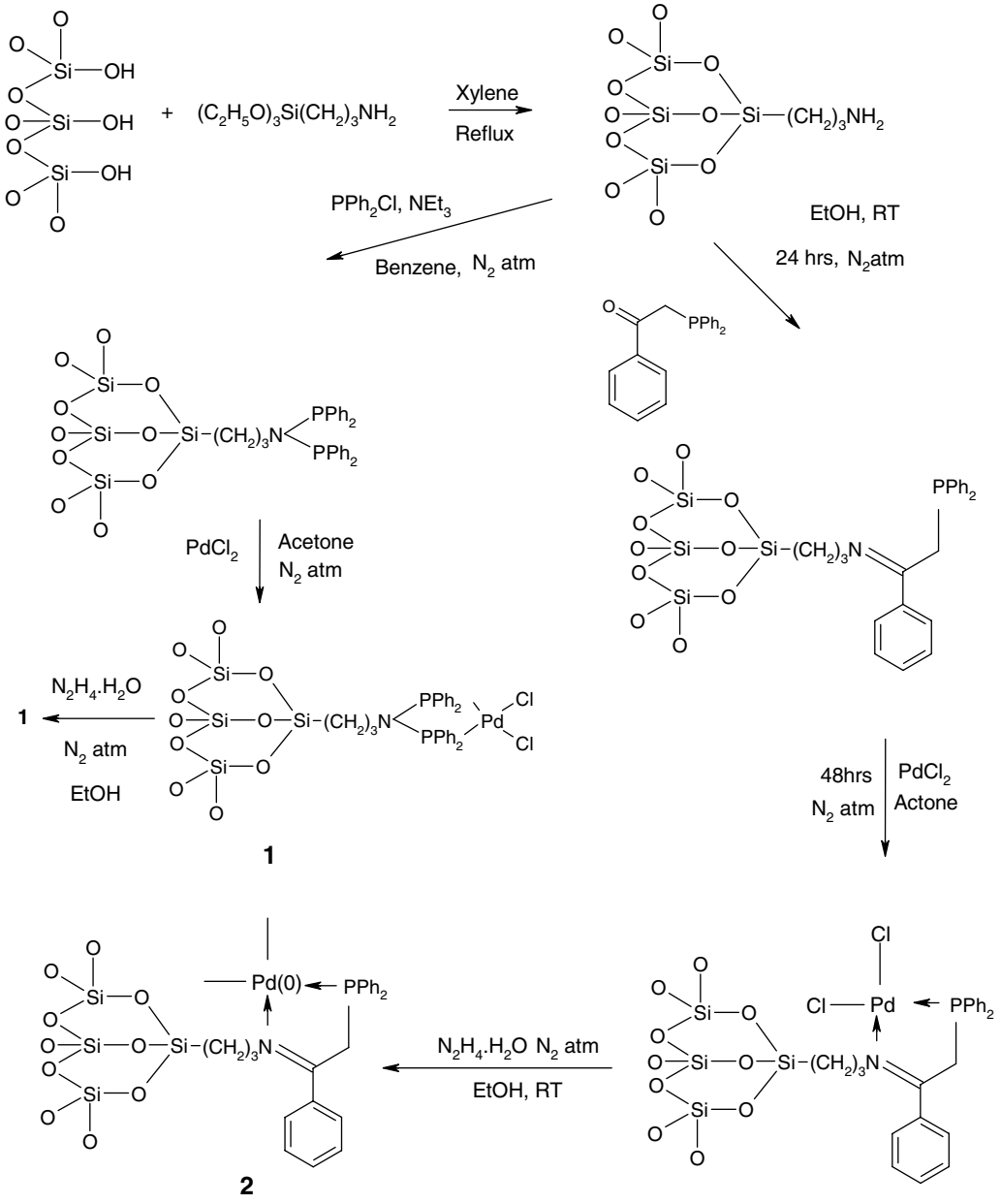
2.10. Synthesis of (*E*)-1-(4-nitrophenyl)-2-phenylethene (**7**)

A mixture of styrene (0.28 g, 2.75 mmol), *p*-iodonitrobenzene (0.62 g, 2.5 mmol)/*p*-bromonitrobenzene (0.50 g, 2.5 mmol) (10 mol% of PPh_3 was added additionally in the case of *p*-bromonitrobenzene), *n*-Bu_3N (0.54 g, 3.0 mmol), *p*-xylene (2.0 cm^3) and catalyst **1**–**3** (37.5 mg) was stirred under nitrogen atmosphere in an oil bath at 110 °C (140 °C for bromonitrobenzene) for 8 h, after which the mixture was cooled to room temperature and treated with chloroform (40 cm^3). The catalyst was filtered, washed with chloroform (3×10 cm^3) followed by acetone (3×10 cm^3), dried in *vacuo* and stored under inert atmosphere for re-use. The filtrate was washed with 5 N HCl (2×15 cm^3), water (2×20 cm^3), brine (2×10 cm^3) and dried over Na_2SO_4. The crude product obtained after the evaporation of the solvent of the filtrate on a rotary evaporator was purified through a silica gel column using hexane–ethylacetate mixture (9:1). The solid product obtained was recrystallized from ethanol to give pure (*E*)-1-(4-nitrophenyl)-2-phenylethene. Mp 157 °C; *Anal*. Calc. for $C_{14}H_{11}NO_2$: C, 74.66; H, 4.88. Found: C, 74.52; H, 4.79%. ^1H NMR ($CDCl_3$, 25 °C): δ (vs TMS) 7.12 (s, 2H Ar–CH), 7.32–7.57 (m, 9H, Ar–H); ^{13}C NMR ($CDCl_3$, 25 °C): δ (vs TMS) 124.1 (Ar–C *o* to NO_2), 126.2 (Ar–CH), 127.0 (O_2N–Ar–CH, Ar–C *o* to CH=CH), 127.8 (Ar–C *p* to CH=CH), 128.8 (Ar–C *m* to CH=CH), 133.3 (Ar–C *m* to NO_2), 136.1 (Ar–CH=), 143.8 (Ar–C *p* to NO_2), 146 (Ar–C–NO_2).

3. Results and discussion

The catalysts **1** and **2** were designed by the sequence of reactions given in Scheme 1 and **3** by those in Scheme 2. We have phosphinated the NH_2 group after anchoring it on silica gel, as doing it earlier resulted in two main side reactions occurring [27]. First the phosphine moieties of the linkers can be quaternized by ethyl groups from the ethoxysilyl functions. Second, the bisphosphinoamine group can rearrange to the corresponding phosphinimine unit that is subsequently hydrolyzed, resulting in the amine and tetraphenyldiphosphine oxide. The catalysts **1** and **2** were stored under a nitrogen atmosphere because due to the presence of Pd(0) their susceptibility to aerial oxidation is very likely. The catalysts do not show any visual sign of decomposition even after six months if stored under nitrogen. The yields of the C–C coupling reactions (Eq. (1)) were also found to be unchanged when aged catalysts were used. For all the catalysts **1**–**3** the anchoring of the ligands/complexes is authenticated by ^{13}C solid state NMR spectra. The ^{13}C CP-MAS NMR spectra of the three catalysts and their intermediates do not indicate the significant presence of unreacted ethoxy groups under the present reaction conditions, which are more drastic [28]. All the catalysts **1**–**3** have been found to be efficient at catalyzing the C–C coupling reaction shown in Eq. (1), and are recyclable. The products **4**–**7** formed by reaction of Eq. (1) have been authenticated by solution ^1H and ^{13}C NMR spectra, elemental analyses and IR spectra.

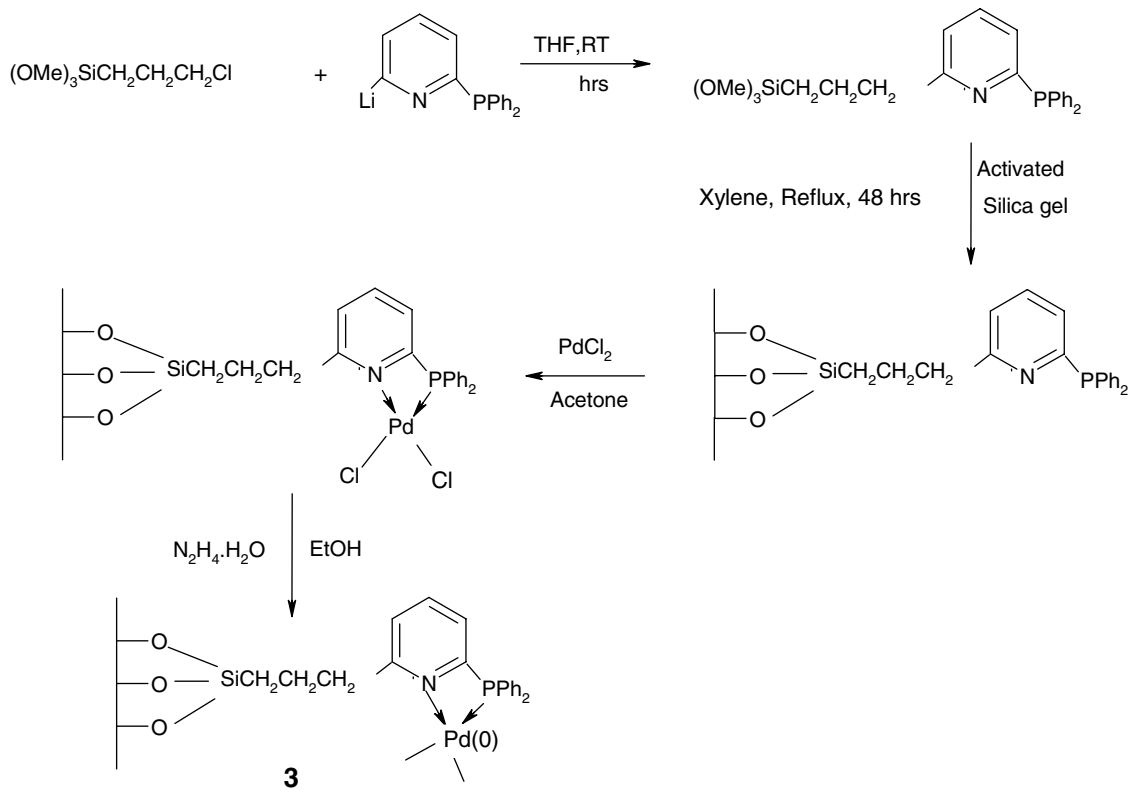
The formation of the *trans* isomer is supported by $^3J(H–H) = 16$ Hz; for a *cis* isomer these coupling constants



Scheme 1.

have values less than 10 Hz. With up to 15–16 re-uses of the catalysts **1**–**3**, the yields of the products do not change significantly as they are within ±3–5%. Thereafter, some small lowering in yields was noticed. They can be used up to 30-times with a reduction in yield of the order of 10–15%. In Table 1 the yields of the products obtained at optimum reaction temperatures are compared. The values of the yields are with respect to aryl halides. In the case of bromo derivatives, the yields are bit lower as expected due to some difficulty of the insertion of Pd into the C–Br bond. Only the *trans* isomer was obtained in all reactions of the type represented by Eq. (1). It appears that the C–C coupling reaction involves the processes given in Scheme 3 and due to steric reasons the organic residues go *trans* to each other.

In the synthesis of **4**–**7**, on lowering the reaction temperatures (oil bath) by 10 °C, a yield decrease of ~7–8% was observed, whereas on raising the temperature of the oil bath by 20 °C above the optimum value the yield does not change. For the catalytic synthesis of **4**–**7** addition of *n*-Bu_3N is essential. It was found to be better than Et_3N as with the later the yields are reduced by half. The effect of the amount of catalysts **1**–**3** on the formation of **4**–**7** was studied. It was found that 37.5 mg of **1**–**3** is sufficient for catalytic formation of **4**–**7** from reactants having concentration levels up to 200 mmol. The yield is reduced by 10–15% if only 20 mg of catalysts **1**–**3** is added. The yields with catalyst **3** are greater than those obtained with **2**. In the case of catalyst **2**, the ring formed with Pd is five membered

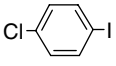
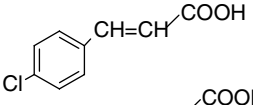
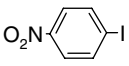
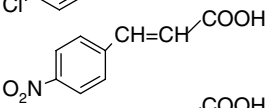
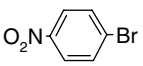
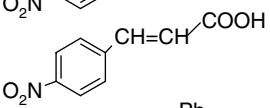
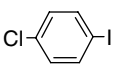
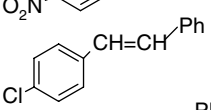
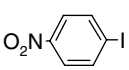
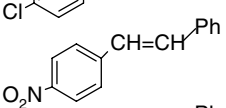
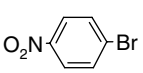
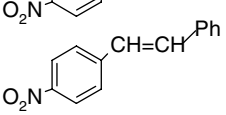


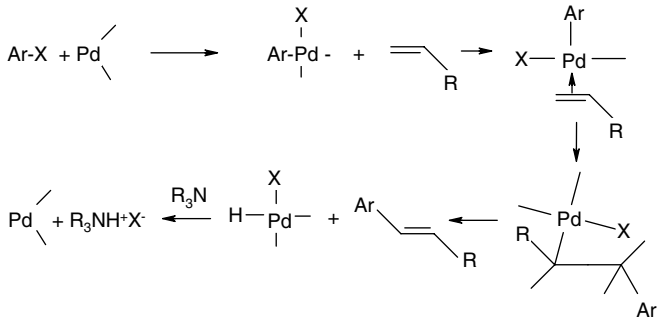
Scheme 2.

while with catalyst **3** four membered ring formation takes place with the metal centre. As the four membered chelate is strained, the ring opening is easier as compared to the five membered chelate. Due to this, the activity of **3** is found to be better than that of catalyst **2**. In the case of **1**, the chelate ring formed is four membered but both donor sites are phosphorus atoms and consequently the stability of the chelate formed with Pd appears to be greater than that of the (P,N) ligand present in catalyst **3**.

The Heck reaction and the form of the palladium catalyst catalyzing it has been a subject of debate in the recent

Table 1
Yields and temperature for the reaction between aryl halides and alkenes (Eq. (1))

Ar–X	Y	Temperature (°C) Catalyst 1/2/3	Product	Yield (%) Catalyst 1/2/3
	COOH	110		79/74/86
	COOH	110		76/82/89
	COOH	140		71/72/76
	Ph	110		83/80/90
	Ph	110		84/78/92
	Ph	140		74/75/79



Scheme 3.

past. De Vries et al. have reported [29,30] that ligand-free $Pd(OAc)_2$ can be used as a catalyst in the Heck reaction of aryl bromides as long as the amount of catalyst is kept between 0.01 and 0.1 mol%. At higher concentrations Pd black forms and the reaction stops. The formation of nanoparticles of palladium has been suggested as a pathway [31] when some palladium complexes of Schiff bases were used as catalyst for the Heck reaction. This reaction has also been demonstrated to be taking place via nanoparticles of palladium in ionic liquids [32]. However, importance of the ligands on the silica surface in retaining palladium catalyzing Heck reactions has not been denied [33]. With our catalysts **1**–**3**, it has been observed that their colour (close to dark red) does not change, even after recycling them. Therefore, it appears that the Pd-complexes in them most probably remain tethered molecular species and stay as such after the catalytic cycle.

4. Conclusion

The catalytic systems **1**–**3** have been designed and found to be suitable for selective Heck reactions as only the *trans* product is obtained in good yield. It appears that the Pd-complexes in them most probably remain tethered molecular species and stay as such after the catalytic cycle.

Acknowledgement

Authors thank Department of Science and Technology, New Delhi (India) for giving research Grant No. SR/S1/IC-16/2002.

References

[1] P.N. Price, J.H. Clark, D.J. Macquarrie, J. Chem. Soc., Dalton Trans. (2000) 110.
[2] J.H. Clark, D.J. Macquarrie, J. Chisem, I. Chisem, J.S. Rafelt, Chem. Commun. (1997) 2203.
[3] I. Chisem, J.S. Rafelt, M.T. Shieh, J. Chisem, J.H. Clark, R. Jachuck, D.J. Macquarrie, C. Ramshaw, K. Scott, Chem. Commun. (1998) 1949.
[4] J.H. Clark, A.P. Kybett, D.J. Macquarrie, K. Martin, J. Chem. Soc., Chem. Commun. (1989) 1355.
[5] P. Battioni, J.P. Lallier, L. Barloy, D. Mansuy, J. Chem. Soc., Chem. Commun. (1989) 1149.
[6] P. Battioni, J.F. Bartoli, D. Mansuy, Y.S. Byun, T.G. Traylor, J. Chem. Soc., Chem. Commun. (1992) 1051.
[7] M.Z. Cai, C.S. Song, X. Huang, Synth. Commun. 27 (1997) 361.
[8] M.Z. Cai, C.S. Song, X. Huang, Synth. Commun. 28 (1998) 693.
[9] M. Lasperas, N. Bellocq, D. Brunel, P. Moreau, Tetrahedron: Asymmetry 9 (1998) 3053.
[10] M. Cai, Y. Huang, H. Zhao, C. Song, J. Orgaomet. Chem. 682 (2003) 20.
[11] C.A. McNamara, M.J. Dixon, M. Bradley, Chem. Rev. 102 (2002) 3275.
[12] C.-A. Lin, F.-T. Luo, Tetrahedron Lett. 44 (2003) 7565.
[13] C.A. McNamara, F. King, M. Bradley, Tetrahedron Lett. 45 (2004) 8239.
[14] K.E. Elson, I.D. Jenkins, W.A. Loughlin, Tetrahedron Lett. 45 (2004) 2491.
[15] P.G. Steel, C.W. Teasdale, Tetrahedron Lett. 45 (2004) 8977.
[16] R.B. Bedford, S.J. Coles, M.B. Hursthouse, V.J.M. Scordia, J. Chem. Soc., Dalton Trans. (2005) 991.
[17] K.C.Y. Lau, H.S. He, P. Chiu, P.H. Toy, J. Comb. Chem. 6 (2004) 955.
[18] H. Nakano, K. Takahashi, Y. Suzuki, R. Fujita, Tetrahedron: Asymmetry 16 (2005) 609.
[19] Y.R. DeMiguel, J. Chem. Soc., Perkin Trans. (2000) 4213.
[20] M. Guino, K.K. Hii, Tetrahedron Lett. 46 (2005) 7363.
[21] M. Guino, K.K. Hii, Tetrahedron Lett. 46 (2005) 6911.
[22] Y. Uozumi, Top. Curr. Chem. 242 (2004) 77, and references therein.
[23] N.E. Leadbeater, M. Marco, Chem. Rev. 102 (2002) 3217.
[24] C. Merckle, J. Blumel, Chem. Mater. 13 (2001) 3617.
[25] Z. Fei, P.J. Dyson, Coord. Chem. Rev. 249 (2005) 2056.
[26] P. Braunstein, J. Organomet. Chem. 684 (2004) 3953.
[27] T. Posset, F. Rominger, J. Blumel, Chem. Mater. 17 (2005) 586.
[28] K.D. Behringer, J. Bluemel, J. Liq, Chromat. Relat. Technol. 19 (1996) 2753.
[29] A.H.M. de Vries, J.M.C.A. Mulders, J.H.M. Mommers, H.J.W. Henderickx, J.G. de Vries, Org. Lett. 5 (2003) 3285.
[30] M.T. Reetz, J.G. de Vries, Chem. Commun. (2004) 1559.
[31] C. Rocaboy, J.A. Gladysz, Org. Lett. 4 (2002) 1993.
[32] C.C. Cassol, A.P. Umpierre, G. Machado, S.I. Wolke, J. Dupont, J. Am. Chem. Soc. 127 (2005) 3298.
[33] C.M. Crudden, M. Sateesh, R. Lewis, J. Am. Chem. Soc. 127 (2005) 10045.

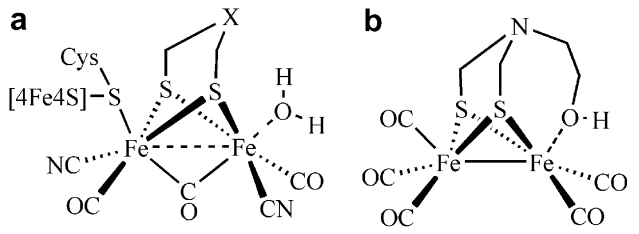


Fig. 1. The H_{ox} state of the Fe-only hydrogenase (a) and the designed model complex (b) that mimics the H_2O-coordination in the H_{ox}.

extension of this work has been conducted by conveniently linking the hydroxy group of **1** to desired ligands such as pyridine. The pyridyl-functionalized ADT-bridged diiron complex [{(μ-SCH_2)$_2$N(CH_2CH_2OOCPy)}Fe_2(CO)$_6$] (**2**) is a potential building block for construction of a photoactive catalyst such as [2Fe2S]–[Ru] catalyst-photosensitizer system for light-driven H_2-production [24–26].

2. Experimental

2.1. Reagents and instruments

All reactions and operations related to organometallic complexes were carried out under a dry, oxygen-free dinitrogen atmosphere with standard Schlenk techniques. All solvents were dried and distilled prior to use according to the standard methods. Isonicotinyl chloride hydrochloride was purchased from Alfa Aesar and $LiEt_3BH$ from Aldrich. Commercially available chemicals, paraformaldehyde, ethanol amine and [$Fe(CO)_5$] were used as received. Complex (μ-SH)$_2$$Fe_2$($CO$)$_6$ was prepared according to the literature procedure [27].

Infrared spectra were recorded on a JASCO FT/IR 430 spectrophotometer. NMR Spectra were collected on a Varian INOVA 400NMR spectrometer. Mass spectra were recorded by electro-spray ionization (ESI) on an HP1100 MSD instrument. Elemental analyses were performed on a THERMOQUEST-FLASH EA 1112 elemental analyzer.

2.2. Synthesis of [{(μ-SCH_2)$_2$N(CH_2CH_2OH)}Fe_2(CO)$_6$] (**1**)

Paraformaldehyde (1.79 g, 0.06 mol) was added to a solution of ethanol amine (1.75 g, 0.03 mol) in THF (25 mL). The reaction mixture was stirred at room temperature for 6 h, and then (μ-HS)$_2$$Fe_2$($CO$)$_6$, prepared in situ from (μ-S_2)Fe_2(CO)$_6$ (1.0 g, 3 mmol) according to the literature [16], was added. The solvent was removed after 1 h. The crude product, a dark red solid, was purified by column chromatography on silica gel using CH_2Cl_2 as eluent. The solvent was completely removed by rotary evaporation to give red solid **1** (0.31 g, 25%). Recrystallization in CH_2Cl_2/hexane afforded crystals of **1** suitable for X-ray crystallography study. *Anal.* Calc. for $C_{10}H_9Fe_2NO_7S_2$ (431.0): C, 27.87; H, 2.10; N, 3.25. Found: C, 28.12; H, 2.17; N, 3.68%. IR (CH_2Cl_2): *ν*CO 2073 (s), 2034 (s), 1999 (s) cm^{-1}. ^1H NMR ($CDCl_3$): δ 3.60 (s, 4H), 3.52 (s, 2H), 2.87 (s, 2H). MS: *m*/*z* 429 [$M-H^+$]$^-$.

2.3. Synthesis of [{(μ-SCH_2)$_2$N(CH_2CH_2OOCPy)}Fe_2(CO)$_6$] (**2**)

Triethylamine (2 mL) was added to a solution of isonicotinyl chloride hydrochloride (0.47 g, 2.65 mmol) in CH_3CN (20 mL) and the mixture was stirred for several minutes. A solution of **1** (0.88 mg, 2.04 mmol) in CH_3CN (40 mL) was then added dropwise at room temperature over 2 h. After the mixture was stirred for 24 h the solvent was removed under vacuum. Pure complex **2** (0.72 g, 66%) was obtained following the same procedure as that for **1**. *Anal.* Calc. for $C_{16}H_{12}Fe_2N_2O_8S_2$ (536.1): C, 35.85; H, 2.26; N, 5.23. Found: C, 35.74; H, 2.33; N, 5.52%. IR (CH_2Cl_2): *ν*CO 2074 (s), 2034 (s), 1999 (s), 1728 (m) cm^{-1}. ^1H NMR (acetone-d_6): δ 9.30 (s, 2H), 7.99 (s, 2H), 4.31 (m, 2H), 3.90 (s, 4H), 3.30 (m, 2H). MS: *m*/*z* 558 [$M+Na$]$^+$.

2.4. Crystal structure determination of complexes *1* and *2*

Single crystal X-ray diffraction measurements were made on a Smart APEX II diffractometer using graphite monochromated Mo Kα radiation (λ = 0.71073 Å). Complete crystal data and parameters for data collection and refinement are listed in Table 1. Data processing was accomplished with the SAINT processing program [28]. Intensity data were corrected for absorption with empirical methods. The structures were solved by direct methods and refined by matrix least-squares methods on F_o^2 by using the SHELXTL crystallographic software package [29]. All hydrogen atoms, except the hydrogen of the OH group in complex **1**, were located by difference maps and their positions were refined isotropically. All non-hydrogen atoms were refined anisotropically.

2.5. Electrochemistry

Acetonitrile (Aldrich, spectroscopy grade) used for performance of electrochemistry was dried with molecular sieve (4 Å) and then freshly distilled from CaH_2 under N_2. A solution of 0.05 M [^{n}Bu$_4$N]PF_6 (Fluka, electrochemical grade) in CH_3CN was used as electrolyte. Electrochemical measurements were recorded using a BAS-100W electrochemical potentiostat. The electrolyte solution was degased by bubbling with dry argon for 10 min before measurement. Cyclic voltammograms were obtained in a three-electrode cell under argon. The working electrode was a glassy carbon disc (diameter 3 mm) successively polished with 3 and 1 μm diamond pastes and sonicated in ion-free water for 10 min. The reference electrode was a non-aqueous Ag/Ag^+ electrode (1.0 mM $AgNO_3$ in CH_3CN) and the auxiliary electrode was a platinum wire.

Table 1
Crystallographic data and refinement parameters for complexes **1** and **2**

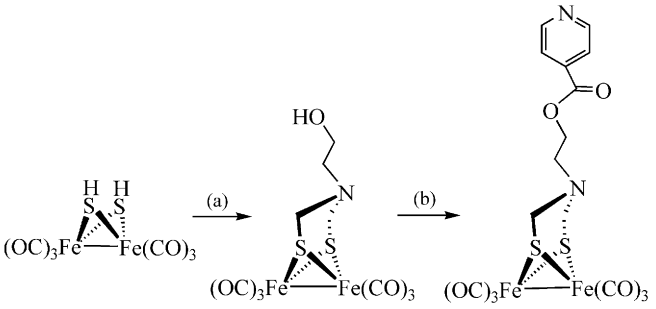
Complex	**1**	**2**
Empirical formula	$C_{10}H_9Fe_2NO_7S_2$	$C_{16}H_{12}Fe_2N_2O_8S_2$
Formula weight	431.00	536.10
Temperature (K)	293(2)	273(2)
Wavelength (Å)	0.71073	0.71073
Crystal system	triclinic	triclinic
Space group	$P\bar{1}$	$P\bar{1}$
Unit cell dimensions		
a (Å)	8.874(2)	9.212(6)
b (Å)	9.165(2)	9.462(6)
c (Å)	10.087(2)	12.759(9)
α (°)	78.566(4)	89.765(8)
β (°)	82.491(4)	69.489(7)
γ (°)	81.757(4)	84.454(8)
Volume (Å)^3	791.3(3)	1036.3(12)
Z	2	2
D_{calc} (Mg/m^3)	1.809	1.718
Absorption coefficient (mm^{-1})	2.126	1.647
$F(000)$	432	540
Crystal size (mm)	$0.3 \times 0.22 \times 0.2$	$0.52 \times 0.3 \times 0.21$
Range for data collection (°)	2.07–26.08	2.16–25.50
Limiting indices	$-10 < h < 10$, $-10 < k < 11$, $-12 < l < 11$	$-10 < h < 11$, $-11 < k < 5$, $-15 < l < 14$
Reflections collected	4300	5306
Independent reflections (R_{int})	2679 (0.0303)	3302 (0.0166)
Completeness to θ	26.08°, 96.6%	25.50°, 97.2%
Absorption correction	multiscan	multiscan
Maximum and minimum transmission	0.654 and 0.521	0.481 and 0.724
Refinement method	full-matrix least-squares on F^2	full-matrix least-squares on F^2
Data/restraints/parameters	3042/0/199	3756/0/272
Goodness-of-fit on F^2	1.055	1.056
Final R indices ($I > 2\sigma(I)$)	$R_1 = 0.0299$, $wR_2 = 0.0800$	$R_1 = 0.0285$, $wR_2 = 0.0743$
R indices (all data)	$R_1 = 0.0338$, $wR_2 = 0.0825$	$R_1 = 0.0337$, $wR_2 = 0.0766$
Largest difference in peak and hole (e Å^{-3})	0.522 and −0.471	0.412 and −0.365

3. Results and discussion

3.1. Synthesis and spectroscopic characterization of complexes *1* and *2*

Complex **1** was successfully obtained by the reaction of freshly prepared $[(\mu\text{-HS})_2Fe_2(CO)_6]$ [27] with *N*-(2-hydroxyethyl)-2-aza-1,3-propanediol, produced in situ by condensation of formaldehyde and ethanol amine in THF. The complex (Fig. 1b), designed as a model of the H_2O-coordinate H_{ox} state of the H-cluster, could not be formed via intramolecular CO-displacement by the OH group of **1** in the presence of CO-removing reagent Me_3NO and/or under irradiation of an ultraviolet lamp. The reaction of complex **1** and isonicotinyl chloride hydrochloride in the presence of excess Et_3N in CH_3CN afforded pyridyl-functionalized diiron complex **2** in a good yield (Scheme 1).

Complexes **1** and **2** were characterized by MS, IR, ^{1}H NMR spectra and elemental analysis. The results of elemental analyses for **1** and **2** are in good agreement with the supposed compositions. The mass spectra show the parent ion peaks at m/z 429 $[M-H]^-$ for **1**, measured by an API-ES negative mode, and at m/z 558 $[M+Na]^+$ for **2** by an API-ES positive mode. Complexes **1** and **2** in CH_2Cl_2 each display three strong νCO bands in the region of 1990–2080 cm^{-1} in IR spectra. The wavenumbers of the νCO bands for complexes **1** and **2** are almost identical. The characteristic frequency for the OH group at 3483 cm^{-1} for **1** and a strong band of the acyl group at 1728 cm^{-1} for **2** were also observed.



Scheme 1. (a) $(CH_2O)_n/H_2NCH_2CH_2OH$, THF; (b) $PyCOCl \cdot HCl$, NEt_3, CH_3CN.

3.2. Molecular structures and intermolecular contacts in the crystals of complexes *1* and *2*

The crystallographic structures of **1** and **2** are given as SHELXL-97 diagrams in Fig. 2. Selected bond lengths and angles are listed in Table 2. Crystallographic studies show the structural resemblance of the framework of **1** and **2** to previously reported 2Fe2S models [5–8]. The central structure of the [2Fe2S] core is in a butterfly conformation and each Fe atom is coordinated with a pseudo-square-pyramidal geometry. The Fe–Fe distances, 2.501 for **1** and 2.503 Å for **2**, are somewhat shorter than that in the structures of Fe-only hydrogenases (ca. 2.6 Å) [3,4], and in good agreement with the Fe–Fe bonds (2.49–2.51 Å) found for other all-CO diiron azadithiolates [19–22]. The bridged-N atoms of **1** and **2** deviate upwards from the plane defined by the C(7), C(8) and C(9) atoms. The sums of the C–N–C angles around N are 352.9° for **1** and 350.9° for **2**. Both hydroxy and pyridyl groups in the crystals of complexes **1** and **2** are in the vertical position.

A packing diagram of molecules in the crystals of complex **1** along the *b*-axis is given in Fig. 3. Hydrogen atoms were generated with isotropic thermal parameters in idealized positions, riding on their carrier atoms, except for the hydrogen atoms of the hydroxyl group, which were located on two different positions from the difference Fourier map and then idealized. As shown in the packing diagram (Fig. 3b), extended networks are constructed by intermolecular H-bonds. In the crystals of complex **1**, in addition to the H-bonds among OH groups, the hydrogen atom of the OH group also form H-bonds with the oxygen atom of the CO ligand, presumably due to the vibration of the OH group. The distances and angles of the two kinds of H-bonds in the crystals of complex **1** are given in Table 3.

A packing diagram of molecules in the crystals of complex **2** along the *a*-axis is given in Fig. 4a. A simplified view of the coupled molecules is given in Fig. 4b to clearly show the assembly geometry and the intermolecular S···O interactions in the crystals of complex **2**. A particularly attractive aspect is the well-arranged centrally symmetric coupling of the molecules, resulting from close S···O intermolecular contacts (3.244 Å) and the π–π stacking of the pyridyl rings (the distance of two adjacent pyridyl rings 2.692 Å). The intermolecular S···O distance in the crystals of complex **2** is slightly shorter than the sum of van der Waals radii but apparently shorter than the observed average value (3.45 Å) of S···O intermolecular contacts reported by Rowland and Taylor [30]. The relative angles

Table 2
Selected bond lengths (Å) and angles (°) for complexes **1** and **2**

Complex	**1**	**2**
Fe(1)–Fe(2)	2.501(7)	2.503(2)
Fe(1)–S(2)	2.271(7)	2.256(2)
Fe(1)–S(1)	2.262(8)	2.256(1)
Fe(2)–S(1)	2.265(7)	2.255(1)
Fe(2)–S(2)	2.260(8)	2.248(1)
Fe(1)–C(1)	1.799(3)	1.793(3)
Fe(1)–C(2)	1.780(3)	1.782(3)
Fe(1)–C(3)	1.799(3)	1.779(3)
Fe(2)–C(4)	1.793(3)	1.791(3)
Fe(2)–C(5)	1.798(3)	1.782(3)
Fe(2)–C(6)	1.798(3)	1.786(3)
Fe(1)–S(1)–Fe(2)	67.07(2)	67.40(4)
Fe(1)–S(2)–Fe(2)	66.99(3)	67.53(5)
S(1)–Fe(1)–S(2)	84.57(3)	84.18(3)
S(1)–Fe(2)–S(2)	84.76(3)	84.38(5)
C(7)–S(1)–Fe(2)	109.8(8)	109.1(1)
C(8)–S(2)–Fe(2)	109.4(9)	108.0(9)
C(7)–N(1)–C(8)	116.0(2)	115.9(2)
C(7)–N(1)–C(9)	118.7(2)	118.7(2)
C(8)–N(1)–C(9)	118.2(2)	116.3(2)
N(1)–C(9)–C(10)	110.7(2)	111.7(2)
C(9)–C(10)–O(7)	111.2(3)	110.5(2)

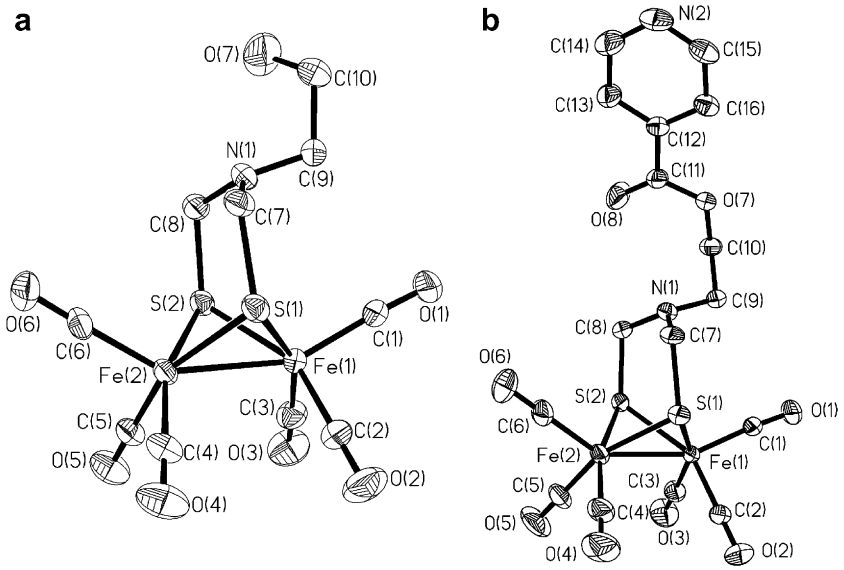


Fig. 2. Molecular structures of **1** (a) and **2** (b).

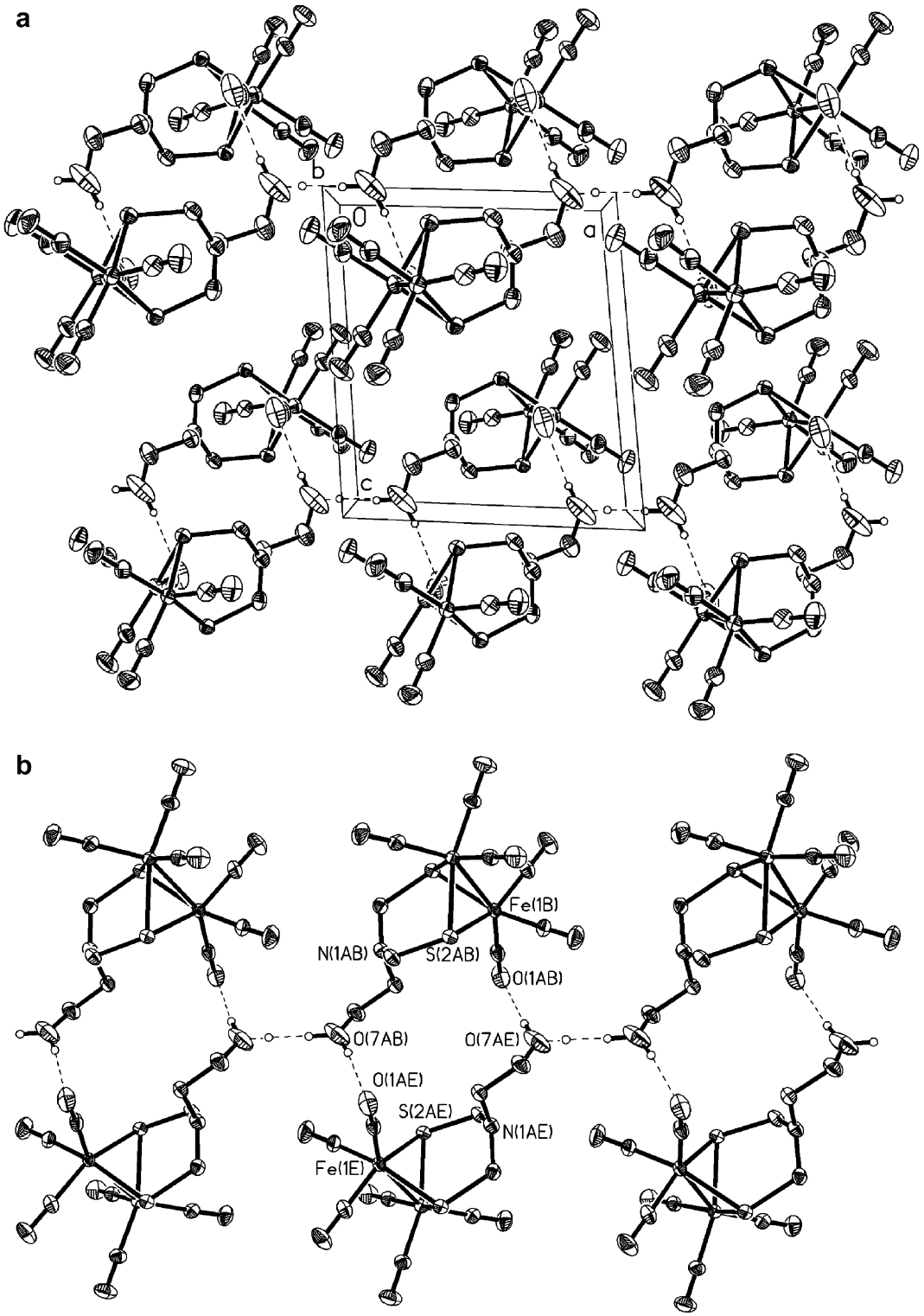


Fig. 3. (a) Stereoplot of the unit cell of **1** along the *b*-axis; (b) a simplified view of packing geometry. The dotted lines represent the intermolecular H-bonds.

Table 3
Distances (Å) and angles (°) for the H-bonds in the crystals of **1**

H-bond	$d_{O\cdots O}$	$d_{O\cdots H}$	O···H–O angle
$O_{CO}\cdots$H–O	3.168	2.263	173.8
$O_{OH}\cdots$H–O	2.927	2.076	177.6

are 139.7° for C–O–S, 165.3° for O–S–Fe(1), 102° for O–S–Fe(2) and 76.4° for O–S–C.

The non-bonded contacts between sulfur and oxygen atoms have been found in crystals of some organic compounds [31–33]. However, most of them are intramolecular

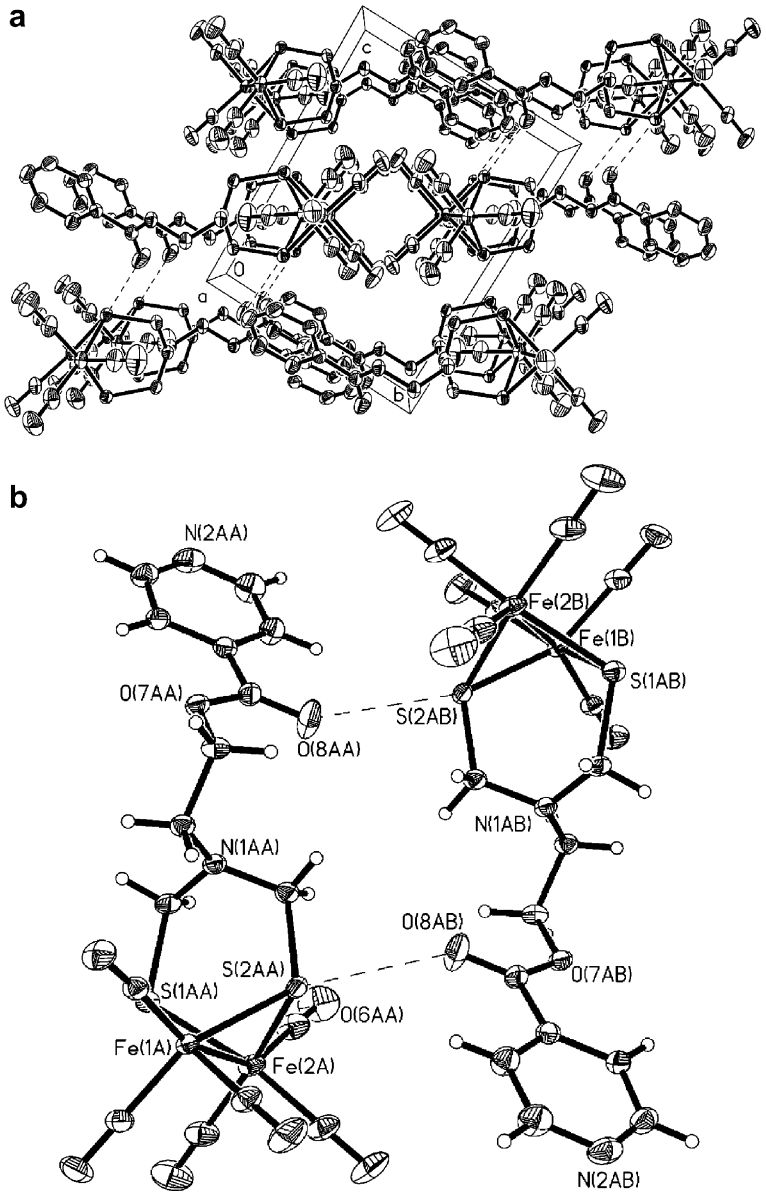


Fig. 4. (a) Stereoplot of the unit cell of **2** along the *a*-axis; (b) a simplified view of packing geometry of the coupled molecules. The dotted lines represent the intermolecular S···O contacts.

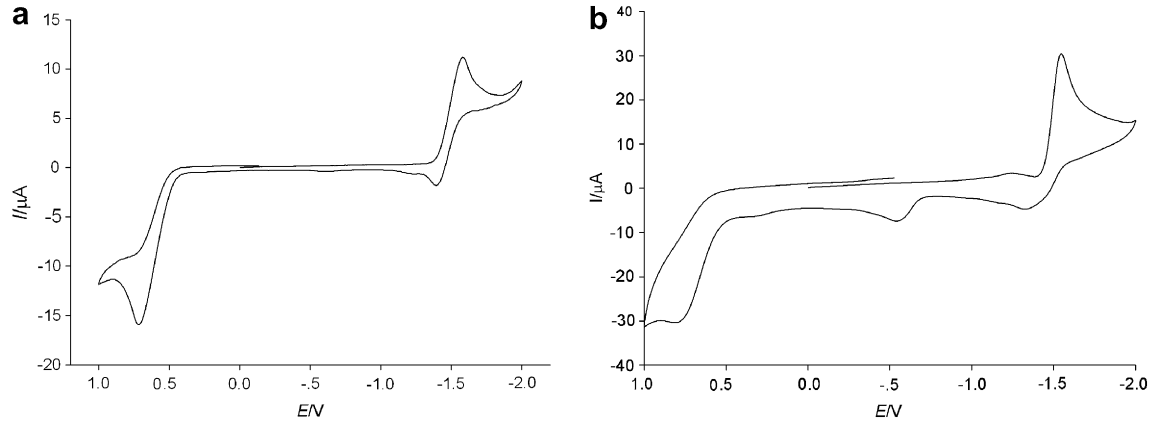


Fig. 5. Cyclic voltammograms of **1** (a) and **2** (b), 1.0 mmol in 0.05 M [^{n}Bu$_4$N]PF$_6$/CH$_3$CN at a scan rate of 100 mV s^{-1}. Potentials are vs. Fc/Fc$^+$.

Table 4
Electrochemical data of complexes **1** and **2**[a]

Complex	E^{ox}_{pirr} (V) Fe(I)Fe(I)/Fe(II)Fe(I)	E_{pc}, E_{pa} (V) Fe(I)Fe(I)/Fe(0)Fe(I)
1	+0.59	−1.66, −1.45
2	+0.61	−1.65, −1.47

[a] All potentials are vs. Fc/Fc^+.

interactions with the S···O non-bonded distances (2.03–3.00 Å) significantly shorter than the sum of the corresponding van der Waals radii (3.25 Å) [33]. To the best of our knowledge, so far there is no report on the intermolecular non-bonded S···O interaction for organometallic complexes. The intermolecular contact between the bridging-sulfur and the oxygen atom of the electro-attracting PyC═O moiety gives a further proof for the nucleophilicity of the bridging-sulfur atoms in the 2Fe2S model complexes, which may play a role of in-site base in the process of enzymetic H_2-evolution [34].

3.3. Cycle voltammograms of model complexes *1* and *2*

Electrochemistry of model complexes **1** and **2** were studied to evaluate their redox properties. The cyclic voltammograms of **1** and **2** were recorded in CH_3CN with 0.05 M *n*-Bu_4NPF_6 as electrolyte (Fig. 5). The electrochemical data are given in Table 4. Complexes **1** and **2** each display an irreversible oxidation peak and an irreversible reduction peak. The oxidation peaks, at +0.59 V versus Fc/Fc^+ for **1** and +0.61 V for **2**, are ascribed to the $Fe(I)Fe(I) \rightarrow Fe(II)Fe(I) + e^-$ process and the reduction peaks, at −1.66 V for **1** and −1.65 V for **2**, are assigned to the one-electron process of $Fe(I)Fe(I) + e^- \rightarrow Fe(0)Fe(I)$, as described for other analogous all-CO diiron complexes reported previously [35]. The redox potentials of diiron complexes are hardly influenced by changing the functional group on the N-bonded ethylene chain. The peak of the second reduction process does not observed within the solvent window.

Acknowledgement

We are grateful to the Chinese National Natural Science Foundation (Grant No. 20471013), the Swedish Energy Agency, the Swedish Research Council and K&A Wallenberg Foundation for financial supports of this work.

Appendix A. Supplementary material

CCDC 619653 and 619654 contain the supplementary crystallographic data for **1** and **2**. These data can be obtained free of charge via http://www.ccdc.cam.ac.uk/conts/retrieving.html, or from the Cambridge Crystallographic Data Centre, 12 Union Road, Cambridge CB2 1EZ, UK; fax: (+44) 1223-336-033; or e-mail: deposit@ccdc.cam.ac.uk. Supplementary data associated with this article can be found, in the online version, at doi:10.1016/j.poly.2006.09.023.

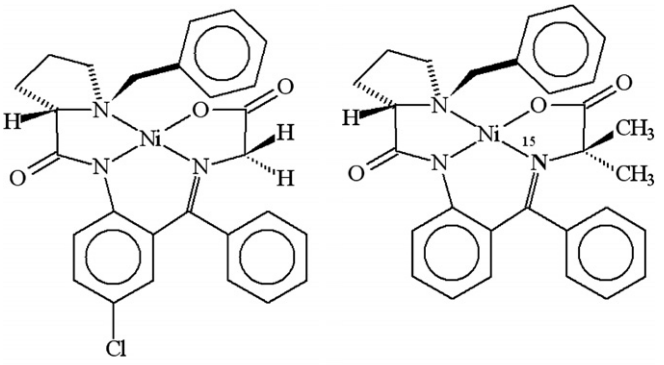
References

[1] R. Cammack, Nature 397 (1999) 214.
[2] M. Frey, ChemBioChem 3 (2002) 153.
[3] J.W. Peters, W.N. Lanzilotta, B.J. Lemon, L.C. Seefeldt, Science 282 (1998) 1853.
[4] Y. Nicolet, C. Piras, P. Legrand, C.E. Hantchikian, J.C. Fontecilla-Camps, Structure 7 (1999) 13.
[5] I.P. Georgakaki, L.M. Thomson, E.J. Lyon, M.B. Hall, M.Y. Darensbourg, Coord. Chem. Rev. 238–239 (2003) 255.
[6] T.B. Rauchfuss, Inorg. Chem. 43 (2004) 14.
[7] X.-M. Liu, S.K. Ibrahim, C. Tard, C.J. Pickett, Coord. Chem. Rev. 249 (2005) 1641.
[8] L.-C. Sun, B. Åkermark, S. Ott, Coord. Chem. Rev. 249 (2005) 1653.
[9] X. Zhao, I.P. Georgakaki, M.L. Miller, R. Mejia-Rodriguez, C.-Y. Chiang, M.Y. Darensbourg, Inorg. Chem. 41 (2002) 3917.
[10] F. Gloaguen, J.D. Lawrence, M. Schmidt, S.R. Wilson, T.B. Rauchfuss, J. Am. Chem. Soc. 123 (2001) 12518.
[11] C.A. Boyke, T.B. Rauchfuss, S.R. Wilson, M. Rohmer, M. Bénard, J. Am. Chem. Soc. 126 (2004) 15151.
[12] P. Li, M. Wang, C.-J. He, G.-H. Li, X.-Y. Liu, C.-N. Chen, B. Åkermark, L.-C. Sun, Eur. J. Inorg. Chem. (2005) 2506.
[13] J. Capon, S. El Hassnaoui, F. Gloaguen, P. Schollhammer, J. Talarmin, Organometallics 24 (2005) 2020.
[14] Y. Nicolet, A.L. Lacey, X. Vemède, V.M. Fernandez, E.C. Hatchikian, J.C. Fontecilla-Camps, J. Am. Chem. Soc. 123 (2001) 1596.
[15] H.-J. Fan, M.B. Hall, J. Am. Chem. Soc. 123 (2001) 3828.
[16] H.-X. Li, T.B. Rauchfuss, J. Am. Chem. Soc. 124 (2002) 726.
[17] L. Schwartz, G. Eilers, L. Eriksson, A. Gogoll, R. Lomoth, S. Ott, Chem. Commun. (2006) 520.
[18] W.-B. Dong, M. Wang, X.-Y. Liu, K. Jin, G.-H. Li, F.-J. Wang, L.-C. Sun, Chem. Commun. (2006) 305.
[19] J.D. Lawrence, H.-X. Li, T.B. Rauchfuss, M. Bénard, M.M. Rohmer, Angew. Chem., Int. Ed. 40 (2001) 1768.
[20] S. Ott, M. Kritikos, B. Åkermark, L.-C. Sun, R. Lomoth, Angew. Chem., Int. Ed. 43 (2004) 1006.
[21] F.-J. Wang, M. Wang, X.-Y. Liu, K. Jin, W.-B. Dong, G.-H. Li, B. Åkermark, L.-C. Sun, Chem. Commun. (2005) 3221.
[22] L.-C. Song, J.-H. Ge, X.-G. Zhang, Y. Liu, Q.-M. Hu, Eur. J. Inorg. Chem. (2006) 3204.
[23] M. Razavet, S.C. Davies, D.L. Hughes, J.E. Barclay, D.J. Evans, S.A. Fairhurst, X.-M. Liu, C.J. Pickett, Dalton Trans. (2003) 586.
[24] S. Ott, M. Borgström, M. Kritikos, R. Lomoth, J. Bergquist, B. Åkermark, L. Hammarström, L.-C. Sun, Inorg. Chem. 43 (2004) 4683.
[25] S. Ott, M. Kritikos, B. Åkermark, L.-C. Sun, Angew. Chem., Int. Ed. 42 (2003) 3285.
[26] L.-C. Song, M.-Y. Tang, F.-H. Su, Q.-M. Hu, Angew. Chem., Int. Ed. 45 (2006) 1130.
[27] D. Seyferth, R.S. Henderson, J. Organomet. Chem. 218 (1981) C34.
[28] Software Packages SMRT and SAINT, Siemens Analytical X-ray Instruments Inc., Madison, WI, 1996.
[29] SHELXTL, Version 5.1, Siemens Industrial Automation, Inc., 1997.
[30] R.S. Rowland, R. Taylor, J. Phys. Chem. 100 (1996) 7384.
[31] R.E. Rosenfield Jr., R. Parthasarathy, J.D. Dunitz, J. Am. Chem. Soc. 99 (1977) 4860.
[32] A. Kálmán, L. Párkányi, Acta Crystallogr., Sect. B 36 (1980) 2372.
[33] J.G. Ángyán, R.A. Poirier, Á. Kucsman, I.G. Csizmadia, J. Am. Chem. Soc. 109 (1987) 2237.
[34] T. Zhou, Y. Mo, A. Liu, Z.-H. Zhou, K.R. Tsai, Inorg. Chem. 43 (2004) 923.
[35] D. Chong, I.P. Georgakaki, R. Mejia-Rodriguez, J. Sanabria-Chinchilla, M.P. Soriaga, M.Y. Darensbourg, Dalton Trans. (2003) 4158.

[11] for positron emission tomography (PET) visualization of cancer cells and in vivo metabolism of 3,4-dioxyphenylalanine (DOPA).

Recently, several stereoselective analogous synthons carrying substituents on the benzyl group were developed [12]. Electronic and steric effects influencing the stereochemistry of alkylation of the synthons were thoroughly investigated by a number of physical–chemical approaches. The conformations of the complexes in solutions were disclosed by NMR [7,13].

A number of X-ray structures of related complexes were published, including pairs of diastereomers with opposite configurations of the α-carbon of the amino acid fragments [14] (for overview, see [13c]). The distribution of the electron density in a single crystal of a glycine synthon was studied by X-ray diffraction by Kožíšek et al. [15]. Ab initio quantum-chemical modelling and topological analysis of electron density were also performed for this molecule [13c,15]. A similar but more acidic Ni(II) complex of the Schiff base of (*S*)-*N*-(2-benzoyl-4-chlorophenyl)-1-benzylpyrrolidine-2-carboxamide and glycine was studied by NMR only [13b]. In spite of their synthetic application as intermediates in the synthesis of α-[^{11}C]methyl amino acids, single crystals of complexes with a quaternary α-carbon of the amino acid fragment have never been studied by X-ray diffraction, neither has complete assignment of their ^{1}H and ^{13}C NMR spectra been done. Here we present X-ray structure determinations for both the Ni(II) complex of the Schiff base of (*S*)-*N*-(2-benzoyl-4-chlorophenyl)-1-benzylpyrrolidine-2-carboxamide and glycine (**1**) and the hemihydrate of the Ni(II) complex of the Schiff base of (*S*)-*N*-(2-benzoylphenyl)-1-benzylpyrrolidine-2-carboxamide and 2-aminoisobutiric acid (**2**), and the full assignment of ^{1}H and ^{13}C NMR spectra of the later structure. These structures are also model compounds for the study of long-range ^{13}C–^{15}N and ^{13}C–^{13}C spin–spin interactions in NMR spectra [13c,16] and circular dichroism [7,17] (see Scheme 1).



1 **2**

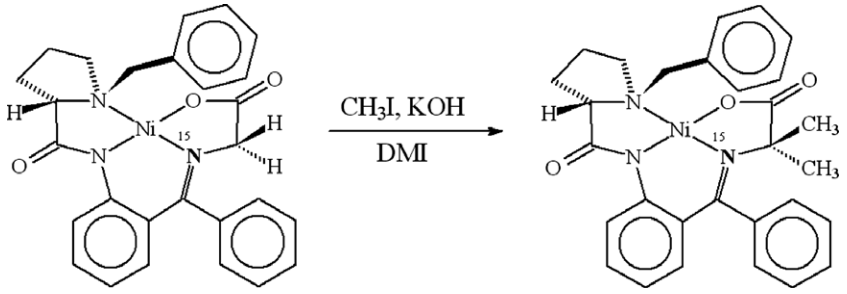
Scheme 1.

2. Experimental

Complex **1** was prepared according to Popkov et al. [13b]. The synthesis of ^{15}N-labelled complex **2**, (^{15}N)Me$_2$GK, was as follows (see also Reaction scheme). To a solution of the Ni(II) complex of the Schiff base of (*S*)-*N*-(2-benzoylphenyl)-1-benzylpyrrolidine-2-carboxamide and (^{15}N)glycine ((^{15}N)GK) (20 mg, 0.04 mmol), cf. Jirman et al. [16], in 1,3-dimethylimidazolidin-2-one (DMI, 1 ml) under an atmosphere of Ar at 20 °C, an excess of KOH and CH_3I (12.6 μl, 0.2 mmol) were added and the reaction mixture was stirred for 30 min. The reaction mixture was poured into 10% aqueous citric acid (30 ml), stirred and the resulting red suspension was filtered off and dried in air. The filter was dried and extracted with chloroform. The extract was evaporated in vacuo. (^{15}N)Me$_2$GK was purified by preparative TLC using silica gel (Merck 60H) eluted with CH_2Cl_2. The obtained complex was then purified by chromatography on Sephadex LH-20 with toluene:MeOH = 2:1 as red crystals. Yield: 15 mg (71% related to (^{15}N)GK), m.p. 212–217 °C (from acetone). Calculated mass for $C_{29}H_{29}N_2{}^{15}NO_3Ni$: $[M^+] = 526.1533$. High resolution FAB MS found $[M^+] = 526.1539$.

NMR spectroscopy: Bruker AMX 360, 23 °C, hexamethyldisiloxane ($\delta(^1H) = 0.05$ ppm) was used as an internal standard. Assigned ^{1}H NMR and ^{13}C NMR spectra for (^{15}N)Me$_2$GK are presented in Table 1.

X-ray analysis: Siemens SMART 1K CCD area detector diffractometer equipped with LT-2 low temperature device, using graphite-monochromated Mo Kα characteristic radiation ($\lambda = 0.71073$ Å). Data were collected at 173 K, with a crystal-to-detector distance 3.97 cm, ω-scans covering whole sphere of reciprocal space with



Reaction scheme.

Table 1
^{1}H and ^{13}C NMR chemical shifts (ppm) for (^{15}N)Me_2GK in $CDCl_3$ at 23 °C

Position	$\delta(^{1}H)$	$\delta(^{13}C)$	$J(^{15}N, ^{13}C)$
1	2.06, 3.66	57.43	
2	2.13, 3.43	23.86	
3	2.46, 2.66	30.61	
4	3.46	69.99	
5		180.46	
6		141.31	1.1
7	7.92	123.96	
8	7.10	131.49	
9	6.62	120.71	
10	6.71	133.24	2.2
11		128.31	2.9
12		171.61	12.1
13		136.32	1.6
14	7.00	128.01	0.8
15	7.39	128.02	
16	7.43	127.14	
17	7.45	129.25	
18	7.28	130.16	1.0
19		74.55	2.7
20		182.49	4.1
21	3.60, 4.46	63.20	
22		133.41	
23	8.08	131.63	
24	7.39	128.03	
25	7.26	128.98	
26	7.39	128.03	
27	8.08	131.63	
28 (C-CH_3)	1.78	29.92	
29 (C-CH_3)	1.08	28.77	

steps of 0.3° [18a]. Data were corrected for absorption effects [18b]. The structures were solved by direct methods [18c] and refined by least-squares method on F^2 with H-atoms constrained to ideal geometries and riding on their respective pivot atoms [18c]. Graphics were produced by DIAMOND [18d].

Crystal data for complex **1**: $C_{27}H_{24}ClN_3NiO_3$, M_r 532.65, triangular red plate, crystal size (mm) = 0.60 × 0.60 × 0.30, monoclinic, space group $P2_1$, $a = 11.4695(1)$ Å, $b = 7.6323(1)$ Å, $c = 13.7066(2)$ Å, $\beta = 98.077(1)°$, $V = 1187.95(3)$ Å^3, $Z = 2$, $D_{calc} = 1.489$ g cm^{-3}, $\mu_{Mo} = 0.965$ mm^{-1}, $\theta_{max} = 32.78°$, $T_{min} = 0.6143$, $T_{max} = 0.7490$. 20736 measured, 8228 independent ($R_{int} = 0.0206$) and 8026 observed ($I > 2\sigma_I$) reflections, 340 parameters, $R_1 = 0.0265$ for observed and $wR(F^2) = 0.0714$ for all reflections, $S = 1.016$, $\Delta\rho_{max} = 0.483$, $\Delta\rho_{min} = -0.286$ e Å^{-3}.

Crystal data for complex **2**: $C_{29}H_{29}N_3NiO_3 \cdot 0.5H_2O$, M_r 535.27, red block crystal, size (mm) = 1.00 × 0.70 × 0.50, trigonal, space group $P3_121$, $a = 14.2295(1)$ Å, $b = 14.2295(1)$ Å, $c = 21.5928(1)$ Å in hexagonal cell, $V = 3786.33(4)$ Å^3, $Z = 6$, $D_{calc} = 1.408$ g cm^{-3}, $\mu_{Mo} = 0.807$ mm^{-1}, $\theta_{max} = 27.12°$, $T_{min} = 0.3113$, $T_{max} = 0.6683$. 45414 measured, 5579 independent ($R_{int} = 0.0728$) and 4778 observed ($I > 2\sigma_I$) reflections, 365 parameters, $R_1 = 0.0343$ for observed and $wR(F^2) = 0.0840$ for all reflections, $S = 0.978$, $\Delta\rho_{max} = 0.278$, $\Delta\rho_{min} = -0.296$ e Å^{-3}.

3. Results and discussion

Crystals of the Ni(II) complex of the Schiff base of (*S*)-*N*-(2-benzoyl-4-chlorophenyl)-1-benzylpyrrolidine-2-carboxamide and glycine (**1**) [GKCl], suitable for X-ray analysis, were obtained by slow evaporation of an acetone solution. Crystals of the Ni(II) complex of the Schiff base of (*S*)-*N*-(2-benzoylphenyl)-1-benzylpyrrolidine-2-carboxamide and 2-aminoisobutiric acid (**2**) [Me_2GK] were grown by the same method. The numbering schemes for complexes **1** and **2** are shown in Figs. 1 and 2, respectively. X-ray structure analysis established unambiguously the absolute structure with Flack parameters [19] being −0.002(5) and −0.031(12), using 3738 and 2452 Friedel pairs for complexes **1** and **2**, respectively. Both complexes show nickel in a square-planar coordination geometry with small pyramidal distortions. In Table 2 we present a selection of bond distances, as well as some stereochemical data. We define the three chelate rings of complexes **1** and **2** as follows: the five-membered ring A is defined by atoms Ni/O2/C20/C19/N3, the six-membered ring B is defined by atoms Ni/N2/C6/C11/C12/N3 and the five-membered ring C is defined by atoms Ni/N1/C4/C5/N2. The conformations of these rings are indicated in Table 2 and they differ substantially between both complexes; while Me_2GK complex **2** adopts an asymmetric λ-envelope/asymmetric δ-boat/asymmetric λ-envelope conformation for rings A/B/C/, respectively,

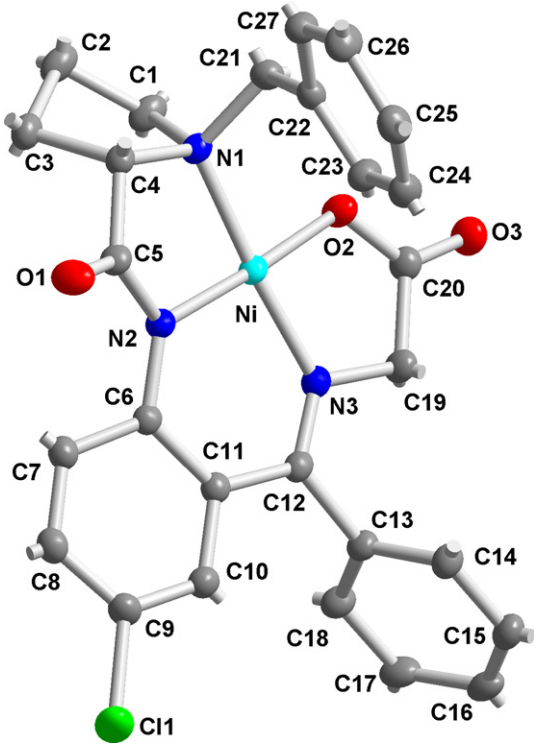


Fig. 1. The numbering scheme of **1** with atomic displacement ellipsoids drawn at the 50% probability level. H atoms are omitted for clarity and indicated by partial bonds only.

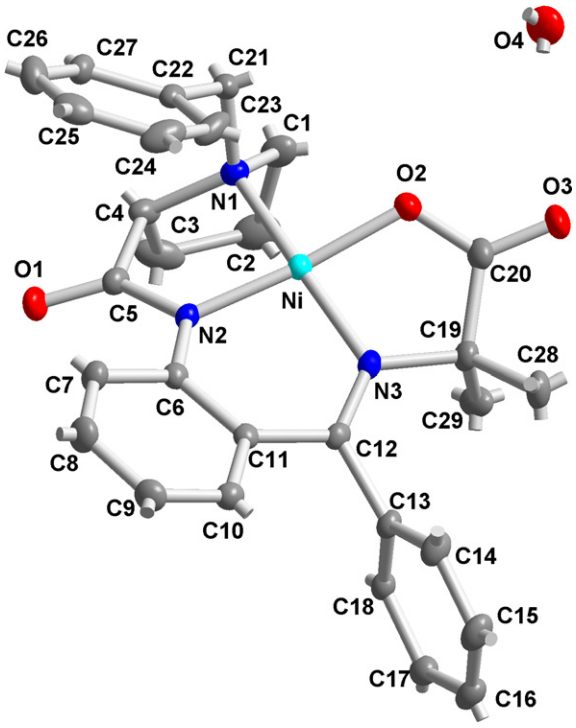


Fig. 2. The numbering scheme of **2** with atomic displacement ellipsoids drawn at the 30% probability level. H atoms are omitted for clarity and indicated by partial bonds only.

Table 2
Selected bond distances (Å) and angles (°) and some structural and stereochemical data

			Complex **1**	Complex **2**
Square-planar centre	Ni–N1		1.941(1)	1.949(2)
	Ni–N2		1.864(1)	1.848(2)
	Ni–N3		1.862(1)	1.880(2)
	Ni–O2		1.869(1)	1.843(2)
	N1–Ni–N2		88.03(4)	86.84(9)
	N2–Ni–N3		95.61(5)	96.69(9)
	N3–Ni–O2		87.52(4)	86.74(9)
	O2–Ni–N1		88.94(4)	90.71(9)
	N1–Ni–N3		175.60(5)	170.24(9)
	N2–Ni–O2		176.12(5)	173.27(9)
RMS deviations from plane			0.036	0.113
Ring A	Ni–O2–C20		116.04(9)	116.1(2)
	O2–C20–C19		114.8(1)	115.8(2)
	C20–C19–N3		109.9(1)	105.4(2)
	C19–N3–Ni		111.50(8)	110.0(2)
Deviation from plane NiN1O2[a]		C19	+0.209(2)	−0.859(4)
		C20	+0.107(2)	−0.358(4)
			asym. δ-env.	asym. λ-env.
Ring B	Ni–N3–C12		129.28(8)	125.4(2)
	N3–C12–C11		122.4(1)	121.3(2)
	C12–C11–C6		123.6(1)	124.0(2)
	C11–C6–N2		122.1(1)	120.4(2)
	C6–N2–Ni		126.09(8)	121.3(2)
Deviation from plane NiN2N3[a]		C12	+0.043(2)	+0.098(4)
		C11	−0.020(2)	+0.607(4)
		C6	−0.125(2)	+0.606(4)
			asym. λ-skew boat	asym. δ-boat
Ring C	Ni–N2–C5		113.73(8)	116.0(2)
	N2–C5–C4		113.1(1)	112.4(2)
	C5–C4–N1		111.08(9)	110.2(2)
	C4–N1–Ni		109.43(8)	106.3(2)
	N2–C5–O1		126.9(1)	127.6(3)
	Ni–N1–C21		113.71(8)	112.9(2)
Deviation from plane NiN1N2[a]		C5	+0.390(2)	−0.250(4)
		C4	+0.167(2)	−0.572(4)
			asym. δ-env.	asym. λ-env.

[a] The deviations are considered positive when the atom is on the same side as the benzyl group atoms (C21 to C27).

the complex GKCl (**1**) adopts an asymmetric δ-envelope/λ-skew boat/asymmetric δ-envelope conformation (for nomenclature see [20]). Thus complex **2** has a similar conformation to the [Ni((*S*)-BBP-L-Ser)] and [Ni((*S*)-BBP-L-aaIm)] complexes reported by Pessoa et al. [17], while complex GKCl (**1**) has a conformation somewhat similar to [Ni((*S*)-BBP-Gly)], reported by the same authors, but published earlier by us [13c,15].

We observed a π-charge delocalization, similar to the recently described structure of the Ni complex of the Schiff base of (*S*)-*N*-(2-benzoylphenyl)-1-benzylpyrrolidine-2-carboxamide and (*S*)-2-amino-3-(1-naphthyl)propanoic acid [7], in the proximity of the N2 atom due to the free π-orbital of this nitrogen atom. The bonds {complex **1**: N2–C6 1.3968(16) Å, N2–C5 1.3910(15) Å; complex **2**: N2–C6 1.398(3) Å, N2–C5 1.371(3) Å} are shorter than the published [21] average value for the N–C(sp^2) bond {$d_{C-N} \approx 1.47(1)$ Å}. We also found a small deviation of the C5–O1 bond {complex **1**: 1.2299(15) Å, complex **2**: 1.230(3) Å} from the published [9] value of $d_{C=O} \approx 1.21(1)$ Å for ketones. The situation is less clear at the N3 atom {complex **1**: N3–C12 1.3059(16) Å, N3–C19 1.4838(16) Å; complex **2**: N3–C12 1.300(3) Å, N3–C19 1.509(3) Å}. These values are in good accordance with the average values for 17 similar structures [1f,14, Refs. [17,19,20,22–24] in 13c,22], namely 1.40(3) Å for N2–C6, 1.37(2) Å for N2–C5, 1.231(9) Å for C5–O1, 1.301(13) for N3–C12 and 1.48(2) Å for N3–C19.

The hydrogen bond schemes of the two complexes are different: complex GKCl (**1**) forms a chain along the *c*-axis (Fig. 3) via weak hydrogen bonds of C–H···O type (for details see Table 3), while the Me_2GK complex **2** forms dimers of molecules, mediated by a water molecule located at the crystallographic twofold axis, see Fig. 4.

In order to assign the ^{1}H NMR and ^{13}C NMR spectra, cross-peaks in 2D NOESY spectra due to a through-space interaction mechanism were obtained for neighbouring protons and, thus, such cross-peaks were found in analogous positions as those observed in the H,H-COSY spectrum based on coupling constants. Conformationally, the most important cross-peaks in the 2D NOESY spectra were found for pairs of resonances at δ 7.00/1.78,

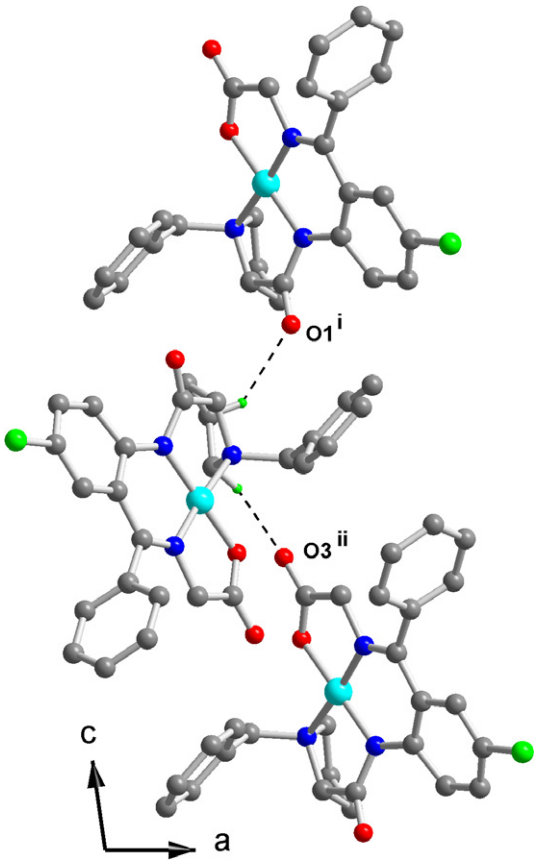


Fig. 3. The hydrogen-bonding pattern in the crystal lattice of **1**. Only H atoms taking part in the presented bonds are shown. For symmetry codes see Table 3. Chains of molecules parallel to c-axis are formed.

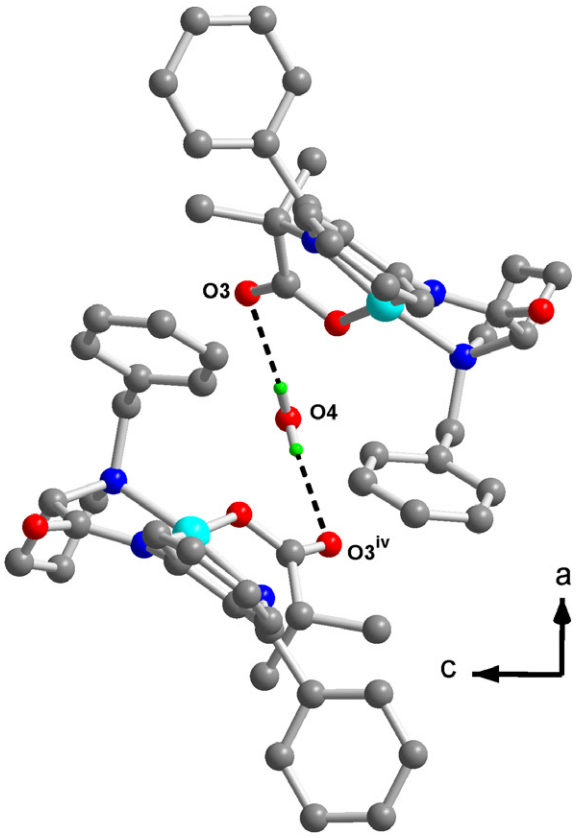


Fig. 4. The hydrogen-bonding pattern in the crystal lattice of **2**. Only H atoms taking part in the presented bonds are shown. Dimers of molecules are formed. Symmetry code: (iv) $-x, -x+y, 1/3-z$.

Table 3
Hydrogen-bonding geometry (Å, °) for GKCl complex (**1**) and Me_2GK complex (**2**)

D–H···A	D–H	H···A	D···A	D–H···A
Complex ***1***				
C2–H2A···O1^{i}	0.99	2.55	3.2946(17)	131.9
C7–H7···O1	0.95	2.25	2.7089(16)	108.5
C21–H21B···O2	0.99	2.38	2.9247(16)	113.8
C1–H1B···O3^{ii}	0.99	2.51	3.4824(19)	167.8
Complex ***2***				
O4–H4A···O3	0.79(4)	2.16(4)	2.942(3)	167(4)
C1–H1B···O2	0.99	2.32	2.893(4)	116.2
C7–H7···O1	0.95	2.27	2.807(3)	115.2
C21–H21B···O3^{iii}	0.99	2.58	3.506(4)	155.9
C28–H28B···O3	0.98	2.40	2.819(4)	105.0

Symmetry codes: (i) $2-x, 1/2+y, 2-z$; (ii) $2-x, 1/2+y, 1-z$; (iii) $-1-x+y, 1-x, z-1/3$.

7.28/1.08, 6.71/7.28, 4.46/3.46 and 8.08/3.46 ppm, corresponding to space proximity of protons H14/H28, H18/H29 (the assignment of these two pairs may be mutually interchanged since an absolute assignment is not clear), H10/H18, H4/H21 and H4/H23,27. From these experimental results it follows that the conformation of the Ni complex in solution should be the same as that in the solid state. Similarity of conformations in $CDCl_3$ solution and in the solid state was previously proved for a similar complex derived from glycine [13a,13b], in the case of the complex derived from (*S*)-2-amino-3-(1-naphthyl)propanoic acid, conformations in $CDCl_3$ solution and in the solid state are significantly different [7].

In complex **2**, the repulsion between the benzyl group and an equatorial methyl group affects the conformation of the benzyl group, distribution of π-electron density in this group and distortion of the internal coordination sphere. In strong contrast to the complex (^{15}N)GK [16] derived from non-substituted (^{15}N)glycine, long range through-space spin–spin interactions are not observed in ^{13}C and ^{15}N NMR spectra of complex **2** (Table 1). A longer distance from the benzyl group to the amino acid and the benzophenone fragments of the molecule is probably responsible for this absence of spin–spin interactions. In (^{15}N)GK, a partial positive charge of the nickel atom leads to polarisation of π-electron density of the benzyl group towards the nickel atom [15]. In several similar complexes, MP2 modelling followed by a topological analysis revealed the formation of weak covalent bonds between carbon atoms in the benzyl group and carbons in the benzophenone fragment or oxygen atoms of the carboxy residue [A. Popkov, M. Breza, unpublished results]. Both polarisation and the weak bond formation could be involved in long range through-space spin–spin interactions. In the complex **2**, these two factors do not play their role due to

a more distant position of the benzyl group compared to complex (^{15}N)GK.

Preparation of a labelled analogue of complex **1** from (^{15}N)glycine is underway.

Appendix A. Supplementary material

CCDC 294429 and 294430 contain the supplementary crystallographic data for this paper. These data can be obtained free of charge via http://www.ccdc.cam.ac.uk/conts/retrieving.html, or from the Cambridge Crystallographic Data Centre, 12 Union Road, Cambridge CB2 1EZ, UK; fax: (+44) 1223-336-033; or e-mail: deposit@ccdc.cam.ac.uk. Supplementary data associated with this article can be found, in the online version, at doi:10.1016/j.poly.2006.09.103.

References

[1] (a) Y.N. Belokon, V.I. Bakhmutov, N.I. Chernoglazova, K.A. Kochetkov, S.V. Vitt, N.S. Garbalinskaya, V.M. Belikov, J. Chem. Soc., Perkin Trans. I (1988) 305;
(b) Y.N. Belokon, V.I. Tararov, V.I. Maleev, T.F. Saveleva, M.G. Ryzhov, Tetrahedron: Asymmetry 9 (1998) 424;
(c) A. Debache, S. Collet, P. Bauchat, D. Danion, L. Euzenat, A. Hercouet, B. Carboni, Tetrahedron: Asymmetry 12 (2001) 761;
(d) M. Nádvorník, A. Popkov, Green Chem. 4 (2002) 71;
(e) H. Ueki, T.K. Ellis, C.H. Martin, T.U. Boettiger, S.B. Bolene, V.A. Soloshonok, J. Org. Chem. 68 (2003) 7104;
(f) X.Y. Gu, J.M. Ndungu, W. Qiu, J.F. Ying, M.D. Carducci, H. Wooden, V.J. Hruby, Tetrahedron 60 (2004) 8233;
(g) S. Vadon-Legoff, S. Dijols, D. Mansuy, J.-L. Boucher, Org. Process Res. Dev. 9 (2005) 677;
(h) V.A. Soloshonok, C. Cai, T. Yamada, H. Ueki, Y. Ohfune, V.J. Hruby, J. Am. Chem. Soc. 127 (2005) 15296.

[2] (a) Z. Han, Y. Yamaguchi, M. Kitamura, K. Maruoka, Tetrahedron Lett. 46 (2005) 8555;
(b) B. Lygo, B. Allbutt, E.H.M. Kirton, Tetrahedron Lett. 46 (2005) 4461;
(c) Y.N. Belokon, N.B. Bespalova, T.D. Churkina, I. Císařová, M.G. Ezernitskaya, S.R. Harutyunyan, R. Hrdina, H.B. Kagan, P. Kočovský, K.A. Kochetkov, O.V. Larionov, K.A. Lyssenko, M. North, M. Polášek, A.S. Peregudov, V.V. Prisyazhnyuk, Š. Vyskočil, J. Am. Chem. Soc. 125 (2003) 12860;
For review, see: (a) B. Lygo, B.I. Andrews, Acc. Chem. Res. 37 (2004) 518;
(b) M.J. O'Donnell, Acc. Chem. Res. 37 (2004) 506;
(c) A. Ma, Angew. Chem., Int. Ed. 42 (2003) 4290;
(d) K. Maruoka, O. Takashi, Chem. Rev. 103 (2003) 3013.

[3] (a) U. Schölkopf, Tetrahedron 39 (1983) 2085;
(b) S.D. Bull, S.G. Davies, S.W. Epstein, M.A. Leech, J.V.A. Ouzman, J. Chem. Soc., Perkin Trans. 1 (1998) 2321;
(c) D.A. Evans, H. Bartroli, T.L. Shih, J. Am. Chem. Soc. 103 (1981) 2127;
(d) D.A. Evans, A.E. Weber, J. Am. Chem. Soc. 108 (1986) 6757;
(e) D. Seebach, A.R. Sting, M. Hoffmann, Angew. Chem., Int. Ed. Engl. 35 (1996) 2708;
(f) T. Hintermann, D. Seebach, Helv. Chim. Acta 81 (1998) 2093;
(g) D. Seebach, M. Hoffmann, Eur. J. Org. Chem. (1998) 1137;
(h) W. Oppolzer, R. Moretti, C. Zhou, Helv. Chim. Acta 77 (1994) 2363;
(i) G.T. Bourne, D. Crich, J.W. Davies, D.C. Horwell, J. Chem. Soc., Perkin Trans. 1 (1991) 1693;
For review, see: (a) R.O. Duthaler, Tetrahedron 50 (1994) 1539;
(b) P.D. Bailey, J. Clayson, A.N. Boa, Contemp. Org. Synth. 2 (1995) 173.

[4] (a) M.D. Fryzuk, B. Bosnich, J. Am. Chem. Soc. 99 (1977) 6262;
(b) A. Miyashita, A. Yasuda, H. Takaya, K. Toriumi, T. Ito, T. Souchi, R. Noyori, J. Am. Chem. Soc. 102 (1980) 7932;
(c) M. Kitamura, M. Tsukamoto, Y. Bessho, M. Yoshimura, U. Kobs, M. Widhalm, R. Noyori, J. Am. Chem. Soc. 124 (2002) 6649;
For review, see: (a) U. Nagel, J. Albrecht, Top. Catal. 5 (1998) 3;
(b) K.V.L. Crepy, T. Imamoto, Adv. Synth. Catal. 345 (2003) 79.

[5] V.I. Tararov, T.F. Saveleva, N.Y. Kuznetsov, N.S. Ikonnikov, S.A. Orlova, Y.N. Belokon, M. North, Tetrahedron: Asymmetry 8 (1997) 79.

[6] Y.N. Belokon, N.I. Chernoglazova, E.V. Ivanova, A.N. Popkov, M.B. Saporovskaya, N.N. Suvorov, V.M. Belikov, Izv. Akad. Nauk. SSSR, Ser. Khim. (1988) 2818 (in Russian); Engl. Trans.: Bull. Acad. Sci. USSR, Div. Chem. Sci. 37 (1989) 2541.

[7] A. Popkov, I. Císařová, J. Sopková, J. Jirman, A. Lyčka, K.A. Kochetkov, Collect. Czech. Chem. Commun. 70 (2005) 1397.

[8] I. Alves, S. Cowell, Y.S. Lee, X.J. Tang, P. Davis, F. Porreca, V.J. Hruby, Biochem. Biophys. Res. Commun. 318 (2004) 335.

[9] N.W. Boaz, S.E. Large, J.A. Ponasik, M.K. Moore, T. Barnette, W.D. Nottingham, Org. Process Res. Dev. 9 (2005) 472.

[10] A. Popkov, M. Nádvorník, P. Kružberská, A. Lyčka, M. Eisenhut, N.M. Gillings, J. Labelled Compd. Radiopharm. 46 (2003) S227.

[11] A. Popkov, M. Nádvorník, J. Jirman, P. Kružberská, A. Lyčka, T. Weidlich, J. Kožíšek, M. Breza, S. Lehel, N.M. Gillings, Czech. J. Phys. 56 (Suppl. D) (2006) D689.

[12] (a) A. Popkov, A. Gee, M. Nádvorník, A. Lyčka, Transition Met. Chem. 27 (2002) 884;
(b) A.S. Saghiyan, H.H. Hambardzumyan, L.L. Manasyan, A.A. Petrosyan, V.I. Maleev, A.S. Peregudov, Synth. Commun. 35 (2005) 449;
(c) A.S. Saghiyan, S.A. Dadayan, S.G. Petrosyan, L.L. Manasyan, A.V. Geolchanyan, S.M. Djamgaryan, S.A. Andreasyan, V.I. Maleev, V.N. Khrustalev, Tetrahedron: Asymmetry 17 (2006) 455.

[13] (a) J. Jirman, A. Popkov, Collect. Czech. Chem. Commun. 60 (1995) 990;
(b) A. Popkov, J. Jirman, M. Nádvorník, P.A. Manorik, Collect. Czech. Chem. Commun. 63 (1998) 990;
(c) A. Popkov, V. Langer, P.A. Manorik, T. Weidlich, Transition Met. Chem. 28 (2003) 475.

[14] O.V. Larionov, T.F. Saveleva, K.A. Kochetkov, N.S. Ikonnokov, S.I. Kozhushkov, D.S. Yufit, J.A.K. Howard, V.N. Khrustalev, Y.N. Belokon, A. de Meijere, Eur. J. Org. Chem. (2003) 869.

[15] J. Kožíšek, M. Fronc, P. Skubák, A. Popkov, M. Breza, H. Fuess, C. Paulmann, Acta Crystallogr., Sect. A 60 (2004) 510.

[16] J. Jirman, M. Nádvorník, J. Sopková, A. Popkov, Magn. Reson. Chem. 36 (1998) 351.

[17] J.C. Pessoa, I. Correia, A. Galvão, A. Gameiro, V. Felix, E. Fiuza, J. Chem. Soc., Dalton Trans. (2005) 2312.

[18] (a) Siemens. SMART and SAINT: Programs for Data Collection and Integration, Madison, USA, 1995;
(b) G.M. Sheldrick, SADABS: Program for Area Detector Absorption and other Corrections, Version 2.03, University of Göttingen, Göttingen, Germany, 2002;
(c) Bruker, SHELXTL: Solution and Refinement Package, Version 6.10, Bruker AXS Inc., Madison, WI, USA, 2001;
(d) K. Brandenburg, DIAMOND: Crystal and Molecular Structure Vizualization, Version 3.0e, Crystal Impact GbR, Bonn, Germany, 2005.

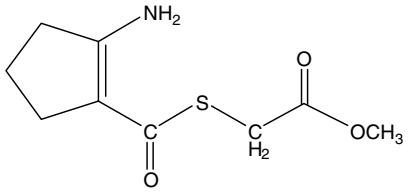
[19] H.D. Flack, Acta Crystallogr., Sect. A 39 (1983) 876.

[20] C.J. Hawkins, in: Absolute Configuration of Metal Complexes, Wiley–Interscience, New York, 1971, pp. 9–13.

[21] J.P. Glusker, M. Lewis, M. Rossi, in: Crystal Structure Analysis for Chemists and Biologists, VCH, New York, 1994, p. 420.

[22] (a) Y.N. Belokon, A.G. Bulychev, M.G. Ryzhov, S.V. Vitt, A.S. Batsanov, Y.T. Struchkov, V.I. Bakhmutov, V.M. Belikov, J. Chem. Soc., Perkin Trans. 1 (1986) 1865;

(b) K. Uytterhoeven, V. Soloshonok, L. van Meervelt, Z. Kristallogr. New Cryst. Struct. (2004) 453;
(c) V.A. Soloshonok, V.P. Kukhar, A.S. Batsanov, M.A. Galakhov, Y.N. Belokon, Y.T. Struchkov, Izv. Akad. Nauk. SSSR, Ser. Khim. (Russ.) (Russ. Chem. Bull.) (1991) 1548;
(d) V.A. Soloshonok, C. Cai, V.J. Hruby, L. Van Meervelt, Tetrahedron 55 (1999) 12045;
(e) Y.N. Belokon, V.I. Maleev, A.A. Petrosyan, T.F. Savel'eva, N.S. Ikonnikov, A.S. Peregudov, V.N. Khrustalev, A.S. Sagiyan, Izv. Akad. Nauk. SSSR, Ser. Khim. (Russ.) (Russ. Chem. Bull.) (2002) 1464;
(f) V.A. Soloshonok, C. Cai, V.J. Hruby, L. Van Meervelt, N. Mischenko, Tetrahedron 55 (1999) 12031.



Scheme 1.

–CH_2COOMe arm was observed; however, weak intermolecular O···H bonds lead to a dimeric arrangement.

2. Experimental

2.1. Materials and physical measurements

All reagents and solvents were commercially obtained, and used without further purification. The ACDA [25,26], ACDASA [6], and ACDASAMe [24] were synthesized by methods in the literature. Infrared spectra were recorded in the range 4000–200 cm^{-1} on a Bruker Vector 22 spectrometer as CsI powder. The ^1H (300 MHz) and ^{13}C (75 MHz) NMR spectra were recorded in DMSO and $CDCl_3$/DMSO (2:1) mixture on a Jeol Eclipse+ 300 spectrometer at room temperature using TMS as reference or solvent signal. EI-mass spectra were performed on a JEOL JMS-AX505HA instrument. UV–Vis spectra were determined in $CHCl_3$ solutions (240–800 nm) on a Spectronic Genesys 5 spectrophotometer using a quartz crystal cell equipped with a Teflon cap. Elemental analyses were obtained from Galbraith Laboratories (Knoxville, TN).

2.2. Ni(ACDASAMe)$_2$ (1)

$NiCl_2 \cdot 6H_2O$ (0.237 g, 1 mmol) was dissolved in ethanol and added to an ethanolic solution of ACDASAMe (0.462 g, 2 mmol). The mixture was stirred for 45 min and the compound that precipitated out as green needles was filtered off and washed with ethanol several times. Yield 0.38 g (73.3%), m.p. 226–227 °C. *Anal.* Calc. for $C_{18}H_{24}N_2NiO_4S_4$: C, 41.63; H, 4.66; N, 5.39. Found: C, 41.37; H, 4.58; N, 5.34%. IR (CsI power) cm^{-1}, 3281s ν(N–H), 1588m ν(N–H) + ν(C=C), 950m and 905m ν_{as}(CSS), 469w and 498w ν(M–N), 320m ν(M–S), 256w δ(N–M–S). EI–MS: m/z 518 (M^+). ^1H NMR in DMSO (assignments according to X-ray atom-labeling), δ: 1.83 (m, 2H, CH_2(6)), 2.50 (m, 7H, CH_2(5 and 7) + DMSO), 3.64 (s, 3H, O–CH_3(9)), 3.99 (s, 2H, S–CH_2(2)–), 7.87 (bs, NH(free)). ^{13}C NMR in DMSO (assignments according to X-ray atom-labeling), δ: 21.7 (C(6)), 31.7 and 34.04 (C(5 and 7)), 37.85 (C(2)), 52.27 (C(9)), 123.08 (C(3)), 154.01 (C(8)), 169.01 (C(4)), 175.18 (C(1)).

2.3. Co(ACDASAMe)$_2$ (2)

ACDASAMe (0.462 g, 2 mmol) was dissolved in ethanol and added to a solution of $CoCl_2 \cdot 6H_2O$ (0.238 g, 1 mmol) in ethanol. The mixture was stirred for 45 min and the brown precipitate was filtered off and washed with ethanol several times. Yield 0.43 g (82.8%), m.p. 191–192 °C. *Anal.* Calc. for $C_{18}H_{24}CoN_2O_4S_4$: C, 41.61; H, 4.66; N, 5.39. Found: C, 41.23; H, 4.55; N, 5.33%. IR (CsI power) cm^{-1}, 3256s ν(N–H), 1592m ν(N–H) + ν(C=C), 943m and 908m ν_{as}(CSS), 460w and 497w ν(M–N), 375w ν(M–S). EI-MS: m/z 518 (M^+).

2.4. X-ray analysis

Suitable crystals for X-ray analysis of Ni(ACDASAMe)$_2$ were obtained from a mixture of CH_2Cl_2 and hexane. The data collection was performed on a Siemens P4/PC diffractometer at room temperature, with graphite-monochromated Mo Kα radiation ($\lambda = 0.71073$ Å). Crystal data: $C_{18}H_{24}N_2NiO_4S_4$, $M = 519.34$, Crystal size $0.52 \times 0.16 \times 0.06$ mm, Monoclinic, $a = 8.808(2)$ Å, $b = 20.393(7)$ Å, $c = 12.476(2)$ Å, $\beta = 92.97°$, $V = 2237.9\ (10)$ Å^3, Density (calculated) 1.541 Mg/m^3, $T = 293(2)$ K, space group $P2_1/n$ (No. 14), $Z = 4$, μ (Mo Kα) = 1.267 mm^{-1}, 4213 reflections collected, 3943 unique ($R_{int} = 0.0565$) which were used in all calculations. Maximum and minimum transmission 0.870 and 0.777, final R values: $R_1 = 0.0531$, $wR_2 = 0.0968$, $R_1 = 0.1110$, $wR_2 = 0.1182$ (all data) ($R_1 = \sum\|F_o|-|F_c\|/\sum|F_o|$, $wR^2 = [\sum w(F_o^2 - F_c^2)^2/\sum w(F_o^2)^2]^{1/2}$), goodness-of-fit 1.030. The structure was solved by direct methods using SHELXS-90 [27] and refined by full-matrix least-squares on F^2 using SHELXL-97 [28]. The hydrogen atoms of the amino moiety were located from the difference map and their positional parameters refined.

3. Results and discussion

The metal complexes were readily obtained by mixing equimolar amounts of metal chloride with the free ligands in ethanol. They exhibit varying degrees of solubility in common organic solvents such as CH_2Cl_2, $CHCl_3$, EtOH, DMSO, ethyl acetate, etc.

The IR spectra of the complexes exhibit characteristic bands that emulate the features observed for the (N,S) coordination mode on diorganosilicon(IV) and indium(III) compounds with an S-alkyl substituted ACDA type ligand [29,30]. The ν(N–H) bands (3281, 1588 and 3256 and 1592) are shifted to higher frequencies in relation to the free ligand (3320 and 1615 cm^{-1}). This is indicative of the deprotonation of NH_2 group on M–NH coordination. In addition, the presence of two signals at 940 and 910 cm^{-1} (ν_{as}(CSS)) provides evidence for the M–S coordination through one sulfur atom. These observations have been further supported by the appearance of new bands at low frequencies, which can be assigned to ν(M–N) and ν(M–S) modes.

In the ^1H NMR spectrum, the lack of the signal at 11 ppm (which corresponds to the proton of the amino group involved in the N–H···S bond in the free ligand

[24]) indicates the removal of that proton on complexation. This is confirmed by a downfield shift of the remaining NH signal at 7.87 (at 6.0 ppm for the free ligand) suggesting an M–N coordination. In addition, the upfield shift of the S–CH_2(2)– proton signals supports the involvement of the sulfur atom on coordination. Similar patterns were also observed in the analogous organosilicon(IV) and indium(III) complexes reported by Sharma [29] and Singh [30] respectively, for which they also suggested a bidentate coordination of the ACDA type ligands through the nitrogen and sulfur atoms.

The UV–Vis spectra of **1** and **2** in $CHCl_3$ solution were obtained, the high intensity bands below 380 nm are probably of ligand origin assignable to intraligand n–π/π–π* transitions. The absorptions observed at 380 and 440 for **1**, and at 397 nm for **2** may be interpreted as ligand to metal charge transfer bands [31]. The lowest energy absorption at 612 for **1** has an intensity consistent with the spin allowed d–d transition $^1A_{1g} \rightarrow {}^1A_{2g}$, as expected for a square planar d^8 species [31]. The second ligand field band ($^1A_{1g} \rightarrow {}^1B_{1g}$), expected to appear at higher energy, may be assigned to the shoulder at 480 nm. Similar spectrum patterns are commonly observed for analogous square-planar Ni(II) complexes with N_2S_2 coordination sphere [15,34]. For cobalt(II) complex **2**, the absorptions associated with the d–d transitions are masked by the tail of the more intense ligand to metal charge transfer bands. The mass spectra show low-intensity signals for the corresponding molecular ions, but rather intense signals for the ligand and fragments containing metal, all exhibiting the expected isotopic distribution patterns.

3.1. Description of the Ni(ACDASAMe)$_2$ (1) structure

Selected bond distances and angles are given in Table 1. Fig. 1 shows a thermal ellipsoid plot of the molecular structure of the Ni(ACDASAMe)$_2$ (**1**) along with the atom-labeling.

The structure consists of independent neutral Ni(ACDASAMe)$_2$ molecules with the nickel(II) exhibiting a slightly distorted square planar coordination. The metal center is coordinated by two ligands through the nitrogen and sulfur atoms showing a *cis* configuration. Both chelate rings are planar (the mean deviations from plane are 0.0174 and 0.0401 Å) with an angle of 8.4° between them. Therefore nickel(II) geometry deviates somewhat from the perfect square planar (mean deviation of 0.0731 Å). A comparable tetrahedrally distorted square planar structure was found in the nickel(II) complex of methyl-2-(β-salicylaldimino-2-hydroxypropyl)cyclopent-1-ene-1-dithiocarboxylate, $(NiHL^3) \cdot H_2O$ [22]. The *trans* N1–Ni–S3 and N2–Ni–S1 angles are 173.7(2) and 174.6(2)°, while the values for the endocyclic N–Ni–S angles are 95.2(2) and 95.0(2)° and the exocyclic N–Ni–S angles are 88.0(2) and 82.3(1)°. This contrast to the corresponding N–Ni–S angles of 180° observed in the *trans*-nickel(II) complex with the S-methyl substituted ACDA-type ligand (ACDE, methyl 2-amino-1-cyclopentenedithiocarboxylic acid) [15].

Table 1
Selected bond distances (Å) and angles (°) for Ni(ACDASAMe)$_2$

Interatomic distances (Å)		Bond angles (°)	
Ni–N(1)	1.875(5)	N(1)–Ni–N(2)	88.0(2)
Ni–N(2)	1.878(5)	N(1)–Ni–S(1)	95.2(2)
Ni–S(1)	2.175(2)	N(2)–Ni–S(1)	174.6(2)
Ni–S(3)	2.176(2)	N(1)–Ni–S(3)	173.7(2)
S(1)–C(8)	1.725(6)	N(2)–Ni–S(3)	95.0(2)
S(2)–C(8)	1.770(6)	S(1)–Ni–S(3)	82.3(1)
S(3)–C(17)	1.714(6)	C(8)–S(1)–Ni	111.7(2)
S(4)–C(17)	1.772(6)	C(8)–S(2)–C(2)	105.3(3)
N(1)–C(4)	1.297(7)	C(17)–S(3)–Ni	112.0(2)
N(2)–C(13)	1.303(8)	C(4)–N(1)–Ni	133.8(4)
C(3)–C(8)	1.364(8)	C(13)–N(2)–Ni	133.5(4)
C(3)–C(7)	1.515(8)	C(8)–C(3)–C(4)	124.5(5)
C(3)–C(4)	1.431(8)	C(3)–C(8)–S(1)	127.1(4)
C(5)–C(6)	1.528(9)	C(3)–C(8)–S(2)	114.8(4)
C(4)–C(5)	1.519(8)	C(17)–C(12)–C(13)	125.8(5)
C(12)–C(13)	1.422(8)	C(17)–C(12)–C(16)	126.1(5)
C(6)–C(7)	1.528(9)	C(12)–C(17)–S(3)	126.2(5)
C(12)–C(17)	1.306(8)	S(3)–C(17)–S(4)	118.1(4)
C(12)–C(16)	1.528(8)		
C(13)–C(14)	1.503(8)		

In comparison with the free ligand a shortening of the N1–C4, C3–C8 bonds distances, and a lengthening of C3–C4, C8–S1 bond lengths within the six-membered chelate ring are observed. This and the angles at C8, which are closer to those of the ideal sp^2 hybridization, are in accordance with a significant electronic delocalization in the chelate rings. The Ni–S and Ni–N bond lengths (av. 2.175 and av. 1.876 Å) are comparable to those observed in the above mentioned *trans*-nickel(II) complex, Ni(ACDE)$_2$ [15].

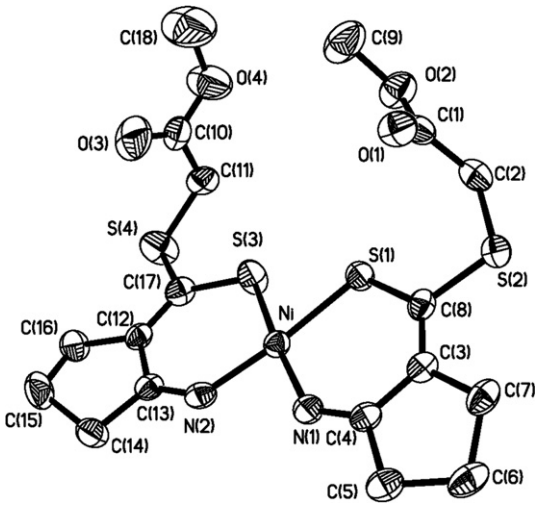


Fig. 1. ORTEP plot of the molecular structure of the Ni(ACDASAMe)$_2$ (**1**) along with the atom-labeling.

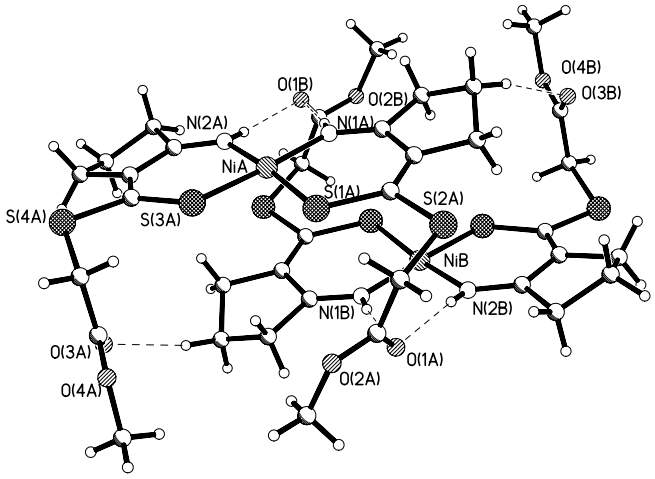


Fig. 2. Dimeric association through hydrogen bonds between two adjacent Ni(ACDASAMe)$_2$ molecules.

In our compound, the most remarkable feature is the *cis* arrangement of the ACDASAMe ligands. The two –CH_2COOMe moieties lie down the coordination plane in a nearly perpendicular fashion (75.2 and 89.5°). Although the potential oxygen donor atom from the –CH_2COOMe arms is available for coordination, no metal interaction is observed. This confirms the observed inherent reluctance on the part of nickel(II) to adopt pentacoordination in the presence of a hard donor atom to occupy the axial position as in $(NiHL^3)\cdot H_2O$ [22,32] where the dangling free pyrazolyl arm exhibits no metal interaction. In our compound, the –C=O group of one of the hanging moieties establishes two hydrogen bonds with the *cis* NH groups of a neighboring molecule. The –C=O group of the remaining arm forms a hydrogen bridge with the C6 atom from the same neighboring molecule. These hydrogen bridges between the two adjacent molecules lead to a dimeric assemblage (see Fig. 2). The O···N distances O(1A)···N(1,2B) = av. 3.19 Å and O(3A)···C(6) = 3.428(2) Å are in the expected range for weak hydrogen bonds [33]. Probably, these hydrogen bonds are responsible of the observed *cis* configuration since they avoid a *trans* ligand arrange similar to that found in the related nickel(II) complex, Ni(ACDE)$_2$ [15]. A comparable *cis*-array was observed in the analogous palladium(II) and platinum(II) complexes of ACDE, where a water molecule hydrogen bonded to both amine protons prevents the claimed favored *trans* configuration observed with nickel(II) [15].

In addition to these intermolecular interactions, there are short S–O distances, which hold the crystal packing.

4. Conclusion

The most remarkable feature is the dimeric assemblage of the Nickel(II) complex, which results from the hydrogen bonds between the dangling –CH_2COOMe arms and the *cis* NH groups and the C6 of the main building of two adjacent molecules. This fact might be the origin of the *cis* configuration of the ACDASAMe ligands on interacting with nickel(II) that avoid the expected ligands *trans* isomerism.

5. Supplementary material

CCDC 286991 contains the supplementary crystallographic data for this paper. These data can be obtained free of charge via www.ccdc.ac.uk/conts/retrieving.html, or from the Cambridge Crystallographic Data Centre, 12 Union Road, Cambridge CB2 1EZ, UK; fax: (+44) 1223-336-033; or e-mail: deposit@ccdc.cam.ac.uk.

Acknowledgements

Support of this work by the UAEM (Project 1428/2000) and the IQ-UNAM is gratefully acknowledged.

References

[1] S.N. Choi, J.R. Wasson, Inorg. Chem. 14 (1975) 1964.
[2] R.P. Hausinger, Biochemistry of Nickel, Plenum Press, New York, 1993.
[3] S.K. Mondal, D.S. Joardar, K. Nag, Inorg. Chem. 17 (1978) 191.
[4] A. Tarassoli, T. Sedaghat, B. Neumüller, M. Ghassemzadeh, Inorg. Chim. Acta 318 (2001) 15.
[5] A.M. Amado, P.J.A. Ribeiro-Claro, J. Inorg. Biochem. 98 (2004) 561.
[6] S.K. Mondal, R. Roy, Sanat K. Mondal, K. Nag, Indian J. Chem. 20A (1981) 982.
[7] S.K. Dutta, S.B. Kumar, S. Bhattacharyya, M. Chaudhury, J. Chem. Soc., Dalton Trans. (1994) 97.
[8] K. Nag, D.S. Joardar, Inorg. Chim. Acta 14 (1975) 133.
[9] L.F. Cappa de Oliveira, P.S. Santos, Vib. Spectrosc. 10 (1995) 57.
[10] M.F. Mackay, M.J. O'Connor, P.J. Oliver, J. Cryst. Mol. Struct. 8 (1978) 161.
[11] P.K. Bharadwaj, W.K. Musker, Inorg. Chem. 26 (1987) 1453.
[12] R. Cea-Olivares, R.A. Toscano, A. Luna, F. Cervantes, Main Group Met. Chem. 16 (1993) 121.
[13] R.D. Bereman, M.R. Churchil, G. Shields, Inorg. Chem. 18 (1979) 3117.
[14] R.D. Bereman, G. Shields, J. Bordner, J.R. Dorfman, Inorg. Chem. 20 (1981) 2165.
[15] E.M. Martin, R.D. Bereman, J. Reibenspies, Inorg. Chim. Acta 191 (1992) 171.
[16] S. Bhattacharyya, S.B. Kumar, S.K. Dutta, E.R.T. Tiekink, M. Chaudhury, Inorg. Chem. 35 (1996) 1967.
[17] G.J.J. Steyn, A. Roodt, I. Poletaeva, Y.S. Varshavsky, J. Organomet. Chem. 536 (1997) 197.
[18] S. Bhattacharyya, D. Ghosh, A. Endo, K. Shimizu, T.J.R. Weakley, M. Chaudhury, J. Chem. Soc., Dalton Trans. (1999) 3859.
[19] S. Bhattacharyya, T.J.R. Weakley, M. Chaudhury, Inorg. Chem. 38 (1999) 633.
[20] S. Bhattacharyya, T.J.R. Weakley, M. Chaudhury, Inorg. Chem. 38 (1999) 5453.
[21] A. Tarassoli, A. Asadi, P.B. Hitchcock, J. Organomet. Chem. 645 (2002) 105.
[22] D. Ghosh, S. Mukhopadhyay, S. Samanta, K-.Y. Choi, A. Endo, M. Chaudhury, Inorg. Chem. 42 (2003) 7189.
[23] A. Tarassoli, T. Sedaghat, M.L. Helm, A.D. Norman, J. Coord. Chem. 56 (2003) 1179.
[24] V. García-Montalvo, M.A. Santana-Valdés, S. Hernández-González, G. Espinosa-Pérez, R. Cea-Olivares, Indian J. Chem. 39B (2000) 177.
[25] B. Bordas, P. Sohar, G. Matolcsy, P. Berencsi, J. Org. Chem. 37 (1972) 1727.

[26] K. Nag, D.S. Joardar, Can. J. Chem. 54 (1976) 2827.
[27] G.M. Sheldrick, Acta Crystallogr.: Sect. A 46 (1990) 467.
[28] G.M. Sheldrick, SHELXL-97, Program for Crystal Structure Refinement, University of Göttingen, Göttingen, Germany, 1997.
[29] R.K. Sharma, Y.P. Singh, A.K. Rai, Indian J. Chem. 38A (1999) 604.
[30] S.K. Singh, Y. Singh, A.K. Rai, R.C. Mehrotra, Polyhedron 8 (1989) 633.
[31] A.B.P. Lever, Inorganic Electronic Spectroscopy, second ed., Elsevier Science, Amsterdam, 1984.
[32] D.C. Goodman, T. Tuntulani, P.J. Farmer, M.Y. Darensbourg, J.H. Reibenspies, Angew. Chem., Int. Ed. Engl. 32 (1993) 116.
[33] B.R. Bhogala, P. Vishweshwar, A. Nangia, Cryst. Growth Design 5 (2005) 1271.
[34] L. Gomes, E. Pereira, B. de Castro, J. Chem. Soc., Dalton Trans. (2000) 1373.

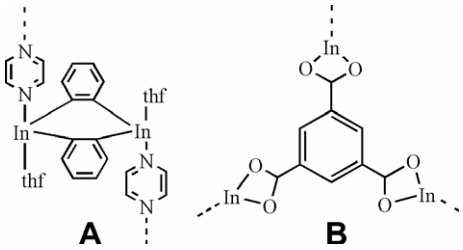


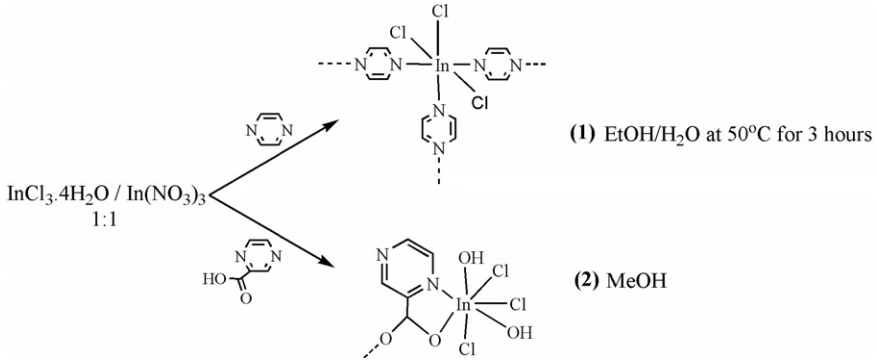
Fig. 1. Examples of reported indium frameworks [8].

(0.22 g, 0.75 mmol) were stirred at 70 °C in a grease free Schlenk flask for 24 h. After filtering the solution to remove any solid particles, the clear solution was stored at room temperature. After 2 days, a white crystalline material was isolated that was suitable for single crystal X-ray analysis. Yield = 36%, based on indium chloride tetrahydrate, melting point >250 °C. IR (KBr pellets, υ cm^{-1}); 3576.4 (w), 1603.4 (m), 1495.6 (m), 1418.4 (m), 1157.7 (m), 118.3 (m), 1054.9 (m), 618.07 (m).

Compound **1** can also be prepared reacting pyrazine (0.04 g, 0.50 mmol) and indium(III) chloride tetrahydrate (0.22 g, 0.75 mmol) in ethanol at 70 °C for 3 days in a grease free Schlenk tube. After filtration and storage at room temperature for 2 days, affords white crystalline material.

4. Preparation of 2

A methanol solution (5 ml) of indium(III) nitrate (0.31 g, 0.8 mmol), pyrazine, 2-carboxylic acid (0.10 g, 0.8 mmol) and indium(III) chloride (0.24 g, 0.8 mmol)



Scheme 1. Synthesis of compounds **1** and **2**.

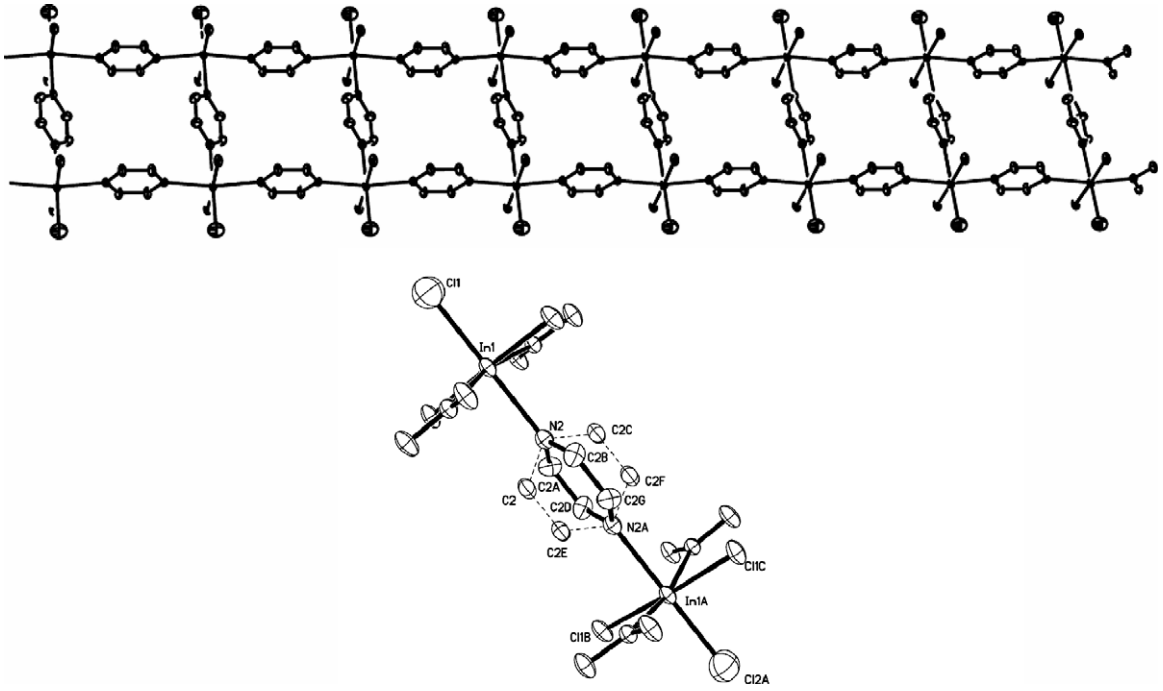


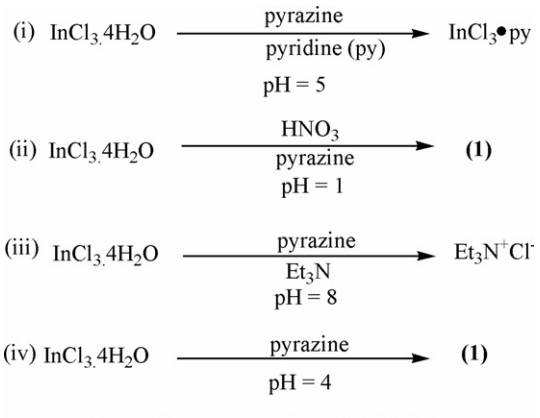
Fig. 2. ORTEP of compound **1**, thermal ellipsoids at 30% probability, hydrogen atoms are omitted for clarity.

Table 1
Crystal data of compounds **1**–**3**

Compound	**1**	**2**	**3**
Chemical formula	$C_6H_6Cl_3InN_3$	$C_5H_6Cl_3InN_2O_3$	$C_{12}H_{28}Cl_6In_2N_2O_4S_4$
Formula weight	341.31	360.26	834.94
Crystal system	tetragonal	orthorhombic	monoclinic
Space group	*P*4(2)/*mnm*	*P*2(1)2(1)2(1)	*P*21/*n*
T (K)	90.2	90.2	90.2
a (Å)	11.8467(8)	6.0291(7)	7.1036(7)
b (Å)	11.8467(8)	11.1140(14)	15.1089(14)
c (Å)	7.5032(10)	13.8525(17)	13.5193(13)
α (°)	90	90	90
β (°)	90	90	94.613(2)
γ (°)	90	90	90
V (Å^3)	1053.03(17)	928.2	1446.3(2)
Z	4	4	2
Reflections collected	2436	7138	8268
Independent reflections	678	1675	2612
Unique data (R_{int})	0.0514	0.0411	0.0395
R Indices (all data)	$R_1 = 0.0642$, $wR_2 = 0.1699$	$R_1 = 0.0682$, $wR_2 = 0.1861$	$R_1 = 0.0458$, $wR_2 = 0.1030$
Final *R* indices [$I > 2\sigma(I)$]	$R_1 = 0.0525$, $wR_2 = 0.1591$	$R_1 = 0.0646$, $wR_2 = 0.1799$	$R_1 = 0.0372$, $wR_2 = 0.0975$

Table 2
Selected bond lengths (Å) and angles (°) of compound **1**

In(1)–N(1)	2.372(9)
In(1)–N(2)	2.327(14)
In(1)–Cl(1)	2.417(3)
In(1)–Cl(2)	2.397(10)
In(1)–In(1a)	7.503
N(1)–In(1)–Cl(1)	89.869(11)
N(1)–In(1)–Cl(2)	95.7(2)
N(2)–In(1)–Cl(2)	180.0
Cl(1)–In(1)–Cl(2)	91.32(9)



Scheme 2. Preparation of **1** at varied pH.

was stirred and heated in a grease free Schlenk for 1 day at 65 °C.

After 1 day, the reaction mixture was filtered and transferred to a beaker for further crystallization. The clear reaction mixture yielded white crystals suitable for X-ray diffraction. Yield = 42% (based on $InCl_3$), Mp >250 °C, the sample shows an evolution of a gas in the interval 100–105 °C (H_2O). The sample did not melt at 250 °C. IR (KBr pellets, υ cm^{-1}); 3413.0 (s), 1067 (m), 1613 (s), 1578 (m), 1383 (m), 784.37 (m), 738.61 (m), 709.0 (m), 568.26 (m).

5. Preparation of 3

An aqueous solution of DMSO (dimethyl sulfoxide) (5 ml) pyrazine (0.04 g, 0.50 mmol), indium(III) chloride tetrahydrate (0.22 g, 0.75 mmol) were stirred at room temperature in an open beaker for 24 h. The solution was filtered to remove any insoluble material. After storage at room temperature for 1 day suitable white crystalline material was obtained. Yield = 49%, based on $InCl_3$, Mp = 137–138 °C. IR (KBr pellets, υ cm^{-1}); 3569.3 (w), 3036.1 (m), 2999.5 (m), 2932.6 (m), 2918.8 (m), 1409.2 (s), 1316.6 (m), 1296.3 (s), 1036.0 (s), 988.15 (s), 951.08 (m).

6. Results and discussion

The reaction of aqueous ethanol or methanol solutions of $InCl_3 \cdot 4H_2O$ with pyrazine ($C_4H_4N_2$) or pyrazine, 2-carboxylic acid (pyz-ca) (1:1.5) at 70 °C for 24 h, is a moderate yielding facile reaction affording $[InCl_3(pyz)]_n$ compound **1**, and $[InCl_3(OH)_2(pyz\text{-}ca)]_n$ compound **2** (Scheme 1). Compound **1** crystallizes as a one-dimensional polymeric material and compound (2) a one-dimensional zigzag framework. Pyrazine and pyz-ca were selected as spacer molecules as are crystalline bidentate molecules, which have good solubility in readily available 'green' solvents such as ethanol and water. Derivatives of the pyrazine molecule, such as pyrazine, 2-carboxylic acid are useful as they promote hydrogen bonding that is often crucial for framework growth.

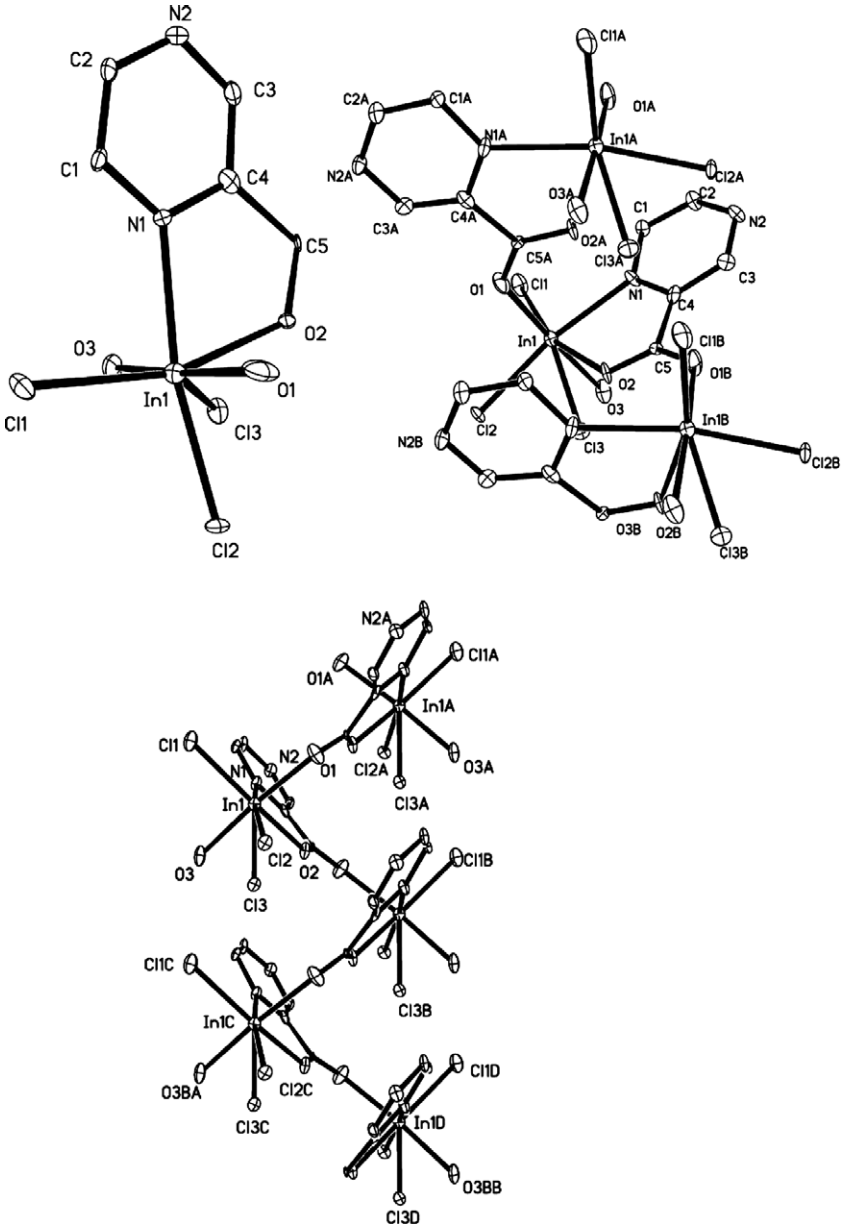


Fig. 3. ORTEP of compound **2**, thermal ellipsoids at 30% probability, hydrogen atoms are removed for clarity.

The solid-state structure of **1** was determined using X-ray crystallography[1] (Fig. 2), and revealed a six-coordinated indium center and a polymeric structure interlinked through pyrazine molecules. Crystal data for compounds **1**–**3** is given in Table 1.

Compound **1** crystallizes in the tetragonal space group, *P*4(2)/*mnm*. The asymmetric unit consists of one indium center, two halves of bridging pyrazine molecules and two terminal chloride ions. One of the bridging pyrazine molecules is disordered over 2 by symmetry equivalent positions. Because of the disorder associated with this pyrazine, the structure was refined with no hydrogen on the carbon atom, C(2). The geometry of both orientations is shown in Fig. 2. The In(III) center is coordinated to three chlorine atoms and three nitrogen atoms. The coordination geometry can be described as a slightly distorted octahedron. Selected bond lengths and angles are given in Table 2.

The In–Cl distances are within the expected range, however the In–N distance of 2.372 Å is shorter than the distances of 2.528–2.540 Å that are found in compound **A** (Fig. 1) [8a]. This shortening of the bond is presumably

[1] Crystal data were collected with a Bruker SMART 1000 diffractometer using graphite monochromated molybdenum radiation ($\lambda = 0.7107$ Å). The data were corrected for absorption. Structures were solved by direct methods using the SHELXS-97 program and refined via full-matrix least squares: (a) G.M. Sheldrick, SHELXS-97, Program for the solution of crystal structures; University of Göttingen, Germany, 1997; (b) G.M. Sheldrick, SHELXL-97, Program for the refinement of crystal structures.

due to packing arrangement of the octahedral geometry. The rectangular distance between the chains is 6.997 by 7.503 Å, which is comparable to a distance of 7.8 Å along the pyrazine linker axis of compound **A** [8a] (Fig. 1).

Previous research [12] has described how pH plays an important role in the assembly process; therefore, the synthesis of **1** was performed under various pH conditions.

Experimental results revealed that an acidic medium is required for the preparation of **1**. Under basic conditions compound **1** could not be isolated, furthermore if the reaction were performed in the presence of a base such as pyridine (Scheme 2, reaction (i)), or triethylamine the products isolated were the adduct, $InCl_3(py)_3$ or $NEt_3{}^+Cl^-$.

The original crystalline material that the X-ray data were collected on was obtained from a reaction mixture of indium(III) chloride and indium(III) nitrate, however further experimental work has shown that compound **1** can also be isolated directly from the reaction of indium(III) chloride with pyrazine under similar reaction conditions.

In a similar manner as was used to prepare compound **1**, compound **2** was isolated as X-ray quality single colorless crystals from methanol. The solid-state structure and key bond lengths and angles are depicted in Fig. 3. Each indium center is coordinated to three chlorides, one nitrogen atom from the pyrazine spacer and three oxygen atoms.

Presumably, the oxygen (OH) coordinated to the indium center arises from the aqueous reaction medium and reaction work-up and aids in the formation of a framework structure through hydrogen bonding.

A seven-coordinated indium atom affords distorted pentagonal bypyramidal geometry. The high coordination number at the indium center is not a new phenomenon and has been previously observed in an indium three-dimensional oxalate polymer [13]. Each indium center is linked by a bridged oxygen atom resulting in an infinite 'zigzag' polymeric structure. The approximate distance between the zigzag chains is 6.029 Å (i.e. from Cl1a–Cl1b, or O3–O3ba). The average In–O distance is 2.171 Å (see Table 3 for pertinent bond lengths and angles) which is comparable to 2.154 Å as observed in similar indium–carboxylate systems [14].

The infra-red spectra of **2** reveals a broad peak centered at 3413 cm^{-1} attributed to the symmetric and asymmetric stretch of the hydroxyl group. At 1067 cm^{-1} the bending mode of μ-OH is observed and at 1613 (s), 1578, 1478 and 1383 cm^{-1} frequencies that correspond to υ asym, υ sym (CO_2H) [14].

In the course of preparing compounds **1** and **2** various solvent systems were investigated. $[InCl_3(dmso_2)(pyz)]_2$, compound **3** (Fig. 4) was isolated from the reaction of $InCl_3 \cdot 4H_2O$ with pyrazine in DMSO (dimethylsulfoxide).

The isolation of compound **3** reveals that in order to obtain a polymeric framework, coordinating solvents must be avoided to prevent blocking potential coordination sites at the metal center. Compound **3** is a dimeric In(III) complex that has a slightly distorted octahedral geometry around both indiums that are linked by a molecule of pyrazine. Each indium center also has two molecules of DMSO coordinated. No noteworthy discrepancies in bond lengths or angles are observed.

Table 3
Selected bond lengths (Å) and angles (°) of compound **2**

In(1)–O(1)	2.186(10)
In(1)–O(2)	2.159(8)
In(1)–O(3)	2.167(11)
In(1)–Cl(1)	2.445(4)
In(1)–Cl(2)	2.388(3)
In(1)–N(1)	2.318(10)
O(3)–In(1)–O(1)	174.0(4)
O(1)–In(1)–N(1)	90.8(4)
N(1)–In(1)–Cl(2)	166.8(3)
O(3)–In(1)–Cl(1)	90.8(3)
N(1)–In(1)–Cl(1)	89.9(3)

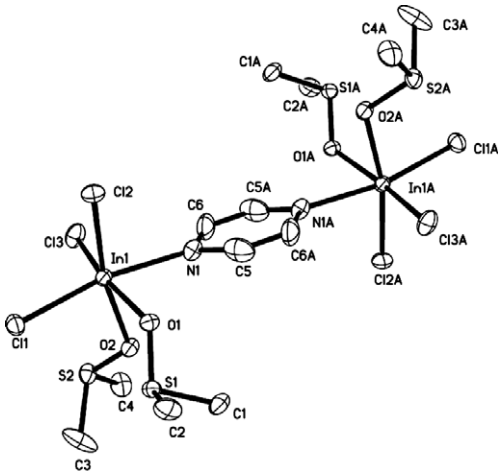


Fig. 4. ORTEP of compound **3**, thermal ellipsoids are at 30% probability, hydrogen atoms are removed for clarity.

Compounds **1**–**3** are insoluble in non-polar solvents, but readily soluble in polar solvents. Compounds **1** and **2** have high thermal stability and show no visible decomposition at temperatures of >250 °C. Compound **3** has a lower melting point of 137–138 °C as anticipated given the DMSO coordination.

Preliminary experiments to exchange the indium atoms with inorganic ions in compounds **1** and **2** have to date been unsuccessful but will be pursued in forthcoming work.

7. Conclusions

The resultant structures **1**–**3** provide an interesting comparison of how changing the functionality of the spacer and the reaction conditions can direct the framework motif. These results will be used in future work to develop the syntheses of a variety of structural frameworks for new chemical systems and will study the application potential of these systems.

8. Supplementary materials

CCDC 610418, 610417 and 610416 contain the supplementary crystallographic data for **1**, **2** and **3**. These data can be obtained free of charge via htpp://www.ccdc.cam.ac.uk/conts/retrieving.html, or from the Cambridge Crystallographic Data Centre, 12 Union Road, Cambridge CB2 1EZ, UK; fax: +44 1223 336 033; or e-mail: deposit@ccdc.cam.ac.uk.

Acknowledgement

Robert A. Welch Foundation, for support of Grant number P-1637.

References

[1] S.L. James, Chem. Soc. Rev. 32 (2003) 276, and references cited therein.
[2] C-D. Wu, A. Hu, L. Zhang, L. Wenbin, J. Am. Chem. Soc 127 (2005) 8940.
[3] (a) G. Férey, M. Latroche, C. Serre, F. Millange, T. Loiseau, A. Percheron-Guégan, A. Percheron-Guégan, Chem. Commun. (2003) 2977;
(b) J.L.C. Rowsell, O.M. Yaghi, Angew. Chem., Int. Ed. Engl. 44 (2005) 4670.
[4] B.H. Hamilton, T.B. Cardon, G.A. Lorigan, C.J. Ziegler, Dalton Trans. (2005) 2941.
[5] M. Dinca, J.R. Long, J. Am. Chem. Soc. 127 (2005) 9376.
[6] S. Kitagawa, R. Kitaura, S. Noro, Angew. Chem., Int. Ed. Engl. (2004) 2334.
[7] (a) Examples include B. Chen, F.R. Fronczek, A.W. Maverick, Inorg. Chem. 43 (2004) 8209;
(b) Y.-B. Dong, Q. Zhang, L. Wang, J.P. Ma, R-Q. Huang, D-Z. Shen, D.Z. Chen, Inorg. Chem. 44 (2005) 6591;
(c) H-F. Zhu, J. Fan, T. Okamura, Z-H. Zhang, G-X. Liu, K-B. Yu, W-Y. Sun, N. Ueyama, Inorg. Chem. 45 (2006) 394.
[8] (a) F. Gabbaï, A. Schier, J. Riede, Angew. Chem., Int. Ed. Engl. 37 (1998) 622;
(b) Y-Q. Tian, C-X. Cai, X-J. Yuan, Y-Z. Li, T-W. Wang, X-Z. You, Chem. Lett. 32 (2003) 796;
(c) K-H. Lii, Y-F. Huang, Inorg. Chem. 38 (1999) 1348;
(d) Z.-Z. Lin, F.-L. Jiang, D.-Q. Yuan, L. Chen, Y.-F. Zhou, M.-C. Hong, Eur. J. Inorg. Chem. (2005) 1927;
(e) Y. Zhang, W. Cheng, D. Wu, H. Zhang, D. Chen, Y. Gong, Z. Kan, J. Zhu, J. Solid State Chem. 179 (2006) 186.
[9] (a) Z.Z. Lin, L. Chen, F.L. Jiang, M.C. Hong, Inorg. Chem. Commun. (2005) 199;
(b) Z.Z. Lin, F.L. Jiang, D.Q. Yuan, L. Chen, Eur. J. Inorg. Chem. 10 (10) (2005) 1927.
[10] (a) Z. Lin, L. Chen, C. Yue, D. Yuan, F. Jiang, M. Hong, J. Solid State Chem. 179 (2006) 1154;
(b) B. Gómez-Lor, E. Gutiérrez-Puebla, M. Iglesias, M.A. Monge, C. Ruiz-Valero, N. Snejko, Inorg. Chem. 41 (2002) 2429.
[11] B. Gómez-Lor, E. Gutiérrez-Puebla, M. Iglesias, M.A. Monge, C. Ruiz-Valero, N. Snejko, Chem. Mater. 17 (2005) 2568.
[12] Z. Lin, F. Jiang, D. Yuan, L. Chen, Y. Zhou, M. Hong, Eur J. Inorg. Chem. (2005) 1927.
[13] S. Yang, G. Li, S. Tian, F. Liao, J. Lin, J. Solid State Chem. 178 (2005) 3703.
[14] Z. Lin, F.L. Jiang, L. Chen, D.Q. Yuan, M.C. Hung, Inorg. Chem. 44 (2005) 73.

2. Experimental

2.1. Material and instrumentation

Infrared spectra were recorded on Nicolet AVATAR 360 FT-IR instrument as KBr plates. Elemental analysis (C, H, N) were performed with Element Analysis system EA 1112 CE Instruments by the Korea Basic Science Institute. $[Fe^{III}(\mathbf{L})_2](ClO_4)$ was prepared according to the literature [5]. All other materials were used as received without further purification.

2.2. Synthesis of $[(Fe^{II}(\mathbf{L})_2)(Mn^{III}(salen))(ClO_4)\cdot 2CH_3CN\cdot CH_3OH]$ ($\mathbf{1}\cdot 2CH_3CN\cdot CH_3OH$)

Method A. A mixture of a solution of $[Fe^{III}(\mathbf{L})_2](ClO_4)$ (0.134 g, 0.2 mmol) in CH_3CN (15 mL) and a solution of $[Mn(salen)(H_2O)](ClO_4)$ (0.088 g, 0.2 mmol) in CH_3OH (10 mL) was refluxed overnight. After cooling at ambient temperature, small amount of precipitate was removed by filtration. Resultant dark brown solution was left without any disturbance. The golden flat crystals were separated. (0.082 g, 46.8%). *Anal.* Calc. for $C_{28}H_{28}B_2ClFeMnN_{20}O_4$ (vacuum-dried powder): C, 38.37; H, 3.22; N, 31.96. Found: C, 37.99; H, 3.58; N, 32.05%. IR (KBr, cm^{-1}): 2512 (w, ν(BH)), 1147, 1095(s, $\nu(ClO_4)$).

Method B. A mixture of $[Fe^{III}(\mathbf{L})_2](ClO_4)$ (0.033 g, 0.05 mmol) and hydroquinone (0.011 g 0.1 mmol) in CH_3CN (5 mL) was mixed up with a solution of $[Mn(salen)(H_2O)](ClO_4)$ (0.022 g, 0.05 mmol) in CH_3OH (5 mL). Resultant dark brown solution was left without any disturbance. The golden flat crystals were separated.

2.3. Crystal structure and determination

The diffraction data for **1** were collected on a Nonius Kappa-CCD diffractometer using Mo Kα radiation ($\lambda = 0.71073$ Å) at 150(1) K. The CCD data were integrated and scaled using the DENZO-SMN software package [6]. The structures were solved by SIR-92 and refined by using SHELXTL/PC V6.12 [7]. There exist two molecules of CH_3CN and one molecule of CH_3OH. But CH_3OH was grossly disordered and was inhibiting the refinement. Therefore, CH_3OH contribution was removed using SQUEEZE (PLATON) [8]. All hydrogen atoms were located in the calculated positions on riding model. Crystallographical data and refinement details for **1** are listed in Table 1.

2.4. X-ray absorption spectroscopy

Fe K-edge X-ray absorption spectra were recorded in the Electrochemistry beam line (BL7C1) of Pohang Accelerater Laboratory (PAL) with a ring current of 120–170 mA at 2.5 GeV. A Si(1 1 1) monochromator crystal was used with detuning to 85% in intensity to eliminate high-order harmonics. The data were collected in transmission mode with the nitrogen (85%) and argon (15%) gas-filled ionization chambers as detectors. Energy calibration was carried out for all measurements using Fe foil placed in front of the third ion chamber, assigning the first inflection point to 7112 eV.

Table 1
Crystal data and refinement data for $\mathbf{1}\cdot 2CH_3CN\cdot CH_3OH$

	$\mathbf{1}\cdot 2CH_3CN\cdot CH_3OH$
Empirical formula	$C_{33}H_{38}B_2ClFeMnN_{22}O_7$
Molecular mass	1022.71
Temperature (K)	150(2)
Crystal system	triclinic
Space group	$P\bar{1}$
a (Å)	12.4710(4)
b (Å)	13.9230(6)
c (Å)	15.7040(6)
α (°)	67.290(2)
β (°)	68.226(2)
γ (°)	85.411(2)
V (Å^3)	2329.52(2)
Z	2
$\rho_{calc.}$ (Mg m^{-3})	1.481
μ(Mo Kα) (mm^{-1})	0.712
F(000)	1064
Crystal size (mm)	$0.32\times 0.30\times 0.07$
Goodness-on-fit	1.029
R_1 [$I > 2\sigma(I)$]	0.0454
wR_2 [$I > 2\sigma(I)$]	0.1128

3. Results and discussion

The reaction of $[Fe^{III}(\mathbf{L})_2](ClO_4)$ with $[Mn(salen)](ClO_4)$ afforded a 1D coordination polymer of $[(Fe^{II}(\mathbf{L})_2)(Mn^{III}(salen))(ClO_4)\cdot 2CH_3CN\cdot CH_3OH]$ ($\mathbf{1}\cdot 2CH_3CN\cdot CH_3OH$) as golden plate crystals. During the reaction, $[Fe^{III}(\mathbf{L})_2]^+$ is reduced to ferrous species of $[Fe^{II}(\mathbf{L})_2]$, due to the strong reducing ability of the borate ligand [9a]. Hydroquinone facilitated the reduction of $[Fe^{III}(\mathbf{L})_2]^+$. It implies that $[Fe^{III}(\mathbf{L})_2](ClO_4)$ should be considered as a good metalloligand which can introduce the spin crossover candidate [9,10]. ($Fe^{II}N_6$) of $[Fe^{II}(\mathbf{L})_2]$ into multidimensional coordination polymers. Although a neutral $[Fe^{II}(\mathbf{L})_2]$ [9a] has been already known, insolubility of this prohibits its participating in further extended architecture. Meanwhile, $[Fe^{III}(\mathbf{L})_2](ClO_4)$ has the advantage of good solubility in CH_3CN and CH_3NO_3. Single crystal X-ray analysis of $\mathbf{1}\cdot 2CH_3CN\cdot CH_3OH$ reveals that among six N_{exo} atoms of $[Fe^{II}(\mathbf{L})_2]$ moiety, only two ones with an inversion symmetry relation on iron centre take part in coordinating the axial sites of $[Mn(salen)]^+$ in a zigzag manner (Fig. 1). This is because the steric bulkiness of $[Mn(salen)]^+$ moiety prohibits all N_{exo} atoms from coordinating to Mn sites. In comparison, in the case of a small well-directed paddle wheel type $[Rh_2(OAc)_4]$, all the free N_{exo} atoms are bound to the axial sites of rhodium moieties. At last unusual neutral 3D 4^66^9 ferrous framework is fabricated, showing incomplete spin transition [5]. The

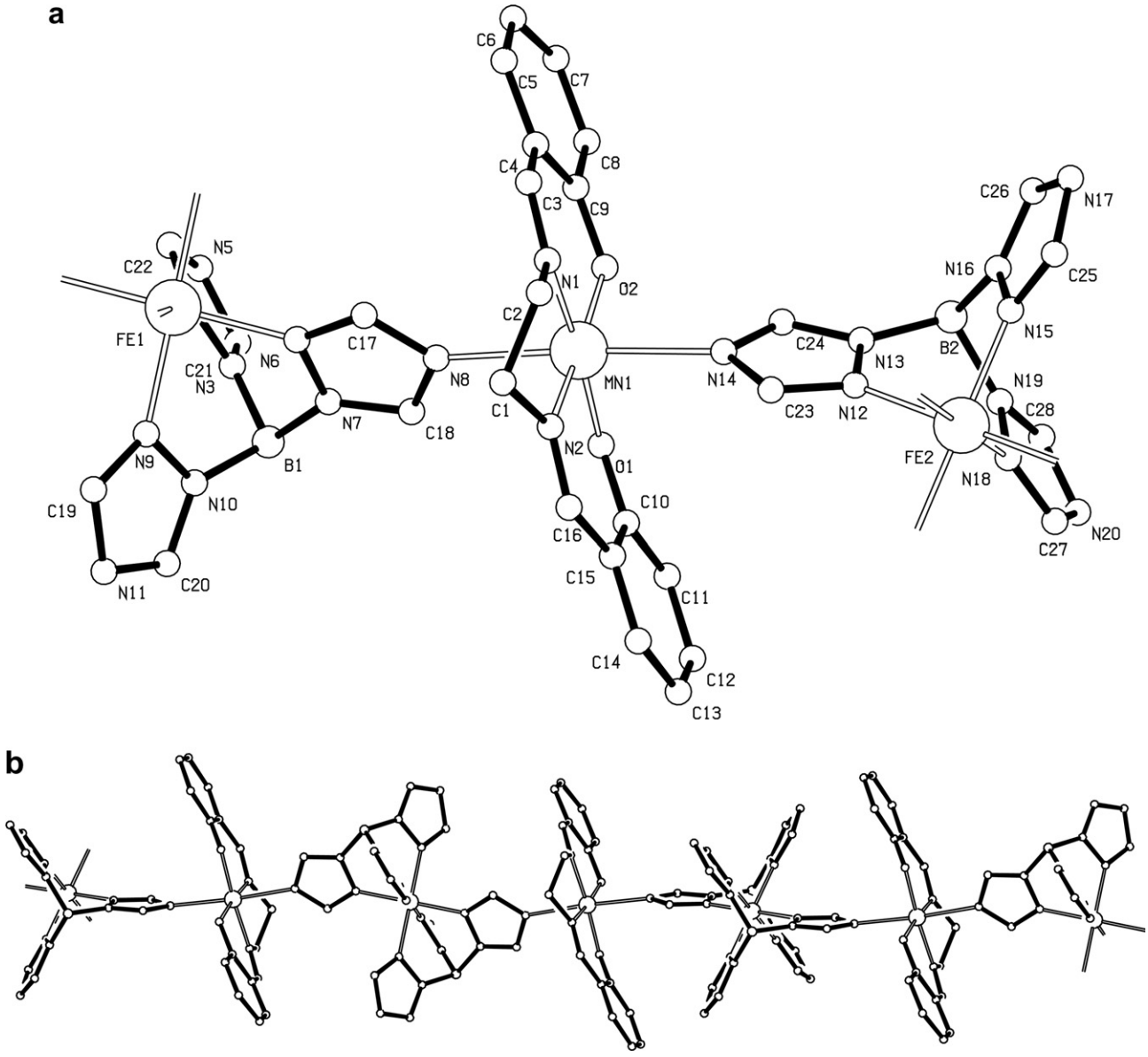


Fig. 1. Asymmetric unit (a) of $\mathbf{1} \cdot 2CH_3CN \cdot CH_3OH$ and 1D infinite chain (b) incorporated with ferrous complex of $[Fe^{II}(\mathbf{L})_2]$. Hydrogen atoms, CH_3CN and CH_3OH were omitted for clarity.

Fe-N bond lengths (1.965(3)–2.018(3) Å) are similar with those of a low spin ferrous complex of $[Fe^{II}(\mathbf{L})_2]$ (avg. 1.99 Å) [9a]. This indicates that the low spin ferrous complex is predominant species at 150 K, comparing with a high spin ferrous complex of $[Fe^{II}(Tp^{3,5\text{-}Me2})_2]$ (2.172 Å) [11] where $Tp^{3,5\text{-}Me2}$ stands for hydrotris(3,5-dimethylpyrazolyl)borate according to the crystallographic evidence. The coordination sphere of Mn^{III} centre comprises N_2O_2 binding system from salen ligand and two N_{exo} atoms of $[Fe^{II}(\mathbf{L})_2]$ moieties with the distances of 2.323(2) and 2.304(2) Å. The angle (176.35(1)°) of N(8)–Mn–N(12) is nearly linear. Consequently, 1D infinite coordination polymer results with Fe^{II}–Mn^{III} set repeating. Selected bond lengths and angles are listed in Table 2. TGA indicate that $\mathbf{1} \cdot 2CH_3CN \cdot CH_3OH$ begins losing CH_3OH and CH_3CN below 26 °C and is completely desolvated above 230°, which related to one CH_3OH and two CH_3CN. Abrupt weight loss at 270 °C is due to the decomposition of **L** and salen. $\mathbf{1} \cdot 2CH_3CN \cdot CH_3OH$ is so efflorescent as to make it difficult to interpret the magnetic property on the ground that XRPD pattern of $\mathbf{1} \cdot 2CH_3CN \cdot CH_3OH$

Table 2
Selected bond lengths (Å) and angles (°) for $\mathbf{1} \cdot 2CH_3CN \cdot CH_3OH$

Fe(1)–N(4)	1.999(3)	Fe(1)–N(6)	1.991(2)
Fe(1)–N(9)	2.018(3)	Fe(2)–N(12)	1.984(2)
Fe(2)–N(15)	1.972(3)	Fe(2)–N(18)	1.965(3)
Mn(1)–N(8)	2.304(2)	Mn(1)–N(14)	2.323(2)
N(4)–Fe(1)–N(6)	86.77(1)	N(4)–Fe(1)–N(9)	90.97(1)
N(6)–Fe(1)–N(9)	92.24(1)	N(12)–Fe(2)–N(15)	88.40(1)
N(12)–Fe(2)–N(18)	90.52(1)	N(15)–Fe(2)–N(18)	91.96(1)
N(8)–Mn(1)–N(14)	176.35(1)		

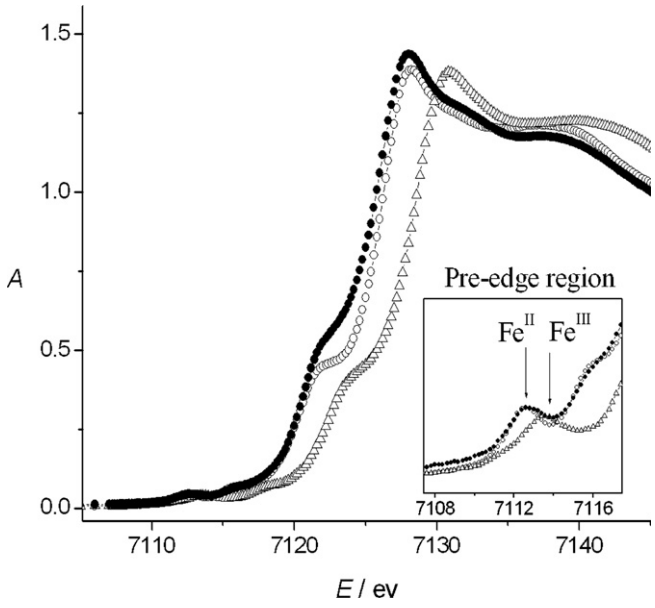


Fig. 2. Fe K-edge XANES spectra of **1** (●), $[Fe^{II}(\mathbf{L})_2]$ (○) and $[Fe^{III}(\mathbf{L})_2](ClO_4)$ (△). The inset shows expanded view of 1s → 3d transition in pre-edge region.

indicates that its 1D framework collapses out of the mother liquor at ambient temperature.

Therefore, we examined the Fe K-edge X-ray absorption structure (XAS) of **1** (vacuum-dried sample), $[Fe^{II}(\mathbf{L})_2]$ and $[Fe^{III}(\mathbf{L})_2](ClO_4)$ for a comparative study at ambient temperature to investigate the oxidation state of the iron centre of **1** (Fig. 2). The features of pre-edge absorption peaks corresponding to 1s → 3d transition in the XAS spectra can inform of the useful structure parameters such as the oxidation state of the chemical species, site symmetry, and covalent bond strength [12,13]. Absorption pattern of **1** in the 1s → 3d pre-edge region (Fig. 2, inset) coincides nearly with that of the low-spin ferrous complex of $[Fe^{II}(\mathbf{L})_2]$ but is far different from that of ferric complex ($[Fe^{III}(\mathbf{L})_2](ClO_4)$). In addition of lower energy absorption of **1** than the ferric $[Fe^{III}(\mathbf{L})_2](ClO_4)$, single 1s → 3d pre-edge absorption peak (7112.6 eV) of **1** is indicative of the low spin ferrous complex like $[Fe^{II}(\mathbf{L})_2]$ (7112.6 eV) because this is able to be assigned as the allowed electric quadrupole transition from $^1A_{1g}$ ground state with an electronic hole configuration of $(e_g)^4$ to ^2E_g excited state with $(e_g)^3$ as a pre-edge feature of a low spin ferrous complex [12].

Acknowledgment

The authors acknowledge the financial support of Korea Science and Engineering Foundation (Grant No. RO1-2001-00053).

Appendix A. Supplementary material

CCDC 604107 contains the supplementary crystallographic data for $\mathbf{1}\cdot 2CH_3CN\cdot CH_3OH$. These data can be obtained free of charge via http://www.ccdc.cam.ac.uk/conts/retrieving.html, or from the Cambridge Crystallographic Data Centre, 12 Union Road, Cambridge CB2 1EZ, UK; fax: (+44) 1223-336-033; or e-mail: deposit@ccdc.cam.ac.uk. Supplementary data associated with this article can be found, in the online version, at doi:10.1016/j.poly.2006.09.011.

References

[1] (a) C. Janiak, Dalton Trans. 14 (2003) 2781;
(b) B. Moulton, M.J. Zaworotko, Chem. Rev. 101 (2001) 1629;
(c) S.R. Batten, R. Robson, Angew. Chem. Int. Ed. 37 (1998) 1460;
(d) P.J. Hagrman, D. Hagrman, J. Zubieta, Angew. Chem. Int. Ed. 38 (1999) 2638;
(e) B.F. Abrahams, B.F. Hoskins, R. Robson, J. Am. Chem. Soc. 113 (1991) 3606.
[2] (a) O.M. Yaghi, M. O'Keeffe, N.W. Ockwig, H.K. Chae, M. Eddaoudi, J. Kim, Nature 423 (2003) 705;
(b) M. Munakata, L.P. Wu, T. Kuroda-Soda, Adv. Inorg. Chem. 46 (1999) 173;
(c) B. Moulton, M.J. Zaworotko, Curr. Opin. Solid State Mater. Sci. 6 (2002) 117;
(d) H.K. Chae, D.Y. Siberio-Pérez, J. Kim, Y. Go, M. Eddaoudi, A.J. Matzger, M. O'Keeffe, O.M. Yaghi, Nature 427 (2004) 523;
(e) D. Maspoch, D. Ruiz-Molina, J. Veciana, J. Mater. Chem. 14 (2004) 2713;
(f) X.-J. Zheng, L.-P. Jin, S.-Z. Lu, Eur. J. Inorg. Chem. (2002) 3356.
[3] (a) S.-I. Noro, S. Kitagawa, M. Yamashita, T. Wada, Chem. Commun. (2002) 222;
(b) R. Kitaura, G. Onoyama, H. Sakamoto, R. Matsuda, S.-I. Noro, S. Kitagawa, Angew. Chem. Int. Ed. 43 (2004) 2684.
[4] K.-T. Youm, S. Huh, Y.J. Park, S. Park, M.G. Choi, M.-J. Jun, Chem. Commun. (2004) 2384.
[5] K.-T. Youm, M.G. Kim, J. Ko, M.-J. Jun, Angew. Chem. Int. Ed. 45 (2006) 4003.
[6] Nonius Kappa-CCD Server software, Nonius B.V. Delft, Netherlands, 1997.
[7] G.M. Sheldrick, SHELXTL/PC Version 6.12 for Windows NT, Bruker AXS Inc., Madison, WI, USA, 2001.
[8] A.L. Spek, PLATON, A Multipurpose Crystallographic Tool, Utrecht University, Utrecht, Netherlands, 2003.
[9] (a) C. Janiak, Chem. Ber. 127 (1994) 1379;
(b) C. Janiak, T.G. Scharmann, J.C. Green, R.P.G. Parkin, M.J. Kolm, E. Riedel, W. Mickler, J. Elguero, R.M. Claramunt, D. Sanz, Chem. Eur. J. 2 (1996) 992;
(c) C. Janiak, T.G. Scharmann, T. Bräuniger, J. Holubová, M. Nádvornik, Z. Anorg. Allg. Chem. 624 (1998) 769.
[10] (a) E. König, Prog. Inorg. Chem. 35 (1987) 527;
(b) P. Gütlich, Y. Garcia, H.A. Goodwin, Chem. Soc. Rev. 29 (2000) 419.
[11] (a) J.D. Oliver, D.F. Mullica, B.B. Hutchinson, W.O. Milligan, Inorg. Chem. 19 (1980) 165;
(b) J.A. Real, M.C. Muñoz, J. Faw, X. Solans, Inorg. Chem. 36 (1997) 3008;
(c) D.L. Reger, C.A. Little, V.G. Young Jr., M. Pink, Inorg. Chem. 40 (2001) 2870.
[12] (a) T.E. Westre, P. Kennepohl, J.G. DeWitt, B. Hedman, K.O. Hodgson, E.I. Solomon, J. Am. Chem. Soc. 119 (1997) 6297;
(b) C. Hannay, M.-J. Hubin-Franskin, F. Grandjean, V. Briois, J.-P. Itié, A. Polian, S. Trofimenko, G.J. Long, Inorg. Chem. 36 (1997) 5580.
[13] (a) V. Briois, P. Sainctavit, G.J. Long, F. Grandjean, Inorg. Chem. 40 (2001) 912;
(b) M.-L. Boillot, J. Zarembowitch, J.-P. Itié, A. Polian, E. Bourdet, J.G. Haasnoot, New J. Chem. 26 (2002) 313.

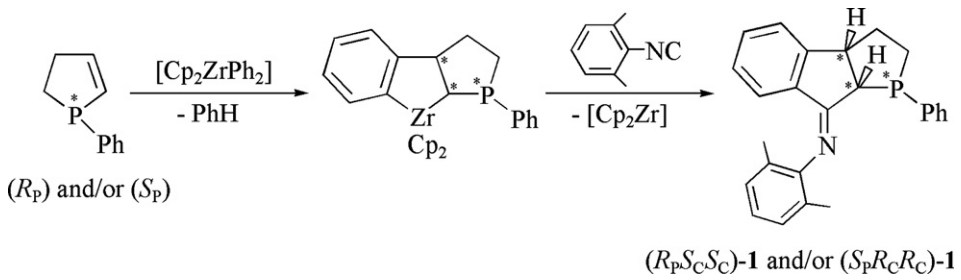
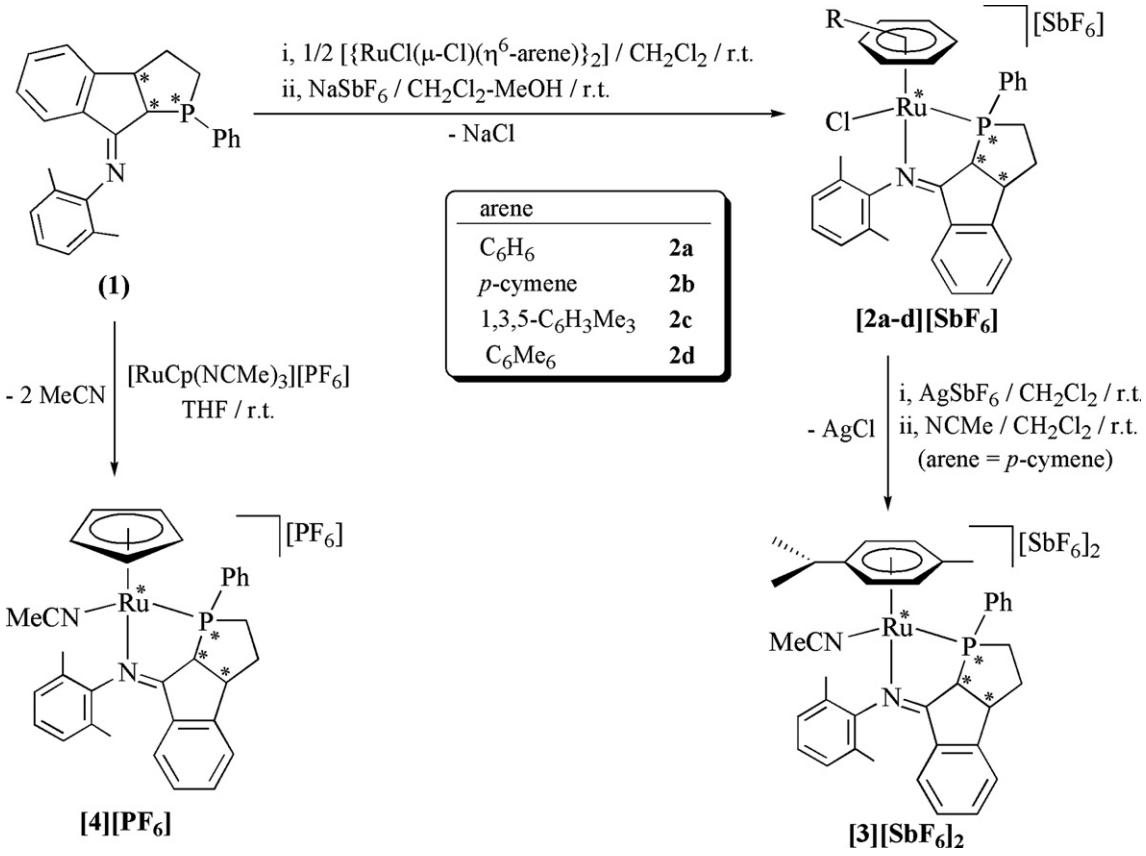


Chart 1. Synthesis of the tricyclic β-iminophosphine ligand **1**.



Scheme 1. Synthesis of half-sandwich ruthenium(II) derivatives containing ligand **1**.

2. Results and discussion

2.1. Synthesis and characterization of the half-sandwich ruthenium(II) compounds [2a–d][SbF6], [3][SbF6]2 and [4][PF6]

The treatment of a dichloromethane solution of dimers $[\{RuCl(\mu\text{-}Cl)(\eta^6\text{-arene})\}_2]$ (arene = C_6H_6, *p*-cymene, 1,3,5-$C_6H_3Me_3$, C_6Me_6) [7] with a twofold excess of ligand **1**[1] leads to the selective formation of the cationic derivatives $[RuCl(\eta^6\text{-arene})(\kappa^2\text{-}P,N\text{-}\mathbf{1})][Cl]$ (**[2a–d][Cl]**), which have been isolated as the corresponding hexafluoroantimonate salts **[2a–d][SbF6]** in 65–88% yield *via* classical Cl^-/SbF_6^- exchange using a methanolic solution of $NaSbF_6$ (Scheme 1). Compounds **[2a–d][SbF6]** have been characterized by means of elemental analyses, conductance measurements, and IR and NMR (^1H, $^{31}P\{^1H\}$ and $^{13}C\{^1H\}$) spectroscopies, all the data being fully consistent with the proposed structure (details are given in Section 4). Remarkably, the chelation of ligand **1**, which implies the generation of a new stereogenic centre on the ruthenium atom, takes place with complete diastereoselectivity as clearly assessed by the appearance of only one set of signals in their NMR spectra. In particular, the $^{31}P\{^1H\}$ NMR spectra display an unique singlet signal at δ 71.1 (**[2a][SbF6]**), 71.4 (**[2b][SbF6]**), 73.0 (**[2c][SbF6]**) and 69.0 (**[2d][SbF6]**) ppm. The coordination of the imine function

[1] Used as the racemic $R_PS_CS_C/S_PR_CR_C$ mixture.

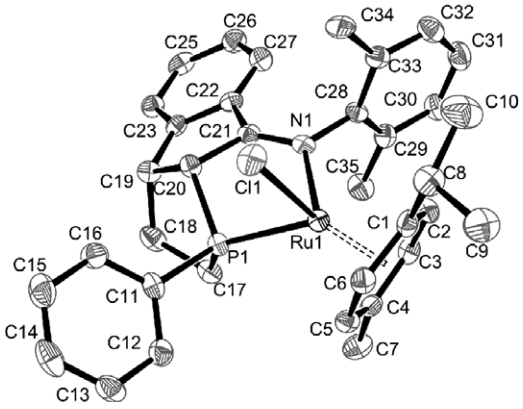


Fig. 1. CAMERON-type view of the structure of cation **[2b]**$^{+}$ showing the crystallographic labelling scheme. Hexafluoroantimonate anion and hydrogen atoms have been omitted for clarity. Thermal ellipsoids are drawn at the 30% probability level. Selected bond distances (Å) and angles (°): Ru–C* = 1.7299(13); Ru–Cl(1) = 2.4090(10); Ru–P(1) = 2.3181(9); Ru–N(1) = 2.145(3); P(1)–C(20) = 1.815(4); C(20)–C(21) = 1.510(5); C(21)–N(1) = 1.293(4); C*–Ru–N(1) = 130.99(9); C*–Ru–Cl(1) = 125.14 (6); C*–Ru–P(1) = 134.68(6); N(1)–Ru–Cl(1) = 88.59(8); N(1)–Ru–P(1) = 78.07(8); P(1)–Ru–Cl(1) = 81.82(4); Ru–P(1)–C(20) = 101.71(12); P(1)–C(20)–C(21) = 104.8(2); C(20)–C(21)–N(1) = 120.3(3); C(21)–N(1)–Ru = 121.3(2). C* = centroid of the *p*-cymene ring (C(1), C(2), C(3), C(4), C(5) and C(6)).

to ruthenium is evidenced by the $^{13}C\{^{1}H\}$ NMR spectra which show a downfield shift of the iminic carbon with respect to the free ligand ($\delta = 190.0$ (**[2a][SbF$_6$]**), 189.8 (**[2b][SbF$_6$]**), 190.0 (**[2c][SbF$_6$]**) and 189.1 (**[2d][SbF$_6$]**) versus 175.0 (**1**) ppm [3b]). Furthermore, the ν(C=N) stretching frequencies (1603 (**[2a][SbF$_6$]**), 1595 (**[2b][SbF$_6$]**), 1580 (**[2c][SbF$_6$]**), 1576 (**[2d][SbF$_6$]**) cm^{-1}) are also in accordance with a metal-bonded imine function [8].

The structure of the cymene compound **[2b][SbF$_6$]** has been unequivocally confirmed by means of an X-ray diffraction study. A drawing of the molecular structure is depicted in Fig. 1; selected bond distances and angles are listed in the caption. Cation **[2b]**$^{+}$ exhibits a classical pseudooctahedral three-legged piano-stool geometry, the coordination sphere around the ruthenium consisting of the *p*-cymene ring, one chloride, and the PhP and imine groups of the bidentate ligand. The distance of the carbon–nitrogen double bond (C(21)–N(1) = 1.293(4) Å) is in the expected range for a coordinated imine function and comparable to that observed in the palladium compound [PdCl$_2$(κ^2-*P*,*N*-**1**)] (C–N = 1.311(12) Å), previously reported by us [5]. The molecule drawn in Fig. 1 shows an $S_{Ru}R_PR_{C(20)}R_{C(19)}$ configuration.[2] As expected, the enantiomer $R_{Ru}S_PS_{C(20)}S_{C(19)}$, not represented here, is also present in the crystal lattice. The preferential formation of the $S_{Ru}R_PR_CR_C/R_{Ru}S_PS_CS_C$ diastereomer versus the $R_{Ru}R_PR_CR_C/S_{Ru}S_PS_CS_C$ one[3] seems to be sterically controlled, the former diastereomer leading to a less congestion between the *p*-cymene ligand substituents and the sterically demanding *P*-phenyl and *N*-mesityl groups. Moreover, in the $S_{Ru}R_PR_CR_C/R_{Ru}S_PS_CS_C$ diastereomer the chloride ligand points in the same direction as the hydrogen atoms C(19)–H and C(20)–H thus minimizing its interaction with the bidentate iminophosphine ligand.

Starting from the *p*-cymene compound **[2b][SbF$_6$]**, the dicationic species [Ru(η^6-*p*-cymene)(NCMe)(κ^2-*P*,*N*-**1**)]-[SbF$_6$]$_2$ (**[3][SbF$_6$]$_2$**) could also be prepared in high yield (71%) through the initial Ag(I)-promoted chloride ligand abstraction and subsequent addition of an excess of acetonitrile (Scheme 1). Compound **[3][SbF$_6$]$_2$** presents spectroscopic data very similar to those of its parent monocationic precursor **[2b][SbF$_6$]**, the most remarkable differences consisting in the appearance of a new resonance at 1.64 ppm in the ^{1}H NMR spectrum, and two singlets at 5.0 and 127.7 ppm in the $^{13}C\{^{1}H\}$ NMR spectrum, attributable to the coordinated acetonitrile molecule. The presence of the acetonitrile ligand is also evidenced in the IR spectrum which exhibits a characteristic C=N absorption at 2242 cm^{-1} [9]. Once again, as inferred by the spectroscopic data (see details in Section 4), the formation of **[3][SbF$_6$]$_2$** takes place with total diastereoselectivity, its stereochemistry being unambiguously determined by a single crystal X-ray diffraction study. As shown in Fig. 2, dication **[3]**$^{2+}$ adopts the expected three-legged piano stool geometry around the ruthenium atom, with values of the interligand angles P(1)–Ru–N(1), P(1)–Ru–N(2), N(1)–Ru–N(2), and those between the centroid of the arene ring C* and the legs in the expected range for this type of complexes. The diastereomer obtained presents a $S_{Ru}S_PS_{C(27)}S_{C(26)}/R_{Ru}R_PR_{C(27)}R_{C(26)}$ configuration[4] (only the former enantiomer is drawn in Fig. 2). The substitution of the chloride ligand by an acetonitrile molecule does not affect significantly the structure of the ruthenacycle, the bond distances within the cyclic skeleton remaining almost unchanged when compared to those shown by **[2b]**$^{+}$ (*ca.* ± 0.04 Å).

As depicted in Scheme 1, the related solvento complex [Ru(η^5-C$_5$H$_5$)(NCMe)(κ^2-*P*,*N*-**1**)][PF$_6$] (**[4][PF$_6$]**) was synthesized (75% yield) by displacement of two labile acetonitrile ligands in the cationic cyclopentadienyl-Ru(II) precursor [Ru(η^5-C$_5$H$_5$)(NCMe)$_3$][PF$_6$] [10]. The most characteristic spectroscopic features of compound **[4][PF$_6$]** are: (i) in the $^{31}P\{^{1}H\}$ NMR spectrum, a sole singlet at 80.3 ppm evidencing the formation of a unique diastereomer, (ii) in the ^{1}H NMR spectrum, two singlets at 1.72 and 4.43 ppm attributable to the coordinated acetonitrile and the η^5-Cp ligand, respectively, and (iii) in the

[2] The priority order to determinate the ruthenium configuration is as follows: η^6-arene > Cl > P > N. Note that, although the spatial disposition remains unchanged, the preference orders for the phosphorus atom change after coordination on the metal inverting the *R*/*S* assignment.

[3] Other diastereoisomers resulting from the epimerization of one of the three stereogenic centres of the ligand **1** are not probable due to its high rigidity.

[4] The priority order to determinate the ruthenium configuration is as follows: η^6-arene > P > N(2) of acetonitrile > N(1) of imine.

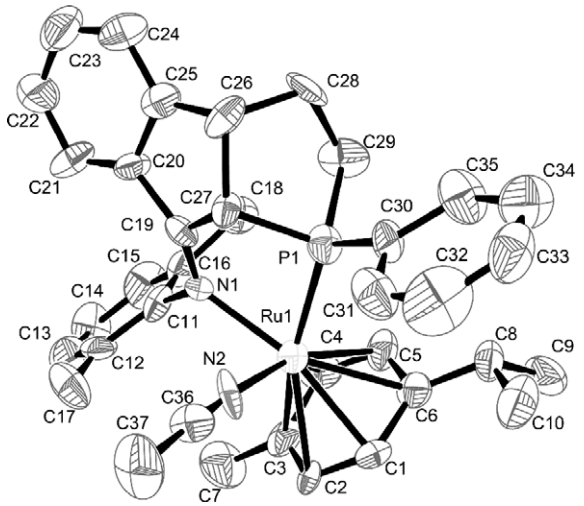


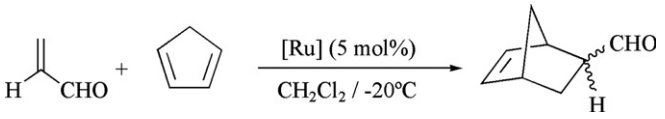
Fig. 2. CAMERON-type view of the structure of dication **[3]**$^{2+}$ showing the crystallographic labelling scheme. Hexafluoroantimonate anions and hydrogen atoms have been omitted for clarity. Thermal ellipsoids are drawn at the 30% probability level. Selected bond distances (Å) and angles (°): Ru–C* = 1.739(4); Ru–N(1) = 2.114(8); Ru–N(2) = 2.058(10); Ru–P(1) = 2.319(3); P(1)–C(27) = 1.822(9); C(27)–C(19) = 1.513(13); C(19)–N(1) = 1.264(12); N(2)–C(36) = 1.131(12); C(36)–C(37) = 1.445(14); C*–Ru–N(1) = 133.7(3); C*–Ru–N(2) = 125.4(3); C*–Ru–P(1) = 130.55(17); N(1)–Ru–N(2) = 84.3(3); N(1)–Ru–P(1) = 77.4(2); N(2)–Ru–P(1) = 88.5(3); Ru–P(1)–C(27) = 100.3(3); P(1)–C(27)–C(19) = 103.5(6); C(27)–C(19)–N(1) = 120.7(10); C(19)–N(1)–Ru = 121.9(7); Ru–N(2)–C(36) = 173.6(10); N(2)–C(36)–C(37) = 175.3(13). C* = centroid of the *p*-cymene ring (C(1), C(2), C(3), C(4), C(5) and C(6)).

$^{13}C\{^{1}H\}$ NMR spectrum, a doublet resonance at 187.2 ppm corresponding to the iminic carbon, and two singlets at 3.9 and 127.0 ppm assignable to the coordinated acetonitrile ligand. Unfortunately, all attempts to obtain crystals suitable for X-ray analysis failed, and therefore the configuration of the diastereomer formed could not be determined.

At this point it should be noted that, apart from the widely studied phosphine-oxazoline containing compounds [11], species $[RuCl(\eta^5\text{-}C_9H_7)\{\kappa^2\text{-}P,N\text{-}2\text{-}Ph_2PC_6H_4C(H)=NBu^t\}]$ (C_9H_7 = indenyl) [12], $[Ru(\eta^5\text{-}C_5Me_5)\{\kappa^3\text{-}P,N,N\text{-}2\text{-}Ph_2PC_6H_4C(H)N(CH_2)_2N=C(H)\text{-}2\text{-}C_6H_4PPh_2\}]_2[ZnCl_4]$ and $[\{Ru(\eta^5\text{-}C_5Me_5)(NCMe)\}_2\{\kappa^4\text{-}P,N,N,P\text{-}2\text{-}Ph_2PC_6H_4C(H)=N(CH_2)_2N=C(H)\text{-}2\text{-}C_6H_4PPh_2\}][ZnCl_4]$ [13] are, as far as we are aware, the only precedents of half-sandwich Ru(II) derivatives containing coordinated iminophosphine ligands reported in the literature [14].

2.2. Catalytic Diels–Alder reactions

Owing to their inherent Lewis-acidity, organometallic ruthenium cations are able to promote Diels–Alder cycloaddition processes [15]. In particular, during the last decade, dicationic (η^6-arene)-ruthenium(II) compounds [11e,16] and monocationic (η^5-cyclopentadienyl)-ruthenium(II) derivatives [17] containing optically active bidentate ligands have proven to be an appealing alternative to the classical Al-, B- or lanthanide-based Lewis-acid catalysts for asymmetric Diels–Alder reactions due to their increased resistance to hydrolysis. With these precedents in mind, we have prepared the optically pure compounds **[2a–d][SbF$_6$]**, **[3][SbF$_6$]$_2$** and **[4][PF$_6$]** starting from the non-racemic iminophosphine ligand ($R_PS_CS_C$)-**1** and we have explored their catalytic performances in the Diels–Alder cycloaddition between acrolein and cyclopentadiene (Scheme 2).



Scheme 2. Diels–Alder reaction of acrolein with cyclopentadiene catalyzed by ruthenium.

Table 1
Diels–Alder reaction of acrolein with cyclopentadiene[a]

Catalyst	Time (h)	Yield[b] (%)	*endo*:*exo*[b]
[2a][SbF$_6$]	20	92	68:32
[2b][SbF$_6$]	20	99	74:26
[2c][SbF$_6$]	20	90	71:29
[2d][SbF$_6$]	20	87	69:31
[3][SbF$_6$]$_2$	20	89	73:27

[a] All reactions were carried out in CH_2Cl_2 at −20 °C using 1.5 mmol of acrolein, 9 mmol of CpH and 5 mol% of ruthenium.
[b] GC determined using *cis*-decaline as internal standard.

We note that starting from the arene–ruthenium(II) precursors **[2a–d][SbF$_6$]**, the catalytically active species, *i.e.* the dications $[Ru(\eta^6\text{-arene})(\kappa^2\text{-}P,N\text{-}\mathbf{1})]^{2+}$, were generated *in situ* upon treatment of **[2a–d][SbF$_6$]** with one equivalent of $AgSbF_6$, while the solvento compounds $[Ru(\eta^6\text{-}p\text{-cymene})(NCMe)(\kappa^2\text{-}P,N\text{-}\mathbf{1})][SbF_6]_2$ (**[3][SbF$_6$]$_2$**) and $[Ru(\eta^5\text{-}C_5H_5)(NCMe)(\kappa^2\text{-}P,N\text{-}\mathbf{1})][PF_6]$ (**[4][PF$_6$]**) were used directly in the catalytic experiments (see details in Section 4). The results obtained are summarized in Table 1.

As shown in Table 1, the use of the arene–ruthenium(II) catalysts **[2a–d][SbF$_6$]** and **[3][SbF$_6$]$_2$** leads to the almost quantitative formation of the expected bicyclo[2.2.1]hept-5-ene-2-carboxaldehyde after 20 h, albeit with moderate diastereoselectivity and with a total lack of enantioselectivity. On the other hand, the cyclopentadienyl compound **[4][PF$_6$]** did not afford the expected cycloadduct, the cyclopentadiene dimer being the only product detected by GC.

3. Conclusion

In this work, we have evidenced the ability of the iminophosphine **1** to chelate half-sandwich ruthenium(II) fragments. In particular, the arene–ruthenium(II) compounds $[RuCl(\eta^6\text{-arene})(\kappa^2\text{-}P,N\text{-}\mathbf{1})][SbF_6]$ (arene = C_6H_6, *p*-cymene, 1,3,5-$C_6H_3Me_3$, C_6Me_6) and $[Ru(NCMe)(\eta^6\text{-}p\text{-cymene})(\kappa^2\text{-}P,N\text{-}\mathbf{1})][SbF_6]_2$, and the cyclopentadienyl derivative $[Ru(NCMe)(\eta^6\text{-}C_5H_5)(\kappa^2\text{-}P,N\text{-}\mathbf{1})][PF_6]$ have been prepared in excellent yields. Remarkably, the chelate

coordination of **1** to ruthenium takes place in all cases with complete diastereoselectivity due probably to the high rigidity and steric requirement of this ligand. Unfortunately, their use in catalytic asymmetric Diels–Alder reactions only affords disappointing diastereo- and enantioselectivities.

4. Experimental

4.1. General information

The manipulations were performed under an atmosphere of dry nitrogen using vacuum-line and standard Schlenk techniques. Solvents were dried by standard methods and distilled under nitrogen before use. All reagents were obtained from commercial suppliers with the exception of ligand **1** [3,4], and derivatives $[\{RuCl(\mu\text{-}Cl)(\eta^6\text{-arene})\}_2]$ (arene = C_6H_6 [18], *p*-cymene [19], 1,3,5-$C_6H_3Me_3$ [18], C_6Me_6 [19]) and $[Ru(\eta^5\text{-}C_5H_5)(NCMe)_3][PF_6]$ [20] which were prepared by following the methods reported in the literature. Infrared spectra were recorded on a Perkin–Elmer 1720-XFT spectrometer. The conductivities were measured at room temperature, in *ca.* 10^{-3} mol dm^{-3} acetone solutions, with a Jenway PCM3 conductimeter. The C, H, and N analyses were carried out with a Perkin-Elmer 2400 microanalyzer. GC measurements were made on a Hewlett–Packard HP6890 equipment using a Supelco Gama-Dex™ 225 (30 m, 250 μm) column. NMR spectra were recorded on a Bruker DPX-300 instrument at 300 MHz (^{1}H), 121.5 MHz (^{31}P) or 75.4 MHz (^{13}C) using $SiMe_4$ or 85% H_3PO_4 as standards. DEPT experiments have been carried out for all the compounds reported.

4.2. Synthesis of compounds *[RuCl(η⁶-arene)(κ²-P,N-**1**)][SbF₆]* (*arene* = C_6H_6 (***[2a][SbF₆]***), *p*-cymene (***[2b][SbF₆]***), 1,3,5-$C_6H_3Me_3$ (***[2c][SbF₆]***), C_6Me_6 (***[2d][SbF₆]***))

A solution of the corresponding dimeric precursor $[\{RuCl(\mu\text{-}Cl)(\eta^6\text{-arene})\}_2]$ (0.2 mmol) in 15 mL of dichloromethane was treated, at room temperature, with ligand **1** (0.150 g, 0.406 mmol) for 1 h. A solution of $NaSbF_6$ (1.035 g, 4 mmol) in methanol (10 mL) was then added and the resulting solution stirred at room temperature for 6 h. The solvents were then removed under vacuum, the crude product extracted with dichloromethane (*ca.* 20 mL), the extract filtered over Kieselguhr, the filtrate evaporated to dryness, and the resulting orange oily residue washed with diethyl ether (3 × 10 mL) and dried in vacuum. **([2a][SbF₆])**: Yield: 65% (0.213 g); *Anal.* Calc. for $RuC_{31}H_{30}F_6ClNPSb$ (819.82 g mol^{-1}): C, 45.42; H, 3.69; N, 1.71. Found: C, 45.29; H, 3.80; N, 1.65%; Conductivity (acetone, 20 °C) 107 Ω^{-1} cm^2 mol^{-1}; IR (KBr) ν = 1603 (C=N); $^{31}P\{^1H\}$ NMR (acetone-d_6) δ = 71.1 (s) ppm; ^{1}H NMR (acetone-d_6) δ = 1.82–2.58 (m, 3H, CH_2), 2.69 and 2.78 (s, 3H each, $C_6H_3Me_2$), 3.25 (m, 1H, CH_2), 4.20 (m, 1H, PCHC*H*), 5.39 (d, 1H, $^2J_{HP}$ = 4.4 Hz, PCH), 5.83 (s, 6H, C_6H_6), 6.03 (d, 1H, $^3J_{HH}$ = 8.1 Hz, CH_{arom}), 7.12–8.15 (m, 11H, CH_{arom}) ppm; $^{13}C\{^1H\}$ NMR (acetone-d_6) δ = 18.1 and 18.7 (s, $C_6H_3Me_2$), 29.2 (d, $^1J_{CP}$ = 19.9 Hz, PCH_2), 32.0 (d, $^2J_{CP}$ = 6.3 Hz, PCH_2CH_2), 43.1 (s, PCH*C*H), 61.5 (d, $^1J_{CP}$ = 37.6 Hz, PCH), 89.5 (d, $^2J_{CP}$ = 2.8 Hz, C_6H_6), 124.2–135.1 (m, CH_{arom} and C_{arom}), 150.8 (s, *C*CC=N), 155.8 (d, $^3J_{CP}$ = 9.1 Hz, *C*C=N), 190.0 (d, $^2J_{CP}$ = 8.3 Hz, C=N) ppm. **([2b][SbF₆])**: Yield: 82% (0.287 g); *Anal.* Calc. for $RuC_{35}H_{38}F_6ClNPSb$ (875.93 g mol^{-1}): C, 47.99; H, 4.37; N, 1.60. Found: C, 47.80; H, 4.41; N, 1.75%; Conductivity (acetone, 20 °C) 115 Ω^{-1} cm^2 mol^{-1}; IR (KBr) ν = 1596 (C=N); $^{31}P\{^1H\}$ NMR (CD_2Cl_2) δ = 71.4 (s) ppm; ^{1}H NMR (CD_2Cl_2) δ = 1.01 and 1.20 (d, 3H each, $^3J_{HH}$ = 7.1 Hz, $CH(CH_3)_2$), 1.19 and 3.13 (m, 1H each, CH_2), 1.68 (s, 3H, CH_3), 2.10 and 2.54 (s, 3H each, $C_6H_3Me_2$), 2.13 (m, 2H, CH_2), 2.61 (m, 1H, C*H*(CH_3)$_2$), 3.87 (m, 1H, PCHC*H*), 4.90 (d, 1H, $^2J_{HP}$ = 5.8 Hz, PCH), 5.10 and 5.19 (br, 2H each, CH of *p*-cymene), 5.94 (d, 1H, $^3J_{HH}$ = 8.1 Hz, CH_{arom}), 7.35–7.99 (m, 11H, CH_{arom}) ppm; $^{13}C\{^1H\}$ NMR (CD_2Cl_2) δ = 18.9 (s, CH_3), 19.4 and 19.5 (s, $C_6H_3Me_2$), 20.8 and 23.3 (s, CH(*C*H$_3$)$_2$), 26.3 (d, $^1J_{CP}$ = 22.6 Hz, PCH_2), 31.1 (s, *C*H(CH$_3$)$_2$), 32.4 (d, $^2J_{CP}$ =3.0 Hz, PCH_2CH_2), 42.8 (s, PCH*C*H), 61.7 (d, $^1J_{CP}$ = 36.2 Hz, PCH), 85.4 (2C) and 88.6 (s, CH of *p*-cymene), 89.7 (d, $^2J_{CP}$ = 4.5 Hz, CH of *p*-cymene), 103.1 (d, $^2J_{CP}$ = 3.0 Hz, C of *p*-cymene), 117.5 (d, $^2J_{CP}$ = 6.8 Hz, C of *p*-cymene), 125.1–135.7 (m, CH_{arom} and C_{arom}), 150.0 (s, *C*CC=N), 155.5 (d, $^3J_{CP}$ = 4.5 Hz, *C*C=N), 189.8 (d, $^2J_{CP}$ = 7.5 Hz, C=N) ppm. **([2c][SbF₆])**: Yield: 71% (0.245 g); *Anal.* Calc. for $RuC_{34}H_{36}F_6ClNPSb$ (861.90 g mol^{-1}): C, 47.38; H, 4.21; N, 1.63. Found: C, 47.12; H, 4.09; N, 1.74%; Conductivity (acetone, 20 °C) 104 Ω^{-1} cm^2 mol^{-1}; IR (KBr) ν = 1580 (C=N); $^{31}P\{^1H\}$ NMR (acetone-d_6) δ = 73.0 (s) ppm; ^{1}H NMR (acetone-d_6) δ = 1.83 (s, 9H, $C_6H_3Me_3$), 1.95–2.43 (m, 3H, CH_2), 2.56 (s, 6H, $C_6H_3Me_2$), 3.31 (m, 1H, CH_2), 4.14 (m, 1H, PCHC*H*), 5.42 (d, 1H, $^2J_{HP}$ = 4.1 Hz, PCH), 5.50 (s, 3H, $C_6H_3Me_3$), 5.90 (d, 1H, $^3J_{HH}$ = 7.9 Hz, CH_{arom}),7.10–8.24 (m, 11H, CH_{arom}) ppm; $^{13}C\{^1H\}$ NMR (acetone-d_6) δ = 17.6 (s, $C_6H_3Me_3$), 18.2 and 18.6 (s, $C_6H_3Me_2$), 25.1 (d, $^1J_{CP}$ = 21.4 Hz, PCH_2), 31.5 (d, $^2J_{CP}$ = 2.7 Hz, PCH_2CH_2), 42.5 (s, PCH*C*H), 59.9 (d, $^1J_{CP}$ = 35.7 Hz, PCH), 88.8 (d, $^2J_{CP}$ = 2.7 Hz, CH of $C_6H_3Me_3$), 103.2 (d, $^2J_{CP}$ = 1.9 Hz, C of $C_6H_3Me_3$), 124.5–135.1 (m, CH_{arom} and C_{arom}), 148.2 (s, *C*CC=N), 155.7 (d, $^3J_{CP}$ = 5.4 Hz, *C*C=N), 190.0 (d, $^2J_{CP}$ = 8.0 Hz, C=N) ppm. **([2d][SbF₆])**: Yield: 88% (0.318 g); *Anal.* Calc. for $RuC_{37}H_{42}F_6ClNPSb$ (903.98 g mol^{-1}): C, 49.16; H, 4.62; N, 1.55. Found: C, 48.89; H, 4.54; N, 1.70%; Conductivity (acetone, 20 °C) 113 Ω^{-1} cm^2 mol^{-1}; IR (KBr) ν = 1576 (C=N); $^{31}P\{^1H\}$ NMR (acetone-d_6) δ = 69.0 (s) ppm; ^{1}H NMR (acetone-d_6) δ = 1.82 (s, 18H, C_6Me_6), 2.16 and 2.53 (s, 3H each, $C_6H_3Me_2$), 2.30 (m, 2H, CH_2), 2.55 and 3.59 (m, 1H each, CH_2), 3.93 (m, 1H, PCHC*H*), 5.26 (d, 1H, $^2J_{HP}$ = 6.4 Hz, PCH), 5.82 (d, 1H, $^3J_{HH}$ = 8.1 Hz, CH_{arom}), 7.04–8.39 (m, 11H, CH_{arom}) ppm; $^{13}C\{^1H\}$ NMR (acetone-d_6) δ = 15.1 (s, C_6Me_6), 19.2 and 19.3 (s, $C_6H_3Me_2$), 22.9

(d, $^1J_{CP} = 22.2$ Hz, PCH_2), 31.5 (d, $^2J_{CP} = 3.0$ Hz, PCH_2CH_2), 42.7 (s, PCHCH), 62.1 (d, $^1J_{CP} = 34.2$ Hz, PCH), 99.3 (s, C_6Me_6), 124.4–134.8 (m, CH_{arom} and C_{arom}), 146.9 (s, CCC=N), 155.3 (d, $^3J_{CP} = 5.0$ Hz, CC=N), 189.1 (d, $^2J_{CP} = 7.0$ Hz, C=N) ppm.

4.3. Synthesis of compound [Ru(NCMe)(η⁶-p-cymene)(κ²-P,N-1)][SbF₆]₂ ([3][SbF₆]₂)

A solution of salt [RuCl(η⁶-*p*-cymene)(κ²-*P*,*N*-**1**)][SbF_6] (**[2b][SbF₆]**) (0.109 g, 0.124 mmol) in 15 mL of dichloromethane was treated, at room temperature and in the absence of light, with $AgSbF_6$ (0.045 g, 0.131 mmol) for 1 h. Acetonitrile (2 mL) was then added and the resulting suspension stirred for 15 min. The AgCl formed was filtered off (Kieselguhr), the filtrate evaporated to dryness, and the resulting yellow oily residue washed with diethyl ether (3 × 10 mL) and dried in vacuum. Yield: 71% (0.099 g); *Anal.* Calc. for $RuC_{37}H_{41}F_{12}N_2Sb_2P$ (1117.28 g mol^{-1}): C, 39.77; H, 3.70; N, 2.51. Found: C, 39.59; H, 3.61; N, 2.70%; Conductivity (acetone, 20 °C) 221 Ω^{-1} cm^2 mol^{-1}; IR (KBr) $\nu = 1590$ (C=N), 2242 (C≡N); $^{31}P\{^1H\}$ NMR (CD_2Cl_2) $\delta = 69.7$ (s) ppm; ^1H NMR (CD_2Cl_2) $\delta = 0.82$ and 1.20 (d, 3H each, $^3J_{HH} = 6.8$ Hz, $CH(CH_3)_2$), 1.64 and 1.86 (s, 3H each, NC*Me* and CH_3), 1.96–2.59 (m, 4H, CH_2 and $CH(CH_3)_2$), 2.45 and 2.70 (s, 3H each, $C_6H_3Me_2$), 3.30 (m, 1H, CH_2), 4.08 (m, 1H, PCHC*H*), 4.95 (d, 1H, $^2J_{HP} = 7.1$ Hz, PCH), 5.25 and 5.82 (d, 1H each, $^3J_{HH} = 6.2$ Hz, CH of *p*-cymene), 5.34 and 5.98 (d, 1H each, $^3J_{HH} = 6.5$ Hz, CH of *p*-cymene), 5.90 (d, 1H, $^3J_{HH} = 8.3$ Hz, CH_{arom}), 7.04–8.01 (m, 11H, CH_{arom}) ppm; $^{13}C\{^1H\}$ NMR (CD_2Cl_2) $\delta = 5.0$ (s, NC*Me*), 18.8 (s, CH_3), 18.9 and 19.1 (s, $C_6H_3Me_2$), 21.2 and 23.6 (s, $CH(CH_3)_2$), 27.5 (d, $^1J_{CP} = 25.0$ Hz, PCH_2), 31.8 (s, $CH(CH_3)_2$), 32.7 (d, $^2J_{CP} = 3.1$ Hz, PCH_2CH_2), 44.1 (s, PCHCH), 61.5 (d, $^1J_{CP} = 33.6$ Hz, PCH), 87.5 (d, 2C, $^2J_{CP} = 3.9$ Hz, CH of *p*-cymene), 91.4 (d, $^2J_{CP} = 1.6$ Hz, CH of *p*-cymene), 91.7 (d, $^2J_{CP} = 3.1$ Hz, CH of *p*-cymene), 112.4 (d, $^2J_{CP} = 3.9$ Hz, C of *p*-cymene), 118.3 (d, $^2J_{CP} = 4.7$ Hz, C of *p*-cymene), 124.5–136.9 (m, CH_{arom} and C_{arom}), 127.7 (s, NCMe), 149.2 (s, CCC=N), 156.5 (d, $^3J_{CP} = 4.7$ Hz, CC=N), 192.9 (d, $^2J_{CP} = 6.3$ Hz, C=N) ppm.

4.4. Synthesis of compound [Ru(η⁵-C₅H₅)(NCMe)-(κ²-P,N-1)][PF₆] ([4][PF₆])

A solution of [Ru(η^5-C_5H_5)$(NCMe)_3$][PF_6] (0.060 g, 0.137 mmol) in 30 mL of THF was treated, at room temperature, with ligand **1** (0.051 g, 0.137 mmol) for 30 min. The solution was then filtered over Kieselguhr, the filtrate evaporated to dryness, and the resulting brown oily residue washed with diethyl ether (3 × 10 mL) and dried in vacuum. Yield: 75% (0.074 g); *Anal.* Calc. for $RuC_{32}H_{32}F_6N_2P_2$ (721.62 g mol^{-1}): C, 53.26; H, 4.47; N, 3.88. Found: C, 53.09; H, 4.35; N, 4.01%; Conductivity (acetone, 20 °C) 117 Ω^{-1} cm^2 mol^{-1}; IR (KBr) $\nu = 1570$ (C=N), 2230 (C≡N) cm^{-1}; $^{31}P\{^1H\}$ NMR (acetone-d_6) $\delta = 80.3$ (s) ppm; ^1H NMR (acetone-d_6) $\delta = 1.72$ (s, 3H, NC*Me*), 2.05, 2.21, 2.60 and 2.83 (m, 1H each, CH_2), 2.48 and 2.51 (s, 3H each, $C_6H_3Me_2$), 4.25 (m, 1H, PCHC*H*), 4.43 (s, 5H, C_5H_5), 5.02 (d, 1H, $^2J_{HP} = 7.4$ Hz, PCH), 6.03 (d, 1H, $^3J_{HH} = 7.9$ Hz, CH_{arom}), 7.09–8.00 (m, 11H, CH_{arom}) ppm; $^{13}C\{^1H\}$ NMR (acetone-d_6) $\delta = 3.9$ (s, NC*Me*), 18.5 and 18.6 (s, $C_6H_3Me_2$), 31.7 (d, $^1J_{CP} = 20.4$ Hz, PCH_2), 33.3 (d, $^2J_{CP} = 3.8$ Hz, PCH_2CH_2), 45.4 (d, $^2J_{CP} = 1.5$ Hz, PCHCH), 63.2 (d, $^1J_{CP} = 27.2$ Hz, PCH), 75.9 (d, $^2J_{CP} = 3.0$ Hz, C_5H_5), 124.7–134.2 (m, CH_{arom} and C_{arom}), 127.0 (s, NCMe), 152.0 (s, CCC=N), 155.8 (d, $^3J_{CP} = 4.5$ Hz, CC=N), 187.2 (d, $^2J_{CP} = 9.8$ Hz, C=N) ppm.

4.5. General procedure for the catalytic Diels–Alder reaction promoted by [2a–d][SbF₆]

A Schlenk tube was charged, under N_2 atmosphere, with the corresponding ruthenium(II) salt (0.075 mmol) and $AgSbF_6$ (0.051 g, 0.15 mmol). Dichloromethane (5 mL) was added and the mixture stirred at room temperature for 30 min, followed by filtration over Kieselguhr to remove the precipitated AgCl. The filtrate was evaporated to dryness, dissolved in 2 mL of CH_2Cl_2 and transferred, under N_2 atmosphere, into a jacketed Schlenk tube refrigerated by a closed ^{i}PrOH circuit kept at −20 °C with a cryostat. Freshly distilled acrolein (0.1 mL, 1.5 mmol), 2,6-lutidine (4 μL, 0.0375 mmol) and *cis*-decaline (0.231 mL, 1.5 mmol) were added. The resulting yellow solution was equilibrated at −20 °C for 30 min before addition of freshly distilled cyclopentadiene (0.6 mL, 9 mmol). The course of the reaction, *i.e.* conversion, *endo:exo* ratio and *ee* excess, was monitored by GC [Supelco Gama-Dex™ 225 (30 m, 250 μm) column; helium 4 mL/min, 60 °C, 10 °C/min to 200 °C: 5.53 min (*cis*-decaline), 5.88 and 6.00 min (*exo* cycloadducts), 6.60 and 6.66 min (*endo* cycloadducts)].

4.6. General procedure for the catalytic Diels–Alder reaction promoted by [3][SbF₆]₂ and [4][PF₆]

A jacketed Schlenk tube refrigerated by a closed ^{i}PrOH circuit kept at −20 °C with a cryostat was charged, under N_2 atmosphere, with the corresponding ruthenium(II) complex (0.075 mmol) and 2 mL of CH_2Cl_2. Freshly distilled acrolein (0.1 mL, 1.5 mmol), 2,6-lutidine (4 μL, 0.0375 mmol) and *cis*-decaline (0.231 mL, 1.5 mmol) were added. The resulting yellow solution was equilibrated at −20 °C for 30 min before addition of freshly distilled cyclopentadiene (0.6 mL, 9 mmol).

4.7. X-ray crystal structure determination of compounds [2b][SbF₆] and [3][SbF₆]₂

Single-crystals suitable for X-ray diffraction analysis were obtained by slow diffusion of diethylether into a

Table 2
Crystal data and structure refinement for **[2b][SbF$_6$]** and **[3][SbF$_6$]$_2$**

	[2b][SbF$_6$]	**[3][SbF$_6$]$_2$**
Empirical formula	$RuC_{35}H_{38}F_6ClNPSb$	$RuC_{37}H_{41}F_{12}N_2\ Sb_2P$
Formula weight	875.90	1117.28
Temperature (K)	180(2)	293(2)
Wavelength (Å)	0.71073	0.71073
Crystal system	monoclinic	monoclinic
Space group	$P2_1/c$	Cc
Unit cell dimensions		
a (Å)	13.0044(10)	18.328(2)
b (Å)	14.0801(13)	15.2979(18)
c (Å)	19.3553(14)	14.8014(18)
α (°)	90	90
β (°)	105.006(8)	90.239(9)
γ (°)	90	90
Volume (Å^3)	3423.2(5)	4150.1(8)
Z	4	4
Calculated density (g cm^{-3})	1.700	1.785
Absorption coefficient (mm^{-1})	1.414	1.773
F(000)	1744	2176
Theta range for data collection (°)	2.17–26.04	3.24–24.66
Index ranges	$-16 \leqslant h \leqslant 15$, $-17 \leqslant k \leqslant 17$, $-23 \leqslant l \leqslant 23$	$-19 \leqslant h \leqslant 21$, $-17 \leqslant k \leqslant 17$, $-17 \leqslant l \leqslant 15$
Reflections collected	26489	13233
Independent reflections [R_{int}]	6667 [0.0788]	5709 [0.0635]
Completeness to theta max. (%)	96.8	99.6
Absorption correction	empirical (DIFABS)	semi-empirical from equivalents
Refinement method	full-matrix least-squares on F^2	
Data/restraints/parameters	6667/0/420	5709/9/479
Goodness-of-fit on F^2	0.904	0.766
R_1 [$I > 2\sigma(I)$]	0.0326	0.0433
wR_2 [$I > 2\sigma(I)$]	0.0564	0.0727
R_1 (all data)	0.0644	0.0846
wR_2 (all data)	0.0630	0.0814
Largest difference peak/hole (e Å^{-3})	0.526/−0.635	0.500/−0.463

saturated solution of **[2b][SbF$_6$]** in dichloromethane or into a solution of **[3][SbF$_6$]$_2$** in a dichloromethane/acetonitrile mixture. The most relevant crystallographic data are collected in Table 2.

Acknowledgements

We are indebted to the Ministerio de Ciencia y Tecnología (MCyT) of Spain (Project BQU2003-00255) and the Gobierno del Principado de Asturias (Projects PR-01-GE-6 and IB05-035) for financial support. P.C. and V.C. thank the MCyT and the European Social Fund for "Ramón y Cajal" contracts. M.Z. thanks the Ministry of Science and Information Society Technologies Poland for financial support (Grant No. 3T09A 15829). A.E.D.A., M.Z. and J.P.M. thank the LEA (Laboratoire Européen Associé, Toulouse-Łódź) for financial support.

Appendix A. Supplementary data

CCDC 615855 and CCDC 615854 contain the supplementary crystallographic data for **[2b][SbF$_6$]** and **[3][SbF$_6$]$_2$**. These data can be obtained free of charge via http://www.ccdc.cam.ac.uk/conts/retrieving.html, or from the Cambridge Crystallographic Data Centre, 12 Union Road, Cambridge CB2 1EZ, UK; fax: (+44) 1223-336-033; or e-mail: deposit@ccdc.cam.ac.uk. Supplementary data associated with this article can be found, in the online version, at doi:10.1016/j.poly.2006.09.030.

References

[1] (a) For reviews on the chemistry of *P*,*N*-donor ligands see: G.R. Newkome, Chem. Rev. 93 (1993) 2067;
(b) P. Espinet, K. Soulantica, Coord. Chem. Rev. 193–195 (1999) 499;
(c) P. Braunstein, F. Naud, Angew. Chem., Int. Ed. 40 (2001) 680;
(d) G. Chelucci, G. Orrù, G.A. Pinna, Tetrahedron 59 (2003) 9471;
(e) P.J. Guiry, C.P. Saunders, Adv. Synth. Catal. 346 (2004) 497;
(f) P. Braunstein, J. Organomet. Chem. 689 (2004) 3953.
[2] For a general review on hemilabile ligands see: C.S. Slone, D.A. Weinberger, C.A. Mirkin, Prog. Inorg. Chem. 48 (1999) 233.
[3] (a) M. Zablocka, N. Cénac, A. Igau, B. Donnadieu, J.-P. Majoral, A. Skowronska, P. Meunier, Organometallics 15 (1996) 5436;
(b) V. Cadierno, M. Zablocka, B. Donnadieu, A. Igau, J.-P. Majoral, A. Skowronska, J. Am. Chem. Soc. 121 (1999) 11086.
[4] M. Zablocka, M. Koprowski, B. Donnadieu, J.-P. Majoral, M. Achard, G. Buono, Tetrahedron Lett. 44 (2003) 2413.
[5] M. Koprowski, R.-M. Sebastián, V. Maraval, M. Zablocka, V. Cadierno, B. Donnadieu, A. Igau, A.-M. Caminade, J.-P. Majoral, Organometallics 21 (2002) 4680.
[6] M.L. Christ, M. Zablocka, S. Spencer, R.J. Lavender, M. Lemaire, J.P. Majoral, J. Mol. Catal. A: Chem. 245 (2006) 210.
[7] (a) For reviews on the chemistry of dimers [{RuCl(μ-Cl)(η^6-arene)}$_2$] see: H. Le Bozec, D. Touchard, P.H. Dixneuf, Adv. Organomet. Chem. 29 (1989) 163;
(b) M.A. Bennett, in: E.W. Abel, F.G.A. Stone, G. Wilkinson (Eds.), Comprehensive Organometallic Chemistry II, vol. 7, Pergamon Press, Oxford, 1995, p. 549;
(c) M.A. Bennett, Coord. Chem. Rev. 166 (1997) 225;
(d) F.C. Pigge, J.J. Coniglio, Curr. Org. Chem. 5 (2001) 757.
[8] (a) See for example: H. Brunner, R. Oeschey, B. Nuber, Organometallics 15 (1996) 3616;
(b) D.L. Davies, O. Al-Duaij, J. Fawcett, M. Giardiello, S.T. Hilton, D.R. Russell, Dalton Trans. (2003) 1.
[9] A. Singh, A.N. Sahay, D.S. Pandey, M.C. Puerta, P. Valerga, J. Organomet. Chem. 605 (2000) 74.
[10] For a review on the chemistry of [Ru(η^5-C$_5$H$_5$)(NCMe)$_3$][PF$_6$] see: C. Slugovc, E. Rüba, R. Schmid, K. Kirchner, K. Mereiter, Monatsh. Chem. 131 (2000) 1241.
[11] (a) See for example: D. Carmona, C. Cativiela, S. Elipe, F.J. Lahoz, M.P. Lamata, M.P. López-Ram de Víu, L.A. Oro, C. Vega, F. Viguri, Chem. Commun. (1997) 2351;
(b) P. Braunstein, M.D. Fryzuk, F. Naud, S.J. Rettig, J. Chem. Soc. Dalton Trans. (1999) 589;
(c) P. Braunstein, F. Naud, S.J. Rettig, New J. Chem. 25 (2001) 32;
(d) M. Lasa, P. López, C. Cativiela, D. Carmona, L.A. Oro, J. Mol. Catal. A: Chem. 234 (2005) 129;
(e) D. Carmona, C. Vega, N. García, F.J. Lahoz, S. Elipe, L.A. Oro, M.P. Lamata, F. Viguri, R. Borao, Organometallics 25 (2006) 1592.

[12] P. Alvarez, J. Gimeno, E. Lastra, S. García-Granda, J.F. Van der Maelen, M. Bassetti, Organometallics 20 (2001) 3762.
[13] (a) W.-K. Wong, Y. Chen, W.-T. Wong, Polyhedron 15 (1996) 1575;
(b) W.-K. Wong, Y. Chen, W.-T. Wong, Polyhedron 16 (1997) 433.
[14] (a) Five- and six-coordinate ruthenium(II) complexes containing bidentate iminophosphine ligands (L = **1** or 2-$Ph_2PC_6H_4C(H)=NR$) of general composition $[RuCl_2(\kappa^2\text{-P,N-L})(PR_3)]$ ($PR_3 = PPh_3$, PPh_2Me, PMe_2Ph), $[RuCl_2(\kappa^2\text{-P,N-L})(DMSO)_2]$ (DMSO = dimethyl sulfoxide) and $[RuCl_2(\kappa^2\text{-P,N-L})_2]$ are also known. See Refs. [5,6] and: P. Crochet, J. Gimeno, S. García-Granda, J. Borge, Organometallics 20 (2001) 4369;
(b) P. Crochet, J. Gimeno, J. Borge, S. García-Granda, New J. Chem. 27 (2003) 414.
[15] (a) For a recent reviews on this topic see: D. Carmona, M.P. Lamata, L.A. Oro, Coord. Chem. Rev. 200–202 (2000) 717;
(b) J.W. Faller, J. Parr, Curr. Org. Chem. 10 (2006) 151.
[16] (a) For recent references see: H. Brunner, F. Henning, M. Weber, M. Zabel, D. Carmona, F.J. Lahoz, Synthesis (2003) 1091;
(b) J.W. Faller, D.G. D'Alliessi, Organometallics 22 (2003) 2749;
(c) A.J. Davenport, D.L. Davies, J. Fawcett, D.R. Russell, Dalton Trans. (2004) 1481;
(d) J.W. Faller, P.P. Fontaine, Organometallics 24 (2005) 4132;
(e) D. Carmona, C. Vega, N. García, F.J. Lahoz, S. Elipe, L.A. Oro, M.P. Lamata, F. Viguri, R. Borao, Organometallics 25 (2006) 1592;
(f) A.E. Díaz-Álvarez, P. Crochet, M. Zablocka, V. Cadierno, C. Duhayon, J. Gimeno, J.-P. Majoral, New J. Chem. 30 (2006) 1295.
[17] (a) For recent references see: E.P. Kündig, C.M. Saudan, F. Viton, Adv. Synth. Catal. 343 (2001) 51;
(b) E.P. Kündig, C.M. Saudan, V. Alezra, F. Viton, G. Bernardinelli, Angew. Chem., Int. Ed. 40 (2001) 4481;
(c) P.G.A. Kumar, P.S. Pregosin, M. Vallet, G. Bernardinelli, R.F. Jazzar, F. Viton, E.P. Kündig, Organometallics 23 (2004) 5410;
(d) V. Alezra, G. Bernardinelli, C. Corminboeuf, U. Frey, E.P. Kündig, A.E. Merbach, C.M. Saudan, F. Viton, J. Weber, J. Am. Chem. Soc. 126 (2004) 4843.
[18] M.A. Bennett, A.K. Smith, J. Chem. Soc. Dalton Trans. (1974) 233.
[19] M.A. Bennett, T.-N. Huang, T.W. Matheson, A.K. Smith, Inorg. Synth. 21 (1982) 74.
[20] E.P. Kündig, F.R. Monnier, Adv. Synth. Catal. 346 (2004) 901.

In this paper, we report four new silver(I) complexes based on PyBIm, namely, $[Ag(PyBIm)\cdot H_2O]\cdot NO_3$ (**1**), $[Ag(PyBIm)\cdot H_2O]\cdot ClO_4$ (**2**), $[Ag_2(PyBIm)_2]\cdot(SiF_6)\cdot 2H_2O$ (**3**) and $[Ag(PyBIm)\cdot(HBDC)]$ (**4**). The Ag(I) atoms are three coordinated in complexes **1** and **2** but two and four coordinated in **3** and **4**, respectively. All the silver(I) atoms of the complexes are bridged by PyBIm via N_{Py} and N_{BIm} into "zigzag" chains. The counter ions have a great effect on the hydrogen bonding systems and coordination spheres, leading to great differences in the crystal packing. Through the hydrogen bonding interactions, the structures of **1**–**3** display a double-layer, a three-dimensional framework and a novel double-chain, respectively. As for complex **4**, the bridging $HBDC^-$ anions connect the $[Ag(PyBIm)]_\infty$ zigzag chain into a two-dimensional coordinate sheet. The counter ions effects and hydrogen-bonding interactions on the polymeric structures represent a new contribution to this active area of study.

2. Experimental

2.1. Materials and methods

The ligand 2-(4-pyridyl)benzimidazole (PyBIm) was synthesized according to the procedure reported by Fieselman [6]. Other reagents and solvents employed were commercially available and used as received without further purification. Elemental analyses were carried out on an EA1110 CHNS-0 CE element analyzer and the IR spectra (KBr pellets) were recorded at a Nicolet Magna 750 FT-IR spectrometer in the range 400-4000 cm^{-1}. Thermogravimetric analyses (TGA) were performed with a Netzsch STA-499C thermoanalyzer under N_2 (30–800 °C range) at a heating rate of 10 °C/min. X-ray powder diffractions (XRPD) were performed on a Bruker D8 Advanced diffractometer with Cu Kα radiation ($\lambda = 1.5418$ Å) at room temperature.

Safety notes. Caution! Perchlorate salts of metal complexes with organic ligands are potentially explosive. Only a small amount of material should be prepared, and it should be handled with great care.

*Synthesis of $[Ag(PyBIm)\cdot H_2O]\cdot NO_3$ (**1**).* An acetonitrile (5 mL) solution of $AgNO_3$ (0.085 g, 0.50 mmol) was slowly diffused into an ethanol (5 mL) solution of PyBIm (0.097 g, 0.50 mmol). Colorless crystals formed in about two weeks (80% yield) *Anal.* Calc. for $C_{12}H_{11}AgN_4O_4$: C, 37.62; H, 2.89; N, 14.62. Found: C, 37.15; H, 3.12; N, 14.13%. IR (KBr pellet, cm^{-1}): 3434s, 1613s, 1559w, 1537w, 1495m, 1480w, 1443, 1414, 1385s, 1357s, 1229m, 1072m, 1041m, 1017w, 838m, 821m, 782s, 700m, 556m, 502w.

*Synthesis of $[Ag(PyBIm)\cdot H_2O]\cdot ClO_4$ (**2**).* An ethanol solution (5 mL) of $AgClO_4$ (0.06 g, 0.30 mmol) was slowly diffused into an ethanol solution of PyBIm (0.06 g, 0.30 mmol). Colorless crystals formed in about three weeks (75% yield). *Anal.* Calc. for $C_{12}H_{11}AgClN_3O_5$: C, 34.27; H, 2.64; N, 9.99. Found: C, 34.15; H, 3.12; N, 10.13%. IR (KBr pellet, cm^{-1}): 3496s, 1612s, 1537w, 1494m, 1481w, 1436s, 1319m, 1285w, 1226m, 1120vs, 1085vs, 969w, 932w, 838m, 816m, 775s, 744w, 672w, 624s, 557w, 500w.

*Synthesis of $[Ag_2(PyBIm)_2]\cdot(SiF_6)\cdot 2H_2O$ (**3**).* A solution of Ag_2SiF_6 (0.22 g, 0.61 mmol), PyBIm (0.24 g, 1.22 mmol), NaF (0.025 g, 0.61 mmol) and H_2O (15 ml) was stirred under ambient conditions, then sealed in a Teflon-lined stainless steel vessel, heated at 150 °C for 5 days and cooled to room temperature. The resulting product was recovered by filtration, washed with distilled water and dried in air (65% yield). *Anal.* Calc. for $C_{24}H_{22}Ag_2F_6N_6O_2Si$: C, 36.75; H, 2.83; N, 10.72. Found: C, 36.54; H, 3.09; N, 10.79%. IR (KBr pellet, cm^{-1}): 3445s, 1614s, 1560w, 1541m, 1496w, 1481w, 1439s, 1384w, 1319m, 1287w, 1227m, 1118s, 1084s, 1065s, 1022s, 839m, 818m, 775s, 745s, 558m, 500w, 473m.

*Synthesis of $[Ag(PyBIm)(HBDC)]$ (**4**).* A solution of Ag_2O (0.069 g, 0.30 mmol), PyBIm (0.24 g, 1.22 mmol), H_2BDC (0.101 g, 0.61 mmol) and H_2O (15 ml) was stirred under ambient conditions, then sealed in a Teflon-lined stainless steel vessel, heated at 150 °C for 5 days and cooled to room temperature. The resulting product was recovered by filtration, washed with distilled water and dried in air (60% yield). *Anal.* Calc. for $C_{20}H_{14}AgN_3O_4$: C, 51.31; H, 3.01; N, 8.97. Found: C, 51.52; H, 3.26; N, 9.06%. IR (KBr pellet, cm^{-1}): 3433s, 1416s, 1566m, 1778w, 1438m, 1384s, 1319m, 1283w, 1228w, 1095w, 1069m, 936m, 839m, 751s, 687m, 539w, 507w.

2.2. X-ray crystallography

Suitable single crystals of **1**–**4** were carefully selected under an optical microscope and glued to thin glass fibers. The diffraction data were collected on a Siemens Smart CCD diffractometer with graphite-monochromated Mo Kα radiation ($\lambda = 0.71073$ Å) at 293 K. An empirical absorption correction was applied using the SADABS program [7]. The structures were solved by direct methods and refined by full-matrix least-squares methods on F^2 by using the SHELXTL-97 program package [8]. Attempts to locate the hydrogen atoms of water in complex **3** failed; the other hydrogen atoms on carbon and nitrogen atoms were generated geometrically. The crystallography details for the structure determination of complexes **1**–**4** are presented in Table 1. Selected bond lengths and bond angles are listed in Table 2.

2.3. Result and discussion

2.3.1. Syntheses and general characterization

Complex **1** can also be obtained by hydrothermal methods, but the crystals obtained were not suitable for X-ray diffraction. As for complex **2**, it can be obtained by hydrothermal methods (the reaction temperature might be better less than 120 °C for security considerations) with the

Table 1
Crystal data and structure refinement parameters for complexes **1**–**4**

	1	**2**	**3**	**4**
Formula	$C_{12}H_{11}AgN_4O_4$	$C_{12}H_{11}AgClN_3O_5$	$C_{24}H_{22}Ag_2F_6N_6O_2Si$	$C_{20}H_{14}AgN_3O_4$
Crystal size (mm^3)	$0.45 \times 0.30 \times 0.15$	$0.50 \times 0.10 \times 0.05$	$0.30 \times 0.10 \times 0.05$	$0.20 \times 0.12 \times 0.10$
Molecular mass	383.12	420.56	784.31	468.21
Crystal system	orthorhombic	orthorhombic	monoclinic	monoclinic
Space group	*Aba*2	*Pbcn*	$P2_1/c$	$P2_1/n$
a (Å)	18.1226(10)	18.4616(8)	15.9922(9)	7.610(2)
b (Å)	13.0426(8)	11.1849(6)	11.6013(6)	13.595(3)
c (Å)	11.0123(6)	13.4372(7)	13.9777(8)	17.471(5)
β (°)	90	90	95.322(3)	92.427(2)
V ($Å^3$)	2602.9(3)	2774.7(2)	2582.1(2)	1805.7(8)
Z	8	8	4	4
T (K)	293(2)	293(2)	293(2)	293(2)
D_{calc} ($g\ cm^{-3}$)	1.955	2.014	2.018	1.722
μ (mm^{-1})	1.572	1.673	1.644	1.149
$T_{min,\ max}$	0.5382, 0.7984	0.4883, 0.9210	0.6383, 0.9223	0.8027, 0.8937
$F(000)$	1520	1664	1544	936
Reflections collected	9603	20154	19463	13463
Independent reflections, R_{int}	2875, 0.0203	3173, 0.0335	5840, 0.0300	4129, 0.0224
Data/restrain/parameters	2875/1/198	3173/0/207	5840/0/370	4129/0/257
Goodness-of-fit on F^2	1.087	1.188	1.165	1.015
R_1, wR_2 [$I > 2\sigma(I)$]	0.0279, 0.0680	0.0333, 0.0740	0.0580, 0.1258	0.0282, 0.0754
R_1, wR_2 (all data)	0.0313, 0.0709	0.0360, 0.0759	0.0708, 0.1330	0.0330, 0.07895
Large difference peak and hole (e $Å^{-3}$)	0.711 and −0.452	0.920 and −0.818	1.110 and −0.833	0.644 and −0.686

Table 2
Selected bond lengths (Å) and angles (°) for complexes **1**–**4**

Complex **1**[a]			
Ag1–O1w	2.596(3)	Ag1–N1	2.222(3)
Ag1–N2	2.172(2)	N1–Ag1–O1w	89.2(1)
N2–Ag1–N1	151.3(1)	N2–Ag1–O1w	114.5(1)
Complex **2**[b]			
Ag1–O1w	2.482(2)	Ag1–N1	2.198(2)
Ag1–N2	2.152(2)	N1–Ag1–O1	90.2(8)
N2–Ag1–N1	153.4(8)	N2–Ag1–O1w	112.6(8)
Complex **3**[c]			
Ag1–N1	2.178(4)	Ag1–N2	2.135(4)
Ag2–N4	2.193(4)	Ag2–N5	2.155(3)
N2–Ag1–N1	157.8(2)	N5–Ag2–N4	155.8(2)
Complex **4**[d]			
Ag1–N1	2.195(2)	Ag1–N2	2.189(2)
Ag1–O1	2.571 (2)	Ag1–O3	2.597(2)
C13–O1	1.223(3)	C13–O2	1.297(3)
N2–Ag1–N1	149.8(6)	N2–Ag1–O1	113.1(6)
N1–Ag1–O1	91.1(6)	N2–Ag1–O3	89.4(6)
N1–Ag1–O3	115.3(6)	O1–Ag1–O3	74.6(5)

[a] $-x+3/2, y+0, z+1/2; -x+3/2, y+0, z-1/2; x, y, z; x, y, z+1; -x+1, -y, z+1$.
[b] $-x+1/2, y+1/2, z; x, y, z; -x+1/2, y-1/2, z; -x+1, -y-1, -z; -x+1, y+1, -z+1/2; x, y+1, z$.
[c] $-x, y+1/2, -z-1/2; -x+1, y-1/2, -z+1/2; -x, y-1/2, -z-1/2; -x+1, y+1/2, -z+1/2$.
[d] $-x+3/2, y+1/2, -z+1/2; -x+5/2, y+1/2, -z+1/2; -x+3/2, y-1/2, -z+1/2; x-1/2, -y+1/2, z-1/2; -x+5/2, y-1/2, -z+1/2$.

production of crystals of excellent quality that are suitable for X-ray diffraction, but for safety considerations, this is not worthy of recommendation. As for complexes **3** and **4**, attempts to get crystals under solution conditions failed. The purities of the four complexes were also identified by XRPD (see supporting information).

The $HBDC^-$ anions bridge the $[Ag_2(PyBIm)_2]_\infty$ chain into a two-dimensional sheet in complex **4**, the protonated carboxylate groups greatly contribute to the crystal packing. Attempts to get a crystal bridged by BDC^{2-} rather than $HBDC^-$ anions failed, the products are only amorphous, and could not be identified easily.

The TGA diagrams show complexes **1**–**3** have similar thermal stabilities and behaviors in the range of 50–220 °C. Complex **1** exhibits loss of one lattice water between 65 and 216 °C (4.91% weight loss observed; 4.70% calculated), complex **2** exhibits loss of the water molecules between 48 and 147 °C (4.05% weight loss observed; 4.28% calculated), while complex **3** exhibits loss of two water molecules between 66 and 195 °C (4.53% weight loss observed; 4.60% calculated). Complex **4** does not show any weight loss up to 262 °C, this is consistent with no lattice or coordinated water in the complex (see supporting information).

2.3.2. Crystal structures

Complex **1** crystallizes in the orthorhombic *Aba*2 space group, the absolute structure was determined from the Flack parameter, refined to be 0.01(3), indicating the complex is of correct absolute structure. X-ray structure analysis reveals that **1** is a one-dimensional zigzag chain based on the $[Ag(PyBIm) \cdot H_2O]$ unit (Fig. 1). The silver(I) atom is three coordinated, by one aqua ligand (Ag1–O1w 2.596(3) Å) and two PyBIm ligands via N_{Py} and N_{BIm} nitrogen donor atoms (Ag1–N1 2.222(3), Ag1–N2 2.172(2) Å), exhibiting

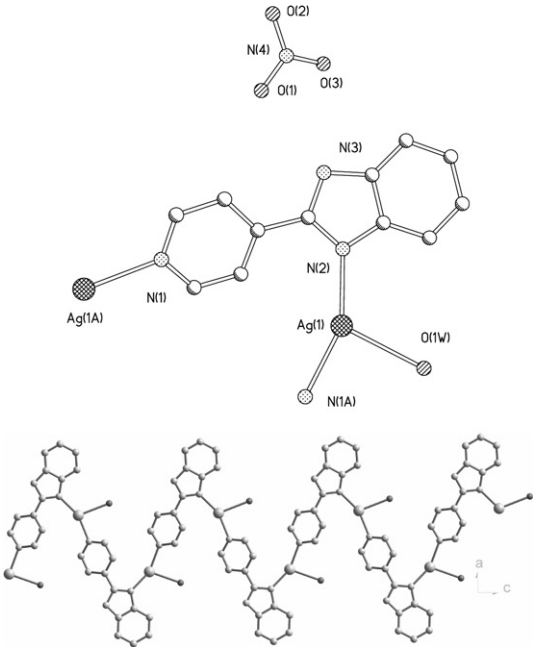


Fig. 1. (Top) Perspective view of the coordination environment of the Ag(I) atom in complex **1**. (Bottom) A view of the "zigzag" chain of $[Ag_2(PyBIm)_2(H_2O)_2]$.

a distorted "T" shaped coordination (N1–Ag1–O1w 89.2(1)°, N2–Ag1–N1 151.3(1)°, N2–Ag1–O1w 114.5(1)°).

The benzimidazolyl rings are almost coplanar in the "zigzag" chain, and the pyridyl ring deviates from the benzimidazolyl ring of the same PyBIm ligand with a dihedral angle of 26.7°. The Ag(I) atoms are bridged by the PyBIm ligands with a separation of 7.111 Å. Strong hydrogen-bonding interactions between the N–H group of benzimidazolyl, lattice water and nitrate (N3···O1 2.901(4) Å, O1w···O1 2.969(4) Å, O1w···O2 2.850(5) Å) as well as π–π (3.36 Å) interactions connect the one-dimensional chains into a two-dimensional double-layer, and the double-layers are further connected into a three-dimensional framework through inter-molecular interactions (Fig. 2), the π–π interactions of the adjacent double-layer are rather weak, as the overlap of the aromatic rings can be neglected (more than 4.5 Å).

In the two-dimensional double-layer, interestingly, the one-dimensional "zigzag" chains are connected by the nitrate groups to the adjacent chains from the other layer

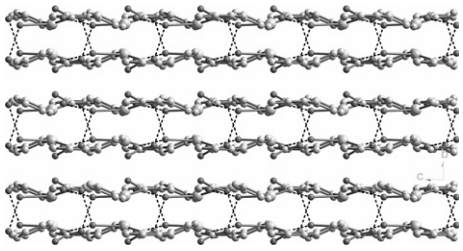


Fig. 2. Perspective view of the 3-D framework of stacked double layer sheets for complex **1**.

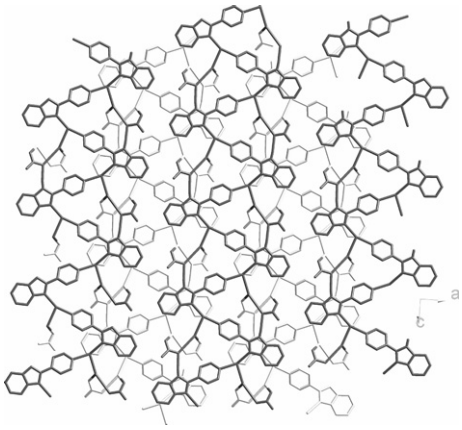


Fig. 3. The hydrogen-bonding interactions connecting the one-dimensional "zigzag" chain into a double-layer in complex **2**.

through hydrogen-bonding as well as strong π–π interactions (3.36 Å) (Fig. 3). This two-dimensional double-layer is not like the common reported ones [9]. In complex **1**, the one-dimensional "zigzag" chains are not directly connected into a two-dimensional sheet, but indirectly. To the best of our knowledge, this phenomenon has not been reported before.

With regard to the influence of the N–H group of the PyBIm ligand, this structure is greatly different from the reported complex $[Ag(2,4\text{-bpy})] \cdot NO_3$ [3a], where the counter ion is weakly coordinated with the silver atom and leads to a two-dimensional sheet without hydrogen-bonding interactions. Although the coordination sphere is similar to that of $[Ag_2(PyBIm)_2(H_2O)_2]SO_4 \cdot H_2O$ [3c], due to the anion effect, great differences occur in the crystal packing.

Complex **2** crystallizes in the orthorhombic *Pbcn* space group, the single-crystal X-ray structure analysis reveals that **2** has the similar one-dimensional zigzag chain based on $[Ag(PyBIm) \cdot H_2O]$ units, as in complex **1**. Similar to complex **1**, the silver(I) atom is also three coordinated by one aqua ligand (Ag1–O1w 2.482(2) Å) and two PyBIm

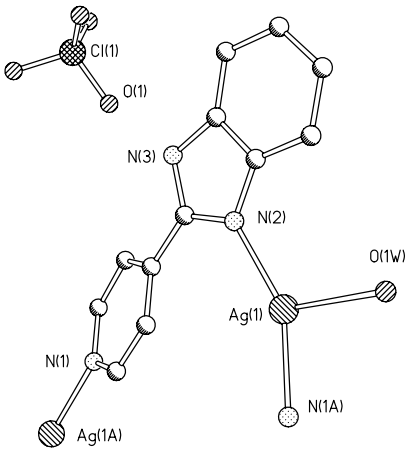


Fig. 4. Perspective view of the coordination environment of the Ag(I) atom in complex **2**.

ligands via N_{Py} and N_{BIm} nitrogen donor atoms (Ag1–N1 2.198(2), Ag1–N2 2.152(2) Å), exhibiting a distorted "T" shaped coordination geometry (N1–Ag1–O1w 90.2(8)°, N2–Ag1–N1 153.4(8)°, N2–Ag1–O1w 112.6(8)°) (Fig. 4).

The benzimidazolyl rings are almost coplanar in the "zigzag" chain, and the pyridyl ring deviates from the benzimidazolyl ring of the same PyBIm ligand with a dihedral angle of 28.8°. The silver atoms are bridged by the PyBIm ligands with a separation of 7.225 Å. Strong hydrogen-bonding interactions involving the N–H group of benzimidazolyl, lattice water and perchlorate (N3···O1 2.881(3) Å, N3···O2 2.945(3) Å, O1w···O2 2.947(3) Å, O1w···O3 2.880(4) Å), as well as π–π interactions (3.35 Å) connect the one-dimensional chains into a three-dimensional framework. Similar to that of complex **1**, the "zigzag" chains in complex **2** are connected by ClO_4^- alternatively with the adjacent layer.

In this three-dimensional framework, for the ordered arrangement of the "zigzag" chains, a one-dimensional channel with a window of 7.7 Å × 10.9 Å is formed, and these channels are filled by ClO_4^- groups and lattice water as guest molecules [10] (see supporting information).

Despite the ClO_4^- also acting as a counter ion in the complex $[Ag(2,4\text{-bpy})]\cdot ClO_4$ [3a], ligand unsupported weak metal–metal interactions occur, whereas this phenomenon does not exist in complex **2**. The abundant hydrogen-bonding interactions in complex **2** lead to a crystal packing that is greatly different from that of $[Ag(2,4\text{-bpy})]\cdot ClO_4$.

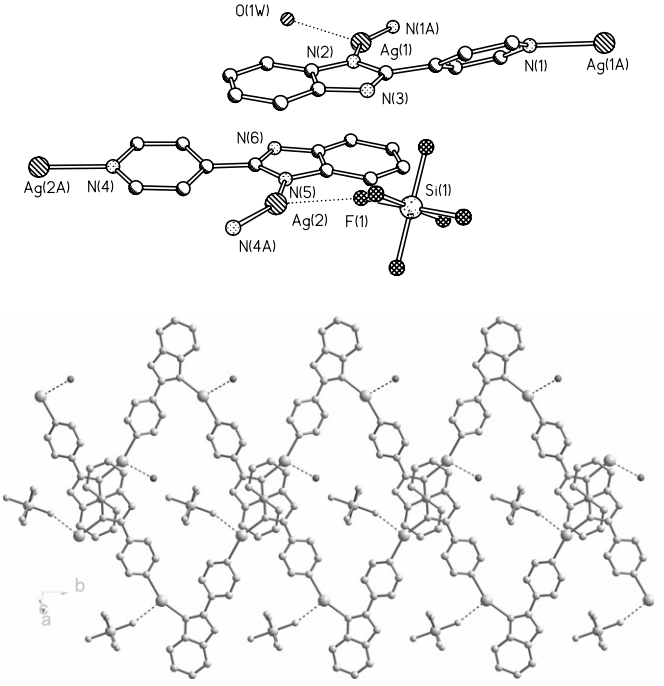


Fig. 5. (Top) Perspective view of coordination sphere of the Ag(I) atoms for complex **3**. (Bottom) Perspective view of the double chain for complex **3**.

Complex **3** consists of a one-dimensional double-chain (Fig. 5), each unit has two distinct silver atoms in the complex. Both of them are two coordinated and bridged by the PyBIm ligands via N_{Py} and N_{BIm} (Ag1–N1 2.178(4), Ag1–N2 2.135(4), Ag2–N4 2.193(4), Ag2–N5 2.155(3) Å) into two "zigzag" chains with adjacent intra-chain Ag···Ag separations of 7.443 and 7.542 Å. The N_{Py}–Ag–N_{BIm} bond angles are slightly larger than those of complexes **1** and **2** (N1–Ag1–N2 157.8(2), N4–Ag1–N5 155.8(2)°), indicating stronger covalent interactions among the silver(I) and nitrogen atoms. The two distinct "zigzag" chains are connected by hydrogen-bonding (O1w···F3 3.019 Å) as well as π–π interactions (3.35–3.40 Å) into a double-chain, unlike the common reported molecular ladder or molecular railroad [11], the double-chain in complex **3** is not jointed by coordination bonds. Besides, O1w and F1 of $[SiF_6]^{2-}$ are also weakly coordinated to the silver(I) atoms with a distance of about 2.610 and 2.605 Å (Ag1···O1w 2.610, Ag2···F1 2.605 Å), respectively. The Ag···F (2.605 Å) distance is much shorter than other silver(I) complexes with the $[SiF_6]^{2-}$ groups acting only as a counter ion (2.702 Å) [12], but longer than the bonded Ag–F distance in the BF_4^- system (2.34–2.53 Å) [13]. The interaction between O1w and Ag1 is comparable to that found in silver(I) carboxylate and oxalate complexes (2.23–2.52 and 2.17–2.61 Å), respectively [14], whilst it is greatly shorter than the sum of van der Waals radii (3.24 Å) of the Ag(I) ion and oxygen atom [15]. The hydrogen-bonding interactions between O1w and F3 (O1w···F3 3.019 Å) also bring the double-chains into a two-dimensional sheet (see supporting information), and these sheets are further aggregated into a three-dimensional framework through strong π–π interactions, with the lattice water and SiF_6^{2-} groups acting as guest molecules [10]. Interestingly, the SiF_6^{2-} groups are connected by the lattice water molecules (O2w) through hydrogen-bonding (O2w···F3 2.708, O2w···F5 2.894 Å) interactions into a one-dimensional chain in the channel (see supporting information).

The single crystal X-ray analysis reveals that complex **4** is attributed with a two-dimensional network. Unlike the former complexes, the silver(I) atom is four coordinated (Ag1–N1 2.195(2) Å, Ag1–N2 2.188(2) Å, Ag1–O1 2.571(2) Å, Ag1–O3 2.597(2) Å), exhibiting a distorted tetrahedral coordination sphere (N2–Ag1–N1 149.8(6)°, N2–Ag1–O1 113.1(6)°, N1–Ag1–O1 91.1(6)°, N2–Ag1–O3 89.4(6)°, N1–Ag1–O3 115.3(6)°, O1–Ag1–O3 74.6(5)°) (Fig. 6). The silver(I) atom deviates from the basic plane formed by N2, N1a and O3a less than 0.0991 Å. The Ag–O bond lengths (2.571(2) and 2.597(2) Å, respectively) are slightly shorter than that in complex **3** (Ag1–O1w 2.610 Å), which is in the normal range for Ag–O bond distances for silver carboxylate and oxalate complexes [14]. The O2 atom of the 1,3-BDC ligand is protoned, C13–O2 (1.297(3) Å) is longer than C13–O1 (1.223(3) Å), and forms hydrogen-bonding interactions with the O3 atom (O2···O3 2.450(2) Å) of the adjacent $HBDC^-$ ligand. The silver(I) atoms are bridged by PyBIm into the similar "zigzag"

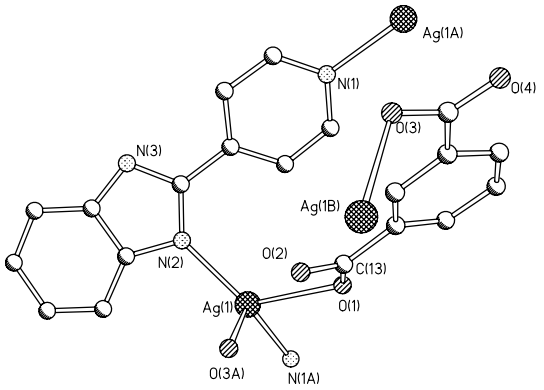


Fig. 6. Perspective view of coordination sphere of the Ag(I) atoms for complex **4**.

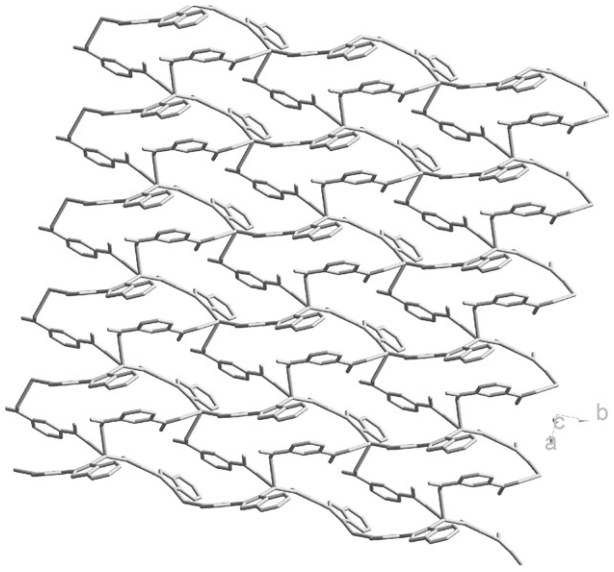


Fig. 7. Bridging HBDC ligands connecting the "zigzag" chain of $[Ag_2(PyBIm)_2(H_2O)_2]^{2+}$ into two-dimensional undulating sheets for complex **4**.

$[Ag(PyBIm)]_\infty$ chain as complexes **1**–**3**, and the chains are further connected by the bridging $HBDC^-$ ligand into a two-dimensional sheet (Fig. 7). The hydrogen-bonding (O2···O3 2.450(2) Å) as well as π–π interactions aggregate the undulating sheets into a three-dimensional framework.

The coordination mode of the HBD^- ligand is greatly different from the reported silver(I) complexes based on benzenecarboxylate derivatives, where the adoption of a bidentate mode for the carboxylate group is very common, leading to weak ligand unsupported Ag···Ag interactions [16]. In complex **4**, either the carboxylate or carboxylic group demonstrates a unidentate bonding fashion.

3. Anion exchange properties of complexes 2 and 3

The ClO_4^- anion does not coordinate to silver(I) in complex **2**, while the F^- of SiF_6^{2-} weakly coordinates to the Ag(I) atom in complex **3**, both anions are only loosely bound to the framework through the hydrogen bonds. To investigate whether these loosely bound ClO_4^- and SiF_6^{2-} anions can be exchanged by other anions, anion exchange reactions were carried out for complexes **2** and **3**. Well-ground powers of complexes **2** and **3** (50 mg) were suspended in aqueous solution (10 ml) of $NaBF_4$ and Na_2SO_4 (1 g), respectively. These mixtures were stirred for one day at room temperature, then filtered, washed with water and dried under vacuum to give a white powder. This procedure was repeated at least three times. The element analyses reveal nearly 100% exchange for both complexes **2** and **3**, the exchanged products gave sharp XPRD patterns, which are similar to that of complexes **2** and **3**, respectively. Indicating the crystal structures have been maintained in both complexes (see supporting information). This phenomenon is similar to the anion properties of cage-like frameworks and cation-layered architectures [17].

4. Conclusions

The PyBIm ligand acts as a bridging ligand rather than a terminal one [18] in the four silver(I) complexes, and bridges the Ag(I) atoms into similar "zigzag" chains, in which the coordination number of the silver(I) atom varies from two to four. Due to the influence of anion symmetry [4b], a great difference in crystal packing is demonstrated. For instance, NO_3^- (D_{3h}) forms hydrogen-bonding interactions greatly different from that of ClO_4^- (D_{4h}) and SiF_6 (D_{6h}), resulting in a double-layer, a three-dimensional framework and a novel double-chain structure, respectively. The $HBDC^-$ anions act not only as counter ions but also as bridging ligands, leading to the formation of a two-dimensional coordinate sheet. Although the N–H groups of the PyBIm ligands do not coordinate to silver(I) atoms, they form strong hydrogen-bonding interactions with the lattice water and anionic counter ions, leading to a great influence on the crystal packing.

Acknowledgements

This work was supported by the 973 program of the MOST (001CB108906), the National Natural Science Foundation of China (20425313, 90206040, 20333070 and 20303021), the Natural Science Foundation of Fujian Province and the Chinese Academy of Sciences.

Appendix A. Supplementary material

CCDC 601880, 601881, 601882 and 601883 contain the supplementary crystallographic data for **1**, **2**, **3** and **4**. These data can be obtained free of charge via http://www.ccdc.cam.ac.uk/conts/retrieving.html, or from the Cambridge Crystallographic Data Centre, 12 Union Road, Cambridge CB2 1EZ, UK; fax: (+44) 1223-336-033; or e-mail: deposit@ccdc.cam.ac.uk. Supplementary data associated with this article can be found, in the online version, at doi:10.1016/j.poly.2006.09.102.

References

[1] (a) J.M. Lehn, Supramolecular Chemistry, VCH, Weinheim, 1995;
(b) D. Braga, L. Brammer, N.R. Champness, CrystEngComm. 6 (2005) 1;
(c) W.S. Li, M.A. Withersby, M. Schröder, Coord. Chem. Rev. 183 (1999) 117;
(d) M. Eddaoudi, D.B. Moler, H. Li, B. Chen, T.M. Reineke, M.O. Keeffe, O.M. Yaghi, Acc. Chem. Res. 34 (2001) 319.

[2] L.S. Felices, P. Vitoria, J.M. Gutièrrez-Zorrilla, S. Reinoso, J. Etxebarria, L. Lezama, Chem. Eur. J. 10 (2004) 5138.

[3] (a) M.L. Tong, S.L. Zheng, X.M. Chen, Chem. Eur. J. 6 (2000) 3729;
(b) G.A. Bowmaker, J.V. Hanna, C.E.F. Richand, A.S. Lipton, J. Chem. Soc., Dalton Trans. (2001) 20;
(c) C.K. Xia, C.Z. Lu, Q.Z. Zhang, X. He, J.J. Zhang, D.M. Wu, Cryst. Growth Des. 5 (2005) 1569;
(d) X.C. Huang, M.H. Zhen, S.W. Ng, Acta Crystallogr., Sect. E: Struct. Rep. (Online) 60 (2004) o939.

[4] (a) J. Zhang, Z.L. Li, Y. Kang, Y.Y. Qin, J.K. Cheng, Y.G. Yao, Cryst. Growth Des. 5 (2005) 73;
(b) N.R. Brooks, A.J. Blake, N.R. Champness, J.W. Cunningham, P. Hubberstey, S.J. Teat, C. Wilson, M. Schröder, J. Chem. Soc., Dalton Trans. (2001) 2530.

[5] (a) R.L. Laduca Jr., R.S. Rarig, P.J. Zapf, J. Zubieta, Solid State Sci. 2 (2000) 39;
(b) M.L. Tong, X.M. Chen, B.H. Ye, S.W. Ng, Inorg. Chem. 37 (1998) 5278.

[6] E. Alcalde, I. Dinares, L. Perez-Garcia, T. Roca, Synthesis (1992) 395.

[7] G.M. Sheldrick, SADABS, University of Göttingen, Göttingen, Germany, 1996.

[8] SHELXTL (version 5.05); Siemens Analytical X-ray Instruments Inc.: Madison, WI, 1994.

[9] (a) Z. Liu, P. Liu, Y. Chen, M.H. Huang, New J. Chem. 29 (2005) 474;
(b) C. Lei, J.G. Mao, Y.Q. Sun, J. Solid State Chem. 177 (2004) 2449;
(c) Z.Z. Lin, F.L. Jiang, L. Chen, D.Q. Yuan, Y.F. Zhou, M.C. Hong, Eur. J. Inorg. Chem. (2005) 71.

[10] (a) R.E. Mulvey, Orangometallices 25 (2006) 1060;
(b) P. Gamez, J. Reedijk, Eur. J. Inorg. Chem. (2006) 29;
(c) N.C. Gianneschi, M.S. Masar, C.A. Mirkin, Acc. Chem. Res. 38 (2005) 825.

[11] (a) M. Fujita, Y.J. Kwon, O. Sasaki, K. Yamaguchi, K. Ogura, J. Am. Chem. Soc. 117 (1995) 7287;
(b) M.L. Tang, H.J. Chen, X.M. Chen, Inorg. Chem. 39 (1997) 2027.

[12] P. Lin, R.A. Henderson, R.W. Harrington, W. Clegg, C.D. Wu, X.T. Wu, Inorg. Chem. 43 (2004) 181.

[13] (a) Y.B. Xie, C. Zhang, J.R. Li, X.H. Bu, J. Chem. Soc., Dalton Trans. (2004) 562;
(b) S.R. Halper, S.M. Cohen, Inorg. Chem. 44 (2005) 486;
(c) F. Haftaradaran, N.D. Draper, D.B. Leznoff, V.E. Williams, J. Chem. Soc., Dalton Trans. (2003) 2105.

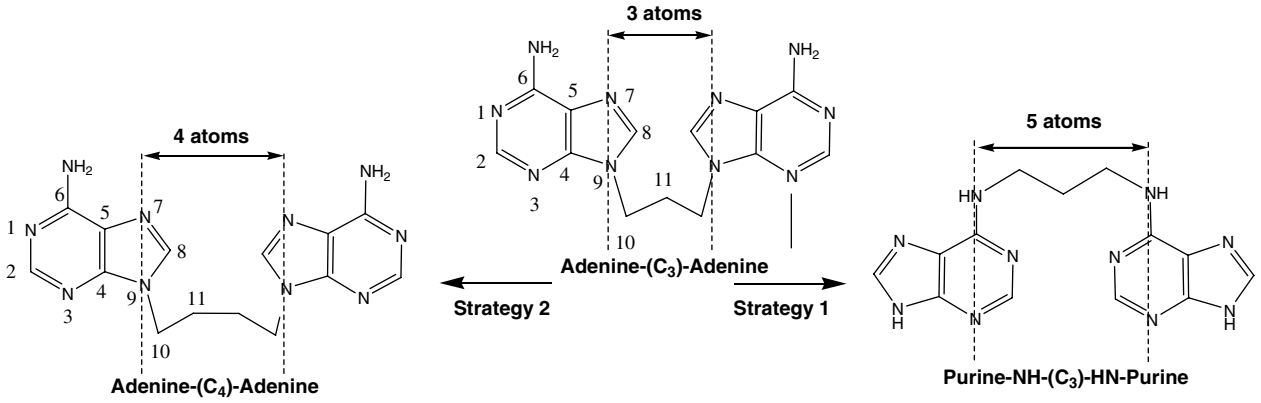
[14] M. Jansen, Angew. Chem., Int. Ed. 26 (1987) 1098.

[15] A. Bondi, J. Phys. Chem. 68 (1964) 441.

[16] (a) D.F. Sun, R. Cao, J.B. Weng, M.C. Hong, Y.C. Liang, J. Chem. Soc., Dalton Trans. (2002) 291;
(b) D.F. Sun, R. Cao, J.B. Weng, M.C. Hong, Y.C. Liang, Inorg. Chim. Acta 357 (2004) 991;
(c) B. Dong, L. Yi, Y. Liu, P. Cheng, Y.B. Dong, J.P. Ma, Inorg. Chem. Commun. 8 (2005) 38;
(d) G. Smith, A.N. Reddy, K.A. Byriel, C.H.L. Kennard, J. Chem. Soc., Dalton Trans (1995) 3565;
(e) M.T. Tong, S.L. Zheng, X.M. Chen, Chem. Eur. J. 6 (2000) 3729.

[17] (a) B. Sui, J. Fan, T. Okamura, W.Y. Sun, N. Ueyama, New J. Chem. 25 (2001) 1378;
(b) L. Raehm, L. Mimassi, C. Guyard-Duhayon, H. Amouri, Inorg. Chem. 42 (2003) 5654;
(c) J. Fan, W.Y. Sun, T. Okamura, Y.Q. Zheng, B. Sui, W.X. Tang, N. Ueyama, Cryst. Growth Des. 4 (2004) 581.

[18] Z.Y. Wang, S.R. Wilson, B.M. Foxman, W.B. Lin, Cryst. Eng. 2 (1999) 91.



Scheme 1.

solved. On the other hand, modifying the reaction conditions, is possible to obtain new zwitterionic inner sphere Zn(II) complexes with polymethylene-bisadenines: $[H\text{-}(Ade)_2C_3(ZnCl_3)]$ (**6**), $[H\text{-}(Ade)_2C_4(ZnCl_3)]\cdot 1.5H_2O$ (**7**) and $[H\text{-}(Ade)_2C_4(ZnCl_3)_2]\cdot 3H_2O$ (**8**). We report here the results of single crystal X-ray diffraction studies on **5**, **5a** and **6** as well as the characterization of **7** and **8** by spectroscopic measurements.

2. Experimental

2.1. Analysis and physical measurements

Elemental analyses were carried out using Carlo-Erba models 1106 and 1108 and Thermo Finnigan Flash 1112 microanalysers. Infrared spectra (KBr pellets) were recorded on a Bruker IFS 66. ^{1}H NMR spectra were obtained with a Bruker AMX 300 spectrometer. Proton chemical shifts in dimethylsulfoxide solution (DMSO-d_6) were referenced to DMSO-d_6 itself [^{1}H NMR, δ(DMSO) = 2.50]. Due to the low solubility of these products the ^{13}C NMR spectra were not clear and do not give useful information. All organic and inorganic (Sigma and Aldrich) reagents were used without further purification.

2.2. Crystallographic studies

Prismatic crystals were selected and mounted on an Enraf-Nonius CAD4 diffractometer. Intensities were collected with graphite monochromatized Mo K_α radiation using $\omega/2\theta$ scan-technique. Three reflections were measured every 2 h as orientation and intensity control, significant intensity decay was not observed. Lorentz-polarization and absorption corrections were made. The structures were solved by Direct methods using SHELXS computer program [4] and refined by full-matrix least-squares method with SHELX97 [5]. Selected crystallographic data are presented in Table 1.

$\{[(H\text{-}Ade)_2C_4][Cd_2Cl_6(H_2O)_2]\cdot 2H_2O\}_n$ (**5**): All non-water hydrogen atoms were computed and refined using a riding model with an isotropic temperature coefficient equals to 1.2 times of equivalent value of carbon or nitrogen atom linked to H.

$\{[(H\text{-}Ade\mathit{N}^3)\text{-}(CH_2)_4\text{-}(H\text{-}Ade\mathit{N}^9)]_2][Cd_3Cl_{10})\cdot 2H_2O\}_n$ (**5a**): 18 H atoms were located from a difference synthesis and refined with an overall isotropic temperature factor and 2 H atoms were computed and refined with an overall isotropic temperature factor using a riding model.

$[H\text{-}(Ade)_2C_3(ZnCl_3)]$ (**6**): All H atoms were computed and refined, using a riding model with an isotropic temperature factor.

2.3. Synthesis of the ligands

2.3.1. Syntheses of $N^9,N^{9'}$-polymethylene-bisadenines (Ade_2C_x) ($x = 3,4$)

The preparation of the ligands was carried out by a method previously described in the literature [1]: a suspension of 2.5 g of adenine and 1 g of NaH (55% dispersion in mineral oil) in 75 ml of dry DMF was stirred at room temperature under Ar atmosphere for 1 h, and then, 0.5 equivalent of the corresponding α,ω-dibromoalkane was added. The resulting suspension was stirred for 2 days, filtered and washed with water and acetone (overall yield 20–30%). The product was purified in boiling water.

2.3.2. $N^9,N^{9'}$-trimethylene-bisadenine (Ade_2C_3) (**1**)

Anal. Calc. for $C_{13}H_{14}N_{10}$: C, 50.3; H, 4.5; N, 45.1. Found: C, 50.4; H, 4.5; N, 45.1%. Selected IR bands (cm^{-1}): 3100vs, 1664vs, 1604vs, 1582sh, 1490m, 1453m, 1422m, 1375m, 1337m, 1303s, 1249m, 1217m, 1066m, 1000w, 797m, 722s, 646m, 606s, 537m. ^{1}H RMN (DMSO-d^6) $\delta = 8.18$ s [2H, H(2)/H(2′)], 8.13 s [2H, H(8)/H(8′)], 7.32 s [4H, NH_2], 4.18 t [4H, H(10)/H(10′), $J = 6.8$ Hz], 2.39 t [2H, H(11), $J = 6.8$ Hz].

The corresponding $Ade_2C_3\cdot 2HCl\cdot H_2O$ (**1a**) was obtained as a crystalline material by evaporation of the ligand dissolved in HCl 1 M. *Anal.* Calc. for $C_{13}H_{18}Cl_2N_{10}O$: C, 38.91; H, 4.52; N, 34.01. Found: C, 38.97; H, 4.45; N, 34.88%. Selected IR bands (cm^{-1}): 3055s, 1690vs, 1626s, 1595s, 1517s, 1441s, 1413s, 1332s, 1222s, 1060w, 823m, 740m, 673m. ^{1}H RMN (DMSO-d^6) $\delta = 8.51$ s [2H, H(2)/

Table 1
Selected crystallographic data

	5	5a	6
Empirical formula	$C_{14}H_{24}Cd_2Cl_6N_{10}O_3$	$C_{28}H_{40}Cd_3Cl_{10}N_{20}O_2$	$C_{13}H_{15}Cl_3N_{10}Zn$
Formula weight	817.93	1380.50	483.07
Crystal system	triclinic	monoclinic	monoclinic
Space group	$P\bar{1}$	$C2/c$	$P2_1/n$
Cell parameters			
a (Å)	10.206(9)	21.535(8)	9.084(10)
b (Å)	12.115(5)	14.385(7)	22.81(9)
c (Å)	12.332(4)	15.246(5)	9.61(9)
α (°)	105.66(3)	90	90
β (°)	113.49(4)	101.38(4)	105.87(9)
γ (°)	95.31(5)	90	90
V (Å^3)	1311.5(13)	4630(3)	1916(3)
D_{calc} (Mg m^{-3})	2.071	1.980	1.675
Z	2	4	4
μ (mm^{-1})	2.272	1.998	1.723
Crystal size (mm)	$0.2 \times 0.1 \times 0.1$	$0.2 \times 0.1 \times 0.1$	$0.20 \times 0.14 \times 0.12$
θ Range (°)	2.14–29.97	2.07–29.97	2.38–30.02
Index ranges	$-14 \leqslant h \leqslant 12$, $-17 \leqslant k \leqslant 16$, $0 \leqslant l \leqslant 17$	$-30 \leqslant h \leqslant 29$, $0 \leqslant k \leqslant 20$, $-1 \leqslant l \leqslant 21$	$-12 \leqslant h \leqslant 12$, $0 \leqslant k \leqslant 32$, $0 \leqslant l \leqslant 13$
Reflections collected	7681	7008	5557
Independent reflections [R_{int}]	7630 [0.0081]	6738 [0.0248]	5557 [0.0000]
Data/restraints/parameters	7630/2/319	6738/2/356	5557/0/244
Final R indices [$I > 2\sigma(I)$]	$R_1 = 0.0415$, $wR_2 = 0.0852$	$R_1 = 0.0483$, $wR_2 = 0.1175$	$R_1 = 0.0573$, $wR_2 = 0.1372$
R indices (all data)	$R_1 = 0.1367$, $wR_2 = 0.1063$	$R_1 = 0.0686$, $wR_2 = 0.1257$	$R_1 = 0.0656$, $wR_2 = 0.1391$
Goodness-of-fit on F^2	0.857	1.092	1.009
Largest difference in peak and hole (e Å^{-3})	1.010 and −0.915	2.307 and −1.070	0.607 and −0.389

H(2′)], 8.48 s [2H, H(8)/H(8′)], 4.31 t [4H, H(10)/H(10′), $J = 6.8$ Hz], 2.48 t [2H, H(11), $J = 6.8$ Hz].

2.3.3. $N^9,N^{9'}$-tetramethylene-bisadenine ($Ade_2C_4 \cdot H_2O$) (**2**)

Anal. Calc. for $C_{14}H_{18}N_{10}O$: C, 49.1; H, 5.2; N, 40.9. Found: C, 49.3; H, 5.2; N, 41.5%. Selected IR bands (cm^{-1}): 3314s, 3153s, 1671vs, 1601vs, 1569s, 1481m, 1440m, 1416s, 1360m, 1328s, 1305s, 1239m, 1196m, 794m, 644m. ^{1}H RMN (DMSO-d^6) $\delta = 8.12$ s [4H, H(2)/H(2′) + H(8)/H(8′)], 7.19 s [4H, NH_2], 4.17 bt [4H, H(10)/H(10′), $J = 6.8$ Hz], 1.76 bm [4H, H(11)/H(11′), $J = 6.8$ Hz].

The corresponding $Ade_2C_4 \cdot 2HCl \cdot 4H_2O$ (**2a**) was obtained as a crystalline material by evaporation of the ligand dissolved in HCl 1 M. *Anal.* Calc. for $C_{14}H_{26}Cl_2N_{10}O_4$: C, 35.83; H, 5.58; N, 29.84. Found: C, 35.79; H, 5.52; N, 29.54%. Selected IR bands (cm^{-1}): 3349s, 3057s, 1692vs, 1650sh, 1612s, 1519m, 1463m, 1417s, 1371m, 1314m, 1217s, 903m, 784m, 715m, 685m, 644m, 531m. ^{1}H RMN (DMSO-d^6) $\delta = 8.46$ s [2H, H(2)/H(2′)], 8.43 s [2H, H(8)/H(8′)], 4.25 bt [4H, H(10)/H(10′), $J = 6.8$ Hz], 1.80 bm [4H, H(11)/H(11′), $J = 6.8$ Hz].

2.4. Preparation of the complexes

As published previously [1,2], ^{1}H NMR spectra of the complexes are very similar to the ligands. Major chemical shift differences are caused by protonation, for this reason the complexes were not characterized by NMR.

2.4.1. Outer sphere complexes: general method [1,2]

To a stirred solution of 2 mmol of the corresponding ligand in 20 ml of HCl 2 M at 50 °C, 2.5 mmol MCl_2 were added, stirred for 30 min and allowed to stay at room temperature. Firstly, a white precipitate of the corresponding complex was formed, filtered and air dried. Suitable crystals for X-ray were obtained, from the resulting solution, after several days.

2.4.1.1. $[(H\text{-}Ade)_2C_3][ZnCl_4] \cdot H_2O$ (**3**) [2]. *Anal.*

Calc. for $C_{13}H_{18}Cl_4N_{10}OZn$: C, 29.0; H, 3.4; N, 26.0. Found: C, 28.9; H, 3.3; N, 26.0%. Selected IR bands (cm^{-1}): 1694vs, 1683vs, 1614s, 1518s, 1441sh, 1416s, 1342m, 1227s, 1062m, 953m, 855m, 820m, 785m, 740w, 726m, 695m, 682m, 643m, 599m, 534m.

2.4.1.2. $[(H\text{-}Ade)_2C_3]_2[Cd_2Cl_8(H_2O)_2] \cdot 4H_2O$ (**4**) [1]. *Anal.*

Calc. for $C_{13}H_{22}CdCl_4N_{10}O_3$: C, 25.1; H, 3.5; N, 22.5. Found: C, 25.0; H, 3.4; N, 22.3%. Selected IR bands (cm^{-1}): 3360s, 3327s, 3275s, 1708vs, 1668s, 1603vs, 1578s, 1488m, 1455m, 1418s, 1358s, 1331m, 1303s, 1259m, 1241m, 1214s, 1192m, 1083w, 1008w, 955w, 802m, 779m, 718m, 642m, 561m.

2.4.1.3. $\{[(H\text{-}Ade)_2C_4][Cd_2Cl_6(H_2O)_2] \cdot 2H_2O\}_n$ (**5**).

The general method only yields microcrystalline samples. Suitable crystals for X-ray were obtained after several weeks in modified conditions: 0.5 mmol of the ligand were stirred with 2.5 mmol of $CdCl_2$ in 20 mL of HCl 0.1 M at

50 °C for 30 min and then allowed to stand at room temperature Yield 60%. *Anal.* Calc. for $C_{14}H_{24}Cd_2Cl_6N_{10}O_3$: C, 20.6; H, 3.0; N, 17.1. Found: C, 20.7; H, 3.0; N, 16.8%. Selected IR bands (cm^{-1}): 3338s, 1693vs, 1635s, 1601s, 1519s, 1438m, 1414s, 1348m, 1321m, 1211s, 933w, 887w, 717s, 670s, 561m, 529m.

2.4.2. Inner sphere complexes

To a stirred solution of 0.5 mmol of the ligand in 20 mL of HCl 0.1 M at 50 °C, 2.5 mmol of $ZnCl_2 \cdot 2H_2O$ were added, stirred 30 min and allowed to stay at room temperature. The resulting precipitate was filtered and air dried.

*2.4.2.1. [H-(Ade)$_2$C$_3$(ZnCl$_3$)] (**6**).* Yield 50%. Crystals suitable for X-ray appeared from filtering waters. *Anal.* Calc. for $C_{13}H_{15}Cl_3N_{10}Zn$: C, 32.3; H, 3.1; N, 29.0. Found: C, 32.5; H, 3.1; N, 28.8%. Selected IR bands (cm^{-1}): 3360s, 3327s, 3275s, 1708vs, 1668s, 1603vs, 1578s, 1488m, 1455m, 1418s, 1358s, 1331m, 1303s, 1259m, 1241m, 1214s, 1192m, 1083w, 1008w, 955w, 802m, 779m, 718m, 642m, 561m.

*2.4.2.2. [H-(Ade)$_2$C$_4$(ZnCl$_3$)] · 1.5H$_2$O (**7**).* Yield 65%. *Anal.* Calc. for $C_{14}H_{20.5}Cl_3N_{10}O_{1.25}Zn$: C, 32.4; H, 3.8; N, 27.0. Found: C, 32.4; H, 3.7; N, 26.6%. Selected IR bands (cm^{-1}): 3516m, 3345s, 3316s, 3090s, 1700vs, 1659s, 1601vs, 1515m, 1486m, 1419s, 1351m, 1326m, 1309s, 1251m, 1227s, 795m, 641m.

*2.4.2.3. [(H-Ade)$_2$C$_4$(ZnCl$_3$)$_2$] · 3H$_2$O (**8**).* With this ligand (N^9,$N^{9'}$-Ade$_2$C$_4$) it is possible to obtain other inner sphere complex in HCl 1 M as a white microcrystalline precipitate. Yield 30%. *Anal.* Calc. for $C_{14}H_{24}Cl_6N_{10}O_3Zn_2$: C, 23.2; H, 3.3; N, 19.3. Found: C, 23.6; H, 3.6; N, 19.1%. Selected IR bands (cm^{-1}): 3093s, 1699vs(br), 1603s(br), 1538m, 1497m, 1421s, 1368m, 1318m, 1309m, 1257m, 1153w, 788m, 772m, 724m, 678m.

3. Results and discussion

Compounds **5**, **5a** and **6** have been characterized by X-ray diffraction and **7**, **8** by comparison of spectroscopic data (IR spectra) with other unequivocally described complexes.

3.1. Cd(II) complexes

Complex $\{[(H\text{-}Ade)_2C_4][Cd_2Cl_6(H_2O)_2] \cdot 2H_2O\}_n$ (**5**) constitutes the first crystal structure isolated with the ligand Ade_2C_4 (Fig. 1).

Its structural analysis reveals the presence of both protonated adenine rings with an anti disposition [dihedral angle N(9)–C(10)–C(10′)–N(9′) = 180°]. The bisadenine molecules are connected among them by two hydrogen bonds N(6)···N(7) producing chains of molecules along the *c*-axis. The structure presents a polymeric chain formed by the union of $[Cd_2Cl_6(H_2O)_2]^{2-}$ units along the *a*-axis. The Cd(II) displays a distorted octahedral geometry with

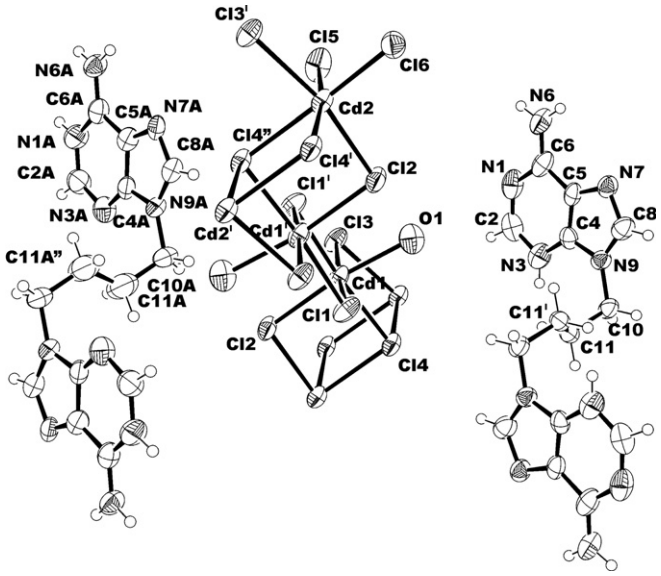


Fig. 1. ORTEP representation of $\{[(H\text{-}Ade)_2C_4][Cd_2Cl_6(H_2O)_2] \cdot 2H_2O\}_n$ (**5**) polymeric structure. Displacement ellipsoids are drawn at the 50% probability level and H atoms are drawn as circles of arbitrary radii.

bridging chlorine atoms. Similar $[Cd_2Cl_8(H_2O)_2]^{4-}$ units were described for the Cd(II) Ade_2C_3 outer sphere complex [1]. The organic and inorganic chains are linked by hydrogen bonds (Fig. 2).

A surprising result related to the reaction between Ade_2C_4 and $CdCl_2$ in acidic media was the isolation – only once – of a single crystal of an inner sphere complex of Cd(II) with an unexpected N^9,$N^{3'}$-tetramethylene-bisadenine: $\{[(H\text{-}Ade N^3)\text{-}(CH_2)_4\text{-}(H\text{-}Ade N^9)]_2][Cd_3Cl_{10}) \cdot 2H_2O\}_n$ **5a** which was suitable for X-ray diffraction analysis (Fig. 3). This complex present an asymmetric and intriguing diprotonated N^9,$N^{3'}$-tetramethylene-bisadenine. Although the details of their formation are not known, several experiences to investigate how the asymmetric ligand is

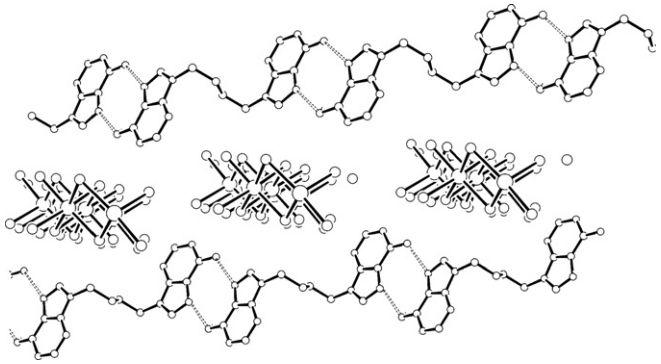


Fig. 2. Crystal structure of 3D network of $\{[(H\text{-}Ade)_2C_4][Cd_2Cl_6(H_2O)_2] \cdot 2H_2O\}_n$ (**5**). A layer: Adenine – Cd(II) polyanion: [N(1A)·Cl(3) = 3.20 Å, N(6A)·Cl(5) = 3.27 Å]; Adenine – Adenine: [N(7)·N(6′) = 2.86 Å]. B layer: Adenine – Adenine: [N(6)·N(7) = 2.98 Å]; Adenine – H_2O: [N(1)···O(4) = 2.84 Å]; H_2O – Cd(II) polyanion: [Cl(6)···O(1) = 3.16 Å, Cl(2)···O(2) = 3.22 Å, Cl(5)···O(4) = 3.21 Å]; H_2O – H_2O: [O(1)···O(2) = 2.78 Å, O(2)···O(4) = 2.84 Å, O3···O(4) = 2.23 Å].

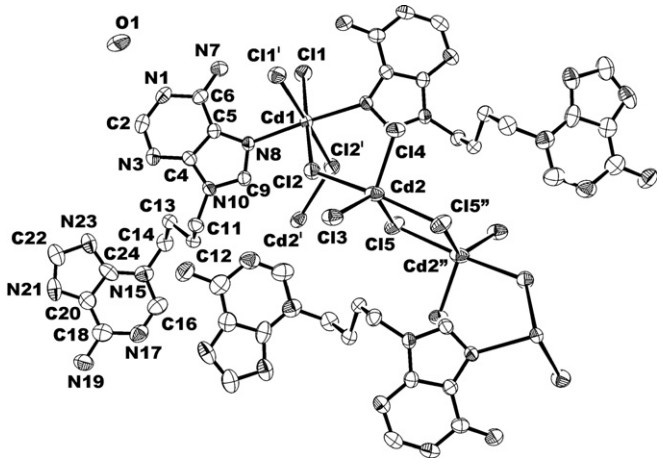


Fig. 3. ORTEP representation of $\{[(\text{H-Ade}N^3)\text{-}(CH_2)_4\text{-}(\text{H-Ade}N^9)]_2\}\text{-}(Cd_3Cl_{10})\cdot 2H_2O\}_n$ (**5a**). Displacement ellipsoids are drawn at the 50% probability level and H atoms are drawn as circles of arbitrary radii.

formed have been undertaken. Additional proofs are under study.

The metal ion forms a polymeric anionic structure with two different types of Cd(II) environments: (i) Cd(II) coordinated directly to two N^9-adenine moieties with an octahedral coordination; (ii) dimeric $[Cd_2Cl_8]^{4-}$ units bridging two octahedral Cd-Adenine moieties (Fig. 4).

The behaviour of the two adenine rings is completely different. The adenine linked through N(9) is protonated at N(1) and coordinated through N(7) to a Cd(II) ion [N(7)···Cd(1) = 2.38 Å]. The adenine linked by N(3) is protonated at N(7) and does not interact with any metal ion. Fig. 5 show the main intermolecular interactions observed.

In order to understand this surprising result, a study of ^{1}H NMR spectra of crude reaction material, obtained in the synthesis of the ligand, show the presence of a minority secondary product, which we have assigned to $N^9,N^{3'}$-trimethylene-bisadenine by comparison of literature data (Fig. 6) [6,7]. In our hands, the best results have been

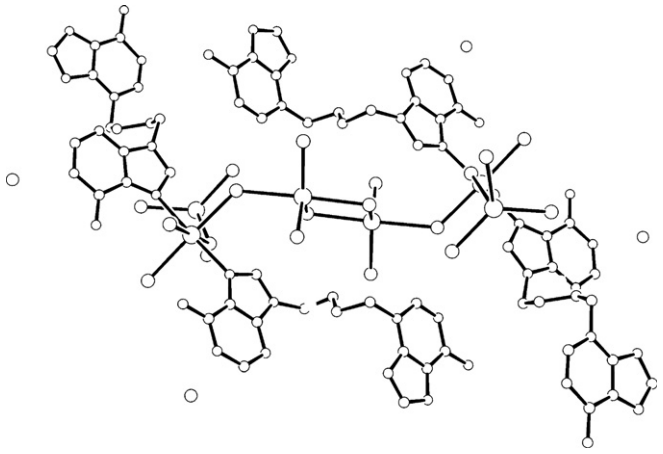


Fig. 4. Polymeric structure of $\{[(\text{H-Ade}N^3)\text{-}(CH_2)_4\text{-}(\text{H-Ade}N^9)]_2\}\text{-}(Cd_3Cl_{10})\cdot 2H_2O\}_n$ (**5a**).

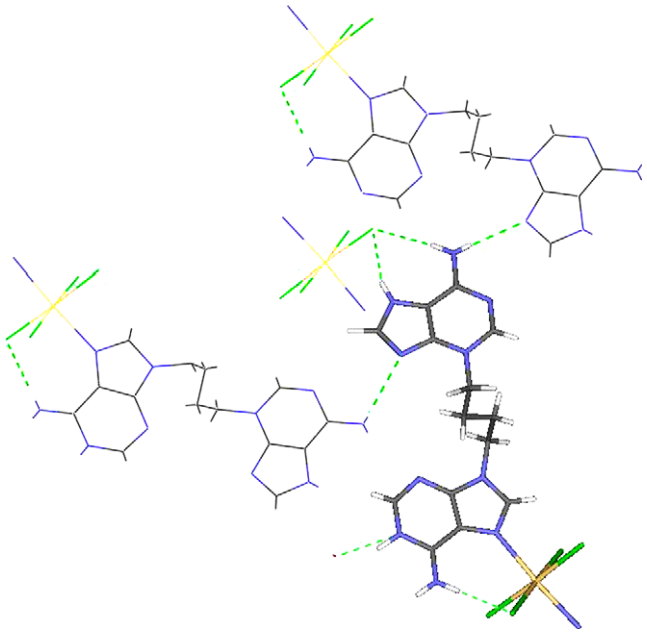


Fig. 5. $\{[(\text{H-Ade}N^3)\text{-}(CH_2)_4\text{-}(\text{H-Ade}N^9)]_2](Cd_3Cl_{10})\cdot 2H_2O\}_n$ (**5a**) additional interactions: [N(19)···N(23) = 3.06 Å]; [N(19)···Cl(1) = 3.3 Å y N(21)···Cl(1) = 3.23 Å]. [N(7)···Cd(1) = 2.38 Å]; [N(1)···O(10) = 2.65 Å]; [N(6)··· Cl(4) = 3.14 Å, N(6)···Cl(1) = 3.27 Å].

obtained with Ade_2C_3 ligand because its higher solubility, although the isolated single crystal was obtained for Ade_2C_4. Thus, a tentative assignation of ^{1}H NMR (DMSO-d^6) would be $\delta = 8.37$ s [1H, H(2′ or 8′) (N^3-Ade)], 8.20 s [1H, H(2) (N^9-Ade)], 8.12 s [1H, H(8) (N^9-Ade)], 7.76 s [1H, H(2′ or 8′) (N^3-Ade)], 7.90 bs [2H, $NH_{2'}$, (N^3-Ade)], 7.21 s [2H, NH_2, (N^9-Ade)], 4.40 t [2H, H(10′), CH_2-(N^3-Ade)], 4.17 t [2H, H(10), CH_2-(N^9-Ade)], 2.39 t [2H, H(11), –CH_2–]. In the literature we can find examples of N^3 substitution of adenines but the experimental conditions (acidic or neutral pH) are very different to those described in this paper [8–10]. In order to optimize the preparation of this new ligand we have modified reaction conditions (use of DMF or anhydrous DMF; addition of drops of water to the reaction mixture; temperature: from r.t. to 100 °C; reaction times from 24 h. to 48 h; different bases: NaOH, K_2CO_3 anhydrous, NaH… or even without base) but, in our hands it has been extremely difficult to obtain a pure sample of this product.

3.2. Zn(II) complexes

Complex $[\text{H-}(Ade)_2C_3(ZnCl_3)]$ (**6**) represents the first inner sphere complex with a $N^9,N^{9'}$-bisadenine. The structure shows a zwitterionic form with one ring protonated at N(1) while the other ring is coordinated to a $ZnCl_3$ moiety, as in other complexes with alkyl-adenines [11,12] (Fig. 7).

Intramolecular hydrogen bonds stabilize the coordination through N(7). Additional intermolecular interactions are present forming dimeric units (see Fig. 8). The two

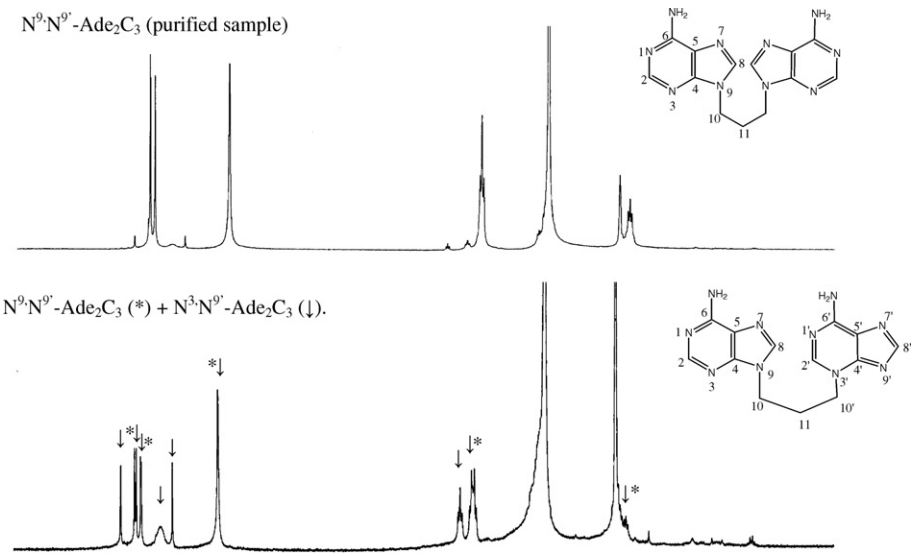


Fig. 6. ^{1}H NMR spectra of N^{9},$N^{9'}$-trimethylene-bisadenine and a sample of reaction crude (best conditions to obtain ^{9},$N^{3'}$-trimethylene-bisadenine: 80 °C, NaH in anhydrous DMF and 48 h).

adenine rings for each molecule present a *s-cis* disposition which allows a *stacking* interaction between the imidazolic rings [average distance 3.39(3) Å], similar to that found in the neutral form [1].

3.3. IR spectra

Although NMR spectroscopy was not useful to characterize the structure of the complexes, the IR data results were very conclusive. The IR spectra of the outer sphere complexes are very similar to the corresponding hydrochlorides. The bands related to δ(NH) are shifted to higher frequencies and the peak at ca. 1328 cm^{-1} assigned to $\nu(C_5–N_7–C_8)$ remains practically unchanged [1,2]. Table 2 shows tentative assignments for the neutral and protonated ligands. Thus, in the infrared spectrum of the zwitterionic inner sphere complex **6**, four bands are exhibited between 1710 and 1570 cm^{-1} (see Fig. 9) which correspond to δ(NH): 1708 and 1668 cm^{-1}, $\delta(NH) + \nu(C_5–C_6)$: 1603 cm^{-1} and $\nu(C_5–N_7–C_8)$: 1578 cm^{-1}. Similar pattern band distribution for [H-(Ade)$_2$C$_4$ZnCl$_3$] (**7**) is indicative of an asymmetric structure and coordination type. The other

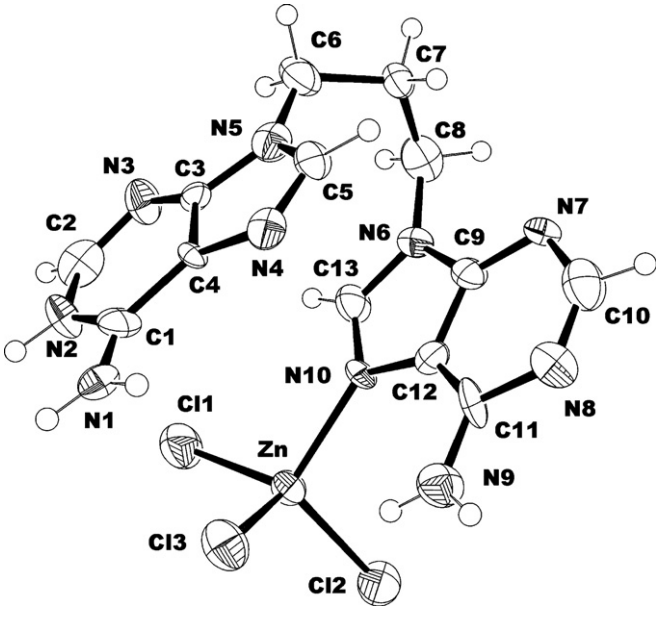


Fig. 7. ORTEP representation of the inner-sphere complex [H-(Ade)$_2$-C$_3$(ZnCl$_3$)] (**6**). Displacement ellipsoids are drawn at the 50% probability level and H atoms are drawn as circles of arbitrary radii.

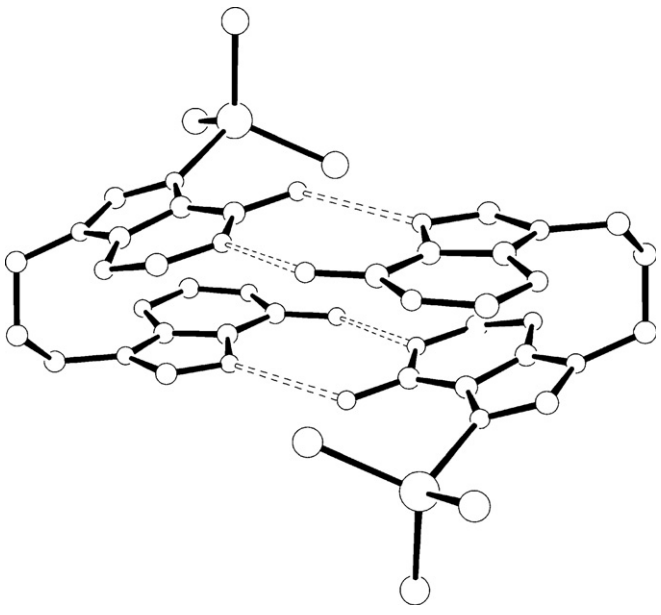


Fig. 8. [H-(Ade)$_2$C$_3$(ZnCl$_3$)] (**6**) additional interactions: Cl(2)···H–N(6′) = 2.41 Å, 160.8°; Cl$^{\#}$···H–N(6′) = 2.46 Å, 168°; Cl$^{\#}$···H–N(1′) = 2.22 Å,157.6°; [N(6$^{\#}$)–H···N(1′) = 2.03 Å, 159.3°; N(7$^{\#}$)···H–N(6′) = 2.13 Å, 171.5°].

Table 2
Tentative assignation of the IR bands

Tentative assignation	Ade_2C_3 (**1**)[a]	$Ade_2C_3 \cdot HCl$ (**1a**)[a]	[H-$(Ade)_2$-$C_3(ZnCl_3)$] (**6**)	Ade_2C_4 (**2**)	$Ade_2C_4 \cdot HCl$ (**2a**)[b]	[H-$(Ade)_2C_4ZnCl_3$] (**7**)	[$(H\text{-}Ade)_2C_4(ZnCl_3)]_2$] (**8**)
δ(NH)	1664vs	1690vs	1708vs, 1668s	1671vs	1692vs	1700vs, 1659s	1699vs, br
δ(NH) + ν(C5–C6)	1604vs	1626s	1603vs	1601vs	1650sh, 1612s	1601vs	1603s, br
ν(N3–C4–C5)	1582sh	1595s	1578s	1569s			
ν(C4N9)+δ(C8–H)	1490m	1517s	1488m	1481m	1519m	1515m,1486m	1497m
δ(C2–H) + ν(C8N9) + δ(C8–H)	1453m	1441s	1455m	1440m	1463m		
ν(N1–C6–N6)	1422m	1413s	1418s	1416s	1417s	1419s	1421s
ν(ring)	1375m			1360m	1371m	1351m	1368m
ν(C5–N7–C8)	1337m	1332*s*	1331m	1328s	1314m	1326m	1318m
ν(C2–N3)+ν(C8–N9)+ δ(C–H)	1303s			1305s		1309s	

[a] Values of **1** and **1a** are equivalent to those previously reported [1,2].
[b] Compound **5** presents a similar IR spectrum to that of **2a**.

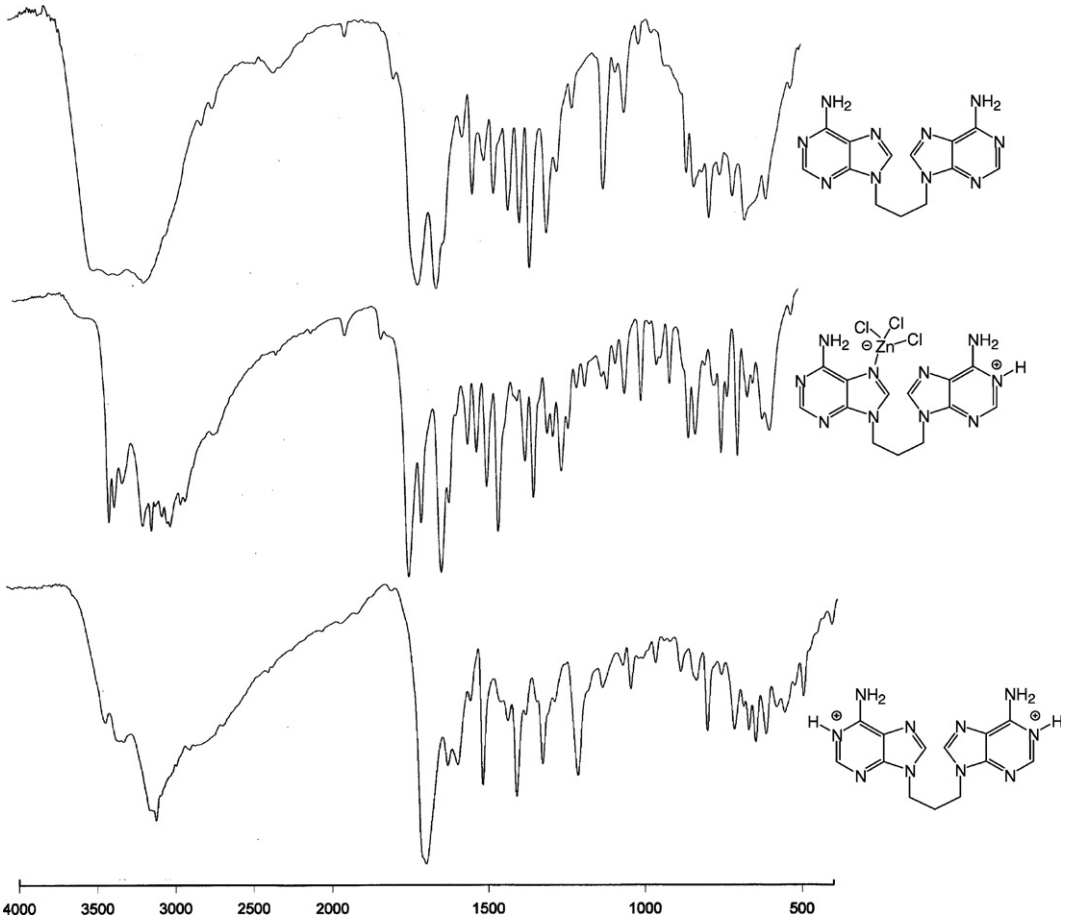


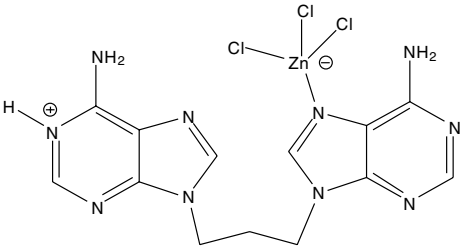
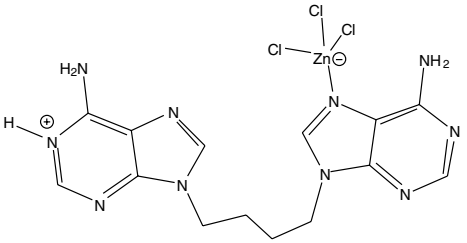
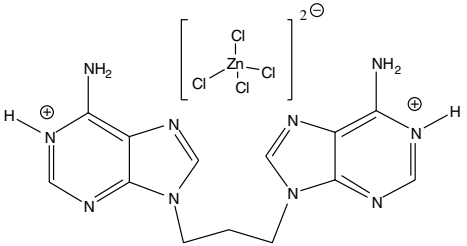
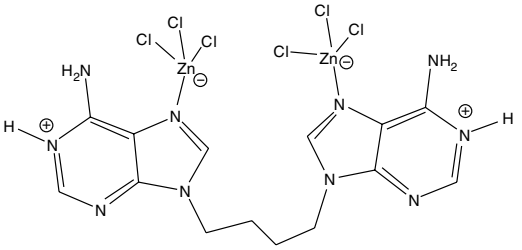
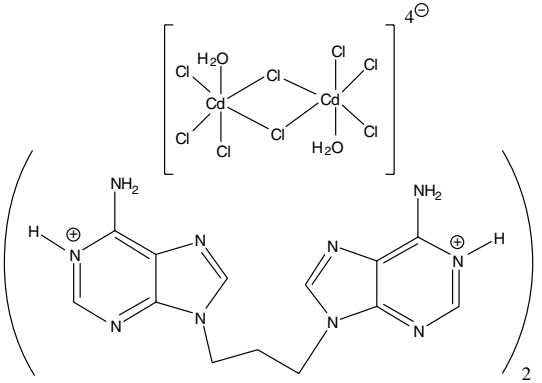
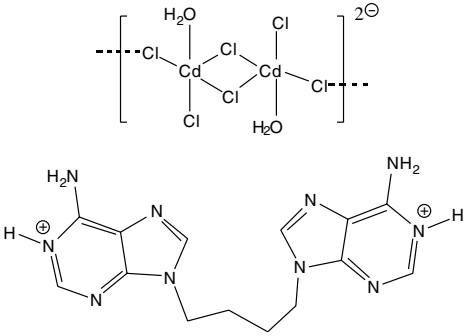
Fig. 9. Comparison of the IR spectra of Ade_2C_3 (**1**), [H-$(Ade)_2C_3(ZnCl_3)$] (**6**) and $Ade_2C_3 \cdot 2HCl$ (**1a**).

inner sphere [$(H\text{-}Ade)_2C_4(ZnCl_3)_2$] (**8**) complex present two broad bands in the same area which can be attributed to the presence of a more symmetric structure equivalent to that found in $N^6,N^{6'}$-[$(H\text{-}Ade)_2C_3(ZnCl_3)_2$] previously described [3].

4. Conclusions

The general behaviour of (tri and tetramethylene)-bisadenines with Zn(II) and Cd(II) in acidic media is shown in Table 3.

Table 3
Proposed structures for the isolated complexes

Experimental conditions		Ade_2C_3	Ade_2C_4
Zn	HCl 0.1 M	$[H\text{-}(Ade)_2C_3(ZnCl_3)]$ (**6**) 	$[H\text{-}(Ade)_2C_4(ZnCl_3)] \cdot 1.5H_2O$ (**7**) 
	HCl $\geqslant$ 1 M	$[(H\text{-}Ade)_2C_3][ZnCl_4] \cdot H_2O$ (**3**) 	$[(H\text{-}Ade)_2C_4(ZnCl_3)_2 \cdot 3H_2O$ (**8**) 
Cd	HCl 0.1 M	$[(H\text{- }Ade)_2C_3]_2[Cd_2Cl_8(H_2O)_2] \cdot 4H_2O$ (**4**) 	$\{[(H\text{- }Ade)_2C_4][Cd_2Cl_6(H_2O)_2] \cdot 2H_2O\}_n$ (**5**) 
	HCl $\geqslant$ 1 M		

These results show:

(i) In our hands, Cd(II) ion only yields outer sphere complexes with N^9,$N^{9'}$-polymethylene-bisadenines in acidic media. Two different anionic species are obtained. The dimeric $[Cd_2Cl_8(H_2O)_2]^{4-}$ with Ade_2C_3 previously described [1] and the polymeric chain based on $[Cd_2Cl_6(H_2O)_2]^{2-}$ units present in the new Ade_2C_4 Cd(II) complex obtained.
(ii) In strong acidic media Ade_2C_3 reactions with Zn(II) only yield outer sphere complexes while Ade_2C_4 yield a bis-zwitterionic inner sphere complex similar to N^6,$N^{6'}$-Ade_2C_3 Zn(II) complex.
(iii) By a modification of the reaction conditions (HCl 0.1 M) is possible to isolate equivalent inner sphere complexes for both ligands: $[H\text{-}(Ade)_2C_x(ZnCl_3)]$ ($x = 3$, 4).

5. Supplementary material

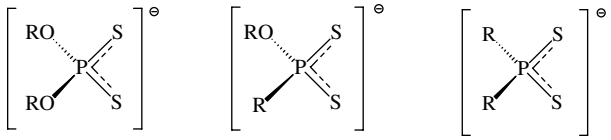
CCDC numbers 612160 , 612161 and 612162 contain the supplementary crystallographic data for **5**, **5a** and **6**. These data can be obtained free of charge via http://www.ccdc.cam.ac.uk/conts/retrieving.html, or from the Cambridge Crystallographic Data Centre, 12 Union Road, Cambridge CB2 1EZ, UK; fax: (+44) 1223-336-033; or e-mail: deposit@ccdc.cam.ac.uk.

Acknowledgements

We are grateful to Spanish CICYT (BQ2002-02546) for financial support and to COST D20 (WG 0006) Project. One of us (F.M.A.), acknowledges a Grant of Conselleria d'Economia, Hisenda i Innovació (Govern de les Illes Balears).

References

[1] A. García-Raso, J.J. Fiol, F. Bádenas, X. Solans, M. Font-Bardia, Polyhedron 18 (1999) 765.
[2] A. García-Raso, J.J. Fiol, F. Bádenas, X. Solans, M. Font-Bardia, Polyhedron 18 (1999) 3077.
[3] A. García-Raso, J.J. Fiol, F. Bádenas, A. Tasada, X. Solans, M. Font-Bardia, M.G. Basallote, M.A. Máñez, M.J. Fernández-Trujillo, D. Sánchez, J. Inorg. Biochem. 93 (2003) 141, and references therein.
[4] G.M. Sheldrick, Acta Crystallogr. Sect. A46 (1990) 467.
[5] G.M. Sheldrick, SHELX-97, A program for crystal structure analysis (Release 97-2), University of Göttingen, Germany, 1997.
[6] S. Balcome, S. Park, D.R. Quirk Door, L. Hafner, L. Phillips, N. Tretyakova, Chem. Res. Toxicol. 17 (2004) 950.
[7] S. Balcome, S. Park, D.R. Quirk Door, L. Hafner, L. Phillips, N. Tretyakova, Chem. Res. Toxicol. 17 (2004) 950.
[8] T. Fujii, G.C. Walker, N.J. Leonard, J. Med. Chem. 22 (1979) 125.
[9] N.J. Leonard, T. Fuji, J. Am. Chem. Soc. 85 (1963) 3719.
[10] J.A. Montgomery, H.J. Thomas, J. Heterocyclic Chem. 1 (1964) 115.
[11] J. Maixner, Acta Crystallogr. Sect. C 49 (1993) 927.
[12] M.J. MacCall, M.R. Taylor, Acta Crystallogr. Sect. B 32 (1976) 1687.



Dithiophosphate, 1 **Dithiophosphonate, 2** **Dithiophosphinate, 3**

Scheme 1.

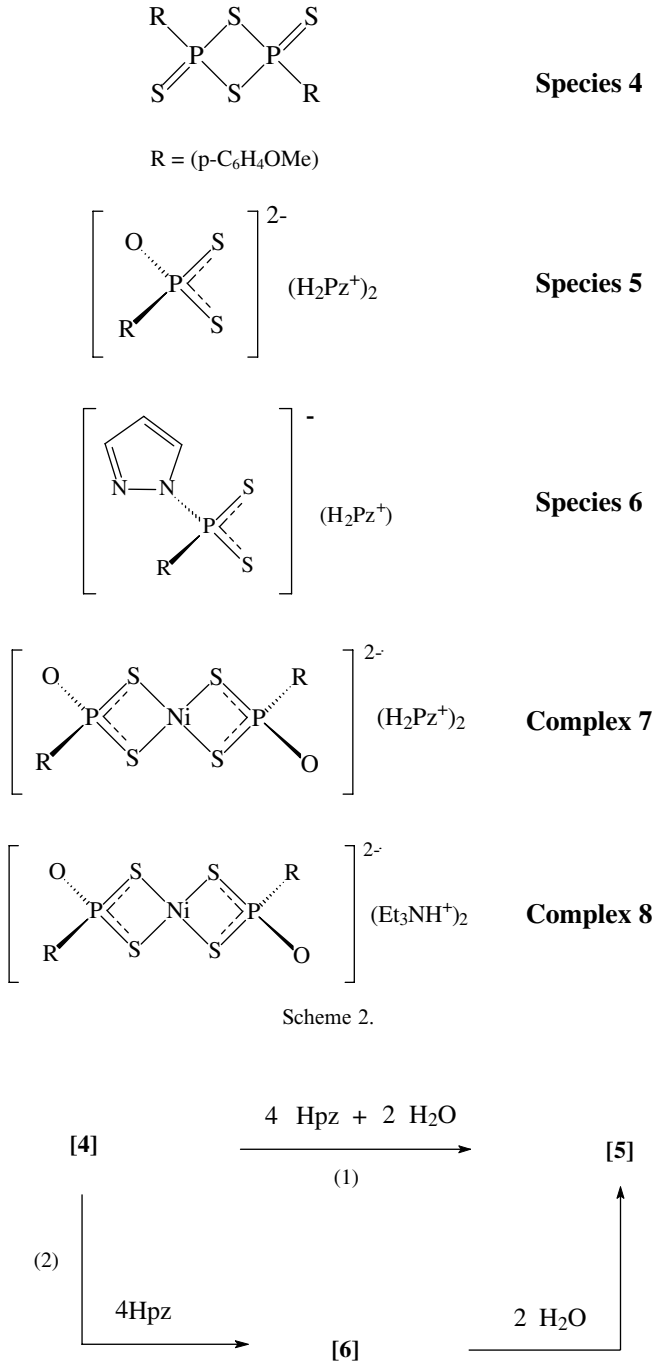
2. Results and discussion

2.1. Synthesis, characterization and solution properties of species 5 and 6

When a suspension of the Lawesson's dimer $[S_2P(p\text{-}C_6H_4OMe)]_2$ (**4**, Scheme 2) in toluene was treated under nitrogen with a large excess of pyrazole (Hpz), a white precipitate formed (**5**, Scheme 3, pathway 1), which, on the basis of elemental analysis, IR and multinuclear spectroscopy, was formulated as an adduct between pyrazole and dithiophosphonic acid (H_2L), with $H_2L \cdot 2Hpz$ formula. Nevertheless, the presence of multiple bonding sites for the acidic proton [the N site(s) on the pz moiety and the S or O sites on the dithiophosphonate ligand] cannot rule out the presence of different tautomers, such as a bispyrazolium salt, $L(H_2pz)_2$, or even a species where the hydrogen atoms are extensively shared between the above quoted N, O and S acceptors.[1]

Species **5** was found to transform from a white solid into a dense liquid if left in air. Why this occurs it is not clear. X-ray powder diffraction (XRPD) indicated the solid to be highly crystalline; yet, as observed by performing a profile fitting of time-dependent XRPD traces, the decomposition has a $t_{1/2}$ value just above 4 h (Fig. 1). GC–MS measurements of the evolved gas fraction did not support any conclusive information, thus leaving the question still open. The XRPD crystalline trace (collected in conventional Bragg–Brentano mode in the air) is nevertheless too complex for an ab initio structural analysis; *inter alia*, this agrees with the presence of two formula units in the asymmetric unit of the crystals, as evidenced by solid state ^{31}P NMR (vide infra). The IR spectrum of solid **5**, recorded in nujol mull, shows a broad absorption at 1869 cm^{-1}, which is likely due to strong hydrogen bonds of the P–O–H–N kind, involving the dithiophosphonic acid and the heteroaromatic ring.

The ^{31}P NMR spectrum of **5** in acetone-d_6 shows one singlet centred at 78.6 ppm (see Table 1). This value shows an upfield shift of about 30 ppm compared to that found earlier for dithiophosphonate ligands [15,16], suggesting the presence of a relatively highly charged (dianionic) form of L for **5**, thus supporting, at least in solution, the formulation of **5** as a bispyrazolium salt, $L(H_2pz)_2$. On lowering the temperature down to 183 K, the ^{31}P NMR spectrum shows only one broader peak at 86.2 ppm, indicating that the system is in the fast exchange regime at room temperature (RT) and that the exchange rate decreases only slightly at low temperature. Unfortunately, the corresponding low temperature ^1H NMR spectrum cannot be employed to follow in detail this process, due to the complexity of the signals in the aromatic region. At room temperature, the ^1H NMR spectrum of **5** (in acetone-d_6) shows two multiplets at 7.9 and 7.1 ppm due to the protons of the aryl group, one singlet centred at 3.8 ppm for the OMe residue and



Species 4

R = (p-C_6H_4OMe)

Species 5

Species 6

Complex 7

Complex 8

Scheme 2.

Scheme 3.

[1] For the sake of completeness, it must be said that even a formulation of the $[(MeO)C_6H_4\text{–}PS_2\text{–}O\text{–}PS_2\text{–}C_6H_4(OMe)](Hpz)_2(H_2pz)_2$ kind cannot be excluded (*Anal.* Calc.: C, 44.95; H, 4.64; N, 16.13), being it consistent even with the ^{31}P CPMAS NMR evidences.

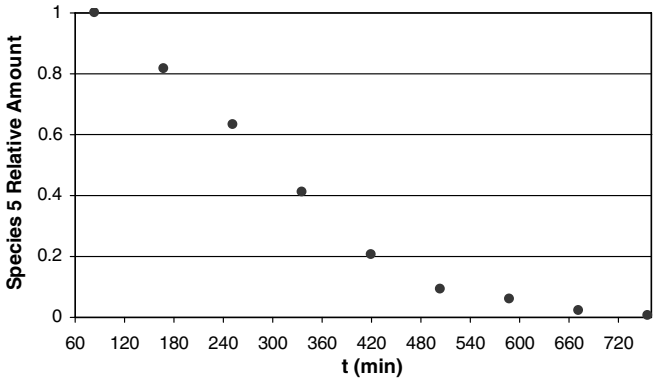


Fig. 1. Time dependence of the solid to liquid decomposition of the (polycrystalline) species **5** if left in air at RT, as followed by the disappearance of the pertinent peaks in the powder diffraction traces.

Table 1
^{31}P chemical shifts (ppm) for species **5**–**8**

Sample	^{31}P solution[a]	^{31}P CPMAS	^{31}P SPE
Species **5**	78.6	97.3	97.3
		94.5	94.5
Species **5** quenched	78.0	97.3	97.2
		94.5	94.4
			89.9
Species **6**	72.8		
Species **6**[*]	78.1	97.2	97.1
	72.8	94.4	94.4
			82.3
Complex **7**	85[b]	77.3	
Complex **8**	69.4[c]	59.7	

[*] Recrystallized from anhydrous toluene (see text).
[a] Spectra recorded in acetone.
[b] Broad peak.
[c] Spectra recorded in methanol.

two signals at 7.7 and 6.3 ppm, assigned to the protons of the pyrazole moiety. The assignment of the signal at 10.3 ppm to acidic (N–H) protons [17] was confirmed by its disappearance after isotopic exchange with D_2O.

The formulation of **5** was also confirmed by the ^{13}C NMR spectrum (recorded at RT in acetone) which shows, beside the phenyl C-atoms signals, only two resonances for the heterocycle at 105.0 and 133.6 ppm, attributed to C(4) and C(3)/C(5), respectively. This excludes any possibility of a P–N bound species.

On the basis of these spectral observations, intermolecular hydrogen bonds between the adducts can be ruled out in solution and, taking into account the elemental analysis, the presence of two molecules of pyrazole *per* molecule of dithiophosphonic acid is implicit.

The fact that no pyrazolium *N*-pyrazolyl-4-methoxyphenyl-phosphonamidodithiolate was obtained when pyrazole alone was reacted with the Lawesson's reagent is here attributed to the specific electron properties of this heterocycle. Indeed, pyrazole can be considered a "hybrid" molecule, the lone pair on N(2) making it nucleophilic, while its aromatic nature transforming it into a good leaving-group.

In order to investigate the role played by Hpz in the reaction with **4**, a new synthesis was carried out in anhydrous conditions. It is well known that aliphatic amines readily react with the Lawesson's dimer forming a stable P–N bond [18]. Accordingly, when a solventless reaction between the Lawesson's reagent and an excess of pyrazole was carried out at 343 K and under nitrogen atmosphere, a new derivative, **6**, could be isolated. Species **6** was formulated as a 4-methoxy-phenylphosphonoaminodithiolate pyrazolium salt (Scheme 2), on the basis of multinuclear NMR spectroscopy. The RT ^{31}P NMR spectrum of **6** recorded in acetone-d_6 shows a sharp signal centred at 72.8 ppm in agreement with the presence of a phosphorus atom directly bound to a nitrogen one [18,19]. In the presence of water, or moisture, compound **6** hydrolyzes very quickly and species **5** is immediately formed, as confirmed by the ^{31}P NMR spectrum of **6**, recorded (in acetone-d_6) after addition of few drops of water and under nitrogen: the latter spectrum shows, beside the signal due to the N-bound P atom, a new peak centred at 78.1 ppm, i.e. that of the phosphorous atom of the P–O bound species **5**. After 30 min, only the signal centred at 78.1 ppm can be observed. This spectroscopic evidence suggests that the first step of the reaction between **4** and pyrazole is the ring opening reaction by nucleophilic attack of the heterocycle to the Lawesson's reagent with the formation of **6**. In the presence of water, the labile species **6** hydrolyzes quickly, forming the more stable derivative **5** (see Scheme 3, pathway 2). The proposed chemical nature of **6** was also confirmed by ^{31}P solid state NMR spectroscopy, as described below.

2.2. Solid state NMR characterization of species 5 and 6

In the absence of samples suitable for conventional X-ray diffraction studies, species **5** and **6** were analysed by solid state NMR spectroscopy, in order to gain some structural information. The ^{31}P CPMAS spectrum of **5** (Fig. 2a, Table 1) shows two distinct peaks at 97.3 ppm and 94.5 ppm, with a downfield shift of about 20 ppm with respect to the single resonance observed in the NMR spectrum in solution (78.6 ppm in acetone). This different chemical shift between the spectra in the solid state and in solution may depend on packing effects, likely the presence of intermolecular hydrogen bonds between the dithiophosphonic acid and the pyrazole.

The chemical shifts of the peaks in the solid state are in agreement with previous studies [19] which report P–O signals resonating in the range 95–110 ppm. The splitting of the ^{31}P signal into two peaks is confirmed by the ^{13}C CPMAS spectrum (Fig. 2b), in which the isolated signals of the O-methyl (at about 55 ppm) and the P-*ipso* (about 160 ppm) carbon nuclei are split into two peaks each. Unfortunately, the extreme peak overlapping in the aromatic region does not allow to unambiguously assign the pyrazole signals. However, it is well known that, in the solid state, pyrazole gives three distinct peaks at

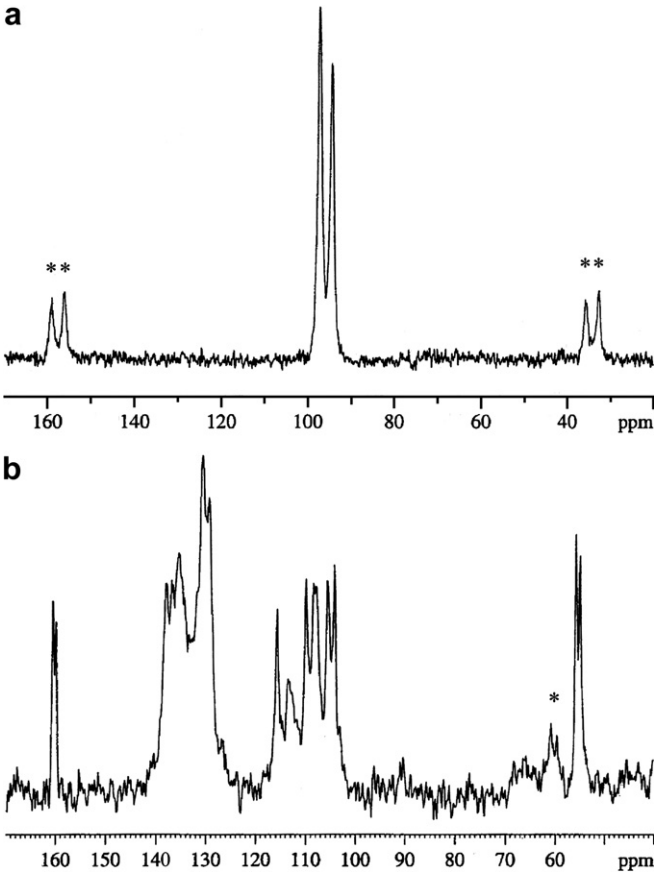


Fig. 2. Solid state NMR spectra of **5**: (a) ^{13}C CPMAS, Number of scans (NS) = 820. (b) ^{31}P CPMAS, NS = 20. Asterisks indicate spinning sidebands.

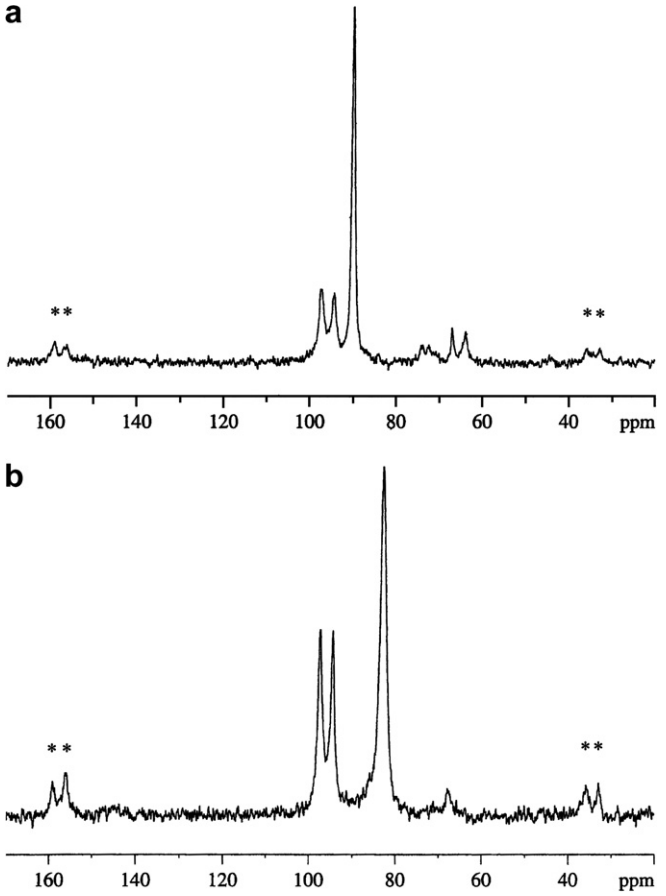


Fig. 3. ^{31}P SPE experiment with recycle delay of 5 s for (a) **5** quenched, Number of scans (NS) = 164, (b) **6***, NS = 48. Asterisks indicate spinning sidebands.

138.7 ppm (C3), 107.0 ppm (C4) and 128.8 ppm (C5) ppm [20]. The clear absence of peaks in the 128 ppm region in the spectrum of **5** seems to indicate that no ''free'' pyrazole is present in species **5**, thus suggesting, in agreement with the above IR results, the presence of a network of hydrogen bonds in the solid.

The presence of split ^{31}P and ^{13}C peaks may suggest either the occurrence of two different phosphorous chemical environments coexisting in a single crystalline phase, or the co-presence of different crystalline forms within the sample. On the basis of the relative intensities of the two peaks (approximately 1:1) the first hypothesis seems more likely. The existence of two crystalline forms in the sample is ruled out by a further experiment in which **5** is obtained by rapidly quenching the reaction mixture down to 273 K before filtering. The ^{31}P CPMAS spectrum recorded on this product was identical to that of species **5**, whereas the ^{31}P SPE spectrum registered with a short recycle delay shows an additional peak at 89.9 ppm (Fig. 3a). The SPE experiment is known to enhance the resonance of those nuclei with a short relaxation time, T_{1P}, i.e. phosphorous nuclei possessing distinct dynamics from those responsible for the peaks in the CPMAS spectrum (in the present case, the two peaks at 97.3 ppm and 94.5 ppm). We suggest that the new peak at 89.9 ppm may belong to an amorphous phase, the formation of which is favoured upon fast cooling and, as expected, is absent in the ^{31}P SPE spectrum of **5** obtained upon slow crystallization. Besides, the presence of the two peaks at 97 and 94 ppm with similar relative intensity, supports the exclusion of the concomitant existence of two crystalline phases.

With the purpose of characterizing the P–N bound species by solid state NMR, **6** was recrystallized using anhydrous toluene, thus changing the consistency of the sample from a sticky material to a solid suitable to be packed in the NMR rotor, **6***. The ^{31}P CPMAS spectrum (not reported) shows two peaks centred at 97.2 ppm and 94.4 ppm, assigned to **5**, which is quickly formed by hydrolysis of **6**. However, an additional peak at 82.2 ppm was found in the ^{31}P SPE spectrum (Fig. 3b), which, on the basis of its chemical shift value [19], is assigned to a phosphorous nucleus of the P–N bound species **6**, thus corroborating the existence of an intermediate P–N species.

2.3. Synthesis and spectroscopic characterization of species 7 and 8

Although both derivatives **5** and **6** can be considered flexible multitopic ligands, the low stability of **6** pushed

us to investigate the coordination properties of species **5** only.

When a suspension of **5** in acetonitrile was treated with $Ni(ClO_4)_2 \cdot 6H_2O$, a violet compound formed, which, on the basis of elemental analysis and spectroscopic data, was formulated as $[NiL_2](H_2Pz)_2$ (**7**). The IR spectrum of **7** (nujol mull) shows one broad band at 1870 cm^{-1}, due to the presence of strong hydrogen bonds of the P–O–H–N kind (as substantiated by the complete structure determination, vide infra).

The RT ^{31}P NMR spectrum of **7** in solution presents one broad peak centred at about 85 ppm, while, on lowering the temperature at 183 K, two sharp peaks at 82.0 and 80.4 ppm appear, suggesting that at low temperatures a slow exchange regime is reached. This fluxional property of **7** may be assigned to the interconversion of the *cis* and *trans* isomers [15].

The RT ^1H NMR spectrum of **7** shows two multiplets centred at 8.1 and 7.1 ppm (phenyl protons), a singlet at 3.9 ppm (methoxo protons) and one broad peak at 4.2 ppm, attributed to an acidic proton. At RT, the protons of pyrazole are undetectable, probably because their signals are so broad to be hidden in the baseline, suggesting an intermediate exchange rate for pyrazole. At 163 K, the ^1H NMR spectrum of **7** shows new signals: one triplet centred at 6.5 ppm, and one doublet at 8.1 ppm, assignable to the protons of the heteroaromatic ring. This indicates that the fluxional process involving pyrazole is substantially slowed down at 163 K. A fundamental role in lowering the rate of the fluxional process may be played by the possibility of formation of strong hydrogen bonds (of P–O–H–N type) even in solution. This was indeed confirmed by the fact that, at RT, after addition of few drops of deuterium oxide, the pyrazole signals do appeared. Apparently, the presence of ^2H versus ^1H nuclei slows down the fluxional process, as does lowering the temperature. Similar isotopic effects have been recently reviewed [21].

On the other hand, when the reaction between **5** and $Ni(ClO_4)_2 \cdot 6H_2O$ was carried out in the presence of triethylamine, a brown precipitate formed, which, on the basis of elemental analysis, IR and ^1H NMR spectroscopy, was formulated as $[NiL_2](Et_3NH)_2$ (**8**), as confirmed by the single crystal X-ray diffraction characterization described below. Species **8** can also be obtained starting from **7** in the presence of triethylamine, showing the stronger basicity of the tertiary amines versus pyrazole.

The RT ^{31}P NMR spectrum of **8** in methanol-d_4 shows one singlet centred at 69.4 ppm while, lowering the temperature at 173 K, two sharp peaks at 73.7 and 72.2 ppm appear. Analogously to what observed for **7**, a slow exchange regime is reached at 173 K, which allows to detect the interconversion process between the *cis* and *trans* isomers.

The RT ^1H NMR spectrum of **8** registered in acetone-d_6 shows two multiplets centred at 8.3 and at 6.7 ppm (aromatic protons), one singlet at 3.8 ppm (methoxo group), and two multiplets centred at 3.2 and 1.3 ppm, due to the triethylamonium ion. On lowering the temperature down to 173 K, these spectral features do not change.

The ^{31}P CPMAS spectra for both nickel complexes **7** and **8** show single peaks at 77.3 ppm and 59.7 ppm, respectively. This large chemical shift difference can be in principle attributed to two distinct, but possibly convergent, effects: the strength of the P–O–H–N interactions, and the electronic reorganization within the RPS_2O fragments, with different hybridization and double bond character of the P=O bond. These subtle effects will be further considered when discussing the X-ray diffraction results (vide infra). The finding of an individual peak for both complexes indicates that only one phosphorus environment is present in the structure, and that the complex must lie about a crystallographic symmetry element. This also suggests that both species crystallize in a unique isomeric form, also in agreement with the crystallographic features which identify the *trans* isomer.

2.4. Crystal and molecular structure of species 7 and 8

Both complexes **7** and **8** crystallize in the triclinic space group $P\bar{1}$. The asymmetric unit of the former species comprises half a Ni(II) ion, lying about a crystallographic inversion centre, one phosphodithiolate ligand (L) and one pyrazole moiety. Whether the latter is a true neutral Hpz molecule, a pyrazolium cation (H_2pz^+) or an intermediate form is not relevant, since an extended network of hydrogen-bonds shows that the acidic hydrogen atoms are shared, in the solid, in the different D–H···A wells.

Also in species **8**, a centrosymmetric $[NiL_2]^{2-}$ complex is present, hydrogen-bonded to one triethylammonium cation on each side. As can be appreciated in Figs. 4 and 5, in both **7** and **8**, the metal centre is tetracoordinated in square planar geometry by four sulfur atoms belonging to two distinct L ligands. Thus, in both compounds, the L moiety acts as a S,S′-chelating ligand, promoting comparable Ni–S bonds of about 2.22 Å and similar S–Ni–S angles of about 88° and 92° (Table 2). Within both $[NiL_2]^{2-}$ complexes, the 4-methoxyphenyl and oxo substituents on each phosphorous atom adopt a *trans* disposition with respect to the mean plane individuated by the NiS_2P_2 moiety, in agreement with the ^{31}P CPMAS NMR observations of a unique isomer and magnetically equivalent P nuclei.

In **7**, the pyrazole ligand is not coordinated to the metal centre. Nevertheless, both nitrogen atoms are involved in hydrogen bond interactions of about 2.65 Å with the oxo substituents of L ligands belonging to two distinct, adjacent $[NiL_2]^{2-}$ complexes (Fig. 6). The presence of such a hydrogen bond implies a slight (yet statistically significant) lengthening of the P–O bond distance, being 1.538(2) Å in complex **7** versus 1.502(2) Å in **8**. It is worth noting that even in species **8** the oxo substituent is involved in a hydrogen bond interaction of about 2.7 Å with the nitrogen atom of an adjacent triethylammonium cation. The different number (and type) of P=O–H–N bonds in **7** and **8** (Table 1) thus affects the local electronic distribution at the P=O

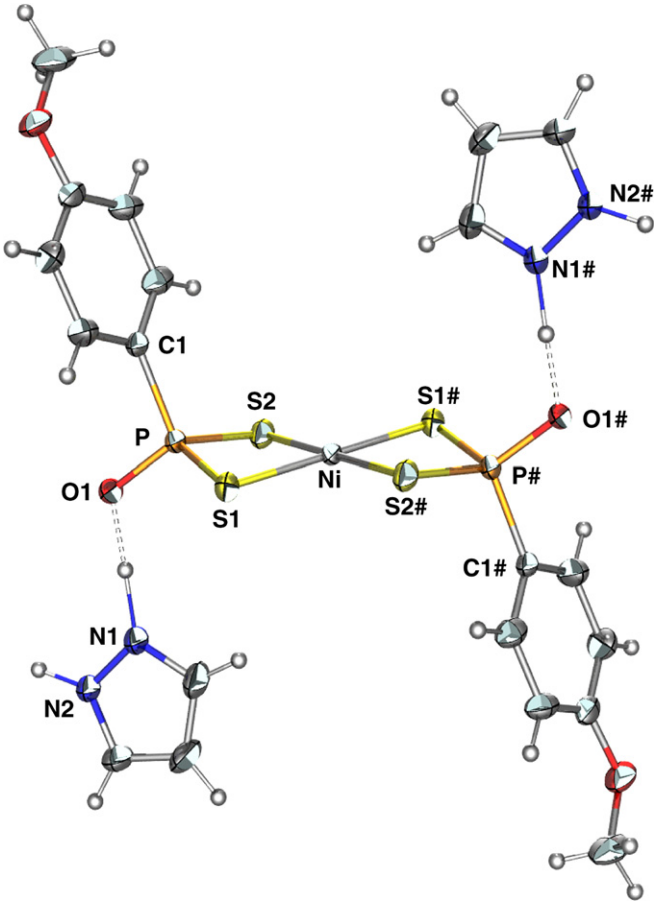


Fig. 4. ORTEP representation (30% probability level) of the molecular structure in complex **7**. Carbon, grey; hydrogen light grey; nitrogen, blue; oxygen, red; phosphorous, orange; sulfur, yellow; nikel, grey. The N–H···O hydrogen bonds between the $[NiL_2]^{2-}$ anion and the pyrazole ligands have been depicted through dashed lines (both the hydrogen atoms involved in this interaction have been arbitrarily assigned to the nitrogen atoms of the pyrazole ligand). #: $[-x, -y, -z]$. (For interpretation of the references to colour in this figure legend, the reader is referred to the web version of this article.)

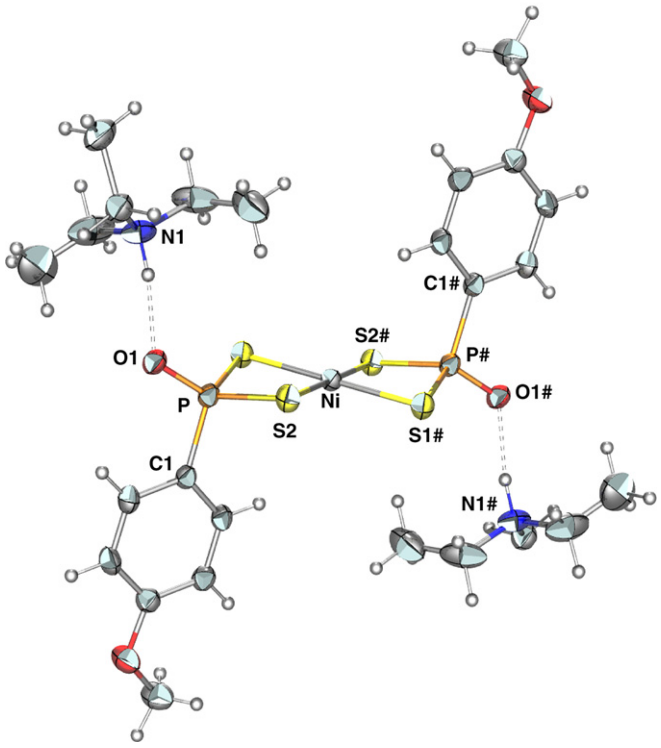


Fig. 5. ORTEP representation (30% probability level) of the $[NiL_2]$-$(HNEt_3)$ moiety present in complex **8**. Carbon, grey; hydrogen light grey; nitrogen, blue; oxygen, red; phosphorous, orange; sulfur, yellow; nickel, grey. The N–H···O hydrogen bond interactions between the $[NiL_2]^{2-}$ anion and the triethylammonium cations have been depicted through dashed lines. The labelling scheme used throughout the manuscript is highlighted. #: $[-x, -y, -z]$. (For interpretation of the references to colour in this figure legend, the reader is referred to the web version of this article.)

fragment; this is also counterbalanced by the slight lengthening (ca. 0.01 Å, i.e. 10σ) of the P–S bonds; these subtle effects may be likely considered responsible for the downfield shift of the ^{31}P peak in the CPMAS spectrum of **7** (with respect to that of **8**), as mentioned above.

As appreciable in Fig. 6, and thanks to the ditopic nature of the pyrazolium cations, the intermolecular interactions present in **7** generate monodimensional chains running in the [1 0 1] direction. At variance, no extended network can exist in **8** and centrosymmetric molecules surrounded each by two triethylammonium cations are present.

3. Experimental

3.1. Materials and methods

Pyrazole (HPz), Lawesson's reagent and salts were used as supplied (Aldrich Chemical Co.). Solvents were dried and distilled by standard methods. All preparations and manipulations were carried out under dinitrogen atmosphere using conventional Schlenk techniques. *Caution:* Perchlorate salts in the presence of transition metal ions

Table 2
Relevant bond distances (Å) and angles (°) for species **7** and **8**

Parameter	7	8
Ni–S1	2.2205(8)	2.218(1)
Ni–S2	2.2243(9)	2.223(1)
P–S1	2.022(1)	2.032(1)
P–S2	2.019(1)	2.031(1)
P–O1	1.538(2)	1.502(2)
P–C1	1.802(3)	1.811(3)
N···O	2.657(3), 2.639(5)	2.689(4)
S1–Ni–S2	87.86(3), 92.14(3)	87.66(4), 92.34(4)
S1–P–S2	99.48(5)	98.36(5)
S1–P–O1	113.91(1)	116.3(1)
S2–P–O1	115.8(1)	116.2(1)
O1–P–C1	106.0(1)	107.7(1)
S1–P–C1	111.1(1)	108.7(1)
S2–P–C1	110.6(1)	109.0(1)
N–H···O	174(4), 177(9)	172(3)

For the labelling scheme, see Figs. 3 and 4.

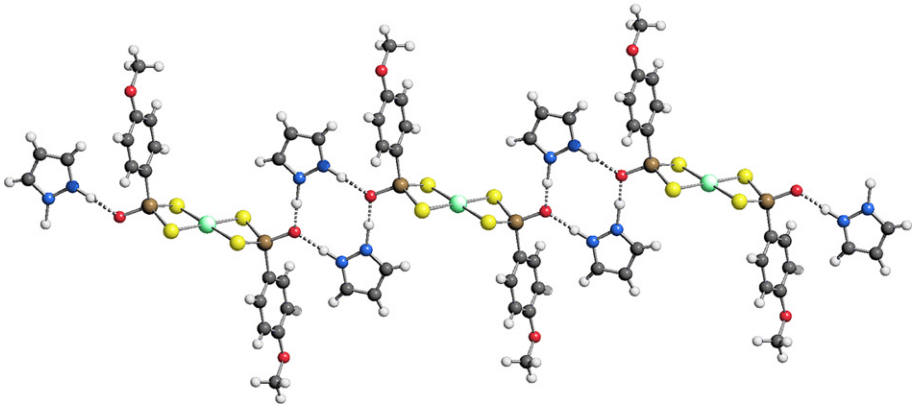


Fig. 6. Schematic representation of the monodimensional chains created by the hydrogen bond interactions (dashed lines) in complex **7**. Carbon, grey; hydrogen light grey; nitrogen, blue; oxygen, red; phosphorous, brown; sulfur, yellow; nickel, light green. (For interpretation of the references to colour in this figure legend, the reader is referred to the web version of this article.)

and organic material are potentially explosive and should be handled with care!

Infrared spectra were recorded on a Shimadzu Prestige-21 instrument. Elemental analyses were carried out on a Perkin–Elmer CHN Analyzer 2400 series II.

NMR spectra were recorded using a Bruker ADVANCE 400 spectrometer, employing for solid state experiments a 4 mm double bearing MAS probe. The standard ^{1}H, ^{13}C and ^{31}P spectra in solution were carried out in acetone (methanol for **8**) at room temperature. For the solid samples ^{31}P cross-polarization magic-angle spinning (CPMAS) spectra were recorded using a recycle time of 4 s, contact times of 1 ms and spinning rates of 10 kHz. ^{31}P single pulse excitation (SPE) experiments with high power proton decoupling were recorded with recycle times of 5 s. The CPMAS experiment select the most hindered carbons, those in the crystalline phase, whereas the SPE experiment acquired with a recycle delay of 5 s selects more mobile carbons (5 s is not enough for complete relaxation of rigid carbons). The ^{31}P spectra were referenced with respect to 85% aqueous H_3PO_4 by setting the ^{31}P NMR peak of poly crystalline ammonium dihydrogenphosphate to +2.5 ppm. The ^{13}C CPMAS spectra were recorded using a recycle time of 5 s, contact times of 1 ms, spinning rates of 7 kHz. Both ^{31}P and ^{13}C solid-state NMR spectra were recorded at room temperature and were transformed using a line broadening of 20 Hz. The number of scans (NS) are indicated in the figure captions.

3.2. Synthesis of species 5–8

3.2.1. Synthesis of 5

To a suspension of the Lawesson's reagent $[S_2P(\mu\text{-}C_6H_4\text{-}OMe)]_2$ (0.404 g; 1.0 mmol) in wet toluene (15 ml), pyrazole was added (0.680 g; 10.0 mmol). The reaction mixture was kept under stirring for 4 h at 333 K, then the white compound was filtered off, washed with toluene and dried under vacuum. IR (nujol): strong and broad absorption band at 1869 cm^{-1} assigned to hydrogen bonds of either the N–H···O, or, for the formulation reported in footnote 1, the N–H···N type [22,23]. *Anal.* Calc. for $C_{13}H_{17}N_4O_2PS_2$ (356.4 g mol^{-1}): C, 43.81; H, 4.81; N, 15.72. Found: C, 44.12; H, 4.67; N, 15.76%. δ_H (400 MHz; CD_3COCD_3; Me_4Si) 9.3 (1H, b s, N–H/O–H), 7.99 (2H, m, Ph), 7.76 (4H, s, $C(3,5)_{pz}$-H), 7.05 (2H, m, Ph), 6.33 (2H, s, $C(4)_{pz}$-H), 3.88 (3H, s, OCH_3) – δ_C (100 MHz; CD_3COCD_3; Me_4Si) 162.7 (Ph), 133.6 ($C_{pz}(3,5)$), 132.7 (Ph), 113.8 (Ph), 105.0 [$C_{pz}(4)$], 55.4 (OCH_3) – δ_P (162 MHz; CD_3COCD_3; H_3PO_4) 78.6 (s) – δ_P (162 MHz; solid state): 97.3 (s), 94.5 (s).

3.2.2. Synthesis of 6

The Lawesson's reagent (0.404 g; 1.0 mmol) and pyrazole (0.680 g; 1.0 mmol) were heated at 75 °C in a sealed flask under nitrogen atmosphere and under stirring for 4 h. The mixture was then allowed to cool and solidify giving a white compound. The residue was then washed many times with anhydrous toluene in order to eliminate excess of pyrazole and to solidify the sample. δ_P (162 MHz; CD_3COCD_3; H_3PO_4) 72.8 (s) – δ_P (162 MHz; solid state): 82.3 (s).

3.2.3. Synthesis of 7

To a solution of $Ni(ClO_4)_2 \cdot 6H_2O$ (0.150 g; 4.2×10^{-1} mmol) in acetonitrile (4 ml), at room temperature and under inert atmosphere, species **5** (0.300 g; 8.4×10^{-1} mmol) was added in one portion. The reaction mixture was kept under stirring for 2 h, then filtered off, washed with acetonitrile and dried under vacuum (yield: 80.2%). IR (nujol): absorption at 1870 cm^{-1}. *Anal.* Calc. for $C_{20}H_{24}N_4O_4S_4P_2Ni$ (633.3 g mol^{-1}): C, 37.93; H, 3.82; N, 8.85. Found: C, 37.82; H, 3.73; N, 8.64%. δ_H (400 MHz; CD_3COCD_3; Me_4Si) 8.12 (2H, m, Ph), 7.12 (2H, m, Ph), 4.19 (1H, b s, N–H/O–H), 3.92 (3H, s, OCH_3) – δ_P (162 MHz; CD_3COCD_3; H_3PO_4) 85 (b s) – δ_P (162 MHz; solid state): 77.3 (s). Crystals suitable for

an X-ray structure determination were obtained by slow diffusion of dichloromethane into an acetone solution of **7**.

3.2.4. Synthesis of 8

To a stirred solution of $Ni(ClO_4)_2 \cdot 6H_2O$ (0.150 g; 4.2×10^{-1} mmol) in acetonitrile (4 ml) at room temperature and under inert atmosphere, **5** (300 g; 8.4×10^{-1} mmol) was added in one portion. After a couple of minutes, Et_3N (0.800 ml) was added dropwise. The brown solid formed was stirred under dinitrogen atmosphere for 2 h, then filtered out, washed with acetonitrile and acetone and dried under vacuum (yield: 84.3%). *Anal.* Calc. for $C_{26}H_{44}N_2O_4S_4P_2Ni$ (699.5 g mol^{-1}): C, 44.63; H, 6.58; N, 4.00. Found: C, 44.82; H, 6.66; N, 4.07%. δ_H (400 MHz; CD_3COCD_3; Me_4Si) 8.24 (2H, m, Ph), 6.98 (2H, m, Ph), 4.83 (1H, b s, N–H/O–H), 3.87 (3H, s, OCH_3), 3.28 (12 H, q, CH_2), 1.35 (18 H, t, CH_3) – δ_P (162 MHz; CD_3COCD_3; H_3PO_4) 69.4 (b s) – δ_P (162 MHz; solid state): 59.7 (s). Crystals suitable for an X-ray structure determination were obtained by slow diffusion of diethyl ether into a methanol solution of **8**.

3.3. X-ray crystallography

Species **7** and **8** crystallize as violet and brown single crystals suitable for X-ray diffraction. Crystals of approximate $0.20 \times 0.14 \times 0.06$ and $0.30 \times 0.20 \times 0.05$ mm dimensions (for **7** and **8**, respectively) were glued on the tip of a glass fibre and mounted on top of a goniometer head. The data were collected using graphite-monochromated Mo Kα radiation ($\lambda = 0.71073$ Å) on Bruker AXS SMART (**7**) or Enraf Nonius CAD-4 (**8**) automated diffractometers. In the first case, the unit cell was determined by acquiring 60 frames (44 reflections) at different ω and ϕ goniometer angles. In the latter, the unit cell was determined on the basis of the setting angles of 25 intense, randomly distributed, reflections with θ in the 9–12° range. A total of 9989 and 3254 reflections, in the $2.3° < \theta < 30.0°$ and $3.0° < \theta < 25.0°$ range (for **7** and **8**, respectively), were collected in the ω-scan mode [SMART: $\Delta\omega = 0.3°$; CAD-4: $\Delta\omega = 0.8 + (0.35\tan\theta)$]. Generator settings: 45 kV, 40 mA (SMART); 50 kV, 30 mA (CAD-4). The data were corrected for Lorenz-polarization and for absorption effects [24,25]. The structure solutions and refinements were performed by direct methods (SIR-97) [26] and full-matrix least-squares procedures on F^2 (SHELX-97) [27], respectively, as implemented in the WinGX suite of programs. All non-hydrogen atoms were treated anisotropically. Hydrogen atoms were made riding on the pertinent parent atoms with an isotropic thermal displacement parameter arbitrarily chosen as 1.2 times that of the parent atom itself. In the case of complex **7** both hydrogen atoms involved in the P–O–H–N hydrogen bond interactions were arbitrarily assigned to the nitrogen atoms. Further details of the crystal structure analyses can be found in Table 3.

Table 3
Crystallographic data and structure refinement parameters for species **7** and **8**

Compound	**7**	**8**
Method	single-crystal XRD	single-crystal XRD
Formula	$C_{20}H_{24}Ni_1N_4O_4P_2S_4$	$C_{26}H_{46}Ni_1N_2O_4P_2S_4$
Formula weight (g mol^{-1})	633.3	699.6
T (K)	298(2)	298(2)
λ (Å)	0.71073	0.71073
Crystal system	triclinic	triclinic
Space group	$P\bar{1}$	$P\bar{1}$
a (Å)	8.484(1)	7.719(3)
b (Å)	9.856(1)	9.122(3)
c (Å)	10.114(1)	13.220(1)
α (°)	109.217(2)	77.81(2)
β (°)	99.837(2)	87.79(2)
γ (°)	113.666(2)	71.70(3)
V (Å^3)	685.1(1)	863.5(4)
Z	1	1
ρ_{calc} (Mg m^{-3})	1.535	1.345
μ (mm^{-1})	1.164	0.928
$F(000)$	326	370
θ Range (°)	2.3–30.0	3.0–25.0
Collected hkl	$-11 \leqslant h \leqslant 11$, $-13 \leqslant k \leqslant 13$, $-14 \leqslant l \leqslant 14$	$0 \leqslant h \leqslant 9$, $-10 \leqslant k \leqslant 10$, $-15 \leqslant l \leqslant 15$
Measured/ independent reflections	9989/3970	3254/3010
Absorption corrections	empirical	empirical
Refinement method	full-matrix least-squares on F^2	full-matrix least-squares on F^2
Data/restrain/ parameter	3970/0/168	3010/0/182
$S(F^2)$[a]	0.900	1.018
$R(F)$, $wR(F^2)$[b] $[I > 2\sigma I]$	0.097, 0.122	0.059, 0.086
$R(F)$, $wR(F^2)$[b] (all)	0.047, 0.105	0.038, 0.078
Maximum and minimum $\Delta\rho$ (e Å^{-3})	0.96 and −0.57	0.40 and −0.26

[a] $S(F^2) = [\sum w(F_o^2 - F_c^2)^2/(n-p)]^{1/2}$ where n is the number of reflections, p the number of parameters and $w = 1/[\sigma^2(F_o^2) + (0.019P)^2 + 1.88P]$ with $P = (F_o^2 + 2F_c^2)/3$.

[b] $R(F) = \sum||F_o| - |F_c||/\sum|F_o|$ and $wR(F^2) = [\sum w(F_o^2 - F_c^2)^2/\sum wF_o^4]^{1/2}$.

4. Conclusions

The syntheses and spectroscopic characterization of the new, S-donor 4-methoxophenyldithiophosphonate ligand (L) have been described. Its coordination properties have been investigated towards the Ni(II) metal centre, and the structural characterization of two salts, containing the centrosymmetric *trans*-$[NiL_2]^{2-}$ anion, has been performed. The extensive solution and solid state multinuclear characterization has allowed to determine the nature of labile intermediates, which could neither be isolated as single crystals nor as *air stable* polycrystalline materials.

Work is in progress, aiming at obtaining distinct thiophosphonate salts of higher stability to be used in the

formation of new metal complexes, by employing differently substituted pyrazoles, and new characterization techniques, such as ab initio X-ray powder diffraction methods [28].

Acknowledgments

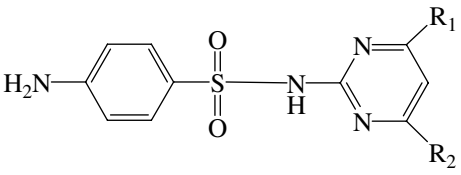
This work was supported by the Ministero dell'Università e della Ricerca (MIUR). We deeply thank Prof. N. Masciocchi, University of Insubria, for helpful discussions.

Appendix A. Supplementary material

Crystallographic data (excluding structure factors) for the two crystal phases have been deposited with the Cambridge Crystallographic Data Centre. CCDC 606670 and 606671 contain the supplementary crystallographic data for this paper. These data can be obtained free of charge via http://www.ccdc.cam.ac.uk/conts/retrieving.html, or from the Cambridge Crystallographic Data Centre, 12 Union Road, Cambridge CB2 1EZ, UK; fax: (+44) 1223-336-033; or e-mail: deposit@ccdc.cam.ac.uk. Supplementary data associated with this article can be found, in the online version, at doi:10.1016/j.poly.2006.09.077.

References

[1] N.K. Roy, Pesticides A 13 (1990) 1989.
[2] A.J. Burn, I. Gosney, C.P. Warrens, J.P. Wastle, J. Chem. Soc., Perkin Trans. 2 (1995) 265.
[3] C.C. Chavdarian, O-(substituted benzyl) dithiophosphonate insecticides. Stauffer Chemical Co., US Patent 4,683,225, 1987.
[4] C.C. Chavdarian, O-(substitued allylic) dithiophosphonate insecticides. Stauffer Chemical Co., US Patent 4,656,164, 1987.
[5] D. Klaman (Ed.), Lubrificants and Related Products, Verlag Chemie, Weinheim, 1984.
[6] J.M. Dumdum, L.T. Mendelson, R.L. Pilling, US Patent 4,908,142, 1990, Chem. Abstr. 112 (1990) 201925.
[7] I. Haiduc, D.B. Sowerby, S.F. Lu, Polyhedron 14 (1995) 3389.
[8] I. Haiduc, J. Organomet. Chem. 623 (2001) 29.
[9] P.G. Harrison, M.J. Begley, T. Kikabhai, F. Killer, J. Chem. Soc., Dalton Trans. (1986) 925.
[10] A.J. Burn, I. Gosney, C.P. Warres, J.P. Wastle, J. Chem. Soc., Perkin Trans. 2 (1995) 265.
[11] (a) E. Livingstone, A.E. Mikhelson, Inorg. Chem. 9 (1970) 2545;
(b) R. Engel, Chem. Rev. 77 (1976) 349;
(c) R. Engel, in: R.L. Heildebrand (Ed.), The Role of Phosphonates in Living System, CRC Press, Boca Raton, FL, 1983, p. 93;
(d) G.R.J. Thatcher, A.S. Campbell, J. Org. Chem. 58 (1993) 2272;
(e) M. de Fernandez, C.P. Vlaas, H. Fan, Y.H. Liu, F.R. Fronczek, R.P. Hammer, J. Org. Chem. 60 (1995) 7390.
[12] (a) W.E. van Zyl, J.P. Fackler, Phosphorus, Sulfur Silicon 167 (2000) 117;
(b) J.R. Wasson, G.M. Woltermann, H. Stoklosa, J. Fortschr. Chem. Forsch. (Top. Curr. Chem.) 35 (1973) 65;
(c) W. Kuchen, H. Hertel, Angew. Chem., Int. Ed. Engl. 8 (1969) 89;
(d) R.C. Mehrotra, G. Svrivastava, B.P.S. Chauhan, Coord. Chem. Rev. 55 (1984) 207.
[13] (a) B. Yed, N.M. Yousif, U. Pedersen, I. Thomsen, S.-O. Lawesson, Tetrahedron 40 (1984) 2047;
(b) S. Scheibye, R. Shabana, S.-O. Lawesson, Tetrahedron 38 (1982) 993.
[14] (a) V.G. Albano, M.C. Aragoni, M. Arca, C. Castellari, F. Demartin, F.A. Devillanova, F. Isaia, V. Lippolis, L. Loddo, G. Verani, Chem. Commun. (2002) 1170;
(b) M.C. Aragoni, M. Arca, F. Demartin, F.A. Devillanova, F. Isaia, V. Lippolis, G. Verani, Inorg. Chim. Acta 358 (2005) 213.
[15] A. Maspero, I. Kain, A.A. Mohamad, M.A. Omary, RJ. Staples, J.P. Fackler, Inorg. Chem. 42 (2003) 311.
[16] W.E. van Zyl, J.P. Fackler, Phosphorus, Sulfur Silicon 167 (2000) 117.
[17] Available from: <http://www.chem.wisc.edu/areas/reich/handouts/nmr-h/data157.gif>.
[18] K. Clausen, A.A. El-Barbary, S.-O. Lawesson, Tetrahedron 37 (1981) 1019.
[19] M.C. Aragoni, M. Arca, F. Demartin, F.A. Devillanova, G. Graiff, F. Isaia, V. Lippolis, A. Tiripicchio, G. Verani, Eur. J. Inorg. Chem. (2000) 2239.
[20] O. Hager, A.L. Llamas-Saiz, C. Foces-Foces, R.M. Claramunt, C. Lopez, J. Elguero, Helv. Chim. Acta 82 (1999) 2213.
[21] H.H. Limbach, G.S. Denisov, S. Golubev, in: A. Kohen, H.H. Limbach (Eds.), Hydrogen Bond Isotope Effects Studied by NMR, CRC Press/Taylor & Francis, Boca Raton, FL/London, 2005, p. 193 (Chapter 7).
[22] M.K. Ehlert, S.J. Rettig, A. Storr, R.C. Thompson, J. Trotter, Can. J. Chem. 68 (1990) 1494.
[23] M.K. Ehlert, S.J. Rettig, A. Storr, R.C. Thompson, J. Trotter, Can. J. Chem. 71 (1993) 1425.
[24] Complex **7**: G. Sheldrick, B. Blessing, Acta Crystallogr., Sect. A 51 (1995) 33.
[25] Complex **8**: A.C.T. North, D.C. Phillips, F.S. Mathews, Acta Crystallogr., Sect. A 24 (1968) 351.
[26] A. Altomare, M.C. Burla, M. Camalli, G.L. Cascarano, C. Giacovazzo, A. Guagliardi, A.G.G. Moliterni, G. Polidori, R. Spagna, J. Appl. Crystallogr. 32 (1999) 115.
[27] G.M. Sheldrick, SHELX-97: Program for Crystal Structure Determination, University of Göttingen, Göttingen, Germany, 1997.
[28] N. Masciocchi, S. Galli, A. Sironi, Comments Inorg. Chem. 26 (2005) 1.



Sulfadiazine (sdr) when R_1 and R_2 are hydrogen (H)
Sulfamerazine (smr) when R_1 is H and R_2 is methyl group (CH_3)
Sulfamethazine (smz) when R_1 and R_2 are methyl group (CH_3)

The diversity of the coordination numbers for the mercury complexes can be found in the literature. In mono-organomercury(II) compounds, the primary bonds leave the Hg atom with enough residual acidity for it to be able to reach a coordination number of six when the donor atoms forming the secondary bonds are small. There are only a small number of Hg complexes with coordination number two [15]. However, Hg(II), has an extremely high affinity for thiol-containing compounds, and forms 1:2 metal: ligand linear complexes with them [16].

In this context, we will discuss the syntheses, spectroscopic characterization and X-ray crystal structure determination of the Hg complexes of sulfa drugs sulfamerazine sulfadiazine and sulfamethazine.

2. Experimental

2.1. General procedures

Analar grade chemicals (SIGMA and BDH) were used as received. CHN microanalysis was carried out using a Perkin–Elmer 2400 CHN elemental analyzer. The IR spectra were recorded on a Nicolet 510 FTIR spectrometer, each compound was pressed into a KBr disk that was prepared in a sample holder by compressing a powdered sample with a 20-fold excess of dry KBr. NMR spectra were recorded on a Bruker Avance AMX-400 spectrometer. ^{1}H and ^{13}C NMR spectra were obtained from a solution of the compounds in d_6-DMSO. The chemical shifts are expressed in ppm relative to internal TMS.

2.2. X-ray crystallography

The crystallographic measurements for the complexes were made at 150 K on a Bruker Nonius Kappa CCD area detector using graphite monochromatised Mo Kα radiation, $\lambda = 0.71073$ Å. The structures were solved by direct methods (SHELXS-97) [17] and refined on F^2 by full-matrix least squares (SHELXL-97) [18] using all unique data and parameters. The absorption correction was made by multi-scan method [19]. The hydrogen atoms on the amino groups of sulfa drugs in the complexes were located from the difference Fourier maps and refined freely.

2.2.1. Preparation of the complex $[Hg(sdz)_2(DMF)_2]$ (1)

Sodium salt of sulfadiazine (0.545 g, 2 mmol) was dissolved in hot methanol and to this, a methanolic solution of $(CH_3COO)_2Hg$ (0.319 g, 1 mmol) was added with constant stirring. A white precipitate was formed and stirring continued for 6 h. It was filtered and dried over silica gel in a dessicator. The precipitate was dissolved in DMF and a few drops of ammonia was added and stirred for 30 min. The solution was filtered and left to crystallize. A few days later, white block crystals were obtained. The compound is soluble in DMF and DMSO but insoluble in water, alcohol and acetonitrile. Anal. Found: C, 36.89, H, 3.85; N, 16.53%. Calc. for $C_{26}H_{32}HgN_{10}O_6S_2$: C, 36.94; H, 3.82; N, 16.57%. IR: (KBr disc): cm^{-1}, 3467(s), 3365(s), 3048(m), 2930, 1655(s), 1614(vs), 1588(vs), 1557(vs), 1506(vs), 1440(sh), 1414(vs), 1342(s), 1291(vs), 1184(w), 1127(sh), 1086(s), 994(w), 958(w), 907(s), 820, 682(s), 651(w), 574(vs), 547(vs), 518(vw), 457(vw), 416(w); ^{1}H NMR (400 MHz, DMSO-d_6): δ 8.50 [2H, d, $J = 4.9$, C(12/14)], 7.78 [2H, d, $J = 8.5$, C(16/20)], 6.98 [1H, t, $J = 4.8$, C(13)], 6.56 [2H, d, $J = 8.6$, C(17/19)], 5.92 [2H, s, (–NH_2)]. ^{13}C NMR (100.6 MHz, DMSO-d_6): δ 162.7 [C(12/14)], 158.8 [C(11)], 153.0 [C18], 130.6 [C(16/20)], 126.1 [C(15)], 114.7 [C(13)], 112.4 [C(17/19)].

2.2.2. Preparation of the complex $[Hg(smr)_2]$ (2)

As with the previous experiment, but sulfamerazine (0.530 g, 2 mmol) was used instead of sodium sulfadiazine. The compound is soluble in DMF and DMSO but insoluble in water, alcohol and acetonitrile. Anal. Found: C, 36.59, H, 3.02; N, 15.57%. Calc. for $C_{22}H_{22}HgN_8O_4S_2$: C, 36.34; H, 3.05; N, 15.41%. IR: (KBr disc): cm^{-1}, 3436(s), 3317(s), 3228(m), 1632(vs), 1598(vs), 1571(vs), 1501(vs), 1465(sh), 1435(vs), 1392(vs), 1371(s), 1332(m), 1310(sh), 1281(vs), 1259(m), 1189(m), 1135(sh), 1093(s), 1010(w), 971(w), 945(w), 917(s), 869(w), 823, 792(s), 769(vw), 716(vw), 689(s), 635(w), 582 (vs) and 546; ^{1}H NMR (400 MHz, DMSO-d_6): δ 8.37 [1H, d, $J = 5.1$, C(14)], 7.84 [2H, d, $J = 8.5$, C(16, 20)], 6.92 [2H, d, $J = 5.1$, C(17, 19)], 6.63 [1H, d $J = 8.8$, C(13)], 5.97 [2H, s, (–NH_2)], 2.39 [3H, s, (CH_3)]. ^{13}C NMR (100.6, DMSO-d_6): δ 168.4 [C(11)], 161.4 [C(12)], 158.3 [C(14)], 152.9 [C(18)], 130.8 [C(15)], 126.2 [C(16/20)], 114.1 [C(17/19)], 112.2 [C(13)], 23.6 [CH_3].

2.2.3. Preparation of the complex $[Hg(smz)_2(DMF)_2]$ (3)

With the same procedure in experiment 2.2.1 except the sodium salt of sulfamethazine (0.601 g, 2 mmol) was used instead of sodium sulfadiazine. The compound is soluble in DMF and DMSO but insoluble in water, alcohol and acetonitrile. Anal. Found: C, 39.72, H, 4.58; N, 15.51%. Calc. for $C_{30}H_{40}HgN_{10}O_6S_2$: C, 39.97; H, 4.47; N, 15.54%. IR: (KBr disc): cm^{-1}, 3457(s), 3360(s), 3247(m), 2919, 1660(vs), 1599(vs), 1577(vs), 1547(vs), 1506, 1429(sh), 1393(vs), 1373(s), 1332(m), 1292(vs), 1258(m), 1194 (w), 1137(sh), 1086(s), 994(w), 965, 897(w), 820, 779(vw), 682(s), 635(w), 589(vs), 549(vs). ^{1}H NMR (400 MHz, DMSO-d_6): δ 7.80 [2H, d, $J = 8.6$ Hz, C(16/20)], 6.57 [2H, d, $J = 8.7$, C(17/19)], 6.69 [1H, s, C(13)], 5.90 [2H, s, (–NH_2)], 2.51 [6H, s, CH_3]. ^{13}C NMR

(DMSO-d_6): δ 167.9 [C(11)], 159.6 [C(12/14)], 152.8 [C(18)], 131.0 [C(15)], 126.3 [C(16/20)], 113.1 [C(17/C19)], 112.0 [C(13)], 23.5 [CH_3].

3. IR spectra

The infrared spectra of the complexes taken in the region 4000–400 cm^{-1} were compared with those of the free ligands. The bands that appear between 3500 and 3400 cm^{-1} due to asym(NH_2) and sym(NH_2) vibrations of the amino (–NH_2) group [13–20] are modified with respect to those of the free respective ligands. These modifications are most probably due to the hydrogen bonding between complexes involving the NH_2 and SO_2 groups.

The peak for the sulfonamidic (N–H) group in the free ligands at around 3125 cm^{-1}, are not present in the spectra of the complexes, confirming the deprotonation of the –SO_2NH– moiety. The scissoring vibrations for the amino (–NH_2) groups appear in the range of 1614–1662 cm^{-1} and peaks due to phenyl ring appear at around 1547 and 1600 cm^{-1}. The peaks around 1325 and 1331 cm^{-1} are assigned to $\nu_{as}(SO_2)$, and those at 1155–1157 cm^{-1} to $\nu_{sy}(SO_2)$, show significant changes upon complexation. The first one splits into two peaks at 1291–1386 cm^{-1} and the second appears at around 1131–1194 cm^{-1} in the complexes.

The 945–965 cm^{-1} bands in the ligands are assigned to ν(S–N) [20] and are at higher frequencies (958–1046 cm^{-1}) in all cases, as a consequence of coordination to the metal. This shift to higher frequencies is in accordance with the shortening of the S–N bond lengths, which have been observed in the crystal structures of complexes (see Table 1).

4. ^{1}H NMR and ^{13}C NMR spectra

Due to these compounds being insoluble in less polar solvents, ^{1}H and ^{13}C NMR spectra were obtained from a solution of the complex in d^6-DMSO. The chemical shifts are expressed in ppm relative to internal TMS. The NMR data is presented in Tables 2–4. The data shows that while the ligands are present in the complex, they only display very small shifts in comparison to the free ligands. The most notable feature is the sulfonamidic proton and correspondingly the relatively large shift of the carbon signal (C11) next to the amide. Whether or not the structure of the complex is retained in solution, or if it exists as solvated cation and ligand anion can not be determined from these spectra.

5. Crystal structure of the complexes 1, 2 and 3

Single crystals suitable for X-ray determination were obtained for the complexes by the slow evaporation of a DMF solution of the complex, in the presence of NH_3. The crystal data and refinement details for the complexes are listed in Table 5.

The crystal structures of the complexes [Hg(sdz)$_2$(DMF)$_2$] (**1**), [Hg(smr)$_2$] (**2**) and [Hg(smz)$_2$(DMF)$_2$] (**3**) are shown in Figs. 1,3, and 5, respectively together with the crystallographic atom numbering scheme used. The selected bond lengths and angles are collected together in Table 6.

The complexes [Hg(sdz)$_2$(DMF)$_2$] (**1**) and [Hg(smz)$_2$(DMF)$_2$] (**3**) have a '2+6' geometry with the Hg atom lying on the two-fold axis. Both molecules contain two short Hg–N(11) amide distances (2.047(3)–2.050(3) Å) as well

Table 1
The IR spectra of the compounds **1**–**3**

Complexes	–NH_2	δNH_2	Phenyl rings	(SO_2)as	(SO_2)sy	S–N
1	3467, 3365	1614	1588, 1557	1342, 1291	1184	994, 958
2	3436, 3317	1632	1598, 1571	1371, 1281	1189	1010, 971
3	3457, 3360	1660	1599, 1577	1373, 1292	1194	994, 965

Table 2
^{1}H NMR and ^{13}C NMR shift assignment of sulfadiazine and its Hg complex [Hg(sdz)$_2$(DMF)$_2$] (**1**) in DMSO-d_6[a]

Assignment	^{1}H(HsdzH)	^{1}H1	^{13}C(HsdzH)	^{13}C1	$\Delta\delta$ (H)[b]	$\Delta\delta$ (C)[b]
N(11)–H	11.35					
C(11)			158.6	162.7		+4.1
C(12)–H/C(14)–H	8.50	8.48	157.5	158.8	−0.02	+1.3
C(13)–H	7.00	6.98	115.9	114.7	−0.02	−1.2
C(15)			125.1	126.1		+1.8
C(16)–H/C(20)–H	7.75	7.78	130.3	130.6	+0.03	+0.3
C(17)–H/C(19)–H	6.58	6.56	112.6	112.4	−0.02	−0.2
C(18)			153.4	153.0		−0.4
NH_2	6.00	5.92			+0.08	

[a] Relative to TMS with DMSO-d_6 peak as reference (^{1}H, 2.60 ppm, ^{13}C, 43.5 ppm).
[b] $\Delta\delta = \delta_{(complex)} - \delta_{(sdz)}$.

Table 3
^{1}H NMR and ^{13}C NMR shift assignment of sulfamerazine and its Hg complex [Hg(smr)$_2$] (**2**) in DMSO-d$_6$[a]

Assignment	^{1}H(smrH)	^{1}H2	^{13}C(smrH)	^{13}C2	$\Delta\delta$ (H)[b]	$\Delta\delta$ (C)[b]
N(11)–H	11.20					
C(11)			164.3	168.4		+4.1
C(12)			157.5	161.4		+3.9
C(13)–H	6.62	6.63	112.1	112.2	+0.01	+0.1
C(14)–H	8.37	8.37	156.8	158.3	0.00	+1.5
C(15)			130.1	130.8		+0.7
C(16)–H/C(20)–H	7.69	7.84	124.9	126.2	+0.15	+1.3
C(17)–H/C(19)–H	6.95	6.92	114.7	114.1	−0.03	−0.6
C(18)			152.9	152.9		0.0
NH_2	6.07	5.97			−0.10	
CH_3	2.41	2.39	23.3	23.6	−0.02	+0.3

[a] Relative to TMS with DMSO-d_6 peak as reference (^{1}H, 2.60 ppm, ^{13}C, 43.5 ppm).
[b] $\Delta\delta = \delta_{(complex)} - \delta_{(smr)}$.

Table 4
^{1}H NMR and ^{13}C NMR shift assignment of sulfamethazine and its mercury complex (**3**) in DMSO-d$_6$[a]

Assignment	^{1}H(smzH)	^{1}H3	^{13}C(smzH)	^{13}C3	$\Delta\delta$ (H)[b]	$\Delta\delta$ (C)[b]
N(11)–H	11.20					
C(11)			165.6	167.9		+2.3
C(12)/C(14)			157.0	159.6		+2.6
C(13)–H	6.45	6.57	112.3	113.1	+0.12	+0.8
C(15)			130.8	131.0		−0.3
C(16)–H/C(20)–H	7.69	7.80	125.4	126.3	+0.11	+0.9
C(17)–H/C(19)–H	6.60	6.69	114.0	112.0	−0.09	−2.0
C(18)			153.2	152.8		−0.4
NH_2	5.98	5.90			−0.08	
CH_3	2.22	2.51	23.4	23.5	+0.29	+0.1

[a] Relative to TMS with DMSO-d_6 peak as reference (^{1}H, 2.60 ppm, ^{13}C, 43.5 ppm).
[b] $\Delta\delta = \delta_{(complex)} - \delta_{(smz)}$.

Table 5
Crystal data and details of data collection and structure refinement for the complexes [Hg(sdz)$_2$ (DMF)$_2$] (**1**), [Hg(smr)$_2$] (**2**) and [Hg(smz)$_2$(DMF)$_2$] (**3**)

	1	**2**	**3**
Empirical formula	$C_{26}H_{32}HgN_{10}O_6S_2$	$C_{22}H_{22}HgN_8O_4S_2$	$C_{30}H_{40}HgN_{10}O_6S_2$
Formula weight	845.33	727.19	901.43
Crystal system	monoclinic	monoclinic	monoclinic
Space group	*C*2/*c*	*C*2/*c*	$P2_1/c$
a (Å)	20.0760(5)	12.8834(5)	12.4196(2)
b (Å)	8.3210(3)	14.5693(5)	8.8066(2)
c (Å)	19.8380(6)	12.7683(6)	17.0090(3)
β (°)	108.6592(16)	97.5505(14)	107.9790(12)
V (Å^{-3})	3139.61(17)	2375.86(17)	1769.22(6)
Z	4	4	2
T (K)	150	150	150
Crystal size (mm)	0.12 × 0.10 × 0.08	0.15 × 0.12 × 0.08	0.16 × 0.12 × 0.10
Shape	block	block	block
Colour	white	white	white
D_{cal}	1.788	2.033	1.692
θ Range for data collection	3.01–27.46	3.19–27.46	2.93–27.48
Reflection collected	14863	16902	14760
Unique reflections	3570	2713	4042
R_{int}	0.0761	0.0866	0.0660
Index ranges	$-26 \leqslant h \leqslant 25$; $-10 \leqslant k \leqslant 10$; $-25 \leqslant l \leqslant 25$	$-16 \leqslant h \leqslant 16$; $-18 \leqslant k \leqslant 18$; $-16 \leqslant l \leqslant 16$	$-16 \leqslant h \leqslant 16$; $-11 \leqslant k \leqslant 11$; $-21 \leqslant l \leqslant 22$
Goodness-of-fit on F^2	1.043	1.107	1.049
Data/parameters	3570/214	2713/177	4042/235
Final *R* indices [$I > 2\sigma(I)$]	0.0373/0.0629	0.0386/0.0843	0.0283/0.0631
R indices (all data)	0.0523/0.0679	0.0465/0.0873	0.0435/0.0685
Largest difference in peak and hole (Å^{-3})	1.248 and −0.895	1.130 and −2.001	0.509 and −0.983

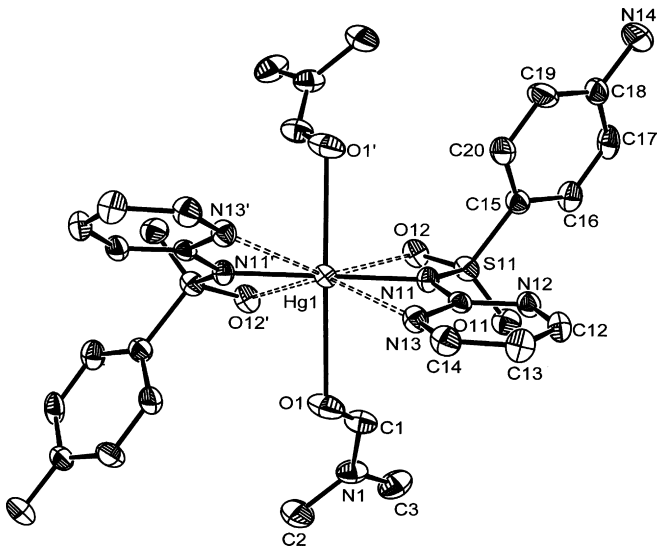


Fig. 1. X-ray structure of $[Hg(sdz)_2(DMF)_2]$ (**1**) showing crystallographic atom numbering scheme used. Thermal ellipsoids are drawn at 50% probability level. The hydrogen atoms are omitted for clarity.

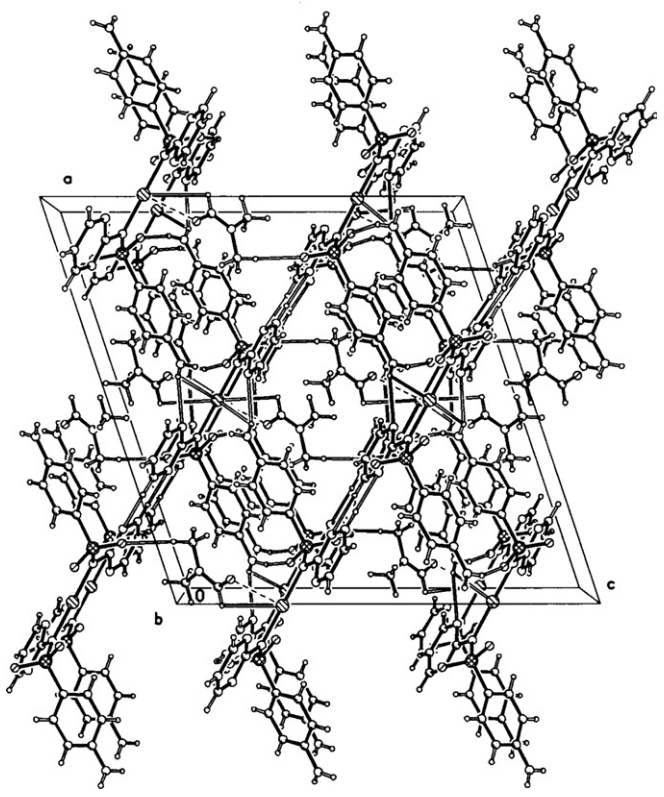


Fig. 2. Packing diagram of the complex $[Hg(sdz)_2(DMF)_2]$ (**1**) showing the hydrogen bonds by dashed lines.

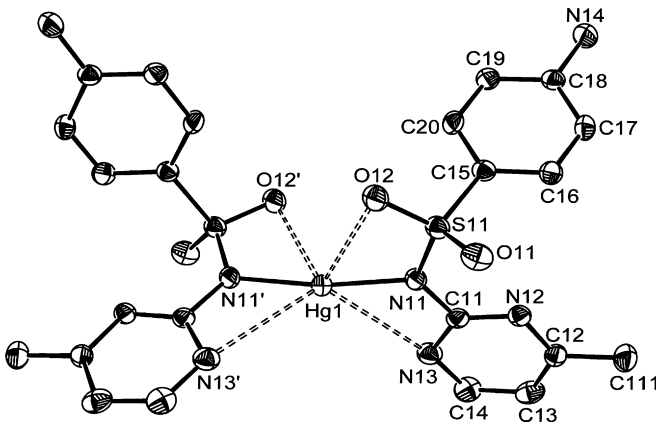


Fig. 3. X-ray structure of $[Hg(smr)_2]$ (**2**) showing crystallographic atom numbering scheme used. Thermal ellipsoids are drawn at 50% probability level. The hydrogen atoms are omitted for clarity.

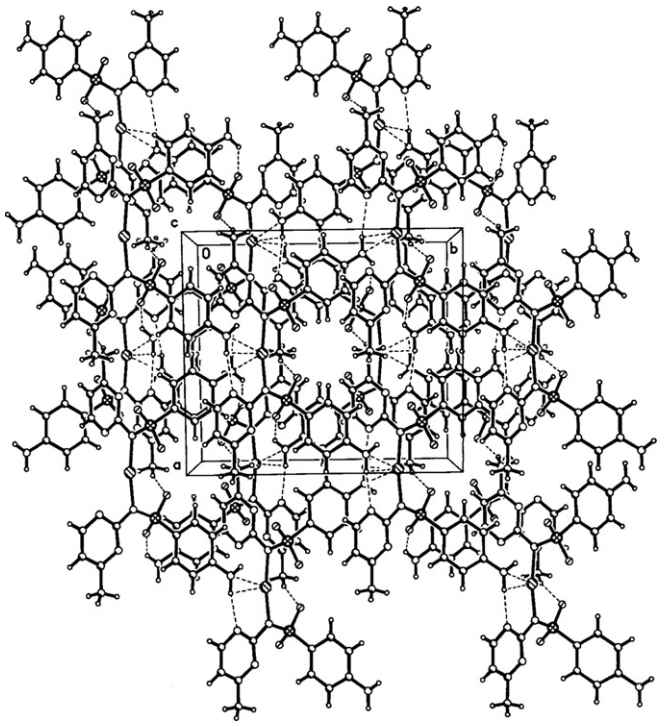


Fig. 4. Packing diagram of the complex $[Hg(smr)_2]$ (**2**) showing hydrogen bonds by open bonds and long interactions by dashed lines.

as six other longer Hg–O/N interactions. These interactions derive from the additional co-ordination of one sulfoxide and one pyrimidine donor of each sulfa drug ligand, as well as two molecules of DMF co-ordinated to each metal. The three donor atoms from each sulfa ligand (N(11), N(13) and O(12)) and the Hg atom all lie within a plane. While at first it might appear that the six donors from the two sulfa ligands might define a distorted hexagonal planar array, the two planes defined by the ligands and the central mercury atom are slightly offset. The DMF molecules are coordinated to the Hg atom and may almost be considered as axial donors to the six equatorial donors of the sulfa ligands.

By contrast, the $[Hg(smr)_2]$ complex **2** has a '2+4' coordination geometry with two molecules of sulfamerazine coordinated with short Hg–N distances through the sulfonamidic nitrogen atoms. Due to the steric constraints of the ligand, the other donors (N(13) and O(12)) are in close

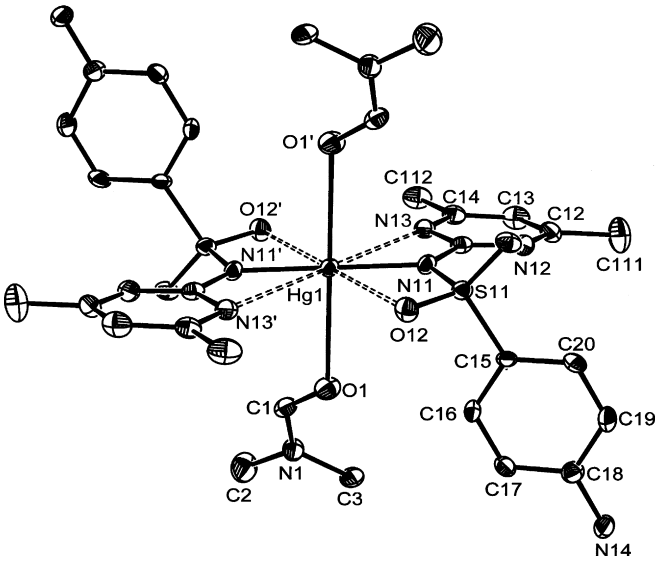


Fig. 5. X-ray structure of $[Hg(smz)_2(DMF)_2]$ (**3**) showing crystallographic atom numbering scheme used. Thermal ellipsoids are drawn at 50% probability level. Hydrogen atoms are omitted for clarity.

Table 6
Selected bond lengths [Å] and angles [°] in the complexes $[Hg(sdz)_2(DMF)_2]$ (**1**), $[Hg(smr)_2]$ (**2**) and $[Hg(smz)_2(DMF)_2]$ (**3**)

	1[a]	**2**[a]	**3**[b]
Bond			
Hg–N(11)	2.047(3)	2.017(4)	2.050(3)
Hg–O(1)	2.713(3)		2.727(2)
Hg–O(12)	2.966(3)	2.832(4)	3.027(2)
Hg–N(13)	2.938(4)	3.014(4)	2.918(3)
S(11)–O(11)	1.443(3)	1.433(4)	1.444(3)
S(11)–O(12)	1.444(3)	1.444(2)	1.445(2)
S(11)–N(11)	1.630(4)	1.648(4)	1.636(3)
S(11)–C(15)	1.759(4)	1.749(5)	1.756(3)
N(11)–C(11)	1.386(6)	1.397(6)	1.392(4)
N(14)–C(18)	1.384(6)	1.369(7)	1.375(4)
Angle			
N(11)–Hg–N(11′)	179.4(2)	171.5(2)	180.0
O(12)–Hg–O(12′)	76.93(12)	97.96(17)	180.0
N(13)–Hg–N(13′)	86.04(14)	119.58(16)	180.0(11)
N(13)–Hg–O(12)	104.34(9)	105.93(11)	104.12(7)
N(13)–Hg–N(11)	50.70(12)	49.33(14)	51.29(9)
N(13)–Hg–O(12′)	128.79(9)	112.71(11)	75.88(7)
N(13)–Hg–N(11′)	128.75(13)	136.59(11)	128.71(9)
N(11)–Hg–O(12′)	126.69(12)	116.93(15)	127.17(9)
N(11)–Hg–O(12)	53.88(12)	56.60(14)	52.83(9)
N(13′)–Hg–O(12)	153.79(9)	112.71(11)	75.88(7)
O(1′)–Hg–O(12)	73.71(10)		92.01(7)
O(1)–Hg–O(1′)	162.73(16)		180.0
N(11)–Hg–O(1)	87.99(12)		94.75(9)
O(1)–Hg–N(11′)	92.09(12)		85.25(9)
O(1)–Hg–O(12)	92.61(10)		87.99(7)
O(1)–Hg–N(13′)	113.06(10)		83.39(8)
O(1)–Hg–N(13)	80.08(11)		96.61(8)
N(13)–C(11)–N(12)	127.1(4)	128.0(5)	127.7(3)

Symmetry transformations used to generate equivalent atoms: ([a]) $-x$, y, $-z+1/2$; ([b]) $-x$, $-y+1$, $-z$.

proximity to the sulfonamidic donor. The closeness of these donors leads to open spaces about the metal centre and an irregular co-ordination sphere. However, the open spaces about the metal centre are apparently not sufficiently large to fit two extra solvent molecule donors. While the comparative steric congestion of the metal centre, as compared to the sulfadiazine complex, might explain the lack of co-ordinated solvent molecules, there is no obvious reason why this molecule would be any more congested than the sulfamethazine complex (with an additional methyl substituent), whose crystal structure also has two co-ordinated solvent molecules. Ultimately, these crystal structures may be determined by crystal packing forces and the observed structures only offer suggestions of their structure in solution. In solution, the structure of **2** may be identical to that of **1** and **3**.

In complexes **1** and **3**, the long Hg–O(1) distances from the DMF donors (2.713(3) Å for **1** and 2.727(2) Å for **3** are slightly shorter than the corresponding bond Hg–O(1) in $[Hg(sdz)_2(DMSO)_2]$ (2.769(7) Å) [11]. The short Hg–N(11) bond distances of 2.047(3) Å for **1**, 2.017(4) Å for **2** and 2.050(3) Å for **3** are also comparable with those of $[Hg(smpz)_2]$ (2.071(4) Å) [13], $[Hg(sdz)_2(DMSO)_2]$ (2.087(4) Å) [11], $[Hg(mq)_2]$ (2.041(6) and 2.031(6) Å) [21] and $[Hg(bpy)_2(NO_2psgly\text{-}N,O)]0.5H_2O$ (2.14(2) Å) [22] (where smpz, sdzH, mq and NO_2psgly are sulfamethoxypiridazine, sulfadiazine, 4-methyl-2(1*H*)-quinoline and *N*-2-nitrophenylsulfonylglycine, respectively).

The C(18)–N(14) bond distances of 1.384(6) Å in **1**, 1.369(7) Å in **2** and 1.375(4) Å in **3** are in good agreement with the corresponding bond in the pure ligands [23]. It is also comparable with the corresponding bond found in the mercury–sulfadiazinato complex $[Hg(sdz)_2(DMSO)_2]$ [11] [1.383(14) Å]. Typically if the terminal amino group is co-ordinated, N–C bond lengths of about 1.413(9)Å are expected [13].

Interestingly, the geometry about the Hg atom in complexes **1** and **3** results in a mutually square planar arrangement of the sulfonamidic and solvent molecules donors. This arrangement is fairly regular showing only minor variations from ideal geometry of the mutually *cis* 90° and *trans* 180° angles. This is evident from the values of *trans* angles for N(11′)–Hg(1)–N(11) (179.4(2)°) and O(1′)–Hg(1)–O(1) (162.7(2)°) for **1** and 180.0° for **3**. The *cis* angles vary from 88.0(1) to 92.1(2)° in the complex **1** and 85.2(2)–94.8(2)° in the complex **3**. Complex **2** lies on a two-fold axis in which the sulfamerazinato ligands are bonded to the Hg-atom through the sulfonamidic nitrogen [N(11)] atom with a N(11)–Hg–N(11′) angle of 171.5(2)° indicating the 'linearity' of the complex.

When bonded to mercury the ligand acts as a tridentate donor, albeit with two very long and one short interaction. Never the less, the 'tridentate' coordination mode of this ligand is particularly rare. Typically, ligands such as pyridyl sulfonamides form complexes where the ligand is monodentate or bidentate. Typical examples are of bidentate co-ordination where the nitrogen of the heterocycle

Table 7
Dimensions of the hydrogen bonds in complexes 1, 2 and 3 [distances in (Å) and angles (°)]

D–H ⋯ A	Compounds	D–H	D ⋯ A	H ⋯ A	<D–H ⋯ A
N14–H14A ... O12[a]	**1**	0.950(8)	3.244(4)	2.346(2)	157.75(3)
N14–H14B ... N13[b]	**1**	0.949(5)	3.210(2)	2.452(1)	136.74(3)
N14–H14A ... N13[c]	**2**	0.931(3)	3.323(7)	2.583(4)	136.78(2)
N14–H14B ... O12[d]	**2**	0.937(6)	3.173(7)	2.399(7)	139.93(5)
N14–H14A ... O11[e]	**3**	0.948(8)	3.031(1)	2.104(8)	165.47(3)
N14–H14B ... O11[f]	**3**	0.949(8)	3.038(7)	2.223(4)	143.46(6)

[a] $-x-1/2, +y+1/2, -z+1/2$.
[b] $x-1/2, +y-1/2, +z$.
[c] $x+1/2, +y-1/2, +z$.
[d] $x, -y, +z+1/2$.
[e] $-x+1, +y-1/2, -z+1/2$.
[f] $x, -y+1/2, +z+1/2$.

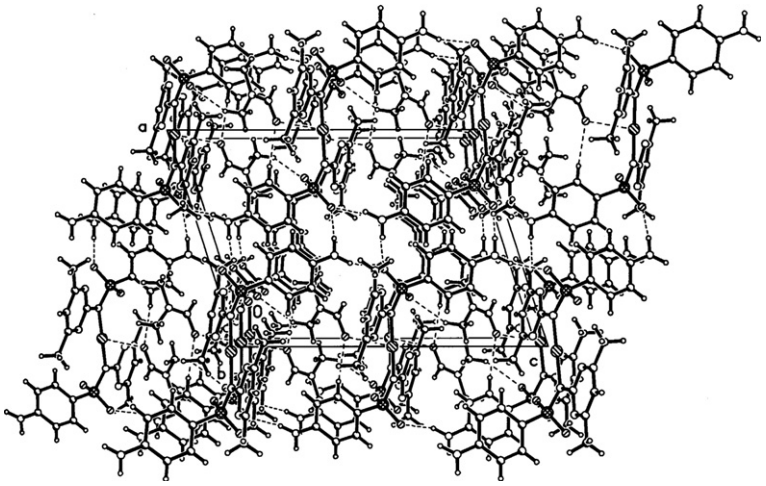


Fig. 6. Packing diagram of the complex $[Hg(smz)_2(DMF)_2]$ (**3**) showing the hydrogen by dashed lines.

and the sulfonamidic nitrogen co-ordinate [24,25] or bidentate co-ordination of nitrogen of the heterocycle and the oxygen of the sulfoxide group co-ordinate [24–26].

The packing of these complexes in the solid state is strongly influenced by the extensive hydrogen bonding between (i) the amino ($-NH_2$) group of one complex unit and the sulfonyl oxygen [N(14)–H(14A) ⋯ O(12) (of other complex unit): 2.346(2) Å with an angle of 157.75(3)°] and (ii) hydrogen bonding between the amino ($-NH_2$) group of one complex unit and the pyrimido nitrogen atoms of the next unit, [N(14)–H(14B) ⋯ N(13) (other complex unit) = 2.452(1) Å with an angle of 136.74(3)°]. The packing diagram of the complex $[Hg(sdz)_2(DMF)_2]$ (**1**) is shown in Fig. 2 and dimensions of the hydrogen bonding is listed in Table 7.

In the packing diagram of the complex **2** the amino group, sulfonyl oxygen and pyrimido nitrogen atoms are hydrogen bonded which is shown in Fig. 4 by dashed lines. Necessarily, the lack of DMF within the lattice leads to a different overall arrangement of hydrogen bonds, though the hydrogen bonding occurs between the same donors and acceptors See Fig. 5. However, on close inspection of the hydrogen binding network in **3**, (Fig. 6), it can be seen that now, the pyrimidine does not participate in hydrogen bonding and now both hydrogens of the amino group are hydrogen bonding to the sulfonyl oxygen of two different ligands. This change in hydrogen bonding is due, in some part, to the additional methyl group on the ligand which will sterically hinder the pyrimidine group.

Acknowledgement

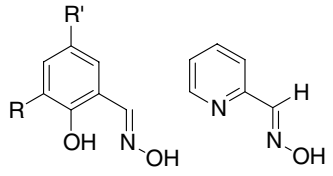
The authors acknowledge the support of the School of Chemistry, Cardiff University, United Kingdom.

Appendix A. Supplementary material

CCDC 293146, 293147 and 293148 contain the supplementary crystallographic data for **1**, **2** and **3**. These data can be obtained free of charge via http://www.ccdc.cam.ac.uk/conts/retrieving.html, or from the Cambridge Crystallographic Data Centre, 12 Union Road, Cambridge CB2 1EZ, UK; fax: (+44) 1223-336-033; or e-mail: deposit @ccdc.cam.ac.uk. Supplementary data associated with this article can be found, in the online version, at doi:10.1016/j.poly.2006.09.056.

References

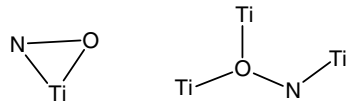
[1] E.C. Constable, Coord. Chem. Rev. 62 (1985) 37.
[2] W. Levason, C.A. McAuliffe, in: C.A. McAuliffe (Ed.), The Chemistry of Mercury, McMillan, London, 1977.
[3] D.K. Breitinger, in: D.E. Fenton, J.A. McCleverty, T.J. Meyer (Eds.), Comprehensive Co-ord. Chem II, Elsevier, Amsterdam, 2003.
[4] C.J. Brown, D.S. Cook, L. Sengier, Acta Crystallogr. C43 (1987) 2332.
[5] N.C. Baenziger, Acta Crystallogr. C39 (1983) 1620.
[6] C.J. Brown, D.S. Cook, L. Sengier, Acta Crystallogr. C41 (1985) 718.
[7] R.–X. Yuan, R.–G. Xiong, Z.–F. Chen, P. Zhang, H.–X. Ju, Z. Dai, Z.–J. Guo, H.–K. Fun, X.–Z. You, J. Chem. Soc. Dalton Trans. (2001) 774.
[8] D.S. Cook, M.F. Turner, J. Chem. Soc. Perkin Trans. 2 (1975) 1021.
[9] N.C. Baenzige, A.W. Struss, Inorg. Chem. 15 (1976) 1807.
[10] L. Menabue, M. Saladini, J. Inorg. Biochem. 49 (1993) 201.
[11] A. Garcia-Raso, J.J. Fiol, G. Martorell, A. Lopez-Zafra, M. Quiros, Polyhedron 16 (1997) 613.
[12] L. Gutierrez, G. Alzuet, J. Borras, A. Castineiras, A. Rodriguez-Fortea, E. Ruiz, Inorg. Chem. 40 (2001) 3089.
[13] A. Garcia-Raso, J.J. Fiol, S. Rigo, A. Lopez-Lopez, E. Molins, E. Espinosa, E. Borras, G. Alzuet, Joaquin Borras, A. Castineiras, Polyhedron 19 (2000) 991.
[14] N. Anand, Sulfonamides and sulfones, in: M.E. Wolff (Ed.), Burger's Medicinal Chemistry, Wiley Interscience, New York, N.Y., 1980, pp. 1–40.
[15] J.S. Casas, M.S. García-Tasende, J. Sordo, Co-ord. Chem. Rev 193-195 (1999) 283.
[16] K.K. Divine, F. Ayala-Fierro, D.S. Barber, D.E. Carter, J. Toxicol. Environ. Health A57 (1999) 489.
[17] G.M. Sheldrick, Acta Crystallogr. A46 (1990) 467.
[18] G.M. Sheldrick, SHELXL-97, Program for Crystal structure determination, University of Göttingen, Germany, 1997.
[19] R.H. Blessing, Acta Crystallogr. A51 (1995) 33.
[20] J. Casanova, G. Aluzet, S. Ferrer, J. Borras, S. Garcia-Granda, E. Perez-Carreno, J. Inorg. Biochem. 51 (1993) 689.
[21] D.M.L. Goodgame, S.P.W. Hill, D.J. Williams, Polyhedron 11 (1992) 1507.
[22] M. Saladini, L. Menabue, E. Ferrari, D. Iacopino, J. Chem. Soc., Dalton Trans. (2001) 1513.
[23] (a) H.S. Shin, G.S. Ihn, H.S. Kim, C.H. Koo, J. Korean Chem. Soc. 18 (1974) 329;
(b) K.R. Acharya, K.N. Kuchela, G. Kartha, J. Cryst. Spect. Res. 12 (1982) 369;
(c) M.R. Caira, R. Mohamed, Acta Cryst. B48 (1992) 492;
(d) A.K. Basak, S.K. Mazumdar and S. Chaudhuri; Acta Crsyt. C39 (1983) 492.
[24] I. Beloso, J. Borras, J. Castro, J.A. Garcia-Vazquez, P. Perez-Lourido, J. Romero, A. Sousa, European J. Inorg. Chem. 3 (2004) 635.
[25] K.K. Narang, J.K. Gupta, J. Inorg. Nucl. Chem. 38 (1976) 589.
[26] (a) I. Beloso, J. Castro, J.A. Garcia-Vazquez, P. Perez-Lourido, J. Romero, A. Sousa, Polyhedron 22 (2003) 1099;
(b) P. Ranganatham, S. Sankara, K. Subbannaya, Indian Drugs 17 (1979) 72.



1H_2 R = R' = H
2H_2 R = R' = Cl
3H_2 R = H, R' = NO_2

4H

Fig. 1. Ligands used in this study.



μ^1-terminal μ^3-triply bridging

Fig. 2. Two different bonding motifs for the oxime ligands with titanium. μ^1-terminal is observed for complex $Ti_2(\mathbf{4})_4(O^iPr)_4$ and μ^3-triply bridging for complexes $Ti_3(\mathbf{1})_2(O^iPr)_8$, $Ti_3(\mathbf{2})_2(O^iPr)_8$ and $Ti_3(\mathbf{3})_2(O^iPr)_8$ respectively.

Pertinent geometric data are given in Table 1. The stoichiometry of the reaction was varied and $Ti_3(\mathbf{1})_2(O^iPr)_8$ was the only isolable complex.

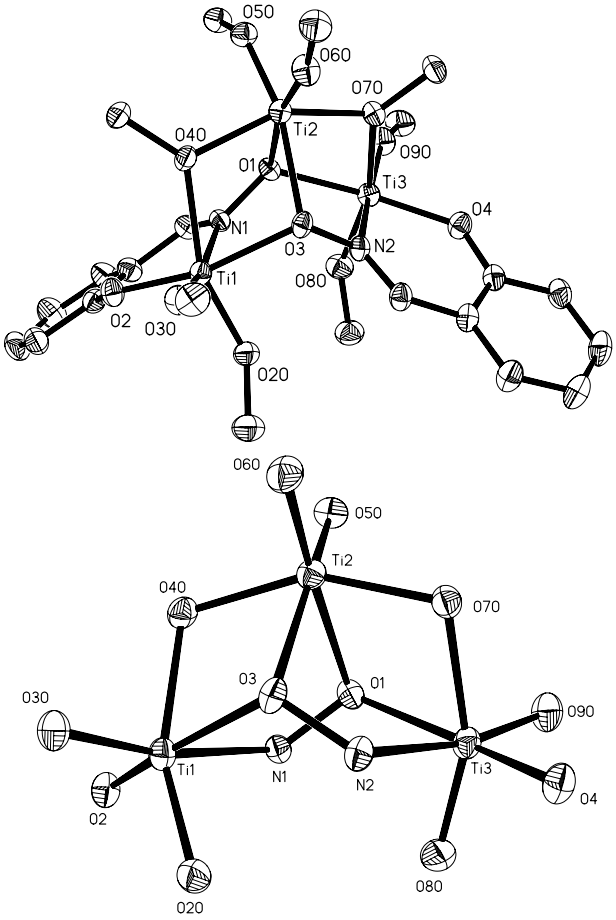


Fig. 3. Top: Molecular structure of complex $Ti_3(\mathbf{1})_2(O^iPr)_8$. Ellipsoids are shown at the 50% probability level, the hydrogen atoms and the isopropoxide methyl groups have been omitted for clarity. Bottom: The trimetallic core of $Ti_3(\mathbf{1})_2(O^iPr)_8$ highlighting the rings present.

Table 1
Key bond lengths (Å) and bond angles (°) for complexes $Ti_3(\mathbf{1})_2(O^iPr)_8$ $Ti_3(\mathbf{2})_2(O^iPr)_8$ and $Ti_3(\mathbf{3})_2(O^iPr)_8$

	$Ti_3(\mathbf{1})_2(O^iPr)_8$	$Ti_3(\mathbf{2})_2(O^iPr)_8$	$Ti_3(\mathbf{3})_2(O^iPr)_8$
Ti(1)–N(1)	2.232(1)	2.249(3)	2.220(4)
Ti(1)–O(2)	1.891(1)	1.924(3)	1.939(4)
Ti(1)–O(3)	2.067(1)	2.060(2)	2.056(3)
Ti(1)–O(20)	1.820(1)	1.770(3)	1.764(4)
Ti(1)–O(30)	1.790(1)	1.786(2)	1.801(4)
Ti(1)–O(40)	2.132(1)	2.083(3)	2.094(4)
Ti(2)–O(1)	2.166(1)	2.188(2)	2.188(3)
Ti(2)–O(3)	2.162(1)	2.199(3)	2.192(3)
Ti(2)–O(40)	1.990(1)	1.981(2)	1.985(4)
Ti(2)–O(50)	1.804(1)	1.793(2)	1.780(4)
Ti(2)–O(60)	1.782(1)	1.775(3)	1.768(4)
Ti(2)–O(70)	1.977(1)	1.966(2)	1.969(4)
Ti(3)–O(1)	2.068(1)	2.054(2)	2.033(4)
Ti(3)–N(2)	2.236(1)	2.249(3)	2.229(4)
Ti(3)–O(4)	1.899(1)	1.916(3)	1.923(4)
Ti(3)–O(70)	2.106(1)	2.073(2)	2.091(3)
Ti(3)–O(80)	1.787(1)	1.776(3)	1.816(3)
Ti(3)–O(90)	1.793(1)	1.788(3)	1.773(3)
O(40)–Ti(1)–O(3)	93.54(5)	92.50(1)	90.99(2)
O(2)–Ti(1)–O(3)	158.91(5)	157.10(1)	157.38(1)
O(40)–Ti(2)–O(70)	153.32(5)	150.43(1)	150.40(1)
O(1)–Ti(2)–O(3)	74.40(4)	74.15(9)	73.70(1)
Ti(2)–O(1)–Ti(3)	101.71(5)	100.68(1)	101.67(1)
Ti(2)–O(3)–Ti(1)	103.18(5)	101.25(1)	101.72(2)
O(70)–Ti(3)–N(2)	73.95(5)	74.57(1)	75.08(1)
O(1)–Ti(3)–N(2)	79.69(5)	79.14(1)	78.56(2)
O(80)–Ti(3)–O(90)	101.21(6)	102.23(1)	102.88(2)

The solid-state structure is comprised of three face sharing distorted Ti(IV) octahedra, with the trimetallic core forming an isosceles triangle with an average non-bonding Ti–Ti distance of 3.641 Å. Two of the metal centres, Ti(1) and Ti(3), are joined in a six-membered ring consisting of the two titanium centres and the two oximate N–O groups {N(1)–O(1) and N(2)–O(3)}. The coordination spheres of Ti(1) and Ti(3) are completed by the phenolic oxygen atoms of the salicylaldoxime ligands, two terminal isopropoxides and a bridging isopropoxide. The third titanium, Ti(2), sits above this six-membered ring and is linked to it by two bridging isopropoxides and two bridging oximate {O(1) and O(3)} oxygen atoms. In total the core, made up of the metal centres, consists of one six-membered ring, two five-membered rings and two Ti_2O_2 four-membered rings. The terminal isopropoxides have Ti–O bond lengths varying between 1.782(1) and 1.820(1) Å, consistent with literature precedent [10–14]. The interactions between the bridging isopropoxides and the two metal centres it bridges differ significantly in nature; for example O(70) binds to Ti(2) and Ti(3) with distances of 1.977(1) Å [Ti(2)–O(70)] and 2.106(1) Å [Ti(3)–O(70)] respectively. These bond lengths are, however, within the expected range for bridging isopropoxides [11,14–17]. The oximato N–O groups bond to all titanium centres, with the nitrogen atom bonding to one titanium and the oxygen atoms bridging the other two; for example N(2) is bonded to Ti(3) and its related oxygen O(3) bridges between Ti(1) and Ti(2). This

structure is the first characterised example of N–O triply bridging coordination known for a titanium oximate. However, it is observed for oximates of other metals for example Ag/Ni [18], Cu/La [19], Fe[20] and V [21]. The Ti–N bond lengths are 2.232(1) Å [Ti(1)–N(1)] and 2.236(1) Å [Ti(3)–N(2)] respectively, which are consistent with the literature [22,23]. The oximate oxygen atoms bridge two titanium centres and, as seen for the bridging alkoxides, these are asymmetric in nature. The bond lengths between the salicylaldoxime phenoxy groups and titanium are 1.891(1) Å [Ti(1)–O(2)] and 1.899(1) Å [Ti(3)–O(4)], which are typical of Ti–O bond lengths in non-bridging phenoxides [24–26], Ti(2) can be considered as part of a 'trapped' $Ti(O^iPr)_4$ molecule, dissociation of which would not lead to any gross structural changes in the remainder of the complex.

The ^1H NMR ($C_6D_5CD_3$) spectrum of $Ti_3(\mathbf{1})_2(O^iPr)_8$ consists of four isopropyl septets of equal intensity (4.63, 4.95, 5.02 and 5.14 ppm). From NOESY and COSY measurements it is possible to assign the resonances at 4.63 and 5.14 ppm to the two sets of terminal isopropoxides adorning Ti(1) and Ti(3) (the A and D sets of protons, Fig. 4). The resonances at 4.95 and 5.02 ppm correspond to either the terminal isopropoxides bound to Ti(2) or the bridging isopropoxide moieties (the B and C sets of protons). Variable temperature ^1H NMR spectroscopic studies (Fig. 4) have shown that dissociation is not observed when heated to 80 °C in deuterated toluene with the only visible dynamic process being exchange between the B and C sets of protons as the temperature is raised. Coalescence begins at 50 °C while at 80 °C the signal begins to sharpen. On cooling, the room temperature spectrum is again observed. ^{13}C NMR spectroscopy also confirms that the solid-state structure is maintained in solution, with four distinct peaks for the separate isopropoxide methine environments. Presumably, the resistance to dissociation is related to the fact that the presence of the $Ti(O^iPr)_4$ group allows the titanium centres to retain their preferred pseudo-octahedral coordination geometry.

Having established the synthetic protocol, attention turned to ligands $\mathbf{2}H_2$ and $\mathbf{3}H_2$ which reacted with $Ti(O^iPr)_4$ to form complexes $Ti_3(\mathbf{2})_2(O^iPr)_8$ and $Ti_3(\mathbf{3})_2(O^iPr)_8$ respectively. Structures were identified from X-ray diffraction and that for $Ti_3(\mathbf{3})_2(O^iPr)_8$ is given in Fig. 5.

Complexes $Ti_3(\mathbf{2})_2(O^iPr)_8$ and $Ti_3(\mathbf{3})_2(O^iPr)_8$ are structurally analogous to complex $Ti_3(\mathbf{1})_2(O^iPr)_8$, as exemplified by the bond lengths (Å) and angles (°) (see Table 1). A very subtle difference between $Ti_3(\mathbf{2})_2(O^iPr)_8$/$Ti_3(\mathbf{3})_2(O^iPr)_8$ and $Ti_3(\mathbf{1})_2(O^iPr)_8$ is that the phenolic-titanium bond is slightly longer for the complexes containing the electron

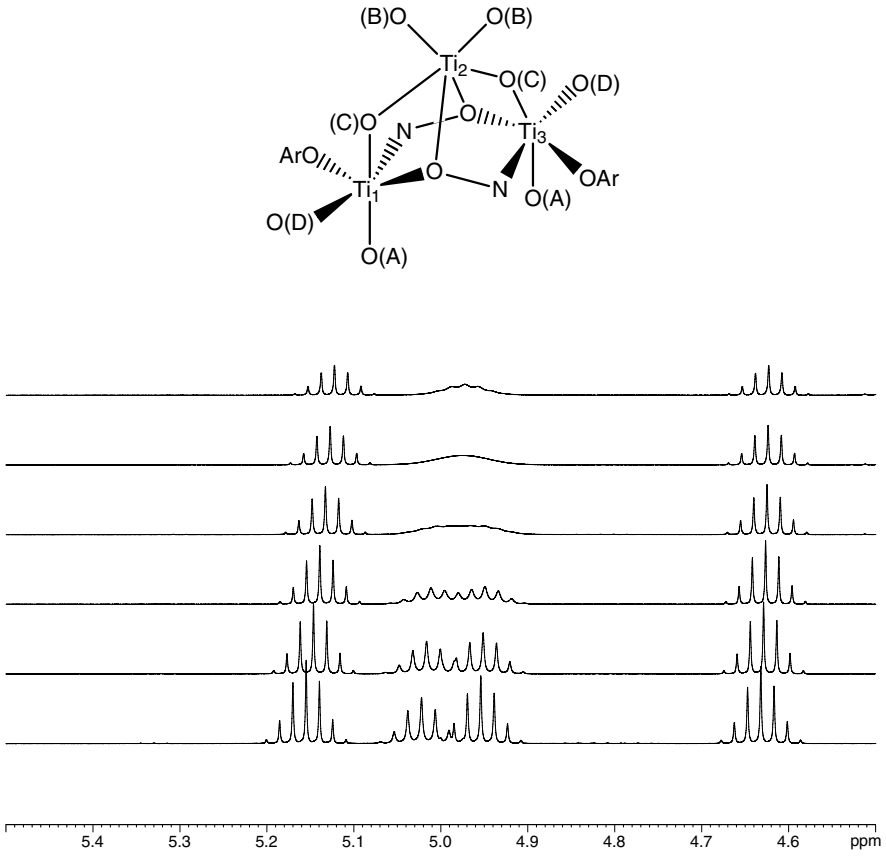


Fig. 4. Top: Representation of the structure of $Ti_3(\mathbf{1})_2(O^iPr)_8$ showing the isopropoxide groups under discussion in the text. Bottom: Variable temperature ^1H NMR spectroscopic studies of $Ti_3(\mathbf{1})_2(O^iPr)_8$, using $C_6D_5CD_3$ as the solvent. The bottom spectrum was acquired at 30 °C going up in 10 °C steps until 80 °C.

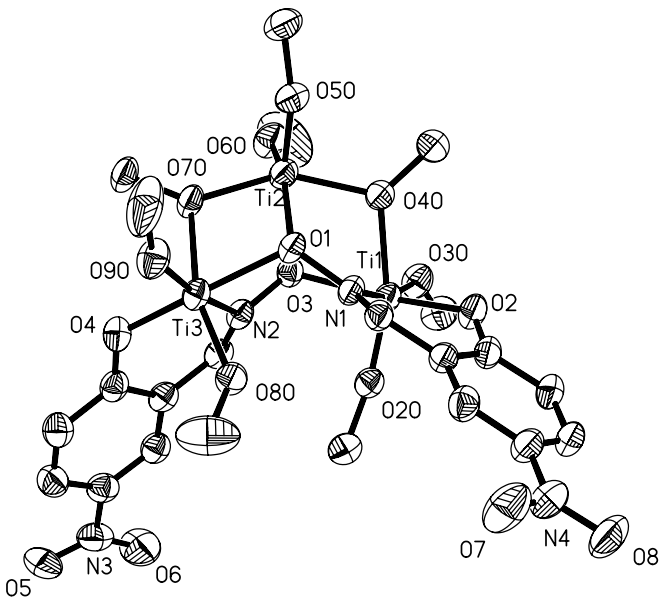


Fig. 5. Molecular structure of complex $Ti_3(\mathbf{3})_2(O^iPr)_8$. Ellipsoids are shown at the 50% probability level. Hydrogen atoms and the isopropoxide methyl groups have been omitted for clarity. The same numbering scheme was applied to complex $Ti_3(\mathbf{2})_2(O^iPr)_8$.

withdrawing groups. Variable temperature ^1H NMR spectroscopy for $Ti_3(\mathbf{3})_2(O^iPr)_8$ yielded similar spectra as shown for $Ti_3(\mathbf{1})_2(O^iPr)_8$ and are given as Supporting information.

As an extension of our studies we endeavoured to examine the reactivity of ligands in which the oxime group is the only potentially anionic group. Thus, 2 equiv. of ligand **4**H were reacted with 1 equiv. of $Ti(O^iPr)_4$. The crystal structure of complex $Ti_2(\mathbf{4})_4(O^iPr)_4$ is given in Fig. 6, pertinent bond lengths and angles are summarised in Table 2.

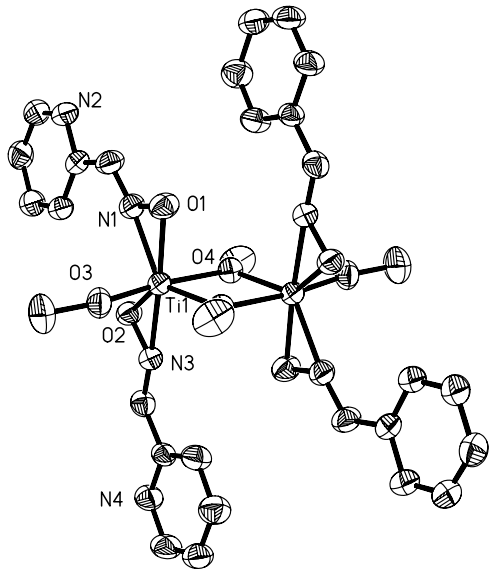


Fig. 6. Molecular structure of complex $Ti_2(\mathbf{4})_4(O^iPr)_4$. Ellipsoids are shown at the 50% probability level, the hydrogen atoms and the isopropoxide methyl groups have been omitted for clarity.

Table 2
Key bond lengths (Å) and bond angles (°) for complex $Ti_2(\mathbf{4})_4(O^iPr)_4$

	$Ti_2(\mathbf{4})_4(O^iPr)_4$
Ti(1)–O(1)	1.978(2)
Ti(1)–O(2)	1.970(2)
Ti(1)–O(3)	1.780(2)
Ti(1)–O(4)	2.083(2)
Ti(1)–O(4A)	1.988(2)
Ti(1)–N(1)	2.047(3)
Ti(1)–N(3)	2.148(2)
O(1)–Ti(1)–N(3)	170.39(8)
O(4)–Ti(1)–O(4A)	75.71(8)
O(1)–Ti(1)–N(1)	39.45(8)
O(2)–Ti(1)–N(3)	38.41(8)
O(2)–Ti(1)–O(3)	93.45(9)
N(1)–Ti(1)–N(3)	131.37(9)
N(1)–Ti(1)–O(2)	92.97(9)
O(3)–Ti(1)–O(1)	94.79(9)
O(3)–Ti(1)–O(4)	173.77(9)

The complex consists of two titanium centres, which are bridged by two isopropoxide ligands. In addition each of the metal centres is ligated by two oximate groups and a terminal isopropoxide ligand completes the coordination sphere of each titanium centre. The oximes are non-bridging and bond to titanium through their oxygen and nitrogen atoms, the pyridyl nitrogen takes no part in bonding. For titanium this bonding mode has only been observed by Thewalt et al. [9]. However, this mode has been observed for other metal oximate complexes; for example Cu [27], Mo [28], Os[29] and Ru [30]. As expected the Ti–oximate bond lengths are shorter than those observed in complexes $Ti_3(\mathbf{1})_2(O^iPr)_8$, $Ti_3(\mathbf{2})_2(O^iPr)_8$ and $Ti_3(\mathbf{3})_2(O^iPr)_8$ due to the non-bridging nature of the oximato group. The ^1H NMR spectrum at 298 K of $Ti_2(\mathbf{4})_4(O\ ^iPr)_4$ only contains one isopropoxide resonance indicating exchange on the NMR time-scale. Upon cooling to 243 K two separate isopropoxide resonances are observed, in agreement with the solid-state structure.

3. Conclusions

In conclusion four new crystal structures of titanium oximes have been determined, which are the first salicylaldoximate complexes of titanium to be crystallographically characterised. These cluster complexes with multiple titanium centres have been shown to be stable at elevated temperatures. In addition these complexes exhibit a triply bridging mode for the oximate ligand, which has not been previously reported for titanium.

4. Experimental

4.1. General

For the preparation and characterisation of complexes, all reactions and manipulations were performed under an inert atmosphere of argon using standard Schlenk or glove-box techniques and all solvents were freshly distilled

over suitable drying agents and degassed prior to use. All ligands were purchased from Aldrich or synthesised using standard literature procedures and recrystallised in petroleum ether prior to use [31]. Ti(O^{i}Pr)$_4$ was purchased from Aldrich and purified by vacuum distillation prior to use. ^{1}H and ^{13}C NMR spectra were recorded on a Bruker Avance 400 or 300 MHz spectrometer, referenced to residual solvent peaks, variable temperature NMR studies were performed in deuterated toluene. Coupling constants are given in Hertz. Elemental analysis was performed by Mr. A.K. Carver at the Department of Chemistry, University of Bath. Crystallographic data were collected on a Nonius KappaCCD area detector diffractometer using Mo Kα radiation ($\lambda = 0.71073$ Å), and all structures were solved by direct methods and refined on all F^2 data using the SHELXL-97 suite of programs [32]. Hydrogen atoms were uniformly included at idealised positions and refined using the riding model. Absorption corrections were applied on merit. See Table 3 for full crystallographic parameters. Complexes Ti$_3$(**1**)$_2$(O^{i}Pr)$_8$ and Ti$_3$(**2**)$_2$(O^{i}Pr)$_8$ have disordered isopropoxide moieties, the carbon atoms of which were modelled over two sites in a 1:1 ratio. The yields quoted are for the first crop of crystals and due to their high solubility in common organic solvents the yields are relatively low. These could be improved by concentrating the filtrate to obtain more material.

4.2. Preparation of *Ti$_3$(**1**)$_2$(O^{i}Pr)$_8$*

A solution of salicylaldoxime (1.37 g, 10 mmol) was prepared in dry toluene (10 ml) under an inert atmosphere. To this Ti(O^{i}Pr)$_4$ (4.5 ml, 15 mmol) was added to give an orange solution. This solution was vigorously stirred for one hour and heated to reflux. The solvent was removed *in vacuo* to give an orange solid product. This product was suspended in hexane and toluene added until dissolution occurred on warming. Standing at room temperature yielded a crop of orange blocks. Yield = 2.12 g (46%), melting point = 147–150 °C. ^{1}H NMR (400 MHz, $CDCl_3$, 25 °C) 0.71 (d, $J = 6$ Hz, 6H, CH_3 (A or D)), 0.81 (d, $J = 6$ Hz, 6H, CH_3 (A or D)), 1.15 (d, $J = 6$ Hz, 6H, CH_3 (B or C)), 1.21 (d, $J = 6$ Hz, 6H, CH_3 (B or C)), 1.23 (d, $J = 6$ Hz, 6H, CH_3 (B or C)), 1.23 (d, $J = 6$ Hz, 6H, CH_3 (B or C)), 1.21 (d, $J = 6$ Hz, 6H, CH_3 (A or D)), 1.34 (d, $J = 6$ Hz, 6H, CH_3 (A or D)), 4.39 (sept, $J = 6$ Hz, 2H, CH (A or D)), 4.73 (sept, $J = 6$ Hz, 2H, CH (B or C)), 4.80 (sept, $J = 6$ Hz, 2H, CH (B or C)), 4.93 (sept, $J = 6$ Hz, 2H, CH (A or D)), 6.68 (m, 4H, Ar–H), 7.09 (m, 2H, Ar–H), 7.18 (m, 2H, Ar–H), 7.96 (s, 2H, imine CH). ^{13}C{^{1}H} NMR, $CDCl_3$: 24.6, 24.9, 25.7, 25.7, 26.0, 26.0, 26.6, 26.7 (CH_3), 75.6, 77.6, 78.7, 79.1 ($CH(CH_3)_2$), 114.3, 118.3, 120.7, 130.8, 132.1 (Ar), 151.2 (NCH), 162.6 (Ar–O). Elemental *Anal.* Calc. for $C_{38}H_{66}N_2O_{12}Ti_3$: C, 51.5; H, 7.50; N, 3.16. Found: C, 50.6; H, 7.27; N, 2.91%.

4.3. Preparation of *Ti$_3$(**2**)$_2$(O^{i}Pr)$_8$*

An analogous procedure to that of Ti$_3$(**1**)$_2$(O^{i}Pr)$_8$ was followed. Ti(O^{i}Pr)$_4$ (0.9 ml, 3 mmol), **2**H$_2$ (0.41 g, 2 mmol). Yield = 0.84 g (84%), melting point = 136–139 °C. ^{1}H NMR (400 MHz, $CDCl_3$, 25 °C) 0.73 (d, $J = 6$ Hz, 6H, CH_3 (A or D)), 0.84 (d, $J = 6$ Hz, 6H, CH_3 (A or D)), 1.10 (d, $J = 6$ Hz, 6H, CH_3 (B or C)), 1.20 (d, $J = 6$ Hz, 6H, CH_3 (B or C)), 1.23 (d, $J = 6$ Hz, 6H, CH_3 (B or C)), 1.24 (d, $J = 6$ Hz, 6H, CH_3 (B or C)), 1.31 (d, $J = 6$ Hz, 6H, CH_3 (A or D)), 1.35 (d ,$J = 6$ Hz, 6H, CH_3 (A or D)), 4.39 (sept, $J = 6$ Hz, 2H, CH (A or D)), 4.66–4.83 (2 overlaying septets, 4H, CH (B or C)), 4.94 (sept, $J = 6$ Hz, 2H, CH (A or D)), 6.97 (d, $J = 2.5$ Hz,

Table 3
Crystallographic data for complexes Ti$_3$(**1**)$_2$(O^{i}Pr)$_8$, Ti$_3$(**2**)$_2$(O^{i}Pr)$_8$, Ti$_3$(**3**)$_2$(O^{i}Pr)$_8$ and Ti$_2$(**4**)$_4$(O^{i}Pr)$_4$

Complex	Ti$_3$(**1**)$_2$(O^{i}Pr)$_8$	Ti$_3$(**2**)$_2$(O^{i}Pr)$_8$	Ti$_3$(**3**)$_2$(O^{i}Pr)$_8$	Ti$_2$(**4**)$_4$(O^{i}Pr)$_4$
Formula	$C_{38}H_{66}N_2O_{12}Ti_3$	$C_{38}H_{62}Cl_4\ N_2O_{12}Ti_3$	$C_{38}H_{64}N_4O_{16}Ti_3$	$C_{18}\ H_{24}N_4O_4Ti$
Formula weight	886.63	1024.40	976.63	408.31
Crystal system	triclinic	monoclinic	monoclinic	monoclinic
Space group	$P\bar{1}$	$P2_1/n$	$P2_1/n$	$C2/c$
Temperature (K)	170(2)	150(2)	150(2)	170(2)
a (Å)	11.6139(2)	12.500(2)	12.275(5)	22.047(4)
b (Å)	11.744(2)	30.770(4)	21.176(9)	9.580(2)
c (Å)	19.3657(4)	13.314(2)	19.067(9)	21.545(4)
α (°)	75.392(1)	90	90	90
β (°)	80.941(1)	101.133(1)	93.22(1)	114.13(3)
γ (°)	61.116(1)	90	90	90
Volume (Å^3)	2236.03(7)	5024.53(1)	4948.4(4)	4152.7(1)
Z	2	4	4	8
D_{calc} (g cm^{-3})	1.317	1.354	1.311	1.306
Reflections collected	35566	51616	44684	21778
θ Range	3.55–27.49	3.64–25.03	3.53–27.45	3.59–25.00
Independent reflections (R_{int})	10224 (0.044)	8829 (0.091)	10632 (0.1459)	3651 (0.0506)
Goodness-of-fit	1.042	1.032	1.118	1.018
R_1, wR_2 [$I > 2\sigma(I)$][a]	0.0364, 0.0871	0.0527, 0.1272	0.0831, 0.1721	0.0473, 0.1204
R_1, wR_2 (all data)[a]	0.0507, 0.0944	0.1007, 0.1475	0.1590, 0.2132	0.0556, 0.1250

[a] $R_1 = \sum |F_o| - |F_c| / \sum |F_o|$, $wR_2 = [\sum (F_o^2 - F_c^2)^2 / \sum w(F_o^2)^2]^{1/2}$.

2H, Ar–H), 7.30 (d, $J = 2.5$ Hz, 2H, Ar–H), 7.88 (s, 2H, imine CH). $^{13}C\{^1H\}$ NMR $CDCl_3$: 23.0, 23.4, 24.2, 24.3, 24.6, 24.9, 25.3, 25.5 (CH_3), 74.7, 78.1, 78.4, 79.0 ($CH(CH_3)_2$), 120.6, 120.7, 123.0, 127.2, 130.5 (Ar), 149.1 (NCH), 155.0 (Ar–O). Elemental *Anal.* Calc. for $C_{38}H_{62}N_2O_{12}Ti_3Cl_4$: C, 44.6; H, 6.10; N, 2.73. Found: C, 43.4; H, 5.96; N, 2.59%.

4.4. Preparation of $Ti_3(\mathbf{3})_2(O^iPr)_8$

An analogous procedure to that of $Ti_3(\mathbf{1})_2(O^iPr)_8$ was followed. $Ti(O^iPr)_4$ (0.9 ml, 3 mmol), $\mathbf{3}H_2$ (0.41 g, 2 mmol). Yield = 0.63 g (65%), melting point = 211–214 °C (dec.). ^1H NMR (400 MHz, $CDCl_3$, 25 °C) 0.71 (d, $J = 6$ Hz, 6H, CH_3 (A or D)), 0.87 (d, $J = 6$ Hz, 6H, CH_3 (A or D)), 1.11 (d, $J = 6$ Hz, 6H, CH_3 (B or C)), 1.21–1.26 (m, 18H, CH_3 (B or C)), 1.32 (d, $J = 6$ Hz, 6H, CH_3 (A or D)), 1.36 (d, $J = 6$ Hz, 6H, CH_3 (A or D)), 4.42 (sept, $J = 6$ Hz, 2H, CH (A or D)), 4.70 (sept, $J = 6$ Hz, 2H, CH (B or C)), 4.77 (sept, $J = 6$ Hz, 2H, CH (B or C)), 4.95 (sept, $J = 6$ Hz, 2H, CH (A or D)), 6.74 (d, $J = 10$ Hz, 2H, Ar–H), 8.00 (s, 2H, imine CH), 8.05–8.10 (m, 4H, Ar–H). $^{13}C\{^1H\}$ NMR $CDCl_3$: 24.5, 24.9, 25.6, 25.7, 25.8, 25.9, 26.6, 26.7 (CH_3), 76.1, 80.0, 80.3, 80.6 ($CH(CH_3)_2$), 119.7, 120.0, 127.7, 128.3, 139.1 (Ar), 150.6 (NCH), 168.5 (Ar–O). Elemental *Anal.* Calc. for $C_{38}H_{64}N_4O_{16}Ti_3$: C, 46.7; H, 6.61; N, 5.74. Found: C, 47.2; H, 6.54; N, 5.66%.

4.5. Preparation of $Ti_2(\mathbf{4})_4(O^iPr)_4$

A solution of *syn*-pyridine-2-aldoxime (1.22 g, 10 mmol) was prepared in dry acetonitrile (10 ml) under an inert atmosphere. To this $Ti(O^iPr)_4$ (1.5 ml, 5 mmol) was added to give a bright orange suspension. This suspension was vigorously stirred at reflux for one hour to give a yellow solution. On cooling this solution yielded a crop of colourless blocks. Yield = 0.90 g (44%), melting point = 132–135 °C. ^1H NMR (400 MHz, $CDCl_3$, 25 °C) 1.17 (br, 24H, CH_3), 4.52 (br, 4H, CH), 7.19–7.32 (m, 4H, Ar–H), 7.63–7.83 (m, 8H, Ar–H), 8.30–8.53 (m, 8H, Ar–H and NCH). $^{13}C\{^1H\}$ NMR $CDCl_3$: 25.9 (CH_3), 77.6 ($CH(CH_3)_2$), 121.4, 122.1, 124.2, 136.9, (Ar), 149.8 (NCH). Elemental *Anal.* Calc. for $C_{36}H_{48}N_8O_8Ti_2$: C, 53.0; H, 5.93; N, 13.72. Found: C, 52.2; H, 5.90; N, 13.60%.

Acknowledgement

We would like to thank the EPSRC and Johnson Matthey for funding this work.

Appendix A. Supplementary material

CCDC 607942, 607943, 607944 and 607945 contain the supplementary crystallographic data for this paper. These data can be obtained free of charge via http://www.ccdc.cam.ac.uk/conts/retrieving.html, or from the Cambridge Crystallographic Data Centre, 12 Union Road, Cambridge CB2 1EZ, UK; fax: (+44) 1223-336-033; or e-mail: deposit@ccdc.cam.ac.uk. Supplementary data associated with this article can be found, in the online version, at doi:10.1016/j.poly.2006.09.055.

References

[1] D. Takeuchi, T. Aida, Macromolecules 33 (2000) 4607.
[2] D.C.H. Oakes, V.C. Gibson, A.J.P. White, D.J. Williams, Inorg. Chem. 45 (2006) 3476.
[3] S. Dayagi, Y. Degani, in: S. Patai (Ed.), The Chemistry of the Carbon Nitrogen Double Bond, Interscience, New York, 1970, p. 61.
[4] S. Mandal, A.K. Dey, J. Inorg. Nucl. Chem. 30 (1968) 1221.
[5] J. Charalambous, M.J. Frazer, J. Chem. Soc. (A) (1968) 2361.
[6] A. Singh, C.K. Sharma, A.K. Rai, V.D. Gupta, R.C. Mehrotra, Indian J. Chem., Sect. A (1971) 2440.
[7] A. Singh, A.K. Rai, R.C. Mehrotra, Indian J. Chem. 12 (1974) 512.
[8] L. Nigam, V.D. Gupta, R.C. Mehrotra, Indian J. Chem., Sect. A 20 (1981) 61.
[9] U. Thewalt, R. Friedrich, Z. Naturforsch., Teil B 46 (1991) 475.
[10] S.D. Bull, M.G. Davidson, A.L. Johnson, D. Robinson, M.F. Mahon, Chem. Commun. (2003) 1750.
[11] R. Ghosh, M. Nethaji, A.G. Samuelson, Chem. Commun. (2003) 2556.
[12] E.Y. Tshuva, I. Goldberg, M. Kol, Z. Goldschmidt, Inorg. Chem. 40 (2001) 4263.
[13] A.J. Chmura, M.G. Davidson, M.D. Jones, M.D. Lunn, M.F. Mahon, Dalton Trans. (2006) 887.
[14] M.G. Davidson, M.D. Jones, M.D. Lunn, M.F. Mahon, Inorg. Chem. 45 (2006) 2282.
[15] J.O. Nolte, M. Schneider, B. Neumann, H.G. Stammler, P. Jutzi, Organometallics 22 (2003) 1010.
[16] D.M. Reis, G.G. Nunes, E.L. Sa, G.R. Friedermann, A.S. Mangrich, D.J. Evans, P.B. Hitchcock, G.J. Leigh, J.F. Soares, New J. Chem. 28 (2004) 1168.
[17] K.M. Waltz, P.J. Carroll, P.J. Walsh, Organometallics 23 (2004) 127.
[18] M.S. Ma, R.J. Angelici, D. Powell, R.A. Jacobson, Inorg. Chem. 19 (1980) 3121.
[19] A.D. Cutland, J.A. Halfen, J.W. Kampf, V.L. Pecoraro, J. Am. Chem. Soc. 123 (2001) 6211.
[20] J.M. Thorpe, R.L. Beddoes, D. Collison, C.D. Garner, M. Helliwell, J.M. Holmes, P.A. Tasker, Angew. Chem., Int. Ed. Engl. 38 (1999) 1119.
[21] V. Zerbib, F. Robert, P. Gouzerh, J. Chem. Soc., Chem. Commun. (1994) 2179.
[22] T.J. Boyle, M.A. Rodriguez, T.M. Alam, Dalton Trans. (2003) 4598.
[23] J. Balsells, P.J. Carroll, P.J. Walsh, Inorg. Chem. 40 (2001) 5568.
[24] M.H. Chisholm, J.H. Huang, J.C. Huffman, W.E. Streib, D. Tiedtke, Polyhedron 16 (1997) 2941.
[25] Y. Kim, J.G. Verkade, Organometallics 21 (2002) 2395.
[26] W.W. Ellis, A. Gavrilova, L. Liable-Sands, A.L. Rheingold, B. Bosnich, Organometallics 18 (1999) 332.
[27] R. Ruiz, J. Sanz, F. Lloret, M. Julve, J. Faus, C. Bois, M.C. Munoz, J. Chem. Soc., Dalton Trans. (1993) 3035.
[28] G.P. Khare, R.J. Doedens, Inorg. Chem. 16 (1997) 907.
[29] R. Castarlenas, M.A. Esteruelas, E. Gutierrez-Puebla, Y. Jean, A. Lledos, M. Martin, J. Tomas, Organometallics 18 (1999) 4296.
[30] H. Werner, T. Daniel, W. Knaup, O. Nurnberg, J. Organomet. Chem. 462 (1993) 309.
[31] G. Stokker, J. Org. Chem. 48 (1983) 2613.
[32] G.M. Sheldrick, SHELXL-97, University of Gottingen, Germany, 1997.

2. Experimental

2.1. General procedures

All reactions and manipulations were carried out using standard Schlenk techniques under an atmosphere of pure nitrogen. Solvents were purified, dried and distilled under a nitrogen atmosphere prior to use. Reactions were monitored by TLC. Chromatographic separations and purification were performed on 200-300 mesh silica gel column. The $Co_2(CO)_8$ was purchased from Aldrich. Published procedures or extensions thereof were used to synthesize initial intermediates $FcC(CH_3)_2Fc'$–C≡CH and FcC≡CH [22–24].

IR spectra were recorded on a Nicolet FT-IR spectrometer, KBr disk. Elemental analyses were carried out on a Elementar var III-type analyzer. ^1H and ^{13}C NMR spectra in $CDCl_3$ were recorded on Inova-500 MHz spectrometer. The mass spectra were determined by using Polaris Q MS, Autospec Ultima-TOF and JMS-T100LC instruments. Melting points were determined by using XT-4 melting point apparatus.

2.2. Synthesis of ligand $FcC(CH_3)_2Fc'$–C≡C–C≡C–Ph ($\mathbf{L}_1$)

$FcC(CH_3)_2Fc'$–C≡CH (80 mg, 0.17 mmol), Ph–C≡CH (40 mg, 0.40 mmol) and CuCl (9 mg, 0.09 mmol) were dissolved in 8 ml pyridine. The mixture solution was stirred for 3 h in air at 60 °C. The solvent was removed under reduced pressure. The resulting mixture was washed with saturated NH_4Cl solution and extracted with CH_2Cl_2. The organic phase was incorporated and then dried using the dehydrated $MgSO_4$ and filtrated. The filtrate was concentrated and the residue was subjected to chromatographic separation on the neutral alumina column (2.0 × 30 cm). Elution with a mixture of hexane–benzene (2:1, v/v) afforded a yellow band. The yellow crystal of ligand $\mathbf{L}_1$ was obtained by recrystallizing from hexane–benzene. Yield: 61% (56 mg, 0.10 mmol). m.p. 158–161 °C. *Anal.* Calc. for $C_{33}H_{28}Fe_2$: C, 73.91; H, 5.26. Found: C, 73.67; H, 5.14%. IR (KBr disk) 3089 [Cp, ν_{C-H}]; 2976, 2930, 2863 [$C(CH_3)_2$, ν_{C-H}]; 2208, 2141 [C≡C, $\nu_{C\equiv C}$]; 1588, 1491, 1440 [C_6H_5, $\nu_{C=C}$]; 1105, 999 [Cp, γ_{C-H}]; 818 [Cp, δ_{C-H}]; 755, 688 [C_6H_5, γ_{C-H}] cm^{-1}. ^1H NMR ($CDCl_3$, δ): 7.3–7.5 (m, 5H, C_6H_5), 4.0–4.4 (m, 17H, Cp), 1.5 [s, 6H, $C(CH_3)_2$]. ^{13}C NMR ($CDCl_3$, δ): 132.3, 128.8, 128.4, 122.2 (C_6H_5); 118.6, 102.8, 70.7, 70.2, 68.3, 67.3 (Cp); 82.5, 78.7, 74.8, 71.0 (–C≡C–C≡C–); 33.2, 30.2 [$C(CH_3)_2$]. MS (EI): 536 (M^+).

2.3. Synthesis of ligand Fc–C≡C–C≡C–Ph ($\mathbf{L}_2$)

Fc–C≡CH (100 mg, 0.50 mmol), Ph–C≡CH (50 mg, 1.00 mmol) and CuCl (12 mg, 0.12 mmol) were dissolved in 20 ml pyridine. The mixture solution was stirred for 3 h in air at 60 °C. The solvent was removed under reduced pressure. The resulting mixture was washed with saturated NH_4Cl solution and extracted with CH_2Cl_2.The organic phase was incorporated and then dried using the dehydrated $MgSO_4$ and filtrated. The filtrate was concentrated and the residue was subjected to chromatographic separation on the neutral alumina column (2.0 × 30 cm). Elution with a mixture of hexane–benzene (3:1, v/v) afforded a yellow band. The yellow crystal of ligand $\mathbf{L}_2$ was obtained by recrystallizing from hexane. Yield: 47% (73 mg, 0.24 mmol). m.p. 114–115 °C. *Anal.* Calc. for $C_{20}H_{14}Fe$: C, 77.45; H, 4.55. Found: C, 77.60; H, 4.70%. IR (KBr disk) 3083 [Cp, ν_{C-H}]; 2218, 2145 [C≡C, $\nu_{C\equiv C}$]; 1593, 1490, 1441 [C_6H_5, $\nu_{C=C}$]; 1104, 1001 [Cp, γ_{C-H}]; 817 [Cp, δ_{C-H}]; 755, 688 [C_6H_5, γ_{C-H}] cm^{-1}. ^1H NMR ($CDCl_3$, δ): 7.3–7.5 (m, 5H, C_6H_5), 4.3, 4.6 (2s, 9H, Cp). ^{13}C NMR ($CDCl_3$, δ): 132.3, 128.8, 128.4, 122.2 (C_6H_5); 82.1, 78.9, 74.7, 72.3 (–C≡C–C≡C–); 70.3, 70.1, 69.6, 63.2 (Cp). MS (EI): 310 (M^+).

2.4. Synthesis of complex $[FcC(CH_3)_2Fc'$–C≡C–C≡C–Ph$][Co_2(CO)_6]$ (**1**)

A benzene solution of $Co_2(CO)_8$ (45 mg, 0.13 mmol) and ligand $\mathbf{L}_1$ (70 mg, 0.13 mmol) was stirred for 12 h at room temperature. The solvent of the resulting mixture was removed in vacuum. The residue was dissolved in a minimal amount of benzene and subjected to chromatographic separation on a silica gel column (2.0 × 40 cm). Elution with hexane–benzene (5:1,v/v) afforded four bands, respectively. The first band is red by-product [Ph–C≡C–C≡C–Ph][$Co_2(CO)_6$]$_2$ (14 mg); the second band is the brown-green complex **2** (15 mg); the third and fourth bands are coordinated isomers [$FcC(CH_3)_2Fc'$–C≡C–C_2–Ph]-[$Co_2(CO)_6$] [brown-green oil, Yield: 28% (30 mg, 0.04 mmol); *Anal.* Calc. for $C_{39}H_{28}O_6Co_2Fe_2$: C, 56.97; H, 3.43. Found: C, 57.69; H, 3.74%. IR (KBr disk) ν (CO) 2089s, 2056vs, 2025vs cm^{-1}; $\nu_{C\equiv C}$ 2172w cm^{-1}]. and [$FcC(CH_3)_2Fc'$–C_2–C≡C–Ph][$Co_2(CO)_6$] [brown-green solid, m.p. 124 °C (dec.), Yield: 19% (20 mg, 0.03 mmol). *Anal.* Calc. for $C_{39}H_{28}O_6Co_2Fe_2$: C, 56.97; H, 3.43. Found: C, 57.46; H, 3.75%. IR (KBr disk) ν (CO) 2090s, 2054 vs, 2026vs cm^{-1}; $\nu_{C\equiv C}$ 2172w cm^{-1}]. The isomer [$FcC(CH_3)_2Fc'$–C_2–C≡C–Ph][$Co_2(CO)_6$] of complex **1**: ^1H NMR ($CDCl_3$, δ): 7.3–7.7 (m, 5H, C_6H_5), 3.9–4.5 (m, 17H, Cp), 1.5 [s, 6H, $C(CH_3)_2$]. ^{13}C NMR ($CDCl_3$, δ): 198.7 (CO); 129.2, 128.9, 113.6 (C_6H_5); 100.8, 91.1 (–C≡C–C≡C–); 65.8-72.3 (Cp); 30.3 [$C(CH_3)_2$]. MS (FAB): 822 (M^+).

2.5. Synthesis of complex $[FcC(CH_3)_2Fc'$–C≡C–C≡C–Ph$][Co_2(CO)_6]_2$ (**2**)

A benzene solution of $Co_2(CO)_8$ (77 mg, 0.22 mmol) and ligand $\mathbf{L}_1$ (60 mg, 0.11 mmol) was stirred for 12 h at room temperature. The solvent of the resulting mixture

was removed in vacuum. The residue was dissolved in a minimal amount of benzene and subjected to chromatographic separation on a silica gel column (2.0 × 40 cm). Elution with hexane–benzene (5:1,v/v) afforded a brown-green band (**2**). The crystal of **2** was obtained by recrystallizing from hexane at −20 °C. Yield: 24% (29 mg, 0.03 mmol) m.p. 105 °C (dec.). *Anal.* Calc. for $C_{45}H_{28}O_{12}Co_4Fe_2$: C, 48.78; H, 2.55. Found: C, 48.31; H, 2.64%. IR (KBr disk) *v*(CO) 2097s, 2077vs, 2054s, 2036vs, 2019vs cm^{-1}. ^1H NMR ($CDCl_3$, δ): 7.3–7.5 (m, 5H, C_6H_5), 4.0–4.3 (m, 17H, Cp), 1.6 [s, 6H, $C(CH_3)_2$]. ^{13}C NMR ($CDCl_3$, δ): 198.8 (CO); 129.3, 128.7, 127.8 (C_6H_5); 65.8–72.3 (Cp); 30.5, 29.5 [$C(CH_3)_2$]. MS (FAB): 1108 (M^+).

2.6. Synthesis of complex [Fc–C≡C–C≡C–Ph]-[$Co_2(CO)_6$] (3)

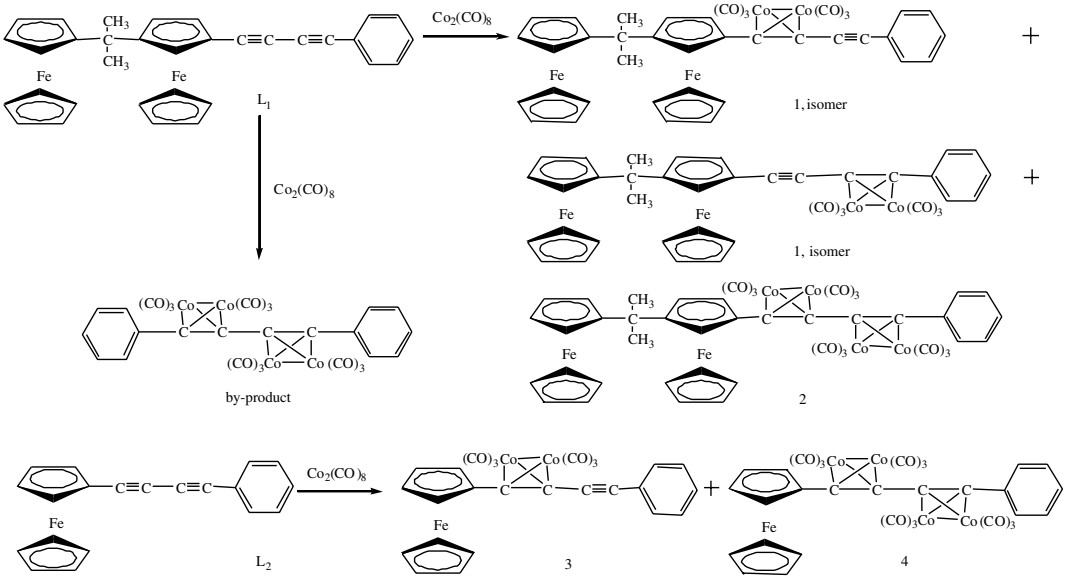
A benzene solution of $Co_2(CO)_8$ (55 mg, 0.16 mmol) and ligand $\mathbf{L}_2$ (50 mg, 0.16 mmol) was stirred for 3 h at room temperature. The solvent of the resulting mixture was removed in vacuum. The residue was dissolved in a minimal amount of benzene and subjected to chromatographic separation on a silica gel column (2.0 × 40 cm). Elution with hexane–benzene (15:1, v/v) afforded a brown-green band (**3**). The complex **3**: Yield: 22% (21 mg, 0.04 mmol). m.p. 83–85 °C. *Anal.* Calc. for $C_{26}H_{14}O_6Co_2Fe$: C, 52.39; H, 2.37. Found: C, 52.46; H, 2.44%. IR (KBr disk) *v* (CO) 2094s, 2058vs, 2038vs, 2011vs cm^{-1}. ^1H NMR ($CDCl_3$, δ): 7.3–7.6 (m, 5H, C_6H_5), 4.3–4.5 (m, 9H, Cp). ^{13}C NMR ($CDCl_3$, δ): 198.7 (CO), 131.4, 128.5 (C_6H_5), 70.1, 69.8, 69.3 (Cp). MS (CSI): 596 (M^+).

2.7. Synthesis of complex [Fc–C≡C–C≡C–Ph]-[$Co_2(CO)_6$]$_2$ (4)

A benzene solution of $Co_2(CO)_8$ (220 mg, 0.64 mmol) and ligand $\mathbf{L}_2$ (100 mg, 0.32 mmol) was stirred for 21 h at room temperature. The solvent of the resulting mixture was removed in vacuum. The residue was dissolved in a minimal amount of benzene and subjected to chromatographic separation on a silica gel column (2.0 × 40 cm). Elution with hexane–benzene (10:1, v/v) afforded a brown-green band (**4**). The crystal of **4** was obtained by recrystallizing from hexane at −20 °C. The complex **4**: Yield: 78% (220 mg, 0.25 mmol). m.p. 135–138 °C. *Anal.* Calc. for $C_{32}H_{14}O_{12}Co_4Fe$: C, 43.58; H, 1.60. Found: C, 43.91; H, 1.68%. IR (KBr disk) *v* (CO) 2075s, 2053vs, 2023vs, 2010s, 2002s cm^{-1}. ^1H NMR ($CDCl_3$, δ): 7.3–7.5 (m, 5H, C_6H_5), 4.3–4.5 (m, 9H, Cp).^{13}C NMR ($CDCl_3$, δ): 199.1 (CO), 138.4, 129.3, 128.6, 128.3 (C_6H_5), 88.3 (–C≡C–C≡C–), 71.1, 69.6, 68.7 (Cp). MS (FAB): 882 (M^+).

2.8. X-ray crystallography of compounds L_1, L_2, 2 and 4

The crystals of $\mathbf{L}_1$, $\mathbf{L}_2$, **2** and **4** were mounted on a glass fiber, respectively. All measurements were made on the Bruker SMART APEX CCD diffractometers with graphite monochromated Mo Kα ($\lambda = 0.71073$ Å) radiation. All data were collected at 20 °C using the φ and ω scan techniques. All structures were solved by direct methods and expanded using Fourier technique [25]. An absorption correction based on the SADABS was applied [26]. All non-hydrogen atoms were refined by the full matrix least-squares on F^2. Hydrogen atoms were located and refined by geometry method. The cell refinement, data collection and reduction were done by Bruker SMART and SAINT [27].



Scheme 1.

Table 1
Crystal data and structure refinement for $\mathbf{L}_1$, $\mathbf{L}_2$, **2** and **4**

Identification code	$\mathbf{L}_1$	$\mathbf{L}_2$	**2**	**4**
Empirical formula	$C_{33}H_{28}Fe_2$	$C_{20}H_{14}Fe$	$C_{45}H_{28}O_{12}Co_4Fe_2$	$C_{32}H_{14}O_{12}Co_4Fe$
Formula weight	536.25	310.16	1108.09	882.00
Temperature (K)	293(2)	293(2)	293(2)	293(2)
Wavelength (Å)	0.71073	0.71073	0.71073	0.71073
Crystal system	triclinic	monoclinic	monoclinic	monoclinic
Space group	$P\bar{1}$	$P2(1)/n$	$P2(1)/n$	$P2(1)/c$
Unit cell dimensions				
a (Å)	6.288(2)	6.2934(17)	18.923(7)	18.079(6)
b (Å)	13.222(5)	12.816(3)	9.572(4)	10.746(3)
c (Å)	15.440(5)	18.460(5)	24.789(10)	16.950(5)
α (°)	84.772(5)	90	90	90
β (°)	83.430(5)	90.498(4)	103.770(6)	101.415(4)
γ (°)	81.642(5)	90	90	90
Volume (Å^3)	1258.0(8)	1488.9(7)	4361(3)	3227.7(17)
Z	2	4	4	4
D_{calc} (Mg/m^3)	1.416	1.384	1.688	1.815
Absorption coefficient (mm^{-1})	1.173	1.002	2.196	2.515
F(000)	556	640	2216	1744
Crystal size (mm)	$0.35 \times 0.15 \times 0.10$	$0.15 \times 0.10 \times 0.10$	$0.30 \times 0.15 \times 0.10$	$0.15 \times 0.15 \times 0.10$
θ Range (°)	1.56–25.01	1.93–26.01	1.22–26.01	1.15–26.01
Limiting indices	$7 \leqslant h \leqslant 7$, $15 \leqslant k \leqslant 12$, $18 \leqslant l \leqslant 16$	$7 \leqslant h \leqslant 7$, $15 \leqslant k \leqslant 15$, $22 \leqslant l \leqslant 8$	$23 \leqslant h \leqslant 23$, $11 \leqslant k \leqslant 10$, $30 \leqslant l \leqslant 24$	$22 \leqslant h \leqslant 21$, $9 \leqslant k \leqslant 13$, $18 \leqslant l \leqslant 20$
Reflections collected	5322	6727	19324	14012
Independent reflections (R_{int})	4377 (0.0168)	2929 (0.0635)	8564 (0.0732)	6313 (0.0334)
Completeness to θ (%)	98.3	99.9	99.8	99.4
Maximum and minimum transmission	0.8917 and 0.6843	0.9065 and 0.8643	0.8103 and 0.5587	0.7870 and 0.7041
Data/restraints/parameters	4377/0/318	2929/0/190	8564/0/570	6313/0/442
Goodness-of-fit on F^2	0.836	0.964	0.840	1.003
Final R indices [$I > 2\sigma(I)$]	$R_1 = 0.0346$, $wR_2 = 0.0638$	$R_1 = 0.0519$, $wR_2 = 0.0905$	$R_1 = 0.0590$, $wR_2 = 0.1303$	$R_1 = 0.0341$, $wR_2 = 0.0665$
R indices (all data)	$R_1 = 0.0569$, $wR_2 = 0.0672$	$R_1 = 0.1227$, $wR_2 = 0.1111$	$R_1 = 0.1488$, $wR_2 = 0.1676$	$R_1 = 0.0558$, $wR_2 = 0.0783$
Largest difference in peak and hole (e Å^{-3})	0.321 and −0.298	0.442 and −0.200	0.911 and −0.574	0.434 and −0.269
Weighing scheme	calc. $w = 1/[\sigma^2(F_o^2) + (0.0285P)^2 + 0.0000P]$, $P = (F_o^2 + 2F_c^2)/3$	calc. $w = 1/[\sigma^2(F_o^2) + (0.0430P)^2 + 0.0000P]$, $P = (F_o^2 + 2F_c^2)/3$	calc. $w = 1/[\sigma^2(F_o^2) + (0.0835P)^2 + 0.0000P]$, $P = (F_o^2 + 2F_c^2)/3$	calc. $w = 1/[\sigma^2(F_o^2) + (0.0289P)^2 + 0.9976P]$, $P = (F_o^2 + 2F_c^2)/3$

The structure solution and refinement were performed by SHELXSL97 [28].

3. Results and discussion

3.1. Synthesis and characterization of compounds L_1, L_2, 1, 2, 3 and 4

The reactions carried out in this work are summarized in Scheme 1. A new ligand $FcC(CH_3)_2Fc'$–C≡C–C≡C–Ph ($\mathbf{L_1}$) was synthesized by the cross coupling reaction of $FcC(CH_3)_2Fc'$–C≡CH and Ph–C≡CH in the presence of catalyst CuCl, and ligand Fc–C≡C–C≡C–Ph ($\mathbf{L_2}$) was obtained by the similar route. Complexes $[FcC(CH_3)_2Fc'–C≡C–C≡C–Ph][Co_2(CO)_6]$ (**1**) and $[Fc–C≡C–C≡C–Ph][Co_2(CO)_6]$ (**3**) were achieved by the reactions of $\mathbf{L_1}$ and $\mathbf{L_2}$ with equal $Co_2(CO)_8$ under mild condition, respectively, and complexes $[FcC(CH_3)_2Fc'–C≡C–C≡C–Ph][Co_2(CO)_6]_2$ (**2**) and $[Fc–C≡C–C≡C–Ph]$- $[Co_2(CO)_6]_2$ (**4**) were provided by the reactions of $\mathbf{L_1}$ and $\mathbf{L_2}$ with excess $Co_2(CO)_8$, respectively. By-product $[Ph–C≡C–C≡C–Ph][Co_2(CO)_6]_2$ is probably produced by the self-coupling of the fragment –C≡C–Ph of ligand $FcC(CH_3)_2Fc'$–C≡C–C≡C–Ph and the reaction with $Co_2(CO)_8$. The coordinated isomers of complex **1**, $[FcC(CH_3)_2Fc'–C≡C–C_2–Ph][Co_2(CO)_6]$ and $[FcC(CH_3)_2Fc'–C_2–C≡C–Ph][Co_2(CO)_6]$ have successfully been separated by the column chromatography technique.

Ligands $\mathbf{L_1}$ and $\mathbf{L_2}$ are yellow and air-stable crystal compound which is soluble in both non-polar solvents such as hexane, petroleum ether, benzene and polar solvents such as diethylether and chloroform. Complexes **2** and **4** are brown-green and air-stable crystal compound which their solubility is similar to ligands $\mathbf{L_1}$ and $\mathbf{L_2}$ and complexes **1** and **3** are also brown-green but air-sensitive. By-product $[Ph–C≡C–C≡C–Ph][Co_2(CO)_6]_2$ is red air-stable crystal compound and the coordinated isomers $[FcC(CH_3)_2Fc'–C≡C–C_2–Ph][Co_2(CO)_6]$ and $[FcC(CH_3)_2Fc'–C_2–C≡C–Ph][Co_2(CO)_6]$ are oil compound, which their solubility is also similar to ligand $\mathbf{L_1}$.

The FTIR spectra in the region 2097–2002 cm^{-1} confirm that there is the coordinated $Co_2(CO)_6$ species and ^1H and ^{13}C NMR reflect that there are Fc, Ph, C≡C, $C(CH_3)_2$ and CO groups in complexes **1**, **2**, **3** and **4**. The structure and composing of compounds $\mathbf{L_1}$, $\mathbf{L_2}$, **1**, **2**, **3** and **4** are further proved by the data of their elemental analysis and MS. The molecular structures of compounds $\mathbf{L_1}$, $\mathbf{L_2}$, **2** and **4** were determined by X-ray crystallography.

3.2. Molecular structures of compounds L_1, L_2, 2 and 4

The molecular structures of compounds $\mathbf{L_1}$, $\mathbf{L_2}$, **2** and **4** were determined by X-ray single crystal analysis. Crystal data and relevant structural parameters are enumerated in Table 1.The structures with the atom numbering scheme are shown in Figs. 1–4, respectively, and the selected bond lengths and angles for $\mathbf{L_1}$, $\mathbf{L_2}$, **2** and **4** are listed in Table 2.

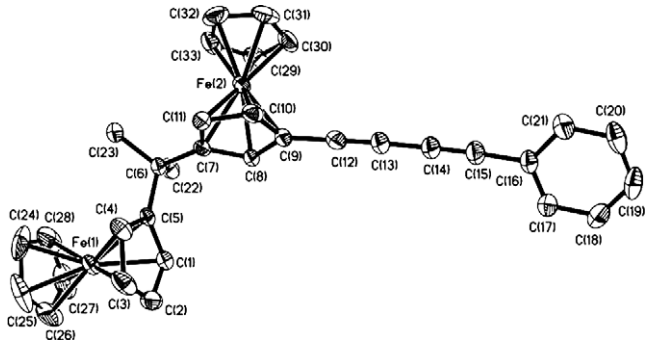


Fig. 1. Molecular structure of ligand L_1.

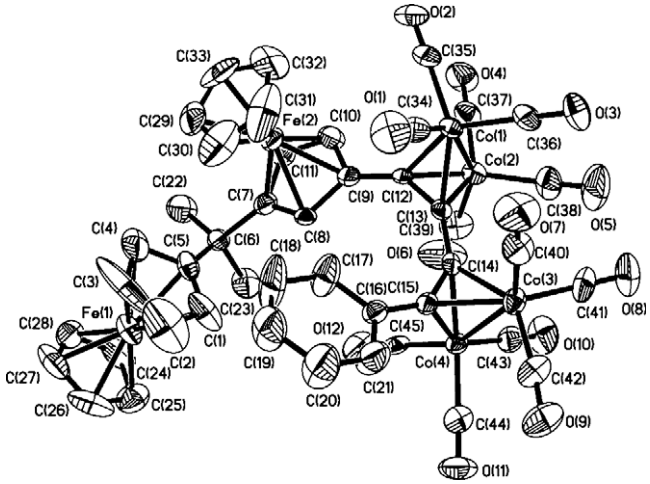


Fig. 2. Molecular structure of complex **2**.

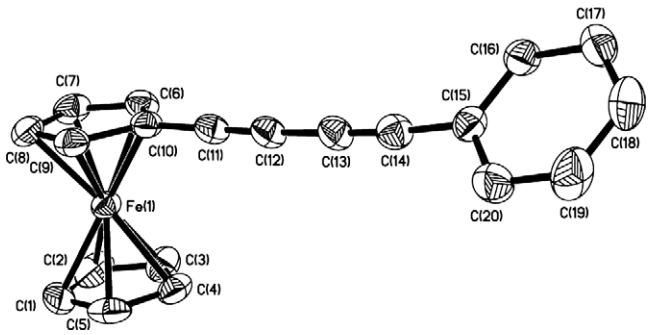


Fig. 3. Molecular structure of ligand L_2.

The molecule of ligand $\mathbf{L_1}$ contains a butadiynyl chain, of which terminals are phenyl and bisferrocenylpropane groups, respectively (see Fig. 1). The bond distances C(12)–C(13) (1.193 Å) and C(14)–C(15) (1.200 Å) show there are carbon–carbon triple bonds in $\mathbf{L_1}$. The shorter C(9)–C(12) (1.436 Å), C(13)–C(14) (1.370 Å) and C(15)–C(16) (1.432 Å) bond distances are the results of electron delocalization of the C_4 diyne chain, phenyl unit and cyclopentadiene ring. The data of the bond angles [C(9)–C(12)–C(13), 174.6°; C(12)–C(13)–C(14), 177.6°; C(13)–C(14)–C(15), 178.0°; C(14)–C(15)–C(16), 177.0°] demonstrate

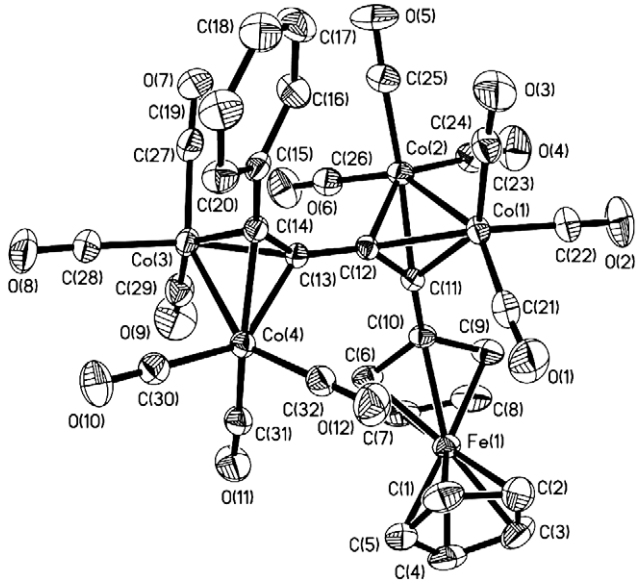


Fig. 4. Molecular structure of complex **4**.

the carbon chain C(9) C(12) C(13) C(14) C(15) C(16) is nearly linear structure. The bond angle C(22)–C(6)–C(23) (108.5°) is close to 109° and other bond angles [C(5)–C(6)–C(7), 105.3°; C(5)–C(6)–C(22), 110.8°; C(5)–C(6)–C(23), 111.0°; C(7)–C(6)–C(22), 111.4°; C(7)–C(6)–C(23), 110.0°] clearly deviate from 109° around the sp^3-hybridized C(6) in $\mathbf{L}_1$ because of the influence of large bulk of ferrocenyl moieties.

In complex **2** the bond angle data [C(9)–C(12)–C(13), 143.4°; C(12)–C(13)–C(14), 145.8°; C(13)–C(14)–C(15), 142.9°; C(14)–C(15)–C(16), 141.4°] and the torsion angle [C(12)–C(13)–C(14)–C(15), −39°] demonstrate the construction of $\mathbf{L}_1$ is altered from the linear to nonlinear structure while $\mathbf{L}_1$ was coordinated to $Co_2(CO)_6$ units. It is noteworthy that $Co_2(CO)_6$ units are coordinated to the alkyne bond in a *cis* configuration and two terminal groups (phenyl and bisferrocenylpropane) are also in a *cis* position (see Fig. 2). Because of a large substituted group bisferrocenylpropane, the molecular structure of **2** is quite different from **4**.

In $\mathbf{L}_1$ the distance of Fe atom to the plane of cyclopentadiene ring [Fe_1 to plane (1) C(1)C(2)C(3)C(4)C(5), 1.65 Å; Fe_1 to plane (2) C(24)C(25)C(26)C(27)C(28), 1.65 Å; Fe_2 to plane (3) C(7)C(8)C(9)C(10)C(11), 1.64 Å; Fe_2 to plane (4) C(29)C(30)C(31)C(32)C(33), 1.66 Å] is nearly equal. The dihedral angles between plane (1) C(1)C(2)C(3)C(4)C(5) and plane (2) C(24)C(25)C(26)C(27)C(28) (3.59°) and between plane (3) C(7)C(8)C(9)C(10)C(11) and plane (4) C(29)C(30)C(31)C(32)C(33) (3.57°) in $\mathbf{L}_1$ reveal that two Cp planes in Fc or Fc′ deviate from parallel because of different substituted Cp ring and steric interaction. It is interesting to note that the dihedral angle between plane (2) and plane (3) is nearly perpendicular(88.98°) as a result of the steric influence. In **2** the distance of Fe atom to the plane

Table 2
Selected bond lengths (Å) and angles (°) for $\mathbf{L}_1$, $\mathbf{L}_2$, **2** and **4**

Bond lengths				Bond angles			
***L*$_1$**							
C(1)–C(5)	1.414(4)	C(12)–C(13)	1.193(4)	C(1)–C(5)–C(6)	127.2(2)	C(12)–C(13)–C(14)	177.6(3)
C(5)–C(6)	1.523(3)	C(13)–C(14)	1.370(4)	C(5)–C(6)–C(7)	105.3(2)	C(13)–C(14)–C(15)	178.0(3)
C(6)–C(22)	1.529(3)	C(14)–C(15)	1.200(4)	C(6)–C(7)–C(8)	126.5(2)	C(14)–C(15)–C(16)	177.0(3)
C(8)–C(9)	1.434(3)	C(15)–C(16)	1.432(4)	C(8)–C(9)–C(12)	127.4(3)	C(15)–C(16)–C(17)	119.8(3)
C(9)–C(12)	1.436(4)	C(16)–C(17)	1.380(4)	C(9)–C(12)–C(13)	174.6(3)	C(15)–C(16)–C(21)	121.5(3)
***L*$_2$**							
C(6)–C(10)	1.430(5)	C(12)–C(13)	1.385(6)	C(6)–C(10)–C(11)	127.9(4)	C(12)–C(13)–C(14)	177.5(4)
C(10)–C(11)	1.423(6)	C(13)–C(14)	1.185(5)	C(10)–C(11)–C(12)	178.3(4)	C(13)–C(14)–C(15)	175.9(4)
C(11)–C(12)	1.191(5)	C(14)–C(15)	1.443(6)	C(11)–C(12)–C(13)	176.8(4)	C(14)–C(15)–C(16)	120.6(4)
2							
C(9)–C(12)	1.441(9)	Co(1)–C(13)	1.981(7)	C(8)–C(9)–C(12)	129.5(7)	Co(2)–C(12)–C(13)	70.4(4)
C(12)–C(13)	1.349(9)	Co(2)–Co(12)	1.973(7)	C(9)–C(12)–C(13)	143.4(6)	Co(2)–C(13)–C(12)	69.7(4)
C(13)–C(14)	1.429(9)	Co(2)–C(13)	1.981(7)	C(12)–C(13)–C(14)	145.8(6)	Co(1)–Co(2)–C(12)	51.2(2)
C(14)–C(15)	1.350(9)	Co(3)–Co(4)	2.449(2)	C(13)–C(14)–C(15)	142.9(6)	C(12)–Co(1)–Co(2)	51.6(2)
C(15)–C(16)	1.448(9)	Co(3)–C(14)	1.970(7)	C(14)–C(15)–C(16)	141.4(6)	Co(3)–C(14)–C(15)	69.2(4)
C(16)–C(17)	1.350(1)	Co(3)–C(15)	1.952(6)	C(15)–C(16)–C(17)	122.4(7)	Co(3)–C(15)–C(14)	70.6(4)
Co(1)–Co(2)	2.457(2)	Co(4)–C(14)	1.982(7)	Co(1)–C(12)–C(13)	70.7(4)	Co(4)–C(14)–C(15)	69.2(4)
Co(1)–C(12)	1.962(6)	Co(4)–C(15)	1.961(7)	Co(1)–C(13)–C(12)	69.3(4)	Co(4)–C(15)–C(14)	70.8(4)
4							
Co(1)–Co(2)	2.459(9)	Co(4)–C(14)	1.942(3)	C(11)–Co(1)–Co(2)	51.95(1)	C(14)–Co(4)–Co(3)	51.86(1)
Co(1)–C(11)	1.954(3)	C(9)–C(10)	1.427(5)	C(11)–Co(2)–Co(1)	50.79(9)	C(9)–C(10)– C(11)	125.7(3)
Co(1)–C(12)	1.996(3)	C(10)–C(11)	1.448(4)	C(12)–Co(1)–Co(2)	51.98(9)	C(10)–C(11)–C(12)	147.4(3)
Co(2)–C(11)	1.985(3)	C(11)–C(12)	1.346(4)	C(12)–Co(2)–Co(1)	51.98(9)	C(11)–C(12)–C(13)	145.8(3)
Co(2)–C(12)	1.996(3)	C(12)–C(13)	1.431(4)	C(13)–Co(3)–Co(4)	52.03(9)	C(12)–C(13)–C(14)	143.5(3)
Co(3)–Co(4)	2.460(9)	C(13)–C(14)	1.343(4)	C(13)–Co(4)–Co(3)	51.45(9)	C(13)–C(14)–C(15)	141.9(3)
Co(3)–C(13)	1.978(3)	C(14)–C(15)	1.464(4)	C(14)–Co(3)–Co(4)	50.46(1)	C(14)–C(15)–C(16)	119.6(3)

of cyclopentadiene ring [Fe(1) to plane(1), 3.32 Å; Fe(1) to plane (2), 6.86 Å; Fe (2) to plane (3), 0.65Å; Fe (2) to plane (4), 2.57Å] is quite different from $\mathbf{L}_1$ because of the coordination effect of Co_2 core with diyne. The dihedral angles between plane (1) and plane (2) (5.27°) and between plane (3) and plane (4) (2.12°) demonstrate that two Cp planes in **2** also deviate from parallel like $\mathbf{L}_1$ but the dihedral angle between plane (2) and plane (3) alters from 88.98° to 67.11° as a result of the diyne coordinated to Co_2 core.

The molecule of ligand $\mathbf{L}_2$ also contains a butadiynyl chain but its terminals are phenyl and ferrocenyl group, respectively (see Fig. 3). The relevant bond distances in $\mathbf{L}_2$ are similar to $\mathbf{L}_1$, which also reveal the electron delocalization among C_4 diyne chain, phenyl and cyclopentadiene ring. The data of bond angles (see Table 2) demonstrate the carbon chain C(10) C(11) C(12) C(13) C(14) C(15) of $\mathbf{L}_2$ is nearly linear structure.

The –C≡C–C≡C– acetylenic linkage in complex **4** is nonlinear, which is proved by the bond angles [C(10)–C(11)–C(12), 147.4°; C(11)–C(12)–C(13), 145.8°; C(12)–C(13)–C(14), 143.5°; C(13)–C(14)–C(15), 141.9°] and the torsion angle [C(11)–C(12)–C(13)–C(14), 159.3°], contrasting sharply with the linear –C≡C–C≡C– carbon chain of $\mathbf{L}_2$. In **4** the two C_2Co_2 units are coordinated to the C_4 diyne chain in a *trans* configuration. The outer C atoms of the diyne chain, C(11) and C(14), carry ferrocenyl and phenyl substituents also orientated *trans* to each other (see Fig. 4). The molecular structure of $\mathbf{L}_2$ and **4** are similar to compounds Fc–C≡C–C≡C–Fc and Fc–C≡C–C≡C–Fc $[Co_2(CO)_6]_2$, respectively [11,29,30].

In $\mathbf{L}_2$ the distance of Fe atom to the plane of cyclopentadiene ring [Fe to plane (1) C(1)C(2)C(3)C(4)C(5), 1.65 Å; Fe to plane (2) C(6)C(7)C(8)C(9)C(10), 1.64 Å] is similar to that in$\mathbf{L}_1$. The dihedral angle (0.26°) between plane (1) and plane (2) shows that two Cp planes are nearly parallel. The dihedral angle between plane (2) and the plane of phenyl ring is 40.98°. Although the distance of Fe atom to the plane of cyclopentadiene ring in **4** is similar to that in $\mathbf{L}_2$, the dihedral angle of **4** is quite different from that of $\mathbf{L}_2$. In **4** the dihedral angle between plane (1) and plane (2) (4.94°) shows that two Cp planes in Fc′ deviate from parallel and the dihedral angle between plane (2) and the plane of phenyl ring (53.02°) become larger because of the steric influences as a result of the diyne coordinated to Co_2 core.

4. Conclusion

Two butadiynyl ligands $FcC(CH_3)_2Fc'$–C≡C–C≡C–Ph ($\mathbf{L}_1$) and Fc–C≡C–C≡C–Ph ($\mathbf{L}_2$) have been synthesized by the cross coupling reaction of terminal alkynes and four corresponding complexes $[FcC(CH_3)_2Fc'–C≡C–C≡C–Ph][Co_2(CO)_6]_n$ [(**1**): $n = 1$; (**2**): $n = 2$] and [Fc–C≡C–C≡C–Ph][$Co_2(CO)_6$]$_n$ [(**3**): $n = 4$ 1; (**4**): $n = 2$] have successfully been obtained by the reaction of ligands $\mathbf{L}_1$ and $\mathbf{L}_2$ with $Co_2(CO)_8$, respectively. The composition and structure of compounds $\mathbf{L}_1$, $\mathbf{L}_2$, **1**, **2**, **3** and **4** have been characterized by elemental analysis, FTIR, ^1H and ^{13}C NMR and MS. The crystal structures of compounds $\mathbf{L}_1$, $\mathbf{L}_2$, **2** and **4** have been determined by X-ray single crystal diffraction. The syntheses and structures of compounds $\mathbf{L}_1$, **1**, **2**, **3** and **4** and the structure of ligand $\mathbf{L}_2$ are firstly reported. The molecular structure data show the butadiynyl groups of ligands $\mathbf{L}_1$ and $\mathbf{L}_2$ are nearly linear structure and the coordinated butadiynyl groups in the complexes **2** and **4** have deviated from linear structure of ligands $\mathbf{L}_1$ and $\mathbf{L}_2$.

Acknowledgments

We are grateful to the Startup Foundation of China Scholar Abroad, the Inner Mongolia Talent Foundation and the Inner Mongolia Science Foundation for financial support of this work.

Appendix A. Supplementary material

CCDC 297322, 297319, 297324 and 297321 contain the supplementary crystallographic data for $\mathbf{L}_1$, $\mathbf{L}_2$, **2** and **4**. These data can be obtained free of charge via http://www.ccdc.cam.ac.uk/conts/retrieving.html, or from the Cambridge Crystallographic Data Centre, 12 Union Road, Cambridge CB2 1EZ, UK; fax: (+44) 1223-336-033; or e-mail: deposit@ccdc.cam.ac.uk. Supplementary data associated with this article can be found, in the online version, at doi:10.1016/j.poly.2006.09.044.

References

[1] F. Barriere, W.E. Geiger, J. Am. Chem. Soc. 128 (2006) 3980.
[2] M.I. Bruce, P.J. Low, F. Hartl, P.A. Humphrey, P. Montigny, M. Jevric, C. Lapinte, G.J. Perkins, R.L. Roberts, B.W. Skelton, A.H. White, Organometallics 24 (2005) 524.
[3] R.C.J. Atkinson, V.C. Gibson, N.J. Long, Chem. Soc. Rev. 33 (2004) 213.
[4] (a) R.D. Adams, B. Qu, M.D. Smith, T.A. Albright, Organometallics 21 (2002) 2970;
(b) R.D. Adams, O.S. Kwon, B. Qu, M.D. Smith, Organometallics 20 (2001) 5225.
[5] A. Tarraga, P. Molina, D. Curiel, V.M. Desamparados, Organometallics 20 (2001) 2145.
[6] L. Cuffe, R.D.A. Hudson, J.F. Gallagher, S. Jennings, C.J. McAdam, R.B.T. Connelly, A.R. Manning, B.H. Robinson, J. Simpson, Organometallics 24 (2005) 2051.
[7] Q.H. Wei, L.Y. Zhang, L.X. Shi, Z.N. Chen, Inorg. Chem. Commun. 7 (2004) 286.
[8] G. Gervasio, P.J. King, D. Marabello, E. Sappa, Inorg. Chim. Acta 350 (2003) 215.
[9] R.D. Adams, B. Qu, M.D. Smith, Inorg. Chem. 40 (2001) 2932.
[10] L.A. Hore, C.J. McAdam, J.L. Kerr, N.W. Duffy, B.H. Robinson, J. Simpson, Organometallics 19 (2000) 5039.
[11] N. Duffy, J. McAdam, C. Nervi, D. Osella, M. Ravera, B. Robinson, J. Simpson, Inorg. Chim. Acta 247 (1996) 99.
[12] T. Ren, Organometallics 24 (2005) 4854.
[13] D. Osella, L. Milone, C. Nervi, M. Ravera, Eur. J. Inorg. Chem. (1998) 1473.
[14] R. Dembinski, T. Bartik, B. Bartik, M. Jaeger, J.A. Gladysz, J. Am. Chem. Soc. 122 (2000) 810.
[15] N. Robertson, C.A. McGowan, Chem. Soc. Rev. 32 (2003) 96.
[16] (a) M.I. Bruce, K. Costuas, T. Davin, B.G. Ellis, J.F. Halet, C. Lapinte, P.J. Low, M.E. Smith, B.W. Skelton, L. Toupet, A.H. White, Organometallics 24 (2005) 3864;

(b) M.I. Bruce, B.G. Ellis, P.J. Low, B.W. Skelton, A.H. White, Organometallics 22 (2003) 3184.
[17] R.D. Adams, U.H.F. Bunz, W. Fu, L. Nguyen, J. Organomet. Chem. 578 (1999) 91.
[18] G. Laus, H. Schottenberger, J. Lukasser, K. Wurst, J. Schutz, K.H. Ongania, L. Zsolnai, J. Organomet. Chem. 690 (2005) 691.
[19] R.D. Adams, B. Qu, Organometallics 19 (2000) 2411.
[20] C.J. McAdam, N.W. Duffy, B.H. Robinson, J. Simpson, Organometallics 15 (1996) 3935.
[21] T.J.J. Muller, J. Blumel, J. Organomet. Chem. 683 (2003) 354.
[22] M.D. Rausch, A. Siegel, L.P. Klemann, J. Org. Chem. 31 (1966) 2703.
[23] J.G. Rodriguez, A. Onate, R.M. Martin-Villamil, I. Fonseca, J. Organomet. Chem. 513 (1996) 71.
[24] M. Rosenblum, N. Brawn, J. Papenmeier, M. Applebaum, J. Organomet. Chem. 6 (1966) 173.
[25] G.M. Sheldrick, Acta Crystallogr., Sect. A 46 (1990) 467.
[26] G.M. Sheldrick, SADABS, Siemens Area Detector Absorption, Correction Software, University of Göttingen, Germany, 1997.
[27] Bruker, SMART and SAINT. Area Detector Control and Integration Software, Bruker Analytical X-ray Instruments Inc., Madison, WI, USA, 1998.
[28] G.M. Sheldrick, SHELXL-97. Program for Crystal Structure Analysis, University of Göttingen, Germany, 1997.
[29] Z. Yuan, G. Stringer, I.R. Jobe, D. Kreller, K. Scott, L. Koch, N.J. Taylor, T.B. Marder, J. Organomet. Chem. 452 (1993) 115.
[30] Q.L. Suo, L.M. Han, Y.B. Wang, J.H. Ye, N. Zhu, X.B. Leng, J. Sun, J. Coord. Chem. 57 (2004) 1591.

Intermolecular interactions analysis in crystalline systems is very important in this field of chemical research. These interactions are responsible for crystal packing, and their understanding could lead to the comprehension of collective properties, providing the design of new structures with specific physical and chemical properties [3]. In crystal engineering, oxocarbon ions have been currently employed as building blocks [3–5], due to the simplicity of these cyclic species. In particular, squarate ion ($C_4O_4^{2-}$) exhibits very unusual electronic and vibrational properties, as can be seen in several investigations in literature [6]. This species presents D_{4h} symmetry and high degree of electronic delocalization, which are very interesting characteristics discussed in many structural [4,7] and spectroscopic investigations [8]. In addition, squarate ion shows both terminal and bridging coordination modes, such as 1,2-bidentate chelating [9] or 1,2-bis(monodentate) [10] and 1,3-bis(monodentate) [11] bridging and even using all four oxygen atoms [2c]. The 1,3-bis(monodentate) bridging coordination mode is very interesting to generate one dimensional (1D) polymeric structures [12,13] and the dimensionality can be expanded to 2D or 3D arrays using multidentate spacer ligands [14]. In this sense, pyridyl-donor ligands, like 1,3-bis(4-pyridyl)propane (BPP), show up as good candidates to generate 2D and 3D network designs [15].

BPP is a very flexible versatile bifunctional ligand [16] due to its aliphatic chain [–$(CH_2)_3$–] between two pyridyl rings. It presents different conformations and consequently different topologies in polymeric structures can be reached by using this ligand [17]. Several determined crystal structures of transition metal and BPP indicate the formation of polymeric structures with 1D, 2D and 3D network designs [18]. This nitrogen ligand can assume different conformations (TT, TG, GG and GG′) that display quite different N–N distances [17,18]. Comparing some crystal structures involving BPP as ligand, Carlucci et al. [19] defined a range of N–N distance in each type of conformation. For instance, for TT this range is 9.1–10.1 Å, for TG is 8.6–9.2 Å, for GG only three examples [20] are found in the literature with distances between 3.9 and 5.3 Å and in GG′ the range is 6.7–8.6 Å.

In this work the synthesis, crystal structure and the vibrational spectra of coordination polymers with BPP and squarate ion ligands and first transition metal ions (M = Mn^{2+}, Co^{2+}, Ni^{2+}, Cu^{2+} and Zn^{2+}) are described. The correlation between crystal data and vibrational spectra is also investigated, with the aim of identifying the intermolecular interactions present in the solid state, as well as their influence on the crystal packing of such structures.

2. Experimental

2.1. Synthesis

$C_{13}H_{14}N_2$ (BPP) (50 mg, 0.25 mmol) and $H_2C_4O_4$ (29 mg, 0.25 mmol) were dissolved in water and mixed. Aqueous solution of metal chloride hydrate (0.25 mmol in 10.0 mL of water) was layered on to the previous solution, and after slow diffusion for a few days, suitable single crystals were obtained and analyzed by vibrational spectroscopy, thermogravimetric analysis and X-ray diffraction techniques. Elemental *Anal.* Calc. for $[C_{13}H_{16}N_2]^{2+}$-$[Mn(C_4O_4)_2(H_2O)_2]^{2-}$ (light yellow, yield = 47%): C, 48.94; N, 5.44; H, 3.88. Found: C, 47.23; N, 4.76; H, 3.82%; *Anal.* Calc. for $[C_{13}H_{16}N_2]^{2+}[Co(C_4O_4)_2(H_2O)_2]^{2-}$ (light pink, yield = 55%): C, 48.56; N, 5.39; H 3.85. Found: C, 48.29; N, 5.26; H, 3.89%; *Anal.* Calc. for $[C_{13}H_{16}N_2]^{2+}$-$[Ni(C_4O_4)_2(H_2O)_2]^{2-}$ (light green, yield = 51%): C, 48.58; N, 5.39; H, 3.86. Found: C, 48.15; N, 5.25; H 4.06%; *Anal.* Calc. for $[C_{13}H_{16}N_2]^{2+}[Cu(C_4O_4)_2(H_2O)_2]^{2-}$ (golden, yield = 50%): C, 48.14; N, 5.35; H, 3.82. Found: C, 46.79; N, 4.70; H 3.91%; *Anal.* Calc. for $[C_{13}H_{16}N_2]^{2+}$-$[Zn(C_4O_4)_2(H_2O)_2]^{2-}$ (colourless, yield = 47%): C, 47.96; N, 5.33; H, 3.81. Found: C, 47.82; N, 5.33; H, 3.85%.

2.2. X-ray diffraction

Single crystal X-ray data were collected in a Nonius Kappa CCD diffractometer with Mo Kα ($\lambda = 0.71073$ Å) at room temperature. Data collection and reduction, and cell refinement were performed by DENZO and SCALEPACK programs [21]. The structures were solved and refined using SHELXL-97 [22]. An empirical isotropic extinction parameter x was refined, according to the method described by Larson [23]. Analytical absorption, Lorentz and polarization effects were corrected. The structures were drawn by ORTEP-3 for Windows [24]. Hydrogen atoms were located from Fourier difference maps. Anisotropic displacement parameters were refined to all non-hydrogen atoms.

2.3. Raman spectra

Fourier-transform Raman spectroscopy was carried out using a Bruker RFS 100 instrument, Nd^{3+}/YAG laser operating at 1064 nm in the near infrared and CCD detector cooled with liquid N_2. Good signal-to-noise ratios were obtained from 2000 scans accumulated over a period of about 30 min, using 4 cm^{-1} as spectral resolution. All spectra were obtained at least twice to show the reproducibility, and no changes in band positions and intensities were observed.

2.4. Infrared spectra

Infrared spectra were obtained in a Bomem MB-102 spectrometer fitted with CsI beam splitter, using KBr disks and spectral resolution of 4 cm^{-1}. Good signal-to-noise ratio was obtained from the accumulation of 128 scans.

2.5. Thermogravimmetric analysis

Thermogravimmetric data were obtained in a Mettler STARe TG50 thermobalance; the samples were heated at

10 °C/min from room temperature to 800 °C in dynamic air flow.

3. Results and discussion

Transition metal complexes of general formulae $\{(H_2BPP)^{2+}[M(C_4O_4)_2(H_2O)_2]^{2-}\}$, where $M = Mn^{2+}$, Co^{2+}, Ni^{2+}, Cu^{2+} and Zn^{2+}, were obtained by slow diffusion of metal chloride aqueous solutions into an aqueous solution containing squaric acid and BPP. In all cases, analytical data suggest the formation of compounds with (1:1:2)/(M^{2+}:BPP:$C_4O_4^{2-}$) stoichiometric ratio. Thermogravimetric curves, which are deposited as Supplementary material, show that Mn^{2+}, Cu^{2+} and Zn^{2+} complexes are stable up to 170 °C, whereas Co^{2+} and Ni^{2+} ones, up to 200 °C. Above these temperatures it can be observed the first weight loss corresponding to two water molecules. The dehydration process occurs at high temperatures indicating the presence of coordination water molecules probably involved in hydrogen bonding. Afterwards, the curves show at least two other weight loss steps attributed to compounds thermodecomposition.

The polymeric nature of compounds was revealed by X-ray single crystal structure analysis. Tables 1 and 2 exhibit crystal data and main geometrical parameters of all transition metal complexes and comparing the listed crystallographic parameters it can be noticed that all compounds are isostructural. Fig. 1 shows the first M^{2+} coordination sphere in a distorted octahedral geometry. Surprisingly, BPP ligands are not coordinated to the metal centers and appear in the cationic form (H_2BPP^{2+}) due to the protonation of pyridyl nitrogen atoms. The formation of H_2BPP^{2+} cation can be explained by the acid-base reaction between squaric acid and BPP.

The metal ions are located in the unit cell inversion center and are surrounded by six oxygen atoms from two squarate ions and two water molecules with average of M–O bond distance of 2.106(2) Å and O–M–O bond angles varying from 83.5° to 96.5°. In the manganese compound it can be observed the longest M–O bond distance to squarate ion, as well as to water molecules (2.174(2) and 2.194(2) Å respectively). However, the shortest M–O bond distances are observed in different complexes: M–O (average of 2.078(2) Å) in nickel and M–O_w (1.980(2) Å) in copper complexes. The average of M–O and M–O_w bond distances are respectively 2.127(2) and 2.085(2) Å. In all compounds the M–O bond distances (M–O2) of one squarate ligand and M–O_w (M–O5) are close to each other when compared to M–O of two squarate ligands (M–O2 and M–O4). Additionally, the two coordination water molecules are involved in medium hydrogen bonds with the non-coordinated oxygen atoms of squarate ligands, as indicated by thermal analysis results, and the average of O···O distance is 2.679(3) Å.

Each squarate ion adopts the 1,3-bis(monodentate) coordination mode and bridges two metal centers giving rise to a two-dimensional (2D) grid with (4,4) topology, as can be seen in Fig. 2. The four-membered rings, formed by metals and squarate ligands, are slightly distorted due to different M–M separations with averages of smaller and larger distances of 8.024 and 8.111 Å, respectively. Squarate rings of four-member topology are almost planar with mean deviation range between 0.011 and 0.016 Å. These rings are not perpendicular to each other, forming an angle around 82° between them. Electronic delocalization is observed in oxocarbon rings since the average of the largest difference in C–C and C–O bond distances is short (respectively 0.006 and 0.018 Å). The oxocarbon rings are within a

Table 1
Crystal data of MH_2BPP complexes

Compound	MnH_2BPP	CoH_2BPP	NiH_2BPP	CuH_2BPP	ZnH_2BPP
Formula	$C_{21}H_{20}N_2O_{10}Mn$	$C_{21}H_{20}N_2O_{10}Co$	$C_{21}H_{20}N_2O_{10}Ni$	$C_{21}H_{20}N_2O_{10}Cu$	$C_{21}H_{20}N_2O_{10}Zn$
Formula weight (g mol^{-1})	515.33	519.32	519.10	523.93	525.76
Crystal system	monoclinic	monoclinic	monoclinic	monoclinic	monoclinic
Space group	*P2/n*	*P2/n*	*P2/n*	*P2/n*	*P2/n*
a (Å)	9.6729(3)	9.5725(4)	9.5262(3)	9.7423(3)	9.6005(3)
b (Å)	8.1471(3)	8.0321(3)	7.9816(3)	7.9262(3)	8.0323(3)
c (Å)	13.4765(6)	13.4487(3)	13.4439(4)	13.5410(6)	13.4436(6)
β (°)	91.774(2)	92.775(2)	93.331(2)	91.571(3)	92.645(3)
V (Å)^3	1061.52(7)	1032.82(6)	1020.47(6)	1045.24(7)	1035.59(7)
Z	2	2	2	2	2
Crystal size (mm)	0.10 × 0.12 × 0.20	0.06 × 0.12 × 0.20	0.06 × 0.09 × 0.21	0.07 × 0.07 × 0.11	0.05 × 0.08 × 0.17
d_{calc} (g cm^{-3})	1.612	1.670	1.689	1.665	1.686
μ(Mo Kα) (cm^{-1})	0.685	0.883	1.003	1.110	1.238
Transmission factors (min/max)	0.891/0.944	0.853/0.948	0.812/0.944	0.906/0.944	0.846/0.946
Reflections measured/unique	13727/2449	11276/2367	11191/2349	9792/2405	10926/2376
Observed reflections [$F_o^2 > 2\sigma(F_o^2)$]	2041	2115	1925	2016	2007
No. of parameters refined	170	170	170	170	170
R	0.0490	0.0399	0.0519	0.0438	0.0443
wR	0.1127	0.1005	0.1154	0.0927	0.1015
S	1.058	1.117	1.077	1.082	1.055
RMS peak (e Å^{-3})	0.149	0.191	0.207	0.178	0.184

Table 2
Selected geometrical parameters of MH_2BPP

	MnH_2BPP	CoH_2BPP	NiH_2BPP	CuH_2BPP	ZnH_2BPP
Bond distance (Å)					
M–O2	2.153(2)	2.091(2)	2.058(2)	2.036(2)	2.092(2)
M–O4	2.194(2)	2.126(2)	2.096(2)	2.277(2)	2.144(2)
M–O5	2.194(2)	2.097(2)	2.069(2)	1.980(2)	2.084(2)
C1–C2	1.458(3)	1.464(3)	1.463(4)	1.461(4)	1.461(4)
C1–C2^{ii}	1.459(3)	1.463(3)	1.466(4)	1.458(4)	1.463(4)
C1–O1	1.254(3)	1.252(3)	1.252(4)	1.249(3)	1.250(3)
C2–O2	1.260(3)	1.256(3)	1.253(4)	1.261(3)	1.258(3)
C3–C4	1.464(3)	1.464(4)	1.456(4)	1.463(4)	1.460(4)
C3–C4^{iv}	1.463(3)	1.470(3)	1.464(4)	1.458(4)	1.460(4)
C3–O3	1.243(3)	1.242(3)	1.244(4)	1.251(4)	1.253(3)
C4–O4	1.263(3)	1.259(3)	1.269(3)	1.261(3)	1.263(3)
N1–N1^{iv}	9.316	9.344	9.357	9.364	9.345
Bond angles (°)					
O2–M–O4	90.50(6)	89.80(6)	90.6(1)	89.30(8)	89.43(8)
O2–M–O5	95.34(6)	96.20(6)	96.4(1)	96.50(9)	96.13(8)
O2–M–O4^{i}	90.58(6)	90.20(6)	90.6(1)	90.70(8)	90.57(8)
O2–M–O5^{i}	84.67(6)	83.82(6)	83.6(1)	83.50(9)	83.87(8)
O5–M–O4	85.75(6)	85.59(6)	85.09(8)	85.56(8)	85.24(8)
O5–M–O4^{i}	94.25(6)	94.41(6)	94.91(8)	94.44(8)	94.76(8)
Hydrogen bond					
D···A (Å)					
O5···O3	2.703(2)	2.688(2)	2.687(3)	2.665(3)	2.687(3)
O5···O1	2.691(2)	2.673(2)	2.670(3)	2.652(3)	2.671(3)
N1···O4^{vi}	2.764(3)	2.773(3)	2.777(4)	2.701(3)	2.762(3)
D–H···A (°)					
O5–H5A···O3	167(4)	173(5)	159(6)	158(4)	159(4)
O5–H5B···O1	164(4)	164(3)	164(7)	167(3)	171(4)
N1–H1···O4	172(4)	166(4)	169(5)	175(4)	172(6)

Symmetry codes: i ($-x$, $-y$, $-z$); ii ($-x$, $-1-y$,$-z$); iv ($1/2-x$, y, $1/2-z$) and vi ($-1/2+x$, $-1-y$, $1/2+z$).

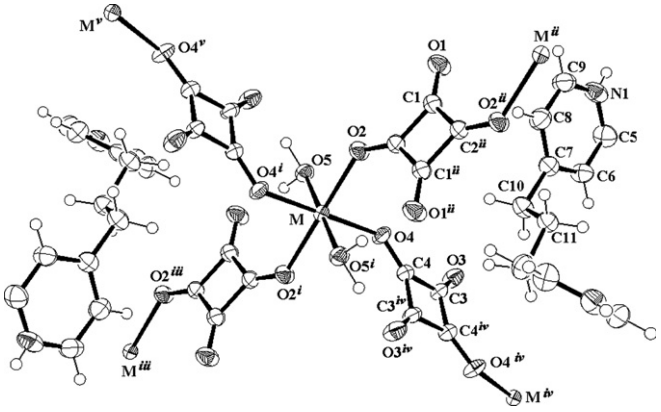


Fig. 1. Crystal structure of MH_2BPP. Symmetry codes: i ($-x$, $-y$, $-z$); ii ($-x$, $-1-y$, $-z$); iii (x, $1+y$, z); iv ($1/2-x$, y, $1/2-z$) and v ($-1/2+x$, $-y$, $-1/2+z$).

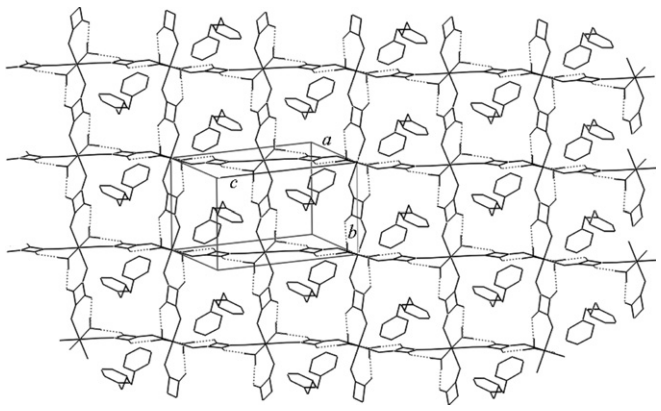


Fig. 2. 2D layer of MH_2BPP showing (4,4) topology and O···O hydrogen bond interactions. Only the hydrogen atoms from water molecules are shown in the figure.

long distance each other and consequently it is not observed π-stacking interaction between them. The supramolecular arrangements are based on single layers, which are not superimposed, showing parallel arrangement of squarate rings along crystallographic *a* axis and ring planes are shifted *ca.* 0.5 Å. Along *b* axis, the squarate rings of adjacent layers are not parallel presenting a rotationz of around 15°.

BPP cationic species are placed inside the four-member ring cavities in two different orientations, inverted to each other, as shown in Fig. 2. In the middle of BPP molecule (C11) is located the twofold axis symmetry. The phenyl rings atoms give rise to planes where the average of deviation of the best plane is 0.004 Å, whereas the range of the angle between phenyl rings is between 76.2° and 78.2°. The smallest angle of phenyl rings is observed for copper

complex and the biggest for manganese. These molecules adopt the TT conformation with N-to-N separation range for all compounds between 9.32 and 9.36 Å. These values are in agreement to other compounds containing BPP ligand in TT conformation structurally characterized [18h,18i,25]. Analysis of topological parameters of π-stacking [1] shows that phenyl rings of adjacent H_2BPP^{2+} layers present centroid–centroid and interplanar distances shorter than 4.0 Å (average of 3.92 and 3.53 Å, respectively), and small horizontal shift (average of 1.19 Å), strongly suggesting π-stacking interaction in these structures. In addition, according to the geometrical parameters of H_2BPP^{2+} displayed in Table 2, BPP cation forms two types of hydrogen bond interactions between layers of four-member rings: N–H···O medium and C–H···O very weak interactions. The presence of all these interactions between two adjacent 2D grids leads to the establishment of a three-dimensional supramolecular array as can be seen in Fig. 3.

Vibrational spectra of these compounds are very similar, and are in agreement with crystal data. The main vibrational modes are listed in Table 3 and Fig. 4 shows the Raman spectra of all compounds. Infrared spectra are deposited as Supplementary materials. In the infrared spectra it can be observed characteristic bands of squarate units around 1500 cm^{-1}, which are related to CC and CO stretching modes, whereas the M–O bond stretching mode is observed at 505 cm^{-1}. Ring breathing of pyridyl group has been assigned to the bands at 995 and 579 cm^{-1} [26,27]. The spectral region between 1600 and 1650 cm^{-1}, where CC and CN stretching modes are expected, is very important in the BPP ligand coordination analysis [17a]. This band shows up at 1605 cm^{-1} for the free ligand and at higher wavenumbers (around 1620 cm^{-1}) when BPP is coordinated to the metal ion. In all investigated compounds infrared spectra it can be seen a medium band at 1640 cm^{-1}, which can be tentatively assigned to the in

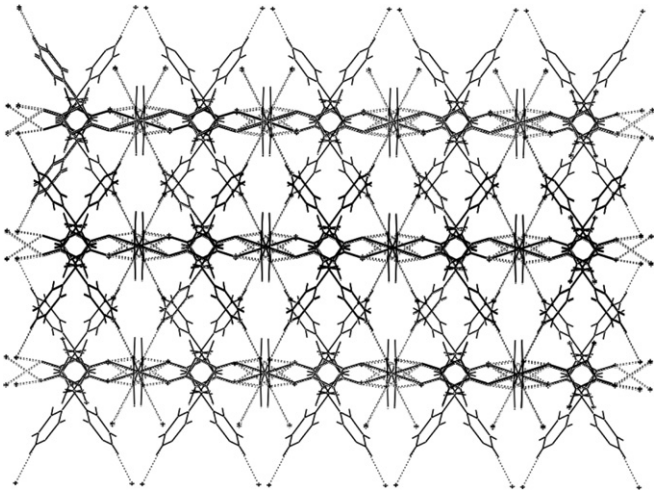


Fig. 3. Three dimensional interactions in MH_2BPP along (1 1 1) direction.

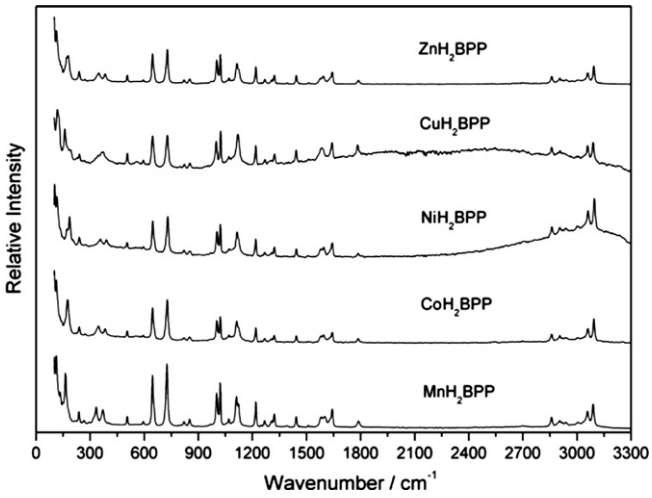


Fig. 4. Raman spectra of MH_2BPP.

Table 3
Vibrational wavenumbers (in cm^{-1}) and tentative assignment of the most important bands observed in the MH_2BPP spectra

MnH_2BPP		CoH_2BPP		NiH_2BPP		CuH_2BPP		ZnH_2BPP		Assignment[a]
IR	R	IR	R	IR	R	IR	R	IR	R	
	333m		346m		358m		343m		346m	δ(CO)
	369m		383m		391m		373m		385vw	
505m	506m	504m	506m	504m	506m	504m	506m	504m	506m	ν(MO)
653w	645s	653m	645s	654w	647s	644w	647s	653w	645s	SQ ring bending
737vw	727vs	736w	728vs	736vw	730vs	736vw	728vs	736vw	728vs	SQ ring breathing
	1021s		1023s		1023s		1023s		1023s	Py ring breathing
1094w	1112s	1095m	1112s	1097m	1116s	1098m	1119s	1096w	1114s	ν(CC)
	1219s		1220m		1218m		1218m		1220s	Py ring bending
1463s		1461vs		1461vs		1462vs		1462vs		ν(CC) + ν(CN)
1498vs		1496vs		1494vs		1488vs		1498vs		
1511vs	1511sh	1510vs	1511sh	1509vs	1509sh	1509sv	1511sh	1510vs	1511sh	
1551s		1548vs		1548vs		1540s		1547s		ν(CC) + ν(CO)
	1602m		1596m		1596m		1598m		1594m	ν(CO)
1639m		1640s		1639s		1638m		1639m		δ(NH)
	1789w		1787w		1787w		1783w		1787w	ν(CO)

[a] SQ = squarate and Py = pyridyl.

plane deformation mode of NH bond, indicating the formation of BPP cationic species, in a very good agreement with the X-ray diffraction data.

Raman spectra of all compounds are also very similar. Ring bending and ring breathing of squarate unit have been observed at 645 and 730 cm^{-1}, respectively. Raman features of pyridyl group at 1220 and 1020 cm^{-1} can also be assigned as described above. An interesting comparison of Raman spectra can be done within squarate alkaline salts [28]. Ring bending and ring breathing modes occur in the same region, indicating that the coordination to metal ions does not affect these specific ring modes. In the Raman spectra of the alkaline salts it can be observed a weak band around 1800 cm^{-1}, assigned to CO bond stretching mode [28]. Similar band is observed around 1790 cm^{-1} in the spectra of all complexes, indicating the presence of non-coordinated CO species in the solid state, which is in agreement with crystal structure where O1 and O3 (Fig. 1) are not bonded to metal site. Previous Raman spectra investigation of transition metal squarates [6d] shows the appearance of two distinct CO stretching modes, observed around 1600–1800 cm^{-1} region. Crystal structures of these squarate complexes [12] show that squarate ion is coordinated to metal sites in a 1,3-bis(monodentate) fashion giving rise to a 1D chain. Those complexes, likewise the ones studied in this work, present both free and coordinated CO groups, which show two different CO stretching wavenumber values. Comparing these data, the band observed around 1600 cm^{-1} can be tentatively assigned to the coordinated CO stretching mode. The CC stretching mode is assigned to a medium band around 1110 cm^{-1} which, in the case of Mn(II), Co(II) and Zn(II) complexes spectra, presents a shoulder at 1120 cm^{-1}; the Ni(II) complex presents a very asymmetric band, and Cu(II) complex do not show any splitting. Previous studies in alkaline squarate salts [29,30] have shown that the bands between 1100 and 1200 cm^{-1} can be used to infer about electronic delocalization in oxocarbon ring. The presence of a single band in the spectra indicates that the squarate ring is very symmetric, with a high degree of electronic delocalization, as observed in the case of rubidium and ammonium salts. On the other hand, in lithium, sodium and potassium squarate, which present small electronic delocalization, the band separation is between 86 and 37 cm^{-1}. In the compounds investigated here, besides the appearance of a shoulder in the high spectral region, the wavenumber separation is not so pronounced when compared within the alkaline squarate compounds, so suggesting an emphasized degree of electronic delocalization in oxocarbon rings. This result is confirmed by X-ray structure data, where the largest C–C bond difference between all squarate ions is very small, around 0.011 Å (Table 2). Similar to the infrared spectra, the CC and CN bond stretching of H_2BPP^{2+} species (*ca.* 1510 cm^{-1}) is observed in low wavenumber values when compared to free (*ca.* 1605 cm^{-1}) and coordinated BPP (*ca.* 1620 cm^{-1}).

4. Conclusion

The new structures involving first transition metal ions ($M = Mn^{2+}$, Co^{2+}, Ni^{2+}, Cu^{2+} and Zn^{2+}), squarate ion and 1,3-bis(4-pyridyl)propane (BPP) are described by means of X-ray diffraction, thermogravimetric and vibrational techniques. All compounds are isostructural and the metal sites are coordinated to squarate ligand in a 1,3-bis(monodentate) fashion and water molecules forming a slightly distorted octahedral geometry. The two water molecules are involved in medium hydrogen bonds with squarate ligands, with O···O distance around 2.680 Å. Crystal structures of these compounds show that the arrangement of metal sites and squarate ligands is in 2D sheets with (4,4) topology. Inside of four-member ring topology are located the cationic BPP molecules, which present two orientations in the same 2D layer, one is inverted related to the other. H_2BPP^{2+} cation forms two types of hydrogen bond interactions with the 2D layers, where one is medium (N–H···O) and another is very weak (C–H···O), in a three dimensional arrangement. Vibrational spectra of these compounds are very similar, in agreement to crystal data. In all infrared spectra a medium band at 1640 cm^{-1} has been observed, assigned to the NH in plane deformation mode, indicative of the formation of H_2BPP^{2+} cation. These metal complexes present free and coordinated CO groups, which show two different CO stretching wavenumbers: one observed at *ca.* 1600 cm^{-1}, assigned to coordinated carbonyl stretching, and another observed at *ca.* 1800 cm^{-1} attributed to the free CO group. The formation of H_2BPP^{2+} cation is probably due to the acid-base reaction between squaric acid and BPP. At last, a very important achievement of this investigation refers to the coordination geometries of all the investigated compounds, which are governed only by the ligands, independently of the different electronic properties of the metal ions.

Acknowledgements

The authors thank CNPq, CAPES and FAPEMIG for financial support, and also to Laboratório de Espectroscopia Molecular (USP-SP) for the Raman facilities. B.L. Rodrigues and R. Diniz are grateful to FAPESP and FAPEMIG respectively for Postdoctoral fellowships. This paper is dedicated to the memory of our great friend Dr. W.M. Teles.

Appendix A. Supplementary material

Thermogravimetric curves (Fig. S1) and infrared spectra (Fig. S2) of all complexes are reported as Supporting Information. CCDC 605611, 605612, 605613, 605614 and 605615 contain the supplementary crystallographic data for the structures reported in the paper. These data can be obtained free of charge via http://www.ccdc.cam.ac.uk/conts/retrieving.html or from the Cambridge

Crystallographic Data Centre, 12 Union Road, Cambridge CB2 1EZ, UK; fax: (+44) 1223-336-033; or e-mail: deposit@ccdc.ac.uk. Supplementary data associated with this article can be found, in the online version, at doi:10.1016/j.poly.2006.09.037.

References

[1] D. Braga, L. Maini, F. Grepioni, Chem. Eur. J. 8 (2002) 1804.

[2] (a) A.N. Khlobystov, A.J. Blake, N.-R. Champness, D.A. Lemenovskii, A.G. Majouga, N.V. Zyk, M. Schröder, Coord. Chem. Rev. 222 (2001) 155;
(b) A. Erxleben, Coord. Chem. Rev. 246 (2003) 203;
(c) S.C. Manna, E. Zangrando, J. Ribas, N.R. Chaudhuri, Inorg. Chim. Acta 358 (2005) 4497;
(d) A.K. Ghosh, D. Ghoshal, T.-H. Lu, G. Mostafa, N.R. Chaudhuri, Cryst. Growth Des. 4 (2004) 851;
(e) M.T. Bujaci, X.T. Wang, S.J. Li, C. Zheng, Inorg. Chim. Acta 333 (2002) 152.

[3] C.K. Lam, T.C.W. Mak, Tetrahedron 56 (2000) 6657.

[4] S. Mathew, G. Paul, K. Shivasankar, A. Choudhury, C.N.R. Rao, J. Mol. Struct. 641 (2002) 263.

[5] F. Dumestre, B. Soula, A.-M. Galibert, P.-L. Fabré, G. Bernardinelli, B. Donnadieu, P. Castan, J. Chem. Soc., Dalton Trans. (1998) 4131.

[6] (a) J.G.S. Lopes, L.F.C. de Oliveira, H.G.M. Edwards, P.S. Santos, J. Raman Spectrosc. 35 (2004) 131;
(b) M.C.C. Ribeiro, L.F.C. de Oliveira, N.S. Goncalves, Phys. Rev. B 63 (2001) 104303;
(c) M.C.C. Ribeiro, L.F.C. de Oliveira, P.S. Santos, Chem. Phys. 217 (1997) 71;
(d) P.S. Santos, J.H. Amaral, L.F.C. de Oliveira, J. Mol. Struct. 243 (1991) 223;
(e) L.F.C. de Oliveira, P.S. Santos, J. Mol. Struct. 245 (1991) 215;
(f) L.F.C. de Oliveira, P.S. Santos, J. Mol. Struct. 269 (1992) 85.

[7] (a) D. Braga, C. Bazzi, F. Grepioni, J.J. Novoa, New J. Chem. 23 (1999) 577;
(b) C. Brouca-Cabarrecq, A. Mohanu, P. Millet, J.C. Trombe, J. Solid State Chem. 177 (2004) 2575;
(c) A. Bulut, I. Ucar, O.Z. Yesilel, H. Icbudak, H. Olmez, O. Buyukgungor, Acta Crystallogr. C 60 (2004) M526;
(d) J.A. Cowan, J.A.K. Howard, Acta Crystallogr. E 60 (2004) M511.

[8] (a) P.S. Santos, O. Sala, L.K. Noda, N.S. Goncalves, Spectrochim. Acta A 56 (2000) 1553;
(b) J.G.S. Lopes, L.F.C. de Oliveira, P.S. Santos, Spectrochim. Acta A 57 (2001) 399;
(c) P.S. Santos, N.S. Goncalves, J. Mol. Struct. 570 (2001) 75;
(d) T.M. Kolev, B.A. Stamboliyska, D.Y. Yancheva, V. Enchev, J. Mol. Struct. 691 (2004) 241.

[9] A. Bouayad, J.-C. Trombe, A. Gleizes, Inorg. Chim. Acta 230 (1995) 1.

[10] (a) Q. Chen, S. Liu, J. Zubieta, Inorg. Chim. Acta 175 (1990) 269;
(b) M.I. Khan, Y.-D. Chang, Q. Chen, J. Salta, Y.-S. Lee, C.J. O'Connor, J. Zubieta, Inorg. Chem. 33 (1994) 6340;
(c) I. Castro, M.L. Calatayad, J. Sletten, F. Lloret, M. Julve, J. Chem. Soc., Dalton Trans. (1997) 811;
(d) I. Castro, M.L. Calatayad, J. Sletten, F. Lloret, M. Julve, Inorg. Chim. Acta 287 (1999) 173.

[11] (a) X. Solans, M. Aguiló, A. Gleizes, J. Fans, M. Julve, M. Verdaguer, Inorg. Chem. 29 (1990) 775;
(b) C.-H. Yang, C.-M. Chuo, G.-H. Lee, C.-C. Wang, Inorg. Chem. Commun. 6 (2003) 135;
(c) D. Cangussu, H.O. Stumpf, H. Adams, J.A. Thomas, F. Lloret, M. Julve, Inorg. Chim. Acta 358 (2005) 2292.

[12] C.R. Lee, C.C. Wang, K.C. Chen, G.H. Lee, Y. Wang, J. Phys. Chem. A 103 (1999) 156.

[13] J.A.C. van Ooijen, J. Reedijk, A.L. Spek, Inorg. Chem. 18 (1979) 1184.

[14] C. Näther, J. Greve, I. Jeß, Chem. Mater. 14 (2002) 4536.

[15] S.R. Batten, J.C. Jeffery, M.D. Ward, Inorg. Chim. Acta 292 (1999) 231.

[16] T.-W. Lee, J.P.-K. Lau, W.-T. Wong, Polyhedron 23 (2004) 999.

[17] (a) M.V. Marinho, M.I. Yoshida, K.J. Guedes, K. Krambrock, A.J. Bortoluzzi, M. Horner, F.C. Machado, W.M. Teles, Inorg. Chem. 43 (2004) 1539;
(b) L. Carlucci, G. Ciani, D.W.v. Gudenberg, D.M. Proserpio, Inorg. Chem. 36 (1997) 3812.

[18] (a) X.J. Luan, Y.Y. Wang, L.J. Zhou, X.H. Cai, C.H. Zhou, Q.Z. Shi, J. Mol. Struct. 750 (2005) 58;
(b) E.Q. Gao, Y.X. Xu, A.L. Cheng, M.Y. He, C.H. Yan, Inorg. Chem. Commun. 9 (2006) 212;
(c) J.Y. Lee, S.J. Hong, C. Kim, S.J. Kim, Y. Kim, Inorg. Chem. Commun. 8 (2005) 692;
(d) Y.B. Dong, M.D. Smith, H.C. zur Loye, J. Solid State Chem. 155 (2000) 143;
(e) M.J. Plater, M.R.S. Foreman, T. Gelbrich, M.B. Hursthouse, Inorg. Chim. Acta 318 (2001) 171;
(f) T.M. Bujici, X.T. Wang, S.J. Li, C. Zheng, Z. Krist.-New Cryst. Struct. 218 (2003) 148;
(g) X.J. Li, R. Cao, W.H. Bi, Y.Q. Wang, Y.L. Wang, X. Li, Polyhedron 24 (2005) 2955;
(h) M.J. Plater, M.R.St.J. Foreman, T. Gelbrich, S.J. Coles, M.B. Hursthouse, J. Chem. Soc., Dalton Trans. (2000) 3065;
(i) M.J. Plater, M.R.St.J. Foreman, T. Gelbrich, M.B. Hursthouse, J. Chem. Soc., Dalton Trans. (2000) 1995;
(j) M.-C. Suen, Z.-K. Chan, J.-D. Chen, J.-C. Wang, C.-H. Hung, Polyhedron 25 (2006) 2325.

[19] L. Carlucci, G. Ciani, D.M. Proserpio, S. Rizzato, CrystEngComm 4 (2002) 121.

[20] (a) E.Q. Gao, S.Q. Bai, Z.M. Wang, C.H. Yan, J. Chem. Soc., Dalton Trans. (2003) 1759;
(b) Y.-B. Chen, J. Zhang, J.-K. Cheng, Y. Kang, Z.-J. Li, Y.-G. Yao, Inorg. Chem. Commun. 7 (2004) 1139.

[21] Z. Otwinowski, W. Minor, Methods Enzymol. 276 (1997) 307.

[22] G.M. Sheldrick, SHELXL-97 – A Program for Crystal Structure Refinement, University of Goettingen, Germany, 1997.

[23] A.C. Larson, Crystallogr. Compd. (1970) 291.

[24] L.J. Farrugia, J. Appl. Crystallogr. 30 (1997) 565.

[25] (a) J. Zhang, Y.-B. Chen, Z.-J. Li, Y.-Y. Qin, Y.-G. Yao, Inorg. Chem. Commun. 9 (2006) 449;
(b) Q.-Y. Liu, L. Xu, CrystEngComm 7 (2005) 87;
(c) X.-Q. Wang, J.-K. Cheng, Y.-H. Wen, J. Zhang, Z.-J. Li, Y.-G. Yao, Inorg. Chem. Commun. 8 (2005) 897;
(d) J. Zhang, Y.-B. Chen, S.-M. Chen, A.-J. Li, J.-K. Cheng, Y.-G. Yao, Inorg. Chem. 45 (2006) 3161;
(e) L. Carlucci, G. Ciani, A. Gramaccioli, D.M. Proserpio, S. Rezzato, CrystEngComm 29 (2000) 1.

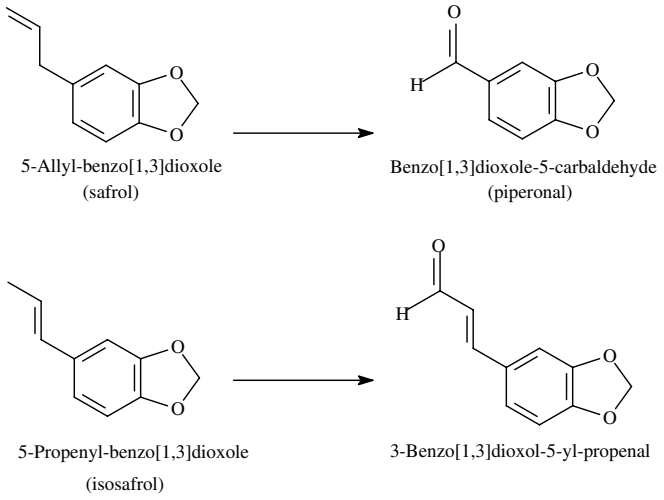
[26] G.L. Cook, F.M. Church, J. Phys. Chem. 61 (1957) 458.

[27] C.H. Kline, J. Turkevich, J. Chem. Phys. 12 (1944) 300.

[28] S.L. Georgopoulos, R. Diniz, B.L. Rodrigues, L.F.C. de Oliveira, J. Mol. Struct. 741 (2005) 61.

[29] S.L. Georgopoulos, R. Diniz, B.L. Rodrigues, M.I. Yoshida, L.F.C. de Oliveira, J. Mol. Struct. 753 (2005) 157.

[30] S.L. Georgopoulos, R. Diniz, M.I. Yoshida, N.L. Speziali, H.F. Dos Santos, G.M.A. Junqueira, L.F.C. de Oliveira, J. Mol. Struct. 794 (2006) 63.



Scheme 1. Structures of substrates and products for the electrooxidations using poly-[*cis*-aquadimethylbipyridyltriphenylphophineruthenium II diphenol anion].

Modified electrodes are useful because they can be applied to several electrochemical systems without modification of their characteristic or efficiency, thus enabling their reuse. Electrodes coated with polymeric films containing reactive groups can be connected to a cell so that they function as working electrodes, leading to the desired organic substrate transformations.

Several modified electrodes containing films bonded to ruthenium complexes from Viologen [14], bipyridyl carbonyl [15,16], bipyridyl ethylamine [17] and other ligands [18,19] were studied and can be used in electrocatalytic oxidations.

In our laboratories we synthesized the allyl ether of *p*-substituted benzenes and we carried out their polymerization so as to obtain chemically and mechanically stable modified electrodes with anionic or cationic ion exchange properties, depending on the nature of the *p*-benzene group [20–22]. Crystallites of noble metals were dispersed in the film which led to the electrocatalytic hydrogenation of unsaturated organic substrates via reduction of H^+ from a mineral acid solution [23,24].

The introduction of a covalent azo bond in the *p*-position of the benzene ring bonded to quinolin-8-ol group, a well known reagent for metal complexation, allows to the preparation of a modified electrode that can be used as metal sensor in the field of the electroanalytical chemistry [25]. Polymerization of this monomer can be accomplished by carrying out anodic scans in a less positive range than that where the redox discharge of the remainder quinoline group occurs. This is possible because the allyl moiety of the monomer polymerizes chemically after electrooxidation at a less positive potential, thus avoiding modification in the structure of the quinoline ligand group. In addition, a large potential window is left untouched in a range corresponding to the reduction potential of transition metals after their complexation with quinoline.

The strategy described above allows the performance of specific electrochemical transformation when these reactions occur at higher potentials in electrocatalytic procedures. Therefore, anchored molecules containing several electrochemical active sites can react with high specificity.

Phenol polymerizes via anodic oxidation, giving a stable film that contains free hydroxyl groups. The electrochemical range of this oxidation is +0.2 to +0.8 V, which is less positive than the potentials for the redox discharges of the ruthenium catalysts [26,27]. Therefore, the above-mentioned strategy can be applied to polyphenol films.

This work presents the transformation of the synthesized *cis*-aquadimethylbipyridyltriphenylphosphineruthenium II perchlorate into its diphenol anion derivative, followed by its electropolymerization to a stable film. We used this film to coat a glassy carbon or a porous carbon felt electrode, and we performed essays to demonstrate the untouched redox activity of this new modified electrode with respect to the aqua and oxo ruthenium group. We also report the use of this modified electrode in the electrocatalytic oxidation of two substrates previously studied in our laboratories (results not yet published).

2. Experimental

2.1. Equipments

Voltammetric measurements were performed using an EG&G PAR 273A potentiostat, connected to an Electrochemical Analysis software model 270. Cyclic voltammetry was carried out in a cylindrical cell (20 mL) using an Ag/AgCl electrode as reference. Glassy carbon (3 mm diameter) was employed as the working electrode, and a platinum wire was used as the auxiliary electrode.

For the electrocatalytic oxidation of the organic substrates, we used a porous carbon felt plate with a surface of 4.7 cm^2 covered with the polymeric film as the working electrode. This electrode was sustained by a platinum wire.

2.2. Reagents

All chemicals used were of analytical grade and were purified when necessary. All solutions were prepared with deionized water (Milli-Q, Millipore Inc., >18 MΩ).

2.3. Analysis

FTIR spectra were recorded in a Perkin Elmer spectrometer model RX series using either liquid film or KBr. Proton nuclear magnetic resonance (^{1}H NMR) spectra were obtained using a Bruker spectrometer model Advance DRX 400 (400 MHz). UV–Vis absorption spectra were recorded on an 8452A HP spectrophotometer 8453 coupled to an 89090A model accessory, at 25 °C. Elemental Analysis measurements were performed on a FISIONS EA1108 model.

2.4. Preparation of cis-aquadimethylbipyridyltriphenylphosphineruthenium II diphenol anion derivative

The complex *cis*-[RuCl(dmbpy)$_2$(PPh$_3$)](PF$_6$) was prepared according to the procedure described in the literature [10], with a global yield of 73%. Then, this material (0.523 g; 0.57 mmol) was dissolved in water (150 mL)/ethanol (150 mL) and an aqueous solution of *p*-silver toluenesulfonate (0.214 g; 0.44 mmol; 100 mL) was added. This mixture was refluxed for 3 h under N_2, the precipitated AgCl was filtered and the volume of the solution was reduced to 1/3 by evaporation. A solution (100 mL) containing phenol (0.269 g; 2.87 mmol) and NaOH (0.114 g; 2.87 mmol) was added slowly, leading to precipitation of the diphenol anion derivative. The dark brown crystalline monomer *cis*-[Ru(dmbpy)$_2$(PPh$_3$)(OH$_2$)](OPh)$_2$ was filtered and washed with cold water and ethyl ether, yielding 0.389 g (0.40 mmol) 70% yield of the product.

^{1}H NMR δ_H (ppm, 400 MHz, CDCl$_3$): 8.8–7.8 (12 H, m, pyridyl hydrogen); 7.3–7.2 (15 H, m, aromatic hydrogen from PPh$_3$); 6.9–7.0 (12 H, m, aromatic hydrogen from phenol) and 2.5 (12 H, methyl).

FTIR (neat, cm^{-1}): 3410 (H$_2$O); 3058 (CH$_3$); 2922 and 2852 (pyridyl and phenyl CH); 1620 and 1436 (C=C and C=N); 1240 and 1092 (PPh$_3$), 728 (pyridyl out of plane CH absorption).

UV–Vis (λ_{max}, nm): 228 (PhO$^-$); 230 (pyridine); 279 (PhO$^-$); 290 (PPh$_3$); 449 (Ru–O).

Elemental *Anal.* Calc. for $C_{54}H_{39}N_4RuPO_3$: C, 70.20; H, 4.03; N, 4.75. Found: C, 77.83; H, 6.06; H, 4.22%.

This monomer was also characterized by cyclic voltammetry with scan ranging from 0.0 to +0.2 V.

2.5. Preparation and characterization of the polymeric film

The monomer (0.053 g; 3.84×10^{-3} mol L^{-1}) was dissolved in a 20 mL cell containing a glassy carbon working electrode and a PTAB/CH_2Cl_2 solution (0.1 mol L^{-1}; 15 mL). Scans from 0.0 to 1.0 V at 25 mV s^{-1} was carried out. To characterize the film scan from 0.0 to +0.9 V was carried out.

The porous carbon felt electrode was prepared in the same way and scans were carried out at 25 mV s^{-1} in the 0.0 to +0.9 V potential range. Characterization was done by comparing the voltammograms obtained here with those described in literature [26,27].

2.6. Electrocatalytic oxidation of safrol (5-allyl-benzo[1,3]dioxole) and isosafrol (5-propenyl-benzo[1,3]dioxole)

A controlled potential of +1.6 V was applied to a 100 mL cell containing the porous carbon felt working electrode coated with the film and a solution (80 mL) of safrol or isosafrol (0.1 mol; 1.6 g) Na_2HPO_4/H_2O 0.05 mol L^{-1} pH 7.

After the current had fallen to low and constant values, the products were extracted with CH_2Cl_2 and dried. Safrol was converted to *piperonal* (5-propenyl-benzo[1,3]dioxole) with 61% yield and isosafrol to 3-benzo[1,3]dioxol-5-yl-propenal with 54% yield. Piperonal: ^{1}H NMR δ_H (ppm, 400 MHz, CDCl$_3$): 9.90 (s, 1H), 7.35–7.10 (m, 3H) and 6.05 (s, 2H).

3-Benzo[1,3]dioxol-5-yl-propenal: ^{1}H NMR δ_H (ppm, 400 MHz, CDCl$_3$): 9.80 (s, 1H), 7.60 (d, 1H), 7.25 (s, 1H), 7.20–6.90 (m, 2H), 6.70 (dd, 1H) and 6.15 (s, 2H).

2.7. Kinetic determinations

From the same experimental conditions described above for the oxidation of the substrates, a new set of experiments was carried out without product extraction. Aliquots were analyzed by UV/Vis spectroscopy until $2 \times t_{1/2}$: the decay observed for the maximum absorbance at 286 nm, in the case of safrol, and at 304 nm, in the case of isosafrol, was converted into concentration values and plotted versus time. Then, the apparent speed constants were calculated (Table 1). The absorbance was converted into concentration taking into account the extinction coefficient ξ for each substrate calculated for the correspondent $\lambda_{max.}$ values. The mass of the substrate that was electrooxidized during the $2 \times t_{1/2}$ experiments was calculated (converted mass, Table 1) from the graphic of the kinetic data, whose abscissas give mass directly.

The mass of ruthenium in the film (2.37×10^{-5} g) prepared over the porous carbon felt electrode was calculated by coulometry (45.18 mC) considering the two electrons for the oxidation peaks showed by voltammetry. The turnover (Table 1) of the ruthenium complex was calculated using the ruthenium equivalent (two electrons = 2.34×10^{-7} eq.) and substrate equivalents (four electrons necessary for the overall transformation, giving the above-indicated products isosafrol = 6.23×10^{-3} eq. and safrol = 5.24×10^{-3} eq.).

3. Results and discussion

The glassy carbon modified electrode coated with the film consisting of poly-[*cis*-aquadimethylbipyridyltriphenylphophineruthenium II diphenol anion] was prepared by scanning the potential range (0.0–1.0 V) corresponding to the phenol anion discharge (0.2–0.75 V), according to the mechanism studied in the literature [26,27].

Fig. 1 A shows that after eight scans the voltammogram remains unchanged, so we assumed that the film formation

Table 1
Kinetic and catalytic parameters for the substrates electrooxidations

Substrates	k for 2 t1/2 (min^{-1})	Coulombs (C)	Turnover	Converted mass (g)
Isosafrol	1.21×10^{-2}	2406 ± 0.25[a]	26623	1.010
Safrol	3.25×10^{-2}	2022 ± 0.22	22393	0.849

[a] Differential theory was used for error calculation.

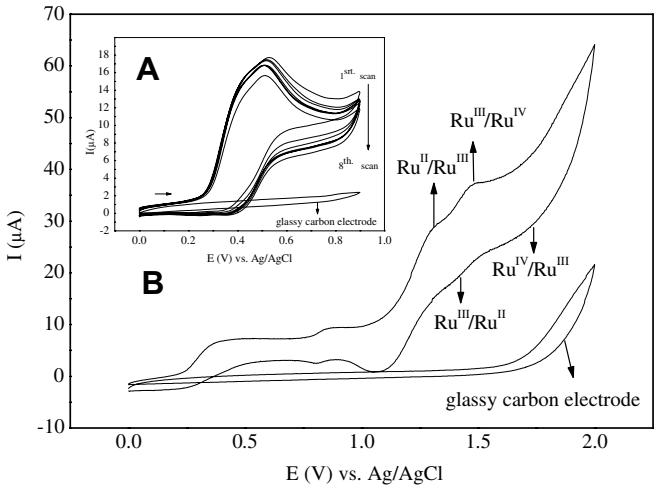


Fig. 1. Cyclic voltammograms of (A) *cis*-aquadimethylbipyridyltriphenylphophineruthenium II diphenolate (polymerization of the film in glassy carbon electrode), scan range from 0.0 to 1.0 V at 25 mV cm^{-1} and (B) characterization of the film, scan range from 0.0 to 1.9 V at 25 mV cm^{-1}.

was completed by them. It was possible to notice the formation of a yellow film on the surface of the electrode. Scanning of the film in the potential range 0.0–2.0 V shows that the discharges of the ruthenium complex (1.0–1.75 V) were not affected by the lower potential range used to polymerization of the phenol anion moiety. Fig. 1B shows that do not occur dissociation in the medium of the positive ruthenium complex associated to the polyphenol anion. This probably is due to the great volume of the complex that remains retained in the lattice of the polymeric chain. This modified electrode was able to catalyze electrooxidation of organic substrates.

The modified carbon felt electrode was prepared in the same way and dedicated in two sets of experiments: electrolysis, from where the reaction products were extracted and analyzed and for the calculation of kinetic and catalytic parameters. Fig. 2 shows the ruthenium complex discharges after the range for phenol oxidation. The voltammogram displays less defined peaks in accordance with the larger surface coated by the film in this electrode.

From the kinetic experiments one can assume that the reactions are pseudo-first order due to the great excess of substrate and the use of a catalytic electrooxidation process. Using the extinction coefficient of the two substrates and the absorbance values obtained by UV/Vis spectroscopy, it was possible to calculate the substrate concentration at various reaction times and plot it versus time, which enable calculation of the apparent speed constants (Table 1), as shown in Fig. 3, with adequate correlation coefficients.

After extraction and analysis of the electrocatalytic oxidation products, the 3-benzo[1,3]dioxol-5-yl-propenal and piperonal obtained from isosafrol and safrol respectively, gives evidence of the occurrence of a 4 electron oxidation. They are interesting from a synthetic point-of-view and are obtained with good yields. The reactions are fast (10^{-2} min^{-1}, Fig. 3). The more stable isosafrol (conjugation between the double bond and aromatic ring: lower speed) had its methyl group oxidized to aldehyde. Safrol (higher speed) underwent a typical organic oxidation of arenes where the $–CH_2$-group close to the aromatic ring was cleaved giving piperonal. In both cases, the selective oxidation to aldehydes and not to the expected carboxylic acids was observed here, as opposed to what occurs in conventional organic oxidation.

The number of Coulombs calculated from the current versus time exponential curve corresponding to $2 \times t_{1/2}$ for safrol and isosafrol for the electrocatalytic oxidation is shown in Table 1 and they are quite similar because these substrates are isomers and their reactions involve four electrons each.

The mass of ruthenium in the film was calculated taking into account the number of Coulombs related to the two-electrons oxidation shown in the voltammogram of Fig. 2.

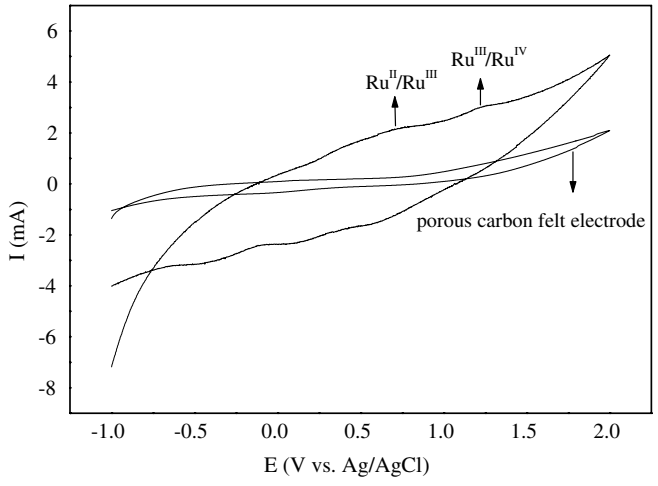


Fig. 2. Characterization of the film that coats the porous carbon felt electrode by cyclic voltammetry, scan range from −1.0 to 1.9 V at 25 mV cm^{-1}.

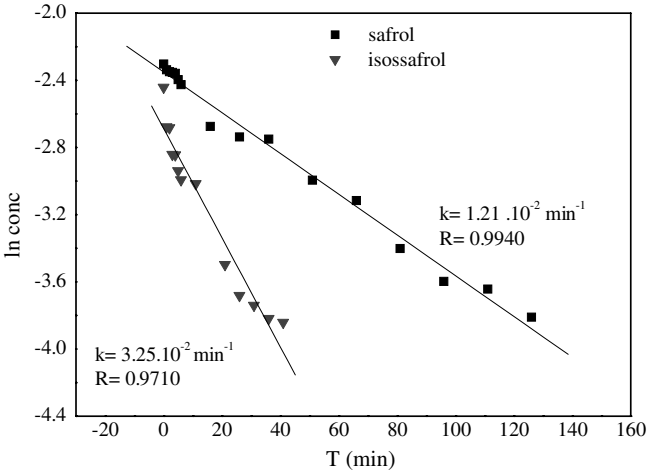


Fig. 3. Linear regression of safrol and isosafrol of the kinetic data analyzed by UV/Vis spectroscopy.

The turnover values calculated from the number of equivalents of substrates and ruthenium (Table 1) are also quite similar and in accordance with the number of Coulombs.

After use this modified electrode presented the same voltammetric properties.

4. Conclusion

The new modified electrode containing ruthenium complex bonded to stable polyphenol film catalyses the rapid electrooxidation of organic substrates, giving products of synthetic interest in good yields. Its preparation can be carried out using a lower potential for oxidation of the phenol moiety, thus avoiding modifications in the electroactive and functional bonded ruthenium complex. Product isolation is very simple and the electrode can be reused. With good turnover, this modified electrode seems to be very convenient for potentially useful electrocatalytic oxidations of organic compounds.

Acknowledgement

The authors are grateful to FAPESP and CNP*q* for the scholarship and financial support.

References

[1] J.M. Madurro, G. Chiericato Jr., W.F. De Giovani, J.R. Romero, Tetrahedron Lett. 29 (1988) 765.
[2] W.F. De Giovani, J.R. Romero, J.M. Madurro, Quím. Nova 11 (1989) 367.
[3] J.L. Campos, W.F. De Giovani, J.R. Romero, Synthesis 7 (1990) 597.
[4] M. Navarro, W.F. De Giovani, J.R. Romero, Synth. Commun. 20 (1990) 399.
[5] M. Navarro, W.F. De Giovani, J.R. Romero, Tetrahedron 47 (1991) 851.
[6] M. Navarro, W.F. De Giovani, J.R. Romero, J. Miller, J. Braz. Chem. Soc. 3 (1992) 70.
[7] R.M.C. Carrijo, J.R. Romero, Synth. Commun. 24 (1994) 433.
[8] L.V. Lavagnoli, M. Navarro, W.F. De Giovani, Quím. Nova 18 (1995) 157.
[9] M. Navarro, S.E. Galembeck, J.R. Romero, W.F. De Giovani, Polyhedron 15 (1996) 153.
[10] E.C. Lima, P.G. Fenga, J.R. Romero, W.F. De Giovani, Polyhedron 17 (1998) 313.
[11] B.A. Moyer, M.S. Thompson, T.J. Meyer, J. Am. Chem. Soc. 102 (1980) 2310.
[12] M.S. Thompson, T.J. Meyer, J. Am. Chem. Soc. 104 (1982) 106.
[13] T.J. Meyer, J. Electrochem. Soc. 131 (1984) 221.
[14] A. Martre, H. Laguitton-Pasquier, A. Deronzier, A. Arriman, J. Phys. Chem. B 107 (2003) 2684.
[15] S. Chardon-Noblat, A. Deronzier, R. Ziessel, D. Zsoldos, Inorg. Chem. 36 (1997) 5384.
[16] S. Chardon-Noblat, G.H. Cripps, A. Deronzier, J.S. Field, S. Gouws, R.J. Haines, F. Southway, Organometallics 20 (2001) 1668.
[17] M. Rodrígues, I. Romero, A. Llobet, Inorg. Chem. 40 (2001) 4150.
[18] E. Eskelinen, M. Haukka, T. Venäläinen, T.A. Pakkanen, M. Wasberg, S. Chardon-Noblat, A. Deronzier, Organometallics 19 (2000) 163.
[19] H. Languitton-Pasquier, A. Martre, A. Deronzier, J. Phys. Chem. B 105 (2001) 4801.
[20] R.C.Z. Lofrano, J.V. Queiroz, J.R. Romero, J. Mol. Catal. A. 174 (2001) 231.
[21] J.O.S. Pontólio, F.L.S. Purgato, J.R. Romero, Quím. Nova 27 (2004) 550.
[22] R.C.Z. Lofrano, J.M. Madurro, L.M. Abrantes, J.R. Romero, J. Mol. Catal. A: Chem. 218 (2004) 73.
[23] A.M. Fundo, M.I.C.F. Costa, J.R. Romero, L.M. Abrantes, Ciência Tecnol. Mater. 17 (2005) 12.
[24] M.I.C.F. Costa, A.M. Fundo, L.M. Abrantes, J.R. Romero, J. Appl. Electrochem. 36 (2006) 43.
[25] José O. Pontólio, N. Ferranti, M. Campos, A.M. Lúcia, J.R. Romero, J. Electroanal. Chem. 584 (2006) 394.
[26] M. Gattrell, D.W. Kirl, J. Electrochem. Soc. 139 (1992) 2736.
[27] M. Gattrell, D.W. Kirl, J. Electrochem. Soc. 140 (1993) 903.

retain their structural integrity upon desolvation–solvation cycles [9].

With these precedents in mind, we undertook hydrothermal synthetic explorations with divalent nickel precursors in the presence of both nicotinic acid and organoimines, which has afforded the 3-D hydrated nickel(II)nicotinate, $[Ni_4(\mu\text{-}H_2O)_2(nic)_8 \cdot 2H_2O]$ (**1**), along with the pillared 3-D material $[Ni_2(H_2O)_2(nic)_4(4,4'\text{-bpy})]$ (**2**). **1** represents a new nickel (II) nicotinate polymorph, contrasting markedly from Lin's previously reported 3-D tetragonal phase $[Ni_2(\mu\text{-}H_2O)(nic)_4] \cdot CH_3CH_2OH \cdot H_2O$ (**3**) [10a], and subtly different from its dehydrated centrosymmetric analog $[Ni_2(\mu\text{-}H_2O)(nic)_4]$ (**4**) [10b]. Herein, we report the syntheses, crystal structures, and thermal properties of these two 3-D coordination polymers along with a magnetochemical investigation of **1**.

2. Experimental

2.1. General considerations

All starting materials were obtained commercially from Aldrich, with the exception of 1,3-di-4-pyridylpropane (TCI America) and 4,4′-dipyridylamine (prepared via literature procedure) [11]. Water was deionized above 3 MΩ in-house. Thermogravimetric analysis was performed on a TA Instruments TGA 2050 Thermogravimetric Analyzer with a heating rate of 5 °C/min up to 900 °C. Elemental analysis was carried out using a Perkin Elmer 2400 Series II CHNS/O Analyzer. IR spectra were recorded on a Mattson Galaxy FTIR Series 3000 using KBr pellets. Variable temperature magnetic susceptibility data (2–300 K) was collected on a Quantum Design MPMS SQUID magnetometer at an applied field of 0.1 T. After each temperature change the sample was kept at the new temperature for 5 min before magnetization measurement to ensure thermal equilibrium. The susceptibility data were corrected for diamagnetism using Pascal's constants [12]. A correction for the diamagnetism of the sample holder was also applied.

2.2. Preparation of $[Ni_4(\mu\text{-}H_2O)_2(nic)_8 \cdot 2H_2O]$ (1)

$NiCl_2 \cdot 6H_2O$ (66 mg, 0.28 mmol), nicotinic acid (68 mg, 0.55 mmol), pyridine (45 μL, 0.56 mmol), and NaOH (1.0 M, 0.42 mL, 0.42 mmol) were mixed into 10 mL distilled H_2O in a 23 mL Teflon-lined Parr acid digestion bomb, which was then sealed and heated at 150 °C for 5 days. The reaction vessel was cooled slowly to 25 °C. Light blue blocks of **1** (60 mg, 68% yield based on Ni) were isolated as a single phase after washing with distilled water and drying in air. As ascertained by unit cell determinations performed on single crystals, **1** could also be prepared by utilizing 1,2-di-4-pyridylethane, 1,3-di-4-pyridylpropane, or 4,4′-dipyridylamine instead of pyridine. However, in all of these cases an insoluble white powder was also produced, which hindered separation of bulk quantities of pure **1**. Single crystals of **1** do not form in the absence of an organoimine. *Anal.* Calc. for $C_{48}H_{40}N_8Ni_4O_{20}$ **1**: C, 44.91; H, 3.14; N, 8.73. Found: C, 44.68; H, 2.98; N, 8.57%. IR (KBr, cm^{-1}): 3445(m), 3143(w), 3085(w), 1638(vs), 1599(m), 1586(m), 1547(w), 1400(vs), 1319(w), 1194(s), 1158(w), 1094(w), 1049(w), 1037(m), 823(m), 765(m), 700(m), 647(w), 575(w), 462(m).

2.3. Preparation of $[Ni_2(H_2O)_2(nicotinate)_4(4,4'\text{-bpy})]$ (2)

$NiCl_2 \cdot 6H_2O$ (66 mg, 0.28 mmol), nicotinic acid (68 mg, 0.55 mmol), 4,4′-bipyridine (87 mg, 0.56 mmol), and NaOH (0.56 mL, 1.0 M, 0.56 mmol) were mixed into 10 mL distilled H_2O in a 23 mL Teflon-lined Parr acid digestion bomb, which was then sealed and heated at 120 °C for 5 days. The reaction vessel was cooled slowly to 25 °C. Large blue blocks of **2** (85 mg, 76% yield based on Ni) were isolated after washing with distilled water and acetone and drying in air. *Anal.* Calc. for $C_{17}H_{14}N_3NiO_5$ **2**: C, 51.17; H, 3.54; N, 10.53. Found: C, 50.24; H, 3.43; N, 10.26%. Carbon analyses were slightly low on several samples, presumably due to incomplete combustion. IR (KBr, cm^{-1}): 3641(w), 2925(m, br), 1615(vs), 1596(m), 1573(m), 1560(m), 1541(w), 1491(w), 1414(s), 1386(vs), 1221(w), 1217(w), 1186(w), 1161(w), 1098(w), 1082(w), 1052(w), 949(w), 834(m), 769(m), 704(m), 635(w), 564(w), 428(w).

3. X-ray crystallography

A blue block crystal of **1** with dimensions 0.52 mm × 0.34 mm × 0.24 mm and a dark blue block crystal of **2** with dimensions 0.70 mm × 0.20 mm × 0.20 mm were subjected to single crystal X-ray diffraction at 173 K using a Bruker-AXS SMART 1k CCD instrument. Reflection data were acquired using graphite-monochromated Mo Kα radiation ($\lambda = 0.71073$ Å). The data were integrated via SAINT [13]. Lorentz and polarization effect and empirical absorption corrections were applied with SADABS [14]. The structures were solved using direct methods and refined on F^2 using SHELXTL [15]. All non-hydrogen atoms were refined anisotropically. Hydrogen atoms bound to carbon atoms were placed in calculated positions and refined isotropically with a riding model. The hydrogen atoms belonging to all water molecules in **1** and **2** were found via Fourier difference maps, then restrained at fixed positions and refined isotropically. The PLATON ADDSYM [16] subroutine indicated the possibility of the centrosymmetric space group $P2_1/m$ for **1**, however, attempts to refine the structure in this higher symmetry space group were unsuccessful (Ni–Ni distances <1 Å). Successful solution and refinement of the crystal structure of **1** was only possible in $P2_1$ using appropriate routines for racemic twinning (TWIN/BASF). This twinning was evident on several crystals of **1** prepared in different batches in the presence of various organoimines (*vide infra*). Relevant crystallographic data for **1** and **2** is listed in Table 1.

Table 1
Crystal and structure refinement data for **1**–**2**

Data	**1**	**2**
Empirical formula	$C_{48}H_{40}N_8Ni_4O_{20}$	$C_{34}H_{28}N_6Ni_2O_{10}$
Formula weight	1283.72	798.04
Collection T (K)	173(2)	173(2)
λ (Å)	0.71073	0.71073
Crystal system	monoclinic	monoclinic
Space group	$P2_1$	$P2_1/n$
a (Å)	10.7155(14)	7.927(5)
b (Å)	19.163(3)	14.795(14)
c (Å)	13.8595(19)	14.634(10)
β (°)	103.952(2)	90.49(8)
V (Å^3)	2762.0(6)	1716.0(20)
Z	2	2
D_{calc} (g cm^{-3})	1.544	1.544
μ (mm^{-1})	1.424	1.164
Minimum/maximum transmission	0.771	0.800
hkl Ranges	$-13 \leqslant h \leqslant 14$, $-24 \leqslant k \leqslant 25$, $-17 \leqslant l \leqslant 18$	$-10 \leqslant h \leqslant 10$, $-19 \leqslant k \leqslant 19$, $-19 \leqslant l \leqslant 19$
Total reflections	33 323	19 596
Unique reflections	13 050	4103
R(int)	0.0231	0.0289
Parameters/restraints	746/13	241/3
R_1 (all data)[a]	0.0349	0.0590
R_1 ($I > 2\sigma(I)$)[a]	0.0308	0.0535
wR_2 (all data)[b]	0.0754	0.1332
wR_2 ($I > 2\sigma(I)$)[b]	0.0738	0.1307
Maximum/minimum residual (e$^-$/Å^3)	0.906/−0.346	0.875/−0.520
Goodness-of-fit	1.198	1.135

[a] $R_1 = \sum||F_o| - |F_c||/\sum|F_o|$.

[b] $wR_2 = \sum\{[w(F_o^2 - F_c^2)^2]/\sum[wF_o^2]_2\}^{1/2}$.

4. Results and discussion

4.1. Syntheses and spectral characterization

Hydrothermal treatment of an aqueous mixture of nickel(II) chloride, nicotinic acid, sodium hydroxide, and pyridine in a 1:2:2:1.5 mole ratio at 150 °C afforded a high yield of **1** as single phase large blue crystals. Eschewing pyridine for 4,4′-bipyridine in the above synthesis resulted in formation of blue blocks of **2** in high yield as a single-phase product. Attempts to prepare other nickel nicotinate/organoimine coordination polymers were subsequently undertaken using 4,4′-dipyridylamine, 1,2-di-4-pyridylethane, and 1,3-di-4-pyridylpropane. In all of these cases, large blue crystals were garnered in addition to variable amounts of an insoluble amorphous white solid. Unit cell determinations via matrix frame collection indicated that in all of these cases **1** was the only single crystalline product. An organoimine was required to successfully prepare single crystals of **1**; only a sea green powder was obtained if the organoimine was omitted. This is consistent with reports where successful hydrothermal synthesis of a desired product requires a reactant that is not incorporated into the final structure, instead serving as a mineralizer or a structure-directing templating agent [17]. The infrared spectra of **1** and **2** show broad, intense O–C–O stretching bands at 1638 cm^{-1} and 1400 cm^{-1}, and 1615 cm^{-1} and 1386 cm^{-1}, respectively, without any bands due to unligated carboxylic acids at ~1710 cm^{-1}. This observation is fully consistent with the presence of only metal-bound carboxylate moieties [18]. Sharper and weaker bands within the

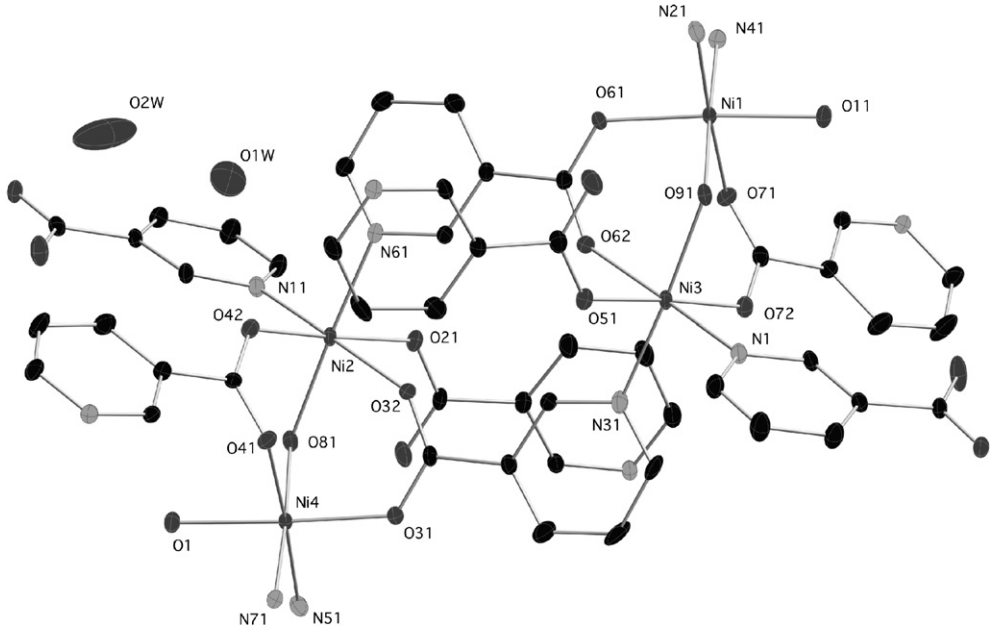


Fig. 1. Thermal ellipsoid plot (50% probability) of the asymmetric unit of **1** with partial atomic number scheme. Hydrogen atoms have been omitted for clarity.

1300–1600 cm^{-1} region correspond to pyridyl ring bending modes [19]. Spectral features between 3000 cm^{-1} and 3400 cm^{-1} in both cases reflect the presence of bound and/or unligated water molecules.

4.2. Crystal structure of $[Ni_4(\mu\text{-}H_2O)_2(nic)_8 \cdot 2H_2O]$ (1)

1 crystallizes in the acentric monoclinic space group $P2_1$, with a large asymmetric unit consisting of four nickel atoms, eight deprotonated nicotinic acid moieties, two μ_2-bridging water molecules, and two water molecules of crystallization (Fig. 1). Each of the four crystallographically distinct Ni atoms displays slightly distorted octahedral $[NiN_2O_4]$ coordination, with standard bond lengths and angles (Table 2). The arrangement of donor atoms about each of the four nickel atoms is identical, albeit with subtly altered bond distances and angles. The two nitrogen donors, one belonging to an exobidentate μ_2-nic ligand and the other to an exotridentate μ_3-nic ligand, are disposed *cis* relative to each other. Oxygen atoms belonging to two different μ_3-nic ligands are also situated in a *cis* orientation. The remaining two coordination sites occupied by oxygen atoms from a μ_2-nic ligand and a μ_2-water molecule, again in a *cis* disposition. The μ_3-nic pyridyl nitrogen donor is arranged *trans* to the μ_2-water molecule that bridge each pair of Ni atoms (Ni–O–Ni angles = 114.2(2)°, 114.9(2)°) into binuclear $[Ni(\mu\text{-}H_2O)(\mu_3\text{-}nic)_2Ni]^{2+}$ units with a Ni–Ni through-space distance of 3.56 Å. Within the two types of binuclear units, the Ni centers are bridged by both carboxylates in a distorted *syn–syn* orientation, with the four sets of Ni–O–O–Ni torsion angles ranging from 28.5° to 41.8° (0° for an idealized *syn–syn* disposition).

Each binuclear unit is turn connected to its neighbors through μ_3-nic ligands to form 1-D $[Ni_2(H_2O)(\mu_3\text{-}nic)_2]$ helical chains that run down the *c* crystal axis. The structure of **1** also contains rippled 2-D cationic $[Ni_4(H_2O)_2(\mu_2\text{-}nic)_4]$ layers coincident with the *bc* crystal plane, built from the junction of the two types of $[Ni_2(\mu_2\text{-}H_2O)]^{4+}$ subunits through all of the μ_2-nic ligands (Fig. 2). This 2-D layer stands in contrast to the $[Co_2(\mu\text{-}H_2O)(\mu_2\text{-}nic)_2]$ 1-D double chain staircase motif observed in the 3-D open framework coordination polymer $[Co_2(\mu\text{-}H_2O)(\mu_2\text{-}nic)_4]$, which contains similar binuclear units [9]. The 2-D cationic layers in **1** are then stitched into the full 3-D crystal structure through the aforementioned helical 1-D $[Ni_2(H_2O)(\mu_3\text{-}nic)_2]$ chains (Fig. 3).

Viewing the 3-D structure down the *c* crystal axis (Fig. 4) of the **1** reveals ~10 Å × ~13 Å "bird-shaped" voids delineated by the nicotinate ligands. The "heads", "tails", and the front parts of the "wings" of the "birds" are demarcated by μ_2-nic moieties, while the rear parts of the "wings" are constructed by the μ_3-nic ligands. As calculated by the PLATON program [16], the void space within the structure occupies 15.1% of its overall volume. Within these incipient void spaces lie dimers of co-crystallized water molecules (O1W···O2W distance = 2.81 Å) which are anchored to the coordination polymer framework via hydrogen bonding from O1W to unligated μ_2-nic carboxylate oxygen atoms (O2 and O62), and from O2W to the ligated μ_3-nic oxygen atom O12. All unligated μ_2-nic oxygen atoms also engage in hydrogen bonding acceptance from the metal-bridging water molecules. Hydrogen bonding distances and angles within **1** are listed in Table 3.

The 3-D framework structure of **1** is very similar to that displayed in the dehydrated phase $[Ni_2(nic)_4(H_2O)]$ (**4**) reported by Lu in 2003 [10b]. However, **1** possesses a slightly smaller unit cell, larger Ni–O–Ni angles, and a wider range of Ni–O–O–Ni torsion angles within its binuclear units, presumably due to the effect of hydrogen

Table 2
Selected bond distance (Å) and angle (°) data for **1**

Ni(1)–O(61)$^{\#1}$	2.013(2)	O(42)–Ni(2)–O(21)$^{\#3}$	176.56(9)
Ni(1)–O(11)	2.069(2)	O(42)–Ni(2)–O(32)	95.75(8)
Ni(1)–N(41)$^{\#2}$	2.076(2)	O(21)$^{\#3}$–Ni(2)–O(32)	82.60(9)
Ni(1)–O(71)	2.094(2)	O(42)–Ni(2)–N(61)	92.53(9)
Ni(1)–N(21)	2.101(3)	O(21)$^{\#3}$–Ni(2)–N(61)	84.49(10)
Ni(1)–O(91)	2.120(2)	O(32)–Ni(2)–N(61)	91.10(8)
Ni(2)–O(42)	2.040(2)	O(42)–Ni(2)–O(81)	91.37(8)
Ni(2)–O(21)$^{\#3}$	2.065(2)	O(21)$^{\#3}$–Ni(2)–O(81)	91.59(8)
Ni(2)–O(32)	2.096(2)	O(32)–Ni(2)–O(81)	88.26(8)
Ni(2)–N(61)	2.100(3)	N(61)–Ni(2)–O(81)	176.09(9)
Ni(2)–O(81)	2.104(2)	O(42)–Ni(2)–N(11)	89.32(9)
Ni(2)–N(11)	2.109(2)	O(21)$^{\#3}$–Ni(2)–N(11)	92.48(9)
Ni(3)–O(72)	2.021(2)	O(32)–Ni(2)–N(11)	174.21(9)
Ni(3)–O(51)$^{\#4}$	2.044(2)	N(61)–Ni(2)–N(11)	91.46(9)
Ni(3)–N(31)$^{\#1}$	2.098(3)	O(81)–Ni(2)–N(11)	88.83(9)
Ni(3)–N(1)	2.108(2)	O(72)–Ni(3)–O(51)$^{\#4}$	176.68(9)
Ni(3)–O(62)$^{\#1}$	2.112(2)	O(72)–Ni(3)–N(31)$^{\#1}$	91.89(9)
Ni(3)–O(91)	2.113(2)	O(51)$^{\#4}$–Ni(3)–N(31)$^{\#1}$	84.89(10)
Ni(4)–O(31)	2.008(2)	O(72)–Ni(3)–N(1)	88.38(9)
Ni(4)–O(1)	2.057(2)	O(51)$^{\#4}$–Ni(3)–N(1)	90.86(9)
Ni(4)–N(71)$^{\#5}$	2.074(2)	N(31)$^{\#1}$–Ni(3)–N(1)	91.15(9)
Ni(4)–N(51)	2.080(3)	O(72)–Ni(3)–O(62)$^{\#1}$	97.00(8)
Ni(4)–O(41)	2.096(2)	O(51)$^{\#4}$–Ni(3)–O(62)$^{\#1}$	83.82(9)
Ni(4)–O(81)	2.120(2)	N(31)$^{\#1}$–Ni(3)–O(62)$^{\#1}$	89.57(9)
O(61)$^{\#1}$–Ni(1)–O(11)	174.36(9)	N(1)–Ni(3)–O(62)$^{\#1}$	174.54(9)
O(61)$^{\#1}$–Ni(1)–N(41)$^{\#2}$	89.96(9)	O(72)–Ni(3)–O(91)	91.15(8)
O(11)–Ni(1)–N(41)$^{\#2}$	88.63(9)	O(51)$^{\#4}$–Ni(3)–O(91)	92.10(8)
O(61)$^{\#1}$–Ni(1)–O(71)	91.39(8)	N(31)$^{\#1}$–Ni(3)–O(91)	176.22(9)
O(11)–Ni(1)–O(71)	83.07(8)	N(1)–Ni(3)–O(91)	91.18(9)
N(41)$^{\#2}$–Ni(1)–O(71)	86.27(9)	O(62)$^{\#1}$–Ni(3)–O(91)	87.83(8)
O(61)$^{\#1}$–Ni(1)–N(21)	90.72(9)	O(31)–Ni(4)–O(1)	175.41(9)
O(11)–Ni(1)–N(21)	94.79(9)	O(31)–Ni(4)–N(71)$^{\#5}$	91.34(9)
N(41)$^{\#2}$–Ni(1)–N(21)	92.33(10)	O(1)–Ni(4)–N(71)$^{\#5}$	87.52(9)
O(71)–Ni(1)–N(21)	177.46(9)	O(31)–Ni(4)–N(51)	91.13(9)
O(61)$^{\#1}$–Ni(1)–O(91)	91.47(8)	O(1)–Ni(4)–N(51)	93.32(9)
O(11)–Ni(1)–O(91)	89.84(8)	N(71)$^{\#5}$–Ni(4)–N(51)	90.00(10)
N(41)$^{\#2}$–Ni(1)–O(91)	178.16(9)	O(31)–Ni(4)–O(41)	91.17(8)
O(71)–Ni(1)–O(91)	92.54(8)	O(1)–Ni(4)–O(41)	84.34(8)
N(21)–Ni(1)–O(91)	88.81(9)	N(71)$^{\#5}$–Ni(4)–O(41)	87.22(9)
		N(51)–Ni(4)–O(41)	176.44(9)
		O(31)–Ni(4)–O(81)	91.56(8)
		O(1)–Ni(4)–O(81)	89.53(8)
		N(71)$^{\#5}$–Ni(4)–O(81)	177.02(9)
		N(51)–Ni(4)–O(81)	90.60(9)
		O(41)–Ni(4)–O(81)	92.06(8)

Symmetry transformations used to generate equivalent atoms: (#1) $x+1$, y, $z+1$; (#2) $x+1$, y, z; (#3) $-x$, $y+1/2$, $-z$; (#4) $-x$, $y-1/2$, $-z+1$; (#5) $x-1$, y, z.

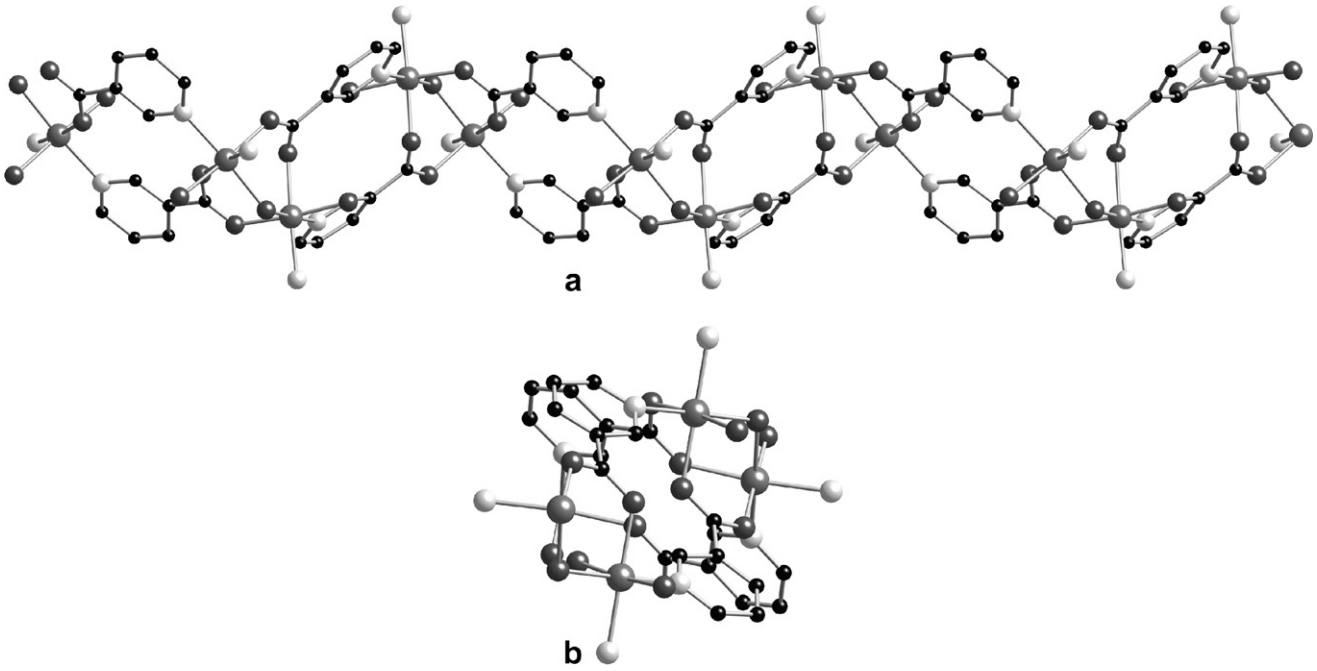


Fig. 2a and 2b. Views of helical 1-D chain of μ_3-nicotinate connected binuclear units in **1** down *a* (top) and *c* (bottom).

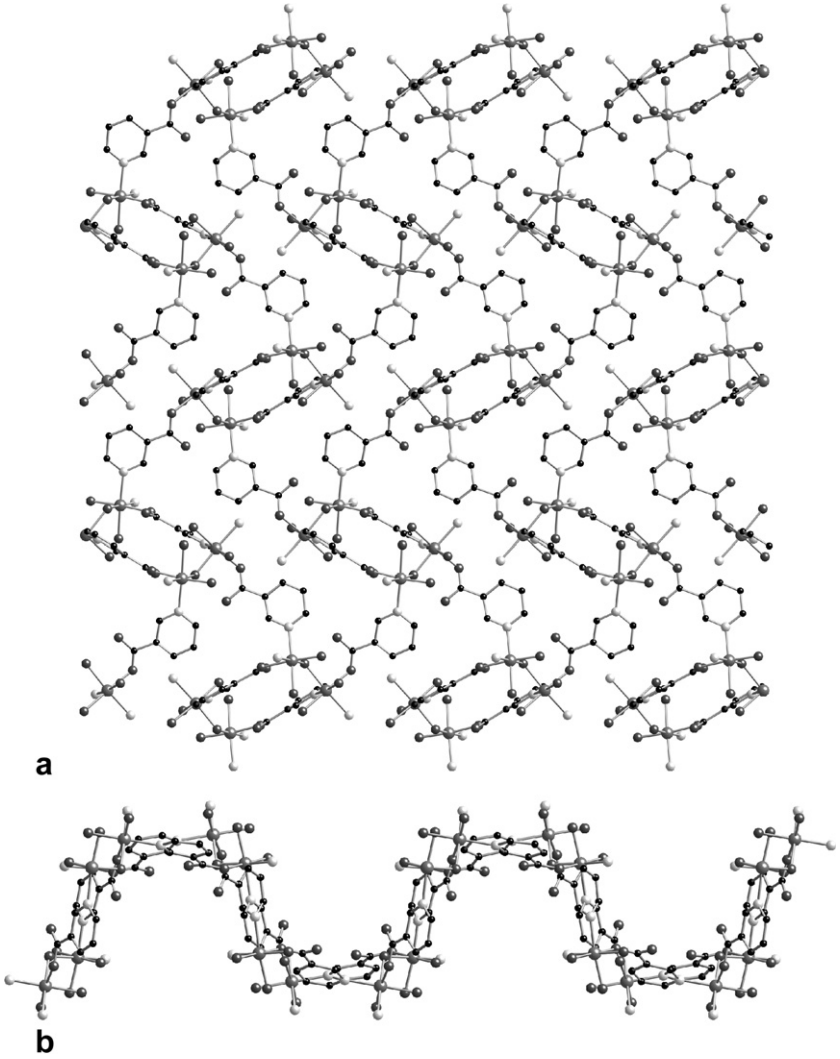
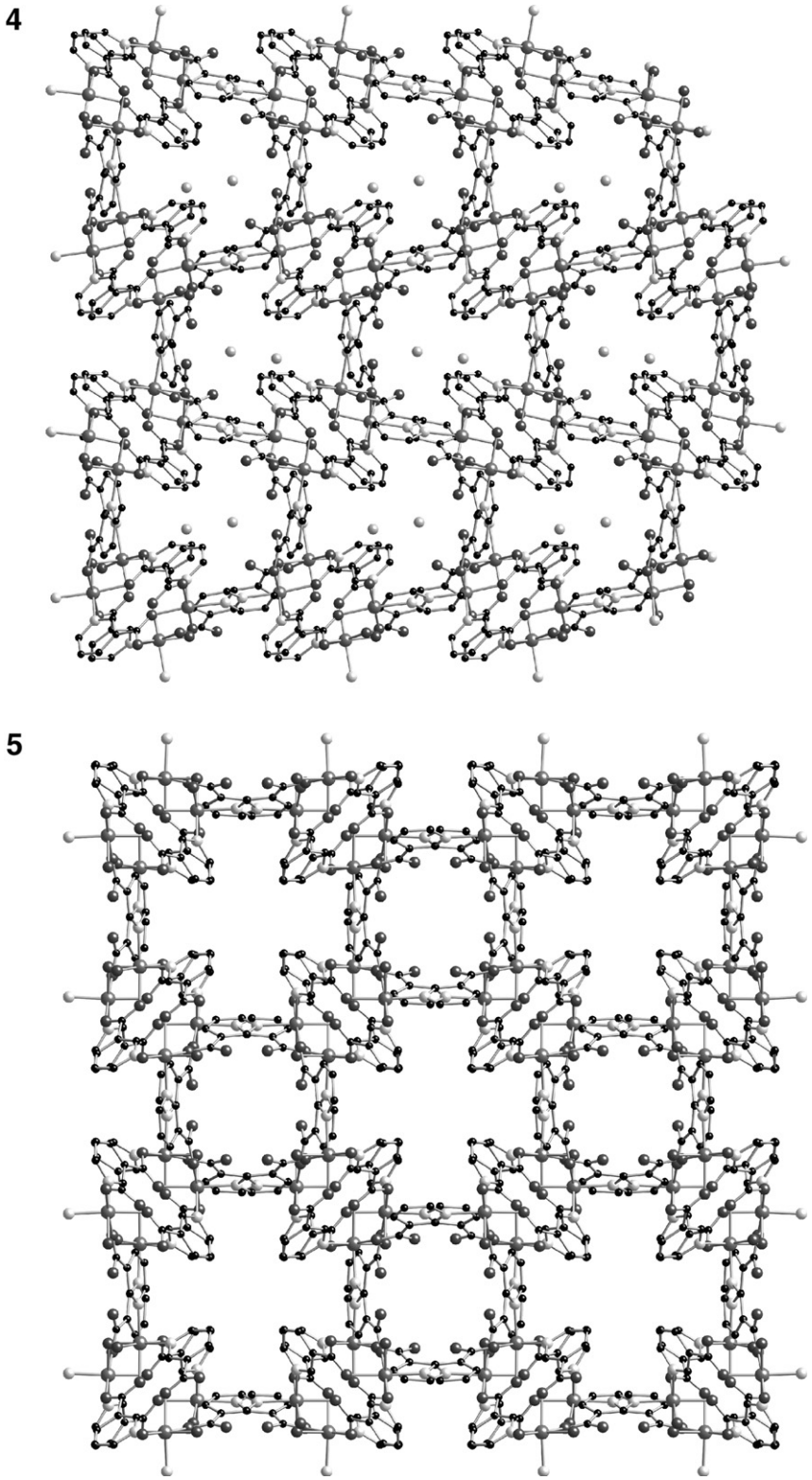


Fig. 3a and 3b. View down *a* (top) and *c* (bottom) of the undulating 2-D network in **1** comprised of μ_2-nicotinate connected binuclear units.



Figs. 4 and 5. Views down *c* of the 3-D network structure of **1** (top) and Lin's tetragonal [Ni_2(nicotinate)$_4$(μ-H_2O)] phase (**3**) (bottom). The 1-D helical chains comprised of binuclear nickel units linked by μ_3-nicotinate ligands run down *c* in both cases. Hydrogen atoms have been omitted for clarity. Waters of crystallization within the "bird" shaped voids in **1** are also shown. Disordered solvent molecules within the structure of **3** are not shown.

bonding between the μ_2-nic and μ_3-nic carboxylate oxygens and the water molecules of crystallization. These variances foment an apparent striking difference in magnetic properties, with **1** manifesting weak antiferromagnetic intradimer coupling, while the nickel ions in the binuclear units in **4** appear to interact in a ferromagnetic fashion (*vide infra*).

1 possesses most of the same structural subunits as in Lin's nickel (II) nicotinate polymorph **3** [10a], yet has a

Table 3
Hydrogen bonding contact distances (Å) and angles (°) within **1** and **2**

D–H···A	*d*(H···A)	<DHA	*d*(D···A)
1			
O1W–H1WA···O2W	1.928	168.55	2.792
O1W–H1WB···O42	2.318	161.92	3.145
O2W–H2WA···O12	2.241	144.67	2.973
O2W–H2WB···O22	2.040	177.46	2.888
O81–H81A···O2	1.757	163.32	2.574
O81–H81B···O22[a]	1.824	164.49	2.633
O91–H91A···O12	1.867	157.85	2.657
O91–H91B···O52[b]	1.756	153.20	2.576
2			
O5–H5C···O4	1.831	161.30	2.661
O5–H5B···O3	1.808	166.27	2.648

Symmetry labels: (a) $-x, y+1/2, -z$; (b) $-x, y-1/2, -z+1$.

remarkably different channel morphology. It is therefore instructive to highlight both the significant similarities and differences between these two phases. The coordination geometry and $[NiN_2O_4]$ arrangement of the donors about the nickel centers are extremely similar in both **1** and **3**, with only minor variations in metrical parameters and torsion angles. Both compounds display triply bridged binuclear $[Ni(\mu\text{-}H_2O)(\mu_3\text{-nic})_2Ni]^{2+}$ subunits, which further conjoin into 1-D helices via μ_3-nic ligands (as seen in Fig. 2 for **1**). However, in **3**, the μ_2-nic ligands bind neighboring binuclear units into tubular 1-D barrels, while this type of ligand propagates a rippled 2-D layered structural motif in **1** (Fig. 3a). The 1-D barrel substructures in **3** are connected into 3-D by μ_3-nic ligands, resulting in a markedly different channel architecture that exhibits "cross-shaped" and "circle-shaped" cavities within the structure (Fig. 5). In **3**, the cross-shaped cavities were found to contain disordered ethanol solvent molecules, while the circular cavities enclathrated water molecules of crystallization.

A comparison of Figs. 4 and 5 shows that neighboring 1-D helical chains in a single plane in **1** (along *bc*, left to right in the figures) spiral in the same direction, while in **3**, the helical chains within a single plane alternate their orientations. Thus, a change in the orientation of the μ_3-nic based helical chains running down the *c*-axis could convert each "cross" and "circle" cavity pair in **3** into two "bird"-type cavities in **1**, or vice versa. It is postulated that the ethanol used in the synthesis of **3** is required as a template for formation of the larger "cross" shaped cavities, which forces the 1-D helical subunits into their necessary orientations during self-assembly. This proposal is corroborated by the structural retention of **1** after refluxing in ethanol for 24 h, as determined by powder XRD.

4.3. Crystal structure of $[Ni_2(H_2O)_2(nicotinate)_4(4,4'\text{-bpy})]$ (2)

The asymmetric unit of **2** (Fig. 6) consists of one nickel atom, one bound aquo ligand, one-half of a 4,4′-bipyridine molecule, and two nicotinate ligands. One of the nicotinate

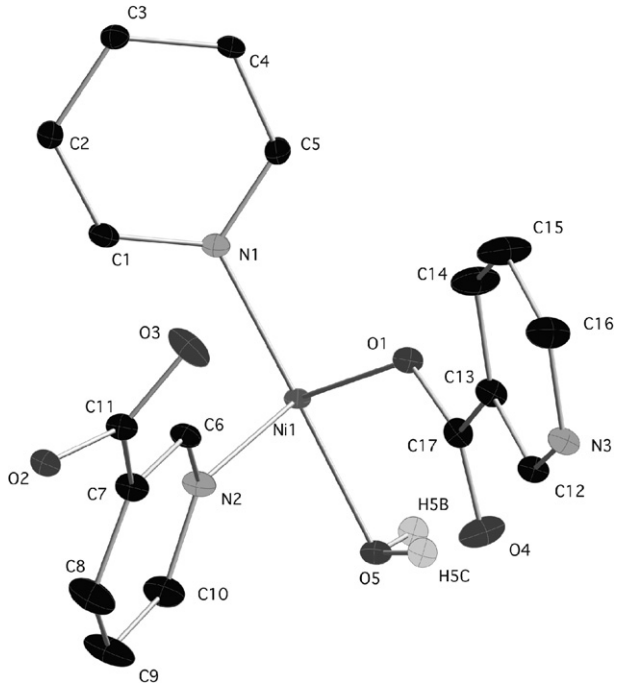


Fig. 6. Asymmetric unit of **2** shown with thermal ellipsoids (50% probability) and atomic numbering scheme. Hydrogen atoms have been omitted for clarity.

anions in the asymmetric unit is bound to Ni through its pyridyl nitrogen atom, while the other is bound in a monodentate manner via a carboxylate oxygen atom. Bond lengths and angles within **2** are typical for $[NiN_3O_3]$ coordination octahedra and are listed in Table 4. At each Ni site, the two *cis*-disposed nicotinate nitrogen donors both are situated *trans* to the two *cis*-oriented monodentate carboxylate oxygen atom donors. The coordination sphere is completed by an aquo ligand and one 4,4′-bpy nitrogen terminus, situated *trans* to each other, and *cis* to the donor atoms from four different μ_2-nic ligands. Thus all three nitrogen donors, and all three oxygen donors, are arranged in a *fac* fashion about the octahedral coordination sphere. Each nickel atom is connected to four others via μ_2-nic ligands, forming a 2-D neutral $[Ni(\mu_2\text{-nic})_2]$ (4,4)-net layer

Table 4
Selected bond distance (Å) and angle (°) data for **2**

Ni1–O1	2.075(3)	O1–Ni1–N1	87.70(13)
Ni1–O2	2.074(3)	O5–Ni1–N1	179.01(11)
Ni1–O5	2.082(3)	O2–Ni1–N3$^{\#1}$	170.20(11)
Ni1–N3$^{\#1}$	2.134(3)	O1–Ni1–N3$^{\#1}$	85.83(12)
Ni1–N1	2.088(3)	O5–Ni1–N3$^{\#1}$	87.89(13)
Ni1–N2$^{\#2}$	2.145(3)	N1–Ni1–N3$^{\#1}$	91.70(13)
		O2–Ni1–N2$^{\#2}$	90.06(12)
O2–Ni1–O1	84.43(11)	O1–Ni1–N2$^{\#2}$	172.59(11)
O2–Ni1–O5	91.55(12)	O5–Ni1–N2$^{\#2}$	91.92(13)
O1–Ni1–O5	93.18(12)	N1–Ni1–N2$^{\#2}$	87.25(13)
O2–Ni1–N1	89.01(13)	N3$^{\#1}$–Ni1–N2$^{\#2}$	99.74(13)

Symmetry transformations: (#1) $x+1/2, -y+3/2, z-1/2$; (#2) $x+1/2, -y+3/2, z+1/2$.

with ~14.6 Å × 7.9 Å 24-membered rectangular-shaped rings (Fig. 7).

The nickel-bound water molecules engage in intralayer hydrogen bonding to two neighboring unligated carboxylate oxygen atoms with H···O distances of 1.81 Å and 1.84 Å (Hydrogen bonding data for **2** is given in Table 3). In order to maximize these hydrogen bonding interactions, the carboxylate subunits of the nicotinate ligands twist to varying degrees (5.15° and 22.0° torsion angles with respect to the pyridyl rings). It is possible that the *cis*-disposition of carboxylate oxygen donors, and therefore the *fac*-type donor arrangement, at each $[NiN_3O_3]$ coordination octahedron may be provoked by the favorability of this hydrogen bonding pattern.

Aided by the conformational twist of the nicotinate ligands, the coordination octahedra about adjacent Ni centers within the same layer are tilted nearly 100° with respect to each other. Each nearly flat 4,4′-bpy tether (1.52° inter-ring torsion angle) points approximately 50° away from the layer plane, connecting each 2-D $[Ni(nic)_2]$ layer to identical layers above and below, thus fostering the full 3-D structure of **2** (Fig. 8). As a result of this rather acute angle, the Ni–Ni contacts through the 4,4′-bpy tether (11.7 Å) are significantly longer than the through-space distances

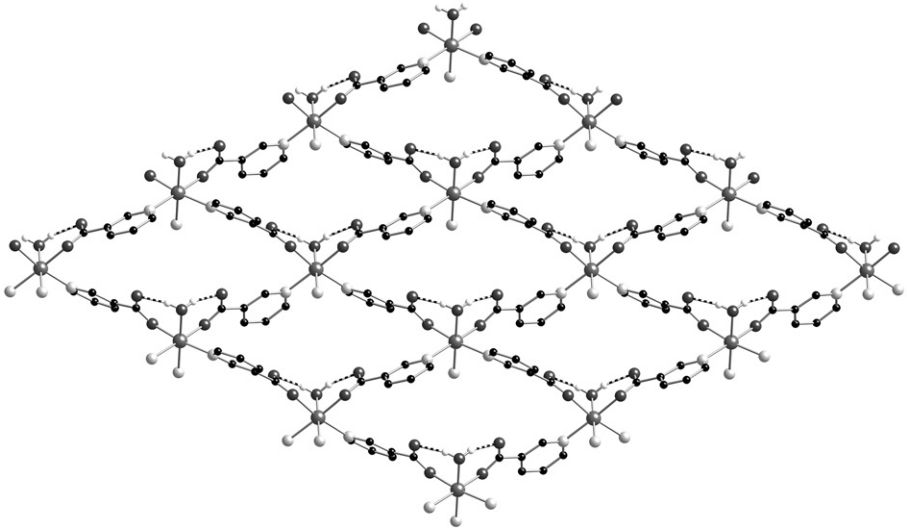


Fig. 7. View of a single 2-D Ni(nicotinate)$_2$ (4,4) layer down *b* in **2**. Bipyridine carbon atoms and most hydrogen atoms have been omitted for clarity. Intralayer hydrogen bonding contacts between aquo ligands and unligated μ_2-nicotinate oxygen atoms are indicated with dashed lines.

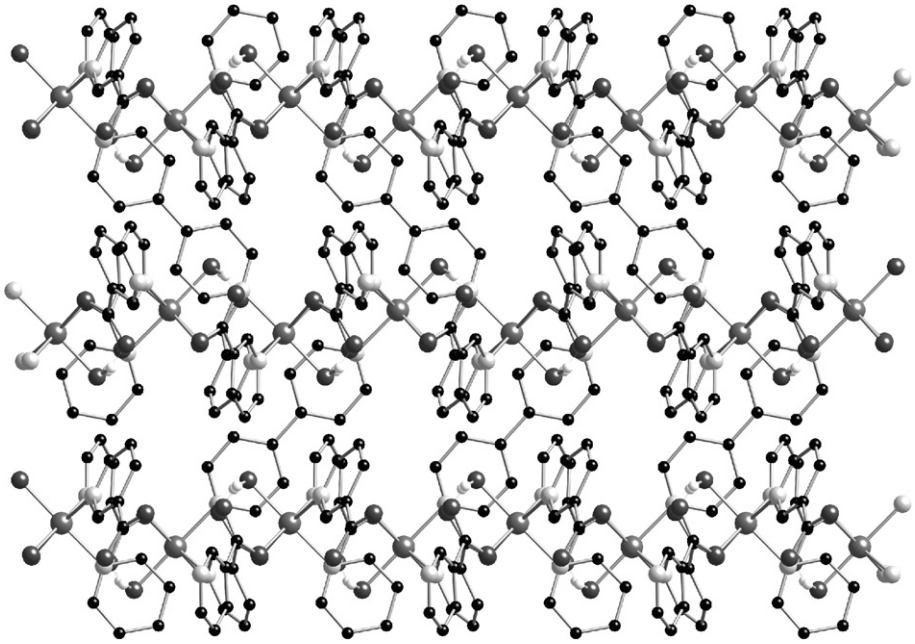


Fig. 8. View of the 3-D structure of **2** down *c*.

between directly overlaid Ni atoms in different layers (6.6 Å, 8.2 Å). As can be seen in Fig. 8, the 4,4′-bpy tethers do not link Ni atoms positioned directly above each other in each pair of layers.

4.4. Thermal properties

Thermogravimetric analysis of **1** (Fig. S1) showed a slight mass loss beginning at room temperature and ending at approximately 75 °C, consistent with unligated water loss (3.0% observed, 2.8% calculated). The mass then remained virtually unchanged until ~330 °C whereupon rapid decomposition commenced. The high thermal stability of **1** can be rationalized by its covalent 3-D network structure, augmented by significant hydrogen bonding. Between 330 °C and 425 °C, a 65.8% mass loss was observed, corresponding to the removal of the bridging water molecules, four nic ligands, and four pyridyl substituents (65.4% calculated). A subsequent mass loss of 11.9% occurred during heating to 650 °C, presumably due to decarboxylation of $NiCO_3$. The final mass loss of 77.7% at 900 °C is consistent with the deposition of NiO (76.7% calculated).

A similar analysis performed on a sample of **2** showed that its 3-D structure is somewhat less thermally robust than that of **1**, with a decomposition onset temperature of ~230 °C. Three distinct degradation steps were seen (Fig. S2). The 21.0% mass loss by 300 °C was consistent with the loss of bound water molecules and 4,4′-bipyridine ligands (24.1% calculated). A further mass loss step of 53.1%, roughly corresponding to the removal of two equivalents of nic ligands and two pyridyl groups (50.4% predicted), was complete by 425 °C. From this point, a slow mass decrease (8.1%) continued until 900 °C, likely marking the expulsion of CO_2 from $NiCO_3$. The total weight loss of 82.2% is in agreement with a remnant of NiO (81.3% calculated).

4.5. Magnetic properties of $[Ni_4(\mu\text{-}H_2O)_2(nic)_8 \cdot 2H_2O]$ (**1**)

Variable temperature magnetochemical investigations were carried out to probe possible spin communication across the triply bridged Ni^{2+} binuclear motifs in **1**. As seen in Fig. 9, a plot of $1/\chi_m$ vs. T (30–300 K) for **1** shows that its variable temperature magnetic susceptibility follows the Curie–Weiss Law ($\chi_m = C/T - \Theta$), with $C = 1.240$ cm^3–K/mol Ni, corresponding to a g value of 2.227 ($g^2 = C/0.125S(S+1)$, with $S = 1$), consistent with published values for pseudo-octahedral Ni^{2+} [20]. The Weiss constant Θ is −1.26 K, which gives a J exchange coupling constant of −0.65 cm^{-1} (via $J = 3\Theta k_B/2S(S+1)$), indicating possible weak antiferromagnetic coupling between the divalent nickel centers in the water-bridged and doubly *syn–syn* carboxylate-bridged binuclear units in **1** (assuming any magnetic interactions through the μ_2-nic or μ_3-nic ligands are very weak). $[M(\mu\text{-}H_2O)M]^{4+}$ units whose M–O–M angles exceed 90°, as is present in **1**, and divalent metal ions bridged by *syn–syn* carboxylate moieties have both previously been shown to promote antiferromagnetic coupling [21,22]. The weakness of the antiferromagnetic coupling in the present case could arise from the deviation of the carboxylate bridges from an idealized *syn–syn* conformation, resulting in poorer interaction between the magnetic e_g-type orbitals of each Ni ion. In addition, the carboxylate bridges in **1** are oriented ~100° apart from each other. It has been previously noted that orthogonality of the bridging groups mitigates antiferromagnetic exchange in a

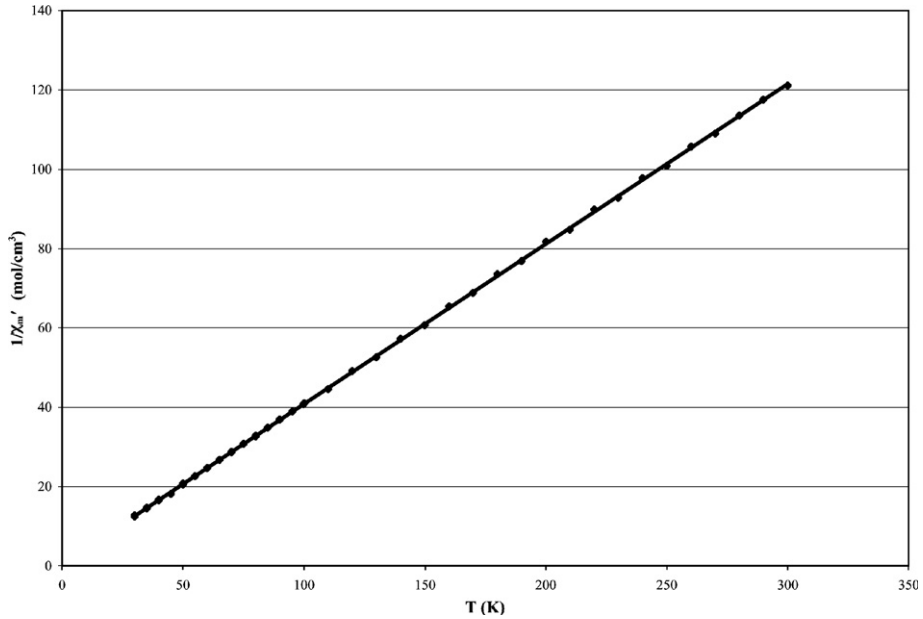


Fig. 9. Curie–Weiss plot for **1** (χ_m^{-1} vs. T)

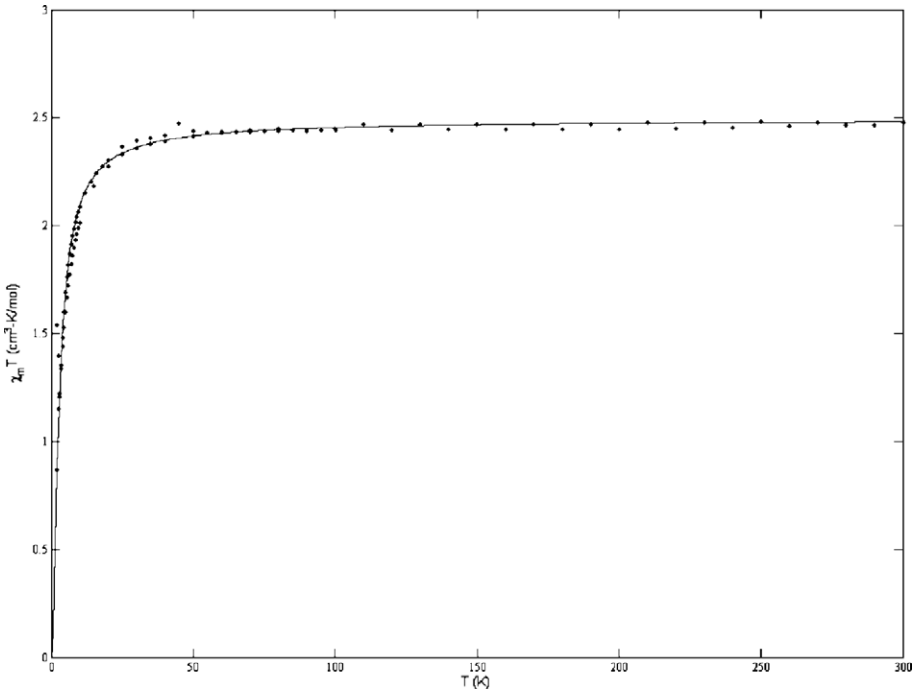


Fig. 10. Plot of $\chi_m T$ vs. T for **1**. Observed data are shown as points. The solid line represents the calculated curve from Eq. (2).

carboxylate- and phenoxo-bridged binuclear nickel complex [23].

A plot of $\chi_m T$ (cm^3–K/mol Ni_2 binuclear units) vs. T for **1** is depicted in Fig. 10. The product $\chi_m T$ at 300 K is 2.49 cm^3–K/mol, almost midway between the calculated values for an uncoupled (1.99 cm^3–K/mol) and coupled (2.99 cm^3–K/mol) pair of Ni^{2+} ions, potentially indicating the presence of antiferromagnetic coupling. This is corroborated by the diminution in the $\chi_m T$ value below 30 K. The Heisenberg Hamiltonian for an isotropically interacting pair of $S = 1$ ions (Eq. (1)) affords the expression for the magnetic susceptibility shown in Eq. (2). Even though there are two crystallographically distinct binuclear units in **1**, the close similarity of their metrical parameters safely allows the two possible intradimer J exchange parameters to be considered equal for ease of treatment.

$$\boldsymbol{H} = -J\boldsymbol{S}_{\mathrm{A}} \cdot \boldsymbol{S}_{\mathrm{B}} \quad (1)$$

$$\chi_m = (2N\beta^2 g^2/kT)(e^x + 5e^{3x}/1 + 3e^x + 5e^{3x})(x = J/kT) \quad (2)$$

The variable temperature susceptibility data were fit to Eq. (2) with the MAGMUN 4.0 software program [24], resulting in the following values: $g = 2.233(2)$, $J = -1.61(2)$ cm^{-1}, and $R = 0.00943$.[1] For *pseudo*-octahedrally coordinated Ni^{2+} ions, a low temperature decrease of $\chi_m T$ due to the single-ion zero-field-splitting parameter D cannot be excluded from consideration. Therefore the reported value of J for **1** should be considered an upper limit.

The magnetochemical behavior of **1** stands in marked contrast to that of its dehydrated structural analog **4** [10b], which displays apparent ferromagnetic coupling ($J = 26.82$ cm^{-1}) between the nickel ions in its binuclear units, with weak antiferromagnetic interactions ($J' = -0.89$ cm^{-1}) through the bridging nic ligands that span the individual binuclear units. Unfortunately no satisfactory empirical correlation exists for bridging ligand geometry and magnetic behavior in Ni^{2+} dimeric systems, as can be made for binuclear Cu^{2+} complexes [25]. It is possible that the observed differences in magnetic behavior between **1** and **4** arise from the slight variances in the Ni–O–Ni bond angles across the bridging water molecule and Ni–O–O–Ni torsion angles through the distorted *syn–syn* carboxylate bridging moieties. Alternatively, it is noted that crystalline samples of **4** were garnered only via manual separation of a multiphase mixture. It is therefore also plausible that the true nature of its susceptibility was masked by the presence of a small amount of ferromagnetic impurity.

5. Conclusion

In summary, hydrothermal treatment of nickel(II) chloride and nicotinic acid in the presence of organoimines has afforded two 3-D nickel(II) nicotinate coordination polymers that exhibit different nicotinate binding modes, highlighting the structural diversity accessible with pyridylcarboxylate ligands. Compound **1** possesses binuclear subunits containing divalent nickel ions bridged by water molecules and *syn–syn* carboxylate groups, further linked by μ_2- and μ_3-nic ligands to form "bird-shaped" cavities. On the other hand **2** displays a pillared 3-D structure

[1] $R = \sum\{[(\chi^2_{\mathrm{obs}} - \chi^2_{\mathrm{calc}})^2]/\sum[\chi^2_{\mathrm{obs}}]^2\}^{1/2}$.

constructed from μ_2-nic based layered motifs connected through 4,4′-bpy tethers. In both compounds, synergistic interactions between carboxylate binding modes and hydrogen bonding patterns serve to provide necessary structure-directing information during nucleation and crystal growth. Both **1** (after dehydration) and **2** display high thermal stability, consistent with their 3-D covalent network structures. In contrast to its previously reported dehydrated analog, **1** manifests possible weak antiferromagnetic coupling across its binuclear subunits. It is certain that further efforts exploring the versatility of carboxylate and dicarboxylate anionic ligands and neutral organoimines will continue to uncover functional coordination polymers with novel structural motifs and intriguing physico-chemical properties.

Acknowledgement

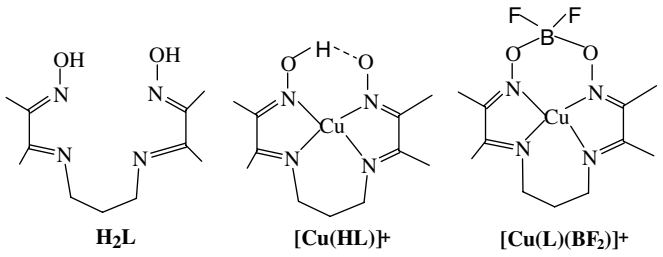
The authors gratefully acknowledge Michigan State University for financial support of this work. We thank Dr. Ronald Supkowski of King's College, Wilkes-Barre, Pennsylvania for performing the thermogravimetric analyses. We are indebted to Dr. Reza Loloee for the SQUID data collection, Dr. Rui Huang for elemental analysis and Dr. James K. McCusker of Michigan State University for helpful discussions. R.L.L. dedicates this paper to his mother Elizabeth Wall LaDuca in honor of her 60th birthday. SDG.

Appendix A. Supplementary material

CCDC 602158 and 602159 contain the supplementary crystallographic data for this paper. These data can be obtained free of charge via http://www.ccdc.cam.ac.uk/conts/retrieving.html, or from the Cambridge Crystallographic Data Centre, 12 Union Road, Cambridge CB2 1EZ, UK; fax: (+44) 1223-336-033; or e-mail: deposit@ccdc.cam.ac.uk. Supplementary data associated with this article can be found, in the online version, at doi:10.1016/j.poly.2006.09.069.

References

[1] (a) J.L.C. Roswell, O.M. Yaghi, Angew. Chem., Int. Ed. Engl. 44 (2005) 4670;
(b) M. Kondo, T. Okubo, A. Asami, S.-I. Noro, T. Yoshitomi, S. Kitagawa, T. Ishii, H. Matsuzaka, Angew. Chem., Int. Ed. Engl. 38 (1999) 140.
[2] (a) J.S. Seo, D. Whang, H. Lee, S.I. Jun, J. Oh, Y.J. Jeon, K. Kim, Nature 404 (2000) 982;
(b) A. Cingolani, S. Galli, N. Masciocchi, L. Pandolfo, C. Pettinari, A. Sironi, J. Am. Chem. Soc. 127 (2005) 6144.
[3] (a) Q.-R. Fang, G.-S. Zhu, M. Xue, J.-Y. Sun, S.-L. Qiu, Shi-Lun, Dalton Trans. (2006) 2399;
(b) X.-M. Zhang, M.-L. Tong, H.K. Lee, X.-M. Chen, J. Solid State Chem. 118 (2001) 118.
[4] (a) S.G. Baca, M.T. Reetz, R. Goddard, I.G. Filippova, Y.A. Simonov, M. Gdaniec, N. Gerbeleu, Polyhedron 25 (2006) 1215;
(b) H. Han, S. Zhang, H. Hou, Y. Fan, Y. Zhu, Eur. J. Inorg. Chem. 8 (2006) 1594;
(c) W. Mori, S. Takamizawa, C.N. Kato, T. Ohmura, T. Sato, Microp. Mesopor. Mater. 73 (2004) 15.
[5] M. Murugesu, R. Clerac, B. Pilawa, A. Mandel, C.E. Anson, A.K. Powell, K. Annie, Inorg. Chim. Acta 337 (2002) 328, and references contained therein.
[6] (a) P. King, R. Clerac, C.E. Anson, C. Coulon, A.K. Powell, Inorg. Chem. 42 (2003) 3492;
(b) T. Tokii, N. Watanabe, M. Nakashima, Y. Muto, M. Morooka, S. Ohba, Y. Saito, Bull. Chem. Soc. Jpn. 63 (1990) 364.
[7] H.W. Roesky, M. Andruh, Coord. Chem. Rev. 236 (2003) 91.
[8] W. Lin, O.R. Evans, R.-G. Xiong, Z. Wang, J. Am. Chem. Soc. 120 (1998) 13272.
[9] Y.-H. Liu, H.-L. Tsai, Y.-L. Lu, Y.-S. Wen, J.-C. Wang, K.-L. Lu, Inorg. Chem. 40 (2001) 6426.
[10] (a) P. Ayyappan, O.R. Evans, W. Lin, Inorg. Chem. 40 (2001) 4627;
(b) C.-D. Wu, C.-Z. Lu, H.-H. Zhuang, J.-S. Huang, Z. Anorg. Allgem. Chem. 629 (2003) 693.
[11] P.J. Zapf, R.L. LaDuca, R.S. Rarig, K.M. Johnson, J. Zubieta, Inorg. Chem. 37 (1998) 3411.
[12] O. Khan, Molecular Magnetism, VCH Publishers, New York, 1993.
[13] SAINT, Software for Data Extraction and Reduction, Version 6.02, Bruker AXS Inc., Madison, WI, 2002.
[14] SADABS, Software for Empirical Absorption Correction, Version 2.03, Bruker AXS Inc., Madison, WI, 2002.
[15] G.M. Sheldrick, SHELXTL, Program for Crystal Structure Refinement, University of Gottingen, Gottingen, Germany, 1997.
[16] A.L. Spek, PLATON, A Multipurpose Crystallographic Tool, Utrecht University, Utrecht, The Netherlands, 1998.
[17] V. Soghomonian, L.A. Meyer, R.C. Haushalter, J. Zubieta, Inorg. Chim. Acta 275–276 (1998) 122.
[18] R.C. Mehrotra, R. Bohra, Metal Carboxylates, Academic Press, New York, 1983.
[19] M. Kurmoo, C. Estournes, Y. Oka, H. Kumagai, K. Inoue, Inorg. Chem. 44 (2005) 217.
[20] C.J. Matthews, K. Avery, Z. Xu, L.K. Thompson, L. Zhao, D.O. Miller, K. Biradha, K. Poirier, M.J. Zaworotko, C. Wilson, A.E. Goeta, J.A.K. Howard, Inorg. Chem. 38 (1999) 5266.
[21] M. Fondo, N. Ocampo, A.M. Garcia-Deibe, R. Vicente, M. Corbella, M.R. Bermejo, J. Sanmartin, Inorg. Chem. 45 (2006) 255.
[22] Y.-Q. Zheng, J.-L. Lin, Z.-P. Kong, Inorg. Chem. 43 (2004) 2590.
[23] K.K. Nanda, R. Das, L.K. Thompson, K. Venkatsubramanian, P. Paul, K. Nag, Inorg. Chem. 33 (1994) 1188.
[24] L.K. Thompson, O. Waldmann, Z. Xu, Coord. Chem. Rev. 249 (2005) 2677.
[25] W.H. Crawford, H.W. Richardson, J.R. Wasson, D.J. Hodgson, W.R. Hatfield, Inorg. Chem. 15 (1976) 1207.



H_2L $[Cu(HL)]^+$ $[Cu(L)(BF_2)]^+$

In our earlier report, we have been able to extend the coordination number of copper(II) under a sterically congested N_4 donor macrocyclic environment [6]. In an extension to such efforts, here, we have considered a comparatively reluctant $[Cu(HL)]^+$ chromophore to investigate its axial interaction with the tetracyanonickelate ion.

Again, the chemistry of cyano-bridged coordination complexes of transitional metal ions is of contemporary interest due to remarkable diversity in their structural topologies and indeed, it is a popular approach for designing the construction of different supramolecular architectures with unusual and interesting properties [7]. Among various cyanometalates, the tetracyanonickelate anion $[Ni(CN)_4]^{2-}$ exhibits bridging character involving either one, two, three or four of the cyano groups and all four possibilities have been found [7]. Although a few copper(II) complexes with tetracyanonickelate bridged 1D [8], 2D [9] and even 3D [9b] structures have been reported recently, the number of structural studies on discrete molecules is surprisingly low [10] and such complexes are prepared mainly by utilizing various N_1, N_2 or N_3 donor ligands. Moreover, there is only a few reports on structural studies of such discrete tetracyanonickelate bridged copper(II) complexes under an N_4 donor ligand environment [11] and to the best of our knowledge this is the first report on an oxime–imine like N_4 donor pseudo-macrocyclic precursor.

On the other hand, from the chemical redox point of view, periodate is thought to be a typical inner-sphere oxidant often featuring diverse mechanistic behavior [12]. Though, there are reports on the oxidation of some inorganic species with a few copper(III) oxime–imine complexes [13], corresponding kinetic studies on the oxidation of copper(II) complexes by inorganic oxidant have not yet been reported. So a kinetic study on the oxidation of the cyano-bridged complex, $[Cu(HL)]_2[Ni(CN)_4]\cdot 4H_2O$ (**2**) along with the parent complex, $[Cu(HL)]ClO_4\cdot 2H_2O$ (**1**) by periodate would be valuable and interesting mechanistically. In this article we report synthesis, crystal structure, electrochemical and kinetic studies on the periodate oxidation on a cyano-bridged Cu(II)–Ni(II)–Cu(II) heterotrinuclear complex **2**. A parallel electrochemical and kinetic studies on the parent complex **1** reveals that there is a distinct difference in behavior of **2** over **1** due to the presence of $[Ni(CN)_4]^-$ in **2**.

2. Results and discussion

2.1. Description of structure of $[Cu(HL)]_2[Ni(CN)_4]\cdot 4H_2O$ (2)

Complex **2** crystallizes in the monoclinic space group *C*2/*c* and exhibits crystallographic C_2 symmetry. The asymmetric unit contains half of the formula unit along with three water molecules. The molecular structure of the complex **2** consists of a discrete hetero-trinuclear species (Cu–Ni–Cu) with the copper–copper separation of 9.778 Å by severely bent cyano bridging [C(8)–N(5)–Cu, 143.7(4)°] of $[Ni(CN)_4]^{2-}$ ion in di-*trans* fashion; along with four water molecules. The bonding arrangement of this trinuclear unit is shown in Fig. 1 and selected bond distances and angles in Table 1. Such type of cyano bridging of $[Ni(CN)_4]^{2-}$, leaves two other *trans* CN groups as terminal, and is comparable to $[Cu(bappz)]_2[Ni(CN)_4]\cdot(ClO_4)_2$ [11a] [bappz = 1,4-bis(3-aminopropyl)piperazine]. The coordination geometry about the copper atom is best described by a square pyramid with the geometrical factor $\tau = 0.01$ [14]. The four nitrogen atoms of the H_2L ligand construct the basal plane and the nitrogen atom of the bridging cyanide occupies the apical position. The copper atom is situated 0.302 Å above the plane towards the apical direction. This makes the basal angles N(1)–Cu–N(3), 161.81(2)° and N(2)–Cu–N(4), 162.64° to deviate significantly from 180° and the four N(5)–Cu–N(*x*) [*x* = 1, 2, 3 and 4] angles are larger than 90° (avg. 98.82(2)^0) indicating that the coordination geometry around each copper(II) atom is a distorted square pyramid. The average Cu–N bond length (1.964(4) Å) at the basal plane is comparable with the complex $[Cu(HL)]ClO_4\cdot 1/2CH_3OH$ [15]. However, in that complex each copper atom of monomeric $[Cu(HL)]ClO_4\cdot 1/2CH_3OH$ unit is further very weakly coordinated to an oxime oxygen (average Cu–O distances of 2.492 (4) Å) of the adjacent equivalent unit to form a singly bridged zigzag chain, whereas, a discrete trinuclear structure is prevailing for complex **2** with no possibility of formation of such oxime oxygen bridged Cu–O bonds.

From the charge balance considerations, it is evident that out of two *cis* oxime groups of each asymmetric unit, one is deprotonated during complex formation and makes intramolecular H-bonding with the remaining –N–OH group. The O(1)–O(2) distance (2.520 Å) is similar to the H-bonded oxygen–oxygen distance observed in other copper–oxime complexes and supports this proposition [15,16]. The Cu–N(5) apical bond length (2.155(4) Å) is comparatively longer than the Cu–N (bridging cyanide)$_{basal}$ (2.040(7) Å) found in $[Cu(Me_6Cy)][Ni(CN)_4]$ [6]. In contrast, Cu–N axial bond lengths for several such cyano bridged copper(II) complexes fall in the range 2.147–2.677 [11a,11b] which are comparable to the Cu–N(5) axial bond length in **2** and indicate the inclination of Cu atom towards the axial site (*vide infra*).

The C-end of the cyano ligand produces a strong field effect, while the N-end behaves as medium ligand with a ligand field lower than that of NH_3. Generally, C–N dis-

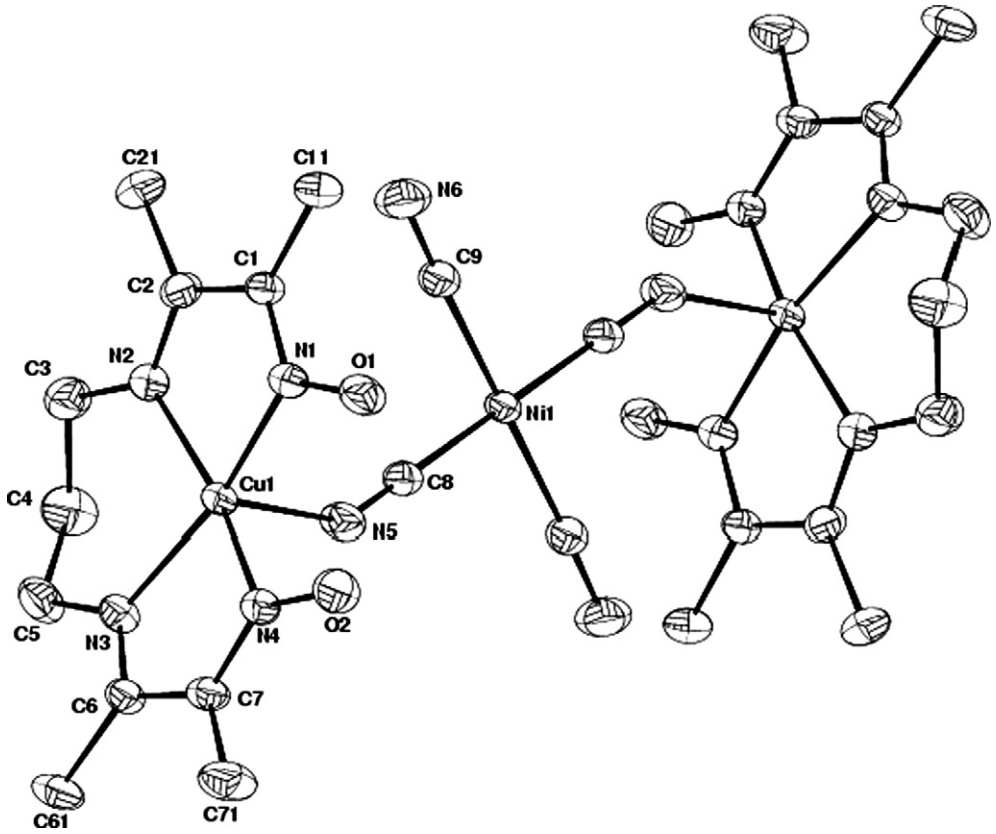


Fig. 1. ORTEP view of the trinuclear unit of **2**. Hydrogen atoms and water molecules are omitted for clarity. (Thermal ellipsoids are represented at the 30% probability level.)

Table 1
Selected bond lengths (Å) and angles (°) for complex **2**

Cu(1)–N(1)	1.961(4)
Cu(1)–N(2)	1.950(4)
Cu(1)–N(3)	1.972(4)
Cu(1)–N(4)	1.972(4)
Cu(1)–N(5)	2.155(4)
N(1)–O(1)	1.336(5)
N(4)–O(2)	1.339(5)
N(5)–C(8)	1.134(6)
N(6)–C(9)	1.152(7)
N(2)–Cu(1)–N(1)	80.9(2)
N(2)–Cu(1)–N(3)	98.7(2)
N(1)–Cu(1)–N(3)	161.8(2)
N(2)–Cu(1)–N(4)	162.6(2)
N(1)–Cu(1)–N(4)	95.1(2)
N(3)–Cu(1)–N(4)	79.7(2)
N(2)–Cu(1)–N(5)	97.1(2)
N(1)–Cu(1)–N(5)	95.2(2)
N(3)–Cu(1)–N(5)	102.8(2)
N(4)–Cu(1)–N(5)	100.2(2)
O(1)–N(1)–Cu(1)	122.2(3)
O(2)–N(4)–Cu(1)	123.2(3)
C(8)–N(5)–Cu(1)	143.7(4)
N(5)–C(8)–Ni(1)	178.3(5)
N(6)–C(9)–Ni(1)	177.8(5)

tances fall in the range 1.12–1.16 and no difference is found whether it is a terminal or bridging ligand [7]. In complex **2**, the C–N distances for the bridging and terminal cyanide groups are 1.134 (6) Å and 1.152(7) Å respectively and conform to the above proposition.

The Ni–C bond distances in $[Ni(CN)_4]^{2-}$ fall in the range 1.856(5)–1.859(5) Å for both bridging and terminal cyano groups and are very close to the ideal value of 1.86 [17]. The $[Ni(CN)_4]^{2-}$ moiety in **2** effectively retains its original square planar geometry and this is evidenced by the fact that all the Ni–C–N bond angles fall in the narrow range of 177.8(5)–178.3(5)°. Such rigidity of the square planer structure is generally seen for $[Ni(CN)_4]^{2-}$ in various bridging structures regardless of different modes of bridging [7].

As it is already known to us that lattice water molecules present in the crystal play a unique and ubiquitous role, not only to impart stability of the complex but simultaneously help to build up the supramolecular as well as the biological architectures. The arrangement of lattice water molecules in the present complex is highly ordered and produces a water column viewed down the *b* axis (Fig. 2).

2.2. IR study

The positions of the relevant IR bands were listed in the experimental section. For cyano complexes the absorption bands due to ν_{CN} stretching vibrations are very characteristic. In the free tetracyanonickelate anion this absorption band appears at 2128 cm^{-1} [17]. On bridging via N atom this band shifts to higher wave number. Here two ν_{CN} IR

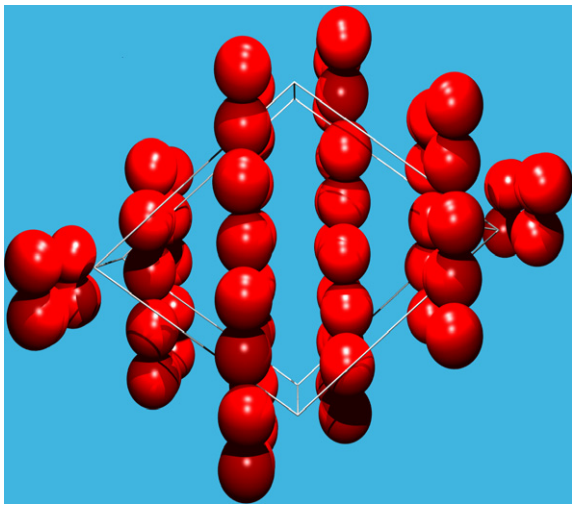


Fig. 2. Water column of the lattice water molecules (viewed down the *b* axis).

bands appeared at 2118(vs) and 2135(s) cm^{-1} for **2** can be assigned to the terminal and bridging cyanides respectively [6]. The broad ν_{O-H} band at 3389 cm^{-1} can assure the presence of O–H···O hydrogen bonded oxime proton [16] as well as the hydrogen bonded lattice water molecules. All the other bands appear more or less at their usual positions.

2.3. Thermal analyses

Thermal decomposition of complex **2** starts at *ca.* 41 °C and consequently, the complex eliminates its uncoordinated four water molecules and the process continues up to *ca.* 58 °C (found/calcd.: 6.45/6.43% with respect to loss of wt%). This is accompanied by a small *endo*-effect on the DTA curve at *ca.* 54 °C. The anhydrous complex $[Cu(HL)]_2[Ni(CN)_4]$ maintains its thermal stability upto *ca.* 171 °C, after which it undergoes an immediate exothermal decomposition with a DTA curve maxima at *ca.* 201 °C. The decomposition of the complex is complete at *ca.* 200 °C, giving CuO and NiO as the final products (found/calcd.: 81.65/81.64% with respect to loss of wt%).

2.4. Magnetic property

The room temperature (298 K) effective magnetic moment per monomer of complex **2** is 1.78μ_B and is comparable with the spin only value (1.73μ_B) for ideally monomeric copper(II) complexes. The large Cu···Cu separation (9.778 Å) in between two monomeric units *via* diamagnetic tetracyanonickelate bridging, weakens the chance of magnetic interactions in the complex.

2.5. EPR studies

Room temperature solid state EPR of the polycrystalline sample of the complex **2** is typical for mononuclear copper(II) complexes with axial distortion and the elongation of axis is characterized by $g_\parallel = 2.134 \pm 0.005$ and $g_\perp = 2.022 \pm 0.002$. Simulation of this signal using the Lorentzian function [18] of the individual EPR line gives: $g_\parallel = 2.13$, $g_\perp = 2.02$, $A_\parallel = 40$ Oe, $A_\perp = 5$ Oe with $\Delta H =$ 40 Oe at $\nu = 9.517$ GHz. The observed values ($g_\parallel > g_\perp$) confirm that the unpaired electron resides in the $d_{x^2-y^2}$ orbital.

2.6. Electrochemical studies

The electrochemical properties of the parent complex $[Cu(HL)]ClO_4 \cdot 2H_2O$ (**1**) and that of complex $[Cu(HL)]_2[Ni(CN)_4] \cdot 4H_2O$ (**2**) were investigated using the cyclic voltammetric technique in aqueous and MeCN solutions. Tetrabutyl ammonium perchlorate (TBAP, 0.1 mol L^{-1}) was used as the supporting electrolyte in MeCN solution, while 0.1 M $NaClO_4$ was used in aqueous solution. For comparison of the data obtained in aqueous solution, cyclic voltammetry of the free ligand (H_2L) was also carried out under similar conditions. All the electrochemical data are summarized in Table 2.

Fig. 3a shows the cyclic voltammogram for complex **2** in MeCN (1.0×10^{-3} mol L^{-1}) with a well defined cathodic wave for copper(II) to copper(I) reduction at a potential *ca.* −0.60 V, for which the reverse scan gave an anodic wave at *ca.* −0.50 V and the corresponding $E_{1/2}$ was estimated as −0.55 V *versus* Ag/AgCl. The peak potentials were invariant of scan rates and i_{pc} *versus* $\nu^{1/2}$ were linear passing through origin, where i_{pc} is the cathodic peak current and ν is the scan rate in V s^{-1}. Though the ΔEp value was slightly higher than that for the Nernstian behavior it may be assumed as a reversible process with a i_{pa}/i_{pc} value approximated to unity. When the scan was continued further to more negative potential, it gave an irreversible reduction peak at potential *ca.* −1.75 V *versus* Ag/AgCl (not shown in the figure). However, this reduction process has not been investigated further. In the anodic potential region, a quasi-reversible one electron oxidation of copper(II) to copper(III) was observed with $\Delta Ep = 0.16$ V and $E_{1/2} = 1.23$ V *versus* Ag/AgCl. It is important to note that the both anodic and cathodic peak positions were invariant with scan rates in the range of 0.05–0.8 V s^{-1}. The diffusion co-efficient [19] value of the complex **2** was determined and shown in Table 2.

Electrochemical reduction and oxidation behavior of the parent complex **1** was found behave similarly in MeCN. Fig. 3b shows a typical voltammogram for the cyclic voltammetry of the parent complex in MeCN with glassy carbon working electrode. The quasi-reversible reduction process appeared at a slightly more positive potential than that in complex **2** under the similar condition and also the voltammetric peak current was consistent with a slightly greater diffusion co-efficient as shown in Table 2. It is important to note that the intensity of the anodic peak for the oxidation of copper(I) to copper(II) in the reverse scan was greatly reduced with the formation of a desorption peak at *ca.* −0.20 V. Here also the second reduction peak, which was again irreversible, was not investigated further.

Cyclic voltammetric studies in MeCN indicate that the complex **2** is reduced at more negative potential (Fig. 3a)

Table 2
Electrochemical parameters[a] of the compounds

Compound	Solvent	Supporting electrolyte (0.1 M)	Ep_c (V)	Ep_a (V)	ΔEp (V)	$E_{1/2}$ (V)	D ($cm^2\ s^{-1}$)
$[CuHL]ClO_4 \cdot 2H_2O$ (**1**)]	MeCN	TBAP	1.12	1.19	0.07	1.15[c]	8.9×10^{-5}
			−0.58	−0.47	0.11	−0.52[d]	2.8×10^{-5}
	water	$NaClO_4$	0.37	0.89	0.52	0.63[b]	
			−0.65	−0.58	0.07	−0.61[d]	
$[Cu(HL)]_2[Ni(CN)_4] \cdot 4H_2O$ (**2**)	MeCN	TBAP	1.15	1.31	0.16	1.23[c]	3.9×10^{-5}
			−0.60	−0.50	0.10	−0.55[d]	6.8×10^{-5}
	water	$NaClO_4$	0.98	1.1	0.12	1.04[c]	2.7×10^{-5}
			0.36	0.84	0.48	0.60[b]	
			−0.63	−0.52	0.11	−0.58[d]	5.3×10^{-5}
H_2L	water	$NaClO_4$	0.49	0.73	0.24	0.61[b]	

[a] Maximum error ± 7%; all potentials are measured against Ag/AgCl reference electrode.
[b] $E_{1/2}$ for ligand oxidation.
[c] $E_{1/2}$ for Cu^{III}/Cu^{II} couple.
[d] $E_{1/2}$ for Cu^{II}/Cu^{I} couple. $E_{1/2}$ is determined as $1/2(Ep_c + Ep_a)$.

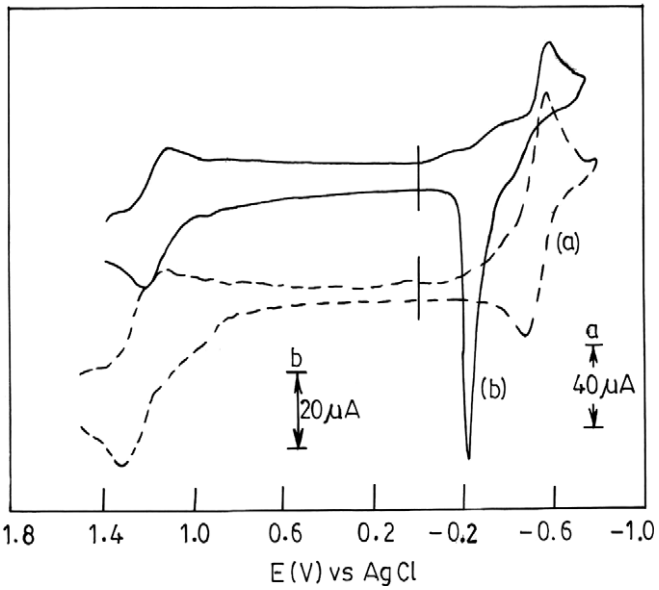


Fig. 3. Cyclic voltammograms of complex **1** (b) and **2** (a) in MeCN using a glassy carbon electrode and TBAP (0.10 M) as supporting electrolyte at 100 mV s^{-1} scan rate.

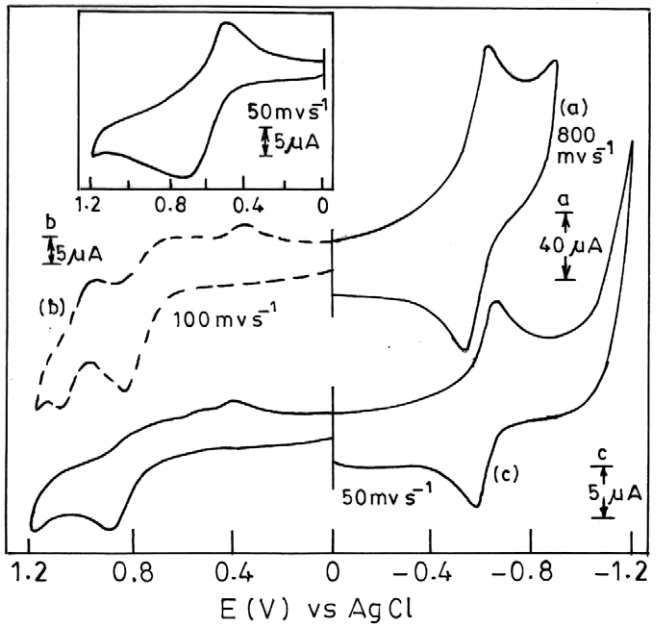


Fig. 4. Cyclic voltammograms of complex **1** (c) and **2** (a and b) in water using a glossy carbon electrode and $NaClO_4$ (0.10 M) as supporting electrolyte at different scan rates. Inset is the cyclic voltammogram of H_2L under the same conditions.

in comparison to that of the parent complex and this is attributed due to the axial ligation of $[Ni(CN)_4]^{2-}$ to $[Cu(HL)]^+$ precursor through nitrogen end (*vide supra*).

In aqueous solution the cyclic voltammetry of the complex **2** (Fig. 4a and b) showed a reduction behavior very similar to that observed in MeCN with a quasi-reversible reduction of Cu^{II}/Cu^{I} at a $E_{1/2}$ of −0.58 V *versus* Ag/AgCl. But in contrast, the oxidation behavior in MeCN was completely different from that in aqueous solution. Oxidation of copper(II) takes place at a $E_{1/2}$ of 1.04 V *versus* Ag/AgCl which was shifted to a lower potential in comparison to that observed in MeCN. Oxidation of copper(II) or reduction of copper(III) involves a fast proton transfer which is facilitated in aqueous solution, and as a result the redox potential is shifted to a lower region. This is a kind of proton-coupled electron transfer reaction and very common for many nickel(II) and iron(II) complexes of analogous ligands [2]. Further, in addition to the oxidation of copper(II) to copper(III) another anodic wave was noticed at $Ep_a = 0.84$ V having a reduction wave in the cathodic scan at *ca.* 0.36 V with $E_{1/2} = 0.60$ V *versus* Ag/AgCl and was assigned to a quasi-reversible oxidation of the copper-bound ligand. It is worth-mentioning here that when the free ligand H_2L was scanned under the similar condition (Fig. 4 inset), an almost identical oxidation of the ligand at $E_{1/2} \sim 0.61$ V was observed. Thus it may be suggested that this quasi-reversible oxidation process is due to oxidation of the copper-bound ligand.

The electrochemical behavior of **1** (Fig. 4c) was also studied in aqueous solution under the similar condition.

It showed a quasi-reversible reduction of copper(II) to copper(I) with a $E_{1/2}$ at around −0.61 V *versus* Ag/AgCl. It also showed an oxidation process having $E_{1/2} \sim 0.63$ V which is assigned to the quasi-reversible oxidation of the metal bound ligand. It is however surprising that we could not get any wave for the oxidation of copper(II) to copper(III) in the potential range up to 1.2 V *versus* Ag/AgCl.

The chemical and electrochemical oxidation of the parent complex is highly pH sensitive and those were studied in detail by Sulfab et al. [3]. They claimed that the $E_{1/2}$ values for the oxidation of copper(II) to copper(III) of the parent complex are 0.955 V, 0.933 V and 0.895 V *versus* SCE at the pH 3.63, 4.00 and 4.59 respectively [3b]. This is in agreement with the decrease of electrode potential with increasing pH. Such consistency holds good over the pH range 1.2–5.0 [13]. However at higher pH the situation seems peculiar. Our cyclovoltammetric study of the parent complex **1** was carried out at pH 6.58 and under such condition the ligand is very likely to undergo fast internal oxidation and consequently destabilize the copper(III) complex. Such ligand oxidation may be the prime reason for the absence of finding any oxidation peak for copper(II) to copper(III) oxidation at ca 1.20 V. However, in complex **2** at pH 6.32, the presence of axial σ-donation from $[Ni(CN)_4]^{2-}$ through N atom may be responsible for stabilization of copper(III) complex under an oxidized ligand environment. Interestingly, at pH < 5.0, no ligand oxidation for both **1** and **2** was observed and this resembles the earlier trend [3b]. And finally, it is noteworthy to mention here that such ligand oxidation in the anodic part dose not arise in complex **1** as well as in **2** in MeCN, and hence the previous claim of ligand oxidation at 1.05 V *versus* SCE by Addison et al. in the same solvent seems surprising [5].

2.7. Kinetic study

The kinetics of oxidation of the complexes **1** and **2** by periodate, I^{VII}, was carried out in the range $[H^+] = (1.0–50.0) \times 10^{-3}$ mol L^{-1}, $[I^{VII}]_t = (0.1–10.0) \times 10^{-3}$ mol L^{-1} (t represents total) at $\mu = 0.50$ mol L^{-1} (Na_2SO_4) and at temperature 25 °C. Kinetics were followed under pseudo-first-order conditions taking complexes as the minor component (2×10^{-4} mol L^{-1}) and by monitoring the increase in absorbance due to the formation of copper(III) complexes at the wavelengths of maximum absorption (515 nm). Fig. 5 represents the time-resolved spectra generated from a kinetic trace. The reactions were clean for more than four half lives, after which kinetic traces become irregular, maybe due to decomposition or for some other reactions. As we are interested to note the chemical redox behavior of these complexes towards periodate as an oxidant, we looked into the initial oxidation process. Pseudo-first-order rate constants (k_{obs}/s^{-1}) were obtained by fitting the kinetic curves with the help of a suitable single exponential computer-fit program and the results obtained in more than two determinations fall in the error limit ± 5%.

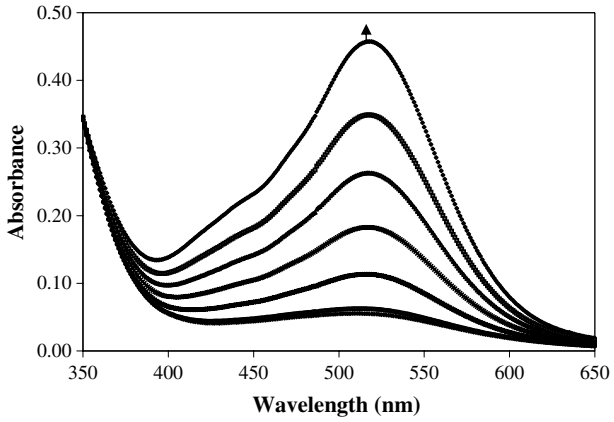
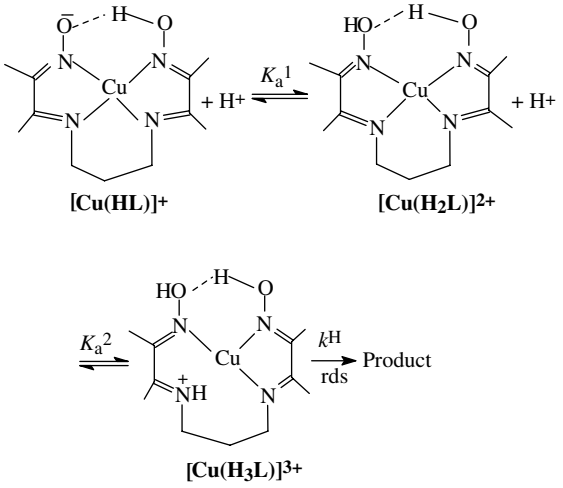


Fig. 5. Spectral scan showing the conversion of copper(II) to copper(III) of the complex **2** under kinetic conditions. First spectrum was for the complex and second was taken immediately after mixing with $[I^{VII}] = 0.0007$ M at $[H^+] = 0.01$ M. Successive spectra were taken in an arbitrary time scale.

2.7.1. Acid catalyzed decomposition of parent complex (*1*) and complex (*2*)

It was observed that both the complexes **1** and **2** undergo acid catalyzed decomposition. So an attempt was taken to study the kinetics of acid catalyzed decomposition these complexes. For this purpose, $[H^+]$ variation experiments were conducted in the range 0.01–0.20 mol L^{-1} at $\mu = 0.50$ mol L^{-1} (Na_2SO_4) and 25 °C, where single exponential decay curves manifests a first-order dependence on the complex. It is interesting to note that this decomposition rate constant (k_{obs}/s^{-1}) is second-order in H^+ and can best be described as the rapid protonation of oximato-oxygen and then second protonation on one of the two imine nitrogen followed by decomposition of the protonated species in a rate determining step and has been described in Eq. (1). Corresponding data have been listed in Table 3. Such protonation weaken both the Cu–N(R)(OH) and Cu–$N(R^1)(R^2)$ bonds and causes the decomposition of the complexes.



(1)

Plots of k_{obs} *versus* $[H^+]$ give non-linear curves (Fig. 6) with increasing slope which were solved by using suitable com-

Table 3
Summary of pseudo-first-order rate constants for the acid catalyzed decomposition of complexes **1** and **2** at $\mu = 0.50$ mol L^{-1} (Na_2SO_4) and 25 °C

$[H^+]$/M	$10^4 \times k_{obs}$ (**1**)/s^{-1}	$10^4 \times k_{obs}$ (**2**)/s^{-1}
0.01	1.46	3.60
0.05	3. 12	9.01
0.10	9.10	21.6
0.15	25.7	52.1
0.20	41.6	90.0

puter-fit program to Eq. (1a) to get $k^H = 0.098 \pm 0.03$ L^2 mol^{-2} s^{-1} and $n = 1.95 \pm 0.17$ for **1** and $k^H = 0.20 \pm 0.05$ L^2 mol^{-2} s^{-1} and $n = 1.93 \pm 0.13$ for **2**

$$k_{obs} = k^H[H^+]^n \quad (1a)$$

The acid catalyzed decomposition rate constant, k^H, for **2** is found to be ~2 times higher than that of complex **1** and can be attributed to the axial coordination of $[Ni(CN)_4]^{2-}$ to the copper(II) center which probably destabilizes the system and facilitates this process.

2.7.2. Oxidation of *1*

The dependence of rate on $[I^{VII}]_t$ was carried out at $[H^+] = 0.01$ mol L^{-1} and a plot of k_{obs} *versus* $[I^{VII}]_t$ shows an initial rapid increase in rate with $[I^{VII}]_t$ followed by slower increase and then becomes almost independent on $[I^{VII}]_t$ (Fig. 7). Such a dependence of rate is best described by Eq. (2). The factor 2 comes from the stoichiometry of the reactions

$$k_{obs} = 2\frac{kQ[I^{VII}]}{1 + Q[I^{VII}]} \quad (2)$$

A non-linear least-square computer-fit program provides $k = (1.37 \pm 0.06) \times 10^{-2}$ s^{-1} and $Q = (1002 \pm 166)$ L mol^{-1}. The dependence of k_{obs} on $[H^+]$ in the range 0.001–0.01 mol L^{-1} at $[I^{VII}]_t = 0.0007$ mol L^{-1}, where a strict first-order dependence on $[I^{VII}]_t$ holds, is shown in

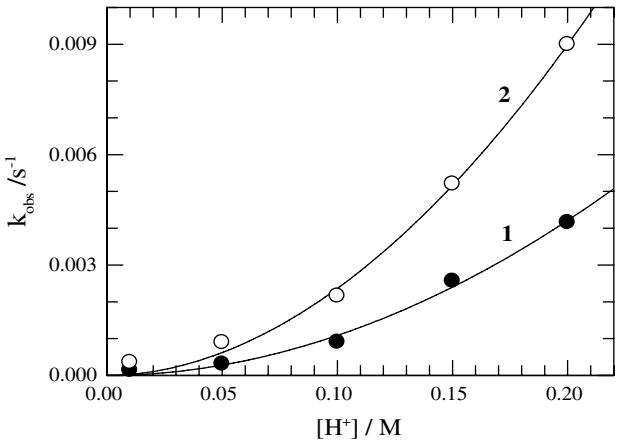


Fig. 6. Plot of pseudo-first-order rate constants (k_{obs}/s^{-1}) *vs.* $[H^+]$ for the acid catalyzed decomposition of complexes **1** and **2** at $\mu = 0.50$ M (Na_2SO_4) and 25 °C.

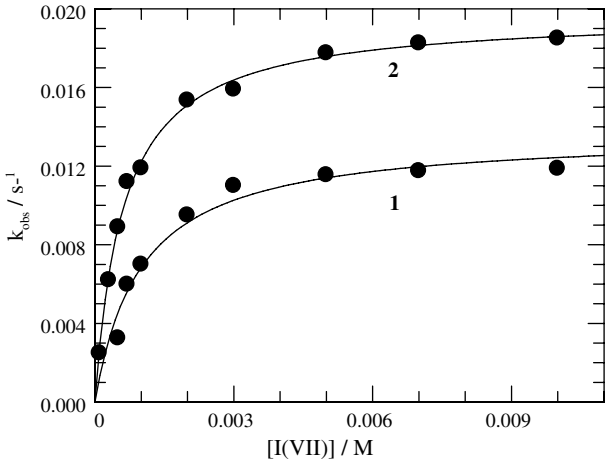


Fig. 7. Plots of k_{obs} *vs.* $[I^{VII}]$ for the oxidation of complexes **1** and **2** at $[H^+] = 0.01$ M.

Fig. 8. The presence of measurable intercept on the rate axis indicates that both protonated (HIO_4) and deprotonated (IO_4^-) species are reactive towards **1**. The following reaction sequence could be framed to explain the above observation:

$$[Cu(HL)]^+ + HIO_4 \overset{Q_1}{\rightleftharpoons} \{[Cu(HL)]^+, HIO_4\} \xrightarrow{k_1} [Cu(L)]^+ + 2H^+ + IO_4^{\cdot -} \quad (3)$$

$$[Cu(HL)]^+ + IO_4^- \overset{Q_2}{\rightleftharpoons} \{[Cu(HL)]^+, IO_4^-\} \xrightarrow{k_2} [Cu(L)]^+ + H^+ + IO_4^{\cdot -} \quad (4)$$

The radical thus generated reacts in a fast step with another copper(II) complex to give $[Cu(L)]^+$ and IO_3^- as the final products (Eq. (5)) to account for an overall 2:1 stoichiometry of the reaction with respect to the complex, which is common to the most of reactions involving periodate as oxidant in acid medium [12]. The fast decomposition of the copper(III) complex generated thereby precludes the

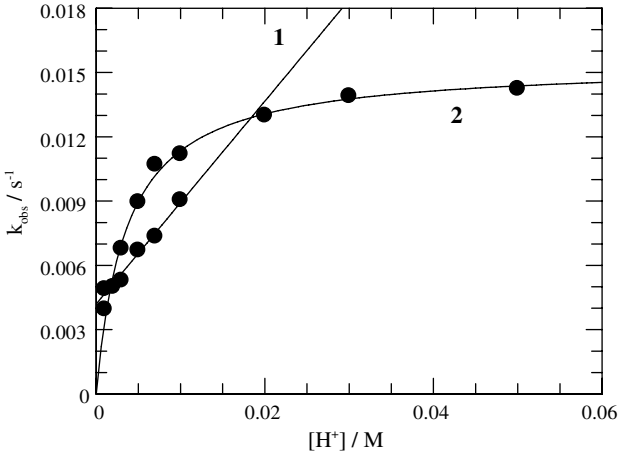


Fig. 8. Plots of k_{obs} *vs.* $[H^+]$ for the oxidation of complexes **1** and **2** at $[I^{VII}] = 0.0007$ M.

determination of the stoichiometry of the reaction under the kinetic conditions

$$[Cu(HL)]^+ + IO_4^{\cdot -} + H^+ \xrightarrow{fast} [Cu(L)]^+ + IO_3^- + H_2O \quad (5)$$

The rate law derived is shown in Eq. (6)

$$k_{obs} = 2\frac{k_1Q_1[H^+] + k_2Q_2K_a}{\{K_a + [H^+]\}}[I^{VII}]_t \quad (6)$$

As, HIO_4 is a strong acid, it is imperative that K_a (0.023) [20] > $[H^+]$ and Eq. (6) where, $k = k_{obs}/2[I^{VII}]_t$, turns to Eq. (7) and easily explains the observed dependence of rate on $[H^+]$,

$$k = (k_1Q_1/K_a)[H^+] + k_2Q_2 \quad (7)$$

The linear fit of data to $[H^+]$ gives parameters as: $k_1Q_1/K_a = (6.75 \pm 0.54) \times 10^2\ s^{-1}$, $k_1Q_1 = 15.5\ L\ mol^{-1}\ s^{-1}$ and $k_2Q_2 = (6.00 \times 0.33)\ L\ mol^{-1}\ s^{-1}$.

2.7.3. Oxidation of **2**

The dependence of rate on $[I^{VII}]_t$ was carried out at $[H^+] = 0.01$ M and a plot of k_{obs} *versus* $[I^{VII}]_t$ shows an initial rapid increase in rate with $[I^{VII}]_t$ followed by slower increase and then becomes almost independent on $[I^{VII}]_t$ (Fig. 7) and best represented by rate law (2). The effect of $[H^+]$ on the oxidation rate was investigated in the range $[H^+] = 0.001$–$0.05\ mol\ L^{-1}$ at $[I^{VII}]_t = 0.0007\ mol\ L^{-1}$, where a strict first-order dependence on it holds good. The rate increases initially rapidly with increasing $[H^+]$, then slowly and finally becomes almost independent of $[H^+]$ resulting in a plateau with a negligibly small or no intercept on the rate axis (Fig. 8). Such a dependence of rate on $[H^+]$ indicates that anionic forms of periodic acid ($H_4IO_6^-$ or IO_4^-) are un-reactive towards the complex leaving H_5IO_6 or $HIO_4 \cdot 2H_2O$ (H_2A) as the sole oxidant. The proton association of periodate anion, which can exist as $H_4IO_6^-$ and IO_4^- and $[HA^-]_t = [IO_4^-] + [H_4IO_6^-]$, can be described by Eq. (8) [12d]

$$HA^- + H^+ \overset{K}{\rightleftharpoons} H_2A \quad (8)$$

thus, K actually represents the apparent proton association constant reported to have value in the range 43–61 $L\ mol^{-1}$ at 25 °C [12d,21]. Considering the foregoing discussion, a reasonable reaction sequence may be proposed to account for the oxidation of $[Cu(HL)]_2[Ni(CN)_4]$ by periodic acid

$$[Cu(HL)]^* + H_5IO_6 \overset{Q}{\rightleftharpoons} \{[Cu(HL)]^*, H_5IO_6\} \quad (9)$$

$$\{[Cu(HL)]^*, H_5IO_6\} \xrightarrow{k} [Cu(L)]^+ + H_3IO_5^{\cdot -} + H_3O^+ \quad (10)$$

Here $[Cu(HL)]^*$ represents the modified species of $[Cu(HL)]_2[Ni(CN)_4]$ where $[Ni(CN)_4]^{2-}$ may be weakly coordinated to a copper center in solution. The radical thus generated reacts with another molecule of the complex in a rapid step to yield $H_3IO_5^{2-}$ as the final reduction product of periodate, which is common to the most of reactions involving periodate as oxidant in acid medium and corresponds to a 2:1 stoichiometric reactions [12]. Here also the fast decomposition of the copper(III) complex precludes the determination of the stoichiometry of the reaction under the kinetic conditions

$$-d[C]/dt = 2\frac{kQ[H_5IO_6]}{1 + Q[H_5IO_6]}[C] \quad (11)$$

Here, $C = [Cu(HL)]_2[Ni(CN)_4]$. While expressing H_5IO_6 in terms of total periodate concentration Eq. (11) turns to Eq. (12).

$$k_{obs} = 2\frac{kQK[H^+][I^{VII}]_t}{1 + \{K[H^+](1 + Q[I^{VII}]_t)\}} \quad (12)$$

Eq. (12) was solved for k and K by fitting k_{obs} as a function of $[I^{VII}]_t$ keeping Q fixed at 100, and the evaluated parameters are: $k = (1.97 \pm 0.03) \times 10^{-2}\ s^{-1}$ and $Q = 3263 \pm 170\ L\ mol^{-1}$. Again fitting k_{obs} as a function of $[H^+]$ with $Q = 3263$ as a fixed parameter gives parameters: $k = (2.21 \pm 0.05) \times 10^{-2}\ s^{-1}$ and $K = (85 \pm 7)\ L\ mol^{-1}$. It is to be mentioned here that very good fitting of two separate sets of data for $[H^+]$ and $[I^{VII}]_t$ indicates the self-consistency of the proposed mechanism. The evaluated proton association equilibrium constant ($K = 85$) for $H_4IO_6^-$ is in reasonable agreement with the literature value of $K = 61$ [12d]. The very large association constant also consistent with an inner-sphere mechanism which may occur either through hydrogen bonding between the hydrogen atom on H_5IO_6 and O^- of the oxime–imine ligand or the oxygen atom of H_5IO_6 and the undissociated H on the oxime–imine ligand. Another possibility is that H_5IO_6 may directly coordinate to the metal center. The main objection of this proposition is the absence of the reactivity of IO_4^- or $H_4IO_6^-$, which may be a better coordinating ligand than H_5IO_6.

It is to be mentioned here that the acidity of reaction media were so chosen for both the reactions that the acid catalyzed decomposition of the complexes is negligible compare to the electron transfer process. The complex $[Cu(HL)]_2[Ni(CN)_4]$ may undergo dissociation to give individual ions $[Cu(HL)]^+$ and $[Ni(CN)_4]^{2-}$; $[Cu(HL)]_2[Ni(CN)_4]$ should then behave identically to that of parent compound prepared separately. As the dependences of rate (k_{obs}/s^{-1}) on $[I^{VII}]_t$ and $[H^+]$ for the reaction with $[Cu(HL)]_2[Ni(CN)_4]$–I^{VII} differ from that of $[Cu(HL)]^+$–I^{VII} reaction, this may arise due to the presence of $[Ni(CN)_4]^{2-}$ ions in the former which may form an ion pair with $[Cu(HL)]^+$ or may be coordinated to the metal center causing this difference. To establish this proposition we checked the dependence of k_{obs} on $[H^+]$ in presence of $[Ni(CN)_4]^{2-}$ in the mole ratio 1:2 = $[Ni(CN)_4]^{2-}$:$[Cu(HL)]^+$ and it was observed that this dependence was almost identical to that observed for $[Cu(HL)]_2[Ni(CN)_4]$–I^{VII} reaction and support our proposition. As the acid catalyzed decomposition of complex **2** is ~2 times higher than complex **1**, it manifests the coordination of $[Ni(CN)_4]^{2-}$ moiety to the copper center destabilizes the system. It indirectly supports the coordination of $[Ni(CN)_4]^{2-}$ moiety to the copper center over the formation of ion pair which rather will stabilize the system.

It is generally accepted that periodate reacts via inner-sphere mechanism and supported by its failure to oxidize $[Fe(Phen)_3]^{2+}$ (phen = phenanthroline), which requires an inner-sphere route [12c]. The oxidation of $[Cr(H_2O)_6]^{3+}$, an inert complex, was proposed to proceed by inner-sphere route assuming $[Cr(H_2O)_5(OH)]^{2+}$ as the reacting species, where the ligated OH^- increases the lability of the metal center [12c]. The substantially high formation constant ($Q = 3263 \pm 170$ L mol^{-1}) suggests that the reaction proceeds through the pre-equilibrium formation of a precursor complex, an inner-sphere adduct, followed by electron transfer. Similar proposition was also advocated in the oxidation of dodecatungstocobaltate(II), a robust outer-sphere reactant, by periodate, where also HIO_4 was the sole reacting species [12d].

3. Conclusion

(1) A cyano-bridged hetero-trinuclear complex, $[Cu(HL)]_2[Ni(CN)_4]\cdot 4H_2O$ (**2**) has been synthesized and characterized by single crystal X-ray structure determination. The square planar $[Cu(HL)]^+$ cation, assumes a square pyramidal geometry through axial ligation by a cyano group of $[Ni(CN)_4]^{2-}$ ion.

(2) The arrangement of lattice water molecules in $[Cu(HL)]_2[Ni(CN)_4]\cdot 4H_2O$ is highly ordered producing water columns viewed down the *b* axis.

(3) Both the complexes **1** and **2** electrochemically behaves very similarly in MeCN as well as in water showing well defined quasi-reversible redox couples for $Cu^{II/I}$ and $Cu^{III/II}$ conversions, with the exception that the latter conversion does not arise in **1** in aqueous medium.

(4) The copper(II) bound ligand oxidation occurs at $E_{1/2} = 0.63$ and 0.60 V *versus* Ag/AgCl for the complexes **1** and **2** respectively only in aqueous solution. The absence of such process in MeCN may be attributed to the fact that it is a proton-coupled electron transfer process, which is only feasible in aqueous medium. Assignment of such a process to the coordinated ligand oxidation was confirmed by carrying out parallel study with the free ligand which showed similar redox process with $E_{1/2} =$ 0.61 V *versus* Ag/AgCl.

(5) Both the complexes **1** and **2** undergo H^+ catalyzed decomposition with a rate second-order in H^+ and can best be described as the rapid protonation of oximato-oxygen and then second protonation on one of the two imine nitrogen followed by decomposition of the protonated species in a rate determining step. Such protonations weaken both the Cu–N(R)(OH) and Cu–N(R^1)(R^2) bonds and causes the decomposition of the complexes.

(6) Periodate oxidation of **1** and **2** reveals that both HIO_4 and IO_4^- are the reacting species for **1** while HIO_4 is the sole reacting species for **2**.

(7) The slightly higher reactivity of **2** over **1** may arise due to the destabilization of complex **2** through axial ligation by $[Ni(CN)_4]^{2-}$. This is in line with the electrochemical behavior in aqueous solution.

4. Experimental

4.1. Materials and methods

All the starting materials like $Cu(CH_3COO)_2\cdot H_2O$, $CuCO_3$, KOH, KCl, CH_3COONa, $NaClO_4$, $HClO_4$, HCl, H_2SO_4, MeOH, diisopropyl ether, *N*,*N*-dimethylformamide, standard buffer solutions (ACROS ORGANICS, USA) of pH 4.0 and 7.0 *etc*. were of reagent grade and used as received. 1,3-Propanediamine (E-Merck, India) was distilled by refluxing over Na metal for about an hour before use. Analytical grade diacetyl monooxime (Merck Germany), KIO_4 (Aldrich) and Na_2SO_4 (Merck Germany) were used after recrystallization. All the experimental solutions of the complexes for electrochemical and kinetic studies were prepared freshly by doubly distilled water.

Elemental analyses were carried out using a Perkin–Elmer 240 elemental analyzer. Infrared spectra (400–4000 cm^{-1}) were recorded from KBr pellets on a Nicolet Magna IR 750 series-II FTIR spectrophotometer. EPR spectra of polycrystalline samples were recorded using a Varian Century Series X-band EPR spectrophotometer (model E 109) with 100 kHz magnetic field modulation. Room temperature magnetic susceptibilities were recorded on a PAR vibrating sample magnetometer using $Hg[Co(NCS)_4]$ as the calibrant. Diamagnetic corrections were estimated from Pascal's constants. TGA and DTA curves were recorded simultaneously on a Perkin–Elmer, Model PyrisDimond TG/DTA in static dry nitrogen at the heating rate of 5 °C min^{-1}. Electrochemical measurements were carried out using a computer controlled PAR model 263A VERSASTAT electrochemical instrument with a glassy carbon disk (4 mm diameter, EG&G) as the working electrode. All the results were collected at 25 ± 0.5 °C with reference to the Ag/AgCl electrode. All the solutions were purged with pure argon gas for at least ten minutes prior to each experiment. Junction potentials are not corrected. Electronic spectra and kinetic experiments were recorded on an Agilent 8453 UV–Vis diode array spectrophotometer with Peltier thermostatic temperature control facility at 25 ± 0.10 °C. The pH (± 0.01) measurements were carried out with a Systronics (model 335, India) digital pH-meter at 25 °C.

4.2. Syntheses

Caution! *Since the perchlorate salts are potentially explosive, only small amounts of the materials should be handled with care.*

$Cu(ClO_4)_2\cdot 6H_2O$ was prepared from $CuCO_3$ and 50% $HClO_4$ by the standard method. $Na_2[Ni(CN)_4]\cdot 3H_2O$ was prepared according to standard literature procedure

[22] taking NaCN instead of KCN, and further characterized by CHN analysis. The ligand H_2L [23] and the parent complex $[Cu(HL)]ClO_4 \cdot 2H_2O$ [5] (**1**) were prepared by using the literature methods and the purity was also checked by CHN analysis.

4.2.1. $[Cu(HL)]_2[Ni(CN)_4] \cdot 4H_2O$ (2)

To a methanolic solution of $[Cu(HL)]^+$ (1.0 mmol, in 40 mL MeOH, generated *in situ* by mixing equimolar quantities of $Cu(ClO_4)_2 \cdot 6H_2O$ and H_2L) $Na_2[Ni(CN)_4] \cdot 3H_2O$ (0.158 g, 0.6 mmol) dissolved in a minimum volume of water, was added drop-wise with constant stirring for 5 min. The precipitate that appeared initially was filtered off and the dark brown filtrate was allowed to undergo slow evaporation at ambient temperature whereupon shiny dark brown crystals suitable for X-ray study were obtained after two weeks. Yield: 52% based on Cu. *Anal.* Calc. for $C_{26}H_{46}N_{12}O_8Cu_2Ni$: C, 37.16; H, 5.52; N, 20.00. Found: C, 37.26; H, 5.51; N, 19.79%.

Selected IR in cm^{-1} (KBr): 3389 (br), 2930 (w), 2135 (s), 2118 (vs), 1630 (m), 1541 (br, m), 1500 (w), 1431 (m), 1379 (m), 1358 (m), 1323 (m),1275 (m),1225 (m), 1115 (br), 1089 (w), 1014 (w), 692 (w), 627 (w). μ_{eff} (per monomer): 1.78μ_B at 25 °C.

4.3. Crystal data collection and refinement

Intensity data for **2** was collected at 293(2) K on a Siemens P4 defractometer using graphite monochromatized Mo Kα radiation ($\lambda = 0.71073$ Å.) and the ω–2θ scan mode in the range $2.06 \leqslant \theta \leqslant 27.51°$. The intensities were corrected for Lorentz-polarization effects and for absorption using ψ-scans. The minimum and maximum transmission factors were 0.154 and 0.235. The structure was solved by direct methods and all non-hydrogen atoms refined anisotropically by full matrix least squares on F^2 using the SHELXTL PLUS-PC version [24] and hydrogen atoms were included geometrically and refined isotropically except the oxime proton and those of water hydrogens of which the former is randomly disordered over its two possible ligand sites in the unit cell. Other additional information concerning the data collection and refinement of the structure is compiled in Table 4.

Table 4
Crystal data and structure refinement for complexes **2**

Empirical formula	$C_{26}H_{46}Cu_2N_{12}NiO_8$
fw	840.25
Crystal system	monoclinic
Space group	*C*2/*c*
a (Å)	13.263(3)
b (Å)	21.255(4)
c (Å)	14.131(3)
β (°)	109.44(3)
V (A^3)	3756.6(13)
Z	4
T (K)	293(2)
λ (Å)	0.71073
d_{calc} ($g\,cm^{-3}$)	1.486
μ (mm^{-1})	1.677
F_{000}	1704
Reflections collected/unique [R_{int}]	4458/4282 [0.0370]
Final *R* indices [$I > 2\sigma(I)$]	$R_1 = 0.0583$, $wR_2 = 0.1408$
R indices [all data]	$R_1 = 0.0937$, $wR_2 = 0.1611$
Goodness-of-fit	1.014

Acknowledgements

Financial support from the Council for Scientific and Industrial Research (CSIR), and University Grant Commission (UGC), New Delhi, India are acknowledged.

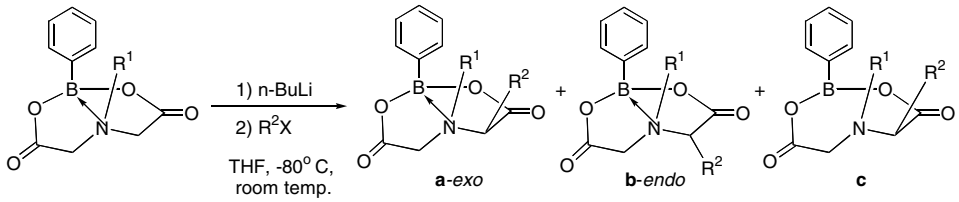
Appendix A. Supplementary material

CCDC 278585 contains the supplementary crystallographic data for the structure reported in the paper. These data can be obtained free of charge via http://www.ccdc.cam.ac.uk/conts/retrieving.html, or from the Cambridge Crystallographic Data Centre, 12 Union Road, Cambridge CB2 1EZ, UK; fax: (+44) 1223-336-033; or e-mail: deposit@ccdc.cam.ac.uk. Supplementary data associated with this article can be found, in the online version, at doi:10.1016/j.poly.2006.09.095.

References

[1] (a) A. Chakravorty, Coord. Chem. Rev. 13 (1974) 1;
(b) V.Y. Kukushkin, D. Tudela, A.J.L. Pombeiro, Coord. Chem. Rev. 156 (1996) 333;
(c) V.Y. Kukushkin, A.J.L. Pombeiro, Coord. Chem. Rev. 181 (1999) 147;
(d) P. Chaudhuri, Coord. Chem. Rev. 243 (2003) 143;
(e) J.A. MeCleverty, T.J. Meyer, Comprehensive Coordination Chemistry II: Ligands, vol. 1, Elsevier Science, Oxford, UK, 2004, Section 1.
[2] (a) J.G. Mohanty, R.P. Singh, A. Chakravorty, Inorg. Chem. 14 (1975) 2178;
(b) A.N. Singh, R.P. Singh, J.G. Mohanty, A. Chakravorty, Inorg. Chem. 16 (1977) 2597;
(c) A.N. Singh, A. Chakravorty, Inorg. Chem. 19 (1980) 969;
(d) K. Nag, A. Chakravorty, Coord. Chem. Rev. 33 (1980) 87;
(e) A. Chakravorty, Isr. J. Chem. 25 (1985) 99;
(f) R.A. Marusak, C. Sharp, A.G. Lappin, Inorg. Chem. 29 (1990) 2298.
[3] (a) Y. Sulfab, M.A. Hussein, N.I. Al-Shatti, Inorg. Chim. Acta 67 (1982) L33;
(b) Y. Sulfab, N.I. Al-Shatti, Inorg. Chim. Acta 87 (1984) L23.
[4] W. Kaim, B. Schwederski, Bioinorganic Chemistry: Inorganic Elements in the Chemistry of Life, John Wiley & Sons, Inc., New York, 2001, Chapter 10.
[5] A.W. Addison, M. Carpenter, L.K.-M. Lau, M. Wicholas, Inorg. Chem. 17 (1978) 1545.
[6] M. Ali, A. Ray, W.S. Sheldrick, H. Mayer-Figge, S. Gao, A.I. Shames, New J. Chem. 28 (2004) 412.
[7] J. Černák, M. Orendáč, I. Potočňák, J. Chomič, A. Orendáčová, J. Skoršepa, A. Feher, Coord. Chem. Rev. 224 (2002) 51.
[8] (a) Z. Smékal, I. Císařová, J. Mroziński, Polyhedron 20 (2001) 3301;
(b) P.S. Mukherjee, T.K. Maji, T. Mallah, E. Zangrando, E.L. Randaccio, N.R. Chaudhuri, Inorg. Chim. Acta 315 (2001) 249;
(c) T.K. Maji, P.S. Mukherjee, G. Mostafa, E. Zangrando, N.R. Chaudhuri, Chem. Commun. (2001) 1368.

[9] (a) T. Miyoshi, T. Iwamoto, Y. Sasaki, Inorg. Chim. Acta 7 (1973) 97;
(b) J. Černák, J. Lipkowski, Monatsh. Chem. 130 (1999) 1195.
[10] (a) H. Kurihara, S. Nishikiori, T. Iwamoto, Acta Crystallogr., Sect. C 53 (1997) 1409;
(b) J. Černák, J. Lipkowski, I. Potočňák, A. Hudák, Monatsh. Chem. 132 (2001) 193;
(c) J. Černák, J. Chomič, M. Dunaj-jurčo, Chem. Pap. 44 (1990) 13;
(d) C. Janiak, H.P. Wu, P. Klüfers, P. Mayer, Acta Crystallogr., Sect. C 55 (1999) 966.
[11] (a) Z. Smékal, Z. Trávníček, J. Mroziński, J. Marek, Inorg. Chem. Commun. 6 (2003) 1395;
(b) N.F. Curtis, H. Puschmann, Acta Crystallogr., Sect. C 60 (2004) 410.
[12] (a) Y. Sulfab, A.I. Abu-Shady, Inorg. Chim. Acta 21 (1977) 115;
(b) A.Y. Kasim, Y. Sulfab, Inorg. Chim. Acta 22 (1977) 16;
(c) A.Y. Kasim, Y. Sulfab, Inorg. Chem. 20 (1981) 506;
(d) M. Ali, S.K. Saha, P. Banerjee, J. Chem. Soc., Dalton Trans. (1991) 2305.
[13] A. Hussein, Y. Sulfab, M. Nasreldin, Inorg. Chem. 28 (1989) 157, and the references therein.
[14] (a) G.A. Mclachlan, G.D. Fallon, R.L. Martin, L. Spiccia, Inorg. Chem. 34 (1995) 254;
(b) A.W. Addison, T.N. Rao, J. Reedijk, R. Van, J. Rijn, G.C. Verschoor, J. Chem. Soc. Dalton Trans. (1984) 1349.
[15] J.A. Bertrand, J.H. Smith, D.G. vanDerveer, Inorg. Chem. 6 (1977) 1484.
[16] O.M. Kanderal, H. Kozlowski, A. Dobosz, J.S. Kozlowska, F. Meyer, I.O. Fritsky, J. Chem. Soc., Dalton Trans. (2005) 1428.
[17] A.G. Sharpe, The Chemistry of the cyano complexes of the Transition Metals, Academic Press, London, 1976.
[18] T. Vanngard, R. Aasa, W. Low (Eds.), Paramagnetic Resonance, vol. II, Academic Press, 1963, p. 509.
[19] A.G. Bard, L.R. Faulkner, Electrochemical Methods Fundamental and Application, John Wiley & Sons, New York, 1980, p. 218.
[20] L.G. Sillen, A.E. Martell, Stability Constants of Metal-Ion Complexes Spl. Publications no. 25, The Chemical Society, 1964, Section I, p. 226.
[21] C.E. Crouthamel, A.M. Hayes, D.S. Martin, J. Am. Chem. Soc. 73 (1951) 82.
[22] C. Fernelius, J. Burbage, W.C. Fernelius (Eds.), Inorganic Syntheses, vol. II, McGraw-Hill Inc., 1946, p. 227, Chapter 8.
[23] E. Uhling, M. Friedrich, Z. Anorg. Allg. Chem. 343 (1966) 299.
[24] G.M. Sheldrick, SHELXL '97, Program for Crystal Structure Refinement, University of Gottingen, Germany, 1997.



1: $R^1 = CH_3$
2: $R^1 = CH_2C_6H_5$

3(**a**-**b**): $R^1 = CH_3$; $R^2 = o\text{-}CH_3C_6H_4CH_2$
4(**a**-**b**): $R^1 = CH_3$; $R^2 = m\text{-}CH_3C_6H_4CH_2$
5(**a**-**b**): $R^1 = CH_3$; $R^2 = p\text{-}CH_3C_6H_4CH_2$
6(**a**-**b**): $R^1 = C_6H_5CH_2$ $R^2 = CH_3$
7(**b**-**c**): $R^1 = C_6H_5CH_2$ $R^2 = CH_3CH_2$
8(**c**): $R^1 = C_6H_5CH_2$ $R^2 = CH_3CH_2CH_2$
9(**b**): $R^1 = C_6H_5CH_2$ $R^2 = CH_3CH_2CH_2CH_2$

Fig. 1. Synthesis of boron heterocycles **3**–**9**.

by ^1H, ^{13}C and ^{11}B NMR, COSY, HETCOR and homonuclear proton decoupling experiments, therefore compounds **8**(**c**) and **9**(**b**) by mass spectrometry and infrared spectroscopy.

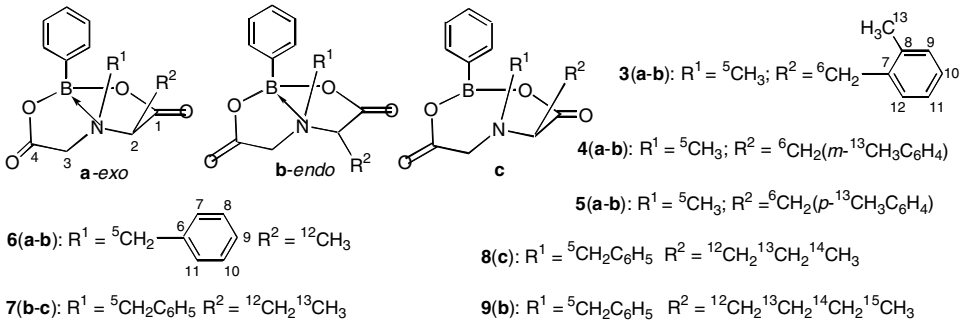
2. Results and discussion

Reactions of (N→B) phenyl[*N*-methyliminodiacetate-*O*,*O*′,*N*]borane **1** with *n*-BuLi and 2-methylbenzyl bromide **a**, 3-methylbenzyl bromide **b**, 4-methylbenzyl bromide **c**, lead to a pair of diasteromers of bicyclic structure **3**–**5**(**a**–**b**), the same is observed under same reaction conditions for (N→B) phenyl[*N*-benzyliminodiacetate-*O*,*O*′,*N*]borane **2** using iodomethane **d**, was obtained the bicyclic structures **6**(**a**–**b**), but in different proportion. However, with iodoethane **e**, lead to the bicyclic structure **7**(**b**) and **7**(**c**), which does not display the intramolecular N→B coordination bond. Whereas compound **8**(**c**) was obtained from the reaction of compound 2 with iodopropane **f**, while **9**(**b**) was obtained with iodobutane **g**.

^1H NMR data of the compounds **3**–**6**(**a**–**b**), **7**(**b**–**c**), **9**(**b**) and **8**(**c**) are summarized in Table 1. The ^1H NMR spectra in $CDCl_3$ of compounds **3**–**5**(**a**–**b**) show two single signals between 2.04 and 2.41 ppm characteristic of *N*-CH_3, indicating the presence of two diasteromers in a ratio 79/21, 76/24 and 82/18, respectively. This in according to the generation of three chiral centers: boron, nitrogen and carbon atoms, four pairs of enantiomers may be expected, but, two of them are eliminated owing to the *cis*-fusion of the ring. In this context the substitute at C2 can be in the *exo* or *endo* position. These spectra exhibit a complex pattern between 3.36 and 4.0 ppm due to the coupling between H2 and H6 showing an ABX system, as well as AB systems of the H-3 protons, showing the presence of two diasteromers. The complete assignment was achieved for the more abundant isomers (*exo*) due to the signals of H-3 and H-6 of the minor isomer are overlapped with those of the more abundant. Structural analysis was achieved by comparison with analogous boron heterocycles [9], where the AB system of H3 of the more abundant isomers appears at lower field than H-3 of the minor isomers. The $\delta(^{11}B)$ values (Table 1) confirm the tetrahedral environment of the ^{11}B nucleus, since they lie in the range reported previously for analogous boron heterocylces [9–11,14–16,18–20].

^1H NMR analyses of the reaction products of compound **2** with iodomethane **d** showed a more complex pattern than compounds **3**–**5**(**a**–**b**). Its spectrum shows two series of signals in a ratio 86/14, where the more abundant isomer has the CH_3 group in the *endo* position, this can be attributed to a steric hindrance of the *N*-benzyl group. The assignment was achieved by homonuclear proton decoupling experiment ^1H $\{^1H\}$, decoupling each quartet signal of H2 at 4.76 and 3.43 ppm, these reduced the doublet signal at 0.98 (CH_3-12 group at *endo* position) and 1.18 ppm, (CH_3-12 group at *exo* position) to a singlet, respectively. The fact that the H2 at *exo* position appears at lower field than H2 at *endo* position can be due to the deshielding of the electronic density of the ring and this effect can be observed for CH_3-12 group at *exo* position, which appears at lower field than CH_3-12 group at *endo* position. Also the spectrum displays two AB systems for H3 at and 4.39 and 3.89 ppm (minor isomer) and 4.21 and 3.96 ppm (more abundant), by comparison of their chemical shift values to those found for compounds **3**–**5** and their analogous [9], the isomer more abundant was assigned to **6**(**b**), where the substituent at 2 is at *endo* position. Furthermore, it was expected that H6 protons of **6**(**b**) showed an AB system; however they exhibited a triplet signal at 4.01, showing a very similar chemical shifts; the (^1H–^1H) COSY spectrum shows correlation between H6 at 4.01 ppm and H_{3A}, which indicates that the H6 protons are close to H_{3A}. This result gives evidence of the steric effect of the *N*-benzyl group obtaining the kinetic diasteromer in mayor proportion. Moreover, a variable temperature experiment in the ^1H NMR of **6**(**a**–**b**) shows coalescence of the AB system at δ 4.21 and 3.96 at 383 K. This is interpreted by a dissociation-inversion mechanism observed bicyclic boron compounds derived from diethanolamines [20,21] and iminodiacetic acids of similar structure [11]. Application of the coalescence temperature was used to calculated the $\Delta G^{\neq}_{coal} = 81.09$ kJ/mol, which is lower in comparison with the corresponding $\Delta G^{\neq}_{coal}$ obtained for a boron heterocycle

Table 1
^{1}H and ^{11}B NMR data for compounds **3**–**6**(**a**–**b**), **7**, **9**(**b**) and **7**–**9**(**c**)

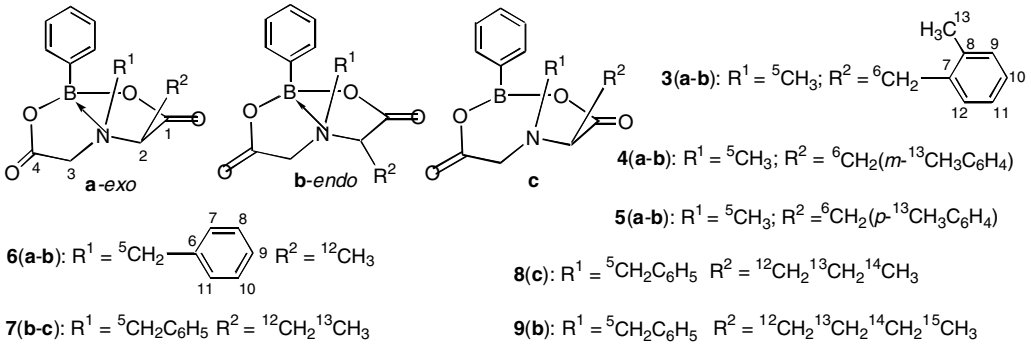


Compound	H2	H3	[b] R^1	[b] R^2	$\delta(^{11}B)$
3a	3.93 (dd) $J_{AX} = 4.70$ $J_{BX} = 9.89$	H_A: 4.08 (d) H_B: 3.57 (d) $J_{AB} = 16.32$	2.04 (s)	H_{6A}: 3.73 (dd), H_{6B}: 3.00 (dd) $J_{AB} = 15.6$, $J_{AX} = 4.70$, $J_{BX} = 9.89$ H_{13}: 2.32 (s)	+10.80
3b	4.19 (dd) $J_{AX} = 4.45$ $J_{BX} = 10.39$	H_A: 3.42 (d) H_B: 3.37 (d) $J_{AB} = 16.50$	2.37 (s)	H_{13}: 2.41 (s)	
4a	3.94 (dd) $J_{AX} = 4.40$ $J_{BX} = 10.00$	H_A: 4.02 (d) H_B: 3.54 (d) $J_{AB} = 16.35$	2.05 (s)	H_{6A}: 3.73 (dd), H_{6B}: 2.94 (dd) $J_{AB} = 15.5$, $J_{AX} = 4.40$, $J_{BX} = 10.0$ H_{13}: 2.31 (s)	+10.76
4b	4.20 (dd) $J_{AX} = 3.70$ $J_{BX} = 11.36$	H_A: 3.38 (d) H_B: 3.31 (d) $J_{AB} = 16.20$	2.34 (s)	H_{13}: 2.42 (s)	
5a	3.91 (dd) $J_{AX} = 4.45$ $J_{BX} = 9.89$	H_A: 4.01 (d) H_B: 3.51 (d) $J_{AB} = 16.32$	2.04 (s)	H_{6A}: 3.73 (dd), H_{6B}: 2.94 (dd) $J_{AB} = 15.5$, $J_{AX} = 4.45$, $J_{BX} = 9.89$ H_{13}: 2.30 (s)	+10.93
5b	4.20 (dd) $J_{AX} = 3.71$ $J_{BX} = 11.13$	H_A: 3.36 (d) H_B: 3.51 (d) $J_{AB} = 16.08$	2.41 (s)	H_{13}: 2.34 (s)	
[a]**6a**	3.43(q) $J = 7$	H_A: 4.39 (d) H_B: 3.89 (d) $J = 17.20$	H_5: 4.01 (t) $J = 6.6$	H_{12}: 1.18 (d) $J = 7.0$	+11.70
[a]**6b**	4.76 (q) $J = 7$	H_A: 4.21 (d) H_B: 3.96 (d) $J = 17.30$	H_{5A}: 4.08 (d) H_{5B}: 3.64 (d) $J = 13.20$	H_{13}: 0.98 (d) $J = 7.0$	
7b	4.13 (t) $J = 7.0$	H_A: 4.04 (d) H_B: 3.53 (d) $J = 16.40$	H_5: 3.60 (s)	H_{12}: 1.69 (m) H_{13}: 1.05 (t) $J = 7.0$	+11.40
7c	3.72 (t) $J = 7.0$	H_A: 3.93 (d) H_B: 3.57 (d) $J = 17.00$	H_{5A}: 3.75 (d) H_{5B}: 3.56 (d) $J = 14.0$	H_{12}: 1.59 (m) H_{13}: 0.85 (t) $J = 7.0$	+29.60
[a]**8c**	3.98 (t) $J = 6.58$	3.54 (s)	3.82 (s)	H_{12}: 1.51 (m) H_{13}: 1.29 (m) H_{14}: 0.85 (t) $J = 7.3$	+28.30
[a]**9b**	4.00 (t) $J = 6.7$	H_A: 4.39 (d) H_B: 3.89 (d) $J = 12.00$	3.82 (s)	$H_{12,13}$: 1.53 (m) H_{14}: 1.31 (m) H_{15}: 0.87 (t) $J = 7.4$	+11.50

$\delta(^{1}H)$ relative to $Si(CH_3)_4$; solvent $CDCl_3$.
[a] Solvent DMSO-d_6.
[b] The signals of the B–Ph group and those of the benzyl group are overlapped, exhibiting an unresolved pattern between 6.9 and 8 ppm. d: double; dd: doublet of doublets; m: unresolved pattern; q: quartet; s: singlet; t: triplet and |j| Hz.

derivate of *N*-alkyliminodiacetic acid (98.4 kJ/mol) [11]. The ^{1}H NMR spectrum at 413 K displays the doublet signals of CH_3-12 groups in a ratio 1/1, suggesting the conversion of the kinetic to the thermodynamic diasteromer. ^{1}H NMR analyses of the reaction products of compound **2** with iodoethane **e** showed two complex pattern for H12 at δ 1.69 and 1.59, and two triplet signals for H13 at δ 1.05 and 0.85 characteristic of ethyl group, respectively in a ratio 50/50. The assignment was achieved by homonuclear proton decoupling experiment ^{1}H $\{^{1}H\}$, decoupling the complex patterns signal at δ 1.69 and 1.59, these reduced the triplet signals at δ 1.05 and 0.85 to a singlet signals, respectively. In addition, the spectrum display the signals for H2, which were assigned by (^{1}H–^{1}H) COSY and confirmed by HETCOR experiment, the triplet signal at δ 4.13 correlates with the complex pattern of H12 at δ 1.59, while the signal at δ 3.72, which is overlapped with a singlet signal, correlated with the complex pattern of H12 at δ 1.69. Additionally the spectrum exhibits two AB systems at δ 4.04 and 3.53, and 3.93 and 3.57 assigned to H3, the first one assigned to compound **7**(**b**) by comparison the chemical shift values of compound **6**(**b**). The spectrum also exhibit two signals for H5 protons, a singlet at δ 3.60 assigned to compound **7**(**b**), giving evidence of a similar electronic environment, and an AB system at δ 3.75 and 3.56 with chemical shift values very close, assigned to **7**(**c**), where the R^2 can give different electronic environment to H5, as well as increase the steric effect to avoid the formation of N→B coordination bond. It is known that N→B bond strength depends strongly on steric effect; bulky substituents at boro or nitrogen tend to weaken the N→B bond [20,21]. ^{11}B NMR spectrum confirm both structures with the signal at δ +11.4 for **7**(**b**) and +29.60 for **7**(**c**) which is characteristic for boron atom tricoordinated [20]. ^{1}H NMR of compound **8**(**c**) clearly showed the triplet signal and two complex pattern for the H14, H13 and H12, respectively, of the propyl group at 2 position, as well as the triple signal characteristic of H2 at δ 3.98. Protons H3 and H5 display a singlet, suggesting that the boron atom is tricoordinated, this is confirmed by its ^{11}B NMR, which exhibits a signal at δ +28.30. ^{1}H NMR spectrum of compound **9**(**b**) clearly shows the signals due to the butyl group at 2 position, a triplet signal at δ 4.0, protons H5 present an AB system and H5 a singlet, these data give

Table 2
^{13}C NMR data for compounds **3**–**6**(**a**–**b**), **7**, **9**(**b**) and **7**–**9**(**c**)



Compound	3a	3b	4a	4b	5a	5b	[a]6a	[a]6b	7b	7c	[a,b]8c	[a,b]9b
C_1	169.0	168.2	168.9	168.1	168.9	168.2	171.6	171.3	170.8	167.5	175.3	176.2
C_2	68.8	68.1	70.6	69.4	70.6	69.5	63.5	63.1	65.4	68.3	63.8	63.7
C_3	55.9	60.2	55.5	60.7	55.5	60.7	57.4	51.1	51.5	57.7	59.3	54.6
C_4	168.8	168.2	168.6	167.7	168.6	168.2	169.9	169.6	168.5	167.5	172.2	172.0
C_5	46.7	47.5	46.9	40.6	46.9	40.6	61.9	61.4	63.3	62.0	59.8	58.0
C_6	30.4	29.6	33.0	31.6	32.7	31.3	134.2	134.0	135.6	133.6	137.4	137.4
C_7	133.0	134.3	133.6	134.8	137.9	141.4	132.1	132.1	131.0	130.9	130.5	130.1
C_8	135.9	134.8	129.4	130.0	128.5	128.3	127.6	127.8	128.0	128.0	127.5	128.5
C_9	129.9	130.1	131.5	132.3	130.2	130.1	129.5	129.6	130.8	130.7	130.2	129.2
C_{10}	128.1	127.4	127.5	127.7	132.1	131.6	127.6	127.8	128.0	128.0	127.5	128.5
C_{11}	126.7	126.0	128.8	129.2	130.2	130.1	132.1	132.1	131.0	130.9	130.5	130.1
C_{12}	129.7	129.6	129.3	129.6	128.5	128.3	13.6	12.3	22.7	22.3	30.8	30.7
C_{13}	19.7	19.9	21.3	21.4	21.0	21.2			12.0	14.1	19.2	30.0
C_{14}											14.1	19.3
C_{15}												14.0
C_o	132.3	134.1	132.4	134.3	132.4	134.2	132.9	132.9	132.6	132.6	134.5	134.5
C_m	128.2	128.0	128.3	125.6	128.3	127.5	128.8	128.7	128.5	128.5	127.7	127.6
C_p	131.3	132.1	129.8	130.2	129.8	130.5	129.7	129.1	129.6	130.1	129.3	128.4

$\delta(^{13}C)$ relative to $Si(CH_3)_4$; solvent $CDCl_3$.
[a] DMSO-d_6.
[b] C_i, 140.1 ppm.

evidence of the formation of intramolecular N→B coordination bond and the butyl group is at *endo* position keeping away from bulky substitute on nitrogen atom. Its ^{11}B NMR shows a signal a δ +11.50 demonstrating the tetrahedral environment of boron atom.

Table 2 shows that compounds **3**–**6**(**a**–**b**), **7**(**b**–**c**), **8**(**c**) and **9**(**b**) exhibit the expected ^{13}C NMR spectra. Structural analysis of the compounds was based on 2D HETCOR NMR data, compounds **6**(**a**–**b**) by COSY NMR data, whereas, by comparison with the chemical shifts of bicyclic analogous [9,16,19].

The 70 eV EI mass spectra of compounds **8**(**c**) and **9**(**b**) do not exhibit the molecular ion. The following important fragment ions are observed, the base peak is at $m/z = 321$ $[C_6H_5CH_2NH_2CH_2C(O)OB(C_6H_5)OCOCH_3]^+$, which correspond to the loss of CHR^2 and rearrangement of the alkyl group, $m/z = 208$ $[C_6H_5CHNNCHC_6H_5]^+$, with relative abundance of 15% and 16%, respectively, the fragment ion at $m/z = 164$ $[C_6H_5CH_2NH(CH_3)CH_2COH]^+$, with relative abundance of 77% and 73%, respectively, and $m/z = 131$ $[C_6H_6CHNCHCH_6]^+$, with relative abundance of 13% and 16%, respectively. The IR spectrum of compound **8**(**c**) exhibits the $\nu_{(CO)}$ carbonyl oxygen band in 1712 and 1600 cm^{-1}, a band due to B–O in 1262 cm^{-1}, as well as the bands due to the $\nu_{C-H\,arom.}$ in 3058 cm^{-1} and $\nu_{C-H\,aliph.}$ in 2920 cm^{-1}. The IR spectrum of compound **9**(**b**) shows the $\nu_{(CO)}$ bands in 1736 and 1602 cm^{-1}, a band attributable to B–O in 1254 cm^{-1}, the bands due to the $\nu_{C-H\,arom.}$ in 3058 cm^{-1} and $\nu_{C-H\,aliph.}$ in 2926 cm^{-1}, also the band due to N→B in 1024 cm^{-1}.

3. Conclusion

The new (N→B) phenyl[*N*-alky-*N*(2-alkyl)aminodiacetate-*O*,*O*′,*N*]boranes **3**–**6**(**a**–**b**), **7**(**b**) and **9**(**b**) and phenyl-[*N*-alkyl-*N*-2-alkyl)aminodiacetate-*O*,*O*′,*N*]boranes **7**(**c**) and **8**(**c**) isomers were characterized by spectroscopic methods, where the compounds **3**–**6**(**a**–**b**), **7**(**b**) and **9**(**b**) exhibit a bicyclic structure due to the presence of an intramolecular N→B coordination bond. Therefore, these compounds show that the substituent can be in *exo* or *endo* position. The existence of steric effects; between the *N*-substituent and the alkyl group at 2 position was indicated by ^1H ^{13}C and ^{11}B NMR data. Moreover, compounds **7**(**c**) and **8**(**c**) do not display intramolecular N→B coordination bond. The study of the intramolecular N→B coordination by dynamic NMR afforded a $\Delta G^{\ddagger}$ value of 81.09 kJ/mol for compound **6**(**b**).

4. Experimental

4.1. General procedure and measurements

The reagents were purchased from Aldrich Co., Boron heterocycles **1** and **2** were prepared according to the literature [14]. ^1H, ^{13}C and ^{11}B NMR spectra were recorded on Jeol GLX-270, Jeol Eclipse-400 and Bruker Avance 300-DPX spectrometers, $CDCl_3$ and DMSO-d_6 were used as solvent. Mass spectra were obtained on a Hewlett-Packard 59940-A spectrometer at 70 eV electron impact. The IR spectra were recorded as KBr pellets on a Perkin–Elmer 16F Pc FT-IR spectrometer. Melting points were measured in open capillary tubes on a Gallemkamp MFB-595 apparatus and have not been corrected.

4.2. Preparation of compounds

The procedure outlined below is general for the preparation of compounds **3**–**6**(**a**–**b**), **7**(**b**–**c**), **8**(**c**) and **9**(**b**).

4.2.1. Synthesis of (N→B) phenyl[N-methyl-N-{2(2-methylbenzyl)}aminodiacetate-O,O′,N]boranes 3(a–b)

A solution of 0.5 g (2.1 mmol) of (N→B) phenyl[*N*-methyliminodiacetate-*O*,*O*′,*N*]borane **1** in 50 ml of THF was cooled to −80 °C and 2.47 ml (2.1 mmol) of *n*-BuLi (0.87 M) in hexane were added dropwise. The reaction mixture was stirred 30 min at −80 °C and 1:30 h at room temperature. After the reaction mixture was cooled with a dry ice acetone bath to −80 °C, 0.28 ml (2.1 mmol) of 2-methylbenzyl bromide **a**, were added. After being warmed at room temperature and stirred 24 h, the solvent was evaporated under vacuum. The solid was treated with a mixture of methylenchloride/petroleum ether to give 0.58 g (80%) of a mixture of **3**(**a**) and **3**(**b**) compounds in a ratio 79/21.

4.2.2. Synthesis of (N→B) phenyl[N-methyl-N-{2(3-methylbenzyl)}aminodiacetate-O,O′,N]boranes 4(a–b)

0.5 g (2.1 mmol) of compound **1**, 2.47 ml (0.87 M) of *n*-BuLi and 0.29 ml (2.1 mmol) of 3-methylbenzyl bromide **b**, gave 0.62 g (85%) of a mixture of **4**(**a**) and **4**(**b**) compounds in a ratio 76/24.

4.2.3. Synthesis of (N→B) phenyl[N-methyl-N-2{(4-methylbenzyl)}aminodiacetate-O,O′,N]boranes 5(a–b)

0.5 g (2.1 mmol) of compound **1**, 2.47 ml (0.87 M) of *n*-BuLi and 0.29 ml (2.1 mmol) and a solution of 0.3 g (2.1 mmol) of 4-methylbenzyl bromide **c** in 2 ml of THF, gave 0.61 g (83%) of a mixture of compounds **5**(**a**) and **5**(**b**) in a ratio 82/18.

4.2.4. Synthesis of (N→B) phenyl[N-benzyl-N-2(methyl)aminodiacetate-O,O′,N] boranes 6(a–b)

0.5 g (1.61 mmol) of (N→B) phenyl[*N*-benzyliminodiacetate-*O*,*O*′,*N*]borane **2** in 25 ml of THF, 1.65 ml (1.61 mmol) 1.01 M of *n*-BuLi and 0.10 ml (1.61 mmol) of iodomethane **d**, gave 0.41 g (75%) of a solid of a mixture of **6**(**a**) and (**6b**) compounds in a ratio 14/86.

4.2.5. Synthesis of (N→B) phenyl[N-benzyl-N-2(ethyl)aminodiacetate-O,O′,N] borane 7(b) and phenyl-[N-benzyl-N-2(ethyl)aminodiacetate-O,O′,N]borane 7(c)

0.5 g (1.61 mmol) of boron heterocycle **2** in 25 ml of THF, 1.60 ml of *n*-BuLi 1.01 M and 0.13 ml (1.61 mmol)

of iodoethane **e**, gave 0.28 g (41%) of a yellow solid of a mixture of **7**(**b**) and **7**(**c**) compounds in a ratio 50/50.

*4.2.6. Synthesis of phenyl[N-benzyl-N-2(propyl)aminodiacetate-O,O′,N]borane **8**(**c**)*

0.5 g (1.61 mmol) of boron heterocycle **2** in 25 ml of THF, 1.60 ml of *n*-BuLi 1.01 M and 0.16 ml (1.61 mmol) of iodopropane **f**, to yield 0.37 g (63%) of compound **8**(**c**) as beige solid with m.p. 189–191 °C.

*4.2.7. Synthesis of (N→B) phenyl[N-benzyl-N-2(butyl)aminodiacetate-O,O′,N] borane **9**(**b**)*

0.5 g (1.61 mmol) of boron heterocycle **2** in 25 ml of THF, 1.60 ml of *n*-BuLi 1.01 M and 0.16 ml (1.61 mmol) of iodobutane **g**, to yield 0.58 g (95%) of compound **9**(**b**) as a solid with m.p. 203–205 °C.

Acknowledgements

The authors thank Consejo Nacional de Ciencia y Tecnología (Conacyt) for financial support and for providing Bachelor scholarship to M.A.C.R and L.A.D. for the development of this work at Centro de Investigación y de Estudios Avanzados del Instituto Politécnico Nacional.

References

[1] G.J. Baum, J. Organomet. Chem. 22 (1970) 269.
[2] S.H. Tung, K.M. Chang, S.L. Tah, C.C. Liu, S.L. Chang, Chem. Abstr. 66 (1967) 37990m.
[3] R. Csuk, H. Hönig, H. Weidmann, H.K. Zimmerman, Arch. Pram. 317 (1984) 336.
[4] M.C. Miller III, A. Sood, B.F. Spielvogel, I.H. Hall, Anticancer Res. 17 (1997) 3299.
[5] S. Karthikeyan, A. Sood, J. Tomas, B.F. Spielvogel, I.H. Hall, Amino Acids 8 (1995) 323.
[6] C.A. Perks, A.J. Mill, G. Constantine, K.G. Harrison, J.A. Gibson, Brit. J. Radiol. 61 (1988) 1115.
[7] H. Nemoto, J. Cai, N. Asao, J. Med. Chem. 38 (1995) 1673.
[8] J.P. Pignol, J.C. Abbe, O. Lefebvre, A. Stampfler, G. Methlin, J.C.R. Sahel, Acad. Sci. III 317 (1994) 543.
[9] T. Mancilla, S.L. Gálvez, Main Group Met. Chem. 15 (1992) 9.
[10] T. Mancilla, Ma. L. Alarcón, L. Carrillo, Heteroatom Chem. 15 (1994) 455.
[11] T. Mancilla, L. Carrillo, Ma. P. Reducindo, Polyhedron 15 (1996) 3777.
[12] G. Shtacher, W. Taub, J. Med. Chem. 9 (1966) 197.
[13] T. Mancilla, L. Carrillo, L.S. Zamudio Rivera, C. Camacho Camacho, D. de Vos, R. Kiss, F. Darro, B. Mahieu, E.R.T. Tiekink, H. Rahier, M. Gielen, M. Kemmer, M. Biesemans, R. Willem, Appl. Organometal. Chem. 15 (2001) 593.
[14] T. Mancilla, R. Contreras, B. Wrackmeyer, J. Organomet. Chem. 307 (1986) 1.
[15] T. Mancilla, R. Contreras, J. Organomet. Chem. 321 (1987) 191.
[16] N. Farfán, T. Mancilla, D. Castillo, G. Uribe, L. Carrillo, P. Joseph-Nathan, R. Contreras, J. Organomet. Chem. 381 (1990) 1.
[17] T. Mancilla, H. Höpfl, G. Bravo, L. Carrillo, Main Group Met. Chem. 20 (1997) 31.
[18] H.I. Beltrán, L.S. Zamudio Rivera, T. Mancilla, R. Santillan, N. Farfán, J. Organomet. Chem. 657 (2002) 194.
[19] T. Mancilla, L.S. Zamudio Rivera, H.I. Beltrán, R. Santillan, N. Farfán, Arkivoc, Part (IV) (2005) 366.
[20] R. Contreras, C. García, T. Mancilla, B. Wrackmeyer, J. Organomet. Chem. 246 (1983) 213.
[21] R. Cusuk, H. Hönig, C. Romanin, Monatsh. Chem. 113 (1982) 1025.

representative compounds are presented, as well as the NMR studies of these paramagnetic nickel(II) complexes.

2. Experimental

2.1. General methods

C, H, and N analyses were carried out with a microanalyzer Carlo Erba model EA 1108. Infrared spectra were recorded on a Perkin–Emer 16F PC FT-IR spectrophotometer using Nujol mulls between polyethylene sheets. The UV–Vis spectra (in acetone) were recorded on a Hitachi 2000V spectrophotometer for 300–700 nm range. The ^{1}H and ^{19}F NMR spectra (in acetone) were recorded on a Bruker AC 200E, Bruker AC 300E or Bruker AV-400 spectrometer. Chemical shifts (in ppm) are reported with respect to the residual solvent signal or $CFCl_3$ (as standard), respectively. The ^{1}H COSY spectrum was obtained at 20 °C for **4** with 256 data points in the F1 dimension and 2048 data points in the F2 dimension with a delay time of 150 or 20 ms. An unshifted sine-bell-squared weighting function was applied prior to Fourier transformation followed by baseline correction in both dimensions and symmetrization. Fast atom bombardment (FAB) mass spectra were run on a Fisons VG Autospec spectrometer operating in the FAB^+ mode. All chemicals were purchased from Aldrich and were used without further purification. Solvents were dried and distilled by general methods before use. The complexes $[Ni(mcN_3)(\mu\text{-}OH)]_2(PF_6)_2$ (mcN_3 = 2,4,4-trimethyl-1,5,9-triazacyclododec-1-ene (Me_3-mcN_3) and its 9-methyl derivative (Me_4-mcN_3)) were prepared by procedures previously described [10,11].

2.2. Syntheses

2.2.1. *[Ni(mcN$_3$)(Bz)](PF$_6$) (mcN$_3$ = Me$_3$-mcN$_3$, Bz = 2-NH$_2$Bz (**1**), 2-NO$_2$Bz (**2**), 4-NH$_2$Bz (**3**); mcN$_3$ = Me$_4$-mcN$_3$, Bz = 2-NH$_2$Bz (**4**), 2-NO$_2$Bz (**5**), 4-NH$_2$Bz (**6**))*

These complexes were prepared by reaction of $[Ni_2(mcN_3)_2(\mu\text{-}OH)_2](PF_6)_2$ (0.12 mmol) with the corresponding carboxylic acid (0.24 mmol) in acetone (25 mL). After stirring for 12 h the solution was concentrated under reduced pressure and the addition of diethyl ether caused the precipitation of a green solid, which was collected by filtration, washed with diethyl ether and air-dried.

$[Ni(Me_3\text{-}mcN_3)(2\text{-}NH_2Bz)](PF_6)$ (**1**): Yield 91 mg (69%). *Anal.* Calc. for $C_{19}H_{31}F_6N_4NiO_2P$: C, 41.41; H 5.67; N, 10.17. Found: C, 41.19; H, 5.72; N, 10.04%. FAB^+, *m/z*: 405 $[M]^+$. IR (cm^{-1}): 3442, 3333 ν(N–H_2), 3290, 3244 ν(N–H), 1660 ν(C=N), 1621 δ (N–H_2), 1504, 1376 ν(CO). UV–Vis in acetone, λ (nm), ε ($M^{-1}\,cm^{-1}$): 622 (72), 380 (174).

$[Ni(Me_3\text{-}mcN_3)(2\text{-}NO_2Bz)](PF_6)$ (**2**): Yield 110 mg (79%). *Anal.* Calc. for $C_{19}H_{29}F_6N_4NiO_4P$: C, 39.27; H, 5.03; N, 9.64. Found: C, 39.14; H, 5.13; N, 9.77%. FAB^+, *m/z*: 435 $[M]^+$. IR (cm^{-1}): 3297, 3267 ν(N–H), 1672 ν(C=N), 1530, 1375 ν(CO). UV–Vis in acetone, λ (nm), ε ($M^{-1}\,cm^{-1}$): 616 (57), 381 (360).

$[Ni(Me_3\text{-}mcN_3)(4\text{-}NH_2Bz)](PF_6)$ (**3**): Yield 87 mg (66%). *Anal.* Calc. for $C_{19}H_{31}F_6N_4NiO_2P$: C, 41.41; H, 5.67; N, 10.17. Found: C, 41.35; H, 5.65; N, 10.14%. FAB^+, *m/z*: 405 $[M]^+$. IR (cm^{-1}): 3418, 3395 ν(N–H_2), 3289, 3256 ν(N–H), 1665 ν(C=N), 1624 δ(N–H_2), 1501, 1375 ν(CO). UV–Vis in acetone, λ (nm), ε ($M^{-1}\,cm^{-1}$): 623 (65), 380 (230).

$[Ni(Me_4\text{-}mcN_3)(2\text{-}NH_2Bz)](PF_6)$ (**4**): Yield 77 mg (57%). *Anal.* Calc. for $C_{20}H_{33}F_6N_4NiO_2P$: C, 42.50; H, 5.89; N, 9.91. Found: C, 42.37; H, 5.96; N, 9.84%. FAB^+, *m/z*: 419 $[M]^+$. IR (cm^{-1}): 3485, 3359 ν(N–H_2), 3265 ν(N–H), 1660 ν(C=N), 1614 δ(N–H_2), 1503, 1376 ν(CO). UV–Vis in acetone, λ (nm), ε ($M^{-1}\,cm^{-1}$): 632 (66), 385 (232).

$[Ni(Me_4\text{-}mcN_3)(2\text{-}NO_2Bz)](PF_6)$ (**5**): Yield 117 mg (82%). *Anal.* Calc. for $C_{20}H_{31}F_6N_4NiO_4P$: C, 40.36; H, 5.25; N, 9.41. Found: C, 40.19; H, 5.34; N, 9.50%. FAB^+, *m/z*: 449 $[M]^+$. IR (cm^{-1}): 3270 ν(N–H), 1666 ν(C=N), 1540, 1376 ν(CO). UV–Vis in acetone, λ (nm), ε ($M^{-1}\,cm^{-1}$): 632 (65), 381 (445).

$[Ni(Me_4\text{-}mcN_3)(4\text{-}NH_2Bz)](PF_6)$ (**6**): Yield 99 mg (73%). *Anal.* Calc. for $C_{20}H_{33}F_6N_4NiO_2P$: C, 42.50; H, 5.89; N, 9.91. Found: C, 42.43; H, 5.85; N, 9.94%. FAB^+, *m/z*: 419 $[M]^+$. IR (cm^{-1}): 3453, 3342 ν(N–H_2), 3280 ν(N–H), 1671 ν(C=N), 1606 δ(N–H_2), 1502, 1375 ν(CO). UV–Vis in acetone, λ (nm), ε ($M^{-1}\,cm^{-1}$): 628 (66), 381 (320).

2.2.2. *[Ni(mcN$_3$)(Bz)(H$_2$O)](PF$_6$) (mcN$_3$ = Me$_3$-mcN$_3$, Bz = 4-NO$_2$Bz (**7**), 2,3,4,5,6-F$_5$Bz (**8**); mcN$_3$ = Me$_4$-mcN$_3$, Bz = 4-NO$_2$Bz (**9**), 2,3,4,5,6-F$_5$Bz (**10**))*

Complexes **7**–**10** were prepared by allowing $[Ni_2(mcN_3)_2(\mu\text{-}OH)_2](PF_6)_2$ (0.12 mmol) to react with the corresponding benzoic acid (0.24 mmol) in acetone (25 mL). After stirring for 12 h the solvent was removed under reduced pressure and the addition of diethyl ether caused the precipitation of a green solid, which was collected by filtration, washed with diethyl ether and air-dried.

$[Ni(Me_3\text{-}mcN_3)(4\text{-}NO_2Bz)(H_2O)](PF_6)$ (**7**): Yield 112 mg (78%). *Anal.* Calc. for $C_{19}H_{31}F_6N_4NiO_5P$: C, 38.08; H, 5.21; N, 9.35. Found: C, 38.01; H, 5.15; N 9.52%. FAB^+, *m/z*: 435 $[M^+-H_2O]$. IR (cm^{-1}): 3577 ν(OH), 3294, 3254 ν(N–H), 1657 ν(C=N), 1555, 1347 ν(CO). UV–Vis in acetone, λ (nm), ε ($M^{-1}\,cm^{-1}$): 621 (63), 381 (483).

$[Ni(Me_3\text{-}mcN_3)(2,3,4,5,6\text{-}F_5Bz)(H_2O)](PF_6)$ (**8**): Yield 112 mg (72%). *Anal.* Calc. for $C_{19}H_{27}F_{11}N_3NiO_3P$: C, 35.43; H, 4.22; N, 6.52. Found: C, 35.30; H, 4.31; N, 6.49%. FAB^+, *m/z*: 480 $[M^+-H_2O]$. IR (cm^{-1}): 3603ν(O–H), 3288, 3272 ν(N–H), 1650 ν(C=N), 1589, 1356 ν(CO). UV–Vis in acetone, λ (nm), ε ($M^{-1}\,cm^{-1}$): 625 (58), 385 (173). ^{19}F NMR ($(CD_3)_2CO$, ppm): δ −109.2 (F_o, 2 F), −144.6 (F_p), −160.7 (F_m, 2F).

$[Ni(Me_4\text{-}mcN_3)(4\text{-}NO_2Bz)(H_2O)](PF_6)$ (**9**): Yield 119 mg (81%). Anal. Found: C, 39.19; H, 5.46; N, 9.12. Calc. for $C_{20}H_{33}F_6N_4NiO_5P$: C, 39.17; H, 5.42; N, 9.14%. FAB^+, *m/z*: 449 $[M-H_2O]^+$. IR (cm^{-1}): 3599 ν(OH), 3287

ν(N–H), 1659 ν(C=N), 1536, 1358 ν(CO). UV–Vis in acetone, λ (nm), ε ($M^{-1}\,cm^{-1}$): 622 (65), 382 (462).

[Ni(Me_4-mcN_3)(2,3,4,5,6-F_5Bz)(H_2O)](PF_6) (**10**): Yield 114 mg (72%). *Anal.* Calc. for $C_{20}H_{29}F_{11}N_3NiO_3P$: C, 36.49; H, 4.44; N, 6.38. Found: C, 36.18; H, 4.53; N, 6.34%. FAB$^+$, *m/z*: 494 [M^+-H_2O]. IR (cm^{-1}): 3590, ν(O–H), 3263 ν(N–H), 1654 ν(C=N), 1604, 1367 ν(CO). UV–Vis in acetone, λ (nm), ε ($M^{-1}\,cm^{-1}$): 626 (57), 384 (169). ^{19}F NMR ($(CD_3)_2CO$, ppm): δ −105.7 (F_o, 2F), −142.9 (F_p), −161.3 (F_m, 2F).

2.3. X-ray data collection and structure determination

Data collection was performed on a Bruker Smart CCD diffractometer with a nominal crystal to detector distance of 4.5 cm. Diffraction data were collected based on a ω scan run. A total of 1371 (complexes **2** and **3**) and 2524 (complexes **4** and **7**) frames were collected at 0.3° intervals and 10 s per frame. The diffraction frames were integrated using the SAINT package [12] and corrected for absorption with SADABS [13]. Data collection for **10** was performed on a Siemens P4 diffractometer. The crystallographic data are shown in Table 1. The structure were solved by direct methods [14] and refined anisotropically on F^2 [13]. Hydrogen atoms were introduced in calculated positions.

3. Results and discussion

3.1. Synthesis

The hydroxo complexes [Ni(mcN_3)(μ-OH)]$_2$(PF_6)$_2$ (mcN_3 = 2,4,4-trimethyl-1,5,9-triazacyclododec-1-ene (Me_3-mcN_3) and its 9-methyl derivative (Me_4-mcN_3)) have been used as starting materials for the preparation of several five-coordinate nickel(II) complexes [15]. When [Ni(mcN_3)(μ-OH)]$_2$(PF_6)$_2$ was treated with substituted benzoic acids HBz-2-NH_2, HBz-2-NO_2, HBz-4-NH_2, HBz-4-NO_2 or HBz-2,3,4,5,6-F_5 in acetone, complexes **1**–**10** were obtained in moderate high yields (Scheme 1). The acid-base reaction occurs at room temperature in acetone with the concomitant liberation of water for **1**–**6** complexes. In contrast, the benzoic acids HBz-4-NO_2 and HBz-2,3,4,5,6-F_5, under the same reaction conditions gave aquo-complexes [Ni(mcN_3)(Bz)(H_2O)](PF_6). Complexes **1**–**10** are all blue-green air-stable solids and they have been characterized by partial elemental analyses, FAB$^+$ mass spectrometry and spectroscopic (IR and NMR) methods.

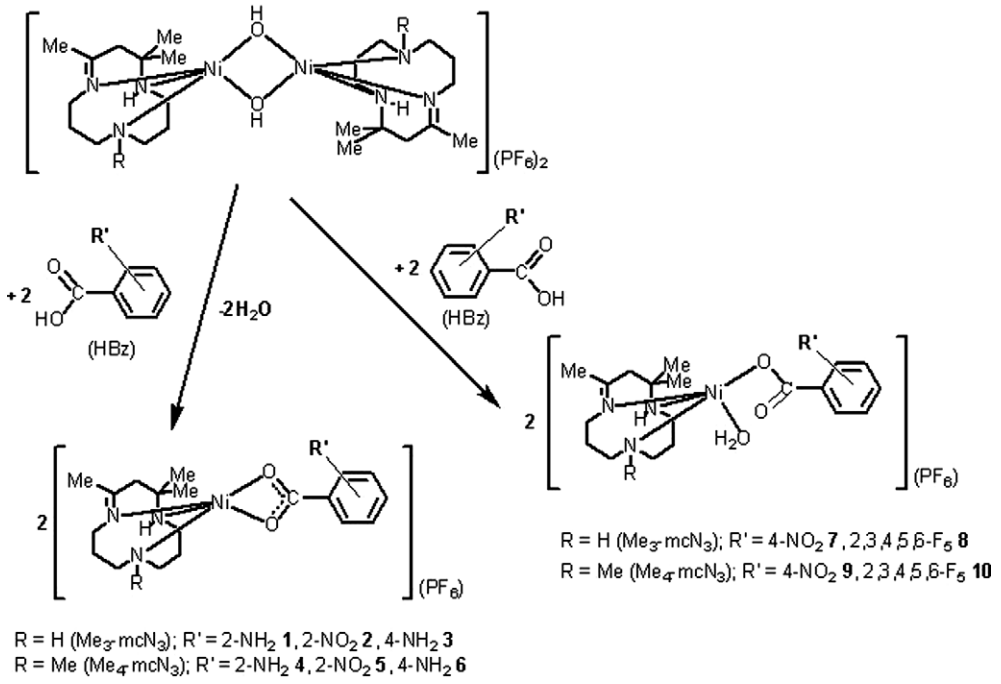
3.2. Infrared and electronic spectra

The IR spectra of complexes **1**–**10** show characteristic absorptions for the mcN_3 ligands [16]: 3297–3244 cm^{-1} ν(N–H), ~1660 cm^{-1} ν(C=N), and two strong bands due to the presence of the PF_6^- ion at 840 and 560 cm^{-1} are also observed. The benzoate ligand in compounds **1**–**6** exhibits κ^2-coordination mode to the nickel atom that is suggested by the IR spectra. The separation between the components of ν(OCO) is in the range 126–164 cm^{-1} and this is consistent with a symmetrical bidentate coordination [17,18]. For complexes **7**–**10** where the carboxylate acts as monodentate ligand, the Δ value is larger (*ca.* 200 cm^{-1}). These coordination modes in **2**, **3**, **4**, **7** and **10** were authenticated by an X-ray crystal structure determination (vide infra). A broad band in the spectra of **7**–**10** in the range 3600–3500 cm^{-1} can be assigned to coordinated water vibrations.

The electronic spectra of the complexes in acetone solution are all similar and show bands in the 620 and 380 nm regions which could be assigned to $^3B_1(F) \rightarrow {}^3E(F)$ and $^3B_1(F) \rightarrow {}^3A_2$, $^3E(P)$ transitions, respectively. The λ_{max} values and molar absorptivities are consistent with a pentacoordinate environment around nickel(II) [15].

Table 1
Crystal data and summary of data collection and refinement for **2**, **3**, **4**, **7** and **10**

Empirical formula	$C_{19}H_{29}F_6N_4NiO_4P$	$C_{19}H_{31}F_6N_4NiO_2P$	$C_{20}H_{33}F_6N_4NiO_2P$	$C_{19}H_{31}F_6N_4NiO_5P$	$C_{20}H_{29}F_{11}N_3NiO_3P$
Formula weight	581.14	551.16	565.18	599.16	658.14
Crystal system	orthorhombic	monoclinic	monoclinic	monoclinic	monoclinic
Unit cell dimensions					
a (Å)	9.5314(5)	9.3203(4)	8.1545(4)	7.6324(3)	12.9840(10)
b (Å)	13.4985(7)	21.1419(9)	15.7841(8)	16.7099(7)	12.8210(10)
c (Å)	18.9838(10)	12.3756(5)	18.8882(10)	19.3507(8)	15.8640(10)
α (°)	90	90	90	90	90
β (°)	90	105.2400(10)	90.6570(10)	92.63	96.100(10)
γ (°)	90	90	90	90	90
Unit cell volume (Å^3)	2442.4(2)	2352.84(17)	2431.0(2)	2465.32(17)	2625.9(3)
Temperature	293(2)	293(2)	293(2)	100(2)	173(2)
Space group	$P2_1cn$	$P2_1/c$	$P2_1/c$	$P2_1/c$	Cc
Z	4	4	4	4	4
μ (mm^{-1})	0.939	0.964	0.935	0.936	0.906
Reflections collected	14698	14505	27675	15298	4616
Independent reflections	5138	5235	5590	5537	4616
R_1 [$I > 2\sigma(I)$]	0.0289	0.0327	0.0462	0.0357	0.0444
wR_2 (all data)	0.0785	0.0870	0.1184	0.0967	0.1330



Scheme 1. Reaction schemes for substituted-benzoate complexes of nickel(II).

3.3. NMR spectroscopy

All of the complexes exhibit relatively sharp hyperfine-shifted ^{1}H NMR signals in acetone solution spanning from 350 to −35 ppm. The ^{1}H NMR spectra of complexes **1**–**10** have been assigned on the basis of our previous studies of paramagnetic nickel(II) macrocyclic complexes [19]. The spectra show (Tables 2 and 3) the expected resonance line pattern because of a dominant spin-polarisation mechanism [20]. The eight α-methylene protons shift downfield whereas the six β-methylene protons shift upfield with regard to the diamagnetic position [21]. The equatorial protons are expected to experience larger contact shifts than the axial protons and therefore the most downfield resonances are due to α-CHeq and the most upfield ones to β-CHeq [22]. The isotropically shifted ^{1}H NMR signals observed for the methyl groups (2-Me, 4-Me(a, b) and 9-Me–N) in Table 2 and phenyl groups of benzoates can be initially assigned by inspection of their peak areas. All the resonances of the phenyl rings (Table 3) are downfield to TMS in accordance with a dominant σ-delocalization pattern of spin density consistent with the ground state

Table 2
^{1}H NMR Chemical shift data (ppm) for the macrocyclic ligands

Complex	H_α	H_β	2-Me	4-Me (a, b)	9-Me
1	338.9 (2H), 231.3 (2H), 218.2 (2H), 106.5 (2H)	−11.3, −12.2 (2H), −25.1, −28.3, −29.8	−15.0	55.4, 18.3	
2	318.7 (2H), 257.0, 222.6 (2H), 194.8, 96.9, 83.9	−12.2 (2H), −15.1, −23.6, −27.6, −32.6	−18.4	51.7, 14.9	
3	342.7 (2H), 229.4 (2H), 224.1, 107.5, 43.5 (2H)	−11.0 (2H), −12.5, −25.6, −27.7, −30.8	−14.5	56.3, 19.6	
4	344.2, 306.0, 287.6, 248.2, 229.7, 100.6, 45.8, 40.9	−9.6 (2H), −13.3, −25.4, −31.5, −32.8	−15.9	62.9, 20.3	129.5
5	335.9, 310.0, 283.2, 248.7, 232.7, 95.5, 51.3 (2H)	−10.0 (2H), −13.3, −25.1, −32.0, −33.8	−17.3	64.6, 19.9	136.2
6	347.2, 301.8, 287.6, 244.6, 224.1, 100.1, 91.1, 43.7, 37.8	−8.7, −9.7, −13.3, −25.4, −31.4, −33.3	−15.9	61.5, 20.7	127.0
7	329.7 (2H), 246.4, 231.4, 206.9, 102.2, 69.3 (2H)	−11.8 (2H), −13.6, −24.3, −28.9, −30.4	−16.8	54.4, 16.6	
8	312.5 (2H), 218.6 (2H), 179.1 (2H), 94.3 (2H)	−12.3 (2H), −15.4, −23.2, −27.4, −33.7	−19.1	48.3, 14.4	
9	341.7 (2H), 307.3, 283.1, 250.1, 232.5, 97.1, 50.2 (2H)	−9.8 (2H), −13.3, −25.0, −32.2, −33.1	−17.0	63.9, 19.9	134.1
10	329.0, 311.0, 284.6, 255.2, 232.1, 93.0, 50.8 (2H)	−9.9 (2H), −13.3, −25.1 −31.7, −34.0	−17.3	63.4, 19.9	135.6

Table 3
^{1}H NMR Chemical shift data (ppm) for the benzoate ligands

Complex	2-H	3-H	4-H	5-H	6-H	Other ligands
1	6.6 (NH_2)	11.1	6.2	8.1	9.8	
2		10.7	5.8	6.5 (5-H + 6-H)		
3	8.9 (2-H + 6-H)	7.8 (3-H + 5-H)	5.4 (NH_2)			
4	7.1 (NH_2)	11.2	6.1	8.1	10.3	
5		10.6 (3-H)	6.1	6.3 (5-H + 6-H)		
6	9.3 (2-H + 6-H)	7.9 (3-H + 5-H)	5.5 (NH_2)			
7	9.4 (2-H + 6-H)	9.9 (3-H + 5-H)				4.7 (H_2O)
8						8.7 (H_2O)
9	9.9 (2-H + 6-H)	10.1 (3-H + 5-H)				5.6 (H_2O)
10						9.8 (H_2O)

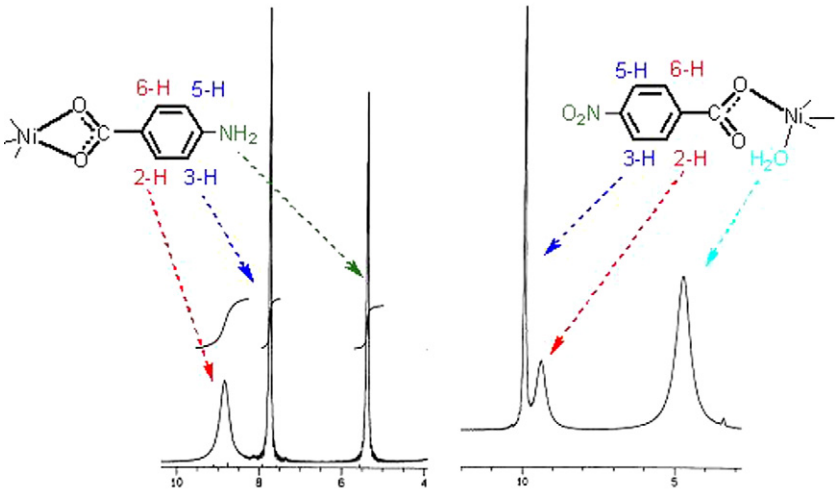


Fig. 1. ^{1}H NMR spectra (in d_6-acetone solution at room temperature) of **3** (left) and **7** (right). Only the phenyl resonances region is shown.

of nickel(II) although the unpaired electrons could polarise the net spin density in the dπ orbitals. A similar behaviour has been observed elsewhere [7]. In spectra of the 4-NH_2 (**3**, **6**) and 4-NO_2 (**7**, **9**) derivatives two resonances for the phenyl protons have been observed (Fig. 1). The broad signal can be assigned to the 2-H and 6-H protons of the aromatic rings nearer to the nickel atom; moreover for the 4-NO_2 derivatives (**7**, **9**) the 3-H and 5-H resonance is more downfield shifted (9.9 and 10.1 ppm) than for 4-NH_2 derivatives (**3**, **6**) (7.8 and 7.9 ppm). Substitution at the position two breaks the ring symmetry so that four phenyl resonances of equal intensity were observed for **1** and **4**. The complete assignment of these isotropically shifted signals required an application of two-dimensional ^{1}H NMR techniques. A magnitude COSY spectrum of **4** (Fig. 2), recorded at 20 °C, clearly shows cross signals between the resonances at 11.2, 8.1 and 6.1 ppm and also between resonances at 10.3 and 8.1 ppm. These signals can be assigned to the phenyl 3-H (11.2), 6-H (10.3), 5-H (8.1), and 4-H (6.1) protons, respectively, of the benzoate ligand. The spectra of 2-NO_2 derivatives (**2**, **5**) show two resonances of intensity corresponding to one and three protons that can be assigned to 3-H and 4,5,6-H (not well-resolved) respectively. Therefore, on the basis of the X-ray structure of **2** and **4** (see below) the distortion in the square pyramidal arrangement of the nickel atom due to the small bite angle of the chelated carboxylate moiety and the substitution on 2-position of the ring result in a larger magnetic anisotropy that in turn induces a larger isotropic shift of the 3-H proton. The ^{19}F NMR spectra of complexes **8** and **10** show the presence of $C_6F_5(OCO)^-$ ring giving three resonances with relative intensities of 2:1:2 due to the *ortho*-, *para*-, and *meta*-F atoms, respectively.

3.4. Solid state structures of the complexes

The single-crystal X-ray diffraction study on [Ni(Me_3-mcN$_3$)(Bz-2-NO_2)](PF_6) (**2**), [Ni(Me_3-mcN$_3$)(Bz-4-NH_2)](PF_6) (**3**) and [Ni(Me_4-mcN$_3$)(Bz-2-NH_2)](PF_6) (**4**) confirms that benzoate formed by deprotonation of the corresponding benzoic acid, is bonded to the nickel atom as a bidentate ligand. The structures of compounds **2**, **3** and **4** are similar. Selected distances angles for these complexes are given in Table 4, and Figs. 3–5 show the thermal ellipsoid diagrams. In these compounds, nickel atoms have distorted square-pyramidal geometry around the metal ion. The Reedijk parameter [23] τ shows values of 0.240, 0.059 and 0.024 for complexes **2**, **3** and **4**, respectively. The three

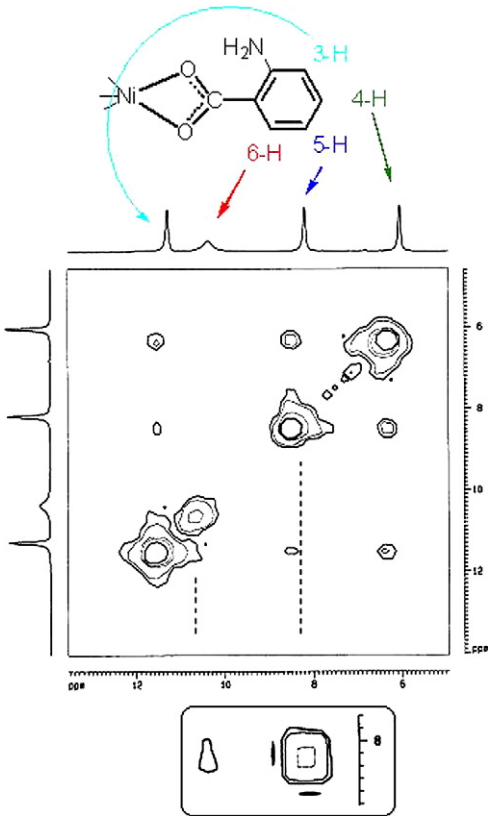


Fig. 2. Magnitude ^{1}H COSY spectrum of complex **4** at 400 MHz at 20 °C in d_6-acetone solution recorded with a delay time of 150 ms. Only the region relevant to the assignment of phenyl resonances is shown in the top trace. The inset on the bottom shows an enlargement of the 5-H–6-H cross-peak area obtained with a delay time of 20 ms.

Table 4
Selected bond lengths (Å) and angles (°) for complexes **2**, **3** and **4**

	2	**3**	**4**
Bond lengths			
Ni(1)–N(1)	1.988(2)	1.993(2)	1.987(2)
Ni(1)–N(2)	2.012(2)	2.026(1)	2.016(2)
Ni(1)–N(3)	2.015(2)	2.020(2)	2.049(2)
Ni(1)–O(1)	2.120(2)	2.103(1)	2.110(2)
Ni(1)–O(2)	2.080(2)	2.062(1)	2.078(2)
Bond angles			
N(1)–Ni(1)–N(2)	95.07(7)	93.93(6)	91.80(8)
N(1)–Ni(1)–N(3)	93.38(8)	94.80(6)	95.42(9)
N(1)–Ni(1)–O(1)	163.78(7)	98.07(5)	100.67(9)
N(1)–Ni(1)–O(2)	101.89(7)	155.55(6)	156.32(8)
N(2)–Ni(1)–N(3)	103.82(7)	102.18(6)	101.34(8)
N(2)–Ni(1)–O(1)	96.52(7)	151.96(5)	157.75(8)
N(2)–Ni(1)–O(2)	149.37(7)	96.62(5)	99.62(8)
N(3)–Ni(1)–O(1)	94.83(7)	101.96(6)	95.80(8)
N(3)–Ni(1)–O(2)	100.46(7)	104.40(6)	102.48(9)
O(2)–Ni(1)–O(1)	62.84(6)	63.52(5)	62.51(8)

nitrogen atoms of the macrocyclic ligand constitute a trigonal face of the pyramid. The two oxygen atoms from the benzoate and two nitrogens of the macrocycle form the basal plane. The nickel ion lies above this plane and is displaced 0.288(1), 0.374(1) and 0.310(1) Å for complexes **2**, **3** and **4**, respectively, towards the N(3) nitrogen, which constitutes the axial donor. The Ni–N distances lie within the range reported in complexes containing the {Ni(mcN$_3$)}

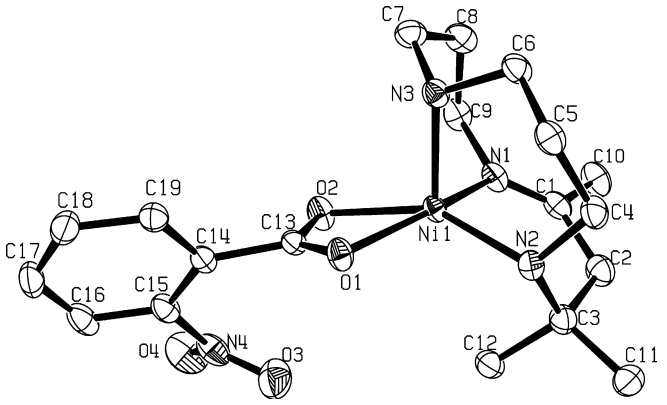


Fig. 3. ORTEP drawing of complex **2** showing the atom numbering scheme. Displacement ellipsoids are drawn at the 50% probability level. For clarity hydrogen atoms of macrocycle are omitted.

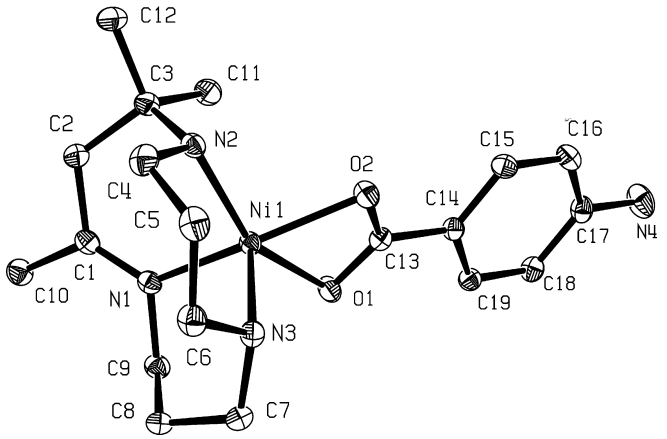


Fig. 4. ORTEP drawing of complex **3** showing the atom numbering scheme. Displacement ellipsoids are drawn at the 50% probability level. For clarity hydrogen atoms of macrocycle are omitted.

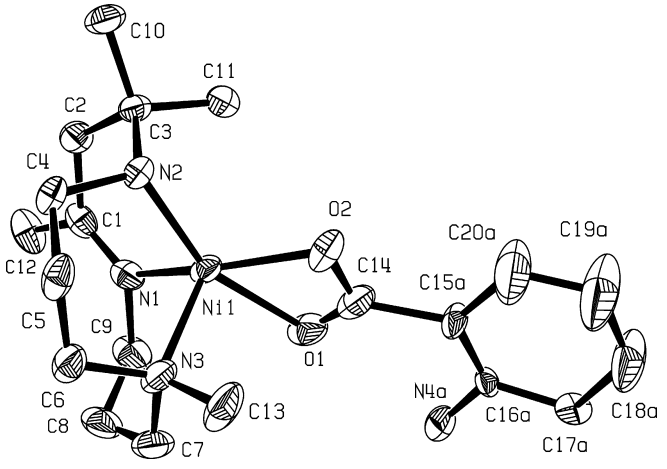


Fig. 5. ORTEP drawing of complex **4** showing the atom numbering scheme. Displacement ellipsoids are drawn at the 50% probability level. For clarity hydrogen atoms of macrocycle are omitted.

moiety [13,15]. The Ni–O bond distances are close to each other (2.0802(15) and 2.1198(17) Å (**2**), 2.0622(12) and 2.1034(12) Å (**3**) and 2.078(2) and 2.1103(18) Å (**4**)) thus the benzoate ligand is bonded in a symmetric (or almost) chelating mode with {[Ni–O(1)]–[Ni–O(2)]} = ΔO values of 0.0396, 0.0412 and 0.0323 Å for **2**, **3** and **4**, respectively. These bond distances are comparable to those reported for other crystallographically characterized nickel-carboxylate complexes with a distorted square pyramidal [24] or octahedral [25,26] geometry. The bite angle of the chelating carboxylate anion shows values of 62.84(6)° **2**, 63.52(5)° **3** and 62.51(8)° **4**, respectively. The torsion angle between the aromatic ring and the nickel-bounded carboxylate group is 57.3 (3) and −8.5 (3)° for complexes **2** and **3**. In addition, there are some interconnections by hydrogen bonds in compound **3** the NH_2 groups in the packing are oriented towards PF_6^- anions with the shortest N···F distances of N4···F3^{i}: 2.937(2) Å and N4···F3^{ii}: 3.084(2) Å (i: $x-1$, $-y+3/2$, $z+1/2$; ii: $-x$, $y+1/2$, $-z+3/2$). In complex **4** the aromatic ring is disordered over two positions with an occupation factor close to 50%. In both positions there is an intramolecular hydrogen bond with a mean O···N distance of 2.682 Å. The molecular structures, with the atom-numbering schemes, of compounds **7** and **10** are shown in Figs. 6 and 7, respectively. Selected bond lengths and angles of complexes **7** and **10** are listed in Table 5. The nickel centre is bonded to a N_3-macrocyclic ligand, a monodentate benzoate and a water molecule in a distorted trigonal bipyramidal geometry for **7** and distorted square-pyramidal geometry for **10**. The τ parameter shows values of 0.593, and 0.175 for complexes **7** and **10**, respectively. The Ni–N (macrocycle) bond distances in **7** and **10** are very similar to those observed in **2**, **3** and **4**. The carboxylate anion acts as a monodentate ligand through the deprotonated hydroxyl oxygen. The Ni–O (benzoate) bond distances are close to each other 2.0472(13) Å for **7** and 2.048(4) Å for **10** and the Ni–O (water) distances are also similar (2.0429(15) Å (**7**) and 2.041(5) Å (**10**)). The nickel atom in **10** is 0.304(2) Å out of de basal plane defined by N1, N2, O1 and O3. The rmsd of this plane is 0.087 Å. The dihedral angle between the carboxylate group and the aromatic ring is 22.6(3)° for **7** and 51.0(5)° for **10**. In compound **7** there is an intramolecular strong hydrogen bond between the water molecule and the carboxylate group with an O5···O2 distance of 2.559(2) Å. In the crystal packing, the complexes appear grouped by pairs (Fig. 8) with a N2···O3^{i} distance (i: $-x+1$, $-y+1$, $-z$) of

Table 5
Selected bond lengths (Å) and angles (°) for complexes **7** and **10**

	7		**10**
Bond lengths			
Ni(1)–N(1)	2.028(2)	Ni(1)–N(1)	2.020(5)
Ni(1)–N(2)	2.026(2)	Ni(1)–N(2)	2.033(4)
Ni(1)–N(3)	2.030(2)	Ni(1)–N(3)	2.054(4)
Ni(1)–O(1)	2.047(1)	Ni(1)–O(1)	2.048(4)
Ni(1)–O(5)	2.043(2)	Ni(1)–O(3)	2.041(5)
Bond angles			
N(1)–Ni(1)–N(2)	91.75(6)	N(1)–Ni(1)–N(2)	91.95(19)
N(1)–Ni(1)–N(3)	90.73(6)	N(1)–Ni(1)–N(3)	93.05(18)
N(1)–Ni(1)–O(1)	179.53(6)	N(1)–Ni(1)–O(1)	167.31(17)
N(1)–Ni(1)–O(5)	92.77(6)	N(1)–Ni(1)–O(3)	92.6(2)
N(2)–Ni(1)–N(3)	101.03(6)	N(2)–Ni(1)–N(3)	102.92(17)
N(2)–Ni(1)–O(1)	87.81(6)	N(2)–Ni(1)–O(1)	82.53(16)
N(2)–Ni(1)–O(5)	143.98(7)	N(2)–Ni(1)–O(3)	156.79(17)
N(3)–Ni(1)–O(1)	89.50(6)	N(3)–Ni(1)–O(1)	99.31(18)
N(3)–Ni(1)–O(5)	114.62(7)	N(3)–Ni(1)–O(3)	99.5(2)
O(5)–Ni(1)–O(1)	87.50(6)	O(3)–Ni(1)–O(1)	88.21(19)

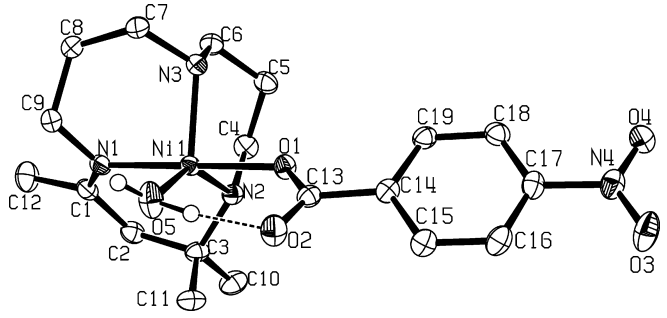


Fig. 6. ORTEP drawing of complex **7** showing the atom numbering scheme. Displacement ellipsoids are drawn at the 50% probability level. For clarity hydrogen atoms of macrocycle are omitted.

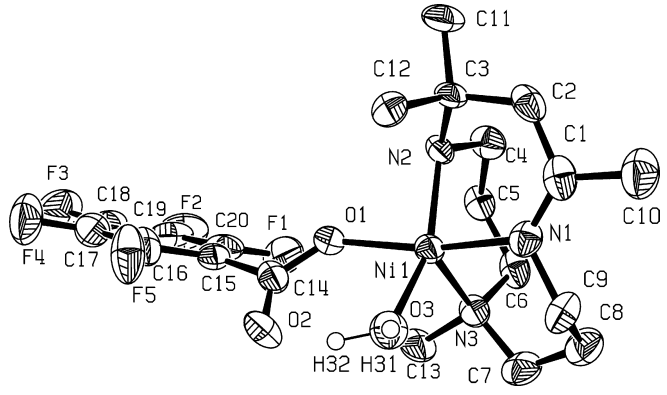


Fig. 7. ORTEP drawing of complex **10** showing the atom numbering scheme. Displacement ellipsoids are drawn at the 50% probability level. For clarity hydrogen atoms of macrocycle are omitted.

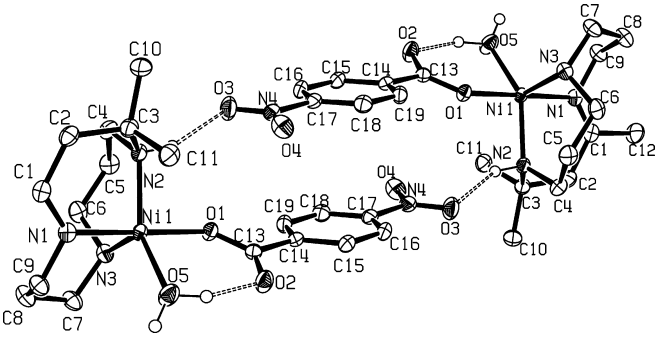


Fig. 8. Molecular grouping in the solid state of complex **7**. Hydrogen atoms of the macrocycle are omitted.

3.054(2) Å and the aromatic rings adopt a parallel orientation having a distance between centroids of 3.741 Å and an angle between the ring normal and the centroid vector of 26.5°. In a similar manner, in **10** there is a strong intramolecular hydrogen bond between the water molecule and the carboxylate group with an O3···O2 distance of 2.580(7) Å. In this case, the O3···F9^{i} distance, 2.720(8) Å, also suggests the existence of a hydrogen bond to the PF_6^- anion (i: $x+1$, y, z). In these complexes Ni atom and N atoms from the macrocycle form three six-membered rings. The conformations adopted for those rings have been used to characterize the conformation of complexes containing these macrocycles [27]. In all the structures reported in this paper the six-membered rings that do not contain the C=N bond have chair-like conformations; this is the most frequent conformation in this kind of complexes [27].

Acknowledgements

We wish to thank Dr. Donaire for his valuable suggestions and to Dr. de Godos for recording the NMR spectra. We thank also the Fundación Séneca de la Región de Murcia (00484/PI/04 and 03010/PI/05) for financial support and the Ministerio de Educación y Ciencia for partial financial support (CTQ2005-09231-C02-01).

Appendix A. Supplementary material

CCDC 613433, 613434, 613435, 613436 and 613437 contain the supplementary crystallographic data for **2**, **3**, **4**, **7** and **10**. These data can be obtained free of charge via http://www.ccdc.cam.ac.uk/conts/retrieving.html, or from the Cambridge Crystallographic Data Centre, 12 Union Road, Cambridge CB2 1EZ, UK; fax: (+44) 1223-336-033; or e-mail: deposit@ccdc.cam.ac.uk. Supplementary data associated with this article can be found, in the online version, at doi:10.1016/j.poly.2006.09.068.

References

[1] R.L. Rardin, W.B. Tolman, S.J. Lippard, New. J. Chem. 15 (1991) 417.
[2] R.H. Holm, P. Kennepohl, E.I. Solomon, Chem. Rev. 96 (1996) 2239.
[3] R.L. Rardin, A. Bino, P. Poganiuch, W.B. Tolman, S. Liu, S.J. Lippard, Angew. Chem., Int. Ed. Eng.l 29 (1990) 812.
[4] D.H. Busch, N.A. Stephenson, Coord. Chem. Rev. 100 (1990) 19.
[5] H. Adams, S. Clunas, D.E. Fenton, S.E. Spey, J. Chem. Soc., Dalton Trans. (2002) 441.
[6] (a) I.L. Eremenko, S.E. Nefedov, A.A. Sidorov, M.A. Golubnichaya, P.V. Danilov, V.N. Ikorskii, Y.G. Shvedenkov, V.M. Novotortsev, I.I. Moiseev, Inorg. Chem. 38 (1999) 3764;
(b) B.S. Hammes, C.J. Carrano, Inorg. Chem. 38 (1999) 3562;
(c) A.J. Blake, J.P. Danks, I.A. Fallis, A. Harrison, W.-S. Li, S. Parsons, S.A. Ross, G. Whittaker, M. Schröder, J. Chem. Soc., Dalton Trans. (1998) 3969.
[7] J.-M. Moratal, J. Salgado, A. Donaire, H.R. Jiménez, J. Castells, Inorg. Chem. 32 (1993) 3587.
[8] S. Wolowiec, L. Latos-Grażyński, D. Toronto, J.-C. Marchon, Inorg. Chem. 37 (1998) 724.
[9] (a) I. Bertini, C. Luchinat, NMR of Paramagnetic Molecules in Biological Systems, Benjamin & Cummings, Menlo Park, CA, 1986;
(b) I. Bertini, P. Turano, A.J. Vila, Chem. Rev. 93 (1993) 2833;
(c) G. La Mar, J.S. de Ropp, NMR Methodology for Paramagnetic Proteins, vol. 12, Plenum Press, New York, 1993, p. 1.
[10] J.W.L. Martin, J.H. Johnston, N.F. Curtis, J. Chem. Soc., Dalton Trans. (1978) 68.
[11] A. Escuer, R. Vicente, J. Ribas, Polyhedron 11 (1992) 453.
[12] SAINT, Version 6.22, Bruker AXS Inc.
[13] G.M. Sheldrick, SADABS, University of Gottingen, 1996.
[14] G.M. Sheldrick, SHELX-97, Programs for Crystal Structure Analysis (Release 97-2), University of Göttingen, Germany, 1998.
[15] (a) M.D. Santana, G. García, A.A. Lozano, G. López, J. Tudela, J. Pérez, L. García, L. Lezama, T. Rojo, Chem. Eur. J. 10 (2004) 1738;
(b) M.D. Santana, G. García, M. Julve, F. Lloret, J. Pérez, M. Liu, F. Sanz, J. Cano, G. López, Inorg. Chem. 43 (2004) 2132;
(c) J. Ruiz, M.D. Santana, A. Lozano, C. Vicente, G. García, G. López, J. Pérez, L. García, Eur. J. Inorg. Chem. (2005) 3049.
[16] M.D. Santana, A. Rufete, G. García, G. López, J. Casabó, A. Cabrero, E. Molins, C. Miravitlles, Polyhedron 16 (1997) 3713.
[17] K. Nakamoto, Infrared and Raman Spectra of Inorganic and Coordination Compounds, Wiley, New York, 1986, p. 236.
[18] H.-L. Zhu, M.-F. Wu, L.-M. Zheng, P. Huang, W.-X. Tang, Transition Met. Chem. 24 (1999) 346.
[19] M.D. Santana, G. García, J. Pérez, E. Molins, G. López, Inorg. Chem. 40 (2001) 5701.
[20] R.H. Holm, C.J. Hawkins, NMR of Paramagnetic Molecules: Principles and Applications, in: G.N. La Mar, W. HorrocksJr., R.H. Holm (Eds.), Academic Press, New York, 1973, p. 243.
[21] M.D. Santana, A.A. Lozano, G. García, G. López, J. Pérez, Dalton Trans. 1 (2005) 104.
[22] A. Dei, M. Wicholas, Inorg. Chim. Acta 166 (1989) 151.
[23] A.W. Addison, T.N. Rao, J. Reedijk, J.V. Rijn, G.C. Verschoor, J. Chem. Soc., Dalton Trans. (1984) 1349.
[24] D.D. LeCloux, M.C. Keyes, M. Osawa, V. Reynolds, W.B. Tolman, Inorg. Chem. 33 (1994) 6361.
[25] B.S. Hammes, C.J. Carrano, Inorg. Chem. 38 (1999) 3562.
[26] A.J. Blake, J.P. Danks, I.A. Fallis, A. Harrison, W.-S. Li, S. Parsons, S.A. Ross, G. Whittaker, M. Schröder, J. Chem. Soc., Dalton Trans. (1998) 3969.
[27] J. Pérez, L. García, A.G. Orpen, M.D. Santana, P. Saez, G. García, New J. Chem. 26 (2002) 726.

Heck reaction [9]. Encouraged by our earlier results and in order to explore new types of 1,1′-diaminoferrocenes, in this paper, we report the synthesis and characterization of 1,1′-bis[(*N*-methyl-*N*-phenyl)aminomethyl(ethyl)]ferrocenes starting from diacylferrocenes (acyl = formyl, acetyl) and anilines. Additionally, the debenzylation phenomenon observed in the synthesis of 1,1′-bis[{(*N*-methyl-*N*-benzyl)-amino}benzyl]ferrocenes, starting from dibenzoylferrocene and benzylamines, will be also discussed.

2. Results and discussion

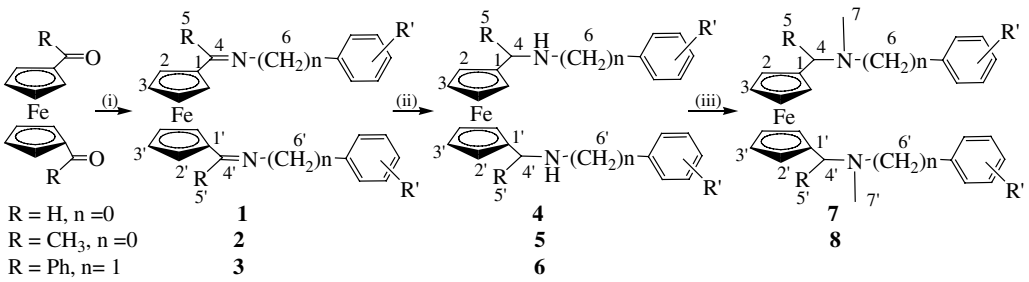
2.1. Synthesis of 1,1′-bis[(N-methyl-N-phenyl)-aminomethyl(ethyl)]ferrocenes 7(8)

The synthetic pathway for 1,1′-bis[(*N*-methyl-*N*-phenyl)aminomethyl(ethyl)]ferrocenes **7**(**8**) is outlined in Scheme 1. Diimine complexes **1** are obtained directly by condensation of diformyl ferrocene and anilines at room temperature in methanol whereas **2**(**3**) are synthesized by condensation of diacetylferrocene (dibenzoylferrocene) and anilines (benzylamines) in toluene using titanium tetrachloride as the catalyst. Although active aluminum oxide as the catalyst in these reactions is also applicable [10], the titanium catalyzed method shows some advantages such as time savings and affording moderate yields of the products, *etc.* Reduction of **1** with sodium borohydride produce quantitatively the 1,1′-bis[(*N*-phenylamino)-methyl]ferrocenes (**4**). However, it is difficult to isolated **5** and **6** due to the incomplete reduction of **2** and **3** with sodium borohydride. Thus, a catalytic reductive system *i.e.*, lithium aluminum hydride–aluminum chloride is chosen to catalyze their reduction, and **5**, **6** are obtained in good yields. Reductive methylation of **4** and **5** with sodium cyanoborohydride and aqueous formaldehyde in the presence of acetic acid [11] yield **7**, **8**, respectively, in moderate yields. Surprisingly, *N*-methylation of **6** with the conditions as mentioned above does not afford the corresponding complexes **9**, in contrast, a sole product, 1,1′-dibenzyl ferrocene [12], is isolated. The same product is also obtained in the *N*-methylation reaction of 1,1′-bis[(*N*-phenylamino)benzyl]ferrocene.

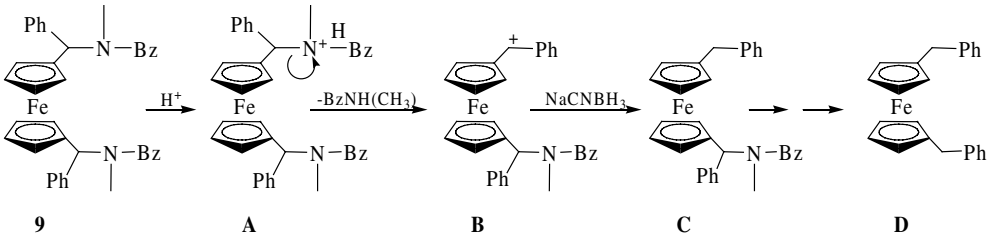
We are puzzled by the above observations. Comparison of the structures of **7**(**8**) and **9** and consideration of the acidic medium in our reactions, it is easily understood that **9** are indeed produced in these reactions. The unsuccessful isolation of **9** is probably attributed to the unique structure of the benzylferrocenyl moiety, causing their debenzylation (Scheme 2), and this result is consistent with Baltzly's observation [13]. As illustrated in Schemes 1 and 2, **7**(**8**) and **9** are in fact *tert*-amines and are easily protonated by acetic acid, particularly for **9**, to give ammonium salts **A**, which is followed by elimination of a neutral benzylamine to afford cations **B**, the latter are better stabilized by both ferrocenyl and phenyl groups. Nucleophilic attack of hydride on **B** will generate **C**. Similarly, the elimination of a second benzylamine, yielding 1,1′-dibenzylferrocene (**D**), is in the same manner as that for the first one (**A** → **C**). Since **9** bear a 1,1′-bis[(*N*-methyl-*N*-benzyl)amino-benzyl] group, the possible elimination of two benzylamines at the same time to generate **D** is also not excluded.

2.2. Spectra characterization of 7(8)

Compounds **1**, **3**–**8** are characterized by elemental analysis, IR and ^{1}H NMR. The elemental analyses are in good agreement with the proposed formula. In the IR spectra, **4** and **6** all display a weak or medium absorption approximate at ν 3340 cm^{-1}, indicating that a N–H group is present in these molecules and this assignment is further confirmed by their ^{1}H NMR where a singlet appears at $\delta \sim 3.90$ ppm in **5** and δ 2.30 ppm in **6** (the peak for **a** N–H group in **4** is missing). In addition, a peak $\delta \sim 4.25$ ppm in **4** is assigned to H4 (H4=H4′=H5=H5′). The satellites correspond to H4 and H5 (H4=H4′, H5=H5′) in **5** (a multiplet $\delta \sim 3.15$ ppm, a doublet $\delta \sim 1.44$ ppm) and **6** (a singlet $\delta \sim 4.37$ ppm, H4=H4′, H5=H5′=0). All of these confirm that diimines **1**–**3** are converted into diamines **4**–**6**, respectively. In the IR spectra of **7**, the absorptions at ν 3340 cm^{-1} observed in **4**, **5** disappear, meanwhile the absorptions at ν 2960, 2870, 1460, 1380 cm^{-1} are present, implying that a N–H group is replaced by N–CH$_3$ in **4** and **5**, and this assignment is consistent with their ^{1}H NMR where H7(7′) display a singlet $\delta \sim 2.80$ ppm in **7** and $\delta \sim 2.45$ ppm in **8**, and these δ values are comparable to those of [(*N*-methyl-*N*-phenyl)aminomethyl]ferrocenes ($\delta \sim 2.70$ ppm) [7]. In addition, the protons in *para*-substituted phenyl rings in **1**, **3**–**8** all display their corresponding splitting patterns.



Scheme 1. Condition: (i) R′C$_6$H$_4$(CH$_2$)$_n$NH$_2$/TiCl$_4$, toluene, reflux for acetyl- and benzoylferrocenes; (ii) LiAlH$_4$–AlCl$_3$/THF; (iii) NaCNBH$_3$, 37%HCHO, AcOH, CH$_3$CN. $n = 0$, R′ = 4-CH$_3$O (a), 4-CH$_3$ (b), C$_6$H$_5$ (c), 3-Cl (d), 4-Cl (e); $n = 1$, R′ = 4-CH$_3$ (f), H (g).



Scheme 2. The possible mechanism for the decomposition of **9**.

2.3. X-ray analysis for the crystal structures of *3g* and *7a*

In order to better understand the structures of the **7**(**8**), complexes, the structures of **3g** and **7a** were determined by X-ray single crystal diffraction. The crystal structures of **3g** and **7a** are presented in Figs. 1 and 2, respectively. Crystallographic data for **3g** and **7a** are given in Table 1, selected bond lengths and angles are listed in Table 2.

Fig. 1 demonstrates that the crystal of **3g** consists of $[Fe\{(\eta^5\text{-}C_5H_4)\text{–}C(C_6H_5)\text{=}NCH_2C_6H_5\}_2]$. However, the crystal of **7a** (Fig. 2) consists of two molecular units $[Fe\{(\eta^5\text{-}C_5H_4)\text{–}CH_2N(CH_3)C_6H_4OCH_3\text{-}4\}_2]$, each being located at a crystallographic center of symmetry. In Fig. 1, the bond lengths of N1–C11 (1.273(3) Å) and N2–C25 (1.278(3) Å) of **3g** correspond to C=N double bonds and are all in the normal range. The phenyl rings attached directly to C11 and C25 are not coplanar with the C=N planes due to the steric hindrance between the phenyl rings and hydrogen atoms of the cyclopentadienyl (Cp) rings. The related dihedral angles between the phenyl planes and the corresponding Cp rings are 63.7° and 102.4°, respectively. In Fig. 2, the bond lengths of N1–C6 (1.502(7) Å) and N2–C20 (1.498(7) Å) in the two molecular units of **7a** are nearly the same. The phenyl plane defined by C8-C13 in one molecular unit is situated above the same side Cp ring, and the dihedral angle between them is 78.5°. A similar location of the phenyl ring and the dihedral angle (with Cp ring, 77.1°) in the other molecular unit is also observed. All of these data are nearly the same as those of [(*N*-methyl-*N*-phenyl)aminomethyl]ferrocenes [14]. The average C–C bond length of the Cp rings in **3g** (1.417 Å) and **7a** (1.453 Å) are similar to the values reported for other ferrocene derivatives [15]. The Fe–C(ring) bond distances range from 2.036 to 2.050 Å in **3g** and from 2.079 to 2.098 Å in **7a**. The two Cp rings of the ferrocenyl fragment in **3g** and **7a** are planar and nearly parallel (interplanar angle 1.7° in **3g**).

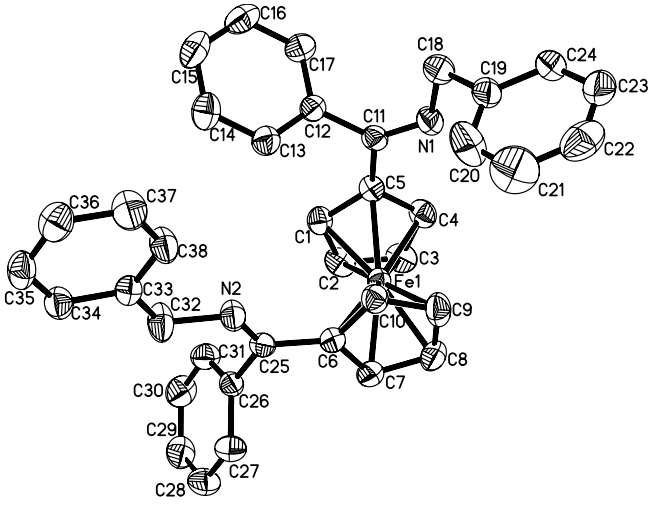


Fig. 1. Perspective view of the independent molecule of **3g** with the atomic numbering scheme (H atoms are omitted for clarity).

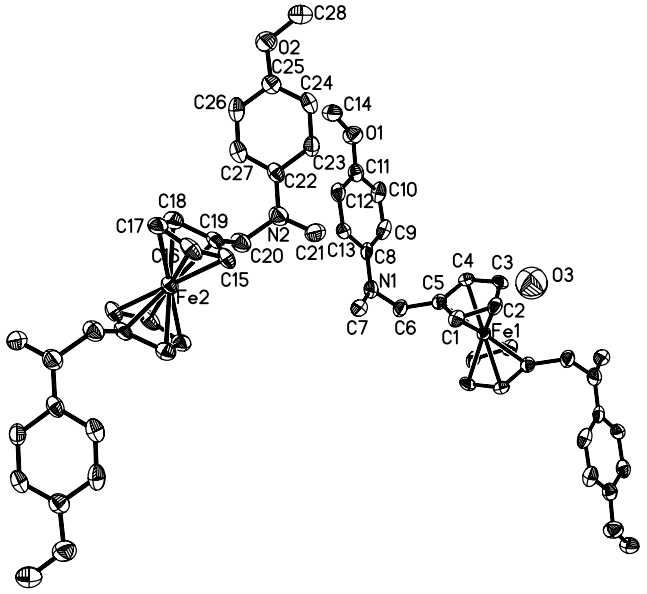


Fig. 2. Perspective view of the independent molecules of **7a** with the atomic numbering scheme (H atoms are omitted for clarity).

3. Experimental

3.1. Materials and instruments

Diformylferrocene [16], diacetylferrocene and dibenzoylferrocene [17] were prepared according to the literature methods. Sodium borohydride, sodium cyanoborohydride were used as received, anilines, titanium tetrachloride, formaldehyde, acetic acid, lithium aluminum hydride, and aluminum chloride were obtained commercially. All of the solvents were purified according standard methods prior to use. Melting points were obtained from a Yanaco micro

Table 1
Crystallographic data for **3g** and **7a**

Compound	**3g**	**7a**
Empirical formula	$C_{38}H_{32}FeN_2$	$C_{28}H_{32.25}FeN_2O_{2.13}$
M	572.51	486.66
Crystal dimensions (mm)	$0.26 \times 0.20 \times 0.18$	$0.24 \times 0.22 \times 0.14$
Crystal system, space group	monoclinic, $P2(1)/c$	monoclinic, $P2(1)/c$
a (Å)	10.763(7)	27.347(1)
b (Å)	26.046(2)	10.043(4)
c (Å)	10.487(7)	9.350(4)
α (°)	90	90
β (°)	91.847(9)	99.672(6)
γ (°)	90	90
V (Å^3)	2938(4)	2531.5(2)
Z	4	4
ρ_{calcd} (Mg m^{-3})	1.294	1.277
μ (mm^{-1})	0.543	0.623
$F(000)$	1200	1029
Reflections collected/unique [R_{int}]	15775/5198 [0.0370]	11972/4409 [0.0906]
Data/restraints/parameters	5198/0/370	4409/6/307
Final R_1, wR_2	0.0353, 0.0781	0.0654, 0.1468
Largest difference in peak and hole (e Å^{-3})	0.188 and −0.218	0.886 and −0.311

Table 2
Selected bond lengths (Å) and angles (°) for **3g** and **7a**

3g		**7a**	
Bond lengths	(Å)	Bond lengths	(Å)
N(2)–C(32)	1.467(3)	C(5)–C(6)	1.544(7)
C(11)–C(12)	1.500(3)	C(19)–C(20)	1.545(7)
C(25)–C(26)	1.502(3)	N(1)–C(7)	1.466(8)
C(5)–C(11)	1.484(3)	N(2)–C(21)	1.486(8)
C(6)–C(25)	1.467(3)	N(1)–C(8)	1.406(7)
N(1)–C(18)	1.470(3)	N(2)–C(22)	1.411(8)
C(4)–C(5)	1.424(3)	C(4)–C(5)	1.452(7)
C(6)–C(7)	1.427(3)	C(18)–C(19)	1.450(7)
Bond angles	(°)	Bond angles	(°)
C(4)–C(5)–C(11)	124.8(2)	C(4)–C(5)–C(6)	125.6(5)
C(7)–C(6)–C(25)	125.6(2)	C(18)–C(19)–C(20)	124.9(5)
C(5)–C(11)–C(12)	117.0(2)	N(1)–C(6)–C(5)	114.0(4)
C(6)–C(25)–C(26)	116.8(2)	N(2)–C(20)–C(19)	113.9(4)
N(1)–C(11)–C(12)	125.7(2)	C(7)–N(1)–C(6)	115.4(5)
N(2)–C(25)–C(26)	125.1(2)	C(21)–N(2)–C(20)	114.8(5)

melting point apparatus and were uncorrected. Elemental analyses were obtained from a Carlo Erba 1106 Elemental analyzer. ^{1}H NMR spectra were measured with a Bruker AV-400 spectrometer by using $CDCl_3$ as a solvent and TMS as internal standard. IR spectra were taken on a BIO-RAD 3000 spectrophotometer.

3.2. Preparation of *7a*, *7b*, *7d* from diformylferrocene (*I*)

3.2.1. Preparation of dialdimines *1a–b*, *1d* from *I*

General procedure: the synthetic procedure for **1a**–**b**, **1d** was the same as described previously [7].

*3.2.1.1. [Fe{(η^5-C_5H_4)–CH=N–$C_6H_4OCH_3$-4}$_2$] (**1a**).* Dark-red solid. M.p. 134–136 °C; Yield 85%. *Anal.* Calc. for $C_{26}H_{24}FeN_2O_2$: C, 69.04; H, 5.35; N, 6.19. Found: C, 68.87; H, 5.33; N, 6.18%. Yield 81%. ^{1}H NMR ($CDCl_3$) δ: 3.81(s, 6H, OCH_3), 4.08(s, 4H, H3, H3′), 4.19(s, 4H, H2, H2′), 6.83(q, 8H, PhH), 8.01(s, 2H, H4, H4′) ppm. IR(KBr) v: 3075(w), 2991(w), 2931(w) 2833(m), 1622(s), 1598(m), 1511(s), 1458(s), 1240(s), 1176(s), 1164(m), 1038(s), 819(vs), 691(w) cm^{-1}.

*3.2.1.2. [Fe{(η^5-C_5H_4)–CH=N–$C_6H_4CH_3$-4}$_2$] (**1b**).* Dark-red solid. M.p. 98–100 °C; Yield 81%. *Anal.* Calc. for $C_{26}H_{24}FeN_2$: C, 74.29; H, 5.76; N, 6.66. Found: C, 74.07; H, 5.73; N, 6.64%. ^{1} H NMR ($CDCl_3$) δ: 1.99(s, 6H, Ar–CH_3), 4.07(s, 4H, H3, H3′), 4.18(s, 4H, H2, H2′), 6.85(q, 8H, PhH), 8.01(s, 2H, H4, H4′) ppm. IR(KBr) v: 3077(w), 3021(w), 2919(w), 2860(w), 1623(vs), 1596(s), 1506(s), 1467(m), 1367(w), 1217(m), 1187(w), 1039(m), 819(s), 778(m) cm^{-1}.

*3.2.1.3. [Fe{(η^5-C_5H_4)–CH=N–C_6H_4Cl-3}$_2$] (**1d**).* Dark-red solid. M.p. 80–82 °C; Yield 83%. *Anal.* Calc. for $C_{24}H_{18}Cl_2FeN_2$: C, 62.51; H, 3.93; N, 6.07. Found: C, 62.43; H, 3.91; N, 6.06%. ^{1} H NMR ($CDCl_3$) δ: 4.08(s, 4H, H3,H3′), 4.21(s, 4H, H2, H2′), 6.88(m, 8H, phH), 8.02(s, 2H, H4, H4′) ppm. IR(KBr) v: 3083(w), 2937(w), 2891(w), 2811(w), 1625(s), 1596(vs), 1498(s), 1361(m), 1251(m), 1094(m), 985(s), 920(w), 761(s), 682(m) cm^{-1}.

3.2.2. Preparation of *4a–b*, *4d* from *1a–b*, *1d*

General procedure: the synthetic procedure for **4a**–**b**, **4d** was the same as described previously [7].

*3.2.2.1. [Fe{(η^5-C_5H_4)–CH_2NH–$C_6H_4OCH_3$-4}$_2$] (**4a**).* Yellow liquid. Yield 90%. *Anal.* Calc. for $C_{26}H_{28}FeN_2O_2$: C, 68.43; H, 6.18; N, 6.14. Found: C, 68.19; H, 6.16; N, 6.13%. IR(KBr) v: 3386(m), 3076(w), 2992(w), 2933(w) 2830(m), 1616(w), 1518(s), 1463(s), 1241(s), 1179(s), 1163(m), 1035(s), 818(vs), 692(w) cm^{-1}. ^{1}H NMR ($CDCl_3$)

δ: 3.75(s, 6H, OCH_3), 4.01(s, 4H, H2, H2′), 4.11(s, 4H, H3, H3′), 4.24(s, 4H, H4, H4′), 6.77(q, 8H, PhH) ppm.

*3.2.2.2. [Fe{(η⁵-C_5H_4)–CH_2NH–$C_6H_4CH_3$-4}$_2$] (**4b**).* Yellow solid. Yield 89%; m.p. 70–72 °C. *Anal.* Calc. for $C_{26}H_{28}FeN_2$: C, 73.59; H, 6.65; N, 6.60. Found: C, 73.41; H, 6.62; N, 6.59%. IR(KBr) *v*: 3401(m), 3089(w), 2912(w), 2857(w), 1613(m), 1517(vs), 1461(w), 1315(m), 1246(m), 1183(w), 1032(w), 805(s) cm^{-1}. ^1H NMR ($CDCl_3$) δ: 2.26(s, 6H, Ar–CH_3), 3.96(s, 4H, H4, H4′), 4.16(s, 4H, H2, H2′), 4.24(s, 4H, H3, H3′), 6.80 (q, 8H, PhH) ppm.

*3.2.2.3. [Fe{(η⁵-C_5H_4)–CH_2NH–C_6H_4Cl-3}$_2$] (**4d**).* Yellow solid. Yield 85%; m.p. 46–48 °C. *Anal.* Calc. for $C_{24}H_{22}Cl_2FeN_2$: C, 61.96; H, 4.77; N, 6.02. Found: C, 61.78; H, 4.71; N, 6.00%. IR(KBr) *v*: 3421(m), 3088(w), 2939(w), 2893(w), 2811(w), 1594(vs), 1557(m), 1495(s), 1362(m), 1251(m), 1098(m), 987(s) 920(w), 831(m), 760(s), 681(m) cm^{-1}. ^1H NMR ($CDCl_3$) δ: 4.10(s, 4H, H2, H2′), 4.14(s, 4H, H3, H3′), 4.25(s, 4H, H4, H4′), 6.62–7.15(m, 8H, PhH) ppm.

3.2.3. Preparation of 7a–b, 7d from 4–b, 4d

General procedure: the synthetic procedure for **7a**–**b**, **7d** was the same as described previously [7].

*3.2.3.1. [Fe{(η⁵-C_5H_4)–$CH_2N(CH_3)$–$C_6H_4OCH_3$-4}$_2$] (**7a**).* Yellow solid. Yield 85%; m.p. 78–80 °C. *Anal.* Calc. for $C_{28}H_{32}FeN_2O_2$: C, 69.42; H, 6.66; N, 5.78. Found: C, 69.31; H, 6.60; N, 5.77%. IR(KBr) *v*: 2980(w), 2939(w), 2893(w), 1509(s), 1456(w), 1332(w), 1243(vs), 1183(m), 1039(m), 917(w), 810(s), 697(m) cm^{-1}. ^1H NMR ($CDCl_3$) δ: 2.73(s, 6H, H7, H7′), 3.76(s, 6H, OCH_3), 4.04(s, 4H, H2, H2′), 4.06(s, 4H, H3, H3′), 4.15(s, 4H, H4, H4′), 6.79(q, 8H, PhH) ppm.

*3.2.3.2. [Fe{(η⁵-C_5H_4)–$CH_2N(CH_3)$–$C_6H_4CH_3$-4}$_2$] (**7b**).* Yellow solid. Yield 78%; m.p. 84–86 °C. *Anal.* Calc. for $C_{28}H_{32}FeN_2$: C, 74.33; H, 7.13; N, 6.19. Found: C, 74.17; H, 7.12; N, 6.18%. IR(KBr) *v*: 3067(w), 3009(w), 2911(w), 2853(w), 1619(m), 1522(s), 1373(m), 1332(m), 1253(m), 1189(m), 1101(w), 830(m), 802(s) cm^{-1}. ^1H NMR ($CDCl_3$) δ: 2.25(s, 6H, Ar–CH_3), 2.80(s, 6H, H7, H7′), 4.05(s, 4H, H2, H2′), 4.09(s, 4H, H3, H3′), 4.22(s, 4H, H4, H4′), 6.72(q, 8H, PhH) ppm.

*3.2.3.3. [Fe{(η⁵-C_5H_4)–$CH_2N(CH_3)$–C_6H_4Cl-3}$_2$] (**7d**).* Yellow liquid. Yield 72%. *Anal.* Calc. for $C_{26}H_{26}Cl_2FeN_2$: C, 63.31; H, 5.31; N, 5.68. Found: C, 63.11; H, 5.29; N, 5.64%. IR (KBr) *v*: 3078(w), 2924(w), 2888(w), 1593(s), 1558(s), 1491(s), 1355(m), 1230(m), 1099(s), 986(s), 827(m), 756(m), 684(m) cm^{-1}. ^1H NMR ($CDCl_3$) δ: 2.89(s, 3H, H7), 2.96(s, 3H, H7, H7′), 4.13(s, 4H, H2, H2′), 4.18(s, 4H, H3, H3′), 4.28(s, 4H, H4, H4′), 6.67-7.19(m, 8H, PhH) ppm.

3.3. Preparation of 8a–c, 8e from diacetylferrocene (II)

3.3.1. Preparation of diketimines 2a–c, 2e from II

General procedure: to the stirred mixtures of diacetylferrocene in toluene and titanium tetrachloride (3% mol), were added 4 equivalents of anilines. The mixtures were refluxed for 6–8 h under argon. After the reactions completed, the mixtures were washed with water three times (3 × 100 ml). The organic phase was dried over anhydrous sodium sulfate and filtered. The solvent was removed under reduced pressure, and the residues were purified by flash chromatography (silica gel, ethyl acetate/hexane = 1:5) to give **2a**–**c**, **2e**.

*3.3.1.1. [Fe{(η⁵-C_5H_4)–$C(CH_3)$=N–$C_6H_4OCH_3$-4}$_2$] (**2a**).* Dark-red solid. Yield 65%; m.p. 182–184 °C (dec.) (lit. [18], >184 °C). IR(KBr) *v*: 3097(w), 2963(w), 2856(w), 1622(vs), 1504(vs), 1465(m), 1361(m), 1236(vs), 1197(m), 1032(m), 850(m), 833(m) cm^{-1}.

*3.3.1.2. [Fe{(η⁵-C_5H_4)–$C(CH_3)$=N–$C_6H_4CH_3$-4}$_2$] (**2b**).* Dark-red solid. Yield 65%; m.p. 144–146°C (lit. [18], 147–147.5 °C). IR(KBr) *v*: 3015(w), 2965(w), 2857(w), 1624(vs), 1504(m), 1460(m), 1287(m), 1117(m), 1036(w), 809(s) cm^{-1}.

*3.3.1.3. [Fe{(η⁵-C_5H_4)–$C(CH_3)$=N–C_6H_5}$_2$] (**2c**).* Dark-red solid. Yield 62%; m.p. 138–140 °C (lit. [18], 141.5–142.5 °C). IR(KBr) *v*: 3021(w), 2968(w), 2858(w), 1623(vs), 1502(m), 1458(m), 1285(m), 1117(m), 1035(w), 809(s) cm^{-1}.

*3.3.1.4. [Fe{(η⁵-C_5H_4)–$C(CH_3)$=N–C_6H_4Cl-4}$_2$] (**2e**).* Dark-red solid. Yield 58%, m.p. 183–185 °C (lit. [18], 184.5–185.5 °C). IR(KBr) *v*: 3023(m), 2969(w), 2861(w), 1623(s), 1494(vs), 1454(w), 1278(m), 1234(w), 1091(m), 825(m) cm^{-1}.

3.3.2. Preparation of 5a–c, 5e from 2a–c, 2e

General procedure: to the stirred solutions of **2a**–**c** and **2e** (10 mmol) in anhydrous THF (50 ml) was added aluminum chloride (3% mmol) and the resulted mixtures were continuously stirred for 30 min at room temperature. Then 20 mmol of lithium aluminum hydride was added in one portion and the mixtures were refluxed for 1 h under argon. The solvent was evaporated under reduced pressure to dryness, dichloromethane (120 ml) was then added and stirred for 1 h. The extraction phase was dried over sodium sulfate and filtered. Removal of solvent yielded residues which were purified by column chromatography (silica gel, ethyl acetate/hexane = 1:3) to yield **5a**–**c**, **5e**.

*3.3.2.1. [Fe{(η⁵-C_5H_4)–$CH(CH_3)NH$–$C_6H_4OCH_3$-4}$_2$] (**5a**).* Yellow liquid. Yield 86%. *Anal.* Calc. for $C_{28}H_{32}FeN_2O_2$: C, 69.42; H, 6.66; N, 5.78. Found: C, 69.31; H, 6.65; N, 5.78 %. IR(KBr) *v*: 3380(w), 3088(w), 2970(m), 2929(m), 2832(m), 1510(vs), 1469(m), 1408(w), 1232(s), 1182(m),

1126(m), 1037(s), 819(s) cm^{-1}. ^1H NMR ($CDCl_3$) δ: 1.43(d, 6H, H5, H5′), 3.75(s, 6H, OCH_3), 3.11(m, 2H, H4, H4′), 3.88(s, 2H, NH), 4.04(s, 4H, H2, H2′), 4.16(s, 4H, H3, H3′), 6.71(q, 8H, PhH) ppm.

*3.3.2.2. [Fe{(η^5-C_5H_4)–CH(CH_3)NH–$C_6H_4CH_3$-4}$_2$] (**5b**).* Yellow liquid. Yield 80%. *Anal.* Calc. for $C_{28}H_{32}FeN_2$: C, 74.33; H, 7.13; N, 6.19. Found: C, 74.19; H, 7.12; N, 6.16%. IR(KBr) *v*: 3404(m), 3094(w), 3023(w), 2961(m), 2913(m), 1616(s), 1517(vs), 1449(m), 1298(m), 1241(m), 1134(m), 1024(w), 807(s) cm^{-1}. ^1H NMR ($CDCl_3$) δ: 1.44(d, 6H, H5, H5′), 2.23(s, 6H, Ar–CH_3), 3.15(m, 2H, H4, H4′), 3.89(s, 2H, NH), 4.06(s, 4H, H2, H2′), 4.20(s, 4H, H3, H3′), 6.90(q, 8H, PhH) ppm.

*3.3.2.3. [Fe{(η^5-C_5H_4)–CH(CH_3)NH–C_6H_5}$_2$] (**5c**).* Yellow liquid. Yield 50%. *Anal.* Calc. for $C_{26}H_{28}FeN_2$: C, 73.59; H, 6.65; N, 6.60. Found: C, 73.40; H, 6.62; N, 6.58%. IR (KBr) *v*: 3405(m), 3083(w), 3047(w), 2970(m), 2924(w), 2863(w), 1601(vs), 1502(vs), 1424(m), 1367(m), 1313(s), 1249(m), 1129(m), 1029(m), 748(s), 691(s) cm^{-1}. ^1H NMR ($CDCl_3$) δ: 1.45(s, 6H, H5, H5′), 3.21(m, 2H, H4, H4′), 3.90(s, 2H, NH), 4.05(s, 4H, H2, H2′), 4.13(s, 4H, H3, H3′), 6.92(m, 10H, PhH) ppm.

*3.3.2.4. [Fe{(η^5-C_5H_4)–CH(CH_3)NH–C_6H_4Cl-4}$_2$] (**5e**).* Yellow liquid. Yield 89%. *Anal.* Calc. for $C_{26}H_{26}Cl_2FeN_2$: C, 63.31; H, 5.31; N, 5.68. Found: C, 63.17; H, 5.29; N, 5.66%. IR (KBr) *v*: 3411(m), 3083(w), 2965(m), 2924(w), 2868(w), 1598(s), 1497(s), 1393(m), 1315(m), 1239(m), 1168(m), 1093(m), 814(s) cm^{-1}. ^1H NMR ($CDCl_3$) δ: 1.46(d, 6H, H5, H5′), 3.10(q, 2H, H4, H4′), 3.91(s, 2H, NH), 4.08(s, 4H, H2, H2′), 4.19(s, 4H, H3, H3′), 7.03(q, 8H, ArH) ppm.

*3.3.3. Preparation of **8a–c, 8e** from **5a–c, 5e***

General procedure: the synthetic procedure for **8a–c**, **8e** was the same as described previously [7].

*3.3.3.1. [Fe{(η^5-C_5H_4)–CH(CH_3)N(CH_3)–$C_6H_4OCH_3$-4}$_2$] (**8a**).* Yellow solid. Yield 58%; m.p. 58–60 °C. *Anal.* Calc. for $C_{30}H_{36}FeN_2O_2$: C, 70.31; H, 7.08; N, 5.47. Found: C, 70.18; H, 7.06; N, 5.45%. IR(KBr) *v*: 3083(w), 2964(m), 2925(m), 2831(m), 1514(vs), 1441(m), 1246(s), 1181(m), 1039(s), 817(s), 683(m) cm^{-1}. ^1H NMR ($CDCl_3$) δ: 1.42(d, 6H, H5, H5′), 2.42(s, 6H, H7, H7′), 3.78(s, 6H, OCH_3), 4.05(s, 4H, H2, H2′), 4.17(s, 4H, H3, H3′), 4.89(m, 2H, H4, H4′), 6.78(q, 8H, PhH) ppm.

*3.3.3.2. [Fe{(η^5-C_5H_4)–CH(CH_3)N(CH_3)–$C_6H_4CH_3$-4}$_2$] (**8b**).* Yellow solid. Yield 55%; m.p. 46–48 °C. *Anal.* Calc. for $C_{30}H_{36}FeN_2$: C, 74.99; H, 7.55; N, 5.83. Found: C, 74.88; H, 7.52; N, 5.82%. IR(KBr) *v*: 3093(w), 2975(m), 2922(m), 2852(m), 2801(m), 1617(s), 1519(vs), 1444(w), 1342(m), 1296(m), 1229(m), 1106(m), 804(s) cm^{-1}. ^1H NMR ($CDCl_3$) δ: 1.45(d, 6H, H5, H5′), 2.26(s, 6H, Ar–CH_3), 2.44(s, 6H, H7, H7'), 4.07(s, 4H, H2, H2′), 4.18(s, 4H, H3, H3′), 4.93(m, 2H, H4, H4′), 6.88(q, 8H, PhH) ppm.

*3.3.3.3. [Fe{(η^5-C_5H_4)–CH(CH_3)N(CH_3)–C_6H_5}$_2$] (**8c**).* Yellow liquid. Yield 56%. *Anal.* Calc. for $C_{28}H_{32}FeN_2$: C, 74.33; H, 7.13; N, 6.19. Found: C, 74.19; H, 7.10; N, 6.17%. IR (KBr) *v*: 3032(w), 2975(w), 2924(w), 2873(w), 1601(vs), 1507(vs), 1439(m), 1346(s), 1224(m), 1188(m), 988(m), 750(s), 691(s) cm^{-1}. ^1H NMR ($CDCl_3$) δ: 1.50(s, 6H, H5, H5′), 2.51(s, 6H, H7, H7′), 4.05(s, 4H, H2, H2′), 4.11(s, 4H, H3, H3′), 5.10(m, 2H, H4, H4′), 6.95–7.21(m, 10H, PhH) ppm.

*3.3.3.4. [Fe{(η^5-C_5H_4)–CH(CH_3)N(CH_3)–C_6H_4Cl-4}$_2$] (**8e**).* Yellow solid. Yield 53%; m.p. 78–80 °C. *Anal.* Calc. for $C_{28}H_{30}Cl_2FeN_2$: C, 64.51; H, 5.80; N, 5.37. Found: C, 64.44; H, 5.80; N, 5.36%. IR (KBr) *v*:3035(w), 2978(w), 2920(w), 2873(w), 1598(s), 1505(s), 1437(m), 1346(s), 1185(m), 986(m), 820(s), 691(s)cm^{-1}. ^1H NMR ($CDCl_3$) δ: 1.47(d, 6H, H5, H5′), 2.49 (s, 6H, H7, H7′), 4.06(s, 4H, H2, H2′), 4.19(s, 4H, H3, H3′), 5.11(s, 2H, H4, H4′), 6.95(q, 8H, PhH) ppm.

*3.4. Preparation of **6f–g** from dibenzoylferrocene (**III**)*

*3.4.1. Preparation of diketimines **3f–g** from **III***

General procedure: the synthetic procedure for **3f–g** was the same as that for **2**.

*3.4.1.1. [Fe{(η^5-C_5H_4)–C(C_6H_5)=N–$CH_2C_6H_4CH_3$-4}$_2$] (**3f**).* Dark-red solid. M.p.101–103 °C; Yield 78%. *Anal.* Calc. for $C_{40}H_{36}FeN_2$: C, 80.00; H, 6.04; N, 4.66. Found: C, 79.89; H, 6.03; N, 4.65%. IR (KBr) *v*: 3028(w), 2916(m). 2862(w), 1622(vs), 1503(m), 1458(m), 1285(m), 1115(m), 1034(w), 810(s). ^1H NMR ($CDCl_3$) δ: 2.01(s, 6H, Ar–CH_3), 3.67(q, 4H, H6, H6′), 3.93(s, 4H, H3, H3′), 4.16(s, 4H, H2, H2′), 6.71(q, 8H, PhH), 7.03(m, 10H, PhH) ppm.

*3.4.1.2. [Fe{(η^5-C_5H_4)–C(C_6H_5)=N–$CH_2C_6H_5$}$_2$] (**3g**).* Red-dark solid. M.p. 99–101 °C; Yield 69%. *Anal.* Calc. for $C_{38}H_{32}FeN_2$: C, 79.72; H, 5.63; N, 4.89. Found: C, 79.67; H, 5.62; N, 4.89%. IR (KBr) *v*: 3024(w), 2918(w), 2858(w), 1623(vs), 1501(m), 1458(m), 1283(m), 1116(m), 1033(w), 821(m), 690(m). ^1H NMR ($CDCl_3$) δ: 3.65(q, 4H, H6, H6′), 3.91(s, 4H, H3, H3′), 4.14(s, 4H, H2, H2′), 7.01 (m, 20H, PhH) ppm.

*3.4.2. Preparation of **6f–g** from **3f–g***

The synthetic procedure for **6f–g** was the same as that for **5**.

*3.4.2.1. [Fe{(η^5-C_5H_4)–CH(C_6H_5)NH–$CH_2C_6H_4CH_3$-4}$_2$] (**6f**).* Yellow liquid. Yield 76%. *Anal.* Calc. for $C_{40}H_{40}FeN_2$: C, 79.46; H, 6.67; N, 4.63. Found: C, 79.28; H, 6.64; N, 4.62%. IR (KBr) *v*: 3394(m), 3083(w), 2917(w), 2859(w), 1515(vs), 1458(w), 1314(m), 1245(m),

1181(w), 1034(w), 806(s) cm^{-1}. ^1H NMR ($CDCl_3$) δ: 2.15(s, 6H, Ar–CH_3), 2.30(m, 2H, NH), 3.49(m, 4H, H6, H6′), 3.90(s, 4H, H2, H2′), 4.13(s, 4H, H3, H3′), 4.37(s, 2H, H4, H4′), 6.66(q, 8H, PhH), 6.98(m, 10H, PhH) ppm.

*3.4.2.2. [Fe{(η^5-C_5H_4)–CH(C_6H_5)NH–$CH_2C_6H_5$}$_2$] (**6g**).* Yellow liquid. Yield 70%. *Anal.* Calc. for $C_{38}H_{36}FeN_2$: C, 79.16; H, 6.29; N, 4.86. Found: C, 79.01; H, 6.25; N, 4.83%. IR (KBr) *v*: 3401(m), 3085(w), 3044(w), 2979(m), 2922(w), 2861(w), 1601(vs), 1500(vs), 1434(m), 1365(m), 1311(s), 1245(m), 1130(m), 1029(m), 748(s), 692(s) cm^{-1}.^1H NMR ($CDCl_3$) δ: 2.28(m, 2H, NH), 3.52(q, 4H, H6, H6′), 3.91(s, 4H, H2, H2′), 4.14(s, 4H, H3, H3′), 4.39(s, 2H, H4, H4′), 6.95(m, 20H, PhH) ppm.

3.5. Crystal structure determination for 3g and 7a

The prismatic single crystals of **3g** and **7a** suitable for X-ray analysis were obtained by slow evaporation of the mixture of ethyl acetate and hexane at room temperature over a period of 1 week. The single crystals of **3g** and **7a** were mounted on a Bruker SMART CCD diffractometer equipped with graphite-monochromated Mo Kα radiation ($\lambda = 0.71073$ Å) at ambient temperature ($T = 293$ K for **3g** and 294 K for **7a**) using the ω-2θ multi-scans technique with the range of $2.05° \leqslant \theta \leqslant 25.03°$ (**3g**), $2.16° \leqslant \theta \leqslant 25.02°$ (**7a**) for data collection. Semi-empirical absorption corrections were applied using the SABABS program [19]. The structures were solved by direct methods and refined by the full-matrix least-squares procedure on F^2 using the SHELX suite of programs [20]. The values of R_1 were given based on F_o with a typical threshold of $F^2 \geqslant 2\sigma(F^2)$. The weighted *R*-factors *wR* were based on F^2 with $w = 1/[\sigma^2(F_o^2) + (0.0376P)^2 + 0.2035P]$ where $P = (F_o^2 + 2F_c^2)/3$ for **3g**, $w = 1/[\sigma^2(F_o^2) + (0.0587P)^2 + 2.9596P]$ where $P = (F_o^2 + 2F_c^2)/3$ for **7a**. Crystallographic data for **3g** and **7a** are summarized in Table 1. Selected bond lengths and angles for **3g** and **7a** are presented in Table 2.

Supplementary material

CCDC 614253 and 613898 contain the supplementary crystallographic data for **3g** and **7a**. These data can be obtained free of charge via http://www.ccdc.cam.ac.uk/conts/retrieving.html, or from the Cambridge Crystallographic Data Centre, 12 Union Road, Cambridge CB2 1EZ, UK; fax: (+44) 1223-336-033; or e-mail: deposit@ccdc.cam.ac.uk.

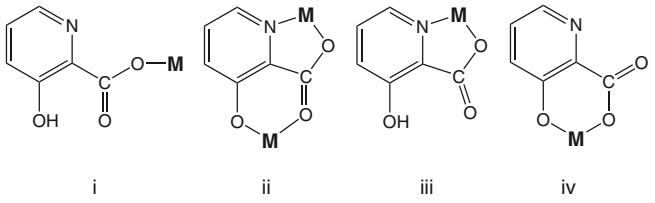
Acknowledgements

We are grateful to the Natural Scientific Foundation of Tianjin Metropolitan Council (Project No. 033609011), People's Republic of China and the Opening Fund from the State Key Laboratory of Elemento-organic Chemistry, Nankai University, People's Republic of China for their generous support for this project.

References

[1] (a) O.B. Sutcliffe, M.R. Bryce, Tetrahedron: Asymmetry 14 (2003) 2297;
(b) L.X. Dai, T. Tu, S.L. You, W.P. Deng, X.L. Hou, Acc. Chem. Res. 36 (2003) 659;
(c) T.J. Colacot, Chem. Rev. 103 (2003) 3101.
[2] (a) S.W. Lee, J. Organomet. Chem. 691 (2006) 1347;
(b) D. Tremblay, F.B. Barrett, N.J. Taylor, J. Organomet. Chem. 691 (2006) 2044;
(c) Z. Weng, S. Teo, L.L. Koh, T.S. Andy Hor, Organometallics 23 (2004) 3603;
(d) V.C. Gibson, N.J. Long, E.L. Marshall, P.J. Oxford, A.J.P. White, D.J. Williams, J. Chem. Soc., Dalton Trans. (2001) 1162.
[3] (a) J. Park, S. Lee, K.H. Ahn, C.W. Cho, Tetrahedron Lett. 36 (1995) 7263;
(b) J. Park, S. Lee, K.H. Ahn, C.W. Cho, Tetrahedron Lett. 37 (1996) 6137;
(c) N.W. Duffy, J. Harper, P. Ramani, R. Ranatunge-Bandarage, B.H. Robinson, J. Simpson, J. Organomet. Chem. 564 (1998) 125;
(d) L. Schwink, P. Knochel, Chem. Eur. J. 4 (1998) 950;
(e) A. Boudier, L.O. Bromm, M. Lotz, P. Knochel, Angew. Chem. Int. Ed. 39 (2000) 4414;
(f) M. Lotz, T. Ireland, J.J.A. Perea, P. Knochel, Tetrahedron: Asymmetry 10 (1999) 1839;
(g) J.J.A. Perea, A. Borner, P. Knochel, Tetrahedron Lett. 39 (1998) 8073;
(h) J.J.A. Perea, M. Lotz, P. Knochel, Tetrahedron: Asymmetry 10 (1999) 375;
(i) J. Kang, J.H. Lee, S.H. Ahn, J.S. Choi, Tetrahedron Lett. 39 (1998) 5523;
(j) O.B. Sutcliffe, M.R. Bryce, Tetrahedron: Asymmetry 14 (2003) 229.
[4] (a) J. Park, Z. Quan, S. Lee, K.H. Ahn, C.-W. Cho, J. Organomet. Chem. 584 (1999) 140;
(b) W. Zhang, Y. Adachi, T. Hirao, I. Ikeda, Tetrahedron: Asymmetry 7 (1996) 451;
(c) W. Zhang, T. Hirao, I. Ikeda, Tetrahedron Lett. 37 (1996) 4545.
[5] (a) Y.J. Wu, X.L. Cui, N. Zhou, M.P. Song, H.Y. Yun, C.X. Du, Y. Zhu, Tetrahedron: Asymmetry 11 (2000) 4877;
(b) R. Bosque, C. Lopez, X. Solans, M. Font-Bardia, Organometallics 18 (1999) 1267;
(c) K. McGrouther, D.K. Weston, D. Fenby, B.H. Robinson, J. Simpson, J. Chem. Soc., Dalton Trans. (1999) 1957;
(d) P.R.R. Ranatunge-Bandarage, B.H. Robinson, J. Simpson, Organometallics 13 (1994) 405.
[6] H.X. Wang, L. Ding, Y.J. Wu, J. Organomet. Chem. 679 (2003) 130.
[7] H.X. Wang, Y.J. Li, R. Jin, J.R. Niu, H.F. Wu, H.C. Zhou, J. Xu, R.Q. Gao, F.Y. Geng, J. Organomet. Chem. 691 (2006) 987.
[8] (a) H.X. Wang, Y.J. Li, R.Q. Gao, H.F. Wu, F.Y. Geng, R. Jin, Inorg. Chem. Commun. 9 (2006) 658;
(b) H.X. Wang, H.F. Wu, H.C. Zhou, R. Jin, R.Q. Gao, F.Y. Geng, J. Xu, Y.J. Li, W.Q. Zhang, Polyhedron 25 (2006) 2530;
(c) H.X. Wang, Y.J. Li, H.F. Wu, R.Q. Gao, F.Y. Geng, X.L. Yang, L.Wan, R.Jin, X.L. Cui, Y.J. Wu, Polyhedron, 25 (2006), in press;
(d) H.X. Wang, H.F. Wu, H.C. Zhou, F.Y. Geng, R.Q. Gao, X.L. Yang, L. Wan, W.Q. Zhang, R. Jin, Inorg. Chim. Acta 359 (2006) 4114.
[9] H.F. Wu, H.X. Wang, R.Q. Gao, F.Y. Geng, X.L. Yang, L. Wan, unpublished results.
[10] (a) S.Q. Huo, Y.J. Wu, X.A. Mao, H.Z. Yuan, Tetrahedron 50 (1994) 10467;
(b) R. Bosque, C. Lopez, J. Sales, X. Solans, J. Organomet. Chem. 483 (1994) 61.
[11] R.F. Borch, A.I. Hassid, J. Org. Chem. 37 (1972) 1673.
[12] M.A. Carroll, A.J.P. White, D.A. Widdowson, D.J. Williams, J. Chem. Soc., Perkin Trans. 1 (2000) 1551.

[13] R. Baltzly, P. Russel, J. Am. Chem. Soc. 75 (1953) 5598.
[14] (a) Y.J. Li, H.X. Wang, H.F. Wu, Acta Crystallogr. E61 (2005) m1579;
(b) H.X. Wang, Y.J. Li, J.F. Hou, Acta Crystallogr. E61 (2005) m1785;
(c) H.X. Wang, Y.J. Li, H.F. Wu, H.C. Zhou, R.Q. Gao, F.Y. Geng, Acta Crystallogr. E61 (2005) m1871;
(d) H.X. Wang, Y.J. Li, H.F. Wu, H.C. Zhou, F.Y. Geng, R.Q. Gao, Acta Crystallogr. E61 (2005) m2322;
(e) H.X. Wang, R.Q. Gao, H.F. Wu, F.Y. Geng, X.L. Yang, Acta Crystallogr. E62 (2006) m1494.
[15] T.H. Allen, O. Kennard, Chem. Design Automation News 8 (1993) 146.
[16] G.G.A. Balavoine, G. Doisneau, T. Fillebeen-Khan, J. Organomet. Chem. 412 (1992) 381.
[17] M. Vogel, M. Rausch, H. Rosenberg, J. Organomet. Chem. 22 (1957) 1016.
[18] Y.H. Liu, Y.J. Wu, H.Y. Yun, L. Yang, Q.S. Zhu, Chem. J. Chinese Univ. 17 (1996) 1225.
[19] G.M. Sheldrick, SADABS, University of Göttingen, 1996.
[20] G.M. Sheldrick, SHELXS-97 and SHELXL-97, programs for crystal structure solution and refinement, University of Göttingen, 1997.



Scheme 1.

manganese and copper [9,10]. In $[CdX(picOH)(HpicOH)(H_2O)]_2$ ($X = Cl^-$, Br^-) we established two modes of HpicOH binding: *N*,*O*-chelating and *O*-monodenate with the pyridine nitrogen atom protonated [11].

Our former investigations pointed out that the mercury(II) ion is capable of forming various binding coordination modes with *N*,*O*-donor atoms when provided by suitable ligands [12–16]. Our present interest on mercury(II) coordination complexes has been directed towards the understanding of the competition between halide ions and ligands containing *N*,*O*-donors for coordination sites of the mercury(II) ion. So far, we found that the tendency of mercury to achieve effective coordination by spatial arrangement of donor atoms of different types of acids, leads to various, mostly highly irregular, coordination polyhedra of mercury. Mono- and dicarboxylic acids containing a pyridine ring, or their hydroxy derivatives, are good ligand systems with *N*,*O*-donor atoms at appropriate sites for modelling various mercury coordination polyhedra in discrete or polymeric complexes of the formulas HgXL, HgX_2L or HgX(L)(LH) (LH and L stand for the protonated and deprotonated form of the ligand, respectively, $X = Cl^-$, Br^-, I^-, SCN^-).

Our wider interest includes investigation of toxicity effects of various metal complexes of the 12th group of elements on microbial communities. For such a study well characterized complexes are needed. This paper describes new mercury(II) complexes with 3-hydroxypicolinic acid. They were synthesized, identified by chemical analysis, characterized by the appropriate spectroscopic methods, both in solution and in the solid state, and two crystal structures were determined by the X-ray diffraction method.

2. Experimental

2.1. Materials and physical measurements

All reagents were supplied by Aldrich Chemical Co. and were used as received without further purification. The CHN-microanalyses were measured by the Central Analytical Service of the Ruđer Bošković Institute, Zagreb. The mercury content in the complexes was determined by complexometric titration with sodium diethyldithiocarbamate of the solution obtained after decomposition of the specimen in *aqua regia* [17].

Pressed KBr pellets were used for IR measurements within the range 4000–400 cm^{-1} with a Perkin–Elmer FT-IR spectrometer 1600 Series.

The one- and two-dimensional homo- and heteronuclear ^1H and ^{13}C NMR spectra were recorded with a Bruker AV 600 spectrometer, operating at 600.133 MHz for the ^1H nucleus and 150.917 MHz for the ^{13}C nucleus. Samples were measured from DMSO-d_6 solutions at 22 °C (295 K) in 5 mm NMR tubes. Chemical shifts, in ppm, are referred to TMS as internal standard. FID resolution in ^1H NMR and ^{13}C NMR spectra was 0.29 and 0.54 Hz per point, respectively. The following measurement techniques were used: standard ^1H, ^{13}C gated proton decoupling, APT, COSY, HMQC and HMBC. The 2D NMR spectra were measured in the pulsed field gradient mode (*z*-gradient).

X-ray and NMR data are given in Tables 1 and 2, respectively.

Table 1
General and crystal data, summary of intensity data collection and structure refinement of compounds **1** and **2**

	1	**2**
Formula	$C_6H_4ClHgNO_3$	$C_6H_5Br_2HgNO_3$
M_r	374.14	499.52
Temperature (K)	293(2)	296(2)
Wavelength (Å)	0.71073	0.71073
Color	colorless	colorless
Crystal system	monoclinic	monoclinic
Space group	$P2_1/c$	$P2_1/c$
Unit cell parameters		
a (Å)	10.4838(19)	10.0030(13)
b (Å)	7.9647(12)	4.1601(5)
c (Å)	9.8583(16)	23.720(3)
β (°)	106.206(18)	97.378(10)
V (Å^3)	790.5(2)	978.9(2)
Z	4	4
D_{calc} (g cm^{-3})	3.144	3.389
F(000)	672	888
Crystal size (mm^3)	$0.173 \times 0.111 \times 0.022$	$0.412 \times 0.111 \times 0.070$
θ Range for data collection (°)	4.8, 30.0	4.66, 26.98
Number of measured reflections	27,119	12,503
Number of independent reflections	2295	2114
Number of observed reflections, $I \geqslant 2\sigma(I)$	2092	2006
Number of parameters	110	123
Absorption correction	integration	integration
μ (mm^{-1})	19.769	23.859
Range of transmission factors	0.027, 0.427	0.050, 0.191
R[a], wR[b] [$I \geqslant 2\sigma(I)$]	0.0266, 0.0308	0.0506, 0.0525
R, wR (all data)	0.0621, 0.0639	0.1320, 0.1347
g_1, g_2 in w[c]	0.0344, 0.9218	0.0768, 5.3103
Goodness-of-fit on F^2, S[d]	1.124	1.134
Minimum and maximum electron density (e Å)[e]	−1.68, 2.61	−3.185, 1.831

[a] $R = \sum||F_o| - |F_c|/\sum|F_o|$.

[b] $wR = \left[\sum(F_o^2 - F_c^2)^2/\sum w(F_o^2)^2\right]^{1/2}$.

[c] $w = 1/[\sigma^2(F_o^2)] + [g_1P + g_2P]$ where $P = (F_o^2 + 2F_c^2)/3$.

[d] $S = \sum[w(F_o^2 - F_c^2)^2/(N_{obs} - N_{param})]^{1/2}$.

[e] The maximum electron density in the last difference Fourier map is near Hg.

2.2. HgCl(picOH) (1)

To an aqueous solution of mercury(II) chloride (0.30 g; 1.1 mmol in 15 ml H_2O) an aqueous solution of 3-hydroxypicolinic acid was added dropwise (0.16 g; 1.15 mmol in 15 ml H_2O). The reaction mixture was allowed to stand for a few days at room temperature to crystallize. The crystalline product was filtered off, washed with cold water and dried in a desiccator. Yield: 0.31 g (75.6%). *Anal.* Calc. for $C_6H_4ClHgNO_3$ (mol. wt. 374.14): C, 19.26; H, 1.08; N, 3.74; Hg, 53.61. Found: C, 19.38; H, 1.18; N, 3.67; Hg, 53.81%. IR max. (cm^{-1}): 3087w, 1621vs, 1601s, 1570s, 1527m, 1476s, 1456vs, 1375vs, 1312vs, 1249s, 1229s, 1149m, 1064w, 893m, 872m-w, 829s, 805m-s, 692s, 578m.

When the same reaction is performed in ethanol **1** is also obtained, however the yield is better from aqueous solution.

2.3. $HgBr_2$(HpicOH) (2)

To an ethanolic solution of mercury(II) bromide (0.3 g; 0.83 mmol in 15 ml of EtOH) an ethanolic solution of 3-hydroxypicolinic acid was added dropwise (0.12 g; 0.86 mmol in 25 ml EtOH). The reaction mixture was left to stand for a few days. The crystalline product was filtered off, washed with cold ethanol and dried. Yield: 0.37 g (90.5%). *Anal.* Calc. for $C_6H_5Br_2HgNO_3$ (mol. wt. 499.52): C, 14.43; H, 1.01; N, 2.80; Hg, 40.16. Found: C, 14.13; H, 1.07; N, 3.15; Hg, 40.07%. IR max. (cm^{-1}): 3585m, sharp, 3526m, sharp, 3065m-w, 2856w, br, 1655s, 1613s, 1534s, 1470s, 1412s, 1377m, 1335s, 1283s, 1252m, 1214m, 1152m, 1120m-w, 1048m-w, 874s, 816vs, 802s, 682s, 667vs, 576w, 549w, 446m.

The same reaction performed in an aqueous solution also results in **2**, but with traces of unreacted $HgBr_2$ which is less soluble in water than ethanol.

2.4. Hg(picOH)$_2$ (3) and Hg(picOH)$_2 \cdot H_2O$ (3a)

To an aqueous solution of mercury(II) acetate (0.3 g; 0.94 mmol in 15 ml H_2O with a few drops of 2 M acetic acid) an aqueous solution of 3-hydroxypicolinic acid was added (0.3 g; 2.15 mmol in 15 ml H_2O). The yellowish product was filtered off, washed with water and dried. Yield (**3**): 0.40 g (88.9%). From the reaction of 3-hydroxypicolinic acid (0.24 g; 1.72 mmol in 15 ml H_2O) and mercury(II) nitrate monohydrate (0.3 g; 0.86 mmol in 15 ml H_2O with a few drops of 20% nitric acid) the 1/1 solvate of $Hg(picOH)_2$ with water was obtained. Yield (**3a**): 0.38 g (87.8%). *Anal.* Calc. for $C_{12}H_8HgN_2O_6$ (mol. wt.

Table 2
^1H and ^{13}C NMR chemical shifts (δ/ppm)[a] and mercury induced chemical shifts ($\Delta\delta$/ppm),[b] H–H coupling constants ($^nJ_{HH}$/Hz)[c] and C–H coupling constants ($^nJ_{CH}$/Hz)[c] of 3-hydroxypicolinic acid (HpicOH) and its mercury compounds

Molecule Atom		HpicOH	HgCl(picOH) **1**	$HgBr_2$(HpicOH) **2**	Hg(picOH)$_2$ **3**
H-2,3	δ	14.81 (bs)	15.42 (bs)	14.34 (bs)	15.31 (bs)
	$\Delta\delta$		0.61	−0.47	0.50
H-4	Δ	7.76	7.65	7.74	7.78
	$^3J_{HH}$	8.55 (d)	8.44 (d)	8.43 (d)	8.46 (d)
	$\Delta\delta$		−0.11	−0.02	0.02
H-5	Δ	7.70	7.74	7.76	7.88
	$^3J_{HH}$	8.61; 5.07 (dd)	8.19; 5.02 (dd)	8.55; 4.93 (dd)	8.05; 5.10 (dd)
	$\Delta\delta$		0.04	0.06	0.18
H-6	Δ	8.05	8.26	8.13	8.29 (bs)
	$^3J_{HH}$	4.94 (d)	4.20 (d)	4.80 (d)	
	$\Delta\delta$		0.21	0.08	0.24
C-2	δ	129.42 (s)	131.21 (s)	129.55 (s)	131.11 (s)
	$\Delta\delta$		1.79	0.13	1.69
C-3	δ	160.17 (s)	160.62 (s)	159.87 (s)	160.63 (s)
	$\Delta\delta$		0.45	−0.30	0.46
C-4	δ	131.92	129.98	131.73	130.04
	J_{CH}	168.06 (d)	169.90 (d)	168.19 (d)	167.34 (d)
	$\Delta\delta$		−1.94	−0.19	−1.88
C-5	Δ	129.63	130.01	129.83	130.41
	J_{CH}	170.48 (d)	167.61 (d)	171.11 (d)	170.25 (d)
	$\Delta\delta$		0.38	0.20	0.78
C-6	Δ	133.56	139.94	135.16	140.02
	J_{CH}	189.93 (d)	190.64 (d)	190.94 (d)	189.94 (d)
	$\Delta\delta$		6.38	1.60	6.46
COOH	δ	165.93 (s)	168.03 (s)	165.93 (s)	168.09 (s)
	$\Delta\delta$		2.46	0.36	2.52

[a] Recorded in DMSO-d_6 solutions. Referred to TMS.
[b] Mercury induced chemical shifts ($\Delta\delta$/ppm) are obtained by subtracting the chemical shifts of the parent compound (HpicOH) from the chemical shifts of the Hg-compounds. Sign (+) denotes deshielding effect, while (−) denotes shielding effect of mercury.
[c] *n* Denotes the number of bonds between nuclei in spin–spin coupling; (s) singlet, (d) doublet.

476.80): C, 30.23; H, 1.69; N, 5.88; Hg, 42.07. Found: C, 30.37; H, 1.75; N, 5.92; Hg, 42.18%. IR max. (cm^{-1}): 3435m, br, 3100m, br, 2935w, 1647vs, 1597s, 1572m, 1470s, 1455s, 1400s, 1380s, 1314s, 1248m, 1230s, 1147m, 1066w, 991w, 939w, 917w-m, 890s, 821s, 691s, 579m-w, 561w. *Anal.* Calc. for $C_{12}H_{10}HgN_2O_7$ (mol. wt. 494.82): C, 29.13; H, 2.04; N, 5.66; Hg, 40.54. Found for: C, 29.25; H, 1.93; N, 5.62; Hg, 40.24%. IR max. (cm^{-1}): 3436m, br, 3030w, 2924w, 1636s, 1590m-s, 1470m, 1455s, 1381s, 1312s, 1229m, 1144m-w, 1040w, 1000w, 980vw, 918w, 886m, 819m, 800m, 687m, 670w, 578w, 542w, 448w.

2.5. X-ray crystallographic structure determination of *1* and *2*

The general and crystal data, and summary of intensity data collection and structure refinement for compounds **1** and **2** are given in Table 1.

The data collection for both structures was carried out on an Oxford Diffraction Xcalibur four-circle kappa geometry single-crystal diffractometer with Sapphire 3 CCD detector, by applying the CrysAlis Software system [18]. A crystal-detector distance of 60 mm and ω scan type was used for both structures. Data reduction, including absorption correction, was done by the CrysAlis RED application of the CrysAlis Software system [18]. Coordinates of the non-hydrogen atoms were determined by direct methods using the SHELXS program [19]. The coordinates and anisotropic thermal displacement parameters for all non-hydrogen atoms were refined by the least-squares methods based on F^2 using the SHELXL97 program [20]. The coordinates of the hydrogen atom belonging to the nitrogen atom in **2** were found by examination of the electron-density Fourier map at the final stages of refinement and were refined freely [the bond distance is 0.8(1) Å]. The other hydrogen atoms which belong to the pyridine carbon atoms, as well as the hydroxyl hydrogen atom, were generated at ideal geometrical positions [Csp^2–H 0.93 Å, $U_{iso}(H) = 1.2\ U_{eq}(C)$; O–H 0.82 Å; $U_{iso}(H) = 1.5\ U_{eq}(O)$], and were refined applying the riding model. The molecular graphics were created by means of the PLATON98 program [21].

3. Results and discussion

3.1. Preparation

Compound **1** HgCl(picOH) was obtained from the reaction of 3-hydroxypicolinic acid (HpicOH) with mercury(II) chloride in an aqueous solution. Similarly, reaction with $HgBr_2$ in ethanolic solution gave $HgBr_2$(HpicOH) (**2**). In both cases the reaction products were not influenced by the molar ratio of reactants (1:1 or 2:1). Both mercury(II) acetate and nitrate monohydrate react with HpicOH in aqueous media giving typical metal carboxylates i.e. $Hg(picOH)_2$ (**3**) and $Hg(picOH)_2 \cdot H_2O$ (**3a**), respectively. All the isolated compounds are soluble in solvents with pronounced coordination properties such as dimethyl sulfoxide (DMSO), *N*,*N*-dimethyl formamide (DMF) or pyridine. Crystals suitable for X-ray diffraction studies were obtained from the mother liquor for compounds **1** and **2**, but all our attempts to prepare crystals of compounds **3** and **3a** failed.

3.2. Structural description of *1* and *2*

In **1** the shortest bonds to Hg are from nitrogen and chlorine atoms (Hg–N 2.143(4) and Hg–Cl 2.298(1) Å) giving a

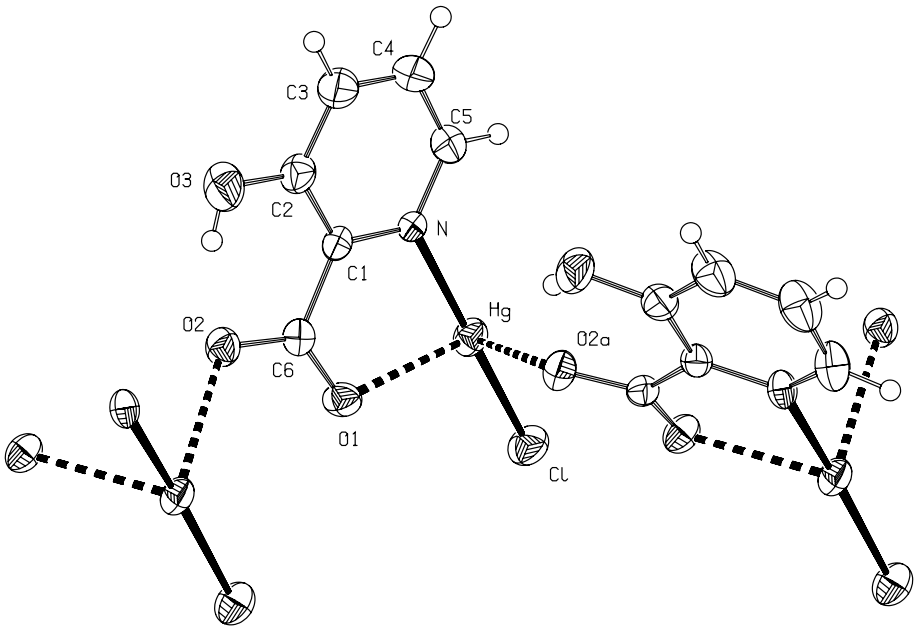


Fig. 1. Drawing of HgCl(picOH) (**1**) with the atom labelling scheme. The thermal ellipsoids are at the 50% probability level. Dashed lines represent Hg···O contacts. Symmetry operation: $a = x$, $0.5 - y$, $z - 0.5$.

Table 3
Selected interatomic distances (Å) and angles (°) for **1**

Interatomic distances		Bond angles	
Hg–N	2.143(4)	N–Hg–Cl	172.68(10)
Hg–Cl	2.2975(13)	N–Hg–O1	73.47(12)
Hg···O1	2.460(3)	Cl–Hg–O1	109.95(8)
Hg···O2^{i}	2.609(3)	N–Hg–O2^{i}	85.13(12)
Hg···O2^{ii}	2.888(3)	Cl–Hg–O2^{i}	101.40(8)
Hg···O1^{iii}	2.904(3)	O1–Hg–O2^{i}	83.38(10)
N–C1	1.345(5)		
N–C5	1.331(6)		
O1–C6	1.248(5)		
O2–C6	1.266(5)		
O3–C2	1.339(6)		

Symmetry transformations used to generate equivalent atoms: (i) x, $0.5 - y$, $z - 0.5$; (ii) $1 - x$, $1 - y$, $2 - z$; (iii) $1 - x$, $1/2 + y$, $3/2 - z$.

Table 4
Selected interatomic distances (Å) and angles (°) for **2**

Bond distances		Bond angles	
Hg–Br1	2.2766(10)	Br1–Hg–Br2	168.22(4)
Hg–Br2	2.3660(10)	Br1–Hg–O1	87.99(18)
Hg···O1	2.602(7)	Br2–Hg–O1	103.63(18)
Hg···Br1^{i}	3.3093(10)		
Hg···Br2^{ii}	3.2469(10)		
Hg···Br2^{iii}	3.8475(10)		
N–C5	1.324(12)		
N–C1	1.492(13)		
O1–C6	1.405(12)		
O2–C6	1.211(12)		
O3–C2	1.481(13)		

Symmetry transformations used to generate equivalent atoms: (i) x, $y - 1$, z; (ii) x, $1 + y$, z; (iii) $-x$, $1/2 + y$, $-1/2 - z$.

slightly distorted characteristic linear coordination, N–Hg–Cl 172.7(1)° [22,23]. These bonds are slightly longer than the sum of the covalent radii of the corresponding atoms because of the additional Hg···O contacts. Both carboxylate oxygen atoms of the deprotonated picolinic acid are involved in coordination to two neighboring mercury atoms (Hg···O1 2.460(3) and Hg···O2 (x, $0.5 - y$, $z - 0.5$) 2.609(3) Å) thus bridging them and forming infinite zigzag chains along the b axis, Fig. 1. Relevant bond distances and bond angles are shown in Tables 3 and 4. Besides the two already mentioned, there are two more long Hg···O contacts (Hg···O2 ($1 - x$, $1 - y$, $2 - z$) 2.888(3) Å and Hg···O1 ($1 - x$, $0.5 + y$, $1.5 - z$) 2.904(3) Å), still shorter than the sum of van der Waals radii (r_{VDW}(Hg) = 1.55–1.65 Å; r_{VDW}(O) = 1.40–1.52 Å) [22–25]. All contacts fulfill the effective coordination sphere of mercury, which is therefore 2 + 4. This behavior is in agreement with Grdenić's classification of a characteristic and effective coordination sphere of mercury in crystal structures [22,23]. Through these contacts (Fig. 2), infinite two-dimensional layers are formed. There is an intramolecular hydrogen bond connecting the hydroxyl and carboxylic group, O3–H···O2 of 2.542(5) Å. The intermolecular hydrogen bonds are very weak (Table 5). A similar coordination, yet with slightly longer covalent Hg–N and Hg–Cl bonds than in **1**, is found in the structure of (pyda · H)$_2$[Hg(pydc)Cl$_2$ · 2H$_2$O] (pyda = 2,6-pyridinediamine; pydc = 2,6-pyridinedicarboxylic acid). In this structure the distances amount to 2.198(6)

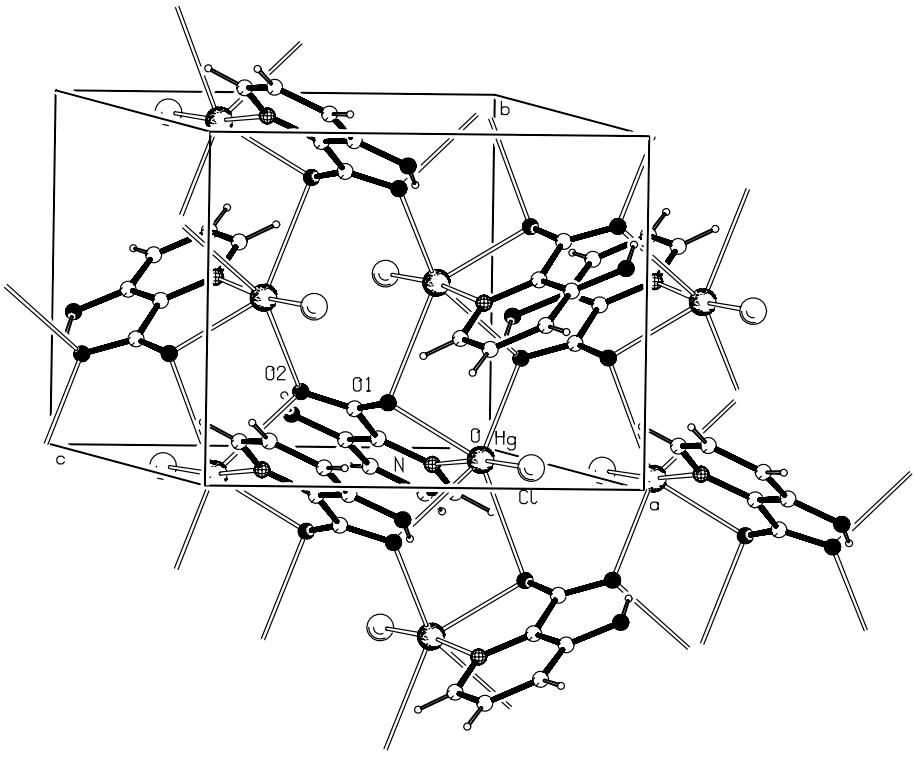


Fig. 2. Packing of molecules of HgCl(picOH) (**1**) in the unit cell, including one polymeric layer. The deformed octahedral geometry around Hg is shown by double lines.

Table 5
Hydrogen bond geometry (distances (Å), angles (°)) in **1** and **2**

D–H···A	D···A	D–H···A
1		
O3–H···O2	2.542(5)	143
C4–H···O3^{i}	3.443(7)	165
C5–H···Cl^{ii}	3.414(5)	131
2		
O3–H···O1	2.334(11)	138
N–H···O2	2.662(10)	116(13)
N–H···O2^{iii}	2.737(12)	133(14)
C3–H···Br2^{iv}	3.495(12)	140

Symmetry transformations used to generate equivalent atoms: (i) $-x$, $1/2+y$, $3/2-z$; (ii) $1-x$, $1-y$, $1-z$; (iii) $-1-x$, $-y$, $-z$; (iv) $-x$, $1-y$, $-z$.

and 2.310(2) Å, respectively [26]. The greater elongation is caused by four Hg···O contacts that are in the range 2.488(5)–2.659(5) Å.

Structure of **2** consists of polymeric chains (Fig. 3). There are two covalent bonds, Hg–Br1 2.277(1) and Hg–Br2 2.366(1) Å forming the linear characteristic coordination, Br1–Hg–Br2 168.22(4)° (Table 4). The effective coordination sphere of mercury can be described as irregular 2 + 3, consisting of three weak additional contacts, two with bromine atoms from adjacent molecules (Hg–Br1 (x, $1+y$, z) 3.309(1) and Hg–Br2 (x, $-1+y$, z) 3.247(1) Å), and one with the carboxylic oxygen of HpicOH in the zwitterionic form (Hg–O1 2.602(7) Å). Interestingly, both covalent Hg–Br bonds are shorter than the sum of the covalent radii for Hg(digonal) and Br atoms (1.30 and 1.14 Å, respectively) [22–25] and also shorter than in the brucite structural type of $HgBr_2$ (Hg–Br of 2.444(7) and 2.445(7) Å, $2\times$Hg···Br of 3.240(5) and $2\times$Hg···Br 3.243(5) Å) [27]. The two bridging mercury to bromine contacts as well as the mercury to oxygen contact are longer than the covalent bond, but shorter than the van der Waals interactions (r_{VDW}(Br) = 1.85–1.95 Å) [22–25]. The coordination polyhedron is best described as very deformed square-pyramidal with an O atom at the apex. The Hg to Br distance at the sixth coordination site of 3.8475(11) Å is too long to be considered as a contact. Analysis of all structures deposited with the Cambridge Crystallographic Data Centre [28] that contain a mercury to bromine bond, showed that the short Hg–Br1 bond in **2** is similar to the shortest one found so far in κ-(d_8-ET)$_4$[$HgBr_2\cdot Hg_2Br_6$] (d_8-ET = wholly deuterated bis(ethylenediothio)tetrathiafulvalene) where Hg–Br is 2.28(2) Å and Br–Hg–Br is 169.7(7)°. There are two additional contacts of 3.41(2) Å at one side of this linear bond, yet the Hg–Br distance of 3.77(2) Å at the other side points to an absence of any additional interactions to Hg [29].

A similar polymeric structural motif to that of **2** was found in the structure of $HgCl_2$(tolnapH), (tolnapH = *N*-*p*-tolyl-2-oxo-1-napthylideneamine) [30]. In the structure of the polymeric HgBr(nic) (nic^- = nicotinate anion, pyridine-3-carboxylate) [15] the effective Hg coordination is a 3 + 2 irregular polyhedron with Hg–Br bond distances of 2.6528(9) and 2.6468(9) Å, which are longer than in **2** and slightly longer than the tetrahedral Hg–Br covalent bond of 2.62 Å [22,23,25].

As in **1**, the O3 hydroxyl atom forms an intramolecular hydrogen bond O3–H···O1 of 2.334(11) Å, yet there is another one involving the protonated nitrogen (N–H···O2

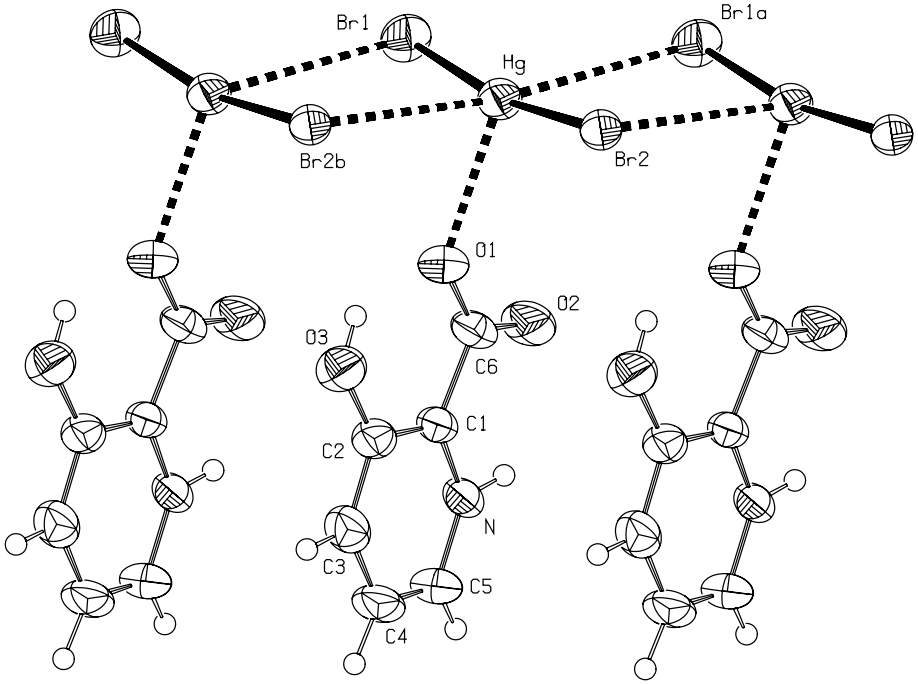


Fig. 3. Drawing of $HgBr_2$(HpicOH) (**2**) with the atom labelling scheme. The thermal ellipsoids are at the 50% probability level. Dashed lines represent Hg···Br and Hg···O contacts. Symmetry operations: $a = x, y-1, z$; $b = x, 1+y, z$.

2.662(10) Å). Two polymeric chains are mutually connected by centrosymmetric pairs via intermolecular hydrogen bonds N–H···O2 ($-1-x$, $-y$, $-z$) of 2.737(12) Å (Fig. 4, Table 5). In such a manner three-center hydrogen bonds are formed and the N–H group is distributed between two proton acceptors.

3.3. Spectral analysis

The infrared spectra of the complexes proved that 3-hydroxypicolinic acid is bound to the mercury(II) ion in the deprotonated form in all the isolated compounds (see ν_a(COO) in the experimental data), however different modes of ligand coordination in **1** and **2** were unambigously confirmed by X-ray structure analysis. Unfortunately, due to overlaping of maxima and vibrational coupling, the observed shifts of absorption bands sensitive to metal coordination relatively to those of the free ligands could not be unambigously assigned.

^{1}H and ^{13}C NMR data of 3-hydroxypicolinic acid and its mercury(II) compounds are given in Table 2 while Scheme 2 shows the labelling of the atoms. The NMR spectra of **1**, **2** and **3** in DMSO solution revealed narrow signals and a lack of long range couplings, which is characteristic of the monomeric form of the molecules. This is not unexpected since in solution the polymers almost certainly break up into monomeric units. On the other hand, the NMR data showed that the ligand is bound as in the solid state with a deprotonated N and O in **1** and **3**, while a neutral O in **2**. The obtained ^{1}H spectra of **1**, **2** and **3** display four groups of signals. The assignments of the protons were supported by COSY spectra. In the ^{1}H NMR spectra, the greatest shifts ($\Delta\delta$) after complexation are observed for OH-protons which are five or six bonds remote from mercury. Interestingly, the OH-proton of compounds **1** and **3** is found to be deshielded, in comparison to the one in **2** which is a shielded proton. Such behavior arises from the different mode of mercury coordination. In all ^{1}H spectra the multiplicity of the signals is alike. The mercury binding does not influence significantly the other protons in the molecules of both compounds **1** and **2**. A small shielding effect is observed on the H-4 atom in complexes **1** and **2**, however deshielding effects are observed on H-5 and H-6 atoms in all three complexes.

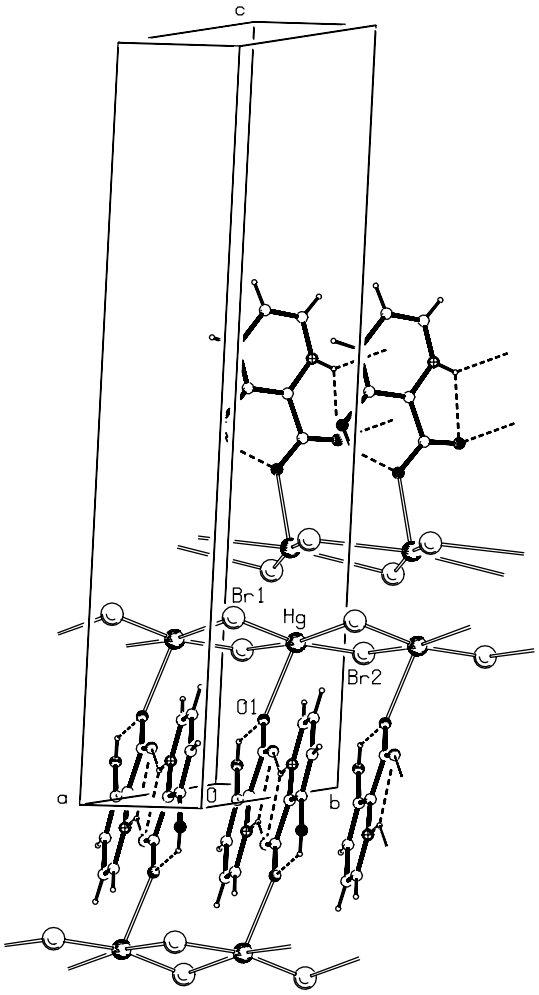
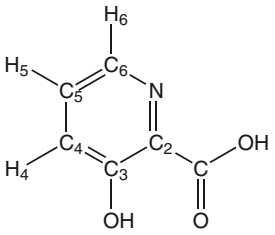


Fig. 4. Packing of $HgBr_2$(HpicOH) (**2**) molecules into polymeric layers. The deformed square pyramidal geometry around Hg is shown by double lines. Hydrogen bonds are shown by dashed lines.



Scheme 2.

The assignments of all the carbon atoms are confirmed by HMQC and HMBC measurements. In the ^{13}C NMR spectra, the greatest change upon complexation with mercury was observed for the chemical shifts of the C-6 atom. In **1** and **3**, C-6 is more deshielded than in **2**, since in complexes **1** and **3** the mercury atom is bonded to the nitrogen atom and the carboxyl group, while in **2** only to the carboxyl group. In all three compounds, carboxyl carbon atom was found to be not so deshielded as the C-6 atom. Shielding effects are observed on C-3 and C-4 atoms (-0.30 and -0.19 ppm, respectively) in complex **2**, and on the C-4 atom in **1** and **3** (-1.94 and -1.88 ppm, respectively). The carbon atom C-2 is deshielded in all three complexes (0.13–1.79 ppm) as expected, since it is close to the mercury binding site. The mercury binding induces electronic redistribution throughout the molecule which makes all the carbon atoms sensitive to mercury binding even if they are distant from mercury.

4. Conclusion

The competition reaction of halide ($X = Cl^-$, Br^-) with the 3-hydroxypyridine-2-carboxylate ligand ($picOH^-$) toward the mercury(II) ion was investigated. It was established that the molar ratio of the reactants did not influence

the type of reaction product, and polymeric $\{HgCl(picOH)\}_n$ or $\{HgBr_2(HpicOH)\}_n$ was always obtained. X-ray crystal structural analysis of these polymeric compounds showed interesting $2+4$ and $2+3$ coordination polyhedra around the mercury atom, and confirmed two different coordination modes of HpicOH. The NMR spectra of all the isolated mercury compounds in DMSO solutions revealed that they exist in the monomeric form.

Acknowledgements

The authors would like to acknowledge the Ministry of Science, Education and Sports of the Republic of Croatia for financial support (Grants Nos. 0119633, 0119632, 0098067 and 0098059).

Appendix A. Supplementary material

CCDC 602643 and 602642 contain the supplementary crystallographic data for **1** and **2**. These data can be obtained free of charge via http://www.ccdc.cam.ac.uk/conts/retrieving.html, or from the Cambridge Crystallographic Data Centre, 12 Union Road, Cambridge CB2 1EZ, UK; fax: (+44) 1223-336-033; or e-mail: deposit@ccdc.cam.ac.uk. Supplementary data associated with this article can be found, in the online version, at doi:10.1016/j.poly.2006.09.094.

References

[1] Y. Kim, G.B. Hurst, M.J. Doktycz, M.V. Buchanan, Anal. Chem. 73 (2001) 2617.
[2] E. Kiss, K. Petrohán, D. Sanna, E. Garribba, G. Micera, T. Kiss, Polyhedron 19 (2000) 55.
[3] V.L. Constantino, L.F.C. de Oliviera, P.S. Santos, H.E. Toma, Trans. Met. Chem. 19 (1994) 103.
[4] P.C.R. Soares-Santos, H.I.S. Nogueira, V. Félix, M.G.B. Drew, R.A. Sá Ferreira, L.D. Carlos, T. Trindade, Chem. Mater. 15 (2003) 100.
[5] S.M.O. Quintal, H.I.S. Nogueira, V. Felix, M.G.B. Drew, New J. Chem. 24 (2000) 511.
[6] S. Gatto, T.I.A. Gerber, G. Bandoli, J. Perils, J.G.H. du Preez, Inorg. Chim. Acta 269 (1998) 235.
[7] A. Shaver, J.B. Ng, D.A. Hall, B.S. Lum, B.I. Posner, Inorg. Chem. 32 (1993) 3109.
[8] S.M.O. Quintal, H.I.S. Nogueira, H.M. Carapuça, V. Félix, M.G.B. Drew, J. Chem. Soc., Dalton Trans. (2001) 3196.
[9] C. Sun, X. Zheng, L. Jin, J. Mol. Struct. 646 (2003) 201.
[10] V.B. Di Marco, A. Tapparo, A. Dolmella, G.G. Bombi, Inorg. Chim. Acta 357 (2004) 135.
[11] Z. Popović, G. Pavlović, M. Vinković, D. Vikić-Topić, M. Rajić Linarić, Polyhedron 25 (2006) 2353.
[12] J. Popović, D. Matković-Čalogović, G. Pavlović, Ž. Soldin, Z. Popović, in: Eleventh Slovenian–Croatian Crystallographic Meeting, Bohinj, Slovenia, June 27–30, 2002, Book of Abstracts, 2002, 35.
[13] D. Matković-Čalogović, I. Picek, Z. Popović, Ž. Soldin, in: Tenth Croatian–Slovenian Crystallographic Meeting, Lovran, Croatia, June 21–24, 2001, Book of Abstracts, 2001, p. 16.
[14] D. Matković-Čalogović, G. Pavlović, Z. Popović, Ž. Soldin, in: 20th European Crystallographic Meeting, ECM 20, Crystallography in Natural Sciences and Technology, Krakow, Poland, August 25–31, 2001, Book of Abstracts, S6.M7.O4. pp. 116.
[15] Z. Popović, G. Pavlović, D. Matković-Čalogović, Ž. Soldin, Acta Crystallogr. C59 (2003) m165.
[16] G. Pavlović, Ž. Soldin, Z. Popović, in: Fourteenth Croatian–Slovenian Crystallographic Meeting, Vrsar, Croatia, June 21–24, 2005, Book of Abstracts, 2005, p. 45.
[17] P. Gouverner, W. Hoedeman, Anal. Chim. Acta 30 (1964) 519.
[18] Oxford diffraction, 2004, Oxford Diffraction Ltd., Xcalibur CCD System, CrysAlis Software System, Version 171.23.
[19] G.M. Sheldrick, Acta Crystallogr. Sect. A 46 (1990) 467.
[20] G.M. Sheldrick, SHELXL97, Program for the refinement of crystal structures. University of Göttingen, Germany, 1997.
[21] A.L. Spek, Acta Crystallogr. Sect. A 46 (1990) 34.
[22] D. Grdenić, Quart. Rev. 19 (1965) 303.
[23] D. Grdenić, Connections in the Crystal Structures of Mercury Compounds, in: G. Dodson, J.P. Glusker, D. Sayre (Eds.), Structural Studies of Molecules of Biological Interest, Clarendon Press, Oxford, 1981, p. 207.
[24] D. Matković-Čalogović, Ph.D. Thesis (in Croatian; Abstract in English) University of Zagreb, 1994.
[25] L. Pauling, The Nature of the Chemical Bond, Third ed., Cornell University Press, Ithaca, NY, 1960.
[26] A. Moghimi, A. Shokrollahi, M. Shamsipur, H. Aghabozorg, M. Ranjbar, J. Mol. Struct. 701 (2004) 49.
[27] V.I. Pakhomov, A.V. Goryunov, I.N. Ivanova-Korfini, A.A. Boguslavskii, R.Sh. Lotfullin, Zh. Neorg. Khim. 35 (1990) 2476.
[28] (a) Cambridge Structural Database V5.27, Cambridge Crystallographic Data Centre, 12 Union Road, Cambridge, England, November, 2002;
(b) F.H. Allen, Acta Crystallogr., Sect. B 58 (2002) 380.
[29] O.A. Dyachenko, V.V. Gritsenko, G.V. Shilov, R.N. Lyubovskaya, R.B. Lyubovskii, Synth. Met. (1994) 193.
[30] Z. Popović, V. Roje, G. Pavlović, D. Matković-Čalogović, M. Rajić, G. Giester, Inorg. Chim. Acta 322 (2001) 65.

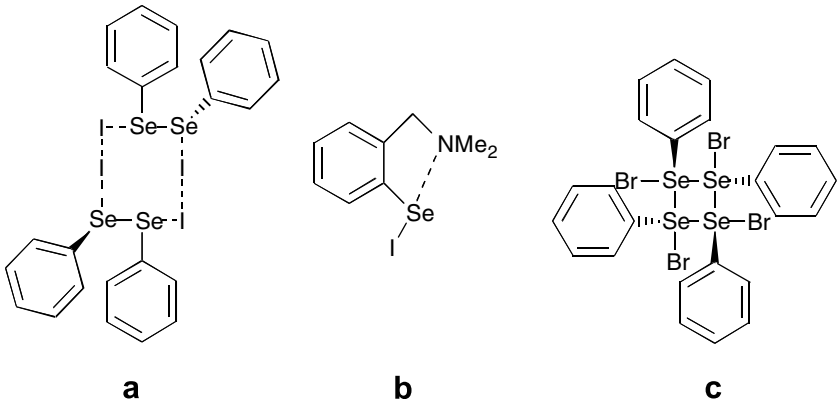


Fig. 1. Examples of different structural motifs observed for ArSeX compounds.

2-(Me_2NCH_2)C_6H_4SeI (Fig. 1(b)) [15]. These compounds feature a linear N···Se–I motif with the selenium atom in a T-shaped geometry. The strong Se···N interactions vary between 2.01(4) and 2.242(5) Å, close to the sum of the covalent radii of selenium and nitrogen (1.80 Å). The Se–I bond lengths in these systems range between 2.7419(9) and 2.8935(8) Å, and are significantly elongated compared with the monomeric RSeI iodoselanes, consistent with a linear N···Se–I system permitting interaction between the lone pair on nitrogen and the σ^* orbital of the Se–I bond.

There are few reported structures of arylselenium bromides or chlorides. The majority of those reported feature structures which are stabilised by non-bonded N···Se–X [10–19], or O···Se–X interactions [20–23], or by hypervalent coordination from either non-bonded halide ions [24] or halogen-substituted groups on the aryl ring [25,26]. Crystallographic reports of unstabilised systems are rarer, and until recently there were no crystallographic reports on PhSeX (X = Cl, Br), although gas-phase electron diffraction data on PhSeBr has appeared [27].

We have recently reported the solid-state structure of PhSeBr [28], which adopts a "square" motif, $Ph_4Se_4Br_4$ (Fig. 1(c)) where four "PhSeBr" units are held together by long Se–Se bonds [Se–Se: 3.004(2) to 3.051(2) Å]. The extended structure is further linked through long Br···Br contacts [Br–Br: 3.693(2) to 3.798(2) Å] to form planar sheets of selenium and bromine atoms. This type of square motif has also been reported for the related tellurium compound, $Ph_4Te_4I_4$ [29], and interestingly, contrasts with the CT structure exhibited by $(Ph_2Se_2I_2)_2$ [9].

There are far fewer structural reports concerning arylselenium pseudohalides. Most of the known examples involve systems where the pseudohalide is cyanide, with structural data reported for RSeCN, where R = C_6F_5 [30], 3-C_5H_4N [31], and 2,4,6-$R_3C_6H_2$ (R = Me, CF_3) [32]. Additionally, the structure of the diselenocyanate *p*-$C_6H_4(SeCN)_2$ [33], has been reported. Other structurally characterised arylselenium pseudohalides include 2,4,6-$(CF_3)_3C_6H_2SeNSO$ [34], the thiocarbamate derivatives $(Me_2NCH_2)C_6H_4SeSC(=S)CNR_2$ (R = Me, Et) [16], and the first stable selenium(II) azide, 2-(Me_2NCH_2)$C_6H_4SeN_3$ [15], which was also stabilised through intramolecular coordination of the NMe_2 group.

With little structural data available for ArSeX compounds which do not feature stabilisation by non-bonded Y···Se–X interactions (Y = N, O, halogen), and in view of the different structural motifs already observed for PhSeX (X = Br, I) [9,28], we have now undertaken a structural study of PhSeCl, and related PhSeX compounds containing pseudohalogens, such as PhSeCN and PhSeSCN, in order to further understand the factors affecting the solid-state structures of such systems.

2. Results and discussion

2.1. Structure of $Ph_4Se_4Cl_4$

PhSeCl is available commercially but may also be synthesised by the 1:1 reaction of diphenyldiselenide with sulfuryl chloride (SO_2Cl_2) in anhydrous diethyl ether. Care should be taken to avoid an excess of SO_2Cl_2 as oxidation readily occurs to the trichloride, $PhSeCl_3$ [35]. The orange solid obtained was characterised by multinuclear NMR spectroscopy, IR spectroscopy and elemental analysis (see Section 3), and the data obtained is consistent with previous literature reports [36]. Crystals of PhSeCl were obtained from a refluxing Et_2O/CH_2Cl_2 (1:1) solution of the compound which was then cooled to form suitable crystals after several days. PhSeCl crystallises in the orthorhombic space group $P2_12_12_1$, and was revealed to adopt a loosely held tetrameric "square" structure, $Ph_4Se_4Cl_4$, see Fig. 2a.

The square motif adopted by $Ph_4Se_4Cl_4$ is analogous to the solid-state structure of $Ph_4Se_4Br_4$ [28], and displays similar structural features. Four "PhSeCl" units are linked by weak selenium-selenium bonds to form an Se_4 square, with the Se–Cl bonds lying in the plane of the square, two phenyl rings located above the plane, and two below. The selenium atoms are thus in a "see-saw" geometry. Some asymmetry is observed for the Se–Se bonds, (as seen for $Ph_4Se_4Br_4$), as there are two shorter bonds, Se(1)–Se(2): 3.002(3) Å/Se(4)–Se(1): 2.993(3) Å, and two longer bonds,

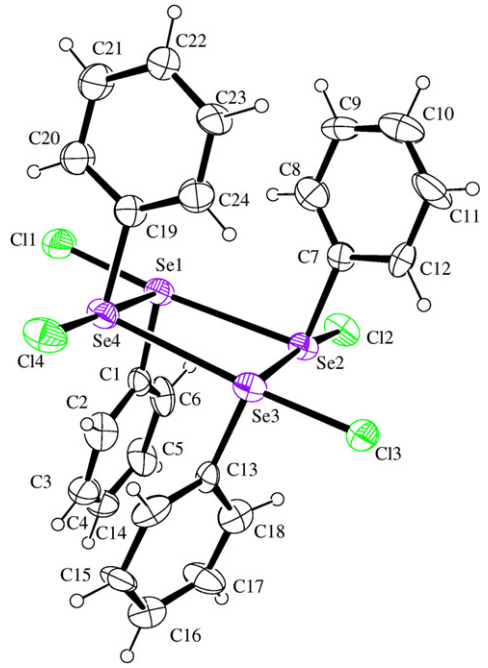


Fig. 2a. Molecular structure of $Ph_4Se_4Cl_4$. Thermal ellipsoids are shown at the 30% probability level. Selected bond lengths (Å) and angles (°): Se(1)–Se(2): 3.002(3), Se(2)–Se(3): 3.035(3), Se(3)–Se(4): 3.031(3), Se(4)–Se(1): 2.993(3), Se(1)–Cl(1): 2.242(5), Se(2)–Cl(2): 2.265(6), Se(3)–Cl(3): 2.251(5), Se(4)–Cl(4): 2.262(6), Se(1)–C(1): 1.929(15), Se(2)–C(7): 1.929(18), Se(3)–C(13): 1.881(18), Se(4)–C(19): 1.944(15), C(1)–Se(1)–Cl(1): 95.2(5), C(7)–Se(2)–Cl(2): 94.7(6), C(13)–Se(3)–Cl(3): 96.9(5), C(19)–Se(4)–Cl(4): 95.7(6), Cl(1)–Se(1)–Se(2): 174.79(16), Cl(1)–Se(1)–Se(4): 92.78(16), C(1)–Se(1)–Se(2): 88.3(5), C(1)–Se(1)–Se(4): 99.8(5), Se(1)–Se(2)–Se(3): 89.86(7), Se(2)–Se(3)–Se(4): 89.08(7), Se(3)–Se(4)–Se(1): 90.11(7), Se(4)–Se(1)–Se(2): 90.42(7).

Se(2)–Se(3): 3.035(3) Å/Se(3)–Se(4): 3.031(3) Å. These Se–Se bonds are well within the sum of the van der Waals radii for two selenium atoms (3.80 Å), and are slightly shorter than those reported for $Ph_4Se_4Br_4$, which vary between 3.004(2) and 3.051(2) Å [28], yet they are considerably longer than the Se–Se bonds in Ph_2Se_2 [Se–Se: 2.29(1) Å] [37], and $(Ph_2Se_2I_2)_2$ [Se–Se: 2.347 Å] [9]. The Se–Se–Se angles in $Ph_4Se_4Cl_4$ vary between 89.08(7) and 90.42(7)°, and are thus very close to the anticipated 90° for a square motif. Similar Se–Se linkages have been reported for 1,2-$C_6H_4(SeCl)_2$ [38], which dimerises, with weak Se–Se bonds of 3.025(1) and 3.039(2) Å between the two 1,2-$C_6H_4(SeCl)_2$ units.

The Se–Cl bonds in $Ph_4Se_4Cl_4$ range in distance between 2.242(5) and 2.265(6) Å, slightly longer than observed for 2,4,6-$R_3C_6H_2SeCl$ [R = Me (Se–Cl: 2.184(1)/2.187(1) Å); R = CF_3 (Se–Cl: 2.177(2) Å)] [32], or 1,2-$C_6H_4(SeCl)_2$ [Se–Cl: 2.185(3)–2.230(3) Å] [38]. These distances are considerably shorter than the Se–Cl bonds observed in ArSeCl compounds with N···Se–Cl interactions present, where distances vary between 2.429(2) and 2.482(8) Å [12,14–16]. Unusually, the Se–C bonds to the phenyl rings in $Ph_4Se_4Cl_4$ show considerable asymmetry, ranging between 1.881(18) and 1.944(15) Å.

The extended structure of $Ph_4Se_4Cl_4$ is similar to $Ph_4Se_4Br_4$ in that the Se_4 squares are further linked by weak chlorine–chlorine contacts (Fig. 2b) to form a planar network of Se_4 and larger Cl_4 squares. However, the Cl···Cl contacts [3.737(7)–3.881(7) Å] are longer than the sum of the van der Waals radii for two chlorine atoms (3.60 Å), but the presence of this extended structural motif might explain the elongation of the Se–Cl bonds compared with 2,4,6-$R_3C_6H_2SeCl$ (R = Me, CF_3), where such contacts are not present [32].

The $^{77}Se\{^1H\}$ NMR spectrum of a solution of the crystals in $CDCl_3$ reveals a single peak at 1045 ppm, in good agreement with previous reports for phenylselenenyl chloride [15], which is suggestive that the aggregation of PhSeCl into an Se_4 square is a solid-state phenomenon, and that the compound is monomeric in solution.

2.2. Structure of PhSeCN

Whilst no PhSeX compounds containing pseudohalogen groups have been structurally characterised, a large number of arylselenocyanates, ArSeCN, are known. The structure of PhSeCN is likely to be of interest as it is a commercially available reagent which has found significant use in organic reactions [1–3] and since the Cl^- and CN^- anions display similar electronegativities, a comparison with the structure of $Ph_4Se_4Cl_4$ would be interesting. PhSeCN is a liquid at room temperature, although crystals suitable for X-ray analysis were obtained in situ by cooling the liquid in capillary tubes at 150(2) K. PhSeCN crystallises in the monoclinic space group $P2_1/n$, with two independent molecules in the unit cell, as shown in Fig. 3a below.

The solid-state structure of PhSeCN is quite different to $Ph_4Se_4Cl_4$, as no aggregation of "PhSeX" units into an Se_4 square is observed. PhSeCN is essentially monomeric, with two independent molecules in the unit cell. The two molecules are loosely linked by Se···N contacts; Se(1)–N(12): 3.329(4) Å, Se(2)–N(11): 3.444(4) Å, both slightly shorter than the sum of the van der Waals radii for selenium and nitrogen (3.45 Å). The Se–C bonds to the cyanide groups [Se–C: 1.849(4)/1.845(4) Å] are considerably shorter than the Se–C bonds to the phenyl rings [Se–C: 1.925(4)/1.936(4) Å], reflecting the increased double bond character in the Se–C bond to the sp hybridised cyanide carbon, compared with the sp^2 hybridised ring carbon. The Se–CN distances are similar to other reported arylselenocyanates [30–33], selenium cyanides such as $Se(CN)_2$ [39], $Se_2(CN)_2$, $Se_3(CN)_2$ [40] and the $[SeCNBr_2]^-$ and $[(SeCN)_2Br]^-$ anions [41]. The C≡N bond lengths [C(11)–N(11): 1.142(5) Å, C(12)–N(12): 1.138(5) Å] are typical for selenocyanates, with Se–C–N angles close to linear, Se(1)–C(11)–N(11): 177.4(4)/Se(2)–C(12)–N(12): 178.7(4)°. The SeCN group is non-planar with respect to the phenyl ring, with torsion angles, C(11)–Se(1)–C(21)–C(31): –35.7(3)° and C(12)–Se(2)–C(22)–C(32): –34.4(3)°.

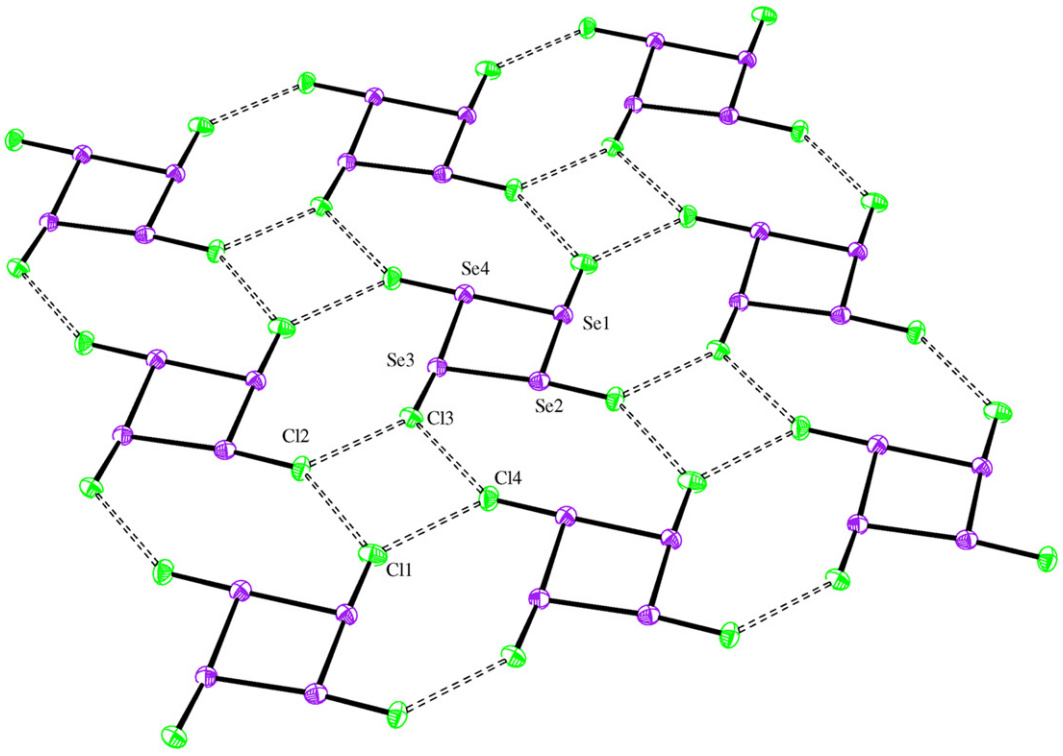


Fig. 2b. Extended solid-state structure of $Ph_4Se_4Cl_4$, showing Se–Se and Cl–Cl contacts. Phenyl rings are omitted for clarity. Contact distances (Å): Cl(1)···Cl(2): 3.791(7), Cl(2)···Cl(3): 3.737(7), Cl(3)···Cl(4): 3.793(7), Cl(4)···Cl(1): 3.881(7).

The loose dimeric structure observed for PhSeCN contrasts with that of the perfluorinated analogue C_6F_5SeCN [30], where the two independent molecules in the unit cell are not linked by any weak Se···N interactions, although a similar dimeric linkage is observed for 3-C_5H_4NSeCN [Se···N: 3.387(6) Å] [31] and 1,4-$C_6H_4(SeCN)_2$ [Se···N: 3.32 Å] [33]. In the extended structure (Fig. 3b) the molecules form infinite one-dimensional chains along the a axis, linked by short Se···N interactions, [Se(1)–N(11_1): 3.023(3) Å, Se(2)–N(12_1): 3.065(4) Å], with C≡N···Se angles close to linear, the deviation being greater in one chain than the other; [C(11)–N(11)···Se(1_2): 172.94(13)°, C(12)–N(12)···Se(2_2): 166.07(14)°]. The Se···N interactions along the chain are thus appreciably shorter than those between the two chains. Additionally, very weak Se···Se contacts of 3.789(7) Å are observed between the chains, just within the sum of the van der Waals radii for two selenium atoms (3.80 Å).

2.3. Structure of PhSeSCN

For comparative purposes we decided to structurally characterise a further PhSeX pseudohalogen system, PhSeSCN. Examples of arylselenium thiocyanates are rare in the literature, but may be prepared by metathesis from RSeX (X = Cl, Br) with alkali metal thiocyanates or Me_3SiNCS [42–47]. PhSeSCN was prepared by the literature method from PhSeCl and Me_3SiNCS in anhydrous

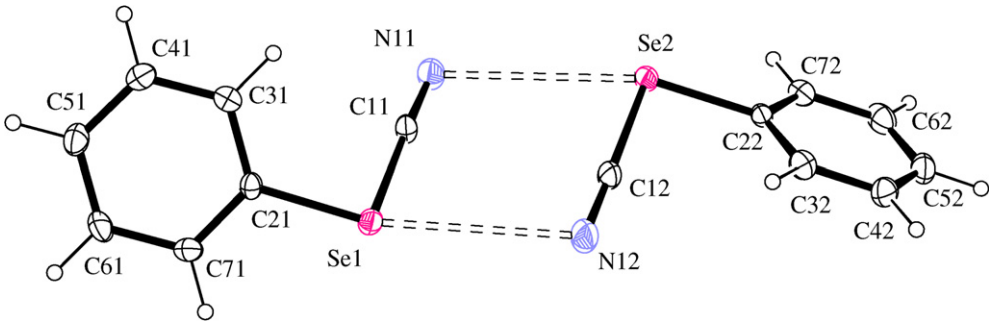


Fig. 3a. Molecular structure of PhSeCN. Thermal ellipsoids are shown at the 30% probability level. Selected bond lengths (Å) and angles (°): Se(1)–C(11): 1.849(4), Se(1)–C(21): 1.925(4), Se(2)–C(12): 1.845(4), Se(2)–C(22): 1.936(4), C(11)–N(11): 1.142(5), C(12)–N(12): 1.138(5), C(21)–Se(1)–C(11): 94.92(15), C(22)–Se(2)–C(12): 95.15(16), Se(1)–C(11)–N(11): 177.4(4), Se(2)–C(12)–N(12): 178.7(4).

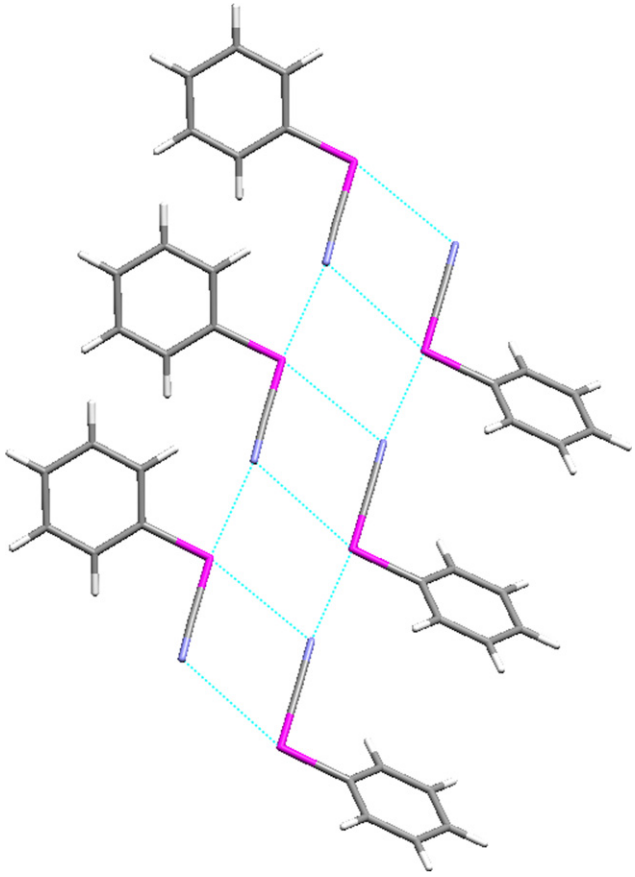


Fig. 3b. Extended structure of PhSeCN, showing Se···N interactions. Selected contact lengths (Å): Se(1)···N(12): 3.329(4), Se(2)···N(11): 3.444(4), Se(1)···N(11_1): 3.023(3), Se(2)···N(12_1): 3.065(4).

dichloromethane [46]. Crystals were obtained by refluxing a Et_2O/CH_2Cl_2 (1:1) solution of the compound, followed by cooling to room temperature, which produced a large crop of orange crystals. PhSeSCN crystallises in the monoclinic space group $P2_1/c$, and the molecular structure is shown in Fig. 4a.

PhSeSCN is, to the best of our knowledge, the first crystallographically characterised selenium-thiocyanate compound, although space-group determinations of 2-RC_6H_4SeSCN (R = NO_2, $COCH_3$) have been reported [43]. The thiocyanato group is coordinated to the selenium through the sulfur atom, and it would appear that the soft selenium centre prefers to bind with sulfur, rather than the harder nitrogen atom. Selenium does bind to nitrogen in the absence of a "softer option", as in 2,4,6-$(CF_3)_3C_6H_2SeNSO$ [34], but clearly the thiocyanato coordination mode is preferred over the isothiocyanato in PhSeSCN, as confirmed in solution by $^{13}C\{^1H\}$ NMR studies, where the SCN carbon resonance is observed at 111.9 ppm (cf. δSCN: 109.6 for C_6F_5SeSCN) [47]. No resonance for the NCS isomer was observed [$^{13}C\{^1H\}$ NMR shifts for NCS groups are typically found at 130–140 ppm] [48]. Additionally, the ν(SCN) band is observed at 2150 cm^{-1} in the IR spectrum, consistent with other reported RSeSCN compounds [46,47].

The Se–S bond in PhSeSCN is 2.2211(11) Å, close to the reported mean for covalent Se–S bonds, 2.193 Å [49], but is slightly shorter than the Se–S bond in the thiocarbamate derivatives 2-$(Me_2NCH_2)C_6H_4SeSC(=S)CNR_2$ [R = Me, Se–S 2.2659(7) Å; R = Et, Se–S: 2.247(1) Å] [16]. The geometry of the SCN group is near linear, S(1)–C(1)–N(1): 176.5(4)°, with S–C and C≡N bond lengths similar to those observed for the free SCN^- ion in KSCN [50]. The bent geometry at both the selenium and sulfur atoms reflects the presence of lone pairs on both atoms with angles S(1)–Se(1)–C(2): 99.30(12)° and Se(1)–S(1)–C(1): 100.49(14)°.

In the extended structure of PhSeSCN individual molecules stack such that a weak interaction, Se(1)···N(1) of 3.348(4) Å is set up, see Fig. 4b. Unlike in PhSeCN, the Se···NC contact angles are non-linear, Se(1)···N(1)–C(1): 102.7(3)°. The shortest Se···N interaction between

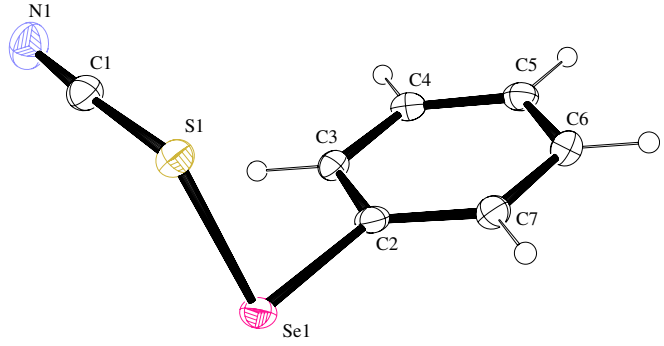


Fig. 4a. Molecular structure of PhSeSCN. Thermal ellipsoids are shown at the 30% probability level. Selected bond lengths (Å) and angles (°): Se(1)–S(1): 2.2211(11), Se(1)–C(2): 1.925(4), S(1)–C(1): 1.696(4), C(1)–N(1): 1.157(6), C(2)–Se(1)–S(1): 99.30(12), Se(1)–S(1)–C(1): 100.49(14), S(1)–C(1)–N(1): 176.5(4).

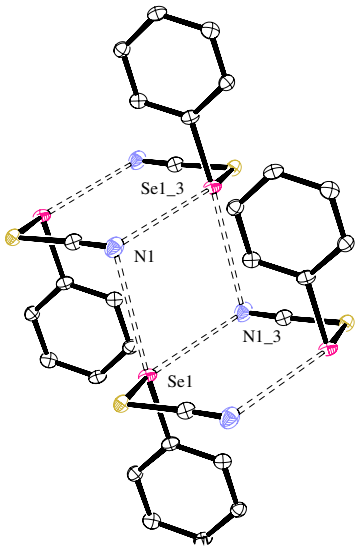


Fig. 4b. Extended structure of PhSeSCN. Thermal ellipsoids are shown at the 30% probability level, and H atoms have been omitted for clarity. Selected contact distances (Å) and angles (°): Se(1)···N(1): 3.348(4) Å, Se(1)···N(1_3): 3.567(4), C(1)–N(1)···Se(1): 102.7(3), C(2)–Se(1)···N(1): 172.10(13), S(1)–Se(1)···N(1): 88.50(7).

adjacent stacks, Se(1)···N(1_3): 3.567(4) Å, is slightly longer than the sum of the van der Waals radii for selenium and nitrogen (3.45 Å).

2.4. Conclusion

The factors influencing the solid-state structures of arylselenium halides are clearly quite subtle, with the structural motif observed being sensitive to both the nature of the R groups bound to selenium, and the identity of the halogen or pseudohalogen in the system. In the absence of bulky aryl groups, monomeric ArSeX structures are seldom observed, and the majority of previously reported structures display intramolecular stabilisation from groups present on the aryl rings. In the phenyl series of compounds, PhSeX, there are no groups present to participate in such interactions, and the solid-state structures of ''PhSeBr'' and ''PhSeI'' are quite different from each other, (square versus centrosymmetric dimer). The results reported herein further illustrate the structural diversity exhibited by ''PhSeX'' compounds. When X = Cl a square motif, $Ph_4Se_4Cl_4$, is observed, analogous to $Ph_4Se_4Br_4$. Both of these compounds consist of a weakly held network of Se_4 squares and larger X_4 (X = Cl or Br) squares. This extended motif is adopted in the absence of any stronger packing forces. The analogous pseudohalogen compounds PhSeCN and PhSeSCN do not exhibit a square motif, but are essentially monomeric, and are linked into chains by Se···N contacts, which are notably shorter in PhSeCN than in PhSeSCN. In the former the Se···NC contact angles are close to linear, whilst for the SCN compound the Se···N interaction is longer, and the Se···NC contact angle non-linear. Such Se···N contacts appear to be the dominant packing force in these compounds, and are strong enough to preclude any formation of the weak lattice of Se_4 squares favoured by $Ph_4Se_4Cl_4$ and $Ph_4Se_4Br_4$.

3. Experimental

3.1. Reagents and physical measurements

$Ph_4Se_4Cl_4$ and PhSeSCN are moisture sensitive, therefore their synthesis was performed under strict anhydrous conditions. Diethyl ether and *n*-hexane (BDH) were distilled over sodium/benzophenone ketyl before use. Anhydrous dichloromethane (Aldrich), diphenyl diselenide (Aldrich), sulfuryl chloride (Aldrich), phenylselenocyanate (Acros) and trimethylsilylisothiocyanate (Aldrich) were all purchased commercially and used as received. ^1H and $^{13}C\{^1H\}$ NMR spectra were recorded on a Bruker DPX400 machine operating at 399.9 and 100.6 MHz, respectively. $^{77}Se\{^1H\}$ NMR spectra were recorded on a Bruker DPX200 machine operating at 38.2 MHz. Peak positions are quoted relative to external TMS $\{^1H/^{13}C\}$ and Me_2Se $\{^{77}Se\}$, using the high frequency positive convention throughout. All spectra were recorded at 300 K. Infrared spectra were recorded on a Nicolet–Nexus combined FT-IR/FT-Raman spectrometer, with the samples for IR prepared as Nujol mulls held between KBr plates ($Ph_4Se_4Cl_4$/PhSeSCN) or as a liquid film (PhSeCN). Melting points were recorded on a Bibby SMP10 melting point apparatus and elemental analyses were performed by the University of Manchester, School of Chemistry Microanalytical Service.

3.2. Crystallographic details

Details of the structural analyses for $Ph_4Se_4Cl_4$, PhSeCN and PhSeSCN are summarised in Table 1. Crystals of $Ph_4Se_4Cl_4$ were twinned by a fourfold rotation about the *c* axis (*a* and *b* axes are almost the same length) and also display racemic twinning. Diffraction data for $Ph_4Se_4Cl_4$ and PhSeSCN were recorded on a Nonius κ-CCD four circle diffractometer at 223(2) and 150(2) K, respectively, and data for PhSeCN on a Bruker Smart APEX CCD diffractometer equipped with an Oxford Cryosystems low-temperature device operating at 150(2) K. Graphite-monochromated Mo Kα radiation ($\lambda = 0.71073$ Å) was used in all cases. The structural data for all the compounds was solved by direct methods (SHELXS97) and refined by full-matrix least squares against F^2 using all data (SHELXL97) [51]. Absorption corrections were carried out with the multiscan method, and were applied either with the SORTAV program [52] (for $Ph_4Se_4Cl_4$ and PhSeSCN), or SADABS [53] (for PhSeCN). Non-hydrogen atoms were refined with anisotropic thermal parameters. Hydrogen atoms for $Ph_4Se_4Cl_4$ and PhSeSCN were refined isotropically. Figures were generated using ORTEP-3 for Windows [54].

3.3. Synthesis of $Ph_4Se_4Cl_4$

1.561 g (5 mmol) of diphenyl diselenide was dissolved in 50 cm^3 of freshly distilled diethyl ether under a nitrogen atmosphere. Sulfuryl chloride (0.480 cm^3, 5 mmol) was added dropwise over several minutes, and the solution turned orange in colour. The reaction was allowed to stir for 24 h, after which time the volume of the solvent was reduced to ca. 20 cm^3 with gradual precipitation of a yellow-orange solid which was isolated using standard Schlenk techniques. Yield = 1.747 g (91 %), mp 63-66°C. Calc. for $C_{24}H_{20}Cl_4Se_4$: C, 37.63; H, 2.64; Cl, 18.51. Found: C, 38.03; H, 2.64; Cl, 18.50%. ^1H NMR ($CDCl_3$): δ 7.36–7.46 [m, 3H], 7.74–7.86 [m, 2H]. $^{13}C\{^1H\}$ NMR ($CDCl_3$): δ 130.0 [s, C_m], 131.0 [s, C_p], 132.1 [s, C_i], 134.8 [s, C_o]. $^{77}Se\{^1H\}$ NMR ($CDCl_3$): δ 1045 [s]. IR (cm^{-1}): 1720, 1578, 1302, 1155, 1022, 687.

3.4. Spectroscopic data for PhSeCN

^1H NMR ($CDCl_3$): δ 7.34–7.49 [m, 3H], 7.61–7.75 [m, 2H]. $^{13}C\{^1H\}$ NMR ($CDCl_3$): δ 102.1 [s, CN], 122.3 [s, C_i], 129.8 [s, C_p], 130.7 [s, C_m], 133.2 [s, C_o]. $^{77}Se\{^1H\}$

Table 1
Crystallographic parameters for $Ph_4Se_4Cl_4$, PhSeCN and PhSeSCN

	$Ph_4Se_4Cl_4$	PhSeCN	PhSeSCN
Empirical formula	$C_{24}H_{20}Cl_4Se_4$	C_7H_5NSe	C_7H_5NSSe
Fw	766.04	182.08	214.14
Colour, habit	yellow, prism	colourless, cylinder	orange, plate
Crystal system	orthorhombic	Monoclinic	monoclinic
Space group	$P2_12_12_1$ (no. 19)	$P2_1/n$ (no. 14)	$P2_1/c$ (no. 14)
Crystal size (mm^3)	$0.10 \times 0.15 \times 0.15$	$0.40 \times 0.40 \times 3.00$	$0.04 \times 0.08 \times 0.20$
Unit cell dimensions			
a (Å)	9.3274(10)	6.0002(8)	5.5043(3)
b (Å)	9.3437(7)	13.1910(17)	17.2890(8)
c (Å)	30.227(3)	17.641(2)	8.3568(4)
α (°)	90	90	90
β (°)	90	94.430(2)	105.986(2)
γ (°)	90	90	90
Volume (Å)	2634.4(4)	1392.1(3)	764.51(7)
T (K)	223(2)	150(2)	150(2)
Z	4	8	4
D_{calc} (mg/m^3)	1.931	1.737	1.861
λ (Å)	0.71073	0.71073	0.71073
μ (Mo Kα) (mm^{-1})	5.989	5.294	5.099
F(000)	1472	704	416
2θ Range (°)	2.97–25.25	1.930–28.987	3.46–25.50
Number of reflections	7095 (3883 unique)	3381 (2429 unique)	1537 (1279 unique)
R_1/wR_2	0.0764/0.1367	0.0343/0.0789	0.0391/0.0917
R_1/wR_2 (all data)	0.1651/0.1787	0.0500/0.0808	0.0511/0.1012
Largest differences in peak and hole (e $Å^{-3}$)	0.79 and −0.854	0.73 and −0.54	0.546 and −0.988

NMR ($CDCl_3$): δ 319.2 [s]. IR (cm^{-1}): 3060, 2154, 1579, 1479, 1441, 1001, 669.

3.5. Synthesis of PhSeSCN

PhSeCl (1.915 g, 10 mmol) was dissolved in 50 cm^3 of anhydrous dichloromethane under a nitrogen atmosphere. Me_3SiNCS (1.41 cm^3, 10 mmol) was added dropwise over several minutes with formation of an orange coloured solution. The reaction was stirred overnight, after which time the solvent and volatile by-products (Me_3SiCl) were removed in vacuo. The resultant orange oil was washed with 30 cm^3 of freshly distilled hexane and left at 0 °C overnight to yield an orange solid which was filtered off using standard Schlenk techniques. Yield = 0.913 g (43%), mp 38–39 °C. Calc. for C_7H_5NSSe: C, 39.62; H, 2.36; N, 6.54; S, 14.97. Found: C, 39.20; H, 2.28; N, 6.47; S, 14.45%. ^1H NMR ($CDCl_3$): δ 7.46–7.53 [m, 3H], 7.82–7.89 [m, 2H]. $^{13}C\{^1H\}$ NMR ($CDCl_3$): δ 111.9 [s, SCN], 130.0 [s, C_i], 130.4 [s, C_m], 131.4 [s, C_p], 135.2 [s, C_o]. $^{77}Se\{^1H\}$ NMR ($CDCl_3$): δ 651 [s]. IR (cm^{-1}): 2150, 739, 686.

4. Supplementary material

CCDC 603331, 603332 and 603333 contain the supplementary crystallographic data for $Ph_4Se_4Cl_4$, PhSeCN and PhSeSCN. These data can be obtained free of charge via http://www.ccdc.cam.ac.uk/conts/retrieving.html, or from the Cambridge Crystallographic Data Centre, 12 Union Road, Cambridge CB2 1EZ, UK; fax: (+44) 1223-336-033; or e-mail: deposit@ccdc.cam.ac.uk.

Acknowledgement

The authors would like to thank EPSRC for a research studentship (RTAH), and also for the UMIST FT IR/Raman facility (Grant No: GR/M30135), NMR facility (Grant No: GR/L52246), and X-ray facility (Research Initiative Grant), and also the University of Edinburgh for facilities to grow crystals of PhSeCN at low temperature. The authors would also like to thank Dr. Alan Brisdon for helpful discussions.

References

[1] C. Paulmier, Selenium Reagents and Intermediates in Organic Synthesis, Pergammon Press, Oxford, 1986.
[2] D. Liotta, Organoselenium Chemistry, John Wiley, New York, 1987.
[3] T. Wirth, Organoselenium Chemistry: Modern Developments in Organic Synthesis, Springer-Verlag, Berlin, 2000.
[4] M. Tiecco, Top. Curr. Chem. 208 (2000) 7, and references cited therein.
[5] T. Wirth, Angew. Chem., Int. Ed. 39 (2000) 3740, and references cited therein.
[6] W-W. du Mont, S. Kubiniok, K. Peters, H-G. von Schnering, Angew. Chem., Int. Ed. 26 (1987) 780.
[7] J. Jeske, P.G. Jones, A.M. von Salzen, W-W. du Mont, Acta Crystallogr., Sect. E 58 (2002) o350.
[8] W-W. du Mont, A. Martens, S. Pohl, W. Saak, Inorg. Chem. 29 (1990) 4847.
[9] S. Kubiniok, W.-W. du Mont, S. Pohl, W. Saak, Angew. Chem., Int. Ed. 27 (1988) 431.

[10] G. Mugesh, A. Panda, H.B. Singh, R.J. Butcher, Chem. Eur. J. 5 (1999) 1411.
[11] G. Mugesh, H.B. Singh, R.J. Butcher, Tetrahedron: Asymmetry 10 (1999) 237.
[12] A. Panda, G. Mugesh, H.B. Singh, R.J. Butcher, Organometallics 18 (1999) 1986.
[13] S. Kumar, K. Kandasamy, H.B. Singh, R.J. Butcher, New J. Chem. 28 (2004) 640.
[14] K. Kandasamy, S. Kumar, H.B. Singh, R.J. Butcher, K.T. Holman, Eur. J. Inorg. Chem. (2004) 1014.
[15] T.M. Klapötke, B. Krumm, K. Polborn, J. Am. Chem. Soc. 126 (2004) 710.
[16] M. Kulcsar, A. Silvestru, J.E. Drake, C.L.B. Macdonald, M.E. Hursthouse, M.E. Light, J. Organomet. Chem. 690 (2005) 3217.
[17] H. Fujihara, H. Mima, M. Ikemori, N. Furukawa, J. Am. Chem. Soc. 113 (1991) 6337.
[18] R. Kaur, H.B. Singh, R.P. Patel, J. Chem. Soc., Dalton Trans. (1996) 2719.
[19] T.G. Back, Z. Moussa, M. Parvez, Phosphorus, Sulfur Silicon Relat. Elem. 179 (2004) 2569.
[20] P.M. Baiwar, G. Llabres, O. Dideberg, L. Dupont, J.L. Piette, Acta Crystallogr., Sect. B 31 (1975) 2188.
[21] T. Takahashi, N. Kurose, S. Kawanami, Y. Arai, T. Koizumi, M. Shiro, J. Org. Chem. 59 (1994) 3262.
[22] N. Kurose, T. Takahashi, T. Koizumi, Tetrahedron 53 (1997) 12115.
[23] M. Iwaoka, H. Komatsu, T. Katsuda, S. Tomoda, J. Am. Chem. Soc. 126 (2004) 5309.
[24] M. Iwaoka, H. Komatsu, T. Katsuda, S. Tomoda, J. Organomet. Chem. 611 (2000) 164.
[25] M. Iwaoka, H. Komatsu, T. Katsuda, S. Tomoda, J. Am. Chem. Soc. 124 (2002) 1902.
[26] M. Iwaoka, H. Komatsu, T. Katsuda, S. Tomoda, J. Org. Chem. 70 (2005) 321.
[27] N.M. Zaripov, M.V. Popik, L.V. Vilkov, T.G. Mannafov, Zh. Strukt. Khim. 21 (1980) 37.
[28] N.A. Barnes, S.M. Godfrey, R.T.A. Halton, I. Mushtaq, R.G. Pritchard, S. Sarwar, Dalton Trans. (2006) 1517.
[29] P.D. Boyle, W.I. Cross, S.M. Godfrey, C.A. McAuliffe, R.G. Pritchard, J.M. Sheffield, Angew. Chem., Int. Ed. 39 (2000) 1796.
[30] T.M. Klapötke, B. Krumm, K. Polborn, Eur. J. Inorg. Chem. (1999) 1359.
[31] S.J. Dunne, L.A. Summers, E.I. von Nagy-Felsobuki, Acta Crystallogr., Sect. C 50 (1994) 971.
[32] T.M. Klapötke, B. Krumm, P. Mayer, H. Piotrowski, M. Vogt, Z. Anorg. Allg. Chem. 629 (2003) 1117.
[33] W.S. McDonald, L.D. Pettit, J. Chem. Soc. (A) (1970) 2044.
[34] N. Bertl, H.W. Roesky, F.T. Edelman, M. Noltemeyer, H.G. Schmidt, Z. Anorg. Allg. Chem. 586 (1990) 7.
[35] N.A. Barnes, S.M. Godfrey, R.T.A. Halton, R.G. Pritchard, Dalton Trans. (2005) 1759.
[36] M.I. Al-Hassan, I.M. Al-Najjar, M.M. Ahmad, Acta Crystallogr., Sect. A 45 (1989) 1011.
[37] E. Marsh, Acta Crystallogr. 5 (1952) 458.
[38] G. Heckmann, G. Wolmershäuser, Chem. Ber. 126 (1993) 1071.
[39] A.C. Hazell, Acta Crystallogr. 16 (1963) 843.
[40] C.J. Burchell, P. Kilian, A.M.Z. Slawin, J.D. Woollins, K. Tersago, C. Van Alsenoy, F. Blockhuys, Inorg. Chem. 45 (2006) 710.
[41] S. Hauge, K. Marøy, Acta Chem. Scand. 46 (1992) 1166.
[42] O. Foss, J. Am. Chem. Soc. 69 (1947) 2236.
[43] R. Eriksen, Acta Chem. Scand. A26 (1972) 1274.
[44] D.G. Garrat, M.D. Ryan, M. Ujjainwalla, Can. J. Chem. 57 (1979) 2145.
[45] W.J.E. Parr, R.C. Crafts, Tetrahedron Lett. 22 (1981) 1371.
[46] T.G. Back, R.G. Kerr, J. Organomet. Chem. 286 (1985) 171.
[47] T.M. Klapötke, B. Krumm, P. Mayer, Z. Naturforsch. 59b (2004) 547.
[48] R.G. Jones, G. Allen, Org. Mag. Reson. 19 (1982) 196.
[49] F.H. Allen, O. Kennard, D.G. Watson, L. Brammer, A.G. Orpen, R. Taylor, J. Chem. Soc., Perkin Trans. 2 (1987) S1.
[50] C. Akers, S.W. Peterson, R.D. Willett, Acta Crystallogr., Sect. B 24 (1968) 1125.
[51] G.M. Sheldrick, SHELX-97, University of Göttingen, Göttingen, Germany, 1997.
[52] R.H. Blessing, Acta Crystallogr., Sect. A 51 (1995) 33.
[53] G.M. Sheldrick, SADABS, version 2004/1, University of Göttingen, Germany.
[54] ORTEP-3 for Windows L.J. Farugia, J. Appl. Crystallogr. 30 (1997) 565.

wires and ion conducting channels [15]. Several Pcs of these types have been designed in order to investigate the complexation behaviour and potential for electronic and ionoelectronic applications [16].

Adam et al. reported that a discotic liquid crystal of triphenylene substituted by alkylthio groups exhibits considerably higher charge carrier mobility in the discotic mesophase, compared with conventional organic semiconductors [17a]. It can be inferred from this example that the sulfur atoms may significantly influence the conductivity of the mesophase. Eichorn and Wöhrle reported the first example of columnar mesomorphism of octakis(octylthio)-substituted Pc zinc and copper complexes [17b]. Ohta et al. reported the synthesis of a series of octakis-(alkylthio)-phthalocyanines [abbreviated as $(C_nS)_8PcH_2$, $n = 8$, 10, 12, 16] and their copper complexes and investigated their mesomorphism. They discussed the influence of sulfur atoms and chain length on the mesomorphism and unique aggregated dimer structures in the columnar mesophase [18]. Although Pcs with methylene bridges showing mesogenic properties which contain O-donors are rather few number [7a,19], there is only one with thioether moieties [20].

There are a large number of different peripherally substituted phthalocyanines and normally they are formed in a single-step reaction from available derivatives of phthalic acid, phthalic anhydride, phthalimide, 2-cyanobenzamide, phthalonitrile, diiminoisoindoline, 1,2-dibromobenzene, or 1,2-dibromo-4,5-dimethylbenzene [1,21]. 1,2-Dibromo-4,5-dimethyl-benzene undergoes the Rosenmund–von Braun reaction effectively and the methyl groups can be brominated using *N*-bromosuccinimide (NBS) to yield 4,5-di(bromomethyl) phthalonitrile [22]. This compound is a valuable starting material for other 4,5-disubstituted phthalonitriles including phthalonitriles appended to thiol [22a], phosphanates [22b], and glycoluril [23]. The particular advantage of performing the Rosenmund–von Braun reaction before the addition of the desired functional groups is that it allows addition of more labile functional groups to the phthalonitrile molecule by avoiding their presence during the harsh cyanodehalogenation reaction. In the bromination reaction of the methyl groups of 4,5-dimethylphthalonitrile, we obtained two products: 4,5-di(bromomethyl) phthalonitrile (**1**) and 4-bromomethyl-5-methylphthalonitrile (**2**). Up until now, the synthesis of 4,5-di(bromomethyl) phthalonitrile (**1**) has been mentioned once in the literature [22a] and in one patent [22b], but 4-bromomethyl-5-methylphthalonitrile (**2**) is not given as a precursor of phthalocyanine. In the literature, Howard and co-workers obtained only compound **1** under reaction conditions similar to ours, but we obtained two products (**1** and **2**). They purified compound **1** with a chromatographic technique using dichloromethane as the eluent. Dichloromethane is very polar solvent for these compounds as an eluent. We separated **1** and **2** on a TLC (silica gel) card using hexane/dichloromethane: 5/2 as the eluent. According to Howard and co-workers, the melting point of compound **1** was between 110 and 122 °C. This is different from our result. The patent concerning compound **1** includes only NMR and IR data and the melting point was not reported. Compound **1** was obtained by crystallization in MeOH after column chromatography [22a]. However, according to our experiences, phthalonitrile derivatives **1** and **2** are crystallized in MeOH as a mixture. We separated the dinitrile derivatives (**1** and **2**) by dissolving in $EtOH/CH_2Cl_2$ (25:1) and then fractional crystallization. It must be emphasized that 4,5-di(bromomethyl) phthalonitrile (**1**) and 4-bromomethyl-5-methylphthalonitrile (**2**) were isolated and characterized clearly for the first time by our group.

In the following, we report the synthesis of new sterically hindered methyl-bridged tetra- and octa-(13,17-dioxa nonacosane-15 sulfanyl)-substituted Pcs using dinitrile derivatives **1** and **2**. The influence of the presence of methylene-bridges in the phthalocyanine core on the mesomorphic properties were determined.

2. Experimental

2.1. Materials

All solvents were purified as described in Perrin and Armarego [24]. 15-Thiol-13,17-dioxa nonacosane [21b] and 4,5-dimethyl phthalonitrile [21a] were prepared according to the reported procedures. All other reagents and solvents were reagent grade quality and were obtained from commercial suppliers.

2.2. Measurements

Elemental analyses were obtained from a Carlo Erba 1106 Instrument. Infrared spectra in KBr pellets were recorded on a Bio-Rad FTS 175C FT-IR spectrophotometer. Optical spectra in the UV–visible region were recorded with a Shimadzu 2001 UV Pc spectrophotometer using 1 cm pathlength cuvettes at room temperature. Electrospray full scan spectra, in the range m/z 50–2000 amu or m/z 2000–3000 amu, were obtained by infusion through fused silica tubing at 2–10 μL min^{-1}. The solutions were analyzed in the positive mode. The LCQ calibration (m/z 50–2000) was achieved according to the standard calibration procedure from the manufacturer (mixture of caffeine, MRFA and Ultramark 1621). An ES-Tuning Mix solution (Agilent) was used to calibrate the spectrometer between 2000 and 3000 amu. The temperature of the heated capillary of the LCQ was set to the range 180–200 °C, the ion spray voltage was in the range 1–7 kV with an injection time of 5–200 ms. Electron ionisation (EI) full scan spectra were obtained from an LCQ-ion trap (Thermofinnigan, San Jose, CA, USA). ^1H and ^{13}C NMR spectra were recorded in $CDCl_3$ solutions on a Varian 500 MHz spectrometer. Transition temperatures were determined at scan rates of 10 °C min^{-1} using Mettler Toledo Star Thermal Analysis System/DSC 822 System differential scanning

calorimeter calibrated with indium under a nitrogen atmosphere. The phase transition behaviours of these compounds were observed with a polarizing microscope, Leitz Wetzler Orthoplan-pol, equipped with the hot stage Linkam TMS 93 and temperature-controller Linkam LNP. X-ray measurements were performed with Cu Kα radiation using a Rigaku Kristalloflex diffractometer (Dmax 2200).

2.3. Synthesis

2.3.1. 4,5-Di(bromomethyl) phthalonitrile (1) and 4-(bromomethyl)-5-methyl phthalonitrile (2)

4,5-Dimethyl phthalonitrile (4.9 g, 31 mmol), NBS (11.2 g, 63 mmol)and benzoyl peroxide (ca. 200 mg) were mixed in carbontetrachloride (50 ml) and the mixture was stirred vigorously, heated under reflux and UV light for 6 h until all the NBS was converted to the succinimide, which floated on the surface of the solution. The solution was cooled to room temperature then filtered and the filtrate was evaporated to dryness. The yellow oily residue was dissolved in methanol, cooled to 5 °C and white solids formed. The solids were filtered. These solids are mixture of the two products. These compounds were detected by thin-layer chromatography [$R_f = 0.24$ (**1**) and $R_f = 0.28$ (**2**)] using dichloromethane:*n*-hexane/2:5 as the mobile phase and separated with the ethanol:dichloromethane 25:1 solvent system using the fractional crystallization technique.

Compound **1** consists of white crystals. Yield: 4 g (41%). m.p. 156 °C. (*Anal.* Calc. for $C_{10}H_6Br_2N_2$ (314) requires: C, 38.25; H, 1.93; N, 8.92. Found: C, 38.13; H, 1.85; N 8.80%.) IR ν_{max}/cm^{-1} (KBr pellet): 3043 (CH_{ar}), 2988–2828 (CH_2), 2236 (C≡N), 608,556 (C–Br). MS (EI) *m*/*z* (%) 314 (15) $[M]^+$, 233 (70) $[M-Br]^+$, 154 (100) [M−2Br], 127 (65), 100 (20). ^{1}H NMR ($CDCl_3$): δ 4.59 (s, 4H, CH_2), 7.81 (s, 2H, CH_{ar}). ^{13}C NMR ($CDCl_3$, APT): δ 26.63 (CH_2), 114.3 (C_{ar}), 116.23 (C≡N), 136.00 ($C_{ar}H$), 142.20 (C_{ar}).

Compound **2** consists of white needle crystals. Yield: 1.50 g (21%). m.p. 170 °C. (*Anal.* Calc. for $C_{10}H_7BrN_2$ (234) requires: C, 51.09; H, 3.00; N, 11.92. Found: C, 51.12; H, 3.10; N, 11.80%.) IR ν_{max}/cm^{-1} (KBr pellet): 3038 (CH_{ar}), 2988–2828 (CH_2), 2240 (C≡N), 1599, 1489, 1457, 909, 608 (C–Br). MS (EI) *m*/*z* (%) 234.9 (85) $[M]^+$, 155.0 (25) $[M-Br]^+$, 151 (100), 127 (40). ^{1}H NMR ($CDCl_3$): δ 2.56 (s, 3H, CH_3), 4.42 (s, 2H, CH_2), 7.66 (s, H, CH_{ar}), 8.30 (s, H, CH_{ar}). ^{13}C NMR ($CDCl_3$, APT): δ 20.71 (CH_3), 35.12 (CH_2), 114.50 (C_{ar}), 114.55 (C_{ar}), 116.20 (C≡N), 134.60 ($C_{ar}H$), 136.00 ($C_{ar}H$), 140.00 (C_{ar}), 145.20 (C_{ar}).

2.3.2. 1,2-Di(13,17-dioxa nonacosane-15-sulfanylmethyl) phthalonitrile (3)

4,5-Di(bromomethyl) phthalonitrile (**1**) (1.57 g, 5 mmol) was dissolved in anhydrous dimethyl sulfoxide (9 ml) under argon and an excess of 15-thiol-13,17-dioxa nonacosane (6.67 g, 15 mmol) was added. After stirring for 15 min at room temperature, dry and finely powdered potassium carbonate (2.50 g, 18 mmol) was added portion wise over 0.5 h with efficient stirring. The reaction mixture was stirred under argon at 50 °C for 48 h. After cooling, the reddish-brown mixture was filtered off and the solvent was evaporated under reduced pressure. The product was purified by column chromatography on silica gel using dichloromethane:*n*-hexane/5:2 as the eluent. Yield: 2.08 g (40%). mp. 26 °C. (*Anal.* Calc. for $C_{64}H_{116}N_2O_4S_2$ (1040) requires :C, 73.60; H, 11.10; N, 2.70. Found: C, 73.79; H, 11.22; N, 2.69%.) IR ν_{max}/cm^{-1} (KBr pellet): 3042 (CH_{ar}), 2985–2855 (CH_2), 2235 (C≡N), 1600, 1464 (C_{ar}=C_{ar}), 1366, 1112 (C–O–C); MS (ES), *m*/*z* (%): 1075.5 (100) $[M+Cl]^-$, 1041 (30) $[M+H]^+$, 924.3 (10) $[M-(C_2H_5)_4]^+$, 855.5 (5) $[M-(OC_{12}H_{25})]^+$, 421.1 (5) $[M-(C_5H_{11})_4]^+$. ^{1}H NMR ($CDCl_3$): δ 0.89 (t, 12H, CH_3), 1.26–1.30 (m, 72H, CH_2), 1.57 (m, 8H, $OCCH_2$), 2.87 (m, 2H, CH), 3.39–3.43 (m, 8H, OCH_2), 3.54–3.61 (m, 8H, CH_2O), 4.07 (s, 4H, CH_2S), 7.82 (s, 2H, CH_{ar}). ^{13}C NMR ($CDCl_3$, decoupled): δ 14.14 (CH_3), 22.17 (CH_2), 26.17 (CH_2), 29.51–29.68 (CH_2), 30.56 (CH_2), 31.94 (CH_2), 45.52 (CH), 71.67 (OCH_2), 71.91 (CH_2O), 114.07 (C≡N), 115.34 (C_{ar}), 135.16 ($C_{ar}H$), 144.03 (C_{ar}).

2.3.3. 4-Methyl-5-(13,17-dioxa nonacosane-15-sulfanylmethyl) phthalonitrile (4)

Compound **4** was prepared by the same procedure as described for the preparation of **3** by starting with 4-(bromomethyl)-5-methyl phthalonitrile (**2**) (0.88 g, 3.76 mmol), an excess of 15-thiol-13,17-dioxa nonacosane (1.77 g, 4.00 mmol) and potassium carbonate (1.96 g, 14.20 mmol). The resulting light-brown oily product was purified by column chromatography on silica gel using dichloromethane:*n*-hexane/4:1 as the eluent. Yield: 450 mg (20%). mp. 29 °C. (*Anal.* Calc. for $C_{37}H_{62}N_2O_2S$ (598) requires: C, 74.19; H, 10.43; N, 4.68%. Found: C, 74.25; H, 10.40; N, 4.50.) IR ν_{max}/cm^{-1} (KBr pellet): 3040 (CH_{ar}), 2957–2853 (CH_2), 2233 (C≡N), 1598, 1462 (C_{ar}=C_{ar}), 1378, 1200, 1120–1135 (C–O–C), 1101, 1080. MS (EI) *m*/*z* (%): 598.70 (20) $[M]^+$, 412.80 (100) $[M-OC_{12}H_{25}]^+$. ^{1}H NMR ($CDCl_3$): δ 0.89 (t, 6H, CH_3), 1.25–1.30 (m, 36H, CH_2), 1.58 (m, 4H, $OCCH_2$), 2.5 (s, 3H, $C_{ar}CH_3$), 2.89 (m, H, CH), 3.40–3.44 (m, 4H, OCH_2), 3.55–3.63 (m, 4H, CH_2O), 3.94 (s, 2H, CH_2S), 7.58 (s, H, CH_{ar}), 7.77 (s, H, CH_{ar}). ^{13}C NMR ($CDCl_3$, APT): δ 14.15 (CH_3), 19.54 ($C_{ar}CH_3$), 22.72 (CH_2), 26.17 (CH_2), 28.51-30.17 (CH_2), 31.95 (CH_2), 33.33 (CH_2), 45.44 (CH), 71.82 (OCH_2), 72.08 (CH_2O), 113.17 (C_{ar}), 114.02 (C_{ar}), 115.34 (C≡N), 133.48 (C_{ar}), 134.24 ($C_{ar}H$), 135.26 ($C_{ar}H$), 143.62 (C_{ar}).

2.3.4. 2,3;9,10;16,17;23,24-Octakis (13,17-dioxa nonacosane-15-sulfanylmethyl) phthalocyaninato nickel (II) (3a)

1,2-Di(13,17-dioxa nonacosane-15-sulfanylmethyl) phthalonitrile (**3**) (400 mg, 0.384 mmol), 1,8-diazabicyclo[5.4.0] undec-7-ene (DBU) (0.08 g, 0.53 mmol), anhydrous $NiCl_2$ (0.102 g, 0.73 mmol) and dried 1-pentanol (6 ml) were

refluxed with stirring under an argon atmosphere for 12 h. 1-Pentanol was removed under reduced pressure. The crude product was passed through a silica gel column using CH_2Cl_2:*n*-hexane 1:1 as the eluent. Furthermore, this product was purified with preparative TLC using the 12:1/*n*-hexane:ethylacetate solvent system. Yield: 70 mg (17%). (*Anal.* Calc. for $C_{256}H_{464}N_8NiO_{16}S_8$ (4222) requires: C, 72.76; H, 11.07; N, 2.65. Found: C, 72.80; H, 11.20; N, 2.25%.) IR ν_{max}/cm^{-1} (KBr pellet): 3040 (CH_{ar}), 2926–2855 (CH_2), 1621 (C_{ar}=C_{ar}), 1464, 1421, 1373, 1340, 1333, 1261 (C–O–C), 1105 (C–N). ^1H NMR ($CDCl_3$): δ 0.89 (t, 48H, CH_3), 1.24–1.29 (m, 288H, CH_2), 1.60 (m, 32H, $OCCH_2$), 3.28 (m, 8H, CH), 3.29–3.48 (m, 32H, OCH_2), 3.75 (t, 32H, CH_2O), 4.66 (s, 16H, CH_2S), 9.16 (s, 8H, CH_{ar}). ^{13}C NMR ($CDCl_3$, decoupled): δ 14.14 (CH_3), 23.19 (CH_2), 27.10 (CH_2), 28.51–31.89 (CH_2), 33.39–33.69 (CH_2), 38.72 (CH_2S), 45.78 (CH), 71.56 (OCH_2), 124.41 ($C_{ar}H$), 136.58 (C_{ar}), 139.25 (C_{ar}), 146.30 ($C_{ar}C$=N).

2.3.5. 2,3;9,10;16,17;23,24-Octakis (13,17-dioxa nonacosane-15-sulfanylmethyl) phthalocyanine (**3b**)

1,2-Di(13,17-dioxa nonacosane-15-sulfanylmethyl) phthalonitrile (**3**) (400 mg, 0.384 mmol), 1,8-diazabicyclo[5.4.0] undec-7-ene (DBU) (0.08 g, 0.53 mmol) and dried 1-penthanol (6 ml) were refluxed with stirring under an argon atmosphere for 12 h. The 1-pentanol was removed under reduced pressure, and the crude product was passed through a silica gel column using CH_2Cl_2:*n*-hexane/2:1 as the eluent. Furthermore, this product was purified with preparative TLC using the 10:1/*n*-hexane:ethylacetate solvent system. Yield: 40 mg (10%). (*Anal.* Calc. for $C_{256}H_{466}N_8O_{16}S_8$ (4165) requires: C, 73.75; H, 11.27; N, 2.69. Found: C, 73.60; H, 11.20; N, 2.40%.) IR ν_{max}/cm^{-1} (KBr pellet): 3235 (NH), 3041 (CH_{ar}), 2926–2855 (CH_2), 1619 (C_{ar}=C_{ar}), 1464, 1368, 1340, 1323, 1261 (C–O–C), 1106,1019 (C–N). ^1H NMR ($CDCl_3$): δ −0.30 (2H, NH), 0.84 (t, 48H, CH_3), 1.11–1.26 (m, 288H, CH_2), 1.60 (m, 32H, $OCCH_2$), 3.29–3.31 (m, 8H, CH), 3.43–3.49 (m, 32H, OCH_2), 3.76 (t, 32H, CH_2O), 4.69 (s, 16H, CH_2S), 9.46 (s, 8H, CH_{ar}). ^{13}C NMR ($CDCl_3$, decoupled): δ 14.09 (CH_3), 22.66–22.71 (CH_2), 28.66 (CH_2), 29.33–29.79 (CH_2), 31.89–31.94 (CH_2), 34.80 (CH_2), 45.85 (CH), 71.24 (OCH_2), 71.58 (CH_2O), 125.33 ($C_{ar}H$), 136.07 (C_{ar}), 127.00 (C_{ar}), 146.30 ($C_{ar}C$=N).

2.3.6. Tetrakis[4-methyl-5-(13,17-dioxa nonacosane-15-sulfanylmethyl)] phthalocyaninato nickel (II) (**4a**)

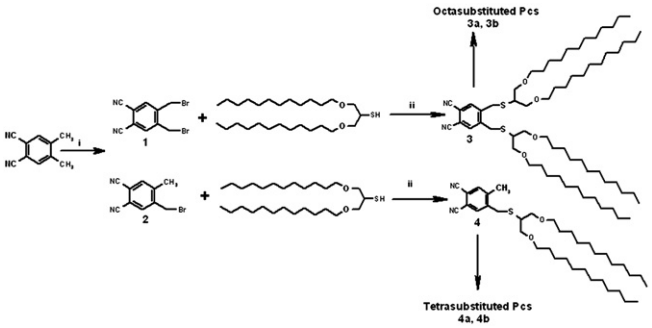
4-Methyl-5-(13,17-dioxa nonacosane-15-sulfanylmethyl) phthalonitrile (**4**) (230 mg, 0.384 mmol), 1,8-diazabicyclo[5.4.0] undec-7-ene (DBU) (0.08 g, 0.53 mmol), anhydrous $NiCl_2$ (0.102 g, 0.73 mmol) and dried 1-penthanol (6 ml) were refluxed with stirring under an argon atmosphere for 8 h. The 1-pentanol was removed under reduced pressure, and the crude product was passed through a silica gel column using CH_2Cl_2:*n*-hexane/2:1 as the eluent. Additionally, this product was purified with preparative TLC using the 12:1/*n*-hexane:ethylacetate solvent system. Yield: 30 mg (13%). (Anal. Calc. for: $C_{148}H_{248}N_8NiO_8S_4$ (2452) requires: C, 72.42; H, 10.18; N, 4.57. Found: C, 72.20; H, 10.20; N, 4.80%.). MS (ES) *m*/*z* (%): 2453 (100) [M+H]. IR ν_{max}/cm^{-1} (KBr pellet): 3040 (CH_{ar}), 2926–2855 (CH_2), 1621 (C_{ar}=C_{ar}), 1464, 1323, 1260 (C–O–C), 1106 (C–N). ^1H NMR ($CDCl_3$): δ 0.76 (t, 24H, CH_3), 0.90–1.30 (m, 144H, CH_2), 1.50 (m, 16H, $OCCH_2$), 2.4 (s, 12H, $C_{ar}CH_3$), 2.60–2.89 (m, 4H, CH), 3.30–3.40 (m, 16H, OCH_2), 3.55–3.63 (m, 16H, CH_2O), 3.94 (s, 8H, CH_2S), 7.80–8.50 (m, 8H, CH_{ar}). ^{13}C NMR ($CDCl_3$, decoupled): δ 13.10 (CH_3), 19.47 ($C_{ar}CH_3$), 21.65 (CH_2), 25.09–25.11 (CH_2), 28.28–28.72 (CH_2), 29.31 (CH_2), 33.22 (CH_2), 38.72–39.43 (CH_2), 44.40 (CH), 70.45 (OCH_2), 70.90 (CH_2O), 122.00 ($C_{ar}H$), 124.02 ($C_{ar}H$), 127.00 (C_{ar}), 134.00 (C_{ar}), 136.10 (C_{ar}), 138.00 (C_{ar}), 146.30 ($C_{ar}C$=N).

2.3.7. Tetrakis[4-methyl-5-(13,17-dioxa nonacosane-15-sulfanylmethyl)] phthalocyanine (**4b**)

4-Methyl-5-(13,17-dioxa nonacosane-15-sulfanylmethyl) phthalonitrile (**4**) (230 mg, 0.384 mmol), 1,8-diazabicyclo[5.4.0] undec-7-ene (DBU) (0.08 g, 0.53 mmol) and dried 1-pentanol (6 ml) were refluxed with stirring under an argon atmosphere for 10 h. The 1-penthanol was removed under reduced pressure, and the crude product was passed through a silica gel column using CH_2Cl_2:*n*-hexane/1:1 as the eluent. Furthermore, this product was purified with preparative TLC using the 12:1/*n*-hexane:ethylacetate solvent system. Yield: 25 mg (11%). (Anal. Calc. for $C_{148}H_{250}N_8O_8S_4$ (2395) requires: C, 74.13; H, 10.51; N, 4.67. Found: C, 74.30; H, 10.20; N, 4.80%.). MS (ES) *m*/*z* (%): 2396 (100) $[M+H]^+$. IR ν_{max}/cm^{-1} (KBr pellet): 3235 (NH), 3040 (CH_{ar}), 2925–2854 (CH_2), 1600, 1464, 1376, 1318, 1261 (C–O–C), 1105,1019 (C–N). ^1H NMR ($CDCl_3$): δ 0.82 (t, 24H, CH_3), 1.02–1.18 (m, 144H, CH_2), 1.47 (m, 16H, $OCCH_2$), 2.85–2.94 (m, 4H, CH), 2.98 (s, 12H, $C_{ar}CH_3$), 3.18–3.40 (m, 16H, OCH_2), 3.62–3.69 (m, 16H, CH_2O), 4.39 (s, 8H, CH_2S), 8.50–9.00 (8H, CH_{ar}). ^{13}C NMR ($CDCl_3$, decoupled): δ 13.10 (CH_3), 19.54 ($C_{ar}CH_3$), 21.65 (CH_2), 28.28–28.72 (CH_2), 29.31 (CH_2), 30.84–33.21 (CH_2), 38.82 (CH_2), 44.30 (CH), 70.45 (OCH_2), 70.90 (CH_2O), 123.80 ($C_{ar}H$), 124.10 ($C_{ar}H$), 134.20 (C_{ar}), 135.80 (C_{ar}), 139.20 (C_{ar}), 146.30 ($C_{ar}C$=N).

3. Results and discussion

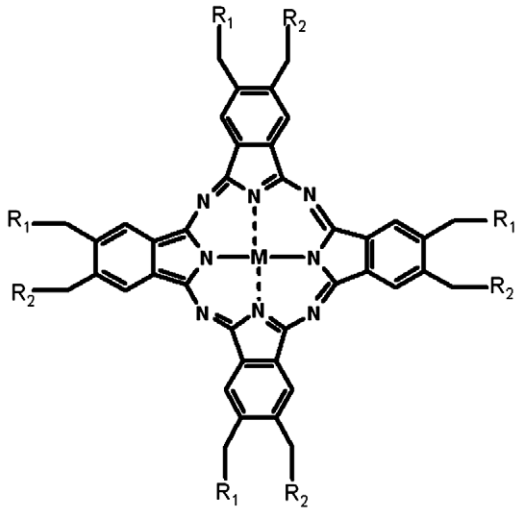
Generally, substituted Pcs are prepared by cyclotetramerization of substituted 1,2-dicyanobenzenes or 1,3-diimino-1*H*-isoindoles [1]. The same route in the literature [21a,25] was applied to prepare the di-substituted dinitrile derivative (**3**) from an excess amount of 15-thiol-13,17-dioxa nonacosane and 4,5-di(bromomethyl) phthalonitrile (**1**). Similarly, the reaction of compound **2** under the same conditions with 15-thiol-13,17-dioxa nonacosane resulted in the expected compound **4** by using the thiol derivative. Starting from 4,5-dimethyl phthalonitrile, the synthetic



Scheme 1. (i) NBS, CCl_4, 6 h reflux under UV light and in an argon atmosphere; (ii) DMSO, K_2CO_3, 50 °C, 48 h.

route is outlined in Scheme 1. The synthesis of methylene-bridged octa-alkylthia substituted phthalocyanine derivatives was reported by Cho and Lim [20]. In their work, 1,2-dibromo-4,5-di(bromomethyl)benzene was substituted with alkylthio chains and then the dibromo derivative was converted into a dinitrile by a Rosenmund–von Braun reaction. However, all efforts to accomplish these reactions failed in the nitrilation step, no dinitriles could be observed, according to our experience on the synthesis of alkylthio substituted dinitrile derivatives [26]. In order to overcome this problem, we used 4,5-di(bromomethyl) phthalonitrile (**1**) and 4-(bromomethyl)-5-methyl phthalonitrile (**2**) as starting compounds for the preparation of alkylthia-substituted phthalonitrile derivatives **3** and **4** respectively, by a nucleophilic displacement reaction.

The preparation of Pc derivatives from the aromatic nitriles occurs under different reaction conditions [1]. A convenient high-yield synthesis requires further consideration. For various substituted dinitriles, the reaction in the presence of strong not nucleophilic bases 1,8-diazabicyclo[5.4.0]undec-7-ene(DBU) or 1,5-diazabicyclo[4.3.0]non-5-ene(DBN), either in 1-pentanol or in bulk, with yields of phthalocyanines of up to 90% is most efficient in comparison to other methods [27]. In addition, these reactions are easy to perform, take place under relatively mild conditions and they yield more pure Pcs. Therefore, metal-free Pc derivatives **3b** and **4b** were obtained directly from the reaction of the dicyano compounds **3** and **4** in 1-pentanol at reflux temperature in the presence of a strong organic base such as DBU (Scheme 1). Also, cyclotetramerization of dinitrile derivatives **3** and **4** in the presence of anhydrous $NiCl_2$ and DBU in 1-pentanol gave the octasubstituted nickel (II) Pc **3a** and **4a**, respectively. The chemical structure of tetra- and octa-substituted phthalocyanine derivatives are given in Fig. 1. We expect that **4a**–**b** were prepared as a statistical mixture of four regioisomers owing to the various possible positions of the alkylthia side chains relative to one another. The four possible isomers can be obtained. By their molecular symmetry as D_{4h}, C_{4h}, C_{2v} and C_s, each isomer would be prepared in a relative yield of 1:1:2:4 respectively [28]. No attempt was made to separate the isomers of **4a**–**b**.



Compound	R_1	R_2	M
3a	$SCH[(CH_2O(C_{12}H_{25})]_2$	$SCH[(CH_2O(C_{12}H_{25})]_2$	Ni
3b	$SCH[(CH_2O(C_{12}H_{25})]_2$	$SCH[(CH_2O(C_{12}H_{25})]_2$	2H
4a	$SCH[(CH_2O(C_{12}H_{25})]_2$	H	Ni
4b	$SCH[(CH_2O(C_{12}H_{25})]_2$	H	2H

Fig. 1. Chemical structure of tetra- and octa-substituted phthalocyanine derivatives.

The methylene-bridged tetra- and octa-Pcs (**3a**–**b**, **4a**–**b**) substituted with the branched thioether were purified in each case by column chromatography (silica gel) and then preparative thin-layer chromatography (TLC) using a mixed solvent system of dichloromethane/*n*-hexane and *n*-hexane/ethylacetate as the eluent respectively. The intense blue waxy products are very soluble in a polar and apolar solvents, such as chloroform, benzene, carbon-tetrachloride and tetrahydrofuran. They were characterized by ^1H and ^{13}C NMR. In addition to elemental analysis results, the mass spectra of the new organic intermediate compounds and Pcs obtained by the ES and EI techniques show relatively intense molecular ion peaks. NMR investigation of all compounds have provided the characteristic chemical shifts for the structures as expected. However, the NH peak was observed in the ^1H NMR spectrum of compound **3b**, but there was no peak belong to NH at the high field for **4b**. A common feature of the ^1H NMR spectra of Pcs (**4a**–**b**) is the broad absorptions when compared with that of octa-substituted Pc derivatives, probably caused by the aggregation of the Pc which is frequently encountered at the concentrations used for NMR measurements. Due to steric hindrance, the octa-substituted Pcs show a lower aggregation tendency than the tetra-substituted Pcs. Also the NH protons of **4b** could not be observed due to this phenomena.

For substances **3a**–**b** and **4a**–**b**, typical absorption spectra of Pcs were observed [29] showing absorption bands in

Table 1
Electronic spectra of the phthalocyanines in chloroform

Compound	λ_{max}/nm (ε/10^4 dm^3 mol^{-1} cm^{-1})	
	Soret band region	Q band region
3a	336.5 (4.79) 462.5 (0.23)	611.5 (3.38) 651[a] (3.54) 679.5 (21.65)
3b	348.5 (7.49)	620.5 (2.85) 653.5[a] (4.62) 673 (13.84) 708.5 (16.56)
4a	334.5 (5.38)	609.5[a] (3.68) 648 (3.98) 676.5 (21.54)
4b	345.5 (14.77)	618.0 (5.44) 650.5[a] (9.09) 669.5 (25.60) 705.5 (29.00)

[a] Shoulder.

the Soret-band region 300–400 nm and Q band transitions at 600–700 nm (Table 1). The metal-free Pcs **3b** and **4b** give a doublet Q band as a result of the D_{2h} symmetry (Fig. 2B for **4b**). The nickel (II) Pcs **3a** and **4a** exhibit intense Q bands around 680 nm with a relatively sharp absorption peak and almost no shoulder on the higher energy side, which correspond to aggregated species. Q bands of the tetra-substituted Pcs (**4a** and **4b**) are at lower wavelengths than those of the octa-substituted Pcs (**3a** and **3b**) as expected (Table 1). For all the phthalocyanines, the effect of thia-substitution was observed as a shift of these intense Q bands to higher wavelengths when compared with unsubstituted, alkyl- or alkoxy-substituted derivatives.

For Pcs, the aggregation behaviour in solution is a good indication of interactions between the aromatic macrocycles. Aggregation is easily detected from optical absorption studies. Any increase in concentration results in aggregation of Pc molecules which is accompanied by a blue shift of the Q band with some decrease in intensity [19a,21b]. It has been concluded that aggregation is enhanced by solvent polarity and the presence of aliphatic side chains [16a,16b,16d,30]. This has indeed been observed with the tetra-substituted derivatives (Fig. 2A for **4a**).

The optical absorption spectra of compounds **3a**–**b** and **4a**–**b** depend on the solvent type. Although, aggregation is not detectable in tetrahydrofuran, chloroform, benzene or pyridine, broad Q bands were observed in the methanol/chloroform (1/1) solvent system. The tendency to form aggregates increases in the order: tetrahydrofuran < chloroform < benzene < pyridine < methanol/chloroform system for tetra-substituted Ni(II) Pc (**4a**) (Fig. 2A). Similar spectra have been obtained in the case of both octa- and tetra-substituted Pc derivatives. The position of the Q band in UV/Vis absorption spectra of the Pc compounds in the methanol/chloroform (1/1) solvent system showing an intermolecular interaction of the Pc core is more prevalent than in other solvents because of the polar solvent system.

3.1. Characterization of the mesophase

The phase transition temperatures were determined by DSC. Table 2 lists the phase transition temperatures established by DSC and polarizing microscopic observations for the octa- and tetra-substituted Pc derivatives (**3a**–**b** and **4a**–**b**). All the thermograms of the Pcs recorded with increasing temperature showed clearly two endothermic peaks. We assume that the first peaks are related to the transitions from the crystal phases to discotic mesophases, and the second ones to the transitions from discotic mesophases to isotropic liquid phases. In addition, the DSC diagrams of the tetra-substituted compounds **4a**–**b** depict a weak peak at about 153 °C (**4a**) and 144 °C (**4b**) in the heating cycle that belongs to the clearing point, and that enthalpy is much smaller than the melting enthalpy, which is due to the fact that for the mesophase to isotropic transition the structural rearrangement of the molecules is far more relevant than for solid to mesophase (Table 2). Similar behaviour was observed in the literature [21a,31]. These investigations indicate that the compounds exhibit a thermotropic liquid crystalline phase between the melting and clearing point (Table 2). The textures observed by polarizing optical microscopy for the compounds studied are very

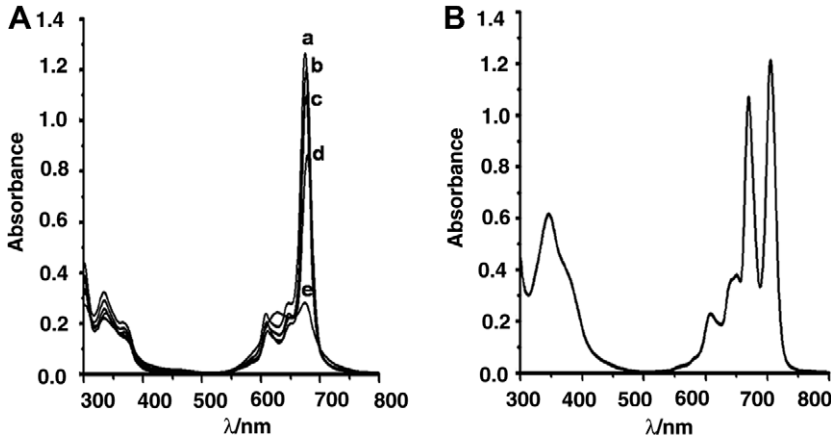


Fig. 2. (A) Visible absorption spectra of tetra-substituted Ni(II) pc derivative (**4a**): (a) in tetrahydrofuran; (b) in chloroform (c) in benzene; (d) in pyridine; (e) in MeOH/chloroform/1:1. (B) Visible absorption spectra of tetra substituted metal-free pc derivative (**4b**) in chloroform.

Table 2
Phase transition temperatures (°C) and in parentheses-enthalpy changes ΔH (in kJ/mol) by DSC (heating and cooling rates are 10 °Cmin^{-1}) for compound **3a**, **3b**, **4a** and **4b**

Compound	Heating		Cooling	
	C → Col_h → I		I → CoI_h → C	
3a	−7.56 (84.76)	28.87 (122.50)	19.07 (74.79)	−15.61 (41.45)
3b	−9.39 (65.41)	23.55 (105.10)	4.24 (54.36)	−15.11 (32.81)
4a	5.02 (127.53)	180.00 (28.88)	179.00 (62.81)	−3.11 (18.64)
4b	8.42 (110.20)	153.10 (3.69)	143.69 (3.11)	1.43 (94.31)

C: solid phase, Col_h: hexagonal discotic columnar mesophase, I: isotropic phase.

similar to those described in Refs. [10,21a]. Excellent textures of samples, preferably fan like textures (Fig. 3) of mesophases were obtained by slowly cooling from the isotropic melt.

The mesophases were identified by microscopic observation and X-ray diffraction measurements at 20 °C. The X-ray data are summarized in Table 3. Powder diffraction patterns of **3a**–**b** and **4a**–**b** contain the typical reflections of a columnar mesophase of substituted Pcs [5]. The Pcs gave five sharp peaks whose spacings are in the ratio of $1{:}\sqrt{3}{:}\sqrt{4}{:}\sqrt{7}\ldots$ in the low angle region, so that each of the mesophases could be established as a discotic hexagonal columnar (Col_h) mesophase. These results suggest a two-dimensional hexagonal lattice with disk-like molecules stacked in columns in the hexagonal arrangement. In the wide angle regions the compounds **3a**–**b** and **4a**–**4b** show a diffuse halo around 4.5 Å which corresponds to the melting of alkyl chains [25c]. An additional reflection at around 3.4 Å is observed which may be assigned to the packing of the macrocyclic subunits in the columns for the compounds

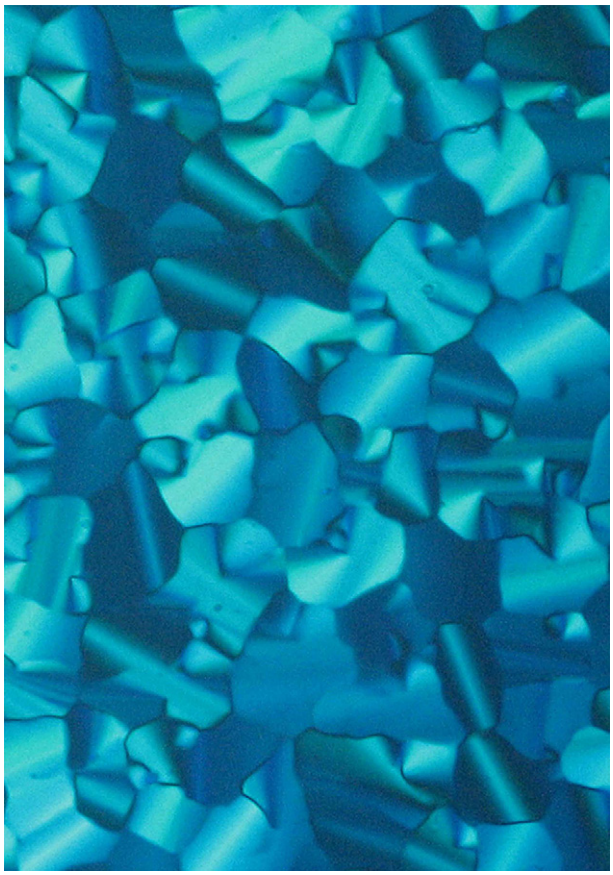


Fig. 3. Optical texture of **4a** observed at 25 °C (magnification ×25).

Table 3
X-ray diffraction data of the Pc derivatives **3a**,**3b**,**4a** and **4b**

Compound	Observed spacings/Å	Theoretical spacings/Å	Lattice constant/Å	Ratio	Miller indices
3a					
	36.90	36.94		1	(100)
	21.55	21.58	$a = 42.61$	$\sqrt{3}$	(110)
	18.63	18.66	Col_{hd} at 20 °C	$\sqrt{4}$	(200)
	13.93	13.96		$\sqrt{7}$	(210)
	12.69	12.72		$\sqrt{9}$	(300)
	10.35	10.38		$\sqrt{12}$	(311)
	7.38				
	4.39				
3b					
	33.95	33.99		1	(100)
	19.70	19.80		$\sqrt{3}$	(110)
	17.10	17.15	$a = 39.20$	$\sqrt{4}$	(200)
	12.75	12.80	Col_{hd} at 20 °C	$\sqrt{7}$	(210)
	11.40	11.42		$\sqrt{9}$	(300)
	4.30				(311)
	3.57				
4a					
	27.39	27.45		1	(100)
	16.06	16.08	$a = 31.63$	$\sqrt{3}$	(110)
	13.96	13.98	Col_{ho} at 20 °C	$\sqrt{4}$	(200)
	10.52	10.55		$\sqrt{7}$	(210)
	9.30	9.34		$\sqrt{9}$	(300)
	7.91	7.93		$\sqrt{12}$	(311)
	4.53	4.60			
4b					
	27.06	27.11		1	(100)
	15.91	15.94		$\sqrt{3}$	(110)
	13.80	13.83		$\sqrt{4}$	(200)
	10.52	10.55	$a = 31.23$	$\sqrt{7}$	(210)
	9.16	9.20	Col_{ho} at 20 °C	$\sqrt{9}$	(300)
	7.81	7.87		$\sqrt{12}$	(311)
	4.51	4.58			

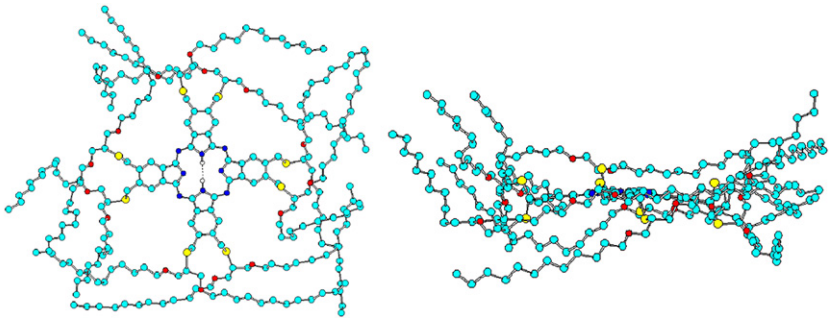


Fig. 4. Molecular structure of metal-free pc **3b**.

3a and **3b**. The sharpness of this reflection suggests good order within the columns and is consistent with the strong intermolecular periodicity associated with the discotic hexagonal ordered Col_h-mesophase [32]. No reflections corresponding to the interdisc distance were observed for **4a–4b**.

The influence of the side chains's nature upon the mesomorphic properties was compared with mesophases of the methylene-bridged octa-alkoxy chain substituted Pc derivatives and their analogues without methylene-bridged derivatives. According to the literature, the mesophase transition temperature of the methylene-bridged alkoxy substituted free Pc was 78 °C, and 83 °C for its without a methylene-bridge derivative [7a,33]. Also, when compared with their octa-substituted branched thioether derivatives, the same behaviour was observed. While the phase transfer temperature of the **3b** analogue without a methylene-bridge was around 0 °C [21a], it was around −9 °C for **3b**. It could be seen that addition of a methylene-bridge to the phthalocyanine core decreases the liquid crystal phase transition temperatures. In addition, comparing the mesophases of the branched thioether Pcs derivatives and their analogous oxoether derivatives, a Col_h mesophase could be seen over a wide temperature region for the thioether Pc derivatives.

Quantum chemical calculations have been applied to predict the electronic and excited states properties of metal free and metallophthalocyanines in recent years [34]. The geometrical data produced from the calculations are usually in good agreement with the data from X-ray analysis. Computer modelling was used to calculate the diameter of the Pc derivatives. The metal free phthalocyanine (**3b**) was subjected to semi-empirical AM1 calculations. Semi-empirical AM1 geometry optimisation calculations were performed in vacuum to obtain the structure with the minimum energy. The conformational changes in the peripheral substituents group, that is methylene-bridged alkylthia, were predicted with molecular dynamics (MD) simulations in vacuum. The starting conformation in molecular dynamics simulations was taken from a geometry optimization with AM1. Twenty picoseconds of MD simulations were run at 300 K constant temperature with 0.001 ps step size, 0.1 ps bath relaxation time and using a molecular mechanics (MM+) force field. At the end of the MD simulations, the diameter of the metal-free Pc was found to be 45 Å. The experimental diameter result from X-ray analysis data is 5 Å less than the calculated one. As shown in Fig. 4, it may be explained that, according to the X-ray diffraction analysis data (Table 3), the alkyl chains do not prefer a straight form but a frizzed form. The geometry optimization with the AM1 method was performed for core the Pc molecule. This was carried out to see the effect of peripheral substituent groups with sulfur atoms on the diameter of the Pc molecule. The diameter of the Pc core is 20 Å. Molecular modelling calculations were performed using HyperChem 7.0 for Windows (Hypercube, FL, USA).

4. Conclusions

Recently we have essentially focused on the synthesis of new Pcs exhibiting gas sensor [35] and liquid crystal properties at room temperature [10d,14d,21b,25c,28b]. Films of the Pcs showing mesomorphic properties at room temperature have been proven to be used as photoconductors and gas sensors in molecular electronic devices and ordered pc films are more sensitive than disordered pc films [35c,36]. In this work, the Pc precursors, 4,5-di(bromomethyl) phthalonitrile (**1**) and 4-bromomethyl-5-methylphthalonitrile (**2**), were isolated and clearly characterized. By using these nitrile derivatives, new methylene-bridged octa- and tetra-branched thioether substituted Pcs Ni(II) and metal-free Pcs were synthesized. These products are soluble in most solvents (carbon tetrachloride, THF, ethylacetate), thermally stable over a wide temperature range and exhibit a hexagonal columnar (Col_h) structure.

The influence of the nature of the side chains upon the mesomorphic properties was compared between mesophases of the Pcs substituted by a methylene-bridged octa-alkoxy chain and their analogues without methylene-bridged derivatives. It could be seen that addition of a methylene-bridge to the phthalocyanine core decreased the liquid crystal phase transition temperatures. In addition, comparing the mesophases of the branched thioether Pcs derivatives and their analogous oxoether derivatives, a Col_h mesophase could be seen over a wide temperature region for the thioether Pc derivatives.

The experimental results of the mesogenic product by X-ray powder analysis were justified by comparison with a computational technique.

Acknowledgement

This work was supported by TUBITAK-TBAG Project 2375 (103T119). The ES mass spectra were taken by Colette Lebrun (DRFMC, CEA-Grenoble).

References

[1] C.C. Leznoff, A.B.P. Lever, Phthalocyanines: Properties and Applications, vols. 1–4, VCH, Weinheim, 1989, 1993 and 1996.
[2] S. Huang, L. Dai, A.W.H. Mau, J. Phys. Chem. B 103 (1999) 4223.
[3] M. Hanack, M. Lang, Adv. Mater. 6 (1994) 819.
[4] P. Matlaba, T. Nyokong, Polyhedron (2002) 2463.
[5] J. Simon, P. Bassoul, in: C.C. Leznoff, A.B.P. Lever (Eds.), Phthalocyanines: Properties and Applications, vol. 2, VCH, Weinheim, 1993, p. 223, Chapter 6.
[6] J. Simon, J.J. Andre, A. Skoulios, New J. Chem. 10 (1986) 295.
[7] (a) C. Piechocki, J. Simon, A. Skoulios, D. Gullion, P. Weber, J. Am. Chem. Soc. 104 (1982) 5245;
(b) J. Barbera, in: J.L. Serrano (Ed.), Metallomesogens, VCH, Weinheim, 1996, p. 164, Chapter 4.
[8] K. Ohta, L. Jacquemin, C. Sirlin, L. Bosio, J. Simon, New. J. Chem. 12 (1988) 751.
[9] D. Masurel, C. Sirlin, J. Simon, New. J. Chem. 11 (1987) 455.
[10] (a) D. Guillon, A. Skoulios, C. Piechocki, J. Simon, P. Weber, Mol. Cryst. Liq. Cryst. 100 (1983) 275;
(b) G.J. Clarkson, N.B. McKeown, K.E. Treacher, J. Chem. Soc., Perkin Trans. 1 (1995) 1817;
(c) J.M. Kroon, R.B.M. Koehorst, M. von Dijk, G.M. Sanders, E.J.R. Sudhölter, J. Mater. Chem. 7 (1997) 615;
(d) A.G. Gürek, M. Durmuş, V. Ahsen, New J.Chem. 28 (2004) 693.
[11] M.J. Cook, M.F. Daniel, K.J. Harrison, N.B. McKeown, A.J. Thompson, J. Chem. Soc., Chem. Commun. (1987) 1086.
[12] A.N. Cammidge, M.J. Cook, K.J. Harrison, N.B. McKeown, J. Chem. Soc., Perkin Trans. 1 (1991) 3053.
[13] N.B. McKeown, J. Painter, J. Mater. Chem. 4 (1994) 1153.
[14] (a) C. Piechocki, J. Simon, J. Chem. Soc., Chem. Commun. (1985) 259;
(b) C. Sirlin, L. Bosio, J. Simon, V. Ahsen, E. Yılmazer, Ö. Bekâroğlu, Chem. Phys. Lett. 139 (1987) 362;
(c) C.F. Van Nostrum, S.J. Picken, R.J.M. Nolte, Angew. Chem., Int. Ed. Engl. 33 (1994) 2173;
(d) F. Yılmaz, D. Atilla, V. Ahsen, Polyhedron 23 (2004) 1931.
[15] F. Von Nostrum, S.J. Picken, A.J. Schouten, R.J.M. Nolte, J. Am. Chem. Soc. 117 (1995) 9957.
[16] (a) O.E. Sielcken, M.M. vonTilborg, M.F.M. Roks, R. Hendriks, W. Drenth, R.J.M. Nolte, J. Am. Chem. Soc. 109 (1987) 4261;
(b) O.E. Sielcken, J. Schram, R.J.M. Nolte, W. Drent, J. Chem. Soc., Chem. Commun. (1988) 108;
(c) O.E. Sielcken, H.C.A. van Lindert, W. Drenth, J. Schoonman, J. Schram, R.J.M. Nolte, Ber. Bunsen-Ges. Phys. Chem. 93 (1989) 702;
(d) N. Kobayashi, A.B.P. Lever, J. Am. Chem. Soc. 109 (1987) 7433;
(e) T. Toupance, V. Ahsen, J. Simon, J. Am. Chem. Soc. 116 (1994) 5352.
[17] (a) D. Adam, P. Schuhmacher, J. Simmerer, L. Haissling, K. Siemensmeyer, K.H. Etzbach, H. Ringsdorf, D. Haarer, Nature 371 (1994) 141;
(b) H. Eichorn, D. Wöhrle, D. Pressner, Liq. Cryst. 22 (1997) 643.
[18] K. Ban, K. Nishizawa, K. Ohta, H. Shirai, J. Mater. Chem. 10 (2000) 1083.
[19] (a) G. Pawlowski, M. Hanack, Synthesis (1980) 28;
(b) C. Piechocki, J. Simon, Nouveau J. Chim. 9 (1985) 159.
[20] I. Cho, Y. Lim, Mol. Cryst. Liq. Cryst. 154 (1988) 9.
[21] (a) H.R. Allcock, T.X. Neenan, Macromolecules 19 (6) (1986) 1495;
(b) A.G. Gürek, V. Ahsen, F. Heineman, P. Zugenmaier, Mol. Cryst. Liq. Cryst. 338 (2000) 75;
(c) D. Atilla, V. Ahsen, J. Porphyrins Phthalocyanines 6 (2002) 593;
(d) F. Yüksel, A.G. Gürek, C. Lebrun, V. Ahsen, New J. Chem. 29 (2005) 726.
[22] (a) C. Wang, M.R. Bryce, A.S. Batsanov, C.F. Stanley, A. Beeby, J.A.K. Howard, J. Chem. Soc., Perkin Trans. 2 (1997) 1671;
(b) Y.J.P. Yasuhiro, Patent, JP 08157489, 1996.
[23] A. Lützen, S.D. Starnes, D.M. Rudkevich, J.R. Rudkevich, Tetrahedron Lett. 41 (2000) 3777.
[24] D.D. Perrin, W.L. Armarego, Purification of Laboratory Chemicals, second ed., Pergamon Press, Oxford, 1980.
[25] (a) A.G. Gürek, Ö. Bekaroğlu, J. Chem. Soc., Dalton Trans. (1994) 1419;
(b) İ. Gürol, V. Ahsen, Ö. Bekaroğlu, J. Chem. Soc., Dalton Trans. (1994) 497;
(c) S. Dabak, V. Ahsen, F. Heineman, P. Zugenmaier, Mol. Cryst. Liq. Cryst. 348 (2000) 111.
[26] A. Gürek, Ö. Bekaroğlu, Helv. Chim. Acta 77 (1994) 1616.
[27] (a) D. Wöhrle, G. Schnurpfeil, G. Knothe, Dyes Pigments 18 (1992) 91;
(b) H. Tomoda, S. Saito, S. Ogawa, S. Shiraishi, Chem. Lett. (1980) 1277;
(c) H. Tomoda, S. Saito, S. Shiraishi, Chem. Lett. (1983) 313.
[28] (a) M. Hanack, G. Schmid, M. Sommerauer, Angew. Chem., Int. Ed. Engl. 32 (1993) 1422;
(b) M. Durmuş, S. Yeşilot, V. Ahsen, New J. Chem. 30 (2006) 675.
[29] N. Kobayashi, in: C.C. Leznoff, A.B.P. Lever (Eds.), Phthalocyanines: Properties and Applications, vol. 2, VCH, Weinheim, 1993, p. 97, Chapter 3.
[30] (a) V. Ahsen, E. Yılmazer, M. Ertaş, Ö. Bekaroğlu, J. Chem. Soc., Dalton. Trans. (1988) 401;
(b) E. Musluoğlu, V. Ahsen, A. Gül, Ö. Bekaroğlu, Chem. Ber. 124 (1991) 2531;
(c) A. Gürek, V. Ahsen, A. Gül, Ö. Bekaroğlu, J. Chem. Soc., Dalton. Trans. (1991) 3367;
(d) M. Koçak, A.İ. Okur, Ö. Bekaroğlu, J. Chem. Soc., Dalton. Trans. (1994) 323.
[31] J. Sleven, C. Görller-Walrand, K. Binnemans, Mater. Sci. Eng. C 18 (2001) 229.
[32] M. Durmuş, C. Lebrun, V. Ahsen, J. Porphyrins Phthalocyanines 8 (2004) 1174.
[33] J.F. Van der Pol, E. Neeleman, J.W. Zwikker, R.J.M. Nolte, W. Drenth, J. Aerts, R. Visser, S.J. Picken, Liq. Cryst. 6 (1989), 5, 577.
[34] (a) M.-S. Liao, J.D. Watts, M.-J. Huang, S.M. Gorun, T. Kar, S. Scheiner, J. Chem. Theor. Comput. 1 (2005) 1201;
(b) M.-S. Liao, J.D. Watts, M.-J. Huang, Inorg. Chem. 44 (2005) 1941;
(c) T.C. Gunaratne, A.V. Gusev, X. Peng, A. Rosa, G. Ricciardi, E.J. Baerends, C. Rizzoli, M.E. Kenney, M.A.J. Rodgers, J. Phys. Chem. A 109 (2005) 2078;
(d) S.P. Keizer, J. Mack, B.A. Bench, S.M. Gorun, M.J. Stillman, J. Am. Chem. Soc. 125 (2003) 7067.
[35] (a) V. Ahsen, M. Özdemir, Z.Z. Öztürk, A. Gül, Ö. Bekaroğlu, J. Chem. Res. (S) 2 (1995) 348;
(b) T.V. Basova, B.A. Kolesov, A.G. Gürek, V. Ahsen, Thin Solid Films 385 (2001) 246;
(c) T.V. Basova, A.G. Gürek, V. Ahsen, Mater. Sci. Eng. C 22 (2002) 99.
[36] T.V. Basova, C. Taşaltın, A.G. Gürek, M.A. Ebeoğlu, Z.Z. Öztürk, V. Ahsen, Sens. Actuators B 96 (2003) 70.

phthalocyanines; the change in symmetry caused by these moieties on periphery is also important. Generally, tetra substituted phthalocyanines are more soluble than symmetrically octasubstituted ones due to the formation of four positional isomers in the case of tetra substituted analogues [13,19,20,26,27]. Thus, a mixture of similar positional isomers may practically be preferred than a single less soluble isomer [28].

Metal phthalocyanine derivatives are known to exhibit high electron transfer properties. The electron transfer properties of phthalocyanines depend on the kind and number of the substituents and are due to the interaction between the phthalocyanine ring and the metal center which is influenced by the conjugated 18π electrons of the phthalocyanine ring [27,29–32]. An electrochemical reaction involves not only electron charge transfer, but also ensues various processes, for instance mass transfer, adsorptions of electroactive species on the electrode, and contribution of coupled chemical reactions. Especially very precise electrochemical analyses are required in the development of functional materials. In this paper, we describe the synthesis and electrochemical properties of soluble biphenyl-malonic ester substituted phthalocyanines. The new compounds were characterized by elemental analyses, ^{1}H NMR, ^{13}C NMR, UV–Vis, and FT-IR spectroscopy, as well as by MASS spectrometry.

2. Experimental

IR spectra were recorded on a Perkin–Elmer Spectrum One FT-IR (ATR sampling accessory) spectrophotometer, electronic spectra on a Unicam UV2 UV–Vis spectrophotometer. Elemental analyses were performed by the Instrumental Analysis Laboratory of the TUBİTAK Marmara Research Centre. ^{1}H NMR and ^{13}C NMR spectra were recorded on a Bruker 250 MHz spectrometer using TMS as internal reference. Mass spectra were measured on a VG Zabspec GC–MS. All reagents and solvents were of reagent grade quality and were obtained from commercial suppliers. The homogeneity of the products was tested in each step by TLC (SiO_2). 4-Nitrophthalonitrile [33], diethyl-3,4-dicyanophenylmalonate [34], potassium salt of diethyl-3,4-dicyanophenylmalonate [34] were synthesized according to the published procedures.

All electrochemical techniques were carried out with a Princeton Applied Research potentiostat/galvanostat controlled by an external PC using the computer program HEADSTRT and utilizing a three-electrode configuration at 25 °C. A Pt wire served as the counter electrode. A saturated calomel electrode (SCE) was employed as the reference electrode and separated from the bulk of the solution by a double bridge containing saturated KCl adjacent to SCE and solvent and carrier adjacent to the solution. Ferrocene/ferrocenium was used as universal reference. The working electrode was a Pt plate with an area of 0.10 cm^2. The surface of the working electrode was polished with a H_2O suspension of Al_2O_3 before each run. The last polishing was done with a particle size of 50 nm. Electrochemical grade tetrabutylammoniumperchlorate (TBAP) in extra pure DCM was employed as the supporting electrolyte at a concentration of 0.1 mol dm^{-3}. High purity N_2 was used for deaeration and to maintain a nitrogen blanket for at least 15 min prior to each run.

2.1. 4-(1,1-Dicarbethoxy-2-(4-biphenyl)-ethyl)-phthalonitrile (1)

To the potassium salt of diethyl-3,4-dicyanophenylmalonate (0.995 g, 3 mmol) in 2:1 acetone:acetonitrile (150 ml) was added 4-(chloromethyl)biphenyl (0.709 g, 3.5 mmol). The mixture was boiled for 20 h under N_2 and then filtered. The solvent was evaporated under reduced pressure to give an oily residue which was washed with water until the product was free of KCl and finally crystallized from diethylether. This compound was soluble in acetone, chloroform, THF, and dichloromethane. Yield: 0.986 g, 71%. Mp 135 °C. IR (KBr), ν (cm^{-1}): 3119 (CH, aromatic), 3059–3032 (CH, aromatic), 2982–2937 (CH, aliphatic), 2237 (C≡N), 1734 (C=O), 1178 (C–O–C); ^{1}H NMR ($CDCl_3$) δ: 7.69–7.32 (m, 10H, aromatic H), 6.84–6.80 (d, 2H, aromatic H), 4.37–4.19 (m, 4H, CH_2), 3.61 (s, 2H, CH_2), 1.28–1.23 (t, 6H, CH_3); ^{13}C NMR ($CDCl_3$) δ: 168.52 (C=O), 142.93, 140.57, 140.23, 133.89, 133.28, 133.14, 132.69, 130.52, 128.79, 127.47, 127.01, 126.96, 115.29 (C–C≡N), 115.16 (C≡N), 115.09 (C≡N), 114.71 (C–C≡N), 63.98 (C–C=O), 62.64 (CH_2–CH_3), 42.56 (C–CH_2–Ph), 13.88 (CH_3); CI-MS (m/z): 453 [M$^+$]; *Anal.* Calc. for $C_{28}H_{24}N_2O_4$: C, 74.32; H, 5.34; N, 6.19. Found: C, 73.98; H, 5.29; N, 6.23%.

2.2. General procedures for phthalocyanine derivatives (2–4)

A mixture of **1** (0.1 g, 0.22 mmol) and the metal salt (0.055 mmol; 0.007 g $CoCl_2$, 0.007 g $CuCl_2$ or 0.009 g $PdCl_2$) was fused in a glass tube (10 × 75 mm) and sealed under N_2. The mixture was heated to 180 °C and stirred for 24 h in an oil bath. After it was cooled to room temperature, the tube was opened and a dark blue solid was obtained. Finally, pure phthalocyanine derivatives were obtained by chromatography on silica gel (first with methanol, then with THF as eluents).

2.2.1. 2,9,17,23-Tetra-(1,1-(dicarbethoxy)-2-(4-biphenyl)-ethyl)phthalocyaninatocobalt (2)

Yield: 0.063 g, 63%. IR (KBr), ν (cm^{-1}): 3027 (CH, aromatic), 2978 (CH, aliphatic), 1724 (C=O), 1165 (C–O–C); UV–Vis λ_{max} (nm) in chloroform: 671, 330; *Anal.* Calc. for $C_{112}H_{96}N_8O_{16}Co$: C, 71.97; H, 5.17; N, 5.99. Found: C, 71.85; H, 5.08; N, 6.10%.

2.2.2. 2,9,17,23-Tetra-(1,1-(dicarbethoxy)-2-(4-biphenyl)-ethyl)phthalocyaninatocopper (3)

Yield: 0.069 g, 71%. IR (KBr), ν (cm^{-1}): 3027 (CH, aromatic), 2978 (CH, aliphatic), 1726 (C=O), 1166 (C–O–C);

UV–Vis λ_{max} (nm) in chloroform: 681, 344; *Anal*. Calc. for $C_{112}H_{96}N_8O_{16}Cu$: C, 71.80; H, 5.16; N, 5.98. Found: C, 71.79; H, 5.12; N, 6.01%.

*2.2.3. 2,9,17,23-Tetra-(1,1-(dicarbethoxy)-2-(4-biphenyl)-ethyl)phthalocyaninatopalladium (**4**)*

Yield: 0.059 g, 61%. IR (KBr), ν (cm^{-1}): 3027 (CH, aromatic), 2920 (CH, aliphatic), 1724 (C═O), 1169 (C–O–C); ^1H NMR ($CDCl_3$) δ: 9.50–9.32 (br, 8H, aromatic H), 8.12–6.98 (m, 40H, aromatic H), 4.46–4.11 (m, 16H, CH_2), 3.66 (s, 8H, CH_2), 1.42–1.23 (q, 24H, CH_3); UV–Vis λ_{max} (nm) in chloroform: 662, 333; MALDI TOF-MS (*m*/*z*): 1916.9 [M^+]; *Anal*. Calc. for $C_{112}H_{96}N_8O_{16}Pd$: C, 70.17; H, 5.04; N, 5.84. Found: C, 70.12; H, 5.01; N, 5.86%.

3. Results and discussion

3.1. Synthesis and characterization

The phthalonitrile derivative **1** was obtained through displacement reaction of 4-nitrophthalonitrile first with diethylmalonate and then in a further reaction with 4-(chloromethyl)biphenyl. Conversion of phthalonitrile derivative **1** into corresponding metallophthalocyanines **2**–**4** was accomplished by reaction with anhydrous salts in fused state [13]. The reaction was complete to give a relatively high yield under these conditions without any need to use ammonium molybdate as the catalyst [27,35]. The yields of the products were 61–71% range which was in accordance with the reported phthalocyanine compounds

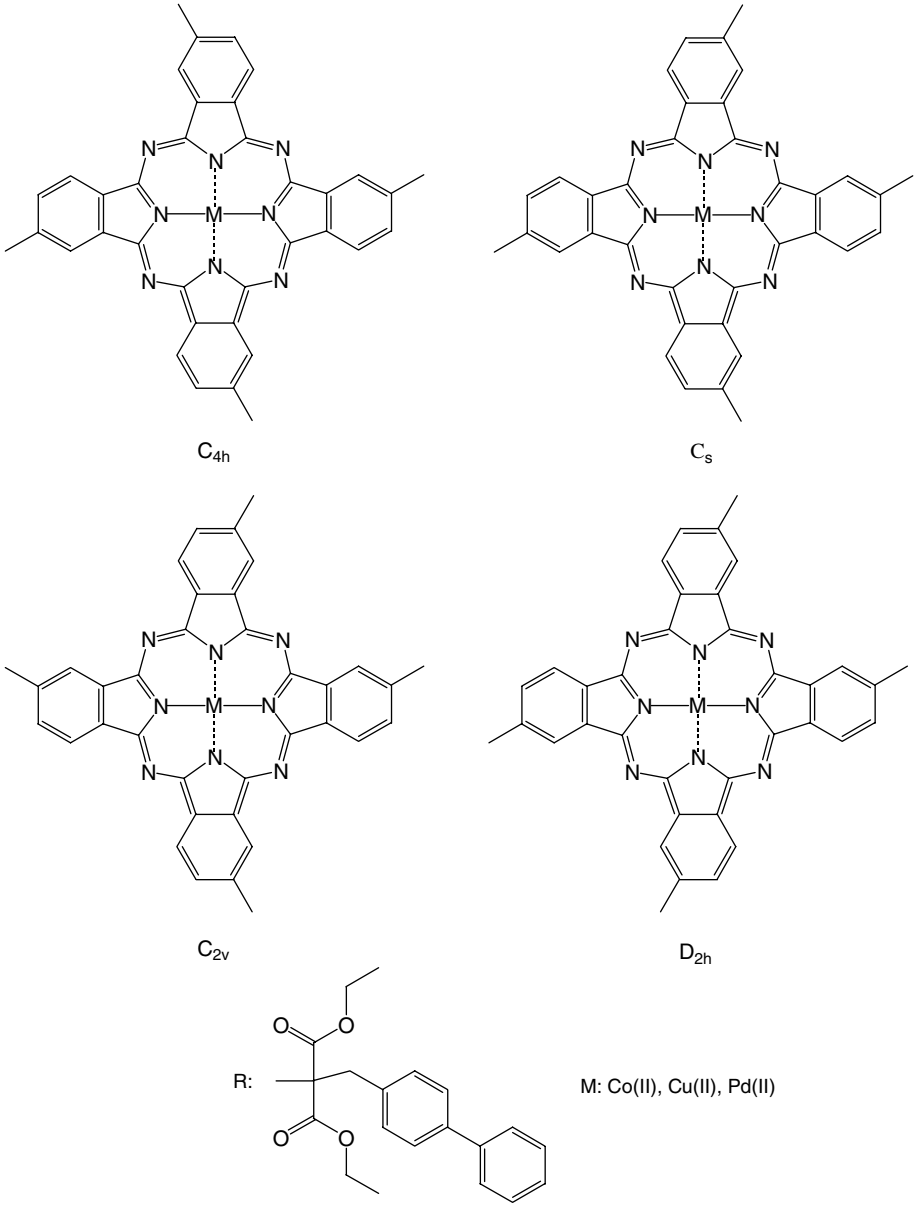


Fig. 1. Isomers of metallophthalocyanines (**2**–**4**).

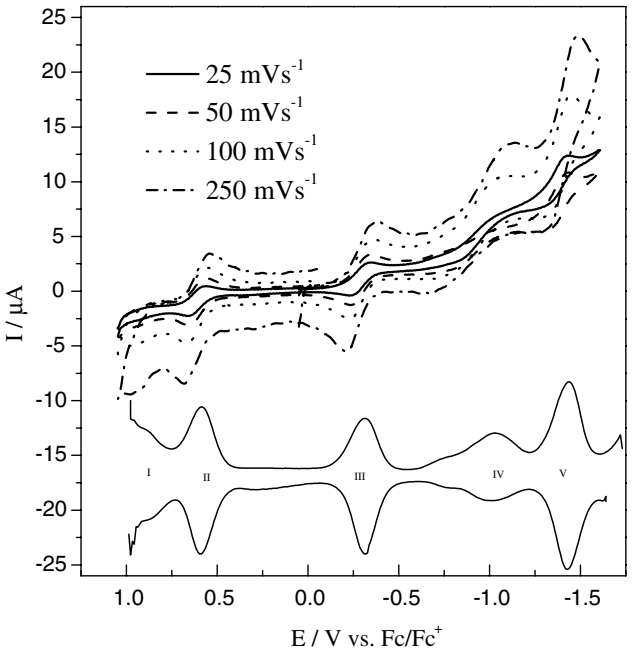


Fig. 2. Cyclic and differential pulse voltammograms of CoPc (**2**) in 0.1 mol dm^{-3} TBAP/DCM electrolyte system at different scan rates.

synthesized directly from the phthalonitrile derivatives and the metal salts without any solvent [36–38]. The phthalocyanines **2**–**4** were purified by column chromatography using silica gel as the stationary phase and methanol, THF as eluents. As a natural consequence of the single substituent on each benzo group, the phthalocyanines **2**–**4** are all a mixture of four constitutional isomers (D_{2h}:C_s:C_{2v}:C_{4h}) (Fig. 1). To the best of our knowledge, there is no literature presently available that reports the successful separation of these four isomers with ordinary column chromatography. Our attempts to separate these isomers by column chromatography are not successful. The blue products are easily soluble in number of solvents such as chloroform, dichloromethane, THF, acetone, DMF, and DMSO.

All of these new compounds were characterized by elemental analyses together with FT-IR, ^{1}H NMR, ^{13}C NMR, UV–Vis, and MASS spectroscopic techniques. Elemental analyses correspond closely with the values calculated for **1**–**4**. In compound **1**, stretching vibrations of C≡N (2237 cm^{-1}), C=O (1734 cm^{-1}), C–O–C (1178 cm^{-1}) appeared at expected frequencies. At the same time, aliphatic CH stretching vibrations are observed at 2982–2937 cm^{-1} and aromatic CH stretching vibrations are observed at 3119–3032 cm^{-1}. The IR spectrum of **1** and those of **2**–**4** were similar, the only difference being the disappearance of C≡N vibration in the latter group.

In the ^{1}H NMR spectrum of **1**, the aromatic protons appear as multiplets and doublet at 7.69–7.32 ppm and 6.84–6.80 ppm. CH_2 protons are observed around 4.37–4.19 ppm as multiplets and singlet at 3.61 ppm. CH_3 protons are observed at 1.28–1.23 ppm as a triplet. The ^{13}C NMR data of **1** confirm the result of the ^{1}H NMR spectrum. In the CI-MS spectrum of **1**, the molecular ion peak appeared at *m*/*z* 453. ^{1}H NMR investigations of compound **4** provided the characteristic chemical shifts for the structures expected. The aromatic protons are observed around 9.50–9.32 ppm as a broad band and 8.12–6.98 ppm as multiplets. CH_2 protons appear at 4.46–3.66 ppm and CH_3 protons appear at 1.37–1.23 ppm. In the MALDI TOF-MS spectrum, we observed a molecular ion peak at *m*/*z* 1916.9 for **4**.

The phthalocyanines display typical electronic spectra with two strong absorption regions, one of them in the UV region at about 300–350 nm (B band) and the other one in the visible region at 600–700 nm (Q band). UV–Vis spectra of all metallophthalocyanines **2**–**4** in chloroform exhibit intense Q bands around 662–681 nm and the B bands in the near UV region, around 330–344 nm, both correlated to π–π* transitions. Because of the bulky substituents on the periphery of phthalocyanines **2**–**4**, Q bands are observed as a sharp absorption peak and almost no shoulder on the higher energy side, which would correspond to aggregated species [39].

3.2. Electrochemical measurements

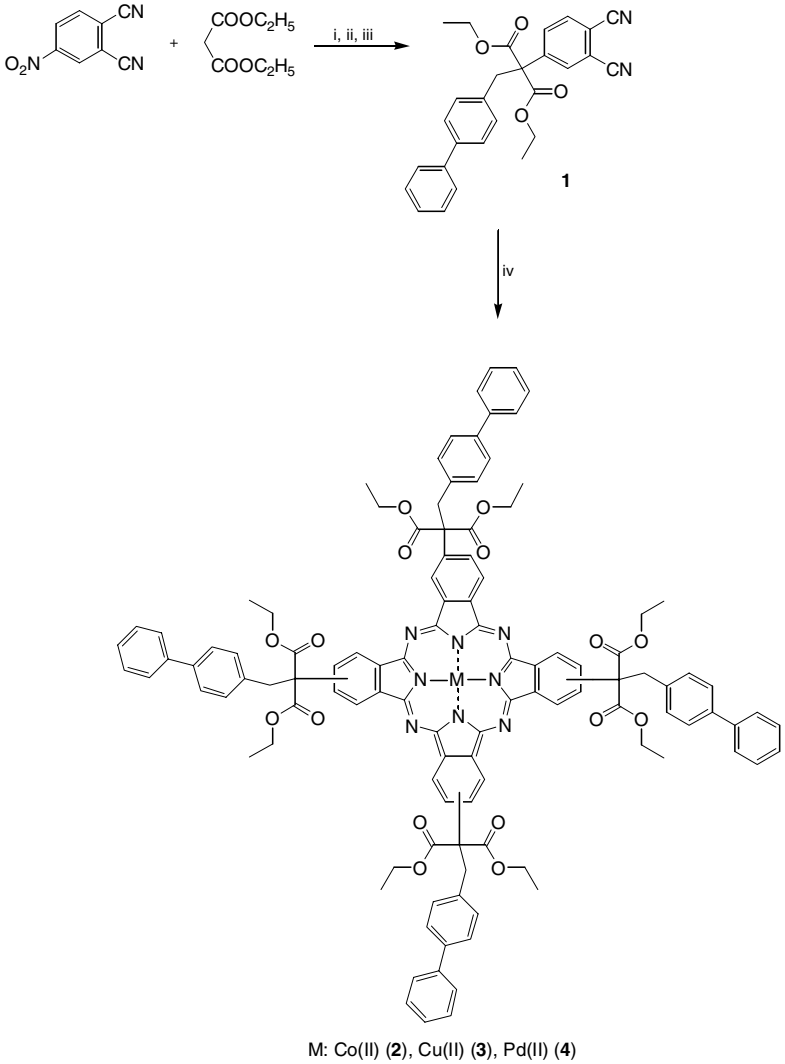
The cyclic voltammograms (CV) of **2** recorded at different scan rates are shown in Fig. 2. The voltammograms of **2** display three reduction couples at −0.29, −0.88, and −1.38 V and two oxidation couples at 0.61 and 0.92 V versus Fc/Fc^+ at 0.100 V s^{-1} scan rate within the available potential range of TBAP/DCM solvent system. Differential pulse voltammetry of the complex confirms the recorded redox processes clearly. The reduction and oxidation behavior of metal-phthalocyanine derivatives is due to the interaction between the phthalocyanine ring and the central metal. The redox properties of metal Pc have been studied by many authors [40–47]. First-row transition metals Pc differ from those of the main-group metals Pc due to the fact that metal "d" orbitals may be positioned between HOMO and LUMO of the phthalocyanine (Pc^{-2}) ligand. This has been well established by several papers published by Lever et al. [27,30–32]. According to this studies, while the first oxidation and first reduction processes occur on the metal center in the metal Pc only for Mn, Fe, and Co derivatives in polar solvent such as DMF and DMSO, the first oxidation process occur on the ring in nonpolar solvent such as DCM and THF. According to Lever et al., for Ni, Cu, and Zn phthalocyanines, redox processes take place on the Pc ring. These studies indicate that first reduction and second oxidation processes of **2** recorded at −0.29 and 0.92 V could be attributed easily to the Co^{II}/Co^{I} and Co^{II}/Co^{III} redox couple, respectively, and the remaining processes to the phthalocyanine ring. All predicted redox processes are given in Eq. 1:

$$[\mathrm{Co(II)Pc}(-1)]^{+} \underset{[\mathrm{Co(III)Pc}(-1)]^{2+}}{\overset{e^{-}\Updownarrow 0.92\ \mathrm{V}}{}} \Longleftrightarrow \overset{e^{-}}{\underset{0.61\ \mathrm{V}}{\Longleftrightarrow}} [\mathrm{Co(II)Pc}(-2)] \overset{e^{-}}{\underset{-0.29\ \mathrm{V}}{\Longleftrightarrow}} [\mathrm{Co(I)Pc}(-2)]^{1-} \overset{e^{-}}{\underset{-0.88\ \mathrm{V}}{\Longleftrightarrow}} [\mathrm{Co(I)Pc}(-3)]^{2-} \underset{[\mathrm{Co(I)Pc}(-4)]^{3-}}{\overset{e^{-}\Updownarrow -1.38\ \mathrm{V}}{}} \quad (1)$$

The separation between the first reduction and first oxidation processes (~0.907 V), which related with the HOMO–LUMO gap of the complex is comparable with the reported CoPc papers [27]. While all redox processes display reversible peak characters only the second reduction process is quasi reversible with a ΔE_p of 0.320 V at 0.100 V s^{-1} scan rate eventhough it has a unity I_{pc}/I_{pa} ratio constant values of $I_p/v^{1/2}$ for all processes suggest diffusion-controlled electron transfer mechanism of redox processes of **2**. For each redox process of **2**, I_{pc}/I_{pa} is almost unity and not changed considerably with the increasing scan rates (Scheme 1).

The voltammograms of **3** (Fig. 3) display three redox processes, assigning to the phthalocyanine ring reduction and oxidation reactions. Scanning the potential to the negative side, two reduction processes at −0.910 and −1.270 V versus Fc/Fc^{+} at 0.1 V s^{-1} scan rate were recorded. Up on scanning anodically an oxidation reaction just at the end of the solvent window (at ~0.560 V) was obtained. All redox processes have quasi reversible peak character with respect to their ΔE_p variation with the scan rate. The separation of the firs reduction and the first oxidation processes (~1.5 V) reflects the HOMO–LUMO gap of the complex. Variation of I_p as a function of $v^{1/2}$ and I_{pc}/I_{pa} ratio suggest diffusion-controlled electron transfer reactions for all redox processes.

Fig. 4 shows the cyclic voltammograms of **4**. Within the available potential range of the solution system, **4** gives only two reversible reduction reactions at −0.895 and −1.280 versus Fc/Fc^{+} at 0.100 V s^{-1} scan rate, respectively. All of these processes are attributed to the phthalocyanine ring electron transfer reactions.



Scheme 1. Synthesis of Pcs. (i) K_2CO_3, DMF, 50 °C; (ii) KOH, ethanol; (iii) acetone/acetonitrile, 4-(chloromethyl)biphenyl, 20 h reflux; (iv) metal salts, 24 h.

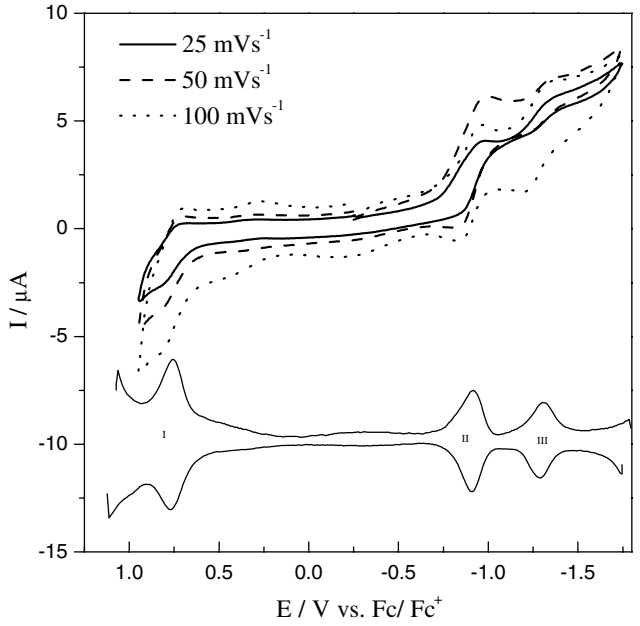


Fig. 3. Cyclic and differential pulse voltammograms of CuPc (**3**) in 0.1 mol dm^{-3} TBAP/DCM electrolyte system at different scan rates.

In conclusion, we have described the synthesis and electrochemical characterization of new metallophthalocyanines. Electrochemical studies show that these compounds have multi-electroned reversible/quasi-reversible redox processes, which are the main requirement for the technological usage of these compounds. The distinctive property of these compounds is that they have a good solubility in polar organic solvents.

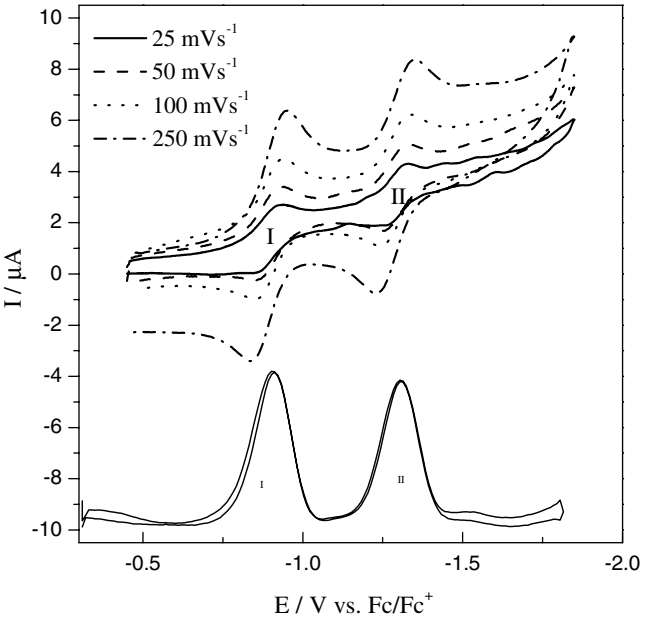


Fig. 4. Cyclic and differential pulse voltammograms of PdPc (**4**) in 0.1 mol dm^{-3} TBAP/DCM electrolyte system at different scan rates.

Acknowledgements

This work was supported by the Research Fund of the Technical University of Istanbul and State Planning Organization (DPT).

References

[1] M. Allmendinger, P. Zell, A. Amin, U. Thewalt, M. Klinga, B. Rieger, Heterocycles 60 (2003) 1065.
[2] J. Gawronski, H. Kolbon, M. Kwit, A. Katrusiak, J. Org. Chem. 65 (2000) 5768.
[3] M.K. Şener, D. Sanchez-Garcia, M. Akkurt, S.Ö. Yıldırım, H. Fun, J.L. Sessler, Turk. J. Chem. 30 (2006) 243.
[4] W.B. Callaway, J.M. Veauthier, J.L. Sessler, J. Porphyrins Phthalocyanines 8 (2004) 1.
[5] R. Öztürk, A. Gül, Tetrahedron Lett. 45 (2004) 947.
[6] J.L. Sessler, J. Jayawickramarajah, A. Gouloumis, T. Torres, D.M. Guldi, S. Maldonado, K.J. Stevenson, Chem. Commun. (2005) 1892.
[7] N.B. McKeown, Phthalocyanine Materials: Synthesis, Structure and Function, Cambridge University Press, Cambridge, 1998.
[8] M. Hanack, M. Lang, Adv. Mater. 6 (1994) 819.
[9] W. Eberhardt, M. Hanack, Synthesis (1997) 95.
[10] Ö. Bekaroğlu, J. Porphyrins Phthalocyanines 4 (2000) 465.
[11] M. Hanack, P. Haisch, Synthesis (1995) 1251.
[12] G. Gümüş, A. Gül, V. Ahsen, New J. Chem. 21 (1997) 589.
[13] M. Koçak, A. Cihan, A.İ. Okur, A. Gül, Ö. Bekaroğlu, Dyes Pigments 45 (2000) 9.
[14] A. Bilgin, B. Ertem, Y. Gök, Supramol. Chem. 17 (2005) 277.
[15] M. Koçak, A. Gürek, A. Gül, Ö. Bekaroğlu, Chem. Ber. 127 (1994) 355.
[16] M. Koçak, A.İ. Okur, Ö. Bekaroğlu, J. Chem. Soc. Dalton Trans. (1994) 323.
[17] S. Gürsoy, A. Cihan, M.B. Koçak, Ö. Bekaroğlu, Monatsh. Chem. 132 (2001) 813.
[18] Z.A. Bayır, Dyes Pigments 65 (2005) 235.
[19] H.A. Dinçer, A. Gül, M.B. Koçak, J. Porphyrins Phthalocyanines 8 (2004) 1204.
[20] M.K. Şener, A. Gül, M.B. Koçak, J. Porphyrins Phthalocyanines 7 (2003) 617.
[21] S.B. Kahl, J. Li, Inorg. Chem. 35 (1996) 3878.
[22] U. Drechsler, M. Pfaff, M. Hanack, Eur. J. Org. Chem. 12 (1999) 3441.
[23] M. Kimura, Y. Sugihara, T. Muto, K. Hanabusa, H. Shirai, N. Kobayashi, Chem. Eur. J. 5 (1999) 3495.
[24] W. Liu, T.J. Jensen, F.R. Fronczek, R.P. Hammer, K.M. Smith, M.G.H. Vicente, J. Med. Chem. 48 (2005) 1033.
[25] C. Choi, P. Tsang, J. Huang, E.Y.M. Chan, W. Ko, W. Fong, D.K.P. Ng, Chem. Commun. 19 (2004) 2236.
[26] C.C. Leznoff, S.M. Marcuccio, S. Grinberg, A.B.P. Lever, K.B. Tomer, Can. J. Chem. (1985) 189.
[27] C.C. Leznoff, A.B.P. Lever (Eds.), Phthalocyanines: Properties and Applications, vol. 1–4, VCH, New York, 1989, 1993, 1996.
[28] C.C. Leznoff, M. Hu, C.R. McArthur, Y. Qin, J.E. van Lier, Can. J. Chem. 72 (1985) 1990.
[29] K.M. Kadish, G. Moninot, Y. Hu, D. Dubois, A. Ibnlfassi, J.M. Barbe, R. Guilard, J. Am. Chem. Soc. 115 (1993) 8153.
[30] A.B.P. Lever, S. Liccocia, P. Minor, B.S. Ramaswamy, S.R. Pickens, K. Magnell, J. Am. Chem. Soc. 103 (1981) 6800.
[31] A.B.P. Lever, P.C. Minor, Inorg. Chem. 20 (1980) 4015.
[32] A.B.P. Lever, Adv. Inorg. Chem. Radiochem. 7 (1965) 27.
[33] J.G. Young, W. Onyebuagu, J. Org. Chem. 55 (1990) 2155.
[34] M.P. Roze, E. Berzins, O. Neilands, Zh. Org. Khim. 28 (1992) 827.
[35] M. Hanack, H. Heckmann, R. Polley, Methods of Organic Chemistry (Houben-Weyl), vol. E9, Georg Thieme Verlag, Stuttgart, 1997, pp. 717–842.

[36] V.N. Nemykin, V.M. Mytsyk, S.V. Volkov, N. Kobayashi, J. Porphyrins Phthalocyanines 4 (2000) 551.
[37] T.M.M. Kumar, B.N. Achar, J. Organometal. Chem. 691 (2006) 331.
[38] M. Lin, J. Wang, N. Chen, J. Huang, J. Coord. Chem. 59 (2006) 607.
[39] N. Kobayashi, A.B.P. Lever, J. Am. Chem. Soc. 109 (1987) 7433.
[40] A.R. Özkaya, E. Hamuryudan, Z.A. Bayır, Ö. Bekaroğlu, J. Porphyrins Phthalocyanines 7 (2000) 689.
[41] A.R. Özkaya, İ. Yılmaz, Ö. Bekaroğlu, J. Porphyrins Phthalocyanines 2 (1998) 483.
[42] A.R. Özkaya, E. Musluoğlu, A. Gül, Ö. Bekaroğlu, J. Chem. Res. (S) (1995) 2721.
[43] A. Koca, M. Şahin, A. Gül, R.Z. Uslu, Monatsh. Chem. 133 (2002) 1135.
[44] A. Koca, Ö.G. Sağlam, A. Gül, Monatsh. Chem. 134 (2003) 11.
[45] A. Kalkan, A. Koca, Z.A. Bayır, Polyhedron 23 (2004) 3155.
[46] A. Koca, M.K. Şener, M.B. Koçak, A. Gül, Transition Met. Chem. 30 (2005) 399.
[47] A. Koca, H.A. Dinçer, M.B. Koçak, A. Gül, Russ. J. Electrochem. 42 (2006) 31.

however, there is a competition between two different ligands for coordination bonds to the same metal, the formation of mixed-ligand coordination compounds gives new and interesting properties [9]. It is known that bipy forms cationic octahedral complexes with divalent transition metal ions, e.g. $[Co(bipy)_3]^{2+}$ [10], while salicylaldehyde ligands form neutral square-planar chelates, e.g. $[Zn(salo)_2]$ and $[Zn(5\text{-Br-salo})_2]$ [11,12].

The Lewis acidity of $[Co^{II}(salo)_2]$ chelates, renders them susceptible to nucleoplilic attack and addition compounds can be obtained. While unidentate nitrogen donor ligands, such as pyridine, may impose tetragonal distortion by occupying *trans* positions $[Co(salo)_2(py)_2]$ [13], structural requirements of the bidentate Lewis base, bipy, dictate occupancy of *cis* positions. Although there are mentioned complexes of Co(II) with 3,5-dichloro-salicylaldehyde and the Lewis base dipyridylamine (dpamH) [14], it has not been reported in the literature any mixed-ligand cobalt(II) compound with 2-hydroxyarylaldehydes and bipyridine, characterized by X-ray diffraction analysis.

For a better understanding of the bonds and structure of mixed-ligand compounds with bipy and substituted salicylaldehydes, we report here the synthesis of a series of new cobalt(II) addition compounds under the formula $[Co^{II}(X\text{-salo})_2bipy]$, where X = 3-$OCH_3$ (**1**), 5-CH_3 (**2**), 5-Cl (**3**) and 5-NO_2 (**4**). The resultant octahedral compounds were characterized by physico-chemical methods and spectroscopic (IR, UV–Vis) studies. Correlation between theoretical results and electronic excitation data were undertaken and the results are presented and discussed. Their structure was verified by X-ray diffraction analysis of a representative compound, the solvated 2,2′-bipyridine-bis(2-hydroxy-5-methoxy-benzaldehydato)cobalt(II), $[Co^{II}(3\text{-}OCH_3\text{-salo})_2\text{-bipy}]\cdot CH_3OH$ (**1**). A cyclic voltammetry (CV) study was employed to investigate their electrochemical behavior, while the thermal behavior for one compound was investigated by simultaneous thermogravimetric-differential thermal analysis (TG-DTA) technique, under nitrogen and oxygen atmosphere. Furthermore, during the synthesis of the titled addition compounds, a side-product was isolated and verified by X-ray analysis as $[Co^{II}(bipy)_3]Br_2\cdot 0.5\text{-(5-chloro-salicylaldehydeH)}\cdot 1.5CH_3OH$ (**5**).

2. Experimental

2.1. Materials

The ligands, substituted 2-OH-benzaldehydes (substituted salicylaldehydes, X-salo), where X = 3-OCH_3, 5-CH_3, 5-Cl or 5-NO_2, the 2,2′-bipyridine (bipy) and the metal salt $CoBr_2\cdot 6H_2O$ were obtained as reagent grade from Aldrich and used as received. The precursor compound $Co(bipy)_2Br_2$ was prepared according to the literature [15]. Solvents for preparation and physical measurements of "extra pure" were obtained from Fluka without further purification.

2.2. Instrumentation/analytical procedures

Microanalyses were obtained using a Perkin–Elmer 240 B CHN microanalyzer. Infrared spectra were recorded on a Perkin–Elmer 1600 FT-IR spectrometer in KBr discs at room temperature and are reported in cm^{-1}. Electronic absorption spectra in solutions were obtained on a Shimatzu 160 A spectrometer. The solid-state electronic spectra were obtained from Nujol mulls. Molar conductivities were measured in CH_3OH, CH_3CN and DMF solutions, employing a WTW conductivity bridge and a calibrated dip type cell. Magnetic susceptibility measurements on powdered samples were performed at 25 °C employing the Faraday method on a home-build balance calibrated against $Hg[Co(SCN)_4]$.

Cyclic voltammetry technique (CV) was used for the electrochemical measurements on a μ-AUTOLAB Potentio-Galvanostat (ECO CHEMIE, Netherlands). A saturated calomel electrode was used as a reference electrode and graphite one as an auxiliary electrode for all measurements. As a working electrode a platinum wire was used. The tests in CH_3CN solution were carried out in the potential region −1900 to +2200 mV at ambient temperature. Recrystallized TEA perchlorate 0.1 M was used as the electrolyte at a scan rate of 100 mV/s. All scans were recorded in degassed solvent and under current of moisture free argon over the solution surface. The thermal behavior of the titled compounds was studied using the simultaneous TG/DTG-DTA technique, over the temperature range ambient-to-1000 °C, using a Setaram Model Setsys-1200 thermogravimetric analyzer. The samples, with mass about 12 mg under nitrogen and 7 mg in oxygen, were heated in platinum crucible, at a heating rate 10 °C/min. Computational techniques: All calculations have been performed using the GAUSSIAN-03 package from Gaussian, Inc. Carnegie Office Park, Building 6 Carnegie, PA 15106, USA. Energy and orbitals calculations were performed using the B3LYP Density Functional Theory approximation (DFT). The basis set used was the LANL2DZ for all atoms. The prediction of the spectrum was calculated using ZINDO option.

2.2.1. Preparation of $[Co^{II}(3\text{-}OCH_3\text{-salo})_2(bipy)]\cdot CH_3OH$ (1)

A solution of 3-methoxy-2-hydroxybenzaldehyde (3-OCH_3-salo), (*o*-vanillin) (152 mg, 1 mmol) and CH_3ONa (54 mg, 1 mmol) in MeOH (25 mL), was added drop-wise to a solution of $Co(bipy)_2Br_2$ (0.266 g, 0.5 mmol) in H_2O (15 mL) at room temperature, under aerobic or inert, under argon, conditions. The solution was stirred for 2 h and then turned darker and an orange-brown solid was formed. The solid was filtered, washed with water and dried under vacuo (0.17 g, 63% yield). The crystalline compound analyzed as *Anal.* Calc. for $C_{27}H_{26}N_2O_7Co$ (MW 549): C, 59.00; H, 4.70; N, 5.10. Found: C, 58.82; H, 4.55; N, 5.08%.

The magnetic value ($\mu_{eff} = 4.26\ \mu_B$) gives the bivalent character of the cobalt ion. The conductivity in freshly

prepared CH_3OH and CH_3CN solutions was found equal to 20 and 27 μS/cm, respectively, denoting the neutral character of the compound, while in DMF equals to 164 μS/cm denoting 2:1 electrolyte. IR spectrum (KBr): selected peaks in cm^{-1}: 3460 m, 1634 and 1616 s (double), 1596 vs, 1093 s, 855 m, 770 and 755 s (double), 729 s, 555 m, 420 m.

2.2.2. Preparation of $[Co^{II}(5\text{-}CH_3\text{-}salo)_2(bipy)] \cdot CH_3OH$ (2)

A solution of 5-methyl-2-hydroxybenzaldehyde (5-CH_3-salo), (136 mg, 1 mmol) and CH_3ONa (54 mg, 1 mmol) in MeOH (25 mL), was added drop-wise to a solution of $Co(bipy)_2Br_2$ (0.266 g, 0.5 mmol) in H_2O (15 mL) at room temperature, under aerobic or inert, under argon, conditions. The solution was stirred for 2 h and then turned darker and an orange-brown solid was formed. The solid was filtered, washed with water and dried under vacuo (0.16 g, 61% yield). The crystalline compound analyzed as *Anal.* Calc. for $C_{27}H_{26}N_2O_5Co$ (MW 517): C, 62.66; H, 5.02; N, 5.41. Found: C, 62.57; H, 4.89; N, 5.25%.

Magnetic value, $\mu_{eff} = 1\,4.10\ \mu_B$, conductivity in CH_3OH and CH_3CN 12 and 15 μS/cm, respectively, while in DMF 167 μS/cm. IR spectrum (KBr): selected peaks in cm^{-1}: 3400 m, 1633 s, 1597 vs, 1148 s, 835 m, 770 s, 547 m, 414 m.

2.2.3. Preparation of $[Co^{II}(5\text{-}Cl\text{-}salo)_2(bipy)] \cdot CH_3OH$ (3)

A solution of 3-chloro-2-hydroxybenzaldehyde (5-Cl-salo), (160 mg, 1 mmol) and CH_3ONa (54 mg, 1 mmol) in MeOH (25 mL), was added drop-wise to a solution of $Co(bipy)_2Br_2$ (0.266 g, 0.5 mmol) in H_2O (15 mL) at room temperature, under aerobic or inert, under argon, conditions. The solution was stirred for 2 h and then turned darker and an orange-brown solid was formed. The solid was filtered, washed with water and dried under vacuo (0.14 g, 52% yield). The crystalline compound analyzed as *Anal.* Calc. for $C_{25}H_{20}N_2O_5Cl_2Co$ (MW 558): C, 52.76; H, 3.58; N, 5.01. Found: C, 52.78; H, 3.53; N, 4.92%.

Magnetic value, $\mu_{eff} = 4.12\ \mu_B$, conductivity in CH_3OH and CH_3CN 15 and 18 μS/cm, respectively, while in DMF 160 μS/cm. IR spectrum (KBr): selected peaks in cm^{-1}: 3401 m, 1638 and 1621 s (double), 1598 vs, 1102 s, 783 and 737 s, 729 s, 544 m, 418 m.

2.2.4. Preparation of $[Co^{II}(5\text{-}NO_2\text{-}salo)_2(bipy)] \cdot H_2O$ (4)

A solution of 5-nitro-2-hydroxybenzaldehyde (5-NO_2-salo), (167 mg, 1 mmol) and CH_3ONa (54 mg, 1 mmol) in MeOH (25 mL), was added drop-wise to a solution of $Co(bipy)_2Br_2$ (0.266 g, 0.5 mmol) in H_2O (15 mL) at room temperature, under aerobic or inert, under argon, conditions. The solution was stirred for 2 h and then turned darker and an orange-brown solid was formed. The solid was filtered, washed with water and dried under vacuo (0.155 g, 55% yield). The crystalline compound analyzed as *Anal.* Calc. for $C_{24}H_{18}N_4O_9Co$ (MW 565): C, 50.97; H, 3.18; N, 9.91. Found: C, 50.47; H, 3.25; N, 9.64%.

Magnetic value, $\mu_{eff} = 4.19\ \mu_B$, conductivity in CH_3OH and CH_3CN 21 and 25 μS/cm, respectively, while in DMF 163 μS/cm. IR spectrum (KBr): selected peaks in cm^{-1}: 3436 m, 1634 s, 1596 vs, 1093 s, 840 m, 764 m, 720 m, 545 w, 495 m, 416 m.

2.2.5. Preparation of $[Co^{II}(bipy)_3]Br_2 \cdot 0.5(5\text{-chloro-salicylaldehydeH}) \cdot 1.5CH_3OH$ (5)

A solution of the ligand 5-chloro-salicylaldehyde (160 mg, 1 mmol) and CH_3ONa (54 mg, 1 mmol) in MeOH (25 mL) was added drop-wise to a solution of $Co(bipy)_2Br_2$ (0.30 g, 0.56 mmol) in H_2O (15 mL) at room temperature. The solution was stirred for 2 h and the orange-brown solid was formed as the main product (compound **3**). In the filtration the deep-brown crystals were isolated upon slow evaporation as the side product (compound **5**). This compound is stable in air, soluble in water, but insoluble in ether and analyzed as *Anal.* Calc. for $C_{35}H_{32.\ 5}N_6O_{2.5}Cl_{0.5}$-$CoBr_2$: C 51.66; H, 3.99; N, 10.33. Found: C, 53.11; H, 3.57; N, 10.45%. The conductivity in CH_3CN equals to 260 μS/cm, denoting 1:2 electrolyte. IR spectrum (KBr): selected peaks in cm^{-1}: 3410 m, 1680 and 1660 vs, 1596 vs, 1470 s, 1276 s, 783 and 737 s, 418 m.

2.3. X-ray crystal structure determinations

Crystals of compounds **1** and **5** were mounted on a Phillips-STOE diffractometer employing Mo Kα radiation. All data were collected at 295 K using the ω–2θ technique. The first matrix was obtained from 25 high theta reflections and leaded to the pronounced space groups. After the centering of the reflections and the definition of the space groups the followed data collection included all reflections with 2θ up to at least 25°. Crystallographic data and other pertinent information are given in Table 1. The data were corrected for Lorentzian polarization effects as usual. For both crystals the first solution came out using the SIR-92 method [16]. Subsequent calculations and data refinement were performed using CRYSTALS version 12.1 [17]. Final unit cell parameters were determined by least-squares method using all observed reflections and finally all data were corrected using DIFABS method [18]. Concerning the compound $[Co(3\text{-}OCH_3\text{-}salo)_2(bipy)] \cdot CH_3OH$ (**1**), all non-hydrogen atoms were refined anisotropically, together with those coming from the solvent molecule. Hydrogen atoms were located in difference Fourrier maps. After refining their positions using fixed thermal parameter values to 0.07 and soft restraints on the bond lengths and angles to regularize their geometry (C···H to 0.98, O···H to 0.82) their positions were finally refined with riding constraints.

For the compound $[Co(bipy)_3]Br_2 \cdot 0.5$(5-chloro-salo-H) $\cdot 1.5CH_3OH$ (**5**), SIR-92 revealed the positions of the atoms forming the moiety $Co(bipy)_3Br_2$, while successive Fourier synthesis revealed the positions of all the rest non-hydrogen atoms and their disordered distribution.

Table 1
Crystal data for compounds **1** and **5**

Compound	**1**	**5**
Empirical formula	$C_{26}H_{22}CoN_2O_6 \cdot CH_4O$	$2(C_{35}H_{32.5}N_6O_{2.5}Cl_{0.5}CoBr_2)$
Formula weight	549.45	1610.13
Wavelength (Å)	0.71070	0.71073
Crystal system	monoclinic	hexagonal
Space group	$P2_1/c$	$P\bar{6}2c$
Unit cell dimensions		
a (Å)	8.389(6)	13.267(2)
b (Å)	15.914(6)	13.267(2)
c (Å)	18.169(8)	22.132(5)
β (°)	91.086(9)	
γ (°)		120
Volume (Å^3)	2425(2)	3373.6(10)
Z	4	2
D_{calc} (Mg/m^3)	1.505	1.585
Absorption coefficient (mm^{-1})	0.759	2.960
F(000)	1140	1618
Crystal size (mm)	$0.12 \times 0.16 \times 0.18$	$0.16 \times 0.22 \times 0.24$
θ Range for data collection (°)	1.70–25.58	1.77–25.11
Limiting indices	$-10 \leqslant h \leqslant 10$, $-15 \leqslant k \leqslant 19$, $-17 \leqslant l \leqslant 22$	$-15 \leqslant h \leqslant 15$, $0 \leqslant k \leqslant 15$, $0 \leqslant l \leqslant 26$
Observed/unique reflections	4790/4548	2650/2020
Completeness to $\theta = 25.58°$ (%)	100.0	99.9
Refinement method	full-matrix least-squares on F^2	full-matrix least-squares on F^2
Weighting scheme	$w = [\text{weight}][1 - (\Delta F/6\sigma F)^2]^2$	$w = [\text{weight}][1 - (\Delta F/6\sigma F)^2]^2$
Data/parameters/restraints	3376/334/0	1766/155/4
Goodness-of-fit on F^2	1.075	1.058
Final R indices	$R_1 = 0.0479$, $wR_2 = 0.0601$ [$I > 0.7\sigma(I)$]	$R_1 = 0.0378$, $wR_2 = 0.0373$ [$I > 1.0\sigma(I)$]
Largest difference in peak and hole (e Å^{-3})	0.31 and −0.47	0.71 and −0.55

Especially for the 5-chloro, salicylaldehyde molecule it was found disordered over three positions as rotating around a C_3 axis passing from the center of the phenyl ring. The carbonyl carbon atom was never located, as it was masked from the chlorine atom as well as all hydrogen atoms due to the disorder rotation. The rest of the hydrogen atoms were positioned geometrically and their positions were finally refined with riding constraints. Soft constraints were also introduced on the bond lengths and angles to regularize geometry of 5-chloro-salicylaldehyde molecule. All disordered atoms coming from the 5-Cl-saloH were refined isotropically. The rest non-hydrogen, non-disordered atoms, were refined anisotropically.

Selected interatomic distances and bond angles are given in Tables 2 and 3, respectively. The figures of the clinographic projections were produced with the CAMERON program [19] and are given in Figs. 1 and 2.

3. Results and discussion

3.1. Synthesis and characterization

The reaction of [Co(II)(bipy)$_2$Br]Br with the anions of the substituted salicylaldehydes (X-salo) and 2,2′-bipyridine (bipy), under proper aerobic or inert conditions, leaded to the formation of the crystalline orange-brownish products. They are stable in air, soluble in almost all the organic solvents but insoluble in water. Their elemental analyses and the absence of electrical conductivity in CH_3CN and CH_3OH solutions indicated neutral compounds, with general formula [Co(II)(X-salo)$_2$(bipy)], while their magnetic moments ($\mu_{eff} = \sim 4.2\ \mu_B$) corroborate with high-spin octahedral coordination of the cobalt(II) ion.

The coordination mode of the ligands in the addition compounds was studied using spectroscopic methods. The X-ray diffraction study of [Co(II)(3-OCH$_3$-salo)$_2$-(bipy)] · CH_3OH, provided evidence regarding the geometry around cobalt(II) ion and the configuration of the ligands.

The successful isolation of these compounds depends on the concentration of the ligand and the precursor compound. When the precursor compound is in excess, a second deep-brown product is always present having the general formula [Co(II)(bipy)$_3$]Br$_2$ · X-saloH. The structure of the latter compounds was elucidated for the compound [Co(II)(bipy)$_3$]Br$_2$ · 0.5(5-chloro-saloH) · 1.5CH_3OH (**5**) by X-ray diffraction study.

3.2. Description of the structure [Co^{II}(3-methoxy-salicylaldehyde)$_2$(bipy)] · CH_3OH (**1**) and [Co^{II}(bipy)$_3$]Br_2 · 0.5(5-chloro-saloH) · 1.5CH_3OH (**5**)

In both compounds the cobalt atom is coordinated to the ligands in a distorted octahedron. In the case of compound [Co(3-OCH$_3$-salo)$_2$(bipy)] (**1**), the most axial vector is this passing through O(4), Co and N(2). If O(4) and N(2) would be considered to occupy the axial positions, then O(5), O(2), N(1) and O(1) would be on the equatorial plane and the geometry could be better described as axially elongated distorted octahedral. All distances and angles are similar with those reported in analogous complexes

Table 2
Selected bond lengths (Å) for compounds **1** and **5**

Compound **1**		Compound **5**	
Co(1)–O(1)	2.098(3)	Co(1)–N(1)	2.143(2)
Co(1)–O(2)	2.049(2)	Co(1)–N(2)	2.089(2)
Co(1)–O(4)	2.074(2)	N(1)–C(1)	1.371(2)
Co(1)–O(5)	2.020(2)	N(1)–C(5)	1.316(2)
Co(1)–N(1)	2.097(3)	N(2)–C(6)	1.418(2)
Co(1)–N(2)	2.084(3)	N(2)–C(10)	1.330(3)
O(1)–C(17)	1.237(4)	C(1)–C(2)	1.363(3)
O(2)–C(12)	1.281(4)	C(2)–C(3)	1.366(3)
O(3)–C(13)	1.361(4)	C(3)–C(4)	1.402(3)
O(3)–C(18)	1.422(5)	C(4)–C(5)	1.382(2)
O(4)–C(25)	1.224(4)	C(5)–C(6)	1.447(3)
O(5)–C(20)	1.287(4)	C(6)–C(7)	1.391(2)
O(6)–C(21)	1.364(4)	C(7)–C(8)	1.424(2)
O(6)–C(26)	1.415(4)	C(8)–C(9)	1.362(3)
O(7)–C(27)	1.342(6)	C(9)–C(10)	1.363(3)
N(1)–C(1)	1.334(4)		
N(1)–C(5)	1.344(4)		
N(2)–C(6)	1.348(4)		
N(2)–C(10)	1.333(4)		
C(1)–C(2)	1.369(5)		
C(2)–C(3)	1.373(5)		
C(3)–C(4)	1.358(5)		
C(4)–C(5)	1.382(5)		
C(5)–C(6)	1.465(4)		
C(6)–C(7)	1.391(5)		
C(7)–C(8)	1.376(5)		
C(8)–C(9)	1.363(5)		
C(9)–C(10)	1.372(5)		
C(11)–C(12)	1.430(5)		
C(11)–C(16)	1.408(5)		
C(11)–C(17)	1.405(5)		
C(12)–C(13)	1.431(5)		
C(13)–C(14)	1.367(5)		
C(14)–C(15)	1.392(6)		
C(15)–C(16)	1.341(6)		
C(19)–C(20)	1.419(5)		
C(19)–C(24)	1.413(5)		
C(19)–C(25)	1.412(6)		
C(20)–C(21)	1.436(5)		
C(21)–C(22)	1.359(5)		
C(22)–C(23)	1.402(6)		
C(23)–C(24)	1.327(6)		

Table 3
Selected bond angles (°) for compounds **1** and **5**

Compound **1**		Compound **5**	
O(1)–Co(1)–O(2)	86.81(9)	N(1)–Co(1)–N(1a)	95.34(6)
O(1)–Co(1)–O(4)	86.02(11)	N(1)–Co(1)–N(2)	77.10(5)
O(2)–Co(1)–O(4)	86.94(10)	N(1)–Co(1)–N(2a)	169.44(5)
O(1)–Co(1)–O(5)	95.79(10)	N(1a)–Co(1)–N(2)	92.73(6)
O(2)–Co(1)–O(5)	171.97(9)	N(2)–Co(1)–N(2a)	95.71(6)
O(4)–Co(1)–O(5)	85.67(10)	Co(1)–N(1)–C(1)	122.46(13)
O(1)–Co(1)–N(1)	167.92(10)	Co(1)–N(1)–C(5)	116.60(11)
O(2)–Co(1)–N(1)	86.01(10)	C(1)–N(1)–C(5)	120.4(2)
O(4)–Co(1)–N(1)	103.27(11)	Co(1)–N(2)–C(6)	114.3(1)
O(5)–Co(1)–N(1)	92.64(11)	Co(1)–N(2)–C(10)	128.4(1)
O(1)–Co(1)–N(2)	94.20(11)	C(6)–N(2)–C(10)	117.1(2)
O(2)–Co(1)–N(2)	99.30(10)	N(1)–C(1)–C(2)	121.9(2)
O(4)–Co(1)–N(2)	173.76(10)	C(1)–C(2)–C(3)	120.2(2)
O(5)–Co(1)–N(2)	88.11(10)	C(2)–C(3)–C(4)	115.8(2)
N(1)–Co(1)–N(2)	77.41(11)	C(3)–C(4)–C(5)	123.3(2)
Co(1)–O(1)–C(17)	123.1(2)	N(1)–C(5)–C(4)	118.2(2)
Co(1)–O(2)–C(12)	125.0(2)	N(1)–C(5)–C(6)	115.3(1)
C(13)–O(3)–C(18)	117.2(3)	C(4)–C(5)–C(6)	126.4(2)
Co(1)–O(4)–C(25)	125.8(2)	N(2)–C(6)–C(5)	116.0(2)
Co(1)–O(5)–C(20)	128.9(2)	N(2)–C(6)–C(7)	120.4(2)
C(21)–O(6)–C(26)	117.5(3)	C(5)–C(6)–C(7)	123.6(2)
Co(1)–N(1)–C(1)	125.4(2)	C(6)–C(7)–C(8)	118.9(2)
Co(1)–N(1)–C(5)	115.8(2)	C(7)–C(8)–C(9)	119.1(2)
C(1)–N(1)–C(5)	118.6(3)	C(8)–C(9)–C(10)	119.7(2)
Co(1)–N(2)–C(6)	116.1(2)	N(2)–C(10)–C(9)	124.8(2)
Co(1)–N(2)–C(10)	125.4(2)		
C(6)–N(2)–C(10)	118.5(3)		
N(1)–C(1)–C(2)	122.5(3)		
C(1)–C(2)–C(3)	118.6(3)		
C(2)–C(3)–C(4)	119.6(3)		
C(3)–C(4)–C(5)	119.4(3)		
N(1)–C(5)–C(4)	121.2(3)		
N(1)–C(5)–C(6)	115.2(3)		
C(4)–C(5)–C(6)	123.6(3)		
N(2)–C(6)–C(5)	115.3(3)		
N(2)–C(6)–C(7)	121.2(3)		
C(5)–C(6)–C(7)	123.4(3)		
C(6)–C(7)–C(8)	118.6(3)		
C(7)–C(8)–C(9)	120.1(3)		
C(8)–C(9)–C(10)	118.4(3)		
N(2)–C(10)–C(9)	123.1(3)		

[13,20]. The atoms forming the equatorial plane present a maximum deviation 0.163(14) Å from it (for O(2)), while the Co(II) cation was found to be 0.015(15) Å lower of the plane with a deviation equal with the error. The bipyridine and the two *o*-vanillin ligands were found to be practically planar with deviations smaller than the error. The dihydral angles formed were 60.86° and 77.73° between the bipy and the two *o*-vanillin moieties, while the angle between the two *o*-vanillins was 54.34°. The bipyridine ligand was found to be nearly perpendicular to the equatorial plane with a formed angle of 85.56°. The two *o*-vanilins form angles of 25.83° and 63.51° with the equatorial plane. No interaction between the complex and the methanol molecule was observed.

In the case of compound, $[Co(bipy)_3]^{2+}2Br^- \cdot 0.5(5\text{-chloro-salicylaldehyde}) \cdot 1.5CH_3OH$ (**5**), the geometry around Co(II) is distorted octahedral due to symmetry reasons. All distances and angles (Tables 2 and 3) are typical as compared with similar complexes previously reported [10,21]. The Br^- anions present no interactions with the complex moiety. In the cell can also be found three disordered methanol molecules, as well as one molecule of 5-chloro-salicylaldehydeH, (badly disordered as previously described) on the symmetry plane $z = 1/4$. The neutral ligand 5-Cl-saloH is completely planar due to symmetry reasons and has no interaction with the cobalt complex (Fig. 2).

3.3. Theoretical calculations and electronic excitation study

Theoretical calculations were performed for structure optimization and assignment of the experimentally observed electronic excitation spectrum for the compound **1**. Specifically, in the crystal structure description, it was

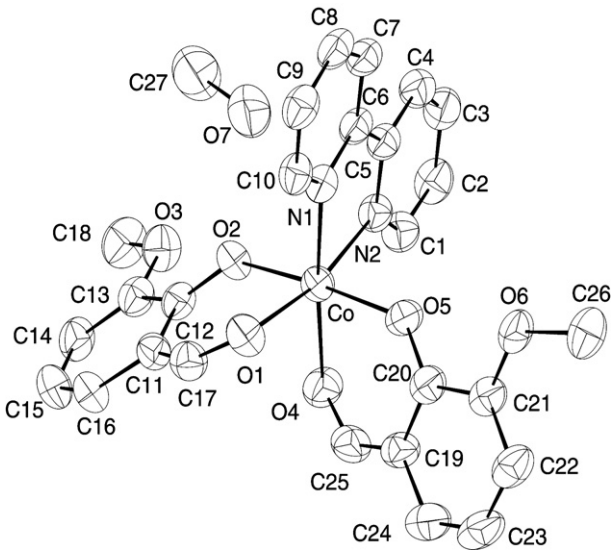


Fig. 1. Molecular structure of $[Co^{II}(3\text{-}OCH_3\text{-}salo)_2(bipy)] \cdot CH_3OH$ (**1**).

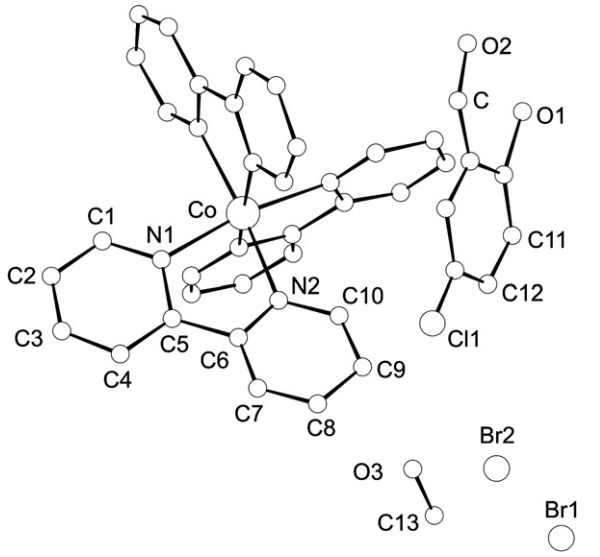


Fig. 2. Molecular structure of $[Co^{II}(bipy)_3]Br_2 \cdot 0.5(5\text{-Cl-saloH}) \cdot 1.5\text{-}CH_3OH$ (**5**).

considered that the complex possessed a coordination sphere with a compressed distorted octahedral arrangement. This resulted considering that the most axial vector was the one passing through N(2), Co and O(4) having an angle of 173.8°. If the vector passing through O(5), Co and O(2), having an angle of 172.0°, would be considered as the most axial, then the geometry could be better described as compressed distorted octahedral. The comparison between the optimized and the "frozen" geometry theoretical spectra, greatly helps to the better assignment of the observed electronic excitation spectra of the compounds recorded in solvents with different dielectric constants, as well as in Nujol mulls.

The experimental UV–Vis spectra of the compound $[Co^{II}(o\text{-vanillin})_2(bipy)]$ (**1**) in the solid state as Nujol mull presented six dominant bands in the region 300–1100 nm (Fig. 3). The two intense bands in the UV region, present at wavelengths 300 and 360 nm (bands I and II, respectively) were assigned to intra-ligand $\pi^* \leftarrow \pi$ or $\pi^* \leftarrow$ n transitions, evidence arising from the position and intensity, as well as from the comparison with the spectra of the corresponding ligands bipy and *o*-vanillin. In the visible region, the three bands at 440, 550 (sh) and 990 nm (bands IV, V, and VI, respectively), are due to the metal suggesting an octahedral arrangement of the ligands around Co(II) [22]. Accordingly, these bands could be assigned to the spin-allowed excitations from the $^4T_{1g}(F)$ ground state to the electronic levels $^4T_{1g}(P)$; $^4A_{2g}$; and $^4T_{2g}$. The band at 396 nm (band III) is the more doubtful to be assigned. It can be either a CT or a d–d transition and its character will be clarified by the theoretical calculations (see below).

As it can be figured out from the electronic spectra of the compound **1** in several solvents (Fig. 3), there is evidence of a solvent effect affording changes in stereochemistry of the cobalt(II) environment. The existence of the octahedral configuration was also concluded for CH_3CN solutions, although the bands II and IV are masked under the single broad band centered at 396 nm (band III). The band at 550 nm (band V) is apparent only in concentrated solutions, while the band at 990 nm (band VI) is clearly seen.

In the cases of DMF and CH_3OH solutions, however, changes either in stereochemistry or in chromophore can be assumed. One new band around 610 nm appears, while the band at 990 nm completely disappears. Changes in the coordination sphere may be accomplished with or without changes in stereochemistry, depending on whether it takes place a nucleophilic substitution or an elimination reaction. Thus, in the case of CH_3OH solution, *possibly* upon oxidation to Co(III), one protonated *o*-vanillin ligand passes in the solution, while a peroxide (O_2^{2-}) group takes its place according to the following equation [23, and references therein]:

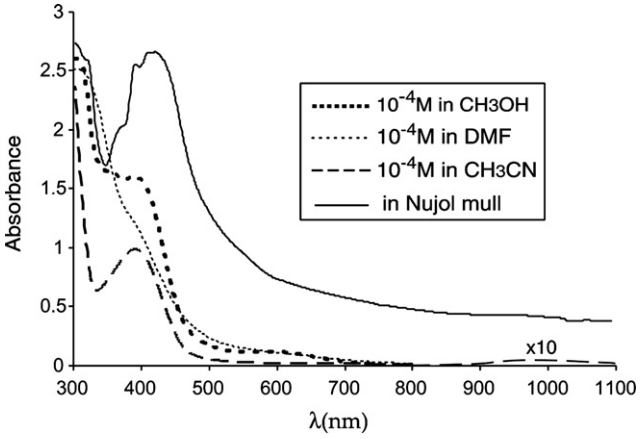


Fig. 3. Electronic excitation (UV–Vis) spectra for $[Co^{II}(3\text{-}OCH_3\text{-salo})_2\text{-}(bipy)] \cdot CH_3OH$ (**1**) in various solvents and in Nujol mull.

$$[Co^{II}(o\text{-vanillin})_2(bipy)] \rightarrow [Co^{III}(o\text{-vanillin})(bipy)(O_2^{2-})] + o\text{-vanillinH}$$

In the case of DMF solutions most possibly upon oxidation to Co (III), an *o*-vanillin ligand was dissociated according to the following equation [24]:

$$[Co^{II}(o\text{-vanillin})_2(bipy)] \rightarrow [Co^{III}(o\text{-vanillin})(bipy)(DMF)]^{2+} + o\text{-vanillinH} + 2X \text{ (or } o\text{-vanillin} + X$$

where X is probably CH_3O)

The two new resulting complexes in solution most probably adopt tetragonal pyramidal geometry of the chromophore. In the case of the more polar DMF molecules a change in configuration is more favorable attributable to the dissociation effect of a ligand. This is also in coincidence to the conductivity measurements especially in the case of DMF, where the transformation seems to be very fast. In the case of CH_3OH the change seems to be slow and the final product occurs from well aerated solutions after a few hours.

In order to find out the influence of the substituents in the benzene ring of the salicylaldehyde ligands, on the electronic spectra of the investigated addition compounds, we recorded them in CH_3CN solutions (Fig. 4). The position of the absorption bands, along with their extinction coefficients (ε values) are given in Table 4. It can be seen that the band VI is present at the same wavelength, around 990 nm for all compounds, while the position and intensity of the band III around 390 nm depends on the substituents of the salicylaldehyde ligand. The bands IV and V found in Nujol spectrum at 440 and 550 nm, respectively, are not clearly observed in CH_3CN solutions with concentration 10^{-4} M.

Theoretical calculations on the crystal structure fixed geometry resulted that the coordination geometry was elongated distorted octahedral. This arises from the d-orbitals arrangement pattern, which was the typical for this

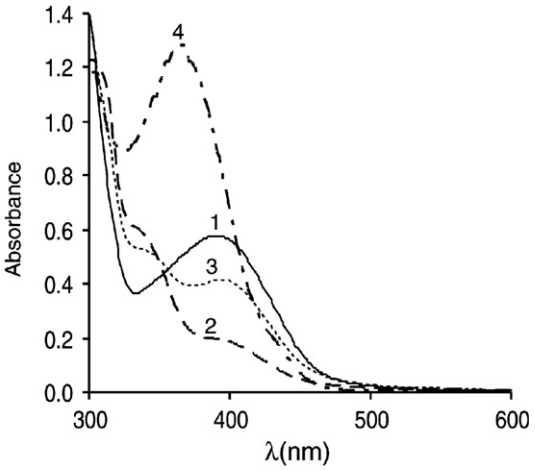


Fig. 4. Electronic excitation (UV–Vis) spectra for the compounds $[Co^{II}(X\text{-salo})_2(bipy)]$, 10^{-4} M in CH_3CN (X = 3-OCH_3 (**1**); 5-CH_3 (**2**); 5-Cl (**3**); 5-NO_2 (**4**)).

Table 4
Electronic excitation (UV–Vis) data for the compounds $[Co^{II}(X\text{-salo})_2(bipy)_2]$ in CH_3CN

Compound	Band I λ (nm), ε	Band II λ (nm), ε	Band III λ (nm), ε	Band VI λ (nm), ε
1	300, 14000	masked	394, 5900	990, 100
2	306, 12100	340, 6100	389, 2180	989, 95
3	301, 13000	330, 5800	390, 4250	989, 95
4	300, 12000	masked	375, 12300	988, 100

geometry. When leaving the complex free to optimize, the final predicted structure was nearly identical with the one observed from the crystal structure with maximum bonds and angles deviations of 0.6 Å and 2°, respectively. The optimized structure had again the same coordination geometry. The d-orbitals arrangement was exactly the same, as the previously observed, with slight differences to the energy calculated values.

The predicted excitation spectrum for the complex **1**, revealed from the coordinates of the optimized structure using the ZINDO approximation, presents six dominant excitation bands in the visible region of the spectrum. These bands were calculated to be at the following excitation maxima: 986.87 nm, 574.77 nm, 507.56 nm, 478.56 nm, 402.70 nm, 399.34 nm. It is resulted that the bands at 987 nm and 478 nm are virtually of d–d character, while the one at around 400 nm is virtually of MLCT character. This is in accordance with the results from the experimental spectrum in the solid state and clarifies the bands character, as one molecular orbital, symmetrically spread over the two vanillin ligands, was found to be located between the e_g and the t_{2g} metal orbitals.

3.4. IR spectra

For all the studied compounds, a plethora of discrete bands appears in their IR spectra, which can be classified as those emanating from crystal water or methanol, from the bipy molecule, from the substituted salicylaldehyde, and those due to the coordination bonds. Thus, the band at 3460–3400 cm^{-1} is indicative of the vibration ν(OH), which is due to the non-coordinated water or methanol. The intense bands at 1596 cm^{-1}, attributable to the stretching vibration of C=N (aromatic bond) are present in all complexes. The intense band at 750 ± 20 cm^{-1}, ascribed to the rocking vibrations of the pyridyl C–H bonds and the band at 870 ± 15 cm^{-1}, attributable to the deformation vibrations of the pyridyl C–H bonds, disclosed the occurrence of the nitrogenous bases in the studied addition compounds. Upon coordination the intense bands stemming from the stretching and bending vibrational modes of the phenolic OH disappear indicating the removal of a hydrogen atom, while the band at ~1640 cm^{-1}attributable to C=O is shifted to lower frequencies indicative of their coordination mode. The bands originating from the C–O stretching vibrations at ~1070 cm^{-1} exhibit small positive shifts, while their intensity is enhanced appreciably. The

medium intensity bands at about 550 and 416 cm^{-1} are attributed to the coordination bonds [25].

3.5. Electrochemical studies

All the studied compounds exhibit the same behavior during the cyclic voltammetry experiments. A typical CV diagram of the compound **1** is, representatively, depicted in Fig. 5, while the experimental data for the studied compounds are presented in Table 5. The CV in the region from −1900 mV to 2200 mV revealed the reversible waves of the couples Co(II)–Co(III) around 400 mV and Co(I)–Co(II) around −850 mV. Both couples present a single electron wave, as compared with the waves generated by equimolar amount of ferrocene solution. These values are very close to them found from the CV of similar compounds [26,27].

The oxidation of the phenolic oxygen is presented with a wave around 1400 mV, while the reduction of the same group takes place at ca. −1800 mV. Both are two electron waves and this suggests that the ligands in the complex are equivalent as expected. The remaining peak in the anodic region at around 1700 mV can be attributed to the oxidation of the bipyridine group. All the results are in accordance with the voltage values of the waves present in the cyclic voltamograms of the free ligands.

In the case of [Co(5-nitro-salicylaldehyde)$_2$bipy] · H_2O (**4**), the CV diagrams in both the free ligand and the complex (Fig. 6), were presented one more reversible wave at −1350 mV, which can be attributed to the oxidation and reduction of the nitro group connected to the phenyl ring of the ligand. This wave is present in the CV of the free ligand with the same pattern.

3.6. Thermal studies

The thermal behaviour of the compound **1** was studied in nitrogen and oxygen atmosphere, over the temperature range ambient to 980 °C by using the simultaneous TG/DTG-DTA technique. As it can be seen from the thermoanalytical curves in nitrogen (Fig. 7), though this compound is very stable at ambient temperature, it is unstable upon heating, decomposing in four successive endothermic stages. The first stage at 25–120 °C is attributed to the elimination of the methanol molecule from the crystal lattice. The second and third decomposition stages possess sharp intense endothermic effects, due to the melting (210 °C) and successive decomposition (270 °C) accompanied by sudden mass loss, about 47%. The decomposition proceeds with the rupture of bonds inside the salicylaldehyde ligands, along with the dissociation of the coordinated bonds.

The small endotherm on the DTA curve at 400 °C, without mass loss, is indicative of possible phase or structural change of the intermediate compound formed at 350 °C. This is probably consisted of the {CoO(bipy)} moiety, as inferred from TG/DTG curves and verified from the IR peaks (760 and 730 cm^{-1}, attributable to the ν(=C–H) of the pyridine molecule).

The gradually elimination of the bipy ligand was followed, leading to the isolation of pure CoO at 500 °C in oxygen atmosphere, verified by IR spectra, while the residue at 980 °C in nitrogen atmosphere was found to be CoO mixed with small amount of carbon. This decomposition mode is in accordance with other analogous nickel(II) addition compounds with bipy and 2-hydroxyaryloximes [28] or cobalt addition compounds with phen and salicylato ligands [29].

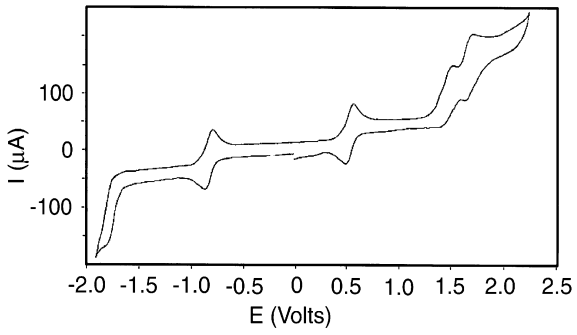


Fig. 5. Cyclic voltammogram of [Co^{II}(3-OCH_3-salo)$_2$(bipy)] (**1**), in CH_3CN with 0.1 M TEAP (scan rate 100 mV/s).

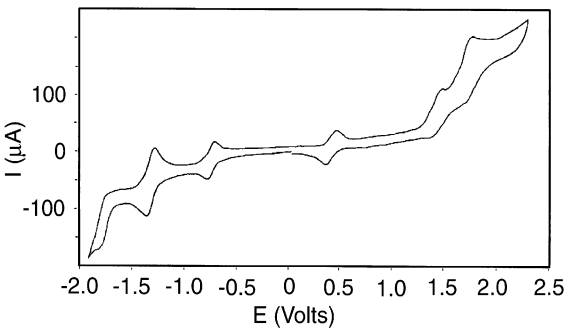


Fig. 6. Cyclic voltammogram of [Co^{II}(5-NO_2-salo)$_2$(bipy)] (**4**) in CH_3CN with 0.1 M TEAP (scan rate 100 mV/s).

Table 5
Cyclic voltammetry data (mV) for all complexes in CH_3CN with 0.1 M TEAP (scan rate 100 mV)/s

	I			II			III			IV	V	VI		
	E_{pa}	E_{pc}	$E_{1/2}$	E_{pa}	E_{pc}	$E_{1/2}$	E_{pa}	E_{pc}	$E_{1/2}$	E_{pa}	E_{pc}	E_{pa}	E_{pc}	$E_{1/2}$
1	−0.87	−0.83	−0.84	0.47	0.51	0.49	1.40	1.48	1.44	1.66	−1.82			
2	−0.88	−0.82	−0.85	0.46	0.51	0.48	1.41	1.48	1.44	1.65	−1.81			
3	−0.86	−0.82	−0.84	0.45	0.49	0.47	1.38	1.46	1.42	1.63	−1.82			
4	−0.82	−0.78	−0.80	0.40	0.46	0.44	1.40	1.46	1.43	1.63	−1.82	−1.43	−1.38	−1.41

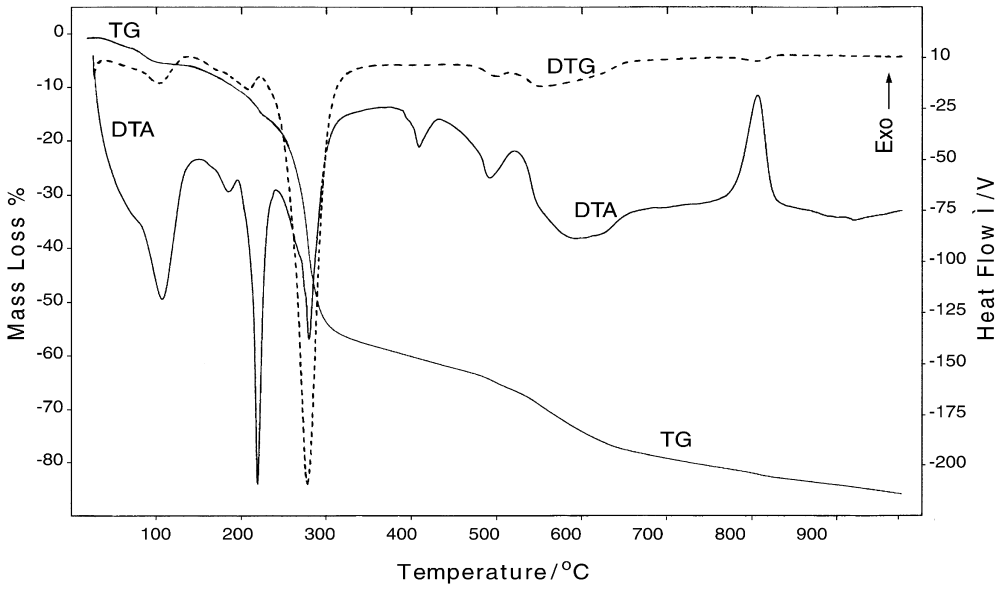


Fig. 7. Thermoanalytical curves (TG/DTG-DTA) of $[Co^{II}(3\text{-}OCH_3\text{-}salo)_2(bipy)] \cdot CH_3OH$ (**1**) in N_2 (heating rate 10 °C/min).

The sharp exothermic peak at 780 °C, accompanied by small mass loss, cannot be assigned with certainty, since in nitrogen atmosphere an exothermic peak maybe due to a sudden decomposition like an explosion or to crystallization.

4. Conclusions

The prepared noval octahedral compounds $[Co^{II}(X\text{-}salo)_2\text{-}(bipy)]$ are stable in air in the solid state and in CH_3CN solutions, while in CH_3OH and DMF solutions are gradually oxidized to Co(III). The theoretical ZINDO investigation with GAUSSIAN-03 for the prediction of the electronic spectrum, gave good correlation with the experimental spectrum in the solid state for the compound **1**. The cyclic voltammogram gave all the expected waves for the redox processes of the metal Co(II) and the ligands bipy and salicylaldehydes. X-ray studies of compounds **1** and **5** verified the existence of two octahedral Co(II) compounds coming from the same reaction. The compound **1** is very stable at ambient temperature, but unstable upon heating, decomposing to CoO at 980 °C in nitrogen, but at 500 °C in oxygen atmosphere.

Acknowledgment

We thank X. Sidiropoulos, Chemistry Department of Aristotle University of Thessaloniki for running the TG-DTA experiments.

Appendix A. Supplementary material

CCDC 267680 and 606952 contain the supplementary crystallographic data for **1** and **5**. These data can be obtained free of charge via http://www.ccdc.cam.ac.uk/conts/retrieving.html, or from the Cambridge Crystallographic Data Centre, 12 Union Road, Cambridge CB2 1EZ, UK; fax: (+44) 1223-336-033; or e-mail: deposit@ccdc.cam.ac.uk. Supplementary data associated with this article can be found, in the online version, at doi:10.1016/j.poly.2006.09.084.

References

[1] R.N. Prasad, A. Agrawal, J. Ind. Chem. Soc. 83 (2006) 75.
[2] R.N. Prasad, M. Agrawal, R. George, J. Ind. Chem. Soc. 82 (2005) 445.
[3] S.T. Hussain, H. Ahmad, M.A. Atta, M. Afzal, M. Saleem, J. Trace Microprobe Tech. 16 (1998) 139.
[4] K. Fujinaga, Y. Sakaguchi, T. Tsuruhara, Y. Seike, M. Okumura, Solvent Extr. Res. Dev. (2001) 144.
[5] P. Sajith, M.T. Ummer, N. Manual, S.K. Mandot, S.L. Agrawal, S. Bandyopadhyay, R. Mukhopadhyay, B. D'Cruz, A.S. Deuri, A.P. Kuriakose, J. Adhes. Sci. Technol. 19 (2005) 1475.
[6] J. Reedijk, in: G. Wilkinson, R.D. Gillard, J.A. Mc-Cleverty (Eds.), Comprehensive Coordination Chemistry, vol. 2, Pergamon Press, Oxford, 1987, p. 73.
[7] S.A. Bedell, A.E. Martell, Inorg. Chem. 22 (1983) 364.
[8] C. Creutz, M. Chou, T.L. Netzel, M. Okumura, N. Sutin, J. Am. Chem. Soc. 102 (1980) 1309.
[9] T.-F. Liu, H.-K. Lin, S.R. Zhu, Z.-M. Wang, H.-G. Wang, X.-B. Leng, Y.-T. Chen, Indian J. Chem. A 41 (2002) 2530.
[10] D.J. Szalda, C. Creutz, D. Mahajan, N. Sutin, Inorg. Chem. 22 (1983) 2372.
[11] Zheng-Ying Xiong, Li-Jiang Liu, Z.-Y. Xiong, L.-J. Liu, Acta Crystallogr., Sect. E 61 (2005) m863.
[12] Q. Chen, Acta Crystallogr., Sect. E 62 (2006) m56.
[13] F. Zhong, S.-H. Zhang, Y.-M. Jiang, X.-X. Zhong, Jiegou Huaxue 22 (2003) 318.
[14] K.N. Patel, N.H. Patel, K.M. Patel, M.N. Patel, Synth. React. Inorg. Met-Org. Chem. 30 (2000) 829, 921,1617.
[15] Th. Kramer, J. Strahle, Z. Naturforsch. B 41 (1986) 692.
[16] A. Altomare, G. Cascarano, G. Giacovazzo, A. Guagliardi, M.C. Burla, G. Polidori, M. Camalli, J. Appl. Crystallogr. 27 (1994) 435.

[17] D.J. Watkin, J.R. Carruthers, P.W. Betteridge, CRYSTALS Program, Chemical Crystallographic Laboratory, Oxford University, Oxford, UK, 1993.
[18] N. Walker, D. Stuart, Acta Crystallogr. Sect., C 39 (1983) 158.
[19] D.J. Walker, C.K. Prout, F.J. Bearch, CAMERON Program, Chemical Crystallographic Laboratory, Oxford University, Oxford, UK, 1996.
[20] C. Tsiamis, St. Karageorgiou, M. Lalia-Kantouri, G. Manoussakis, Gazz. Chim. Ital. 117 (1987) 317.
[21] J.-Y. Niu, Z.-L. Wang, J.-P. Wang, Polyhedron 23 (2004) 773.
[22] R.P. John, A. Steekanth, R. Maliyekal, P. Kurup, S.M. Mobin, Polyhedron 21 (2002) 2515.
[23] K. Kurtzak, J. Solution Chem. 27 (1998) 621.
[24] A.B.P. Lever, Inorganic Electronic Spectroscopy, 2nd ed., Elsevier, Amsterdam, 1984.
[25] R.M. Silverstein, G.C. Bassler, G. Morvill, Spectrometric Identification of Organic Compounds, 3rd ed., Wiley, New York, 1974.
[26] H. Shimakoshi, M. Koga, Y. Hisaeda, Bull. Chem. Soc. Jpn. 75 (2002) 1553.
[27] S.K.H. Rahaman, H. Chowdhury, D. Bose, R. Ghosh, Chen-H. Hung, B.K. Ghosh, Polyhedron 24 (2005) 1755.
[28] M. Lalia-Kantouri, A.G. Hatzidimitriou, M. Uddin, Polyhedron 18 (1999) 3441.
[29] H. Olmez, F. Arslam, H. Icbudak, J. Therm. Anal. Calorim. 76 (2004) 793.

applications in design of new biologically active metal–biomolecule compounds on the other hand. The importance of the effects of metal ions in stabilizing particular conformations in peptides has been shown for the copper(II) and zinc(II) complexes with *N*-phthaloylglycylglycine, in which the *N*-protected dipeptide adopted β-pleated conformations in the solid state [9]. While the zinc(II) complex was monomeric, the copper(II) complex had a polymeric structure formed by bridging carboxylates [9].

The steric van der Waals interactions between the aliphatic groups in the copper(II) chelates with *N*,*N*-dimethylated L-isoleucine, L-valine and L-leucine were suggested to be the cause for different EPR parameters measured for these complexes dissolved in hydrogen-bond making solvents [10–12]. The steric intramolecular and crystal lattice effects rather than electronic effects were attributed to cause the geometry differences found between the experimental crystalline molecular structures and the vacuum molecular structures (calculated applying the hybrid density functional method B3LYP [13–16]; the electronic properties were calculated using the natural population analysis (NPA) method [17]) for a series of anhydrous and aqua copper(II) complexes with amino acids [18,19]. These effects can be studied and modeled with the molecular mechanics method [18–20].

There have been a number of reported experimental crystal structures of bis-copper(II) complexes with glycine and *N*-alkylated glycine derivatives. These are: *cis* bis-(glycinato)copper(II) hydrate [21], *trans* diaquabis-(sarcosinato)copper(II) [22], *trans* aquabis(*N*,*N*-dimethylglycinato)copper(II) dihydrate [23], *trans* aquabis(*N*-*tert*-butyl-*N*-methylglycinato)copper(II) [24], *cis* and *trans* bis-(glycinato)copper(II) [25], *trans* bis(glycinato)copper(II) hydrate [25], and *trans* bis(*N*-*tert*-butyl-*N*-benzylglycinato)copper(II) [26]. The structural and electronic properties of the first four listed complexes were investigated [19], as well as of (di- and more) hydrated copper(II) chelates with glycine [27,28] by using the quantum chemical B3LYP [13–16] and NPA [17] methods. The mechanism of the *cis* to *trans* isomerism of bis(glycinato)copper(II) was theoretically studied in the gas phase [29] and related with the observed solid state *cis* to *trans* bis(glycinato)copper(II) geometry rearrangements [29,30].

The UV–Vis and IR characterizations of *trans* bis-(*N*,*N*-diethylglycinato)copper(II), $Cu(Et_2Gly)_2$, and *trans* bis(*N*,*N*-dibutylglycinato)copper(II) were reported by Nash and Scheafer [31]. They noticed that these two complexes as well as *trans* bis(D,L-*N*,*N*-diethylalaninato)-copper(II) formed red solutions when dissolved in benzene or ethylene chloride solutions. While bis(D,L-*N*,*N*-diethylalaninato)copper(II) retained the red color in the crystalline state, the two glycinato complexes changed the color from red to bluish upon cooling the solution and crystallization. Nash and Sheaffer concluded that the red color would mean truly four-coordinate complex, while blue color indicated the copper(II) coordination number greater than four [31]. Indeed the X-ray determination and refinement of the crystal structure of *trans* $Cu(Et_2Gly)_2$ presented for the first time in this Article revealed that the coordination about the copper atom was a distorted pyramid with carbonyl oxygen atom from neighboring molecule occupying the fifth copper(II) coordination position at a relatively short distance of 2.312 Å. To our best knowledge, such type of the copper(II) coordination geometry has not yet been observed for anhydrous *trans* bis copper(II) amino acid complexes in the crystalline state. It may be obvious that the copper(II) coordination geometry changed from four-coordinate to five-coordinate upon crystallization. Similar pyramidal coordination pattern with axially placed carbonyl oxygen was found in the crystal structures of *cis* bis(D-alaninato)copper(II) [32], *cis* bis(L-alaninato)copper(II) [33], and *cis* bis(glycinato)copper(II) [25] in which the carbonyl oxygen was 2.37 Å away from the copper(II). In the solid state structures of earlier reported *trans* bis copper(II) chelates with *N*,*N*-dialkylated amino acids, the copper(II) was either truly four-coordinate or with a water molecule at the fifth coordination position [19]. Conversely, in anhydrous *trans* bis copper(II) complexes with *N*-unsubstituted aliphatic amino acids the copper(II) coordination geometry was either an irregular square-planar or a distorted planar, with two carbonyl oxygen atoms from adjacent molecules in the crystal lattice completing an elongated octahedron [19].

This paper examines the ability of recently reported molecular mechanics (MM) force field FFW [19,20] developed for modeling anhydrous and aqua copper(II) amino acid complexes in simulated crystalline surroundings and in vacuo to reproduce the unit cell dimensions and molecular conformation of the novel crystal structure of $Cu(Et_2Gly)_2$. The study has been aimed at investigating the effects of steric interactions caused by the replacement of amino hydrogen atoms with flexible ethyl substitutents on the structural properties of the copper(II) glycinato complex in the solid state and vacuum. The conformational analysis of $Cu(Et_2Gly)_2$ showed that the experimentally obtained conformer was not the most stable in vacuo. The result has motivated us to study the intermolecular interactions of different conformers in the crystal state to elucidate the processes that governed the appearance of experimentally observed conformer in the real crystal structure.

2. Experimental

2.1. Syntheses and crystal structure determination

The *N*,*N*-diethylglycine ligand was prepared by condensation of glycine with acetaldehyde. The catalytic hydrogenation was carried out over three days at room temperature and 1.5 bar in ethanol/water (1:1) solution following the procedure of Bowman and Stroud [34]. After removing the catalyst, the product was recrystallized from ethanol/ether solution giving *N*,*N*-diethylglycine (m.p. 131–132 °C). The elemental analysis confirmed the composition

of the ligand. The $Cu(Et_2Gly)_2$ complex was prepared according to the modified procedure of Nash and Schaefer [31], i.e., by reaction of copper(II) acetate monohydrate with the sodium salt of *N*,*N*-diethylglycine in dichloromethane. The blue anhydrous crystals appeared upon slow evaporation from red-violet methylene chloride solution. Single blue crystals of polymeric $Cu(Et_2Gly)_2$ were obtained by recrystallization from water solution by slow evaporation at room temperature. The cell and refinement data were collected at room temperature using diffractometer with serial detector. The F^2 reflection data were prepared by standard data reduction procedure including the absorption correction.

The crystal structure of *catena*-poly[(*N*,*N*-diethylglycinato-κ*O*,κ*N*)copper(II)-μ-[*N*,*N*-diethylglycinato-κO^1,κ*N*:O^2]] was solved in the classical way using the heavy-atom method. Non-hydrogen atoms were allowed for anisotropic thermal motion. The hydrogen atom positions were calculated as riding atoms at default effective non-H-to-H atom distances according to corresponding sterteochemical requests. All calculations were performed and the figures were drawn using WinGX suite of programs [35].

Crystal data. $C_{12}H_{24}CuN_2O_4$, $M = 323.87$, monoclinic, $a = 9.9151(8)$ Å, $b = 7.4321(8)$ Å, $c = 21.2665(19)$ Å, $\beta = 103.122(7)°$, $V = 1526.2(2)$ Å^3, $T = 293(2)$ K, space group $P2_1/c$ (No. 14), $Z = 4$, μ(Mo Kα) = 1.44 mm^{-1}, 3693 reflections measured, 3331 unique reflections ($R_{int} = 0.017$). The final $R_1 = 0.0369$ (based on 2333 reflections with $I \geqslant 2\sigma I$), and 0.0704 (all data), $wR_2 = 0.1102$.

2.2. Molecular mechanics calculations

The conformational (strain) potential energy of the molecule was calculated from the following basic formula:

$$V_{\text{strain}} = \sum_{\text{bonds}} D_e(e^{-2\alpha(b-b_0)} - 2e^{-\alpha(b-b_0)}) + \frac{1}{2}\sum_{\text{valence angles}} k_\theta(\theta-\theta_0)^2 + \frac{1}{2}\sum_{\text{torsion angles}} V_\varphi(1 \pm \cos n\varphi) + \frac{1}{2}\sum_{\text{out-of-plane angles}} k_\chi\chi^2 + \sum_{i<j}\left(A_iA_jr_{ij}^{-12} - B_iB_jr_{ij}^{-6}\right) + \sum_{l<m} q_lq_mr_{lm}^{-1}$$

Here b, θ, φ, χ and r are bond lengths, valence, torsion, and out-of-plane angles, and nonbonded distances. D_e, α and b_0 are empirical parameters for bond stretching (a Morse function), k_θ and θ_0 for valence-angle bending, and k_χ for the out-of-plane deformational potential for the carboxyl group. Torsional interactions are specified with V_φ and n (height and multiplicity of the torsional barrier, respectively). One torsion per bond was calculated. A and B are one-atom empirical parameters for the van der Waals interactions (a Lennard-Jones 12-6 function). The q is a charge parameter. Intramolecular interactions separated by three and more bonds were considered nonbonded and calculated with the Lennard-Jones and electrostatic potentials. The interactions inside the copper(II) coordination sphere were modeled using the Morse potential between the copper and ligand donor atoms (two nitrogens and two oxygens), the repulsive electrostatic potential between the four donor atoms, and a torsion-like potential dependent on the "torsion" angle O–N–N–O, with two minima at 0° and 180° that correspond to the *cis*- and the *trans*-planar CuN_2O_2 configurations, respectively. It is a model without any explicit valence-angle bending potential for the angles around copper.

All MM calculations were performed using the modified [36] Lyngby version of the CFF program for conformational analysis [37–39], and with the force field FFW [19,20] suited for modeling anhydrous and aqua copper(II) complexes with aliphatic amino acids with *trans*- or *cis*-CuN_2O_2 coordination polyhedron.

In the Lyngby-CFF program [37–39], the input charge parameters are used for an assignment of fractional atomic charges. The assignment is done by a special charge redistribution algorithm, which keeps the total charge of the molecules neutral and distributes the charge values in a manner supposed to mimic ab initio results [36,39]. For the copper(II) amino acid complexes the charge redistribution algorithm has been adapted to yield the assigned fractional charges close to the charges resulting from NPA calculated for the bis-copper(II) complexes with L-*N*,*N*-dimethylvaline, L-alanine, L-leucine [18], as well as with glycine, sarcosine, *N*,*N*-dimethylglycine, and *N*-*tert*-butyl-*N*-benzylglycine [19].

A detailed description of the FFW's development as well as of the discussion on the efficacy of the force field in simulation and prediction of experimental crystal and molecular structures and quantum-chemically calculated vacuum structures can be found in our earlier paper [19]. Specifically, the modeling included experimental molecular and crystal structures of 13 anhydrous and 10 aqua copper(II) complexes with aliphatic amino acids and their alkyl derivatives. The efficacy of the force field expressed by means of the root-mean-square (rms) deviations between the experimental and theoretical crystal values of 23 copper(II) amino acid complexes were 0.018 Å in the bond lengths, 2.2° in the valence angles, 5.5° in the torsion angles (the hydrogen atoms were omitted in the internal coordinates' comparisons), 0.395 Å in the unit cell lengths, and the unit cell volumes were reproduced in the range from −8.1% to 9.6% [19].

The conformational potential energy was minimized for an isolated molecular system (in vacuo or a gas-phase approximation), and for a molecule surrounded with other molecules in the crystal lattice (a condensed-phase approximation). During the energy minimization of a crystal, all degrees of freedom (i.e., six lattice constants and 3N position coordinates of the N atoms in the asymmetric unit) were allowed to vary, except α and γ unit cell angles and all three unit cell angles in the cases of a monoclinic and an orthorhombic crystal, respectively. The chosen lattice constants were kept unchanged to preserve the presumed symmetry of the crystals. The other asymmetric units in the simulated crystalline environment were generated from

the original asymmetric unit by symmetry operations of a specific space group assigned to the crystal lattice. The intermolecular atom–atom interactions between the atoms of the original asymmetric unit of $Cu(Et_2Gly)_2$, and the atoms of surrounding asymmetric units, $V_{intermolecular}$, were calculated using the same functional forms (Lennard-Jones 12-6 function and coulombic potential) and empirical parameters as for the intramolecular nonbonded interactions. The crystal simulations were carried out by using the Williams variant of the Ewald lattice summation method [40,41] with a spherical and abrupt cut-off limit of 14 Å, and convergence constants of 0.2 $Å^{-1}$, 0.2 $Å^{-1}$, and 0.0 for Coulomb, dispersion, and repulsion lattice summation terms. A detailed description of the crystal simulations is given elsewhere [41]. The potential energy of the $Cu(Et_2Gly)_2$ molecule in the simulated crystal surroundings, $V_{crystal}$, was calculated as a sum of the intramolecular strain potential energy, V_{strain}, and the intermolecular van der Waals and electrostatic contribution (lattice energy), $V_{intermolecular}$, i.e., $V_{crystal} = V_{strain} + V_{intermolecular}$.

3. Results and discussion

3.1. The X-ray molecular and crystal structure

The asymmetric unit contains the copper atom coordinated in distorted square-planar fashion with two glycine ligands' oxygen and nitrogen atoms, respectively, attached to the metal center in *trans* position (Fig. 1). Selected bond distances and angles in polymeric $Cu(Et_2Gly)_2$ are listed in Table 1.

The displacement of copper from calculated best plane through the donor O and N atoms may be considered significant being 0.1749(4) Å. The deviation of the O(11)–Cu–O(21) and N(1)–Cu–N(2) from linearity is considerable (Table 1). Five-membered chelate rings have the conformation of an open envelope with different ring atoms on the flap. Nitrogen atom N(1) is moved out of the plane calculated through the Cu, O(11), C(11), and C(12), respectively, for 0.724(2) Å, while methylene carbon atom C(22) is shifted for 0.429(3) Å out of the best plane through the Cu, O(21), N(2), and C(21), respectively. The copper atom is coordinatively unsaturated. Oxygen atom $O(22^i)$ [(i): $1-x$, $y-1/2$, $-z+1/2$] from the neighboring molecule increases the Cu coordination number to 5 turning its coordination sphere from square-planar to distorted square-pyramidal. The chelate bidentate ligand containing O(22) serves as the bridging moiety between neighboring copper atoms developing the discrete endless coordination polymer chains spreading along the *y*-axis (Figs. 2 and 3). Neighboring parallel polymeric chains are held together by standard van der Waals interatomic interactions and through very weak C–H···O(12) and C–H···O(22) hydrogen bonding (i.e., close carbon to carbonyl oxygen atoms' intermolecular contacts are from 3.152 to 3.657 Å).

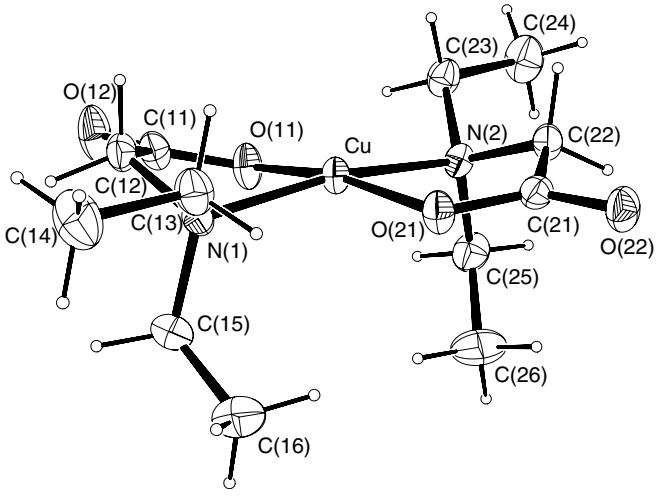


Fig. 1. An ORTEP-3 figure of the asymmetric unit with thermal ellipsoids drawn at 30% probability level.

The apical Cu–$O(22^i)$ bond distance is significantly longer than the basal Cu–O(11) and Cu–O(21) bond lengths (Table 1) and represents an average bond distance found in corresponding aqua copper(II) complexes with *N*-alkylated amino acids having water molecule placed in the apex of a square pyramid (bordering values from 2.206 to 2.464 Å) [23,24,42–46]. As expected, the copper atom is shifted out of the basal plane to the square-pyramid vertex. There are no significant discrepancies from standard non-hydrogen atoms bond lengths and bond angles values [20,22,24,31,42–46]. The intermolecular copper-to-oxygen linkage effects to the spatial orientation of the nitrogen atoms ethyl substituents (Fig. 3).

3.2. The MM simulation of the experimental molecular and crystal structure

The experimental atomic coordinates and the unit cell lengths and angles were taken as the starting point for geometry optimization using the crystal simulator of the Lyngby-CFF program [38,41]. All degrees of freedom were allowed to relax during the geometry optimization except the α and γ unit cell angles were kept equal to 90° to preserve required $P2_1/c$ unit cell symmetry.

According to the FFW input charge parameters given elsewhere [20], the fractional charges assigned to the atoms of $Cu(Et_2Gly)_2$ by the charge redistribution algorithm of the Lyngby-CFF program (see Section 2.2) are as follows: 1.31044 e (Cu), −0.61612 e [N(1) and N(2)], −0.85348 e [O(11) and O(21)], −0.65548 e [O(12) and O(22)], −0.26148 e [C(12), C(13), C(15), C(22), C(23), and C(25)], −0.57328 e [C(14), C(16), C(24), and C(26)], 0.86262 e [C(11) and C(21)], and 0.21152 e to the hydrogen atoms.

The FFW force field reproduces well the X-ray crystal data as it may be seen from the fit between the experimental and theoretical molecular and crystal structures depicted in Figs. 4 and 5. Table 1 lists selected theoretical internal coordinates of the simulated FFW(crystal) structure (we named it also as the 1-3 conformer) in line with their experimental values.

Table 1
Selected experimental bond distances (Å) and angles (°) in polymeric $Cu(Et_2Gly)_2$ and their corresponding theoretical FFW(crystal) and FFW(vacuum) values for two conformers named 1-3 (observed experimentally) and 12-12

	Experimental	FFW			
	Crystal 1-3	Crystal 1-3	Vacuum 1-3	Crystal 12-12	Vacuum 12-12
Bond distances					
Cu–O(11)	1.928(2)	1.931	1.926	1.929	1.923
Cu–O(21)	1.945(2)	1.927	1.921	1.930	1.923
Cu–N(2)	2.044(2)	2.027	2.025	2.021	2.020
Cu–N(1)	2.056(2)	2.027	2.025	2.021	2.020
Cu–O(22^i)	2.312(2)	2.599			
O(11)–C(11)	1.288(4)	1.271	1.272	1.276	1.277
O(12)–C(11)	1.222(4)	1.225	1.221	1.225	1.221
O(21)–C(21)	1.277(3)	1.270	1.271	1.276	1.227
O(22)–C(21)	1.241(3)	1.224	1.221	1.222	1.221
Bond angles					
O(11)–Cu–O(21)	169.9(1)	178.2	176.8	173.5	172.9
O(11)–Cu–N(2)	92.58(9)	94.5	92.9	94.6	94.7
O(21)–Cu–N(2)	85.41(9)	85.3	85.9	85.0	85.4
O(11)–Cu–N(1)	83.32(9)	81.8	84.0	85.0	85.4
O(21)–Cu–N(1)	96.91(9)	98.4	97.5	95.2	97.7
N(2)–Cu–N(1)	169.36(9)	176.2	174.6	178.3	177.4
O(11)–Cu–O(22^i)	96.07(9)	90.3			
O(21)–Cu–O(22^i)	94.06(9)	91.5			
N(2)–Cu–O(22^i)	99.31(9)	93.8			
N(1)–Cu–O(22^i)	90.91(9)	86.9			
C(21)–O(22)–Cu^{ii}	143.7(2)	141.9			
Torsion angles					
O(11)–Cu–N(1)–C(13)	−152.5(2)	−152.1	−145.6	139.9	137.1
O(21)–Cu–N(2)–C(23)	−141.3(2)	−137.6	−133.5	140.1	137.1
C(16)–C(15)–N(1)–Cu	73.3(4)	67.6	63.0	59.2	59.3
C(14)–C(13)–N(1)–Cu	177.3(3)	178.9	178.4	−49.5	−46.4
C(26)–C(25)–N(2)–Cu	−53.0(3)	−48.8	−51.0	60.0	59.3
C(24)–C(23)–N(2)–Cu	177.1(2)	177.8	177.4	−45.9	−46.4
C(11)–C(12)–N(1)–Cu	39.1(3)	37.2	34.2	−23.4	−21.4
C(21)–C(22)–N(2)–Cu	28.3(3)	24.7	21.5	−24.9	−21.4
O(21)–N(2)–N(1)–O(11)	179.3	−178.9	−172.6	175.3	170.2

Symmetry codes: (i) = $1 - x$, $y - 1/2$, $-z + 1/2$; (ii) = $x + 1$, y, z.

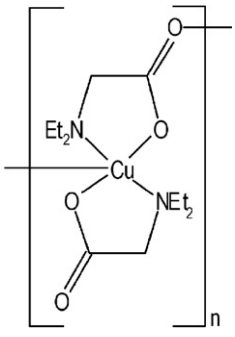


Fig. 2. Two-dimensional sketch showing the way the monomeric $Cu(Et_2Gly)_2$ units link together via Cu–O intermolecular bonding producing the polymeric chains.

As mentioned in Section 1, the short distance of 2.312 Å between the copper(II) and carbonyl oxygen atom of the neighboring complex has not been so far observed for the anhydrous *trans* bis-copper(II) amino acid complexes. The FFW force field yields the distance to be 2.599 Å. This value is in accord with the mean value of experimental intermolecular distances $Cu\cdots O_{carbonyl} = 2.79 \pm 0.23$ Å observed in 8 copper(II) complexes with aliphatic amino acids included in the modeling and parametrization of the FFW force field (FFW yielded the corresponding mean of Cu to carbonyl oxygen distances to be 2.72 ± 0.11 Å) [19]. The equilibrium Cu to O(22^i) distance yielded by FFW is the result of the interplay of intramolecular and intermolecular forces during the energy minimization. Generally, the intermolecular distances are reproduced with lower accuracy than the intramolecular bond lengths. The longer than observed Cu to O(22^i) distance and consequently less pronounced influence of the axially placed carbonyl oxygen on the distortion of the copper(II) coordination polyhedron are most probably the cause that the copper(II) coordination geometry is less distorted in FFW(crystal) than in the experimental crystal structure (Fig. 4, Table 1).

The shortage in the reproduction of the Cu to O(22^i) distance as well as of the extent of copper(II) coordination polyhedron distortion did not influence correct reproduction of the molecules' packing in the unit cell (Fig. 5).

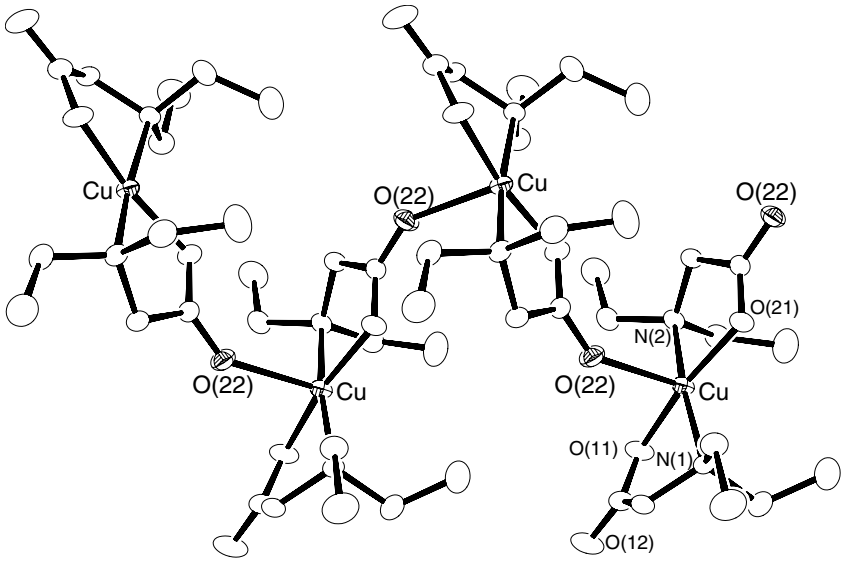


Fig. 3. An ORTEP-3 presentation of the discrete chain of the coordination polymer of *catena*-poly[(*N*,*N*-diethylglycinato-κ*O*,κ*N*)copper(II)-μ-[*N*,*N*-diethylglycinato-κO^1,κ*N*:O^2]] spreading along the *y*-axis. The hydrogen atoms are excluded because of clarity.



Fig. 4. The fit between the experimental X-ray crystal (in white) and theoretical FFW(crystal) (in black) molecular structures. Depicted in grey is the FFW(vacuum) structure calculated without the influence of the intermolecular forces. The molecule orientation is as in Fig. 1.

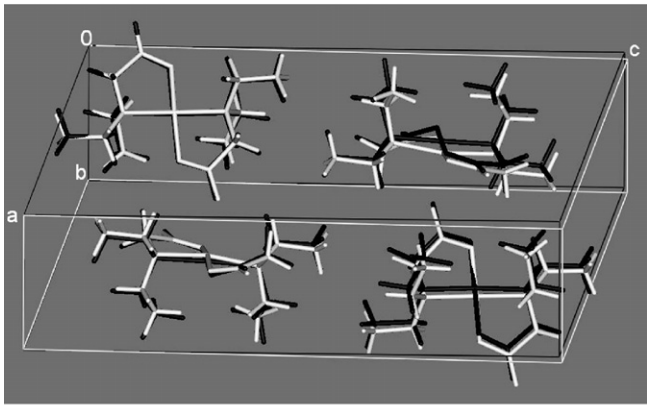


Fig. 5. The match of the unit cell dimensions and molecules' packing between the experimental X-ray crystal data (in white) and theoretical FFW(crystal) results (in black, $a = 9.8774$ Å, $b = 7.5125$ Å, $c = 21.1378$ Å, $\beta = 104.147°$, $V = 1520.9$ Å^3).

The relative error in reproducing the unit cell volume is 0.3%, showing that FFW models well the intermolecular aliphatic–aliphatic interactions between the ethyl groups, and the C–H···O(12) and C–H···O(22) hydrogen bonding. Namely, the differences between the experimental and theoretical close intermolecular contacts between the carbon atoms and carbonyl oxygen atoms are in the range from −0.057 Å up to 0.096 Å.

The rms deviations and maximum errors between the X-ray experimental and FFW(crystal) bond lengths, *b*, valence angles, *θ*, and torsion angles, *φ* (hydrogen atoms were not taken into account) are as follows: rms(Δ*b*) = 0.019 Å, $\Delta b_{max} = -0.053$ Å [for the C(13)–C(14) bond length], rms(Δ*θ*) = 2.9°, $\Delta\theta_{max} = -8.3°$ [for the O(11)–Cu–O(21) angle], and rms(Δ*φ*) = 3.2°, $\Delta\varphi_{max} = 5.7°$ [for the C(16)–C(15)–N(1)–Cu torsion]. These values are within the range of the maximum errors obtained for previously studied copper(II) amino acid complexes [19]. Specifically, the maximum differences calculated between the experimental and FFW internal coordinates for previously studied 13 anhydrous copper(II) chelates were −0.073 Å for the bond lengths, −8.3° for the valence angles, and −11.7° for the torsion angles [19]. By including $Cu(Et_2Gly)_2$ to the set of 23 anhydrous and aqua copper(II) amino acid complexes on which the FFW force field has earlier been examined [19], the total rms errors in the reproduction of experimental crystal data of currently 24 copper(II) chelates are 0.018 Å in the bond lengths, 2.3° in the valence

Table 2
Vacuum minimum strain energy, V_{strain}, for the conformers of $Cu(Et_2Gly)_2$ having the same conformations of the two chelate rings, and the characteristic torsion angle values of conformer minimum[a]

Conformer name	C(14)–C(13)–N(1)–Cu C(24)–C(23)–N(2)–Cu	C(16)–C(15)–N(1)–Cu C(26)–C(25)–N(2)–Cu	O(11)–Cu–N(1)–C(13) O(21)–Cu–N(2)–C(23)	V_{strain}
1-1	176.7	59.6	−143.0	10.80
2-2	149.6	174.8	−145.2	38.13
3-3	176.2	−56.0	−137.3	6.95
4-4	−87.9	39.9	−141.1	38.15
5-5	−61.0	172.3	−136.4	25.96
6-6	−51.4	−56.0	−132.2	11.72
7-7	51.1	50.0	−145.3	8.30
8-8	44.8	172.3	−134.5	13.02
9-9	46.6	−59.2	−137.2	0.16
10-10	−50.2	−49.6	145.3	8.62
11-11	−44.8	−172.2	134.3	12.73
12-12	−46.4	59.3	137.1	0.00
13-13	−176.5	−59.6	143.0	10.90
14-14	−177.8	142.0	141.2	39.97
15-15	−175.9	56.0	137.4	7.05
16-16	66.9	−30.5	153.1	30.15
17-17	63.1	−172.7	140.9	26.29
18-18	70.3	59.7	132.3	20.65

[a] Torsion angles are in °, and strain energies are in kcal mol^{-1}. Zero strain energy: −4221.69 kcal mol^{-1}.

angles, and 5.4° in the torsion angles. The presented results in reproducing the molecular and crystal structure of $Cu(Et_2Gly)_2$ additionally prove that the FFW force field is well suited for modeling bis-copper(II) complexes with aliphatic amino acids.

The impact of the crystal packing forces on the molecule geometry may be examined from the fit between the FFW(vacuum) and crystalline molecular structures (Fig. 4), and credited to be the most noticeable for the ethyl chain geometry (Table 1), i.e., for the groups that took part in the aliphatic–aliphatic interactions in the crystal lattice, and to more strained (i.e., more non-planar) five-atom chelate ring geometry in crystal than in vacuo.

3.3. Conformational analysis in vacuo

FFW was also used to study the strain energy distribution among the conformers of $Cu(Et_2Gly)_2$ in vacuo without the influence of the intermolecular interactions. From theoretical sterochemical considerations, it can be proposed that each chelate ring has 18 possible conformations; that is, two possible conformations of the five-atom chelate ring (characterized by the torsion angle $C'–C^{\alpha}–N–Cu \approx \pm 30°$) and nine combinations of the ethyl group orientations (as each ethyl group can adopt any of three possible orientations that correspond to the C–C–N–Cu torsion angle values close to 180°, 60°, or −60°). Table 2 lists the minimum strain energy values of the conformers having the same conformations of the two chelate rings, the minima's torsion angle values characterizing these conformers, and the number-names we assigned to the conformers. The conformation found in the experimental crystal structure (Figs. 1 and 4) corresponds to the conformation mixed between the 1-1 and 3-3 conformers (Table 2), and accordingly we called it as the 1-3 conformer (Fig. 6).

In the gas phase the 1-3 conformer is predicted to have the strain energy, V_{strain}, greater than the most stable conformer 12-12 (Table 2, Fig. 6) by 9.21 kcal mol^{-1}. In vacuo the most stable conformers 12-12 and 9-9 (Table 2) have the ethyl groups oriented perpendicularly to the chelate ring planes, shielding the copper coordination site for axial bonding (Fig. 6). As we initially supposed four-coordinate complex in the red-violet solution, the forming of close intramolecular van der Waals aliphatic–aliphatic contacts between the C–H

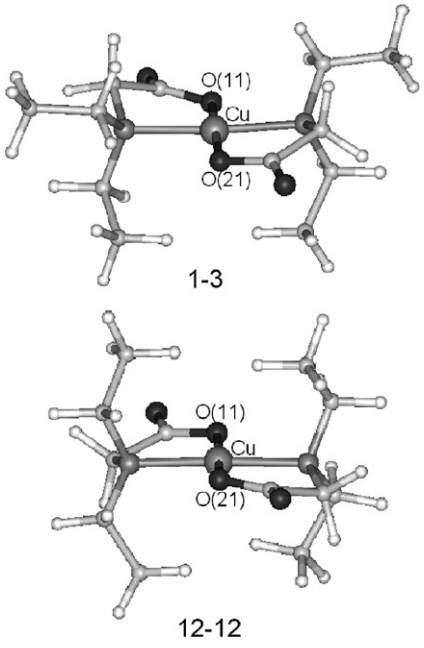


Fig. 6. FFW(vacuum) minimum structures of the 1-3 and 12-12 conformers (selected internal coordinates are given in Table 1).

groups, and the inaccessibility of the fifth copper(II) coordination site make these conformers stereochemically and energetically suited to be prevailing conformers in solution too. Conversely, the 1-3 conformer has the ethyl groups oriented to make possible bonding of the carbonyl oxygen atom to the copper(II) as well as forming intermolecular aliphatic–aliphatic interactions between the ethyl groups in the crystal lattice (Figs. 3, 5 and 6). Therefore, we supposed that not only the change in the copper(II) coordination geometry but also in the molecular conformation occurred upon crystallization.

3.4. Unit cell packings and intermolecular interactions of different conformers

To verify the supposition that a conformer having the ethyl group orientations so as to make the fifth copper(II) coordination site accessible for axial bonding (i.e., the conformer with at least one ethyl group torsion angle C–C–N–Cu ≈ 180°) is better suited for crystal packing than the vacuum most stable conformers 12-12 and 9-9, we extended the conformational analysis to the calculations of crystal lattice packings of selected conformers (mostly of

Table 3
Minimum potential energy values $V_{crystal}$ and $V_{intermolecular}$ (see Section 2.2) calculated for the listed conformers of $Cu(Et_2Gly)_2$ in simulated crystalline surroundings (space group $P2_1/c$) using the FFW force field[a]

Conformer $V_{crystal}$[b] / kcal mol^{-1} $V_{intermolecular}$ / kcal mol^{-1}								
1-1 *6.58* *–42.40*	**1-3** *1.45* *–46.93*	**1-7** *7.61* *–42.18*	**1-9** *8.09* *–34.71*	**1-10** *9.44* *–40.94*	**2-2** *33.12* *–44.89*	**1-12** *2.12* *–41.76*	**1-13** *8.94* *–40.97*	**1-15** *11.49* *–34.20*
3-1 *4.06* *–45.49*	**3-3** *–0.07* *–45.47*	**3-7** *7.48* *–38.60*	**3-9** *6.16* *–34.91*	**3-10** *9.80* *–35.57*	**3-11** *9.90* *–38.87*	**3-12** *5.79* *–36.02*	**3-13** *5.31* *–43.15*	**3-15** *6.92* *–37.29*
7-1 *7.33* *–41.85*	**7-3** *5.79* *–43.63*	**7-7** *10.34* *–41.29*	**4-4** *35.15* *–41.13*	**5-5** *25.73* *–38.11*	**6-6** *11.33* *–39.41*	**7-12** *11.99* *–31.82*	**7-13** *12.27* *–36.44*	**7-15** *10.90* *–34.25*
9-1 *4.12* *–40.08*	**9-3** *3.87* *–38.21*	**8-8** *13.26* *–38.36*	**9-9** *0.07* *–37.94*	**9-10** *8.30* *–33.20*	**12-11 (min 2)** *8.14* *–35.45*	**12-12 (min 2)** *4.61* *–32.69*	**9-13** *6.13* *–38.16*	**9-15** *7.25* *–34.48*
10-1 *7.87* *–42.23*	**10-3** *7.21* *–38.87*	**10-7** *9.20* *–36.55*	**10-9** *5.61* *–36.45*	**10-10** *10.66* *–35.31*	**10-3 (min 2)** *7.39* *–41.76*	**10-12** *9.05* *–33.32*	**10-13** *11.51* *–36.34*	**10-15** *12.06* *–33.27*
14-14 *32.52* *–47.06*	**11-3** *7.30* *–43.48*	**16-16** *27.98* *–39.20*	**14-3** *16.07* *–45.84*	**11-10** *11.97* *–36.60*	**11-11** *10.76* *–41.37*	**11-12** *9.04* *–33.85*	**3-13 (min 2)** *4.62* *–42.36*	**16-16** 27.98 *–39.20*
12-1 *5.56* *–39.02*	**12-3** *5.90* *–37.09*	**12-7** *5.61* *–37.91*	**6-1** *7.87* *–42.23*	**12-10** *8.93* *–32.68*	**12-11** *9.64* *–33.46*	**12-12** *0.00* *–37.84*	**12-13** *7.01* *–38.34*	**12-15** *7.93* *–32.86*
13-1 *9.83* *–41.92*	**13-3** *4.46* *–43.05*	**13-7** *10.71* *–40.47*	**13-9** *8.79* *–34.11*	**13-10** *4.90* *–44.37*	**13-11** *12.28* *–37.30*	**13-12** *8.36* *–34.50*	**13-13** *11.54* *–37.14*	**13-15** *6.11* *–40.66*
15-1 *4.54* *–42.42*	**15-3** *1.84* *–44.64*	**15-7** *6.19* *–42.16*	**15-9** *4.68* *–40.05*	**15-10** *6.25* *–41.48*	**17-17** *29.63* *–35.88*	**15-12** *2.91* *–38.79*	**15-13** *10.93* *–38.03*	**15-15** *7.97* *–36.55*

[a] Thicken line marks the conformers with the lowest energies calculated.
[b] Zero $V_{crystal}$ value corresponds to −4258.44 kcal mol^{-1}.

the conformers having lower in vacuo strain energy, Table 2). The energy minimizations were started from equilibrium vacuum Cartesian coordinates for a series of conformers, and from the same unit cell dimensions, $P2_1/c$ space group symmetry operations, and molecule's orientation as in the experimental structure. For instance, the 12-1 conformer had the initial orientation such that its chelate ring conformations 12 and 1 (defined in Table 2) were in place of experimental chelate ring conformations 1 and 3, respectively. The in-crystal energy values for the obtained minima are given in Table 3. The geometry optimizations for the conformers with the same combination of the chelate ring conformations were started from their two possible orientations (e.g., 1-12 and 12-1) and usually led to different minima (Table 3), revealing the dependence of the energy minimization result on the initial orientation. For some conformers, a conformational change occurred during energy minimization, e.g., the 9-12 conformer transformed into the 12-12 conformer (the minimum denoted as 12-12 (min 2) in Table 3). Table 4 lists the unit cell dimensions of 9 minima having lowest V_{cystal} energies obtained (the unit cell dimensions of the 1-3 minimum are given in Fig. 5).

It seems reasonable to assume that during the process of crystallization from solution the $Cu(Et_2Gly)_2$ molecules tended to arrange themselves in the solid state so as to form as many aliphatic–aliphatic close contacts between the C–H groups, the C–H···O hydrogen bonds as well as the axial coordinative bonds between the copper(II) and carbonyl oxygen atoms as possible. Indeed systematically the lowest $V_{\text{intermolecular}}$ energy values were yielded by FFW for the conformers that could form close axial Cu to O(22) intermolecular bonding (Tables 3 and 4). The energy differences between the V_{cystal} values obtained for most of the conformers having the same combination of the chelate ring conformations are up to 3–4 kcal mol^{-1} (Table 3). Larger energy differences were obtained only for the conformers having the chelate ring conformation 15, and for the 7-12 and 12-7 conformers (Table 3). One more $P2_1/c$ minimum of 12-12 (denoted as 12-12 (min 3) in Table 4; relative V_{crystal} = 1.50 kcal mol^{-1}, $V_{\text{intermolecular}}$ = −37.02 kcal mol^{-1}), and two predicted crystal packing minima of the 12-12 conformer in space group $P2_12_12_1$ (for which the molecule orientation and the unit cell lengths of the $P2_1/c$ 12-12 and 12-12 (min 3) minima (Table 4), respectively, were taken as the input data prior to energy minimization) are also within the energy difference range of 3 kcal mol^{-1}. Namely, V_{cystal} of one $P2_12_12_1$ minimum differed by −0.79 kcal mol^{-1} ($V_{\text{intermolecular}}$ = −38.53 kcal mol^{-1}; a = 6.799 Å, b = 15.830 Å, c = 13.955 Å, V = 1502.1 Å^3) and of the second one differed by 0.77 kcal mol^{-1} ($V_{\text{intermolecular}}$ = −37.03 kcal mol^{-1}; a = 10.760 Å, b = 7.826 Å, c = 18.541 Å, V = 1561.3 Å^3) from the lowest energy 12-12 minimum calculated in space group $P2_1/c$ (Tables 3 and 4) and illustrated in Fig. 7.

For some conformers other space group symmetry operations and differently chosen initial conditions prior to energy minimization may lead to more energetically favorable minimum. However, on the basis of the achieved in-crystal results for the conformers of $Cu(Et_2Gly)_2$ and within the MM calculation approximations applied, we expect that if there is any energetically more favored crystal packing than already found for the 12-12 and 9-9 conformers, its $V_{\text{intermolecular}}$ is unlikely to overcome the intermolecular potential energy difference of about 7–9 kcal mol^{-1} between the in-crystal minima of 12-12 and 9-9 on one side

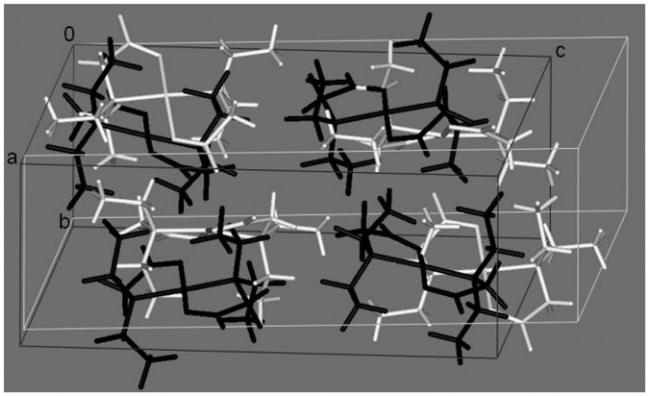


Fig. 7. The predicted unit cell packing of the 12-12 conformer in space group $P2_1/c$ (denoted in black; unit cell dimensions are given in Table 4) compared with the experimental X-ray crystal unit cell (denoted in white).

Table 4
The unit cell a, b, c lengths (Å), angle β (°) and volume V (Å^3), and intermolecular Cu(II) to axial (or approximate axial) O(22) distances (Å) of the conformers having the lowest energy minima calculated in space group $P2_1/c$ using the FFW force field[a]

Conformer	a	b	c	β	V	Cu–O(22)
3-1	11.453	6.535	20.977	104.01	1523.3	2.710, 4.410
3-3	9.960	7.359	21.324	104.22	1515.0	2.620, 5.138
15-3	10.070	7.346	20.741	95.23	1527.9	2.620, 5.236
1-12	7.472	10.324	21.077	109.74	1530.4	2.842
9-1	12.022	6.896	19.474	104.62	1562.2	3.607, 4.604
12-12	10.645	7.801	18.331	98.07	1507.1	4.274, 4.363
12-12 (min 3)	7.031	14.087	16.669	103.86	1602.9	
15-12	10.407	7.606	20.119	98.29	1575.9	4.049, 4.254
9-9	10.639	7.790	18.339	98.09	1504.7	4.272, 4.350

[a] Vacuum strain energy values for the conformers not listed in Table 2 are as follows (relative to −4221.69 kcal mol^{-1}): 9.21 kcal mol^{-1} for 3-1; 5.47 kcal mol^{-1} for 9-1; 4.37 kcal mol^{-1} for 1-12; 3.43 kcal mol^{-1} for 15-12; 6.38 kcal mol^{-1} for 15-3.

and the conformers having the ethyl groups' orientation that allows close axial coordinative bonding to the copper(II) on the other side (Tables 3 and 4).

The 14-14 conformer had the most favorable intermolecular interactions (-47.06 kcal mol^{-1}, Table 3) but too large intramolecular strain (Table 2) to allow the possibility of its crystallization in the real case. The next conformer with the lowest intermolecular interaction energy is the 1-3 conformer (Fig. 5), followed by the 3-3 conformer (Tables 3 and 4). The theoretical results confirmed what we would expect, that both intramolecular stability and crystal lattice close packing affect the occurrence of specific conformer in the solid state. As the 1-3 conformer has been observed in the real crystal structure, and FFW predicts its V_{crystal} as well as $V_{\text{intermolecular}}$ among the most favorable ones (Table 3), we choose the 1-3 minimum (Fig. 5, Table 1) to discuss its crystal packing in relation to the 12-12 minimum (Fig. 7, Table 1). Hence, the 1-3 and 12-12 conformers are selected to represent the conformers that can have and cannot have the axial Cu to carbonyl oxygen atom coordinative bonding in the solid state, respectively.

The energy difference between the 1-3 and 12-12 theoretical structures dropped from 9.21 kcal mol^{-1} in the vacuum to 1.43 kcal mol^{-1} in the simulated crystal surroundings. The energy drop is due to the intermolecular potential energy contribution, $V_{\text{intermolecular}}$, as the difference between the 1-3 and 12-12 intramolecular V_{strain} energy contributions to V_{crystal} amounts 10.52 kcal mol^{-1}. Therefore, the possibility of the 1-3 conformer to form both the aliphatic–aliphatic interactions and the Cu to axial O coordinative bonding lowered the in-crystal potential energy difference relative to the 12-12 conformer. As already mentioned, FFW overestimated the Cu to carbonyl oxygen distance in the simulated crystal structure of the 1-3 conformer (Table 1), and thus most probably underestimated the energy contribution of the interaction between Cu(II) and axially placed O(22^{i}) that might have decreased (or even increased in favor to 1-3) the difference between the potential energy of this particular conformer and other conformers in the crystal lattice. Whether further reparametrization of the FFW force field (which might be a rather complicated task [19]) may offer more definite answer on the energetic problem of this particular interaction remains to be examined in forthcoming studies. However, the difference between the intermolecular energy contributions of 12-12 and 1-3 equals 9.09 kcal mol^{-1} (8.40 kcal mol^{-1} for the $P2_12_12_1$ 12-12 minimum) and gives a quantitative proof that the crystal packing forces favor the 1-3 conformation over the 12-12 one.

4. Conclusions

The X-ray diffraction measurements of the crystal structure of *catena*-poly[(*N*,*N*-diethylglycinato-κ*O*,κ*N*)copper(II)-μ-[*N*,*N*-diethylglycinato-κO^1,κ*N*:O^2]] reveal that five-coordinate copper(II) coordination geometry and coordination polymer chain formation can occur in the crystal structures of anhydrous *trans* bis-copper(II) amino acid complexes. Good match between the experimental and simulated crystal structures of the title compound confirms the reliability of the FFW force field for modeling steric aliphatic–aliphatic interactions in the copper(II) amino acid complexes. The MM results suggest that intermolecular aliphatic–aliphatic interactions between flexible ethyl groups replacing the amino hydrogen atoms in glycine affected the changes in the molecular conformation and consequently in the copper(II) coordination sphere upon crystallization of $Cu(Et_2Gly)_2$. The MM force field applied for the conformational analysis in vacuo and in crystal yielded the results to assist in understanding the crystallization process from solution.

Acknowledgements

We thank Nevenka Paulić for the ligand synthesis and Andreja Sironić for the complex synthesis and the crystal preparation. This work was supported by the Croatian Ministry of Science, Education and Sport (Project Nos. 0022107 and 0119630).

Appendix A. Supplementary material

CCDC 604154 contains the supplementary crystallographic data for this paper. These data can be obtained free of charge via http://www.ccdc.cam.ac.uk/conts/retrieving.html, or from the Cambridge Crystallographic Data Centre, 12 Union Road, Cambridge CB2 1EZ, UK; fax: (+44) 1223-336-033; or e-mail: deposit@ccdc.cam.ac.uk. Supplementary data associated with this article can be found, in the online version, at doi:10.1016/j.poly.2006.09.087.

References

[1] M. DiDonato, B. Sarkar, Biochim. Biophys. Acta 1360 (1997) 3.
[2] E.D. Harris, Prog. Clin. Biol. Res. 380 (1993) 163.
[3] J. Gažo, I.B. Bersuker, J. Garaj, M. Kabešová, J. Kohout, H. Langfelderová, M. Melník, M. Serátor, F. Valach, Coord. Chem. Rev. 19 (1976) 253.
[4] B. Murphy, B. Hathaway, Coord. Chem. Rev. 243 (2003) 237.
[5] M. Tanaka, J. Synth. Org. Chem. Jpn. 60 (2002) 125.
[6] M. Cirilli, V.M. Coiro, A. Di Nola, F. Mazza, Biopolymers 46 (1998) 239.
[7] M. Tanaka, S. Nishimuru, M. Oba, Y. Demizu, M. Kurihara, H. Suemune, Chem. Eur. J. 9 (2003) 3082.
[8] N. Paulić, N. Raos, J. Coord. Chem. 31 (1994) 181.
[9] N. Barooah, R.J. Sarma, J.B. Baruah, Eur. J. Inorg. Chem. (2006) 2942.
[10] V. Noethig-Laslo, N. Paulić, R. Pogni, R. Bassosi, Polyhedron 21 (2002) 1643.
[11] J. Sabolović, V. Noethig-Laslo, Cell. Mol. Biol. Lett. 7 (2002) 151.
[12] K. Mirosavljević, J. Sabolović, V. Noethig-Laslo, Eur. J. Inorg. Chem. (2004) 3930.
[13] A.D. Becke, J. Chem. Phys. 98 (1993) 5648.
[14] C. Lee, W. Yang, R.G. Parr, Phys. Rev. B 37 (1988) 785.
[15] S.H. Vosko, L. Wilk, M. Nusair, Can. J. Phys. 58 (1980) 1200.
[16] P.J. Stephens, F.J. Devlin, C.F. Chabalowski, M.J. Frisch, J. Phys. Chem. 98 (1994) 11623.

[17] A.E. Reed, R.B. Weinstock, F. Weinhold, J. Chem. Phys. 83 (1985) 735.
[18] J. Sabolović, K.R. Liedl, Inorg. Chem. 38 (1999) 2764.
[19] J. Sabolović, C.S. Tautermann, T. Loerting, K.R. Liedl, Inorg. Chem. 42 (2003) 2268.
[20] B. Kaitner, N. Paulić, G. Pavlović, J. Sabolović, Polyhedron 18 (1999) 2301.
[21] H.C. Freeman, M.R. Snow, I. Nitta, K. Tomita, Acta Crystallogr. 17 (1964) 1463.
[22] R.V. Krishnakumar, S. Natarajan, S.A. Bahadur, T.S. Cameron, Z. Kristallogr. 209 (1994) 443.
[23] T.S. Cameron, K. Prout, F.J.C. Rossotti, D. Steele, J. Chem. Soc., Dalton Trans. (1973) 2626.
[24] B. Kaitner, G. Ferguson, N. Paulić, N. Raos, J. Coord. Chem. 26 (1992) 95.
[25] S.M. Moussa, R.R. Fenton, B.A. Hunter, B.J. Kennedy, Aust. J. Chem. 55 (2002) 331.
[26] B. Kaitner, G. Ferguson, N. Paulić, N. Raos, J. Coord. Chem. 29 (1993) 247.
[27] T.J.M. de Bruin, T.M. Marcelis, H. Zuilhof, E.J.R. Sudhölter, Phys. Chem. Chem. Phys. 1 (1999) 4157.
[28] T. Hattori, T. Toraishi, T. Tsuneda, S. Nagasaki, S. Tanaka, J. Phys. Chem. A 109 (2005) 10403.
[29] C.S. Tautermann, J. Sabolović, A. Voegele, K.R. Liedl, J. Phys. Chem. B 108 (2004) 2098.
[30] B.W. Delf, R.D. Gillard, P. O'Brien, J. Chem. Soc., Dalton Trans. (1979) 1301.
[31] C.P. Nash, W.P. Schaefer, J. Am. Chem. Soc. 91 (1969) 1319.
[32] R.D. Gillard, R. Mason, G.B. Robertson, J. Chem. Soc. (A) 12 (1969) 1864.
[33] S.M. Moussa, R.R. Fenton, B.J. Kennedy, R.O. Piltz, Inorg. Chim. Acta 288 (1999) 29.
[34] R.E. Bowman, H.H. Stroud, J. Chem. Soc. (1950) 1342.
[35] L.J. Farrugia, J. Appl. Crystallogr. 32 (1999) 837.
[36] J. Sabolović, Ž. Mrak, S. Koštrun, A. Janeković, Inorg. Chem. 43 (2004) 8479.
[37] S.R. Niketić, Kj. Rasmussen, The Consistent Force Field: A Documentation, Lectures Notes in Chemistry, vol. 3, Springer, Berlin, 1977.
[38] Kj. Rasmussen, Potential Energy Functions in Conformational Analysis, Lectures Notes in Chemistry, vol. 37, Springer, Berlin, 1985.
[39] Kj. Rasmussen, S.B. Engelsen, J. Fabricius, B. Rasmussen, in: R. Fausto (Ed.), Recent Experimental and Computational Advances in Molecular Spectroscopy, NATO ASI Series C: Mathematical and Physical Sciences, vol. 406, Kluwer Academic Publisher, Dordrecht, 1993, pp. 381–419.
[40] D.E. Williams, Top. Curr. Phys. 26 (1981) 3.
[41] L.-O. Pietilä, Kj. Rasmussen, J. Comput. Chem. 5 (1984) 252.
[42] B. Kamenar, M. Penavić, A. Škorić, N. Paulić, N. Raos, Vl. Simeon, J. Coord. Chem. 17 (1988) 85.
[43] B. Kaitner, N. Paulić, N. Raos, J. Coord. Chem. 25 (1992) 337.
[44] B. Kaitner, G. Ferguson, N. Paulić, N. Raos, J. Coord. Chem. 30 (1993) 233.
[45] B. Kaitner, G. Pavlović, N. Paulić, N. Raos, J. Coord. Chem. 36 (1995) 327.
[46] B. Kaitner, G. Pavlović, N. Paulić, N. Raos, J. Coord. Chem. 43 (1998) 309.

Recently, our group has paid attention to the study of new tin sulfur-based compounds with oxygen or other ligands [9]. We have reported the first octanuclear tin oxy-sulfide clusters $[Sn_8S_{12}O_4(SPh)_6]^{6-}$ [9a], and subsequently developed a simple route to prepare $[Sn_8S_{12}(\mu_4\text{-}O)_2(\mu_2\text{-}OH)_2Cl_6]^{6-}$ and $[Sn_{10}S_{16}(\mu_4\text{-}O)_4Cl_4]^{4-}$ [9b]. During our investigation on the reaction behavior of $(Bu_4N)_2[Sn_3S_4(edt)_3]$, two novel trinuclear tin(IV) oxy-sulfide complexes of $(Bu_4N)[Sn_3(\mu_3\text{-}OH)S_3(edt)_3]\cdot DMF$ (**1**) and $(Bu_4N)[Sn_3(\mu_3\text{-}OH)S_3(edt)_3]\cdot H_2O$ (**2**) were unexpectedly obtained. Herein, the syntheses, structures and characterizations of complexes **1** and **2** are reported.

2. Experimental

2.1. Materials and instrumentation

All synthetic operations were performed in air. $(Bu_4N)_2[Sn_3S_4(edt)_3]$ [10], $Zn(SCN)_2$ [11] and $Cd(SCN)_2$ [12] were synthesized according to the literature. The other chemicals and reagents were of reagent grade and were used as received without further purification. Carbon, hydrogen and nitrogen analyses were performed on a Vario EL III Elemental Analyzer. The infrared and far-infrared spectra were recorded on a Nicolet Magna 750 FT-IR spectrometer using pressed KBr and CsI pellets, respectively. The samples for Raman spectra were diluted with KBr powder and placed in an NMR tube. The Raman spectra were taken on a Nicolet Magna 950 Raman spectrometer. Mass spectra (ES-MS) were measured on a Finngan LCQ mass spectrometer using CH_2Cl_2 as solvent. ^1H NMR spectra were obtained on a Unity 500 MHz NMR spectrometer.

2.2. Synthesis of $(Bu_4N)[Sn_3(\mu_3\text{-}OH)S_3(edt)_3]\cdot DMF$ (1)

2.2.1. Method 1

To the colorless solution of $(Bu_4N)_2[Sn_3S_4(edt)_3]$ (0.125 g, 0.1 mmol) in 10 ml of CH_3CN, a 1 ml solution of DMF containing CuI (0.019 g, 0.1 mmol) and KI (0.017 g, 0.1 mmol) were rapidly added while stirring. The resulting mixture was stirred for 1 h, followed by filtration to remove brown deposits. The pink filtrate was allowed to crystallize in air. Three weeks later, a lot of colorless prismatic crystals were obtained, washed with *i*-propanol and dried in air. Yield: 0.032 g (30% based on $(Bu_4N)_2[Sn_3S_4(edt)_3]$) Elemental *Anal.* Calc. for $C_{25}H_{56}N_2O_2S_9Sn_3$: C, 28.29; H, 5.32; N, 2.64. Found: C, 28.93; H, 5.48; N, 2.76%. IR (KBr pellet) and far-IR (CsI pellet) spectra: (cm^{-1}): 3563w, 3374w, 2958s, 2906s, 2872s, 1641m, 1467m, 1413m, 1382m, 1284m, 1247w, 1160w, 921m, 845m, 737w, 640w, 440m, 357s, 306m, 255w, 222w, 198w. Raman spectrum (cm^{-1}): 2991s, 1117m, 557w. ^1H NMR (Unity 500, $CDCl_3$, $-NCH_2^dCH_2^cCH_2^bCH_3^a$): δ 1.041–1.070 (12H, $^3J(^1H\text{–}^1H) = 15$ Hz, $-CH_3^a$), 1.520–1.564 (8H, $^3J(^1H\text{–}^1H) = 15$ Hz, $-CH_2^b$), 1.693–1.707 (8H, $-CH_2^c$), 2.888, 2.963 (6H, $-NCH_3$), 3.009–3.164 (12H, $^3J(^1H\text{–}^1H) = 77.5$ Hz, $1SCH_2$), 3.219 (1H, –OH), 3.284–3.317 (8H, $^3J(^1H\text{–}^1H) = 16.5$ Hz, $-CH_3^d$), 8.022 (1H, –COH).

2.2.2. Method 2

$(Bu_4N)_2[Sn_3S_4(edt)_3]$ (0.125 g, 0.1 mmol) and $CuCl_2$ (0.013 g, 0.1 mmol) were dissolved in 5 ml of DMF to give a red solution. This red solution was allowed to stand in air for one day, resulting in a brown precipitate. The precipitate was removed by filtration. The colorless filtrate was placed on a surface utensil to crystallize in air. Three days later, lots of colorless crystals were obtained, washed with ether and dried in air. Yield: 0.010 g (9.4% based on $(Bu_4N)_2[Sn_3S_4(edt)_3]$).

2.3. Synthesis of $(Bu_4N)[Sn_3(\mu_3\text{-}OH)S_3(edt)_3]\cdot H_2O$ (2)

2.3.1. Method 1

$Zn(SCN)_2$ (0.020 g, 0.11 mmol) and 1,10-phen · $2H_2O$ (0.020 g, 0.1 mmol) were dissolved in 10 ml of CH_3CN/CH_2Cl_2 (1:1) and stirred for 3 h. $(Bu_4N)_2[Sn_3S_4(edt)_3]$ (0.125 g, 0.1 mmol) was added into the solution, resulting in a white turbid solution. The mixture was stirred for 2 h and then filtered. The colorless filtrate was allowed to crystallize in air. Three weeks later, lots of colorless block crystals were obtained and washed with *i*-propanol and dried in air. Yield: 0.036 g (35.4% based on $(Bu_4N)_2[Sn_3S_4(edt)_3]$). Element *Anal.* Calc. for $C_{22}H_{51}NO_2S_9Sn_3$: C, 26.26; H, 5.11; N, 1.39. Found: C, 26.59; H, 5.05; N, 1.60%. IR (KBr pellet) and far-IR (CsI pellet) spectra (cm^{-1}): 3629m, 3561m, 3403m, 3162w, 2958s, 2904s, 2871s, 1477m, 1467m, 1416w, 1379m, 1288w, 1250w, 1180w, 922w, 891w, 735w, 669w, 640w, 441m, 357s, 307w, 251w, 199m; Raman spectrum (cm^{-1}): 2991m, 1120s, 561m; ^1H NMR (Unity 500, $CDCl_3$, $-NCH_2^dCH_2^cCH_2^bCH_3^a$): δ 1.041–1.069 (12H, $^3J(^1H\text{–}^1H) = 14$ Hz, $-CH_3^a$), 1.550 (8H, $-CH_2^b$), 1.707 (8H, $-CH_2^c$), 3.010–3.168 (12H, $^3J(^1H\text{–}^1H) = 79$ Hz, $-SCH_2$), 3.221 (1H, –OH), 3.284–3.312 (8H, $^3J(^1H\text{–}^1H) = 14$ Hz, $-CH_3^d$).

2.3.2. Method 2

$Cd(SCN)_2$ (0.020 g, 0.09 mmol) and 1,10-phen · $2H_2O$ (0.020 g, 0.1 mmol) were added into 20 ml of CH_3CN/CH_2Cl_2 (1:1). The mixture was stirred for 3 h. To the mixture $(Bu_4N)_2[Sn_3S_4(edt)_3]$ (0.125 g, 0.1 mmol) was added. The mixture was stirred for another 2 h and then filtered. The colorless filtrate was left in air. Three weeks later, lots of colorless block crystals were obtained. The crystals were filtered and washed with *i*-propanol and dried in air. Yield: 0.016 g (16.0% based on $(Bu_4N)_2[Sn_3S_4(edt)_3]$).

2.4. X-ray crystallography

Crystal data for compound **1** was collected at 130.15 K on a Rigaku RAXIS IIc Smart/CCD diffractometer with Mo Kα radiation ($\lambda = 0.71073$ Å). Data reduction, cell

refinements and absorption correction were performed with CrystalClear software (Rigaku Corp., 2000). Crystal data for compound **2** was collected at 293(2) K on a Siemens Smart/CCD diffractometer with Mo Kα radiation ($\lambda = 0.71073$ Å). Data reduction and cell refinements were performed with Smart-CCD software. An absorption correction was applied by using SADABS software [13].

In the two compounds, all non-hydrogen atoms and the hydrogen atoms of OH were located through direct methods. All non-hydrogen atoms, except disordered atoms, were refined anisotropically by full-matrix least-squares methods. All hydrogen atoms, except the hydrogen atom of OH, were generated geometrically. All calculations were performed by SHELXL-97 [14]. Final $R = \sum\|F_o| - |F_c\|/\sum|F_o|$ and $Rw = [\sum[w(F_o^2 - F_c^2)^2]/\sum w(F_o^2)^2]^{1/2}$ with $w = 1/[\sigma^2(F_o^2) + (aP)^2 + bP]$ (where $P = (F_o^2 + 2F_c^2)/3$). A summary of crystal data and structure refinement for the two compounds is provided in Table 1. Selected bond lengths and angles for **1** and **2** are summarized in Table 2. H-bond data of the two compounds are listed in Table 3.

3. Results and discussion

3.1. Syntheses

As shown in Scheme 1, compound **1** was obtained through the reaction of $[Sn_3S_4(edt)_3]^{2-}$ with $CuCl_2$ or $KCuI_2$ in the presence of DMF, while compound **2** was formed by the reaction of $[Sn_3S_4(edt)_3]^{2-}$ with Zn(1,10-phen)$(SCN)_2$ or Cd(1,10-phen)$(SCN)_2$ in CH_3CN/CH_2Cl_2 (1:1). Our original aim was to prepare cubane-like clusters through the addition reaction of $[Sn_3S_4(edt)_3]^{2-}$ with metal blocks. However, two new compounds containing the same

Table 2
Selected bond lengths and bond angles for complexes **1** and **2**

*Selected bond lengths and bond angles for complex **1***	
Sn–O(1)	2.287(4)–2.346(4)
Sn–O(2)	2.284(4)–2.331(4)
Sn–$S_{(equatorial)}$	2.3911(17)–2.4163(16)
Sn–$S_{(axial)}$	2.4407(18)–2.4662(16)
O–Sn–$S_{(equatorial)}$	80.76(10)–88.30(10)
O–Sn–$S_{(axial)}$	175.22(10)–179.54(11)
$S_{(axial)}$–Sn–$S_{(equatorial)}$	90.44(6)–101.52(6)
$S_{(equatorial)}$–Sn–$S_{(equatorial)}$	112.32(6)–125.81(5)
*Selected bond lengths and bond angles for complex **2***	
Sn–O(1)	2.310(4)–2.348(4)
Sn–$S_{(equatorial)}$	2.399(2)–2.4232(17)
Sn–$S_{(axial)}$	2.449(2)–2.4718(18)
O(1)–Sn–$S_{(equatorial)}$	80.66(10)–86.84(10)
O(1)–Sn–$S_{(axial)}$	173.47(11)–175.94(11)
$S_{(axial)}$–Sn–$S_{(equatorial)}$	90.79(6)–102.96(8)
$S_{(equatorial)}$–Sn–$S_{(equatorial)}$	111.87(6)–125.57(7)
Sn–O(1)–H(1)	113(5)–124(5)

Table 1
Crystal data collection and structure refinement parameters for **1** and **2**

	1	**2**
Empirical formula	$C_{25}H_{56}N_2O_2S_9Sn_3$	$C_{22}H_{51}NO_2S_9Sn_3$
Formula weight	1061.33	1006.25
Radiation	Mo Kα 0.71073 Å	Mo Kα 0.71073 Å
Temperature (K)	130.15	293(2)
Crystal description	prism, colorless	block, colorless
Dimensions	$0.35 \times 0.30 \times 0.30$	$0.40 \times 0.40 \times 0.38$
Crystal system	monoclinic	monoclinic
Space group	*P*2(1)	*P*2(1)/*n*
Unit cell dimensions		
a (Å)	10.799(3)	12.1947(2)
b (Å)	16.704(4)	22.8503(3)
c (Å)	23.359(6)	14.4198(2)
β (°)	102.383(3)	104.638(1)
V (Å^3)	4115.7(19)	3887.69(10)
Z	4	4
Index ranges of measured data	−14 to 14, −14 to 21, −30 to 29	−14 to 8, −27 to 14, −17 to 17
θ Range for data collection (°)	2.29–27.48	1.71–25.03
μ (mm^{-1})	2.288	2.417
Density (g cm^{-3})	1.713	1.719
F(000)	2120	2000
Reflections measured	31951	12145
Observed reflection (>2*σ*(*I*))	14367	5948
Independent reflections (R_{int})	14847 (0.0284)	6783 (0.0214)
R	0.0313	0.0398
Rw	0.0715	0.0879
Goodness-of-fit on F^2	1.088	1.358
Largest and mean *Δ*/*σ*	0.001, 0.000	0.001, 0.000
Largest difference peak (e/Å^3)	0.811, −0.481	0.461, −0.554

$R = \sum\|F_o| - |F_c\|/\sum|F_o|$ and $Rw = [\sum[w(F_o^2) - (F_c^2)^2]/\sum w(F_o^2)^2]^{1/2}$ with $w = 1/[\sigma^2(F_o^2) + (aP)^2 + bP]$, where $P = (F_o^2 + 2F_c^2)/3$ **1**: $a = 0.0261$, $b = 5.1062$; **2**: $a = 0.000$, $b = 11.4412$. Flack parameter for **1** is 0.002(15).

Table 3
Hydrogen bonds for complexes **1** and **2**

D–H	$d_{(D-H)}$ (Å)	$d_{(H\cdots A)}$ (Å)	⟨DHA (°)	$d_{(D\cdots A)}$ (Å)	*A*
H-bond in complex ***1***					
O1–H1	0.78(6)	1.98(6)	166(7)	2.739(5)	O3[a]
O2–H2	0.84(2)	1.98(4)	157(7)	2.774(5)	O4[b]
Symmetry code: a: $x-1, y, z$; b: $x+1, y, z$					
H-bond in complex ***2***					
O1–H1	0.887	1.950	173.90	2.834	O2
O2–H2	0.941	2.468	168.47	3.396	S2[a]
Symmetry code: a: $x-1/2, -y+1/2, z-1/2$					

$$[Sn_3S_4(edt)_3]^{2-} + DMF \xrightarrow[\text{or } KCuI_2]{CuCl_2} [Sn_3(OH)S_3(edt)_3]^-DMF \quad (1)$$

$$[Sn_3S_4(edt)_3]^{2-} + H_2O \xrightarrow[\text{or Cd(phen)(SCN)}_2]{Zn(phen)(SCN)_2} [Sn_3(OH)S_3(edt)_3]^-H_2O \quad (2)$$

Scheme 1. Replacement of μ_3-S by μ_3-OH in the anion cluster of $[Sn_3S_4(edt)_3]^{2-}$ in the presence of proper desulfurizing agents.

incomplete cubane-like anion clusters of $[Sn_3(\mu_3\text{-}OH)S_3(edt)_3]^-$ capped by μ_3-OH and with different H-bond acceptors were unexpectedly obtained. This may because Zn^{2+}, Cu^{2+} or Cd^{2+} play the role of sulfide scavengers in the reactions. A similar phenomenon has been reported previously in the literature [15]. The mechanism may be that the looser μ_3-S–Sn bond was first cleft by Zn^{2+} (Cu^{2+} or Cd^{2+}), and then OH^- was incorporated into the three tin atoms to form $[Sn_3(\mu_3\text{-}OH)S_3(edt)_3]^-$. The bridging OH^- in the two compounds might come from trace water in the solvents.

3.2. Description of the crystal structures of complexes *1* and *2*

As shown in Fig. 1, there are two crystallographically independent but chemically equivalent DMF molecules, two anions and two cations in the asymmetric unit. ORTEP drawing of anions A and B are shown in Fig. 2. In anion A three tin atoms are connected by a central μ_3–OH and three μ_2-S atoms, affording an incomplete cubane-like skeleton. The skeleton is similar to that of $[Sn_3S_4(edt)_3]^{2-}$ [10] except that the central μ_3-S is replaced by μ_3-OH. The average Sn···Sn separation (Sn(1)···Sn(2) 3.533 Å, Sn(1)···Sn(3) 3.559 Å, Sn(2)···Sn(3) 3.563 Å) is 3.552 Å, and is shorter than that of $(Et_4N)_{2n}[Sn_3S_7]_n$ (3.6053 Å) [3d], but is longer than that of $\{[(c\text{-}C_5H_9)_7Si_7O_{12}Sn]_3(OH)_4\}^-$ (3.512 Å) [17]. All tin atoms are five-coordinated by two sulfur atoms of $SC_2H_4S^{2-}$, two μ_2-S and one μ_3-OH in a trigonal bipyramidal geometry. The sum of the equatorial angles are 356.96° (S(2)–Sn(1)–S(9) 120.85(6)°, S(2)–Sn(1)–S(7) 120.12(6)°, S(7)–Sn(1)–S(9) 115.99(5)°) for Sn(1), 356.29° (S(7)–Sn(2)–S(3) 123.36(6)°, S(7)–Sn(2)–S(8) 113.89(6)°, S(3)–Sn(2)–S(8) 119.04(5)°) for Sn(2) and 355.39° (S(8)–Sn(3)–S(5) 119.02(5)°, S(8)–Sn(3)–S(9) 113.97(6)°, S(9)–Sn(3)–S(5) 122.40(5)°) for Sn(3). They are all less than 360°, indicating that all the Sn atoms are slightly deviated from the corresponding equatorial plane. All the axial angles of O(1)–Sn(1)–S(1) (179.54(11)°), O(1)–Sn(2)–S(4) (177.03(11)°) and O(1)–Sn(3)–S(6) (177.18(10)°) are also slightly deviated from 180°. Thus the coordination geometry of each tin atom can be described as a distorted trigonal bipyramid.

The average axial Sn–S bond length (2.4507(15) Å) is obviously longer than that of equatorial Sn–S

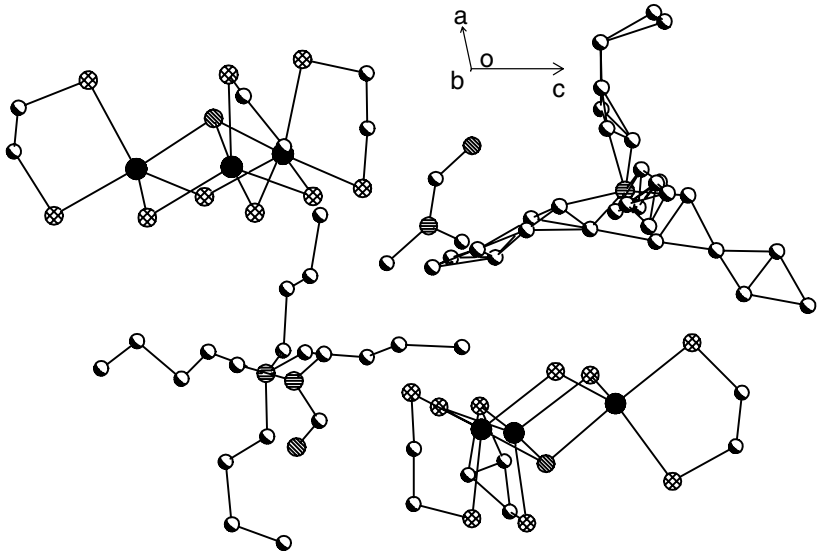


Fig. 1. Perspective view of complex **1** showing two crystallographically independent but chemically equivalent anions, two cations and two DMF molecules in the asymmetric unit.

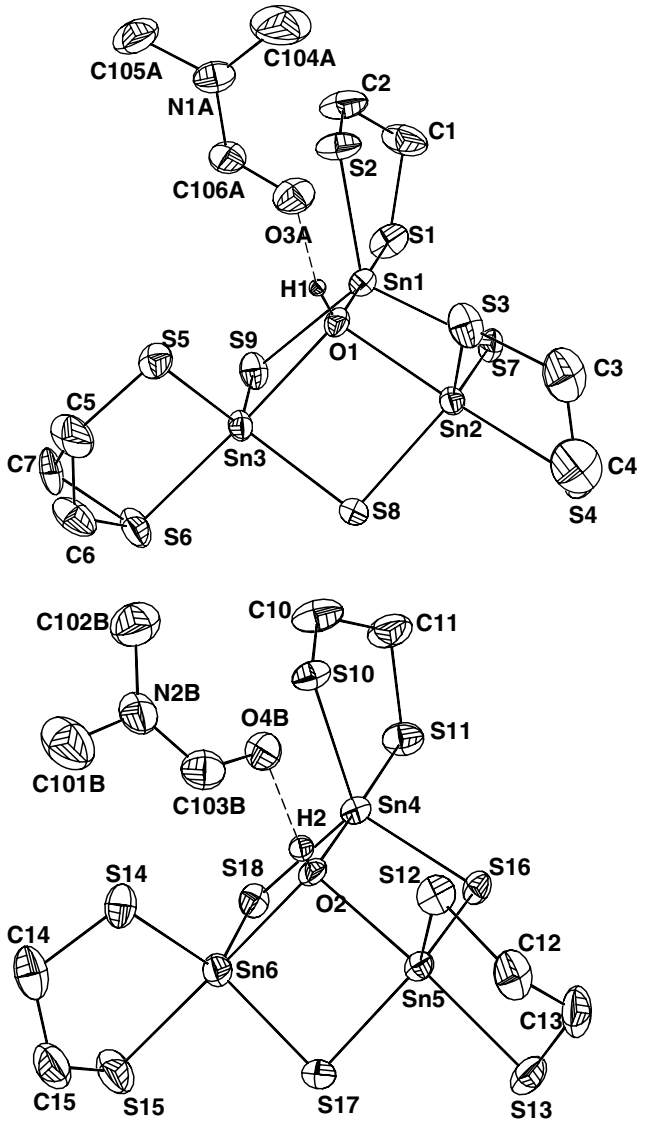


Fig. 2. ORTEP diagrams of anion A (top) and anion B (bottom) in the asymmetric unit of complex **1** with the atom numbering scheme (all non-hydrogen atoms are represented by ellipsoids at 50% probability). Symmetry code: A: $x-1$, y, z; B: $x+1$, y, z.

(2.4040(15) Å). The Sn–O bond lengths fall in the range of 2.287(4)–2.346(4) Å, and their average bond length (2.310 Å) is longer than that of $\{[(c\text{-}C_5H_9)_7Si_7O_{12}Sn]_3(OH)_4\}^-$ (2.276 Å) [17]. The separation of O(1)–O(3A) is 2.739(5) Å, suggesting the presence of an intermolecular H-bond between the cluster of $[Sn_3(\mu_3\text{-}OH)S_3(edt)_3]^-$ and the neighboring DMF molecule.

As shown in Fig. 2, anion B also possesses an incomplete cubane-like metal skeleton. The average Sn···Sn separation is 3.55 Å, and the average bond lengths of Sn–O(2), $Sn–S_{axial}$ and $Sn–S_{equatorial}$ are 2.313, 2.4543 and 2.406 Å, respectively. They are all comparable with those in anion A. The separation of O(2)–O(4B) of 2.774(5) Å is slightly longer than that in anion A.

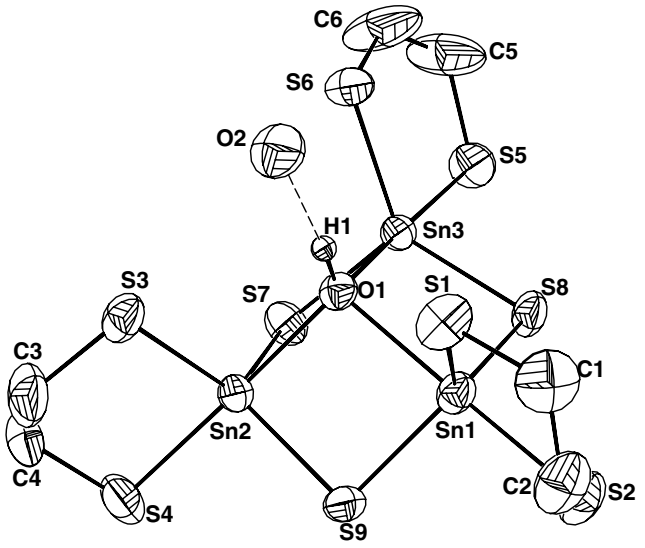


Fig. 3. ORTEP diagram of the anion of complex **2** with the atom numbering scheme (all non-hydrogen atoms are represented by ellipsoids at 40% probability).

Different from anion B, disorder (C6) exists in anion A. In addition, serious disorders are present in one cation of Bu_4N^+ (the details can be seen in Supplemental CIF file).

The anion structure of complex **2**, as shown in Fig. 3, is similar to that of **1** except that the hydrogen acceptor is the water molecule. The H-bond data for complexes **1** and **2** are summarized in Table 3.

3.3. Spectrum

The broad band around 3400 cm^{-1} in the IR spectra of the two compounds suggests the presence of the OH group. For complex **1**, the characteristic stretching vibration of C=O, occurring about 1640 cm^{-1}, is shifted to lower frequency by 35 cm^{-1} with respect to the standard IR spectrum of DMF film, owing to the formation of an intermolecular H-bond. The band around 198 cm^{-1} in the spectra of the two compounds could be attributed to νSn–O [8b]. The medium absorption bands in the region of 300–450 cm^{-1} should be ascribed to the Sn–S stretching vibrations [8b,16].

In the Raman spectra of **1** and **2**, an obvious medium peak for νC–S is found at 557 and 561 cm^{-1}, respectively. The peak around 1120 cm^{-1} could be attributed to the stretching vibration of νC–N.

It can be seen from Table 4 that the ^1H NMR chemical shift (δ) of Sn–OH varies greatly in the range of 1.60–8.90 ppm depending on their various chemical and physical environments [17–24]. The ^1H NMR chemical shift (δ) of Sn–OH for complexes **1** and **2** was found at 3.219 and 3.221 ppm, respectively.

The ES-MS spectra for the two compounds show the molecular ion peak of $[Sn_3(\mu_3\text{-}OH)S_3(edt)_3]^-$ at around 744.6 (m/z).

Table 4
^{1}H NMR chemical shift of Sn–OH in some organotin oxo clusters

Compound	δ(Sn–OH)	Solvent	Ref.
{*n*-BuSnCl ($O_2CC_5H_4$–Fe–C_5H_5)}$_3$(O)(OH)	7.10–7.30	$CDCl_3$ 200 MHz	[17]
{[Ph(HO)$SnCH_2$Sn(I)Ph]O}$_4$	3.74	$CDCl_3$ 400 MHz	[18]
[*n*-BuSn(OH)$(OH_2)Cl_2$]$_2$	1.6	$CDCl_3$ 300 MHz	[19]
[(*n*-Bu)$_2Sn_2Cl_2$(OH)$(O_2PPh_2)_3$]$_2$ · $2CH_2Cl_2$	4.73	$CDCl_3$ 300 MHz	[20]
{Sn(CH_2Ph)(OH)[$O_2P(C_6H_{11})_2$]$_2$}	4.90	$CDCl_3$ 200 MHz	[21]
[{Sn(CH_2Ph)(OH)[$O_2P(C_6H_{11})_2$]}$_3$O][$O_2P(C_6H_{11})_2$]	8.90	$CDCl_3$ 200 MHz	[21]
{[(*c*-$C_5H_9)_7Si_7O_{12}Sn$]$_3$(μ-OH)$_4$} · $\{HNEt_3\}^+$	5.61 (μ_2–OH) 6.33 (μ_3–OH)	$CDCl_3$ 400 MHz	[22]
[(*n*-BuSn(OH)$O_2Pcyc_2)_3$OI(*n*-$BuSnCl_2O_2Pcyc_2)_2$OH]	6.13	$CDCl_3$, 300 MHz	[20]
[*t*-Bu_2SnOH(OTf)(H_2O)]$_2$	5.20	CD_3CN 300 MHz	[23]
[*t*-Bu_2Sn(OH)(NO_3)]$_2$	1.60	Acetone-*d* 300 MHz	[23]
[*n*-Bu_2SnOH(OTf)(H_2O)]$_2$	5.48	CD_3CN 300 MHz	[23]
[{$C_2S_3N_2(CH_3)_2$Sn}$_2$O$(CH_3)_2$Sn(OH)$_2$] · $1.5H_2O$	5.15	$CDCl_3/D_2O$ 300 MHz	[24]
[{$C_2S_3N_2(PhCH_2)_2$Sn}$_2$O$(PhCH_2)_2$Sn(OH)(OEt)]	5.15	$CDCl_3/D_2O$ 300 MHz	[24]

4. Conclusion

In summary, two new incomplete cubane-like trinuclear tin (IV) oxy-sulfide clusters $(Bu_4N)[Sn_3(\mu_3\text{-}OH)S_3(edt)_3]\cdot DMF$ (**1**) and $(Bu_4N)[Sn_3(\mu_3\text{-}OH)S_3(edt)_3]\cdot H_2O$ (**2**) were prepared by a cluster-skeleton substitution reaction based on the precursor $(Bu_4N)_2[Sn_3S_4(edt)_3]$. The two compounds differ only in controlling the nature of the solvate molecule which is hydrogen bonded to the cluster in the resulting solid. $CuCl_2$, $KCuI_2$, Cd(1,10-phen)$(SCN)_2$ or Zn(1,10-phen)$(SCN)_2$ were found to act as a mild desulfurizing agent under the appropriate conditions. This may provide a convenient method for preparing new tin oxy-sulfides.

Acknowledgements

This research was supported by grants from the State Key Laboratory of Structure Chemistry, the National Science Foundation of China (20333037, 90206040, 90406024) and Fujian Province (2005HZ01-1, 2004HZ01-1, 2004J041).

Appendix A. Supplementary material

CCDC 286953 and 286954 contain the supplementary crystallographic data for **1** and **2**. These data can be obtained free of charge via http://www.ccdc.cam.ac.uk/conts/retrieving.html, or from the Cambridge Crystallographic Data Centre, 12 Union Road, Cambridge CB2 1EZ, UK; fax: (+44) 1223-336-033; or e-mail: deposit@ccdc.cam.ac.uk. Supplementary data associated with this article can be found, in the online version, at doi:10.1016/j.poly.2006.09.098.

References

[1] (a) R.L. Bedard, L.D. Vail, S.T. Wilson, E.M. Flanigen, US Patent, 4 880 761, 1989;
(b) R.L. Bedard, L.D. Vail, S.T. Wilson, E.M. Flanigen, US Patent, 4 933 068, 1990.
[2] (a) T. Jiang, G.A. Ozin, J. Mater. Chem. 8 (1998) 1099;
(b) W.S. Sheldrick, J. Chem. Soc., Dalton Trans. (2000) 3041;
(c) T. Jiang, G.A. Ozin, A. Verm, R.L. Bedard, J. Mater. Chem. 8 (1998) 1649.
[3] (a) Y. Ko, K. Tan, D.M. Nellis, S. Koch, J.B. Parise, J. Solid State Chem. 114 (1995) 506;
(b) J.B. Parise, Y. Ko, J. Rijssenbeek, D.M. Nellis, K. Tan, S. Koch, J. Chem. Soc., Chem. Commun. (1994) 527;
(c) T. Jiang, A. Lough, G.A. Ozin, D. Young, R.L. Bedard, Chem. Mater. 7 (1995) 245;
(d) T. Jiang, A. Lough, G.A. Ozin, R.L. Bedard, R.W. Broach, J. Mater. Chem. 8 (1998) 721;
(e) T. Jiang, A. Lough, G.A. Ozin, Adv. Mater. 10 (1998) 42.
[4] (a) J.B. Parise, Y. Ko, Chem. Mater. 6 (1994) 718;
(b) J.B. Parise, Y. Ko, K. Tan, D.V. Nellis, S. Koch, J. Solid State Chem. 117 (1995) 219.
[5] (a) C. Zimmermann, M. Melullis, S. Dehnen, Angew. Chem., Int. Ed. 41 (2002) 4269;
(b) C. Zimmermann, C.E. Anson, F. Weigend, R. Cle'rac, S. Dehnen, Inorg. Chem. 44 (2005) 5686.
[6] Y.-L. An, M. Ji, M.-H. Baiyin, X. Liu, C.-Y. Jia, D.-H. Wang, Inorg. Chem. 42 (2003) 4248.
[7] (a) J.-H. Liao, G.M. Marking, K.F. Hsu, Y. Matsushita, M.D. Ewbank, R. Borwick, P. Cunningham, M.J. Rosker, M.G. Kanatzidis, J. Am. Chem. Soc. 125 (2003) 9484;
(b) O. Palchik, R.G. Iyer, J.H. Liao, M.G. Kanatzidis, Inorg. Chem. 42 (2003) 5052;
(c) M.J. Manos, R.G. Iyer, E. Quarez, J.H. Liao, M.G. Kanatzidis, Angew. Chem., Int. Ed. 44 (2005) 3552.
[8] (a) W. Schiwy, B. Krebs, Angew. Chem. 87 (1975) 451;
(b) K.C.K. Swamy, R.O. Day, R.R. Holmes, J. Am. Chem. Soc. 110 (1988) 7543;
(c) O.R. Floeck, M. Draeger, Organometallics 12 (1993) 4623;
(d) W. Bubenheim, U. Muller, Z. Anorg. Allg. Chem. 619 (1993) 779.
[9] (a) L.-M. Wu, L. Chen, J.-C. Dai, C.-P. Cui, Z.-Y. Fu, X.-T. Wu, Inorg. Chem. Commun. 4 (2001) 574;
(b) J.-J. Zhang, S.-M. Hu, X.-T. Wu, W.-X. Du, R.-B. Fu, L.-S. Wang, Inorg. Chem. Commun. 6 (2003) 744.
[10] B. Krebs, T. Lindner, L. Stork, Z. Kristallogr. 174 (1986) 125.
[11] V. Aslanov, M. Ionov, K. Kynev, Z. Kristallogr. 21 (1976) 1198.
[12] M. Cannas, G. Carta, A. Cristini, G. Marongiu, J. Chem. Soc., Dalton Trans. (1976) 300.
[13] G.M. Sheldrick, SADABS, University of Göttiongen, Germany, 1996.

[14] G.M. Sheldrick, SHELXT-97, Program for Crystal Structure Refinement, University of Göttingen, Germany, 1997.
[15] (a) W.-J. Zhang, A. Behens, J. Catjens, M. Ebel, X.-T. Wu, D. Rehder, Inorg. Chem. 43 (2004) 3020;
(b) W.-J. Zhang, X.-T. Wu, B. Wu, S.-Y. Yu, D. Rehder, Inorg. Chem. 42 (2003) 1130.
[16] D. Dakternieks, B.F. Hpskins, E.R.T. Tiekink, G. Winter, Inorg. Chim. Acta 85 (1984) 215.
[17] K.C.K. Swamy, S. Nagabrahmanandachari, K. Raghuraman, J. Organomet. Chem. 587 (1999) 132.
[18] M. Mehring, G. Gabriele, S. Hadjikakou, M. Schürmann, D. Dakternieks, K. Jurkschat, Chem. Commun. (2002) 834.
[19] R. Holmes, S. Shafieezad, V. Chandrasekhar, J.M. Holmes, R.O. Day, J. Am. Chem. Soc. 110 (1988) 1174.
[20] K.C. Kumara Swamy, R.O. Day, R.R. Holmes, Inorg. Chem. 31 (1992) 4184.
[21] K.C.K. Swamy, M.A. Said, S. Nagabrahmanandachari, D.M. Poojary, A. Clearfield, J. Chem. Soc., Dalton Trans. (1998) 1645.
[22] R. Duchateau, T.W. Dijkstra, J.R. Severn, R.A. van Santen, I.V. Korobkov, J. Chem. Soc., Dalton Trans. (2004) 2677.
[23] K. Sakamoto, H. Ikeda, H. Akashi, T. Fukuyama, A. Orita, J. Otera, Organometallics 19 (2000) 3242.
[24] C.-L. Ma, J.-H. Zhang, F. Li, R.-F. Zhang, Eur. J. Inorg. Chem. (2004) 2775.

the use of squarate afforded notable works through versatile bridging modes [6]. On the contrary, the number of reports relating to the coordination chemistry of the croconate dianion is limited. A few structures of first row transition metal-croconate systems, $[M(II)(C_5O_5)(H_2O)_3]$ [M = Cu, Zn, Mn, Fe and Co] [7] and of some croconate complexes associated with co-ligands such as imidazole [8], histamine [9], 2,2′-bipyridine [10], 4,4′-bipyridine, [11] bis(2-pyridylcarbonyl)amido anion, [12], etc. are reported. A literature survey reveals different binding modes (Scheme 1) of croconate: bidentate chelate (**I**) [5f,7a,8–10,13], bridging bidentate/monodentate (**II**) [7a,7b,7c], bridging bis-bidentate ligand through either four (**III**) [12,14] or three adjacent (**IV**) [14,15] croconate oxygen atoms and bidentate chelate/bridging bis-bidentate chelate (μ_5) (**V**) [11]. Recently our group reported three new different bridging modes of croconate, acting as a tridentate (**VI**) and tetradentate ligand (**VII**) [5a,16] in Cd(II)- and Ag(I)–Na(I) complexes, respectively, and bridging bidentate chelate/monodentate (**VIII**) [17] in a Cu(II) complex where C–H···O interactions contribute to control the coordination bond formation in the metal-organic framework (MOF). Moreover we have also reported the croconate dianion sitting as a lattice moiety in the solid state architecture, which stabilizes the MOF through H-bonding occurring between its oxygens and coordinated water molecules [18]. The present contribution reports the synthesis, crystal structure and thermal behavior of $\{[Co(4,4'\text{-bipy})(H_2O)_4]\cdot(C_5O_5)\cdot(H_2O)_2\}_n$ (**1**), $\{[Fe(4,4'\text{-bipy})(H_2O)_4]\cdot(C_5O_5)\cdot(H_2O)_2\}_n$ (**2**) and $\{[Co_2(bpds)_2(C_5O_5)_2(H_2O)_4]\cdot(H_2O)_3\}_n$ (**3**) networks [4,4′-bipy = 4,4′-bipyridyl, bpds = 4,4′-bipyridyl disulfide, $C_5O_5^{2-}$ = croconate dianion], all having a 3D supramolecular architecture.

2. Experimental

2.1. Materials

High purity 4,4′-bipyridyl (98%), 4,4′-bipyridyl disulfide (aldrithiol-4; 98%) and the disodium salt of croconic acid were purchased from the Aldrich Chemical Co. Inc. and were used as received. All other chemicals were of AR grade.

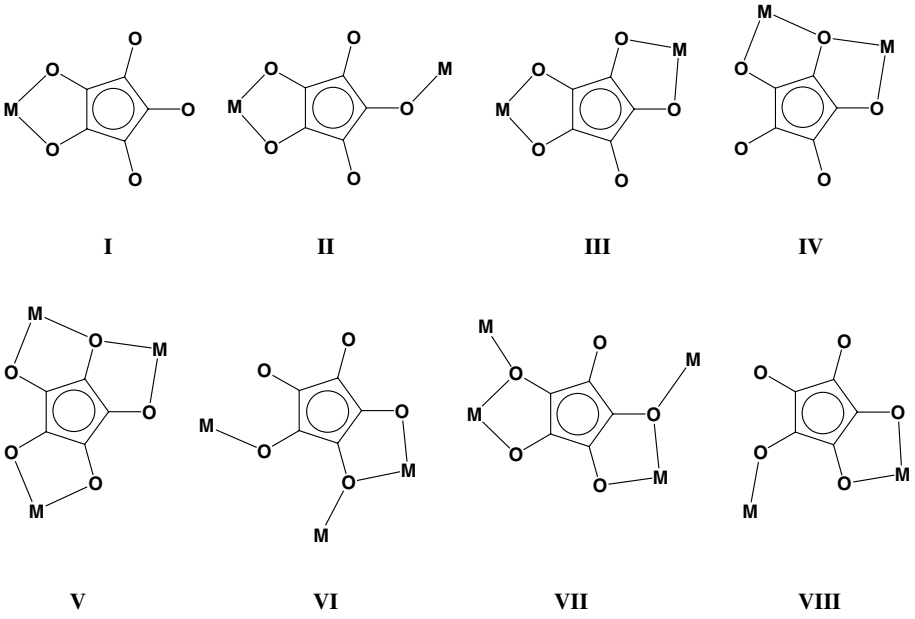
2.2. Physical measurements

Elemental analyses (carbon, hydrogen and nitrogen) were performed using a Perkin–Elmer 240C elemental analyzer. IR spectra were measured using KBr pellets on a Nicolet 520 FTIR spectrometer. The magnetic susceptibility was measured at 27 °C using an EG and G PAR-155 vibrating sample magnetometer, using $Hg[Co(SCN)_4]$ as reference material; a diamagnetic correction was made by using Pascal's constants. The UV–Vis reflectance spectra were recorded between 200 and 1400 nm on a Perkin–Elmer Lambda 950 spectrophotometer at room temperature in the solid state. Thermogravimetric analyses were carried out on a Mettler Toledo Star system.

2.3. Synthesis

2.3.1. $\{[Co(4,4'\text{-bipy})(H_2O)_4]\cdot(C_5O_5)\cdot(H_2O)_2\}_n$ (1)

The complex was synthesized by slow diffusion of a mixture of a methanolic solution (10 ml) of 4,4′-bipyridyl (1 mmol, 0.156 g) and the disodium salt of croconic acid (1 mmol, 0.186 g, dissolved in a minimum amount of water) over an aqueous solution (10 ml) of $Co(NO_3)_2\cdot 6H_2O$ (1 mmol, 0.291 g). Single crystals suitable for X-ray



Scheme 1.

analysis were obtained at the junction of the layers after a few days. Yield: 70%. *Anal.* Calc. for $C_{15}H_{20}CoN_2O_{11}$ (463.26): C, 38.85; H, 4.31; N, 6.04. Found: C, 38.84; H, 4.33; N, 6.05%. μ_{eff} at 300 K = 5.05 BM.

*2.3.2. $\{[Fe(4,4'\text{-bipy})(H_2O)_4]\cdot(C_5O_5)\cdot(H_2O)_2\}_n$ (**2**)*

A methanolic solution (10 ml) of 4,4′-bipy (1 mmol, 0.156 g) was gently poured into an aqueous solution (5 ml) of the disodium salt of croconic acid (1 mmol, 0.186 g). Ferrous ammonium sulfate hexahydrate (1 mmol, 0.393 g) in water (5 ml) was added to this solution dropwise with constant stirring. A deep red complex separated out. Single crystals suitable for X-ray analysis were obtained by diffusing the aqueous solution (5 ml) of ferrous ammonium sulfate hexahydrate on a water–methanol (1:2) layer (15 ml) of the disodium salt of croconic acid and 4,4′-bipy (1:1) in a corked tube. The red colored single crystals were deposited at the junction of the two solutions after a few weeks. Yield: 70%. *Anal.* Calc. for $C_{15}H_{20}FeN_2O_{11}$ (460.18): C, 39.14; H, 4.35; N, 6.09. Found: C, 39.09; H, 4.31; N, 6.05%. μ_{eff} at 300 K = 5.52 BM.

*2.3.3. Complex $\{[Co_2(bpds)_2(C_5O_5)_2(H_2O)_4]\cdot(H_2O)_3\}_n$ (**3**)*

A methanolic solution (5 ml) of $Co(NO_3)_2\cdot 6H_2O$) (1 mmol, 0.291 g) was added to a methanolic solution (5 ml) of bpds (1 mmol, 0.220 g) dropwise with constant stirring. To this reaction mixture an aqueous solution (10 ml) of the disodium salt of croconic acid (1 mmol, 0.186 g) was added and stirred for 30 min. It was filtered and deep brown single crystals suitable for X-ray analysis were obtained from the filtrate kept in a $CaCl_2$ desiccator after a few days. Yield: 75%. *Anal.* Calc. for $C_{30}H_{30}Co_2N_4S_4O_{17}$ (964.68): C, 37.32; H, 3.11; N, 5.81. Found: C, 36.66; H, 3.24; N, 5.71%. μ_{eff} at 300 K = 5.00 BM.

2.4. Crystallographic data collection and refinement

Crystal data and details of data collection and refinement for the structures reported are summarized in Table 1. The data collections were carried out using Mo Kα radiation ($\lambda = 0.71073$ Å) at 293(3) K on a Nonius DIP-1030H system (complexes **1** and **2**) and at 100(3) K on a Bruker SMART (complex **3**) equipped with a CCD area detector. Cell refinement, indexing and scaling of the data sets were performed using the program MOSFLM [19]. All the structures were solved by the Patterson method and Fourier analyses and refined by the full-matrix least-squares method based on F^2 with all observed reflections [20]. The calculations were performed using the WinGx System, Ver 1.64.05 [21].

3. Results and discussion

3.1. IR spectroscopy

The IR spectra of complexes **1** and **2** in the 1400–1800 cm^{-1} region, where characteristic bands for the different binding modes of the croconate dianion are observed,

Table 1
Crystal data and details of the structure determination for complexes **1**, **2** and **3**

Complex	**1**	**2**	**3**
Empirical formula	$C_{15}H_{20}CoN_2O_{11}$	$C_{15}H_{20}FeN_2O_{11}$	$C_{30}H_{30}Co_2N_4O_{17}S_4$
Formula weight (g mol^{-1})	463.26	460.18	964.68
Crystal system	monoclinic	monoclinic	monoclinic
Space group	$P2_1/m$	$P2/c$	$P2_1/c$
a (Å)	6.724(3)	6.770(3)	16.858(2)
b (Å)	12.048(4)	11.437(3)	13.6388(19)
c (Å)	11.325(3)	12.383(4)	17.692(2)
β (°)	96.00(2)	103.73(2)	113.899(3)
V (Å^3)	912.4(6)	931.4(6)	3719.1(9)
Z	2	2	4
D_{calc} (g cm^{-3})	1.686	1.641	1.723
μ (Mo Kα) (mm^{-1})	1.006	0.874	1.198
$F(000)$	478	476	1968
θ Range (°)	2.48–29.60	2.46–29.58	1.99–27.10
Number of collected data	10012	9926	24657
R_{int}	0.0470	0.0570	0.1079
Unique data	2417	2570	8120
Data $I > 2\sigma(I)$	1837	1686	5045
Refined parameters	160	153	556
R_1[a] $[I > 2\sigma(I)]$	0.0446	0.0363	0.0694
wR_2[a] $[I > 2\sigma(I)]$	0.1276	0.0882	0.1285
Goodness-of-fit[b]	1.047	0.921	1.024
Residuals (e Å^{-3})	0.696, −0.381	0.293, −0.227	1.241, −0.625

[a] $R_1 = \sum||F_o|-|F_c||/\sum|F_o|$, $wR_2 = [\sum w(F_o^2 - F_c^2)^2/\sum w(F_o^2)^2]^{1/2}$.

[b] Goodness-of-fit $= \{\sum[w(F_o^2 - F_c^2)^2]/(n-p)\}^{1/2}$.

exhibit a very strong and broad band (ca. 1500 cm^{-1} for **1**; 1502 cm^{-1} for **2**) and one sharp band (1662 cm^{-1} for **1**; 1660 cm^{-1} for **2**). The former band is assigned to a mixture of ν(C–C) and ν(C–O) stretching vibrations and the latter to ν(C=O) of croconate [8], which hints that the oxocarbon species function as a counter anion rather than being involved in the coordination sphere. IR spectra of complex **3** in the same region possess some different bands: a very strong band at 1514 cm^{-1} and three strong bands at 1540, 1591 and 1485 cm^{-1}. The broad band (3500–3200 cm^{-1}) in all the complexes confirms the presence of water molecules. The IR spectra also show bands corresponding to ρ_r (H_2O) [735, 731 and 725 cm^{-1} for **1**, **2** and **3**, respectively] and $\rho_w(H_2O)$ [636, 636 and 625 cm^{-1} for **1**, **2** and **3**, respectively] which indicate the presence of coordinated water molecules.

3.2. Description of the structures

3.2.1. $\{[Co(4,4'\text{-bipy})(H_2O)_4]\cdot(C_5O_5)\cdot(H_2O)_2\}_n$ (**1**) and $\{[Fe(4,4'\text{-bipy})(H_2O)_4]\cdot(C_5O_5)\cdot(H_2O)_2\}_n$ (**2**)

The crystal structures having the same stoichiometry are described together in order to compare the subtle details that differentiate their geometry. The iron derivative (complex **2**) is isomorphous to that containing manganese(II), reported by this laboratory a couple of years ago [18]. A drawing of the packing with the atom labelling scheme is shown in Figs. 1 and 2, and a selection of bond lengths and angles is given in Tables 2 and 3. The present complexes reveal Co$(H_2O)_4^{2+}$ and Fe$(H_2O)_4^{2+}$ units bridged by 4,4′-bipy ligands with the occurrence of 1D coordination polymeric chains (Figs. 1 and 2). Four water molecules (O(1w), O(2w) and the symmetry related ones) form the equatorial plane and the 4,4′-bipy nitrogen atoms N1 and N2 occupy the *trans* axial positions. The metal and 4,4′-bipy nitrogen donors are positioned on a mirror plane in complex **1** and on a twofold axis in **2**. This different symmetry site leads to a N–Co–N bond angle of 177.90(12)°, while the N–Fe–N fragment is collinear. The Fe–N distances (Table 3) are slightly shorter than the values of 2.237 Å found in the mononuclear complex, $[Fe(H_2O)_4(bipy)_2]$(disaccharinate) [22].

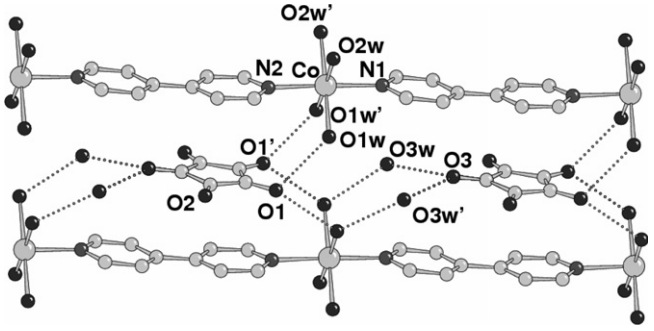


Fig. 1. Coordination polymer in complex **1** developed along the *c*-axis with the encapsulated croconate dianion (dotted lines indicate H-bonds).

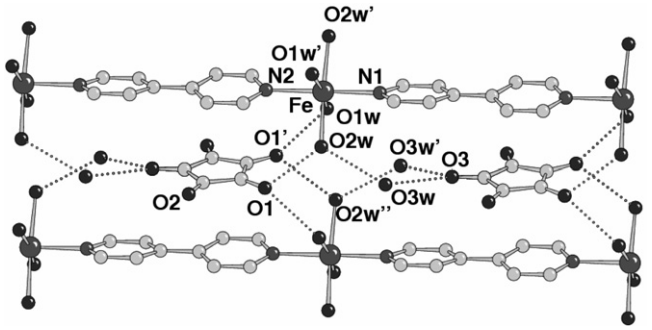


Fig. 2. Coordination polymer in complex **2** running along the *b* axis with the encapsulated croconate dianion (dotted lines indicate H-bonds).

Table 2
Selected bond lengths (Å) and angles (°) for complex **1**

Co–O(1w)	2.085(2)	Co–N(1)	2.107(3)
Co–O(2w)	2.137(2)	Co–N(2)	2.128(3)
O(1w)–Co–O(1w′)	90.16(14)	O(1w)–Co–N(2)	87.78(9)
O(1w)–Co–O(2w)	177.53(9)	O(2w)–Co–O(2w′)	86.54(14)
O(1w)–Co–O(2w′)	91.62(10)	N(1)–Co–O(2w)	90.94(9)
O(1w)–Co–N(1)	90.74(9)	N(2)–Co–O(2w)	90.59(9)
		N(1)–Co–N(2)	177.90(12)

Symmetry operation: (′) x, $-y+1/2$, z.

Table 3
Selected bond lengths (Å) and angles (°) for complex **2**

Fe–O(1w)	2.117(2)	Fe–N(1)	2.159(2)
Fe–O(2w)	2.163(2)	Fe–N(2″)	2.186(2)
O(1w)–Fe–O(1w′)	172.47(9)	O(1w)–Fe–N(2″)	86.24(5)
O(1w′)–Fe–O(2w)	87.96(8)	O(2w′)–Fe–O(2w)	176.36(9)
O(1w)–Fe–O(2w)	92.27(8)	N(1)–Fe–O(2w)	88.18(5)
O(1w)–Fe–N(1)	93.76(5)	O(2w)–Fe–N(2″)	91.82(5)
		N(1)–Fe–N(2″)	180.0

Symmetry operations: (′) $-x+1$, y, $-z+3/2$; (″) x, $y-1$, z.

The water oxygens of the equatorial plane are coplanar in complex **1** and exhibit a slight distortion in complex **2** (±0.104 Å), with the metal ion displaced from this mean plane by 0.031(2) Å (Co) and 0.035(1) Å (Fe) towards N(1). From a careful analysis of Tables 2 and 3 it is worth noting in both cases there are differences between the M–O bond distances for the two independent H_2O ligands (~30σ) and between the two M–N distances (~10σ). We do not have an explanation for this feature, the packing and the environment of the cited atoms not being indicative for these apparent discrepancies. The rings of the 4,4′-bipy ligand are almost coplanar in complex **1**, but rather tilted by about 12° in the iron derivative (**2**).

The intermetallic distances connected by the 4,4′-bipy ligand are 11.325(3) Å (Co–Co) and 11.437(3) Å (Fe–Fe), which are to be compared with the value found in the Mn derivative of 11.531(4) Å; these values follow the increasing ionic radius of the metal(II).

The croconate dianions, encapsulated between contiguous polymeric chains at a distance of about 3.4 Å from

the N(2) pyridine rings of 4,4′-bipy, give rise to a H-bonding scheme involving coordinated and lattice water molecules (Figs. 1 and 2). However, the H-bonding pattern leading to the supramolecular architecture in the two crystals is slightly different. H-bonds are formed between the croconate O(1) and coordinated water molecules, while croconate oxygen O(3) is connected to the lattice water molecules O(3w), but in such a way that the latter interact with water molecules of the same chain in complex **1**, but with aqua ligands of different polymers in complex **2**. The three dimensional structure is achieved through O(2) of an adjacent croconate that behaves as a H-bond acceptor with respect to O(1w) and O(3w). The latter interactions are not shown in Figs. 1 and 2.

3.2.2. $\{[Co_2(bpds)_2(C_5O_5)_2(H_2O)_4]\cdot(H_2O)_3\}_n$ (**3**)

The structural determination evidences two crystallographic independent metal ions in a severely distorted octahedral coordination with O_4N_2 chromophore (Fig. 3), embracing a chelating croconate dianion, two water molecules and two nitrogens, all arranged in *cis* positions. The octahedral coordination spheres are highly distorted with deviations of up to 10° from ideal angles (Table 4). It is worth noting that the pyridine rings present an unsymmetrical coordination, as evident from Fig. 3, with a Co–N···S angle that varies from 168.62° to 174.02°, the pyridine ring N(4) being the most bent. The Co–OH_2 bond lengths, falling in the range 2.051(4)–2.093(4) Å, are about 0.05–0.10 Å shorter than the Co–N [2.106(4)–2.150(5) Å] and the Co–O(croconate) ones [2.133(4)–2.196(4) Å]. The involvement of oxygen atoms in H-bonding (*vide supra*) may account for these differences.

Table 4
Selected bond lengths (Å) and angles (°) for complex **3**

Co(1)–O(1w)	2.091(4)	Co(2)–O(3w)	2.093(4)
Co(1)–O(2w)	2.063(4)	Co(2)–O(4w)	2.051(4)
Co(1)–N(1)	2.106(4)	Co(2)–N(2)	2.115(5)
Co(1)–N(3)	2.150(5)	Co(2)–N(4′)	2.129(5)
Co(1)–O(1)	2.160(4)	Co(2)–O(8)	2.133(4)
Co(1)–O(2)	2.153(4)	Co(2)–O(9)	2.196(4)
O(1w)–Co(1)–O(2w)	90.37(16)	O(3w)–Co(2)–O(4w)	85.72(16)
O(1w)–Co(1)–N(1)	172.67(16)	O(3w)–Co(2)–N(2)	88.99(17)
O(1w)–Co(1)–N(3)	89.88(17)	O(3w)–Co(2)–N(4′)	174.04(17)
O(1w)–Co(1)–O(1)	87.34(15)	O(3w)–Co(2)–O(8)	86.85(15)
O(1w)–Co(1)–O(2)	84.45(15)	O(3w)–Co(2)–O(9)	88.93(15)
O(2w)–Co(1)–N(1)	96.79(16)	O(4w)–Co(2)–N(2)	94.48(18)
O(2w)–Co(1)–N(3)	90.82(16)	O(4w)–Co(2)–N(4′)	96.21(17)
O(2w)–Co(1)–O(1)	86.53(15)	O(4w)–Co(2)–O(8)	93.23(16)
O(2w)–Co(1)–O(2)	167.42(15)	O(4w)–Co(2)–O(9)	172.26(16)
N(1)–Co(1)–N(3)	91.59(17)	N(2)–Co(2)–N(4′)	96.45(18)
N(1)–Co(1)–O(1)	91.51(15)	N(2)–Co(2)–O(8)	170.94(16)
N(1)–Co(1)–O(2)	88.22(15)	N(2)–Co(2)–O(9)	91.00(16)
N(3)–Co(1)–O(1)	176.14(15)	N(4′)–Co(2)–O(8)	87.42(16)
N(3)–Co(1)–O(2)	100.61(16)	N(4′)–Co(2)–O(9)	88.58(16)
O(1)–Co(1)–O(2)	81.79(14)	O(8)–Co(2)–O(9)	80.88(14)

Symmetry operation: (′) $x-1, y-1, z$.

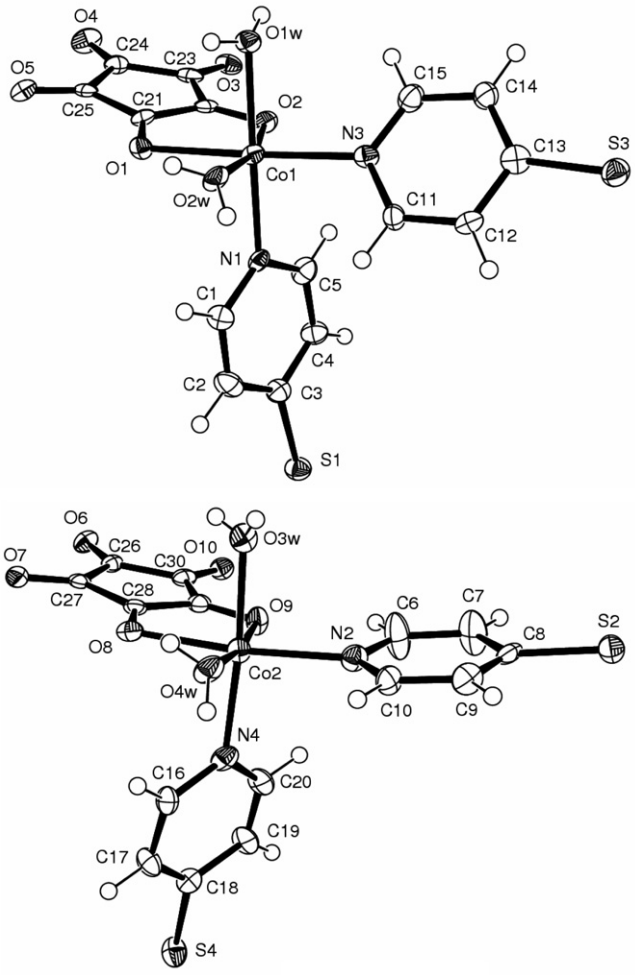


Fig. 3. ORTEP view of the metal coordination sphere of the two independent cobalt ions in complex **3** (ellipsoid at the 40% probability level).

The crystal structure comprises of a 1D undulating polymeric chain of $[Co(H_2O)_2(C_5O_5)]$ neutral units linked by bpds spacers (Fig. 4). Along the –Co–(bpds)–Co– array the metal ions are alternatively separated by 11.598(2) and 10.999(2) Å, with a Co–Co–Co angle of 147.32(1)°. The different Co–Co distance is caused by the slightly dissimilar conformation of the two bpds ligands. These present a C–S–S–C torsion bond angle of 91.8(3)° and 101.7(3)°, leading to a slightly different N–N bridging distance, 7.840, and 8.452 Å, respectively.

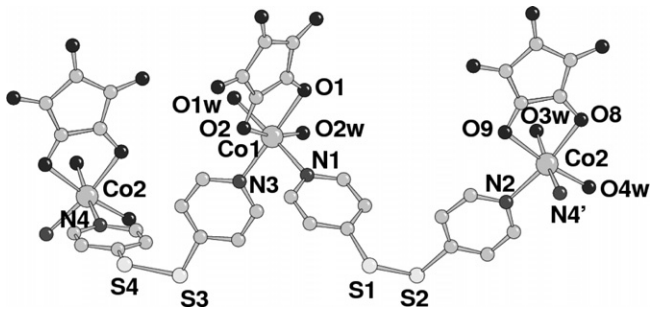


Fig. 4. Coordination polymer of complex **3**.

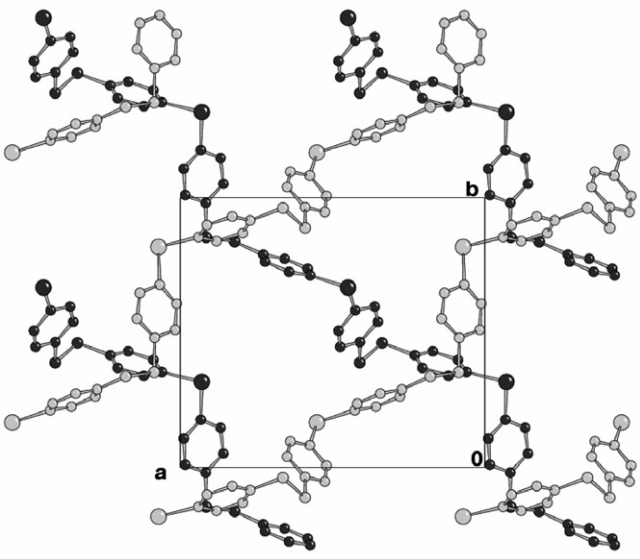


Fig. 5. Packing diagram of Co(dpds) polymers in complex **3** projected down the *c* axis (water molecules and croconate not shown for the sake of clarity).

The torsion angles of bpds linkers are well within or slightly above the range of values [83.8(6)–95.5(8)°] reported for a series of metal complexes [23], where the authors stated that bpds is "a rather conformationally rigid linker".

Series of coordination polymers running in different directions are piled parallel to the [0 0 1] plane and a different conformation of the bpds ligands may be caused in order to favor the crystal packing (Fig. 5). Finally, a H-bonding interaction occurring among coordinated and lattice water molecules as well as croconate oxygens (Table 5) leads to a 3D supramolecular architecture. It is interesting to note that in the crystal the shortest intermetallic distance between different polymers is 6.851 Å [Co(1) and Co(2) at $-x$, $1/2 + y$, $1/2 - z$].

3.3. Thermal analysis

Thermogravimetric analysis of complex **1** shows desolvation in the temperature range 100–156 °C. The TG profile (Fig. 6) hints loss of two lattice and four coordinated water molecules (Fig. 1) taking place simultaneously (mass loss: experimental, 23.31% and calculated, 23.32%) without showing any intermediate step. The deaquation temperature range corroborates the involvement of H-bonding among the coordinated/lattice water molecules and the croconate dianion (Fig. 1). The deaquated species (**1a**, blue) is stable up to 270 °C. The IR spectral bands of the

Table 5
H-bonds involving water molecules in complexes **1**, **2** and **3**

D–H	*d*(D–H)	*d*(H···A)	∠DHA	*d*(D···A)	A	Symmetry operation
1[a]						
O1w–H1	0.851	1.941	173.12	2.789	O1	$[-x, -y+1, -z]$
O1w–H2	0.853	1.942	162.90	2.769	O2	$[x, y-1, z]$
O2w–H1	0.829	1.944	169.55	2.763	O3w	$[-x+1, -y+1, -z+1]$
O2w–H2	0.842	2.005	174.42	2.844	O1	$[-x+1, y-1/2, -z]$
O3w–H1	0.830	2.085	166.29	2.898	O3	
O3w–H2	0.839	2.093	158.52	2.890	O2	$[-x, y-1/2, -z+1]$
2[a]						
O1w–H1	0.810	2.008	177.38	2.817	O1	$[x-1, y-1, z]$
O1w–H2	0.830	1.943	166.56	2.757	O2	$[-x+1, -y-1, -z+1]$
O2w–H1	0.824	1.984	170.11	2.800	O1	$[x, y-1, z]$
O2w–H2	0.857	1.962	167.82	2.806	O3w	
O3w–H1	0.819	2.138	177.17	2.956	O3	
O3w–H2	0.821	2.066	164.38	2.864	O2	$[-x+2, -y-1, -z+1]$
3[b]						
O1w–H1	0.715	2.033	142.20	2.635	O7	$[-x, -y+1, -z]$
O1w–H2	0.911	1.774	164.92	2.664	O3	$[-x+1, -y+1, -z]$
O2w–H1	0.783	1.934	172.05	2.711	O6w	$[-x+1, y+1/2, -z+1/2]$
O2w–H2	0.784	1.952	170.63	2.728	O6	$[-x, -y+1, -z]$
O3w–H1	0.654	2.069	160.81	2.696	O5	$[-x, -y+1, -z]$
O3w–H2	1.123	1.624	173.30	2.743	O5w	$[x-1, y, z]$
O4w–H1	0.827	1.976	157.67	2.759	O10	$[x, -y+1/2, z+1/2]$
O4w–H2	0.843	1.858	170.87	2.694	O7w	$[x-1, y, z]$
O5w–H1	0.810					
O5w–H2	1.165	1.954	136.95	2.916	O9	$[-x+1, y+1/2, -z+1/2]$
O6w–H1	0.781	2.234	160.48	2.981	O7	$[x+1, y, z]$
O6w–H2	0.795	2.197	151.25	2.919	O3	
O7w–H1	0.846	1.996	177.05	2.841	O6w	
O7w–H2	0.659	2.537	149.00	3.120	O4	$[-x+1, -y+1, -z]$

[a] O3w = lattice water molecule.
[b] O5w–O7w = lattice water molecules.

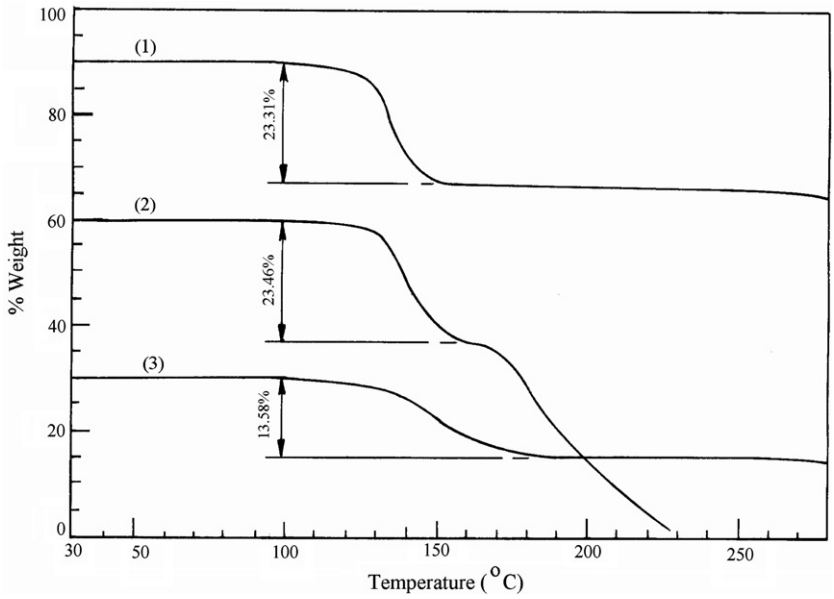


Fig. 6. Thermogravimetric curves for complexes **1**, **2** and **3**.

dehydrated complex, assigned to ν(C–C) and ν(C–O) stretch vibrations of the croconate moiety, shift towards lower wavenumber, splitting at 1481 and 1413 cm^{-1}. The band corresponding to ν(C=O) weakens and shifts to 1637 cm^{-1}. One additional band at 1604 cm^{-1}, assigned to ν(C=C), is obtained. These facts indicate linkage of the croconate dianion with the cobalt(II) center. It is interesting to note that **1a** looks transparent when observed under an optical microscope with a polarizer, but X-ray powder diffraction analysis indicates an amorphous material. Moreover, the croconate dianion may function as a bridging ligand to satisfy the tetrahedral coordination geometry of Co(II) in **1a** [solid state electronic spectra (19445, ~16646 and 8495 cm^{-1} for **1**) and (19275, 17970, 13990–15475 and 8798 cm^{-1} for **1a**) and room temperature magnetic measurements (μ_{eff} for **1** 5.05 BM and for **1a** 4.81 BM (at 300 K)]. On exposure to humid atmosphere (RH ~ 80%) **1a** reverts at ambient temperature showing thermochromism due to octahedral ⇌ tetrahedral geometrical transformation. X-ray powder diffraction analysis also corroborates the above facts.

Complex **2** is thermally stable up to 130 °C and shows deaquation beyond this temperature and gets deaquated (mass loss: experimental, 23.46%; calculated, 23.47%) at 160 °C. The deaquated species collapses immediately upon further heating as the iron(II) centers fail to attain the required geometry after removal of water molecules.

Upon heating complex **3** up to 100 °C there is no mass change, then upon further heating coordinated and lattice water molecules are released in two steps, overlapping each other, in the temperature range ~100 to ~185 °C, yielding blue species, **3a** (mass loss: experimental, 13.58%; calculated, 13.07%). The deaquation temperature range corroborates the structural results which evidence the existence of H-bonding among the coordinated/lattice water molecules and croconate dianion. The species **3a** is stable up to 300 °C and does not revert on exposure to humid atmosphere (RH ~ 80%) at ambient temperature. Room temperature magnetic susceptibility measurement of **3a** was carried out but the difference of magnetic moment between **3** and **3a** is negligible. There is difference in the electronic mull spectral bands, though, which indicate a tetrahedral geometry around Co(II) in **3a**. It is to note that the color change upon deaquation is not prominent like **1**.

4. Conclusion

Three supramolecular architectures using the croconate dianion and bipyridyl spacers have been investigated. The presence of oxocarbons dianions as lattice species or as metal ligands leads to 1D coordination polymeric chains of different topology. Structure determination of complexes **1** and **2** shows $Co(H_2O)_4$ and $Fe(H_2O)_4$ units connected by bridging 4,4′-bipy. The adjacent chains undergo H-bonding with the lattice croconate dianion and water molecules to form a 3D supramolecular architecture. In contrast, the polymer of complex **3** is built of bridging bpds, with metals coordinated by chelating croconate and two water molecules. The resulting chains undergo H-bonding with the lattice water molecules resulting in a 3D supramolecular network in the solid state. Thermal study shows octahedral–tetrahedral transformations taking place in complexes **1** and **3** in the solid state.

Supplementary material

CCDC 617097, 617098 and 617099 contain the supplementary crystallographic data for this paper. These data can be obtained free of charge via http://www.ccdc.cam.ac.uk/conts/retrieving.html, or from the Cambridge

Crystallographic Data Centre, 12 Union Road, Cambridge CB2 1EZ, UK; fax: (+44) 1223-336-033; or e-mail: deposit@ ccdc.cam.ac.uk.

Acknowledgements

The authors are thankful to the Council of Scientific and Industrial Research, New Delhi, for financial support and acknowledge National Facility on Single Crystal X-ray Diffraction of IIT Kanpur for data collection of one complex.

References

[1] (a) G.R. Desiraju, in: Crystal Engineering: Design of Organic Solids, Elsevier, Amsterdam, 1989. Angew. Chem., Int. Ed. Engl. 34 (1995) 2311;
(b) J.M. Lehn, Supramolecular Chemistry, VCH, Weinheim, 1985 (Chapter 9);
(c) R. Robin, B.F. Abrahams, R.R. Barten, R.W. Gable, B.F. Huskiness, J. Lieu, Supramolecular Architecture, ACS, Washington, DC, 1992 (Chapter 19);
(d) B. Moulton, M.J. Zaworotko, Chem. Rev. 101 (2001) 1629;
(e) R.K. Seddon, M.J. Zaworotko, Crystal Engineering: The Design and Application of Functional Solids, NATO Science Series.

[2] (a) I.G. Dance, in: G.R. Desiraju (Ed.), The Crystals as a Supramolecular Entity, John Wiley, NewYork, 1996;
(b) D.J. Hill, M.J. Mio, R.B. Prince, T.S. Hughes, J.S. Moore, Chem. Rev. 101 (2001) 3893;
(c) D. Ghoshal, T.K. Maji, G. Mostafa, T.-H. Lu, N. Ray Chaudhuri, Cryst. Growth Des. 3 (2003) 9;
(d) A.K. Ghosh, D. Ghoshal, T.-H. Lu, G. Mostafa, N. Ray Chaudhuri, Cryst. Growth Des. 4 (2004) 851;
(e) D. Ghoshal, T.K. Maji, G. Mostafa, S. Sain, J. Ribas, E. Zangrando, T.-H. Lu, N. Ray Chaudhuri, J. Chem. Soc., Dalton Trans. (2004) 1687.

[3] (a) K. Maruoka, N. Murase, H. Yamamoto, J. Org. Chem. 58 (1993) 2938;
(b) C. Chen, K.S. Suslick, Coord. Chem. Rev. 128 (1993) 293;
(c) B.F. Hoskins, R. Robson, J. Am. Chem. Soc. 112 (1990) 1546;
(d) M. Kondo, T. Yoshitomi, K. Seki, H. Matsuzaka, S. Kitagawa, Angew. Chem., Int. Ed. Engl. 36 (1997) 1725;
(e) A.K. Ghosh, A.D. Jana, D. Ghoshal, G. Mostafa, N. Ray Chaudhuri, Cryst. Growth Des. 6 (2006) 701;
(f) A. Yuan, J. Zou, B. Li, Z. Zha, C. Duan, Y. Liu, Z. Xu, S. Keizer, Chem. Commun. (2000) 1279.

[4] (a) J.-M. Lean, Angew. Chem., Int. Ed. Engl. 29 (1990) 1304;
(b) A.R.A. Palmans, J.A.M.A. Vekemans, H. Kooijman, A.L. Speck, E.W. Meijer, Chem. Commun. (1997) 2247;
(c) G. Desiraju, Acc. Chem. Res. 35 (2002) 565;
(d) D. Ghoshal, A.K. Ghosh, J. Ribas, E. Zangrando, G. Mostafa, N. Ray Chaudhuri, Cryst. Growth Des. 5 (2005) 941.

[5] (a) T.K. Maji, G. Mostafa, S. Sain, J.S. Prasad, N. Ray Chaudhuri, CrystEngComm. 3 (2001) 155;
(b) D. Das, A. Ghosh, N. Ray Chaudhuri, Bull. Chem. Soc. Jpn. 70 (1997) 789;
(c) T.K. Maji, D. Das, N. Ray Chaudhuri, J. Therm. Anal. Calorim. 63 (2001) 617;
(d) S.C. Manna, E. Zangrando, J. Ribas, N. Ray Chaudhuri, Inorg. Chim. Acta 358 (2005) 4497;
(e) T.K. Maji, D. Ghoshal, E. Zangrando, J. Ribas, N. Ray Chaudhuri, CrystEngComm. 6 (2004) 623;
(f) C.-C. Wang, C.-H. Yang, G.-H. Lee, Inorg. Chem. 41 (2002) 1015.

[6] (a) A. Weiss, E. Riegler, I. Alt, H. Bohme, C. Robl, Z. Naturforsch. B41 (1986) 18;
(b) C.R. Lee, C.C. Wang, Y. Wang, Acta Crystallogr. Sect. B52 (1996) 966;
(c) R. West, H.Y. Niu, J. Am. Chem. Soc. 85 (1963) 2589;
(d) M. Habenschuss, B.C. Gerstein, J. Chem. Phys. 61 (1974) 854;
(e) A. Weiss, E. Riegler, C. Robl, Z. Naturforsch. B41 (1986) 1329;
(f) A. Weiss, E. Riegler, C. Robl, Z. Naturforsch. B41 (1986) 1333;
(g) O.M. Yaghi, G. Li, T.L. Groy, J. Chem. Soc., Dalton Trans. (1995) 727;
(h) J. Greve, I. Jess, C. Nather, J. Solid State Chem. 175 (2003) 328;
(i) J. Sletten, H. Daraghmeh, F. Lloret, M. Julve, Inorg. Chim. Acta 279 (1998) 127;
(j) I. Castro, J. Sletten, L.K. Glaerum, J. Cano, F. Lloret, J. Faus, M. Julve, J. Chem. Soc., Dalton Trans. (1995) 3207;
(k) H. Grove, J. Sletten, M. Julve, F. Lloret, J. Cano, J. Chem. Soc., Dalton Trans. (2001) 259;
(l) C. Nather, J. Greve, I. Jess, Chem. Mater. 14 (2002) 4536.

[7] (a) M.D. Glick, G.L. Downs, L.F. Dahl, Inorg. Chem. 3 (1964) 1712;
(b) M.D. Glick, L.F. Dahl, Inorg. Chem. 5 (1966) 289;
(c) A. Cornia, A.C. Fabretti, A. Giusti, F. Ferraro, D. Gatteschi, Inorg. Chim. Acta 212 (1993) 87;
(d) F. Dumestre, B. Soula, A.M. Galibert, P.L. Fabre, G. Bernardinelli, B. Donnadieu, P. Castan, J. Chem. Soc., Dalton Trans. (1998) 4131.

[8] D. Deguenon, G. Bernardinelli, J.P. Tuchagues, P. Castan, Inorg. Chem. 29 (1990) 3031.

[9] P. Castan, D. Deguenon, F. Dahan, Acta Crystallogr. Sect. C 47 (1991) 2656.

[10] I. Castro, J. Sletten, J. Faus, M. Julve, J. Chem. Soc., Dalton Trans. (1992) 2271.

[11] C.-C. Wang, C.-H. Yang, S.-M. Tseng, G.-H. Lee, Y.-P. Chiang, H.-S. Sheu, Inorg. Chem. 42 (2003) 8294.

[12] I. Castro, J. Sletten, J. Faus, M. Julve, Y. Journaux, F. Lloret, S. Alvarez, Inorg. Chem. 31 (1992) 1889.

[13] (a) I. Castro, J. Sletten, L.K. Glærum, F. Lloret, J. Faus, M. Julve, J. Chem. Soc., Dalton Trans. (1994) 2777;
(b) J. Sletten, O. Bjørsvik, Acta Chem. Scand. 32 (1998) 770;
(c) D. Deguenon, P. Castan, F. Dahan, Acta Crystallogr. Sect. C 47 (1991) 433;
(d) Q. Chen, S. Liu, J. Zubieta, Inorg. Chim. Acta 175 (1990) 241.

[14] I. Castro, M.L. Calatayud, F. Lloret, J. Sletten, M. Julve, J. Chem. Soc., Dalton Trans. (2002) 2397.

[15] I. Castro, M.L. Calatayud, J. Sletten, M. Julve, F.C.R. Lloret, Acad. Sci., Ser. IIc: Chim. 4 (2001) 235.

[16] T.K. Maji, S. Konar, G. Mostafa, E. Zangrando, T.-H. Lu, N. Ray Chaudhuri, J. Chem. Soc., Dalton Trans. (2003) 171.

[17] D. Ghoshal, A.K. Ghosh, J. Ribas, G. Mostafa, N. Ray Chaudhuri, CrystEngComm. 7 (2005) 616.

[18] S. Sain, T.K. Maji, N. Ray Chaudhuri, E. Zangrando, Transition Met. Chem. 27 (2002) 716.

[19] Collaborative Computational Project, Number 4, Acta Crystallogr. Sect. D 50 (1994) 760.

[20] G.M. Sheldrick, SHELX97 Programs for Crystal Structure Analysis (Release 97-2), University of Göttingen, Germany, 1998.

[21] L.J. Farrugia, J. Appl. Crystallogr. 32 (1999) 837.

[22] P.A.M. Williams, E.G. Ferrer, E.J. Baran, O.E. Piro, J.A. Ellena, E.E. Castellano, An. Asoc. Quim. Argent. 90 (2002) 109.

[23] R. Horikoshi, T. Mochida, N. Maki, S. Yamada, H. Motiyama, J. Chem. Soc., Dalton Trans. (2002) 28, and refs. therein.

Surprisingly, urea derivatives of 1,4,7,10-tetraazacyclododecane (cyclen) and 1,4,8,11-tetraazacyclotetradecane (cyclam) have, to the best of our knowledge, been reported in the literature by a unique example [13]. Although the introduction of carbamoyl groups at the nitrogen atoms reduces their basicity and binding ability irreversibly, the clean and high-yielding reaction is useful for receptor synthesis [13].

Herein we present the synthesis and structure determination of novel tetrafunctional *N*-thiophosphorylated thiourea, based on a cyclam backbone. The syntheses and studying of its salts with sodium and potassium ions, and the complex with the $[Cu(PPh_3)_2]^+$ cation is also reported.

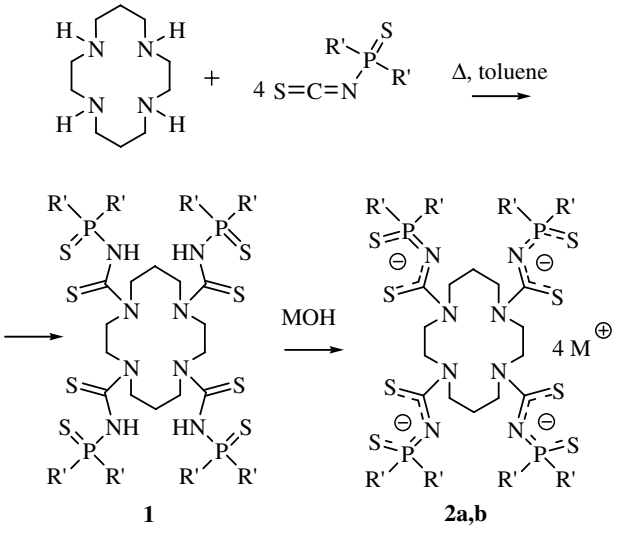
2. Results and discussion

2.1. Synthesis

Thiourea **1** was prepared by the reaction of cyclam with the isothiocyanate of diisopropyl-thiophosphoric acid in toluene (Scheme 1). The compound was obtained as a crystalline solid, soluble in most polar solvents. Its composition has been confirmed by elemental analysis.

IR, ^{31}P and ^{1}H NMR spectroscopy data have shown that thiourea **1** partially decomposes in solution with elimination of isothiocyanate $(i\text{PrO})_2\text{P(S)NCS}$ molecules, while the four-substituted product **1** has been isolated in the solid state.

Addition of acceptor groups to the cyclam nitrogen atoms results in the substantial decrease of the donor abilities of the cyclic nitrogens [13] and the macrocyclic cavity loses its efficacy to coordinate metal ions. In our case, hydrogens of cyclam NH groups are substituted by acylamidophosphate.



R' = O*i*Pr M = Na+ (**2a**), K+(**2b**)

Scheme 1.

It was found that deprotonation of the exocyclic functions prevents the dissociation of the $(i\text{PrO})_2\text{P(S)NCS}$ moiety, as is the case in the sodium and potassium M_4L salts **2a**,**b**. Salts **2a**,**b** were prepared by the reaction of the hydroxide of the corresponding metal in aqueous ethanol (Scheme 1). The compounds obtained are polycrystalline solids soluble in water and acetone. The salt **2b** has been used for copper(I) complex synthesis by the reaction with $Cu(PPh_3)_3I$ in aqueous ethanol–dichloromethane solution (Scheme 2).

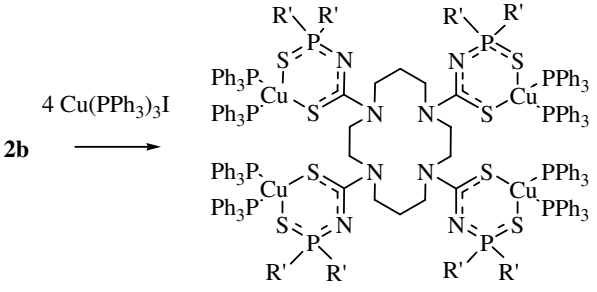
Chelating C(S)NP(S) units are coordinated with the copper(I) cation with a {*S*,*S*′}-bidentate donor set of thiocarbonyl and thiophosphoryl groups. Compound **3** is a stable polycrystalline solid, soluble in dichloromethane, chloroform, acetone and DMF.

2.2. IR and NMR spectroscopy

The IR spectrum of **1** in Nujol contains the unique absorption band of the NH group at 3110 cm^{-1}. There are two absorption bands at 1496 and 1518 cm^{-1} corresponding to the S=C–N group. The absorption band assigned to the P=S group is displayed in the characteristic area at 660 cm^{-1}. The wide absorption band of the ester POC unit of **1** at 1000 cm^{-1} unequivocally confirms the presence of the substituted thiophosphoryl moiety.

The IR spectrum in Nujol does not exhibit any band in the 1980–2200 m^{-1} range. In a CCl_4 solution of **1** there is a band at 1988 cm^{-1}, corresponding to the absorption of the S=C=N group. It may indicate that thiourea **1** partially dissociates in solution with elimination of isothiocyanate $(i\text{PrO})_2\text{P(S)NCS}$ molecules. ^{31}P and ^{1}H NMR spectroscopy data confirm this suggestion. There are two singlet signals at $\delta = 59.7$ and 43.1 ppm in the $^{31}P\{^1H\}$ NMR spectrum of **1**. The major signal at $\delta = 59.7$ ppm is in the region that is characteristic for *N*-thiophosphorylated thioamides and thioureas [9], whereas the second one corresponds to the isothiocyanate $(i\text{PrO})_2\text{P(S)NCS}$ [14].

The ^{1}H NMR spectrum of **1** contains a double set of signals assigned to $(i\text{PrO})_2\text{P(S)}$ protons. The signals of CH_3 and OCH protons of acylamidophosphate fragments are at $\delta = 1.37$ ppm with $^3J_{H,H} = 6.0$ Hz and 4.86 ppm with



3, R' = O*i*Pr

Scheme 2.

$^3J_{H,H} = 6.2$ Hz and $^3J_{POCH} = 12.4$ Hz. The signals of CH_3 and OCH protons of $(i\text{PrO})_2\text{P(S)NCS}$ are broad singlets at $\delta = 1.56$ and 4.93 ppm, respectively. The set of multiplets corresponding to CH_2 protons at $\delta = 1.78$–4.43 ppm, derives from the cyclam moiety.

The broadened signal corresponding to the NHP(S) proton of thiourea **1** is observed at 6.99 ppm. The broad peak of the $NHCH_2$ proton is also observed, supporting the presence of an unsubstituted nitrogen in the cyclam moiety.

The IR spectrum of **2a** in Nujol is similar to that of **2b**. The absorption bands of the P=S group of the anionic forms of thiourea **1** in salts **2a**,**b** are shifted by approximately 35 cm^{-1} to lower frequencies relative to the band of the parent ligand **1**. This confirms the deprotonation of the exocyclic fragments [9]. The NH band is not seen in the IR spectra of the **2a** and **2b** salts. There are intensive absorption bands of the deprotonated thioamide groups around 1532 (**2a**) and 1538 (**2b**) cm^{-1} [9]. These bands and those observed for POC at 991 (**2a**) and 998 (**2b**) cm^{-1} indicate the preservation of the ligand structure.

The $^{31}P\{^1H\}$ NMR signals of both **2a**,**b** salts appear at $\delta = 62.0$ and 62.1 ppm, respectively, showing a downfield shift when compared to the free ligand **1**.

The ^1H NMR spectra contain a single set of signals for the CH_3 protons at $\delta = 1.32$ (**2a**) and 1.34 (**2b**) ppm. The signals of OCH protons are overlapped by the solvent signal. The CH_2 band, corresponding to the cyclam fragment, appears at $\delta = 1.60$–4.46 ppm. The signal for the NHP(S) proton was not observed. The integrated intensities of the signals of CH_3 and CH_2 protons with a ratio of 48:20 support the tetra-N-substituted cyclam ligand. No bands were observed for the proton corresponding to the mono-, di- or tri-N-substituted cyclam moiety.

The IR bands of P=S in **3** are shifted by 43 and 11 cm^{-1} to lower frequencies relatively to the parent ligand **1** and the salt **2b**, respectively. This confirms the chelate formation with Cu^I. The intensive absorption band of the conjugated thioamide group in the spectrum of **3** is observed at 1508 cm^{-1} and it is shifted to lower frequencies when compared to **2b**.

The ^{31}P NMR spectrum of **3** contains two singlet signals at $\delta = -1.1$ and 52.0 ppm. The broad resonance band at 52.0 ppm corresponds to the phosphorus of the thiophosphoryl group and is in the characteristic region for similar complexes [10]. The signal at −1.1 ppm corresponds to the triphenylphosphine and it is downfield compared to free PPh_3.

The exchange between free and bound triphenylphosphine in solutions of the studied complex **3** results in the phosphine signal broadening in the ^{31}P NMR spectrum, as was observed for Cu(I) thioether complexes (see [15] and references therein). The ratio of the integral intensity in the ^1H NMR spectrum reveals the composition of the complex **3**. The ratio of OCH protons (OPri) signal intensity to phenyl protons of PPh_3 is 1:15 while the intensities of OCH protons correlates to the total intensity of the NCH_2 multiplet as 1:2.

2.3. EI and ES mass spectrometry

The electron impact mass spectrum (EI-MS) of **1** contains the $[\text{cyclam}]^+$ (100%) and $[(i\text{PrO})_2\text{P(S)NCS}]^+$ (36%) structure ion peaks. The molecular ion of **1** is unstable under the measurement conditions.

ES-MS (electrospray method) of **1** shows peaks for the following ions: $[\text{cyclam}+H]^+$ (24%) и $[(i\text{PrO})_2\text{P(S)NCS}+H]^+$ (17%), $[M-3(i\text{PrO})_2\text{P(S)NCS}+H]^+$ (100%), $[M-2(i\text{PrO})_2\text{P(S)NCS}+K]^+$ (9%), $[M-(i\text{PrO})_2\text{P(S)NCS}+K]^+$ (11%) and $[M+CH_3OH+K]^+$ (8%). Positive ions with a greater weight in the ES-MS of **1** were absent.

There is a peak for the molecular ion of **2a** $[M+H_2O+Na]^+$ with an intensity of 18%. The molecular ion peak of **2b** is absent in the ES-MS. Their electrospray spectra contain all ions characteristic of the mono-, di- and tri-N-substituted derivatives of cyclam: $[M-3(i\text{PrO})_2\text{P(S)NCS}-2Me+3H]^+$ (37%, Me = Na, **2a**; 100%, Me = K, **2b**), $[M-2(i\text{PrO})_2\text{P(S)NCS}-Me+2H]^+$ (100% **2a**, Me = Na; 46%, Me = K, **2b**) and $[M-(i\text{PrO})_2\text{P(S)NCS}+H]^+$ (14%) (**2b**).

The ES spectrum of complex **3** contains rather intensive peaks of mono- and di-N-substituted derivatives: $[M-3(i\text{PrO})_2\text{P(S)NCS}-3Cu(PPh_3)_2+4H]^+$ (32%) and $[M-2(i\text{PrO})_2\text{P(S)NCS}-2Cu(PPh_3)_2+K+2H]^+$ (58%). The are also peaks of cations of the composition $[\text{cyclam}]^+$ (100%) and $[(i\text{PrO})_2\text{P(S)NCS}+H]^+$ (23%). The ES-MS does not show any peak for the molecular ion of **3**.

3. Experimental

3.1. Physical measurements

Infrared spectra (Nujol) were recorded with a Specord M-80 spectrometer in the range 400–3600 cm^{-1}. NMR spectra were obtained on a Varian Unity-300 NMR spectrometer at 25 °C. ^1H and $^{31}P\{^1H\}$ spectra were recorded at 299.948 and 75.429 MHz, respectively. Chemical shifts are reported with reference to Me_4Si (^1H) and H_3PO_4 ($^{31}P\{^1H\}$). The electron ionisation mass spectrum of thiourea **1** was measured on a TRACE MS Finnigan MAT instrument. The ionisation energy was 70 eV. The substance was injected directly into the ion source at 150 °C. Heating was carried out in a programmed mode from 35 to 200 °C at a rate of 35 °C/min. Electrospray ionisation mass spectra were measured with a Finnigan-Mat TCQ 700 mass spectrometer on a 10^{-6} M solution in CH_3OH. The speed of sample submission was 2 μL/min. The ionisation energy was 4.5 kV. The capillary temperature was 200 °C. Elemental analyses were performed on a Perkin–Elmer 2400 CHN microanalyser.

3.2. Synthesis of *1*

A suspension of cyclam (100 mg, 0.5 mmol) in toluene (10 cm^3) was mixed with a toluene solution of the isothiocyanate of *O*,*O*′-diisopropylthiophosphoric acid (525.8 mg,

2.2 mmol). The mixture was boiled for 10 min. The solvent was then removed in vacuo. A colourless precipitate of **1** (520.0 mg, 90%) was isolated from dichloromethane by *n*-hexane (Found: C, 39.48; H, 7.03; N, 9.66. $C_{38}H_{80}N_8O_8P_4S_8$ requires C, 39.43; H, 6.97; N, 9.68%); mp 66 °C (from CH_2Cl_2/*n*-C_6H_{14}); IR ν_{max}(Nujol)/cm^{-1} 660 (P═S), 1000 (POC), 1496, 1518 (S═C–N) and 3110 (NH); ν_{max} (CCl_4)/cm^{-1} 656 (P═S), 998 (POC), 1480 (S═C–N), 1988 (S═C═N) and 2870–3000 (NH); NMR δ_H ($CDCl_3$/ppm, *J* in Hz) 1.37 (36H, t, $^3J_{H,H}$ 6.0, CH_3), 1.56 (12H, br s, CH_3, (*i*PrO)$_2$P(S)NCS), 1.78–4.43 (20H, m, CH_2), 4.86 (6H, d sept, $^3J_{POCH}$ 12.4, $^3J_{H,H}$ 6.2, OCH), 4.93 (2H, br s, OCH, (*i*PrO)$_2$P(S)NCS), 6.99 (3H, br s, P(S)NH) and 8.18 (1H, s, NH); δ_P($CDCl_3$/ppm) 43.1 (s, (*i*PrO)$_2$P(S)NCS) and 59.7 (br s, P(S)NH); *m*/*z* (EI) 200 (cyclam, 100%)$^+$ and 239 [(*i*PrO)$_2$P(S)NCS, 36]$^+$; *m*/*z* (ES) 201.5 (cyclam+H, 24%)$^+$, 240.6 [(*i*PrO)$_2$P(S)NCS+H, 17]$^+$, 441.2 (M−3(*i*PrO)$_2$P(S)NCS+H, 100)$^+$, 718.2 (M−2(*i*PrO)$_2$P(S)NCS+K, 9)$^+$, 957.8 (M−(*i*PrO)$_2$P(S)-NCS+K, 11)$^+$ and 1229.1 (M+CH_3OH+K, 8)$^+$.

3.3. Synthesis of *2a,b*

A suspension of **1** (115.6 mg, 0.1 mmol) in aqueous ethanol (10 cm^3) was mixed with an ethanol solution of sodium (17.6 mg, 0.44 mmol) or potassium hydroxide (24.6 mg, 0.44 mmol). The mixture was stirred at room temperature for 30 min. The solvent was then removed in vacuo.

A colourless precipitate of **2a** (113.2 mg, 91%) was isolated from aqueous ethanol by *n*-hexane (Found: C, 36.73; H, 6.10; N, 8.86. $C_{38}H_{76}N_8Na_4O_8P_4S_8$ requires C, 36.65; H, 6.15; N, 9.00%); mp 195 °C (from EtOH/*n*-C_6H_{14}); IR ν_{max}/cm^{-1} 623 (P═S), 991 (POC) and 1532 (S···C···N); NMR δ_H (D_2O/ppm) 1.32 (48H, br s, CH_3) and 1.60–4.41 (20H, m, CH_2); δ_P(D_2O/ppm) 62.0; *m*/*z* (ES) 485.1 (M−3(*i*PrO)$_2$P(S)NCS−2Na+3H, 37%)$^+$, 746.2 (M−2(*i*PrO)$_2$P(S)NCS−Na+2H, 100)$^+$ and 1286.6 (M+H_2O+Na, 18)$^+$.

A colourless precipitate of **2b** (107.3 mg, 82%) was isolated from aqueous ethanol by *n*-hexane (Found: C, 34.89; H, 5.79; N, 8.61. $C_{38}H_{76}N_8K_4O_8P_4S_8$ requires C, 34.84; H, 5.85; N, 8.55%); mp 183 °C (from EtOH/*n*-C_6H_{14}); IR ν_{max}/cm^{-1} 628 (P═S), 998 (POC) and 1538 (S···C···N); NMR δ_H (D_2O/ppm) 1.34 (48H, br s, CH_3) and 1.67–4.46 (20H, m, CH_2); δ_P(D_2O/ppm) 62.1; *m*/*z* (ES) 517.1 (M−3(*i*PrO)$_2$P(S)NCS−2K+3H, 100%)$^+$, 794.3 (M−2(*i*PrO)$_2$P(S)NCS−K+2H, 46)$^+$ and 1071.7 (M−(*i*PrO)$_2$P(S)NCS+H, 14)$^+$.

3.4. Synthesis of *3*

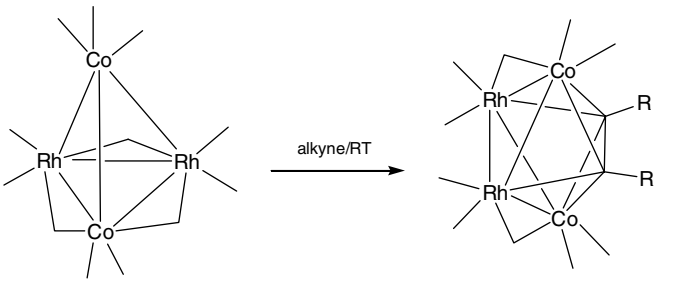
A suspension of **2b** (105 mg, 0.08 mmol) in aqueous ethanol (10 cm^3) was mixed with a dichloromethane solution of Cu(PPh_3)$_3$I (312.6 mg, 0.32 mmol). The mixture was stirred at room temperature for 4 h. The solvent was then removed in vacuo. A colourless precipitate of **3** (874.6 mg, 78%) was isolated from dichloromethane by *n*-hexane (Found: C, 62.23; H, 5.69; N, 3.36. $C_{182}H_{196}Cu_4N_8O_8P_{12}S_8$ requires C, 62.35; H, 5.63; N, 3.30%); mp 148 °C (from CH_2Cl_2/*n*-C_6H_{14}); IR ν_{max}/cm^{-1} 617 (P═S), 1002 (POC) and 1508 (S═C–N); NMR δ_H ($CDCl_3$/ppm) 1.27 (48H, br s, CH_3), 1.46–4.38 (20H, m, CH_2) and 4.71 (8H, br s, OCH) and 7.28–7.49 (120H, m, PPh_3); δ_P($CDCl_3$) −1.1 (br s, PPh_3) and 52.0 (s, P(S)N); *m*/*z* (ES) 201.2 (cyclam+H, 100%)$^+$, 240.4 [(*i*PrO)$_2$P(S)NCS+H, 23]$^+$, 1027.3 (M−3(*i*PrO)$_2$P(S)NCS− 3Cu(PPh_3)$_2$+4H, 32)$^+$ and 1891.2 (M−2(*i*PrO)$_2$P(S)NCS−2Cu(PPh_3)$_2$+K+2H, 58)$^+$.

Acknowledgements

This work was supported by the Russian Foundation for Basic Research (Grant Nos. 03-03-32372-a, 03-03-96225-r2003tatarstan_a), the joint program of CRDF and the Russian Ministry of Education (BHRE 2004 Y2-C-07-02, grants REC-007). D.A. Safin and M.G. Babashkina wish to thank the Faculty of Chemistry of the University of Wroclaw for a scholarship.

References

[1] (a) T.A. Kaden, Topics Curr. Chem. 121 (1984) 154;
(b) P.V. Bernhardt, G.A. Lawrance, Coord. Chem. Rev. 104 (1990) 297.
[2] T.A. Kaden, Pure Appl. Chem. 60 (1988) 1117.
[3] F.C.J.M. Van Veggel, W. Verboom, D.N. Reinhoudt, Chem. Rev. 94 (1994) 279.
[4] M. Kruppa, B. König, Chem. Rev. 106 (2006) 3520.
[5] K.P. Wainwright, Adv. Inorg. Chem. 52 (2001) 293.
[6] A.E.V. Gorden, J. Xu, K.N. Raymond, P. Durbin, Chem. Rev. 103 (2003) 4207.
[7] (a) P.D. Beer, E.J. Hayes, Coord. Chem. Rev. 240 (2003) 167;
(b) V. Amendola, M. Bonizzoni, D. Esteban-Gomez, L. Fabbrizzi, M. Licchelli, F. Sancenon, A. Taglietti, Coord. Chem. Rev. 250 (2006) 1451.
[8] K.P. Wainwright, Coord. Chem. Rev. 166 (1997) 35.
[9] F.D. Sokolov, V.V. Brusko, N.G. Zabirov, R.A. Cherkasov, Curr. Org. Chem. 10 (2006) 27.
[10] A.Yu. Verat, F.D. Sokolov, N.G. Zabirov, M.G. Babashkina, D.B. Krivolapov, V.V. Brusko, I.A. Litvinov, Inorg. Chim. Acta 359 (2006) 475.
[11] F.D. Sokolov, N.G. Zabirov, V.V. Brusko, D.B. Krivolapov, I.A. Litvinov, Mendeleev Commun. 13 (2003) 72.
[12] N.G. Zabirov, V.V. Brusko, A.Y. Verat, D.B. Krivolapov, I.A. Litvinov, R.A. Cherkasov, Phosphorus Sulfur Silicon 177 (2002) 1869.
[13] B. König, M. Pelka, M. Subat, I. Dix, P.G. Jones, Eur. J. Org. Chem. 10 (2001) 1943.
[14] M.G. Zimin, R.M. Kamalov, R.A. Cherkasov, A.N. Pudovik, Phosphorus, Sulfur Silicon Relat. Elem. 13 (1982) 371.
[15] C. Ohrenberg, L.M. Liable-Sands, A.L. Rheingold, C.G. Riordan, Inorg. Chem. 40 (2001) 4276.



(1)

The reaction depicted in Eq. (1) initially captured our attention because, with the exception of bis(pentafluorophenyl)acetylene [7a], all of the alkyne ligands studied for their reactivity with cluster **1** have possessed electron-donating substituents. Accordingly, this prompted our earlier study on the reaction of **1** with the electron-poor alkyne dimethyl acetylenedicarboxylate (dmad), where facile cluster fragmentation and specific metal redistribution to give $Co_3Rh(CO)_{10}(\mu\text{-dmad})$ and $CoRh_3(CO)_9(\mu\text{-dmad})_3$ were demonstrated [8]. Interestingly no evidence for the expected butterfly cluster $Co_2Rh_2(CO)_{10}(\mu\text{-dmad})$ was observed, suggesting that once formed $Co_2Rh_2(CO)_{10}(\mu\text{-dmad})$ is unstable and fragments in solution to give $Co_3Rh(CO)_{10}(\mu\text{-dmad})$ and $CoRh_3(CO)_9(\mu\text{-dmad})_3$. If the electronic character of the alkyne is important in controlling the stability of the initially formed butterfly cluster $Co_2Rh_2(CO)_{10}(\mu\text{-alkyne})$, the use of an alkyne ligand that is not as electron deficient as dmad might allow us to trap and/or observe $Co_2Rh_2(CO)_{10}(\mu\text{-alkyne})$ before any fragmentation of the $Co_2Rh_2(\mu\text{-alkyne})$ cluster. Herein we report our results on the reaction between cluster **1** and methyl propiolate, which gives $Co_3Rh(CO)_{12}$ (**2**), $Co_3Rh(CO)_{10}(\mu\text{-HCCCO}_2\text{Me})$ (**3**), $Co_2Rh_2(CO)_{10}(\mu\text{-HCCCO}_2\text{Me})$ (**4**), and $CoRh_3(CO)_9(\mu\text{-HCCCO}_2\text{Me})_3$ (**5**) as the principal products. These products have been characterized by a combination of methods including comparison to independently prepared samples, spectroscopic methods, and FAB mass spectrometry. The solid-state structure of $Co_2Rh_2(CO)_{10}(\mu\text{-HCCCO}_2\text{Me})$ (**4**) and the regiospecific insertion of the methyl propiolate ligand into the Co–Co bond of **1** was established by X-ray crystallography.

2. Experimental

2.1. General

The mixed-metal cluster $Co_2Rh_2(CO)_{12}$ was prepared from $Co_2(CO)_8$ and $Rh_2(CO)_4Cl_2$ [9], with the latter chemical synthesized by carbonylation of hydrated $RhCl_3$ [10]. Thermolysis of $Co_2Rh_2(CO)_{12}$ in hexane gave the sample of pure $Co_3Rh(CO)_{12}$ that was used as a standard for cluster **2** and in the independent synthesis of cluster **3** [9]. The chemicals $Co_2(CO)_8$ and methyl propiolate were purchased from Strem Chemical Co. and Aldrich Chemical Co., respectively, and were used as received. All reaction and NMR solvents were distilled from an appropriate drying agent using Schlenk techniques and stored under argon in storage vessels equipped with a high-vacuum Teflon stopcock [11].

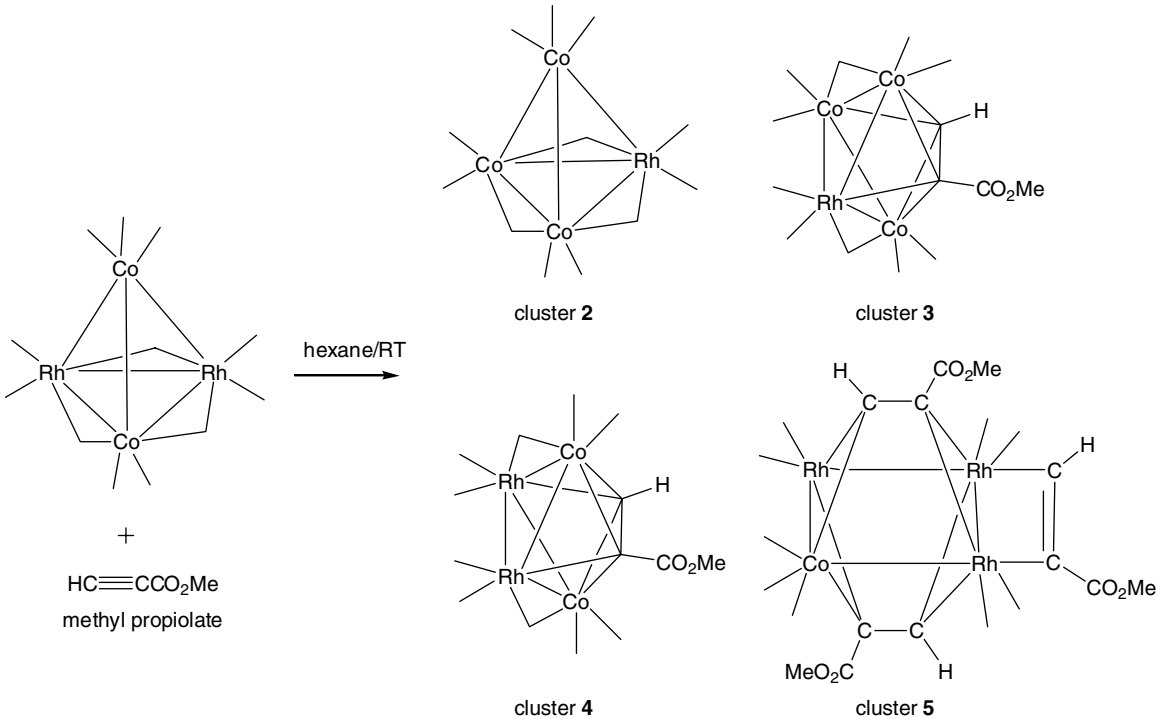
The IR spectral data were recorded on a Nicolet 20 SXB FT-IR spectrometer in sealed 0.1 mm NaCl cells, while the ^1H spectral data were recorded at 200 MHz on a Varian Gemini-200 spectrometer. The ESI-APCI mass spectrum of cluster **5** was recorded at the UC San Diego Mass Spectrometry Center in the positive ionization mode.

2.2. Reaction of $Co_2Rh_2(CO)_{12}$ with methyl propiolate

To a small Schlenk vessel containing 0.13 g (0.21 mmol) of $Co_2Rh_2(CO)_{12}$ in 40 mL of hexane was added 36 mg (0.43 mmol) of methyl propiolate under argon flush. The vessel was capped and stirred for 3.0 h at room temperature, during which time some precipitate corresponding to $CoRh_3(CO)_9(\mu\text{-HCCCO}_2\text{Me})_3$ was observed. TLC examination of the reaction solution at this point revealed the presence of three spots ($R_f = 0.95$ for cluster **2**; $R_f = 0.80$ for clusters **3** and **4**; $R_f = 0.10$ for cluster **5**) using CH_2Cl_2 as the mobile phase. The hexane was removed in vacuo and the residue dissolved in a minimum amount of CH_2Cl_2, followed by chromatographic separation over silica gel. Cluster **2** was eluted using hexane, followed by clusters **3** and **4** as overlapping bands using a mixture of hexane/CH_2Cl_2 (1:2), after which cluster **5** was obtained by changing the eluent to ethyl acetate/CH_2Cl_2 (1:9). The IR data spectrum for the isolated $Co_3Rh(CO)_{12}$ exactly matched that of the independently prepared sample of cluster **2**, as did the TLC properties. The amount of **2** isolated from the column was ca. 15 mg. The cluster mixture composed of $Co_3Rh(CO)_{10}(\mu\text{-HCCCO}_2\text{Me})$ and $Co_2Rh_2(CO)_{10}(\mu\text{-HCCCO}_2\text{Me})$ was isolated as a brown-purple colored solid (47 mg). IR (hexane): ν(CO) 2102 (m), 2072 (vs), 2056 (vs), 2047 (vs), 2030 (m), 2005 (m), 1897 (m), 1878 (sh, m), 1716 (w, ester) cm^{-1}. ^1H NMR ($CDCl_3$): δ 3.68 (s, Me), 8.72 (s, alkyne CH, cluster **3**), 9.20 (s, alkyne CH, cluster **4**). $CoRh_3(CO)_9(\mu\text{-HCCCO}_2\text{Me})_3$ was isolated as a dark red solid (50 mg). IR (CH_2Cl_2): ν(CO) 2095 (m), 2061 (vs), 2022 (s), 1911 (b, w), 1729 (s, ester) cm^{-1}. ^1H NMR ($CDCl_3$): δ 3.93 (s, 9H, CO_2Me), 7.74 (d, 1H, $J = 7.74$ Hz), 8.19 (d, 1 H, $J = 7.74$ Hz), 8.42 (s, 1H). ESI-APCI MS (m/z): 894.71 $[\mathbf{5}+Na]^+$.

2.3. X-ray diffraction structure for $Co_2Rh_2(CO)_{10}(\mu\text{-HCCCO}_2\text{Me})$

Single crystals of $Co_2Rh_2(CO)_{10}(\mu\text{-HCCCO}_2\text{Me})$ were grown from a hexane solution containing $Co_3Rh(CO)_{10}(\mu\text{-HCCCO}_2\text{Me})$ and $Co_2Rh_2(CO)_{10}(\mu\text{-HCCCO}_2\text{Me})$ at 0 °C. The reported X-ray data were collected on a Bruker SMART™ 1000 CCD-based diffractometer at 213 K. The frames were integrated with the available SAINT software package using a narrow-frame algorithm [12], and the structure was solved and refined using the SHELXTL program package [13]. The molecular structure



Scheme 1.

was checked by using PLATON [14], and solved by direct methods with all nonhydrogen atoms refined anisotropically. All carbon-bound hydrogen atoms were assigned calculated positions and allowed to ride on the attached heavy atom, unless otherwise noted. Refinement for $Co_2Rh_2(CO)_{10}(\mu\text{-}HCCCO_2Me)$ converged at $R = 0.0511$ and $R_w = 0.1497$ for 2742 independent reflections with $I > 2\sigma(I)$.

3. Results and discussion

3.1. Reaction of $Co_2Rh_2(CO)_{12}$ with methyl propiolate and spectroscopic characterization of clusters 2–5

The reaction between the cluster compound $Co_2Rh_2(CO)_{12}$ and methyl propiolate proceeds rapidly at room temperature in hexane. The brown color of cluster **1** changes to that of red-purple with the accompanying formation with a red precipitate of cluster **5**, which is relatively insoluble in hexane. TLC examination of the reaction solution revealed the presence of four new spots belonging to clusters **2**–**5**. Of these products, clusters **3** and **4** not exhibit distinct separation on silica gel or alumina chromatographic supports and were consequently isolated together as an inseparable mixture. This chromatographic behavior mirrors that reported by Tunik et al. for the closely related alkyne clusters $Co_3Rh(CO)_{10}(\mu\text{-}PhCCPh)$ and $Co_2Rh_2(CO)_{10}(\mu\text{-}PhCCPh)$ that could not be separated by column chromatography [15]. The products were subsequently isolated by chromatography using silica gel as described in the experiment section. Scheme 1 outlines this reaction and the nature of the resulting products.

The identity of cluster **3** was ascertained by its independent synthesis [9], with the TLC and IR spectral data perfectly matching that of the cluster isolated from the reaction. The observed fragmentation of cluster **1**, along with the formation of cluster **2**, has been documented by us in our earlier study involving the reaction of cluster **1** with the alkyne dmad [8]. The mixture composed of clusters **3** and **4** was characterized in solution by IR and ^1H NMR spectroscopies. While the IR spectral data are of little help in the characterization of these two closed related compounds, the ^1H NMR data do allow us to comment on the unequivocal composition of the mixture. Despite the appearance of a single methyl resonance at δ 3.68 for both products, the two down-field alkyne resonances at δ 8.72 (cluster **3**) and 9.20 (cluster **4**) are consistent with the proposed products [7b,16]. These assignments were further strengthened by the independent synthesis of cluster **3** starting from $Co_3Rh(CO)_{12}$ (**2**) and methyl propiolate. The expected alkyne-substituted cluster **3** was indeed produced and its ^1H NMR spectrum was in excellent agreement with those data obtained from the cluster mixture containing **3** and **4**. The presence of **4** in the mixture was confirmed by X-ray diffraction analysis (*vide infra*). Based on the area associated with the terminal alkyne hydrogens in the mixture of **3** and **4**, the major product was determined to be cluster **4** (ca. 70%).

The lability of clusters **3** and **4** towards added methyl propiolate was next probed. Treatment of a hexane solution containing **3** and **4** with excess methyl propiolate led

Table 1
X-ray crystallographic data and processing parameters $Co_2Rh_2(CO)_{10}$-(μ-$HCCCO_2Me$)

CCDC entry no.	608087
Space group	triclinic, $P\bar{1}$
a (Å)	8.692(1)
b (Å)	9.359(1)
c (Å)	12.482(2)
α (°)	88.032(2)
β (°)	70.039(2)
γ (°)	87.514(2)
V (Å^3)	953.2(2)
Molecular formula	$C_{14}H_4Co_2O_{12}Rh_2$
fw	687.85
Formula units per cell (Z)	2
D_{calcd} (Mg/m^3)	2.397
λ (Mo Kα) (Å)	0.71073
μ (mm^{-1})	3.473
R_{merge}	0.0273
Absorption correction	empirical
Absorption correction factor	0.927/0.673
Total reflections	5905
Independent reflections	2742
Data/resolution/parameters	2742/0/276
R	0.0511
R_w	0.1497
Goodness-of-fit on F^2	1.069
Largest difference peak and hole (e/A^3)	1.298 and −2.063

to the slow consumption of both **3** and **4** (ca. 50%) and concomitant formation of cluster **5** and material decomposition, as assessed by TLC. The metal redistribution observed here is in keeping with our premise of enhanced metal scrambling and alkyne activation reactivity in this genre of cluster in the presence of electron-deficient alkynes.[1] The reactivity of clusters **1**, **3**, and **4** with different alkyne ligands is currently under study by groups.

The 64e-cluster $CoRh_3(CO)_9$(μ-$HCCCO_2Me)_3$, which is analogous to the dmad-substituted cluster $CoRh_3(CO)_9$-(μ-dmad)$_3$ prepared by us, was characterized in solution (IR and NMR) and by mass spectrometry. The IR spectrum exhibits terminal carbonyl stretching bands from 2095 to 1911 cm^{-1}, with the ester carbomethoxy groups displaying a strong ν(CO) band at 1729 cm^{-1}. The ^{1}H NMR spectrum provides valuable information concerning the coordination of the three methyl propiolate ligands to the planar metallic frame. The observation of three distinct alkyne hydrogen resonances at δ 7.74, 8.19, and 8.42, each of which integrates for a single hydrogen, immediately rules out the below cluster isomers. These particular isomers possess equivalent face-capping μ_4-alkyne groups that would display two ^{1}H resonances in a 2:1 ratio for the alkyne hydrogens instead of the three CH moieties spectroscopically found. The two face-capping alkyne ligands must be bound to the cluster in a head-to-tail fashion, as depicted in Scheme 1. Cluster **5** was also examined by ESI mass spectrometry in order to unequivocally establish the $CoRh_3$ metallic composition of the cluster. The mass spectrum exhibited a strong m/z peak at 894.71 that is consistent with the formation of the singly charged sodium adduct of cluster **5**, $[CoRh_3(CO)_9(\mu\text{-}HCCCO_2Me)_3{+}Na]^+$.

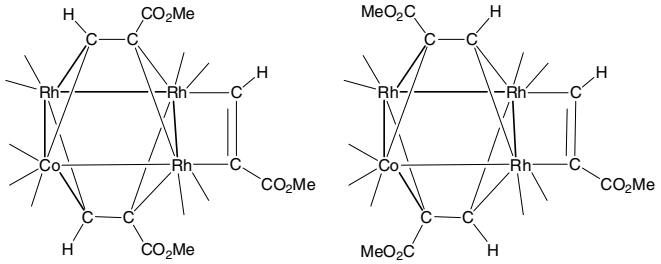


Table 2
Selected bond distances (Å) and angles (°) in $Co_2Rh_2(CO)_{10}$-(μ-$HCCCO_2Me$)[a]

Bond distances			
Rh(1)–Rh(2)	2.645(1)	Rh(1)–Co(1)	2.530(2)
Rh(1)–Co(2)	2.547(2)	Rh(2)–Co(1)	2.541(2)
Rh(2)–Co(2)	2.565(2)	Rh(1)–C(11)	1.86(2)
Rh(1)–C(10)	1.91(1)	Rh(1)–C(1)	2.03(1)
Rh(1)–C(9)	2.06(1)	Rh(2)–C(12)	1.92(2)
Rh(2)–C(13)	1.93(1)	Rh(2)–C(2)	2.10(1)
Rh(2)–C(14)	2.12(1)	Co(1)–C(6)	1.75(1)
Co(1)–C(5)	1.79(1)	Co(1)–C(9)	1.89(1)
Co(1)–C(1)	2.02(1)	Co(2)–C(2)	2.12(1)
Co(2)–C(8)	1.79(1)	Co(2)–C(7)	1.80(1)
Co(2)–C(14)	1.88(1)	Co(2)–C(2)	2.12(1)
Co(2)–C(1)	2.09(1)	C(1)–C(2)	1.39(2)
C(2)–C(3)	1.51(1)		
Bond angles			
C(1)–Rh(1)–Co(1)	51.1(3)	C(1)–Rh(1)–Co(2)	52.9(4)
Co(1)–Rh(1)–Co(2)	90.05(5)	C(1)–Rh(1)–Rh(2)	72.6(4)
Co(1)–Rh(1)–Rh(2)	58.76(4)	Co(2)–Rh(1)–Rh(2)	59.14(4)
C(2)–Rh(2)–Co(1)	53.3(3)	C(2)–Rh(2)–Co(2)	50.0(3)
Co(1)–Rh(2)–Co(2)	89.39(5)	C(2)–Rh(2)–Rh(1)	71.7(3)
Co(1)–Rh(2)–Rh(1)	58.35(4)	Co(2)–Rh(2)–Rh(1)	58.50(4)
C(1)–Co(1)–C(2)	39.1(5)	C(1)–Co(1)–Rh(1)	51.6(3)
C(2)–Co(1)–Rh(1)	73.9(3)	C(1)–Co(1)–Rh(2)	75.3(4)
C(2)–Co(1)–Rh(2)	52.6(3)	Rh(1)–Co(1)–Rh(2)	62.89(4)
C(2)–Co(2)–C(1)	39.4(4)	C(2)–Co(2)–Rh(1)	75.1(3)
C(1)–Co(2)–Rh(1)	50.8(3)	C(2)–Co(2)–Rh(2)	52.8(3)
Rh(1)–Co(2)–Rh(2)	62.31(4)	C(2)–C(1)–Co(1)	74.3(7)
C(2)–C(1)–Rh(1)	109.3(9)	Co(1)–C(1)–Rh(1)	77.3(4)
C(2)–C(1)–Co(2)	67.3(7)	Co(1)–C(1)–Co(4)	121.8(7)
Rh(1)–C(1)–Co(2)	76.2(4)	C(1)–C(2)–C(3)	123(1)
C(1)–C(2)–Co(2)	73.3(6)	C(1)–C(2)–Rh(2)	106.0(7)
C(1)–C(2)–Co(1)	66.7(6)	Co(2)–C(2)–Co(1)	120.7(5)
Rh(2)–C(2)–Co(1)	74.2(3)	Rh(2)–C(14)–Co(2)	79.5(4)
Rh(1)–C(9)–Co(1)	79.5(4)		

[a] Numbers in parentheses are estimated standard deviations in the least significant digit.

[1] The reaction of cluster **1** with excess dmad (ca. 12 mol equiv.) in hexane leads to complete cluster fragmentation and coupling of three alkyne molecules to furnish the dirhodium flyover compound $Rh_2(CO)_4$-[μ-C(CO_2Me)C(CO_2Me)C(CO_2Me)C(CO_2Me)C(CO_2Me)C(CO_2Me)]. Unpublished results.

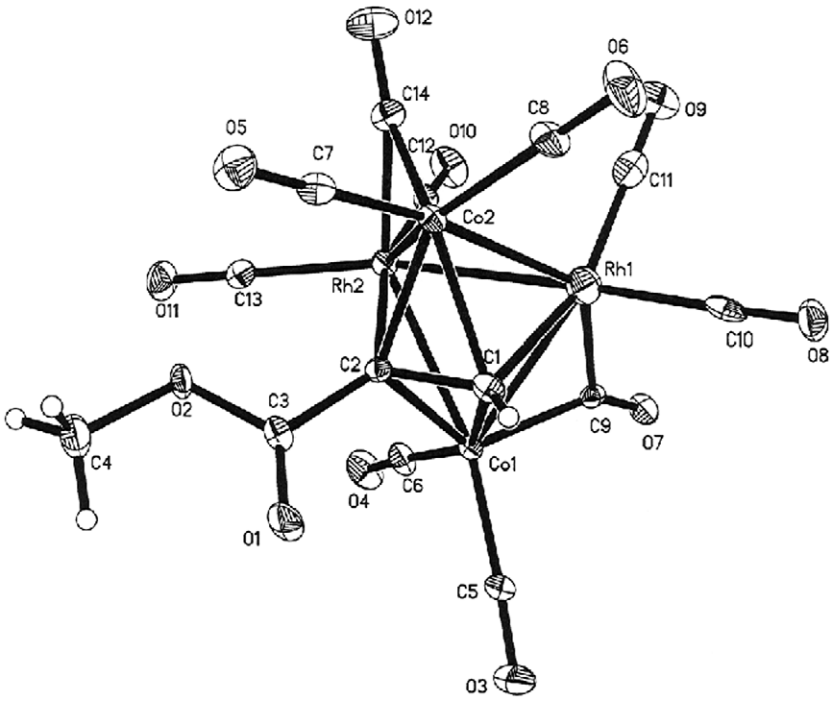


Fig. 1. Thermal ellipsoid plot of $Co_2Rh_2(CO)_{10}(\mu\text{-}HCCCO_2Me)$ showing the thermal ellipsoids at the 50% probability level.

3.2. X-diffraction structure of $Co_2Rh_2(CO)_{10}(\mu\text{-}HCCCO_2Me)$

The solid-state structure of $Co_2Rh_2(CO)_{10}(\mu\text{-}HCCCO_2Me)$ was established by X-ray crystallography. Single crystals of $Co_2Rh_2(CO)_{10}(\mu\text{-}HCCCO_2Me)$ were found to exist as discrete molecules in the unit cell with no unusually short inter- or intramolecular contacts. Tables 1 and 2 report the X-ray data collection and processing parameters and selected bond distances and angles, respectively.

The thermal ellipsoid plot of $Co_2Rh_2(CO)_{10}(\mu\text{-}HCCCO_2Me)$ is shown in Fig. 1, where the polyhedral expansion or opening of the original cluster tetrahedron and the formal insertion of the methyl propiolate ligand into the Co–Co bond of the cluster **1** are confirmed. This 60e-cluster may be viewed as either a butterfly or *arachno* cluster derived from the regiospecific opening of the original Co–Co bond in **1** or as a *closo* six-vertex based on a $Co_2Rh_2C(alkyne)_2$ core [17]. The two rhodium atoms are situated parallel to the 4e-methyl propiolate donor ligand, as found in the $Co_2Rh_2(CO)_{10}(\mu\text{-alkyne})$ clusters that have been structurally characterized [7]. The Rh(1)–Rh(2) bond length of 2.645(2) Å is slightly longer in comparison to the mean distance of 2.546 Å exhibited by the four Co–Rh bonds in cluster **4**. The experimentally determined metal–metal bond distances in **4** are in good agreement with those distances found in other mixed-metal Co_xRh_n containing clusters [7,8,15,18]. The six metal–C(alkyne) bond distances range from 2.02(1) Å [Co(2)–C(2) and Co(1)–C(1)] to 2.12(1) Å [Co(1)–C(2)] and display an average length of 2.06 Å. The C(1)–C(2) distance of 1.39(2) Å is longer than the corresponding C–C bond distance of 1.202 Å associated with the analogous distance of a free alkyne ligand [19]. Of the ten ancillary CO ligands, the C(9)O(7) and C(14)O(12) groups function as bridging groups and span the Co(1)–Rh(1) and Co(2)–Rh(2) vectors, respectively. The distances and angles exhibited by the two bridging CO groups and the remaining eight linear CO groups are unremarkable and require no comment.

4. Conclusions

The mixed-metal cluster $Co_2Rh_2(CO)_{12}$ reacts with methyl propiolate to give the clusters $Co_3Rh(CO)_{12}$ (**2**), $Co_3Rh(CO)_{10}(\mu\text{-}HCCCO_2Me)$ (**3**), $Co_2Rh_2(CO)_{10}(\mu\text{-}HCCCO_2Me)$ (**4**), and $CoRh_3(CO)_9(\mu\text{-}HCCCO_2Me)_3$ (**5**) as the principal products. The solid-state structure of **4** unequivocally was established by X-ray crystallography, and with it the first structurally characterized $Co_2Rh_2(alkyne)$ butterfly cluster containing an electron-withdrawing alkyne ligand.

Acknowledgements

Financial support from the Robert A. Welch Foundation (Grants P-0074-WHW and B-1093-MGR) is appreciated. Dr. Yongxuan Su (UCSD) is thanked for recording the ESI-ACPI mass spectrum of cluster **5**.

Appendix A. Supplementary material

Crystallographic data have been deposited with the Cambridge Crystallographic Data Centre (CCDC). These

data can be obtained free of charge via http://www.ccdc.cam.ac.uk/conts/retrieving.html, or from the Cambridge Crystallographic Data Centre, 12 Union Road, Cambridge CB2 1EZ, UK; fax: (+44) 1223-336-033; or e-mail: deposit@ccdc.cam.ac.uk. Supplementary data associated with this article can be found, in the online version, at doi:10.1016/j.poly.2006.09.086.

References

[1] (a) I. Ojima, I.N. Clos, R.J. Donovan, P. Ingallina, Organometallics 10 (1991) 38;
(b) O. Ojima, Z. Li, in: R.D. Adams, F.A. Cotton (Eds.), In Catalysis by Di- and Polynuclear Metal Cluster Compounds, Wiley-VCH, New York, 1998;
(c) I. Ojima, Z. Li, R.J. Donovan, P. Ingallina, Inorg. Chim. Acta 270 (1998) 279;
(d) I. Ojima, E.S. Vidal, Organometallics 18 (1999) 5103.

[2] K.H. Park, I.G. Jung, Y.K. Chung, Org. Lett. 6 (2004) 1183.

[3] (a) F. Azzaroni, P. Biscarini, S. Bordini, G. Longoni, E. Venturini, J. Organomet. Chem. 508 (1996) 59;
(b) L. Huang, Y. Xu, G. Piao, A. Liu, W. Zhang, Catal. Lett. 23 (1993) 87.

[4] (a) N. Eliau, D. Avnir, M.S. Eisen, J. Blum, J. Sol–Gel Sci. Technol. 35 (2005) 159;
(b) F. Gelman, J. Blum, D. Avnir, J. Am. Chem. Soc. 124 (2002) 14460;
(c) L. Alvila, T.A. Pakkanen, T.T. Pakkanen, O. Krause, J. Mol. Catal. 75 (1992) 333;
(d) F. Gelman, D. Avnir, H. Schumann, J. Blum, J. Mol. Catal. A 171 (2001) 191.

[5] (a) M. Garland, P. Pino, J. Organomet. Chem. 417 (1991) 121;
(b) M. Garland, P. Pino, Organometallics 10 (1991) 2643;
(c) I.T. Horváth, M. Garland, G. Bor, P. Pino, J. Organomet. Chem. 358 (1988) C17;
(d) G. Bor, Pure Appl. Chem. 58 (1986) 543.

[6] (a) I.T. Horváth, Organometallics 5 (1986) 2333;
(b) M. Bojczuk, B.T. Heaton, S. Johnson, C.A. Ghilardi, A. Orlandini, J. Organomet. Chem. 341 (1988) 473.

[7] (a) I.T. Horváth, L. Zsolnai, G. Huttner, Organometallics 5 (1986) 180;
(b) I. Ojima, N. Clos, R.J. Donovan, P. Ingallina, Organometallics 10 (1991) 3211;
(c) I.T. Horváth, Polyhedron 7 (1988) 2345;
(d) B.-H. Zhu, W.-Q. Zhang, Q.-Y. Zhao, Z.-G. Bian, B. Hu, Y.-H. Zhang, Y.-Q. Yin, J. Sun, J. Organomet. Chem. 650 (2002) 181;
(e) B.-H. Zhu, B. Hu, W.-Q. Zhang, Y.-H. Zhang, Y.-Q. Yin, J. Sun, J. Organomet. Chem. 681 (2003) 275.

[8] W.H. Watson, B. Poola, M.G. Richmond, Organometallics 24 (2005) 4687.

[9] S. Martinengo, P. Chini, V.G. Albano, F. Cariati, T. Salvatori, J. Organomet. Chem. 59 (1973) 379.

[10] J.A. McCleverty, G. Wilkinson, Inorg. Synth. 8 (1966) 211.

[11] D.F. Shriver, The Manipulation of Air-Sensitive Compounds, McGraw-Hill, New York, 1969.

[12] Saint Version 6.02, Bruker Analytical X-ray Systems, Inc. Copyright 1997–1999.

[13] SHELXTL Version 5.1, Bruker Analytical X-ray Systems, Inc. Copyright 1998.

[14] PLATON – A Multipurpose Crystallographic Tool, Utrecht University, Utrecht, The Netherlands, Spek, A.L., 2001.

[15] S.P. Tunik, V.R. Krym, G.L. Starova, A.B. Nikol'skii, I.S. Podkorytov, S. Ooi, M. Yamasaki, M. Shiro, J. Organomet. Chem. 481 (1994) 83.

[16] P. Srinivasan, W.K. Leong, Eur. J. Inorg. Chem. (2006) 464.

[17] (a) Cluster **4** contains seven skeletal electron pairs according to Polyhedral Skeletal Electron Pair (PSEP) theory and depending whether the alkyne moiety is included in the vertex count or not leads one to either an arachno (butterfly) or the closo polyhedral designation;
(b) D.M.P. Mingos, D.J. Wales, Introduction to Cluster Chemistry, Prentice-Hall, Englewood Cliffs, NJ, 1990.

[18] (a) V.G. Albano, D. Braga, F. Grepioni, R.D. Pergola, L. Garlaschelli, A. Fumagalli, J. Chem. Soc., Dalton Trans. (1989) 879;
(b) M. Ebihara, M. Liba, S. Higashi, N. Tsuzuki, T. Kawamura, T. Morioka, S. Ozawa, T. Yamabe, H. Masuda, Polyhedron 22 (2003) 3413;
(c) P. Braunstein, H. Lehner, D. Matt, A. Tirpicchio, M.T. Camellini, New J. Chem. 9 (1985) 597;
(d) T. Albiez, A.K. Powell, H. Vahrenkamp, Chem. Ber. 123 (1990) 667.

[19] R.C. Weast (Ed.), Handbook of Chemistry and Physics, 56th ed., CRC Press, Cleveland, OH, 1975.

V-shaped building block [Cu(dbsf)]. Using these V-shaped building blocks, with the help of different auxiliary ligands, we have successfully obtained five new copper coordination compounds: $[Cu(dbsf)(H_2O)]_n \cdot 0.5n(i\text{-}C_3H_7OH)$ (**1**), $[Cu(dbsf)(4,4'\text{-bpy})_{0.5}]_n \cdot nH_2O$ (**2**), $[Cu(dbsf)(2,2'\text{-bpy})(H_2O)]_2 \cdot (n\text{-}C_3H_7OH) \cdot 0.5H_2O$ (**3**), $[Cu(dbsf)(phen)(H_2O)]_2 \cdot 1.5H_2O$ (**4**) and $[Cu(dbsf)(2,2'\text{-bpy})(H_2O)]_n \cdot n(i\text{-}C_3H_7OH)$ (**5**).

2. Experimental

2.1. Materials and apparatus

All reagents were used as received without further purification (H_2dbsf from TCL). The C, H, N microanalyses were carried out with a Vario EL elemental analyzer. The IR spectra were recorded with a Nicolet Avatar 360 FT-IR spectrometer using the KBr pellet technique. The thermal analyses were performed on a ZRY-2P thermal analyzer using a heating rate of 20 °C/min from room temperature to 900 °C.

2.2. Synthesis

2.2.1. Synthesis of $[Cu(dbsf)(H_2O)]_n \cdot 0.5n(i\text{-}C_3H_7OH)$ (*1*)

A mixture of $CuCl_2 \cdot 6H_2O$ (0.017 g, 0.1 mmol), H_2dbsf (0.030 g, 0.1 mmol), NaOH aqueous solution (0.05 mL, 0.65 M), HCl aqueous solution (0.05 mL, 1.20 M), distilled water (5 mL), isopropanol (5 mL) and *N*,*N*-dimethyl formamide (0.1 mL) was sealed in a Teflon-lined stainless vessel (25 mL) and heated at 180 °C for 72 h under autogenous pressure. The vessel was then cooled slowly to room temperature. Blue strip crystals were obtained by filtration, washed with distilled water and isopropanol, and dried in air. Yield: 0.002 g (4.8%). Additionally a lot of blue polycrystals were also obtained (~50%. Found: C, 42.09; H, 4.11%). *Anal.* Calc. for $C_{15.5}H_{14}CuO_{7.5}S$ (415.87): C, 44.77; H, 3.39. Found: C, 44.70; H, 3.64%. IR data (KBr pellet, cm^{-1}): 3441s, 1633s, 1409s, 1169m, 1140w, 1100w, 742m, 727w, 523w.

2.2.2. Synthesis of $[Cu(dbsf)(4,4'\text{-bpy})_{0.5}]_n \cdot nH_2O$ (*2*)

A mixture of $CuCl_2 \cdot 6H_2O$ (0.017 g, 0.1 mmol), H_2dbsf (0.030 g, 0.1 mmol), 4,4′-bpy · $2H_2O$ (0.019 g, 0.1 mmol), NaOH aqueous solution (0.05 mL, 0.65 M), HCl aqueous solution (0.05 mL, 1.20 M), distilled water (5 mL) and *N*,*N*-dimethyl formamide (0.1 mL) was sealed in a Teflon-lined stainless vessel (25 mL) and heated at 180 °C for 72 h under autogenous pressure. The vessel was then cooled slowly to room temperature. Green strip crystals were obtained by filtration, washed with distilled water and dried in air. Yield: 0.015 g (32.3%). *Anal.* Calc. for $C_{19}H_{14}CuNO_7S$ (463.91): C, 49.19; H, 3.04; N, 3.02. Found: C, 49.48; H, 3.18; N, 3.05%. IR data (KBr pellet, cm^{-1}): 3439s, 1644s, 1608m, 1570m, 1408s, 1326w, 1302w, 1169m, 1100m, 1015w, 739s, 726w, 620w, 520m.

2.2.3. Synthesis of $[Cu(dbsf)(2,2'\text{-bpy})(H_2O)]_2 \cdot (n\text{-}C_3H_7OH) \cdot 0.5H_2O$ (*3*)

The synthesis of complex **3** was the same as that for complex **2** but substituting 2,2′-bpy (0.016 g, 0.1 mmol) for 4,4′-bpy · $2H_2O$, and *n*-propanol (5 mL) was also added to the reaction mixture. Blue block crystals were obtained by filtration, washed with distilled water and *n*-propanol, and dried in air. Yield: 0.020 g (34.7%). *Anal.* Calc. for $C_{25.5}H_{22.5}CuN_2O_{7.75}S$ (576.55): C, 53.13; H, 3.92; N, 4.86. Found: C, 53.56; H, 4.34; N, 4.53%. IR data (KBr

Table 1
Crystal data and structure refinement parameters of complexes **1**–**5**

Complex	**1**	**2**	**3**	**4**	**5**
Empirical formula	$C_{15.5}H_{14}CuO_{7.5}S$	$C_{19}H_{14}CuNO_7S$	$C_{25.5}H_{22.5}CuN_2O_{7.75}S$	$C_{26}H_{19.5}CuN_2O_{7.75}S$	$C_{27}H_{26}CuN_2O_8S$
Formula weight	415.87	463.91	576.55	579.54	602.10
Crystal system	orthorhombic	orthorhombic	triclinic	triclinic	monoclinic
Space group	*Cmcm*	*Cmcm*	$P\bar{1}$	$P\bar{1}$	$P2_1/n$
a (Å)	22.073(5)	12.694(4)	6.936(4)	6.975(5)	6.8069(9)
b (Å)	12.689(2)	13.983(4)	12.137(6)	12.115(10)	16.574(2)
c (Å)	11.592(2)	21.823(7)	16.324(9)	16.749(13)	23.762(3)
α (°)	90	90	79.717(9)	82.469(13)	90
β (°)	90	90	88.063(10)	85.658(12)	92.146(2)
γ (°)	90	90	73.418(9)	74.148(13)	90
V ($Å^3$)	3246.9(12)	3874(2)	1295.5(12)	1348.5(18)	2678.8(6)
Z	8	8	2	2	4
F(000)	1696	1888	593	593	1244
D_{calc} (Mg m^{-3})	1.701	1.591	1.478	1.427	1.493
T (K)	293(2)	293 (2)	293(2)	293(2)	293(2)
θ Range (°)	1.85–26.30	1.87–26.46	1.78–25.01	2.26–25.01	1.50–26.39
μ (mm^{-1})	1.514	1.278	0.974	0.937	0.946
Goodness-of-fit	1.054	1.087	1.073	1.020	1.046
Final *R* indices [$I > 2\sigma(I)$]	$R_1 = 0.0413$, $wR_2 = 0.1036$	$R_1 = 0.0617$, $wR_2 = 0.1221$	$R_1 = 0.0570$, $wR_2 = 0.1550$	$R_1 = 0.0562$, $wR_2 = 0.1475$	$R_1 = 0.0374$, $wR_2 = 0.0852$

pellet, cm^{-1}): 3431s, 1600s, 1560s, 1474w, 1447w, 1398s, 1319w, 1297m, 1163s, 1133m, 1101m, 1054w, 1012w, 773w, 744s, 731m, 718w, 692w, 624m, 576w.

2.2.4. Synthesis of [Cu(dbsf)(phen)(H_2O)]$_2$ · 1.5H_2O (4)

The synthesis of complex **4** followed a similar process as for complex **2** except that 4,4′-bpy · 2H_2O was replaced by phen·H_2O (0.020 g, 0.1 mmol), and isopropanol (5 mL) was added to the reaction mixture. Blue strip crystals were obtained by filtration, washed with distilled water and isopropanol, and dried in air. Yield: 0.031 g (53.5%). *Anal.* Calc. for $C_{26}H_{19.5}CuN_2O_{7.75}S$ (579.54): C, 53.89; H, 3.39; N, 4.83. Found: C, 53.53; H, 3.76; N, 4.74%. IR data (KBr pellet, cm^{-1}): 3423s, 1604s, 1563s, 1518w, 1426m, 1398s, 1380s, 1344m, 1298m, 1161s, 1102m, 856w, 746s, 724s, 624m, 585w.

2.2.5. Synthesis of [Cu(dbsf)(2,2′-bpy)(H_2O)]$_n$ · n(i-C_3H_7OH) (5)

The synthesis of complex **5** followed the same procedure as that for complex **2** except using 2,2′-bpy (0.016 g, 0.1 mmol) instead of 4,4′-bpy · 2H_2O, and isopropanol (5 mL) was added to the reaction mixture. Blue board crystals were obtained by filtration, washed with distilled water and isopropanol, and dried in air. Yield: 0.051 g (84.7%). *Anal.* Calc. for $C_{27}H_{26}CuN_2O_8S$ (602.10): C, 49.69; H, 3.07; N, 3.05. Found: C, 49.72; H, 3.11; N, 3.01%. IR data (KBr pellet, cm^{-1}): 3418s, 1600s, 1560s, 1475w, 1447m, 1399s, 1298m, 1163s, 1133m, 1101m, 744m, 731w, 623w.

In the syntheses of the complexes **1**–**5**, HCl and NaOH solutions were added to adjust the pH of the reaction system. Propanol and DMF were added to enhance the solubility of the H_2dbsf ligand. Complexes **1**, **4** and **5** were synthesized in the mixed solvent of water, isopropanol and DMF, and **2** was formed in the mixed solvent of water and DMF, while complex **3** was obtained in the mixed solvent of water, *n*-propanol and DMF, showing that selectivity of the solvent plays an important role in the formation of the complexes.

2.3. X-ray diffraction determination

Diffraction data for complexes **1**–**5** were collected at 294 K on a Bruker SMART 1000 CCD diffractometer with a graphite-monochromatized Mo Kα radiation (λ = 0.71073 Å), using the ω and φ scan technique. A semi-empirical absorption correction was applied with the SADABS program. The structures were solved by direct methods and refined by full-matrix least-squares on F^2 using the SHELXS-97 and SHELXL-97 programs [12–14], respectively. All non-hydrogen atoms were refined anisotropically. Hydrogen atoms were placed in geometrically calculated positions. Crystallographic data for complexes **1**–**5** are summarized in Table 1, and selected bond lengths (Å) and bond angles (°) are listed in Table 2 while selected hydrogen bond lengths (Å) and bond angles (°) are presented in Table 3.

Table 2
Selected bond lengths (Å) and bond angles (°) for complexes **1**–**5**[a]

Complex ***1***			
Cu(1)–O(1)	1.952(3)	Cu(1)–O(3)#2	1.981(3)
Cu(1)–O(4)	2.153(4)		
O(1)–Cu(1)–O(4)	100.9(1)	O(1)#1–Cu(1)–O(3)#2	89.8(1)
O(1)–Cu(1)–O(1)#1	89.9(2)	O(3)#2–Cu(1)–O(4)	90.1(1)
O(1)–Cu(1)–O(3)#2	168.8(1)	O(3)#2–Cu(1)–O(3)#3	88.3(2)
Complex ***2***			
Cu(1)–O(1)	1.987(5)	Cu(2)–O(2)	1.966(5)
Cu(1)–N(2)#4	2.10(1)	Cu(2)–N(1)	2.12(1)
O(1)–Cu(1)–O(1)#1	88.7(3)	O(2)–Cu(2)–O(2)#1	90.0(3)
O(1)–Cu(1)–O(1)#2	89.9(3)	O(2)–Cu(2)–O(2)#2	88.9(3)
O(1)–Cu(1)–O(1)#3	167.6(3)	O(2)–Cu(2)–O(2)#3	168.8(3)
O(1)–Cu(1)–N(2)#4	96.2(1)	O(2)–Cu(2)–N(1)	95.6(1)
Complex ***3***			
Cu(1)–O(1)	1.929(4)	Cu(1)–N(1)	1.992(5)
Cu(1)–O(7)	2.303(4)	Cu(1)–N(2)	1.996(5)
Cu(1)–O(5)#1	1.924(4)		
O(1)–Cu(1)–O(7)	95.5(2)	O(5)#1–Cu(1)–N(1)	93.3(2)
O(1)–Cu(1)–N(1)	169.8(2)	O(5)#1–Cu(1)–N(2)	164.7(2)
O(1)–Cu(1)–N(2)	93.5(2)	N(1)–Cu(1)–O(7)	93.0(2)
O(5)#1–Cu(1)–O(1)	90.6(2)	N(1)–Cu(1)–N(2)	80.4(2)
O(5)#1–Cu(1)–O(7)	101.0(2)	N(2)–Cu(1)–O(7)	93.4(2)
Complex ***4***			
Cu(1)–O(1)	1.951(4)	Cu(1)–N(1)	2.014(4)
Cu(1)–O(7)	2.353(4)	Cu(1)–N(2)	2.020(4)
Cu(1)–O(5)#1	1.941(4)		
O(1)–Cu(1)–O(7)	95.1(2)	O(5)#1–Cu(1)–N(1)	92.6(2)
O(1)–Cu(1)–N(1)	171.8(2)	O(5)#1–Cu(1)–N(2)	167.1(2)
O(1)–Cu(1)–N(2)	92.5(2)	N(1)–Cu(1)–O(7)	91.1(2)
O(5)#1–Cu(1)–O(1)	91.9(2)	N(1)–Cu(1)–N(2)	81.8(2)
O(5)#1–Cu(1)–O(7)	98.9(2)	N(2)–Cu(1)–O(7)	92.8(2)
Complex ***5***			
Cu(1)–O(1)	1.943(2)	Cu(1)–N(1)	2.011(2)
Cu(1)–O(8)	2.273(2)	Cu(1)–N(2)	2.016(2)
Cu(1)–O(5)#1	1.955(2)		
O(1)–Cu(1)–O(8)	96.82(8)	O(5)#1–Cu(1)–N(1)	91.20(9)
O(1)–Cu(1)–O(5)#1	92.52(8)	O(5)#1–Cu(1)–N(2)	162.82(8)
O(1)–Cu(1)–N(1)	168.43(8)	N(1)–Cu(1)–O(8)	93.83(8)
O(1)–Cu(1)–N(2)	93.04(8)	N(1)–Cu(1)–N(2)	80.41(9)
O(5)#1–Cu(1)–O(8)	94.18(8)	N(2)–Cu(1)–O(8)	101.28(8)

[a] Symmetry transformations used to generate equivalent atoms: For **1**, #1 $-x$, y, z; #2 $-x$, $y-1$, z; #3 x, $y-1$, z. For **2**, #1 x, y, $-z+1/2$; #2 $-x+2$, y, z; #3 $-x+2$, y, $-z+1/2$; #4 x, $y+1$, z. For **3**, #1 $-x+1$, $-y$, $-z+1$. For **4**, #1 $-x+1$, $-y+1$, $-z+2$. For **5**, #1 $-x+1/2$, $y-1/2$, $-z+1/2$.

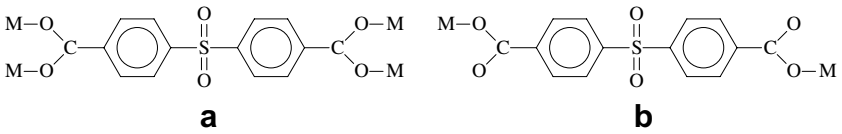
3. Results and discussion

3.1. Description of the structures

In complexes **1**–**5**, the dbsf^{2-} ligands are completely deprotonated and are largely bent at the sulfone-sulfur sites (C–S–C = 103.0(2)–106.5(3)°, O–S–O = 119.1(2)–120.2(3)°). Each of them displays a V-shaped configuration, and assembles with the Cu(II) ion to form the V-shaped building block [Cu(dbsf)]. The coordination

Table 3
Selected hydrogen bond lengths (Å) and bond angles (°) for complexes **1**–**5**

D–H···A	*d*(D–H)	*d*(H···A)	*d*(D···A)	∠DHA	Symmetry code
*Complex **1***					
O(4)–H(4A)···O(5wA)	0.849	1.998	2.785	153.62	[*x*, *y*, *z*−1]
O(4)–H(4A)···O(5′wB)	0.849	2.133	2.905	150.97	[−*x*, *y*, −*z* + 1/2]
O(4)–H(4A)···O(5′wB)	0.849	2.133	2.905	150.97	[*x*, *y*, *z* − 1]
O(4)–H(4B)···O(3)	0.852	2.172	3.013	169.44	[*x*, −*y* + 1, −*z*]
*Complex **3***					
O(7)–H(7B)···O(6)	0.850	2.337	2.803	114.87	[−*x*, −*y*, −*z* + 1]
C(13)–H(13)···O(4)	0.930	2.547	3.232	130.80	[−*x* + 1, −*y* − 1, −*z* + 1]
C(22)–H(22)···O(3)	0.930	2.376	3.253	157.30	[−*x* + 1, −*y*, −*z*]
C(21)–H(21)···O(6)	0.930	2.403	3.318	168.00	[*x* − 1, *y* + 1, *z*−1]
*Complex **4***					
O(7)–H(7B)···O(6)	0.849	2.346	2.784	112.58	[−*x*, −*y* + 1, −*z* + 2]
O(7)–H(7A)···O(8w)	0.849	1.995	2.825	165.52	[−*x*, −*y* + 1, −*z* + 1]
C(19)–H(19)···O(6)	0.930	2.487	3.130	126.40	[*x* − 1, *y* + 1, *z*−1]
C(20)–H(20)···O(6)	0.930	2.683	3.228	118.10	[*x* − 1, *y* + 1, *z*−1]
C(4)–H(4)···O(2)	0.930	2.542	3.304	99.70	[*x* + 1, *y*, *z*]
*Complex **5***					
O(7)–H(7A)···O(6)	0.820	2.152	2.914	154.48	[−*x* − 1/2, *y* − 1/2, −*z* + 1/2]
O(8)–H(8A)···O(6)	0.845	1.920	2.720	157.58	[−*x* + 1/2, *y* − 1/2, −*z* + 1/2]
O(8)–H(8B)···O(2)	0.845	1.996	2.788	155.72	[*x* + 1, *y*, *z*]
C(4)–H(4)···O(2)	0.930	2.306	3.197	160.30	[−*x* + 1, −*y* + 1, −*z*]



Scheme 1. The coordination modes of the $dbsf^{2-}$ ligand in complexes **1**–**5**.

modes of the $dbsf^{2-}$ ligand in complexes **1**–**5** are represented in Scheme 1.

3.1.1. [Cu(dbsf)(H$_2$O)]$_n$ · 0.5n(i-C$_3$H$_7$OH) (**1**)

In complex **1**, each Cu(II) ion is coordinated to five oxygen atoms, four oxygen atoms from four $dbsf^{2-}$ ligands and one oxygen atom from a water molecule, as shown in Fig. 1a. O(1), O(1C), O(3B) and O(3C) atoms form an equatorial plane and one oxygen atom (O(4)) occupies the axial position, giving a slightly distorted square-pyramidal geometry. In complex **1**, each $dbsf^{2-}$ ligand adopts a bis(bridging-bidentate) mode (Scheme 1a) to coordinate to four Cu(II) ions. V-Shaped building blocks [Cu(dbsf)] are joined to form 1D double-chains, as shown in Fig. 1b. The single 1D double-chain possesses rhombic voids with dimensions of about 8 × 8 Å. All these double-chains are parallel to each other. Along the *c*-axis, these double-chains are arranged in an ABAB fashion and there is a displacement between the adjacent chains, which leads to the formation of small 1D channels (Fig. 1c). Hydrogen bonds are observed between the coordinated water molecules and the carboxylate oxygen atoms of $dbsf^{2-}$ ligands among the adjacent chains along the *c*-axis (Table 3), and there are π–π stacking interactions in the *ab*-plane, with a distance of 3.507 Å between the phenyl rings of $dbsf^{2-}$ ligands. Hydrogen bonds and π–π stacking interactions result in the formation of the porous supramolecular network of complex **1**. Isopropanol molecules are accommodated in the channels (see Fig. 1c). There are hydrogen bonds between the oxygen atom (O(5w)) of isopropanol molecules and coordinated water molecules of the chains (Table 3).

3.1.2. [Cu(dbsf)(4,4′-bpy)$_{0.5}$]$_n$ · nH$_2$O (**2**)

In complex **2**, there are two kinds of crystallographically independent Cu(II) ions, as shown in Fig. 2a. Both Cu(1) and Cu(2) are five-coordinated, and their coordination environments are similar but the bond lengths and bond angles around Cu(1) and Cu(2) are different. Each Cu(II) ion is coordinated to four oxygen atoms of four different $dbsf^{2-}$ ligands and one nitrogen atom of one 4,4′-bpy molecule. In complex **2**, the $dbsf^{2-}$ ligands adopt a bis(bridging-bidentate) mode (Scheme 1a), linking the Cu(II) ions into a 1D double-chain structure along the *a*-axis, which is similar to that in complex **1**. However, because of the introduction of 4,4′-bpy molecules, these 1D [Cu(dbsf)]$_n$ double-chains are pillared to generate 2D square-grids (Fig. 2b). Unexpectedly, two such grids interpenetrate each

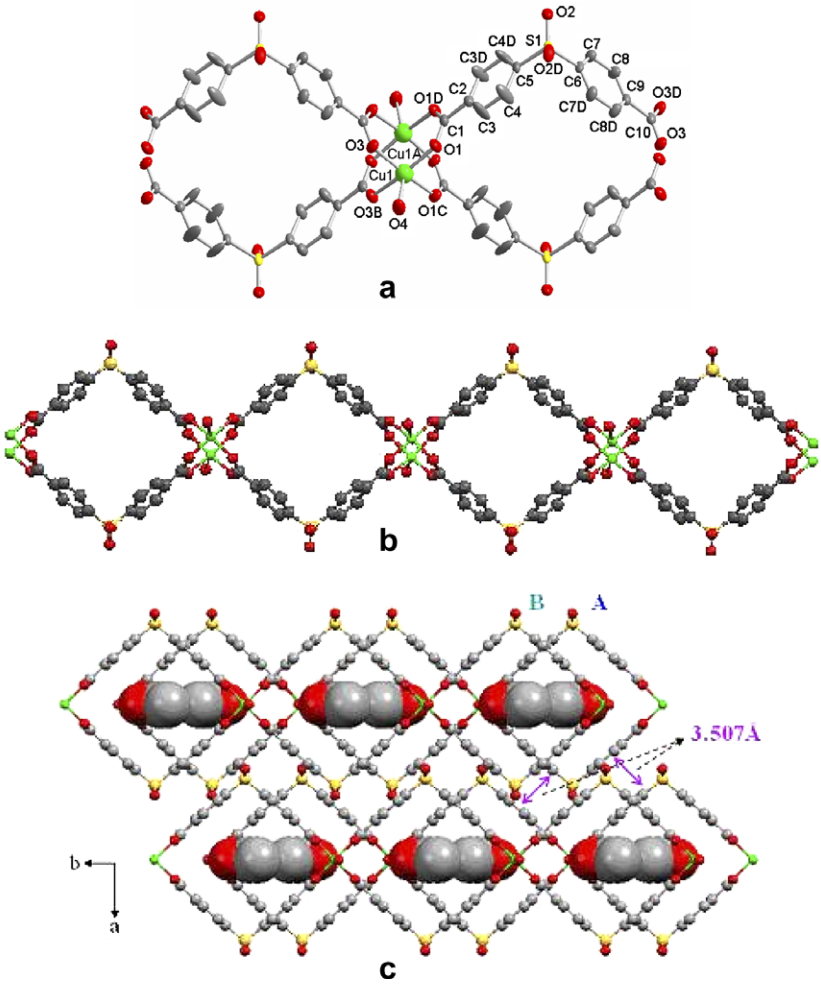


Fig. 1. (a) The coordination environment of the Cu(II) ion in complex **1** with 30% thermal ellipsoids, all hydrogen atoms are omitted for clarity. (b) The 1D double-chain structure with rhombic voids. (c) View of the supramolecular network of complex **1** along the *c*-direction (space-filling model represents isopropanol molecules).

other to generate a novel catenane-like 2D layer (Fig. 2c). Such catenane-like layers are unusual [15]. These catenane-like 2D structures stack in an ABAB fashion along the *c*-axis with some displacement between A and B, resulting in the formation of a 3D supramolecular network. There are lattice water molecules accommodated between the layers.

3.1.3. *[Cu(dbsf)(2,2′-bpy)(H$_2$O)]$_2$ · (n-C$_3$H$_7$OH) · 0.5H$_2$O* (**3**) *and [Cu(dbsf)(phen)(H$_2$O)]$_2$ · 1.5H$_2$O* (**4**)

X-ray diffraction analysis reveals that complexes **3** and **4** possess similar structures, except that the 2,2′-bpy ligand in complex **3** is replaced by a phen ligand in complex **4**, and the guest molecules are different in the two complexes (*n*-C_3H_7OH and H_2O for **3**, H_2O for **4**). So only the structure of complex **3** will be described here. The coordination environment of the Cu(II) ion in complex **3** is shown in Fig. 3a. The Cu(II) ion is five-coordinated, with two oxygen atoms from two $dbsf^{2-}$ ligands, two nitrogen atoms from one 2,2′-bpy ligand and one oxygen atom from a coordinated water molecule. The coordination geometry of the Cu(II) ion can be described as a distorted square-pyramid. The Cu–N bond lengths are 2.014(4) and 2.020(4) Å, and the Cu–O bond lengths are in the range of 1.941(4)–2.353 (4) Å (the Cu–N bond lengths are 1.992(5) and 1.996(5) Å, and the Cu–O bond lengths are in the range of 1.924(4)–2.303 (4) Å for complex **4**). In complex **3**, every $dbsf^{2-}$ ligand adopts a bis(monodentate) mode (Scheme 1b), so that two V-shaped building blocks encircle to form a macrocyclic dimer unit (Fig. 3a). All the dimer units are parallel, and plenty of hydrogen bonds exist between them. Along the *a*-axis, there exists O–H···O hydrogen bonds [O(7)–H(7B)···O(6)] between the coordinated water molecule and the oxygen atom of the uncoordinated carboxyl group. In addition, three kinds of C–H···O hydrogen bonds, such as C(13)–H(13)···O(4), C(22)–H(22)···O(3) and C(21)–H(21)···O(6) exist in the adjacent dimers in the *bc*-plane. Moreover, a π–π stacking interaction exists between 2,2′-bpy ligands (the face-to-face distance is 3.639 Å). These hydrogen bonds and π–π stacking interactions lead to the

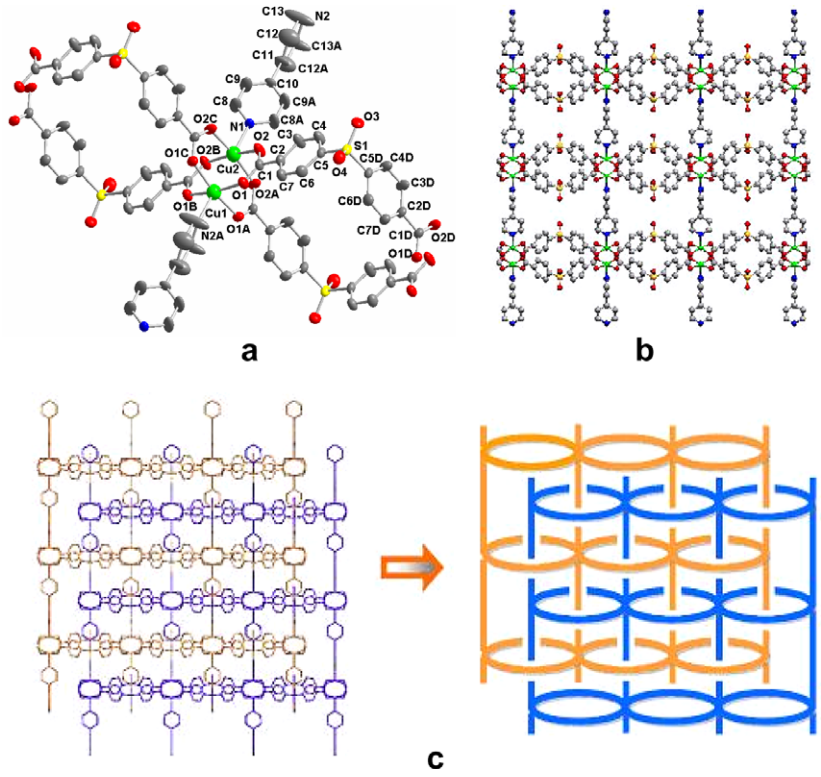


Fig. 2. (a) The coordination environments of the Cu(II) ions in complex **2** with 30% thermal ellipsoids, all hydrogen atoms are omitted for clarity. (b) The 2D layer framework of complex **2**. (c) Interpenetrated catenane-like 2D layers and its schematic view.

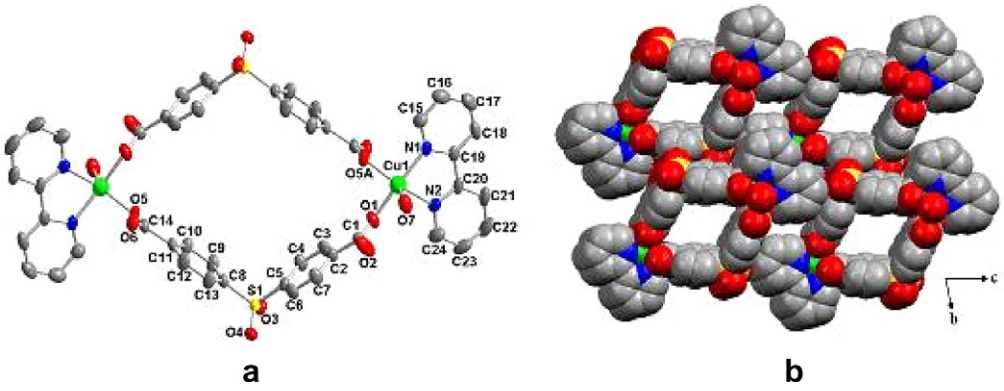


Fig. 3. (a) The coordination environment of the Cu(II) ion in complex **3** with 30% thermal ellipsoids, all hydrogen atoms are omitted for clarity. (b) View of the 3D porous supramolecular structure along the *a*-axis, all the atoms except hydrogen atoms are shown as a space-filling model.

formation of a 3D porous supramolecular architecture [16], as shown in Fig. 3b. Water molecules and *n*-propanol molecules alternately occupy the 1D channels along the *a*-axis. But they are so far away from the dimers that no hydrogen bonds are formed between the guest molecules and the dimers.

3.1.4. $[Cu(dbsf)(2,2'\text{-bpy})(H_2O)]_n \cdot n(i\text{-}C_3H_7OH)$ (**5**)

The X-ray crystallographic analysis shows that complex **5** possesses 1D tooth-like chains. There is one crystallographically independent Cu(II) center in the crystal structure. As shown in Fig. 4a, the Cu(II) ion is five-coordinated and displays a distorted square-pyramidal geometry, which is completed by two nitrogen atoms from one chelating 2,2′-bpy ligand, two oxygen atoms from two $dbsf^{2-}$ ligands, and one oxygen atom from one coordinated water molecule. In complex **5**, the $dbsf^{2-}$ ligands adopt a bis(monodentate) mode (Scheme 1b), the same as that in complex **3**, but they connect the Cu(II) ions into a completely different structure. V-Shaped building blocks are joined head-to-tail to form infinite tooth-like chains (Fig. 4b). Among these chains, there are plenty of hydro-

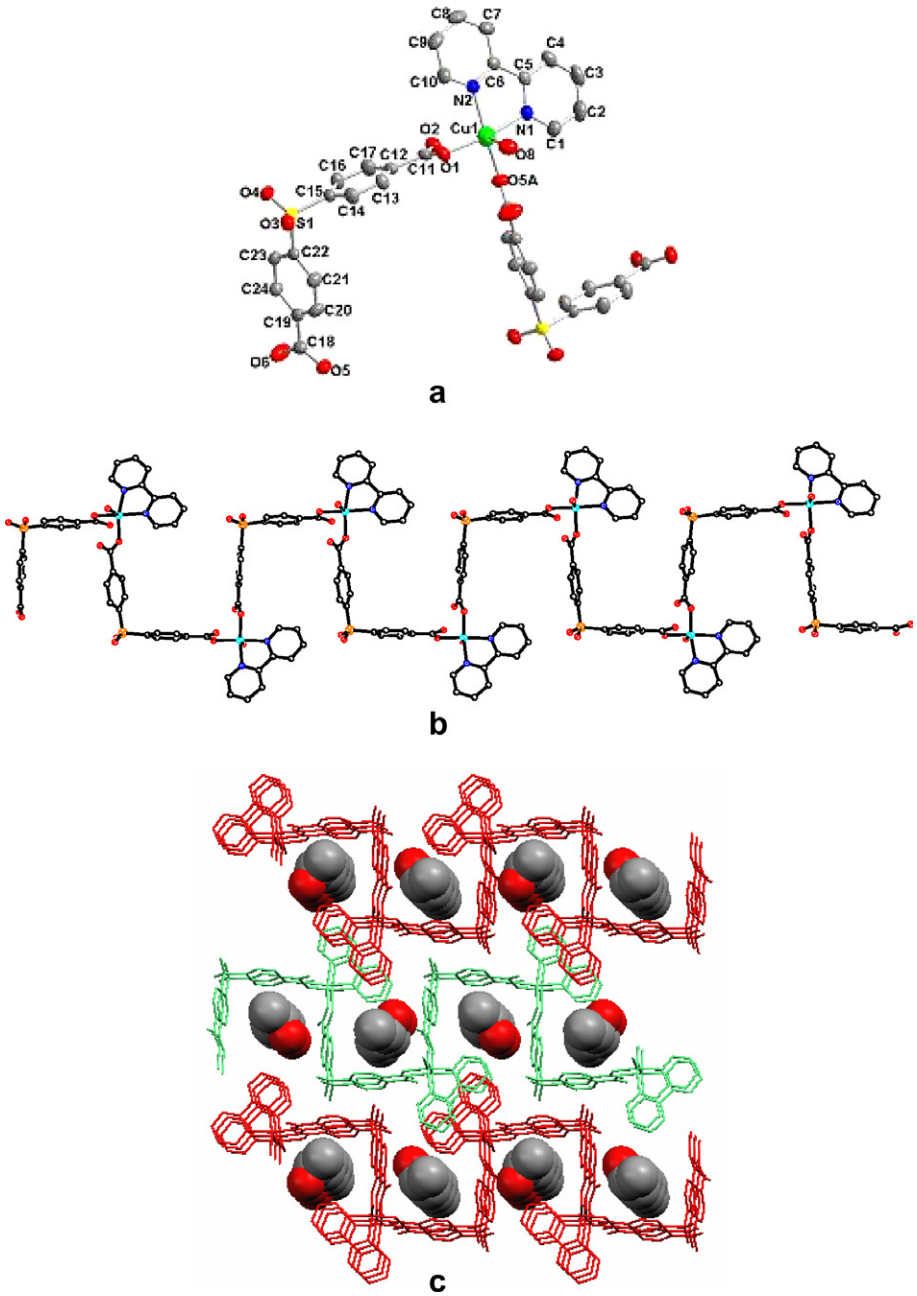
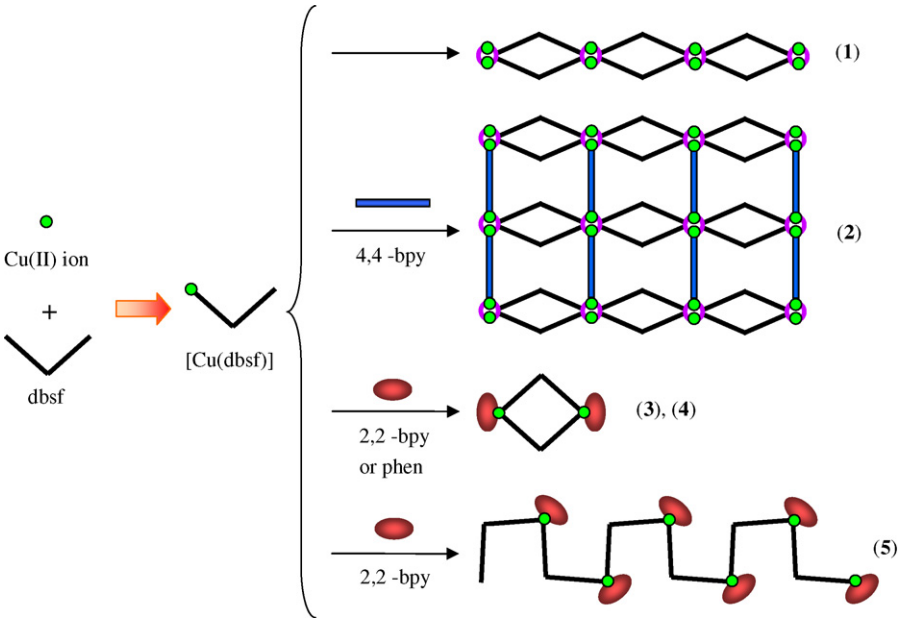


Fig. 4. (a) The coordination environment of the Cu(II) ion in complex **5** with 30% thermal ellipsoids, all hydrogen atoms are omitted for clarity. (b) The infinite 1D chain structure formed by V-shaped building blocks of [Cu(dbsf)]. (c) View of the 3D supramolecular structure along *a*-axis (space-filling model represents solvent molecules).

gen bonds. O–H···O hydrogen bonds are observed between the uncoordinated oxygen atoms (O(6)) and coordinated water molecules of the adjacent chains. Additionally, C–H···O hydrogen bonds are observed between C···H (H(4)) of the 2,2′-bpy molecule and the other uncoordinated carboxylate oxygen atoms (O(2)) of the adjacent chain (Table 3). The 2,2′-bpy molecules also participate in face-to-face π–π stacking interactions with a separation at the closest contact of 3.267 Å, and the pyridyl planes of the 2,2′-bpy ligands are parallel to ones in the adjacent chains. Thus a 3D supramolecular structure is formed via hydrogen bonds and π–π stacking interactions. In the 1D channels along the *a*-axis, isopropanol molecules are accommodated (Fig. 4c). They form O–H···O hydrogen bonds with the non-coordinated oxygen atoms (O(6)) of the $dbsf^{2-}$ ligands. The formation of these hydrogen bonds prevents the $dbsf^{2-}$ ligands encircling to form a dimer fragment. Besides, isopropanol molecules occupy the voids of the tooth-like chains, functioning as important supports to the shape of the chains.

3.1.5. Comparison of the structures of complexes *1*–*5*

By self-assembly from V-shaped building blocks [Cu(dbsf)], we obtained five new complexes with structure described as



Scheme 2. The simplified representation of the structures of the five complexes.

0D metallocyclic, 1D chain and 2D catenane-like layer. From the above descriptions, it is obvious that the introducing of different auxiliary ligands has a crucial effect on the assembly of the [Cu(dbsf)] building block and the formation of the final structures. The simplified structures of these five complexes are represented in Scheme 2. In complexes **1**–**5**, the $dbsf^{2-}$ ligand shows two coordination modes (Scheme 1). It adopts a bis(bridging-bidentate) mode (Scheme 1a) in complexes **1** and **2**, and the bis(monodentate) mode (Scheme 1b) in complexes **3**–**5**. In complex **1**, V-shaped building blocks [Cu(dbsf)] are joined to form 1D double-chains. While in complex **2**, when the bridging auxiliary ligand 4,4′-bpy is introduced, these 1D double-chains are pillared into 2D layers. When terminal auxiliary ligands phen/2,2′-bpy were introduced into the Cu/dbsf system, 0D dimeric complexes **3** and **4** were obtained, in which every two V-shaped building blocks [Cu(dbsf)] encircle to form metallocyclic units in which the terminal ligands phen/2,2′-bpy prevent the structures extending to a higher dimension.

In addition, solvent molecules impact the structure too. It is worth noting that complexes **3** and **5** were obtained from the same reactants in different solvents, they possess very different structures [17]. Complex **3** is composed of dimetal macrocyclic molecules with two V-shaped building blocks of [Cu(dbsf)], while in complex **5**, V-shaped building blocks of [Cu(dbsf)] are linked in a head-to-tail model, and 1D tooth-like chains are organized. This may be attributed to the dissimilar solvent molecules included. In complex **5**, the free isopropanol molecules form hydrogen bonds with the main chain so as to prevent the $dbsf^{2-}$ ligands encircling to form dimer fragments (see Fig. 4c), occupying the voids of the tooth-like chains, and acting as important supports to the shape of the chains.

3.2. Thermal analyses

Thermogravimetric analyses of the complexes **2**–**5** were carried out to examine their thermal stabilities. The observed TG curve reveals that complex **2** looses its lattice water molecules at the first weight loss of 3.0% (calc. 3.8%) from 64 °C to 172 °C. For complex **3**, the TG curve shows that the uncoordinated solvent molecules and coordinated water molecules are lost at the first weight loss, 9.0% (calc. 9.1%) from 109 °C to 201 °C. While for complex **4**, the uncoordinated and coordinated water molecules are lost from 73 °C to 112 °C at the first weight loss of 6.2% (calc. 5.4%). In complex **5**, the first weight loss of 9.9% from 169 °C to 206 °C corresponds to the loss of uncoordinated isopropanol molecules (calc. 9.9%).

The TG curves of the complexes **3** and **5** show that further decomposition starts when the solvent was removed, indicating that the host framework collapses when the solvent is absent.

4. Conclusions

In summary, a series of Cu/dbsf complexes were prepared under hydro/solvothermal conditions. The crystal structures of the title complexes are the first report on metal complexes of 4,4′-dicarboxybiphenyl sulfone. Different structures of complexes **1**–**5** indicate that the V-shaped dicarboxylate ligand $dbsf^{2-}$ has the ability of adjusting its coordination configuration in different reaction systems

intelligently. Complexes **1**–**5** are all built up from V-shaped building blocks [Cu(dbsf)] with diverse auxiliary ligands. Our studies show that the configuration of the building blocks of [Cu(dbsf)] together with the help of auxiliary ligands has a crucial effect on the topology and configuration of the final structures of the Cu(II) complexes. Additionally, the solvent molecule acting as a guest is another notable factor for the arrangement of the 3D supramolecular networks.

5. Supplementary material

CCDC 611527, 611528, 611529, 611530 and 611531 contain the supplementary crystallographic data for **1**, **2**, **3**, **4** and **5**. These data can be obtained free of charge via http://www.ccdc.cam.ac.uk/conts/retrieving.html, or from the Cambridge Crystallographic Data Centre, 12 Union Road, Cambridge CB2 1EZ, UK; fax: (+44) 1223-336-033; or e-mail: deposit@ccdc.cam.ac.uk.

Acknowledgement

This project is supported by National Nature Science Foundation of China (20331010, 20501003).

References

[1] (a) M. Eddaoudi, D.B. Moler, H.L. Li, B.L. Chen, T.M. Reineke, M. O'Keeffe, O.M. Yaghi, Acc. Chem. Res. 34 (2001) 319;
(b) O.M. Yaghi, M. O'Keeffe, N.W. Ockwig, H.K. Chae, M. Eddaoudi, J. Kim, Nature 423 (2003) 705;
(c) L. Carlucci, G. Ciani, D.M. Proserpio, Coord. Chem. Rev. 246 (2003) 247;
(d) M. O'Keeffe, M. Eddaoudi, H. Li, T. Reineke, O.M. Yaghi, J. Solid State Chem. 152 (2000) 3;
(e) K. Biradha, CrystEngComm 5 (2003) 374;
(f) R.J. Hill, D.L. Long, N.R. Champness, P. Hubberstey, M. Schröder, Acc. Chem. Res. 38 (2005) 337.

[2] (a) B.L. Chen, N.W. Ockwig, A.R. Millward, D.S. Contreras, O.M. Yaghi, Angew. Chem., Int. Ed. 44 (2005) 4745;
(b) D.N. Dybtsev, H. Chun, S.H. Yoon, D. Kim, K. Kim, J. Am. Chem. Soc. 126 (2004) 32;
(c) E. Herrero, M.V. Cabanas, J. Alonso, F. Conde, J.M. Gonzalez-Calbet, M. Vallet-Regi, Chem. Mater. 11 (1999) 3521;
(d) B. Gomez-Lor, E. Gutierrez-Puebla, M. Iglesias, M.A. Monge, C. Ruiz-Valero, N. Snejko, Chem. Mater. 17 (2005) 2568;
(e) H. Chun, D.N. Dybtsev, H. Kim, K. Kim, Chem. Eur. J. 11 (2005) 3521;
(f) P. Lobinger, H. Jarzina, H.W. Roesky, S. Singh, S.S. Kumar, H.-G. Schmidt, M. Noltemeyer, H.C. Freyhardt, Inorg. Chem. 44 (2005) 9192;
(g) R.Q. Zou, H. Sakurai, Q. Xu, Angew. Chem., Int. Ed. 45 (2006) 2542;
(h) K.L. Wong, G.L. Law, Y.Y. Yang, W.T. Wong, Adv. Mater. 18 (2006) 1051;
(i) B.L. Chen, C.D. Liang, J. Yang, D.S. Contreras, Y.L. Clancy, E.B. Lobkovsky, O.M. Yaghi, S. Dai, Angew. Chem., Int. Ed. 45 (2006) 1390.

[3] (a) M. Eddaoudi, J. Kim, N. Rosi, D. Vodak, J. Wachter, M. O'Keeffe, O.M. Yaghi, Science 295 (2002) 469;
(b) A.K. Cheetham, G. Férey, T. Loisean, Angew. Chem., Int. Ed. 38 (1999) 3268.

[4] (a) H.L. Li, M. Eddaoudi, M. O'Keeffe, O.M. Yaghi, Nature 402 (1999) 276;
(b) H. Li, C.E. Davis, T.L. Groy, D.G. Kelley, O.M. Yaghi, J. Am. Chem. Soc. 120 (1998) 2186;
(c) O.M. Yaghi, C.E. Davis, G. Li, H. Li, J. Am. Chem. Soc. 119 (1997) 2861;
(d) T.M. Reineke, M. Eddaoudi, D. Moler, M. O'Keeffe, O.M. Yaghi, J. Am. Chem. Soc. 122 (2000) 4843.

[5] E.Y. Lee, M.P. Suh, Angew. Chem., Int. Ed. 43 (2004) 2798.

[6] (a) M.L. Tong, X.M. Chen, B.H. Ye, S.W. Ng, Inorg. Chem. 37 (1998) 5278;
(b) S.Q. Zang, Y. Su, Y.Z. Li, H.Z. Zhu, Q.J. Meng, Inorg. Chem. 45 (2006) 2972;
(c) L. Pan, M.B. Sander, X.Y. Huang, J. Li, M. Smith, E. Bittner, B. Bockrath, J.K. Johnson, J. Am. Chem. Soc. 126 (2004) 1308.

[7] (a) X.L. Wang, C. Qin, E.B. Wang, Y.G. Li, Z.M. Su, Chem. Commun. (2005) 5450;
(b) X.L. Wang, C. Qin, E.B. Wang, Y.G. Li, Z.M. Su, L. Xu, L. Carlucci, Angew. Chem., Int. Ed. 44 (2005) 5824;
(c) X.L. Wang, C. Qin, E.B. Wang, Z.M. Su, Chem. Eur. J. 12 (2006) 2680;
(d) J. Tao, J.X. Shi, M.L. Tong, X.X. Zhang, X.M. Chen, Inorg. Chem. 40 (2001) 6328;
(e) X.M. Chen, G.F. Liu, Chem. Eur. J. 8 (2002) 4811.

[8] (a) S.R. Batten, R. Robson, Angew. Chem., Int. Ed. 37 (1998) 1460;
(b) J. Kim, B.L. Chen, T.M. Reineke, H.L. Li, M. Eddaoudi, D.B. Moler, M. O'Keeffe, O.M. Yaghi, J. Am. Chem. Soc. 123 (2001) 8239;
(c) S.M. Chen, C.Z. Lu, Q.Z. Zhang, J.H. Liu, X.Y. Wu, Eur. J. Inorg. Chem. (2005) 423;
(d) P.M. Forster, N. Stock, A.K. Cheetham, Angew. Chem., Int. Ed. 44 (2005) 7608;
(e) Y.F. Zhou, B.Y. Lou, D.Q. Yuan, Y.Q. Xu, F.L. Jiang, M.C. Hong, Inorg. Chim. Acta 358 (2005) 3057.

[9] (a) V.S.S. Kumar, F.C. Pigge, N.P. Rath, New J. Chem. 28 (2004) 1192;
(b) A.J. Blake, N.R. Brooks, N.R. Champness, M. Crew, A. Deveson, D. Fenske, D.H. Gregory, L.R. Hanton, P. Hubberstey, M. Schröder, Chem. Commun. (2001) 1432;
(c) Y.J. Qi, Y.H. Wang, C.W. Hu, M.H. Cao, L. Mao, E.B. Wang, Inorg. Chem. 42 (2003) 8519.

[10] (a) X.L. Wang, C. Qin, E.B. Wang, Z.M. Su, L. Xu, S.R. Batten, Chem. Commun. (2005) 4789;
(b) B. Chen, F.R. Fronczek, B.H. Courtney, F. Zapata, Cryst. Growth Des. 6 (2006) 825;
(c) C.A. Williams, A.J. Blake, P. Hubberstey, M. Schröder, Chem. Commun. (2005) 5435.

[11] (a) Z.H. Zhou, J.M. Yang, H.L. Wan, Cryst. Growth Des. 5 (2005) 1825;
(b) S.L. Childs, L.J. Chyall, J.T. Dunlap, V.N. Smolenskaya, B.C. Stahly, G.P. Stahly, J. Am. Chem. Soc. 126 (2004) 13335;
(c) P. Vishweshwar, A. Nangia, V.M. Lynch, Cryst. Growth Des. 3 (2003) 783;
(d) C. Livage, C. Egger, G. Ferey, Chem. Mater. 11 (1999) 1546;
(e) A. Dimos, D. Tsaousis, A. Michaelides, S. Skoulika, S. Golhen, L. Ouahab, C. Didierjean, A. Aubry, Chem. Mater. 14 (2002) 2616;
(f) D.T. de Lill, N.S. Gunning, C.L. Cahill, Inorg. Chem. 44 (2005) 258;
(g) L.A. Borkowski, C.L. Cahill, Inorg. Chem. 42 (2003) 7041.

[12] G.M. Sheldrick, SADABS: A Program for Empirical Absorption Correction of Area detector Data, University of Göttingen, Göttingen, Germany, 1997.

[13] G.M. Sheldrick, SHELXS 97: Program for Crystal Structure Solution, University of Göttingen, Göttingen, Germany, 1997.
[14] G.M. Sheldrick, SHELXL 97: Program for Crystal Structure Refinement, University of Göttingen, Göttingen, Germany, 1997.
[15] (a) D.M.L. Goodgame, S. Menzer, A.M. Smith, D.J. Williams, Angew. Chem., Int. Ed. 34 (1995) 574;
(b) J.L. Sagué, K.M. Fromm, Cryst. Growth Des. 6 (2006) 1566.
[16] L.J. Barbour, Chem. Commun. (2006) 1163.
[17] (a) E. Tynan, P. Jensen, P.E. Kruger, A.C. Lees, Chem. Commun. (2004) 776;
(b) E. Tynan, P. Jensen, N.R. Kelly, P.E. Kruger, A.C. Lees, B. Moubaraki, K.S. Murray, J. Chem. Soc., Dalton Trans. (2004) 3440;
(c) E. Tynan, P. Jensen, A.C. Lees, B. Moubaraki, K.S. Murray, P.E. Kruger, CrystEngComm 7 (2005) 90.

structural novelty has resulted in the synthesis of a series of compounds with NiP_nX (X = halogens or N or C or S) chromophores. Dithiocarbamates have proven to be versatile metal chelates and in particular nickel(II) dithiocarbamates with a planar NiS_4 chromophore are found to show interesting variations in reactivity towards soft Lewis bases such as phosphines and hard bases such as nitrogenous ligands. As a continuation of our interest [5,6] in exploring the synthetic and structural chemistry of transition metal dithiocarbamates and to understand the influence of phosphines and nitrogenous ligands on the NiS_2PX (X = C or N or P) chromophore and on the S_2–C N< bond we investigated the following compounds: [Ni(4-mpzdtc)-(PPh_3)(NCS)] (**1**), [Ni(4-mpzdtc)(PPh_3)(CN)] (**2**), [Ni-(4-mpzdtc)(PPh_3)$_2$]$ClO_4 \cdot H_2O$ (**3**) and [Ni(4-mpzdtc)-(dppe)]ClO_4 (**4**), where 4-mpzdtc = 4-methylpiperazinecarbodithioato anion, PPh_3 = triphenylphosphine and dppe = 1,2-bis((diphenylphosphino)ethane). In this paper, we report the synthesis, spectral and electrochemical properties of the compounds **1**–**4** along with the single crystal X-ray structures of **1** and **3** which crystallized out as single crystals.

2. Experimental

All the reagents and solvents employed were commercially available analytical grade materials and were used as supplied, without further purification. IR spectra were recorded on an ABB Bomem MB 104 spectrophotometer (range 4000–400 cm^{-1}) as KBr pellets. The UV–Vis spectra were recorded in CH_2Cl_2 on a HITACHI U-2001 spectrophotometer. Cyclic voltammetric studies were carried out using an ECDA-001, Basic Electrochemistry system. A three-electrode configuration was used, comprising of glassy carbon as the working electrode, a platinum wire as the counter electrode and Ag|AgCl as the reference electrode. Experiments were carried out at room temperature using 0.01 M tetrabutylammonium perchlorate as the supporting electrolyte under a nitrogen atmosphere. NMR spectra were recorded on a Bruker 400 MHz spectrometer at room temperature, using $CDCl_3$ as solvent. ^{13}C NMR spectra were recorded in the proton decoupled mode.

2.1. Preparation of the complexes

2.1.1. Bis(4-methylpiperazinecarbodithioato) nickel(II)

2.1.1.1. [Ni(4-mpzdtc)$_2$]. A mixture of 1-methylpiperazine (100 mg, 1 mmol) and CS_2 (76 mg, 1 mmol) in ethanol (50 mL) was kept under ice cold conditions (−5 °C) for 10 min and to this pale yellow solution $NiCl_2 \cdot 6H_2O$ (120 mg, 0.5 mmol) in water (25 mL) was added slowly with vigorous stirring. The dark green precipitate obtained was filtered, washed with ether and water. It was kept for evaporation and dried over anhydrous calcium chloride (Yield: 95%, dec.: >250 °C).

2.1.2. (4-Methylpiperazinecarbodithioato)(thiocyanato-N)-(triphenylphosphine) nickel(II)

*2.1.2.1. [Ni(4-mpzdtc)(PPh_3)(NCS)] (**1**).* A mixture of Ni(4-mpzdtc)$_2$ (205 mg, 0.5 mmol), PPh_3 (260 mg, 1 mmol), $NiCl_2 \cdot 6H_2O$ (120 mg, 0.5 mmol) and NH_4SCN (75 mg, 1 mmol) was refluxed for 3 h in an acetonitrile–methanol solvent mixture (2:1, 75 cm^3) and was then concentrated to ca. 25 cm^3. The dark purple-red solution obtained was filtered and was kept for evaporation. After 2 days, a solid separated out, was filtered, and then dried over anhydrous calcium chloride. Single crystals suitable for X-ray analysis were obtained by recrystallization from the same solvent mixture (Yield: 75%, dec.: 189 °C). *Anal.* Calc. for $C_{25}H_{26}N_3NiPS_3$: C, 54.16; H, 4.72; N, 7.58. Found: C, 54.01; H, 4.59; N, 7.44%.

2.1.3. (Cyano)(4-methylpiperazinecarbodithioato)-(triphenylphosphine) nickel(II)

*2.1.3.1. [Ni(4-mpzdtc)(PPh_3)(CN)] (**2**).* A mixture of Ni(4-mpzdtc)$_2$ (205 mg, 0.5 mmol), PPh_3 (260 mg, 1 mmol), $NiCl_2 \cdot 6H_2O$ (120 mg, 0.5 mmol) and KCN (65 mg, 1 mmol) was refluxed for 3 h in an acetonitrile–methanol solvent mixture (2:1, 75 cm^3) and then concentrated to ca. 25 cm^3. The pale orange-red solution obtained was filtered and kept for evaporation. After 2 days, an orange-red solid separated out. It was dried over anhydrous calcium chloride and recrystallized from the same solvent mixture (Yield: 65%, dec.: 180 °C). *Anal.* Calc. for $C_{25}H_{26}N_3NiPS_2$: C, 57.49; H, 5.01; N, 8.04. Found: C, 57.38; H, 4.90; N, 7.94%.

2.1.4. Bis(triphenylphosphine)(4-methylpiperazine-carbodithioato)nickel(II) perchlorate monohydrate

*2.1.4.1. [Ni(4-mpzdtc)(PPh_3)$_2$]$ClO_4 \cdot H_2O$ (**3**).* A mixture of Ni(4-mpzdtc)$_2$ (205 mg, 0.5 mmo1), PPh_3 (520 mg, 2 mmol), $NiCl_2 \cdot 6H_2O$ (120 mg, 0.5 mmol) and NH_4ClO_4 (115 mg, 1 mmol) was refluxed for about 2 h in a methanol–dichloromethane solvent mixture (1:1, 50 cm^3), and then concentrated to ca. 25 cm^3. The purple-red solution obtained was filtered and left for evaporation. The separated solid was filtered and dried, and single crystals suitable for X-ray analysis were obtained by repeated recrystallization from the same solvent mixture (Yield: 65%, dec.: 183 °C). *Anal.* Calc. for $C_{42}H_{43}ClN_2NiO_5P_2S_2$: C, 57.58; H, 4.94; N, 3.19. Found: C, 57.42; H, 4.84; N, 3.10%.

2.1.5. 1,2-Bis((diphenylphosphino)ethane)(4-methyl-piperazinecarbodithioato) nickel(II) perchlorate

*2.1.5.1. [Ni(4-mpzdtc)(dppe)]ClO_4 (**4**).* A mixture of Ni(4-mpzdtc)$_2$ (410 mg, 1 mmol), dppe (790 mg, 2 mmol), $NiCl_2 \cdot 6H_2O$ (240 mg, 1 mmol) and NH_4ClO_4 (230 mg, 2 mmol) was refluxed for about 4 h in a methanol-dichloromethane solvent mixture (1:1, 50 cm^3). The solution was then concentrated to ca. 25 cm^3. The purple-red solution obtained was filtered and kept for evaporation. After 2 days, a purple-red solid separated out and it was recrystallized from the same solvent mixture (Yield: 65%,

Table 1
Crystal data, data collection and refinement parameters for **1** and **3**

Complex	**1**	**3**
Empirical formula	$C_{25}H_{26}N_3NiPS_3$	$C_{84}H_{86}Cl_2N_4Ni_2O_{10}P_4S_4$
FW	554.3	1752.0
Crystal dimensions (mm)	$0.19 \times 0.23 \times 0.24$	$0.22 \times 0.25 \times 0.29$
Crystal system	monoclinic	monoclinic
Colour	purple red	orange red
Habit	needle	column, irregular
Space group	$P2_1/c$	$P2_1/c$
a (Å)	7.86(2)	31.819(3)
b (Å)	31.011(3)	11.323(3)
c (Å)	11.033(2)	24.464(3)
α (°)	90	90
β (°)	90.31 (2)	105.31(3)
γ (°)	90	90
U (Å^3)	2689(7)	8501(3)
Z	4	8
D_c (g cm^{-3})	1.290	1.367
μ (cm^{-1})	9.53	7.38
$F(000)$	1088	3640
λ (Å)	Mo Kα (0.71073)	Mo Kα (0.71069)
θ Range (°)	1.31–27.53	3.03–28.01
Scan type	ω–2θ	ω–2θ
Index ranges	$-3 \leqslant h \leqslant 3, -40 \leqslant k \leqslant 40, -1 \leqslant l \leqslant 14$	$0 \leqslant h \leqslant 42, 0 \leqslant k \leqslant 14, -32 \leqslant l \leqslant 31$
Reflections collected	2649	20311
Observed reflections $F_o > 4\sigma(F_o)$	1474	6357
Weighting scheme	$W = 1/[\sigma^2(F_o^2) + (0.0470P)^2 + 0.00P]$, where $P = (F_o^2 + 2F_c^2)/3$	$W = 1/[\sigma^2(F_o^2) + (0.0051P)^2 + 0.00P]$, where $P = (F_o^2 + 2F_c^2)/3$
Number of parameters refined	402	1355
Final R, R_w (observed, data)	0.0354, 0.1033	0.0660, 0.0598
Goodness-of-fit	1.009	0.877

Table 2
Selected bond distances and bond angles for **1** and **3**

1		**3**	
Bond distances			
Ni(1)–N(31)	1.859(6)	Ni(1A)–S(2A)	2.1937(15)
Ni(1)–S(2)	2.1809(19)	Ni(1A)–P(11A)	2.2149(16)
Ni(1)–P(12)	2.207(3)	Ni(1A)–P(30A)	2.2333(16)
Ni(1)–S(3)	2.213(4)	Ni(1A)–S(1A)	2.2272(16)
S(2)–C(4)	1.714(8)	S(1A)–C(3A)	1.710(5)
S(3)–C(4)	1.706(7)	S(2A)–C(3A)	1.707(5)
C(4)–N(5)	1.316(8)	C(3A)–N(4A)	1.306(5)
N(8)–C(11)	1.477(13)	N(7A)–C(10A)	1.471(8)
N(31)–C(32)	1.152(7)	N(4A)–C(9A)	1.493(6)
C(32)–S(33)	1.619(7)	N(4A)–C(5A)	1.486(6)
Bond angles			
N(31)–Ni(1)–P(12)	92.15(19)	S(2A)–Ni(1A)–P(11A)	91.02(6)
S(2)–Ni(1)–P(12)	97.35(8)	P(11A)–Ni(1A)–P(30A)	99.82(6)
N(31)–Ni(1)–S(3)	92.2(2)	S(2A)–Ni(1A)–S(1A)	78.44(5)
S(2)–Ni(1)–S(3)	78.86(8)	P(30A)–Ni(1A)–S(1A)	90.72(6)
C(4)–S(2)–Ni(1)	86.3(2)	C(3A)–S(1A)–Ni(1A)	85.31(18)
C(4)–S(3)–Ni(1)	85.5(3)	C(3A)–S(2A)–Ni(1A)	86.42(17)
N(5)–C(4)–S(3)	125.3(6)	N(4A)–C(3A)–S(1A)	123.7(4)
N(5)–C(4)–S(2)	125.4(6)	N(4A)–C(3A)–S(2A)	126.5(4)
S(3)–C(4)–S(2)	109.3(4)	S(1A)–C(3A)–S(2A)	109.8(3)
C(32)–N(31)–Ni(1)	168.6(6)	C(3A)–N(4A)–C(9A)	122.5(5)
N(31)–C(32)–S(33)	179.5(9)	C(3A)–N(4A)–C(5A)	124.1(5)

dec.: 193 °C). *Anal.* Calc. for $C_{32}H_{35}ClN_2NiO_4P_2S_2$: C, 52.51; H, 4.82; N, 3.82. Found: C, 52.41; H, 4.70; N, 3.71%.

2.2. X-ray crystallography

Details of the crystal data, data collection and refinement parameters for **1** and **3** are summarized in Table 1. Intensity data were collected at ambient temperature (295 K) on Bruker AXS (with CCD) (for **1**) [7] and Philips PW 1100 (for **3**) diffractometers [8], using graphite monochromated Mo Kα radiation ($\lambda = 0.71073$ Å and 0.71069 Å for **1** and **3**, respectively). All the non-hydrogen atoms were refined anisotropically and all the hydrogen atoms were refined isotropically. The absorption corrections were performed with the method in SHELXTL-NT V5.1 [7] for **1** and with the North, Phillips and Mathews method for **3** [9]. The ORTEP diagram was drawn with the ORTEP-3 program [10]. Selected bond distances and bond angles are given in Table 2.

3. Results and discussion

3.1. Electronic spectra

The d–d transition bands are observed at 483, 465, 483 and 467 nm for complexes **1**, **2**, **3** and **4**, respectively. The

bands are assigned to $d_{z^2}/d_{xy} \rightarrow d_{x^2-y^2}$ transitions [11]. The cyanide ion exerts a larger LFSE and hence the lowest λ_{max} value is associated with **2**. The observed red shift in **2** when compared to similar complexes with a NiS_2PN chromophore [6] is significant.

3.2. IR spectral studies

For complexes **1**, **2**, **3** and **4**, the ν_{C-N} (S_2–C=N<) bands are observed at 1547, 1529, 1534 and 1519 cm^{-1}, respectively. The increase in wavenumber for the mixed ligand complexes compared to that observed for the parent complex [Ni(4-mpzdtc)$_2$] (1503 cm^{-1}) is attributed to the mesomeric drift of electron density towards the nickel atom through the S_2–C=N< bond from the dithiocarbamate. The ν_{C-S} stretching vibrations are observed around 1000 cm^{-1} (**1**–**4**) without any splitting, supporting the bidentate coordination of the dithiocarbamate ligand. The observed stretching frequencies at 2093 cm^{-1} for complex **1** and at 2115 cm^{-1} for complex **2** are attributed to the 'N'-coordinated thiocyanate and 'C'-coordinated cyanide anions, respectively. The intense signals observed in the fingerprint region for complexes **3** and **4** [1095 cm^{-1} for **3** and 1089 cm^{-1} for **4**] are due to the presence of $\nu_{ClO_4^-}$ stretching in both cases.

3.3. Cyclic voltammetric studies

The reduction potential for the parent [Ni(4-mpzdtc)$_2$] complex is observed at −1548 mV. All the mixed ligand complexes showed lower one electron reduction potentials. (−1189, −972 and −754 mV for complexes **1**, **2** and **3** respectively). For the chelating phosphine complex **4**, quasi-reversible reduction potentials are observed at $-998(E_p^c)/-790(E_p^a)$ mV and it is due to the chelating nature of the phosphine, which is not completely delinked from the Ni^I-species formed as a result of the electrochemical reduction. Lower reduction potentials observed for complexes **1**–**3** indicate the ease of electron addition in the mixed ligand complexes and this is because of the presence of PPh_3, NCS^- and CN^- around the nickel atom [5].

3.4. NMR spectral studies

NMR chemical shifts of the synthesized complexes are summarized in Table 3.

3.4.1. ^1H NMR

For all the four mixed ligand complexes (**1**–**4**), the aromatic protons resonate in the region 7.31–7.91 ppm. The α(methylene) protons are greatly deshielded and are observed in the downfield region due to complexation. However, the β-CH_2 and N–CH_3 proton signals are observed closely and the assignments are made on the basis of proton integral values obtained for the corresponding signals. For complex **4**, the signal due to the methylene protons of the chelating phosphine appears at 2.67 ppm.

3.4.2. ^{13}C NMR

For all the four complexes, the N–CH_3 carbon signal is observed around 45.0 ppm and this deshielding is due to the minor deshielding effect of the nearby electronegative nitrogen. The β-CH_2 carbon signals are observed around 53.0 ppm with a small upfield shift of about 3 ppm compared to that of the corresponding carbon signal in *N*-methylpiperazine [56.4 ppm]. Signals due to α-carbons are only slightly deshielded. Aromatic carbon signals are observed in the downfield region of 126.9–137.3 ppm for all the four synthesized complexes. The N–$^{13}CS^-$ and $^{13}CN^-$ carbon signals are observed at 143.9 and ~131 ppm for complexes **1** and **2**, respectively (for complex **2**, the $^{13}CN^-$ signal at 131 ppm, is merged with the aromatic carbon signals). For complex **4**, the methylene carbon present in the chelating phosphine is observed at

Table 3
NMR chemical shifts of the complexes (in ppm)

Compound	NMR	α-CH_2[a]	β-CH_2[a]	δ-CH_3	PPh_x[b]	>N $^{13}CS_2$	S–^{13}C–N^-	$^{13}CN^-$
1	^1H	3.78 (t)	2.46 (t)	2.17 (s)	7.46–7.70 (m)			
	^{13}C	46.6	53.2	45.2	128.8–134.9	202.8	143.9	
	^{31}P				20.5			
2	^1H	3.74 (t)	2.43 (t)	2.30 (s)	7.40–7.81 (m)			
	^{13}C	46.0	53.7	45.5	128.6–134.1	204.2		~131
	^{31}P				22.1			
3	^1H	3.73 (t)	2.63 (t)	2.43 (s)	7.31–7.66 (m)			
	^{13}C	46.3	53.4	45.3	128.8–137.3	199.2		
	^{31}P				30.9			
4	^1H	3.89 (t)	2.63(t)	2.40 (s)	7.52–7.91 (m)[c]			
	^{13}C	46.3	53.3	45.1	126.9–132.8[d]	201.7		
	^{31}P				61.8			

[a] Chemical shifts due to a, e protons.
[b] Where $x = 3$ for **1**, **2** and **3** and 2 for **4**.
[c] The (>P–CH_2–)$_2$ signal is observed at 2.67 ppm.
[d] The (>P–$^{13}CH_2$–)$_2$ signal is observed at 26.4 ppm.

26.4 ppm. Finally, the most important ^{13}C NMR signals of the $S_2-^{13}C{=}N<$ carbons are observed at 202.8, 204.2, 199.2 and 201.7 ppm for complexes **1**, **2**, **3** and **4**, respectively with a very weak intensity characteristic of the quaternary carbon signals. The mesomeric shift of electron density from the dithiocarbamate moiety towards the metal centre contributes to the upfield shift from the normal chemical shift values of $Ni(dtc)_2$ complexes (206–210 ppm) [12]. The $S_2-^{13}C{=}N<$ chemical shifts of the three complexes with PPh_3 follow the order: **3** < **1** < **2**, indicating the influence of PPh_3, NCS and CN, respectively on the mesomeric drift of electron density towards nickel.

3.4.3. ^{31}P NMR

^{31}P chemical shifts are observed at 20.5, 22.1, 30.9 and 61.8 ppm for complexes **1**, **2**, **3** and **4**, respectively. A good extent of deshielding of about 75 ppm is observed for the ^{31}P signal of complex **4**, compared to the free chelating dppe ^{31}P signal observed at −13 ppm [13]. In the case of complexes **1**, **2** and **3** signals are also observed in the deshielded region compared to the free PPh_3 signal at −5 ppm [14]. A very high deshielding of signals observed in all the cases is attributed to the movement of electron density from the phosphorus towards the nickel atom on complexation. The PPh_3 complexes show the following order of increasing ^{31}P chemical shifts: **3** (30.9 ppm) > **2** (22.1 ppm) > **1** (20.5 ppm). The observed order clearly establishes the ease with which the back bonding interaction takes place. The back bonding electron donation is the best in the case of **3**, containing the NiP_2 chromophore.

3.5. Structural analysis

The single crystal X-ray structure of **1** contains four discrete molecules per unit cell. The ORTEP diagram of the molecule is shown in Fig. 1. The observed distortion of the square planar coordination around nickel is attributed to the small bite angle of 78.86(8)°. The planarity is supported by the observed diamagnetism of the complex. Delocalization of π electron density over the S_2CN moiety leads to a decrease in the C–N [S_2–C=N<] distance [1.316(8) Å] and also an increase in the S–C–N angles [125.3(6)° and 125.4(6)°] over the S–C–S angle [109.3(4)°]. The observed difference in Ni–S distances [2.213(4) and 2.1809(19) Å] is attributed to the difference in the *trans* influencing properties of PPh_3 and NCS^-. PPh_3 being a good π acceptor has a greater *trans* influence and hence the Ni–S bond *trans* to PPh_3 is longer than the other Ni–S bond.

The Ni–N distance [1.859(6) Å] is quite short, showing the effective bonding between the nickel atom and the thiocyanate-*N*. The C–N bond distance in N–C–S [1.152(7) Å] is significantly shorter than the S_2–C=N< N–C bond distance of 1.316(8) Å. The C–S bond length in N–C–S is 1.619(7) Å, which is similar to the C=S distance of 1.69 Å. The N–C–S bond is [179.5(9)°] and is almost linear. In the dithiocarbamate part, the piperazine ring is in a sterically favoured chair conformation with the normal C–C and C–N bond lengths. The *N*-methyl group in the terminal position is equatorially oriented to avoid the 1,3-diaxial steric interactions with the axial hydrogens. Phenyl groups in triphenylphosphine show normal bond parameters.

$[Ni(4\text{-mpzdtc})(PPh_3)_2]ClO_4 \cdot H_2O$ is discrete and monomeric. One molecule of water is co-crystallized with the complex. Eight formula units are present in the unit cell. Each asymmetric unit has two molecules and the bond parameters of one molecule are listed. The ORTEP diagram of **3** is shown in Fig. 2. Distortions with respect to the idealized geometry are observed in the coordination angles: the P–Ni–P angle is very large [99.82(6)°] due to steric interactions between two PPh_3 groups, while the S–Ni–S bite angle is low, 78.44(5)° as observed in similar compounds [6]. The observed shortening of the >N–CS_2 C–N distance is in line with the bond parameters observed for $[Ni(dtc)(PPh_3)_2]^+$ (where, dtc = dmdtc or dedtc or pipdtc) complexes [6]. Among the mixed ligand complexes, those

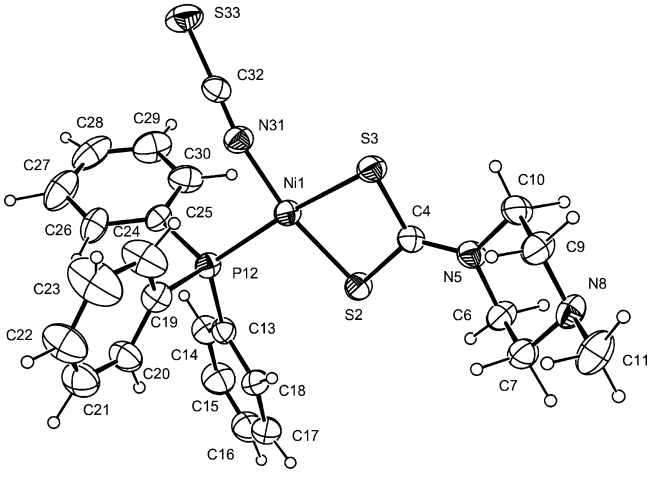


Fig. 1. Thermal ellipsoid plot of $[Ni(4\text{-mpzdtc})(PPh_3)(NCS)]$ (30% probability).

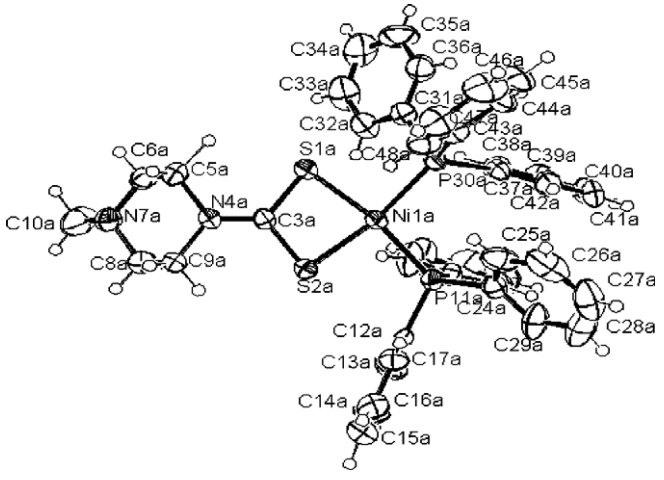


Fig. 2. Thermal ellipsoid plot of $[Ni(4\text{-mpzdtc})(PPh_3)_2]ClO_4 \cdot H_2O$ (30% probability) (H_2O and the ClO_4^- ion are omitted for clarity).

of the NiS_2P_2([Ni(dtc)$(PPh_3)_2]^+$) chromophore show very short S_2–C---N< distances due to the π-acidic nature of the triphenylphosphine. The two S–C–N angles [123.7(4)° and 126.5(4)°] are observed to be larger than the S–C–S angle [109.8(3)°]. Ni–P distances are very similar [2.2333(16) and 2.2149(16) Å]. The two Ni–S and S–C distances are comparable, showing that the negative charge of the bidentate ligand is equally distributed over the two donor atoms. The perchlorate ion shows thermal disorder as reported earlier [5]. The disordered perchlorate ion shows extensive short contacts ranging from 2.5 to 2.9 Å with H atoms of the piperazine ring and similarly with the oxygen atom of the water molecule O1W in the same range. Two hydrogen atoms of the water molecule attached to O2W could not be located in the Fourier map. Also, the disorder associated with ClO_4^- has been modelled such that each oxygen atom is positioned at two coordinate positions of 50% site occupancy at distances of 0.552, 0.336, 0.465, 0.391 Å (for molecule A) and 0.912, 0.815, 0.778, 1.223 Å. (for molecule B). Probable contacts indicating H-bonded interactions in the distance range of 2.4–2.8 Å are observed. Approximately 32 such interactions were noted [15,16]. The very large number of short contacts observed is a result of the modelled oxygen atoms of the perchlorate ion (eight oxygens of 50% site occupancy for every perchlorate ion). The triphenylphosphine and piperazine ring in the dithiocarbamate ligand show normal bond parameters. As observed in complex **1**, the methyl group in the terminal position prefers the equatorial orientation.

Comparison of bond parameters of **1** and **3** indicates a similarity in shortening of the N–CS_2 (N–C) distance for both complexes. The Ni–P distance in the NiS_2PN chromophore [2.207(3) for **1**] is slightly shorter than that of the NiS_2P_2 chromophore [the mean value is 2.2241(16) Å for **3**]. The observed decrease in P–Ni–N angle of about 8° for **1** [92.15(19) versus 99.82(6)] compared to that of the P–Ni–P angle in **3** is due to the decrease in steric crowding around metal centre by the replacement of bulky PPh_3 with NCS^-. The S–C–S and S–Ni–S angles are however similar.

Appendix A. Supplementary material

CCDC 263874 and 263875 contain the supplementary crystallographic data for **1** and **3**. These data can be obtained free of charge via http://www.ccdc.cam.ac.uk/conts/retrieving.html, or from the Cambridge Crystallographic Data Centre, 12 Union Road, Cambridge CB2 1EZ, UK; fax: (+44) 1223-336-033; or e-mail: deposit@ccdc.cam.ac.uk. Supplementary data associated with this article can be found, in the online version, at doi:10.1016/j.poly.2006.10.006.

References

[1] Y. Nan, Z. Yang, Tetrahed. Lett. 40 (1999) 2323.
[2] J. Sorgl, W. Liu, D. Marshal, Liebshkind, J. Am. Chem. Soc. 121 (1999) 9449.
[3] T. Sombaih, D. Huang, J. Lin, D. Rayabarajac, K. Cheng, J. Org. Chem. 64 (1999) 3663.
[4] P.S. Jarrett, O.M.N. Dhubhghaill, P.J. Sadler, J. Chem. Soc., Dalton Trans. (1993) 1863.
[5] K. Ramalingam, G. Aravamudan, M. Seshasayee, Inorg. Chim. Acta 128 (1987) 231.
[6] B. Arul Prakasam, K. Ramalingam, G. Bocelli, R. Olla, Z. Anorg. Allg. Chem. 630 (2004) 301.
[7] Bruker Axs Inc., 6300 Enterprise Lane, Madison, WI 53719-1173, USA.
[8] D. Belletti, New hardware and software systems for controlling a Philips PW1100 single crystal diffractometer, Parma, Italy, Internal report (1996) 1.
[9] A.C.T. North, D.C. Phillips, F.S. Mathews, Acta Crystallogr., Sect. A 24 (1968) 351.
[10] L.J. Farrugia, ORTEP-3 for Windows, University of Glasgow, Scotland, UK, 1999.
[11] M.V. Rajasekaran, G.V.R. Chandramouli, P.T. Manoharan, Chem. Phys. Lett. 162 (1989) 110.
[12] H.L.M. Van Gaal, J.W. Diesveld, F.W. Pijpers, J.G.M. Van Der Lindon, Inorg. Chem. 18 (1979) 3251.
[13] E.P. Garrou, Chem. Rev. 81 (1981) 229.
[14] R.M. Silverstein, F.X. Webster, Spectrometric Identification of Organic Compounds, 6th ed., Wiley, New York, 1998, p. 55, 226, 294.
[15] G.A. Jeffrey, L. Lewis, Carbohydr. Res. 60 (1978) 179.
[16] R. Taylor, O. Kennard, Acta Crystallogr., Sect. B 39 (1983) 133.

macrocyclic cavity and periphery can be chosen independently, thus giving rise to physical properties not seen in the phthalocyanine or metal fragment alone. Using these strategies, so far many novel substituted phthalocyanines have been synthesized [18–22]. The family of reactive phthalocyanine molecules has been an interesting target for the development of further chemical reactions with the phthalocyanine complexes [11,23]. Designed peripheral moieties on the phthalocyanines bearing heteroatoms (N, O, S) are used to bind an exocyclic metal ion, design desired geometries and confer solubility [7,11,13,14,17]. These functionally designed phthalocyanines/porphyrazines perturb pc optical transitions by shifting the absorption from the visible to near-IR or UV-region. For example, phthalocyanines bearing the thia functionality show optical changes when they bind transition metal ions, while phthalocyanines bearing a crown ether are well suited to binding alkaline and alkaline-earth metal ions [11–14,24].

In our previous studies, we have synthesized and characterized octasubstituted ionophore metallophthalocyanines bearing reactive propane 1,2-diolsulfanyl and water-soluble metalloporphyrazines with peripherally functionalized bis [thioethoxy (ethoxy)ethanol] moieties. To increase the solubility in polar solvents and the polarity to bind a metal ion peripherally, in this paper we report the preparation, optical, electrochemical and specific cation binding properties of the functional receptor phthalocyanines having a peripheral thiohexylalcohol functionality, $\{M[Pc(S–C_6H_{13}OH)_4]\}$ (M = Zn(II), Cu(II), Co(II)). To extend the application of the complexes we have also investigated the electrochemical properties of the designed complexes.

2. Experimental

2.1. Materials and equipment

$Zn(O_2CMe)_2$, $CuCl_2$ and $CoCl_2$ were purchased from Aldrich and Alfa Aesar and were used as received. 4-Nitro phthalonitrile was prepared according to the literature procedure [25]. All other reagents were obtained from Merck, Aldrich, Fluka, and Alfa Aesar, Chemical Co. and were used without purification. All reactions were carried out under a dry nitrogen atmosphere. ^1H NMR and ^{13}C NMR spectra were recorded on Bruker 300 spectrometer instruments. Multiplities are given as s (singlet), d (doublet), t (triplet) and m (multiplet). FTIR (Thin Solution Film) were recorded on anATI UNICOM-Mattson 1000 Spectrophotometer. Elemental analysis (C, H, N and S) was performed at the Instrumental Analysis Laboratory of Marmara University. Routine UV–Vis spectra were obtained in a quartz cuvette on a Unicom UV-2 spectrometer. Chromatography was performed with silica gel (Merck grade 60 and sephadex) from Aldrich. The homogenities of the products were tested in each step by TLC (SiO_2, $CHCl_3$ and MeOH).

2.2. Electrochemical method

The cyclic voltammetry (CV), differential pulse voltammetry (DPV) and controlled potential chronocoulometry (CPC) measurements were carried out with a Princeton Applied Research Model VersaStat II potentiostat/galvanostat controlled by an external PC and utilizing a three-electrode configuration at 25 °C. The working electrode was a Pt plate with a surface area of 0.10 cm^2. The surface of the working electrode was polished with a H_2O suspension of Al_2O_3 before each run. The last polishing was done with a particle size of 50 nm. A Pt wire served as the counter electrode. A saturated calomel electrode (SCE) was employed as the reference electrode and separated from the bulk of the solution by a double bridge. Ferrocene was used as an internal reference. Electrochemical grade tetrabutylammonium perchlorate (TBAP) in extra pure dimethylsulfoxide (DMSO) was employed as the supporting electrolyte at a concentration of 0.10 mol dm^{-3}. High purity N_2 was used for deaeration for at least 15 min prior to each run and to maintain a nitrogen blanket during the measurements. During voltammetric measurements, the reference electrode tip was moved as close as possible to the working electrode so that uncompensated resistance of the solution was a smaller fraction of the total resistance, and therefore the potential control error was low. IR compensation was also applied to the CV scans to further minimize the potential control error.

For controlled potential chronocoulometric (CPC) studies, a Pt gauze working electrode (10.5 cm^2 surface area), a Pt wire counter electrode separated by a glass bridge and a SCE reference electrode separated by a glass bridge were used.

2.3. MALDI sample preparation and MALDI mass spectrometry

3-Indole acrylic acid (IAA) (20 mg/mL in acetonitrile) and α-cyano-4-hydroxy cinnamic acid (ACCA) (15 mg/mL 1:1 water–acetonitrile) MALDI matrices for **2**, **3** and **4** were prepared. MALDI samples were prepared by mixing complexes (2 mg/mL in acetonitrile) with the matrix solution (1:10 v/v) in a 0.5 mL eppendorf® micro tube. Finally, 1 μL of this mixture was deposited on the sample plate, dried at room temperature and then analyzed. Mass spectra were acquired on a Voyager-DE™ PRO MALDI-TOF mass spectrometer (Applied Biosystems, USA) equipped with a nitrogen UV-Laser operating at 337 nm. Spectra were recorded in the reflectron mode with average of 50 shots.

2.4. Synthesis

2.4.1. 4′-(6-Hydroxyhexylsulfanyl)-1,2-dicyanobenzene (*1*)

6-Mercapto-1-hexanol (0.77 g, 5.78 mmol) and 4-nitrophthalonitrile (1.00 g, 5.78 mmol) were dissolved in dry DMF and heated at 40 °C in N_2 atmosphere for 1 h.

Then finely ground anhydrous potassium carbonate (~1.20 g, 8.67 mmol) was added portionwise to the mixture over 0.5 h. The reaction mixture was stirred efficiently under nitrogen at 40–45 °C for 3 days. After the reaction mixture was cooled to room temperature it was poured into ca. 200 cm^3 ice-water. The creamy precipitate thus formed was filtered and washed with water until the washings became neutral. The crude product was dissolved in chloroform and washed with 5% $NaHCO_3$ to remove starting unreacted compounds. The creamy solution was then dried with anhydrous Na_2SO_4, and filtered. The solvent, chloroform, was removed under reduced pressure giving a creamy powder. It was chromatographed over a silica gel column using a mixture of $CHCl_3$:MeOH (10/1) as eluent, giving a hydroscopic solid, 4′-(6-hydroxyhexylsulfanyl)-1,2-dicyanobenzene (**1**). Finally, the pure powder was dried in a vacuum. Yield: 0.93 g (61.89%); m.p.: 74 °C, IR (thin film) ν/cm^{-1}: 2233 (–CN), 3342 (CH_2–OH), 3104, 3023 (Ar–H), 2929, 2888, 2859 (Aliph-CH_2) 1710 (H–O···H, weak), 1581 (st), 1544, 1473, 1390, 1286, 1191, 1128, 1072, 983, 873, 831, 719, 572; ^{1}H NMR ([d_6]-DMSO) J/Hz, δ/ppm: 7.78 (dd, $^3J = 7.5$, 1H, *ortho* to SR, phenyl H5) 7.67 (1H, *ortho* to CN and SR, phenyl H3), 7.60 (dd, $^3J = 7.0$, 1H, *ortho* to SR and Ar–H, phenyl H6), 4.19 (t, q, –CH_2–OH, D_2O exchangeable), 3.57 (t, 2H, –CH_2OH), 3.00 (CH_2–CH_2–S–), 1.65 (m, 2H, CH_2–S–Ar), 1.50 (m, 2H, $CH_2CH_2CH_2$–OH), 1.40 (m, 2$x$$CH_2CH_2CH_2$); ^{13}C NMR ([300 MHz, d_6]-DMSO + $CDCl_3$) δ/ppm: 147.81, 133.73, 130.43, 130.35, 116.20, 116.20, 115.95, 115.75, 110.30, 78.23 ($CDCl_3$), 61.68 (–CH_2OH), 40.44 (DMSO), 32.77 (S–CH_2), 31.63 (CH_2CH_2OH), 28.72 (SCH_2CH_2), 28.30 ($SCH_2CH_2CH_2$), 25.57 ($CH_2CH_2CH_2CH_2$OH). *Anal.* Calc. for $C_{14}H_{16}N_2OS$ (%): C, 64.62; H, 6.15; N, 10.77. Found: C, 64.04; H, 6.05; N, 10.28%. MS (ESI-MS): m/z: 261.1 $[M+H]^+$ (45%), 278.1 $[M+H_2O]^+$ (10%), 284.1 $[M+Na]^+$ (20%).

2.4.2. 2,9,16,23-Tetrakis(6-hydroxyhexylsulfanyl)phthalocyaninatozinc(II) (**2**)

A mixture of **1** (0.25 g, 0.96 mmol), anhydrous $Zn(O_2CMe)_2$ (0.04 g, 0.24 mmol) and DBU (0.05 cm^3) in a sealed tube was pulverized and transferred to a sealed tube and heated with efficient stirring at 170 °C for 8 h under a nitrogen atmosphere. The deep green-blue product was cooled to room temperature, and solid was washed successively with CH_3CN, *i*-PrOH, and HAc, to remove any inorganic and organic impurities, until the filtrate was clear. The green-blue product was isolated by silica gel column chromatography with THF–MeOH (50/1 v/v) as eluent. Pure **2** was obtained as a viscous yellow oil following column chromatography over sephadex (1/20 (v/v) $CH_3OH/CHCl_3$, eluent) and then dried in a vacuum. Complex **2** is soluble in THF, MeOH, DMF, DMSO, DMAA and pyridine. Yield: 0.087 g (32.80%). *Anal.* Calc. for $C_{56}H_{64}N_8O_4S_4Zn$ (1105 g/mol): C, 60.81; H, 5.79; N, 10.14. Found: C, 60.08; H, 5.80; N, 9.77%. IR (thin film) ν/cm^{-1}: 3640 (free OH, w), 3287 (br, H-bonded), 2927, 2855, 1737 (H–O···H, weak), 1612 (w), 1597, 1484, 1433, 1365, 1303, 1229, 1217, 1138, 1069, 1034, 909, 814,759,742. ^{1}H NMR ([d_6]-DMSO) J/Hz δ/ppm: 7.83 (broad, 1H, *ortho* to SR, $^3J = 7.0$, phenyl H5) 7.82 (s, isomer, 1H, *ortho* to CN and SR, $^3J = 7.2$, phenyl H3), 7.61(dd, 1H, *ortho* to SR and Ar–H, $^3J = 7.0$, phenyl H6), 4.22 (s, t, br, –CH_2–OH, D_2O exchangable), 3.59 (t, 2H, –CH_2OH), 3.01 (CH_2–S–), 1.65 (m, 2H, CH_2–S–Ar), 1.47 (m, 2H, $CH_2CH_2CH_2$–OH), 1.40 (m, 2$x$$CH_2$-$CH_2CH_2$). UV–Vis (THF), λ_{max}/nm: 681 (6.00), 615 (1.22), 582 (sh, 0.57), 345 (5.7); MS (Maldi-TOF, α-cyano-4-hydroxy cinnamic acid (CHCA) as matrix): m/z (100%): 1105.20 $[M+H]^+$, 1149.20 $[M-H+2Na]^+$, 1189.20 $[M-2H+3Na+H_2O]^+$, 1151.20 $[M+2Na]^+$, 1192 $[M+3Na+H_2O]^+$, 1129.20 $[M-3H+4Na+2H_2O]^+$.

2.4.3. 2,9,16,23-Tetrakis(6-hydroxyhexylsulfanyl)phthalocyaninatocopper(II) (**3**)

4′-(6-Hydroxyhexylsulfanyl)-1,2-dicyanobenzene (**1**) (0.25 g, 0.96 mmol), anhydrous copper (II) chloride (0.03 g, 0.24 mmol) and dbu (0.05 cm^3) in 1-hexanol (~1 cm^3) were heated to reflux in a sealed tube under N_2 for 8 h. The green-blue mixture was cooled to room temperature after which the mixture was diluted with petroleum ether. The crude precipitate was washed several times successively with first *i*-PrOH, CH_3CN and then HAc to remove any organic and inorganic impurities. Finally, the product was redissolved in $MeOH/CHCl_3$ and further purified by silica gel chromatography (eluent: $MeOH/CHCl_3$ (10/100)) and sephadex (10/100 $MeOH/CHCl_3$). After washing the resulting oily product with copious amounts of hexane, diethylether and finally *i*-PrOH, it was then dried in a vacuum. This product is moderately soluble in MeOH and THF, and soluble in DMF, DMSO and pyridine. Yield: 0.06 g (24.16%). *Anal.* Calc. for $C_{56}H_{64}N_8O_4S_4Cu$ (1103.5 g/mol): C, 60.90; H, 5.80; N, 10.15. Found: C, 60.69; H, 5.77; N, 9.58%. IR (thin film) ν/cm^{-1}: 3638 (free OH, w), 3250 (H-bonded, OH), 3010, 2973, 2951, 2856, 1732 (H–O···H, weak), 1657 (w), 1598, 1433 (w), 1364 (st), 1364, 1310, 1229, 1217, 1137, 1118, 1034, 910, 887, 873, 811, 742, 687; UV–Vis (THF), λ_{max}/nm: 684 (15.70), 622 (3.76), 582 (1.18), 351 (9.80); MS (Maldi-TOF, CHCA as matrix): m/z (100%): 1103.20 $[M+H]^+$, 1187 $[M-2H+3Na+H_2O]^+$, 1227 $[M-3H+4Na+2H_2O]^+$, 1267 $[M-4H+5Na+3H_2O]^+$.

2.4.4. 2,9,16,23-Tetrakis(6-hydroxyhexylsulfanyl)phthalocyaninatocobalt(II) (**4**)

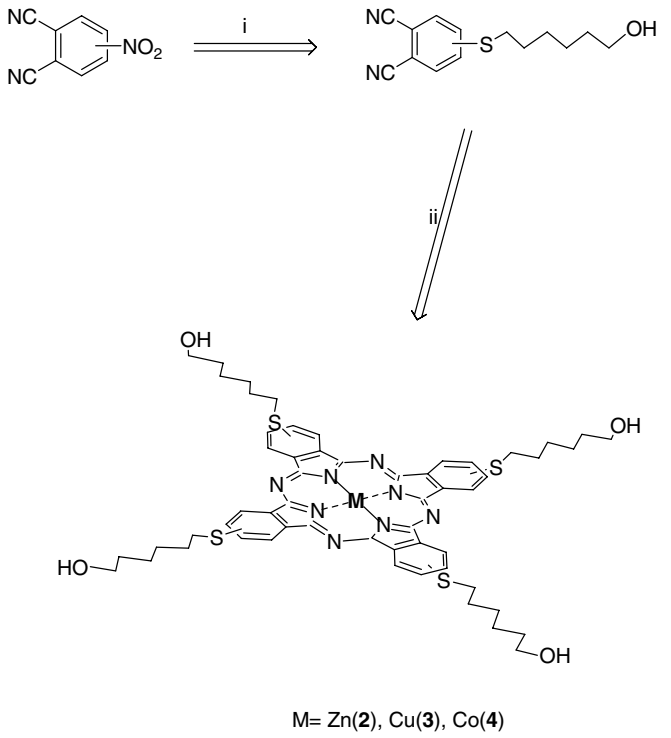
Compound **1** (0.25 g, 0.96 mmol), anhydrous $CoCl_2$ (left overnight in an oven at 110 °C) (0.03 g, 0.24 mmol) and DBU (0.05 cm^3) were pulverized and transferred to a tube and sealed under nitrogen atmosphere. The temperature of the reaction mixture was raised to 150–160 °C and kept at this value for 12 h. After cooling to room temperature and diluting with *i*-PrOH, the reaction mixture was filtered. The dark green-blue crude product

formed during the reaction was treated with *i*-PrOH several times and filtered off. It was then successively washed with H_2O, acetonitrile and dried. It was further purified by column chromatography (flash column) with silica gel ($CHCl_3$/MeOH as eluent, (5/100)) and dried in a vacuum. Blue star phthalocyanine (**4**) is slightly soluble in 2-propanol and acetonitrile, and well soluble in THF, MeOH, EtOH, DMF and DMSO. Yield: 0.07 g (27.30%). *Anal.* Calc. for $C_{56}H_{64}N_8O_4S_4Co$ (1099 g/mol): C, 61.15; H, 5.82; N, 10.19. Found: C, 60.56; H, 5.56; N, 9.59%. IR (KBr thin film) ν/cm^{-1}: 3639 (free OH), 3243 (H-bonded, OH), 3017, 2976, 2927, 2856, 1727 (H–O···H, weak), 1603 (w), 1505, 1432 (w), 1364 (st), 1314, 1229, 1216, 1141, 1105, 1040, 931, 873, 781, 750, 740, 690. UV–Vis (THF), λ_{max}/nm: 678 (12.08), 628 (6.34), 334 (16.11); MS (MALDI-TOF, CHCA as matrix): *m*/*z* (100%): 1099 $[M+H]^+$, 1117 $[M+H+H_2O]^+$.

3. Result and discussion

3.1. Synthesis and characterization

The synthesis of the metallophthalocyanines (**2**–**4**) required the preparation of the key phthalonitrile precursor (**1**) (Scheme 1). We used nucleophilic aromatic displacement of the nitro group of 4-nitrophthalonitrile [25] with the –SH functional site of 6-mercapto-hexanol, which is more preferable than –OH nucleophiles, to afford compound **1**, 4′-(6-hydroxyhexylsulfanyl)-1,2-dicyanobenzene,



Scheme 1. Synthetic route of 2,9,16,23-tetrakis(6-hydroxyhexylsulfanyl)-phthalocyanine M[Pc(S–$C_6H_{13}OH)_4$] (M = Zn(II), Cu(II), Co(II)). (i) K_2CO_3, 6-mercapto-1-hexanol, DMF, 40 °C, 3 days. (ii) anhydrous $Zn(O_2CMe)_2$, $CuCl_2$, $CoCl_2$, DBU.

in good yield at reflux temperature in THF in the presence of K_2CO_3. Receptor metallophthalocyanines M[Pc-(S–$C_6H_{13}OH)_4$] (M = Zn^{II}, Cu^{II}, Co^{II}) (**2**–**4**) in the present work were obtained from the cyclotetramerization reaction of **1** with the corresponding appropriate anhydrous metal salt in the presence of hexanol and 1,8-diazabicyclo [5.4.0] undec-7-ene (DBU) as a strong base (Scheme 1), followed by chromatographic purification on silica gel and size exclusion columns. The green-blue cyclotetramerization products (**2**–**4**), were isolated as a mixture of isomers and purified by column chromatography in workable yields (32.80% for **2**, 24.16% for **3**, and 27.30% for **4**). Purification steps were tedious because of peripheral polar reactive end-groups. The peripheral OH– and sulfur donor atom have a profound influence on physical and chemical properties of the phthalocyanine macrocycle. The four polar peripheral groups confer good solubility on these macromolecules in polar media such as MeOH, THF, DMF, DMSO and DMAE.

3.2. Spectroscopic characterization

The characterization of each phthalocyanine was carried out by FTIR, ^{1}H NMR (except **3** and **4**), UV–Vis and MALDI-MS spectroscopic methods, as well as by elemental analysis. All the analytical and spectral data are consistent with the predicted structures.

In the IR spectra of **2**, **3** and **4**, the major strong –CN band at 2233 cm^{-1} belonging to **1** disappeared after conversion to the metallophthalocyanines (**2**–**4**). A very weak band in all phthalocyanines above 3000 cm^{-1} is due to the aromatic C–H stretchings. In the IR spectra of all the phthalocyanines, the most intense bands of the spectra are the absorption at ca. 2930 and 2855–2860 cm^{-1} due to the C–H stretching vibrations of the $-CH_2$ groups for the 1-hydroxyhexyl moieties. Primary aliphatic –OH peaks at around 3240 and 3640 cm^{-1} (free (w) and H-bonded OH) and the rest of the spectra are closely similar to that of former one's and are diagnosed easily. The most instinctive indicators for **1** are the signals belonging to the aromatic protons *ortho* to the cyano group in the lower field region of the ^{1}H NMR (DMSO-d_6) and six different aromatic carbon atoms between 110 and 148 ppm in the ^{13}C APT spectrum. As the ^{1}H NMR spectrum of compound **1** was recorded in $CDCl_3$, it showed only broad signals for the substituents, while the aromatic proton signals were not observed. However, in the presence of DMSO-d_6, the aromatic proton signals emerged as relatively broad signals in the downfield region of the spectrum. In compound **1**, bearing substituents in the four-positions, the aromatic protons *ortho* to the cyano group appeared at 7.67 ppm as one slightly broad singlet in the downfield region of the ^{1}H NMR spectrum, in addition to a doublet of doublets at 7.78 and 7.60, while broad deuterium exchangeable –OH protons came out at 3.57 ppm. The ^{1}H NMR spectrum of **2** was almost identical to the starting compound **1** except for small shifts and slight broadening. The broad

signals in **2** are probably due to the chemical exchange associated with aggregation–disaggregation equilibria which occur at the high concentrations used in the NMR measurements or because of it being an isomeric mixture [1]. The substitution of **2**–**4** with 6-mercaptohexanol results in the formation of positional isomers, which causes the splitting of the signals for the peripheral aromatic protons in the downfield of the aromatic region. Slightly broad signals for primary aliphatic –OH exchangeable protons of the phthalocyanines at 3.57 ppm disappeared after addition of D_2O.

UV–Vis spectra of the phthalocyanine complexes (**2**–**4**) exhibited characteristic absorptions in the Q-band region at around 650–700 nm, attributed to the π–π^* transition from the HOMO (highest occupied molecular orbital) to the LUMO (lowest unoccupied molecular orbital) of the Pc^{2-} ring, and in the B band region (UV region) at around 300–400 nm, arising from the deeper π–π^* transitions. In the UV–Vis absorption spectra of all phthalocyanines, the Q-band absorptions were observed as a single band of high intensity at 686, 686 and 674 nm, respectively. There was also a shoulder at the slightly higher energy side of the Q band for each phthalocyanine. In the phthalocyanines bearing sulfanyl substituted moieties on the periphery, the Q band absorption was shifted to the lower energy side as a result of the electron-donating thioether substituents compared to that of phthalocyanines bearing oxa substituted moieties, whereas the position of the soret-like π–π^* bands of all the phthalocyanines was only slightly shifted. Any increase in the concentration results in the aggregation of the phthalocyanine molecules, which is accompanied by a blue shift of the Q-band with a decrease in intensity (ε_{max}). The extent of aggregation is slightly stronger for the phthalocyanines bearing tetrasubstituents on the periphery than that for the octasubstituted ones [13,20,26].

3.3. MALDI-MS spectra

The mass spectra of **2**, **3** and **4** confirmed the proposed structures. The protonated molecular ion peaks were easily identified at *m*/*z*: 1105.20 $[M+H]^+$ for **2**, and *m*/*z*: 1103.20 $[M+H]^+$ for **3**. The protonated molecular ion peak for **4** was observed at 1099 Da which exactly overlapped with the mass of the cobalt complex calculated theoretically from the elemental composition of the complex (Fig. 1). Beside the protonated molecular ion peak of the complex, additional peaks were observed at 1100, 1101, 1102, 1103 and 1104 in the high mass range, representing the isotopic distribution of the metal and carbon. Following the protonated molecular ion peak, a peak group was observed at 18 Da mass higher than the protonated molecular ion peak group, with almost the same pattern. This peak is the result of a water adduct with the protonated ion peak of complex **4**. The MALDI spectra of **2** and **3** showed very clear and low fragmentations in the MALDI-MS.

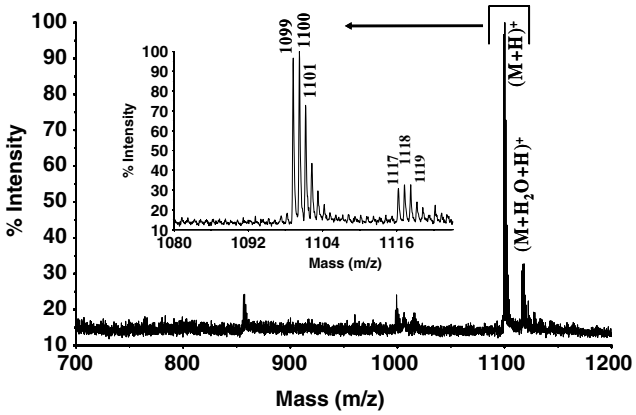


Fig. 1. Positive ion and reflectron mode MALDI-MS spectrum of **4** was obtained in 3-indoleacrylic acid MALDI matrix using nitrogen laser accumulating 50 laser shots. Inset spectrum shows the expanded molecular mass region of the complex.

3.4. Spectroscopic metal ion binding titrations

The sulfur groups on the periphery of the metallophthalocyanine complexes (MPc's) are optically sensitive to soft metal ions, such as Ag^I and Pd^{II}. Therefore, we have employed UV–Vis spectroscopic titrations to monitor the capability of our MPc's for sensing/coordinating transition metal ions of different size. Each titration experiment was carried out using a MeOH/THF solution of MPc's (10/90, v/v) to ensure complete dissolution of the analyte salts, $AgNO_3$, Na_2PdCl_4, $Cd(O_2CMe)_2$ and $Hg(NO_3)_2$ dissolved in MeOH. Here, the concentration of each MPc and the metal salt was ca 10^{-5} and 10^{-3} mol dm^{-3}, respectively. The reason for the higher concentration of the metal salt was to produce negligible changes by dilution after its addition to the phthalocyanine solution. Sulfur donor atoms of 1-hydroxyhexylsulfanyl moieties of **2**–**4** coordinate Ag^I and Pd^{II}, exhibiting optical changes. However, no optical changed were observed when the complexes were titrated with Cd^{II} and Hg^{II}.

The titration of **2**–**4** with Pd^{II} showed similar optical changes, as shown in Fig. 2. The room temperature gradual addition (μl) of Pd^{II} to the solution of **2**–**4** caused a gradual color change, from blue-green to intractable dark-green, suggesting the complex formation of the complexes with Pd^{II}. As shown in Fig. 2, Pd^{II} binding to the donor atoms of the complexes results in pronounced effects in the Q and B-bands, and in the n–π^* transitions (attributed to the non-bonding sulfur electron (n) to the π^* phthalocyanine orbital) [14]. While addition of small increments of Pd^{II} to **2**–**4** leads to a gradual disappearance of the monomeric species, which show absorptions at 686, 686 and 674 nm, simultaneously enhancing the intensity of the oligomeric aggregated species with absorptions around 654, 655 and 640 nm, respectively. B-bands of all the complexes shift to the higher energy side by about 15–20 nm, without change in intensity. As in Fig. 2, the titration shows clear isobestic points at 345, 384, 487, 607, 624, 662 and

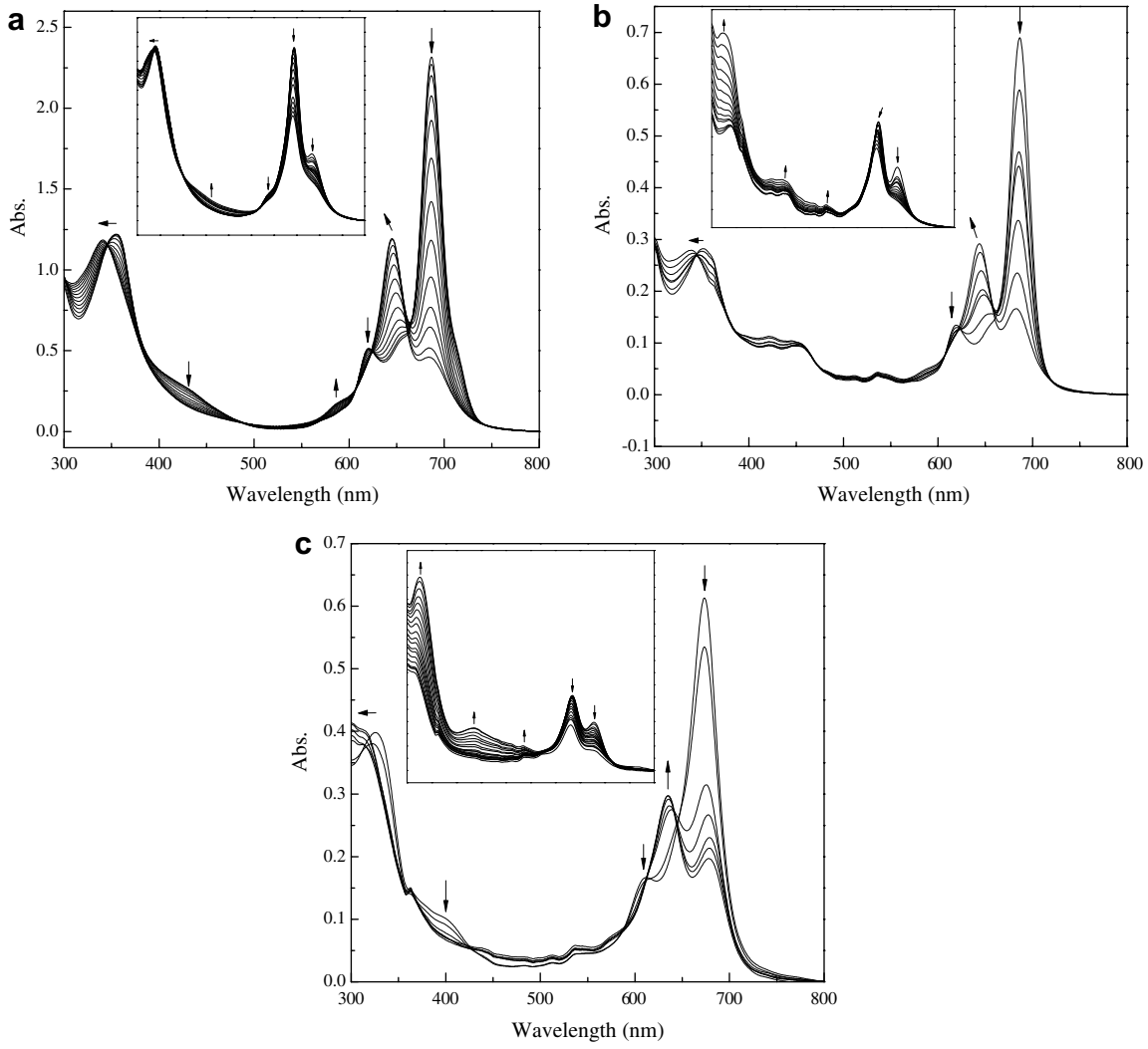


Fig. 2. UV–Vis spectra of **2** (a), **3** (b) and **4** (c) in THF/MeOH during titration by Pd^{2+} (in MeOH).

740 nm for **2**, 345, 377, 467, 607, 623, 661 and 720 nm for **3** and 315, 363, 425, 590, 612 and 645 nm for **4**. This type of spectroscopic behavior probably results from the complexation of Pd^{II} with the phthalocyanine complexes and the aggregation-disaggregation equilibrium of the Pd^{II}–Pc complexes. This observation is in harmony with previously reported studies [14,17,23,26]. However, further addition of Pd^{II} indicates very distinct spectroscopic changes as shown in the inset of Fig. 2. While the intensities of the Q-bands of monomeric and oligomeric aggregated species start to decrease, the intensity of B-bands and the n–π^* transition-bands (attributed to the non-bonding sulfur electron (n) to the π^* phthalocyanine orbital) at around 400–500 nm increase. These uncommon spectroscopic changes indicate that the overall complexation behavior of the complexes likely to be more complex. These uncommon changes may be the result of the formation of a Pd^{II}–Pc complex exhibiting a different geometry, the decomposition of the aggregates and the formation of square planar complexes (inset figures in Fig. 2a–c).

Fig. 3 shows the initial and end points of the titration of **2** and **3** with Ag^{I}, representing the optical changes of the complexes with Ag^{I}. The addition (μl) of Ag^{I} to a solution of **2**–**4** caused a gradual color change, from blue-green to intractable dark-blue, suggesting complex formation of the complexes with Ag^{I}. As shown in Fig. 3, addition of Ag^{I} to the solution of the complexes leads to a gradual disappearance of the monomeric species, simultaneously enhancing the intensity of the oligomeric aggregated species observed at the higher energy side of the Q-band of the monomeric species. A blue shift of about 15–20 nm without change in intensity for the B-bands of the all complexes was also recorded. The titration shows clear isobestic points at 330, 478, 607, 655 and 715 nm for **2**, 335, 387, 486, 615, 656 and 715 nm for **3** and 335, 380, 470, 620, 656 and 716 nm for **4**. These spectroscopic changes indicate the coordination of Ag^{I} by the donor atoms of the phthalocyanines and the formation of network type polymer units due to the aggregation of complexes. Further addition of Ag^{I} did not change the spectra. The results of the titration

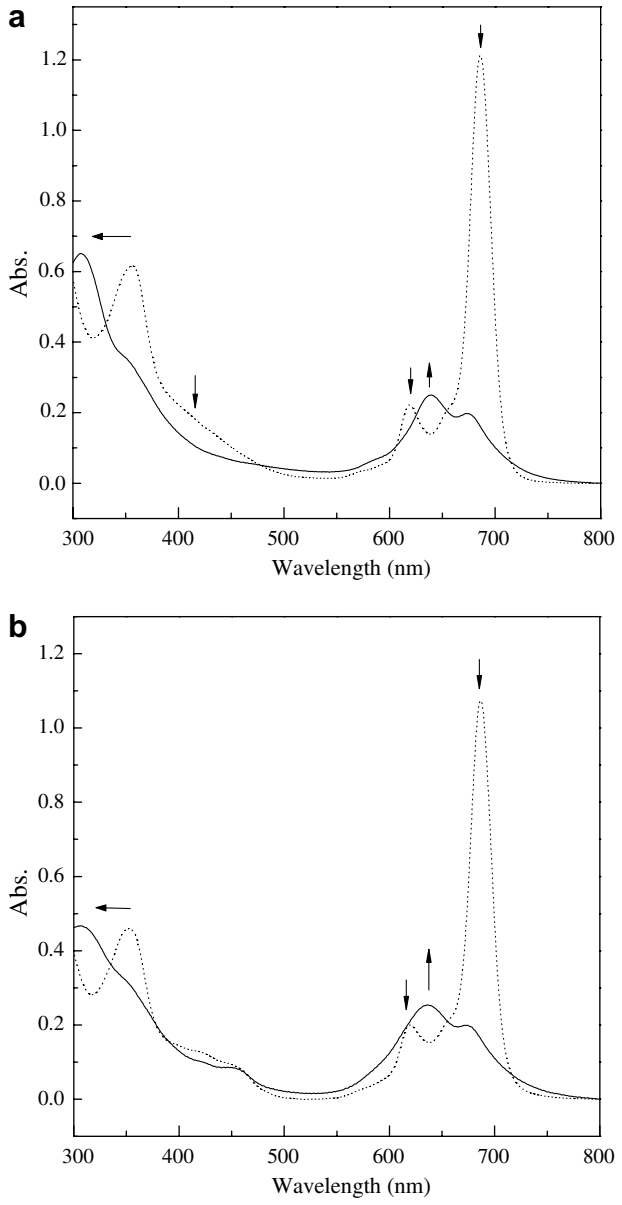


Fig. 3. UV–Vis spectra of **2** (a) and **3** (b) in THF/MeOH during titration by Ag^{+} (in MeOH).

with Ag^{I} ion closely followed those obtained in previous works [14,17,23,26].

3.5. Electrochemical measurements

The electrochemical behavior of all of the phthalocyanines was investigated by cyclic voltammetry (CV) and differential pulse voltammetry (DPV) on a platinum working electrode in DMSO. The half-wave redox potential values ($E_{1/2}$) versus SCE are summarized in Table 1. Fig. 4 shows the cyclic voltammograms and differential pulse voltammograms of **3** and **4**, as typical representatives of the compounds.

Within the electrochemical window of TBAP/DMSO, compound **4** undergoes a quasi-reversible one-electron

Table 1
Voltammetric data for the complexes

Complexes	Oxd. 1			Red. 1			Red. 2			Red. 3			Reference
	$E_{1/2}$ (V)[a]	ΔE_p (mV)[b]	I_{pc}/I_{pa}[c]	$E_{1/2}$ (V)[a]	ΔE_p (mV)[b]	I_{pc}/I_{pa}[c]	$E_{1/2}$ (V)[a]	ΔE_p (mV)[b]	I_{pc}/I_{pa}[c]	$E_{1/2}$ (V)[a]	ΔE_p (mV)[b]	I_{pc}/I_{pa}[c]	
2	0.73	65	0.92	−0.74	63	0.98	−1.10	65	0.86	−1.43			Tw
3	0.18	72	0.52	−0.73	64	0.95	−1.03	65	0.90	−1.42			Tw
4	0.46	95	0.95	−0.36	96	1.00	−1.27	103	0.98				Tw
[d]CoPc	0.12			−0.50			−0.93			−1.30			[17]
[d]CuPc	0.15			−0.85			−1.06			−1.90			[17]
[d]NiPc	0.64			−0.97			−1.14			−2.04			[17]
[e]NiPc				−0.62			−1.21			−1.67			[29]
[e]CoPc	0.60			−0.61			−1.04			−1.26			[29]

[a] $E_{1/2} = (E_{pa} + E_{pc})/2$ at 100 mV s^{-1}.
[b] $\Delta E_p = E_{pa} + E_{pc}$ at 100 mV s^{-1}.
[c] I_{pa}/I_{pc} for reduction, I_{pc}/I_{pa} for oxidation processes at 100 mV s^{-1}.
[d] Substituted with tetra-propandiolsulfanyl moieties.
[e] Substituted with tetra-aminophenyl sulfanyl moieties. Tw: This work.

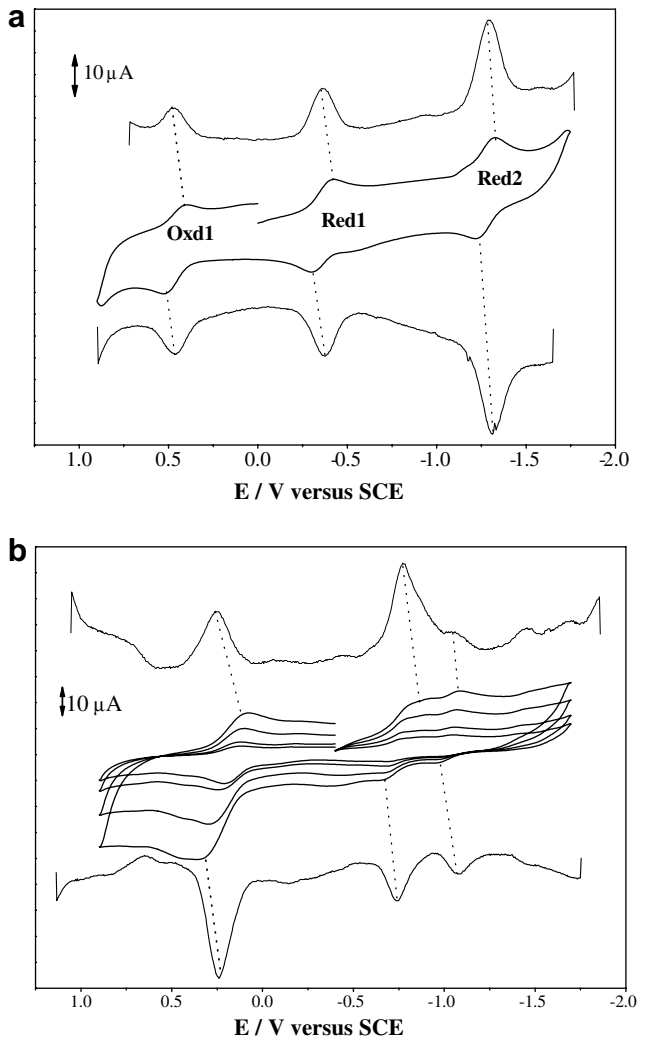


Fig. 4. Cyclic and differential pulse voltammograms of **4** (a) and **3** (b) at various scan rates on Pt in DMSO/TBAP.

oxidation and two quasireversible one-electron reductions at 0.47, −0.36 and −1.27 V versus SCE at a 0.100 V s^{-1} scan rate, respectively. Differential pulse voltammetry of the complex confirms the recorded redox processes clearly. Reversibility is illustrated by the similarity in the forward and reverse DPV scans (inset in Fig. 4) [27]. First-row transition metal Pcs differ from the main-group metal Pcs due to the fact that metal "d" orbitals may be positioned between the HOMO and LUMO of the phthalocyanine (Pc^{-2}) ligand. The first oxidation and first reduction processes occur on the metal center in the metal Pc only for Mn, Fe and Co derivatives in polar solvents such as DMF and DMSO. For Ni, Cu and Zn phthalocyanines, redox processes take place on the Pc ring [27,28]. This study indicates that the first reduction and first oxidation processes of **4**, recorded at 0.465 and −0.360 V, could easily be assigned to the Co^{II}/ Co^{I} and Co^{II}/ Co^{III} redox couples, respectively, and the remaining processes to the phthalocyanine ring. All predicted redox processes are given in Eq. (1). Furthermore, both the first oxidation and the first reduction of **4** are recorded at almost the same potentials relative to those of the reported CoPc with a slight shift as a result of the electron-donating substituents, with the separation between the metal center reduction and oxidation processes also remaining unchanged (Table 1). The separation between the metal center reduction and oxidation processes (∼0.825 V) is comparable with the CoPc papers [28–32]. As shown in Table 1, the redox processes are shifted towards a positive potential as a result of the electron releasing ability of the tetra –(6-mercapto 1-hexanol) substituents with respect to the tetra-(propanediolsulfanyl) tetrachloro substituted CoPc characterized in our previous study [17].

$$[\mathrm{Co(III)Pc}(-2)]^{+} \underset{0.47\ \mathrm{V}}{\overset{e^-}{\Longleftrightarrow}} [\mathrm{Co(II)Pc}(-2)] \Longleftrightarrow \overset{e^-}{\underset{-0.36\ \mathrm{V}}{}}[\mathrm{Co(I)Pc}(-2)]^{1-} \underset{-1.27\ \mathrm{V}}{\overset{e^-}{\Longleftrightarrow}} [\mathrm{Co(I)Pc}(-3)]^{2-} \quad (1)$$

Within the electrochemical window of TBAP/DMSO, **2** and **3** undergo a one-electron oxidation and three one-electron reductions. Because of the electro-inactive metal center of the complexes, all of these processes are attributed to successive removal of electrons from, or addition of electrons to, the macrocycle orbitals. Differential pulse voltammetry of the complex confirms the recorded redox processes clearly. Moreover the oxidation process of **3** has adsorption character due to the very intense anodic current and the linear variation of the anodic peak current with scan rate. Copper macrocycles generally showed adsorption behavior in our previous studies [33,34]. As a result of the adsorption of the complexes on the electrode surface, the oxidation couple of the complexes shift to a less positive potential with respect to common copper phthalocyanine studied in the literature. Adsorption of the complexes results in a significantly decreased potential difference between the first reduction and first oxidation redox processes, i.e., a decreased HOMO–LUMO gap (0.910 V) of the compounds. However, the HOMO–LUMO gap (∼1.470 V) of **2** is comparable with those of common metallophthalocyanines (∼1.300–1.700 V). A positive potential shift of the redox processes for **2** and **3** with respect to tetra-propanediolsulfanyl tetra-chloro substituted CuPc, characterized in our previous study [17], was also observed.

4. Conclusions

We have synthesized novel phthalocyanine derivatives bearing peripheral tetrakis(6-hydroxyhexylsulfanyl) substituents which are soluble in a range of especially polar organic solvents. The peripherally modified phthalocyanines have been fully characterized with various spectroscopic and electrochemical methods in this work, representing a unique class of selective metal–ion chelators that absorb in the visible region. The thio donors as a soft-base, which are distributed on benzene moieties of the phthalocyanine, are coordinated with metal ions,

such as Ag^{I} and Pd^{II}, so resulting in a polymeric assembly. The thio groups on the periphery provide good donor capabilities for soft metal ions, resulting in the red shift of the Q-band. Thus, the ease of altering of the chemical and spectroscopic properties of these phthalocyanines through peripheral variation allows continuing studies to focus on the development of the next generation of sensor complexes for the targeting of particular metal cations. Peripheral and center metal variation of the complexes also affect the redox properties in solution. Electrochemical studies establish that the phthalocyanine derivatives undergo up to four quasi-reversible one-electron diffusion controlled metal and/or ligand-based oxidation/reduction electron transfer reactions, differing with potential shift as a result of the electron withdrawing/releasing effect of the substituents and the metal–ligand interactions.

Acknowledgements

We thank The Research Fund of Sakarya University, TÜBİTAK (Project No. TBAG-2241 (102T167)) and DPT-2004 (Project No. 2003K120970).

References

[1] (a) C.C. Leznoff, A.B.P. Lever, in: C.C. Leznoff, A.B.P. Lever (Eds.), Phthalocyanines: Properties and Applications, vols. 1–4, VCH, Weinheim, 1989–1996;
(b) N. Kobayashi, H. Miwa, H. Isago, T. Tomura, Inorg. Chem. 38 (1999) 479;
(c) N.B. Mc Keown, Phthalocyanine Materials, Cambridge University Press, 1998;
(d) M. Hanack, M. Lang, Adv. Mater. 6 (1994) 819.

[2] (a) B.J. Vesper, K. Salaita, H. Zong, C.A. Mirkin, A.G.M. Barrett, B.M. Hoffman, J. Am. Chem. Soc. 126 (2004) 16653;
(b) C.G. Claessens, W.J. Blau, M. Cook, M. Hanack, R.J.M. Nolte, T. Torres, D. Wöhrle, Monatsh. Chem. 132 (2001) 3;
(c) M. Kimura, K. Wada, Y. Iwashima, K. Ohta, K. Hanabusa, H. Shirai, N. Kobayashi, Chem. Commun. 19 (2003) 2504.

[3] (a) Ş. Abdurrahmanoğlu, A.R. Özkaya, M. Bulut, Ö. Bekaroğlu, J. Chem. Soc., Dalton Trans. (2004) 4022;
(b) J.P. Fox, D. Goldberg, Inorg. Chem. 42 (2003) 8181.

[4] E.S. Schmith, T.S. Calderwood, T.C. Bruice, Inorg. Chem. 25 (1986) 3718.

[5] (a) T. Toupance, P. Bassoul, L. Mineau, J. Simon, J. Phys. Chem. 100 (28) (1996) 11704;
(b) S. Makhseed, A. Bumajdad, B. Ghanem, K. Msayib, N.B. McKeown, Tetrahedron Lett. 45 (2004) 4865;
(c) M.J. Cook, A. Jafari-Fini, Tetrahedron 56 (2000) 4085;
(d) T. Komatsu, K. Ohta, T. Fujimoto, I. Yamamoto, J. Mater. Chem. (1994) 4.

[6] (a) X. Li, L.E. Sinks, B. Rybtchinski, M.R. Wasielewski, J. Am. Chem. Soc. 126 (2004) 10810;
(b) J. Sleven, C. Görller-Walrand, K. Binnemans, Mater. Sci. Eng. C 18 (2001) 229.

[7] M. Zhao, C. Zhong, C. Stern, A.G.M. Barrett, B.M. Hoffman, Inorg. Chem. 43 (2004) 3377.

[8] (a) V. Mantareva, D. Petrova, L. Avramov, I. Angelov, E. Borisova, M. Peeva, D. Wöhrle, J. Porphyr. Phthalocya. 9 (2005) 47;
(b) D. Gonzalez-Rodriguez, C.G. Claessens, T. Torres, S.G. Liu, L. Echegoyen, N. Vila, S. Nonell, Chemistry – A Eur. J. 11 (2005) 3881.

[9] A.N. Cammidge, M.J. Cook, D.L. Hughes, F. Nekelson, M. Rahman, Chem. Commun. 7 (2005) 930.

[10] (a) M. Kandaz, I. Yılmaz, Ö. Bekaroğlu, Polyhedron 19 (2000) 115;
(b) T. Ceyhan, A. Altındal, M.K. Erbil, Ö. Bekaroğlu, Polyhedron 25 (2006) 737;
(c) M. Özer, A. Altindal, A.R. Ozkaya, M. Bulut, O. Bekaroglu, Synth. Met. 155 (1) (2005) 222.

[11] (a) A.R. Koray, V. Ahsen, Ö. Bekaroglu, J. Chem. Soc., Chem. Commun. 12 (1986) 932;
(b) M. Kandaz, S.L.J. Michel, B.M. Hoffman, J. Porphyr. Phthalocya. 7 (2003) 700;
(c) M. Kandaz, Ö. Bekaroğlu, Chem. Ber. 135 (1997) 1833.

[12] A.E. Pullen, C. Faulmann, P. Casoux, Eur. J. Inorg. Chem. (1999) 269.

[13] (a) S. Dabak, O. Bekaroglu, New J. Chem. 21 (2) (1997) 267;
(b) D.P. Goldberg, S.L.J. Michel, A.J.P. White, D.J. Williams, A.G.M. Barrett, B.M. Hoffman, Inorg. Chem. 37 (1998) 2100.

[14] S.L.J. Michel, A.G.M. Barrett, B.M. Hoffman, Inorg. Chem. 42 (2003) 814.

[15] M. Kimura, T. Kuroda, K. Ohta, K. Hanabusa, H. Shirai, N. Kobayashi, Langmuir 19 (2003) 4825.

[16] B.A. Minch, W. Xia, C.L. Donley, R.M. Hernandez, C. Carter, M.D. Carducci, A. Dowson, D.F. O'Brien, N.R. Armstrong, Chem. Mater. 17 (2005) 1618.

[17] M. Kandaz, H.S. Çetin, A. Koca, A.R. Özkaya, Dyes Pigments, in press. doi:10.1016/j.dyepig. 2006.02.008.

[18] Y. Bian, L. Li, J. Dou, D.Y.Y. Cheng, R. Li, C. Ma, D.K.P. Ng, N. Kobayashi, J. Jiang, Inorg. Chem. 43 (2004) 7539.

[19] M. Kandaz, Ö. Bekaroğlu, J. Porphyr. Phthalocya. 3 (1999) 339.

[20] Ş. Merey, Ö. Bekaroğlu, J. Chem. Soc., Dalton Trans. (1999) 4503.

[21] A.B.P. Lewer, S.R. Pickens, P.C. Minor, S. Cicoccia, B.S. Ramamswamy, K. Magnell, J. Am. Chem. Soc. 103 (1981) 6800.

[22] M.A. Diaz Garcia, I. Ledoux, J.A. Duro, T. Tores, F. Agullo-Lopez, J. Zyss, J. Phys. Chem. 98 (1994) 8761.

[23] S.J. Lange, J.W. Sibert, A.G.M. Barrett, B.M. Hoffman, Tetrahedron 56 (2000) 7371.

[24] (a) O.E. Sielcken, M.M. Vantilborg, M.F.M. Roks, R. Hendriks, W. Drenth, R.J.M. Nolte, J. Am. Chem. Soc. 109 (1987) 4261;
(b) C. Zhong, C. Stern, A.G.M. Barrett, B.M. Hoffman, J. Am. Chem. Soc. 127 (27) (2005) 9769.

[25] J.G. Young, W. Onyebuagu, J. Org. Chem. 55 (1990) 2155.

[26] İ. Gürol, V. Ahsen, Ö. Bekaroğlu, J. Chem. Soc., Dalton Trans. (1994) 497.

[27] A.B.P. Lever, E.R. Milaeva, G. Speier, The Redox Chemistry of Metallophthalocyanines in Solution, in: C.C. Leznoff, A.B.P. Lever (Eds.), Phthalocyanines: Properties and Applications, vol. 3, VCH, New York, 1993.

[28] N. Kobayashi, H. Ogata, N. Nonaka, E.A. Luk'yanets, Chem. Eur. J. 9 (2003) 5123.

[29] M. Kandaz, M.N.U. Yaraşır, A. Koca, Ö. Bekaroğlu, Polyhedron 21 (2002) 255.

[30] A. Kalkan, A. Koca, Z.A. Bayır, Polyhedron 23 (2004) 3155.

[31] A. Koca, M.K. Şener, M.B. Koçak, A. Gül, Transition Met. Chem. 30 (4) (2005) 399.

[32] A. Koca, H.A. Dinçer, M.B. Koçak, A. Gül, Russ. J. Electrochem. 41 (1) (2006) 36.

[33] İ. Yılmaz, M. Kandaz, A.R. Özkaya, A. Koca, Monatsh. Chem. 133 (2002) 609.

[34] M. Kandaz, A.R. Özkaya, A. Koca, Transition Met. Chem. 29 (8) (2004) 847.

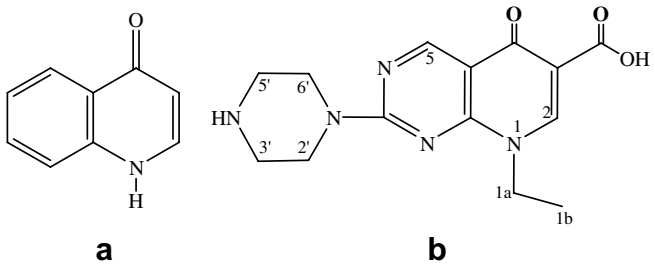


Fig. 1. (a) The 4-oxo-1,4-dihydroquinoline skeleton. (b) Pipedimic acid (8-ethyl-5,8-dihydro-5-oxo-2-(1-piperazinyl)pyrido(2,3-d)pyrimidine-6-carboxylic acid = HPPA) and atom labelling.

rofloxacin complexes as polyoxometalates have been characterized [25], while no quinolone complexes of $Mo(VI)O_2^{2+}$ and $U(VI)O_2^{2+}$ have been reported yet, although their role as bioelements is well established [26–29].

Pipemidic acid, HPPA (Fig. 1b), a 4-quinolone product, is an antibacterial agent used to treat gram-negative urinary tract infections [30] and severely damages DNA in the absence of an exogenous metabolizing system [31]. Pipemidic acid can act as a bidentate ligand through the quinolone oxygen and one carboxylate oxygen atom. In the literature, complexes of protonated pipemidic acid are reported with Ca^{2+}, Sr^{2+}, Ba^{2+}, Sn(IV) [32] and with the lanthanides La(III), Ce(III), Pr(III), Nd(III), Sm(III), Tb(III), Dy(III) and Y(III) [33] as well as of the deprotonated pipemidic acid with pentacoordinate Cu(II) and Mn(II) [34]. The reported results suggest that metal ion coordination might be involved in the antibacterial activity of HPPA [35].

We have initiated the study of the structure, spectroscopic and biological properties of transition metal complexes of diverse quinolone antibacterial drugs [36–39]. In this context we have studied the interaction of deprotonated pipemidic acid with the transition metal ions $V^{IV}O^{2+}$, Mn(II), Fe(III), Co(II), Ni(II), Zn(II),Cd(II), $Mo^{VI}O_2^{2+}$ and $U^{VI}O_2^{2+}$ in an attempt to examine the mode of binding and possible synergetic effects. The resulting mononuclear complexes have been characterized with elemental analysis and diverse spectroscopic techniques (IR, UV–Vis, NMR and EPR spectroscopy). Molecular modelling techniques have been employed so as to propose a low energy model for the most favorable isomer of the VO^{2+}, Fe^{3+} and MoO_2^{2+} complexes based on molecular mechanics calculations in the gas phase. The interaction of complexes with calf-thymus (CT) DNA has been studied with UV and circular dichroism (CD) spectroscopy. The antibacterial activity of the complexes has been also investigated against three microorganisms.

2. Experimental

2.1. Materials

All the chemicals for the synthesis of the compounds were used as purchased. DMF was distilled from calcium hydride (CaH_2) and CH_3OH from Mg, and stored over 3 Å molecular sieves. Diethyl ether, anhydrous grade and absolute ethanol were used without any further purification. Pipemidic acid and CT DNA were purchased from Sigma and $VOSO_4 \cdot 5H_2O$, $CoCl_2 \cdot 6H_2O$, $MnCl_2 \cdot 4H_2O$, $FeCl_3 \cdot 3H_2O$, $NiCl_2 \cdot 6H_2O$, $ZnCl_2$, $CdCl_2 \cdot 2.5H_2O$, $UO_2(NO_3)_2 \cdot 6H_2O$, $MoO_2(acac)_2$, KOH and all the solvents were purchased from Aldrich Co. Agarose was purchased from BRL. Tryptone and yeast extract were purchased from Oxoid (Unipath, Hampshire, UK). All chemicals and solvents were reagent grade.

DNA stock solutions (5 mM) were prepared by dilution of CT DNA with buffer (containing 150 mM NaCl and 15 mM trisodium citrate at pH 7.0) followed by exhaustive stirring at 4 °C for three days [40] and the solutions were kept at 4 °C for no longer than a week. The nucleotide concentrations were determined by their absorption at 260 nm using $\varepsilon = 6600\ M^{-1}\ cm^{-1}$ (expressed as phosphate).

2.2. Synthesis of the complexes

2.2.1. $VO(PPA)_2(H_2O)$ (1)

A warm methanolic solution (15 mL) of deprotonated pipemidic acid (0.4 mmol, 121 mg) was added to a methanolic solution (10 mL) of $VOSO_4 \cdot 5H_2O$ (0.2 mmol, 51 mg) and the reaction mixture was refluxed for 2 h. The solution was filtered and left for slow evaporation. After a few days a brown-green microcrystalline product was deposited, collected with filtration, washed with methanol and dried. Yield: 104 mg, ~75%. *Anal.* Calc. for $VO(PPA)_2(H_2O)$ ($C_{28}H_{34}N_{10}O_8V$) (MW = 689.58): C, 48.77; H, 4.97; N, 20.31. Found: C, 49.05; H, 5.03; N, 20.10%. The complex is soluble in DMSO and DMF and is a non-electrolyte.

In a similar way complexes **2**–**9** were prepared with the use of the corresponding metal salt.

2.2.2. $Mn(PPA)_2(H_2O)_2$ (2)

$MnCl_2 \cdot 4H_2O$ (0.2 mmol, 40 mg) was used. A yellow microcrystalline product was collected. Yield: 97 mg, ~70%. *Anal.* Calc. for $Mn(PPA)_2(H_2O)_2$ ($C_{28}H_{36}N_{10}O_8Mn$) (MW = 695.59): C, 48.35; H, 5.22; N, 20.13. Found: C, 48.62; H, 5.30; N, 19.89%. The complex is soluble in DMSO, DMF, CH_3CN and acetone and is a non-electrolyte.

2.2.3. $Fe(PPA)_3$ (3)

$FeCl_3 \cdot 3H_2O$ (0.2 mmol, 44 mg) and pipemidic acid (0.6 mmol, 192 mg) were used. An orange microcrystalline product was collected. Yield: 140 mg, ~67%. *Anal.* Calc. for $Fe(PPA)_3$ ($C_{42}H_{48}N_{15}O_9Fe$) (MW = 962.79): C, 52.39; H, 5.03; N, 21.82. Found: C, 51.93; H, 4.91; N, 22.03%. The complex is soluble in DMSO, DMF and H_2O and is a non-electrolyte.

2.2.4. $Co(PPA)_2(H_2O)_2$ (4)

$CoCl_2 \cdot 6H_2O$ (0.2 mmol, 48 mg) was used. An orange-yellow microcrystalline product was collected. Yield: 90 mg, ~65%. *Anal.* Calc. for $Co(PPA)_2(H_2O)_2$

($C_{28}H_{36}N_{10}O_8Co$) (MW = 699.59): C, 48.07; H, 5.18; N, 20.02. Found: C, 47.76; H, 5.37; N, 19.65%. The complex is soluble in DMSO and DMF and is a non-electrolyte.

2.2.5. $Ni(PPA)_2(H_2O)_2$ (5)

$NiCl_2 \cdot 6H_2O$ (0.2 mmol, 48 mg) was used. A light green microcrystalline product was collected. Yield: 98 mg, ~70%. *Anal.* Calc. for $Ni(PPA)_2(H_2O)_2$-($C_{28}H_{36}N_{10}O_8Ni$) (MW = 699.37): C, 48.09; H, 5.19; N, 20.03. Found: C, 48.41; H, 5.01; N, 20.17%. The complex is soluble in DMSO, DMF, ethanol and H_2O and is a non-electrolyte.

2.2.6. $Zn(PPA)_2(H_2O)_2$ (6)

$ZnCl_2$ (0.2 mmol, 28 mg) was used. A pale yellow microcrystalline product was collected. Yield: 105 mg, ~75%. *Anal.* Calc. for $Zn(PPA)_2(H_2O)_2$ ($C_{28}H_{36}N_{10}O_8Zn$) (MW = 706.04): C, 47.63; H, 5.14; N, 19.84. Found: C, 47.75; H, 5.21; N, 19.98%. The complex is soluble in DMSO, CH_3CN, acetone and H_2O and is a non-electrolyte.

2.2.7. $MoO_2(PPA)_2$ (7)

$MoO_2(acac)_2$ (0.2 mmol, 66 mg) was used. A pale yellow microcrystalline product was collected. Yield: 100 mg, ~69%. *Anal.* Calc. for $MoO_2(PPA)_2$ ($C_{28}H_{32}N_{10}O_8Mo$) (MW = 732.56): C, 45.91; H, 4.40; N, 19.12. Found: C, 46.19; H, 4.62; N, 19.00%. The complex is soluble in DMSO and DMF and is a non-electrolyte.

2.2.8. $Cd(PPA)_2(H_2O)_2$ (8)

$CdCl_2 \cdot 2.5H_2O$ (0.2 mmol, 46 mg) was used. A yellow microcrystalline product was collected. Yield: 100 mg, ~66%. *Anal.* Calc. for $Cd(PPA)_2(H_2O)_2$ ($C_{28}H_{36}N_{10}O_8Cd$) (MW = 753.07): C, 44.66; H, 4.82; N, 18.60. Found: C, 45.07; H, 4.75; N, 18.45%. The complex is soluble in DMSO, DMF, H_2O, $CHCl_3$ and acetone and is a non-electrolyte.

2.2.9. $UO_2(PPA)_2$ (9)

$UO_2(NO_3)_2 \cdot 6H_2O$ (0.2 mmol, 100 mg) was used. A pale yellow microcrystalline product was collected. Yield: 125 mg, ~70%. *Anal.* Calc. for $UO_2(PPA)_2$ ($C_{28}H_{32}$-$N_{10}O_8U$) (MW = 874.65): C, 38.45; H, 3.69; N, 16.01. Found: C, 38.88; H, 3.80; N, 15.87%. The complex is soluble in DMSO, DMF, CH_3CN, acetone and H_2O and is a non-electrolyte.

2.3. Physical measurements

IR spectra (400–4000 cm^{-1}) were recorded on a Nicolet Magna-IR 550 with samples prepared as KBr pellets. UV–Vis spectra were recorded on a Thermo Electron Corporation Helios α dual beam spectrophotometer. C, H, and N elemental analysis were performed on a Perkin–Elmer 240B elemental analyzer. Electric conductance measurements were carried out with a WTW model LF 530 conductivity outfit and a type C cell, which had a cell constant of 0.996. This represents a mean value calibrated at 25 °C with potassium chloride. NMR spectra were recorded with a Bruker Avance 500 MHz instrument and were processed by X-WIN NMR 2.6 (Bruker Analytik GmbH). X-band EPR spectra at liquid helium temperatures were recorded on a Bruker ER 200D EPR spectrometer equipped with an Oxford Instruments ESR900 cryostat and an Anritsu microwave frequency counter. Simulations of EPR spectra were carried out with a computer program written by Prof. Michael P. Hendrich, Department of Chemistry, Carnegie Mellon University, Pittsburgh, USA [41,42].

All CD spectra were recorded on a Jasco J-700 spectropolarimeter using a 1.0 cm path quartz cell and the following acquisition parameters: $\lambda = 190$–400 nm, scan speed 50 nm min^{-1}, resolution step 0.2 nm, sensitivity 50 mdeg, response 1 s, bandwidth 1.0 nm, accumulations 10. In some cases, the spectra were averaged over an appropriate number of scans. All CD spectra were recorded at 25 °C after the complexes had been incubated with CT DNA for 24 h at 37 °C.

2.4. Molecular modelling

With the aim to present a molecular model for each new complex that is unbiased by the starting structure, we have used Langevin dynamics with a simulated annealing protocol. Using this method, the mean total energy of an ensemble of structures guides the selection of the most favorable configuration for each complex. The starting structures were constructed using the program HyperChem and the MM+ force field that is based on the Allinger's MM2 force field [43]. For all the metal ions we used a default parameter set with $R^* = 2.20$ Å and $e^* = 0.02$ kcal mol^{-1}, since their van der Waals interactions are not expected to play a major role in such bonded representations as in octahedral complexes. Metal–ligand bond lengths were corrected in the final models using harmonic restraints with equilibrium values that were extracted from crystallographic data of similar compounds [44–56] (Tables S1, S3, and S5). Non-bonded interactions were calculated in vacuo with no cutoff and the electrostatic energy term was treated using bond dipoles. Initial energy minimizations were carried out by a conjugate gradient method with rms gradient <0.01 as convergence criterion.

Each model (Schemes S1–S3) was subjected to 20 individual rounds of simulated annealing setting a different value to the seed for the assignment of the starting velocities. To integrate the Langevin equation [57] the step size was set to 1fs and the collision frequency to 1 ps^{-1}. The annealing calculation comprised three phases: (i) raising the temperature of the system from 10 to 1000 K over 2 ps, (ii) keeping the system at 1000 K for 3 ps, and (iii) cooling the system down to 0 K over 15 ps. A tight coupling of the system with temperature (0.1 ps) was used for the heating and equilibration

phases. During the cooling phase the bath relaxation time was gradually decreased from 5.0 ps (7000 steps), 2.0 ps (3000 steps), 1.0 ps (2000 steps), 0.5 ps (2000 steps) to 0.05 ps (1000 steps). At the final step all structures had rms gradient < 0.01 and their total energy was recorded (Tables S2, S4, and S6). The models presented herein were selected from among the lowest energy structures that were generated for each starting geometry. A final minimization of their energy was performed as above, but having applied the metal–ligand distance restraints.

2.5. Antibacterial activity – minimum inhibitory concentration

The antibacterial activity of the compounds (ligands, metal salts and complexes) was studied against *S. aureus*, *E. coli* and *P. aeruginosa*. The microorganisms were maintained in the laboratory of "Inorganic Materials and Biomolecules" of NCSR "Demokritos". Screening was performed by determining the minimum inhibitory concentration (MIC). Two different media [Luria broth medium (=LB, containing 1% w/v tryptone, 0.5% w/v NaCl and 0.5% w/v yeast extract) and minimal medium salts broth (=MMS, containing 1.5% w/v glucose, 0.5% w/v NH_4Cl, 0.5% w/v K_2HPO_4, 0.1% w/v NaCl, 0.01% w/v $MgSO_4 \cdot 7H_2O$ and 0.1% w/v yeast extract)] were used. The compounds were dissolved in distilled water with twofold serial dilutions from 128 to 4 $\mu g\,mL^{-1}$. All cultures were incubated at 37 °C. Control tests with no active ingredients were also performed.

The MIC was determined using twofold serial dilutions in liquid media containing 4–128 $\mu g\,mL^{-1}$ of the compound being tested. The solvent used was water where the solubility of the compound permits and DMSO in the remaining cases. The activity of DMSO has been also investigated and no activity at the quantities used in this work has been found. A preculture of bacteria was grown in LB overnight at the optimal temperature of each species. Two milliliters of MMS were inoculated with 20 mL of this preculture. This culture was used as a control to examine if the growth of the bacteria tested is normal. In a similar second culture, 20 μL of the bacteria as well as the tested compound at the desired concentration were added. A third sample containing 2 mL MMS supplemented with the same compound concentration was used as a second control to check the effect of the compound on MMS. All samples were in duplicate. We monitored bacterial growth by measuring the turbidity of the culture after 12 and 24 h. If a certain concentration of a compound inhibited bacterial growth, half the concentration of the compound was tested. This procedure was carried on to a concentration that bacteria grow normally. The lowest concentration that inhibited bacterial growth was determined as the MIC value. All equipment and culture media were sterile.

3. Results and discussion

3.1. Synthesis of the complexes

All the complexes have been prepared at high yield (65–75%) via the addition of a methanolic solution of deprotonated pipemidic acid to a methanolic solution of the metal ion at a ratio 3:1 for Fe^{3+} and 2:1 for the remaining divalent metal ions according to the reaction:

$$M^{n+} + n\mathrm{PPA} \rightarrow M(\mathrm{PPA})_n(H_2O)_x$$

where $M^{n+} = VO^{2+}$, Mn^{2+}, Co^{2+}, Ni^{2+}, Zn^{2+}, MoO_2^{2+}, Cd^{2+}, UO_2^{2+} ($n = 2$) and Fe^{3+} ($n = 3$), $x = 0$, 1 or 2. All complexes were collected as microcrystalline products. Although diverse crystallization techniques were employed, we did not manage to obtain crystals suitable for determination of structures with X-ray crystallography.

3.2. Infrared spectroscopy

In Table 1 the characteristic absorptions of the IR spectra of all the complexes are listed. In the IR spectra of complexes **1**–**9** the band at 1723 cm^{-1} in the HPPA spectrum attributed to the absorption of $\nu(C{=}O)_{carb}$ has disappeared and has been replaced by two very strong characteristic bands in the ranges 1600–1615 cm^{-1} and 1370–1360 cm^{-1}, that can be assigned as asymmetric, $\nu(CO_2)_{asym}$, and symmetric, $\nu(CO_2)_{sym}$, stretching ν(O–C–O) vibrations. The difference $\Delta = \nu_{asym}(CO_2) - \nu_{sym}(CO_2)$ is a useful characteristic for determining the coordination mode of the ligands. The Δ values fall in the range 238–252 cm^{-1}, indicating a monodentate coordination mode of the carboxylato group [58–60]. Finally, the pyridone stretch $\nu(C{=}O)_p$ is shifted from 1617 to 1634 cm^{-1} upon bonding. These changes of the IR spectra suggest that PPA is coordinated to the metal via the pyridone oxygen and one carboxylate oxygen atom [5].

The existence and the number of the $\nu(M{=}O)$ absorptions is a useful diagnostic tool of complex characterization. The appearance of the V=O stretching frequency in complex **1** at ~954 cm^{-1} suggests that a monoanionic ligand lies in a *trans* position to O_v ($O_{vanadyl}$) [61]. This acceptance is indicative of the arrangement of one O_{carb} ($O_{carboxylate}$) or O_{pyr} ($O_{pyridone}$) atom in the axial position of the octahedron around the V atom and excludes the O_w (O_{water}) atom. The existence of two $\nu(M{=}O)$ absorptions for MoO_2^{2+} and UO_2^{2+} complexes are indicative of a *cis* arrangement of two oxygen atoms around Mo and U atoms, respectively [26]. The band at ~3400–3420 cm^{-1} in the IR spectra of the complexes **1**, **2**, **4**, **5**, **6** and **8** can be attributed to the ν(O–H) vibration of one or two coordinated water molecules [59].

3.3. Electronic spectroscopy

The UV–Vis spectra of the complexes have been recorded as nujol mulls and in solution. The solvent has

Table 1
Characteristic absorptions (in cm^{-1}) of the IR spectra of the complexes

	$\nu(C{=}O)_p$	$\nu(CO_2)_{asym}$	$\nu(CO_2)_{sym}$	Δ[a]	$\nu(M=O)$
HPPA	1617	1723[b]			
$VO(PPA)_2(H_2O)$	1629	1606	1368	238	950
$Mn(PPA)_2(H_2O)_2$	1634	1608	1362	246	
$Fe(PPA)_3$	1637	1615	1363	252	
$Co(PPA)_2(H_2O)_2$	1625	1604	1362	242	
$Ni(PPA)_2(H_2O)_2$	1628	1608	1361	247	
$Zn(PPA)_2(H_2O)_2$	1626	1609	1362	247	
$MoO_2(PPA)_2$	1625	1603	1365	238	930, 900
$Cd(PPA)_2(H_2O)_2$	1624	1605	1360	245	
$UO_2(PPA)_2$	1634	1614	1365	249	910, 870

[a] $\Delta = \nu(CO_2)_{asym} - \nu(CO_2)_{sym}$.
[b] As ν(COOH).

been chosen based on the solubility of each complex. Practically, the spectra in solution are identical with those in nujol with the exception of a few nm shifts in some cases. In Table 2, the UV–Vis spectral data of all the complexes in the different solvents are given.

The UV spectra of the complexes are practically identical with that of the pipemidato ligand but slightly shifted, indicative of coordination through the pyridone and one carboxylate oxygen atom.

In the visible spectra, there are characteristic bands attributed to d-d transitions only for VO^{2+}, Fe^{3+}, Co^{2+} and Ni^{2+} complexes. For the $V^{IV}O^{2+}$ complex three low-intensity bands at ~802 (band I), 600 (band II) and 495 (band III) nm attributed to d–d transitions are observed. Band I at $\lambda = 802$ nm ($\varepsilon = 12\ M^{-1}\ cm^{-1}$) can be attributed to a $b_2(d_{xy}) \rightarrow e^*_\pi(d_{xz}, d_{yz})$ transition of the $V^{IV}O^{2+}$ and band II at $\lambda = 600$ nm ($\varepsilon = 20\ M^{-1}\ cm^{-1}$) to a $b_2(d_{xy}) \rightarrow b_1^*(d_{x^2-y^2})$ transition [62]. Band III at $\lambda = 495$ nm ($\varepsilon = 26\ M^{-1}\ cm^{-1}$) is also observed and can be attributed to a $d_{xy} \rightarrow d_{z^2}$ transition, although it usually lies under the much stronger ligand-to-metal charge-transfer (=LMCT) transition at $\lambda = 425$ nm ($\varepsilon = 100\ M^{-1}\ cm^{-1}$) and can be difficult to distinguish [63,64]. These bands are typical for distorted octahedral VO^{2+} complexes [46,48,61].

The spectrum of $Fe(PPA)_3$ exhibits two bands that can be attributed to d–d transitions: one weak band (as a shoulder) at ~600 nm ($\varepsilon = 30\ M^{-1}\ cm^{-1}$) which can be assigned as a $^6A_{1g} \rightarrow {}^5T_{1g}$ transition and an intense one at $\lambda = 500$ nm ($\varepsilon = 95\ M^{-1}\ cm^{-1}$) assigned as a $^6A_{1g} \rightarrow T_{2g}(G)$ transition [65,66]. These bands are typical for distorted octahedral Fe^{3+} complexes [49–51]. Additionally, a band at $\lambda = 436$ nm ($\varepsilon = 135\ M^{-1}\ cm^{-1}$), observed as a shoulder, can be attributed to a LMCT transition.

In the visible spectra of $Co(PPA)_2(H_2O)_2$ and $Ni(PPA)_2(H_2O)_2$ one band at ~555 ($\varepsilon = 40\ M^{-1}\ cm^{-1}$) and ~625 nm ($\varepsilon = 45\ M^{-1}\ cm^{-1}$), respectively, attributed to a d–d transition has been found as expected for octahedral Co^{2+} [67] and Ni^{2+} [68] high-spin complexes. Similar behavior has been observed for the octahedral high-spin Co^{2+} [12] and Ni^{2+} [11] cinoxacin complexes.

All the complexes also exhibit an absorption band at ~425–435 nm which can be assigned to the LMCT transition for the quinolone ligand [36–39].

3.4. NMR spectroscopy

^1H NMR spectra of HPPA, $Zn(PPA)_2(H_2O)_2$ and $UO_2(PPA)_2$ have been recorded in d_6-DMSO. The assignment of every signal has been achieved by comparing the

Table 2
Characteristic bands λ_{max} (nm) (ε, $M^{-1}\ cm^{-1}$) in the UV–Vis spectra of the complexes in different solvents

	IL bands		Band CT	Bands d–d		
HPPA[a]	330 (1900)	359 (1350)				
$VO(PPA)_2(H_2O)$[a]	331 (2200)	370 (1350)	425(sh)[d] (100)	495(sh) (26)	600 (20)	802 (12)
$Mn(PPA)_2(H_2O)_2$[a]	332 (2250)	370 (1230)	425(sh) (135)			
$Fe(PPA)_3$[b]	329 (2400)	375 (1250)	436(sh) (135)	500 (95)	600 (30)	
$Co(PPA)_2(H_2O)_2$[c]	327 (2150)	368 (1430)	425(sh) (120)		555 (40)	
$Ni(PPA)_2(H_2O)_2$[c]	342 (2350)	372 (1180)	430(sh) (125)		625 (45)	
$Zn(PPA)_2(H_2O)_2$[c]	330 (2150)	369 (1190)	425(sh) (145)			
$MoO_2(PPA)_2$[a]	329 (2150)	370 (1420)	423(sh) (115)			
$Cd(PPA)_2(H_2O)_2$[a]	334 (2350)	370 (1450)	420(sh) (145)			
$UO_2(PPA)_2$[a]	342 (1780)	368 (1380)	422(sh) (120)			

[a] In DMSO.
[b] In H_2O.
[c] In DMF.
[d] (sh) = shoulder.

^{1}H NMR spectra of the complexes to that of the ligand and spectra reported in the literature [69]. The results are shown in Table 3.

Comparison of the ^{1}H NMR spectra of $Zn(PPA)_2(H_2O)_2$ and $UO_2(PPA)_2$ with that of HPPA shows a significant perturbation of the chemical shift (up to 0.7 ppm) of the aromatic protons H2 and H5, indicating that H2 and H5 are close to the coordination site of the ligand. The signals for the aliphatic and piperazine protons are practically unchanged since they lie far from the binding site of the ligand.

The overall changes of the NMR spectra of the complexes are indicative of coordination of the pipemidato ligand to the metal via the pyridone and carboxylate oxygen atoms.

3.5. EPR spectroscopy

The EPR spectrum of $VO(PPA)_2(H_2O)$ in DMSO at 12 K is shown in Fig. 2. The spectrum is typical for a mononuclear VO^{2+} complex. We have simulated the spectrum assuming an $S = 1/2$ species interacting with a nucleic spin of $I = 7/2$ through the usual spin Hamiltonian:

$$H = \beta \mathbf{SgB} + \mathbf{IAS}$$

where β is the Bohr magneton and **A** is the tensor of the hyperfine interaction. The spectrum is well reproduced with axial **g**- and **A**-tensors with the values $g_{\|}$=1.942(2), $g_{\perp} = 1.976(2)$, $g_{iso} = (2g_{\perp} + g_{\|})/3 = 1.965$, $A_{\|} = 170(1) \times 10^{-4}$ cm^{-1}, $A_{\perp} = 59.7(1) \times 10^{-4}$ cm^{-1} and $A_{iso} = (2A_{\perp} + A_{\|})/3 = 96.5 \times 10^{-4}$ cm^{-1}. The experimentally deduced pair of values ($g_{\|} = 1.942(2)$ and $A_{\|} = 170(1) \times 10^{-4}$ cm^{-1}) support an O_4 basal plane of the octahedron [60].

The value of $A_{\|}$ is helpful in predicting the nature of the equatorial ligands of the VO^{2+} moiety through the "additivity principle" [70–72]. In the present case, the ligands involved are two O_{carb} and two O_{pyr} atoms of PPA ligands and one O_w atom. From the literature we obtained $A_{\|}(O_{pyr}) = 38.6 \times 10^{-4}$ cm^{-1}, $A_{\|}(O_{carb}) = 42.7 \times 10^{-4}$ cm^{-1} and $A_{\|}(O_w) = 45.7 \times 10^{-4}$ cm^{-1} [71,72]. By making use of these values, the three possible configurations and the respective $A_{\|}$ values are: (i) two O_{carb} and two O_{pyr} atoms of PPA with O_w at the axial position and $A_{\|} = 162.6 \times 10^{-4}$ cm^{-1}, (ii) two O_{pyr}, one O_{carb} atoms of PPA and one O_w with the other O_{carb} at the axial position and $A_{\|} = 165.6 \times 10^{-4}$ cm^{-1} and (iii) two O_{carb}, one O_{pyr} atoms of PPA and one O_w with the other O_{pyr} at the axial position and $A_{\|} = 169.7 \times 10^{-4}$ cm^{-1}. We observe that the configuration with an axial O_w gives rise to a relatively low $A_{\|}$ value in comparison to the experimental value of $A_{\|} = 170(1) \times 10^{-4}$ cm^{-1}, suggesting that O_w occupies an equatorial position, lying *cis* to O_v. Among the other two configurations, the conformation with O_{pyr} at the axial position is more consistent with the EPR parameters and in agreement with that observed in the crystal structure of the complex VO(ciprofloxacinato)$_2$(H_2O) [45] where $A_{\|} = 173 \times 10^{-4}$ cm^{-1}, leading us to the conclusion that the equatorial sites of the octahedron around V are occupied by two O_{carb} and one O_{pyr} atoms of PPA ligands and one O_w, with the second O_{pyr} at the axial position *trans* to O_v.

The EPR spectrum of $Fe(PPA)_3$ in DMSO at 12 K shows a signal at $g \sim 4.3$, characteristic for a high-spin Fe^{3+} ion in an almost rhombic environment. The EPR spectrum of $Mn(PPA)_2(H_2O)_2$ in DMSO consists of a six line pattern at $g \sim 2.0$, typical for a mononuclear Mn^{2+} ($S = 5/2$) complex. The EPR spectrum of $Co(PPA)_2(H_2O)_2$ in DMF at 10 K is rather complicated; it exhibits multiple signals, has a maximum at $g \sim 5.7$ and is consistent for a mononuclear octahedral high-spin Co^{2+} ($S = 3/2$) complex.

Table 3
Chemical shifts (ppm) in ^{1}H NMR spectra of HPPA, $Zn(PPA)_2(H_2O)_2$ and $UO_2(PPA)_2$ in d_6-DMSO

	HPPA	$Zn(PPA)_2(H_2O)_2$	$UO_2(PPA)_2$
H2 and H5	8.90 (2H)	8.16 (2H)	8.16 (2H)
H1a	4.39 (2H)	4.39 (2H)	4.40 (2H)
H1b	1.36 (3H)	1.35 (3H)	1.35 (3H)
H2′, H6′ or	3.14–3.25 (4H)	3.15–3.23 (4H)	3.15–3.26 (4H)
H3′, H5′	3.86(4H)	3.81(4H)	3.70 (4H)
H4′	9.19 (1H)	8.91 (1H)	8.91 (1H)

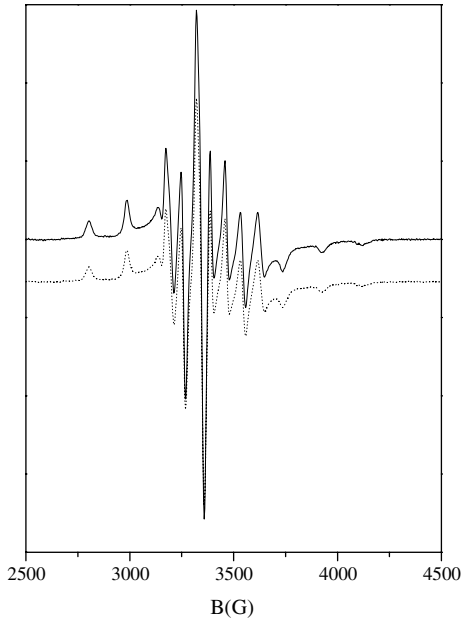


Fig. 2. Experimental (——) and theoretical (·····) EPR spectrum for complex $VO(PPA)_2(H_2O)$ in DMSO. EPR conditions: $T = 12$ K; microwave power = 0.13 mW; modulation amplitude = 5 Gpp; microwave frequency = 9.42 GHz.

3.6. Molecular dynamics

3.6.1. $Fe(PPA)_3$

In order to present a model for the complex we have constructed the two *fac*- and the two *mer*-$Fe(PPA)_3$

enantiomers (Scheme S1). The average energy of each set of enantiomers is almost equal, as is expected from such molecular mechanics calculations. However, the final structures of *mer*-[Fe(PPA)$_3$] exhibit lower energies by less than 0.3 kcal mol^{-1} in comparison to the energies of the *fac* isomers. For the *mer* models we have applied a set of harmonic restraints at the metal–ligand bonds during an additional minimization phase (Table S1) [49–52]. Based on these results we present the lowest energy model of one *mer*-[Fe(PPA)$_3$] enantiomer as the favorable configuration of the complex (Fig. S1). However, we can neither exclude the formation of any of the other isomers, nor unambiguously distinguish between the favorable enantiomers.

3.6.2. VO(PPA)$_2$(H$_2$O)

Using the same approach as above, 8 diastereoisomers of the VO(PPA)$_2$(H$_2$O) complex have been constructed (Scheme S2). In all these models the water molecule occupies a *cis* position with respect to V = O, in accordance with our EPR results and just as in similar vanadyl complexes [45–48]. Again, the resultant models of all VO(PPA)$_2$(H$_2$O) isomers exhibit comparable average total energy with the two *transOc* enantiomers (as are arbitrarily designated in Scheme S2) being more stable by more than 2 kcal mol^{-1} (Table S4). After application of the distance restraints to the M–L bonds (Table S3) and their geometry correction by minimizing the energy of the complex, the structure of the predicted most stable isomer is obtained (Fig. 3).

3.6.3. MoO$_2$(PPA)$_2$

Three pairs of enantiomers have been constructed as starting models of MoO$_2$(PPA)$_2$ (Scheme S3). After the Langevin dynamics simulated annealing calculations, we obtained the total energy results of 20 different conformations for each starting model, which guide us to select the *transOc* isomers as the more favorable. Their average energy is almost equal, as expected, and is lower than the other four isomers by more than 3 kcal mol^{-1} (Table S6). The lowest energy model structure found is illustrated in Fig. S3.

3.7. Antimicrobial activity

The efficiencies of the complexes have been tested against two Gram(−), *Escherichia coli* (*E. coli*) and *Pseudomonas aeruginosa* (*P. aeruginosa*), and one Gram(+), *Staphylococcus aureus* (*S. aureus*), microorganisms. The results are presented in Table 4.

It is evident (Table 4) that the ligand and the complexes have inhibitory action against all microorganisms tested and the coordination of HPPA (MIC = 16–64 μg mL^{-1}) with transition metal ions results in diverse biological activity (MIC for the complexes = 8–64 μg mL^{-1}). The activity of complexes VO(PPA)$_2$(H$_2$O), Mn(PPA)$_2$(H$_2$O)$_2$, MoO$_2$(PPA)$_2$ and Cd(PPA)$_2$(H$_2$O)$_2$ is equal to that of HPPA against all microorganisms tested. Complexes Fe(PPA)$_3$

Table 4
MIC in μg mL^{-1}

	E. coli	*P. aeruginosa*	*S. aureus*
HPPA	64	64	16
VO(PPA)$_2$(H$_2$O)	64	64	16
Mn(PPA)$_2$(H$_2$O)$_2$	64	64	16
Fe(PPA)$_3$	64	64	32
Co(PPA)$_2$(H$_2$O)$_2$	64	64	32
Ni(PPA)$_2$(H$_2$O)$_2$	64	32	32
Zn(PPA)$_2$(H$_2$O)$_2$	32	32	32
MoO$_2$(PPA)$_2$	64	64	16
Cd(PPA)$_2$(H$_2$O)$_2$	64	64	16
UO$_2$(PPA)$_2$	8	8	8

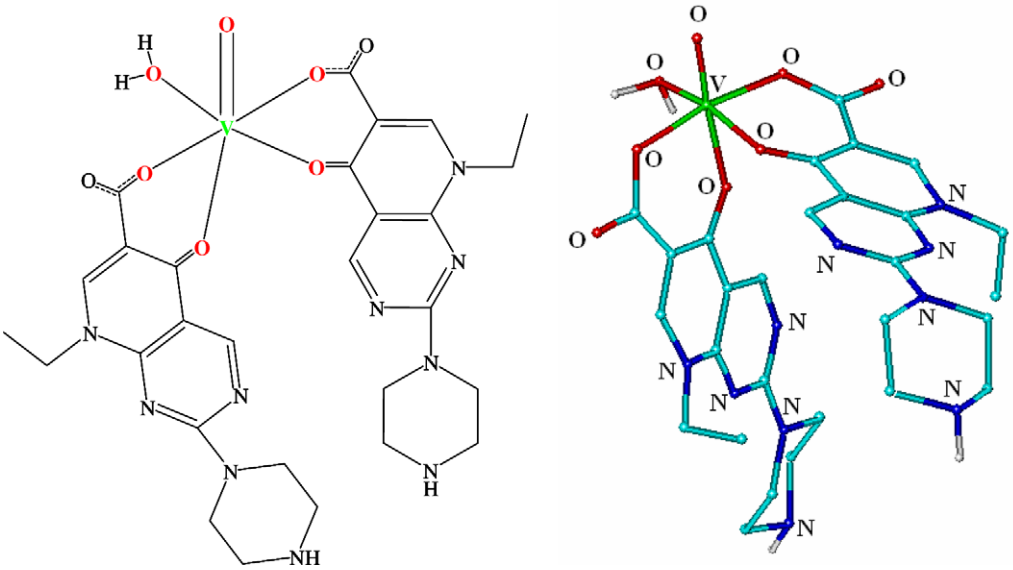


Fig. 3. Lowest energy model of VO(PPA)$_2$(H$_2$O).

and $Co(PPA)_2(H_2O)_2$ have antibacterial activity against *E. coli* and *P. aeruginosa* similar to that of HPPA (MIC = 64 μg mL^{-1}), but they are twice less active against *S. aureus* (MIC = 32 μg mL^{-1}). The antibacterial activity of $Ni(PPA)_2(H_2O)_2$ against *E. coli* is equal to that of HPPA. $Ni(PPA)_2(H_2O)_2$ is twice more active than HPPA against *P. aeruginosa* and twice less active against *S. aureus*. $Zn(PPA)_2(H_2O)_2$ is twice more active than HPPA against two Gram(−) microorganisms but twice less active against *S. aureus*. Finally, $UO_2(PPA)_2$ is four and two times more active than HPPA against two Gram(−) microorganisms and *S. aureus*, respectively.

The antimicrobial activity of the metal salts has also been investigated. It has been found that the metal salts do not exhibit antimicrobial activity at the concentration range used to assay the activity of the complexes in this work. When the antimicrobial activity of the metal complexes is investigated, the following principal factors [73,74] should be considered: (i) the chelate effect of the ligands; (ii) the nature of the *N*-donor ligands; (iii) the total charge of the complex; (iv) the existence and the nature of the ion neutralizing the ionic complex; (v) the nuclearity of the metal center in the complex. For complexes **1**–**9**, only the first of these factors is present, i.e. the chelate effect of the ligand. This is probably one of the main reasons for the diverse antibacterial activity shown by the complexes while the nature of the metal ion coordinated to PPA may have a significant role in this diversity. The significant improvement of the activity of PPA when coordinated to the uranyl complex is simply an evidence of the role of the coordinated metal ion [45]. On the other hand, further biological experiments in order to clarify the possible mechanism of action of the complexes are under investigation.

In conclusion, the best inhibition of the complexes is provided by $UO_2(PPA)_2$ (MIC = 8 μg mL^{-1}) against the three microorganisms tested.

3.8. Interaction of the complexes with CT DNA

DNA can provide three distinctive binding sites for the quinolone complexes; namely, groove binding, binding to phosphate group and intercalation [75]. This behavior is of great importance with regard to the relevant biological role of fluoroquinolone antibiotics in the human body [76,77].

3.8.1. Study of the complexes – CT DNA interaction with UV spectroscopy

The absorption spectra of the interaction of the complexes with CT DNA have been recorded for a constant CT DNA concentration (3.125×10^{-4} M) in different mixing ratios. Representative UV spectra of the complexes **1**, **2** and **9** with CT DNA derived for diverse complex:CT DNA mixing ratios (*r*) are shown in Fig. 4 while UV spectra of all the complexes with CT DNA are shown in Fig. S4. The changes observed in the absorption spectra

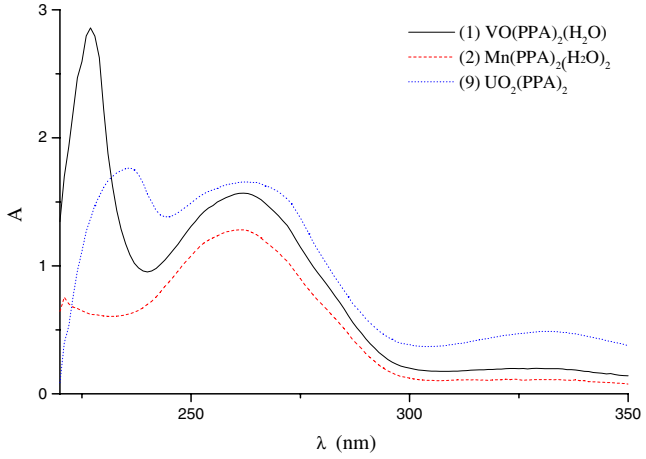


Fig. 4. Absorption spectra of complexes **1**, **2** and **9** in the presence of CT DNA. The *r* value is 1:200. The spectra were recorded at 25 °C after complexes had been incubated with CT DNA for 24 h at 37 °C.

of the complexes after mixing with CT DNA indicate that the interaction of the complexes with CT DNA takes place by a direct formation of a new complex with double-helical CT DNA [78].

3.8.2. Study of the complexes – CT DNA interaction with CD spectroscopy

The CD spectra of the complexes with double-stranded CT DNA for different *r* values can provide us with useful information concerning the complex–nucleotide interaction. The CD spectra of the interaction of the free ligand with CT DNA do not show any transitions because there is not any asymmetry or chirality in the molecules [78].

The CD spectrum of free CT DNA is conservative and consists of a negative band at 245 nm and a positive one at 275 nm, characteristic of the B-form of DNA [79]. The CD spectra of CT DNA in the presence of complex **1** are shown in Fig. 5a. They consist of a positive band I at 275 nm and a strong negative one II at 246 nm. When *r* increases, the λ_{max} of band I is shifted from 275 nm to higher wavelengths (up to 282 nm) followed by a decrease of the intensity, indicating that the DNA-form changes from the B- to A-form (B → A transition). This change (CD Cotton effect) is characteristic of reduced DNA helicity which is attributed to complex interstrand crosslinking to the DNA pairs [80]. Quite similar behavior is observed in the CD spectra of CT DNA in the presence of complex $MoO_2(PPA)_2$.

The CD spectra of CT DNA in the presence of complex **2** are shown in Fig. 5b. The increase of *r* leads to a raise in the intensity of band I at 275 nm and a shift of the λ_{max} from 280 nm to lower wavelengths (up to 274 nm) while the negative band at 246 nm remains practically unchanged. The overall changes in the CD spectra indicate the existence of a B → A CT DNA transition that can be attributed to intrastrand linking of adjacent

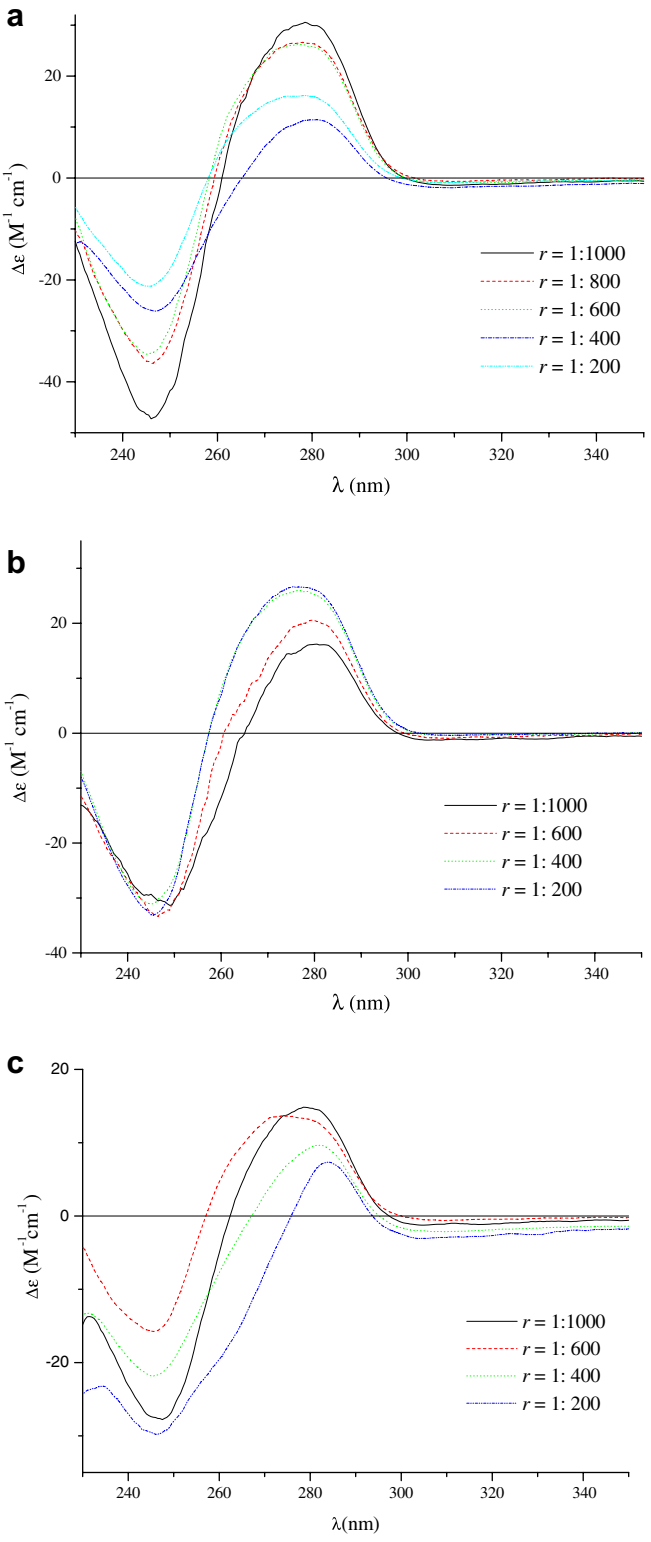


Fig. 5. CD spectra of CT DNA in 5 mM buffer (containing 150 mM NaCl and 15 mM trisodium citrate at pH 7.0) in the presence of: (a) complex $VO(PPA)_2(H_2O)$ (**1**), (b) complex $Mn(PPA)_2(H_2O)_2$ (**2**) and (c) complex $UO_2(PPA)_2$ (**9**), with different r values. The spectra were recorded at 25 °C after samples had been incubated with CT DNA for 24 h at 37 °C.

guanines so that the DNA conformation is modified and destacking of the adjacent bases occurs [81–83]. Similar behavior is observed in the CD spectra of CT DNA in the presence of complexes $Fe(PPA)_3$, $Co(PPA)_2(H_2O)_2$, $Ni(PPA)_2(H_2O)_2$, $Zn(PPA)_2(H_2O)_2$ and $Cd(PPA)_2(H_2O)_2$.

The CD spectra of CT DNA in the presence of complex $UO_2(PPA)_2$ (**9**) are shown in Fig. 5c. The λ_{max} of positive band I is shifted from 275 nm to higher wavelengths (up to 285 nm) followed by a decrease in the intensity upon increase of r, while the intensity of the negative band II at 246 nm increases indicating that the DNA-form changes from the B- to A-form (B → A transition) [81].

4. Conclusions

The synthesis and characterization of nine mononuclear complexes of the first-generation quinolone antibacterial drug pipemidic acid with the ions VO^{2+}, Mn^{2+}, Fe^{3+}, Co^{2+}, Ni^{2+}, Zn^{2+}, MoO_2^{2+}, Cd^{2+} and UO_2^{2+} has been realized with physicochemical and spectroscopic methods. In all the complexes, the pipemidato ligand is bound to the metal via the pyridone oxygen and one carboxylate oxygen atom. Each metal is six-coordinate and its environment could be described as a distorted octahedron. With the use of molecular modelling, we have proposed a low energy model for the structures of $Fe(PPA)_3$, $VO(PPA)_2(H_2O)$ and $MoO_2(PPA)_2$. The antimicrobial activity of the complexes has been tested on three different microorganisms. The complexes show diverse biological activity in comparison to the free pipemidic acid. The best inhibition of the complexes is provided by $UO_2(PPA)_2$ ($MIC = 8\ \mu g\ mL^{-1}$) against the three microorganisms tested. The investigation of the interaction of the complexes with CT DNA has been performed with diverse spectroscopic techniques and showed that the complexes can be bound to CT DNA. For all the complexes, a B → A CT DNA transition has been observed.

Acknowledgements

The authors are grateful to E.L.K.E (70/4/6495) and the "Excellence in the Research Institutes" Program (Action 3.3.1 co-funded by the Greek Ministry of Development and E.U.) for financial support. We thank Prof. M.P. Hendrich, Department of Chemistry, Carnegie Melon University, Pittsburgh, USA for providing us with the EPR simulation program and Dr. I. Eskioglou, Department of Medical Laboratories, Technological and Educational Institution of Larissa, Larissa, Greece for the supply of the microorganisms.

Appendix A. Supplementary material

IR and UV–Vis spectral data for HPPA and all the complexes and ^1H NMR chemical shifts for HPPA, $MoO_2(PPA)_2$ and $UO_2(PPA)_2$. Three schemes (Schemes S1–S3) for the diastereoisomers of $Fe(PPA)_3$, $VO(PPA)_2(H_2O)$ and $MoO_2(PPA)_2$ employed in the simulated annealing calculations. Three Tables (Table S1, S3, and S5)

for the metal–ligand distance restraints applied during the energy minimization phase in order to adjust the geometry of $Fe(PPA)_3$, $VO(PPA)_2(H_2O)$ and $MoO_2(PPA)_2$ models. Three Tables (Table S2, S4, and S6) for the energy statistics from the simulated annealing results of $Fe(PPA)_3$, $VO(PPA)_2(H_2O)$ and $MoO_2(PPA)_2$ diastereoisomers, respectively. Three figures (Figs. S1–S3) for the lowest energy models of $[Fe(PPA)_3]$, $VO(PPA)_2(H_2O)$ and $MoO_2(PPA)_2$ enantiomers. One figure (Fig. S4) for representative UV spectra of all the complexes with CT DNA. Supplementary data associated with this article can be found, in the online version, at doi:10.1016/j.poly.2006.10.017.

References

[1] A. Albert, The Physico-Chemical Basis of Therapy: Selective Toxicity, 6th ed., Chapman & Hall, London, 1979.
[2] M.N. Hughes (Ed.), The Inorganic Chemistry of Biological Processes, 2nd ed., Wiley, New York, 1981.
[3] J. Liu, E.B. Wang, J. Peng, Y.S. Zhou, J. Rare Earths 17 (1999) 139.
[4] S. Chakrabarti, D. Dasgupta, D. Bhattacharyya, J. Biol. Phys. 26 (2000) 203.
[5] I. Turel, Coord. Chem. Rev. 232 (2002) 27.
[6] D. Rehder, J. Costa Pessoa, C.F.G.C. Geraldes, T. Kabanos, T. Kiss, B. Meier, G. Micera, L. Pettersson, M. Rangel, A. Salifoglou, I. Turel, D. Wang, J. Biol. Inorg. Chem. 7 (2002) 384.
[7] S.C. Wallis, L.R. Gahan, B.G. Charles, T.W. Hambley, Polyhedron 14 (1995) 2835.
[8] I. Turel, I. Leban, N. Bukovec, J. Inorg. Biochem. 56 (1994) 273.
[9] I. Turel, L. Golic, O.L. Ruiz Ramirez, Acta Chim. Slov. 46 (1999) 203.
[10] C. Chulvi, M.C. Munoz, L. Perello, R. Ortiz, M.I. Arriortua, J. Via, K. Urtiaga, J.M. Amigo, L.E. Ochando, J. Inorg. Biochem. 42 (1991) 133.
[11] M. Ruiz, R. Ortiz, L. Perello, A. Castineiras, M. Quiros, Inorg. Chim. Acta 211 (1993) 133.
[12] M. Ruiz, R. Ortiz, L. Perello, J. Latorre, J. Server-Carrio, J. Inorg. Biochem. 65 (1997) 87.
[13] M. Ruiz, L. Perello, R. Ortiz, A. Castineiras, C. Maichle-Mossmer, E. Canton, J. Inorg. Biochem. 59 (1995) 801.
[14] M. Ruiz, R. Ortiz, L. Perello, S. Garcia-Granda, M.R. Diaz, Inorg. Chim. Acta 217 (1994) 149.
[15] M. Ruiz, L. Perello, J. Server-Carrio, R. Ortiz, S. Garcia-Granda, M.R. Diaz, E. Canton, J. Inorg. Biochem. 69 (1998) 231.
[16] A. Koppenhofer, U. Hartmann, H. Vahrenkamp, Chem. Ber. 128 (1995) 779.
[17] B. Macias, M.V. Villa, I. Rubio, A. Castineiras, J. Borras, J. Inorg. Biochem. 84 (2001) 163.
[18] Z.-F. Chen, R.-G. Xiong, J. Zhang, X.-T. Chen, Z.-L. Xue, X.-Z. You, Inorg. Chem. 40 (2001) 4075.
[19] G. Mendoza-Diaz, L.M.R. Martinez-Aguilera, R. Perez-Alonso, Inorg. Chim. Acta 138 (1987) 41.
[20] G. Mendoza-Diaz, L.M.R. Martinez-Aguilera, R. Moreno-Esparza, K.H. Pannell, F. Cervantes-Lee, J. Inorg. Biochem. 50 (1993) 65.
[21] S.C. Wallis, L.R. Gahan, B.G. Charles, T.W. Hambley, P.A. Duckworth, J. Inorg. Biochem. 62 (1996) 1.
[22] I. Turel, K. Gruber, I. Leban, N. Bukovec, J. Inorg. Biochem. 61 (1996) 197.
[23] Z.-F. Chen, B.-Q. Li, Y.-R. Xie, R.-G. Xiong, X.-Z. You, X.-L. Feng, Inorg. Chem. Commun. 4 (2001) 346.
[24] L.Z. Wang, Z.F. Chen, Z.S. Wang, H.Y. Li, R.G. Xiong, X.Z. You, Chin. J. Inorg. Chem. 18 (2002) 1185.
[25] D.J. Wang, Z.D. Fang, D.Y. Han, Chem. Res. Chin. Univ. 21 (2005) 258.
[26] E.I. Steifel, in: G. Wilkinson (Ed.), Comprehensive Coordination Chemistry, vol. 3, Pergamon Press, Oxford, 1989, pp. 1375–1420.
[27] P. Testillano, M. Sanchez-Pina, A. Olmedilla, M. Ollacarizqueta, C. Tandler, M. Risueno, J. Histochem. Cytochem. 39 (1991) 1427.
[28] P.E. Nielsen, C. Hiort, S.H. Sonnichsen, O. Buchardt, O. Dahl, B. Norden, J. Am. Chem. Soc. 114 (1992) 4967.
[29] A. Papakyriakou, A. Anagnostopoulou, A. Garnier-Suillerot, N. Katsaros, Eur. J. Inorg. Chem. (2002) 1146.
[30] K.G. Naber, J. Antimicrob. Chemother. 46 (2000) 49.
[31] V. Mersch-Sundermann, K.H. Hauff, P. Braun, W. Lu, Int. J. Oncol. 5 (1994) 855.
[32] L. Yang, W. Li, D.L. Tao, Y.F. Li, X.L. Yang, Synth. React. Inorg. Met.-Org. Chem. 29 (1999) 1485.
[33] L. Yang, D. Tao, X. Yang, Y. Li, Y. Guo, Chem. Pharm. Bull. 51 (2003) 494.
[34] B. Szymanska, D. Skrzypek, D. Kovala-Demertzi, M. Staninska, M.A. Demertzis, Spectrochim. Acta A 63 (2006) 518.
[35] B. Qiao, Y. Lu, C. Xuan, Chem. Res. Chin. Univ. 10 (1994) 341.
[36] E.K. Efthimiadou, Y. Sanakis, M. Katsarou, C.P. Raptopoulou, A. Karaliota, N. Katsaros, G. Psomas, J. Inorg. Biochem. 100 (2006) 1378.
[37] E.K. Efthimiadou, Y. Sanakis, C.P. Raptopoulou, A. Karaliota, N. Katsaros, G. Psomas, Bioorg. Med. Chem. Lett. 16 (2006) 3864.
[38] G. Psomas, A. Tarushi, E.K. Efthimiadou, Y. Sanakis, C.P. Raptopoulou, N. Katsaros, J. Inorg. Biochem. 100 (2006) 1764.
[39] E.K. Efthimiadou, H. Thomadaki, Y. Sanakis, C.P. Raptopoulou, N. Katsaros, A. Scorilas, A. Karaliota, G. Psomas, J. Inorg. Biochem. (2006) (doi: doi:10.1016/j.jinorgbio.2006.07.019).
[40] E. Tselepi-Kalouli, N. Katsaros, J. Inorg. Biochem. 37 (1989) 271.
[41] A.P. Golombek, M.P. Hendrich, J. Magn. Reson. 165 (2003) 33.
[42] A.K. Upadhyay, A.B. Hooper, M.P. Hendrich, J. Am. Chem. Soc. 128 (2006) 4330.
[43] N.L. Allinger, J. Am. Chem. Soc. 99 (1977) 8127.
[44] P. Christofis, M. Katsarou, A. Papakyriakou, Y. Sanakis, N. Katsaros, G. Psomas, J. Inorg. Biochem. 99 (2005) 2197 (and references therein).
[45] I. Turel, A. Golobic, A. Klavzar, B. Pihlar, P. Buglyo, E. Tolis, D. Rehder, K. Sepcic, J. Inorg. Biochem. 95 (2003) 199.
[46] I. Correia, J. Costa Pessoa, M.T. Duarte, R.T. Henriques, M.F.M. Piedade, L.F. Veiros, T. Jakusch, T. Kiss, A. Dornyei, M.M.C.A. Castro, C.F.G.C. Geraldes, F. Avecilla, Chem. Eur. J. 10 (2004) 2301.
[47] S.S. Amin, K. Cryer, B. Zhang, S.K. Dutta, S.S. Eaton, O.P. Anderson, S.M. Miller, B.A. Reul, S.M. Brichard, D.C. Crans, Inorg. Chem. 39 (2000) 406.
[48] J. Costa Pessoa, I. Cavaco, I. Correia, I. Tomaz, T. Duarte, P.M. Matias, J. Inorg. Biochem. 80 (2000) 35.
[49] M. Scarpellini, A. Neves, A.J. Bortoluzzi, I. Vencato, V. Drago, W.A. Ortiz, C. Zucco, J. Chem. Soc., Dalton Trans. (2001) 2616.
[50] L. Westerheide, F.K. Muller, R. Than, B. Krebs, J. Dietrich, S. Schindler, Inorg. Chem. 40 (2001) 1951.
[51] J.M. Rowland, M. Olmstead, P.K. Mascharak, Inorg. Chem. 40 (2001) 2810.
[52] K. Matsumoto, T. Ozawa, K. Jitsukawa, H. Einaga, H. Masuda, Inorg. Chem. 40 (2001) 190.
[53] E.J. Brown, A.C. Whitwood, P.H. Walton, A.-K. Duhme-Klair, J. Chem. Soc., Dalton Trans. (2004) 2458.
[54] Z.-H. Zhou, S.-Y. Hou, Z.-X. Cao, H.-L. Wan, S.-W. Ng, J. Inorg. Biochem. 98 (2004) 1037.
[55] S.-M. Chen, C.-Z. Lu, Y.-Q. Yu, Q.-Z. Zhang, X. He, Acta Crystallogr., Sect. C 60 (2004) m437.
[56] A.-K. Duhme-Klair, G. Vollmer, C. Mars, R. Frohlich, Angew. Chem., Int. Ed. 39 (2000) 1626.
[57] M.P. Allen, D.J. Tildesley (Eds.), Computer Simulation of Liquids, Oxford University Press, Oxford, 1989.
[58] C. Dendrinou-Samara, G. Tsotsou, C.P. Raptopoulou, A. Kortsaris, D. Kyriakidis, D.P. Kessissoglou, J. Inorg. Biochem. 71 (1998) 171.

[59] K. Nakamoto, Infrared and Raman Spectra of Inorganic and Coordination Compounds, 4th ed., Wiley, New York, 1986.
[60] G.B. Deacon, R.J. Phillips, Coord. Chem. Rev. 33 (1980) 227.
[61] E.J. Tolis, V.I. Teberekidis, C.P. Raptopoulou, A. Terzis, M.P. Sigalas, Y. Deligiannakis, T.A. Kabanos, Chem. Eur. J. 7 (2001) 2698.
[62] E. Garribba, G. Micera, A. Panzanelli, D. Sanna, Inorg. Chem. 42 (2003) 3981.
[63] H. Kelm, H.-J. Kruger, Inorg. Chem. 35 (1996) 3533.
[64] M. Nakai, M. Obata, F. Sekiguchi, M. Kato, M. Shiro, A. Ichimura, I. Kinoshita, M. Mikuriya, T. Inohara, K. Kawabe, H. Sakurai, C. Orvig, S. Yano, J. Inorg. Biochem. 98 (2004) 105.
[65] W.O. Koch, V. Schunemann, M. Gerdan, A.X. Trautwein, H.-J. Krüger, Chem. Eur. J. 4 (1998) 1255.
[66] H. Chun, C.N. Verani, P. Chaudhuri, E. Bothe, E. Bill, T. Weyhermuller, K. Wieghardt, Inorg. Chem. 40 (2001) 4157.
[67] D.A. Buckingham, C.R. Clark, in: G. Wilkinson (Ed.), Comprehensive Coordination Chemistry, vol. 4, Pergamon Press, Oxford, 1989, pp. 635–900.
[68] L. Sacconi, F. Mani, A. Bencini, in: G. Wilkinson (Ed.), Comprehensive Coordination Chemistry, vol. 5, Pergamon Press, Oxford, 1989, pp. 1–347.
[69] M. Sakai, A. Hara, S. Anjo, M. Nakamura, J. Pharm. Biomed. Anal. 18 (1999) 1057.
[70] N.D. Chasteen (Ed.), Biological Magnetic Resonance, Plenum, New York, 1981, pp. 53–119 (Chapter 2).
[71] T.S. Smith, R. LoBrutto, V.L. Pecoraro, Coord. Chem. Rev. 228 (2002) 1 (and references therein).
[72] T.S. Smith, C.A. Root, J.W. Kampf, P.G. Rasmussen, V.L. Pecoraro, J. Am. Chem. Soc. 122 (2000) 767.
[73] A.D. Russell, in: S.S. Block (Ed.), Disinfection, Sterilization and Preservation, 4th ed., Lea & Febiger, Philadelphia, PA, 1991, pp. 27–59.
[74] H.W. Rossmore, in: S.S. Block (Ed.), Disinfection, Sterilization and Preservation, 4th ed., Lea & Febiger, Philadelphia, PA, 1991, pp. 290–321.
[75] A. Rodger, B. Norden (Eds.), Circular Dichroism and Linear Dichroism, Oxford University Press, Oxford, 1997.
[76] G. Song, Y. He, Z. Cai, J. Fluoresc. 14 (2004) 705.
[77] P. Drevensek, I. Turel, N.P. Ulrih, J. Inorg. Biochem. 96 (2003) 407.
[78] G.S. Son, J-.A. Yeo, M.-S. Kim, S.K. Kim, A. Holmen, B. Akerman, B. Norden, J. Am. Chem. Soc. 120 (1998) 6451.
[79] W. Curtis-Johnson, in: K. Nakanishi, N. Berova, R.W. Woody (Eds.), CD of Nucleic Acids in Circural Dichroism, Principles and Applications, VHS, New York, 1994, pp. 523–540.
[80] C.K.S. Pillai, U.S. Nandi, Biochim. Biophys. Acta 474 (1977) 11.
[81] N. Nikolis, C. Methenitis, G. Pneumatikakis, J. Inorg. Biochem. 95 (2003) 177.
[82] T.C. McGregor, Z. Balcharova, Y. Qu, M.-C. Tran, R. Zadulova, V. Brabec, N. Farrel, J. Inorg. Biochem. 77 (1999) 43.
[83] T.C. Jenkins, in: K.R. Fox (Ed.), Drug–DNA Interaction Protocols, Humana Press, Totowa, NJ, 1997, pp. 195–218.

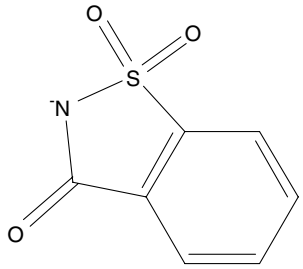


Fig. 1. The structure of the saccharinate anion.

A suggestion has been made that the importance of saccharin complexes lies in the potential use of saccharin as an antidote for metal poisoning [11,13]. Metal complexes of saccharin could also play a role in understanding human metabolic processes [6].

Since very little information has been reported on mixed-ligand complexes containing saccharin and tridentate sulfur–nitrogen chelating agents as co-ligands, we report herein the synthesis, characterization and bioactivity of mixed-ligand copper (II) complexes of three HNNS ligands formed between *S*-benzyldithiocarbazate with 2-acetylpyridine, 2-benzoylpyridine and 6-methyl pyridine-2-aldehyde (Fig. 2) with saccharinate anion as a co-ligand.

2. Experimental

All chemicals and solvents were of analytical grade and were used as received. The *S*-benzyldithiocarbazate (SBDTC), its Schiff bases (HNNS′, HNNS″ and HNNS‴ and $[Cu(sac)_2(H_2O)_4]\cdot 2H_2O$ were prepared by the following literature methods [6,14–16].

2.1. General method of synthesis of the complexes

$[Cu(sac)_2(H_2O)_4]\cdot 2H_2O$ [6] (0.536 g, 0.001 mol) dissolved in boiling water (25 ml) was mixed with a solution of the appropriate Schiff base (0.001 mol) in ethanol (40 ml), and the resulting mixture was heated on a water bath for 30 min. On standing overnight, the mixture yielded crystalline complexes which were filtered, washed with ethanol and dried in a desiccator over silica gel for 24 h. Yield: (ca. 75%). Crystals of [Cu(NNS′)(sac)] (where NNS′ = *S*-benzyl-β-*N*-(2-acetylpyrid-2-yl)methylenedithiocarbazate) suitable for X-ray diffraction analysis were obtained from an acetonitrile solution.

2.2. Physical measurements

Microanalyses for carbon, hydrogen, nitrogen and sulphur were carried out using a LECO CHNS-932 instrument. The IR spectra as KBr pellets were recorded using a Perkin–Elmer FT IR 1750X spectrophotometer (4000–400 cm^{-1}). The molar conductance of 10^{-3} M solutions of the metal complexes in DMSO were measured at 29 °C using a Jenway 4310 conductivity meter and a dip-type cell with a platinized electrode. Magnetic susceptibilities at room temperature were measured using a Sherwood Scientific MSB-AUTO magnetic susceptibility balance. The UV–Vis spectra were run on a Shimadzu UV-2501 PC Recording Spectrophotometer (900–200 nm).

2.3. X-ray structure determination of [Cu(S-benzyl-β-N-(2-acetylpyrid-2-yl)methylenedithiocarbazate)(sac)]

Beautiful green-brown crystals of the metal complex were formed after the acetonitrile solution was allowed to slowly evaporate for a few weeks. A selected crystal was mounted on a glass fibre using perfluoropolyether oil and cooled rapidly to 150 K in a stream of cold N_2 using an Oxford Cyrosystems CYROSTREAM unit. Diffraction data were measured using an Enraf-Nonius Kappa CCD diffractometer (graphite-monochromated Mo Kα radiation, $\lambda = 0.71073$ Å). Intensity data were processed using the DENZO-SMN package [17]. The structures were solved using the direct-methods program [18] to locate all non-hydrogen atoms. Subsequent full-matrix least-squares refinement on *F* was carried out using CRYSTALS Program Suite [19]. Coordinates and anisotropic thermal parameters of all non-hydrogen atoms were refined. Hydrogen atoms were positioned geometrically after each cycle of refinement. A five-term Chebychev polynomial weighting scheme

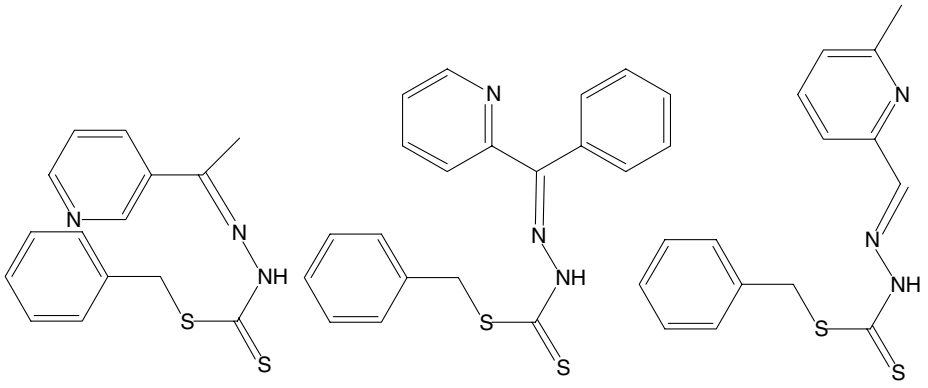


Fig. 2. Structure of HNNS′, HNNS″ and HNNS‴ ligands, respectively (in thione form).

was applied. Refinement converged satisfactorily to give $R = 0.0301$ and $R_w = 0.0360$ with residual electron density minimum and maximum of −0.49 and 0.44 e Å^{-3}. Further crystallographic and refinement details are shown in Table 3.

2.4. Bioactivity

2.4.1. Target microorganisms

Eight pathogenic microbials were used to test the biological potential of the complexes. They were *Methicillin resistant staphylococcus* (MRSA), *Bacillus subtilis* wild type (B29), *Subtilis mutant* (mutant defective DNA repair-B28), *Pseudomonas aeruginosa* (60690), *Candida albicans* (CA), *Aspergillus ochraceous* (398), *Saccaromyces ceciricaee* (20341) and *Candida lypolytica* (2075). The source of microbes and culture maintenance were as previously described [20].

2.4.2. Qualitative antimicrobial assay

Antimicrobial activity of each sample was qualitatively determined by a modified disc diffusion method [21] as previously detailed [22]. A lawn of microorganisms was prepared by pipetting and evenly spreading inoculum (10^{-4} cm^3, adjusted turbidometrically to 10^5–10^6 cfu cm^{-3} (cfu: colony forming units) on to agar set in Petri dishes, using Nutrient agar (NA) for the bacteria and potato dextrose agar (PDA) for fungi. Whatman No. 1 filter paper discs of 6 mm diameter were impregnated with stock solution of the compound (100 mg cm^{-3}) and dried under sterile conditions. The dried discs were then placed on the previously inoculated agar surface. The plates were inverted and incubated for 24 h at 30 °C for bacteria and 37 °C for fungi. Antimicrobial activity was indicated by the presence of clear inhibition zones around the discs. Commercially available streptomycin (Sigma, USA) was used for the antibacterial control while nystatin (Sigma, USA) was used as the antifungal control.

2.4.3. Quantitative antimicrobial assay

Compounds that showed positive (>15 mm) anti-microbial inhibition with the disc diffusion assay were subjected to the broth dilution method for the quantitative measurement of microbiostatic (inhibitory) activity as described by Hufford and Clark [23]. The lowest concentration that completely inhibited visible microbial growth was recorded as the minimum inhibitory concentration (MIC, μg cm^{-3}). Streptomycin and nystatin were used as positive controls for bacteria and fungi, respectively.

2.4.4. Cytotoxic assay

The HL-60 (Human T-lymphoblastic leukemia) and MCF-7 cell lines were obtained from the National Cancer Institute, USA. The cells were cultured in RPMI-1640 (Sigma) medium supplemented with 10% fetal calf serum. Cytotoxicity was determined using the microtitration of 3-(4,5-dimethylthiazol-2-yl)-2,5-diphenyltetrazolium bromide (MTT) assay (Sigma, USA) as reported by Mosmann [20]. Controls that contained only cells were included for each sample. Cytotoxicity was expressed as CD_{50}, i.e. the concentration that reduced the absorbance of treated cells by 50% with reference to the control (untreated cells). Doxorubicin, Tamoxifen and Cisplatin were used as standard cytotoxins.

3. Results and discussion

The reaction of $[Cu(sac)_2(H_2O)_4]$ with the Schiff bases in boiling ethanol afforded crystalline complexes containing one Schiff base and one saccharinate ligand. The physicochemical properties of the complexes together with their analytical data are shown in Table 1. The analytical data support the proposed formulations for the complexes. The complexes are sparingly soluble in most organic solvents but dissolve readily in donor solvents such as DMSO and DMF. They appear to be stable in air.

3.1. Magnetic and conductivity data

The complexes exhibit room temperature magnetic moments in the 1.8–1.87 BM range (Table 1), which is normal for a $3d^9$ metal ion in a magnetically dilute environment [8]. Their molar conductance values in DMSO (Table 1) fall in the range of 9.31–27.4 ohm^{-1} cm^2 mol^{-1} indicating that, although some dissociation of these complexes seems to occur in this solvent, the conductance values are much lower than that expected for a 1:1 electrolyte [24]. The con-

Table 1
Analytical data and physical properties of the Cu(II) complexes

Compound[a]	Colour	M.p. (°C)	Λ[b]	μ[c]	Analytical data[d] (%)				
					C	H	N	S	Cu
[Cu(NNS′)(sac)]	brown-green	212	27.41	1.87	48.11 (48.29)	3.30 (3.50)	10.37 (10.24)	17.41 (17.58)	11.35 (11.61)
[Cu(NNS″)(sac)]	dark green	230	9.31	1.80	52.42 (53.32)	3.31 (3.31)	10.22 (9.21)	14.94 (15.82)	10.41 (10.45)
[Cu(NNS‴)(sac)]	green	146	13.41	1.84	47.64 (48.30)	3.75 (3.50)	10.61 (10.24)	17.27 (17.58)	11.77 (11.61)

[a] NNS′ = *S*-benzyl-β-*N*-(2-acetylpyrid-2-yl)methylenedithiocarbazate, NNS″ = *S*-benzyl-β-*N*-(2-benzoylpyrid-2-yl)methylenedithiocarbazate and NNS‴ = *S*-benzyl-β-*N*-(6-methylpyrid-2-yl)methylenedithiocarbazate.
[b] Molar conductance (ohm^{-1} cm^2 mol^{-1}) of ca. 10^{-3} M solutions in DMSO.
[c] Magnetic moments at 298 K.
[d] Calculated values are given in parentheses.

ductivity data, therefore, support that both the saccharinate anion and the Schiff base are coordinated to the central copper (II) ion as uninegatively charged ligands [25].

3.2. Electronic and infrared spectra

The IR spectra of the ligands exhibit the ν(C=N), ν(N–N) and ν(CSS) bands at ca. 1580, 1050–1100 and 800–900 cm^{-1} (Table 2), respectively, which are shifted in the spectra of the metal complexes indicating coordination of the ligands to the copper (II) ions via the pyridyl nitrogen, the azomethine nitrogen and the thiolate sulphur atom. The coordination of the azomethine nitrogen to the metal is indicated by the shift of the ν(C=N) band and the ν(N=N) band to higher frequencies (Table 2). Generally, evidence of coordination of thiosemicarbazone and dithiocarbazate ligands to metal ions via the azomethine nitrogen has been based on the shifting of the azomethine C=N band of the free ligand from higher to lower wavenumbers in the spectra of the metal complexes [26]. However, shifting of this band to both higher and lower frequencies has been reported [27]. The ν(N=N) bands of all the free ligands were shifted to higher wavenumbers on complexation as a result of a reduction in the repulsion between the lone pairs of electrons on the nitrogen atoms due to coordination via the azomethine nitrogen atom [28]. The lowering of the ν(CSS) band in the spectra of the copper (II) complexes as compared to the frequencies for the free ligands indicates coordination through one of the sulphur atoms. The pyridine ring deformation mode at ca. 600 cm^{-1} in the spectra of the free ligands is shifted to higher wavenumbers in the spectra of the complexes indicating coordination of the pyridine ring nitrogen atom to the copper (II) ion. The spectra of the complexes do not exhibit the ν(NH) bands of the free ligands supporting the fact that deprotonation of the ligands occurs during their coordination to the copper (II) ion. In addition to showing the characteristic bands due to the Schiff bases, the IR spectra of the present copper (II) complexes also show the $\nu(SO_2)_{sym}$, $\nu(SO_2)_{assym}$ and ν(C=O) bands for the saccharinate ion at ca. 1150, 1290 and 1640 cm^{-1}, respectively [11,29–31]. An X-ray crystallographic structural analysis of [Cu(*S*-benzyl-β-*N*-(2-acetylpyrid-2-yl)methylenedithiocarbazate)(sac)] agrees with the interpretation of the above IR spectral data.

The electronic spectra of the copper (II) complexes (Table 2) exhibit intra-ligand bands attributable to $n \rightarrow \pi^*$ transition in the range 328–354 nm, $S \rightarrow Cu(II)$ charge transfer band in the 422–400 nm and a d–d band in the 700–640 nm range. The presence of the $S \rightarrow Cu(II)$

Table 3
Crystallographic data and structure refinement details for [Cu(NNS′)(sac)]

Empirical formula	$C_{22}H_{18}CuN_4O_3S_3$
Formula weight	546.15
Temperature (K)	150
Wavelength (Å)	0.71073
Crystal system	triclinic
Space group	$P\bar{1}$
Unit cell dimensions	
a (Å)	8.4795(2)
b (Å)	9.5364(2)
c (Å)	15.5272(4)
α (°)	97.56(9)
β (°)	92.93(1)
γ (°)	115.373(1)
Volume (A^3)	1116.50(5)
Z	2
Absorption coefficient (mm^{-1})	1.293
F(000)	558.00
Crystal size (mm)	$0.08 \times 0.12 \times 0.18$
Reflections collected/unique [R_{int}]	9001/5068 [0.0002]
Maximum and minimum transmission	0.90, 0.86
Data/restraints/parameters	4070/0/298
Goodness-of-fit on F^2	1.063
Final R indices [$I > 3D_i$]	$R = 0.0301$, $R_w = 0.0360$
Largest differential peak and hole (e $Å^{-3}$)	0.44 and −0.49

Table 2
Selected IR bands and electronic spectral data for the ligands and their copper (II)-saccharinate complexes

Compound[a]	IR bands								Electronic spectra[b]
	νNH	νCN	νNN	νCSS	$\nu_s SO_2$	$\nu_{as} SO_2$	νCO	ν(py)	$\lambda_{max}(\log\varepsilon)$ nm(L mol^{-1} cm^{-1})
HNNS′	3175w	1579m	1063s	890w				622m	339(4.4)
HNNS″	3024w 2916w	1582m	1040s	848m				600m	354(4.5)
HNNS‴	3080w 2910w	1584m	1052s	838w				608m	342(4.6)
[Cu(NNS′)(sac)(H_2O)]		1592m	1074m	816w	1154s	1294s	1674s	630m	640(2.7), 398(4.1) 328(4.6)
[Cu(NNS″)(sac)(H_2O)]		1592m	1090m	816m	1156s	1306s	1648s	607m	651(2.4), 422(3.9) 340(4.2)
[Cu(NNS‴)(sac)(H_2O)]		1592m	1057w	789m	1146s	1288vs	1641s	612m	700(2.5) 342(4.2)

[a] NNS′ = *S*-benzyl-β-*N*-(2-acetylpyrid-2-yl)methylenedithiocarbazate, NNS″ = *S*-benzyl-β-*N*-(2-benzoylpyrid-2-yl)methylenedithiocarbazate and NNS‴ = *S*-benzyl-β-*N*-(6-methylpyrid-2-yl)methylenedithiocarbazate.
[b] $\log\varepsilon$ (L mol^{-1} cm^{-1}) are given in parentheses.

LMCT band at ca. 420 nm in all these spectra is indicative of the coordination of the Schiff base to the copper (II) ion via the thiolate sulphur atom [32]. Such LMCT bands are common in the electronic spectra of copper (II) complexes of related tridentate NNS thiosemicarbazone ligands [33]. The presence of a d–d band in the 690–640 nm range agrees well with the position of the d–d band in the electronic spectra of other square-planar copper (II) complexes that contain the CuN_3S chromophore, some structures of which have been established by X-ray diffraction [2,10,22,34,35].

4. The structure of the [Cu(*S*-benzyl-β-*N*-(2-acetylpyrid-2-yl)methylenedithiocarbazate)(sac)] complex

The thermal ellipsoid drawing of the [Cu(NNS′)(sac)] molecule with the atom numbering scheme is shown in Fig. 3. The bond lengths and bond angles are given in Table 4. The complex crystallizes as a monomeric species. As implied by the physicochemical results, the copper (II) ion is of distorted four-coordinate geometry with the donor atoms of the Schiff base being the pyridine nitrogen atom, the azomethine nitrogen atom and the mercapto-sulphur atom. The nitrogen of the saccharinate anion occupies the fourth coordination position. The Schiff base is coordinated to the copper (II) ion in its iminothiolate form. Tautomerism of the dithiocarbazate ligand to its iminothiolate form is expected to convert the C=S bond to a single C–S bond, but the length of the C–S bond in the present complex falls between a C–S single bond and C=S double bond, indicating extensive delocalization over the C–N–N–C–S chain. This is also evident in the interatomic bond distances, C(7)–N(8) [1.295(2) Å], N(8)–N(9)[1.389(2) Å], and C(10)–N(9) [1.301(3) Å]. The C(10)–S(11) bond [1.739(19) Å] retains its partial double bond character with the length between that of a C–S single bond [1.82 Å] and a C=S double bond [1.62 Å]. It is longer than that found in

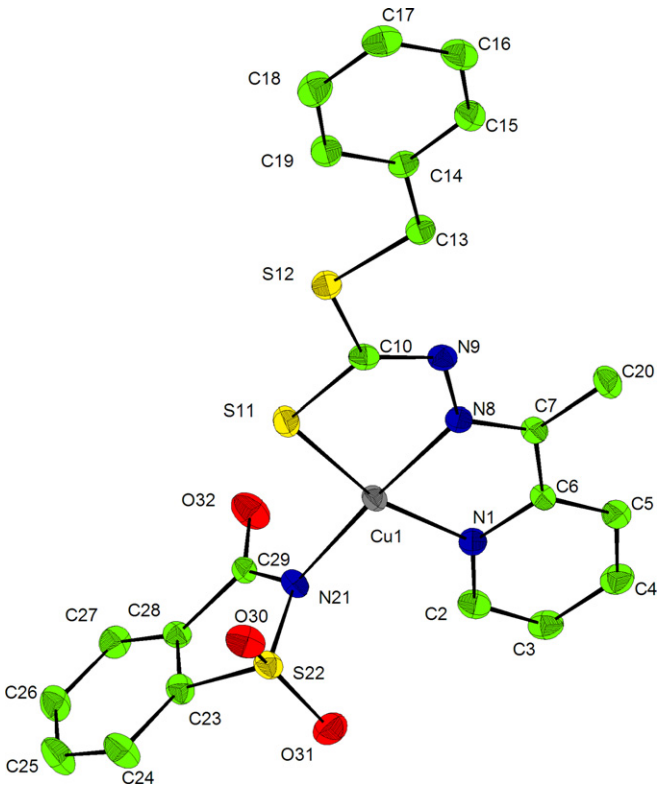


Fig. 3. ORTEP diagram of $C_{22}H_{18}CuN_4O_3S_3$ (with 50% probability displacement ellipsoids) with atomic numbering scheme.

Table 4
Selected bond lengths (Å) and bond angles for [Cu(NNS′)(sac)]

Bond lengths		Bond angles	
Cu(1)–N(1)	2.016(16)	N(1)–Cu(1)–N(1)	165.22(5)
Cu(1)–N(8)	1.958(16)	N(21)–Cu(1)–S(11)	97.51(5)
Cu(1)–S(11)	2.243(5)	N(8)–Cu(1)–S(11)	85.02(5)
Cu(1)–N(21)	1.966(16)	N(21)–Cu(1)–N(1)	96.99(7)
C(7)–N(8)	1.295(2)	N(8)–Cu(I)–N(1)	80.68(7)
N(8)–N(9)	1.389(2)	N(8)–Cu(1)–N(21)	175.76(7)
C(10)–N(9)	1.301(3)		
C(10)–S(11)	1.739(19)		

Table 5
Comparison of bond lengths in some copper (II)-saccharinate complexes

Compound[a]	Cu–N_{sac}	Cu–S	Cu–N_{py}	Cu–N_{azo}	Cu–O_{sac}	Ref.
$[Cu(pytsc)(sac)(H_2O)]\cdot 0.5H_2O$	1.974(8)	2.264(3)	2.020(8)	1.956(8)		[10]
[Cu(pysme)(sac)(MeOH)]	1.967(2)	2.295(9)	2.062(2)	1.958(2)		[35]
$[Cu(6mpsme)(sac)(H_2O)]$	2.004(2)	2.304(8)	2.113(2)	1.973(2)		[34]
$[Cu(sac)(NH_3)_4]$					2.113(8)	[37]
$[Cu(sac)(NH_3)_4]\cdot sac\cdot H_2O$	2.328(2)				2.715(2)	[37]
	2.309(2)				2.705(3)	[37]
$[Cu(sac)_2(mpy)_2]$	2.335(15)		1.9667(13)			[8]
[Cu(NNS′)(sac)]	1.966(16)	2.243(5)	2.016(16)	1.958(16)		this work
$[Cu(sac)(PPh_3)_2]\cdot CH_2Cl_2$	1.933(2)				2.130(2)	[37]
$[Cu(sac)(PPh_3)_2]\cdot \frac{3}{4}CHCl_3$	1.965(5)					[37]
trans-$[Cu(sac)_2(NH_3)_4]$	2.508(12)		2.07(12)			[37]
			2.042(12)			
$[Cu(sac)_2(H_2O)_4]\cdot 2H_2O$	2.061(2)					[2]

[a] pytsc = pyridine-2-aldehydethiosemicarbazone, pysme = pyridine-2-aldehyde SMDTC, 6mpsme = 6-methylpyridine-2-aldehyde SMDTC, mpy = 2-pyridylmethanol.

the free methylpyruvate Schiff base of SMDTC [1.652(6) Å] [25] and pyridine-2-carboxaldehydethiosemicarbazone [1.698(3) Å] [28]. The Cu–S [2.243(5) Å], Cu–$N_{azomethine}$ [1.958(16) Å} and Cu–N_{py} [2.016(16) Å] bond lengths compare well with other copper (II)-saccharinate complexes regardless of the geometry around the central Cu(II) ion, as shown in Table 5.

An examination of the bond angle data in Table 4 shows that the [Cu(NNS′)(sac)] complex does not have ideal square-planar geometry. The angles N(21)–Cu(1)–S(11), N(8)–Cu(1)–S(11), N(21)–Cu(1)–N(1) and N(8)–Cu(1)–N(1) deviate substantially from that expected for an ideal square-planar structure. This distortion could be due to the restricted bite size of the deprotonated tridentate Schiff base ligand.

5. Biological activities

5.1. Antimicrobial activities

These copper (II) complexes have been assayed against several selected pathogens to evaluate their antibacterial and antifungal properties. The results collected in Table 6 indicate that the complexes are weakly active against all the bacteria and fungi chosen (inhibitory zones < 15 mm). The values are lower than those found for both SBDTC and SMDTC [28,36]. The [Cu(NNS‴)(sac)(H_2O)] complex is completely inactive against the bacteria and fungi assayed whereas the [Cu(NNS″)(sac)] complex is completely inactive towards the bacterial strains and weakly active against the fungal strains. This is in contrast with the antimicrobial activities of the complexes of SMDTC that have been shown to exhibit moderate to strong activities against the bacteria and fungi assayed [34]. It appears that the coordination of the saccharinate anion to the copper (II) in the complexes of the present tridentate Schiff base ligands diminishes the antibacterial and antifungal activities of the Schiff bases which were previously found to be active against several bacteria and fungi [34].

5.2. Cytotoxic activities

The measure of cytoxicity used in this work, CD_{50}, is the concentration required to reduce growth of cancer cells by 50%. CD_{50} values <5.0 μg cm^{-3} indicate that the complex is strongly active; CD_{50} values of 5.0–10.0 μg cm^{-3} indicate that the complex is moderately active, values of 10.0–25.0 μg cm^{-3} indicate that the complex is weakly active and values above 25 μg cm^{-3} indicate that the complex is inactive. The complexes, [Cu(NNS″)(sac)] and [Cu(NNS‴)(sac)] exhibit marked activity against the HL-60 cell line (Human Myeloid leukemic cells) with CD_{50}(μg cm^{-3}) values of 0.25 and 0.5, respectively, whereas the complex [Cu(NNS′)(sac)] is inactive. *S*-benzyldithiocarbazate from which the Schiff bases are derived [34] and the simple $CuCl_2 \cdot 2H_2O$ salt are both inactive. Since complexes with bulkier ligands are expected to be thermodynamically less stable, it is possible that the saccharinate ligand from [Cu(NNS″)(sac)] and [Cu(NNS‴)(sac)] are more easily displaced in solution making available a site through which coordination can occur with a suitable donor atom in the cancer cells. All of the Cu(II) complexes reported herein are inactive against the MCF-7 cell line (human breast carcinoma with positive estrogen receptor). The values for the standards, Doxorubicin, Tamoxifen and cisplatin are 0.8, 1.8 and 1.00 μg cm^{-3}, respectively (see Table 7).

Table 7
Cytotoxic activities of the copper (II)-saccharinate complexes

Compound[a]	HL-60	MCF-7	Caov-3
[Cu(NNS′)(sac)]	–	–	0.40
[Cu(NNS″)(sac)]	0.25	–	40.0
[Cu(NNS‴)(sac)]	0.50	–	13.5
Doxorubicin (standard)	0.80		
Tamoxifen (standard)		1.80	
Cisplatin (standard)			1.00

HL-60 = Human Myeloid Leukemic Cells, MCF-7 = Human Breast Carcinoma Cells with Positive Estrogen Receptor, Caov-3 = Human Ovarian Papillary Adenocarcinoma Cancer Cells, – ,inactive.

[a] CD_{50} < 5.0 μg cm^{-3} – strongly active, CD_{50} 5.0 < 10.0 μg cm^{-3} – moderately active, CD_{50} 10.0 < 25.0 μg cm^{-3} – weakly active, CD_{50} > 25.0 μg cm^{-3} – not active. CD_{50} (μg cm^{-3}) = Cytotoxic dose at 50%, i.e. the concentration to reduce growth of cancer cells by 50%.

6. Conclusion

The reaction of $[Cu(sac)_2(H_2O)_4] \cdot 2H_2O$ with the tridentate Schiff bases derived from *S*-benzyldithiocarbazate and heterocyclic ketones in a methanol–water mixture produces crystalline green complexes in high yields which are mixed-

Table 6
Qualitative antimicrobial assay results[a] (diameter in mm)

Compound	MRSA	B29	60690	S-T	C.A	398	20341
[Cu(NNS′)(sac)]	12	13	14	12	12	11	12
[Cu(NNS″)(sac)]	–	–	–	–	8	7	7
[Cu(NNS‴)(sac)]	–	–	–	–	–	–	–
Streptomycin (antibacterial control)	31	30	30	30			
Nystatin (antifungal control)					21	25	24

Methicillin resistant staphylococcus (MRSA); *Bacillus subtilis* wild type (B29), *P. aeruginosa* (60690); *S. typhimurium* (S-T), *C. albicans* (C.A), *A. ochraceous* (398), *S. ceciricaee* (20341).

[a] Diameter of 15 mm and above is considered active; –, inactive.

ligand binary copper (II) complexes containing the saccharinate anion and the tridentate NNS^- Schiff bases. An X-ray crystal structure determination of [Cu(NNS′)(sac)] shows that it has a distorted square-planar geometry. In view of the similarity of the IR and electronic spectra of the [Cu(NNS″)(sac)] and [Cu(NNS‴)(sac)] complexes with that of the [Cu(NNS′)(sac)], it is proposed that the former complexes also have a distorted square-planar geometry.

Of the three mixed-ligand complexes, the ones with methyl and phenyl groups in the ligands exhibit marked anticancer activity against the leukemic HL-60 cell lines, the activities being higher than the standard anticancer drug, Doxorubicin. The high selectivity towards this cell line is of particular interest and is worthy of further investigation.

7. Supplementary data

Crytallographic data for the structural analysis have been deposited with the Cambridge Crystallographic Data Centre, CCDC No. 262373 A copy of this information may be obtained free of charge from The Director, CCDC, 12 Union Road, Cambridge, Cb2 1EZ, UK (fax: +44 1223 336 033; e-mail: deposit@ccdc.cam.ac.uk or www: http://www.ccdc.ac.uk).

Acknowledgements

We thank the Department of Chemistry and Laboratory of Molecular and Cell Biology, Institute of Biosciences, Universiti Putra Malaysia, for the provision of laboratory facilities and the University of Oxford for providing X-ray crystallographic services. We also thank Md. Uwaisulqarni Osman for technical assistance. The research was funded by a grant from the Ministry of Science and Environment, Malaysia, under the Intensification of Research in Priority Areas Scheme (IRPA Grant Nos. 09-02-04-0296 and 09-02-04-0755-EA001).

References

[1] M.J. Allen, E. Bayland, C.E. Dukes, E.S. Horning, J.G. Watson, Brit. J. Cancer 11 (1975) 212.
[2] C.T. Supuran, M.D. Banciu, Rev. Roum. Chim. 36 (1991) 1345.
[3] W. Henderson, B.K. Nicholson, L.J. McCaffrey, Inorg. Chim. Acta 285 (1999) 145.
[4] J.M. Law, W. Henderson, B.K. Nicholson, J. Chem. Soc., Dalton Trans. (1997) 4587.
[5] S.Z. Haider, K.M.A. Malik, K.J. Ahmed, Inorg. Synth. 23 (1985) 47.
[6] S.Z. Haider, K.M.A. Malik, K.J. Ahmad, H. Hess, H. Riffel, M.B. Hursthouse, Inorg. Chim. Acta 72 (1983) 21.
[7] B. Kamenar, G. Jovanski, Cryst. Struct. Commun. 11 (1982) 257.
[8] F.A. Cotton, G.E. Lewis, C.A. Murillo, W. Schwotzer, G. Vale, Inorg. Chem. 23 (1984) 4038.
[9] F.A. Cotton, L.R. Falvello, R. Llusar, E. Libby, C.A. Murillo, W. Schwotzer, G. Valle, Inorg. Chem. 25 (1986) 3423.
[10] F.A. Cotton, L.R. Falvello, C.A. Murillo, G. Valle, Z. Anorg. Allg. Chem. 540 (1986) 67.
[11] E.W. Ainscough, E.N. Baker, A.M. Brodie, R.J. Cresswell, J.D. Ranford, J.M. Waters, Inorg. Chim. Acta 172 (1990) 185.
[12] Y. Zhang, Transit. Met. Chem. 19 (1994) 446.
[13] K.M.A. Malik, S.Z. Haider, M.A. Hossain, M.B. Hursthouse, Acta Crystallogr., Sect. C 40 (1984) 1696.
[14] M. Akbar Ali, M.T.H. Tarafder, J. Inorg. Nucl. Chem. 39 (1977) 1785.
[15] M. Akbar Ali, S.M.M.H. Majumder, R.J. Butcher, J.P. Jasinski, J.M. Jasinski, Polyhedron 16 (1997) 2749.
[16] M.E. Hossain, J. Begum, M.N. Alam, M. Nazimuddin, M.A. Ali, Transit. Met. Chem 18 (1993) 497.
[17] Z. Otwinski, W. Minor, in: C.W. Carter, R.M. Sweet (Eds.), Processing X-ray Diffraction Data Collected in Oscillation Mode, Methods in Enzymology, vol. 276, Academic Press, New York, 1997, p. 276.
[18] A. Altomare, J. Appl. Crystallogr. 27 (1994) 435.
[19] P.W. Betteridge, J.R. Carruthers, R.I. Cooper, K. Prout, D.J. Watkin, J. Appl. Crystallogr. 36 (2003) 1487.
[20] T. Mosmann, J. Immunol. Methods 65 (1983) 55.
[21] A.W. Bauer, Am. J Clin. Pathol. 45 (1966) 493.
[22] Zhang Yugeng, Wang Yebin, Yu Heng, Cryst. Res. Technol. 30 (1995) 831.
[23] C.D. Hufford, A.M. Clark, in: A. Ur-Rahman (Ed.), Studies in Natural Product Chemistry, vol. 2, Elsevier, Amsterdam, 1988, p. 421.
[24] W.J. Geary, Coord. Chem. Rev. 7 (1971) 81.
[25] M.A. Ali, A.H. Mirza, R.J. Butcher, Polyhedron 20 (2001) 1037.
[26] M. Mohan, P. Sharma, Inorg. Chim. Acta 106 (1985) 197.
[27] M.A. Ali, D.J. Phiilips, S.E. Livingstone, Coord. Chem. Rev. 5 (1971) 119.
[28] M.T.H. Tarafder, A. Kasbollah, K.A. Crouse, A.M. Ali, B.M. Yamin, H.K. Fun, Polyhedron 20 (2001) 2363.
[29] C. Jovanovski, S. Tancera, B. Soptrajanov, Spectrosc. Lett. 28 (1995) 1095.
[30] V.T. Vilmaz, Synth. React. Inorg. Met. Org. Chem. 29 (1999) 621.
[31] V.T. Yilmaz, A. Karadag, C. Thoene, J. Coord. Chem. 55 (2002) 609.
[32] B.P. Straughan, S. Walker, Spectroscopy, vol. 1, John Wiley & Sons, Inc., USA, 1976.
[33] M.E. Hossain, J. Begum, M.N. Alam, M. Nazimuddin, M.A. Ali, Transit. Met. Chem. 18 (1993) 497.
[34] Thahira B.S.A. Ravoof, K.A. Crouse, M. Ibrahim M. Tahir, A. Cowley, M.A. Ali, Polyhedron 23 (2004) 2491.
[35] M.A. Ali, A.H. Mirza, Thahira B.S.A. Ravoof, P.V. Bernhardt, Polyhedron 23 (2004) 2031.
[36] Chew Kar Beng, M.T.H. Tarafder, K.A. Crouse, A.M. Ali, B.M. Yamin, H.K. Fun, Polyhedron 23 (2004) 1385.
[37] L.R. Falvello, J. Gomez, I. Pascual, M. Thomas, E.P. Urriolabeitia, A.J. Schultz, Inorg. Chim. Acta 40 (2001) 4455.

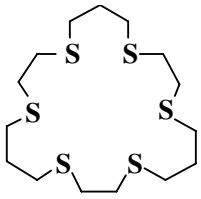


Fig. 1. [21]aneS$_6$.

1,4,7,10,13,16-hexathiacyclohexadecane ([18]aneS$_6$) have shown that these ligands may be capable of producing transition metal complexes with some unique properties [12a]. It is also well documented that the low-spin states of Co(II) and Fe(II) as well as some unusual oxidation states such as Pd(III), Pt(III) and Rh(II) are stabilized by S_6 ligand sphere [12a]. However, macrocyclic six-coordinate copper hexathiaether complexes have not been explored extensively except, for some work by Cooper and coworkers [7], Schroder et al. [9c], de Groot and Leob [12a], Desper and Gellman [13j], and Rogers and Nunez [14].

In this paper, we wish to present our work on copper(II/I) complexes with a new hexathiaether ligand 1,4,8,11,15,18-hexathiacyclo-henicosane ([21]aneS$_6$) (Fig. 1). Herein, we describe the stability constant and electrochemical potential data obtained for Cu([21]aneS$_6$)$^{2+}$, Cu([21]aneS$_6$)$^{+}$ complexes and the crystal structure of the latter complex, and compare the data with that of similar homoleptic copper complexes reported to date. Interestingly, this is the first report of synthesis and characterization of a metal coordinated [21]aneS$_6$ complex.

2. Experimental

Ultraviolet and visible spectra were obtained using a Hewlett-Packard 8452A diode array spectrophotometer. Stability constant measurements were determined using a Cary model 17D dual-beam spectrophotometer equipped with a thermostated (at 25 ± 0.2 °C) cell holder. Cyclic voltammetric studies were determined by using a BAS 100 electrochemical work station (Bioanalytical Systems, Lafayette, IN) operated at ambient temperature, by means of slow scan cyclic voltammetry ($v = 10$–$100\ \mathrm{mV\ s^{-1}}$). A three-electrode electrochemical cell was used and consisted of a 3-mm glassy carbon disk working electrode, a Pt wire electrode, and a Ag/AgCl (3 M NaCl) reference electrode (Bioanalytical Systems; $E^f = 0.228$ V versus SHE). A standard solution of ferroin (Fe(phen)$_3 \cdot 3ClO_4$ in 0.05 M KCl) was used as an external reference. The potential of ferroin has been accurately determined as $E^f = 1.117$ V versus SHE [15]. Nuclear magnetic resonance spectra were recorded on a Varian U 500 (500 MHz) FT-NMR Spectrometer. All NMR spectra for copper(II/I) complexes were obtained in D_2O at room temperature and the chemical shifts are reported in δ values (ppm) relative to TMS.

Ligand [21]aneS$_6$ was synthesized by Dr. Leo Ocrymowycz as reported previously [16]. Copper(II)perchlorate hexahydrate was synthesized as reported earlier [17]. (*Warning! Metal perchlorate salts are potentially explosive; the isolated salts should never be dried and should not be subjected to shock!*). Solutions of copper([21]aneS$_6$)$^{2+}$ were prepared as reported prevoiusly [18,8d]. Ionic strength of solutions was maintained at 0.1 M by adding $HClO_4$. On formation of the Cu([21]aneS$_6$)$^{2+}$ complex, the solution turned dark green and a new peak appeared in the ultraviolet and visible spectra at 410 nm confirming the formation of the copper([21]aneS$_6$)$^{2+}$ complex. All spectral observations were made at 410 nm. ^{1}H NMR (D_2O): δ 2.96 (s, 12H), 2.90 (t, 12H), 2.21 (p, 6H): ^{13}C NMR (D_2O): δ 33.01, 31.43, 30.36. A crystal of Cu([21]aneS$_6$)$^{+}$ was grown by preparing a stoichiometric solution of Cu([21]aneS$_6$)$^{2+}$ by mixing Cu(ClO_4)$_2$ and [21]aneS$_6$ in 1:1 ratio, and reducing the solution of Cu([21]aneS$_6$)$^{2+}$ under argon using copper shot, followed by slow evaporation of the solvent. The crystals appeared as colorless needles. Crystal structure data have been deposited at the Cambridge Crystallographic Data Center by Dr. Mary Jane Heeg [19], and allocated the deposition number CCDC 268931.

3. Results and discussion

Copper combines with ligands according to the following general equation (Eq. (1)). L designates the ligand, and the Cu^{II}L designates the Copper–ligand complex

$$Cu^{2+} + L \rightleftarrows Cu(II)L \tag{1}$$

$$K_{Cu^{II}L} = [Cu^{II}L]/([Cu^{2+}][L]) \tag{2}$$

In general, copper(II) thiaether complexes exhibit strong S-to-Cu charge transfer bands in the vicinity of 390 nm, which facilitate monitoring of the Cu(II)complex concentration in solution. In aqueous media, Cu([21]aneS$_6$)$^{2+}$ showed a strong absorbance peak at 410 nm and this peak was used to obtain absorbance data for stability constant determinations. Cu([21]aneS$_6$)$^{2+}$ forms a weak complex in aqueous solution. Therefore, we used the method of McConnell and Davidson [20] to determine the molar absorptivity (ε) and stability constant ($K_{Cu^{II}L}$) of the complex (Eq. (2)). This method allows convenient, simultaneous determination of both molar absorptivity and stability constant for a given weak metal–ligand complex. The applicable relationship, as derived from mass balance expressions and Beer's law, may be written in the form (Eq. (3)),

$$\frac{bC_L}{A} = \frac{1}{\varepsilon_{ML}} + \frac{1}{\varepsilon_{ML} K_{ML} C'_M} \tag{3}$$

where b represents the path length of the spectrophotometric cell; C_L is the total concentration of ligand added; M represents the metal of interest, which is Cu in this case, and ML represents the metal–ligand complex; ε_{ML} is the molar absorptivity of the Cu^{II}L complex; A is the measured absorbance corrected for any contribution from uncomplexed Cu(II); K_{ML} is the stability constant of the

metal–ligand complex; C_M is the concentration of the free metal ion (uncomplexed) in solution. The value of C_M (in Eq. (3)), which is equivalent to $C_{Cu^{II}} - [Cu^{II}L]$ (in Eq. (4)), was calculated by using a computer software program [21]. A more appropriate equation for the current copper–ligand complex could be written as (4) as derived from Eq. (3)

$$\frac{bC_L}{A} = \frac{1}{\varepsilon_{Cu^{II}L}} + \frac{1}{\varepsilon_{Cu^{II}L} K_{Cu^{II}L'}(C_{Cu^{II}} - [Cu^{II}L'])} \quad (4)$$

In the above eqution, the primed quantity ($Cu^{II}L'$) indicates any anion complexes that may form in 0.10 M $HClO_4$. By plotting bC_L/A against $1/(C_{Cu^{II}} - [Cu^{II}L'])$ yields ε_{CuL} as the reciprocal intercept and $K_{Cu^{II}L}$ as the intercept/slope ratio. By employing this method, molar absorptivity of Cu([21]aneS$_6$)$^{2+}$ was determined to be 6000 $M^{-1}\,cm^{-1}$ and the stability constant of Cu([21]aneS$_6$)$^{2+}$ was found to be 1.26×10^1 M^{-1} (Table 1). This indicates that Cu^{2+} forms a weak complex with [21]aneS$_6$ in aqueous medium. Our earlier studies with a similar homoleptic macrocycle namely, [18]aneS$_6$, gave a stability constant value of 2.5×10^3 M^{-1} for Cu([18]aneS$_6$)$^{2+}$ [22], which agrees well with the value reported ($\sim 5 \times 10^3$ M^{-1}) in a recent study [8b].

Cyclic voltammetry of Cu([21]aneS$_6$)$^{2+/+}$ at scan rates between 50 and 100 mV/s generated cyclic voltammograms where ΔE_{pp} was 64 mV indicating the reversible nature of the copper complex. Similar reversible electrochemical behavior has been reported for Cu([18]aneS$_6$)$^{2+/+}$ in aqueous solution [8b] and nitromethane [7]. Reversible behavior requires that electron transfer process determines the rate of the redox process [7]. The formal potential of Cu([21]aneS$_6$)$^{2+/+}$ complex was found to be 0.89 V (versus SHE). This is the highest potential reported to date for a macrocyclic $Cu^{2+/+}$ complex in aqueous solution. High potential values of 0.79 V (versus SHE) and 0.72 V (versus SCE) have been reported for Cu([18]aneS$_6$)$^{2+/+}$ in aqueous [8b] and non-aqueous media [7]. Similar high potentials (as high as 0.83 V versus SHE) have been reported for acyclic ligands bearing thiaether donor atoms [22,23], and a series of acyclic pentadentate N_2S_3 donor atom system [24].

The stability constant of Cu([21]aneS$_6$)$^{+}$ was calculated by using the Nernst equation in the form (Eq. (5)) by employing the formal potential value for the $Cu^{2+/+}$ complex and the stability constant obtained for Cu([21]aneS$_6$)$^{2+}$

$$E^f_{Cu^{II/I}L} = E^f_{Cu^{II/I}solv} - \frac{2.303RT}{F} \log \frac{K_{Cu^{II}L'}}{K_{Cu^{I}L'}} \quad (5)$$

In the above equation, $E^f_{Cu^{II}L}$ represents the formal potential of the $Cu^{II/I}L$ complex (assumed to be identical with the half-wave potential) [8b], $E^f_{Cu^{II/I}solv}$ represents the potential for the solvated Cu(II/I) redox couple which was determined to be 0.13 V (relative to SHE) in water in the presence of 0.1 M $HClO_4$ [18]. $KCu^{II}L'$ and $KCu^{I}L'$ are the conditional stability constants for the oxidized and reduced species, respectively. The calculated value for the stability constant of Cu([21]aneS$_6$)$^{+}$ was 7.9×10^{13} M^{-1}. A similar high value of 6×10^{14} M^{-1} has been reported for the stability constant of Cu([18]aneS$_6$)$^{+}$ in aqueous solution [8b]. Furthermore, high stability constant values in the order of $\sim 10^{15}$ for Cu(I) complexes have been determined for various acyclic and macrocyclic ligands containing both sulfur and amine nitrogen donor atoms [25].

High formal potentials indicate a significant difference in stability of the $Cu^{2+/+}$ complexes. Such high potentials reflect thermodynamic stabilization of Cu(I) over Cu(II) by either electronic or stereochemical properties of the ligands and result, for example, when a ligand forces Cu(II) to assume a geometry (e.g., tetrahedral) more appropriate to Cu(I) [26]. Hartman and Cooper [7], as well as Chaka et al. [8b], obtained high redox potentials for $Cu^{2+/+}$ [18]aneS$_6$ system. According to Hartman and Cooper [7], the very high redox potentials are attributed to the π acidity of the sulfur donor atoms. Interestingly, according to Rorabacher [6a,8b], Cu(II/I) redox potentials are primarily a function of the stability of the Cu(II) complex. This has been clearly demonstrated in a study which involved measuring potentials and stability constants of Cu(II/I) complexes for a wide variety of copper complexes involving thiaether sulfurs as well as imine and amine nitrogen donor atoms [25]. Accordingly, for about 35 different uncharged terdentate, quadridentate and quindentate ligands, the stability constants of Cu(I)L complexes remained in the narrow range of 10^{12}–10^{16}, with few exceptions, regardless of large differences in coordination geometry and donor strength. For these same 35 ligands, the Cu(II)L stability constants spanned 26 orders of magnitude. Thus the study revealed that the Cu(II/I) potentials, which covered a range of 1.5 V, were inversely related to the logarithmic values of the Cu(II)L stability constants for a wide range of ligand types. Since Cu(II) complexes where $K_{Cu^{II}L} < 10$ cannot be forced to form completely under reasonable solution conditions, the practical upper limit for formal potentials of Cu(II/I)L systems maybe very close to the potential obtained for Cu([21]aneS$_6$)$^{2+/+}$ (0.89 V versus SHE) [25]. This can be shown clearly by using the Nernst equation, Eq. (5) [25].

By comparing stability constant and electrochemical potential data obtained for similar homoleptic $Cu^{2+/+}$ systems such as [14]aneS$_4$ and related 12-13-15-16-membered S$_4$ macrocycles, Rorabacher [6a,8b] points out clearly that the larger 18-membered macrocycle has more flexibility to

Table 1
Physical parameters for $Cu^{II/I}$([21]aneS$_6$) in aqueous solution at 25 °C, $\mu = 0.10$ M[a]

E^f (V)	0.89[b]
λ_{max} (nm) ($Cu^{II}L$)	410
$\varepsilon_{Cu^{II}L}$ ($M^{-1}\,cm^{-1}$) ($Cu^{II}L$)	6×10^3
$K_{Cu^{I}L}$ (M^{-1})	7.9×10^{13}
$K_{Cu^{II}L}$ (M^{-1})	1.26×10^1

[a] Ionic strength maintained with 0.1 M $HClO_4$ in aqueous solution.
[b] Relative to SHE.

Table 2
Comparative values for stability constant and formal potential of Cu(II)- and Cu(I)-macrocyclic homoleptic polythiaether complexes in aqueous solution at 25 °C, $\mu = 0.10$ M

Complexed ligand	E^f (H_2O)[a] (V)	$K_{Cu^{II}L}$ (M^{-1})	$K_{Cu^{I}L}$ (M^{-1})	$K_{Cu^{I}L}/K_{Cu^{II}L}$	Reference
[12]aneS$_4$	0.69	2.5×10^{3}	$<7\times10^{12}$	$\sim10^{9}$	[8f]
[13]aneS$_4$	0.52	2.8×10^{3}	1.1×10^{10}	$\sim10^{7}$	[8f]
[14]aneS$_4$	0.59	2.1×10^{4}	1.3×10^{12}	$\sim10^{8}$	[8f]
[15]aneS$_4$	0.64	1.5×10^{3}	6.2×10^{11}	$\sim10^{8}$	[8f]
[15]aneS$_5$	0.69	1.5×10^{4}	4.5×10^{13}	$\sim10^{9}$	[8f]
[16]aneS$_4$	0.71	1.6×10^{2}	1.1×10^{12}	$\sim10^{10}$	[8f]
[18]aneS$_6$	0.79	$\sim5\times10^{3}$	6×10^{14}	$\sim10^{11}$	[8b]
[18]aneS$_6$	nd	2.5×10^{3}	nd	nd	[22]
[21]aneS$_6$	0.89	1.3×10^{1}	7.9×10^{13}	$\sim10^{12}$	this work

nd = not determined.
[a] Relative to SHE.

accommodate the tetrahedral geometry commonly encountered by Cu(I) complexes than do the smaller macrocycles (stability constants and redox potentials of some of these systems are listed in Table 2 for comparison). Similarly, the large stability constant of Cu([21]aneS$_6$)$^+$ implies that the larger 21-membered ring, [21]aneS$_6$, favors the Cu(I) tetrahedral geometry to a greater extent than its smaller macrocyclic counterparts (Table 2). This can be demonstrated by comparing the difference in magnitude of stability constants for a given Cu(II/I) macrocyclic system. For the large [21]aneS$_6$ macrocycle, the stability constant of the Cu(I) complex (7.9×10^{13} M^{-1}) is 12 orders of magnitude greater than that of the Cu(II) complex (1.3×10^{1} M^{-1}). Similarly for the large [18]aneS$_6$ system, the stability constant of the Cu(I) complex (6×10^{14} M^{-1}) is 11 orders of magnitude greater than that of the Cu(II) complex (5×10^{3} M^{-1}). For a smaller macrocycle such as [14]aneS$_4$, this difference between the Cu(II/I) complexes is much less and eight orders of magnitude. This shows clearly that as the size of the macrocycle increases the strength of the Cu(I) complex increases favoring its easy formation in solution (Table 2). This is ample evidence to show that larger macrocycles have more flexibility to accommodate the tetrahedral geometry commonly encountered for Cu(I) complexes than do the smaller macrocycles.

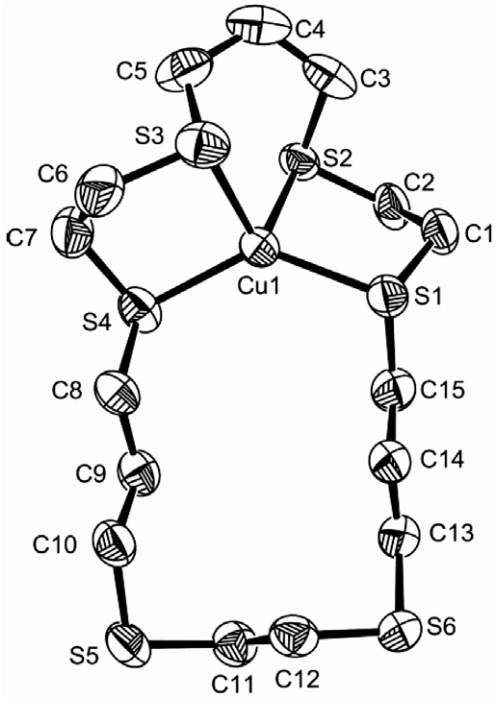


Fig. 2. ORTEP drawing of the cationic unit of Cu^I([21]aneS$_6$)ClO$_4$ showing the labeling scheme for atoms at 50% probability (hydrogen atoms removed for clarity).

The crystal structure of Cu([21]aneS$_6$)$^+$ (Fig. 2) shows that four sulfur atoms adjacent to one another are coordinated to the Cu$^+$ ion in this complex. The Cu$^+$ ion is encapsulated by [21]aneS$_6$ ligand bonding directly to S1, S2, S3 and S4 at distances of 2.2756 (8), 2.3522 (8), 2.3576 (9) and 2.2773 (8) Å, respectively (Table 3). The copper ion is not coordinated to the remaining two sulfur atoms. Bond distances and angles calculated for the crystal (Table 3) show that it is a distorted tetrahedron, which is a common geometry encountered by Cu(I)L complexes. A similar structure has been reported for Cu([18]aneS$_6$)$^+$ [7], while a slightly different crystal structure has been reported for Cu([16]aneS$_6$)$^+$ [12a]. Crystal structures of many other copper(I) complexes we studied earlier showed Cu(I) complex adopting a distorted tetrahedron [6a,6g,8a,8e,22]. Similar distorted tetrahedral structures of copper(I) have been well documented [6a].

In general, as a d^9 system, Cu(II) tends to adopt a six-coordinate tetragonal (distorted octahedral) geometry or a five-coordinate (square pyramidal or trigonal bipyramidal) geometry, whereas Cu(I), as a d^{10} system, is found to be four-coordinate (tetrahedral) [6a].

Copper(I) structures are known to be strongly influenced by the nature of coordinating groups [6a]. The first crystal structure of a macrocyclic Cu(I) complex, 1,4,8,11-tetrathiacyclotetra-decancopper(I) (Cu([14]-aneS$_4$)$^+$), was reported by Rorabacher et al. in 1977 [27]. Accordingly, copper(I) complex attained an irregular tetrahedron where Cu(I) was coordinated to three sulfur donor atoms from one ligand molecule and another sulfur donor atom from an adjacent ligand molecule. This has been attributed

Table 3
Selected bond lengths (Å) and angles (°) for [Cu^I([21]aneS$_6$)ClO$_4$

Cu(1)–S(1)	2.2756(8)
Cu(1)–S(4)	2.2773(8)
Cu(1)–S(2)	2.3522(8)
Cu(1)–S(3)	2.3576(9)
S(1)–Cu(1)–S(4)	131.80(3)
S(1)–Cu(1)–S(2)	93.18(3)
S(4)–Cu(1)–S(2)	115.84(3)
S(1)–Cu(1)–S(3)	121.03(3)
S(4)–Cu(1)–S(3)	94.33(3)
S(2)–Cu(1)–S(3)	96.51(3)

to the inability of [14]aneS$_4$ ligand to distort sufficiently to accommodate a tetrahedral geometry [27]. Rogers et al. reported a tercoordinate polymeric crystal structure for copper(I)complex of [18]aneS$_6$ ligand, where one copper atom was bound to two sulfur atoms of one ligand and one sulfur atom of the other [14]. We obtained similar crystal structures of 1:2 (copper:ligand), and polymers for copper(I) complexes of dibz-[14]aneS$_4$, bz-cis-cyhx-[14]aneS$_4$ and bz-trans-cyhx-[14]aneS$_4$ [22] (dibz = dibenzo, cyhx = cyclohexyl). Polymeric structures involving Copper(I) are not uncommon [22,28].

Hartman and Cooper [7] determined the crystal structures of both Cu(II) and Cu(I) complexes of [18]aneS$_6$. In the Cu([18]aneS$_6$)$^{2+}$ complex, all six sulfur donor atoms were coordinated to the copper atom and it crystallized as a centrosymmetric meso isomer, in which each triad of adjacent sulfur atoms coordinates to a trigonal face of the coordination octahedron. This arrangement is known to maximize the number of gauche placements at the C–S bonds, a marked tendency of macrocyclic thiaethers [29]. Cu([18]aneS$_6$)$^{2+}$ was a tetragonally-distorted octahedron with four short and two long Cu–S bonds where the axial elongation was due to Jahn–Teller distortion [7].

The Cu([18]aneS$_6$)$^{+}$ adopted a severely distorted tetrahedral geometry [7]. This was reminiscent of that found for the Cu([14]aneS$_4$)$^{+}$ [27] and Cu([15]aneS$_5$)$^{+}$ [8g]. In Cu([18]aneS$_6$)$^{+}$, four adjacent sulfur atoms were bonded to the copper atom indicating that the other two adjacent Cu–S bonds have been ruptured upon reduction. The crystal structure of Cu([21]aneS$_6$)$^{+}$ shows a similar conformation as described for Cu([18]aneS$_6$)$^{+}$, where four adjacent sulfurs are coordinated to the copper(I) atom. In fact, the bond distances and bond angles around the copper ion in Cu([21]aneS$_6$)$^{+}$ (Table 3) match very well with those of Cu([18]aneS$_6$)$^{+}$ [7]. The crystal structure reported for a Cu(I) complex of a similar homoleptic hexathiaether ligand, Cu([16]aneS$_6$)$^{+}$ [12a], is different to both Cu([21]aneS$_6$)$^{+}$ and Cu([18]aneS$_6$)$^{+}$ [7]. In Cu([16]aneS$_6$)$^{+}$, four sulfur donor atoms are bonded to the copper atom but the two non-bonded sulfur atoms do not lie adjacent to each other. They are separated from each other by two pairs of bonded sulfur atoms. This forms a symmetric crystal structure, which consists of two identical components. However, the Cu–S bond distances reported for the Cu([16]aneS$_6$)$^{+}$ crystal match very well with those of Cu([21]aneS$_6$)$^{+}$ and Cu([18]aneS$_6$)$^{+}$.

In Cu([18]aneS$_6$)$^{2+}$octahedral complex, two adjacent Cu–S bonds break upon reduction to yield the tetrahedral Cu([18]aneS$_6$)$^{+}$ [7]. Considering the similarity of the structures between [18]aneS$_6$ and [21]aneS$_6$ ligands as well as their Cu(I) complexes, in the absence of a crystal structure for Cu([21]aneS$_6$)$^{2+}$, we can speculate a similar analogy for breaking of Cu–S bonds during reduction of Cu([21]-aneS$_6$)$^{2+}$ to Cu([21]aneS$_6$)$^{+}$. It implies that Cu([21]aneS$_6$)$^{2+}$ may also form a six-coordinate complex, where all six sulfur atoms are bonded to the copper atom, which could undergo a similar Cu–S bond rupture in adjacent Cu–S bonds upon reduction to give a four-coordinate Cu([21]-aneS$_6$)$^{+}$.

As noted earlier, blue copper proteins are known to display high redox potentials [1]. Considering type 1 ''blue'' copper proteins structurally characterized to date, rusticyanin bears the highest redox potential (0.68 V), while stellacyanin bears the lowest redox potential (0.18 V) [30]. The significant difference in redox potential of these ''blue'' copper proteins is attributed to the type of axial ligand, which is bonded to the copper atom [30]. It has also been suggested earlier that the reason for this variation is that the protein constrain the distance between the copper ion and the axial ligands to different values, and its unusual cupric geometry [30]. The role of the axial ligand has been extensively debated in terms of its function in the fine-tuning of the redox potential and spectroscopic properties of type1 'blue' copper proteins [30]. Studies carried out during the last decade [31], and more recent studies [32], however, challenge the earlier speculation. It maybe interesting to investigate whether the significant difference in redox potential of these ''blue'' copper proteins bears any relationship to the degree of stabilization created by their surrounding ligands for Cu(I) geometry over Cu(II) by a similar phenomenon as discussed herein.

In summary, we present the first synthesis and characterization of a metal coordinated [21]aneS$_6$ complex. The Cu([21]aneS$_6$)$^{2+/+}$ system shows a formal potential of 0.89 V (vs. SHE), which is the highest reported to date for a Cu(II/I) system in aqueous media. By employing the Nernst equation we can infer that the practical upper limit for formal potential of Cu(II/I)L systems maybe close to this high value. The stability constant obtained for Cu([21]aneS$_6$)$^{+}$ is 12 orders of magnitude greater than that of Cu([21]aneS$_6$)$^{2+}$ indicating the flexibility of this large macrocyclic ligand to accommodate the tetrahedral geometry commonly encountered for Cu(I) complexes more favorably, than Cu(II) complexes. Recent studies carried out on a Cu(II/I) system in aqueous media with a similar homoleptic ligand, [18]aneS$_6$, reported a comparable trend with a high formal potential value (0.79 V versus SHE) and large difference in stability constants where Cu(I) has been favored 11 orders of magnitude greater than that of Cu(II) [8b]. The results of the current study further support the conclusions drawn earlier by Rorabacher [6a,8b,25] that the Cu(II/I) redox potentials are primarily a function of the stability of the Cu(II) complex, and that the larger macrocyclic ligands have more flexibility to accommodate the tetrahedral geometry commonly encountered for Cu(I) complexes than do the smaller macrocycles.

Acknowledgments

I thank Dr. Leo Ochrmowycz for preparing the ligand [21]aneS$_6$, and Dr. Mary Jane Heeg for resolving the crystal structure of Cu([21]aneS$_6$)$^{+}$. I also thank Dr. Mark A. Whitener for the ORTEP diagram, and Dr. David J. Szalda for assistance with structural parameters of the crystal.

The valuable comments and suggestions of the reviewers are gratefully acknowledged.

References

[1] (a) A.G. Sykes, Adv. Inorg. Chem. 36 (1990) 377;
(b) E.T. Adman, Adv. Protein Chem. 42 (1991) 145;
(c) E.I. Solomon, J.W. Hare, D.M. Dooley, J.H. Dawson, P.J. Stephens, H.B. Gray, J. Am. Chem. Soc. 102 (1980) 168;
(d) H. Beinert, Coord. Chem. Rev. 33 (1980) 55.

[2] P.M. Coleman, H.C. Freeman, J.M. Guss, M. Murata, V.A. Norris, J.A.M. Ramshaw, M.P. Venkatappa, Nature 272 (1978) 319.

[3] J.M. Guss, H.C. Freeman, J. Mol. Biol. 169 (1983) 521.

[4] E.T. Adman, R.E. Stenkamp, L.C. Seiker, L.H. Jensen, J. Mol. Biol. 169 (1983) 521.

[5] I. Harvey, Q. Hao, E.M. Duke, W.J. Ingledew, S.S. Hasnain, Acta. Crystallogr., Sect. D 54 (1998) 629.

[6] (a) D.B. Roarabacher, Chem. Rev. 104 (2004) 651;
(b) R. Balamurugan, M. Palaniandavar, M.A. Halcrow, Polyhedron 25 (2006) 1077;
(c) R. Balamurugan, M. Palaniandavar, H. Stoeckli-Evans, M. Neuburger, Inorg. Chim. Acta 359 (2006) 1103;
(d) R. Balamurugan, M. Palaniandavar, R.S. Gopalan, G.U. Kulkarni, Inorg. Chim. Acta 357 (2004) 919;
(e) R. Balamurugan, M. Palaniandavar, Inorg. Chem. 40 (2001) 2246;
(f) M. Vaidyanathan, R. Balamurugan, U. Sivagnanam, M. Palaniandavar, J. Chem. Soc., Dalton Trans. (2001) 3498;
(g) K. Krylova, C.P. Kulatilleke, M.J. Heeg, C.A. Salhi, L.A. Ochrymowycz, D.B. Rorabacher, Inorg. Chem. 38 (1999) 4322;
(h) T. Adman, in: P. Harrison (Ed.), Topics in Molecular and Structural Biology, Metalloproteins, Macmillan, New York, 1985;
(i) S.G. Murray, F.R. Hartley, Chem. Rev. 81 (1981) 365;
(j) K.D. Karlin, J. Zubieta (Eds.), Copper Coordination Chemistry: Biochemical and Inorganic Perspectives, Adenine Press, Guilderland, New York, 1983;
(k) P.J.M.W.L. Birker, E.F. Godefroi, J. Helder, J. Reedijk, J. Am. Chem. Soc. 104 (1982) 7556;
(l) J. van Rijn, W.L. Dreissen, J. Reedijk, J.-M. Lehn, Inorg. Chem. 23 (1984) 3584;
(m) J.V. Dagdigian, V. McKee, C.A. Reed, Inorg. Chem. 21 (1982) 1332;
(n) N. Aoi. G.E. Matsubayashi, T. Tanaka, J. Chem. Soc., Dalton Trans. (1984) 1349;
(o) J.F. Richardson, N.C. Payne, Inorg. Chem. 17 (1978) 2111.

[7] J.R. Hartman, S.R. Cooper, J. Am. Chem. Soc. 108 (1986) 1202.

[8] (a) S.H. Kakos, L.T. Dressel, J.F. Bushendorf, C.P. Kotarba, P. Wijetunge, C.P. Kulatilleke, M.P. McGillivary, G. Chaka, M.J. Heeg, L.A. Ochrymowycz, D.B. Rorabacher, Inorg. Chem. 45 (2006) 923;
(b) G. Chaka, L.A. Ochrymowycz, D.B. Rorabacher, Inorg. Chem. 44 (2005) 9105;
(c) A. Kandegedara, K. Krylova, T.J. Nelson, R.R. Schroeder, L.A. Ochrymowycz, D.B. Rorabacher, J. Chem. Soc., Dalton Trans. (2002) 792;
(d) Q. Yu, C.A. Salhi, E.A. Ambundo, M.J. Heeg, L.A. Ochrymowycz, D.B. Rorabacher, J. Am. Chem. Soc. 123 (2001) 5720;
(e) P. Wijetunge, C.P. Kulatilleke, L.T. Dressel, M.J. Heeg, L.A. Ochrymowycz, D.B. Rorabacher, Inorg. Chem. 39 (2000) 2897;
(f) M.M. Bernardo, R.R. Schroeder, D.B. Rorabacher, Inorg. Chem. 30 (1991) 1241;
(g) P.W.R. Corfield, C. Ceccarelli, M.D. Glick, I.W.-Y. Moy, L.A. Ochrymowycz, D.B. Rorabacher, J. Am. Chem. Soc. 107 (1985) 2399.

[9] (a) N.R. Brooks, A.J. Blake, N.R. Champness, P.A. Cooke, P. Hubbersty, D.M. Proserpio, C. Wilson, M. Schroder, J. Chem. Soc., Dalton Trans. (2001) 456;
(b) L.R. Sutton, A.J. Blake, P.A. Cooke, M. Schroder, Chem. Commun. (2000) 563;
(c) A.J. Blake, R.O. Gould, A.J. Holder, A.J. Lavery, M. Schroeder, Polyhedron 9 (1990) 2919;
(d) R.O. Gould, A.J. Lavery, M. Schroeder, Chem. Commun. (1985) 1492.

[10] (a) M. Delgado, R.E. Wolf Jr., J.R. Hartman, G. McCafferty, R. Yagbasan, S.C. Rawle, D.J. Watkin, S.R. Cooper, J. Am. Chem. Soc. 114 (1992) 8983;
(b) D.J. White, H.-J. Kuppers, A.J. Edwards, D.J. Watkin, S.R. Cooper, Inorg. Chem. Soc. 31 (1992) 5351;
(c) P.J. Blower, J.A. Clarkson, S.C. Rawle, J.R. Hartman, R.E. Wolf Jr., R. Yagbasan, S.G. Bott, S.R. Cooper, Inorg. Chem. 28 (1989) 4040;
(d) S.R. Cooper, Acc. Chem. Res. 21 (1988) 141;
(e) E.J. Hintsa, J.R. Hartman, S.R. Cooper, J. Am. Chem. Soc. 105 (1983) 3738;
(f) J.R. Hartman, R.E. Wolf, B.M. Foxman, S.R. Cooper, J. Am. Chem. Soc. 105 (1983) 131;
(g) S.R. Cooper, S.C. Rawle, J.R. Hartman, E.J. Hintza, G.A. Admans, Inorg. Chem. 27 (1988) 1209;
(h) R.E. Wolf Jr., J.R. Hartman, J.M.E. Storey, B.M. Foxman, S.R. Cooper, J. Am. Chem. Soc. 107 (1987) 4328.

[11] (a) H. Sanaullah, H. Hungerbuhler, C. Schoneich, M. Morton, D.G. Vander Velde, G.S. Wilson, K.-D. Asmus, R.S. Glass, J. Am. Chem. Soc. 119 (1997) 2134;
(b) R.S. Glass, L.K. Steffen, D.D. Swanson, G.S. Wilson, R. de Gelder, R.A.G. de Graaff, R. Reedijk, Inorg. Chim. Acta 207 (1993) 241;
(c) W.N. Setzer, C.A. Ogle, G.S. Wilson, R.S. Glass, Inorg. Chem. 22 (1983) 266;
(d) R.S. Glass, G.S. Wilson, W.N. Setzer, J. Am. Chem. Soc. 102 (1980) 5068.

[12] (a) B. de Groot, S.J. Loeb, Inorg. Chem. 28 (1989) 3573;
(b) J. Casabo, T. Flor, M.N. Stuart Hill, H.A. Jenkins, J.C. Lockhart, S.J. Loeb, I. Romero, F. Teixidor, Inorg. Chem. 34 (1995) 5410;
(c) J.E. Kickham, J. Inorg. Chem. 33 (1994) 4351;
(d) B. de Groot, S.J. Loeb, G.K.H. Shimizu, Inorg. Chem. 33 (1994) 2663;
(e) J.E. Kickham, S.J. Loeb, S.H. Murphy, J. Am. Chem. Soc. 115 (1993) 7031;
(f) J.E. Kickham, S.J. Loeb, Inorg. Chem. 33 (1994) 4351;
(g) S.J. Loeb, D.L. Smith, Inorg. Chem. 32 (1993) 1297;
(h) S.J. Loeb, G.K.H. Shimizu, Inorg. Chem. 32 (1993) 1001;
(i) B. de Groot, H.A. Jenkins, S.J. Loeb, Inorg. Chem. 31 (1992) 203;
(j) S.J. Loeb, G.K.H. Shimizu, Chem. Commun. (1991) 1119;
(k) S.J. Loeb, G.K.H. Shimizu, Can. J. Chem. 69 (1991) 1141;
(l) S.L. Murphy, S.J. Loeb, G.K.H. Shimizu, Tetrahedron 54 (1998) 15137.

[13] (a) J. Nishijo, A. Miyazaki, T. Enoki, Bull. Chem. Soc. Jpn. 77 (2004) 715;
(b) R.D. Adams, R. Layland, K. McBride, Organometallics 15 (1996) 5425;
(c) C.R. Lucas, L. Shuang, M.J. Newlands, J.-P. Charland, E.J. Gabe, Can. J. Chem. 67 (1989) 639;
(d) C.R. Lucas, L. Shuang, M.J. Newlands, J.-P. Charland, E.J. Gabe, Can. J. Chem. 66 (1988) 1506;
(e) H. Meliani, C. Vinas, F. Teixidor, R. Silnappaa, R. Kivekas, Polyhedron 20 (2001) 2517;
(f) L. Escriche, M.P. Almajano, J. Casabo, F. Teixidor, J. Ruis, C. Miravitles, R. Kivekas, R. Sillanappa, J. Chem. Doc., Dalton Trans. (1993) 2969;
(g) Silanappaa, R. Kivekas, Polyhedron 20 (2001) 2517;
(h) R. Yagbasan, J. Phys. Astrophys 12 (1988) 244;
(i) J. Shen, J. Pickard, Z. Naturforsch. Chem. Sci. 47 (1992) 1736;
(j) J.J.M. Desper, S.H. Gellman, J. Am. Chem. Soc. 113 (1991) 704;
(k) L. Escriche, M.-P. Almajano, J. Casabo, F. Teixidor, J.C. Lockhart, G.A. Forsyth, R. Kivekas, M. Sundberg, Polyhedron 15 (1996) 4203;

(l) W.K. Musker, M.M. Ohmstead, R.M. Kessler, Inorg. Chem. 23 (1984) 1764;
(m) M. Munakata, L.P. Wu, M. Yamamoto, T. Kuroda-Sowa, M. Maekawa, J. Chem. Soc., Dalton Trans. (1995) 3215.
[14] R.D. Rogers, L. Nunez, J. Coord. Chem. 21 (1990) 111.
[15] E.L. Yee, R.J. Cave, K.L. Guyer, P.D. Tyma, M.J. Weaver, J. Am. Chem. Soc. 101 (1980) 1131.
[16] L.A. Ochrymowycz, C.-P. Mak, J.D. Michna, J. Org. Chem. 39 (1974) 2079.
[17] L.L. Diaddario Jr., L.A. Ochrymowycz, D.B. Rorabacher, Inorg. Chem. 31 (1992) 2347.
[18] L. Aronne, B.C. Dunn, J.R. Vyvyan, C.W. Souvignier, M.J. Mayer, T.A. Howard, C.A. Salhi, S.N. Goldie, L.A. Ochrymowycz, D.B. Rorabacher, Inorg. Chem. 34 (1995) 357.
[19] M.J. Heeg, C.P. Kulatilleke, L.A. Ochrymowycz, D.B. Rorabacher, Private Communication (1078), 2005.
[20] (a) H. McConell, N. Davidson, J. Am. Chem. Soc. 72 (1950) 3164;
(b) H.A. Benesi, J.H. Hilderbrand, J. Am. Chem. Soc. 71 (1949) 2703.
[21] B.C. Dunn, Ph.D. Dissertation, Wayne State University, Detroit, Michigan, 1996.
[22] B.A.C.P. Kulatilleke, Ph.D. Dissertation, Wayne State University, Detroit, Michigan, 2000.
[23] B.C. Dunn, P. Wijetunge, J.R. Vyvyan, T.A. Howard, A.J. Grall, L.A. Ochrymowycz, D.B. Rorabacher, Inorg. Chem. 36 (1997) 4484.
[24] B. Adhikary, C.R. Lucas, Inorg. Chem. 33 (1994) 1376.
[25] E.A. Ambundo, M.-V. Deydier, A.J. Grall, N. Aguera-Vega, L.T. Dressel, T.H. Cooper, M.J. Heeg, L.A. Ochrymowycz, D.B. Rorabacher, Inorg. Chem. 38 (1999) 4233.
[26] G.S. Patterson, R.H. Holm, Bioinorg. Chem. 4 (1975) 257.
[27] E.R. Dockal, L.L. Diaddario Jr., M.D. Glick, D.B. Rorabacher, J. Am. Chem. Soc. 99 (1977) 4530.
[28] (a) Polymeric Cu(I) complexes have also been observed in the presence of chloride ion: Ref. [14] listed in this paper;
(b) A.J. Blake, V. Lippolis, S. Parsons, M. Schröder, Acta Crystallogr., Sect. C 57 (2001) 36.
[29] (a) J.R. Hartman, R.E. Wolf Jr., B.R. Foxman, S.R. Cooper, J. Am. Chem. Soc. 105 (1983) 131;
(b) D.St. C. Black, I.A. McLean, Tetrahedron Lett. (1969) 3961;
(c) D.St. C. Black, I.A. McLean, Aust. J. Chem. 24 (1971) 1401.
[30] M.A. Hough, J.F. Hall, L.D. Kanbi, S.S. Hasnain, Acta Crystallogr., Sect. D 57 (2001) 355.
[31] (a) M.H.M. Olsson, U. Ryde, B.O. Roos, K. Pierloot, J. Biol. Inorg. Chem. 3 (1998) 109;
(b) U. Ryde, M.H.M. Olsson, K. Pierloot, B.O. Roos, J. Mol. Biol. 261 (1996) 586.
[32] (a) U. Ryde, M.H.M. Olsson, B.O. Roos, J.O.A. De Kerpel, K. Pierloot, J. Biol. Inorg. Chem. 5 (2000) 565;
(b) M.H.M. Olsson, U. Ryde, J. Biol. Inorg. Chem. 4 (1999) 654.

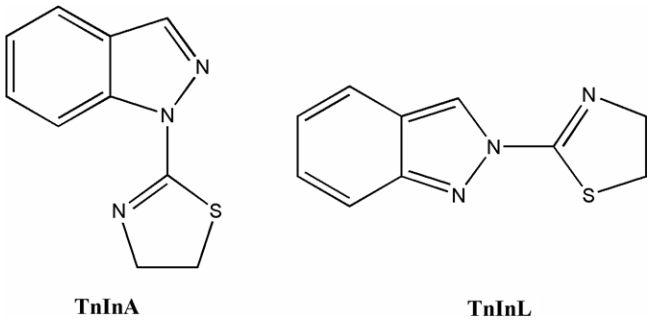


Fig. 1. Structure of TnInA and TnInL.

and were recrystallized from ethanol 96% (3.63 g, 35%) and acetone (2.54 g, 25%), respectively.

2.2. Preparation of $[Cu(NO_3)(TnInA)_2(H_2O)](NO_3)\cdot(H_2O)$ (1)

$Cu(NO_3)_2\cdot 3H_2O$ (121 mg, 0.5 mmol) dissolved in an ethanol–water was added to an ethanol–water solution of TnInA (100 mg, 0.5 mmol). The resulting solution was allowed to evaporate slowly at room temperature. After a few days, green crystals were isolated from the solution (122 mg, 38.7%). The crystals were first separated by filtration, then washed with cold ether and finally air-dried. *Anal*. Calc. for $C_{20}H_{22}CuN_8O_8S_2$: C, 38.12; H, 3.52; N, 17.79; S, 10.18. Found: C, 38.03; H, 3.33; N, 17.61; S, 10.12%.

2.3. Preparation of $[Cu(NO_3)_2(TnInL)(H_2O)]$ (2)

This complex was prepared by reacting an ethanol–water solution of $Cu(NO_3)_2\cdot 3H_2O$ (121 mg, 0.5 mmol) with an ethanol–water solution of TnInL (100 mg, 0.5 mmol), giving green crystals after a slow evaporation of the solution at room temperature (117.3 mg, 57.4%). The crystals were filtered and washed with cold ether and air-dried. *Anal*. Calc. for $C_{10}H_{11}CuN_5O_7S$: C, 29.38; H, 2.71; N, 17.13; S, 7.83. Found: C, 29.23; H, 2.67; N, 16.80; S, 7.80%.

2.4. Instrumental procedures

Chemical analyses of carbon, hydrogen, nitrogen and sulphur were performed by microanalytical methods using a Leco CHNS-932 microanalyser. IR spectra were recorded on a Perkin–Elmer FT-IR 1720 spectrophotometer, from KBr pellets in the 4000–370 cm^{-1} range and on a Perkin–Elmer FT-IR 1700X spectrophotometer, from polyethylene pellets in the 500–150 cm^{-1} range. UV–Vis–NIR reflectance spectra for complexes in the 200–1500 nm range were obtained from pellets of the samples, using a Shimadzu UV-3101 PC spectrophotometer and $BaSO_4$ as a reference. Magnetic susceptibility measurements were performed on polycrystalline samples using a magnetometer with pendulum MANICS DSM8, equipped with helium continuous-flow cryostat and an electromagnetometer DRUSCH EAF 16 UE. Data were corrected for temperature independent paramagnetism and diamagnetic contributions, which were estimated from the Pascal constants. The EPR spectra were recorded at room temperature in solid state and at 77 K in DMSO solution employing a BRUKER ESP-300E spectrometer using the X band of microwave.

2.5. Crystal structure determinations

Experimental details of crystal structure determinations including crystal data, data collection, structure determinations and refinement parameters for **1** and **2** are listed in Table 1. X-ray diffraction measurements were performed using a Bruker SMART CCD diffractometer equipped with graphite-monochromated Mo Kα radiation ($\lambda = 0.71073$ Å) using the ϕ–ω scan technique for **1** and an Enraf–Nonius CAD4 diffractometer equipped with graphite-monochromated Cu Kα radiation ($\lambda = 1.5418$ Å) using the ω–2θ scan technique for **2**. Empirical absorption

Table 1
Crystal data, data collection and refinement details for $[Cu(NO_3)(TnInA)_2(H_2O)](NO_3)(H_2O)$ (**1**), $[Cu(NO_3)_2(TnInL)(H_2O)]$ (**2**)

	1	**2**
Crystal shape	prism	plate
Colour	green	green
Size (mm)	$0.49\times0.49\times0.28$	$0.60\times0.50\times0.08$
Chemical formula	$C_{20}H_{22}CuN_8O_8S_2$	$C_{10}H_{11}CuN_5O_7S$
Formula weight	630.1	408.8
Crystal system	monoclinic	monoclinic
Space group	$P21$	$P21/n$
Unit cell dimensions		
a (Å)	7.679(1)	7.094(1)
b (Å)	16.376(1)	23.624(2)
c (Å)	9.744(1)	9.224(1)
β (°)	94.494(1)	111.70(1)
Cell volume (Å^3)	1221.6(1)	1436.4(3)
Z	2	4
D_{calc} (g cm^{-3})	1.713	1.891
μ (mm^{-1})	1.130	3.993
$F(000)$	646	828
θ Range	2.1–28.2	3.7–74.8
Index ranges	$-10\leqslant h\leqslant 10$, $-21\leqslant k\leqslant 21$, $-12\leqslant l\leqslant 12$	$-8\leqslant h\leqslant 8$, $-29\leqslant k\leqslant 0$, $-11\leqslant l\leqslant 0$
Independent reflections	5533	2940
Observed reflections $[F>4\sigma(F)]$	5484	2880
Data completeness	0.948	0.996
Maximum/minimum transmission	0.728/0.595	0.726/0.149
Number of refined parameters	368	225
$R\ [F>4\sigma(F)]$[a]	0.023	0.049
$wR\ [F>4\sigma(F)]$[b]	0.061	0.139
Goodness-of-fit[c]	0.972	1.098
ρ_{max}/ρ_{min} (e Å^{-3})	0.315/−0.270	1.092/−1.112

[a] $R=\sum\|\|F_o\|-|F_c\|\|/\sum|F_o|$.
[b] $R=\{\sum[w(F_o^2-F_c^2)^2]/\sum[w(F_o^2)^2]\}^{1/2}$.
[c] The goodness-of-fit (GOF) equals $\{\sum[w(F_o^2-F_c^2)^2]/(N_{rflns}-N_{params})\}^{1/2}$.

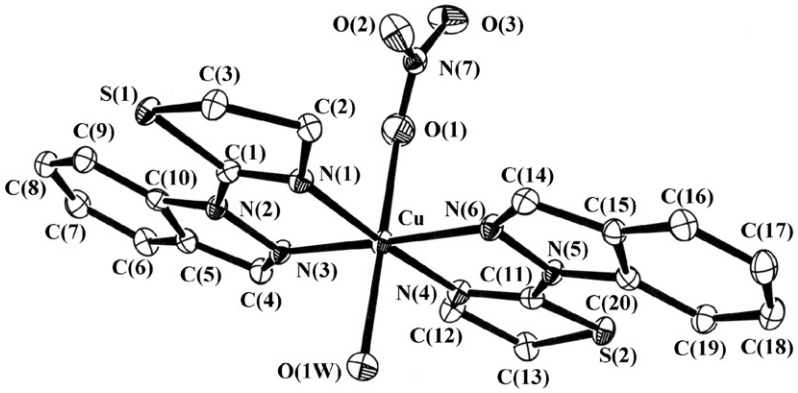


Fig. 2. Molecular structure of cation complex $[Cu(NO_3)(TnInA)_2(H_2O)]^+$, showing the atom-numbering scheme. The thermal ellipsoids are plotted at the 50% probability level.

corrections were applied using the SADABS [8] program for **1** whereas semiempirical absorption corrections were made based on psi-scan application using the WINGX [9] package for **2**. The structure of **1** was solved by Patterson methods and subsequent Fourier differences, whereas the structure of **2** was solved by direct methods and subsequent Fourier differences using, in all cases, the WINGX package [9] and refined by full-matrix least-squares on F^2. All non-hydrogen atoms were refined with anisotropic displacement parameters. Hydrogen atoms attached to carbon and nitrogen atoms were positioned geometrically, with U_{iso} values derived from U_{eq} values of the corresponding carbon and nitrogen atoms. However, hydrogen atoms of the water molecules were detected by Fourier differences and were refined with isotropic displacement parameters.

3. Results and discussion

3.1. Crystal structures

Complex **1** crystallizes into monoclinic unit cells, each one containing two $[Cu(NO_3)(TnInA)_2(H_2O)]^+$ cations, two nitrate anions and two water molecules held by a three-dimensional hydrogen bonds network. The overall view and labelling of the atoms of complex cation are displayed in Fig. 2. Table 2 lists the selected bond lengths, angles and hydrogen-bond parameters.

The environment around the copper(II) atom may be described as a distorted octahedral geometry with the ligand–metal–ligand bite angles varying between 80.6(1)° [N(1)–Cu–N(3)] and 99.8(1)° [N(1)–Cu–N(6)]. The metallic atom is coordinated by two thiazoline nitrogen atoms [av. Cu–N = 1.981 Å], two indazole nitrogen atoms [av. Cu–N = 2.054 Å], one oxygen atom from a monodentate nitrate group [Cu–O(1) = 2.446(2) Å] and one oxygen atom from a water molecule [Cu–O(1W) = 2.333(1) Å].

The $Cu–O_{water}$ bond distance is shorter to the calculated mean value [2.47(19) Å] calculated using the data of 130 six-coordinate copper(II) complexes with an N_4O_2 environment, obtained with the CONQUEST software [10] from the Cambridge Structural Database (CSD) [11] and likewise, the $Cu–O_{nitrate}$ bond length is similar to the average value [2.51(16) Å] calculated from the data of 67 complexes. The $Cu–N_{thiazoline}$ bond lengths are in good agreement with the mean value [1.96(4) Å] found for 15 copper(II) complexes with this type of bond in the CSD. Finally, the $Cu–N_{indazole}$ bond lengths are slightly shorter to those found in bis(Hydrogen tris(indazol-1-yl)borato)-copper(II)-chloroform solvate [2.132 Å] [12] and bis(Hydrogen–tris(indazol-1-yl)borato)-copper(II)-tetrahydrofuran solvate [2.127 Å] [12].

The chelate ring Cu–N(1)–C(1)–N(2)–N(3) is essentially planar with maximum mean plane deviation for N(3) (0.058 Å). However, the chelate ring Cu–N(4)–C(11)–N(5)–N(6) shows a conformation near to envelope with the apex at N(6), deviating 0.198 Å from the mean plane formed by Cu, N(4), C(11) and N(5). This geometry is

Table 2
Selected bond lengths (Å), angles (°) and hydrogen-bond parameters for $[Cu(NO_3)(TnInA)_2(H_2O)](NO_3)(H_2O)$ (**1**)

Cu–O(1)	2.446(2)	Cu–O(1W)	2.333(1)
Cu–N(1)	1.979(2)	Cu–N(3)	2.048(2)
Cu–N(4)	1.983(2)	Cu–N(6)	2.060(2)
N(5)–N(6)	1.389(2)	N(3)–N(2)	1.383(2)
C(1)–N(1)	1.282(2)	N(2)–C(1)	1.382(2)
N(4)–C(11)	1.280(2)	N(5)–C(11)	1.377(2)
N(1)–Cu–N(4)	175.0(1)	N(3)–Cu–O(1W)	97.2(1)
N(1)–Cu–N(3)	80.6(1)	N(6)–Cu–O(1W)	85.6(1)
N(4)–Cu–N(3)	98.6(1)	N(1)–Cu–O(1)	92.8(1)
N(1)–Cu–N(6)	99.8(1)	N(4)–Cu–O(1)	82.2(1)
N(4)–Cu–N(6)	80.8(1)	N(3)–Cu–O(1)	78.9(1)
N(3)–Cu–N(6)	177.2(1)	N(6)–Cu–O(1)	98.3(1)
N(1)–Cu–O(1W)	91.3(1)	O(1W)–Cu–O(1)	173.9(1)
N(4)–Cu–O(1W)	93.8(1)		

Bond A···H–D	Position of A	A···D (Å)	A···H–D (°)
O(2)···H(4W)–O(2W)	x, y, z	2.861(2)	161(2)
O(4)···H(2W)–O(1W)	x, y, z	2.877(2)	178(1)
O(4)···H(3W)–O(2W)	$x-1, y, z-1$	2.915(2)	158(2)
O(3)···H(1W)–O(1W)	$x+1, y, z$	2.803(2)	155(2)

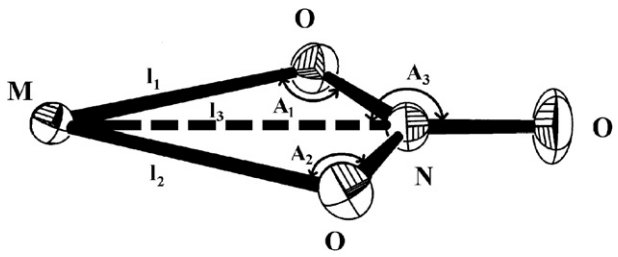


Fig. 3. Parameters used for assigning nitrate coordination modes [14].

Table 3
Criteria for assigning nitrate coordination modes [14]

	Monodentate	Anisobidentate	Bidentate
l_2–l_1 (Å)	>0.6	0.3–0.6	<0.3
A_1–A_2 (°)	>28	14–28	<14
l_3–l_2 (Å)	<0.1	0.1–0.2	>0.2
A_3 (°)	<162	162–168	>168

proved by the puckering parameters $q = 0.127$ Å and $\phi = 142.7°$ calculated according to Cremer and Pople [13].

The thiazoline rings S(1)–C(1)–N(1)–C(2)–C(3) [$q = 0.256$ Å; $\phi = -44.3°$] [13] and S(2)–C(11)–N(4)–C(12)–C(13) [$q = 0.165$ Å; $\phi = -49.9°$] [13] show an intermediate conformation between envelope and half-chair. In the first thiazoline ring, C(2) and C(3) are deviating −0.133 and 0.285 Å, respectively, from the plane formed by S(1), N(1) and C(1). Likewise, in the second thiazoline ring, C(12) and C(13) are deviating −0.133 and 0.136 Å, respectively, from the plane formed by S(2), C(11) and N(4).

According to the criteria for the assignment for nitrate binding modes introduced by Kleywegt et al. [14] (see also Fig. 3, Tables 3 and 4), the nitrate binding mode in **1** has been classified as monodentate.

The crystal structure presents a three-dimensional hydrogen-bond network in which oxygen atoms O(2), O(3) and O(4) from nitrate groups act as acceptors of hydrogen, whereas water molecules act as donors. A diagram showing this network is given in Fig. 4.

The crystal structure of **2** is built up of neutral $[Cu(NO_3)_2(TnInL)(H_2O)]$ entities linked through hydrogen bonds involving water molecules and nitrate groups. The structure of the complex is shown in Fig. 5, together with the atomic numbering scheme. Selected bond lengths, angles and hydrogen-bond parameters are given in Table 5.

The stereochemistry of the complex centre is basically five coordinate, but with the second oxygen of the nitrate group occupying the sixth coordination position at a potentially bonding distance of 2.685 Å, to give a $(4 + 1 + 1^*)$ type coordination [15,16]. The ligand geometry around copper(II) centre is best described as distorted square

Table 4
Parameters for complexes

Complex	Nitrate group	l_2–l_1 (Å)	A_1–A_2 (°)	l_3–l_2 (Å)	A_3 (°)	Classification
1	N(7), O(1), O(2), O(3)	0.990	50.0	−0.139	150.4	monodentate
2	N(4), O(1), O(2), O(3)	0.723	32.9	0.024	160.4	monodentate
	N(5), O(4), O(5), O(6)	0.961	49.0	−0.104	157.7	monodentate

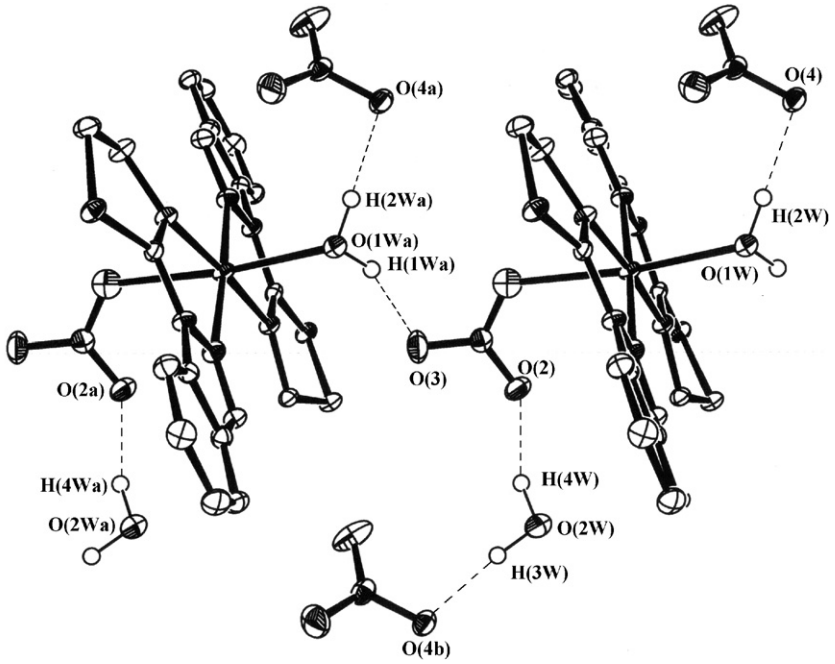


Fig. 4. View of the hydrogen bond network of **1**.

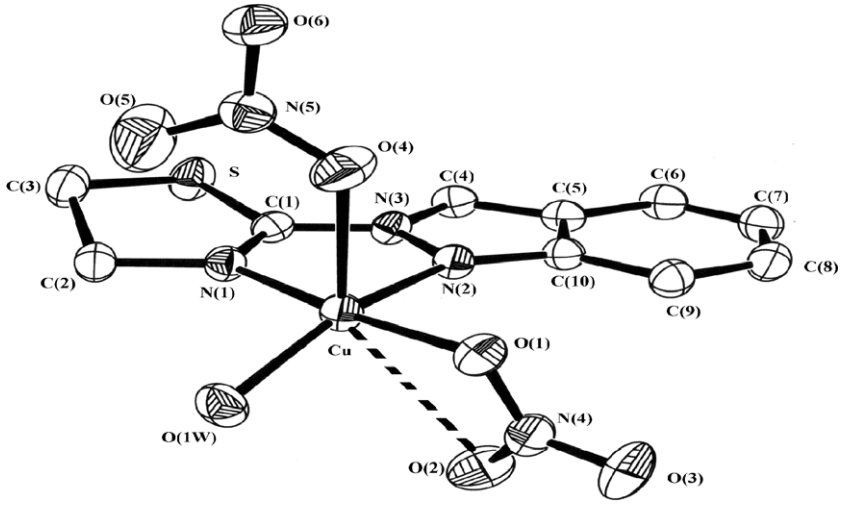


Fig. 5. Crystal structure of **2**, showing the atom-numbering scheme. The thermal ellipsoids are plotted at the 50% probability level.

pyramidal with a τ value of 0.26, indicating a geometry closer to a regular square pyramid ($\tau = 0$) than a regular trigonal bipyramid ($\tau = 1$) [17]. The equatorial positions are occupied by one water molecule [Cu–O(1W) = 1.964(2) Å], one nitrate oxygen atom [Cu–O(1) = 1.962(2) Å], one thiazolinic nitrogen atom [Cu–N(1) = 1.996(2) Å] and one indazolic nitrogen atom [Cu–N(2) = 2.034(2) Å]. The axial position is occupied by one nitrate oxygen atom at a distance of 2.342(2) Å from copper atom. The O(4)–metal–basal ligand angles vary from the ideal value for a square pyramid (90°) and they are comprised between 106.7(1)° [O(4)–Cu–O(1W)] and 83.1(1)° [O(4)–Cu–O(1)]. Likewise, the basal ligand–metal–basal ligand angles differ from the ideal value of 90°, varying between 95.1(1)° [O(1W)–Cu–N(1)] and 80.3(1)° [N(1)–Cu–N(2)].

The Cu–$O_{nitrate}$ basal bond distance is similar to the average value [1.99(4) Å] calculated for 29 square pyramidal copper(II) complexes with an N_2O_3 environment in CSD. In the same way, the Cu–$O_{nitrate}$ axial bond distance is in good agreement with the mean value 2.35(11) Å obtained for 53 complexes and the Cu–O_{water} distance is comparable to the mean values 1.97(2) Å found for 68 complexes. Finally, the Cu–$N_{thiazoline}$ and Cu–$N_{indazole}$ bond lengths are similar to those found in **1**.

Table 5
Selected bond lengths (Å), angles (°) and hydrogen-bond parameters for $[Cu(NO_3)_2(TnInL)(H_2O)]$ (**2**)

Cu–O(1)	1.962(2)	Cu–O(1W)	1.964(2)
Cu–O(4)	2.342(2)	Cu–N(1)	1.996(2)
Cu–N(2)	2.034(2)	N(1)–C(1)	1.263(4)
N(2)–N(3)	1.368(3)	N(3)–C(1)	1.402(4)
O(1)–Cu–O(1W)	91.0(1)	O(1)–Cu–N(1)	173.9(1)
O(1W)–Cu–N(1)	95.1(1)	O(1)–Cu–N(2)	94.1(1)
O(1W)–Cu–N(2)	158.1(1)	N(1)–Cu–N(2)	80.3(1)
O(4)–Cu–O(1)	83.1(1)	O(4)–Cu–O(1W)	106.7(1)
N(1)–Cu–O(4)	95.1(1)	N(2)–Cu–O(4)	95.1(1)

Bond A···H–D	Position of A	A···D (Å)	A···H–D (°)
O(6)···H(1W)–O(1W)	$x-1, y, z$	2.756(3)	168.4(2)
O(6)···H(2W)–O(1W)	$x-1/2, -y+1/2, z+1/2$	2.832(4)	166.5(2)

The five-membered chelate ring Cu–N(1)–C(1)–N(3)–N(2) is essentially planar with maximum mean plane deviation for C(1) (0.030 Å). For the thiazoline ring, the puckering parameters $q = 0.308$ Å and $\phi = 137.6°$ [13] indicate a conformation near to envelope with the C(3) atom deviating 0.478 Å above the mean plane formed by S, C(1), N(1) and C(2).

The nitrate binding mode has been classified in a similar form to **1**. Thus, the results showed in Table 4 indicate that the nitrate group N(5), O(4), O(5), O(6) acts undoubtedly as monodentate, whereas nitrate group N(4), O(1), O(2), O(3) exhibits values of monodentate but close to anisobidentate.

In fact, focusing our attention on the N(4)–O(1)–Cu angle, we see that its values differs significantly from linearity, amounting to 110.7(2)°. Likewise, the mean plane formed by the atoms O(1), O(2), O(3) and N(4) of monodentate nitrate ligand forms an angle of 83.4° with the plane constituted by O(1W)–Cu–N(2). Both facts may possibly be explained in terms of crystal packaging effects, but as they facilitate the approach from O(2) to the central ion, it cannot be excluded that they are conditioned by the existence of a O(2)–Cu weak interaction [2.685(3) Å].

It should be pointed out that the main difference in both complexes with respect to the structure of free ligands TnInA and TnInL is due to the different degree of rotation of the thiazoline ring around the C(1)–N(2) [or C(11)–N(5)] and C(1)–N(3) bond, respectively, which permits the coordination through N(1) [torsion angle N(1)–C(1)–N(2)–N(3) = −2.6° and N(4)–C(11)–N(5)–N(6) = −11° in **1**; −176.9° in TnInA free; torsion angle N(1)–C(1)–N(3)–N(2) = 8.7° in **2**; 178.8° in TnInL free].

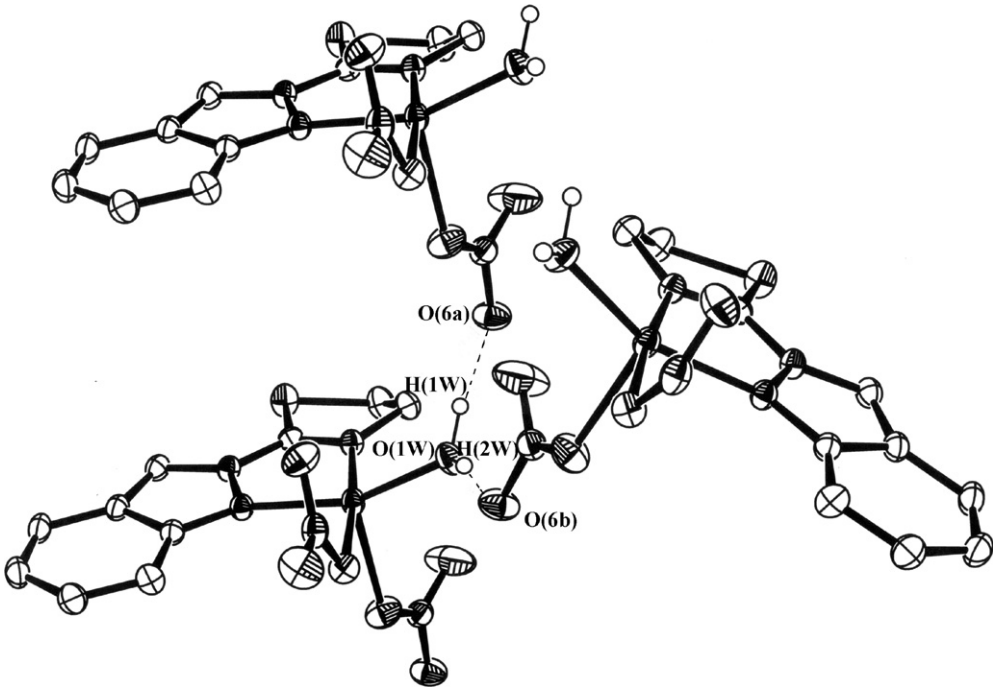


Fig. 6. View of the hydrogen bonds of **2**.

Finally, the crystal structure is stabilized by a two-dimensional hydrogen-bond system perpendicular to the b direction in which the water molecule is involved in two intermolecular hydrogen bonds, each of them linking to a nitrate group belonging to two different neighbouring $[Cu(NO_3)_2(TnInL)(H_2O)]$ entities. A diagram showing this network is given in Fig. 6.

3.2. Spectroscopic properties

The reflectance spectrum of **1** exhibits one broad asymmetric band centred at $\sim$14 250 cm^{-1} with a low energy shoulder assigned to the $^2T_{2g}(D) \leftarrow {}^2E_g(D)$ transition in agreement with the octahedral stereochemistry [18–20]. Moreover, the spectrum shows other strong band at $\sim$30 490 cm^{-1} what is assigned to a charge-transfer band [21]. The reflectance spectrum of **2** consists of a very broad d-d asymmetric band centred at $\sim$13 330 cm^{-1} with a shoulder at $\sim$10 800 cm^{-1} assigned to the $^2B_1[(d_{x^2-y^2})^1] \rightarrow {}^2A_1[(d_{z^2})^1]$ and $^2B_1[(d_{x^2-y^2})^1] \rightarrow {}^2B_2[(d_{xy})^1]$, $^2E[(d_{xz})^1]$, $^2E[(d_{yz})^1]$ transitions, respectively. This spectral pattern is typical of the square-pyramidal stereochemistry [21]. Likewise, the spectrum shows a strong absorption at $\sim$27 170 cm^{-1} with a shoulder at $\sim$35 460 cm^{-1} which may be associated with a charge-transfer band and with the $\pi \rightarrow \pi^*$ transitions of the organic ligand, respectively.

The EPR spectra of polycrystalline samples at 298 K (Fig. 7 for **1** and Fig. 8 for **2**) and at 77 K in DMSO solution (Fig. 9 for **1** and Fig. 10 for **2**) of complexes were recorded in the X-band, using the 100 kHz field modulation.

In the solid state, complex **1** exhibits a typically axial spectrum ($g_\parallel = 2.28$ and $g_\perp = 2.09$). The geometric parameter $G = (g_\parallel - 2)/(g_\perp - 2)$ value is found to be in the range 3.5–5.0 and $g_\parallel > g_\perp > 2.0023$, which is consistent with a $d_{x^2-y^2}$ ground state having a negligible exchange coupling [21,22]. In frozen solution the spectrum ($g_\parallel = 2.32$ and $g_\perp = 2.08$) cannot be simulated by only one species. An other species should be formed directly when the solution of DMSO is prepared and this species may involve DMSO in the coordination sphere. One of these signals affords g

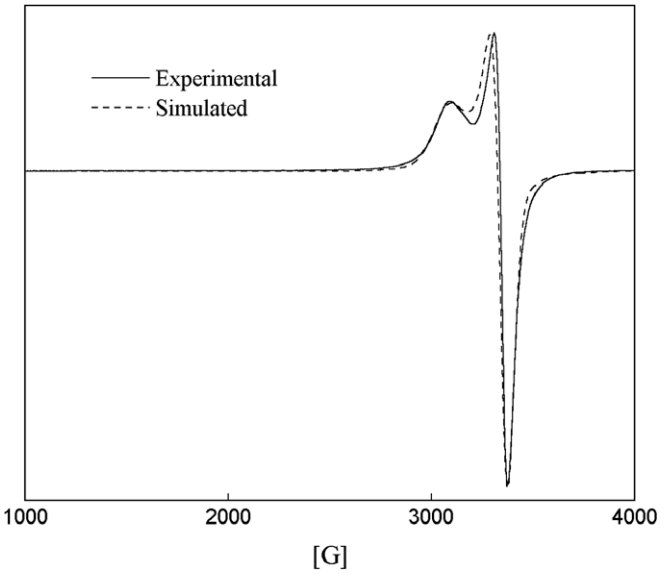


Fig. 7. EPR spectrum of **1** in the polycrystalline state at 298 K.

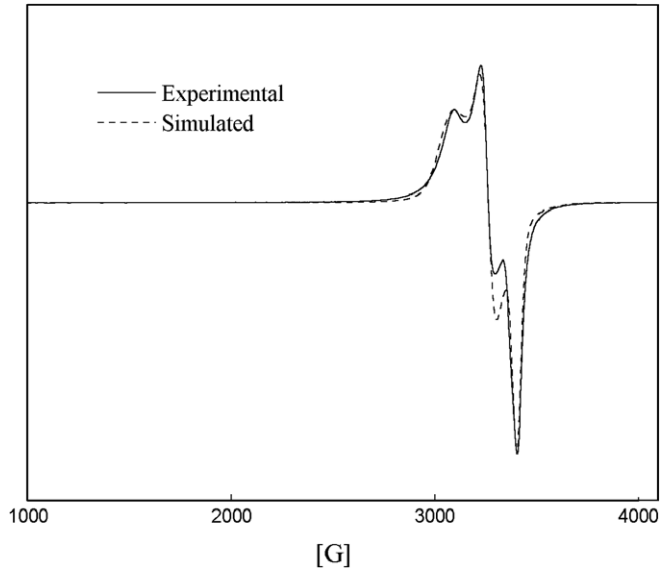


Fig. 8. EPR spectrum of **2** in the polycrystalline state at 298 K.

values that resemble those of **1** in the powder which shows that this complex have a static structure in the solid, and that their molecular and electronic structures in the solid state and in solution are the same. The other signal of spectrum cannot be well simulated.

The spectrum of **2** in the solid state at 298 K is typically rhombic ($g_1 = 2.06$, $g_2 = 2.15$ and $g_3 = 2.28$). The geometric parameter $R = (g_2 - g_1)/(g_3 - g_2)$ value is 0.69, which is consistent with a square-pyramidal or octahedral geometry with a $d_{x^2-y^2}$ ground state [15,21,23,24]. The spectrum in DMSO solution of this complex at 77 K changes to an axially elongated form with $g_{\|} = 2.33$ and $g_{\perp} = 2.08$, indicating a square pyramidal geometry and showing four hyperfine lines corresponding to monomeric copper(II) species (no superhyperfine structure is observed). The g values that resemble those of **1** in the powder which shows that this complex have a static structure in the solid, and that their molecular and electronic structures in the solid state and in solution are the same. The other signal of spectrum cannot be well simulated.

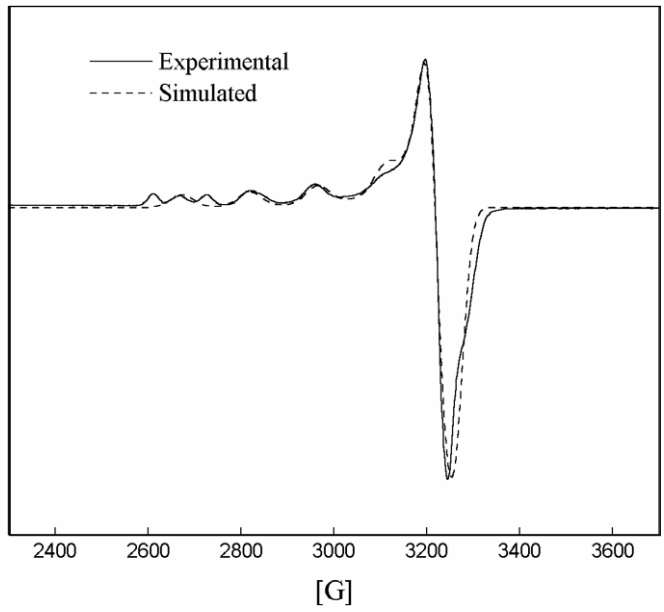


Fig. 9. EPR spectrum of **1** in DMSO solution at 77 K.

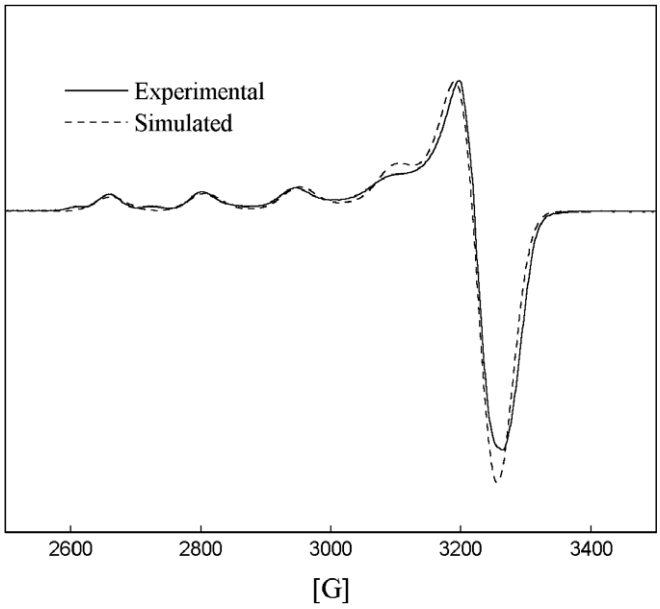


Fig. 10. EPR spectrum of **2** in DMSO solution at 77 K.

ues in the solid state at room temperature and in frozen solution are not much different from each other, hence the geometry around the copper ion is unaffected on cooling the solution to liquid nitrogen temperature, which gives no information indicative to a fluxional behaviour.

The IR spectra of **1** and **2** in the 4000–370 cm^{-1} region show the presence of bands due to the organic moiety. In both complexes the bands assigned to ν(C=N) skeletal vibration of the indazole ring (1598 cm^{-1} for **1** and 1622 cm^{-1} for **2**) and ν(C=N) skeletal vibration of the thiazoline ring (W_1) (1615 cm^{-1} for **1** and 1633 cm^{-1} for **2**), undergoes a negative shift when compare with that for the uncoordinated respective ligand (TnInA: ν(C=N) = 1614 cm^{-1}, $W_1 = 1632$ cm^{-1}; TnInL: ν(C=N) = 1637 cm^{-1}, $W_1 = 1641$ cm^{-1}). From all this can be deduced a coordination via these nitrogen atoms of the ligands [25–28].

In addition, the IR spectra of the complexes were investigated to obtain evidence for ionic or coordinated nitrate ions. This question has been the subject of considerable study. The most commonly used for determining coordination of the nitrate ion is the method based on the ($\nu_1 + \nu_4$) combination bands [29–32]. In this way, the bands registered at 1763, 1717 and 1707 cm^{-1} for **1** are assigned to ($\nu_1 + \nu_4$) combination bands. The first one is assignable to combination band of group nitrate ionic [30]. The value of the splitting ($\Delta = 10$ cm^{-1}) for the last two bands reveals the presence of one monodentate nitrate group in agreement with Lever's criteria [30]. For **2** the ($\nu_1 + \nu_4$) region shows bands at 1763 and 1752 cm^{-1} and at 1735 and 1716 cm^{-1} with the separation of 11 cm^{-1} and of 19 cm^{-1}. These bands can be assigned to one monodentate nitrate group and one anisobidentate nitrate group, respectively [30]. These results are in good accord with the X-ray structural determination data.

Table 6
Far IR bands (cm^{-1}) with tentative assignments

Compound	ν(Cu–O_{water})	ν(Cu–$N_{indazole}$)	ν(Cu–$N_{thiazoline}$)	ν(Cu–ONO_2)
$[Cu(NO_3)(TnInA)_2(H_2O)](NO_3)\cdot(H_2O)$ (**1**)	341	306	249 235	323
$[Cu(NO_3)_2(TnInL)(H_2O)]$ (**2**)	326	291	249	254

Besides, other bands due to monodentate nitrate ligands are registered at 707 and 697 cm^{-1} (ν_4), 1395 cm^{-1} (ν_3), 840 cm^{-1} (ν_2) and 1015 cm^{-1} (ν_1) for **1** and at 730 and 707 cm^{-1} (ν_4), 1435 and 1299 cm^{-1} (ν_3), 820 cm^{-1} (ν_2) and 1034 cm^{-1} (ν_1) for **2** [30]. Bands at 1387, 1056 and 826 cm^{-1} can be assigned to the nitrate ion group for the complex **1** and the bands at 719 and 690 cm^{-1} (ν_4) can be attributed to anisobidentate nitrate group for complex **2**.

The far IR spectra of these complexes show the appearance of bands due to metal–ligand stretching vibrations. Tentative assignments are listed in Table 6. The strong bands in the region 325–340 cm^{-1} are assigned to ν(Cu–O_{water}) vibration [33,34], whereas new bands at 305–290 cm^{-1} can be tentatively attributed to ν(Cu–$N_{indazole}$) vibration [35]. Likewise, bands due to ν(Cu–$N_{thiazoline}$) vibration [33,36,37] are found in the 250–235 cm^{-1} range. Finally, ν(Cu–ONO_2) vibrations [38–42] are registered in spectra at 325–255 cm^{-1}.

3.3. Magnetic measurements

The observed molar magnetic susceptibility for Cu(II) complexes was corrected for diamagnetism and temperature-independent paramagnetism to provide the fully corrected magnetic moment at room temperature ($\mu = 2.46$ BM for **1**; $\mu = 1.91$ BM for **2**). These values are slightly over or in the range 1.75–2.2 BM, which allows to exclude metal–metal interactions, supporting a monomeric structural formulation for these compounds [43].

4. Conclusion

For Cu(II)/TnInA and Cu(II)/TnInL systems, both with a 1:1 ligand/metal ratio, it was obtained complexes with six and five coordination numbers, respectively. Thus, $[Cu(NO_3)(TnInA)_2(H_2O)](NO_3)(H_2O)$ (**1**) shows an environment around the copper atom that may be described as distorted octahedral geometry with two organic ligands coordinated to metal centre. However, in $[Cu(NO_3)_2(TnInL)(H_2O)]$ (**2**) the geometry around the metal atom is adequately described as a square pyramid with only one organic ligand linked to ion copper.

From these results, we can conclude that the linear arrangement of heterocycles in TnInL ligand generate a greater steric impediment on the coordination sphere than the angular one in TnInA ligand. This fact hinder the access of a second organic ligand in complex **2**.

Likewise, these results are in good agreement with the cadmium(II) complexes preliminary reported [1], where complexes exhibited similar triangulated dodecahedral geometry that was more distorted in complex $[Cd(NO_3)_2(TnInL)_2]$ than in complex $[Cd(NO_3)_2(TnInA)_2]$, which was attributed to packing effects. The difference stoichiometry in copper complexes can be explained because of the presence of a smaller metal ion that intensifies the structural difference between TnInA and TnInL ligands.

Acknowledgements

We thank the Junta de Extremadura (Consejería de Educación, Ciencia y Tecnología) and the FEDER [Project 2PR04A011] for financial support.

Appendix A. Supplementary material

CCDC 619126 and 619127 contain the supplementary crystallographic data for $[Cu(NO_3)_2(TnInL)(H_2O)]$ and $[Cu(NO_3)(TnInA)_2(H_2O)](NO_3)(H_2O)$. These data can be obtained free of charge via http://www.ccdc.cam.ac.uk/conts/retrieving.html, or from the Cambridge Crystallographic Data Centre, 12 Union Road, Cambridge CB2 1EZ, UK; fax: (+44) 1223-336-033; or e-mail: deposit@ccdc.cam.ac.uk. Supplementary data associated with this article can be found, in the online version, at doi:10.1016/j.poly.2006.10.001.

References

[1] F.J. Barros-García, F. Luna-Giles, M.A. Maldonado-Rogado, E. Viñuelas-Zahínos, Polyhedron 25 (2006) 43.
[2] F.J. Barros-García, A. Bernalte-García, F. Luna-Giles, M.A. Maldonado-Rogado, E. Viñuelas-Zahínos, Polyhedron 25 (2006) 52.
[3] S. Bräse, C. Gil, K. Knepper, Bioorgan. Med. Chem. 10 (2002) 2415.
[4] G. Daidone, D. Raffa, B. Maggio, M.V. Raimondi, F. Plescia, D. Schillaci, Eur. J. Med. Chem. 39 (2004) 219.
[5] M.-H. Shih, F.-H. Ke, Bioorg. Med. Chem. 12 (2004) 4633.
[6] C.G. Bonde, N.J. Gaikwad, Bioorgan. Med. Chem. 12 (2004) 2151.
[7] S.H. Kim, H. Son, G. Nam, D.Y. Chi, J.H. Kim, Bioorg. Med. Chem. Lett. 10 (2000) 1143.
[8] Bruker AXS Inc., SADABS, Version 2.03, Bruker AXS Inc., Madison, WI, 2001.
[9] L.J. Farrugia, J. Appl. Cryst. 32 (1999) 837.
[10] F.H. Allen, Acta Crystallogr. B 58 (2002) 380.
[11] I.J. Bruno, J.C. Cole, P.R. Edington, M. Kessler, C.F. Macrae, P. McCabe, J. Pearson, R. Taylor, Acta Crystallogr. B 58 (2002) 389.
[12] C. Janiak, S. Tenizdemir, S. Dechert, W. Deck, F. Girgsdies, J. Heinze, M.J. Kolm, T.G. Scharmann, O.M. Zipffel, Eur. J. Inorg. Chem. (2000) 1229.
[13] D. Cremer, J.A. Pople, J. Am. Chem. Soc. 97 (1975) 1354.
[14] G.J. Kleywegt, W.G.R. Wiesmeijer, G.J. Van Driel, W.L. Driessen, J. Reedijk, J.H. Noordik, J. Chem. Soc., Dalton Trans. (1985) 2177.
[15] W. Fitzgerald, B.J. Hathaway, J. Chem. Soc., Dalton Trans. (1981) 567.
[16] R. Ballesteros, B. Abarca, A. Samadi, J. Server-Carrió, E. Escrivá, Polyhedron 18 (1999) 3129.

[17] A.W. Addison, T.N. Rao, J. Reedijk, J. van Rijn, G.C. Verschoor, J. Chem. Soc., Dalton Trans. (1984) 1349.
[18] S. Menon, M.V. Rajasekharan, Polyhedron 17 (1998) 2463.
[19] B.J. Hathaway, D.E. Billing, Coord. Chem. Rev. 5 (1970) 143.
[20] L.K. Thompson, B.S. Ramaswamy, R.D. Dawe, Can. J. Chem. 56 (1978) 1311.
[21] B.J. Hathaway, in: G. Wilkinson, R.D. Gill, J.A. McCleverty (Eds.), Comprehensive Coordination Chemistry, vol. 5, Pergamon Press, Oxford, 1987.
[22] B.J. Hathaway, J. Chem. Soc., Dalton Trans. (1972) 1196.
[23] S. Tyagi, B.J. Hathaway, J. Chem. Soc., Dalton Trans. (1981) 2029.
[24] R.J. Fereday, P. Hodgson, S. Tyagi, B.J. Hathaway, J. Chem. Soc., Dalton Trans. (1981) 2070.
[25] M. Shakir, S.P. Varkey, F. Firdaus, P.S. Hameed, Polyhedron 13 (1994) 2319.
[26] B. Singh, R.N. Singh, R.C. Aggarwal, Polyhedron 4 (1985) 401.
[27] M.M. Mostafa, M.A. Khattab, K.M. Ibrahim, Polyhedron 2 (1983) 583.
[28] J. Nelson, S. Martin Nelson, W.D. Perry, J. Chem. Soc., Dalton Trans. (1976) 1282.
[29] K. Nakamoto, Infrared and Raman Spectra of Inorganic and Coordination Compound, fifth ed., Wiley, New York, 1997.
[30] A.B.P. Lever, E. Mantovani, B.S. Ramaswamy, Can. J. Chem. 49 (1971) 1957.
[31] C.C. Addison, D. Sutton, Prog. Inorg. Chem. 8 (1967) 195.
[32] B.N. Gaterhouse, S.E. Livingstone, R.S. Nyholm, J. Chem. Soc. (1957) 4222.
[33] F.J. Barros-García, A. Bernalte-García, F.J. Higes-Rolando, F. Luna-Giles, M.A. Maldonado-Rogado, E. Viñuelas Zahínos, Inorg. Chim. Acta 357 (2004) 3574.
[34] G. Sartori, C. Furlani, A. Damiani, J. Inorg. Nucl. Chem. 8 (1959) 119.
[35] C. Santini, C. Pettinari, M. Pellei, G. Gioia-Lobbia, A. Pifferi, M. Camalli, A. Mele, Polyhedron 18 (1999) 2255.
[36] A. Bernalte-García, A.M. Lozano-Vila, F. Luna-Giles, R. Pedrero-Marín, Polyhedron 25 (2006) 1399.
[37] F.J. Barros-García, A. Bernalte-García, F. Luna-Giles, A.M. Pizarro-Galán, E. Viñuelas-Zahínos, Z. Anorg. Allg. Chem. 631 (2005) 1898.
[38] M.C. García-Cuesta, A.M. Lozano, J.J. Meléndez-Martínez, F. Luna-Giles, A.L. Ortiz, L.M. González-Meléndez, F.L. Cumbrera, J. Appl. Cryst. 37 (2004) 993.
[39] K. Madhukar, B. Madhu, B.A. Sastry, G. Ponticelli, M. Massacessi, Polyhedron 8 (1989) 935.
[40] D.X. West, R.J. Hartley, J. Inorg. Nucl. Chem. 43 (1981) 957.
[41] D.X. West, R.J. Hartley, J. Inorg. Nucl. Chem. 43 (1981) 963.
[42] R.H. Nuttall, D.W. Taylor, J. Chem. Soc., Chem. Commun. (1968) 1417.
[43] G. Albertin, E. Bordignon, A.A. Orio, Inorg. Chem. 14 (1975) 1411.

donation from O to Mo, as indicated by the short Mo–O bond length. Results of electrochemical studies show that the complexes of the type $[\{M(NO)(Tp^{Me2})X\}_n(QH_{2-n})]$ undergo one-electron reduction when $n = 1$ thereby generating 17*e* species, or two distinct one-electron reduction processes when $n = 2$. These redox processes may be reversible, depending on X [13].

Many bimetallic complexes $[\{M(NO)(Tp^{Me2})X\}_2(Q)]$ (M = Mo or W, X = halide, Q = bifunctionalised hydrocarbons or related aromatic ring systems) have been reported. Examples include species where Q = 1,*x*-O_2C_n-H_{2n-2} ($n = 6$, $x = 2$–4; $n = 5$, $x = 3$) [14]; Q = *para*- or *meta*-OC_6H_4O; $OC_6H_4YC_6H_4O$ (Y = none, O, S, SO_2, CO, $COC_6H_4C_6H_4CO$) [15]; Q = $OC_6H_4(C_6H_4)_nC_6H_4O$ ($n = 1$ or 2), $OC_6H_4CR{=}CRC_6H_4O$ (R = H or Et), and $OC_6H_4CH{=}CHC_6H_4CH{=}CHC_6H_4O$ [16]; Q = 4,4′-bipyridines [17]; Q = α,ω-bis(4-pyridyl)polyenes [18]; Q = $OC_6H_4(CH_2)_nO$ ($n = 1$–3) or $NHC_6H_4(CH_2)_nO$ ($n = 2$, 3) [19]; Q = $(NHCH_2)_2Z$ (Z = none, CH_2 or $\{CH_2OCH_2\}_2$) [20]; Q = *ortho*-, *meta*- and *para*-$[C_6H_4(NH)_2]^{2-}$ [21–23]; Q = NHC_6H_4O [15]; Q = 4-(imidazol-1-yl)phenol [24]; Q = pyrazine [25]. Dinuclear complexes incorporating short bridge O^{2-} have also been reported [26]. However, little work has been presented on species containing short saturated hydrocarbyl ligand systems, for example ethane-1,2-diol. Earlier synthetic and spectroscopic characterization of bimetallic Mo complexes was carried out some time ago [13f] but most of the results were not published because of difficulties with separation of diastereoisomers and determination of the crystal structure of a doubly bridged complex.

In order to further develop our studies of the dinuclear nitrosyl complexes of Mo and W with the bridge coordinated to metals by oxygen donor we have returned to our research involving ethane-1,2-diol. We have now been able to separate singly bridged diastereoisomers and have determined the crystal structure of *anti*-$[\{Mo(NO)(Tp^{Me2})(OCH_2CH_2O)\}_2]\cdot 4CHCl_3$. Additionally, we prepared $[\{M(NO)(Tp^{Me2})X\}_n(OCH_2CH_2OH_{2-n})]$ (M = Mo, X = Br, $n = 1$ or 2; M = W, X = Cl, $n = 1$ or 2) complexes. All compounds were characterized electrochemically using cyclic voltammetry (CV) and differential pulse voltammetry (DPV).

2. Results and discussion

2.1. Syntheses

The bimetallic species $[\{M(NO)(Tp^{Me2})X\}_2(OCH_2CH_2O)]$ (M = Mo, X = Cl, Br, I; M = W, X = Cl) were obtained by two different routes: (i) reaction between $[M(NO)(Tp^{Me2})X_2]$ and $HOCH_2CH_2OH$ in dichloromethane or diethyl ether in the presence of silver acetate or hexamethylenetetramine, and (ii) by direct reaction between the main reagents. The first route afforded a mixture of diastereoisomers of $[\{Mo(NO)(Tp^{Me2})X\}_2(OCH_2CH_2O)]$ (each metal centre is chiral, possible types are *R*–*R*/*S*–*S* and *R*–*S*/*S*–*R*)[1] which are difficult to separate chromatographically. Diastereoisomer I could be separated by taking advantage of its better stability at higher temperatures. Thus, refluxing a mixture of diastereoisomers in toluene allowed isolation of pure diastereoisomer I. Analogously, it was also possible to obtain one diastereoisomer of $[\{Mo(NO)(Tp^{Me2})I\}_2(OCH_2CH_2O)]$ by directly reacting $[Mo(NO)(Tp^{Me2})I_2]$ with $HOCH_2CH_2OH$ in refluxing benzene. This method gave the highest yield. Also a single diastereoisomer has been obtained from the direct reaction between $[W(NO)(Tp^{Me2})Cl_2]$ with $HOCH_2CH_2OH$ in refluxing toluene. In the separation of tungsten bimetallic isomers we have taken advantage of the fact that one isomer is much more soluble in CH_2Cl_2 than the other.

Substitution of both iodides in $[Mo(NO)(Tp^{Me2})I_2]$ by $HOCH_2CH_2OH$ in the presence of NEt_3 provided the doubly-bridged bimetallic complex, whose structure was established by X-ray crystallographic study to be the *anti*-isomer.

The monometallic species $[Mo(NO)(Tp^{Me2})X(OCH_2CH_2OH)]$ (X = Cl, I), which were described previously [13f,27] and for X = Br, may be also obtained from the reaction between $[Mo(NO)(Tp^{Me2})X_2]$ and $HOCH_2CH_2OH$ in dichloromethane in the presence of silver acetate. These complexes, eluted as the second fractions in chromatographic separation, have spectroscopic data identical with those published before. The monometallic $[Mo(NO)(Tp^{Me2})(OCH_2CH_2OH)_2]$ [27] was prepared by substitution of ethoxy groups in $[Mo(NO)(Tp^{Me2})(OEt)_2]$ by the more acidic ethane-1,2-diol in boiling toluene.

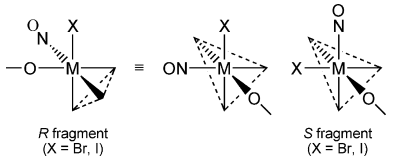
The analytical data for the new bimetallic complexes are given in Table 1.

2.2. Spectroscopic studies

IR spectra of the mono- and dinuclear compounds exhibit absorptions which are characteristic for the $[HB(3,5\text{-}Me_2pz)_3]^-$ ligand: ν(BH) at ca. 2550 cm^{-1} and ν(C–Me) in the range 1365–1451 cm^{-1}. Molybdenum monometallics and singly-bridged complexes show one ν(NO) in the range 1672–1675 cm^{-1}, that of the tungsten dinuclear complex at 1630 cm^{-1} and of the molybdenum doubly bridged complex at 1642 cm^{-1} (Table 1). These values are consistent with trends observed earlier [13f].

The mass spectra (Table 1) of the compounds contain ion clusters which span a wide mass range due to the presence of a large number of possible isotope combinations.

[1] According to the Cahn–Ingold–Prelog rules, the relative configurations of the metal fragments are assigned as shown:



when X = Cl then the assignment of the configuration is opposite.

Table 1
Characterisation data for the new complexes

Compound[a]	Analysis [b]/(%)			IR[d] ν(NO)/cm^{-1}	Mass spectrum		^{1}H NMR		
							δ_H/ppm (integral multiplicity)[h]		
	C	H	N		m/z[e]	Assign.	CH (pz)	Me (pz)	Q
$\{MoCl\}_2(Q)$	39.35 (39.33)	4.62 (4.95)	20.63 (20.07)	1672	999.20[f] (1000.16)	$M^+ + Na$	*Diastereoisomer I*[i]		
							5.86 (2s)	2.50 (6s)	
					943.18[f] (942.20)	$M^+ - Cl$	5.80 (2s)	2.39 (6s)	
							5.66 (2s)	2.37 (6s)	
								2.36 (6s)	
								2.28 (6s)	
								2.16 (6s)	6.35 (2m)
							Diastereoisomer II		6.02 (2m)
							5.85 (2s)	2.49 (6s)	
							5.69 (2s)	2.37 (6s)	
							5.59 (2s)	2.36 (12s)	
								2.18 (6s)	
								2.07 (6s)	
{MoBr}(QH)	36.42 (36.20)	4.78 (4.82)	17.23 (17.38)	1675	588.1[g] (588.04)	$M^+ + Na$	5.91 (1s)	2.52 (3s)	6.01 (1m)
							5.88 (1s)	2.41 (3s)	5.77 (2m)
					486.2[g] (486.14)	$M^+ - Br$	5.80 (1s)	2.40 (3s)	4.14 (2m)
								2.38 (9s)	
							Diastereoisomer I		
$\{MoBr\}_2(Q)$	37.24 (37.30)	4.70 (4.85)	17.98 (17.91)	1673	1088.0[g] (1087.06)	$M^+ + Na$	5.86 (2s)	2.50 (6s)	
					985.1[g] (985.15)	$M^+ - Br$	5.76 (2s)	2.39 (6s)	
							5.65 (2s)	2.38 (6s)	
								2.37 (6s)	
								2.18 (6s)	6.29 (2m)
								2.15 (6s)	5.86 (2m)
							Diastereoisomer II		
							5.84 (2s)	2.49 (6s)	
							5.72 (2s)	2.39 (6s)	
							5.51 (2s)	2.36 (12s)	
								2.24 (6s)	
								1.92 (6s)	
$\{MoI\}_2(Q)$	33.39 (33.13)	4.24 (4.17)	16.64 (16.90)	1674	1130.1[g] (1131.05)	$M^+ - NO$	*Diastereoisomer I*		
							5.84 (2s)	2.48 (6s)	
					1034.2[g] (1035.14)	$M^+ - I$	5.70 (2s)	2.40 (6s)	
							5.65 (2s)	2.38 (6s)	
								2.35 (6s)	
								2.12 (6s)	
								2.06 (6s)	6.15 (2m)
							Diastereoisomer II		5.58 (2m)
							5.83 (2s)	2.46 (6s)	
							5.76 (2s)	2.43 (6s)	
							5.41 (2s)	2.35 (6s)	
								2.34 (6s)	
								2.32 (6s)	
								1.75 (6s)	
$\{Mo(Q)\}_2$	31.47 (31.61)	3.96 (3.91)	12.10 (13.58)[c]	1642	967.21[f,g] (967.26)	M^+	5.81 (6s)	2.94 (6s)	6.16 (4m)
								2.62 (12s)	5.33 (4m)
								2.34 (6s)	AB pair;
								2.32 (12s)	$J_{AB} = 11.0$ Hz
$\{WCl\}_2(Q)$	33.59 (33.33)	3.96 (4.20)	16.76 (17.01)	1630	1175.3[g] (1175.25)	$M^+ + Na$	*Diastereoisomer I*		
							5.86 (2s)	2.57 (6s)	
					1117.4[g] (1119.30)	$M^+ - Cl$	5.79 (2s)	2.37 (6s)	
							5.69 (2s)	2.37 (6s)	
								2.35 (6s)	
								2.34 (6s)	
								2.18 (6s)	6.14 (2m)

Table 1 (*continued*)

Compound[a]	Analysis [b]/(%)			IR[d] ν(NO)/cm^{-1}	Mass spectrum		^{1}H NMR		
							δ_H/ppm (integral multiplicity)[h]		
	C	H	N		m/z[e]	Assign.	CH (pz)	Me (pz)	Q
							Diastereoisomer II		5.82 (2m)
							5.85 (2s)	2.56 (6s)	
							5.74 (2s)	2.36 (6s)	
							5.62 (2s)	2.34 (6s)	
								2.33 (6s)	
								2.24 (6s)	
								2.22 (6s)	

[a] {Mo} or {W} = Mo(NO)(Tp^{Me2}) or W(NO)(Tp^{Me2}); Q = OCH_2CH_2O.

[b] Calculated values in parentheses; complexes may be isolated containing n moles of C_6H_{14} or $CHCl_3$ (which was also seen in the ^{1}H NMR spectrum) as determined for $\{MoBr\}_2(Q) \cdot 1/3C_6H_{14}$ and $\{Mo(Q)\}_2 \cdot 4CHCl_3$.

[c] The results of elemental analysis of freshly prepared sample. Results of the repeated elemental analysis after few weeks: $C_{34}H_{52}B_2Mo_2N_{14}O_6 \cdot 2/5CHCl_3$ requires: C, 34.66; H, 4.34; N, 15.50; found: C, 34.18; H, 4.08; N, 15.12% indicate, along with the presence of diffuse streaks in the diffraction pattern, that the crystals were losing solvent slowly.

[d] Recorded from KBr discs.

[e] Most intense peak of clusters; values in parentheses based on isotopic distribution calculated by ChemCalc [28].

[f] MALDI spectrum.

[g] ESI spectrum.

[h] Spectra were recorded at 300 MHz in $CDCl_3$; s = singlet, m = multiplet.

[i] Diastereoisomer I is thermodynamically more stable.

The most intense peak of the cluster does not always correspond exactly to the value based on most abundant isotopes. The spectra provide parent molecular ions (or alkali metal adducts) in addition to fragment ions consistent with the loss of halide and/or NO.

The ^{1}H NMR spectra (Table 1) are consistent with the formulations of the complexes and contain two groups of signals characteristic for the $[HB(3,5\text{-}Me_2pz)_3]^-$ ligand. In the spectra of the diastereoisomers (I and II) of $[\{M(NO)(Tp^{Me2})X\}_2(OCH_2CH_2O)]$ [M = Mo, X = Cl, Br or I; M = W, X = Cl] the pyrazolyl proton resonances occur in the range δ 5.86–5.41 (Mo) and 5.86–5.62 (W) as three signals of relative intensity 2:2:2, whilst the 3,5-methyl protons appear as five or six resonances of relative area 6:6:6:6:6:6 or 6:6:12:6:6 in the range δ 2.50–1.75 (Mo) and 2.57–2.18 (W). This behaviour is consistent with the absence of a plane of symmetry through {Mo(NO)-(Tp^{Me2})} centre. These spectra suggest the presence of the same centre of symmetry as found in $[\{Mo(NO)(Tp^{Me2})\text{-}Cl\}_2(NHCH_2CH_2NH)]$, i.e. antiperiplanar arrangement with respect to the bridge [20].

The spectrum of *anti*-$[\{Mo(NO)(Tp^{Me2})(OCH_2\text{-}CH_2O)\}_2]$ is exceptional and contains *one* resonance (δ 5.81) due to protons attached to C^4 atom of the pyrazolyl rings (probably by a reason of accidental degeneracy; normally, for related bis-alkoxides [13f] two singlets 2:1 are expected), and four signals of relative area 6:12:6:12 in the range δ 2.94–2.92, due to the twelve 3,5-methyl groups. This indicates that the complex contains a plane of symmetry. It shows, along with the crystal structure, that the metal centres are equivalent.

As had been observed previously [13f], the diastereotopic protons attached to the α-carbon atom in all the complexes resonate at low field with respect to free α,ω-diol. This effect is due to the strong electronegativity of the {M(NO)-(Tp^{Me2})X} centre (M = Mo or W, X = halide or none).

2.3. Electrochemical studies

The electrochemical properties of the bimetallic compounds and related monometallic species were investigated by CV and DPV in dichloromethane (Table 2). The monometallic complexes $[M(NO)(Tp^{Me2})X(OCH_2CH_2OH)]$ exhibit a single one-electron quasi-reversible reduction wave at potentials within the range of -1.05 to -1.11 V (M = Mo, X = Cl, Br or I) and -1.63 V (M = W, X = Cl) versus ferrocene–ferrocenium. The $E_{1/2}$-values, for mono- and bimetallic complexes, become more negative in the sequence I < Br < Cl, due to p(π) → d(π) donation from X to Mo, consistently with electronegativity effects. The bis-alkoxide $[Mo(NO)(Tp^{Me2})(OCH_2CH_2OH)_2]$ is reduced at -1.62 V which is consistent with the lower value of ν(NO) which, in turn, reflects electron density at the metal centre. As a result of p(π) → d(π) donation from O to Mo the LUMO orbital is destabilised and shifts the $E_{1/2}$ of the complex to more cathodic value [29]. All the species reveal $E_{1/2}$-values in the regions expected for related mono-alkoxides [30] and bis-alkoxides [31].

The bimetallic complexes $[\{M(NO)(Tp^{Me2})X\}_2(OCH_2\text{-}CH_2O)]$ [M = Mo, X = Cl, Br or I; M = W, X = Cl] exhibit two one-electron reductions waves, with separations ΔE_{dpv} of the order of 300 mV. The comproportionation constants[2] (in the range 10^4–10^5) for formation of mixed-oxidation-state complexes [12] indicate substantial interactions between the two metal-based redox centres. These

[2] Comproportionation constant calculated from $K_c = \exp(F\Delta E_{1/2}/RT)$.

Table 2
Electrochemical data for the complexes

Complex	$E_{1/2}$[a] (V)	ΔE_p[b] (mV)	$\Delta E_{1/2}$[c] (mV)	ΔE_{dpv}[d] (mV)
$[Mo(NO)(Tp^{Me2})Cl(OCH_2CH_2OH)]$	−1.11	97		
$[\{Mo(NO)(Tp^{Me2})Cl\}_2(OCH_2CH_2O)]$	−1.17, −1.47	110, 185	294	310
$[Mo(NO)(Tp^{Me2})Br(OCH_2CH_2OH)]$	−1.09	114		
$[\{Mo(NO)(Tp^{Me2})Br\}_2(OCH_2CH_2O)]$	−1.12, −1.44	147, 295	312	320
$[Mo(NO)(Tp^{Me2})I(OCH_2CH_2OH)]$	−1.05[e]	62		
$[\{Mo(NO)(Tp^{Me2})I\}_2(OCH_2CH_2O)]$	−1.11[e,f], −1.36[e,f]	76, 72	251	260
$[Mo(NO)(Tp^{Me2})(OCH_2CH_2OH)_2]$	−1.62	258		
$[W(NO)(Tp^{Me2})Cl(OCH_2CH_2OH)]$	−1.63	107		
$[\{W(NO)(Tp^{Me2})Cl\}_2(OCH_2CH_2O)]$	−1.70, −1.95	121, 213	253	270

[a] Formal potentials versus the ferrocene–ferrocenium couple measured in CH_2Cl_2 with a scan rate of 0.1 V s^{-1}; ca. 10^{-3} mol dm^{-3} in complex.
[b] Difference between anodic and cathodic peak potentials (for Fc/Fc^+ couple $\Delta E_p = 60$–80 mV).
[c] Separation between the two one-electron reduction potentials, determined by cyclic voltammetry.
[d] Difference between first and second reduction potentials determined by differential pulse voltammetry; pulse amplitude 50 mV.
[e] Practically irreversible ($i_c > i_a$).
[f] A new anodic wave is observed at −0.85 V.

interactions are dependent on the nature of M, and that in tungsten complex being smaller than its molybdenum analogue. The $E_{1/2}$-values of the *first* and second reduction processes are more *cathodic* (the first ca. 30–60 mV) than the $E_{1/2}$-value for the reduction of the corresponding monometallic species. The reduction processes for the chloro and bromo complexes are chemically reversible, whereas those in iodo species were practically irreversible as a result of dissociation of I^-. The large values of ΔE_p indicate that electron transfer processes are kinetically slow. The significant metal–metal interactions detected electrochemically in the bimetallic complexes incorporating the saturated bridging ligand could arise from through-σ-bond inductive effects and coulombic through-space interactions [14]. For the bimetallic iodo-complex the absolute magnitude of ΔE_{dpv} should be treated with caution because of the irreversible nature of the reduction processes. The tungsten complexes are reduced at potentials ca. 500 mV more *cathodic* than their Mo analogues. It was checked in the case of isolated diastereoisomers that they showed identical electrochemical behaviour.

The complex *anti*-$[\{Mo(NO)(Tp^{Me2})(OCH_2CH_2O)\}_2]$ was insoluble in solvents other than chloroform, which is unsuitable for electrochemical studies.

2.4. Crystal structure of anti-$[\{Mo(NO)(Tp^{Me2})(OCH_2CH_2O)\}_2]\cdot 4CHCl_3$

In the crystal structure of *anti*-$[\{Mo(NO)(Tp^{Me2})(OCH_2CH_2O)\}_2]\cdot 4CHCl_3$ two nonequivalent dinuclear molecules were found, with identical Mo centres and chloroform solvates (2 Mo atoms:4 solvent molecules) held together by weak van der Waals forces. The complex is constructed from two $\{Mo(NO)(Tp^{Me2})\}$ distorted octahedral units linked by two (OCH_2CH_2O) bridges (Fig. 1). The short Mo–O bond lengths (1.86, 1.91 Å) as well as Mo–O–C angles (136.3°, 137.0°), which suggest a significant degree of $p(\pi) \rightarrow d(\pi)$ donation from O to Mo, are comparable with those found in the related alkoxide complexes $[Mo(NO)(Tp^{Me2})X(Y)]$ [$X = OPr^i$, $Y = OPr^i$ or OEt; $X = I$, $Y = O(CH_2)_3Br$] [32]. The molybdenum-nitrosyl system is slightly bent from linearity (175.0°). The nitrosyl substituents are oriented *antiperiplanar* with respect to each other. Simplified representation of the metal first coordination sphere is shown in Fig. 2. The asymmetric unit contains two tetrahedral fragments of complex and two independent molecules of $CHCl_3$ (typical geometry and no short contact to the complex). The small crystal size and the presence of disordered solvent molecules in crystal (diffuse streaks in the diffraction pattern are observed) resulted in relatively poor refinement ($R = 10.89\%$). However the atoms positions in the main part of elementary cell (see Fig. 3) were found with a good precision. That is why the bonds length and the values of angles (Table 3) are comparable with values which were obtained for similar structures.

The point group of molecule $2/m$ (C_{2h}) confirms the presence of a plane of symmetry which is reflected in ^1H NMR spectra.

3. Experimental

3.1. Materials and instrumentation

Precursors $[M(NO)(Tp^{Me2})X_2]$ (M = Mo, X = Cl, Br, I or OEt; M = W, X = Cl) [33] and monometallic species $[M(NO)(Tp^{Me2})X(OCH_2CH_2OH)]$ (M = Mo or W; X = Cl, I) [13f,27] were prepared according to previously described methods. All reactions were carried out under pure argon (BOC, N5.0) using Schlenk techniques. Commercial solvents and triethylamine were purified by distillation under argon; dichloromethane from CaH_2, toluene and benzene from sodium-benzophenone and triethylamine from sodium. Anhydrous, 99.8% ethane-1,2-diol was supplied from Aldrich and used directly. Column

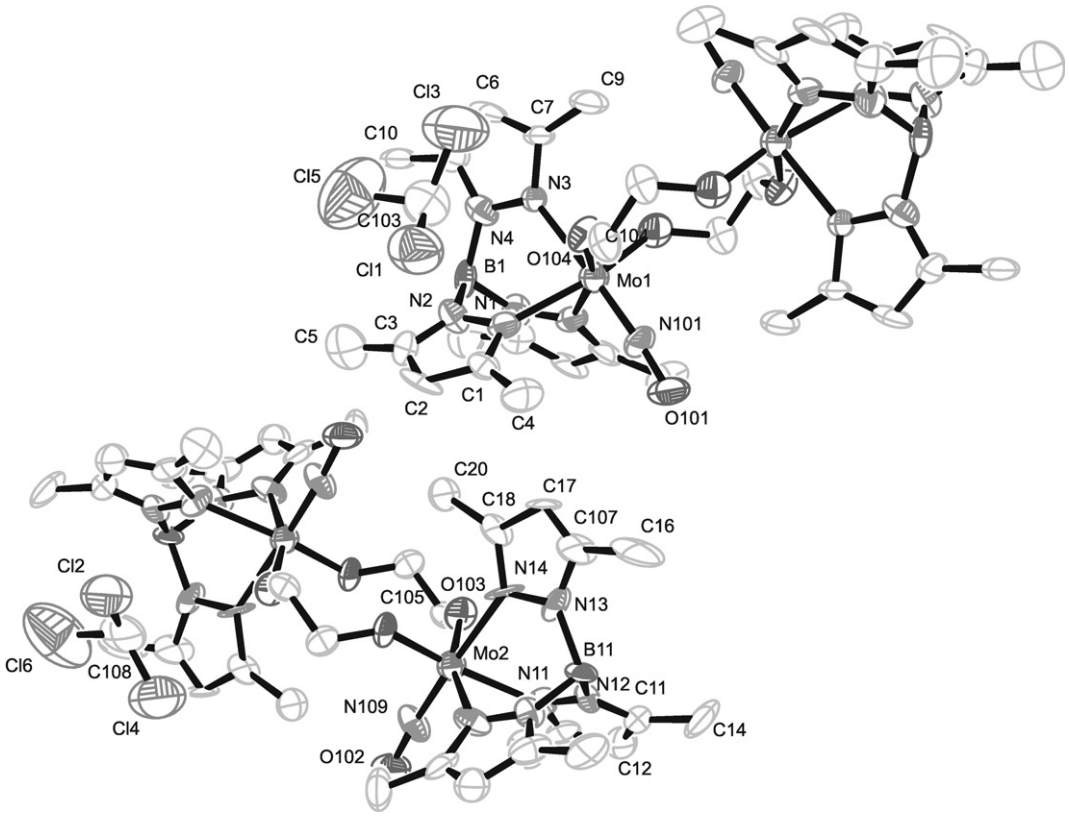


Fig. 1. ORTEP plot of the complex unit of *anti*-[{Mo(NO)(Tp^{Me2})(OCH_2CH_2O)}$_2$] · 4$CHCl_3$ with 2 molecules $CHCl_3$, showing thermal ellipsoids at the 50% probability level. All hydrogen atoms are omitted.

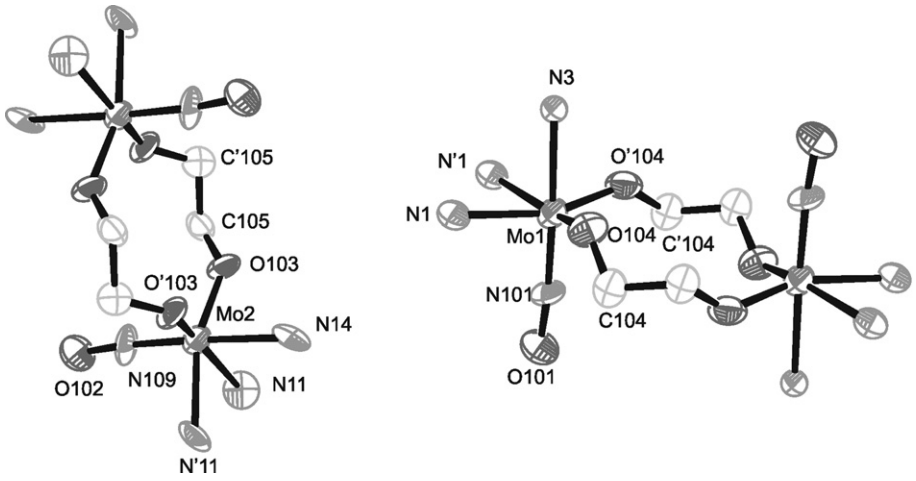


Fig. 2. Illustration of the dinuclear core in the structure of *anti*-[{Mo(NO)(Tp^{Me2})(OCH_2CH_2O)}$_2$] · 4$CHCl_3$.

chromatography was carried out in glass columns with Merck silica gel 60 (70-230 mesh) as the stationary phase. The reaction's progress and purity of compounds were monitored by TLC analysis using Merck silica gel (60) F_{254} plates. Elemental analyses were performed by the Microanalytical Laboratory of the Faculty of Chemistry at Jagiellonian University.

IR spectra were recorded using a Bio-Rad FTS 175C spectrophotometer in KBr discs and ^{1}H NMR spectra using a Varian Mercury-Vx 300 MHz spectrometer. Mass spectra were collected on a Bruker-Daltonics Esquire 3000 (ESI) and Reflex IV (MALDI). Cyclic and differential pulse voltammetry measurements were carried out using a BAS 100B/W electrochemical workstation (BioAnalytical Systems), under argon in 10^{-3} M solution of complex in dry dichloromethane, containing 0.1 M [NBu^n_4][PF_6] as base electrolyte. A standard three-electrode cell was used, with a platinum-bead working electrode, a platinum wire secondary electrode, and a Ag/AgCl electrode as the reference. Ferrocene was added at the end of each experiment as an

Table 3
Selected bond lengths (Å) and angles (°) for *anti*-[{Mo(NO)(Tp^{Me2})(OCH_2CH_2O)}$_2$]·4$CHCl_3$

Mo(1)–N(1)	2.200(18)	Mo(2)–N(11)	2.220(17)
Mo(1)–N(3)	2.26(2)	Mo(2)–N(14)	2.26(3)
Mo(1)–N(101)	1.77(3)	Mo(2)–N(109)	1.731(13)
Mo(1)–O(104)	1.860(14)	Mo(2)–O(103)	1.910(14)
N(101)–O(101)	1.25(3)	N(109)–O(102)	1.24(2)
O(104)–C(104)	1.46(2)	O(103)–C(105)	1.39(2)
C(104)–C′(104)	1.49(4)	C(105)–C′(105)	1.52(4)
N(1)–Mo(1)–N′(1)	75.5(9)	N(11)–Mo(2)–N′(11)	76.3(10)
N(1)–Mo(1)–N(3)	84.2(7)	N(11)–Mo(2)–N(14)	84.4(7)
N(101)–Mo(1)–N(1)	93.9(8)	N(109)–Mo(2)–N(11)	93.6(9)
N(101)–Mo(1)–N(3)	177.6(10)	N(109)–Mo(2)–N(14)	177.4(8)
N(101)–Mo(1)–O(104)	99.7(6)	N(109)–Mo(2)–O(103)	99.0(9)
O(104)–Mo(1)–N(1)	89.6(6)	O(103)–Mo(2)–N(11)	89.2(7)
O(104)–Mo(1)–N′(1)	160.5(7)	O(103)–Mo(2)–N′(11)	161.3(6)
O(104)–Mo(1)–N(3)	81.8(6)	O(103)–Mo(2)–N(14)	82.6(6)
O(104)–Mo(1)–O′(104)	101.7(9)	O(103)–Mo(2)–O′(103)	102.2(9)
C(104)–O(104)–Mo(1)	137.0(12)	C(105)–O(103)–Mo(2)	136.3(13)
O(101)–N(101)–Mo(1)	175(2)	O(102)–N(109)–Mo(2)	175.0(15)

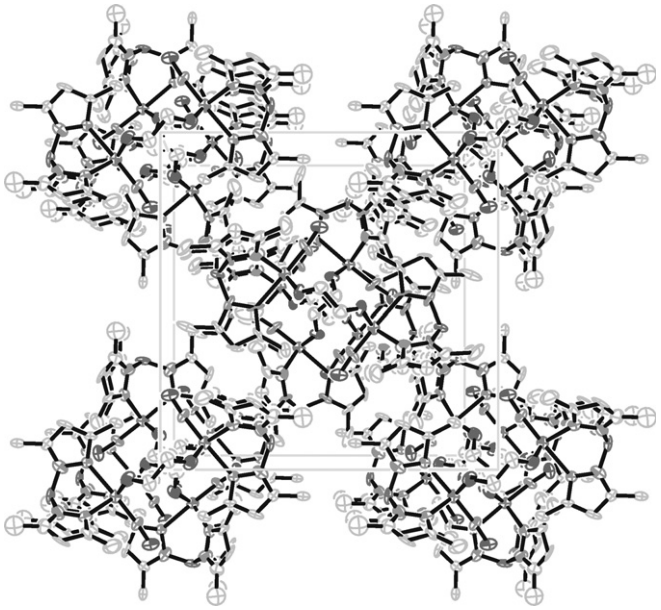


Fig. 3. View of compound *anti*-[{Mo(NO)(Tp^{Me2})(OCH_2CH_2O)}$_2$]·4$CHCl_3$ along direct [0 0 1] (without solvent molecules).

internal standard; all potentials are quoted versus the ferrocene–ferrocenium couple. The number of electrons in each transfer was estimated by comparison with [{Mo(NO)(Tp^{Me2})Cl}$_2$O], for which a one electron process has been shown [26a].

3.2. Synthetic procedures

3.2.1. Synthesis of [{Mo(NO)(Tp^{Me2})Cl}$_2$(OCH_2CH_2O)]

To a solution of [Mo(NO)(Tp^{Me2})Cl_2] (0.50 g, 1.0 mmol) in dry dichloromethane (80 cm^3) AgOCOMe (0.20 g, 1.2 mmol) and ethane-1,2-diol (0.26 g, 4.2 mmol) were added. The mixture was stirred and refluxed overnight affording a deep blue solution. The precipitate of inorganic salts was filtered off and the filtrate evaporated in vacuo. The residue was dissolved in the minimum volume of dichloromethane and chromatographed on silica gel using dichloromethane as eluant. Two blue bands were observed on the column (bi- and monometallic species). The first major fraction was collected, the solvent was partially evaporated in vacuo and *n*-hexane was added. The volume of the mixture was further reduced in vacuo until precipitation began. The resulting blue product was filtered off, washed with *n*-hexane, dried at ca. 80 °C for 1 h and then in vacuo for 12 h (mixture of diastereoisomers, 0.13 g, 26%).

3.2.2. Synthesis of [{Mo(NO)(Tp^{Me2})Br}$_2$(OCH_2CH_2O)] and [Mo(NO)(Tp^{Me2})Br(OCH_2CH_2OH)]

Method 1. These compounds were prepared as blue-green powders as described above using [Mo(NO)(Tp^{Me2})Br_2] (0.50 g, 0.86 mmol), ethane-1,2-diol (0.22 g, 3.5 mmol) and AgOCOMe (0.15 g, 0.90 mmol) in dichloromethane (60 cm^3), but heating was finished after 8 h. The first and the second blue fractions were collected and precipitated from CH_2Cl_2/*n*-hexane (0.12 g, 27%, mixture of bimetallic diastereoisomers; 0.05 g, 10%, monometallic).

Method 2. [Mo(NO)(Tp^{Me2})Br_2] (0.50 g, 0.86 mmol) together with ethane-1,2-diol (1.1 g, 18 mmol) and hexamethylenetetramine (0.12 g, 0.86 mmol) in diethyl ether–dichloromethane mixture (50 cm^3; 5:1 v/v) was stirred and refluxed for 2 h. The resulting blue solution was decanted from an oily deposit, filtered and cooled to −10 °C overnight. The mixture was decanted again and the supernatant liquid evaporated to dryness. The residue was chromatographed on silica gel using dichloromethane as eluant (0.08 g, 18%, mixture of bimetallic diastereoisomers; 0.07 g, 14%, monometallic).

3.2.3. Synthesis of [{Mo(NO)(Tp^{Me2})I}$_2$(OCH_2CH_2O)]

Method 1. This compound was prepared as a green powder according to the procedure described above using [Mo(NO)(Tp^{Me2})I_2] (0.50 g, 0.74 mmol), ethane-1,2-diol (0.22 g, 3.5 mmol) and AgOCOMe (0.13 g, 0.78 mmol) in

dichloromethane (60 cm^3), but heating was finished after 4 h (mixture of diastereoisomers, 0.07 g, 16%).

Method 2. A mixture of [Mo(NO)(Tp^{Me2})I_2] (0.50 g, 0.74 mmol) and ethane-1,2-diol (0.55 g, 8.9 mmol) was stirred and refluxed in benzene (50 cm^3) for 10 h and then stirred overnight at RT. The resulting green solution was decanted and filtered and an oily deposit was discarded. The filtrate was reduced in volume and left to crystallise diastereoisomer I (0.22 g, 51%).

Method 3. A mixture of [Mo(NO)(Tp^{Me2})I_2] (0.50 g, 0.74 mmol) and ethane-1,2-diol (2.2 g, 35 mmol) was stirred and refluxed in diethyl ether (50 cm^3) for 2 h. The resulting green solution was decanted from an oily deposit, filtered and cooled to −10 °C overnight. The mixture was decanted again and the supernatant liquid evaporated to dryness. The residue was chromatographed on silica gel using dichloromethane as eluant. The first green fraction was collected and precipitated from CH_2Cl_2/*n*-hexane as a green powder (mixture of diastereoisomers, 0.06 g, 14%).

3.2.4. Synthesis of [{Mo(NO)(Tp^{Me2})(OCH_2CH_2O)}$_2$]

A mixture of [Mo(NO)(Tp^{Me2})I_2] (1.0 g, 1.5 mmol) and ethane-1,2-diol (0.11 g, 1.8 mmol) in dry toluene (100 cm^3) was brought to reflux and then triethylamine (3.5 ml) was added. After 1 h ethane-1,2-diol (0.066 g, 1.1 mmol) was added affording a red-brown solution, and a precipitate was formed. Then, refluxing was continued for 30 min. The mixture was then cooled to −10 °C and the pink precipitate which formed was filtered off and washed with *n*-hexane, dichloromethane and dried at ca. 80 °C for 1 h and then in vacuo for 12 h (*anti* isomer, 0.16 g, 23%). The complex was recrystallised from chloroform as a red crystals.

3.2.5. Synthesis of [Mo(NO)(Tp^{Me2})(OCH_2CH_2OH)$_2$]

To a solution of [Mo(NO)(Tp^{Me2})($OEt)_2$] (0.10 g, 0.20 mmol) in dry toluene (30 cm^3) ethane-1,2-diol (0.11 g, 1.8 mmol) was added. The mixture was stirred and refluxed for 6 h, the solution was cooled and evaporated in vacuo to one third of its volume. The mixture was cooled to −10 °C overnight and the pink crystals which formed were filtered off, washed with dichloromethane, *n*-hexane, dried at ca. 80 °C for 1 h and then in vacuo for 12 h (0.047 g, 44%).

3.2.6. Synthesis of [{W(NO)(Tp^{Me2})Cl}$_2$(OCH_2CH_2O)]

A mixture of [W(NO)(Tp^{Me2})Cl_2] (0.5 g, 0.86 mmol) and ethane-1,2-diol (1.1 g, 18 mmol) in dry toluene (100 cm^3) was stirred and refluxed for 6 h. The resulting purple solution was decanted from an oily deposit, filtered, and cooled to −10 °C overnight. The mixture was decanted again and the supernatant liquid evaporated to dryness. The residue was redissolved in CH_2Cl_2 and the purple precipitate which formed was filtered off (diastereoisomer I, 0.04 g, 8%) and the filtrate evaporated in vacuo to low volume and chromatographed using dichloromethane as eluant. The first fraction was collected and precipitated from CH_2Cl_2/*n*-hexane as a purple powder (diastereoisomer II, 0.05 g, 10%).

3.2.7. Crystal structure determination of anti-[{Mo(NO)(Tp^{Me2})(OCH_2CH_2O)}$_2$]

The red crystals were grown by slow evaporation of a solvent from concentrated solution of the complex in $CHCl_3$. Selected crystal had dimensions $0.2 \times 0.15 \times 0.1$ mm^3. X-ray data were collected on a Nonius Kappa CCD with graphite monochromated Mo Kα radiation ($\lambda = 0.71070$ Å). 2651 reflections were measured ($2\theta_{max} = 40°$) at 20 °C. Corrections for Lorentz and polarization were applied. The structure was solved by direct methods and refined by the full-matrix least-squares method on all F^2 data using the SHELXL-97 suite of programs. The model, accepted as the 'correct' structure, gave final R $[=\sum(F_o - F_c)/\sum(F_o)]$ and wR $[=\sum\{w(F_o^2 - F_c^2)^2\}/\sum\{w(F_o^2)^2\}]^{1/2}$ values of 0.1875 and 0.2425, respectively, for 377 parameters and all 2651 data. The corresponding R values for 1579 data with $I > 2\sigma(I)$ were 0.1089 and 0.2153. Weighting scheme, $w = 1/[\sigma^2(F_o^2) + (0.0512P)^2 + 113.8839P]$, where $P = (F_o^2 + 2F_c^2)/3$. All non-hydrogen atoms were refined with anisotropic thermal parameters; hydrogen atoms were included in calculated positions and refined isotropically.

Crystal data. $C_{34}H_{52}B_2Mo_2N_{14}O_6 \cdot 4CHCl_3$, $M = 1443.89$, tetragonal, space group $P4_2/m$, $a = b = 17.1770(4)$ Å, $c = 20.8570(7)$ Å, $V = 6153.84(3)$ $Å^3$, $Z = 2$, $D_c = 1.562$ g cm^{-3}, $F(000) = 2924$, μ(Mo Kα) = 0.981 mm^{-1}.

4. Conclusion

The characterization of dinuclear complexes derived from the {M(NO)(Tp^{Me2})X}$^+$ (M = Mo or W; X = halide) moiety and ethane-1,2-diol is difficult because of isomeric forms which may be present. It is possible to obtain the thermodynamically more stable isomer I by using benzene as the solvent in the synthesis of the bimetallic iodo-complex or by prolonged boiling of the isomeric mixture in toluene. In the separation of tungsten bimetallic isomers we have taken advantage of the fact that one isomer is much more soluble in CH_2Cl_2 than the other.

Results of cyclic voltammetry studies of the bimetallic complexes have revealed $\Delta E_{1/2}$ ca. 300 mV (M = Mo, X = Cl or Br), which reflects the extent of interactions between metal centres comparable with that obtained from analogous complexes containing cyclohexane-1,2-diol as the bridge.

The doubly bridged complex, [{Mo(NO)(Tp^{Me2})(OCH_2-CH_2O)}$_2$], should exist as the *syn* and *anti* isomers, but as yet, only *anti* isomer has been obtained and its molecular structure has been determined.

Acknowledgements

We are grateful to the Chemical Company Dwory S.A. for the partial support of this work and thank the Joint X-Ray Laboratory, Faculty of Chemistry and ŚLAFiBS, Jagiellonian University for making the Nonius KappaCCD

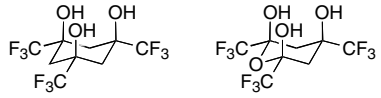
diffractometer available. One of us (A.W.) is especially grateful to Professor J.A. McCleverty for providing the opportunity to advance the work on this topic and a very long lasting and very fruitful scientific collaboration.

Appendix A. Supplementary material

CCDC 605526 contains the supplementary crystallographic data for this paper. These data can be obtained free of charge via http://www.ccdc.cam.ac.uk/conts/retrieving.html, or from the Cambridge Crystallographic Data Centre, 12 Union Road, Cambridge CB2 1EZ, UK; fax: (+44) 1223-336-033; or e-mail: deposit@ccdc.cam.ac.uk. Supplementary data associated with this article can be found, in the online version, at doi:10.1016/j.poly.2006.10.004.

References

[1] J.A. McCleverty, M.D. Ward, in: J.A. McCleverty, T.J. Meyer (Eds.), Comprehensive Coordination Chemistry II, vol. 2, Elsevier, Amsterdam, 2003, pp. 743–757.
[2] M.B. Robin, P. Day, Adv. Inorg. Chem. Radiochem. 10 (1967) 247.
[3] N.S. Hush, Trans. Faraday. Soc. 57 (1961) 155.
[4] N.S. Hush, Electrochim. Acta 13 (1968) 1005.
[5] H. Taube, Electron Transfer Reactions of Complex Ions in Solution, Academic Press, New York, 1970.
[6] G.M. Tom, C. Creutz, H. Taube, J. Am. Chem. Soc. 96 (1974) 7827.
[7] C. Creutz, Prog. Inorg. Chem. 30 (1983) 1.
[8] D.E. Richardson, H. Taube, Inorg. Chem. 20 (1981) 1278.
[9] M.D. Ward, Chem. Ind. (1996) 568.
[10] M.D. Ward, Chem. Ind. (1997) 640.
[11] J.A. Thomas, A. Włodarczyk, C.J. Jones, J.A. McCleverty, M.G. Hutchings, Polyhedron 15 (1996) 1409.
[12] D.N. Beratan, J.N. Betts, J.N. Onuchic, Science 252 (1991) 1285.
[13] (a) J.A. McCleverty, D. Seddon, N.A. Bailey, N.W. Walker, J. Chem. Soc., Dalton Trans. (1976) 898;
(b) J.A. McCleverty, A.E. Rae, I. Wolochowicz, N.A. Bailey, J.M.A. Smith, J. Chem. Soc., Dalton Trans. (1982) 951;
(c) J.A. McCleverty, A. Wlodarczyk, in: 24th International Conference on Coordination Chemistry, Athens, 1986;
(d) J.A. McCleverty, A. Wlodarczyk, Chimika Chronika New Series (1986) 404;
(e) A. Wlodarczyk, A.J. Edwards, J.A. McCleverty, Polyhedron 7 (1988) 103;
(f) J.A. McCleverty, A. Wlodarczyk, Polyhedron 7 (1988) 449;
(g) R. Cook, J.P. Maher, J.A. McCleverty, M.D. Ward, A. Wlodarczyk, Polyhedron 12 (1993) 2111.
[14] S.L.W. McWhinnie, C.J. Jones, J.A. McCleverty, L.J. Yellowlees, J. Chem. Soc., Dalton Trans. (1996) 4401.
[15] S.M. Charsley, C.J. Jones, J.A. McCleverty, B.D. Neaves, S.J. Reynolds, G. Denti, J. Chem. Soc., Dalton Trans. (1988) 293.
[16] A. Abdul-Rahman, A.A. Amoroso, T.N. Branston, A. Das, J.P. Maher, J.A. McCleverty, M.D. Ward, A. Wlodarczyk, Polyhedron 16 (1997) 4353.
[17] S.L.W. McWhinnie, C.J. Jones, J.A. McCleverty, D. Collison, F.E. Mabbs, J. Chem. Soc., Chem. Commun. (1990) 940.
[18] A. Das, J.P. Maher, J.A. McCleverty, J.A. Navas Badiola, M.D. Ward, J. Chem. Soc., Dalton Trans. (1993) 681.
[19] A. Das, C.J. Jones, J.A. McCleverty, Polyhedron 12 (1993) 327.
[20] N.J. AlObaidi, C.J. Jones, J.A. McCleverty, Polyhedron 9 (1990) 693.
[21] A. Wlodarczyk, J.P. Maher, J.A. McCleverty, M.D. Ward, J. Chem. Soc., Chem. Commun. (1995) 2397.
[22] A. Wlodarczyk, J.P. Maher, J.A. McCleverty, M.D. Ward, J. Chem. Soc., Dalton Trans. (1997) 3287.
[23] N.J. AlObaidi, S.L.W. McWhinnie, T.A. Hamor, C.J. Jones, J.A. McCleverty, J. Chem. Soc., Dalton Trans. (1992) 3299.
[24] J.P. Maher, J.A. McCleverty, M.D. Ward, A. Wlodarczyk, J. Chem. Soc., Dalton Trans. (1994) 143.
[25] A. Wlodarczyk, G.A. Doyle, J.P. Maher, J.A. McCleverty, M.D. Ward, Chem. Commun. (1997) 769.
[26] (a) A. Wlodarczyk, J.P. Maher, S. Coles, D.E. Hibbs, M.H.B. Hursthouse, K.M. Abdul Malik, J. Chem. Soc., Dalton Trans. (1997) 2597;
(b) A. Wlodarczyk, S.J. Coles, M.B. Hursthouse, K.M. Abdul Malik, H.F. Lieberman, J. Chem. Soc., Dalton Trans. (1997) 2921.
[27] G. Denti, J.A. McCleverty, A. Włodarczyk, J. Chem. Soc., Dalton Trans. (1981) 2021.
[28] M. Krompiec, L. Patiny, in: Fifth International Electronic Conference on Synthetic Organic Chemistry (ECSOC-5), 2001. Available from: <http://www.mdpi.org/ecsoc-5.htm>.
[29] N.J. AlObaidi, M. Chaudhury, D. Clague, C.J. Jones, J.C. Pearson, J.A. McCleverty, S.S. Salam, J. Chem. Soc., Dalton Trans. (1987) 1733.
[30] C.J. Jones, J.A. McCleverty, B.D. Neaves, S.J. Reynolds, H. Adams, N.A. Bailey, G. Denti, J. Chem. Soc., Dalton Trans. (1986) 733.
[31] N.J. AlObaidi, S.S. Salam, P.D. Beer, C.D. Bush, T.A. Hamor, F.S. McQuillan, C.J. Jones, J.A. McCleverty, Inorg. Chem. 31 (1992) 263.
[32] J.A. McCleverty, A.E. Rae, I. Wołochowicz, N.A. Bailey, J.M.A. Smith, J. Chem. Soc., Dalton Trans. (1982) 951.
[33] S.J. Reynolds, C.F. Smith, C.J. Jones, J.A. McCleverty, D.C. Bower, J.L. Templeton, Inorg. Synth. 23 (1985) 4.



Scheme 1. Ligands H_3TTFTCH (**1**) and H_3TTPT (**2**).

The tetranuclear structure of **6** is largely similar in structure to that observed for the reported structure **4** with the exception that now four copper ions constitute the tetranuclear core. The coordination pattern of the ligand **2** is identical to the one found in **4**. Its formation is accomplished by reaction of copper-hexafluoroacetylacetonate with 3-methyl-1*H*-pyrazole (=3-Hmpz). For both complexes **4** and **6** no attempt as to the isolation of the free ligands **1** and **2**, respectively, has been reported and thus no proof was provided for their stability in their fully protonated forms. While **1** displays a C_{3v} symmetry, **2** belongs to the point group C_s.

We present here a greatly simplified synthetic access to **3** avoiding the electrolytic pathway (Scheme 2) [10], full characterisation of the neutral, isolated form of **2**, and unequivocal evidence for the presence of **2**, rather than **1**, in the tetranuclear complex (**4** → **5**), thus in fact contesting the structural interpretation of the diffraction data obtained for this complex, as given in Ref. [4].

2. Experimental

2.1. General

Reagents were purchased from commercial suppliers and used without further purification. All solvents except tetrahydrofuran (THF) were used without purification. THF was distilled from sodium-benzophenone and, when mentioned, degassed thoroughly by freeze–thaw–vacuum cycles. NMR spectra were recorded on a Bruker Avance 200 (operating at 200.13 MHz for ^{1}H, 50.32 MHz for ^{13}C and 188.31 MHz for ^{19}F). For ^{1}H and ^{13}C, chemical shifts (δ) are reported in parts per million relative to TMS, using the solvent line as secondary internal reference. For ^{19}F spectra, chemical shifts are reported in parts per million (δ) relative to $CFCl_3$, using $CFCl_3$ in $CDCl_3$ as external reference. The IR spectra were recorded on a Mattson 3000 FT-IR spectrometer between 3500 and 500 cm^{-1} using KBr disks (w: weak, m: medium, s: strong, vs: very strong, sh: shoulder). The UV–Vis spectra were recorded on a Jasco V-550 spectrometer.

2.2. Synthesis

2.2.1. 1,10-Phenanthroline-bis(pyrimidine-2-thionato)-cadmium(II) (3)

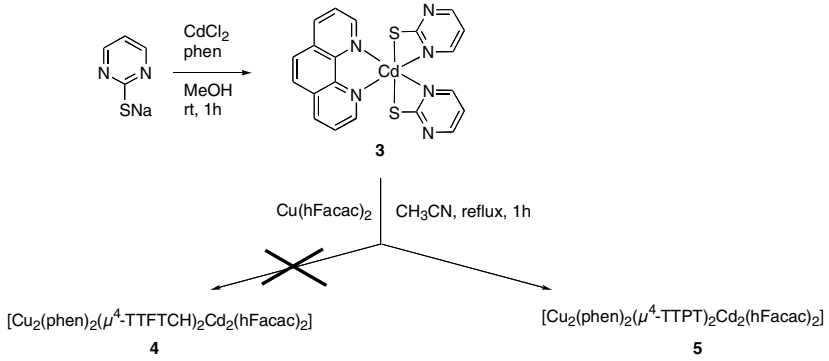
$CdCl_2$ (2.0 g, 10.80 mmol) and 204 mL of methanol were placed into a 500 mL round-bottom flask. The mixture was heated to reflux until all the cadmium chloride was dissolved (*ca.* 2 h). Separately, a freshly prepared MeONa solution (0.24 M, 595 mg Na, 106 mL MeOH) in a 250 mL round-bottom flask was treated with 2-mercaptopyrimidine (2.86 g, 25.0 mmol) and 1,10-phenanthroline monohydrate (0.89 g, 4.48 mmol) was added successively. The resulting yellow thiolate solution was added dropwise to the $CdCl_2$ solution at room temperature. An off-white solid immediately precipitated. After stirring for one additional hour, the reaction mixture was filtered, the precipitate was successively washed with 30 mL of methanol, 30 mL of water and 10 mL of methanol and then dried *in vacuo* to afford 4.78 g of a white powder (9.28 mmol, 85%). The crude material was recrystallised in boiling acetonitrile (*ca.* 2.5 L), and 3.56 g of **3** were isolated as yellow crystals (6.91 mmol, 64%).

Anal. Calc. for $C_{20}H_{14}CdN_6S_2$: C, 46.65; H, 2.74; N, 16.32; S, 12.45. Found: C, 46.91; H, 2.94; N, 16.28; S, 12.53%.

^{1}H NMR (DMSO-d_6, 200 MHz) δ 9.26 (1H, d, $^3J = 4.5$ Hz) 8.86 (1H, d, $^3J = 8.0$ Hz); 8.26 (2H, d, $^3J = 5.0$ H) 8.24 (1H, s) 8.11 (1H, dd, $^3J = 8.0$, 4.5 Hz) 6.90 (1H, t, $^3J = 5.0$ Hz); ^{13}C NMR ($CDCl_3$, 50 MHz) δ 115.0, 126.5, 128.5, 130.2, 140.4, 142.1, 151.2, 157.8.

2.2.2. [Cu$_2$(phen)$_2$(μ^4-TTPT)$_2$Cd$_2$(hFacac)$_2$]CH$_3$CN (5)

Into a 6 L round-bottom flask were introduced complex **3** (1.49 g, 2.89 mmol), Cu(hFacac)$_2 \cdot x$H$_2$O (2.98 g, 6 mmol) and 4.7 L of acetonitrile. The green reaction mixture was



Scheme 2. Synthetic procedure for tetranuclear complex **5**.

refluxed for 1 h in order to dissolve **3**. After hot filtration, the resulting orange solution was allowed to slowly evaporate at room temperature over one month which resulted in a loss of approx. 1.5 L. 740 mg of dark blue, X-ray quality crystals were collected (0.39 mmol, 27% based on **3**) (see Figs. 1 and 2).

Anal. Calc. for $C_{50}H_{26}Cd_2Cu_2F_6N_4O_{12}CH_3CN$: C, 33.99; H, 1.59; N, 3.81. Found: C, 33.93; H, 1.73; N, 3.93%. IR (KBr): 3098 w, 2971 w, 2265 w, 1655 s, 1607 w, 1589 m, 1551 m, 1522 s, 1501 s, 1462 m, 1431 m, 1343 w, 1260 vs, 1191 sh, 1182 vs, 1147 vs, 1133 sh, 1092 m, 1060 m, 1024 w, 968 m, 927 w, 890 w, 845 m, 791 m, 737 w, 724 m, 665 m, 609 w, 580 w, 552 w cm^{-1}. UV–Vis (THF): $\lambda_1 = 296$ nm ($\varepsilon = 22{,}300$ L^{-1} mol cm^{-1}); $\lambda_2 = 273$ nm ($\varepsilon = 35{,}400$ L^{-1} mol cm^{-1}); $\lambda_3 = 225$ nm ($\varepsilon = 34{,}100$ L^{-1} mol cm^{-1}); $\lambda_4 = 208$ nm ($\varepsilon = 35{,}100$ L^{-1} mol cm^{-1}).

2.2.3. 2,4,6-tris(trifluoromethyl)tetrahydropyran-cis,cis-2,4,6-triol (2)

In a 25 mL round-bottomed flask, **5** (280 mg, 0.149 mmol) was treated with Et_2O (5 mL) and 3 N H_2SO_{4aq} (5 mL). The reaction mixture was vigourously stirred at room temperature until complete disappearance of the blue crystals (*ca.* 1 h). The aqueous phase was extracted two times with Et_2O, and the combined organic phases were dried over anhydrous Na_2SO_4, filtered, and concentrated *in vacuo*. Purification by silica gel column chromatography (ethyl acetate/hexane = 1:50–1:2, R_F (1:2) = 0.3, stains colourless (!) with $KMnO_4$) gave 95 mg of **2** as colorless crystals (0.281 mmol, 94%). Recrystallisation in hot hexane afforded diffraction quality crystals (see Fig. 2b).

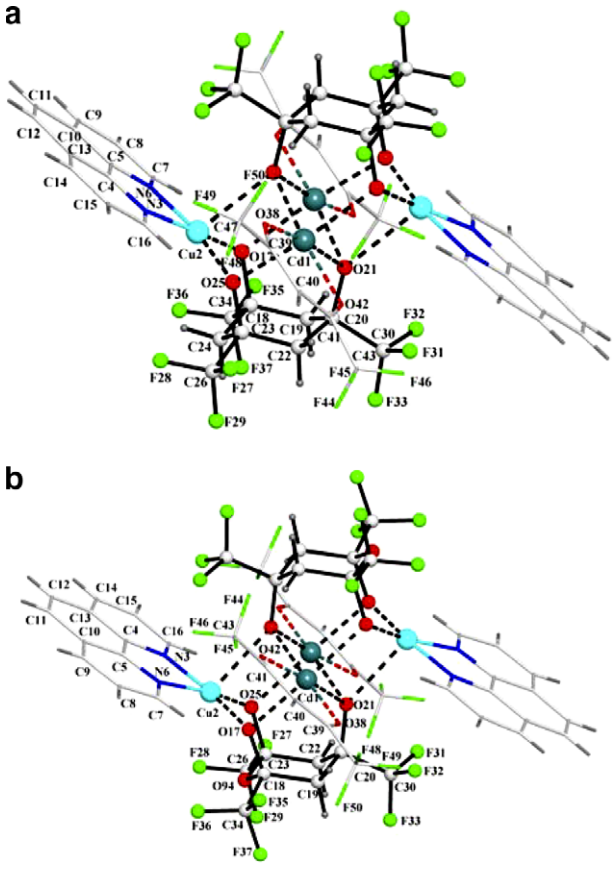


Fig. 1. Structure proposed for X-ray analysis of **4**/**5**. (a) containing ligand **1** (→**4**); (b) containing ligand **2** (→**5**) (a statistical disorder of O94 is considered for refinement over positions C19 and C22 as well, but not shown here for clarity). Color codes: copper (light blue), cadmium (gray), oxygen (red), nitrogen (blue), fluorine (green). (For interpretation of the references to colour in this figure legend, the reader is referred to the web version of this article.)

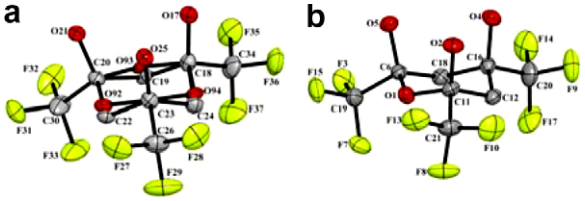


Fig. 2. (a) A perspective rendering of the tridentate ligand TTPT (**2**) with a statistically disordered oxygen atom. (b) X-ray crystal structure of *isolated* 2,4,6-tris(trifluoromethyl)-tetrahydropyran-*cis*,*cis*-2,4,6-triol (H_3TTPT, **2**) (30% probability thermal ellipsoids; hydrogen atoms omitted for clarity). (For interpretation of the references to colour in this figure legend, the reader is referred to the web version of this article.)

^{1}H NMR ($CDCl_3$, 200 MHz) δ 2.40 (1H, 1/2AB, $J = 14.1$ Hz) 2.15 (1H, 1/2AB, $J = 14.1$ Hz); ^{19}F NMR ($CDCl_3$, 188 MHz) δ −86.05 (1F, s) −88.15 (2F, s); ^{13}C NMR (CD_3OD, 100 MHz) δ 126.0 (1C, q, $J_{C-F} = 295$ Hz) 123.2 (2C, q, $J_{C-F} = 283$ Hz) 96.2 (2C, q, $J_{C-F} = 33$ Hz) 71.9 (1C, q, $J_{C-F} = 30$ Hz) 31.2 (1C, s);

HR-MS: $C_8H_6F_9O_4$ $[M-H]^-$ calcd 337.0122, found 337.0119. $C_8H_4F_9O_3$ $[M-H-H_2O]^-$ calcd 319.0017, found: 319.0019.

IR (KBr): 3450 br, 2961 m, 2926 m, 2855 w, 1716 m, 1637 w, 1466 m, 1439 m, 1383 m, 1289 sh, 1273 vs, 1194 vs, 1132 vs, 1118 sh, 1058 s, 1035 sh, 1024 s, 810 m cm^{-1}.

2.2.4. General procedures for decomplexation and ligand isolation

2.2.4.1. Typical aqueous conditions. A 50 mL Schlenk tube charged with 45 mg of **5** (0.024 mmol) was vacuum-purged several times with Ar (or H_2). Then, Et_2O (10 mL) and distilled water (5 mL) containing the reagent (HCl, NH_4Cl or Na_2EDTA) were added. The reaction mixture, monitored by TLC, was stirred at room temperature for the prescribed time stated in Table 1. The aqueous phase was extracted two times with Et_2O, the combined organic phases dried over anhydrous Na_2SO_4, filtered, and concentrated *in vacuo*. The crude organic residue was analysed by ^{1}H and ^{19}F NMR spectroscopy.

2.2.4.2. Typical anhydrous conditions. **5** (45 mg, 0.024 mmol) was placed in a 15 mL flame-dried Schlenk tube which was subsequently vacuum-purged several times with Ar. The addition of degassed THF and stirring for a short period of time (*ca.* 15 min) at room temperature led to complete dissolution of **5**. The resulting blue solution was then treated by several means with the gaseous reagent: direct bubbling into the solution, dropwise addition in

Table 1
Experimental procedures employed for the liberation of the presumed ligand TTFTCH (**2**)

Entry	Experimental conditions[a]	Organic residue
1	2 M HCl_{aq} Et_2O 2 h	**2** + hFacac
2	2 M HCl_{aq} Et_2O H_2 atmosphere 24 h	**2** + hFacac
3	NH_4Cl_{sat} Et_2O 6 d	no reaction
4	NH_4Cl_{sat} Et_2O H_2 atmosphere 6 d	no reaction
5	NH_4Cl_{sat} Et_2O air condition 6 d	no reaction
6[c]	HCl_{gas} bubbling degassed THF 10 min	**2** + hFacac
7[c]	HCl_{gas} dissolved in THF degassed THF 20 min	**2** + hFacac
8[b]	degassed THF H_2S_{gas} atmosphere 3 h	**2** + thio-hFacac
9[c]	H_2S_{gas} bubbling degassed THF 3 min	**2** + thio-hFacac
10[b]	25 equiv. *i*-PrMgCl THF 3 h 30 min	**2** + hFacac
11	4 equiv. Na_2EDTA Et_2O/H_2O 2 months	no reaction

[a] If no mention, experiment carried out under inert atmosphere.
[b] Filtration under air.
[c] Filtration under inert atmosphere.

gas-saturated THF or streaming on the liquid surface. The reaction mixture was allowed to react until total disappearance of the blue colour. After purging the system with Ar for 15 min, the crude reaction mixture was filtered in order to remove all metal precipitates ($CdCl_2$, $CuCl_2$, CuS or CdS, respectively). The solvent was evaporated, and the resulting residue in solution in $CDCl_3$ was subjected to NMR analysis.

2.3. Mass spectrometry

Mass spectra were acquired on a ThermoFinnigan LCQ Advantage ion trap instrument, detecting positive ions (+) or negative ions (−) in the ESI mode. Samples (in methanol:dichloromethane:water, 45:40:15, v/v/v) were infused directly into the source (5 μL/min) using a syringe pump. As a control experiment, **2** (respectively **4/5**) was dissolved in acetonitrile (respectively in THF) and introduced into the ESI source at a flow rate of 5 μL/min: no major modification of the spectra could be observed. The following source parameters were applied: spray voltage 3.0–3.5 kV, nitrogen sheath gas flow 5–20 arbitrary units. The heated capillary was held at 200 °C. A high-resolution mass spectrum (HR-MS) of compound **2** was obtained using a ThermoFinnigan MAT95XL double-focusing mass spectrometer equipped with a ESI III source.

2.4. X-ray crystallography

Suitable crystals were mounted on a Nonius Kappa CCD diffractometer using Mo Kα radiation ($\lambda = 0.71073$ Å) and equipped with a CCD area detector. Intensities for **2** and **4/5** were collected at room temperature by means of the program COLLECT [11]. Cell-refinement and data reduction were carried out with the EVALCCD [12] program. An analytical absorption correction was achieved by modeling the crystal faces [13] through the WINGX gui [14]. The resulting set of *hkl* was used for structure solution with SIR97 [15]. All non-hydrogen atoms were refined anisotropically with the program CRYSTALS [16]. Hydrogen atoms were placed geometrically and then refined using riding constraints. Crystallographic data details on data collection and structure refinement are listed in Table 2.

3. Results and discussion

Castro et al. proposed that, while conducting the reaction between the two starting materials (Scheme 2), **1** was generated in a metal-assisted mechanism starting from

Table 2
Crystallographic data and structural refinement parameters for compounds **2** and **4/5**

	Compound **4/5**			Compound **2**
	Structure **4** (previous data set [4])	Structure **4** (newly collected data)	Structure **5** (newly collected data)	H_3TTPT
Chemical formula	$C_{56}H_{36}Cd_2Cu_2F_{30}N_6O_{10}$	$C_{54}H_{33}Cd_2Cu_2F_{30}N_5O_{10}$	$C_{52}H_{29}Cd_2Cu_2F_{30}N_5O_{12}$	$C_8H_7F_9O_4$
a (Å)	12.238(2)	11.849(5)	11.849(5)	8.010(5)
b (Å)	12.707(5)	12.226(5)	12.226(5)	8.423(5)
c (Å)	11.853(3)	12.714(5)	12.714(5)	10.403(5)
α (°)	92.95(3)	63.451(5)	63.451(5)	67.428(5)
β (°)	104.45(2)	86.894(5)	86.894(5)	83.080(5)
γ (°)	63.41(2)	75.535(5)	75.535(5)	66.779(5)
V (Å^3)	1592.3	1591.9(11)	1591.9(11)	595.2(6)
Z	1	1	1	2
Formula weight	1874.79	1833.72	1837.66	338.14
Space group	$P\bar{1}$	$P\bar{1}$	$P\bar{1}$	$P\bar{1}$
T (K)	293	293	293	293
λ (Å)	1.54056	0.71069	0.71069	0.71069
D_{calc} (g cm^{-3})	1.955	1.913	1.917	1.887
μ (mm^{-1})	7.550	1.471	1. 471	0.232
Number of reflections collected	9221	19284	19284	6683
Number of independent reflections	7000	7506	7506	2781
R_1 ($I > 3\sigma(I)$)	0.039	0.045	0.043	0.037
wR_2	0.042	0.057	0.051	0.039

hexafluoroacetylacetonate (hFacac). As a consequence of our interest in **1**, we have opted for a "quick" access to a sample of it by resynthesizing $[Cu_2(phen)_2(\mu^4\text{-TTFTCH})_2\text{-}Cd_2(hFacac)_2]$ (**4**), rather than conducting new metal-free experiments with unknown outcome. Simple hydrolysis of **4** would then afford the desired H_3TTFTCH (**1**).

Initially, we needed to make 1,10-phenanthroline-bis(pyrimidine-2-thionato)cadmium(II) (**3**), precursor for the tetranuclear complex **4/5** (Scheme 2). Rather than pursuing the published electrochemical approach [17] using Cd plate as the anode, we developed a simpler and more high-yielding (85%) procedure based on $CdCl_2$ and the thiol in its fully deprotonated form. With [Cd(pymt)$_2$phen] (**3**) in hand, we reproduced on a larger scale the exact experimental conditions proposed by Castro et al. for the formation of **4/5** allowing **3** and bis(hexafluoroacetylacetonato)Cu(II) to react in refluxing acetonitrile. It is imperative to use recrystallised **3** (in hot acetonitrile) in order to observe the formation of **4/5**. Furthermore, optimisation of the speed of solvent evaporation during the crystallisation period of **4/5** turned out to be crucial: an elevated evaporation rate only led to an unknown green precipitate. Once the solubility limit of **4/5** was reached, further evaporation caused the formation of an undesired yellow precipitate. Under optimal conditions, **4/5** could be obtained as deep blue crystals in 27% yield (calculation based on **3**). Mono-crystals were subjected to a routine X-ray diffraction analysis and the presence of **1** was confirmed in the resulting tetranuclear complex structure (Fig. 1a).

The deep blue crystals of **4/5** were subsequently destroyed in a biphasic mixture of 3 N H_2SO_4 and diethyl ether. Column chromatography of the organic residue isolated from the ethereal phase afforded partially hydrated hexafluoroacetylacetone and a colorless crystalline solid. Surprisingly, all NMR data (1H, 13C, and 19F) for the latter compound supported a C_2-symmetry incompatible with the C_{3v} space group of **1** (Scheme 1). Additional characterisation by ESI-MS, and HR-MS supported a tetrahydropyran structure rather than a cyclohexyl moiety. A subsequent X-ray analysis of the isolated ligand (Fig. 2b) confirmed the tetrahydropyran structure **2**. Remarkably, treatment with 3 N H_2SO_4 did not lead to the formation of a mixture of an entirely *cis*-configured acetal and its *cis–trans*-configured counterpart by thermodynamic equilibration : the stereoconfiguration found in the crystals of **4/5** was retained.

Although no usual mechanistic pathway could explain a possible *in situ* transformation of **1** into **2** (two C–C bonds broken and two C–O bonds formed under reasonably mild conditions), the high yield of **2** (94% based on **4/5**) led us to explore the possibility that TTFTCH (**1**) was getting quantitatively oxidized during hydrolysis. We thus decided to

Table 3
Selected bond distances (Å) and angles (°) for compounds **2** and **4/5**[a]

Structure **4** (previous data set)		Structure **4** (newly collected data)		Structure **5** (newly collected data)		H_3TTPT (**2**)	
Bond distances (Å)							
C31–C32	1.492(5)	C18–C19	1.485(5)	C18–C19	1.530(7)	O1–C6	1.418(3)
C32–C33	1.478(5)	C18–C24	1.496(6)	C18–C24	1.541(7)	O1–C11	1.412(3)
C33–C35	1.495(6)	C19–C20	1.485(5)	C18–O93	1.422(9)	C6–C18	1.522(3)
C35–C36	1.496(6)	C20–C22	1.489(5)	C18–O94	1.418(9)	C11–C12	1.520(4)
C36–C38	1.479(6)	C22–C23	1.480(5)	C19–C20	1.521(7)	C12–C16	1.514(4)
C38–C31	1.490(5)	C23–C24	1.499(5)	C20–C22	1.529(7)	C16–C18	1.518(4)
				C20–O92	1.419(9)		
				C20–O93	1.424(9)		
				C22–C23	1.522(7)		
				C23–C24	1.538(7)		
				C23–O92	1.417(9)		
				C23–O94	1.420(9)		
Bond angles (°)							
C32–C31–C38	110.1(3)	C24–C18–C34	108.3(4)	C19–C18–C24	109.4(8)	C6–O1–C11	118.48(18)
C31–C32–C33	116.1(3)	C18–C19–C20	115.2(3)	C19–C18–O94	111.2(9)	O1–C6–C18	113.8(2)
C32–C33–C35	110.1(3)	C19–C20–C22	110.2(3)	C24–C18–O93	110.6(5)	O1–C11–C12	112.6(2)
C33–C35–C36	111.0(3)	C20–C22–C23	115.3(3)	C18–C19–C20	110.0(6)	C11–C12–C16	110.0(2)
C35–C36–C38	110.4(3)	C22–C23–C24	109.2(3)	C19–C20–C22	110.8(8)	C12–C16–C18	109.8(2)
C31–C38–C36	116.2(4)	C23–C24–C18	110.0(3)	C19–C20–O92	110.6(9)	C6–C18–C16	110.9(2)
				C22–C20–O93	110.9(8)		
				C20–C22–C23	110.2(5)		
				C22–C23–C24	108.5(8)		
				C22–C23–O94	110.4(9)		
				C24–C23–O92	109.2(9)		
				C23–C24–C18	105.0(5)		
				C23–O92–C20	123.8(9)		
				C18–O93–C20	123.0(8)		
				C23–O94–C18	118.8(8)		

[a] Estimated standard deviations in the least significant digits are given in brackets.

perform a series of rigorous experiments to liberate the ligand using reagents as various as HCl_{gas}, H_2S_{gas}, or EDTA, while partially or entirely excluding oxygen and water as possible oxygen sources (Table 1). The resulting highly insoluble compounds with copper and cadmium ($CdCl_2$, $CuCl_2$, CuS and CdS) provided a powerful driving force for TTFTCH liberation. Under inert and reductive atmosphere, the biphasic system HCl_{aq}/Et_2O led to the "oxidised" compound **2**. The softer reagent NH_4Cl was found to be inert toward **4/5**. Tetrahydrofuran turned out to be an excellent solvent to dissolve **4/5** which greatly aided in tests with various reagents. Use of hydrogen sulfide (reaction time: 3 min) was particularly powerful in cleaving the complex while ensuring perfectly reductive conditions. In all these attempts, only the acetal **2** was obtained despite rigorous exclusion of oxygen. These results made any oxidation of **1**–**2** increasingly unlikely. Two subsequent liberation attempts with orthogonal conditions were carried out, one using a Grignard reagent, the other EDTA, the former leading to exclusive formation of **2**, the latter having no impact on crystalline **4/5** in the absence of THF.

Keeping in mind the very unusual way how **1** was formed and the reported X-ray structure of a similar complex containing **2** in place of **1**, we started to doubt the original X-ray diffraction assignment corresponding to

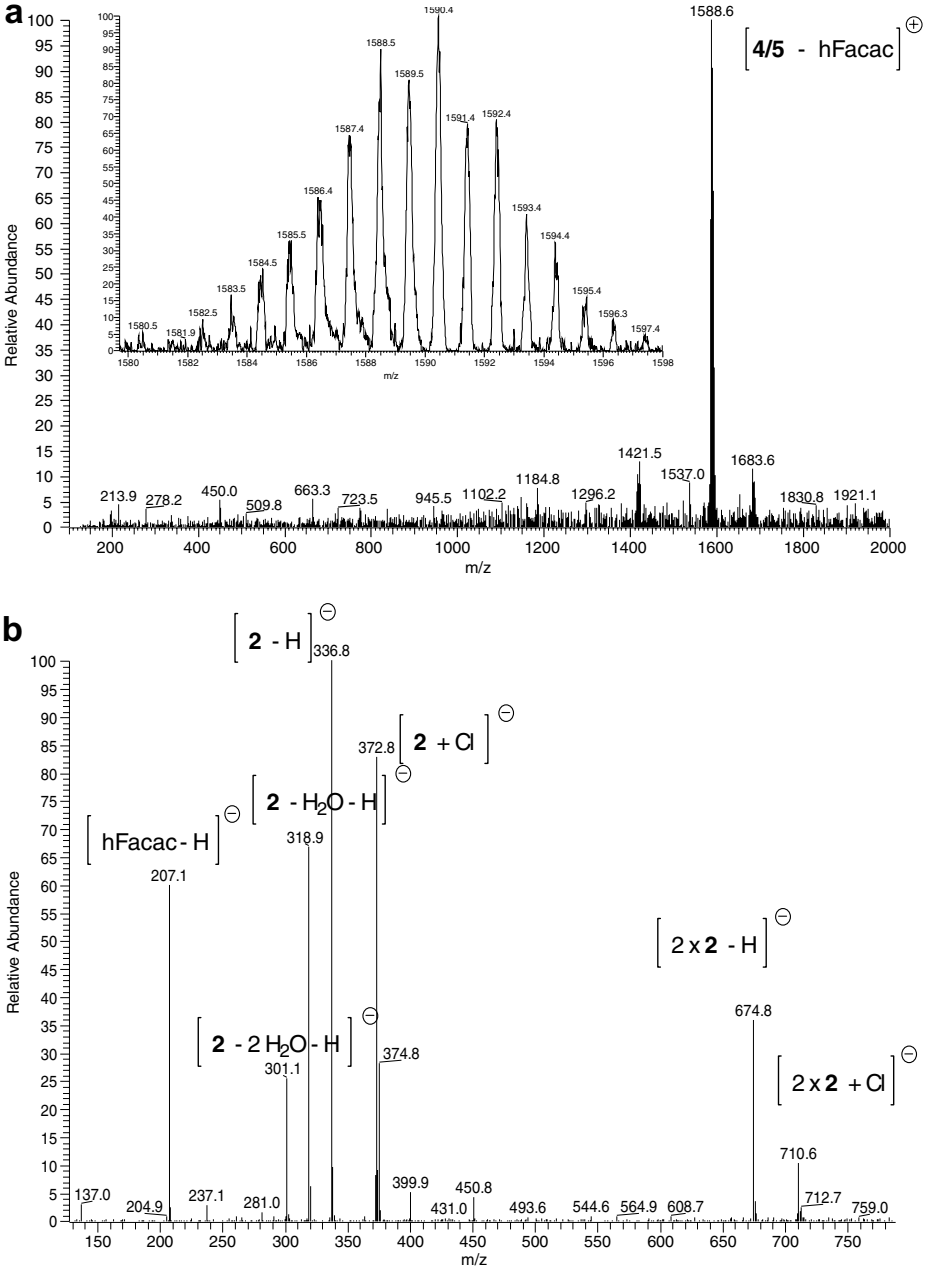


Fig. 3. ESI-MS of cpd. **4/5** dissolved in THF: (a) positive mode (inlet: expansion of peak [**4/5**-hFacac]$^+$), (b) negative mode.

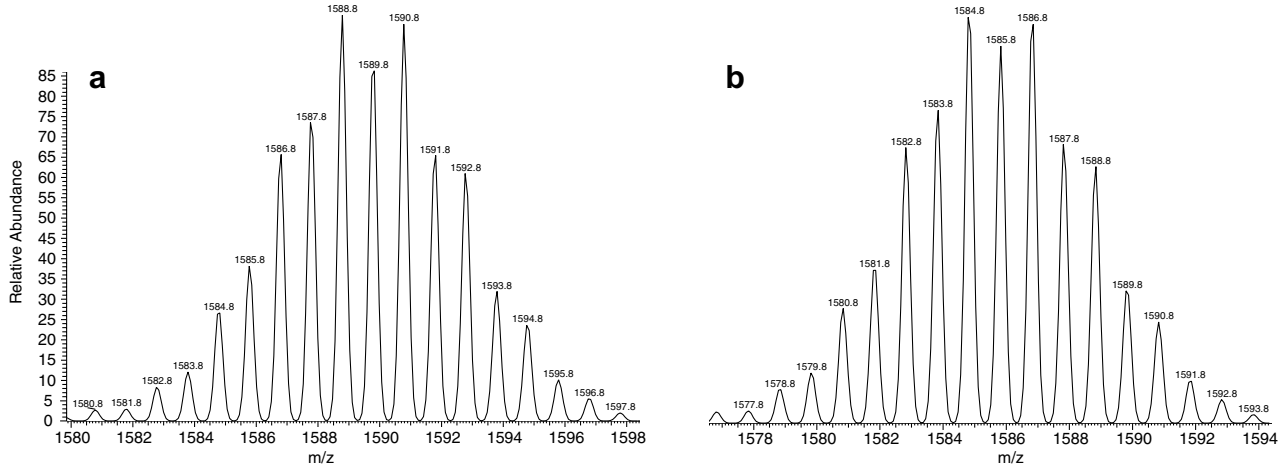


Fig. 4. Expansion of the peak [**4**/**5**-hFacac]$^+$: (a) calculated isotopic distribution for [**5**-hFacac]$^+$ and (b) calculated isotopic distribution for [**4**-hFacac]$^+$.

structure **4**, reported by Castro et al. and redetermined by us. Newly collected crystallographic data (space group, cell volume, cell parameters) from crystals of **4**/**5** were in full agreement with Ref. [4]. The data collected for **4**/**5** were used to reinvestigate the identity of the atoms constituting the presumed cyclohexane ring of ligand **1**. We explored the effect of interchanging one methylene group with an oxygen. Refinement as an oxygen atom led to a similar *R* factor but the equivalent displacement parameter was slightly high ($U_{eq} = 0.059$) compared to those of the atoms forming the 6-membered ring ($U_{eq} \sim 0.030$). Consequently, the structure containing a located oxygen on the cycle as reported for the tetra-copper complex **6** was discarded. Another refinement was achieved by modelling an oxygen atom delocalised over the three available positions (Figs. 1 and 2a) using soft restraints on bond length. This procedure led to a slight improvement of the *R* factor (4.3%) compared to the one obtained using a cyclohexane structure (4.5%). Thus, the refinement results tend to show that the oxygen atom is present and delocalised on three positions revealing a statistical disorder. This is confirmed by the fact that a low temperature measurement (150 K) did not allow to localise the oxygen atom on a given position. Relevant bonding distances and angles for structure **4** (with previous reported values), **5** and **2**, as well as crystal parameters and basic information pertaining to data collection are given in Section 2 (see Table 3).

Elemental analysis of **4**/**5** turned out to be very different from the one published (C, 33.93; H, 1.73; N, 3.93 versus C, 36.0; H, 1.8; N, 4.3) and tends to validate structure **5** with one molecule of solvent as found in the crystal lattice. Nevertheless, we looked for additional analytical methods to support our assumptions: liquid and solid NMR spectroscopy had to be ruled out due to the paramagnetic character of copper(II). IR spectroscopy did not furnish clear evidence for a tetrahydropyran ring: the characteristic C–O–C stretching band of such a structure being possibly masked by the very broad C–OH and C–F stretching bands around 1150 cm^{-1}. Since **4**/**5** was soluble enough in THF, we thus turned to mass analysis for independent data.

It is worthy to note that cadmium as well as copper present several abundant isotopes which lead to unambiguous peak patterns aiding in structure assignment [18]. Ionisation of **4**/**5** dissolved in THF was achieved using the soft electrospray-ionisation technique. Although no molecular ion peak could be detected, relevant fragmentation ions were identified, especially [**4**/**5**-hFacac]$^+$ (Fig. 3a). A "zoom" scan in the region of *m*/*z* 1589 was compared to the calculated isotopic mass distribution for [Cu_2(phen)$_2$-(μ^4-TTFTCH)$_2$$Cd_2$(hFacac)]$^+$ (**4**) and [Cu_2(phen)$_2$-(μ^4-TTPT)$_2$$Cd_2$(hFacac)]$^+$ (**5**) (Fig. 4): the experimental set of peaks perfectly corresponded to the simulated spectrum of **5**, thus rendering the presence of ligand **2** indisputable. The unique loss of one hexafluoroacetylacetonate unit from the molecular ion rules out any rearrangement or oxidation process during ionisation. Importantly, detection in negative mode only gave rise to derivatives of **2** and hexafluoroacetylacetonate [hFacac]$^-$ without traces of **1** (Fig. 3b). The ESI-MS spectrum of free tetrahydropyran **2** (not shown) was in full agreement with this fragmentation pattern.

4. Conclusions

An improved large-scale synthesis of [Cu_2(phen)$_2$-(μ^4-TTPT)$_2$$Cd_2$(hFacac)$_2$] in the form of deep-blue crystals (**5**) and the isolation and characterisation of the free ligand, *cis*,*cis*-2,4,6-tris(trifluoromethyl)tetrahydropyran-2,4,6-triol (**2**) is presented.[1] Structure **4** was previously attributed to the crystals by an X-ray structure determination. A newly conducted X-ray analysis does not provide sufficient data to assign structure **4** or **5** to these same blue crystals.

[1] The coordinating properties of compound **2** are currently under investigation.

However, three sets of independent data (elemental analysis, chemical reactivity and mass spectral analysis) unequivocally establish their identity as being structure **5** rather than **4**, thus proving this study a case where diffraction data interpretation meets its limits.

5. Supplementary material

CCDC 618989 and 616292 contain the supplementary crystallographic data for **2** and **5**. These data can be obtained free of charge via http://www.ccdc.cam.ac.uk/conts/retrieving.html, or from the Cambridge Crystallographic Data Centre, 12 Union Road, Cambridge CB2 1EZ, UK; fax: (+44) 1223-336-033; or e-mail: deposit@ccdc.cam.ac.uk.

Acknowledgements

This work was supported by the CNRS and the French Research Ministry. We thank Laurence Arzel for help with the mass spectral analysis.

References

[1] CAS registry: 380-93-8.
[2] (a) F. Smith, M. Stacey, J.C. Tatlow, Fluoroketones, Patent GB 773402 19570424, 1957.;
(b) S. Resconich, Ph.D Thesis, Purdue University, 1961.
[3] M.M. Dhingra, K.R. Tatta, Org. Mag. Res. 9 (1977) 23–28.
[4] R. Castro, M.L. Duran, J.A. Garcia-Vasquez, J. Romero, A. Sousa, A. Castineiras, W. Hiller, J. Strahle, Polyhedron 11 (1992) 1195–1200.
[5] (a) For observations of other tetranuclear Cd–Cu complexes, see: E.A. Buvaylo, V.N. Kokozay, O.Y. Vassilyeva, B.W. Skelton, Inorg. Chem. Commun. 7 (2004) 1061–1064;
(b) E.A. Vinogradova, O.Y. Vassilyeva, V.N. Kokozay, B.W. Skelton, J.K. Bjernemosee, P.R. Raithby, J. Chem. Soc., Dalton Trans. 22 (2002) 4248–4252.
[6] For a general introduction to high-nuclearity complexes, see: P. Braunstein, L.A. Oro, P.R. Raithby (Eds.), Metal Clusters in Chemistry, Wiley-VCH, Weinheim, 1999.
[7] T. Kogane, K. Harada, R. Hirota, A. Urushiyama, Polyhedron 15 (1996) 4093–4101.
[8] For polyfluorinated diketones see: M.V. Nikonov, D.L. Chizhov, V.G. Ratner, K.I. Pashkevich, J. Fluorine Chem. 106 (2000) 115–116.
[9] For perfluorinated diketones see: J.D.O. Anderson, W.T. Pennington, D.D. DesMarteau, Inorg. Chem. 32 (1993) 5079–5083.
[10] For the advantages of an electrochemical approach, see: J.A. Garcia-Vazquez, J. Romero, A. Sousa, Coord. Chem. Rev. 195 (1999) 691–745.
[11] Nonius 2001, COLLECT, Nonius BV, Delft, The Netherlands.
[12] A.J.M. Duisenberg, L.M.J. Kroon-Batenburg, A.M.M. Schreurs, J. Appl. Cryst 36 (2003) 220–229.
[13] N.W. Alcock, Cryst. Comput. (1970) 271–278.
[14] L.J. Farrugia, J. Appl. Cryst. 32 (1999) 837–838.
[15] A. Altomare, M.C. Burla, M. Camalli, G.L. Cascarano, C. Giacovazzo, A. Guagliardi, A.G.G. Moliterni, G. Polidori, R. Spagna, J. Appl. Cryst. 32 (1999) 115–119.
[16] P.W. Betteridge, J.R. Carruthers, R.I. Cooper, K. Prout, D. Watkin, J. Appl. Cryst. 36 (2003) 1487.
[17] (a) R. Castro, M.L. Duran, J.A. Garcia-Vasquez, J. Romero, A. Sousa, A. Castineiras, W. Hiller, J. Strähle, Z. Naturforsch. Sect. B 47 (1992) 1067–1074;
(b) J.J. Habeeb, D.G. Tuck, F.H. Walters, J. Coord. Chem. 8 (1978) 27–33.
[18] W. Henderson, J. Scott McIndoe, Mass Spectrometry of Inorganic, Coordination and Organometallic Compounds, Wiley, Chichester, 2005.

2.2. Physical measurements

FT-IR spectra in the 400–4000 cm^{-1} range were recorded on a Perkin–Elmer FT-IR spectrometer using KBr pellets. Optical diffuse-reflectance spectra were measured on a Perkin–Elmer instrument Lambda 900 UV/Vis spectrometer equipped with an integrating sphere at 293 K, and the $BaSO_4$ plate was used as the reference. The C, H and N analyses were carried out on an Elemental Vario EL III analyzer. Room-temperature fluorescence spectra were measured on a FLS920P spectrometer with a laser at 397 nm as the excitation light. Thermogravimetric analyses were carried out on a NETZSCH STA 449C unit at a heating rate of 15 °C min^{-1} under a nitrogen atmosphere.

2.3. Preparation of 1–3

2.3.1. $[Et_4N]_2[WOS_3Cu(dppe)]_2 \cdot H_2O$ (1)

A mixture of $[Et_4N]_2[WOS_3CuCN]$ (0.20 mmol, 129.20 mg) and dppe (0.20 mmol, 79.60 mg) in DMF (4 mL) was stirred for 20 min and then filtered. By slow diffusion of *i*-PrOH into the filtrate gave air stable yellow crystals of **1**. Yield: 42%. *Anal*. Calc. for $C_{68}H_{90}Cu_2N_2O_3P_4S_6W_2$: C, 45.51; H, 5.05; N, 1.56. Found: C, 45.44; H, 5.13; N, 1.63%. IR (KBr pellet, cm^{-1}): 1629 w, 1482 s, 1457 w, 1434 s, 1394 w, 1171 w, 1099 w, 1000 w, 892 vs, 880 sh, 746 m, 721 m, 696 s, 514 s, 482 m, 471 s, 438 s, 414 sh.

2.3.2. $[WS_4Cu_2(dppe)_2]_n$ (2)

A mixture of **1** (0.02 mmol, 35.89 mg) and AgI (0.04 mmol, 9.39 mg) was placed in a glass tube and 2 mL of DMF was added. The tube was sealed after evacuation and heated to 120 °C for 1 day. Upon slowly cooling to room temperature over 2 days, yellow crystals of **2** were obtained in 17% yield (based on W). *Anal*. Calc. for $C_{52}H_{48}Cu_2P_4S_4W$: C, 50.53; H, 3.91. Found: C, 50.49; H, 3.98%. IR (KBr pellet, cm^{-1}): 1482 m, 1433 s, 1165 w, 1098 m, 1026 w, 999 w, 882 w, 740 m, 718 m, 692 vs, 514 m, 481 m, 455 s, 447 sh.

2.3.3. $[Et_4N]_2[WEE'S_2Ag(dppe)]_2 \cdot CH_3CN$ (3)

The synthetic procedure was similar to that of **1** with $[Et_4N]_2[WOS_3AgCN]$ (0.20 mmol, 138.10 mg) instead of $[Et_4N]_2[WOS_3CuCN]$. Yield: 35%. *Anal*. Calc. for $C_{70}H_{91}Ag_2N_3O_{1.89}P_4S_{6.11}W_2$: C, 44.07; H, 4.81; N, 2.20. Found: C, 43.96; H, 4.86; N, 2.12%. IR (KBr pellet, cm^{-1}): 1662 m, 1482 m, 1457 w, 1433 vs, 1393 w, 1170w, 1095 m, 900 s, 884 sh, 755 m, 735 m, 719 m, 696 s, 510 m, 473 s, 442 s, 431 s.

2.4. X-ray crystallography

The data for **1**–**3** were collected on a RIGAKU MERCURY CCD area-detector diffractometer with graphite-monochromated Mo Kα radiation ($\lambda = 0.71073$ Å). The structures were solved by direct methods and refined on F^2 by full-matrix least-squares procedures using the SHELXTL software suite [31]. All non-hydrogen atoms were refined anisotropically except for those with disordered positions of the $[Et_4N]^+$ and CH_3CN in **3**. The positions of H atoms were generated geometrically (C–H bond fixed at 0.96 Å), assigned isotropic thermal parameters, and allowed to ride on their parent carbon atoms before the final cycle of refinement. Hydrogen atoms have not been included in the disordered part of the model. The hydrogen atoms of the water molecule in **1** could not be located theoretically and were not located. The occupancies of the disordered S and O atoms in **3** were refined freely with the sum of occupancies being 1.000 at each site of E or E′. The occupancies of the disordered components of the $[Et_4N]^+$ and CH_3CN in **3** were assumed to be 0.50 for each disordered atom. A summary of the crystallographic data of **1**–**3** is presented in Table 1.

Table 1
Crystallographic data for compounds **1**, **2** and **3**

Compound	**1**	**2**	**3**
Empirical formula	$C_{68}H_{90}Cu_2N_2O_3P_4S_6W_2$	$C_{52}H_{48}Cu_2P_4S_4W$	$C_{70}H_{91}Ag_2N_3O_{1.89}P_4S_{6.11}W_2$
Formula mass	1794.44	1235.95	1907.90
Crystal system	monoclinic	triclinic	monoclinic
Space group	*C*2/*c*	$P\bar{1}$	*C*2/*c*
a (Å)	23.703(1)	11.480(1)	18.260(1)
b (Å)	10.823(1)	12.940(1)	16.550(1)
c (Å)	29.238(2)	17.850(2)	26.960(2)
α (°)	90.00	99.640(3)	90.00
β (°)	101.974(1)	102.800(5)	102.370(3)
γ (°)	90.00	95.970(4)	90.00
V (Å^3)	7337.4(6)	2521.6(5)	7958.2(9)
Z	4	2	4
D_{calc} (g cm^{-3})	1.624	1.628	1.592
μ (Mo Kα) (mm^{-1})	4.000	3.439	3.649
T (K)	130(2)	130(2)	293(2)
R_1[a] $[I > 2\sigma(I)]$	0.0224	0.0464	0.0609
wR_2[b] $[I > 2\sigma(I)]$	0.0473	0.0848	0.1602

[a] $R_1 = \sum \| F_o| - |F_c| / \sum |F_o|$.
[b] $wR_2 = [\sum w(F_o^2 - F_c^2)^2 / \sum w(F_o^2)^2]^{1/2}$.

3. Results and discussion

3.1. Syntheses

Treatment of $[Et_4N]_2[WOS_3MCN]$ (M = Cu or Ag) with one equiv. of dppe in DMF produced **1** and **3**. Crystals of **1** and **3** could be obtained via slow diffusion of *i*-PrOH into their DMF solutions. In addition, reactions using MCN or MSCN (M = Cu or Ag) with $[Et_4N]_2[WOS_3]$ in the presence of dppe also led to the same results. Compound **2** was isolated in the attempt to make W/Cu/Ag clusters by the reaction of **1** and AgI in DMF under vacumm. It is possible that an equilibrium $2WOS_3^{2-} \rightleftharpoons WO_2S_2^{2-} + WS_4^{2-}$ exists in solution and it will be reasonable for the transformation from WOS_3^{2-} to WS_4^{2-}. The reaction of **1** with AgI also produced a large amount of Ag_2S and some unidentified precipitate, which resulted in the decrease of the yield of **2**. The measurements of the ^1H and ^{31}P NMR spectra of **1**–**3** were not done due to their poor solubility in solvents.

3.2. Crystal structures of 1–3

The molecular structure of **1** was confirmed by a single-crystal X-ray diffraction study. The structure of the anion of **1** is shown in Fig. 1 and selected bond lengths and angles are listed in Table 2. The molecule is situated on an inversion center. In the asymmetric unit of **1**, the WOS_3^{2-} dianion acts as a bidentate ligand to coordinate one Cu atom through two bridging S atoms leaving the other S and O atoms uncoordinated. The W=O bond length [1.756(2) Å] is slightly greater than those observed for $[W_2O_2S_6Cu_4(PPh_3)_4]$ [1.696(1) Å] [32] and $[WOS_3Cu_3(PPh_3)_2(SC_4H_9)]_2$ [1.695(5) Å] [33]. The W=S_t bond length is characteristic of a typical double bond. The two W–S_{br} bond lengths are within the normal range of the W–μ-S bonds observed in other W/Cu/S clusters and are considered to be single bonds. The W···Cu distance [2.779(1) Å], which is comparable to those found for $[WOS_3Cu_3(S_2COEt)(PPh)_3]$ [2.752(2) Å] (av) [33] and $[W_2O_2S_6Cu_4(PPh_3)_4]$ [2.780(1) Å] (av) [32], suggests the

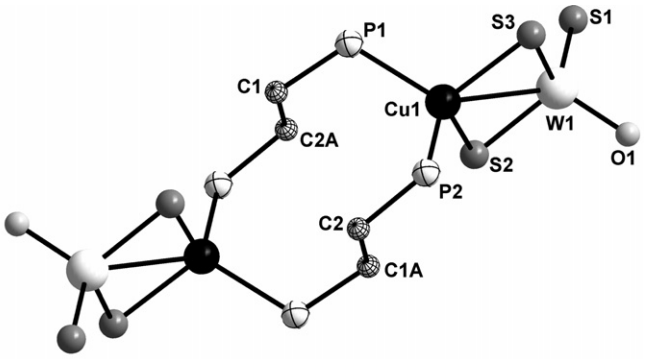


Fig. 1. Structure and labeling of the $[WOS_3Cu(dppe)]_2^{2-}$ anion of **1**. Hydrogen atoms and the phenyl rings bound to phosphorous atoms are omitted for clarity. Symmetry code: #A $-x, -y+1, -z$.

Table 2
Selected bond lengths (Å) and angles (°) for complexes **1**–**3**

Complex **1**[a]			
W(1)–O(1)	1.756(2)	S(1)–W(1)–Cu(1)	125.9(1)
W(1)–S(1)	2.192(1)	S(2)–W(1)–Cu(1)	53.6(1)
W(1)–S(2)	2.236(1)	S(3)–W(1)–Cu(1)	53.7(1)
W(1)–S(3)	2.232(1)	P(1)–Cu(1)–P(2)	107.7(1)
W(1)–Cu(1)	2.779(1)	P(1)–Cu(1)–S(2)	111.9(1)
Cu(1)–P(1)	2.292(1)	P(1)–Cu(1)–S(3)	111.8(1)
Cu(1)–P(2)	2.280(1)	P(2)–Cu(1)–S(2)	111.7(1)
Cu(1)–S(2)	2.312(1)	P(2)–Cu(1)–S(3)	111.7(1)
Cu(1)–S(3)	2.316(1)	S(2)–Cu(1)–S(3)	102.1(1)
O(1)–W(1)–S(1)	110.0(1)	P(2)–Cu(1)–W(1)	126.0(1)
O(1)–W(1)–S(2)	109.4(1)	P(1)–Cu(1)–W(1)	126.3(1)
O(1)–W(1)–S(3)	109.5(1)	S(2)–Cu(1)–W(1)	51.1(1)
S(1)–W(1)–S(3)	110.3(1)	S(3)–Cu(1)–W(1)	51.0(1)
S(1)–W(1)–S(2)	110.4(1)	W(1)–S(2)–Cu(1)	75.3(1)
S(2)–W(1)–S(3)	107.3(1)	W(1)–S(3)–Cu(1)	75.3(1)
O(1)–W(1)–Cu(1)	124.1(1)		
Complex **2**[b]			
W–S(1)	2.209(1)	S(4)–W–Cu(1)	124.5(1)
W–S(2)	2.208(1)	Cu(1)–W–Cu(2)	174.0(1)
W–S(3)	2.202(1)	P(1)–Cu(1)–P(2)	112.0(1)
W–S(4)	2.217(1)	P(1)–Cu(1)–S(2)	107.0(1)
W–Cu(1)	2.783(1)	P(2)–Cu(1)–S(2)	119.5(1)
W–Cu(2)	2.774(1)	P(1)–Cu(1)–S(1)	113.5(1)
Cu(1)–P(1)	2.282(1)	P(2)–Cu(1)–S(1)	103.8(1)
Cu(1)–P(2)	2.307(1)	S(1)–Cu(1)–S(2)	100.6(1)
Cu(1)–S(1)	2.329(1)	P(1)–Cu(1)–W	124.4(1)
Cu(1)–S(2)	2.309(1)	P(2)–Cu(1)–W	123.3(1)
Cu(2)–P(3)	2.290(1)	S(2)–Cu(1)–W	50.3(1)
Cu(2)–P(4)	2.262(1)	S(1)–Cu(1)–W	50.3(1)
Cu(2)–S(3)	2.329(1)	P(3)–Cu(2)–P(4)	112.5(1)
Cu(2)–S(4)	2.322(1)	P(4)–Cu(2)–S(4)	113.2(1)
S(1)–W–S(3)	107.7(1)	P(3)–Cu(2)–S(4)	111.9(1)
S(1)–W–S(3)	109.0(1)	P(4)–Cu(2)–S(3)	105.1(1)
S(1)–W–S(4)	110.8(1)	P(3)–Cu(2)–S(3)	112.9(1)
S(2)–W–S(3)	111.1(1)	S(3)–Cu(2)–S(4)	100.5(1)
S(3)–W–S(4)	108.1(1)	P(3)–Cu(2)–W	122.0(1)
S(2)–W–S(4)	110.1(1)	P(4)–Cu(2)–W	125.3(1)
S(1)–W–Cu(2)	120.1(1)	S(3)–Cu(2)–W	50.2(1)
S(2)–W–Cu(2)	132.2(1)	S(4)–Cu(2)–W	50.6(1)
S(3)–W–Cu(2)	54.3(1)	W–S(1)–Cu(1)	75.6(1)
S(4)–W–Cu(2)	54.1(1)	W–S(2)–Cu(1)	76.0(1)
S(1)–W–Cu(1)	54.1(1)	W–S(3)–Cu(2)	75.5(1)
S(2)–W–Cu(1)	53.6(1)	W–S(4)–Cu(2)	75.3(1)
S(3)–W–Cu(1)	127.5(1)		
Complex **3**[c]			
W(1)–S(1)	2.210(1)	E–W(1)–Ag(1)	117.8(1)
W(1)–S(2)	2.231(1)	S(1)–W(1)–Ag(1)	57.1(1)
W(1)–E	2.082(2)	S(2)–W(1)–Ag(1)	56.2(1)
W(1)–E′	1.969(3)	P(1)–Ag(1)–S(1)	102.9(1)
W(1)–Ag(1)	3.062(1)	P(1)–Ag(1)–S(2)	110.4(1)
Ag(1)–P(1)	2.493(1)	P(1)–Ag(1)–P(2)	121.0(1)
Ag(1)–P(2)	2.495(1)	P(2)–Ag(1)–S(1)	117.8(1)
Ag(1)–S(1)	2.627(1)	P(2)–Ag(1)–S(2)	110.9(1)
Ag(1)–S(2)	2.600(1)	S(1)–Ag(1)–S(2)	89.4(1)
S(1)–W(1)–S(2)	111.7(1)	P(1)–Ag(1)–W(1)	121.4(1)
S(1)–W(1)–E	111.6(1)	P(2)–Ag(1)–W(1)	117.6(1)
S(1)–W(1)–E′	110.1(1)	S(2)–Ag(1)–W(1)	45.5(1)
S(2)–W(1)–E	110.3(1)	S(1)–Ag(1)–W(1)	44.9(1)
S(2)–W(1)–E′	114.7(1)	W(1)–S(1)–Ag(1)	78.0(1)
E–W(1)–E′	97.6(1)	W(1)–S(2)–Ag(1)	78.3(1)
E′–W(1)–Ag(1)	144.5(1)		

Symmetry transformations used to generate equivalent atoms: [a]For **1**: #1 $-x, -y+1, -z$. [b]For **2**: #1 $-x+1, -y+1, -z+1$; #2 $-x, -y, -z$. [c]For **3**: #1 $-x+2, y, -z+3/2$; #2 $-x+3/2, -y+5/2, -z+1$; #3 $-x+1, -y+2, -z+1$.

existence of metal–metal interaction. Two cluster cores (WOS_3Cu), orientated in opposite direction, are linked via two dppe bridging ligands to form a 10-membered ring [–Cu–P–C–C–P–]$_2$. The distance between the two Cu atoms of the ring is 5.929(1) Å. The flexible dppe adopts a twisted chair conformation. The P1–C1–C2A and P2–C2–C1A angles are 110.2(2)° and 111.1(2)°, respectively. There is a H_2O molecule around the O atom of the [WOS_3] unit. The O1···O2 distance is 2.854(3) Å, suggesting the existence of O–H···O interaction. Thus, as shown in Fig. 2, a helical chain forms through the O–H···O interaction. The pitch (length per turn) of the helical chain is 29.2 Å.

Fig. 3 shows the structure of **2** and selected bond lengths and angles are listed in Table 2. The crystallographic structure of **2** extends in a one-dimensional way as a neutral chain. The WS_4^{2-} dianion coordinates two Cu atoms and acts as a bridging block in the polymeric chain. The W–μ-S bond distances [2.209(1) Å] (av) are typical for W–S single bonds. The W···Cu distance [2.779(1) Å] (av) is a little longer than those observed for [$WS_4Cu_4(dppm)_4$][PF_6]$_2$ [2.760(1) Å] [23] and [$WS_4Cu_2(PPh_3)_3$]·0.8CH_2Cl_2 [2.740(1) Å] (av) [28]. The Cu–P bond [2.285(1) Å] (av) and the Cu–S bond [2.322(1) Å] (av) are comparable to those in other W/S/Cu compounds. The [$CuWS_4Cu$] units are bridged by the dppe ligands to give repeating 10-membered [–Cu–P–C–C–P–]$_2$ rings. The dppe ligand also adopts a twisted chair conformation as observed in **1**, with the P1–C1–C2A, P2–C2–C1A, P3–C3–C4B and P4–C4–C3B angles being 113.3(3)°, 109.6(3)°, 110.2(3)° and 113.1(3)°, respectively. As shown in Fig. 4, the tungsten and copper atoms of **2** form a helical chain with the Cu atoms acting as the turning points. The pitch (length per turn) of the helical chain is 20.5 Å.

The crystal structure of **3** was determined by a single-crystal X-ray diffraction study. The structure of the anion of **3** is shown in Fig. 5. Selected bond lengths and angles are listed in Table 2. The terminal S and O atoms of the [$WEE'S_2Ag$] unit are disorderd with different occupancies at the site of E or E′ (E = 0.636S + 0.364O, E′ = 0.581O + 0.419S), which are in consistent with the bond lengths of W=E [2.082(2) Å] and W=E′ [1.969(3) Å]. The W=E bond length is a little shorter than that of a normal W=S_t double bond, while the W=E′ bond length is somewhat longer than that of a standard W=O bond. The

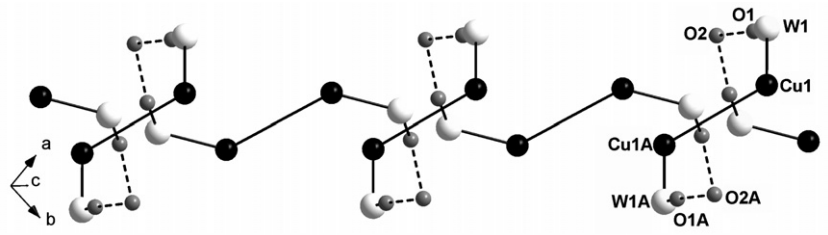


Fig. 2. Simplified diagram of the helical chain of **1** formed through the O–H···O interaction. For clarity, only tungsten, copper and oxygen atoms which form the chain are displayed. Symmetry code: #A $-x$, $-y+1$, $-z$.

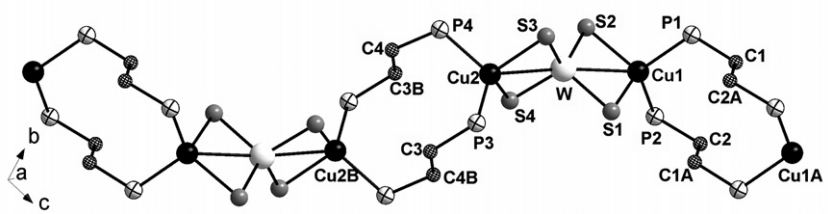


Fig. 3. Structure and labeling of the polymeric chain of **2**. Hydrogen atoms and the phenyl rings bound to phosphorous atoms are omitted for clarity. Symmetry code: #A $-x+1$, $-y+1$, $-z+1$; #B $-x$, $-y$, $-z$.

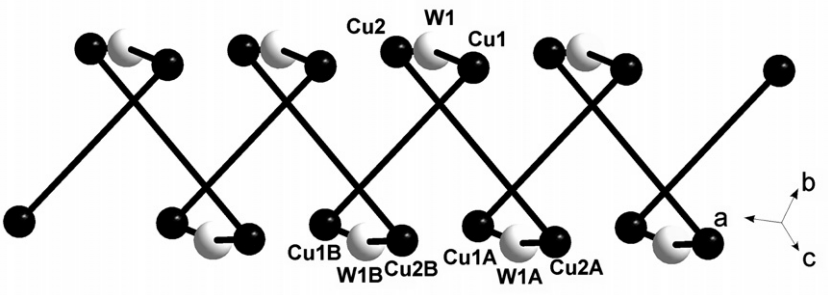


Fig. 4. Simplified diagram of the helical chain of **2**. For clarity, only tungsten and copper atoms which form the chain are displayed. Symmetry code: #A $-x+1$, $-y+1$, $-z+1$; #B $-x$, $-y$, $-z$.

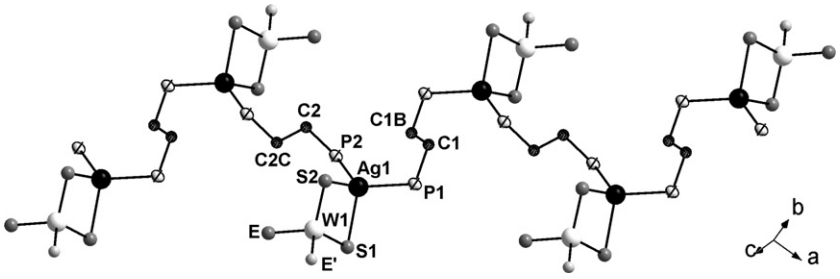


Fig. 5. Structure and labeling of the polymeric anionic chain of **3**. Hydrogen atoms and the phenyl rings bound to phosphorous atoms are omitted for clarity. Symmetry code: #A $-x+2$, y, $-z+3/2$; #B $-x+3/2$, $-y+5/2$, $-z+1$; #C $-x+1$, $-y+2$, $-z+1$.

W···Ag distance [3.062(1) Å] is slightly longer than those found for $[(WS_4)_2Ag_4(PPh_3)_4]$ [2.977(1) Å] [34] and $[W_2S_8Ag_2(dppm)_3](CH_2Cl_2)$ [2.947(1) Å] [25]. The Ag–S bond lengths [2.613(1) Å] (av) and Ag–P bond lengths [2.494(1) Å] (av) are comparable to those found for other W/S/Ag compounds. The [WEE′S_2Ag] units are bridged by bidentate dppe ligands to form a zig-zag chain. The bidentate dppe also adopts a twisted chair conformation with the P1–C1–C1B and P2–C2–C2C angles being 109.4(3)° and 112.2(2)°, respectively.

3.3. Infrared spectra and optical absorption spectra

The infrared spectra of these complexes show typical absorptions around 515 cm^{-1} due to the Cu–P bonds and around 510 cm^{-1} due to the Ag–P bonds. Other bands at ca. 500 cm^{-1} can be assigned to the vibrations ν(M═S) according to the literature data and those at lower frequencies are attributed to the bridging sulfur atoms [35]. As expected, the vibrations ν(W═O) are observed at ca. 900 cm^{-1}.

Optical absorption spectra of compounds **1**–**3** (Fig. 6) have been measured by diffuse-reflectance experiments. The UV–Vis absorption data were calculated from the reflectance data using the Kubelka–Munk function [36,37]: $\alpha/S = (1-R)^2/2R$, where R is the experimentally observed reflectance, α the absorption coefficient and S the scattering coefficient. The absorption edges for **1**–**3** are about 2.46, 2.33 and 2.54 eV, respectively, determined as the intersection point by $(\alpha/S)^2 = 0$ in a $(\alpha/S)^2$ versus E plot [38]. These results show that the present compounds may be classed as semiconductors.

3.4. Luminescent properties and TGA study

Fig. 7 depicts the luminescent emission spectra of compounds **1**–**3** in the solid state at 298 K. With excitation of laser at 397 nm, the emissions observed for **1**–**3** are 578, 574 and 652 nm, respectively, which are much higher than that of free ligand dppe (434 nm), but near to those of $[Cu_3(dppm)_3WS_4](ClO_4)$ (615 nm) [22] and $[Cu_4(dcpm)_4WS_4](ClO_4)_2$ (619 nm) [24] in the solid state. With reference to $[Cu_3(dppm)_3WS_4](ClO_4)$ [22] and $[Cu_4(dcpm)_4WS_4](ClO_4)_2$ [24], the origin of the emission may be assigned as $^3[\psi(M,P)^1\sigma^*(W\text{–}S)^1]$ (M = Cu, Ag) triplet MMCT excited states. The red shift of emission from compound **1** (or **2**) to **3** is consistent with the higher energy of the 4d (Ag) orbital than that of the 3d (Cu) orbital.

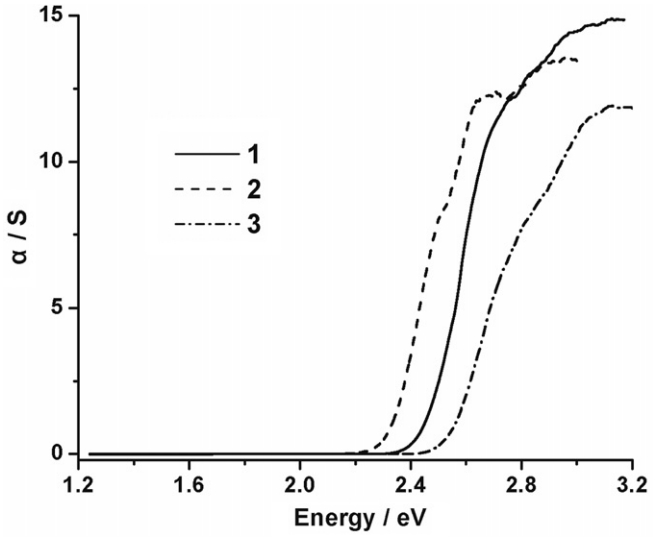


Fig. 6. Optical absorption spectra for **1**–**3**.

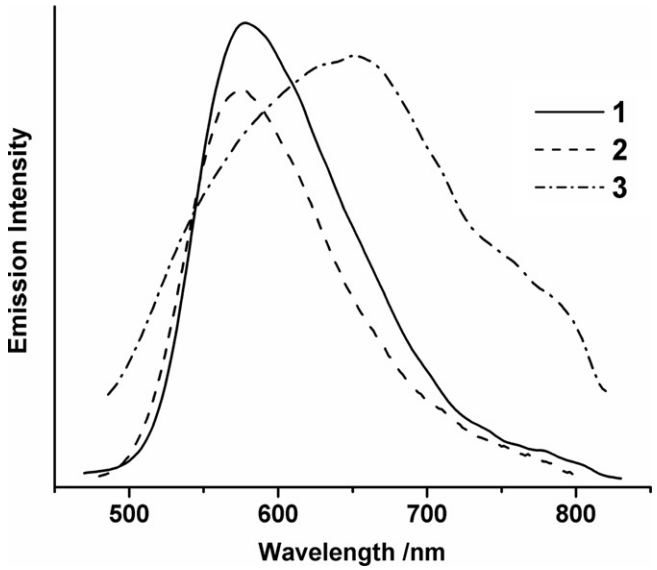


Fig. 7. Solid-state emission spectra of **1**–**3** at 298 K.

The thermogravimetric analysis (TGA) study shows that compounds **1**–**3** are stable up to 216 °C, 291 °C, and 215 °C, respectively.

4. Conclusion

Three W/Cu(Ag)/S complexes containing bridging diphosphine ligands, varying from tetranuclear cluster **1** to one-dimentional polymeric clusters **2** and **3**, have been prepared. To the best of our knowledge, **2** and **3** are the first two examples of polymers containing bridging diphosphine ligands for the W/Cu(Ag)/S system. The optical absorption spectra show that compounds **1**–**3** may be classed as semiconductors. With excitation of laser at 397 nm, complexes **1**–**3** are luminescent at room temperature in the solid state.

Acknowledgments

This research was supported by grants from the State Key Laboratory of Structural Chemistry, Fujian Institute of Research on the Structure of Matter, Chinese Academy of Sciences (CAS), the Ministry of Science and Technology of China (2001CB108906) and the National Science Foundation of China (20333070 and 20673117).

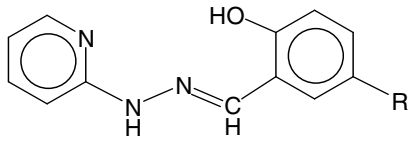
Appendix A. Supplementary material

CCDC 618364, 618365 and 618366 contain the supplementary crystallographic data for **1**, **2** and **3**. These data can be obtained free of charge via http://www.ccdc.cam.ac.uk/conts/retrieving.html, or from the Cambridge Crystallographic Data Centre, 12 Union Road, Cambridge CB2 1EZ, UK; fax: (+44) 1223-336-033; or e-mail: deposit@ccdc.cam.ac.uk. Supplementary data associated with this article can be found, in the online version, at doi:10.1016/j.poly.2006.10.013.

References

[1] S. Leininger, B. Olenyuk, Peter J. Stang, Chem. Rev. 100 (2000) 853.
[2] G.F. Swiegers, T.J. Malefetse, Chem. Rev. 100 (2000) 3483.
[3] B. Moulton, M.J. Zaworotko, Chem. Rev. 101 (2001) 1629.
[4] R.H. Holm, Chem. Soc. Rev. 10 (1981) 455.
[5] L.J. Laughlin, D. Coucouvanis, J. Am. Chem. Soc. 117 (1995) 3118.
[6] S.H. Laurie, Eur. J. Inorg. Chem. (2000) 2443.
[7] S. Shi, W. Ji, S.H. Tang, J.P. Lang, X.Q. Xin, J. Am. Chem. Soc. 116 (1994) 3615.
[8] Q. Huang, X.T. Wu, T.L. Sheng, Q.M. Wang, Inorg. Chem. 34 (1995) 4931.
[9] Q. Huang, X.T. Wu, Q.M. Wang, T.L. Sheng, J.X. Lu, Angew. Chem., Int. Ed. Engl. 35 (1996) 868.
[10] Q. Huang, X.T. Wu, J.X. Lu, Inorg. Chem. 35 (1996) 7445.
[11] Q. Huang, X.T. Wu, J.X. Lu, Chem. Commun. (1997) 703.
[12] H. Yu, W.J. Zhang, X.T. Wu, T.L. Sheng, Q.M. Wang, P. Lin, Angew. Chem., Int. Ed. Engl. 37 (1998) 2520.
[13] L. Chen, X.T. Wu, X.C. Gao, W.J. Zhang, P. Lin, J. Chem. Soc., Dalton Trans. (1999) 4303.
[14] C. Zhang, Y.L. Song, Y. Xu, H.K. Fun, G.Y. Fang, Y.X. Wang, X.Q. Xin, J. Chem. Soc., Dalton Trans. (2000) 2823.
[15] J.P. Lang, C.M. Jiao, S.B. Qiao, W.H. Zhang, B.F. Abrahams, Inorg. Chem. 44 (2005) 3664.
[16] J.M. Manoli, C. Potvin, F. Secheresse, S. Marzak, J. Chem. Soc., Chem. Commun. (1986) 1557.
[17] C. Potvin, J.M. Manoli, F. Secheresse, S. Marzak, Inorg. Chem. 26 (1987) 4370.
[18] J.P. Lang, Q.F. Xu, R.X. Yuan, B.F. Abrahams, Angew. Chem., Int. Ed. Engl. 43 (2004) 4741.
[19] K. Liang, H.G. Zheng, Y.L. Song, M.F. Lappert, Y.Z. Li, X.Q. Xin, Z.X. Huang, J.T. Chen, S.F. Lu, Angew. Chem., Int. Ed. Engl. 43 (2004) 5776.
[20] Z.H. Li, S.W. Du, X.T. Wu, Inorg. Chem. 43 (2004) 4776.
[21] Z.H. Li, S.W. Du, X.T. Wu, Inorg. Chem. Commun. 9 (2006) 79.
[22] C.K. Chan, C.X. Guo, R.J. Wang, T.C.W. Mak, C.M. Che, J. Chem. Soc., Dalton Trans. (1995) 753.
[23] J.P. Lang, K. Tatsumi, Inorg. Chem. 37 (1998) 6308.
[24] C.M. Che, B.H. Xia, J.S. Huang, C.K. Chan, Z.Y. Zhou, K.K. Cheung, Chem. Eur. J. 7 (2001) 3998.
[25] H. Yu, Q.F. Xu, Z.R. Sun, S.J. Ji, J.X. Chen, Q. Liu, J.P. Lang, K. Tatsumi, Chem. Commun. (2001) 2614.
[26] Y. Cai, Y.L. Song, H.G. Zheng, Y.Y. Niu, C.H. Du, X.X. Quan, Chem. Lett. (2002) 508.
[27] W.J. Zhang, A. Behrens, J. Ga1tjens, M. Ebel, X.T. Wu, D. Rehder, Inorg. Chem. 43 (2004) 3020.
[28] D. Rehder, W.J. Zhang, X.T. Wu, M. Ebel, C. Bader, Inorg. Chim. Acta 358 (2005) 1981.
[29] J.W. McDonald, G.D. Friesen, L.D. Rosenhein, W. Newton, Inorg. Chim. Acta 72 (1983) 205.
[30] S.F. Gheller, T.W. Hambley, J.R. Rodgers, R.T.C. Brownlee, M.J. O'Connor, M.R. Snow, A.G. Wedd, Inorg. Chem. 23 (1984) 2519.
[31] G.M. Sheldrick, Bruker SHELSTL-PC, University of Göttingen, Göttingen, Germany, 1997.
[32] A. Müller, H. Bogge, T.K. Hwang, Inorg. Chim. Acta 39 (1980) 71.
[33] S.W. Du, N.Y. Zhu, P.C. Cheng, X.T. Wu, Angew. Chem., Int. Ed. 31 (1992) 1085.
[34] A. Müller, H. Bogge, E. Koniger-Ahlborn, J. Chem. Soc., Chem. Commun. (1978) 739.
[35] H.W. Hou, X.Q. Xin, S. Shi, Coord. Chem. Rev. 153 (1996) 25.
[36] G. Kotüm, Reflectance Spectroscopy, Springer, New York, 1969.
[37] W.W. Wendlandt, Reflectance Spectroscopy, Interscience, New York, 1966.
[38] G. Cao, L.K. Rabenberg, C.M. Nunn, T.E. Mallouk, Chem. Mater. 3 (1991) 149.

with the general formula [VO_2(phsalR)]. In the following account, we have described the synthesis, characterization and physical properties of these complexes. The molecular structure of a representative complex has been determined by X-ray crystallography.



Hphsal (R = H)
HphsalOMe (R = OCH_3)
HphsalCl (R = Cl)
HphsalBr (R = Br)
HphsalNO_2 (R = NO_2)

2. Experimental

2.1. Materials

The Schiff bases (HphsalR) were prepared in 70–80% yield by condensation reactions of 2-hydrazinopyridine with the corresponding 5-substituted salicylaldehyde in methanolic media [15–17]. All other chemicals and solvents used in this work were of analytical grade available commercially and were used without further purification.

2.2. Physical measurements

Microanalytical (C, H, N) data were obtained with a Thermo Finnigon Flash EA1112 series elemental analyzer. Infrared spectra were collected by using KBr pellets on a Jasco-5300 FT-IR spectrophotometer. A Sherwood Scientific balance was used for magnetic susceptibility measurements. A Shimadzu 3101-PC UV/Vis/NIR spectrophotometer was used to record the electronic spectra. The ^1H ($Si(CH_3)_4$ as internal standard) and ^{51}V ($VOCl_3$ as external standard) NMR spectra were recorded with the help of a Bruker 400 MHz NMR spectrometer. A Jeol JES-FA200 spectrometer was used for EPR experiments. Solution electrical conductivities were measured with a Digisun DI-909 conductivity meter.

2.3. Synthesis of [VO_2(phsal)] (1)

An aqueous solution (15 ml) of $VOSO_4 \cdot 5H_2O$ (100 mg, 0.4 mmol) was added to an acetonitrile solution (20 ml) of Hphsal (85 mg, 0.4 mmol) and $N(C_2H_5)_3$ (0.07 ml, 51 mg, 0.5 mmol). The mixture was refluxed for 1 h. The resulting brown solution was kept in air at room temperature for slow evaporation. Dark brown crystalline material separated in about 2 days was collected by filtration, washed with acetonitrile and finally dried in air. Yield: 60 mg (51%).

The other four complexes [VO_2(phsalOMe)] (**2**), [VO_2-(phsalCl)] (**3**), [VO_2(phsalBr)] (**4**) and [VO_2(phsalNO_2)] (**5**) reported in this work were synthesized by using one mole equivalent each of $VOSO_4 \cdot 5H_2O$, $N(C_2H_5)_3$ and the corresponding Schiff base in 50–60% yields by following the same procedure as described above.

2.4. X-ray crystallography

Single crystal of [VO_2(phsal)] (**1**) was collected directly from the product precipitated in the synthetic reaction mixture. The unit cell parameters and the intensity data were obtained on a Bruker-Nonius SMART APEX CCD single crystal diffractometer, equipped with a graphite monochromator and a Mo Kα fine-focus sealed tube ($\lambda = 0.71073$ Å) operated at 2.0 kW. The detector was placed at a distance of 6.0 cm from the crystal. Data were collected at 298 K with a scan width of 0.3° in ω and an exposure time of 5 s/frame. The SMART software was used for data acquisition and the SAINT-Plus software was used for data extraction [18]. The SADABS program [19] was used for the absorption correction. The complex crystallizes in the space group $P\bar{1}$. The structure was solved by direct method and refined on F^2 by full-matrix least-squares procedures. All non-hydrogen atoms were refined anisotropically. The hydrogen atom of the NH group in the hydrazine fragment of the ligand was located on a difference map and refined with $U_{iso}(H) = 1.2U_{eq}(N)$. The other hydrogen atoms were added at idealized positions by using a riding model. The SHELX-97 programs [20] were used for structure solution and refinement. The ORTEX6a [21] and PLATON [22] packages were used for molecular graphics. Selected crystallographic data for **1** are listed in Table 1.

Table 1
Crystallographic data for [VO_2(phsal)] (**1**)

Chemical formula	$VC_{12}H_{10}N_3O_3$
Formula weight	295.17
Crystal system	triclinic
Space group	$P\bar{1}$
a (Å)	6.9432(13)
b (Å)	7.8457(15)
c (Å)	11.359(2)
α (°)	91.024(3)
β (°)	99.877(3)
γ (°)	101.149(3)
V (Å^3)	597.3(2)
Z	2
ρ (g cm^{-3})	1.641
μ (mm^{-1})	0.837
Reflections collected	6960
Reflections unique	2768
Reflections [$I \geqslant 2\sigma(I)$]	2260
Parameters	175
R_1, wR_2 [$I \geqslant 2\sigma(I)$]	0.0459, 0.1054
R_1, wR_2 (all data)	0.0598, 0.1113
Goodness-of-fit on F^2	1.080
Largest difference in peak and hole (e Å^{-3})	0.506 and −0.256

Table 2
Elemental analysis[a] and electronic spectroscopic[b] data

Complex	C (%)	H (%)	N (%)	λ_{max} (nm) ($10^{-4} \times \varepsilon$ (M^{-1} cm^{-1}))
$[VO_2(phsal)]$ (**1**)	48.72 (48.83)	3.35 (3.41)	14.18 (14.24)	505 (1.18), 480[c] (1.11), 418[c] (0.89), 380[c] (1.55), 360 (1.75), 280[c] (2.58)
$[VO_2(phsalOMe)]$ (**2**)	47.83 (48.01)	3.62 (3.72)	12.79 (12.92)	510 (1.09), 485[c] (0.99), 385[c] (1.16), 370 (1.31), 272 (2.13)
$[VO_2(phsalCl)]$ (**3**)	43.65 (43.73)	2.71 (2.75)	12.66 (12.75)	510 (0.96), 480[c] (0.82), 385[c] (0.84), 365 (0.93), 270 (1.58)
$[VO_2(phsalBr)]$ (**4**)	38.41 (38.53)	2.45 (2.42)	11.15 (11.23)	507 (1.60), 485[c] (1.38), 385[c] (1.50), 368 (1.66), 275 (2.59)
$[VO_2(phsalNO_2)]$ (**5**)	42.14 (42.37)	2.38 (2.67)	16.33 (16.47)	512 (1.13), 488[c] (1.03), 375[c] (1.62), 350 (1.93), 275[c] (1.44)

[a] Calculated values are in parentheses.
[b] In dimethylformamide.
[c] Shoulder.

3. Results and discussion

3.1. Synthesis and some properties

The complexes were synthesized in moderate yields by reacting equimolar amounts of $VOSO_4 \cdot 5H_2O$, HphsalR and $N(C_2H_5)_3$ in water–acetonitrile mixture under aerobic conditions. The elemental analysis data are consistent with the general molecular formula $[VO_2(phsalR)]$ (Table 2). The complexes are insoluble in common organic solvents except dimethylsulphoxide and dimethylformamide. In solutions, they are electrically non-conducting. The EPR silence and the room temperature magnetic susceptibilities indicate the diamagnetic character of these complexes. Thus the metal ion in each of the five complexes is in +5 oxidation state. Most likely during the formation of these complexes from oxovanadium(IV) starting material, the aerial oxygen acts as the oxidizing agent.

It is interesting to note that our previously reported ternary oxovanadium(IV) complexes, [VO(phsalR)(acac)], were also synthesized under aerobic conditions from equimolar amounts of $[VO(acac)_2]$ and HphsalR in acetonitrile [15]. Thus the synthetic procedures for $[VO_2(phsalR)]$ and [VO(phsalR)(acac)] differ in (i) the oxovanadium(IV) starting material, (ii) use of base $N(C_2H_5)_3$, and (iii) the reaction medium. Perhaps the chelated acetylacetonate instead of the non-coordinating or weakly coordinating sulphate in the oxovanadium(IV) starting material used for the synthesis of [VO(phsalR)(acac)] stabilizes the +4 oxidation state of the metal centre by forming the mixed-ligand species.

3.2. Spectroscopic characteristics

The infrared spectra of **1**–**5** display a broad band centred at ~3400 cm^{-1}. This band is possibly due to the N–H stretch of the hydrazine fragment of the ligand [23]. The strong band observed in the range 1632–1636 cm^{-1} is most likely associated with the C=N stretch of the tridentate Schiff base ligand [10–15,24]. The complexes of dioxovanadium(V) with tridentate ligands display two strong to medium bands in the ranges 930–970 and 900–940 cm^{-1} [12–14,25–28]. The higher energy band is assigned to the ν_{as} stretch and the lower energy band is assigned to the ν_s stretch of the *cis*-VO_2^+ moiety. The coordination geometry of the metal ion in these complexes varies between trigonal-bipryamidal and distorted octahedral. The latter is due to either coordination of an additional monodentate ligand or formation of weakly associated di(μ-oxo) bridged dimeric species from two square-pyramidal molecules. The present series of complexes **1**–**5** also displays a strong and sharp band at ~942 cm^{-1}. This band is attributed to the ν_{as} stretch of the *cis*-VO_2^+ moiety. All the spectra show a very strong band at ~890 cm^{-1} with a shoulder at ~910 cm^{-1}. Perhaps the ν_s stretch of the *cis*-VO_2^+ unit is the origin of this shoulder.

Electronic spectra were recorded using dimethylformamide solutions of **1**–**5**. The spectral profiles of all the complexes are very similar. A representative spectrum is shown in Fig. 1. The complexes display several absorptions in the wavelength range 512–270 nm (Table 2). The absorptions in the range 512–350 nm are possibly due to the ligand-to-metal charge transfer transitions [10–14,25–28]. The highest energy absorption observed in the range 280–270 nm is most likely due to a ligand centred transition [15].

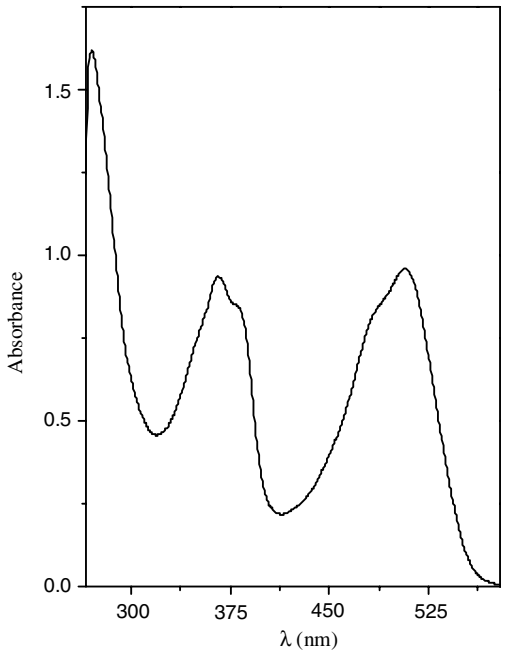


Fig. 1. Electronic spectrum of $[VO_2(phsalCl)]$ (**3**) in dimethylformamide solution.

The dimethylsulphoxide-d_6 solutions of **1**–**5** were used to record the proton NMR spectra. The aromatic protons appear as multiplets in the range δ 8.5–6.8 ppm. The protons of the methyl group of the methoxy substituent in $[VO_2(phsalOMe)]$ (**2**) resonate as a singlet at δ 3.74 ppm. The –NH– proton of the hydrazine fragment in all the complexes appears as a broad singlet within δ 12.65–12.87 ppm. The azomethine (–CH=N–) proton is observed as a singlet in the range δ 8.55–8.59 ppm. We have also recorded the ^{51}V NMR spectra of **1**–**5** in dimethylsulphoxide-d_6. All the complexes show a resonance between δ −549 and −555 ppm. These chemical shifts are comparable with those reported for similar dioxovanadium(V) complexes [25,27–29].

3.3. Structure of $[VO_2(phsal)]$ (*1*)

Dioxovanadium(V) complexes with planar tridentate ligands can have either trigonal-bipyramidal or square-pyramidal geometry [12–14,25–27,29–31]. In the solid state, trigonal-bipyramidal complexes remain mononuclear while square-pyramidal complexes can dimerise and form di(μ-oxo) bridged dinuclear species. Examples of such di(μ-oxo) bridged species are rare [12,25,29–31]. Complex **1** belongs to this category of dioxovanadium(V) complexes. The structure of **1** is depicted in Fig. 2. The bond parameters associated with the metal ion are listed in Table 3. The metal ion is in a square-pyramidal N_2O_3 coordination sphere. One of the two oxo groups and the pyridine-N, the imine-N and the phenolate-O donor $phsal^-$ form the N_2O_2 basal plane (mean deviation 0.07 Å). The second oxo group satisfies the apical coordination site. As commonly observed for square-pyramidal complexes [10–12,25,29–33], the metal centre in **1** is displaced by 0.367(1) Å from the N_2O_2 basal plane toward the apical oxo group. The distortion of a square-pyramidal geometry toward a trigonal-bipyramidal geometry can be indicated by the value of τ which is defined as $(\beta - \alpha)/60$, where α is the smaller and β is the larger *trans* bond angles in the basal plane [33]. For a perfect square-pyramidal geometry the value of τ is zero and for an ideal trigonal-bipyramidal geometry the value of τ is unity. In the case of **1**, the τ is found to be 0.02. Thus the N_2O_3 coordination sphere in **1** is very close to an ideal square-pyramidal shape. As expected the V–O(phenolate) (1.8797(18) Å) and V–N (pyridine) (2.112(2) Å) bond lengths in **1** (Table 3) are shorter than these bond lengths (1.935(2) and 2.121(4) Å) observed in the previously reported ternary oxovanadium(IV) complex with $phsal^-$ [15]. However, the V–N(imine) bond length (2.1706(19) Å) in **1** is longer than that (2.066(2) Å) in [VO(phsal)(acac)] [15]. This difference is possibly due to the greater *trans* effect of the oxo group in **1** compared to that of the acetylacetonate-O in [VO(phsal)(acac)]. In general, the V–O(phenolate), the V–N(pyridine) and the V–N(imine) bond lengths in **1** are comparable with the bond lengths observed in VO^{3+} and VO_2^+ complexes containing the same coordinating atoms [10–14,25–31]. In **1**, the V=O bond length (1.6736(17) Å) in the basal plane is significantly longer than the apical V=O bond length (1.600(2) Å). This is due to the formation of a centrosymmetric dimeric species via sharing of the basal plane oxo groups by the metal centres of two molecules of **1** (Fig. 3). In $[VO_2(phsal)]_2$, the $\{V_2(\mu\text{-}O)_2\}$ unit is planar and unsymmetrical with respect to the V–O distances (V–O(2), 1.6736(17) Å and V–O(2a), 2.5193(19) Å). Such unsymmetrical $\{V_2(\mu\text{-}O)_2\}$ unit is common in dinuclear species formed by similar square-pyramidal dioxovanadium(V) complexes with tridentate ligands [12,25,29–31]. The V–O(2)–V(a) and the O(2)–V–O(2a) angles are 103.08(8)° and 76.92(8)°, respectively. The metal···metal

Table 3
Selected bond lengths (Å) and angles (°) for $[VO_2(phsal)]_2$

Bond lengths (Å)			
V–O(1)	1.8797(18)	V–N(1)	2.1706(19)
V–O(2)	1.6736(17)	V–N(3)	2.112(2)
V–O(3)	1.600(2)	V–O(2a)	2.5193(19)
Bond angles (°)			
O(1)–V–O(2)	102.27(8)	O(1)–V–O(3)	101.51(10)
O(1)–V–N(1)	83.06(8)	O(1)–V–N(3)	152.99(8)
O(1)–V–O(2a)	83.32(8)	O(2)–V–O(3)	107.55(9)
O(2)–V–N(1)	151.53(9)	O(2)–V–N(3)	93.05(8)
O(2)–V–O(2a)	76.92(8)	O(3)–V–N(1)	98.53(9)
O(3)–V–N(3)	94.74(9)	O(3)–V–O(2a)	172.31(8)
N(1)–V–N(3)	73.22(8)	N(1)–V–O(2a)	75.97(6)
N(3)–V–O(2a)	78.62(7)	V–O2–V(a)	103.08(8)

Symmetry transformation used to generate the equivalent atoms: $-x$, $-y$, $-z+1$.

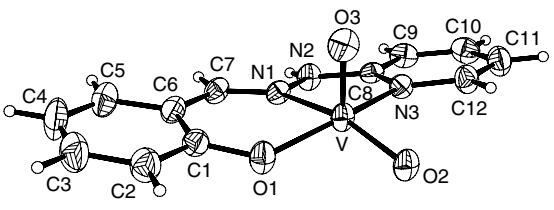


Fig. 2. Structure of $[VO_2(phsal)]$ (**1**) with the atom labeling scheme. All non-hydrogen atoms are represented by their 40% probability thermal ellipsoids.

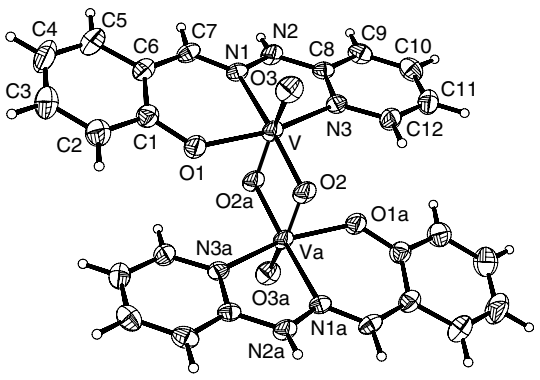


Fig. 3. Centrosymmetric dimer of $[VO_2(phsal)]$ (**1**). All non-hydrogen atoms are represented by their 40% probability thermal ellipsoids.

distance is 3.325(1) Å. The long V–O(2a) distance suggests weak coordination at the *trans* position to the apical oxo group. Thus the metal centres are in distorted octahedral N_2O_4 coordination spheres in $[VO_2(phsal)]_2$ and the dimeric species resembles two edge-shared octahedra.

3.4. Intermolecular hydrogen bonding and self-assembly

The complexes **1**–**5** described in this work possess an acceptor as well as a donor group for conventional hydrogen bonding interaction. These are the metal coordinated oxo group and the N–H group of the hydrazine fragment of phsal$^-$. The vanadium(IV/V) bound oxo group is fairly strong basic centre and is known to participate in intermolecular conventional as well as non-conventional hydrogen bonding interactions [14,15,34]. It has been observed before that the acidity of the N–H proton increases significantly in aryl- or aroylhydrazine based Schiff bases when the adjacent imine-N is coordinated to a metal ion [35,36]. It may be noted that for the ternary oxovanadium(IV) complex of phsal$^-$, [VO(phsal)(acac)], the strong intermolecular N–H···O=V hydrogen bonding interaction plays the decisive role in providing the infinite one-dimensional supramolecular structure [15]. The same self-assembly pattern via intermolecular N–H···O=V hydrogen bonding interaction is also observed in the crystal lattice of **1** (Fig. 4). The dimeric species $[VO_2(phsal)]_2$ forms a one-dimensional chain structure due to the involvement of the N–H group of phsal$^-$ and the metal bound oxo group at the basal plane of the square-pyramidal monomeric unit in intermolecular N–H···O=V hydrogen bonding interaction. The N(2)–H, H···O(2) and N(2)···O(2) distances and the N(2)–H···O(2) angle are 0.82(3), 1.94(3) and 2.745(3) Å and 168(3)°, respectively. There is no other significant non-covalent interaction between the parallel one-dimensional structures.

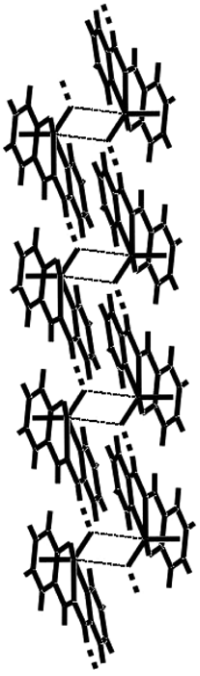


Fig. 4. One-dimensional ordering of the dimers of $[VO_2(phsal)]$ (**1**) via intermolecular N–H···O=V hydrogen bonds in the crystal lattice.

4. Conclusion

A new series of dioxovanadium(V) complexes of general formula $[VO_2(phsalR)]$ (HphsalR = 4-R-2-(pyridin-2-yl-hydrazonomethyl)-phenols) has been synthesized. The complexes have been characterized with the help of microanalytical, magnetic susceptibility, various spectroscopic and X-ray crystallographic measurements. All the complexes are diamagnetic and NMR active. The electronic spectra of the complexes display several bands due to ligand-to-metal charge transfer and ligand centred transitions. The crystal structure of $[VO_2(phsal)]$ (R = H) reveals that the metal centre is in an essentially perfect square-pyramidal N_2O_3 coordination sphere assembled by the pyridine-N, the imine-N and the phenolate-O donor planar phsal$^-$ and two oxo groups. Dimerisation of $[VO_2(phsal)]$ leads to the formation of a di(μ-oxo)-bridged species in which the metal centres are in two edge-shared distorted octahedral N_2O_4 coordination spheres. In the crystal lattice, these dimers form an intermolecular N–H···O=V hydrogen bond assisted one-dimensional supramolecular assembly.

5. Supplementary material

CCDC 618872 contains the supplementary crystallographic data for $[VO_2(phsal)]$ (**1**). These data can be obtained free of charge via http://www.ccdc.cam.ac.uk/conts/retrieving.html, or from the Cambridge Crystallographic Data Centre, 12 Union Road, Cambridge CB2 1EZ, UK; fax: (+44) 1223-336-033; or e-mail: deposit@ccdc.cam.ac.uk.

Acknowledgements

Financial assistance received from the Council of Scientific and Industrial Research (CSIR) (Grant No. 01(1880)/03/EMR-II) is gratefully acknowledged. Ms. A. Sarkar thanks the CSIR for a research fellowship. X-ray structure determination was performed at the National Single Crystal Diffractometer Facility, School of Chemistry, University of Hyderabad (established by the Department of Science and Technology). We thank the University Grants Commission for the facilities provided under the UPE and CAS programs.

References

[1] N.D. Chasteen (Ed.), Vanadium in Biological Systems, Kluwer, Dordrecht, 1990.
[2] A. Butler, C.J. Carrano, Coord. Chem. Rev. 109 (1991) 148.
[3] D.C. Crans, C.M. Simone, J.S. Blanchard, J. Am. Chem. Soc. 114 (1992) 4926.

[4] H. Sigel, A. Sigel (Eds.), Metal Ions in Biological Systems: Vanadium and its Role in Life, Marcel Dekker, New York, 1995.
[5] D. Rehder, Coord. Chem. Rev. 182 (1999) 297.
[6] S. Macedo-Ribeiro, W. Hemrika, R. Renirie, R. Wever, A. Messerschmidt, J. Biol. Inorg. Chem. 4 (1999) 209.
[7] A. Butler, M.J. Clague, G.E. Meister, Chem. Rev. 94 (1994) 625.
[8] C. Slebodnick, B.J. Hamestra, V.L. Pecoraro, Struct. Bond. (Berlin) 89 (1997) 51.
[9] M.R. Maurya, Coord. Chem. Rev. 237 (2003) 163.
[10] N.R. Sangeetha, V. Kavita, S. Wocadlo, A.K. Powell, S. Pal, J. Coord. Chem. 51 (2000) 55.
[11] N.R. Sangeetha, S. Pal, Bull. Chem. Soc. Jpn. 73 (2000) 357.
[12] S.N. Pal, S. Pal, J. Chem. Crystallogr. 30 (2000) 329.
[13] S.N. Pal, S. Pal, Acta Crystallogr., Sect. C 57 (2001) 141.
[14] S.N. Pal, K.R. Rahika, S. Pal, Z. Anorg. Allg. Chem. 627 (2001) 1631.
[15] A. Sarkar, S. Pal, Polyhedron 25 (2006) 1689.
[16] M.F. Zady, J.L. Wong, J. Org. Chem. 41 (1976) 2491.
[17] C.C. Blanco, F.G. Sánchez, Anal. Chem. 56 (1984) 2035.
[18] SMART version 5.630 and SAINT-plus version 6.45, Bruker-Nonius Analytical X-ray Systems Inc., Madison, WI, USA, 2003.
[19] G.M. Sheldrick, SADABS: Empirical Absorption Correction Program, University of Göttingen, Göttingen, Germany, 1997.
[20] G.M. Sheldrick, SHELX-97: Structure Determination Software, University of Göttingen, Göttingen, Germany, 1997.
[21] P. McArdle, J. Appl. Crystallogr. 28 (1995) 65.
[22] A.L. Spek, PLATON: A Multipurpose Crystallographic Tool, Utrecht University, Utrecht, The Netherlands, 2002.
[23] W. Kemp, Organic Spectroscopy, Macmillan, Hampshire, 1987, p. 66.
[24] S.G. Sreerama, S. Pal, Inorg. Chem. 44 (2005) 6299.
[25] X. Li, M.S. Lah, V.L. Pecoraro, Inorg. Chem. 27 (1988) 4657.
[26] X.-M. Zhang, X.-Z. You, X. Wang, Polyhedron 15 (1996) 1793.
[27] A.G.J. Ligtenbarg, A.L. Spek, R. Hage, B.L. Feringa, J. Chem. Soc., Dalton Trans. (1999) 659.
[28] M.R. Maurya, S. Khurana, C. Schulzke, D. Rehder, Eur. J. Inorg. Chem. (2001) 779.
[29] C.A. Root, J.D. Hoeschele, C.R. Cornman, J.W. Kampf, V.L. Pecoraro, Inorg. Chem. 32 (1993) 3855.
[30] L.M. Mokry, C.J. Carrano, Inorg. Chem. 32 (1993) 6119.
[31] C.A. Duncan, E.P. Copeland, I.A. Kahwa, A. Quick, D.J. Williams, J. Chem. Soc., Dalton Trans. (1997) 917.
[32] B.F. Hoskins, F.D. Whillans, Coord. Chem. Rev. 9 (1972) 365.
[33] A.W. Addison, T.N. Rao, J. Reedijk, J. van Rijn, G.C. Verschoor, J. Chem. Soc., Dalton Trans. (1984) 1349.
[34] S.P. Anthony, L. Srikanth, T.P. Radhakrishnan, Mol. Cryst. Liq. Cryst. 381 (2002) 133.
[35] B. Mondal, S. Chakraborty, P. Munshi, M.G. Walawalkar, G.K. Lahiri, J. Chem. Soc., Dalton Trans. (2000) 2327.
[36] S.N. Pal, S. Pal, J. Chem. Soc., Dalton Trans. (2002) 2102.

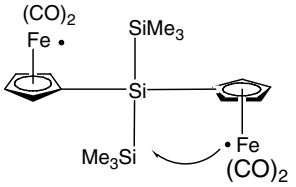


Fig. 1. Iron-centered free radicals from Fe–Fe bond homolysis of **1**.

bonds attached to the Cp rings [16,17], which furnished strong evidence to rule out the stepwise pathway of the free radical mechanism [24]. To further examine the regiospecific feature, a study on systems containing non-bridging Si–Si bonds attached to other positions, such as at the bridge, is desirable. In this aspect, we have in a recent study [25] occasionally isolated the silicon-bridged complex $[\eta^5,\eta^5\text{-}C_5H_4\text{–}Si(Me)(SiMePh_2)\text{–}C_5H_4]Fe_2(CO)_2(\mu\text{-}CO)_2$ that contains a non-bridging exocyclic Si–Si bond at the silicon bridge. Unfortunately, the complex has been obtained as a by-product in a too small amount to study its chemistry.

In this paper, we report the first designed synthesis of such complexes by choosing the 1,1,1,3,3,3-hexamethyltrisilanylene-bridged complex $[\eta^5,\eta^5\text{-}C_5H_4\text{–}Si(SiMe_3)_2\text{–}C_5H_4]Fe_2(CO)_2(\mu\text{-}CO)_2$ (**1**) and its CO ligand substitution derivatives $[\eta^5,\eta^5\text{-}C_5H_4\text{–}Si(SiMe_3)_2\text{–}C_5H_4]Fe_2(CO)L(\mu\text{-}CO)_2$ [L = $P(OPh)_3$ (**2**), $P(OMe)_3$ (**3**), PPh_3 (**4**), PMe_3 (**5**)] that contain two exocyclic Si–Si bonds at the silicon bridge as the target molecules. Examination of the chemical properties of these complexes under various conditions demonstrated that these Si–Si bonds could not be cleaved by the intramolecular iron centers, providing further evidence to rule out the possibility of activation of Si–Si bonds by the iron-centered free radicals from homolysis of the Fe–Fe bond (Fig. 1). On the contrary, the inertness of the Si–Si bonds towards the metal centers could be rationally explained in terms of the oxidative addition mechanism of activation of Si–Si bonds [26,27].

2. Experimental

2.1. General

All the reactions were carried out under a nitrogen or argon atmosphere by using vacuum line and Schlenk techniques. THF, *p*-xylene and hexane were dried and distilled from sodium/benzophenone. IR spectra were recorded with a Bio-Rad FTS 135 spectrometer. ^1H and ^{13}C NMR spectra were recorded with a Varian UNITY Plus-400 or a Bruker AC-P200 spectrometer. Elemental analysis was performed using an Elementar Vario EL instrument. $(Me_3Si)_2SiCl_2$ was prepared according to the literature procedures [28].

2.2. Synthesis of complex *1*

To a flask containing 1.9 g (29 mmol) of cyclopentadiene and 50 ml of THF was added 14 ml (1.77 M in hexane, 25 mmol) of *n*-butyllithium at −78 °C. The mixture was stirred at room temperature for 1 h, then, 3.0 g (12 mmol) of $Me_3SiSiCl_2SiMe_3$ was added dropwise at −78 °C. The mixture was allowed to warm to room temperature, stirred at this temperature overnight and then refluxed for 2 h. After cooling to room temperature, the mixture was hydrolyzed with a saturated solution of NH_4Cl, extracted with ether, washed with water and dried over anhydrous magnesium sulfate. Evaporation of the solvent under reduced pressure gave $Me_3SiSi(C_5H_5)_2SiMe_3$ as an oil, which was used directly, without further purification, for the next step of reaction.

To a flask containing the oil product obtained above and 50 ml of *p*-xylene was added 4.9 g of $Fe(CO)_5$ (25 mmol). The mixture was refluxed with stirring overnight. The solvent was removed under reduced pressure (unreacted $Fe(CO)_5$ should be collected in a liquid nitrogen trap) to give a solid residue, which was separated through a neutral alumina column. Elution with petroleum ether/dichloromethane (4:1) gave a red band, from which 1.2 g of **1** (28% yield) was obtained as a dark-red crystalline solid, m.p. 220 °C (dec). *Anal.* Calc. for $C_{20}H_{26}O_4Fe_2Si_3$: C, 45.63; H, 4.94. Found: C, 45.64; H, 5.00%. ^1H NMR ($CDCl_3$): δ 0.26 (s, 9H, SiMe), 4.99 (t, $J = 2.1$ Hz, 2H, Cp), 5.46 (t, $J = 2.1$ Hz, 2H, Cp). ^{13}C NMR ($CDCl_3$): δ 0.64 (SiMe), 86.45, 86.83, 101.38 (Cp), 209.83 (terminal CO), 272.65 (bridging CO). IR (KBr, cm^{-1}): ν_{co} 1993 (s), 1949 (s), 1774 (s).

2.3. Synthesis of complexes *2*–*5*

2.3.1. Thermal reactions of *1* with $P(OPh)_3$ and $P(OMe)_3$

To a flask charged with 100 mg (0.19 mmol) of **1** and 10 ml of *p*-xylene was added 92 mg (0.74 mmol) of $P(OPh)_3$. The mixture was refluxed for 16 h with magnetic stirring. The solvent was removed under reduced pressure. The residue was separated through a neutral alumina column. Elution with petroleum ether/dichloromethane (4:1) developed a green band, from which 46 mg (36% yield) of **2** was afforded as black crystals. In a similar fashion, **3** was prepared (32% yield) from **1** and $P(OMe)_3$ after refluxing for 24 h.

For **2**: m.p. 210 °C (dec). *Anal.* Calc. for $C_{37}H_{41}O_6Fe_2PSi_3$: C, 54.95; H, 5.07. Found: C, 54.88; H, 5.08%. ^1H NMR ($CDCl_3$): δ 0.23 (s, 18H, SiMe), 4.29, 4.49, 4.97, 5.41 (br s, 2H:2H:2H:2H, Cp), 7.16–7.33 (m, 15H, Ph). ^{13}C NMR ($CDCl_3$): δ 0.69 (SiMe); 83.56, 85.68, 86.34, 88.32, 98.09, 99.82 (Cp); 121.75 (d, $J = 3.6$ Hz, Ph), 124.70 (Ph), 129.59 (Ph), 151.51 (d, $J = 9.9$ Hz, Ph), 213.96 (terminal CO), 278.62 (d, $J = 21.5$ Hz, bridging CO). IR (KBr, cm^{-1}): ν_{co} 1993 (s), 1964 (s), 1777 (s), 1746 (s).

For **3**: m.p. 208 °C (dec). *Anal.* Calc. for $C_{22}H_{35}O_6Fe_2Si_3P$: C, 42.44; H, 5.63. Found: C, 42.48; H, 5.61%. ^1H NMR ($CDCl_3$): δ 0.26 (s, 18H, $SiMe_3$), 3.55 (d, $J = 11.1$ Hz, 9H, OCH_3), 4.81, 4.90, 4.91, 5.32 (br s, 2H:2H:2H:2H, Cp). ^{13}C NMR ($CDCl_3$): δ 0.75 (SiMe),

52.06 (d, $J = 4.93$ Hz, OCH_3), 82.63, 85.40, 85.76, 87.13, 99.11, 100.28 (Cp), 214.51 (terminal CO), 281.90 (d, $J = 24.65$ Hz, bridging CO). IR (KBr, cm^{-1}): ν_{co} 1995 (s), 1963 (s), 1774 (s), 1730 (s).

*2.3.2. Photochemical reactions of **1** with PPh_3 and PMe_3*

A solution containing 100 mg (0.19 mmol) of **1**, 199 mg (0.76 mmol) of PPh_3 and 20 ml benzene in a Pyrex tube was irradiated with a high-pressure mercury lamp (500 W) for 10 h at room temperature. The solvent was removed under reduced pressure and the residue was separated through a column (neutral alumina, petroleum ether/ether, 10:1). Collection of the dark green band gave black crystals of **4** (90 mg, 62% yield). In a similar fashion, **5** was obtained by using PMe_3 in place of PPh_3 as grey crystals in 53% yield.

For **4**: m.p. 220 °C (dec). *Anal.* Calc. for $C_{37}H_{41}Fe_2O_3PSi_3$: C, 58.42; H, 5.43. Found: C, 58.41; H, 5.40%. ^1H NMR ($CDCl_3$): δ 0.27 (s, 18H, SiMe), 4.19, 4.90, 4.91, 5.12 (br s, 2H:2H:2H:2H, Cp), 7.24–7.53 (m, 15H, Ph). ^{13}C NMR ($CDCl_3$): δ 0.77 (SiMe); 82.00, 86.36, 88.84, 90.00, 97.72, 98.61 (Cp); 128.65 (d, $J = 9.9$ Hz, Ph), 129.77 (Ph), 134.21 (d, $J = 9.2$ Hz, Ph), 135.84 (d, $J = 41.7$ Hz, Ph), 212.88 (terminal CO), 284.11 (d, $J = 14.8$ Hz, bridging CO). IR: (KBr, cm^{-1}): ν_{co} 1955 (s), 1766 (s), 1730 (s).

For **5**: m.p. 230 °C (dec) *Anal.* Calc. for $C_{22}H_{35}Fe_2O_3PSi_3$: C, 46.0; H, 6.14. Found: C, 45.87; H, 5.90%. ^1H NMR ($CDCl_3$): δ 0.26 (s, 18H, SiMe), 1.00 (d, $J = 9.0$ Hz, 9H, CH_3), 4.77, 4.88, 4.94, 5.29 (br s, 2H:2H:2H:2H, Cp). ^{13}C NMR ($CDCl_3$): δ 0.76 (SiMe), 18.78 (d, $J = 28.2$ Hz, CH_3); 80.89, 85.60, 85.81, 88.57, 99.24 (Cp); 217.20 (terminal CO), 283.80 (d, $J = 16.0$ Hz, bridging CO). IR (KBr, cm^{-1}): ν_{co} 1933 (s), 1767 (s), 1729 (s).

Table 1
Crystallographic data of **1** and **2**

	1	**2**
Formula	$C_{20}H_{26}Fe_2O_4Si_3$	$C_{37}H_{41}Fe_2O_6PSi_3$
Formula weight	526.38	808.64
Temperature (K)	293(2)	293(2)
Crystal size (mm)	$0.20 \times 0.16 \times 0.10$	$0.24 \times 0.22 \times 0.18$
Crystal system	orthorhombic	monoclinic
Space group	*Pnma*	*P*2(1)/*n*
a (Å)	21.295(8)	13.167(4)
b (Å)	12.203(4)	17.500(5)
c (Å)	9.363(3)	17.057(5)
α (°)	90	90
β (°)	90	99.681(5)
γ (°)	90	90
V (Å^3)	2433.2(15)	3874.5(18)
Z	4	4
D_{cal} (g cm^{-3})	1.437	1.386
Instrument	Bruker Smart 1000	Bruker Smart 1000
Wavelength (Å)	0.71073	0.71073
F(000)	1088	1680
θ Range (°)	1.91–26.37	1.81–25.00
N_{total}	13304	19358
$N_{independent}$	2612	6714
$N_{observed}$	1693	3131
Parameters	157	442
Restrains	8	0
Goodness-of-fit	1.036	0.926
R	0.0471	0.0566
R_w	0.0819	0.0819

*2.4. X-ray molecular structure determination of **1** and **2***

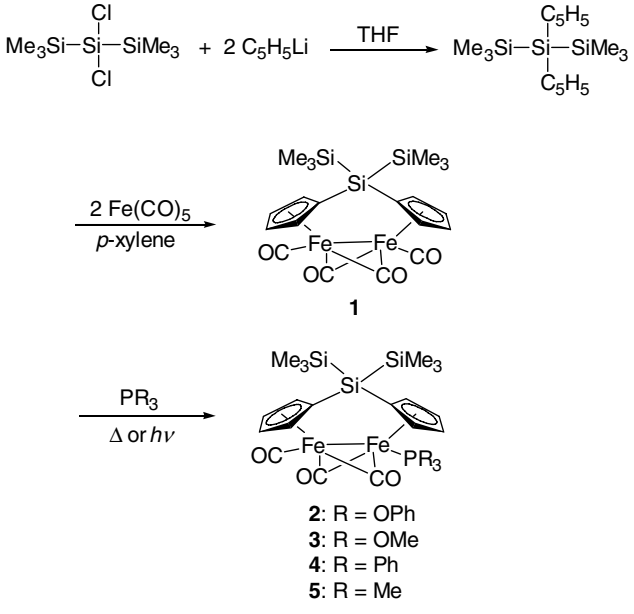
Single crystals of **1** and **2** suitable for X-ray diffraction analyses were obtained from *n*-hexane/dichloromethane solutions. Data collections were performed on a BRUKER SMART 1000 diffractometer at room temperature using $2\theta/\omega$ scan techniques with Mo Kα radiation ($\lambda = 0.71073$ Å). The structures were solved by direct methods using the SHELX-90 program and refined by least square methods on F^2. All non-hydrogen atoms were refined anisotropically. Hydrogen atoms were added theoretically and included in the refinement processes in an isotropic manner. Crystal data and selected experimental information have been listed in Table 1.

3. Results and discussion

3.1. Synthesis of complexes

Synthesis of complex **1** was accomplished through the reaction of $(Me_3Si)_2Si(C_5H_5)_2$, prepared from $(Me_3Si)_2SiCl_2$ and two equivalents of C_5H_5Li in THF, with $Fe(CO)_5$ in refluxing *p*-xylene in a total yield of 28% (Scheme 1).

When **1** was heated in refluxing *p*-xylene in the presence of $P(OPh)_3$ or $P(OMe)_3$, CO-substituted derivatives **2** and **3** were obtained, respectively. The CO substitution reaction with PPh_3, which did not occur under thermal conditions



Scheme 1. Synthesis of the complexes.

due to steric hindrance, could be carried out under photochemical conditions, to provide complex **4**. The same kind of reaction of **1** with PMe_3, which is too volatile to be used at high temperatures, could be effected photochemically at room temperature to afford complex **5** (Scheme 1).

Complexes **1**–**5** were characterized by elemental analyses and spectroscopic methods. The ^1H NMR spectrum of **1** showed a singlet at 0.26 ppm for the SiMe protons and two sets of pseudotriplets at 4.99 and 5.46 ppm for protons of the Cp groups. After substitution of CO by a phosphite or phosphine ligand, the singlet due to the SiMe groups remained little changed, whereas the signals due to the Cp protons split into four sets, demonstrating successful substitution of CO by a phosphorus ligand. Signals due to PR_3 were also observed. The ^{13}C NMR spectrum of **1** exhibited one signal at 0.64 ppm for the SiMe carbons, three signals at 86.45, 86.83 and 101.38 ppm for Cp carbons, and two signals at 209.83 and 272.65 ppm for terminal and bridging CO carbons, respectively. The spectra of the PR_3-substituted derivatives showed generally one signal for SiMe carbons, six signals due to Cp carbons, a singlet and a doublet for terminal and bridging CO, respectively, along with those attributable to the PR_3 ligands. The doublet signal for the bridging CO was due to coupling with the adjacent phosphorus nucleus. IR spectra of these complexes showed absorption bands for both terminal and bridging CO groups, just as expected.

3.2. Stability of the Si–Si bonds

It was found that the Si–Si bonds of **1** were stable under the conditions of refluxing in *p*-xylene. This is in sharp contrast to the case of the $–Me_2SiSiMe_2–$ bridged complexes [11,12], in which the bridging Si–Si bond could be readily broken under the same conditions. Moreover, the Si–Si bonds of **1** were also stable under UV irradiation. The stability of the Si–Si bonds has allowed the CO substitution reactions of **1** to be operated under either thermal or photochemical conditions. The Si–Si bonds in the ligand substituted derivatives **2**–**5** were also found to be stable under both thermal and photochemical conditions. Since it has been well established that the phosphorus ligands can considerably accelerate the Si–Si bond activation in the Si–Si bond-bridged systems [12], the present results could further strengthen the conclusion that these exocyclic Si–Si bonds could not be activated by the intramolecular transition metal centers.

Since iron-centered free radicals could easily be produced under the thermal and photochemical conditions [29,30], the stableness of the Si–Si bonds means that these radicals are not able to activate the Si–Si bonds. Also formed under these conditions could be the coordinatively unsaturated iron species from dissociation of the appropriate ligands [30–32]. Although these species are believed to be responsible for activation of the bridging Si–Si bond as concluded in the previous paper [15], they are apparently not able to cleave the non-bridging exocyclic Si–Si bonds in the present systems. This should be attributed to the fact that these Si–Si bonds are located in a position such that they could not be approached by the intramolecular iron center, due to restriction of the cyclic structure. Such spatial restriction, however, does not exist in the structure of the iron-centered free radical (Fig. 1), because the cyclic structure has been opened after breaking the Fe–Fe bond.

3.3. Molecular structures

The molecular structures of **1** and **2** have been determined by X-ray diffraction methods. The molecule of **1** (Fig. 2) contains a disordered Me_3Si group that has two rotational positions (each at 50% occupancy). The overall molecule has C_s symmetry. The symmetrical plane goes through three silicon atoms and the center of the Fe–Fe

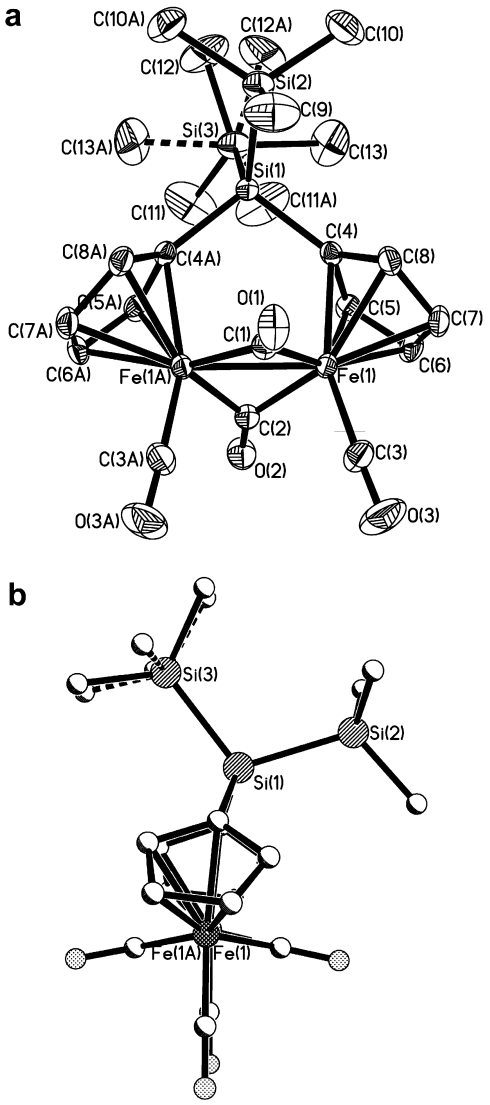


Fig. 2. (a) ORTEP drawing of $[\eta^5,\eta^5\text{-}C_5H_4–Si(Me_3Si)_2–C_5H_4]Fe_2(\mu\text{-}CO)_2(CO)_2$ (**1**). Thermal ellipsoids are at the 30% probability level. Hydrogen atoms are omitted for clarity. (b) Side view of **1**.

bond. The bridging silicon atom, however, is not located on the top of the molecule but moves away from the plane defined by two iron and two bridged-head Cp carbon atoms by a distance of 0.58 Å (see Fig. 2b). This results

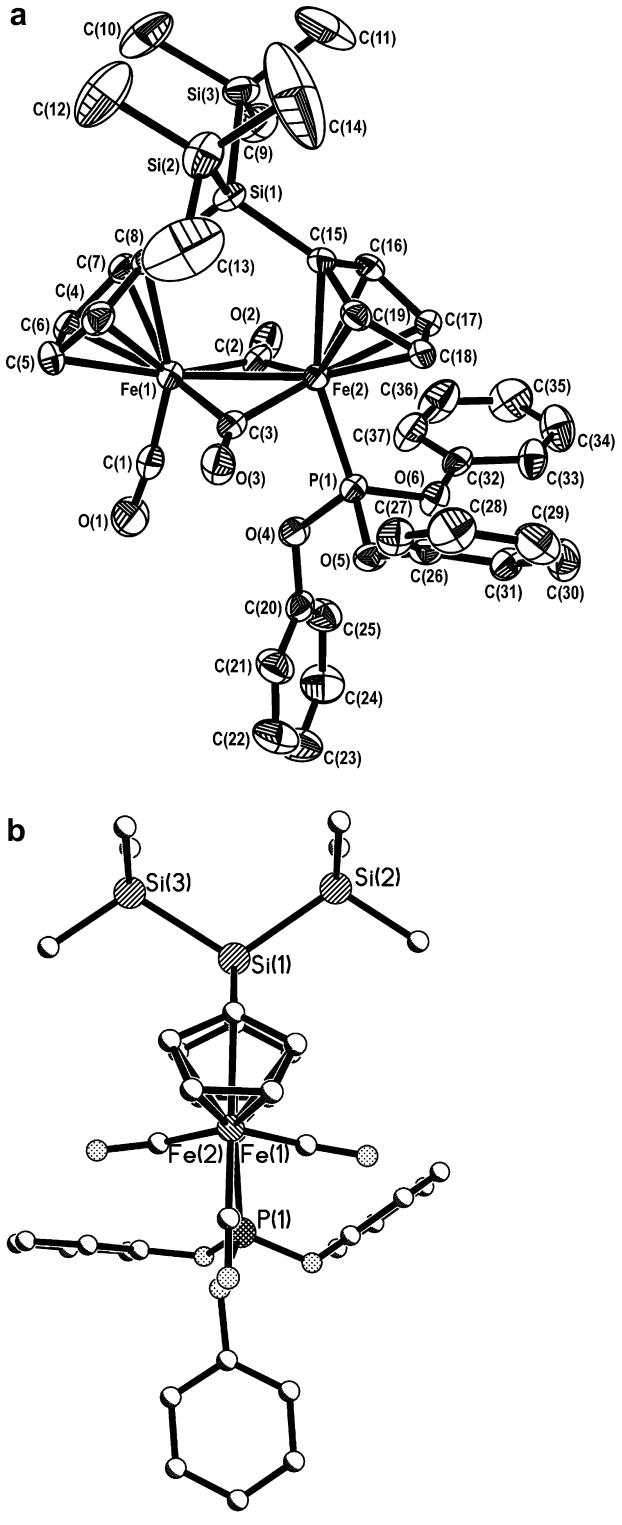


Fig. 3. (a) ORTEP drawing of $[\eta^5,\eta^5\text{-}C_5H_4\text{–}Si(Me_3Si)_2\text{–}C_5H_4]Fe_2(\mu\text{-}CO)_2(CO)P(OPh)_3$ (**2**). Thermal ellipsoids are at the 30% probability level. Hydrogen atoms are omitted for clarity. (b) Side view of **2**.

Table 2
Selected bond lengths (Å) and angles (°) for **1**

Fe(1)–Fe(1A)	2.523(1)	Si(1)–C(4)	1.886(4)
Si(1)–Si(2)	2.361(2)	Si(1)–Si(3)	2.362(2)
Fe(1)–C(4)	2.143(4)	Fe(1)–C(3)	1.752(5)
Fe(1)–C(2)	1.939(5)	Fe(1)–C(1)	1.930(4)
C(4)–Si(1)–C(4A)	103.7(2)	Si(2)–Si(1)–Si(3)	110.4(1)
C(4)–Si(1)–Si(2)	111.3(1)	C(4)–Si(1)–Si(3)	110.0(1)
Si(1)–C(4)–Fe(1)	121.2(2)	C(4)–Fe(1)–Fe(1A)	95.9(1)

Table 3
Selected bond lengths (Å) and angles (°) for **2**

Fe(1)–Fe(2)	2.531(1)	Fe(2)-P(1)	2.123(2)
Si(1)–Si(2)	2.351(2)	Si(1)–Si(3)	2.355(2)
Si(1)–C(8)	1.870(5)	Si(1)–C(15)	1.880(5)
Fe(1)–C(8)	2.146(5)	Fe(2)–C(15)	2.138(5)
Fe(1)–C(1)	1.735(7)	Fe(1)–C(2)	1.922(6)
Fe(1)–C(3)	1.933(5)	Fe(2)–C(2)	1.915(6)
Fe(2)–C(3)	1.906(5)		
Si(2)–Si(1)–Si(3)	113.0(1)	C(8)–Si(1)–C(15)	105.3(2)
C(8)–Si(1)–Si(2)	109.1(2)	C(15)–Si(1)–Si(2)	111.0(2)
C(8)–Si(1)–Si(3)	108.6(2)	C(15)–Si(1)–Si(3)	109.6(2)
C(8)–Fe(1)–Fe(2)	97.2(1)	C(15)–Fe(2)–Fe(1)	94.9(1)
P(1)–Fe(2)–Fe(1)	105.6(1)	Si(1)–C(15)–Fe(2)	122.3(2)
Si(1)–C(8)–Fe(1)	120.2(2)		

in the five-membered ring composed of the bridging silicon, two iron and two the bridged-head Cp carbon atoms taking an envelope-like conformation. This type of conformation has previously been observed in other silicon- and carbon-bridged complexes [2,7,8]. Interestingly, in complex **2** the bridging silicon atom has moved onto the top of the molecule (Fig. 3). Thus, the molecule has C_1 symmetry in the crystalline state. The five-membered cyclic skeleton is basically planar, with a mean deviation of only 0.011 Å (Fig. 3b). This is, to our knowledge, the first example of a silicon-bridged complexes to have such a conformation.

The shift of the bridge onto the top of the molecule is likely caused by the steric effect of the $P(OPh)_3$ ligand. Meanwhile, the bulkiness of $P(OPh)_3$ makes the Fe–Fe bond slightly lengthened from 2.5227 Å for **1** to 2.5311 Å for **2**. The Cp–Si–Cp angle is also increased from 103.7° for **1** to 105.3° for **2**. Interestingly, the bridging Si–Cp bonds have been slightly shortened from 1.886 Å for **1** to 1.870/1.880 Å for **2**, implying that the original strain that may exist in the five-membered cyclic structure may have been released to some extent. The lengths of the Si–Si bonds are 2.362/2.361 Å for **1** and 2.355/2.351 Å for **2**, which are rather close to one another. Other selected bond lengths and angles for **1** and **2** have been listed in Tables 2 and 3, respectively.

4. Summary

According to the results observed above, it seems that an appropriate position of the Si–Si bonds with respect to the transition metal centers should be an important factor that may control the intramolecular Si–Si bond

activation. Without such a position that is approachable by the intramolecular coordinatively unsaturated transition metal centers, the Si–Si bond would remain stable, although Si–Si bonds should be highly susceptible towards oxidative addition to intramolecular transition metal centers [33,34].

Acknowledgements

We thank the National Natural Science Foundation of China for financial support of this work (Project Nos. 29872020, 20372036 and 20421202) and the Natural Science Foundation of Tianjin (Project No. 05YFJMJC06800).

Appendix A. Supplementary material

CCDC 280002 and 280003 contain the supplementary crystallographic data for **1** and **2**, respectively. These data can be obtained free of charge via http://www.ccdc.cam.ac.uk/conts/retrieving.html, or from the Cambridge Crystallographic Data Centre, 12 Union Road, Cambridge CB2 1EZ, UK; fax: (+44) 1223-336-033; or e-mail: deposit@ccdc.cam.ac.uk. Supplementary data associated with this article can be found, in the online version, at doi:10.1016/j.poly.2006.10.026.

References

[1] T.E. Bitterwolf, J. Organomet. Chem. 547 (1997) 23.
[2] W. van den Berg, J.A.M.T.C. Cromsigt, W.P. Bosman, J.M.M. Smits, R. de Gelder, A.W. Gal, J. Heck, J. Organomet. Chem. 524 (1996) 281.
[3] B. Callan, M.G. Cox, A. McCabe, A.R. Manning, P. Sayal, P. Soye, S.C. Wade, F.S. Stephens, P. McArdle, D. Cunningham, J. Organomet. Chem. 466 (1994) 185.
[4] F.A. Cotton, D.L. Hunter, P. Lahuerta, A.J. White, Inorg. Chem. 15 (1976) 557.
[5] R.B. King, M.B. Bisnette, Inorg. Chem. 3 (1964) 801.
[6] H. Tobita, H. Habazaki, M. Shimoi, H. Ogino, Chem. Lett. (1985) 1044.
[7] J. Weaver, P. Woodward, J. Chem. Soc., Dalton Trans. (1973) 1439.
[8] P.A. Wegner, V.A. Uski, R.P. Kiester, S. Dabestani, V.W. Day, J. Am. Chem. Soc. 99 (1977) 4846.
[9] K.D. Janda, W.W. McConnell, G.O. Nelson, M.E. Wright, J. Organomet. Chem. 259 (1983) 139.
[10] M. Moran, M.C. Pascual, I. Cuadrado, J. Losada, Organometallics 12 (1993) 811.
[11] H. Sun, S. Xu, X. Zhou, H. Wang, X. Yao, J. Organomet. Chem. 444 (1993) C41.
[12] H. Sun, X. Teng, X. Huang, Z. Hu, Y. Pan, J. Organomet. Chem. 595 (2000) 268.
[13] H. Sun, Z. Zhang, Y. Pan, J. Yang, X. Zhou, Inorg. Chem. 42 (2003) 4076.
[14] H. Sun, Z. Zhang, X. Zhou, Chin. J. Chem. 21 (2003) 839.
[15] H. Sun, Y. Pan, X. Huang, Z. Zhang, Z. Guo, H. Zhang, J. Li, F. Wang, Organometallics 25 (2006) 133.
[16] H. Sun, X. Huang, Z. Hu, Z. Zhang, X. Leng, L. Weng, Inorg. Chim. Acta 348 (2003) 8.
[17] H. Sun, X. Zhou, X. Yao, H. Wang, Polyhedron 15 (1996) 4489.
[18] W. Xie, B. Wang, X. Dai, S. Xu, X. Zhou, Organometallics 17 (1998) 5406.
[19] W. Xie, B. Wang, X. Dai, S. Xu, X. Zhou, J. Chem. Soc., Dalton Trans. 7 (1999) 1141.
[20] Y. Zhang, S. Xu, X. Zhou, Organometallics 16 (1997) 6017.
[21] Y. Zhang, S. Xu, G. Tian, X. Zhou, J. Sun, Organometallics 17 (1998) 1122.
[22] B. Wang, Y. Zhang, S. Xu, X. Zhou, Organometallics 16 (1997) 4620.
[23] Y. Zhang, B. Wang, S. Xu, X. Zhou, J. Sun, J. Organomet. Chem. 584 (1999) 356.
[24] X. Zhou, Y. Zhang, W. Xie, S. Xu, J. Sun, Organometallics 16 (1997) 3474.
[25] H. Sun, H. Zhang, Z. Zhang, Chin. J. Chem. 24 (2006) 1476.
[26] H.K. Sharma, K.H. Pannell, Chem. Rev. 95 (1995) 1351.
[27] M. Suginome, Y. Ito, J. Chem. Soc., Dalton Trans. (1998) 1925.
[28] K.A. Jackson, C.J. Rhodes, J. Organomet. Chem. 336 (1987) 45.
[29] M.C. Baird, Chem. Rev. 88 (1988) 1217.
[30] T.J. Meyer, J.V. Caspar, Chem. Rev. 85 (1985) 187.
[31] M.O. Joseph, P.C. Charles, Chem. Rev. 87 (1987) 307.
[32] M.J. Calhorda, C.C. Romao, L.F. Veiros, Chem. Eur. J. 8 (2002) 868.
[33] A. Bottoni, A.P. Higueruelo, G.P. Miscione, J. Am. Chem. Soc. 124 (2002) 5506.
[34] S. Sakaki, M. Ieki, J. Am. Chem. Soc. 115 (1993) 2373.

a *N*,*N*′-chelating system like bpy (2,2′-bipyridine), phen (1,10-phenanthroline) have been reported [11,20]. The scarcity of the rhenium nitrosyl core with the azoimine function has created profound interest in studying the reactivity of the $Re(NO)^{3+}$ moiety towards arylazoheterocycles.

In order to explore the rhenium–nitrosyl chemistry of RaaiR′ we have used the reductive nitrosylation process. In an aqueous alkaline medium ReO_4^- undergoes reductive nitrosylation by $NH_2OH \cdot HCl$, furnishing the $Re(NO)^{3+}$ moiety in solution. The moiety is isolable as $M[Re(NO)(OH)_4]$ (M = Ph_4P or Ph_4As) salts or as $[Re(NO)(OH)_3(L\text{-}L')]$ (L-L = diimine ligand like bpy or phen) [11]. Addition of RaaiR′ to this solution has separated a brown red solid complex of the composition $[Re(NO)(OH)_3(N,N')]$ (*N*,*N*′) = azoimine ligand, RaaiR′ where R = H; R′ = H (Pai-H; 2-(phenylazo)imidazole, **1a**), Me (Pai-Me; 1-methyl-2-(phenylazo)imidazole, **1b**), Et (Pai-Et; 1-ethyl-2-(phenylazo)imidazole, **1c**): R = Me; R′ = H (Tai-H; 2-(*p*-tolylazo)imidazole, **2a**), Me (Tai-Me; 1-methyl-2-(*p*-tolylazo)imidazole, **2b**), Et (Tai-Et; 1-ethyl-2-(*p*-tolylazo)imidazole, **2c**)]. The spectroscopic characterisation and reactivity of the compounds are reported in this work.

2. Experimental

2.1. Materials

The starting material, $K[ReO_4]$, was of extra-pure quality and obtained from Aldrich. The AR grade solvents used for physicochemical studies were further purified by a literature method [21]. Water of high purity was obtained by distilling deionized water from $K[MnO_4]$. The ligands, 2-(arylazo)imidazoles (RaaiH) and 1-alkyl-2-(arylazo)imidazoles (RaaiR′) were prepared by the reported procedure [15].

2.2. Physical measurements

UV–Vis spectra were recorded on a Lambda 25, Perkin–Elmer UV–Vis spectrophotometer. IR spectra (KBr disk) were recorded on RX-1 Perkin–Elmer FT-IR (4000–450 cm^{-1}) and JASCO Model 420 FT-IR (4000–200 cm^{-1}) spectrophotometers. Electrical conductivity in a MeCN solution was measured with a Systronics 304 digital conductivity meter with a solution concentration of ca. 10^{-3} mol dm^{-3}. Magnetic susceptibilities were obtained from a vibrating sample magnetometer PAR 155 model. Microanalytical (C, H, N) data were collected on a Perkin–Elmer 2400C elemental analyzer. ESR spectra were measured in MeCN solution at 298 K using a Bruker ESR spectrophotometer model EMX 10/12, X-band ER 4119 MS cylindrical resonator. All pH measurements were made with an E.C. (India) digital pH meter (model 5651). Electrochemical measurements were carried out with the use of a computer controlled EG&G PARC VersaStat model 250 Electrochemical instrument using a Pt-disk working electrode and Pt-wire auxiliary electrode. The solution was IR compensated and the results were collected at 298 K. The reported results are referenced to SCE in MeCN and are uncorrected for junction potentials. $[n\text{-}Bu_4N][ClO_4]$ was used as the supporting electrolyte.

2.2.1. Preparation of tri-hydroxo-nitrosyl-{*N*(1)-methyl-2-(phenylazo)-imidazole}rhenium(II) hydrate, $[Re(NO)(OH)_3(Pai\text{-}Me)] \cdot H_2O$, (*1b*) generation of the $Re(NO)^{3+}$ moiety

A mixture of $K[ReO_4]$ (0.11 g, 0.38 mmol) and $NH_2OH \cdot HCl$ (0.36 g, 5.25 mmol) was dissolved in 25 ml water. The solution was heated to ca. 80 °C for 10 min with constant stirring. Solid NaOH beads were gradually added to the stirred solution until it turned red and the pH increased to ca. 10.5. The red solution was stirred at 80 °C for half an hour and cooled.

$$ReO_4^-(aq) \xrightarrow[\text{Excess } OH^-]{NH_2OH \cdot HCl} Re(NO)^{3+} \quad (1)$$

2.2.2. Preparation of $[Re(NO)(OH)_3(Pai\text{-}Me)]$

The pH of the red solution was lowered to ca. 5–6 by adding 1:1 HCl. To an ethanolic solution of 1-methyl-2-(phenylazo)imidazole (Pai-Me) (0.13 g, 0.70 mmol) the red solution was added dropwise whilst stirring. Immediately a buff coloured precipitate appeared. The solution was stirred for ca. 10 min and the precipitate was filtered, washed with water, ethanol and diethyl ether, and finally dried over fused $CaCl_2$ under vacuum. The yield was 0.12 g (67%). All the other complexes were prepared by the same procedure and yield varied from 60% to 70%.

$$Re(NO)^{3+}(aq) + \text{Pai-Me} \rightarrow [Re(NO)(OH)_3(\text{Pai-Me})] \quad (2)$$

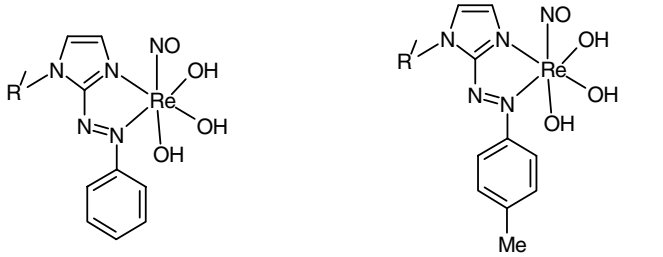
Anal. Calc. for $C_9H_{13}N_5O_5Re$ (**1a**): C, 23.60; H, 2.84; N, 15.34. Found: C, 23.68; H, 2.80; N, 15.43%. UV–Vis spectral data in MeCN (λ_{max}) (nm) (10^{-3}) ∈ (dm^3 mol^{-1} cm^{-1}): 470 (2.30), 375 (8.48). FT-IR data (KBr) (ν, cm^{-1}): 1700 (NO), 1605 (C=N), 1437 (N=N). *Anal.* Calc. for $C_{10}H_{15}N_5O_5Re$ (**1b**): C, 25.44; H, 3.18; N, 14.84. Found: C, 25.53; H, 3.24; N, 14.93%. UV–Vis spectral data in MeCN (λ_{max}) (nm) (10^{-3}) ∈ (dm^3 mol^{-1} cm^{-1}): 465 (1.20), 368 (9.23). FT-IR data (KBr) (ν, cm^{-1}): 1697 (NO), 1600 (C=N), 1444 (N=N). *Anal.* Calc. for $C_{11}H_{17}N_5O_5Re$ (**1c**): C, 27.18; H, 3.50; N, 14.42. Found: C, 27.32; H, 3.40; N, 14.52%. UV–Vis spectral data in MeCN (λ_{max}) (nm) (10^{-3}) ∈ (dm^3 mol^{-1} cm^{-1}): 460 (2.72), 370 (15.80). FT-IR data (KBr) (ν, cm^{-1}): 1700 (NO), 1600 (C=N), 1438 (N=N). *Anal.* Calc. for $C_{10}H_{15}N_5O_5Re$ (**2a**): C, 25.44; H, 3.18; N, 14.84. Found: C, 25.40; H, 3.14; N, 14.80%. UV–Vis spectral data in MeCN (λ_{max}) (nm) (10^{-3}) ∈ (dm^3 mol^{-1} cm^{-1}): 463 (1.90), 372 (9.30). FT-IR data (KBr) (ν, cm^{-1}): 1698 (NO), 1600 (C=N), 1445 (N=N). *Anal.* Calc. for $C_{11}H_{17}N_5O_5Re$ (**2b**): C, 27.18; H, 3.50; N, 14.42. Found: C, 27.27; H, 3.43; N, 14.50%. UV–Vis spectral data in MeCN (λ_{max}) (nm)

(10^{-3}) ∈ ($dm^3\ mol^{-1}\ cm^{-1}$): 446 (2.30), 368 (10.70). FT-IR data (KBr) (υ, cm^{-1}): 1698 (NO), 1600 (C=N), 1438 (N=N). *Anal.* Calc. for $C_{12}H_{19}N_5O_5Re$ (**2c**): C, 28.82; H, 3.80; N, 14.01. Found: C, 28.70; H, 3.72; N, 14.12%. UV–Vis spectral data in MeCN (λ_{max}) (nm) (10^{-3}) ∈ ($dm^3\ mol^{-1}\ cm^{-1}$): 462 (7.20),383 (13.80). FT-IR data (KBr) (υ, cm^{-1}): 1689 (NO), 1598 (C=N), 1444 (N=N).

3. Results and discussion

3.1. Synthesis

An aqueous solution of $K[ReO_4]$ was treated with $NH_2OH \cdot HCl$ and NaOH to prepare a red solution of the $Re(NO)^{3+}$ moiety (Solution-A). An ethanolic solution of 1-alkyl-2-(arylazo)imidazole (RaaiR′) was added dropwise to Solution-A whilst stirring at room temperature. Brown red complexes of the composition $[Re(NO)(OH)_3(RaaiR')]$, namely $[Re(NO)(OH)_3(Pai\text{-}H)] \cdot H_2O$ (**1a**), $[Re(NO)(OH)_3(Pai\text{-}Me)] \cdot H_2O$ (**1b**), $\{Re(NO)(OH)_3(Pai\text{-}Et)] \cdot H_2O$ (**1c**), $[Re(NO)(OH)_3(Tai\text{-}H)] \cdot H_2O$ (**2a**), $[Re(NO)(OH)_3(Tai\text{-}Me)] \cdot H_2O$ (**2b**) and $[Re(NO)(OH)_3(Tai\text{-}Et)] \cdot H_2O$ (**2c**), were separated.



[Re(NO)(OH)$_3$(Pai-R′)] [Re(NO)(OH)$_3$(Tai-R′)]

Pai-R′ = Pai-H (**1a**), Pai-Me (**1b**), Pai-Et (**1c**); Tai-R′ = Tai-H (**2a**), Tai-Me (**2b**), Tai-Et (**2c**)

The complexes were filtered, washed and recrystallised from a 2-methoxy-ethanol-EtOH mixture. The composition and molecularity of the complexes have been supported by microanalytical data. Molar conductance measurements in MeCN suggest non-conductivity of the complexes. Thermogravimetric (TG and DTA) analyses of the compounds reveal that one water molecule in each case is very loosely held, and this is released at 80–85 °C. Although three different isomers are possible, with $[Re(NO)(OH)_3(RaaiR')]$ having an unsymmetrical *N*,*N*′ chelating ligand, we have not been able to separate them.

3.2. IR and electronic spectra

The isolated complexes are all monomeric as is evident from the microanalytical data. The hydroxo group and lattice held water molecules together show a single and slightly broad υ(OH) IR band at ca. 3400 cm^{-1}, but the $\partial(H_2O)$ band is apparently occluded in the low energy tail of the υ(NO) vibrational band. All the complexes exhibit a sharp and symmetrical υ(NO) vibrational band at ca. 1700 cm^{-1}. The υ(NO) stretch suffers a blue shift by 10–15 cm^{-1} relative to the corresponding bpy and phen complexes [11,20]. The complexes exhibit a moderately intense band at 1435–1445 cm^{-1} which may be ascribed to υ(N=N) vibrations. The said frequency is also blue shifted by 40–65 cm^{-1} in the complexes relative to the free ligand values. The chelated azoimine function receives electrons by $d\pi(M) \rightarrow \pi^*(azo)$ means which usually lowers the υ(N=N) stretch [17–19,22]. In the present series of complexes two π-acidic groups, NO^+ and N=N, are competing for same $d\pi$(Re(II)) electrons. The stronger π-acidic NO^+ accepts π-electrons more efficiently than the azoimine grouping and probably weakens the π back donation that raises the υ(N=N) stretching frequency. Other bands at 790, 775, 700–600 cm^{-1} corresponding to the imidazole moiety are observed.

The solution electronic spectra of the complexes were recorded in the range 900–200 nm in MeCN. The complexes show absorption bands in the ranges 320–330, 365–385 and 440–450 nm (Fig. 1). The transitions below 400 nm are of high intensity and are ascribed to intraligand charge-transfer, $\pi \rightarrow \pi^*$ and $n \rightarrow \pi^*$ transitions [15,16] of the chelated ligand (RaaiR′). The longer wavelength transition may correspond to the combination of MLCT ($d\pi(Re) \rightarrow \pi^*$(azoimine)) and $b_2 \rightarrow e$ transitions [23]. The said bands also appear in the complexes but are blue shifted by ca. 55 and 35 nm, respectively.

3.3. Magnetic properties and e.s.r data

The complexes exhibit a μ_{eff} value of ca. 1.8 BM at 298 K. A slightly higher value than the spin-only value expected for a single electron [Re(II), d^5, low-spin octahedral case] may be due to the negative value of the spin–orbit coupling constant and orbital non-degeneracy of the singly occupied molecular orbital (s.o.m.o) involved.

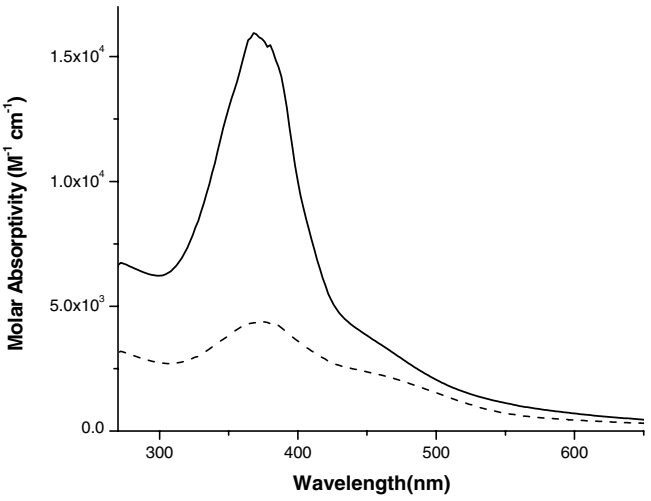
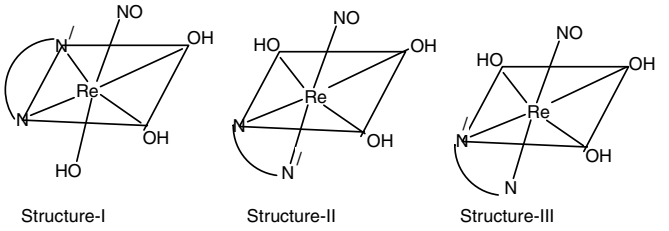


Fig. 1. Electronic spectra of $[Re(NO)(OH)_3(Pai\text{-}H)]$ (····) and $[Re(NO)(OH)_3(Pai\text{-}Et)]$ (—) in MeCN solution.



The e.s.r spectra (Fig. 2) are difficult to explain in terms of molecular symmetry. There may be three (**I**–**III**) structures; of them, structure-**I** is asymmetric and **II**, **III** posses C_s symmetry. The axial e.s.r. spectra may be more appropriately described by structure **II** or **III** than that of **I**. A well defined sextet is observed which arises from hyperfine coupling with the spin-active ^{185}Re and ^{187}Re nuclei [both have $I = 5/2$, Fig. 2] [24].

3.4. Electrochemical studies

Cyclic voltammetry was carried out in a MeCN solution using a Pt-working electrode in the potential range 1.8 V to −1.8 V in the presence of $[NBu_4][ClO_4]$ as the supporting electrolyte. The cyclic voltammogram shows quasireversible to irreversible responses at 0.7–0.8 (couple I), 0.2–0.3 (couple II), −0.1 to −0.2 (couple III), −0.5 to −0.6 (couple IV) and −1.3 to −1.4 V (couple V) (Table 1, Fig. 3). The couples I and II do not have a well defined cathodic peak on scan reversal from positive to negative. Separate voltammetric drawings at variable scan rates for couples I and II exhibit similar behaviour. This suggests that the redox performances are independent of scan speed or asking potential. At slow scan rates (10–50 mV s^{-1})ΔE_P remains almost constant, as do the E_{Pa} and the E_{Pc} values. However, the peak-to-peak separation of the redox couples III–V is largely dependent on the scan rate and increases from 120 mV at 10 mV s^{-1} to 600 mV at 1000 mV s^{-1}. This observation suggests a low heterogeneous electron-transfer rate constant which has been influenced by the applied potential. The arylazoimidazoles (RaaiR′) do not show any oxidation but irreversible reductive responses, in general two quasireversible couples at −0.8 and −1.3 V are ascribed to [—N═N—]/[—N⁻—N—]$^-$ and [—N⁻—N—]/[—N⁻—N⁻—]$^=$, respectively [22]. Thus, couples IV and V are reductive responses of the chelated azoimine ligand. The anodic shift of these two couples (IV and V) compared to the free ligand values may be due to electron drifting to Re(II) from the coordinated ligand. The first three couples (couples I, II and III) may be assigned to [Re(NO)] centred redox responses. Couple I is assigned to $[Re(NO)(OH)_3(RaaiR')]^+/[Re(NO)(OH)_3(RaaiR')]$ [11]. Couples II and III are assigned to successive one electron reductions of the coordinated NO^+ unit; $[Re–NO]^+ \rightarrow [Re–NO]$ (couple II), $[Re–NO] \rightarrow [Re–NO]^-$ (couple III). These three couples are irreversible in nature indicating the instability of the reduced species.

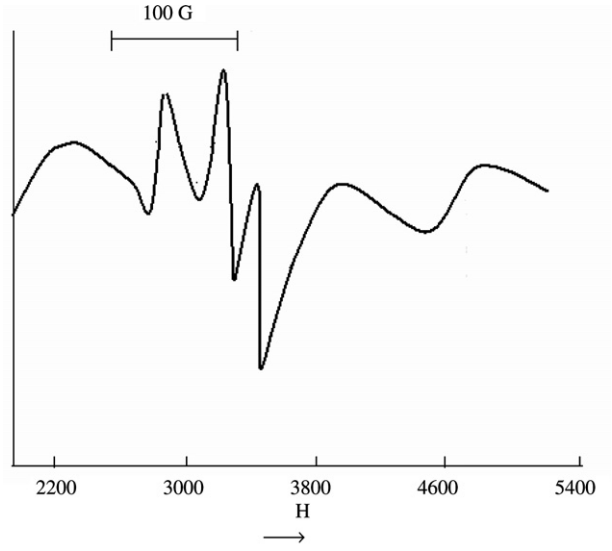


Fig. 2. X-band ESR spectrum of $[Re(NO)(OH)_3(Tai\text{-}Me)]$, polycrystalline, 298 K.

Table 1
E.s.r. parameters of the complexes at 298 K

Compound[a]	g_s[b]	$g_\parallel$[c]	$g_\perp$[c]	g_{av}[d]	$\langle A\rangle_{Re}$(G)
1a	2.00	1.98	2.07	2.04	340–620
1b	2.01	1.97	2.04	2.03	350–640
1c	2.00	1.96	2.11	2.06	330–610
2a	2.00	1.96	2.05	2.02	330–620
2b	2.02	1.98	2.09	2.05	320–610
2c	2.00	1.98	2.03	2.01	340–630

[a] In the polycrystalline state.
[b] g_s represents the g value of the derivative curve in the polycrystalline state.
[c] For spin paired d^5 system $g_\perp > g_\parallel$ and $g_\parallel < 2$.
[d] $g_{av} = (2g_\perp + g_\parallel)/3$.

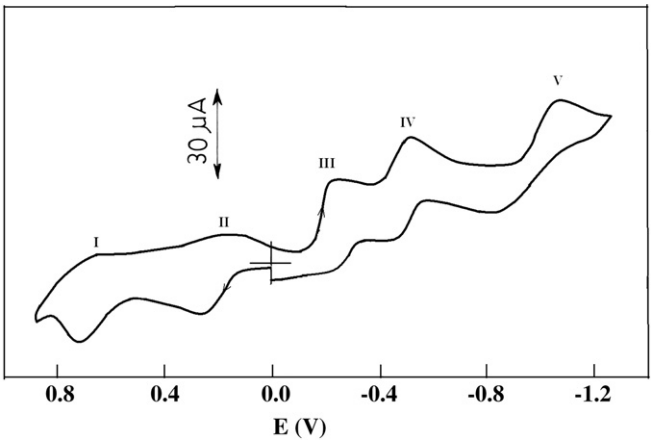
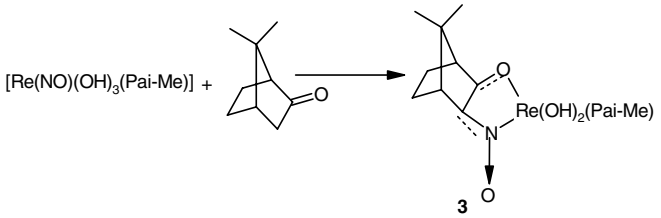


Fig. 3. Cyclic voltammogram of $[Re(NO)(OH)_3(Tai\text{-}Et)]$ (**2c**) in MeCN using a Pt-working electrode, SCE reference and a Pt-wire auxiliary electrode in the presence of $[n\text{-}Bu_4N][ClO_4]$ as the supporting electrolyte.

4. Reactivity of [Re(NO)(OH)$_3$(Tai-Me)]

The nitrosyl complexes exhibit a high degree of electrophilic character [25] of the coordinated NO ligand. The electrophilic behaviour of these new complexes has been investigated by reacting with camphor (cmp), a compound having an active methylene group. An acetonitrile solution of [Re(NO)(OH)$_3$(Tai-Me)] reacted smoothly with camphor in the presence of NaOMe, and the solution colour changed from brown-red to red-violet. The progress of the reaction was followed by monitoring ν(NO), which decreased steadily from 1700 cm^{-1}, and the composition of the reaction mixture was followed by thin-layer chromatography, collecting portions of the reaction solution from time-to-time. The product analyses are in accordance with reaction (3). The reaction involves electrophilic addition of the coordinated NO to the activated



(3)

–CH$_2$– group, forming a bound oxime (camphorquinone monoxime). Deprotonation of the active methylene (–CH$_2$–) leads to the generation of a carbanion which subsequently attacks the electrophilic NO$^+$, with the synthesis of camphorquinone monoxime. The disappearance of ν(NO) (1700 cm^{-1}) and the growth of ν(N → O) at 1220 cm^{-1} strongly support the reaction. Microanalytical, spectroscopic and electrochemical results of the camphorquinone monoxime complex (**3**) suggest a structure of the complex which supports this coupling reaction of the coordinated NO. The compound shows a very complex pattern of proton signals in the aliphatic region, 0.8–1.0, 1.28–1.40, 2.20, 2.40 and 4.00 ppm. Camphor –CH$_2$– and –CH– may be assigned to 0.8–1.0 and 1.28–1.40 ppm. 9-Me and 1-Me of the coordinated Tai-Me appear at 2.35 and 4.11 ppm, respectively. In the aromatic region (6.00–9.00 ppm) imidazole protons 4-H and 5-H appear as broad singlets at ca. 7.18 and 6.92 ppm, respectively. Broadening of the signals may be due to rapid proton exchange with solvent ($CHCl_3$ from $CDCl_3$). *p*-Tolyl protons (7-H to 11-H) appear at 8.32 ($J = 7.5$ Hz, 7, 11-H, doublet) and 7.44 ppm ($J = 7.5$ Hz, 8, 10-H, doublet). The cyclic voltammogram shows a peak, E_{Pa}, at 0.62 V, which suggests a Re(III)/Re(II) couple, and ligand reductions at −0.73 ($\Delta E_p = 140$ mV) and −1.3 V ($\Delta E_p = 220$ mV).

5. Conclusion

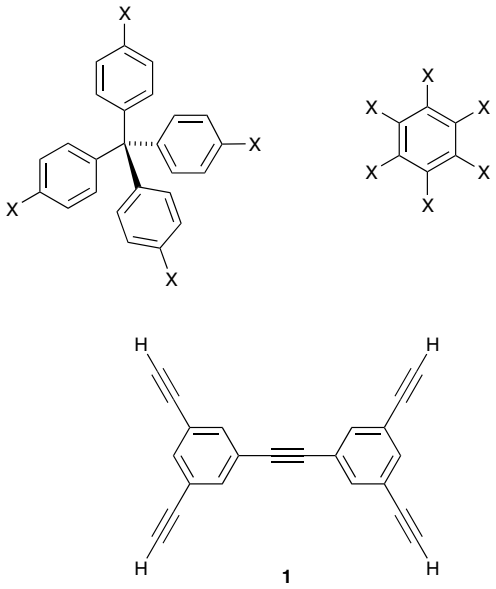
Rhenium–nitrosyl complexes of arylazoimidazoles are synthesized by reductive nitrosylation of ReO_4^- in aqueous alkaline medium by $NH_2OH \cdot HCl$. The ligands are bidentate *N*,*N*′ chelating type. The complexes exhibit υ(NO) at ca. 1700 cm^{-1}, which upon reaction with camphor in alkaline medium vanishes with appearance of a new impression at 1220 cm^{-1}. This and other spectroscopic properties suggest a C–N coupling reaction of the coordinated NO and formation of a camphoroxime complex. The precursors [Re(NO)(OH)$_3$(azoimidazole)] are magnetically active and show $\langle g_{av} \rangle \approx 2.0$. Cyclic voltammetry exhibits irreversible metal oxidation, and NO$^+$ and azo reductions.

Acknowledgments

One of us (A.D.M.) thanks the University Grants Commission (UGC), New Delhi for financial support under a minor research scheme. C.S. thanks CSIR, New Delhi for funding. Miss Pampa Pratihar also thanks UGC for a fellowship.

References

[1] K.K. Pandey, Coord. Chem. Rev. 51 (1983) 69;.
[2] J.A. McCleverty, Chem. Rev. 104 (2004) 403.
[3] K.M. Miranda, Coord. Chem. Rev. 249 (2005) 433.
[4] B. Machura, Coord. Chem. Rev. 249 (2005) 2277.
[5] G.B. Richter-Addo, P. Legzdins, Metal Nitrosyls, Oxford University Press, New York, 1992.
[6] B.L. Wescott, J.H. Enemark, in: A.B.P. Lever, E.I. Solomon (Eds.), Transition Metal Nitrosyls in Inorganic Electronic Structure and Spectroscopy, vol. 2, Wiley& Sons, New York, 1999, Chap 7.
[7] R.W. Adams, J. Chatt, N.E. Hooper, G.L. Leigh, J. Chem. Soc., Dalton Trans. (1974) 1075.
[8] P. Bandyopadhyay, S. Rakshit, Indian J. Chem. 11 (1973) 496.
[9] F. Zingales, A. Trovati, F. Cariati, P. Uguagliati, Inorg. Chem. 10 (1971) 507.
[10] P. Byabartta, S.k. Jasimuddin, B.K. Ghosh, C. Sinha, A.M.Z. Slawin, J.D. Woollins, New J. Chem. 26 (2002) 1415.
[11] R.G. Bhattacharyya, P.S. Roy, A.K. Dasmahapatra, J. Chem. Soc., Dalton Trans. (1988) 793.
[12] D. Dutta, A. Chakravorty, Inorg. Chem. 22 (1983) 1085.
[13] G.K. Lahiri, S. Goswami, L.R. Falvello, A. Chakravorty, Inorg. Chem. 26 (1987) 3365.
[14] B.K. Ghosh, A. Mukhopadhyay, S. Goswami, S. Ray, A. Chakravorty, Inorg. Chem. 23 (1984) 4633.
[15] G.K. Routh, S. Pal, D. Das, C. Sinha, A.M.Z. Slawin, J.D. Woollins, Polyhedron 20 (2001) 363, and references therein.
[16] P.K. Santra, P. Byabarta, S. Chattopadhyay, G. Mostafa, L.R. Falvello, C. Sinha, Eur. J. Inorg. Chem. (2002) 1124, and references therein.
[17] S.K. Jasimuddin, P. Byabarta, C. Sinha, G. Mostafa, T.H. Lu, Inorg. Chim. Acta 357 (2004) 2015.
[18] U.S. Ray, B.G. Chand, A.K. Dasmahapatra, G. Mostafa, T.-H. Lu, C. Sinha, Inorg. Chem. Commun. 6 (2003) 634.
[19] J. Dinda, S. Senapoti, T. Mondal, A.D. Jana, M. Chiang, T.-H. Lu, C. Sinha, Polyhedron 25 (2006) 1125.
[20] S. Banerjee, S. Bhattacharyya, B.K. Dirghangi, M. Menon, A. Chakravorty, Inorg. Chem. 39 (2000) 6.
[21] A.I. Vogel, A Text Book of Practical Chemistry, third ed., Longman, New York, 1959.
[22] T.K. Misra, D. Das, C. Sinha, P. Ghosh, C.K. Pal, Inorg. Chem. 37 (1998) 1672.
[23] J.H. Enemerk, R.D. Feltham, Coord. Chem. Rev. 13 (1974) 339.
[24] B.A. Goodman, J.B. Raynor, Adv. Inorg. Chem. Radiochem. 13 (1970) 135.
[25] T. Suganuma, A. Tanada, H. Tomizawa, M. Tanaka, E. Miki, Inorg. Chim. Acta 320 (2001) 2341.



Scheme 1. Central cores for four- or six-armed stars and dendrimers.

3,5-Dibromonitrobenzene [23], 3,5-diiodonitrobenzene [24] and compound **1** [22] were made by published routes or slight modifications thereof.

2.2. Compound 2

Compound **2** was prepared as previously reported [27], except that a catalytic amount of CuI was added before the addition of KI. Spectroscopic data were in accord with those published [27].

2.3. Compound 3

Compound **2** (345 mg, 1.15 mmol), CuCl (4.10 mg, 0.0414 mmol) and $[Pd(PPh_3)_2Cl_2]$ (28.8 mg, 0.0410 mmol) were dissolved in Et_3N (25 ml). Compound **1** (75.0 mg, 0.273 mmol) was then added and the reaction mixture heated to 60 °C and stirred at this temperature for 24 h. After cooling to room temperature, solvent was removed under reduced pressure and the residue was purified by column chromatography (alumina, hexanes: CH_2Cl_2 1:0 changing to 3:1 during elution). Compound **3** was isolated as a brown solid (81.5 mg, 0.0846 mmol, 32.4%). ^{1}H NMR (400 MHz, $CDCl_3$) δ/ppm 7.63 (s, 6H, H^B), 7.47 (s, 16H, H^A),0.28 (s, 36H, C^{Me}). ^{13}C NMR (100 MHz, $CDCl_3$) δ/ppm 134.3, 134.2, 131.9, 131.5, 123.9, 123.5, 123.3, 122.7, 104.5 ($C^{C\equiv CTMS}$), 96.6 ($C^{C\equiv CTMS}$), 90.3 ($C^{C\equiv C}$), 89.5 ($C^{C\equiv C}$), 88.9 ($C^{C\equiv C}$), −0.1 (C^{Me}). FAB-MS *m/z* 963 $[M]^+$, 766 $[M–C_2C_6H_4C_2TMS]^+$, 73 $[TMS]^+$ (base peak). IR (ν, cm^{-1}) 2955w, 2153m, 1581s, 1505m, 1404w, 1246s, 1102w, 1018w, 859vs, 832vs, 757s, 677s.

2.4. Compound 4

The method used differs from that published [25] but gave a similar yield of **4**; more recently, another modification has been published [26]. 3,5-Dibromonitrobenzene (1.00 g, 3.56 mmol) was dissolved in Et_3N (50 ml) with CuCl (53.5 mg, 0.540 mmol) and $[Pd(PPh_3)_2Cl_2]$ (379 mg, 0.540 mmol). After the addition of TMSC≡CH (1.52 ml, 10.8 mmol), the mixture was heated to 60 °C and was stirred at this temperature for 20 h. After cooling to room temperature, solvent was removed under reduced pressure and the residue was extracted with a solution of 10% CH_2Cl_2 in hexanes (150 ml). The crude material was purified by column chromatography (alumina, hexanes: CH_2Cl_2 1:0 gradually changing to 10:1). Compound **4** was isolated as a light brown solid (613 mg, 1.94 mmol, 54.6%). ^{1}H NMR (400 MHz, $CDCl_3$) δ/ppm 8.21 (s, 2H, H^2), 7.82 (s, 1H, H^4), 0.28 (s, 18H, H^{Me}). ^{13}C NMR (100 MHz, $CDCl_3$) δ/ppm 148.2 (C^1), 140.6 (C^4), 126.3 (C^2), 125.4 (C^3), 101.6 ($C^{C\equiv C}$), 98.4 ($C^{C\equiv C}$), −0.2 (C^{Me}). FAB-MS *m/z* 315 $[M]^+$, 300 $[M–CH_3]^+$ (base peak). IR (ν, cm^{-1}) 2959m, 2160m, 1537vs, 1410w, 1352vs, 1250s, 843vs, 746vs, 775s, 760s, 669s. Previously reported spectroscopic data [25] are for an acetone solution of **4**.

2.5. Compound 5

Compound **5** was prepared by a modification of that reported [25]. 3,5-Diiodoaniline (1.15 g, 3.33 mmol) was dissolved in Et_3N (50 ml) with CuCl (49.5 mg, 0.500 mmol) and $[Pd(PPh_3)_2Cl_2]$ (351 mg, 0.500 mmol). TMSC≡CH (1.18 ml, 8.38 mmol) was then added and the mixture was heated to 60 °C and was stirred at this temperature for 20 h. After cooling to room temperature, solvent was removed under reduced pressure and the crude residue was purified by column chromatography (alumina, hexanes: CH_2Cl_2 1:0 changing to 3:1). Compound **5** was isolated as a light brown solid (891 mg, 3.12 mmol, 93.7%). ^{1}H NMR (400 MHz, $CDCl_3$) δ/ppm 7.00 (t, *J* 1.6 Hz, 1H, H^4), 6.71 (d, *J* 1.6 Hz, 2H, H^2), 3.52 (br, NH_2), 0.23 (s, 18H, C^{Me}). ^{13}C NMR (100 MHz, $CDCl_3$) δ/ppm 146.4 (C^1), 126.5 (C^4), 124.3 (C^2), 118.8 (C^3), 104.8 ($C^{C\equiv C}$), 94.5 ($C^{C\equiv C}$), 0.4 (C^{Me}). FAB-MS *m/z* 285 $[M]^+$, 270 $[M–CH_3]^+$ (base peak). IR (ν, cm^{-1}) 3381m, 2959m, 2899m, 2152m, 1587s, 1553m, 1429m, 1410m, 1248s, 839vs, 756s, 648s. Previously reported spectroscopic data [25] are for an acetone solution of **5**.

2.6. Compound 6

Compound **5** (70.0 mg, 0.245 mmol) was suspended in water (25 ml), concentrated HCl (5 ml) was added and the brown solution was cooled to 0 °C. A solution of $NaNO_2$ (17.3 mg, 0.251 mmol) in water (10 ml) was added to the reaction mixture and this was stirred at 0 °C for 1 h. A catalytic amount of CuI (10 mg) was added, followed by KI (105 mg, 0.633 mmol). The reaction mixture was stirred at 0 °C for 6 h, during which time THF (total 30 ml) was added in small amounts to increase the solubility of the reactants. After warming to room temperature, water and Et_2O (1:2, 75 ml) were

added to the vigorously stirred reaction mixture. Two layers were allowed to separate, and the aqueous layer was extracted with Et_2O (100 ml), and the organic layer was collected, washed with brine, and dried over $MgSO_4$. After removal of solvent under reduced pressure, the crude residue was purified by column chromatography (alumina, hexanes: CH_2Cl_2 1:0 changing to 10:1). Compound **6** was isolated as a yellow solid (72.8 mg, 0.184 mmol, 75.1%). ^{1}H NMR (400 MHz, $CDCl_3$) δ/ppm 7.74 (d, J 1.6 Hz, 2H, H^2), 7.52 (t, J 1.6 Hz, 1H, H^4),0.23 (s, 18H, C^{Me}). ^{13}C NMR (100 MHz, $CDCl_3$) δ/ppm 140.2 (C^2), 134.4 (C^4), 125.0 (C^3), 102.2 ($C^{C\equiv C}$), 96.6 ($C^{C\equiv C}$), 92.8 (C^1), −0.2 (C^{Me}). FAB-MS m/z 396 $[M]^+$, 381 $[M–CH_3]^+$ (base peak). IR (ν, cm^{-1}) 3086w, 2955m, 2924m, 2854w, 2214w, 2160w, 1898m, 1774m, 1574s, 1481s, 1411s, 1396m, 1272m, 1250m, 1072m, 1011m, 864s, 817vs, 756s, 679s.

2.7. Compound 7

Compound **6** (325 mg, 0.821 mmol), CuCl (3.0 mg, 0.030 mmol) and $[Pd(PPh_3)_2Cl_2]$ (21.1 mg, 0.0301 mmol) were dissolved in Et_3N (25 ml). Compound **1** (55.0 mg, 0.201 mmol) was then added. The reaction mixture was heated at 60 °C for 18 h. After cooling to room temperature, solvent was removed and the residue was purified by column chromatography (alumina, hexanes: CH_2Cl_2 1:0 changing to 5:1). Compound **7** was isolated as a brown solid (71.4 mg, 0.0523 mmol, 26.0%). ^{1}H NMR (400 MHz, $CDCl_3$) δ/ppm 7.57 (m, 18H, $H^{A,B}$), 0.25 (s, 72H, C^{Me}). ^{13}C NMR (100 MHz, $CDCl_3$) δ/ppm 135.2, 135.1, 134.6, 134.4, 123.9 (overlapping signals), 123.1, 122.9, 103.0 ($C^{C\equiv CTMS}$), 95.9 ($C^{C\equiv CTMS}$), 89.1 ($C^{C\equiv C}$), 88.9 ($C^{C\equiv C}$), 88.5 ($C^{C\equiv C}$), −0.1 (C^{Me}). MALDI-MS m/z 1346 $[M]^+$, 1331 $[M–CH_3]^+$ (base peak). IR (ν, cm^{-1}) 2958w, 2152w, 1740w, 1558w, 1473m, 1404w, 1377w, 1248s, 1191m, 945w, 873sh, 839vs, 760s, 702w, 644m.

2.8. Compound 8

Compound **3** (20.0 mg, 0.0208 mmol) was dissolved in CH_2Cl_2 (35 ml), and $Co_2(CO)_8$ (142 mg, 0.415 mmol) was added to the solution. The reaction mixture was stirred at room temperature for 3 h. Solvent was then removed under reduced pressure, and the crude product was purified by column chromatography (silica, hexanes) to yield **8** as a red solid (67.5 mg, 0.0191 mmol, 91.8%). ^{1}H NMR (400 MHz, $CDCl_3$) δ/ppm 7.50 (m, 22H, $H^{A,B}$), 0.42 (s, 36H, C^{Me}). ^{13}C NMR (100 MHz, $CDCl_3$) δ/ppm 199.8 (C^{CO}), 198.6 (C^{CO}), 198.4 (C^{CO}), 140.2, 140.1, 138.2, 137.7, 130.5, 129.6, 129.5, 128.0, 104.4 ($C^{C\equiv CTMS}$), 94.2 ($C^{C\equiv CTMS}$), 91.1 ($C^{C\equiv C}$), 90.4 ($C^{C\equiv C}$), 79.8 ($C^{C\equiv C}$), 0.8 (C^{Me}). MALDI-MS m/z 987 $[M–18Co–54CO + Na]^+$. IR (ν, cm^{-1}) 2085s, 2046s, 1988vs, 1730w, 1573m, 1481m, 1402m, 1247s, 1109m, 885m, 833vs, 758w, 687w.

2.9. Compound 9

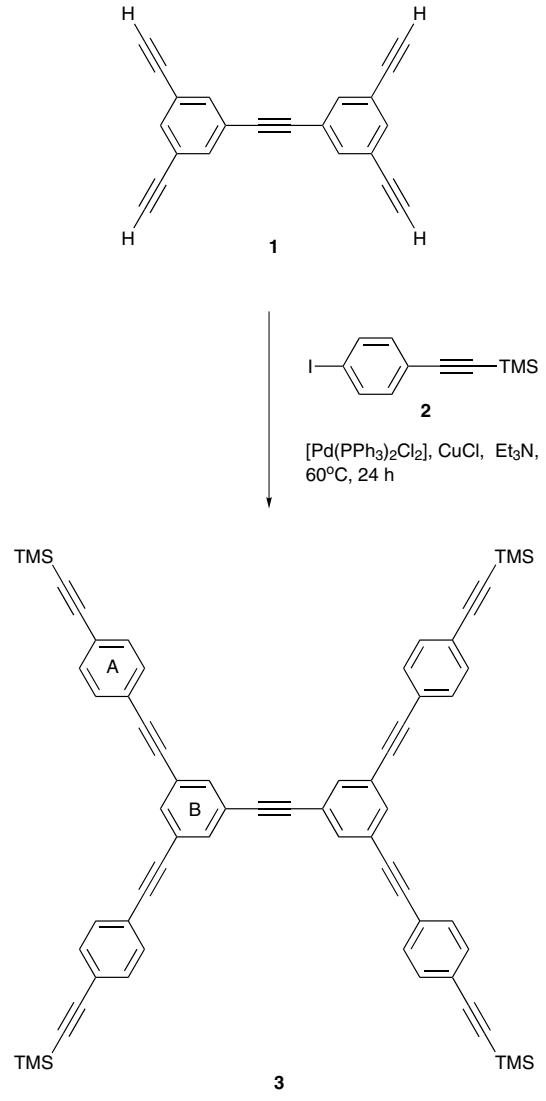
Compound **7** (35.0 mg, 0.0257 mmol) was dissolved in CH_2Cl_2 (50 ml), and $Co_2(CO)_8$ (253 mg, 0.740 mmol) was added to the solution. The reaction mixture was stirred at room temperature for 3 h. Solvent was removed, and the crude product was purified by column chromatography (silica, hexanes: CH_2Cl_2 1:0 changing to 10:1 during elution) to yield **9** as a red solid (101 mg, 0.0199 mmol, 77.3%). ^{1}H NMR (400 MHz, $CDCl_3$) δ/ppm 7.39 (m, 18H, $H^{A,B}$), 0.25 (s, 72H, C^{Me}). ^{13}C NMR (100 MHz, $CDCl_3$) δ/ppm 199.6 (C^{CO}), 199.0 (C^{CO}), 198.5 (C^{CO}), 140.5, 140.0, 139.9, 139.8, 133.4, 131.7, 131.5, 129.6, 103.8 ($C^{C\equiv CTMS}$), 93.3 ($C^{C\equiv CTMS}$), 93.0 ($C^{C\equiv C}$), 88.2 ($C^{C\equiv C}$), 80.3 ($C^{C\equiv C}$), 0.9 (C^{Me}). MALDI-MS see text. IR (ν, cm^{-1}) 2091s, 2044s, 1998vs, 1767w, 1573m, 1497w, 1404m, 1250s, 1011w, 833vs, 756m, 679m.

2.10. Crystal structure determination of 4

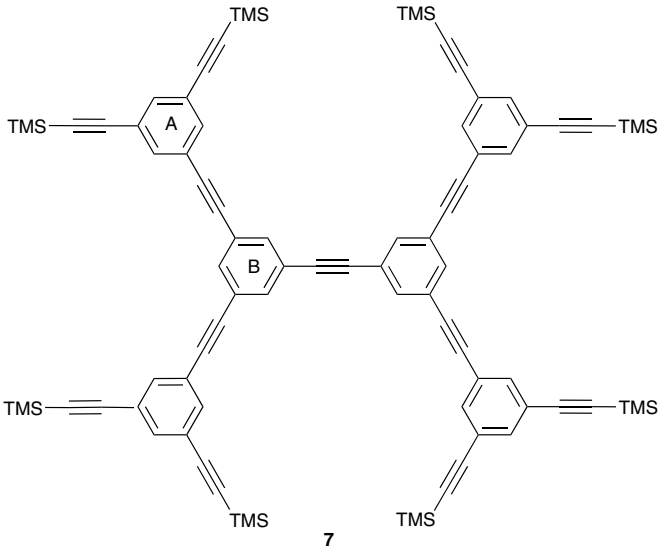
Data were collected on an Enraf Nonius Kappa CCD instrument; data reduction, solution and refinement used the programs COLLECT [28], SIR92 [29] and CRYSTALS [30]. Crystal data for **4**: $C_{16}H_{21}NO_2Si_2$, $M = 315.52$, monoclinic, space group $C2$, $a = 30.8355(3)$, $b = 8.4122(1)$, $c = 17.9490(2)$ Å, $\beta = 99.1107(7)°$; $U = 4597.13(9)$ Å^3, $Z = 10$, $D_c = 1.140$ g cm^{-3}, μ(Mo Kα) = 0.196 mm^{-1}, $T = 173$ K, 19 002 reflections collected, 5616 unique reflections. Refinement of 477 parameters against F^2 using all data converged to a final $R_1 = 0.0515$ ($I > 2.0\sigma$, 0.0619 all data), $wR_2 = 0.1711$ ($I > 2.0\sigma$, 0.1740 all data), Goodness-of-fit = 0.9827.

3. Results and discussion

We have previously reported the preparation and characterization of compound **1** (Scheme 1) as part of a study of small polyalkyne frameworks and their cobalt cluster-decorated derivatives [22]. We now report the use of **1** as an alkyne-centred core for the construction of a first generation star and dendrimer. Each terminal alkyne in **1** is easily coupled to the linear, protected alkyne **2** by Sonogashira methodology [31,32] (Scheme 2). We observed that coupling occurred more effectively using the iodo-derivative **2** rather than the analogous bromo-compound. A slight excess over the stoichiometrically required four equivalents of **2** was needed to optimize the yield of product **3**. Compound **3** was characterized by spectroscopic and mass spectrometric methods. The highest mass peak in the FAB mass spectrum of **3** at m/z 963 corresponded to the parent ion, although facile loss of the TMS protecting group led to a base peak at m/z 73. The ^{1}H NMR spectrum confirmed the expected symmetry of the product, with singlets at δ 7.63 and 7.47 ppm assigned on the basis of relative integrals to protons H^B and H^A, respectively. Four equivalent TMS groups gave rise to a singlet at δ 0.28 ppm. The ^{13}C NMR spectrum was also consistent with the expected



Scheme 2. Synthetic route to compound **3** (first generation star), and ring labelling for the NMR spectroscopic assignments.



Scheme 3. Compound **7** (first generation dendrimer), and ring labelling for the NMR spectroscopic assignments.

symmetry of **3**, with the appearance of five signals in the region for the alkyne carbon atoms. Following from our earlier observations for related systems [22], we assign the carbons for the outermost alkyne groups to the signals of highest frequency (δ 104.5 and 96.6 ppm) with the innermost alkyne carbons coming at δ 90.3, 89.5 and 88.9 ppm.

For the formation of the first generation dendrimer **7** shown in Scheme 3, the most desirable unit to react with **1** was iodo-derivative **6**. The first strategy that we adopted for the synthesis of **6** was the conversion of 3,5-dibromonitrobenzene to the bis(alkyne) derivative **4**, followed by reduction to amine **5**, and final conversion to **6**. The initial Sonogashira coupling was successful, and produced **4** in 54.6% yield. Although this compound has been reported previously [25,26], its solid state structure has not been determined. X-ray quality crystals of **4** were grown from CH_2Cl_2 solution. Interestingly, although achiral, **4** crystallizes in the chiral space group *C*2 [33,34]. There are three independent molecules in the unit cell, one of which (molecule A) is located on a special position and thus contains a 2-fold axis. The independent molecules B and C and half of molecule A together form a chiral building block that assembles into a chiral structure. The three molecules are structurally similar, and one molecule (type B) is shown in Fig. 1. Selected bond lengths and angles are given in the figure caption and are unexceptional. For the two molecules (molecules B and C) that do not lie on special positions, the nitro group is twisted with respect to the aryl ring (angles between the least squares planes of NO_2 and C_6 ring are 13.5(7)° (molecule B, Fig. 1) and 4.6(6)° (molecule C). These angles compare with a range of 5.6–17.0° in other 1-NO_2-3,5-(RC≡C)$_2$C$_4$H$_3$-type compounds [26,35,36] found in a search of the Cambridge Structural Database

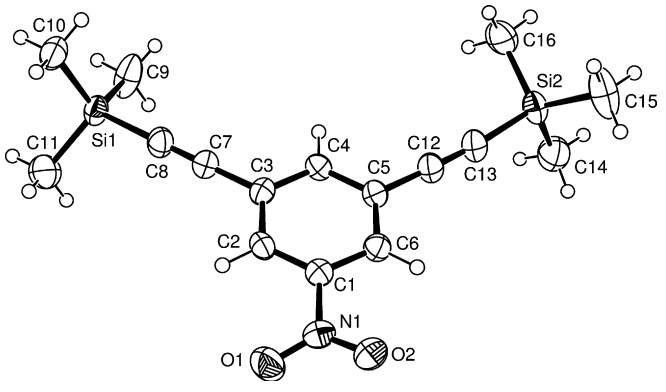


Fig. 1. The molecular structure of one of three crystallographically independent (but structurally similar) molecules of **4**. Selected bond parameters: O1–N1 = 1.223(6), O2–N1 = 1.212(6), N1–C1 = 1.480(7), C3–C7 = 1.447(7), C5–C12 = 1.445(7), C7–C8 = 1.193(7), C12–C13 = 1.196(7), Si–C range 1.846(6)–1.863(8) Å; O1–N1–O2 = 123.5(5), O1–N1–C1 = 118.2(5), O2–N1–C1 = 118.3(5), C3–C7–C8 = 177.8(5), Si1–C8–C7 = 174.1(5), C5–C12–C13 = 178.1(6), Si2–C13–C12 = 174.0(5)°.

[37,38]. The packing of the molecules in the solid state deserves a mention. Fig. 2a views the unit cell down the crystallographic *b*-axis. Each molecule lying on a special position is the central member of a group of three (BAB) molecules, while molecules C are arranged in pairs. Extension of these motifs generates triple or double layers of molecules, respectively. This is shown for the triple layers in Fig. 2b. All molecules within one type of layer are oriented in the same direction (Fig. 2b and c), whereas molecules in triple and double layers are oriented in opposite directions (Fig. 2a). Within each layer, the principal intermolecular interactions arise from the fact that each NO_2 group lies directly over an aromatic ring (Fig. 2c). In the double layers, the C···N distance is 3.23 Å, and the C···O distances are 3.36 and 3.19 Å. In the triple layers, the stacking of molecules leads to alternating NO_2···aryl···NO_2 (C···N = 3.34 Å) and aryl···NO_2···aryl (C···N = 3.32 Å) sandwiches.

Attempts to reduce compound **4** to amine **5** were unsuccessful, and this strategy to building block **6** was therefore abandoned. Our second approach was to start with an amino precursor, but required the use of the more reactive iodo- rather than bromo-derivative for reaction with TMSC≡CH. Compound **5** was obtained in almost quantitative yield by the Sonogashira coupling of 3,5-diiodoaniline with two equivalents of TMSC≡CH. Conversion of **5** to **6** (Scheme 4) was carried out using Sandmeyer conditions, and **6** was obtained in 75.1% yield. In its FAB mass spectrum, the highest mass peak at *m*/*z* 396 was assigned to the parent ion, with the base peak (*m*/*z* 381) arising from loss of a methyl group. ^{1}H and ^{13}C NMR spectroscopic data were fully in accord with the symmetry of **6**, confirming the introduction of two alkyne functionalities. With an efficient route to **6** established, we were able to proceed to the assembly of the first generation dendrimer **7** (Scheme 3). Reaction of **1** with just over four equivalents of **6** under Sonogashira conditions gave, after workup, polyyne **7** in 26.0% yield. The highest mass peak (*m*/*z* 1346) in the MALDI mass spectrum of the product was assigned to the parent ion, but as with other protected alkynes reported here, facile loss of a methyl group generated the base peak (*m*/*z* 1331). The ^{1}H NMR spectrum was simple, exhibiting only two signals at δ 7.57 and 0.25 ppm, consistent with complete functionalization of the dendrimer core **1**, and

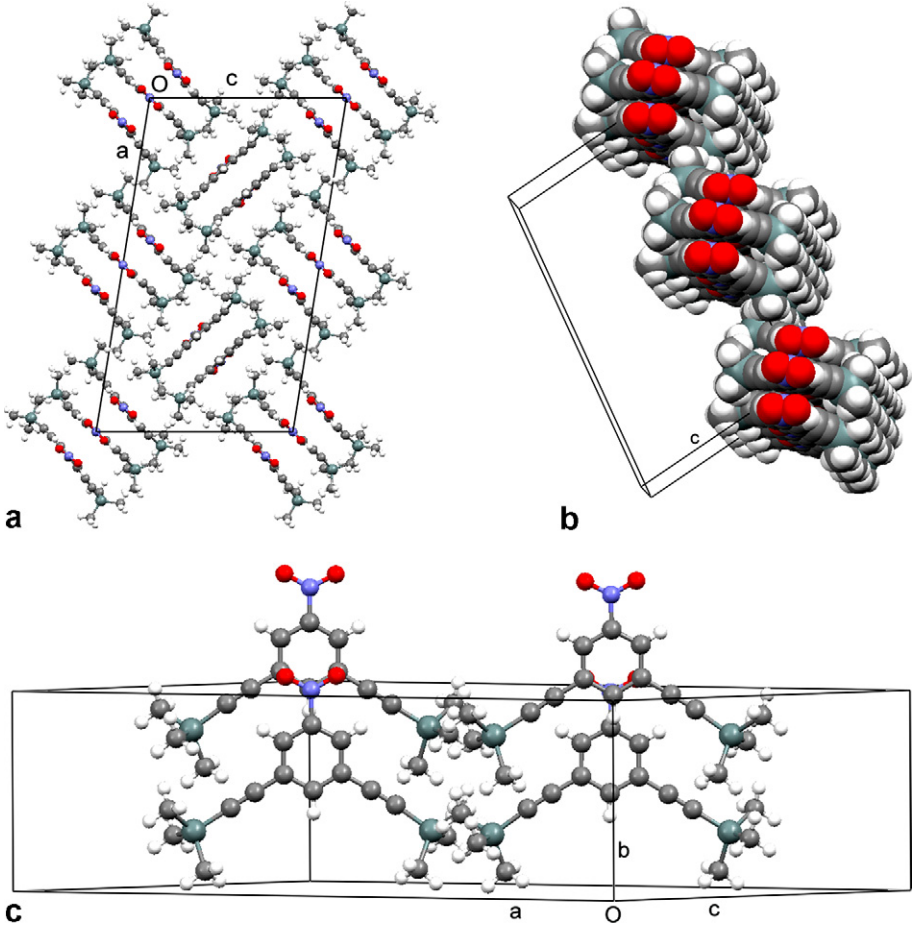
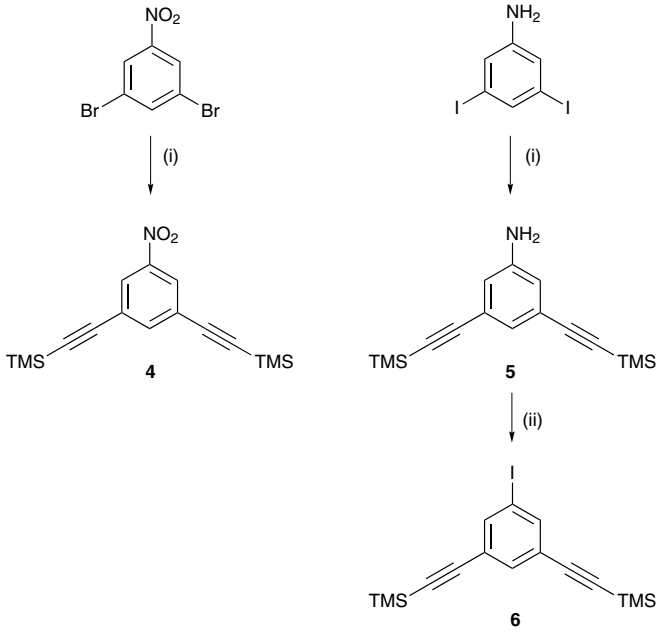


Fig. 2. Packing of molecules of **4**: (a) the unit cell viewed along the *b*-axis; (b) triple layers of molecules running parallel to the *b*-axis; (c) double layers are formed by stacking of molecules C.

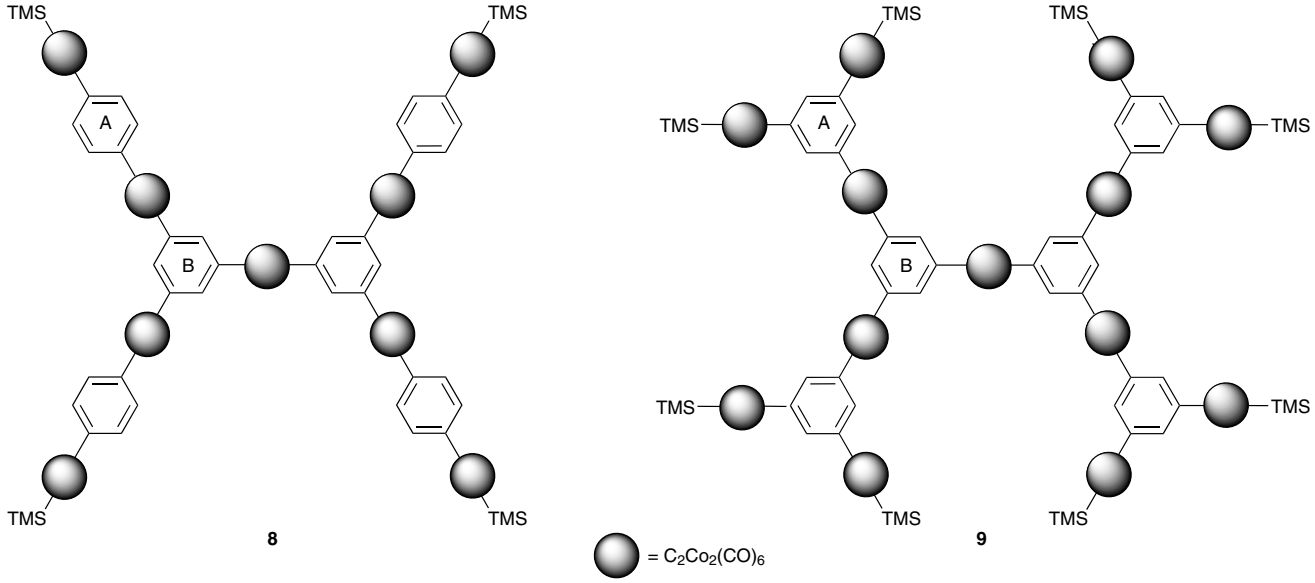


Scheme 4. Synthetic conditions for the formation of **4** and **6**: (i) $[Pd(PPh_3)_2Cl_2]$, CuCl, TMSC≡CH, Et_3N, 60 °C, 20 h; (ii) $NaNO_2$, HCl, CuI, KI, 0 °C, 6 h.

the formation of a monodispersed product. The ^{13}C NMR spectrum was also in accord with the degree of molecular symmetry expected for **7**.

Each of polyynes **3** and **7** reacted with $Co_2(CO)_8$ in CH_2Cl_2 solution at room temperature. A significant excess of $Co_2(CO)_8$ was needed in order to achieve complete functionalization of the alkyne domains (ratio **3**: $Co_2(CO)_8 \approx 1{:}20$, and **7**: $Co_2(CO)_8 \approx 1{:}29$). Chromatographic workup resulted in **8** and **9** (Scheme 5) being isolated in high yield, but all attempts to grow X-ray quality crystals led to decomposition of the materials, and good elemental analytical data could not be obtained. Characterization of the compounds therefore relied on spectroscopic techniques.

The IR spectra of **8** and **9** showed the characteristic signature of a $C_2Co_2(CO)_6$ unit in the carbonyl region. The ^1H NMR spectrum of **9** exhibited a multiplet at δ 7.39 ppm and a singlet at δ 0.25 ppm; the presence of one TMS environment was consistent with a symmetrical product. A well-resolved ^{13}C NMR spectrum of **9** was particularly informative. The ^{13}C NMR spectra of asymmetrical clusters of type $Co_2(CO)_6C_2RR'$ typically exhibit only one signal for the six carbonyl ^{13}C nuclei [39]. For **9**, the ^{13}C NMR spectrum revealed three CO environments (δ 199.6, 199.0 and 198.5 ppm with approximate relative integrals of 8:1:4). These data support the presence of three cluster environments and the symmetry of the structure for **9** shown in Scheme 5. The ^1H NMR spectrum of **8** exhibited a multiplet at δ 7.50 ppm and singlet at δ 0.42 ppm, but the latter signal had a shoulder at δ 0.44 ppm. The relative integrals of these signals were approximately 10:1. Examination of the spectrum revealed a low intensity signal at δ 6.4 ppm [22] that was assigned to a C≡CH proton, indicating that a degree of deprotection had occurred. This, together with the relative integrals of the aryl: TMS signals (≈24:38) suggested the presence of compound **8** and approximately 10% of a derivative of **8** in which one C≡CTMS group had been converted to C≡CH, or smaller amounts of derivatives with more than one deprotected terminal alkyne. Further support for this came from the carbonyl region of the ^{13}C NMR spectrum which exhibited signals at δ 199.8, 198.6 and 198.4 ppm with relative integrals 4:4:1, with additional low intensity signals at δ 198.9 and 198.2 ppm. A clean sample of **9** could not be obtained. On going from **3** to **8**, and from **7** to **9**, five ^{13}C NMR resonances are retained in the alkyne region for



Scheme 5. Cobalt carbonyl derivatives **8** (star) and **9** (first generation dendrimer), with ring labelling for the NMR spectroscopic assignments.

each compound. Signals in the ^{13}C NMR spectrum of **8** for the deprotected derivative could not be resolved. Although the addition of the $Co_2(CO)_6$ unit to the alkyne functionality causes only a small shift in the associated ^{13}C signals, it is sufficient to indicate that Co_2C_2-cluster formation has occurred [22].

We have previously observed that either FAB-MS or MALDI-TOF mass spectrometry is suited to the characterization of cobalt-cluster functionalized polyynes, depending on the size of the molecule [22]. The highest mass peak in the MALDI-TOF of **8** was observed at *m*/*z* 987 and could be assigned to $[M–18Co–54CO + Na]^+$, i.e. total loss of the nine $Co_2(CO)_6$ units appears to be facile under laser irradiation conditions. For compound **9**, we did not observe a well-resolved MALDI-TOF spectrum, although a low intensity peak corresponding to the polyyne framework (*m*/*z* 1349) was detected; attempts with and without matrix were made. We conclude that we have reached the upper limits of the usefulness of MALDI-TOF mass spectrometry for the characterization of compounds of this family.

4. Conclusions

We have reported synthetic strategies for the construction of alkyne-centred first generation star and dendritic polyynes, and their reactions with $Co_2(CO)_8$ to produce fully decorated cobalt-cluster containing species. Characterization of the latter is not trivial. Crystal growth tends to lead to decomposition, and MALDI-TOF mass spectrometry (which has proven invaluable for related, but smaller, molecules) fails to give definitive information. The most useful technique for characterization of the compounds is ^{13}C NMR spectroscopy. In particular, well-resolved spectra allow one to distinguish between the core, inner and peripheral cluster domains, adding to the correlation data that we have previously reported [22].

Acknowledgements

We thank the Swiss National Science Foundation and the University of Basel for financial support.

Appendix A. Supplementary material

CCDC 620904 contains the supplementary crystallographic data for **4**. These data can be obtained free of charge via http://www.ccdc.ac.uk/conts/retrieving.html, or from the Cambridge Crystallographic Data Centre, 12 Union Road, Cambridge CB2 1EZ, UK; fax: (+44) 1223-336-033; or e-mail: deposit@ccdc.cam.ac.uk. Supplementary data associated with this article can be found, in the online version, at doi:10.1016/j.poly.2006.10.037.

References

[1] N.J. Long, C.K. Williams, Angew. Chem., Int. Ed. 42 (2003) 2586.
[2] R.P. Kingsborough, T.M. Swager, Prog. Inorg. Chem. 48 (1999) 123.
[3] U.H.F. Bunz, Chem. Rev. 100 (2000) 1605.
[4] U.H.F. Bunz, Y. Rubin, Y. Tobe, Chem. Soc. Rev. 28 (1999) 107.
[5] S. Szafert, J.A. Gladysz, Chem. Rev. 103 (2003) 4175.
[6] P.F.H. Schwab, M.D. Levin, J. Michl, Chem. Rev. 99 (1999) 1863.
[7] T. Ren, Organometallics 24 (2005) 4854.
[8] W.-Y. Wong, J. Inorg. Organomet. Polym. Mater. 15 (2005) 197.
[9] J.-F. Nierengarten, Pure Appl. Chem. 78 (2006) 847.
[10] S. Leininger, P.J. Stang, Organometallics 17 (1998) 3981.
[11] A.M. McDonagh, C.E. Powell, J.P. Morrall, M.P. Cifuentes, M.G. Humphrey, Organometallics 22 (2003) 1402.
[12] J.G. Rodríguez, J. Esquivias, A. Lafuente, C. Diaz, J. Org. Chem. 68 (2003) 8120.
[13] J.G. Rodríguez, J. Esquivias, Tetrahedron Lett. 44 (2003) 4831.
[14] M. Osawa, M. Hoshino, S. Horiuchi, Y. Wakatsuki, Organometallics 18 (1999) 112.
[15] N. Ohshiro, F. Takei, K. Onitsuka, S. Takahashi, J. Organomet. Chem. 569 (1998) 195.
[16] C. Chi, J. Wu, X. Zhao, J. Li, F. Wang, Tetrahedron Lett. 42 (2001) 2181.
[17] C. Chi, J. Wu, X. Wang, X. Zhao, J. Li, F. Wang, Macromolecules 34 (2001) 3812.
[18] E.C. Constable, O. Eich, C.E. Housecroft, L.A. Johnston, Chem. Commun. (1998) 2661.
[19] E.C. Constable, O. Eich, C.E. Housecroft, J. Chem. Soc., Dalton Trans. (1999) 1363.
[20] E.C. Constable, O. Eich, C.E. Housecroft, Inorg. Chem. Commun. 2 (1999) 431.
[21] E.C. Constable, O. Eich, D. Fenske, C.E. Housecroft, L.A. Johnston, Chem. Eur. J. 6 (2000) 4364.
[22] E.C. Constable, D. Gusmeroli, C.E. Housecroft, M. Neuburger, S. Schaffner, Polyhedron 25 (2006) 421.
[23] P. Wautelet, J. Le Moigne, V. Videva, P. Turek, J. Org. Chem. 68 (2003) 8025.
[24] G.-J. ten Brink, J.M. Vis, I.W.C.E. Arends, R.A. Sheldon, Tetrahedron 58 (2002) 3977.
[25] F. Chimenti, A. Bolasco, D. Secci, P. Chimenti, A. Granese, Synth. Commun. 34 (2004) 2549.
[26] B. Traber, T. Oeser, R. Gleiter, Eur. J. Org. Chem. (2005) 1283.
[27] O. Lavastre, L. Ollivier, P.H. Dixneuf, Tetrahedron 52 (1996) 5495.
[28] COLLECT Software, Nonius BV 1997–2001.
[29] A. Altomare, G. Cascarano, G. Giacovazzo, A. Guagliardi, M.C. Burla, G. Polidori, M. Camalli, J. Appl. Crystallogr. 27 (1994) 435.
[30] P.W. Betteridge, J.R. Carruthers, R.I. Cooper, K. Prout, D.J. Watkin, J. Appl. Crystallogr. 36 (2003) 1487.
[31] K. Sonogashira, Y. Tohda, N. Hagihara, Tetrahedron Lett. 16 (1975) 4467.
[32] K. Sonogashira, J. Organomet. Chem. 653 (2002) 46.
[33] H.D. Flack, Helv. Chim. Acta 86 (2003) 905.
[34] E. Pidcock, Chem. Commun. (2004) 3457.
[35] D.L. An, T. Nakano, A. Orita, J. Otera, Angew. Chem. Int.Ed. 41 (2002) 171.
[36] K. Xu, D.M. Ho, R.A. Pascal Jr., J. Org. Chem. 60 (1995) 7186.
[37] F.H. Allen, Acta Crystallogr., Sect. B 58 (2002) 380.
[38] I.J. Bruno, J.C. Cole, P.R. Edgington, M.K. Kessler, C.F. Macrae, P. McCabe, J. Pearson, R. Taylor, Acta Crystallogr., Sect. B 58 (2002) 389.
[39] S. Aime, L. Milone, R. Rossetti, P.L. Stanghellini, Inorg. Chim. Acta 22 (1977) 135.

Arguably the most extensively studied luminescent lanthanide complexes are those with β-diketonate ligands [6]. When three β-diketonate ligands coordinate a trivalent lanthanide ion, an electrically neutral complex is produced. Unless a sterically encumbering β-diketonate ligand is used, additional ligands such as water and other Lewis bases are necessary in order to fulfill the high coordination requirement of these large metal ions. For practical applications, non-aqua neutral ligands are typically used, as high phonon energy OH oscillators can bridge off at very high rates the energy of the excited states of a lanthanide ion, leading to low quantum efficiency of light emission [7].

The property of the Lewis base adduct of a lanthanide β-diketonate depends on not only the diketonate but also the accompanying neutral ligand(s). Specifically, while the wavelength of light emission is inherently metal-dependent, its quantum efficiency is heavily dependent on how well the energetic levels of the ligand singlet, triplet, and the lanthanide emissive states are matched, a direct consequence of the ligand-assisted transfer of excitation energy [3,4,8]. Other properties such as thermal stability, solubility, and film-forming characteristics (for the fabrication of light-emitting devices) are also strongly dependent on the nature of the ligands.

We have been interested in the design and synthesis of lanthanide β-diketonates for applications as light-emitting materials in organic electroluminescent devices, as they offer a number of advantages over the much studied conducting polymers and other non-lanthanide materials [9]. Specifically, we have been looking at ligand design as a fundamental means of enhancing the thermal stability of a complex and improving its charge-carrier transporting ability in a working device [10]. For example, a terbium complex with acetylacetonate ligand modified with an electron-withdrawing oxadiazolyl group has been shown to possess higher thermal stability than its unmodified counterpart. More importantly, significantly improved electroluminescence device performance was also achieved [10]. In comparison, the unmodified complex barely produced any green emission using an otherwise identically configured device. Work by others has also validated this ligand design approach for producing improved electroluminescent lanthanide materials [11].

The neutral ligands are equally important in modifying the properties of luminescent lanthanide β-diketonates. Just like the negatively charged ligands, neutral ligands contribute to the overall stability of the resulting complex. They may also serve to promote energy transfer for light emission. Based on such considerations, we have recently started the quest for adducts of lanthanide β-diketonates with unique neutral ligands [12]. One of the ligands of interest is 2,4,6-tri(2-pyridyl)-1,3,5-triazine (TPTZ), a bulky aromatic compound featuring three 2-pyridyl rings fixed on a central 1,3,5-triazine platform [13]. This ligand has been studied previously for its application in actinide–lanthanide group separations in a synergistic extraction system [14]. There also exist a few structurally characterized lanthanide complexes in which TPTZ acts as a tridentate ligand [15,16]. However, TPTZ adducts of lanthanide β-diketonates are unknown prior to our work. In addition to the novelty of such complexes, the bulky ligand, by offering three coordinating atoms, helps protect the lanthanide ion from interacting with solvent molecules, and therefore, suppressing solvent-based vibrational coupling and luminescence quenching [17]. Furthermore, the remaining nitrogen atoms allow for further coordination to other metals, transition metals in particular. Thus, structurally sophisticated heterometallic complexes may be envisioned, for which novel magnetic as well as luminescence properties can be expected [18,19].

As a first step to many of the research opportunities elaborated above, we have prepared the TPTZ adducts of several lanthanide β-diketonates, wherein the lanthanide ion is Eu^{3+}, Tb^{3+}, or Er^{3+}, and the β-diketone is dibenzoylmethane (DBM), 1-benzoylacetone (BA), thenoyltrifluoroacetone (TTA), or 4,4,4-trifluoro-1-phenyl-1,3-butanedione (BTFA). The Eu^{3+} and Tb^{3+} complexes are synthesized as potential red- and green-emitting materials, respectively, while their Er^{3+} cognate is potentially useful in developing integrated lasers or fiber amplifiers due to its near infrared emission [20,21]. In this report, we describe in detail the synthesis, structural characterization by single-crystal diffraction, and photoluminescence studies of these new members of the lanthanide β-diketonate family.

2. Experimental

Reagents were of commercial origin (Aldrich) and were used as received. The recently reported procedure [12] for the synthesis of $Eu(DBM)_3TPTZ$ was adopted with modifications where necessary. Elemental analysis (CHN) was performed by Desert Analytics Laboratory, Tucson, Arizona.

2.1. Synthesis of $Tb(DBM)_3TPTZ$

A mixture of TPTZ (0.312 g, 1.00 mmol) and $TbCl_3 \cdot 6H_2O$ (0.265 g, 1.00 mmol) in 15 mL of absolute ethanol was stirred under reflux for 30 min to afford a clear solution. To this mixture was added over 10 min a solution of $KOBu^t$ (0.800 g, 7.130 mmol) and DBM (0.672 g, 3.00 mmol) in 20 mL of absolute ethanol, and the resulting mixture was stirred at 50 °C for 1 h, and then at room temperature for an additional 30 min. Ethanol was removed under vacuum, and the residue was washed with copious de-ionized water. The crude product thus obtained was dissolved in a minimum amount of chloroform, and the solution was dried over anhydrous $MgSO_4$. The filtrate was collected, from which a yellow solid was obtained upon removal of the solvent. Upon recrystallization from ethanol/chloroform (v/v 2:1), analytically pure product was obtained as a yellow crystalline solid (0.73 g, 64.0%). *Anal.* Calc. for $C_{63}H_{45}N_6O_6Tb$: C, 66.32; H, 3.98; N, 7.36. Found: C, 66.44; H, 3.96; N, 7.08%.

2.2. Synthesis of Er(DBM)$_3$TPTZ

This compound was prepared by starting with $ErCl_3 \cdot 6H_2O$ (0.382 g, 1.00 mmol) and adopting otherwise identical preparative and purification procedures to those for Tb(DBM)$_3$TPTZ. The product was obtained as a pale yellow crystalline solid (1.02 g, 88.8%). *Anal.* Calc. for $C_{63}H_{46}N_6O_{6.5}Er$: C, 65.32; H, 4.00; N, 7.25. Found: C, 65.45; H, 4.33; N, 7.28%.

2.3. Synthesis of Eu(BA)$_3$TPTZ

A mixture of TPTZ (0.312 g, 1.00 mmol) and $EuCl_3 \cdot 6H_2O$ (0.366 g, 1.00 mmol) in 20 mL of absolute ethanol was stirred at 50 °C for 10 min to afford a clear solution. To this mixture was added with stirring a solution of $KOBu^t$ (0.600 g, 5.347 mmol) and BA (0.487 g, 3.00 mmol) in 15 mL of absolute ethanol. The resulting mixture was stirred at 60 °C for 0.5 h, and then at room temperature under nitrogen for an additional 1.5 h. Purification of the reaction mixture followed the procedures detailed above for Tb(DBM)$_3$TPTZ. Analytically pure product was obtained as a pale yellow crystalline solid (0.57 g, 60.0%) upon recrystallizing the crude product from ethanol: chloroform:hexane (v/v/v 2:1:1). *Anal.* Calc. for $C_{48}H_{40}N_6O_{6.5}Eu$: C, 60.25; H, 4.11; N, 8.80. Found: C, 60.25; H, 4.34; N, 9.01%.

2.4. Synthesis of Eu(BTFA)$_3$TPTZ

$EuCl_3 \cdot 6H_2O$ was allowed to react with TPTZ as described above. To this mixture was added with stirring a solution of $KOBu^t$ (0.336 g, 3.00 mmol) and BTFA (0.648 g, 3.00 mmol) in 20 mL of absolute ethanol. The resulting mixture was stirred at 60 °C for 30 min, and then at room temperature under nitrogen for an additional 3 h. The mixture was filtered and the solid was washed with copious de-ionized water to remove KCl byproduct. The crude product thus obtained was washed with hexane (3 mL), dissolved in acetone (50 ml), and the solution was dried over anhydrous $MgSO_4$. The filtrate was collected, from which a pale yellow solid was obtained upon removal of the solvent. Recrystallization from ethanol:acetone (v/v 1:1) afforded analytically pure product as a pale yellow crystalline solid (0.63 g, 57.0%). *Anal.* Calc. for $C_{48}H_{30}N_6O_6F_9Eu$: C, 51.95; H, 2.72; N, 7.57. Found: C, 51.56; H, 2.54; N, 7.37%.

2.5. Synthesis of Eu(TTA)$_3$TPTZ

Starting with $EuCl_36H_2O$ (0.366 g, 1.00 mmol) and adopting otherwise identical preparative and purification procedures described for Eu(BTFA)$_3$TPTZ, the product was obtained as a pale yellow crystalline solid (1.00 g, 78.0%). *Anal.* Calc. for $C_{42}H_{24}N_6O_6F_9S_3Eu$: C, 44.72; H, 2.14; N, 7.45. Found: C, 44.38; H, 2.20; N, 7.45%.

2.6. X-ray structure determinations

Single crystals of Tb(DBM)$_3$TPTZ and Er(DBM)$_3$-TPTZ suitable for X-ray diffraction studies were obtained by directly layering their respective saturated chloroform solutions with diethyl ether at room temperature. Single crystals of Eu(BTFA)$_3$TPTZ and Eu(TTA)$_3$TPTZ were produced by slow evaporation of their respective solutions in ethanol:acetone (v/v 1:1), while single crystals of Eu(BA)$_3$TPTZ were obtained from its solution in ethanol:chloroform:hexane (v/v/v 2:1:1).

The crystals were mounted on a glass fiber in a random orientation. Examination of the crystal was carried out on a Bruker SMART 1000 CCD detector X-ray diffractometer at 170(2) K and a power setting of 50 kV, 40 mA. Data were collected on the SMART1000 system using graphite monochromated Mo Kα radiation ($\lambda = 0.71073$ Å). The frames were integrated using the Bruker SAINT [22] software package's narrow frame algorithm, and empirical absorption and decay corrections were applied using the program SADABS [23]. The structures were solved using SHELXS in the Bruker SHELXTL (Version 5.0) software package [22]. Refinements were performed using SHELXL and illustrations were made using XP.

Solution was achieved by using direct methods followed by Fourier synthesis. Hydrogen atoms were added at idealized positions, constrained to ride on the atom to which they are bonded and given thermal parameters equal to 1.2 or 1.5 times U_{iso} of that bonded atom. Details on data collection and structure refinements are given in Table 1.

2.7. Photophysical studies

Electronic absorption spectra in the solid state and chloroform solutions were recorded on a Perkin–Elmer Lambda 10 spectrophotometer. Photoluminescence studies were carried out with a Fluorolog-3 fluorometer. The measured solid-state and solution-phase luminescence for the Tb^{3+} and Eu^{3+} complexes was excited by the light from a Xe-Arc lamp and detected using a photo multiplier tube at an angle of 90° with respect to the incident beam. Near infrared emission spectrum of Er(DBM)$_3$TPTZ was obtained at room temperature by excitation using a 980-nm laser diode (ADC Telecommunications), a grating monochromator, and an InGaAs detector (Thorlabs). A chopper and a lock-in amplifier were used for signal amplification.

Photoluminescence quantum yields were measured and calculated using cresyl violet perchlorate (quantum yield $\varphi = 0.54$ in methanol [24]) and rhodamin 6G ($\varphi = 0.95$ in ethanol [25]) as the standards. Corrections were made for the instrumental parameters and differing refractive indices of the solvents used [26,27]. The relative quantum yields were calculated using the following established equation where Abs, A, and n denote the absorbance at the excitation wavelength, integrated area of the corrected emission

Table 1
Crystal data and structure refinement for $Er(DBM)_3(TPTZ)$, $Tb(DBM)_3(TPTZ)$, $Eu(TTA)_3(TPTZ)$, $Eu(BA)_3(TPTZ)$, and $Eu(BTFA)_3(TPTZ)$

	$Er(DBM)_3(TPTZ)$	$Tb(DBM)_3(TPTZ)$
Empirical formula	$C_{65}H_{50}ErN_6O_6$	$C_{63}H_{45}TbN_6O_6$
Formula weight (g mol^{-1})	1186.37	1140.97
Temperature (K)	170(2)	170(2)
Wavelength (Å)	0.71073	0.71073
Crystal system	monoclinic	monoclinic
Space group	*I*2/*a*	*P*21/*c*
Unit cell dimensions		
a (Å)	25.3385(12)	9.5880(10)
b (Å)	17.0616(8)	23.062(3)
c (Å)	26.3956(13)	24.482(3)
β (°)	109.8140(10)	96.617(2)
Volume (Å^3)	10735.7(9)	5377.3(10)
Z	8	4
D_{calc} (mg/m^3)	1.468	1.409
Absorption coefficient (mm^{-1})	1.625	1.374
F(000)	4816	2312
Crystal size (mm^3)	$0.19 \times 0.19 \times 0.18$	$0.30 \times 0.20 \times 0.10$
θ Range for utilized data (°)	1.45–28.32	1.22–26.00
Limiting indices	$-33 \leqslant h \leqslant 33$, $-22 \leqslant k \leqslant 22$, $-35 \leqslant l \leqslant 35$	$-11 \leqslant h \leqslant 11$, $-28 \leqslant k \leqslant 28$, $-30 \leqslant l \leqslant 30$
Reflections utilized	67549	57456
Independent reflections [R_{int}]	13252 [0.1232]	10559 [0.1650]
Completeness to $\theta = 28.32°$ (%)	99.1	100.0
Absorption correction	semi-empirical from equivalents	semi-empirical from equivalents
Maximum and minimum transmission	0.7567 and 0.7470	0.8749 and 0.6834
Refinement method	full-matrix least-squares on F^2	full-matrix least-squares on F^2
Data/restraints/parameters	13251/250/730	10559/243/685
Goodness-of-fit on F^2	0.905	0.980
Final *R* indices [$I > 2\sigma(I)$]	$R_1 = 0.0346$, $wR_2 = 0.0717$	$R_1 = 0.0634$, $wR_2 = 0.1143$
R indices (all data)	$R_1 = 0.0559$, $wR_2 = 0.0765$	$R_1 = 0.1292$, $wR_2 = 0.1356$
Largest difference in peak and hole (e Å^{-3})	1.260 and −0.586	1.162 and −1.425
RMS difference in density (e Å^{-3})	0.109	0.134

	$Eu(TTA)_3(TPTZ)$	$Eu(BA)_3(TPTZ)$	$Eu(BTFA)_3(TPTZ)$
Empirical formula	$C_{46}H_{36}EuF_9N_6O_8S_3$	$C_{48}H_{39}EuN_6O_6$	$C_{50}H_{36}EuF_9N_6O_7$
Formula weight (g mol^{-1})	1219.95	947.81	1155.81
Temperature (K)	170(2)	170(2)	170(2)
Wavelength (Å)	0.71073	0.71073	0.71073
Crystal system	orthorhombic	monoclinic	triclinic
Space group	*P*212121	*P*21/*n*	$P\bar{1}$
Unit cell dimensions			
a (Å)	10.4683(8)	12.265(3)	11.0603(10)
b (Å)	15.5897(12)	27.548(6)	15.0588(13)
c (Å)	30.023(2)	12.472(3)	15.3027(14)
β (°)	90	93.576(5)	92.666(2)
Volume (Å^3)	4899.7(7)	4205.9(17)	2418.8(4)
Z	4	4	2
D_{calc} (mg/m^3)	1.654	1.497	1.587
Absorption coefficient (mm^{-1})	1.5014	1.549	1.390
F(000)	2440	1920	1156
Crystal size (mm^3)	$0.294 \times 0.174 \times 0.071$	$0.228 \times 0.223 \times 0.101$	$0.269 \times 0.310 \times 0.370$
θ Range for utilized data (°)	1.36–26.47	1.80–23.27	1.33–26.42
Limiting indices	$-13 \leqslant h \leqslant 13$, $-19 \leqslant k \leqslant 19$, $-37 \leqslant l \leqslant 37$	$-13 \leqslant h \leqslant 13$, $-28 \leqslant k \leqslant 30$, $-13 \leqslant l \leqslant 12$	$-13 \leqslant h \leqslant 13$, $-18 \leqslant k \leqslant 18$, $-19 \leqslant l \leqslant 19$
Reflections utilized	54175	25900	26593
Independent reflections [R_{int}]	10075 [0.1213]	6045 [0.1742]	9826 [0.0329]
Completeness to $\theta = 28.32°$ (%)	99.6	99.9 ($\theta = 23.27°$)	98.8
Absorption correction	semi-empirical from equivalents	semi-empirical from equivalents	semi-empirical from equivalents
Maximum and minimum transmission	1.0 and 0.895317	1.0 and 0.633047	0.7062 and 0.6274
Refinement method	full-matrix least-squares on F^2	full-matrix least-squares on F^2	full-matrix least-squares on F^2
Data/restraints/parameters	10075/855/725	6045/115/554	9826/0/662
Goodness-of-fit on F^2	1.108	1.095	1.080
Final *R* indices [$I > 2\sigma(I)$]	$R_1 = 0.0593$, $wR_2 = 0.1352$	$R_1 = 0.0663$, $wR_2 = 0.1532$	$R_1 = 0.0490$, $wR_2 = 0.1120$

Table 1 (*continued*)

	$Eu(TTA)_3(TPTZ)$	$Eu(BA)_3(TPTZ)$	$Eu(BTFA)_3(TPTZ)$
R indices (all data)	$R_1 = 0.1236$, $wR_2 = 0.1786$	$R_1 = 0.1777$, $wR_2 = 0.2247$	$R_1 = 0.0633$, $wR_2 = 0.1180$
Largest difference in peak and hole (e Å^{-3})	2.304 and −1.069	2.004 and −1.680	1.674 and −0.639
RMS difference in density (e Å^{-3})	0.183	0.172	0.096

spectrum, and refractive index of the solvent, respectively. Subscript R and S refer to the reference and the unknown sample, respectively [28,29]. The experiments were performed using chloroform solutions ($1–5 \times 10^{-5}$ M) of the title complexes whose absorbance values are less than 0.2. The experimental uncertainty for the quantum efficiency calculations was found to be 10%.

$$\varphi_S = \varphi_R(\mathrm{Abs}_R/\mathrm{Abs}_S)(A_S/A_R)(n_S^2/n_R^2)$$

The stoichiometry of each of the title complexes in the solution phase was evaluated by titration of the specific lanthanide chloride solution ($1–5 \times 10^{-5}$ M) with TPTZ and the corresponding β-diketone. A stock solution of the ligand was freshly prepared by deprotonation of the β-diketone using a stoichiometric amount of $KOBu^t$. Following each addition of the ligand (both TPTZ and β-diketonate) solution, the integrated emission intensities of the $^5D_0 \rightarrow {}^7F_2$ (for Eu^{3+} at 614 nm) and $^5D_4 \rightarrow {}^7F_5$ (for Tb^{3+} at 544 nm) transitions were monitored. Details of the experiments can be found in Supporting Information. The lanthanide (Eu^{3+} or Tb^{3+}):TPTZ ratio was found to be 1:1, while the ratio of Eu^{3+}:diketonate (BTFA, TTA, or BA) were found to be 1:3. However, the sensitization of Tb^{3+} luminescence by DBM is too weak to allow a reliable determination of the Tb^{3+}:DBM ratio. This finding is consistent with the results, presented below, of the spectroscopic and luminescence studies of $Tb(DBM)_3TPTZ$ in chloroform.

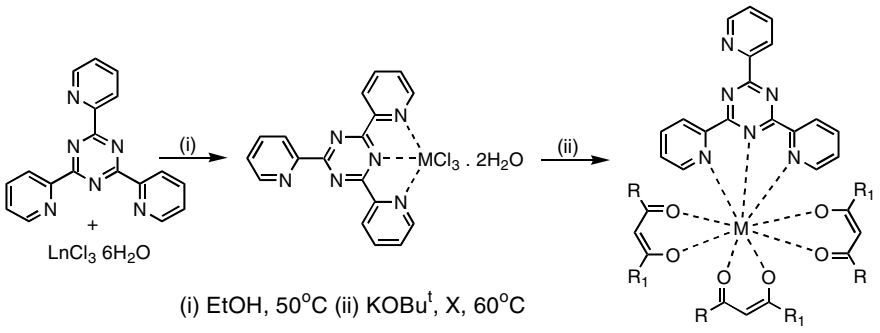
3. Results and discussion

3.1. Synthesis and structural characterization

As noted in our previous work, the Lewis base ligand (TPTZ) is introduced prior to the coordination of DBM, BA, TTA, or BTFA ligands (Scheme 1) to avoid possible adventitious hydrolysis which has been shown to produce unexpected polynuclear oxo/hydro complexes [30]. The pre-occupation of part of the coordination sphere by the rather bulky TPTZ ligand also helps prevent more than three β-diketonate ligands from being incorporated [31]. Thus, electrically neutral and coordinatively saturated complexes were obtained. All compounds were produced in good to excellent yields. They are readily soluble in solvents such as acetone, chloroform, and dichloromethane, but sparingly soluble in alcohols. Product purification by recrystallization from alcohol and one of these solubilizing solvents proved to be facile. Satisfactory microanalysis results (CHN) were obtained for all complexes.

The crystal structures of all five complexes have been established by single crystal X-ray diffraction, and are shown in Figs. 1–5, respectively. Selected metric values of bond distances and angles are summarized in Table 2.

In each of these complexes, the lanthanide ion is situated in a coordination sphere composed of six oxygen atoms of the β-diketonate ligands and three nitrogen atoms of the TPTZ ligand. The coordination polyhedron can be best



$Tb(DBM)_3TPTZ$: Ln=Tb; X=DBM; R=R_1=C_6H_5

$Er(DBM)_3TPTZ$: Ln=Er; X=DBM; R=R_1=C_6H_5

$Eu(TTA)_3TPTZ$: Ln=Eu; X=TTA; R=C_4H_3S, R_1=CF_3

$Eu(BA)_3TPTZ$: Ln=Eu; X=BA; R=C_6H_5, R_1=CH_3

$Eu(BTFA)_3TPTZ$: Ln=Eu; X=BTFA; R=C_6H_5, R_1=CF_3

Scheme 1. Synthesis of LnL_3TPTZ (Ln = Eu, Tb, Er; L = DBM, BA, TTA, BTFA).

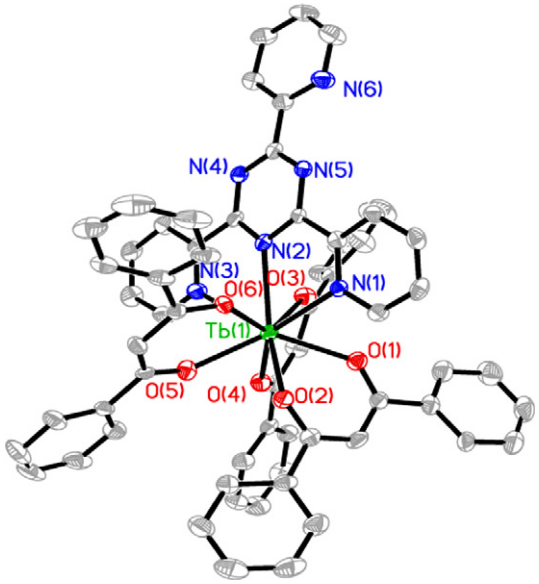


Fig. 1. An ORTEP view of the crystal structure of $Tb(DBM)_3(TPTZ)$ with partial atomic labeling. Thermal ellipsoids are drawn at the 30% probability level.

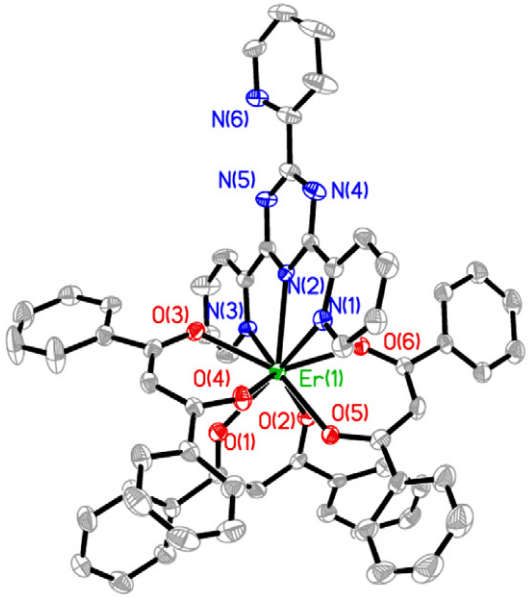


Fig. 2. An ORTEP view of the crystal structure of $Er(DBM)_3(TPTZ)$ with partial atomic labeling. Thermal ellipsoids are drawn at the 30% probability level.

described as a distorted square antiprism monocapped by the central coordinating nitrogen atom. The rather crowded coordination environment effectively protects the lanthanide center from any substantial interactions with potentially luminescence-quenching solvent molecules.

The aromatic rings of the TPTZ ligand are nearly coplanar in each of the five complexes. Within the same complex, the Ln–N bond to the central coordinating N is the shortest (indicated in bold face in Table 2), in agreement with our previous observation [12,32] and those made by

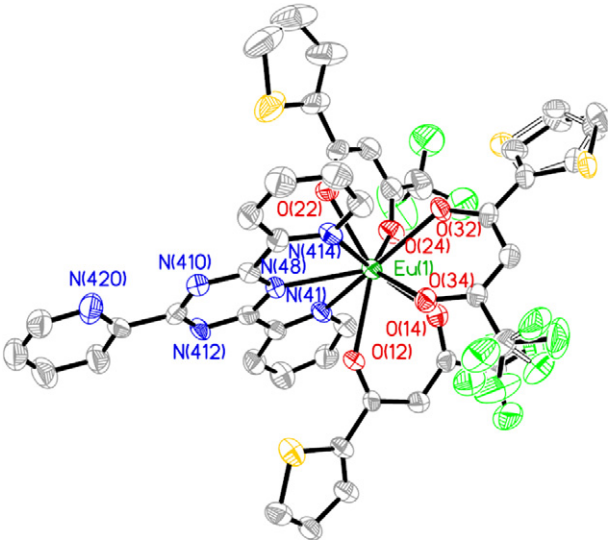


Fig. 3. An ORTEP view of the crystal structure of $Eu(TTA)_3(TPTZ)$ with partial atomic labeling. Thermal ellipsoids are drawn at the 50% probability level.

others [14–16,33]. It is also of interest to note that the Eu–N(central) bonds [2.6757(16) Å for $Eu(DBM)_3TPTZ$; 2.618(11) Å for $Eu(BA)_3TPTZ$; 2.580(7) Å for $Eu(TTA)_3$-TPTZ; 2.607(3) Å for $Eu(BTFA)_3TPTZ$] are all noticeably longer than that of $[Eu(TPTZ)Cl_3(MeOH)_2]$ [2.555(4) Å], the only other Eu–TPTZ complex [14]; the TPTZ ligand is understandably forced further away from the metal center by the bulkier diketonate ligands than if it is in a less coordinatively congested environment. By a similar argument, the presence of a bulky TPTZ ligand causes noticeably longer Eu–O distance (average) in the present adducts than those of closely related complexes with smaller neutral ligands. For example, the average Eu–O distance of $Eu(DBM)_3(TPTZ)$ is 2.384 Å versus 2.348 Å of $Eu(DBM)_3L$ [L = 2-(4′-dimethylaminophenyl)imidazo-[4,5-f]1,10-phenanthroline] [34]; the corresponding value for $Eu(BTFA)_3TPTZ$ is 2.405 Å versus 2.360 Å for $Eu(BTFA)_3(2,2'$-dipyridyl) [35].

The non-coordinating "arm" of the TPTZ ligand in $Eu(BA)_3TPTZ$ and $Eu(BTFA)_3TPTZ$ is close in space to a corresponding arm of a second molecule. As such, π-dimers are formed, with a separation between two TPTZ ligands of 3.155 and 3.285 Å, shown in Figs. 4 and 5, respectively. The formation of such π-dimers raises an interesting question of whether excimers can form in the solid state, a point inviting further investigation.

3.2. Electronic spectroscopic and photoluminescence studies

Electronic spectroscopic and photoluminescence studies have been carried out for the title complexes in both chloroform solutions and the solid state, from which very similar results have been obtained. In addition, luminescence titration experiments utilizing solutions with concentrations comparable to those for the luminescence quantum

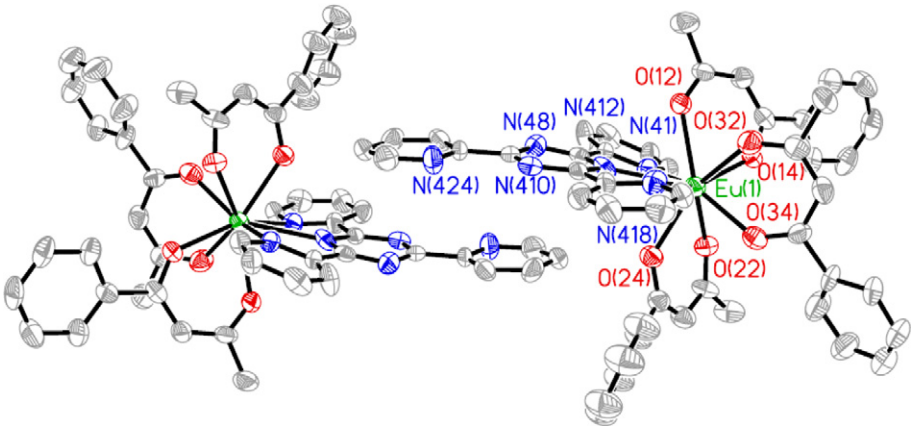


Fig. 4. The TPTZ ligands stack to form a centrosymmetric "dimer" in the crystal structure of $Eu(BA)_3TPTZ$. The closest contact between the TPTZ ligands is 3.155 Å.

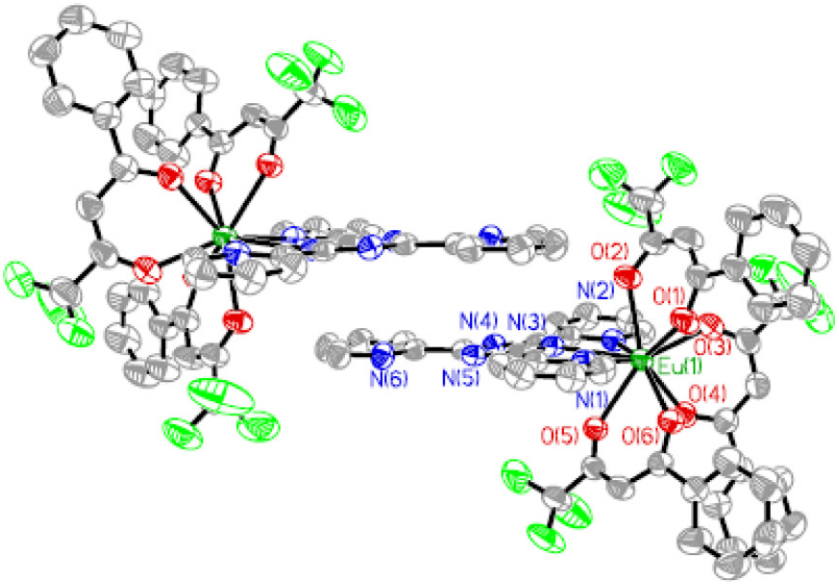


Fig. 5. The TPTZ ligands stack to form a centrosymmetric "dimer" in the crystal structure of $Eu(BTFA)_3TPTZ$. The closest contact between the TPTZ ligands is 3.285 Å.

yield measurements were also conducted. The observed ratio of 1:1:3 (TPTZ:Ln^{3+}:diketonate) is consistent with the molecular and crystal structures of the title complexes. In other words, the complexes remained un-dissociated in solution, even at the relatively low concentrations utilized.

The electronic absorption spectra of $Er(DBM)_3TPTZ$ and $Tb(DBM)_3TPTZ$ in chloroform each show three maxima at 250, 285, and 353 nm, independent of the central lanthanide metal. This observation is consistent with ligand-based absorptions [DBM (250 and 352 nm) and TPTZ (250 and 285 nm)] of these complexes. Complexes $Eu(BA)_3TPTZ$, $Eu(TTA)_3TPTZ$, and $Eu(BTFA)_3TPTZ$ also show ligand-based absorption in the range of 230–385 nm (Supporting Information).

The electronic excitation and photoluminescence of $Tb(DBM)_3TPTZ$, $Eu(BA)_3TPTZ$, $Eu(TTA)_3TPTZ$, and $Eu(BTFA)_3TPTZ$ were also studied in chloroform solutions.

It is clear that the excitation of these complexes is mostly ligand based. The maximum emission of the terbium complex was observed when the complex was excited at 290 nm, suggesting that ligand-to-Tb^{3+} energy transfer is mainly mediated by the TPTZ ligand (Fig. 6). In contrast, the strongest emissions of $Eu(BA)_3TPTZ$, $Eu(TTA)_3TPTZ$, and $Eu(BTFA)_3TPTZ$ were observed when the complexes were excited at 345, 355, and 342 nm, respectively. These excitation wavelengths match the absorption spectra of the corresponding β-diketonate ligands [12] (Supporting Information), suggesting that energy transfer originates from the β-diketonate ligands to Eu^{3+} ion. Only the excitation and emission spectra of $Eu(BA)_3TPTZ$ are shown in Fig. 7 as representatives. Those for $Eu(TTA)_3TPTZ$ and $Eu(BTFA)_3TPTZ$ are deposited in Supporting Information. These observations are in line with the commonly accepted notion of "antenna effect" for lanthanide luminescence [36,37].

Table 2
Selected bond distances (Å) and angles (°) of $Tb(DBM)_3(TPTZ)$, $Er(DBM)_3(TPTZ)$, $Eu(BA)_3TPTZ$, $Eu(TTA)_3TPTZ$, and $Eu(BTFA)_3TPTZ$

$Tb(DBM)_3TPTZ$		$Er(DBM)_3TPTZ$	
Tb(1)–O(1)	2.380(4)	Er(1)–O(1)	2.308(2)
Tb(1)–O(2)	2.335(4)	Er(1)–O(2)	2.373(2)
Tb(1)–O(3)	2.394(5)	Er(1)–O(3)	2.376(2)
Tb(1)–O(4)	2.327(4)	Er(1)–O(4)	2.314(2)
Tb(1)–O(5)	2.322(4)	Er(1)–O(5)	2.294(2)
Tb(1)–O(6)	2.421(4)	Er(1)–O(6)	2.326(2)
Tb(1)–N(1)	2.626(5)	Er(1)–N(1)	2.655(2)
Tb(1)–N(2)	**2.596(5)**	**Er(1)–N(2)**	**2.568(2)**
Tb(1)–N(3)	2.640(5)	Er(1)–N(3)	2.582(2)

$Eu(BA)_3TPTZ$		$Eu(TTA)_3TPTZ$		$Eu(BTFA)_3TPTZ$	
Eu(1)–O(34)	2.324(10)	Eu(1)–O(12)	2.602(7)	Eu(1)–O(1)	2.418(3)
Eu(1)–O(14)	2.349(9)	Eu(1)–O(14)	2.347(6)	Eu(1)–O(2)	2.397(3)
Eu(1)–O(24)	2.385(9)	Eu(1)–O(22)	2.404(6)	Eu(1)–O(3)	2.394(4)
Eu(1)–O(12)	2.406(9)	Eu(1)–O(24)	2.397(6)	Eu(1)–O(4)	2.433(3)
Eu(1)–O(32)	2.426(10)	Eu(1)–O(32)	2.399(6)	Eu(1)–O(5)	2.416(3)
Eu(1)–O(22)	2.466(9)	Eu(1)–O(34)	2.425(6)	Eu(1)–O(6)	2.373(3)
Eu(1)–N(41)	2.661(11)	Eu(1)–N(41)	2.602(7)	Eu(1)–N(1)	2.631(4)
Eu(1)–N(412)	**2.618(11)**	**Eu(1)–N(48)**	**2.580(7)**	**Eu(1)–N(3)**	**2.607(3)**
Eu(1)–N(418)	2.684(11)	Eu(1)–N(414)	2.634(8)	Eu(1)–N(2)	2.629(4)

$Tb(DBM)_3TPTZ$		$Er(DBM)_3TPTZ$	
O(1)–Tb(1)–O(2)	71.0(2)	O(1)–Er(1)–O(2)	70.7(1)
O(3)–Tb(1)–O(4)	73.0(2)	O(3)–Er(1)–O(4)	70.6(1)
O(5)–Tb(1)–O(6)	70.6(1)	O(5)–Er(1)–O(6)	75.1(1)
O(1)–Tb(1)–N(2)	113.5(2)	O(1)–Er(1)–N(2)	138.0(1)
O(3)–Tb(1)–N(2)	66.4(2)	O(3)–Er(1)–N(2)	69.7(1)
O(5)–Tb(1)–N(2)	114.0(2)	O(5)–Er(1)–N(2)	132.6(1)

$Eu(BA)_3TPTZ$		$Eu(TTA)_3TPTZ$		$Eu(BTFA)_3TPTZ$	
O(12)–Eu(1)–O(14)	73.3(3)	O(12)–Eu(1)–O(14)	72.5(2)	O(1)–Eu(1)–O(2)	71.0(1)
O(22)–Eu(1)–O(24)	70.1(3)	O(22)–Eu(1)–O(24)	68.9(2)	O(3)–Eu(1)–O(4)	68.0(1)
O(32)–Eu(1)–O(34)	70.1(3)	O(32)–Eu(1)–O(34)	70.6(2)	O(5)–Eu(1)–O(6)	71.5(1)
O(12)–Eu(1)–N(412)	68.9(3)	O(12)–Eu(1)–N(48)	67.0(2)	O(1)–Eu(1)–N(2)	138.7(1)
O(22)–Eu(1)–N(412)	109.6(3)	O(22)–Eu(1)–N(48)	72.9(2)	O(3)–Eu(1)–N(2)	79.8(1)
O(32)–Eu(1)–N(412)	116.3(3)	O(32)–Eu(1)–N(48)	143.8(2)	O(5)–Eu(1)–N(2)	82.4(1)

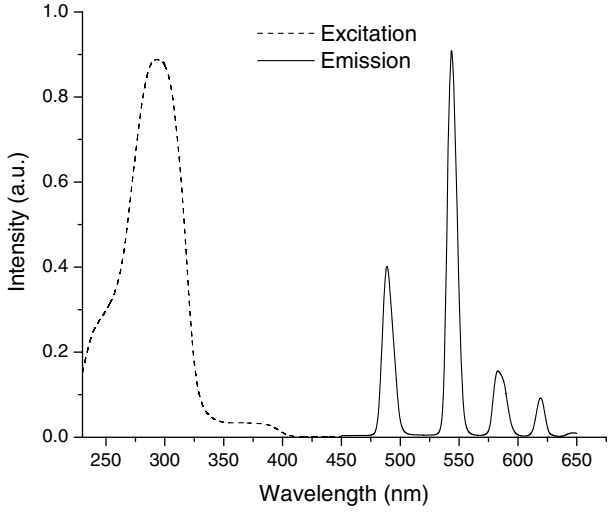


Fig. 6. The excitation (---) and emission (—) spectra of $Tb(DBM)_3TPTZ$ in $CHCl_3$.

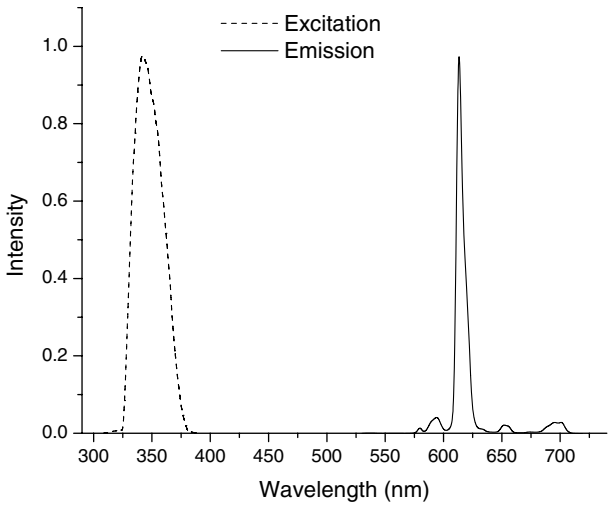


Fig. 7. The excitation (---) and emission (—) spectra of $Eu(BA)_3TPTZ$ in $CHCl_3$.

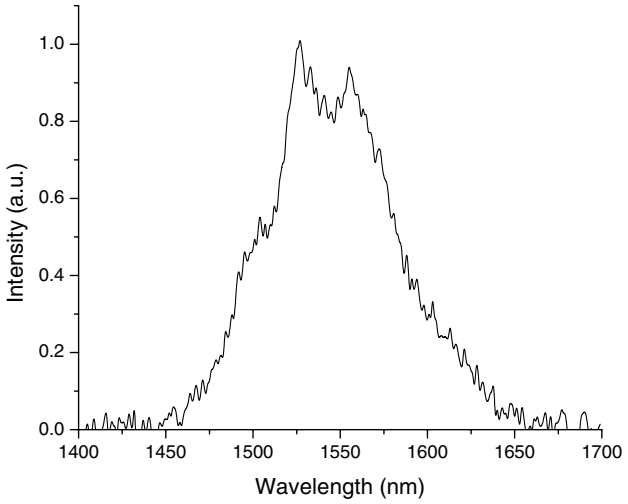


Fig. 8. The emission spectrum of $Er(DBM)_3TPTZ$ in $CHCl_3$.

The photoluminescence quantum yields of $Tb(DBM)_3$-TPTZ, $Eu(DBM)_3TPTZ$, $Eu(BA)_3TPTZ$, $Eu(TTA)_3TPTZ$, and $Eu(BTFA)_3TPTZ$ were found to be 3.4%, 17.4%, 15.5%, 40.2%, and 69.7% respectively. As expected, these lanthanide β-diketonate adducts with TPTZ display higher emission quantum yields than their aqua analogs [17,38]. In terms of photoluminescence quantum yield, $Eu(BTFA)_3$-TPTZ is among the most efficient Eu^{3+} complexes that are without substitution of H for D.

When the chloroform solution of $Er(DBM)_3TPTZ$ was excited by a 980-nm pump laser, near infrared emission, shown in Fig. 8, was observed. The maximum intensity peak is located at 1527 nm, assigned to $^4I_{13/2} \rightarrow {}^4I_{15/2}$, with a full width at half-maximum (FWHM) of about 81 nm. The value is greater than those of erbium-doped phosphate glass (55 nm) [39] and an erbium complex doped in epoxy resin polymers (47 nm) [40], but comparable to those of erbium polydentate cage complexes (70 nm) in organic solutions [41] and erbium tris(8-hydroxy)quinoline (73 nm) doped in sol–gels [20]. A broad spectrum enables a wide gain bandwidth for optical amplification in telecommunication systems.

4. Conclusion

Several new lanthanide β-diketonate adducts with the neutral ligand TPTZ were synthesized and their structures were established using single crystal X-ray diffraction. In each case, the lanthanide center is coordinatively saturated with three β-diketonate ligands and a TPTZ ligand. π–π interactions involving TPTZ ligands were observed with the formation of dimers of both $Eu(BA)_3TPTZ$ and $Eu(BTFA)_3TPTZ$. Photoluminescence studies confirmed that excitation of the complexes is originated from the ligand absorption of photons, and the emission is characteristic of the lanthanide ion of the complex. It is likely that the bulky TPTZ ligand enhances the luminescence efficiency of the title complexes over their aqua species by effectively shielding the lanthanide ions from interacting with luminescence-quenching solvent molecules.

Acknowledgements

This work was supported by NSF CAREER Grant No. CHE-0238790. Acknowledgment is also made to the Donors of The Petroleum Research Fund, administered by the American Chemical Society, for partial support of this research. We thank Professors S.S. Saavedra and K. Miranda for the use of fluorometers, Mr. H. Gan for experimental assistance, and Dr. G.S. Nichol for X-ray crystallographic assistance. The CCD-based X-ray diffractometer was purchased through an NSF Grant (CHE-96103474, USA).

Appendix A. Supplementary material

Details of spectroscopic and photoluminescence studies in both solution and the solid states. CCDC 238124, 238125, 618401, 618402 and 618403 contain the supplementary crystallographic data for $Tb(DBM)_3TPTZ$, $Er(DBM)_3TPTZ$, $Eu(TTA)_3TPTZ$, $Eu(BA)_3TPTZ$, and $Eu(BTFA)_3TPTZ$. These data can be obtained free of charge via http://www.ccdc.cam.ac.uk/conts/retrieving.html, or from the Cambridge Crystallographic Data Centre, 12 Union Road, Cambridge CB2 1EZ, UK; fax: (+44) 1223-336-033; or e-mail: deposit@ccdc.cam.ac.uk. Supplementary data associated with this article can be found, in the online version, at doi:10.1016/j.poly.2006.10.049.

References

[1] (a) J.-C.G. Bünzli, C. Piguet, Chem. Soc. Rev. 34 (2005) 1048;
(b) D. Parker, J.A.G. Williams, J. Chem. Soc., Dalton Trans. (1996) 3613;
(c) N. Sabbatini, M. Guardogi, J.M. Lehn, Coord. Chem. Rev. 123 (1993) 201.
[2] C. Görller-Walrand, K. Binnemans, Spectral intensities of f–f transitions, in: K.A. GschneidnerJr., L. Eyring (Eds.), Handbook on the Physics and Chemistry of Rare Earths, vol. 25, North-Holland, Amsterdam, 1998.
[3] (a) R.E. Whan, G.A. Crosby, J. Mol. Spectrosc. 8 (1962) 315;
(b) G.A. Crosby, R.E. Whan, R.M. Alire, J. Chem. Phys. 34 (1961) 743;
(c) G.A. Crosby, R.E. Whan, J.J. Freeman, J. Am. Chem. Soc. 66 (1962) 2493.
[4] M.L. Bhaumik, H. Li, B. Marciniiak, Coord. Chem. Rev. 99 (1990) 55.
[5] C. Yang, L.M. Fu, Y. Wang, J.P. Zhang, W.T. Wong, X.C. Ai, Y.F. Qiao, B.S. Zou, L.L. Gui, Angew. Chem. Int. Ed. 43 (2004) 5010.
[6] K. Binnemans, Rare-earth beta-diketonates, in: K.A. GschneidnerJr., J.-C.G. Bünzli, V.K. Pecharsky (Eds.), Handbook on the Physics and Chemistry of Rare Earths, vol. 35, B.V. Elsevier, 2005, pp. 107–252 (Chapter 225).
[7] W.D.W. Horrocks, D.R. Sudnick, Acc. Chem. Res. 14 (1981) 384.
[8] M. Latva, H. Takalo, V.-M. Mukkala, C. Matachescu, J.C. Rodriguez-Ubis, J. Kankare, J. Lumin. 75 (1997) 149.
[9] S. Dirr, A. Böhler, S. Wiese, H.H. Johannes, W. Kowalsky, Jpn. J. Appl. Phys. 37 (1998) 1457.

[10] R. Wang, R. Wang, J. Yang, Z. Zheng, M.D. Carducci, T. Cayou, N. Peyghambarian, G.E. Jabbour, J. Am. Chem. Soc. 123 (2001) 6179.
[11] (a) C.H. Huang, F.Y. Li, W. Huang, Introduction to Organic Light-Emitting Materials and Devices, Fudan Press, Shanghai, China, 2005 (Chapter 8);
(b) X. Gao, H. Cao, C. Huang, B. Li, S. Umitani, Appl. Phys. Lett. 72 (1998) 2217.
[12] C.R. De Silva, J. Wang, M.D. Carducci, S.A. Rajapakshe, Z. Zheng, Inorg. Chim. Acta 357 (2004) 630.
[13] G. Ionova, C. Raber, R. Guillaumont, S. Ionov, C. Madic, J.C. Krupa, D. Guillaneux, New J. Chem. 26 (2002) 234.
[14] R. Wietzke, M. Mazzanti, J. Latour, J. Pecaut, Inorg. Chem. 38 (1999) 3581.
[15] M.G.B. Drew, M.J. Hudson, P.B. Iverson, C. Madic, Acta Cryst. C56 (2000) 434.
[16] G.Y.S. Chan, M.G.B. Drew, M.J. Hudson, N.S. Isaacs, P. Byers, Polyhedron 15 (1996) 3385.
[17] E. Niyama, H.F. Brito, M. Cremona, E.E.S. Teotonio, R. Reyes, G.E.S. Brito, M.C.F.C. Felinto, Spectrochim. Acta A 61 (2005) 2643.
[18] R. Zibaseresht, R.M. Hartshorn, Aust. J. Chem. 58 (2005) 345.
[19] (a) H.B. Xu, L.X. Shi, L.Y. Zhang, Q.H. Wei, Z.N. Chen, Chem. Commun. (2006) 1601;
(b) I. Coppo, M. Duati, V.N. Kozhevnikov, J.W. Hofstraat, L. De Cola, Angew. Chem. Int. Ed. 44 (2005) 1806;
(c) I. Klink, H. Keizer, F.C.J.M. van Veggle, Angew. Chem. Int. Ed. 39 (2000) 4319;
(d) G.M. Davies, S.J.A. Pope, H. Adams, S. Faulkner, M.D. Ward, Inorg. Chem. 44 (2005) 4656.
[20] O. Park, S. Seo, B. Bae, J.H. Shin, Appl. Phys. Lett. 82 (2003) 2787.
[21] W.P. Gillin, R.J. Curry, Appl. Phys. Lett. 74 (1999) 798.
[22] Bruker SAINT Reference Manual Version 5.0; Bruker AXS Inc.: Madison, Wisconsin, USA, 1997.
[23] SADABS: Area-Detector Absorption Correction, Siemens Industrial Automation, Inc., Madison, WI, USA, 1996.
[24] F.R.G. Silva, O.L. Malta, C. Reinhard, H. Gudel, C. Piguet, J.E. Moser, J. Bünzli, J. Phys. Chem. A 106 (2002) 1670.
[25] R.F. Kubin, A.N. Fletcher, J. Lumin. 27 (1982) 455.
[26] J.N. Demas, G.A. Crosby, J. Phys. Chem. 75 (1971) 991.
[27] J.V. Caspar, T.J. Meyer, J. Am. Chem. Soc. 105 (1983) 5583.
[28] M. Shi, F. Li, T. Yi, D. Zhang, H. Hu, C. Huang, Inorg. Chem. 44 (2005) 8929.
[29] S. Quici, M. Cavazzini, G. Marzanni, G. Accorsi, N. Armaroli, B. Ventura, F. Barigelletti, Inorg. Chem. 44 (2005) 529.
[30] R. Wang, D. Song, S. Wang, Chem. Commun. (2002) 368.
[31] L.R. Melby, N.J. Rose, E. Abramson, J.C. Caris, J. Am. Chem. Soc. 86 (1964) 5117.
[32] C.R. De Silva, R. Wang, Z. Zheng, Polyhedron 25 (2006) 3449.
[33] S.A. Cotton, V. Franckevicius, M.F. Mahon, L.L. Ooi, P.R. Raithby, S.J. Teat, Polyhedron 25 (2006) 1057.
[34] Z. Bian, K. Wang, L. Jin, Polyhedron 21 (2002) 315.
[35] H.J. Batista, A.V.M. de Andrade, R.L. Longo, A.M. Simas, G.F. de Sa, N.K. Ito, L.C. Thompson, Inorg. Chem. 37 (1998) 3542.
[36] S. Quici, G. Marzanni, A. Forni, G. Accorsi, F. Barigelletti, Inorg. Chem. 43 (2004) 1294.
[37] F.J. Steemers, W. Verboom, D.N. Reinhoudt, E.B. van der Tol, J.W. Verhoeven, J. Am. Chem. Soc. 117 (1995) 9408.
[38] G.F. De Sa, O.L. Malta, C.M. Donega, A.M. Simas, R.L. Longo, P.A. Santa-Cruz, E.F. da Silva Jr., Coord. Chem. Rev. 196 (2000) 165.
[39] S. Jiang, M. Myers, N. Peyghambarian, J. Non-Cryst. Solids 239 (1998) 143.
[40] W.H. Wong, E.Y.B. Pun, K.S. Chan, Appl. Phys. Lett. 84 (2004) 176.
[41] L.H. Slooff, A. van Blassderen, A. Polman, G.A. Hebbink, S.I. Klink, F.C.J.M. van Veggel, D.N. Reinhoudt, J.W. Hofstraat, J. Appl. Phys. 91 (2002) 3955.

Furthermore, the use of volatile and/or toxic organic solvents is considered to be undesirable from the green chemistry point of view. Thus, solvent-free reactions or reactions carried out in innocuous solvents are thought to provide an environmentally friendly route to chemical synthesis. From this standpoint it will be highly desirable to find ways in which water can be used as a reaction medium. Herein, we describe the preparation and characterization of a tetrameric cubane complex of cobalt(III), viz. $Co_4^{III}(\mu_3\text{-}O)_4(\mu\text{-}O_2CCH_3)_4(4\text{-}CNpy)_4$ (**I**) which homogeneously catalyses the oxidation of *p*-xylene under mild conditions with molecular oxygen as the oxidant in aqueous media.

2. Experimental

2.1. Materials and methods

All materials used in this work were obtained from commercial sources and used without further purification. $Co(NO_3)_2 \cdot 6H_2O$, sodium acetate and hydrogen peroxide were obtained from E. Merck (India), 4-cyanopyridine was purchased from Aldrich (USA) and *p*-xylene was purchased from SRL (India). Methanol used was of reagent grade. C, H, N analysis was performed using a Perkin–Elmer 2400 CHNS/O Analyser, while the determination of the cobalt content was done by standard gravimetric procedure. UV–Vis spectrum was recorded on a Hitachi U-3210 spectrophotometer. Infrared spectra of the complex in the mid-IR region (4000–450 cm^{-1}) were recorded using a Perkin–Elmer RX1 FT-IR spectrophotometer for KBr pellets. The ^1H NMR spectrum of compound **I** was recorded using a Bruker 400 MHz instrument. Tetramethylsilane (TMS) was used as an internal standard. Chemical shifts reported are in parts per million (ppm) taking the TMS signal as 0.00. A Bruker Daltonics Esquire 300 Plus ESI instrument was used to obtain the mass spectrum.

Cyclic and differential pulse voltammetric measurements were performed using an EG&G PAR model 253 VersaStat potentiostat/galvanostat (with electrochemical analysis software 270) having a three-electrode setup consisting of a glassy carbon working, platinum wire auxiliary and a saturated calomel reference electrode (SCE). All electrochemical studies were carried out at room temperature using TBAP as the supporting electrolyte dissolved in dichloromethane at a concentration 50 times higher than that of complex **I**. The sample solutions were purged with and kept under an atmosphere of N_2. The $E_{1/2}$ values quoted for the CV experiments correspond to the midpoints of the forward (anodic, E_{pa}) and reverse (cathodic, E_{pc}) peak potentials [$E_{1/2} = (E_{pc} + E_{pa})/2$]. The reversibility of the redox couples was determined from peak-to-peak separations [$\Delta E_p = E_{pa} - E_{pc}$] observed and by estimating the ratio of the cathodic peak current (i_{pc}) and anodic peak current (i_{pa}) at various scan rates (v). The stoichiometry of the electron transfer processes was determined from the peak current measurements and by comparing the results with data obtained for related systems using ferrocene as a standard [9].

2.2. Preparation of $Co_4^{III}(\mu_3\text{-}O)_4(\mu\text{-}O_2CCH_3)_4(4\text{-}CNpy)_4$ (**I**)

$Co(NO_3)_2 \cdot 6H_2O$ (2.91 g, 10 mM) and sodium acetate (2.72 g, 20 mM) are stirred in methanol (30 mL) and then 4-cyanopyridine (1.04 g, 10 mM) is added to the solution. The stirred reaction mixture is then heated to boiling and 30% hydrogen peroxide (2 mL, 20 mM diluted with MeOH to 10 mL) is slowly added drop wise into it. Stirring under reflux is continued for 4 h. The cooled reaction mixture is filtered and concentrated to ca. 15 mL. CH_2Cl_2 (30 mL) is added to the concentrated solution whereupon a light pink aqueous layer separates out on top. The green dichloromethane layer is separated and petroleum ether (60–80° fraction) is added into it to obtain an olive green product. The product is dried in a vacuum desiccator over fused calcium chloride. Yield: 1.24 g (~52%). Analysis for $C_{32}H_{28}N_8O_{12}Co_4$, *Anal.* Calc.: C, 40.36; H, 2.96; N, 11.77, Co, 24.75. Found: C, 40.73; H, 3.03; N, 11.92; Co, 24.46%. Electronic spectra [λ_{max} (CH_2Cl_2), nm (ε, $M^{-1}\,cm^{-1}$)]: 634 (sh), 445 (8017), 362 (sh), 259 (22 500). IR spectral data [ν_{max}/cm^{-1}, (KBr)]: –C≡N stretch: 2250; ν_{asym} (COO^-), 1533; ν_{sym} (COO^-), 1411; pyridyl ring stretches, 1611, 1492; μ_3-oxo-bridge, 634. ^1H NMR data [δ/ppm (DMSO-D_6)]: 8.56 (d, $J = 6.2$ Hz, 8H), 7.69 (d, $J = 6.1$ Hz, 8H), 1.93 (s, 12H). ESI-MS data (m/z): 953 (M^+), 849 ('M^+−4-CNpy', most intense peak).

2.3. Conversion of p-xylene to p-toluic acid

All reactions were carried out in a medium pressure batch reactor supplied by BERGHOF GmbH, Germany with reaction vessel capacities ranging from 75 to 250 mL. It is electronically controlled with an external heating system and has internally stirring magnetic devices. The experimental temperature is also maintained electronically.

A mixture of *p*-xylene, water and the catalyst were taken in a PTFE container. This was then put into the reactor. The reactor was closed and then oxygen was purged through it. Desired O_2 pressure was applied from an O_2-cylinder and the temperature of the reaction mixture was raised to 130 °C. The reaction was carried out for 4 h at this temperature. The reaction mixture was stirred continuously during the course of the reaction. When the reaction time was over, (time period counts from the moment the reactor reaching 130 °C to the moment the heating was switched off) the reactor was allowed to cool down to room temperature without any help of cooling device.

After completion of the reaction, the reaction mixture was taken out from the reactor. It was extracted out with diethyl ether and water. The product *p*-toluic acid contained in the organic layer was separated and the solvent

was removed by rotary vacuum evaporation and finally by using a high vacuum pump to remove the last traces of volatile liquids. The product so obtained was weighed to determine the percentage yield on the basis of moles of *p*-xylene used and *p*-toluic acid obtained. Formation of terephthalic was detected and estimated by isolating and analysing the solid residue left in the PTFE container after solvent extraction.

3. Results and discussion

3.1. Synthesis and characterization of $Co_4^{III}(\mu_3\text{-}O)_4(\mu\text{-}O_2CCH_3)_4(4\text{-}CNpy)_4$ (I)

The tetrameric cobalt(III) complex has been prepared by oxidizing cobalt(II) ions in the presence of the nitrogen base ligand 4-cyanopyridine and acetate ion.

$$Co^{2+} + CH_3CO_2^- + 4\text{-CNpy} \xrightarrow[MeOH]{H_2O_2} Co_4^{III}(\mu_3\text{-O})_4(\mu\text{-O}_2CCH_3)_4(4\text{-CNpy}_4)$$

The substituted pyridine ligand stabilises the higher oxidation state of the metal. Although a dark olive green complex can be isolated from the concentrated reaction mixture, the isolated yield of the product is relatively low due to its high solubility in the solvent system used. However, isolation of complex **I** via precipitation by adding petroleum ether to a CH_2Cl_2 extract of the reaction mixture leads to a much higher yield without affecting the purity of the product.

The complex has been studied by infrared and UV–Vis spectroscopy. In the KBr phase IR spectrum of complex **I** it is possible to identify bands due to the bridging acetate anions as well as for the pyridyl N-bound 4-cyanopyridine ligands. The asymmetric –COO stretching (ν_{asym}) and symmetric –COO stretching (ν_{sym}) bands appear at 1531 cm^{-1} and 1411 cm^{-1}, respectively. The separation of the asymmetric and symmetric stretching vibrations ($\nu_{asym} - \nu_{sym} = \Delta\nu = 120\ cm^{-1}$) of the carboxyl group is consistent with this ligand bonding in a bridging fashion. A weak but sharp band at 2250 cm^{-1} indicates the presence of 4-cyanopyridine ligand in the complex.

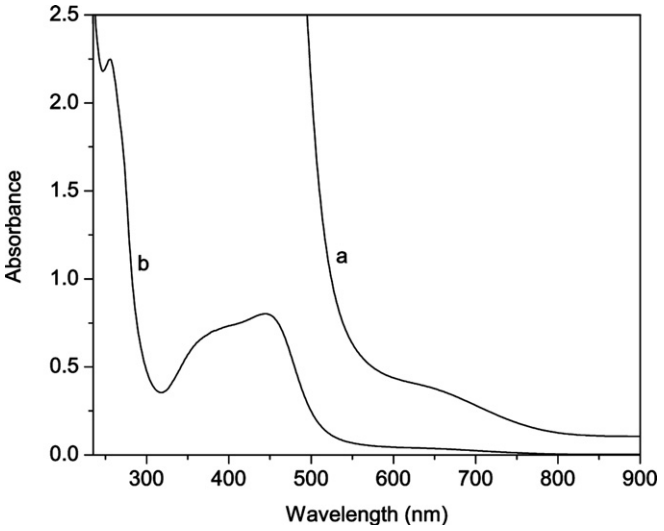


Fig. 1. UV–Vis spectrum recorded for $Co_4^{III}(\mu_3\text{-O})_4(\mu\text{-O}_2CCH_3)_4(4\text{-CNpy})_4$ (**I**) at two different concentrations in CH_2Cl_2: (a) 10^{-3} M; (b) 10^{-4} M.

The UV–Vis spectrum of complex **I** is shown in Fig. 1. The spectral band at 634 nm is likely to be due to a spin allowed d–d transition, while the stronger absorption at

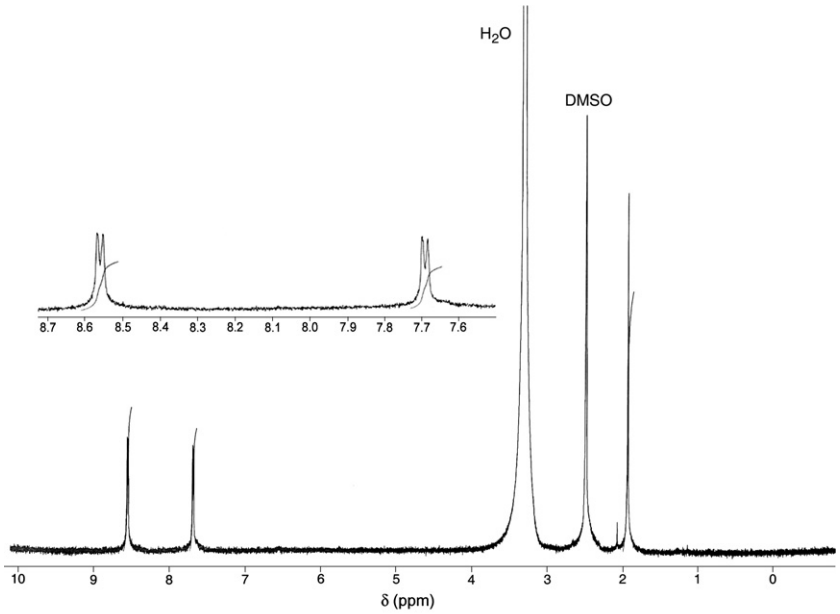


Fig. 2. ^1H NMR spectrum recorded for $Co_4^{III}(\mu_3\text{-O})_4(\mu\text{-O}_2CCH_3)_4(4\text{-CNpy})_4$ (**I**) in DMSO-D_6.

445 nm having a shoulder at 362 nm is likely to have its origin in charge transfer transitions of the MLCT type. Based on X-ray crystallographic studies on related complexes prepared under similar conditions in this laboratory [9,10] it appears likely that complex **I** has four cobalt atoms along with four oxygen atoms occupying the alternate corners of an approximate cube and thus this complex belongs to the class of compounds commonly referred to as 'cubane clusters' [11]. All four cobalt atoms are in the +3 oxidation state to result in a diamagnetic compound for the d^6-Co^{3+} system. The diamagnetic nature is shown up in the ^{1}H NMR spectrum recorded for complex **I** dissolved in DMSO-D_6 (Fig. 2). Apart from the signals due to the residual DMSO and water admixed with it, there is one sharp singlet at 1.93 ppm due to the methyl group of the acetato ligand and in addition, a pair of sharp doublets centred at 8.56 and 7.69 ppm are observed as expected for the pyridyl ring of 4-cyanopyridine. This suggests that complex **I** also has a similar molecular structure with $[Co_4(\mu_3\text{-}O)_4(\mu\text{-}O_2CR)_4(py)_4]$ with R = CH_3 and C_6H_5 [9]. This formula is also supported by elemental analysis. Conclusive evidence regarding the tetrameric formula of complex **I** comes from the appearance of an intense peak corresponding to the *m*/*z* value 953 in the electrospray ionization mass spectrum (ESI-MS). This peak is assigned to the molecular ion peak for complex **I**. Based on experimental evidences given above, we believe that the molecular structure of $[Co_4(\mu_3\text{-}O)_4(\mu\text{-}O_2CCH_3)_4(4\text{-}CNpy)_4]$ is as shown in Fig. 3.

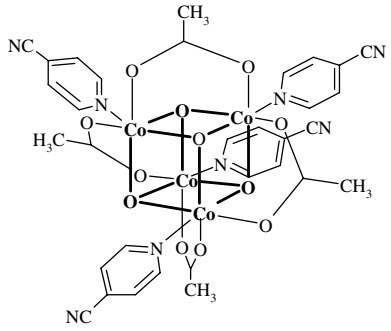


Fig. 3. Proposed molecular structure of $Co_4^{III}(\mu_3\text{-}O)_4(\mu\text{-}O_2CCH_3)_4(4\text{-}CNpy)_4$ (**I**).

Electrochemical properties of the tetrameric oxo-bridged complex **I** have been studied by cyclic and differential pulse voltammetric techniques using a three electrode assembly. The results are shown in Fig. 4.

Electrochemical studies on $Co_4^{III}(\mu_3\text{-}O)_4(\mu\text{-}O_2CCH_3)_4(4\text{-}CNpy)_4$ (**I**) show a one-electron oxidation process with $E_{1/2} = 1.003$ V and $\Delta E_p = 90$ mV versus SCE at 5 mV s^{-1}. No other notable electrochemical response was observed in the potential range −1.3 to +1.3 V. The electron transfer process is quasireversible in nature as judged from the high ΔE_p values as well as from the dependence of the peak-to-peak potential separation on scan rate ($\Delta E_p = 128$ mV at 20 mV s^{-1}). The differential pulse voltammetric study also shows a single redox response with a peak potential of 1.02 V, which is close to the value obtained with cyclic voltammetry. Based on results published [12] for related systems, it is believed that the following couple involving the tetrameric Co_4O_4 core in complex **I** gives rise to the redox activity

$$[Co_4^{III}(\mu_3\text{-}O)_4]^{4+} \overset{-e}{\underset{+e}{\rightleftharpoons}} [Co_3^{III}Co^{IV}(\mu_3\text{-}O)_4]^{5+}.$$

3.2. Catalytic oxidation of p-xylene

Production of terephthalic acid from homogeneous liquid phase oxidation of *p*-xylene is an industrially important reaction. A large number of investigations have been carried out to refine the process as well as to understand the kinetics and mechanism of the important industrial reaction. Cobalt salts or their combinations with activators and/or co-catalysts are commonly used as catalysts. Almost all the commercial processes use acetic acid as solvent for the oxidation of methyl substituted benzene. One of the problems of current manufacturing processes for terephthalic acid is the corrosive medium (acetic acid, Co, Mn and Br) in which the reaction takes place [4]. In view

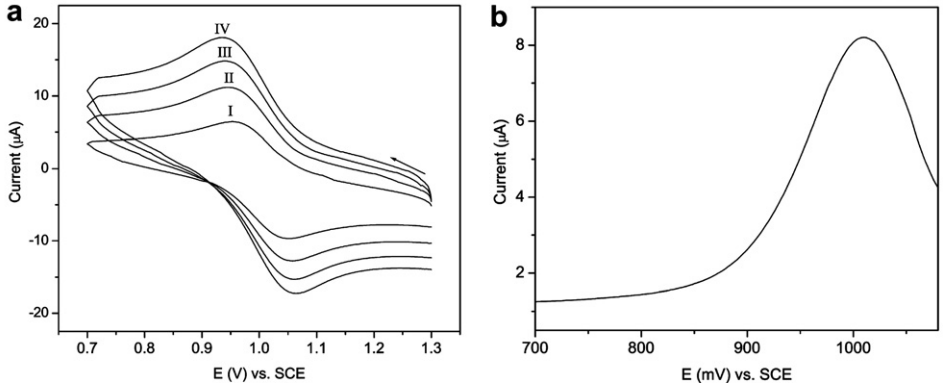
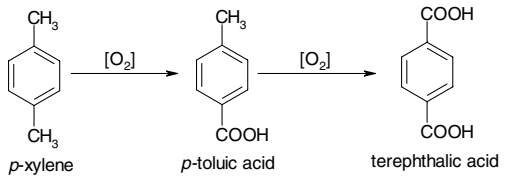


Fig. 4. Cyclic voltammograms for $Co_4^{III}(\mu_3\text{-}O)_4(\mu\text{-}O_2CCH_3)_4(4\text{-}CNpy)_4$ (**I**) in CH_2Cl_2–0.2 M TBAP: (a) at scan rates [I] 5, [II] 10, [III] 15, [IV] 20 mV s^{-1}; (b) Differential pulse voltammogram of **I** at 5 mV s^{-1}.

of various environmental issues, research on the development of catalysts for such processes is still live and relevant.



In absence of a promoter cobalt-catalysed autoxidation of *p*-xylene is a sluggish process because the methyl groups in the intermediate, i.e., *p*-methylbenzoic (*p*-toluic) acid are deactivated by the electron withdrawing nature of the carboxyl group and thus the remaining methyl group is particularly resistant to further oxidation. Even in presence of bromide ion promoter which significantly affects the kinetics of the reaction, faster rates are observed only at high temperatures (typically at ~200 °C). Cobalt(II) acetate alone in catalytic concentrations is a poor catalyst for one-step oxidation of *p*-xylene to terephthalic acid in most solvents. It is also relevant to note here that an inordinately long induction period is often observed in the catalytic conversion of *p*-xylene to terephthalic acid because the Co(II) to Co(III) oxidation is a slow process.

In view of the above facts, it is important to investigate if a cobalt(III) catalyst such as complex **I** can be used as a catalyst for the oxidation of *p*-xylene. We studied the effect of pressure and catalyst concentration on *p*-xylene oxidation using water as a solvent to find that *p*-toluic is the principal product with terephthalic acid forming only in traces (~1%). Our results on the homogeneous catalysis of the oxidation of *p*-xylene by dioxygen are presented below under two separate headings.

3.3. Effect of pressure

The effect of pressure was studied at applied pressures of 10, 15, 20 and 25 bar, the actual pressure during the reaction being ~5 bar higher than the initially applied pressure in each case. The data are presented in Fig. 5. It is found that the formation of *p*-toluic acid form terephthalic acid is linearly dependent on applied pressure. The amount of *p*-toluic acid increases with increase of pressure (Fig. 4).

3.4. Effect of catalyst concentration

Effect of catalyst concentration was investigated at 130 °C under the reaction pressure of 20 bar. Highest yield of the product, *p*-toluic acid is obtained at the maximum catalyst concentration. As evidenced by the linear increase of product yield with increasing catalyst concentration (Fig. 6), the reaction is likely to follow first order kinetics with respect to catalyst concentration.

Although the formation of terephthalic acid could be observed only in very low yield, keeping in view the fact that the reaction is carried out without addition of any promoter, it is still a significant result from the fact that at least the first oxidation step is occurring in a selective manner. Our results are also interesting in view of the fact that the reactions are carried out in the environmentally benign solvent water.

Effect of added water on the rate of *p*-xylene oxidation by cobalt(II) and manganese(II) catalysts has been addressed by other authors [13]. On the other hand, Higashijima [14] reported a ruthenium-substituted heteropolyanion $[SiW_{11}O_{39}Ru^{III}(H_2O)]^{5-}$, which is very active as a water soluble catalyst for the oxidation of *p*-xylene to terephthalic acid at 200 °C. This reaction was also found to

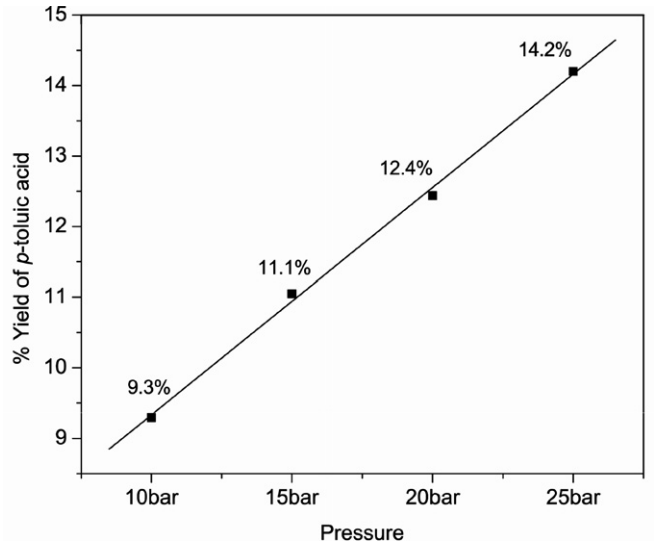


Fig. 5. Effect of pressure on *p*-toluic acid formation catalysed by $Co_4^{III}(\mu_3\text{-}O)_4(\mu\text{-}O_2CCH_3)_4(4\text{-}CNpy)_4$ (**I**) in water. [*Conditions*: *p*-xylene = 2 mL (16 mmol); H_2O = 48 mL; amount of catalyst = 0.05 g; oxidant, O_2; T = 130 °C; reaction time = 4 h.]

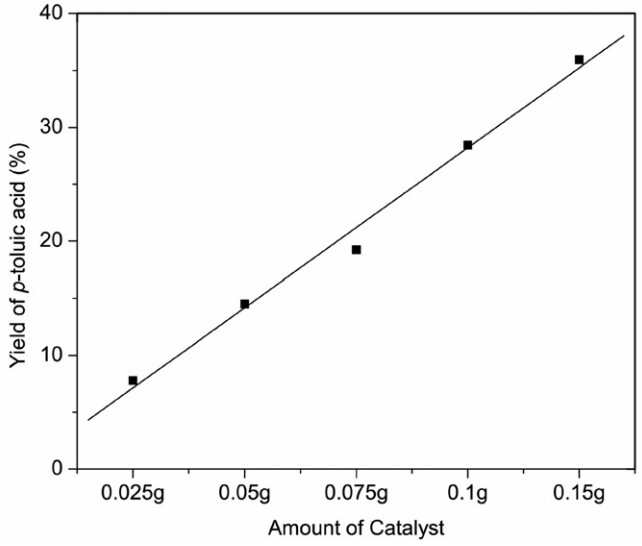


Fig. 6. Effect of catalyst concentration on toluic acid formation catalysed by $Co_4^{III}(\mu_3\text{-}O)_4(\mu\text{-}O_2CCH_3)_4(4\text{-}CNpy)_4$ (**I**) in water. [*Conditions*: *p*-xylene = 2 mL (16 mmol); H_2O = 48 mL; pO_2 = 20 bar; oxidant, O_2; T = 130 °C; reaction time = 4 .]

give *p*-toluic acid as a co-product. Water has also been suggested as a viable medium for terephthalic acid synthesis at 300 °C by Dunn et al. [15]. At the same time, it also has been the subject of patent literature [16]. Comparing our observations with results described in the published literature, we are led to believe that if complex **I** remains intact at higher temperatures, it may be possible to improve the *p*-toluic acid yield beyond what is being reported here. Formation of terephthalic acid is also likely to become more significant under such conditions.

4. Conclusion

The present work has shown that carboxylate bridged cobalt(III) oxo clusters can be generated by H_2O_2 oxidation of Co(II) in presence of pyridine based ligands. Effectiveness of a cobalt(III) system for homogeneously catalysed oxidation of *p*-xylene by O_2 in aqueous media has been demonstrated. Because the catalyst is appreciably soluble in both water as well as *p*-xylene, it may be assumed that the conversion of the substrate to *p*-toluic acid occurs in the rapidly stirred liquid medium. Electrochemical results described in this paper also suggests that both cobalt(III) and cobalt(IV) may be involved in the catalytic cycle leading to the selective oxidation of *p*-xylene to form *p*-toluic acid as the principal product.

Acknowledgements

Financial support was received from in the form of a research grant from DST, India (Grant No. SR/S1/IC-51/2003) and a research fellowship (to R.C.) from UGC, India are gratefully acknowledged. D.K. thanks the Head, Chemistry Department, GU for permitting her to use the catalytic reactor during her Master's project dissertation work, which forms a part of this paper.

Appendix A. Supplementary material

Supplementary data associated with this article can be found, in the online version, at doi:10.1016/j.poly.2006.10.014.

References

[1] R.A. Sheldon, J.A. Kochi, Metal Catalysed Oxidations of Organic Compounds, Academic Press, New York, 1981.
[2] P. Raghavendrachar, S. Ramachandran, Ind. Eng. Chem. Res. 31 (1992) 453.
[3] (a) P.M. Price, J.H. Clark, D.J. Macquarrie, J. Chem. Soc., Dalton Trans. (2000) 101;
(b) B.K. Das, J.H. Clark, Chem. Commun. (2000) 605.
[4] (a) W. Partenheimer, Catal. Today 23 (1995) 69;
(b) A.K. Suresh, M.M. Sharma, T. Sridhar, Ind. Eng. Chem. Res. 39 (2000) 3958.
[5] R.E.P. Winpenny, in: J.A. McCleverty, T.J. Meyer (Eds.), Comprehensive Coordination Chemistry, vol. 7, Pergamon Press, Oxford, 2004, pp. 125–175 [Chapter 7.3].
[6] (a) C.E. Sumner Jr., Inorg. Chem. 27 (1988) 1320;
(b) C.E. Sumner Jr., G.R. Steinmetz, Inorg. Chem. 28 (1989) 4290.
[7] C.E. Sumner Jr., G.R. Steinmetz, J. Am. Chem. Soc. 107 (1985) 6124.
[8] (a) S.A. Chavan, D. Srinivas, P. Ratnasamy, Chem. Commun. (2001) 1124;
(b) S.A. Chavan, D. Srinivas, P. Ratnasamy, J. Catal. 204 (2001) 409;
(c) S.A. Chavan, S.B. Halligudi, D. Srinivas, P. Ratnasamy, J. Mol. Catal. A: Chemical 161 (2000) 49.
[9] R. Chakrabarty, Ph.D. Thesis, Gauhati University (2006).
[10] R. Chakrabarty, B.K. Das, J. Mol. Catal. A: Chem. 223 (2004) 39.
[11] T. Ama, M.M. Rashid, T. Yonemura, H. Kawaguchi, A. Takeuchi, T. Yasui, Coord. Chem. Rev. 198 (2000) 101.
[12] K. Dimitrou, A.D. Brown, T.E. Concolino, A.L. Rheingold, G. Christou, Chem. Commun. (2001) 1284.
[13] (a) Z. Cvengrošová, M. Hronec, J. Kizlink, L. Malík, J. Ilavský, J. Mol. Catal. 40 (1987) 235;
(b) Q. Wang, X. Li, L. Wang, Y. Cheng, G. Xie, Ind. Eng. Chem. Res. 44 (2005) 4518.
[14] M. Higashijima, Chem. Lett. 28 (1999) 1093.
[15] J.B. Dunn, P.E. Savage, Environ. Sci. Technol. 39 (2005) 5427.
[16] J.S. Plotkin (Dow Chemical) U.S. Patent 6,759,550 (2004).

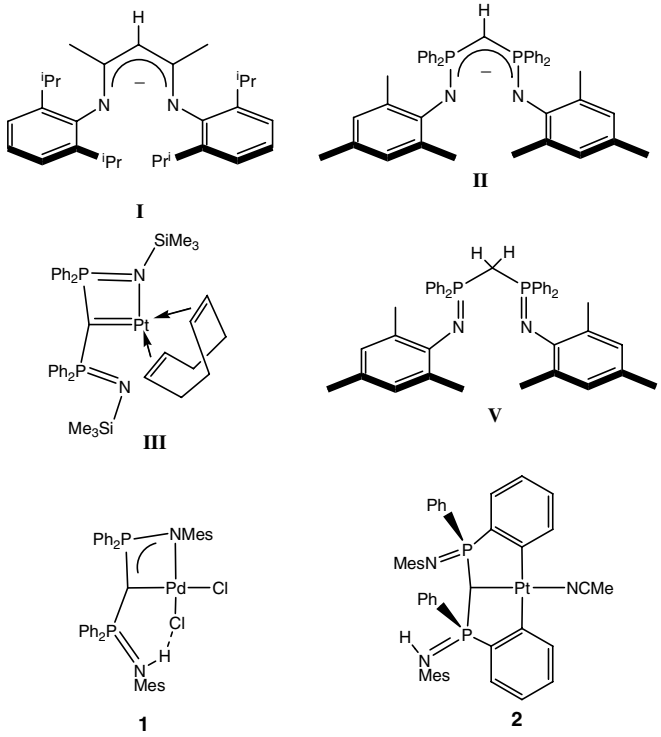


Chart 1.

formation of the singly metallated complex [Pd(**II**)Cl]. The solution spectroscopic data were not however consistent with this, likely, square planar and symmetrical configuration. The ^{1}H NMR spectrum revealed two singlet resonances for each of the *ortho*- and *para*-methyls as well as the *meta*-methine centres of two inequivalent *N*-mesityl substituents. The *P*-phenyl region of the spectrum was also considerably more complex than anticipated. The $^{31}P\{^{1}H\}$ NMR spectrum indicated an unsymmetrical disposition of the bis(phosphinimino)methanide ligand and appeared as an AX pair of doublet signals centred at 39.9 and 27.6 ppm [$^{2}J_{PP} = 15.4$ Hz].

This inference was confirmed by a single crystal X-ray diffraction analysis, which revealed that, although deprotonation of the ligand precursor had occurred under these mild conditions, compound **1** also contained the HCl liberated during the deprotonation process and may be best described as a dichloropalladate(II). The molecular structure of **1** is illustrated in Fig. 1. Details of the X-ray analysis are provided in Table 1, while selected bond lengths and angles are provided in Tables 2 and 3, respectively. Coordination around the palladium centre is approximately square planar. Two of the coordination sites about Pd are occupied by the three-membered chelate provided by the methanide carbon (C1) centre and one of the phosphinimino substituents of the κ-C,κ-N bis(phosphinimo)methanide ligand. The chlorides occupy the two remaining sites. Despite the restricted bite angle of the three-membered N(1)–P(1)–C(1) chelate [N(1)–Pd–C(1),

Table 1
Selected data collection parameters for compounds **1** and **2**

	1	**2**
Chemical formula	$C_{43}H_{44}Cl_2N_2P_2Pd$	$C_{45}H_{42}D_3N_3P_2Pt(C_2D_3N)$
Formula weight	828.06	931.9
T (K)	173(2)	173(2)
Crystal size (mm^3)	$0.30 \times 0.25 \times 0.20$	$0.25 \times 0.20 \times 0.10$
Crystal system	monoclinic	monoclinic
Space group	$P2_1/c$ (No. 14)	$P2_1/c$ (No. 14)
a (Å)	22.0530(3)	10.6441(1)
b (Å)	11.2115(1)	17.3375(2)
c (Å)	16.7783(2)	22.4742(3)
α (°)	90	90
β (°)	106.964(1)	97.576(1)
γ (°)	90	90
Z	4	4
V (Å^3)	3967.88(8)	4111.23(8)
d_{calc} (Mg m^{-3})	1.38	1.51
μ (mm^{-1})	0.72	3.53
θ Range (°)	3.72–27.49	3.75–25.70
R_1; wR_2 [$I > 2\sigma(I)$]	0.036, 0.068	0.032, 0.072
$R1$; wR_2 all data	0.053, 0.073	0.035, 0.073
Measured/independent reflections/R_{int}	49405/9050/0.055	65986/7674/0.053
Reflections with $I > 2\sigma(I)$	7456	7092

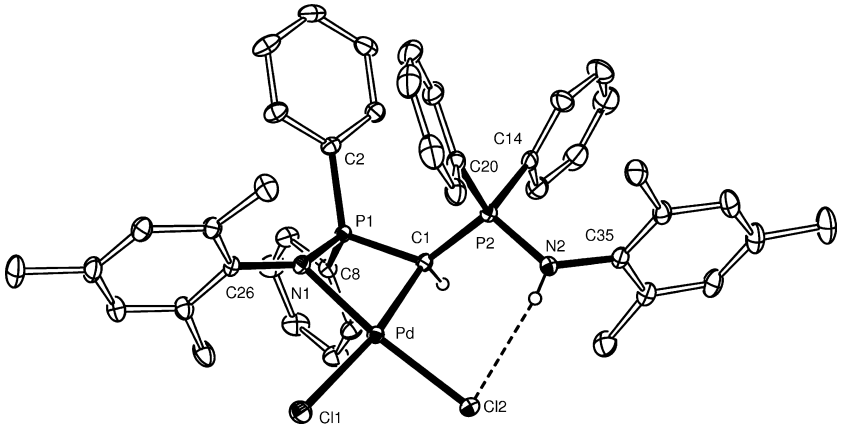


Fig. 1. ORTEP drawing (30% ellipsoids) of compound **1**. Hydrogen atoms except those attached to C1 and N2 removed for clarity.

Table 2
Selected bond lengths (Å) for compounds **1** and **2**

	1	2
Pd–N(1)	2.043(2)	
Pt–N(3)		2.003(4)
M–C(1)	2.103(2)	2.051(4)
Pd–Cl(2)	2.3177(6)	
Pd–Cl(1)	2.3257(6)	
Pt–C(15)		2.051(4)
Pt–C(3)		2.074(4)
P(1)–N(1)	1.594(2)	1.643(4)
P(1)–C(1)	1.784(2)	1.789(4)
P(1)–C(2)	1.803(2)	1.771(4)
P(1)–C(8)	1.807(2)	1.805(5)
P(2)–N(2)	1.639(2)	1.572(4)
P(2)–C(1)	1.768(2)	1.804(4)
P(2)–C(14)	1.797(3)	1.801(4)
P(2)–C(20)	1.801(2)	1.829(5)
N(1)–C(26)	1.425(3)	1.437(6)
N(2)–C(35)	1.441(3)	1.407(6)

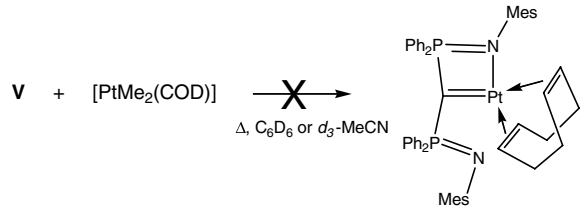
Table 3
Selected bond angles (°) for compounds **1** and **2**

	1	2
N(1)–Pd–C(1)	75.74(8)	
N(3)–Pt–C(1)		178.84(16)
N(3)–Pt–C(15)		93.19(16)
N(1)–Pd–Cl(2)	172.33(6)	
C(1)–Pd–Cl(2)	96.62(6)	
N(1)–Pd–Cl(1)	94.91(6)	
C(1)–Pd–Cl(1)	169.38(7)	
Cl(2)–Pd–Cl(1)	92.63(2)	
C(1)–Pt–C(15)		85.83(16)
N(3)–Pt–C(3)		92.37(17)
C(1)–Pt–C(3)		88.59(17)
C(15)–Pt–C(3)		174.29(17)
N(1)–P(1)–C(1)	97.62(10)	111.5(2)
N(1)–P(1)–C(2)	114.29(10)	110.9(2)
C(1)–P(1)–C(2)	118.32(11)	104.9(2)
N(1)–P(1)–C(8)	117.54(11)	110.6(2)
C(1)–P(1)–C(8)	106.27(11)	107.7(2)
C(2)–P(1)–C(8)	103.27(11)	111.1(2)
N(2)–P(2)–C(1)	107.42(11)	108.1(2)
N(2)–P(2)–C(14)	104.24(11)	121.1(2)
C(1)–P(2)–C(14)	112.19(12)	99.3(2)
N(2)–P(2)–C(20)	110.44(12)	112.9(2)
C(1)–P(2)–C(20)	111.31(11)	109.7(2)
C(14)–P(2)–C(20)	110.95(12)	104.7(2)
C(26)–N(1)–P(1)	136.76(17)	119.9(3)
C(26)–N(1)–Pd	126.16(15)	
P(1)–N(1)–Pd	94.14(9)	
C(35)–N(2)–P(2)	124.22(18)	134.2(3)
P(2)–C(1)–P(1)	125.87(13)	119.4(2)
P(2)–C(1)–M	115.63(12)	109.1(2)
P(1)–C(1)–M	86.78(10)	108.3(2)

75.74(8)°], the remaining angles provided by the *cis*-disposed ligands are close to 90°. The Pd–Cl bond distances [Pd–Cl(1) 2.3257(6), Pd–Cl(2) 2.3177(6) Å] are similar despite the increased coordination number of the Cl(2) centre which displays an additional hydrogen bonded interaction to the N(2) proton of the 'free' P(2)–N(2) arm of the chelated ligand. Any effect is probably offset by the relative *trans* influences of the C(1) and N(1) donors.

It did not prove possible to enforce any further deprotonation of the C(1) centre within compound **1**, to produce palladium carbenoid species analogous to **III**, either by heating (100 °C) or by addition of an external base (DBU, Et_3N). Monitoring of these reactions by $^{31}P\{^1H\}$ NMRin d_8-toluene indicated either decomposition to complex mixtures of products or no apparent reaction respectively.

Although the directly analogous reaction of **V** and $[PtCl_2(NCMe)_2]$ has not yet yielded identifiable products, reaction of $[Pt(PPh_2Me)Cl(\mu\text{-}Cl)]_2$ and a closely related *N*-tolyl-substituted bis(phosphinimino)methane has been reported by Elsevier and co-workers to produce the similarly *N*,*C*-coordinated complex $[PtCl(PPh_2Me)\{CH(Ph_2PNC_6H_4\text{-}4\text{-}Me)(Ph_2P{=}N(H)C_6H_4\text{-}4\text{-}Me)\}]^+Cl$ [7]. This cation was also formed irrespective of added base and, for this reason, we attempted the alternative methane-elimination route to the platinum carbenoid species illustrated in Scheme 1. Extended heating and NMR (^1H, $^{31}P\{^1H\}$) monitoring of an NMR-scale reaction of $[PtMe_2(COD)]$ and **V** in C_6D_6 indicated that no reaction had occurred. In contrast, a similar reaction performed in d_3-MeCN resulted in the complete disappearance of Pt–Me resonance at 0.63 ppm in the ^1H NMR spectrum after 18 h at 100 °C. These conditions also resulted in the loss of the characteristic methylene triplet of **V** centred at 4.01 ppm and the appearance of a series of resonances consistent with the formation of unligated COD. Attempted ^{31}P NMR monitoring of this reaction at regular intervals over a 7 day period was not informative and revealed only the resonances due to the starting material and several unidentifiable resonances, which, once apparent, did not alter in relative intensity. Upon slow cooling, however, colourless crystals of compound **2** deposited within the NMR tube, and we assume that plausible intermediates (vide infra) are either short-lived or present in too low concentration as to be observable, while the ultimate product, compound **2**, deposits and is depleted from solution as the reaction proceeds and is thus not observed. The crystalline material would not redissolve in d_3-MeCN, but proved to be highly soluble in $CDCl_3$ enabling the full spectroscopic characterisation of compound **2**. Although the $^{31}P\{^1H\}$ NMR spectrum consisted of a single resonance at 46.0 ppm, indicative of symmetrical coordination of the deprotonated ligand, it was apparent that the desired



Scheme 1.

synthesis of a carbenoid species had again been unsuccessful. Compound **2** did not contain coordinated COD and it was clear that the PCH_2P methylene of **V** had not been doubly deprotonated as evidenced by a triplet resonance (1H by integration) at 3.26 ppm ($^2J_{PP} = 9.2$ Hz) in the ^1H NMR spectrum. Attempts to acquire ^{195}Pt NMR data were unsuccessful, most likely due to the anisotropic magnetic environment of the metal centre.

The origin of these solution data was made clear by a single crystal X-ray analysis performed on crystals of compound **2**. The results of this study, illustrated in Fig. 2, were consistent with the solution data and revealed that **V** had undergone a triple C–H activation reaction. Details of the X-ray analysis are provided in Table 1, while selected bond lengths and angles are provided in Tables 2 and 3 respectively. Three coordination sites about the square planar platinum centre are provided by the deprotonated C(1) methanide carbon and two bonds to sp^2 carbon atoms which have been formed by *ortho*-metallation of two of the P-bound phenyl rings. A coordinated molecule of acetonitrile, *trans* to the methanide carbon centre, occupies the remaining coordination site. Charge balance is maintained by protonation of one of the non-coordinated phosphinimine (N1) nitrogen atoms. The resulting chemical inequivalence of the phosphorus nuclei was not, however, apparent in the NMR spectra most likely due to rapid exchange of the proton between the two phosphinimino nitrogen centres and the development of apparent C_2 symmetry. Although the bond lengths and angles within the structure itself are entirely normal and consistent with previously reported Pt(II) alkyl and aryl derivatives [8], and such intramolecular aromatic substitution by late transition metal complexes has been known to occur for over 40 years [9], a transformation of a neutral bis(phosphinimino)methane into a formally trianionic chelate is unique. It is interesting to note that Cavell has reported that **III** underwent thermally initiated *ortho*-metallation of a single *P*-phenyl with concomitant protononation of the carbenoid C=Pt bond [6a]. This latter process occurred diastereoselectively to generate P and C stereocentres with fixed relative absolute configurations and it was speculated that metallation involved the intermediacy of an undetectable platinum(IV) hydride intermediate. The formation of compound **2** occurred with similar diastereoselectivity and, although we have not yet definitively identified any intermediates and a number of viable alternative pathways may be envisaged, it is plausible that **2** results from a similar mechanism (Scheme 2) and the intermediacy of a carbenoid species similar to that depicted in Scheme 1.

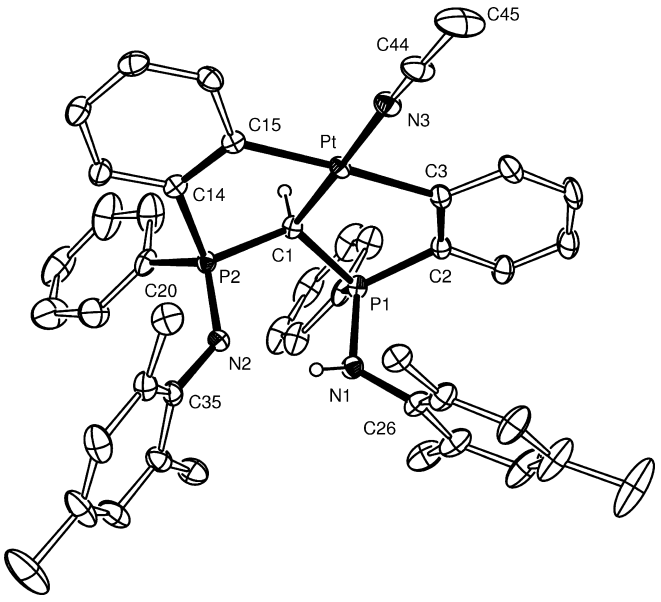
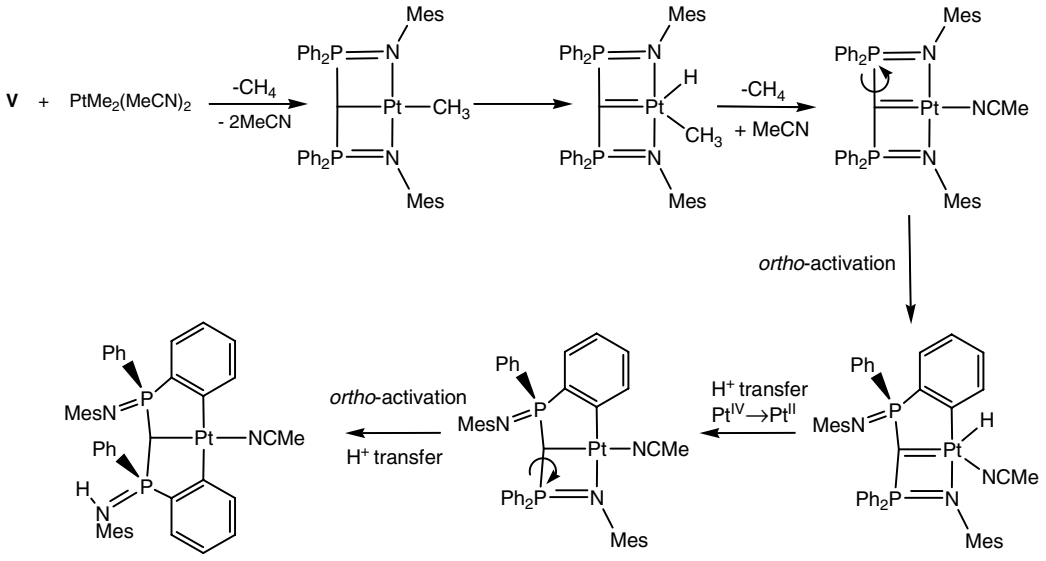


Fig. 2. ORTEP drawing (30% ellipsoids) of compound **2**. Hydrogen atoms except those attached to C1 and N1 removed for clarity.



Scheme 2. Proposed 'carbenoid' pathway to compound **2**.

We are continuing to investigate this hypothesis and will report the outcome of these studies in a future publication.

3. Experimental section

All manipulations were carried out using standard Schlenk and glovebox techniques under an inert atmosphere of either nitrogen or argon. All solvents were distilled under nitrogen and dried with conventional drying agents. NMR spectra were recorded at 270 or 500 (^{1}H), 125.8 (^{13}C) and 202.5 (^{31}P) MHz from samples in either C_6D_6 or d_8-toluene or $CDCl_3$; chemical shifts are given relative to $SiMe_4$. Mass spectra were recorded under fast atom bombardment (FAB) on samples in a matrix of nitrobenzyl alcohol. In spectral assignments Mes = 2,4,6-trimethylphenyl. The ligand precursor **V** was synthesised by a literature procedure [4g].

3.1. Preparation of compound *1*

A solution of **V** (0.25 g, 3.8 mmol), in CH_2Cl_2 (10 cm^3) was added at room temperature to a CH_2Cl_2 (10 cm^3) solution of $[PdCl_2(NCMe)_2]$ (0.1 g, 3.8 mmol), resulting in an immediate colour change from yellow to orange/red. This solution was stirred for 14 h before complete removal of volatiles. The red solid was crystallised from hexane at room temperature to yield **1** as dark red crystals (0.25 g, 79%). Anal. Calc. for $C_{43}H_{44}Cl_2N_2P_2Pd$: C, 62.38; H, 5.31; N, 3.38. Found: C, 62.55; H, 5.50; N, 3.23%. ^{1}H NMR ($CDCl_3$); δ 1.39 (s, 3H, *p-Me*, mesN), 1.54 (s, 3H, *p-Me*, mesN=P), 1.96 (s, 6H, *o-Me*, mesN), 1.99 (s, 6H, *p-Me*, mesN=P), 2.78 (dd, 1H, $^{2}J_{PH} = 14.8$, 1.6 Hz, PC*H*P), 5.25 (s, 1H, N*H*), 6.39 (s, 2H, *m*-C*H*, mesN), 6.39 (s, 2H, *m*-C*H*, mesN=P), 6.80–8.20 (m, 20H, *Ph*–P). ^{13}C NMR ($CDCl_3$): δ −15.5 (dd, $^{1}J_{PP} = 79.2$, 75.5 Hz, P*C*P), 20.4 (*o*-Me), 20.7 (*o*-Me), 20.8 (*p*-Me), 122.1 (d, $^{1}J_{PP} = 93.1$ Hz, *i*–CP), 125.2 (Ar), 125.4 (d, $^{1}J_{PP} = 106.9$ Hz, *i*–CP), 127.9 (d, $J_{PP} = 12.5$ Hz, PhP), 128.1 (Ar), 128.4 (d, $J_{PP} = 11.3$ Hz, PhP), 128.4, 128,7, 128.8 (Ar), 129.5 (d, $J_{PP} = 11.3$ Hz, PhP), 131.8 (d, $J_{PP} = 23.9$ Hz, PhP), 131.8 (Ar), 132.6 (Ar), 132.9 (d, $J_{PP} = 12.0$ Hz, PhP), 133.4 (d, $J_{PP} = 16.3$ Hz), 133.8 (Ar), 134.4 (d, $J_{PP} = 11.0$ Hz, PhP), 135.9 (Ar), 136.3, 136.4 (Ar), 136.7 (d, $J_{PP} = 8.9$ Hz, PhP), 137.8 (Ar). ^{31}P{^{1}H} NMR ($CDCl_3$): δ 27.6 (d, $^{2}J_{PP} = 15.4$ Hz), 39.9 (d, $^{2}J_{PP} = 15.4$ Hz). MS (FAB: *m*/*z*): 792 [2, M^+−HCl], 756 [5, M^+−HCl−Cl], 651 [5], 440 [100], 330 [40], 183 [35], 147 [55].

4. Preparation of compound 2

A mixture and $[PtMe_2(COD)]$ (0.035 g, 0.11 mmol) and **V** (0.070 g, 0.11 mmol) were dissolved in d_3-MeCN and transferred to an NMR tube equipped with a Youngs tap. Initial NMR analysis of the pale yellow solution indicated that no reaction had occurred. The NMR tube was then heated to 100 °C for 18 hours, after which time the Pt–Me signal (0.62 ppm) in the ^{1}H spectrum and the ^{31}P NMR (−17 ppm) signal for V had completely disappeared. Upon standing at room temperature overnight colourless crystals of compound **2** deposited and were isolated by filtration (0.07 g, 70%). A sample for analysis was prepared by grinding and exposure to a dynamic vacuum. Anal. Calc. for $C_{43}H_{43}D_3N_3P_2Pt$: C 60.86, H 4.78, N 4.73. Found: C 60.65, H 4.65, N 4.80. ^{1}H NMR ($CDCl_3$); δ 2.11 (s, 6H, *p-Me*), 2.14 (s, 12H, *o-Me*), 3.26 (t, 1H, $^{2}J_{HP} = 9.2$ Hz, $^{2}J_{HPt} = 54$ Hz, PC*H*P), 6.60 (s, 4H, *m*-C*H,mes*), 6.82 (4, 6H, *o*-C*H*,PhP), 7.16–7.51 (m, 18H, *Ph*–P). ^{13}C NMR ($CDCl_3$): δ 19.9 (*p*-Me), 20.9 (*o*-Me), 30.9 (CHP) 122.3 (Ar), 127.9 (Ar), 128.4 (Ar), 130.8 (Ar), 131.8 (Ar), 136.5. ^{31}P{^{1}H} NMR ($CDCl_3$): δ 46.0. MS (FAB: *m*/*z*): 888 [30, M^+], 844 [10, M^+−d_3-MeCN], 650 [5], 277 [100], 57 [70].

5. Crystal structure determinations

Data for **1** and **2** were collected at 173 K on a Nonius KappaCCD diffractomer, λ(Mo-Kα) = 0.71073 Å. An absorption correction (MULTISCAN) was applied. The structures were solved by direct methods (SHELXS-97) [10] and refined by full matrix least squares (SHELXL-97) [11] with non-H atoms anisotropic and H atoms included in riding mode except for the H atoms on C1 and N1 of compound **1**, and C1 and N1 of compound **2** which were refined.

Acknowledgement

We thank the Royal Society for a University Research Fellowship (M.S.H.).

Appendix A. Supplementary material

CCDC 285813 and 285814 contain the supplementary crystallographic data for **1** and **2**. These data can be obtained free of charge via http://www.ccdc.cam.ac.uk/conts.retrieving.html, or from the Cambridge Crystallographic Data Centre, 12 Union Road, Cambridge CB2 1EZ, UK; fax: (+44) 1223-336-033; or e-mail: deposit @ccdc.cam.ac.uk. Supplementary data associated with this article can be found, in the online version, at doi:10.1016/j.poly.2006.10.020.

References

[1] For a general review of β-diketiminate chemistry, see: L. Bourget-Merle, M.F. Lappert, J.R. Severn, Chem. Rev. 102 (2002) 3031.
[2] (a) Examples of s-block bis(phosphinimino)methanide complexes: M.T. Gamer, P.W. Roesky, Z. Anorg. Allg. Chem. 627 (2001) 877;
(b) R.P.K. Babu, A. Kasani, R. McDonald, R.G. Cavell, Inorg. Chem. 39 (2000) 4981;
(c) R.P.K. Babu, A. Kasani, R. McDonald, R.G. Cavell, Organometallics 20 (2001) 1451;
(d) P. Wei, D. Stephan, Organometallics 22 (2003) 601;
(e) M.S. Hill, P.B. Hitchcock, Chem. Commun. (2003) 1758;
(f) T.K. Panda, A. Zulys, M.T. Gamer, P.W. Roesky, J. Organomet. Chem. 690 (2005) 5078.

[3] (a) Examples of p-block bis(phosphinimino)methanide complexes: K. Aparna, R. McDonald, M. Ferguson, R.G. Cavell, Organometallics 18 (1999) 4241;
(b) M.S. Hill, P.B. Hitchcock, S.M.A. Karagouni, J. Organomet. Chem. 689 (2004) 722.
[4] (a) Examples of d-block bis(phosphinimino)methanide complexes: K.V. Katti, U. Seseke, H.W. Roesky, Inorg. Chem. 26 (1987) 814;
(b) P. Imhoff, C.J. Elsevier, J. Organomet. Chem. 361 (1989) C61;
(c) P. Imhoff, G.H. Guelpen, K. Vrieze, W.J.J. Smeets, A.L. Spek, C.J. Elsevier, Inorg. Chim. Acta 235 (1995) 77;
(d) P. Imhoff, R. Van Asselt, C.J. Elsevier, M.C. Zoutberg, C.H. Stam, Inorg. Chim. Acta 184 (1991) 73;
(e) M.W. Avis, C.J. Elsevier, N. Veldman, H. Koojiman, A.L. Spek, Inorg. Chem. 35 (1996) 1518;
(f) A. Kasani, R.P.K. Babu, R. McDonald, R.G. Cavell, Organometallics 18 (1999) 3775;
(g) S. Al-Benna, M.J. Sarsfield, M. Thornton-Pett, D.L. Ormsby, P.J. Maddox, P. Brès, M. Bochmann, J. Chem. Soc., Dalton Trans. (2000) 4247;
(h) M.S. Hill, P.B. Hitchcock, J. Chem. Soc., Dalton Trans. (2002) 4694;
(i) D.J. Evans, M.S. Hill, P.B. Hitchcock, Dalton Trans. (2003) 570;
(j) P. Wei, D. Stephan, Organometallics 21 (2002) 1308;
(k) C. Bibal, M. Pink, Y.D. Smurnyy, J. Tomaszewski, K.G. Caulton, J. Am. Chem. Soc. 126 (2004) 2312.
[5] U. Fekl, W. Kaminsky, K.I. Goldberg, J. Am. Chem. Soc. 123 (2001) 6423.
[6] (a) N.D. Jones, G. Lin, R.A. Gossage, R. McDonald, R.G. Cavell, Organometallics 22 (2003) 2832;
(b) G. Lin, N.D. Jones, R.A. Gossage, R. McDonald, R.G. Cavell, Angew. Chem., Int. Ed. 42 (2003) 4054.
[7] M.W. Avis, K. Vrieze, H. Kooikman, N. Veldman, A.L. Spek, C.J. Elsevier, Inorg. Chem. 34 (1995) 4092.
[8] See, for example, Ref. [6a] and references cited therein.
[9] G.W. Parshall, Acc. Chem. Res. 3 (1970) 139.
[10] G.M. Sheldrick, SHELXS-97, Program for the Solution of Crystal Structures, Göttingen, 1997.
[11] G.M. Sheldrick, SHELXL-97, Program for the Refinement of Crystal Structures, Göttingen, 1997.

Our interest is continuation of investigating coordinating properties of Cu(II) with pyridine-2-carboxylate ligand. Until now, aside from the violet form of the formula Cu(2-pca)$_2$ obtained by us earlier [4a], only a few 1:1 mononuclear adducts of bis(pyridine-2-carboxylate)copper(II) [6] have been reported for which structural data are available.

In this work, we present a synthesis, the spectral and magnetic properties, and the X-ray single-crystal analysis of a blue-violet form of Cu(2-pic)$_2$, where 2-pic = pyridine-2-carboxylate. We would like to emphasize that the compound studied is another new complex of copper(II) with pyridine-2-carboxylate structurally and magnetically characterized by us. The anhydrous Cu(pyridine-2-carboxylate)$_2$ prepared directly from picolinic acid was previously obtained by others [7] and the square-planar environment was proposed, but the crystal structure was not determined. This compound was obtained by us using a procedure slightly modified with respect to those described in the literature.

In view of the structural data, it should be expected that exchange interactions between copper(II) ions occur through double out-of-plane carboxylate bridges. Hence, the object of our interest was an investigation of the magnetic properties of this compound and an estimation of the value of the exchange interaction.

Here, we describe the results of spectroscopic and magnetic studies of blue-violet form of Cu(pyridine-2-carboxylate)$_2$ in the light of structure description.

2. Experimental

2.1. Reagents and physical measurements

Starting materials and solvents for the synthesis were obtained commercially and used as received. Metal content was determined using a Carl-Zeiss-Jena atomic absorption spectrophotometer. Elemental analyses were carried out using a Perkin–Elmer elemental analyzer 2400CHN.

Infrared spectra (100–4000 cm^{-1}) were recorded on a Bruker IFS 113v spectrophotometer using KBr pellets, and solid-state electronic spectra (28 000–4000 cm^{-1}) were performed on a Cary 500 spectrophotometer.

The EPR spectra of powder samples were recorded (at 295 and 77 K) on a Bruker ESP 300E spectrometer operating at X-band and equipped with a Bruker NMR gaussmeter ER 035 M and a Hewlett–Packard microwave frequency counter HP 5350B. The EPR parameters were calculated by computer simulation of the experimental spectra of the powder samples using Bruker's WIN-EPR SimFonia Version 1.25.

Magnetic measurements of polycrystalline sample were carried out with a Quantum Design SQUID magnetometer (MPMSXL-5 type). Measurements were recorded at magnetic field of 0.5 T over the temperature range 1.8–300 K. The correction for diamagnetism of the experimental susceptibility was based on subtracting the sample-holder signal and estimating the contribution χ_D from Pascal constants [8]. The effective magnetic moments were calculated from $\mu_{eff} = 2.83(\chi_M T)^{1/2}$ using temperature-independent paramagnetism of 60×10^{-6} cm^3 mol^{-1} for Cu(II).

2.2. X-ray crystallography

All measurements of crystal were performed on a Kuma KM4CCD κ-axis diffractometer [9a] with graphite-monochromated Mo Kα radiation. The crystal was positioned at 65 mm from the KM4CCD camera. Frames (612) were measured at 0.75° intervals with a counting time of 45 s. No absorption correction was applied. Data reduction and analysis were carried out with KUMA DIFFRACTION (Wrocław) programs. The structure was solved by direct methods (program SHELXS97 [9b]) and refined by the full-matrix least-squares method on all F^2 data using the SHELXL97 [9c] programs. Non-hydrogen atoms were refined with anisotropic displacement parameters; hydrogen atoms were included from geometry and were fixed.

2.3. Synthesis

This compound was obtained by us with a procedure similar to those described in literature [7] but modified by us. Copper(II) acetate monohydrate (1 mmol) was dissolved in DMF (40 cm^3) and tetrahydrofuran (THF, 5 cm^3) was added to a solution of picolinic acid (2 mmol) in DMF (20 cm^3). After ca. 30 min of stirring the blue solution was filtered. Single blue crystals suitable for X-ray analysis were obtained by slow evaporation of the solvent.

Anal. Calc. for [$C_{12}H_8N_2O_4Cu$]: C, 46.84; H, 2.62; N, 9.10; Cu 20.65. Found: C, 46.32; H, 2.58; N, 8.95; Cu, 20.79%.

3. Results and discussion

3.1. Description of the structure

Crystallographic parameters are summarized in Table 1 and selected bond distances and angles are listed in Table 2.

The structure of the Cu(2-pic)$_2$ compound with crystallographic numbering is depicted in Fig. 1.

The Cu(2-pic)$_2$ molecule, as a whole, is nearly planar and forms obliquely stacked planes. The copper(II) ion has nearly square-planar coordination with *trans* positioned oxygen and nitrogen donor atoms of two N,O-chelating picolinate ligands (2-pic = pyridine-2-carboxylate) to form a complex involving a five-membered stable chelate ring. The copper(II) ion is slightly deviating from the basal plane (0.02 Å). No unusual bond angles and bond lengths are observed for the coordinated picolinate anion. Both axial and planar Cu–O bond lengths are identical within experimental error (3σ). The Cu–O and Cu–N distances in the basal plane agree well with those found in other square-planar copper(II) complexes [10]. Additionally, there are weak axial interactions between copper

Table 1
Crystal data and structure refinement of $Cu(2\text{-pic})_2$

Empirical formula	$C_{12}H_8N_2O_4Cu$
Formula weight	307.74
T (K)	100(1)
λ (Å)	0.71073
Crystal system	monoclinic
Space group	$P2_1/c$
Unit cell dimensions	
a (Å)	5.163(2)
b (Å)	24.658(6)
c (Å)	8.452(2)
β (°)	92.22(3)
V (Å^3)	1075.2(6)
Z	4
D_{calc} (Mg m^{-3})	1.901
μ (mm^{-1})	2.043
$F(000)$	620
Crystal size (mm)	$0.10 \times 0.10 \times 0.04$
Diffractometer	Kuma KM4CCD
θ Range for data collection (°)	3.46 −28.40
h,k,l Ranges	$-6 \rightarrow 5$, $-28 \rightarrow 29$, $-10 \rightarrow 10$
Reflections collected	6192
Independent reflections (R_{int})	1881 (0.1248)
Data/parameters	1881/172
Goodness-of-fit (F^2)	1.247
Final R_1/wR_2 indices ($I > 2\sigma I$)	0.1227/0.1994
Largest difference in peak and hole (e Å^{-3})	1.601 and −0.722

Table 2
Selected bond lengths (Å) and angles (°) of $Cu(2\text{-pic})_2$

Cu(1)–O(1)	1.944(7)	N(2)–Cu(1)–O(11)	83.6(3)
Cu(1)–N(2)	1.949(9)	N(1)–Cu(1)–O(11)	95.6(4)
Cu(1)–N(1)	1.960(9)	O(1)–Cu(1)–O(2A)	97.9(3)
Cu(1)–O(11)	1.960(7)	N(1)–Cu(1)–O(2A)	84.8(3)
Cu(1)–O(2A)	2.745(8)	N(2)–Cu(1)–O(2A)	98.0(3)
		O(11)–Cu(1)–O(2A)	81.8(3)
Cu(1)–O(12B)	2.770(8)	O(1)–Cu(1)–O(12B)	82.2(3)
O(1)–Cu(1)–N(2)	96.5(3)	N(1)–Cu(1)–O(12B)	95.0(3)
O(1)–Cu(1)–N(1)	84.4(3)	N(2)–Cu(1)–O(12B)	82.2(3)
N(2)–Cu(1)–N(1)	176.9(4)	O(11)–Cu(1)–O(12B)	98.0(3)
O(1)–Cu(1)–O(11)	179.7(4)		

atoms of one plane and carboxylic oxygens of neighboring planes ($Cu\cdots O(2A) = 2.745(8)$, $Cu\cdots O(12B) = 2.770(8)$ Å). Because axial bonding interactions to the copper(II) ion are reported up to 3.3 Å [11] and the angle between the Cu–O(2A) vector and the normal to the equatorial plane, which is the measure of overlap of metal–ligand orbitals, is 0°, the axial interaction must be considered as bonding [12], though the interaction is assumed to be very weak. The spectroscopic evidence supports the axial bonding (see Section 3.2). Therefore, the polyhedron can be described as a tetragonally distorted ($CuN_2O_2O'_2$ chromophore) octahedron, elongated along in the axial direction with a long Cu–O distance, as is expected for apical bond lengths in six-coordinated, strongly tetragonally distorted copper(II) complexes [13]. The most important features of the structure result from the fact that the copper(II) ions

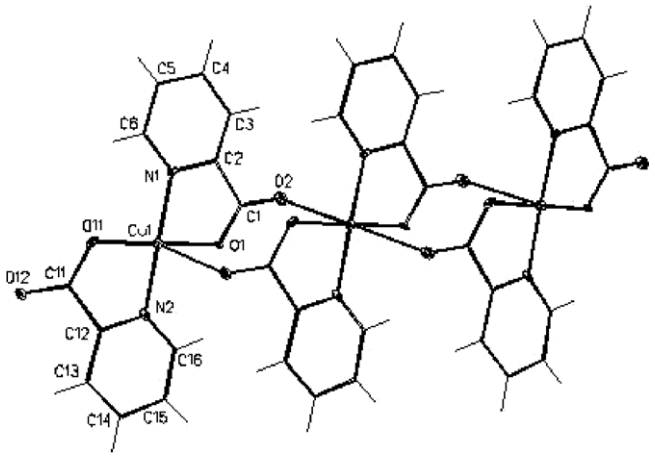


Fig. 1. One-dimensional structure of $Cu(2\text{-pic})_2$ with crystallographic numbering. Cu···Cu distances are 5.163 Å.

are sequentially doubly bridged by carboxylate groups to form an infinite linear one-dimensional polymeric chain extended along the crystallographic x-axis (Fig. 1). The crystal packing is shown in Fig. 2.

Each polymeric chain is linked to other ones by very weak hydrogen bonds C(3)–H(3)···O(2) $(2-x, 1-y, -z)$ [C(3)···O(2) 3.277(13) Å; H(3)···O(2) 2.49 Å; ∠C(3)–H(3)···O(2) 140°] and C(15)–H(15)···O(12) $(1+x, 1/2-y, -1/2+z)$ [C(15)···O(12) 3.162(13) Å; H(15)···O(12) 2.40 Å; ∠C(15)–H(15)···O–(12) 137°]. These bonds

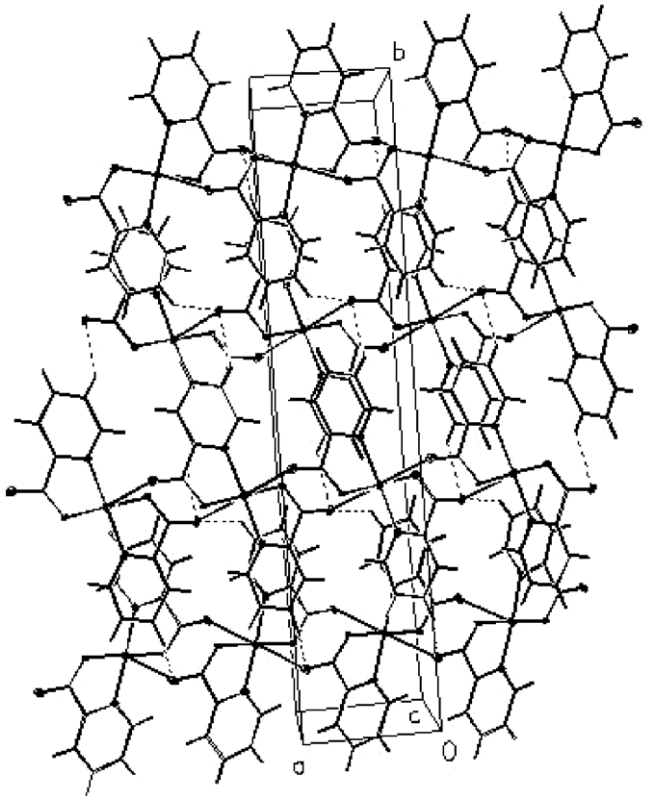


Fig. 2. Crystal packing of $Cu(2\text{-pic})_2$ showing hydrogen bonds (dashed lines).

arise from interaction of a CH from pyridine and an O atom from the carboxylate group. These hydrogen bond interactions, linked in a zigzag chain arrangement, lead to the formation of a 2D sheet structure (Fig. 3a,b). The shortest interchain Cu···Cu separations are 7.43 and 8.09 Å.

As previously noted, each carboxylate group bridges two copper(II) ions through the O(2A) and O(12B) oxygen atoms of the equatorial and the axial position on the copper(II) coordination polyhedron, respectively. This coordination behavior causes the non-planarity of the Cu–O–C–O–Cu′ fragment and gives rise to the formation of a chair-like eight-membered ring Cu–O–C–O–Cu′–O–C–O–Cu with the Cu·Cu distance of 5.163 Å. This distance is near the range of reported values of ca. 5 Å observed for polyatomic bridges [14]. The bridging pathway Cu–O–C–O–Cu′ is asymmetric not only in its conformation but also with respect to Cu–O bond lengths. The intermolecular Cu···Cu distance (5.163 Å) suggests magnetic interactions between the copper(II) centers (see Section 3.3).

3.2. Spectroscopic properties

The IR spectrum of the $Cu(2\text{-pic})_2$ compound shows asymmetric and symmetric stretching vibrations of the coordinated carboxylate groups, $\nu_{as}(COO)$ and $\nu_s(COO)$, at 1649 and 1351 cm^{-1}, respectively. The difference between the two bands, $\Delta\nu$, which gives information on the bonding mode of the carboxylate group [15], is equal for the complex to 298 cm^{-1}, and may suggest a monodentate coordination. Owing to the non-symmetric bonding mode of the carboxylate group, a large splitting ($\Delta\nu$) of the COO stretching frequencies should be expected [15a]. In other words, large $\Delta\nu$ values (>200 cm^{-1}) indicate highly asymmetrical bridging, i.e. a "pseudo-monodentate" coordination, which may be approaching a monodentate coordination. So, the large $\Delta\nu$ value observed in our compound can be viewed as a pseudo-monodentate coordination, which is consistent with the structure. Generally, the number, shape and position of the corresponding absorption bands are strongly affected by some hydrogen bonding interactions of the carboxyl group of pyridine-carboxylate [16]. So, the shoulder observed on the broad band of $\nu_{as}(COO)$ stretch about 1650 cm^{-1}, overlapping with the stretching vibration of $\nu(C{=}N)$ of the pyridine ring, may be responsible for the presence of hydrogen bonding as confirmed by the crystal structure (Fig. 3).

The characteristic band attributed to the out-of-plane ring deformation vibration of the pyridine ring $\delta(C{=}N)$, which occurs for a free ligand at 407 cm^{-1}, is shifted in the complex to a higher frequency (419 cm^{-1}), indicating bond formation between the copper ion and the nitrogen atom of the heterocyclic ring. The bands associated with Cu–N and Cu–O vibrations at 257 and 340 cm^{-1}, respectively, were tentatively assigned on the basis of previous studies of pyridines as N-donor ligands, carboxylate compounds and by comparison with free ligands [17]. For $Cu(2\text{-pic})_2$, where CuN_2O_2 chromophore has *trans* square-planar geometry, only a single band corresponding to Cu–O and Cu–N stretches is observed. However, for the *cis*-isomer two absorption bands would be expected. This is consistent with the criteria published by Herlinger et al. [18] and with the reported crystal structure.

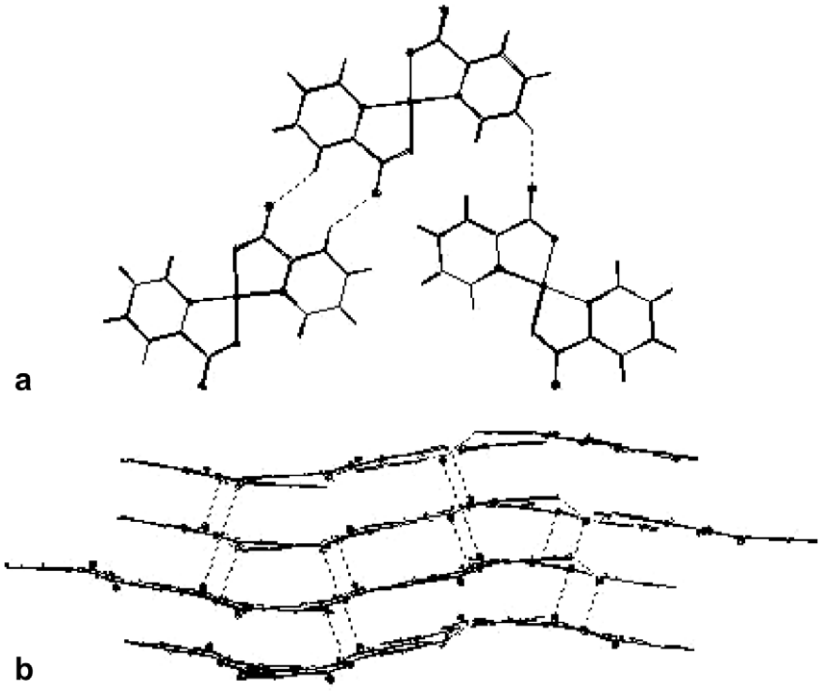


Fig. 3. (a, b) Two views of the 2D sheet structure of $Cu(2\text{-pic})B_2$ showing the sites of hydrogen bonding between the molecules (dashed lines).

The X-band EPR spectrum of a polycrystalline sample of Cu(2-pic)$_2$ (**1**) is of axial type with no hyperfine structure. As a result of a computer simulation procedure (powder spectrum simulation) the following values of the spectroscopic splitting factors were obtained: $g_{\|} = 2.22_8$, $g_{\perp} = 2.05_2$ (Fig. 4). The spectra are independent of temperature. The g-values obtained from the simulations indicate basically a d($x^2 - y^2$) ground state for Cu(II) as observed for other copper–aminoacid complexes [19].

The hyperfine structure expected for Cu(II) ions is not observed, suggesting the existence of exchange interactions coupling the paramagnetic ions [20]. The $g_{\|}$ value is in agreement with that observed for CuN_2O_2 chromophores with strong planar and weaker axial bonds [21].

The ligand-field spectrum shows one broad asymmetric band centered at 16 670 cm^{-1}, characteristic of a tetragonally distorted octahedral with a $CuN_2O_2O'_2$ chromophore [22], consistent with the structural analysis.

3.3. Magnetic properties

Because the results of structural determination of Cu-(2-pic)$_2$ clearly indicate that in this complex there are carboxylate bridging groups through which an exchange interaction may be mediated, we performed a magnetic study of them. In general, the ability of the carboxylate group to propagate exchange interactions between two copper(II) ions separated by more than 5 Å has been well demonstrated [23]. Additionally, because the interchain Cu···Cu separations of 7.43 and 8.09 Å are in the range, up to 11 Å, in which magnetic exchange has been observed [24], a weak exchange interaction mediated by an H-bond system is also expected.

The magnetic properties of the Cu(2-pic)$_2$ were investigated in the temperature range of 1.8–300 K. The magnetic susceptibility results for polycrystalline sample obey the Curie–Weiss law between 25 and 300 K, $\chi = C/(T - \theta)$, where χ is the magnetic susceptibility per copper atom, the Curie constant $C = Ng^2\beta^2S(S+1)/3k$ and $S = 1/2$. The best fit values of the Curie (C) and Weiss (θ) constants are equal to 0.42 cm^3 K mol^{-1} and −1.9 K, respectively. Negative Weiss constant value suggests a weak antiferromagnetic interaction between the copper(II) ions. The temperature variation of χT is depicted in Fig. 5.

The magnetic moment at room temperature (1.83 μ_B) is typical of the normal value for an uncoupled copper(II) system and might suggest the absence of spin exchange, but the χT value decreases slowly with temperature, lowering from 0.418 cm^3 K mol^{-1} at 300 K to 0.291 cm^3 K mol^{-1} at 1.8 K. This suggests the existence of a weak antiferromagnetic exchange between the copper(II) ions at low temperatures.

Taking into account the crystal structure of the compound, the magnetic properties could be explained by the Heisenberg linear-chain model of magnetic interaction arising from the isotropic model $S = 1/2$ described by the Hamiltonian $H = -2J\sum_{i=1}^{n} S_i \cdot S_{i+1}$. The magnetic data were analyzed using the Bonner–Fisher expression [25a], assuming a first-order molecular-field correction to account for the interchain interaction, Eq. (1) [25b]:

$$\chi_{Cu}^{coor} = \frac{\chi_{Cu}}{1 - \frac{2zJ'}{N\beta^2 g^2}\chi_{Cu}} \quad (1)$$

where χ_{Cu} is the susceptibility of copper(II) centers in an isolated Heisenberg chain, $J'$is the interchain exchange, and z is the number of nearest neighbors chains. In the frame of this model, the best-fit parameters obtained by the least-squares fit are the following: $J = -0.73$ cm^{-1}, $zJ' = -0.06$ cm^{-1}, $g = 2.08$ with the value of R=3.93 × 10^{-5}, where R is the agreement factor defined as $R = \sqrt{\sum \frac{1}{(\chi_i^{exp})^2}(\chi_i^{exp} - \chi_i^{calc})^2 / \sum \frac{1}{(\chi_i^{exp})^2}}$

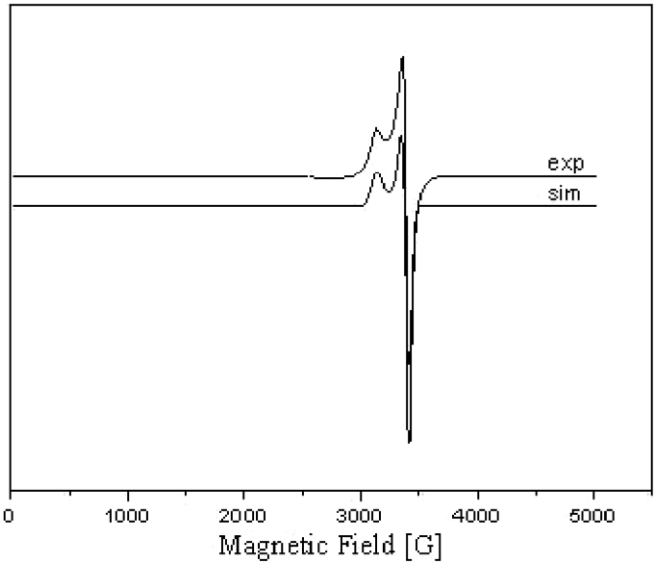


Fig. 4. The experimental EPR powder spectrum of Cu(2-pic)$_2$ obtained at 9.5 GHz (exp) and computer simulation (sim).

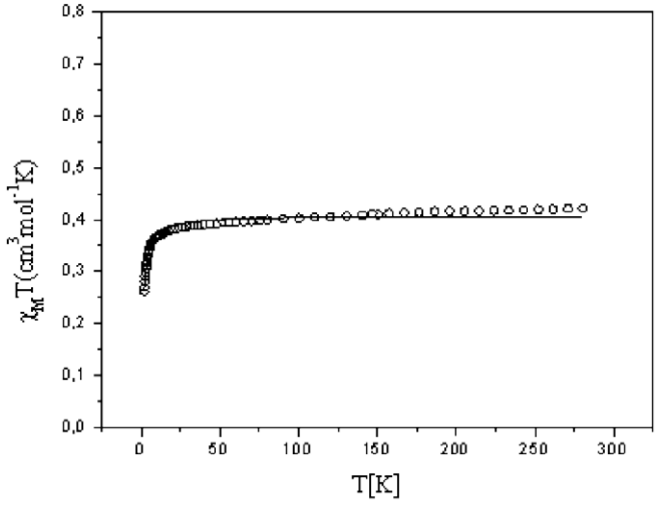


Fig. 5. Plot of $\chi_{Cu}T$ (O) *vs.* T for Cu(2-pic)$_2$. The solid line represents the best fit of the experimental data to the Bonner–Fisher chain model with the parameters reported in the text.

The temperature variation of experimental and calculated values of $\chi_M T$ of the Cu(2-pic)$_2$ is shown in Fig. 5.

3.4. Magneto-structural correlations

Different coordination modes of carboxylato groups lead to the formation of mononuclear and polynuclear structures. From the magnetic point of view, the range of magnetic behaviour as a function of different coordination modes was pointed out, from strongly coupled to moderate or weak antiferromagnetic compounds and even ferromagnetic ones.

For copper(II) complexes, the *syn–syn* conformation mediates strong antiferromagnetic interactions (singlet–triplet separation value $\sim -300\ cm^{-1}$). Weak antiferro- or ferromagnetic interactions are observed in carboxylato-bridged copper(II) complexes in which the carboxylate group adopts the *syn–anti* conformation [4b]. In an *anti–anti* carboxylate bridge, a weak to moderate antiferromagnetic coupling is observed [26].

It is worth noticing that a large number of dinuclear and polynuclear copper(II) geometries, planar or parallel planar, especially those bridged by hydroxide [27] and chloride [28] ions, have been reported. These compounds are often divided into two types (Fig. 6): (i) parallel plane bridging in which the bridging ligands are equatorially bound to both metal ion and (ii) perpendicular plane bridging in which the bridging ligands are axially bound to one metal ion and equatorially bound to the other, characteristic for hydroxo- and chloro-bridged systems, respectively. The carboxylato-bridged compound studied in this work belong to (ii) type, i.e. with a double out-of-plane bridging framework and parallel planar geometry of copper(II) ion.

Generally, magnetic coupling for all known out-of-plane polynuclear compounds is relatively weak, because of the near-orthogonality of magnetic orbitals, as it has been shown for chloro- [28d,29], carbonato- [30] and oximato- [31] bridged compounds. In the case of interactions in apical-equatorial bond modes, the orthogonality of magnetic orbitals leads to a coupling which must be very weakly antiferromagnetic, zero or weakly ferromagnetic.

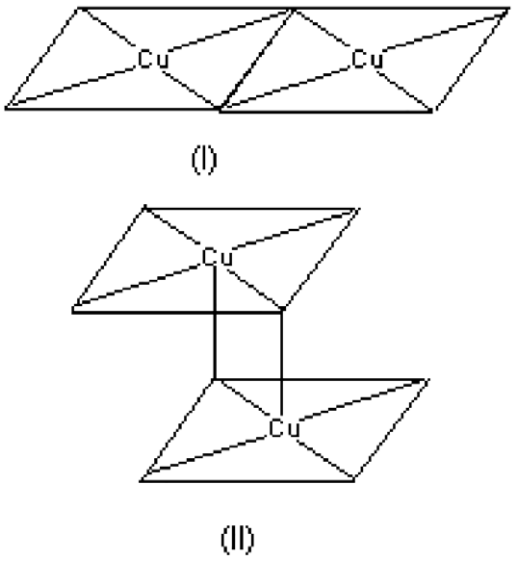


Fig. 6. Relative orientation of the coordination planes in the copper(II) compounds of in the plane (I) and out-of-plane (II) bridging modes type.

It is worthy of note that the weak interaction between copper(II) centers has been previously observed for some carboxylato-bridged complexes (J from ~ 0.5 to ~ -1 cm^{-1}) in which the carboxylate group bridges from the basal to the axial position with a long Cu–O distance (2.28–2.68 Å) [5b]. The value of J is small as expected for this kind of compounds exhibiting an out-of-plane bridging framework.

In the case of the Cu(2-pic)$_2$, the very weak antiferromagnetic coupling observed between the copper atoms is expected in the light of the following electronic and structural features: (i) relatively long Cu–O axial distance, (ii) non planarity of the Cu–O–C–O–Cu′ fragment (an out-of-phase exchange pathway), and (iii) each carboxylate bridge involves an axial position on a copper(II) ion, where the spin density of the unpaired electron is very small, in square-based geometry the unpaired electron is in $d(x^2 - y^2)$. In other words, the bridge links the axial-equatorial coordination sites of the square-planar neighboring Cu(II) centers via both superexchange pathways, and the delocalization of unpaired electron density along the axial coordination site should be very poor, and magnetic orbitals are almost orthogonal. All these features are unfavorable to the propagation of strong interactions.

The magnitude of the interaction in Cu(2-pic)$_2$ is much less than in the di-chlorobridged series [28d,29], because of the greater distance through which exchange effects have to be transmitted in the carboxylate group. The results indicate that the carboxylate group is less effective in allowing for electron spin delocalization than the pathways between ligands and Cu(II) ions involving a chloro-bridge.

In summary, a comparison between the values of J for Cu(2-pic)$_2$ analyzed here and those for out-of-plane single carboxylato-bridged compounds [5b] reveals that the monocarboxylato-bridged series exhibit weaker antiferromagnetic coupling. This is consistent with the simple orbital model proposed by Kahn et al. [32], in which magnetic coupling is proportional to the square of the overlapping integral. So, for mono-out-of-plane bridged copper(II) compounds, the values of coupling constant are smaller due to a decreasing number of the bridging groups.

Finally, although the distance between the donor and the acceptor of C–H···O hydrogen bonds is relatively short, only very weak antiferromagnetic interactions are possible due to large Cu···Cu separations. It is worth of mentioning, that despite large axial Cu–O bond distances, a covalent carboxylate bridge is more effective in allowing for electron spin delocalization than pathways involving non-covalent hydrogen bonds. These results are important in view of the fact that those chemical pathways are present in most metalloproteins.

4. Concluding remarks

In summary, a new example of copper(II) compound (blue-violet form) with the pyridine-2-carboxylate ligand of the formula $Cu(2\text{-pic})_2$ is reported in this paper. We would like to emphasize that the compound here studied and a violet form of $Cu(2\text{-pca})_2$ obtained by us earlier [4a] are the polymorphic forms of Cu(pyridine-2-carboxylate)$_2$.

Two key factors control the crystal structure of $Cu(2\text{-pic})_2$ and provide superexchange paths for magnetic interactions between the copper ions, the bridging coordination and the interchain hydrogen bonds. The hydrogen bonds generate a supramolecular structure and governing stability of the complexes, and have an important role in the magnetism by a further increase in the dimensionality of the overall structure.

Finally, it was interesting to design a new polynuclear copper(II) compound with parallel planar geometry and with an out-of-plane framework of carboxylate bridges.

Acknowledgements

This work was supported by the Polish Ministry of Science and Higher Education (Grant No. 1T09A 12430). We thank Professor Julia Jezierska (Faculty of Chemistry, University of Wrocław, Wrocław, Poland) for the simulation of EPR spectra and helpful discussions.

Appendix A. Supplementary material

CCDC 255026 contains the supplementary crystallographic data for the structures reported in this paper. These data can be obtained free of charge via http://www.ccdc.cam.ac.uk/conts/retrieving.html, or from the Cambridge Crystallographic Data Centre, 12 Union Road, Cambridge CB2 1EZ, UK; fax: (+44) 1223-336-033; or e-mail: deposit@ccdc.cam.ac.uk. Supplementary data associated with this article can be found, in the online version, at doi:10.1016/j.poly.2006.10.019.

References

[1] (a) B.P. Murphy, B.J. Hathaway, Coord. Chem. Rev. 124 (1993) 63;
(b) B.J. Hathaway, in: G. Wilkinson, R.D. Gillard, J.A. McCleverty (Eds.), Comprehensive Coordination Chemistry, vol. 5, Pergamon Press, Oxford, 1987, p. 553.
[2] (a) M. Melník, Coord. Chem. Rev. 42 (1982) 259;
(b) M. Kato, Y. Muto, Coord. Chem. Rev. 92 (1988) 45.
[3] (a) B. Kozlevčar, N. Lah, I. Leban, Croat. Chim. Acta 73 (2000) 733;
(b) M. Melník, M. Koman, D. Hudecová, J. Moncol, B. Dudová, T. Głowiak, J. Mroziński, C. Holloway, Inorg. Chim. Acta 308 (2000) 1;
(c) J. Moncol', M. Palicová, P. Segl'a, M. Koman, M. Melník, M. Valko, T. Głowiak, Polyhedron 21 (2002) 365.
[4] (a) B. Żurowska, J. Ochocki, Z. Ciunik, J. Mroziński, J. Reedijk, Inorg. Chim. Acta 357 (2004) 755;
(b) B. Żurowska, J. Mroziński, Inorg. Chim. Acta 342 (2003) 23, and references therein.
[5] (a) C.J. O'Connor, E.E. Eduok, F.R. Fronczek, O. Kahn, Inorg. Chim. Acta 105 (1985) 107;
(b) P.R. Levstein, R. Calvo, Inorg. Chem. 29 (1990) 1581.
[6] (a) F.S. Stephens, J. Chem. Soc. A (1970) 2377;
(b) A. Takenaka, H. Utsumi, T. Yamamoto, A. Furusaki, I. Nitta, J. Chem. Soc. Jpn. Pure Chem. 91 (1970) 928.
[7] (a) R.D. Gillard, S.H. Laurie, F.S. Stephens, J. Chem. Soc. A (1968) 2588;
(b) A. Kleinstein, G.A. Webb, J. Inorg. Nucl. Chem. 33 (1971) 405;
(c) M. Inoue, M. Kubo, J. Magn. Reson. 4 (1971) 175;
(d) M. Hernández-Molina, J. González-Platas, C. Ruiz-Pérez, F. Lloret, M. Julve, Inorg. Chim. Acta 284 (1999) 258, and references therein.
[8] E. König, Magnetic Properties of Coordination and Organometallic Transition Metal Compounds, Springer, Berlin, 1966.
[9] (a) Oxford Diffraction, Poland Sp. z o.o., CRYSALIS CCD and CRYSALIS RED Programs, Wrocław, 2002.;
(b) G.M. Sheldrick, SHELXS97, Program for Solution of Crystal Structures, University of Göttingen, 1997;
(c) G.M. Sheldrick, SHELXL97, Program for Crystal Structure Refinement, University of Göttingen, 1997.
[10] (a) M. Melnik, M. Kabešová, M. Dunaj-Jurčo, C.E. Holloway, J. Coord. Chem. 41 (1997) 35;
(b) M.E. Bluhm, M. Ciesielski, H. Gorls, O. Walter, M. Doring, Inorg. Chem. 42 (2003) 8878;
(c) H. Masuda, A. Odani, O. Yamauchi, Inorg. Chem. 28 (1989) 624.
[11] A. Walsh, B.J. Hathaway, J. Chem. Soc., Dalton Trans. (1984) 15.
[12] L.P. Battaglia, A.B. Corradi, L. Menabue, Inorg. Chem. 22 (1983) 3251.
[13] G. Davey, F.S. Stephens, J. Chem. Soc. A (1971) 103.
[14] E. Colacio, J.P. Costes, R. Kivekäs, J.P. Laurent, J. Ruiz, M. Sundberg, Inorg. Chem. 30 (1991) 1475.
[15] (a) G.B. Deacon, R.J. Philips, Coord. Chem. Rev. 33 (1980) 227;
(b) K. Nakamoto, Infrared and Ramann Spectra of Inorganic and Coordination Compounds, Wiley, New York, 1997.
[16] G. Marcotrigiano, L. Menabue, G.C. Pellacani, J. Inorg. Nucl. Chem. 40 (1978) 165.
[17] (a) M. Cadene, A.M. Vergnoux, Spectrochim. Acta, Part A 28 (1972) 1663;
(b) C.W. Frank, L.B. Rogers, Inorg. Chem. 5 (1966) 619.
[18] A.W. Herlinger, S.L. Wenhold, T.V. Long II., J. Am. Chem. Soc. 92 (1970) 6474.
[19] O.R. Nascimento, A.J. Costa-Filho, D.I. De Morais, J. Ellena, L.F. Delboni, Inorg. Chim. Acta 312 (2001) 133.
[20] D. Gatteschi, A. Bencini, Electron Paramagnetic Resonance of Exchange Coupled Systems, Springer-Verlag, Berlin, 1990.
[21] A.C. Fabretti, G. Franchini, P. Zannini, M. Divaira, Inorg. Chim. Acta 105 (1985) 8.
[22] L. Abuhijleh, C. Woods, Y. Amed, Inorg. Chim. Acta 130 (1991) 11.
[23] E. Colacio, J.M. Dominguez-Vera, R. Kivekäs, J. Ruiz, Inorg. Chim. Acta 218 (1994) 109.
[24] (a) B.J. Hathaway, Struct. Bond. 14 (1973) 49;
(b) B.J. Hathaway, D.E. Billing, Coord. Chem. Rev 5 (1970) 143;
(c) T.D. Smith, J.R. Pilbrow, Coord. Chem. Rev. 13 (1974) 73.
[25] (a) J.C. Bonner, M.E. Fisher, Phys. Rev., Sect. A 135 (1964) 640;
(b) J.W. Stout, R.C. Chisholm, J. Chem. Phys. 36 (1962) 979.
[26] (a) A. Rodriguez-Fortea, P. Alemany, S. Alvarez, E. Ruiz, Chem. Eur. J. 7 (2001) 627;
(b) S. Youngme, C. Pakawatchai, W. Somjitsripunya, K. Chinnakali, H.-K. Fun, Inorg. Chim. Acta 303 (2000) 181;
(c) E. Colacio, J.M. Domínguez-Vera, M. Ghazi, R. Kivekäs, M. Klinga, J.M. Moreno, Eur. J. Inorg. Chem. (1999) 441;
(d) M. Inoue, M. Kubo, Inorg. Chem. 9 (1970) 2310;
(e) E. Colacio, J.M. Domínguez-Vera, R. Kivekäs, J.M. Moreno, A. Romerosa, J. Ruiz, Inorg. Chim. Acta 212 (1993) 115.
[27] (a) P. Hay, J. Thibeault, R. Hoffmann, J. Am. Chem. Soc. 97 (1975) 4884;
(b) D.J. Hodgson, Prog. Inorg. Chem. 19 (1975) 173;
(c) E. Ruiz, P. Alemany, S. Alvarez, J. Cano, J. Am. Chem. Soc. 119 (1997) 1297;

(d) E. Ruiz, P. Alemany, S. Alvarez, J. Cano, Inorg. Chem. 36 (1997) 3683;
(e) V.H. Crawford, H.W. Richardson, J.R. Wasson, D.J. Hodgson, W.E. Hatfield, Inorg. Chem. 15 (1976) 2107.
[28] (a) S.G.N. Roundhill, D.M. Roundhill, D.R. Bloomquist, C. Landee, R.D. Willet, D.M. Dooley, H.B. Gray, Inorg. Chem. 18 (1979) 831;
(b) J.V. Folgado, E. Coronado, D. Beltrán, J. Chem. Soc., Dalton Trans. (1986) 1061, and references therein;
(c) R. Faure, H. Loiseleur, G. Thomas-David, Acta Crystallogr., Sect. B 29 (1973) 1890;
(d) P. Segl'a, M. Jamnický, M. Koman, J. Šima, T. Głowiak, Polyhedron 17 (1998) 4525.
[29] (a) J.V. Folgado, E. Coronado, D. Beltrán, J. Chem. Soc., Dalton Trans. (1986) 1061;
(b) K. Hara, M. Inoue, S. Emori, M. Kuto, J. Magn. Reson. 4 (1971) 337.
[30] S. Youngme, N. Chaichit, P. Kongsaeree, G.A. van Albada, J. Reedijk, Inorg. Chim. Acta 324 (2001) 232.
[31] B. Cervera, R. Ruiz, F. Lloret, M. Julve, J. Cano, J. Faus, C. Bois, J. Mroziński, J. Chem. Soc., Dalton Trans. (1997) 1061.
[32] (a) O. Kahn, M.F. Charlot, Nouv. J. Chim. 4 (1980) 567;
(b) J.J. Girerd, M.F. Charlot, O. Kahn, Mol. Phys. 34 (1977) 1063;
(c) O. Kahn, B. Briat, J. Chem. Soc., Faraday Trans. 2 (1976) 268.

investigation and the density functional theory (DFT) calculations for the complex [{$ReOBr_4$}(μ-O){$ReO(3,5\text{-}Me_2pzH)_4$}]. The UV–Vis spectrum of the dirhenium complex has been discussed on the basis of the spin-allowed electronic transitions calculated for [{$ReOBr_4$}(μ-O){$ReO(3,5\text{-}Me_2pzH)_4$}] with the time-dependent DFT (TDDFT) method.

Recent calculations with the TDDFT method for open- and closed-shell 5d-metal complexes (including rhenium complexes) have supported the TDDFT method to be applicable for such systems, giving a good assignment of experimental spectra [9–14].

Gancheff and co-workers [15] have performed extended tests of the ability of the B3LYP method in the LANL2DZ basis set for rhenium oxo complexes in a geometry optimization and calculation of spectral properties. Although this is not a very extended basis set, its use with the DFT has shown it to be sufficient for geometry optimization and calculation of spectral properties. It gives good agreement with the experimental data and its use is especially justified in the case of large molecules.

2. Experimental

2.1. General procedure

All the reagents used in the synthesis were commercially available and were used without further purification. The complex [$ReOBr_3(PPh_3)_2$] and 3,5-Me_2pzH were prepared according to the literature methods [16,17].

The IR spectrum was recorded on a Nicolet Magna 560 spectrophotometer in the spectral range 4000–400 cm^{-1} with the sample in the form of KBr pellets. The electronic spectrum was measured on a spectrophotometer Lab Alliance UV–VIS/8500 in the range 800–200 nm in deoxygenated dichloromethane solution. The ^1H NMR spectrum was obtained in $CDCl_3$ using an Inova 300 spectrometer. Elemental analyses (CHN) were performed on a Perkin–Elmer CHN-2400 analyzer.

2.2. Preparation of [{$ReOBr_4$}(μ-O){$ReO(3,5\text{-}Me_2pzH)_4$}]

[$ReOBr_3(PPh_3)_2$] (1 g, 1.03 mmol) was suspended in acetone (30 ml), acidified by four drops of concentrated HBr and then 3,5-Me_2pzH (0.5 g, 5.2 mmol) in acetone (5 ml) was added dropwise to the stirred suspension. The mixture was stirred for 24 h at room temperature. The reaction solution was concentrated to ~10 ml and diethyl ether (30 ml) was added. Blue crystals of [{$ReOBr_4$}(μ-O){$ReO(3,5\text{-}Me_2pzH)_4$}], suitable for X-ray structure determination, were obtained by slow recrystallization from acetonitrile. Yield 55%.

Anal. Calc. for $C_{20}H_{32}Br_4N_8O_3Re_2$: C, 21.36; H, 2.87; N, 9.96. Found: C, 21.54; H, 3.00; N, 9.86%. IR (KBr, cm^{-1}) 3186 (s), 3137 (s), 3035 (w), 2970 (w), 1574 (s), 1479 (m), 1406 (m), 1368 (w), 1259 (m), 1221 (w), 1186 (m), 1148 (m), 1094 (w), 1064 (m), 1029 (w), 969 (m), 812 (s), 778 (s), 752 (m), 698 (vs), 614 (m), 445 (w).

^1H NMR (20 °C, $CDCl_3$, ppm): $\delta = 1.91$ (s, 12H, CH_3), 2.68 (s, 12H, CH_3), 6.04 (s, 4H, CH), 11.58 (s, 4H, NH).

2.3. Crystal structure determination and refinement

A blue crystal of [{$ReOBr_4$}(μ-O){$ReO(3,5\text{-}Me_2pzH)_4$}] was mounted on a KM-4-CCD automatic diffractometer equipped with a CCD detector, and used for data collection. X-ray intensity data were collected with graphite monochromated Mo Kα radiation ($\lambda = 0.71073$ Å) at a temperature of 293.0(2) K, with the ω scan mode. Exposure time (34 s) was used and all the Ewald sphere reflections were collected up to $2\theta = 50.2°$. The unit cell parameters were determined from least-squares refinement of the setting angles of the 4248 strongest reflections. Details concerning crystal data and refinement are given in Table 1. Lorentz, polarization and numerical absorption corrections [18] were applied. The structure was solved by means of the Patterson method and subsequently completed by difference Fourier recycling. All the non-hydrogen atoms were refined anisotropically using the full-matrix, least-squares technique. All the hydrogen atoms were found from difference Fourier synthesis after four cycles of anisotropic refinement, and refined as "riding" on the adjacent carbon atom with an individual isotropic temperature factor equal to 1.2 times the value of the equivalent temperature factor of the endocyclic parent atom and equal to 1.5 times the value of the equivalent temperature factor of the methyl parent carbon atom. During refinement the methyl groups were allowed to rotate about their local threefold axis. SHELXS97 [19], SHELXL97 [20] and SHELXTL [21] programs were used for all the calculations. Atomic scattering factors were those incorporated in the computer programs.

2.4. Magnetic measurements

The magnetic measurements of the powdered samples were measured over the temperature range 1.8–300 K using a Quantum Design SQUID-based MPMSXL-5-type magnetometer. The superconducting magnet was generally operated at a field strength ranging from 0 to 0.5 T. Measurements of a sample of the compound were made at a magnetic field of 0.5 T.

The SQUID magnetometer was calibrated with a palladium rod sample. Corrections are based on subtracting the sample-holder signal.

2.5. Computational details

The GAUSSIAN03 program [22] was used in the calculations. The geometry of [{$ReOBr_4$}(μ-O){$ReO(3,5\text{-}Me_2pzH)_4$}] was optimized in a singlet state using the DFT method with the B3LYP functional [23,24]. The electronic spectrum was calculated with the TDDFT method [25].

Table 1
Crystal data and structure refinement for the complex [{$ReOBr_4$}(μ-O){$ReO(3,5\text{-}Me_2pzH)_4$}]

Empirical formula	$C_{20}H_{32}Br_4N_8O_3Re_2$
Formula weight	1124.58
Temperature (K)	293.0(2)
Wavelength (Å)	0.71073
Crystal system	tetragonal
Space group	*I*4
Unit cell dimensions	
a (Å)	10.3282(9)
b (Å)	10.3282(9)
c (Å)	15.1065(17)
Volume (Å^3)	1611.4(3)
Z	2
D_{calc} (Mg/m^3)	2.318
Absorption coefficient (mm^{-1})	12.499
F(000)	1044
Crystal size (mm)	$0.21 \times 0.19 \times 0.15$
θ Range for data collection (°)	3.88–25.11
Index ranges	$-12 \leqslant h \leqslant 12$, $-11 \leqslant k \leqslant 12$, $-18 \leqslant l \leqslant 18$
Reflections collected	8571
Independent reflections (R_{int})	1453 (0.0752)
Completeness to $2\theta = 50°$ (including systematically absent reflections)	100%
Maximum and minimum transmission	0.2292 and 0.0883
Data/restraints/parameters	1453/1/91
Goodness-of-fit on F^2	1.146
Final *R* indices [$I > 2\sigma(I)$]	$R_1 = 0.0322$ $wR_2 = 0.0796$
R indices (all data)	$R_1 = 0.0327$ $wR_2 = 0.0799$
Absolute structure parameter	0.00(3)
Largest difference in peak and hole (e Å^{-3})	1.283 and −0.986

The calculations were performed using an ECP basis set on the rhenium atom and the standard 6-31G basis set for the other atoms. For bromine, oxygen, nitrogen and carbon atoms, diffuse and polarization functions were added. The Xe core electrons of Re were replaced by an effective core potential and a DZ quality Hay and Wadt Los Alamos ECP basis set (LANL2DZ) [26] was used for the valence electrons. An additional *d* function with exponent $\alpha = 0.3811$ and *f* function with exponent $\alpha = 2.033$ on the rhenium atom were added.

3. Results and discussion

3.1. Preparation

The compound [{$ReOBr_4$}(μ-O){$ReO(3,5\text{-}Me_2pzH)_4$}] has been isolated in the reaction of [$ReOBr_3(PPh_3)_2$] with 3,5-dimethylpyrazole in acidified acetone at room temperature. The reaction was carried out in a system open to the atmosphere, and water is the source of the bridging oxo group.

3.2. Infrared data

The elemental analysis of the complex is in good agreement with its formulation. The infrared spectrum confirms the presence of terminal and bridging oxo ligands and 3,5-Me_2pzH in the coordination sphere. A sharp band at 969 cm^{-1} is assignable to the symmetric Re═O stretch, and a strong multicomponent band at 698 cm^{-1} with the same shape as that illustrated in the article of Cotton et al. [27] results from overlapping of the antisymmetric Re–O–Re stretching modes with the aromatic ring out-of-plane deformation vibrations. The ν(Re═O) and ν_{as}(Re–O–Re) observed for [{$ReOBr_4$}(μ-O){$ReO(3,5\text{-}Me_2pzH)_4$}] agree well with the appropriate values found previously in similar dirhenium oxocompounds. The electron-withdrawing effect of the terminal Re═O group in complexes with an O═Re─O─Re═O framework results in a relative weakening of the bridging Re–O_b bonds and leads to the reduction in the frequency of the ν(Re–O–Re) stretching mode in comparison with $[Re_2OCl_{10}]^{4-}$. The antisymmetric ν(Re–O–Re) stretching mode of the last compound occurs as a strong band at 850–855 cm^{-1} [28]. The strong bands in the range 3200–3100 cm^{-1}, assignable to N–H vibrations, indicate the coordination of the pyrazole ligands in the neutral monodentate form [29]. Such coordination of the 3,5-dimethylpyrazole molecules is also supported by ^{1}H NMR studies; the singlet at 11.58 ppm corresponds to NH protons.

3.3. Magnetic properties

The magnetic data of the [{$ReOBr_4$}(μ-O){$ReO(3,5\text{-}Me_2pzH)_4$}] complex under the form χ_g versus *T* (χ_g being the experimental gram magnetic susceptibility) are shown in Fig. 1. The relation of χ_g versus *T* indicates

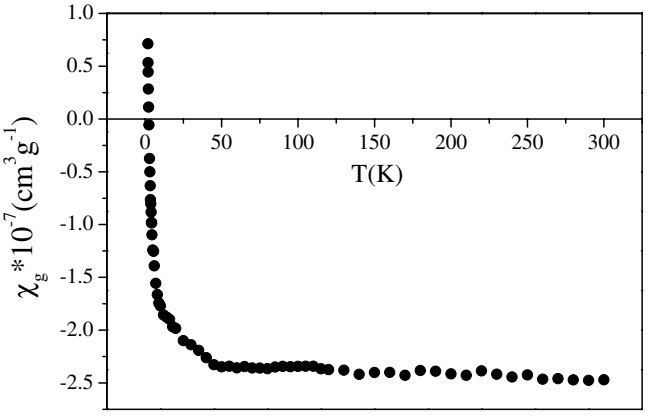


Fig. 1. Plot of the experimental magnetic data χ_g (●) vs. T for complex [{$ReOBr_4$}(μ-O){$ReO(3,5\text{-}Me_2pzH)_4$}].

diamagnetism of the complex in the temperature range ⩾2.5–300 K and very high purity of the sample.

The magnetic properties of the complex evidence coupling electrons in the O═Re—O—Re═O core and confirm the $5d^2$ electronic configuration of both rhenium (V) centers.

3.4. Crystal structure

A definite proof for the structure is provided by the X-ray diffraction results. A perspective drawing of [{$ReOBr_4$}-(μ-O){$ReO(3,5\text{-}Me_2pzH)_4$}] is given in Fig. 2, and the most important bond lengths and angles are reported in Table 2. The [{$ReOBr_4$}(μ-O){$ReO(3,5\text{-}Me_2pzH)_4$}] complex takes a dinuclear structure in which two rhenium atoms are bridged by the oxo ligand. The rhenium and oxygen (terminal and bridging) atoms occupy special positions *a* of *I*4 (No.79) space group at 0, 0, *z* [30]. This forces the molecule

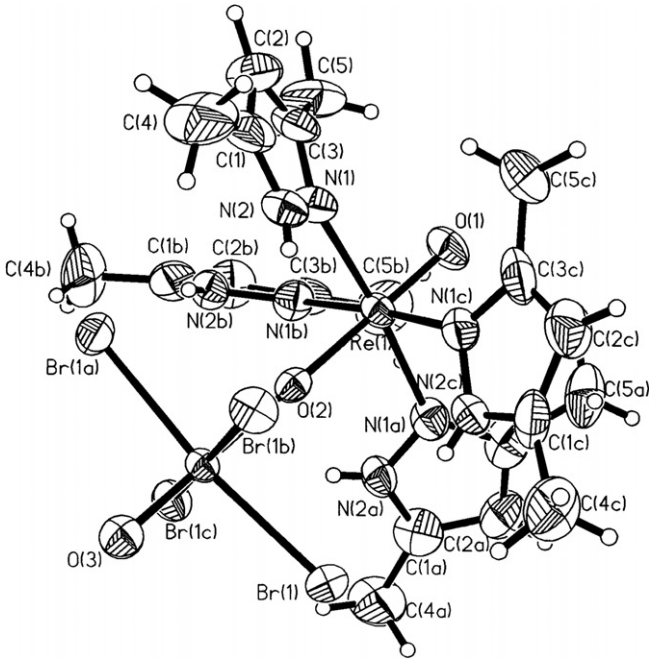


Fig. 2. The molecular structure of [{$ReOBr_4$}(μ-O){$ReO(3,5\text{-}Me_2pzH)_4$}].

to occupy four asymmetric units. The molecules are linked *via* two intermolecular hydrogen bonds: medium strength N(2)–H(2N)···Br(1)#(−*y*, *x*, *z*) (D···A distance 3.366(8) Å and D–H···A angle 164.2°) and weak C(2)–H(2)···O(3)#(*x* − 0.5, *y* − 0.5, *z* − 0.5) (D···A distance 3.496(13) Å and D–H···A angle 163.6°) [31,32]. The intramolecular hydrogen bond linkage C(5)–H(5)···O(1) (D···A distance 3.207(16) Å and D–H···A angle 126.1°) provides additional stabilisation of the [{$ReOBr_4$}(μ-O){$ReO(3,5\text{-}Me_2pzH)_4$}] molecule [31,32].

Each rhenium ion of [{$ReOBr_4$}(μ-O){$ReO(3,5\text{-}Me_2pzH)_4$}] is in a distorted octahedral geometry. The equatorial plane of the Re(1) center is occupied by four 3,5-Me_2pzH molecules, whereas the equatorial plane of the Re(2) atom consists of four bromide ligands. The axial positions of Re(1) and Re(2) centers are occupied by terminal (O_t) and bridging (O_b) oxo ligands. Because of the crystallographic symmetry, the O═Re—O—Re═O core is perfect linear.

The Re(1)–O_t bond is shorter (by 0.037 Å) in comparison with the Re(2)–O_t distance, and the Re(1)–O_b is shorter (by 0.06 Å) than the Re(2)–O_b distance. Both Re–O_t bond lengths fall in the range 1.639–1.76 Å [33], typical of mononuclear complexes of rhenium(V) having a $[ReO]^{3+}$ core, and suggest a considerable degree of triple bond character due to $O_t \rightarrow Re_\pi$ bonding. On the other hand, the Re–O_b bond distances in the dirhenium complex are shorter than a single Re–O length. An ideal single Re–O bond distance, predicted by the use of Pauling's oxygen covalent radius and Cotton and Lippard's value for the Re(V) octahedral covalent radius, should be *ca.* 2.04 Å [34]. It indicates some redistribution of the d_π–p_π interaction along the O_t–Re–O_b unit in the discussed dinuclear rhenium complexes.

The Re–N and Re–Br and bond lengths of [{$ReOBr_4$}-(μ-O){$ReO(3,5\text{-}Me_2pzH)_4$}] are unexceptional, they agree well with appropriate values found previously in similar rhenium compounds [8,35].

A mixed oxidation state formulation involving Re(III) and Re(VII) centers could be proposed for the unsymmetrical [{$ReOBr_4$}(μ-O){$ReO(3,5\text{-}Me_2pzH)_4$}] complex. However, Re(VII) is generally found in complexes including a {ReO_3} moiety and Re(III) coordination compounds are not normally associated with a terminal oxo ligand [36]. A mixed oxidation state formulation involving Re(III) and Re(VII) centers is also inconsistent with the magnetic susceptibility measurements. It seems that the diamagnetic [{$ReOBr_4$}(μ-O){$ReO(3,5\text{-}Me_2pzH)_4$}] complex can be best formulated as the $[Re^VOBr_4][Re^VO_2(3,5\text{-}Me_2pzH)_4]$ adduct. Such a formulation is supported by general features of rhenium coordination compounds and is in accordance with the magnetic studies and DFT calculations for [{$ReOBr_4$}(μ-O){$ReO(3,5\text{-}Me_2pzH)_4$}].

3.5. Optimised geometry

The geometry of [{$ReOBr_4$}(μ-O){$ReO(3,5\text{-}Me_2pzH)_4$}] was optimized in a singlet state using the DFT method

Table 2
The experimental and optimized bond lengths (Å) and angles (°) for [{$ReOBr_4$}(μ-O){$ReO(3,5\text{-}Me_2pzH)_4$}]

	Bond lengths			Bond angles	
	Experimental	Optimized		Experimental	Optimized
Re(1)–N(1)	2.123(7)	2.150	O(1)–Re(1)–O(2)	180.0	179.79
Re(1)–N(1)#1	2.123(7)	2.151	O(1)–Re(1)–N(1)#1	92.8(2)	92.07
Re(1)–N(1)#2	2.123(7)	2.151	O(2)–Re(1)–N(1)#1	87.2(2)	87.81
Re(1)–N(1)#3	2.123(7)	2.151	O(1)–Re(1)–N(1)	92.8(2)	91.98
Re(1)–O(1)	1.654(15)	1.726	O(2)–Re(1)–N(1)	87.2(2)	88.14
Re(1)–O(2)	1.91(2)	1.849	N(1)#1–Re(1)–N(1)	174.5(5)	175.96
Re(2)–O(2)	1.97(2)	2.131	O(1)–Re(1)–N(1)#2	92.8(2)	91.89
Re(2)–O(3)	1.691(14)	1.659	O(2)–Re(1)–N(1)#2	87.2(2)	87.93
Re(2)–Br(1)	2.5578(8)	2.622	N(1)#1–Re(1)–N(1)#2	89.87(2)	89.93
Re(2)–Br(1)#1	2.5578(8)	2.615	N(1)–Re(1)–N(1)#2	89.87(2)	90.05
Re(2)–Br(1)#2	2.5578(8)	2.618	O(1)–Re(1)–N(1)#3	92.8(2)	92.17
Re(2)–Br(1)#3	2.5578(8)	2.618	O(2)–Re(1)–N(1)#3	87.2(2)	88.00
			N(1)#1–Re(1)–N(1)#3	89.87(2)	89.86
			N(1)–Re(1)–N(1)#3	89.87(2)	90.00
			N(1)#2–Re(1)–N(1)#3	174.5(5)	175.93
			Re(1)–O(2)–Re(2)	180.0	179.78
			O(3)–Re(2)–O(2)	180.000(2)	179.90
			O(3)–Re(2)–Br(1)#1	93.72(2)	95.44
			O(2)–Re(2)–Br(1)#1	86.28(2)	84.59
			O(3)–Re(2)–Br(1)	93.72(2)	95.40
			O(2)–Re(2)–Br(1)	86.28(2)	84.59
			Br(1)#1–Re(2)–Br(1)	172.55(5)	169.17
			O(3)–Re(2)–Br(1)#2	93.72(2)	95.52
			O(2)–Re(2)–Br(1)#2	86.28(2)	84.57
			Br(1)#1–Re(2)–Br(1)#2	89.758(3)	89.58
			Br(1)–Re(2)–Br(1)#2	89.758(3)	89.62
			O(3)–Re(2)–Br(1)#3	93.72(2)	95.39
			O(2)–Re(2)–Br(1)#3	86.28(2)	84.51
			Br(1)#1–Re(2)–Br(1)#3	89.758(3)	88.36
			Br(1)–Re(2)–Br(1)#3	89.758(3)	89.38
			Br(1)#2–Re(2)–Br(1)#3	172.55(5)	169.08

#1 $-x, -y, z$; #2 $y, -x, z$; #3 $-y, x, z$.

with the B3LYP functional. The optimized geometric parameters are gathered in Table 2. Considerable differences between experimental and calculated values can be noticed for the Re–O_t and Re–O_b bond lengths. To some extent the differences are ascribed to the crystallographic symmetry of [{$ReOBr_4$}(μ-O){$ReO(3,5\text{-}Me_2pzH)_4$}]. The optimized geometry seems to represent the chemically reasonable structure [$Re^{V}OBr_4$][$Re^{V}O_2(3,5\text{-}Me_2pzH)_4$] for the title complex. The calculated Re(1)–O(1) and Re(1)–O(2) bonds are similar to those observed in $[ReO_2L_4]^+$ complexes and the Re(2)–O_b bond is considerable weaker in comparison with the Re(1)–O_b one.

3.6. Charge distribution

Table 3 presents the atomic charges from the Natural Population Analysis (NPA) for [{$ReOBr_4$}(μ-O){$ReO(3,5\text{-}Me_2pzH)_4$}]. The calculated charges on the rhenium atoms are considerable lower than the formal charge of +5. The populations of the $5d_{xy}$, $5d_{xz}$, $5d_{yz}$, $5d_{x^2-y^2}$ and $5d_z^2$ orbitals of the central atoms in [{$ReOBr_4$}(μ-O){$ReO(3,5\text{-}Me_2pzH)_4$}] are as follows: Re(1): 0.862, 0.862, 0.916, 1.061 and 1.532; Re(2): 0.814, 0.814, 1.492, 1.048 and 1.394. This is a result of significant charge donation from the oxo ligands, bromine ions and N-heterocyle molecules. The Re(2) center, with the bromide ions in the equatorial plane, is less positive in comparison with the Re(1) ion. Considerable differences in the values of charges are

Table 3
Atomic charges from the natural population analysis (NPA) for [{$ReOBr_4$}(μ-O){$ReO(3,5\text{-}Me_2pzH)_4$}]

Atom	Atomic charge
Re(1)	1.424
Re(2)	0.944
O(1)	−0.566
O(2)	−0.830
O(3)	−0.353
Br(1)	−0.407
Br(2)	−0.404
Br(3)	−0.405
Br(4)	−0.405
N(1)	−0.347
N(2)	−0.354
N(3)	−0.347
N(4)	−0.354
N(5)	−0.347
N(6)	−0.354
N(7)	−0.347
N(8)	−0.354

observed for the terminal and bridging oxo ligands – less negative terminal oxo ligands indicates higher electron density delocalization from the terminal ligands towards the rhenium centers and corresponds to differences in the Re–O_t and Re–O_b bonds lengths. Some differences are also visible in the values of the charges of the terminal oxo ligands – the oxo ligand coordinated to the Re(2) atom is less negative. It corresponds to populations of the 2s, $2p_x$, $2p_y$ and $2p_z$ orbitals of the oxo ligands: O(1): 1.839, 1.769, 1.473 and 1.473; O(3): 1.831, 1.705, 1.399 and 1.399; O(2): 1.780, 1.767, 1.632 and 1.633. An increase in the p orbital population is observed for the bridging oxo ligand.

Table 4
The occupancies and hybridization of the calculated Re–O natural bond orbitals (NBOs) for [{$ReOBr_4$}(μ-O){$ReO(3,5\text{-}Me_2pzH)_4$}]

BD	Occupancy	Hybridization of NBO
Re(1)–O(1)	1.961 (0.304)	$0.437(sd^{2.82})_{Re(1)} + 0.899(sp^{1.53})_{O(1)}$
Re(1)–O(1)	1.987 (0.350)	$0.559(d)_{Re(1)} + 0.829(p)_{O(1)}$
Re(1)–O(1)	1.986 (0.350)	$0.559(d)_{Re(1)} + 0.829(p)_{O(1)}$
Re(2)–O(3)	1.967 (0.263)	$0.877(sp^{1.92})_{O(3)} + 0.480(sd^{4.42})_{Re(2)}$
Re(2)–O(3)	1.988 (0.225)	$0.817(p)_{O(3)} + 0.576(d)_{Re(2)}$
Re(2)–O(3)	1.992 (0.227)	$0.816(p)_{O(3)} + 0.578(d)_{Re(2)}$

3.7. NBO analysis

Each natural bond orbital (NBO) σ_{AB} can be written in terms of two directed valence hybrids (HHOs) h_A i h_B on atoms A and B:

$$\sigma_{AB} = c_A h_A + c_B h_B$$

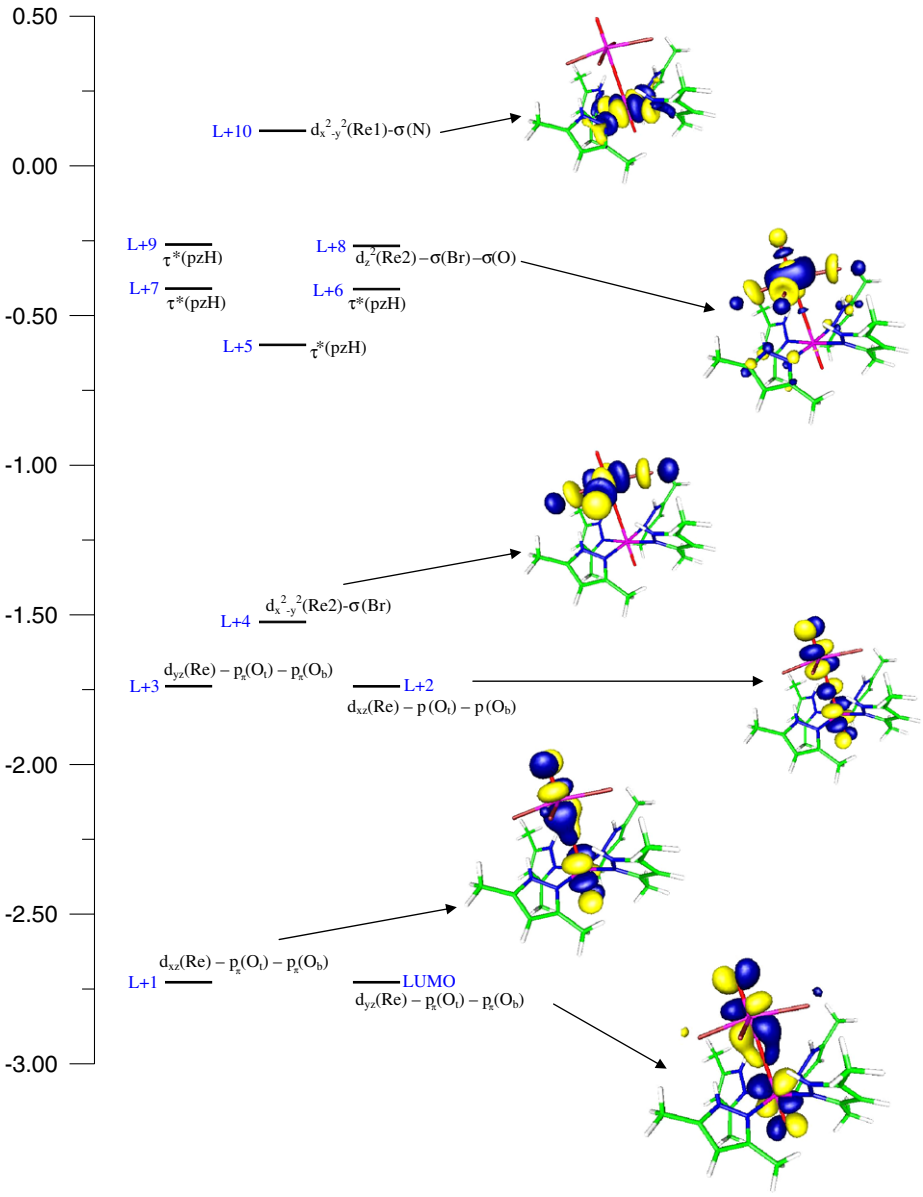


Fig. 3a. The energy (eV), character and contours of the selected unoccupied molecular orbitals of [{$ReOBr_4$}(μ-O){$ReO(3,5\text{-}Me_2pzH)_4$}].

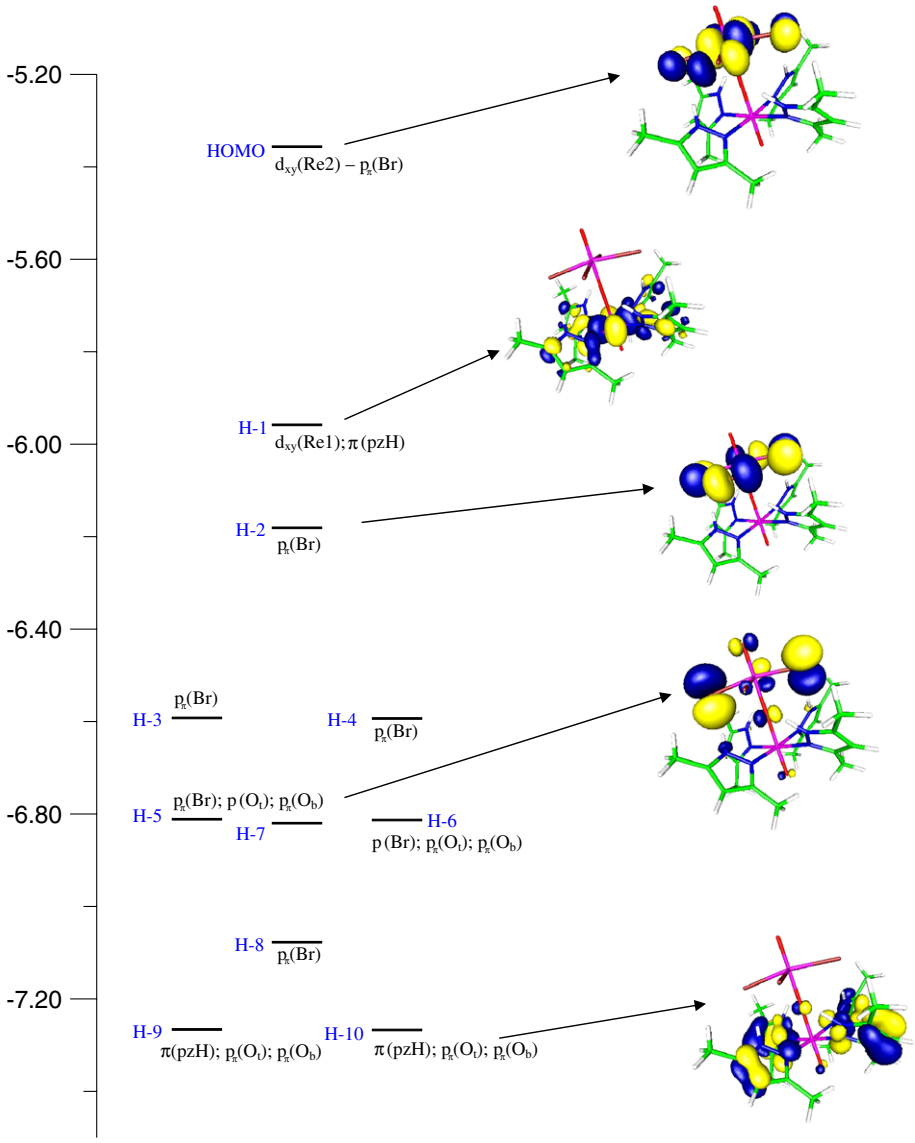


Fig. 3b. The energy (eV), character and contours of the selected occupied molecular orbitals of [{$ReOBr_4$}(μ-O){$ReO(3,5\text{-}Me_2pzH)_4$}].

where c_A i c_B are polarization coefficients. Each valence bonding NBO must in turn be paired with a corresponding valence *anti*-bonding NBO:

$$\sigma^*_{AB} = c_B h_A - c_A h_B$$

to complete the span of the valence space. The Lewis-type (donor) NBOs are thereby complemented by the non-Lewis-type (acceptor) NBOs that are formally empty in an idealized Lewis picture. The interactions between 'filled' Lewis-type NBOs and 'empty' non-Lewis NBOs lead to a loss of occupancy from the localized NBOs of the idealized Lewis structure into the empty non-Lewis orbitals, and they are referred to as 'delocalization' corrections to the zeroth-order natural Lewis structure. The stabilization energy ΔE_{ij} (kcal/mol) associated with the delocalization is estimated by the second-order perturbative as

$$\Delta E_{ij} = q_i(F(i,j)^2)/(\varepsilon_j - \varepsilon_i)$$

where q_i is the donor orbital occupancy, ε_i, ε_j are diagonal elements (orbital energies) and $F(i,j)$ is the off-diagonal NBO Fock or Kohn–Sham matrix element [37].

In the case of the complex [{$ReOBr_4$}(μ-O){$ReO(3,5\text{-}Me_2pzH)_4$}], three Re–$O_t$ natural bond orbitals were detected for each Re atom. The occupancies and hybridization of the calculated Re–O_t natural bond orbitals (NBOs) are given in Table 4. The Re–O_t bonds are all strongly polarized towards the oxygen atom. The *s* and *p* oxygen orbitals and s and d rhenium orbitals take part in the $\sigma_{Re\text{–}Ot}$ bond formation, whereas the $\pi_{Re\text{–}Ot}$ bond orbitals result from overlapping of the empty d_{xz} and d_{yz} rhenium orbitals with the occupied p_x and p_y orbitals of the terminal oxygen ligands. Each terminal oxo ligand of [{$ReOBr_4$}-(μ-O){$ReO(3,5\text{-}Me_2pzH)_4$}] has one lone pair with an occupancy close to 2. The Re–O_b bonds were not detected, indicating predominantly Coulomb-type interactions between the central ion and the bridging oxo ligand [38].

Table 5 presents the occupancies and atomic orbital compositions of the lone pairs (LP) orbitals detected on the bridging oxygen atom, as well as the character of the acceptor orbital and stabilization energies (ΔE_{ij}) for the corresponding donor–acceptor interactions. The O_b ligand has four lone pairs orbitals (LP) and electron density from LP orbitals of the bridging oxygen is mainly delocalized into the antibonding Re(1)–O(1) bond orbitals (Table 5). It explains the considerable differences in the calculated Re(1)–O(2) and Re(2)–O(2) bond lengths and supports the formulation of the title complex as Re(V) species.

3.8. Electronic structure

The energies, characters and contours of selected unoccupied and occupied molecular orbitals of the investigated complex are presented in Figs. 3a and 3b, respectively. The z axis goes along the O═Re—O—Re═O linkage, and the local symmetry of the rhenium centers is considered in the discussion.

The two highest MOs of [{$ReOBr_4$}(μ-O){$ReO(3,5\text{-}Me_2pzH)_4$}] are predominantly localized on the d_{xy} orbitals of the Re(1) and Re(2) atoms, and the remaining eight d-type orbitals of the rhenium ions are found among unoccupied MOs. The LUMO, LUMO + 1, LUMO + 2 and LUMO + 3 can be ascribed as π-antibonding rhenium–oxygen molecular orbitals.

Each rhenium atom uses six valence orbitals, $5d^{2^2}_{x-y}$, $5d^2_z$, 6s, $6p_x$, $6p_y$ and $6p_z$, to form σ-bonds with the six ligands, the occupied $5d_{xy}$ orbitals of both rhenium ions remains non-bonding, and the empty $5d_{yz}$ and $5d_{xz}$ orbitals interact with the filled $2p_x$ and $2p_y$ orbitals of the terminal and bridging oxo ligands to give four π-bonding, two π-non-bonding and four π-antibonding molecular orbitals. In total, there are four σ and four π bonding orbitals describing the Re_2O_3 unit.

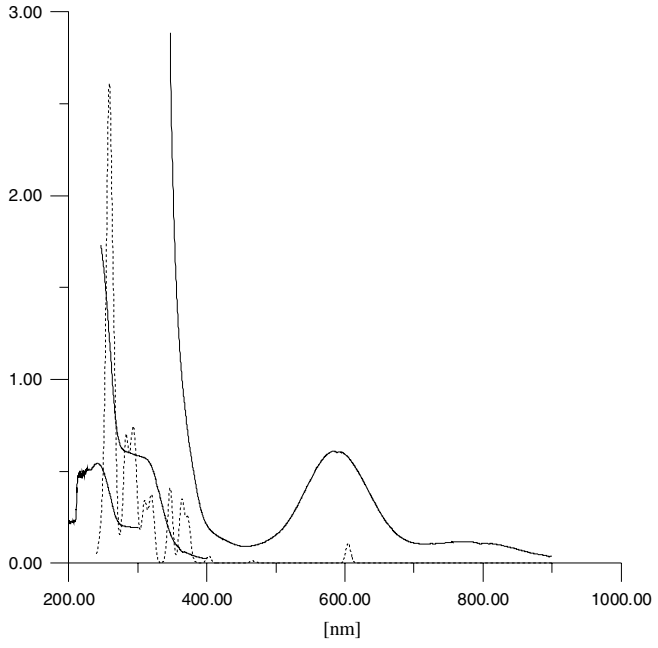


Fig. 4. The experimental (——) and calculated (- - - -) electronic absorption spectra of [{$ReOBr_4$}(μ-O){$Re(O)(3,5\text{-}Me_2pzH)_4$}].

3.9. Electronic spectrum

The experimental and calculated electronic spectra of [{$ReOBr_4$}(μ-O){$ReO(3,5\text{-}Me_2pzH)_4$}] are presented in Fig. 4. Each calculated transition is represented by a gaussian function $y = ce^{-bx^2}$ with the height (c) equal to the oscillator strength and b equal to 0.04 nm^{-2}.

Table 6 shows the spin-allowed singlet–singlet electronic transitions calculated with the TDDFT method for [{$ReOBr_4$}(μ-O){$ReO(3,5\text{-}Me_2pzH)_4$}]. For the high energy part of the spectrum, only transitions with oscillator strengths larger than 0.050 are listed in Table 6.

The investigated complex is of large size, and a hundred electron transitions calculated by the TDDFT method do not comprise all the experimental absorption bands. The UV–Vis spectrum of [{$ReOBr_4$}(μ-O){$ReO(3,5\text{-}Me_2pzH)_4$}] was calculated to 240 nm, so the shortest wavelength experimental band cannot be assigned completely to the calculated transitions. Some additional mainly intraligand and interligand transitions are expected to be found at higher energies in the calculation for [{$ReOBr_4$}-(μ-O){$ReO(3,5\text{-}Me_2pzH)_4$}].

The assignment of the calculated transitions to the experimental bands is based on the criterion of the energy and oscillator strength of the calculated transitions. Only the main components of the molecular orbital are taken into consideration for the description of the electronic transitions.

The two longest wavelength experimental bands are attributed to the transitions of d → d character with small oscillator strengths.

Table 5
The occupancies and atomic orbital compositions of the lone pairs (LP) detected on the bridging oxygen atom and the character of the acceptor orbital, as well as stabilization energies (ΔE_{ij}) for the corresponding donor–acceptor interactions

Donor orbital	Occupancy of donor orbital	Acceptor orbital	ΔE_{ij} (kcal/mol)
$(sp^{0.69})$	1.810	$0.899(sd^{2.82})_{Re(1)} - 0.437(sp^{1.53})_{O(1)}$; $0.480(sp^{1.92})_{O(3)} - 0.877(sd^{4.42})_{Re(2)}$	26.13; 91.96
$(sp^{1.45})$	1.739	$0.899(sd^{2.82})_{Re(1)} - 0.437(sp^{1.53})_{O(1)}$; $0.480(sp^{1.92})_{O(3)} - 0.877(sd^{4.42})_{Re(2)}$	175.65; 4.74
$p_{O(2)}$	1.633	$0.829(d)_{Re(1)} - 0.559(p)_{O(1)}$; $0.576(p)_{O(3)} - 0.817(d)_{Re(2)}$	58.02; 16.29
$p_{O(2)}$	1.633	$0.829(d)_{Re(1)} - 0.559(p)_{O(1)}$; $0.576(p)_{O(3)} - 0.817(d)_{Re(2)}$	58.01; 16.66

Table 6
The energy and molar absorption coefficients of absorption bands and the electronic transitions calculated with the TDDFT method for [{$ReOBr_4$}-(μ-O){$ReO(3,5\text{-}Me_2pzH)_4$}]

The most important orbital excitations	Character	λ (nm)	E (eV)	f	Experimental Λ (nm)(E (eV))ε
H → L + 1	d → d	885.3	1.40	0.0002	805.0 (1.54) 95
H − 1 → L	d → d	604.7	2.05	0.0036	
H − 1 → L + 1	d → d	604.7	2.05	0.0036	595.0 (2.08) 520
H → L + 2	d → d	473.7	2.62	0.0001	
H → L + 3	d → d	473.7	2.62	0.0001	
H − 4 → L	π(Br) → d	402.6	3.08	0.0026	
H − 3 → L					
H − 7 → L	π(Br) → d	373.0	3.32	0.0069	
H − 7 → L + 1	π(Br) → d	372.9	3.32	0.0068	
H − 1 → L + 3	d → d	370.3	3.35	0.0015	
H − 1 → L + 2	d → d	370.2	3.35	0.0015	
H − 6 → L + 1	π (Br)/π(O) → d	363.5	3.41	0.0224	
H − 5 → L					
H − 8 → L	π(Br) → d	346.8	3.57	0.0135	
H − 8 → L + 1	π(Br) → d	346.7	3.58	0.0137	
H − 1 → L + 4	d → d	323.7	3.83	0.0003	
H − 9 → L	π(pzH) → d	320.6	3.87	0.0072	
H − 9 → L + 1	π(pzH) → d	320.6	3.87	0.0073	306.8 (4.04) 10160
H − 10 → L + 1	π(pzH) → d	317.9	3.90	0.0064	
H − 9 → L					
H − 12 → L + 1	π(pzH)/π(O)/σ(Br) → d	310.0	4.00	0.0145	
H − 11 → L					
H − 12 → L + 1	π(pzH)/π(O)/σ(Br) → d	308.9	4.01	0.0065	
H − 11 → L					
H − 3 → L + 4	π(Br) → d	296.6	4.19	0.0137	
H − 4 → L + 4	π (Br) → d	295.5	4.20	0.0138	
H − 1 → L + 10	d → d	294.5	4.21	0.0030	
H − 15 → L + 1	σ(Br)/π (Br)/π(O) → d	290.5	4.27	0.0256	
H − 14 → L					
H − 6 → L + 2	π (Br)/π(O) → d	282.5	4.38	0.0214	
H − 5 → L + 3					
H − 5 → L + 4	π (Br)/π(O) → d	282.4	4.39	0.0093	
H − 6 → L + 4	π (Br)/π(O) → d	282.3	4.39	0.0097	
H − 16 → L	π(pzH) → d	264.8	4.68	0.0335	
H − 16 → L + 1	π(pzH) → d	264.8	4.68	0.0332	
H − 1 → L + 6	d → π*(pyzH)	258.4	4.80	0.0704	
H − 1 → L + 7	d → π*(pyzH)	258.3	4.80	0.0706	
H − 17 → L	π (Br) → d	257.2	4.82	0.0064	
H − 17 → L + 1	π (Br) → d	257.1	4.82	0.0069	239.6 (5.17) 46170
H − 20 → L	σ(O) → d π(pzH) → d	252.1	4.92	0.0107	
H − 9 → L + 3					
H − 20 → L + 1	σ(O) → d	252.1	4.92	0.0105	
H − 9 → L + 2	π(pzH) → d				
					218.4 (5.68) 42000

The broad and intense experimental band with a maximum at 306.8 nm can be assigned to the *LMCT* transitions occurring from the bromine and oxo ligands to the *d* orbitals of the rhenium centers. In this range, the calculated d → d transitions are significantly weaker in comparison with the *LMCT* transitions, which means they are hidden by the latter transitions.

The experimental band at 239.6 nm can mainly be attributed to transitions of *MLCT* character occurring from the rhenium centers to the π-antibonding orbitals of the pyrazole ligands. However, contribution of the *LMCT* transitions into this band is also confirmed by the calculations.

4. Conclusions

A novel dinuclear oxo complex, [{$ReOBr_4$}(μ-O){$ReO(3,5\text{-}Me_2pzH)_4$}], has been prepared and structurally as well as spectroscopically and magnetically characterized. X-ray studies confirm a distorted octahedral geometry of the rhenium centers and the presence of a prefect linear O═Re—O—Re═O core. The diamagnetic [{$ReOBr_4$}(μ-O){$ReO(3,5\text{-}Me_2pzH)_4$}] complex can be best formulated as the [$Re^{V}OBr_4$][$Re^{V}O_2(3,5\text{-}Me_2pzH)_4$] adduct. Such a formulation is supported by general features of coordination rhenium compounds and is in accordance with the DFT calculations for [{$ReOBr_4$}(μ-O){$ReO(3,5\text{-}Me_2pzH)_4$}].

5. Supplementary material

CCDC 622582 contains the supplementary crystallographic data for $C_{38}H_{47}Cl_4N_8O_2PRe_2$. These data can be obtained free of charge via http://www.ccdc.cam.ac.uk/conts/retrieving.html, or from the Cambridge Crystallographic Data Centre, 12 Union Road, Cambridge CB2 1EZ, UK; fax: (+44) 1223-336-033; or e-mail: deposit@ccdc.cam.ac.uk.

Acknowledgements

The GAUSSIAN03 calculations were carried out in the Wrocław Centre for Networking and Supercomputing, WCSS, Wrocław, Poland Under Calculational Grant No51/96.

The crystallographic part was financed by funds allocated by the Ministry of Scientific Research and Information Technology to the Institute of General and Ecological Chemistry, Technical University of Łódź.

References

[1] S. Trofimenko, Inorg. Chem. 34 (1986) 115.
[2] G. La Monica, G.A. Ardizzoia, Prog. Inorg. Chem. 46 (1997) 151.
[3] G.A. Ardizzoia, G. La Monica, A. Maspero, M. Moret, N. Masciocchi, Eur. J. Inorg. Chem. (1998) 1503.
[4] S. Fortin, A.L. Beauchamp, Inorg. Chim. Acta 279 (1998) 159.
[5] E. Alessio, E. Zangrando, E. Iengo, M. Macchi, P.A. Marzilli, L.G. Marzilli, Inorg. Chem. 39 (2000) 294.
[6] S. Fortin, A.L. Beauchamp, Inorg. Chem. 39 (2000) 4886.
[7] A. Lazzaro, G. Vertuani, P. Bergamini, N. Mantovani, A. Marchi, L. Marvelli, Roberto Rossi, V. Berolasi, V. Ferretti, J. Chem. Soc., Dalton Trans. (2002) 2843.
[8] B. Machura, J.O. Dzięgielewski, R. Kruszynski, T.J. Bartczak, J. Kusz, Inorg. Chim. Acta 357 (2004) 1011.
[9] M.C. Aragoni, M. Arca, T. Cassano, C. Denotti, F.A. Devillanova, F. Isaia, V. Lippolis, D. Natali, L. Niti, M. Sampietro, R. Tommasi, G. Verani, Inorg. Chem. Commun. 5 (2002) 869.
[10] P. Romaniello, F. Lelj, Chem. Phys. Lett. 372 (2003) 51.
[11] P. Norman, P. Cronstrand, J. Ericsson, Chem. Phys. 285 (2002) 207.
[12] J. Bossert, N.B. Amor, A. Strich, C. Daniel, Chem. Phys. Lett. 342 (2001) 617.
[13] C.E. Powell, M.P. Cifuentes, A.M. McDonagh, S.K. Hurst, N.T. Lucas, C.D. Delfs, R. Stranger, M.G. Humphrey, S. Houbrechts, I. Asselberghs, A. Persoons, D.C.R. Hockless, Inorg. Chim. Acta 352 (2003) 9.
[14] J.P. Morral, C.E. Powell, R. Stranger, M.P. Cifuentes, M.G. Humphrey, G.A. Heath, J. Organomet. Chem. 670 (2003) 248.
[15] J. Gancheff, C. Kremer, E. Kremer, O.N. Ventura, J. Mol. Struct. (Theochem) 580 (2002) 107.
[16] G. Rouschias, G. Wilkinson, J. Chem. Soc. A (1966) 465.
[17] A.I. Vogel, Textbook of Practical Organic Chemistry, Longman Group Limited, 1978.
[18] STOE & Cie, X-RED. Version 1.18. STOE & Cie GmbH, Darmstadt, Germany, 1999.
[19] G.M. Sheldrick, Acta Crystallogr. A46 (1990) 467.
[20] G.M. Sheldrick, SHELXL97. Program for the Solution and Refinement of Crystal Structures, University of Gööttingen, Germany, 1997.
[21] G.M. Sheldrick, SHELXTL: Release 4.1 for Siemens Crystallographic Research Systems, 1990.
[22] M.J. Frisch, G.W. Trucks, H.B. Schlegel, G.E. Scuseria, M.A. Robb, J.R. Cheeseman, J.A. Montgomery Jr., T. Vreven, K.N. Kudin, J.C. Burant, J.M. Millam, S.S. Iyengar, J. Tomasi, V. Barone, B. Mennucci, M. Cossi, G. Scalmani, N. Rega, G.A. Petersson, H. Nakatsuji, M. Hada, M. Ehara, K. Toyota, R. Fukuda, J. Hasegawa, M. Ishida, T. Nakajima, Y. Honda, O. Kitao, H. Nakai, M. Klene, X. Li, J.E. Knox, H.P. Hratchian, J.B. Cross, C. Adamo, J. Jaramillo, R. Gomperts, R.E. Stratmann, O. Yazyev, A.J. Austin, R. Cammi, C. Pomelli, J.W. Ochterski, P.Y. Ayala, K. Morokuma, G.A. Voth, P. Salvador, J.J. Dannenberg, V.G. Zakrzewski, S. Dapprich, A.D. Daniels, M.C. Strain, O. Farkas, D.K. Malick, A.D. Rabuck, K. Raghavachari, J.B. Foresman, J.V. Ortiz, Q. Cui, A.G. Baboul, S. Clifford, J. Cioslowski, B.B. Stefanov, G. Liu, A. Liashenko, P. Piskorz, I. Komaromi, R.L. Martin, D.J. Fox, T. Keith, M.A. Al-Laham, C.Y. Peng, A. Nanayakkara, M. Challacombe, P.M.W. Gill, B. Johnson, W. Chen, M.W. Wong, C. Gonzalez, J.A. Pople, GAUSSIAN 03, Revision B.03, Gaussian, Inc., Pittsburgh, PA, 2003.
[23] A.D. Becke, J. Chem. Phys. 98 (1993) 5648.
[24] C. Lee, W. Yang, R.G. Parr, Phys. Rev. B 37 (1988) 785.
[25] M.E. Casida, in: J.M. Seminario (Ed.), Recent Developments and Applications in Modern Density Functional Theory, Theoretical and Computational Chemistry, vol. 4, Elsevier, Amsterdam, 1996.
[26] P.J. Hay, W.R. Wadt, J. Chem. Phys. 82 (1985) 299.
[27] F.A. Cotton, W.R. Robinson, R.A. Walton, Inorg. Chem. 6 (1967) 223.
[28] W.P. Griffith, T.D. Wickins, J. Chem. Soc. A (1967) 675.
[29] K. Nakamoto, Infrared and Raman Spectra of Inorganic and Coordination Compounds, 4th ed., Wiley-Interscience, New York, 1986.
[30] T. Hahn (Ed.), International Tables for Crystallography, vol. I, D. Reidel Publishing Company, Dordrecht, Holland, 1983, pp. 326–327.
[31] G.A. Jeffrey, W. Saenger, Hydrogen Bonding in Biological Structures, Springer-Verlag, 1994.
[32] G.R. Desiraju, T. Steiner, The Weak Hydrogen Bond in Structural Chemistry and Biology, Oxford University Press, 1999.
[33] J.M. Mayer, Inorg. Chem. 27 (1988) 3899.
[34] S.R. Flechter, A.C. Skapski, J. Chem. Soc., Dalton Trans. (1972) 1073.
[35] B. Machura, Coord. Chem. Rev. 249 (2005) 591.
[36] U. Abram, Compr. Coord. Chem. II 5 (2003) 371–402.
[37] A.E. Reed, L.A. Curtiss, F. Weinhold, Chem. Rev. 88 (1988) 899.
[38] M.L. Kuznestov, A.J.L. Pombeiro, J. Chem. Soc., Dalton Trans. (2003) 738.

synthetic therapeutics [6,7], or, not infrequently, by a combination therapy. There is therefore a need for research efforts to seek effective active drugs that mimic or enhance the properties of insulin.

Vanadium and organovanadium complexes have been proposed as adjuncts in the treatment of diabetes mellitus and the efficacy of vanadium as an insulin-mimicking transition metal has been reported [8,9]. Several clinical studies have been performed with organovanadium complexes using low doses of vanadium (2 mg/kg/day) in order to improve the insulinomimetic efficacy of vanadium without increasing its toxicity in diabetic patients [9,10].

Insulin mimetic VO compounds are described in the literature and several of them are sugar-derived substances [11–15]. Different types of coordination involving the vanadyl ion have also been investigated [16,17]. However, poor absorption from the gastrointestinal tract into the bloodstream and the optimal effectiveness in vivo are current limitations to administering vanadate to diabetic patients. Some vanadium complexes have been shown to increase potency over inorganic vanadium in induced-diabetic rats [18]. One example is bis(maltolato)oxovanadium(IV) which offers significant water solubility, neutral charge, and lipophilicity and may therefore enhance gastrointestinal tract absorption [19,20].

Saccharides belong to an interesting class of chemical compounds that plays an important role in various forms of living systems by being present as small integral parts of diverse biological molecules, including nucleic acids, polysaccharides, antibiotics, glycoproteins, glycolipids and aminosugars. Saccharide molecules posses several functional hydroxyl groups that may play key roles in complexing with transition metal ions to produce a variety of metal–saccharide complexes differing in their nature and utility [21–23].

In this approach we characterized the species of sugar chelated with vanadium in the VO–HGlu system, at physiological pH, in order to study its anti-diabetic effect in an acute treatment of hyperglycemic rats by intraperitoneal injection or oral gavage. The aim of this study was to investigate the use of sugars as a chelating agent in a vanadium complex with the aim of presenting an insulin mimetic compound, which would be expected to have a low toxicity.

2. Experimental

2.1. Materials

The monossaccharides D-Gluconic acid (potassium salt), D-ribose, D-ribono-1,4-lactone, D-galactone-1,4-lactone and 2-deoxy-D-glucose and the metallic salts of analytic grade ($VOSO_4$) were purchased from commercial sources (Sigma and Aldrich) and used without further purification. The stock solution of VO(IV) (1×10^{-2} mol L^{-1}) was standardized by titration with a standard solution of $KMnO_4$ (potassium permanganate) through the oxi-reduction method [24]. The exact amount of the acid added to prevent the cation precipitation was calculated using Gran's Plot [25]. Purity of all the ligands was established by potentiometric titration. Carbonate-free solutions of 0.100 mol L^{-1} KOH were prepared from Baker Dilut-It ampoles and were standardized by titration with potassium acid phthalate purchased from Sigma.

2.2. Animals

Male Wistar rats (160–190 g) were used. They were bred in our animal facility and housed in an air-conditioned room (approximately 22 °C) with controlled lighting 12:12 h light/dark cycle (lights on from 06:00 to 18:00 h). The animals were maintained with food pellets (Nuvital, Nuvilab CR1, Curitiba, PR, Brazil), while tap water was available ad libitum. Fasted animals were deprived of food for at least 16 h but allowed free access to water. All the animals were carefully monitored and maintained in accordance with ethical recommendations of the Brazilian Veterinary-Medicine Council (CMV) and the Brazilian College of Animal Experimentation (COBEA). Rats fasted for 16 h received 70 mg/kg body weight of alloxan (Sigma, St. Louis, MO, USA) by a single intravenous injection. The diabetic state was assessed, by measuring serum glucose levels 3 days later [26]. Rats that died during the experiment (around 8%) were excluded from the analysis.

2.3. Synthesis of the VO–HGlu complex

The VO–HGlu complex was synthesized following a modified procedure describe in the literature [27]. The solids were prepared by mixing concentrated solutions of $VOSO_4$ and D-Gluconic acid (potassium salt) in aqueous media at neutral pH value and the solvent was evaporated until a solid was formed. The solid was purified after successive recrystallizations.

2.4. Potentiometric titrations

The potentiometric titrations were carried out in a sealed thermostated vessel at 25 °C, under inert atmosphere (Ar) with continuous magnetic stirring. The pH meter (Corning) with glass and reference electrodes (Ingold) was calibrated with standard HCl and KOH solutions to directly read $-\log[H^+]$, designated as pH. The experimental solutions, adjusted to 0.1000 mol L^{-1} ionic strength by addition of KCl, were titrated with 0.100 mol L^{-1} standard CO_2-free KOH solution. Equilibrium measurements of sugars were carried out in the presence and absence of VO^{2+}. The problem solutions contained 0.100 mmol of saccharides and the metal system had a molar ratio of 1:1 and 1:2 (metal:ligand) with 0.1000 mmol of VO^{2+}. All the potentiometric studies were

carried out with 40.00 mL of experimental solution and each system was titrated at least three times. The pH range for accurate measurements was considered to be 2.5–11.0.

All equilibrium constants were calculated using the program BEST7 [28a]. Mole and millimole units were used to express the quantities of reagents, and the hydrolysis constants in water for the metal ion were obtained from the literature [28b] and were fully employed in all calculations. The species distribution curves were drawn with the SPE and SPEPLOT programs [28a].

2.5. EPR

EPR spectra were obtained at 298 K and 77 K for the metal–ligand complex solution at pH 3.6, 7.25 and 10.6, on a Bruker ESP300E instrument operating at 9.5 GHz (X-band) with 100 kHz field modulation.

2.6. TGA–DSC

Thermal analysis was carried out using a Shimadzu system (DSC – 50 and TGA – 50) at a heating rate of 10 °C min^{-1} and under N_2 atmosphere (50 mL min^{-1}). The sample mass used was 6.730 mg. Standard indium (156.6 °C) and hydrate calcium oxalate were used for DSC and TGA calibration, respectively.

2.7. Time-course of VO–HGlu complex effects on hyperglycemia in alloxan-induced diabetic rats

Animals for which the development of hyperglycemia was confirmed (around 98%) 72 h after the alloxan injection were randomized into four groups of six rats: Group I, normal rats that received a saline solution by oral gavages (0.5 mL); Group II, diabetic rats that received VO(IV) (0.0607 mol/L; 0.5 mL) intraperitoneally; Group III, diabetic rats that received 0.5 mL of VO–HGlu at 100 mg/kg intraperitoneally and Group IV, diabetic rats that received 0.5 mL of VO–HGlu at 100 mg/kg by oral gavages. The VO–HGlu complex was prepared immediately prior to its use and was kept in a physiological pH solution to be administered to the animals. The serum glucose was measured before the animals received the complex solution and at 1, 2 and 3 h subsequent to the treatment [29].

2.8. Determination of serum glucose concentration

Blood samples were collected from the cannula previously implanted in the jugular vein as described by [30], and centrifuged. Serum glucose levels were determined by the oxidase method [31]. The absorbencies were measured with a Pharmacia LKB-Ultrospec III spectrophotometer (Pharmacia LKB Biotechnology, Inc., Uppsala, Sweden) at 505 nm. A serum glucose range of 480–570 mg/dL was used for the experiment.

2.9. Statistical analysis

Data were expressed as mean ± SEM. One-way analysis of variance (ANOVA) followed by the Bonferroni post-test, with the aid of the INSTAT program (version 1.121) was carried out. Differences were considered to be significant at $p \leqslant 0.05$.

3. Results and discussion

3.1. Equilibrium of the D-gluconic acid and the vanadyl cation VO^{2+}

The potentiometric titration profile of HGlu in the presence and absence of VO^{2+} in the 1:1 (metal:ligand) ratio, is given in Fig. 1. Complexation began around pH 3, requiring almost three moles of protons per mole of sugar to reach the break point. The buffer region above pH 7 shows the consumption of over one addition mole of titrant (totally 4.5) per mole of the ligand (sugar). Only this system presented a solubility feature up to pH 11, while the other systems studied precipitated. The negative values in the abscissa represent the neutralization of the acid excess in the metallic solution.

The equilibria in the VO–Hglu system are represented by Eqs. (1)–(7) where HL and L^- are the protonated and deprotonated species of the D-Gluconic acid, respectively;

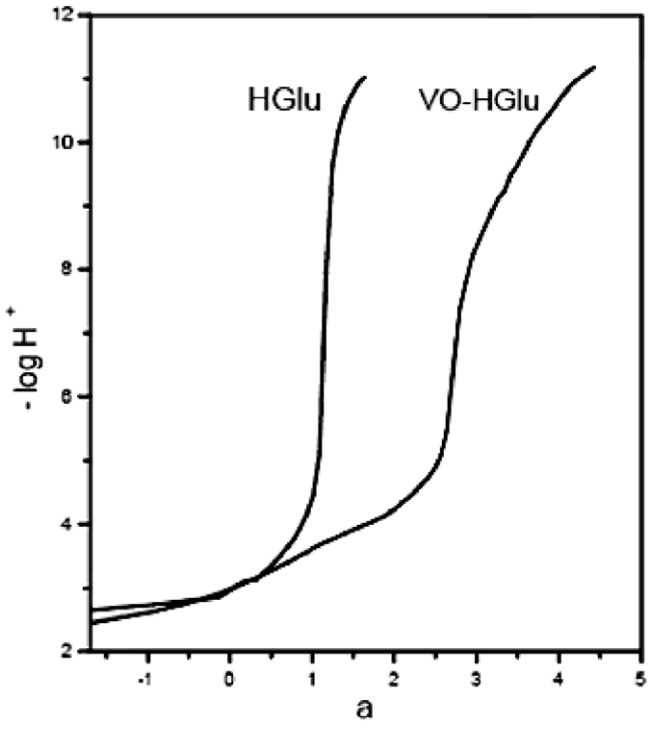


Fig. 1. Potentiometric pH profiles of D-gluconic acid (HGlu) in the presence and absence of VO^{2+}, in the metal to ligand ratio of 1:1 (M:L), at 25.0 °C and $I = 0.100$ mol/L (KCl). Negative values in the abscissa represent the neutralization of mineral acid added to the system. In the abscissa **a** stands for number of moles of KOH per number of moles of ligand.

VO^{2+} is the aqueous oxovanadium and VOL^{+}, $VOH_{-1}L$, $VOH_{-2}L^{-}$, $VOH_{-3}L^{2-}$ and $VOH_{-4}L^{3-}$ are the mononuclear species formed with none, one, two, three and four hydroxyl groups from the D-gluconic acid, which were deprotonated in the complexation by the metal ion. The values for the equilibrium constants defined by Eqs. (1)–(7) are presented in Table 1.

$$L^{-} + H^{+} \rightleftharpoons HL \quad (1)$$

$$VO^{2+} + L^{-} \rightleftharpoons VOL^{+} \quad (2)$$

$$VOL^{+} \rightleftharpoons VOH_{-1}L + H^{+} \quad (3)$$

$$VOH_{-1}L \rightleftharpoons VOH_{-2}L^{-} + H^{+} \quad (4)$$

$$VOH_{-2}L^{-} \rightleftharpoons VOH_{-3}L^{-2} + H^{+} \quad (5)$$

$$VOH_{-3}L^{2-} \rightleftharpoons VOH_{-4}L^{-3} + H^{+} \quad (6)$$

$$2VOH_{-2}L \rightleftharpoons (VO)_2H_{-5}L_2 + H^{+} \quad (7)$$

The potentiometric pH profile of D-galactone-1,4-lactone (Galac) in the presence of VO^{2+}, in the 1:1 (metal ligand) ratio is given in Fig. 2. The curves for Riblac and dGlu in the presence of the VO^{2+} ion are similar to that shown in Fig. 2 and they are not shown here. The titration curves for Galac, Riblac and dGlu in the presence of the VO^{2+} ion were interrupted around pH 4.6 due to the precipitation of the metal ion hydrolysis products.

The logarithms of the constants defined by Eqs. (8) and (9) are displayed in Table 2 and they refer to the sugars: Galac, Riblac, and dGlu in the presence of the VO^{2+} ion.

$$VO^{2+} + L^{-} \rightleftharpoons VOH_{-1}L + H^{+} \quad (8)$$

$$VOH_{-1}L \rightleftharpoons VOH_{2-}L + H^{+} \quad (9)$$

It can be seen from the values in Table 2 that the closed chain sugars do not chelate well to the metal ion studied, although there is the formation of insoluble hydrolysis products of the metal species. Since the cyclic sugars complex the vanadyl ion weakly, the other analytical assays were performed only with the HGlu sugar molecule.

The species distribution diagram of the HGlu and VO^{2+} system is given in Fig. 3. For this sugar, more species are formed than in the case of the others, because this is an open chain sugar and its hydroxyl groups are in appropriate positions to complex with the metal ion yielding five-member rings, thus, inhibiting its hydrolysis and precipitation. We did not detect in solution complexes in a molar ratio of 1:2 metal:ligand, as reported in the literature in solid state and characterized by IR and UV–Vis spectroscopies [32]. In that publication the authors detected the presence of a deprotonated carboxylate molecule and also a deprotonated hydroxyl group coordinated to the metal ion given rise to the $[OV(gluconate)_2]^{2-}$ ion complex. The formation of the 1:2 metal:ligand complex in the solid state, is most probably due to some packing effects which are contributing to the formation of this species and thus the authors were able to isolate this compound in the solid state when they used an excess of ligand.

The formation of 48% VOL species at pH 2.8 and 42% $VOH_{-1}L$ species at pH 3.8 can be seen in Fig. 3. Formation of the $VOH_{-2}L$ predominates above pH 4.0 until pH

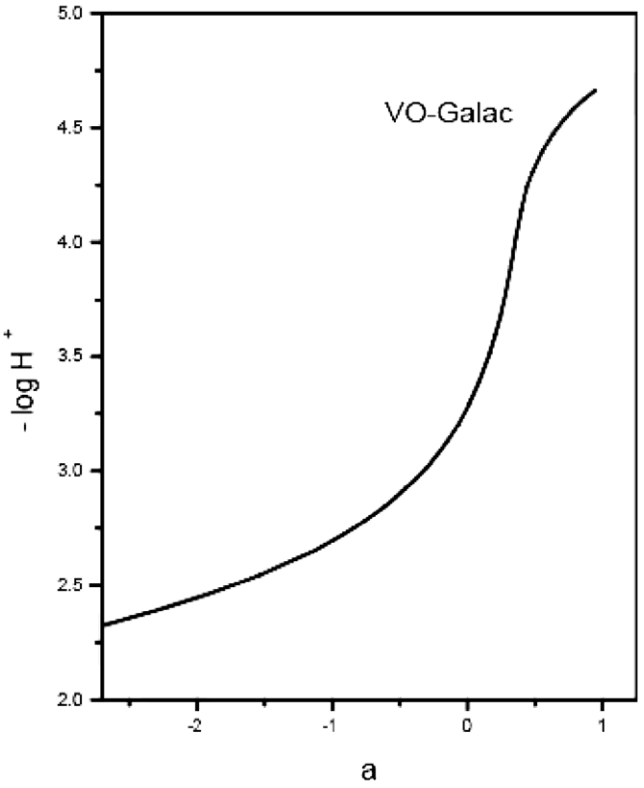


Fig. 2. Potentiometric pH profiles of D galactone-1,4-lactone (Galac) and VO^{2+}, in the metal to ligand ratio of 1:1 (M:L), at 25.0 °C and $I = 0.100$ mol/L (KCl). Negative values in the abscissa represent the neutralization of mineral acid added to the system. In the abscissa **a** stands for number of moles of KOH per number of moles of ligand.

Table 1
Logarithms of stability constants ($\log K$) for the acid–base and complex equilibriums for HGlu and the metal ion VO(IV)

Species	$\log K$[a]
$[HL]/[H^{+}]\,[L^{-}]$	3.60 (3) (3.46)[b]
$[VOL^{+}]/[VO^{2+}]\,[L^{-}]$	3.90 (3)
$[VOH_{-1}L]\,[H^{+}]/[VOL^{+}]$	−3.46 (5)
$[VOH_{2-}L^{-}]\,[H^{+}]/[VOH_{-1}L]$	−4.00 (5)
$[VOH_{-3}L^{2-}]\,[H^{+}]/[VOH_{-2}L^{-}]$	−8.84 (5)
$[VOH_{-4}L^{3-}]\,[H^{+}]/[VOH_{-3}L^{2-}]$	−11.18 (6)
$[(VO)_2H_{-5}L_2]\,[H^{+}]/[VOH_{-2}L]^2$	−6.60 (5)

$T = 25.0$ °C, and $\mu = 0.100$ mol/L (KCl).
[a] The numbers in parenthesis represent the absolute error of the last digit of the value.
[b] Ref. [27].

Table 2
Values for the logarithms of the formation constants for the ligands Galac, Riblac, dGlu with VO^{2+}; 25.0 °C and $I = 0.100$ mol/L

Species	$\log K$		
	Galac	Riblac	dGlu
$[VOH_{-1}\,L]\,[H^{+}]/[VO^{2+}][L]$	−0.78 (6)	−0.64 (6)	−0.88 (6)
$[VOH_{2-}\,L]\,[H^{+}]/[VOH_{-1}L]$	−4.92 (6)	−4.93 (6)	−5.32 (6)

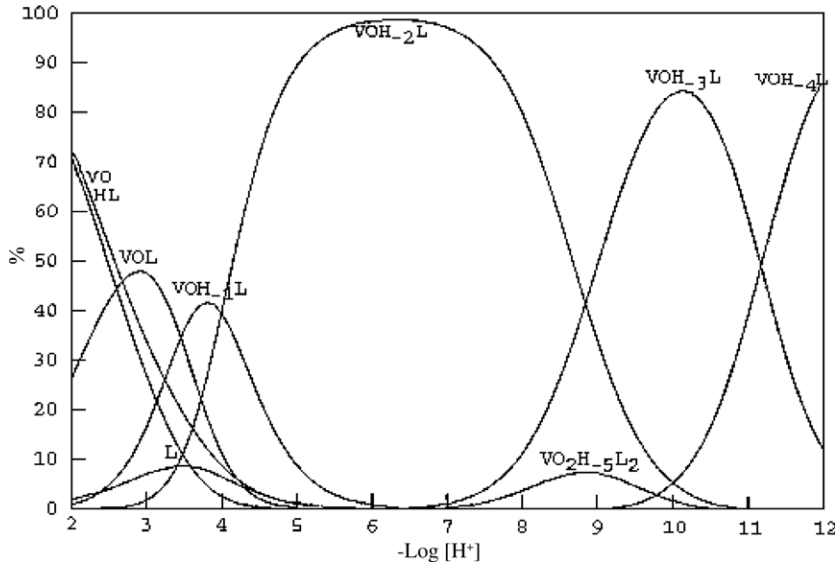
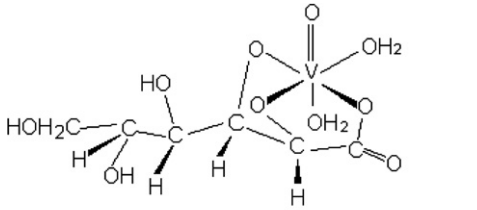


Fig. 3. Species distribution diagram for the species formed in the HGlu–VO system, in the ligand to metal ratio of 1:1 according to pH variation. VO is the free concentration of the oxocation, HL is the fully protonated sugar molecule and VOL is the complex in 1:1 stoichiometry, $VOH_{-1}L$, $VOH_{-2}L$, $VOH_{-3}L$ and $VOH_{-4}L$ are the mono-, di-, tri- and tetra- hydroxyl deprotonated species and $VO_2H_{-5}L_2$ represents the dinuclear $(VO)_2H_{-5}L_2$ species. The ligand concentration is 2.5×10^{-3} mol/L, $T = 25.0$ °C and $I = 0.100$ mol/L (KCl).

values close to 9. This species has two deprotonated OH groups complexed to the metal ion. This is the major species present at physiological pH (7.4). In this species the ligand does not occupy all the coordination sites of the metal ion, leaving two positions where water molecules can be coordinated to the octahedral vanadium(IV) ion (Fig. 4). At pH values above 7.0 there is the formation of a small amount of the dinuclear complex species presenting a hydroxo bridge linking two metal ions. Above a pH value of 8.8 $VOH_{-3}L$ and $VOH_{-4}L$ species predominate, as three and four alcohol groups of the sugar molecule are deprotonated, respectively.



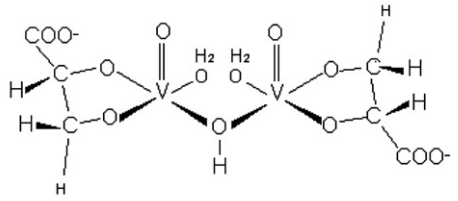


Fig. 4. Proposed structure for the species represented as $VOH_{-2}L$ and $(VO)_2H_{-5}L_2$, between the HGlu ligand and vanadyl ion.

3.2. EPR spectra

The Hglu–VO complexes are EPR-active in liquid (300 K) or in frozen (77 K) water solution. Experimental spectra of the frozen water solutions of the complexes at pH 3.6, 7.25 and 10.6 are shown in Fig. 5. The g values and hyperfine splitting constants of the Hglu–VO complexes were obtained from computer simulation (Simfonia®, Bruker). According to the species distribution diagram (Fig. 3) at pH 3.6 there are two main types of complexes, VOL and VOH_{-1} L. The best g and hyperfine splitting constant values for the two complexes are: $g\| = 1.9405$,

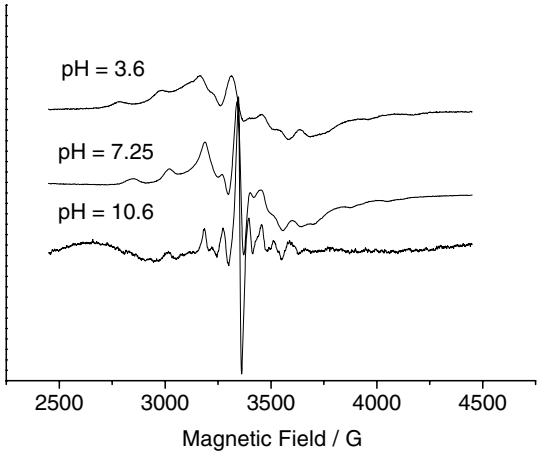


Fig. 5. EPR spectra at X-band ($\nu \approx 9.5$ GHz) of the frozen water solution of the Hglu–VO complexes at pH 3.6, 7.25 and 10.6. Instrument settings for the experimental spectra: power, 20 mW; modulation 100 kHz; sweep centre, 3450 G; sweep width, 2000 G.

$g\perp = 1.9827$, $A\| = 180 \times 10^{-4}\ cm^{-1}$, $A\perp = 70 \times 10^{-4}\ cm^{-1}$. The orders ($g\| < g\perp$ and $A\| \gg A\perp$) are consistent with the oxovanadium(IV) site of C_{4v} symmetry with a $^2B_2$ ground state (unpaired electron on a d_{xy} vanadium orbital). The magnitude of the EPR parameters $g\|$ and $A\|$ are consistent with four oxygen atoms as equatorial ligands. These could be one from the Hglu carboxylate group and three from water molecules or, alternatively, two from water molecules and two from the Hglu molecule. $VO(acac)_2$ has been previously study and it was found that this compound has four oxygen atoms as equatorial ligands, $g\| = 1.944$ and $A\| = 174 \times 10^{-4}\ cm^{-1}$ [33a]. This result is consistent with those for the VOL and $VOH_{-1}L$ complexes. The EPR parameters for the Hglu–VO complexes at pH 7.25 and 10.6 are analogous ($g\| = 1.9495$, $g\perp = 1.9810$, $A\| = 156 \times 10^{-4}\ cm^{-1}$, $A\perp = 58 \times 10^{-4}\ cm^{-1}$) and support a different set of equatorial donor atoms for the VO^{2+} group, with a stronger coordination ligand field than those for the complexes formed at pH 3.6, using two or three hydroxyl groups of the Hglu ligand as donor atoms ($VOH_{-2}L$ and $VOH_{-3}L$) and perhaps with a little distortion of the C_{4v} symmetry around the vanadyl centre [33b]. The different degree of distortion for the two complexes could bring the EPR parameters for the two complexes to the same values.

Fig. 6 represents the DSC curve for the VO–HGlu complex isolated at neutral pH showing one endothermic transition at 118.82 °C, corresponding to 12.5% of a molecular weight of 296 g mol^{-1}, corresponding to two water molecules coordinated to the metal ion in the complex as shown in Fig. 4. The two water molecules can be replaced during the association of the complex with a receptor site of the insulin. In other words, it has two free positions for coordination. The second endothermic transition (at 345.77 °C) is assigned to a break in the sugar chain [34,35].

3.3. Biological assays

Taking into account our previous results performed with this experimental approach [36,37] we chose the optimal time-course procedure to investigate the short-term action of this new complex. Table 3 shows the glycemia profiles for normal animals (control group) and diabetic animals treated with VO(IV) solution (0.0607 mol/L) intraperitoneally or a single dose of VO–HGlu complex (100 mg/kg) intraperitoneally or by oral gavage, over time (from zero to 3 h). This dose of VO–HGlu complex showed a significant hypoglycemic effect from 0 to 3 h when compared to the respective zero time when the animals were treated intraperitoneally, but after oral administration of the complex only a slight lowering in glucose serum levels was observed.

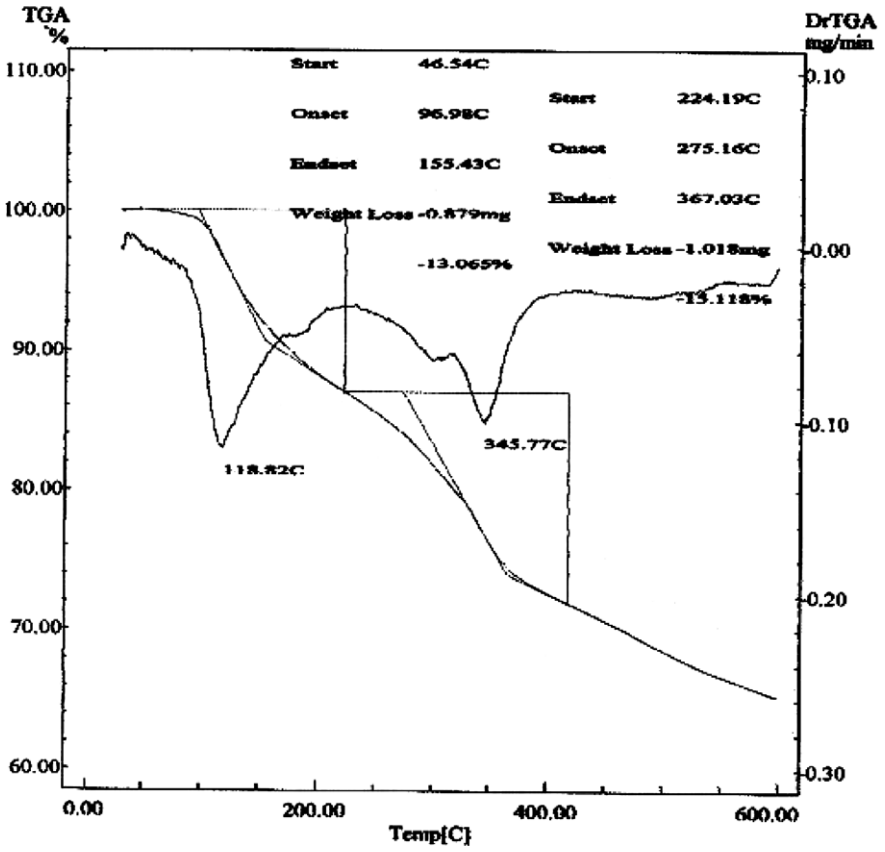


Fig. 6. TGA–DSC of HGlu–VO complex showing one endothermic transition at 118.82 °C, with a 12.5% water weight loss (2 mol) and another endothermic transition at 345.77 °C, corresponding to the decomposition of the complex.

Table 3
Time-course for the effect of VO–HGlu on glycemia in diabetic rats[a]

Time (h)	Group I	Group II	Group III	Group IV
	Normal + saline solution (oral gavage)	Diabetic + VO(IV) (0.0607 mol/L) (intraperitoneal)	Diabetic + VO–Hglu (100 mg/kg) (intraperitoneal)	Diabetic + VO–Hglu (100 mg/kg) (oral gavage)
0	130 ± 2	505 ± 3	516 ± 8	502 ± 24
1	117 ± 2	434 ± 32[b]	459 ± 8[b]	410 ± 12[b]
2	115 ± 6	418 ± 16 [b]	413 ± 9[b]	497 ± 6
3	130 ± 4	430 ± 10[b]	397 ± 12[b]	487 ± 20

[a] Values are expressed as mean ± SEM; $n = 6$ in duplicate for each group.
[b] Statistically significant difference in relation to the corresponding zero time value; $p \leqslant 0.05$.

According to the literature, results from glycemia studies in diabetic animals, using acute screening trials of the complexes bis(maltolato)oxovanadium(IV); (BMOV), bis(maltolato)-zinc(II) dihydrate, *cis*-bis(maltolato)dioxomolybdenum(IV), tris(maltolato)chromium(III) monohydrate, bis(maltolato)copper(II) and bis(maltolato)cobalt (II), indicate that only vanadyl maltol, when administered by oral gavage, lower plasma glucose levels compared to untreated diabetic animals (zero time) [38]. BMOV has been experimentally used as a representative standard in several biological studies due to its approval for clinical experiments [18]. However, a pharmacologically beneficial dose of BMOV is associated with some toxicity and hence attempts are underway to evolve vanadium complexes with fewer side effects while retaining their enhanced therapeutic activities [39]. Additionally, besides the BMOV complex, many vanadium complexes have been reported to be more effective when introduced by intraperitoneal administration than by oral gavage treatment [40].

Vanadium alone, in the form of vanadyl, was effective in lowering glucose levels in a similar concentration (0.0607 mol/L) to that used to prepare the sugar complex (0.0788 mol/L). The maximum percentage reduction in the case of simultaneous administration, HGlu–VO complex, at a dose of 100 mg/kg administered intraperitoneally in diabetic animals was 23%. As demonstrated in this preliminary study the HGlu–VO(IV) complex has a pharmacological potential to be efficient as an organically chelated vanadium complex. One of the advantages of this sugar complex is that, unlike the cyclic sugar complexes, it keeps the metal ion in solution at physiological pH at the concentrations used in the potentiometric studies. There is no metal ion hydrolysis and undesirable precipitates are therefore not formed. Increasing the vanadium or HGlu doses with the aim of observing synergy is unlikely to be advantageous due to the potential toxicity of high doses of vanadium. However, studies on the efficiency of this new complex toward hyperglycemia, as well as investigations into its toxicity, are in progress, using the chronic treatment approach in diabetic animals.

References

[1] D. Rehder, Angew. Chem., Int. Ed. Engl. 30 (1991) 148.
[2] E. Tisiani, I.G. Fantus, Trends Endocrinol. Metab. 8 (1997) 51.
[3] A. Butler, C.J. Carrano, Coord. Chem. Ver. 109 (1991) 61.
[4] P. Zimmet, K.G.M.M. Alberti, J. Shaw, Nature 414 (2001) 782.
[5] G.S. Eisenbarth, New Engl. J. Med. 314 (1992) 1360.
[6] R.A. De Fronzo, R.C. Banadonna, E. Ferrannini, Diabetes Care 15 (1992) 318.
[7] B. Zhang, G. Salituro, D. Szalkowski, Z. Li, Y. Zhang, I. Royo, D. Vilella, M.T. Diez, F. Pelaez, C. Ruby, R.L.R.L. Kendall, X. Mao, P. Griffin, J. Calaycay, J.R. Zierath, J.V. Heck, R.G. Smith, D.E. Moller, Science 284 (1999) 974.
[8] A.B. Goldfine, D.C. Simonson, F. Folli, M.E. Patti, C.R. Kahn, Mol. Cell. Biochem. 153 (1995) 217.
[9] Y. Schechter, I. Goldwaser, M. Mironckik, M. Fridkin, D. Gefel, Coord. Chem. Rev. 237 (2003) 3.
[10] K.H. Thompson, J.H. McNeill, C. Orvig, Chem. Rev. 99 (1999) 2561.
[11] G.R. Willsky, A.B. Goldfine, P.J. Kostyniak, J.H. McNeill, L.Q. Yang, H.R. Khan, D.C. Crans, J. Inorg. Biochem. 85 (2001) 33.
[12] H. Sakurai, A. Tsuji, in: J.O. Nriagu (Ed.), Vanadium, a Versatile Biochemical Effector in Chemical Rat Mammary Carcinogenisis, Wiley, London, 1998.
[13] H. Sakurai, Y. Kojima, Y. Yoshikawa, K. Kawabe, H. Yasui, Coord. Chem. Rev. 226 (2002) 187.
[14] H. Yasui, A. Tamura, T. Takino, H. Sakurai, J. Inorg. Biochem. 91 (2002) 327.
[15] H. Sakurai, A. Tamura, J. Fugono, H. Yasui, T. Kiss, Coord. Chem. Rev. 245 (2003) 31.
[16] E.J. Baran, J. Inorg. Biochem. 80 (2000) 1.
[17] K.H. Thompson, C. Orvig, J. Inorg. Biochem. 85 (2001) 33.
[18] V.G. Yuen, C. Orvig, J.H. McNeill, Can. J. Physiol. Pharmacol. 73 (1995) 55.
[19] I.A. Setyawati, K.H. Thompson, V.G. Yuen, Y. Sun, M. Battell, D.M. Lyster, C. VO, T.J. Ruth, S. Zeisler, J.H. McNeill, C. Orvig, J. Appl. Physiol. 84 (1998) 569.
[20] P. Caravan, L. Gelmini, N. Glover, F.G. Herring, H. Li, J.H. McNeill, S.J. Rettig, I.A. Setyawati, E. Shuter, Y. Sun, A.S. Tracey, V.G. Yuen, C. Orvig, J. Am. Chem. Soc. 117 (1995) 12759.
[21] B. Gyurcsik, L. Nagy, Coord. Chem. Ver. 203 (2000) 81.
[22] S.B. Etcheverry, P.A.M. Williams, E.J. Baran, Carbohydr. Res. 302 (1997) 131.
[23] A. Sreedhara, M.S. Raghavan, C.P. Rao, Carbohydr. Res. 264 (1994) 227.
[24] N. Furnan, in: D. Van (Ed.), Standard Methods of Chemical Analysis, Vol. 1, Nortand Company Inc., 1962, pp. 1211–1213.
[25] F.J.C. Rossoti, H. Rossoti, J. Chem. Educ. 42 (7) (1965) 375.
[26] E.J. Verspohl, Planta Med. 68 (2002) 581.
[27] P.A.M. Williams, S.B. Etcheverry, E.J. Baran, Carbohydr. Res. 329 (2000) 41.
[28] (a) A.E. Martell, R.J. Motekaitis, in: The Determination and Use of Stability Constants, 2nd ed., VCH, New York, 1992;
(b) C.F. Baes, R.E. Mesmer, The Hydrolysis of Cations, Wiley Interscience, New York, 1976.
[29] E. De Sousa, L. Zanatta, I. Seifriz, T.B. Creczynski-Pasa, M.G. Pizzolatti, B. Szpoganicz, F.R.M.B. Silva, J. Nat. Prod. 67 (2004) 829.
[30] P.G. Harms, S.R. Ojeda, J. Appl. Physiol. 36 (1974) 275.

[31] H. Varley, A.H. Gowenlick, M. Bell, in: I.W. Heinemann (Ed.), Practical Biochemistry, 5th ed., Vol. 1, Willian Heinemann Medical Books, London, 1976, p. 389.
[32] P.A.M. Williams, D.A. Barrio, S.B. Etcheverry, E.J. Baran, J. Inorg. Biochem. 98 (2004) 333.
[33] (a) A.J. Tasiopoulos, A.N. Troganis, A. Evangelou, C.P. Raptopoulou, A. Terzis, Y. Deligiannakis, T.A. Kabanos, Chem. Eur. J. 5(3)(1999)910; (b) F.C.S. de Paula, S. Carvalho, H.A. Duarte, E.B. Paniago, A.S. Mangrich, E.C. Pereira-Maia, J. Inorg. Biochem. 76 (1999) 221.
[34] M.M. Meier, M.T.B. Luiz, B. Szpoganicz, V. Soldi, Thermochim. Acta 375 (2001) 153.
[35] A.L.R. Mercê, E. Fernandes, A.S. Mangrich, M.R. Sierakowski, B. Szpoganicz, J. Braz. Chem. Soc. 12 (6) (2001) 791.
[36] F.R.M.B. Silva, B. Szpoganicz, M.G. Pizzolatti, M.A.V. Willrich, E. De Sousa, J. Ethnopharmacol. 83 (2002) 33.
[37] A.P. Jorge, H. Horst, E. De Sousa, M.G. Pizzolatti, F.R.M.B. Silva, Chem. Biol. Interact. 149 (2004) 89.
[38] K.H. Thompson, J. Chiles, V.G. Yuen, J. Tse, J.H. McNeill, C. Orvig, J. Inorg. Biochem. 98 (2004) 683.
[39] K.H. Thompson, C. Orvig, Science 300 (2003) 936.
[40] L.C.Y. Woo, V.G. Yuen, K.H. Thompson, J.H. McNeill, C. Orvig, J. Inorg. Biochem. 76 (1999) 251.

Hg(II) halide complexes of a BPMO ligand 1,2-bis(diphenylphosphino)ethane monoxide (dppeO).

2. Experimental

All reactions were carried out under an atmosphere of dry nitrogen. Reactants and reagents were obtained from Aldrich Chemical Company and used without further purification. The solvents were dried and distilled using standard methods [13].

2.1. Instrumentation

The ^{1}H and ^{31}P–$\{^{1}H\}$NMR spectra were recorded in $CDCl_3$ solution on a Bruker DPX400 spectrometer at 400.13 and 161.98 MHz, referenced relative to residual $CHCl_3$ and external 85% H_3PO_4, respectively. The IR spectra in the interval of 4000–400 cm^{-1} were recorded on a Perkin–Elmer 1720X FT-IR spectrometer using KBr pellets. Elemental analyses were performed at the Ecole d'ingénieurs de Fribourg, Switzerland.

2.2. Synthesis of compounds

2.2.1. 1,2-Bis(diphenylphosphino)ethane monoxide (dppeO)

The phosphonium salt obtained by the reaction of 1,2-bis(diphenylphosphino)ethane (dppe) with benzyl bromide in dry toluene, was hydrolysed with aqueous sodium hydroxide to yield the ligand, as reported previously [14]. IR (cm^{-1}): 3052, 1937, 2903, 1588, 1480, 1435, 1182, 1122, 1106, 1069, 1025, 997, 881, 783, 727, 692, 712, 536, 513, 504, 474. ^{1}H NMR : 2.28 (br, 4H), 7.29–7.71 (m, 20H). ^{31}P NMR : −11.68 (d, $^{3}J_{P-P} = 48.4$), 33.18 (d, $^{3}J_{P-P} = 48.4$).

2.2.2. $[HgCl_2(dppeO)]_n$ (1)

To a methanolic solution of mercury(II) chloride (0.13 g, 0.48 mmol), solid dppeO (0.2 g, 0.48 mmol) was added in portions and allowed to stir overnight. The white precipitate obtained was filtered, washed with cold methanol and recrystallized from acetonitrile. Yield: 0.27 g, 83%; m.p.: 253–255 °C. *Anal.* Calc. for $C_{26}H_{24}Cl_2HgOP_2$: C, 45.53; H, 3.53. Found. C, 45.93; H, 3.51%. IR (cm^{-1}): 3054, 2913, 1589, 1436, 1160, 1121, 1103, 997, 741, 725, 690, 540, 516, 506, 476. ^{1}H NMR : 2.87–2.97 (m, 2H), 3.08–3.13 (m, 2H), 7.40–7.91 (m, 20H). ^{31}P NMR : 33.40 (d, $^{3}J_{P-P} = 58.9$), 37.12 (d, $^{3}J_{P-P} = 58.9$, $^{1}J_{Hg-P} = 7449$).

2.2.3. $[HgBr_2(dppeO)]_n$ (2)

The reaction was carried out as for **1** using mercury(II) bromide (0.17 g, 0.48 mmol). The product obtained was recrystallized by slow evaporation of a chloroform solution. Yield: 0.32 g, 87%; m.p.: 225–227 °C. *Anal.* Calc. for $C_{26}H_{24}Br_2HgOP_2$: C, 40.30; H, 3.12. Found. C, 40.21; H, 3.08%. IR (cm^{-1}): 3054, 2907, 1589, 1483, 1435, 1409, 1164, 1121, 1101, 1069, 1026, 997, 739, 726, 690, 540, 515, 476. ^{1}H NMR : 2.89 (br, 2H), 3.06 (br, 2H), 7.42–7.89 (m, 20H). ^{31}P NMR : 29.46 (d, $^{3}J_{P-P} = 57.5$), 33.38 (d, $^{3}J_{P-P} = 57.5$, $^{1}J_{Hg-P} = 6422$).

2.2.4. $[HgI_2(dppeO)]_n$ (3)

Complex **3** was obtained in the same way as **1** using mercury(II) iodide (0.22 g, 0.48 mmol) and dppeO (0.2 g, 0.48 mmol). The product obtained was recrystallized by slow evaporation of a chloroform solution. Yield: 0.35 g, 83%; m.p.: 212–214 °C. *Anal.* Calc. for $C_{26}H_{24}Hg\ I_2OP_2$: C, 35.94; H, 2.78. Found. C, 35.87; H, 2.75%. IR (cm^{-1}): 3053, 2906, 1588, 1484, 1436, 1411, 1156, 1120, 1098, 998, 739, 726, 691, 538, 507, 494, 474. ^{1}H NMR: 2.75 (br, 2H), 2.92 (br, 2H), 7.45–7.86 (m, 20H). ^{31}P NMR: 6.34 (br, $^{1}J_{Hg-P} = 4366$), 32.93 (d, $^{3}J_{P-P} = 54.9$).

2.2.5. $[HgCl_2(dppeO)_2]$ (4)

A solution of mercury(II) chloride (0.098 g, 0.36 mmol) in methanol was added dropwise to a solution of dppeO (0.3 g, 0.72 mmol) in dichloromethane. The mixture was stirred for 3 h. White feathery crystals obtained after slow evaporation of the solvent were washed with cold methanol and dried *in vacuo*. Yield: 0.29 g, 75%; m.p.: 250 °C. *Anal.* Calc. for $C_{52}H_{48}Cl_2HgO_2P_4$: C, 56.76; H, 4.40. Found. C, 56.47; H, 4.35%. IR (cm^{-1}): 3051, 2912, 1573, 1484, 1436, 1188, 1121, 1104, 997, 738, 728, 693, 540, 517, 506, 479. ^{1}H NMR: 2.90 (br, 8H), 7.27–7.91 (m, 40H). ^{31}P NMR: 28.75 (br, $^{1}J_{Hg-P} = 4654$), 34.08 (br).

2.2.6. $[HgBr_2(dppeO)_2]$ (5)

Complex **5** was prepared in the same way as for **4** using mercury(II) bromide (0.13 g, 0.36 mmol). Yield: 0.29 g, 70%. m.p.: 216–218 °C. *Anal.* Calc. for $C_{52}H_{48}Br_2HgO_2P_4$: C, 52.52; H, 4.07. Found. C, 51.92; H, 4.06%. IR (cm^{-1}): 3429, 3051, 2910, 1573, 1484, 1436, 1190, 1121, 1103, 996, 737, 727, 693, 539, 516, 507, 478. ^{1}H NMR: 2.88 (br, 8H), 7.45–7.93 (m, 40H). ^{31}P NMR: 21.19 (br, $^{1}J_{Hg-P} =$ 3874), 33.21 (br).

2.2.7. $[HgI_2(dppeO)_2]$ (6) · $CHCl_3$

Complex **6** was prepared in the same way as for **4** using mercury(II) iodide (0.16 g, 0.36 mmol). The product was crystallized in chloroform. Yield: 0.35 g, 75%; m.p.: 196–198 °C. *Anal.* Calc. for $C_{53}H_{49}Cl_3HgI_2O_2P_4$: C, 45.38; H, 3.52. Found. C, 45.82; H, 3.53%. IR (cm^{-1}): 3052, 2942, 1589, 1483, 1436, 1184, 1120, 1103, 997, 736, 692, 538, 508, 478. ^{1}H NMR: 2.70–2.83 (m, 8H), 7.27–7.88 (m, 40H). ^{31}P NMR: 4.32 (br, $^{1}J_{Hg-P} = 3042$), 33.14 (br).

2.3. X-ray crystallography

Single crystals of **2** and **3** were obtained by slow evaporation of a chloroform solution. Well formed crystals of **4** were obtained as a DMSO solvate by mixing two equivalents of dppeO, 1 equiv. of $HgCl_2$ and one equivalent of dimethyltin dichloride, in DMSO and allowed to stand. Crystals of **5** were grown from a dichloromethane solution by vapour diffusion of hexane. The intensity data were

collected at 173 K (−100 °C) on a Stoe Mark II-Image Plate Diffraction System [15] equipped with a two-circle goniometer using Mo Kα graphite monochromated radiation. The structures were solved by Direct methods using the programme SHELXS-97 [16]. The refinement and all further calculations were carried out using SHELXL-97 [17]. The H-atoms were included in calculated positions and treated as riding atoms using SHELXL default parameters. The non-H atoms were refined anisotropically, using weighted full-matrix least-squares on F^2. In complex **2**, disorder was noted in one of the ligand molecules in the atoms C53, C54, P6, O3 and the phenyl rings C67–C72 and C73–C78; two sets of positions were refined for the above atoms (occupancies 0.47(A) and 0.53(B)). The phenyl ring atoms C42, C43, C45 and C46 were also found to be disordered over two positions and refined with occupancies 0.5 for both the positions (A and B). In the co-crystallised chloroform molecule, the chlorine atoms were found to be disordered over two positions (occupancies 0.566 (A) and 0.434 (B)), the C–Cl distances were constrained to their theoretical values and the thermal parameters made equal. All the phenyl rings, except ring C21–C26, have been constrained to have thermal parameters equal to that of their respective *ipso* carbon atom. Complex **3** crystallized in the non-centrosymmetric triclinic space group $P\bar{1}$ and was refined as an inversion twin (final BASF value =0.418(13)). In complexes **3** and **4**, the phenyl rings were constrained to have thermal parameters equal to that of their respective *ipso* carbon atom. Disorder was also found in the phenyl rings and in atoms P2 and O1 of complex **5**. Two sets of positions (A and B) were refined with occupancies of 0.5,

Table 2
Selected bond lengths (Å) and bond angles (°)

Complex **2**			
Hg(1)–P(1)	2.395(2)	Hg(1)–O(3A^{i})	2.56(2)
Hg(2)–P(3)	2.404(2)	Hg(2)–O(1)	2.526(6)
Hg(3)–P(5)	2.411(2)	Hg(3)–O(2)	2.566(6)
Br(1)–Hg(1)	2.491(1)	Br(4)–Hg(2)	2.590(1)
Br(2)–Hg(1)	2.609(1)	Br(5)–Hg(3)	2.521(1)
Br(3)–Hg(2)	2.510(1)	Br(6)–Hg(3)	2.557(1)
O(1)–P(2)	1.489(6)	O(2)–P(4)	1.497(7)
O(3A)–P(6A)	1.51(2)		
P(1)–Hg(1)–O(3A^{i})	88.2(5)	P(3)–Hg(2)–O(1)	81.42(14)
P(1)–Hg(1)–Br(1)	134.95(6)	P(3)–Hg(2)–Br(3)	134.13(6)
P(1)–Hg(1)–Br(2)	114.17(5)	P(3)–Hg(2)–Br(4)	118.62(6)
Br(1)–Hg(1)–Br(2)	107.87(4)	Br(3)–Hg(2)–Br(4)	104.51(4)
O(3A^{i})–Hg(1)–Br(2)	92.7(4)	Br(3)–Hg(2)–O(1)	107.91(14)
Br(1)–Hg(1)–O(3A^{i})	105.5(5)	O(1)–Hg(2)–Br(4)	98.78(14)
P(5)–Hg(3)–O(2)	86.67(16)	Br(5)–Hg(3)–Br(6)	107.92(6)
P(5)–Hg(3)–Br(5)	127.60(7)	Br(5)–Hg(3)–O(2)	102.45(15)
P(5)–Hg(3)–Br(6)	121.91(7)	Br(6)–Hg(3)–O(2)	97.94(14)
Symmetry operation, i = x, $y-1$, z.			
Complex **3**			
Hg(1)–P(1)	2.468(8)	Hg(1)–I(2)	2.699(2)
Hg(2)–P(3^{i})	2.477(7)	Hg(1)–I(1)	2.732(3)
Hg(1)–O(2)	2.480(19)	Hg(2)–I(3)	2.700(3)
Hg(2)–O(1)	2.49(2)	Hg(2)–I(4)	2.709(3)
O(1)–P(2)	1.531(19)	O(2)–P(4)	1.467(17)
P(1)–Hg(1)–O(2)	90.8(5)	P(3^{i})–Hg(2)–O(1)	91.7(4)
P(1)–Hg(1)–I(2)	124.4(2)	P(3^{i})–Hg(2)–I(3)	122.2(2)
P(1)–Hg(1)–I(1)	118.1(2)	P(3^{i})–Hg(2)–I(4)	117.7(2)
I(2)–Hg(1)–I(1)	110.29(9)	I(3)–Hg(2)–I(4)	114.31(9)
O(2)–Hg(1)–I(1)	106.6(5)	O(1)–Hg(2)–I(4)	102.8(5)
O(2)–Hg(1)–I(2)	100.4(5)	O(1)–Hg(2)–I(3)	100.0(5)
Symmetry operation, i = x, y, $z-1$			

Table 1
Crystal data and refinement details for complexes **2**–**5**

	2	**3**	**4**	**5**
Empirical formula	$C_{78}H_{72}Br_6Hg_3O_3P_6$, $CHCl_3$	$C_{52}H_{48}Hg_2I_4O_2P_4$	$C_{52}H_{48}Cl_2HgO_2P_4$, $(CH_3)_2SO$	$C_{52}H_{48}Br_2HgO_2P_4$
Formula weight	2443.77	1737.56	1178.40	1189.19
Crystal system	triclinic	triclinic	orthorhombic	orthorhombic
Space group	$P\bar{1}$ (No. 2)	$P\bar{1}$ (No. 1)	*Pbcm* (No. 57)	*Pbcm* (No. 57)
Unit cell dimensions				
a (Å)	11.9992(9)	9.282(2)	8.8571(5)	8.8042(5)
b (Å)	17.8071(12)	10.667(2)	23.6279(17)	23.320(2)
c (Å)	21.2026(14)	15.108(3)	24.4130(12)	24.2351(16)
α (°)	71.616(5)	108.594(15)	90	90
β (°)	81.423(6)	90.358(17)	90	90
γ (°)	78.554(6)	102.191(17)	90	90
V (Å^3)	4195.4(5)	1381.4(5)	5109.0(5)	4975.7(6)
Z	2	1	4	4
Absorption coefficient (mm^{-1})	8.588	7.938	3.326	4.866
Collected reflections	57012	11767	45912	20451
Independent reflections	22579	8184	4687	4540
R_{int}	0.0845	0.1151	0.0899	0.1174
Observed reflections [$I > 2\sigma(I)$]	12462	4892	3675	3157
R_1 (observed data)	0.0587	0.0782	0.0536	0.0544
WR_2 (all data)	0.1369	0.2078	0.1273	0.1228

Table 3
Selected bond lengths (Å) and bond angles (°)

Complex **4**			
Hg(1)–P(2)	2.453(2)	Cl(2)–Hg(1)	2.587(3)
Cl(1)–Hg(1)	2.594(3)	O(1)–P(1)	1.481(5)
P(2)–Hg(1)–P(2^{i})	143.93(8)	P(2)–Hg(1)–Cl(1)	106.09(4)
P(2)–Hg(1)–Cl(2)	95.59(5)	Cl(2)–Hg(1)–Cl(1)	98.16(10)
Symmetry operation, i = x, y, $-z-1/2$			
Complex **5**			
Hg(1)–P(1)	2.456(2)	Br(2)–Hg(1)	2.664(1)
Br(1)–Hg(1)	2.725(1)	O(1)–P(2)	1.483(13)
P(1)–Hg(1)–P(1^{i})	142.34(10)	P(1)–Hg(1)–Br(1)	92.92(6)
P(1)–Hg(1)–Br(2)	107.11(6)	Br(2)–Hg(1)–Br(1)	105.19(5)
Symmetry operation, i = x, y, $-z+3/2$			

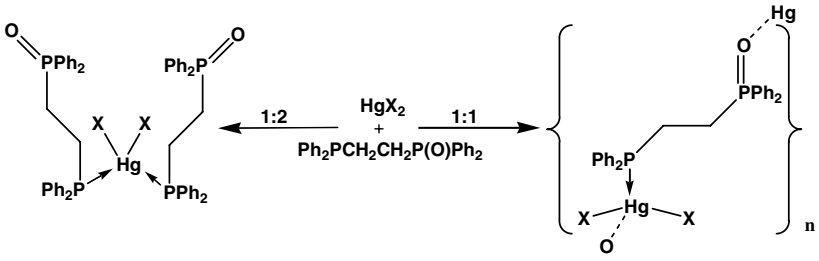
and the bond distances have been constrained to their theoretical values. Semi-empirical absorption corrections were applied using MULscanABS (PLATON) for **2** ($T_{min}/T_{max} = 0.080/0.178$) and **5** ($T_{min}/T_{max} = 0.621/0.895$). Empirical absorption corrections were applied using DELrefABS (PLATON) for **3** ($T_{min}/T_{max} = 0.167/0.639$) and **4** ($T_{min}/T_{max} = 0.401/0.796$). Further crystallographic data are given in Table 1 and selected bond distances and angles are given in Tables 2 and 3. The molecular structure and crystallographic numbering schemes are illustrated in ORTEP III [18] and PLATON [19] drawings, Figs. 1–5.

3. Results and discussion

The reaction of 1,2-bis(diphenylphosphino)ethane monoxide (dppeO) with various mercury(II) halides has been carried out. Different coordination modes have been observed with different metal to ligand stoichiometry. The reactions are represented in Scheme 1.

3.1. Hg(II)–dppeO 1:1 complexes

The reaction of HgX_2 (X = Cl, Br, I) and dppeO in equimolar ratio in methanol yielded white precipitates immediately. The IR spectra of the products show strong



Scheme 1. Reaction of dppeO with Hg(II) halides.

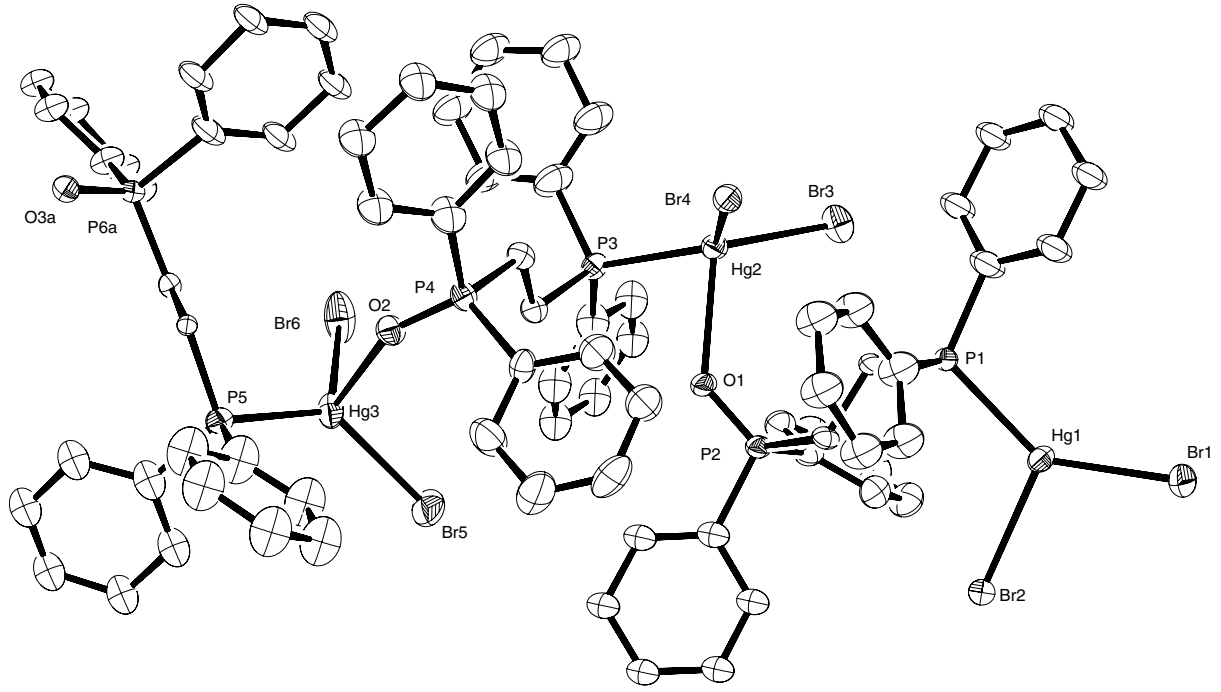


Fig. 1. Asymmetric unit of **2** at 30% probability ellipsoids. The hydrogen atoms, the disordered components and the solvent molecule of $CHCl_3$ have been omitted for clarity.

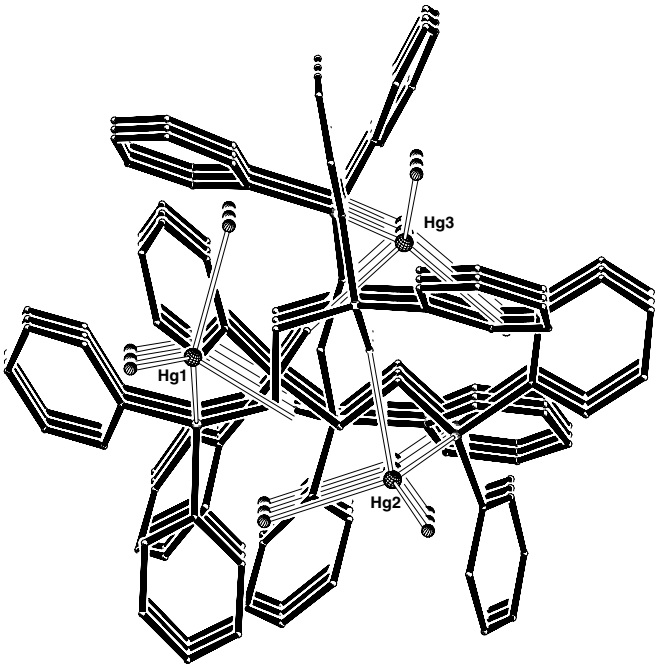


Fig. 2. A view of complex **2** along crystallographic *b*-axis. The figure shows the pseudo three-fold screw axis leading to an helical arrangement.

bands at 1160, 1164 and 1156 cm^{-1} for **1**, **2** and **3**, respectively, attributed to the coordinated (P = O) group. The ^{1}H NMR spectra exhibit two broad multiplets for two magnetically non-equivalent methylene protons in the ligand. Of the two signals in the ^{31}P NMR spectra, the ones exhibiting satellite signals due to ^{199}Hg (16.4% natural abundance, $I = 1/2$), are assigned to the coordinated 'PPh_2'. The chemical shifts and the coupling constants decrease going from chloride to iodide (see Table 4) as observed previously for $[HgX_2(PPh_3)_n]$ (X = Cl, Br,I) ($n = 1, 2$) [20,21]. The ^{31}P NMR signals due to '$Ph_2P = O$' are not shifted much from the corresponding free ligand resonance (+33.18 ppm), suggesting the dissociation of the Hg–O bond in solution.

3.2. Hg(II)–dppeO 1:2 complexes

When 1 equiv. of HgX_2 (X = Cl, Br, I) was added dropwise to two equivalents of dppeO, the 1:2 complexes were obtained in which the ligand coordinates exclusively with the phosphine moiety. The IR and ^{31}P NMR spectra are in accordance with the observed coordination mode. Interestingly, the coordination chemical shifts ($\Delta\delta = \delta_{complex} - \delta_{ligand}$) and the Hg–P coupling constants are lower for the 1:2 complexes (Table 4). The difference in the spectral parameters for the 1:1 and 1:2 complexes is most probably dominated by the steric interactions [20] due to the proximity of bulky phenyl groups to the metal center in the latter. Indeed, complex **6** with bulky iodide ligands appears very labile in solution. Repeated attempts to obtain single crystals of complex **6** lead to the formation

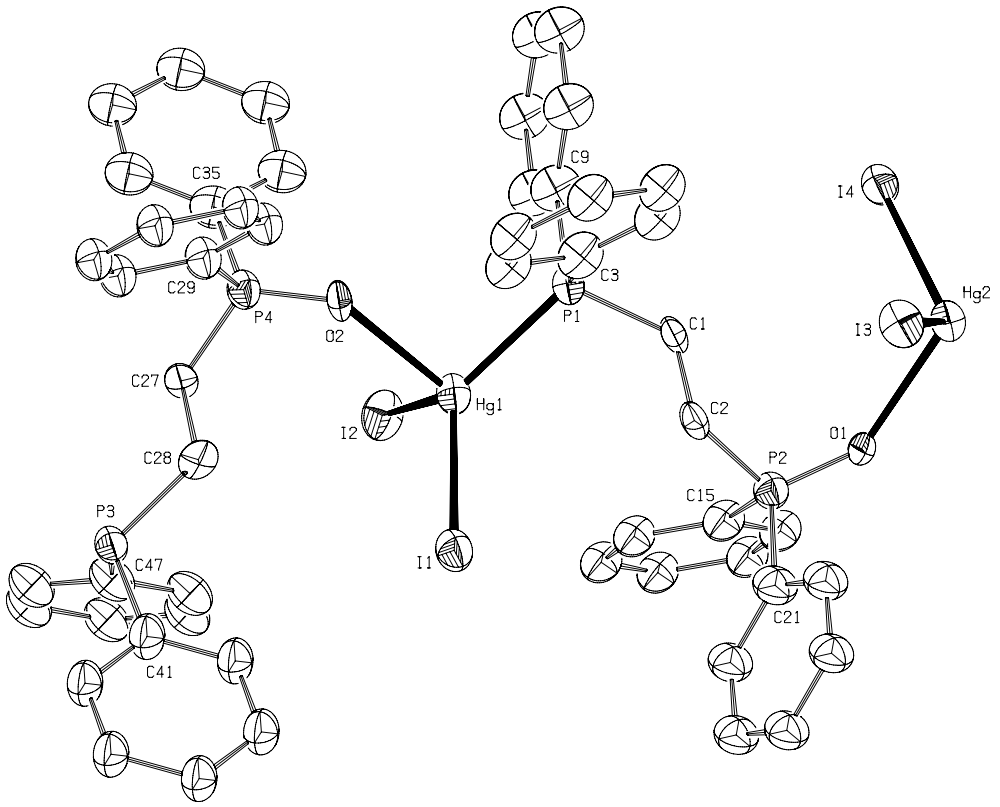


Fig. 3. Asymmetric unit of **3** at 30% probability ellipsoids. The hydrogen atoms have been omitted for clarity.

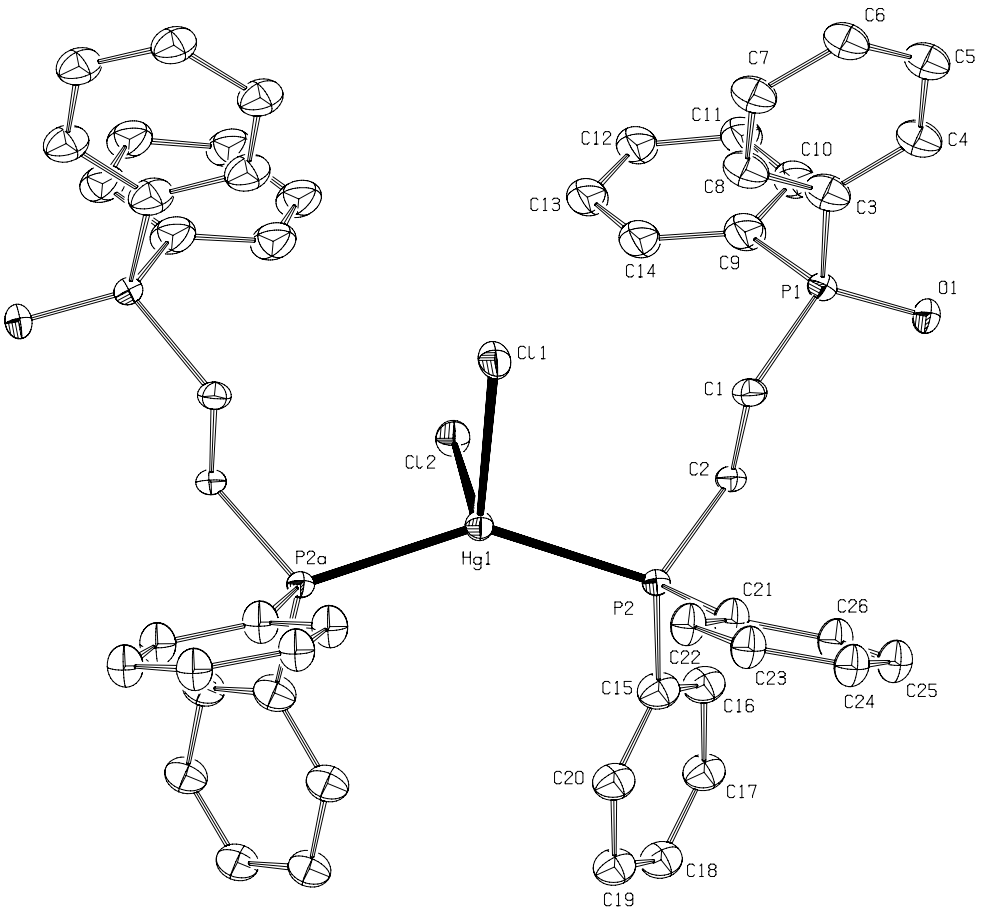


Fig. 4. Molecular structure of **4** at 30% probability ellipsoids. Atoms Hg1, Cl1 and Cl2 lie in the mirror plane. The hydrogen atoms and the DMSO solvent molecule have been omitted for clarity.

of complex **3**, as confirmed by the unit cell parameters derived from the preliminary X-ray diffraction data. In the ^{1}H NMR spectra, the methylene protons of the dppeO framework appear as a single peak for complexes **4** and **5**, while the same protons show two broad resonances for complex **6**.

A noteworthy feature of the ^{31}P NMR spectra is the increased intensity of the phosphine oxide signal which seems to have merged peaks. This may be attributed to the presence of $Ph_2P(O)CH_2CH_2P(O)Ph_2$ (dppeO_2) in solution, formed due to the oxidation of dissociated dppeO by Hg^{2+}. Catalytic oxidation of bis(diphenylphosphino)methane (dppm) by Hg^{2+} to dppmO and dppmO_2 has been noted previously [22].

3.3. Molecular structures of the 1:1 complexes *2* and *3*

The molecular structures of complexes **2** and **3** are shown in Figs. 1 and 3, respectively, and selected bond distances and angles are given in Table 2. The asymmetric unit of **2** is composed of three $HgBr_2$ units bridged by three dppeO ligands and a molecule of chloroform solvent. The X-ray analysis reveals the coordination of both 'P' and 'O' atoms of the ligand to mercury thereby forming an infinite one dimensional polymeric chain. The chain contains a pseudo three-fold screw axis which propagates along the crystallographic *b*-axis, thus exhibiting a pseudo-helical arrangement (Fig. 2).

The geometries around the three Hg centers are highly distorted tetrahedral. The bond angles range from 88.2(5)° to 134.95(6)°, 81.42(14)° to 134.13(6)° and 86.67(16)° to 127.62(7)° for Hg(1), Hg(2) and Hg(3), respectively. Similar range has been observed in $[Hg\{Ph_2P(S)CH_2PPh_2\}I_2]$ [10]. The geometry around Hg in the above complex was considered as flattened tetrahedral, since the metal deviates by only 0.3823(8) Å from the least-squares plane defined by the two I atoms and one P atom in the direction of the capping S atom. In the present case the Hg atom deviations from the best least-squares plane defined by the two Br atoms and one P atom are 0.244, 0.234, 0.229 Å for Hg(1), Hg(2) and Hg(3), respectively, from the direction of the capping O atom. Such type of flattening from the tetrahedral geometry could be the result of several factors including the steric interactions. While the Hg–P distances (2.395(2)–2.411(2) Å) are comparable to the same distance in the P,O-chelate complex *trans*-$[Hg\{Ph_2PNP(O)Ph_2\text{–}P,O\}_2]$ [7], the Hg–O bonds (mean distance 2.55(9) Å) are longer than the *normal*

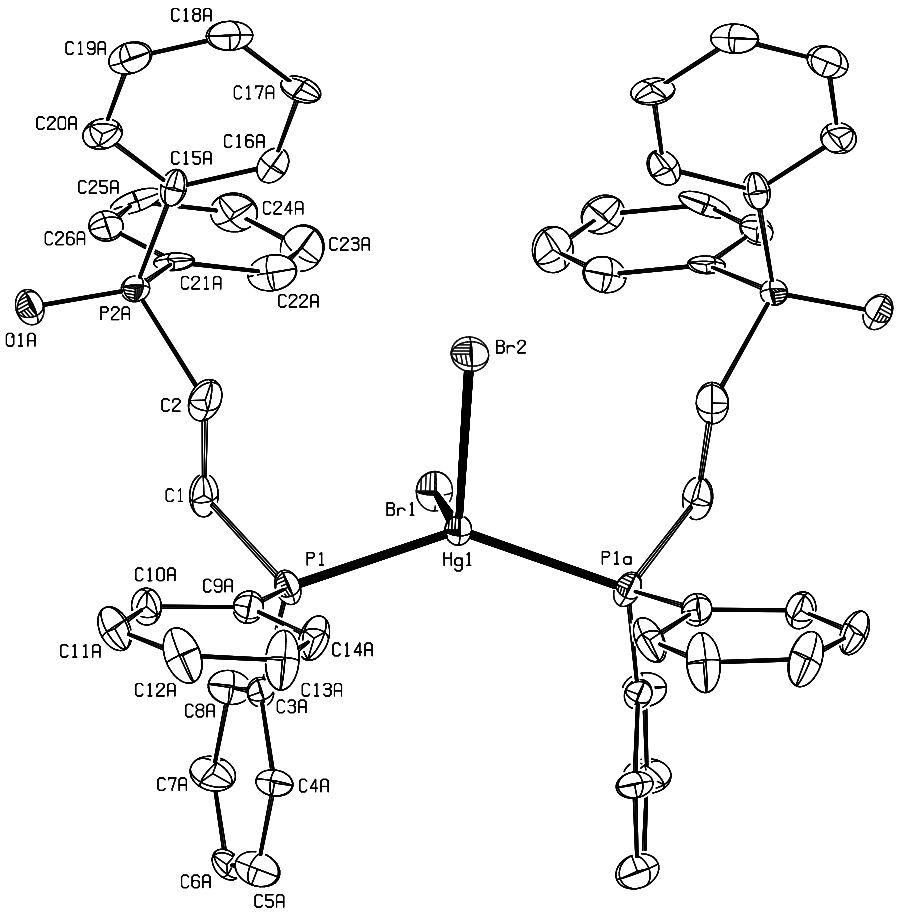


Fig. 5. Molecular structure of complex **5** at 30% probability ellipsoids. Atoms Hg1, Br1 and Br2 lie in the mirror plane. The hydrogen atoms and the disordered components have been omitted for clarity.

Hg–O covalent bond (ca. 2.1 Å), thus accounting for its dissociation in solution as noted in the ^{31}P NMR spectra.

Complex **3** crystallizes in the non-centrosymmetric triclinic space group $P\bar{1}$. The asymmetric unit consists of two HgI_2 units bridged by two dppeO molecules, resulting in the formation of a linear zig-zag polymeric chain. A similar distorted arrangement is observed as that of **2**. However, compared to **2,** the deviations of the Hg(1) and Hg(2) atoms from the least-squares plane described by two I atoms and one P atom are high being equal to 0.406 and 0.367 Å, respectively. The average Hg–P distance of 2.472(7) Å is longer than the values observed in **2**, while the average Hg–O distance of 2.485(2) Å is shorter.

It is interesting to note that although the precursor ligand, dppe and its fully oxidized form $dppeO_2$ have the pronounced tendency to act as a bridging ligands, the bridging tendency of dppeO has not been, to the best of our knowledge, previously confirmed [23] crystallographically with any metal. Hence, complexes **2** and **3** represent the first examples of structurally characterized polymeric complexes where dppeO acts as a bridging bidentate ligand.

Table 4
IR and ^{31}P NMR spectral parameters [ν (cm^{-1}), δ (ppm), J (Hz)]

	ν(P = O)	δ PPh_2	δ $Ph_2P=O$	$^3J_{(P-P)}$	$^1J_{(Hg-P)}$	$\Delta\delta$[a] (PPh_2)
dppeO	1182	−11.68	33.18	48.4		
1	1160	37.12	33.40	58.9	7449	48.7
2	1164	29.46	33.38	57.5	6422	41.1
3	1156	6.34	32.93	54.9	4366	18.0
4	1188	28.75	34.08		4654	40.4
5	1190	21.19	33.21		3874	32.9
6	1184	4.32	33.14		3042	16.0

[a] ($\Delta\delta = \delta_{complex} - \delta_{ligand}$).

3.4. Molecular structures of 1:2 complexes **4** and **5**

The molecular structures of the 1:2 complexes **4** and **5** are shown in Figs. 4 and 5, respectively. Table 3 contains selected bond distances and angles. The mercury atom is coordinated to two halogens and two phosphorus atoms. The P = O groups in both complexes remain free and no significant interaction with the metal has been observed. The mercury and the two halogen atoms lie in the mirror plane. Complex **4** crystallizes as a DMSO solvate. The geometry around mercury is distorted tetrahedral. The Hg–P distances of 2.453(2) and 2.456(2) Å in **4** and **5**, respectively, are in the range of 2.39(1)–2.574(3) Å reported previously for 1:2 mercuric halide–phosphine complexes [24,25]. The P–Hg–P angles 143.93(8)° and 142.34(10)° in **4** and **5**, respectively, are significantly higher than the tetrahedral angle. Such a trend was observed in the complexes $[HgCl_2(PPh_3)_2]$ [24] and $[HgCl_2(PEt_3)_2]$ [26], where the P–Hg–P angles are 134° and 158°, respectively. These were interpreted in terms of strong Hg–P bonding and weaker Hg–Cl interactions. It seems reasonable to include steric effects as well as the tendency of Hg(II) to acquire primary coordination of valency of two, to account for the higher P–Hg–P angles.

In summary, we have prepared and characterized mercury(II)–dppeO complexes with different molecular structures and geometries. The P, O-coordinated infinite one- dimensional polymers were obtained when 1:1 molar ratio of metal to ligand was used. Complexes **2** and **3** represent the first crystallographically characterized examples containing dppeO ligand in bridging bidentate coordination mode. The Hg(II) center is located in a highly distorted tetrahedral environment. The change in the halogen from bromide to iodide has a marked influence in the structure of the polymeric chain from pseudo helical to a zig-zag arrangement. On the other hand exclusively P, P-coordinated complexes were obtained when two equivalents of ligand were added to one equivalent of the metal salt . The complexes were discretely monomeric containing uncoordinated phosphine oxide group. The results suggest that the interaction of Hg(II) with different phosphines remain an active field of research leading to complexes with unusual structures.

Acknowledgement

M.M.E. thanks the Swiss Federal Commission for a scholarship to study at the University of Neuchatel.

Appendix A. Supplementary material

CCDC 617574, 617575, 617576 and 617577 contain the supplementary crystallographic data for **2**, **3**, **4** and **5**. These data can be obtained free of charge via http://www.ccdc.cam.ac.uk/conts/retrieving.html, or from the Cambridge Crystallographic Data Centre, 12 Union Road, Cambridge CB2 1EZ, UK; fax: (+44) 1223-336-033; or e-mail: deposit@ccdc.cam.ac.uk. Supplementary data associated with this article can be found, in the online version, at doi:10.1016/j.poly.2006.10.030.

References

[1] K. Brodersen, H.-U. Hummel, in: G. Wilkinson (Ed.), Comprehensive Coordination Chemistry, vol. 5, Pergamon Press, Oxford, 1987, pp. 1047–1097.
[2] D.J. Eisler, R.J. Puddephatt, Dalton Trans. (2003) 3567, and references therein.
[3] V.V. Grushin, Chem. Rev. 104 (2004) 1629.
[4] C. Abu-Gnim, I. Amer, J. Organomet. Chem. 516 (1996) 235.
[5] R.W. Wegman, A.G. Abatjoglou, A.M. Harrison, J. Chem. Soc., Chem. Commun. (1987) 1891.
[6] S.O. Grim, L.C. Satek, C.A. Tolman, J.P. Jesson, Inorg. Chem. 14 (1975) 655.
[7] R. Haid, R. Gutmann, G. Czermak, C. Langes, W. Oberhauser, H. Kopacka, K.-H. Ongania, P. Bruggeller, Inorg. Chem. Commun. 6 (2003) 61.
[8] P.K.S. Gupta, L.W. Houk, D. van der Helm, M.B. Hossain, Inorg. Chim. Acta 44 (1980) L235.
[9] T.S. Lobana, P.K. Sharma, Ind. J. Chem. 27A (1988) 732.
[10] T.S. Lobana, M.K. Sandhu, M.J. Liddell, E.R.T. Tiekink, J. Chem. Soc., Dalton Trans. (1990) 691.
[11] P. Barbaro, F. Cecconi, C.A. Ghilardi, S. Midollini, A. Orlandini, A. Vacca, Inorg. Chem. 33 (1994) 6163.
[12] D.C. Bebout, A.E. DeLanoy, D.E. Ehmann, M.E. Kastner, D.A. Parrish, R.J. Butcher, Inorg. Chem. 37 (1998) 2952.
[13] W.L.F. Armarego, D.D. Perrin, Purification of Laboratory Chemicals, 4th ed., Butterworth Heinemann, Oxford, 1996.
[14] D.S. Amenta, B.R. Ayras, J. Jurica, J.W. Gilje, Inorg. Chim. Acta 336 (2002) 115.
[15] Stoe, X-AREA V1.17 & X-RED32 V1.04 Software, Stoe & Cie GmbH, Darmstadt, Germany, 2002.
[16] G.M. Sheldrick, Acta Crystallogr. A46 (1990) 467.
[17] G.M. Sheldrick, SHELXL-97, Universität Göttingen, Göttingen, Germany, 1999.
[18] L.J. Farrugia, J. Appl. Crystallogr. 30 (1997) 565.
[19] A.L. Spek, J. Appl. Crystallogr. 36 (2003) 7.
[20] E.C. Alyea, S.A. Dias, R.G. Goel, W.O. Ogini, P. Pilon, D.W. Meek, Inorg. Chem. 17 (1978) 1697.
[21] H.B. Buergi, R.W. Kunz, P.S. Pregosin, Inorg. Chem. 19 (1980) 3707.
[22] W. Oberhauser, T. Stampfl, R. Haid, G. Langes, C. Bachmann, H. Kopacka, K.-H. Ongania, P. Bruggeller, Polyhedron 20 (2001) 727.
[23] The complex $[(\mu\text{-dppeO})Eu(acac\text{-}F_6)_3(\mu\text{-dppeO})PdCl_2]_n$ has been formulated as a polymer based on spectroscopic studies V.A. Petrov, W.J. Marshall, V.V. Grushin, Chem. Commun. (2002) 520.
[24] N.A. Bell, T.D. Dee, M. Goldstein, P.J. McKenna, I.W. Nowell, Inorg. Chim. Acta 71 (1983) 135.
[25] M. Kubicki, S.K. Hadjikakou, M.N. Xanthopoulou, Polyhedron 20 (2001) 2179.
[26] N.A. Bell, T.D. Dee, P.L. Goggin, M. Goldstein, R.J. Goodfellow, T. Jones, K. Kessler, D.M. McEwan, I.W. Nowell, J. Chem. Res. (S)2 (M) (1981) 201.

2. Experimental

2.1. Materials and physical methods

The complexes $[M(CO)_4L_2]$ and $Ph_4P[MCl(CO)_3L_2]$ were freshly prepared by the published method [7], and all other chemicals were purchased from commercial sources and used without further purification. Experiments were carried out under an N_2 atmosphere. Infrared spectra were recorded on a Perkin–Elmer 781 spectrometer using samples prepared as nujol mulls on sodium chloride discs. The ^1H NMR spectra were obtained for solutions in dimethylsulfoxide-d_6 and were referenced to the solvent as internal standard.

2.2. Synthesis of $[MoCl(CO)_2(\eta^3\text{-}CH_2C(COCl)C{=}CH_2)L_2]$ (L_2 = bipy **4a**, L_2 = phen **4b**)

A mixture of $[Mo(CO)_4L_2]$ (2.0 mmol), Ph_4PCl (824 mg, 2.2 mmol) and excess 1,4-dichloro-2-butyne (**3**) (0.2 ml) was refluxed in CH_2Cl_2 (10 ml) for 6 h, cooled to room temperature and then stored at 5 °C for 3 days. The orange product was filtered from solution and dried *in vacuo*. Yields = 69% **4a**, 73% **4b**.

2.3. Synthesis of $[WCl(CO)_2(\eta^3\text{-}CH_2C(COCl)C{=}CH_2)(2,9\text{-}Me_2phen)]$ (**4c**)

A mixture of $[W(CO)_4(2,9\text{-}Me_2phen)]$ (504 mg, 1.0 mmol) and Ph_4PCl (400 mg, 1.07 mmol) in 1,2-$C_2H_4Cl_2$ (25 ml) was refluxed for 6 h with an excess of **3** (0.1 ml). Reduction of the solvent volume under reduced pressure followed by storage at 5 °C for 3 days gave the orange title product. This was filtered from solution and dried *in vacuo*. Yield = 76%.

2.4. Attempted preparation of **4a**

$Mo(CO)_6$ (264 mg, 1.0 mmol), phen (180 mg, 1.0 mmol), Ph_4PCl (400 mg, 1.1 mmol) and **3** (0.1 ml) were refluxed in CH_2Cl_2, $CHCl_3$ or CH_2Br_2 (25 ml) and monitored by IR spectroscopy for 3–72 h.

2.5. Thermal study of **4a**

Method a: Mixtures of $[Mo(CO)_4(phen)]$ (**1a**) (50 mg, 0.13 mmol) and Ph_4PCl (60 mg, 0.16 mmol) were refluxed with **3** (0.1 ml) in CH_2Cl_2, $CHCl_3$, 1,1,1-$C_2H_3Cl_3$, 1,2-$C_2H_4Cl_2$, CH_2Br_2 or C_6H_5Cl (25 ml) for 3–6 h. *Method b:* The reaction was carried out as *a*, but **1a** and Ph_4PCl were replaced by **4a** (60 mg, 0.12 mmol). For both methods, the complex $[MoCl_2(CO)(\eta^2\text{-}ClCH_2C{\equiv}CCH_2Cl)(phen)]$ (**5**) was obtained from those solvents boiling in the range 61–96 °C. For **5**: ^1H NMR in DMSO-d_6, 5.41 (brs, 4H), 8.05–9.35 (m, 8H); IR (Nujol) 1956 cm^{-1}; elemental *Anal.* Calc. for ($\cdot 0.5CH_2Cl_2$): C, 38.85; H, 2.40; N 5.18. Found: C, 39.70; H, 2.34; N 5.43.

2.6. Synthesis of $[MoCl(CO)_2(\eta^3\text{-}CH_2C(COBr)C{=}CH_2)(phen)]$

A suspension of **4a** (365 mg, 0.5 mmol) and potassium bromide (595 mg, 5.0 mmol) in refluxing acetone (50 ml) was stirred for 18 h. The resulting mixture was poured into water (20 ml), and then extracted twice with dichloromethane (25 ml). The separated organic layer was dried over $MgSO_4$, and removal of solvent in vacuo gave the orange-red product. Yield = 45%.

2.7. Synthesis of $[MoCl(CO)_2(\eta^3\text{-}CH_2C(COX)C{=}CH_2)L_2]$ ($X = NHCH_2CH{=}CH_2$, L_2=bipy **6** or phen **7**; $X = NC_5H_{10}$, L_2 = bipy **8**; $X = NHCH_2C{\equiv}CH$, L_2 = bipy **9**)

Method a: A mixture of $[Mo(CO)_4L_2]$ (1.0 mmol) and Ph_4PCl (393 mg, 1.05 mmol) was stirred in CH_2Cl_2 (10 ml) with an excess of allyl amine, piperidine or propargyl amine (0.25 ml), and to this was added **3** (0.1 ml). The mixture darkened on addition, and after refluxing for 7 h, the volume was reduced by half using a flow of N_2. Storage overnight at low temperature gave the product as orange-red microcrystals. These were filtered from solution, and recrystallized from methanol or CH_2Cl_2–petrol mixtures. *Method b*: The acyl chloride complex was prepared as given in Section 2.2, and to this was added the amine. After a further 1 h reaction under reflux, the product was isolated as described above. *Method c*: The reaction was carried out as described in *a*, but $[Mo(CO)_4L_2]$ and Ph_4PCl were replaced by $Ph_4P[MoCl(CO)_3L_2]$ (1.0 mmol). Yields of each complex obtained by methods *a–c* were similar, and in the range 42–68%.

2.8. Synthesis of $[WCl(CO)_2(\eta^3\text{-}CH_2C(COX))C{=}CH_2\text{-}(2,9\text{-}Me_2phen)]$ ($X = N(CH_2CH{=}CH_2)_2$ **10** or $NHCH(Ph)CO_2Me$ **11**)

The synthesis was carried out as described in Section 2.7 method *a*, but using 1,2-$C_2H_4Cl_2$ and the appropriate amine. Yields = 49% **10**, 54% **11**.

2.9. Synthesis of $MoCl(CO)_2(\eta^3\text{-}CH_2C(CO_2CH_2C{\equiv}CH)C{=}CH_2)(phen)]$ (**12**) and $[MoCl(CO)_2(\eta^3\text{-}CH_2C(COS(CH_2)_2SH)C{=}CH_2)(phen)]$ (**13**)

The reaction was carried out as described in Section 2.7 method *a*, with the amine replaced by propargyl alcohol or 1,2-ethanedithiol (0.5 ml) and triethylamine (0.1 ml). Yields = 54% **12**, 47% **13**.

2.10. X-ray crystallography

A single orange crystal of **9** ($0.50 \times 0.20 \times 0.12$ mm) was grown from a CH_2Cl_2–petrol mixture and mounted on a glass fibre in paratone oil. Data were collected at 120 K on an Nonius KappaCCD area detector diffractometer located at the window of a Nonius FR591 rotating anode

X-ray generator, equipped with a molybdenum target (λ Mo Kα = 0.71073 Å). The structure was solved and refined using the SHELX-97 suite of programs and data were corrected for absorption effects by means of comparison of equivalent reflections using the program SADABS [8,9]. Non-hydrogen atoms were refined anisotropically, whilst hydrogen atoms were fixed in idealised positions with their thermal parameters riding on the values of their parent atoms. Positional disorder (180° rotation) was found to be present in the propargyl chain (C18–C20) with an occupancy ratio of 66:34, and only one orientation of this chain is shown in Fig. 1 for clarity. $C_{20}H_{16}ClMoN_3O_3$, monoclinic, $P2_1/c$, $a = 7.4910(1)$, $b = 16.9292(3)$, $c = 15.2343(2)$ Å, $\beta = 93.9620(10)°$, volume = 1927.35(5) Å^3, $Z = 4$, $D_c = 1.646$ Mg/m^3, $\mu = 0.846$ mm^{-1}, 29 518 measured, 4422 unique ($R_{int} = 0.0358$) and 3827 ($F_o > 4\sigma(F_o)$) reflections, R_1 (obs) = 0.0287 and wR_2 (all data) = 0.0732 $\rho_{max}/\rho_{min} = 0.650/-0.933$ e Å^{-3}.

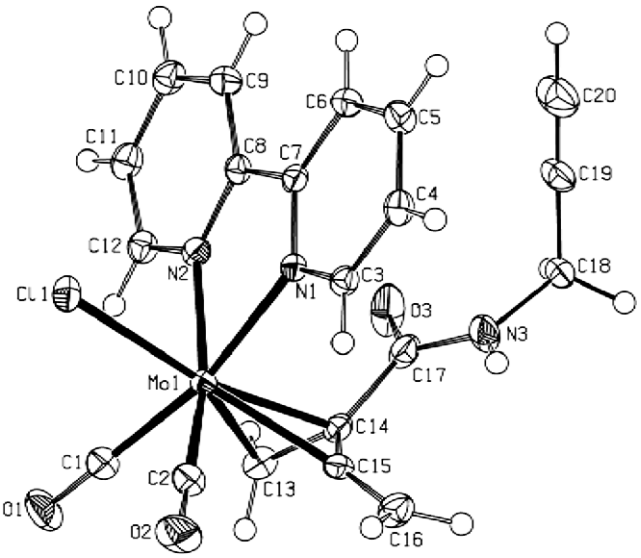


Fig. 1. The crystal structure of [MoCl(CO)$_2$(η^3-CH$_2$C(CONHCH$_2$C≡CH)C=CH$_2$)(2,2′-bipyridine)] (**9**), with the second component of the disordered propargyl chain (C18′–C20′) omitted for clarity.

3. Results and discussion

3.1. Synthesis of substituted butadienyl complexes

A mixture of [Mo(CO)$_4$L$_2$] (L$_2$ = phen, **1a**, bipy **1b**), Ph$_4$PCl and 1,4-dichloro-2-butyne (**3**) was refluxed in CH$_2$Cl$_2$, and the product was monitored by IR and NMR spectroscopy over time. After 3 h approximately equal quantities of unreacted **1** and [MoCl(CO)$_2$-(η^3-CH$_2$C(COCl)C=CH$_2$)L$_2$] (**4a**,**4b**) were obtained, and complete conversion of **1** to **4** was achieved after a further 3 h (Eq. (1), Scheme 1). During this period the orange reaction mixture showed no signs of darkening due to formation of purple Ph$_4$P[MoCl(CO)$_3$L$_2$] (**2a**,**2b**), nor was there evidence of this compound in the spectra. This was not unexpected, since **2** reacted rapidly with **3** at 20 °C, and at elevated temperatures would be consumed on formation. Whilst yields of **4** were similar to the previous two stage process (Eqs. (2) and (3)), the new reaction time exceeds the latter by 3 h. A mixture of [W(CO)$_4$(2,9-Me$_2$phen)] (**1c**), Ph$_4$PCl and **3** heated in CH$_2$Cl$_2$, CHCl$_3$ or 1,1,1-C$_2$H$_3$Cl$_3$ (40–72 °C) over the same 6 h period showed no spectroscopic change. However increasing the temperature to 81 °C (1,2-C$_2$H$_4$Cl$_2$) afforded the acyl chloride (**4c**) in good yield, and this new reaction time compares favourably with the previous two stage total of 18 h (Eqs. (2) and (3)). The practical and environmental advantages of transferring to the one pot method are therefore, (i) isolation of products in good yield using minimum glassware and cleaning solvents, (ii) complete elimination of MeCN (Eq. (2)), (iii) reduction of solvent temperatures by 60–70 °C (previously 110 °C Mo and 140 °C W, Eq. (2))

$$\underset{\mathbf{1}}{M(CO)_4L_2} + Ph_4PCl + \underset{\mathbf{3}}{ClCH_2C{\equiv}CCH_2Cl} \rightarrow \underset{\mathbf{4}}{[MCl(CO)_2(\eta^3\text{-}CH_2C(COCl)C{=}CH_2)L_2]} \quad \text{(eqn. 1)}$$

$$\mathbf{1} + Ph_4PCl \rightarrow \underset{\mathbf{2}}{Ph_4P[MCl(CO)_3L_2]} \quad \text{(eqn. 2)}$$

$$\mathbf{2} + \mathbf{3} \rightarrow \mathbf{4} \quad \text{(eqn. 3)}$$

$$\mathbf{1} + Ph_4PCl + \mathbf{3} \rightarrow \underset{\mathbf{5}}{[MCl_2(CO)(\eta^2\text{-}ClCH_2C{\equiv}CCH_2Cl)L_2]} \quad \text{(eqn. 4)}$$

$$\mathbf{4} + \mathbf{3} \rightarrow \mathbf{5} \quad \text{(eqn. 5)}$$

$$\mathbf{1} + Ph_4PCl + \mathbf{3} + XH \rightarrow \underset{\mathbf{6\text{-}13}}{[MCl(CO)_2(\eta^3\text{-}CH_2C(COX)C{=}CH_2)L_2]} \quad \text{(eqn. 6)}$$

Scheme 1. Conditions: Eq. (1) Δ CH$_2$Cl$_2$ (Mo, 6 h) or 1,2-C$_2$H$_4$Cl$_2$ (W, 6 h), Eq. (2) Δ toluene (Mo, 1 h) or xylene (W, 16 h) and MeCN, Eq. (3) RT CH$_2$Cl$_2$2 h, Eqs. 94) and (5) Δ CHCl$_3$6 h, Eq. (6) Δ CH$_2$Cl$_2$ (Mo, 7 h) or 1,2-C$_2$H$_4$Cl$_2$ (W, 7 h).

and (iv) reaction time for tungsten complexes reduced by 12 h.

In an effort to decrease the time required to convert $[Mo(CO)_4L_2]$ to **4**, reactions of **1a**, Ph_4PCl and **3** were carried out in higher boiling point solvents. Coordinating solvents were avoided in view of their potential reaction with **1** to form solvated compounds of the type $[M(CO)_3(L_2)(S)]$ [10], and chlorinated solvents were selected for their ability to dissolve reactants and products. After 4 h in $CHCl_3$ (61 °C), peaks due to carbonyl stretching in **1a** had been replaced by those of **4a** and an additional peak of almost equal intensity at 1956 cm^{-1}. The latter predominated on raising the temperature to 96 °C (CH_2Br_2), and the complex $[MoCl_2(CO)(\eta^2\text{-}ClCH_2C{\equiv}CCH_2Cl)(phen)]$ (**5**) was isolated from solution. This product was also obtained on refluxing a mixture of **4a** and excess 1,4-dichloro-2-butyne in this solvent (Eqs. (4) and (5), Scheme 1), and one pot production of **5** occurred in solvents of higher boiling point until onset of decomposition of intermediate **2** occurred at 129 °C (C_6H_5Cl). Dichloroalkyne **3** is not expected to undergo rearrangement within this temperature range [11], and therefore the additional chlorine in **5** originates from decomposition of **4a**. On refluxing **4a** in acetone containing bromide ions, the derivative $[MoCl(CO)_2(\eta^3\text{-}CH_2C(COBr)C{=}CH_2)(phen)]$ was obtained,[1] and thus both **4a** and its acyl bromide analogue were stable at 56 °C. Isolation of **5** from one pot reactions of **1a**, Ph_4PCl and **3** in solvents boiling within the range 61–129 °C was therefore attributable to destabilization at these higher temperatures.

Attempts to prepare **4a** or **4b** by a one pot method using $[Mo(CO)_6]$, L_2, Ph_4PCl and **3** in refluxing CH_2Cl_2 over several days were less successful. Loss of CO from the hexacarbonyl was found to be slow at this temperature, and 12 h were required to form uncontaminated **1**. The diimine ligands bipy and phen, being weaker pi acceptors than CO, labilize $[M(CO)_4L_2]$ complexes towards dissociative ligand loss from the position *cis* to them. This *cis* labilization results in reaction substitution rates several orders of magnitude larger for these chelate complexes than for $Mo(CO)_6$. After 24 h the IR solution spectrum showed carbonyl stretching absorptions due to **1** and acyl chloride complex **4** of approximately equal intensity. However continued reaction times resulted in decreasing strength of these bands, suggesting the acyl chloride was thermally unstable over extended periods. A good yield of **4** could not be obtained via this method after 48 h (21%), and little remained in solution after refluxing for 72 h. Increasing the reaction temperature by use of $CHCl_3$ or CH_2Br_2 was found to accelerate formation of **1** and **4**, but also resulted in more rapid decomposition of the latter.

[1] For $[MoCl(CO)_2(\eta^3\text{-}CH_2C(COBr)C{=}CH_2)phen]$: ^1H NMR in DMSO-d_6 1.91 (s, H), 3.79 (s, H), 5.67 (d, 1.38H), 6.19 (d, 1.38H), 7.99 (m, 2H), 8.18 (s, 2H), 8.82 (m, 2H), 9.13 (d, 4.42H), 9.29 (d, 4.66H); IR (Nujol), cm^{-1}. 1989, 1912, 1650.

Addition of primary or secondary amines XH to the one pot reaction mixture of **1**, Ph_4PCl and **3** in CH_2Cl_2 afforded substituted complexes of the type $[MCl(CO)_2(\eta^3\text{-}CH_2C(COX)C{=}CH_2)L_2]$ (**6**–**11**), and in the presence of triethylamine and alcohol or thiol, the corresponding ester and thioester complexes could also be achieved (X = $OCH_2C{\equiv}CH$ **12**, $S(CH_2)_2SH$ **13**). These were characterized by their IR and NMR spectra (Tables 1 and 2), and the stereochemistry of **9** was investigated by a single crystal X-ray analysis. In some cases, where complexes were only soluble in DMSO, reproducible elemental analyses could not be obtained since oxidation to $[Mo_2Cl_2O_4(L_2)_2]$ occurred readily on recrystallization [12]. Complete replacement of CH_2Cl_2 by water in this one pot method was not possible due to insolubility of **1**. However **4** and **6**–**9** could be achieved from a two phase CH_2Cl_2/H_2O system, and where small volumes of the former were used, water assisted mixing and filtration. For example, similar yields of **4a** and **6** were obtained when 10 ml CH_2Cl_2 was replaced by 10 ml water and 0.5 ml CH_2Cl_2 in Sections 2.2 and 2.7, respectively. The tungsten complexes however proved more sensitive to water, and on heating **1c**, Ph_4PCl and **3** to 80 °C in an equivolume mixture of 1,2-$C_2H_4Cl_2$ and water (2.3), a mixture of **4c** and the known complex $[WCl_2(CO)_3(2,9\text{-}Me_2phen)]$ was obtained.

3.2. Characterization of complexes

3.2.1. Spectroscopic data

All the η^3-butadienyl complexes exhibited a pair of strong absorptions in their IR spectra between 1982 and 1894 cm^{-1} due to the metal *cis*-dicarbonyl fragment. A band of medium intensity near 1710 cm^{-1} arising from ν(C=O) of the acyl chloride **4** was shifted to lower wavenumber in **6**–**13**, and weak peaks near 3400 or 3250 cm^{-1} were assigned to ν(NH) or ν(C≡CH), respectively. The ^1H NMR spectra showed two singlets near 1.8 and 3.7 ppm due to the methylene terminus of the η^3-bonded butadienyl, and a pair of doublets arising from the double bond of this unit appeared near 5.7 and 6.2 ppm, with coupling constants of 2.2 Hz. Amide complexes containing NH gave rise to a triplet between 6.1 and 6.6 ppm, and a further triplet at 2.84 ppm was attributable to the terminal propargyl proton of **9**. Other signals due to aliphatic substituents of the butadienyl and aromatic protons of the L_2 ligand were unexceptional. As a result of their low solubilities, the ^{13}C NMR spectra of **6**–**13** were not recorded.

3.2.2. Crystal structure determination of 9

A solid-state crystal structure determination of $[MoCl(CO)_2(\eta^3\text{-}CH_2C(CONHCH_2C{\equiv}CH)C{=}CH_2)(2,2'\text{-bipyridine})]$ was carried out to determine the stereochemistry of the substituted η^3-butadienyl fragment. Fig. 1 shows a view of the molecule and the atomic labeling scheme used, and selected bond lengths and angles for **9** are given in Table 3. The coordination geometry about the Mo centre may be considered to be that of a slightly distorted octahedron

Table 1
Selected infrared and analytical data for $[MCl(CO)_2(\eta^3\text{-}CH_2C(COX)C{=}CH_2)L_2]$[g]

No.	X	L_2	Infrared data[a]			Analysis, found (calculated) %		
			ν(C≡O)	ν(C=O)	ν(NH)	C	H	N
6	$NHCH_2CH{=}CH_2$	bipy	1958, 1881	1639	3402	50.10 (50.05)	3.47 (3.75)	8.65 (8.75)
7	$NHCH_2CH{=}CH_2$	phen	1964, 1888	1647	3429		[e]	
8	NC_5H_{10}	bipy	1960, 1890	1609		51.38 (51.15)	4.64 (4.81)	7.63 (7.78)[f]
9[b]	$NHCH_2C{\equiv}CH$	bipy	1958, 1882	1654	3412	50.20 (50.26)	3.31 (3.35)	8.47 (8.79)
10	$N(CH_2CH{=}CH_2)_2$	Me_2phen	1980, 1896	1628			[e]	
11	$NHCH(Ph)CO_2Me$	Me_2phen	1970, 1890	1644, 1745	3408	47.81 (47.51)	3.54 (3.76)	5.46 (5.45)
12[c]	$OCH_2C{\equiv}CH$	phen	1973, 1897	1701			[e]	
13[d]	SCH_2CH_2SH	phen	1968, 1891	1637		46.37 (46.62)	2.84 (3.14)	5.55 (5.18)

[a] As nujol mulls, cm^{-1}.
[b] ν(C≡CH) 3256 cm^{-1}.
[c] ν(C≡CH) 3249 cm^{-1}.
[d] ν(SH) 2593 cm^{-1}.
[e] Non-reproducible results, highly insoluble or unstable.
[f] Calc. MeOH.
[g] M = Mo for all complexes, except **10**, **11** where M = W.

Table 2
^{1}H NMR data for complexes **6**–**13**[a]

No.	H'_{anti} H'_{syn}	H''_{anti} H''_{syn}	NH	Aliphatic	Aromatic
6	1.79 (s, H), 3.70 (s, H)	5.63 (d, 2.2, H), 6.27 (d, 1.9, H)	6.30 (t, 5.5, H)	2.79 (m, H), 3.02 (m, H), 4.77 (m, 2H), 5.13 (m, H)	7.96 (m, 2H), 8.17 (m, 2H), 8.50 (m, 2H), 8.69 (d, 4.4, H), 8.81 (d, 4.9, H)
7	1.86 (s, H), 3.84 (s, H)	5.74 (d, 2.2, H), 6.29 (d, 2.2, H)	6.15 (t, 5.8, H)	2.24 (m, H), 2.43 (m, H), 4.47 (m, 2H), 4.54 (m, H)	8.00 (m, 2H), 8.17 (s, 2H), 8.80 (m, 2H), 9.11 (d, 4.9, H), 9.24 (d, 4.9, H)
8	1.94 (s, H), 3.91 (s, H)	5.54 (d, 2.3, H), 6.09 (d, 2.4, H)		1.77 (m, 6H), 2.12 (m, H), 3.18 (m, H), 3.53 (m, 2H)	7.83 (m, 2H), 8.08 (m, 2H), 8.42 (m, 2H), 8.66 (m, H), 8.81 (m, H)
9	1.78 (s, H), 3.68 (s, H)	5.63 (d, 2.2, H), 6.25 (d, 2.5, H)	6.58 (t, 5.5, H)	2.84 (t, 2.22H), 3.07 (m, 2H),	7.64 (m, 2H), 8.16 (m, 2H), 8.5 (m, 2H), 8.68 (d, 4.4, H), 8.81 (d, 4.7, H)
10	1.91 (s, H), 3.69 (s, H)	5.62 (d, 2.2, H), 6.16 (d, 2.2, H)		3.30 (s, 3H), 3.35 (s, 3H), 3.75 (d, 5.502H), 4.05 (d, 5.50,2H), 5.14 (m, 4H), 5.71 (m, 2H)	7.78 (m, 2H), 7.90 (s, 2H), 8.40 (m, 2H)
11	1.88 (s, H), 1.95 (s, H), 3.46 (s, H), 3.70 (s, H)	5.43 (d, 1.3, H), 5.49 (d, 1.5, H), 6.34 (d, 1.5, H), 6.48 (d, 1.5, H)	5.79 (d, 7.5, H), 6.37 (d, 6.4, H)	3.20 (s, 3H), 3.32 (s, 3H), 3.33 (s, 3H), 3.35 (s, 3H), 3.43 (s, 3H), 3.62 (s, H), 3.66 (s, 3H), 3.86 (brs, H)	6.85–7.15 (m, 10H), 7.65–7.89 (m, 10H), 8.33 (d, 2.4, H), 8.36 (d, 2.4, H)
12	1.97 (s, H), 3.74 (s, H)	5.71 (d, 2.2, H), 6.23 (d, 2.2, H)		2.96 (m, H), 3.13 (m, 2H)	8.04 (m, 2H), 8.20 (s, 2H), 8.84 (m, 2H), 9.14 (m, H), 9.33 (m, H)
13	1.93 (s, H), 3.85 (s, H)	5.78 (d, 2.2, H), 6.31 (d, 2.2, H)		2.16 (m, 2H), 2.34 (m, 2H)	8.09 (m, 2H), 8.19 (s, 2H), 8.82 (m, 2H), 9.12 (d, 4.9, H), 9.28 (d, 4.9, H)

[a] Spectra recorded in DMSO-d_6. Data reported in ppm, multiplicity, coupling constant (Hz), number of protons.

if the central atom of the butadienyl based ligand (C14) is considered to be the point of attachment. The central molybdenum atom is bonded to two carbonyl groups [Mo1–C1 1.980(2) Å; Mo1–C2 1.976(2) Å], two nitrogens of 2,2′-bipyridine [Mo1–N1 2.2309(17) Å; Mo1–N2 2.2246(16) Å], a chlorine atom [Mo1–Cl1 2.4997(5) Å] and a 2-substituted butadienyl unit, C_8H_8NO. The metal–CO and carbonyl bond lengths [C1–O1 1.150(3) Å; C2–O2 1.147(3) Å] and angles [Mo1–C1–O1 179.3(2)°; Mo1–C2–O2 178.5(2)°], and the C1–Mo1–C2 bond angle [82.22(9)°], are all typical of a pair of mutually *cis* carbonyl groups. The rings of the bipyridine unit are approximately planar within experimental error, and their bond lengths and angles are similar to values found for related molybdenum η^3-allyl and η^3-pentadienyl bipyridyl complexes [13–15].

Within the butadienyl moiety, the C13–C14–C15 angle of 113.27(19)°, the C13–C14 and C14–C15 bond lengths

Table 3
Selected bond lengths (Å) and angles (°) for [MoCl(CO)$_2$(η^3-CH$_2$C(CONHCH$_2$C≡CH)C=CH$_2$)(bipy)] (**9**)

Mo1–C1	1.980(2)	Mo1–C13	2.300(9)
Mo1–C2	1.976(2)	Mo1–C14	2.228(8)
Mo1–N1	2.2309(17)	Mo1–C15	2.208(9)
Mo1–N2	2.2246(16)	C13–C14	1.423(3)
Mo1–Cl1	2.4997(5)	C14–C15	1.414(3)
C14–C17	1.495(3)	C15–C16	1.317(3)
C17–O3	1.226(3)	C1–O1	1.150(3)
C17–N3	1.346(3)	C2–O2	1.147(3)
N3–C18	1.456(4)	C18–C19	1.458(6)
		C19–C20	1.180(4)
C1–Mo1–C2	82.22(9)	C13–C14–C15	113.27(19)
N1–Mo1–N2	73.37(6)	C14–C15–C16	141.6(2)
O1–C1–Mo1	179.3(2)	O2–C2–Mo1	178.5(2)
C14–C17–O3	121.2(2)	O3–C17–N3	122.9(2)
C17–N3–C18	117.9(2)	N3–C18–C19	110.8(4)
C14–Mo1–N1	87.25(7)	C18–C19–C20	178.9(4)
C2–Mo1–C15	69.71(8)	C1–Mo1–C15	109.90(8)
C2–Mo1–N2	165.93(8)	C1–Mo1–N2	99.56(8)
C15–Mo1–N2	121.85(7)	C2–Mo1–C14	104.34(8)
C1–Mo1–C14	102.18(8)	C15–Mo1–C14	37.26(7)
N2–Mo1–C14	88.99(7)	C2–Mo1–N1	102.37(8)
C1–Mo1–N1	168.27(7)	C15–Mo1–N1	81.83(7)
C2–Mo1–C13	107.51(9)	C1–Mo1–C13	66.94(9)
C15–Mo1–C13	63.39(8)	N2–Mo1–C13	85.84(7)
C14–Mo1–C13	36.52(8)	N1–Mo1–C13	120.77(7)
C2–Mo1–Cl1	85.62(6)	C1–Mo1–C11	86.67(6)
C15–Mo1–C11	147.29(5)	N2–Mo1–C11	80.58(4)
C14–Mo1–C11	167.36(5)	N1–Mo1–C11	82.96(4)
C13–Mo1–C11	147.83(6)		

of 1.423(3) and 1.414(3) Å respectively, and the Mo1–C13 and Mo1–C14 separations of 2.300(9) and 2.228(8) Å are all similar to 1- and 2-substituted η^3-allyl complexes of molybdenum [16–18]. However the shorter Mo1–C15 distance of 2.208(9) Å may reflect an intermediate bond order between **1** and **2** that is not expected within an η^3-allyl system. (Compare [Mo(CO)$_2$(η^3-1-RC$_3$H$_4$)(phen)(O$_2$CCF$_3$)] R = H 2.316(5) Å, R = Me 2.411(13) Å.) Although the C15–C16 bond length of 1.317(3) Å is slightly longer than that observed for the related selenoester 2-substituted complex [1.242(13) Å], this value is consistent with related dienyl complexes of the type [Mo(CO)$_2$(η^3-CH$_2$CHC=CR^{1}R^2)L$_3$] (L$_3$ = Cp, Tp; R^1, R^2 = H, Me) [4,5,19]. A non-planar arrangement of hydrogen atoms at terminal atoms C13 and C16 suggests the double bond C15–C16 is not conjugated with respect to the C13–C14–C15 unit, and this should be reflected in the chemical reactivity. The amide group of the butadienyl fragment is approximately planar, with the carbonyl orientated away from the C=CH$_2$ terminus, and the propargyl substituent extends over the bipy ring system. The C18–C19–C20 angle of 178.9(4)° and the C19–C20 bond length of 1.180(6) Å are both in accord with this linear chain.

Asymmetry at the metal centre may occur in related complexes of the type [Mo(CO)$_2$(η^3-allyl)L$_2$Y] due to a non-dissociative trigonal twist rearrangement of L$_2$Y against the M(CO)$_2$(allyl) unit, and this may give rise to dynamic NMR spectra. For example, an asymmetric arrangement of L$_2$Y at the metal has been found in solution and solid states for bipy and phen complexes [Mo(CO)$_2$(η^3-RC$_3$H$_4$)L$_2$Y] (R = H, 1-Me) [13,16]. In contrast, solid state structures of **9** and its phen thioester (M = W, X = SBu) and selenoester (M = Mo, X = SePh) analogues all exhibit a symmetrical arrangement of the M(CO)$_2$L$_2$Cl unit [20,21] and their NMR solution spectra are non-complex and invariant over the temperature range −50 to 20 °C. Whilst allyl complexes [W(CO)$_2$(η^3-CH$_2$CRCH$_2$)L$_3$]$^+$ (L$_3$ = bis(2-methylpyridyl)amine) exhibit dynamic behaviour in solution at room temperature for both R = H and Me, and an asymmetric arrangement of the tridentate ligand has been shown in the solid state [22], fluxionality has not been reported for either [Mo(CO)$_2$(η^3-CH$_2$CHC=CH$_2$)Cp] or [Mo(CO)$_2$(η^3-CH$_2$CMeC=CH$_2$)Tp] [4,5]. A more detailed molecular orbital description of bonding in metal η^3-butadienyl complexes is required to explain these differences.

4. Conclusions

Complexes containing the η^3-CH$_2$C(COCl)C=CH$_2$ moiety can be synthesized from 1,4-dichloro-2-butyne by a one pot reaction with [M(CO)$_4$L$_2$] and Ph$_4$PCl. Chlorinated solvents with boiling points in the range 40–60 °C (M = Mo) or 83–96 °C (M = W) are required for this conversion, and at elevated temperatures destabilization of the butadienyl complex can occur to afford [MCl$_2$(CO)(η^2-ClCH$_2$C≡CCH$_2$Cl)L$_2$]. Preparation of the η^3-dienyl complex from one pot reactions involving [M(CO)$_6$] are hindered by this temperature requirement. Loss of CO below 60 °C (Mo) or 96 °C (W) is relatively slow and rate determining, and over the necessarily extended periods, increasing decomposition of dienyl product occurs. In contrast, conversion of the tetracarbonyl to [MCl(CO)$_3$L$_2$]$^-$ occurs more rapidly, and reaction in situ with the dichloroalkyne is fast. Thus under conditions for successful one pot production of the acyl chloride, addition of alcohols, amines or thiols generates the analogous ester, amide and thioester complexes, and in general these are found to have greater thermal stability below 120 °C. Both Mo and W complexes can also be obtained in the presence of water, however for the latter, formation of [WCl$_2$(CO)$_3$L$_2$] as a co-product reduces final yields. Comparison of the structure of propargyl amide **9** with related selenoester and thioester reveals a common arrangement of the acyl substituent and non-coordinated double bond. Isomers of these forms have not been observed in solution or solid states, and a combination of steric and electrostatic factors may explain the preferred orientation. Crystallographic data of all three complexes suggest pi-delocalization within the metal bound C1C2C3 unit is unconjugated with respect to C3=C4, and whilst these complexes may undergo similar reactions to substituted η^3-allyl analogues, the unusually short M–C3 bond length suggests direct parallels can't be assumed. Their behaviour with nucleophilic and electrophilic reagents is under investigation.

Appendix A. Supplementary material

CCDC 612555 contains the supplementary crystallographic data for the crystal structure reported in this paper. These data can be obtained free of charge via http://www.ccdc.cam.ac.uk/conts/retrieving.html, or from the Cambridge Crystallographic Data Centre, 12 Union Road, Cambridge CB2 1EZ, UK; fax: (+44) 1223-336-033; or e-mail: deposit@ccdc.cam.ac.uk. Supplementary data associated with this article can be found, in the online version, at doi:10.1016/j.poly.2006.10.040.

References

[1] (a) O. Boutry, M.L. Poveda, E. Carmona, J. Organomet. Chem. 528 (1997) 143;
(b) C.P. Casey, S. Chung, Y. Ha, D.R. Powell, Inorg. Chim. Acta 265 (1997) 127.
[2] (a) M. Ogasawara, H. Ikeda, T. Hayashi, Angew. Chem., Int. Ed. 39 (2000) 1042;
(b) M. Ogasawara, H. Ikeda, T. Nagano, T. Hayashi, Org. Lett. 3 (2001) 2615;
(c) M. Ogasawara, H. Ikeda, T. Nagano, T. Hayashi, J. Am. Chem. Soc. 123 (2001) 2089.
[3] S. Kezuka, K. Kanemoto, R. Takeuchi, Tetrahedron Lett. 45 (2004) 6403.
[4] N. Vinson, C.S. Day, M.E. Welker, Organometallics 19 (2000) 4356.
[5] D.R. Lantero, A.G. Glenn, C.S. Day, M.E. Welker, Organometallics 22 (2003) 1998.
[6] A.G.W. Hodson, R.K. Thind, O. Granville-George, J. Organomet. Chem. 689 (2004) 2114.
[7] B.J. Brisdon, D.A. Edwards, J.W. White, J. Organomet. Chem. 156 (1978) 427.
[8] G.M. Sheldrick, SHELX-97: Programs for Structure Solution and Refinement, University of Göttingen, Germany, 1997.
[9] G.M. Sheldrick, SADABS, Version 2.10, Bruker AXS Inc., Madison, WI, USA, 2003.
[10] L.W. Houk, G.R. Dobson, Inorg. Chem. 5 (1966) 2119.
[11] A.G.W. Hodson, J. Organomet. Chem. 691 (2006) 4747.
[12] (a) H.K. Saha, M.C. Halder, J. Inorg. Nucl. Chem. 34 (1972) 3097;
(b) P.C.H. Mitchell, J. Inorg. Nucl. Chem. 25 (1963) 963.
[13] J.R. Ascenso, C.G. de Azevedo, M.J. Calhorda, M.A.A.F. de C.T. Carrondo, P. Costa, A.R. Dias, M.G.B. Drew, V. Felix, A.M. Galvão, C.C. Romão, J. Organomet. Chem. 632 (2001) 197.
[14] S. Lush, S. Wang, G. Lee, S. Peng, S. Wang, R. Liu, Organometallics 9 (1990) 1862.
[15] M.D. Curtis, N.A. Fotinos, J. Organomet. Chem. 272 (1984) 43.
[16] L. Eriksson, M.P.T. Sjogren, B. Akermark, Acta Crystallogr. C 52 (1996) 77.
[17] P. Powell, J. Organomet. Chem. 129 (1977) 175.
[18] C. Borgmann, C. Limberg, E. Kaifer, H. Pritzkov, L. Zsolnai, J. Organomet. Chem. 580 (1999) 214.
[19] S.A. Benyunes, R.J. Deeth, A. Fries, M. Green, M. McPartlin, C.B.M. Nation, J. Chem. Soc., Dalton Trans. (1992) 3453.
[20] A.G.W. Hodson, R.K. Thind, M. McPartlin, J. Organomet. Chem. 664 (2002) 277.
[21] A.G.W. Hodson, G. Conole, Organometallics 17 (1998) 5347.
[22] B.J. Brisdon, M. Cartwright, A.G.W. Hodson, M.F. Mahon, K.C. Molloy, J. Organomet. Chem. 435 (1992) 319.

complexes with X-ray studies, $[M(ox)_2]$, for some divalent metals (Cu, Ni, Pd), reveal the bidentate monoanion mode of the ligand, resulting in a slightly distorted trans square-planar configuration for the chromophore MN_2O_2. Strong intramolecular hydrogen bonds between the phenolic oxygen and the hydrogen of the oximic hydroxyl were observed in all the cases [12–15]. In the case of cobalt, however, 2-hydroxy-aryloximato complexes were not reported systematically and crystal structures are limited to the square pyramidal complexes of the type $[Co(saox)_2NO]$ [16], and to the octahedral adducts with dimethylsulfoxide $[Co(saox)_2(dmso)_2]$ [17]. An analogous structure had been reported previously by us, for Ni adducts with phenanthroline $[Ni(saox)_2phen]$ [18].

Moreover, cobalt plays an important role among biologically active ions [3]. It has been found that the $[Co(III)(saox)_2(CH_3COO)]$ [19], inhibits 50% of leukemic cell proliferation, binds DNA strongly and also inhibits the relaxation activity to topoisomerase II. The biological activities of cobalt can be increased when mixed-ligand complexes with heterocyclic bases, such as bipy are involved. For example, the complex $[Co(III)(bipy)_2L]^{2+}$, where L = benzoylhydrazone derivative, a ligand with N and O donor atoms, shows DNA binding and antitumor activity [20].

Based on the above-mentioned applications and in order to fill the gap on structurally characterized cobalt 2-hydroxy-aryloximates, we report here the synthesis and structural study of 12 new mixed-ligand cobalt(III) complexes, under the general formula $[Co(oxime)(enR)_2]Br$, where oxime is the dianion of a 2-hydroxy-aryloxime (H_2oxime) and enR an α-diimine (bipy or phen). It is known that H_2saox usually behaves as bidentate monoanion [15] or as bridging dianion ligand between two metal centers in polynuclear complexes [21–24]. To the best of our knowledge, this is the second example of mononuclear 2-hydroxy-aryloximato complexes, where the ligand H_2saox acts as dianion (saox). The first example was reported for the complex [Co(III)(saox)triethyl tetramine]-Cl [25].

The new cationic Co(III) compounds were characterized by physicochemical and spectroscopic methods. The octahedral environment with CoN_5O chromophore was confirmed by X-ray diffraction analysis of the compound $[Co(saox)(bipy)_2]Br$ (**1**). Correlation between theoretical results and electronic excitation data were undertaken for the compound **1** and the results are presented and discussed. Cyclic voltammetry (CV) study was employed to investigate the electrochemical behavior of the prepared complexes.

The ligands 2-OH-aryloximes (H_2oxime) used in this work are: 2-OH, $C_6H_4CR{=}NOH$ [R = H (salicylaldoxime, H_2saox); R = CH_3 (acetophenonoxime, H_2apox); R = C_2H_5 (propiophenonoxime, H_2ppox); R = C_6H_5 (benzophenonoxime, H_2bpox)] or 2-OH, 3-MeO, $C_6H_3CH{=}NOH$ (3-methoxy-salicylaldoxime or *o*-vanillinoxime (H_2vanox)) and 2-OH, 5-Me, $C_6H_3C(CH_3){=}NOH$ (5-methyl-acetophenonoxime, H_2mpox) The crystal structure of one of the investigated oxime ligand, the 2-hydroxy-benzophenonoxime (H_2bpox) was also determined by X-ray analysis, verifying the strong intra-and intermolecular hydrogen bonds.

2. Experimental

2.1. Materials

The ligand 2-OH-benzaldoxime (salicylaldoxime, H_2saox), the 2,2′-bipyridine (bipy), the 1,10′-phenanthroline (phen) and the metal salt $CoBr_2 \cdot 6H_2O$ were obtained as reagent grade from Aldrich and used as received. The other 2-OH-aryloxime ligands (H_2oxime) and the precursor compounds $Co(bipy)_2Br_2$ and $Co(phen)_2Br_2$ were prepared according to the literature methods [26,27]. Solvents for preparation and physical measurements of "extra pure" were obtained from Fluka without further purification.

2.2. Instrumentation/analytical procedures

Microanalyses were obtained using a Perkin–Elmer 240 B CHN microanalyzer. Infrared spectra were recorded on a Perkin–Elmer 1600 FT-IR spectrometer in KBr discs at room temperature and are reported in cm^{-1}. Electronic absorption spectra in solutions were obtained on a Shimatzu 160 A spectrometer. The solid-state electronic spectrum was obtained from Nujol mull. The H NMR spectrum was recorded on a Bruker AM 300 (300 MHz) in $CDCl_3$ solution with TMS as internal standard. Molar conductivity was measured in DMF solution employing a WTW conductivity bridge and a calibrated dip type cell. Magnetic susceptibility measurement on powdered sample was performed at 25 °C employing the Faraday method on a home-build balance calibrated against $Hg[Co(SCN)_4]$. CV was used for the electrochemical measurements on a μ-AUTOLAB Potentio-Galvanostat (ECO CHEMIE, Netherlands). A saturated calomel electrode was used as a reference electrode and graphite one as an auxiliary electrode for all measurements. As a working electrode a platinum wire one was used. The tests in CH_3CN solution were carried out in the potential region −1800 to +2200 mV at ambient temperature. Recrystallized TEA perchlorate 0.1 M was used as the electrolyte at a scan rate of 100 mV/s. All scans were recorded in degassed solvent and under current of moisture free argon over the solution surface.

Computational techniques. All calculations have been performed using the GAUSSIAN-98 revision A11 package from Gaussian, Inc. Carnegie Office Park, Building 6 Carnegie, PA 15106, USA. Energy and orbitals calculation were performed using the B3LYP Density Functional Theory approximation. The basis set used was the LANL2DZ for all atoms. The prediction of the spectrum was calculated using CIS and ZINDO options.

2.3. Preparation of the complexes $[Co(oxime)(enR)_2]Br \cdot 2H_2O$

2.3.1. $[Co(saox)(bipy)_2]Br \cdot 2H_2O$

A solution of H_2saox (68.5 mg, 0.5 mmol) and CH_3ONa (54 mg, 1 mmol) in MeOH (20 mL), was added drop-wise to a solution of $Co(bipy)_2Br_2$ (0.266 g, 0.5 mmol) in H_2O (20 mL) at room temperature, under air. The brown solution (pH 8) was stirred for 2 h and then turned darker and a dark green solid was formed. The solid was filtered and washed with diethyl ether and dried under vacuum (0.22 g, 65% yield). The resulting powder analyzed as solvent free and bipyridine free. *Anal.* Calc. for $C_{27}H_{21}N_5O_2CoBr \cdot 2H_2O$ (MW 622): C, 52.09; H, 4.02; N, 11.25. Found: C, 51.82; H, 4.13; N, 10.80%. Conductivity in DMF = 65 μS/cm, $\mu_{eff} = 0$. IR (KBr): selected peaks in cm^{-1}: 3407 m, ν(OH crystal water); 1604 s and 1604 and 1590 s, ν(C=N); 1325 s, ν(–C–O); 1033 m and 916 m, ν(=N–O); 756, 773 s (double) and 729 s (pyridine molecules); 524 m, ν(Co–O); 474 m, ν(Co–N).

The newly prepared microcrystalline Co(III) compound is stable in air, soluble in almost all the organic solvents and in water, but insoluble in diethyl ether. Single crystals suitable for X-ray analysis were separated from the mother liquid by slow evaporation and characterized as $[Co^{III}(saox)(bipy)_2]Br \cdot 0.166bipy \cdot 0.15CH_3OH \cdot 1.75H_2O$.

2.3.2. $[Co(vanox)(bipy)_2]Br \cdot 2H_2O$

A solution of H_2vanox (83.5 mg, 0.5 mmol) and CH_3ONa (54 mg, 1 mmol) in MeOH (20 mL), was added drop-wise to a solution of $Co(bipy)_2Br_2$ (0.266 g, 0.5 mmol) in H_2O (20 mL) at room temperature, under air. The brown solution (pH 7.8) was stirred for 2 h and then turned darker and a dark green solid was formed. The solid was filtered and washed with diethyl ether and dried under vacuum (0.19 g, 58% yield). *Anal.* Calc. for $C_{28}H_{23}N_5O_3CoBr \cdot 2H_2O$ (MW 652): C, 51.53; H, 4.14; N, 10.73. Found: C, 52.31; H, 4.34; N, 10.40%. Conductivity in DMF = 68 μS/cm, $\mu_{eff} = 0$. IR (KBr): selected peaks in cm^{-1}: 3395 m, ν(OH crystal water); 1605 s and 1605 and 1596 s, ν(C=N); 1322 s, ν(–C–O); 1035 m and 896 m, ν(=N–O); 738, 767 s (double) and 730 s (pyridine molecules); 541 m, ν(Co–O); 446 m, ν(Co–N).

2.3.3. $[Co(apox)(bipy)_2]Br \cdot 2H_2O$

A solution of H_2apox (75.5 mg, 0.5 mmol) and CH_3ONa (54 mg, 1 mmol) in MeOH (20 mL), was added drop-wise to a solution of $Co(bipy)_2Br_2$ (0.266 g, 0.5 mmol) in H_2O (20 mL) at room temperature, under air. The brown solution (pH 7.8) was stirred for 2 h and then turned darker and a dark green solid was formed. The solid was filtered and washed with diethyl ether and dried under vacuum (0.24 g, 73% yield). *Anal.* Calc. for $C_{28}H_{23}N_5O_2CoBr \cdot 2H_2O$ (MW 636): C, 52.83; H, 4.24; N, 11.00. Found: C, 53.80; H, 4.20; N, 10.52%. Conductivity in DMF = 73 μS/cm, $\mu_{eff} = 0$. IR (KBr): selected peaks in cm^{-1}: 3401 m, ν(OH crystal water); 1605 s and 1605 and 1590 s, ν(C=N); 1315 s, ν(–C–O); 1018 m and 896 m, ν(=N–O); 738, 767 s (double) and 730 s (pyridine molecules); 513 m, ν(Co–O); 422 m, ν(Co–N).

2.3.4. $[Co(ppox)(bipy)_2]Br \cdot 2H_2O$

A solution of H_2ppox (82.5 mg, 0.5 mmol) and CH_3ONa (54 mg, 1 mmol) in MeOH (20 mL), was added drop-wise to a solution of $Co(bipy)_2Br_2$ (0.266 g, 0.5 mmol) in H_2O (20 mL) at room temperature, under air. The brown solution (pH 8) was stirred for 2 h and then turned darker and a dark green solid was formed. The solid was filtered and washed with diethyl ether and dried under vacuum (0.17 g, 52% yield). *Anal.* Calc. for $C_{29}H_{25}N_5O_2CoBr \cdot 2H_2O$ (MW 650): C, 53.53; H 4.46; N, 10.76. Found: C, 54.20; H, 4.52; N, 10.80%. Conductivity in DMF = 67 μS/cm, $\mu_{eff} = 0$. IR (KBr): selected peaks in cm^{-1}: 3400 m, ν(OH crystal water); 1604 s and 1604 and 1592 s, ν(C=N); 1319 s, ν(–C–O); 1020 m and 922 m, ν(=N–O); 742, 759 s (double) and 735 s (pyridine molecules); 530 m, ν(Co–O); 460 m, ν(Co–N).

2.3.5. $[Co(bpox)(bipy)_2]Br \cdot 2H_2O$

A solution of H_2bpox (106.5 mg, 0.5 mmol) and CH_3ONa (54 mg, 1 mmol) in MeOH (20 mL), was added drop-wise to a solution of $Co(bipy)_2Br_2$ (0.266 g, 0.5 mmol) in H_2O (20 mL) at room temperature, under air. The brown solution (pH 7.5) was stirred for 2 h and then turned darker and a dark green solid was formed. The solid was filtered and washed with diethyl ether and dried under vacuum (0.19 g, 54% yield). *Anal.* Calc. for $C_{33}H_{29}N_5O_2CoBr \cdot 2H_2O$ (MW 698): C, 56.73; H, 4.15; N, 10.02. Found: C, 57.78; H, 4.17; N, 10.08%. Conductivity in DMF = 78 μS/cm, $\mu_{eff} = 0$. IR (KBr): selected peaks in cm^{-1}: 3395 m, ν(OH crystal water); 1603 s and 1603 and 1585 s, ν(C=N); 1321 s, ν(–C–O); 1034 m and 951 m, ν(=N–O); 763, 781 s (double) and 736 s (pyridine molecules); 550 m, ν(Co–O); 498 m, ν(Co–N).

2.3.6. $[Co(mpox)(bipy)_2]Br \cdot 2H_2O$

A solution of H_2mpox (82.5 mg, 0.5 mmol) and CH_3ONa (54 mg, 1 mmol) in MeOH (20 mL), was added drop-wise to a solution of $Co(bipy)_2Br_2$ (0.266 g, 0.5 mmol) in H_2O (20 mL) at room temperature, under air. The brown solution (pH 7.6) was stirred for 2 h and then turned darker and a dark green solid was formed. The solid was filtered and washed with diethyl ether and dried under vacuum (0.21 g, 64% yield). *Anal.* Calc. for $C_{29}H_{25}N_5O_2CoBr \cdot 2H_2O$ (MW 650): C, 53.54; H, 4.46; N, 10.765. Found: C 54.43; H, 4.66; N, 10.76%. Conductivity in DMF = 67 μS/cm, $\mu_{eff} = 0$. IR (KBr): selected peaks in cm^{-1}: 3403 m, ν(OH crystal water); 1604 s and 1604 and 1576 s, ν(C=N); 1323 s, ν(–C–O); 1018 m and 892 m, ν(=N–O); 762, 780 s (double) and 736 s (pyridine molecules); 526 m, ν(Co–O); 497 m, ν(Co–N).

2.3.7. [Co(saox)(phen)$_2$]Br · 2H$_2$O

A solution of H$_2$saox (68.5 mg, 0.5 mmol) and CH$_3$ONa (54 mg, 1 mmol) in MeOH (20 mL), was added drop-wise to a solution of Co(phen)$_2$Br$_2$ (0.289 g, 0.5 mmol) in H$_2$O (20 mL) at room temperature, under air. The brown solution (pH 8) was stirred for 2 h and then turned darker and a dark green solid was formed. The solid was filtered and washed with diethyl ether and dried under vacuum (0.27 g, 80% yield). *Anal.* Calc. for $C_{31}H_{21}N_5O_2CoBr \cdot 2H_2O$ (MW 670): C, 55.52; H, 3.73; N, 10.44. Found: C, 56.18; H, 3.94; N, 10.03%. Conductivity in DMF = 69 μS/cm, $\mu_{eff} = 0$. IR (KBr): selected peaks in cm^{-1}: 3420 m, *ν*(OH crystal water); 1604 s and 1615 and 1589 s, *ν*(C=N); 1320 s, *ν*(–C–O); 1034 m and 913 m, *ν*(=N–O); 756, 842 s (double) and 719 s (pyridine molecules); 535 m, *ν*(Co–O); 473 m, *ν*(Co–N).

2.3.8. [Co(vanox)(phen)$_2$]Br · 2H$_2$O

A solution of H$_2$vanox (83.5 mg, 0.5 mmol) and CH$_3$ONa (54 mg, 1 mmol) in MeOH (20 mL), was added drop-wise to a solution of Co(phen)$_2$Br$_2$ (0.289 g, 0.5 mmol) in H$_2$O (20 mL) at room temperature, under air. The brown solution (pH 7.8) was stirred for 2 h and then turned darker and a dark green solid was formed. The solid was filtered and washed with diethyl ether and dried under vacuum (0.19 g, 54% yield). *Anal.* Calc. for $C_{32}H_{23}N_5O_2CoBr \cdot 2H_2O$ (MW 700): C, 54.85; H, 3.85; N, 10.00. Found: C, 54.07; H, 4.06; N, 10.72%. Conductivity in DMF = 70 μS/cm, $\mu_{eff} = 0$. IR (KBr): selected peaks in cm^{-1}: 3405 m, *ν*(OH crystal water); 1610 s and 1610 and 1587 s, *ν*(C=N); 1330 s, *ν*(–C–O); 1077 m and 966 m, *ν*(=N–O); 775, 844 s (double) and 719 s (pyridine molecules); 535 m, *ν*(Co–O); 433 m, *ν*(Co–N).

2.3.9. [Co(apox)(phen)$_2$]Br · 2H$_2$O

A solution of H$_2$apox (75.5 mg, 0.5 mmol) and CH$_3$ONa (54 mg, 1 mmol) in MeOH (20 mL), was added drop-wise to a solution of Co(phen)$_2$Br$_2$ (0.289 g, 0.5 mmol) in H$_2$O (20 mL) at room temperature, under air. The brown solution (pH 7.9) was stirred for 2 h and then turned darker and a dark green solid was formed. The solid was filtered and washed with diethyl ether and dried under vacuum (0.17 g, 49% yield). *Anal.* Calc. for $C_{32}H_{23}N_5O_2CoBr \cdot 2H_2O$ (MW 684): C, 56.14; H, 3.95; N, 10.23. Found: C, 56.13; H, 4.07; N, 10.86%. Conductivity in DMF = 78 μS/cm, $\mu_{eff} = 0$. IR (KBr): selected peaks in cm^{-1}: 3417 m, *ν*(OH crystal water); 1610 s and 1610 and 1590 s, *ν*(C=N); 1365 s, *ν*(–C–O); 1017 m and 940 m, *ν*(=N–O); 753, 841 s (double) and 720 s (pyridine molecules); 507 m, *ν*(Co–O); 449 m, *ν*(Co–N).

2.3.10. [Co(ppox)(phen)$_2$]Br · 2H$_2$O

A solution of H$_2$ppox (82.5 mg, 0.5 mmol) and CH$_3$ONa (54 mg, 1 mmol) in MeOH (20 mL), was added drop-wise to a solution of Co(phen)$_2$Br$_2$ (0.289 g, 0.5 mmol) in H$_2$O (20 mL) at room temperature, under air. The brown solution (pH 7.5) was stirred for 2 h and then turned darker and a dark green solid was formed. The solid was filtered and washed with diethyl ether and dried under vacuum (0.21 g, 60% yield). *Anal.* Calc. for $C_{33}H_{25}N_5O_2CoBr \cdot 2H_2O$ (MW 698): C, 56.73; H, 4.15; N, 10.02. Found: C, 56.63; H, 4.07; N, 9.70%. Conductivity in DMF = 73 μS/cm, $\mu_{eff} = 0$. IR (KBr): selected peaks in cm^{-1}: 3410 m, *ν*(OH crystal water); 1607 s and 1607 and 1580 s, *ν*(C=N); 1315 s, *ν*(–C–O); 1018 m and 920 m, *ν*(=N–O); 754, 846 s (double) and 719 s (pyridine molecules); 520 m, *ν*(Co–O); 476 m, *ν*(Co–N).

2.3.11. [Co(bpox)(phen)$_2$]Br · 2H$_2$O

A solution of H$_2$bpox (106.5 mg, 0.5 mmol) and CH$_3$ONa (54 mg, 1 mmol) in MeOH (20 mL), was added drop-wise to a solution of Co(phen)$_2$Br$_2$ (0.289 g, 0.5 mmol) in H$_2$O (20 mL) at room temperature, under air. The brown solution (pH 7.3) was stirred for 2 h and then turned darker and a dark green solid was formed. The solid was filtered and washed with diethyl ether and dried under vacuum (0.28 g, 75% yield). *Anal.* Calc. for $C_{37}H_{25}N_5O_2CoBr \cdot 2H_2O$ (MW 746): C, 59.51; H, 3.88; N, 9.38. Found: C, 59.84; H, 4.02; N, 8.88%. Conductivity in DMF = 75 μS/cm, $\mu_{eff} = 0$. IR (KBr): selected peaks in cm^{-1}: 3415 m, *ν*(OH crystal water); 1610 s and 1610 and 1585 s, *ν*(C=N); 1318 s, *ν*(–C–O); 1035 m and 950 m, *ν*(=N–O); 754, 841 s (double) and 729 s (pyridine molecules); 525 m, *ν*(Co–O); 458 m, *ν*(Co–N).

2.3.12. [Co(mpox)(phen)$_2$]Br · 2H$_2$O

A solution of H$_2$mpox (82.5 mg, 0.5 mmol) and CH$_3$ONa (54 mg, 1 mmol) in MeOH (20 mL), was added drop-wise to a solution of Co(phen)$_2$Br$_2$ (0.289 g, 0.5 mmol) in H$_2$O (20 mL) at room temperature, under air. The brown solution (pH 7.4) was stirred for 2 h and then turned darker and a dark green solid was formed. The solid was filtered and washed with diethyl ether and dried under vacuum (0.23 g, 66% yield). *Anal.* Calc. for $C_{33}H_{25}N_5O_2CoBr \cdot 2H_2O$ (MW 698): C, 56.73; H, 4.15; N, 10.02. Found: C, 57.08; H, 4.24; N, 9.76%. Conductivity in DMF = 70 μS/cm, $\mu_{eff} = 0$. IR (KBr): selected peaks in cm^{-1}: 3427 m, *ν*(OH crystal water); 1604 s and 1604 and 1592 s, *ν*(C=N); 1364 s, *ν*(–C–O); 1032 m and 900 m, *ν*(=N–O); 778, 843 s (double) and 720 s (pyridine molecules); 512 m, *ν*(Co–O); 455 m, *ν*(Co–N).

2.4. X-ray crystallography

Data for single crystals of titled compounds [Co(saox)(bipy)$_2$]Br · 0.166bipy · 0.15CH$_3$OH · 1.75H$_2$O and H$_2$bpox (Table 1) were collected with a Bruker SMART APEX CCD system with Mo Kα radiation ($\lambda = 0.7107$ Å) and corrected for absorption by semi-empirical methods (multi-scan). Both structures were solved by direct methods.

For the [Co(saox)(bipy)$_2$]Br structure the assignment of non-hydrogen atoms was immediate except for those present in the crystallographic mirror plane at $y = 1/4$. Many peaks appear at this plane in the ΔFmaps, the assignment

of which was not obvious, indicating considerable disorder of the structure at this plane. The two most intense peaks were assigned to bromine atoms with partial occupancy: after some trial and error, occupancies were fixed to optimize the refinement while keeping electrical neutrality of the compound. After this, a set of 12 weak peaks which roughly formed two hexagons were assigned as a non-coordinated bipyridine molecule with partial occupancy, which was introduced with fixed bond distances. Other weak peaks in this plane were assigned as partial occupancy water or methanol molecules (the latter introduced with constrained C–O distance). All full-occupancy non-hydrogen atoms were refined anisotropically as well as partial occupancy bromine atoms. Other partial occupancy atoms were refined isotropically. Hydrogen atoms of the organic moieties at general positions were placed at ideal positions as well as those of the bipy molecule at the mirror plane. Those belonging to water and methanol molecules were found by ΔFmaps and refined using soft constraints. Finally, all hydrogen positions were refined using riding constraints. The refinement on F^2 was performed using CRYSTALS version 12 [28] under a Chebyshev weighting scheme.[1]

All non-hydrogen atoms of the H_2bpox structure were refined anisotropically and all hydrogen atoms were found by ΔFmaps at their expected positions. The oximic and the phenoxy hydrogen atoms were refined using soft constraints to regularize their geometries. Finally, all hydrogen atoms were positioned at their ideal positions and refined using riding constraints. The refinement on F^2 was performed using SHELX-97 [29].

3. Results and discussion

3.1. Synthesis and characterization

The reaction of $[Co^{II}(enR)_2Br]Br$ with 2-hydroxy-aryloximes (H_2oxime) and nitrogenous bases enR, such as 2,2′-bipyridine (bipy) or 1,10′-phenanthroline (phen) under proper aerobic conditions lead to the formation of the green cobalt compounds. The elemental analyses, the electrical conductivity and the absence of magnetic moment (diamagnetic), indicated 1:1 electrolyte of the type $[Co^{III}(oxime)(enR)_2]Br \cdot 2H_2O$. The rare dianionic nature of the oximes, such as salicylaldoxime ($saox^{-2}$) in mononuclear complexes, is inferred from the absence of the stretching mode of the oximino hydroxyl group in the IR spectrum and the absence of the oximic proton signal, in the H NMR spectrum in $CDCl_3$, while for the free ligand is observed at ~3380 cm^{-1} and ~10.44 ppm, respectively [10]. This is further verified from the X-ray analysis discussed later.

3.2. Theoretical calculations and electronic excitation study

The excitation spectra of all the complexes presented five dominant bands in the region 200–900 nm in a series of solvents with different dielectric constant and as Nujol spreads. Two of them at the higher energies with high ε values (established at the region around 255 nm and 300 nm depending on the solvent) were attributed to intraligand $\pi^* \leftarrow \pi$ or $\pi^* \leftarrow n$ excitations and will not be further discussed. The three remaining bands around 340 nm, 400 nm and 670 nm can be attributed as follows: for the first as presenting an MLCT character (see below) and as d ← d transitions of Co(III) for the latest two. Table 2 presents the excitation bands (in wave lengths) together with the ε values for all the studied complexes. Table 3 presents the excitation and ε values in all the studied solvents for the complex $[Co(saox)(bipy)_2]Br$.

When recording the spectrum in organic solvents the arrangement effects of the dissolution, change the positions of the observed bands presenting a solvatochromic effect. The shape of the electronic spectra in the visible region even in solution or as a spread, as well as the low extinction coefficients, are suggestive of an octahedral configuration around the cobalt(III) ion. The positions of the absorption bands in the visible are in good agreement with other octahedral coordination compounds of Co(III) [20,30,31]. The bands II and III show a red shift due to the solvent polarity according to the solvent order Nujol > $CHCl_3$ > CH_3OH > CH_3CN > DMF as it can be seen in Fig. 1. The above d–d excitations in the visible can be attributed to the transition terms $^3T_{2g} \leftarrow {}^1A_{1g}$, and $^1T_{2g} \leftarrow {}^1A_{1g}$, respectively. The position of the Band I (MLCT), which is observed as shoulder at 340 nm is stable and does not depend on the solvent.

The main objective of the theoretical calculations was to explain the electronic excitation spectrum of the complexes using the geometry of the X-ray molecular structure determination of $[Co(saox)(bipy)_2]Br$, as well as the geometry of a slightly modified model in order to obtain a C_{4v} symmetry of the coordination sphere.

The predicted spectrum of the two slightly different complexes of $[Co(saox)(bipy)_2]Br$ in the asymmetric unit of the molecular structure, presents three dominant excitation bands in the visible region of the spectrum using the CIS theoretical approximation. For the one of the complexes in the asymmetric unit (see Section 3.3) these bands were calculated to be at 403 nm, 473 nm and 670 nm. For the second complex the three bands were predicted at 412 nm, 465 nm and 695 nm. All the above bands became of singlet excitations and their symmetry was undetermined. These transitions found all to have main participation from cobalt(III) d orbitals. Especially the orbitals involved are the $d_{xy} \leftarrow d_{z^2}$ for the transition at 670–695 nm, $d_{x^2-y^2} \leftarrow d_{z^2}$ for the one at 465–473 nm and

[1] Method, part 1, Chebychev polynomial (Watkin, 1994, Prince, 1982) $[weight] = 1.0/[A \sim 0 \sim {}^*T \sim 0 \sim (x) + A \sim 1 \sim {}^*T \sim 1 \sim (x) + \cdots + A \sim n-1 \sim]^*T \sim n-1 \sim (x)$ where $A \sim i \sim$ are the Chebychev coefficients listed below and $x = F_{calc}/F_{max}$. Method = Robust Weighting (Prince, 1982) $A \sim i \sim$ are: 9.68, 13.3, 4.23.

Table 1
Crystal data for $[Co(saox)(bipy)_2]Br \cdot 0.166bipy \cdot 0.15CH_3OH \cdot 1.75H_2O$ and H_2bpox

Empirical formula	$C_{28.81}H_{26.43}BrCoN_{5.33}O_{3.90}$	$C_{13}H_{11}NO_2$
Formula weight	648.67	213.23
Wavelength (Å)	0.71073	0.71073
Crystal system	orthorhombic	orthorhombic
Space group	*Pnma*	*Pbca*
Unit cell dimensions		
a (Å)	17.7483(1)	9.4668(7)
b (Å)	36.829(2)	8.8177(6)
c (Å)	17.3196(1)	25.9413(18)
Volume (Å^3)	11320.9(11)	2165.5(3)
Z	16 (8 asymmetric units and 2 formulas per asymmetric unit)	8
D_{calc} (Mg/m^3)	1.522	1.308
Absorption coefficient (mm^{-1})	2.062	0.089
$F(000)$	5277.6	896
Crystal size (mm)	$0.59 \times 0.37 \times 0.08$	$0.56 \times 0.37 \times 0.34$
θ Range for data collection (°)	1.11–28.34	1.57–28.29
Limiting indices	$-18 \leqslant h \leqslant 23$, $-49 \leqslant k \leqslant 48$, $-20 \leqslant l \leqslant 23$	$-12 \leqslant h \leqslant 12$, $-11 \leqslant k \leqslant 9$, $-33 \leqslant l \leqslant 31$
Reflections collected/unique (R_{int})	69 254/13 500 (0.0542)	12 832/2532 (0.0221)
Completeness	to $\theta = 26.92°$, 99.7%	to $\theta = 27.30°$, 98.9%
Absorption correction	semi-empirical from equivalents	none
Maximum and minimum transmission	0.8522 and 0.4242	
Refinement method	full-matrix least-squares on F^2	full-matrix least-squares on F^2
Weighting scheme	$w = [\text{weight}][1 - (\delta F/6\sigma F)^2]^2$	$w = 1/[\sigma^2(F_o^2) + (0.07P)^2 + 0.35P]$ where $P = (F_o^2 + 2F_c^2)/3$
Data/restraints/parameters	8040/23/745	2532/2/151
Goodness-of-fit on F^2	1.103	1.033
Final R indices [$I > 2\sigma(I)$]	$R_1 = 0.0306$, $wR_2 = 0.0728$	$R_1 = 0.0467$, $wR_2 = 0.1264$
R indices (all data)	$R_1 = 0.0406$, $wR_2 = 0.0870$	$R_1 = 0.0584$, $wR_2 = 0.1347$
Largest difference in peak and hole (e Å^{-3})	1.80 and −1.59	0.210 and −0.210

Table 2
Electronic excitation data for the [Co(oxime)(enR)$_2$]Br 10^{-4} M in CH_3CN

a/a	Compound	Band I, sh		Band II		Band III	
		λ (nm)	logε	λ (nm)	logε	λ (nm)	logε
1	[Co(saox)(bipy)$_2$]Br · 2H$_2$O	340	3.81	407	2.90	674	2.32
2	[Co(vanox)(bipy)$_2$]Br · 2H$_2$O	332	3.69	403	2.72	677	2.24
3	[Co(apox)(bipy)$_2$]Br · 2H$_2$O	338	3.72	401	2.88	672	2.19
4	[Co(ppox)(bipy)$_2$]Br · 2H$_2$O	339	3.85	409	2.80	675	2.30
5	[Co(bpox)(bipy)$_2$]Br · 2H$_2$O	337	3.86	406	2.84	679	2.36
6	[Co(mpox)(bipy)$_2$]Br · 2H$_2$O	341	3.78	411	2.96	676	2.20
7	[Co(saox)(phen)$_2$]Br · 2H$_2$O	330	3.72	400	2.64	678	2.19
8	[Co(vanox)(phen)$_2$]Br · 2H$_2$O	324	3.72	396	2.53	682	2.08
9	[Co(apox)(phen)$_2$]Br · 2H$_2$O	324	3.67	402	2.61	680	2.14
10	[Co(ppox)(phen)$_2$]Br · 2H$_2$O	320	3.73	398	2.55	685	2.11
11	[Co(bpox)(phen)$_2$]Br · 2H$_2$O	328	3.70	394	2.58	683	2.10
12	[Co(mpox)(phen)$_2$]Br · 2H$_2$O	322	3.72	400	2.59	686	2.15

Table 3
Electronic excitation data for the [Co(saox)(bipy)$_2$]Br in various solvents

Solvent	Band I, sh		Band II		Band III	
	λ (nm)	logε	λ (nm)	logε	λ (nm)	logε
$CHCl_3$	340	4.10	386	3.80	646	2.47
CH_3OH	340	3.31	400	2.92	653	2.30
CH_3CN	340	3.81	407	2.90	674	2.32
DMF	340	3.81	412	2.97	680	2.35

$d_{x^2-y^2} \leftarrow d_{yz}$ for the one at 403–415 nm. The two of the three doubly occupied obritals of Co(III), the HOMO − 1 (d_{yz}) and the HOMO − 2 (d_{xz}), were calculated to have nearly the same energy, while the energy of the HOMO (d_{z^2}) was considerably higher. As LUMO in both cases were found π^* orbitals from the ligands and further higher were found the d_{xy} and the $d_{x^2-y^2}$ orbitals. In this case it is clear that the equatorial plane contains the following four nitrogen atoms N1, N2, N3, N4. The axial positions were occupied from the rest bipy nitrogen, N5 and the phenolic oxygen from the oxime, O1. The final geometry of the model could be better described as compressed distorted octahedral.

Better results have been obtained when calculating the transition energies using the ZINDO approximation through GAUSSIAN-98. The calculated excitations in the visible were established at 594 nm (singlet-no symmetry), 442 nm (singlet-no symmetry) and 408 nm (triplet-no symmetry) while the orbitals were involved as follows: $d_{z^2} \leftarrow d_{xy}$ for the transition at 594 nm, $d_{x^2-y^2} \leftarrow d_{xy}$ for the one at 442 nm and $d_{x^2-y^2} \leftarrow d_{yz}$ for the one at 408 nm. The two cationic cobalt(III) complexes in this case were calculated to have excitation maxima difference less than 1 nm. The two of the three doubly occupied orbitals of Co(III), the HOMO − 1 (d_{yz}) and the HOMO − 2 (d_{xz}), were calculated to have nearly the same energy with values considerably lower than the energy value of the HOMO (d_{xy}). As LUMO and NLUMO π^* orbitals from the ligands were found, while the d_{z^2} and the $d_{x^2-y^2}$ orbitals lied at higher energies. The geometry in this case was assumed to be elongated distorted octahedral. The nitrogen atoms N1 and N3 are placed on the axial positions while the equatorial plane is formed from the atoms N2, O1, N4 and N5 with respect to the crystal molecular structure numbering. The orbitals arrangement also suggests that

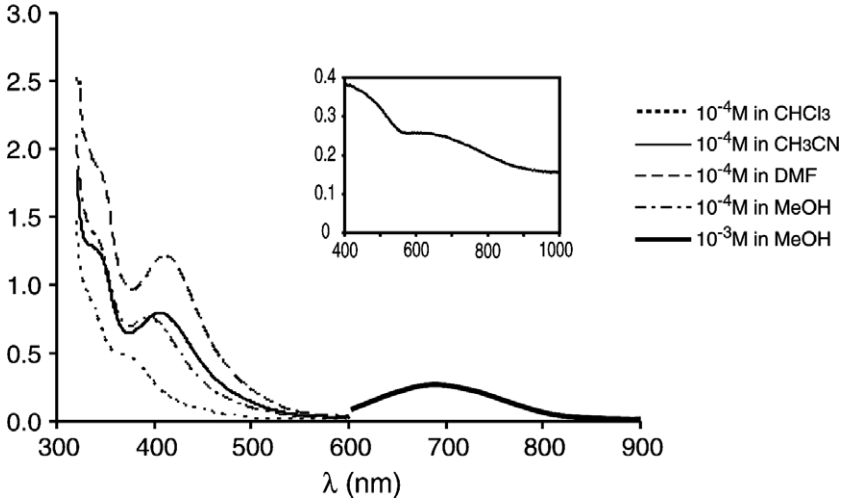


Fig. 1. Electronic excitation (UV/Vis) spectra for [Co(saox)(bipy)$_2$]Br in various solvents and in Nujol mull (in the window).

the bands present around 350 nm are mainly of MLCT character and this is in fairly agreement with the results found in analogous Co(III) complex with the Schiff-base salen (390 nm) [32].

The excitation energies especially from the ZINDO calculations were very close to those found from the experimental visible excitation spectrum of the complex in Nujol. The only difference is that the band around 442 nm was not clearly recorded as it was probably masked from the one around 408 nm which was much more intense. This is why the suggested complex geometry was elongated distorted octahedral as described previously.

In the case of a theoretical model, a mean distance of 1.94 Å from Co(III) for all nitrogen and oxygen atoms has been used. The symmetry of the coordination sphere was C_{4v}. After performing a ZINDO calculation the arrangement of the d orbitals of cobalt(III) differs from the one found from the crystal structure, obtaining the typical octahedral form and the excitations calculated were the following: 470 nm (singlet-B1) representing the $d_{x^2-y^2} \leftarrow d_{xy}$ transition and two nearly equal excitations around 400 nm both singlets with E symmetry representing the $d_{z^2} \leftarrow d_{xz}$ and the $d_{z^2} \leftarrow d_{yz}$ transitions. The energy difference between the HOMO (d_{xy}) and HOMO − 2 (d_{xz}) orbitals in this case was 0.001 eV while HOM − 1 (d_{yz}) and HOMO − 2 had equal energies. Both d_{z^2} and $d_{x^2-y^2}$ orbitals were found at higher positions (compared to the LUMO orbital which was a ligand antibonding orbital) with practically equal calculated energy values.

3.3. Description of the structures

The asymmetric unit of $[Co(saox)(bipy)_2]Br \cdot 0.166bipy \cdot 0.15CH_3OH \cdot 1.75H_2O$ contains two unicationic mononuclear Co(III) complexes with similar geometries. Each Co(III) is coordinated to one bis deprotonated dianionic oxime ligand and two bipy ligands in an octahedral arrangement of the coordination sphere. All distances and angles (Table 4) around cobalt have typical values for Co(III)–nitrogen and Co(III)–oxygen bonds and bonding angles [16a,33,34]. The charge of the complex cations is balanced by bromide anions, two of them placed at general positions with full and 0.2 occupancy, respectively, and the others disordered on three positions with occupancies 0.35, 0.30 and 0.15 on the mirror plane at $y = 1/4$; this adds up to two bromides per asymmetric unit (one per complex cation). The structure is completed by interstitial full occupancy water molecules at general positions and by disordered methanol and non-coordinated bipyridine molecule, both of them with partial occupancy on the mirror plane at $y = 1/4$. A strong hydrogen bonding net is present through all the water molecules hydrogen atoms and the bromine anions.

Concerning the two cobalt(III) complexes the geometry around the metal can be described as distorted octahedral. The nitrogen atoms N1 and N3 (Fig. 2) are placed on the axial positions. The equatorial plane is formed from the atoms N2, O1, N4 and N5. The cobalt(III) ion is placed on this plane with a deviation smaller than the error, while the maximum deviation is coming from the N(1) atom being 0.073(7) Å. The coordination sphere can then be described as elongated distorted octahedral. The two coordinated bipy molecules are planar as expected forming a dihedral angle of 93.86(12)° between them.

Table 4
Selected bond lengths (Å) and angles (°) for $[Co(saox)(bipy)_2]Br \cdot 0.166bipy \cdot 0.15CH_3OH \cdot 1.75H_2O$

Co(1)–N(1)	1.907(2)
Co(1)–N(2)	1.940(2)
Co(1)–N(3)	1.972(2)
Co(1)–N(4)	1.934(3)
Co(1)–N(5)	1.935(2)
Co(1)–O(1)	1.886(2)
N(1)–C(7)	1.299(4)
N(1)–O(2)	1.379(3)
O(1)–C(2)	1.315(3)
C(1)–C(2)	1.407(4)
C(1)–C(7)	1.449(4)
N(1)–Co(1)–N(2)	93.10(10)
N(1)–Co(1)–N(3)	175.55(10)
N(2)–Co(1)–N(3)	82.98(10)
N(1)–Co(1)–N(4)	86.38(11)
N(2)–Co(1)–N(4)	177.84(10)
N(3)–Co(1)–N(4)	97.62(11)
N(1)–Co(1)–N(5)	93.21(10)
N(2)–Co(1)–N(5)	94.61(10)
N(3)–Co(1)–N(5)	89.21(10)
N(4)–Co(1)–N(5)	83.33(10)
N(1)–Co(1)–O(1)	94.30(10)
N(2)–Co(1)–O(1)	91.06(9)
N(3)–Co(1)–O(1)	83.71(9)
N(4)–Co(1)–O(1)	91.07(10)
N(5)–Co(1)–O(1)	170.33(9)

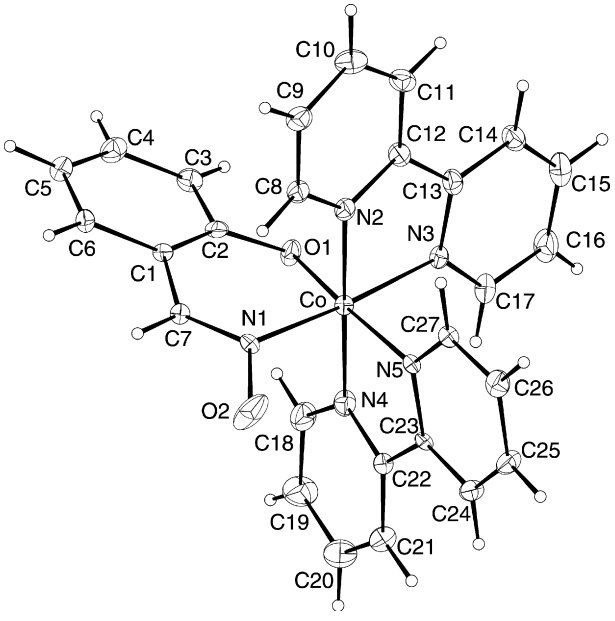


Fig. 2. Molecular structure of one of the cationic complexes $[Co(saox)(bipy)_2]^+$ in the asymmetric unit.

The bond distances between N1 and O2 as well as those between all atoms forming the oximic chelate ring are not equal to those found in two structures of similar compounds presented previously [25,35]. In our case they all have an intermediate value between the normal double and single bond. This fact lead to the conclusion that the oximic chelate ring in both complexes can be better described as an extended delocalized π system. This bis deprotonated oxime ligand is not quite planar presenting a maximum deviation from the mean plane of 0.238(7) Å for the oximic oxygen. The formed dihedral angles of the oxime mean plane with the two bipy ligands have values of 111.30(13)° and 85.15(12)°. Analogous plane distances and angles were obtained when studying the second Co(III) complex in the asymmetric unit.

The unit cell of the neutral ligand H_2bpox consists of eight molecules. All distances and angles (Table 5) are similar to those found in other oxime molecules in the literature. The phenoximic group (excluding the phenyl substitution) is planar with maximum deviation of 0.080(2) Å coming from C(7). The phenyl group is completely planar with deviations from the mean plane equal or smaller than the error and the formed angle between the planes was found to be 63.96(2)°. Strong intra-molecular hydrogen bond is formed between H(1) and N(1) with a distance between O(1) and N(1) of 2.558(2) Å. Inter-molecular hydrogen bond was also found between H(2) and O'(1) with symmetry operator $(1/2 + x,\ 1/2 - y,\ 1 - z)$. The distance O(2) to O′(1) was found to be 2.779(1) Å. These hydrogen bondings is keeping close pairs of molecules in the cell, forming four pairs in each cell, while each pair connected to its neighboring one, is finally forming a zig-zag chain of paired molecules along the a axis of the crystal (Fig. 3).

Table 5
Bond lengths (Å) and angles (°) for H_2bpox

C(1)–O(1)	1.3610(16)
C(1)–C(6)	1.382(2)
C(1)–C(2)	1.4068(18)
C(2)–C(3)	1.3960(18)
C(2)–C(7)	1.4767(18)
C(3)–C(4)	1.376(2)
C(4)–C(5)	1.374(2)
C(5)–C(6)	1.374(2)
C(7)–N(1)	1.2855(16)
C(7)–C(1P)	1.4959(17)
N(1)–O(2)	1.3922(14)
C(1P)–C(2P)	1.383(2)
C(1P)–C(6P)	1.387(2)
C(2P)–C(3P)	1.384(2)
C(3P)–C(4P)	1.369(3)
C(4P)–C(5P)	1.375(3)
C(5P)–C(6P)	1.379(2)
O(1)–C(1)–C(6)	117.80(12)
O(1)–C(1)–C(2)	121.99(12)
C(6)–C(1)–C(2)	120.21(12)
C(3)–C(2)–C(1)	117.21(12)
C(3)–C(2)–C(7)	120.79(11)
C(1)–C(2)–C(7)	122.00(11)
C(4)–C(3)–C(2)	121.95(13)
C(5)–C(4)–C(3)	119.80(14)
C(4)–C(5)–C(6)	119.85(14)
C(5)–C(6)–C(1)	120.95(14)
N(1)–C(7)–C(2)	116.81(11)
N(1)–C(7)–C(1P)	123.20(12)
C(2)–C(7)–C(1P)	119.94(11)
C(7)–N(1)–O(2)	113.97(10)
C(2P)–C(1P)–C(6P)	119.49(13)
C(2P)–C(1P)–C(7)	120.24(13)
C(6P)–C(1P)–C(7)	120.27(13)
C(1P)–C(2P)–C(3P)	120.00(17)
C(4P)–C(3P)–C(2P)	120.00(19)
C(3P)–C(4P)–C(5P)	120.50(16)
C(4P)–C(5P)–C(6P)	119.89(18)
C(5P)–C(6P)–C(1P)	120.10(17)

3.4. Electrochemical study

Cyclic voltammetry experiments were performed with pre-purified crystalline fine powder solutions of the compounds (crystals treated with diethyl ether in order to get the compound free from the crystalline bipy or phen and solvent). A typical voltavogram gave primarily three well separated reversible anodic waves close to 0.39 V, 0.73 V and 1.07 V (Fig. 4). Two more irreversible waves

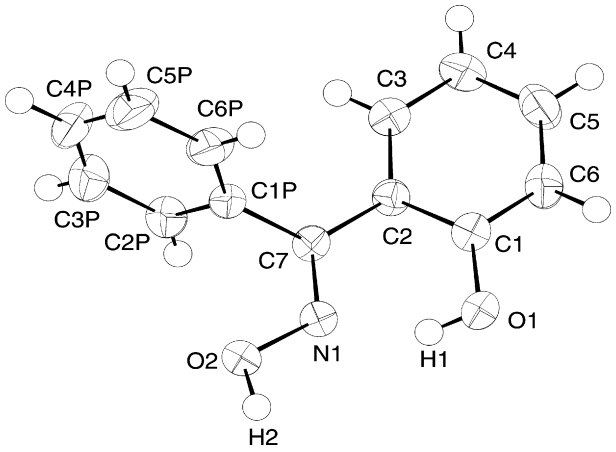


Fig. 3. Molecular structure of H_2bpox.

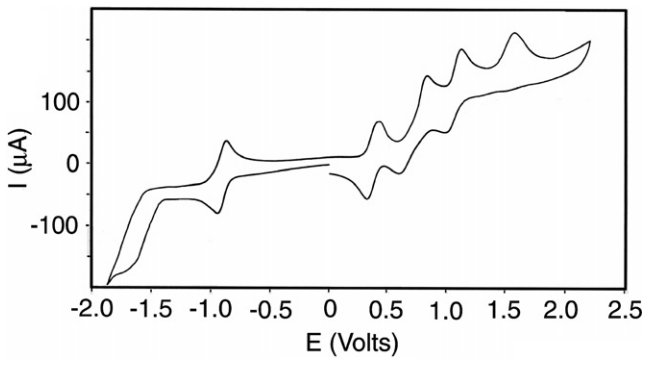


Fig. 4. Cyclic voltammogram of $[Co(saox)(bipy)_2]Br$ in CH_3CN with 0.1 M TEAP (scan rate 100 mV/s).

Table 6
Cyclic voltammetry data (mV) for [Co(oxime)(enR)$_2$]Br in CH_3CN with 0.1 M TEAP (scan rate 100 mV/s)

Compound	Potentials (V)													
	I			II			III			IV			V	VI
	E_{pa}	E_{pc}	$E_{1/2}$	E_{pa}	E_{pc}	$E_{1/2}$	E_{pa}	E_{pc}	$E_{1/2}$	E_{pa}	E_{pc}	$E_{1/2}$	E_{pa}	E_{pc}
1	−0.85	−0.93	−0.89	0.44	0.34	0.39	0.84	0.60	0.72	1.14	0.98	1.06	1.58	−1.77
2	−0.85	−0.91	−0.88	0.43	0.35	0.39	0.85	0.60	0.73	1.14	0.99	1.06	1.49	−1.63
3	−0.86	−0.94	−0.90	0.44	0.33	0.38	0.84	0.62	0.71	1.15	1.00	1.07	1.56	−1.71
4	−0.85	−0.93	−0.89	0.45	0.35	0.40	0.85	0.61	0.72	1.14	0.99	1.06	1.74	−1.55
5	−0.84	−0.92	−0.88	0.44	0.35	0.40	0.82	0.59	0.72	1.16	0.97	1.05	1.61	−1.64
6	−0.86	−0.94	−0.90	0.42	0.35	0.38	0.82	0.58	0.71	1.15	0.98	1.06	1.58	−1.71
7	−0.84	−0.92	−0.88	0.43	0.33	0.38	0.89	0.65	0.75	1.15	1.02	1.08	1.57	−1.75
8	−0.86	−0.93	−0.90	0.44	0.35	0.40	0.92	0.66	0.74	1.18	1.00	1.09	1.50	−1.63
9	−0.85	−0.91	−0.88	0.43	0.34	0.39	0.91	0.66	0.73	1.17	1.00	1.09	1.55	−1.69
10	−0.85	−0.92	−0.89	0.43	0.34	0.39	0.93	0.65	0.74	1.18	1.01	1.09	1.71	−1.54
11	−0.85	−0.93	−0.89	0.43	0.34	0.38	0.92	0.65	0.74	1.17	0.99	1.08	1.59	−1.65
12	−0.86	−0.94	−0.90	0.44	0.34	0.39	0.94	0.66	0.75	1.19	1.00	1.10	1.57	−1.73

were present at ca 1.50 V and at −1.75. Finally, the last reversible wave was in the cathodic region at ca −0.89 V as shown in Table 6, which contains the full experimental data of the electrochemical behavior of the studied compounds.

The waves at −0.89 V and 0.39 V are corresponding to the couples Co(I/II) and Co(II/III), respectively. These values are very close to them found from the cyclic voltammetry of similar compounds [36–38]. The rest of the reversible waves at 0.72 V and 1.06 V are assigned to the oxidation of the bipyridine rings, while the phenanthroline rings seemed to be oxidized a little higher at ca 0.74 V and 1.09 V. The oxidation of the oxime ligands could be attributed to the waves at ca 1.50 V up to 1.80 V, while the reductions appear at ca −1.4 V down to −1.8 V depending on the oxime ligand. The latest is in accordance with the waves found when studying the electrochemical behavior of the free oxime ligands under the same experimental conditions. The oxidation waves in the cases of [Co(saox)(bipy)$_2$]Br and [Co(ppox)(phen)$_2$]Br were found at 1.58 V and 1.74 V, respectively, while the reduction waves were found to be at −1.77 V and −1.55 V (Figs. 4 and 5).

The waves assigned to the redox potentials of the free oxime ligands, as well as of the oxime ligands in the complexes, represent two-electron fermentations for ppox, apox, mpox and bpox. For vanox and saox, however, we observe one-electron oxidation waves and two-electron reduction waves. It is possible that the second oxidation wave is outside the studied voltage region. It is worthy to be mentioned that in the voltamograms of H_2ppox and H_2apox free ligands, two well separated oxidation waves were observed, each one representing one-electron, while in the cases of H_2bpox and H_2mpox one wave representing two electrons. All the rest waves on the voltavograms of the complexes represent one-electron transformations, as compared with the waves generated by equimolar amount of ferrocene solution.

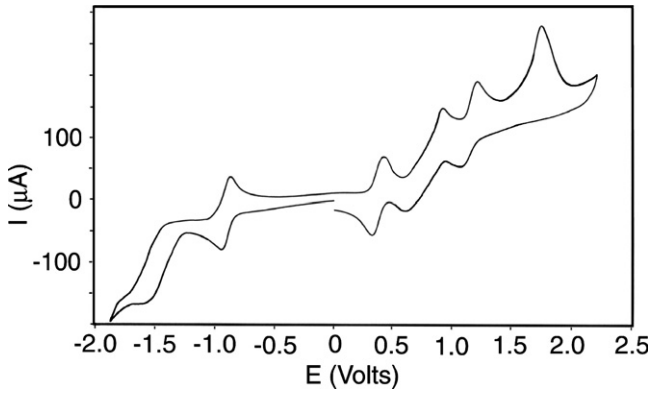


Fig. 5. Cyclic voltammogram of [Co(ppox)(phen)$_2$]Br in CH_3CN with 0.1 M TEAP (scan rate 100 mV/s.).

4. Conclusions

In the novel complexes [Co(oxime)(enR)$_2$]Br · 2H_2O, with octahedral arrangement of the chromophore CoN_5O, the rare for mononuclear Co(III) complexes, bidentate dianion character of the oxime ligand is established. The theoretical investigation with GAUSSIAN-98 for the prediction of the electronic spectrum and especially the ZINDO calculations, gave good correlation with the experimental spectrum in the solid state of the complex [Co(saox)(bipy)$_2$]Br. The cyclic voltammetry study gave all the expected waves for the redox processes of the metal Co(III) and the oxime ligands, as well as for the α-diimines bipy and phen.

Appendix A. Supplementary material

CCDC 292952 and 622386 contain the supplementary crystallographic data for this paper. These data can be obtained free of charge via http://www.ccdc.cam.ac.uk/conts/retrieving.html, or from the Cambridge Crystallographic Data Centre, 12 Union Road, Cambridge CB2 1EZ, UK; fax: (+44) 1223-336-033; or e-mail: deposit@ccdc.cam.ac.uk. Supplementary data associated with this article can be found, in the online version, at doi:10.1016/j.poly.2006.10.047.

References

[1] M.E. Keeney, K. Osseo-Asare, K.A. Woode, Coord. Chem. Rev. 59 (1984) 141.
[2] V.Yu. Kukuskin, D. Tudela, A.J.J. Pombeiro, Coord. Chem. Rev. 156 (1996) 333.
[3] V.Yu. Kukuskin, A.J.J. Pombeiro, Coord. Chem. Rev. 181 (1999) 147.
[4] M. Lalia-Kantouri, in: G. Ondrejovic, A. Sirota (Eds.), Monograph Series of the International Conferences on Coordination Chemistry, vol. 4, Slovak Technical University Press, Bratislava, 1999, p. 97.
[5] J. Szymanowski, Al. Borowiak-Resterna, Crit. Rev. Anal. Chem. 22 (1991) 519.
[6] S. Nishihama, N. Sakaguchi, T. Hirai, I. Komasawa, Ind. Eng. Chem. Res. 39 (2000) 4986.
[7] Y. Zhu, Q. Yang, H. Zheng, W. Yu, Y. Quian, Mater. Chem. Phys. 91 (2005) 293.
[8] M. Lalia-Kantouri, M. Hartophylles, Polyhedron 11 (1992) 789.
[9] M. Lalia-Kantouri, M. Hartophylles, Thermochim. Acta 224 (1993) 203.
[10] M. Lalia-Kantouri, M. Hartophylles, P.D. Jannakoudakis, G.P. Voutsas, Z. Anorg. Allg. Chem. 621 (1995) 645.
[11] (a) M. Hartophylles, M. Lalia-Kantouri, J. Therm. Anal. 48 (1997) 1365;
(b) M. Lalia-Kantouri, J. Therm. Anal. Cal. 82 (2005) 791.
[12] G.P. Voutsas, K.G. Keramidas, M. Lalia-Kantouri, Polyhedron 15 (1996) 147.
[13] A.G. Hatzidimitriou, M. Uddin, M. Lalia-Kantouri, Z. Anorg. Allg. Chem. 623 (1997) 627.
[14] G.P. Voutsas, K.G. Keramidas, E. Dova, M. Lalia-Kantouri, M. Hartophylles, Z. Kristallogr. NCS 214 (1999) 33.
[15] A. Smith, P. Tasker, D. White, Coord. Chem. Rev. 241 (2003) 61.
[16] (a) L.F. Larkworthy, D.C. Povey, J. Crystallogr. Spectrosc. Res. 13 (1983) 413;
(b) M. Gallagher, M.F.C. Ladd, L.F. Larkworthy, D.C. Povery, K.A.R. Sailo, J. Crystallogr. Spectrosc. Res. 16 (1986) 967.
[17] D. Cupertino, M. McParitin, A.M. Zissimos, Polyhedron 20 (2001) 3239.
[18] M. Lalia-Kantouri, A. Hatzidimitriou, M. Uddin, Polyhedron 18 (1999) 3441.
[19] D. Jayaraju, Y.N. Vashisht Gopal, A.K. Kondapi, Arch. Biochem. Biophys. 369 (1999) 68.
[20] S. Srinirasam, J. Annaraj, PR. Athappan, J. Inorg. Biochem. 99 (2005) 876.
[21] E. Bill, C. Krebs, M. Wintwer, M. Gerdan, A.X. Trautwein, U. Florke, H.J. Haupt, P. Chaudhuri, Chem. Eur. J. 3 (1997) 193.
[22] P. Chaudhuri, M. Hess, T. Weyhermuller, E. Bill, H.J. Haupt, U. Florke, Inorg. Chem. Commun. 1 (1998) 39.
[23] J. Thorpe, R.L. Beddoes, D. Collison, C.D. Garner, M. Helliwell, J.M. Holmes, P.A. Tasker, Angew. Chem., Int. Ed. 38 (1999) 1119.
[24] C.P. Raptopoulou, Y. Sannakis, A.K. Boudalis, V. Psycharis, Polyhedron 24 (2005) 711.
[25] E. Toyota, K. Umakoshi, Y. Yamamoto, Bull. Chem. Soc. Jpn. 68 (1995) 858.
[26] G.N. Walker, R.T. Smith, J. Org. Chem. 36 (1971) 305.
[27] Th. Kramer, J. Strahle, Z. Naturforsch. B 41 (1986) 962.
[28] P.W. Betteridge, J.R. Carruthers, R.I. Cooper, K. Prout, D.J. Watkin, J. Appl. Crystallogr. 36 (2003) 1487.
[29] G.M. Sheldrick, SHELX-97, University of Göttingen, Göttingen, Germany, 1997.
[30] N.Ch. Saha, R.J. Butcher, S. Chaudhuri, N. Saha, Polyhedron 22 (2003) 383.
[31] A. Bottcher, T. Takeuchi, K.I. Hardcastle, Th.J. Meade, H.B. Gray, Inorg. Chem. 36 (1997) 2498.
[32] A.A. Khandar, B. Shaabani, F. Belaj, A. Bakhtiari, Polyhedron 25 (2006) 1893.
[33] R.P. John, A. Streekanth, M.R.P. Kurup, S.M. Mobin, Polyhedron 21 (2002) 2515.
[34] Xi-Xue Hu, Ch.-Ling Pan, Ji-Qung Xu, Xiao-Bing Cui, Guang-Di Yang, Tie-Gang Wang, Eur. J. Inorg. Chem. (2004) 1566.
[35] P.S. Reddy, K.H. Reddy, Polyhedron 19 (2000) 1687.
[36] H. Shimakoshi, M. Koga, Y. Hisaeda, Bull. Chem. Soc. Jpn. 75 (2002) 1553.
[37] S.K.H. Rahaman, H. Chowdhury, D. Bose, R. Ghosh, Chen-H. Hung, B.K. Ghosh, Polyhedron 24 (2005) 1755.
[38] K.M. Kadish, in: St.J. Lippard (Ed.), Progress in Inorganic Chemistry, vol. 34, Wiley, New York, 1986, p. 515.

ing Q^- and a tridentate Schiff-base, interesting chemistry was observed. When $Ti(O^iPr)_4$ reacted with (2-hydroxyphenyl)salicylideneimine in the presence of a large excess of 8-hydroxyquinoline, only Ti(IV)-Schiff-base complex precipitate was obtained initially. However, another Ti(IV) complex containing both Schiff-base and 8-hydroxyquinolinate was obtained only after standing for a long period of time. The mechanism of the delayed formation of the mixed-ligand complex was investigated and the results are reported herein. Though Schiff-bases are well known as versatile ligands [9], the literature on their complexes with Ti(IV) are limited, more specifically there are only few Ti(IV) complexes with tridentate Schiff-base being reported so far [10].

2. Experimental

2.1. Physical measurement

^1H NMR spectra were recorded on a Bruker AC-400 spectrometer. ^{13}C NMR spectra were measured on a Bruker Avence 600 NMR spectrometer. Elemental analyses were carried out in a Heraeus CHN Rapid Analyzer. Mass spectrum was recorded on a JOEL JMS-SX 102 high resolution mass spectrometer.

2.2. Synthesis of *N*-(2-hydroxyphenyl)salicylideneimine$_2$ Sap [11]

In a round bottom flask, 2-aminophenol 5.45 g (50 mmol) was dissolved in 90 mL dried THF at elevated temperature under nitrogen atmosphere. Salicylaldehyde 6.11 g (50 mmol) in THF was added drop-wise to this THF solution. The reaction mixture was heated under refluxing condition. Orange precipitates were observed within 10 min. Reaction was continued for 1 h. Filtering, washing the precipitate with toluene, and drying in a vacuum oven at 60 °C, orange crystal (9.34 g, 89%) was obtained. M.p. 110 °C. Elemental *Anal.* Calc. for $C_{13}H_{11}NO_2$: C, 73.23; H, 5.20; N, 6.57. Found: C, 73.28; H, 5.33; N, 6.61%. The ^1H NMR data are consistent with the literature values.

2.3. Synthesis of bis[*N*-(2-oxophenyl)-salicylideneiminato]titanium(IV), Ti(Sap)$_2$

Under nitrogen atmosphere, $Ti(O^iPr)_4$ 0.16 mL (0.50 mmol) was transferred to a 90 mL dried methanol solution containing *N*-(2-hydroxyphenyl)salicylideneimine (H_2Sap) 0.21 g (1.0 mmol). Red solid suspension formed immediately. Reaction was continued for 1.5 h. Filtering, washing with methanol, and drying in a vacuum oven at 80 °C, red solid product 0.21 g (0.45 mmol) was obtained. Yield: 90%. Decomposition temperature: 375 °C. δ_H (400 MHz, CD_3OD:CD_2Cl_2 (3:1), Me_4Si) 6.395 (2H, d, Ar), 6.634 (2H, d, Ar), 6.825 (2H, t, Ar), 6.980 (2H, t, Ar), 7.066 (2H, t, Ar), 7.465 (2H, m, Ar), 7.534 (2H, d, Ar), 7.705 (2H, d, Ar), 9.136 (2H, s, CH=N). δ_C (150 MHz, DMSO-d_6, Me_4Si) 113.81, 115.83, 116.12, 119.49, 120.21, 121.94, 130.08, 135.08, 136.99, 138.43, 159.05, 160.92, 162.78. Elemental *Anal.* Calc. for $TiC_{26}H_{18}N_2O_4$: C, 66.40; H, 3.86; N, 5.96. Found: C, 66.30; H, 3.86; N, 5.86%. HRMS. M^+: 470.0740 (calc. 470.0746).

2.4. Synthesis of *N*-(2-oxophenyl)salicylideneiminato-8-hydroxyquinolinato methoxotitanium(IV), Ti(Sap)Q(OMe)

2.4.1. Method I

Under a nitrogen atmosphere, a 5 mL dried methanol solution containing $Ti(O^iPr)_4$ 0.18 mL (0.58 mmol) was added to a 5 mL dried methanol solution containing 8-hydroxyquinoline 0.15 g (1.03 mmol). Then a 90 mL dried methanol solution containing *N*-(2-hydroxyphenyl)salicylideneimine (H_2Sap) 0.11 g (0.52 mmol) was added to the reaction mixture. The solution became cloudy immediately with red solid suspension, which then precipitated. After stirring for additional 1.5 h, the solution was left standing overnight. Fine red crystals grew on the wall of the reaction vessel. These crystals were collected, washed with methanol and dried in air. The single crystals were subjected to X-ray diffraction studies.

2.4.2. Method II

$Ti(O^iPr)_4$ 0.10 mL (0.31 mmol) was added to a 80 mL methanol solution containing *N*-(2-hydroxyphenyl)salicylideneimine (H_2Sap) 57 mg (0.27 mmol). The solution became turbid with red solid suspension, then became clear after heating to 60 °C for 10 min. A 5 mL methanol solution containing HQ 0.39 g (2.69 mmol) was added to this clear solution. The resulting clear red solution was maintained at 60 °C under stirring for 30 min. The solution was then chilled down rapidly to 10 °C by immersing in cold water. The resulting small amount of precipitates identified by ^1H NMR to be Ti(Sap)$_2$ were removed by filtering. The volume of the filtrate was then reduced to 30 mL, solid product Ti(Sap)Q(OMe) 0.043 g (0.10 mmol) was then obtained by filtration and drying in a vacuum oven. Yield: 32% based on Ti. δ_H 400 MHz, (400 MHz, CD_3OD:CD_2Cl_2 (3:1), Me_4Si) 6.343 (1H, d, Ar), 6.488 (1H, d, Ar), 6.784 (1H, t, Ar), 6.863 (1H, t, Ar), 6.972 (1H, d, Ar), 7.023 (1H, t, Ar), 7.310–7.368 (3H, m, Ar), 7.557 (1H, t, Ar), 7.588 (2H, d, Ar), 8.232 (1H, d, Ar), 8.293 (1H, d, Ar), 9.109 (1H, s, CH=N). δ_C (150 MHz, CD_3OD:CD_2Cl_2 (3:1), Me_4Si) 53, 111.36; 111.41; 115.04; 115.35; 115.63; 117.13; 117.32; 119.27; 119.68; 121.76; 121.95; 129.37; 129.80; 129.99; 130.54; 134.76; 136.66; 138.61; 138.82; 145.66; 146.04; 158.08. Elemental *Anal.* Calc. for $TiC_{23}H_{18}N_2O_4$: C, 63.61; H, 4.18; N, 6.45. Found: C, 64.55; H, 4.03; N: 6.42%.

2.5. Preparation of (μ-oxo)-bis[N-(2-oxophenyl)-salicylideneiminato-8-hydroxyquinolinatotitanium(IV)]

Under nitrogen atmosphere, a 5.0 mL dried methanol solution containing $Ti(O^iPr)_4$ 0.018 mL (0.058 mmol) was added to a 5 mL dried methanol solution containing 8-hydroxyquinoline 0.075 g (0.50 mmol) in a round bottom flask. Then a 90 mL methanol dried solution containing *N*-(2-hydroxyphenyl)salicylideneimine 0.011 g (0.052 mmol) was added to the round bottom flask. Red suspension of $Ti(Sap)_2$ was formed immediately. The reaction mixture was stirred for additional 1.5 h. To this mixture, 100 mL of acetonitrile (not going through rigorous drying procedure) was added. After standing for two days, few pieces of red single crystals were formed on the wall of the round bottom flask. These single crystals were characterized by X-ray diffraction method to be $[Ti(Sap)Q]_2(\mu\text{-}O)$. δ_H (400 MHz, CD_3OD:CD_2Cl_2 (3:1), Me_4Si) 6.339 (2H), 6.475 (2H), 6.954 ~ 7.043 (6H), 7.074 (2H), 7.271 (2H), 7.343 (2H), 7.576 (2H), 7.639 (2H), 7.661 (2H), 7.706 (2H), 8.362 (2H), 8.522 (2H), 9.193 (2H).

2.6. X-ray crystallography

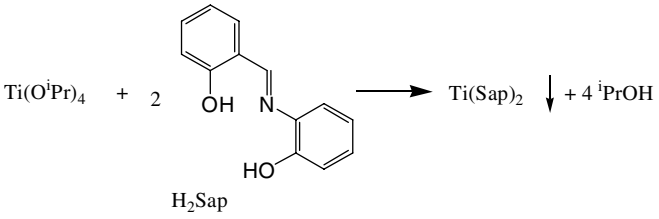
The red prism single crystal ($0.58 \times 0.62 \times 0.80$ mm) of Ti(Sap)Q(OMe) was obtained directly from its preparative solution of method I. Red plate single crystal ($0.20 \times 0.40 \times 0.60$ mm) of $[Ti(Sap)Q]_2(\mu\text{-}O)$ were also obtained directly from its preparative solution. Both crystals of Ti(Sap)Q(OMe) and $[Ti(Sap)Q]_2(\mu\text{-}O)$ were sealed in glass capillaries. Diffraction data measurements were recorded on Rigaku AFC7S diffractometer with graphite monochromated Mo Kα radiation for both Ti(Sap)Q(OMe) and $[Ti(Sap)Q]_2(\mu\text{-}O)$. Empirical absorption corrections were made. The structures were solved by direct method [12], and expanded using Fourier techniques. All non-hydrogen atoms were refined anisotropically. The imine moieties of the Sap^{2-} ligands in both structures were disordered. They were refined with fixed s.o.f's (0.65/0.35 for Ti(Sap)-Q(OMe) and 0.5/0.5 and 0.65/0.35 for the two Sap^{2-} ligands in $[Ti(Sap)Q]_2(\mu\text{-}O)$, respectively). All hydrogen atoms (including those on disordered imine moieties) assumed their calculated positions with riding model. The crystal data, important information on the diffraction data collections and refinements of structural data are presented in Table 1.

Table 1
Some crystallographic data and results of structural refinements for Ti(Sap)Q(OMe) and [Ti(Sap)Q](μ-O)

	Ti(Sap)Q(OMe)	$[Ti(Sap)Q]_2(\mu\text{-}O)$
Formula	$C_{23}H_{18}N_2O_4Ti$	$C_{44}H_{30}N_4O_7Ti_2 \cdot (CH_3CN)$
Temperature	298	298
Crystal system	triclinic	triclinic
Space group	$P\bar{1}$	$P\bar{1}$
a (Å)	7.828(1)	10.626(2)
b (Å)	10.221(1)	12.521(3)
c (Å)	13.547(2)	15.851(3)
α (°)	111.46(1)	76.79(2)
β (°)	90.38(2)	72.52(3)
γ (°)	105.11(1)	76.52(3)
V (Å^3)	967.5(3)	1927.4(8)
Z	2	2
Number of reflections collected	3609	7936
Number of independent reflections (R_{int})	3403(0.009)	7572(0.025)
Number of observed/ restraint/parameters	2592/0/301	4250/0/577
R_1	0.036	0.042
wR_2	0.097	0.108
Goodness-of-fit	1.05	1.00
Maximum difference in peak and hole/(e Å^{-3})	0.24 and −0.26	0.32 and −0.29

3. Results and discussion

The reaction between $Ti(O^iPr)_4$ and *N*-(2-hydroxyphenyl)salicylideneimine (H_2Sap), a tridentate Schiff-base ligand, in a stoichiometric ratio in dried methanol solution, produced a red solid product with high yield 90%. The product was identified by ^1H NMR, $^{13}C\{1H\}$ NMR, high resolution mass spectrometry and elemental analysis to be consistent with $Ti(Sap)_2$. This reaction can be summarized by



H_2Sap

(1)

Attempt to prepare titanium complexes containing both Sap^{2-} and Q^- (8-hydroxyquinolinate) failed when the amounts of the reactants were in the stoichiometric ratio of $Ti(O^iPr)_4$:H_2Sap:HQ = 1:1:1. Only a red precipitate, identified by ^1H NMR to be $Ti(Sap)_2$, was obtained. When the amount of HQ was increased up to 10 equiv. reaching a reactant molar ratio of $Ti(O^iPr)_4$:H_2Sap:HQ = 1:1:10, again only red precipitates $Ti(Sap)_2$ were obtained. We tried several combinations of the ratios of reactants, even with less than stoichiometric H_2Sap, $Ti(Sap)_2$ precipitate was always obtained as the only initial product. However, when the reaction mixture with 2 equiv. HQ was left in the reaction vessel overnight, some small red single crystals formed on the wall of reaction vessel. These single crystals were identified by X-ray diffraction study to be Ti(Sap)Q(OMe). The methoxide group in this compound originated from solvent. If wet acetonitrile was added to a reaction mixture with 10-fold excess of HQ before standing for two days, then different red single crystals, identified by X-ray diffraction study to be $Ti[(Sap)Q]_2(\mu\text{-}O)$, were grown on the wall of reaction vessel.

The color of Ti(Sap)Q(OMe) is red which is different from the orange color of $TiQ_2(O^iPr)_2$. Therefore, introducing the Schiff-base ligand into the coordination sphere of Ti(IV) do change its color as expected. The problem is how to prepare Ti(Sap)Q(OMe) in large quantity. This can be accomplished only after the mechanism of the reaction of $Ti(OR)_4$ with HQ and H_2Sap is understood.

One approach to obtain Ti complex containing both Sap^{2-} and Q^- as major product is to use $TiQ_2(O^iPr)_2$ as a starting reactant. This approach would work if the reason for failing to obtain Ti(Sap)Q(OR) from a mixture of $Ti(O^iPr)_4$, H_2Sap and HQ in methanol was because H_2Sap had a high reaction rate in coordinating to Ti(IV) center to precipitate out as $Ti(Sap)_2$ before HQ can coordinate to Ti(IV), i.e., the rate of reaction of H_2Sap to Ti(IV) is much faster than that of HQ. When Ti(IV) is pre-coordinated with two Q^- ligands, then the rate of the reaction of HQ with Ti(IV) played no role in forming Ti(IV) complex with both Sap^{2-} and Q^-. Therefore, if the ratio of reactants $TiQ_2(O^iPr)_2$:H_2Sap is 1:1, one would expect to see a mixed ligand complex Ti(Sap)Q(OMe) as a major product. Experimentally, the direct reaction between $TiQ_2(O^iPr)_2$ and H_2Sap yielded $Ti(Sap)_2$ as the initial precipitate even in the presence of excess $TiQ_2(O^iPr)_2$ up to 10-fold excess.

To understand the unusual behavior of the reaction between $TiQ_2(OR)_2$ and H_2Sap, it was monitored by ^1H NMR spectra. The ^1H NMR spectrum of a solution of $TiQ_2(O^iPr)_2$ in CD_3OD:CD_2Cl_2 (3:1) mixed solvent, recorded three minutes after the addition of H_2Sap with a molar ratio of 1 to 1 showed the presence of $Ti(Sap)_2$ together with HQ and unreacted $TiQ_2(OR)_2$ (OR is most likely OCD_3 due to rapid exchange with solvent) and H_2Sap. Red solid suspension of $Ti(Sap)_2$ could be seen in the reaction mixture. However, there was no sign of the formation of Ti(Sap)Q(OR). After 10 min of reaction, the ^1H NMR spectrum indicated that the reaction of H_2Sap with $TiQ_2(OR)_2$ proceeded continuously, signals of HQ increased, H_2Sap decreased and a set of small new signals corresponding to Ti(Sap)Q(OR) was detected. After 30 min of reaction, the ^1H NMR spectrum was similar to that obtained at 10 min reaction time except the relative intensities corresponding to H_2Sap and $TiQ_2(OR)_2$ were decreasing, while those for HQ and Ti(Sap)Q(OR) were increasing and those for $Ti(Sap)_2$ remained unchanged. After 1 h reaction time, the ^1H NMR signals became steady. At this stage, three drops of deuterated water was added to the NMR tube. The signals of $Ti(Sap)_2$ and Ti(Sap)Q(OR) disappeared. After standing for additional hour, signals attributed to $[Ti(Sap)Q]_2(\mu\text{-}O)$ and $[TiQ_2(\mu\text{-}O)]_4$ were observed.

These ^1H NMR results provided insight into the mechanistic pathways for the formation of the products obtained in our experiment. One interesting finding in the ^1H NMR spectral monitoring of the reaction between H_2Sap and $TiQ_2(OR)_2$ was that no trace of Ti(Sap)Q(OR) was detected initially. One expects that formation of $Ti(Sap)_2$ from the reaction between $TiQ_2(OR)_2$ and H_2Sap should be a stepwise process, as depicted in Eqs. (2) and (3), instead of simultaneous reaction of two molecules of H_2Sap with $TiQ_2(OR)_2$

$$TiQ_2(OR)_2 + H_2Sap \rightleftharpoons Ti(Sap)Q(OR) + HQ + ROH \quad (2)$$

$$Ti(Sap)Q(OR) + H_2Sap \rightleftharpoons Ti(Sap)_2 + HQ + ROH \quad (3)$$

To be consistent with the observation of the initial absence of Ti(Sap)Q(OR), this compound must be formed and reacted immediately with H_2Sap. In other word, the rate of reaction of H_2Sap toward Ti(Sap)Q(OR) is much higher than that toward $TiQ_2(OR)_2$. In this initial stage, most Ti(Sap)Q(OR) formed reacts immediately with H_2Sap leading to the absence of its ^1H NMR signal. As the reaction proceeds to completion, the concentration of H_2Sap decreases leading to reduced forward rates for both Eqs. (2) and (3). In the mean time, the concentration of HQ increases resulting in increased reverse rates. If the reverse rate of Eq. (3) is fast, then one expect to see the build-up of Ti(Sap)Q(OR) at sufficient low concentration of H_2Sap and sufficient high concentration of HQ.

To investigate the reversibility of the reaction in Eq. (3), the ^1H NMR spectra of a saturated solution of $Ti(Sap)_2$ in CD_3OD:CD_2Cl_2 (3:1) were examined in the presence of large amount of HQ with a molar ratio greater than 5. Immediately after the addition of HQ to the $Ti(Sap)_2$ solution, signals due to $Ti(Sap)Q(OCD_3)$ and H_2Sap appeared besides those of saturated $Ti(Sap)_2$. In addition, the integrated intensities of signals indicated that $Ti(Sap)Q(OCD_3)$ and H_2Sap were formed with equal concentrations. The ^1H NMR spectrum remained unchanged after the initial measurement. It indicated that the equilibrium in Eq. (3) was reached within the time scale of sample preparation for NMR measurement. From the integrated intensities of the four species in solution, the apparent equilibrium constant K_3 in Eq. (3) is calculated to be 60 M. This experiment demonstrated unequivocally that the reaction in Eq. (3) is reversible. In this experiment, $TiQ_2(OR)_2$ was not observed within experimental limit, it implies that the apparent equilibrium constant K_2 for Eq. (2) is in favor of products under these experimental conditions. To estimate K_2, the ^1H NMR spectra used to monitor the reaction of excess $TiQ_2(OR)_2$ with H_2Sap were examined. The integrated intensities of non-overlapping signals for $TiQ_2(OR)_2$, Ti(Sap)Q(OR), HQ and H_2Sap at equilibrium in CD_3OD (18 M)/CD_2Cl_2 (3/1) allowed us to determine the apparent equilibrium constants $K_2 = 10$ M. Based on the concentration-calibrated ^1H NMR integrated signal intensities of the above two ^1H NMR experiments, the apparent solubilities of $Ti(Sap)_2$ and $Ti(Sap)Q(OCD_3)$ are 5.0×10^{-3} M and 1.4×10^{-2} M, respectively. Obviously, the solubilitiy of $Ti(Sap)_2$ is about three times lower than that Ti(Sap)Q(OR). When D_2O is added to the reaction mixture of $TiQ_2(O^iPr)_2$ and H_2Sap, the ^1H NMR spectra showed the disappearance of $Ti(Sap)_2$ and Ti(Sap)Q(OR) and appearance of $[Ti(Sap)Q]_2(\mu\text{-}O)$ and $[TiQ_2(\mu\text{-}O)]_4$.

The disappearance of $Ti(Sap)_2$ was due to its reduced solubility in the presence of water. The disappearance of Ti(Sap)Q(OR) was due to its reaction with water to form $[Ti(Sap)Q]_2(\mu\text{-O})$ as depicted in:

$$2Ti(Sap)Q(OR) + D_2O \rightarrow [Ti(Sap)Q]_2(\mu\text{-O}) + 2ROD \quad (4)$$

This equation can be used to account for the formation of the red single crystals of $[Ti(Sap)Q]_2(\mu\text{-O})$ when wet acetonitrile was added to the reaction mixture of $Ti(O^iPr)_4$, H_2Sap and HQ. The formation of $[TiQ_2(\mu\text{-O})]_4$ is due to the known reaction between $TiQ_2(OR)_2$ with water as depicted in [7]:

$$4TiQ_2(OR)_2 + 4H_2O \rightarrow [TiQ_2(\mu\text{-O})]_4 + 8ROH \quad (5)$$

Therefore, the formation of $Ti(Sap)_2$, Ti(Sap)Q(OMe) and $[Ti(Sap)Q]_2(\mu\text{-O})$ from the reaction of $Ti(O^iPr)_4$ and H_2Sap and HQ can be satisfactorily accounted for by Eqs. (2)–(4). To isolate large amount of Ti(Sap)Q(OMe), we tried to overcome the formation of precipitate of $Ti(Sap)_2$ by elevating the reaction temperature to 60 °C. When H_2Sap (0.27 mmol) was added to 80 mL methanol solution of $Ti(O^iPr)_4$ (0.31 mmol), the precipitates of $Ti(Sap)_2$ were formed immediately. When the solution temperature was raised to 60 °C, the precipitate dissolved. At this temperature, a clear red solution was obtained when large excess of HQ (2.69 mmol) was added. After the resulting mixture was cooled down to 10 °C, some initial precipitate, identified to be $Ti(Sap)_2$, was removed by filtration. When the volume was reduced to 30 mL, precipitates of Ti(Sap)Q(OMe) were obtained at 32% yield based on Ti. Thus we have found a procedure to prepare large amount of the Ti(IV) complex coordinated simultaneously by tridentate, bidentate and monodentate ligands.

The structure of Ti(Sap)Q(OMe) and its atomic numbering are shown in Fig. 1. Some relevant bond distances and bond angles are collected in Table 2. The Ti atom is octahedrally coordinated by one nitrogen atom and one oxygen atom of 8-hydroxyquinolinate ligand, one nitrogen atom and two oxygen atoms of *N*-(2-oxophenyl)salicylideneiminate ligand, and one oxygen atom of methoxide ligand. The two oxygen atoms of Sap^{2-} are *trans* to each other, as expected from the planar structure of this ligand. Indeed, all atoms on the Sap^{2-} ligand are essentially co-planar with mean deviation of 0.08 Å. However, the O2–Ti1–O3 angle of 157.6° is far from the ideal 180; presumably because Ti atom is too large to fit into the linear position. This may be one of the main reason why Sap^{2-} is labile when coordinated to Ti(IV). Both nitrogen atoms are trans to oxygen atoms; ∠O1–Ti1–N2 (161.4) and ∠O4–Ti1–N1 (169.6) are closer to 180 than ∠O2–Ti1–O3. N1–Ti1–O4 is particularly close to linear because the methoxide ligand can adjust its position without constraint. The bite angle of Q^- is 75°. This is quite close to the O3–N2 bite angle of Sap^{2-}. On the other hand, the bite angle of O2–N2 with Ti atom is 86° which is substantially larger than those for the five-member rings.

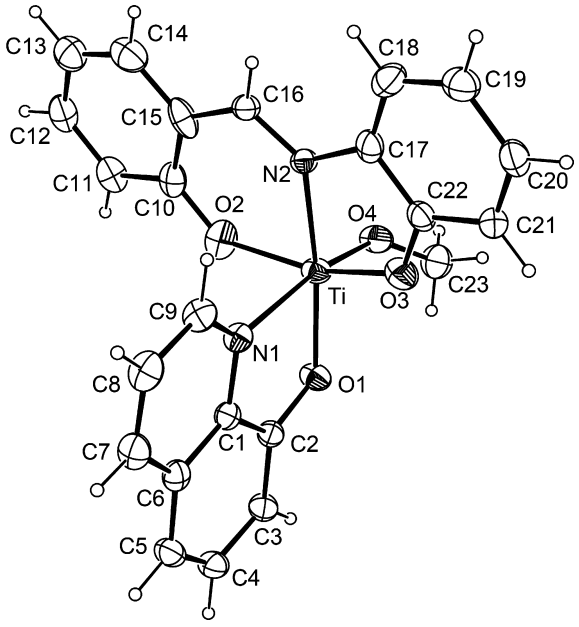


Fig. 1. Molecular plot of Ti(Sap)Q(OMe). Thermal ellipsoids represent 30% probability.

The Ti–O distances are at least 0.3 Å shorter than any Ti–N distance. This is due to the formation of partial double Ti–O bond by the donation of oxygen lone-paired electrons into the empty π-orbitals on Ti(IV). Ti1–O4 is particularly short because the methoxide can be positioned to maximize the formation of partial double bond. The detailed comparison of Ti–N distances is somewhat unreliable due to the fact that the imine group is disordered. The bond angles between O4–Ti1 and the four *cis* atoms are all larger than 90° (O1: 94.2°; O2: 96.1°; N2: 103.6°/N2A: 105.5°; O3: 95.1°), indicating that Ti is situated above the O1–O2–N2–O3 plane toward O4. Indeed Ti is 0.24(8) Å above the least square plane O1–O2–N2–O3 whose maximum planar deviation is within 0.09 Å.

The disorder in the Ti(Sap)Q(OMe) complex resulted from the 180° flip-over of the Sap^{2-} ligand. Their occupancies (s.o.f's) for the two orientations are fixed to 0.65 for N2/C16/H16 and 0.35 for N2A/C16A/H16A, respectively.

The structure of $[Ti(Sap)Q]_2(\mu\text{-O})$ and its atomic numbering are shown in Fig. 2. Some relevant bond distances and bond angles are collected in Table 1. Both Ti1 and Ti2 are octahedrally coordinated by one oxygen atom and one nitrogen atom of Q^- ligand, two oxygen atoms and one nitrogen atom of Sap^{2-} ligand, and one oxygen atom of the bridging oxide ligand. The bond distances and bond angles around the two Ti(IV) centers are remarkably similar to the corresponding ones in Ti(Sap)Q(OMe) when the bridging oxide ligand is viewed as taking the place of methoxide ligand. The similarities around each Ti center, taking Ti1 as an example, include: (a) N1–Ti1–O4 is the one that is closest to the linear arrangement comparing to other *trans* atom1–Ti1–atom2 arrangements; (b) the bite angles for five-member rings are all very similar; (c) the

Table 2
Relevant bond distances and bond angles of Ti(Sap)Q(OMe) and $[Ti(Sap)Q]_2(\mu\text{-}O)$

	Ti(Sap)Q(OMe)	$[Ti(Sap)Q]_2(\mu\text{-}O)$	
Ti1–O1	1.910(2)	1.891(2) [Ti1–O2]	1.897(2) [Ti2–O5]
Ti1–N1	2.297(2)	2.298(3)	2.317(3) [Ti2–N3]
Ti1–O2	1.898(2)	1.894(3) [Ti1–O3]	1.880(3) [Ti2–O7]
Ti1–O3	1.895(2)	1.915(3) [Ti1–O4]	1.906(3) [Ti2–O6]
Ti1–N2	2.20(1)[a]	2.21(5)[a] [Ti1–N2]	2.20(1)[a] [Ti2–N4]
Ti1–O4	1.790(2)	1.806(2) [Ti1–O1]	1.814(2) [Ti2–O1]
N2–C16	1.29(2)[a]	1.28(3)[a]	1.27(3)[a] [N4–C38]
∠O1–Ti1–N2	158(3)	157(1) [∠O2–Ti1–N2]	156(2) [∠O5–Ti2–N4]
∠N1–Ti1–O4	169.60(8)	176.8(1) [∠N1–Ti1–O1]	174.9(1) [∠N3–Ti2–O1]
∠O2–Ti1–O3	157.6(1)	157.7(1) [∠O3–Ti1–O4]	157.5(1) [∠O6–Ti2–O7]
∠O1–Ti1–N1	75.44(7)	75.6(1) [∠O2–Ti1–N1]	75.6(1) [∠O5Ti–2N3]
∠O2–Ti1–N2	86.0(2)	89.5(2) [∠O4–Ti1–N2]	86.7(2) [∠O7–Ti2–N4]
∠O3–Ti1–N2	72.5(1)	69.8(2)	72.2(2) [∠O6–Ti2–N4]
∠O4–Ti1–O1	94.21(8)	101.2(1) [∠O1–Ti1–O2]	100.1(1) [∠O1–Ti1–O5]
∠O4–Ti1–O2	96.1(1)	96.3(1) [∠O1–Ti1–O4]	95.0(1) [∠O1–Ti2–O6]
∠O4–Ti1–N2	103.6(1)	100.6(2) [∠O1–Ti1–N2]	100.9(2) [∠O1–Ti2–N4]
∠O4–Ti1–O3	95.1(1)	95.7(1) [∠O1–Ti1–O3]	95.0(1) [∠O1–Ti2–O6]
∠Ti1–O4–Ti2		154.0(2)	

[a] Averaged value of two disordered parts.

Ti1–O4 bond distance is particularly short; (d) the Ti1–N2 distance is noticeably shorter than that of Ti1–N1; (e) the Ti1 is above the O1–O2–N2–O3 plane toward the O4 atom. The Ti1–O4–Ti2 angle is 154.0° indicating the Sap^{2-} ligands are not parallel to each other; a dihedral angle 7.2° exists between these two ligands.Similar flip-over disorders in Sap^{2-} were found in the $[Ti(Sap)Q]_2(\mu\text{-}O)$ complex. The two Sap^{2-} ligands were assigned with different ratio of occupancies (s.o.f's): 0.5/0.5 (N2/C16/H16 vs. N2A/C16A/H16A) for one ligand, 0.65/0.35 (N4/C38/H38 versus N4A/C38A/H38A) for another.

The bonding parameters of some known structures of titanium(IV) complexes containing 8-hydroxyquinolinate ligand [7,8,13–17] fall in the narrow ranges: Ti–O(Q): 1.87–1.96 Å; Ti–N(Q): 2.20–2.29 Å; and bite angle: 75–77°. The structural parameters between Ti and Q^- of

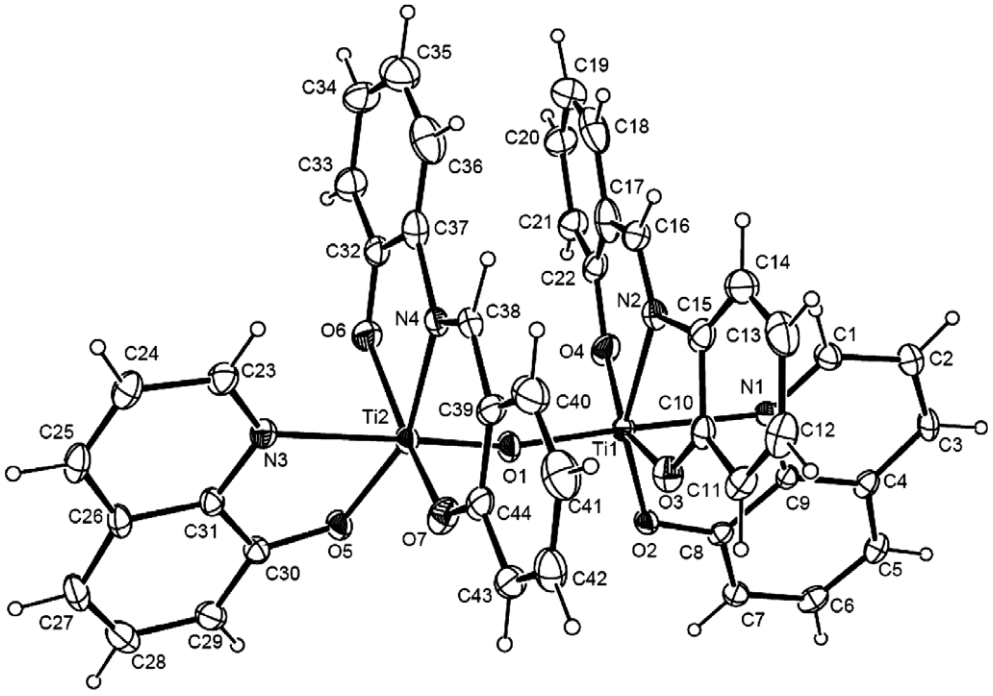


Fig. 2. Molecular plot of $[Ti(Sap)Q]_2(\mu\text{-}O)$. Thermal ellipsoids represent 30% probability.

the two compounds reported in this work are also in these narrow ranges. The bonding parameters between Ti(IV) and the Sap^{2-} ligand in both Ti(Sap)Q(OMe) and $[Ti(Sap)Q]_2(\mu\text{-}O)$ are comparable to those reported in $Ti[4,6\text{-}^tBu\text{-}2\text{-}\{CH{=}N(2\text{-}C_6H_4O)\}C_6H_3O]_2$ [9a]. However, large biting angles for the six member rings (86° versus 81°) and small biting angles (ca. 70° versus 76°) for the five-member rings are observed in this work in comparison with those in the work of Owiny et al. [10a].

It has been shown by Bickley and Serpone [18] that $TiQ_2(OR)_2$ is fluxional via a Ti–N bond rupture mechanism. We have further established that both Q^- in $TiQ_2(OR)_2$ can be substituted by Sap^{2-} and the Sap^{2-} ligand in $Ti(Sap)_2$ can be substituted by Q^- in a time scale of minutes. Therefore, in Ti(IV) complexes both Q^- and Sap^{2-} are substitutional labile in spite of being multidentate chelating ligands. While $TiQ_2(OR)_2$ and Ti(Sap)Q(OR) are air stable, the substitutional lability of Q^- and Sap^{2-} is a desirable feature for their potential application as precursors for metal oxide based materials via sol–gel process.

4. Conclusion

The reaction of $Ti(O^iPr)_4$ in the simultaneous presence of tridentate Schiff-base H_2Sap and 8-hydroxyquinoline HQ in methanol at room temperature, is not a viable method for the preparation of Ti(Sap)Q(OMe) because $Ti(Sap)_2$ precipitate can be formed immediately. Then small amount of the desired product can be formed only slowly through a set of equilibrating reactions. These reactions were established and their equilibrium constants were evaluated. However, when the reaction was carried out at 60 °C, at which the $Ti(Sap)_2$ precipitate was soluble, Ti(Sap)Q(OMe) was obtained conveniently after rapid chilling to 10 °C and following workup procedure.

Acknowledgement

We thank the National Science Council of Taiwan (Grant: 93-2113-M-007-009) and Tajen University (94080) for financial support.

Appendix A. Supplementary material

CCDC 273730 and 273731 contain the supplementary crystallographic data for Ti(Sap)Q(OMe) and $[Ti(Sap)Q]_2(\mu\text{-}O)$. These data can be obtained free of charge via http://www.ccdc.cam.ac.uk/conts/retrieving.html, or from the Cambridge Crystallographic Data Centre, 12 Union Road, Cambridge CB2 1EZ, UK; fax: (+44) 1223-336-033; or e-mail: deposit@ccdc.cam.ac.uk. Supplementary data associated with this article can be found, in the online version, at doi:10.1016/j.poly.2006.10.048.

References

[1] Y. Hamada, T. Sano, M. Fujita, T. Fujii, Y. Nishio, K. Shibata, Jpn. J. Appl. Phys 32 (Part 2) (1993) L514.
[2] A. Caillet, D. Bauer, Tetrahedron Lett. 46 (1973) 4629.
[3] (a) H. Schmidbaur, J. Lettenbauer, D.L. Wilkinson, G. Müller, O.Z. Kumberger, Z. Naturforsch. B 46 (1991) 901;
(b) I. Fujii, N. Hirayama, J. Ohtani, K. Kodama, Anal. Sci 12 (1996) 153;
(c) M. Brinkmann, G. Gadret, M. Muccini, C. Taliani, N. Mascinocchi, D. Sironi, J. Am. Chem. Soc. 122 (2000) 5147;
(d) M. Cölle, J. Gmeiner, W. Milius, H. Hillebrecht, W. Brütting, Adv. Funct. Mater. 13 (2003) 108;
(e) M. Cölle, R.E. Dinnebier, W. Brütting, Chem. Commun. (2002) 2908.
[4] (a) L.S. Sapochak, F.E. Benincasa, R.S. Schofield, J.L. Baker, K.K.C. Riccio, D. Fogarty, H. Kohlmann, K.F. Ferris, P.E. Burrows, J. Am. Chem. Soc. 124 (2002) 6119;
(b) N. Donze, P. Pechy, M. Gratzel, M. Schaer, L. Zuppiroli, Chem. Phys. Lett. 315 (1999) 405;
(c) T.A. Hopkins, K. Meerholz, S. Shaheen, M.L. Anderson, A. Schmidt, B. Kippelen, A.B. Padias, H.K. Hall Jr., N. Peyghambarian, N.R. Armstrong, Chem. Mater. 8 (1996) 344.
[5] M.A. Katkova, Y.A. Kurskii, G.K. Fukin, A.S. Averyushkin, A.N. Artamonov, A.G. Vitukhnovsky, M.N. Bochkarev, Inorg. Chim. Acta 385 (2005) 3625.
[6] (a) C.W. Tang, S.A. Van Slyke, Appl. Phys. Lett. 51 (1987) 913;
(b) S.A. Van Slyke, C.W. Tang, US Patent 1985 4539507;
(c) J.H. Burroughes, D.C. Bradley, A.R. Brown, R.N. Marks, K.D. Mackay, R.H. Friend, P.L. Burn, A.B. Holmes, Nature 347 (1990) 539.
[7] W.F. Zeng, Y.S. Chen, M.Y. Chiang, S.S. Chern, C.P. Cheng, Polyhedron 21 (2002) 1081.
[8] M.M. Amini, M. Mirzaee, Appl. Organomet. Chem 19 (2005) 339.
[9] (a) L. Sacconi, Coord. Chem. Rev 1 (1996) 126;
(b) S. Yamada, Coord. Chem. Rev 1 (1966) 415;
(c) M. Calligaries, L. Randaccio (Eds.), Comprehensive Coordination Chemistry, vol. 2, Pergamon, Oxford, 1987, pp. 715–738.
[10] (a) D. Owiny, S. Parkin, F.T. Ladipo, J. Organomet. Chem 678 (2003) 134;
(b) J. Strauch, T.H. Warren, G. Erker, R. Frolich, P. Saarenketo, Inorg. Chim. Acta 300–302 (2000) 810;
(c) P.R. Woodman, N.W. Alcock, I.J. Munslow, C.J. Sanders, P. Scott, J. Chem. Soc., Dalton Trans. 19 (2000) 3340;
(d) S.J. Coles, M.B. Hursthouse, D.G. Kelly, A.J. Toner, Polyhedron 19 (2000) 177;
(e) J.P. Corden, W. Errington, P. Moore, M.G.H. Wallbridge, Chem. Commun. (1999) 323.
[11] (a) D.C. Freeman, C.E. White, J. Am. Chem. Soc. 78 (1956) 2678;
(b) E.C. Alyea, A. Malek, Can. J. Chem. 53 (1975) 939.
[12] SIR 92 Program: A. Altomare, G. Cascarano, C. Giacovazzo, A. Guagliardi, J. Appl. Cryst. 26 (1993) 343.
[13] B.F. Studd, A.G. Swallow, J. Chem. Soc. A (1968) 1961.
[14] J.D. Matthews, N. Singer, A.G. Swallow, J. Chem. Soc. A (1970) 2545.
[15] P.H. Bird, A.R. Frazer, C.F. Llau, Inorg. Chem. 12 (1973) 1322.
[16] M.M. Amini, M. Mirzaee, S.W. Ng, Acta Crystallogr., Sect. E 60 (2004) m145.
[17] I. Demakopoulos, N. Klouras, C.P. Raptopoulou, A. Terzis, Z. Anorg. Allg. Chem. 621 (1995) 1761.
[18] D.G. Bickley, N. Serpone, Inorg. Chem. 18 (1979) 2200.

In the course of our ongoing exploration of the use of hydrothermal techniques to prepare mixed-valence polyoxovanadates, we have isolated a series of discrete hexadecavanadates by introducing bigger N-containing chelate ligands (such as 1,10′-phenanthroline and 2,2′-bipyridine) to the reaction system [14b,22]. While the hydrothermal synthesis, as an extremely convenient method, has been proven to be well suited for the preparation of metastable mixed-valence polyoxometalates, the reactive mechanism has not been understood yet [23]. Herein, we report the hydrothermal synthesis, single crystal investigation and chemical and physical characterization of a new "hexadecavanadate" from the stoichiometric point of view, that can be formulated as $[Ni(phen)_3]_2\{[V_{15}O_{36}(Cl)]_{0.5}[V_{17}O_{40}(Cl)]_{0.5}\}\cdot H_2O$ (**1**), in which two kinds of architectures $\{V_{17}O_{40}(Cl)\}$ and $\{V_{15}O_{36}(Cl)\}$ coexist. One of these two clusters, $\{V_{17}O_{40}(Cl)\}$, has never been previously observed in polyoxovanadate chemistry.

2. Experimental

2.1. Materials, instruments and analytical methods

All the chemicals purchased were of reagent grade and were used as received. The hydrothermal synthesis was carried out in a polytetrafluoroethylene lined stainless steel container under autogeneous pressure. The oxalic acid used in the reaction system acts as the reducing agent that generates V(IV) from the V(V) used in the synthesis. The reaction vessel was filled to approximately 60% of its volume capacity. Distilled water was used in the reactions.

Elemental analyses (C, H and N) were performed on a Perkin–Elmer 2400 CHN Elemental Analyzer. V and Ni were determined by a Leaman inductively coupled plasma (ICP) spectrometer. The IR spectrum was recorded in the range 400–4000 cm^{-1} on an Alpha Centaurt FT/IR spectrophotometer using KBr pellets. The XPS spectrum was recorded on an ESAY ESCA spectrometer with a Mg Kα achromatic X-ray source. TG analysis was performed on a Thermal Analyzer DT-30B instrument in an air atmosphere at a heating rate of 10 °C min^{-1}. Variable temperature susceptibility measurements were carried out in the temperature range 2–300 K at an applied magnetic field of 0.1 T on polycrystalline samples with a Quantum Design MPMS-XL-5 SQUID magnetometer. The susceptibility data were corrected for the sample holder, previously measured using the same conditions, and for the diamagnetic contributions of the salt as deduced using Pascal's constant tables (-1318.8×10^{-6} emu mol^{-1} per $\{V_{16}\}$ cluster). Q-band ESR spectra were recorded on a polycrystalline sample with a Bruker E-500 ELEXSYS spectrometer in the temperature range 300–4.2 K.

2.2. Syntheses

$[Ni(phen)_3]_2\{[V_{15}O_{36}(Cl)]_{0.5}[V_{17}O_{40}(Cl)]_{0.5}\}\cdot H_2O$ (**1**). A mixture of V_2O_5 (0.90 g, 5.0 mmol), $Ni(NO_3)_2\cdot 6H_2O$ (0.30 g, 1.0 mmol), phen (0.60 g, 3.3 mmol), $H_2C_2O_4\cdot 2H_2O$ (0.20 g, 2.2 mmol), CH_3COONa (0.60 g, 7.3 mmol), Tris (Tris = Trishydroxymethylaminomethane) (0.36 g, 3.0 mmol) and H_2O (10 mL, 555 mmol) in the presence of HCl (4 M) in a molar ratio of 5:1:3:2:7:3:555 was sealed in a 20 mL Teflon-lined autoclave and heated at 165 °C for 36 h. The initial pH was around 4.0 and the final pH was close to 4.3. After slow cooling to room temperature, black prismatic crystals of the title compound were filtered and washed with distilled water (55% yield based on V). *Anal.* Calc. (%): C, 32.25; H, 1.80; N, 6.27; Ni, 4.39; V, 30.49. Found (%): C, 31.85; H, 1.79; N, 6.22; Ni, 4.30; V, 30.48%. IR (solid KBr pellet/cm^{-1}): 3440.3 (s), 1603.9 (m), 1519.2 (s), 1458.2 (s), 1420.5 (s), 994.1 (s), 845.2 (s), 717.4 (w), 637.6 (m).

2.3. X-ray crystallography

Black single crystals of **1**, with dimensions $0.37\times0.25\times0.18$ mm, were selected and mounted on a Rigaku RAXIS RAPID IP diffractometer equipped with a graphite-monochromated Mo Kα (λ = 0.71073 Å) radiation source at 293 K. A total of 8045 independent reflections were collected among which 4993 reflections with $I > 2\sigma(I)$ were considered observed. The structure was solved by direct methods and refined on F^2 by full-matrix least squares methods using SHELXTL 97 [24,25]. V8, V9 and V10 atoms in this compound are disordered and all have 50% occupancy. Anisotropic refinements were employed for the non-hydrogen atoms. A summary of the crystallographic data is listed in Table 1. Atomic coordinates and equivalent isotropic displacement parameters as well as selected bond lengths and angles for compound **1** are listed in the tables of supplementary material.

Table 1
Crystal data and structure refinement for compound **1**

Empirical formula	$C_{288}H_{192}O_{156}N_{48}Cl_4V_{64}Ni_8$
Formula weight	10693.02
Temperature (K)	293(2)
Wavelength (Å)	0.71073
Crystal system	monoclinic
Space group	*C*2/*c*
a (Å)	16.683(3)
b (Å)	20.199(4)
c (Å)	27.222(5)
α (°)	90.00
β (°)	90.14(3)
γ (°)	90.00
Volume ($Å^3$)	9173(3)
Z	1
D_{calc} (Mg/m^3)	1.936
Absorption coefficient (mm^{-1})	2.066
F (000)	5268
Θ Range for data collection	2.99–25.00
Largest difference in peak and hole (e $Å^{-3}$)	1.450 and −0.710
Goodness-of-fit on F^2	1.019
Final *R* indices [$I > 2\sigma(I)$]	R_1 = 0.0625, $wR_2 = 0.1589$
R indices (all data)	$R_1 = 0.1086$, $wR_2 = 0.1786$

3. Results and discussion

3.1. Description of the structure

The single-crystal X-ray diffraction analysis reveals that compound **1** (Fig. 1) is composed of one stoichiometric $[V_{16}O_{38}Cl]^{4-}$ anion, two $[Ni(phen)_3]^{2+}$ cations and one lattice water molecule. The $[Ni(phen)_3]^{2+}$ cation exhibits the typical tris-chelated structure where the Ni(II) ion is surrounded by three bidentate phen ligands. All the Ni–N distances are very similar (2.073(5)–2.109(6) Å) and the N–Ni–N angles are close to 180° for the *trans* positions (172.0(2)°–173.2(2)°) and close to 90° for the *cis* positions (90.1(2)°–97.5(2)°), except for the three chelate angles, which are smaller and identical within experimental error (79.8(2)°, 79.9(2)° and 80.2(2)°). These distances and angles are very similar to those found for this complex in other salts [26].

The polyanion exhibits a host shell structure containing one Cl^- ion in its center with approximate C_{2v} symmetry. The atoms V8, V9 and V10 (and those in the symmetry-related positions) in the cluster present a positional disorder, having 50% occupancy. This positional disorder means that in every two POM units one must have the V8 (and V8A) and V9 (and V9A) atoms whereas the other must have the V10 (and V10A) atom, leading to the presence of a $\{V_{15}\}$ and a $\{V_{17}\}$ cluster coexisting in the structure. This assumption means that both architectures coexist in the crystal (co-crystallize) probably as a result of a coexistence of both species in similar concentrations in the solution under the hydrothermal conditions. Note that any other possible combination where V10 (and V10A) coexist with V8 (and V8A) or V9 (and V9A) atoms is not realistic since the V8–V10 and V9–V10 distances (1.94 and 1.47 Å, respectively) are much shorter than the average V–V distance in the cluster (ca. 3.0 Å), and than the V8–V9 distance (3.26 Å). Note also that the possibility of a rotational disorder of only one $\{V_{16}\}$ cluster could also explain the presence of the disorder in the V8, V9 and V10 positions by a rotation around the C_2 axis. This $\{V_{16}\}$ polyoxovanadate should have the three V atoms present simultaneously on different sides of the cluster (i. e., V8 and V9 on one side and V10 on the other side) since the presence of the three V atoms on the same side of the cluster is unrealistic given the short V8–V10 and V9–V10 distances (see above). Albeit in this hypothetical $\{V_{16}\}$ cluster, the C_2 axis would be removed. Finally, as a consequence of the described disorder, the oxygen atom O21, which is very close to the C_2 axis, appears in two very close positions at a distance of 0.96 Å with an occupancy factor of 50% each. This O21 atom is bonded to the V9 atoms and, therefore it presents a similar positional disorder to that of the V9 atom.

Note that this disorder is similar to that found for the V1 atom in the related compound $H_2[C(CH_2OH)_3NH_3]_{0.5}$-$[Cd(phen)_3]\{[Cd(H_2O)(phen)_2]_2(V_{16}O_{38}Cl)\}_{0.5}\{[Cd(H_2O)$-$(phen)_2]_2(V_{16}O_{39}Cl)\}_{0.5} \cdot 2H_2O$ [22b].

In summary, the only remaining possible distribution implies that the crystal structure must contain two different kinds of POM fragments: $\{V_{15}\}$ and $\{V_{17}\}$. Since these two clusters differ only in the presence or absence of three kinds of V atoms (V8, V9 and V10), this means that the two clusters have a common portion of $\{V_{13}\}$ (Fig. 2a). The $\{V_{13}\}$ fragment also has a crystallographic twofold symmetry (C_{2v}) with the C_2 axis aligned along the V7–Cl1 axis. Obviously there are two big cavities on each side of the $\{V_{13}\}$ fragment, thus it can accommodate two more V–O groups {V10–O18} to form the $\{V_{15}\}$ cluster (Fig. 2b) or four more V–O groups ({V8–O20} and {V9–O19}), leading to the$\{V_{17}\}$ cluster (Fig. 2c). Therefore, compound **1** can be considered as a fused product of architectures $\{V_{15}\}$ and $\{V_{17}\}$.

The $\{V_{15}\}$ cluster is similar to the classical $[V_{15}O_{36}]^{5-}$ [12] anion and is formed by fifteen $\{VO_5\}$ square pyramids, encapsulating a Cl^- anion, sharing edges and corners via three μ_2- and eighteen μ_3-oxygen atoms, respectively. Remarkably, owing to the disorder of the V10 group, the observed distance between V10 and O18 is unusually short (1.415(6) Å) for the expected vanadyl bond (V=O). Besides the terminal oxygen atom O18, the square pyramid $\{V(10)O_5\}$ configuration is accomplished by other four μ_3-oxygen atoms O16, O12, O17 and O14 with two long (V10–O16 = 2.162(7) Å and V10–O12 = 2.167(7) Å) and two short (V10–O17 = 1.971(6) Å and V10–O14 = 1.997(5) Å) bond distances.

As depicted in Fig. 2c, the $\{V_{17}\}$ cluster is built up from seventeen $\{VO_5\}$ square pyramids encapsulating a central Cl^- ion. The seventeen $\{VO_5\}$ square pyramids share edges and corners through two μ_2- and twenty-one μ_3-oxygen atoms, respectively, giving rise to a cage-like cluster. To the best of our knowledge, the topology of this $\{V_{17}\}$ cluster is unprecedented in polyoxovanadate chemistry.

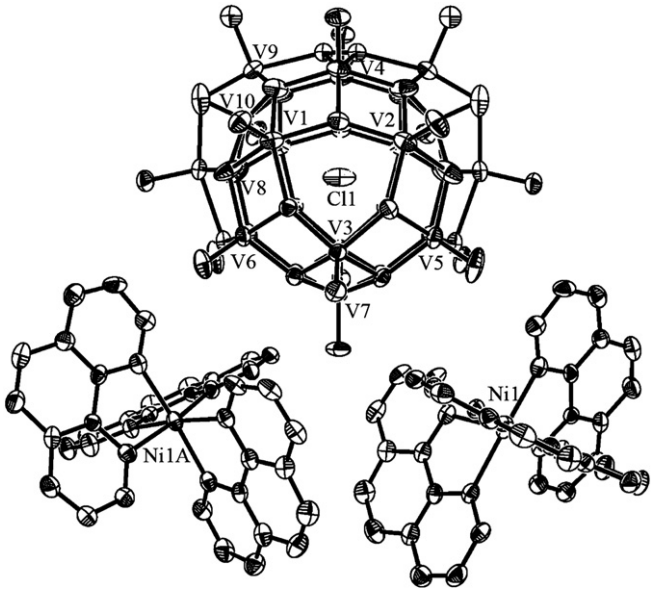


Fig. 1. ORTEP plot of compound **1** with thermal ellipsoids at 30% probability. The crystal lattice waters are omitted for clarity.

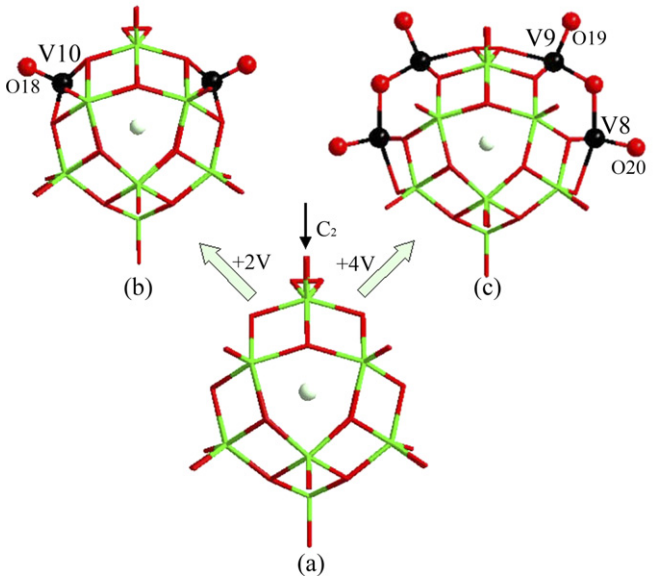


Fig. 2. The scheme of the transformation of architectures $\{V_{15}O_{36}(Cl)\}$ (b) and $\{V_{17}O_{40}(Cl)\}$ (c) from the common portion of $\{V_{13}\}$ (a).

Fig. 3 shows the topology comparison of these two clusters, in which the skeletons are built up via short V–V contacts of ca. 3.0 Å. Although they have the common portion of $\{V_{13}\}$, their geometrical features are quite different. In the $\{V_{15}\}$ cluster (Fig. 3a), the added V10 atoms enhance the whole symmetry from C_{2v} to D_{3h}. This cluster exhibits two kinds of vanadium atom nodes: the 3-connected (V1, V2 and V3) one and the 2-connected (V4, V5, V6, V7 and V10) one. While in the $\{V_{17}\}$ cluster (Fig. 3b), the added V8 and V9 atoms just retain the original C_{2v} symmetry. Three kinds of vanadium atom nodes are present in it, that is the 4-connected (V4) nodes, the 3-connected (V3, V5 and V6) nodes and the 2-connected (V1, V2, V7, V8 and V9) nodes. This framework differs from all other known polyoxovanadate structures in that it has one quadrangle, three octagons and four hexagons [14c].

Based on the type of bonded oxygen atoms in the $\{V_{17}\}$ framework, the coordination environments around the V atoms may be classified into two types of square pyramids (as shown in Fig. 2c): (i) those formed by a terminal, three μ_3- and one μ_2-oxygen atom: $\{(O{=})V(\mu_3\text{-}O)_3(\mu_2\text{-}O)\}$ such as V8 and V9 and (ii) those formed by one terminal oxygen atom and four μ_3-oxygen atoms:$\{(O{=})V(\mu_3\text{-}O)_4\}$, as observed in all the other V atoms. In the first type of square pyramid, the bond distances are 1.581(9)–1.645(2) Å, 1.769(5)–2.201(6) Å and 1.729(6)–2.022(8) Å for the terminal, μ_3- and μ_2-oxygen atoms, respectively. The second type of pyramid presents distances of 1.584(5)–1.598(5) Å and 1.846(4)–2.018(5) Å for the terminal and μ_3- oxygen atoms, respectively.

In this cluster, the mean distance from the central Cl^- anion to the bridging oxygen atoms of the periphery is 3.556 Å and to the vanadium atoms is 3.609 Å. The template effect of the encapsulated Cl^- ion in an anionic

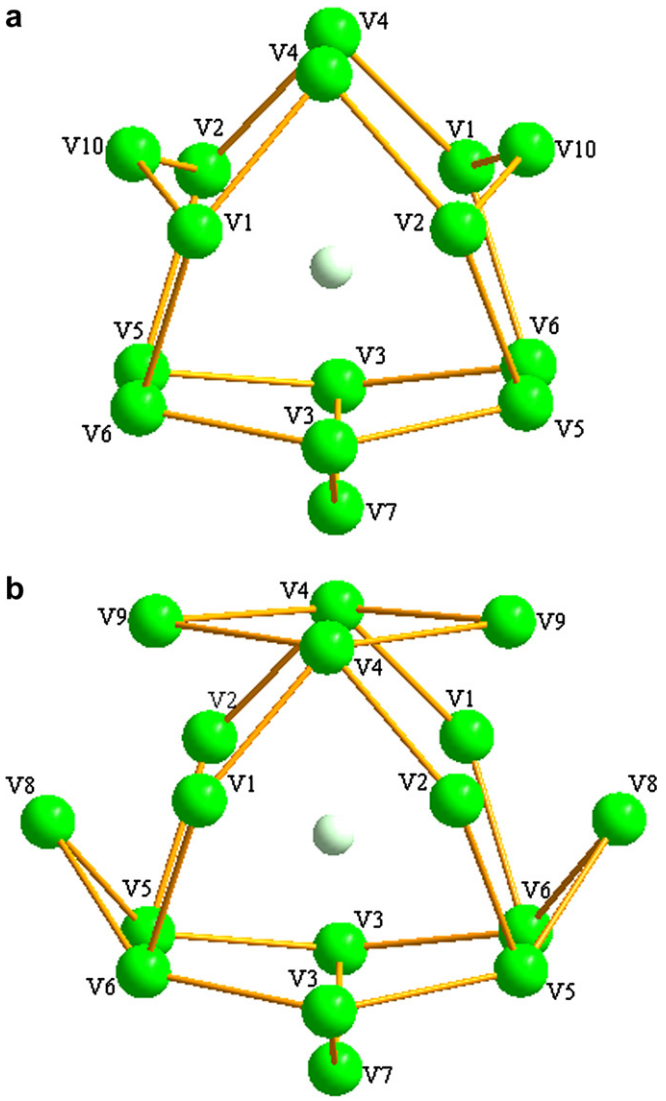


Fig. 3. The representations of the metal frameworks of $\{V_{15}O_{36}(Cl)\}$ (a) and $\{V_{17}O_{40}(Cl)\}$ (b) built up via V–V close contacts of ca. 3.0 Å. Short contacts between vanadium atoms: in (a), V1–V4 2.890(2) Å, V1–V6 2.958(2) Å, V1–V10 2.988(3) Å, V2–V4 2.931(2) Å, V2–V5 2.983(2) Å, V2–V10 2.999(4) Å, V3–V5 2.915(2) Å, V3–V6 2.866(2) Å, V3–V7 3.016(2) Å; in (b), V1–V4 2.890(2) Å, V1–V6 2.958(2) Å, V2–V4 2.931(2) Å, V2–V5 2.983(2) Å, V3–V5 2.915(2) Å, V3–V6 2.866(2) Å, V3–V7 3.016(2) Å, V4–V9 3.074(3) Å, V5–V8 2.891(3) Å,V6–V8 2.880(3) Å, V9–V4, 3.045(3) Å.

molecular oxide host has previously been discussed in many polyoxovanadate clusters with hollow structures [27].

Examination of the intermolecular contacts between the clusters reveals an unusual one-dimensional zigzag chain along the *c*-axis which is constructed by hydrogen-bonding interactions between terminal oxygen atoms O20 in adjacent clusters [O20···O20 = 2.967 Å] (see Fig. S1). Between the polyoxoanions and the Ni complexes, there exist extensive C···O short contacts ranging from 3.008 to 3.215 Å.

The assignment of the oxidation state of the V atoms can be done according to their coordination geometries and bond valence sum calculations. With this method we can estimate a global charge of −2.8 for the $[V_{17}O_{40}Cl]^{n-}$

cluster and of −4.4 for the $[V_{15}O_{36}Cl]^{n-}$ cluster. Consequently, the whole cluster can be approximately formulated as $\{[V_{15}O_{36}(Cl)]_{0.5}[V_{17}O_{40}(Cl)]_{0.5}\}^{3.6-}$. Note that due to the above-mentioned disorder problems this method may not be adequate in calculating the charge on those V atoms presenting disorder, but when it is applied to the whole cluster the relative errors are diluted and minimized and we can assume that the obtained results are acceptable. In fact the estimated value of −3.6 is in agreement with the expected charge of −4, calculated by taking into account that there are two Ni^{2+} cations per cluster. Thus, the "average" polyanion can be formulated as $[V_{16}O_{38}Cl]^{4-}$, indicating the presence of seven reduced V(IV) atoms: $[V_7^{IV}V_9^{V}O_{38}Cl]^{4-}$. The manganometric titration of the reduced vanadium indicates the presence of seven V^{IV} sites per formula unit in agreement with the estimations of the bond valence sum calculation analysis and the cationic charges in the structure. The XPS spectrum (see Fig. S2) of **1** gives two overlapped peaks at 515.51 and 516.95 eV, attributed to V^{IV} and V^{V}, respectively [28], confirming the presence of reduced V(IV) atoms.

3.2. Thermal stability of compound *1*

Thermogravimetric analysis of **1** was carried out in air atmosphere with a heating rate of 10 °C min^{-1} in the temperature range 50–1000 °C. It shows two distinct weight loss stages on the TGA curve (Fig. 4). The first weight loss of 31.2% takes place in the range 50–483 °C. This is attributed to the loss of one lattice water and five phen molecules (calc. 34.12%). The second weight loss of 8.3% at 483–570 °C is in good agreement with the loss of one phen molecule and one Cl^- (calc. 7.9%). Since the TG analysis was carried out in air atmosphere, the V(IV) ions must be oxidized to V_2O_5. Therefore, assuming the residue corresponds to V_2O_5 and NiO, the observed residue (60.36%) is in good agreement with the calculated value (59.97%). Exact elemental analysis of the residue after the calcination of **1** at 1000 °C shows a V:Ni molar ratio of 8.18 (close to the expected value of 8.0), confirming the formula of **1**. As the DTA curve shows, between 400 and 550 °C there are two strong exothermic peaks which correspond to the decomposition of the water molecule, phen molecules and Cl^-. An endothermal peak at 646 °C is attributed to the melting point peak of vanadium pentoxide.

3.3. FT-IR spectrum for compound *1*

The IR spectrum (Fig. S3) of **1** exhibits intense bands at 845.2, 717.4 and 637.6 cm^{-1} that can be ascribed to the ν(V–O–V) vibrations. The strong bands at 994.1 cm^{-1} can be assigned to the stretching vibrations of ν(V=O) bonds, which are consistent with that of some known polyoxovanadates [17,22c,29]. The bands appearing in the 1603–1104 cm^{-1} region can be attributed to the characteristic vibrations of phen molecules. Finally, the broad band at 3440 cm^{-1} is characteristic of the water molecules.

3.4. Magnetic properties

The thermal variation of the product of the molar magnetic susceptibility times the temperature, $\chi_M T$, per $[V_{16}O_{38}Cl]^{4-}$ cluster shows at room temperature a value of 3.67 emu K mol^{-1} which decreases almost linearly with decreasing temperature to reach a plateau of ca. 2.8 emu K mol^{-1} between ca. 10 and 5 K. Below ca. 5 K the $\chi_M T$ product shows a more abrupt decrease to reach a value of ca. 1.5 emu K mol^{-1} at 2 K (Fig. 5). Since the title compound presents two Ni(II) ions per $[V_{16}O_{38}Cl]^{4-}$ cluster, its magnetic moment is expected to be the sum of the magnetic contribution from the two Ni(II) ions plus that of the $[V_{16}O_{38}Cl]^{4-}$ cluster. If we assume that the two Ni(II) complexes are paramagnetic and, therefore, their expected contribution is ca. 2.2 emu K mol^{-1} (expected value for two $S = 1$ ions with a g value of ca. 2.1), then the magnetic contribution of the $[V_{16}O_{38}Cl]^{4-}$ cluster is estimated to be ca. 1.5 emu K mol^{-1} at room temperature and ca. 0.8 emu K mol^{-1} at low temperature.

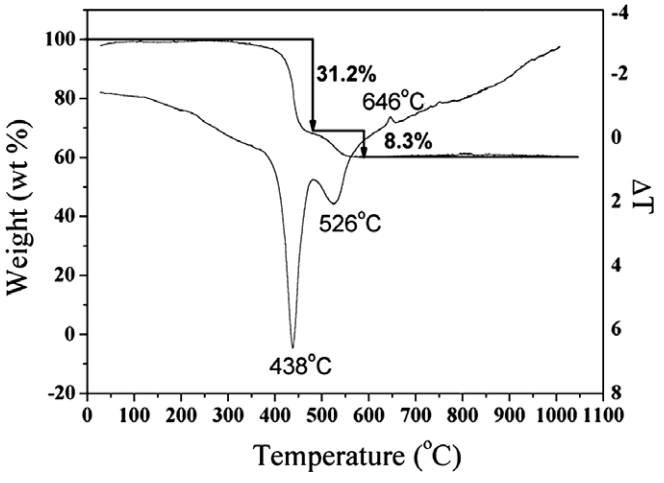


Fig. 4. Thermogravimetric analysis for compound **1**.

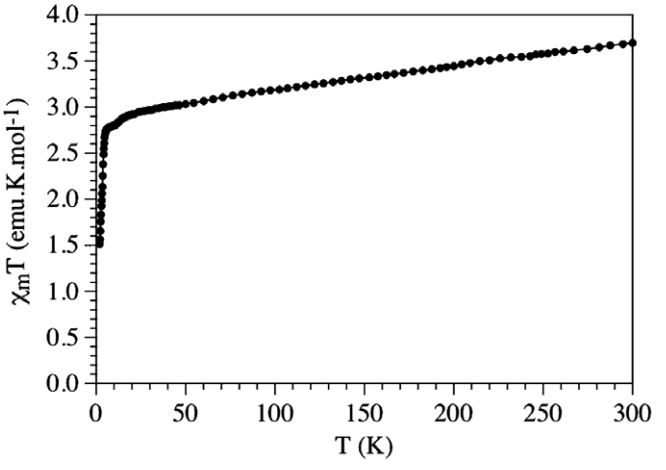


Fig. 5. Thermal variation of the product of the magnetic susceptibility and temperature per $[V_{16}O_{38}Cl]^{4-}$ cluster.

Note that the abrupt decrease observed at low temperatures, typical of Ni(II) complexes with zero field splitting (ZFS), precludes the exact determination of the contribution from the POM at low temperatures. The behavior deduced for the POM is very close to that observed in many other reduced polyoxovanadates [27a,30], where the room temperature magnetic moment is well below the expected value (in the title compound the expected value for seven independent unpaired electrons with $g = 2$, coming from the seven reduced V(IV) centers, is $7*0.375 = 2.625$ emu K mol^{-1}). This lower value of the magnetic moment is attributed to the strong antiferromagnetic coupling due to a large degree of delocalization. As in many other reduced vanadates, the magnetic moment of the title compound shows an almost linear decrease when decreasing the temperature, indicating the presence of the population of thermally accessible excited spin states at high temperature. The sharp decrease observed below ca. 5 K can be attributed to the presence of a zero field splitting (ZFS) in the two Ni(II) ions and/or to the presence of antiferromagnetic coupling between the reduced V(IV) in the POM. Due to the complexity of the possible exchange pathways there is no magnetic model available to date to fit the magnetic behavior of the reduced polyoxovanadate cluster.

The Q-band ESR spectrum of the title compound at room temperature shows only one wide signal with a line width, ΔH, of ca. 550 G (55 mT), centered at ca. 12360 G (1.236 T) ($g = 1.959$) that can be attributed to the presence of the delocalized electrons of the reduced polyoxovanadate (Fig. 6), since the Ni(II) ion is ESR silent in octahedral complexes due to the ZFS. The intensity of the ESR signal increases with decreasing temperature in a similar way to that found in the SQUID measurements. At low temperatures, the product of the spin susceptibility times the temperature ($\chi_{spin}T$, χ_{spin} being the area of the ESR signal) shows a sharp decrease starting at ca. 30 K that can be attributed to the presence of antiferromagnetic exchange interactions appearing at this temperature due to a progressive localization of the delocalized electrons of the POM. This progressive localization is also observed in the thermal variation of the line width (ΔH) and the g factor. Thus, ΔH linearly increases with decreasing temperature from a room temperature value of ca. 55 mT down to ca. 25 K where ΔH is ca. 80 mT (slope of ca. 0.1 mT K^{-1}) and then sharply increases, also linearly, below ca. 25 K to reach a value of ca. 112 mT at 4.2 K (slope of ca. 1.5 mT K^{-1}) (Fig. 7). The g value remains constant from room temperature down to ca. 25 K and below this temperature it sharply increases to reach a value of 1.980 at 4.2 K (inset in Fig. 7). These changes in the thermal variations of the g value and in ΔH below ca. 25 K suggest that the added electrons in the reduced polyoxovanadate remain delocalized over the V atoms in the polyoxovanadate clusters in the temperature range 300–25 K and that at low temperatures they start a progressive localization process. This localization process should lead to an axial signal with two components

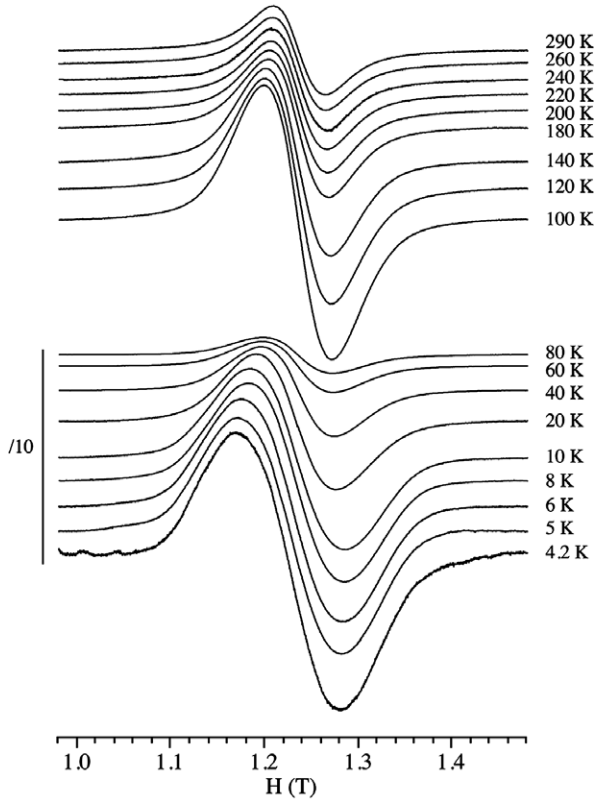


Fig. 6. Thermal variation of the Q-band ESR signal of the title compound.

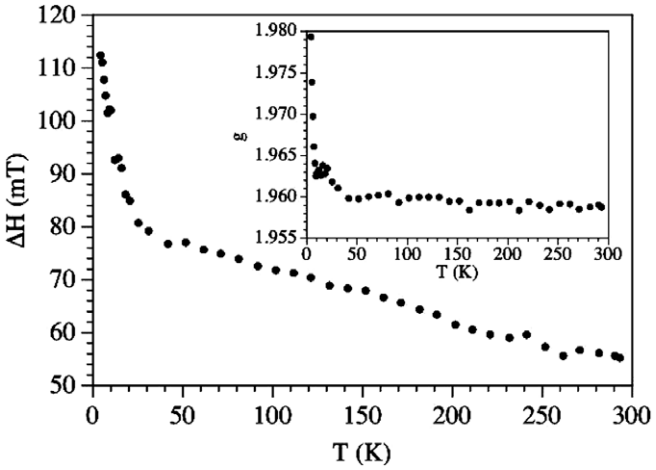


Fig. 7. Thermal variation of the ΔH value of the Q-band ESR signal of the title compound. **Inset:** thermal variation of the g value of the Q-band ESR signal of the title compound.

($g_{\parallel}$ and $g_{\perp}$) splitting into eight signals each due to the hyperfine coupling with the ^{51}V nucleus ($I = 7/2$, natural abundance 99.75%). Since there are several crystallographically different V atoms in the clusters, this localization process should give rise to several groups of eight signals each overlapping in the $g = 2$ region. The observed signal would be, therefore, the sum of all these signals. Three facts support this idea: (i) the signal becomes asymmetric below ca. 25 K (as expected, since $g_{\parallel} \neq g_{\perp}$), (ii) the line width at low

temperatures (ca. 112 mT) corresponds to the range where the two groups of eight signals expand in other V(IV) ions in a similar coordination environment [31] and (iii) the spectrum at 4.2 K shows weak features at both sides of the central signal that can be attributed to the extreme signals of one of the several groups of eight signals expected.

4. Conclusions

In summary, we have discovered a new polyoxovanadate which contains two different architectures: $\{V_{17}O_{40}(Cl)\}$ and $\{V_{15}O_{36}(Cl)\}$. The $\{V_{17}O_{40}(Cl)\}$ cluster represents a new vanadium oxide framework in polyoxometalate chemistry. The magnetic behavior of **1** indicates that the extra seven electrons of the reduced polyoxovanadate skeleton are delocalized at room temperature and are progressively localized at low temperature.

Acknowledgements

The authors acknowledge financial support from the National Science Foundation of China (20671016). C.J.G.G. thanks the Generalitat Valenciana for financial support.

Appendix A. Supplementary material

CCDC 293662 contains the supplementary crystallographic data for this paper. These data can be obtained free of charge via http://www.ccdc.cam.ac.uk/conts/retrieving.html, or from the Cambridge Crystallographic Data Centre, 12 Union Road, Cambridge CB2 1EZ, UK; fax: (+44) 1223-336-033; or e-mail: deposit@ccdc.cam.ac.uk. Supplementary data associated with this article can be found, in the online version, at doi:10.1016/j.poly.2006.10.050.

References

[1] (a) P. Kögerler, L. Cronin, Angew. Chem., Int. Ed. Engl. 44 (2005) 844;
(b) D.E. Katsoulis, Chem. Rev. 98 (1998) 359;
(c) E. Coronado, J.R. Galán-Mascarós, C. Giménez-Saiz, C.J. Gómez-García, E. Martínez-Ferrero, M. Almeida, E.B. Lopes, Adv. Mater. 16 (2004) 324;
(d) M.T. Pope, A. Müller, Angew. Chem., Int. Ed. Engl. 30 (1991) 34;
(e) T. Liu, E. Diemann, H. Li, A. Dress, A. Müller, Nature 426 (2003) 59;
(f) E. Coronado, C.J. Gómez-García, Chem. Rev. 98 (1998) 273.
[2] (a) A. Müller, F. Peters, M.T. Pope, D. Gatteschi, Chem. Rev. 98 (1998) 239;
(b) W.G. Klemperer, T.A. Marquart, O.M. Yaghi, Angew. Chem., Int. Ed. Engl. 31 (1992) 49.
[3] E. Hamilton, P.E. Fanwick, J.J. Wilker, J. Am. Chem. Soc. 124 (2002) 78.
[4] J. Fuchs, S. Mahjour, J. Pickardt, Angew. Chem., Int. Ed. Engl. 15 (1976) 374.
[5] V.W. Day, W.G. Klemperer, O.M. Yaghi, J. Am. Chem. Soc. 111 (1989) 4518.
[6] A. Bino, S. Cohen, C.H. Wirguin, Inorg. Chem. 21 (1982) 429.
[7] V.W. Day, W.G. Klemperer, D.J. Maltbie, J. Am. Chem. Soc. 109 (1987) 2991.
[8] Y.P. Zhang, R.C. Haushalter, J. Zubieta, Inorg. Chim. Acta. 277 (1998) 263.
[9] V.W. Day, W.G. Klemperer, O.M. Yaghi, J. Am. Chem. Soc. 111 (1989) 5959.
[10] D. Hou, K.S. Hagen, C.L. Hill, J. Am. Chem. Soc. 114 (1992) 5864.
[11] L. Chen, F.L. Jiang, Z.Z. Lin, Y.F. Zhou, C.Y. Yue, M.C. Hong, J. Am. Chem. Soc. 127 (2005) 8588.
[12] A. Müller, M. Penk, R. Rohlfing, E. Krickemeyer, J. Döring, Angew. Chem., Int. Ed. 29 (1990) 926.
[13] D. Hou, K.S. Hagen, C.L. Hill, J. Chem. Soc., Chem. Commun. (1993) 426.
[14] (a) S.X. Liu, L.H. Xie, B. Gao, C.D. Zhang, C.Y. Sun, D.H. Li, Z.M. Su, Chem. Commun. 40 (2005) 5023;
(b) Y.H. Chen, X.J. Gu, J. Peng, Z.Y. Shi, H.Q. Yu, E.B. Wang, N.H. Hu, Inorg. Chem. Commun. 7 (2004) 705;
(c) D.L. Long, D. Orr, G. Seeber, P. Kögerler, L.J. Farrugia, L. Cronin, J. Clust. Sci. 14 (2003) 313.
[15] J. Marrot, K. Barthelet, C. Simonnet, D. Riou, C.R. Chim 8 (2005) 971.
[16] M.I. Khan, S. Ayesh, R.J. Doedens, M.H. Yu, C.J. O'Connor, Chem. Commun. (2005) 4658.
[17] Y. Hayashi, K. Fukuyama, T. Takatera, A. Uehara, Chem. Lett. (2000) 770.
[18] B.E. Koene, N.J. Taylor, L.F. Nazar, Angew. Chem., Int. Ed. 38 (1999) 2888.
[19] A. Müller, J. Döring, H. Bögge, E. Krickemeyer, Chimia 42 (1988) 300.
[20] (a) A. Müller, E. Diemann, E. Krickemeyer, S. Che, Naturwissenschaften 80 (1993) 77;
(b) A. Müller, E. Krickemeyer, M. Penk, R. Rohlfing, A. Armatage, H. Bögge, Angew. Chem., Int. Ed. 30 (1991) 1674;
(c) A. Müller, R. Rohlfing, E. Krickemeyer, H. Bögge, Angew. Chem., Int. Ed. 32 (1993) 909.
[21] A. Müller, R. Rohlfing, J. Döring, M. Penk, Angew. Chem., Int. Ed. Engl. 30 (1991) 588.
[22] (a) Y.H. Chen, J. Peng, H.Q. Yu, Z.G. Han, X.J. Gu, Z.Y. Shi, E.B. Wang, N.H. Hu, Inorg. Chim. Acta. 358 (2005) 403;
(b) B.X. Dong, Y.H. Chen, J. Peng, Y.M. Kong, Z.G. Han, J. Mol. Struct. 748 (2005) 171;
(c) B.X. Dong, J. Peng, Y.H. Chen, Y.M. Kong, A.X. Tian, H.S. Liu, J.Q. Sha, J. Mol. Struct. 788 (2006) 200.
[23] P.J. Hagrman, D. Hagrman, J. Zubieta, Angew. Chem., Int. Ed. 38 (1999) 2638.
[24] G.M. Sheldrick, SHELXS 97, Program for Crystal Structure Solution, University of Göttingen, Göttingen, Germany, 1997.
[25] G.M. Sheldrick, SHELXS 97, Program for Crystal Structure Refinement, University of Göttingen, Göttingen, Germany, 1997.
[26] (a) Y.G. Li, Y. Lu, G.Y. Luan, E.B. Wang, Y.B. Duan, C.W. Hu, N.H. Hu, H.Q. Jia, Polyhedron 21 (2002) 2601;
(b) M. Yuan, Y.G. Li, E.B. Wang, C.G. Tian, L. Wang, C.W. Hu, N.H. Hu, H.Q. Jia, Inorg. Chem. 42 (2003) 3670.
[27] (a) A. Müller, Inorg. Chem. 36 (1997) 5239;
(b) M.I. Khan, E. Yohannes, R.J. Doedens, Inorg. Chem. 42 (2003) 3125.
[28] R. Larsson, B. Folkesson, G. Schoen, Chem. Scripta 3 (1973) 88.
[29] T. Kurata, Y. Hayashi, A. Uehara, K. Isobe, Chem. Lett. (2003) 1040.
[30] S.T. Zheng, J. Zhang, G.Y. Yang, Eur. J. Inorg. Chem. (2004) 2004.
[31] Z. Shi, J. Peng, C.J. Gómez-García, S. Benmansour, X. Gu, J. Solid State Chem. 179 (2006) 253.

either as KBr pellets or as a solution in a cell provided with a KBr window, using a Perkin–Elmer Spectra GX 2000 spectrometer. ^{1}H NMR spectra were recorded on a Bruker 200 MHz FT NMR (model: Avance-DPX 200) using $CDCl_3$ as the solvent and tetramethylsilane (TMS) as an internal standard. Electronic spectra were recorded with a Shimadzu UV-3101 PC or a Cary 500 Scan UV–Vis-NIR spectrometer; while room temperature luminescence spectra were recorded with a Perkin–Elmer LS 50B luminescence spectrofluorimeter. Electrochemical experiments were performed on a CH-660A (USA) electrochemical instrument with a conventional three-electrode cell assembly. Saturated Ag/AgCl as a reference and platinum as a working electrode were used for all measurements. Ferrocene was added at the end of each experiment as an internal standard and all potentials are quoted versus the ferrocene/ferrocenium (Fc/Fc^+) couple. X-ray single crystal data for $\mathbf{L}_2$ was collected using Mo Kα ($\lambda = 0.7107$ Å) radiation on a SMART APEX diffractometer equipped with a CCD area detector. Data collection, data reduction [10] and structure solution/refinement [11,12] were carried out using the software package of SMART APEX. The structure was solved by direct methods and refined in a routine manner. All hydrogen atoms were geometrically fixed at their idealized position. Graphics were generated using Mercury 1.4.1 [13].

2.3. Synthesis

2.3.1. 1-Hydroxy-2-methoxy-anthraquinone ($\mathbf{L}_1$)

1.0 g (4.16 mM) of 1,2-dihydroxy-9,10-anthraquinone was dissolved in 30 ml of acetone. To this, 1.6 g of anhydrous K_2CO_3 was added and the mixture was stirred at room temperature for a few minutes. Then 1.049 g dimethyl sulfate (8.33 mM) dissolved in 5 ml of acetone was added from a dropping funnel over 30 min. The resulting solution was then refluxed for 4 h. Then acetone was partially removed under reduced pressure (~5 ml). To this about 25 ml of diethylether was added and the undesired compounds were discarded in the water layer by solvent extraction. The ether solution was then dried over anhydrous $MgSO_4$ and ether was removed to yield the crude product. Purification of the desired product was achieved by gravity chromatography using SiO_2 as the stationary phase and *n*-hexane–$CHCl_3$ (3:7; v/v) as the eluent. Yield: 0.25 g (23%). ^{1}H NMR (200 MHz, $CDCl_3$): 13.05 (s, 1H, –OH), 8.25–8.2 (m, 2H, H^5, H^8), 8.078 (d, 1H, $J = 8.4$ Hz, H^4), 7.89–7.83 (m, 2H, H^6, H^7), 7.24 (1H, d, $J = 8.4$ Hz, H^3), 3.94 (s, 3H, $-OCH_3$). FT-IR (KBr; cm^{-1}): 3329 (NH), 3272 (NH), 1651 (–C=O). ESI MS [*m*/*z* (positive ion mode)]: 278 (M^++Na^+, 20%), 255 (M^+, 38%). Elemental analysis for $C_{15}H_{10}O_4$: *Anal.* Calc.: C, 70.86; H, 3.96. Found: C, 70.7; H, 4.0%. UV–Vis spectra (DMF, λ_{max} nm (ε M^{-1} cm^{-1})): 278 (1.10×10^5), 369 (4.44×10^4).

2.3.2. 1,2-Dimethoxy-anthraquinone ($\mathbf{L}_2$)

2 g (34 mM) of 1,2-dihydroxy-9,10-anthraquinone and 12.4 g anhydrous K_2CO_3 were mixed in 40 ml of acetone and then stirred at room temperature for a few minutes. To this resulting mixture, 14 ml dimethyl sulfate (150 mM) dissolved in 20 ml of acetone was added from a dropping funnel over 30 min. The resulting solution was then refluxed for 4 h. Then acetone was partially removed under reduced pressure (~15 ml) and about 50 ml of diethyl ether was added. The starting compound and any $\mathbf{L}_1$ formed due to partial conversion were removed in the water layer, whose pH was maintained at 9.5. The ether was dried under reduced pressure to recover the crude product. This was further purified by chromatography using a SiO_2 column and *n*-hexane–$CHCl_3$ (1:1; v/v) as eluent. Yield: 0.7 g (39%). ^{1}H NMR (200 MHz, $CDCl_3$): 8.28–8.23 (m, 2H, H^5, H^8), 8.174 (d, 1H, $J = 8.6$ Hz, H^4), 8.78–8.74 (m, 2H, H^6, H^7), 7.28 (1H, d, $J = 8.6$ Hz, H^3), 4.0 (s, 3H, $-[OCH_3]^1$), 3.03 (s, 3H, $-[OCH_3]^2$) . FT-IR (KBr; cm^{-1}): 1336, 1270 (O–CH_3), 1670 (–C=O). ESI MS [*m*/*z* (positive ion mode)]: 291 (M+Na^+, 50%); 269 (M+H^+; 90%); Elemental analysis for $C_{15}H_{10}O_4$: *Anal.* Calc.: C, 71.64; H, 4.52. Found: C, 72.0; H, 4.5%. UV–Vis spectra (DMF, λ_{max} nm (ε M^{-1} cm^{-1})): 279 (1.59×10^4), 328 (7.6×10^3), 425 (9.20×10^3). The structure for $\mathbf{L}_2$ was further established by single crystal X-ray studies.

2.4. Spectrophotometer titrations

A 1.0×10^{-3} M solution of the receptor $\mathbf{L}_1$ and a 1.0×10^{-3} M solution of the receptor $\mathbf{L}_2$ in DMF were prepared and stored in the dark. These solutions were used for all spectroscopic studies after the appropriate dilution. 1.0×10^{-3} M solutions of $MClO_4$ (M is an alkali metal ion) or $M'(ClO_4)_2$ (M′ is an alkaline earth metal ion) were prepared in dried and distilled DMF, and were stored under an inert atmosphere. All titration experiments were performed using 1.0×10^{-4} M solutions of receptor $\mathbf{L}_1$ and 1.35×10^{-5} M solutions of receptor $\mathbf{L}_2$ in DMF and various concentrations of the cations (5.0×10^{-6} to 5.0×10^{-4} M) in DMF. Affinity constants were evaluated after calculating the concentrations of the respective species, like free $\mathbf{L}_1$, $\mathbf{L}_2$, $\mathbf{M}^{2+}$ and the associated complexes, e.g. $\mathbf{L}_1 \cdot \mathbf{M}^{2+}/\mathbf{L}_2 \cdot \mathbf{M}^{2+}$. The effect of the ionic strength on the affinity constant value was also examined by repeating the studies at various 0–0.1 M [(^{t}Bu$_4$N)ClO_4] supporting electrolyte concentrations. The affinity constant values were evaluated from the absorbance data of the titration curve using 519 nm as the probe wavelength.

2.5. Luminescence titration

The standard solutions mentioned above were also used for luminescence titration studies. For all measurements, λ_{ext} used was 517 nm ($\mathbf{L}_1$)/514 nm ($\mathbf{L}_2$) with an excitation and emission slit width of 5 nm. All titration experiments were performed using 2.5×10^{-5} M solutions of receptors $\mathbf{L}_1$ and $\mathbf{L}_2$ in DMF (thoroughly degassed before measurement with IOLAR grade dinitrogen gas) and solutions of various cations (3.0×10^{-5} to 5.0×10^{-4} M) in DMF.

2.6. Computational details

All calculated geometries were fully optimized at the RHF/6-31G* level of theory using the JAGUAR program [14,15]. These structures were a true minimum at this level of theory and were characterized by harmonic vibrational frequencies.

3. Results and discussion

$\mathbf{L}_1$ and $\mathbf{L}_2$ were synthesized following standard reaction procedures. Both these receptors were characterized by standard analytical and spectroscopic techniques. The structure of $\mathbf{L}_2$ was further confirmed by single crystal X-ray diffraction (Fig. 1) studies. X-ray quality crystals were obtained by the slow evaporation of $\mathbf{L}_2$ from a CH_3CN solution at room temperature. Single crystal X-ray analysis revealed that $\mathbf{L}_2$ belongs to a non-centrosymmetric monoclinic space group $P2_1$. The asymmetric unit comprises of one molecule of $\mathbf{L}_2$, and the methyl C-atom of one of the methoxy groups is oriented above the plane containing the anthraquinone moiety and the other methoxy group. In the crystal structure the oxygen atoms of the anthraquinone moiety of $\mathbf{L}_2$ display non-bonded interactions with the neighboring molecule through C–H···O interactions thereby forming a helical chain parallel to the *c*-axis (Fig. 1b). The helical nature of $\mathbf{L}_2$ is due to the inclined packing of the adjacent molecules at an angle of 52.1° parallel to the *c*-axis. Such helical chains are further packed parallel to the *a*-axis via various C–H···O non-bonded interactions.

Receptor $\mathbf{L}_1$ shows a strong absorption band at 278 nm and a shoulder at 328 nm; while for $\mathbf{L}_2$ this shoulder is barely detectable in this region (Figs. 2 and 3). In the visible region, for $\mathbf{L}_1$ a well defined absorption band at 427 nm was observed, however, for $\mathbf{L}_2$ a shoulder at 369 nm was observed. This absorption band in the visible region was due to charge transfer from the donor –OH/–OCH_3 unit to the acceptor quinone units [16]. On addition of Mg^{2+} a set of new absorption bands appeared in the range 500–575 nm for both receptors and, consequently, a visual color change from yellow to red was noticed (Figs. 2 and 3).

However, the changes were more prominent for $\mathbf{L}_1$ as compared to $\mathbf{L}_2$. Similar experiments were performed for all the metal ions of the groups IA and IIA. Group IA metal ions do not show any color change upon addition to receptor solutions (SI Figure 1). Other group IIA metal ions show a mild color change with receptors $\mathbf{L}_1$ and $\mathbf{L}_2$ (SI Figure 2). Luminescence spectra for $\mathbf{L}_1$ and $\mathbf{L}_2$ were also recorded. Both were found to be weakly emitting on excitation at their respective charge transfer spectral band ($\lambda_{ext} = 369$ nm for $\mathbf{L}_1$ and 425 nm for $\mathbf{L}_2$; Figs. 2 and 3). The weak emission property was due to photoinduced

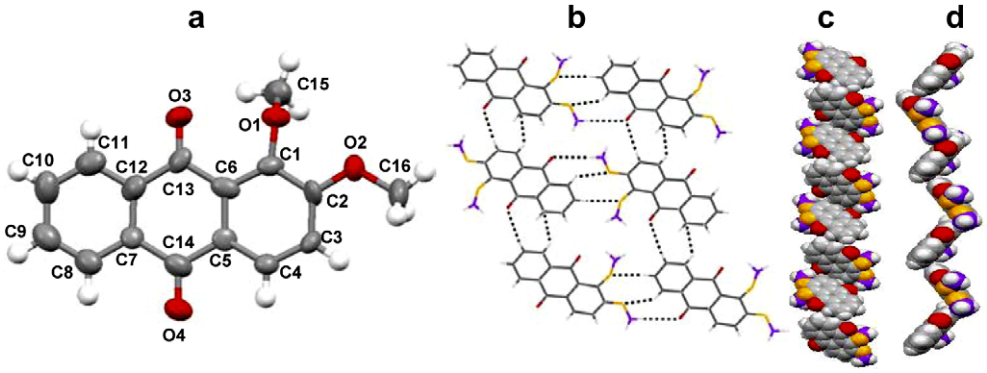


Fig. 1. (a) ORTEP diagram of $\mathbf{L}_2$ (50% probability); (b) illustration of various non-bonded interactions between the C–H of $\mathbf{L}_2$ and oxygen atoms; (c) helical arrangement of $\mathbf{L}_2$ along the *c*-axis; (d) packing of the helical network, view down the *a*-axis. Color code: Oxygen atom of the methoxy group (orange), C-atoms of the methoxy group (purple) and oxygen atom of the anthraquinone (red). (For interpretation of the references to color in this figure legend, the reader is referred to the web version of this article.)

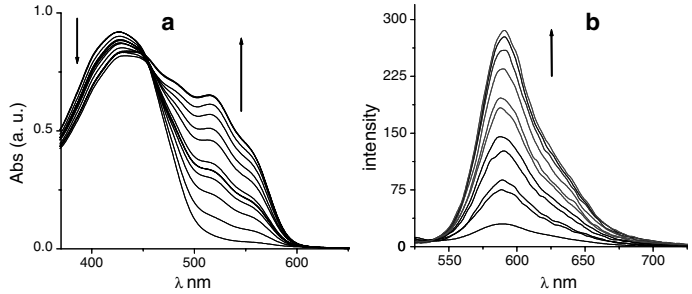


Fig. 2. Spectral changes for $\mathbf{L}_1$ at varying [Mg^{2+}] in DMF at 25 °C: (a) Absorption spectral changes $\mathbf{L}_1$ (1.0×10^{-4} M) with [Mg^{2+}] (5.0×10^{-6} to 5.0×10^{-4} M); (b) fluorescence spectral changes ($\lambda_{ext} = 517$ nm) of $\mathbf{L}_1$ (2.5×10^{-4} M) with [Mg^{2+}] (3.0×10^{-6} to 5.0×10^{-4} M).

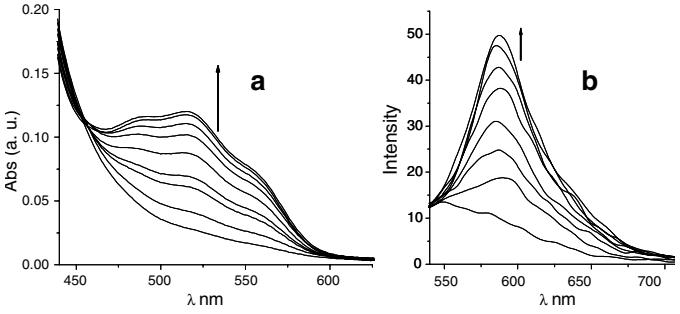


Fig. 3. Spectral changes for $\mathbf{L}_2$ at varying [Mg^{2+}] in DMF at 25 °C: (a) Absorption spectral changes $\mathbf{L}_2$ (1.35×10^{-5} M) with [Mg^{2+}] (5.0×10^{-6} to 3.75×10^{-4} M); (b) fluorescence spectral changes ($\lambda_{ext} = 515$ nm) of $\mathbf{L}_2$ (2.5×10^{-4} M) with [Mg^{2+}] (3.0×10^{-5} to 5.0×10^{-4} M).

electron transfer between the donor (–OH/–OCH_3) and acceptor (quinone) centers [16,17]. For, $\mathbf{L}_1$, the possibility of intra- and inter-molecular excited state proton transfer may cause a highly efficient radiationless deactivation of the excited states to the ground state and this might also have contributed to the observed low steady state emission quantum yield for $\mathbf{L}_1$ [17]. However, for both these receptors an appreciable increase in emission intensity was observed on addition of excess alkaline earth metal ions – especially Mg^{2+}, when excited at their respective new absorption maximum (517 nm for $\mathbf{L}_1$ and 515 nm for $\mathbf{L}_2$). The excitation spectra of the complexes matched well with the respective absorption spectra. This result suggests that the observed fluorescence was due to the formation of new complexes, $\mathbf{L}_1\cdot\mathbf{Mg}^{2+}$ and $\mathbf{L}_2\cdot\mathbf{Mg}^{2+}$. Thus changes in electronic and emission spectra suggest a binding of the alkaline earth metal ions to the receptor molecules. Significant spectral changes on addition of Mg^{2+} ions suggest a stronger binding to $\mathbf{L}_1$ and $\mathbf{L}_2$. The association constants for the respective group IIA metal ions, towards $\mathbf{L}_1$ and $\mathbf{L}_2$, were obtained from systematic spectrophotometric titrations (Table 1). Representative spectrophotometric titration profiles for Mg^{2+} with $\mathbf{L}_1$ and $\mathbf{L}_2$ are shown in Figs. 2 and 3. Association constants for the metal ions, evaluated from spectrophotometric titrations, for the specific receptors ($\mathbf{L}_1$ and $\mathbf{L}_2$) are presented in Table 1.

Table 1
Constants[a] of the complex formation equilibrium

M^{n+}	K_1 (10^3 M^{-1})	K_2 (10^3 M^{-1})
Mg^{2+}	102 (4)	20.0 (1)
	139 (5)[b]	24.0 (1)[b]
Ca^{2+}	13.6 (0.4)	7.8 (0.4)
Sr^{2+}	12.0 (0.4)	6.0 (0.3)
Ba^{2+}	1.30 (0.2)	0.6 (0.1)

Perchlorate salts of the respective metal ions were used for the studies.

[a] K value reported (K_1 and K_2 values are for receptors $\mathbf{L}_1$ and $\mathbf{L}_2$, respectively) is the average of five independent data evaluated from each individual UV–Vis titration data for the respective receptor and cation.

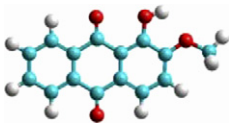
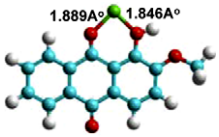
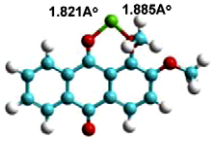
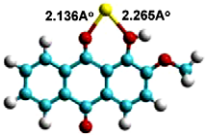
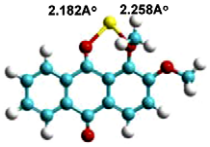
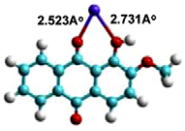
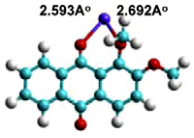
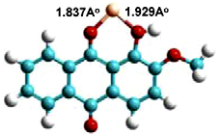
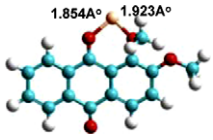
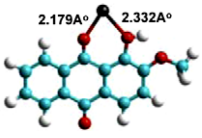
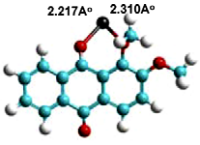
[b] Values obtained from the fluorescence titration data. The value provided in the parentheses is the uncertainty.

The job plot for each titration signified the stoichiometry for the binding of the respective metal ion to each receptor and in all cases a 1:1 complex formation was observed (SI Figure 3). The association constant for the Mg^{2+} ion to each receptor was also evaluated from the emission titration data (Figs. 2b and 3b). The values obtained thus were found to match well with the spectrophotometric titration data and are shown in Table 1. Stability constant values showed the following order for the group IIA metal ions: $K_{Mg^{2+}} \gg K_{Ca^{2+}} > K_{Sr^{2+}} \gg K_{Ba^{2+}}$. Data presented in Table 1 also revealed that $\mathbf{L}_1$ binds these ions more strongly as compared to $\mathbf{L}_2$.

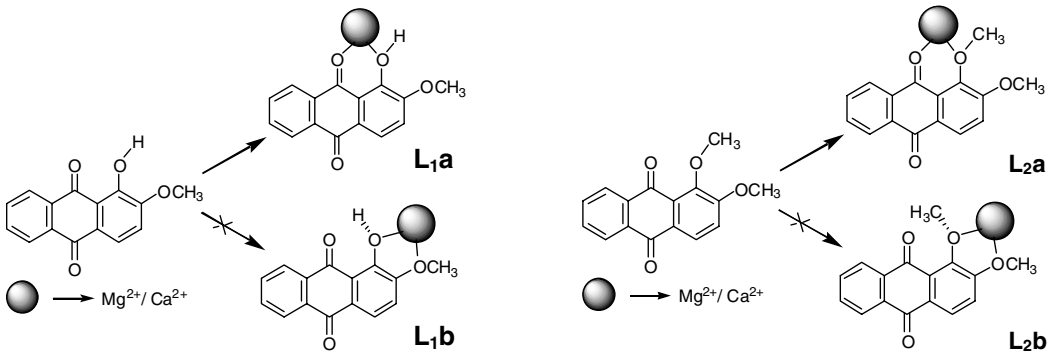
Electrochemical studies revealed that binding of the Mg^{2+} ion to $\mathbf{L}_1$ and $\mathbf{L}_2$ also caused a change in the reduction potential for the quinone fragment of the receptor units. The anthraquinone moiety is known to undergo a reversible two electron reduction process to generate 9,10-dihydroxy anthracene in the presence of protic solvents – as this redox process involves a simultaneous 2e-$2H^+$ transfer reaction [18]. Thus, as expected, $\mathbf{L}_1$ and $\mathbf{L}_2$ showed an irreversible redox process in aprotic solvent (DMF) at −0.07 and −0.20 V (versus Fc/Fc^+ couple), respectively. The potential values were evaluated from differential pulse voltammetric (DPV) studies. In the presence of the Mg^{2+} ion, these respective potential values shifted to −0.01 and −0.16 V (versus Fc/Fc^+ couple), respectively. Comparison of the potential data before and after addition of the Mg^{2+} ion revealed that reduction of the quinone fragment became more facile on binding the metal ion to the receptor units. The change in potential data for $\mathbf{L}_1\cdot\mathbf{Mg}^{2+}$ (60 mV), as compared to that for $\mathbf{L}_2\cdot\mathbf{Mg}^{2+}$ (40 mV), clearly indicates that the binding of the Mg^{2+} ion to $\mathbf{L}_1$ is stronger than that to $\mathbf{L}_2$. Thus, the data obtained from the electrochemical studies also corroborate our observation of the spectrometric titration experiments. Further, lower reduction potential data also signified the lowering of the LUMO energy level for the anthraquinone fragment, which presumably accounts for the observed red shift of the charge transfer absorption band in $\mathbf{L}_1\cdot\mathbf{Mg}^{2+}$ and $\mathbf{L}_2\cdot\mathbf{Mg}^{2+}$ as compared to $\mathbf{L}_1$ and $\mathbf{L}_2$, respectively. The observed increase in emission intensity for $\mathbf{L}_1$ and $\mathbf{L}_2$ on addition of an increasing amount of Mg^{2+} suggests that metal ion complexation suppresses the intramolecular photoinduced electron transfer from the non-bonding orbitals of the donor fragment to the LUMO of the acceptor fragment [16,17].

The calculated results for the complexation of the metal ions with the receptors $\mathbf{L}_1$ and $\mathbf{L}_2$ are shown in Table 2. The complexation study has been performed with the following metal ions, i.e., Li^+, Na^+, K^+, Mg^{2+} and Ca^{2+}. Alkali metal ions show relatively poor binding affinity towards the receptors $\mathbf{L}_1$ and $\mathbf{L}_2$ compared to that of Mg^{2+} and Ca^{2+} ions (Table 2). The calculated parent geometry of $\mathbf{L}_2$ has been found to be in good agreement with the observed X-ray structure. The orientation of the methoxy groups of $\mathbf{L}_2$, shown in Table 2, has a good match with the orientations obtained in the X-ray structure (Fig. 1).

Table 2
RHF/6-31G* calculated structures for L_1 and L_2 and their corresponding metal complexes with Li^+, Na^+, K^+, Mg^{2+} and Ca^{2+}

L_1	Energy	L_2	Energy
	(0.26881)		(0.27569)
	−71.69 (0.34903)		−71.862 (0.34827)
	−53.04 (0.33214)		−50.29 (0.33602)
	−31.11 (0.32777)		−35.18 (0.33362)
	−192.19 (0.24833)		−191.16 (0.24949)
	−128.08 (0.26515)		−126.297 (0.26716)

Binding energies are in kcal/mol and the HOMO–LUMO energy gaps in eV are shown in parentheses.
Color code used is as follows: green: Li^+; yellow: Na^+; violet: K^+; orange: Mg^{2+}; black: Ca^{2+}.
For interpretation of the references to color in this table legend, the reader is referred to the web version of this article.



Scheme 1. Schematic presentation of the binding of Mg^{2+} and Ca^{2+} ions to L_1 and L_2.

Calculations further show that this geometry is a minimum on the potential energy surface. In the calculated structures, metal ions prefer to bind with one of the carbonyl oxygen atoms and the OH/OMe groups (Table 2). A shift of the stretching frequency to lower energy for the carbonyl functionality in the FTIR spectra, recorded for $\mathbf{L}_1$ and $\mathbf{L}_2$ in the absence and presence of Mg^{2+} in DMF solution, confirmed the binding of the C=O unit to the Mg^{2+} ion. It is known in the literature that Mg^{2+} binds to the oxygen of a carbonyl functionality in a chelating ligand. For coumarin an appreciable bathochromic shift in the absorption spectra was observed on binding to the Mg^{2+} ion [19,20].

Further, support to the presumption of the coordination by the carbonyl oxygen and adjacent OH/OCH_3 functionalities came from the energy optimized structures for $\mathbf{L}_1 \cdot \mathbf{Mg}^{2+}$ and $\mathbf{L}_2 \cdot \mathbf{Mg}^{2+}$. The possibility of two binding modes for Mg^{2+} and Ca^{2+} towards $\mathbf{L}_2$ was examined theoretically. The calculated binding energy values revealed that the binding modes shown in Scheme 1: (L_1b & L_2b) are less favored than those of Scheme 1: (L_1a & L_2a). The RHF/6-31G* calculated results show that the resultant binding of Mg^{2+} in $\mathbf{L}_2\mathbf{a}$ is preferred by 24.32 kcal/mol than $\mathbf{L}_2\mathbf{b}$ and Ca^{2+} shows the same preferential binding by 15.59 kcal/mol. Additional calculations performed with $\mathbf{L}_1$ also showed a similar trend of interaction energies with Mg^{2+} and Ca^{2+} ions. $\mathbf{L}_1\mathbf{a}$ has been found to be preferred by 6.7 kcal/mol for Mg^{2+} and 20.8 kcal/mol for Ca^{2+} (Supporting information). Importantly, in the case of the Mg^{2+} ion, interaction with –OH and –OMe groups of $\mathbf{L}_1$ leads to the transfer of the hydroxyl proton to the carbonyl oxygen atom (Supporting information). However, this optimized geometry has been found to be a minimum on the potential energy surface. The binding energy for the alkaline earth metal ions with receptor $\mathbf{L}_1$ has been found to be slightly higher than that of $\mathbf{L}_2$ and this result qualitatively corroborates the experimental observation that the stability constants for the binding of alkaline earth metal ions are higher with receptor $\mathbf{L}_1$. It can be assumed that electron correlated calculations could lead to a better prediction for the relative interaction of $\mathbf{L}_1$ with the metal ions compared to that of $\mathbf{L}_2$, this, however, would be expensive for this size of system and hence it has not been calculated in this study. Further, the HOMO–LUMO energy gap calculated at the RHF/6-31G* level of theory suggests that the preferential binding of alkaline earth metal ions reduces this energy gap compared to the corresponding parent geometries and supports the observation of visual color change in the case of these metal ions (Table 2).

4. Conclusions

Two chromogenic receptors, $\mathbf{L}_1$ and $\mathbf{L}_2$, bind with alkaline earth metal ions with a subsequent change in the electronic and luminescence spectral patterns. Binding of different group IIA metal ions follows the order $K_{Mg(II)} \gg K_{Ca(II)} > K_{Sr(II)} \gg K_{Ba(II)}$. A binding induced change in color could be detected for group IIA metal ions; while it was more prominent for Mg^{2+}. Relative affinities of the metal ions towards $\mathbf{L}_1$ and $\mathbf{L}_2$ were rationalized by ab initio calculations. X-ray study reveals an interesting helical structure for $\mathbf{L}_2$.

Acknowledgement

The Department of Science and Technology and Board of Research in Nuclear Science, Government of India, support this work. Authors, DAJ and DKK wish to acknowledge CSIR for a SRF. BG and AD wish to thank Dr. P.K. Ghosh (CSMCRI, Bhavnagar) for his keen interest in this work.

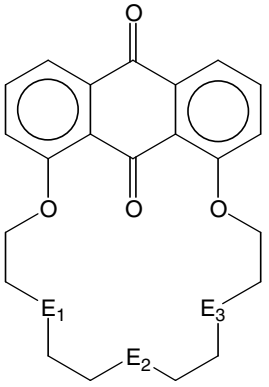
Appendix A. Supplementary material

Change in absorption spectra of $\mathbf{L}_1$ and $\mathbf{L}_2$ with group IA and IIA metal ions, spectrophotometric titration profile for $\mathbf{L}_1$ and $\mathbf{L}_2$ on addition of different group IIA metal ions, visual color change on addition of different group IA and IIA metal ions, binding energies and optimized structure of $\mathbf{L}_1\mathbf{b} \cdot \mathbf{Mg}^{2+}/\mathbf{L}_2\mathbf{b} \cdot \mathbf{Mg}^{2+}$ and $\mathbf{L}_1\mathbf{b} \cdot \mathbf{Ca}^{2+}/\mathbf{L}_2\mathbf{b} \cdot \mathbf{Ca}^{2+}$, coordinates of the optimized structures. Supplementary data associated with this article can be found, in the online version, at doi:10.1016/j.poly.2006.10.051.

References

[1] J.A. Cowan, Introduction to the Biological Chemistry of Magnesium, VCH, New York, 1995.
[2] E. Cooper, J. Cell Biol. 153 (2001) 9.
[3] J.A. Cowan, Biometals 15 (2002) 225–235.
[4] G.A. Rude, Am. J. Cardiol. 63 (1989) 316.
[5] P. Bühlmann, E. Pretsch, E. Bakker, Chem. Rev. 98 (1998) 1593.
[6] H. Miyaji, W. Sato, J.L. Sessler, Angew. Chem., Int. Ed. 39 (2000) 1777.
[7] S. Das, A. Bhattacharya, P.C. Mandal, M.C. Rath, T. Mukherjee, Radiat. Phys. Chem. 65 (2002) 93.
[8] D.A. Jose, D. Krishna Kumar, B. Ganguly, Amitava Das, Tetrahedron Lett. 46 (2005) 5343.
[9] D.A. Jose, D. Krishna Kumar, Bishwajit Ganguly, Amitava Das, Org. Lett. 6 (2004) 3445.
[10] SAINT+, 6.02 ed., Bruker AXS, Madison, WI, 1999.
[11] G.M. Sheldrick, SHELXTL Reference Manual, Version 5.1, Bruker AXS, Madison, WI, 1997.
[12] G.M. Sheldrick, SHELXL-97: Program for Crystal Structure Refinement, University of Göttingen, Göttingen, Germany, 1997.
[13] Mercury 1.4.1 Supplied with Cambridge Structural Database, Copyright CCDC, 2005–2006.
[14] JAGUAR, 5.5 ed., Schrodinger, Inc., Portland, OR, 2004.
[15] W.J. Hehre, L. Radom, P.v.R. Schleyer, Ab Initio Molecular Orbital Theory, Wiley, New York, 1986.
[16] Y. Liu, Z.-Y. Duan, H.-Y. Zhang, X.-L. Jiang, J.-R. Han, J. Org. Chem. 70 (2005) 1450.
[17] L. Prodi, F. Bolletta, M. Montalti, N. Zaccheroni, Tetrahedron Lett. 39 (1998) 5451.
[18] D. Ghosh, A.D. Shukla, R. Banerjee, A. Das, J. Chem. Soc., Dalton Trans. (2002) 1220.
[19] L.F. Capitán-Vallvey, M.D. Fernández-Ramos, A. Lapresta-Fernández, E. Brunet, J.C. Rodŕiguez-Ubis, O. Juanes, Talanta 68 (2006) 1663.
[20] L.H. Jiwan, C. Branger, J.-P. Soumillion, B. Valeur, J. Photochem. Photobiol. A 80 (1998) 169.

The scaffold we have employed integrates an anthraquinone lumophore with a receptor that incorporates an intraannular carbonyl oxygen. Complexation by a metal cation of sufficiently high charge binds with the carbonyl oxygen and results in inversion of the non-radiative n–π* and radiative π–π* transitions, resulting in luminescence turn-on. Recent examples that utilize the PCT photodynamic mechanism include: the detection of alkaline earth metals by a xanthone macrocycle that also contains an intraannular carbonyl oxygen [31,32]; the detection of Ca^{2+} and alkali metals by a tetranaphthylcalixarene [29,30]; and the detection of Hg^{2+} by a 8-hydroxybenzoate [33]. A novel fluorogenic probe that senses reaction chemistry by inversion of n–π* and π–π* states has also been described [34]. Already we have demonstrated selective detection of Pb(II) by **1**, the complete oxygen-containing analog [35]. With relative synthetic ease, we have achieved both the selective detection of Cd(II) and the selective detection of Hg(II) using different thia-substituted macrocycles **2** and **3**. Crystallographic results are presented, including an unusual Hg_2^{2+} crown ether dimer complex which forms upon mercury(II) reduction by the solvent DMF.



1: $E_1,E_2,E_3 = O$
2: $E_1,E_3 = S$ $E_2 = O$
3: $E_1,E_2,E_3 = S$

2. Experimental

2.1. Materials and instrumentation

The metal salts cadmium(II) perchlorate monohydrate (Sigma–Aldrich), mercury(II) perchlorate trihydrate (Alfa-Aesar) and magnesium perchlorate hexahydrate (Sigma–Aldrich), were used as purchased. 1,8-oxybis(ethyleneoxyethyleneoxy)anthracene-9,10-dione (**1**), 1,8-oxybis(ethylenethioethyleneoxy)anthracene-9,10-dione (**2**), and 1,8-thiobis(ethylenethioethyleneoxy)anthracene-9,10-dione (**3**) were synthesized using previously reported procedures [36]. Elemental analyses for carbon and hydrogen were conducted using an Exeter CE-440 Elemental Analyzer. Microanalyses for sulfur were conducted by MHW Laboratories of Phoenix, AZ. All samples were previously dried at 100 ° C under vacuum before elemental analyses to remove solvates. LC-ESI-MS was conducted using a Micromass (Manchester, UK) mass spectrometer. Spectroscopic data including fitting routines for binding constants were conducted according to Ref. [35]. Ref. [37] describes determination of quantum yields. Absorbance data was collected using a HP 8452A diode array spectrophotometer and luminescence titrations conducted using a SPEX Fluoromax fluorimeter. *Caution*. Although we have experienced no difficulties with the perchlorate salts, these should be regarded as potentially explosive and handled with care.

2.2. Synthesis of $[Cd \cdot \mathbf{2}](ClO_4)_2$ (**4**)

0.2 g (0.47 mmol) of **2** was dissolved in 20 mL of dichloromethane, and cadmium (II) perchlorate monohydrate (0.15 g, 0.47 mmol), dissolved in 15 mL of acetonitrile, was added drop wise and stirred for 2 h. All the solvents were evaporated under reduced pressure and the residue dissolved in 20 mL of CH_2Cl_2–methanol (8:2) mixture and layered with diethyl ether. Bright yellow crystals were obtained. Yield ~0.29 g (72%). Melting point 190–194 °C (dec). Elemental *Anal.* Calc. for $C_{22}H_{22}O_{13}S_2CdCl_2$: C, 35.63; H, 2.97; S, 8.65. Found: C, 35.53; H, 3.29; S, 8.74%. ^{1}H NMR (CD_3CN, 22 °C): δ 3.24 (*t*, 4H, CH_2–O, $J = 5.5$ Hz); 3.42 (*t*, 4H, CH_2–O, $J = 5.5$ Hz); 3.89 (*t*, 4 H, CH_2–O, $J = 5.5$ Hz); 4.39 (*t*, 4H, CH_2–O, $J = 5.5$ Hz); 7.35 (*t*, 2H, Ar–H, $J = 5$); 7.69–7.78 (*m*, 4H, Ar–H). ^{13}C NMR (CD_3CN, 25 °C): δ 38.2, 33.9, 67.4, 68.3, 120.4, 120.6, 122.8, 135.4, 131.4, 159.7, 183.4, 185.6. ESI-S *m*/*z*: Found 642.88 (M^+, 100%); Calc. 642.4.

2.3. Synthesis of $[Hg \cdot \mathbf{2}](ClO_4)_2$ (**5**)

0.2 g (0.47 mmol) of **2** was dissolved in 20 mL of dichloromethane and mercury (II) perchlorate trihydrate (0.21 g, 0.47 mmol), in 15 mL of acetonitrile, was added drop wise stirred for 2 h. All the solvents were evaporated under reduced pressure. The residue was dissolved in 5 mL of acetonitrile and mixed with excess diethyl ether (40 mL). A yellow colored precipitate was obtained which was dissolved in 25 mL of acetonitrile and layered with diethyl ether. Yellow colored fibrous crystals were obtained. Yield ~0.19 g (48%). Melting point: 228–230 °C (dec). Elemental *Anal.* Calc. for $C_{22}H_{22}O_{13}S_2HgCl_2$: C, 31.84; H, 2.65; S, 7.73. Found: C, 31.86; H, 2.69; S, 8.04%. ^{1}H NMR (d^6-DMSO, 22 °C): δ 3.51–3.59 (*bm*, 4H, CH_2–O); 3.94–4.01 (*bm*, 8H, CH_2–O); 4.58–4.63 (*bm*, 4H, CH_2–O); 7.62 (*d*, 2H, Ar–H, $J = 7.8$); 7.77–7.89 (*bm*, 4H, Ar–H). ^{13}C NMR (CD_3CN, 25 °C): δ 35.8, 37.3, 64.1, 65.9, 119.4, 119.7, 123.5, 133.7, 135.2, 157.3, 182.6, 185.5. ESI-S *m*/*z*: Found 730.93 (M^+, 100%); Calc. 730.6.

2.4. Synthesis of $[Cd \cdot \mathbf{3}](ClO_4)_2$ (**6**)

0.2 g (0.45 mmol) of **3** was dissolved in 25 mL of dichloromethane and cadmium (II) perchlorate monohydrate (0.14 g, 0.45 mmol), dissolved in 15 mL of acetonitrile,

was added drop wise and stirred for 2 h. All the solvents were evaporated under reduced pressure and the residue dissolved in 20 mL of acetonitrile and layered with diethyl ether. A yellow solid was obtained. Yield ~0.20 g (60%). Melting point: 222–224 °C (dec). Elemental *Anal.* Calc. for $C_{22}H_{22}O_{12}S_3CdCl_2$: C, 34.87; H, 2.91; S, 12.69. Found: C, 35.02; H, 3.23; S, 13.57%. ^{1}H NMR (d^6-DMSO, 22 °C): δ 2.93 (*t*, 4H, CH_2–O, $J = 5$ Hz); 3.03 (*t*, 4H, CH_2–O, $J = 5$ Hz); 3.12 (*t*, 4H, CH_2–O, $J = 5$ Hz); 4.31 (*t*, 4H, CH_2–O, $J = 5$ Hz); 7.5–7.54 (*d*, 2H, Ar–H, $J = 9.8$ Hz); 7.66–7.76 (*bm*, 4H, Ar–H). ^{13}C NMR (DMSO-d_6, 25 °C): δ 30.4, 32.4, 32.7, 71.8, 118.7, 120.4, 123.4, 134.2, 134.4, 158.1, 180.9, 183.3. ESI-MS *m*/*z*: Found 658.82 (M^+, 100%); Calc. 658.5.

2.5. Synthesis of [Hg · 3](ClO$_4$)$_2$ (7)

0.2 g (0.45 mmol) of **3** was dissolved in 20 mL of dichloromethane and mercury (II) perchlorate trihydrate (0.2 g, 0.45 mmol), in 15 mL of acetonitrile, was added dropwise and stirred for 2 h. The precipitate that formed was dissolved again in 25 mL of 617 acetonitrile–methanol (8:2) and layered with diethyl ether. A flaky, yellow solid was obtained. Yield ~0.25 g (65%). Melting point: 165–68 °C (dec). Elemental *Anal.* Calc. for $C_{22}H_{22}O_{12}S_3HgCl_2$: C, 31.24; H, 2.60; S, 11.37. Found: C, 31.36; H, 2.96; S, 11.86%. ^{1}H NMR (d^6-DMSO, 22 °C): δ 3.30–3.54 (*bm*, 12H, CH_2–O,); 4.38–4.49 (*bm*, 4H, CH_2–O); 7.5–7.54 (*d*, 2H, Ar–H, $J = 9.4$ Hz); 7.66–7.79 (*bm*, 4H, Ar–H). ^{13}C NMR (d^6-DMSO, 25 °C): δ 30.8, 31.9, 32.3, 68.4, 119.1, 120.1, 123.3, 133.9, 134.9, 157.4, 180.1, 182.7. ESI-MS *m*/*z*: Found 746.65 (M^+, 100%); Calc. 746.6.

2.6. Synthesis of [Hg$_2$ · (3)$_2$](ClO$_4$)$_2$ (8)

0.1 g (0.12 mmol) of **7** was dissolved in 5 mL of dimethylformamide. Over time, yellow crystals were obtained along with elemental mercury. Yield ~0.25 g (65%). Melting point 195–198 °C (dec). Elemental *Anal.* Calc. for $C_{44}H_{44}O_{16}S_6Hg_2Cl_2$: C, 35.40; H, 2.95; S, 12.89. Found: C, 35.31; H, 3.35; S, 12.80%. Due to poor solubility, no NMR spectra were obtained. ESI-MS *m*/*z*: Found 1393.15 (M^+, 100%); Calc. 1393.8.

2.7. Synthesis of [Mg · 1](ClO$_4$)$_2$ (9)

0.15 g (0.37 mmol) of **1** was dissolved in 15 mL of acetonitrile and a solution of 0.125 g (0.37 mmol) of magnesium (II) perchlorate hexahydrate in 10 mL of acetonitrile was slowly added. The mixture was stirred for 2 h and the solvent evaporated under reduced pressure. The residue was dissolved in 10 mL of acetonitrile and layered with diethyl ether which produced a yellow crystalline solid. Yield: 55%. Melting point >300 °C. Elemental *Anal.* Calc. for [Mg · **1** · (H_2O)](ClO$_4$)$_2$: $C_{22}H_{24}O_{16}MgCl_2$: C, 41.32; H, 3.75. Found: C, 40.83; H, 3.64%. ^{1}H NMR (CD_3CN, 22 °C): δ 3.19 (*bm*, 20H, CH_2–O + H_2O (coordinated to magnesium); 4.24 (*t*, 4H, CH_2–O, $J = 4.4$ Hz); 7.34 (*t*, 2H, Ar–H, $J = 5$); 7.63–7.67 (*m*, 4H, Ar–H). ^{13}C NMR (CD_3CN, 25 °C): δ 69.6, 70.1, 70.2, 70.6, 120.5, 121.4, 122.2, 135.4, 136.5, 159.7. ESI-MS *m*/*z*: Found 522.04 (M^+, 100%), Calc. 522.18.

2.8. X-ray crystallography

A crystal of compound **4**, grown by vapor diffusion of diethyl ether in methanol, was mounted on a Bruker SMART CCD diffractometer for data collection at 173(2) K using Mo Kα radiation. Final cell constants were calculated from the *xyz* centroids of 2947 reflections from the data collection after integration [38]. Structures were solved by direct methods using SIR92 [39] or SHELXS-97 [40] and refined using SHELXL-97 [41]. There is a compositional disorder in one coordination site around the Cd atom. The site is occupied 71% of the time by a methanol molecule and 29% of the time by a water molecule, hydrogen bonded to another water molecule. The perchlorate (Cl2–O14) was modeled as disordered over two positions (57:43). The dichloromethane was modeled as disordered over two positions (69:31). Crystallographic data for compound **8** and **9** were collected at 295 K, using Mo Kα radiation on a Nonius CAD4 diffractometer. Psi-scan data collection was used for absorption corrections. Refinement was completed using the WINGX suite of crystallographic software [41,42]. Compound **9** has one perchlorate, Cl(2), disordered over two positions in a 62:38 ratio. Table 1 lists additional crystal and refinement information.

3. Results

3.1. Synthesis and crystallography

Addition of equal molar amounts of macrocycles **2** and **3** to cadmium and mercury perchlorate salts yield 1:1 adducts as confirmed by NMR, elemental analyses and ESI-MS. Characterization of compound **4** by single-crystal X-ray crystallography also confirms that Cd^{2+} is encapsulated by macrocycle **2** (Fig. 1). The metal center has octahedral geometry that includes bonds to the three ring heteroatoms, the intraannular carbonyl, a perchlorate anion, and either a methanol or water solvent molecule in compositional disorder (71:29%). The dihedral angle formed between the two aromatic rings of the anthraquinone is 0.0°, requiring a planar anthraquinone that also participates in π-stacking (~3.5 Å) within the unit cell. Important bond distances and angles of **4** are listed in Table 2.

Both compound **3** and its mercury(II) adduct have poor solubility in most organic solvents. For this reason, crystals were grown in the polar solvent DMF. Upon slow evaporation of the solvent, yellow crystals of **8** formed in addition to very fine droplets of elemental mercury. Subsequent structural analysis revealed that **3** does not contain the Hg(II) cation, but surprisingly ligates Hg_2^{2+}

Table 1
Crystallographic and refinement data for $[Cd \cdot \mathbf{2} \cdot H_2O \cdot ClO_4]ClO_4 \cdot CH_2Cl_2$ (**4**), $[Hg_2 \cdot (\mathbf{3})_2](ClO_4)_2$ (**8**), and $[Mg \cdot \mathbf{1} \cdot (H_2O)_2](ClO_4)_2$ (**9**)

	4	**8**	**9**
Empirical formula	$C_{24}H_{28}CdCl_4O_{14}S_2$	$C_{44}H_{44}O_{16}S_6Hg_2Cl_2$	$C_{22}H_{26}Cl_2MgO_{17}$
Formula weight	859.90	1493.2	657.6
Temperature (K)	173(2)	295(2)	295(2)
Diffractometer	Smart Bruker	Nonius CAD4	Nonius CAD4
Crystal system	triclinic	monoclinic	monoclinic
Space group	$P\bar{1}$	$P2_1/c$	$P2_1/c$
a (Å)	9.2809(11)	9.197(3)	9.941(1)
b (Å)	11.5038(14)	17.843(3)	11.880(4)
c (Å)	15.5084(18)	14.690(6)	22.727(6)
α (°)	77.098(2)		
β (°)	80.722(2)	91.88(3)	93.53(1)
γ (°)	82.401(2)		
Volume (Å^3)	1584.9(3)	2409(13)	2678.9
Z	2	2	4
Density (calc) (g cm^{-3})	1.802	2.058	1.631
Absorption coefficient (mm^{-1})	1.225	6.801	0.350
$F(000)$	865	1452	680
θ Range	1.36–25.06	1.0–25.0	1.8–25.0
Index ranges	$-11 \leqslant h \leqslant 11$, $-13 \leqslant k \leqslant 13$, $-18 \leqslant l \leqslant 18$	$0 \leqslant h \leqslant 10$, $0 \leqslant k \leqslant 21$, $-17 \leqslant l \leqslant 17$	$0 \leqslant h \leqslant 11$, $0 \leqslant k \leqslant 14$, $-26 \leqslant l \leqslant 26$
Independent reflections [R_{int}]	5603 [0.0436]	4228 [0.0940]	4709 [0.0344]
Observed reflections	4251	2747	2928
Maximum/minimum transmission	0.838/0.749	0.281/0.235	
Data/restr./parameters	5603/13/449	4228/0/316	4709/0/427
Goodness-of-fit	1.02	1.03	1.02
Final R indices [$I>2\sigma(I)$]	$R_1 = 0.0486$ $wR_2 = 0.1014$	$R_1 = 0.0515$ $wR_2 = 0.1073$	$R_1 = 0.0572$ $wR_2 = 0.1428$
R indices (all data)	$R_1 = 0.0740$ $wR_2 = 0.1030$	$R_1 = 0.1146$ $wR_2 = 0.1258$	$R_1 = 0.1190$ $wR_2 = 0.1716$
Peak and hole (e Å^{-3})	0.93 and −0.80	2.36 and −1.09	0.35 and −0.53

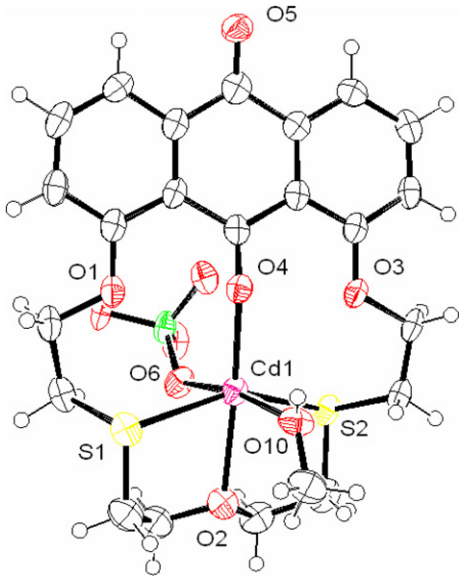


Fig. 1. Thermal ellipsoid (50%) diagram of $[Cd(II) \cdot \mathbf{2} \cdot MeOH \cdot ClO_4]^+$ cation. The second perchlorate counteranion and the CH_2Cl_2 solvent molecule have been removed for clarity.

instead, bridged by two molecules of **3** (Fig. 2). The ring structure is significantly bent to accommodate a trigonal arrangement of sulfur atoms that bind to a Hg(I) atom within each macrocycle. The anthraquinone also adopts a slightly bent conformation where the two aromatic rings are related by a dihedral angle of 10.7°. The Hg–Hg bond in this structure is 2.550(1) Å, on the same order as that found in $Hg_2(NO_3)_2$ (2.508(2) Å) [43]. The Hg_2^{2+} unit has previous been found bridging oxygen-containing crown ethers [44] and has also been found bridging nitrogen-containing phenanthroline [45] and selenaaza complexes [46]. Only two sulfur-containing Hg_2^{2+} complexes have been reported [47,48]. Poor solubility of **8** restricted study by NMR spectroscopy, and luminescence of the Hg_2^{2+}-containing complex was not observed.

The crystal structure of the magnesium(II) perchlorate complex **9** is shown in Fig. 3. Compound **1** has been distorted to accommodate a pseudo pentagonal bipyramidal geometry around the central magnesium(II) ion. While the Mg–O4 bond distance is longer (2.716(3) Å) than the bonds to the ether or carbonyl oxygens (Table 2), this bond is significantly shorter than the bond to the second phenolic type oxygen (Mg–O3 = 3.767(4) Å). Although crystals were grown by vapor diffusion of diethyl ether into acetonitrile, the oxophilic magnesium remains capped by two water molecules, present as hydrates from the metal salt or other water present in the solvent. The planarity of the anthraquinone in this structure is midway between the previous two structures with a dihedral angle of 4.7°.

Table 2
Selected bond distances (Å) and angles

	4 (Cd^{2+})	**8** (Hg^{+})	**9** (Mg^{2+})
Temperature (K)	173	295	295
M—O=C	(O4) 2.198(4)	(O2) 2.874(3)	(O2) 2.000(3)
M–E1	(S1) 2.621(2)	(S1) 2.654(3)	(O5) 2.186(3)
M–E2	(O2) 2.434(4)	(S2) 2.838(3)	(O6) 2.110(3)
M–E3	(S2) 2.608(2)	(S3) 2.741(3)	(O7) 2.244(3)
Cd–$OClO_3$	(O6) 2.375(4)		
Cd–MeOH	(O10) 2.28(4)		
Hg–Hg		2.550(1)	
Mg–OH_2			(O16) 2.048(4)
Mg–OH_2			(O17) 2.021(4)
O=C intraannular	O4–C13 1.237(6)	O2–C3 1.224(11)	O2–C3 1.229(5)
O=C extraannular	O5–C6 1.218(6)	O1–C10 1.224(12)	O1–C10 1.227(5)
O–M–E2	O4–Cd–O2 175.6	S2–Hg–O2 141.8	O2–Mg–O6 154.1
E1–M–E3	S1–Cd–S2 152.1	S1–Hg–S3 93.6	O5–Mg–O7 146.5

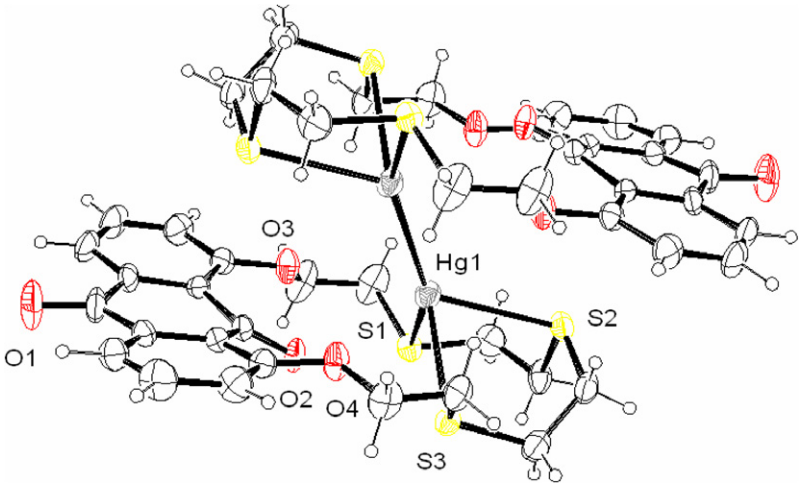


Fig. 2. Thermal ellipsoid (30%) diagram of $[Hg_2 \cdot \mathbf{3}_2]^{2+}$ cation showing the Hg–Hg bond. The perchlorate counteranions have been removed for clarity.

3.2. Spectroscopy

A shift to longer wavelength occurs in the optical absorption spectrum upon titration of **2** with $Cd(ClO_4)_2$ in acetonitrile (Fig. 4). Concomitant with the shift in the absorbance maximum of **2** is the corresponding increase in fluorescence at 506 nm. We observe a clean isosbestic point in the titration of Cd(II) with **2**, that produces a $\log K_{binding}$ of 4.1(2), representing: $\mathbf{2} + Cd^{2+} \leftrightarrow [Cd \cdot \mathbf{2}]^{2+}$ (Table 3 and fitting plot provided in the Supplemental material). Fluorescence enhancement ($\lambda_{max} = 522$ nm) is also observed when Hg^{2+} ion is combined with **3** (Supplemental material); however the binding properties could not be determined in this case since isosbestic behavior was not observed. We attribute initial Hg^{2+} complex formation to a 1:2 metal:ligand sandwich complex, $[Hg \cdot \mathbf{3}_2]^{2+}$, before conversion into the 1:1 $[Hg \cdot \mathbf{3}]^{2+}$ product at higher Hg^{2+} concentration. Fig. 5 shows the luminescence changes exhibited by **2** and **3** in the presence of two equivalents of metal perchlorate salts in acetonitrile and compared to changes previously observed for **1** [13]. While **1** has good selectivity for Pb(II), **2** and **3** are almost exclusively selec-

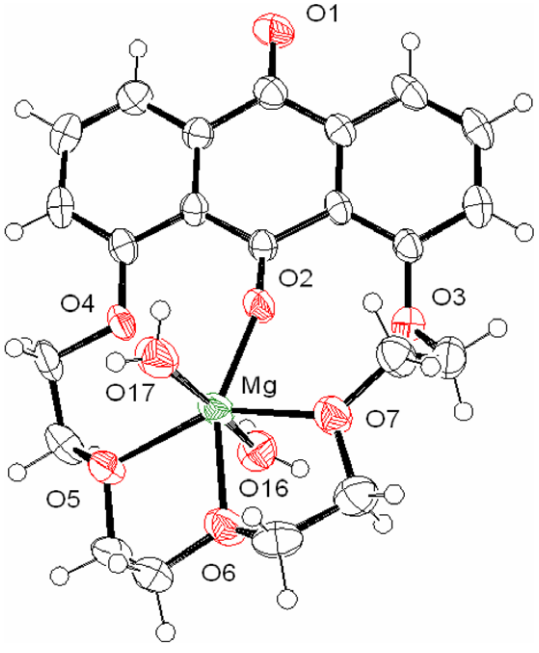


Fig. 3. Thermal ellipsoid (50%) diagram of $[Mg \cdot \mathbf{1} \cdot (H_2O)_2]^{2+}$ cation. The two perchlorate counteranions have been removed for clarity.

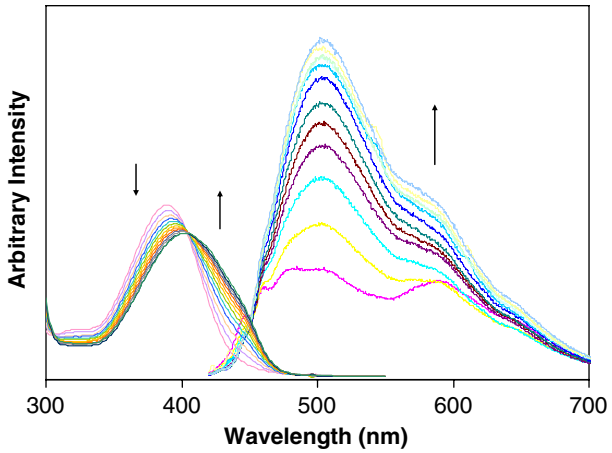


Fig. 4. UV/Vis and fluorescence titration of **2** with $Cd(ClO_4)_2$ in acetonitrile. Each addition equals 0.2 equiv. of Cd^{2+}. Excitation at 404 nm ($\varepsilon_{404} = 7100\ M^{-1}\ cm^{-1}$). $\mathbf{2} = 1.0 \times 10^{-4}$ M.

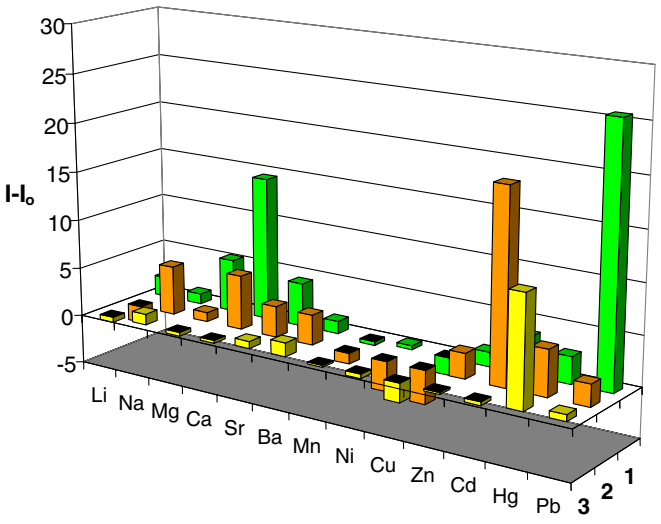


Fig. 5. Fluorescence changes of **1**–**3** after addition of two equivalents of metal perchlorate salts. Excitation wavelength was 420 nm and the emission intensity changes were calculated λ_{max} at 515 nm (Pb^{2+}), 510 nm (Cd^{2+}) and 520 nm (Hg^{2+}). **1**–**3** $= 1.0 \times 10^{-4}$ M; $M^{n+} = 2.0 \times 10^{-4}$ M. Data for **1** are from Ref. [35]. A digital picture showing luminescence is part of the TOC graphic.

tive for Cd(II) and Hg(II), respectively. A photograph for comparison is provided in the TOC graphic and the Supplemental material.

4. Discussion

Addition of **2** and **3** to cadmium(II) and mercury(II) perchlorate salts in acetonitrile produces selective luminescence that is different from that previously observed for **1** in the presence of lead(II) [35]. Each macrocycle has unique emission properties that are cation dependent. We have also observed that interference from alkaline earth metals decrease with increasing number of sulfur atoms in the lumophore. This is quite apparent in Fig. 5 which shows the change in luminescence going across each series and supports previous knowledge that alkaline earth metals tend to be more oxophilic, and supported by the coordination of two water molecules in the Mg^{2+} complex (Fig. 3). Results are consistent with the soft mercuric ion showing preference for the macrocycle with the greatest number of soft sulfur atoms. Also, transition metals with partially filled d-orbitals always quench luminescence in these cases. Metal ions such as Mn^{2+}, Ni^{2+} and Cu^{2+} show complete quenching in fact, where luminescence is even less than the macrocycle alone in acetonitrile solvent. This quenching mechanism using available d–d transitions has previously been observed in other luminescence systems [49].

X-ray crystallography of these complexes reveals that a variety of coordination geometries can exist for the central metal in the solid-state. Previous work with Pb(II) has two perchlorates coordinated to the metal center, one above and one below macrocycle **1**, and the Zn and Mn structures of **1** reveal that both a water molecule and an acetonitrile molecule cap the metal above and below the plane of the same encapsulating macrocycle [35]. Two different cases are presented here; (A) where one perchlorate anion and one solvent molecule are coordinated in the case of Cd^{2+} (Fig. 1), and (B) a second case where two water molecules coordinate to Mg^{2+} (Fig. 3). In the case of magnesium, this structure is essentially isostructural to that found for Zn and Mn where an acetonitrile has been replaced by either methanol or water (71:29% compositional disorder). The space group and cell parameters are quite similar in these two structure types, and suggest the magnesium metal center prefers the harder oxygen-containing ligands.

Previous work has demonstrated that Hg_2^{2+} extraction can be accomplished using thiacarbamoyl substituted calix[4]arenes [50]. The Hg_2^{2+} adduct formed in this case however, **8** (Fig. 2), does not result from the addition of

Table 3
Photophysical data for complexes in acetonitrile

Ligand	**1**	**2**	**3**	Pb^{2+} **1**[a]	Cd^{2+} +**2**	Hg^{2+} +**3**
λ_{vis} (acetonitrile, nm)	385	388	390	404	402	406
log K_b				5.5 ± 0.3	4.1 ± 0.2	
λ_{em} (acetonitrile, nm)	480	476	481	515	506	522
Quantum yield	<0.001[b]	0.004	0.0016	0.022	0.010	0.006

[a] Data in this column from Ref. [13].
[b] Quantum yield from Ref. [37].

mercurous ion, but certainly via reduction of added mercuric ion by the solvent DMF. This has previously been observed in the formation of silver nanocrystals by the reduction of Ag^{+} ion in DMF [51]. The presence of **3** is also not necessary for reduction since Hg^{0} is still formed when Hg^{2+} is the only species added to DMF. Reduction by DMF is also observed for other Hg(II) salts. Formation of Hg^{0} is postulated based upon the known mercurous ion disproportionation reaction: $Hg_2^{2+} \leftrightarrow Hg^{0} + Hg^{2+}$. This also does not occur in other polar solvents such as CH_3CN or DMSO, which do not contain an aldehyde group available for oxidation as is the case with DMF. Reduction of Hg^{2+} has also been observed in the structural characterization of a Hg_2^{2+} complex containing a tripodal nitrogen ligand [52]. The authors concluded that oxidation of the ligand by Hg^{2+} happens in this case, where the production of Hg^{0} was not observed and isolation of the Hg_2^{2+} complex occurs in low yield. Using DMF as the media in this case, production of Hg_2^{2+} and the resulting sulfur-mercury(I) adduct occur in high yield.

5. Conclusions

Photoinduced charge transfer (PCT) sensors of this type provide a means of imparting cation selectivity. Whereas other systems typically incorporate standard size macrocycles (i.e. 18-crown-6, 15-crown-5, and their heteroatom-substituted analogs), the intraannular carbonyl in this system changes the receptor size and alters binding properties of potential guests, distinctive from previously studied macrocycles. With relative ease of synthesis as well, we have been able to tailor the PCT macrocycle and fine tune selectivity with excellent control using rings of the same size that contain different combinations of heteroatoms. The charge-to-size ratio of the metal cation in combination with receptor composition results in variation in emission properties, specific for Cd^{2+}, Hg^{2+} and Pb^{2+} in these examples. We are currently investigating new receptors that will further refine selectivity and solubility for this family of luminescence sensors.

Acknowledgments

The authors thank the National Science Foundation (0082978) and the South Dakota 2010 Initiative for financial support. We also thank the University of South Dakota and NSF-EPSCOR (9720642 and 0091948) for the purchase and upgrade of a Nonius CAD4 X-ray diffractometer. Benjamin Kucera at the University of Minnesota X-ray Diffraction Laboratory completed the structure determination of $[Cd \cdot \mathbf{2} \cdot H_2O \cdot ClO_4]ClO_4 \cdot CH_2Cl_2$ (**4**). The elemental analyzer was purchased using NSF-URC funding (CHE-0532242).

Appendix A. Supplementary material

Hg(II) absorbance and luminescence spectra are available as supplementary data. CCDC 296855, 296853, and 296854 contain the supplementary crystallographic data for **4**, **8** and **9**. These data can be obtained free of charge via http://www.ccdc.cam.ac.uk/conts/retrieving.html, or from the Cambridge Crystallographic Data Centre, 12 Union Road, Cambridge CB2 1EZ, UK; fax: (+44) 1223-336-033; or e-mail: deposit@ccdc.cam.ac.uk. Supplementary data associated with this article can be found, in the online version, at doi:10.1016/j.poly.2006.10.046.

References

[1] R.L. Chaney, J.A. Ryan, Y.M. Li, S.L. Brown, in: M.J. McLaughlin, B.R. Singh (Eds.), Cadmium in Soils and Plants, Kluwer, Boston, 1999.
[2] A. Renzoni, F. Zino, E. Franchi, Environ. Res. 77 (1998) 68.
[3] O. Malm, Environ. Res. 77 (1998) 73.
[4] EPA Fact Sheet EPA-823-F-01-011; EPA, Office of Water, Washington, DC, 2001.
[5] N. Rifai, G. Cohen, M. Wolf, L. Cohen, C. Faser, J. Savory, L. DePalma, Ther. Drug Monit. 15 (1993) 71, and references within.
[6] S. Dobson, Cadmium-Environmental Aspects, World Health Organization, Geneva, 1992.
[7] D.W. Boening, Chemosphere 40 (2000) 1335.
[8] P.W. Davidson, G.J. Myers, C. Cox, C.F. Shamlaye, D.O. Marsh, M.A. Tanner, M. Berlin, J. Sloane-Reeves, E. Cernichiari, O. Choisy, A. Choi, T.W. Clarkson, Neurotoxicology 16 (1995) 677.
[9] M. Choi, M. Kim, K.D. Lee, K.N. Han, I. Yoon, H.J. Chung, J. Yoon, Org. Lett. 3 (2001) 3455.
[10] M. Narita, Y. Higuchi, F. Hamada, H. Kumagai, Tetrahedron Lett. 39 (1998) 8687.
[11] J. Bourson, F. Badaoui, B. Valeur, J. Fluoresc. 4 (1994) 275.
[12] N. Higuchi, T. Niimi, N. Ogawa, F. Hamada, K. Hitoshi, I. Nobuhiko, S. Miyano, C. Kabuto, Tetrahedron 56 (2000) 4659.
[13] N.J. Youn, S.K. Chang, Tetrahedron Lett. 46 (2005) 125.
[14] G. Hennrich, H. Sonnenschein, U. Resch-Genger, J. Am. Chem. Soc. 121 (1999) 5073.
[15] L. Prodi, M. Montalti, N. Zaccheroni, J.S. Bradshaw, R.M. Izatt, P.B. Savage, Tetrahedron Lett. 42 (2001) 2941.
[16] S.H. Yang, O.J. Shon, K.M. Park, S. S Lee, H.J. Park, M.J. Kim, J.H. Lee, J.S. Kim, Bull. Korean Chem. Soc. 23 (2002) 1585.
[17] A.M. Costero, R. Andreu, E. Monrabal, R. Martinez-Manez, F. Sancenon, J. Soto, J. Chem. Soc., Dalton Trans. (2002) 1769.
[18] C.T. Chen, W.P. Huang, J. Am. Chem. Soc. 124 (2002) 6246.
[19] W.S. Xia, R.H. Schmehl, C.J. Li, J.T. Mague, C.P. Luo, D.M. Guldi, J. Phys. Chem. B 106 (2002) 833.
[20] K. Rurack, U. Resch-Genger, J.L. Bricks, M. Spieles, Chem. Commun. (2000) 2103.
[21] J. Bourson, J. Pouget, B. Valeur, J. Phys. Chem. 97 (1993) 4552.
[22] B. Valeur, J. Pouget, J. Bourson, M. Kaschke, N.P. Ernsting, J. Phys. Chem. 96 (1992) 6545.
[23] A. Caballero, R. Martinez, V. Lioveras, I. Ratera, J. Vidal-Gancedo, K. Wurst, A. Tarraga, P. Molina, J. Veciana, J. Am. Chem. Soc. 127 (2005) 15666.
[24] Y. Yu, L. Lin, K. Yang, X. Zhong, R. Huang, L. Zheng, Talanta (2006), articles online.
[25] E.M. Nolan, S.J. Lippard, J. Am. Chem. Soc. 125 (2003) 14270.
[26] Y. Yang, K. Yook, J. Tae, J. Am. Chem. Soc. 127 (2005) 16760.
[27] S. Yoon, A. Albers, A. Wong, C. Chang, J. Am. Chem. Soc. 127 (2005) 16030.
[28] Y. Miyake, A. Ono, Tetrahedron Lett. 46 (2005) 2441.
[29] I. Leray, J. P Lefevre, J.-F. Delouis, J. Delaire, J.B. Valeur, Chem. Eur. J. 7 (2001) 4590.
[30] I. Leray, F.O. O'Reilly, J.L. Habib Jiwan, J.P. Soumillion, B. Valeur, Chem. Commun. (1999) 795.
[31] M. Montalti, L. Prodi, N. Zaccheroni, J. Fluoresc. 10 (2000) 71.

[32] L. Prodi, F. Bolletta, N. Zaccheroni, I.F. Watt, N.J. Mooney, Chem. Eur. J. (1998) 1090.
[33] H. Zhang, L.F. Han, K.A. Zachariasse, Y.B. Jiang, Org. Lett. 7 (2005) 4217.
[34] Z. Zhou, C.J. Farrni, J. Am. Chem. Soc. 126 (2004) 8862.
[35] M. Kadarkaraisamy, A.G. Sykes, Inorg. Chem. 45 (2006) 779.
[36] M. Kadarkaraisamy, E. Dufek, D. Lone Elk, A.G. Sykes, Tetrahedron 61 (2005) 479.
[37] B. Kampmann, Y. Lian, K. Klinkel, P.A. Vecchi, H.L. Quiring, C.C. Soh, A.G. Sykes, J. Org. Chem. 67 (2002) 3878.
[38] SAINT V6.1, Bruker Analytical X-ray Systems, Madison, WI, 1999.
[39] A. Altomare, M.C. Burla, M. Camalli, G. Cascarano, C. Giacovazzo, A. Guagliardi, A.G.G. Moliterni, G. Polidori, R. Spagna, J. Appl. Cryst. 32 (1998) 115.
[40] SHELXTL-Plus V5.10, Bruker Analytical X-ray Systems, Madison, WI, 1998.
[41] G.M. Sheldrick, SHELX97 – Programs for Crystal Structure Analysis (Release 97-2), Institüt für Anorganische Chemie der Universität, Göttingen, Germany, 1998.
[42] WINGX: An Integrated System of Windows Programs for the Solution, Refinement, and Analysis of Single Crystal X-ray Diffraction Data, Ver. 1.70, L.J. Farrugia, J. Appl. Cryst. 32 (1999) 837.
[43] D. Grdenic, M. Sikirica, I. Vickovic, Acta Crystallogr. B31 (1975) 2174.
[44] R. Malleier, H. Kopacka, W. Schuh, K. Wurst, P. Peringer, Chem. Commun. (2001) 51.
[45] V.J. Catalano, M.A. Malwitz, B.C. Noll, Inorg. Chem. 41 (2002) 6553.
[46] S. Panda, H.B. Singh, R.J. Butcher, Inorg. Chem. 43 (2004) 8532.
[47] K. Brodensen, A. Knorr, Z. Naturforsch. Teil. B 45 (1990) 1193.
[48] K. Brodensen, G. Liehr, W. Rolz, Z. Anorg. Allg. Chem. 428 (1977) 166.
[49] L.J. Larson, J.I. Zink, Inorg. Chim. Acta 169 (1990) 71, and references within.
[50] A.T. Yordanov, D.M. Roundhill, J.T. Mague, Inorg. Chim. Acta 250 (1996) 295.
[51] I. Pastoriza-Santos, L.M. Liz-Marzan, Pure Appl. Chem. 72 (2000) 83.
[52] D.C. Bebout, J.F. Bush, E.M. Shumann, J.A. Viehweg, M.E. Kastner, D.A. Damon, S.M. Baldwin, J. Chem. Crystallogr. 33 (2003) 457.

On the other hand, the design of transition-metal clusters with novel magnetic properties is considerable interest from the standpoint of material chemistry and condensed matter physics [27–30]. Although a great effort has been made to study magnetic properties of dinuclear Cu(II) complexes, there has been comparatively little work reported on higher nuclearity isolated compounds, especially for these with more than four metal ions. Structural and magnetic data have been reported for pentanuclear Cu(II) complex, in which four metal centers are arranged in a square Cu_4O_4 alkoxide bridged grid and one external Cu(5) ion is connected via diazine N–N group to Cu(2) [31]. Antiferromagnetic intramolecular interactions between external Cu(II) and Cu(2) ions are predominant, whilst those between Cu(1)–Cu(4) and Cu(4)–Cu(3) within the triangular grouping of coppers are weak ferromagnetic ($J_1 = 1.9$ and $J_2 = -90$).

A chiral hexanuclear complex having a propeller structure has been studied [32]. Its core structure consists of six Cu(II) ions and five oxygen atoms and resembles a cryptand, and has a proton trapped inside. Magnetic susceptibility measurements show the complex has antiferromagnetically coupled ground state. Similarly, hexanuclear compound $[Cu_6(tmen)_6(\mu\text{-}N_3)_2(\mu\text{-}C_2O_4)_3(H_2O)_2][ClO_4]_4$ with *N*,*N*,*N*′,*N*′-tetramethylethane-1,2-diamine [33] and sulfato-bridged hexanuclear dimer show significant antiferromagnetic coupling [34]. On the contrary, the six copper(II) ions in the core of the hexanuclear cluster – $[PhSiO_2Cu_6(O_2SiPh)_6]\cdot 6EtOH$ are ferromagnetically coupled with $J = 42\ cm^{-1}$ [35]. Antiferromagnetic exchange between copper(II) ions has been also observed in octanuclear macrocyclic complexes [36]. The structural and magnetic studies for the dodecanulcear macrocyclic complex $[Cu_6L(\mu_2\text{-}OH)_3](ClO_4)_3\cdot 4H_2O$ have been reported [37]. The structure of the dimeric cation consists of two almost flat, hexagonal macrocyclic rings, each involving an array of six Cu(II) centers. Two macrocyclic rings are connected by four hydroxide groups. The magnetic behavior and calculated exchange integrals indicate significant antiferromagnetic interactions.

This paper deals with the structural, spectroscopic and magnetic studies of new decanuclear copper(II), in which two pentanuclear subunits are linked through chloride bridges.

2. Experimental

2.1. Synthesis

The complex of the formula $[Cu_5(\beta\text{-alaha})_4Cl_2]_2\cdot 2HCl\cdot 15H_2O$ was synthesized in reaction of $CuCl_2$ (0.1 M) and β-alaninehydroxamate hydrochloride $C_3H_8N_2O_2\cdot HCl$ (0.1 M) in water solution. The deep blue solution was adjusted to pH ≈ 5.5. The solution kept at stable temperature provided dark green single crystals suitable for X-ray analysis. The size of the crystals was appropriate for absorption spectra measurements.

2.2. X-ray structure determination

The structure of the title compound was determined by single-crystals X-ray diffraction. Crystal data are given in Table 1, together with the refinement details. All X-ray measurements of the crystal were performed at low temperature using an Oxford Cryosystem device on a Kuma KM4CCD κ-axis diffractometer with graphite-monochromated MoKα radiation. The crystal was positioned at 65 mm from the CCD camera. 612 frames were measured at 0.75° intervals with a counting time of 15 s. Accurate cell parameters were determined and refined by least-squares fit of 4200 the strongest reflections. The data were corrected for Lorentz and polarization effects. Analytical absorption correction was applied. Data reduction and analysis were carried out with the Oxford Diffraction (Poland) Sp. z o.o (formerly Kuma Diffraction Wrocław, Poland) programs. The structure was solved by direct methods (program SHELXS97 [38]) and refined by the full-matrix least-squares method on all F^2 data using the SHELXL97 [39] programs. Non-hydrogen atoms were refined with anisotropic displacement parameters; all hydrogen atoms from the $>CH_2$ and $>NH_2$ groups were included from geometry of molecules and four hydrogen atoms only from the water molecules were identified in $\Delta\rho$ maps. During refinement all hydrogen atoms parameters, including isotropic displacement factors, were fixed.

2.3. Magnetic and spectroscopic measurements

The magnetic susceptibility of solid sample was recorded using a SQUID MPMS5 magnetometer in the temperature range 1.8–300 K at external field of 0.5 T and 200 G. All data were corrected for diamagnetism estimated from Pascal's constants.

Absorption spectra were measured at 293 and 4 K on a Carry-Varian 500 Scan spectrophotometer equipped with a helium flow cryostat (OXFORD CF 1204).

3. Results and discussion

The crystal structure of the title compound consists of discrete decanuclear molecules of complex: $[Cu_5(\beta\text{-alaha})_4Cl_2]_2$ composed of two pentanuclear clusters bridged by chloride ions, chloride anions and non-coordinated water molecules. Coordination of copper(II) ions in pentanuclear subunit as well as the atom labeling are given in Fig. 1. Table 2 contains the selected bond distances and angles relevant to the metal coordination sphere. All nitrogen and oxygen atoms of four β-alaninehydroxamate ligands are involved in coordination of five copper(II) ions. The pentanuclear cluster with symmetry close to C_{4v} is formed by four copper(II) ions (Cu(2)–Cu(4)) in the basal plane (±0.0368 Å) and a Cu(1) ion in apex, situated 0.54 Å above this plane. The center-to-center distances are in the range 3.2805–6.5262 Å. The distances between the central and peripheral copper(II) ions vary from 3.2805 (Cu1–Cu2) to

Table 1
Crystal data and structure refinement for $[Cu_5(\beta\text{-alaha})_4Cl_2]_2 \cdot 2HCl \cdot 15H_2O$

Empirical formula	$C_{24}H_{80}C_{16}Cu_{10}N_{16}O_{31}$
Formula weight	1937.14
Temperature (K)	100(2)
Wavelength (Å)	0.71073
Crystal system	monoclinic
Space group	*C*2/*c*
a (Å)	25.901(5)
b (Å)	15.127(3)
c (Å)	17.636(4)
alpha (°)	90
beta (°)	116.65(3)
gamma (°)	90
Volume (Å^3)	6176(2)
Z	4
D_{calc} (Mg m^{-3})	2.083
Absorption coefficient (mm^{-1})	3.725
F(000)	3904
Crystal size (mm)	$0.15 \times 0.10 \times 0.10$
Theta range for data collection (°)	3.30–28.80
Ranges of *h*,*k*,*l*	$-33 \geqslant 29$, $-19 \geqslant 20$, $-21 \geqslant 23$
Reflections collected	19442
Independent reflections (R_{int})	7427 (0.0422)
Absorption correction	analytical
Data/parameters	7427/394
Goodness-of-fit (F^2)	1.144
Final R_1/wR_2 indices ($I > 2sI$)	0.0577/0.1755
Largest difference in peak and hole (e A^{-3})	3.074 and −2.162

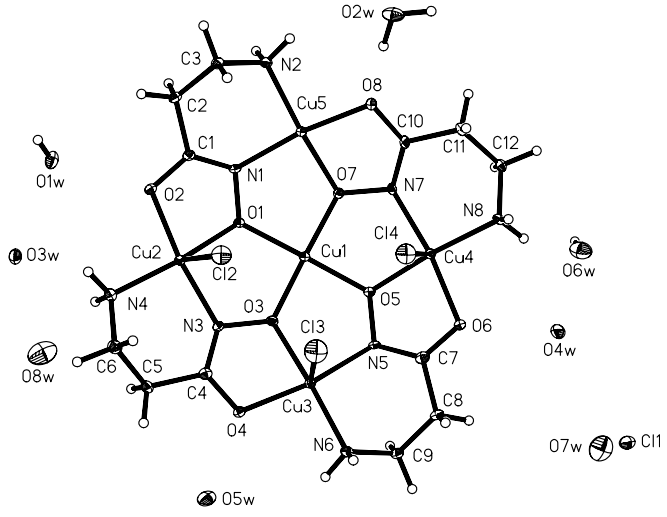


Fig. 1. X-ray crystal structure of the pentameric subunit of complex $[Cu_5(\beta\text{-alaha})_4Cl_2]_2 \cdot 2HCl \cdot 15H_2O$.

3.3335 Å (Cu1–Cu3), while those between peripheral copper(II) ions are longer and vary from 4.5731 (Cu3–Cu4) to 4.610 Å (Cu4–Cu5). All peripheral Cu(II) ions are coordinated in the similar manner. The two nitrogen donors of β-alaninehydroxamate ligand are bound to Cu(II) ion while the two oxygen atoms chelate the adjacent metal ion. In this way tetrameric unit comprising four six-membered as well as five-membered chelate rings is created. In the center of the tetrameric unit, the fifth Cu1 ion is centered, which is bridged to peripheral Cu(II) ions (Cu2–Cu5) by four oxygen atoms of the hydroxamic groups (–NHOH). It causes formation of next four five-membered rings in pentanuclear species. The central metal ion adopts a nearly square planar environment, what can be confirmed by the fact that a sum of the valence angles (O–Cu1–O) is 360.06°. The Cu2, Cu3, Cu4, Cu5 ions are additionally linked to chloride atoms acting as bridges coupling the metal ions from two pentameric subunits. Fig. 2 shows the view of decanuclear complex with four chloride bridges. The average Cu···Cl distance equals to 2.708 Å, thus it is much longer then Cu···O and Cu···N distances, which are equal to 1.942 and 1.988 Å, respectively. The distances between two metal centers coupled by chloride bridges are as follows: Cu2–Cu2′ = 4.8596 Å, Cu3–Cu5′ = 5.1275 Å, Cu4–Cu4′ = 5.0982 Å and Cu5–Cu3′ = 5.1275 Å. The position of two hydrogen cations was not localized by

Table 2
Selected distances (Å) and angles (°) for $[Cu_5(\beta\text{-alaha})_4Cl_2]_2 \cdot 2HCl \cdot 15H_2O$

Cu(1)–O(3)	1.892(3)	Cu(4)–O(5)	1.936(3)
Cu(1)–O(7)	1.920(3)	Cu(4)–N(7)	1.984(3)
Cu(1)–O(1)	1.929(3)	Cu(4)–N(8)	1.987(4)
Cu(1)–O(5)	1.944(3)	Cu(4)–O(6)	1.991(3)
Cu(2)–O(1)	1.952(3)	Cu(4)–Cl(4)	2.7062(11)
Cu(2)–O(2)	1.967(3)	Cu(5)–O(8)	1.945(3)
Cu(2)–N(3)	1.978(3)	Cu(5)–O(7)	1.952(3)
Cu(2)–N(4)	1.991(4)	Cu(5)–N(1)	1.973(4)
Cu(2)–Cl(2)	2.6696(11)	Cu(5)–N(2)	2.013(3)
Cu(3)–O(3)	1.911(3)	Cu(5)–Cl(3)#1	2.751(2)
Cu(3)–O(4)	1.969(3)	Cl(2)–Cu(2)#1	2.6696(11)
Cu(3)–N(6)	1.988(4)	Cl(3)–Cu(5)#1	2.751(2)
Cu(3)–N(5)	1.997(3)	Cl(4)–Cu(4)#1	2.7062(11)
Cu(3)–Cl(3)	2.708(2)		
O(3)–Cu(1)–O(7)	178.40(12)	O(4)–Cu(3)–Cl(3)	90.43(9)
O(3)–Cu(1)–O(1)	91.14(12)	N(6)–Cu(3)–Cl(3)	97.91(12)
O(7)–Cu(1)–O(1)	90.37(12)	N(5)–Cu(3)–Cl(3)	91.71(11)
O(3)–Cu(1)–O(5)	88.78(12)	O(5)–Cu(4)–N(7)	90.11(13)
O(7)–Cu(1)–O(5)	89.77(12)	O(5)–Cu(4)–N(8)	173.54(15)
O(1)–Cu(1)–O(5)	173.55(12)	N(7)–Cu(4)–N(8)	94.73(15)
O(1)–Cu(2)–O(2)	81.10(12)	O(5)–Cu(4)–O(6)	80.95(12)
O(1)–Cu(2)–N(3)	91.35(13)	N(7)–Cu(4)–O(6)	170.56(13)
O(2)–Cu(2)–N(3)	172.28(13)	N(8)–Cu(4)–O(6)	93.97(14)
O(1)–Cu(2)–N(4)	170.06(14)	O(5)–Cu(4)–Cl(4)	91.79(10)
O(2)–Cu(2)–N(4)	94.09(14)	N(7)–Cu(4)–Cl(4)	90.39(10)
N(3)–Cu(2)–N(4)	93.62(14)	N(8)–Cu(4)–Cl(4)	92.45(14)
O(1)–Cu(2)–Cl(2)	90.17(9)	O(6)–Cu(4)–Cl(4)	92.92(10)
O(2)–Cu(2)–Cl(2)	93.58(9)	O(8)–Cu(5)–O(7)	81.77(12)
N(3)–Cu(2)–Cl(2)	98.85(12)	O(8)–Cu(5)–N(1)	170.81(13)
N(4)–Cu(2)–Cl(2)	81.81(12)	O(7)–Cu(5)–N(1)	91.94(13)
O(3)–Cu(3)–O(4)	81.81(12)	O(8)–Cu(5)–N(2)	94.72(13)
O(3)–Cu(3)–N(6)	176.30(14)	O(7)–Cu(5)–N(2)	173.62(14)
O(4)–Cu(3)–N(6)	95.38(13)	N(1)–Cu(5)–N(2)	92.15(14)
O(3)–Cu(3)–N(5)	88.91(13)	O(8)–Cu(5)–Cl(3)#1	84.10(10)
O(4)–Cu(3)–N(5)	170.24(13)	O(7)–Cu(5)–Cl(3)#1	88.80(10)
N(6)–Cu(3)–N(5)	93.76(14)	N(1)–Cu(5)–Cl(3)#1	89.10(11)
O(3)–Cu(3)–Cl(3)	84.56(10)	N(2)–Cu(5)–Cl(3)#1	96.15(11)

Symmetry transformations used to generate equivalent atoms: #1 $-x$, y, $-z + 1/2$.

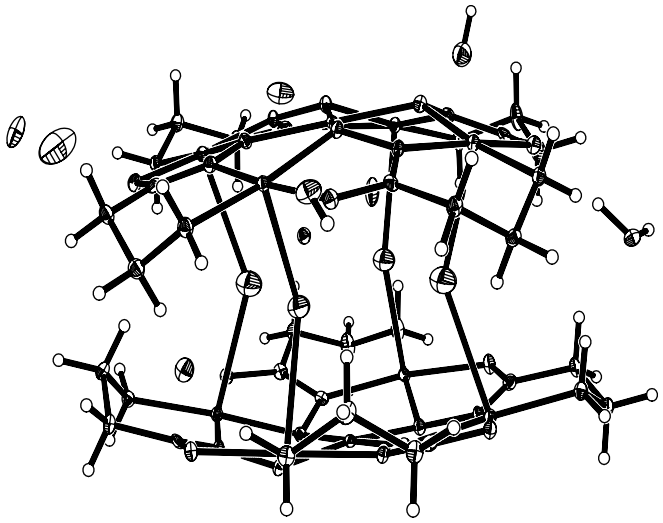


Fig. 2. X-ray crystal structure of the complex $[Cu_5(\beta\text{-alaha})_4Cl_2]_2 \cdot 2HCl \cdot 15H_2O$.

X-ray refinement. In our opinion the Cl^- ion and water molecules could be occupied by both hydrogen atoms.

The hydrogen-bonding system in this structure is complex due to the presence of water molecules. Non-coordinated water molecules and chloride anions participate in hydrogen-bonds with nitrogen atoms from amine groups, carboxyl oxygen atoms and other water molecules (see Table 3).

The structure of the pentanuclear cluster unit shows some common features with another cooper(II) compound, published by Kurzak et al. [26]. In earlier reported structure of a general formula $[Cu_5(\beta\text{-alaha})_4](ClO_4)_2 \cdot 5H_2O$, pentameric subunits are also created and the same coordination mode of β-alaninehydroxamate anions is observed. All copper(II) ions are additionally connected to fifth oxygen atom of water molecule, perchlorate anion or alaninehydroxamate ligand (distances vary from 2.363 to 2.675 Å). Moreover, the central metal ion (Cu5) exhibits a long interactions with oxygen atom $O(5^{II})$, which also interacts with one of the peripheral copper(II) ion (Cu4) leading to an increase of the coordination number of the latter to CN = 6. Contrary to our system with chloride bridges, the perchlorate bridges between cooper(II) ions from two different pentameric subunits are not present. In this case two pentanuclear clusters are joined only by one hydroxamic oxygen atom. It is worth to notice that the structure of our system is more ordered in comparison to that reported by Kurzak et al. [26]. It is probably caused by the presence of chloride bridges playing important role in stabilization of the crystal structure. Deformation of the pentameric cluster from C_{4v} symmetry is stronger in the earlier published complex what is manifested mainly in larger deviation from basal plane of four peripheral Cu(II) ions (±0.10 [26] and 0.039 for our compound). It was also observed in now investigated compound that the central copper(II) ion is situated higher above the plane formed by four peripheral metal ions (0.54 Å) then in $[Cu_5(\beta\text{-alaha})_4](ClO_4)_2 \cdot 5H_2O$ (0.4 Å) [26].

Fig. 3 shows the absorption spectra of $[Cu_5(\beta\text{-alaha})_4Cl_2]_2 \cdot 2HCl \cdot 15H_2O$ single crystal obtained at room and liquid-helium temperature. The electronic spectra consist of overlapped d–d absorption bands of Cu(II) ions with different symmetry sites and the charge-transfer band (L → M). The broad band centered at UV region, with some shoulders indicating unresolved bands (15 848 cm^{-1}, 16 886 cm^{-1}, 18 188 cm^{-1}), consists of the bands of four slightly different copper(II) optical centers with very low symmetry (peripheral metal ions) and the bands of cooper(II) ion with a symmetry close to D_{4h} (central metal ion). As the result of splitting of energy levels for a d^9 metal ion with D_{4h} symmetry the d–d hole transitions: $x^2 - y^2 \rightarrow xy$, $x^2 - y^2 \rightarrow z^2$, $x^2 - y^2 \rightarrow (xz, yz)$ may be expected, but in C_1 the transitions depend on magnitude of energy levels' splitting. In fact, appropriate transitions should be observed for pentagonal coordination of Cu^{2+} ion: $x^2 - y^2 \rightarrow z^2$, $x^2 - y^2 \rightarrow xy$, $x^2 - y^2 \rightarrow (xz, yz)$. Overlapping of these transitions for four non-equivalent five-coordinated Cu(II) centers (Cu2–Cu5) and four-coordinated Cu(II) (Cu1) center leads to a complex, unresolved absorption spectrum, which does not became

Table 3
Hydrogen-bonds for $[Cu_5(\beta\text{-alaha})_4Cl_2]_2 \cdot 2HCl \cdot 15H_2O$ (Å and °)

D–H···A	d(D–H)	d(H···A)	d(D···A)	∠(DHA)
N(2)–H(2B)···Cl(1)#2	0.92	2.65	3.536(4)	160.7
N(4)–H(4A)···O(3W)	0.92	2.17	2.999(5)	150.2
N(4)–H(4B)···O(8W)	0.92	2.21	3.004(7)	143.8
N(6)–H(6A)···O(2W)#1	0.92	2.20	3.043(5)	152.6
N(6)–H(6B)···Cl(1)#3	0.92	2.58	3.428(4)	153.8
N(8)–H(8A)···O(4W)#1	0.92	2.39	3.153(6)	140.7
N(8)–H(8B)···O(6W)	0.92	2.10	2.960(6)	155.8
O(1W)–H(11W)···Cl(1)#4	0.72	2.54	3.251(4)	171.2
O(2W)–H(21W)···O(8)	0.96	1.76	2.715(4)	174.7
O(2W)–H(22W)···O(5W)#5	0.94	1.94	2.870(6)	171.4
O(6W)–H(61W)···O(6)#6	0.96	2.37	3.041(6)	126.4

Symmetry transformations used to generate equivalent atoms: #1 $-x, y, -z + 1/2$; #2 $x - 1/2, -y + 1/2, z - 1/2$; #3 $-x + 1/2, y - 1/2, -z + 1/2$; #4 $-x, y - 1, -z + 1/2$; #5 $x - 1/2, y + 1/2, z$; #6 $-x, -y + 1, -z$.

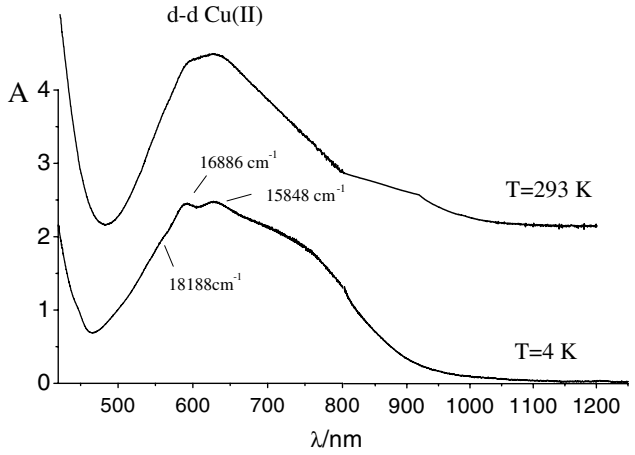


Fig. 3. The absorption spectra of single crystal of $[Cu_5(\beta\text{-alaha})_4Cl_2]_2 \cdot 2HCl \cdot 15H_2O$ at 298 and 4 K.

resolved even at liquid-helium temperature. Moreover, stronger electron–phonon coupling than in f-electron systems can lead to a broadening of the optical lines, too.

The EPR spectra of title compound at room as well as at nitrogen liquid temperature show broad copper(II) signals having $g = 2.01$ (298 K) and 2.17 (77 K), and no resolution of g_{II} and $g_{\perp}$ is observed.

The molar magnetic susceptibilities χ_M of $[Cu_5(\beta\text{-alaha})_4Cl_2]_2 \cdot 2HCl \cdot 15H_2O$ are measured on a powdered sample in the temperature range 1.9–300.5 K under the applied magnetic field of 0.5 T, and the results are shown in Fig. 4 in the form of $\chi_M T$ versus T. The inset in this figure presents the temperature dependence of $\chi_M T$ (1.9–50 K) registered under the applied magnetic field of 200 G. The value of $\chi_M T$ at 300.5 K is 1.09 $cm^3\,mol^{-1}$ K, which is lower than the spin only value of five uncoupled Cu(II) ions (1.875 $cm^3\,mol^{-1}$ K for $g = 2$), thus indicating the presence of strong antiferromagnetic interaction. As the temperature is lowered the $\chi_M T$ decreases gradually, reaching a value of 0.42 $cm^3\,mol^{-1}$ K at 38 K (as expected for five Cu(II) ions AF coupled, the value for one copper(II) ($S = 1/2$) with g different from 2) (Fig. 4). On further cooling it decreases very slowly to reach a plateau below 18 K at about 0.39 $cm^3\,mol^{-1}$ K (Fig. 4). Below 5 K a further decrease of $\chi_M T$ is observed (0.30 $cm^3\,mol^{-1}$ K at 1.9 K), which can be attributed to interactions between two pentanuclear units ($S = 1/2$) in complex $[Cu_5(\beta\text{-alaha})_4Cl_2]_2 \cdot 2HCl \cdot 15H_2O$. The profile of the curve indicates predominant antiferromagnetic interactions between the Cu(II) centers within the pentameric Cu_5 core and weaker antiferromagnetic interactions between Cu(II) ions from two pentanuclear Cu_5 units bridged by chloride anions. The temperature dependence of reciprocal susceptibilities χ_M^{-1} is also indicative on the antiferromagnetic interactions (Fig. 5). It is almost linear in the temperature range of 50–300.5 K, the Curie constant (C) is 1.47 $cm^3\,mol^{-1}$ K and the Curie-Weiss temperature is −111.71 K. Similar magnetic behavior has been reported for a sulfato-bridged hexanuclear dimer $[Cu_3(MeImds)(SO_4)(H_2O)_3]_2$, where MeImds stands for bis(salicylaldehyde)methylimino-diacetylhydrazone [34]. The decrease of $\chi_M T$ on lowering the temperature indicates quite strong antiferromagnetic coupling within trinuclear unit. Below 40 K, the curve reaches plateau at $\chi_M T = 0.42$ $cm^3\,mol^{-1}$.The further decrease at lower temperature was attributed to a weak antiferromagnetic interactions between the trimetallic units mediated by sulfate bridges. For another trinuclear complex with bis(2-hydroxybenzyl)-1,3diamnopropane the second decrease of $\chi_M T$ at temperature below 10 K was attributed to intermolecular interactions between $S = 1/2$ trimeric units [40].

Considering that there are not significant differences between Cu(1) and peripheral Cu ions distances, and also between neighboring peripheral Cu ions laying in almost planar square, we assumed the four exchange integrals for interactions between central Cu(1) ion and Cu(2), Cu(3), Cu(4), Cu(5) as the same one (J). Similarly, we

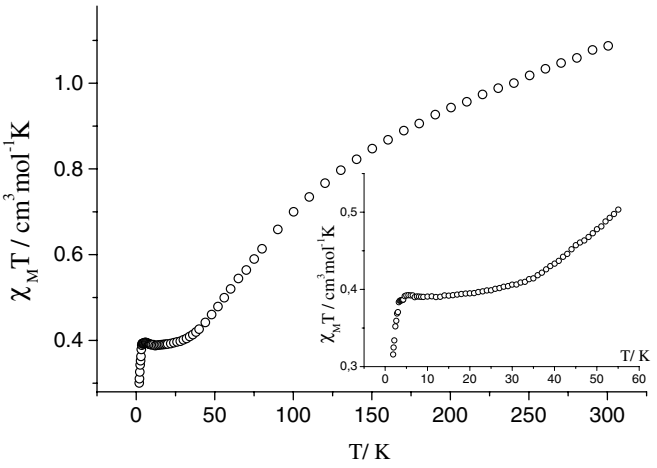


Fig. 4. Experimental magnetic data plotted as $\chi_M \cdot T$ vs. T calculated per molecule of complex $[Cu_5(\beta\text{-alaha})_4Cl_2] \cdot HCl \cdot 7.5H_2O$; from measurements performed at 0.5 T. The inset shows $\chi_M \cdot T$ vs. T from measurements performed at 200 G.

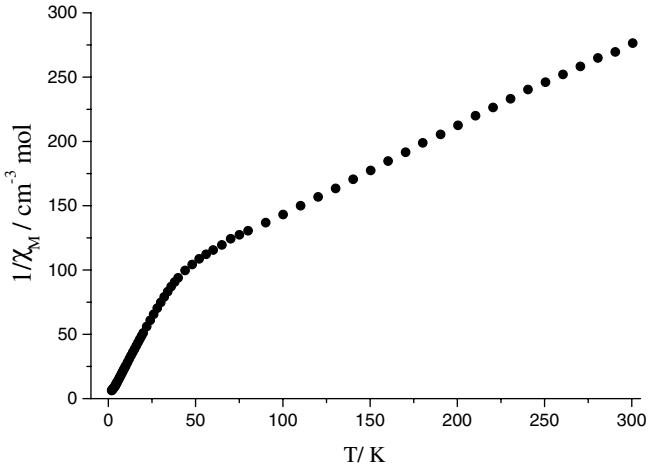


Fig. 5. Experimental magnetic data plotted as χ_M^{-1} vs. T for $[Cu_5(\beta\text{-alaha})_4Cl_2] \cdot HCl \cdot 7.5H_2O$.

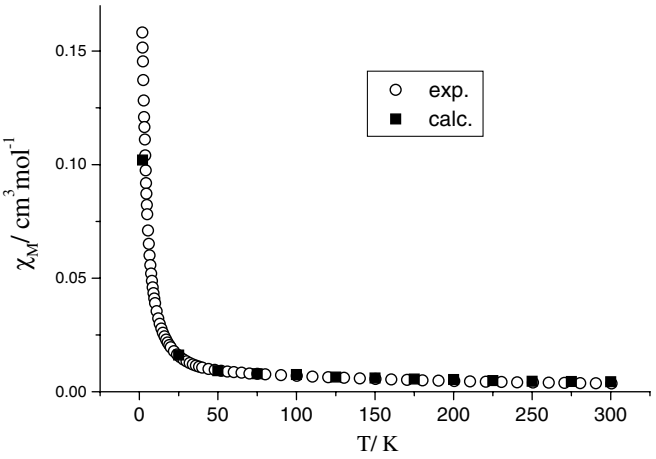


Fig. 6. Experimental and calculated magnetic susceptibility χ_M for $[Cu_5(\beta\text{-alaha})_4Cl_2]\cdot HCl\cdot 7.5H_2O$.

assumed one exchange integral (J′) for interactions between peripheral copper ions. Calculations of the dependence of magnetic susceptibility versus temperature were undertaken using the following expression:

$$\chi_M = N\frac{\mu_B^2 g^2}{kT}\left\{\frac{30\exp(2y-11x)+6\exp(-2y-11x)+6\exp(-11x)+6\exp(-15x)}{5\exp(2y-11x)+3\exp(-2y-11x)+3\exp(-11x)+4\exp(-15x)+\exp(-2y-15x)}\right\},$$

where J describes interactions between Cu1 ion and remaining Cu(II) ions (2, 3, 4, 5) (Fig. 1) and J' describes interactions between four peripheral Cu(II) ions (2, 3, 4, 5) creating a square (Fig. 1)

$$x = J'/2kT, \quad y = J/kT.$$

This equation relates to the system of five interacting copper(II) ions (pentanuclear cluster) with C_{4v} symmetry. The interactions between peripheral Cu(II) ions of two pentanuclear cluster joined by chloride bridges were not taken into account. The best fit was obtained for the following parameters set: $H = 5000$ G, $g = 2.15$, $J = 25\ cm^{-1}$ and $J' = -55\ cm^{-1}$. The calculated data do not fit very well to experimental results (see Fig. 6), what shows that the interaction of two clusters Cu_5 through chloride bridges influences the magnetic properties of the investigated system. These super-exchange interactions seem to be antiferromagnetic in character and they are displayed at very low temperatures (1.8–5 K). It is worth to mention that interactions between neighboring clusters can be mostly ferromagnetic or antiferromagnetic as it was reported earlier by Cukerblat [41]. More precise explanation of the magnetic behavior of our complex compound requires further, more detailed theoretical investigations.

4. Supplementary material

CCDC 233518 contains the supplementary crystallographic data for this paper. These data can be obtained free of charge via http://www.ccdc.cam.ac.uk/conts/retrieving.html, or from the Cambridge Crystallographic Data Centre, 12 Union Road, Cambridge CB2 1EZ, UK; fax: (+44) 1223-336-033; or e-mail: deposit@ccdc.cam.ac.uk.

References

[1] C.P. Brink, A.L. Crumbliss, Inorg. Chem. 23 (1984) 4708.
[2] S.J. Barclay, B.H. Huynh, K.N. Raymond, Inorg. Chem. 23 (1984) 2011.
[3] D.A. Brown, M.V. Chidambaram, J.D. Glennon, Inorg. Chem. 19 (1980) 3260.
[4] J.B. Nejlands, in: G. Eichron (Ed.), Inorganic Biochemistry, Elsevier, New York, 1973, p. 167 (Chapter 5).
[5] J.B. Nejlands, Science 156 (1967) 1443.
[6] J.B. Nejlands, Struct. Bonding 1 (1966) 59.
[7] C.G. Pitt, A.E. Martell, ACS Symp. Ser. 140 (1980) 279.
[8] R.T. Coutts, Can. J. Pharm. Sci. 2 (1967) 27.
[9] J.C. Powers, J.W. Harper, in: A.J. Barett, G. Salvesen (Eds.), Proteinase Inhibitors, Elsevier, 1986, p. 244.
[10] D.A. Brown, A.L. Roche, Inorg. Chem. 22 (1983) 2199.
[11] H. Kehl, Chemistry and Biology of Hydroxamic Acids, Karger, New York, 1982.
[12] K. Munakata, K. Kobashi, S. Takebe, J. Hase, J. Pharm. Dyn. 3 (1980) 451.
[13] K.N. Raymond, C.J. Carrano, Acc. Chem. Res. 12 (1997) 183.
[14] E.B. Paniago, S. Carvalho, Inorg. Chim. Acta 92 (1984) 253.
[15] E. Farkas, J. Szöke, T. Kiss, H. Kozłowski, W. Bal, J. Chem. Soc., Dalton Trans. (1989) 2247.
[16] B. Kurzak, K. Kurzak, J. Jezierska, Inorg. Chim. Acta 125 (1986) 77.
[17] B. Kurzak, K. Kurzak, J. Jezierska, Inorg. Chim. Acta 130 (1987) 189.
[18] D. Kroczewska, B. Kurzak, E. Matczak-Jon, Polyhedron 21 (2002) 2183.
[19] D.A. Brown, A.L. Roche, T.A. Pakkanen, T.T. Pakkanen, K. Smolander, Chem. Commun. (1982) 676.
[20] C.O.B. De Miranda-Pinto, Y.P. Mascarenhas, S. Carvalho, E.B. Paniago, Ciência e Cultura Suppl. 35 (1982) 422.
[21] M. Julien-Pouzol, S. Jaulmes, P. Laruelle, S. Carvalho, E.B. Paniago, Acta Crystallogr., Sect. C 41 (1985) 712.
[22] C.O.B. De Miranda-Pinto, E.B. Paniago, S. Carvalho, M. Tabak, Y.P. Mascarenhas, Inorg. Chim. Acta 137 (1987) 145.
[23] T. Głowiak, M. Koralewicz, School Symposium on Inorganic Biochemistry and Molecular Biophysics, Wrocław-Karpacz, 1985.
[24] J. Legendziewicz, P. Gawryszewska, E. Gałdecka, Z. Gałdecki, J. Lumin. 559 (1997) 72.
[25] J. Legendziewicz, P. Gawryszewska, A. Waśkowska, Spectrochim. Acta A 54 (1998) 2087.
[26] B. Kurzak, E. Farkas, T. Głowiak, H. Kozłowski, J. Chem. Soc., Dalton Trans. (1991) 163.
[27] D. Gatteschi, Adv. Mater. 6 (1994) 635.
[28] R. Neuman, M. Dahan, Nature 388 (1997) 353.
[29] E. Coronado, F. Palacio, J. Veciana, Angew. Chem. Int. Ed. 42 (2003) 2570.
[30] O. Yaghi, G. Li, H. Li, Nature 378 (1995) 703.
[31] L.K. Thompson, C.J. Matthews, L. Zhao, Z. Xu, D.O. Miller, C. Wilson, M.A. Leech, J.A.K. Howard, S.L. Heath, A.G. Whittaker, R.E.P. Winpenny, J. Solid State Chem. 159 (2001) 308.
[32] S. Wang, Z. Pang, J.C. Zheng, M.J. Wagner, Inorg. Chem. 32 (1993) 5975.
[33] R. Vincente, A. Escuer, X. Solans, M. Font-Bardia, J. Chem. Soc., Dalton Trans. (1996) 1835.

[34] A. Bacchi, M. Carcelli, G. Pelizzi, C. Solinas, L. Sorace, Inorg. Chim. Acta 359 (2006) 2275.
[35] E. Rentschler, D. Gatteschi, A. Cornia, A.C. Fabretti, A.-L. Barra, O.I. Shchegolikhina, A.A. Zhdanov, Inorg. Chem. 35 (1996) 4427.
[36] P. Guerrino, S. Tamburini, P.A. Vigato, Coord. Chem. Rev. 139 (1995) 17.
[37] S.S. Tandon, L.K. Thompson, J.N. Bridson, C. Benelli, Inorg. Chem. 34 (1995) 911.
[38] G.M. Sheldrick, SHELXS97, Program for Solution of Crystal Structures, University of Göttingen, 1997.
[39] G.M. Sheldrick, SHELXL97, Program for Crystal Structure refinement, University of Göttingen, 1997.
[40] Y. Song, P. Gamez, O. Roubeau, I. Mutikainen, U. Turpeinen, J. Reedijk, Inorg. Chim. Acta 358 (2005) 109.
[41] B.S. Cukerblat, M.I. Bielinskii, Magnetokhimia i radiospektroskopia obmiennykh klasterow, Sztinca, Kishynyev, 1983.

ligands with functional groups have been comparatively little synthesized and investigated. In contrast to the coordination polymers with flexible imidazole ligands, the coordination polymers containing rigid π-conjugated imidazole ligands have potential applications in the fields of electrooptical devices [3c]. Therefore, more efforts should be focused on the design and synthesis of rigid imidazole ligand by functional group modifications.

In addition, in construction of the infinite supramolecular networks, multidentate ligand thiocyanate is usually employed to bridge between metal centers to form polymeric structures. Thiocyanate is a highly versatile ambidentate ligand with a polarizable π system and two different donor atoms, which can coordinate to metals through either the nitrogen or the sulfur atoms, or both [15]. The various bridging modes of the thiocyanate ligand not only generate new types of network structures but also offer the opportunity for forming hetero-metallic complexes involving various combinations of metal ion node points. Such combinations could lead to the formation of materials with useful properties deriving from the presence of the hetero-metallic arrays [16,17].

We have rationally designed and synthesized a functional imidazole ligand with good electron donor and acceptor through a conjugated bridge [18]. Based on the bridging potential of the hard and soft coordination centers of the ambidentate thiocyanate ligand, we obtained a series of organic-inorganic hybridized supramolecular polymers containing functional rigid imidazole ligands, which is original and different from the other reported imidazole-containing coordination polymers [19]. The combination of inorganic and functional organic moieties leads to both new structural architectures and excellent properties. In this article, we report the synthesis, structures and photoluminescence of three new supramolecular coordination polymers $[Cd(SCN)_2L_2]_n$ (**1**), $[CdHg(SCN)_4L_2]_n$ (**2**) and $[MnHg(SCN)_4L_2]_n$ (**3**).

2. Experimental

2.1. General

All commercially available chemicals are of analytical grade and used without further purification. The solvents were purified by conventional methods before use. *trans*-4-Imidazolyl-4′-(*N*,*N*-diethylamino)stilbene (L) was synthesized according to the methods reported [18]. IR spectra were recorded on a Nicolet FT-IR instrument by using KBr discs in the 4000–400 cm^{-1} range. Elemental analyses were carried out on Perkin–Elmer 240 analyzer. UV–Vis spectra were recorded with a UV-265 spectrophotometer. Luminescence spectra were recorded on a Perkin–Elmer LS55B fluorescence spectrophotometer at room temperature. Thermal stability studies from room temperature to 600 °C in nitrogen atmosphere with a heating rate of 10 °C min^{-1} were executed on a Perkin–Elmer pyres-1 DMDA-V1 instrument.

2.2. Synthesis

2.2.1. Preparation of $[Cd(SCN)_2L_2]_n$ (*1*)

The complex was synthesized by layering method at room temperature. A clear methanol solution (15 mL) of $Cd(NO_3)_2 \cdot 4H_2O$ (30.8 mg, 0.1 mmol) and NaSCN (16.4 mg, 0.2 mmol) was carefully layered onto a solution of L (73.4 mg, 0.2 mmol) in chloroform (15 mL). Yellow needle-shaped crystals suitable for X-ray diffraction were obtained by slow interlayer diffusion. Yield: 67.3 mg (70%). *Anal.* Calc. for $[CdC_{44}H_{46}N_8S_2]_n$: C, 61.21; H, 5.37; N, 12.98. Found: C, 61.18; H, 5.39; N, 12.94%. IR (KBr, cm^{-1}): 3421 m, 2088 s, 1598 s, 1523 s, 1468 w.

2.2.2. Preparation of $[CdHg(SCN)_4L_2]_n$ (*2*)

Methanol solution of $CdHg(SCN)_4$ was prepared by reaction of $Cd(NO_3)_2 \cdot 6H_2O$ (34.2 mg, 0.1 mmol), $Hg(NO_3)_2 \cdot H_2O$ (34.3 mg, 0.1 mmol) and NaSCN (32.8 mg, 0.4 mmol) in 20 mL of methanol. The white precipitate of KNO_3 was removed by filtration. The methanol solution of $CdHg(SCN)_4$ was carefully layered onto a solution of L (73.4 mg, 0.2 mmol) in chloroform (15 mL). Yellow sheet-like crystals suitable for X-ray diffraction were obtained by slow interlayer diffusion. Yield: 83.1 mg (65%). *Anal.* Calc. for $[CdHgC_{46}H_{46}N_{10}S_4]_n$: C, 46.81; H, 3.93; N, 11.78. Found: C, 46.85; H, 3.97; N, 11.82%. IR (KBr, cm^{-1}): 3438 m, 2119 s, 1620 s, 1591 s, 1426 w.

2.2.3. Preparation of $[MnHg(SCN)_4L_2]_n$ (*3*)

The same synthetic procedure as for **2** was used except that $Cd(NO_3)_2 \cdot 4H_2O$ was replaced by $Mn(NO_3)_2 \cdot 6H_2O$ and a 1:2 metal-to-ligand molar ratio was adopted, giving yellow rhomboid single crystals. Yield: 70.9 g (60%). *Anal.* Calc. for $[MnHgC_{46}H_{46}N_{10}S_4]_n$: C, 49.21; H, 4.13; N, 12.48. Found: C, 49.19; H, 4.15; N, 12.53 (%). IR (KBr, cm^{-1}): 3421 m, 2119 s, 1620 s, 1591 m, 1426 w.

2.3. X-ray crystallography

The X-ray diffraction measurements were performed on a Bruker SMART CCD area detector using graphite-monochromated Mo Kα radiation ($\lambda = 0.71073$ Å) at 298(2) K. Intensity data were collected in the variable ω-scan mode. The structures were solved by direct methods and difference Fourier syntheses. All non-hydrogen atoms were refined anisotropically and hydrogen atoms were introduced geometrically. Calculations were performed with the SHELXTL-97 program package [20]. All crystallographic data for complexes **1**, **2** and **3** are summarized in Table 1. Selected bond lengths and bond angles are listed in Table 2.

3. Results and discussion

3.1. Spectroscopic characterization

The organic ligand, *trans*-4-imidazolyl-4′-(*N*,*N*-diethylamino)stilbene (L) is the first reported imidazole derivative

Table 1
Crystal data and structure refinement for complexes **1**, **2** and **3**

Complex	**1**	**2**	**3**
Empirical formula	$C_{44}H_{46}CdN_8S_2$	$C_{46}H_{46}HgCdN_{10}S_4$	$C_{46}H_{46}MnHgN_{10}S_4$
Formula weight	863.41	1180.16	1122.70
Temperature (K)	298(2)	298(2)	298(2)
Wavelength (Å)	0.71073	0.71073	0.71073
Crystal system	triclinic	triclinic	monoclinic
Space group	$P\bar{1}$	$P\bar{1}$	$P2_1/c$
a (Å)	5.785(3)	14.430(8)	18.584(2)
b (Å)	10.100(4)	18.61(1)	19.071(3)
c (Å)	17.664(4)	19.25(1)	14.408(3)
α (°)	96.364(3)	92.310(9)	
β (°)	94.458(2)	90.869(8)	111.925(2)
γ (°)	95.808(2)	111.778(7)	
Volume (Å^3)	1016.4(7)	4793(5)	4737.2(4)
Z	1	2	4
ρ_{calc} (g/cm^3)	1.411	1.636	1.574
$F(000)$	446	2336	2244
Crystal size (mm)	$0.53 \times 0.24 \times 0.07$	$0.42 \times 0.37 \times 0.19$	$0.35 \times 0.29 \times 0.13$
Reflections collected	4941	22264	24448
Unique reflections	3439	15357	8348
Parameters	340	1117	559
S on F^2	0.941	1.005	1.021
R_1 $[I > 2\sigma(I)]$	0.0724	0.1092	0.0539
wR_2 $[I > 2\sigma(I)]$	0.1438	0.2436	0.1226
$\Delta\rho_{min/max}$ (e Å^{-3})	1.083/−0.843	5.163/−1.188	0.817/−0.743

with π-conjugated system and functional group [19]. The IR spectrum of free ligand shows absorption at 1480 cm^{-1}, attributing to the vibration of the C=N of imidazole [18a]. Compared with the double peaks 1496, 1436 cm^{-1}, 1490, 1427 cm^{-1} and 1492, 1426 cm^{-1} assigned to the C=N of imidazole in complexes **1**, **2** and **3**, respectively, the shifts and splits of the band suggest coordination of the imidazole groups in the complexes [21]. The C–N stretching vibrations of SCN^- at 2126 and 2128 cm^{-1} for **2** and **3**, suggest bridging modes of SCN^- ligands [22]. The absorption peak at lower wave numbers (2088 cm^{-1}) was for ν(C–N) of the thiocyanate in complex **1**, implying a different binding mode in accordance with the results of X-ray analysis. The electronic absorption spectra of all compounds were measured in DMF solutions (10^{-5} mol L^{-1}). The free L ligand displays strong absorption peak at 369 nm, which is assigned as K band absorption arising from $\pi \rightarrow \pi^*$ transitions within the extended π-conjugated system. The large molar absorption coefficient ($\log\varepsilon = 4.29$) is indicative of highly π-conjugated system [18a]. Complexes **1**, **2** and **3** display absorption peaks at 368 ($\log\varepsilon = 4.65$), 363 ($\log\varepsilon = 4.65$) and 365 ($\log\varepsilon = 4.65$) nm, also arising from $\pi \rightarrow \pi^*$ transitions of L ligands.

3.2. Thermal stability

Thermal stabilities for the title compounds were determined by TG technique. The TG curves exhibited that $[Cd(SCN)_2L_2]_n$ (**1**), $[CdHg(SCN)_4L_2]_n$ (**2**) and $[MnHg(SCN)_4L_2]_n$ (**3**) were stable up to their decomposition temperatures of 327.9, 316.6 and 326.8 °C, respectively, without showing any melting process, indicating the high stabilities of them. The decomposition temperatures of coordination polymers are much higher than that of the free ligand (289.3 °C). Therefore, coordination of the ligand to the metal ion results in greater thermal stability. The higher thermal stabilities indicate the potential applications of complexes **1**, **2** and **3**.

3.3. Crystal structures

3.3.1. Crystal structure of $[Cd(SCN)_2L_2]_n$ (1)

Complex **1** was obtained as yellow needle crystals by layering methanol solution of $Cd(NO_3)_2 \cdot 4H_2O$ and NaSCN onto L in chloroform. The structural unit and the one-dimensional chain for complex **1** are shown in Fig. 1a and b. Cd^{II} ion, being in between soft and hard acid, exhibits both (S and N) bonding modes [15,23]. Each Cd^{II} ion lies at a center of symmetry surrounded by six related atoms. The equatorial positions are occupied by two nitrogen atoms and two sulfur atoms from four thiocyanate anions (the Cd–N bond lengths are 2.291(7) Å, the Cd–S bond lengths are 2.750(2) Å), and two nitrogen atoms of imidazole groups from two different ligands occupy the axial positions with Cd–N bond lengths of 2.304(5) Å, therefore, the polyhedron can be described as a distorted octahedron. From Table 2, it can be seen that the S–C–N bond angles are 179.3(7)°, that is, the SCN^- group is almost perfectly linear. The S–C and C–N distances of 1.622(8) and 1.150(9) Å in SCN^- indicate a π-delocalization along the metal–thiocyanate chains [15]. This observation is consistent with the fact that the SCN^- ligand is easily polarizable ($^-$S–C≡N ↔ S=C=N$^-$).

Table 2
Selected bond distances (Å) and angles (°) for complexes **1**, **2** and **3**

Complex **1**			
Bond lengths (Å)			
Cd(1)–N(4)	2.291(7)	Cd(1)–S(1)#1	2.751(2)
S(1)–Cd(1)#4	2.750(2)	Cd(1)–N(1)	2.304(5)
S(1)–C(22)	1.622(8)	N(4)–C(22)	1.150(9)
N(3)–C(20)	1.41(2)		
Bond angles (°)			
N(4)–C(22)–S(1)	179.3(7)	N(4)–Cd(1)–N(1)	90.9(2)
N(4)–Cd(1)–S(1)#2	88.0(2)	N(1)–Cd(1)–S(1)#2	89.7(2)
Complex **2**			
Bond lengths (Å)			
Cd(1)–N(9)	2.23(1)	Cd(1)–N(4)#1	2.29(2)
Cd(2)–N(8)#2	2.30(1)	Cd(2)–N(7)#3	2.33(2)
N(7)–Cd(2)#4	2.33(2)	N(8)–Cd(2)#2	2.30(1)
Cd(1)–N(12)	2.29(2)	Cd(1)–N(1)	2.35(2)
Cd(1)–N(5)	2.36(2)	Cd(1)–N(6)	2.44(2)
Hg(2)–S(7)	2.507(5)	Hg(2)–S(6)	2.531(6)
Hg(2)–S(5)	2.554(8)	Hg(2)–S(8)	2.567(7)
Bond angles (°)			
N(9)–Cd(1)–N(4)#1	93.3(6)	N(9)–Cd(1)–N(12)	172.8(5)
N(4)#1–Cd(1)–N(12)	87.3(6)	N(9)–Cd(1)–N(1)	87.2(6)
N(4)#1–Cd(1)–N(1)	89.3(7)	N(12)–Cd(1)–N(1)	100.0(6)
N(9)–Cd(1)–N(5)	94.8(6)	N(4)#1–Cd(1)–N(5)	171.1(7)
N(12)–Cd(1)–N(5)	85.2(7)	N(1)–Cd(1)–N(5)	87.5(6)
N(9)–Cd(1)–N(6)	85.3(6)	N(4)#1–Cd(1)–N(6)	100.9(7)
N(12)–Cd(1)–N(6)	87.5(6)	N(1)–Cd(1)–N(6)	167.7(6)
N(5)–Cd(1)–N(6)	83.4(6)	N(18)–Cd(2)–N(15)	171.2(5)
N(18)–Cd(2)–N(3)	81.7(6)	N(15)–Cd(2)–N(3)	97.2(6)
N(18)–Cd(2)–N(2)	85.9(5)	N(15)–Cd(2)–N(2)	85.3(5)
S(7)–Hg(2)–S(5)	104.9(2)	S(6)–Hg(2)–S(5)	115.5(3)
S(7)–Hg(2)–S(8)	111.2(2)	S(6)–Hg(2)–S(8)	107.9(3)
S(5)–Hg(2)–S(8)	108.4(3)		
Complex **3**			
Bond lengths (Å)			
Hg(1)–S(2)	2.492(3)	Hg(1)–S(4)	2.546(3)
Hg(1)–S(3)	2.557(3)	Mn(1)–N(4)	2.217(8)
Hg(1)–S(1)	2.551(3)	Mn(1)–N(10)#3	2.301(9)
Mn(1)–N(9)#3	2.221(9)	Mn(1)–N(1)	2.218(8)
Mn(1)–N(7)	2.229(9)	Mn(1)–N(8)#3	2.228(8)
S(1)–C(43)	1.67(1)	S(2)–C(44)	1.65(1)
S(3)–C(45)	1.65(1)	S(4)–C(46)	1.62(1)
N(7)–C(43)	1.12(1)	N(8)–C(44)	1.15(1)
Bond angles (°)			
S(4)–Hg(1)–S(1)	107.4(1)	S(1)–Hg(1)–S(3)	105.5(1)
S(2)–Hg(1)–S(4)	111.38(9)	S(2)–Hg(1)–S(1)	112.2(1)
S(2)–Hg(1)–S(3)	107.1(1)	S(4)–Hg(1)–S(3)	113.3(1)
N(9)#3–Mn(1)–N(7)	172.6(3)	N(1)–Mn(1)–N(10)#3	87.1(3)
N(7)–Mn(1)–N(10)#3	99.0(3)	N(9)#1–Mn(1)–N(10)#3	84.8(3)
N(4)–Mn(1)–N(10)#3	84.7(3)	N(4)–Mn(1)–N(1)	171.8(3)
N(1)–Mn(1)–N(9)#3	86.2(3)	N(9)#1–Mn(1)–N(8)#2	87.7(3)
N(8)#2–Mn(1)–N(10)#3	170.8(3)	N(1)–Mn(1)–N(7)	87.7(3)
N(8)#2–Mn(1)–N(7)	89.1(3)	N(1)–Mn(1)–N(8)#2	97.7(3)
N(4)–Mn(1)–N(7)	93.6(3)	N(4)–Mn(1)–N(8)#2	90.4(3)
N(4)–Mn(1)–N(9)#3	93.0(3)	C(43)–N(7)–Mn(1)	169.2(9)
C(45)–S(3)–Hg(1)	91.0(3)	C(46)–S(4)–Hg(1)	97.8(3)
C(43)–S(1)–Hg(1)	97.4(4)	C(44)–S(2)–Hg(1)	98.5(3)
N(7)–C(43)–S(1)	179(1)	N(8)–C(44)–S(2)	177(1)
N(10)–C(46)–S(4)	176(1)	N(9)–C(45)–S(3)	180(1)

Equivalent atoms generated by complex **1**: #1 $-x+2$, $-y+2$, $-z+2$; #2 $x-1$, y, z; #3 $-x+3$, $-y+2$, $-z+2$; #4 $x+1$, y, z. By complex **2**: #1 $-x+1$, $-y+1$, $-z$; #2 $-x+1$, $-y+1$, $-z+1$; #3 $x-1$, y, z; #4 $x+1$, y, z. By complex **3**: #1 $-x+1$, $-y+1$, $-z$; #2 $-x+2$, $-y$, $-z+1$; #3 $-x+2$, $y+1/2$, $-z+1/2$.

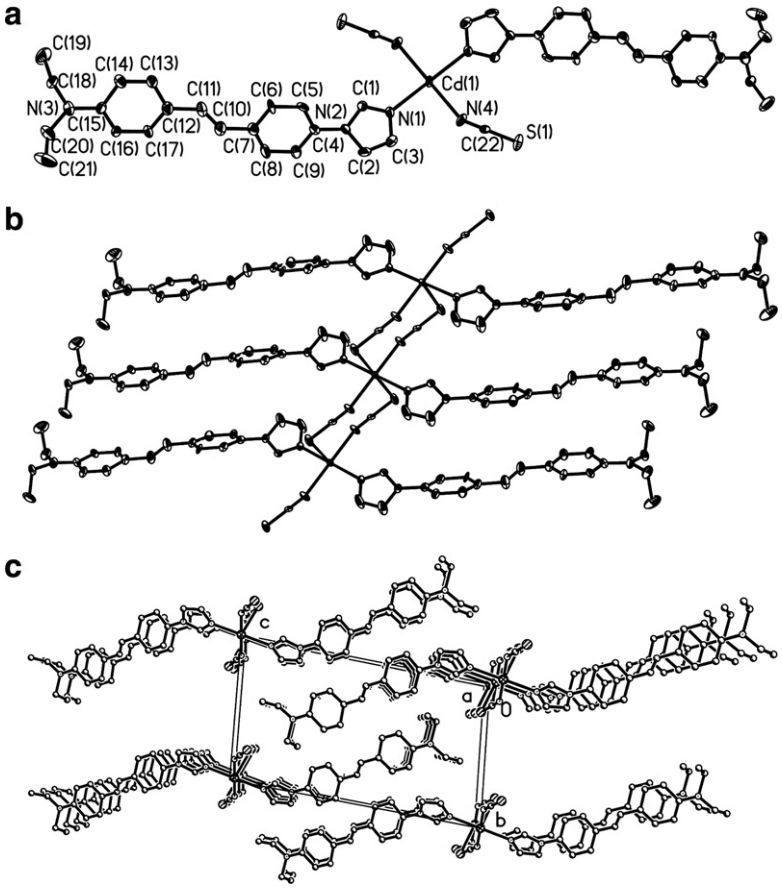


Fig. 1. (a) The structural unit of complex **1**. (b) One-dimensional zigzag chain fragment of complex **1**. (c) Perspective view of molecular packing of complex **1** (hydrogen atoms are omitted for clarity).

Adjacent Cd^{II} ions are linked by two bridging SCN^- ligands with the Cd···Cd distance of 5.785 Å, creating a one-dimensional polymeric chain structure along the *a*-axis comprising eight-membered $(N–C–S–Cd)_2$ rings, which have been well documented in Cd–NCS systems [24]. The molecular packing is shown in Fig. 1c.

In this complex, the molecular structure of L is almost planar, least-square plane calculations show that the dihedral angle between the two benzene rings is 8.3°, indicating they are nearly coplanar. The geometry around N(3) is planar. The bond lengths of N(3)–C(18) (1.57(2) Å) and N(3)–C(20) (1.41(2) Å) are longer than that of N(3)–C(15) (1.362(9) Å), indicating π conjugation from the lone pair of N(3) to the adjacent phenyl ring [25]. The C–C bond lengths are located between the normal C–C single-bond distance of 1.54 Å and double-bond distance of 1.34 Å, which also show that L has a highly delocalized π-electron system in the molecule.

3.3.2. Crystal structure of $[CdHg(SCN)_4L_2]_n$ (**2**)

To extend metal–thiocyanate coordination chains into higher dimensional architectures, Hg^{II} ions were added. By layering methanol solution of $Cd(NO_3)_2 \cdot 4H_2O$, $Hg(NO_3)_2 \cdot H_2O$ and NaSCN onto L in chloroform, yellow sheet-like crystals were obtained. The structure of complex **2** is two-dimensional hetero-metallic framework sheet. The coordination modes in the structure can be rationalized in terms of the hard–soft acid–base (HSAB) concept [24]. Hg^{II} ion, being a soft acid, is preferentially coordinated by the soft base (S) terminus of the SCN^- ligand [15,23]. As shown in Fig. 2a, each Cd^{II} ion is placed in a distorted octahedral environment, being coordinated by six N atoms, two N atoms from two L and other four N atoms from four NCS^- ligands. The Cd–N bond lengths are in the range between 2.23(1) and 2.44(2) Å. The Cd–N–C angles are range between 171(2)° and 141(1)°, respectively. Each Hg^{II} ion is in a distorted tetrahedral geometry, being coordinated by four thiocyanate sulfur atoms. The Hg–S bond lengths are in the range between 2.566(7) and 2.508(5) Å. The Hg–S–C angles are in the range between 101.1(6)° and 92.4(6)°. The SCN^- ligands are virtually linear with average S–C and N–C bond lengths of 1.64(2) and 1.16(2) Å, respectively, indicating a π-delocalization in the metal–thiocyanate frameworks.

Cd^{II} and Hg^{II} ions are bridged by NCS^- groups to form two-dimensional sheets in the *ac*-plane, containing

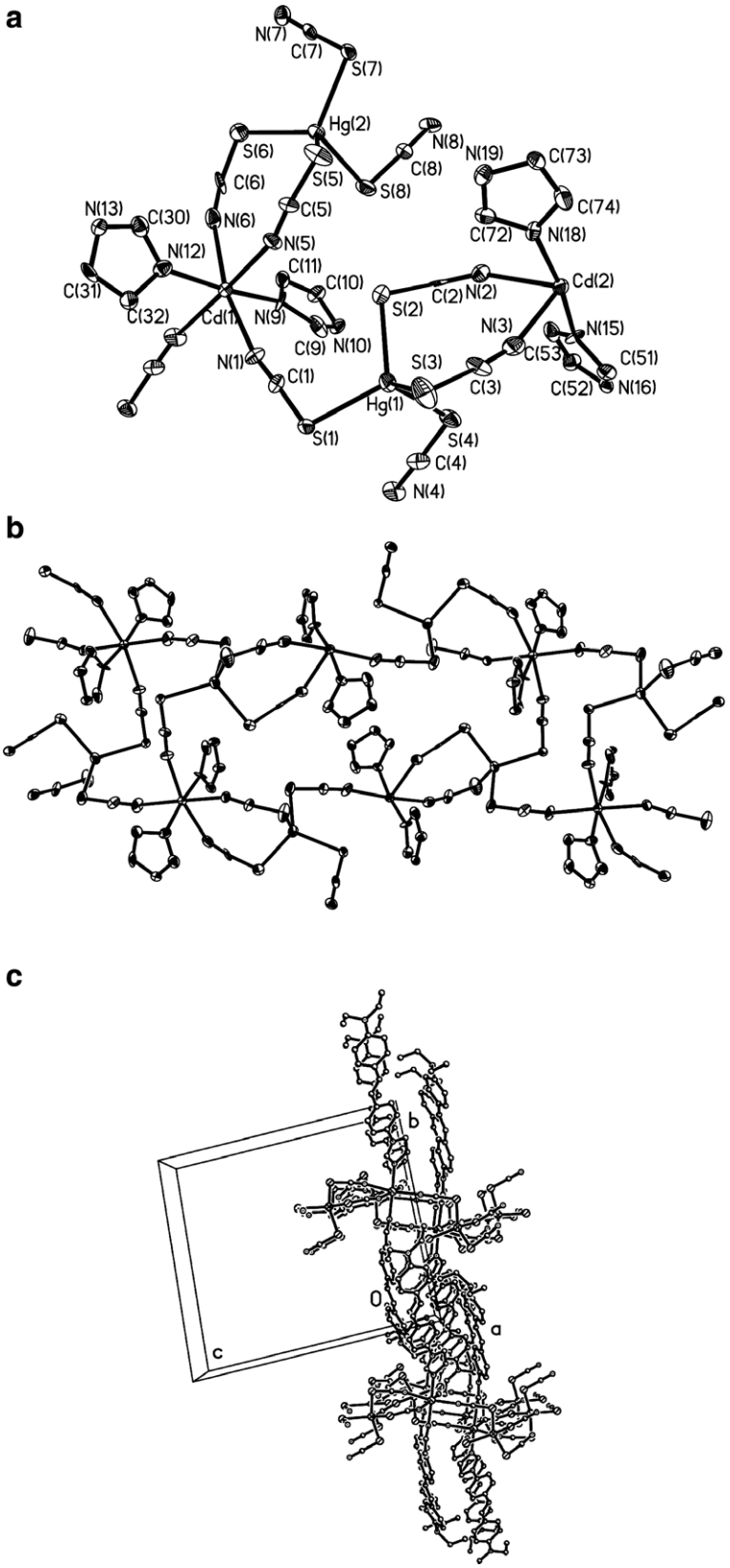


Fig. 2. (a) The coordination environment of Cd^{II} and Hg^{II} in complex **2**. (b) The polymeric sheet of complex **2** (hydrogen atoms and *trans*-4-(4-diethylamino styryl)phenyl are omitted for clarity). (c) Perspective view of molecular packing of complex **2** (hydrogen atoms are omitted for clarity).

16-membered $[Cd_2Hg_2(SCN)_4]$ and 32-membered $[Cd_4Hg_4(SCN)_8]$ cycles as subunits, which adopt pseudo-chair conformations, as shown in Fig. 2b. To our knowledge, such arrangements of the subunits have not been reported in Cd–SCN–Hg system. The molecular packing is shown in Fig. 2c.

The C–C bond lengths of the imidazole ligands in complex **2** are located between the normal C–C single-bond dis-

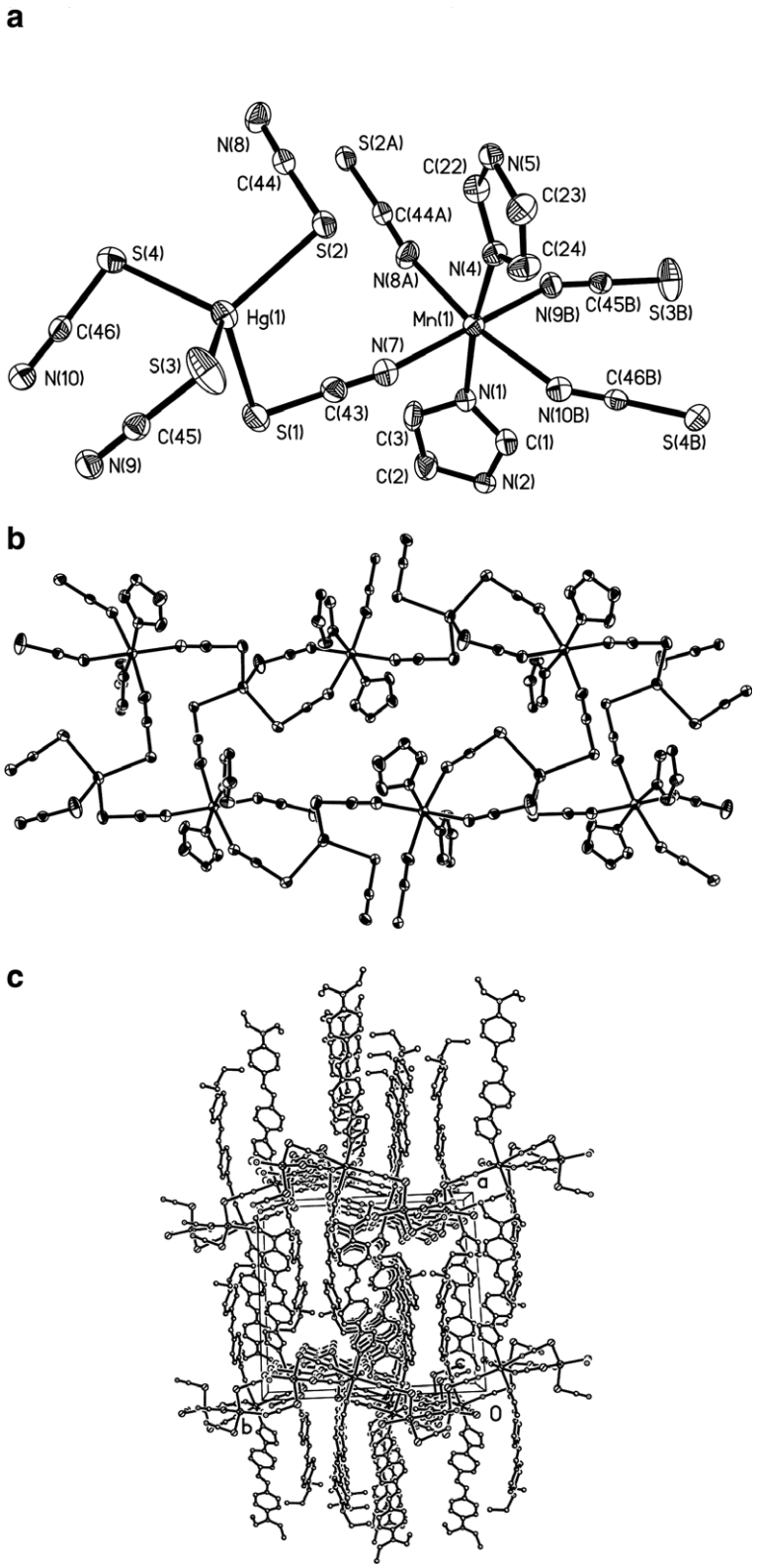


Fig. 3. (a) The coordination environment of Mn^{II} and Hg^{II} in complex **3**. (b) The 2D polymeric sheet of complex **3** (hydrogen atoms and *trans*-4-(4-diethylamino styryl)phenyl are omitted for clarity). (c) Perspective view of molecular packing of complex **3** (hydrogen atoms are omitted for clarity).

tance and double-bond distance, which show that they have delocalized π-electron systems.

3.3.3. Crystal structure of $[MnHg(SCN)_4L_2]_n$ (3)

The yellow rhomboid single crystals of complex **3** were obtained using the same synthetic procedure as for **2** except that Cd^{II} ions were replaced by Mn^{II} ions. The structure of **3** is two-dimensional hetero-metallic framework sheet. The coordination modes in the structure can be rationalized in terms of the hard–soft acid–base (HSAB) concept. Mn^{II}, being a metal in the first transition series, exhibits only N-coordination. As shown in Fig. 3a, each Mn^{II} ion is in a N_6 distorted octahedral geometry, being coordinated by two nitrogen atoms from two imidazole ligands and four thiocyanate nitrogen atoms. The Mn–N bond lengths are in the range between 2.218(8) and 2.301(9) Å. Each Hg^{II} ion is in a S_4 distorted tetrahedral geometry, being coordinated by four thiocyanate sulfur atoms. The Hg–S bond lengths are in the range between 2.492(3) and 2.557(3) Å. The dihedral angle between the two benzene rings of the two ligands (L) in the complex is 10.8° and 13.7°, respectively. As shown in Fig. 3b, the Mn^{II} and Hg^{II} ions are linked by bridging NCS^- groups to form two-dimensional sheets in the *bc*-plane, containing 16-membered $[Mn_2Hg_2(SCN)_4]$ and 32-membered $[Mn_4Hg_4(SCN)_8]$ cycles to adopt pseudo-chair conformation as subunits. The molecular packing is shown in Fig. 3c.

Comparing the three structures, we have observed the difference in dimensions and geometries with variation of the center metals. The thiocyanate links the center metals in various fashions to form different polymeric constructions. The conjugated systems of ligands (L) are also different in the three structures.

3.4. Photoluminescene

The photoluminescence properties of compounds have been studied in the solid state at room temperature. The measurements were carried out under the same experimental conditions and the results are shown in Fig. 4. The maxima emissions observed in complexes **1**, **2** and **3** are assigned to the $\pi \rightarrow \pi^*$ transitions of the L ligands due to their close resemblance to that of the free ligand [26]. Compared with that of the free ligand, the maximum wavelength of **1** is red-shifted by 2 nm from 475 to 477 nm upon excitation over the range of 300–450 nm, accompanied by a decreased luminescent intensity. However, the maxima emission wavelengths of **2** and **3** are red-shifted by 8 and 9 nm from 475 to 483 and 484 nm, respectively, relative to that of the free ligand, accompanied by the increased luminescent intensity. The results indicate that photoluminescence properties of complexes can been controlled by the frameworks and coordination of different center metals.

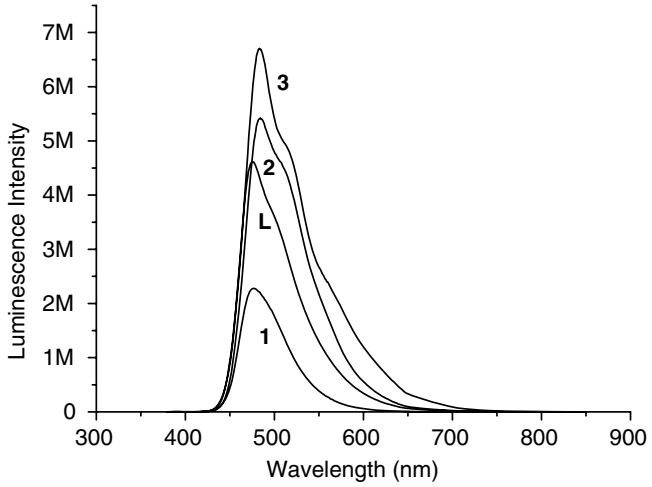


Fig. 4. Solid-state emission spectra of the compounds.

4. Conclusions

Three new coordination polymers containing functional rigid imidazole ligand with one- and two-dimensional frameworks have been obtained. The study shows that rational design metal-organic frameworks constructed from metals and functional π-conjugated ligands have prepared supramolecular polymers with both new structural architectures and unusual properties. By supramolecular self-assembly of different metals with the same ligands, different types of frameworks can be obtained. In $[Cd(SCN)_2L_2]_n$ (**1**), Cd^{II} ions are linked by bridging SCN^- ligands to form a one-dimensional polymeric chain structure. In $[CdHg(SCN)_4L_2]_n$ (**2**) and $[MnHg(SCN)_4L_2]_n$ (**3**), hetero-metals are linked by SCN^- ligands to form 2D coordination polymers, which show that the choice of metal ions is critical in determining the architecture of the complex. The title crystals posses better stabilities and do not show any decomposition and hygroscopic at room temperature. Their high thermal stabilities and excellent optical properties make them suitable to be used as potential optical materials. Further studies on related properties and synthesis of other functional rigid imidazole ligands with metals are under way.

5. Supplementary material

CCDC 257858, 255806 and 257859 contain the supplementary crystallographic data for **1**, **2** and **3**. These data can be obtained free of charge via http://www.ccdc.cam.ac.uk/conts/retrieving.html, or from the Cambridge Crystallographic Data Centre, 12 Union Road, Cambridge CB2 1EZ, UK; fax: (+44) 1223-336-033; or e-mail: deposit@ccdc.cam.ac.uk.

Acknowledgements

This work was supported by the National Natural Science Foundation of China (50532030, 50335050, and 50325311), Person with Ability Foundation of Anhui Province (2002Z021), Doctoral Program Foundation of the Ministry of Education of China, Education Committee of Anhui Province (2006KJ032A, 2006KJ135B, and 2006KJ158B),

The Team for Scientific Innovation Foundation of Anhui Province (2006KJ007TD), Key Laboratory of Opto-Electronic Information Acquisition and Manipulation (Anhui University), Ministry of Education, Person with Ability Foundation of Anhui University.

References

[1] (a) Z.M. Xue, Y.P. Tian, W. Wang, M.H. Jiang, J. Chem. Soc., Dalton Trans. (2003) 1373;
(b) H.P. Zhou, Y.P. Tian, J.Y. Wu, J.Z. Zhang, D.M. Li, M.H. Jiang, Y. Xie, Eur. J. Inorg. Chem. (2005) 4976;
(c) H.P. Zhou, Y.M. Zhu, C.M. Cui, J.Y. Wu, Y. Xie, M.H. Jiang, X.T. Tao, Y.P. Tian, Inorg. Chem. Commun. 9 (2006) 351;
(d) E. Cariati, D. Roberto, R. Ugo, P.C. Ford, S. Galli, A. Sironi, Inorg. Chem. 44 (2005) 4077;
(e) H.P. Zhou, J.Z. Zhang, D.M. Li, J.Y. Wu, Y. Xie, M.H. Jiang, X.T. Tao, Y.P. Tian, J. Mol. Struct. 743 (2005) 93.

[2] (a) H.F. Zhu, W. Zhao, T.-a. Okamura, J. Fan, W.Y. Sun, N. Ueyama, New J. Chem. 28 (2004) 1010;
(b) O.R. Evans, W.B. Lin, Acc. Chem. Res. 35 (2002) 511;
(c) C.L. Chen, A.M. Goforth, M.D. Smith, C.Y. Su, H.C.Z. Loye, Inorg. Chem. 44 (2005) 8762.

[3] (a) J.F. Berry, F.A. Cotton, L.M. Daniels, C.A. Murillo, J. Am. Chem. Soc. 124 (2002) 3212;
(b) M. Yoshizawa, S. Miyagi, M. Kawano, K. Ishiguro, M. Fujita, J. Am. Chem. Soc. 126 (2004) 9172;
(c) E. Cariati, X.H. Bu, P.C. Ford, Chem. Mater. 12 (2000) 3385.

[4] C. Janiak, J. Chem. Soc., Dalton Trans. (2003) 2781.

[5] O.R. Evans, R.G. Xiong, Z. Wang, G.K. Wong, W. Lin, Angew. Chem., Int. Ed. 38 (1999) 536.

[6] S.Y. Wang, Y.Z. Li, T.-a. Okamura, J. Fan, W.Y. Sun, N. Ueyama, Eur. J. Inorg. Chem. (2003) 3783.

[7] M. Eddaoudi, D.B. Moler, H.L. Li, B. Chen, T.M. Reineke, M. O'Keeffe, O.M. Yaghi, Acc. Chem. Res. 34 (2001) 319.

[8] B. Moulton, M.J. Zaworotko, Chem. Rev. 101 (2001) 1629.

[9] (a) X.J. Zhang, Y.P. Tian, S.L. Li, M.H. Jiang, Polyhedron 22 (2003) 397;
(b) Y.P. Tian, W.T. Yu, C.Y. Zhao, M.H. Jiang, Z.G. Cai, H.G. Fun, Polyhedron 21 (2002) 1217.

[10] R.O. Evans, W.B. Lin, Chem. Mater. 13 (2001) 3009.

[11] J.M. Rivera, H. Reyes, R. Santillan, Chem. Mater. 18 (2006) 1174.

[12] C. Elena, D. Roberto, R. Ugo, P.C. Ford, S. Galli, A. Sironi, Inorg. Chem. 44 (2005) 4077.

[13] G. Yang, H.G. Zhu, B.H. Liang, X.M. Chen, J. Chem. Soc., Dalton Trans. (2001) 580.

[14] H.K. Liu, C.Y. Su, C.M. Qian, J. Liu, H.Y. Tan, B.S. Kang, J. Chem. Soc., Dalton Trans. (2001) 1167.

[15] H. Zhang, X.M. Wang, K. Zhang, B.K. Teo, Coord. Chem. Rev. 183 (1999) 157.

[16] H. Zhang, D.E. Zelmon, G.E. Price, B.K. Teo, Inorg. Chem. 39 (2000) 1868.

[17] (a) H. Zhang, X.M. Wang, H. Zhu, W. Xiao, K. Zhang, B.K. Teo, Inorg. Chem. 38 (1999) 886;
(b) H. Zhang, X.M. Wang, D.E. Zelmon, B.K. Teo, Inorg. Chem. 40 (2001) 1501;
(c) H. Zhang, X.M. Wang, K. Zhang, B.K. Teo, Inorg. Chem. 37 (1998) 3490;
(d) M.A.S. Goher, Q.C. Yang, T.C.W. Mak, Polyhedron 19 (2000) 615;
(e) S.L. Li, J.Y. Wu, Y.P. Tian, H. Ming, M.H. Jiang, H.K. Fun, Eur. J. Inorg. Chem. 14 (2006) 2900.

[18] (a) F. Jin, F.Y. Hao, J.L. Ma, J.Y. Wu, Y.P. Tian, Chinese J. Struct. Chem. 25 (11) (2006) 1303;
(b) F. Jin, J. Ma, J.L. Ma, Y.M. Cui, J.Y. Wu, Y.P. Tian, Chem. J. Chin. Univ. 27 (9) (2006) 1599.

[19] (a) W. Zhao, J. Fan, T.-a. Okamura, W.Y. Sun, N. Ueyama, New J. Chem. 28 (2004) 1142;
(b) J. Fan, L. Gan, H. Kawaguchi, W.Y. Sun, K.B. Yu, W.X. Tang, Chem. Eur. J. 9 (2003) 3965;
(c) W.Y. Sun, J. Fan, T.-a. Okamura, N. Ueyama, Inorg. Chem. Commun. 3 (2000) 541;
(d) H.F. Zhu, Z. Wei, T.-a. Okamura, J. Fan, W.Y. Sun, N. Ueyama, New J. Chem. 28 (2004) 1010;
(e) J. Fan, B. Sui, T.-a. Okamura, W.X. Tang, W.Y. Sun, N. Ueyama, J. Chem. Soc., Dalton Trans. (2002) 3868.

[20] G.M. Sheldrick, SHELXTL V. 5.1 Software Reference Manual, Bruker AXS, Inc., Madison, WI, USA, 1997.

[21] L. Shen, D.J. Xu, J.G. Liu, Y.Z. Xu, J. Coord. Chem. 55 (3) (2002) 301.

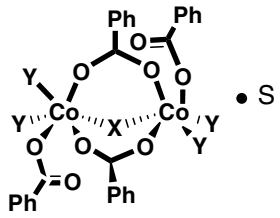
[22] K. Nakamoto, Infrared and Roman Spectra of Inorganic and Coordination Compounds, 4th ed., Wiley, New York, 1986.

[23] (a) R.G. Pearson, J. Am. Chem. Soc. 85 (1963) 3533;
(b) R.G. Pearson, J. Am. Chem. Soc. 89 (1967) 1827;
(c) R.G. Pearson, Science 151 (1966) 172.

[24] (a) M. Taniguchi, Y. Sugita, A. Ouchi, Bull. Chem. Soc. Jpn. 60 (1987) 179;
(b) M. Taniguchi, A. Ouchi, Bull. Chem. Soc. Jpn. 62 (1987) 424;
(c) H.J. Chen, G. Yang, X.M. Chen, Acta Crystallogr., Sect. C 55 (1999) 2012;
(d) G. Yang, H.G. Zhu, B.H. Liang, X.M. Chen, J. Chem. Soc., Dalton Trans. (2001) 580.

[25] F. Cariati, U. Caruso, R. Centore, W. Marcolli, A. De Maria, B. Panunzi, A. Roviello, A. Tuzi, Inorg. Chem. 41 (2002) 6597.

[26] (a) C.M. Che, C.W. Wan, K.Y. Ho, Z.Y. Zhou, New J. Chem. 25 (2001) 63;
(b) C.M. Che, C.W. Wan, W.Z. Lin, W.Y. Yu, Z.Y. Zhou, W.Y. Lai, S.T. Lee, Chem. Commun. (2001) 721.



where X= H_2O; Y = pyridine

Ph = C_6H_5 and	S= $C_6H_5CO_2H$. C_6H_6	1a
Ph = C_6H_5 and	S = 1.5 C_6H_6	1b
Ph = p-ClC_6H_4	S= none	1c

Fig. 1. Aqua-bridged dinuclear cobalt (II) benzoate complexes.

toluene, methanol and acetonitrile were distilled and used. The X-ray diffraction data were collected at 296 K with Mo Kα radiation ($\lambda = 0.71073$ Å) using a Bruker Nonius SMART CCD diffractometer equipped with graphite monochromator. The SMART software was used for data collection and also for indexing the reflections and determining the unit cell parameters; the collected data were integrated using SAINT software. The structures were solved by direct methods and refined by full-matrix least-squares calculations using SHELXTL software. All the non-H atoms were refined in the anisotropic approximation against F^2 of all reflections. The H-atoms, except those attached to N, O, and F were placed at their calculated positions and refined in the isotropic approximation; those attached to heteroatoms (N and O) were located in the difference Fourier maps, and refined with isotropic displacement coefficients. In case of complex **1a**, the included benzene molecule was solved in the isotropic approximation. Moreover, in the case of compound **2**, only one of the hydrogen atoms of the hydrogen bonded water molecule could be located in the difference Fourier (for crystal data see Table 1).

2.2. Synthesis of the complexes

2.2.1. Synthesis of $[Co_2(\mu\text{-}H_2O)(\mu\text{-}OBz)_2(OBz)_2(Py)_4]\cdot(C_6H_6)(BzOH)$ (**1a**)

In a typical experiment, benzoic acid (0.24gm, 2 mmol), sodium hydroxide (0.08gm, 2 mmol) and cobalt (II) chloride hexahydrate (0.238gm, 1 mmol) were finely ground in mortar and heated at 100 °C for 15 min, the pink colour turns blue. The solid mixture was cooled to room temperature transferred into a round bottom flask and benzene (20 ml) was added to it and the heterogeneous mixture was stirred at room temp for 5 min followed by the addition of pyridine (0.158 g, 2 mmol). The blue supernatant liquid turned pink

Table 1
Crystal data and refinement parameters for **1** and **2**

	1a	1b	1c	2
Formulae	$C_{61}H_{54}Co_2N_4O_{11}$	$C_{57}H_{51}Co_2N_4O_9$	$C_{48}H_{38}Cl_4Co_2N_4O_9$	$C_{56}H_{56}Co_4N_8O_{16}$
Molecular weight	1136.94	1053.88	1074.48	1332.81
Crystal system	monoclinic	monoclinic	monoclinic	orthorhombic
Space group	$P2_1/c$	$P2_1/c$	$P2_1/c$	$Fddd$
Temperature (K)	296	296	296	296
Wavelength (Å)	0.71073	0.71073	0.71073	0.71073
Unit cell dimensions				
a (Å)	10.5613(3)	10.8300(4)	21.8994(10)	21.1772(6)
b (Å)	26.0992(7)	38.4304(15)	20.5157(10)	25.7730(12)
c (Å)	21.1667(6)	12.6302(6)	12.0381(6)	22.5183(6)
α (°)	90	90	90	90
β (°)	95.750(2)	91.559(3)	92.1440(10)	90
γ (°)	90	90	90	90
V (Å^3)	5805.1(3)	5254.8(4)	5404.7(5)	12290.5(7)
Z	4	4	4	8
Density (Mg m^{-3})	1.301	1.332	1.320	1.441
Absorption coefficient (mm^{-1})	0.633	0.691	0.864	1.132
Absorption correction	none	none	none	none
F(000)	2360	2188	2192	5472
Total number of reflections	52884	37792	55233	30772
Reflections, $I > 2\sigma(I)$	14382	13907	13454	3841
Maximum 2θ (°)	28.29	29.16	28.34	28.34
Ranges (h, k, l)	$-13 \le h \le 14$ $-29 \le k \le 34$ $-28 \le l \le 27$	$-14 \le h \le 13$ $-44 \le k \le 52$ $-15 \le l \le 17$	$-29 \le h \le 28$ $-28 \le l \le 27$ $-16 \le l \le 16$	$-28 \le h \le 28$ $-34 \le k \le 33$ $-30 \le l \le 30$
Completeness to 2θ (%)	99.8	98.1	99.8	99.7
Refinement method	full-matrix least-squares on F^2	full-matrix least-squares on F^2	full-matrix least-squares on F^2	full-matrix least-squares on F^2
Data/restraints/parameters	14382/0/669	13907/0/657	13454/0/612	3841/0/197
GOOF (F^2)	1.021	1.104	1.048	0.952
R indices [$I > 2\sigma(I)$]	0.0704	0.0616	0.0551	0.0323
R indices (all data)	0.1574	0.1079	0.0828	0.0743

in colour. The residue was filtered off and the pink filtrate was left undisturbed. Pink crystals were collected after 3 days and dried in air. Yield: 34%. *Anal.* Calc. for $C_{61}H_{54}Co_2N_4O_{11}$: C, 64.37; H, 4.74. Found: C, 64.58; H, 4.82%. IR (KBr, cm^{-1}): 3063(s), 1614(s), 1568(s), 1537(s), 1487(m), 1403(s), 1219(m), 1070(m), 853(s), 766(s), 717(s), 701(s). Magnetic moment: 6.54BM at 25 °C; UV–Vis: λ_{max} (MeOH) 519 nm, $\varepsilon = 40.10\ M^{-1}\ cm^{-1}$.

2.2.2. Synthesis of $[Co_2(\mu\text{-}H_2O)(\mu\text{-}OBz)_2(OBz)_2(Py)_4]\cdot 1.5(C_6H_6)$ (**1b**)

Sodium benzoate (0.29 g, 2 mmol) and cobalt (II) chloride hexahydrate (0.238 g, 1 mmol) were finely ground in the mortar and heated at 100 °C for 15 min, during which the pink colour became blue. The mixture was cooled to room temperature and transferred into a round bottom flask. To this mass, benzene (20 ml) was added and the heterogeneous mixture was stirred at room temp for 5 min followed by the addition of pyridine (0.158 g, 2 mmol). The blue supernatant liquid turned pink in colour. The residue was filtered off and the pink filtrate was left undisturbed. Pink crystals were obtained after 3 days that were collected and dried in air. Yield: 23%. *Anal.* Calc. for $C_{57}H_{51}Co_2N_4O_9$: C, 64.90; H, 4.83. Found: C, 64.98, H, 4.94%. IR (KBr, cm^{-1}): 3446(b), 3066(bs), 2361(b), 1627(s), 1601(s), 1573(s), 1537(m), 1485(m), 1393(s), 1068(m), 1038(m), 812(ms), 757(ms), 716(s), 701(s), 677(m). Magnetic moment: 6.52 BM at 25 °C; UV–Vis: λ_{max}(MeOH) 519 nm, $\varepsilon = 40.32\ M^{-1}\ cm^{-1}$.

2.2.3. Compound $[Co_2(\mu\text{-}H_2O)(\mu\text{-}p\text{-}Cl\text{-}OBz)_2(p\text{-}Cl\text{-}OBz)_2(Py)_4]$ (**1c**) (where p-Cl-OBz = para-chlorobenzoate)

It was prepared in a similar procedure as adopted for **1a**. Yield 39%. *Anal.* Calc. for $C_{48}H_{38}Cl_4Co_2N_4O_9$: C, 53.58; H, 3.53. Found: C, 54.52; H, 3.50%. IR (KBr, cm^{-1}): 3069(bs), 1608(s), 1561(s), 1486(ms), 1446(ms), 1403(s), 1219(m), 1169(m), 1091(ms), 1014(ms), 856(m), 772(s), 699(s), 537(s). Magnetic moment: 5.93 BM at 25 °C; UV–Vis: λ_{max}(MeOH) 518 nm, $\varepsilon = 37.06\ M^{-1}\ cm^{-1}$.

2.2.4. Synthesis of complex $Co_4O_4(Py)_4(O_2CPh)_4\cdot 4CH_3CN\cdot 4H_2O$ (**2**)

Complex **1a** (0.114 g, 0.1 mmol) was dissolved in acetonitrile (10 ml) and H_2O_2 (0.4 ml; 30% v/v) was added dropwise. On addition of hydrogen peroxide the pink solution became dark green. The solution was filtered to remove undissolved material (if any) and the filtrate was left undisturbed for 2 days. Dark green crystals were obtained after 2 days, which were found suitable for single crystal X-ray diffraction studies. Yield: 52%; IR (KBr, cm^{-1}): 3412(b), 3060(b), 2368(ms), 1602(bs), 1527(s), 1448(ms), 1384(s), 1212(ms), 1070(ms), 1026(ms), 757(ms), 718(s), 691(s). ^1H NMR ($CDCl_3$, 400 MHz) 8.73 (8H, d, $J = 6.0$ Hz), 8.02 (8H, d, $J = 8.0$ Hz), 7.46 (4H, t, $J = 7.2$ Hz), 7.32 (4H, t, $J = 7.2$ Hz), 7.22 (8H, m), 6.97 (8H, t, $J = 7.2$ Hz).

2.2.5. Synthesis of $[Co(H_2O)(Py)_2(OBz)_2]$ (**3**)

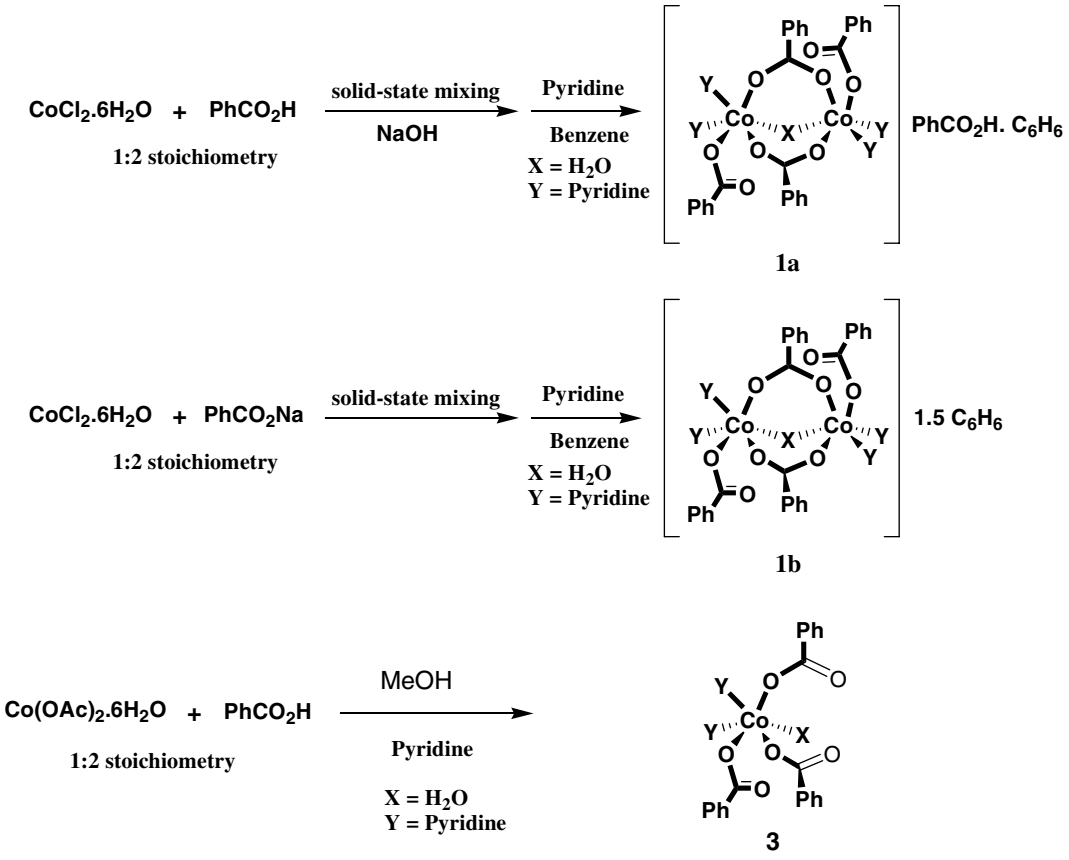
To a well-stirred solution of benzoic acid (0.24 g, 2 mmol) in methanol (20 ml) cobalt (II) acetate tetrahydrate (0.25 g, 1 mmol) was added and stirred for 12 h at room temperature. After that pyridine (0.158 g, 2 mmol) was added and at room temperature for half an hour. On standing pink crystals were precipitated after 6 days. The crystals were dried in air. Crystalline yield: 42% (based on Co). *Anal.* Calc. for $C_{24}H_{22}N_2O_5Co$: C, 60.37; H, 4.61. Found: C, 60.29; H, 4.62%. IR (KBr, cm^{-1}): 3265(wb), 3058(w), 1593(s), 1540(s), 1572(m), 1485(w), 1445(m), 1408(s), 1374(s), 1065(m), 1039(m), 856(m), 756(w), 722(s), 701(s), 625(m). Magnetic moment (27 °C) 4.04 BM UV–Vis: λ_{max}(MeOH) 517 nm = 25.07 $m^{-1}\ cm^{-1}$. *Crystal parameters*. Formula: $C_{24}\ H_{22}N_2O_5Co$; Temperature, 296(2) K; Density ($Mg\ m^{-3}$): 1.410; Monoclinic; $P21/c$; $a = 9.33(2)$, $b = 20.67(3)$, $c = 13.05(2)$, $\alpha = 90.00$, $\beta = 116.78(10)$, $\gamma = 90.00$; $V = 2248.44(7)$ Å^3, $Z = 4$, $\mu = 0.801$; GOOF (F^2) 0.884; R indices [$I > 2\sigma(I)$], 0.0293 R indices (all data) 0.0715.

3. Result and discussion

We have found that the reaction of cobalt (II) chloride hexahydrate, benzoic acid and sodium hydroxide in the solid-state (Scheme 1) followed by addition of pyridine (in 1:2:2 stoichiometry) gave the cobalt (II) benzoate complex, $[Co_2(\mu\text{-}H_2O)(\mu\text{-}OBz)_2(OBz)_2(Py)_4]\cdot(C_6H_6)(BzOH)$ (**1a**). The complex is soluble in chloroform, benzene or toluene and could subsequently be crystallised from benzene as pink plates in the $P2_1/c$ space group.

Crystal structure of **1a** shows this complex to be a binuclear cobalt (II) assembly (Fig. 2), where each of the cobalt centres have octahedral geometries, such that Co(1)···Co(2) distance is 3.597(3) Å. The binuclear structure of the cobalt (II) complex is stabilised by two μ-benzoate molecules, which are present in the bridging mode along with a bridging water molecule. In this regard it may be pointed out that these binuclear cobalt complexes having two bridging carboxylate groups and the aqua bridge have close structural similarities to the biological relevant system aminopetidase [3a]. Each cobalt (II) centre in complex **1a** is coordinated to two pyridine molecules and a monodentate benzoate group thereby completing the 6-coordination environment about the metal ion.

The monodentate benzoate groups are intramolecularly hydrogen bonded to the water molecule through O9–H···O8 (2.583 Å, 169.4°) and O9–H···O6 (2.546 Å, 163.9°) interactions. The Co1–$O9_{aqua}$ and Co2–$O9_{aqua}$ bond distances in this complex are 2.135(3) and 2.129(3) Å while the corresponding the Co1–O_{aqua}–Co2 bond angle is 115.03(12)°. The important bond distances and bond angles for this complex are given in Table 2. Solid state FT-IR spectra of the complex **1a** shows a sharp absorption at 3063 cm^{-1} due to O–H stretching and is an indication of the strong hydrogen bonding interactions involving the bridging aqua ligand. In methanol, the



Scheme 1.

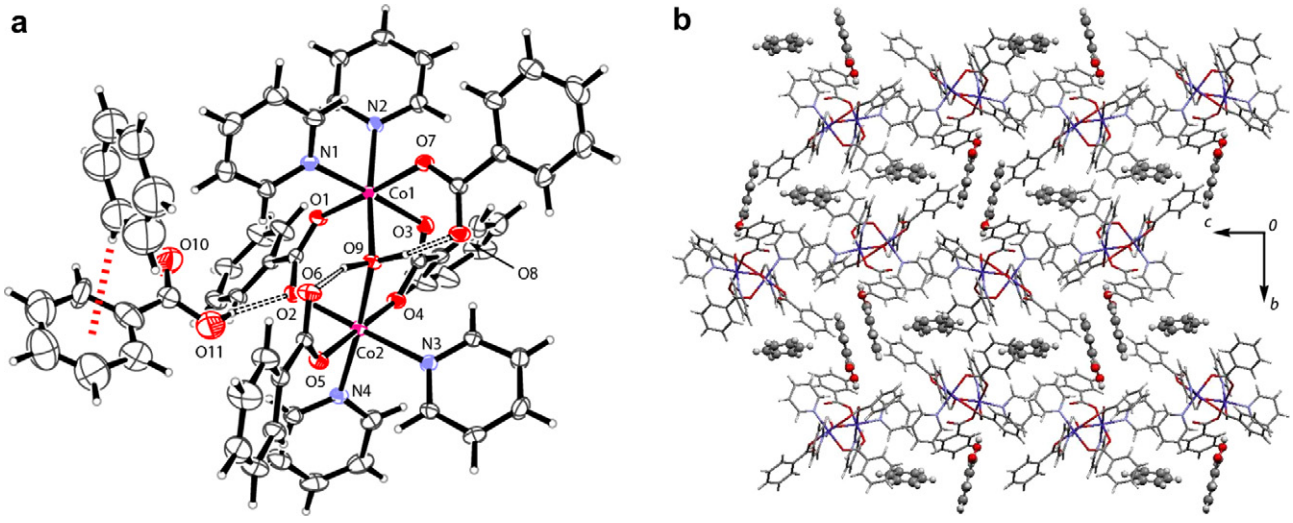


Fig. 2. (a) Crystal structure of **1a** (thermal ellipsoids drawn to 30% probability) and (b) inclusion of benzoic acid and benzene molecules.

UV–Vis spectrum of **1a** shows a weak absorption band at 512 nm that is assigned to the $^4T_1(F) \rightarrow {}^4A_2(F)$ transition [3a]. The absorption spectra have a shoulder at 414 nm, which is attributed to the $^4T_1(F) \rightarrow {}^4T_1(P)$.

This aqua-bridged binuclear cobalt (II) benzoate complex **1a** leads to the inclusion of free benzoic acid molecules as well as benzene molecules in the crystal lattice via self-assembly. This is because *in situ* preparation of sodium benzoate by reacting benzoic acid and sodium hydroxide in the solid phase possibly leaves unreacted neutral benzoic acid molecules. These benzoic acid molecules readily dissolve in benzene and are held in the lattice through intermolecular O10–H···O2 (2.722 Å, 164.9°) hydrogen bonding interactions to one of the bridging benzoate ligand of the complex. Weak aromatic C–H···π interactions ($d_C \cdots \pi$ 3.87 Å) involving the C60–H of the benzene

Table 2
Selected inter-nuclear distances (in Å) and angles (in °) in **1a**

Bond distances		Bond angles		Bond angles	
Co(1)–O(1)	2.075(3)	O(1)–Co(1)–O(7)	175.65(12)	O(4)–Co(2)– O(5)	177.78(13)
Co(1)–O(7)	2.082(3)	O(1)–Co(1)–O(3)	88.11(13)	O(4)–Co(2)–O(2)	88.64(12)
Co(1)–O(3)	2.093(3)	O(7)–Co(1)–O(3)	90.65(13)	O(5)–Co(2)–O(2)	91.29(12)
Co(1)–O(9)	2.135(3)	O(1)–Co(1)–O(9)	95.88(12)	O(4)–Co(2)– O(9)	94.19(12)
Co(1)–N(1)	2.136(4)	O(7)–Co(1)–O(9)	88.18(12)	O(5)–Co(2)–O(9)	88.03(12)
Co(1)–N(2)	2.148(4)	O(3)–Co(1)–O(9)	85.79(13)	O(2)–Co(2)–O(9)	88.74(13)
Co(2)–O(4)	2.086(3)	O(1)–Co(1)–N(1)	90.65(14)	O(4)–Co(2)–N(4)	91.95(14)
Co(2)–O(5)	2.088(3)	O(7)–Co(1)–N(1)	90.78(14)	O(5)–Co(2)–N(4)	85.84(14)
Co(2)–O(2)	2.127(3)	O(3)–Co(1)–N(1)	177.09(15)	O(2)–Co(2)–N(4)	89.57(14)
Co(2)–O(9)	2.129(3)	O(9)–Co(1)–N(1)	91.73(14)	O(9)–Co(2)–N(4)	173.60(14)
Co(2)–N(3)	2.168(4)	O(1)–Co(1)–N(2)	89.47(13)	O(4)–Co(2)–N(3)	90.82(13)
Co(2)–N(4)	2.148(4)	O(7)–Co(1)–N(2)	86.40(12)	O(5)–Co(2)–N(3)	89.28(13)
Co(1) ⋯ Co(2)	3.597(3)	O(3)–Co(1)–N(2)	91.55(14)	O(2)–Co(2)–N(3)	178.88(15)
Co1–O9–Co2	115.03(12)	O(9)–Co(1)–N(2)	173.94(14)	O(9)–Co(2)–N(3)	90.31(14)
		N(1)–Co(1)–N(2)	91.07(15)	N(4)–Co(2)–N(3)	91.44(15)

molecule as donor and the aromatic ring of the benzoic acid molecule as acceptor stabilises the solid-state assembly of **1a**.

Addition of pyridine to a mixture of cobalt (II) chloride hexahydrate and preformed sodium benzoate in the solid phase in 2:1:2 stoichiometries gave a pink solid, which was dissolved in benzene. The benzene soluble component was found to be the corresponding aqua-bridged binuclear complex, $[Co_2(\mu\text{-}H_2O)(\mu\text{-}OBz)_2(OBz)_2(Py)_4]\cdot 1.5C_6H_6$. Subsequent crystallisation of the complex from benzene gave the benzene inclusion compound as shown in Fig. 3, which also crystallises in $P2_1/c$ space group.

Crystal structure of the complex **1b** shows that the two cobalt (II) centres are bridged by one water molecule and two benzoates. The coordination environment of **1b** is similar to that of complex **1a** wherein each cobalt (II) centre is coordinated to a monodentate benzoate and two N-donor pyridine ligands. The bridging aqua group in **1b** is hydrogen bonded to the carboxyl group of the monodentate benzoate ligand through intramolecular O9–H9A⋯O8 (2.571 Å, 172.2°) and O9–H9B⋯O8 (2.579 Å, 166.9°) interactions as shown in Fig. 3. The Co1–$O9_{aqua}$ and Co2–$O9_{aqua}$ bond distances are 2.139(2) and 2.143(2) Å while the corresponding Co1–$O9_{aqua}$–Co2 bond angle is 111.87(11)°. Although the Co1–$O9_{aqua}$ and Co2–$O9_{aqua}$ bond distances in **1b** are only slightly longer than **1a**, (∼0.05 Å) the Co1–$O9_{aqua}$–Co2 bond angle is smaller by ∼4°. Important bond angles and bond distances for structure of complex **1b** is shown in Table 3. The observed parameters of the Co–O_{aqua}–Co motif in **1a** and **1b** are comparable with structural analogs reported elsewhere [7d,7e,7f,7g,7h].

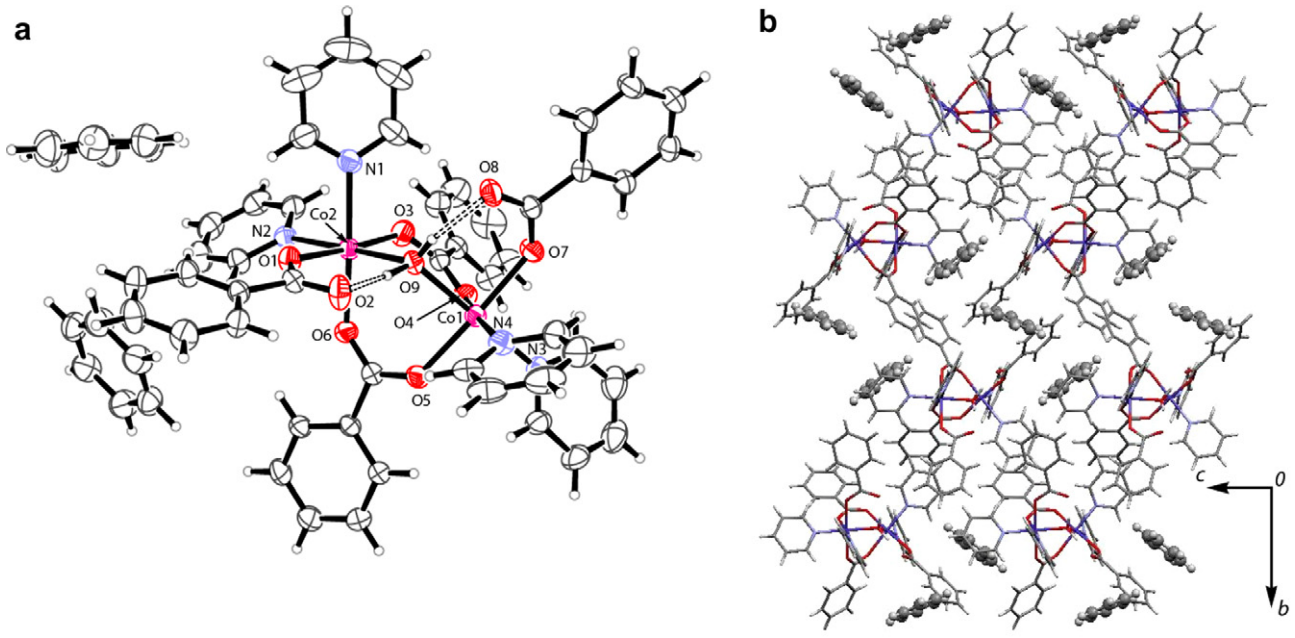


Fig. 3. (a) Crystal structure of **1b** (thermal ellipsoids drawn to 30% probability) and (b) inclusion of benzene molecules in **1b** .

Table 3
Selected inter-nuclear distances (in Å) and angles (in °) in **1b**

Bond distances		Bond angles		Bond angles	
Co(1)–O(4)	2.070(2)	O(6)–Co(1)–O(7)	177.19(9)	O(1)–Co(2)–O(3)	175.58(10)
Co(1)–O(6)	2.065(2)	O(4)–Co(1)–O(6)	91.55(8)	O(1)–Co(2)–O(5)	89.09(9)
Co(1)–O(7)	2.107(2)	O(4)–Co(1)–O(7)	87.20(9)	O(3)–Co(2)–O(5)	94.46(9)
Co(1)–O(9)	2.139(2)	O(6)–Co(1)–O(9)	88.81(10)	O(1)–Co(2)–O(9)	89.88(9)
Co(1)–N(3)	2.146(3)	O(4)–Co(1)–O(9)	98.72(9)	O(5)–Co(2)–O(9)	89.80(9)
Co(1)–N(4)	2.164(3)	O(7)–Co(1)–O(9)	88.89(10)	O(3)–Co(2)–O(9)	92.75(1)
Co(2)–O(1)	2.066(2)	O(4)–Co(1)–N(3)	84.40(10)	O(1)–Co(2)–N(2)	88.71(9)
Co(2)–O(3)	2.050(2)	O(6)–Co(1)–N(3)	91.19(10)	O(3)–Co(2)–N(2)	88.69(10)
Co(2)–O(5)	2.099(2)	O(7)–Co(1)–N(3)	91.20(10)	O(5)–Co(2)–N(2)	89.49(9)
Co(2)–O(9)	2.143(2)	O(9)–Co(1)–N(3)	176.88(10)	O(9)–Co(2)–N(2)	178.44(11)
Co(2)–N(1)	2.174(3)	O(4)–Co(1)–N(4)	170.32(10)	O(1)–Co(2)–N(1)	89.98(11)
Co(2)–N(2)	2.165(3)	O(6)–Co(1)–N(4)	91.79(10)	O(3)–Co(2)–N(1)	86.40(11)
Co(1) ··· Co(2)	3.547(2)	O(7)–Co(1)–N(4)	89.84(10)	O(5)–Co(2)–N(1)	178.13(11)
Co1–O9–Co2	111.87(11)	O(9)–Co(1)–N(4)	90.43(10)	O(9)–Co(2)–N(1)	91.81(11)
		N(3)–Co(1)–N(4)	86.45(10)	N(1)–Co(2)–N(2)	88.87(11)

It is noteworthy that solid state self-assembly of the binuclear complex **1a** leads to the inclusion of both benzoic acid and benzene molecules in the lattice while in **1b** inclusion of benzene is observed. The absence of benzoic acid in the lattice of **1b** may be rationalised by the fact that sodium benzoate, which has poor solubility in benzene, was used as the benzoate source. In this case, the self-assembly of binuclear cobalt (II) benzoate complex leads to the inclusion of two benzene molecules in the crystal lattice that are stabilised by weak intermolecular C–H···π interactions. The magnetic moments of complexes **1a** and **1b** at room temperature are found to be 6.54 and 6.52BM, respectively, which corresponds to octahedral geometry about the cobalt (II) centre and the presence of orbital contribution to the spin-only value for a Co^{2+} ion [8].

Mild oxidation of **1a** with H_2O_2 in acetonitrile under neutral conditions gave dark green complex **2**, which could be crystallised from acetonitrile. Crystallographic studies of the **2** shows the structure is derived from a composition $Co_4O_4(Py)_4(O_2CPh)_4 \cdot 4CH_3CN \cdot 4H_2O$ as shown in Fig. 5a. The complex has a core comprising of Co_4O_4 cluster in which the Co···Co distances are 2.7093(5), 2.7111(5) and 2.8191(5) Å as shown in Fig. 5b. The corresponding Co–O bond distances are found to be 1.9539(14), 1.9600(14) and 1.8661(13) Å, which indicates that the Co_4O_4 cluster has a cubic geometry. Each of the cobalt centres is attached to a pyridine ligand and μ-benzoate group bridges each two alternate cobalt centres. The tetranuclear cobalt (III)–benzoate complex **2** are held in the lattice through intermolecular O4–H···O3 (2.756 Å, 175.1°) hydrogen bonding interactions involving the included water molecule and the bridging oxo-groups of the Co_4O_4 units of **2**. This results in the formation three-dimensional networks in which the acetonitrile molecules are included as guests in the lattice. The complex is diamagnetic and shows broad absorptions at 639 nm in the visible spectrum, which is assigned to $^1A_1 \rightarrow {}^1T_1$ transition. It may be mentioned that the tetrameric cobalt (III) complexes are reported in the literature [9] and have interesting catalytic oxidative properties [9d].

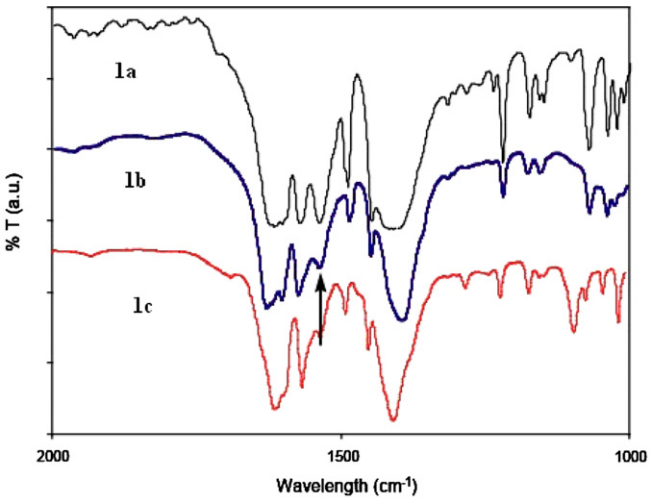


Fig. 4. FT-IR spectra of **1a**, **1b** and **1c** (solid-state) showing the absorption bands (1538 cm^{-1}) due to inclusion of aromatic guest molecules in the lattice.

To understand the effect of substituents on the benzoic acid molecule on the formation of binuclear cobalt (II) complexes, similar reactions were performed with *o*-nitrobenzoic acid and *p*-chlorobenzoic acid.

The complex $[Co_2(\mu\text{-}H_2O)(\mu\text{-}p\text{-Cl–OBz})_2(p\text{-Cl–OBz})_2(Py)_4]$ (**1c**) was prepared by reacting cobalt (II) chloride hexahydrate with *p*-chlorobenzoic acid in the presence of sodium hydroxide, and subsequent addition of pyridine (Fig. 6). The complex obtained was a pink solid, which could be crystallised from toluene. It may be mentioned that although the complex dissolves in benzene, diffraction quality crystals containing benzene could not be isolated. The structure of this aqua-bridged binuclear complex, **1c** is similar to **1a**–**b**, wherein, the two cobalt (II) centres are bridged by two bidentate benzoate groups and an aqua bridge. There is slight variation in the Co1–O_{aqua}–Co2

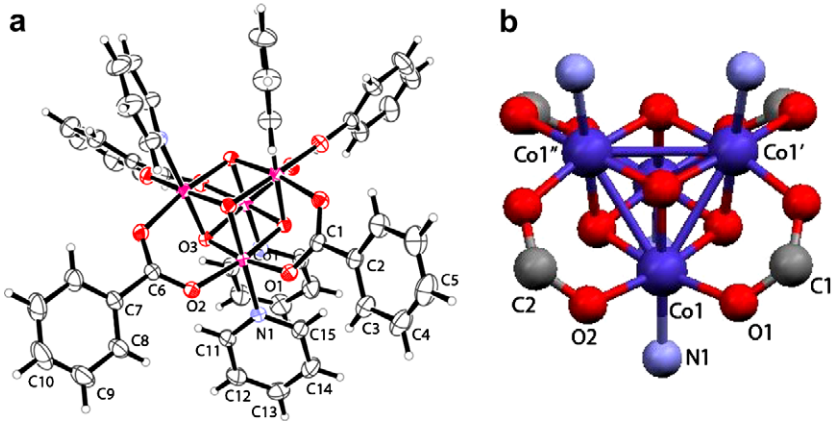


Fig. 5. (a) Crystal structure of **2** (thermal ellipsoids drawn to 30% probability) and (b) the Co_4O_4 core, where Co1···Co1′ 2.7093(5) Å, Co1···Co1″ 2.7111(5) Å, and Co1′···Co1″ 2.8191(5) Å. Solvent molecules are not shown for clarity. Symmetry equivalence $^{\#1}-x+1/4, -y+1/4, z$; $^{\#2}x, -y+1/4, -z+1/4$; $^{\#3}-x+1/4, y, -z+1/4$.

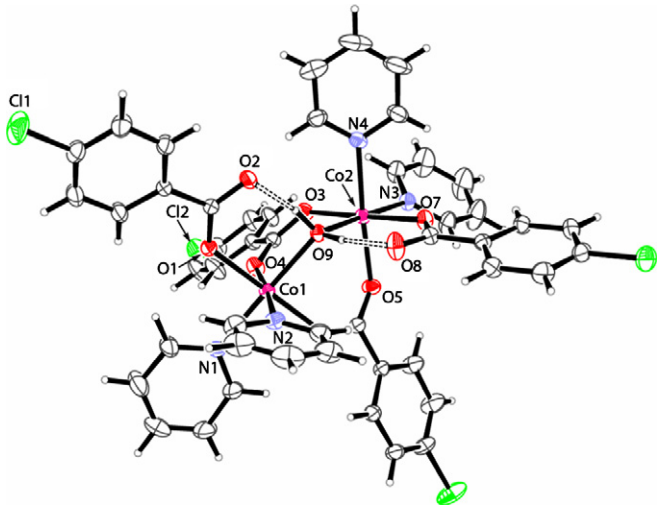


Fig. 6. Crystal structure of **1c** (thermal ellipsoids drawn to 30% probability).

separation due to electronic effect (see Table 4) and due to the different environment created by guest molecule but the observed distances are within the expected bond distances of systems that are reported [5a,7e]. Aqua-bridged Co–O–Co frame having pyridine as axial ligands with trifluoroacetate and stearate are reported in the literature and have similar co-ordination features to the one reported in this study [7o,7p].

Absence of aromatic guest molecules in the crystal lattice is also apparent in the solid state IR spectra as shown in Fig. 4. The presence of aromatic guests such as benzoic acid and benzene in the lattice of **1a** and **1b** give rise to a strong absorption band at 1538 cm^{-1}. This absorption band is absent in the solid state FT-IR spectrum of **1c**.

The bond distances and bond angles for the Co1–O_{aqua}–Co2 motif in the complexes, **1a**–**1c**, shows slight variation

Table 5
Comparison of bond distances and angles

	1a	1b	1c
Co(1)–O_{aqua}	2.135(3)	2.139(2)	2.156(2)
Co(2)–O_{aqua}	2.129(3)	2.143(2)	2.160(2)
Co(1)–O_{aqua}–Co(2)	115.03(12)	111.87(11)	115.20(10)
Co(1)···Co(2)	3.597(3)	3.547(2)	3.644(2)

Table 4
Selected inter-nuclear distances (in Å) and angles (in °) in **1c**

Bond distances		Bond angles		Bond angles	
Co(1)–O(1)	2.099(2)	O(1)–Co(1)–O(6)	176.31(10)	O(3)–Co(2)–O(5)	91.89(10)
Co(1)–O(4)	2.064(2)	O(1)–Co(1)–O(4)	90.50(10)	O(3)–Co(2)–O(7)	177.87(9)
Co(1)–O(6)	2.044(2)	O(4)–Co(1)–O(6)	93.13(10)	O(5)–Co(2)–O(7)	88.73(11)
Co(1)–O(9)	2.156(2)	O(6)–Co(1)–O(9)	88.42(10)	O(3)–Co(2)–O(9)	92.07(9)
Co(1)–N(1)	2.193(3)	O(4)–Co(1)–O(9)	91.77(9)	O(5)–Co(2)–O(9)	92.02(9)
Co(1)–N(2)	2.183(3)	O(1)–Co(1)–O(9)	90.84(9)	O(7)–Co(2)–O(9)	89.94(9)
Co(2)–O(3)	2.062(2)	O(1)–Co(1)–N(1)	90.27(9)	O(3)–Co(2)–N(3)	90.77(10)
Co(2)–O(5)	2.080(2)	O(4)–Co(1)–N(1)	87.42(10)	O(5)–Co(2)–N(3)	87.36(10)
Co(2)–O(7)	2.095(2)	O(6)–Co(1)–N(1)	90.52(10)	O(7)–Co(2)–N(3)	87.23(10)
Co(2)–O(9)	2.160(2)	O(9)–Co(1)–N(1)	178.63(10)	O(9)–Co(2)–N(3)	177.11(10)
Co(2)–N(3)	2.155(3)	O(1)–Co(1)–N(2)	87.87(10)	O(3)–Co(2)–N(4)	90.37(10)
Co(2)–N(4)	2.180(3)	O(4)–Co(1)–N(2)	176.08(11)	O(5)–Co(2)–N(4)	176.23(10)
Co(1)···Co(2)	3.644(2)	O(6)–Co(1)–N(2)	88.54(10)	O(7)–Co(2)–N(4)	88.90(11)
Co1–O–Co2	115.20(10)	O(9)–Co(1)–N(2)	91.82(10)	O(9)–Co(2)–N(4)	90.91(10)
		N(1)–Co(1)–N(2)	89.02(11)	N(4)–Co(2)–N(3)	89.60(11)

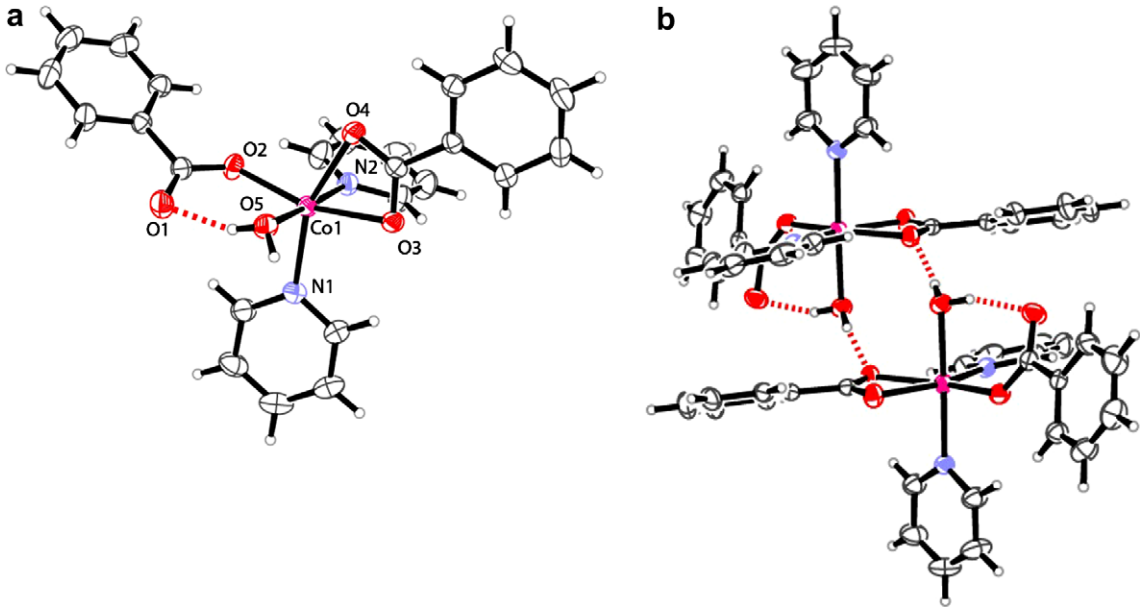


Fig. 7. (a) Crystal structure of $[Co(H_2O)(Py)_2(OBz)_2]$ (**3**) and (b) its hydrogen bonded dimer (thermal ellipsoids drawn to 30% probability).

in the distances and angles (Table 5). This happens due to subtle electronic factors, while the supramolecular assembly as in the case of **1a** and **1b** controls the inclusion properties.

When similar reaction of cobalt (II) acetate tetrahydrate in methanolic solution were carried out in the presence of benzoic acid and pyridine a mononuclear cobalt complex $[Co(H_2O)(Py)_2(OBz)_2]$ (**3**) is formed. The crystal structure of the complex is shown in Fig. 7. The compound remains as dimeric units through hydrogen bonding interaction between the O–H···O interaction between the C=O of carboxylate with a water molecule. The magnetic moment and the visible spectral features support the structure.

4. Conclusions

We have described a solid-state synthetic route to a few binuclear cobalt (II) complexes, and method of synthesis leads to either acid inclusion or inclusion of aromatic solvent. The aqua bridge in these binuclear structures is stabilised by intramolecular O–H···O hydrogen bonding interactions between the bridging aqua group and the monodentate benzoate/substituted benzoate groups. The solution state synthesis of similar complexes led to the formation of mononuclear cobalt (II) complex.

5. Supplementary material

CCDC 608661, 608662, 608663, 608664 and 620811 contain the supplementary crystallographic data for **1a**, **1b**, **1c**, **2** and **3**. These data can be obtained free of charge via http://www.ccdc.cam.ac.uk/conts/retrieving.html, or from the Cambridge Crystallographic Data Centre, 12 Union Road, Cambridge CB2 1EZ, UK; fax: (+44) 1223-336-033; or e-mail: deposit@ccdc.cam.ac.uk.

Acknowledgement

We are thankful to DST (India) for financial support.

References

[1] (a) J.B. Vincent, G.L. Olivier-Lilley, B.A. Averill, Chem. Rev. 90 (1990) 1447;
(b) D.E. Wilcox, Chem. Rev. 96 (1996) 2435;
(c) J.T. Groves, L. Ann Baron, J. Am. Chem. Soc. 111 (1989) 5442;
(d) H. Shim, F.M. Raushel, Biochemistry 39 (2000) 7357;
(e) A. Messerschmidt, A. Huber, T. Poulos, K. Wieghardt (Eds.), Handbook of Metalloproteins, Wiley, Chichester, UK, 2001.
[2] W.T. Lowther, D.A. McMillen, A.M. Orville, B.W. Matthews, Proc. Natl. Acad. Sci. USA 95 (1998) 12153.
[3] (a) R.C. Holz, Coord. Chem. Rev. 232 (2002) 5;
(b) M.P. Allen, A.H. Yamada, F.H. Carpenter, Biochemistry 22 (1983) 3778.
[4] (a) S. Hikichi, M. Yoshizawa, Y. Sasakura, M. Akita, Y. Moro-oka, J. Am. Chem. Soc. 120 (1998) 10567;
(b) M.N. Mortensen, B. Jensen, A. Hazell, A.D. Bond, C.J. McKenzie, J. Chem. Soc., Dalton Trans. (2004) 3396.
[5] (a) R. Lachicotte, A. Kitaygorodskiy, K.S. Hagen, J. Am. Chem. Soc. 115 (1993) 8883;
(b) D.M. Kurtz, Chem. Rev. 96 (1996) 585;
(c) C. He, S.J. Lippard, J. Am. Chem. Soc. 120 (1998) 105;
(d) A.M. Barrios, S.J. Lippard, J. Am. Chem. Soc. 122 (2000) 9172.
[6] R.A. Reynolds III, W.R. Dunham, D. Coucouvanis, Inorg. Chem. 37 (1998) 1232.
[7] (a) B.-H. Ye, I.D. William, X.-Y. Li, J. Inorg. Biochem. 92 (2002) 128;
(b) K.S. Hagen, R. Lachicotte, J. Am. Chem. Soc. 114 (1992) 8741;
(c) D. Coucouvanis, R.A. Reynolds III, W.R. Dunham, J. Am. Chem. Soc. 117 (1995) 7570;
(d) A. Caneschi, F. Ferraro, D. Gatteschi, M.C. Melandui, P. Rey, R. Sessoli, Angew. Chem., Int. Ed. Engl. 89 (1989) 1365;
(e) S.B. Yu, S.J. Lippard, I. Shweky, A. Bino, Inorg. Chem. 31 (1992) 3502;
(f) U. Turpeinen, Finn. Chem. Lett. (1977) 36;
(g) M. Ahlgren, U. Turpeinen, R. Hämäläinen, Acta Chem. Scan. 32 (1978) 189;
(h) H. Uekusa, S. Ohba, T. Tokii, Acta Crystallogr. C51 (1995) 625;

(i) D. Lee, P.-L. Hung, B. Spingler, S.J. Lippard, Inorg. Chem. 41 (2002) 521;
(j) V. Calvo-Perez, S. Ostrovsky, A. Vega, J. Pelikan, E. Spodine, W. Haase, Inorg. Chem. 45 (2006) 644;
(k) Y.-H. Liu, H.-L. Tsai, Y.-L. Lu, Y.-S. Wen, J.-C. Wang, K.-L. Lu, Inorg. Chem. 40 (2001) 6426;
(l) U. Turpeinen, R. Hämäläinen, J. Reedijk, Polyhedron 6 (1987) 1603;
(m) H. Muhonen, Inorg. Chem. 25 (1986) 4693;
(n) M.G.B. Drew, J. Nelson, F. Esho, V. McKee, S.M. Nelson, J. Chem. Soc., Dalton Trans. (1982) 1837;
(o) R.W. Corkery, D.C.R. Hockless, Acta Crystallogr. C53 (1997) 840;
(p) T.J. Prior, J.C. Burley, Acta. Crystallogr. E61 (2005) m1424.

[8] B.N. Figgis (Ed.), Introduction to Ligand Fields, John Wiley, New York, 1966.

[9] (a) K. Dimitrou, K. Flotting, W.E. Streib, G. Cristou, J. Am. Chem. Soc. 115 (1993) 6432;
(b) J.K. Beattie, T.W. Humbley, J.A. Kelpetko, A.F. Master, P. Turner, Polyhedron 17 (1998) 1343;
(c) T. Ama, M.M. Rashid, T. Yonemura, H. Kawaguchi, A. Takeuchi, T. Yasui, Coord. Chem. Rev. 198 (2000) 101;
(d) R. Chakrabarty, B.K. Das, J. Mol. Catal. A: Chem. 223 (2004) 39.

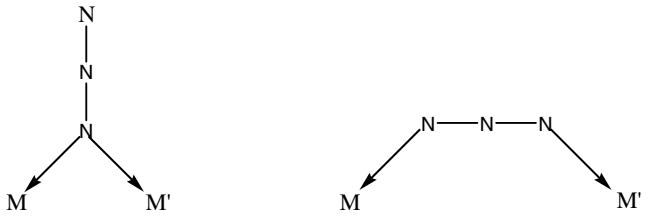


Fig. 1. The different kind of bridging mode of the azide ligand.

The main rationale for such studies stems from the understanding of the magneto-structural correlations in molecular systems and developing new functional molecule-based materials [8].

We report here the synthesis of an asymmetric μ-1,3-EE doubly azido bridged copper(II) complex incorporating a new tridentate Schiff base ligand. It is noteworthy that only a very few cases of the end-to-end azido bridged polynuclear copper(II) complexes reported so far have shown ferromagnetic coupling. The complex has been completely characterized with micro-analytical techniques, FT-IR, UV–Vis, EPR spectra and structure with single crystal X-ray diffraction analysis. Cryomagnetic susceptibility measurement (2–300 K) shows a ferromagnetic interaction with $J = 13.6\ cm^{-1}$.

2. Experimental

2.1. Materials

Analytical reagent grade $Cu(ClO_4)_2 \cdot 6H_2O$, 2-dimethylaminoethylamine and 1,1,1-trifluoropentane-2,5-dione were purchased from Aldrich Chemical Co. and used as received without further purification. All the solvents used were of reagent grade and super dried before use.

2.2. Syntheses

Caution! Perchlorate salts of metal complexes in the presence of organic ligands are potentially explosive. Though no problem has been encountered during the synthesis of the reported materials, they should be prepared in small quantities and must be handled with proper care.

2.2.1. Synthesis of the Schiff base ligand LH

The ligand LH was synthesized by refluxing a mixture of a 25 ml dry methanolic solution of 3 mmol 1,1,1-trifluoropentane-2,5-dione with a 25 ml methanolic solution of 3 mmol 2-dimethylaminoethylamine for 50 min. The resulting yellow solution containing the Schiff base ligand (LH) was cooled and used without further purification.

2.2.2. Synthesis of $[CuL(\mu_{1,3}\text{-}N_3)]_2$ (1)

To a 30 ml, 1.11 g stirred methanolic solution of $Cu(ClO_4)_2 \cdot 6H_2O$, the liquid Schiff base solution was slowly added, followed by a sodium azide (5 mmol) solution prepared with a minimum volume of water in methanol. The resulting mixture was stirred for an additional 35 min, and the final filtrate was kept undisturbed at room temperature. Deep green block shaped crystals of **1** were obtained after three days. Suitable X-ray diffraction quality single crystals were mechanically isolated from the bulk materials. Yield: 86% with respect to the metal substrate. *Anal.* Calc. for $C_{18}H_{28}Cu_2F_6N_{10}O_2$: C, 32.88; H, 4.29; N, 21.30; Cu, 19.33. Found: C, 32.82; H, 4.25; N, 21.20; Cu, 19.53%.

2.3. Physical measurements

Elemental analyses (carbon, hydrogen and nitrogen) were performed on a Perkin–Elmer 2400 CHN Elemental Analyser. Copper has been estimated quantitatively by a standard iodometric procedure. The Fourier Transform infrared spectrum was recorded on a Perkin–Elmer RX I FT-IR spectrophotometer in the range 4000–400 cm^{-1} as a solid KBr disc and the electronic spectrum on a Perkin–Elmer $\lambda - 40$ UV–Vis spectrometer at 300 K in 1 cm quartz cuvettes using HPLC grade acetonitrile as the solvent. Magnetic susceptibility measurements for **1** were carried out on polycrystalline samples at the Servei de Magnetoquímica of the Universitat de Barcelona, with a Quantum Design SQUID MPMS-XL susceptometer apparatus working in the range 2–300 K under a magnetic field of approximately 500G (2–30 K) and 1000 G (35–300 K). Diamagnetic corrections were estimated from Pascal's tables. The EPR spectrum has been recorded on an X-band Bruker Spectrometer (ESR 300E), working with an Oxford helium liquid cryostat for variable temperature.

2.4. X-ray crystallography

A good quality dark green air stable single crystal with dimensions $0.01 \times 0.02 \times 0.03$ mm was mounted on a Nonius Kappa CCD Diffractometer equipped with a graphite monochromated focused X-ray tube bearing a molybdenum target ($\lambda_{MoK\alpha} = 0.71069$ Å). Intensity data were collected at 293 K. A total of 5346 reflections (unique reflections, 3060; $R_{int} = 0.03$) were measured and 2097 data were observed [$I/\sigma(I) > 3$] for **1**. The crystal showed almost no decomposition under X-ray exposure during data collection. Preliminary orientation matrices and unit cell parameters were obtained from the peaks of the first 10 frames and refined using the whole data set. Frames were integrated and corrected for Lorentz and polarization effects using DENZO. The scaling as well as the global refinement of the crystal parameters was performed by SCALEPACK. Reflections that were partly measured on previous and following frames were used to scale the frames on each. Whole data processing was performed using the Kappa CCD analysis software [9a]. The lattice constants were refined by least-square refinement using 2646 reflections ($1.00° < \theta < 27.48°$). No absorption correction was applied

Table 1
Crystal data and structure refinements for **1**

Complex	**1**
Formula	$C_9H_{14}CuF_3N_5O$
F.W.	328.80
Crystal system	monoclinic
Space group	$P2_1/n$ (No. 14)
Unit cell dimensions	
a (Å)	10.679(5)
b (Å)	9.706(5)
c (Å)	13.635(5)
α (°)	90
β (°)	107.939(5)
γ (°)	90
V (Å^3)	1344.6(11)
Z	4
T (K)	293
Diffractometer used	Nonius Kappa CCD
$\lambda_{MoK\alpha}$ (Å)[a]	0.71069
D_{calc} (g cm^{-3})	1.620
μ (mm^{-1})	1.659
$F(000)$	668
θ (°)	2.13, 27.49
Absorption corrections	none
Total data	5346
Unique data	3060
R_{int}	0.030
Observed data [$I > 3\sigma(I)$]	2097
N_{ref}; N_{par}	2097; 173
R[b]	0.0415
Rw[c]	0.0473
Goodness-of-fit on F^2	1.12
$\Delta\rho_{max}$ (e$^-$ Å^{-3})	0.45
$\Delta\rho_{min}$ (e$^-$ Å^{-3})	−0.35

[a] All data collected with Mo Kα radiation ($\lambda = 0.71069$ Å).
[b] $R = \sum(|F_o - F_c|)/\sum|F_o|$.
[c] $Rw = \{\sum[w(|F_o - F_c|)^2]/\sum[w|F_o|^2]\}^{1/2}$.

to the data sets. According to the observed systematic extinctions, the structure has been solved in the monoclinic system with the H–M space group $P2_1/n$. The structure has been solved by direct methods with the SIR 97 program [9b], combined with Fourier difference syntheses and refined against F using reflections with [$I/\sigma(I) > 3$] using the CRYSTALS program [9c]. All non-hydrogen atoms were successfully refined with anisotropic thermal parameters. The hydrogen atoms were placed geometrically and refined with isotropic thermal parameters. All calculations and graphical works have been done using WinGX [9d], ORTEP [9e] and PLATON [9f] programs. Selected crystallographic data, experimental conditions and some features of the structural refinements are summarized in Table 1.

3. Results and discussion

3.1. Infrared spectrum

The solid state Fourier Transform infrared spectrum of the complex was recorded on a FT-IR spectrophotometer for the range 4000–400 cm^{-1} and is fully consistent with the structure confirmed from single crystal X-ray diffraction studies. The sample was studied as powder dispersed in a KBr pellet. The metal bonded ν_{str}(CH=N) frequency was observed as intense bands at 1597 and 1625 cm^{-1} [10a]. Sharp transitions for the ν_{str}(C–O) frequency appeared at 1275 and 1285 cm^{-1} [10b]. Schiff base ligand coordination to the Cu(II) metal center is substantiated by two bands at 425 and 400 cm^{-1} corresponding to ν_{str}(Cu–N) and ν_{str}(Cu–O) respectively [10c]. $\nu_{sym}(CF_3)$ and $\nu_{asym}(CF_3)$ frequencies were supported by well resolved peaks at 1140 and 1200 cm^{-1} respectively [10a]. The broad bands observed in the range 3520 and 1600 cm^{-1} are attributable to the ν_{str}(O–H) and δ(O–H) frequencies for the adhered water. The IR spectrum of **1** shows the most intense absorption band at 2070 cm^{-1} corresponding to the N_3^- ligand. The $\delta(N_3^-)$ vibration is splitted (635–610 cm^{-1}), indicating the existence of a bridged group in it [10a], though it cannot be used to ascertain the exact nature of the bridging mode of the azide anion.

3.2. UV–Vis spectrum

Although the electronic spectra of copper(II) complexes with multidentate Schiff base ligands are not in general good indicators of geometry, they can help to support it. The electronic spectrum of complex **1** in acetonitrile solution shows two strong absorption bands in the region 211 and 275 nm. These bands are clearly charge transfer in origin [11a]. The bands in the region 460–330 nm are assigned to the n–π^* transition of the azomethine group. In the spectrum of the complex, the bands of the azomethine chromophore n–π^* transition are shifted to lower frequencies indicating that the imine nitrogen atom is involved in coordination to the metal ion [11a]. The UV absorption band observed at 380 nm can be attributed to the ligand to Cu(II) charge transfer transition (LMCT) [11b,11c]. The visible spectrum of the azido complex displays a single broad band between 530 and 630 nm. These spectral features are consistent with the five-coordinate geometry of the Cu(II) complex. In general typical Cu(II) complexes of SP or distorted SP geometries exhibit a band in the range 550–660 nm, whereas the corresponding TBP complexes usually show a maximum at $\lambda > 800$ nm with a higher energy shoulder [12]. This indicates that the solution spectrum of the complex ion is adequately explained by a d–d transition for the Cu(II) ion in a distorted SP geometry where the absorption maximum band observed in the visible region results from a $^2E \rightarrow {}^2B_1$ transition.

3.3. X-ray crystal structure of $[CuL(\mu_{1,3}\text{-}N_3)]_2$ (**1**)

The crystal structure of complex **1** has been determined. The most relevant features of the structure with the asymmetric unit and symmetry related fragments, has been shown as an ORTEP diagram with atom numbering scheme in Fig. 2. A few selected bonding parameters also have been included in Table 2.

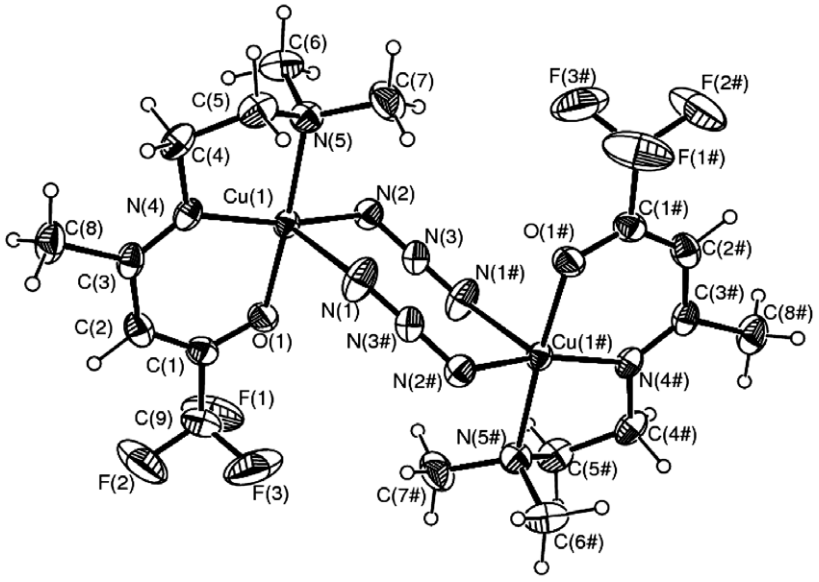


Fig. 2. ORTEP view of the dimeric unit (non-hydrogen atoms shown with 40% ellipsoid probability).

Table 2
Selected bond lengths and bond angles of **1**

Bond lengths	(Å)	Bond angles	(°)
Cu(1)–O(1)	1.924(2)	O(1)–Cu(1)–N(1)	94.21(14)
Cu(1)–N(1)	2.394(3)	O(1)–Cu(1)–N(2)	89.08(12)
Cu(1)–N(2)	1.992(3)	O(1)–Cu(1)–N(4)	93.73(12)
Cu(1)–N(4)	1.958(3)	O(1)–Cu(1)–N(5)	174.89(12)
Cu(1)–N(5)	2.040(3)	N(1)–Cu(1)–N(2)	97.22(12)
		N(1)–Cu(1)–N(4)	98.65(13)
		N(1)–Cu(1)–N(5)	90.87(14)
		N(4)–Cu(1)–N(5)	85.01(15)
		N(3)–N(1)–Cu(1)	129.6(3)
		N(3)–N(2)–Cu(1)	118.2(2)
		N(2)–N(3)–N(1)	176.5(3)

The structure determination reveals that the complex is a centrosymmetric dimer in which the metal atoms are five-coordinated, being bonded to three coordinating donor sites from the corresponding tridentate Schiff base ligand, *L*, and two bridging azide anions as shown in Fig. 2. As can be seen, each azide ion bridges the metal centers in an end-to-end (EE) fashion making an intra-metal Cu–Cu distance of 5.096(4) Å within the dimeric part, with an inversion center placed midway between them. It is the most striking structural feature of the reported dimer due to the fact that despite being an EE-doubly azido bridged copper(II) complex it shows a significant ferromagnetic interaction, which is not very common. The Cu atoms [Cu(1) and Cu(2)] adopt a distorted square pyramidal geometry with a CuN_4O chromophore furnished by three ligating atoms N(4), N(5) and O(1) of the corresponding tridentate Schiff base ligand and a nitrogen atom, N(1), forming the basal plane [Cu(1)–N(4) = 1.958(3), Cu(1)–N(5) = 2.040(3), Cu(1)–O(1) = 1.924(2), Cu(1)–N(1) = 2.394(3) Å] and the elongated apical position is occupied by the nitrogen atom N(2) from the other centrosymmetrically related EE azide bridge [Cu(1)–N(2) = 1.992(3) Å]. The longer Cu(1)–N(2) bond length is clearly associated with the pseudo Jahn-Teller effect on the Cu(II) ion [13,14]. The Cu atom is displaced by an amount of 0.181(2) Å from the basal plane towards the apical atom N(2). The distortions of the coordination polyhedron from square pyramidal to trigonal bipyramidal is expressed as τ, an index of the degree of trigonality; τ is defined as $(\beta - \alpha)/60$ where β and α are the two *trans*-basal angles. For a perfectly square pyramidal geometry the value is equal to 0, while it becomes 1 for a perfect trigonal bipyramidal geometry. The τ value calculated for the reported complex is 0.19, which supports well the geometry of the Cu atoms in the dimeric entity. In the diazo bridged Cu(II) dimeric complex two adjacent Cu centers are interconnected via two azide anions in an end-to-end bridging fashion. The EE bridging azide is quasilinear with a N–N–N bond angle of 176.52° and the N–N bond lengths in the azide anion are 1.154(5) and 1.185(4) Å with Cu–N_{axial}–N, 129.6(3)° and Cu–N_{eq}–N, 118.2(2)° respectively. The μ-(1,3)-azido ligand is almost linear [N–N–N angle: 176.5(3)°]. The EE azide bridges form a closed and puckered eight membered ring in very stable chair form incorporating Cu(1)–N(1)–N(3)–N(2)–Cu(1*)–N(1*)–N(3*)–N(2*) atoms. The packing diagram of the complex shows no significant intramolecular covalent or hydrogen bonding interactions present in the complex.

3.4. Magneto-structural correlation

End-on (EO) dibridged azido complexes are well known in the literature and magneto-structural correlations have determined that the coupling is ferromagnetic for bridging Cu–N–Cu angles <108° [15]. In end-to-end (EE) dibridged azido complexes with Cu(II) exhibiting its common

elongated octahedral or square pyramidal coordination geometry in its 6 or 5 coordination environment, the EE linkage can occur via two different routes: in the equatorial–equatorial configuration (*equatorial–equatorial*), where the azido group coordinates via the equatorial bonds to both the copper atoms, strong antiferromagnetic coupling can occur since the σ orbitals on the azido group couple directly with the unpaired electron density in the $d_{x^2-y^2}$ orbitals [16]. In contrast, if the bridging conformation involves an equatorial linkage to one of the Cu ions and an axial linkage to the second (*equatorial–axial*), the coupling is expected to be a weak one, since there is a little overlap of the azido σ and π orbitals with the magnetic $d_{x^2-y^2}$ orbital via the axial interaction.

The magnetic behaviour of the complex is shown in Fig. 3, as a $\chi_M T$ versus T plot. At room temperature the $\chi_M T$ value is 0.860 cm^3 K mol^{-1}, which is close to the expected value for two uncoupled copper(II) ions, with $g = 2.12$. $\chi_M T$ increases slightly with lowering of temperature and reaches a maximum of 1.034 cm^3 K mol^{-1} at *ca.* 9.5 K. Below this temperature $\chi_M T$ decreases to a value of 0.851 cm^3 K mol^{-1} at 2 K. The shape of this curve indicates dominant ferromagnetic coupling until 9.5 K, which results from the interaction of the copper(II) ions through the double end-to-end azide bridge. The decrease in $\chi_M T$ observed at low temperature may be due to an intradimer antiferromagnetic exchange and/or the presence of a zero field splitting of the $S = 1$ ground state. To determine the exchange parameters *via* the double (μ-1,3) azide bridge, $\chi_M T$ was fit to the Bleaney–Bowers expression for an isotropically coupled pair of $S = 1/2$ ions, [17] [Eq. (1)] in conjunction with an additional mean-field correction term, χ_{MF}, [Eq. (2)] where N is Avogadro's number, μ_B is the Bohr magneton, k_B is the Boltzmann constant and z is the number of nearest neighbours [18]. The best fit parameters for reproducing satisfactorily the experimental data, as shown in Fig. 4, are $J_1 = +13.6$ cm^{-1}, $zJ' = -0.52$ cm^{-1}

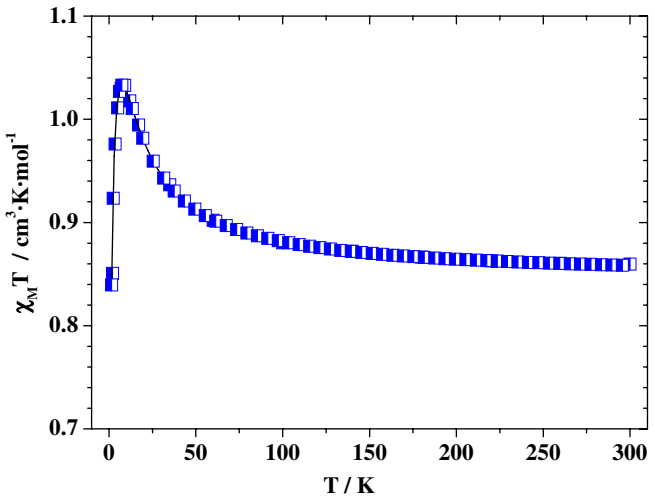


Fig. 3. Plot of $\chi_M T$ vs. T for complex **1** (per Cu–Cu) (solid line shows the best fit of the data).

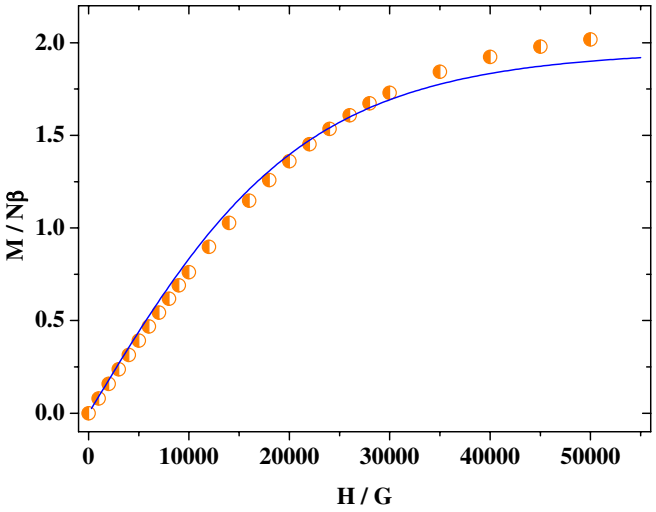


Fig. 4. The field dependence of the magnetization at 2 K for complex **1** (per Cu–Cu) (solid line shows the best fit of the data).

and $g = 2.12$ with $R = 3.4 \times 10^{-5}$ ($R = \sum_i (\chi T_{icalc} - \chi T_{iexp})^2 / (\chi T_{iexp})^2$). During the regression analysis the temperature independent paramagnetism was fixed as $2 \times 30 \times 10^{-6}$.

$$\chi_M = \frac{Ng^2\mu_B^2}{k_B T} \frac{2\exp(J/k_B)}{1 + 3\exp(J/k_B)} \quad (1)$$

$$\chi_{MF} = \frac{\chi_M}{1 - \chi_M(zJ'/Ng^2\mu_B^2)} \quad (2)$$

The weak ferromagnetic coupling found in the complex can be compared to that previously reported by Xie et al. [19a] for an analogous double asymmetric $\mu_{1,3}$-(N_3) bridged dimeric copper(II) system $[Cu_2(bben)_2(N_3)_4]_n$. EE azido bridges are well known to mediate antiferromagnetic interactions. However, ferromagnetic interactions are favored for complexes with very large M–$\mu_{1,3}(N_3)$–M bond and torsion angles, according to theoretical calculations [19b,19c,20]. Escuer et al. have recently elaborated in a nice way the topic of ferromagnetism in these kinds of doubly azido bridged copper(II) complexes with all relevant current references [5a].

The field dependence of magnetization (0–5.5 T) measured at 2 K is shown in Fig. 4, in the form of M/Nβ (per Cu_2 unit) versus H. The magnetization reaches a value of 1.92 Nβ at 5.5 T which is close to the expected $S = 1$ value of 2 Nβ for the Cu_2 system, indicating the presence of a ferromagnetic interaction between the nearest copper(II) ions.

3.5. EPR spectrum

The room temperature X-band EPR spectrum of complex **1** shows the typical axial pattern for distorted copper(II) species with $d_{x^2-y^2}$ ground state ($g_\parallel > g_\perp > 2.0$) (Fig. 5) in agreement with crystal data. Two bands are observed at $g_\parallel = 2.16$ and $g_\perp = 2.07$ (3205.2 and 3373.3 Gauss for $\nu = 9.7878$ GHz), corresponding to the transi-

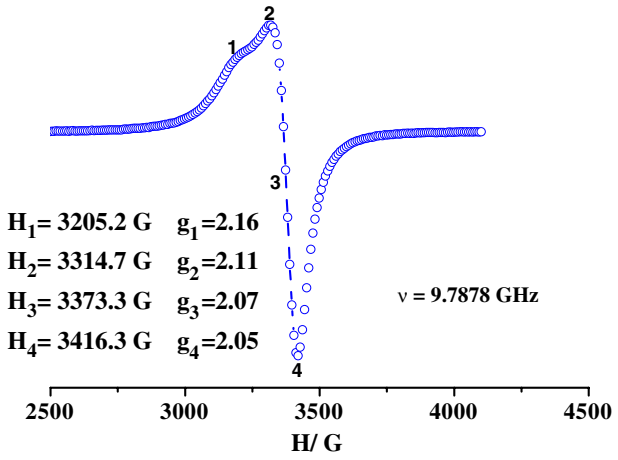


Fig. 5. EPR spectrum recorded at room temperature for complex **1**.

tion $\Delta M_S = \pm 1$ [4c,14]. The possible half-field transition $\Delta M_S = \pm 2$, rather frequent in copper(II) dimers, is not observed.

4. Conclusion

In conclusion, the results of the X-ray structure determination for the complex **1** are consistent with dinuclear doubly bridged azido groups in an end-to-end bonding fashion. The copper centers are penta-coordinated with a slight distortion from SP geometry, which was also confirmed through the UV studies in solution. The experimental observations suggest that the stretching frequencies of the azide group alone cannot be used to make a diagnosis of their exact bonding coordination modes in the complex. Cryomagnetic susceptibility measurements reveals a ferromagnetic interaction of $J = 13.6\ cm^{-1}$ is operating via the double azido bridges between the paramagnetic centers.

Acknowledgements

Financial assistance from Defence Research and Development Organisation (DRDO), New Delhi is gratefully acknowledged. J.C. is thankful to the University Grants Commission, New Delhi for providing a Senior Research Fellowship to him. This work is also supported by grants given by the Ministerio de Educación y Ciencia (Programa Ramón y Cajal) and BQU2003/00539 of Spain.

Appendix A. Supplementary material

CCDC 615174 contains the supplementary crystallographic data for **1**. These data can be obtained free of charge via htpp://www.ccdc.cam.ac.uk/conts/retrieving.html, or from the Cambridge Crystallographic Data Centre, 12 Union Road, Cambridge CB2 1EZ, UK; fax: (+44) 1223-336-033; or e-mail: deposit@ccdc.cam.ac.uk. Supplementary data associated with this article can be found, in the online version, at doi:10.1016/j.poly.2006.11.013.

References

[1] P. Manikandan, R. Muthukumaran, K.R. Justin Thomas, B. Varghese, G.V.R. Chandramouli, P.T. Manoharan, Inorg. Chem. 40 (2001) 2378.
[2] B. Woodard, R.D. Willett, S. Haddad, B. Twamley, C.J. Gomez-Garcia, E. Coronado, Inorg. Chem. 43 (2004) 1822.
[3] (a) R. Neumann, M. Dahan, Nature 388 (1997) 353;
(b) M. Fujita, Y.J. Kwon, S. Washizu, K. Ogura, J. Am. Chem. Soc. 116 (1994) 1151;
(c) M. Fujita, J. Yazaki, K. Ogura, Tetrahedron Lett. 32 (1991) 5589;
(d) O.M. Yaghi, G.M. Li, H.L. Li, Nature 378 (1995) 703.
[4] (a) J. Ribas, M. Monfort, C. Diaz, C. Bastos, C. Mer, X. Solans, Inorg. Chem. 34 (1995) 4986;
(b) A. Escuer, R. Vicente, J. Ribas, M.S.El. Fallah, X. Solans, M. Font-Bardia, Inorg. Chem. 33 (1994) 1842;
(c) J. Ribas, M. Monfort, B.K. Ghosh, R. Cortes, X. Solans, M. Font-Bardia, Inorg. Chem. 35 (1996) 864;
(d) T.K. Maji, P.S. Mukherjee, G. Mostafa, T. Mallah, J.C. Boquera, N.R. Chaudhuri, Chem. Commun. (2001) 1012.
[5] (a) A. Escuer, M. Font-Bardía, S.S. Massoud, F.A. Mautner, E. Penālba, X. Solans, R. Vicente, New J. Chem. 28 (2004) 681;
(b) L. Li, Z. Jiang, D. Liao, S. Yan, G. Wang, Q. Zhao, Transit. Metal Chem. 25 (2000) 630;
(c) L. Li, D. Liao, Z. Jiang, S. Yan, Polyhedron 20 (2001) 681.
[6] A. Escuer, M. Font-Bardia, E. Penālba, X. Solans, R. Vicente, Inorg. Chim. Acta 298 (2000) 195.
[7] H.-R. Wen, C.-F. Wang, Y. Song, J.-L. Zuo, X.-Z. You, Inorg. Chem. 44 (2005) 9039.
[8] (a) D. Gatteschi, O. Kahn, J.S. Miller, F. Palacio, Magnetic Molecular Materials, NATO ASI Series, Kluwer, Dordrecht, 1991;
(b) J.S. Miller, M. Drillon, Magnetism: Molecules to Materials, Wiley-VCH, Weinheim, 2002;
(c) O. Kahn, Molecular Magnetism, VCH, New York, 1993.
[9] (a) Nonius COLLECT, DENZO, SCALEPACK, SORTAV: KappaCCD Program US B.V., Delft, The Netherlands, 1999.;
(b) G. Cascarano, A. Altomare, C. Giacovazzo, A. Guagliardi, A.G.G. Moliterni, D. Siliqi, M.C. Burla, G. Polidori, M. Camalli, Acta Crystallogr., Sect. A 52 (1996) C-79;
(c) D.J. Watkin, C.K. Prout, J.R. Carruthers, P.W. Betteridge, CRYSTALS, Issue 11, Crystallography Laboratory, Oxford, UK, 1999;
(d) L.J. Farrugia, WinGX, J. Appl. Cryst. 32 (1999) 837;
(e) L.J. Farrugia, ORTEP-3 for Windows, J. Appl. Cryst. 30 (1997) 565;
(f) A.L. Spek, PLATON for Windows, 1.081, Acta Crystallogr., Sect. A 46 (1990) C-34.
[10] (a) K. Nakamoto, Infrared and Raman Spectra of Inorganic and Coordination Compounds, fifth ed., John Wiley, New York, 1997, Part A and B;
(b) R.T. Conley, Infrared Spectroscopy, Allyn & Bacon, Boston, 1966;
(c) L.K. Singh, S. Mitra, J. Chem. Soc., Dalton Trans. (1987) 2089.
[11] (a) A.B.P. Lever, Inorganic Electronic Spectroscopy, second ed., Elsevier, Amsterdam, 1984;
(b) P. Dapporto, M. Formica, V. Fusi, L. Giothi, M. Micheloni, P. Paoli, R. Pontellini, P. Rossi, Inorg. Chem. 40 (2001) 6186;
(c) T. Gajda, A. Jancsó, S. Mikkola, H. Lönnberg, H. Sirges, J. Chem. Soc., Dalton Trans. (2002) 1757.
[12] (a) U. Mukhopadhyay, I. Bernal, S.S. Massoud, F.A. Mautner, Inorg. Chim. Acta 357 (2004) 3673;
(b) Y. Song, D.-R. Zhu, K.-L. Zhang, Y. Xu, C.-Y. Duan, X.-Z. You, Polyhedron 19 (2000) 1461.

[13] P.S. Mukherjee, S. Dalai, G. Mostafa, T.-H. Lu, E. Rentschler, N.R. Chaudhuri, New J. Chem. 25 (2001) 1203.
[14] P. Talukder, A. Datta, S. Mitra, G. Rosair, M. Salah El Fallah, J. Ribas, Dalton Trans. (2004) 4161.
[15] (a) S.S. Tandon, L.K. Thompson, M.E. Manuel, I.N. Bridson, Inorg. Chem. 33 (1994) 5555;
(b) L.K. Thompson, S.S. Tandon, M.E. Manuel, Inorg. Chem. 34 (1995) 2356.
[16] (a) J. Comarmond, P. Plumeré, J.M. Lehn, Y. Agnus, R. Louis, R. Weiss, O. Kahn, J. Am. Chem. Soc. 104 (1982) 6330;
(b) Y. Agnus, R. Louis, J.P. Gisselbrecht, R. Weiss, J. Am. Chem. Soc. 106 (1984) 93.
[17] B. Bleaney, K.D. Bowers, Proc. R. Soc. London, Ser. A 214 (1952) 451.
[18] B.E. Myers, L. Berger, S.A. Friedberg, J. Appl. Phys. 40 (1968) 1149.
[19] (a) Y. Xie, Q. Liu, H. Jiang, C. Du, X. Xu, Y. Zhu, New J. Chem. 26 (2002) 176;
(b) A. Escuer, R. Vicente, X. Solans, M. Font-Bardía, Inorg. Chem. 33 (1994) 6007;
(c) M. Monfort, I. Resino, M. Salah El. Fallah, J. Ribas, M. Font-Bardia, H. Stoeckli-Evans, Chem. Eur. J. 7 (2001) 280.
[20] F. Fabrizi de Biani, E. Ruiz, J. Cano, J.N. Novoa, S. Alvarez, Inorg. Chem. 39 (2000) 3221.

1182, 1024, 918 and 727. Magnetic moment at 298 K, 3.29 B.M.

2.1.2. Preparation of $[Cu(dipicH_2)(OH_2)_3][Ce(dipic)_3]\cdot 3H_2O$ (2)

This compound was prepared by similar method to that of **1**, with $(NH_4)_2Ce(NO_3)_6$ (0.552 g, 1.01 mmol), $Cu(NO_3)_2\cdot 3H_2O$ (0.241 g, 0.998 mmol) and dipicH_2 (0.670 g, 4.01 mmol). Pale blue blocks were formed in 4–5 days (0.740 g, 76%). During the preparation a small amount of blue coloured crystals, identified as Cu(dipic)-(dipicH_2)$\cdot 3H_2O$ was also formed. The pale blue blocks of **2** were separated and recrystallized from hot water. *Anal.* Calc. for $C_{28}H_{26}CeCuN_4O_{22}$: C, 34.52; H, 2.69; N, 5.75. Found: C, 34.56; H, 2.50; N, 5.76%. ν_{max}(KBr)/cm^{-1} 3084, 1645, 1477, 1431, 1361, 1273, 1176, 1072, 1022, 923, 765 and 733. Magnetic moment at 298 K, 1.94 B.M.

2.1.3. Preparation of $[Zn(dipicH_2)(OH_2)_3][Ce(dipic)_3]\cdot 3H_2O$ (3)

The preparation was similar to that of **1** and **2** with $(NH_4)_2Ce(NO_3)_6$ (0.550 g, 1.00 mmol), $Zn(NO_3)_2\cdot 6H_2O$ (0.310 g, 1.04 mmol) and dipicH_2 (0.672 g, 4.02 mmol). Pale yellow blocks were formed in 4–5 days (0.770 g, 78%). These blocks were recrystallized from hot water. *Anal.* Calc. for $C_{28}H_{26}CeN_4O_{22}Zn$: C, 34.45; H, 2.68; N, 5.74. Found: C, 34.14; H, 2.41; N, 5.02%. ν_{max}(KBr)/cm^{-1} 3406, 1647, 1427, 1383, 1178, 1078, 1024, 916 and 729.

2.2. X-ray crystallography

X-ray data were collected for compounds **1** and **2** on an Enraf Nonius CAD-4 diffractometer and for **3** on a Bruker SMART APEX CCD X-ray diffractometer, using graphite-monochromated Mo Kα radiation ($\lambda = 0.71073$ Å). Data of **1** and **2** were reduced using XCAD4 [3] and psi-scan [4] absorption corrections were applied. For **3** the data was reduced using SAINTPLUS [5] and a multiscan absorption correction using SADABS [6] was performed. The structure was solved using SHELXS-97 and refined using SHELXL-97 [7]. All ring hydrogens were assigned on the basis of geometrical considerations and were allowed to ride upon the respective carbon atoms. Drawings were made using ORTEP3 for Windows [8] and Mercury [9]. In compound **3**, one lattice water molecule was disordered in two positions. The crystal data for the three compounds are presented in Table 1 and selected bond lengths and angles in Tables 2–4.

Powder diffractograms were measured using a PW3710 model Philips Analytical X-ray diffractometer.

2.3. Physical measurements

EPR spectra were measured on a JEOL JES – FA 200 spectrometer. Powder simulations were done using a previously described computer program [10]. Electronic Reflectance spectra were measured by using a Shimadzu UV-3100 spectrometer equipped with an ISR-3100 integrating sphere attachment. Thermogravimetric analysis was per-

Table 1
Crystal data and structure refinement for **1**, **2** and **3**

	1	**2**	**3**
Formula	$C_{28}H_{26}CeN_4NiO_{22}$	$C_{28}H_{26}CeCuN_4O_{22}$	$C_{28}H_{26}CeN_4O_{22}Zn$
Formula weight	969.36	974.19	976.02
Crystal system	triclinic	triclinic	triclinic
a (Å)	10.5250(8)	10.5553(14)	10.5178(5)
b (Å)	11.6839(14)	11.561(3)	11.4883(5)
c (Å)	14.851(3)	14.923(3)	14.9564(7)
α (°)	68.362(16)	68.221(16)	67.9900(10)
β (°)	88.539(10)	88.552(13)	88.9330(10)
γ (°)	87.983(8)	88.23(2)	88.5350(10)
V (Å^3)	1696.4(5)	1690.1(6)	1674.87(13)
Z	2	2	2
Space group	$P\bar{1}$	$P\bar{1}$	$P\bar{1}$
T (K)	298(2)	298(2)	100(2)
Crystal size (mm)	$0.56\times0.24\times0.24$	$0.60\times0.56\times0.52$	$0.45\times0.39\times0.29$
μ (mm^{-1})	1.981	2.060	2.160
Reflections collected	7904	7842	19 574
Unique reflections, R_{int}	7757, 0.0018	7704, 0.003	7841, 0.0161
Completeness to $2\theta = 25.0$ (%)	99.7	99.5	99.6
Refinement method	full-matrix least squares on F^2	full-matrix least squares on F^2	full-matrix least squares on F^2
$R(F_o^2)$[a] $[I > 2\sigma(I)]$	0.0279	0.0224	0.0199
$R_w(F_o^2)$[b] $[I > 2\sigma(I)]$	0.0759	0.0619	0.0524

[a] $R = \sum \|F_o| - |F_c\| / \sum |F_o|$.

[b] $R_w = \left[\sum w(F_o^2 - F_c^2)^2 / \sum (wF_o^4)\right]^{1/2}$.

Table 2
Selected bond lengths (Å) and angles (°) for **1**

Ce–O(11)	2.323(3)	Ce–O(21)	2.339(3)	Ce–O(13)	2.345(3)
Ce–O(31)	2.346(3)	Ce–O(33)	2.366(3)	Ce–O(23)	2.368(3)
Ce–N(21)	2.498(3)	Ce–N(11)	2.520(3)	Ce–N(31)	2.525(3)
Ni–N(41)	1.994(3)	Ni–O(52)	2.030(3)	Ni–O(53)	2.030(3)
Ni–O(51)	2.049(3)	Ni–O(43)	2.172(3)	Ni–O(41)	2.178(3)

N(41)–Ni–O(52)	177.22(13)	N(41)–Ni–O(53)	94.74(13)
O(52)–Ni–O(53)	84.85(12)	N(41)–Ni–O(51)	95.76(13)
O(52)–Ni–O(51)	84.74(13)	O(53)–Ni–O(51)	169.39(12)
N(41)–Ni–O(43)	77.11(12)	O(52)–Ni–O(43)	105.63(12)
O(53)–Ni–O(43)	89.92(12)	O(52)–Ni–O(41)	100.92(12)
O(51)–Ni–O(43)	90.92(12)	N(41)–Ni–O(41)	76.35(12)
O(53)–Ni–O(41)	94.06(12)	O(51)–Ni–O(41)	89.92(13)
O(43)–Ni–O(41)	153.40(11)		

Table 3
Selected bond lengths (Å) and angles (°) for **2**

Ce–O(31)	2.3308(18)	Ce–O(21)	2.3331(18)	Ce–O(33)	2.3337(18)
Ce–O(13)	2.3524(17)	Ce–O(23)	2.3768(17)	Ce–O(11)	2.3835(17)
Ce–N(11)	2.4996(19)	Ce–N(31)	2.523(2)	Ce–N(21)	2.5258(19)
Cu–O(52)	1.9595(19)	Cu–O(53)	1.9683(19)	Cu–O(51)	1.9967(19)
Cu–N(41)	2.014(2)	Cu–O(43)	2.338(2)	Cu–O(41)	2.350(2)

O(52)–Cu–O(53)	86.62(8)	O(52)–Cu–O(51)	86.26(8)
O(53)–Cu–O(51)	172.26(8)	O(52)–Cu–N(41)	176.31(8)
O(53)–Cu–N(41)	93.36(8)	O(51)–Cu–N(41)	93.94(8)
O(52)–Cu–O(43)	108.52(8)	O(53)–Cu–O(43)	89.43(8)
O(51)–Cu–O(43)	89.96(8)	N(41)–Cu–O(43)	75.17(8)
O(52)–Cu–O(41)	101.50(8)	O(53)–Cu–O(41)	95.51(8)
O(51)–Cu–O(41)	88.88(8)	N(41)–Cu–O(41)	74.82(8)
O(43)–Cu–O(41)	149.81(7)		

Table 4
Selected bond lengths (Å) and angles (°) for **3**

Ce–O(31)	2.3306(12)	Ce–O(33)	2.3321(12)	Ce–O(21)	2.3402(12)
Ce–O(11)	2.3426(12)	Ce–O(13)	2.3648(12)	Ce–O(23)	2.3692(12)
Ce–N(11)	2.5011(14)	Ce–N(31)	2.5236(14)	Ce–N(21)	2.5259(14)
Zn–O(52)	2.0341(13)	Zn–O(51)	2.0465(13)	Zn–N(41)	2.0659(15)
Zn–O(53)	2.0831(13)	Zn–O(43)	2.2100(13)	Zn–O(41)	2.2635(13)

O(52)–Zn–O(51)	85.76(5)	O(52)–Zn–N(41)	172.16(5)
O(51)–Zn–N(41)	96.04(5)	O(52)–Zn–O(53)	83.96(5)
O(51)–Zn–O(53)	169.14(5)	N(41)–Zn–O(53)	94.62(5)
O(52)–Zn–O(43)	111.97(5)	O(51)–Zn–O(43)	89.02(5)
N(41)–Zn–O(43)	75.74(5)	O(53)–Zn–O(43)	91.56(5)
O(52)–Zn–O(41)	98.13(5)	O(51)–Zn–O(41)	95.60(5)
N(41)–Zn–O(41)	74.11(5)	O(53)–Zn–O(41)	89.33(5)
O(43)–Zn–O(41)	149.81(5)		

formed using a NETZSCH STA 409 PC/PG instrument. Room temperature magnetic susceptibilities of the powdered samples were measured using a Sherwood Scientific magnetic susceptibility balance.

2.4. Computational details

DFT along with geometry optimizations and time dependent DFT (TDDFT) have been performed using the B3LYP exchange correlation functional [11] as implemented in the Gaussian-03 [12]. The spin-unrestricted version was employed for open shell ions. For both types of calculations, triple-ζ basis sets [13] were used for Ni, Cu and Zn atoms and double-ζ basis sets [14] were used for all other atoms. Other basis sets in the Gaussian-03 suite were also used for comparison.

Ligand field theory calculations based on the angular overlap model (AOM) [15] were done using the AOMX program [16].

EPR g and A tensors were calculated using the program package ORCA [17] at the B3LYP level of DFT. A triple-ζ basis set [13] was used for all atoms.

3. Results and discussion

3.1. Synthesis

All three compounds are obtained in good yield by mixing the reagents in the appropriate molar ratio. The initial crystalline blocks obtained from aqueous methanolic solution and the crystals formed from hot water were found to be identical by comparing their X-ray powder patterns. The powder patterns also matched with those calculated based on the crystal structure.

$DipicH_2$ can coordinate in the neutral form as well as in monoanionic ($dipcH^-$) and dianionic ($dipic^{2-}$) forms. The following complex species have been previously reported: $M(dipicH)_2$ M = Ni, Zn [18], $M(dipic)_2^{2-}$ M = Ni, Cu, Zn [19], $Cu(dipic)(dipicH_2)$ [18b,20], $Cu(dipic)(OH_2)_2$ [21] and $Cu(dipic)(OH_2)_3$ [21b,22]. In the preparation of **2**, a small amount of $Cu(dipic)(dipicH_2)\cdot 3H_2O$ was formed along with the main compound. Besides this, no other side products were formed in the present synthesis. The presence of $Ce(dipic)_3^{2-}$ appears to ensure the crystallization of cationic complexes containing the neutral form of the ligand in all cases.

3.2. Structures

All the three compounds **1**–**3** are obtained as isomorphous ionic crystals containing $[M(dipicH_2)(OH_2)_3]^{2+}$ and $[Ce(dipic)_3]^{2-}$ ions (Figs. 1–3). The tri-capped trigonal prismatic Ce(IV) chelate has also been observed in Ce(IV)-alkaline earth-dipic complexes [2]. However, in all these cases some of the free oxygen atoms of the chelate coordinate to M(II) ions forming chains and networks. In the present cases there is no coordination link between the anions and cations. Instead, the free oxygen atoms form H-bonds with carboxylic groups and coordinated water molecules of the cation.

All the three cations, $[M(dipicH_2)(OH_2)_3]^{2+}$, have very similar 4+2 coordination polyhedra. The equatorial plane contains the nitrogen atom of $dipicH_2$ and the O atoms of the three water molecules, while the axial positions are occupied by the carbonyl oxygen atoms of $dipicH_2$. The major difference is that the axial elongation is significantly more in the case of the copper complex. The average equatorial and axial distances (Å) are 2.026(3), 2.175(3) (Ni); 1.984(2), 2.344(2) (Cu); 2.057(1), 2.236(1) (Zn). It would

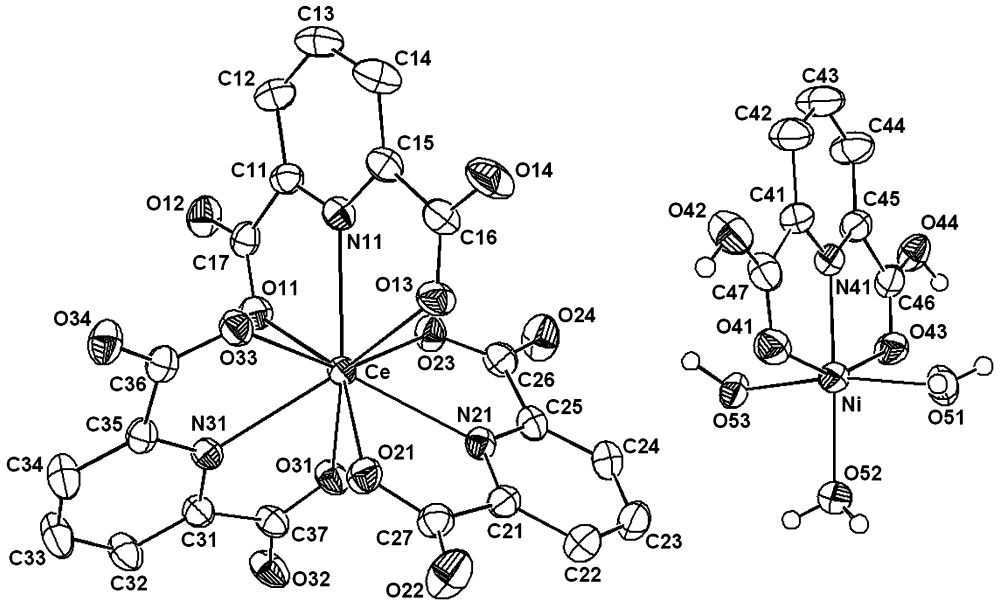


Fig. 1. ORTEP view of compound **1** showing the atom labeling. Thermal ellipsoids are drawn at the 50% probability level and ring hydrogen atoms and lattice water molecules have been omitted for clarity.

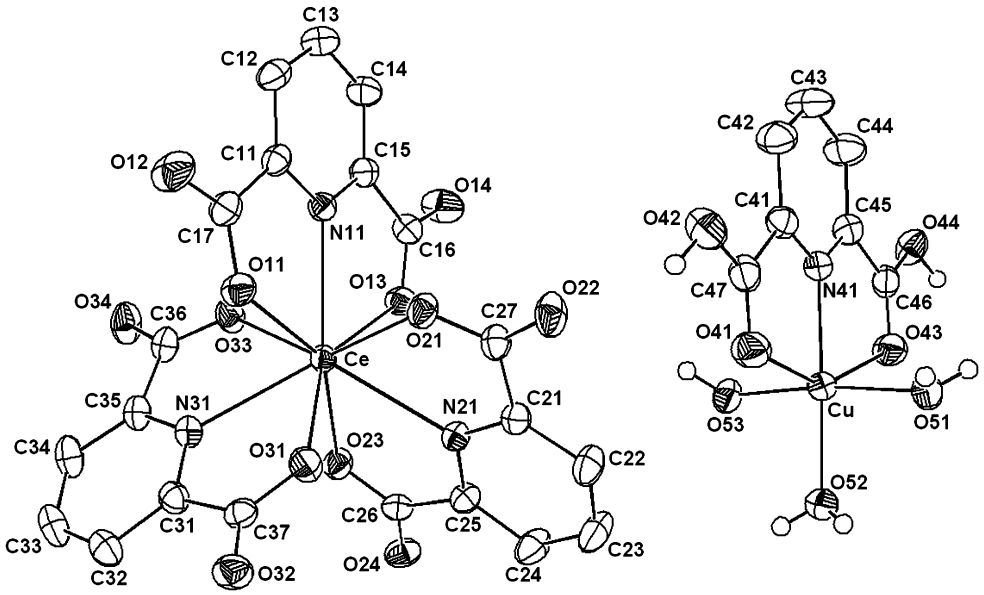


Fig. 2. ORTEP view of compound **2**, showing the atom labeling. Thermal ellipsoids are drawn at the 50% probability level and ring hydrogen atoms and lattice water molecules have been omitted for clarity.

appear that the expected vibronic effects are superimposed on the steric requirements of the ligand to produce the observed static structure in the case of the copper complex. The average off-axis deviation (°) of the axial ligand atoms are 13.5 (Ni) and 15.1 (Cu, Zn). The equatorial atoms including the metal atoms are very nearly coplanar in all cases with a largest deviation of the atoms (Å) from the mean plane 0.038(3) (Ni), 0.062(2) (Cu) and 0.111(2) (Zn). The deviations amount to a very slight tetrahedral distortion with the following inter planar angles (°): 3.3(2) (Ni); 4.6(1) (Cu); 8.2(1) (Zn).

Hydrogen bonding interactions between cations and anions generate a one-dimensional chain in all three crystals (Fig. 4). Further H-bonding involving lattice water molecules generates a three-dimensional network.

3.3. Electronic spectra

Assuming a tetragonal symmetry for the d^8 complex ion, the broad features in the solid state spectrum of **1** in the range 8000–20 000 cm^{-1} may be assigned to transitions arising from the ground state ($^3A_2$) to the split components

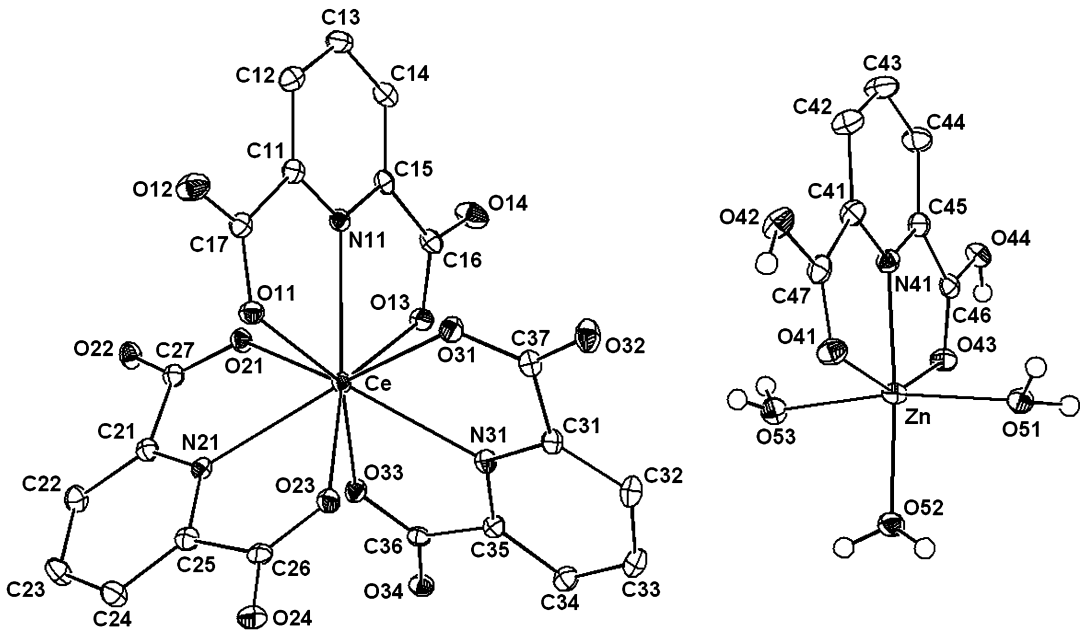


Fig. 3. ORTEP view of compound **3** showing the atom labeling. Thermal ellipsoids are drawn at the 50% probability level and ring hydrogen atoms and lattice water molecules have been omitted for clarity.

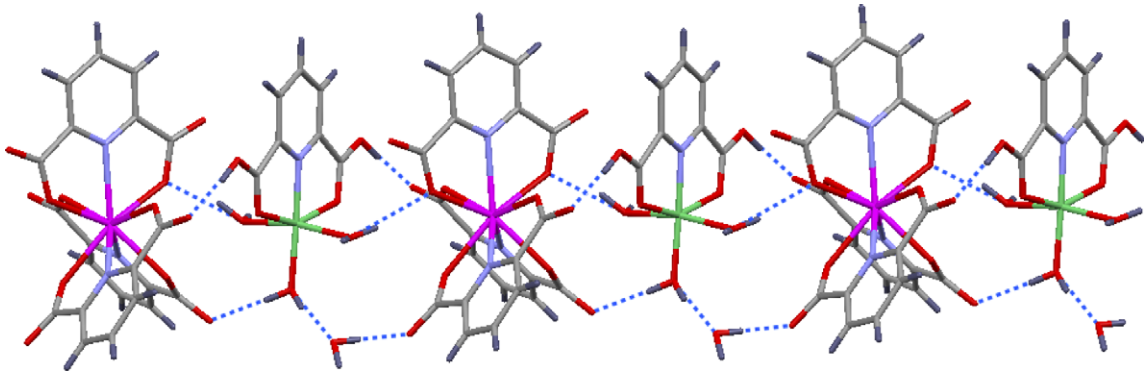


Fig. 4. 1D chain formed by H-bond interactions of cation and anion units.

of $^3T_2$ and $^3T_1$. The band positions and assignments are shown in Table 5. In the case of the copper complex **2**, two broad bands are seen which are assigned to excitations from d_z^2 and d_{xy} to $d_{x^2-y^2}$. Higher energy transitions could not be measured for these compounds due to the presence of strongly absorbing $[Ce(dipic)_3]^{2-}$ ions. The assignments are in general agreement with the calculations based on the AOM model as well as TDDFT theory. As indicated in Table 5, the axial perturbation in the case of the Cu(II) complex is only about one-fourth of the corresponding interaction in the Ni(II) complex. The excitation energies obtained from TDDFT calculations for the Cu(II) complex are in satisfactory agreement with the AOM calculations. The agreement is less than satisfactory in the case of the Ni(II) complex. It has been reported that transitions involving double excitations are not well represented in the TDDFT model [23]. In a low-symmetry six-coordinate d^8 complex, transitions to the split components of $^3T_2$ and $^3T_1(F)$ are essentially single electron excitations. The six lowest energy excitations quoted in Table 5 correspond to these. It is seen that the energies are overestimated by about 2000–3000 cm^{-1}. All the eight different basis sets used gave similar results.

3.4. EPR Spectrum of 2

The packing of the Cu(II) complex cations alternating with the bulky diamagnetic anions in the crystals lead to magnetic dilution. The EPR spectrum of the polycrystalline sample is shown in Fig. 5, in which the hyperfine splitting is fully resolved in the parallel region. The EPR parameters derived by computer simulation of the experimental spectra are given in Table 6. The parameters are consistent with the tetragonally distorted Cu(II) complex. Included in the table are the EPR parameters derived using DFT calculations with the experimental geometry. The calculated *g*-values

Table 5
Electronic spectral data

Compound	Band maxima/1000 cm^{-1}			
	Experimental	AOM[a]	TDDFT[b]	Assignment[c]
$[Cu(dipicH_2)(OH_2)_3]^{2+}$	8.8	8.89	7.99	$^1A_1 \leftarrow {}^2B_1$
		13.44	13.70	$^2B_2 \leftarrow {}^2B_1$
	13.0	14.21, 14.36	15.75, 15.87	$^2E \leftarrow {}^2B_1$
$[Ni(dipicH_2)(OH_2)_3]^{2+}$	7.6	7.49, 7.95	10.30, 10.79	$^3E \leftarrow {}^3B_1$
		12.32	13.98	$^3B_2 \leftarrow {}^3B_1$
	13.6	13.57	16.84	$^3A_2 \leftarrow {}^3B_1$
		16.78, 16.85	20.28, 23.43	$^3E \leftarrow {}^3B_1$
	15.2	25.12		$^3A_2 \leftarrow {}^3B_1$
		26.78, 26.91		$^3E \leftarrow {}^3B_1$

[a] The bonding parameters (cm^{-1}) used: Cu(II) complex, $e_\sigma(N) = 4900$, $e_\pi(N) = 800$, $e_\sigma(O) = 4800$, $e_\sigma(O_{axial}) = 400$. Ni(II) complex, $e_\sigma(N) = 4900$, $e_\pi(N) = 600$, $e_\sigma(O) = 4200$, $e_\sigma(O_{axial}) = 1700$, $B = 850$, $C = 3400$.
[b] The values quoted are for the basis set B3LYP/TZV+DZ – see text. Other basis sets gave similar results.
[c] The labels correspond to D_{4h} symmetry. The pattern of calculated splittings shows that D_{4h} is a good approximation to the molecular symmetry, which in fact, is not higher than C_s.

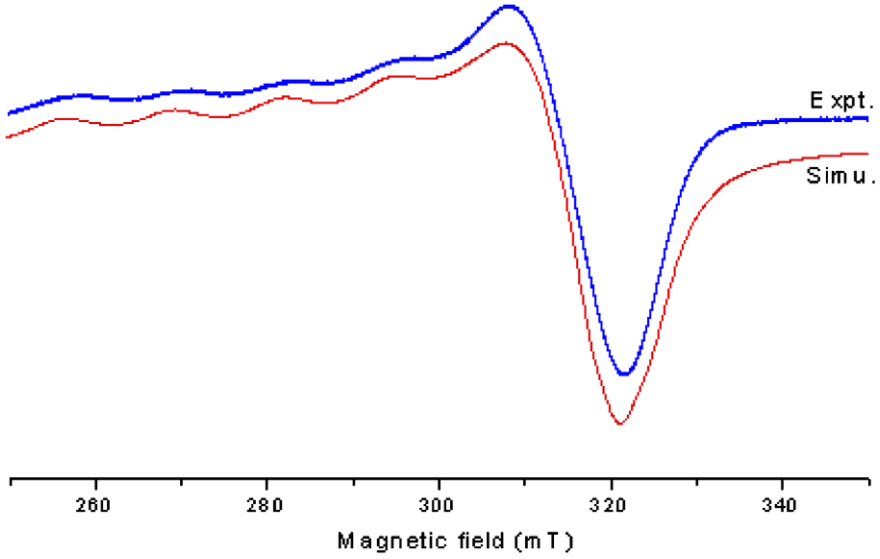


Fig. 5. EPR spectrum (X band, $\nu = 9.158$ GHz) of a powder sample of **2** at room temperature.

Table 6
EPR parameters of **2**[a]

	Experimental	DFT	LFT[b]
g_x	2.050	2.056	
g_y	2.100	2.099	
g_z	2.383	2.237	
A_x	⩽20	37	
A_y	⩽20	76	
A_z	140	−159	
A_F		−72.4	−102
A_x^D		124.4	99
A_y^D		64.4	99
A_z^D		−189.0	−198
A_x^{so}		24.3	23
A_y^{so}		44.9	23
A_x^{so}		102.0	161

[a] A-values in units of 10^{-4} cm^{-1} (sign of A not determined).
[b] Spin–orbit parameters (λ) = −828 cm^{-1}, $\langle r^{-3}\rangle = 7.64$ a.u. See text for covalency factors.

are within 1% (g_x, g_y) and 6% (g_z) of the experimental value. The parallel component (g_z) is the one most influenced by spin–orbit perturbation. To a first approximation, its deviation from the free spin value is directly proportional to the square of the coefficient of the metal d-orbital in the SOMO and inversely proportional to the energy gap between the molecular orbitals based on $d_{x^2-y^2}$ (SOMO) and d_{xy}. Simple ligand field analysis [24] assuming axial symmetry and using the proposed electronic spectral assignments (*vide infra*) leads to the following values for the d-orbital coefficients in the molecular orbitals: 0.98 ($d_{x^2-y^2}$), 0.94 (d_{xy}) and 0.89 (d_{xz}, d_{yz}). The values of the different contributions to the metal hyperfine splitting *viz.* Fermi contact (A_F), Spin dipolar (A_z^D, A_x^D, A_y^D) and spin–orbit ($A_z^{so}, A_x^{so}, A_y^{so}$) based on this analysis are included in Table 6. It is seen that the agreement of the hyperfine splitting components calculated by DFT with the ligand field

analysis is poor. The deviations in the calculated values are as much as 200% for the in-plane component and 13% for the axial component. It is seen that the better agreement in the case of the axial component in mainly due to the cancellation of errors in A_F and A_z^D having a negative sign and A_z^{so}, which makes a positive contribution. A similar observation has been made earlier with regard to hyperfine splitting calculations using the program ORCA [25]. In spite of the poor agreement of the magnitude of the calculated hyperfine tensor components with the experiment, the orientation of the *g*- and *A*-tensor are collinear with each other (within 1°) and the in-plane components are along the Cu–N and Cu–O bonds (within 3°). While this orientation is reasonable for the observed structure (all in plane bond angles being $90 \pm 2°$), the powder spectrum does not afford the orientation of the *g* and *A* principal directions.

3.5. Thermal analysis

The thermogravimetric analyses of all compounds show the same trend. The weight loss begins at 50 °C and the loss of five water molecules is complete at 160 °C (wt. loss calculated 9.28%, found 9.39% for **1**; 9.23% and 9.59% for **2**; 9.22% and 10.28% for **3**). The loss of the last coordinated water takes place gradually and the structures were found to completely break down above 270 °C. This indicates that the four-coordinate structures are thermally stable relative to the six-coordinate ones at temperatures higher than about 160 °C.

3.6. Geometry optimization

The geometry of the cationic part of **1**, **2** and **3** were optimized without any constraints. The optimized structures of the isolated cations are superimposed on the crystallographic structures in Fig. 6. The bond distances in the optimized geometry are within 0.06 Å of the crystallographic values in all cases. It is noteworthy that the DFT calculation captures the essential feature of the static Jahn–Teller distortion in the case of the Cu(II) complex, *viz.*, elongation of the axial bonds [26]. In this context, it is worth investigating the structural changes associated with the deprotonation of $dipicH_2$ in these complexes. The results are shown in Fig. 7, wherein the calculated minimum energy structures of $M(dipic)(OH_2)_3$ are superimposed on the corresponding $[M(dipicH_2)(OH_2)_3]^{2+}$ structures. In the case of Ni(II), there was only a small

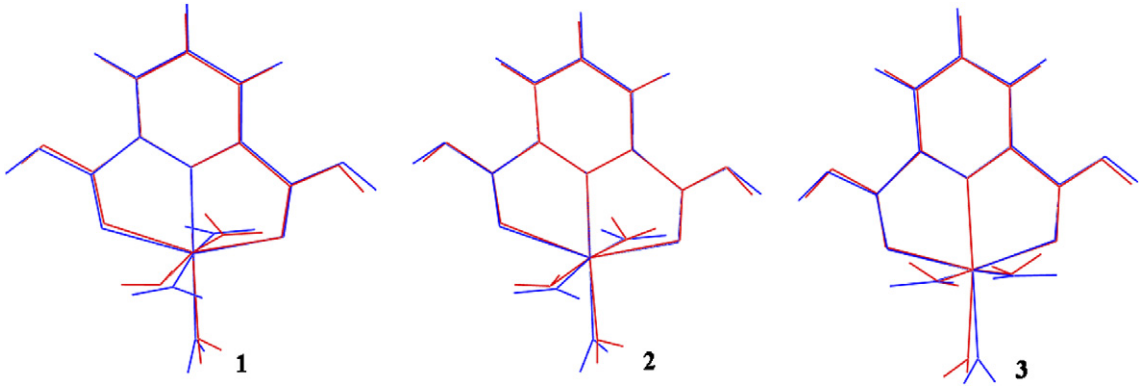


Fig. 6. Optimized structures of the isolated cations, superimposed on the crystallographic structures.

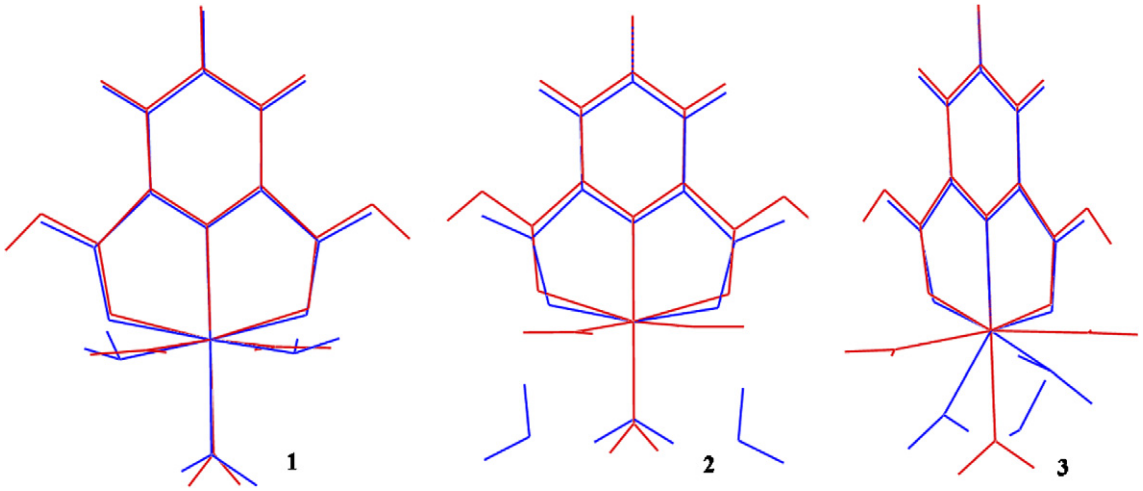


Fig. 7. Optimized structures of $M(dipic)(OH_2)_3$ and $[M(dipicH_2)(OH_2)_3]^{2+}$ (see text for description).

reduction in the two axial bond distances, by 0.05 and 0.1 Å. In the case of Cu(II), there is a switch of the elongation axis. The carboxylate oxygen atoms close in on copper with a simultaneous weakening of the two *trans* bonds to water molecules. The final structure is square planar, the two water molecules which are no longer in the coordination sphere of Cu(II) are involved in H-bonding on the periphery of the complex. The $Cu–O_{carboxylate}$ bonds are shortened by 0.3 Å. The crystal structure of Cu(dipic)-$(OH_2)_3$ [22] differs from the computed gas phase structure. It consists of six-coordinated molecules with weak axial bonds to water molecules. Nevertheless, the present result shows that the calculation is able to model the switch of the Jahn–Teller axis accompanying the deprotonation of the ligand. The Zn(II) complex transforms to a five-coordinate structure upon deprotonation in which the $Zn–O_{carboxylate}$ bonds are shortened by 0.2 Å.

4. Conclusion

The cations $[M(dipicH_2)(OH_2)_3]^{2+}$, containing strongly acidic hydrogen atoms, are stabilized in crystals by bulky $[Ce(dipic)_3]^{2-}$ anions. Even though the three crystals with M = Ni, Cu, Zn are isomorphous, the cations maintain the structural features characteristic of their electronic configurations. This is especially prominent for the Cu(II) complex in which a vibronic distortion is superimposed on the steric distortion. This complex also affords well-resolved EPR spectra due to magnetic isolation of the cations provided by the bulky anions. It is shown that TDDFT calculations are able to reproduce the electronic transition energies with reasonable accuracy for the d^9 complex. The agreement is not satisfactory for the d^8 complex. Geometry optimizations using DFT are able to model static Jahn–Teller elongation of the Cu(II) complex ion as well as changes accompanying the deprotonation of the coordinated $dipicH_2$. While DFT is able to model the structure, electronic transition and *g*-anisotropy of the d^9 complex, the agreement of the hyperfine splitting constants is poor. Various contributions to hyperfine coupling are not satisfactorily modelled at the present level of theory.

Acknowledgements

The X-ray data were collected at the diffractometer facility at the University of Hyderabad, established by the Department of Science and Technology, Government of India. Computations were performed at CMSD. Infrastructure support from UGC (UPE program) is also acknowledged. This work was supported by CSIR, India. T.K.P. thanks the CSIR for the award of a research fellowship.

Appendix A. Supplementary material

CCDC 622453, 622454 and 622455 contain the supplementary crystallographic data for this paper. These data can be obtained free of charge via http://www.ccdc.cam.ac.uk/conts/retrieving.html, or from the Cambridge Crystallographic Data Centre, 12 Union Road, Cambridge CB2 1EZ, UK; fax: (+44) 1223-336-033; or e-mail: deposit@ccdc.cam.ac.uk. Supplementary data associated with this article can be found, in the online version, at doi:10.1016/j.poly.2006.11.029.

References

[1] (a) X.-P. Yang, R.A. Jones, W.-K. Wong, V. Lynch, M.M. Oye, A.L. Holmes, Chem. Commun. (2006) 1836;
(b) J.-P. Costes, F. Dahan, W. Wernsdorfer, Inorg. Chem. 45 (2006) 5;
(c) J.-C.G. Bunzli, C. Piguet, Chem. Soc. Rev. 34 (2005) 1048;
(d) C.M. Zaleski, E.C. Depperman, J.W. Kampf, M.L. Kirk, V.L. Pecoraro, Angew. Chem., Int. Ed. 43 (2004) 3912.
[2] (a) T.K. Prasad, M.V. Rajasekharan, Inorg. Chem. Commun. 8 (2005) 1116;
(b) T.K. Prasad, S. Sailaja, M.V. Rajasekharan, Polyhedron 24 (2005) 1487;
(c) S. Sailaja, M.V. Rajasekharan, Acta Crystallogr., Sect. E 57 (2001) m341;
(d) G. Swarnabala, M.V. Rajasekharan, Inorg. Chem. 37 (1998) 1483.
[3] K. Harms, S. Wocadlo, XCAD4-CAD4 Data Reduction, University of Marburg, Marburg, Germany, 1995.
[4] A.C.T. North, D.C. Phillips, F.S. Mathews, Acta Crystallogr., Sect. A 24 (1968) 351.
[5] SAINTPLUS, Bruker AXS Inc., Madison, WI, USA, 2003.
[6] G.M. Sheldrick, SADABS Program for Empirical Absorption Correction, University of Gottingen, Germany, 1996.
[7] G.M. Sheldrick, SHELXS-97, SHELXL-97, University of Gottingen, Gottingen, Germany, 1997.
[8] L.J. Farrugia, J. Appl. Crystallogr. 30 (1997) 565.
[9] C.F. Macrae, P.R. Edgington, P. McCabe, E. Pidcock, G.P. Shields, R. Taylor, M. Towler, J. van de Streek, J. Appl. Crystallogr. 39 (2006) 453.
[10] G. Swarnabala, M.V. Rajasekharan, Inorg. Chem. 28 (1989) 662.
[11] A.D. Becke, J. Chem. Phys. 98 (1993) 5648.
[12] M.J. Frisch, G.W. Trucks, H.B. Schlegel, G.E. Scuseria, M.A. Robb, J.R. Cheeseman, J.A. Montgomery Jr., T. Vreven, K.N. Kudin, J.C. Burant, J.M. Millam, S.S. Iyengar, J. Tomasi, V. Barone, B. Mennucci, M. Cossi, G. Scalmani, N. Rega, G.A. Petersson, H. Nakatsuji, M. Hada, M. Ehara, K. Toyota, R. Fukuda, J. Hasegawa, M. Ishida, T. Nakajima, Y. Honda, O. Kitao, H. Nakai, M. Klene, X. Li, J.E. Knox, H.P. Hratchian, J.B. Cross, C. Adamo, J. Jaramillo, R. Gomperts, R.E. Stratmann, O. Yazyev, A.J. Austin, R. Cammi, C. Pomelli, J.W. Ochterski, P.Y. Ayala, K. Morokuma, G.A. Voth, P. Salvador, J.J. Dannenberg, V.G. Zakrzewski, S. Dapprich, A.D. Daniels, M.C. Strain, O. Farkas, D.K. Malick, A.D. Rabuck, K. Raghavachari, J.B. Foresman, J.V. Ortiz, Q. Cui, A.G. Baboul, S. Clifford, J. Cioslowski, B.B. Stefanov, G. Liu, A. Liashenko, P. Piskorz, I. Komaromi, R.L. Martin, D.J. Fox, T. Keith, M.A. Al-Laham, C.Y. Peng, A. Nanayakkara, M. Challacombe, P.M.W. Gill, B. Johnson, W. Chen, M.W. Wong, C. Gonzalez, J.A. Pople, Gaussian 03, Revision B.05, Gaussian, Inc., Pittsburgh PA, 2003.
[13] A. Schaefer, C. Huber, R. Ahlrichs, J. Chem. Phys. 100 (1994) 5829.
[14] A. Schaefer, H. Horn, R. Ahlrichs, J. Chem. Phys. 97 (1992) 2571.
[15] B.N. Figgis, M.A. Hitchman, Ligand Field Theory and its Applications, Wiley-VCH, New York, 2000.
[16] H. Adamsky, AOMX, 09-Jun-96 Version, an Angular Overlap Model Computer Program, Department of Theoretical Chemistry, Heinrich-Heine-Universitat, Dusseldorf, Germany.
[17] F. Neese, ORCA – An Ab initio, Density Functional and Semi-Empirical Program Package Version 2.4, Max-Planck-Insitut für Bioanorganische Chemie, Mülheim, der Ruhr, 2004.
[18] (a) L.C. Nathan, T.D. Mai, J. Chem. Crystallogr. 30 (2000) 509;
(b) N. Okabe, N. Oya, Acta Crystallogr., Sect. C 56 (2000) 305;

(c) K. Hakansson, M. Lindahl, G. Svensson, J. Albertsson, Acta Chem. Scand. 47 (1993) 449;
(d) P. Quaglieri, H. Loiseleur, G. Thomas, Acta Crystallogr., Sect. B 28 (1972) 2583.

[19] (a) S.K. Ghosh, J. Ribas, P.K. Bharadwaj, Cryst. Growth Des. 5 (2005) 623;
(b) S.K. Ghosh, P.K. Bharadwaj, Inorg. Chem. 44 (2005) 5553;
(c) A.-Y. Fu, D.-Q. Wang, D.-Z. Sun, Acta Crystallogr., Sect. E 61 (2005) m401;
(d) N.W. Alcock, G.J. Clarkson, G.A. Lawrance, P. Moore, Aust. J. Chem. 57 (2004) 565;
(e) J.C. MacDonald, T.-J.M. Luo, G.T.R. Palmore, Cryst. Growth Des. 4 (2004) 1203;
(f) A. Moghimi, M. Ranjbar, H. Aghabozorg, F. Jalali, M. Shamsipur, R.K. Chadah, J. Chem. Res. 477 (2002) 1047;
(g) M. Ranjbar, M. Taghavipur, H. Aghabozorg, A. Moghimi, F. Jalali, M. Shamispur, Pol. J. Chem. 76 (2002) 785;
(h) J.C. MacDonald, P.C. Dorrestein, M.M. Pilley, M.M. Foote, J.L. Lundburg, R.W. Henning, A.J. Schultz, J.L. Manson, J. Am. Chem. Soc. 122 (2000) 11692;
(i) J.G.H.du. Preez, H.E. Rohwer, B.J. van Brecht, M.R. Caira, J. Chem. Soc., Dalton Trans. (1984) 975.

[20] E.E. Sileo, M.A. Blesa, G. Rigotti, B.E. Rivero, E.E. Castellano, Polyhedron 15 (1996) 4531.

[21] (a) M. Koman, J. Moncol, D. Hudecova, B. Dudova, M. Melnik, M. Korabik, J. Mrozinski, Pol. J. Chem. 75 (2001) 957;
(b) E.E. Sileo, G. Rigotti, B.E. Rivero, M.A. Blesa, J. Phys. Chem. Solids 58 (1997) 1127.

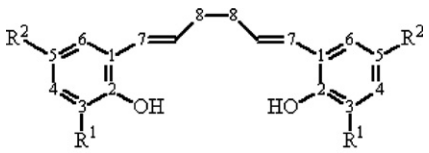
[22] (a) L. Mao, Y. Wang, Y. Qi, M. Cao, C. Hu, J. Mol. Struct. 668 (2004) 197;
(b) A.J. Blake, M. Felloni, P. Hubberstey, C. Wilson, M. Schroder, Acta Crystallogr., Sect. E 58 (2002) 43.

[23] P.W. Thulstrup, L. Broge, E. Larsen, J. Springborg, J. Chem. Soc., Dalton Trans. (2003) 3199.

[24] B.A. Goodman, J.B. Raynor, Adv. Inorg. Chem. Radiochem. 13 (1970) 135.

[25] P. Comba, Y.D. Lampeka, A.I. Prikhodko, G. Rajaraman, Inorg. Chem. 45 (2006) 3632.

[26] (a) As a check on this procedure, we optimized the structure of $[Cu(OH_2)_6]^{2+}$ starting with a regular octahedral geometry having a bond distance 2.12 Å. The water molecules were constrained with O–H = 0.96 Å and H–O–H = 105°. The optimized structure is of tetragonal symmetry with axial and equatorial distances of 2.20 and 1.99 Å, respectively. The structure is stabilized to the extent of 23.4 kJ mol^{-1} with respect to the regular octahedral structure. Similar optimizations in the case of $[Ni(OH_2)_6]^{2+}$ and $[Zn(OH_2)_6]^{2+}$ results in regular octahedral geometries with bond distances 2.04 Å (Ni^{2+}) and 2.07 Å (Zn^{2+}). The optimized structure of $[Cu(OH_2)_6]^{2+}$ compares well with the previous ab initio SCF calculations [26b]: bond distances, 2.24 Å (axial), 2.06 Å (equatorial), stabilization energy = 7.0 kJ mol^{-1};
(b) R. Akesson, L.G.M. Pettersson, M. Sandstrom, U. Wahlgren, J. Phys. Chem. 96 (1992) 150.



R^1	R^2	Ligand
H	H	H_2L^1
H	Br	H_2L^2
H	Cl	H_2L^3
H	MeO	H_2L^4
H	NO_2	H_2L^5
Br	Br	H_2L^6
Cl	Cl	H_2L^7
I	I	H_2L^8

Fig. 1. Ligands used in this study and the ^{13}C NMR numbering system.

to bring about apoptosis in lymphocyte cell cultures [36]. The (salen)chromium(III)/DMAP catalyst system is used in the fixation of CO_2 with epoxides to form carbonates [37].

As part of the ongoing investigations [38] by our group of metal–salen catalyzed oxidations and of insulin-mimetic complexes [39] we prepared complexes of chromium–salen. In this paper we describe chromium(III) complexes of the tetradentate Schiff bases, *N*,*N*′-bis(salicylidene) ethylene-diamine, H_2L^1; *N*,*N*′-bis(5-bromosalicylidene) ethylenediamine, H_2L^2; *N*,*N*′-bis(5-chlorosalicylidene)ethylenediamine, H_2L^3; *N*,*N*′-bis(5-methoxysalicylidene)ethylenediamine, H_2L^4; *N*,*N*′-bis(5-nitrosalicylidene)ethylenediamine, H_2L^5; *N*,*N*′-bis(3,5-diclorosalicylidene)ethylenediamine, H_2L^6; *N*,*N*′-bis(3,5-dibromo-salicylidene)ethylenediamine, H_2L^7; and *N*,*N*′-bis(3,5-diiodosalicylidene)ethylenediamine, H_2L^8. A structural representation of the ligands, their abbreviations, and numbering system of the carbons for ^{13}C NMR are given in Fig. 1.

2. Experimental

2.1. Reagents

Ethylenediamine, 99%; salicylaldehyde, 98%; 5-bromosalicylaldehyde, 98%; 5-chlorosalicylaldehyde, 98%; 5-methoxyosalicylaldehyde, 98%; 5-nitrosalicylaldehyde, 99%; 3,5-dibromosalicylaldehyde, 98%; 3,5-dichlorosalicylaldehyde, 99%; 3,5-diiodosalicylaldehyde, 97%; (methyl sulfoxide)-d_6, 99.9 atom% D, DMSO-d_6; chloroform-*d* 99.8 atom% D, $CDCl_3$ (Aldrich Chemical Co.) and $CrCl_3 \cdot 6H_2O$ (Riedel-de-Haën Inc.) were used as received. All other solvents and reagents were obtained commercially and were used without further purification.

2.2. Preparation of the Schiff bases

The Schiff bases were prepared in a similar manner [40] by the following procedure: to a stirred solution of 4.0 mmol of the appropriate substituted salicylaldehyde in ethanol (50 ml) was added dropwise an ethanolic solution (10 ml) of 2.0 mmol ethylenediamine. This mixture was then heated for 2 h. Afterwards the mixture was cooled to room temperature, then cooled for 24 h at 5 °C. The solid was filtered and washed with cold ethanol (5 ml at 5 °C) and dried over silica. The ligands were used without further purification.

2.2.1. Ligand H_2L^1

Brilliant yellow flakes. Yield: 0.498 g, 92.8%. m.p.: 125–126 °C (uncorrected). *Anal*. Calc. for $C_{16}H_{16}N_2O_2$: C, 71.6; H, 6.0; N, 10.4. Found: C, 71.7; H, 6.0; N, 10.4%. Selected IR bands (KBr, cm^{-1}): 1634s, $\nu_{C=N}$; 1576m, $\nu_{C=C}$; 1371m, ν_{C-N}; 1283m, ν_{C-O}. UV–Vis spectrum in DMSO [λ_{max} (nm), ε (M^{-1} cm^{-1})]: 317 (8420), 402 (465). Mass spectrum, ESI/MS in DMSO [*m*/*z*(%)]: 267(18), 245(19), 227(51), 172(73), 157(39), 141(100).

2.2.2. Ligand H_2L^2

Light yellow crystals. Yield: 0.794 g, 93.2%. m.p.: 171–173 °C (uncorrected). *Anal*. Calc. for $C_{16}H_{14}N_2O_2Br_2$: C, 45.1; H, 3.3; N, 6.6. Found: C, 45.5; H, 3.3; N, 6.7%. Selected IR bands (KBr, cm^{-1}): 1632s, $\nu_{C=N}$; 1565m, $\nu_{C=C}$; 1360m, ν_{C-N}; 1274s, ν_{C-O}; 1072m, ν_{C-Br}. UV–Vis spectrum in DMSO [λ_{max} (nm), ε (dm^3 cm^{-1} mol^{-1})]: 329 (7050), 421 (735). Mass spectrum, ESI/MS, in DMSO [*m*/*z*(%)]: 425(43), 385(6), 339(25), 325(37), 249(46), 201(100).

2.2.3. Ligand H_2L^3

Light yellow crystals. Yield: 0.560 g, 83.0%. m.p.: 155–157 °C (uncorrected). *Anal*. Calc. for $C_{16}H_{14}N_2O_2Cl_2$: C, 57.0; H, 4.2; N, 8.3. Found: C, 57.0; H, 4.2; N, 8.4%. Selected IR bands (KBr, cm^{-1}): 1633s, $\nu_{C=N}$; 1570m, $\nu_{C=C}$; 1362m, ν_{C-N}; 1275m, ν_{C-O}; 1092m ν_{C-Cl}. UV–Vis spectrum in DMSO [λ_{max} (nm), ε (dm^3 cm^{-1} mol^{-1})]: 328 (7510), 423 (670). Mass spectrum, ESI/MS, in DMSO [*m*/*z*(%)]: 338(4), 254(36), 215(30), 179(100).

2.2.4. Ligand H_2L^4

Yellow powder. Yield: 0.560 g, 85.4%. m.p.: 150–152 °C (uncorrected). *Anal*. Calc. for $C_{18}H_{20}N_2O_4$: C, 65.8; H, 6.1; N, 8.5. Found: C, 66.1; H, 6.0; N, 8.4%. Selected IR bands (KBr, cm^{-1}): 1638s, $\nu_{C=N}$; 1587m, $\nu_{C=C}$; 1357m, ν_{C-N}; 1274m, ν_{C-O}; 1228m, ν_{C-O-C}. UV–Vis spectrum in DMSO [λ_{max} (nm), ε (dm^3 cm^{-1} mol^{-1})]: 346 (8630), 430 (140).

2.2.5. Ligand H_2L^5

Yellow powder. Yield: 0.580 g, 81.0%. m.p.: 261–263 °C (uncorrected). *Anal*. Calc. for $C_{16}H_{14}N_4O_6$: C, 53.6; H, 3.9; N, 15.6. Found: C, 53.3; H, 3.8; N, 15.8%. Selected IR bands (KBr, cm^{-1}): 1646s, $\nu_{C=N}$; 1614s, $\nu_{C=C}$; 1542m, ν_{NO_2}; 1353m, ν_{C-N}; 1324s ν_{NO_2}. UV–Vis spectrum in DMSO [λ_{max} (nm), ε (dm^3 cm^{-1} mol^{-1})]: 365 (15100), 420 (17400). Mass spectrum, ESI/MS, in DMSO [*m*/*z*(%)]: 359(11), 259(6), 228(10), 179(58), 157(100).

2.2.6. Ligand H_2L^6

Yellow powder. Yield: 1.036 g, 88.7%. m.p.: 238–241 °C (uncorrected). *Anal.* Calc. for $C_{16}H_{12}N_2O_2Br_4$: C, 32.9; H, 2.1; N, 4.8. Found: C, 33.1; H, 2.2; N, 4.9%. Selected IR bands (KBr, cm^{-1}): 1636s, $\nu_{C=N}$; 1592m, $\nu_{C=C}$; 1356w, ν_{C-N}; 1287w, ν_{C-O}. UV–Vis spectrum in DMSO [λ_{max} (nm), ε ($dm^3\,cm^{-1}\,mol^{-1}$)]: 289 (6180), 335 (4340), 431 (6340).

2.2.7. Ligand H_2L^7

Yellow powder. Yield: 0.696 g, 85.7%. m.p.: 208–210 °C (uncorrected). *Anal.* Calc. for $C_{16}H_{12}N_2O_2Cl_4$: C, 47.3; H, 3.0; N, 6.9. Found: C, 47.0; H, 2.7; N, 6.7%. Selected IR bands (KBr, cm^{-1}): 1639s, $\nu_{C=N}$; 1552w, $\nu_{C=C}$; 1369w, ν_{C-N}; 1289w, ν_{C-O}. UV–Vis spectrum in DMSO [λ_{max} (nm), ε ($dm^3\,cm^{-1}\,mol^{-1}$)]: 286 (5600), 334 (4570), 431 (5610).

2.2.8. Ligand H_2L^8

Yellow powder. Yield: 0.854 g, 55.0%. m.p.: 240–242 °C (uncorrected). *Anal.* Calc. for $C_{16}H_{12}N_2O_2I_4$: C, 24.9; H, 1.6; N, 3.6. Found: C, 24.6; H, 1.6; N, 3.3%. Selected IR bands (KBr, cm^{-1}): 1630s, $\nu_{C=N}$; 1580m, $\nu_{C=C}$; 1353m, ν_{C-N}; 1281m, ν_{C-O}. UV–Vis spectrum in DMSO [λ_{max} (nm), ε ($dm^3\,cm^{-1}\,mol^{-1}$)]: 296 (5800), 344 (5000), 438 (6520).

2.3. Preparation of the chromium(III) complexes

The chromium(III) complexes were prepared essentially as described [41]. The following procedure was used: ethylenediamine (0.12 g, 2.0 mmol) and the appropriate salicylaldehyde (4.0 mmol) were added to a solution of chromium(III) chloride hexahydrate (0.53 g, 2.0 mmol) in ethylene glycol–water–methanol (1:1:3, 50 ml). After the mixture was refluxed for 30 min, potassium carbonate (0.21 g, 1.5 mmol) was gradually added to the solution, then refluxing the solution for about 3–4 h. The precipitate was filtered, washed with cold water (5 ml) and cold ethanol (5 ml) and dried over silica. The complex was recrystallized from 95% ethanol and dried over silica in a desiccator at room temperature.

2.3.1. Preparation of $[Cr(L^1)(OH)(H_2O)]$

Brown powder. Yield: 0.253 g, 35.8%. m.p.: 245–250 °C decomposition (uncorrected). *Anal.* Calc. for $C_{16}H_{17}N_2O_4Cr$: C, 54.4; H, 4.9; N, 7.9. Found: C, 54.7; H, 5.2; N, 7.95%. Selected IR bands (KBr, cm^{-1}): 1638s, $\nu_{C=N}$; 1540m, $\nu_{C=C}$; 1372m, ν_{C-N}; 1295m, ν_{C-O}; 538w, ν_{Cr-O}; 375w, ν_{Cr-N}. UV–Vis spectrum in DMSO [λ_{max} (nm), ε ($dm^3\,cm^{-1}\,mol^{-1}$)]: 277 (14000), 334 (3420), 393 (3700). Mass spectrum, ESI/MS, in DMSO [m/z(%)]: 474(60), 428(17), 319(20), 241(22), 215(20), 179(100), 153(88). μ_{eff}(298 K): 3.92 BM.

2.3.2. Preparation of $[Cr(L^2)(OH)(H_2O)]$

Brown powder. Yield: 0.358 g, 35.0%. m.p.: >360 °C. *Anal.* Calc. for $C_{16}H_{15}N_2O_4Br_2Cr$: C, 37.6; H, 2.95; N, 5.5. Found: C, 37.8; H, 2.6; N, 5.3%. Selected IR bands (KBr, cm^{-1}): 1627s, $\nu_{C=N}$; 1592m, $\nu_{C=C}$; 1377m, ν_{C-N}; 1300m, ν_{C-O}; 582w, ν_{Cr-O}; 378w, ν_{Cr-N}. UV–Vis spectrum in DMSO [λ_{max} (nm), ε ($dm^3\,cm^{-1}\,mol^{-1}$)]: 284 (12400), 341 (1294), 407 (980). Mass spectrum, ESI/MS, in DMSO [m/z(%)]: 633(10), 521(16), 470(9), 339(52), 325(54), 311(42), 283(51), 249(100). μ_{eff}(298 K): 4.13 BM.

2.3.3. Preparation of $[Cr(L^3)(OH)(H_2O)]$

Brown powder. Yield 0.372 g, 44.0%. m.p.: >360 °C. *Anal.* Calc. for $C_{16}H_{15}N_2O_4Cl_2Cr$: C, 45.5; H, 3.6; N, 6.6. Found: C, 45.1; H, 3.2; N, 6.4%. Selected IR bands (KBr, cm^{-1}): 1629s, $\nu_{C=N}$; 1599m, $\nu_{C=C}$; 1379m, ν_{C-N}; 1302m, ν_{C-O}; 584w, ν_{Cr-O}; 376w, ν_{Cr-N}. UV–Vis spectrum in DMSO [λ_{max} (nm), ε ($dm^3\,cm^{-1}\,mol^{-1}$)]: 344 (2000), 413 (1570). Mass spectrum, ESI/MS, in DMSO [m/z(%)]: 543(8), 319(10), 257(10), 215(10), 184(27), 179(100), 153(63), 145(19). μ_{eff}(298 K): 3.92 BM.

2.3.4. Preparation of $[Cr(L^4)(OH)(H_2O)]$

Brown powder. Yield: 0.445 g, 53.8%. m.p.: >360 °C. *Anal.* Calc. for $C_{18}H_{21}N_2O_6Cr$: C, 52.3; H, 4.8; N, 6.8. Found: C, 52.2; H, 5.1; N, 6.6%. Selected IR bands (KBr, cm^{-1}): 1628s, $\nu_{C=N}$; 1563m, $\nu_{C=C}$; 1388m, ν_{C-N}; 1305m, ν_{C-O};. 5 69w, ν_{Cr-O}; 380w, ν_{Cr-N}. UV–Vis spectrum in DMSO [λ_{max} (nm), ε ($dm^3\,cm^{-1}\,mol^{-1}$)]: 357 (2010), 430 (1380). μ_{eff}(298 K): 4.00 BM.

2.3.5. Preparation of $[Cr(L^5)(H_2O)_2]Cl$

Brown powder. Yield: 0.409 g, 46.0%. m.p.: >360 °C. *Anal.* Calc. for $C_{16}H_{16}N_4O_8ClCr$: C, 40.1; H, 3.4; N, 11.7. Found: C, 40.6; H, 3.3; N, 12.0%. Selected IR bands (KBr, cm^{-1}): 1638s, $\nu_{C=N}$; 1580m, $\nu_{C=C}$; 1390m, ν_{C-N}; 1304m, ν_{C-O}; 569w, ν_{Cr-O}; 375w, ν_{Cr-N}. UV–Vis spectrum in DMSO [λ_{max} (nm), ε ($dm^3\,cm^{-1}\,mol^{-1}$)]: 375 (19200). Mass spectrum, ESI/MS, in DMSO solutions [m/z(%)]: 564(12), 476(13), 359(32), 305(56), 275(52), 259(68), 227(100), 215(21). μ_{eff}(298 K): 3.51 BM.

2.3.6. Preparation of $[Cr(L^6)(H_2O)_2]Cl$

Brown powder. Yield: 0.363 g, 25.7%. m.p.: >360 °C. *Anal.* Calc. for $C_{16}H_{14}N_2O_4ClBr_4Cr$: C, 27.2; H, 2.0; N, 4.0. Found: C, 27.5; H, 1.8; N, 3.7%. Selected IR bands (KBr, cm^{-1}): 1634s, $\nu_{C=N}$; 1578m, $\nu_{C=C}$; 1358w, ν_{C-N}; 1298w, ν_{C-O}; 575w, ν_{Cr-O}; 370w, ν_{Cr-N}. UV–Vis spectrum in DMSO [λ_{max} (nm), ε ($dm^3\,cm^{-1}\,mol^{-1}$)]: 286 (16400), 336 (4570), 410 (4180). μ_{eff}(298 K): 4.19 BM.

2.3.7. Preparation of $[Cr(L^7)(H_2O)_2]Cl$

Brown powder. Yield: 0.522 g, 53.0%. m.p.: >360 °C. *Anal.* Calc. for $C_{16}H_{14}N_2O_4Cl_5Cr$: C, 36.4; H, 2.7; N, 5.3. Found: C, 36.2; H, 2.7; N, 5.5%. Selected IR bands (KBr, cm^{-1}): 1628s, $\nu_{C=N}$; 1519w, $\nu_{C=C}$; 1376w, ν_{C-N}; 1290w, ν_{C-O}; 580w, ν_{Cr-O}; 357w, ν_{Cr-N}. UV–Vis spectrum in DMSO [λ_{max} (nm), ε ($dm^3\,cm^{-1}\,mol^{-1}$)]: 319 (4060), 415 (2370). μ_{eff}(298 K): 4.05 BM.

2.3.8. Preparation of $[Cr(L^8)(H_2O)_2]Cl \cdot H_2O$

Brown powder. Yield: 0.245 g, 13.4%. m.p.: >360 °C. *Anal.* Calc. for $C_{16}H_{164}N_2O_5ClI_4Cr$: C, 21.1; H, 1.8; N, 3.1. Found: C, 21.0; H, 2.0; N, 3.2%. Selected IR bands (KBr cm^{-1}): 1637s, $\nu_{C=N}$; 1566w, $\nu_{C=C}$; 1372w, ν_{C-N}; 1391m, ν_{C-O}; 569w, ν_{Cr-O}; 375w, ν_{Cr-N}. UV–Vis spectrum in DMSO [λ_{max} (nm), ε ($dm^3\ cm^{-1}\ mol^{-1}$)]: 292 (9940), 346 (3410), 415 (2370). μ_{eff}(298 K): 4.03 BM.

2.4. Physical measurements

Elemental microanalyses (C, H, N) were performed by the Microanalytical Laboratory of the Departamento de Química of the Universidade Federal de São Carlos, with a Faison EA 1108 CHNS-O instrument. Melting points were determined using a Mel-Temp II Laboratory Devices USA. The molar conductance was determined with a Cole-Parmer Model 1481-90 conductivity meter. IR spectra were recorded in KBr pressed discs (1% by weight) with a Bomem Michelson 102 FT-IR instrument. The ^1H and ^{13}C NMR spectra of the free ligand in $CDCl_3$ and DMSO-d_6, with tetramethylsilane as an internal standard, were obtained using a Bruker ARX 400 MHz 9.4 T spectrophotometer. All chemical shifts (^1H and ^{13}C) are given in ppm versus tetramethylsilane (TMS). Magnetic susceptibility measurements were made on a powered sample at 298 K using a Johnson–Matthey Magnetic Susceptibility Balance model Mark II using the magnetic susceptibility standard $HgCo(NCS)_4$.

All the mass spectra were performed by the mass spectrometry Laboratory of the Departamento de Química of the Universidade Federal de São Carlos using a QuattroLC triple-quadrupole mass spectrometer (Micromass, Manchester, UK) coupled with an liquid chromatograph; the data were acquired using Masslynx software (version 3.2). The electrospray ionization capillary voltage was maintained between 4 and 4.2 kV, and the cone voltage was kept at 30 V unless otherwise stated. Nitrogen was used as the desolvation and nebulization gas. The source and desolvation temperatures were kept at 100 °C. The ESI mass spectra were recorded by scanning MS1. The mass spectra of these compounds were performed on 15 ng dm^{-3} DMSO solutions.

Electronic spectra were recorded in the 260–800 nm range using a Shimadzu MultSpec-1501 instrument. These spectra of the DMSO solutions were obtained at room temperature using matched 1.0 cm quartz cells. The electronic spectra were resolved by deconvolution using the Voigt function, amplitude, Gaussian/Lorentzian widths, of the Jandel Scientific Software PeakFit™ program [42]. In this version of the Voigt function, the Gaussian and Lorentzian widths were calculated as well as the amplitude and center of each peak. The width and area of each peak were allowed to vary without using a background function. A reliability factor, defined as $R = \sum|y_{obs.,i} - y_{calc.,i}|/\sum y_{obs.,i}$, was used to determine the goodness of fit between the measured and the calculated spectra. A degree of freedom adjusted coefficient of determination of the Jandel Scientific Software PeakFit™ program [42] was also used in the determination of the goodness of fit [43].

3. Results and discussion

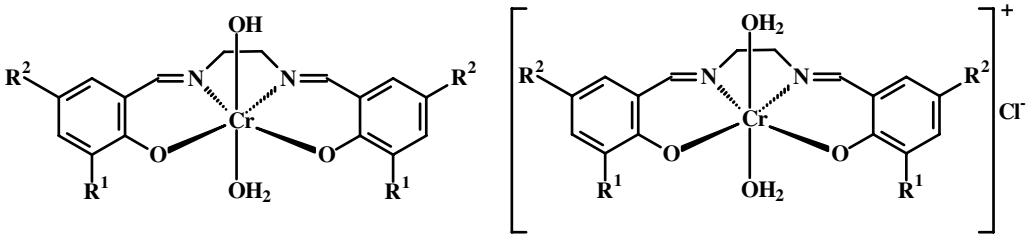
The complexes of chromium(III) are stable in air, both in solution and in the crystalline state. The solids are various shades of brown. The yields of the purified complexes varied from 13.7% to 53.7%. The variation is due to differences in the solubility of the starting ligands and the final complexes. The complexes showed magnetic moment in the range of 3.5–4.2 BM which corresponds to three unpaired electrons [44].

The molar conductance of the complexes was an aid for proposing their formulas. For pure DMSO the measured conductivity was 15.1 S $cm^2\ mol^{-1}$, for a 1:1 electrolyte, KCl, 1.00×10^{-3} mol L^{-1} in DMSO, the molar conductivity was 46.0 S $cm^2\ mol^{-1}$ and 126.5 S $cm^2\ mol^{-1}$ for the 2:1 electrolyte, $MgCl_2$, 1.00×10^{-3} mol L^{-1} in DMSO. The molar conductances in DMSO solutions, at 25 °C, with a concentration of 1×10^{-3} mol L^{-1}, are: $[Cr(L^5)(H_2O)_2]Cl$, 54 S $cm^2\ mol^{-1}$; $[Cr(L^6)(H_2O)_2]Cl$, 39 S $cm^2\ mol^{-1}$; $[Cr(L^7)(H_2O)_2]Cl$, 45 S $cm^2\ mol^{-1}$ and $[Cr(L^8)(H_2O)_2]Cl$, 50 S $cm^2\ mol^{-1}$. These data are, as expected, for a 1:1 electrolyte. The complexes, $[Cr(L^1)(OH)(H_2O)]$, 14 S $cm^2\ mol^{-1}$; $[Cr(L^2)(OH)(H_2O)]$, 13 S $cm^2\ mol^{-1}$; $[Cr(L^3)(OH)(H_2O)]$, 26 S $cm^2\ mol^{-1}$ and $[Cr(L^4)(OH)(H_2O)]$, 18 S $cm^2\ mol^{-1}$, are neutral electrolytes. Solutions of the complexes were also tested with $AgNO_3$ for free chloride íon with the results confirming the proposed structures. The proposed structural representations of the complexes and their abbreviations are given in Fig. 2.

The results of the microanalyses, the molar conductance and tests with $AgNO_3$ indicate that two series of complexes are formed by the same synthetic procedure [41]. The first series of complexes $[Cr(L^n)(H_2O)_2]Cl$, is the expected product of the synthesis. The second series, $[Cr(L^m)(OH)(H_2O)]$, is related to the first series by the deprotonation of a coordinated water forming a neutral complex. A slow addition rate results in the expected $[Cr(L^n)(H_2O)_2]Cl$ product. However, either if the potassium carbonate is added too fast or if amount is larger than the value calculated, the product is $[Cr(L^n)(OH)(H_2O)]$. The potassium carbonate is used in the synthesis to deprotonate the Schiff base H_2L^n.

3.1. IR spectra

The IR spectra of the free ligands and the complexes exhibit various bands in the 250–4000 cm^{-1} region. A typical spectrum of the free ligand and the corresponding chromium(III) are shown in Fig. 3. The O–H stretching frequency of the ligand is expected in the 3300–3800 cm^{-1} region, however, this frequency is generally displaced to the 2840–2960 cm^{-1} region due to the internal hydrogen bridge OH···N=C [45,46]. As the hydrogen bond becomes stronger, the bandwidth increases, and this band sometimes is not detected. Hydrogen bonds in these Schiff bases are



R^1	R^2	L	Complexes
H	H	OH	$[Cr(L^1)(OH)(H_2O)]$
H	Br	OH	$[Cr(L^2)(OH)(H_2O)]$
H	Cl	OH	$[Cr(L^3)(OH)(H_2O)]$
H	MeO	OH	$[Cr(L^4)(OH)(H_2O)]$

R^1	R^2	L	Complexes
H	NO_2	H_2O	$[Cr(L^5)(H_2O)_2]Cl$
Br	Br	H_2O	$[Cr(L^6)(H_2O)_2]Cl$
Cl	Cl	H_2O	$[Cr(L^7)(H_2O)_2]Cl$
I	I	H_2O	$[Cr(L^8)(H_2O)_2]Cl$

Fig. 2. Complexes prepared in this study.

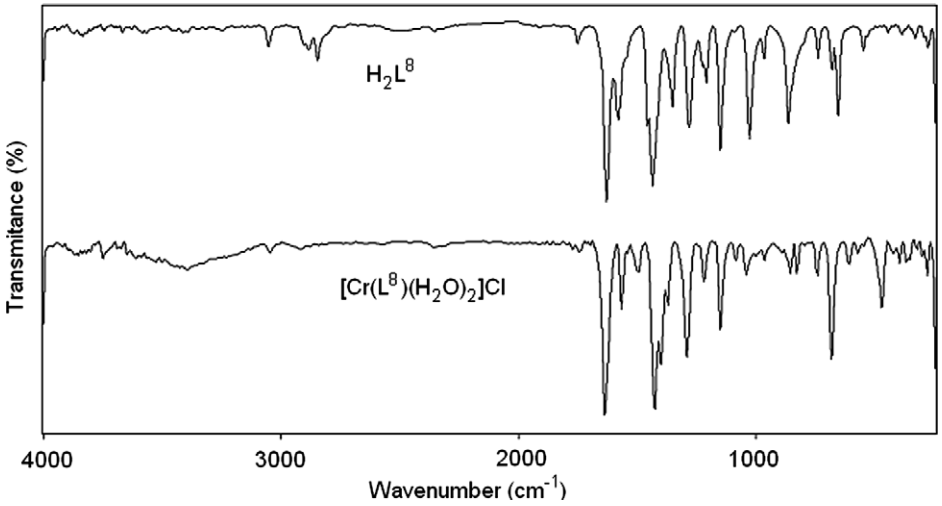


Fig. 3. IR spectra (250–4000 cm^{-1}) of H_2L^8 and $[Cr(L^8)(H_2O)_2]Cl$.

usually very strong. The ligands are relatively planar with adequate intramolecular distance that favors intramolecular hydrogen bond formation [47]. Electron-donating groups on the phenolic ring increase the electron density on the hydroxyl oxygen making the H–O bond stronger, the absorption usually appears as a broad band in the IR spectrum. For the chromium(III) complexes, the disappearance of this band is expected due to the substitution of hydrogen for the metal on the complex formation.

The C=N stretching frequencies are in the 1592–1640 cm^{-1} region as reported for similar ligands [48,49]. The ligands exhibit the characteristic C=N band in 1630–1646 cm^{-1} region, while the complexes the C=N were observed in the 1628–1638 cm^{-1} region. The C=N stretching frequency is generally shifted to a lower frequency, indicating a decrease in the C=N bond order due to the coordinate bond of the metal with the imine nitrogen lone pair [50,51].

In the 1500–1600 cm^{-1} region, the observed bands were attributed to aromatic C=C vibrations. On coordination these bands shift to lower frequencies for the chromium complexes of ligands H_2L^1, H_2L^7 and H_2L^8 and to higher frequencies for H_2L^2, H_2L^3, H_2L^4 and H_2L^6 [52].

The C–N stretching frequency has been reported [52–54] in the 1350–1410 cm^{-1} region. For the free ligands, the band occurs in the 1290–1310 cm^{-1}region and for the complexes, 1350–1390 cm^{-1} region. The C–O stretching frequency appears as a weak band within the 1290–1340 cm^{-1} range as reported for similar ligands [45,46,55]. This band occurs in the 1280–1300 cm^{-1} region for the free ligands and in the 1290–1310 cm^{-1} region for the complexes. The C–O stretching frequency is generally shifted to a higher frequency, indicating the formation of bond oxygen of phenolic group with the metal ion [50,51].

Evidence regarding the bonding of the chromium with the nitrogen and/or oxygen atom of the Schiff base is provided by the appearance of bands in the 250–600 cm^{-1} region. The band at 570–590 cm^{-1} is assigned to ν(Cr–O),

while band at 260–390 cm^{-1} is assigned to ν(Cr–N). These bands are observed as new peaks for the complexes and are not present in the spectrum of the free ligand. As pointed out by Percy and Thornton [55], the metal–oxygen and metal–nitrogen frequency assignments are at times very difficult.

3.2. Nuclear magnetic resonance spectra

The ^{1}H NMR spectra of the free ligands were recorded in $CDCl_3$ and DMSO-d_6. The chemical shifts, expressed in ppm downfield form tetramethylsilane, are given in Table 1. ^{1}H NMR spectra of similar Schiff base ligands have been reported [40,52,56–58]. The free ligands exhibit a broad peak between 14 and 12.5 ppm, which is due to hydrogen-bonded phenolic protons. This peak is due to hydrogen bonded phenolic protons [56,59–61] and the integration is generally less than 2.0 due to this intramolecular hydrogen bonding [40,61,45]. Signals for the methine protons of the azomethine group, –N=C(H)– were observed between 8.4 and 8.2 ppm. In the region of 7.6–6.8 ppm were assigned chemical shifts for hydrogen of the aromatic ring. The alkyl protons =N–CH_2–CH_2–N= were observed between 4.2 and 3.9 ppm. For H_2L^4, the signal for the –OCH_3 group was observed at 3.75 ppm.

The ^{13}C NMR spectra of the free ligands were recorded in $CDCl_3$ or DMSO-d_6. The chemical shifts, expressed in ppm downfield form tetramethylsilane, are given in Table 2. Our numbering system follows that of Fig. 1. The ^{13}C spectra allow an assignment of the peaks based on ^{13}C shifts in μ-oxobis(disalicyldeneiminato) complexes [40,62] and in similar tetradentate Schiff base ligands and their complexes [40,52]. The chemical shifts for carbon C(8) of =N–CH_2CH_2-N=, were recorded between 59.7 and 54.2 ppm. The signals for carbon C(7) from imine group –N=C(H)– were observed between 166.8 and 165.2 ppm with no noticeable influence of the substituent groups. The signal for C(OCH_3) of ligand H_2L^4 is 55.8 ppm.

Table 1
^{1}H NMR data of free ligands with tetramethylsilane, TMS, as internal standard (chemical shifts in ppm and J in Hz)

	H_2L^{1a}	H_2L^{2a}
δOH	>12.00	>12.00
δ–N=*C*(*H*)–	8.57 (s, 2H)	8.56 (s, 2H)
δPh		
C_4H	7.41 (dd, $J = 7.6$, $J = 1.7$, 2H)	7.64 (d, $J = 2.6$, 2H)
C_6H	7.30 (ddd, $J = 8.3$, $J = 7.3$, $J = 1.7$, 2H)	7.44 (dd, $J = 8.8$, $J = 2.6$, 2H)
C_5H	6.86 (ddd, $J = 7.6$, $J = 7.3$, $J = 1.1$, 2H)	
C_3H	6.84 (dd, $J = 8.3$, $J = 1.1$, 2H)	6.83 (d, $J = 8.8$, 2H)
δ=N–CH_2–	3.90 (s, 4H)[b]	3.91 (s, 4H)
	H_2L^{3c}	H_2L^{4c}
δOH	13.13 (s, 1.3H)	12.72 (s, 1.2H)
δ–N=C(H)–	(s) 8.31 (s, 2H)	8.32 (s, 2H)
δPh		
C_4H	7.51 (d, $J = 2.8$, 2H)	7.26 (d, $J = 1.6$, 2H)
C_3H	7.23 (dd, $J = 8.8$, $J = 2.8$, 2H)	6.85 (dd, J =9.6, $J = 1.6$, 2H)
C_6H	6.90 (d, $J = 8.8$, 2H)	6.74 (d, $J = 9.6$, 2H)
δ=N–CH_2–	3.97 (s, 4H)	3.95 (s, 4H)
δOCH_3		3.75 (s,6H)
	H_2L^{5a}	H_2L^{6a}
δOH	>12.00	>12.00
δ–N=C(H)–	8.75 (s, 2H)	8.56 (s, 2H)
δPh		
C_4H	8.42 (d, $J = 3.0$, 2H)	7.80 (d, $J = 2.6$, 2H)
C_6H	8.07 (dd, $J = 9.5$, $J = 3.0$, 2H)	7.60 (d, $J = 2.6$, 2H)
C_3H	7.73 (d, $J = 9.5$, 2H)	
δ=N–CH_2–	4.00 (s, 4H)	3.98 (s, 4H)
	H_2L^{7c}	H_2 L^{8a}
δOH	13.98 (s, 1.1H)	>12.00
δN=C(H)–	8.29 (s, 2H)	8.46 (s, 2H)
δPh		
C_4H	7.41 (d, $J = 2.4$, 2H)	8.02 (d, $J = 2.3$, 2H)
C_6H	7.16 (d, $J = 2.4$, 2H)	7.70 (d, $J = 2.3$, 2H)
δN–CH_2–	4.01 (s, 4H)	3.95 (s, 4H)

[a] DMSO-d_6.
[b] s = singlet, d = doublet, dd = doublet of doublets, ddd = doublet of doublet of doublets.
[c] $CDCl_3$.

Table 2
^{13}C NMR data of free ligands with tetramethylsilane, TMS, as internal standard (chemical shifts in ppm)

	H_2L^{1a}	H_2L^{2b}	H_2L^{3a}	H_2L^{4a}	H_2L^{5b}	H_2L^{6b}	H_2L^{7a}	H_2L^{8b}
C(1)	118.6	119.5	119.3	118.2	122.0	118.7	118.3	118.6
C(2)	161.0	160.5	159.5	155.0	167.2	162.1	159.5	164.8
C(3)	116.9	120.7	118.6	117.5	121.2	114.1	119.4	92.6
C(4)	132.3	135.3	132.3	119.4	130.7	138.5	132.3	149.0
C(5)	118.7	109.4	123.3	151.9	135.6	106.5	130.5	110.1
C(6)	131.4	133.9	130.5	114.8	128.9	134.4	123.4	141.3
C(7)	166.6	166.1	165.3	166.2	166.2	166.8	165.2	166.7
C(8)	59.7	58.8	59.6	59.7	54.2	55.3	59.6	56.4
$C(OCH_3)$				55.8				

[a] $CDCl_3$.
[b] DMSO-d_6.

Other chemical shifts are for the aromatic carbons and depend on the substituent group when compared to ligand H_2L^1 with hydrogens on C(3), C(4), C(5), and C(6). The signal for C(1) bonded to the imine group is observed between 118.3 and 122.0. This signal is the least affected by the substituent groups. The largest shift is only 3.4 ppm due the nitro group. The chemical shifts for the carbon C(2) bonded to the oxygen of the phenolic group were observed between 167.2 and 155 ppm. The methoxy group causes the greatest upfield shift of 6.0 ppm and the nitro group, the greatest downfield shift of 6.2 ppm when compared to hydrogen as the substituent. This is reasonable since methoxy is an electron donating group and nitro an electron withdrawing group and both being *para* to C(2).

The signal for C(3) varies between 92.6 and 121.2 ppm. The greatest effect occurs when iodine is bonded to this carbon. The nitro group, which is *meta* to this position, has the next largest effect. The presence of the substituent groups on C(3) and C(5) has a variable effect on the signal of C(4), which occurs between 119.4 and 149.0. When C (4) is *ortho* to methoxy, the signal suffers an upfield shift of 12.9 ppm and a downfield shift of 16.7 when *ortho* to two iodides in positions 3 and 5. The chemical shifts for the carbon C(5) also suffer a wide variation, from 109.4 for Br to 151.9 for MeO. All the substituents affect this signal. The signal of C(6) is most affected by the methoxy group *ortho* to this carbon.

All the substituents affect the chemical shifts of the aromatic carbons. For the mono-substituted ligands, the methoxy and nitro groups present the greatest influence. The methoxy group on C(5) causes a upfield shift of the signals of C(2), C(4), and C(6) and a downfield shift for C(5) in comparison with the ^{13}C spectrum of H_2L^1. The nitro group on C(5) causes a downfield shift of the signals of C(1), C(2), C(3) and C(5) and an upfield shift for C(4) and C(6). For the di-substituted ligands, the order of influence is I > Br > Cl.

3.3. Electronic spectra

The electronic spectra of the DMSO solutions of the free ligands, recorded in the 250–800 region, exhibit one or two bands. Bands due to the $n \rightarrow \pi^*$ transition of the C=C and C=N chromophores normally occur between 270 and 300 nm [63]. These bands shift to the red when the chromophores are in a conjugated system. These are observed as a shoulder only for H_2L^6, 289 nm; H_2L^7, 286 nm; and H_2L^8, 296 nm. The strong intramolecular hydrogen bond occurring in the Schiff base ligands may also account in part for the shift of these bands that occurs between 400 and 440 nm [64]. Molecular orbital calculations indicate that this band in the 400–440 nm region is an $n \rightarrow \pi^*$ transition type, involving the promotion of an electron of the free electron pair on the nitrogen to an antibonding π-orbital of imine group [64]. Another factor to be considered in the assignment of this transition is its absence in spectra of the corresponding complex as shown in Figs. 4 and 5.

The isolated benzene ring exhibits three characteristic absorptions at 184, 204 and 256 nm; all assigned to $\pi \rightarrow \pi^*$-type transitions [63]. Substitutions on the ring, by auxochromes and chromophores, shift this band to the red. The ligand band between 317 and 370 nm is assigned as a $\pi \rightarrow \pi^*$ transition involving molecular orbitals of C=N chromophore and the benzene ring [65]. Electron-donating

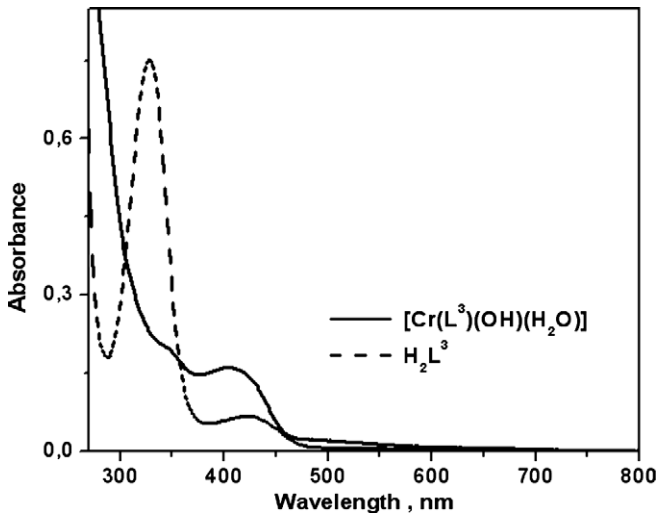


Fig. 4. Electronic spectra (260–800 nm) of H_2L^3 and $[Cr(L^3)(OH)(H_2O)]$ in DMSO.

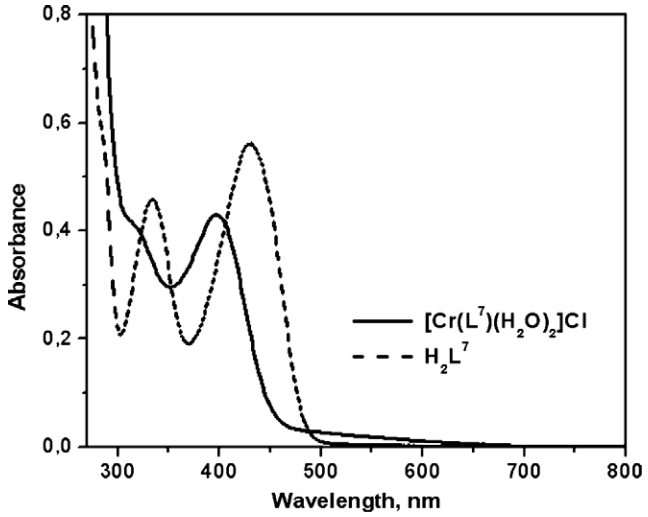


Fig. 5. Electronic spectra (260–800 nm) of H_2L^7 and $[Cr(L^7)(H_2O)_2]Cl$ in DMSO.

groups on the aromatic ring generally result in a bathochromic shift in all observed bands. The $\pi \rightarrow \pi^*$-type transition due to the C=N chromophore shifts to lower energies on complexation. In general, the $\pi \rightarrow \pi^*$-type transition due to the aromatic ring undergoes a similar smaller shift.

Another difference observed in the electronic spectra of the chromium(III) complexes, compared to the spectra of the corresponding free ligand, is associated with the appearance of a broad low intensity band at ca. 500 nm. This band is attributed to the d–d transitions of the chromium ion. These bands are of low molar absorptivity, ε, being Laporte 'forbidden' transitions. Another important characteristic is the absence of the $n \rightarrow \pi^*$ band. The formation of the metal–nitrogen bond stabilizes the electron pair on the nitrogen atom [64]. The appearance of a strong band between 390 and 430 nm is attributed to ligand-to-metal charge-transfer bands. These charge-transfer transitions probably occur form the π-orbitals of the Schiff bases to the d-orbitals of chromium.

The Gaussian/Lorentzian analysis of the visible portion, 11 760–25 000 cm^{-1} of the optical absorption spectrum yields three peaks, due to a symmetry that is less than octahedral in a six-coordinate complex. Each of the triply degenerate T terms is split into two new terms, an E and an A or B, with the result that six transitions are now expected instead of three [66,67]. For the chromium(III) complexes with C_{2v} symmetry six transitions I: $^4B_{1g} \rightarrow {}^4E_g(^4T_{2g})$; II: $^4B_{1g} \rightarrow {}^4B_{2g}(^4T_{2g})$; III: $^4B_{1g} \rightarrow {}^4E_g(^4T_{1g})$; IV: $^4B_{1g} \rightarrow {}^4A_{2g}(^4T_{1g})$; V: $^4B_{1g} \rightarrow {}^4A_{2g}(^4T_{1g}(P))$; VI: $^4B_{1g} \rightarrow {}^4E_g(^4T_{1g}(P))$ were proposed. The three transitions appear at higher energies and are covered by ligand-to-metal charge-transfer bands. Thus, only the three first transitions are calculated as shown in Fig. 6. The calculated values for the absorption maximum, the molar absorptivity, and the oscillator strength [68] for each peak are given in Table 3.

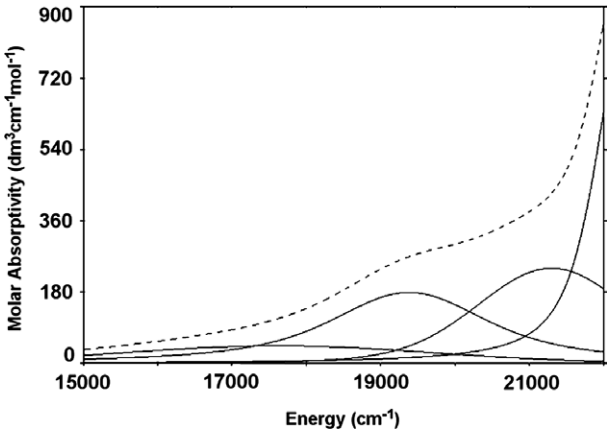


Fig. 6. Gaussian/Loretzian analysis of $[Cr(L^2)(OH)(H_2O)]$ for the DMSO electronic spectrum.

A consistent treatment for the bands is to assign the band near 15 600–17 600 cm^{-1} as the $^4B_{1g} \rightarrow {}^4E_g(^4T_{2g})$ transition; the band at ca. 18 400–20 400 cm^{-1} as the $^4B_{1g} \rightarrow$

Table 3
Gaussian/Loretzian band components for the visible spectra of the chromium(III) complexes in DMSO

Complexes	Band[a]	$\lambda_{max} \times 10^3$ (cm^{-1})	ε_{max} (dm^3 mol^{-1} cm^{-1})	Oscillator strength[b]
$[Cr(L^1)(OH)(H_2O)]$	($R = 0.13\%$)[c]			
	I	16.14	61.5	9.27×10^{-4}
	II	20.39	281.6	3.99×10^{-3}
	III	23.11	374.6	1.62×10^{-3}
$[Cr(L^2)(OH)(H_2O)]$	($R = 0.10\%$)			
	I	15.67	75.9	1.39×10^{-3}
	II	19.45	143.6	2.88×10^{-3}
	III	22.78	147.9	3.32×10^{-3}
$[Cr(L^3)(OH)(H_2O)]$	($R = 0.05\%$)			
	I	15.85	53.0	9.27×10^{-4}
	II	20.11	188.9	3.99×10^{-3}
	III	22.43	282.6	1.62×10^{-3}
$[Cr(L^4)(OH)(H_2O)]$	($R = 0.07\%$)			
	I	15.59	91.1	1.47×10^{-3}
	II	19.06	205.1	3.75×10^{-3}
	III	21.52	294.2	2.95×10^{-3}
$[Cr(L^5)(H_2O)_2]Cl$	($R = 0.66\%$)			
	I	16.20	75.9	1.05×10^{-3}
	II	18.35	117.7	1.46×10^{-3}
	III	19.95	629.3	8.54×10^{-3}
$[Cr(L^6)(H_2O)_2]Cl$	($R = 0.65\%$)			
	I	17.62	44.7	1.01×10^{-3}
	II	19.37	179.5	2.10×10^{-3}
	III	21.29	240.6	2.63×10^{-3}
$[Cr(L^7)(H_2O)_2]Cl$	($R = 0.35\%$)			
	I	16.54	24.1	1.98×10^{-4}
	II	18.46	116.7	1.74×10^{-3}
	III	21.58	239.9	4.30×10^{-3}
$[Cr(L^8)(H_2O)_2]Cl$	($R = 0.15\%$)			
	I	16.46	64.7	1.25×10^{-3}
	II	19.79	194.0	3.57×10^{-3}
	III	22.52	204.3	5.27×10^{-3}

[a] Assignments I, $^4B_{1g} \rightarrow {}^4E_g(^4T_{2g})$; II, $^4B_{1g} \rightarrow {}^4B_{2g}(^4T_{2g})$; III, $^4B_{1g} \rightarrow {}^4E_g(^4T_{1g})$.
[b] Ref. [70].

$4B_{2g}(^4T_{2g})$ transition and that 20000–23100 cm^{-1} as the $^4B_{1g} \rightarrow {}^4E_g(^4T_{1g})$ transition.

3.4. Mass spectra

A preliminary study of ESI mass spectra of the free ligands and their corresponding complexes gave promising results. The negative ion ESI mass spectrum of the H_2L^1 ligand in DMSO showed the ion $[M-H]^-$ at 267 *m/z* and for H_2L^2 the ion $[M-H]^-$ at 425 *m/z*. The positive ion ESI mass spectrum of the H_2L^3 ligand in DMSO presented the ion $[M+H]^+$ at 338 *m/z* and for H_2L^5 the ion $[M+H]^+$ at 359 *m/z*. For both types of complexes, $[Cr(L)(OH)(H_2O)]$ or $[Cr(L)(H_2O)_2]$ Cl, the results indicated the presence of the $[Cr(L^n)(DMSO)_2]^+$ ion in DMSO solution. The positive ion ESI mass spectrum of the $[Cr(L^1)]^+$ complex showed an ion at 474 *m/z* corresponding to $[Cr(L^1)(DMSO)_2]^+$; for $[Cr(L^2)]^+$, an ion at 633 *m/z*, $[Cr(L^2)(DMSO)_2]^+$; for $[Cr(L^3)]^+$, an ion at 543 *m/z*, $[Cr(L^3)(DMSO)_2]^+$ and for $[Cr(L^5)]^+$, an ion at 564 *m/z*, $[Cr(L^5)(DMSO)_2]^+$. Such coordination of solvent molecules to the central metal atom in the ESI process has been reported [69,70]. A detailed study of the complexes including a study of the daughter ions of $[Cr(L^n)(DMSO)_2]^+$ complex will be undertaken to determine the behavior of fragmentations of these compounds.

4. Conclusions

A series of symmetrical tetradentate Schiff bases containing the N_2O_2 donor set and their corresponding chromium(III) complexes have been synthesized and spectrally characterized. The same synthetic procedure gives two series of complexes depending on the amount and rate of addition of potassium carbonate used to deprotonate the Schiff base. The initial mass spectra study indicates that for the two series of complexes in DMSO that the same species, $[Cr(L^n)(DMSO)_2]^+$ is present.

Acknowledgements

Financial support from the Conselho Nacional de Desenvolvimento Cientifico e Tecnológico, CNPq, and the Fundação de Amparo à Pesquisa do Estado de São Paulo, FAPESP, is gratefully acknowledged. We thank FAPESP for providing an undergraduate scholarship to P.E.A. and the CNPq for graduate scholarships to M.P. dos S. and S.R. We thank Prof. Alzir A. Batista for the use of the magnetic susceptibility balance and Dr. Gustavo Von Poelhsitz for his help with these measurements.

References

[1] M. Wang, L.F. Wang, Y.Z. Li, Q.X. Li, Z.D. Xu, D.Q. Qu, Transition Met. Chem. 26 (2001) 307.
[2] S.D. Dhumwad, K.B. Gudasi, T.R. Goudar, Indian J. Chem. A 33 (1994) 320.
[3] N.N. Gulerman, S. Rollas, H. Erdeniz, M. Kiraj, J. Pharm. Sci. 26 (2001) 1.
[4] K.H. Reddy, P.S. Reddy, P.R. Babu, Transition Met. Chem. 25 (2000) 154.
[5] P. Tarasconi, S. Capacchi, G. Pelosi, M. Corina, R. Albertini, A. Bonati, P.P. Dall'Aglio, P. Lunghi, S. Pinelli, Bioorg. Med. Chem. 8 (2000) 154.
[6] H. Singh, L.D.S. Yadav, S.B.S. Mishra, J. Inorg. Nucl. Chem. 42 (1981) 1701.
[7] J. Charo, J.A. Lindencrona, L.M. Carlson, J. Hinkula, R. Kiessling, J. Virol. 78 (2004) 11321.
[8] D.X. West, S.L. Dietrich, I. Thientananvanich, C.A. Brown, A.E. Liberta, Transition Met. Chem. 19 (1994) 320.
[9] N.K. Singh, S.B. Singh, Indian J. Chem. A 40 (2001) 1070.
[10] V. Mishra, S.N. Pandeya, S. Anathan, Acta Pharm. Turc. 42 (2000) 139.
[11] D. Jamal, M.A. Quaraishi, J. Electrochem. Soc. India 49 (2000) 56.
[12] E.J. Baran, J. Inorg. Biochem. 80 (2000) 1.
[13] F. Velde, I.W.C.E. Arends, R.A. Sheldon, J. Inorg. Biochem. 80 (2000) 81.
[14] X.D. Zhu, C.G. Wang, Y.L. Dang, H.B. Zhou, Z.S. Wu, Z.J. Liu, D.L. Ye, Q.C. Zhou, Synth. React. Inorg. Met.-Org. Chem. 30 (2000) 625.
[15] M. Kanthimathi, A. Dhathathreyan, B.U. Nair, Chem. Phys. Lett. 324 (2000) 43.
[16] H. Zhang, Y. Zhang, C. Li, J. Catal. 238 (2006) 369.
[17] B. Bahramian, V. Mirkhani, M. Moghadam, S. Tangestaninejad, Appl. Catal. A 301 (2006) 169.
[18] J. Wen, J. Zhao, X. Wang, J. Dong, T. You, J. Mol. Catal. A 245 (2006) 242.
[19] E. Konig, S. Herzog, J. Inorg. Nucl. Chem. 32 (1970) 585.
[20] K.A. Biedermann, J.R. Landolph, Cancer Res. 50 (1990) 7835.
[21] R.A. Anderson, Regul. Toxicol. Pharmacol. 26 (1997) S25.
[22] W. Mertz, J. Nutr. 123 (1993) 626.
[23] K. Govindaraju, T. Ramasami, D. Ramaswamy, J. Inorg. Biochem. 35 (1989) 127.
[24] K. Govindaraju, T. Ramasami, D. Ramaswamy, J. Inorg. Biochem. 35 (1989) 137.
[25] E.G. Samsel, K. Srinivasan, J.K. Kochi, J. Am. Chem. Soc. 107 (1985) 7606.
[26] E.M. McGarrigle, D.M. Murphy, D.G. Gilheany, Tetrahedron: Asymmetry 15 (2004) 1343.
[27] N.J. Kerrigan, H. Muller-Bunz, D.G. Gilheany, J. Mol. Catal. A 227 (2005) 163.
[28] Z.K. Li, L. Liang, L. Yang, H. Chen, X.G. Zhou, J. Mol. Catal. A 235 (2005) 108.
[29] W. Adam, F.G. Gelacha, C.R. Saha-Möller, V.R. Stegmann, J. Org. Chem. 65 (2000) 1915.
[30] M. Bandini, P.G. Cozzi, A. Umani-Ronchi, Angew. Chem., Int. Ed. 39 (2000) 2327.
[31] M. Bandini, P.G. Cozzi, A. Umani-Ronchi, Tetrahedron 57 (2001) 835.
[32] S.E. Schaus, J. Branalt, E.N. Jacobsen, J. Org. Chem. 63 (1998) 403.
[33] M. Malinowska, P. Kwiatkowski, J. Jurczak, Tetrahedron Lett. 45 (2004) 7693.
[34] R. Vijayalakshmi, M. Kanthimathi, V. Subramanian, B.U. Nair, Biochim. Biophys. Acta 1475 (2000) 157.
[35] V.G. Vaidyanathan, T. Weyhermuller, B.U. Nair, J. Subramanian, J. Inorg. Biochem. 99 (2005) 2248.
[36] R. Rajaram, B.U. Nair, T. Ramasami, Biochem. Biophys. Res. Commun. 210 (1995) 434.
[37] R.L. Paddock, S.T. Nguyen, J. Am. Chem. Soc. 123 (2001) 11498.
[38] A.P. de A. Marques, E.R. Dockal, F.C. Skrobot, I.L.V. Rosa, Inorg. Chem. Commun. (in press).
[39] A.C. Barbosa, M.Sc. Thesis, Universidade Federal de São Carlos, Brazil, 2004.
[40] O. Signorini, E.R. Dockal, G. Castellano, G. Oliva, Polyhedron 15 (1995) 245.

[41] S. Yamada, K. Iwasaki, Bull. Chem. Soc. Jpn. 42 (1969) 1463.
[42] "Peak Fit v.4.0 Documentation", AISN Software Inc., San Rafael, CA, 1995, pp. 8-7–8-9.
[43] "Peak Fit v.4.0 Documentation", AISN Software Inc., San Rafael, CA, 1995, p. B-1.
[44] J.E. Huheey, E.A. Keiter, R.L. Keiter, Inorganic Chemistry Principles of Structure and Reactivity, 4th ed., HaperCollins College Publishers, New York, 1993, p. 465.
[45] K. Ueno, A.E. Martel, J. Phys. Chem. 60 (1956) 1270.
[46] J.A. Faniran, K.S. Patel, J.C. Bailar Jr., J. Inorg. Nucl. Chem. 36 (1974) 1547.
[47] H.H. Freedman, J. Am. Chem. Soc. 83 (1961) 2900.
[48] A. Vogt, S. Wolowiec, R.L. Prasas, A. Gupta, J. Skarzeviski, Polyhedron 17 (1998) 1231.
[49] J.R. Zamian, E.R. Dockal, Transition Met. Chem. 21 (1996) 370.
[50] G.A. Kohawole, K.S. Patel, J. Chem. Soc., Dalton Trans. (1981) 1241.
[51] P. Gluvchinsky, G.M. Mocler, Spectrochim. Acta A 32 (1976) 1615.
[52] F.A. Bottino, P. Finocchiaro, E. Libertini, J. Coord. Chem. 16 (1988) 341.
[53] P. Gluvchinsky, G.M. Mocler, E. Sinn, Spectrochim. Acta A 33 (1977) 1073.
[54] X. Wang, X.M. Zang, H.X. Lin, Polyhedron 14 (1993) 293.
[55] G.C. Percy, J. Thornton, J. Inorg. Nucl. Chem. 35 (1973) 35, 2319.
[56] M. Gullotti, A. Pasini, P. Fantucci, R. Ugo, R.D. Gillard, Gazz. Chim. Ital. 102 (1972) 855.
[57] B.N. Ghose, R.A. Bako, Acta Chim. Hung. 124 (1987) 459.
[58] R.C. Felicio, E.T.G. Cavalheiro, E.R. Dockal, Polyhedron 20 (2001) 261.
[59] C. Condorelli, I. Fragala', S. Giuffrida, A. Cassol, Z. Anorg. Allg. Chem. 412 (1975) 251.
[60] N.M.D. Brown, D.C. Nonhebel, Tetrahedron 24 (1968) 5655.
[61] R.M. Silverstein, G.C. Bassler, T.C. Morril, Spectrometric Identification of Organic Compounds, 5th ed., Wiley, New York, 1991, pp. 183–184.
[62] K.S. Murray, J. Chem. Soc., Dalton Trans. (1975) 1538.
[63] R.M. Silverstein, G.C. Bassler, T.C. Morril, Spectrometric Identification of Organic Compounds, 5th ed., Wiley, New York, 1991, pp. 110–111.
[64] B. Bosnich, J. Am. Chem. Soc. 90 (1968) 627.
[65] S.M. Grawford, Spectrochim. Acta 19 (1963) 255.
[66] L. Dubicki, M.A. Hitchman, P. Day, Inorg. Chem. 9 (1970) 188.
[67] J.E. Huheey, E.A. Keiter, R.L. Keiter, Inorganic Chemistry Principles of Structure and Reactivity, 4th ed., HaperCollins College Publishers, New York, 1993, pp. 442–449.
[68] A.B.P. Lever, Inorganic Electronic Spectroscopy, 2nd ed., Elsevier, Amsterdam, 1984, pp. 161–162.
[69] M.K. Kumar, S. Prabhakar, M.R. Kumar, T.J. Reddy, S. Premsingh, S. Rajagopal, M. Vairamani, Rapid Commun. Mass Spectrom. 18 (2004) 1103.
[70] V. Katta, S.K. Choudhury, B.T. Chait, J. Am. Chem. Soc. 112 (1990) 5348.

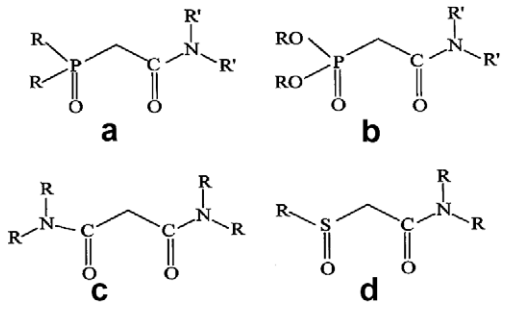


Fig. 1. Different bi-functional ligands: (a) CMPO; (b) CMP; (c) malanonamide and (d) CMSO.

[28a] and $[UO_2(DBM)_2 \cdot 2H_2O]$ [28b] (DBM = $C_6H_5COCHCOC_6H_5$) were prepared according to the reported methods. FTIR spectra were recorded on a JASCO-610 spectrometer and the samples were mounted as nujol mulls. The ^1H NMR spectra were recorder on Brucker AC-300 or 500 MHz spectrometers and the peaks were calibrated with respect to an internal $CHCl_3$ peak. The Analytical Chemistry Division of Bhabha Atomic Research Center, Mumbai, performed the elemental analysis.

2.1. Synthesis of $[UO_2(DBM)_2C_6H_5CH_2SOCH_2CONHC_6H_5]$ (1)

To a solution of $[UO_2(DBM)_2 \cdot 2H_2O]$ (300 mg, 0.408 mmol) in chloroform, $C_6H_5CH_2SOCH_2CONHC_6H_5$ was added (111.6 mg, 0.408 mmol) and refluxed for 5 h. The solution was filtered, layered with dodecane and allowed to evaporate slowly overnight. The orange colored product obtained was filtered, washed with hexane and dried. Yield: 370 mg (91.5%). Elemental *Anal.* Calc. (%) for $[UO_2(DBM)_2C_6H_5CH_2SOCH_2CONHC_6H_5]$; $C_{45}H_{37}O_8SNU$: C, 54.6: H, 3.7; N, 1.4. Found: C, 54.4; H, 3.8; N, 1.2%. IR (KBr, ν cm^{-1}): 3350 (NH), 1674 (CO of CMSO), 1590 (CO of DBM), 1007 (SO), 904 (O=U=O); ^1H NMR ($CDCl_3$, δ ppm): 3.58 (d, 14 Hz, 1H, OS–CH_2–CO), 4.08 (d, 14 Hz, 1H, OS–CH_2–CO), 4.66 (br, 2H, –CH_2–SO–), 7.09–8.43 (m, 33H, C_6H_5 + CH + NH).

2.2. Synthesis of $[UO_2(DBM)_2C_6H_5SOCH_2CON^iPr_2]$ (2)

This was prepared similar to **1** by taking $UO_2(DBM)_2 \cdot 2H_2O$] and $C_6H_5SOCH_2CON^iPr_2$in a 1:1 ratio and the final orange colored product was recrystallized from a $CHCl_3$/iso-octane mixture as an orange colored powder. Yield: 91%. Elemental *Anal.* Calc. (%) for $[UO_2(DBM)_2C_6H_5SOCH_2CON^iPr_2]$; $C_{44}H_{43}O_8SNU$: C, 53.7; H, 4.4; N, 1.4. Found: C, 54.0; H, 4.1; N, 1.0%. IR (KBr, ν cm^{-1}): 1640 (CO of CMSO), 1590 (CO of DBM), 990 (SO), 906 (O=U=O); ^1H NMR ($CDCl_3$, δ ppm): 0.87 (d, 6 Hz, 3H, CH_3), 1.26 (d, 6 Hz, 3H, CH_3), 1.67 (m, 6H, CH_3), 3.48 (m, 2H, CH), 4.29 (d, 14 Hz, 1H, OS–CH_2–CO), 4.87 (d, 14 Hz, 1H, OS–CH_2–CO), 7.23 (s, CH, 2H, DBM), 7.43–8.48 (br, m, 25H, C_6H_5).

2.3. Synthesis of $[\{UO_2(DBM)_2\}_2C_6H_5CH_2SOCH_2CONHC_6H_5]$ (3)

This was prepared by taking 2 equiv. of $[UO_2(DBM)_2 \cdot 2H_2O]$ (300 mg, 0.408 mmol) and 1 equiv. of $C_6H_5CH_2SOCH_2CONHC_6H_5$ (55.8 mg, 0.204 mmol). The final orange colored product was recrystallized from $CHCl_3$/iso-octane as a red-orange crystalline solid. Yield: 315 mg (90.4%). Elemental *Anal.* Calc. (%) for $[\{UO_2(DBM)_2\}_2C_6H_5CH_2SOCH_2CONHC_6H_5]$; $C_{75}H_{59}O_{14}SNU_2$: C, 52.7; H, 3.5; N, 0.8. Found: C, 52.4; H, 3.7; N, 0.9%. IR (KBr, ν cm^{-1}): 3255 (NH), 1638 (CO of CMSO), 1590 (CO of DBM), 999 (SO), 914 (O=U=O); ^1H NMR ($CDCl_3$, δ ppm): 3.81 (d, 12 Hz, 1H, OS–CH_2–CO), 4.31 (d, 12 Hz, 1H, OS–CH_2–CO), 4.64 (br, 2H, –CH_2–SO), 6.98–8.42 (m, 55H, C_6H_5 + CH + NH).

2.4. Synthesis of $[\{UO_2(DBM)_2\}_2C_6H_5SOCH_2CON^iPr_2]$ (4)

This was prepared similarly to **3** by taking 2 equiv. of $[UO_2(DBM)_2 \cdot 2H_2O]$ and 1 equiv. of $C_6H_5SOCH_2CON^iPr_2$, and the final product was recrystallized from a $CHCl_3$/iso-octane mixture as an orange colored powder. Yield: 87%. Elemental *Anal.* Calc. (%) for $[\{UO_2(DBM)_2\}_2C_6H_5SOCH_2CON^iPr_2]$; $C_{74}H_{65}O_{14}SNU_2$: C, 52.2; H, 3.8; N, 0.8. Found: C, 52.0; H, 4.0; N, 0.7%. IR (KBr, ν cm^{-1}): 1600 (CO of CMSO), 1590 (CO of DBM), 990 (SO), 905 (O=U=O); ^1H NMR ($CDCl_3$, δ ppm): 1.07 (d, 6 Hz, 3H, CH_3), 1.27 (d, 6 Hz, 3H, CH_3), 1.92 (m, 6H, CH_3), 3.55 (m, 2H, CH), 4.61 (d, 13 Hz, 1H, OS–CH_2–CO), 5.02 (d, 12 Hz, 1H, OS–CH_2–CO), 7.20 (s, 4H, CH, DBM) 7.5–8.41 (br, m, 45H, C_6H_5).

2.5. Solvent extraction studies

Distribution studies were performed by using a pre-equilibrated solution of HTTA (thenoyl trifluoroacetone), CMSO ($C_6H_5SOCH_2CONBu_2$) and a HTTA + CMSO mixture in toluene (pre-equilibrated with 1 M HNO_3) with the required aqueous phase (0.02 M HNO_3 + 0.1 M $NaNO_3$) spiked with a ^{233}U tracer in a thermostated water bath for 1 h at 25 ± 0.1 °C. Assays of organic and aqueous phases were done in duplicate by alpha counting using a dioxane based liquid scintillator. The distribution ratio (D) is defined as the ratio of the concentration of uranium in the organic phase to that of the aqueous phase.

2.6. X-ray diffraction studies of 3

The X-ray diffraction data for compound **3** were collected on a Siemens SMART CCD diffractometer fitted with graphite monochromated Mo Kα radiation (λ = 0.71073 Å) at 297(2)°. Data collection, indexing and initial cell refinement were handled using SMART software [33]. Frame integration and final cell refinement were carried out using SAINT software [34]. The SADABS software

Table 1
Crystal and Structural refinement details for compound **3**

Empirical formula	$C_{77}H_{64}NClO_{15}SU_2$
Formula weight	1786. 86
Crystal system	triclinic
Space group	$P\bar{1}$ (no 2)
Unit cell dimensions	
a (Å)	13.6064(7)
b (Å)	13.8588(7)
c (Å)	20.4243(10)
α (°)	87.830(1)
β (°)	79.498(1)
γ (°)	79.399(1)
Volume (Å^3)	3722.2(3)
Z (formula unit)	2
Calculated density (g/cm^3)	1.594
2θ Range for data collection (°)	2.34–28.28
Reflections collected/unique	23 800/17 541
Data/restraints/parameters	17 541/0/754
Goodness-of-fit on F^2	0.997
Final R indices [$I > 2\sigma(I)$]	0.0485
R indices (all data)	0.1141
Largest difference in peak and hole (e Å^3)	1.466 and −1.125

$w = 1/[\sigma_2(F_o^2) + (0.0513P)^2 + 5.3717P]$; $P = (F_o^2 + 2F_c^2)/3$ for **3**.

[35] package was used to perform the absorption corrections. The structures were solved by direct methods, completed by subsequent difference Fourier syntheses and refined by full-matrix least-squares procedures on F^2 using SHELXTL [36] version 5.1. The non-hydrogen atoms were refined anisotropically. The hydrogen atoms were refined with geometrical constraints with ideal bond lengths and angles, and were treated as riding atoms. All computations were carried out on a PC using the SHELXTL-PC program package. Selected crystallographic and refinement details are given in Table 1.

3. Results and discussion

3.1. Complexation study of $C_6H_5CH_2SOCH_2CONHC_6H_5$ and $C_6H_5SOCH_2CON^iPr_2$ with uranyl bis(β-diketonate) (1:1 compounds)

The reaction of $C_6H_5CH_2SOCH_2CONHC_6H_5$ or $C_6H_5SOCH_2CON^iPr_2$ with uranyl bis(β-diketonate) in a 1:1 ratio yielded **1** or **2**. IR spectra of the compounds show that the ligand is bonded only through the sulfoxo oxygen atom to the uranyl group ($\Delta\nu_{co}$ is close to zero, $\Delta\nu_{co} = \nu_{\text{free ligand}} - \Delta\nu_{\text{complex}}$, see Supplementary material) and acts as a monodentate ligand. The observed frequency differences for the sulfoxo groups ($\Delta\nu_{SO} = 11\ cm^{-1}$ and 48 cm^{-1} for **1** and **2** respectively) agree well with the supposition that the sulfoxo group is bonded to the uranyl group directly [28,37,38] in the reported compounds. ^{1}H NMR spectra of **1** and **2** also support the IR spectral observations by showing downfield shifts (ca $\Delta\delta = 0.45$ ppm for $C_6H_5CH_2$ of **1** and 0.27–0.35 and 0.59–0.84 ppm for $SOCH_2CO$ of **1** and **2** respectively, $\Delta\delta = \delta_{\text{free ligand}} - \delta_{\text{complex}}$) for the CH_2 protons adjacent to the sulfoxo group. We could not get suitable crystals for **1** and **2** to confirm our spectroscopic observations.

3.2. Complexation study of $C_6H_5CH_2SOCH_2CONHC_6H_5$ and $C_6H_5SOCH_2CON^iPr_2$ with uranyl bis(β-diketonate) (1:2 compounds)

The 1:2 reaction of $C_6H_5CH_2SOCH_2CONHC_6H_5$ or $C_6H_5SOCH_2CON^iPr_2$ with uranyl bis(β-diketonate) yielded **3** or **4**. IR spectra of the compounds show that the CMSO ligand is bonded through both the sulfoxo and carbamoyl oxygen atoms to the uranyl group. The observed frequency differences for the sulfoxo ($\Delta\nu_{SO} = 19\ cm^{-1}$ for **3** and 48 cm^{-1} for **4**) [28,37,38] and carbamoyl ($\Delta\nu_{CO} = 36\ cm^{-1}$ for **3** and 42 cm^{-1} for **4**) [14–28] groups agree well with the supposition that the sulfoxo and carbamoyl groups are bonded to the uranyl group directly in the reported compounds. The ^{1}H NMR spectra of **3** and **4** also support the coordination of both the sulfoxo and carbamoyl oxygen atoms to the uranyl group by showing downfield shifts for the CH_2 protons adjacent to the donor groups SO and CO ($C_6H_5CH_2SO$ and $SOCH_2CO$). It is interesting to note that the coordination chemical shifts ($\Delta\delta = \delta_{\text{free ligand}} - \delta_{\text{compound}}$) for the CH_2 protons of the $C_6H_5CH_2SO$ group in **1** and **3** are almost same (0.45 and 0.43 ppm respectively) and those of the $SOCH_2CO$ group are different (0.27–0.35 and 0.50–0.58 ppm respectively, see Supplementary material). The compounds **2** and **4** (0.59–0.84 and 0.91–1.01 ppm respectively for **2** and **4**) also show similar results for the $SOCH_2CO$ protons. The structure for compound **3** was determined by single crystal X-ray diffraction methods and shows a bridging bidentate mode of bonding for the CMSO ligand.

3.3. Molecular structure of 3

The molecular structure of **3** is given in Fig. 2 (there is a solvent molecule in the crystal lattice which is not shown in the figure for clarity) and selected interatomic bond distances and angles are given in Table 2. The structure shows that the CMSO ligand $C_6H_5CH_2SOCH_2CONHC_6H_5$ is bonded through both sulfoxo and carbamoyl oxygen atoms to two different uranyl bis(β-dibenzoyl methanate) units and acts as a bridging bidentate ligand. The observed uranium to sulfoxo oxygen distance [U–O(S), 2.402(5) Å] is slightly longer compared to those observed in $[UO_2(DBM)_2PhCH_2SOCH_3]$ (2.375(6) Å) [39] and $[UO_2(NO_3)_2(^iPrO)_2POCH_2SO(p\text{-}MeC_6H_4)]$ (2.36(2) Å) [20] and shorter compared to those observed in $[UO_2(NO_3)_2C_6H_5SOCH_2CONBu_2]$ (2.442(9) Å) [28] and $[UO_2(DBM)_2PhSOPh]$ (2.427(6) Å) [40]. The U–O (amide) distance (2.492(5) Å) is longer in magnitude compared to those observed in $[UO_2(NO_3)_2Ph(EtO)POCH_2CONEt_2]$ (2.426(8) Å), $[UO_2(NO_3)_2Ph_2POCH_2CONEt_2]$ (2.404(5) Å) [17], $[UO_2(NO_3)_2{}^iPr_2NCOCH_2CON^iPr_2]$ (2.41(2) Å) [27] and $[UO_2(NO_3)_2C_6H_5SOCH_2CONBu_2]$ (2.408(9) Å) [28] and comparable with

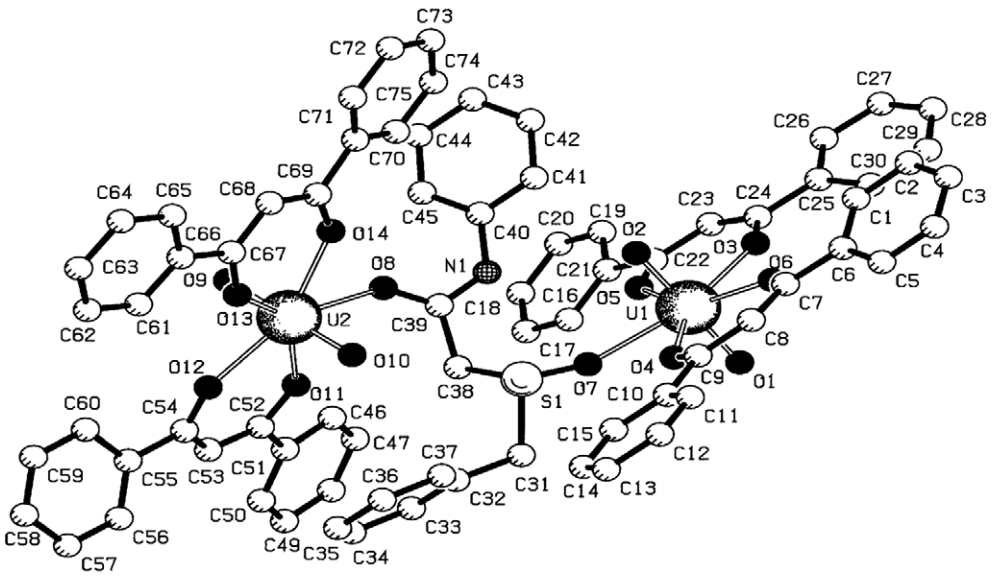


Fig. 2. Molecular structure of $[\{UO_2(DBM)_2\}_2C_6H_5CH_2SOCH_2CONHC_6H_5]$.

Table 2
Selected interatomic bond distances (Å) and angles (°) for **3**

U1–O1	1.783(5)	U1–O2	1.766(5)	U1–O3	2.296(5)
U1–O4	2.368(5)	U1–O5	2.398(5)	U1–O6	2.336(5)
U1–O7	2.402(5)	U2–O8	2.492(5)	U2–O9	1.774(6)
U2–O10	1.778(6)	U2–O11	2.350(6)	U2–O12	2.324(6)
U2–O13	2.340(6)	U2–O14	2.325(5)		
O1–U1–O2	178.1(2)		O3–U1–O4		71.25(18)
O4–U1–O7	74.57(17)		O7–U1–O5		70.23(16)
O5–U1–O6	69.12(17)		O6–U1–O3		75.00(18)
O9–U2–O10	178.4(3)		O11–U2–O12		70.6(2)
O12–U2–O13	74.3(2)		O13–U2–O14		71.0(2)
O14–U2–O8	71.8(2)		O8–U2–O11		72.5(2)

those observed in $[\{UO_2(DBM)_2\}_2C_6H_5NHCOCH_2CONHC_6H_5]$ (2.495(7) Å) [41]. The average bond distances for U–O (β-diketonate) [2.349(5) Å for U1 and 2.334(6) Å for U2] [39–41] and U=O (uranyl) [1.774(5) Å for U1 and 1.776(6) Å for U2] [14–28,39–41] are normal. The whole molecule is stabilized in the solid state by various intra [N1–H1···O5, 3.084(7) Å, 155.67°; N1–H1···O7, 3.175(8) Å, 126.78°] and inter [C11–H11···O10, 3.374(10) Å, 154.26°; C59–H59···O9, 3.501(10) Å, 169.38°; C73–H73···O2, 3.386(10) Å, 143.91°] molecular hydrogen bonding interactions to give a polymeric arrangement in the solid state.

3.4. Extraction studies on U(VI) with HTTA and $C_6H_5SOCH_2CONBu_2$

Extraction studies for the uranyl ion in the tracer level by using a mixture of HTTA (thenoyl trifluoroacetone) and CMSO ($C_6H_5SOCH_2CONBu_2$) were carried out to explore the possibility of separation from nitric acid medium. The distribution ratio data for the uranyl ion from nitric acid medium with various concentrations of CMSO at a constant HTTA concentration of 0.1 F is shown in Fig. 3. This shows clearly that CMSO or HTTA alone did not show any appreciable extraction for the uranyl ion (D_U for 0.1 F HTTA is 0.062 and for 0.01 F CMSO is negligible) under the conditions studied. However, it shows an appreciable extraction when a mixture was employed ($D_U = 3.2$ when a mixture of 0.1 F HTTA + 0.01 F CMSO was used).

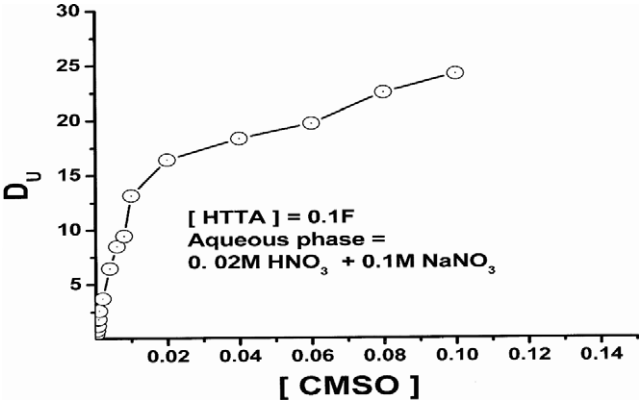


Fig. 3. Variation of D_U with [CMSO] at constant [HTTA].

In order to establish the nature of the species extracted during the solvent extraction process, the distribution ratios were measured as a function of CMSO and HTTA at constant HTTA and CMSO respectively in the linear region of the curve. The plots of $\log D_U$ versus log[HTTA] at constant [CMSO] and $\log D_U$ versus log[CMSO] at constant [HTTA] are given in Figs. 4 and 5 respectively (see Supplementary material). These plots show that the slopes of the straight lines obtained were found to be closer to **2** and **1** respectively for HTTA and CMSO. These results suggest that the species extracted under the conditions studied has the composition $[UO_2(TTA)_2 \cdot CMSO]$ in the

organic phase, which is in agreement with the reported studies [42,43].

4. Conclusions

Complexation studies of CMSO with uranyl bis(β-diketonate) show that it acts as a monodentate ligand in 1:1 compounds and bonds through the sulfoxo oxygen atom to the uranyl group. It shows further that CMSO acts as a bridging bidentate ligand in 1:2 compounds and bonds through both the sulfoxo and carbamoyl oxygen atoms to two different uranyl bis(β-diketonate) units. Extraction studies show that there is an enhancement in the extraction of the uranyl ion from nitric acid medium when a mixture of CMSO and HTTA are used.

Acknowledgements

We wish to thank the Head, Analytical Chemistry Division, BARC for carbon, hydrogen and nitrogen analysis, the Head, National NMR facilities, TIFR, Mumbai for NMR spectra and the Head, Fuel Chemistry Division, BARC for his support. H.K.F would like to thank the Malaysian Government and Universiti Sains Malaysia for research grant R&D No. 305/pfizik/610961. A.U. thanks the Universiti Sains Malaysia for a visiting Post-Doctoral Fellowship.

Appendix A. Supplementary material

CCDC 205003 contains the supplementary crystallographic data for this paper. These data can be obtained free of charge via htpp://www.ccdc.cam.ac.uk/conts/retrieving.html, or from the Cambridge Crystallographic Data Centre, 12 Union Road, Cambridge CB2 1EZ, UK; fax: (+44) 1223-336-033; or e-mail: deposit@ccdc.cam.ac.uk. Supplementary data associated with this article can be found, in the online version, at doi:10.1016/j.poly.2006.11.019.

References

[1] L.R. Morss, N.M. Edelstein, J. Fuger, J.J. Katz (Eds.), The Chemistry of the Actinide and Transactinide Elements, Springer, Netherlands, 2006.
[2] C.J. Burns, M.P. Neu, H. Boukhalfa, K.E. Gutowski, N.J. Bridges, R.D. Rogers, in: J.A. McCleverty, T.J. Meyer, G.F.R. Parkin (Eds.), Comprehensive Coordination Chemistry II, vol. 3, Elsevier, Oxford, 2004, p. 189.
[3] M. Ephritikhine, J. Chem. Soc., Dalton Trans. (2006) 2501.
[4] J.N. Mathur, M.S. Murali, K.L. Nash, Solvent Extr. Ion Exch. 19 (2001) 357.
[5] G.R. Choppin, A. Morgenstern, J. Radioanal. Nucl. Chem. 243 (2000) 45.
[6] K.L. Nash, G.R. Choppin, Sep. Sci. Technol. 32 (1997) 255.
[7] (a) C. Musikas, Inorg. Chim. Acta 140 (1987) 197;
(b) C. Cuillerdier, C. Musikas, P. Hoel, L. Nigond, X. Vitart, Sep. Sci. Technol. 26 (1991) 1229.
[8] E.P. Horwitz, H. Diamond, A. Martin, Solvent Extr. Ion Exch. 5 (1987) 447.
[9] W.W. Schulz, E.P. Horwitz, Sep. Sci. Technol. 23 (1988) 1191.
[10] (a) C. Musikas, Inorg. Chim. Acta 140 (1987) 197;
(b) C. Cullerdier, C. Musikas, P. Hoel, in: L. Cecille, M. Cesarci, L. Pietrelli (Eds.), New Separation Technique for Radioactive Waste and Other Specific Applications, Elsevier Applied Science, Oxford, 1991, p. 41.
[11] L. Nigond, C. Musikas, C. Cuillerdier, Solvent Extr. Ion Exch. 12 (1994) 297.
[12] L. Nigond, C. Musikas, C. Cuillerdier, Solvent Extr. Ion Exch. 12 (1994) 261.
[13] L. Nigond, N. Condamines, P.Y. Cordier, J. Livet, C. Madic, C. Cuillerdier, C. Musikas, Sep. Sci. Technol. 30 (1995) 2075.
[14] S.M. Bowen, E.N. Duesler, R.T. Paine, Inorg. Chem. 21 (1982) 261.
[15] S.M. Bowen, E.N. Duesler, R.T. Paine, Inorg. Chim. Acta 61 (1982) 55.
[16] S.M. Bowen, E.N. Duesler, R.T. Paine, Inorg. Chem. 22 (1983) 286.
[17] L.J. Caudle, E.N. Duesler, R.T. Paine, Inorg. Chim. Acta 110 (1985) 91.
[18] D.J. McCabe, A.A. Russell, S. Karthikeyan, R.T. Paine, R.R. Ryan, B.F. Smith, Inorg. Chem. 26 (1987) 1230.
[19] S. Karthikeyan, R.T. Paine, R.R. Ryan, Inorg. Chim. Acta 144 (1988) 135.
[20] D.T. Cromer, R.R. Ryan, S. Karthikeyan, R.T. Paine, Inorg. Chim. Acta 172 (1990) 165.
[21] P. Byers, M.G.B. Drew, M.J. Hudson, N.S. Isaacs, C. Madic, Polyhedron 13 (1994) 349.
[22] G.Y.S. Chan, M.G.B. Drew, M.J. Hudson, P.B. Iveson, J.O. Liljenzin, M. Skalberg, L. Spjuth, C. Madic, J. Chem. Soc., Dalton Trans. (1997) 649.
[23] P. Thuery, M. Nierlich, M.C. Charbonnel, C.D. Auwer, J.P. Dognon, Polyhedron 18 (1999) 3599.
[24] P.B. Iveson, M.G.B. Drew, M.J. Hudson, C. Madic, J. Chem. Soc., Dalton Trans. (1999) 3605.
[25] B.M. Rapko, B.K. McNamara, R.D. Rogers, G.J. Lumetta, B.P. Hay, Inorg. Chem. 38 (1999) 4585.
[26] C.D. Auwer, M.C. Charbonnel, M.G.B. Drew, M. Grigoriev, M.J. Hudson, P.B. Iveson, C. Madic, M. Nierlich, M.T. Presson, R. Revel, M.L. Russell, P. Thuery, Inorg. Chem. 39 (2000) 1487.
[27] G.J. Lumetta, B.K. McNamara, B.M. Rapko, R.L. Sell, R.D. Rogers, G. Broker, J.E. Hutchison, Inorg. Chim. Acta 309 (2000) 103.
[28] (a) S. Kannan, K.V. Chetty, V. Venugopal, M.G.B. Drew, J. Chem Soc., Dalton Trans. (2004) 3604;
(b) K.M. Abubacker, N.S.K. Prasad, J. Inorg. Nucl. Chem. 16 (1961) 296.
[29] S.R. Mohanthy, A.S. Reddy, J. Inorg. Nucl. Chem. 37 (1975) 1791.
[30] A.S. Reddy, V.V. Ramakrishna, S.K. Patil, Radiochem. Radioanal. Lett. 28 (1977) 445.
[31] C. Musikas, Sep. Sci. Technol. 23 (1988) 1211.
[32] N. Condamines, C. Musikas, Solvent Extr. Ion Exch. 10 (1992) 69.
[33] SMART, Siemens Analytical X-ray System, Madison, Wisconsin, USA, 1996.
[34] SAINT, Siemens Analytical X-ray System, Madison, Wisconsin, USA, 1996.
[35] G.M. Sheldrick, SADABS, University of Gottingen, Germany, 1996.
[36] SHELXTL Version 5.1, Software reference Manual, Brucker Analytical X-ray Systems, Madison, Wisconsin, USA, 1997.
[37] P.J. Alvey, K.W. Bagnall, O.V. Lopez, D. Brown, J. Chem. Soc., Dalton Trans. (1975) 1277.
[38] U. Casellato, P.A. Vigato, M. Vidali, Coord. Chem. Rev. 36 (1981) 183.
[39] S. Kannan, V. Venugopal, M.R.A. Pillai, P.A. Dreoge, C.L. Barnes, Polyhedron 15 (1996) 97.
[40] S. Kannan, S. Shanmugasundara Raj, H.K. Fun, Acta Crystallogr., Sect. C 56 (2000) E545.
[41] S. Kannan, G. Ferguson, Inorg. Chem. 36 (1997) 1724.
[42] S.K. Patil, V. Bhandiwad, M. Kusumakumari, R. Swarup, J. Inorg. Nucl. Chem. 43 (1981) 1647.
[43] M.S. Subramanian, S.A. Pai, J. Inorg. Nucl. Chem. 32 (1970) 6377.

Table 1
Crystal data and structure refinement for compounds **4**, **5** and **6**

Compound	**4**	**5**	**6**
Empirical formula	$C_{20}H_{15}FN_4O_2Pd$	$C_{20}H_{15}ClN_4O_2Pd$	$C_{22}H_{20}N_4O_2Pd$
Formula weight	468.76	485.21	478.82
Temperature (K)	170(2)	293(2)	170(2)
Space group	$P2_1/n$	$P2_1/c$	$C2/c$
a (Å)	23.6192(15)	11.777(2)	15.7152(11)
b (Å)	7.3320(5)	21.096(4)	13.2781(9)
c (Å)	40.194(3)	22.791(4)	10.0203(7)
β (°)	90.706(1)	103.345(3)	114.556(1)
Volume (Å^3)	6960.2(8)	5509.4(17)	1901.8(2)
Z	16	12	4
D_{calc} (Mg/m^3)	1.789	1.755	1.672
Absorption coefficient (mm^{-1})	1.102	1.181	1.003
Crystal size (mm)	$0.15 \times 0.10 \times 0.08$	$0.20 \times 0.05 \times 0.05$	$0.30 \times 0.15 \times 0.15$
Reflections collected	37520	30455	5265
Independent reflections (R_{int})	13566 (0.0530)	10805 (0.0664)	1868 (0.0226)
Data/restraints/parameters	13566/0/1017	10805/0/773	1868/0/134
Goodness-of-fit on F^2	1.042	1.021	1.082
Final R indices [$I > 2\sigma(I)$]	$R_1 = 0.0498$, $wR_2 = 0.1157$	$R_1 = 0.0500$, $wR_2 = 0.0975$	$R_1 = 0.0244$, $wR_2 = 0.0618$
R indices (all data)	$R_1 = 0.0871$, $wR_2 = 0.1277$	$R_1 = 0.1005$, $wR_2 = 0.1112$	$R_1 = 0.0266$, $wR_2 = 0.062$
Largest difference in peak and hole (e Å^{-3})	1.158 and −0.521	1.199 and −0.544	0.324 and −0.549

rigid and N4-tetradentate ligand, shows unprecedented reactivity towards Suzuki–Miyaura cross-coupling reactions under mild conditions, whilst N4-type saturated Pd complexes have never been used for C–C coupling reactions.

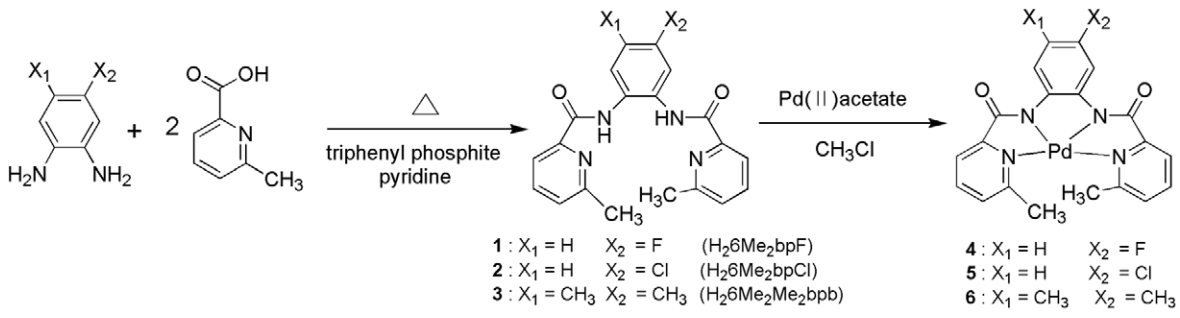
2. Experimental

2.1. General

Elemental analysis for carbon, nitrogen and hydrogen was carried out using an EA1108 (Carlo Erba Instrument, Italy) in the Organic Chemistry Research Center of Sogang University, Korea. Product analyses for the Suzuki–Miyaura cross-coupling reaction were performed on either a Hewlett–Packard 5890 II Plus gas chromatograph interfaced with Hewlett–Packard Model 5989B mass spectrometer or a Donam Systems 6200 gas chromatograph equipped with a FID detector using a 30-m capillary column (Hewlett–Packard, HP-1, HP-5 and Ultra 2). Diamines, 6-methyl-2-picolinic acid, and triphenylphosphite were purchased from Aldrich and were used as received.

2.2. Syntheses of ligands *1*, *2* and *3* and of complexes *4*, *5* and *6*

Ligands **1** ($6Me_2bpF$) and **2** ($6Me_2bpCl$) were prepared by the reactions of the appropriate diamines (10 mmol) with 6-methyl-2-picolinic acid (20 mmol) in pyridine in the presence of triphenylphosphite (20 mmol), according to the literature method [5]. For **1**, ^{1}H NMR ($CDCl_3$, 300 MHz) δ: 2.42 (s, 3H, CH_3), 2.62 (s, 3H, CH_3), 6.88–8.22 (m, 9H, aromatic-H), 10.08 (s, 1H, N–H), 10.58 (s, 1H, N–H). IR (KBr): ν(N–H) 3299 and ν(C=O) 1686 cm^{-1}. *Anal.* Calc. for $C_{20}H_{17}FN_4O_2$ (364.36): C, 65.92; H, 4.71; N, 15.38. Found: C, 66.03; H, 4.55; N, 15.12%. For **2**, ^{1}H NMR ($CDCl_3$, 300 MHz) δ: 2.46 (s, 6H, $2CH_3$), 6.32–8.11 (m, 8H, aromatic-H), 10.34 (s, 2H, 2N–H). IR (KBr): ν(N–H) 3274 and ν(C=O) 1688 cm^{-1}. *Anal.* Calc. for $C_{20}H_{17}ClN_4O_2$ (380.83): C, 63.07; H, 4.51; N, 14.72. Found: C, 63.25; H, 4.32; N, 14.73%. Ligand **3** ($6Me_2Me_2bpb$) was obtained as in the previous study [5]. Complexes **4**–**6** were obtained from the reaction of each ligand (0.5 mmol) with palladium(II) acetate (0.11g, 0.5 mmol) in CH_3Cl (20 mL) in good yields. Crystals of



Scheme 1. Syntheses of the ligands and their Pd complexes.

the complexes **4**–**6** were grown by slowly evaporating their solutions in CH_3CN/ether. For **4** (Pd(6Me$_2$bpF)), ^{1}H NMR (DMSO-d_6, 300 MHz) δ: 2.52 (s, 6H, 2CH_3), 6.71–8.18 (m, 9H, aromatic-H). IR (KBr): ν(C=O) 1630 cm^{-1}. *Anal*. Calc. for $C_{22}H_{20}N_4O_2Pd$ (478.82): C, 55.18; H, 4.22; N, 11.70. Found: C, 54.98; H, 4.00; N, 11.91%. For **5** (Pd(6Me$_2$bpCl)), IR (KBr): ν(C=O) 1635 cm^{-1}. *Anal*. Calc. for $C_{22}H_{20}N_4O_2Pd$ (478.82): C, 55.18; H, 4.22; N, 11.70. Found: C, 54.97; H, 4.20; N, 11.64%. For **6** (Pd(6Me$_2$Me$_2$bpb)), ^{1}H NMR (DMSO-d_6, 300 MHz) δ: 2.13 (s, 6H, 2CH_3), 7.64–8.13 (m, 8H, aromatic-H). IR (KBr): ν(C=O) 1623 cm^{-1}. *Anal*. Calc. for $C_{22}H_{20}N_4O_2Pd$ (478.82): C, 55.18; H, 4.22; N, 11.70. Found: C, 55.16; H, 4.33; N, 11.75%.

2.3. Catalytic activity of compound 5

Catalytic reaction conditions: Under air atmosphere, aryl halide (25 mM, 0.1 mmol) was added to a mixture of aryl boronic acid (50 mM, 0.2 mmol), catalyst **5** (0.1 mM, 4×10^{-4} mmol) and K_3PO_4 (50 mM, 0.2 mmol) in ethanol at room temperature. The reaction mixture was agitated in a shaking incubator at 50 °C. Conversions and yields were determined by GC/Mass analysis of 20 μL aliquots

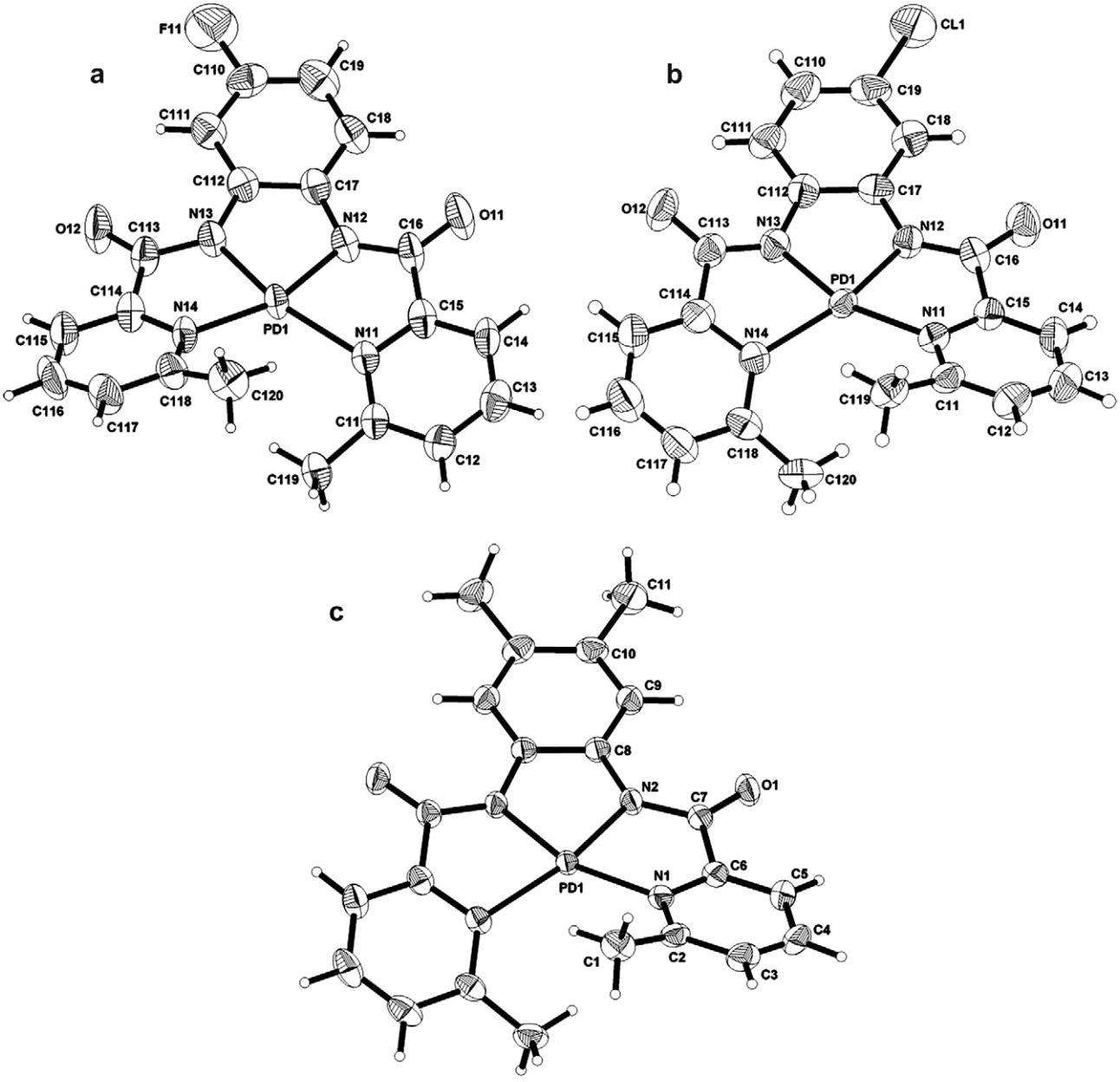


Fig. 1. Building blocks for compounds **4** (a), **5** (b) and **6** (c). Only one unit for each compound is present, but there are four independent Pd complex units in compound **4** and three independent Pd complex units in compound **5**.

Table 2
Selected bond lengths (Å) and angles (°) for compound **4**

Pd(1)–N(13)	1.941(4)
Pd(1)–N(12)	1.970(4)
Pd(1)–N(11)	2.098(4)
Pd(1)–N(14)	2.100(4)
Pd(2)–N(23)	1.946(4)
Pd(2)–N(22)	1.949(4)
Pd(2)–N(21)	2.082(4)
Pd(2)–N(24)	2.087(4)
Pd(3)–N(33)	1.952(4)
Pd(3)–N(32)	1.954(4)
Pd(3)–N(31)	2.097(4)
Pd(3)–N(34)	2.102(4)
Pd(4)–N(43)	1.952(4)
Pd(4)–N(42)	1.963(4)
Pd(4)–N(44)	2.105(4)
Pd(4)–N(41)	2.108(4)
N(13)–Pd(1)–N(12)	83.57(19)
N(13)–Pd(1)–N(11)	162.67(17)
N(12)–Pd(1)–N(11)	80.21(18)
N(13)–Pd(1)–N(14)	79.97(17)
N(12)–Pd(1)–N(14)	162.01(19)
N(11)–Pd(1)–N(14)	116.85(17)
N(23)–Pd(2)–N(22)	83.67(18)
N(23)–Pd(2)–N(21)	161.55(17)
N(22)–Pd(2)–N(21)	80.20(18)
N(23)–Pd(2)–N(24)	80.53(17)
N(22)–Pd(2)–N(24)	162.23(18)
N(21)–Pd(2)–N(24)	116.59(17)
N(33)–Pd(3)–N(32)	82.81(19)
N(33)–Pd(3)–N(31)	161.70(18)
N(32)–Pd(3)–N(31)	80.03(18)
N(33)–Pd(3)–N(34)	81.19(18)
N(32)–Pd(3)–N(34)	161.31(18)
N(31)–Pd(3)–N(34)	116.77(17)
N(43)–Pd(4)–N(42)	83.19(18)
N(43)–Pd(4)–N(44)	80.54(18)
N(42)–Pd(4)–N(44)	161.55(17)
N(43)–Pd(4)–N(41)	161.88(18)
N(42)–Pd(4)–N(41)	79.91(17)
N(44)–Pd(4)–N(41)	117.12(17)

Table 3
Selected bond lengths (Å) and angles (°) for compound **5**

Pd(1)–N(12)	1.944(4)
Pd(1)–N(13)	1.955(4)
Pd(1)–N(14)	2.084(4)
Pd(1)–N(11)	2.106(4)
Pd(2)–N(22)	1.950(4)
Pd(2)–N(23)	1.953(4)
Pd(2)–N(24)	2.090(4)
Pd(2)–N(21)	2.103(4)
Pd(3)–N(33)	1.944(4)
Pd(3)–N(32)	1.945(5)
Pd(3)–N(34)	2.089(5)
Pd(3)–N(31)	2.098(5)
N(12)–Pd(1)–N(13)	83.45(18)
N(12)–Pd(1)–N(14)	162.93(16)
N(13)–Pd(1)–N(14)	80.54(18)
N(12)–Pd(1)–N(11)	80.91(17)
N(13)–Pd(1)–N(11)	162.48(18)
N(14)–Pd(1)–N(11)	115.72(17)
N(22)–Pd(2)–N(23)	83.0(2)
N(22)–Pd(2)–N(24)	162.80(19)
N(23)–Pd(2)–N(24)	81.35(19)
N(22)–Pd(2)–N(21)	80.73(18)
N(23)–Pd(2)–N(21)	161.78(17)
N(24)–Pd(2)–N(21)	115.72(17)
N(33)–Pd(3)–N(32)	83.02(19)
N(33)–Pd(3)–N(34)	80.6(2)
N(32)–Pd(3)–N(34)	159.77(18)
N(33)–Pd(3)–N(31)	162.31(19)
N(32)–Pd(3)–N(31)	80.43(18)
N(34)–Pd(3)–N(31)	116.90(19)

Table 4
Selected bond lengths (Å) and angles (°) for compound **6**

Pd(1)–N(2)#1	1.9442(17)
Pd(1)–N(2)	1.9442(17)
Pd(1)–N(1)#1	2.0880(19)
Pd(1)–N(1)	2.0881(19)
N(2)#1–Pd(1)–N(2)	83.60(10)
N(2)#1–Pd(1)–N(1)#1	80.78(7)
N(2)–Pd(1)–N(1)#1	162.41(7)
N(2)#1–Pd(1)–N(1)	162.40(7)
N(2)–Pd(1)–N(1)	80.78(7)
N(1)#1–Pd(1)–N(1)	115.74(10)

Symmetry transformations used to generate equivalent atoms: #1 $-x$, y, $-z+3/2$.

withdrawn periodically from the reaction mixture, using an internal standard (dodecane). Control reactions carried out in the absence of the catalysts showed trace amounts of conversion of the reactant to the corresponding product in the same time period.

2.4. X-ray crystallography

The X-ray diffraction data for all three compounds were collected on a Bruker SMART APX diffractometer equipped with a monochromater in the Mo Kα ($\lambda = 0.71073$ Å) incident beam. Each crystal was mounted on a glass fiber. The CCD data were integrated and scaled using the Bruker-SAINT software package, and the structures were solved and refined using SHEXTL V6.12 [6]. All hydrogen atoms were placed in calculated positions. The crystallographic data for compounds **4**, **5** and **6** are listed in Table 1.

3. Results and discussion

Ligands **1**–**3** were prepared in good yields (40–60%) by the reactions between the appropriate diamines with 6-methyl-2-picolinic acid in pyridine (Scheme 1) according to the literature method [5] or its modified method. Complexes **4** and **5** were obtained from the reactions of ligands **1** and **2**, respectively, with palladium(II) acetate in CH_3Cl in excellent yields and their structures were determined by X-ray crystallography. We also prepared a Pd(II) complex **6** containing the non-halogen and dimethyl-substituted

ligand ($6Me_2Me_2bpb$) for comparison to compounds **4** and **5**.

All three compounds **4**, **5** and **6** contain simple building blocks that are four-coordinated Pd(II) complex units (Fig. 1). The four nitrogen atoms of the ligands coordinate to the Pd(II) ions to form mononuclear complex building blocks, and selected bond distances and angles are listed in Tables 2–4 for compounds **4**, **5** and **6**, respectively. The molecules are much distorted from square planar because of steric hindrance of the methyl groups of the pyridyl rings. The torsion angles of C11–N11–Pd1–N14, C21–N21–Pd2–N24, C31–N31–Pd3–N34 and C41–N41–Pd4–N44 for compound **4** are −17.5(5)°, −26.3(5)°, 34.0(6)° and −33.8(6)°, respectively. The torsion angles of C11–N11–Pd1–N14, C21–N21–Pd2–N24 and C31–N31–Pd3–N34 for compound **5** are −17.6(5)°, 24.2(5)° and −31.0(5)°, respectively. The torsion angle of C2–N1–Pd1–N1#1 for compound **6** is −23.57 (17)°. In compound **4**,

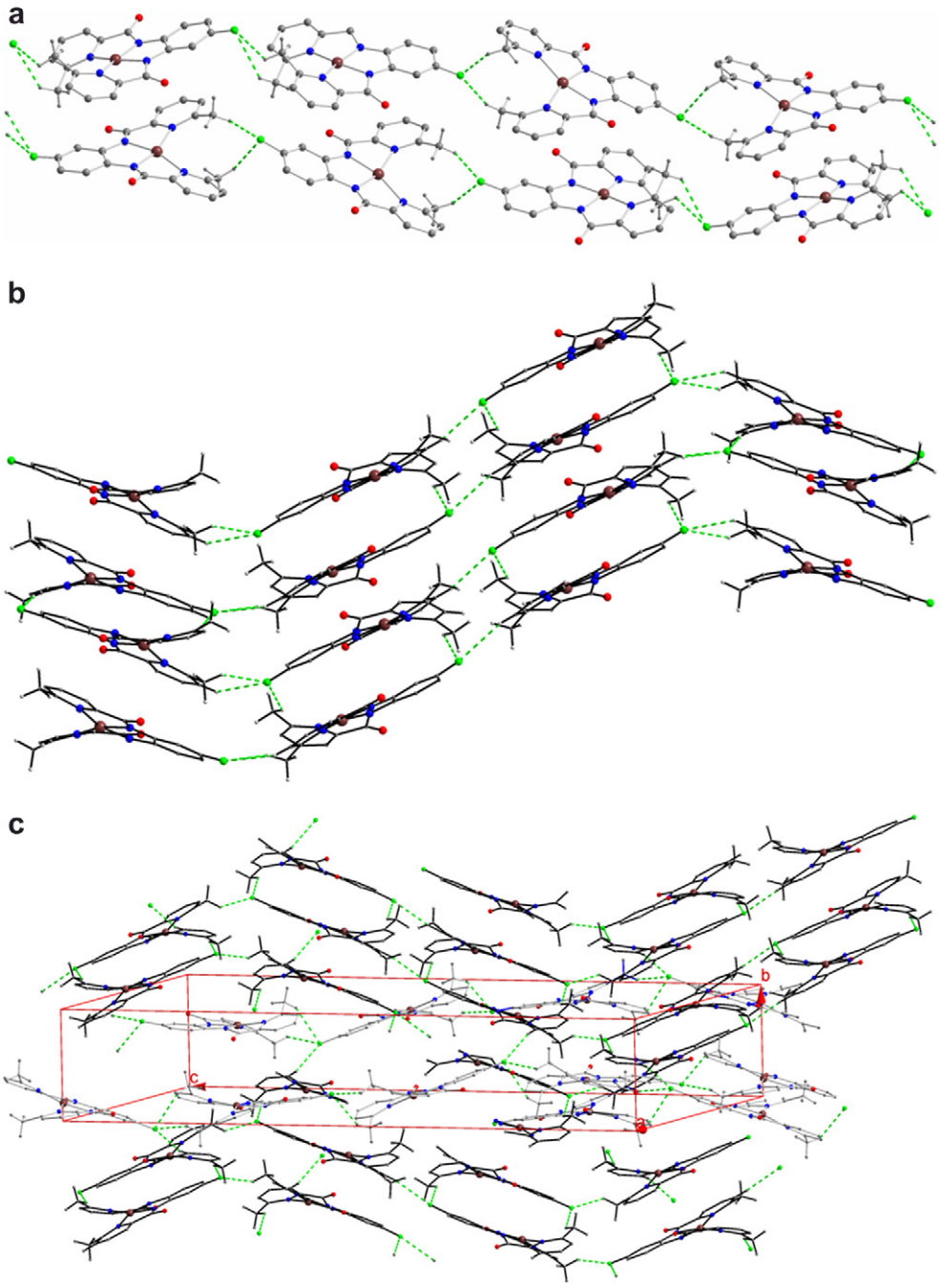


Fig. 2. (a) One-dimensional chains containing Pd1 and Pd2 complex units coloured in grey. (b) A two-dimensional sheet containing Pd3 and Pd4 complex units coloured in black. (c) Packing view of compound **4** showing C(methyl, pyridyl)–H···F–C interactions leading to a three-dimensional structure. H atoms not involved in intermolecular interactions have been omitted for clarity. Green dotted lines represent C(methyl)–H···F–C interactions. (For interpretation of the references to colour in this figure legend, the reader is referred to the web version of this article.)

Table 5
Hydrogen bond distances and angles for compounds **4**, **5** and **6**

	F···H (Å)	F···C (Å)	F···H–C (°)
*Compound **4***			
F21···H12C–C120(2 − *x*, 1 − *y*, 1 − *z*)	2.798(1)	3.221(1)	107.55(1)
F21···H11B–C119(2 − *x*, 1 − *y*, 1 − *z*)	2.646(1)	3.339(1)	129.46(1)
F11···H22C–C220(1.5 − *x*, −0.5 + *y*, 0.5 − *z*)	2.815(1)	3.317(1)	113.51(1)
F11···H21C–C219(1.5 − *x*, −0.5 + *y*, 0.5 − *z*)	2.817(1)	3.55(1)	133.81(1)
F41···H31A–C319	2.735(1)	3.432(1)	130.02(1)
F31···H41A–C419	2.772(1)	3.474(1)	130.55(1)
F31···H417–C417(pyridyl)(− *x*, 2 − *y*, −*z*)	2.855(1)	3.681(1)	148.58(1)
F41···H317–C317(pyridyl)(0.5 − *x*, −0.5 + *y*, 0.5 − *z*)	2.845(1)	3.566(1)	135.20(1)
F41···H32B–C320(0.5 − *x*, −0.5 + *y*, 0.5 − *z*)	2.507(1)	3.305(2)	140.54(1)
F11···H34–C34(pyridyl)(0.5 − *x*, 0.5 + *y*, 0.5 − *z*)	2.810(1)	3.684(1)	157.02(1)
	Cl/O···H (Å)	Cl/O···C (Å)	Cl/O···H–C (°)
*Compound **5***			
Cl1···H11C–C119(1 − *x*, 0.5 + *y*, 0.5 − *z*)	2.923(3)	3.752(3)	145.25(1)
Cl3···H21A–C219(1 − *x*, 1 − *y*, −*z*)	2.884(1)	3.595(1)	131.72(2)
Cl22···H31B–C319(*x*, −1 + y, *z*)	2.829(1)	3.719(1)	154.62(2)
O32···H32B–C320(1 − *x*, 2 − *y*, −*z*)	2.399(2)	3.209(2)	141.88(1)
	O···H (Å)	O···C (Å)	O···H–C (°)
*Compound **6***			
O1···H4–C4(pyridyl)(0.5 − *x*, −0.5 − *y*, 2.5 − *z*)	2.456(1)	3.235(1)	141.44(1)

there are four independent Pd(II) complex building units, and Pd(1) and Pd(2) complex units are connected altenatively by C(methyl)–H···F–C intermolecular interactions to form one-dimensional chains, and Pd(3) and Pd(4) complex units are also connected by C(methyl or pyridyl)–H···F–C intermolecular interactions to produce two-dimensional zigzag sheets. These Pd(1)–Pd(2) chains and Pd(3)–Pd(4) zigzag sheets are stacked by weak C–H···F–C interactions as shown in Fig. 2 (Tables 2 and 5). Only C(methyl)–H···F–C interactions contribute to the construction of compound **4** even though C=O acceptor groups coexist. In compound **5** there are three independent Pd(II) complex building units, and Pd(1) complex units are connected by weak C(methyl)–H···Cl–C interactions to form a one-dimensional chain. Pd(2) and Pd(3) complex units are connected by both C–H···Cl–C and C(methyl)–H···O=C interactions to form Pd(2)–Pd(3)–Pd(2)–Pd(3) tetranuclear rings. These Pd(1) chains and Pd(2)–Pd(3)–Pd(2)–Pd(3) rings are stacked alternatively as shown in Fig. 3 (Tables 3 and 5). The C–Cl sites do compete with C=O groups, and both C–H···Cl–C and C–H···O=C interactions do contribute to the crystal structure in compound **5**. In compound **6**, there is no halogen atom for intermolecular C–H···X–C interactions, and instead there is C(pyridyl)–H···O=C hydrogen bonding. The carbonyl oxygen atoms interact with a methyl hydrogen atom and with a pyridyl hydrogen atom of the neighbouring molecule to form a two-dimensional compound as shown in Fig. 4 (Tables 4 and 5).

Usually, it is well known that the ''organic fluorine'', C–F groups cannot form hydrogen bonds if there coexist O and N atom acceptors in the molecule, in spite of the high electronegativity of the F atom [4]. As we have shown above, however, C–H···F–C interactions contribute exclusively to the crystal structure of Pd(II) compound **4** in the presence of stronger C=O hydrogen acceptor groups, suggesting that the F atom does not act like ''organic fluorine'' in our Pd complex. In addition, in the case of compound **5**, both C–H···O=C and C–H···Cl–C interactions were observed in construction of the crystal structure. This phenomenon might stem from the similar electronegativity of Cl and O atoms. Pd(II) complex **6** containing a non-halogen and dimethyl-substituted ligand produces a two-dimensional network through intermolecular C–H···O interactions as one can expect. All these results indicate that weak intermolecuar C–H···X–C interactions can contribute to the crystal packing and stabilize the multi-dimensional structures, and the C–X (X = F, Cl) sites can form hydrogen bonds although stronger C=O acceptor groups coexist, in particular in these Pd(II) complexes.

3.1. Catalytic activity

The Suzuki–Miyaura cross-coupling reaction represents one of the most widely used processes for the synthesis of biaryls, that are versatile intermediates in organic synthesis and a recurring functional group in many natural products and bioactive compounds [7]. Therefore, considerable effort has been directed towards the development of efficient and selective methods for the synthesis of biaryls. Phosphine ligands are generally used to complex and activate the palladium species, and excellent results have been reported for the palladium-catalyzed Suzuki–Miyaura cross-coupling reaction [8]. However, certain phosphine-complexed palladium catalysts are air- and moisture-sensitive, and the reactions have to be handled under an inert atmosphere [9].

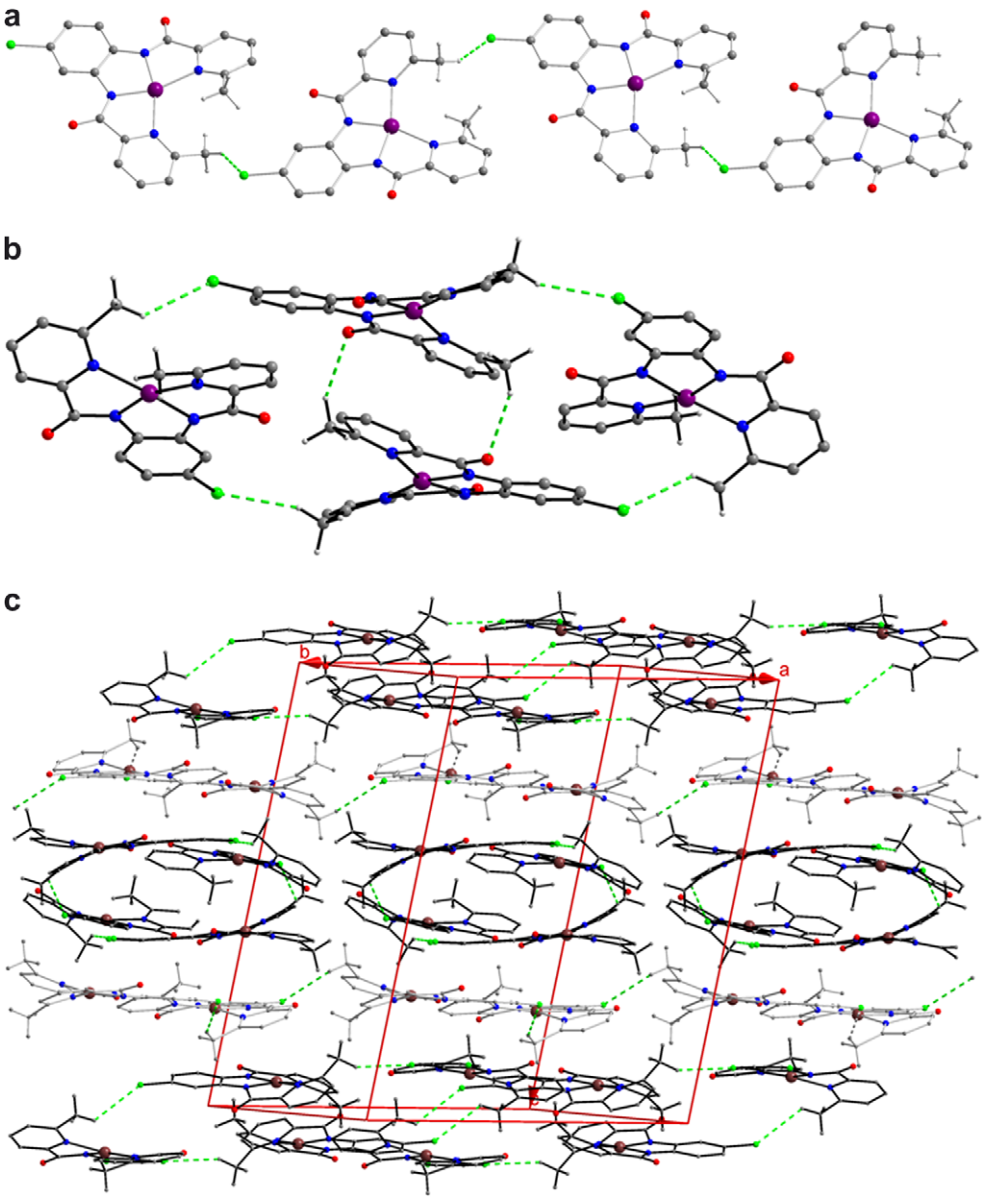
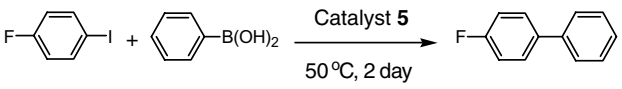


Fig. 3. (a) One-dimensional chain containing the Pd1 complex unit coloured in grey. (b) A tetranuclear ring containing Pd2 and Pd3 complex units coloured in black. (c) Packing diagram of compound **5** showing both C(methyl)–H···Cl–C and C(methyl)–H···O=C interactions. H atoms not involved in intermolecular interactions have been omitted for clarity. Green dotted lines represent C(methyl)–H···Cl–C and C(methyl)–H···O=C interactions. (For interpretation of the references to colour in this figure legend, the reader is referred to the web version of this article.)

Therefore, the development of phosphine-free palladium catalysts, which are insensitive to air, would be significant. Very recently, nitrogen ligands such as diazabutadiene, oxime, *N*-acylamidine and di-2-pyridylmethylamine have emerged as efficient partners for the Suzuki reaction in order to circumvent the problems associated with tertiary phosphine derivatives [10]. These facts inspired us to test complexes **4**–**6** in the Suzuki reaction under aerobic conditions in consideration of their beneficial air- and moisture-stability properties, whilst N4-type saturated Pd complexes have never been used for C–C coupling reactions.

We first tested the catalytic activity of all complexes in the Suzuki–Miyaura reaction between 4-fluoroiodobenzene (25 mM) and phenylboronic acid (50 mM) with K_3PO_4 (50 mM) as a base in EtOH (5 mL) *at low temperature* (50 °C; bath temperature) (Eq. (1)).



(1)

Complex **5** catalyzed almost quantitatively the C–C coupling reaction with a 2 day reaction time (entry 1 of Table 6), whilst **4** did not show any catalytic activity and **6** only catalyzed the C–C coupling reaction slowly (25 days).

Based on these results, next we tested the catalytic efficacy of catalyst **5** in the Suzuki reaction using 4-substituted aryl iodides as the substrate and 4-substituted aryl boronic

Table 6
5-catalyzed cross-coupling reactions of aryl iodides with arylboronic acids at 50 °C[a]

Entry	Ar-I	$ArB(OH)_2$	Time (days)	Conversion[b] (%)	Yield[c] (%)
1	4-flooroiodobenzene	phenylboronic acid	2	96.2	95.0
2	iodobenzene	phenylboronic acid	4	94.4	94.0
3	4-methyliodobenzene	phenylboronic acid	6	83.7	81.3
4	4-flooroidobenzene	4-flooroPhenylboronic acid	4	90.0	89.5
5	iodobenzene	4-flooroPhenylboronic acid	6	90.8	90.0
6	4-methyliodobenzene	4-flooroPhenylboronic acid	6	83.8	78.0
7	4-flooroiodobenzene	4-methylphenyiboronic acid	4	92.3	92.0
8	iodobenzene	4-methylphenyiboronic acid	4	90.3	85.0
9	4-methyliodobenzene	4-methylphenyiboronic acid	6	89.8	86.2

[a] Unless otherwise indicated, the reaction conditions were as follows: aryl iodide (25 mM, 0.1 mmol), aryl boronic acid (50 mM, 0.2 mmol), catalyst **5** (0.1 mM, 4×10^{-4} mmol) and K_3PO_4 (50 mM, 0.2 mmol) in ethanol at 50 °C. Control reactions carried out in the absence of the catalysts showed trace amounts of conversion of the reactant to the corresponding product in the same time period.
[b] Conversion was determined by GC using an internal standard (dodecane).
[c] Yield was determined by GC using an internal standard (dodecane).

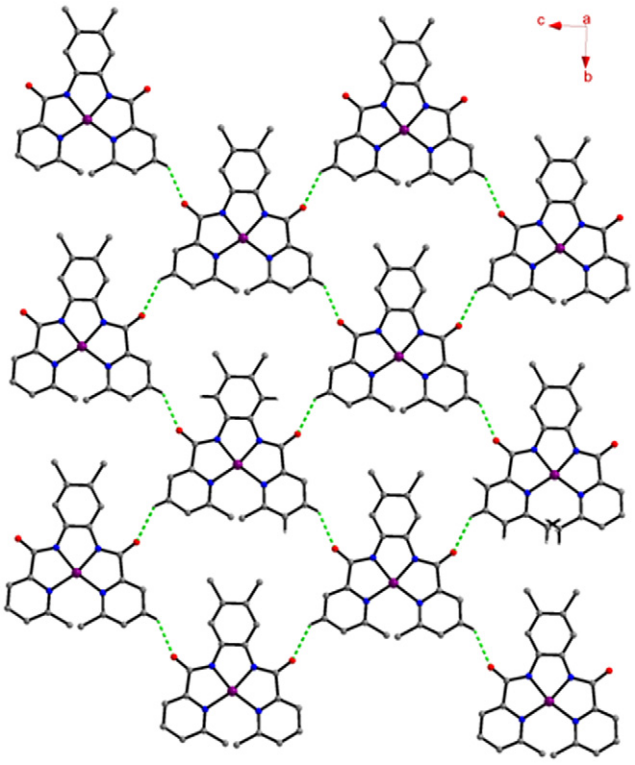


Fig. 4. Two-dimensional structure of compound **6** showing intermolecular C–H···O=C interactions. H atoms not involved in intermolecular interactions have been omitted for clarity. Green dotted lines represent C(pyridyl)–H···O=C interactions. (For interpretation of the references to colour in this figure legend, the reader is referred to the web version of this article.)

acids under aerobic conditions, and the coupling results are listed in Table 6. As illustrated in Table 6, various aryl iodides, including both electron-poor and -rich aryl iodides, were readily converted to the corresponding coupled products in excellent yields within 2–6 days. It is worth noting that this reaction was performed without the protection of inert gas. In particular, electron-poor 4-fluoroiodobenzene underwent the fastest C–C coupling reaction (entries 1, 4 and 7 of Table 6), whilst electron-rich 4-methyliodobenzene was the most slow to be converted to the corresponding biaryls (entries 3, 6 and 9 of Table 6). In addition, catalyst **5** was found to be thermally stable in subsequent catalytic runs, not sensitive to air or moisture, and easily accessible from inexpensive starting materials. Further detailed studies regarding the C–C coupling mechanism by new N4-type Pd systems,[2] as well as the influence of the steric and electronic factors of the ligands are ongoing.

4. Conclusion

In summary, we have reported the synthesis and characterization of new palladium polymeric compounds containing novel tetradentate ligands, 1,2-bis(6-methylpyridine-2-carboxamide)-4,5-substituted-benzene, and in the cases of the halogen-substituted compounds **4** and **5**, non-classical C(methyl or pyridyl)–H···X–C interactions play important roles for the construction of crystal structures in the presence of stronger C=O hydrogen acceptor groups in the molecule. In case of the non-halogen and methyl-substituted compound **6**, C(pyridyl)–H···O=C interactions can generate a two-dimensional structure. We have also reported that the novel catalyst **5** was used to carry out Suzuki coupling reactions with aryl iodides and aryl boronic acids *at low temperature* (50 °C), whilst **4** showed no catalytic activity and **6** only catalyzed the C–C coupling reaction slowly. This novel catalyst **5** is air- and moisture-stable, and the reaction can be readily conducted under aerobic conditions. In addition, the use of the catalyst **5** for the Suzuki–Miyaura cross-coupling

[2] At this stage, we do not know the exact reaction mechanism for the C–C coupling reaction. However, based on the olefin polymerization mechanism proposed with N4-type Zr complexes (J. Chem. Soc., Dalton Trans. (1997) 2487–2484), we assume that the 6-methylpyridyl moiety of catalyst **5** could dissociate to produce one or two labile sites during the catalytic reaction, and then the C–C coupling reaction may go through a reductive elimination step.

reaction represents an interesting alternative to existing catalytic systems based on the use of tertiary phosphine ligands. Moreover, this system shows unprecedented reactivity for a N4-type ligand system with regard to reactivity with the C–C coupling reaction. Furthermore, the fact that the catalyst can be synthesized from inexpensive and readily available starting materials using a straightforward procedure makes these complexes very promising catalysts.

Acknowledgements

Financial support from The SEOUL R & BD Program, the Korea Research Foundation (2002-070-C00053) and the Korean Science and Engineering Foundation (R01-2005-000-10490-0(2005) and ABRL R14-2003-014-01-001-0) is gratefully acknowledged.

Appendix A. Supplementary material

CCDC 623688, 623687 and 623689 contain the supplementary crystallographic data for **4**, **5** and **6**. These data can be obtained free of charge via http://www.ccdc.cam.ac.uk/conts/retrieving.html, or from the Cambridge Crystallographic Data Centre, 12 Union Road, Cambridge CB2 1EZ, UK; fax: (+44) 1223-336-033; or e-mail: deposit @ccdc.cam.ac.uk. Supplementary data associated with this article can be found, in the online version, at doi:10.1016/j.poly.2006.11.020.

References

[1] (a) X.J. Luan, Y.-Y. Wang, D.-S. Li, P. Liu, H.-M. Hu, Q.-Z. Shi, S.-M. Peng, Angew. Chem., Int. Ed. 44 (2005) 3864;
(b) B.-B. Ding, Y.-Q. Weng, Z.-W. Mao, C.-K. Lam, X.-M. Chen, B.-H. Ye, Inorg. Chem. 44 (2005) 8836;
(c) A. Angeloni, P.C. Crawford, A.G. Orpen, T.J. Podesta, B.J. Shore, Chem. Eur. J. 10 (2004) 3783;
(d) V. Balamurugan, M.S. Hundal, R. Mukherjee, Chem. Eur. J. 10 (2004) 1683;
(e) Y. Wang, J. Yu, Y. Li, Z. Shi, R. Xu, Chem. Eur. J. 9 (2003) 5048;
(f) D. Braga, F. Grepioni, G.R. Desiraju, Chem. Rev. 98 (1998) 1375.

[2] (a) C. Janaik, T.G. Scharmann, Polyhedron 22 (2003) 1123;
(b) L. Brammer, E.A. Bruton, P. Sherwood, Cryst. Growth Des. 1 (2001) 277;
(c) G.R. Desiraju, Acc. Chem. Res. 35 (2002) 565.

[3] (a) A.J. Mountford, D.L. Hughes, S.J. Lancaster, Chem. Commun. (2003) 2148;
(b) J.L. Alonso, S. Antolinez, S. Blanco, A. Lesarri, J.C. Lopez, W. Caminati, J. Am. Chem. Soc. 126 (2004) 3244;
(c) M.C.W. Chan, S.C.F. Kui, J.M. Cole, G.J. McIntyre, S. Matsui, N. Zhu, K.-H. Tam, Chem. Eur. J. 12 (2006) 2607;
(d) A. Abad, C. Agullo, A.C. Cunat, C. Vilanova, M. Carmen Ramirez de Arellano, Cryst. Growth Des. 6 (2006) 46.

[4] (a) V.R. Thalladi, H.-C. Weiss, D. Bläser, R. Boese, A. Nangia, G.R. Desiraju, J. Am. Chem. Soc. 120 (1998) 8702, and references therein;
(b) H. Lee, C.B. Knobler, M.F. Hawthorne, Chem. Commun. (2000) 2485;
(c) A.J. Mountford, S.J. Lancaster, S.J. Coles, P.N. Horton, D.L. Hughes, M.B. Hursthouse, M.E. Light, Inorg. Chem. 44 (2005) 5921;
(d) A.R. Choudhury, T.N. Guru Row, Cryst. Growth Des. 4 (2004) 47.

[5] (a) S.H. Nam, H. Kwak, Y.M. Lee, S.J. Hong, C. Kim, Y. Kim, Anal. Sci. 22 (2006) x37;
(b) D.H. Lee, J.Y. Lee, J.Y. Ryu, Y. Kim, C. Kim, I.-M. Lee, Bull. Korean Chem. Soc. 27 (2006) 1031.

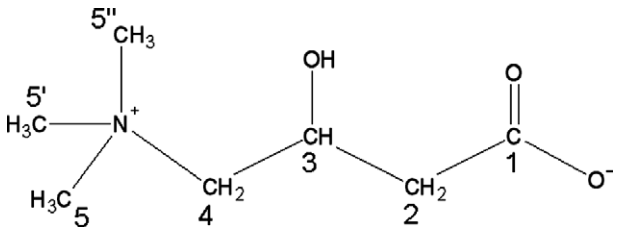
[6] G.M. Sheldrick, SHELXTL/PC. Version 6.12 for Windows XP, Bruker AXS Inc., Madison, WI, 2001.

[7] (a) A. Zapf, M. Beller, Chem. Commun. (2005) 431;
(b) G. Bringmann, C. Gunther, M. Ochse, O. Schupp, S. Tasler, in: W. Herz, H. Falk, G.W. Kirby, R. Moore (Eds.), Progress in the Chemistry of Organic Natural Products, 82, Springer, New York, 2001, p. 1.

[8] E.B. Tomothy, S.D. Walker, J.R. Martinelli, S.L. Buchwald, J. Am. Chem. Soc. 127 (2005) 4685.

[9] (a) Z. Xiong, N. Wang, M. Dai, A. Li, J. Chen, Z. Yang, Org. Lett. 6 (2004) 3337;
(b) L. Liu, Y. Zhang, Y. Wang, J. Org. Chem. 70 (2005) 6122.

[10] (a) D.A. Alonso, C. Najera, M.C. Pacheco, J. Org. Chem. 67 (2002) 5588;
(b) G.A. Grasa, A.C. Hiller, S.P. Nolan, Org. Lett. 3 (2001) 1077;
(c) J. Silberg, T. Schareina, R. Kempe, K. Wurst, M.R. Buchmeiser, J. Organomet. Chem. 622 (2001) 6;
(d) J.-H. Li, W.-J. Liu, Org. Lett. 6 (2004) 2809.



Scheme 1. Structure of L-carnitine zwitterion.

copper ions with biologically interesting ligands have been investigated in detail. Copper is involved in the activation and hydroxylation of various substrates via free radical reactions [31,32]. Copper(II) complexes with diverse drugs and their synergetic activity have been the subject of a large number of research studies [33–36]. We have recently reported the synthesis, the structure characterization and the biological activity of copper(II) complexes with coumarin and quinolone derivatives [37–39].

In a recent work, Chang et al. reported that oxidative stress elicited from copper accumulation, increases the amount of free fatty acids, thereby inducing mitochondrial dysfunction. L-carnitine treatment can inhibit this mitochondrial injury [40]. Therefore the investigation of copper and L-carnitine interaction is biologically important.

In the present study, two copper complexes with L-carnitine were isolated and characterized using several spectroscopic techniques. One of the complexes was also characterized using X-ray crystallography. To our knowledge this is the first example of crystal structure characterization of a metal complex containing L-carnitine.

2. Experimental

2.1. Materials and methods

All reagents were purchased from Aldrich without any further purification. Deuterated solvents for use in the NMR (D_2O and DMSO-d_6) were purchased from Merck. ESMS spectra were recorder on a Fisons Instruments VG BIO-Q quadrupole mass spectrometer, with the solution injected via a Rheodyne injector valve directly through the 10 μL loop in the OCP-V4.06 QUATT 4000 spectrometer. Nitrogen was the nebulizing and drying gas. Focus voltage was set to 10 V, the capillary voltage at 3.00 kV and HV Lens Voltage at 0.46 kV. 20–50 spectra combination was required for acceptable S/N ratio. Sample flow rate was 3 μL/min, with CH_3CN or CH_3OH used as mobile phase, while the electrostatic ion source operated at atmospheric pressure. ^1H and ^{13}C NMR spectra were recorded on a Varian UNITYplus operating at 300 MHz spectrometer in D_2O solution with TSP as internal standard and DMSO-d_6 using the solvent peak as an internal reference (2.50 ppm). Thermogravimetric and differential thermal analysis were carried out on a Mettler Toledo S R apparatus in N_2 atmosphere (temperature range: 40–1000 °C; heating rate: 20 °C/min). IR spectra were recorded in a KBr pellet on a Perkin-Elmer 880 IR spectrophotometer. High-frequency Raman spectra were recorded with a Perkin-Elmer GX Fourier transform spectrometer with a diode pumped Nd:YAG laser at 1064 nm as the excitation source. EPR spectra in solid state (298 and 40 K) or aqueous solution (298 and 11 K) were recorded on a Bruker ER-200D-SRC X-band spectrometer interfaced to a personal computer and equipped with an Oxford EPR 900 cryostat, an Anritsu MF76A frequency counter and a Bruker 035N NMR gaussmeter. UV–Vis spectra were recorded with 1-cm cuvette on a Hitachi U-2000 spectrophotometer. Elemental analysis (C, H, N) was carried out at the Organic Chemistry Laboratory of the National Technical University of Athens, Greece while Cu was determined by atomic absorption.

2.2. Synthesis

2.2.1. Synthesis of $[Cu_2(L\text{-carnitine})_2Cl_2(H_2O)_2]Cl_2$ (1)

L-Carnitine (0.16 g, 1 mmol) was dissolved in ethanol (20 ml) and was added to an ethanol (20 ml) solution of $CuCl_2 \cdot 2H_2O$ (0.18 g, 1 mmol), under stirring. After the mixing, a green product was precipitated. It was filtered off and dried over $CaCl_2$ (yield: 0.16 g, 45%). *Anal.* Calc. for $Cu_2C_{14}H_{34}N_2Cl_4O_8$: C, 26.92; H, 5.49; N, 4.49; Cu, 20.0. Found: C, 27.22; H, 5.88; N, 4.20; Cu, 19.6%. IR (KBr): 3418 (*v* O–H), 3021, 2955, 2918 (*v* C–H), 1619 (v_{as} COO^-), 1421 (v_{sym} COO^-), 561, 431 (Cu–O) cm^{-1}. ^1H NMR (300 MHz, D_2O, 25 °C): 1.29 (–CH_2–COO^-), 3.24 [$(CH_3)_3N^+$], 3.87 (–CH–OH) ppm. ^{13}C NMR (300 MHz, D_2O, 25 °C): 19.55 (C2), 56.62 (C5), 59.81 (C4), 81.73 (C3) ppm. UV–Vis (H_2O): $\lambda = 240$, 400, 790 nm ($\varepsilon = 30.7\ M^{-1}\ cm^{-1}$).

2.2.2. Synthesis of $[Cu_2(L\text{-carnitine})_4(H_2O)_2] \cdot (ClO_4)_4 \cdot H_2O \cdot CH_2Cl_2$ (2)

L-carnitine (0.31 g, 2 mmol) was added to an aqueous (10 ml) solution of $Cu(ClO_4)_2 \cdot 6H_2O$ (0.37 g, 1 mmol), under stirring and a blue-green solution was resulted. Slow evaporation of the solvent resulted a blue-green precipitate, which after dilution to a 10 ml acetonitrile/dichloromethane (1:1) solution and layering with 10 ml ether gave a small quantity of blue-green crystals, suitable for X-ray determination. *Anal.* Calc. for $Cu_2C_{29}H_{68}N_4Cl_6O_{31}$: C, 26.62; H, 5.24; N, 4.28. Found: C, 26.77; H, 5.38; N, 4.40%. IR (KBr): 3432 (*v* O–H), 3019, 2948, 2921 (*v* C–H), 1620 (v_{as} COO^-), 1420 (v_{sym} COO^-), 1148, 1096 (*v* Cl–O), 626 (Cu–O) cm^{-1}. ^1H NMR (300 MHz, DMSO, 25 °C): −51, −5, −2, 28 ppm.

2.3. X-ray crystallography

The complex **2** crystals were mounted in air at the temperature of 150 K. Diffraction measurements were made on a Bruker SMART diffractometer using graphite monochromated Mo Kα radiation. Unit cell dimensions were determined by the angular settings of 9352 reflections in

the range $3 < 2\theta < 28°$. The structure was solved by direct methods and refined in full-matrix least-squares procedure on F^2 with DIRDIF-96 [41]. Hydrogen atoms placed geometrically after each cycle and were not placed on the OH side-groups of the carnitine ligands or the ligated water molecules. The Me_3N^+ group of carnitine molecule #1 is disordered. The two sets of methyl positions were refined in the occupancy ratio 0.7:0.3. The part weight atoms were refined with a common overall isotropic displacement parameter. Similarity restraints were applied to the distances, angles and displacement parameters in the carnitine ligands. The Me_3N^+ groups were additionally restrained to have local 3-fold symmetry. The ClO_4^- anions were badly disordered, and these and the solvents of crystallisation (CH_2Cl_2 and H_2O) were treated by the SQUEEZE procedure.

3. Results and discussion

Complex **1** was prepared in ethanol by mixing equimolar amounts of L-carnitine and $CuCl_2 \cdot 2H_2O$, while complex **2** was prepared in aqueous solution by mixing L-carnitine and $Cu(ClO_4)_2 \cdot 6H_2O$ in a molar ratio of 2:1. The resulted precipitate was dissolved in an acetonitrile/dichloromethane solution which was layered with ether.

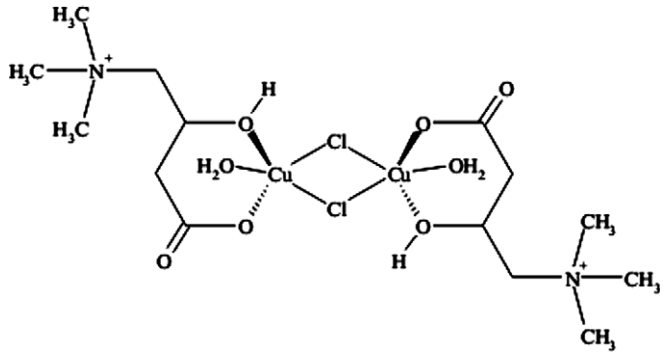
The proposed structure of complex **1** cation is presented in Scheme 2. The two metal ions are connected through two chloro-bridges. The ligand is coordinated with the carboxyl oxygen atom monodentately and the hydroxyl group of carbon atom 3, forming a six membered chelate ring. An analogue coordination mode of L-carnitine has been proposed for a zinc complex [28].

In the solid state IR spectrum of the complex, the replacement of the valence stretching carboxylic vibration $\nu(C{=}O)_{carb}$ of L-carnitine zwitterion at 1600 cm^{-1} by the asymmetric, $\nu(CO_2)_{asym}$, at 1619 cm^{-1} and the symmetric stretching ν(O–C–O) vibration, $\nu(CO_2)_{sym}$, at 1421 cm^{-1} as well as the Δ value of 198 cm^{-1} ($\Delta = \nu(CO_2)_{asym} - \nu(CO_2)_{sym}$) are indicative of the monodentate coordination mode of the carboxylato group. This is not a large Δ value for such coordination mode and probably the acetate oxygen is hydrogen bonded to water or a hydroxyl group of another ligand molecule, giving what may be regarded as a ''pseudo-bridging'' arrangement [42]. Peaks due to the C–H vibration of the methyl- and methylene-groups appear in the region 2900–3100 cm^{-1}. The Cu–O stretching frequencies are observed at 431 and 561 cm^{-1} [43]. It is noteworthy that no band in the region of 320–350 cm^{-1} appears, indicating the absence of a $Cu–Cl_{terminal}$ bond. The ν(Cu–Cl–Cu) band which corresponds to the bridging character of the Cu–Cl bond could not be observed as it appears at higher energies and out of the spectrometer scan limit. However, using Raman spectroscopy in the range of 10–3500 cm^{-1} a peak was observed at 166 cm^{-1} that can be connected to the chloro-bridge symmetric vibration.

The TG and DTG analysis curves of the complex were carried out in the temperature range of 40–1000 °C (Supplementary material). The first weight loss (8.6%) at the temperature range of 50–180 °C is attributed to the evaluation of the two coordinated water molecules and one probably to moisture (theor.: 8.6). The second major weight loss (52.2%) occurs between 180 and 390 °C and corresponds to the extraction of the two ligand molecules (theor.: 51.4%). The final residue (21.9%) at 1000 °C consists of the two remaining copper atoms (theor.: 20.2%) [31,44].

The solid state EPR spectrum of complex **1** (Fig. 1) did not give any signal at room temperature, while at lower temperature (40 K) comprised a broad weak signal with $g = 2.13$ with no hyperfine interactions even at 10 K and higher power. The absence of hyperfine structure in the powder spectra points to a significant inter-dimer interaction of the two copper(II) ions via the chloro-bridge.

The complex dissolved in water was also EPR silent at room temperature. At lower temperatures (11 K) the spectrum reveals two signals at $g \sim 2$, around 3100 G, and at $g \sim 4$, around 1500 G. The first one is an unsaturated signal without hyperfine interactions, which decreases upon increase of temperature following the Curie law (Fig. 2). The appearance of an additional very weak signal at lower field (near half-field) is characteristic of binuclear copper complexes [45] due to a singlet–triplet transition of



Scheme 2. The proposed structure of complex **1**.

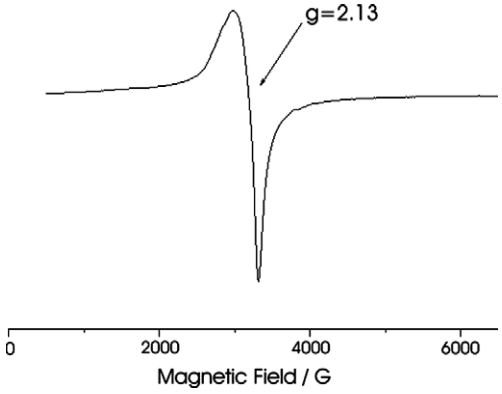


Fig. 1. EPR spectrum of complex **1** in solid state.

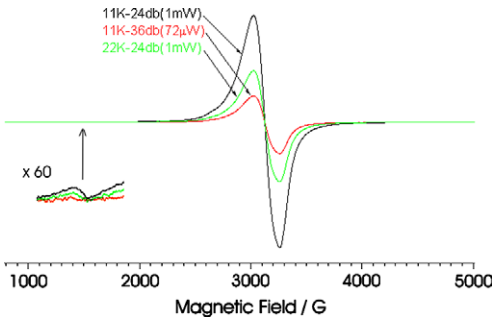


Fig. 2. EPR spectra of complex **1** in aqueous solution ($T = 11$ and 22 K) and different energy parameters. The appearance of a half-field transition is also presented (inset).

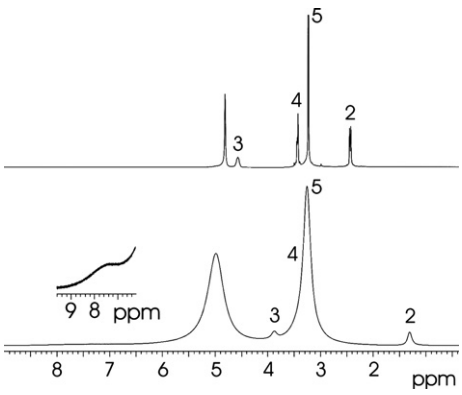


Fig. 3. ^{1}H NMR spectra of complex **1** (bottom) and L-carnitine (upper), in D_2O solution.

$\Delta M_s = 2$ (Fig. 2, inset) and implies that the binuclear complex is not totally dissociated in aqueous solution.

The NMR experiments confirmed the coordination mode of the ligand and therefore the proposed structure. The NMR data are presented in Table 1. The ^{1}H NMR spectrum of the complex in D_2O was compared to that of free L-carnitine (Fig. 3). The spectrum shows a weak paramagnetic effect that can happen after the degradation of even a small part of the complex to monomeric copper(II) complex (represented by a wide peak at 7.5 ppm). The H2 and H3 protons are expected to be the most affected since they are nearest to the Cu–O coordination points (Table 1). The two protons (H2) of the methylene group attached to the carboxylic group are shifted upfield ($\Delta\delta = 1.15$ ppm) as well as the H3 proton ($\Delta\delta = 0.7$ ppm). The H4 protons are less affected and overlapped in the spectrum by the methyl-group protons (H5) that are not shifted. The ^{13}C NMR spectrum of the complex and free L-carnitine were also obtained with analogous results for the carbon shifts where C1 and C3 are affected most, since they participate in the six-membered chelation ring.

In DMSO-d_6 solution, the ^{1}H NMR spectrum is paramagnetic with a characteristic broad peak at 18 ppm. This spectrum suggests that the dimeric complex has been degraded due to DMSO that can coordinate to copper(II) leading to dissociation of dimers.

The electronic spectrum of the complex has been recorded in aqueous solution. A shoulder at 240 nm is attributed to $\pi \rightarrow \pi^*$ transitions within the ligands, while at 300 nm to a ligand-to-metal charge transfer band corresponding to the $Cl \rightarrow Cu(II)$ transition [45]. The complex exhibits also a d–d transition weak and very broad band in the region 650–900 nm which is typical for a distorted square pyramidal geometry in an equilibrium towards a trigonal bipyramid [46,47].

The ESMS of complex **1** (cationic and anionic mode) was obtained in aqueous solution and the identified fragments are presented in Table 2. For both modes the parent ion could not be observed indicating that the complex was dissociated in the experimental conditions and therefore gave rise to low mass fragments with high relative abundance. In the cationic mode (Fig. 4), the peak of L-carn^{+} (m/z 162) is observed. The main fragment (m/z 145) is due to the loss of a hydroxyl group from L-carnitine. The fragment with many isotopes at m/z 267 is due to $[Cu_2Cl_2(H_2O)_2(OOH^-)]^+$, a hydroperoxo dimeric copper(II) complex without the ligand. The similarity of the theoretical and experimental isotopic allocation patterns is obvious for this fragment, which maintains the binuclear form of the complex. The hydroperoxo group is produced under the electrospray experimental conditions. From the spectrum the simultaneous release and degradation of the ligand are shown. The most of the observed fragments are the same with those referred in bibliography for the ESMS spectrum of L-carnitine in aqueous solution [48]. Fragments resulting from the degradation of L-carnitine are observed at m/z 118, 103, 85 and 60 due to glycine betaine, the loss of trimethyl-amine from L-carnitine, the sequential dehydrogenation and trimethyl-amine, respectively. In the anionic mode (Fig. 5), the main fragment appears at m/z 170 due to $[CuCl_3]^-$ and its theoretical pattern is schematized (Fig. 5, inset). The ESMS, under these

Table 1
^{1}H and ^{13}C NMR chemical shifts of L-carnitine and complex **1** in D_2O solution using TSP as internal standard

		Assignment				
		1 (–COO^-)	2 (–CH_2–COO^-)	3 (–CH–OH)	4 (–CH_2–N^+–)	5 ((CH_3)$_3$–N^+–)
L-Carnitine	^{1}H(ppm)		2.43–2.45	4.57	3.43–3.45	3.24
	^{13}C(ppm)	180.64	45.71	72.85	66.52	56.92
Copper complex	^{1}H(ppm)		1.29	3.87	overlapped	3.24
	^{13}C(ppm)	not shown	19.55	81.73	59.81	56.62

Table 2
ESMS fragments of complex **1** in the cationic and anionic mode (aqueous solution)

m/z (experimental)	Fragment	*m/z* (theoretical)	Relative abundance
Cationic mode			
267.1	$[Cu_2Cl_2(H_2O)_2(OOH^-)]^+$	267.1	42
186.2	$[Cu^{II}Cl(CH_3CH_2CH_2COOH)]^+$	186.0	41
162.3	$(CH_3)_3N^+–CH_2–CH(OH)–CH_2–COOH$	162.2	75
145.2	$[(CH_3)_3N–CH_2–CH(OH)–CH_2–COOH–OH]^+$	145.2	100
118.1	$(CH_3)_3N^+–CH_2–COOH$	118.2	18
102.4	$^+CH_2–CH(OH)–CH_2–COOH$	103.1	27
85.3	$^+CH_2–CH=CH–COOH$	85.1	3
60.4	$(CH_3)_3NH^+$	60.1	7
Anionic mode			
170.1	$[Cu^{II}Cl_3]^-$	169.9	100

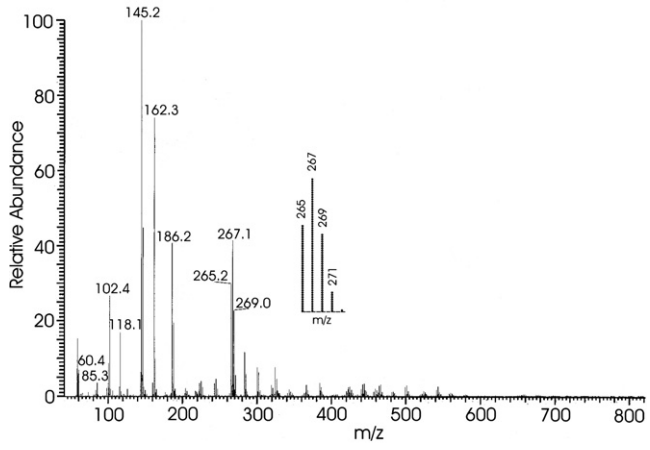


Fig. 4. ESMS spectrum of complex **1** in the cationic ES mode (inset: the theoretical pattern of $[Cu_2Cl_2(H_2O)_2(OOH^-)]^+$).

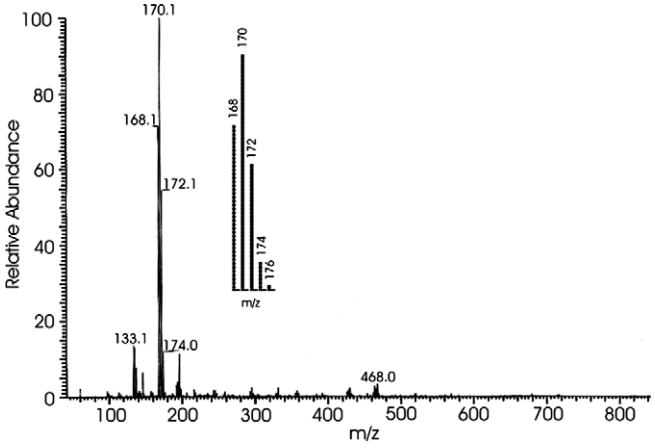


Fig. 5. ESMS spectrum of complex **1** in the anionic ES mode (inset: the theoretical pattern of $CuCl_3^-$).

experimental conditions and although it did not provide the parent complex ion, was indicative of the binuclear form with chloro-bridges from the fragment $[Cu_2Cl_2(H_2O)(OOH)]^+$. It was also informative of the $Cu_2Cl_2^{2+}$ core stability and the degradation path of the carnitine ligand.

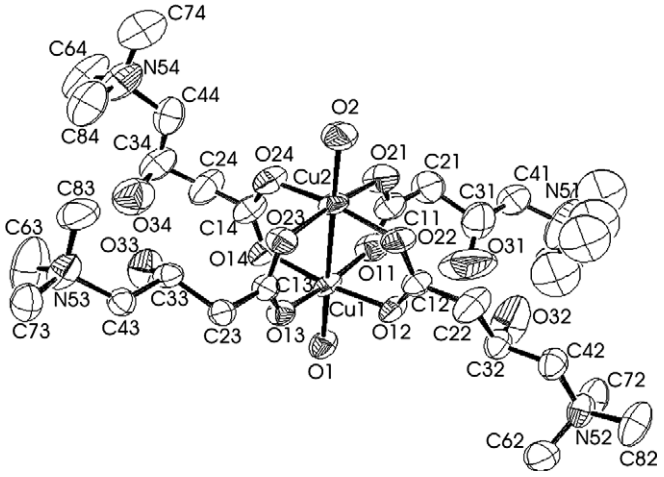


Fig. 6. The structure of complex **2** cation as it was identified from X-ray analysis showing the atomic labeling (50% thermal probability ellipsoids).

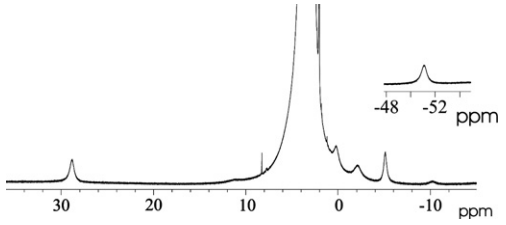


Fig. 7. ^1H NMR spectrum of complex **2** in DMSO-d_6 solution.

Efforts to obtain crystals of complex **1** had no satisfactory results using copper(II) chloride. When copper(II) perchlorate was used in aqueous solution, crystals were isolated and the X-ray analysis demonstrated the binuclear complex cation presented in Fig. 7. The small quantity of the crystals prevented further experiments as in complex **1** except for IR and NMR spectroscopy. The IR spectrum (Supplementary material) shows a broad band of medium intensity around 3700–3100 cm^{-1}, due to the symmetric and asymmetric O–H stretching vibrations. The stretching frequencies for C–H bonds in the aliphatic CH, CH_2 and CH_3 groups of the ligand are observed at 2900–3100 cm^{-1}, while bands attributed to aliphatic CH bending

Table 3
Crystallographic data summaries for complex **2**

Empirical formula	$Cu_2C_{29}H_{54}Cl_6N_4O_{31}$
Formula weight	1294.57
Crystal size	$0.20 \times 0.30 \times 0.80$
T (K)	150
Crystal system	monoclinic
Space group	$P2_1$
Unit cell dimensions	
a (Å)	13.0938(4)
b (Å)	15.3026(5)
c (Å)	13.5100(4)
α (°)	90
β (°)	94.949(2)
γ (°)	90
V (Å^3)	2696.90(14)
Z	2
D_{calc} (g/cm^3)	0.985
μ(Mo Kα) (mm^{-1})	1.178
F(000)	844
Reflections collected	14815
Independent reflections (R_{int})	14815 (0.032)
Goodness-of-fit (on F^2)	1.0235
R[a]	0.0626[c]
R_w[b]	0.0786[d]

[a] $R = \sum\|F_o| - |F_c\|/\sum|F_o|$.
[b] $R_w = [\sum w(|F_o|^2 - |F_c|^2)^2/\sum w(|F_o|^2)^2]^{1/2}$.
[c] For 8288 reflections with $F > 4\sigma(F)$.
[d] F^2 and all data.

are verified in the region of 990–920 cm^{-1}. The asymmetrical carboxylate C–O vibration for complex **2** appears at 1620 cm^{-1} with the symmetric one observed at 1472 cm^{-1}. Additional bands at 1096 and 626 cm^{-1} are characteristic of perchlorate anions. The ^{1}H NMR spectrum of the complex in DMSO-d_6 (Fig. 7) reveals strong paramagnetism since broad peaks are observed at +28, −2, −5 and −51 ppm, indicating that the dimer is dissociated to a mononuclear complex.

The crystallographic details of complex **2** blue-green crystal are presented in Table 3. The structure of complex **2** cation (Fig. 6) consists of dinuclear *paddle-wheel* units in which four carnitine ligands are bridging the two copper atoms in a *syn–syn* disposition (the hydrogen atoms have been omitted for clarity). The copper(II) ions are close enough with a Cu...Cu distance value of 2.5957(8) Å. Each ligand is connected to both metal ions via its carboxylate group making a bridge, while a water molecule occupies the axial position of each copper atom. Each copper atom lies in a square-planar pyramidal coordination with the four oxygen atoms in the basal plane and the water oxygen atom at the apex [Cu1–O1, 2.160(4) Å; Cu2–O2, 2.160(5) Å]. As expected, the axial bonds are the longest. Cu(1) lies 0.182 Å and Cu(2) lies 0.175 Å out of their respective least-squares basal planes towards O(1) and O(2), respectively. A number of *paddle-wheel* complexes have been reported in the literature. This structural type is associated with metal–metal interactions that vary from no interactions, weak or moderate spin-pairing in the copper(II) carboxylates, various orders of metal–metal bonding, to "super-short" metal–metal bonds. For Cu...Cu distances that have been reported, this distance in complex **2** is at the lower limit [49]. Some selected bond lengths and angles are listed in Table 4.

Table 4
Selected atomic distances (Å) and bond angles (°) for complex **2**

Cu1–O1	2.160(4)	Cu2–O2	2.160(5)
Cu1–O11	1.930(4)	Cu2–O21	1.948(4)
Cu1–O12	1.961(3)	Cu2–O22	1.963(4)
Cu1–O13	1.940(3)	Cu2–O23	1.943(3)
Cu1–O14	1.950(4)	Cu2–O24	1.908(2)
O1–Cu1–O11	91.73(18)	O21–Cu2–O22	89.9(2)
O1–Cu1–O12	95.89(15)	O2–Cu2–O23	92.59(17)
O11–Cu1–O12	89.79(19)	O21–Cu2–O23	169.96(19)
O1–Cu1–O13	99.04(16)	O22–Cu2–O24	169.36(17)
O11–Cu1–O13	169.23(18)	O2–Cu2–O24	96.5(2)

4. Conclusions

Two binuclear copper(II) complexes of L-carnitine were synthesized and characterized. The X-ray structural characterization of a L-carnitine metal complex is the first to be reported. The knowledge of L-carnitine's coordination mode with copper(II) as well as the spectroscopic study of the thermodynamic and kinetic stability in aqueous solution of these complexes are important for the biological activity of L-carnitine with copper(II) in mitochondria.

Acknowledgements

The project is co-financed within Op. Education by the ESF (European Social Fund) and National Resources (research program: HERAKLEITOS, EPEAEK II). The authors are grateful to Dr. L. Leondiadis, Asst. Prof. A. Moutsatsou, Prof. K. Viras and Ms. A. Maniatakou for their kind assistance.

Appendix A. Supplementary material

CCDC 609928 contains the supplementary crystallographic data for **2**. These data can be obtained free of charge via http://www.ccdc.cam.ac.uk/conts/retrieving.html, or from the Cambridge Crystallographic Data Centre, 12 Union Road, Cambridge CB2 1EZ, UK; fax: (+44) 1223-336-033; or e-mail: deposit@ccdc.cam.ac.uk. Supplementary data associated with this article can be found, in the online version, at doi:10.1016/j.poly.2006.11.010.

References

[1] R.R. Ramsay, R.D. Gandour, F.R. van der Leij, Biochim. Biophys. Acta 1546 (2001) 21.
[2] S. Harpaz, Aquaculture 249 (2005) 3.
[3] J. Arenas, J.C. Rubio, M.A. Martin, Y. Campos, Early Human Develop. 53 (1998) S43.
[4] P. Walter, A.O. Schffhauser, Ann. Nutr. Metab. 44 (2000) 75.
[5] H. Karlic, A. Lohninger, Nutrition 20 (2004) 709.
[6] M. Speich, A. Pineau, F. Ballereau, Clin. Chim. Acta 312 (2001) 1.

[7] J. Arenas, J.R. Ricoy, A.R. Encinas, P. Pola, S. D'Iddio, M. Zeviani, S. Didonato, M. Corsi, Muscle Nerve 14 (1991) 598.
[8] A. Dayanandan, P. Kumar, C. Panneerselvam, J. Nutr. Biochem. 12 (2001) 254.
[9] R.J. Thiel, S.W. Fowkes, Med. Hypotheses 62 (2004) 35.
[10] M. Seven, M. Cengiz, S. Tuzgen, M.Y. Iscan, Am. J. Hum. Biol. 13 (2001) 721.
[11] L.A. Calo, E. Pagnin, P.A. Davis, A. Semplicini, R. Nicolai, M. Calvani, A.C. Pessina, Int. J. Cardiol. 107 (2006) 54.
[12] M.A. Arsenian, Progr. Cardiovasc. Dis. 40 (1997) 265.
[13] S. Savitha, J. Tamilselvan, M. Anusuyadevi, C. Panneerselvam, Clin. Chim. Acta 355 (2005) 173.
[14] S. Moretti, E. Alesse, L. Di Marzio, F. Zazzeroni, B. Ruggeri, S. Marcellini, G. Famularo, S.M. Steinberg, A. Boschini, M.G. Cifone, C. De Simone, Blood 91 (1998) 3817.
[15] R. Bueno, M.A. de Sotomayor, C. Perez-Guerrero, L. Gomez-Amores, C.M. Vazquez, M.D. Herrera, Life Sci. 77 (2005) 2082.
[16] K. Carnajal, R. Moreno-Sanchez, Arch. Med. Res. 34 (2003) 89.
[17] J.M. Hurot, M. Cucherat, M. Haugh, D. Fouque, J. Am. Soc. Nephrol. 13 (2002) 708.
[18] Y. Matsumoto, I. Amano, S. Hirose, Y. Tsuruta, S. Hara, M. Murata, T. Imai, Blood Purif. 19 (2001) 24.
[19] U. Wenzel, A. Nickel, H. Daniel, J. Nutr. 135 (2005) 1510.
[20] C.S. Yeh, J.Y. Wang, T.L. Cheng, C.H. Juan, C.H. Wu, S.R. Lin, Cancer Lett. 233 (2006) 297.
[21] G. Peluso, R. Nicolai, E. Reda, P. Benatti, A. Barbarisi, M. Calvani, J. Cell. Physiol. 182 (2000) 339.
[22] B.J. Chang, M. Nishikawa, E. Sato, K. Utsumi, M. Inoue, Arch. Biochem. Biophys. 405 (2002) 55.
[23] A. Giancaterini, A. de Gaetano, G. Mingrone, D. Gniuli, E. Liverani, E. Capristo, A.V. Greco, Metabolism 149 (2000) 704.
[24] F. Giannessi, P. Pessotto, E. Tassoni, P. Chiodi, R. Conti, F. de Angelis, N. Dell'Uomo, R. Catini, R. Deias, M.O. Tinti, P. Carminati, A. Arduini, J. Med. Chem. 46 (2003) 303.
[25] G. Mingrone, Ann. N.Y. Acad. Sci. 1033 (2004) 99.
[26] J.M. Duran, M.J. Peral, M.L. Calonge, A.A. Ilundain, J. Membr. Biol. 185 (2002) 65.
[27] E. Mokhova, E. Arrigoni-Martelli, M. Bellei, V. Dedukhova, U. Muscatello, A. Starkov, V. Bobyleva, FEBS Lett. 289 (1991) 187.
[28] Y. Yoshikawa, E. Ueda, H. Sakurai, Y. Kojima, Chem. Pharm. Bull. 51 (2003) 230.
[29] A.K. Reznick, V.E. Kagen, R. Ransey, M. Tsuchiya, E.A. Serbinova, L. Packer, Arch. Biochem. Biophys. 296 (1992) 349.
[30] L. Packer, M. Valenza, E. Serbinova, P. Starkereed, K. Frost, V. Kagan, Arch. Biochem. Biophys. 288 (1991) 533.
[31] C.J. Feng, Q.H. Luo, Z.L. Wang, M.C. Shen, H.W. Wang, M.H. Zhao, J. Inorg. Biochem. 75 (1999) 1.
[32] L. Zhou, J.R.J. Sorenson, J. Inorg. Biochem. 72 (1998) 217.
[33] D.J. Hodgson, Prog. Inorg. Chem. 19 (1975) 173.
[34] M. Melnik, Coord. Chem. Rev. 42 (1982) 259.
[35] M. Kato, Y. Muto, Coord. Chem. Rev. 92 (1988) 45.
[36] J.E. Weder, C.T. Dillon, T.W. Hambley, B.J. Kennedy, P.A. Lay, J.R. Biffin, H.L. Regtop, N.M. Davies, Coord. Chem. Rev. 232 (2002) 95.
[37] E. Efthimiadou, Y. Sanakis, C. Raptopoulou, A. Karaliota, N. Katsaros, G. Psomas, Bioorg. & Med. Chem. Lett. 16 (2006) 3864.
[38] E. Efthimiadou, Y. Sanakis, M. Katsarou, C. Raptopoulou, A. Karaliota, N. Katsaros, G. Psomas, J. Inorg. Biochem. 100 (2006) 1378.
[39] A. Karaliota, O. Kretsi, C. Tzougraki, J. Inorg. Biochem. 84 (2001) 33.
[40] B.-J. Chang, M. Nishikawa, S. Nishiguchi, M. Inoue, Int. J. Cancer 113 (2005) 719.
[41] P.T. Beurskens, G. Beurskens, W.P. Bosman, R. de Gelder, S. Garcia Granda, R.O. Gould, R. Israel, J.M.M. Smits, University of Nijmegen, Toernooiveld 1, 6525 ED Nijmegen, The Netherlands, 1996.
[42] G.B. Deacon, R.J. Phillips, Coord. Chem. Rev. 33 (1980) 227.
[43] Y. Mathey, D.R. Greig, D.F. Shriver, Inorg. Chem. 21 (1982) 3409.
[44] B.A. Vaartstra, J.A. Samuels, E.H. Barash, J.D. Martin, W.E. Streib, C. Gasser, K.G. Gaulton, J. Organomet. Chem. 449 (1993) 191.
[45] W.A. Alves, R.H. de Almeida Santos, A. Paduan-Filho, C.C. Becerra, A.C. Borin, A.M. da Costa Ferreira, Inorg. Chim. Acta 357 (2004) 2269, and references therein.
[46] S. Tiraddo-Guerra, N.A. Cuevas-Garibay, M.E. Sosa-Torres, R. Zamorano-Ulloa, J. Chem. Soc., Dalton Trans. (1998) 2431.
[47] M. Rodriguez, A. Llobet, M. Corbella, Polyhedron 19 (2000) 2483.
[48] C. Tallarico, S. Pace, A. Longo, Rapid Commun. Mass Spectrom. 12 (1998) 403.
[49] K. Skorda, G.S. Papaefstathiou, A. Vafiadis, A. Lithoxoidou, C.P. Raptopoulou, A. Terzis, V. Psycharis, E. Bakalbassis, V. Tangoulis, S.P. Perlepes, Inorg. Chim. Acta 326 (2001) 53.

stereoelectronic effects that reduce the exothermicity of the reaction, inhibit the approach of another enR molecule and may render the $[Cu(enR)_2]^{2+}$ entity unattainable [9], while the approach of different molecules or ions with compatible spatial requirements, such as the anions of β-diketonates, is not impeded and in many instances is actually favored leading to the formation of mixed ligand chelates. The mixed-ligand entity $[Cu(enR)\beta]^{2+}$ has attracted appreciable attention because of solvatochromism influenced by the species that effect electrical neutrality either forming covalent bond or acting as counteranions, while in the $[Cu(enR)\beta_2]$ addition compounds, the structure of several of which has been elucidated by crystallographic methods, coordination saturation of copper(II) is achieved [10,11].

Previous studies revealed that addition of 1,2-diaminoethane, en, and its *N*-substituted derivatives, enR (such as the *N*,*N*-dimethyl-1,2-diaminoethane, Me_2en), to bis(β-diketonato)copper(II) chelates cleaves the oxygen–copper(II) bonds and coordination of the 1,2-diamine predominates resulting in the formation of the distorted octahedral CuN_4O_2 chromophore [5,12,13]. Total cleavage of the oxygen–copper(II) bonds also takes place [14] when Me_2en reacts with bis(3-cyano-2,4-pentanedionato)copper(II), $Cu(NC–acac)_2$, and the $CuN_4N'_2$ chromophore prevails with the anion $NC–acac^-$ interacting through the cyano nitrogen and attaining the $S(E,Z)$ conformation instead of the commonly encountered $U(Z,Z)$.

The variable coordination mode and conformation of the substituted 2,4-pentanedionato anions prompted the present investigation in order to get acquainted with the factors influencing the mode of interaction and the conformation of anions β-diketonates in the presence of copper(II) and 1,2-diamines and related nitrogenous bases. Density functional calculations were carried out as an elegant means to probe the consequences of substitution within the 2,4-pentanedionato moiety as regards their likely bonding sites and conformation. Further, the bis(pentane-2,4-dionato)copper(II), $Cu(acac)_2$, and its substituted derivatives ($Cu(NC–acac)_2$ $Cu(O_2N\text{-}acac)_2$, and $Cu(tfac)_2$) were reacted with 1,2-ethanediamine, en, several of its *N*-alkyl derivatives, enR, and 1,2-propanediamine, pn, and the resulting chelates were studied in order to obtain information regarding: (a) the reactivity of the $Cu\beta_2$ chelates towards 1,2-diamines, enR, (b) the influence of substituents within the β-diketonates on the interactions with enR, (c) the occurrence and the role of hydrogen bonding, (d) the effect of functional groups on the interactions and the conformation of the anion of the β-ketoenol, and (e) the changes in the electronic excitation energies as a result of substituent effects and the ensuing changes in group vibrations. Additionally, the crystal structure of $[Cu(MeenMe)_2(NC–acac)_2]\cdot 2H_2O$ was elucidated and is reported.

2. Results and discussion

The reaction of *N*-substituted 1,2-ethanediamines, enR, and 1,2- propanediamine, pn, with the resonance-stabilized bis(β-diketonato)copper(II) chelates, $Cu\beta_2$ (β = acacH, O_2N–acacH, NC–acacH, tfacH) leads to addition compounds, the structure and composition of which depends on the nature and the concentration of the reactants [11,12]. The preference for the formation of the $[Cu\beta_2(enR)_2]$ addition compounds is exemplified in the case of $Cu(NC–acac)_2$. The 1:2 adducts $[Cu(NC–acac)_2(enR)_2]$ were obtained even when the concentration of the sterically unhindered enR was below the required amount for the formation of the 1:1 adduct. The existence of unreacted $Cu(NC–acac)_2$ species in the reaction sediment was revealed by the intense absorption band (due to the cyano group) at 2196 cm^{-1} while in $[Cu(NC–acac)_2(enR)_2]$ this band is split. It transpires that in dilute solutions equilibrium involving the $[Cu(NC–acac)_2enR]$ species pertains and implies that disproportionation takes place upon loss of solvent.

There are distinct differences in the physicochemical properties between the present series of compounds corresponding to the general composition $[Cu(enR)_2\beta_2]$ and the $[Cu(enR)\beta_2]$ adducts. The molar conductivity values Λ_M, of the 1:2 addition compounds, $[Cu(enR)_2\beta_2]$, in nitromethane are in the range 15–60 S cm^2 M^{-1} and in water span a rather wide range indicating that the extent and the nature of interactions of the bifunctional anions of the β-diketonates, β^-, are altered and suggest that fission of copper–oxygen bonds has apparently taken place. As has been reported [5,11,14] and the infrared spectra suggest, the β-diketonato chelate rings no longer exist and the anions β^-, that essentially counterbalance the charge of the evolving $[Cu(enR)_2]^{2+}$ species, do not necessarily retain their $U(Z,Z)$ conformation.

2.1. Infrared spectra

The extensive investigations on the infrared spectra of the $Cu\beta_2$ chelates and the species resulting from covalent interactions of copper(II) cations with 1,2-diamines [15] facilitate the assessment of the structural changes incurred upon addition of enR to $Cu\beta_2$ and their effect on group vibrations. Regarding the partially substituted 1,2-diamines, the absence of bands at frequencies above 3300 cm^{-1} in the infrared spectra of $[Cu(enR)_2\beta_2]$ and suggests that the enR species coordinate as bidentate ligands (Table 1). The bands due to the 1,2-diamines in the 900–750 cm^{-1} region are regarded as indicative of the spatial disposition of the 1,2-diamine. The pattern of these bands in the compounds under investigation suggests chelation and *gauche* conformation since it is closely related to the pattern observed in the spectra of the $[Cu(enR)_2]^{2+}$ entity as well as in 1,2-diamine addition compounds of $Cu\beta_2$ for which the structure has been elucidated by X-ray diffraction.

Coordination of the 1,2-diamine also induces changes in absorptions associated with the anion of the β-diketonate. In the compounds $[Cu(enR)_2\beta_2]$ the frequency of the bands emanating from certain groups within the β-diketonato moiety is of particular importance. For instance, the band

Table 1
Band maxima ($\tilde{\nu}/cm^{-1}$) of the main absorptions in the IR spectra of addition compounds resulting from the reaction of some bis(β-diketonato) copper(II) chelates with 1,2-diamines

	Compound	C⇢O	C⇢C	CH_3	N–H	N–H	C⇢X
1	$[Cu(en)_2(acac)_2](H_2O)_2$	1570	1525	1480, 1422	3275, 3215	3130	
2	$[Cu(en)_2(NC–acac)_2]$	1615	1500	1390	3275	3145	2182
3	$[Cu(Meen)_2(NC–acac)_2]$	1608	1560	1378	3245	3165	2178
4	$[Cu(Meen)_2(tfac)_2]$	1675	1605	1420	3260, 3220	3130	
5	$[Cu(MeenMe)_2(acac)_2]$	1645, 1625	1525	1425, 1390	3215	3175	
6	$[Cu(MeenMe)_2(NC–acac)_2](H_2O)_2$	1605	1528	1375	3235	3165	2179
7	$[Cu(MeenMe)_2(O_2N\text{-}acac)_2]$	1680, 1603	1450, 1428	1360	3205	3162	1397
8	$[Cu(MeenMe)_2(tfac)_2]$	1670, 1635	1550, 1510	1460, 1440	3195	3175	
9	$[Cu(Me_2en)_2(NC–acac)_2]$	1623	1525	1380	3225	3123	2173
10	$[Cu(Me_2en)_2(O_2N\text{-}acac)_2]$	1645, 1602	1460, 1425	1360	3180	3072	1395
11	$[Cu(Me_2en)_2(tfac)_2]$	1608	1525	1465	3170	3075	
12	$[Cu(pn)_2(acac)_2\ (H_2O)_2]$	1595	1465, 1445	1370, 1355	3342	3112	
13	$[Cu(pn)_2(NC–acac)_2]$	1622	1530	1380	3270	3140	2184
14	$[Cu(pn)_2(O_2N\text{-}acac)_2]$	1670	1555,1430	1380, 1330	3270, 3235	3140	1410, 1385
15	$[Cu(pn)_2(tfac)_2]$	1635	1495	1380	3290, 3240	3120	

due to the asymmetric vibration of the C–C–C segment is shifted to lower frequency while the absorption associated with the perturbed C⇢O and the conjugated C⇢C bonds is shifted to higher frequency relative to that of the parent compounds $Cu\beta_2$ (Table 1). The large shifts in such adducts were understood [16] as indicative of hydrogen bonded β-ketoenolato-anions and unidentate coordination through one of the carbonyl oxygens. Apparently, upon ligation of the diamine a weakening of the copper–oxygen bond and even cleavage takes place, as the conductivity results imply. Shifts in the absorptions associated with skeletal vibrations of the carbon chain were rather difficult to interpret and are attributed to changes in the conformation suggesting that the skeletal carbon atoms of the β-diketonato-moiety are not coplanar.

Groups such as the –CN and the $–NO_2$ that are also capable of covalent interactions with the metal center and are attached to the β-diketonato anion make the IR spectra more interesting. In the case of $[Cu(MeenMe)_2(NC–acac)_2]$ the band emanating from the stretching vibration of the cyano group peaks at 2173 cm^{-1} compared to 2196 cm^{-1} in $Cu(NC–acac)_2$. This diminution of frequency is attributed to bonding interactions of the terminal nitrogen atom with the metal ion. In the case of $[Cu(Me_2en)_2(O_2N–acac)_2]$ and $[Cu(MeenMe)_2(O_2N–acac)_2]$ the interactions of β-diketonato anion with copper(II) apparently do not involve the oxygens of the $–NO_2$ group since the band at 1525 cm^{-1}, assigned to the asymmetric stretching vibration (ν_{as}) of the $–NO_2$ group, as well as the bands at 1395 cm^{-1} and 826 cm^{-1} attributed to the symmetric stretching vibrations (ν_s) and the scissoring deformation of the $–NO_2$ group, respectively, are present in virtually the same position as those in the spectra of the parent compound.

2.2. Electronic excitation spectra

The diffuse reflectance spectra of the $[Cu(enR)_2\beta_2]$ addition compounds are different from those of the $[Cu\beta_2(enR)]$ compounds and the $[Cu\beta_2]$ chelates and are characterized by a broad structureless envelope in the visible having width at half-height ~3.8 μm^{-1} under which all of the ligand field transitions in the copper chelates are congregated. The Jahn–Teller theorem requires any non-linear system with a degenerate ground state to undergo such a distortion as will remove the degeneracy. The d^9 configuration of the copper(II) ion precludes regular octahedral structures since the single unpaired electron would reside in the doubly degenerate e_g orbital manifold. Tetragonal distortions that remove the orbital degeneracy are very common, especially with σ-bonding ligands such as the 1,2-diamines and the extremum of the envelope in the region 1.74–1.87 μm^{-1} compares favorably with the wavenumber of maximum absorption occurring in the cationic species $[Cu(enR)_2]^{2+}$. Previous studies of $[Cu(enR)_2\beta_2]$ compounds revealed the presence of the CuN_4 entity in either D_{2h} or D_{4h} microsymmetry depending on the substitution of the 1,2-diamine, and for the sake of brevity, a D_{4h} symmetry of the CuN_4 chromophore with $^2B_{1g}$ ground state was assumed for the compounds under consideration. Under these circumstances the energy required for the transition $^2A_{1g} \leftarrow {}^2B_{1g}$ reflects the degree of tetragonal distortion. The distortion involves elongation of the axial bonds, a measure of which is the ratio $T = R_S/R_L$, where R_S is the mean in-plane copper–ligand bond length and R_L is the mean out-of plane (axial) bond length. The tetragonal distortion T resulting from crystallographic data on a large number of copper(II) chelates is not dependent on the ligands present and in tetragonally distorted octahedral copper(II) compounds involving unidentate ligands diminishes below 0.6, when the axial ligands are merely positioned by lattice packing factors. The T value is about 0.8 whenever the axial ligands are weakly bonded, and the term ''semi-coordination'' has been introduced to describe this structural situation. In order to gain additional information an unsuccessful attempt was made to analyze the room temperature low-energy envelope into

three components attributed to transitions $^2A_{1g} \leftarrow {}^2B_{1g}$, $^2B_{2g} \leftarrow {}^2B_{1g}$, $^2E_g \leftarrow {}^2B_{1g}$ and to obtain a reasonable fit and a consistent sequence of band intensities. While a number of alternative sets of bands with reasonable fit were obtained, no consistency of intensities was realized.

A plausible alternative for explaining the observed ligand field excitation energy seems to be the existence of a $CuN_4N'_2$ chromophore in $[Cu(MeenMe)_2(NC–acac)_2]$ as in $[Cu(Me_2en)_2(NC–acac)_2]$ that result from the coordination of $NC–acac^-$ through the cyano nitrogen. Irrefutable proof that this rarely occurring mode of coordination actually occurs was obtained by elucidating the crystal structure of $[Cu(Me_2en)_2(NC–acac)_2]$ and was reaffirmed by resolving the structure of $[Cu(MeenMe)_2(NC–acac)_2]$ reported here.

2.3. Description of the Structure of $[Cu(MeenMe)_2(NC–acac)_2]\cdot 2H_2O$

The experimental results are in accord with the existence of an $[Cu(enR)_2]^{2+}$ entity that interacts with two β-ketoenolato anions to achieve electrical neutrality. Consideration of the interatomic distances in $[Cu(MeenMe)_2(NC–acac)_2]\cdot 2H_2O$ reveals that the copper ion is surrounded by nitrogen donor atoms (Table 2). The distances between the diamine nitrogens and the copper atom are slightly unequal being 2.028(2) and 2.049(2) Å. The CuN_4 chromophore exists in a plane (the basal plane) that is expressed by the equation $8.323x - 4.405y - 8.705z = 1.718$. The apical positions are occupied by the cyano nitrogens of the $NC–acac^-$ anion at a distance of 2.617(2) Å from the copper ion. Covalent interactions through the nitrogen of the cyano group are rare and have only been observed before in [16] and [17]. The interatomic distances and bond angles within the β-diketonato moiety indicate extensive electron delocalization. The lengthy separation of the carbonyl oxygens signifies change of conformation to the rarely encountered $S(E,Z)$ one.

The nearest oxygen atom to the metal center is that of a water molecule at a distance of 4.137(3) Å that precludes any direct covalent interactions with copper. Further away at a distance of 5.485(3) Å is the oxygen of a carbonyl group that also abstains from covalent interactions with copper. The absence of interactions of the carbonyl oxygen with the copper atom is in contrast to numerous $[Cu(enR)\beta_2]$ addition compounds and two of the $[Cu(enR)_2\beta_2]$ species in which carbonyl oxygens occupy the apical positions in a tetragonally distorted octahedral arrangement about copper (see Fig. 1).

The disposition of the donor atoms stipulates that the central metal ion exists in a tetragonally distorted octahedral arrangement and microsymmetry approaching D_{2h}. The tetragonal distortion, T, is appreciable ($T = 0.78$) and is more pronounced than that in $[Cu(Me_2en)_2(NC–acac)_2]$ in which $T = 0.82$. However the R_L distance of 2.617(2) Å is appreciably shorter than the values found out in $[Cu(en)_2(acac)_2]\cdot 2H_2O$ and in $[Cu(Me_2en)_2(hfac)_2]$ where the β^- anions retaining the $U(Z,Z)$ conformation interact with the copper center through only one of the carbonyl oxygens at a distance of ~2.79 Å. These are in accord with the notion that the copper ion has a prolate ellipsoidal shape the eccentricity of which is continuously variable, but does not support suggestions that the elongation of the axial bonds is accompanied by simultaneous contraction of the in-plane ones [7].

Hydrogen bonds have been observed in $[Cu(Me_2en)_2(hfac)_2]$ and reexamination of the crystallographic data for $[Cu(Me_2en)_2(NC–acac)_2]$ indicates the occurrence of intramolecular hydrogen bonds involving the hydrogens of the amino group and one of the carbonyl oxygens. In the

Table 2
Selected bond lengths (Å) and bond angles (°) for $[Cu(MeenMe)_2(NC–acac)_2]\cdot 2H_2O$

Cu(1)–N(2)	2.049(2)	N(3)–Cu(1)–N(3a)	180.00
Cu(1)–N(3)	2.028(2)	N(3)–Cu(1)–N(2a)	85.10(8)
Cu(1)–N(1)	2.617(2)	N(3)–Cu(1)–N(2)	94.90(8)
C(1)–C(2)	1.479(4)	C(4)–C(3)–C(2)	126.5(2)
C(2)–C(3)	1.458(3)	C(6)–C(3)–C(2)	118.1(2)
C(2)–O(1)	1.228(3)	C(6)–C(3)–C(4)	115.4(2)
C(3)–C(4)	1.423(4)	C(3)–C(2)–C(1)	116.7(2)
C(3)–C(6)	1.426(3)	O(1)–C(2)–C(1)	120.3(2)
C(4)–C(5)	1.531(4)	O(1)–C(2)–C(3)	122.8(2)
C(4)–O(2)	1.248(3)	C(5)–C(4)–C(3)	122.3(2)
C(6)–N(1)	1.148(3)	O(2)–C(4)–C(3)	121.5(2)
C(7)–N(2)	1.478(3)	O(2)–C(4)–C(5)	116.1(3)
C(8)–C(9)	1.504(3)	N(1)–C(6)–C(3)	178.3(2)
C(8)–N(2)	1.476(3)	C(6)–N(1)–Cu(1)	159.9(2)
C(9)–N(3)	1.495(2)	N(2)–C(8)–C(9)	108.8(2)
C(10)–N(3)	1.506(2)	N(3)–C(9)–C(8)	107.5(1)
N(1)–Cu(1)–N(1a)	180.00	C(7)–N(2)–Cu(1)	119.6(1)
N(1)–Cu(1)–N(2)	88.69(6)	C(8)–N(2)–Cu(1)	107.2(1)
N(1)–Cu(1)–N(2a)	91.31(6)	C(8)–N(2)–C(7)	110.7(2)
N(1)–Cu(1)–N(3)	96.20(7)	C(9)–N(3)–Cu(1)	107.1(1)
N(1)–Cu(1)–N(3a)	83.80(7)	C(10)–N(3)–Cu(1)	116.1(1)
N(2)–Cu(1)–N(2a)	180.00	C(10)–N(3)–C(9)	110.7(2)

The atoms marked "a" are symmetry related to the corresponding atoms.

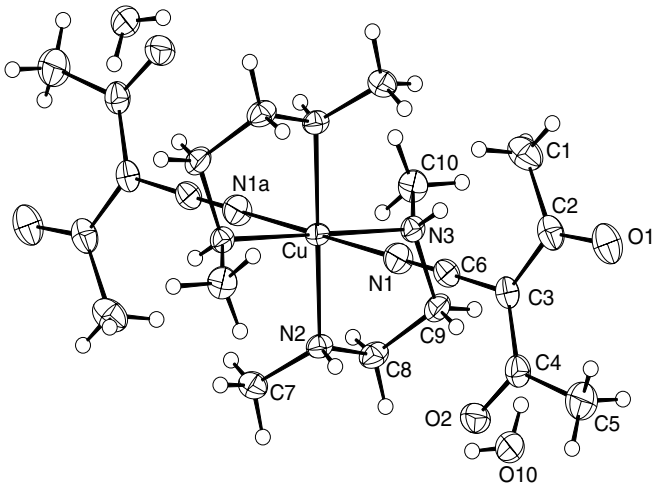


Fig. 1. ORTEP diagram of $[Cu(MeenMe)_2(NC–acac)_2]\cdot 2H_2O$.

compound under consideration the orientation of the NC–acac$^-$ anion does not bring any of the carbonyl oxygens in the environs of the diamine nitrogens that are bonded to the same metal center. However intermolecular hydrogen bonds are observed between the remote carbonyl oxygens of the [Cu(MeenMe)$_2$(NC–acac)$_2$] entity and the diamine nitrogens bonded to other copper centers . Additionally, the second carbonyl oxygen and the second diamine nitrogen are also implicated in intermolecular hydrogen bonding albeit in a different manner involving the water molecules. In fact a network of hydrogen bonding interlinks all the entities in the unit cell and brings about a supramolecular structure. The network of hydrogen bonds in the unit cell is portrayed in Fig. 2.

2.4. Theoretical considerations

Study of the β-*diketonato ligands*. The β-diketonates and their anions have been known to exhibit multiple active sites and attain various conformations. Since diffraction data are not always available nor easily obtainable, we undertook quantum chemical calculations in order to further understand their chemistry. Thus, the series of symmetrically and non-symmetrically substituted β-diketonates and the conformers of their anions, β$^-$, listed in Scheme 1, were fully optimized without imposing any constraint. Frequency calculations were performed on the optimized structures in order to determine the nature of the stationary point found. $W(E,E)$ conformers of the β-diketonato anions have not been observed in [Cuβ$_2$(enR)$_2$] compounds, therefore only the results of the S and U conformers are presented here. The results reaffirm that the $U(Z,Z)$ conformer of the free β-diketonates has enhanced stability due to the strong intramolecular hydrogen bond. Removal of the labile hydrogen enhances the keto form and in most cases β$^-$ adopts the lower energy $S(E,Z)$ conformation with the two oxygen atoms being placed on either side of the carbon chain. The calculated electronic energy E, the relative energy ΔE, the corrected zero-point vibrational energy (ZPVE) denoted E_{corr}, and the free energy, G, of the conformers are listed in Table 3. For instance, the energy of the $U(Z,Z)$ conformer of the NC–acac$^-$ anion exceeds the energy of the $S(E,Z)$ conformer by 18.98 kJ/mol, while the energy of the $U(Z,Z)$ conformer of the acac$^-$ anion exceeds the energy of the $S(E,Z)$ conformer by 26.02 kJ/mol. The ZPVE corrected energy, as well as the free energy, shows the same relative energy order. In the case of the hfac$^-$ anion its $U(Z,Z)$ conformer is more stable by 5 kJ/mol, because in this manner close contacts between the electronegative fluorine and oxygen atoms are avoided.

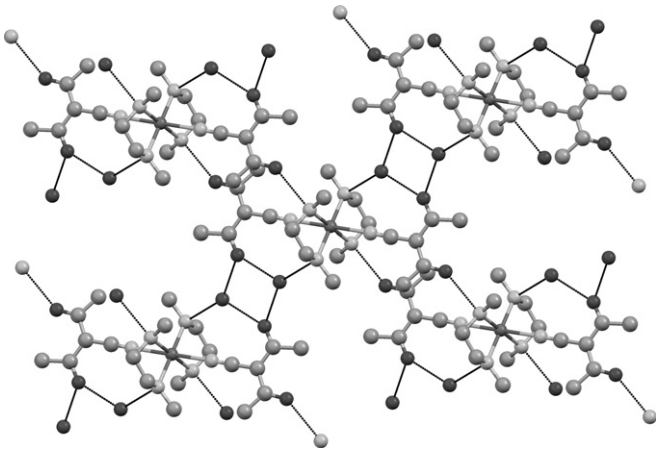


Fig. 2. Network of hydrogen bonds in the unit cell of [Cu(MeenMe)$_2$(NC–acac)$_2$] · 2H$_2$O.

The reactions described here took place in ethanol solutions and for this reason the solvent effect was studied in the frame of the COSMO model. The relative energy order is preserved even though the $U(Z,Z)$ and $S(E,Z)$ conformers lay closer in energy with the $U(Z,Z)$ conformers exhibiting lower solvation energies (ΔG_{solv}) and thus acquiring additional stabilization. In the case of the acac$^-$ anion, the present calculations suggest that while the energy difference between the $U(Z,Z)$ and $S(E,Z)$ conformers in the gas phase is substantial (26.02 kJ/mol), it diminishes to only 2.91 kJ/mol in solution.

The condensed Fukui function value, f_k^-, was advantageously employed to assess the relative reactivity of different sites in the ligands. In the case of the hfac$^-$ anion, the condensed Fukui functions for all the fluorine atoms of the U conformer were calculated. Although the fluorine atom that lies on the carbon plane is predicted to have higher charge with respect to the other fluorine atoms (−0.385 versus −0.377), the f_k^- are equal for all these atoms. Selected atomic charges (NPA) and f_k^- values for the $S(E,Z)$ and $U(Z,Z)$ conformers of the β-diketonato anions are presented in Table 4. The f_k^- values point to the oxygen atoms as the most favorable reactive sites whenever the NC–acac$^-$ anion achieves its U conformation. However, upon change of conformation to $S(E,Z)$ there is a steep increase in the f_k^- value of the nitrogen atom whereas an unsymmetrical sharp drop is observed in the f_k^- values of the carbonyl oxygen atoms. These findings are corroborated from the experimental data of the crystal structures of the [Cu(Me$_2$en)$_2$(NC–acac)$_2$] and [Cu(MeenMe)$_2$(NC–acac)$_2$] · 2(H$_2$O)$_2$ chelates that are in accord with the adoption by NC–acac$^-$ of the $S(E,Z)$ conformation and the interaction through the cyano nitrogen atom.

Study of the [Cuβ$_2$(*enR*)$_2$]. Further, we probed certain [Cu(enR)$_2$β$_2$] systems for which reliable crystallographic data exist. The systems [Cu(MeenMe)$_2$(NC–acac)$_2$] (**S1**) and [Cu(Me$_2$en)$_2$(NC–acac)$_2$] (**S2**) were surveyed in which the anion NC–acac$^-$ was allowed to adopt the $S(E,Z)$ conformation. In the calculations for [Cu(Me$_2$en)$_2$(hfac)$_2$] (**U$_F$**) the conformation of the hfac$^-$ anion was settled to $U(Z,Z)$ as experimentally observed. While the B3LYP/LanL2MB calculations predict rather elongated Cu–ligand bonds, the structures obtained from the B3LYP/LanL2DZ model chemistry are in better agreement with solid state X-ray crystal structures. Therefore, the focus will be on the results

Table 3
Electronic energy (E), ZPVE corrected energy (E_{corr}), free energy (G), electronic energy in ethanol solution (E_{CPCM}) and ΔG of solvation for the $S(E,Z)$ and $U(Z,Z)$ conformers of some β-diketonato anions calculated at the B3LYP/6-31+G(d,p) level

Anion conformer	acac$^-$		Hfac$^-$		NO_2-acac$^-$		NC–acac$^-$		Cl-acac$^-$	
	U	*S*	*U*	*S*	*U*	*S*	*U*	*S*	*U*	*S*
E (a.u.)	−345.26352	−345.27350	−940.76349	−940.76156	−549.79914	−549.80009	−437.53804	−437.54527	−804.86118	−804.87213
ΔE (kJ/mol)	26.02	0.0	0.0	5.07	2.49	0.0	18.98	0.0	28.75	0.0
E_{corr} (a.u.)	−345.14692	−345.15674	−940.69060	−940.68682	−549.67714	−549.67799	−437.42078	−437.42770	−804.75283	−804.76339
ΔE_{corr} (kJ/mol)	25.78	0.0	0.0	9.92	2.23	0.0	18.17	0.0	27.73	0.0
G (a.u.)	−345.18813	−345.19838	−940.73754	−940.73920	−549.72406	−549.72449	−437.46665	−437.47271	−804.79663	−804.80686
ΔG (kJ/mol)	26.91	0.0	4.36	0.0	1.13	0.0	15.91	0.0	26.86	0.0
E_{CPCM} (a.u.)	−345.36383	−345.36494	−940.83991	−940.83634	−549.88364	−549.88340	−437.62515	−437.62962	−804.95010	−804.95657
ΔE_{CPCM} (kJ/mol)	2.91	0.0	0.0	9.37	0.0	0.63	11.74	0.0	16.99	0.0
ΔG_{solv} (kJ/mol)	−255.43	−233.22	−181.63	−177.44	−209.74	−206.85	−216.40	−209.91	−223.68	−212.46
	Ac-acac$^-$		dbm$^-$		tfac$^-$		bzac$^-$		tfbzac$^-$	
	U	*S*	*U*	*S*	*U*	*S*	*U*	*S*	*U*	*S*
E (a.u.)	−497.92583	−497.94106	−728.77017	−728.77346	−643.01569	−643.02502	−537.01711	−537.02735	−834.76778	−834.77022
ΔE (kJ/mol)	39.99	0.0	8.64	0.0	24.50	0.0	26.89	0.0	6.41	0.0
E_{corr} (a.u.)	−497.76841	−497.78318	−728.54095	−728.54411	−642.92001	−642.92916	−536.84424	−536.85424	−834.61576	−834.61809
ΔE_{corr} (kJ/mol)	−38.78	0.0	8.30	0.0	24.03	0.0	26.25	0.0	6.12	0.0
G (a.u.)	−497.81785	−497.83123	−728.59793	−728.60105	−642.96852	−642.97584	−536.89354	−536.90307	−834.67121	−834.67303
ΔG (kJ/mol)	−38.78	0.0	8.19	0.0	19.22	0.0	25.02	0.0	4.78	0.0
E_{CPCM} (a.u.)	498.01512	−498.02188	−728.87066	−728.86786	−643.10410	−643.10607	−537.12170	−537.12184	−834.85402	−834.85683
ΔE_{CPCM} (kJ/mol)	17.75	0.0	0.0	7.35	5.17	0.0	0.37	0.0	7.38	0.0
ΔG_{solv} (kJ/mol)	−222.09	−202.51	−253.63	−238.11	−218.49	−200.29	−266.19	−240.33	−222.76	−213.80

Table 4
Selected net atomic charges $q_k(N)$ and condensed Fukui function values f_k^- of the conformers of some β-diketonato anions

Anion conformer	$acac^-$				$Hfac^-$				NO_2-$acac^-$				NC–$acac^-$			
	U		*S*		*U*		*S*		*U*		*S*		*U*		*S*	
	q_k	f_k^-	q_k	f_k^-	q_k	f_k^-	q_k	f_k^-	q_k	f_k^-	q_k	f_k^-	q_k	f_k^-	q_k	f_k^-
Atom k																
O1	−0.685	0.279	−0.740	0.298	−0.618	0.281	−0.639	0.231	−0.613	0.154	−0.631	0.170	−0.633	0.289	−0.686	0.191
O2	−0.685	0.279	−0.715	0.322	−0.618	0.281	−0.645	0.254	−0.613	0.154	−0.677	0.193	−0.633	0.289	−0.664	0.178
Other									−0.515[1]	0.166	−0.489	0.133	−0.484[3]	0.156	−0.465	0.253
									−0.515[2]	0.166	−0.429	0.130				

Anion conformer	Cl-$acac^-$				Ac-$acac^-$				dbm^-			
	U		*S*		*U*		*S*		*U*		*S*	
	q_k	f_k^-	q_k	f_k^-	q_k	f_k^-	q_k	f_k^-	q_k	f_k^-	q_k	f_k^-
Atom k												
O1	−0.653	0.190	−0.686	0.194	−0.606	0.113	−0.683	0.260	−0.658	0.181	−0.707	0.199
O2	−0.653	0.190	−0.707	0.205	−0.663	0.182	−0.683	0.076	−0.658	0.181	−0.686	0.181
Other	−0.151[4]	0.172	−0.109	0.175	−0.706[5]	0.209	−0.683	0.300				

Anion conformer	tfac$^-$				bzac$^-$				tfbzac$^-$			
	U		*S*		*U*		*S*		*U*		*S*	
	q_k	f_k^-	q_k	f_k^-	q_k	f_k^-	q_k	f_k^-	q_k	f_k^-	q_k	f_k^-
Atom k												
O1	−0.645	0.244	−0.701	0.272	−0.670	0.192	−0.727	0.211	−0.645	0.172	−0.683	0.257
O2	−0.659	0.203	−0.684	0.211	−0.673	0.202	−0.701	0.201	−0.634	0.232	−0.667	0.183
Other												

The numbers indicate the relevant atom:
[1]: O(a) oxygen atom of the –NO_2 group.
[2]: O(b) oxygen atom of the –NO_2 group.
[3]: N atom of the –NC group.
[4]: Cl atom.
[5]: O oxygen atom of the $CH_3C(O)$-group.

obtained from the latter DFT calculations (i.e. B3LYP/LanL2DZ). Selected optimized structural parameters of **S1**, **S2** and $\mathbf{U_F}$ are presented in Table 5 together with the experimental ones. Our calculations further predict intramolecular hydrogen bonding for all complexes involving amino hydrogen H(N2-1) and one carbonyl oxygen, O2. Upon formation of the $[Cu(enR)_2]^{2+}$ entity the β-diketonato ligand is oriented in such a way so as to enhance its interactions with the metal atom and to maximize hydrogen bonding. The NC–acac$^-$ anion approaches the $[Cu(enR)_2]^{2+}$ entity and assumes the $S(E,Z)$ conformation enabling the cyano nitrogen (N1) to be in the neighborhood of the metal center and as the Cu–N1 distance diminishes weak interactions prevail. Simultaneously, the carbonyl oxygens are involved in hydrogen bonding. The results of the DFT calculations for $[Cu(Me_2en)_2(NC–acac)_2]$ (**S2**) are in harmony with the findings of the X-ray crystallographic data and the outcome of the DFT calculations for $[Cu(MeenMe)_2(NC–acac)_2]$ in the (**S1**) conformation deviate only imperceptibly from the X-ray structure favoring a shorter distance of the axially positioned cyano nitrogen. Shorter distances of the axially positioned carbonyl oxygens are also envisaged for $[Cu(Me_2en)_2(hfac)_2]$ ($\mathbf{U_F}$) in discord with the X-ray crystallographic data. These discrepancies may be attributed to the fact that the theoretical results refer to the isolated molecule in the gas phase while the experimental data refer to the solid state. Additionally, since the water molecules in $[Cu(MeenMe)_2(NC–acac)_2]\cdot 2H_2O$ induce charge redistribution and bring about multiple hydrogen bonding, the disagreement between theoretical and experimental results could be attributed to the exclusion of the water molecules from the calculations.

In order to probe the influence of conformation of the β-diketonato ligands on the energetics of the $[Cu(MeenMe)_2(NC–acac)_2]$ and $[Cu(Me_2en)_2(NC–acac)_2]$ systems, the $Cu(MeenMe)_2(NC–acac)_2$ (**U1**) and $[Cu(Me_2en)_2(NC–acac)_2]$ (**U2**) compounds were also studied with the NC–acac$^-$ anion constrained to $U(Z,Z)$ conformation. Selected geometric, energetic and electronic parameters for **S1**, **U1**, **S2**, and **U2** are compiled in Table 6. It was revealed that the **U1** and **U2** appear to be slightly more stable (by 0.3 and 1.5 kcal/mol, respectively) forming stronger intramolecular hydrogen bonds between the NC–acac$^-$ and the $[Cu(enR)_2]^{2+}$ entity. When the β-diketonato ligand assumes the $U(E,Z)$ conformation, it comes closer to the equatorial plane of the $[Cu(enR)_2]^{2+}$ entity. The distance between the copper ion and the carbonyl oxygen atoms (O1) occupying the apical positions is 2.497 for **U1** and 2.445 for **U2**. Stronger intramolecular bonding is observed relative to **S1** and **S2**, implicating the second carbonyl oxygen (O2) and the hydrogens of the amino group.

The association of the two β-diketonato ligands with the $[Cu(enR)_2]^{2+}$ entity to afford the $[Cu\beta_2(enR)_2]$ compounds implicates a rather strong interaction. The computed association energies ΔE_1 amount to 118.6–143.9 kcal/mol, and are higher for the **U1** and **U2** compounds. Further, the net charges on the Cu atoms calculated by NPA are +1.364, +1.378, +1.327 and 1.341 for the **U1**, **U2**, **S1** and the **S2** structures, respectively. The smaller net charge on the Cu atom of the latter complexes implies enhanced electron density transfer from all ligands to the copper atom, i.e. enhanced sigma bonding when they coordinate through the cyano nitrogen. This electron transfer is located mainly in the 4s orbital of the Cu atoms as shown by the natural electron configuration in Table 6.

Regarding the elongated axial Cu–N distance and the consequences on the nature of interaction of the NC–acac$^-$ with the metal center, the molecular orbital (MO) composition of the systems under investigation was considered. The MO composition reveals that the highest occupied molecular orbital (HOMO) of the (**S1**), (**S2**) structures comes mainly from an orbital of the β$^-$ diketonato anion

Table 5
Selected experimental and calculated (B3LYP/LanL2DZ) interatomic distances (Å) and bond angles (°) of some mixed-ligand copper(II) chelates, $[Cu\beta_2(enR)_2]$

Compound	$[Cu(MeenMe)_2(NC–acac)_2]$		$[Cu(Me_2enme)_2(NC–acac)_2]$		$[Cu(Me_2en)_2(hfac)_2]$	
	Calculated (**S1**)	Experimental	Calculated (**S2**)	Experimental	Calculated ($\mathbf{U_F}$)	Experimental
Cu–O1					2.428	2.793
Cu–N2	2.098	2.049(2)	2.199	2.139	2.183	2.064
Cu–N3	2.090	2.028(2)	2.020	1.9902	2.027	1.989
Cu–N1	2.496	2.617(2)	2.534	2.514		
N3–O2	2.470	4.924	2.758	2.940	2.806	2.03
N2–Cu–N2a	179.98	180.00	179.754	180.00	179.98	179.97
N3–Cu–N3a	179.99	180.00	179.212	179.90	179.88	179.98
N1–Cu–N1a	179.99	180.00	179.3	179.9		
N1–Cu–N2	98.06	88.69(6)	85.503	86.570		
N1–Cu–N3	89.64	96.20(7)	90.052	86.56		
N1–C6–C3	174.2	178.3(2)	173.910	177.27		
N1–C6–Cu	134.5	159.9(2)	131.94	136.80		
O1–Cu–N3					87.41	83.7
O1–Cu–N2					84.85	73.8

Table 6
Selected geometric, energetic and electronic parameters for **S1**, **U1**, **S2**, and **U2** calculated at B3LYP/LanL2DZ level

	S1	U1	S2	U2
E (a.u.)	−1609.22645	−1609.22698	−1609.22674	−1609.22494
ΔE (kcal/mol)	0.3	0	1.5	0
ΔE_1[a] (kcal/mol)	138.3	143.9	118.6	122.4
Cu–X_{apical}[b] (Å)	2.436	2.497	2.533	2.445
O2–N2 (Å)	2.758	2.712	2.756	2.716
q(Cu)	+1.327	+1.364	+1.341	+1.378
nec(Cu)[c]	[core], 3d[9.40], 4s[0.25], 4p[0.02]	[core], 3d[9.39], 4s[0.23], 4p[0.02]	[core], 4s[0.25], 3d[9.38], 4p[0.02]	[core], 4s[0.22], 3d[9.37], 4p[0.02]

[a] $\Delta E_1 = \frac{1}{2}[(2E_{\beta^-} + E_{[Cu(enR)_2]^{2+}}) - E_{Cu(enR)_2\beta_2}]$.
[b] Cu–X_{apical}: Cu–N13 for **S1** and **S2** and Cu–O1 for **U1** and **U2**.
[c] nec: natural electron configuration.

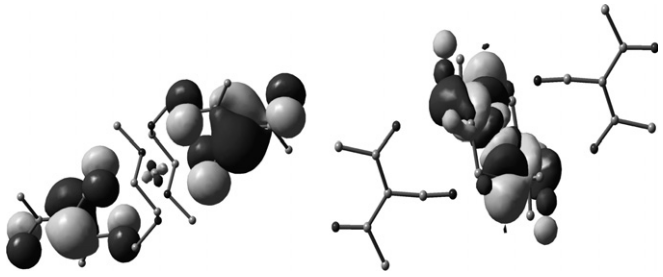


Fig. 3. HOMO and LUMO of **S1**.

with negligible contributions from the atomic orbitals (AO) of the Cu atom and orbitals from the nitrogen donor atoms of the diamine ligand. On the other hand, the main contribution to the lowest unoccupied molecular orbital (LUMO) comes mainly from the Cu atom and the nitrogen atoms of the diamine ligand and essentially no contribution from the β^- diketonato anion. These findings suggest a small degree of covalency (see Fig. 3).

3. Conclusions

The reaction of bis(2,4-pentadionato)copper(II) and cognate compounds with ethanediamine and some of its *N*-derivatives, enR, culminates in the dissolution of the copper–oxygen bond and subsequent formation of copper-nitrogen bonds with the anions of the β-diketonates interacting through atoms placed in apical positions of the square planar $[Cu(enR)_2]^{2+}$ entity. Substituents within the β-diketonate anion affect its mode of interaction and conformation. DFT calculations suggest that when the β-diketonato anion acts as a monodentate ligand, it binds through one of the carbonyl oxygens, while in the case of the NC–acac$^-$ anion binding is envisaged through the nitrogen atom of the cyano group. Further the results indicate that the conformation of the β-diketonato ligand is affected by the formation of hydrogen bonds. The presence of solvent molecules, especially when the solvent is capable of hydrogen bonding, may influence appreciably the conformation of the β-diketonate anion. Water exemplifies this case by participating in extensive hydrogen bonding. The present elucidation of the crystal structure of $[Cu(Me\text{-}en)_2(NC\text{-}acac)_2]\cdot 2H_2O$ supports the results of the DFT calculations. The NC–acac$^-$ anion interacts through the terminal nitrogen atom and attains the $S(E,Z)$ conformation. Extensive intermolecular hydrogen bonding involving the hydrogen atoms of the amino groups and the water molecules present culminates in supramolecular structure.

4. Experimental

4.1. Reagents

1,2-diaminoethane (ethylenediamine, en) and its *N*-alkyl substituted derivatives *N*,*N*-dimethyl-1,2-diaminoethane, Me_2en, its symmetric isomer *N*,*N*′-dimethyl-1,2-diaminoethane, MeenMe, and 1,2-diaminopropane, pn, were purchased from Aldrich and Alfa Aesar. The β-ketoenols (β), 2,4-pentanedione (acetylacetone acacH) and trifluoroacetylacetone (1,1,1-trifluoro-2,4-pentanedione, tfacH), were purchased from Lancaster Synthesis and Aldrich.

4.2. Physical measurements and determinations

Details on the methods and the instruments employed for elemental analyses are given elsewhere [12,16]. Melting points were determined on a Reichert heated plate apparatus and are uncorrected. Molar conductivities were measured on a Metrohm 660 conductivity bridge employing a calibrated dip type cell. The measurements were performed in a series of solutions of analytical grade nitrobenzene and nitromethane and concentrations ranging from 10^{-4} M to 10^{-2} M were employed in order to examine the likelihood of concentration dependence. Molecular mass determinations were accomplished on a Knauer apparatus. Magnetic susceptibility measurements in powdered samples were performed at 25 °C employing the Faraday method on a home-build balance calibrated against $Hg[Co(SCN)_4]$. Diamagnetic corrections were estimated employing the experimental values obtained for Me_2en, MeenMe, $(CH_3COCHCOCH'_3)$Na, and $(CH_3COCCNCOCH'_3)$Na, and from Pascal's constants. The effective magnetic moments, $\mu_{eff}(m_B)$, were calculated using the expression

$\mu_{eff} = 49(\chi_M^{corr})^{1/2}$ $(T = 298\ K)$.

Electronic spectra in solution were measured on a Shimatzu 160A spectrophotometer using 10 mm teflon stoppered quartz cells. The solid state electronic spectra were obtained from nujol mulls. Infrared spectra were obtained by the KBr disc technique and were recorded on a Perkin–Elmer 1430IR spectrophotometer with a range 4000–200 cm^{-1} calibrated against polystyrene.

4.3. Synthesis

The synthesis of 3-cyano-2,4-pentanedione (Traube's acetylacetone, CN-acacH) was performed by reacting acetylacetone with cyanogen employing the procedure described by Fackler [1] while the 3-nitro-2,4-pentanedione (NO_2–acacH) was prepared by Collman's procedure [12]. The homoleptic bis(ß-diketonato)copper(II) chelates, $Cuß_2$, and 1:2 addition compounds, $[Cuß_2(enR)_2]$, were prepared as described in the literature [14,17,18]. The $[Cu(enR)_2(NC–acac)_2]$ compounds are obtained as colored crystals while the $[Cu(enR)_2(tfac)_2]$ and the $[Cu(enR)_2(O_2N–acac)_2]$ compounds are separated as amorphous solids.

[Cu(en)$_2$(acac)$_2$](H$_2$O)$_2$. Yield: 82%. Colour: purple. M.p.: 164–166 °C. *Anal.* Calc. for $C_{14}CuN_4O_6H_{34}$: C, 43.67; N, 14.51; H, 8.88. Found: C, 43.43; H, 8.90; N, 14.30%. IR (KBr): 3275, 3215, 3130, 1570, 1525, 1480, 1422 cm^{-1}. $\Lambda_M(H_2O)$: 123 S cm^2 M^{-1}. UV/Vis: (nujol) $\nu_{max} = 1.894\ \mu m^{-1}$; ($CH_3NO_2$) $\nu_{max} = 1.613\ \mu m^{-1}$; ($C_2H_5OH$) $\nu_{max} = 1.458\ \mu m^{-1}$; ($CH_3CN$) $\nu_{max} = 1.764$, $1.582\ \mu m^{-1}$; (H_2O) $\nu_{max} = 1.789\ \mu m^{-1}$; (DMSO) $\nu_{max} = 1.603\ \mu m^{-1}$. $\mu_{eff} = 1.84\ m_B$.

[Cu(en)$_2$(NC-acac)$_2$]. Yield: 88%. Colour: violet. M.p.: 191–193 °C. *Anal.* Calc. for $C_{16}CuN_6O_4H_{28}$: C, 44.49; H, 6.53; N, 19.45. Found: C, 44.7; H, 6.3; N, 19.2%. IR (KBr): 3275, 3145, 2182, 1615, 1500, 1390 cm^{-1}. $\Lambda_M(H_2O)$: 147 S cm^2 M^{-1}. UV/Vis: (nujol) $\nu_{max} = 1.828\ \mu m^{-1}$; ($CH_3NO_2$) $\nu_{max} = 1.678\ \mu m^{-1}$; ($C_2H_5OH$) $\nu_{max} = 1.773\ \mu m^{-1}$; ($CH_3CN$) $\nu_{max} = 1.754\ \mu m^{-1}$; ($H_2O$) $\nu_{max} = 1.821\ \mu m^{-1}$; (DMSO) $\nu_{max} = 1.802\ \mu m^{-1}$. $\mu_{eff} = 1.79\ m_B$.

[Cu(Meen)$_2$(NC-acac)$_2$]. Yield: 81%. Colour: violet. M.p.: 205–207 °C. *Anal.* Calc. for $C_{18}CuN_6O_4H_{32}$: C, 47.00; H, 7.01; N, 18.26. Found: C, 46.9; H, 7.1; N, 18.6%. IR (KBr): 3245, 3165, 2178, 1608, 1560, 1378 cm^{-1}. $\Lambda_M(H_2O)$: 140 S cm^2 M^{-1}. UV/Vis: (nujol) $\nu_{max} = 1.821\ \mu m^{-1}$; ($CH_3NO_2$) $\nu_{max} = 1.592\ \mu m^{-1}$; ($C_2H_5OH$) $\nu_{max} = 1.709\ \mu m^{-1}$; ($CH_3CN$) $\nu_{max} = 1.773\ \mu m^{-1}$; ($H_2O$) $\nu_{max} = 1.802\ \mu m^{-1}$; (DMSO) $\nu_{max} = 1.782\ \mu m^{-1}$. $\mu_{eff} = 1.80\ m_B$.

[Cu(Meen)$_2$(tfac)$_2$]. Yield: 83%. Colour: violet. M.p.: 195–197 °C. *Anal.* Calc. for $C_{16}CuN_4O_4H_{28}F_6$: C, 37.10; H, 5.45; N, 10.82. Found: C, 36.8; H, 6.0; N, 10.4%. IR (KBr): 3260, 3220, 3130, 1675, 1605, 1420 cm^{-1}. $\Lambda_M(H_2O)$: 220 Scm^2M^{-1}. UV/Vis (nujol) $\nu_{max} = 1.739\ \mu m^{-1}$; ($CH_3NO_2$) $\nu_{max} = 1.508\ \mu m^{-1}$; ($C_2H_5OH$) $\nu_{max} = 1.613\ \mu m^{-1}$; ($CH_3CN$) $\nu_{max} = 1.709\ \mu m^{-1}$; ($H_2O$) $\nu_{max} = 1.802\ \mu m^{-1}$; (DMSO) $\nu_{max} = 1.724\ \mu m^{-1}$. $\mu_{eff} = 1.80\ m_B$.

[Cu(MeenMe)$_2$(acac)$_2$]. Yield: 74%. Colour: blue violet. M.p.: 111–114 °C. *Anal.* Calc. for $C_{18}CuN_4O_4H_{38}$: C, 49.35; H, 8.74; N, 12.78. Found: C, 49.4; H, 8.8; N, 12.6%. IR (KBr): 3235, 3165, 2179, 1605, 1528, 1375 cm^{-1}. $\Lambda_M(H_2O)$: 127 S cm^2 M^{-1}. UV/Vis: (nujol) $\nu_{max} = 1.808\ \mu m^{-1}$; ($CH_3NO_2$) $\nu_{max} = 1.536\ \mu m^{-1}$; ($C_2H_5OH$) $\nu_{max} = 1.696\ \mu m^{-1}$; ($CH_3CN$) $\nu_{max} = 1.523\ \mu m^{-1}$; ($H_2O$) $\nu_{max} = 1.795\ \mu m^{-1}$; (DMSO) $\nu_{max} = 1.732\ \mu m^{-1}$. $\mu_{eff} = 1.83\ m_B$.

[Cu(MeenMe)$_2$(NC-acac)$_2$]·2H$_2$O. Yield: 77%. Colour: blue violet. M.p.: 156–158 °C. *Anal.* Calc. for $C_{20}CuN_6O_6H_{40}$: C, 45.83; H, 7.69; N, 16.03. Found: C, 45.6; H, 7.7; N, 16.2%. IR (KBr): 3235, 3165, 2179, 1605, 1528, 1375 cm^{-1}. $\Lambda_M(H_2O)$: 108 S cm^2 M^{-1}. UV/Vis: (nujol) $\nu_{max} = 1.858\ \mu m^{-1}$; ($CH_3NO_2$) $\nu_{max} = 1.600\ \mu m^{-1}$; ($C_2H_5OH$) $\nu_{max} = 1.680\ \mu m^{-1}$; ($CH_3CN$) $\nu_{max} = 1.689\ \mu m^{-1}$; ($H_2O$) $\nu_{max} = 1.760\ \mu m^{-1}$; (DMSO) $\nu_{max} = 1.718\ \mu m^{-1}$. $\mu_{eff} = 1.72\ m_B$.

[Cu(MeenMe)$_2$(NO$_2$–acac)$_2$]. Yield: 81%. Colour: blue violet. M.p.: 125–126 °C. *Anal.* Calc. for $C_{18}CuN_6O_8H_{36}$: C, 40.94; H, 6.87; N, 15.91. Found: C, 41.0; H, 7.0; N, 16.0%. IR (KBr): 3205, 3162, 1680, 1603, 1450, 1428, 1397, 1360 cm^{-1}. $\Lambda_M(H_2O)$: 215 S cm^2 M^{-1}. UV/Vis: (nujol) $\nu_{max} = 1.818\ \mu m^{-1}$; ($CH_3NO_2$) $\nu_{max} = 1.733\ \mu m^{-1}$; ($C_2H_5OH$) $\nu_{max} = 1.672\ \mu m^{-1}$; ($CH_3CN$) $\nu_{max} = 1.678\ \mu m^{-1}$; ($H_2O$) $\nu_{max} = 1.763\ \mu m^{-1}$; (DMSO) $\nu_{max} = 1.695\ \mu m^{-1}$. $\mu_{eff} = 1.86\ m_B$.

[Cu(MeenMe)$_2$(tfac)$_2$]. Yield: 74%. Colour: blue. M.p.: 188–190 °C. *Anal.* Calc. for $C_{18}CuN_4O_4H_{32}F_6$: C, 39.60; H, 5.91; N, 10.26. Found: C, 40.4; H, 6.0; N, 10.1%. IR (KBr): 3195, 3175, 1670, 1635, 1550, 1510, 1460, 1440 cm^{-1}. $\Lambda_M(H_2O)$: 296 S cm^2 M^{-1}. UV/Vis: (nujol) $\nu_{max} = 1.750\ \mu m^{-1}$; ($CH_3NO_2$) $\nu_{max} = 1.520\ \mu m^{-1}$; ($C_2H_5OH$) $\nu_{max} = 1.616\ \mu m^{-1}$; ($CH_3CN$) $\nu_{max} = 1.529\ \mu m^{-1}$; ($H_2O$) $\nu_{max} = 1.763\ \mu m^{-1}$; (DMSO) $\nu_{max} = 1.681\ \mu m^{-1}$. $\mu_{eff} = 1.73\ m_B$.

[Cu(Me$_2$en)$_2$(NC–acac)$_2$]. Yield: 80%. Colour: blue violet. M.p.: 164–165 °C. *Anal.* Calc. for $C_{20}CuN_6O_4H_{36}$: C, 49.42; H, 7.44; N, 17.21. Found: C, 49.2; H, 7.4; N, 17.2%. IR (KBr): 3225, 3123, 2173, 1623, 1525, 1380 cm^{-1}. $\Lambda_M(H_2O)$: 110 S cm^2 M^{-1}. UV/Vis: (nujol) $\nu_{max} = 1.869\ \mu m^{-1}$; ($CH_3NO_2$) $\nu_{max} = 1.534\ \mu m^{-1}$; ($C_2H_5OH$) $\nu_{max} = 1.680\ \mu m^{-1}$; ($CH_3CN$) $\nu_{max} = 1.608\ \mu m^{-1}$; ($H_2O$) $\nu_{max} = 1.767\ \mu m^{-1}$; (DMSO) $\nu_{max} = 1.736\ \mu m^{-1}$. $\mu_{eff} = 2.02\ m_B$.

[Cu(Me$_2$en)$_2$(NO$_2$–acac)$_2$]. Yield: 85%. Colour: violet. M.p.: 132–133 °C. *Anal.* Calc. for $C_{18}CuN_6O_8H_{36}$: C, 40.94; H, 6.87; N, 15.91. Found: C, 40.6; H, 7.1; N, 15.4%. IR (KBr): 3180, 3072, 1645, 1602, 1450, 1425, 1395, 1360 cm^{-1}. $\Lambda_M(H_2O)$: 154 S cm^2 M^{-1}. UV/Vis: (nujol) $\nu_{max} = 1.802\ \mu m^{-1}$; ($CH_3NO_2$) $\nu_{max} = 1.623\ \mu m^{-1}$; ($C_2H_5OH$) $\nu_{max} = 1.658\ \mu m^{-1}$; ($CH_3CN$) $\nu_{max} = 1.653\ \mu m^{-1}$; ($H_2O$) $\nu_{max} = 1.760\ \mu m^{-1}$; (DMSO) $\nu_{max} = 1.698\ \mu m^{-1}$. $\mu_{eff} = 1.78\ m_B$.

[Cu(Me$_2$en)$_2$(tfac)$_2$]. Yield: 80%. Colour: blue. M.p.: 145–147 °C. *Anal.* Calc. for $C_{18}CuN_4O_4H_{32}$ F_6: C, 39.60; H, 5.91; N, 10.26. Found: C, 38.9; H, 6.2; N, 9.8%. IR

(KBr): 3170, 3075, 1608, 1525, 1465 cm^{-1}. $\Lambda_M(H_2O)$: 222 S cm^2 M^{-1}. UV/Vis: (nujol) $\nu_{max} = 1.802$ μm^{-1}; (CH_3NO_2)$\nu_{max} = 1.802$ μm^{-1}; (C_2H_5OH) $\nu_{max} = 1.590$ μm^{-1}; (CH_3CN) $\nu_{max} = 1.558$ μm^{-1}; (H_2O) $\nu_{max} = 1.742$ μm^{-1}; (DMSO) $\nu_{max} = 1.553$ μm^{-1}. $\mu_{eff} = 1.90$ m_B.

[Cu(pn)$_2$(acac)$_2$](H$_2$O)$_2$. Yield: 75%. Colour: violet. M.p.: 74–76 °C. *Anal.* Calc. for $C_{16}CuN_4O_6H_{38}$: C, 43.08; H, 8.59; N, 12.55. Found: C, 42.8; H, 8.5; N, 12.4%. IR (KBr): 3342, 3112, 1595, 1465, 1445, 1370, 1355 cm^{-1}. $\Lambda_M(H_2O)$: 180 S cm^2 M^{-1}. UV/Vis: (nujol) $\nu_{max} = 1.825$ μm^{-1}; (CH_3NO_2) $\nu_{max} = 1.603$ μm^{-1}; (C_2H_5OH) $\nu_{max} = 1.736$ μm^{-1}; (CH_3CN) $\nu_{max} = 1.636$ μm^{-1}; (H_2O) $\nu_{max} = 1.876$ μm^{-1}; (DMSO) $\nu_{max} = 1.698$ μm^{-1}. $\mu_{eff} = 1.70$ m_B.

[Cu(pn)$_2$(NC–acac)$_2$]. Yield: 77%. Colour: blue violet. M.p.: 194–195 °C. *Anal.* Calc. for $C_{18}CuN_6O_4H_{32}$: C, 47.00; H, 7.01; N, 18.27. Found: C, 47.6; H, 7.1; N, 18.5%. IR (KBr): 3270, 3140, 2184, 1622, 1530, 1380 cm^{-1}. $\Lambda_M(H_2O)$: 156 S cm^2 M^{-1}. UV/Vis: (nujol) $\nu_{max} = 1.894$ μm^{-1}; (CH_3NO_2)$\nu_{max} = 1.642$ μm^{-1}; (C_2H_5OH) $\nu_{max} = 1.789$ μm^{-1}; (CH_3CN) $\nu_{max} = 1.795$ μm^{-1}; (H_2O) $\nu_{max} = 1.828$ μm^{-1}; (DMSO) $\nu_{max} = 1.795$ μm^{-1}. $\mu_{eff} = 1.79$ m_B.

[Cu(pn)$_2$(NO$_2$–acac)$_2$]. Yield: 81%. Colour: violet. M.p.: 156–157 °C. *Anal.* Calc. for $C_{16}CuN_6O_8H_{32}$: C, 38.44; H, 6.45; N, 16.80. Found: C, 37.9; H, 6.5; N, 16.9%. IR (KBr): 3270, 3235, 3140, 1670, 1555, 1430, 1410, 1385, 1380, 1330 cm^{-1}. $\Lambda_M(H_2O)$: 219 S cm^2 M^{-1}. UV/Vis: (nujol) $\nu_{max} = 1.862$ μm^{-1}; (CH_3NO_2) $\nu_{max} = 1.730$ μm^{-1}; (C_2H_5OH) $\nu_{max} = 1.812$ μm^{-1}; (CH_3CN) $\nu_{max} = 1.792$ μm^{-1}; (H_2O) $\nu_{max} = 1.869$ μm^{-1}; (DMSO) $\nu_{max} = 1.805$ μm^{-1}. $\mu_{eff} = 1.87$ m_B.

[Cu(pn)$_2$(tfac)$_2$]. Yield: 72%. Colour: violet. M.p.: 136–137 °C. *Anal.* Calc. for $C_{16}CuN_4O_4H_{28}F_6$: C, 37.10; H, 5.45; N, 10.81. Found: C, 36.9; H, 5.3; N, 10.6%. IR (KBr): 3290, 3240, 3120, 1635, 1495, 1380 cm^{-1}. $\Lambda_M(H_2O)$: 159 Scm^2M^{-1}. UV/Vis: (nujol) $\nu_{max} = 1.754$ μm^{-1}; (CH_3NO_2) $\nu_{max} = 1.626$ μm^{-1}; (C_2H_5OH) $\nu_{max} = 1.631$ μm^{-1}; (CH_3CN) $\nu_{max} = 1.698$ μm^{-1}; (H_2O) $\nu_{max} = 1.825$ μm^{-1}; (DMSO) $\nu_{max} = 1.786$ μm^{-1}. $\mu_{eff} = 1.88$ m_B.

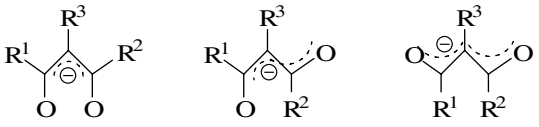
4.4. X-ray crystallographic measurements of [Cu(MeenMe)$_2$(NC–acac)$_2$] · 2H$_2$O

The dark blue crystal selected for lattice constant determination and intensity data collection was a rectangular prism with dimensions $0.22 \times 0.35 \times 0.42$ mm. The crystal was mounted in an arbitrary orientation on a Enraf-Nonius CAD4 four cycles automatic diffractometer using graphite monochromator and Mo Kα radiation. The lattice parameters were calculated by least squares refinement of 25 strong reflections ($17 < \theta < 19°$) which were specifically measured for this purpose. The collection of 3448 reflections as accomplished by operating the diffractometer in the $\omega/2\theta$ scan mode between $2 < \omega < 28°$. Three reference reflections did not show any intensity fluctuations during the measurements. Systematic absences led to space group $P2_1/c$.

All heavy atoms were readily found from a three-dimensional synthesis map using the SIR-92 program [19]. After least-squares refinements with the non-hydrogen atoms, the hydrogen atom were also located in the difference Fourier map. The coordinates for all hydrogen atoms were refined using slack constraints to regularize their geometry, while all non-hydrogen atoms have been refined anisotropically. All calculations were performed employing the CRYSTALS program [20]. Refinement was carried out by full-matrix least-squares on F^2. Details of crystal analysis, data collection and structure refinement are given in Table 7, together with the final values for the unit cell. The figures of the clinographic projections were produced with the program ORTEPII [21].

Table 7
Crystal data and experimental details for the structural study of [Cu(MeenMe)$_2$(NC–acac)$_2$] · 2H$_2$O

Formula	$C_{20}H_{36}N_6O_4Cu \cdot 2H_2O$
Molecular mass, M_r	524.12
Crystal parameters	
Crystal shape	blue violet prisms
Crystal size (mm)	$0.22 \times 0.35 \times 0.42$
Crystal system	monoclinic
Space group	$P2_1/c$
Reflections for cell measurement	25 with $17° \leqslant \theta \leqslant 19°$
Unit-cell dimensions	
a (Å)	10.7874(2)
b (Å)	11.5471(2)
c (Å)	11.6148(3)
β (°)	111.40(3)
V_c (Å^3)	1347.1(3)
Molecules per cell, Z	2
D_x (Mg m^{-3})	1.29 (calculated)
Linear absorption coefficient, μ (mm^{-1})	0.853
Measurement of intensity data	
Instrument	CAD4-F
Monochromator	graphite
Radiation (Mo Kα) (λ, Å)	0.71073
Scan mode	$\omega/2\theta$
ω range (°)	2.03–27.38
Reflections measured	3448
Independent reflections	3052
Reflections observed	1801 reflected [$I \geqslant 2\sigma(I)$]
Parameters refined	151
Indices limits	$-13 \leqslant h \leqslant 13$, $0 \leqslant k \leqslant 14$, $0 \leqslant l \leqslant 15$
F(000)	558
Refinement	
Completeness to $\theta = 27.38$ (%)	100
Weighting scheme	$w = 1/[\sigma^2(F^2) + (0.03P)^2 + 0.00P]$, where $P = (\max(F_o^2, 0) + 2F_c^2)/3$
Goodness-of-fit on F^2	1.097
Final R indices	$R_1 = 0.0263$, $wR_2 = 0.0675$
Largest difference in peak and hole (e Å^{-3})	0.30 and −0.20



U(Z,Z) S(E,Z) W(E,E)

abbreviation	R^1	R^2	R^3
Acac	Me	Me	H
hfac	CF_3	CF_3	H
O_2N-acac	Me	Me	O_2N-
NC-acac	Me	Me	NC-
Cl-acac	Me	Me	Cl-
acacac	Me	Me	$H_3C(O)C$-
dbm	Ph	Ph	H
tfac	CF_3	Me	H
bzac	Ph	Me	H
tfbzac	CF_3	Ph	H

Scheme 1. $S(E,Z)$, $U(Z,Z)$ and $W(E,E)$ conformers of the anions β^-.

4.5. Computational procedure

All quantum chemical calculations were performed using the GAUSSIAN 98W Rev. A.11 program [22].

4.5.1. Study of the β-diketonato ligands

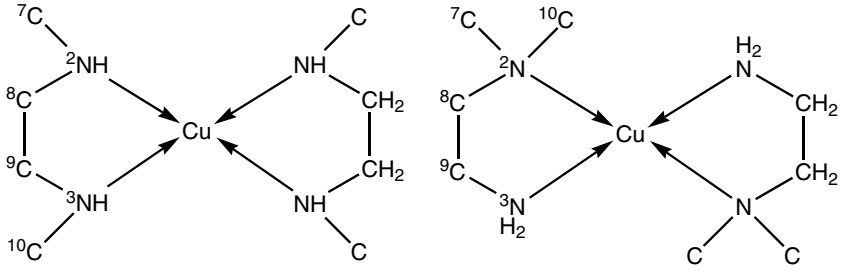
Full geometry optimizations and harmonic frequency calculations for certain β-diketonates and the *S*, *U*, and *W* conformers of their anions, β^-, have been performed in the framework of density functional theory with Becke's three-parameter hybrid functional and the correlation functional of Lee, Yang and Parr B3LYP [23,24] (Scheme 1). The medium sized split valence 6–31G(d,p) basis set, improved with one diffuse function, was implemented. This combination of method and basis set is considered sufficient for an estimate of conformational energy difference [25]. To analyze the nature of bonding the natural population analysis of Weinhold and Carpenter [26] was employed. To study the effect of the solvent (ethanol) on the stability of the anions, the conductor-like screening solvation model (COSMO) was applied using the CPCM keyword [27]. The condensed Fukui functions were employed to predict the most probable reactive sites of the systems under consideration. These reactivity descriptors are derived from the density functional theory as function of the electron density. In the case of electrophilic attack, the Fukui function f_k^- of an atom k in a molecule is expressed by the equation[28]: $f_k^- = q_k(N) - q_k(N-1)$ where $q_k(N)$, $q_k(N-1)$ are atomic charges for atom k in the N and $(N-1)$ electron systems, respectively. These atomic charges were computed from single point calculations at the optimized geometries for the N and $(N-1)$ electron systems.

4.5.2. Study of the $[Cu\beta_2(enR)_2]$

Full geometry optimizations have also been performed for the following chemical entities: $[Cu(MeenMe)_2]^{2+}$ (denoted **M**), $Cu(MeenMe)_2(NC–acac)_2$ (**S1**), $Cu(Me_2en)_2(NC–acac)_2$ (**S2**) in which the NC–acac$^-$ adopts the $S(E,Z)$ conformation, and $Cu(Me_2en)_2(hfac)_2$ ($\mathbf{U_F}$) in which the hfac$^-$ anion is constrained to the $U(Z,Z)$ conformation (see Scheme 2). Furthermore, the compounds $Cu(MeenMe)_2(NC–acac)_2$ (**U1**) and $[Cu(Me_2en)_2(NC–acac)_2]$ (**U2**) were also studied with the conformation of the NC–acac$^-$ anion constrained to $U(Z,Z)$. The B3LYP scheme was employed, since it has been shown to provide accurate results for many transition metal containing systems. Two different basis sets were considered: LanL2MB and LanL2DZ. The LanL2MB basis set specifies the STO-3G basis set [29] for first-row atoms and the Los Alamos effective core potential (ECP) [30] plus MBS on Na–Bi. The LanL2DZ basis set specifies the D95 basis set [31] for first-row atoms and the Los Alamos effective core potential (ECP) plus DZ on Na–Bi. When available, initial geometries were obtained from X-ray structures. The stationary points found from the B3LYP/LanL2MB optimization have been characterized by frequency analysis. No frequency analysis of the optimized points found from the B3LYP/LanL2DZ was attempted due the considerable computational effort required to calculate second derivatives. In order to get an understanding of the main features of the Cu–ligand bonding in this family of compounds the Natural Population Analysis was implemented.

Appendix A. Supplementary material

CCDC 267832 contains the supplementary crystallographic data for this paper. These data can be obtained free of charge via http://www.ccdc.cam.ac.uk/conts/retrieving.html, or from the Cambridge Crystallographic Data Centre, 12 Union Road, Cambridge CB2 1EZ, UK; fax:

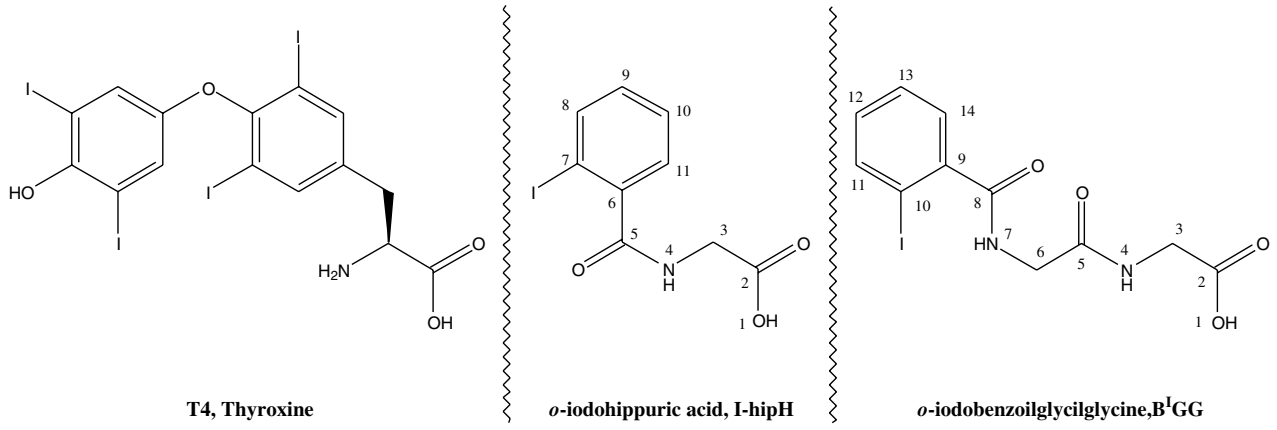


Scheme 2. Atom numbering of the $[Cu(MeenMe)_2]^{2+}$ and the $[Cu(Me_2en)_2]^{2+}$ entities.

(+44) 1223-336-033; or e-mail: deposit@ccdc.cam.ac.uk. Supplementary data associated with this article can be found, in the online version, at doi:10.1016/j.poly.2006.11.008.

References

[1] J.P. Fackler Jr., Prog. Inorg. Nucl. Chem. 6 (1966) 361.
[2] M.V. Veidis, G.H. Schreiber, T.E. Gough, G.J. Palenik, J. Am. Chem. Soc. 91 (1969) 1859.
[3] T.M. Shepherd, J. Chem. Soc. A (1972) 813.
[4] L.L. Funck, T.R. Ortolano, Inorg. Chem. 7 (1968) 567.
[5] M.A. Bush, D.E. Fenton, R.S. Nyholm, M.R. Truter, Chem. Commun. (1970) 1335.
[6] D.P. Graddon, W.K. Ong, J. Inorg. Nucl. Chem. 37 (1975) 469.
[7] (a) B.J. Hathaway, J. Chem. Soc., Dalton Trans. (1972) 1196;
(b) B.J. Hathaway, P.G. Hodgson, J. Inorg. Nucl. Chem. 35 (1973) 4071.
[8] E.J. Corey, J.C. Bailar, J. Am. Chem. Soc. 81 (1959) 2620.
[9] K. Sone, Y. Fukuda, Rev. Inorg. Chem. 11 (1990) 123.
[10] C. Tsiamis, A. Hatzidimitriou, L.C. Tzavellas, Inorg. Chem. 37 (1998) 2903.
[11] T. Kurauchi, M. Matsui, Y. Nakamura, S. Ooi, S. Kawaguchi, H. Kuroya, Bull. Chem. Soc. Jpn. 47 (12) (1974) 3049.
[12] J.P. Collman, Angew. Chem. 77 (1965) 105.
[13] G.M. Sheldrick, Acta Crystallogr., Sect. A 46 (1990) 467.
[14] D.K. Venetopoulou, K.G. Keramidas, G.P. Voutsas, P.I. Rentzeperis, K. Goubitz, C. Tsiamis, Z. Kristallogr. 261 (1993) 1572.
[15] (a) B.P. Kennedy, A.B.P. Lever, J. Am. Chem. Soc. 95 (1973) 6907;
(b) B.J. Hathaway, Struct. Bonding (Berlin) 57 (1984) 55;
(c) S. Ahuja, S. Tripathi, J. Chem. Educ. 88 (1991) 681;
(d) H.F. Holtzclaw, J.P. Collman, J. Am. Chem. Soc. 79 (1957) 3318;
(e) M. Mikami, I. Nakagawa, T. Shimanouchi, Spectrochim. Acta A 23 (1967) 1037;
(f) H. Junge, H. Musso, Spectrochim. Acta A 24 (1967) 1219.
[16] C. Tsiamis, L.C. Tzavellas, A. Stergiou, V. Anesti, Inorg. Chem. 35 (1996) 4984.
[17] O. Angelova, G. Petrov, J. Macicek, Acta Crystallogr., Sect. C 45 (1989) 710.
[18] A. Thornton, Coord. Chem. Rev. 104 (1990) 173, and references therein.
[19] A. Altomare, G. Cascarano, G. Giacovazzo, A. Guagliardi, M.C. Burla, G. Polidori, M. Camalli, J. Appl. Cryst. 27 (1994) 435.
[20] D.J. Watkin, J.R. Carruthers, P.W. Betteridge, CRYSTALS, An Advanced Crystallographic Computer Program, Crystallographic Laboratory, Oxford University, England, 1976.
[21] Johnson, ORTEP II, Report ORNL-5138, Oak Ridge National Laboratory, TN, USA, 1976.
[22] M.J. Frisch, G.W. Trucks, H.B. Schlegel, G.E. Scuseria, M.A. Robb, J.R. Cheeseman, V.G. Zakrzewski, J.A. Montgomery Jr., R.E. Stratmann, J.C. Burant, S. Dapprich, J.M. Millam, D. Daniels, K.N. Kudin, M.C. Strain, O. Farkas, J. Tomasi, V. Barone, M. Cossi, R. Cammi, B. Mennucci, C. Pomelli, C. Adamo, S. Clifford, J. Ochterski, G.A. Petersson, P.Y. Ayala, Q. Cui, K. Morokuma, P. Salvador, J.J. Dannenberg, D.K. Malick, D. Rabuck, K. Raghavachari, J.B. Foresman, J. Cioslowski, J.V. Ortiz, A.G. Baboul, B.B. Stefanov, G. Liu, A. Liashenko, P. Piskorz, I. Komaromi, R. Gomperts, R.L. Martin, D.J. Fox, T. Keith, M.A. Al-Laham, C.Y. Peng, A. Nanayakkara, M. Challacombe, P.M.W. Gill, B. Johnson, W. Chen, M.W. Wong, J.L. Andres, C. Gonzalez, M. Head-Gordon, E.S. Replogle, J.A. Pople, GAUSSIAN 98, Revision A.11, Gaussian, Inc., Pittsburgh, PA, 2001.
[23] D. Becke, J. Chem. Phys. 98 (1993) 5648.
[24] Lee, W. Yang, R.G. Parr, Phys. Rev. B 37 (1988) 785.
[25] J.B. Foresman, A.E. Frisch, Exploring Chemistry with Electronic Structure Methods, second ed., Gaussian Inc., Pittsburgh, PA, 1996.
[26] J.E. Carpenter, F. Weinhold, J. Mol. Struct. (Theochem) 169 (1998) 41.
[27] V. Barone, M. Cossi, J. Phys. Chem. A 102 (1998) 1995.
[28] W. Yang, W.J. Mortier, J. Am. Chem. Soc. 108 (1986) 5708.
[29] W.J. Hehre, R.F. Stewart, J.A. Pople, J. Chem. Phys. 51 (1969) 2657.
[30] P.J. Hay, W.R. Wadt, J. Chem. Phys. 82 (1985) 270.
[31] T.H. Dunning Jr., P.J. Hay, in: H.F. SchaeferIII (Ed.), Modern Theoretical Chemistry, vol. 3, Plenum, New York, 1976, p. 1.



Scheme 1. Formulae of thyroxine and two model compounds of it: *o*-iodohippuric acid and *o*-iodobenzoylglycilglycine.

the new results obtained and the previously reported by us, in three binary and four ternary complexes involving *ortho*-iodohippuric acid derivatives and acyclovir (acv) or 1,10-phenanthroline (phen).

2. Experimental

Elemental microanalyses were carried out using a Thermo Finnigan model Flash 1112 microanalyzer. IR spectra in the solid state (KBr pellets) were measured in the 4000–400 cm^{-1} range on a Bruker IFS 66 spectrometer. ^1H NMR spectra were recorded at room temperature on a Bruker AMX 300 (300 MHz). Proton chemical shifts in deuterated dimethylsulfoxide ([D_6] DMSO) were referenced to [D_6] DMSO (δ[D_6] DMSO: 2.47 ppm).

Reagents were used as received from Sigma, Merck or Aldrich. *o*-Iodohippuric acid (*o*-iodobenzoylglicine) was prepared according to the literature procedure [20,21] or supplied by Aldrich. *o*-Iodobenzoylglycilglycine (B^IGG) was also synthesized according to the general procedure for hippuric acid [20,21] (see below).

Synthesis of binary complexes, $[Zn(I\text{-}hip)_2(OH_2)_2]_2 \cdot 3H_2O$ (**1**) [17], $[Ag(I\text{-}hip)] \cdot 1.25H_2O$ (**2**) [18] and $[Cu(I\text{-}hip)_2(OH_2)_3] \cdot 2H_2O$ (**3**) [19] are reported previously. Moreover, we have tried to form some ternary complexes between these compounds and others ligands: [(Co, Ni or Zn)$(I\text{-}hip)_2(acv)(OH_2)_3$] (**4**) [17], $[Cu(I\text{-}hip)(phen)_2]^+$-$(I\text{-}hip^-) \cdot 7H_2O$ (**5**) [19], $[Cu(I\text{-}hip)(bpy)_2]^+(I^-) \cdot 1.5H_2O$ (**6**) and $[Cu(B^IGG)(bpy)_2]^+(I^-) \cdot 4H_2O$ (**7**).

2.1. Synthesis of o-iodobenzoilglycilglycinate sodium salt (B^IGG)

Sodium bicarbonate (42 mmol) was added to a solution of glycilglycine (20 mmol) in water (35 ml). The mixture was stirred for 1 h until complete solution and *o*-iodobenzoyl chloride (20 mmol) was added together with acetone (5 ml) (in order to increase the solubility and reactivity of the *o*-iodobenzoil chloride). The reaction was slightly heated at 50 °C and stirred for 4 h. Subsequently, the reaction mixture was neutralized with HCl of 1 N, stirred for 15 min, and the resulting precipitate was filtered off and washed with cold water. The neutralization-washing process was repeated three times and finally the crude *o*-iodobenzoylglycilglycinate sodium salt were washed with diethyl ether, filtered off and dry at room temperature (yield: 65%).

The isolated product, white powder, was the monohydrated sodium salt: sodium *o*-iodobenzoylglycilglycinate (B^IGG) monohydrate. *Anal.* Calc. for $C_{11}H_{12}IN_2NaO_5$: C, 32.86; H, 3.01; N, 6.97. Found: C, 32.73; H, 3.12; N, 6.95%. IR (cm^{-1}): 414vw, 433vw, 546m, 586m, 611m, 637m, 680m, 728w, 749m, 775w, 872w, 914vw, 943vw, 985m, 999s, 1015m, 1041w, 1093m (br), 1239s, 1263m, 1293m, 1347m, 1432s, 1443s, 1463m, 1535s, 1587m, 1620vs, 1664s, 1711s, 2043m, 3343vs. ^1H NMR ([D_6] DMSO): δ 12.03 [bs, 1H, C(2)OO(1)-H], 8.61 [t, 1H, N(7)-H, $J = 5.7$ Hz], 8.08 [t, 1H, N(4)-H, $J = 5.4$ Hz], 7.85 [d, 1H, H(14), $J = 7.8$ Hz], 7.42 [s(br), 2H, H(11 and 12)], 7.15 [m, 1H, H(13)], 3.85 [d, 2H, C(6)-H_2, $J =$ 5.7 Hz], 3.76 [d, 2H, C(3)-H_2, $J = 5.4$ Hz].

2.2. $[Cu(I\text{-}hip)(bpy)_2]^+(I^-) \cdot 1.5H_2O$ (6)

Basic copper carbonate $[CuCO_3 \cdot Cu(OH)_2]$ (1 mmol) and I-hipH (3 mmol) in water (100 ml) were refluxed for 2 h, then the excess of insoluble reactants were filtered off, followed by the addition of solid bpy (3 mmol) and subsequently the mixture was refluxed for two more hours. Finally, sodium iodide (1.5 mmol) was added to the solution to assist the crystallization. This synthesis is similar to that previously reported to prepare acyclovir ternary compounds [17]. Green crystals of $[Cu(I\text{-}hip)(bpy)_2]^+(I^-) \cdot 1.5H_2O$ (**6**) suitable for X-ray diffraction studies were obtained after 4–5 days from the parental solution and has been separated one-to-one of others brown crystals corresponding to the non-desired reaction by-product $[Cu(I)(bpy)_2]^+ \cdot I^-$ [22]. The ternary complex obtained decomposes on air by lose of water molecules (yield: ca. 30%). Repetitions of this synthesis without sodium iodide addition yield a mixture of two types of crystals corresponding to $[Cu(I\text{-}hip)(bpy)_2]^+(I\text{-}hip^-) \cdot 4H_2O$ and a certain quantity of the previously described ternary complex

$[Cu(I\text{-}hip)(bpy)_2]^+(I^-)\cdot 1.5H_2O$ where the origin of the iodide counter ion is not clear (an impurity or a decomposition of I-hip).

*$[Cu(I\text{-}hip)(bpy)_2]^+(I^-)\cdot 1.5H_2O$ (**6**)*: Green crystals. *Anal*. Calc. for $C_{29}H_{23}CuI_2N_5O_3$ (completely dehydrated sample): C, 43.17; H, 2.87; N, 8.68; I, 31.46. Found: C, 43.19; H, 2.89; N, 7.86; I, 32.14%. IR (cm^{-1}): 417vw, 482vw, 568w, 636w, 661w, 689w, 730m, 745m, 770vs, 831vw, 870vw, 914vw, 949vw, 985vw, 999w, 1014m, 1059vw, 1101w, 1121vw, 1164m, 1254m, 1297m, 1318m, 1382s, 1430m, 1445s, 1459m, 1473s, 1497s, 1513s, 1582vs, 1601s, 1648vs, 1669s, 3059m, 3379m.

$[Cu(I\text{-}hip)(bpy)_2]^+(I\text{-}hip^-)\cdot 4H_2O$: Blue crystals. *Anal*. Calc. for $C_{38}H_{38}CuI_2N_6O_{10}$: C, 43.22; H, 3.63; N, 7.96. Found: C, 42.50; H, 3.54; N, 7.96%. IR (cm^{-1}): 416vw, 440vw, 456vw, 532w, 579w, 624w, 636w, 652w, 663w, 672w, 715w, 732m, 762m, 772m, 867vw, 955vw, 1013m, 1031vw, 1062vw, 1086vw, 1106vw, 1158vw, 1175w, 1232w, 1253m, 1261m, 1311m, 1398vs, 1448m, 1457m, 1470m, 1506s, 1582s, 1600s, 1634s, 1652vs, 3061w, 3313m, 3394m, 3486m.

2.3. $[Cu(B^IGG)(bpy)_2]^+(I^-)\cdot 4H_2O$ (7)

Basic copper carbonate (1 mmol) and B^IGG sodium salt (3 mmol) in water (100 ml) were refluxed for 2 h, then the excess of insoluble reactants were filtered off, followed by the addition of solid bpy (3 mmol) and subsequently the mixture was refluxed for two more hours. An oily complex material was obtained in all attempts. Only one crystal suitable for X-ray diffraction studies could be obtained.

2.4. X-ray crystallographic study

Suitable crystals of **6** and **7** were selected for X-ray single crystal diffraction experiments and mounted at the tip of glass fibres on an Enraf-Nonius CAD4 diffractometer producing graphite-monochromated Mo Kα radiation ($\lambda = 0.71073$ Å). In each case, after the random search of 25 reflections, the indexation procedure gave rise to the cell parameters (see Table 1 for a summary of the crystal data). Data were collected in the ω-2θ scan mode. Absorption correction for **6** was performed following the empirical DIFABS method. The structural resolution procedure was made using the WinGX package [23]. Solving for structure factor phases was performed by SHELXS-97 [24] for **6** and SIR-2004 [25] for **7**, and the full matrix refinement by SHELXL-97 [26]. Non-H atoms were refined anisotropically and H-atoms were introduced in calculated positions and refined riding on their parents atoms. A summary of refinements parameters can also be seen in Table 1. H-atoms of water molecules could not be located in any

Table 1
Selected crystallographic data for compounds **6** and **7**

Identification code	**6**	**7**
Empirical formula	$C_{58}H_{52}Cu_2I_4N_{10}O_9$	$C_{31}H_{34}CuI_2N_6O_8$
Formula weight	1667.78	935.98
Temperature (K)	294(2)	293(2)
Wavelength (Å)	0.71073	0.71073
Crystal system	monoclinic	triclinic
Space group	$P2_1/n$	$P\bar{1}$
Unit cell dimensions		
a (Å)	15.912(3)	12.515(3)
b (Å)	17.705(4)	12.993(3)
c (Å)	22.472(4)	13.662(4)
α (°)	90	66.144(16)
β (°)	101.474(14)	65.31(2)
γ (°)	90	71.84(2)
Volume ($Å^3$)	6204(2)	1818.6(8)
Z	4	2
D_{calc} (Mg/m^3)	1.785	1.709
Absorption coefficient (mm^{-1})	2.738	2.353
$F(000)$	3248	922
Crystal size (mm)	$0.46\times0.38\times0.21$	$0.46\times0.42\times0.29$
θ Range for data collection (°)	1.44–24.98	1.73–24.98
Index ranges	$-18\leqslant h\leqslant 18$, $-21\leqslant k\leqslant 0$, $0\leqslant l\leqslant 26$	$-14\leqslant h\leqslant 13$, $-15\leqslant k\leqslant 14$, $-16\leqslant l\leqslant 0$
Reflections collected	11182	6606
Independent reflections (R_{int})	10888 (0.0397)	6309 (0.0295)
Completeness to final θ (%)	99.9	98.7
Maximum and minimum transmission	0.5971 and 0.3657	
Refinement method	full-matrix least-squares on F^2	full-matrix least-squares on F^2
Data/parameters	10888/748	6309/457
Goodness-of-fit on F^2	1.024	1.299
Final R indices [$I>2\sigma(I)$]	$R_1 = 0.0666$, $wR_2 = 0.1746$	$R_1 = 0.0765$, $wR_2 = 0.2488$
R indices (all data)	$R_1 = 0.1257$, $wR_2 = 0.2099$	$R_1 = 0.1263$, $wR_2 = 0.3253$
Largest difference in peak and hole (e $Å^{-3}$)	1.767 and −1.686	2.072 and −2.050

case. Largest diffraction peaks and holes were located close to heavy atoms in Fourier difference map. The ORTEP [27] representations of the two complexes were made at 50% probability.

The software used to generate the figures and to calculate the distances and angles values are MERCURY 1.4.1 [28], which can be obtained free of charge from CCDC, and Accelrys DS Viewer Pro 5.0 [29], which a 30-days trial version can also be obtained free of charge.

D_{pln}, D_{Atn} and D_{lim} distances as well as θ, φ and ω angles in C–I···π interactions are calculated as defined by Prasanna and Guru-Row [30].

In order to measure the distortions of the coordination polyhedron from the square pyramid to the trigonal bipyramid (CN = 5), the Addison parameter (τ) has been calculated according to the literature procedures [31], as an indication of the degree of trigonality. τ is defined as $(\beta - \alpha)/60$, where β and α are the two *trans*-basal angles. For a perfectly square pyramidal geometry τ is equal to zero, while it becomes unity for a perfectly trigonal-bipyramidal geometry.

3. Results and discussion

3.1. Crystal structure of $[Cu(I\text{-}hip)(bpy)_2]^+(I^-)\cdot 1.5H_2O$ (6)

In X-ray crystal structure of $[Cu(I\text{-}hip)(bpy)_2]^+(I^-)\cdot 1.5H_2O$ (**6**) (Fig. 1), we detect, in a first approach, that the coordination environment is coincident with that for compound $[Cu(I\text{-}hip)(phen)_2]^+(I\text{-}hip^-)\cdot 7H_2O$ (**5**). Two complex units are present in the asymmetrical unit where the two copper(II) ions present distorted octahedral coordinations. These ions are linked to two oxygen atoms of the carboxylate anion of I-hip by means of a strong and an ancillary bonds [Cu–O distances: O(9), 2.100(8) and O(10), 2.71 Å for Cu(1); O(43), 2.217(9) and O(44), 2.47 Å for Cu(2)] and to the four nitrogen atoms from two bpy molecules [Cu–N distances: N(11), 1.972(8); N(22), 2.064(7); N(23), 2.164(8) and N(34), 1.975(7) Å for Cu(1); N(45), 2.131(8); N(56), 1.990(7); N(57), 1.982(7) and N(68), 2.089(8) Å for Cu(2)]. The positive charges of complex units are compensated by the presence of iodide atoms (one per formula unit). The structure is completed by three water molecules per asymmetrical unit.

In this compound, the Addison parameter (τ) presents a value of $\tau = 0.41$. It means that, considering a coordination number CN = 5, the real coordination polyhedron is about halfway between a square pyramidal and a trigonal bipyramidal coordinations.

The 3D structure of this compound is formed by bidimensional layers coincident with the *a*–*c*-plane.

There is not present any intramolecular interaction, but the crystal unit is built by means of a lot of intermolecular interactions among complex units and also with the water molecules. The more relevant interactions should be:

(a) Stacking [32] between bipyridyl rings in the couple of complexes in the asymmetrical unit [distance C(27)···C(50) or C(29)···C(52), ca. 3.34 Å; torsion, 179°] strengthened by $C_{aromatic}$–H···π interactions

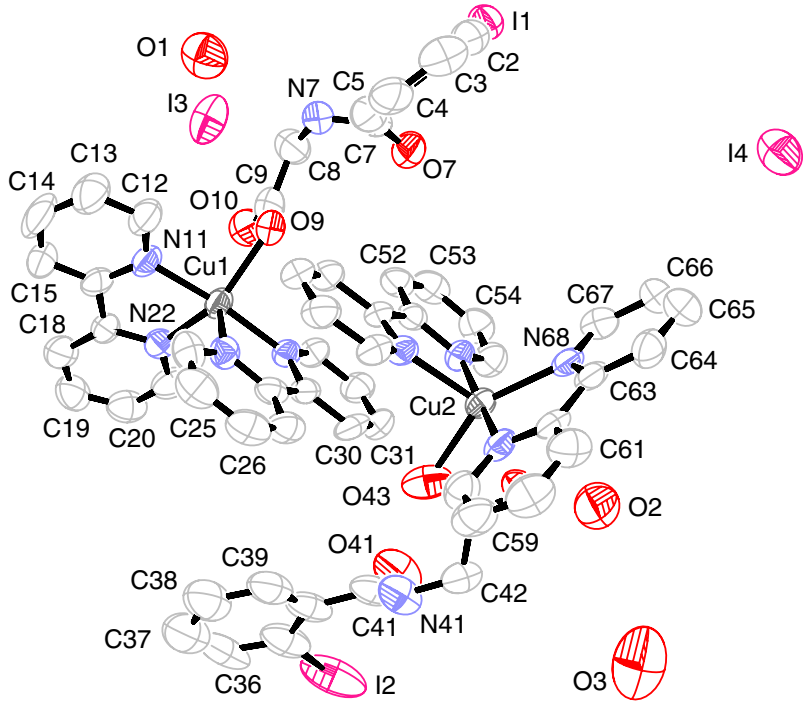


Fig. 1. ORTEP representation (50% probability) of the asymmetrical unit in $[Cu(I\text{-}hip)(bpy)_2]^+(I^-)\cdot 1.5H_2O$ (**6**). Numeration of several atoms has been omitted for clarity.

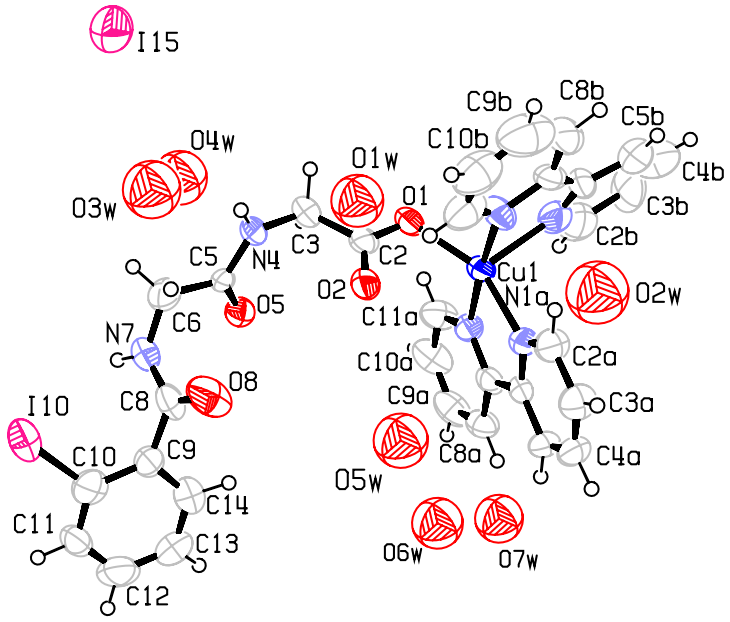


Fig. 2. ORTEP representation (50% probability) of the complex $[Cu(B^{I}GG)(bpy)_2]^{+}(I^{-}) \cdot 4H_2O$ (**7**).

for each bipyridyl [distance H(2)···C(28), H(36)···C(50) and H(36)···C(51); 2.79, 2.70 and 2.87 Å], which yields a more extended and complex C–H···π···π···H–C interaction.

(b) An extended stacking, normal to the described C–H···π···π···H–C units, between four aromatic rings, two *o*-iodobenzoyl rings, which are part of the C–H···π contact, at the inside [distance C(2)···C(38) or C(4)···C(36), ca. 3.36 Å; torsion, 175°], and two bipyridyl ligands which do not participate in that interaction at the outside of the group [distance C(2)···C(21) or C(3)···C(21), ca. 3.25 Å and torsion, 158°; distance C(67)···C(36), ca. 3.31 Å and torsion, 157°]. This π-cluster unit, is extended along the *a* direction, like a wire, assisted by the formation of another stacking between the winger bipyridyl rings [distance C(16)···C(64), ca. 3.49 Å and torsion 173°] and strengthened by contacts between O(44)···H(18) and O(10)···H(64) (see below). These infinite stacking chains are intertwined by orthogonal C–H···π···π···H–C clusters which grow from the two central *o*-iodobenzoyl rings to right and left sides. These crisscrossed strings form 2D networks which are piled in the *b* direction related, for instance, by the iodine anions and water molecules (for more information see Section 3.3.1.5).

(c) An interesting $C_{aromatic}$–H···O hydrogen bonds[1] between carboxylate or carboxamide from I-hip ligand and bipyridyl [distance and angle: C(27)–H(27)···O(43), 3.34 Å and 153°; C(52)–H(52)···O(9), 3.41 Å and 144°; C(47)–H(47)···O(7), 3.22 Å and 127°;C(32)–H(32)···O(41), 3.39 Å and 146°; C(18)–H(18)···O(44), 3.33 and 143°; and C(64)–H(64)···O(10), 3.46 Å and 158°].

(d) And finally, iodine atoms interact with their environment: thus, iodine from *o*-iodobenzoyl rings, shows an intramolecular contact between this halogen and the oxygen atom from amide bond [distances I(1)···O(7) and I(2)···O(41), 3.42 and 3.26 Å]. Although the contact angle is not very adequate [angle C=O···I, 80°], we observe a decrease in the torsion between the aryl ring and the peptidic bond of the I-hip ligand, with regard to the binary I-hip complexes, which could be explained by the presence of this interaction. And finally, the iodide anions interact with I–$C_{aromatic}$ [distance I(4)···I(1), 3.89 Å] and H–$C_{aromatic}$ moieties [distance I(4)···H(41), 2.83; I(4)···H(58), 3.08; I(3)···H(14), 3.07; and I(3)···H(48), 3.10 Å]. All these contacts are shorter than the corresponding van der Waals values [I···I, 3.96; I···O, 3.50; and I···H, 3.18 Å] calculated by Bondi [33].

3.2. Crystal structure of $[Cu(B^{I}GG)(bpy)_2]^{+}(I^{-}) \cdot 4H_2O$ (7)

In this X-ray structure, the copper(II) ion present a distorted octahedral coordination (see Fig. 2), being linked to the two O atoms of the carboxylate in I-hip [Cu(1)–O distances: O(1), 2.012(7) and O(2), 2.74 Å] and to the four N atoms from two bpy molecules [Cu(1)–N distances: N(1A), 2.041(8); N(12A), 1.993(9); N(1B), 2.175(10) and N(12B), 2.016(9) Å]. The coordination environment is again coincident with the

[1] All hydrogen bond distances are given between the donor and the acceptor atoms; angles of interaction correspond to D–H···A.

corresponding to compounds **5** and **6** and the complex unit is positively charged and compensated by the presence of one iodide atom. The presence of seven water molecules completes the structure (water molecules O1W and O2W have complete occupancy (100%); but O3W, O4W and O5W have only 40%; O6W, 30%; and O7W, 50% occupancy). The 3D structure of this compound is also formed by bi-dimensional layers in the *a*–*b*-plane.

The Addison parameter (τ) relating to this compound presents a value of $\tau = 0.33$. In this compound, the geometry is a little nearer to a square pyramid than those for compound **6**, but anyway it is also faraway from any of the two perfect geometries.

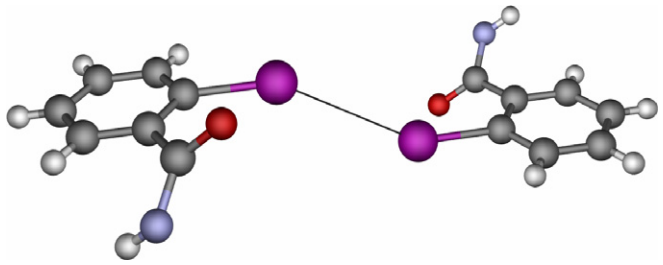


Fig. 3. Iodine–iodine interaction in compound $[Cu(I\text{-}hip)_2(OH_2)_3]\cdot 2H_2O$ (**3**). In order to centre this short contact with a value of 3.78 Å, only the nearness of iodine atoms has been represented (more structural information in Ref. [19]).

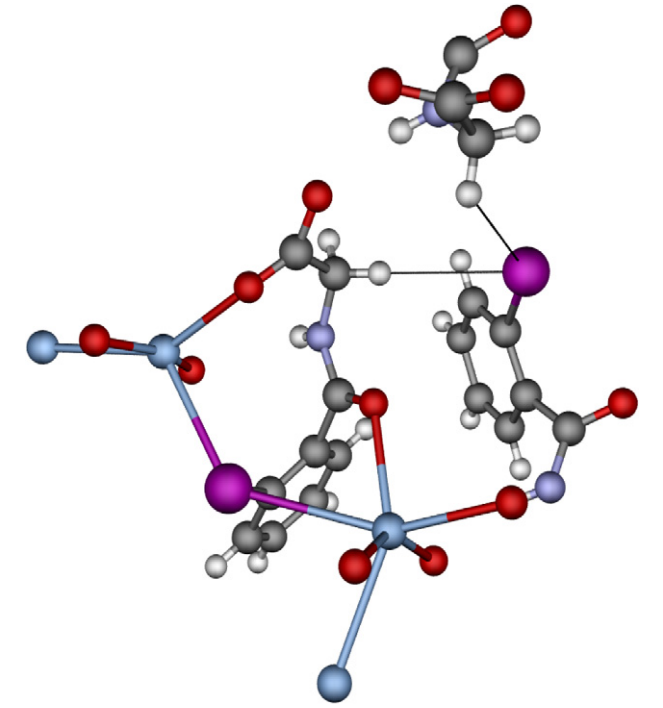


Fig. 4. Iodine–hydrogen interaction (depicted with black lines) and iodine–metal bond (depicted as a standard bond) in compound **2** [18]. (For interpretation of the references to colour in this figure legend, the reader is referred to the web version of this article.)

Every cationic complex recognizes another one (head to tail) by means of a tandem of hydrogen bonds between peptide moieties [distance and angle O(5)···H(7)–N(7), 2.94 Å and 167°] and each of these couples interacts with another one via water molecules and iodide atoms. In order to form the molecular planes within the crystal structure, each bipiridyl ring of one couple interacts with the corresponding one of other couple by means of stacking interactions [distance C(10A)···C(4A) and C(4A)···C(10A), 3.35 Å; distance C(6A)···C(8A) and C(8A)···C(6A), 3.43 Å; torsion 170°] [distance C(6B)···C(9B) and C(9B)···C(6B), 3.33 Å; distance C(7B)···C(8B) and C(8B)···C(7B), 3.36 Å; torsion 171°].

With regard to iodine interactions, one short contact between iodine moiety and iodide anion are present [distance I(10)···I(15), 3.81 Å], shorter than the corresponding van der Waals distance must be mentioned and the iodide anion also interacts with H–$C_{aromatic}$, as in compound **6** [distance I(15)···H(9B), 3.09 Å].

Finally, two $C_{aromatic}$–H···O hydrogen bonds are also present between O atoms from carboxylato/peptide and bipyridyl (type A) moieties [distance and angle: C(4A)–H(4A)···O(5), 2.98 Å and 119.9°; C(5A)–H(5A)···O(2), 3.52 Å and 166.1°; and C(8A)–H(8A)···O(2), 3.46 Å and 163.5°].

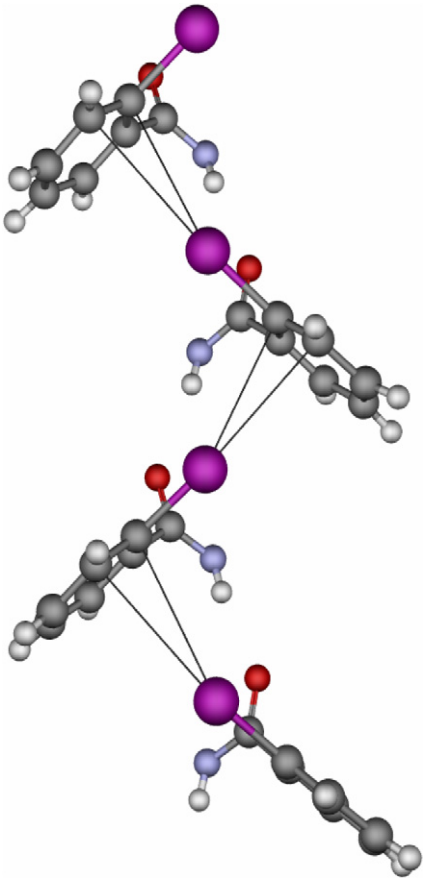


Fig. 5. C–I···π interaction in compound $[Zn(I\text{-}hip)_2(OH_2)_2]_2\cdot 3H_2O$ (**1**) [17]. The I···$C_{aromatic}$ distance values are 3.56 and 3.74 Å alternatively.

3.3. Iodine interactions present in these compounds

Different levels of interactions and self-assemblies involving iodine atoms have been detected in the seven compounds previously described.

3.3.1. A simple type of recognition patterns

3.3.1.1. Iodine–iodine interaction (I···I). $[Cu(I\text{-}hip)_2(OH_2)_3]\cdot 2H_2O$ (**3**) presents a short contact between two iodine atoms in I-hip rings (Fig. 3). The bond distance is about 0.2 Å shorter than de van der Waals value and the final 3D structure is generated by means those reported iodine contacts which yields different planes in the *c* direction.

Similar type of interaction is also present in compound $[(Co, Ni \text{ or } Zn})(I\text{-}hip)_2(acv)(OH_2)_3]$ (**4**). Likewise, an equivalent contact Ph-I···I^- appears in compounds $[Cu(I\text{-}hip)(bpy)_2]^+(I^-)\cdot 1.5H_2O$ (**6**) and $[Cu(B^IGG)(bpy)_2]^+(I^-)\cdot 4H_2O$ (**7**). In all cases, these iodide interactions are very important to maintain the 3D crystal structure.

3.3.1.2. Iodine–hydrogen interaction (I···H–C). Another type of interaction is present between iodine and hydrogen(-C) atoms as, for instance, in complex $[Ag(I\text{-}hip)]\cdot 1.25H_2O$ (**2**), where iodine moiety is closed to two hydrogen atoms from glycine moieties (Fig. 4). These distances are approximately 3.10 Å whereas the calculated van der Waals distance is 3.18 Å.

In the other compounds, as in $[(Co, Ni \text{ or } Zn})(I\text{-}hip)_2(acv)(OH_2)_3]$ (**4**), $[Cu(I\text{-}hip)(bpy)_2]^+(I^-)\cdot 1.5H_2O$ (**6**) and $[Cu(B^IGG)(bpy)_2]^+(I^-)\cdot 4H_2O$ (**7**), is also detected this kind of interaction, where the hydrogen atoms belong to aromatic rings instead of aliphatic chains.

3.3.1.3. Iodine–metal bond (I–Ag). Complex $[Ag(I\text{-}hip)]\cdot 1.25H_2O$ (**2**) also presents direct bonds between iodine (I-hip) and two silver atoms at 3.15 and 3.36 Å (Fig. 4). These contacts are in the levels described in the literature for Ag–I short contact or large bond. Iodine bonded to metals is only present in silver complexes.

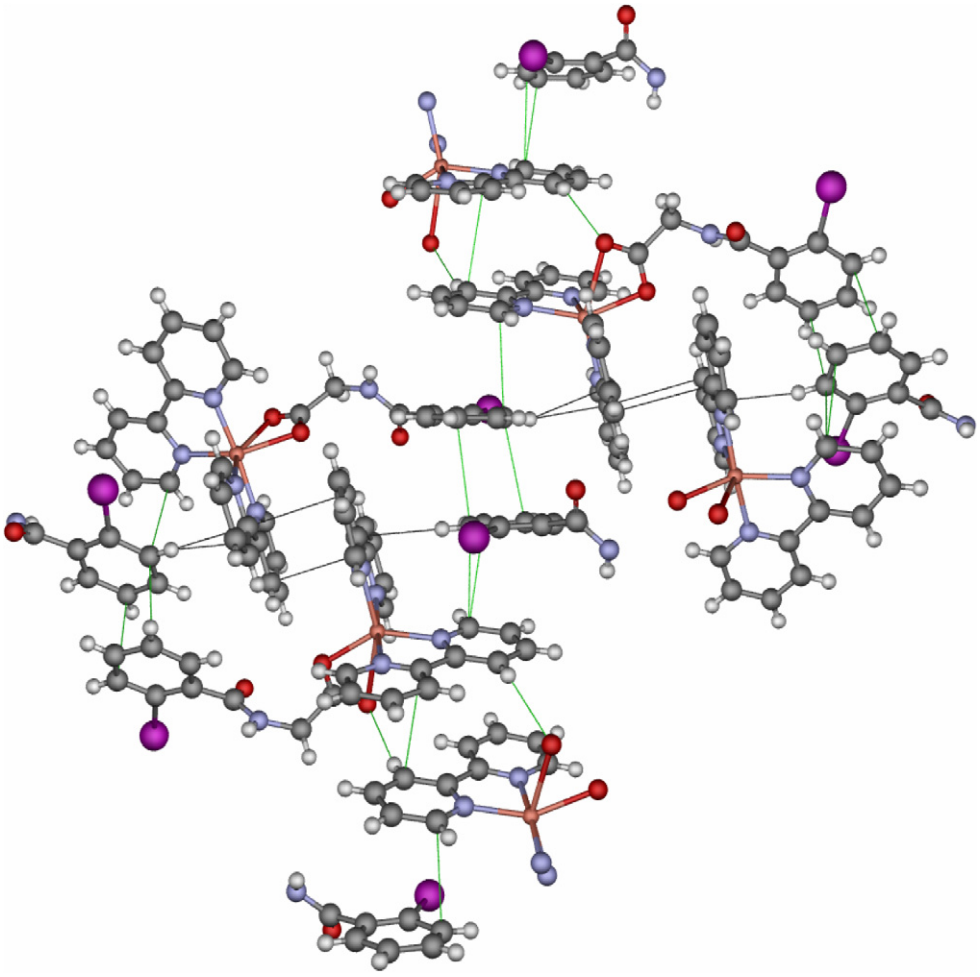


Fig. 6. Two types of connected interactions which direct the formation of a planar structure in compound $[Cu(I\text{-}hip)(bpy)_2]^+(I^-)\cdot 1.5H_2O$ (**6**). The stacking piled along the *a* direction extended to all the crystal is depicted with green lines (vertical in the center of the figure) and the C–H···π···π···H–C patterns which are observed in horizontal and indicated with black lines (one on the left side and another one on the right side). (For interpretation of the references to colour in this figure legend, the reader is referred to the web version of this article.)

3.3.1.4. Iodine–π system interaction (C–I···π). Binary derivative $[Zn(I\text{-hip})_2(OH_2)_2]_2 \cdot 3H_2O$ (**1**) holds, in its crystal structure, a close contact between iodine atoms and aromatic rings which remember us a C–H···π interaction. In these complex an extended C–I···π interaction (Fig. 5) where one iodine moiety of I-hip contacts closely with the aromatic ring of another I-hip molecule is present. The interaction occurs in the neighbourhood of the iodine moieties (see Fig. 5). This fact tells us than the iodine atom is important in the interaction not only to bond another ring, but also to active the aromatic ring in order to be bonded.

A recent publication [30] has been defined various parameters (three distances and three angles) in order to explore and compare this interaction type. In compound **1**, the six parameter values are (for shorter/longer interactions): D_{pln}, 3.577/3.778 Å; D_{Atn}, 3.559/3.739 Å; D_{lim}, 3.493/3.709 Å; θ, 78.13–78.02°/80.70–77.93°; φ, 79.70–79.40°/78.33–81.16° and ω, 84.10°/84.22°. In the cited paper, is also defined de maximum distance at which a iodine–aromatic ring contact can be considered as interaction: D_{max}, identified as sum of the van der Waals radii of iodine and half-thickness of aromatic ring with an added tolerance of 5% of this sum in order to address electrostatic contributions to the interaction, has a value of 3.86 Å. Our results, confirm the directional preference of the C–I···π interactions.

3.3.1.5. Interactions promoted by iodine atoms which do not directly participate in them. Iodine substitution in aromatic rings improves the capability of interaction between these aromatic rings. Thus, in $[Cu(I\text{-hip})(bpy)_2]^+(I^-) \cdot 1.5H_2O$ (**6**) is not possible to detect any important iodine interaction, but there are very important stacking self-assemblies. In Fig. 6 are depicted the 2D plane formed by these interactions. In green colour represent the stacking along the *a* direction, which crosses all the crystal, whereas in black colour two C–H···π···π···H–C cluster patterns are shown. Detailed distances of these interactions have been reported in Section 3.1.

There are other examples in which the presence of a iodine substitution in the aromatic rings helps to stabilize the formation or reinforcement of stacking interactions. For instance, in compound $[(Co, Ni \text{ or } Zn)(I\text{-hip})_2(acv)(OH_2)_3]$ (**4**), it is possible to detect a stacking interaction between acyclovir and I-hip which enforce the formation of two enantiomeric structures.

3.3.2. A complex pattern of recognition factors

3.3.2.1. Iodine–iodine (I···I) plus iodine–hydrogen (I···H–C) interactions. $[(Co, Ni \text{ or } Zn)(I\text{-hip})_2(acv)(OH_2)_3]$ (**4**) show two types of described single recognition patterns involving iodine atoms (Fig. 7). Thus, the resulting iodine network is formed by iodine–hydrogen(aromatic) contacts at 3.15 Å [van der Waals value, 3.18 Å] and iodine–iodine bonds at 3.80 Å [van der Waals value, 3.96 Å]. In the picture, the first ones are indicated in green thin lines, and the second ones are indicated in black thin lines.

3.3.2.2. C–I···π···π···I–C. Another interesting way of interaction between iodine atoms is by means a long

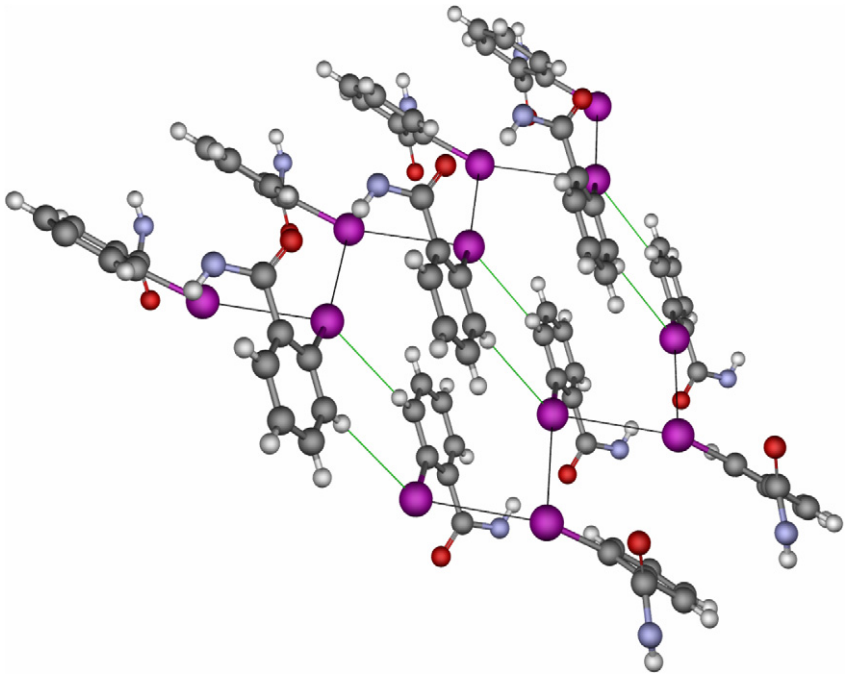


Fig. 7. Network of interactions in complex $[(Co, Ni \text{ or } Zn)(I\text{-hip})_2(acv)(OH_2)_3]$ (**4**) [17]. There are hydrogen–iodine interactions depicted with green lines and iodine–iodine contacts indicated with black lines. These two types of recognitions form to chains of iodine atoms which are related to each other by means of tandems of C–H···I interactions. (For interpretation of the references to colour in this figure legend, the reader is referred to the web version of this article.)

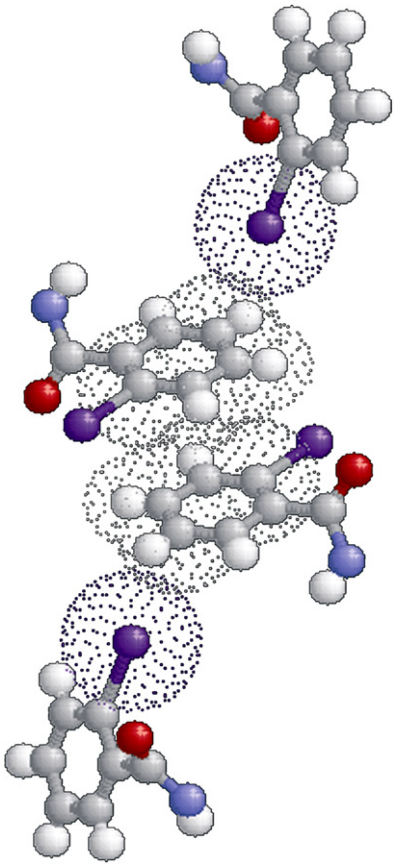


Fig. 8. New C–I···π···π···I–C cluster pattern presents in complex [Cu-(I-hip)(phen)$_2$]$^+$(I-hip$^-$) · 7H$_2$O (**5**) [19]. As it is the most complex iodine interactions observed in the family of compounds presented in this work, we have represented the implied atoms as boundary surfaces in order to well understand the composition of recognition patterns.

distance C–I···π···π···I–C as can be observed in [Cu(I-hip)-(phen)$_2$]$^+$(I-hip$^-$) · 7H$_2$O (**5**). Fig. 8 illustrates these ideas and show this new pattern of molecular recognition: an stacking interaction between two aryl rings from I-hip [distance, 3.39 Å; torsion, 180°] reinforced by two interesting C–I···C(ring) interactions [distance, 3.60 and 3.55 Å], similar to a C–H···π one, on each stacked ring. We can also understand this cluster as two C–I···π interactions locked by a stacking between two other *o*-iodobenzoyl rings (four iodophenyl moieties are implied in these kind of interaction).

The six distance parameters for compound **5** are: D_{pln}, 4.158 Å; D_{Atn}, 3.551–3.602 Å; D_{lim}, 3.509 Å; θ, 54.90–57.26°; φ, 106.64–103.88° and ω, 115.04°. These results are also in agreement with the discussion about this type of interaction, made for compound **1**.

4. Conclusion

Different and interesting patterns of molecular recognition involving iodine atoms are shown in this paper. Among these interactions it is possible to include: I···I, I···H–C(aromatic or aliphatic), I···M(metal ion), I···π (like C–H···π) and aromatic self-assemblies assisted by iodine atoms. These interactions could be similar to their formed between thyroxine and its binding molecules because of the similarity between thyroxine and the different iodohippurate compounds studied in the present work.

Acknowledgments

One of us, Miquel Barceló-Oliver, is grateful to "Conselleria d'Economia, Hisenda i Innovació" of the Government of Balearic Islands for a Ph.D. fellowship [FPI05-34068589T]. The authors also thank the "Vicerectorat de Investigació i Política Científica" of the University of Balearic Islands (project number UIB2005/5), the "Conselleria d'Economia, Hisenda i Innovació" (competitive groups grant) of the Government of Balearic Islands and the "Dirección General de Investigación Científica y Técnica" of the Spanish authorities (project number CTQ2006-09339/BQU) for their generous financial support.

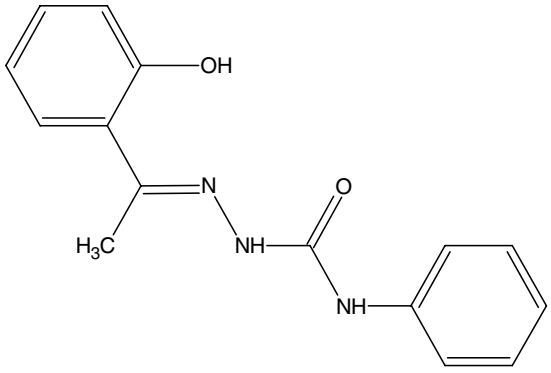
Appendix A. Supplementary material

CCDC 237826, 269073, 285764, 237828, 237827, 285763, 624402 and 624403 contain the supplementary crystallographic data for **1**, **2**, **3**, **4** (Co complex), **4** (Zn complex), **6** and **7**. These data can be obtained free of charge via http://www.ccdc.cam.ac.uk/conts/retrieving.html, or from the Cambridge Crystallographic Data Centre, 12 Union Road, Cambridge CB2 1EZ, UK; fax: (+44) 1223-336-033; or e-mail: deposit@ccdc.cam.ac.uk. Supplementary data associated with this article can be found, in the online version, at doi:10.1016/j.poly.2006.11.024.

References

[1] F. Zhang, W. Nianqing, X. Wang, L. Zhu, Z. Chai, Biol. Trace Elem. Res. 97 (2004) 125.
[2] J. Hemberger, M. Orlando, PCT Int. Appl. (2003) 38 [Application: WO 2003-EP2083 20030228].
[3] M.G. Wade, S. Parent, K.W. Finnson, W. Foster, E. Younglai, A. McMahon, D. Cyr, G. Daniel, C. Hughes, Toxicol. Sci. 67 (2002) 207.
[4] S. Farr, PCT Int. Appl. (2001) 222 [Application: WO 2000-US30474 20001103].
[5] B. Kochel, R. Andrzejak, M. Jurga, T. Tomkalsli, J. Lesczyszyn, B. Radomska, Proc. Int. Symp. Met. Ions Biol. Med. (1998) 539.
[6] F. Gao, C. Niu, J. Ni, T. Jin, R.WangX. Wang, Wuji Huaxue Xuebao 13 (1997) 119 [CAN 127:161601 AN 1997:441156 CAPLUS].
[7] M.D. Chen, P.Y. Lin, W.H. Lin, Gaoxiong Yixue Kexue Zazhi 7 (1991) 628 [CAN 116:212346 AN 199:212346 CAPLUS].
[8] W. Cash, D. William, H.E. Harold, S.W. Cox, E.A. Ekong, J.S. Epstein, S.G. Gabbe, R.M. Sigel, Endocrinology 81 (1967) 291.
[9] W. Cash, D. William, M. Gardy, H.E. Carlson, E.A. Ekong, J. Biol. Chem. 241 (1966) 1745.
[10] A. Wahlborg, E. Frieden, Arch. Biochem. Biophys. 111 (1965) 672.
[11] G. Litwack, J. Biol. Chem. 228 (1957) 823.
[12] E.C. Wolff, E.G. Ball, J. Biol. Chem. 224 (1957) 1083.
[13] F. Zhang, Y.-Z. Li, X. Gao, H.-L. Chen, Q.-T. Liu, A. Odani, O. Yamauchi, Chem. Lett. 33 (2004) 556.
[14] F. Zhang, A. Odani, H. Masuda, O. Yamauchi, Inorg. Chem. 35 (1996) 7148.

[15] F. Zhang, T. Yajima, H. Masuda, A. Odani, O. Yamauchi, Inorg. Chem. 36 (1997) 5777.
[16] F. Zhang, T. Yajima, A. Odani, O. Yamauchi, Inorg. Chim. Acta 278 (1998) 136.
[17] M. Barceló-Oliver, A. Terrón, A. García-Raso, J.J. Fiol, E. Molins, C. Miravitlles, J. Inorg. Biochem. 98 (2004) 1703.
[18] M. Barceló-Oliver, A. Tasada, J.J. Fiol, A. García-Raso, A. Terrón, E. Molins, Polyhedron 25 (2006) 71.
[19] M. Barceló-Oliver, A. García-Raso, A. Terrón, E. Molins, M.J. Prieto, V. Moreno, J. Martínez, V. Lladó, I. López, A. Gutiérrez, P.V. Escribá, J. Inorg. Biochem. (accepted for publication).
[20] A.H. Blatt, Organic Synthesis Collective, vol. 2, Wiley, New York, 1943.
[21] F. Wild, Identificación de Compuestos Orgánicos (Spanish translation of Characterization of Organic Compounds, Cambridge University Press, Cambridge), S.A. Gustavo Gili (Ed.), Spain, 1951, pp. 186–200.
[22] G.A. Barclay, B.F. Hoskins, C.H.L. Kennard, J. Chem. Soc. (1963) 5691 [CCDC code: IBIPCI].
[23] L.J. Farrugia, J. Appl. Crystallogr. 32 (1999) 837.
[24] G.M. Sheldrick, SHELXS-97: Program for the Solution of Crystal Structures, University of Göttingen, Göttingen, Germany, 1997.
[25] M.C. Burla, R. Caliandro, M. Camalli, B. Carrozzini, G.L. Cascarano, L. De Caro, C. Giacovazzo, G. Polidori, R. Spagna SIR-2004: an improved tool for crystal structure determination and refinement, J. Appl. Crystallogr. 38 (2005) 381.
[26] G.M. Sheldrick, SHELXL-97: Program for Crystal Structure Analysis (Release 97-2), University of Göttingen, Göttingen, Germany, 1997.
[27] L.J. Farrugia, J. Appl. Crystallogr. 30 (1997) 565.
[28] C.F. Macrae, P.R. Etgington, P. McCabe, E. Pidcock, G.P. Shields, R. Taylor, M. Towler, J. van de Streek, J. Appl. Crystallogr. 39 (2006) 453.
[29] Accelrys DS Viewer Pro 5.0. Available from: <http://www.accelrys.com>.
[30] M.D. Prasanna, T.N. Guru-Row, Cryst. Eng. 3 (2000) 135.
[31] A.W. Addison, T. Nageswara-Rao, J. Reedijk, J. van Rijn, G.C. Verschoor, J. Chem. Soc., Dalton Trans. (1984) 1349.
[32] O. Yamauchi, A. Odani, M. Takani, J. Chem. Soc., Dalton Trans. (2002) 3411, and references therein.
[33] A. Bondi, J. Phys. Chem. 68 (1964) 441.



Scheme 1.

(BDH) were used without further purification. All solvents obtained commercially were distilled before use.

2.2. Synthesis of the ligand and its metal complexes

The semicarbazone was synthesized as per the earlier reported method [5]. The structural formula of the ligand (H_2L) is depicted in Scheme 1.

The mixed ligand complexes CuLphen and CuLpy [where L is the dianion of 2-hydroxyacetophenone-*N*(4)-phenyl semicarbazone, phen is 1,10-phenanthroline and py is pyridine] were synthesized by the following method. A hot solution of H_2L (0.540 g, 2 mmol) in methanol (20 cm^3) was mixed with 2 mmol of the appropriate heterocyclic base in methanol. To this a hot filtered solution of $Cu(OAc)_2 \cdot H_2O$ (0.398 g, 2 mmol) in methanol was added with constant stirring. The mixture was then stirred for 3 h. The complexes, separated as microcrystals, were filtered and thoroughly washed with water, methanol and ether and finally dried over P_4O_{10} *in vacuo*.

Complexes Cu(HL)Cl and $Cu_2(HL)_2SO_4$ were synthesized by the direct reaction of the copper salt with the ligand. A solution of the appropriate copper salt (1 mmol) in methanol was added to a hot methanolic solution of the ligand, H_2L (1 mmol) and the mixture was then stirred for 3 h. The resulting microcrystals were filtered and thoroughly washed with water, methanol and then ether and finally dried over P_4O_{10} *in vacuo.*

The compound Cu_2L_2 was obtained when a hot solution of H_2L (0.540 g, 2 mmol) in methanol (20 cm^3) was mixed with a hot filtered solution of $Cu(OAc)_2 \cdot H_2O$ (0.398 g, 2 mmol) in methanol with constant stirring. The mixture was then stirred for 3 h. The complexes, separated as microcrystals, were filtered and thoroughly washed with water, methanol and ether and finally dried over P_4O_{10} *in vacuo*.

Single crystals of CuLphen suitable for X-ray diffraction were obtained by the slow evaporation of its solution in a mixture of acetonitrile and methanol.

2.3. Physical methods

Elemental analyses were carried out using a Vario EL III CHNS analyzer at SAIF, Kochi, India. IR spectra were recorded on a Thermo Nicolet AVATAR 370 DTGS model FT-IR Spectrophotometer with KBr pellets and the ATR technique at SAIF, Kochi, India. Electronic spectra were recorded on a Cary 5000, version 1.09 UV–Vis-NIR Spectrophotometer from solutions in DMSO. Magnetic moment measurements were carried out in the polycrystalline state on a Vibrating Sample Magnetometer at 5 kOe field strength. EPR spectra were recorded in a Varian E-112 X-band EPR spectrometer using TCNE as a standard at SAIF, IIT, Bombay, India.

2.4. X-ray crystallography

Single crystals of the compound CuLphen suitable for X-ray diffraction studies were grown from its solution in a mixture of acetonitrile and methanol (1:1) by slow evaporation in air. A single crystal of dimension $0.45 \times 0.30 \times 0.20$ mm was selected and mounted on a Bruker SMART APEX diffractometer, equipped with a graphite crystal incident-beam monochromator and a fine focus sealed tube Mo Kα ($\lambda = 0.71073$ Å) X-ray source. The crystallographic data along with details of structure solution refinements are given in Table 1. The unit cell

Table 1
Crystal refinement parameters of CuLphen

Empirical formula	$C_{27}H_{21}CuN_5O_2$
Formula weight	511.3
Color	greenish brown
Temperature, T (K)	173(2)
Wavelength (Mo Kα) (Å)	0.71073
Crystal system	monoclinic
Space group	$P21/c$
Lattice constants	
a (Å)	13.4877(19)
b (Å)	25.891(4)
c (Å)	14.1496(19)
α (°)	90
β (°)	113.73
γ (°)	90
Volume V (Å^3)	4523.4 (1)
Z	8
Calculated density (ρ) (Mg m^{-3})	1.504
Absorption coefficient, μ (mm^{-1})	1.002
$F(000)$	2104.0 (2107.02)
Crystal size (mm)	$0.45 \times 0.30 \times 0.20$
θ Range for data collection (°)	1.76–28.33
Limiting indices	$-17 \leqslant h \leqslant 16$, $-27 \leqslant k \leqslant 34$, $-8 \leqslant l \leqslant 18$
Reflections collected	27970
Unique reflections (R_{int})	10749 (0.0229)
Completeness to θ	28.33° (95.5%)
Absorption correction	semi-empirical from equivalents
Maximum and minimum transmission	0.8247 and 0.6612
Refinement method	full-matrix least-squares on F^2
Data/restraints/parameters	10749/0/799
Goodness-of-fit on F^2	1.031
Final R indices [$I > 2\sigma(I)$]	$R_1 = 0.0336$, $wR_2 = 0.0850$
R indices (all data)	$R_1 = 0.0440$, $wR_2 = 0.0898$
Largest difference peak and hole (e Å^{-3})	0.485 and −0.400

dimensions were measured and the data collection was performed at 173 K. Bruker SMART software was used for data acquisition and Bruker SAINT software for data integration [6]. Absorption corrections were carried out using SADABS based on Laue symmetry using equivalent reflections [7]. The structure was solved by direct methods and refined by full-matrix least-squares calculations with the SHELXTL-PLUS software package (version 5.1) [8]. The graphics used was diamond version 3.0 [9]. All non-hydrogen atoms were refined anisotropically, and all hydrogen atoms were located from the difference Fourier map and refined isotropically.

3. Result and discussion

The principal ligand H_2L was synthesized by the direct condensation of 2-hydroxyacetophenone with *N*(4)-phenyl semicarbazide. The elemental analysis data obtained is in good agreement with the stoichometry of 2-hydroxyacetophenone-*N*(4)-phenyl semicarbazone. H_2L can exist in the keto or enol form or an equilibrium mixture of the two since it has an amide –NH–C═(O) function. However, the IR spectrum of H_2L indicates that in the solid state it remains in the keto form. The IR spectra of complexes, however, do not show any intense absorption band at 1696 cm^{-1} due to the carbonyl stretching of the semicarbazone moiety. This shows that in solution, it converts to the enol form and coordinates to the metal in the enolate form.

The complexes CuLphen and CuLpy were readily formed by the reaction of the ligand and heterocyclic base with copper acetate. The complexes Cu(HL)Cl and $Cu_2(HL)_2SO_4$ were formed by the reaction of the ligand with copper chloride and copper sulfate, respectively.

The principal ligand H_2L undergoes double deprotonation to L^{2-} and acts as a tridentate ligand in CuLphen, whilst 1,10-phenanthroline acts as a bidentate ligand and occupies the fourth and fifth coordination positions of copper. In the case of CuLpy, L acts as a tridentate ligand thus occupying three positions and pyridine completes the fourth coordination position. In Cu(HL)Cl and $Cu_2(HL)_2SO_4$, the principal ligand acts as a monoanionic tridentate ligand.

The colours, elemental analyses, stoichiometries of H_2L and its complexes are presented in Table 2. The complexes are insoluble in most polar and non-polar solvents. They are soluble in DMF, acetonitrile and DMSO. The conductivity measurements were made in DMSO solutions and all the complexes were found to be non-electrolytes [10].

The room temperature magnetic susceptibilities of the complexes in the polycrystalline state fall in the range 1.80–2.00 BM, which are very close to the spin-only value of 1.73 BM for a d^9 copper system.

3.1. Electronic and IR spectra

The significant electronic absorption bands in the spectra of the ligand and all the complexes recorded in DMSO solution are presented in Table 3.

The semicarbazone and copper(II) complexes have two bands; one centered around 40 000 cm^{-1} and another around 28 000 cm^{-1}. These bands are assigned to $\pi \rightarrow \pi^*$ and $n \rightarrow \pi^*$ transitions of the phenyl rings and semicarbazide moiety, respectively [11]. The charge transfer bands are observed around 25 000 cm^{-1}, and their broadness can be explained as being due to the combination of $O \rightarrow Cu$ and $N \rightarrow Cu$ LMCT transitions [12]. For the Cu(II) complexes there are three spin allowed transitions, $B_{1g} \rightarrow A_{1g}$, $B_{1g} \rightarrow B_{2g}$ and $B_{1g} \rightarrow E_g$, but it is very difficult to resolve them into separate bands due to the very low energy difference between these bands.

The band $n \rightarrow \pi^*$, which is found at 27 770 cm^{-1} in the spectrum of the uncomplexed semicarbazone, was slightly shifted on complexation. This is an indication of the enolization followed by the deprotonation of the ligand during complexation. All the complexes gave d–d bands in the 15 000–16 000 cm^{-1} range [13,14]. In the chloro complex,

Table 3
Electronic spectral assignments, λ (cm^{-1}) for H_2L and its copper(II) complexes

Compound	d–d	LMCT	$n \rightarrow \pi^*$	$\pi \rightarrow \pi^*$
H_2L			27 770	43 103
CuLphen	16 212	24 570	28 735	41 666
CuLpy	16 949	24 875	28 535	39 062
CuHLCl	15 830	25 188	28 653	41 152
		31 446		
$Cu_2(HL)_2SO_4$	15 620	24 937	28 900	39 062
Cu_2L_2	15 625	21 231	26 737	33 003

Table 2
Colours, elemental analyses and magnetic susceptibility of 2-hydroxyacetophenone-*N*(4)-phenyl semicarbazone and its copper(II) complexes

Compound	Colour	Empirical formula	Found (Calc.)%			μ (BM)
			C	H	N	
H_2L	pale yellow	$C_{15}H_{15}N_3O_2$	66.70(66.90)	5.57(5.61)	15.60(15.60)	
CuLphen	dark green	$C_{27}H_{25}N_5O_2Cu$	62.96(63.46)	4.89(4.14)	13.56(13.70)	1.93
CuLpy	pale green	$C_{20}H_{20}N_4O_2Cu$	58.28(58.60)	4.38(4.43)	13.55(13.67)	1.87
Cu(HL)Cl	brown	$C_{15}H_{14}N_3O_2ClCu$	49.20(49.05)	3.77(3.84)	11.49(11.44)	1.75
$Cu_2(HL)_2SO_4$	pale green	$C_{30}H_{28}N_6SO_8Cu_2$	46.72(47.43)	3.27(3.71)	10.98(11.06)	1.81
Cu_2L_2	green	$C_{30}H_{26}N_6O_4Cu_2$	54.38(54.46)	4.04(3.96)	12.60(12.70)	1.71

a shoulder observed at 31 446 cm^{-1} is assigned as a Cl → Cu charge–transfer transition [15].

The tentative assignments for the IR spectral bands, useful for determining the ligand's mode of coordination, are listed in Table 4. A sharp band at 1621 cm^{-1} in the semicarbazone can be attributed to the characteristic >C=N group. This band shifts slightly (20–40 cm^{-1}) towards lower frequencies in the copper(II) complexes [16,17] indicating the coordination of azomethine nitrogen to copper. It is further supported by the appearance of new bands at 421–450 cm^{-1}, assignable to ν(Cu–N) for these complexes [18].

The increase in the ν(N–N) value in the spectra of the complexes is due to the increase in double bond character, off-setting the loss of electron density via donation to the metal and it is a confirmation of the coordination of the ligand through the azomethine nitrogen. The appearance of bands in the 1496–1546 cm^{-1} range in the complexes is due to the asymmetric stretching vibration of the newly formed N=C bond as a result of the enolization of the principal ligand. The ν(N–H) band of the semicarbazone disappears in the complexes, except in Cu(HL)Cl and $Cu_2(HL)_2SO_4$, also indicating the enolization and deprotonation of H_2L followed by coordination of the enolate to Cu. This is further supported by the appearance of a new peak in the range 365–375 cm^{-1} indicating ν(Cu–O).

A broad absorption band observed in the 3500–3050 cm^{-1} region for H_2L is due to the phenolic OH. This band, however, disappears in the complexes, thereby indicating the coordination of the phenolic oxygen to the copper atom. Bands in the region 950–550 cm^{-1} are due to the substituted benzene ring. These bands correspond to out-of-plane bending of C–H ring protons and C–C bonds of the aromatic rings.

Thus it is seen that the principal ligand H_2L acts as a dianionic tridentate ligand in the complexes CuLphen, Cu_2L_2 and CuLpy. In complexes Cu(HL)Cl and $Cu_2(HL)_2SO_4$, it is acting as a monoanionic tridentate ligand.

The fourth (and fifth) coordination sites in complexes CuLphen and CuLpy are occupied by N atom(s) of the heterocyclic base and these bands are assignable in the 243–336 cm^{-1} region of the spectra. The IR spectra of the complexes CuLphen and CuLpy display bands characteristic of coordinated heterocyclic bases [19].

In the spectrum of the complex Cu(HL)Cl, a peak at 331 cm^{-1} indicates the terminal nature of the chlorine atom. The sulfato complex $Cu_2(HL)_2SO_4$ has bands at 997, 1039 and at 1119 cm^{-1}, indicating the presence of bidentate bridging sulfato group [20].

3.2. EPR spectra

The EPR spectra of polycrystalline samples at 298 K, DMF solution at 298 and 77 K were recorded in the X-band, using 100-kHz modulation; g factors were quoted relative to the standard marker TCNE ($g = 2.00277$). The EPR parameters of the copper(II) complexes are presented in Table 5.

The EPR spectra of the complexes recorded in the polycrystalline state at room temperature provide information about the coordination environment around copper(II) in these complexes.

The EPR spectra of CuLphen and Cu_2L_2 in the polycrystalline state at 298 K show only one broad signal at $g_{iso} = 2.099$ and 2.096, respectively. Such isotropic spectra, consisting of only one broad signal and hence only one g value (g_{iso}), arises from extensive exchange coupling through misalignment of the local molecular axes between different molecules in the unit cell (dipolar broadening) and enhanced spin lattice relaxation. This type of spectra unfortunately give no information on the electronic ground state of the copper(II) ions present in the complexes. For Cu_2L_2 we got a half field signal at $g = 4.192$, indicating dimeric species [21]. The spectra of CuLpy and $Cu_2(HL)_2SO_4$ showed axial spectra with well defined $g_{\|}$ and $g_{\perp}$ features. The variation in the $g_{\|}$ and $g_{\perp}$ values indicate that the

Table 4
Infrared spectroscopic assignments (cm^{-1}) for 2-hydroxyacetophenone-*N*(4)-phenyl semicarbazone and its copper(II) complexes

Compound	ν(C=N)	ν(N=C)	ν(C=O)	ν(C–O)	ν(N–N)	Bands due to heterocyclic bases	ν(CN)azo	ν(Cu–O)	ν(NH)
H_2L	1621 s		1644 s		1030 m				3327 m
CuLphen	1591 s	1544 s		1139 m	1033 m	657 w 726 m 845 m 1425 s 282 m	438 w	372 w	
CuLpy	1597 s	1556 m		1145 w	1002 w	348 440 w 695 w 1298 m	421 w	375 w	
Cu(HL)Cl	1577 s	1497 m		1122 m	1035 w		449 w	365 w	3052 w
$Cu_2(HL)_2SO_4$	1597 s	1499 m		1119 m	1039 w		450 w	368 w	
Cu_2L_2	1596 s	1564 s		1150 m	1031 m		464 w	371 w	

s = strong, m = medium, w = weak.

Table 5
Spin Hamiltonian and bonding parameters of copper(II) 2-hydroxyacetophenone-*N*(4)-phenyl semicarbazones

	CuLphen	CuLpy	Cu(HL)Cl	$Cu_2(HL)_2SO_4$	Cu_2L_2
Polycrystalline (298 K)					
$g_\parallel$		2.163	2.236	2.32	
$g_\perp$		2.076	2.098	2.078	
g_{iso}	2.099				2.096
G		2.14	2.40	4.10	
DMF (77 K)					
$g_\parallel$	2.220	2.212	2.200	2.233	$g_3 = 2.193$
$g_\perp$	2.076	2.066	2.057	2.073	$g_1 = 2.032$
					$g_2 = 2.081$
$A_\parallel/A_3$	198	197	174	197	221
A_2					20.4
A_1					16.9
α^2	0.8385	0.8147	0.8005	0.8472	0.8682
β^2	0.8363	0.8960	0.8571	0.8902	0.7734
$\gamma 2$	0.9712	0.9687	0.8993	0.9831	0.8243
$K_\parallel$	0.7013	0.7330	0.6865	0.7542	0.6715
$K_\perp$	0.8144	0.7892	0.7199	0.8329	0.7157
A_N					15.3
DMF (298 K)					
g_{iso}					2.115
A_{iso}					80.6
A_N					20.4

A values in 10^{-4} cm^{-1}.

geometry of the compounds in the solid state are affected by the nature of the coordinating gegenions.

For the complex CuLpy, the $g_\parallel > g_\perp > 2$ and a G value falling within the range 2.1–3.8 are consistent with a $d_{x^2-y^2}$ ground state.

The geometric parameter G, which is a measure of the exchange interaction between copper centers in the polycrystalline compound, is calculated using the equation, $G = (g_\parallel - 2)/(g_\perp - 2)$. G values < 4.4, are consistent with a $d_{x^2-y^2}$ ground state having a small exchange coupling [22]. If $G > 4$, the exchange interaction is negligible [23].

The EPR spectrum of the complex Cu_2L_2 in DMF solution at 298 K (Fig. 1) is isotropic with hyperfine splitting into four lines. In addition, the high field signal ($M_I = -3/2$) is split into three lines by the bonding of the azomethine nitrogen atom with copper. The g_{iso} value is found to be 2.115 and A_N is found to be 20.4×10^{-4} cm^{-1}. However, the spectrum of this compound in DMF solution at 77 K shows typical rhombic features with three g values g_1, g_2 and g_3 (Fig. 2). All the parallel hyperfine lines split into three with a superhyperfine coupling constant, $A_N = 15.3 \times 10^{-4}$ cm^{-1}. These indicate the involvement of the azomethine nitrogen in coordination. The presence of a weak line, lower in the field, is due to the less abundant ^{65}Cu isotope [24].

In the EPR spectrum of the five coordinate copper(II) complex, CuLphen in frozen DMF, the expected superhyperfine lines of three N atoms (one azomethine nitrogen and two nitrogens from phenanthroline) are not observed but shows four fairly resolved hyperfine lines [^{63,65}Cu, $I = 3/2$] corresponding to $-3/2$, $-1/2$, 1/2 and 3/2 transi-

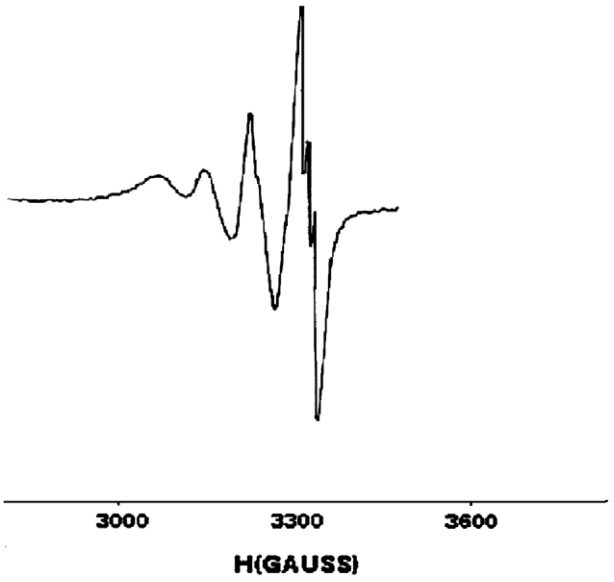


Fig. 1. EPR spectrum of Cu_2L_2 in DMF at 298 K.

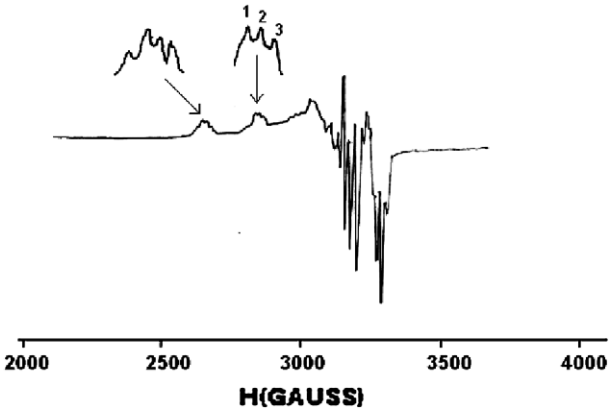


Fig. 2. EPR spectrum of Cu_2L_2 in DMF at 77 K. The $M_I = +3/2$ and $+1/2$ are expanded.

tions. The $g_\parallel > g_\perp$ value suggest a distorted square pyramidal structure and rules out the possibility of a trigonal bipyramidal structure which would be expected to have $g_\perp > g_\parallel$. Thus the coordination polyhedron comprises of one phenanthroline nitrogen, an azomethine nitrogen, an enolate oxygen and a phenolate oxygen of the semicarbazone which forms the base of the pyramid and the remaining phenanthroline nitrogen occupies the axial position, as the results obtained from the crystal study.

The EPR spectra of the four coordinate copper(II) complexes, CuLpy, Cu(HL)Cl and $Cu_2(HL)_2SO_4$, in DMF at 77 K show resolved four copper hyperfine lines. The expected superhyperfine splitting of nitrogen atoms are also not observed here. The $g_\parallel > g_\perp$ suggests a square planar geometry for these complexes. The EPR spectrum of the compound Cu(HL)Cl in DMF solution at 77 K is given in Fig. 3.

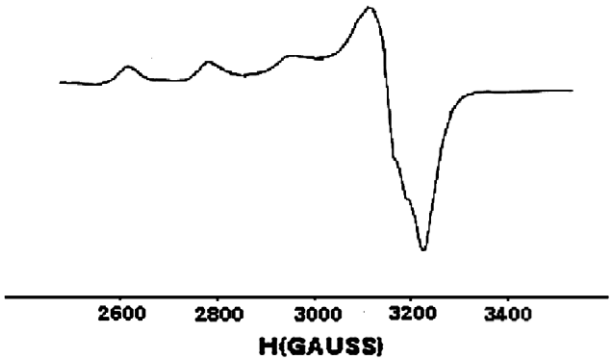


Fig. 3. EPR spectrum of Cu(HL)Cl in DMF at 77 K.

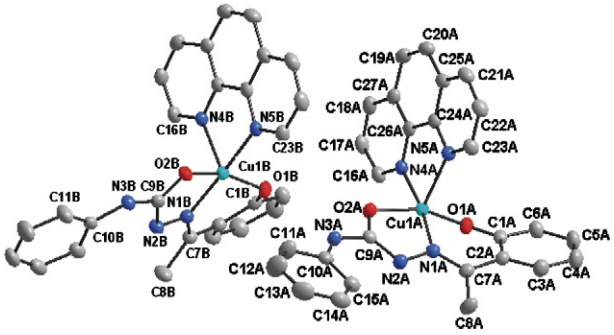


Fig. 4. The molecular structure of CuLphen along with the atom numbering scheme. The hydrogen atoms are omitted for clarity.

The $g_{\|}$ values are nearly the same for all the complexes indicating that the bonding is dominated by the semicarbazone moiety. In all the complexes, $g_{\|} > g_{\perp} > 2.00$. The fact that $g_{\|}$ values are less than 2.3 is an indication of significant covalent character to the M–L bond [25,26].

The EPR parameters $g_{\|}$, $g_{\perp}$, $A_{\|}$(Cu) and the energies of d–d transitions were used to evaluate the bonding parameters α^2, β^2 and γ^2 which may be regarded as measures of the covalency in the in-plane σ-bonds, in-plane π-bonds and out-of-plane π-bonds. The value of the in-plane σ-bonding parameter α^2 is estimated from the expression:

$$\alpha^2 = -A_{\|}/0.036 + (g_{\|} - 2.00277) + 3/7(g_{\perp} - 2.00277) + 0.04 \text{ [27,28]}.$$

The following simplified parameters were used to evaluate the bonding parameters [29],

$$K_{\|}^2 = (g_{\|} - 2.00277)E_{\text{d–d}}/8\lambda_o$$

$$K_{\perp}^2 = (g_{\perp} - 2.00277)E_{\text{d–d}}/2\lambda_o$$

Where $K_{\|}^2 = \alpha^2\beta^2$ and $K_{\perp}^2 = \alpha^2\gamma^2$, $K_{\|}$ and $K_{\perp}$ are orbital reduction factors and λ_o represents the one electron spin orbit coupling constant which equals $-828\ \text{cm}^{-1}$.

Hathaway [30] has pointed out that for pure sigma bonding, $K_{\|} \approx K_{\perp} \approx 0.77$ and for in plane π-bonding, $K_{\|} < K_{\perp}$, while for out-of-plane π-bonding $K_{\perp} < K_{\|}$. In all the complexes, it is observed that $K_{\|} < K_{\perp}$ which indicates the presence of significant in-plane π bonding. Furthermore α^2, β^2 and γ^2 have values less than 1.0, which is expected for 100% ionic character of the bonds, and become smaller with increasing covalent character. Therefore, the evaluated values α^2, β^2 and γ^2 of the complexes are consistent with both strong in-plane σ- and in-plane π-bonding.

3.3. Crystal structure of CuL phen

The molecular structure of the complex along with atom numbering scheme is given in Fig. 4, and selected

Table 6
Selected bond lengths (Å) and bond angles (°) of CuLphen

Cu(1)A–O(1)A	1.9227(13)	Cu1B–O1B	1.8947(14)
Cu(1)A–N(1)A	1.9514(15)	Cu(1)B–N(1)B	1.9424(17)
Cu(1)A–N(4)A	2.0320(17)	Cu(1)B–N(4)B	2.0302(16)
Cu(1)A–N(5)A	2.2216(17)	Cu(1)B–N(5)B	2.2874(16)
Cu(1)A–O(2)A	1.9517(14)	Cu(1)B–O(2)B	1.9859(14)
N(1)A–C(7)A	1.300(3)	N(1)B–C(7)B	1.308(3)
N(1)A–N(2)A	1.393(2)	N(1)B–N(2)B	1.391(2)
N(3)A–C(10)A	1.409(3)	N(3)B–C(10)B	1.412(3)
O(1)A–C(1)A	1.326(2)	O(1)B–C(1)B	1.321(3)
C(9)A–O(2)A	1.294(2)	C(9)B–O(2)B	1.282(2)
N(2)A–C(9)A	1.328(2)	N(2)B–C(9)B	1.330(3)
N(3)A–C(9)A	1.373(3)	N(3)B–C(9)B	1.377(3)
C(2)A–C(7)A	1.468(3)	C(2)B–C(7)B	1.469(3)
C(7)A–C(8)A	1.509(4)	C(7)B–C(8)B	1.502(3)
O(2)A–Cu(1)A–N(1)A	81.00(6)	O(2)B–Cu(1)B–N(1)B	81.68(6)
N(1)A–Cu(1)A–N(5)A	105.07(6)	N(1)B–Cu(1)B–N(5)B	99.78(6)
O(1)A–Cu(1)A–N(1)A	92.41(6)	O(1)B–Cu(1)B–N(1)B	92.57(6)
O(1)A–Cu(1)A–N(5)A	98.94(6)	O(1)B–Cu(1)B–N(5)B	109.05(6)
O(1)A–Cu(1)A–O(2)A	159.53(6)	O(1)B–Cu(1)B–O(2)B	157.24(6)
N(4)A–Cu(1)A–N(5)A	78.75(6)	N(4)B–Cu(1)B–N(5)B	77.03(6)
O(2)A–Cu(1)A–N(5)A	101.48(6)	O(2)B–Cu(1)B–N(5)B	93.66(6)
O(1)A–Cu(1)A–N(4)A	95.16(6)	O(1)B–Cu(1)B–N(4)B	91.44(6)
N(1)A–Cu(1)A–N(4)A	170.91(7)	N(1)B–Cu(1)B–N(4)B	175.54(6)
O(2)A–Cu(1)A–N(4)A	90.18(6)	O(2)B–Cu(1)B–N(4)B	95.34(6)

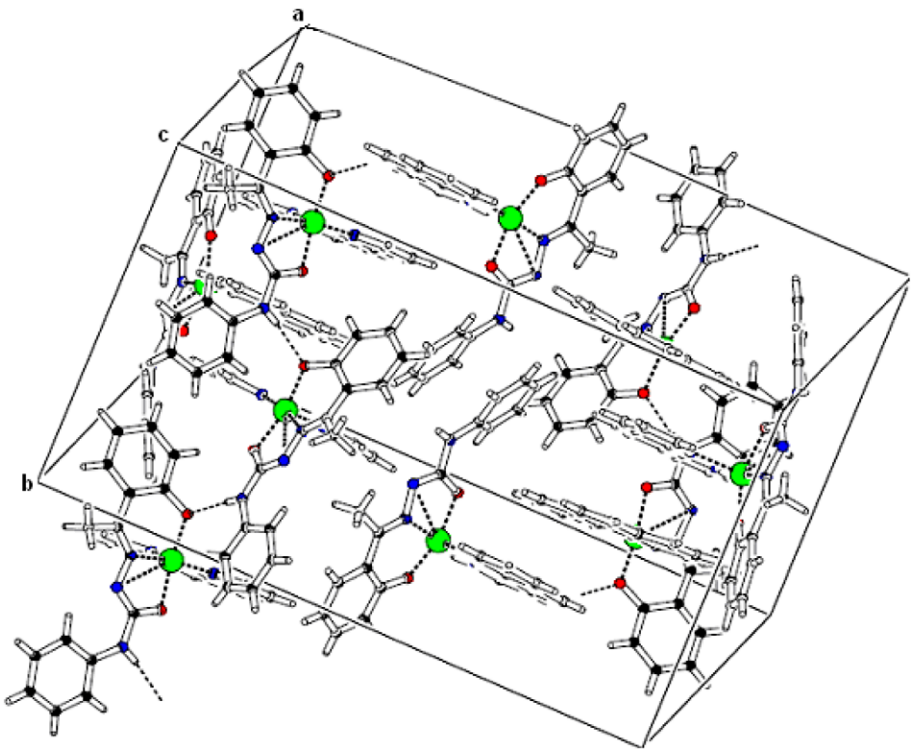


Fig. 5. Packing diagram of CuLphen showing intermolecular hydrogen bonding.

bond lengths and bond angles are summarized in Table 6. The compound crystallizes in a monoclinic lattice with space group $P2_1/c$. The asymmetric unit contains two molecules. The two discrete molecules differ from each other in the orientation of the *N*-phenyl rings – the molecular unit with an A residue has a *transoidal* orientation while that with B residue has a *cisoidal* orientation. The unit cell contains eight molecules. The copper in the mononuclear complex is five coordinate and has a distorted square pyramidal geometry in both the molecules. The basal coordination positions are occupied by the phenolate oxygen O(1), azomethine nitrogen N(1), enolate oxygen O(2) of the semicarbazone and the phen nitrogen, N(4). The apical position is occupied by the second nitrogen of phen, N(5)A, at a larger distance (2.2216 Å) compared to N(4)A (2.0321 Å). In molecule B, these distances are 2.2874 and 2.0302 Å, respectively. The four base atoms are coplanar, showing a significant distortion from a square geometry as indicated by the O(1)A–Cu(1)A–O(2)A bond angle of 159.53°. The corresponding angle for the second molecule is slightly less at 157.24°. The deviation of the central copper atom from the basal plane in the direction of the axial nitrogen is evident from the bond angles of N(1)A–Cu(1)A–N(4)A (170.90°) and O(1)A–Cu(1)A–N(1)A (92.42°). The corresponding angles in molecule B are 175.54° and 92.57°, respectively. Most of the angles involving the central copper atoms are widely different, from 90° and 180°, indicating significant distortion from the square pyramidal geometry. One of the reasons for the deviation from an ideal stereochemistry is the restricted bite angle imposed both by the H_2L and phen ligands. The trigonality index τ is calculated using the equation $\tau = (\beta - \alpha)/60$ [31] (for perfect square pyramidal and triogonal bipyramidal geometries the values of τ are zero and unity, respectively). The value of τ for molecules A and B are 0.19 and 0.30, respectively. This shows that both have distorted square pyramidal geometries and molecule B has more distortion than molecule A.

The variation in Cu–N the bond distances, Cu(1)A–N(1)A (1.9514 Å), Cu(1)A–N(4)A (2.0321 Å), Cu(1)A–N(5)A (2.2215 Å), Cu(1)B–N(1)B (1.9424 Å), Cu(1)B–N(4)B (2.0302 Å) and Cu(1)B–N(5)B (2.2874 Å), indicate the differences in the strength of the bonds formed by each of the coordinating N atoms. The difference in the bond lengths can be attributed to the difference in the π back bonding between the phen and the semicarbazone moieties. However, the large bond distances at the axial Cu(1)A–N(4)A position supports the lack of significant out-of-plane π-bonding. This fact is in accordance with the absence of superhyperfine splitting due to N(4) in the EPR spectrum of the compound.

All the phenanthroline rings are arranged parallel to each other within the unit cell (Fig. 5). The phenanthroline rings Cg [5] and Cg [15] are involved in π–π interactions with a distance of 3.4277 Å in CuLphen. The *cisoid*al *N*-phenyl rings Cg [18] and Cg [18] of the neighboring molecules in the unit cell are also involved in π–π interactions with a distance of 3.8825 Å. In addition to the π–π stacking, C–H···π interactions of the phen hydrogen with the

Table 7
Hydrogen bonding

D–H···A	D–H (Å)	H···A (Å)	D···A (Å)	∠D–H···A (°)
N(3A)–H(3A)···O(1A)	0.84(2)	2.11(2)	2.935(2)	170.5(19)

Equivalent position code; x, $-y+1/2$, $z+1/2$.

[π···π Interactions]

Cg(I)–Res(I)···Cg(J)	Cg–Cg (Å)	α (°)	β (°)	γ (°)
Cg(5)···[1]···Cg(15)[a]	3.4277(12)	4.28	10.60	10.84
Cg(18)···[2]···Cg(18)[b]	3.8825(16)	0.02	21.88	21.88
Cg(4)···[1]···Cg(15)[c]	3.5429(13)	4.87	24.11	19.55
Cg(4)···[1]···Cg(19)[d]	3.7698(14)	4.76	27.66	27.81
Cg(15)···[2]···Cg(4)[e]	3.5429(13)	4.87	24.11	19.55
Cg(15)···[2]···Cg(5)[f]	3.4276(12)	4.28	10.60	10.84
Cg(19)···[2]···Cg(4)[g]	3.7698(14)	4.76	27.81	27.66
Cg(19)···[2]···Cg(8)[h]	3.7323(13)	5.03	21.61	26.63

Equivalent position code; a: x, y, z; b: $1-x$, $-y$, $2-z$; c: x, $1/2-y$, $1/2+z$; d: x, $1/2-y$, $-1/2+z$; e: x, $1/2-y$, $1/2+z$; f: x, y, z; g: x, $1/2-y$, $1/2+z$; h: x, $1/2-y$, $1/2+z$.

Cg (4) = N(4)A, C16(A), C(17)A, C(18)A, C(27)A, C(26)A
Cg (8) = C(19)A, C(20)A, C(25)A, C(24)A, C(26)A, C(27)A
Cg (19) = C(19)B, C(20)B, C(25)B, C(24)B, C(26)B, C(27)B
Cg (5) = N5A, C(23)A, C(22)A, C(21)A, C(25)A, C(24)A
Cg (15) = N(4)B, C(16)B, C(17)B, C(18)B, C(27)B, C(26)B
Cg (18) = C(10)B, C(11)B, C(12)B, C(13)B, C(14)B, C(15)B

C–H··· π interactions

X–H(I)···Cg(J)	H···Cg (Å)	X···Cg (Å)	∠X–H–Cg (°)
C(13)B–H(13)B[2]···Cg(5)[a]	2.96	3.759	148
C(22)A–H(22)A[1]··· Cg(12)[b]	2.92	3.6483	136

Equivalent position code; a: $1-x$, $1-y$, $1-z$; b: x, y, z.

Cg (15) = N(4)B, C(16)B, C(17)B, C(18)B, C(27)B, C(26)B
Cg(5) = N(5)A, C(23)A, C(22)A, C(21)A, C(25)A, C(24)A
Cg (12) = Cu(1)B, O(2)B, C(9)B, N(2)B, N(1)B

D, donor; A, acceptor; Cg, centroid; α, dihedral angles between planes I and J; β, angle Cg(I) and Cg(J).

rings of neighboring molecules contribute to the stability of the unit cell packing (Table 7).

Ring puckering analysis and least square plane calculations show that the Cg(3) ring comprising of Cu(1)A, O(1)A, C(1)A, C(2)A, C(7)A, N(1)A adopts a S (screw-boat) conformation in the complex and the centroid Cg(12) comprising of Cu(1)B–O(2)B–C(9)B, N(2)B–N(1)B is twisted on the N(1)B–Cu(1)B axis. The Cg [14] ring comprising of Cu(1)B, O(1)B, C(1)B, C(2)B, C(7)B, N(1)B adopts an envelope conformation.

Acknowledgements

M.R.P. Kurup is thankful to the Department of Science and Technology, New Delhi, India for financial support. The authors are thankful to the Sophisticated Analytical Instrumentation Facility, Cochin University of Science and Technology, Kochi 22, India for elemental analyses and IIT, Bombay, India for EPR spectra. U.L. Kala and S. Suma acknowledge the University Grants Commission, New Delhi, India for financial support.

Appendix A. Supplementary material

CCDC 612867 contains the supplementary crystallographic data for CuLphen. These data can be obtained free of charge via http://www.ccdc.ac.uk/conts/retrieving.html, or from the Cambridge Crystallographic Data Centre, 12 Union Road, Cambridge CB2 1EZ, UK; fax: (+44) 1223-336-033; or e-mail: deposit@ccdc.cam.ac.uk. Supplementary data associated with this article can be found, in the online version, at doi:10.1016/j.poly.2006.11.035.

References

[1] M. Akkurt, S. Ozfuric, S. Ide, Anal. Sci. 16 (2000) 667.
[2] J. R Dimmock, R.N. Puthucode, J.M. Smith, M. Hetherington, J.W. Quil, U. Pugazhenthi, J. Med. Chem. 39 (1996) 3984.
[3] J. R Dimmock, K.K. Sidhu, S.D. Thumber, S.K. Basran, M. Chen, J.W. Quil, Eur. J. Chem. 30 (1995) 287.
[4] H. Beraldo, D. Gaminob, Mini. Rev. Med. Chem. 4 (2004) 31.
[5] A. Sreekanth, U.L. Kala, C.R. Nayar, M.R.P. Kurup, Polyhedron 23 (2004) 41.
[6] SMART, SAINT, Area Detector Software Package and SAX Area Detector Integration Program, Bruker Analytical X-ray, Madison, WI, USA, 1997.

[7] SADABS, Area Detector Absorption Correction Program, Bruker Analytical X-ray, Madison, WI, 1997.
[8] G.M. Sheldrick, SHELXTL-PLUS, Crystal Structure Analysis Package, Bruker Analytical X-ray, Madison, WI, USA, 1997.
[9] K. Bramdenburg, Diamond Version 3.0, Crystal Impact GbR, Bonn, Germany, 1997–2004.
[10] W.J. Geary, Coord. Chem. Rev. 7 (1971) 81.
[11] C.R.K. Rao, P.S. Zacharias, Polyhedron 16 (1997) 1201.
[12] H. Sacconi, G. Speroni, J. Am Chem. Soc. 87 (1965) 3102.
[13] R.P. John, A. Sreekanth, V. Rajakannan, T.A. Ajith, M.R.P. Kurup, Polyhedron 23 (2004) 2549.
[14] M. Joseph, M. Kuriakose, M.R.P. Kurup, E. Suresh, A. Kishore, G. Bhat, Polyhedron 25 (2006) 61.
[15] M.J.M. Campbell, Coord. Chem. Rev. 15 (1975) 279.
[16] B.S. Garg, M.R.P. Kurup, S.K. Jain, Y.K. Bhoon, Transit. Met. Chem. 13 (1988) 92.
[17] B.S. Garg, M.R.P. Kurup, S.K. Jain, Y.K. Bhoon, Transit. Met. Chem. 13 (1988) 247.
[18] K. Nakamoto, Infrared and Raman Spectra of Inorganic and Coordination Compounds, Part B, fifth ed., Wiley, New York, 1997.
[19] R.P. John, A. Sreekanth, M.R.P. Kurup, H.-K. Fun, Polyhedron 24 (2005) 601.
[20] V. Philip, V. Suni, M.R.P. Kurup, M. Nethaji, Polyhedron 25 (2006) 1931.
[21] P.F. Rapheal et al., Polyhedron (2006), doi:10.1016/j.poly.2006.09.091.
[22] A.H. Maki, B.R. McGarvey, J. Chem. Phys. 29 (1958) 31.
[23] J.R. Wasson, C. Trapp, J. Phys. Chem. 73 (1969) 3763.
[24] J.A. De Bolfo, T.D. Smith, J.F. Boas, J.R. Pilbrow, J. Chem. Soc., Faraday II 72 (1976) 481.
[25] M.J. Bew, B.J. Hathaway, R.R. Faraday, J. Chem. Soc., Dalton Trans. (1972) 1229.
[26] A. Sreekanth, M.R.P. Kurup, Polyhedron 22 (2003) 3321.
[27] A.H. Maki, B.R. McGarvey, J. Chem. Phys. 29 (1958) 35.
[28] D. Kivelson, R. Neiman, J. Chem. Soc., Dalton Trans. (1961) 49.
[29] B.N. Figgis, Introduction to Ligand Fields, Interscience, New York, 1996, p. 295.
[30] B.J. Hathaway, in: G. Wilkinson, R.D. Gillard, J.A. McCleverty (Eds.), Comprehensive Coordination Chemistry, vol. 5, Pergamon, Oxford, 1987, p. 533.
[31] A.W. Addison, J.N. Rao, J. Reedijk, G.C. Vershoor, J. Chem. Soc., Dalton Trans. (1984) 1349.

groups. An ionic $[MeAl(OR)_2AlMe_2]^+(MeAlCl_3)^-$ complex and monomeric organoaluminum complexes $R'Al(OR)_2$ and R'_2AlOR (where OR = (*S*)-α,α-diphenyl-2-pyrrolidinyl-methoxide as a ligand possessing a "magic" group, R′ = Me, Et, 1-Nor, ^{t}Bu) were obtained in reactions of (*S*)-α,α-diphenyl-2-pyrrolidinyl-methanol with Me_2AlCl and R'_3Al, respectively [7]. The reaction of a cyclopropene analog of aluminum $LAl[\eta^2\text{-}C_2(SiMe_3)_2]$ (L = HC[(CMe)-(NAr)]$_2$, Ar = 2,6-*i*-$Pr_2C_6H_3$) with Ph_2CO yielded the complex $LAl[OC(Ph)_2C_2(SiMe_3)_2]$ possessing the "magic" group. The complex was the result of an insertion of the carbonyl into an Al–C (vinyl) bond [8]. Treatment of the bridging hydride complex $(\mu,\eta^1\text{:}\eta^1\text{-}Ph_2pz)(Al^iBu_2)_2(\mu\text{-}H)$ with diphenylmethanol or benzophenone afforded the diphenylmethoxide compound $(\mu,\eta^1\text{:}\eta^1\text{-}Ph_2pz)(Al^iBu_2)_2(\mu\text{-}OCHPh_2)$ [9]. Aluminum macrocyclic structures with the Ph_2CO group were synthesised in reactions of diphenylglycolic acid with Me_3Al [10]. Among the diphenylmethoxo aluminum complexes, the four-coordinated monomeric complex (EDBP)Al(OCHPh$_2$)(THF) (EDBP-H_2 = 2,2′-ethylidene-bis(4,6-di-*tert*-butylphenol)) is the only example to possess efficient catalytic activity in the ROP of lactones [11].

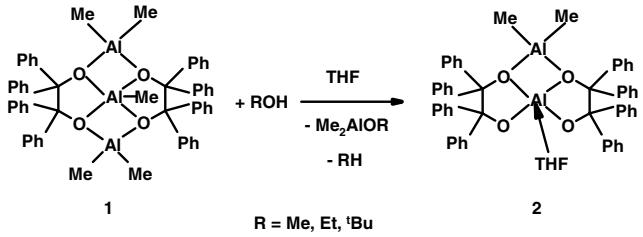
Considering the ability of the Ph_2CO group to enhance the catalytic activities of organometallic complexes and our last results involving the catalytic activity of dinuclear alkylaluminum benzopinacolates in the ROP of ε-caprolactone, we found it imperative to study group 13 complexes with diphenylmethoxo ligands. In this work we present the reactions of ^{t}Bu$_3$M (M = Al, Ga, In), Me_3Ga and Me_3In with benzopinacol. We report the unusual structure of a methylmethoxo indium benzopinacolate and the results of alcoholysis reactions of group 13 benzopinacolates.

2. Results and discussion

2.1. Reactions of $Me_5Al_3[OC(C_6H_5)_2C(C_6H_5)_2O]_2$ (1) with alcohols

As described in Section 1, the partial hydrolysis reaction of compound **1** led to the formation of the dinuclear complex $Me_2Al_2[OC(C_6H_5)_2C(C_6H_5)_2O]_2(C_4H_8O)$ (**2**). In this study, we showed that the reaction of the compound **1** with 1 equiv. of alcohol ROH (R = Me, Et, ^{t}Bu) resulted with the formation of the same product **2** in 80–90% yield (Scheme 1).[1]

Compound **2** was isolated from the post reaction mixture as a precipitate after addition of *n*-hexane. The presence of signals at −1.85 (AlCH_3), −1.06 (AlCH_3), 1.45 (THF) and 3.52 (THF) ppm and aromatic proton signals in the ^{1}H NMR spectrum indicated that the structure of compound **2** was the same as that of the earlier reported



Scheme 1.

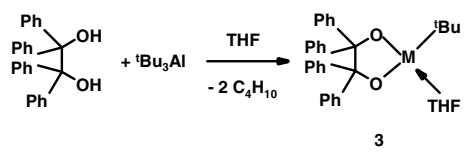
partial hydrolysis product [4]. Similarly to water, the alcohols played the role of the factor formally eliminating a Me_3Al molecule (in a form of a methylaluminum alkoxide) from the trinuclear compound **1**.

2.2. Reactions of benzopinacol with ^{t}Bu$_3$M (M = Al, Ga, In)

^{t}Bu$_3$Al reacted with an equimolar amount of benzopinacol to form the complex ^{t}BuAl[OC(C$_6$H$_5$)$_2$C(C$_6$H$_5$)$_2$O]-(C$_4$H$_8$O) (**3**) (Scheme 2).

In contrast to the trinuclear methyl- and ethylaluminum benzopinacolates $R_5Al_3[OC(C_6H_5)_2C(C_6H_5)_2O]_2$ (R = Me (**1**), Et) [4], the *tert*-butyl compound **3** was monomeric. The molecular structure of **3** has been determined by X-ray crystallography and it is shown in Fig. 1. Data collection and structure analysis are presented in Table 1. The molecule of **3** consists of a diolate unit, ^{t}Bu group bonded to the aluminum atom and a THF molecule coordinated to the Al atom. The aluminum atom is in a four coordinate highly distorted tetrahedral environment. The Al–O(3)$_{THF}$ bond [1.889(2) Å] is much longer than the Al–O(2) [1.745(2) Å] and Al–O(1) [1.724(2) Å] bonds. Fundamental studies have recently produced a number of trimetallic diolates [3], however compound **3** is the first mononuclear product of the reaction of aliphatic diols with alkylalanes. Several monomeric alane aromatic diolates were prepared by Lin [12] and Okuda [13]. Recently Lewiński [14] has reported a monomeric methylaluminum(bisphenoxide)-ε-caprolactone complex.

In contrast to the dimeric aluminum benzopinacolates $R_2Al_2[OC(C_6H_5)_2C(C_6H_5)_2O]_2(C_4H_8O)$ [R = Me (**2**), Et] [4], the monomeric compound **3** demonstrated very low activity in the polymerisation of ε-caprolactone. An attempt to activate **3** by replacing the ^{t}Bu with an alkoxyl group failed. Reactions of compound **3** with *iso*-propyl- and benzyl alcohols resulted in the formation of a mixture of *tert*-butylaluminum alkoxides and benzopinacol. In the presence of dioxygen, compound **3** underwent transformation into a complicated mixture of products instead of the expected *tert*-butoxoaluminum benzopinacolate.



Scheme 2.

[1] Alcohols are more soluble in organic solvents than water. Therefore, the cost of the synthesis of complexes $\{R_2Al_2[OC(C_6H_5)_2C(C_6H_5)_2O]_2(B)\}$ (R = alkyl group, B = Lewis base) in reactions of compounds $\{R_5Al_3[OC(C_6H_5)_2C(C_6H_5)_2O]_2\}$ with alcohols, is lower due to the small amount of solvents needed for the process.

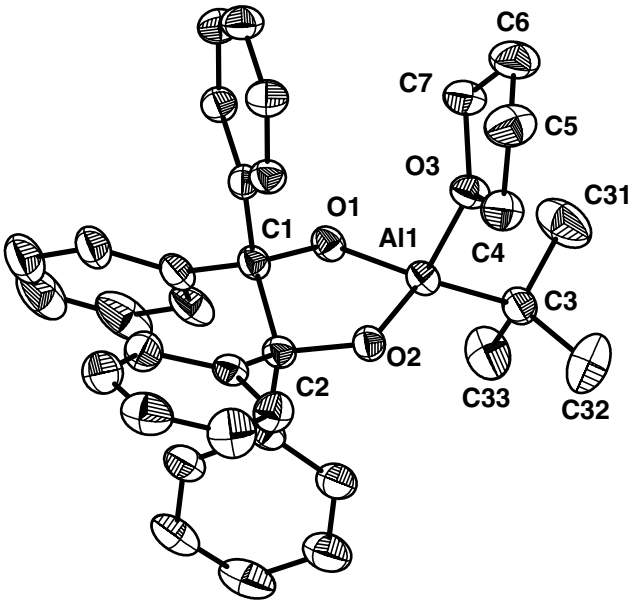


Fig. 1. Molecular structure of ^{t}BuAl[OC(C$_6$H$_5$)$_2$C(C$_6$H$_5$)$_2$O](C$_4$H$_8$O) (**3**). Thermal ellipsoids are shown at the 30% level. Hydrogen atoms are omitted for clarity. Selected bond lengths (Å) and bond angles (°): Al–O(2) 1.745(2), Al–O(1) 1.724(2), Al–O(3) 1.889(2), Al–C(3) 1.961(2), O(1)–C(1) 1.431(2), O(2)–C(2) 1.423(3), C(1)–C(2) 1.645(3); O(2)–Al–O(1) 93.9(1), O(2)–Al–O(3) 100.9(1), O(1)–Al–O(3) 111.6(1), O(2)–Al–C(3) 130.2(1), O(1)–Al–C(3) 115.7(1), O(3)–Al–C(3) 103.6(1).

Reactions of benzopinacol with ^{t}Bu$_3$Ga and ^{t}Bu$_3$In were carried over 3 h upon refluxing in toluene. We found that benzopinacol did not react with ^{t}Bu$_3$Ga, which was in agreement with our earlier observation of less reactivity of ^{t}Bu$_3$Ga and ^{t}Bu$_3$In in comparison with ^{t}Bu$_3$Al [15,16]. The ^{1}H NMR spectrum of the post reaction mixture revealed the signals of unreacted benzopinacol and ^{t}Bu$_3$Ga only. On the other hand, the reaction of ^{t}Bu$_3$In with benzopinacol resulted in the precipitation of indium and oxygenation of benzopinacol to benzophenone. The presence of benzophenone in the post reaction mixture was confirmed on the basis of the *C*O carbon signal at 77.21 ppm in the ^{13}C NMR spectrum.

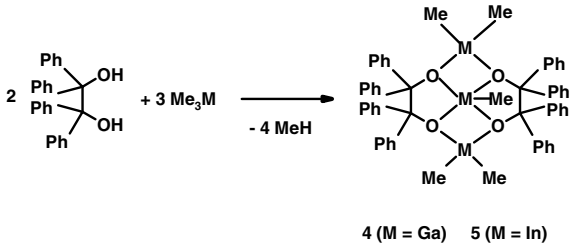
2.3. Methylgallium- and methylindium benzopinacolates

Independently of the molar ratio of the reagents, reactions of Me$_3$M (M = Ga, In) with benzopinacol afforded trinuclear complexes Me$_5$M$_3$[OC(C$_6$H$_5$)$_2$C(C$_6$H$_5$)$_2$O]$_2$ [**4** (M = Ga), **5** (M = In)], containing two diolate units (Scheme 3).

Compound **4** was crystallised from a post reaction mixture in 90% yield. The molecular structure of **4** was determined on the basis of a X-ray diffraction study and it is shown in Fig. 2. Data collection and structure analysis

Table 1
Crystal data and data collection parameters for **3**, **4** · 2CH$_2$Cl$_2$ and **6** · 2CH$_2$Cl$_2$

	3	**4** · 2CH$_2$Cl$_2$	**6** · 2CH$_2$Cl$_2$
Empirical formula	C$_{34}$H$_{37}$AlO$_3$	C$_{57}$H$_{55}$Ga$_3$O$_4$ · 2CH$_2$Cl$_2$	C$_{60}$H$_{64}$In$_4$O$_6$ · 2CH$_2$Cl$_2$
Formula weight	520.62	1183.02	1510.24
Temperature (K)	293(2)	100(2)	293(2)
Wavelength Å	0.71073	0.71073	0.71073
Crystal system	monoclinic	monoclinic	triclinic
Space group	$P2_1/c$	$P2_1/c$	$P\bar{1}$
a (Å)	12.843(1)	20.994(2)	10.956(2)
b (Å)	16.768(1)	10.807(1)	11.856(2)
c (Å)	14.916(1)	23.905(2)	12.862(3)
α (°)	90	90	100.35(2)
β (°)	115.33(1)	106.046(8)	97.15(2)
γ (°)	90	90	110.21(2)
V (Å^3)	2903.4(3)	5212.4(9)	1510.7(5)
Z	4	4	1
D_{calc} (g cm^{-3})	1.191	1.508	1.660
Absorption coefficient (mm^{-1})	0.102	1.792	1.733
F(000)	1112	2424	752
Crystal size (mm)	0.20 × 0.20 × 0.15	0.20 × 0.15 × 0.15	0.20 × 0.20 × 0.15
Θ Range for data collection (°)	2.77–25.00	3.06–25.00	3.29–25.00
Index ranges	$-15 \leqslant h \leqslant 15$, $-19 \leqslant k \leqslant 19$, $-17 \leqslant l \leqslant 17$	$-24 \leqslant h \leqslant 24$, $-12 \leqslant k \leqslant 12$, $-28 \leqslant l \leqslant 28$	$-13 \leqslant h \leqslant 13$, $-14 \leqslant k \leqslant 14$, $-15 \leqslant l \leqslant 15$
Reflections collected	22089	36778	21863
Independent reflections [R_{int}]	5088 [0.0881]	9144 [0.0809]	5300 [0.0682]
Refinement method	full-matrix least-squares on F^2		
Data/restraints/parameters	5088/0/346	9144/0/693	5300/0/348
Goodness-of-fit on F^2	0.834	1.022	1.083
Final R indices [$I > 2\sigma(I)$]	$R_1 = 0.0438$, $wR_2 = 0.0917$	$R_1 = 0.0552$, $wR_2 = 0.1374$	$R_1 = 0.0440$, $wR_2 = 0.1113$
R indices (all data)	$R_1 = 0.1109$, $wR_2 = 0.1079$	$R_1 = 0.0765$, $wR_2 = 0.1504$	$R_1 = 0.0547$, $wR_2 = 0.1198$
Maximum/minimum of residual electron density	0.204 and −0.188	0.961 and −1.047	0.778 and −0.919



Scheme 3.

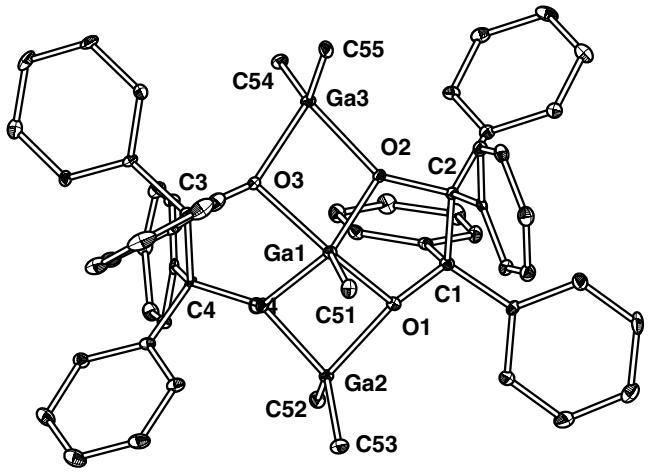


Fig. 2. Molecular structure of $Me_5Ga_3[OC(C_6H_5)_2C(C_6H_5)_2O]_2 \cdot 2CH_2Cl_2$ ($\mathbf{4} \cdot 2CH_2Cl_2$). Thermal ellipsoids are shown at the 20% level. Hydrogen atoms and molecules of CH_2Cl_2 are omitted for clarity. Selected bond lengths (Å) and bond angles (°): Ga(1)–O(4) 1.924(3), Ga(1)–O(2) 1.932(3), Ga(1)–C(51) 1.951(5), Ga(1)–O(3) 1.986(3), Ga(1)–O(1) 2.013(3), Ga(2)–O(1) 1.964(3), Ga(2)–O(4) 1.992(3), Ga(3)–O(3) 1.978(3), Ga(3)–O(2) 1.994(3); O(4)–Ga(1)–O(2) 122.0(1), O(4)–Ga(1)–O(3) 79.6(1), O(2)–Ga(1)–O(3) 79.4(1), O(4)–Ga(1)–O(1) 80.6(1), O(2)–Ga(1)–O(1) 79.5(1), O(3)–Ga(1)–O(1) 137.2(1), O(4)–Ga(1)–C(51) 113.6(2), O(2)–Ga(1)–C(51) 124.2(2), C(51)–Ga(1)–O(3) 116.4(2), C(51)–Ga(1)–O(1) 106.3(2).

are presented in Table 1. Two molecules of CH_2Cl_2 are present in the formula unit of **4**. The molecule of **4** consists of a tetracyclic structure formed from two Ga_2O_2 four-membered rings and two GaO_2C_2 five-membered rings. A central Ga(1) atom is five-coordinate, residing in the distorted square pyramidal geometry with the basal plane consisting of four oxygen atoms of the diol units and the methyl group residing in an apical position. The coordination sphere geometry of the central metal atom is closer to a square pyramidal structure [i.e., O(3)–Ga(1)–O(1) 137.2(1)°, O(4)–Ga(1)–O(2) 122.0(1)°] than to a trigonal bipyramidal geometry. The same geometry around the central metal atom was observed for related trinuclear aluminum complexes [4,17–20]. The sums of the angles about the oxygen atoms {$\sum$[O(1)] 350.3°; $\sum$[O(2)] 358.9°; $\sum$[O(3)] 358.8°; $\sum$[O(4)] 359.9°} were slightly less than 360°, which indicates a small steric strain in the molecule.

The ^{1}H NMR spectrum of **4** revealed three singlets of CH_3Ga group protons (at −0.15, −0.67 and −0.71 ppm) and multiplet of aromatic protons at 7.33–7.01 ppm with the integration ratio of 6:6:3:40, which were in agreement with the measured structure. The signal of *C*O carbons at 91.29 ppm in the ^{13}C NMR spectrum was situated in the region of the *C*O signals (ppm) of alkylaluminum benzopinacolates {**1** (93.31); $Et_5Al_3[OC(C_6H_5)_2C(C_6H_5)_2O]_2$ (93.30); **2** (92.81, 87.73); $Et_2Al_2[OC(C_6H_5)_2C(C_6H_5)_2O]_2$(THF) (92.62, 87.78)} [4]. In comparison with *C*O signals of alkylalane-[2] and alkygallane aliphatic diolates (ppm), ^{t}Bu$_4$Ga$_2$(OCH$_2$C$_6$H$_4$CH$_2$OH)$_2$ (67.49); ^{t}Bu$_5$Ga$_3$(OCH$_2$C$_6$H$_4$CH$_2$O)$_2$ (68.30); ^{t}Bu$_4$MeGa$_3$(OCH$_2$C$_6$H$_4$CH$_2$O)$_2$ (67.58); ^{t}Bu$_2$Me$_3$Ga$_3$(OCH$_2$C$_6$H$_4$CH$_2$O)$_2$ (67.44, 65.63) [15]; $Me_5Ga_3[OC(CH_3)_2CH_2C(CH_3)_2O]_2$ (74.86) [21]; ^{t}Bu$_5$Ga$_3$[OCH$_2$C(CH$_3$)$_2$CH$_2$O]$_2$ (78.4) [20], the *C*O carbon signal of **4** is dramatically shifted downfield, which is caused by the electron withdrawing effect of the aromatic rings.

The methylindium benzopinacolate **5** was not isolated as a pure compound. The ^{1}H NMR spectrum of a white solid crystallised in the post reaction mixture, besides signals of compound **5**, exhibited several small singlets in the region from 0.0 to −1.0 ppm. It indicated the presence of indium methyls, which crystallised together with **5**. Attempts to isolate the pure compound **5** failed, because it underwent easy decomposition and became dark. The elemental analysis, molecular weight and melting point were not measured due to the impurity and the instability of compound **5**. The structure of **5** was proposed on the basis of ^{1}H and ^{13}C NMR spectra. Similarly to the spectra of compounds **1** [4] and **4**, the ^{1}H NMR spectrum of **5** revealed three singlets at −0.21, −0.47 and −0.72 ppm with a 2:2:1 integration ratio, assigned to the protons of five methyl groups bonded to indium atoms. The signal of *C*O carbons (at 89.94 ppm) in the ^{13}C NMR spectrum was situated in the same region as those of aluminum- and gallium benzopinacolates. The presence of one signal of *C*O carbons in the spectrum indicated the equivalence of the CO groups, which was in agreement with the proposed structure of **5**. The analogy of the spectra of compounds **1**, **4** and **5** showed that **5** was isostructural to the compounds **1** and **4**.

Attempts to synthesise the dinuclear complexes $Me_2M_2[OC(C_6H_5)_2C(C_6H_5)_2O]_2(C_4H_8O)$ (M = Ga, In), isostructural to the aluminum derivative **2**, failed. In contrast to the partial hydrolysis and alcoholysis reactions of the aluminum benzopinacolate **1**, reactions of the methylgallium- and methylindium benzopinacolates (**4** and **5**) with water and alcohols resulted in the decomposition of the compounds to benzopinacol and metalloxanes or a mixture of alkoxides, respectively. The ^{1}H NMR spectra of the post reaction mixtures revealed a singlet of O*H* group protons at 3.04 ppm and a multiplet of aromatic protons (7.37–7.21 ppm) characteristic for benzopinacol. The reaction carried out under milder reaction conditions (at 0 °C in a diluted solution) resulted in the same products. In our opinion, the digallium complex $Me_2Ga_2[OC(C_6H_5)_2C(C_6H_5)_2O]_2(C_4H_8O)$ was formed as a very unstable inter-

[2] For chemical shift of CO signals of alkylalane aliphatic diolates see Ref. [4], p. 2933.

mediate product, undergoing decomposition. In the reaction of the indium compound **5** with water and alcohols, benzopinacol underwent an oxidation to benzophenone, whereas organoindium compounds were reduced to indium (for details see Section 3.5). Two singlets of CH_3M protons characteristic for the expected $Me_2M_2[OC(C_6H_5)_2C(C_6H_5)_2O]_2(C_4H_8O)$ (M = Ga, In) products were not observed in the ^1H NMR spectra, which indicated that these products were not formed in the reactions. For comparison, the ^1H NMR spectrum of the aluminum derivative **2** revealed the signals of CH_3Al protons as two singlets at −1.06 and −1.85 ppm [4].

2.4. Methylmethoxo indium benzopinacolate

The reaction of benzopinacol with Me_3In and Me_2InOMe in a 1:1:1 molar ratio afforded an unusual methylmethoxo indium benzopinacolate $Me_6In_4[OC(C_6H_5)_2C(C_6H_5)_2O]_2(OCH_3)_2$ (**6**) (Scheme 4). The pure compound **6** was isolated by crystallisation from the post reaction mixture in 35% yield. It has been spectroscopically and crystallographically characterised. Data collection and structure analysis are presented in Table 1. The molecular structure of **6** is shown in Fig. 3 (top).

The centrosymmetric tetranuclear molecule of **6** consists of a pentacyclic structure formed from three In_2O_2 four-membered rings and two InO_2C_2 five-membered rings. The tetranuclear compound is formed by the alkoxide termini of two diolate ligands and two methoxyl groups bridging two Me_2In units and two central MeIn units. The five-coordinate In(1) atoms reside in a distorted square pyramidal geometry with the basal plane consisting of three oxygen atoms of the diolate units and one atom of the OMe group. The Me group is situated in an apical position. The angles $O(2)^{\#1}$–In(1)–O(1) 135.4(1)° and O(2)–In(1)–O(3) 121.1(1)° indicate that the coordination geometry of the In(1) atoms is closer to a square pyramidal structure than to a trigonal bipyramidal geometry.

It is worthy of note, that the two terminal In_2O_2 rings deviate highly from a plane tetragon {sums of the angles about the oxygen atoms $\sum$[O(1)]: 349.8° and $\sum$[O(3)]: 342.8°; torsion angle O(3)–In(1)–O(1)–In(2): −16.8(1)°}.

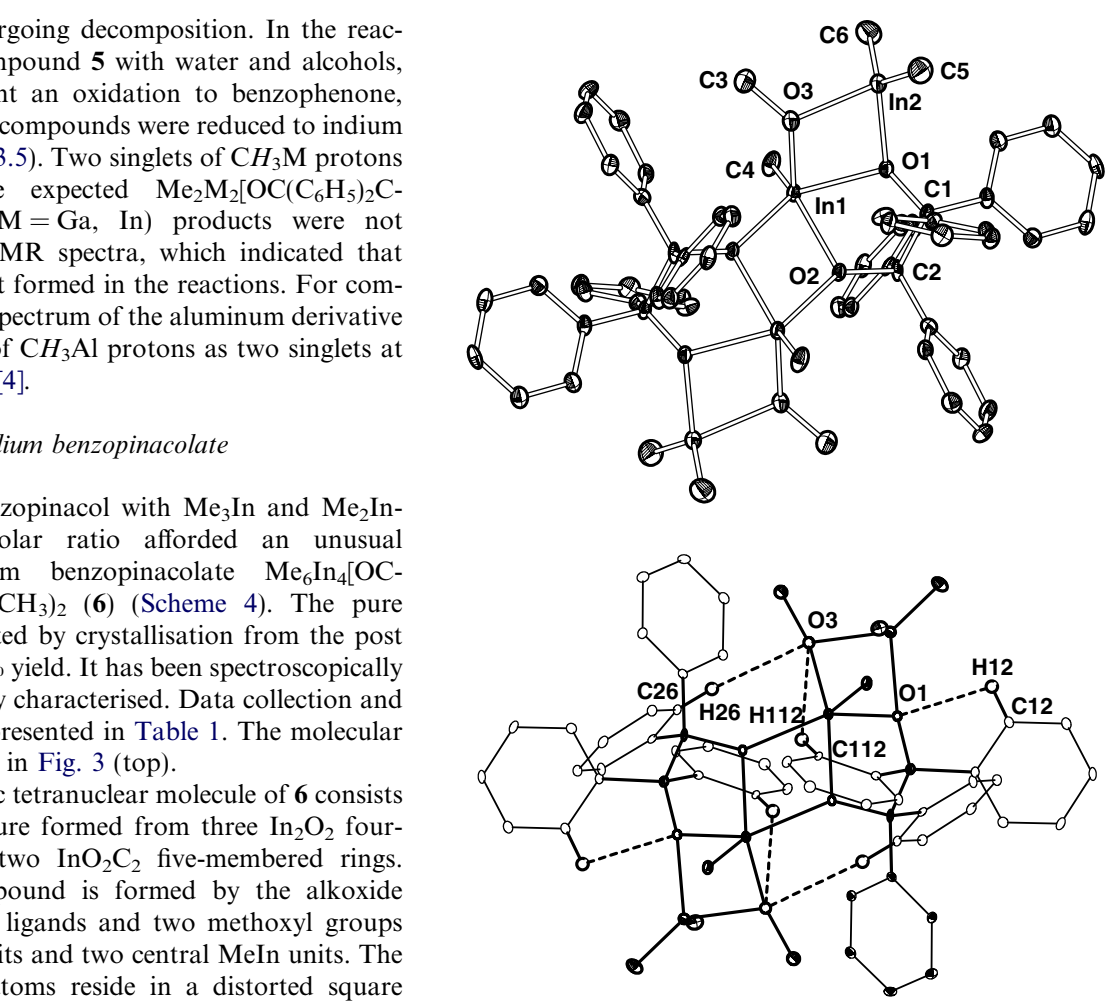
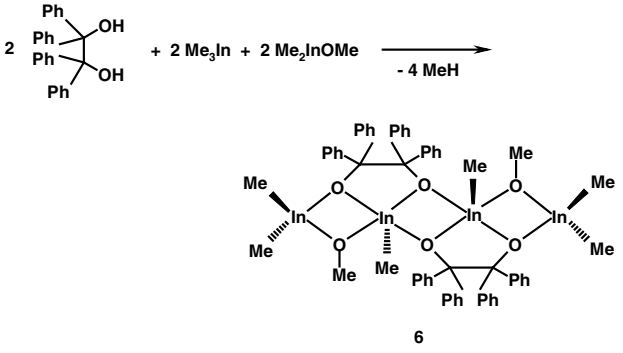


Fig. 3. Molecular structure of $Me_6In_4[OC(C_6H_5)_2C(C_6H_5)_2O]_2(OCH_3)_2 \cdot 2CH_2Cl_2$ (**6** · $2CH_2Cl_2$). (Top) Thermal ellipsoids are shown at the 40% level. Hydrogen atoms and molecules of CH_2Cl_2 are omitted for clarity. Selected bond lengths (Å) and bond angles (°): In(1)–O(1) 2.217(3), In(1)–O(2) 2.156(3), In(1)–O(3) 2.176(3), In(1)–$O(2)^{\#1}$ 2.182(3), C(4)–In(1) 2.138(5), C(5)–In(2) 2.131(6), C(6)–In(2) 2.148(6), In(2)–O(1) 2.157(3), In(2)–O(3) 2.193(3); $O(2)^{\#1}$–In(1)–O(1) 135.4(1), O(2)–In(1)–O(3) 121.1(1), C(4)–In(1)–$O(2)^{\#1}$ 116.3(2), C(4)–In(1)–O(1) 106.8(2), C(4)–In(1)–O(2) 125.8(2), C(4)–In(1)–O(3) 110.5(2), C(5)–In(2)–C(6) 134.8(2), C(5)–In(2)–O(1) 116.5(2), C(6)–In(2)–O(1) 99.2(2), C(5)–In(2)–O(3) 112.7(2), C(6)–In(2)–O(3) 101.5(2), O(1)–In(2)–O(3) 76.3(1). (Bottom) A view of the intramolecular hydrogen bonds in the molecule of **6** · $2CH_2Cl_2$. Hydrogen atoms are omitted excluding those involved in the H-bond formation. The dashed lines represent C–H···O hydrogen bonds.



Scheme 4.

A detailed examination of the structural data showed that very probably the deviation is the result of intramolecular interactions of *ortho*-positioned hydrogens with O(1) and O(3) oxygen atoms [(O(1)–H(12): 2.40 Å, C(12)–H(12)···O(1): 102°, O(3)–H(26): 2.55 Å, C(26)–H(26)···O(3): 174°, O(3)–H(112): 2.64 Å, C(112)–H(112)···O(3): 138°) (Fig. 3 bottom). The hydrogen atoms were placed in calculated positions, however short distances between the confirmed *ortho*-positioned carbons and O(1) and O(3) oxygen atoms [C(26)–O(3): 3.499(6) Å, C(112)–O(3): 3.406(7) Å, C(12)–O(1): 2.760(5) Å] indicated the possibility of involving the hydrogen atoms H(12), H(26) and

H(112) in hydrogen bond interactions with the oxygen atoms O(1) and O(3). Intermolecular hydrogen interactions in the crystal structure were not found. Moreover long-distances donor–acceptor interactions were absent in the supramolecular structure. Recently Lewinski has presented the substantial role of non-covalent interactions ($C–H_{aryl}\cdots O$, $C–H_{aliph}\cdots O$ and $C–H\cdots\pi$ hydrogen bonds) in molecular assembly and the structure of metal complexes [22].

Compound **6** was more stable than the compound **5**. It demonstrated very low solubility in solvents. The ^1H NMR spectrum of **6** revealed one singlet at 2.17 ppm of OCH_3 protons and three singlets (at −0.14, −0.81 and −1.05 ppm) of $InCH_3$ protons with a 1:1:1:1 integration ratio, which is in agreement with the measured structure of the compound. The presence of two signals of *C*O carbons (at 87.22 and 82.98 ppm) in the ^{13}C NMR spectrum indicate the inequivalence of the CO groups. In comparison with the *C*O signals of group 13 metal benzopinacolates: **1** (93.31 ppm), **2** (92.81 and 87.73 ppm), **3** (88.85 ppm), **4** (91.29 ppm) and **5** (89.94 ppm), the *C*O signal of **6** at 82.98 ppm is shifted upfield. It is the result of weakening of the electron withdrawing effect of the aromatic rings by a donating effect of the methoxyl groups.

Group 13 alkylalkoxides incorporating diolate ligands are rare. Earlier Chisholm and Lin [23] reported one dimeric methylalkoxo aluminum biphenolate (μ-biphenolate)AlMe(μ)–OCH(^{i}Pr)$_2$AlMe$_2$, prepared from the reaction of biphenolate-H_2 with 2 mol equiv. of Me_3Al in the presence of 1 mol equiv. of 2,4-dimethyl-3-pentanol. The compound demonstrates a catalytic activity in ROP of *rac*-lactide.

In conclusion, trinuclear alkylaluminum benzopinacolates react with alcohols to yield binuclear complexes $R_2Al_2[OC(C_6H_5)_2C(C_6H_5)_2O]_2(C_4H_8O)$. Alcohols, as well as water, play the role of a factor formally eliminating a R_3Al molecule (as an alkylaluminum alkoxide) from the trinuclear benzopinacolates. The compounds **4** and **5** were studied as starting materials for the syntheses of dinuclear complexes $Me_2M_2[OC(C_6H_5)_2C(C_6H_5)_2O]_2(C_4H_8O)$ (M = Ga, In), a potential ROP of cyclic esters. Unfortunately, in the presence of water and alcohols compounds **4** and **5** underwent a decomposition reaction to benzopinacol and mixtures of metalloxanes and alkoxides. Contrary to the stable aluminum compound **2**, presumably the gallium and indium derivatives $Me_2M_2[OC(C_6H_5)_2C(C_6H_5)_2O]_2$-$(C_4H_8O)$ were formed as unstable intermediate products. Further attempts with substituted benzopinacols will be undertaken to obtain stable dinuclear complexes.

We found that the reaction of benzopinacol with Me_3In and Me_2InOMe in a 1:1:1 molar ratio afforded the unusual tetranuclear methylmethoxo indium benzopinacolate **6**. The reaction of diols with a mixture of group 13 trialkyl metals and dialkyl metal alkoxides can be regarded as the general method of synthesis of alkylalkoxo group 13 metal diolates. Diolate alkylmetal complexes supported by additional alkoxide ligands are potential useful reagents in organic transformations and polymerisation. Further studies on the syntheses and characteristics of alkylalkoxo group 13 metal diolates will be continued.

3. Experimental

All manipulations were carried out using standard Schlenk techniques under an inert gas atmosphere. The solvents were distilled over a blue benzophenone-K complex. Prof. K.B. Starowieyski (Warsaw University of Technology) kindly supported us with Me_3Ga and Me_3In. Compound **1**, benzopinacol and $^tBu_3Al$ were synthesised as described in the literature [4,24,25]. ^1H and ^{13}C NMR spectra were run on Mercury-400BB spectrometer. ^1H NMR spectra were recorded at 400.09 MHz. Chemical shifts were referenced to the residual proton signals of $CDCl_3$ (7.26 ppm). ^{13}C NMR spectra were run at 100.60 MHz (standard: chloroform $^{13}CDCl_3$, 77.20 ppm). Elemental analysis of **6** was obtained on a Perkin–Elmer 2400 analyser.

3.1. Reactions of $Me_5Al_3[OC(C_6H_5)_2C(C_6H_5)_2O]_2 \cdot 2CH_2Cl_2$ (**1** · $2CH_2Cl_2$) with alcohols

A solution of MeOH (0.016 g, 0.5 mmol) in THF (4 cm^3) was added to solid compound **1** · $2CH_2Cl_2$ (0.528 g, 0.5 mmol). The mixture was set aside for ca. 24 h. Volatiles were removed in vacuo. A resulting glassy solid consisting of **2** and Me_2AlOMe was washed with *n*-C_6H_{14} (5 cm^3) two times, then dried in vacuo furnishing a white solid of **2** · THF (0.421 g, 88%). The ^1H NMR spectrum of products washed away from **2** · THF and soluble in *n*-C_6H_{14} revealed signals of Me_2AlOMe. ^1H NMR ($CDCl_3$): δ 3.63 [3H, s, $(CH_3)_2AlOCH_3$], −0.95 [6H, s, $(CH_3)_2AlOCH_3$] ppm. The spectrum of Me_2AlOMe obtained in the reaction of **1** · $2CH_2Cl_2$ with MeOH was similar to that published elsewhere [26].

Similarly, from of EtOH (0.023 g, 0.5 mmol) and **1** · $2CH_2Cl_2$ (0.528 g, 0.5 mmol) the white solid of **2** · THF (0.392 g, 82%) was obtained. The ^1H NMR spectrum of products washed away from **2** · THF and soluble in *n*-C_6H_{14} revealed signals of Me_2AlOEt. ^1H NMR ($CDCl_3$): δ 3.94 [2H, q, $(CH_3)_2AlOCH_2CH_3$], 1.39 [3H, t, $(CH_3)_2AlOCH_2CH_3$], −0.86 [6H, s, $(CH_3)_2AlOCH_2CH_3$] ppm. The spectrum of Me_2AlOEt obtained in the reaction of **1** · $2CH_2Cl_2$ with EtOH was similar to that published elsewhere [27].

The reaction of ^tBuOH (0.037 g, 0.5 mmol) with **1** · $2CH_2Cl_2$ (0.528 g, 0.5 mmol) afforded **2** · THF (0.430 g, 90%). The ^1H NMR spectrum of products washed away from **2** · THF and soluble in *n*-C_6H_{14} revealed signals of Me_2AlO^tBu. ^1H NMR ($CDCl_3$): δ 1.27 [9H, s, $(CH_3)_2AlOC(CH_3)_3$], −0.51 [6H, s, $(CH_3)_2AlOC(CH_3)_3$] ppm. The spectrum of Me_2AlO^tBu obtained in the reaction of **1** · $2CH_2Cl_2$ with ^tBuOH was similar to that published elsewhere [28].

The ^1H NMR spectrum of **2** obtained in the above reactions was the same as described earlier [4].

3.2. Synthesis of $^tBuAl[OC(C_6H_5)_2C(C_6H_5)_2O](C_4H_8O)$ (3)

A solution of $^tBu_3Al \cdot OEt_2$ (0.544 g, 2 mmol) in THF (10 cm^3) was added to a stirred solution of benzopinacol (0.732 g, 2.0 mmol) in THF (30 cm^3) at 0 °C. The reaction mixture was allowed to warm to room temperature and refluxed (1 h). Volatiles were removed in vacuo, then a white colourless solid of **3** (0.718 g, 69%) was sublimed off in vacuo. A solution of **3** in *n*-C_6H_{14} upon cooling at −25 °C furnished X-ray quality crystals. M.p.: 171 °C.

^{1}H NMR ($CDCl_3$): δ 7.64–7.00 (20H, m, H aromat), 3.71 [broadened, 4H, m, CH_2O (THF)], 1.15 (9H, s, (CH_3)$_3$C), 1.76 [broadened, 4H, m, CH_2 (THF)] ppm. ^{13}C NMR ($CDCl_3$): δ 150.31, 148.22, 129.37, 129.33, 126.78, 126.00, 125.49, 125.21 (*C* aromat), 88.85 (*C*O), 65.80 [*C*H$_2$O (THF)], 30.41 [(*C*H$_3$)$_3$C], 24.94 [*C*H$_2$ (THF)], 15.25 [(CH$_3$)$_3$*C*] ppm.

Molecular weight: found: 504, calc.: 520. Elemental *Anal.* Calc.: Al, 5.19; ^{t}Bu, 10.96 wt%. Found: Al, 5.30; hydrolysable *tert*-butyl groups, 10.62.

3.3. Synthesis of $Me_5Ga_3[OC(C_6H_5)_2C(C_6H_5)_2O]_2 \cdot 2CH_2Cl_2$ ($4 \cdot 2CH_2Cl_2$)

A solution of benzopinacol (1.098 g, 3 mmol) in CH_2Cl_2 (30 cm^3) was added to a stirred solution of Me_3Ga (0.541 g, 4.7 mmol) in Et_2O (20 cm^3) at −78 °C. The reaction mixture was allowed to warm to room temperature (2 h). The post reaction mixture was stored at −5 °C, yielding colourless crystals of $4 \cdot 2CH_2Cl_2$ (1.860 g, 1.35 mmol, 90%). m.p.: 186–189 °C.

^{1}H NMR ($CDCl_3$): δ 7.33–7.01 (40H, m, H aromat), −0.15 (6H, s, GaCH_3), −0.67 (6H, s, GaCH_3), −0.71 (3H, s, GaCH_3). ^{13}C NMR ($CDCl_3$): δ 145.28, 144.92, 130.63, 130.59, 128.56, 127.28, 126.93, 126.52, 126.46,126.40 (*C* aromat) 91.29 (*C*O), −0.14, −0.31 (Ga*C*H$_3$) ppm. Anal. Calc. for $C_{59}H_{59}Ga_3O_4Cl_4$: C, 59.85; H, 4.99%. C, 59.40; H, 5.30%.

3.4. Synthesis of $Me_5In_3[OC(C_6H_5)_2C(C_6H_5)_2O]_2$ (5)

A solution of benzopinacol (0.732 g, 2 mmol) in CH_2Cl_2 (20 cm^3) was added to a stirred solution of Me_3In (0.525 g, 3.3 mmol) in Et_2O (20 cm^3) at −78 °C. The reaction mixture was allowed to warm to room temperature (2 h). The post reaction mixture was stored at −25 °C (one week), yielding a white solid (0.340 g) sensitive to light and higher temperature. The solid undergoes a slow decomposition and becomes dark. NMR spectra revealed the signals of **5** (main product) and a mixture of methylindium compounds. An attempt to isolate the pure compound **5** by recrystallisation failed.

^{1}H NMR (**5**) ($CDCl_3$): δ 7.85–7.04 (40H, m, H aromat), −0.21 (6H, s, InCH_3), −0.47 (6H, s, GInCH_3), −0.72 (3H, s, InCH_3). ^{13}C NMR (**5**) ($CDCl_3$): δ 147.78, 130.61, 130.52, 127.17, 126.80, 126.32 (*C* aromat), 89.94 (*C*O), 0.98, 0.49 (In*C*H$_3$) ppm.

3.5. Reactions of compounds 4 and 5 with water and alcohols

The reaction of compound **4** with water was carried out as described in Section 3.1. using 0.592 g (0.5 mmol) of $4 \cdot 2CH_2Cl_2$ and 0.0045 g (0.25 mmol) of water. After removal of THF from the post reaction mixture, *n*-C_6H_{14} (10 cm^3) was added to the reaction products. A white solid precipitated. The solution was filtered to separate the solid. The solvent was removed from the filtrate under reduced pressure and products, soluble in *n*-C_6H_{14}, were obtained. The products soluble in *n*-C_6H_{14} and the solid were studied by NMR spectroscopy. ^{1}H NMR (reaction product of **4** with water, soluble in *n*-C_6H_{14}) ($CDCl_3$): δ 7.5–6.9 (H aromat, m), 3.04 (O*H*, s, benzopinacol), 0.0 to −1.0 (CH_3, m, broad, galloxanes) ppm. ^{1}H NMR (white solid insoluble in *n*-C_6H_{14}) ($CDCl_3$): δ 7.37–7.21 (20H, m, H aromat, benzopinacol), 3.04 (2H, s, OH, benzopinacol) ppm.

Reactions of compound **5** with water and workup of the products were carried out as described above for **4**, using 0.574 g (0.5 mmol) of **5** and 0.0045 g (0.25 mmol) of water at 0 and −40 °C. The reaction mixtures were allowed to warm to room temperature. After addition of *n*-C_6H_{14} to the post reaction mixture, a grey solid precipitated. ^{1}H NMR (reaction product of **5** with water, soluble in *n*-C_6H_{14}) ($CDCl_3$): δ 7.45–7.82 (H aromat, m, benzophenone, benzopinacol) 3.04 (O*H*, s, benzopinacol) ppm. ^{13}C NMR (reaction product of **5** with water, soluble in *n*-C_6H_{14}) ($CDCl_3$): δ 77.21 (*C*═O, benzophenone) ppm. The grey solid insoluble in *n*-C_6H_{14}, probably containing indium, was a complicated mixture of products. The products of the reactions carried out at 0 and −40 °C were the same.

Reactions of **4** with alcohols were carried out as described in Section 3.1 using 0.592 g (0.5 mmol) of $4 \cdot 2CH_2Cl_2$ and 0.5 mmol of alcohol (0.023 g of EtOH, 0.016 g of MeOH). After addition of *n*-C_6H_{14} to the post reaction mixture, a white solid appeared. The solution was filtered to separate the solid. The solvent was removed from the filtrate under vacuum and products soluble in *n*-C_6H_{14} were obtained. The products soluble in *n*-C_6H_{14} and the solid were studied by NMR spectroscopy.

^{1}H NMR (reaction product of **4** with EtOH, soluble in *n*-C_6H_{14}) ($CDCl_3$): δ 7.17–7.81 (H aromat, m), 3.87 (OCH_2CH$_3$, m), 1.26 (OCH$_2$CH_3, m), −0.2 to −0.5 (CH_3Ga, broad, m, oligomeric methylgallium compounds), 3.04 (O*H*, s, benzopinacol), −0.15, −0.67 and −0.71 (CH_3Ga, three singlets, unreacted compound **4**) ppm. ^{1}H NMR (white solid, insoluble in *n*-C_6H_{14}) ($CDCl_3$): δ 7.37–7.21 (20H, m, H aromat, benzopinocol), 3.04 (2H, s, OH, benzopinacol) ppm. Similarly, from **4** and MeOH, products soluble in *n*-C_6H_{14} and a white solid were obtained. ^{1}H NMR (reaction product of **4** with MeOH, soluble in *n*-C_6H_{14}) ($CDCl_3$): δ 7.02–7.32 (H aromat, m), 3.58 (OCH_3, m), −0.2 to −0.6 (CH_3Ga, broad, m, oligomeric methylgallium compounds), 3.04 (O*H*, s, benzopinacol), −0.15, −0.67

and −0.71 (CH_3Ga, three singlets, unreacted compound **4**) ppm. ^1H NMR (white solid, insoluble in n-C_6H_{14}) ($CDCl_3$): δ 7.37–7.21 (20H, m, H aromat, benzopinacol), 3.04 (2H, s, OH, benzopinacol) ppm.

The spectra indicated that the post reaction mixtures of **4** with EtOH and MeOH consisted of benzopinacol, methylgallium alkoxides and unreacted compound **4**.

The reaction of compound **5** with MeOH was carried out as described above using 0.574 g (0.5 mmol) of **5** and 0.016 g (0.5 mmol) of MeOH. A grey solid of indium precipitated from the post reaction mixture of **5** with MeOH in THF. After filtration the grey solid was removed. THF was distilled off from the filtrate and reaction products were studied by ^1H NMR spectroscopy. ^1H NMR ($CDCl_3$): δ 7.48–7.83 (H aromat, m, benzophenone, benzopinacol), 3.69, 3.51 (OCH_3, m, broad), −0.07, −0.35 ($InCH_3$, m, broad, methylindium methoxides), −0.21, −0.47 −0.72 ($InCH_3$, s, unreacted compound **5**) ppm. Similarly to the partial hydrolysis products of **5**, the post reaction mixture of **5** with MeOH contained indium, benzophenone, benzopinacol and unreacted **5**.

3.6. Synthesis of $Me_6In_4[OC(C_6H_5)_2C(C_6H_5)_2O]_2(OCH_3)_2 \cdot 2CH_2Cl_2$ ($\mathbf{6} \cdot 2CH_2Cl_2$)

A solution of methanol (0.096 g, 3 mmol) in Et_2O (2 cm^3) was added to a solution of Me_3In (0.960 g, 6 mmol) in Et_2O (10 cm^3) at −78 °C. A reaction mixture was allowed to warm to room temperature (1 h), then cooled to −78 °C. A solution of benzopinacol (1.098 g, 3 mmol) in CH_2Cl_2 (20 cm^3) was added dropwise to the mixture. A reaction mixture was allowed to warm to room temperature (2 h). Colourless, X-ray quality crystals of $\mathbf{6} \cdot 2CH_2Cl_2$ (0.790 g, 0.53 mmol) were obtained after crystallisation from the post reaction mixture at 5 °C (yield 35%). The compound undergoes decomposition at 163 °C without melting.

^1H NMR ($CDCl_3$): δ 7.00–7.40 (m, H aromat), 2.17 (6H, s, OCH_3), −0.14 (6H, s, $InCH_3$), −0.81 (6H, s, $InCH_3$), −1.05 (6H, s, $InCH_3$). ^{13}C NMR ($CDCl_3$): δ 144.11, 130.84, 128.58, 127.29 (C aromat), 87.22, 82.98 (CO), 52.80 (OCH_3), −4.26, −4.51 ($InCH_3$) ppm. *Anal.* Calc. for $C_{62}H_{68}In_4O_6Cl_4$: C, 49.77; H, 4.50. Found: C, 49.02; H, 4.76%.

3.7. X-ray crystal structure analyses

Crystals of compounds **3**, **4** and **6** were mounted in inert oil and sealed in glass capillaries under argon. Determination of the crystal structures of **3**, **4** and **6** was performed on a KUMA KM4CCD κ-axis diffractometer with graphite-monochromated Mo Kα radiation. The crystals of **3**, **4** and **6** were positioned 65 mm from the KM4CCD camera. For compound **3** 1000 frames were measured in 0.6° intervals with a counting time of 10 s. For compound **4** 600 frames were measured in 1.0° intervals with a counting time of 25 s. For compound **6** 1000 frames were measured in 1.2° intervals with a counting time of 25 s. All of the data were corrected for Lorentz and polarisation effects. No absorption correction was applied. Data reduction and analysis were carried out using the KUMA Diffraction (Wrocław) programs. The structures of the investigated crystals were solved by direct methods [29] and refined using the SHELXS/SHELXL computer programs [30]. All hydrogen atoms were placed in calculated positions and their thermal parameters were refined isotropically. Scattering factors were taken from the literature [31, Tables 6.1.1.4 and 4.2.4.2].

Absorption corrections were not made for compounds **4** and **6** because, following our experience, for such values of absorption coefficients, the corrections do not lead to a significant improvement of the final results. According to [32], for $0 < \mu < 25$ cm^{-1} ($0 < \mu < 2.5$ mm^{-1}) an absorption correction is not usually necessary unless a crystal with a very unfavorable shape is used, since if applied the absorption corrections will not significantly improve in accuracy of the results. In our case the crystals were rather small with no big differences in the three dimensions.

The X-ray structures were measured in the Crystallography Unit of the Physical Chemistry Laboratory at the Chemistry Department of the University of Warsaw.

Acknowledgement

The scientific work was financed by the Polish State Committee for Scientific Research as Research Project 3 T08E 026 27.

Appendix A. Supplementary material

CCDC 602048, 602049 and 602050 contain the supplementary crystallographic data for **3**, **4** and **6**. These data can be obtained free of charge via http://www.ccdc.cam.ac.uk/conts/retrieving.html, or from the Cambridge Crystallographic Data Centre, 12 Union Road, Cambridge CB2 1EZ, UK; fax: (+44) 1223-336-033; or e-mail: deposit@ccdc.cam.ac.uk. Supplementary data associated with this article can be found, in the online version, at doi:10.1016/j.poly.2006.11.032.

References

[1] (a) M. Endo, T. Aida, S. Inoue, Macromolecules 20 (1987) 2982;
(b) A. Duda, Z. Florjanczyk, A. Hofman, S. Słomkowski, S. Penczek, Macromolecules 23 (1990) 1640;
(c) Ph. Dubois, C. Jakobs, R. Jerome, Ph. Teyssie, Macromolecules 24 (1991) 2266;
(d) Ph. Dubois, C. Jakobs, R. Jerome, Ph. Teyssie, Macromolecules 26 (1993) 2730;
(e) Ph. Dubois, C. Jakobs, R. Jerome, Ph. Teyssie, Macromolecules 26 (1993) 4407;
(f) M. Akatsuka, T. Aida, S. Inoue, Macromolecules 28 (1995) 1320;
(g) N. Ropson, Ph. Dubois, R. Jerome, Ph. Teyssie, Macromolecules 28 (1995) 7589;
(h) T. Aida, S. Inoue, Acc. Chem. Res. 29 (1996) 39;
(i) A. Duda, Macromolecules 29 (1996) 1399;

(j) Ph. Dubois, N. Ropson, R. Jerome, Ph. Teyssie, Macromolecules 29 (1996) 1965;
(k) M. Gadzinowski, S. Sosnowski, S. Słomkowski, Macromolecules 29 (1996) 6404;
(l) S. Penczek, A. Duda, Macromol. Symp. 107 (1996) 1;
(m) A. Kowalski, A. Duda, S. Penczek, Macromol. Rapid Commun. 19 (1998) 567;
(n) B. Ko, C.-C. Lin, Macromolecules 32 (1999) 8296;
(o) E. Martin, P. Dubois, R. Jerome, Macromolecules 33 (2000) 1530;
(p) Y.-C. Liu, B.-T. Ko, C.-C. Lin, Macromolecules 34 (2001) 6196;
(q) M.-L. Hsueh, B.-H. Huang, C.-C. Lin, Macromolecules 35 (2002) 5763;
(r) H.-L. Chen, B.-T. Ko, B.-H. Huang, C.-C. Lin, Organometallics 20 (2001) 5076.

[2] (a) O. Mekasuwandumrong, P. Praserthdam, M. Inoue, V. Pavarajarn, W. Tanakurungsank, J. Mater. Sci. 39 (2004) 2417;
(b) T. Hinklin, B. Toury, C. Gervais, F. Babonneau, J.J. Gislason, R.W. Morton, R.M. Laine, Chem. Mater. 16 (2004) 21;
(c) W. Koh, S.J. Ku, Y. Kim, Thin Solid Films 304 (1997) 222.

[3] W. Ziemkowska, Coord. Chem. Rev. 249 (2005) 2176.

[4] W. Ziemkowska, S. Kucharski, A. Kołodziej, R. Anulewicz-Ostrowska, J. Organomet. Chem. 689 (2004) 2930.

[5] (a) M. Braun, Angew. Chem., Int. Ed. 35 (1996) 519;
(b) M. Braun, R. Flaischer, B. Mai, M.-A. Schneider, S. Lachenicht, Adv. Synth. Catal. 346 (2004) 474;
(c) P.J. Walsh, A.E. Lurain, J. Balsells, Chem. Rev. 103 (2003) 3297;
(d) D. Seebach, A.K. Beck, A. Heckel, Angew. Chem., Int. Ed. 40 (2001) 92.

[6] (a) C. Bolm, K. Muniz, Chem. Commun. (1999) 1295;
(b) C. Bolm, J.P. Hildebrand, K. Muniz, N. Hermans, Angew. Chem., Int. Ed. 40 (2001) 3284;
(c) C. Bolm, J. Rudolf, J. Am. Chem. Soc. 124 (2002) 14850.

[7] (a) E. Hecht, T. Gelbrich, K.-H. Thiele, J. Sieler, Z. Anorg. Allg. Chem. 626 (2000) 180;
(b) T. Gelbrich, E. Hecht, K.-H. Thiele, J. Sieler, J. Organomet. Chem. 595 (2000) 21.

[8] C. Cui, S. Köpke, R. Herbst-Irmer, H.W. Roesky, M. Noltemeyer, H.-G. Schmidt, B. Wrackmeyer, J. Am. Chem. Soc. 123 (2001) 9091.

[9] Z. Yu, J.M. Wittbrodt, A. Xia, M.J. Heeg, H.B. Schlegel, C.H. Winter, Organometallics 20 (2001) 4303.

[10] C. Redshaw, M.R.J. Elsegood, K.E. Holmes, Angew. Chem., Int. Ed. 44 (2005) 1850.

[11] T.-C. Liao, Y.-L. Huang, B.-H. Huang, C.-C. Lin, Macromol. Chem. Phys. 204 (2003) 885.

[12] (a) C.-H. Lin, L.-F. Yan, F.-C. Wang, Y.-L. Sun, C.-C. Lin, J. Organomet. Chem. 587 (1999) 151;
(b) B.-T. Ko, Y.-C. Chao, C.-C. Lin, Inorg. Chem. 39 (2000) 1463.

[13] (a) W. Braune, H. Ma, T.S. Spaniol, J. Okuda, Organometallics 24 (2005) 1953;
(b) H. Ma, G. Melillo, L. Oliva, T.P. Spaniol, U. Englert, J. Okuda, J. Chem. Soc., Dalton Trans. (2000) 721.

[14] J. Lewiński, P. Horeglad, E. Tratkiewicz, W. Grzenda, J. Lipkowski, E. Kołodziejczyk, Macromol. Rapid Commun. 25 (2004) 1939.

[15] W. Ziemkowska, M. Buźniak, S. Kwaśniewska, K.B. Starowieyski, R. Anulewicz-Ostrowska, J. Organomet. Chem. 688 (2003) 246.

[16] W. Ziemkowska, P. Stella, R. Anulewicz-Ostrowska, J. Organomet. Chem. 690 (2005) 722.

[17] W. Ziemkowska, S. Pasynkiewicz, T. Głowiak, J. Organomet. Chem. 562 (1998) 3.

[18] W. Ziemkowska, S. Pasynkiewicz, R. Anulewicz-Ostrowska, M. Frączak, Main Group Metal Chem. 23 (2000) 169.

[19] W. Ziemkowska, Main Group Metal Chem. 23 (2000) 389.

[20] C.N. McMahon, S.J. Obrey, A. Keys, S.G. Bott, A.R. Barron, J. Chem. Soc., Dalton Trans. (2000) 2151.

[21] W. Ziemkowska, R. Anulewicz-Ostrowska, J. Organomet. Chem. 689 (2004) 2056.

[22] J. Lewiński, J. Zachara, I. Justyniak, M. Dranka, Coord. Chem. Rev. 249 (2005) 1185.

[23] M.H. Chisholm, C.-C. Lin, J.C. Gallucci, B.-T. Ko, J. Chem Soc., Dalton Trans. (2003) 406.

[24] A.I. Vogel, Preparatyka Organiczna, Wydawnictwa Naukowo-Techniczne, Warsaw 1984, Poland, p. 303, Polish Ed. A solution of benzophenone in 2-propanol was irradiated by means of UV lamp to yield benzopinacol (Yield 80%).

[25] W. Uhl, Z. Anorg. Allg. Chem. 570 (1989) 37.

[26] H. Vahrenkamp, H. Nöth, J. Organomet. Chem. 12 (1968) 281.

[27] E.G. Hoffman, Trans. Faraday Soc. 58 (1962) 42.

[28] H. Schmidbaur, F. Schindler, Chem. Ber. 99 (1966) 2178.

[29] G.M. Sheldrick, Acta Crystallogr., Sect. A 46 (1990) 467.

[30] (a) G.M. Sheldrick, SHELXL 97. Program for the Refinement of Crystal Structures, University of Göttingen, Germany, 1997;
(b) G.M. Sheldrick, SHELXL 93. Program for Refinement of Crystal Structure, University of Göttingen, Germany, 1993.

[31] A.I.C. Wilson (Ed.), International Tables for X-ray Crystallography, vol. C15, Kluwer Dordrecht, 1992.

[32] Walter de Gruyter, (Ed.), Modern X-ray Analysis on Single Crystals, Berlin, New York, 1980, p. 207.

dinitrogen and freeze–pump–thaw degassed immediately prior to use. The ^{1}H, $^{13}C\{1H\}$, $^{31}P\{^{1}H\}$ NMR spectra were recorded at 300, 75.4 and 121.4 MHz, respectively, at 295 K, using a Bruker Avance DRX 300 MHz NMR spectrometer. ^{1}H NMR and $^{13}C\{^{1}H\}$ NMR chemical shifts are reported in ppm downfield from TMS. ^{1}H NMR chemical shifts are referenced to the residual hydrogen signal of the deuterated solvents and in $^{13}C\{^{1}H\}$ NMR the ^{13}C signal of the deuterated solvents was used as a reference. $^{31}P\{^{1}H\}$ NMR chemical shifts are reported in ppm downfield from H_3PO_4 and referenced to the high frequency of 85% H_3PO_4. GC analyses were carried out in a Shimadzu GCMS-QP5000 Electron Ionization (EI) system. Elemental analyses were determined on a Heraeus CHN-O-RAPID elemental analyzer. The starting materials 1,3-benzenedimethanol, chlorodiisopropylphosphine, 4-(dimethylamino)pyridine (DMAP), $PdCl_2$, $CDCl_3$ were purchased from Aldrich Chemical Co. and used without further purification. The complex $[PdCl_2(COD)]$ was synthesized according to the published procedure [5].

2.2. Preparation and procedure

The synthesis and characterization of the pincer ligand 1,3-bis[(di-isopropylphosphinite)methyl]benzene$\{C_6H_4(CH_2\text{-}OPPr^{i})_2\text{-}1,3\}$ (**2**), its palladium derivative **3** and catalytic experiments were done as follows.

2.2.1. Synthesis and characterization of $\{C_6H_4(CH_2OPPr^{i})_2\text{-}1,3\}$ (2)

To a stirred solution of 1,3-benzenedimethanol (0.4145 g, 3 mmol) and DMAP (0.7451 g, 6.1 mmol) in THF (60 mL) was added $ClPPr^{i}_2$ (0.95 mL, 6 mmol) *via* a syringe at 0 °C. After the addition was completed the cooling bath was removed and stirring was continued at room temperature overnight. The solvent was then evaporated and the crude product dissolved in toluene and passed through a short path of silica gel. Toluene was evaporated under vacuum to afford a colorless oil of **3** (1.056 g, 2.85 mmol, 95%). This compound was used in the next step without further purification. ^{1}H NMR (299.847 MHz, $CDCl_3$): $\delta = 0.72$ (dd, $^{3}J_{HP} = 15.3$ Hz, $^{3}J_{CHCH_3} = 7.2$ Hz, 12H, $CH(CH_3)_2$), 0.84 (dd, $^{3}J_{HP} = 10.2$ Hz, $^{3}J_{CHCH_3} =$ 6.9 Hz, 12H, $CH(CH_3)_2$), 1.40 (m, 4H, $CH(CH_3)_2$), 4.47 (d, $J_{HP} = 8.40$ Hz, 4H, CH_2O), 6.73–7.13 (m, 4H, ArH). $^{31}P\{^{1}H\}$ NMR (121.379 MHz, $CDCl_3$): $\delta = 155.23$ (s). $^{13}C\{^{1}H\}$ NMR (75.404 MHz, $CDCl_3$): $\delta = 17.22$ (d, $J = 8.6$ Hz, $CH(CH_3)_2$), 18.13 (d, $J = 20.1$ Hz, $CH(CH_3)_2$), 28.43 (d, $J = 17.7$ Hz, $CH(CH_3)_2$), 74.52 (d, $J =$ 21.2 Hz, CH_2O), 126.80, 128.43, 129.27, 140.11 (d, $J = 7.4$ Hz), Ar.

2.2.2. Synthesis and characterization of $[PdCl\{C_6H_3(CH_2OPPr^{i}_2)\text{-}2,6\}]$ (3)

A solution of **2** (1.056 g, 2.85 mmol) in toluene (20 mL) was added dropwise to a suspension of $[PdCl_2(COD)]$ (0.815 g, 2.85 mmol) in toluene (30 mL) and set up for reflux for 5 h. The solution was filtered over a short pad of silica gel, washed with diethyl ether and pumped off to dryness. The resulting solid was extracted with diethyl ether and then the solvent was removed under vacuum. Recrystallization of the crude product in CH_2Cl_2/hexane resulted in the formation of a colorless crystalline solid, (1.026 g, 2 mmol, 70%). ^{1}H NMR (299.847 MHz, $CDCl_3$): $\delta = 1.11$ (dd, $^{3}J_{HP} = 14.40$ Hz, $^{3}J_{CHCH_3} = 6.70$ Hz, 12H, $CH(CH_3)_2$), 1.40 (dd, $^{3}J_{HP} = 17.40$ Hz, $^{3}J_{CHCH_3} =$ 6.70 Hz, 12H, $CH(CH_3)_2$), 2.40 (m, 4H, $CH(CH_3)_2$), 4.77 (d, $J_{HP} = 19.2$ Hz, 2H, CH_2O), 6.82–7.21 (m, 3H, Ar). $^{31}P\{^{1}H\}$ NMR (121.392 MHz, $CDCl_3$): $\delta = 144.88$ (s). $^{13}C\{^{1}H\}$ NMR (75.404 MHz, $CDCl_3$): $\delta = 15.02$ (brs, CH_3), 16.50 (brs, CH_3), 18.28 (brs, CH_3), 26.78 (brs, CH), 80.55 (CH_2O), 124.56, 127.74, 139.72 (vt, $J = 6.33$ Hz), 145.86. *Anal.* Calc. for $C_{20}H_{35}Cl_1O_2P_2Pd_1$ ($M_r = 511.311$): C, 46.98; H, 6.90. Found: C, 47.05; H, 6.93%.

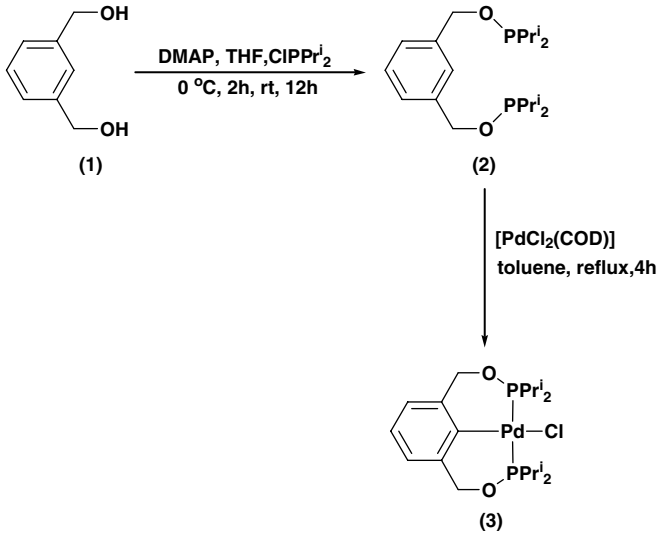
2.2.3. General procedure for heck coupling reactions

A solution (solvent, 3–5 ml) of 5.0 mmol of halobenzene, 6.0 mmol of alkene, and the prescribed amount of **3** as catalyst was introduced into a Schlenk tube. The tube was charged with a magnetic stir bar and 1.1 equiv. of base, sealed, and fully immersed in a 180 °C silicon oil bath. After the prescribed reaction time, the mixture was cooled to room temperature and the organic phase was analyzed by gas chromatography.

3. Results and discussion

The overwhelming majority of the reported PCP pincer complexes are based on the same structural principle, namely a bis-chelating metallacycle incorporating an aromatic carbon formed by C–H activating a 1,3-di(phosphinomethyl)benzene moiety. Except $[MBr\{C_6H_3(CH_2\text{-}CH_2PPh_2)_2\text{-}2,6\}]$ (M = Pd, Pt) [6], which is the only reported example of a PCP bis(phosphino)pincer complex with two six-membered metallacycles by Venanzi and coworkers, so far all other reported PCP pincer complexes are mainly five-membered metallocycles. To the best of our knowledge there are no reports on the synthesis and usage of bis(phosphinite) PCP pincer complexes with two six-membered metallocycles. We have previously reported on the synthesis of a new class of unsymmetric PCP′ pincer complexes which are useful for the Heck coupling reaction of aryl iodides [7]. Herein, we report the synthesis and catalytic activity of the first bis(phosphinite) PCP pincer complex with two six-membered metallacycles, showing that complex **3** has excellent catalytic activity in the Heck coupling reaction of halo-benzenes, including aryl chlorides.

The synthesis of the ligand 1,3-bis[(di-isopropylphosphinite)methyl]benzene (**2**) is outlined in Scheme 1. Thus 1,3-benzenedimethanol **1** is converted into **2** by using $ClPPr^{i}_2$ in THF in the presence of DMAP as a base. The $^{31}P\{^{1}H\}$ NMR spectrum of this compound shows a sharp singlet at 155.23 ppm. Refluxing **2** with $[PdCl_2(COD)]$ in



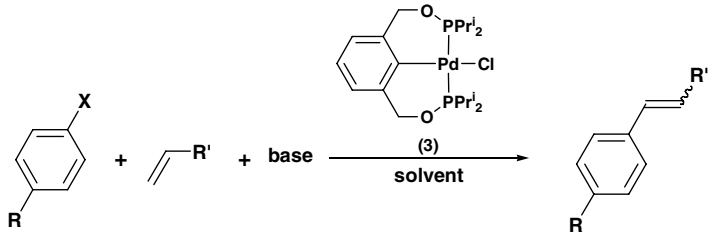
Scheme 1. Synthesis of the two six-membered Pd complex **3**.

toluene for 5 h affords the palladium complex [PdCl{C_6H_3-($CH_2OPPr^i_2$)-2, 6}] (**3**) in 85% yield. The $^{31}P\{^1H\}$ NMR spectrum of this complex shows a singlet at 144.88 ppm. The palladium complex **3** is thermally stable up to 180 °C and in the open air (oxygen and moisture).

Reaction conditions were found where complex **3** exhibited very good catalytic activity with excellent results on the Heck coupling of iodobenzene with styrene. Hence, we decided to extend the study to other substrates, in order to determine whether our catalyst could be operative in the C–C coupling of less reactive C–Br and C–Cl bonds. The results obtained are presented in Table 1. In general, complex **3** exhibits higher activity than the previously reported bis(phosphine) PCP pincer complexes [PdCl-{C_6H_3-2, 6-($CH_2PPr^i_2$)$_2$}] (**4**) and bis(phosphinito) PCP pincer complex [PdCl{C_6H_3-2, 6-($OPPr^i_2$)$_2$}] (**5**) (Scheme 2) [8,9]. In these cases, compound **4** is not effective at all with arylchlorides while complex **5** only showed TON's (Turn Over Numbers) 100 times lower with aryl chlorides when compared to complex **3**. Thus, while both complexes **4** and **5** have two five-membered palladacycle rings, complex **3** differs not only with respect to the phosphorous donor atoms but also to the size of the chelate rings. Based on the results shown in Table 1, complex **3**, with two phosphinite groups and two six-membered palladacycle rings (in principle more flexible), has higher activity than either complex **4** or **5**. Although complex **3** has the higher ring size of the three compounds, the fact that the phosphorous donor atoms in complex **3** are $OPPr^i_2$ makes it electronically different from complex **4** with $CH_2PPr^i_2$ donating groups.

There has been a considerable debate in the literature about the oxidation states of the species involved in the catalytic cycle, with Pd(IV)/Pd(II) and Pd(II)/Pd(0) both being proposed at various times [4,8]. Another feasible proposal for the present case is that it might be possible that

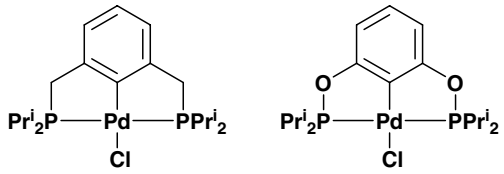
Table 1
Heck couplings of halobenzenes with different olefins using the complex [PdCl{$C_6H_3(CH_2OPPr^i)_2$-2,6}] (**3**) as a catalyst



Entry	Aryl halide	Olefin R′	Base	Catalyst (mol %)	Solvent	Yield (%)[a]	TON
1	PhCl	Ph	Na_2CO_3	0.01	NMP	94	9400
2	PhCl	Ph	Na_2CO_3	0.01	DMF	89	8900
3	PhCl	Ph	Na_2CO_3	0.05	NMP	99	1980
4	PhCl	Ph	Na_2CO_3	0.05	DMF	99	1980
5	PhCl	Ph	Cs_2CO_3	0.05	dioxane	99	1980
6	PhCl	Ph	Cs_2CO_3	0.05	dioxane	99	1980
7	PhCl	4-MeOPh	Na_2CO_3	0.01	NMP	94	9400
8	PhCl	4-MeCOPh	Na_2CO_3	0.01	DMF	89	8900
9	PhI	*n*-butyl methacrylate	Na_2CO_3	0.006	NMP	100[b]	16667
10	PhI	*n*-butyl methacrylate	Na_2CO_3	0.006	DMF	99[b]	16500
11	PhBr	*n*-butyl methacrylate	Na_2CO_3	0.006	NMP	100[b]	16667
12	PhBr	*n*-butyl methacrylate	Na_2CO_3	0.006	DMF	97[b]	16167

[a] Yields obtained at 180 °C by GC analysis are based on aryl halide and product. In all experiments with styrene only the *trans* configured product was detected.

[b] Using *n*-butylmethacrylate the product is a mixture of *n*-butyl-2-benzylacrylate, *n*-butyl-(E)-2-methylcinnamate and *n*-butyl (Z)-2-methylcinnamate. The yields reported are total.



Scheme 2. Five-membered Pd(II) PCP pincer complexes.

one or both arms may delicate at some stage enabling the compound to catalyze the reaction, thus behaving as a hemilabile ligand [10]. However, as it has been shown recently it is possible that complex **3** would not be the true catalyst but merely a catalyst precursor able to generate nanoparticles in the media [11]. Thus, although the precise mechanism of the catalytic reaction using complex **3** remains to be elucidated, efforts aimed at shedding some further light regarding this are currently under progress in our laboratories.

In summary, so far the catalyst described here is among the most active yet reported in Heck coupling reactions. This complex is ideal to catalyze the coupling of deactivated and sterically hindered aryl bromides and chlorides as they are comparatively inexpensive, very easily synthesized and can be used to give high conversion at low concentrations of catalyst. By comparing catalysts **3**, **4** and **5** it is clear that increasing the ring size from five to six-membered and also using phosphinite instead of phosphine groups both lead to the more active catalyst **3**.

Acknowledgements

The support of this research by the Ministry of Science, Research and Technology of Iran is gratefully acknowledged. Ali Naghipour thanks Prof. S.J. Sabounchei and Prof. C. M. Jensen for their help. D. C.-G. and D. M.-M. would like to thank CONACYT (J41206-Q) and DGAPA-UNAM (IN114605).

References

[1] (a) L.N. Lewis, J.F. Smith, J. Am. Chem. Soc. 108 (1986) 2728;
(b) L.N. Lewis, J. Am. Chem. Soc. 108 (1986) 743.
[2] (a) J. Dupont, M. Pfeffer, J. Spencer, Eur. J. Inorg. Chem. (2001) 1917;
(b) G. Dyker, Angew. Chem., Int. Ed. 38 (1999) 1698.
[3] (a) M. Gupta, W.C. Kaska, R.E. Cramer, C.M. Jensen, J. Am. Chem. Soc. 119 (1997) 840;
(b) M. Gupta, W.C. Kaska, C.M. Jensen, Chem. Commun. (1997) 2273;
(c) R.A. Gossage, L.A. van de Kuil, G. van Koten, Acc. Chem. Res. 31 (1998) 423;
(d) L.A. van de Kuil, D.M. Grove, R.A. Gossage, J.W. Zwikker, L.W. Jenneskens, W. Drenth, G. van Koten, Organometallics 16 (1997) 4985;
(e) F.E. Hahn, M.C. Jahnke, V. Gómez-Benítez, D. Morales-Morales, T. Pape, Organometallics 24 (2005) 6458;
(f) Z. Wang, S. Sugiarti, C.M. Morales, C.M. Jensen, D. Morales-Morales, Inorg. Chim. Acta 359 (2006) 1923;
(g) V. Gómez-Benítez, O. Baldovino-Pantaleón, C. Herrera-Álvarez, R.A. Toscazo, D. Morales-Morales, Tetrahedron Lett. 47 (2006) 5059;
(h) V. Gómez-Benítez, R.A. Toscazo, D. Morales-Morales, Inorg. Chem. Commun. 10 (2007) 1;
(i) O. Baldovino-Pantaleón, S. Hernández-Ortega, D. Morales-Morales, Adv. Synth. Catal. 348 (2006) 236.
[4] I.P. Beletskaya, A.V. Cheprakov, Chem. Rev. 100 (2000) 3009.
[5] D. Drew, J.R. Doyle, Inorg. Synth. 28 (1990) 348.
[6] Q.-N. Lu, S. Chaloupka, L.M. Venanzi, Wuji Huaxue 17 (2001) 227.
[7] A. Naghipour, S.J. Sabounchei, D. Morales-Morales, S. Hernández-Ortega, C.M. Jensen, J. Organomet. Chem. 689 (2004) 2494.
[8] D. Morales-Morales, R. Redón, C. Yung, C.M. Jensen, Chem. Commun. (2000) 1619.
[9] M. Ohff, A. Ohff, M.E. van der Boom, D. Milstein, J. Am. Chem. Soc. 119 (1997) 11687.
[10] (a) E. Poverenov, G. Leitus, L.J.W. Simón, D. Milstein, Organometallics 24 (2005) 5937;
(b) E. Poverenov, M. Gandelman, L.J.W. Shimon, H. Rozenberg, Y. Ben-David, D. Milstein, Organometallics 24 (2005) 1082;
(c) E. Poverenov, M. Gandelman, L.J.W. Shimon, H. Rozenberg, Y. Ben-David, D. Milstein, Chem. Eur. J. 10 (2004) 4673.
[11] (a) N.T.S. Phan, M. van der Sluy, C.W. Jones, Adv. Synth. Catal. 348 (2006) 609;
(b) J. Dupont, C.S. Consorti, J. Spencer, Chem. Rev. 105 (2005) 2527;
(c) V. Farina, Adv. Synth. Catal. 346 (2004) 1553.

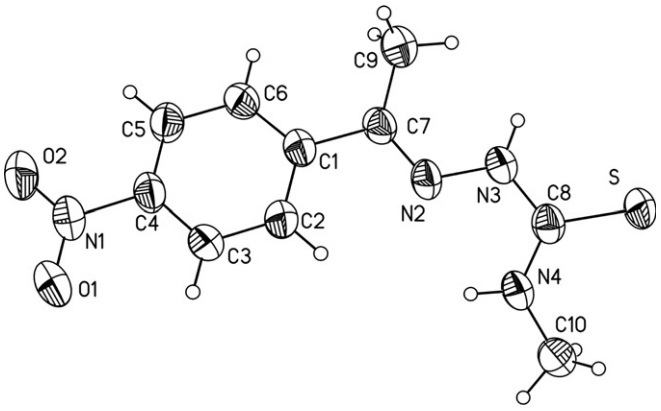


Fig. 1. Perspective view of the structure of H4NO$_2$Ac4M (**1**).

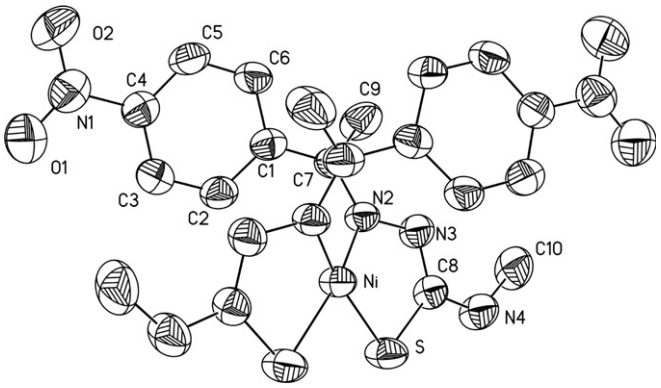


Fig. 2. Perspective view of the structure of [Ni(4NO$_2$Ac4M)$_2$] (**2**).

2. Experimental

2.1. Apparatus

Melting points were measured with a Mettler FP90 equipment. Partial elemental analyses were performed on a Perkin Elmer CHN 2400 analyzer. Electronic spectra were recorded on a Hewlett Packard 8453 spectrometer using dimethylformamide (DMF) solutions and 1 cm cells. Infrared spectra were recorded on a Perkin Elmer FT-IR Spectrum GX spectrometer using nujol mulls between CsI plates as support. An YSI model 31 conductivity bridge was employed for molar conductivity measurements.

^{1}H and ^{13}C NMR spectra in solution were recorded on a Bruker DRX 400 ADVANCE spectrometer using tetramethylsilane (TMS) as internal standard. The samples (15 mg) were dissolved in $CDCl_3$ or DMSO-d_6 (~0.5 mL). Chemical shifts are given in ppm (δ units).

Solid-state NMR spectra were recorded on a Bruker AMX 400 wide-bore NMR spectrometer using a commercial triple resonance MAS 4 mm probe. Proton-decoupled ^{13}C MAS NMR spectra were acquired using cross polarization [10]. Typical acquisition parameters were the following: spin lock time 2.0 ms, recycle delay 3 s, ^{1}H B1 field 91 kHz, 3072 data points, 25000 acquisitions, and spectral width of 50 kHz. The spectra were acquired at 298 K with a spinning speed of 10 kHz. Adamantane was used as reference (high field signal at 29.5 ppm).

Solid-state MAS NMR spectra were recorded at different temperatures on a Bruker AMX 500 wide-bore NMR spectrometer using commercial triple resonance MAS probes (3.2 mm for ^{13}C and 2.5 mm for ^{1}H experiments). Proton-decoupled ^{13}C MAS NMR spectra were acquired using cross polarization [10]. Typical acquisition parameters were the following: spin lock time 3.0 ms, recycle delay 3 s, ^{1}H B1 field 83 kHz, 10240 data points, 5000 acquisitions, and spectral width of 66 kHz. The ^{13}C NMR spectra were acquired at 323 and 343 K with a spinning speed of 20 kHz. ^{1}H MAS NMR spectra were acquired at 298 K with a spinning speed of 30 kHz. Typical acquisition parameters were the following: recycle delay 5 s, ^{1}H B1 field 114 kHz, 4096 data points, 32 acquisitions, and spectral width of 20 kHz.

The crystal structures of H4NO$_2$Ac4M (**1**) and its nickel(II) complex (**2**) were investigated. Data for **1** were obtained using the XSCANS software [11] and for **2** with the Collect package [12]. Crystal data and refinement for **1** and **2** are shown in Table 1. Cell dimensions of the

Table 1
Crystal data for H4NO$_2$Ac4M (**1**) and [Ni(4NO$_2$Ac4M)$_2$] (**2**)

Compound	H4NO$_2$Ac4M (**1**)	[Ni(4NO$_2$Ac4M)$_2$] (**2**)
Empirical formula	$C_{10}H_{12}N_4O_2S$	$C_{20}H_{22}N_8NiO_4S_2$
Formula weight	252.30	561.29
Temperature (K)	293 (2)	
Crystal system	triclinic	monoclinic
Space group	$P\bar{1}$	$C2/c$
Unit cell dimensions		
a (Å)	8.605(3)	12.857(3)
b (Å)	9.015(4)	8.670(2)
c (Å)	9.529(4)	22.502(5)
α (°)	65.18(3)	90
β (°)	72.51(3)	105.16(3)
γ (°)	63.96(3)	90
Volume (Å^3)	596.7(4)	2421.1(8)
Z, D_{calc} (Mg/m^3)	2, 1.404	4, 1.540
Absorption coefficient (mm^{-1})	0.267	1.018
F(000)	264	1160
Crystal size (mm)	0.15 × 0.15 × 0.20	0.09 × 0.08 × 0.01
Crystal color, shape	yellow, prismatic	brown, prismatic
Diffractometer, scan	SIEMENS P4/θ–2θ	Kappa CCD
Graphite-monochromated radiation	Mo Kα, λ = 0.71073 Å	
θ Range for data collected (°)	2.38–25.00	3.65–26.49
Index range, θ	$-1 \leqslant h \leqslant 10$ $-9 \leqslant k \leqslant 9$ $-11 \leqslant l \leqslant 11$	$-14 \leqslant h \leqslant 16$ $-10 \leqslant k \leqslant 10$ $-28 \leqslant l \leqslant 28$
Reflections collected/unique (R_{int})	2500/ 2046(0.0395)	20387/ 2503(0.1416)
Observed reflections [$I > 2\sigma(I)$]	1516	1432
Restraints/parameters	0/154	0/159
R_{obs}, R_{all}	0.0619/0.0851	0.0522/0.1232
wR_{2obs}, wR_{2all}	0.1660/0.1839	0.1183/0.1467
Goodness-of-fit on F^2	1.254	0.982
Largest difference in peak and hole (e Å^{-3})	0.380/−0.304	1.113/−0.343

crystals of **1** and **2** were found by least-squares fit of 27 and 20387 accurate centred reflections respectively, with 2θ values ranging from 10 to 25 (**1**) and from 7.3 to 53.0 (**2**). Three standard reflections measured periodically for **1** showed no decrease in intensity during data collection. Data were corrected for Lorentz and polarization effects, but not for absorption. The structures were solved by direct methods and refined on F^2 by full-matrix least-squares using the SHELX97 [13] program in a WinGX system [14]. Although some of the hydrogen atoms could be identified in a Fourier difference map, in the final model they were geometrically positioned and refined using a riding model. All non-H atoms were anisotropically refined.

2.2. Synthesis of *N*(4)-methyl-4-nitroacetophenone thiosemicarbazone (*1*) and its nickel(II) complex (*2*)

N(4)-Methyl thiosemicarbazide and 4-nitroacetophenone have been purchased from Aldrich Chem. Co. and used without further purification. The thiosemicarbazone **1** was obtained by mixing equimolar amounts (6.6 mmol) of 4-nitroacetophenone and *N*(4)-methyl thiosemicarbazide in absolute ethanol (40 mL) with addition of two drops of concentrated sulfuric acid as catalyst. The reaction mixture was kept under reflux for 7 h. The resulting solids were filtered at room temperature and then washed with ethanol followed by diethyl ether and dried under reduced pressure.

N(4)-Methyl-4-nitroacetophenone thiosemicarbazone (**1**): Yellow solid. Mp: 216.3–217.6 °C; *Anal.* Calc. for $C_{10}H_{12}N_4O_2S$: C, 47.61; H, 4.79; N, 22.21. Found: C, 47.55; H, 4.69; N, 22.26%. UV–Vis λ_{max} (cm^{-1}): 36900, 27400. IR (nujol mulls, cm^{-1}): 3342 ν_{ass}(NH), 3182 ν_s(NH), 1590 ν(C=N), 1538 $\nu_{ass}(NO_2)$, 1330 $\nu_s(NO_2)$, 819 ν(C=S). ^{1}H and ^{13}C NMR data are shown in Tables 4 and 5, respectively.

Complex **2** was obtained by reacting of **1** (2.0 mmol in 15 mL of ethanol) with nickel(II) acetate (1.0 mmol in 15 mL of ethanol). The reaction mixture was kept under reflux for 3 h. The resulting solid was filtered at room temperature and then washed with ethanol followed by diethyl ether.

N(4)-Methyl-4-nitroacetophenone thiosemicarbazonatonickel(II) (**2**): Brown solid. 257.0–258.4 °C (dec); *Anal.* Calc. for $C_{20}H_{22}N_8NiO_4S_2$: C, 42.80; H, 3.95; N, 19.96. Found: C, 42.77; H, 3.97; N, 19.78%. UV–Vis λ_{max} (cm^{-1}): 32050, 27100, 24070, 17600. IR (nujol mulls, cm^{-1}): 1578 ν(C=N), 1532 $\nu_{ass}(NO_2)$, 1332 $\nu_s(NO_2)$, 768 ν(C–S), 460 ν(M–N), 390 ν(M–S). Molar conductivity (1×10^{-3} mol L^{-1} DMF): 0.96 Ω^{-1} cm^2 mol^{-1}; ^{1}H and ^{13}C NMR data of **2** in DMSO-d_6 are shown in Tables 6 and 7 respectively.

2.3. Theoretical methodology

Theoretical studies were carried out using the GAUSSIAN03W software package [15]. HF and DFT geometry optimizations were performed using the geometries previously obtained by the PM3 semi-empirical method [16]. BLYP and B3LYP functionals with the standard Pople's split valence 6-31G* basis set [17] were used in the DFT calculations. The optimized geometries were characterized as true minima on the potential energy surface (PES) with all harmonic frequencies being real. The electronic-nuclear energies (E) were calculated by means of the HF and DFT methods. Solvent effects ($CHCl_3$, $\varepsilon = 6.66$, and DMSO, $\varepsilon = 46.7$) in the geometry optimizations were taken into consideration using the Polarizable Continuum Model (PCM) [17a,17b,18] as implemented in the HF/6-31G* and DFT/B3LYP/6-31G* GAUSSIAN03 software package.

DFT/BLYP/6-31G* optimized geometries of **1** were used for the hydrogen ($^{Calc}\delta_H$) and carbon ($^{Calc}\delta_C$) chemical shift calculations. Hydrogen and carbon calculated chemical shifts of **1** were obtained in relation to the correspondent DFT/BLYP/6-31G* calculated values for tetramethylsilane ($^{Calc}\delta_H$ 32.44 and $^{Calc}\delta_C$ 190.90). For **2** the HF/6-31G* method has been used. In this case, the values for tetramethylsilane are $^{Calc}\delta_H$ 32.09 and $^{Calc}\delta_C$ 201.19.

3. Results and discussion

Microanalyses of the nickel(II) complex (see Section 2) suggest the formation of $[Ni(4NO_2Ac4M)_2]$ (**2**) in which two anionic ligands coordinate to the metal. The molar conductivity data indicate that the complex is a non-electrolyte, in accordance with the proposed formulation.

The π–π^* absorption at ca. 37000 cm^{-1} in the electronic spectrum of **1** was not significantly modified upon complexation. The n–π^* transitions attributed to the azomethine and thioamide groups overlap at 27400 cm^{-1} in the electronic spectrum of **1**, but were found separately at 32050 and 27100 cm^{-1} in the spectrum of **2**. The N–Ni(II) and S–Ni(II) ligand-to-metal charge transfer transitions occur probably under the same envelope at ca. 24070 cm^{-1}. Ligand field transitions were observed at 17600 cm^{-1} [19,20].

The ν(C=N) stretching vibration at 1590 cm^{-1} in the infrared spectrum of **1** shifts to 1578 cm^{-1} in the spectrum of **2**, indicating coordination of the imine nitrogen. The absorption at 819 cm^{-1} attributed to ν(C=S) in the spectrum of **1** shifts to 768 cm^{-1} in that of **2**, indicating complexation through a thiolate sulfur. Absorptions at 390 cm^{-1} and at 460 cm^{-1} in the spectrum of **2** were attributed to the ν(Ni–S) and ν(Ni–N) vibrations respectively. Hence the infrared spectra indicate coordination of the thiosemicarbazones through the N–S chelating system [19,20].

3.1. Structural characterization of *1* and *2*

ORTEP3 views [21] of the structures of $H4NO_2Ac4M$ (**1**) and $[Ni(4NO_2Ac4M)_2]$ (**2**) can be seen in Figs. 1 and 2 respectively. Table 2 shows selected bond distances (Å) and angles (°). Both compounds form hydrogen bonds and the geometry parameters are presented in Table 3.

Table 2
Selected bond lengths (Å) and angles (°) for $H4NO_2Ac4M$ (**1**) and $[Ni(4NO_2Ac4M)_2]$ (**2**)

Bond lengths (Å)			Angle (°)		
Atoms	$H4NO_2Ac4M$	$[Ni(4NO_2Ac4M)_2]$	Atoms	$H4NO_2Ac4M$	$[Ni(4NO_2Ac4M)_2]$
S–C8	1.682(3)	1.755(4)	N4–C8–S	123.5(3)	117.4(3)
C8–N4	1.330(4)	1.336(5)	N3–C8–S	119.7(3)	123.4(3)
C8–N3	1.364(5)	1.298(5)	N2–N3–C8	118.3(3)	112.0(3)
N3–N2	1.377(4)	1.394(4)	C7–N2–N3	119.6(3)	114.6(3)
C7–N2	1.275(4)	1.296(5)	N2–C7–C9	125.3(3)	121.2(4)
C7–C9	1.509(5)	1.494(6)	N2–C7–C1	114.6(3)	120.0(4)
C7–C1	1.494(4)	1.475(6)	C9–C7–C1	120.1(3)	118.8(4)
N1–O1	1.233(4)	1.223(5)	O1–N1–O2	123.1(3)	123.5(4)
N1–O2	1.209(4)	1.223(5)	N2–Ni–N2[a]		100.8(2)
Ni–N2		1.937(3)	N2–Ni–S[a]		164.2(1)
Ni–S		2.156(1)	N2–Ni–S		85.8(1)
			S–Ni–S[a]		91.5(1)

[a] Symmetry operation $-x+1, y, -z+1/2$.

Table 3
Hydrogen bonding geometry, H···A $\langle r(A) + 2.000$ A and $\angle DHA \rangle$ 110, for $H4NO_2Ac4M$ (**1**) and $[Ni(4NO_2Ac4M)_2]$ (**2**)

Compound	D–H···A	d(D–H)	d(H···A)	d(D–H···A)	∠D–H···A
$H4NO_2Ac4M$	N3–H–S$^{\#}$	0.86	2.70	3.533(3)	163.5
	N4–H–O1*	0.86	2.45	3.141(4)	138.2
$[Ni(4NO_2Ac4M)_2]$	N4–H4···O1′	0.86	2.34	3.067(6)	142.7

Symmetry operation: (#1) $-x+1, -y+1, -z+1$; (*) $-x+1, -y-1, -z+2$ and (′) $x, -y, z+1/2$.

Compound **1** crystallizes in the *EE* configuration in relation to the C7–N2 and N3–C8 bonds, respectively. Compound **2** crystallizes in the *EZ* configuration, in which a twisting of approximately 180° in the N3–C8 bond occurs, to match the steric requirements of bidentate coordination through the N2–S system.

In **1** the hydrogen at N4 forms an intermolecular hydrogen bond with O1, and the hydrogen at N3 forms an intermolecular hydrogen bond with the sulfur of a second molecule. The N4–H···O1 hydrogen bond observed in the crystal structure of **1** remains in the structure of **2**, forming a polymeric chain.

In the complex the sulfurs are approximately in *cis* positions to each other. The Ni atom lies on a twofold axis (1y 1/4). Different angles were found between the metal and the atoms in the two ligands: N2–Ni–N2* = 100.8(2)°, N2–Ni–S = 85.8(1)°, N2–Ni–S* 164.2(1)°, S–Ni–S* 91.5(1)° (* symmetry operation $-x+1, y, -z+1/2$), indicating that the geometry around the metal centre is distorted quadratic or distorted tetrahedral.

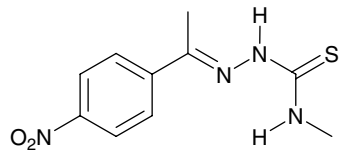
In the complex the two thiosemicarbazone molecules present the same bond distances and angles. The C8–S bond distance goes from 1.682(3) Å in the free thiosemicarbazone to 1.755(4) Å in the complex, in accordance with the C–S bond changing from mainly double in **1** to predominantly single in **2**. The C8–N3 bond varies from 1.364(5) Å in **1** to 1.298(5) Å in **2**, indicating the formation of a new predominantly double bond, in agreement with deprotonation at N3. The N2–N3 bond goes from 1.377(4) Å in **1** to 1.394(4) Å in **2**; C7–N2 goes from 1.275(4) in **1** to 1.296(5) Å in **2**; C7–C1 goes from 1.494(4) Å in **1** to 1.475(6) Å in **2**.

The angles in the thiosemicarbazone moiety undergo significant changes on coordination (see Table 2). The N4–C8–S angle goes from 123.5(3)° in **1** to 117.4(3)° in **2**, the N3–C8–S angle goes from 119.7(3)° in **1** to 123.4(3)° in **2**; the N3–N2–C7 angle goes from 119.6(3)° in **1** to 114.6(3)° in **2** and the N2–N3–C8 angle from 118.3(3)° in **1** to 112.0(3)° in **2**. The angle between the aromatic ring and the thiosemicarbazone chain goes from 24.7(2)° in the free thiosemicarbazone to 30.4(1)° in the complex.

3.2. Experimental and theoretical NMR studies of *1*

DFT/BLYP/6-31G* and DFT/B3LYP/6-31G* calculations were used for geometry optimizations of **1** in the gas phase as well as with consideration of solvent ($CHCl_3$ and DMSO) effects. Fig. 3 shows the differences in the electronic-nuclear energies (E) between the various geometries of **1**. DFT/BLYP/6-31G* calculations indicate that the **1-*E*,*E*** isomer presents the lowest energy as compared to **1-*Z*,*E***, **1-*E*,*Z*** and **1-*Z*,*Z***, with $\Delta E = 3.16$, 10.58 and 13.74 kcal/mol, respectively. DFT/B3LYP/6-31G* calculations revealed the same order of energy for these geometries, with differences of $\Delta E = 2.81$, 10.67 and 13.60 kcal/mol, of **1-*E*,*E*** in relation to **1-*Z*,*E***, **1-*E*,*Z*** and **1-*Z*,*Z*** respectively.

DFT/BLYP/6-31G*/$CHCl_3$ calculations considering the effect of $CHCl_3$ show that **1-*E*,*E*** is still the geometry of lowest energy, with differences in energy of $\Delta E = 1.98$, 6.55 and 9.10 kcal/mol, respectively in relation to **1-*Z*,*E***, **1-*E*,*Z*** and **1-*Z*,*Z***. A lower difference in energy was found between the optimized geometries (DFT/BLYP/6-31G*/DMSO) considering the effect of DMSO with $\Delta E = 1.91$,



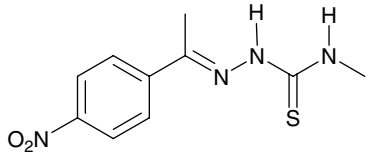
1-*E*,*E*

E(DFT/BLYP/6-31G*)= -1155.56683929 au

E(DFT/B3LYP/6-31G*)= -1155.82698458 au

E(DFT/B3LYP/6-31G*/$CHCl_3$)= -1155.84187092 au

E(DFT/B3LYP/6-31G*/DMSO)= -1155.84894957 au



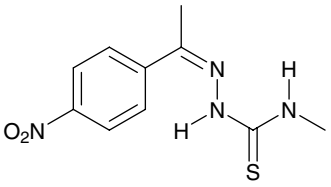
1-*E*,*Z*

E(DFT/BLYP/6-31G*)= -1155.54998509 au

E(DFT/B3LYP/6-31G*)= -1155.80997389 au

E(DFT/B3LYP/6-31G*/$CHCl_3$)= -1155.83143581 au

E(DFT/B3LYP/6-31G*/DMSO)= -1155.84238363 au



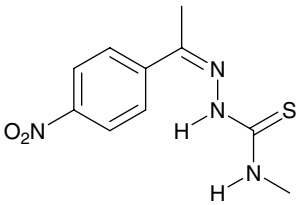
1-*Z*,*E*

E(DFT/BLYP/6-31G*)= -1155.56180947 au

E(DFT/B3LYP/6-31G*)= -1155.82250732 au

E(DFT/B3LYP/6-31G*/$CHCl_3$)= -1155.83872204 au

E(DFT/B3LYP/6-31G*/DMSO)= -1155.84590320 au



1-*Z*,*Z*

E(DFT/BLYP/6-31G*)= -1155.54494482 au

E(DFT/B3LYP/6-31G*)= -1155.80531321 au

E(DFT/B3LYP/6-31G*/$CHCl_3$)= -1155.82737638 au

E(DFT/B3LYP/6-31G*/DMSO)= -1155.83934354 au

Fig. 3. Electronic-nuclear energy (*E*) of the DFT/BLYP/6-31G* and DFT/B3LYP/6-31G* optimized geometries of **1** in the gas phase and considering solvent ($CHCl_3$ and DMSO) effects (PCM).

4.12 and 9.10 kcal/mol, respectively. The results indicate a decrease in energy of the optimized geometries in the order DFT/BLYP/6-31G*, DFT/B3LYP/6-31G*, DFT/BLYP/6-31G*/$CHCl_3$ and DFT/B3LYP/6-31G*/DMSO. However, all theoretical calculations suggest a lower relative energy for the **1-*E*,*E*** isomer. The theoretical calculations did not indicate stabilization effects of $CHCl_3$ on any of the studied geometries.

Fig. 4 shows partial ^{1}H NMR spectra of **1** in DMSO-d_6 and $CDCl_3$. The NMR signals were attributed based on 1D (^{1}H, ^{13}C and DEPT 135) and 2D (COSY, NOESY, HSQC and HMBC) experiments. The spectrum in DMSO-d_6 (Fig. 4a) exhibits only one signal (singlet) in the aromatic region (δ_H 8.20). This signal integrates for four hydrogens and shows HSQC correlation with signals of the methine carbons at δ_C 127.74 (C2/C6) and 123.39 (C3/C5). The singlet observed at δ_H 10.46 (integration for one hydrogen) does not correlate with any carbon in the HSQC contour map. This signal shows HMBC correlations with the signals at δ_C 145.13 (C7) and 178.87 (C8). Therefore, the signal at δ_H 10.46 can be assigned to H–N3. In the HSQC contour map the singlet at δ_H 2.34 (integration for three hydrogens) shows a correlation with the signal for at δ_C 14.02 (C9). In the HMBC contour map this signal correlates with only a carbon signal at δ_C 145.13 (C7), via $^2J_{H,C}$. The NOESY contour map shows correlations between the signals at δ_H 10.46 (H–N3) and 2.34 (H–C9). These long range interactions are spatially permitted only for the *E*-configuration in relation to the imino group and for the *E*- and *Z*-configurations in relation to the thioamide group, i.e. for isomers **1-*E*,*E*** and **1-*E*,*Z***, respectively (Fig. 3).

Fig. 4b shows the ^{1}H NMR spectrum of **1** in $CDCl_3$. The aromatic hydrogens are observed at δ_H 8.26 (H–C3/H–C5) and 7.87 (H–C2/H–C6). The NOESY contour map of **1** did not allow the determination of its stereochemistry. However, the existence of two signals assigned to the aromatic hydrogens in the ^{1}H NMR spectrum of **1** could indicate a different geometry from that observed in DMSO-d_6, since in the latter only one signal was noticed (Fig. 4a).

Table 4 shows the experimental ^{1}H NMR chemical shifts ($^{Exp}\delta_H$) for **1** in $CDCl_3$ and DMSO-d_6, as well as the DFT/BLYP/6-31G* calculated ^{1}H NMR chemical shifts ($^{Calc}\delta_H$) for the **1-*E*,*E***, **1-*Z*,*E***, **1-*E*,*Z*** and **1-*Z*,*Z*** optimized geometries at the same theoretical level. The experimental chemical shifts of H–C2, H–C6, H–N3 and H–N4 in DMSO-d_6 are found at higher frequencies than in $CDCl_3$. Similarly, the calculated chemical shifts of the same hydrogens ($^{Calc}\delta_H$) were obtained at higher frequencies for **1-*E*,*E*** and **1-*E*,*Z*** than for **1-*Z*,*E*** and **1-*Z*,*Z***. In addition, the experimental chemical shifts for H–C3/H–C5 in DMSO-d_6 were found at lower frequency than in $CDCl_3$. Similarly, the calculated chemical shifts of these hydrogens in **1-*E*,*E*** and **1-*E*,*Z*** were found at lower frequencies than the

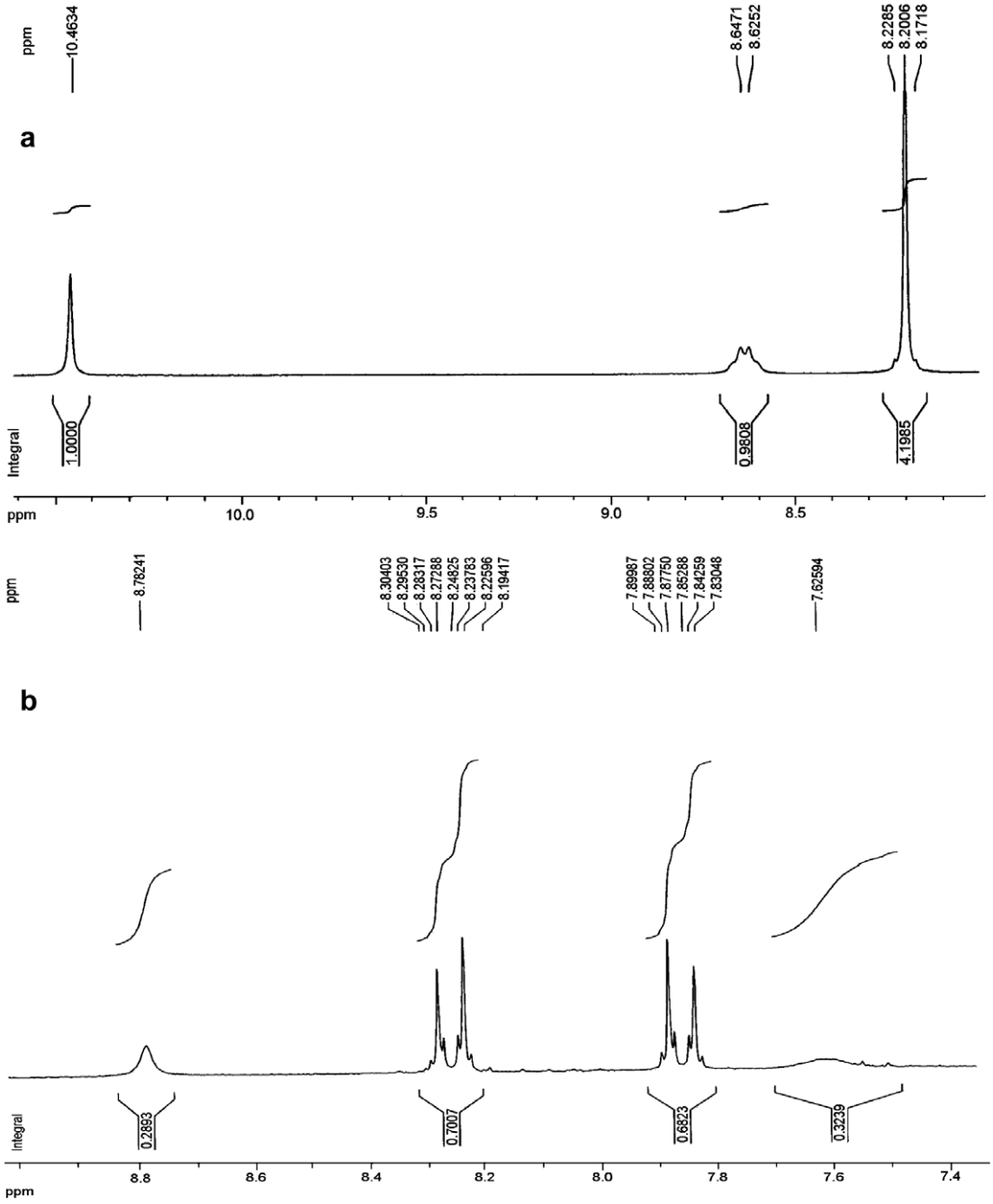


Fig. 4. Partial ^{1}H NMR spectra (400 MHz, TMS) of **1** in (a) DMSO-d_6 and (b) $CDCl_3$.

corresponding values in **1**-*Z*,*E* e **1**-*Z*,*Z*. Therefore the calculated chemical shifts are closer to the experimental values for **1**-*E*,*E* and **1**-*E*,*Z* in DMSO-d_6 and for **1**-*Z*,*E* and **1**-*Z*,*Z* in $CDCl_3$.

Table 5 shows the experimental ^{13}C NMR chemical shifts ($^{Exp}\delta_C$) for **1** in $CDCl_3$ and DMSO-d_6, as well as DFT/BLYP/6-31G* calculated ^{13}C NMR chemical shifts ($^{Calc}\delta_C$) for the carbons of the **1**-*E*,*E*, **1**-*Z*,*E*, **1**-*E*,*Z* and **1**-*Z*,*Z* optimized geometries at the same theoretical level. The C1, C2, C4, C6 and C7 chemical shifts in DMSO-d_6 were observed at higher frequencies than the corresponding values in $CDCl_3$. Similarly, the calculated chemical shifts for the same carbons of the **1**-*E*,*E* and **1**-*E*,*Z* isomers were found at higher frequencies than the corresponding carbons of **1**-*Z*,*E* and **1**-*Z*,*Z*. In addition, the C3, C5, C8 and C10 chemical shifts in DMSO-d_6 were found at lower frequencies than the shifts of the corresponding carbons in $CDCl_3$. The calculated shifts of these carbons were found at lower frequencies for the **1**-*E*,*E* and **1**-*E*,*Z* isomers than for **1**-*Z*,*E* and **1**-*Z*,*Z*. Hence the calculated values ($^{Calc}\delta_C$) for **1**-*E*,*E* and **1**-*E*,*Z* are closer to the experimental data ($^{Exp}\delta_C$) in DMSO-d_6. In $CDCl_3$ the calculated values of carbon chemical shifts were closer to the experimental data for **1**-*Z*,*E* and **1**-*Z*,*Z*.

Table 4
^{1}H NMR chemical shifts ($^{Exp}\delta_H$) of **1** in $CDCl_3$ and DMSO-d_6 (400 MHz, TMS) and DFT/BLYP/6-31G* calculated ^{1}H NMR chemical shifts ($^{Calc}\delta_H$[a]) for the optimized geometries of **1** given in Fig. 3

Atom	Solvent/$^{Exp}\delta_H$		Geometry/$^{Calc}\delta_H$[a]			
	$CDCl_3$	DMSO-d_6	**1-*E*,*E***	**1-*E*,*Z***	**1-*Z*,*E***	**1-*Z*,*Z***
H–C2	7.87	8.20	7.84	8.67	7.36	7.36
H–C3	8.26	8.20	8.13	8.21	8.33	8.25
H–C5	8.26	8.20	8.19	8.14	8.32	8.34
H–C6	7.87	8.20	8.34	8.27	7.55	7.35
H–N3	8.78	10.46	7.85	7.62	7.02	7.64
H–N4	7.60	8.64	6.56	4.43	6.53	3.92
H–C9	2.33	2.34	2.18	2.02	2.38	2.49
H–C10	3.30	3.05	3.18	3.24	3.19	3.10

[a] Values obtained relative to the calculated chemical shift of the hydrogens of tetramethylsilane TMS (δ_H 32.44) using DFT/BLYP/6-31G*.

Table 5
^{13}C NMR chemical shifts ($^{Exp}\delta_C$) of **1** in $CDCl_3$ and DMSO-d_6 (100 MHz, TMS) and DFT/BLYP/6-31G* calculated ^{13}C NMR chemical shifts ($^{Calc}\delta_C$[a]) of the optimized geometries of **1** (see Fig. 3)

Atom	Solvent/$^{Exp}\delta_C$		Geometry/$^{Calc}\delta_C$[a]			
	$CDCl_3$	DMSO-d_6	**1-*E*,*E***	**1-*E*,*Z***	**1-*Z*,*E***	**1-*Z*,*Z***
C1	143.34	144.01	136.15	136.20	131.84	133.16
C2	127.01	127.74	120.50	120.74	120.41	120.18
C3	123.85	123.39	116.80	117.14	118.17	116.94
C4	143.78	147.45	149.19	149.31	139.71	139.48
C5	123.85	123.39	117.24	116.71	117.31	118.46
C6	127.01	127.74	119.06	117.67	120.30	121.41
C7	143.34	145.13	145.57	142.46	140.03	139.60
C8	179.04	178.87	164.33	165.41	165.44	165.07
C9	13.44	14.02	13.16	10.70	26.33	26.54
C10	31.47	31.30	32.52	31.89	32.36	32.53

[a] Values obtained relative to the calculated chemical shift of the carbons of TMS (δ_C 190.90) using DFT/BLYP/6-31G*.

As already mentioned, the lowest energy isomer is **1-*E*,*E*** and the energy difference between **1-*E*,*E*** and **1-*E*,*Z*** is of 4.12 Kcal/mol in DMSO-d_6, suggesting that in this solvent the **1-*E*,*E*** isomer is the most plausible. In $CDCl_3$ the energy difference between **1-*E*,*E*** and **1-*Z*,*E*** is small (1.98 kcal/mol). Since the NMR spectra in the two solvents are not the same, the **1-*Z*,*E*** isomer is probably present in $CDCl_3$. The presence of **1-*Z*,*Z*** in $CDCl_3$ seems improbable considering the significant energy difference between **1-*E*,*E*** and **1-*Z*,*Z*** (9.10 kcal/mol).

3.3. Experimental and theoretical NMR studies of (2)

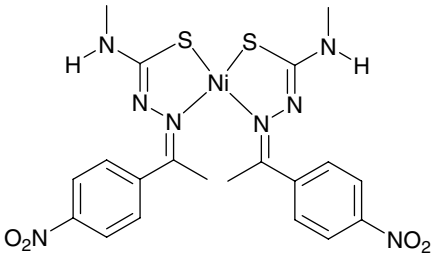
HF/3-21G* and HF/6-31G* theoretical calculations were employed for the geometry optimization of **2** in the gas phase as well as considering the effect of DMSO. Fig. 5 shows the electronic-nuclear energies of the different geometries of **2**. In all geometries of **2** the thiosemicarbazone must adopt the *Z*-configuration in relation to the N3–C8 bond to match the steric requirements of bidentate coordination. Hence only the configuration in relation to the C7–N2 bond is considered hereafter. The HF/3-21G* optimized geometry for **2-*cis*(*E*-Ni-*E*)** presents lower energy in relation to **2-*cis*(*Z*-Ni-*Z*)**, **2-*cis*(*E*-Ni-*Z*)**, **2-*trans*(*E*-Ni-*E*)**, **2-*trans*** (***E*-Ni-*Z***) and **2-*trans*** (***Z*-Ni-*Z***), with $\Delta E = 7.59$, 4.22, 2.01, 9.37 and 4.01 kcal/mol, respectively. HF/6-31G* calculations of the differences in energy between the optimized geometry for **2-*cis*(*E*-Ni-*E*)** in relation to **2-*cis*(*Z*-Ni-*Z*)**, **2-*cis*(*E*-Ni-*Z*)**, **2-*trans*(*E*-Ni-*E*)**, **2-*trans*** (***E*-Ni-*Z***) and **2-*trans*** (***Z*-Ni-*Z***)gave $\Delta E = 5.45$, 2.91, −1.83, 9.27 and −2.23 kcal/mol, respectively.

Table 6 shows the ^{1}H NMR data for **2** in DMSO-d_6 (**2** was insoluble in $CDCl_3$). The NMR signals were attributed based on 1D (^{1}H, ^{13}C and DEPT 135) and 2D (COSY, NOESY, HSQC and HMBC) experiments. NOESY correlations may occur either between the hydrogens of one of the ligands or between hydrogens located in the two ligands. The observed NOESY correlations between H–C2/H–C6, H-C9 and H–C10 could be attributed to all isomeric forms of **2**. However, the ^{1}H and ^{13}C NMR data (Tables 6 and 7) indicate that the chemical shifts for the atoms of the two ligands are equal. In this case, both ligands in **2** should adopt the same configuration, which cannot be attributed to **2-*trans*(*Z*-Ni-*E*)** and **2-cis** (***Z*-Ni-*E***). Therefore the NMR data of **2** can only be assigned to **2-*cis*(*E*-Ni-*E*)**, **2-*cis*(*Z*-Ni-*Z*)**, **2-*trans*(*Z*-Ni-*Z*)**, or **2-*trans*(*E*-Ni-*E*)**.

Table 6 also shows the HF/6-31G* hydrogen calculated chemical shifts for the geometries of **2** optimized at the same theoretical level. Since both thiosemicarbazones adopt the same configuration in the complex only one value of the calculated chemical shifts is reported. The calculated ^{1}H chemical shifts for **2-*cis*(*E*-Ni-*E*)** and **2-*trans*-(*E*-Ni-*E*)** deviate too much from the experimental shifts in DMSO-d_6 (mean deviations between the experimental and calculated shifts, $\Delta\delta_H$, are 12.49 and 11.66 respectively). The mean deviation of each hydrogen is smaller for the **2-*trans*** (***Z*-Ni-*Z***) ($\Delta\delta_H = 2.52$) and **2-*cis*(*Z*-Ni-*Z*)** ($\Delta\delta_H = 4.10$).

Table 7 shows ^{13}C NMR experimental data of **2**, along with HF/6-31G* calculated ^{13}C NMR chemical shifts ($^{Calc}\delta_C$) of the geometries of **2** optimized at the same theoretical level. Since both thiosemicarbazones adopt the same configuration in the complex only one value of the calculated chemical shifts is reported. The calculated ^{13}C chemical shifts for **2-*cis*(*E*-Ni-*E*)** and **2-*trans*(*E*-Ni-*E*)** deviate too much from the experimental shifts in DMSO-d_6. (mean deviations between the experimental and calculated shifts, $\Delta\delta_c$, are 7.99 and 13.50 respectively). The mean difference between the experimental and calculated chemical shifts of each carbon is smaller for the **2-*trans*** (***Z*-Ni-*Z***) ($\Delta\delta_C = 5.08$) and **2-*cis*** (***Z*-Ni-*Z***) ($\Delta\delta_C = 5.05$).

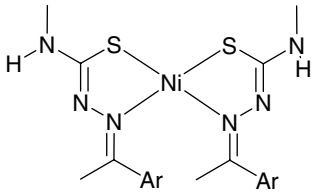
The solid-state ^{1}H MAS NMR does not provide information on the stereochemistry of **2**. Fig. 6 shows the solid-state ^{13}C MAS NMR of **2** at different temperatures. At room temperature the spectrum of the powder is similar to that obtained in DMSO-d_6, indicating the possible presence of the same isomer in both media. However, in the



2-*cis*(*Z*-Ni-*Z*)

E(HF/3-21G*)= -3787.39687827 au

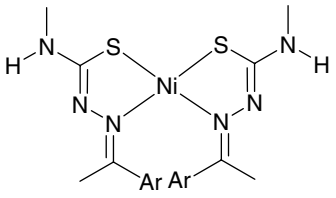
E(HF/6-31G*)= -3806.58064163 au



2-*cis*(*E*-Ni-*Z*)

E(HF/3-21G*)= -3787.40224997 au

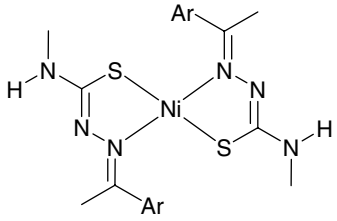
E(HF/6-31G*)= -3806.58469459 au



2-*cis*(*E*-Ni-*E*)

E(HF/3-21G*)= -3787.40896999 au

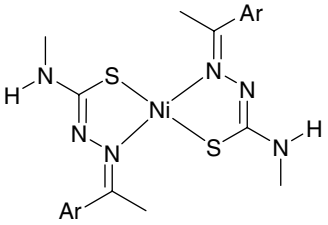
E(HF/6-31G*)= -3806.58932744 au



2-*trans*(*E*-Ni-*E*)

E(HF/3-21G*)= -3787.40576726 au

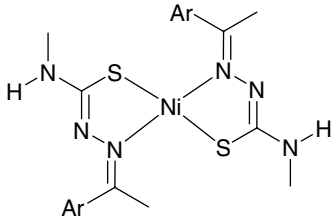
E(HF/6-31G*)= -3806.59224346 au



2-*trans*(*Z*-Ni-*Z*)

E(HF/3-21G*)= -3787.40257674 au

E(HF/6-31G*)= -3806.59288555 au



2-*trans*(*Z*-Ni-*E*)

E(HF/3-21G*)= -3787.39404357 au

E(HF/6-31G*)= -3806.57456236 au

Fig. 5. Electronic-nuclear energy (*E*) of the HF/3-21G* and HF/6-31G* optimized geometries of **2**, in the gas phase and considering solvent (DMSO) effects (PCM).

Table 6
^{1}H NMR chemical shifts ($^{Exp}\delta_H$) of **2** in DMSO-d_6 (400 MHz, TMS) and HF/6-31G*, calculated ^{1}H NMR chemical shifts ($^{Calc}\delta_H$[a]) of the optimized geometries of **2** (see Fig. 5) and deviation between the experimental and calculated shifts $\Delta = |^{Exp}\delta_{H\ DMSO} - {}^{Calc}\delta_H|$

Atom	$^{Exp}\delta_H$	Geometry/$^{Calc}\delta_H$[a]							
		2-*cis* (*E*-Ni-*E*)	**Δ**	**2-*cis* (*Z*-Ni-*Z*)**	**Δ**	**2-*trans* (*E*-Ni-*E*)**	**Δ**	**2-*trans* (*Z*-Ni-*Z*)**	**Δ**
H–C2	8.94	73.56	64.52	2.26	6.68	−30.89	39.83	5.05	3.89
H–C3	8.35	20.45	12.10	7.22	1.13	4.77	3.58	8.76	0.41
H–C5	8.35	7.68	0.67	7.50	0.85	17.44	9.09	9.09	0.74
H–C6	8.94	1.66	7.28	3.83	5.11	15.19	6.25	8.11	0.83
H–C9	1.81	−3.38	5.19	12.41	10.60	−15.52	17.33	5.67	3.86
H–C10	2.49	1.23	1.26	2.10	0.39	13.99	11.50	2.08	0.41
H–N4	7.27	−1.50	8.77	−0.77	8.04	1.59	5.68	−2.78	10.05
Mean deviation			12.49		4.10		11.66		2.52

[a] Values obtained relative to the calculated chemical shift of the hydrogens of tetramethylsilane TMS (δ_H 32.09) using HF/6-31G*.

powder two signals were observed for C2/C6, suggesting that the non-equivalency of these two carbons is probably due to the more rigid arrangement in the solid. As mentioned before, the crystal structure of **2** shows that the complex adopts the **2-*cis*(*E*-Ni-*E*)**-configuration. Since the crystal has been obtained from a solution made from the

Table 7
^{13}C NMR chemical shifts ($^{Exp}\delta_C$) of **2** in DMSO-d_6 (100 MHz, TMS) and HF/6-31G* calculated ^{13}C NMR chemical shifts ($^{Calc}\delta_C$[a]) of the optimized geometries of **2** (see Fig. 5) and deviation between the experimental and calculated shifts $\Delta = |^{Exp}\delta_{C\ DMSO} - {}^{Calc}\delta_C|$

Atom	$^{Exp}\delta_C$ powder	$^{Exp}\delta_C$ DMSO	Geometry/$^{Calc}\delta_C$[a]							
			2-*cis*(*E*-Ni-*E*)	**Δ**	**2-*cis*(*Z*-Ni-*Z*)**	**Δ**	**2-*trans*(*E*-Ni-*E*)**	**Δ**	**2-*trans*(*Z*-Ni-*Z*)**	**Δ**
C1	145.11	145.50	152.57	7.07	141.86	3.64	138.92	6.58	147.56	2.06
C2	131.00–128.60	129.20	158.87	29.67	118.25	10.95	93.56	35.64	123.43	5.77
C3	125.02	123.40	140.83	17.43	121.61	1.79	122.90	0.50	124.56	1.16
C4	148.33	147.30	146.12	1.18	139.71	7.59	146.99	0.31	141.70	5.60
C5	125.02	123.40	124.66	1.26	121.85	1.55	133.93	10.53	123.86	0.46
C6	131.00–128.60	129.20	117.74	11.46	123.66	5.54	134.35	5.15	125.73	3.47
C7	165.78	163.30	159.75	3.55	160.34	2.96	191.59	28.09	149.84	13.46
C8	172.81	173.50	170.72	2.78	174.14	0.64	203.39	29.89	167.08	6.42
C9	20.69	19.60	17.09	2.51	33.46	13.86	14.36	5.24	28.16	8.56
C10	33.86	30.70	27.69	3.01	28.68	2.02	43.61	12.91	26.90	3.80
Mean deviation				7.99		5.05		13.50		5.08

[a] Values obtained relative to the calculated chemical shift of the carbons of TMS (δ_C 201.19) using HF/6-31G*.

powder dissolved in DMF, we suggest that in the powder a *cis* isomer is probably present, which would be **2-*cis*(*Z*-Ni-*Z*)**,considering that the theoretical and experimental chemical shifts for this isomer were in good agreement. Therefore **2-*cis*(*Z*-Ni-*Z*)** → **2-*cis*(*E*-Ni-*E*)** conversion probably occurs during crystallization, since **2-*trans*(*Z*-Ni-*Z*)** → **2-*cis*(*E*-Ni-*E*)** conversion would require coordination of the solvent to the metal centre with displacement of one

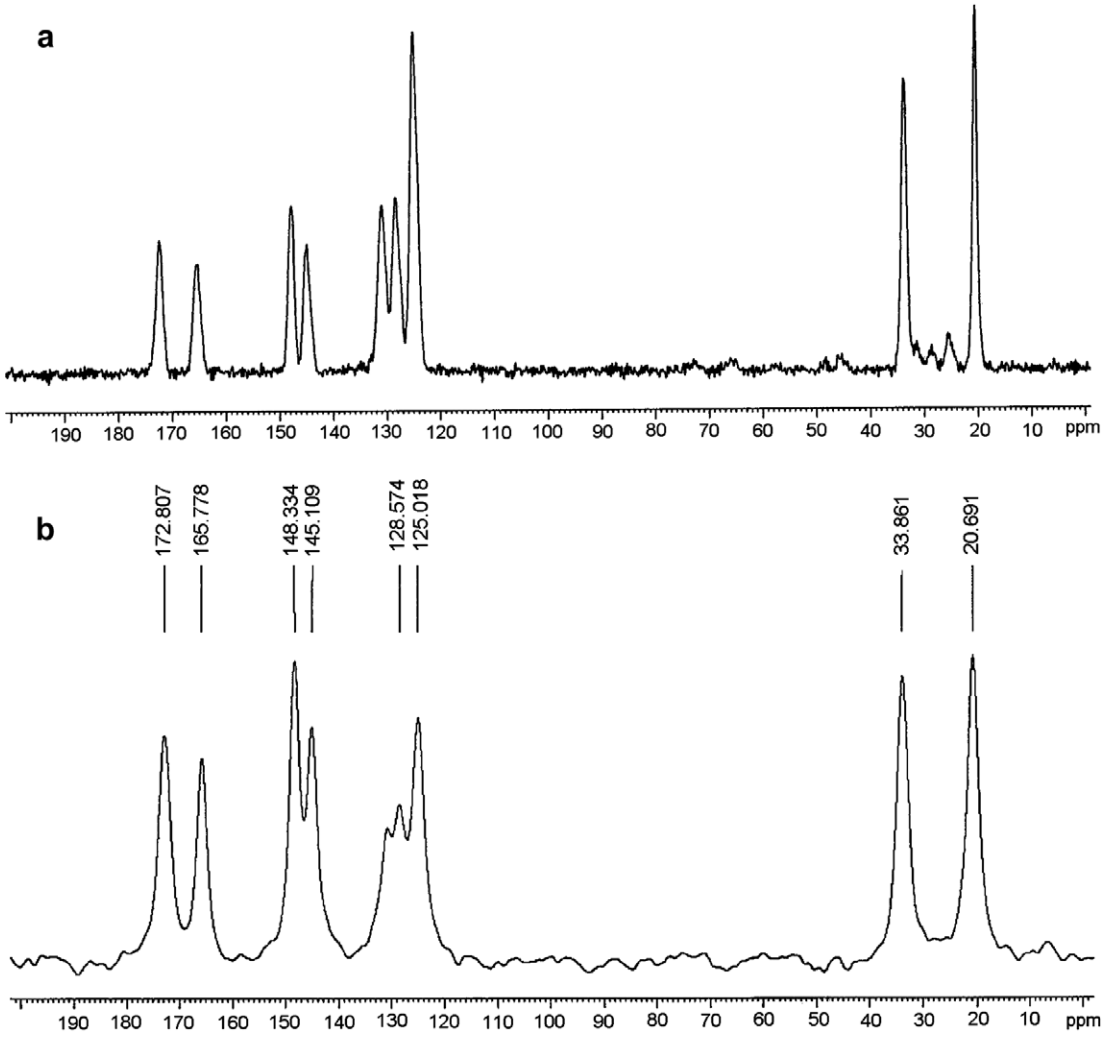


Fig. 6. Solid-state ^{13}C MAS NMR of **2** at: (a) 323 K (100 MHz; adamantane) and (b) 343 K (125 MHz; adamantane).

of the ligands, followed by re-coordination of the thiosemicarbazone in a different configuration.

Fig. 6b shows the solid-state ^{13}C MAS NMR spectrum of **2** at 343 K. When the temperature goes from 323 to 343 K the signal at ca. δ_C 131.0 decreases in intensity whereas the intensity of the signal at δ_C 128.6 increases, probably due to the motion of the aromatic rings through rotation along the C7–C1 bond. As a consequence, coalescence of the signals of C2 and C6 occurs because of the similar chemical ambiance of these two carbons. The PM3 calculated rotational barrier of C7–C1 for **2-*cis*(*E*-Ni-*E*)** is $\Delta E = 24.47$ kcal/mol which is too high to allow rotation to occur, corroborating that this configuration is not present in the powder. For the other configurations this barrier is ca. 10 kcal/mol, which is small enough to allow rotation to occur, with coalescence of the C2 and C6 signals with rising the temperature. Hence **2-*cis*(*Z*-Ni-*Z*)** is the most probable configuration in the powder.

4. Conclusion

X-ray structural studies of *N*(4)-methyl-4-nitroacetophenone thiosemicarbazone, $H4NO_2Ac4M$ (**1**) and its nickel(II) complex, $[Ni(4NO_2Ac4M)_2]$ (**2**) revealed that the **1-*E*,*E*** isomer of the thiosemicarbazone and the **2-*cis*** (**E-Ni-*E***) isomer of the complex are formed in the crystal. Analyses of experimental NMR data along with HF and DFT theoretical calculations of energies and of ^1H and ^{13}C NMR chemical shifts for the optimized geometries of **1** suggest that the **1-*E*,*E*** isomer probably exists in DMSO-d_6, and the **1-*Z*,*E*** isomer in $CDCl_3$. Analyses of solid state (powder) as well as solution (DMSO-d_6) NMR data along with HF and DFT calculations of chemical shifts for the optimized geometries of **2** indicate the presence of **2-*cis*(*Z*-Ni-*Z*)** in DMSO-d_6 as well as in the powder, indicating that **2-*cis*(*Z*-Ni-*Z*)** → **2-*cis*(*E*-Ni-*E*)** conversion probably occurs during crystallization.

5. Supplementary material

CCDC 622046 and 622047 contain the supplementary crystallographic data for **1** and **2**. These data can be obtained free of charge via http://www.ccdc.cam.ac.uk/conts/retrieving.html, or from the Cambridge Crystallographic Data Centre, 12 Union Road, Cambridge CB2 1EZ, UK; fax: (+44) 1223-336-033; or e-mail: deposit@ccdc.cam.ac.uk.

Acknowledgement

Financial support from Capes and CNPq from Brazil is acknowledged.

References

[1] H. Beraldo, D. Gambino, Mini. Rev. Med. Chem. 4 (2004) 31.
[2] G. Aguirre, L. Boiani, H. Cerecetto, M. Fernandez, M. González, A. Denicola, L. Otero, D. Gambino, C. Rigol, C. Olea-Azar, M. Faundez, Bioorg. Med. Chem. 12 (2004) 4885.
[3] L. Otero, M. Vieites, L. Boiani, A. Denicola, C. Rigol, L. Opazo, C. Olea-Azar, J.D. Maya, A. Morello, R.L. Krauth-Siegel, O.E. Piro, E. Castellano, M. González, D. Gambino, H. Cerecetto, J. Med. Chem. 49 (2006) 3322.
[4] N. Bharti, Shailendra, S. Sharma, F. Naqvi, A. Azam, Bioorg. Med. Chem. 11 (2003) 2923.
[5] N. Bharti, F. Athar, M.R. Maurya, A. Azam, Bioorg. Med. Chem. 12 (2004) 4679.
[6] J.S. Binkley, J.A. Pople, W.J. Hehre, J. Am. Chem. Soc. 102 (1980) 939.
[7] R.G. Parr, W. Yang, Density Functional Theory of Atoms and Molecules, Oxford, New York, 1989.
[8] A.M. Barreto, A.F.C. Alcântara, H. Beraldo, Tetrahedron 61 (2005) 7045.
[9] A.F.C. Alcântara, D. Piló-Veloso, W.B. De Almeida, C.R.A. Maltha, L.C.A. Barbosa, J. Mol. Struct. 791 (2006) 180.
[10] A. Pines, M.G. Gibby, J.S.J. Waugh, Chem. Phys. 59 (1973) 569.
[11] Siemens XSCANS Users Manual, Siemens Analytical X-ray Instruments, Madison, WI, 1994.
[12] Enraf-Nonius, Nonius, B.V. Collect, Deft, The Netherlands, 1997–2000.
[13] G.M. Sheldrick, SHELX97, Program for the Refinement of Crystal Structures, University of Göttingen, Germany, 1997.
[14] L.J. Farrugia, J. Appl. Crystallogr. 32 (1999) 837.
[15] M.J. Frisch, G.W. Trucks, H.B. Schlegel, G.E. Scuseria, M.A. Robb, J.R. Cheeseman, J.A. Montgomery Jr., T. Vreven, K.N. Kudin, J.C. Burant, J.M. Millam, S.S. Iyengar, J. Tomasi, V. Barone, B. Mennucci, M. Cossi, G. Scalmani, N. Rega, G.A. Petersson, H. Nakatsuji, M. Hada, M. Ehara, K. Oyota, R. Fukuda, J. Hasegawa, M. Ishida, T. Nakajima, Y. Honda, O. Kitao, H. Nakai, M. Klene, X. Li, J.E. Knox, H.P. Hratchian, J.B. Cross, C. Adamo, J. Jaramillo, R. Gomperts, R.E. Stratmann, O. Yazyev, A.J. Austin, R. Cammi, C. Pomelli, J.W. Ochterski, P.Y. Ayala, K. Morokuma, G.A. Voth, P. Salvador, J.J. Dannenberg, V.G. Zakrzewski, S. Dapprich, A.D. Daniels, M.C. Strain, O. Farkas, D.K. Malick, A.D. Rabuck, K. Raghavachari, J.B. Foresman, J.V. Ortiz, Q. Cui, A.G. Baboul, S. Clifford, J. Cioslowski, B.B. Stefanov, G. Liu, A. Liashenko, P. Piskorz, I. Komaromi, R.L. Martin, D.J. Fox, T. Keith, M.A. Al-Laham, C.Y. Peng, A. Nanayakkara, M. Challacombe, P.M.W. Gill, B. Johnson, W. Chen, M.W. Wong, C. Gonzalez, J.A. Pople, GAUSSIAN 03, Revision B.04, Gaussian Inc., Pittsburgh, PA, 2003.
[16] M.J.S. Dewar, E.G. Zoebish, E.F. Healy, J.J.P. Stewart, J. Am. Chem. Soc. 107 (1985) 902.
[17] (a) R. Ditchfield, W.J. Hehre, J.A. Pople, J. Chem. Phys. 54 (1971) 724;
(b) W.J. Hehre, R. Ditchfield, J.A. Pople, J. Chem. Phys. 56 (1972) 2257;
(c) P.C. Hariharan, J.A. Pople, Mol. Phys. 27 (1974) 209;
(d) M.S. Gordon, Chem. Phys. Lett. 76 (1980) 163;
(e) P.C. Hariharan, J.A. Pople, Theor. Chim. Acta 28 (1973) 213.
[18] (a) M. Cossi, V. Barone, R. Camimi, J. Tomasi, Chem. Phys. Lett. 255 (1996) 327;
(b) V. Barone, M. Cossi, J. Tomasi, J. Chem. Phys. 107 (1997) 3210.
[19] H. Beraldo, W. Nacif, L.R. Teixeira, J.S. Reboucas, Transition Met. Chem. 27 (2002) 85.
[20] R.F.F. Costa, A.P. Rebolledo, T. Matencio, H.D.R. Calado, J.D. Ardisson, M.E. Cortes, B.L. Rodrigues, H. Beraldo, J. Coord. Chem. 58 (2005) 1307.
[21] C.K. Johnson, ORTEP 11, Report ORNL-5135. Oak ridge National Laboratory, TN, 1976.

$[Cu(en)_3]^{2+}$ (en = 1,2-ethanediamine), $[Cu(OMPA)_3]^{2+}$ (OMPA = octamethylpyrophosphoramide), $[Cu(bpy)_3]^{2+}$ (bpy = 2,2′-bipyridyl) and $[Cu(phen)_3]^{2+}$ (phen = 1,10-phenanthroline). Within the copper chromophore, complexes containing three equivalent didentate chelate ligands, $[Cu(en)_3]SO_4$ [5] and $[Cu(OMPA)_3](ClO_4)_2$ [6], have been found to involve D_3 site symmetry with six apparently equivalent bonds as a consequence of the dynamic Jahn-Teller effect [8–12] and show partially statically and dynamically distorted CuN_6 octahedra for the lower symmetry C_2 or C_1 complexes. The most likely form of the vibronically induced distortion or dynamic Jahn-Teller distortion consistent with C_2 symmetry is the elongated tetragonal distortion [13], producing the most common type of static stereochemistry of the copper(II) ion, namely elongated rhombic or tetragonal octahedral.

In cases of copper(II) complexes with two equivalent didentate chelate ligands and some sulfur oxoanions including those of the ClO_4^-, BF_4^- and PF_6^- anions, the structures displayed four-, five- or six-coordinated chromophores with the monodentate, chelate, didentate polymeric bridge (along the anion) or non-coordinating natures of these anions depending on the nature of the chelate ligands. The examples are $[Cu(dpyam)_2](ClO_4)_2$ [14], $[Cu(dpyam)_2](BF_4)_2$ [15], $[Cu(dpyam)_2](PF_6)_2$ [present work], $[Cu(bpy)_2(OH_2)](S_2O_6)$ [16], $[Cu(dpyam)_2(OH_2)](S_4O_6)$ [17], $[Cu(bpy)_2(O_2ClO_2)](ClO_4)$ [18], $[Cu(bpy)_2(F_2BF_2)](BF_4)$ [18,19], [Cu(bpy or phen)$_2$(OS_4O_5)] [20], $[Cu(bpy)_2(S_3O_6)]$ [20,21] and $[Cu(bpy)_2(OS_2O_7)]H_2O$ [16]. In order to continue the investigation on the coordination properties and the correlation of the stereochemistry and electronic properties of the tris and bis-chelate copper(II) complexes with these anions, the structures and electronic properties of two new tris-chelate complexes, $[Cu(phen)_3](S_4O_6)(S_8)$ (**1**) and $[Cu(phen)_3](BF_4)_2$ (**2**), and two new bis-chelate complexes, $[Cu(phen)_2(OS_2O_7)]$ (**3**) and $[Cu(phen)_2(FBF_3)](BF_4)$ (**4**), are now reported and discussed in comparison with other relevant complexes. The latter two complexes display some differences in Cu(II) environment and binding modes of $S_2O_8^{2-}$ and BF_4^- anions.

2. Experimental

2.1. General

The ligand 1,10-phenanthroline and all reagents are commercial grade materials and were used without further purification. Elemental analyses (C, H, N) were determined on a Perkin-Elmer PE 2400 CHNS Analyzer.

IR spectra were recorded on a Perkin-Elmer Spectrum One FT-IR spectrophotometer as KBr discs in the 4000–450 cm^{-1} spectral range. Solid-state (diffuse reflectance) electronic spectra were measured as polycrystalline samples on a Perkin-Elmer Lambda2S spectrophotometer, within the range 8000–18 000 cm^{-1}. ESR spectra were recorded using a Bruker ESR-300 X-band instrument operating at room temperature with DPPH ($g = 2.0036$) as a reference.

2.2. Syntheses of the compounds

2.2.1. $[Cu(phen)_3](S_4O_6)(S_8)$ (1)

A hot DMF solution (10 ml) of phen (0.198 g, 1.0 mmol) was added to a warm aqueous solution (10 ml) of $Cu(NO_3)_2 \cdot 3H_2O$ (0.241 g, 1.0 mmol). Then an aqueous solution (10 ml) of $Na_2S_2O_3 \cdot 5H_2O$ (0.248 g, 1.0 mmol) was added to the mixture, yielding a brown solution. After a month, blue polygon-shaped crystals of compound **1** were obtained which were filtered off, washed with the mother liquid and air-dried. Yield ca. 60%. $C_{36}H_{24}CuN_6O_6S_8$: *Anal.* Calc. C, 45.20; H, 2.53; N, 8.79. Found: C, 45.50; H, 2.61; N, 8.84%.

2.2.2. $[Cu(phen)_3](BF_4)_2$ (2)

This compound was prepared by adding a hot ethanol solution (10 ml) of phen (0.198 g, 1.0 mmol), to a warm aqueous solution (5 ml) of $Cu(BF_4)_2 \cdot nH_2O$ (0.118 g, 0.5 mmol). The resulting blue solution was allowed to evaporate at room temperature. After two weeks, needle blue crystals of compound **2** were obtained which were filtered off, washed with the mother liquid and air-dried. Yield ca. 85%. $C_{36}H_{24}CuF_8N_6B_2$: *Anal*. Calc. C, 55.59; H, 3.11; N, 10.81. Found: C, 55.62; H, 3.25; N, 10.67%.

2.2.3. $[Cu(phen)_2(OS_2O_7)]$ (3)

Compound **3** was prepared by adding an aqueous solution (10 ml) of $Cu(CH_3COO)_2 \cdot nH_2O$ (0.091 g, 0.5 mmol) to a solution of phen (0.198 g, 1.0 mmol) in acetonitrile (20 ml), then an aqueous solution (5 ml) of $K_2S_2O_8$ (0.109 g, 1.0 mmol) was added, yielding a blue solution. The solution was allowed to evaporate at room temperature. After a week, bluish green rod crystals of compound **3** were formed. They were filtered off, washed with the mother liquid and air-dried. Yield ca. 92%. $C_{24}H_{16}S_2CuN_4O_8$: *Anal.* Calc. C, 46.79; H, 2.61; N, 9.10. Found: C, 46.45; H, 2.54; N, 9.14%.

2.2.4. $[Cu(phen)_2(FBF_3)](BF_4)$ (4)

Compound **4** was prepared by adding an aqueous solution (20 ml) of $Cu(BF_4)_2 \cdot nH_2O$ (0.236 g, 1.0 mmol) to a solution of phen (0.346 g, 2.5 mmol) in ethanol (20 ml), yielding a blue solution. The solution was allowed to evaporate at room temperature. After a week, bluish green crystals of compound **4** were formed. They were filtered off, washed with the mother liquid and air-dried. Yield ca. 74%. $C_{24}H_{16}B_2CuN_4F_8$: *Anal*. Calc. C, 48.25; H, 2.70; N, 9.38. Found: C, 48.18; H, 2.61, N, 9.45%.

2.3. Crystallography

The X-ray single-crystal data were collected at 293 K for compounds **1**–**4** on a 4K Bruker SMART APEX CCD area-detector diffractometer (rotating anode, graphite-monochromated Mo Kα radiation, $\lambda = 0.71073$ Å) using the SMART program [22]. Raw data frame integration was performed with SAINT [23], which also applied correction

for Lorentz and polarization effects. An empirical absorption correction using the SADABS [24] program was applied, which resulted in transmission coefficients ranging from 1.000 to 0.733 for **1**, 1.000 to 0.739 for **2**, 1.000 to 0.768 for **3** and 1.000 to 0.740 for **4**.

The structures were solved by direct methods and refined by the full matrix least-squares method on $(F_{obs})^2$ with anisotropic thermal parameters for all non-hydrogen atoms, except disordered *F* atoms of the BF_4^- groups in **2**, using the SHELXTL-PC V 6.12 software package. For the structure determination of compound **1**, the sulfur atoms of the S_8 group showed disorder; the occupancies of the disordered positions were initially refined and later fixed at 0.50 and 0.50. The two F atoms of each BF_4^- group in **2** showed disorder, with occupancies of 0.5. All hydrogen atoms of the phen ligand in **1** were fixed and allowed to ride on the attached atoms, while those of compounds **2**–**4** were located geometrically and refined isotropically. The molecular structure pictures were created by using the SHELXTL-PC package [25]. The crystal and refinement details for compounds **1**–**4** are listed in Table 1.

3. Results and discussion

3.1. Description of $[Cu(phen)_3](S_4O_6)(S_8)$ (1) and $[Cu(phen)_3](BF_4)_2$ (2)

The asymmetric unit of complexes **1** and **2** involves $[Cu(phen)_3]^{2+}$ cations and $S_4O_6^{2-}$ and BF_4^- anions, respectively. In addition, **1** has S_8 molecules in the lattice. The ORTEP views of the asymmetric units of **1** and **2** are shown in Fig. 1, together with the numbering scheme. Selected bond distances and angles are listed in Table 2. The cationic species $[Cu(phen)_3]^{2+}$ in **1** and **2** are similar in stereochemistry, in which the copper(II) ion is six-coordinated by six nitrogen atoms from three phenanthroline ligands. The coordination geometry around the copper ion can be described as elongated rhombic octahedral with four equatorial Cu–N bond distances being markedly different in the case of **1** (2.026(3) to 2.115(3) Å, $\Delta N_{in} = 0.089(3)$ Å) as compared to those of **2** (2.031(3) to 2.054(3) Å, $\Delta N_{in} = 0.023(3)$ Å), with the remaining two nitrogens occupying the apical sites at significantly larger distances (2.295(4) and 2.328(4) Å for **1**; 2.269(3) and 2.346(4) Å for **2**). This leads to a slight difference in tetragonalities (*T*), 0.892 for **1** and 0.886 for **2** (*T* = the average four-in-plane distance/the axial out-of-plane distance [26]), the tetragonality increasing with increasing in-plane bond distances. Compound **1** has a high ΔN_{in} value of 0.089 Å, corresponding to a high in-plane rhombic distortion, and there is very little in-plane rhombic distortion in **2**, attributed to a low ΔN_{in} value of 0.023 Å. The basal CuN_4 planes of both compounds are slightly twisted, with dihedral angles (CuN_2/CuN_2) of 20.4(1)° for **1** and 19.3(1)° for **2**. The phenanthroline moieties do not display any unusual features with regard to bond lengths and angles in either of the two compounds studied compared with the free molecule [27]. However, they do exhibit meaningful deviations from

Table 1
Crystal and refinement data for complexes **1**, **2**, **3** and **4**

Complex	1	2	3	4
Molecular formula	$[Cu(phen)_3](S_4O_6)(S_8)$	$[Cu(phen)_3](BF_4)_2$	$[Cu(phen)_2(OS_2O_7)]$	$[Cu(phen)_2(FBF_3)](BF_4)$
Molecular weight	956.63	777.77	616.07	597.57
T/K	293(2)	293(2)	293(2)	293(2)
Crystal system	monoclinic	monoclinic	triclinic	triclinic
Space group	*P*2(1)/*n*	*P*2(1)/*n*	$P\bar{1}$	$P\bar{1}$
a (Å)	17.1531(9)	9.3179(5)	7.6058(14)	7.4427(2)
b (Å)	13.3857(7)	30.0654(17)	9.6820(18)	10.8338(3)
c (Å)	18.7461(10)	12.8879(7)	15.577(3)	16.1079(3)
α (°)	90.0000	90.0000	79.244(3)	98.8740(10)
β (°)	114.1690(10)	110.4250(10)	81.927(3)	102.8510(10)
γ (°)	90.0000	90.0000	83.155(3)	105.7510(10)
V (Å^3)	3926.9(4)	3383.5(3)	1168.1(3)	1186.43(5)
Z	4	4	2	2
D_c/(g cm^3)	1.618	1.527	1.752	1.673
μ/mm^{-1}	1.037	0.727	1.176	1.006
F(000)	1948	1572	626	598
Crystal size/mm	$0.25 \times 0.14 \times 0.11$	$0.38 \times 0.23 \times 0.13$	$0.28 \times 0.12 \times 0.03$	$0.38 \times 0.23 \times 0.13$
Number of reflection collected	32558	29647	10356	8932
Number of unique reflections [R_{int}]	8606 [0.0492]	8137 [0.0534]	5404 [0.0256]	6495 [0.0150]
Data/restraints/parameters	8606/12/646	8137/0/647	5404/0/418	6495/0/416
Goodness-of-fit	1.048	1.049	1.050	1.072
Final *R* indices [$I > 2\sigma(I)$]	$R_1 = 0.0677$, $wR_2 = 0.1526$	$R_1 = 0.0663$, $wR_2 = 0.1325$	$R_1 = 0.0502$, $wR_2 = 0.1012$	$R_1 = 0.0526$, $wR_2 = 0.1176$
R indices (all data)	$R_1 = 0.0962$, $wR_2 = 0.1676$	$R_1 = 0.1185$, $wR_2 = 0.1529$	$R_1 = 0.0734$, $wR_2 = 0.1103$	$R_1 = 0.0734$, $wR_2 = 0.1308$
Largest difference peak and hole (e Å^3)	0.814, −0.523	0.319, −0.308	0.503, −0.351	0.474, −0.620

$R = \sum \| |F_o| - |F_c| \| / \sum |F_o|$, $R_w = [\sum w\{|F_o| - |F_c|\}^2 / \sum w|F_o|]^{1/2}$.

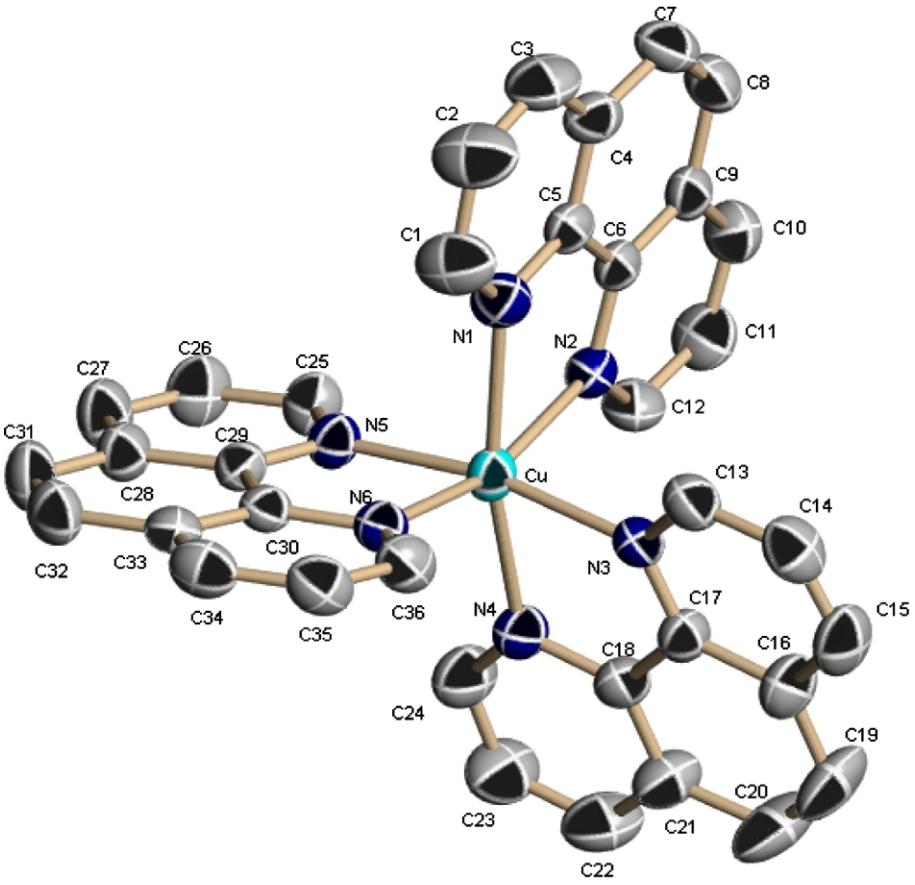


Fig. 1. The representative structure of $[Cu(phen)_3]^{2+}$ in $[Cu(phen)_3](S_4O_6)(S_8)$ (**1**) and $[Cu(phen)_3](BF_4)_2$ (**2**). Hydrogen atoms are omitted for clarity.

Table 2
Selected bond lengths (Å) and angles (°) with e.s.d.s. in parentheses of $[Cu(phen)_3](S_4O_6)(S_8)$ (**1**) and $[Cu(phen)_3](BF_4)_2$ (**2**)

	1	**2**
Cu–N(1)	2.328(4)	2.346(3)
Cu–N(2)	2.115(3)	2.031(3)
Cu–N(3)	2.029(3)	2.044(3)
Cu–N(4)	2.295(4)	2.269(3)
Cu–N(5)	2.026(3)	2.051(3)
Cu–N(6)	2.080(3)	2.054(3)
N(1)–Cu–N(2)	75.8(1)	76.4(1)
N(1)–Cu–N(3)	97.1(1)	103.1(1)
N(1)–Cu–N(4)	167.0(1)	178.6(1)
N(1)–Cu–N(5)	93.8(1)	87.1(1)
N(1)–Cu–N(6)	87.2(1)	87.0(1)
N(2)–Cu–N(3)	92.5(1)	91.7(1)
N(2)–Cu–N(4)	92.4(1)	102.5(1)
N(2)–Cu–N(5)	95.4(1)	163.3(1)
N(2)–Cu–N(6)	162.4(1)	95.8(1)
N(3)–Cu–N(4)	97.7(1)	77.6(1)
N(3)–Cu–N(5)	167.9(1)	94.1(1)
N(3)–Cu–N(6)	94.2(1)	168.6(1)
N(4)–Cu–N(5)	92.7(1)	94.1(1)
N(4)–Cu–N(6)	105.0(1)	92.3(1)
N(5)–Cu–N(6)	81.0(1)	81.1(1)

Table 3
Selected bond lengths (Å) and angles (°) with e.s.d.s. in parentheses of $[Cu(phen)_2(OS_2O_7)]$ (**3**) and $[Cu(phen)_2(FBF_3)](BF_4)$ (**4**)

	3	**4**
Cu–N(1)	2.027(3)	2.060(2)
Cu–N(2)	2.002(2)	1.999(2)
Cu–N(3)	1.985(2)	2.078(2)
Cu–N(4)	2.034(3)	2.019(2)
Cu–X(1)	2.353(2)	2.184(2)
Cu–X(2)	3.182(2)	3.110(2)
N(1)–Cu–N(2)	82.4(1)	81.8(1)
N(1)–Cu–N(3)	100.2(1)	137.5(1)
N(1)–Cu–N(4)	148.6(1)	100.1(1)
N(2)–Cu–N(3)	167.0(1)	98.5(1)
N(2)–Cu–N(4)	102.1(1)	177.0(1)
N(3)–Cu–N(4)	82.4(1)	81.7(1)
X(1)–Cu–N(1)	109.4(1)	122.7(1)
X(1)–Cu–N(2)	84.5(1)	89.3(1)
X(1)–Cu–N(3)	82.7(1)	99.8(1)
X(1)–Cu–N(4)	101.9(1)	87.7(1)
X(2)–Cu–N(1)	79.0(1)	68.3(1)
X(2)–Cu–N(2)	88.5(1)	75.6(1)
X(2)–Cu–N(3)	104.5(1)	70.7(1)
X(2)–Cu–N(4)	70.1(1)	107.3(1)
X(1)–Cu–X(2)	168.1(1)	160.3(1)

X = O and F for **3** and **4**, respectively.

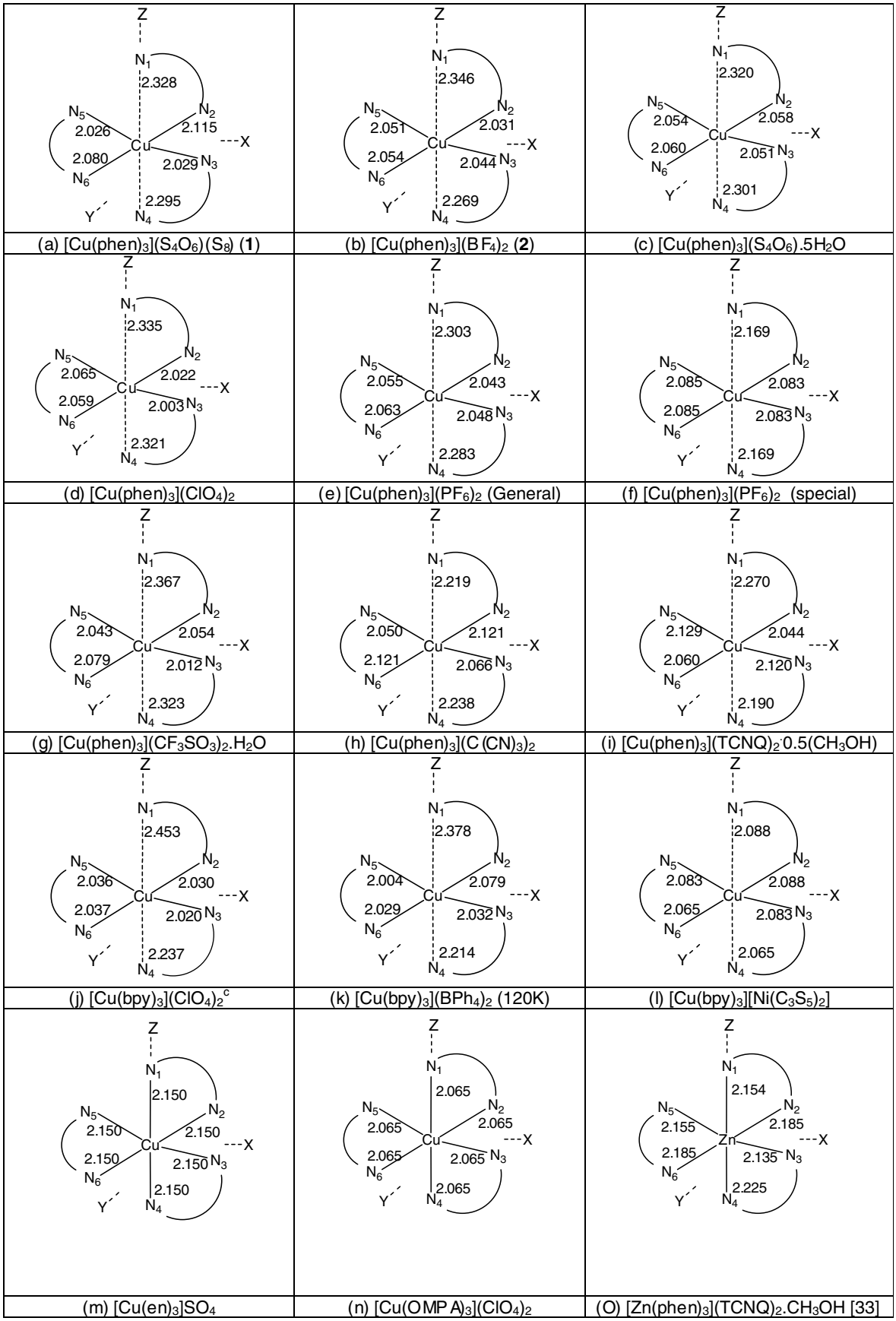


Fig. 2. Comparison of $[M(phen)_3]^{2+}$ coordination geometries.

planarity, as measured by the dihedral angle between opposite pyridine groups [2.3(1)°, 3.0(1)° and 3.8(1)° for **1** and 2.4(1)°, 3.9(1)° and 1.3(1)° for **2**]. The angles between the least-square phenanthroline planes are [phen(N(1)–N(2))]–[phen(N(3)–N(4))] = 85.9(1)°, [phen(N(1)–N(2))]–[phen(N(5)–N(6))] = 82.3(1)° and [phen(N(3)–N(4))]–[phen(N(5)–N(6))] = 68.4(1)° for **1** and [phen(N(1)–N(2))]–[phen(N(3)–N(4))] = 87.3(1)°, [phen(N(1)–N(2))]–[phen(N(5)–N(6))] = 75.1(1)° and [phen(N(3)–N(4))]–[phen(N(5)–N(6))] = 81.4(1)° for **2** (See Table 3).

Complexes **1** and **2** are the most common type of tris-chelate copper(II) complexes with three equivalent ligands. The appearance of regular CuN_6 or CuO_6 are rare and are found in few complexes: $[Cu(en)_3](SO_4)$ [5], $K_2Pb[Cu(NO_2)_6]$ [28] and $[Cu(OMPA)_3](ClO_4)_2$ [6] in which their Cu(II) chromophore has either D_3 or T_d site symmetries, in apparent violation of the Jahn-Teller theorem due to the dynamic Jahn-Teller effect. Complexes **1** and **2** exhibit lower symmetry of C_1, distorted from the parent dynamic Jahn-Teller complex D_3 symmetry, and produce the most common type of static stereochemistry ($T < 0.9$) [26], an elongated rhombic octahedron. The elongated octahedral CuN_6 chromophores in **1** and **2** are somewhat different; **1** is much more rhombic and only a few examples have been observed with this feature, Fig. 2h and i. This can rationalized using the approximate forms of the Q_ε and Q_θ components of the JT active e vibration of a trigonal tris-chelate $[Cu(chelate)_3]^{2+}$ chromophore with D_3 symmetry and a ^2E electronic ground state and a_{2u} [12], as shown in Fig. 3. For both compounds a linear combination of the separate Q_ε and Q_θ components of the JT active e vibration is in operation for which the Q_ε component in **1** is big when compared to that of **2**. The Q_ε component can introduce a rhombic distortion of the CuN_6 chromophore, although the component itself is small as compared to Q_θ. A distortion along the Q_θ component results in a tetragonally distorted CuN_6 octahedron for both compounds. In addition, the molecule of both compounds distorts along the a_{2u} coordinate, resulting in the unequivalent Cu–N_{ax} bond distances. The most relevant complexes to **1** and **2** are found in the elongated rhombic octahedral complexes $[Cu(phen)_3]X_2$ where $X = (S_4O_6^{2-})_{0.5} \cdot 5H_2O$ [2], $C(CN)_3^-$ [29], ClO_4^- [30], $CF_3SO_3^- \cdot H_2O$ [31], PF_6^- [32] and $TCNQ^- \cdot (CH_3OH)_{0.5}$ [33]; $[Cu(bipy)_3](ClO_4)_2$ [34–36], $[Cu(bipy)_3](BPh_4)_2$ [3], $[Cu(bpy)_3][Ni(C_3S_5)_2]$ [37] and $\{C_{14}H_{19}N_2\}[Cu(hfacac)_3]$ [38]; the copper(II) chromophores are compared in Table 4 and Fig. 2.

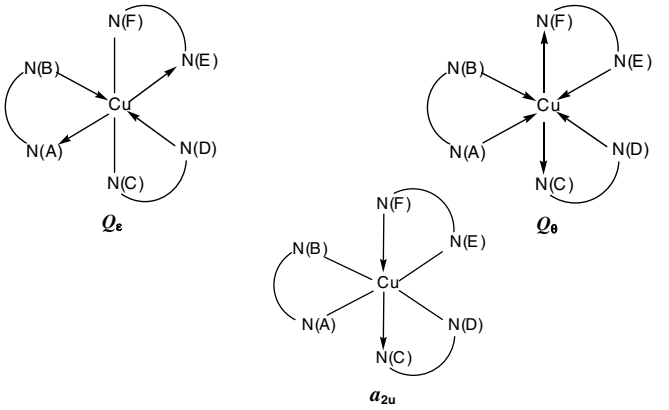


Fig. 3. The approximate forms of Q_ε and Q_θ components of the active JT e vibration of the trigonal tris-chelate $[Cu(chelate)_3]^{2+}$ chromophore. D_3 symmetry: chelate = (N–N) or (O–O), and a_{2u}.

The lattice of compound **1** is stabilized by hydrogen bonding between the amine-C and $O(S_4O_6^{2-})$ (C...O distances 3.030(1)–3.367(2) Å). For compound **2**, the lattice is stabilized by hydrogen bonding between the amine-C and $F(BF_4^-)$ (C...F distances 3.094(1)–3.321(2) Å).

3.2. Description of $[Cu(phen)_2(OS_2O_7)]$ (3) and $[Cu(phen)_2(FBF_3)](BF_4)$ (4)

The structures of **3** and **4** consist of chains of $[Cu(phen)_2(OS_2O_7)]$ and $[Cu(phen)_2(FBF_3)]^+$ units, parallel to an axis, respectively with uncoordinated, disordered BF_4^- anions for **4.** The copper(II) ions are linked into infinite chains by the asymmetrically bridging peroxodisulfato groups (Cu–O 2.353(2), Cu–O′ 3.182(2) Å) in **3** across the anion, and the asymmetrically bridging tetrafluoroborate groups (Cu–F 2.184(2), Cu–F′ 3.110(2) Å) in **4**. However, the sixth axial coordination sites of the bridging $S_2O_8^{2-}$ in **3** and BF_4^- in **4** are too long to be considered even as semi-coordination to the Cu(II) ion, 3.182(2) and 3.110(2) Å for **3** and **4**, respectively. Consequently, the local molecular structure of both compounds, Figs. 4 and 5, involves five-coordinate CuN_4O and CuN_4F chromophores, which can be best described as having a distorted square pyramidal geometry with $\tau = 0.31$ for **3** and a distorted trigonal bipyramidal geometry with $\tau = 0.66$ for **4** ($\tau = (\beta - \alpha)/60$, $\tau = 0$ for square pyramid and $\tau = 1$ for trigonal bipyramidal) [39]. In **3** the equatorial Cu–N distances are not significantly different, ranging from 1.985(2) to 2.034(3) Å. The axial position is occupied by an O atom of the peroxodisulfate at 2.353(2) Å. The CuN_4 chromophore is non-planar with a marked tetrahedral twist of 36.0(1)°. The Cu atom lies above the basal CuN_4 plane, 0.162(1) Å toward the O atom of peroxodisulfate. The Cu ... Cu distance is 7.540(3) Å. The bonding parameters for the S_2O_8 ligand are very close to those found for a previously reported coordinated peroxodisulfate group [18]. The bond lengths in the terminal SO_3 groups are 1.415(3)–1.440(3) Å, the longest, S(1)–O(1) = 1.440(3) Å, is significantly longer than the rest, consistent with the involvement of O(1) in semi-coordination to the Cu(II) atom at 2.353(2) Å [40]. The lattice of compound **3** is stabilized by hydrogen bonding between the amine-C and $OS_2O_8^{2-}$ (C...O distances 3.137(1)–3.444(2) Å) and a very weak interaction between the Cu atom and O′ atom of the neighbouring $S_2O_8^{2-}$ group (Cu–O′, 3.182(2) Å).

In the case of **4**, the local molecular structure involves a five-coordinate CuN_4F chromophore with a distorted trigonal bipyramidal geometry, $\tau = 0.66$, Fig. 5. The out of trigonal plane Cu–N(2) and Cu–N(4) distances are only just

Table 4
Structural data and electronic spectra of tris(chelate)copper(II) complexes

Complex	Cu–N1/Å (ax.)	Cu–N4/Å (ax.)	Cu–N2/Å (eq.)	Cu–N3/Å (eq.)	Cu–N5/Å (eq.)	Cu–N6/Å (eq.)	T[e]	Band maxima (kK)[f]	Polycrystalline e.s.r. spectrum			Reference
									g_1	g_2	g_3	
$[Cu(phen)_3](S_4O_6)(S_8)$ (**1**)	2.328(4)	2.295(4)	2.115(3)	2.029(3)	2.026(3)	2.080(3)	0.892	14.57, 8.63		2.108[h]		this work
$[Cu(phen)_3](BF_4)_2$ (**2**)	2.346(3)	2.269(3)	2.031(3)	2.044(3)	2.051(3)	2.054(3)	0.886	14.86, 8.62		2.098[h]		this work
$[Cu(phen)_3](S_4O_6) \cdot 5H_2O$	2.320(4)	2.301(4)	2.058(4)	2.051(4)	2.054(4)	2.060(4)	0.890	15.74, 10.66	2.310		2.054	[2]
$[Cu(phen)_3](ClO_4)_2$	2.335(12)	2.321(11)	2.022(13)	2.003(13)	2.065(12)	2.059(14)	0.875	14.23, 10.63		2.083[h]		[30]
$[Cu(phen)_3](PF_6)_2$ (general)	2.303(9)	2.283(10)	2.043(9)	2.048(9)	2.055(9)	2.063(10)	0.895	14.97, 7.73[g]				[32]
$[Cu(phen)_3](PF_6)_2$ (special)	2.169(10)	2.169(10)	2.083(11)	2.083(11)	2.085(10)	2.085(10)	0.961					[32]
$[Cu(phen)_3](CF_3SO_3)_2 \cdot H_2O$	2.367(3)	2.323(3)	2.054(3)	2.012(3)	2.043(2)	2.079(3)	0.873	14.68, 7.84[g]				[31]
$[Cu(phen)_3](C(CN)_3)_2$	2.219(3)	2.238(3)	2.121(3)	2.066(3)	2.121(3)	2.050(3)	0.938					[29]
$[Cu(phen)_3](TCNQ)_2 \cdot 0.5(CH_3OH)$	2.270(10)	2.190(10)	2.044(9)	2.120(9)	2.129(9)	2.060(10)	0.936					[33]
$[Cu(bpy)_3](ClO_4)_2$[a]	2.450(7)	2.226(7)	2.026(5)	2.030(8)	2.034(8)	2.035(3)	0.869	14.23,10.63[g]		2.083[h]		[34]
$[Cu(bpy)_3](ClO_4)_2$[b]	2.469(6)	2.222(7)	2.020(5)	2.018(6)	2.027(6)	2.037(5)	0.864					[37]
$[Cu(bpy)_3](ClO_4)_2$[c]	2.453(3)	2.237(3)	2.030(3)	2.020(3)	2.036(3)	2.037(3)	0.866					[36]
$[Cu(bpy)_3](BPh_4)_2$ (120 K)	2.378(6)	2.214(6)	2.079(5)	2.032(5)	2.004(5)	2.029(5)	0.887	15.01, 7.97[g]				[3]
$\{C_{14}H_{19}N_2\}[Cu(hfacac)_3]$	2.156(1)[d]	2.201(1)[d]	1.981(1)[d]	2.028(1)[d]	2.002(1)[d]	2.035(1)[d]	0.923					[38]
$[Cu(bpy)_3][Ni(C_3S_5)_2]$	2.088(2)	2.065(2)	2.088(2)	2.083(2)	2.083(2)	2.065(2)	1.002					[37]
$[Cu(OMPA)_3](ClO_4)_2$	2.065(2)	2.065(2)	2.065(2)	2.065(2)	2.065(2)	2.065(2)	1.000					[6]
$[Cu(en)_3]SO_4$	2.150(2)	2.150(2)	2.150(2)	2.150(2)	2.150(2)	2.150(2)	1.000					[5]

When[a–c] carried out in temperature range 283–303 K.
ax., axial; eq., equatorial.
[a] $R1 = 0.091$.
[b] $R1 = 0.062$.
[c] $R1 = 0.035$.
[d] Cu–O distances.
[e] T, tetragonality.
[f] $kK = 1000\ cm^{-1}$.
[g] Present work at room temperature.
[h] g_1 (determination from pseudo-isotropic spectra).

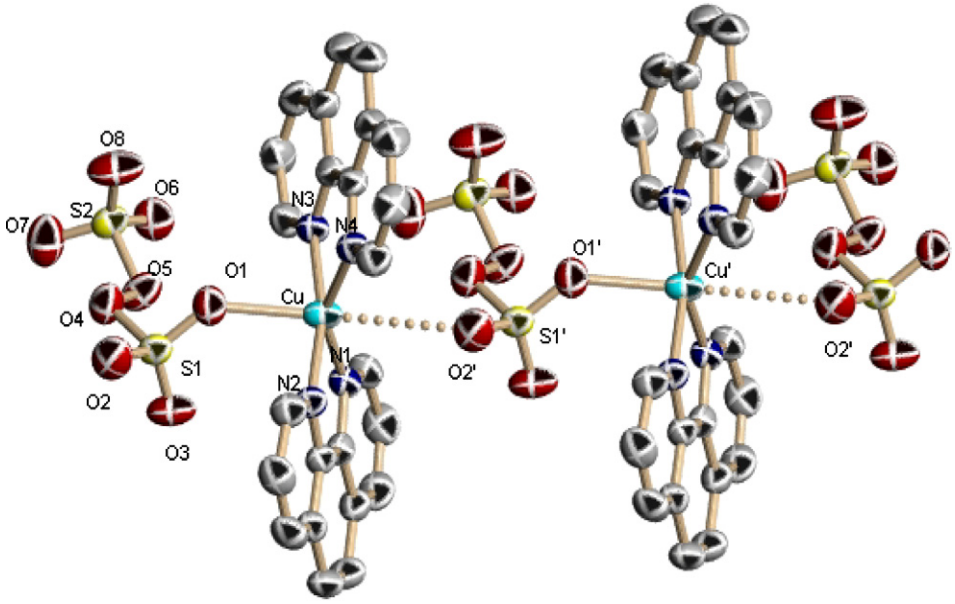


Fig. 4. Thermal ellipsoid (50% probability) plot of $[Cu(phen)_2(OS_2O_7)](S_2O_8)$ (**3**). Hydrogen atoms are omitted for clarity.

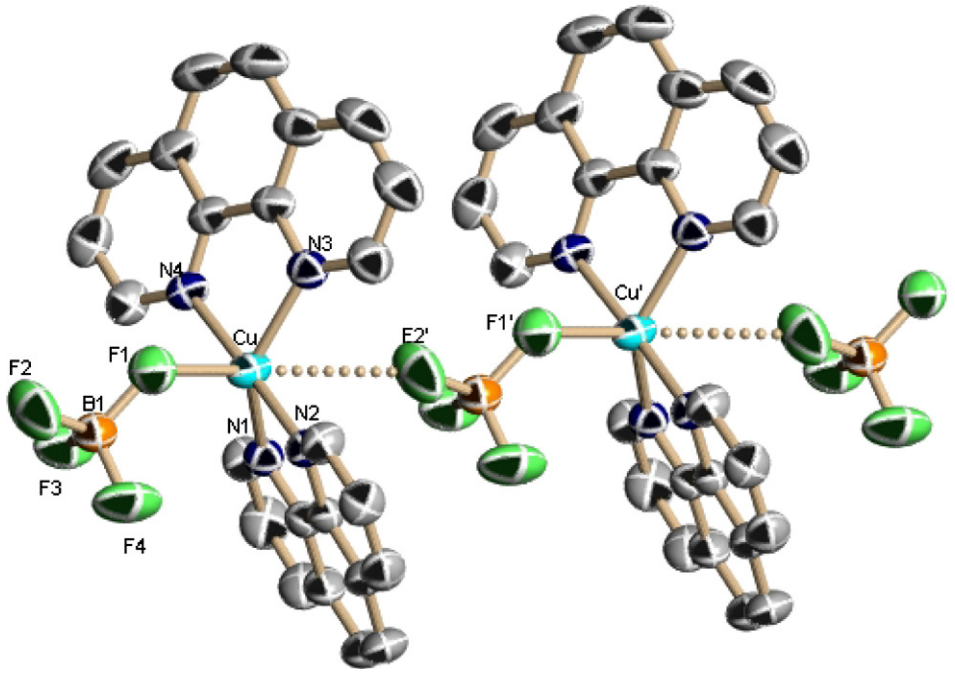


Fig. 5. Thermal ellipsoid (50% probability) plot of $[Cu(phen)_2(FBF_3)](BF_4)$ (**4**). Hydrogen atoms and uncoordinating BF_4^- are omitted for clarity.

significantly different (2.019(2) and 1.999(2) Å) and are almost linear, with N(2)–Cu–N(4) = 177.0(1)°. The three in-plane Cu–N distances are significantly different (2.060(2), 2.078(2) and 2.184(2) Å) and longer than the out of plane Cu–N distances by 0.060 Å, only slightly less than the difference of 0.1 Å previously observed in trigonal-bipyramidal Cu(II) complexes [41]. The much shorter in-plane Cu–F(1) distance of 2.184(2) Å suggests the non-involvement in axial sites of the typical elongated octahedral geometry as compared with the elongated, previously observed, Cu–F distance of 2.560(2) Å in $[Cu(bpy)_2(F_2BF_2)](BF_4)$ [19]. The octahedral units in this analogous compound are linked into infinite chains by the bridging didentate tetrafluoroborate group. For compound **4**, the lattice is stabilized by hydrogen bonding between the amine-C and $F(BF_4^-)$ (C…F distances 3.107(4)–3.345(1) Å) and a very weak interaction between Cu atoms and F′ atoms of the neighbouring BF_4^- groups (Cu–F′, 3.110(2) Å).

The coordination geometries of the corresponding $Cu(chelate)_2X_2$ or, $Cu(chelate)_2Y$, where chelate = phen [42–44], dpyam [16,44,45] or bpy [13,20]; X = BF_4^-,

Table 5
Structural data and electronic spectra of bis(chelate)copper(II) complexes

Complex	Chromophore	Coordination number and geometry	T[a]	τ[b]	Band maxima (kK[c])	Polycrystalline e.s.r. spectrum			Reference
						g_1	g_2	g_3	
$[Cu(phen)_2(OS_2O_7)]$ (**3**)	CuN_4O	5, SPy		0.31	13.48	2.210		2.062	this work
$[Cu(phen)_2(FBF_3)](BF_4)$ (**4**)	CuN_4F	5, TBP		0.66	12.82, 10.07(sh)		2.180[d]		this work
$[Cu(phen)_2(S_4O_6)]$	CuN_4O_2	6, Oct	0.81						[4]
$[Cu(bpy)_2(OS_2O_7)]\cdot H_2O$	CuN_4O	5, interm.		0.52	13.62				[16]
$[Cu(bpy)_2(S_4O_6)]$	CuN_4O_2	6, Oct	0.760		14.70	2.062[e]	2.067[e]	2.228[e]	[20]
$[Cu(bpy)_2(O_2ClO_2)](ClO_4)$	CuN_4O_2	6, Oct	0.757		15.10	2.054[e]	2.065[e]	2.255[e]	[18]
$[Cu(bpy)_2(F_2BF_2)](BF_4)$	CuN_4F_2	6, Oct	0.763		15.20	2.055[e]	2.070[e]	2.243[e]	[18,19]
$[Cu(bpy)_2(OH_2)](S_2O_6)$	CuN_4O	5, TBP		0.92	12.45	2.011	2.158	2.225	[16,18]
$[Cu(dpyam)_2](ClO_4)_2$	CuN_4	4, Tet			18120, 15500(sh), 13160(sh), 10420				[14]
$[Cu(dpyam)_2](BF_4)_2$	CuN_4	4, Tet			18180, 15630(sh), 13330(sh), 10530	2.29	2.29	2.07	[15]
$[Cu(dpyam)_2](PF_6)_2$[f]	CuN_4	4, Tet			18050, 15920(sh) 13050(sh), 10390				
$[Cu(dpyam)_2(OH_2)_2](SO_4)\cdot 7H_2O$	CuN_4O_2	6, Oct	0.81		17.52, 1450				[15]
$[Cu(dpyam)_2(OH_2)_2](S_4O_6)$	CuN_4O_2	6, Oct	0.82		17.98, 14.79	2.26		2.09	[17]
$[Cu(dpyam)_2(SO_4)][Cu(dpyam)_2(OH_2)_2](PF_6)_2\cdot 2H_2O$	CuN_4O_2	6, *cis*-Oct[g]			14.97, 10.13	2.47		2.08	[17]

[a] T, tetragonality.
[b] τ, trigonal distortion index ($\tau = (\beta - \alpha)/60$).
[c] $kK = 1000\ cm^{-1}$.
[d] g_1 (determination from pseudo-isotropic spectra).
[e] Single crystal e.s.r. values.
[f] Present work.
[g] The first chromophore, Spy, square pyramidal; TBP, trigonal bipyramidal; Oct, octahedral; Tet, tetrahedral; interm, intermediate geometry between Spy and TBP.

ClO_4^- and PF_6^- and $Y = S_4O_6^{2-}$, $S_2O_6^{2-}$, $S_3O_6^{2-}$ and $S_2O_8^{2-}$, are compared with those of the title complexes as in Table 5. The binding behaviour of the anions and the geometries are different depending on types of the chelate ligands.

3.3. Spectral characterization

The IR spectra of compounds **1**–**4** show broad and intense bands of the ionic $S_4O_6^{2-}$ (1249 and 1215 cm^{-1} for **1**), $S_2O_8^{2-}$ (1285 cm^{-1} for **3**) and BF_4^- anions (1059 cm^{-1} for **2** and 1066 cm^{-1} for **4**). The electronic reflectance spectra of compounds **1** and **2** show two well-resolved bands with nearly equal intensity at approximately 14570 and 8630 cm^{-1} for **1**; 14860 and 8620 cm^{-1} for **2**, which are assigned as the $d_{z^2} \rightarrow d_{xy}$ and $d_{xz} \approx d_{yz} \approx d_{x^2-y^2} \rightarrow d_{xy}$ transitions, respectively, corresponding to an elongated octahedral geometry with high tetragonalities of ca. 0.89. This yields a tentative one-electron orbital sequence of $d_{xy} > d_{z^2} > d_{xz} \approx d_{yz} \approx d_{x^2-y^2}$, an order which is comparable to that previously deduced for the elongated octahedral complexes [38,46]. The electronic reflectance spectrum of **3** consists of a single broad peak at 13820 cm^{-1}. This spectral character of the compound is consistent with the distorted square pyramidal geometry ($\tau = 0.31$), but with a slightly lower energy than expected due to a high tetrahedral twist of the square base (36.0°) [15]. The one-electron ground state configuration is $d_{x^2-y^2} > d_{z^2} > d_{xy} > d_{xz} \approx d_{yz}$. The transition may be assigned as $d_{xy}, d_{xz}, d_{yz}, d_{z^2} \rightarrow d_{x^2-y^2}$. Complex **4** with $\tau = 0.66$ displays a single $d \rightarrow d$ transition at 12820 cm^{-1}, with some evidence for a possible low-energy shoulder at 10700 cm^{-1}, consistent with a distorted TBP stereochemistry [46]. The one-electron ground-state configuration is $d_{z^2} > d_{xy} \approx d_{x^2-y^2} > d_{xz} \approx d_{yz}$ and the principal absorption may be assigned as a $d_{xz} \approx d_{yz} \rightarrow d_{z^2}$ transition, with the low-energy shoulder assigned as a $d_{xy} \approx d_{x^2-y^2} \rightarrow d_{z^2}$ transition.

The polycrystalline ESR spectrum of **3** is axial with $g_\parallel \gg g_\perp > 2.0 = 2.210 \gg 2.062 > 2.0$, consistent with a $d_{x^2-y^2}$ ground state for the distorted square-based pyramidal geometry of the CuN_4O' chromophore [46]. However, X-band EPR measured on polycrystalline samples of **1**, **2** and **4** at RT showed a broad isotropic signal with a g_{iso} at around 2.108, 2.098 and 2.180, respectively which give no information regarding to the electronic ground state.

4. Supplementary material

CCDC 616539, 616540, 616541 and 616542 contain the supplementary crystallographic data for **1**, **2**, **3** and **4**. These data can be obtained free of charge via http://www.ccdc.cam.ac.uk/conts/retrieving.html, or from the Cambridge Crystallographic Data Centre, 12 Union Road, Cambridge CB2 1EZ, UK; fax: (+44) 1223-336-033; or e-mail: deposit@ccdc.cam.ac.uk.

Acknowledgements

The authors thank the The Thailand Research Fund (Agreement Numbers RTA 4880008 and BRG 4980007), Khon Khaen University and the Higher Education Development Project: Postgraduate Education and Research Program in Chemistry (PERCH) for financial support.

References

[1] S. Youngme, N. Chaichit, C. Pakawatchai, S. Booncoon, Polyhedron 21 (2002) 1279.
[2] D. Reinen, C. Friebel, Struct. Bond. (Berlin) 37 (1979) 1.
[3] B. Murphy, M. Aljabri, A.M. Ahmed, G. Murphy, B.J. Hathaway, M.E. Light, T. Geilbrich, M.B. Hursthouse, J. Chem. Soc., Dalton Trans. (2006) 357.
[4] E. Freire, S. Baggio, R. Baggio, M.T. Garland, Acta Crystallogr., Sect. C 54 (1998) 464.
[5] D.L. Cullen, E.C. Lingafelter, Inorg. Chem. 9 (1970) 1858.
[6] M.D. Joesten, M.S. Hussain, P.G. Lenhert, Inorg. Chem. 9 (1970) 151.
[7] J.M. Seco, M.J. Garmendia, M. Quiros, J. Coord. Chem. 55 (2002) 345.
[8] H.A. Jahn, E. Teller, Proc. Roy. Soc., Ser. A 161 (1937) 220.
[9] H.A. Jahn, Proc. Roy. Soc., Ser. A 164 (1938) 117.
[10] I.B. Bersuker, Chem. Rev. 101 (2001) 1067.
[11] P.T. Miller, P.G. Lenhert, M.D. Joesten, Inorg. Chem. 11 (1972) 2221.
[12] C.J. Simmons, New. J. Chem. 17 (1993) 77.
[13] S. Takagi, P.G. Lenhert, M.D. Jöesten, J. Am. Chem. Soc. 96 (1974) 6606.
[14] Miao Du, Xian-He Bu, Lin-Hong Weng, Xue-Bing Leng, Ya-Mei Guo, Acta Crystallogr., Sect. E E57 (2001) 25.
[15] S. Youngme, K. Poopasit, K. Chinnakali, S. Chantrapromma, Hoong-Kun Fun, Inorg. Chim. Acta 292 (1999) 57.
[16] W.D. Harrison, B.J. Hathaway, Acta Crystallogr., Sect B 36 (1980) 1069.
[17] S. Youngme, N. Chaichit, Polyhedron 21 (2002) 247.
[18] J. Foley, D. Kennefick, D. Phelan, S. Tyagi, B. Hathaway, J. Chem. Soc., Dalton Trans. (1983) 2333.
[19] Nakai Hisayoshi, Bull. Chem. Soc. Jpn. 56 (1983) 1637.
[20] W.D. Harrison, B.J. Hathaway, Acta Crystallogr., Sect. B 35 (1979) 2910.
[21] M.B. Ferrari, G.G. Fava, C. Pelizzi, J. Chem. Soc., Chem. Comm. 1 (1977) 8.
[22] Bruker, SMART (version 5.6), Bruker AXS Inc., Madison, WI, USA, 2000.
[23] Siemens, SAINT, Version 4 Software Reference Manual, Siemens Analytical X-Ray Systems, Inc., Madison, WI, USA, 2000.
[24] G.M. Sheldrick, SADABS, Program for Empirical Absorption correction of Area Detector Data, University of Göttingen, Göttingen, Germany, 2000.
[25] Siemens, SHELXTL, 2000, Version 6.12 Reference Manual, Siemens Analytical X-Ray Systems, Inc., Madison, WI, USA, 2000.
[26] A. Murphy, B.J. Hathaway, T.J. King, J. Chem. Soc., Dalton Trans. (1979) 1646.
[27] S. Nishigaki, H. Yoshioka, K. Nakatsu, Acta Crystallogr., Sect. B 34 (1978) 875.
[28] (a) N.W. Isaacs, C.H.L. Kennard, J. Chem. Soc. A (1969) 386;
(b) S. Takagi, M.D. Joesten, P.G. Lenhert, Acta Crystallogr., Sect. B 32 (1976) 326;
(c) D.L. Cullen, E.C. Lingafelter, Inorg. Chem. 10 (1971) 1264.
[29] I. Potočňák, M. Pohlová, C. Wagner, L. Jäger, Acta Crystallogr., Sect. E 58 (2002) 595.
[30] O.P. Anderson, J. Chem. Soc., Dalton Trans. (1973) 1237.
[31] J. Sletten, M. Julve, Acta Chem. Scand. 53 (1999) 631.
[32] J.M. Seco, M.J. Garmendia, M. Quiros, J. Coord. Chem. 55 (2002) 345.
[33] A. Bencini, S. Midollini, C. Zanchini, Inorg. Chem. 28 (1989) 1963.
[34] (a) O.P. Anderson, J. Chem. Soc., Dalton Trans. (1972) 2597;
(b) B.J. Hathaway, P.G. Hodgson, P.C. Power, Inorg. Chem. 13 (1974) 2009.
[35] Z.-M. Liu, Z.-H. Jiang, D.-Z. Liao, G.-L. Wang, Polyhedron 10 (1991) 101.
[36] P. Majumdar, A.K. Ghosh, L.R. Falvello, S.-M. Peng, S. Goswami, Inorg. Chem. 37 (1998) 1651.
[37] C. Faulman, Y.S.J. Veldhuizen, J.G. Haasnot, J. Reedijk, P. Cassoux, Acta Crystallogr., Sect. C 54 (1998) 1827.
[38] M.R. Truter, B.L. Vickery, J. Chem. Soc., Dalton Trans. (1972) 395.
[39] A.W. Addison, T. Nageswara Rao, J. Reedijk, J. van Run, G.C. Verschoor, J. Chem. Soc., Dalton Trans. (1984) 1340.
[40] F. Huq, A.C. Skapski, J. Chem. Soc. A (1971) 1927.
[41] G. Murphy, P. Nagle, B. Murphy, B. Hathaway, J. Chem. Soc., Dalton Trans. (1997) 2645.
[42] O.J. Parker, S.L. Aubol, G.L. Breneman, Acta Crystallogr., Sect. C 52 (1996) 39.
[43] O.J. Parker, J.L. Manson, G.L. Breneman, Acta Crystallogr., Sect. C 50 (1994) 1201.
[44] (a) J. Sletten, K. Svardal, A. Sfrensen, Acta Chem. Scand. 47 (1993) 1091;
(b) J.E. Johnson, T.A. Beineke, R.A. Jacobson, J. Chem. Soc., Sect. A (1971) 1371.
[45] M. Dua, Y.M. Guo, S.T. Chen, X.H. Bu, J. Ribas, Inorg. Chim. Acta 346 (2003) 207.
[46] B.J. Hathaway, Comprehensive Coordination Chemistry, in: G. Wilkinson, R.D. Gillard, J.A. McCleverty (Eds.), The Synthesis, Reactions, Properties and Applications of Coordination Compounds, vol. 5, Pergamon Press, Oxford, 1987, pp. 533–774 (Section 53).

and anions [4–11]. BPP is a flexible ligand that can adopt different conformations with respect to relative orientations of CH_2 groups, such as TT, TG, GG and GG' (where T = trans and G = gauche) [7b,9a,11a]. A wide variety of network topologies and structural motifs, including one-dimensional (1-D) chains [9c–11a] two-dimensional (2-D) open-framed, interpenatrated or interdigitated sheets [5a,5b–9a,9b,10a,10b,11] and three-dimensional (3-D) arrays [5a,5c,9b,9d,10b,10c] can be obtained using BPP ligand due to its flexibility.

In addition, several investigations have shown the potencial application of oxocarbon species, in particular squarate ($C_4O_4^{2-}$) and croconate ($C_5O_5^{2-}$) ions, as building blocks in crystal engineering to the construction of desired arrangements using supramolecular structures self-assembly [11c,12]. On the other hand, 3,5-bis(dicyanomethylene)-cyclopentane-1,2,4-trionate dianion, namely Croconate Violet (CV^{2-}), an interesting member of the so-called pseudo-oxocarbon family [13], has received much less attention in coordination chemistry studies. CV^{2-} species shows extended π electron delocalization, strong absorption in the visible region, reversible electrochemical behavior as well as electrical conductivity typical of semiconductors materials [14]. It has been observed that CV^{2-} dianion exhibits basically two different coordination modes; through the vicinal oxygen atoms in a chelating fashion [15] or through nitrogen atoms of dicyanomethylene groups in a bridging mode [16].

From this point of view, in this work, the synthesis, spectroscopic properties and crystal structure of a novel Zn(II) two-dimensional coordination polymer containing both versatile structural components BPP and Croconate Violet dianion, are reported.

2. Experimental

2.1. Materials and physical measurements

1,3-Bis(4-pyridyl)propane was purchased from Aldrich Chemical Co. and used without further purification. $(NBu_4)_2CV$ was prepared according to the published method [15c]. Elemental analyses for C, H and N were carried out on a Perkin–Elmer 2400 analyzer. Zinc was measured with an atomic absorption spectrophotometer Hitachi Z-8200. Thermogravimetric analysis (TG/DTG) was obtained on a TG-50 Mettler STARe. Sample was heated at 10 °C/min from room temperature to 800 °C in a dynamic nitrogen atmosphere (flow rate = 200 mL/min). Infrared spectra were recorded on a FT-IR Bomem MB102 spectrometer in the wavenumber range 4000–400 cm^{-1} using KBr pellets. Raman spectra were obtained in the solid state in a Bruker RFS 100 instrument equipped with Nd^{3+}/YAG laser operating at 1064 nm in the near infrared and CCD detector cooled with liquid N_2 with an average of 1000 scans and 4 cm^{-1} of spectral resolution.

2.2. Synthesis of $\{[Zn(\mu\text{-}BPP)(BPP)(CV)(H_2O)]\cdot H_2O\}_n$ (1)

To 30 mL of a methanolic solution containing 106 mg (0.356 mmol) of $Zn(NO_3)_2\cdot 6H_2O$ at 65 °C, 256 mg (0.356 mmol) of $(NBu_4)_2CV$ dissolved in 20 mL of methanol were added. After 15 min, 20 mL of a methanolic solution containing 140 mg (0.712 mmol) of BPP were added. The resulting solution was kept under stirring at 65 °C for 1 h and after this time, 10 mL of water were added. The solution was set aside and a week later the formation of dark green crystals and a small amount of golden crystals was observed. The crystals were recovered by filtration and the golden ones were identified as $(NBu_4)_4[Zn(CV)_3]$ already described in the literature [15c]. The crystals were washed several times with methanol, dichloromethane and acetone to eliminate $(NBu_4)_4[Zn(CV)_3]$ and the prismatic dark green single crystals of $\{[Zn(\mu\text{-}BPP)(BPP)(CV)(H_2O)]\cdot H_2O\}_n$ were isolated and used in the X-ray diffraction data collection. Yield: 50%. m.p. = 180 °C (d). *Anal.* Calc. for $C_{37}H_{32}N_8O_5Zn$: C, 60.54; H, 4.39; N, 15.27; Zn, 8.90. Found: C, 60.39; H, 4.42; N, 16.03; Zn, 8.71%. IR (KBr, cm^{-1}): $\nu(CH_{arom})$, 3037 (w); $\nu(CH_{aliph})$, 2951 (w), 2858 (w); ν(CN), 2210 (s), 2200 (s); ν(CO), 1688 (w); ν(CC/CN), 1619 (s), 1577 (sh); ν(CO + CC + CC(CN)), 1600 (s); 1526 (s), 1482 (s), 1432 (m); δ_{oop}(CH), 822 (m), 808 (w), 619 (w), 590 (w). Raman

Table 1
Crystallographic data and structure refinement parameters for compound **1**

Minimum formula	$C_{37}H_{32}N_8O_5Zn$
Formula weight	734.08
Temperature (K)	295(2)
Crystal system, space group	triclinic, $P\bar{1}$
Unit cell dimensions	
a (Å)	11.8730(6)
b (Å)	12.2415(7)
c (Å)	13.845(2)
α (°)	71.988(7)
β (°)	66.436(8)
γ (°)	79.506(4)
Volume (Å^3)	1750.1(3)
Z	2
D_{calc} (g cm^{-3})	1.393
Absorption coefficient (mm^{-1})	0.757
$F(000)$	760
θ Range for data collection (°)	1.66–25.07
Index ranges	$-14 \leqslant h \leqslant 12$, $-14 \leqslant k \leqslant 13$, $-16 \leqslant l \leqslant 0$
Reflections colleted/unique	6496/6217
Reflections observed/parameters	4596/464
Refinement method	full-matrix least-square on F^2
Goodness-of-fit on F^2	1.043
Final R indices $[I > 2\sigma(I)]$[a,b]	$R_1 = 0.0345$, $wR_2 = 0.0770$
R indices (all data)[a,b]	$R_1 = 0.0722$, $wR_2 = 0.0818$
Largest difference in peak and role (e Å^{-3})	0.233 and −0.231

[a] $R = \sum \||F_o| - |F_c|\| / \sum |F_o|$.
[b] $R_w = \left\{\sum[w(F_o^2 - F_c^2)^2] \Big/ \sum w(F_o^2)^2]\right\}^{1/2}$; $w = [\sigma^2(F_o^2) + (aP)^2 + bP]^{-1}$, where $P = (F_o^2 + 2F_c^2)/3$.

(1064 nm, cm^{-1}): $\nu(CH_{arom})$, 3074 (w), 3063 (w), 3051 (w); $\nu(CH_{aliph})$, 2953 (w), 2918 (w), 2882 (w); ν(CN), 2209 (s), 2196 (m); ν(CO), 1684 (w); ν(CC/CN), 1611 (m), 1573 (w); ν(CO + CC + CC(CN)), 1492 (s), 1459 (w); δ_{oop}(CH), 624 (w), 601(w).

2.3. X-ray data collection and structure determination

Single-crystal X-ray diffraction measurement of complex **1** was carried out on an Enraf-Nonius *CAD*-4 diffractometer with a graphite-monochromated Mo Kα radiation ($\lambda = 0.71073$ Å) at 295(2) K. The structure was solved by direct methods with SHELXS97 [17] and refined by full-matrix least-square procedure based on F^2 using SHELXL97 program [18]. Crystal data and structure refinement parameters are summarized in Table 1.

3. Results and discussion

3.1. Synthesis and general characterization

Reaction of $Zn(NO_3)_2 \cdot 6H_2O$, $(NBu_4)_2CV$ and BPP ligand in methanolic media has afforded $\{[Zn(\mu\text{-BPP})(BPP)(CV)(H_2O)] \cdot H_2O\}_n$ (**1**). Recently, it has been reported the synthesis of a Zn(II) complex with the dianion CV^{2-} namely $K_2[Zn(CV)_2(H_2O)_2] \cdot 2H_2O$ containing the core $[Zn(CV)_2]^{2-}$ that can be used as a building block for coordination polymers construction [15d]. In the present work, the original idea was the replacement of coordinated water molecules in $[Zn(CV)_2(H_2O)_2]^{2-}$ by the nitrogen ligand BPP to generate an anionic coordination polymer. In this sense, the precursor $(NBu_4)_2CV$ was used to afford a great cation (NBu_4^+) that could stabilize the anionic polymeric chain. However, the analytical data have indicated the formation of a neutral compound with (1:1:2)/(Zn^{2+}:CV^{2-}:BPP) molar ratio in which tetrabutylammonium cations are not present.

The results of thermogravimetric analysis show two weight losses at 80 and 110 °C, indicating the presence of two distinct water molecules in the structure (Obs., 5.1% and Calc., 4.9%) corresponding to coordination and lattice water molecules. Above 180 °C, the complete thermodecomposition takes place and at 800 °C there is a residue consistent with metallic zinc in association with a black amorphous material.

The IR and Raman spectra of compound **1** are shown in Fig. 1. It can be verified that the stretching modes at 2210 and 2200 cm^{-1} assigned to ν(CN) vibrations are little affected in comparison to free CV^{2-} dianion [15c], indicating that dicyanomethylene groups do not participate in the coordination to Zn(II) centers. On the other hand, ν(CO) mode originally at 1635 cm^{-1} in the $(NBu_4)_2CV$ spectrum [15c], is absent in the spectrum of **1**, although it can be observed the presence of a low intensity band at 1688 cm^{-1}. These results suggest the pseudo-oxocarbon coordination to the metal center through the vicinal oxygen atoms O1 and O2, in a bidentate fashion, as observed for

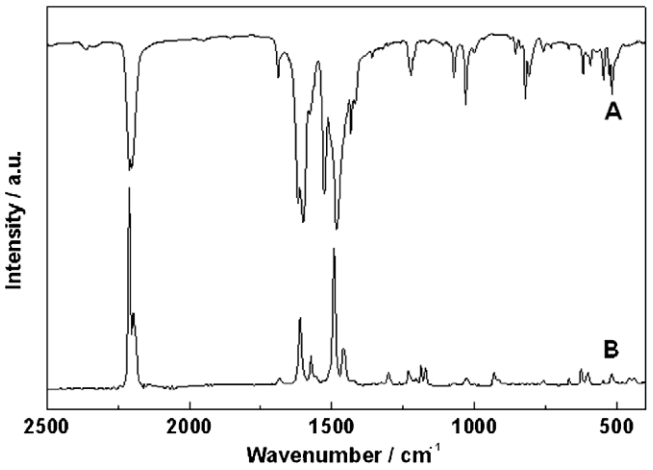


Fig. 1. Infrared (A) and Raman (B) spectra of $\{[Zn(\mu\text{-BPP})(BPP)(CV)(H_2O)] \cdot H_2O\}_n$ (**1**).

other complexes with CV^{2-} dianion coordinated in a O,O-bonding mode, described in the literature [15]. It should be noticed that in **1**, the pyridine ring vibrational band shifts from 1605 cm^{-1} in free BPP to 1619 cm^{-1}. In fact, the presence of ν(CC/CN) in higher wavenumber is indicative of metal coordination [19] to BPP pyridine nitrogen atoms, as observed for previous structurally characterized compounds [9a,20].

3.2. Description of the crystal structure of *1*

The asymmetric unit of **1**, shown in Fig. 2, is constituted by a Zn(II) ion coordinated to three pyridine nitrogen atoms (N21, N41 and N51) from two different BPP ligands as well as to two oxygen atoms (O1 and O2) from one CV^{2-} dianion and one *aqua* ligand (OW1). Additionally, there is one lattice water molecule in the structure as was indicated by thermal analysis. The donor atoms are arranged around the metal center in a distorted octahedral geometry with a *facial* local isomery (ZnN_3O_3). As was suggested by spectroscopic data, the pseudo-oxocarbon CV^{2-} is coordinated to the Zn(II) center in a O,O-bonding bidentate fashion with no participation of the dicyanomethylene ($-C(CN)_2$) groups. Selected bond distances and angles are presented in Table 2.

It can be noticed that Zn–O bond distances are not equivalent, corresponding to an asymmetrical bidentate coordination mode. The Zn–O2 bond distance (2.0772(15) Å) is much shorter than Zn–O1 (2.3510(15) Å) and the latter one is longer than Zn–OW1 bond distance (2.2067(16) Å). This asymmetrical bidentate coordination mode has been already observed for other complexes containing the CV^{2-} dianion described in the literature [15a,15b,15d]. In addition, the coordination promotes great perturbations in Croconate Violet C–O bonds. In fact, all C–O bonds are equivalent in the free CV^{2-} with mean distances of 1.244(6) Å for $K_2CV \cdot 2H_2O$ [13b] and 1.239(2) Å for $(NBu_4)_2CV$ [15c], characterizing a delocalized electronic system. On the other hand, in **1**, C2A–O2

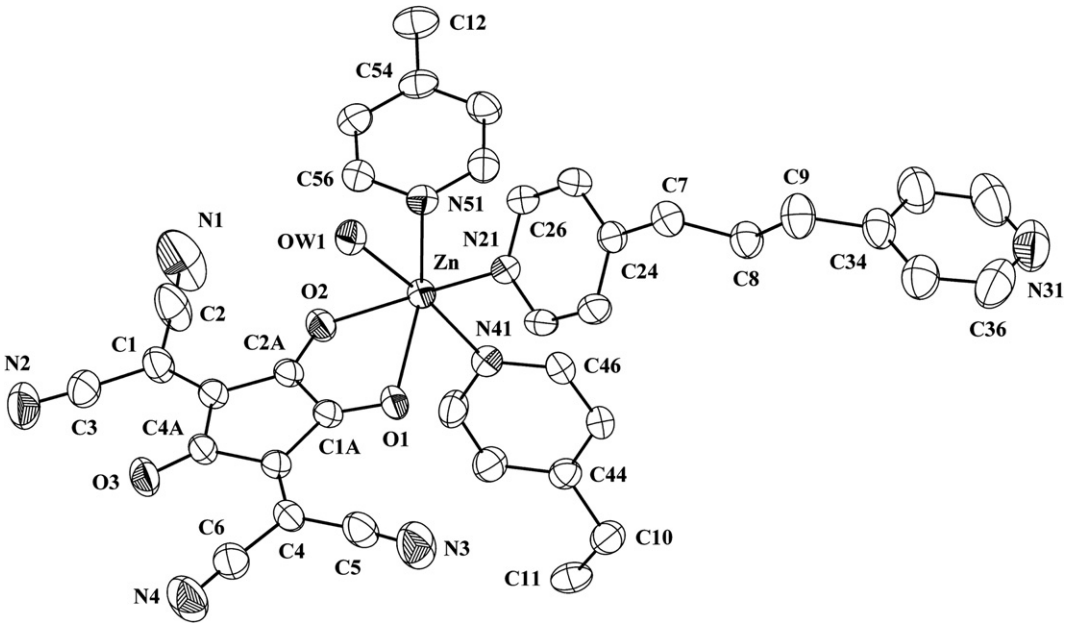


Fig. 2. Projection of the asymmetric unit of **1** with the atomic numbering scheme [21]. Displacement ellipsoids drawn at the 50% probability level. Hydrogen atoms and lattice water molecule oxygen atom (OW2) were omitted for clarity.

bond distance, in which the oxygen atom is more strongly bonded to Zn(II), is longer than C1A–O1, assuming the values of 1.264(3) and 1.246(3) Å, respectively. However, C4A–O3 bond length (1.221(3) Å), which oxygen atom is not involved in the coordination to the metal center, is much shorter than C2A–O2 and C1A–O1 and even than those observed in the free ligand, indicating a great carbonyl character for C4A–O3 bond. In this sense, it can be concluded that the pseudo-oxocarbon exhibits a partial localization of the π electrons upon complexation. This fact can be responsible for the low intensity stretching bands in 1688 and 1684 cm^{-1}, assigned to ν(CO), observed in IR and Raman spectra respectively.

The one-dimensional (1-D) polymeric nature of $\{[Zn(\mu\text{-BPP})(BPP)(CV)(H_2O)]\cdot H_2O\}_n$, shown in Fig. 3, was revealed through the connection of asymmetric units metallic centers by BPP ligands. It must be pointed out that there are two kinds of BPP ligands in the structure. The BPP ligands, which contain N41 and N51 pyridine nitrogen atoms, act in a bridging coordination mode toward the Zn(II) centers and are responsible for the 1-D polymeric chain formation along the crystallographic *a* axis. On the other hand, the BPP ligands, which contain N21 and N31 nitrogen atoms, are pendants and coordinate the metal ions through N21 atom in a monodentate fashion, with no participation of N31.

Table 2
Selected bond distances (Å) and angles (°) for compound **1**

Zn–O1	2.3510(15)	C1A–O1	1.246(3)
Zn–O2	2.0772(15)	C2A–O2	1.264(3)
Zn–OW1	2.2067(16)	C4A–O3	1.221(3)
Zn–N21	2.0841(18)	C2–N1	1.146(3)
Zn–N41	2.1542(19)	C3–N2	1.134(3)
Zn–N51	2.1215(18)	C5–N3	1.141(3)
		C6–N4	1.141(3)
O1–Zn–O2	77.37(6)	N21–Zn–OW1	83.77(7)
O1–Zn–OW1	86.27(6)	N21–Zn–N41	96.50(7)
O1–Zn–N21	90.31(6)	N21–Zn–N51	102.29(7)
O1–Zn–N41	86.43(6)	N41–Zn–OW1	172.69(6)
O1–Zn–N51	167.00(6)	N41–Zn–N51	95.18(7)
O2–Zn–OW1	83.41(6)		
O2–Zn–N21	162.75(6)		
O2–Zn–N41	94.76(7)		
O2–Zn–N51	89.63(7)		

The BPP ligands that act in a bridging coordination mode adopt a TG (*trans–gauche*) conformation along the 1-D polymeric chain exhibiting a N41-to-N51′ separation of 8.73(3) Å (symmetry code (′) $1 + x$, y, z). On the other hand, it can be noticed that the pendant BPP ligands assume the TT (*trans–trans*) conformation which is associated to a maximum separation between the pyridine nitrogen atoms (d(N21···N31) = 10.023(4) Å). These values are in accordance to other metal compounds containing BPP ligand structurally characterized [7b]. Additionally, the intra-chain distance between two adjacent metallic centers is equivalent to the crystallographic *a* axis length corresponding to 11.8730(6) Å.

Among the several known coordination polymers constructed through the interaction of metal cations with the flexible ligand BPP [4–11] there is a Mn(II) complex namely $[\{Mn(bpp)_3Cl_2\}(H_2O)_2]_n$ reported in the literature [9d] which has bridging and pendant BPP ligands. However, in contrast to **1** structure, in the manganese complex the bridging BPP molecules adopt a TT conformation (d(N···N) = 9.962 Å) and, the pendant ones assume a TG conformation (d(N···N) = 8.985 Å).

The most prominent structural feature of **1** is that, besides the metal–ligand (Zn–N) interaction, responsible for the 1-D chain formation along the crystallographic *a*

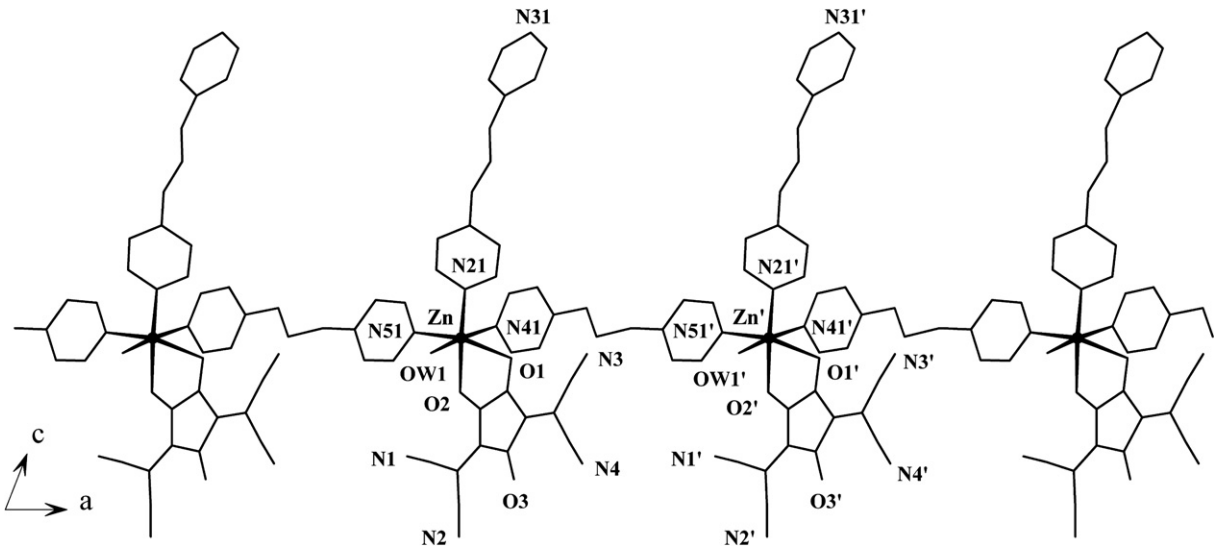


Fig. 3. One-dimensional (1-D) polymeric chain of $\{[Zn(\mu\text{-BPP})(BPP)(CV)(H_2O)]\cdot H_2O\}_n$ extended along the crystallographic *a* axis. Hydrogen atoms and lattice water molecule oxygen atom (OW2) were omitted for clarity. Symmetry transformations used to generate equivalent atoms: (′) $1+x, y, z$.

axis, it can be noticed other interactions like hydrogen bonding. Normally, these interactions are weaker than those of coordination, however, as in the present case, they play an essential role in the establishment of multi-dimensional networks in the solid state. In this sense, as can be seen in Fig. 4, the 1-D polymeric chains are connected through cooperative hydrogen bonding involving N31, OW2 and OW1 atoms giving rise to a two-dimensional (2-D) supramolecular array along the crystallographic *c* axis. In fact, each N31 atom, which is not coordinated to metal ion, from terminal BPP ligands, forms hydrogen bonding with the non-coordinated water molecules present in the crystalline lattice. In this hydrogen bond (OW2$\cdots$N31″ = 2.841(3) Å, OW2–H3 = 0.935(2) Å, H3$\cdots$N31″ = 1.909(3) Å, OW2–H3$\cdots$N31″ = 174.6(2)°, symmetry code (″) $x, y, 1-z$) the separation between nitrogen and oxygen atoms is much shorter than the van der Waals radii sum (3.07 Å). In addition, the non-coordinated water molecules are involved in stronger hydrogen bonds with the coordination water molecules (OW1$\cdots$OW2 = 2.725(3) Å, OW1–H1 = 0.932(2) Å, H1$\cdots$OW2 = 1.794(2) Å, OW1–H1$\cdots$OW2 = 177.1(1)°).

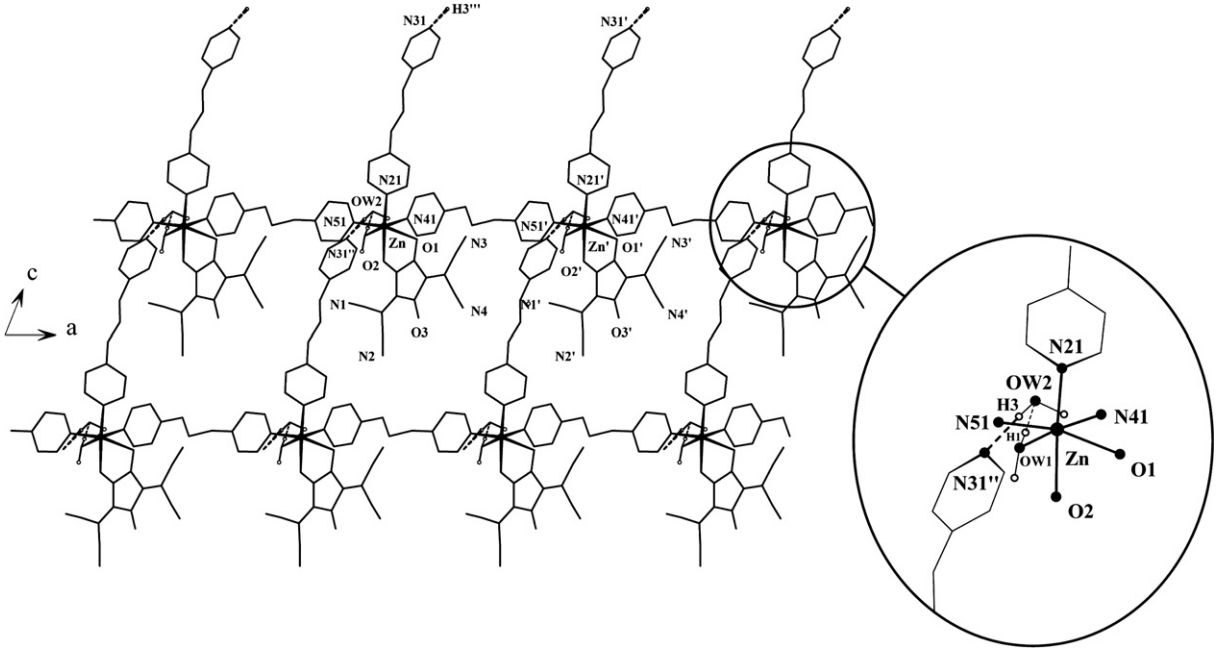


Fig. 4. Two-dimensional (2-D) supramolecular network of $\{[Zn(\mu\text{-BPP})(BPP)(CV)(H_2O)]\cdot H_2O\}_n$, **1**, extended through cooperative hydrogen bonding involving N31, OW2 and OW1 atoms. Symmetry transformations used to generate equivalent atoms: (′) $1+x, y, z$; (″) $x, y, -1+z$; (‴) $x, y, 1+z$.

The separation between two inter-chain Zn(II) centers, along the terminal BPP ligands, is equivalent to the crystallographic *c* axis, leading to a 2-D network extended by hydrogen bonding with (4,4) type structural topology, similar to a distorted square grid. The lowest closed path represents a parallelogram of $a \times c$ (11.8730(6) × 13.845(2) Å) dimensions.

In addition, an interesting interdigitation phenomenon can be observed in the compound **1** structure. Since the BPP ligands in TT and TG conformations are oriented to opposite sides in the network lowest closed path, the parallelogram exhibits two concave sides and two convex ones, resulting in an extremely undulated rhombohedral grid. Two complementary grids fit each other, without being interpenetrated, giving rise to a bilayer supramolecular structure. π–π interactions between Croconate Violet rings of adjacent sheets with an interplanar distance of 3.618(4) Å, as well as, hydrogen bonds between CV^{2-} non-coordinated oxygen atoms (O3) and coordinated water molecules (OW1···O3$''''$ = 3.018(2) Å, OW1–H2 = 0.982(2) Å, H2···O3$''''$ = 2.272(2) Å, OW1–H2···O3$''''$ = 131.9(1)°, symmetry code ($''''$) $-1+x, -y, -z+1$), can be identified. Although these interactions are much weaker than those discussed before, they seem to be very important in the (4,4) networks interdigitation to maintain the bilayer supramolecular structure.

It must be pointed out that there is only one example of a coordination polymer containing Croconate Violet dianion reported in the literature [16], namely $\{[Fe(\mu\text{-CV})(H_2O)_2]\cdot 2H_2O\}_n$, and therefore $\{[Zn(\mu\text{-BPP})(BPP)(CV)(H_2O)]\cdot H_2O\}_n$, described in this work, is the first 2-D coordination polymer involving Zn(II), the CV^{2-} ion and an ancillary nitrogen ligand.

4. Conclusion

In summary, the present study provides an interesting example of Zn(II) coordination polymer constructed from the flexible nitrogen ligand BPP and Croconate Violet dianion namely $\{[Zn(\mu\text{-BPP})(BPP)(CV)(H_2O)]\cdot H_2O\}_n$ (**1**). Thermogravimetric results have shown the presence of coordination and lattice water molecules in the complex structure. According to vibrational spectroscopic data, the Croconate Violet dianion is coordinated to Zn(II) center through the vicinal oxygen atoms O1 and O2 in a chelating fashion with no involvement of CN moieties. All these facts were confirmed by single crystal X-ray diffraction analysis. The asymmetric unit consists on a Zn(II) center surrounded by three nitrogen atoms from two different BPP ligands, two oxygen atoms from one Croconate Violet dianion and one *aqua* ligand, adopting a distorted octahedral geometry in a *facial* arrangement (ZnN_3O_3). The one-dimensional (1-D) polymeric nature of **1** was revealed through the connection of asymmetric units metallic centers by BPP ligands, which adopt a TG conformation. The 1-D polymeric chains are connected through cooperative hydrogen bonding, giving rise to a two-dimensional (2-D) supramolecular array with (4,4) structural topology. Two complementary 2-D sheets fit each other exhibiting an interdigitation phenomenon, affording a bilayer supramolecular structure.

5. Supplementary material

CCDC 615919 contains the supplementary crystallographic data for $\{[Zn(\mu\text{-BPP})(BPP)(CV)(H_2O)]\cdot H_2O\}_n$ (**1**). These data can be obtained free of charge via http://www.ccdc.cam.ac.uk/conts/retrieving.html, or from the Cambridge Crystallographic Data Centre, 12 Union Road, Cambridge CB2 1EZ, UK; fax: (+44) 1223-336-033; or e-mail: deposit@ccdc.cam.ac.uk.

Acknowledgements

The authors are grateful to the Brazilian agencies CAPES, CNPq and FAPEMIG for financial support, to Laboratório de Espectroscopia Molecular USP for Raman facilities and to Dr. Renata Diniz for crystallographic data discussions. The authors and specially Flávia C. Machado dedicate this article to the beloved memory of Dr. Wagner Magno Teles, an enthusiast for coordination polymers and supramolecular chemistry studies, who suddenly and prematurely left us in December 2004.

References

[1] (a) S.R. Batten, R. Robson, Angew. Chem., Int. Ed. 37 (1998) 1461;
(b) N.R. Champness, M. Schröder, Curr. Opin. Solid State Mater. Sci. 3 (1998) 419;
(c) A.J. Blake, N.R. Champness, P. Hubberstey, W.-S. Li, M.A. Withersby, M. Schröder, Coord. Chem. Rev. 183 (1999) 117;
(d) M.A. Withersby, A.J. Blake, N.R. Champness, P.A. Cooke, P. Hubberstey, W.-S. Li, M. Schröder, Inorg. Chem. 38 (1999) 2259;
(e) D.A. McMorran, P.J. Steel, J. Chem. Soc., Dalton Trans. (2002) 3321.

[2] (a) H.O. Stumpf, L. Ouahab, Y. Pei, P. Bergerat, O. Kahn, J. Am. Chem. Soc. 116 (1994) 3866;
(b) O.-S. Jung, Y.J. Kim, Y.-A. Lee, J.K. Park, H.K. Chae, J. Am. Chem. Soc. 122 (2000) 9921;
(c) O.R. Evans, W. Lin, Acc. Chem. Res. 35 (2002) 511;
(d) X. Meng, Y. Song, H. Hou, Y. Fan, G. Li, Y. Zhu, Inorg. Chem. 42 (2003) 1306;
(e) O.M. Yaghi, H. Li, T.L. Groy, Inorg. Chem. 36 (1997) 4292;
(f) M. Eddaoudi, H. Li, O.M. Yaghi, J. Am. Chem. Soc. 122 (2000) 1391;
(g) S. Noro, R. Kitaura, M. Kondo, S. Kitagawa, T. Ishii, H. Matsuzaka, M. Yamashita, J. Am. Chem. Soc. 124 (2002) 2568;
(h) M. Fujita, Y.J. Kwon, S. Washizu, K. Ogura, J. Am. Chem. Soc. 116 (1994) 1151;
(i) T. Sawaki, T. Dewa, Y. Aoyama, J. Am. Chem. Soc. 120 (1998) 8539;
(j) J.S. Seo, D. Whang, H. Lee, S.I. Jun, J. Oh, Y.J. Jeon, K. Kim, Nature 404 (2000) 982;
(k) B. Moulton, M.J. Zaworotko, Curr. Opin. Solid State Mater. Sci. 6 (2002) 117;
(l) X.J. Li, X.Y. Wang, S. Gao, R. Cao, Inorg. Chem. 45 (2006) 1508.

[3] (a) R.L. Paul, S.M. Couchman, J.C. Jeffery, J.A. McCleverty, Z.R. Reeves, M.D. Ward, J. Chem. Soc., Dalton Trans. (2000) 845;
(b) S.R. Batten, Curr. Opin. Solid State Mater. Sci. 5 (2001) 107;

(c) A. Erxleben, Coord. Chem. Rev. 246 (2003) 203;
(d) S.A. Barnett, N.R. Champness, Coord. Chem. Rev. 246 (2003) 145.
[4] (a) L. Carlucci, G. Ciani, D.W.v. Gudenberg, D.M. Proserpio, Inorg. Chem. 36 (1997) 3812;
(b) S.R. Batten, J.C. Jeffery, M.D. Ward, Inorg. Chim. Acta 292 (1999) 231;
(c) M.J. Plater, M.R.St.J. Foreman, A.M.Z. Slawin, J. Chem. Res. (S) (1999) 74.
[5] (a) M.J. Plater, M.R.St.J. Foreman, T. Gelbrich, S.J. Coles, M.B. Hursthouse, J. Chem. Soc., Dalton Trans. (2000) 3065;
(b) M.J. Plater, M.R.St.J. Foreman, T. Gelbrich, M.B. Hursthouse, J. Chem. Soc., Dalton Trans. (2000) 1995;
(c) L. Carlucci, G. Ciani, M. Moret, D.M. Proserpio, S. Rizzato, Angew. Chem., Int. Ed. 39 (2000) 1506.
[6] (a) M.J. Plater, M.R.St.J. Foreman, T. Gelbrich, M.B. Hursthouse, Inorg. Chim. Acta 318 (2001) 171;
(b) M.J. Plater, M.R.St.J. Foreman, R.A. Howie, J.M.S. Skakle, Inorg. Chim. Acta 318 (2001) 175;
(c) M.J. Plater, M.R.St J. Foreman, J.M.S. Skakle, Cryst. Eng. 4 (2001) 293;
(d) F.M. Tabellion, S.R. Seidel, A.M. Arif, P.J. Stang, J. Am. Chem. Soc. 123 (2001) 11982;
(e) F.M. Tabellion, S.R. Seidel, A.M. Arif, P.J. Stang, J. Am. Chem. Soc. 123 (2001) 11982.
[7] (a) M.-L. Tong, Y.-M. Wu, J. Ru, X.-M. Chen, H.-C. Chang, S. Kitawaga, Inorg. Chem. 41 (2002) 4846;
(b) L. Carlucci, G. Ciani, M. Moret, D.M. Proserpio, S. Rizzato, CrystEngComm 4 (2002) 121;
(c) K. Jin, X. Huang, L. Pang, J. Li, A. Appel, S. Wherland, Chem. Commun. (2002) 2872.
[8] (a) S. Konar, E. Zangrando, M.G.B. Drew, T. Mallah, J. Ribas, N.R. Chaudhuri, Inorg. Chem. 42 (2003) 5966;
(b) E.Q. Gao, S.Q. Bai, Z.M. Wang, C.H. Yan, J. Chem. Soc., Dalton Trans. (2003) 1759.
[9] (a) M.V. Marinho, M.I. Yoshida, K.J. Guedes, K. Krambrock, A.J. Bortoluzzi, M. Hörner, F.C. Machado, W.M. Teles, Inorg. Chem. 43 (2004) 1539;
(b) F.A. Almeida, J. Klinowski, Inorg. Chem. 43 (2004) 3882;
(c) Y. Kang, Z.-J. Li, Y.-G. Yao, Inorg. Chem. Commun. 7 (2004) 1139;
(d) A.K. Ghosh, D. Ghoshal, T.-H. Lu, G. Mostafa, N.R. Chaudhuri, Cryst. Growth Des. 4 (2004) 851.
[10] (a) Q.-Y. Liu, L. Xu, CrystEngComm 7 (2005) 87;
(b) S. Hu, M.-L. Tong, J. Chem. Soc., Dalton Trans. (2005) 1165;
(c) X.-J. Li, R. Cao, W.-H. Bi, Y.-Q. Wang, Y.-L. Wang, X. Li, Polyhedron 24 (2005) 2955.
[11] (a) F. Li, X. Li, T. Li, W. Su, R. Cao, J. Mol. Struct. 782 (2006) 116;
(b) J. Zhang, Y.-B. Chen, S.-M. Chen, Z.-J. Li, J.K. Cheng, Y.-G. Yao, Inorg. Chem. 45 (2006) 3161;
(c) C.C. Corrêa, R. Diniz, L.H. Chagas, B.L. Rodrigues, M.I. Yoshida, W.M. Teles, F.C. Machado, L.F.C. de Oliveira, Polyhedron, in press, 10.1016/j.poly.2006.09.037.
[12] (a) J.A.C. van Ooijen, J. Reedijk, A.L. Spek, Inorg. Chem. 18 (1979) 1184;
(b) C.-K. Lam, T.C.W. Mak, Tetrahedron 56 (2000) 6657;
(c) S. Mathew, G. Paul, K. Shivasankar, A. Choudhury, C.N.R. Rao, J. Mol. Struct. 641 (2002) 263;
(d) C.-C. Wang, C.-H. Yang, G.-H. Lee, Inorg. Chem. 41 (2002) 1015;
(e) D. Braga, L. Maini, F. Grepioni, Chem. Eur. J. 8 (2002) 1804;
(f) D. Cangussu, H.O. Stumpf, H. Adams, J.A. Thomas, F. Lloret, M. Julve, Inorg. Chim. Acta 358 (2005) 2292.
[13] (a) G. Seitz, P. Imming, Chem. Rev. 92 (1992) 1227;
(b) V.L. Himes, A.D. Mighell, C.R. Hubbard, A.J. Fatiadi, J. Res. Natl. Bur. Stand. 85 (1980) 87;
(c) G. Seitz, R. Sutrisno, B. Gerecht, G. Offermann, R. Schmdt, W. Massa, Angew. Chem., Int. Ed. 21 (1982) 283;
(d) P.-L. Fabré, C. Pena, A.-M. Galibert, B. Soula, G. Bernardinelli, B. Donnadieu, P. Castan, Can. J. Chem. 78 (2000) 280.
[14] (a) P.V. Kamat, M.A. Fox, Chem. Phys. Lett. 92 (1982) 595;
(b) P.V. Kamat, M.A. Fox, A.J. Fatiadi, J. Am. Chem. Soc. 106 (1984) 1191;
(c) P.-L. Fabré, F. Dumestre, B. Soula, A.-M. Galibert, Eletrochim. Acta 45 (2000) 2697.
[15] (a) F. Dumestre, B. Soula, A.-M. Galibert, P.-L. Fabré, G. Bernardinelli, B. Donnadieu, P. Castan, J. Chem. Soc., Dalton Trans. (1998) 4131;
(b) B. Soula, A.-M. Galibert, B. Donnadieu, P.-L. Fabré, Inorg. Chim. Acta 324 (2001) 90;
(c) W.M. Teles, R.A. Farani, D.S. Maia, N.L. Speziali, M.I. Yoshida, L.F.C. de Oliveira, F.C. Machado, J. Mol. Struct. 783 (2006) 52;
(d) W.M. Teles, R.A. Farani, N.L. Speziali, M.I. Yoshida, L.F.C. de Oliveira, F.C. Machado, Inorg. Chim. Acta 359 (2006) 3384.
[16] B. Soula, A.-M. Galibert, B. Donnadieu, P.-L. Fabré, J. Chem. Soc., Dalton Trans. (2003) 2449.
[17] G.M. Sheldrick, SHELXS97, Program for the Solution of Crystal Structures, University of Göttingen, Göttingen, Germany, 1997.
[18] G.M. Sheldrick, SHELXL97, Program for the Refinement of Crystal Structures, University of Göttingen, Göttingen, Germany, 1997.
[19] R. Scopelliti, G. Bruno, C. Donato, G. Tresoldi, Inorg. Chim. Acta 313 (2001) 43.
[20] M.T. Bujaci, X. Wang, S. Li, C. Zheng, Inorg. Chim. Acta 333 (2002) 152.
[21] K. Brandenburg, DIAMOND Version 3.1. Crystal Impact GbR, Bonn, Germany, 2004–2005.

Tertiary amine ligands offer considerable flexibility in the reactivity of the OsO_4/ligand mixture. In using OsO_4, as an effective reagent, in *cis*-hydroxylation of alkenes as well as in a variety of catalytic systems, the critical step depends on the formation of an osmium(VI) cycloadduct which is promoted by bases such as pyridine [10–12].

On the other hand, nitrogen ligands are important chemicals in chemistry [13]. The pyridines' substituted derivatives are also a family of donors commonly used in coordination chemistry. The 2- and 2,6-substituted derivatives invariably have steric problems with Lewis acids. Derivatives of pyridine in the *meta* and *para* positions provide a set of ligands with a constant steric requirement toward bulky Lewis acids. Since steric problems are often encountered in transition metal ion chemistry, the pyridine family is often used to determine electronic influences on the chemistry.

Despite the importance of OsO_4 in catalytic processes, a field where the Lewis acidity of OsO_4 plays an important role, it is surprising that no quantitative information exists on the acidity strength of this important compound in the literature. A particular question that this study attempts to address is to find the Lewis acidity of osmium tetroxide using three simple and straightforward scales, pK_a of N-donors, the Hammett reaction constant and the ECW model. This article concerns the reaction (1), the formation of an $OsO_4 \cdot L$ complex. We have measured the relative coordination ability of different N-donor ligands (shown in Scheme 1) toward OsO_4. We have also measured the enthalpies of the adduct formation in CCl_4. Carbon tetrachloride is an excellent solvent in the present study, as it has a very poor solvating effect and the compounds have good solubility in this solvent. The Drago's E_A and C_A parameters for OsO_4 are also obtained. This is particularly significant because of the importance of OsO_4 in inorganic, organometallic, and catalytic chemistry. These parameters also allow the chemists to predict and correlate quantitatively the enthalpies of $OsO_4 \cdot$ Lewis base interactions.

2. Experimental

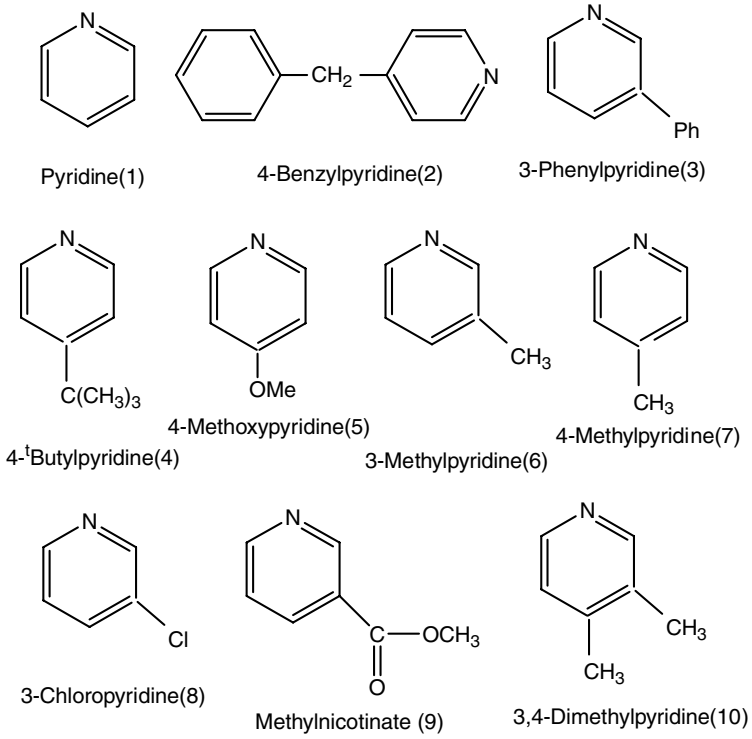
Caution: Osmium tetroxide presents an especial hazard to the eyes. Appropriate care should be taken in handling this compound.

2.1. Materials

Osmium tetroxide was obtained from Merck. Pyridine and its substituted derivatives were purchased from commercial sources and used without further purification. CCl_4 (Merck; quality for spectroscopy) was used as a solvent throughout this study.

2.2. Instruments

Equilibrium measurements were performed with conventional UV–vis spectrophotometer (Perkin–Elmer Lambda 25). Quartz cuvettes with 1 cm optical path lengths were used. Equilibrium measurements were carried out at different temperatures, maintained by a circulating water thermostatic system (EYELA NCB-3100 constant-temperature bath).



Scheme 1. Structural formulas of pyridine and its derivatives.

2.3. Measurements

The stepwise titration of the OsO_4 with 10 ring-substituted pyridines in CCl_4 according to Eq. (1) was followed spectrophotometrically at corresponding wavelength. Eqs. (3) and (4) were fitted to data of equilibrium absorbances to give the equilibrium constants and the enthalpies [14,15].

$$\mathrm{Abs}_{eq} = \left\{\frac{\varepsilon_{OsO_4} + \varepsilon_{OsO_4\cdot L}K_{eq}[L]}{1 + K_{eq}[L]}\right\}[Os]_T \quad (3)$$

Here, Abs_{eq} is the absorbance of a solution at equilibrium; ε_{OsO_4} and $\varepsilon_{OsO_4\cdot L}$ are molar absorptivities for OsO_4 and $OsO_4 \cdot L$ species, respectively at corresponding wavelength; $[Os]_T$ is the total concentration of OsO_4 and $OsO_4 \cdot L$ in the solution, and [L] represents the equilibrium ligand concentration. Such solutions contained L at a known concentration because $[L]_T \cong [L]_{eq} \gg [Os]_T$.

$$\ln K_{eq} = \frac{-\Delta H}{RT} + \frac{\Delta S}{R} \quad (4)$$

3. Results and discussion

We have previously reported that methyltrioxorhenium (MTO) forms only 1:1 complexes in solution with a variety of substituted pyridines [14,15]. The equilibrium constants for the MTO reactions show both $\log K_{eq}$ versus pK_a and Hammett-type correlations. We now report equilibrium constants for the formation of the corresponding OsO_4 complexes [Eq. (1)] and try to find the Lewis acidity of OsO_4 using three scales.

3.1. Scale 1: Acidity order based on pK_a of N-donors

In a similar manner, as shown previously [14,15] for MTO, OsO_4 forms only 1:1 pyridine adducts, in agreement with other studies [11,12]. Table 1 gives the equilibrium constants, for reaction (1) in CCl_4 solvent. The non-linear least square analysis was used to determine K_{eq} by fitting of absorbance–concentration data to Eq. (3).

The acidity of OsO_4 has been compared with MTO and Zn(TPP). Equilibrium data for MTO and Zn(TPP) are reported in the literature [15,19]. The excellent linear relationship was observed between the equilibrium constants and the pK_a values of the ligands. Fig. 1 shows the linear relationship of $\log K_{eq}$ for three acids, OsO_4 (in CCl_4), MTO (in CCl_4) and Zn(TPP) (in toluene) with the pK_a of the base, which is of the form $\log K_{eq} = m(pK_a) + b$. For OsO_4, MTO and Zn(TPP), $m = 0.33$, 0.43 and 0.65, respectively. This equation has been widely used as an empirical representation of equilibrium constant data [14,15,20,21].

It has been suggested that m is related to the σ-polarizing power of a cation [21], which we find to be $Zn^{II} > Re^{VII} > Os^{VIII}$. From Fig. 1, an extrapolation shows that the Zn(TPP) adducts will become more stable than OsO_4 or MTO as ligand basicity increases. The higher ligand basicities place more electron density on the pyridine nitrogen making it more polarizable. This increased polarizability has more effect for the more polarizing metal ion, i.e., $Zn^{II} > Re^{VII} > Os^{VIII}$, or in the order of increasing m values.

3.2. Scale 2: The Hammett reaction constant (ρ)

The Hammett σ values of substituted pyridines are shown in Table 1. Fig. 2 shows that the equilibrium data fit a Hammett correlation of the form shown in Eq. (5).

$$\log \frac{K_{eq}}{K_0} = \rho\sigma \quad (5)$$

In this equation K_0 is for $OsO_4 \cdot$ pyridine, K_{eq} is for $OsO_4 \cdot$ substituted pyridines, and σ is the Hammett substituent constant. The ρ constant values for different acids and the corresponding R^2 (correlation coefficient) values are collected in Table 2.

Gasperini and Ragaini have recently reported [24], for the first time, that ρ can be considered as a measure of

Table 1
Equilibrium constants[a] and ΔH values for the complex formation reactions [Eq. (1)] between OsO_4 and pyridines (shown in Scheme 1) in CCl_4

Ligand	σ[b]	pK_a[c]	$10^{-1}K_{eq}$/L mol^{-1}					ΔH/kJ mol^{-1}
			10 °C	20 °C	25 °C	30 °C	40 °C	
1	0	5.23	11.2	8.5	7.5	6.5	5.3	−18.77 ± 0.34
2	[d]	5.59	15.0	11.9	9.9	8.51	7.1	−18.96 ± 1.16
3	0.06	4.85	8.45	6.3	5.6	5.0	4.0	−18.38 ± 0.41
4	−0.20	5.98	20.2	15.8	13.4	11.5	9.4	−19.32 ± 0.81
5	−0.27	6.59	31.1	23.0	20.3	17.5	14.2	−19.46 ± 0.54
6	−0.07	5.52	14.2	11.0	9.3	8.0	6.7	−19.06 ± 0.91
7	−0.17	5.94	19.6	15.2	12.9	11.3	9.1	−19.21 ± 0.57
8	0.37	2.95	1.8	1.4	1.3	1.2	0.9	−17.15 ± 1.29
9	0.32	3.13	2.2	1.7	1.5	1.3	1.1	−17.68 ± 0.43
10	−0.24	6.46	29.3	22.4	19.3	16.3	13.4	−19.66 ± 0.82

[a] Estimated error in K_{eq} is ±10%.
[b] The σ_m and σ_p parameters were used for *meta* and *para* substituents, respectively. The sum of the individual σ values is reported when two substituents are present on the pyridine ring.
[c] K_a applies to the reaction $HL^+ = H^+ + L$ in aqueous solution.
[d] Not defined.

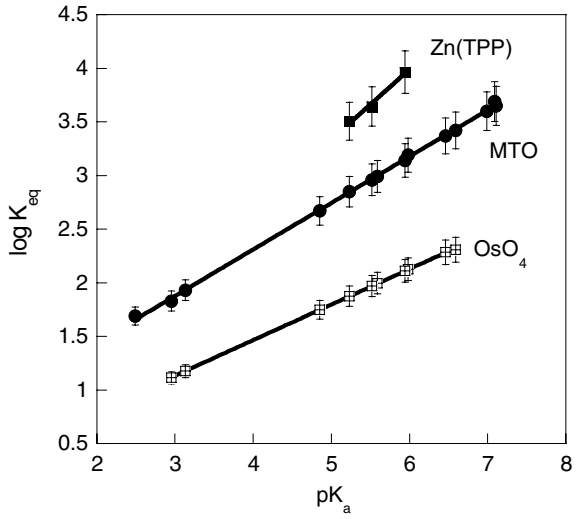


Fig. 1. Plot of $\log K_{eq}$ for the complexation of OsO_4 with N-donors as a function of the pK_a of the N-donors.

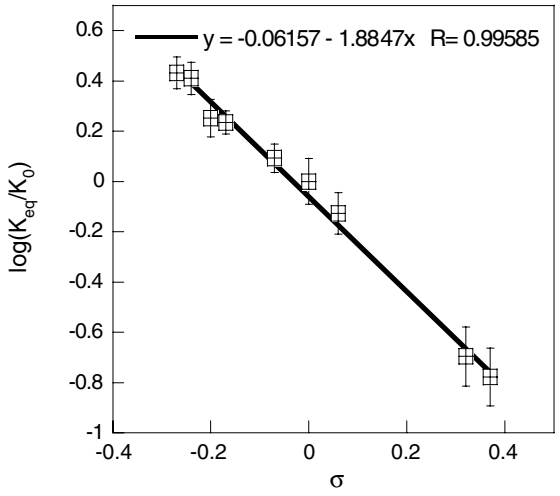


Fig. 2. Plot of $\log(K_{eq}/K_0)$ vs. the Hammett σ constants at 298 K for the complexation of OsO_4 with pyridine and its derivatives.

Table 2
Values of ρ (reaction constant) for different acids

Acids[a]	ρ	R^2 (ρ)	Solvent	Ref.
OsO_4	−1.9	0.996	CCl_4	this work
MTO	−2.5	0.996	CCl_4	[15]
OsO_4	−1.9	0.991	toluene	[11]
Phenol	−1.0	0.997	CCl_4	[16]
o-Chloranil	−3.2	0.993	CCl_4	[17]
$[Cu(PhMePh)_2]$	−1.7	0.998	$CHCl_3$	[18]
Zn(OEP)	−2.0	0.987	toluene	[19]
Zn(TPP)	−2.7	0.992	toluene	[19]
H^+	−5.6	0.996	water	[22]
C_{60}-fullerene	−2.9	0.997	CCl_4	[23]

[a] MTO = Methyltrioxorhenium, *o*-Chloranil = 3,4,5,6-tetrachloro-1,2-benzoquinone, PhMePh = 1-hydroxy-3-phenyl-4,5-dimethylpyrazole 2-oxide, OEP = octaethylporphyrin, TPP = tetraphenylporphyrin.

the Lewis acidity of the metal complexes bearing completely different ligands and having metals with different oxidation states. They have also reported that there is very little experimental quantitative information on the Lewis acidity of transition metal complexes, in the literature. In this section, we attempt to make a comparison between the ρ constants of different acids including OsO_4 (see Table 2). The data in Table 2 can be used to give an experimental answer to an important question i.e., acidity of OsO_4.

3.2.1. The sign of ρ

A negative reaction constant ($\rho < 0$) means that the reaction center is more positive and the reaction is favored by electron-donating substituents or ligand to metal σ-bonding influences, while vice versa a positive reaction constant ($\rho > 0$) indicates the development of a negative charge at reaction center. The data reported in Table 2 show that ρ is negative for the pyridine equilibria with acids and it shows that a positive charge expands on the pyridine nitrogen in the complex as compared with the free ligand. The metal center, so, acts as an electron acceptor and attracts electrons upon coordination.

3.2.2. The magnitude of ρ

The magnitude of the reaction constant (ρ) is also essentially a measure of the susceptibility of a reaction to the polar effect of substituents in the adjacent benzene ring – the larger the value of ρ, the greater the susceptibility of the reaction. The important point that is obvious from the data in Table 2, is that the values of ρ constants are greatly variable and range from −1.0 to −5.6. In general terms, the ρ values show the OsO_4 reactions to be less sensitive to substituent effects than those of MTO or Zn(TPP). The more negative ρ values of MTO and Zn(TPP) compared to OsO_4 indicates that in the complex the pyridine nitrogen on MTO (or Zn(TPP)) has a higher formal positive charge than that on the nitrogen in the OsO_4 complex. Thus a given electron-donating group on pyridine will have more effect (greater sensitivity) in stabilizing the higher positive charge on the nitrogen adjacent to MTO than in the corresponding OsO_4 species. The higher positive charge on the pyridine nitrogen in MTO results from the Re^{VII} accepting relatively more of the electron pair from nitrogen than did Os^{VIII}. In other words, the Re^{VII} is a better σ polarizer than Os^{VIII}, a conclusion reached earlier on the basis of the *m* values.

In a similar method, to compare the Lewis acidity of OsO_4, the Hammett correlation for other acids has been used and shown in Table 2. Obviously, the acid strength order on the basis of data collected in Table 2 is as follow:

$$H^+ > \text{o-Chloranil} > C_{60}\text{-fullerene} > \text{Zn(TPP)} > \text{MTO} > \text{Zn(OEP)} > OsO_4 > [Cu(PhMePh)_2] > \text{Phenol}$$

3.3. Scale 3: The ECW model

The third scale that has been used to make an acidity scale for OsO_4 is the ECW model. We have measured values of the enthalpy change from the temperature dependency of the equilibrium constant for reaction shown in

Eq. (1). The enthalpy values were evaluated from the corresponding temperature data by applying a linear $\ln K_{eq}$ least squares analysis according to van't Hoff equation [Eq. (4) and Fig. 3] and listed in Table 1.

Drago et. al. have introduced [25] an empirical four-parameter equation to describe and predict the enthalpy change accompanying the reaction of neutral acids with neutral bases in poorly solvating solvents (e.g. CCl_4) or in the gas phase. This equation takes the form

$$-\Delta H = E_A E_B + C_A C_B \quad (6)$$

where E_A and C_A are parameters for the acid (arbitrarily set as $E_A = 0.50$ and $C_A = 2.00$ for I_2) and where E_B and C_B are parameters for the base (E_B for dimethylacetamide (DMA) was set at 2.35 and C_B for $(C_2H_5)_2S$ was set at 3.92). It is felt that the $E_A E_B$ term reflects the electrostatic part of the acid-base interaction and that the $C_A C_B$ term reflects the covalent part. The beauty of the Drago equation lies in its minimum of constraints, which in turn allows the best possible fitting of the enthalpy data by an equation of its form [26].

In this section, we try to obtain the values for E_A and C_A parameters of OsO_4 and establish another scale for acidity of OsO_4. Cramer and Bopp [27] have reported a graphical representation of the E and C equation that can result for OsO_4 when the base is varied. Thus, factoring Eq. (6) and extracting $(C_B + E_B)$ gives Eq. (7).

$$\frac{-\Delta H}{C_B + E_B} = \left(\frac{C_A + E_A}{2}\right) + \left(\frac{C_A - E_A}{2}\right) R_B \quad \text{where}$$

$$R_B = \left(\frac{C_B - E_B}{C_B + E_B}\right) \quad (7)$$

Note that this is the equation for a straight line, $y = ax + b$. Using the values of $-\Delta H$ (in kcal/mol) for Lewis bases (shown in Scheme 1) from Table 1, $-\Delta H/(C_B + E_B)$ is calculated and plotted versus the value of R_B calculated for N-donor ligands from their parameters in Table 3 (see Fig. 4). Fitting of the data to Eq. (7) gives values of $E_A = 2.01$ (kcal/mol)$^{1/2}$ and $C_A = 0.25$ (kcal/mol)$^{1/2}$ for OsO_4. The results are basically important because they create an acidity scale for OsO_4. Another very important use of these parameters is the calculation of enthalpy of OsO_4 interactions for hundreds of systems which have not been examined experimentally.

To put the acidity of OsO_4 on an external scale, it is better to compare OsO_4 with other famous acids. For this comparison, I_2, H_2O, BMe_3, BF_3, C_6H_5OH, $AlMe_3$, Me_3SnCl, CoPPIXDME {cobalt^{II} protoporphyrin IX dimethyl ester}, MTO {methyltrioxorhenium}, Zn(TPP) {zinc^{II} tetraphenylporphyrin}, $Cu(HFacac)_2$ {HFacac = hexafluoroacetylacetonato}, $VO(acac)_2$ {vanadyl acetyl-

Table 3
Selected parameters of the ECW model[a]

Base	E_B	C_B	Acid	E_A	C_A
1-Methylimidazole	1.16	4.92	I_2	0.50	2.00
Pyridine	1.78	3.54	phenol	2.27	1.07
4-Benzylpyridine	1.80	3.65	$AlMe_3$	8.66	3.68
3-Phenylpyridine	1.75	3.41	BF_3	6.10	2.87
4-^{t}Butylpyridine	1.84	3.70	BMe_3	2.90	3.60
4-Methoxypyridine	1.83	3.83	Zn(TPP)[b]	2.72	1.45
3-Methylpyridine	1.81	3.67	H_2O	1.31	0.78
4-Methylpyridine	1.83	3.73	$Cu(HFacac)_2$[c]	1.82	2.86
3-Chloropyridine	1.66	3.08	$VO(acac)_2$[d]	1.60	1.96
Methylnicotinate	1.70	3.24	$Mo_2(PFB)_4$[e]	3.15	1.05
3,4-Dimethylpyridine	1.86	3.86	CoPPIXDME[f]	2.32	1.34
C_5H_5NO	2.29	2.23	Me_3SnCl	2.87	0.71
C_6H_5CN	1.65	0.75	MTO[g]	2.38	1.15

[a] Data from Ref. [25c]. Units for E_B, C_B, E_A and C_A are (kcal/mol)$^{1/2}$.
[b] Zinc(II) tetraphenylporphyrin.
[c] HFacac = hexafluoroacetylacetonato.
[d] Vanadyl acetylacetonate, data from Ref. [28].
[e] Molybdenum(II) perfluorobutyrate.
[f] Cobalt(II) protoporphyrin IX dimethyl ester.
[g] Methyltrioxorhenium, data from Ref. [15].

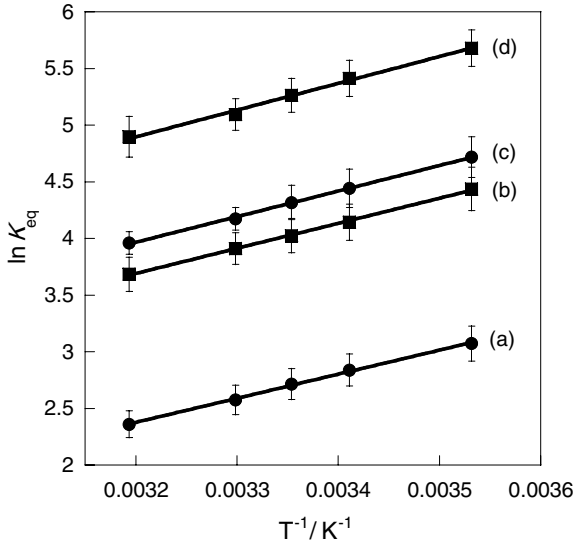


Fig. 3. van't Hoff plots for complexation of OsO_4 with (a) methylnicotinate, (b) 3-phenylpyridine, (c) pyridine and (d) 3,4-dimethylpyridine in CCl_4.

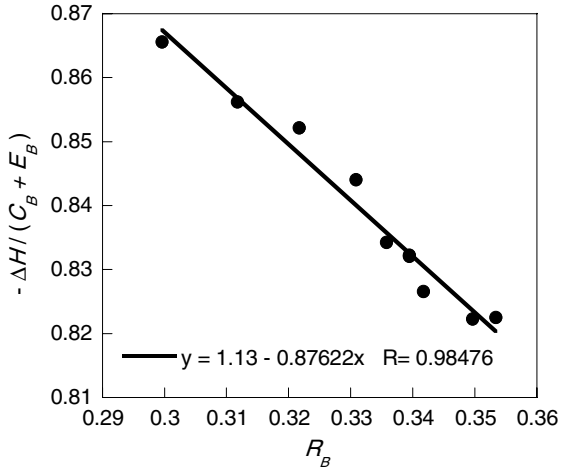


Fig. 4. A plot of Eq. (7) for pyridine derivatives reacting with OsO_4.

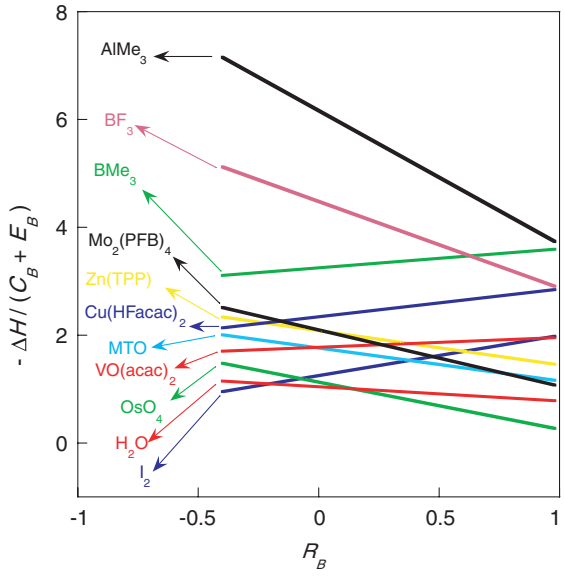


Fig. 5. The E and C plot according to Eq. (7) for a series of different acids reacting with bases. The lines for Me_3SnCl, CoPPIXDME and phenol have been omitted for more clarity.

acetonate} and $Mo_2(PFB)_4$ {molybdenium(II) perfluorobutyrate} were chosen. E_A and C_A parameters of these acids are listed in Table 3. Using parameters from Table 3 and Eq. (7), $-\Delta H$ (in kcal/mol) is calculated for a given acid, (e.g. BF_3) interacting with a base (e.g. pyridine). This value of $-\Delta H$ (in kcal/mol) divided by $(C_B + E_B)$ for pyridine {i.e. $-\Delta H/(C_B + E_B)$} is plotted versus the value of R_B calculated for pyridine from its parameters in Table 3, according to Eq. (7). Next, $-\Delta H$ is calculated for BF_3 interacting with methylnicotinate using Eq. (6). Dividing $-\Delta H$ by $(C_B + E_B)$ and calculating R_B for methylnicotinate give a second point on the BF_3 line. More points can be obtained using parameters for other bases listed in Table 3. A straight-line characteristic of the acid results by connecting the two or more plotted points. The line for BF_3 is shown in Fig. 5, along with those obtained in a similar fashion for a series of different acids (listed in Table 3) including OsO_4. Bases can range from a covalent base, ($R_B = 1.0$ for $E_B = 0$) to an electrostatic base ($R_B = -1.0$ for $C_B = 0$). The acceptor order toward any base whose E_B and C_B values are known can be determined from the corresponding plot. The value of R_B is calculated for the base, and a line parallel to the vertical axis is drawn. Listing the acceptors' intersection with this parallel line in order of decreasing $-\Delta H/(C_B + E_B)$ produces the acceptor order. For an electrostatic base with $R_B = -1.0$, $AlMe_3$ is the strongest acceptor and the acceptor order toward this electrostatic base is read off the graph in decreasing order as

$$AlMe_3 > BF_3 > Mo_2(PFB)_4 > BMe_3 > Me_3SnCl > Zn(TPP) > MTO > CoPPIXDME > C_6H_5OH > OsO_4 > Cu(HFacac)_2 > VO(acac)_2 > H_2O > I_2$$

For a covalent base with $R_B = 1.0$, the order is as follow:

$$AlMe_3 > BMe_3 > BF_3 > Cu(HFacac)_2 > I_2 > VO(acac)_2 > Zn(TPP) > CoPPIXDME > MTO > C_6H_5OH > Mo_2(PFB)_4 > H_2O > Me_3SnCl > OsO_4$$

For different amount of covalency in the base, the R_B value varies and different acceptor order results. Toward a base like pyridine ($C_B = 3.54$, $E_B = 1.78$ and $R_B = 0.33$) the acid strength order is

$$AlMe_3 > BF_3 > BMe_3 > Cu(HFacac)_2 > Zn(TPP) > VO(acac)_2 > Mo_2(PFB)_4 > CoPPIXDME > MTO > I_2 > C_6H_5OH > Me_3SnCl > H_2O > OsO_4$$

and for a base like C_5H_5NO ($C_B = 2.33$, $E_B = 2.29$ and $R_B = 0.01$) the order is

$$AlMe_3 > BF_3 > BMe_3 > Cu(HFacac)_2 > Mo_2(PFB)_4 > Zn(TPP) > CoPPIXDME > VO(acac)_2 > Me_3SnCl > MTO > C_6H_5OH > I_2 > OsO_4 > H_2O$$

and toward C_6H_5CN ($C_B = 0.75$, $E_B = 1.65$ and $R_B = -0.38$) the acceptor order is

$$AlMe_3 > BF_3 > BMe_3 > Mo_2(PFB)_4 > Zn(TPP) > Me_3SnCl > Cu(HFacac)_2 > CoPPIXDME > MTO > C_6H_5OH > VO(acac)_2 > OsO_4 > H_2O > I_2$$

When the acceptor lines for two different acids cross, the acceptor order changes towards bases on opposite sides of the intersection. If the lines do not cross over the range of R_B from -1 to $+1$ (e.g. OsO_4 and BF_3 in Fig. 5), the acceptor order for these two acids will never change for a σ-bonding interaction as the base varies (e.g. BF_3 is always a stronger σ acceptor than OsO_4). Generally, ECW model has provided an acidity scale that accommodates a multitude of acceptor orders towards different kinds of bases.

4. Conclusion

The results presented here clarify the acidity of osmium tetroxide using three simple and straightforward scales.

(i) Donor ability of N-donors: The excellent linear relationship was observed between the equilibrium constants and the pK_a values of the ligands as $\log K_{eq} = m(pK_a) + b$. The m values are related to the σ-polarizing power of metal ion and so the acidity order is $Zn(TPP) > MTO > OsO_4$.

(ii) The Hammett reaction constant: A linear correlation between the relative coordination strength and the Hammett σ constant of the substituents on the pyridine ring was also found. This allowed one to measure the Lewis acidity of OsO_4 using reaction constant, ρ. Obviously OsO_4 is a weaker acid than MTO and Zn(TPP) toward substituted pyridines.

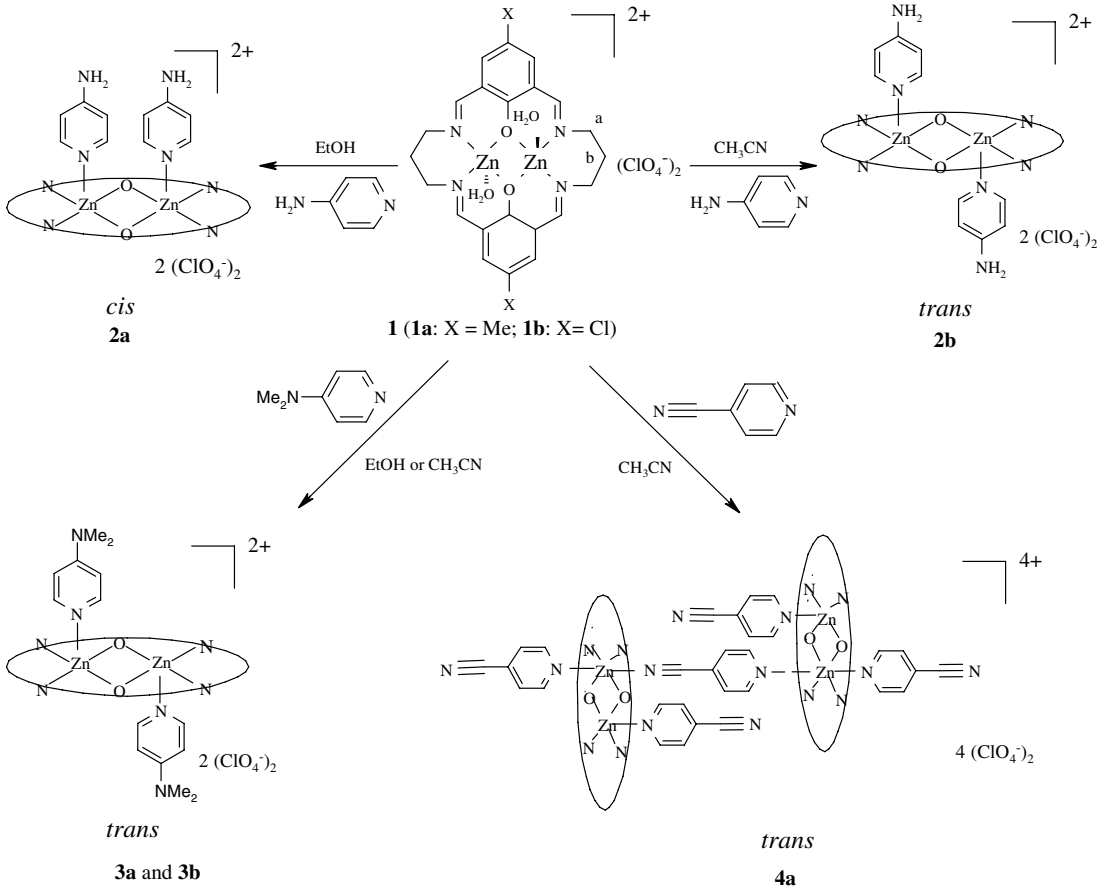
(iii) The ECW model: Comparing E_A and C_A parameters of OsO_4 with parameters for other well-known acids, the following results can be obtained: (1) Since both E_A and C_A values are greater for BMe_3, MTO, BF_3 and Zn(TPP) as compared to those for OsO_4, they are the stronger acids toward all bases. (2) In the case of OsO_4, $Cu(HFacac)_2$, $VO(acac)_2$, H_2O and I_2, the situation is ambiguous. Thus OsO_4 is more acidic than I_2 toward bases with $E_B \gg C_B$, but is a weaker acid for bases where $C_B \gg E_B$.

Acknowledgements

The authors gratefully acknowledge financial support from the Shiraz University Research Council through Grants No. 84-GR-SC-12 and No. 83-SC-172-C276. Mr. Hamidreza Samouei is gratefully acknowledged for exploring the initial interactions between N-donors and osmium tetroxide and Dr. Majid Hashemi of the Persian Gulf University for a generous gift of OsO_4.

References

[1] J.C. Riemersma, Biochim. Biophys. Acta 152 (1968) 718.
[2] A. Dehestani, W.H. Lam, D.A. Hrovat, E.R. Davidson, W.T. Borden, J.M. Mayer, J. Am. Chem. Soc. 127 (2005) 3423.
[3] B.C. Bales, P. Brown, A. Dehestani, J.M. Mayer, J. Am. Chem. Soc. 127 (2005) 2832.
[4] J.M. Schomaker, B.R. Travis, B. Borhan, Org. Lett. 5 (2003) 3089.
[5] H.K. Desai, H.P. Chokshi, S.W. Pelletier, J. Nat. Prod. 52 (1989) 1296.
[6] W. Herz, R.C. Ligon, J. Org. Chem. 37 (1972) 1400.
[7] M. Zelikoff, H.A. Taylor, J. Am. Chem. Soc. 72 (1950) 5039.
[8] A.R. Bader, J. Am. Chem. Soc. 70 (1948) 3938.
[9] (a) J. Rudolph, P.C. Sennhenn, C.P. Vlaar, K.B. Sharpless, Angew. Chem., Int. Ed. Engl. 35 (1996) 2810;
(b) P. O'Brien, Angew. Chem., Int. Ed. Engl. 38 (1999) 326;
(c) G. Li, H-T. Chang, K.B. Sharpless, Angew. Chem., Int. Ed. Engl. 35 (1996) 451;
(d) O. Reiser, Angew. Chem., Int. Ed. Engl. 35 (1996) 1308;
(e) M.A. Andersson, R. Epple, V.V. Fokin, K.B. Sharpless, Angew. Chem., Int. Ed. Engl. 41 (2002) 472;
M.A. Andersson, R. Epple, V.V. Fokin, K.B. Sharpless, Angew. Chem. 114 (2002) 490;
(f) K. Muniz, Chem. Soc. Rev. 33 (2004) 166.
[10] (a) M. Schröder, Chem. Rev. 80 (1980) 187;
(b) H.C. Kolb, M.S. VanNieuwenzhe, K.B. Sharpless, Chem. Rev. 94 (1994) 2483;
(c) A.H. Éll, S.Y. Jonsson, A. Börje, H. Adolfsson, J.-E. Bäckvall, Tetrahedron Lett. 42 (2001) 2569;
(d) S.Y. Jonsson, H. Adolfsson, J.-E. Bäckvall, Chem. Eur. J. 9 (2003) 2783;
(e) S.Y. Jonsson, K. Färnegårdh, J.-E. Bäckvall, J. Am. Chem. Soc. 123 (2001) 1365;
(f) J.L. Courtney, in: W.J. Mijs, C.R.H.I. de Jones (Eds.), Organic Syntheses by Oxidation with Metal Compounds, Plenum, New York, 1986, p. 449.
[11] D.W. Nelson, A. Gypser, P.T. Ho, H.C. Kolb, T. Kondo, H-L. Kwong, D.V. McGrath, A.E. Rubin, P. Norrby, K.P. Gable, K.B. Sharpless, J. Am. Chem. Soc. 119 (1997) 1840.
[12] R.J. Collin, J. Jones, W.P. Griffith, J. Chem. Soc., Dalton Trans. (1974) 1094.
[13] (a) A. Togni, L.M. Venanzi, Angew. Chem., Int. Ed. Engl. 33 (1994) 497;
A. Togni, L.M. Venanzi, Angew. Chem. 106 (1994) 517;
(b) F. Fache, E. Schulz, M.L. Tommasino, M. Lemaire, Chem. Rev. 100 (2000) 2159.
[14] (a) S.M. Nabavizadeh, Inorg. Chem. 42 (2003) 4204;
(b) S.M. Nabavizadeh, A. Akbari, M. Rashidi, Eur. J. Inorg. Chem. (2005) 2368;
(c) S.M. Nabavizadeh, Dalton Trans. (2005) 1644.
[15] S.M. Nabavizadeh, M. Rashidi, J. Am. Chem. Soc. 128 (2006) 351.
[16] J. Rubin, G.S. Panson, J. Phys. Chem. 69 (1965) 3089.
[17] A.K. Ray, S. Bhattacharya, M. Banerjee, A.K. Mukherjee, Spectrochim. Acta: Part A 58 (2002) 1375.
[18] F. Kai, H. Haraga, H. Kobayashi, Polyhedron 4 (1985) 947.
[19] G. Szintay, A. Horváth, Inorg. Chim. Acta 310 (2000) 175.
[20] (a) M.M. Jones, Elementary Coordination Chemistry, Prentice-Hall Inc., Englewood Cliffs, NJ, 1964, p. 340;
(b) G. Schwarzenbach, G. Anderegg, W. Schnieder, H. Senn, Helv. Chim. Acta 88 (1955) 1147;
(c) C.H. Kirksey, P. Hambright, C.B. Storm, Inorg. Chem. 8 (1969) 2141;
(d) C.H. Kirksey, P. Hambright, Inorg. Chem. 9 (1970) 958;
(d) L.E. Kapinos, B. Song, H. Sigel, Chem. Eur. J. 5 (1999) 1794.
[21] (a) J.G. Jones, J.B. Poole, J.C. Tomkinson, R.J.P. Williams, J. Chem. Soc. (1958) 2001;
(b) S. Ahrland, J. Chatt, N.R. Davies, Quart. Rev. (London) 12 (1958) 265.
[22] D.R. Lide, CRC Handbook of Chemistry and Physics, 81st ed., CRC Press, Boca Raton, FL, 2000.
[23] S. Bhattacharya, M. Banerjee, A.K. Mukherjee, Spectrochim. Acta: Part A 58 (2002) 2563.
[24] M. Gasperini, F. Ragaini, Organometallics 23 (2004) 995.
[25] (a) R.S. Drago, Struct. Bonding 15 (1973) 73;
(b) R.S. Drago, Coord. Chem. Rev. 33 (1980) 251;
(c) R.S. Drago, Applications of Electrostatic-Covalent Models in Chemistry, Surfside Scientific Publishers, Gainesville, FL, 1994.
[26] (a) The most modern inorganic textbooks have also discussed the ECW model. For a summary of the significance of this model, see for instance: G.L. Miessler, D.A. Tarr, Inorganic Chemistry, Prentice-Hall, Englewood Cliffs, NJ, 2003, p. 189;
(b) J.E. Huheey, E.A. Keiter, R.L. Keiter, Inorganic Chemistry, Principles of Structure and Reactivity, Harper-Collin, New York, 1993, p. 336;
(c) D.F. Shriver, P.W. Atkins, Inorganic Chemistry, Oxford University Press, London, 1999, p. 169;
(d) F.A. Cotton, G. Wilkinson, P.L. Gaus, Basic Inorganic Chemistry, John Wiley and Sons, New York, 1994, p. 219;
(e) B.E. Douglas, D. McDaniel, J. Alexander, Concepts and Models of Inorganic Chemistry, Wiley, New York, 1994, p. 343.
[27] R.E. Cramer, T.T. Bopp, J. Chem. Educ. 54 (1977) 612.
[28] R.S. Drago, Polyhedron 13 (1994) 2017.



Scheme 1. Schematic illustration for the preparation of the macrocyclic complexes.

For the dinuclear Zn(II) centers $[Zn_2L(H_2O)_2](ClO_4)_2$ (**1**) (Scheme 1), prepared from the [2+2] sodium template condensation of 1,3-diaminopropane and 2,6-diformyl-4-substitutedphenol, both penta-coordinate and hexa-coordinate modes are common, depending on the ligands used [5]. Weakly coordinated water molecules at each side of the macrocyclic framework [6] can be replaced by an additive ligand bearing strong coordination atoms. If small or linear ligands such as CH_3COO^- [7a] and N_3^- [7b] anions are applied to react with **1**, the *trans* positional isomers will be the dominant products in order to minimize the spatial hindrance, since the two zinc(II) ions are positioned in a distance less than 3.3 Å. Nevertheless, if ligands containing aromatic rings are involved, *cis* and *trans* conformations, with respect to the rigid macrocylic skeletons, are accessible upon interaction at the supramolecular level. Compared to conventional means, X-ray single-crystal diffraction is the most powerful tool to characterize these two possible isomers. In our previous reports, we have described two *cis* molecular ladder elements by using 4-aminopyridine and 4-pyridinecarboxylate [8] as well as two infinite coordinative bond driven 1D ladders in which macrocyclic platforms are connected by 4,4-bipyridine [9]. All of these complexes are further stabilized by complementary hydrogen binding and face-to-face π–π interactions.

Recently, there have been a few reports on 1D chains of this type of macrocycle with mono μ_2-bridging ligands, such as formate bridged dinuclear Zn(II) [10], 1,3-diaminopropane bridged dinuclear Ni(II) [11], acetylenedicarboxylate [12] and 7,7,8,8-tetracyanoquinodimethane bridged dinuclear Cu(II) complexes [13]. Moreover, several sandwich-like dimacrocyclic complexes with double μ_2-oxygen bridges like tetranuclear Zn(II) [14] and tetranuclear Fe(III) [15] complexes have also been documented. Additionally, we have reported two coordinative bond free donor-acceptor hydrogen-bond-supported layer complexes bearing 2-methylquinoline [14a] and 8-methylquinoline [16]. However, the motif of a molecular stair, where two aromatic rings adopt a *trans* conformation with respect to the macrocyclic plane, is a relatively new topology that is rarely reported to date [17]. Moreover, the study of regulating the *cis* and *trans* macrocyclic subunits has not been mentioned. In this paper, we report the self-assembly study of macrocyclic complexes having pendant 4-aminopyridine (4-ampy), 4-dimethylaminopyridine (4-dmampy) and isonicotinonitrile (4-cnpy) groups, in which these pyridine rings are *trans* relative to the rigid macrocyclic plane. Controlled synthesis of the *cis* and *trans* isomers can be achieved for the 4-ampy subunits and the experimental result is supported by DFT calculations.

2. Experimental

2.1. Materials and general methods

All solvents and chemicals were of analytical grade and were used without further purification. 4-Ampy, 4-dmampy and 4-cnpy were purchased as commercial chemicals from Aldrich. 4-Methyl-2,6-diformylphenol was prepared in high yield by an improved oxidation method using active manganese(IV) dioxide [6b]. Dinuclear macrocyclic zinc complexes **1** were synthesized via a sodium template method described previously [6a]. Elemental analyses for carbon, hydrogen and nitrogen were performed on a Perkin–Elmer 1400C analyzer. Infrared spectra (4000–400 cm^{-1} and 600–100 cm^{-1}) were recorded on a Nicolet FTIR 170X spectrophotometer at 298 K using KBr plates. UV–visible (UV–vis) spectra were recorded with a Shimadzu UV-3150 double-beam spectrophotometer using a Pyrex cell with a path length of 10 mm. ^1H NMR spectra were obtained on a Bruker 500 MHz NMR spectrometer. Electrospray ionization mass spectra (ESI-MS) were recorded on a Finnigan MAT SSQ 710 mass spectrometer in the scan range of 100–1200 amu.

All the Density Function Theory computations were carried out with the Gaussian 03, Revision C.02 programs [18]. The fixed atom coordinates given by their CIFs were used in these cases where the number, type of atoms and the charge of molecules were kept the same. The B3LYP method and the LanL2DZ basis set were used for the zinc(II) macrocyclic *cis* and *trans* isomers, i.e. two monocations ([**2a**-ClO_4]$^+$ and [**2b**-ClO_4]$^+$) as well as two dications ([**2a**-2ClO_4]$^{2+}$ and [**2b**-2ClO_4]$^{2+}$), in order to compare the total energy differences of these isomers.

Caution: Although no problem was encountered in all our experiments, transition metal perchlorates are potentially explosive and should be handled in small quantities.

2.2. Synthesis of complex *2b*

An acetonitrile solution (10 cm^3) of 4-ampy (0.094 g, 1 mmol) was added to a stirred solution of polycrystalline **1b** [$Zn_2L_b(H_2O)_2$](ClO_4)$_2$ (0.405 g, 0.5 mmol) in hot acetonitrile (40 cm^3, 50 °C). The mixture was heated under reflux for 1 h, after which it was cooled to room temperature and filtered. The filtrate was slowly evaporated in air to near 5 cm^3, and then yellow single crystals, suitable for X-ray diffraction measurements, were collected in a yield of 87% (0.418 g). *Anal.* Calc. for [($Zn_2C_{22}H_{20}N_4O_2Cl_2$)-($C_5H_6N_2$)$_2$] · ($ClO_4$)$_2$: C, 39.98; H, 3.36; N, 11.66. Found: C, 40.02; H, 3.32; N, 11.57%. Main FT-IR (KBr disk, cm^{-1}): 3458 and 3365 (NH_2), 1641 (C=N), 1095, 1081 and 625 cm^{-1} (ClO_4^-), 408 and 242 cm^{-1} (Zn-py). ^1H NMR (500 MHz, DMSO-d^6, 298 K, TMS): $\delta = 8.52$ (s, 4H, HC=N), 7.82 (d, 8H, py-H), 7.79 (s, 4H, phenyl), 6.48 (s, 4H, NH_2), 3.86 (t, 8H, $^aCH_2$), 1.98 (m, 4H, $^bCH_2$). UV–vis: (λ_{max} in MeOH), 371, 246, 212 nm (**1b**: 365, 245, 216 nm). ESI-MS: *m*/*z* 671 [$Zn_2L_bClO_4$]$^+$, 286 [Zn_2L_b]$^{2+}$/2.

2.3. Synthesis of complex *3a*

A 10 cm^3 methanol solution of 4-dmampy (0.122 g, 1.0 mmol) was added to a stirred solution of **1a** [Zn_2L_a(H_2O)$_2$](ClO_4)$_2$ (0.384 g, 0.5 mmol) dissolved in 40 cm^3 methanol. The mixture was heated under reflux for 2 h, after which it was cooled to room temperature and filtered. The filtrate was slowly evaporated in air to near 10 cm^3, and yellow crystalline solids, suitable for X-ray diffraction measurements, were obtained in a yield of 86% (0.420 g). *Anal.* Calc. for [($Zn_2C_{24}H_{26}N_4O_2$)($C_7H_{10}N_2$)$_2$] · (ClO_4)$_2$: C, 46.74; H, 4.75; N, 11.47. Found: C, 46.71; H, 4.91; N, 11.39%. Main FT-IR (KBr disk, cm^{-1}): 3011 (C–H), 2925 and 2859 (alkyl), 1639 (C=N), 1561 and 1541 (C=C), 1415 (alkyl), 1093, 1084 and 623 cm^{-1} (ClO_4^-), 408 and 243 cm^{-1} (Zn-py). ^1H NMR (500 MHz, CD_3OD, 298 K, TMS): $\delta = 8.44$ (s, 4H, HC=N), 8.02 (d, 4H, py-H), 7.46 (s, 4H, phenyl), 6.71 (d, 4H, py-H), 4.02 (t, 8H, $^aCH_2$), 3.07 (s, 12H, py-NMe_2), 2.32 (m, 6H, PhMe), 2.07 (m, 4H, $^bCH_2$). UV–vis: (λ_{max} in MeOH), 366, 252, 203 nm (**1a**: 362, 251, 208 nm). ESI-MS: *m*/*z* 633 [Zn_2L_a-ClO_4]$^+$, 266 [Zn_2L_a]$^{2+}$/2.

2.4. Synthesis of complex *3b*

The procedure is similar to **3a** except that **1b** [$Zn_2L_b(H_2O)_2$](ClO_4)$_2$ (0.405 g, 0.5 mmol) was used and the yield is 88% (0.450 g). In our reference experiments, single crystals having the same structures as **3a** and **3b** can also be obtained from their acetonitrile solutions. *Anal.* Calc. for [($Zn_2C_{22}H_{20}N_4O_2Cl_2$)($C_7H_{10}N_2$)$_2$] · ($ClO_4$)$_2$: C, 42.50; H, 3.96; N, 11.01. Found: C, 42.51; H, 3.99; N, 11.08%. Main FT-IR (KBr disk, cm^{-1}): 2929 (alkyl), 1641 (C=N), 1625, 1583, 1559 and 1542 (C=C), 1442 and 1412 (alkyl), 1094, 1079 and 623 cm^{-1} (ClO_4^-), 407 and 242 cm^{-1} (Zn-py).^1H NMR (500 MHz, CD_3OD, 298 K, TMS): $\delta = 8.43$ (s, 4H, HC=N), 8.02 (d, 4H, py-H), 7.66 (s, 4H, phenyl), 7.00 (d, 4H, py-H), 4.03 (t, 8H, $^aCH_2$), 3.07 (s, 12H, py-NMe_2), 2.15 (m, 4H, $^bCH_2$). UV–vis: (λ_{max} in MeOH), 370, 245, 213 nm. ESI-MS: *m*/*z* 671 [$Zn_2L_bClO_4$]$^+$, 286 [Zn_2L_b]$^{2+}$/2.

2.5. Synthesis of complex *4a*

The procedure is similar to **2b**. A 10 cm^3 methanol solution of 4-cnpy (0.104 g, 1.0 mmol) was added to a stirred solution of **1a** [$Zn_2L_a(H_2O)_2$](ClO_4)$_2$ (0.384 g, 0.5 mmol) in 40 cm^3 methanol, and finally yellow crystalline solids, suitable for X-ray diffraction measurements, were obtained in a yield of 84% (0.473 g). *Anal.* Calc. for [($Zn_2C_{24}H_{26}$-N_4O_2)($C_6H_4N_2$)$_3$] · (ClO_4)$_2$ · (CH_3CN)$_2$: C, 49.04; H, 3.94; N, 14.92. Found: C, 49.01; H, 3.99; N, 14.78%. Main FT-IR (KBr disk, cm^{-1}): 3029 (C–H), 2914 and 2853 (alkyl), 2131 (C≡N), 1642 (C=N), 1593 and 1559

(C=C), 1412 (alkyl), 1097, 1085 and 627 cm^{-1} (ClO_4^-), 409 and 244 cm^{-1} (Zn-py). ^1H NMR (500 MHz, CD_3OD, 298 K, TMS): $\delta = 8.79$ (d, 6H, py-H), 8.47 (s, 4H, HC=N), 7.75 (d, 6H, py-H), 7.49 (d, 4H, phenyl), 4.05 (t, 8H, $^aCH_2$), 2.33 (s, 6H, PhMe), 2.19 (s, 6H, CH_3CN), 2.03 (m, 4H, $^bCH_2$). UV–vis: (λ_{max} in MeOH), 365, 252, 202 nm. ESI-MS: m/z 633 $[Zn_2L_aClO_4]^+$, 266 $[Zn_2L_a]^{2+}/2$.

2.6. X-ray data collection and solution

Single-crystal samples of **2b**, **3a**, **3b** and **4a** were glue-covered and mounted on glass fibers and then used for data collection. Crystallographic data of **2b** were collected at 291(2) K on a Bruker SMART 1 K CCD diffractometer, while those of **3a**, **3b** and **4a** were collected at 120(2) K on a Rigaku Mercury CCD area-detector, using graphite monochromated Mo Kα radiation ($\lambda = 0.71073$ Å). In the case of the Rigaku system, the original data files generated by Crystalclear were transformed to SHELXTL97 format by the TEXSAN program [19]. The crystal systems were determined by laue symmetry and the space groups were assigned on the basis of systematic absences using XPREP. Absorption corrections were performed to all data and the structures were solved by direct methods and refined by full-matrix least-squares method on F^2_{obs} by using the SHELXTL-PC software package [20]. All non-H atoms were anisotropically refined and all hydrogen atoms were inserted in calculated positions, assigned fixed isotropic thermal parameters and allowed to ride on their respective parent atoms. The middle carbon atom of the 1,3-diaminopropane unit (C9) in **3a** and atoms O3 and O4 of the perchlorate anions in **4a** are found to be disordered over two positions with different site occupancy factors. A summary of crystal data, experimental details and refinement results for macrocyclic complexes **2b**, **3a**, **3b** and **4a** is listed in Table 1, while selected bond distances and bond angles around every zinc(II) center are given in Table 2.

3. Results and discussion

3.1. Synthesis and general characterization

All the macrocyclic complexes described herein are facilely synthesized in high yields under mild conditions (Scheme 1) and are fully characterized. In comparison with the starting materials, several nanometer red shifts are

Table 1
Crystal and refinement data for macrocyclic complexes **2b**, **3a**, **3b** and **4a**

Compound	**2b**	**3a**	**3b**	**4a**
Empirical formula	$Zn_2C_{32}H_{32}N_8O_{10}Cl_4$	$Zn_2C_{38}H_{46}N_8O_{10}Cl_2$	$Zn_2C_{36}H_{40}N_8O_{10}Cl_4$	$Zn_2C_{46}H_{44}N_{12}O_{10}Cl_2$
Formula weight	961.20	976.47	1017.30	1126.57
T (K)	291(2)	120(2)	120(2)	120(2)
Wavelength (Å)	0.71073	0.71073	0.71073	0.71073
Crystal size (mm)	$0.40 \times 0.40 \times 0.30$	$0.20 \times 0.10 \times 0.10$	$0.20 \times 0.10 \times 0.10$	$0.20 \times 0.10 \times 0.10$
Crystal system	monoclinic	monoclinic	monoclinic	triclinic
Space group	$P2_1/c$ (no. 14)	$P2_1/n$ (no. 14)	$P2_1/n$ (no. 14)	$P\bar{1}$ (no. 2)
a (Å)	10.770(1)	9.984(2)	10.056(2)	10.359(2)
b (Å)	18.212(2)	12.139(2)	12.162(2)	11.288(2)
c (Å)	19.920(1)	16.934(3)	16.643(3)	12.067(2)
α (°)	90.00	90	90.00	109.47(3)
β (°)	93.72(1)	94.65(3)	92.97(3)	113.02(3)
γ (°)	90.00	90	90.00	90.44(3)
V (Å^3)	1941.7(4)	2045.8(7)	2032.7(6)	1208.9(4)
Z/D_{calc} (g/cm^3)	2/1.644	2/1.585	2/1.662	1/1.547
F (000)	976	1008	1040	578
μ (mm^{-1})	1.576	1.371	1.511	1.174
Absorption corrections	multi-scan	multi-scan	multi-scan	multi-scan
Maximum/minimum transmissions	0.621/0.475	0.875/0.771	0.864/0.752	0.892/0.799
Refinement method	full-matrix least-squares on F^2	full-matrix least-squares on F^2	full-matrix least-squares on F^2	full-matrix least-squares on F^2
h_{min}/h_{max}	−13/13	−11/11	−11/11	−11/12
k_{min}/k_{max}	−20/23	−14/14	−14/14	−13/13
l_{min}/l_{max}	−12/12	−18/20	−19/17	−12/14
Parameters/restraints	253/0	284/0	274/0	371/0
$R_{int}/R(\sigma(I)/(I))$	0.0534/0.0823	0.0616/0.0334	0.0502/0.0357	0.0951/0.0707
Total/Unique data	11 551/4520	16 742/3542	16 916/3543	10 067/4124
Final R indices [$I > 2\sigma(I)$]	$R_1 = 0.0536$, $wR_2 = 0.1125$	$R_1 = 0.0422$, $wR_2 = 0.0881$	$R_1 = 0.0561$, $wR_2 = 0.1091$	$R_1 = 0.0565$, $wR_2 = 0.1471$
R indices (all data)	$R_1 = 0.0974$, $wR_2 = 0.1224$	$R_1 = 0.0472$, $wR_2 = 0.0901$	$R_1 = 0.0678$, $wR_2 = 0.1134$	$R_1 = 0.0581$, $wR_2 = 0.1486$
Goodness-of-fit on F^2	0.930	1.201	1.107	1.036
Maximum/minimum, $\Delta\rho$ (e Å^{-3})	0.570/−0.313	0.427/−0.531	1.369/−0.416	1.340/−0.770

$R_1 = \sum||F_o| - |F_c||/\sum|F_o|$, $wR_2 = [\sum[w(F_o^2 - F_c^2)^2]/\sum w(F_o^2)^2]^{1/2}$.

Table 2
Selected bond distances (Å) and angles (°) for complexes **2b**, **3a**, **3b** and **4a**

Bond distances		Bond angles	
2b			
Zn1–O1	2.090(2)	N3–Zn1–O1	98.89(12)
Zn1–O1A$^{\#1}$	2.068(2)	N3–Zn1–O1A$^{\#1}$	101.10(12)
Zn1–N1	2.080(3)	N3–Zn1–N1	104.35(14)
Zn1–N2	2.050(3)	N3–Zn1–N2	110.74(14)
Zn1–N3	2.022(3)		
Zn1–Zn1A$^{\#1}$	3.285		
3a			
Zn1–O1	2.049(2)	N3–Zn1–O1	103.17(9)
Zn1–O1A$^{\#2}$	2.092(2)	N3–Zn1–O1A$^{\#2}$	76.07(8)
Zn1–N1	2.071(2)	N3–Zn1–N1	103.43(9)
Zn1–N2	2.056(3)	N3–Zn1–N2	106.64(10)
Zn1–N3	2.046(2)		
Zn1–Zn1A$^{\#2}$	3.261		
3b			
Zn1–O1	2.098(3)	N3–Zn1–O1	100.99(14)
Zn1–O1A$^{\#3}$	2.059(3)	N3–Zn1–O1A$^{\#3}$	103.64(14)
Zn1–N1	2.066(4)	N3–Zn1–N1	104.63(14)
Zn1–N2	2.077(3)	N3–Zn1–N2	103.24(14)
Zn1–N3	2.030(5)		
Zn1–Zn1A$^{\#3}$	3.275		
4a			
Zn1–O1	2.045(2)	N3–Zn1–O1	92.77(11)
Zn1–O1A$^{\#1}$	2.069(2)	N3–Zn1–O1A$^{\#1}$	92.68(10)
Zn1–N1	2.032(2)	N3–Zn1–N1	93.81(10)
Zn1–N2	2.042(3)	N3–Zn1–N2	96.42(11)
Zn1–N3	2.248(3)		
Zn1–N5B$^{\#4}$	2.644(4)		
Zn1–Zn1A$^{\#1}$	3.174		

Symmetry transformations used to generate equivalent atoms: $^{\#1}[1-x, -y, 1-z]$, $^{\#2}[-x, 2-y, -z]$, $^{\#3}[1-x, 1-y, 1-z]$, $^{\#4}[x, -1+y, z]$.

observed for all the complexes in their electronic spectra, indicative of axial complexation with pyridine-based ligands. ^{1}H NMR, IR spectra and C H N elemental analyses are consistent with their structures. ESI-MS spectral studies of **2b**, **3a**, **3b** and **4a** in methanol show that only mono and doubly charged peaks corresponding to the production of macrocyclic units of **1a** and **1b** are found. In addition, the ESI-MS peaks have been calculated and verified by using the numbers and natural isotopic abundance of the atoms [21].

The syntheses of **2a** and **2b** are reproducible in our experiments. In view of the difficulties of distinguishing the *cis* and *trans* isomers by IR, EA and UV–vis methods, X-ray single-crystal diffraction was used as the main approach to check the stereo configurations. We found that controlled synthesis of the *cis* or *trans* isomers **2a** or **2b**, where the same rigid macrocyclic platform and counterion are used, can be achieved merely by the substitution of a protonic solvent (ethanol) for a non-protonic solvent (acetonitrile). When the hydrogen atoms of the amino group are substituted by methyl groups, i.e. in the case of 4-dmampy, only the *trans* isomers (**3a** and **3b**) can be isolated no matter what solvent is used (protonic or non-protonic) because there is no strong H-bond donor present in the 4-dmampy molecule. In other words, this reference experiment demonstrates the importance of the participancy of the H-bond in our case. Furthermore, when a 4-cnpy molecule, which has a stronger coordination ability and may act as a bidentate bridging ligand, is used, an infinite 1D macrocycle-based stair **4b** is generated via compensatory coordinative bonds as well as hydrogen bonding and face-to-face π–π stacking interactions. One can see that subtle change of the 4-substitution group of pyridine-based ligands yields different molecular arrays and packing fashions.

3.2. Single-crystal structures of *2b*, *3a*, *3b* and *4a*

The X-ray determination results of **2b** reveal that each asymmetric unit contains half of the molecule and each zinc(II) center displays a five-coordinate pyramidal configuration consisting of four macrocyclic donors and an apical nitrogen atom from 4-ampy. As illustrated in Fig. 1a, two 4-ampy molecules in a *trans* mode are perpendicular to the macrocyclic platform. The bond lengths and bond angles of **2b** are analogous to those of **2a**. It is of much interest to note that the amino group of 4-ampy is uncoordinatedly naked, which makes the compound look like a molecular stair element. Effective N–H...O hydrogen contacts (Fig. 2) are found between the oxygen atoms of one perchlorate anion and two adjacent 4-ampy molecules (Table 3), which are obviously different from those in the *cis* isomer where a 12-membered N–H...O hydrogen-bonded ring stands on the top of macrocyclic plane [9]. Moreover, weak C–H...O type H-bonds are observed in **2b** between the imino H atom of the macrocyclic unit and one perchlorate oxygen atom. In addition, weak offset π–π stacking interactions are present between the vicinal phenyl rings of the macrocycles in a head-to-tail fashion. The shortest intermolecular contact distance between them is 3.851 Å.

X-ray diffraction analyses for **3a** and **3b** reveals that they have the same molecular symmetry as **2b**, as can be seen in Fig. 1b and Fig. 1c. They are isomorphous structures although **3a** and **3b** have different substituted groups (Me or Cl) in their macrocyclic backbones. Both central zinc(II) ions display five-coordinate pyramidal configurations consisting of four macrocyclic donors and an axial nitrogen atom of 4-dmampy. The macrocyclic dications are countered by two perchlorate ions and no solvent molecule is present in their crystal structures. The bond lengths and bond angles related to one central zinc(II) ion in **3a** are as follows: Zn1–O1, 2.049(2), Zn1–O1A $[-x, 2-y, -z]$, 2.092(2), Zn1–N1, 2.071(2), Zn1–N2, 2.056(3), Zn1–N3, 2.046(2) Å; N3–Zn1–O1, 103.17(9), N3–Zn1–O1A, 76.07(8), N3–Zn1–N1, 103.43(9), N3–Zn1–N2, 106.64(10)°. In contrast, those in **3b** are listed as follows: Zn1–O1, 2.098(3), Zn1–O1A $[1-x, 1-y, 1-z]$, 2.059(3), Zn1–N1, 2.066(4), Zn1–N2, 2.077(3), Zn1–N3, 2.030(5) Å; N3–Zn1–O1, 100.99(14), N3–Zn1–O1A, 103.64(14), N3–Zn1–N1, 104.63(14), N3–Zn1–N2, 103.24(14)°. 4-Dmampy

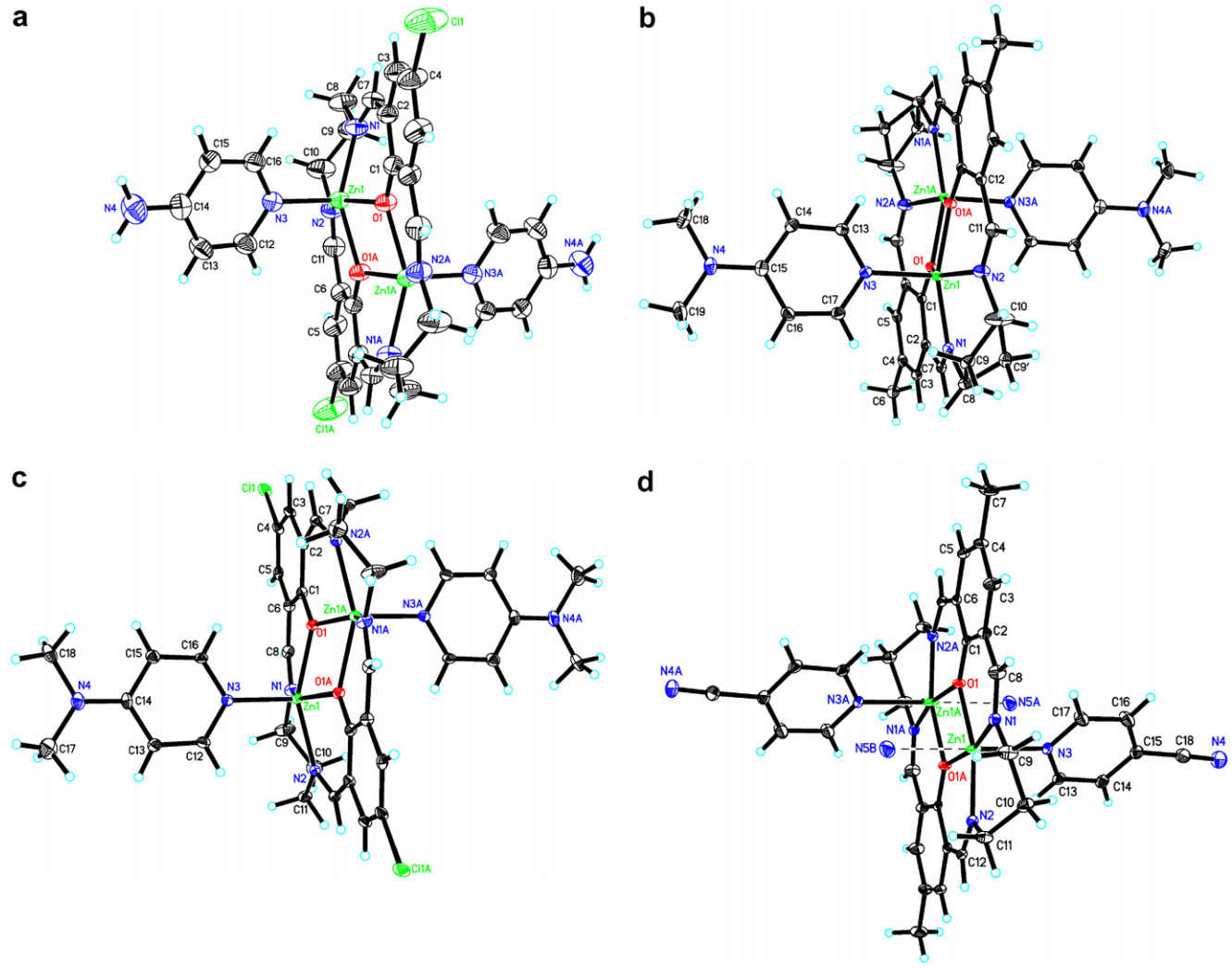


Fig. 1. ORTEP diagrams (30% thermal probability level) of the molecular structures of **2b** (a), **3a** (b), **3b** (c) cations and the polymeric unit of **4a** (d) cation with a partial atom-numbering scheme. The perchlorate anions and solvent molecules are omitted for simplicity.

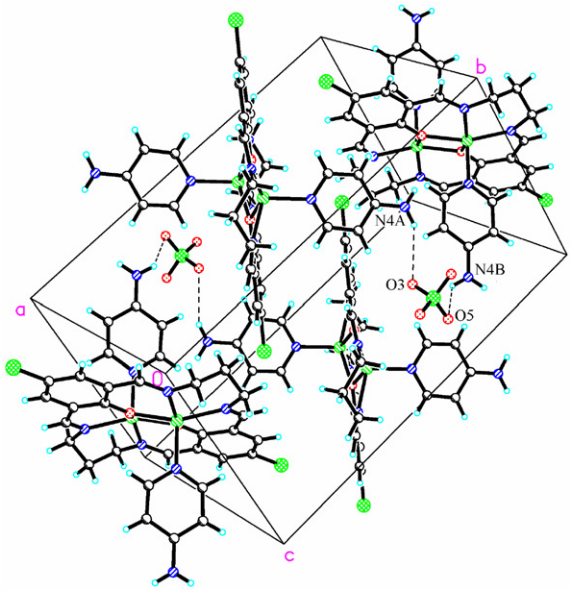


Fig. 2. A perspective view of the π–π stacking and hydrogen bonding interactions in **2b** with the unit cell.

molecules in **3a** and **3b** serve as monodentate ligands at each side of the macrocyclic plane and similar macrocycle-based molecular stair elements are formed.

The crystal packing structures of **3a** and **3b** are also very similar. Nevertheless, different from **2a** and **2b**, only weak C–H...O hydrogen bonds are found between the neighboring molecules in **3a** and **3b** after the H atoms of amino group are substituted by two methyl groups (Table 3). The lack of strong hydrogen bonds present in **2b** that fix the contiguous 4-ampy molecules to a certain degree makes the axial Zn–N σ-bond rotate to a parallel mode so as to minimize the spatial repulsion between the neighboring macrocyclic units. Accordingly, adjacent pyridine rings are parallel via the offset π–π stacking interactions with intermolecular separations of 3.652 Å in **3a** and 3.714 Å in **3b**. Thus similar quasi 1D molecular stairs based mainly on π–π stacking interactions are formed, as can be seen in Fig. 3.

From the outcome of the X-ray single-crystal diffraction study, complex **4a** crystallizes in the triclinic space group $P\bar{1}$. Like **2b**, **3a** and **3b**, each asymmetric unit of **4a** contains half

Table 3
Hydrogen bonding interactions (Å, °) in macrocyclic complexes **2b**, **3a**, **3b** and **4a**

D–H...A	H...A	D...A	∠DHA	Symmetry *trans*
2b				
N4A–H4AA...O5	2.57	3.172(9)	128.0	$-x, -1/2+y, 3/2-z$
N4B–H4BB...O3	2.57	3.339(8)	149.0	$-x, -y, 2-z$
C8–H8B...O4	2.46	3.311(8)	146.0	$x, 1/2-y, -1/2+z$
3a				
C6–H6A...O4	2.58	3.181(4)	120.0	$2-x, 2-y, 1-z$
C8–H8A...O3	2.55	3.361(4)	143.0	$-1/2+x, 3/2-y, -1/2+z$
C11–H11...O2	2.44	3.366(4)	166.0	$-3/2+x, 3/2-y, -1/2+z$
C17–H17...O3	2.52	3.371(4)	149.0	$-1/2+x, 3/2-y, -1/2+z$
3b				
C8–H8...O2	2.42	3.340(6)	163.0	$1/2+x, 3/2-y, -1/2+z$
C10–H10A...O5	2.54	3.455(7)	153.0	$1-x, 1-y, 1-z$
C11–H11A...O4	2.59	3.351(6)	134.0	$-1/2+x, 3/2-y, -1/2+z$
C15–H15...O2	2.58	3.363(6)	140.0	$x, y, 1+z$
4a				
C9–H9A...N4	2.58	3.401(6)	140.0	$x, -1+y, z$
C23–H23A...N1	2.62	3.158(9)	117.0	$x, 1+y, z$
C9–H9A...N4	2.58	3.401(6)	140.0	$x, -1+y, z$
C23–H23A...N1	2.62	3.158(9)	117.0	$x, 1+y, z$
C5–H5...O2	2.51	3.407(6)	159.0	$x, y, 1+z$
C8–H8...O4	2.30	2.897(10)	120.0	$1-x, -y, 1-z$
C17–H17...O3	2.56	3.308(9)	135.0	$1+x, y, 1+z$
C20–H20A...O5	2.24	3.119(11)	154.0	
C22–H22A...O5	2.31	3.004(11)	129.0	$1-x, 1-y, 1-z$
C26–H26B...O3	2.48	3.160(2)	127.0	$-x, 1-y, 1-z$

of the macrocyclic platform and two 4-cnpy molecules are situated at each side of the macrocyclic plane. There is another 4-cnpy molecule that lies across a crystallographic inversion center positioned at the phenyl carbon atom bonded to the cyano group, which results in the same separation with two contiguous macrocycles. Two six-coordinate zinc(II) ions are located essentially on the coordination plane (mean deviation from the basal plane is 0.126 Å), which is different from those pyramids in **1a**, **1b**, **2b**, **3a** and **3b** but analogous to the macrocyclic ladders [6]. The change of the coordination geometry makes the separation between the two metal centers shorter (3.174 Å) than those in **2b** (3.285 Å), **3a** (3.261 Å) and **3b** (3.275 Å). Each 4-cnpy plane is perpendicular to the macrocyclic plane to minimize steric crowding (Fig. 1d). It should be mentioned that two apical coordinative bonds connecting zinc(II) ions are obviously different, generating asymmetric and elongated octahedron configurations. However, both of the axial Zn–N bonds are longer than those in the three above-mentioned structures (2.022–2.046 Å).

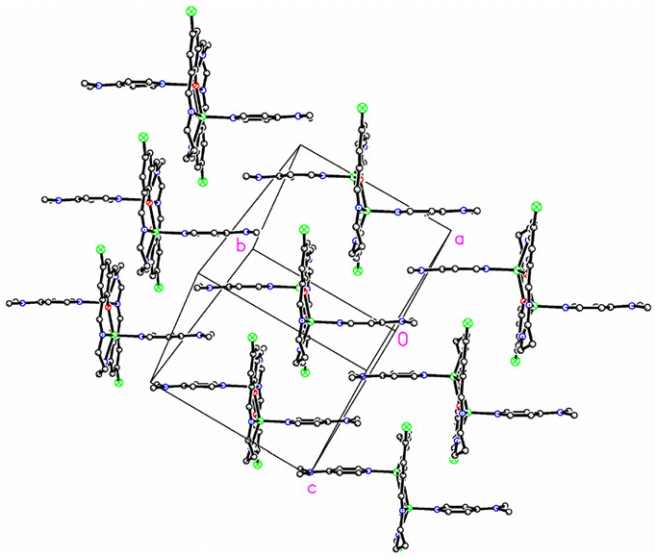


Fig. 3. A perspective view of the π–π packing structure in **3b** with the unit cell. The perchlorate anions and the hydrogen atoms are omitted for clarity.

It is noteworthy that two 4-cnpy moieties on one side of a macrocycle have different coordination modes, one serves as a bridge to connect two neighboring macrocyclic metal centers by using its head and tail nitrogen atoms, while the other is only mono-coordinated to a metal ion via its pyridyl nitrogen atom, leaving the cyanic group uncoordinated. As a significant result, an infinite 1D polymeric stair is constituted (Fig. 4), where all 4-cnpy planes are nearly parallel one another. 4-Cnpy molecules bend a little bit to the opposite side with a dihedral angle of 9.4° between two pyridine rings, and their centroid–centroid separation is 3.555 Å, exhibiting typical π–π stacking interactions. As shown in Fig. 5, the molecular stairs are further stabilized by intermolecular C–H...O and C–H...N hydrogen bonds, where oxygen atoms of perchlorate anions, macrocyclic nitrogen atoms and cyanic groups of 4-cnpy serve as acceptors while hydrogen atoms of 1,3-diaminopropane units and 4-cnpy act as donors (see also Table 3).

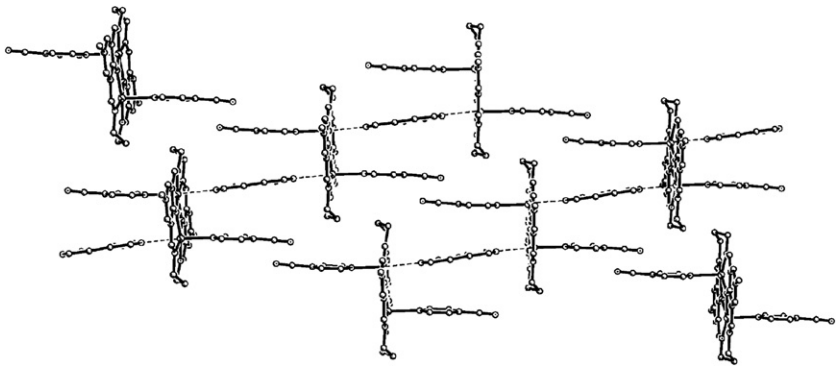


Fig. 4. A perspective view of the 1D molecular stairs in **4a** where the perchlorate anions and the solvent acetonitrile molecules are left out for simplicity.

3.3. Density function theory (DFT) calculations

Now that our experiments hint that it is possible to regulate the orientation (*cis* or *trans*) of the organic subunits by controlling the reaction conditions, namely the alteration of the solvent used can lead to the different topologies of **2a** and **2b**, we have tried to seek some other support by performing theoretical computations. Firstly, DFT calculations were carried out to get the total "Energy" of the isolated *cis* and *trans* isomers with fixed atom coordinates given by their CIFs, where substituted groups of the phenyl rings were replaced by hydrogen atoms to keep the same amount of atoms, and only the dications were retained. When the B3LYP method and the LanL2DZ basis set were used, the program gave the close total energies of −1228940.68 and −1228903.03 Kcal/mol for $[\mathbf{2a}\text{-}2ClO_4]^{2+}$ and $[\mathbf{2b}\text{-}2ClO_4]^{2+}$, respectively, which indicated that the *cis* dicationic species is somewhat more thermally stable than the *trans* one. However, the energy difference (37.65 Kcal/mol) is not so large, which means that both of them are accessible isomers. Furthermore, when the perchlorate anion was introduced for the same calculation in order to investigate the contribution of hydrogen bonding and face-to-face π–π stacking interactions, the resulting total energy gap (219.63 Kcal/mol) became larger, also in favor of the *cis* isomer, (−1426756.94 Kcal/mol for $[\mathbf{2a}\text{-}ClO_4]^{+}$ and −1426537.31 Kcal/mol for $[\mathbf{2b}\text{-}ClO_4]^{+}$). Thus it can be concluded that the presence of the 12-membered N–H...O hydrogen-bonded ring between the perchlorate anions and 4-ampy as well as the face-to-face π–π stacking interactions in **2a**, probably induced by the protonic ethanol molecules encapsulated in the crystal and causing such a big energy difference, have contributed significantly to the formation of the *cis* isomer in the solid state.

Secondly, in order to compare the differences between the energy-minimized and crystal structures, optimized structures for the above-mentioned dications and monocations were carried out. The energy-minimized structures show a very small energy difference of 1.13 Kcal/mol for dications $[\mathbf{2a}\text{-}2ClO_4]^{2+}$ (−1229347.10 Kcal/mol) and $[\mathbf{2b}\text{-}2ClO_4]^{2+}$ (−1229345.97 Kcal/mol), and 7.77 Kcal/mol for monocations $[\mathbf{2a}\text{-}ClO_4]^{+}$ (−1427359.08 Kcal/mol) and (−1427351.31 Kcal/mol) $[\mathbf{2b}\text{-}ClO_4]^{+}$, also favoring the formation of the *cis* isomer. However, compared with the energy generated from the structural parameters determined by the X-ray diffraction method, the larger ΔE values from the dications (405.29 and 444.07 Kcal/mol) to the monocations (602.14 and 814.00 Kcal/mol) also show clearly the contribution of hydrogen bonding and π–π stacking interactions in **2a** and **2b**.

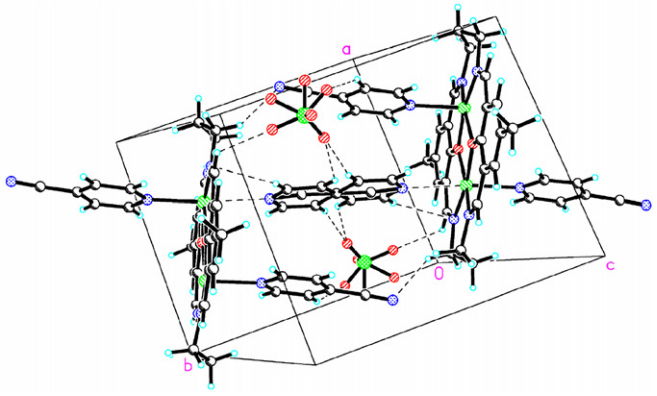


Fig. 5. A perspective view of the self-complementary π–π stacking and hydrogen bonding interactions in **4a**.

4. Conclusions

In summary, self-assembly of dinuclear zinc(II) macrocyclic species with three different linear 4-substituted pyridyl ligands (4-ampy, 4-dmampy and 4-cnpy) results in three *trans* molecular stair elements and one 1D molecular stair. The self-assembly study of these *trans* macrocyclic staircases is novel, and the driving forces in the formation of these molecular aggregations are synergistic interactions of metal–ligand bonding, hydrogen bonding and π–π stacking interactions in the solid state. Controlled synthesis of the *cis* or *trans* isomers (**2a** or **2b**), where the same rigid macrocyclic platform and counterion are used, can be achieved merely by the substitution of a protonic solvent for a non-protonic solvent since hydrogen bonding and π–π stacking interactions play a significant role here. This

is further verified by theoretical calculations and subsequent comparison between the energy-minimized and crystal structures for different monocations or dications.

Furthermore, when the two hydrogen atoms of the amino group are replaced by methyl groups in order to block the formation of effective hydrogen bonds, only the *trans* isomer can be obtained either in protonic or non-protonic solvents. Additionally, weak offset π–π stacking interactions are observed in the packing structures of **2b**, **3a** and **3b**. In contrast, strong face-to-face π–π stacking interactions are found in the packing structure of 1D stair **4a** because of the confinement of coordinative bonds to a small separation (<3.3 Å) between two zinc(II) centers. Compared with the starting materials, complexes **2b**, **3a** and **3b** retain the five-coordinate pyramidal configurations, while **4a** undergoes a configuration transformation to a six-coordinate elongated octahedron. The outcome demonstrates that the subtle change of the 4-substitution group of the pyridine-based ligand yields different molecular arrays and packing fashions, and that hydrogen bonding and π–π stacking interactions play an important role in the formation of the resultant complexes. Further studies are in progress for the preparation and the physical properties of Schiff-base macrocyclic complexes having different backbones, sizes and nuclearities.

Acknowledgements

W.H. would like to acknowledge the Major State Basic Research Development Program (No. 2006CB806104) and the National Natural Science Foundation of China (No. 20301009) for financial aid. Special thanks go to Dr. Hirokazu Sato of Ebara Research Co. Ltd., for his kind help in GAUSSIAN 03 calculations.

Appendix A. Supplementary material

CCDC 276339, 295420, 295421, and 276340 contain the supplementary crystallographic data for **2b**, **3a**, **3b** and **4a**. These data can be obtained free of charge via http://www.ccdc.cam.ac.uk/conts/retrieving.html, or from the Cambridge Crystallographic Data Centre, 12 Union Road, Cambridge CB2 1EZ, UK; fax: (+44) 1223-336-033; or e-mail: deposit@ccdc.cam.ac.uk. Supplementary data associated with this article can be found, in the online version, at doi:10.1016/j.poly.2006.11.055.

References

[1] (a) A. Erxleben, Coord. Chem. Rev. 246 (2003) 203;
(b) B. Moulton, M.J. Zaworotko, Chem. Rev. 101 (2001) 1629;
(c) F.A. Cotton, C. Lin, C.A. Murillo, Acc. Chem. Res. 34 (2001) 759;
(d) S. Leininger, B. Olenyuk, P.J. Stang, Chem. Rev. 100 (2000) 853;
(e) H. Li, M. Eddaoudi, M. O Keeffe, O.M. Yaghi, Nature 402 (1999) 276;
(f) M. Fujita, Chem. Soc. Rev. 27 (1998) 417;
(g) S.R. Batten, R. Robson, Angew. Chem., Int. Ed. 37 (1998) 1460;
(h) P.J. Stang, B. Olenyuk, Acc. Chem. Res. 30 (1997) 502;
(i) R. Robson, B.F. Abrahams, S.R. Batten, R.W. Gable, B.F. Hoskins, J. Liu, Supramolecular Architecture, ACS, Washington, DC, 1992.
[2] (a) B. Dutta, P. Bag, U. Florke, K. Nag, Inorg. Chem. 44 (2005) 147;
(b) B. Dutta, P. Bag, B. Adhikary, U. Florke, K. Nag, J. Org. Chem. 69 (2004) 5419;
(c) J. Gao, J.H. Reibenspies, A.E. Martell, Angew. Chem., Int. Ed. 42 (2003) 6008;
(d) R.G. Xiong, X.Z. You, B.F. Abrahams, Z. Xue, C.M. Che, Angew. Chem., Int. Ed. 40 (2001) 4422.
[3] D. Braga, L. Brammer, N.R. Champness, CrystEngComm. 7 (2005) 1.
[4] (a) P.A. Vigato, S. Tamburini, Coord. Chem. Rev. 248 (2004) 1717;
(b) J. Nelson, V. McKee, G. Morgan, Prog. Inorg. Chem. 47 (1998) 167;
(c) H. Okawa, H. Furutachi, D.E. Fenton, Coord. Chem. Rev. 174 (1998) 51;
(d) B. Dietrich, P. Viout, J.M. Lehn, Macrocyclic Chemistry, VCH, Weinheim, 1993;
(e) V. McKee, Adv. Inorg. Chem. 40 (1993) 323;
(f) J.D. Lamb, R.M. Izatt, J.J. Christensen, D.J. Eatough, in: G.A. Melson (Ed.), Coordination Chemistry of Macrocyclic Compounds, Plenum Press, New York, 1979;
(g) N.H. Pilkington, R. Robson, Aust. J. Chem. 23 (1970) 2226.
[5] W. Huang, H. Zhu, S. Gou, Coord. Chem. Rev. 250 (2006) 414.
[6] (a) W. Huang, S. Gou, D. Hu, Y. Xu, S. Chantrapromma, Q. Meng, J. Mol. Struct. 561 (2001) 121;
(b) W. Huang, S. Gou, D. Hu, Q. Meng, Synth. Commun. 30 (2000) 1555.
[7] (a) A.J. Atkins, D. Black, R.L. Finn, A. Marin-Becerra, A.J. Blake, L. Ruiz-Ramirez, W.-S. Li, M. Schroder, J. Chem. Soc., Dalton Trans. (2003) 1730;
(b) H. Adams, N.A. Bailey, P. Bertrand, C.O.R. de Barbarin, D.E. Fenton, S. Gou, J. Chem. Soc., Dalton Trans. (1995) 275.
[8] W. Huang, S. Gou, D. Hu, S. Chantrapromma, H.-K. Funm, Q. Meng, Inorg. Chem. 40 (2001) 1712.
[9] W. Huang, S. Gou, D. Hu, S. Chantrapromma, H.-K. Funm, Q. Meng, Inorg. Chem. 41 (2002) 864.
[10] W. Huang, D. Hu, S. Gou, S. Chantrapromma, H.-K. Fun, Y. Xu, Q. Meng, Inorg. Chim. Acta 342 (2003) 9.
[11] A. Asokan, B. Varghese, A. Caneschi, P.T. Manoharan, Inorg. Chem. 37 (1998) 228.
[12] M. Pascu, M. Andruh, A. Muller, M. Schmidtmann, Polyhedron 23 (2004) 673.
[13] P.G. Lacroix, J.C. Daran, J. Chem. Soc., Dalton Trans. (1997) 1369.
[14] (a) W. Huang, S. Gou, H. Qian, D. Hu, S. Chantrapromma, H.-K. Fun, Q. Meng, Eur. J. Inorg. Chem. (2003) 947;
(b) N.D.J. Branscombe, A.J. Blake, A. Marin-Becerra, Wan-Sheung Li, S. Parsons, L. Ruiz-Ramirez, M. Schroder, Chem. Commun. (1996) 2573.
[15] Y. Miyasato, Y. Nogami, M. Ohba, H. Sakiyama, H. Okawa, Bull. Chem. Soc. Jpn. 76 (2003) 1009.
[16] J. Fang, W. Huang, S. Chantrapromma, S.S.S. Raj, I.A. Razak, H.-K. Fun, S. Gou, H. Wang, Acta Crystallogr. C 56 (2000) 1429.
[17] P. Gabbai, A. Schier, J. Riede, Angew. Chem., Int. Ed. 37 (1998) 622.
[18] M.J. Frisch, G.W. Trucks, H.B. Schlegel, G.E. Scuseria, M.A. Robb, J.R. Cheeseman, J.A. Montgomery Jr., T. Vreven, K.N. Kudin, J.C. Burant, J.M. Millam, S.S. Iyengar, J. Tomasi, V. Barone, B. Mennucci, M. Cossi, G. Scalmani, N. Rega, G.A. Petersson, H. Nakatsuji, M. Hada, M. Ehara, K. Toyota, R. Fukuda, J. Hasegawa, M. Ishida, T. Nakajima, Y. Honda, O. Kitao, H. Nakai, M. Klene, X. Li, J.E. Knox, H.P. Hratchian, J.B. Cross, C. Adamo, J. Jaramillo, R. Gomperts, R.E. Stratmann, O. Yazyev, A.J. Austin, R. Cammi, C. Pomelli, J.W. Ochterski, P.Y. Ayala, K. Morokuma, G.A. Voth, P. Salvador, J.J. Dannenberg, V.G. Zakrzewski, S. Dapprich, A.D. Daniels, M.C. Strain, O. Farkas, D.K. Malick, A.D. Rabuck, K. Raghavachari, J.B. Foresman, J.V. Ortiz, Q. Cui, A.G. Baboul, S.

Clifford, J. Cioslowski, B.B. Stefanov, G. Liu, A. Liashenko, P. Piskorz, I. Komaromi, R.L. Martin, D.J. Fox, T. Keith, M.A. Al-Laham, C.Y. Peng, A. Nanayakkara, M. Challacombe, P.M.W. Gill, B. Johnson, W. Chen, M.W. Wong, C. Gonzalez, J.A. Pople, GAUSSIAN 03, Revision C.02, Gaussian, Inc., Pittsburgh, PA, 2004.

[19] (a) Molecular structure Coorporation & Rigaku Coorporation, Crystalclear. Version 1.3. MSC, 9009 New Trails Drive, The Woodlands, TX 77381-5209, USA, and Rigaku, Toyko, Japan, 2001.; (b) Molecular structure Corporation & Rigaku Corporation, TEXSAN. Version 1.11. MSC, 9009 New Trails Drive, The Woodlands, TX 77381-5209, USA, and Rigaku, Toyko, Japan, 2000.

[20] Bruker, SHELXTL (Version 6.10), Bruker AXS Inc., Madison, Wisconsin, USA, 2000.

[21] J.D. Lee, Talanta 20 (1973) 1029.

tubing inserted inside a furnace. Pt–Rh thermocouples and eurotherm heat controllers monitored the temperatures of all gas inlet lines. Tungsten hexachloride (99.9%-W) was purchased from Strem Chemicals, Inc. and ethanol (denatured) was purchased from Aldrich. WCl_6 and the ethanol were placed into separate heated stainless steel bubblers and the vapours generated introduced into the gas streams by passing hot nitrogen gas through the bubblers. Gas flows were adjusted using suitable regulators and flow controllers. The exhaust from the reactor was vented directly into the extraction system of a fume cupboard. All of the apparatus was baked out with nitrogen at 150 °C for 60 min before deposition. Deposition experiments were conducted by heating the horizontal-bed reactor and the bubblers to the required temperatures before diverting the nitrogen line through the bubblers and hence to the reactor. At the end of the deposition the bubbler-lines were closed and only nitrogen passed over the sensor. The sensor was allowed to cool with the graphite block to ca. 150 °C before it was removed. Coated sensors were handled and stored in air. The samples were analysed using X-ray Photoelectron Spectroscopy (XPS), Scanning Electron Microscopy (SEM), Raman spectroscopy and X-ray Diffraction (XRD).

X-ray powder diffraction patterns were measured on a Siemens D8 diffractometer using monochromated Cu Kα1 radiation (Cu Kα1 = 1.5406 Å) utilising a large angle detector. The diffractometer was used in low incident geometry (5°). Data manipulation were performed using Bruker EVA software and samples were indexed using Unit Cell and compared to database standards. SEM were obtained on a Jeol 6301F (accelerating voltage 20 kV) using Oxford Instruments ISIS software. Raman spectra were acquired on a Renishaw Raman System 1000 using a helium–neon laser of wavelength 632.8 nm. The Raman system was calibrated against the emission lines of neon. X-ray photoelectron spectra were recorded with a VG ESCALAB 220i XL instrument using focused (300 μm spot) monochromatic Al Kα radiation at a pass energy of 20 eV. Scans were acquired with steps of 50 meV. A flood gun was used to control charging and the binding energies were referenced to an adventitious C 1s peak at 284.8 eV. Depth profile measurements were obtained using argon beam sputtering (etch voltage 5 kV). Electrical conductivity was determined by 4-probe measurement on glass substrates.

Gas-sensing measurements were carried out using an apparatus of in house design, comprising a glass flow-through cell to which three heated devices could be connected and sealed. Gases were applied using computer operated mass flow controllers (Tylan General) through two separate lines. The first carried pre-mixed gases in air of known concentration (100 ppm EtOH, 500 ppm NO_2), purchased directly from source (BOC Special Gases). The remaining line carried dry air ('zero grade' compressed air purchased directly from BOC). In this way the gas concentration of the air supplied to the sensors could be controlled (EtOH 1–100 ppm). Gas-sensing experiments were performed at sensor temperatures of 300, 400, 500 and 600 °C, with the total resistance of the WO_3 film being measured using a digital multimeter (Keithley 175A).

3. Results and discussion

The APCVD reaction of WCl_6 with ethanol was examined. It was found that the use of ethanol as the co-reactant in a molar ratio of 1:10 (W:ethanol) at a substrate temperature of 625 °C with a total N_2 carrier flow of 15 l/min caused the deposition of blue films on the sensor substrates. The films were adherent to the substrate and passed the 'Scotch tape test'. The deposition time was 30 s.

SEM was used to examine the film microstructures. The films deposited using ethanol as the co-reactant (Fig. 1) appeared as a 'mat' of discrete needles orientated parallel to the substrate.

These morphologies are unlike those seen in the literature for films deposited from tungsten hexaphenoxide via aerosol-assisted (AA-) CVD on glass substrates, from tungsten(VI) ethoxide via sol–gel on silicon substrates, from tungsten hexacarbonyl via LPCVD on silicon or from tungsten hexaphenoxide deposited onto a sensor substrate under the application of an electric field [3,10–12]. The change in film morphology with different co-reactants is an exciting avenue for developing gas sensors because the sensor morphology plays a critical role in the response characteristics.

The films deposited at 625 °C were analysed using glancing-angle XRD. The films deposited from ethanol ($a = 7.36(9)$, $b = 7.42(9)$, $c = 3.87(9)$ Å) indexed as monoclinic WO_3 ($a = 7.285$, $b = 7.517$, $c = 3.835$ Å) but showed striking preferred orientation with the $\langle 0\,2\,0\rangle$ and $\langle 0\,4\,0\rangle$ diffraction peaks greatly enhanced (Fig. 2) [13].

Further analysis was performed using Raman spectroscopy (Fig. 3). The films deposited using ethanol had the

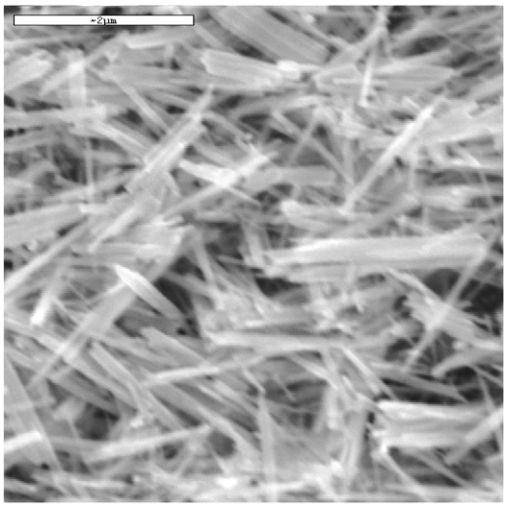


Fig. 1. Micrograph of film deposited using ethanol.

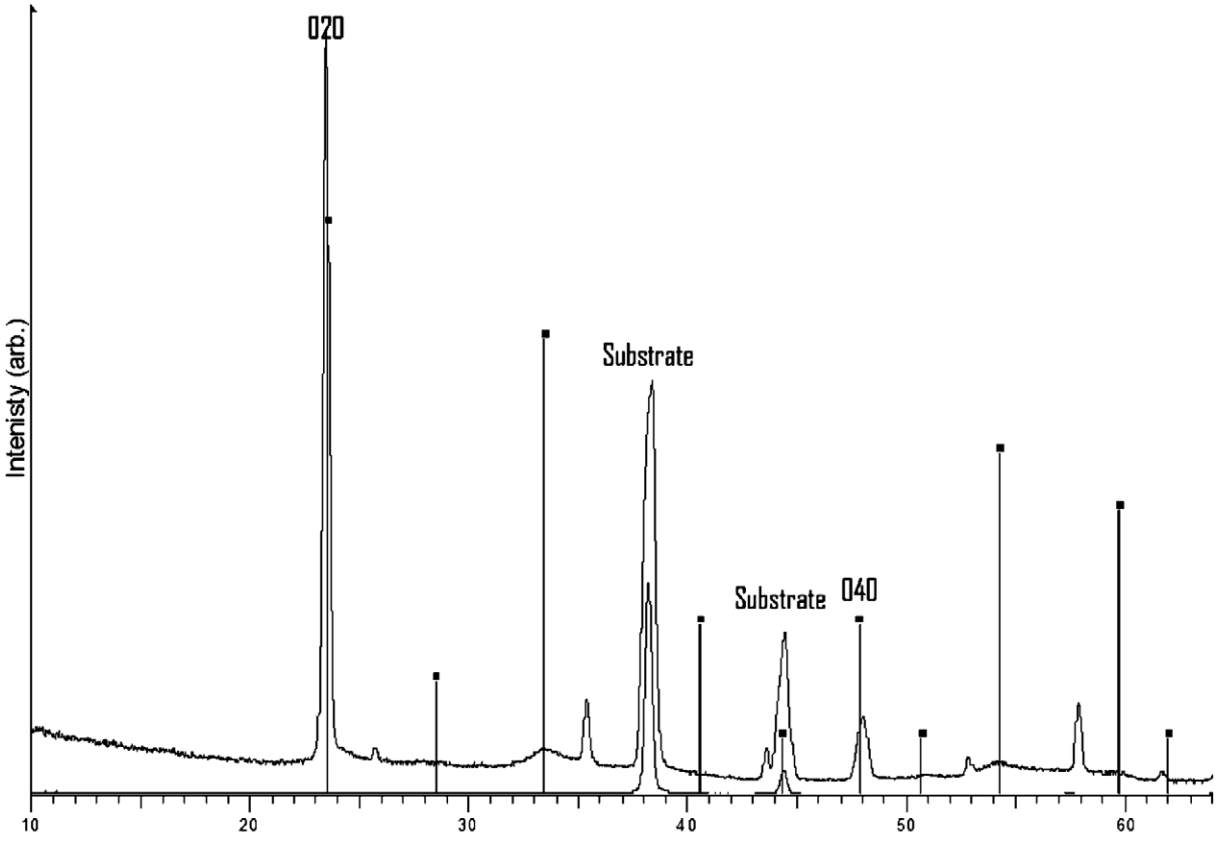


Fig. 2. X-ray diffraction pattern of film deposited using ethanol (substrate pattern also shown).

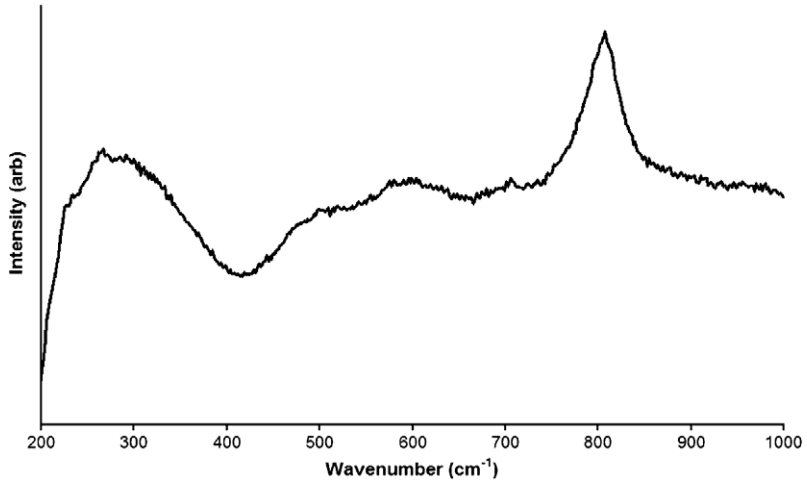


Fig. 3. Raman spectrum of film deposited using ethanol.

approximate form of crystalline WO_3 but with an amorphous appearance, with broad poorly defined peaks [14,15]. The films had a significantly different spectrum in the region 200–400 cm^{-1}. This region has been identified as containing W^{4+}–O and W^{5+}–O vibrations in amorphous WO_{3-x} tungsten oxides and may suggest the presence of reduced species in this film [16].

XPS was used to analyse the surface of the as-deposited films. The films were exposed to air after deposition and prior to XPS analysis. The film deposited from WCl_6 and ethanol had a very poor peak shape in the W4f region, being very broad and asymmetric. Deconvolution of the peak, using FWHM and peak area constraint, revealed 3 $W4f_{7/2}$ peaks. The peak fitting did not precisely model the experimental data, with slight deviation at the high energy side, but it was clear that there was a W^{6+} environment (35.5 eV), a W^{5+} environment (34.4 eV) and a W^{4+} (33.3 eV) environment in an approximate ratio of 3:2:1 [17]. The presence of such a large relative amount of reduced tungsten species would explain the very deep blue

colour observed in this film. No chlorine contamination was detected in the deposited films but carbon contamination was significant at the surface (~15–20%). An exact determination of the bulk carbon contamination was not made, however, it was shown that the carbon was graphitic rather than carbide and was reduced even after short etch periods, indicating that the film bulk probably had low levels of carbon contamination.

The gas-sensing properties of the deposited films were examined. The sensors were not annealed or treated prior to measurements on their response to repeated treatments of 20 ppm ethanol in flowing air (Fig. 4). It can be seen that after an initial 'burn-in' period (up to 200 min, effectively annealing the sensor) that the sensor behaves as a typical n-type sensor on exposure to the reducing gas ethanol at an operating temperature of 400 °C. In gas-sensing experiments conducted at operating temperatures of 300, 500 and 600 °C no response was observed. The sensor reaches its maximum response within 60 s of exposure. The magnitude of response remains stable during the exposure and returns to 50% of the initial resistance value within 60 s of the exposure ending. The response of the sensor to 20 ppm ethanol (defined as R/R_0, the maximum resistance on exposure to test gas/baseline resistance) was $R/R_0 = 1.84$. Some baseline drift was observed over the 30 h analysis period, although the baseline stabilised towards the end of the experiment. The response was found to be consistent and reproducible.

The response of the sensor to exposure to different concentrations of ethanol was examined (Fig. 5). It can be seen

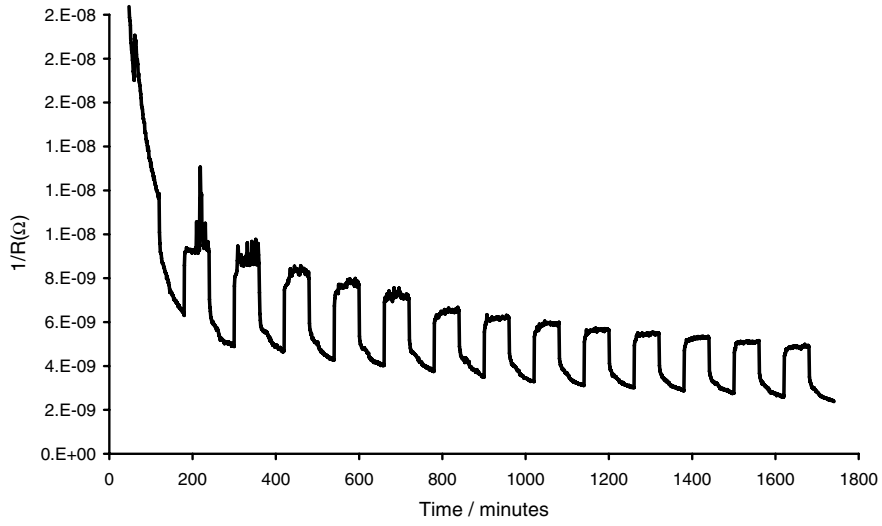


Fig. 4. CVD sensor response upon repeated exposure to 20 ppm ethanol vapour at an operating temperature of 400 °C.

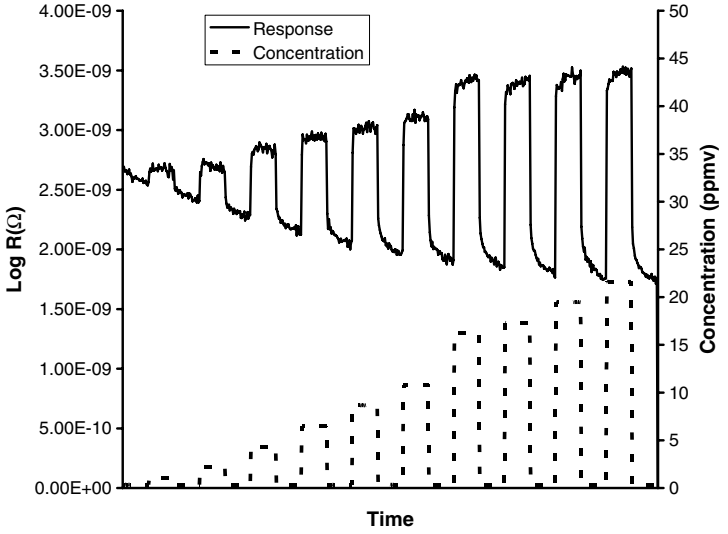


Fig. 5. The change in CVD prepared sensor resistance upon exposure to varying concentrations of ethanol vapour at an operating temperature of 400 °C.

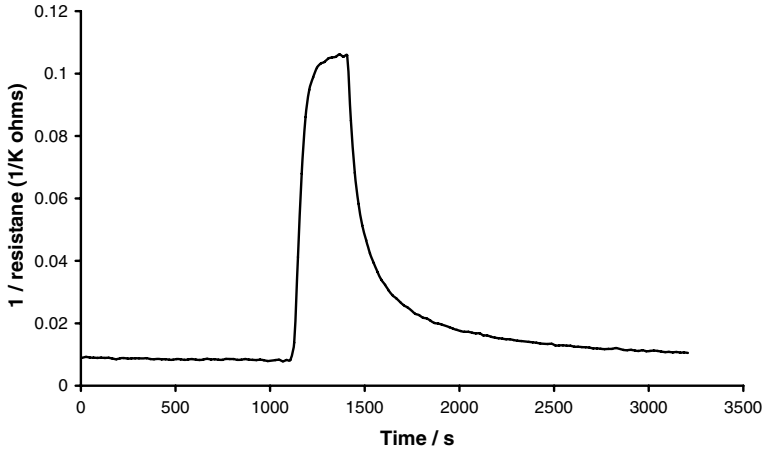


Fig. 6. Commercially produced screen-printed sensor response upon exposure to 100 ppm ethanol vapour at an operating temperature of 400 °C.

that the sensor response increases upon increasing ethanol concentration. Indeed it was found that the sensor response increases linearly over the concentration range examined (1–25 ppm) of ethanol.

In all cases the peak response was square and similar to the response produced by other sensors produced via CVD routes [18]. In all cases the response is fairly "clean" and free from noise. The response shape indicates that some of the resistivity change is a result of contributions from the bulk of the material; dense films, such as those produced by CVD, have relatively fewer absorption sites than porous films, such as those produced by screen-printing; hence they tend to saturate much more quickly in line with the network resistor model [19] (see Fig. 6).

Indeed, direct comparison to a commercially produced screen-printed WO_3 sensor, tested on the same experimental set up, indicates some key differences. The response is an order of magnitude larger, 10.32 versus 1.84 for the CVD produced centre though it should be noted the concentration of test gas is higher. Also the screen-printed sensor does not saturate as quickly and has a more familiar "shark fin" response shape this is because screen-printed sensors have a generally porous and open microstructure that leads to a greater number of potential surface absorption sites. The CVD produced sensor had a faster response time; this is likely to be because the ratio of surface sites to test gas molecules is lower.

All the tests show that production of a gas sensor using the newly developed CVD technique for the deposition of tungsten oxide show great promise. The future challenges will be to tailor film thickness and microstructure to optimise the gas response to a particular scenario and to stabilise the resistance baseline.

4. Conclusions

The gas-sensing characteristics of a particular material are governed by a great number of factors, such as stoichiometry, density/porosity, grain size and thickness. CVD gives direct control over these properties from the deposition conditions allowing a material to be deposited for specific sensing roles. These results demonstrate that a gas sensor made from CVD tungsten oxide is sensitive and gives a linear response to a reducing vapour (ethanol).

Acknowledgement

The EPSRC is thanked for providing the grant for this work. Pilkington Glass is thanked for the supply of substrates, Mr. Kevin Reeves of UCL Archaeology, and Mr. Robert Palgrave of UCL Chemistry are thanked for assistance with SEM and XPS techniques, respectively. I.P.P. thanks the Royal Society/Wolfson Trust for a merit award.

References

[1] S.K. Deb, Philos. Mag. 27 (1973) 801.
[2] P.M.S. Monk, R.J. Mortimer, D.R. Rosseinsky, Electrochromism: Fundamentals and Applications, VCH, New York, 1995.
[3] C. Cantalini, M.Z. Atashbar, Y. Li, M.K. Ghantasala, S. Santucci, W. Wlodarski, M.J. Passacantando, J. Vac. Sci. Technol. A 17 (1999) 1873.
[4] M. Regragui, M. Addou, A. Outzourhit, J.C. Bernede, E.L.B. El Iddrissi, E. Benseddik, A. Kachouane, Thin Solid Films 358 (2000) 40.
[5] A. Rougier, F. Portemer, A. Quede, M. El Marssi, Appl. Surf. Sci. 153 (1999) 1.
[6] R.U. Kirss, L. Meda, Appl. Organomet. Chem. 12 (1998) 155.
[7] C.S. Blackman, I.P. Parkin, Chem. Mater 17 (2005) 1583.
[8] C.G. Granqvist, Handbook of Inorganic Electrochromic Materials, Elsevier, New York, 1995.
[9] C.G. Granqvist, Sol. Energ. Mater. Sol. Cells 60 (2000) 201.
[10] G. Shaw, I.P. Parkin, K.F. E Pratt, D.E. Williams, J. Mater. Chem. 15 (2005) 149.
[11] W.B. Cross, I.P. Parkin, S.A. O'Neill, Chem. Mater. 15 (2003) 2786.
[12] K.K. Lai, H.H. Lamb, Thin Solid Films 370 (2000) 114.
[13] G. Andersson, Acta Chem. Scand. 7 (1953) 154.
[14] E. Salje, Acta Crystallogr., Sect. A 31 (1975) 360.
[15] M.F. Daniel, B. Desbat, C.J. Lassegues, B. Gerand, M. Figlarz, J. Solid State Chem. 67 (1987) 235.

[16] S.H. Lee, H.M. Cheong, C.E. Tracy, A. Mascarenhaus, D.K. Benson, S.K. Deb, Electrochim. Acta 44 (1999) 3111.
[17] B. Yous, S. Robin, A. Donnadieu, G. Dufour, C. Maillot, H. Roulet, C. Senemaud, Mat. Res. Bull. 19 (1984) 1349.
[18] R. Binions, C.J. Carmalt, I.P. Parkin, K.F.E. Pratt, G.A. Shaw, Chem. Mater. 16 (2004) 2489.
[19] S.C. Naisbitt, K.F.E. Pratt, D.E. Williams, I.P. Parkin, Sens. Actuat. B 114 (2006) 969.

Recently, the use of NHC ligands has emerged as replacements for organophosphanes in organometallic catalysts [9] and PDT (propanedithiolates) hydrogenase models [10,11]. NHCs are superior to a "phosphane mimic", as they often show a greater electron-donating power than phosphine ligand. Unlike other carbenes, the electronic and steric effects of the *N*-substituents make these compounds stable.

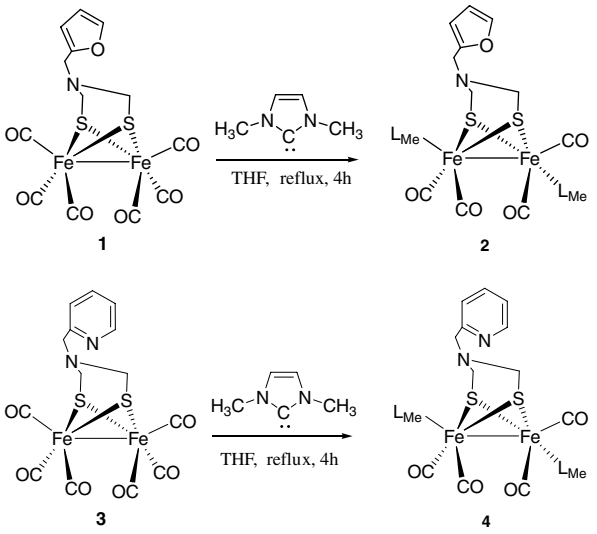
On the other hand, numerous possibilities of nitrogen functionalization induce a great structural versatility. We have previously described the furan-containing Fe_2S_2 complex [12]. Owing to its electron-rich property, this complex exhibited electrochemically favorable positive potential under acid ambient. We would like to know the behavior of pyridine analogues, with the electronic property contrary to that of furan. Our interest in pyridine stems also from the idea that the protonation of pyridine *N* atom would be a convenient route to increase the water-solubility of the corresponding metal complexes, with the ultimate objective being the homogeneous catalytic H_2 production. To the best of our knowledge, the use of NHC's as powerful ligands for the design of new diiron systems relevant to the furan- and pyridine-containing azadithiolate active site of the Fe-only hydrogenase has not been reported. We describe here our results concerning the novel NHC disubstituted diiron azadithiolate complexes $[\{(\mu\text{-}SCH_2)_2NCH_2(2\text{-}C_4H_3O)\}Fe_2(CO)_4(L_{Me})_2]$ (**2**) and $[\{(\mu\text{-}SCH_2)_2NCH_2(2\text{-}C_5H_4N)\}Fe_2(CO)_4(L_{Me})_2]$ (**4**) (L_{Me} = 1,3-dimethyl imidazol-2-ylidene).

2. Results and discussion

2.1. Synthesis and spectroscopy

The reaction of the diiron azadithiolate precursor $[\{(\mu\text{-}SCH_2)_2NCH_2(2\text{-}C_4H_3O)\}Fe_2(CO)_6]$ (**1**) [12] with excess of 1,3-dimethylimidazol-2-ylidene [13] (L_{Me}) (8 equiv.) smoothly afforded $[\{(\mu\text{-}SCH_2)_2NCH_2(2\text{-}C_4H_3O)\}Fe_2(CO)_4(L_{Me})_2]$ (**2**) (Scheme 1). The pyridine-containing carbene ligands substituted complex $[\{(\mu\text{-}SCH_2)_2NCH_2(2\text{-}C_5H_4N)\}Fe_2(CO)_4(L_{Me})_2]$ (**4**) was obtained in a similar manner from complex **3**, which was prepared from *C*-pyridin-2-yl-methylamine and $[(\mu\text{-}S_2)Fe_2(CO)_6]$ according to the literature [12]. These two products must be purified scrupulously by neutral Al_2O_3 column chromatography, and were characterized by ^1H NMR, IR spectra and X-ray diffraction method.

The IR spectra of the NHC disubstituted derivatives **2** and **4** displayed, respectively, three strong bands in the carbonyl region (1964, 1919, 1886 cm^{-1} and 1963, 1918, 1886 cm^{-1}) in a frequency ranging lower than those of the trimethylphosphine disubstituted PDT (propanedithiolate) (1979–1898 cm^{-1}) [14], the same ligand substituted PDT (1967–1888 cm^{-1}) [10], and very close to those of the bis-cyanide compound $[Fe_2(\mu\text{-}S(CH_2)_3S)(CN)_2(CO)_4]_2$ (ν(CO) 1965–1884 cm^{-1}) [15,16]. Overall, these IR spectra data confirmed the expected greater electron-donating



Scheme 1. Preparation of complexes **2** and **4**.

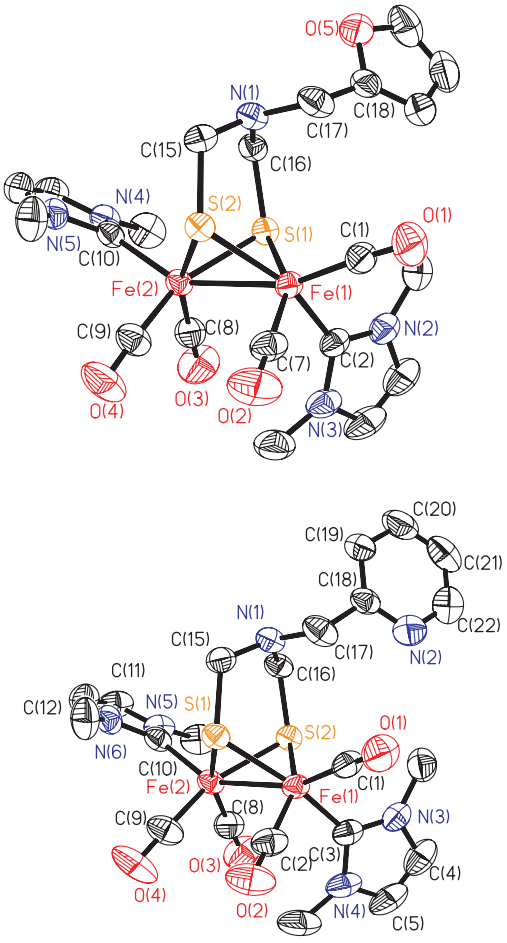


Fig. 1. ORTEP view (ellipsoids at 30% probability level) of **2** (upper) and **4** (lower). Selected bond distances (Å) and angles (°): complex **2**: Fe1–Fe2, 2.5314(6), Fe–S, 2.2828(6)–2.3037(8), Fe–C, 1.747(3)–1.985(3), Fe1–S1–Fe2, 67.28(2), Fe1–S2–C15, 115.85(9), Fe2–S2–C15, 109.16(10), Fe1–S2–Fe2, 66.88(2), C15–N1–C16, 113.4(2), C15–N1–C17, 114.7(2), C16–N1–C17, 118.6(2); complex **4**: Fe1–Fe2, 2.5341(8), Fe–S, 2.2822 (10)–2.2964(9), Fe–C, 1.751(4)–1.992(3), Fe2–S2–Fe1, 67.13(3), C15–N1–C16, 112.7(2), C15–N1–C17, 115.2(2), C16–N1–C17, 117.4(2).

ability of the NHC ligand (L_{Me}) was superior to that of the trimethylphosphine ligand and almost the same to the cyanide ligand.

2.2. Molecular structure

Fig. 1 shows the crystal structures of **2** and **4** with selected bond lengths and angles. The Fe_2S_2 skeletons of **2** and **4** are the well known butterfly structures found in related diiron complexes [17,18]. Each iron center displays approximately the square-pyramidal coordination geometry. The Fe–Fe distances in **2** (2.5314(6) Å) and **4** (2.5341(8) Å) are very close to those of other diiron dithiolate analogues. It is worth noting that the Fe–Fe distances are notably lengthened in the disubstituted species than those of complex **1** and **3** by ca. 0.02 Å [12]. One of the NHC group in **2** and **4** lies in the apical position, and the other in the basal positions (*cis* to the Fe–Fe axis) as expected, due to the spatial effect. The Fe–C (carbene L_{Me}) distances in **2** and **4** (1.981(3), 1.985(3), 1.979(3) and 1.992(3) Å) are longer than others. The sum of C–N–C angles around the *N*-bridged atom is respectively 346.7° and 345.3°, 10° larger than **1** (334.5°) and **3** (331.29°). The N(1)–C(17)–C(18) locates in the same side with the basal NHC, since such arrangement ensures that the furan and the basal NHC adopt the sterically less demanding position.

2.3. Eletrochemistry and protonation

Cyclic voltammetry (CV) experiments in MeCN–Bu_4NPF_6 indicated a totally irreversible one-electron reduction of **2** ($E_{red} = -2.53$ V versus Fc/Fc^+) (Fig. 2). In comparison to the parent hexacarbonyl complex **1** ($E_{red} = -1.55$ V versus Fc/Fc^+), the replacement of the two CO for two 1,3-dimethylimidazol-2-ylidenes resulted in a negative shift of the reduction potential by 980 mV. Similarly, the irreversible one-electron reduction of **4** ($E_{red} = -2.49$ V versus Fc/Fc^+) (Fig. 2) had the 950 mV shift comparison to that of **3**. The shifts were significantly larger by contrast with the reductive potentials of the disubstituted PMe_3 (410 mV) [19] and disubstituted PTA (1,3,5-triaza-7-phosphaadamantane) of PDT (440 mV) [16c], and even larger than that of the same disubstituted *N*-heterocyclic carbene ligands of PDT (810 mV) [9]. Attributing to the strong electron-donating ligand L_{Me},

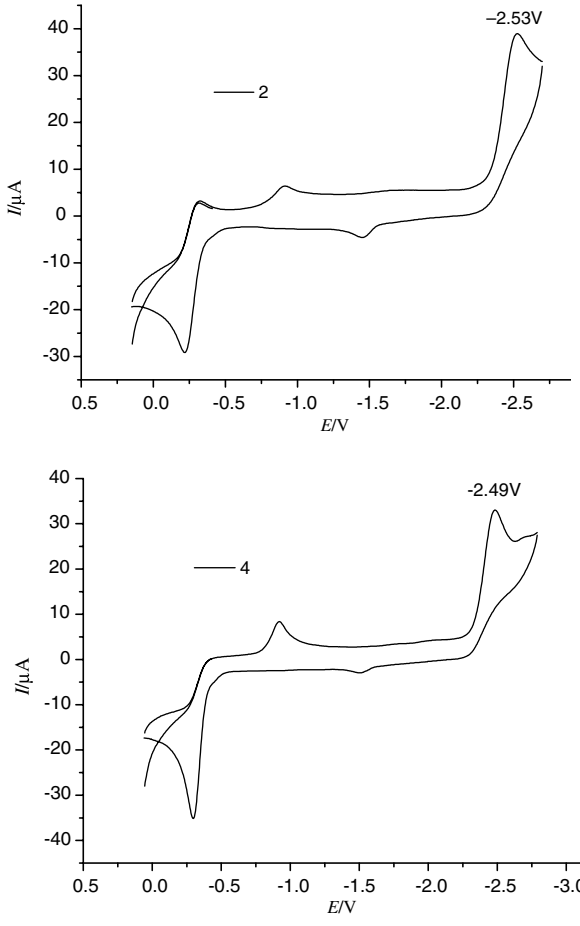


Fig. 2. Cyclic voltammograms of **2** and **4**: 1.0 mmol in 0.05 M *n*-Bu_4NPF_6/CH_3CN at a scan rate of 100 mV s^{-1}. All potentials given are vs. Fc/Fc^+.

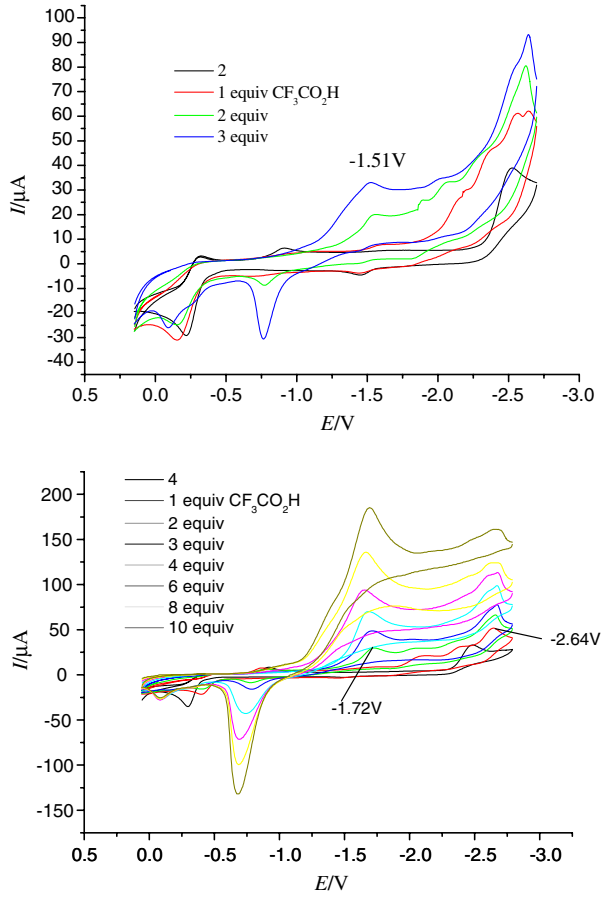


Fig. 3. Cyclic voltammograms of **2** and **4** in the presence of CF_3CO_2H in different concentrations, and sample concentration is 1.0 mmol in 0.05 M *n*-Bu_4NPF_6/CH_3CN, scan rate = 100 mV s^{-1}, working electrode: glassy carbon. All potentials are given vs. Fc/Fc^+.

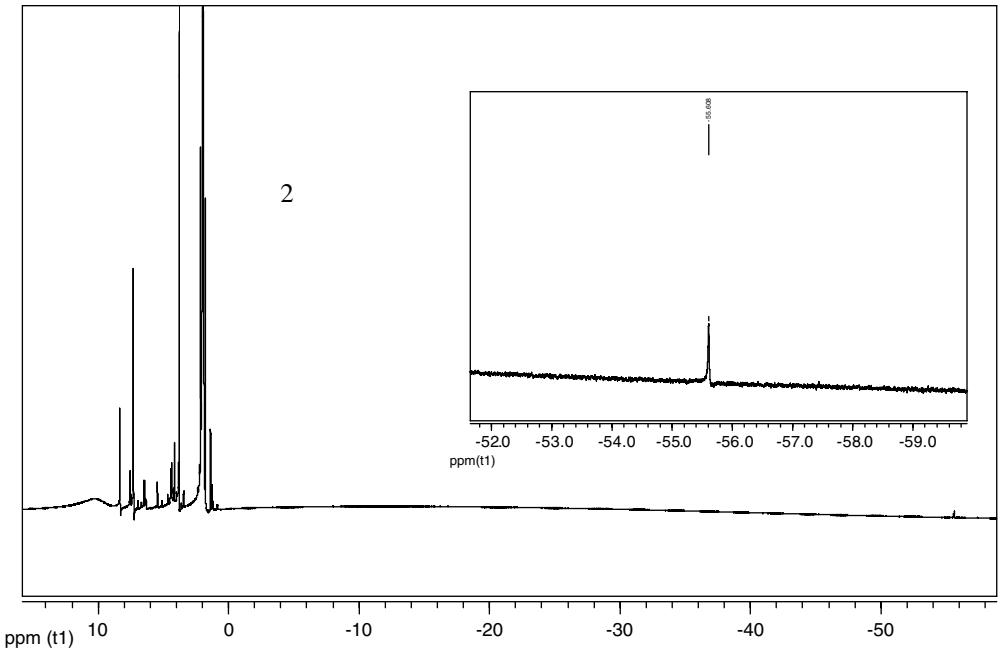


Fig. 4. The ^{1}H NMR of **2** in the presence of CF_3CO_2H.

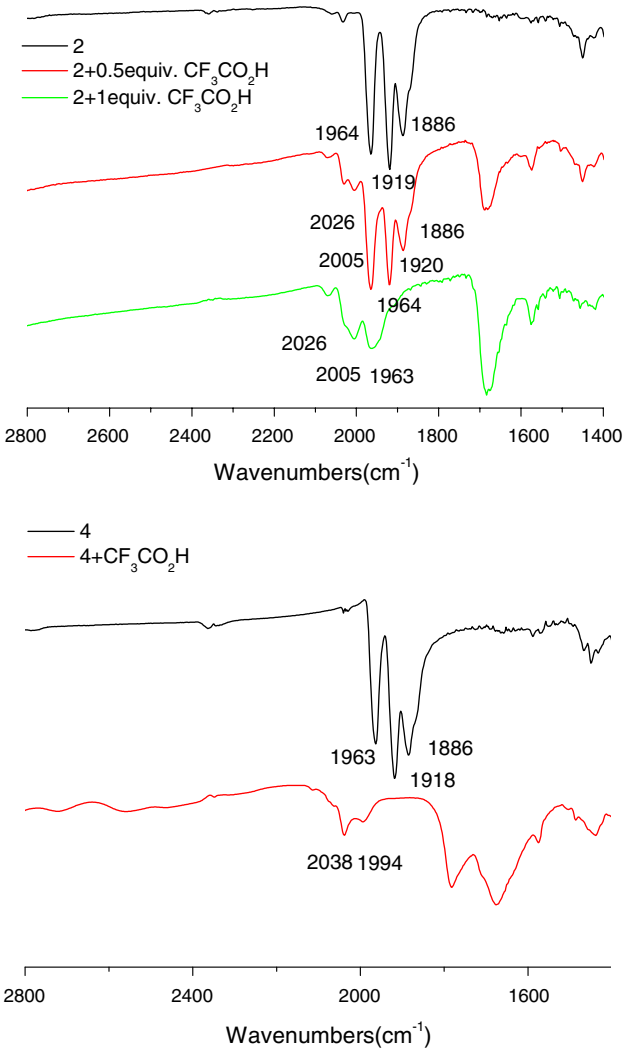


Fig. 5. The IR spectra of **2** and **4** in the presence of CF_3CO_2H.

the more negative potential was expected thanks to the changed electron density of diiron atoms. Moreover, it seemed that the results were also related to furan and pyridine heterocycles. Therefore, IR spectra data and electrochemical data clearly indicated that the Fe–Fe bonds in **2** and **4** were rendered sufficiently rich electron density to catch proton and produce hydrogen further.

The electrochemical performance was further investigated in the presence of CF_3CO_2H. Upon addition of one equivalent acid to **2** and **4**, the new reduction peaks were observed at $E_{red} = -1.51$ V and $E_{red} = -1.72$ V in the CV graphs (Fig. 3), with 1.02 V and 0.77 V less negative by comparison to those before the ligands exchanged. The new electrochemical events were assigned to the reduction of $\mathbf{2H}^+$ and $\mathbf{4H}^+$. The current intensity of the new peak enhanced gradually with the increment of the acid, suggesting the electrochemically catalytic proton reduction. The new peaks indicated the formation of Fe–H–Fe bond, which could be detected for the negative H signal at −55 ppm and −27 ppm respectively in ^{1}H NMR (Fig. 4, taking **2** as an example), and the hydride signal showed the rich electron density of diiron nuclear. In addition, the detected shifts of IR spectra data for **2** (from 1964, 1919, 1886 to 2026, 2005, 1963 cm^{-1}) and **4** (from 1963, 1918, 1886 to 2038, 1994 cm^{-1}) also indicated the formation of Fe–H–Fe bond according to the shift wavenumbers after protonation between Fe–Fe reported (Fig. 5).

3. Experimental

3.1. Reagents and instruments

The reactions and operations related to organometallic complexes were carried out under a dry, oxygen-free

nitrogen atmosphere. THF was dried and distilled by standard methods. Commercially available reagents, *N*-methylimidazole and CH_3I were used without further purification. The reagent potassium *tert*-butoxide was purchased from Aldrich. [{(μ-SCH_2)$_2$$NCH_2$(2-$C_4H_3O$)}$Fe_2$-$(CO)_6$] was prepared according to the described method [12]. IR spectra were recorded on a JASCO FT/IR 430 spectrophotometer. ^{1}H NMR spectra were collected with a Varian INOVA 400 NMR spectrometer. Elemental analyses were performed on a CARLO ERBA MOD-1106 elemental analyzer. Diffraction measurements were made on a Siemens SMART CCD diffractometer using graphite monochromated Mo Kα radiation ($\lambda = 0.71073$ Å).

3.2. Synthesis of [{(μ-SCH_2)$_2$$NCH_2$(2-$C_4H_3O$)}-$Fe_2(CO)_4(L_{Me})_2$] (**2**) ($L_{Me}$ = 1,3-dimethyl imidazol-2-ylidene)

A Schlenk flask was charged with 1-methylimidazole (0.58 mL, 7.25 mmol). The solution was cooled and maintained at 0 °C while CH_3I (0.45 mL, 7.25 mmol) was added dropwise. After stirring for 20 min at room temperature, the imidazolium iodide salt was yielded. Potassium *tert*-butoxide (1.2 g, 10.6 mmol) in THF (40 mL) was added to give a light yellow solution and turned to pink 3 h later. The reaction solution was filtered through Celite and eluted with THF. After the combined filtrates were concentrated to ca. 40 mL and transferred into Schlenk flask, **1** (0.47 g, 1 mmol) was added. After refluxing for 5 h, it gave a dark red solution. After evaporation of the solvent, the crude product was purified by column chromatography with neutral Al_2O_3 by using hexane/CH_2Cl_2 (3:1) as eluent to give complex **2** as a red solid (0.37 g, 80%). Recrystallization in the mixture solvent of hexane and CH_2Cl_2 (1:1) afforded crystals suitable for X-ray crystallography study. ^{1}H NMR ($CDCl_3$) δ (ppm): 7.25 (s, 1H), 6.21 (s, 1H), 5.97 (s, 1H), 6.96 (s, 4H), 4.01 (s, 12H), 3.5 (s, 2H), 3.2 (s, 4H); ESI-MS: *m*/*z*: 604.4 $[M + H]^+$, IR (cm^{-1}): *ν*(CO) 1964, 1919, 1886 cm^{-1}; *Anal.* Calc. for $C_{21}H_{25}Fe_2N_5O_5S_2$: C, 41.81; H, 4.18; N, 11.61. Found: C, 41.67; H, 4.20; N, 11.72%.

3.3. Synthesis of [{(μ-SCH_2)$_2$$NCH_2$(2-$C_5H_4N$)}-$Fe_2(CO)_6$] (**3**)

The hydroxylation product (1.68 g, 10 mmol), prepared from 2-pyridinemethylamine (1.08 g, 10 mmol) and HCHO/H_2O (2 mL, 20 mmol) in THF (20 mL), was added to a THF solution (20 mL) of [(μ-Li_2S_2)$Fe_2(CO)_6$], freshly derived from [(μ-S)$_2$$Fe_2(CO)_6$] (0.344 g, 1.0 mmol), and $LiEt_3BH$ (1 M in THF, 1.0 mL, 1.0 mmol) at −78 °C. The mixture was stirred for 1 h at −78 °C, then 2 h at room temperature. During the course of the reaction, the color of the solution turned dark red. After evaporation of the solvent, the crude product was purified by column chromatography with silica gel by using CH_2Cl_2 as eluent to give complex **3** as a red solid (0.22 g, 45%). Recrystallization in hexane afforded crystals of **3** suitable for X-ray crystallography study. ^{1}H NMR ($CDCl_3$) δ 8.60 (s, 1H), 7.64 (s, 1H), 7.25 (s, 2H), 3.95 (s, 2H), 3.52 (s, 4H); ^{13}C NMR ($CDCl_3$) δ 207.9, 160.0, 156.7, 149.4, 137.0, 123.0, 77.5, 77.2, 76.9, 63.5, 52.8; ESI-MS: *m*/*z*: 478.9 $[M + H]^+$; IR (cm^{-1}): *ν*(CO) 2070, 2014, 1993; *Anal.* Calc. for $C_{14}H_{10}N_2O_6S_2Fe_2$: C, 35.17; H, 2.11; N, 5.86. Found: C, 35.39; H, 2.13; N, 5.91%.

3.4. Synthesis of [{(μ-SCH_2)$_2$$NCH_2$(2-$C_5H_4N$)}-$Fe_2(CO)_4(L_{Me})_2$] (**4**)

This complex was prepared from **3** (0.38 g, 8 mmol) in a similar manner as complex **2** to give complex **4** as a red solid (0.40 g, 82%). Recrystallization in hexane and CH_2Cl_2 afforded crystals suitable for X-ray crystallography study. ^{1}H NMR ($CDCl_3$) δ (ppm): 8.43 (s, 1H), 7.54 (s, 1H), 7.08 (s, 1H), 6.68 (s, 1H), 6.96 (s, 4H), 4.06 (s, 12H), 3.60 (s, 2H), 3.09 (s, 4H); ESI-MS: *m*/*z*: 615.4 $[M + H]^+$, IR (cm^{-1}): *ν*(CO) 1963, 1918, 1886 cm^{-1}; *Anal.* Calc. for $C_{22}H_{26}Fe_2N_6O_4S_2$: C, 43.01; H, 4.27; N, 13.68. Found: C, 42.67; H, 4.40; N, 13.72%.

4. Conclusion

In summary, the combined use of furan and NHC has led to the preparation of complex **2**, which shows a very low reduction potential at −2.53 V. Pyridine analogue **4** is also obtained in a similar manner with a reduction potential at −2.49 V. Our preliminary studies have shown that this two model complexes exhibited some desirable properties with the strong electron-donating capability. The ^{1}H NMR, IR spectra and electrochemical data clearly show that the *N*-heterocyclic carbene ligands possess electron-donating properties, even superior to those of phosphane ligands and very close to the cyanide ligands. Thanks to the versatility of the *N*-heterocyclic carbene ligands, these carbene disubstituted furan- and pyridine-containing Fe-only azathiolate hydrogense models represent a new class of hydrogenase active site mimics with desirable catalytic reduction properties.

5. Supplementary material

CCDC 276212, 272295 and 604776 contain the supplementary crystallographic data for this paper. These data can be obtained free of charge via http://www.ccdc.cam.ac.uk/conts/retrieving.html, or from the Cambridge Crystallographic Data Centre, 12 Union Road, Cambridge CB2 1EZ, UK; fax: (+44) 1223-336-033; or e-mail: deposit@ccdc.cam.ac.uk.

Acknowledgements

We are grateful to the Ministry of Science and Technology of China and the Chinese National Natural Science Foundation (Grant No. 20128005) for financial supports of this work. We are also grateful to the Swedish Engergy

Agency, K&A Wallenberg Foundation, the Swedish Research Council and the Scientific Research Foundation for the Returned Overseas Chinese Scholars, Ministry of Education.

References

[1] J.W. Peters, W.N. Lanzilotta, B.J. Lemon, L.C. Seefeldt, Science 282 (1998) 1853.
[2] Y. Nicolet, C. Piras, P. Legrand, C.E. Hatchikian, J.C. Fontecilla-Camps, Structure 7 (1999) 13.
[3] (a) M.Y. Darensbourg, E.J. Lyon, J.J. Smee, Coord. Chem. Rev. 206–207 (2000) 533;
(b) R.B. King, T.E. Bitterwolf, Coord. Chem. Rev. 206–207 (2000) 563;
(c) I.P. Georgakaki, L.M. Thomson, E.J. Lyon, M.B. Hall, M.Y. Darensbourg, Coord. Chem. Rev. 238–239 (2003) 255;
(d) D.J. Evans, C.J. Pickett, Chem. Soc. Rev. 32 (2003) 268;
(e) T.B. Rauchfuss, Inorg. Chem. 43 (2004) 14.
[4] F. Wang, M. Wang, X. Liu, K. Jin, W. Dong, G. Li, B. Åkermark, L. Sun, Chem. Commun. 25 (2005) 3221.
[5] W. Dong, M. Wang, X. Liu, K. Jin, G. Li, F. Wang, L. Sun, Chem. Commun. 26 (2006) 305.
[6] X. Zhao, I.P. Georgakaki, M.L. Miller, R. Mejia-Rodriguez, C. Chiang, M.Y. Darensbourg, Inorg. Chem. 41 (2002) 3917.
[7] F. Gloaguen, J.D. Lawrence, T.B. Rauchfuss, M. Bénard, M.-M. Rohmer, Inorg. Chem. 41 (2002) 6573.
[8] S. Ott, M. Borgström, M. Kritikos, R. Lomoth, J. Bergquist, B. Åkermark, L. Hammarström, L. Sun, Inorg. Chem. 43 (2004) 4683.
[9] (a) W.A. Herrmann, Angew. Chem., Int. Ed. 41 (2002) 1290;
(b) W.A. Herrmann, T. Weskamp, V.P.W. Böhm, Adv. Organomet. Chem. 48 (2002) 1;
(c) T. Weskamp, V.P.W. Böhm, W.A. Herrmann, J. Organomet. Chem. 600 (2000) 12;
(d) L. Jafarpour, S.P. Nolan, J. Organomet. Chem. 617–618 (2001) 27.
[10] J.-F. Capon, S.E. Hassnaoui, F. Gloaguen, P. Schollhammer, J. Talarmin, Organometallics 24 (2005) 2020.
[11] J.W. Tye, J. Lee, H.-W. Wang, R. Mejia-Rodriguez, J.H. Reibenspies, M.B. Hall, M.Y. Darensbourg, Inorg. Chem. 44 (2005) 5550.
[12] S. Jiang, J. Liu, L. Sun, Inorg. Chem. Commun. 9 (2006) 290.
[13] A.J. Arduengo, H.V.R. Dias, R.L. Harlow, M. Kline, J. Am. Chem. Soc. 114 (1992) 5530.
[14] X. Zhao, I.P. Georgakaki, M.L. Miller, J.C. Yarbrough, M.Y. Darensbourg, J. Am. Chem. Soc. 123 (2001) 9710.
[15] A. Le Cloirec, S.P. Best, S. Borg, S.C. Davies, D.J. Evans, D.L. Hughes, C.J. Pickett, Chem. Commun. 20 (1999) 2285.
[16] (a) J.D. Lawrence, T.B. Rauchfuss, S.R. Wilson, Inorg. Chem. 41 (2002) 6193;
(b) J.L. Nehring, D.M. Heinekey, Inorg. Chem. 42 (2003) 4288;
(c) R. Mejia-Rodriguez, D. Chong, J.H. Reibenspies, M.P. Soriaga, M.Y. Darensbourg, J. Am. Chem. Soc. 126 (2004) 12004.
[17] E.J. Lyon, I.P. Georgakaki, J.H. Reibenspies, M.Y. Darensbourg, Angew. Chem., Int. Ed. 38 (1999) 3178.
[18] (a) G. Hogarth, M. O'Brien, D.A. Tocher, J. Organomet. Chem. 672 (2003) 29;
(b) C. He, M. Wang, X. Zhang, Z. Wang, C. Chen, J. Liu, B. Åkermark, L. Sun, Angew. Chem., Int. Ed. 43 (2004) 3571;
(c) L. Song, Z. Yang, H. Bian, Q. Hu, Organometallics 23 (2004) 3082.
[19] D. Chong, I.P. Georgakaki, R. Mejia-Rodriguez, J. Sanabria-Chinchilla, M.P. Soriaga, M.Y. Darensbourg, Dalton Trans. (2003) 4158.

constant [15] of the corresponding phosphorus(V) selenide, [16,17] prepared by the oxidation of the phosphine with elemental selenium, where phosphorus(V) selenides incorporating electron-withdrawing groups exhibit larger coupling constants that those for phosphorus(V) selenides incorporating electron-donating groups. Here, we report data for a comprehensive series of phosphorus(V) selenides, which offer a clearer insight into the effect of perfluoroalkyl groups on the electronic properties of phosphines used in fluorous catalysis.

2. Experimental

Proton, ^{19}F and ^{31}P NMR spectroscopies were carried out on a Bruker ARX250 spectrometer at 250.13, 235.34 and 101.26 MHz or a Bruker DPX300 spectrometer at 300.14, 282.41 and 121.50 MHz, respectively, and were referenced to external $SiMe_4$ (^1H), external $CFCl_3$ (^{19}F) and to external H_3PO_4 (^{31}P) using the high frequency positive convention. Abbreviations for NMR spectral multiplicities are as follows: s = singlet, d = doublet, t = triplet, q = quartet, m = multiplet. Elemental analyses were performed by the Elemental Analysis Service at the University of North London. Mass spectra were recorded on a Kratos Concept 1H mass spectrometer.

$P(4\text{-}C_6H_4R)_3$ (R = H, F, Cl, Me, OMe and NMe_2) and BINAP were commercial samples and used as received, whilst *cis*-$[PtCl_2(MeCN)_2]$ was prepared by the literature route [18].

2.1. General procedure for the preparation of phosphines

n-BuLi (2.0 mmol, 1.6 M solution in hexane) was added dropwise over 1 h to a solution of the required bromobenzene (2.0 mmol) in diethyl ether at −78 °C. This solution was then stirred at −78 °C for 3 h. The requisite chlorophosphine (2.0 mmol for diphenylchlorophosphines, 1.0 mmol for dichlorophenylphosphines or 0.66 mmol for PCl_3) was then added dropwise in a solution of diethyl ether over 1 h and the solution allowed to warm to room temperature overnight. The solution was then washed well with water, the organic layer separated, dried and the solvent removed in vacuo. The resulting phosphine was purified by column chromatography using petroleum ether as the eluent. Uniquely, **1f** was prepared by a modification of the literature route for **3f**, [6b] by the reaction of the chlorosilane with the lithiate formed from the reaction of $Ph_2P(C_6H_4\text{-}4\text{-}Br)$ with BuLi at low temperature in diethylether. Many of the phosphines prepared in this work have been described previously (**1b**, [7]; **2b**, [7]; **3a**, [15]; **3b**, [7]; **3d**, [8b]; **3e**, [11]; **3f**, [6b]; **3g**, [9a]; **3h**, [9b]; **3j**, [19]; **3k**, [20]; **3l**, [21]; **4b**, [14]; **5b**, [14]; **6b**, [22]; **7a**, [23]; **7b**, [24]; **7c**, [24]; **8a**, [24]; **8b**, [24]; **9a**, [22,23]; **10a**, [24]; **10b**, [24]; **11b**, [25]; **11d**, [25]), and here we just report data for new ligands and additional data for established species where appropriate.

2.1.1. 4-(Trifluoromethylphenyl)diphenylphosphine (*1a*)

M.p. = 53–54 °C (Lit. 51–53 °C) [26]. *m/z* (FAB) 330 (M^+). ^1H NMR ($CDCl_3$) 7.50 (2H, d, $^3J_{HH}$ 10.0, ArH), 7.30 (2H, d, $^3J_{HH}$ 10.0, ArH), 7.28 (10H, m, ArH). $^{19}F\{^1H\}$ NMR ($CDCl_3$) −63.20 (s). $^{31}P\{^1H\}$ NMR ($CDCl_3$) −5.4 (s).

2.1.2. 4-(Heptadecafluoro-n-octylphenyl)diphenylphosphine (*1c*)

M.p. = 89–91 °C. *Anal.* Calc. for $C_{26}H_{14}F_{17}P$: C, 45.88; H, 2.06. Found: C, 45.89; H, 1.95%. *m/z* (FAB) 680 (M^+). ^1H NMR ($CDCl_3$) 7.45 (2H, d, $^3J_{HH}$ 8.0, ArH), 7.31 (12H, m, ArH). $^{19}F\{^1H\}$ NMR ($CDCl_3$) −80.76 (3F, t, $^4J_{FF}$ 10.0, CF_3), −110.78 (2F, t, $^4J_{FF}$ 14.4, α-CF_2), −121.21 (2F, m, CF_2), −121.84 (6F, m, 3 × CF_2), −122.68 (2F, m, CF_2), −126.12 (2F, m, CF_2). $^{31}P\{^1H\}$ NMR ($CDCl_3$) −5.4 (s).

2.1.3. 4-(1H,1H,2H,2H-tridecafluoro-n-octyldimethylsilylphenyl)diphenylphosphine (*1f*)

M.p. = 186 °C dec. *Anal.* Calc. for $C_{28}H_{24}F_{13}PSi$: C, 50.37; H, 3.60. Found: C, 50.51; H, 3.58%. *m/z* (FAB) 667 (MH^+). ^1H NMR ($CDCl_3$) 7.31 (2H, dd, $^3J_{PH}$ 10.9, $^3J_{HH}$ 8.0, ArH-2,6), 7.20 (12H, m, ArH), 1.87 (2H, m, CH_2), 0.85 (2H, m, CH_2Si), 0.18 (6H, s, CH_3). $^{19}F\{^1H\}$ NMR ($CDCl_3$) −81.30 (3F, t, $^4J_{FF}$ 10.1, CF_3), −116.45 (2F, t, $^4J_{FF}$ 14.0, α-CF_2), −122.48 (2F, m, CF_2), −123.40 (2F, m, CF_2), −123.66 (2F, m, CF_2), −126.67 (2F, m, CF_2). $^{31}P\{^1H\}$ NMR ($CDCl_3$) −5.7 (s).

2.1.4. Tris-(4-heptadecafluoro-n-octylphenyl)phosphine (*3c*)

M.p. = 92 °C (Lit. 92–95 °C) [27]. *m/z* (FAB) 1516 (M^+). ^1H NMR ($CDCl_3$) 7.53 (6H, d, $^3J_{HH}$ 7.9, ArH-3,5), 7.35 (6H, t, $^3J_{HH}$ 7.7, $^3J_{PH}$ 7.7, ArH-2,6). $^{19}F\{^1H\}$ NMR ($CDCl_3$) −80.76 (9F, t, $^4J_{FF}$ 8.9, CF_3), −110.99 (6F, t, $^4J_{FF}$ 14.0, α-CF_2), −121.17 (6F, m, CF_2), −121.72 (18F, m, 3 × CF_2), −122.67 (6F, m, CF_2), −126.08 (6F, m, CF_2). $^{31}P\{^1H\}$ NMR ($CDCl_3$) −6.2 (s).

2.1.5. 3-(Heptadecafluoro-n-octylphenyl)diphenylphosphine (*4c*)

Oil. *Anal.* Calc. for $C_{26}H_{14}F_{17}P$: C, 45.88; H, 2.06. Found: C, 45.72; H, 2.00%. *m/z* (FAB) 680 (M^+). ^1H NMR ($CDCl_3$) 7.46 (2H, m, ArH), 7.37 (2H, m, ArH), 7.22 (10H, m, ArH). $^{19}F\{^1H\}$ NMR ($CDCl_3$) −80.78 (3F, t, $^4J_{FF}$ 10.0, CF_3), −110.89 (2F, t, $^4J_{FF}$ 14.2, α-CF_2), −121.31 (2F, m, CF_2), −122.04 (6F, m, 3 × CF_2), −122.78 (2F, m, CF_2), −126.20 (2F, m, CF_2). $^{31}P\{^1H\}$ NMR ($CDCl_3$) −5.1 (s).

2.1.6. Tris-(3-heptadecafluoro-n-octylphenyl)phosphine (*5c*)

M.p. = 77–78 °C (Lit. 84–86 °C) [27]. *m/z* (FAB) 1516 (M^+). ^1H NMR ($CDCl_3$) 7.59–7.46 (9H, m, ArH), 7.35 (3H, d, $^3J_{HH}$ 6.3, ArH). $^{19}F\{^1H\}$ NMR ($CDCl_3$) −80.92 (9F, t, $^4J_{FF}$ 9.4, CF_3), −111.47 (6F, t, $^4J_{FF}$ 14.0, α-CF_2), −121.45 (6F, m, CF_2), −122.10 (18F, m, 3 × CF_2),

Table 1
NMR spectral data for phosphorus(V) selenides[a]

Phosphine	M.p. (°C)	Elemental analysis[b]	m/z[c]	^{1}H	$^{19}F\{^{1}H\}$	$^{31}P\{^{1}H\}$
1a	88–91	C, 55.63 (55.88); H, 3.36 (3.43)	409 (M^+)	7.76 (2H, dd, $^{3}J_{PH}$ 12.4, $^{3}J_{HH}$ 8.4, ArH-2,6), 7.61 (6H, m, ArH), 7.40 (6H, m, ArH)	−63.09 (3F, s, CF_3)	35.1 (s, $^{1}J_{SeP}$ 741), 35.5 (s, $^{1}J_{SeP}$ 774)[d]
1b	39–40	C, 43.64 (43.77); H, 1.97 (2.13)	661 (MH^+)	7.79 (2H, dd, $^{3}J_{PH}$ 12.9, $^{3}J_{HH}$ 8.5, ArH-2,6), 7.65 (6H, m, ArH), 7.42 (6H, m, ArH)	−81.32 (3F, t, $^{4}J_{FF}$ 9.9, CF_3), −111.55 (2F, t, $^{4}J_{FF}$ 13.7, α-CF_2), −121.93 (4F, m, 2 × CF_2), −123.25 (2F, m, CF_2), −126.62 (2F, m, CF_2)	34.9 (s, $^{1}J_{SeP}$ 743), 34.7 (s,$^{1}J_{SeP}$ 774)[d]
1c	88–89	C, 41.38 (41.11); H, 1.92 (1.84)	759 (M^+)	7.78 (2H, dd, $^{3}J_{PH}$ 12.8, $^{3}J_{HH}$ 8.3, H-2,6), 7.67 (6H, m, ArH), 7.46 (6H, m, ArH)	−80.75 (3F, t, $^{4}J_{FF}$ 10.0, CF_3), −111.05 (2F, t, $^{4}J_{FF}$ 14.2, α-CF_2), −121.15 (2F, m, CF_2), −121.47 (2F, m, CF_2), −121.82 (4F, m, 2 × CF_2), −122.66 (2F, m, CF_2), −126.10 (2F, m, CF_2)	35.1 (s, $^{1}J_{SeP}$ 742), 35.5 (s, $^{1}J_{SeP}$ 775)[d]
1f	99–101	C, 45.10 (45.16); H, 3.13 (3.23)	747 (MH^+)	7.64–7.54 (6H, m, ArH), 7.45–7.31 (8H, m, ArH), 1.88 (2H, m, CH_2CF_2), 0.87 (2H, m, CH_2Si), 0.20 (6H, s, CH_3)	−81.27 (3F, t, $^{4}J_{FF}$ 9.0, CF_3), −116.71 (2F, t, $^{4}J_{FF}$ 12.0, α-CF_2), −122.49 (2F, m, CF_2), −123.66 (2F, m, CF_2), −124.04 (2F, m, CF_2), −126.68 (2F, m, CF_2)	35.0 (s, $^{1}J_{SeP}$ 730), 36.8 (s, $^{1}J_{SeP}$ 766)[d]
2b	Oil	C, 37.08 (36.89); H, 1.25 (1.33)	979 (MH^+)	7.78 (4H, dd, $^{3}J_{PH}$ 12.9, $^{3}J_{HH}$ 8.5, ArH-2,6), 7.64 (5H, m, ArH), 7.44 (4H, m, ArH)	−81.38 (6F, t, $^{4}J_{FF}$ 9.6, CF_3), −111.72 (4F, t, $^{4}J_{FF}$ 13.58, α-CF_2), −121.95 (8F, m, 2 × CF_2), −123.28 (4F, m, CF_2), −126.64 (4F, m, CF_2)	34.5 (s, $^{1}J_{SeP}$ 756), 34.7 (s, $^{1}J_{SeP}$ 782)[d]
3b	76–77	C, 33.48 (33.38); H 0.71 (0.93)	1297 (MH^+)	7.79 (6H, dd, $^{3}J_{PH}$ 13.0, $^{3}J_{HH}$ 8.3, ArH-2,6), 7.64 (6H, dd, $^{3}J_{HH}$ 8.3, $^{4}J_{PH}$ 2.9, ArH-3,5)	−81.40 (9F, t, $^{4}J_{FF}$ 9.8, CF_3), −111.74 (6F, t, $^{4}J_{FF}$ 13.6, α-CF_2), −121.99 (12F, m, 2 × CF_2), −123.29 (6F, m, CF_2), −126.67 (6F, m, CF_2)	34.0 (s, $^{1}J_{SeP}$ 769), 33.9 (s, $^{1}J_{SeP}$ 792)[d]
3c	126–127	C, 31.67 (31.62); H, 0.78 (0.75)	1596 (MH^+)	7.80 (6H, dd, $^{3}J_{PH}$ 13.2, $^{3}J_{HH}$ 8.5, ArH-2,6), 7.62 (6H, dd, $^{3}J_{HH}$ 8.5, $^{4}J_{PH}$ 2.1, ArH-3,5)	−81.19 (9F, t, $^{4}J_{FF}$ 9.8, CF_3), −111.56 (6F, t, $^{4}J_{FF}$ 13.3, α-CF_2), −121.57 (6F, m, CF_2), −121.92 (6F, m, CF_2), −122.24 (12F, m, 2 × CF_2), −123.07 (6F, m, CF_2), −126.50 (6F, m, CF_2)	35.8 (s, $^{1}J_{SeP}$ 793)[d]
3d	71–72	C, 36.60 (36.57); H, 1.89 (1.74)	1380 (MH^+)	7.59 (6H, dd, $^{3}J_{PH}$ 13.3, $^{3}J_{HH}$ 8.2, ArH-2,6), 7.22 (6H, dd, $^{3}J_{HH}$ 8.2, $^{4}J_{PH}$ 2.5, ArH-3,5), 2.88 (6H, m, CH_2), 2.32 (6H, m, CH_2)	−80.82 (9F, t, $^{4}J_{FF}$ 9.8, CF_3), −114.51 (6F, t, $^{4}J_{FF}$ 14.5, α-CF_2), −121.86 (6F, m, CF_2), −123.42 (6F, m, CF_2), −123.47 (6F, m, CF_2), −126.12 (6F, m, CF_2)	33.8 (s, $^{1}J_{SeP}$ 733), 34.2 (s, $^{1}J_{SeP}$ 767)[d]
3e	118–120	C, 38.14 (38.03); H, 2.03 (2.11)	1423 (MH^+)	7.58 (6H, dd, $^{3}J_{PH}$ 13.3, $^{3}J_{HH}$ 8.2, ArH-2,6), 7.19 (6H, m, ArH-3,5), 2.67 (6H, m, CH_2), 1.97 (12H, m, 2 × CH_2)	−80.77 (9F, t, $^{4}J_{FF}$ 10.0, CF_3), −114.10 (6F, t, $^{4}J_{FF}$ 14.8, α-CF_2), −121.89 (6F, m, CF_2), −122.85 (6F, m, CF_2), −123.35 (6F, m, CF_2), −126.08 (6F, m, CF_2)	33.8 (s, $^{1}J_{SeP}$ 725), 34.2 (s, $^{1}J_{SeP}$ 764)[d]
3g	112–114	C, 32.84 (32.73); H, 1.00 (1.17)	1537 (MH^+)	7.59 (6H, dd, $^{3}J_{PH}$ 12.9, $^{3}J_{HH}$ 9.1, ArH-2,6), 6.92 (6H, dd, $^{3}J_{HH}$ 9.1 $^{4}J_{PH}$ 2.1 ArH-3,5), 4.42 (6H, t, $^{3}J_{HF}$ 12.60, OCH_2)	−81.36 (9F, t, $^{4}J_{FF}$ 10.1, CF_3), −119.84 (6F, m, α-CF_2), −122.53 (12F, m, 2 × CF_2), −122.79 (6F, m, CF_2), −123.58 (6F, m, CF_2), −126.73 (6F, m, CF_2)	31.1 (s, $^{1}J_{SeP}$ 729), 33.3 (s, $^{1}J_{SeP}$ 759)[d]
3h	80–81 (dec)		1770 (MH^+)	7.56 (6H, dd, $^{3}J_{PH}$ 12.9, $^{3}J_{HH}$ 8.8, ArH-2,6), 6.85 (6H, dd, $^{3}J_{HH}$ 8.8, $^{4}J_{PH}$ 2.0, ArH-3,5), 4.00 (6H, m, OCH_2), 2.18 (6H, m, CH_2), 2.09 (6H, m, CH_2)	−81.25 (9F, t, $^{4}J_{FF}$ 9.0, CF_3), −114.83 (6F, t, $^{4}J_{FF}$ 15.0, α-CF_2), −122.69 (18F, m, 3 × CF_2), −123.58 (6F, m, CF_2), −124.46 (6F, m, CF_2), −126.58 (6F, m, CF_2)	31.4 (s, $^{1}J_{SeP}$ 715), 33.2 (s, $^{1}J_{SeP}$ 754)[d]
3l	121–123	C, 37.25 (37.44); H, 1.98 (2.08)	579 (MH^+)	7.52–7.43 (12H, m, ArH)		33.7 (s, $^{1}J_{SeP}$ 748), 35.4 (s, $^{1}J_{SeP}$ 778)[d]
4a	Oil	C, 55.69 (55.75); H, 3.50 (3.42)	411 (MH^+)	7.94 (1H, d, $^{3}J_{PH}$ 13.4, ArH-2), 7.81 (1H, dd, $^{3}J_{PH}$ 12.9 $^{3}J_{HH}$ 7.6, ArH-6), 7.64 (5H, m, ArH), 7.39 (7H, m, ArH)	−62.75 (s, CF_3)	35.3 (s, $^{1}J_{SeP}$ 742)
4b	Oil		661 (MH^+)	7.92 (1H, dd, $^{3}J_{PH}$ 13.0, $^{3}J_{HH}$ 7.6, ArH-6), 7.82 (1H, d, $^{3}J_{PH}$ 13.5, ArH-2), 7.67–7.42 (12H, m, ArH)	−80.86 (3F, t, $^{4}J_{FF}$ 9.5, CF_3), −111.01 (2F, t, $^{4}J_{FF}$ 14.1, α-CF_2), −121.38 (2F, m, CF_2), −121.91 (2F, m, CF_2), −122.80 (2F, m, CF_2), −126.15 (2F, m, CF_2)	35.3 (s, $^{1}J_{SeP}$ 744), 35.7 (s, $^{1}J_{SeP}$ 774)[d]

(*continued on next page*)

Table 1 (*continued*)

Phosphine	M.p. (°C)	Elemental analysis[b]	*m*/*z*[c]	^{1}H	^{19}F{^{1}H}	^{31}P{^{1}H}
4c	0Oil		760 (MH^+)	7.93 (1H, dd, $^{3}J_{PH}$ 12.9, $^{3}J_{HH}$ 7.5, ArH-6), 7.83 (1H, d, $^{3}J_{PH}$ 13.8, ArH-2), 7.70–7.35 (12H, m, ArH)	−80.83 (3F, t, $^{4}J_{FF}$ 9.1, CF_3), −111.28 (2F, t, $^{4}J_{FF}$ 14.0, α-CF_2), −121.20 (2F, m, CF_2), −121.73 (2F, m, CF_2), −121.89 (2F, m, CF_2), −122.54 (2F, m, CF_2), −122.68 (2F, m, CF_2), −126.14 (2F, m, CF_2)	35.3 (s, $^{1}J_{SeP}$ 744)
5b	157–158	C, 33.14 (33.38); H, 0.98 (0.93)	1297 (MH^+)	8.09 (3H, dd, $^{3}J_{PH}$ 13.7, $^{3}J_{HH}$ 7.6, ArH-2), 7.69 (9H, m, ArH)	−81.45 (9F, t, $^{4}J_{FF}$ 9.3, CF_3), −112.07 (6F, t, $^{4}J_{FF}$ 14.0, α-CF_2), −122.13 (6F, m, CF_2), −122.48 (6F, m, CF_2), −123.57 (6F, m, CF_2), −126.86 (6F, m, CF_2)	34.7 (s, $^{1}J_{SeP}$ 772), 35.8 (s, $^{1}J_{SeP}$ 796)[d]
5c	126–127	C, 31.82 (31.62); H, 0.67 (0.75)	1596 (M^+)	8.16 (3H, dd, $^{3}J_{PH}$ 13.8, $^{3}J_{HH}$ 7.2, ArH-2), 7.61 (9H, m, ArH)	−80.75 (9F, t, $^{4}J_{FF}$ 8.5, CF_3), −111.08 (6F, t, $^{4}J_{FF}$ 14.1, α-CF_2), −121.15 (6F, m, CF_2), −122.00 (18F, m, 3 × CF_2), −122.68 (6F, m, CF_2) −126.10 (6F, m, CF_2)	34.6 (s, $^{1}J_{SeP}$ 773)
6a	97–100	C, 55.86 (55.75); H, 3.51 (3.42)	411 (MH^+)[e]	7.75 (4H, m, ArH), 7.55 (2H, m, ArH), 7.40 (8H, m, ArH)	−53.52 (d, $^{4}J_{PF}$ 3, CF_3)	38.0 (q, $^{4}J_{PF}$ 3, $^{1}J_{SeP}$ 752)
6b	108–109	C, 43.59 (43.77); H, 2.13 (2.13)		7.70 (4H, m, ArH), 7.55 (2H, m, ArH), 7.38 (8H, m, ArH)	−80.81 (3F, t, $^{4}J_{FF}$ 11.3, CF_3), −99.69 (2F, dt, $^{4}J_{PF}$ 10.0, $^{4}J_{FF}$ 15.3, α-CF_2), −117.62 (2F, m, CF_2), −121.41 (2F, m, CF_2), −122.88 (2F, m, CF_2), −126.17 (2F, m, CF_2)	40.4 (t, $^{4}J_{PF}$ 10, $^{1}J_{SeP}$ 757), 39.9 (t, $^{4}J_{PF}$ 10, $^{1}J_{SeP}$ 791)
7a	Oil	C, 50.69 (50.42); H, 2.60 (2.73)	477 (M^+)	8.09 (2H, d, $^{3}J_{PH}$ 12.6, ArH-2,6), 7.91 (1H, s, ArH-4), 7.63 (4H, m, ArH), 7.44 (6H, m, ArH)	−62.84 (s, CF_3)	35.0 (s, $^{1}J_{SeP}$ 755), 35.8 (s, $^{1}J_{SeP}$ 784)[d]
7b	Oil	C, 36.72 (36.89); H, 1.30 (1.33)	977 (M^+)	8.08 (2H, d, $^{3}J_{PH}$ 12.7, ArH-2,6), 7.82 (1H, s, ArH-4), 7.63 (4H, m, ArH), 7.59 (6H, m, ArH)	−80.82 (6F, t, $^{4}J_{FF}$ 9.7, CF_3), −111.08 (4F, t, $^{4}J_{FF}$ 14.0, α-CF_2), −121.30 (4F, m, CF_2), −121.89 (4F, m, CF_2), −122.73 (4F, m, CF_2), −126.11 (4F, m, CF_2)	35.2 (s, $^{1}J_{SeP}$ 758), 35.8 (s, $^{1}J_{SeP}$ 785)[d]
7c	Oil	C, 34.44 (34.66); H, 1.00 (1.10)		8.08 (2H, d, $^{3}J_{PH}$ 12.9, ArH-2,6), 7.83 (1H, s, ArH-4), 7.53 (10H, m, ArH)	−81.78 (6F, t, $^{4}J_{FF}$ 10.4, CF_3), −111.21 (4F, t, $^{4}J_{FF}$ 14.2, α-CF_2), −121.11 (8F, m, 2 × CF_2), −121.90 (8F, m, 2 × CF_2), −122.67 (4F, m, CF_2), −126.06 (4F, m, CF_2)	35.2 (s, $^{1}J_{SeP}$ 758)
8a	Oil	C, 43.15 (43.14); H, 1.82 (1.80)	613 (M^+)	8.09 (4H, d, $^{3}J_{PH}$ 13.0, ArH-2,6), 7.99 (2H, s, ArH-4), 7.54 (5H, m, ArH)	−63.04 (s, CF_3)	34.6 (s, $^{1}J_{SeP}$ 779), 35.2 (s, $^{1}J_{SeP}$ 801)[d]
8b	Oil	C, 31.54 (31.27); H, 0.59 (0.68)	1613 (M^+)	8.03 (4H, d, $^{3}J_{PH}$ 12.8, ArH-2,6), 7.89 (2H, s, ArH-4), 7.49 (5H, m, ArH)	−81.09 (12F, t, $^{4}J_{FF}$ 9.8, CF_3), −111.74 (8F, t, $^{4}J_{FF}$ 14.2, α-CF_2), −121.50 (8F, m, CF_2), −122.12 (8F, m, CF_2), −122.96 (8F, m, CF_2), −126.40 (8F, m, CF_2),	34.7 (s, $^{1}J_{SeP}$ 785), 35.3 (s, $^{1}J_{SeP}$ 806)[d]
9a[16]				8.11 (6H, d, $^{3}J_{PH}$ 13.1 ArH-2,6), 8.09 (3H, s, ArH-4),	−63.50 (s, CF_3)	34.3 (s, $^{1}J_{SeP}$ 803), 34.3 (s, $^{1}J_{SeP}$ 817)[d]
10a	Oil	C, 34.59 (34.53); H, 0.90 (0.99)		8.08 (2H, d, $^{3}J_{PH}$ 13.0, ArH-2′,6′), 7.99 (1H, s, ArH-4'), 7.80 (4H, m, C_6H_4), 7.70 (4H, m, C_6H_4)	−62.93 (6F, s, CF_3), −80.78 (6F, t, $^{4}J_{FF}$ 9.8, CF_3), −111.29 (4F, t, $^{4}J_{FF}$ 14.3, α-CF_2), −121.33 (4F, m, CF_2), −121.70 (4F, m, CF_2), −122.82 (4F, m, CF_2), −126.08 (4F, m, CF_2)	34.2 (s, $^{1}J_{SeP}$ 780), 34.8 (s, $^{1}J_{SeP}$ 801)[d]
10b	Oil	C, 31.48 (31.27); H, 0.55 (0.68)	1613 (M^+)	8.01 (2H, d, $^{3}J_{PH}$ 13.0, ArH-2′,6′), 7.87 (1H, s, ArH-4'), 7.78 (4H, dd, $^{3}J_{PH}$ 13.2, $^{3}J_{HH}$ 8.3, ArH-2,6), 7.66 (4H, dd, $^{3}J_{HH}$ 8.3, $^{4}J_{PH}$ 2.2, ArH-3,5)	−81.21 (12F, t, $^{4}J_{FF}$ 10.7, CF_3), −111.45 (4F, t, $^{4}J_{FF}$ 14.2, α-CF_2), −111.72 (4F, t, $^{4}J_{FF}$ 14.2, α-CF_2), −121.56 (8F, m, CF_2), −122.14 (8F, m, CF_2), −123.0 (8F, m, CF_2), −126.42 (8F, m, CF_2)	34.0 (s, $^{1}J_{SeP}$ 785), 34.3 (s, $^{1}J_{SeP}$ 803)[d]

11b[f]	125–127	1417 [MH]+[e]	7.96 (2H, s, ArH), 7.89 (2H, dd, $^3J_{HH}$ 10.0, $^4J_{HH}$ 2.5, ArH), 7.66–7.54 (8H, m, PhH), 7.52 (2H, d, $^3J_{HH}$ 7.5, ArH), 7.35–7.21 (12H, m, PhH), 6.64 (2H, d, $^3J_{HH}$ 10.0, ArH), 6.59 (2H, d, $^3J_{HH}$ 10.0, ArH)	−81.18 (6F, t, $^4J_{FF}$ 9.8, CF_3), −110.77 (4F, m, α-CF_2), −121.48 (4F, m, CF_2), −121.80 (4F, m, CF_2), −123.16 (4F, m, CF_2), −126.48 (4F, m, CF_2)	32.7 (s, $^1J_{SeP}$ 749)
11d[g]	127–131	C, 49.14 (48.91); H, 2.48 (2.58) 1473 [MH]+[e]	7.69 (6H, m, PhH), 7.56 (4H, m, PhH), 7.50 (2H, s, ArH), 7.40 (2H, dd, J_{HH} 12.2, J_{HH} 8.8, ArH), 7.34–7.13 (12H, m, ArH and PhH), 6.58 (2H, d, $^3J_{HH}$ 8.7, ArH), 6.33 (2H, dd, $^3J_{HH}$ 8.8, $^4J_{HH}$ 1.5, ArH), 2.84 (4H, m, CH_2), 2.25 (4H, m, CH_2)	−80.75 (6F, t, $^4J_{FF}$ 10.4, CF_3), −114.52 (4F, m, α-CF_2), −121.79 (4F, m, CF_2), −122.80 (4F, m, CF_2), −123.38 (4F, m, CF_2), −126.08 (4F, m, CF_2)	32.8 (s, $^1J_{SeP}$ 743)
11i[h]	> 300	781 [MH]+[e]	7.71–7.53 (12H, m, ArH and PhH), 7.43 (2H, m, ArH), 7.29–7.09 (14H, m, ArH and PhH), 6.69 (2H, d, $^3J_{HH}$ 8.4, ArH), 6.63 (2H, m, ArH)		33.7 (s, $^1J_{SeP}$ 739)

[a] Spectra recorded in $CDCl_3$ unless otherwise stated. Data given as δ (intensity, multiplicity, J (Hz), assignment.
[b] Calculated values in parentheses.
[c] FAB spectra unless otherwise stated.
[d] Spectra recorded in diethyl ether.
[e] ES^+ spectra.
[f] $[\alpha]_D$ ($CHCl_3$) 20.7° ($c = 1.2$).
[g] $[\alpha]_D$ ($CHCl_3$) 17.72° ($c = 0.9$).
[h] $[\alpha]_D$ ($CHCl_3$) 19.0° ($c = 1.6$).

−122.90 (6F, m, CF_2) −126.29 (6F, m, CF_2). $^{31}P\{^1H\}$ NMR ($CDCl_3$) −6.9 (s).

2.2. General procedure for the preparation of phosphorus(V) selenides

The phosphine (0.20 g) was dissolved in chloroform (10 ml) and selenium powder added (0.30 g, 3.8 mmol). The mixture was heated to 70 °C overnight. After cooling, the excess selenium was removed by filtration through a cotton wool plug and the solvent removed in vacuo to give the phosphorus(V) selenide in a 64–89% yield. A few of the phosphorus(V) selenides used in this study have been reported previously; tris(4-*N*,*N*-dimethylaminophenyl) phosphine selenide, [28] tris(4-methoxyphenyl)phosphine selenide, tris(4-methylphenyl)phosphine selenide, trisphenylphosphine selenide, tris(4-fluorophenyl)phosphine selenide, tris(4-trifluoromethylphenyl)phosphine selenide, tris (3-trifluoromethylphenyl)phosphine selenide and tris(3,5-trifluoromethylphenyl)phosphine selenide, [15] and tris(4-chlorophenyl)phosphine [29]. Table 1 summarises all the analytical and NMR spectroscopic data for the new phosphorus(V) selenides prepared in this work.

2.3. General procedure for the preparation of $[PtCl_2L_2]$ complexes

The phosphine (0.1 mmol) and $[PtCl_2(CH_3CN)_2]$ (0.05 mmol) were dissolved in dichloromethane (10 ml) and heated to reflux for 2 h. After cooling, the solvent was removed and the resulting solid washed well with petroleum ether to give a pale yellow solid in 84–91% yield.

2.3.1. cis- and trans-$[PtCl_2\{Ph_2P(C_6H_4\text{-}4\text{-}CF_3)\}_2]$

Anal. Calc. for $C_{38}H_{28}Cl_2F_6P_2Pt$: C, 49.30; H, 3.03. Found: C, 49.15; H, 3.03%. *m/z* (FAB) 891 $(M-Cl)^+$. ^1H NMR ($CDCl_3$) 7.96 (8H, m, ArH), 7.36 (12H, m, ArH), 7.19 (8H, m, ArH). $^{19}F\{^1H\}$ NMR ($CDCl_3$) −63.00 (s, *trans*), −63.10 (s, *cis*). $^{31}P\{^1H\}$ NMR ($CDCl_3$) 20.5 (s, $^1J_{PtP}$ 2656, *trans*), 14.7 (s, $^1J_{PtP}$ 3653, *cis*).

2.3.2. cis- and trans-$[PtCl_2\{Ph_2P(C_6H_4\text{-}4\text{-}C_8F_{17})\}_2]$

m/z (FAB) 1591 $(M-Cl)^+$. ^1H NMR ($CDCl_3$) 7.70 (4H, d, $^3J_{HH}$ 7.8, ArH-3,5), 7.53 (4H, t, $^3J_{HH} = {}^3J_{PH}$ 7.8, ArH-2,6), 7.34 (16H, m, PhH), 7.19 (4H, m, PhH). $^{19}F\{^1H\}$ NMR ($CDCl_3$) −80.73 (6F, t, $^4J_{FF}$ 9.8, CF_3), −111.09 (4F, t, $^4J_{FF}$ 13.7, α-CF_2), −121.17 (4F, m, CF_2), −121.54 (4F, m, CF_2), −121.84 (8F, m, $2 \times CF_2$), −122.64 (4F, m, CF_2), −126.06 (2F, m, CF_2). $^{31}P\{^1H\}$ NMR ($CDCl_3$) 20.5 (s, $^1J_{PtP}$ 2664, *trans*), 14.5 (s, $^1J_{PtP}$ 3653, *cis*).

2.3.3. cis- and trans-$[PtCl_2\{Ph_2P(C_6H_4\text{-}4\text{-}SiMe_2C_2H_4C_6F_{13})\}_2]$

Anal. Calc. for $C_{56}H_{48}Cl_2F_{26}P_2Pt$: C, 42.08; H, 3.01. Found: C, 42.06; H, 2.89%. *m/z* (FAB) 1563 $(M-Cl)^+$. ^1H NMR ($CDCl_3$) 7.63–7.08 (28H, m, ArH), 1.89 (4H, m, CH_2CF_2), 0.88 (4H, m, CH_2Si), 0.23 (12H, s, CH_3).

$^{19}F\{^1H\}$ NMR ($CDCl_3$) −81.30 (6F, t, $^4J_{FF}$ 9.9, CF_3), −116.68 (4F, t, $^4J_{FF}$ 14.1, α-CF_2), −123.06 (4F, m, CF_2), −123.63 (4F, m, CF_2), −124.02 (4F, m, CF_2), −126.67 (4F, m, CF_2). $^{31}P\{^1H\}$ NMR ($CDCl_3$) 19.9 (s, $^1J_{PtP}$ 2632, *trans*), 13.8 (s, $^1J_{PtP}$ 3673, *cis*).

2.3.4. cis- and trans-[$PtCl_2\{P(C_6H_4$-4-$CH_2CH_2CH_2C_6F_{13})_3\}_2$]

Anal. Calc. for $C_{90}H_{60}Cl_2F_{78}P_2Pt$: C, 36.61; H, 2.03. Found: C, 36.70; H, 1.96%. *m/z* (FAB) 2915 $(M-Cl)^+$. ^1H NMR ($CDCl_3$) 7.34 (12H, dd, $^3J_{PH}$ 11.2, $^3J_{HH}$ 8.2, ArH-2,6), 6.90 (12H, m, ArH-3,5), 2.60 (12H, m, CH_2), 1.87 (24H, m, CH_2). $^{19}F\{^1H\}$ NMR ($CDCl_3$) −81.10 (18F, t, $^4J_{FF}$ 9.9, CF_3), −114.31 (12F, t, $^4J_{FF}$ 12.3, α-CF_2), −122.09 (12F, m, CF_2), −122.68 (12F, m, CF_2), −123.06 (12F, m, CF_2), −126.42 (12F, m, CF_2). $^{31}P\{^1H\}$ NMR ($CDCl_3$) 18.6 (s, $^1J_{PtP}$ 2614, *trans*), 12.8 (s, $^1J_{PtP}$ 3679, *cis*).

2.3.5. cis-[$PtCl_2\{Ph_2P(C_6H_4$-3-$CF_3)\}_2$]

Anal. Calc. for $C_{38}H_{28}Cl_2F_6P_2Pt$: C, 49.24; H, 3.02. Found: C, 49.18; H, 2.96%. *m/z* (FAB) ^1H NMR ($CDCl_3$) 7.46 (14H, m, ArH), 7.27 (4H, m, ArH), 7.18 (10H, m, ArH). $^{19}F\{^1H\}$ NMR ($CDCl_3$) −62.69 (s, CF_3). $^{31}P\{^1H\}$ NMR ($CDCl_3$) 15.1 (s, $^1J_{PtP}$ 3653).

2.3.6. cis- and trans-[$PtCl_2\{Ph_2P(C_6H_4$-3-$C_8F_{17})\}_2$]

Anal. Calc. for $C_{52}H_{28}Cl_2F_{34}P_2Pt$: C, 35.35; H, 1.72. Found: C, 34.15; H, 1.73%. *m/z* (FAB) 1591 $(M-Cl)^+$. ^1H NMR ($CDCl_3$) 8.00–7.20 (28H, m, ArH). $^{19}F\{^1H\}$ NMR ($CDCl_3$) −80.91 (6F, m, CF_3), −111.01 (4F, m, α-CF_2), −121.19 (4F, m, CF_2), −121.81 (12F, m, $3\times CF_2$), −122.67 (4F, m, CF_2), −126.08 (4F, m, CF_2). $^{31}P\{^1H\}$ NMR ($CDCl_3$) 21.2 (s, $^1J_{PtP}$ 2663, *trans*), 16.1 (s, $^1J_{PtP}$ 3650, *cis*).

2.3.7. cis- and trans-[$PtCl_2\{P(C_6H_4$-4-$C_8F_{17})_3\}_2$]

Anal. Calc. for $C_{84}H_{24}Cl_2F_{102}P_2Pt$: C, 30.58; H, 0.73. Found: C, 30.50; H, 0.64%. *m/z* (MALDI-TOF) 3227 $(M-2Cl)^+$. ^1H NMR (C_6D_6/C_6F_6) 7.98 (6H, dd, $^3J_{HH}$ 8.2, $^3J_{PH}$ 5.5, ArH-2,6), 7.79 (6H, dd, $^3J_{HH}$ 8.2, $^3J_{PH}$ 8.5, ArH-2,6), 7.72 (12H, d, $^3J_{HH}$ 8.2, ArH-3,5). $^{19}F\{^1H\}$ NMR (C_6D_6/C_6F_6) −83.48 (18F, t, $^4J_{FF}$ 10.0, CF_3), −113.30 (6F, t, $^4J_{FF}$ 14.6, α-CF_2), −113.43 (6F, t, $^4J_{FF}$ 15.5, α-CF_2), −122.92 (12F, m, CF_2), −123.33 (24F, m, $2\times CF_2$), −123.49 (12F, m, CF_2), −124.34 (12F, m, CF_2), −128.04 (12F, m, CF_2). $^{31}P\{^1H\}$ NMR (C_6D_6/C_6F_6) 20.5 (s, $^1J_{PtP}$ 2741, *trans*), 15.2 (s, $^1J_{PtP}$ 3570, *cis*).

2.3.8. cis- and trans-[$PtCl_2\{Ph_2P(C_6H_3$-3,5-$[CF_3]_2)\}_2$]

Anal. Calc. for $C_{40}H_{26}Cl_2F_{12}P_2Pt$: C, 45.24; H, 2.45. Found: C, 45.03; H, 2.38%. *m/z* (FAB) 1027 $(M-Cl)^+$. ^1H NMR ($CDCl_3$) 7.66 (2H, s, ArH-4), 7.60 (2H, d, $^3J_{PH}$ 11.6, ArH-2,6), 7.58 (2H, d, $^3J_{PH}$ 11.1, ArH-2,6), 7.42 (12H, m, PhH), 7.25 (8H, m, PhH). $^{19}F\{^1H\}$ NMR ($CDCl_3$) −62.96 (s, CF_3). $^{31}P\{^1H\}$ NMR ($CDCl_3$) 22.1 (s, $^1J_{PtP}$ 2685, *trans*), 15.9 (s, $^1J_{PtP}$ 3630, *cis*).

3. Results and discussion

Measuring $^1J_{PtP}$ for *cis*-[$PtCl_2L_2$] (L = triarylphosphine) is a very useful tool for the characterisation of platinum complexes, with the magnitude of the coupling constant being a predictive function of the triarylphosphine ligand, and Pringle et al. have shown that these values correlate very well with the Hammett σ_p parameter of the substituent

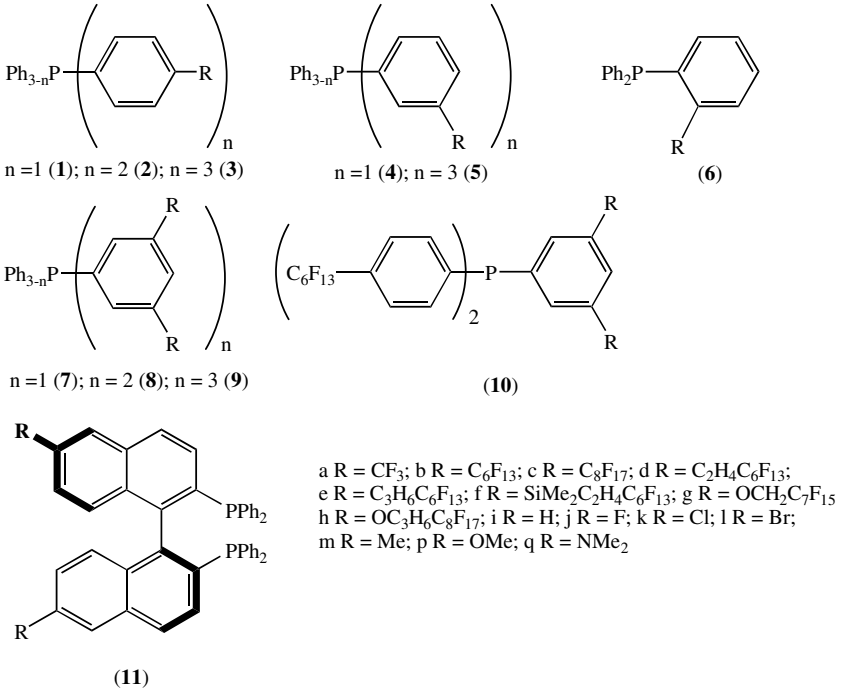


Fig. 1. Phosphines used in this study.

on the aryl ring [30]. We have previously used this technique to probe the effect of perfluoroalkylation on the donor properties of triarylphosphines [13]. However, systematic comparison of the electronic impact of the perfluoroalkyl-substituent is not always possible since, as a consequence of steric constraints, some *cis*-$[PtCl_2L_2]$ complexes are not available. Furthermore, even where the complexes can be formed, it is difficult to be certain that the effect being probed is entirely electronic. For example, the $^1J_{PtP}$ values for the *cis*-$[PtCl_2L_2]$ complexes derived from $Ph_2P(C_6H_4\text{-}4\text{-}C_6F_{13})$ and $Ph_2P(C_6H_4\text{-}3\text{-}C_6F_{13})$ are 3653 Hz [13] and 3635 Hz [14], respectively, although it

Table 2
Coupling constant data for phosphorus(V) selenides and *cis*-/*trans*-$[PtCl_2L_2]$ complexes[a]

Phosphine	Substituent	$\lvert^1J_{SeP}\rvert$	ΔJ_{SeP}[b]	$\lvert^1J_{SeP}\rvert$[c]	$\lvert^1J_{PtP}\rvert$[d]	$\lvert^1J_{PtP}\rvert$[e]
3q	NMe_2	683[f]	−53		3747[g]	
3p	OMe	710[h]	−20	746	3707[g]	
3m	Me	715[h]	−15		3691[g]	
3h	$OC_3H_6C_8F_{17}$	715	−15	754		
3e	$C_3H_6C_6F_{13}$	725	−5	764	3679	2614
3g	$OCH_2C_7F_{15}$	729	−1	759	3680[i]	
3i	H	730	0	767	3675[g]	2635[j]
1f	$SiMe_2C_2H_4C_6F_{13}$	730	0	766	3673	2632
3d	$C_2H_4C_6F_{13}$	733	3	767	3679[k]	
3j	F	741[h]	11	772	3666[l]	
3k	Cl	748	18	775	3648[g]	
3l	Br	748	18	778	3646	
1a	CF_3	741	11	774	3653	2656
1b	C_6F_{13}	743	13	774	3653[m]	
1c	C_8F_{17}	742	12	775	3653	2664
4a	CF_3	742	12		3653	
4b	C_6F_{13}	744	14	774	3633[n]	2646[n]
4c	C_8F_{17}	744	14		3650	2663
6a	CF_3	752	22			2805[o]
6b	C_6F_{13}	757	27	791		2826[o]
2b	C_6F_{13}	756	26	782	3635[m]	
7a	CF_3	755	25	784	3630	2685
7b	C_6F_{13}	758	28	785	3630[p]	2692[p]
7c	C_8F_{17}	758	28		3622[p]	2695[p]
3a	CF_3	765[h]	35		3611[g]	
3b	C_6F_{13}	769	39	792	3615[m]	2712[m]
3c	C_8F_{17}	insol.		793	3570	2741
5a	CF_3	766[h]	36		3608[l]	2720[l]
5b	C_6F_{13}	772	42	796		2723[n]
5c	C_8F_{17}	773	43			
8a	CF_3	779	49	801		2739[p]
8b	C_6F_{13}	785	55	806		2741[p]
10a	CF_3/C_6F_{13}	780	50	801	3591[p]	2741[p]
10b	C_6F_{13}	785	55	803	3576[p]	2744[p]
9a	CF_3	803	73	817	3621[l]	2786[l]
11i	H	739	0[q]		3665[r]	
11d	$C_2H_4C_6F_{13}$	743	4[q]		3665[r]	
11b	C_6F_{13}	749	10[q]		3636[r]	

[a] Data (Hz) recorded for compounds dissolved in $CDCl_3$ unless otherwise stated.
[b] $\Delta J_{SeP} = \lvert^1J_{SeP}\rvert(L) - \lvert^1J_{SeP}\rvert(PPh_3)$ unless otherwise stated.
[c] Diethyl ether.
[d] *cis*-$[PtCl_2L_2]$.
[e] *trans*-$[PtCl_2L_2]$.
[f] Data from Ref. 28.
[g] Data from Ref. 30.
[h] Data from Ref. 16.
[i] Data from Ref. 31.
[j] Data from Ref. 32.
[k] Data from Ref. 33.
[l] Data from Ref. 22.
[m] Data from Ref. 13.
[n] Data from Ref. 14.
[o] Data from Ref. 34.
[p] Data taken from Ref. 22.
[q] $\Delta J_{SeP} = \lvert^1J_{SeP}\rvert(L) - \lvert^1J_{SeP}\rvert$ (**11i**).
[r] Data taken from Ref. 25.

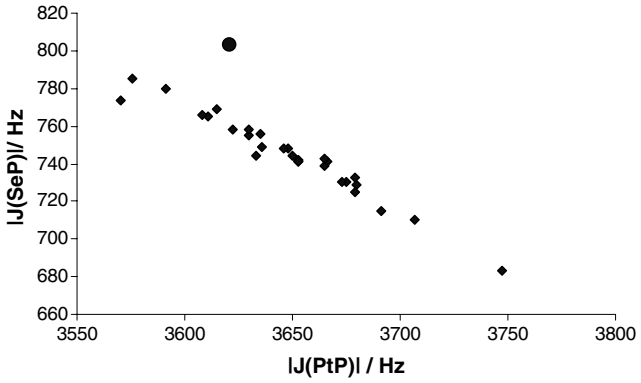
would be anticipated that placing the perfluoroalkyl group in the *para*- or *meta*-position would have little effect on the electronic properties of the phosphine and, indeed, Howell et al. report that the electron-withdrawing effect of the purely inductive CF_3 is felt almost equally at the *ortho*-, *meta*- and *para*-positions [16].

In order to fully understand the electronic influence of perfluoroalkyl substituents on the donor properties of triarylphosphines, we have prepared a comprehensive series of phosphorus(V) selenides from a range of triaryl phosphines (Fig. 1). NMR spectroscopic data for these compounds, alongside those for the *cis*-$[PtCl_2L_2]$ complexes and selected values from the literature, are presented in Table 2. The NMR data, in particular the $|^1J_{SeP}|$ coupling constants, [15] are solvent dependent and this must be borne in mind in any comparison. Unfortunately, not all the phosphorus(V) selenides are soluble in either $CDCl_3$ or diethyl ether so, in order to offer a comprehensive analysis, data for many of the compounds are reported for both solvents; the correlations discussed below apply equally well to both sets of data.

These data reveal a number of significant facts. Firstly, as reported previously for the CF_3-derivatised aryl phosphines, [16] the $|^1J_{SeP}|$ values for the C_6F_{13} derivatised phosphorus(V) selenides are cumulative. So, ΔJ_{PSe} (relative to $Se=PPh_3$) for the selenide derived from $P(C_6H_4\text{-}4\text{-}C_6F_{13})_3$, **3b**, is three times that for the selenide derived from $Ph_2P(C_6H_4\text{-}4\text{-}C_6F_{13})$, **1b**. Similarly, that from **8b** gives a value four times greater than that from **1b**. Secondly, despite various anecdotal, spectroscopic and catalytic evidence to the contrary, the lengths of the perfluoroalkyl substituents have no impact upon the electronic environment at phosphorus since ΔJ_{SeP} for related series (phosphines = **1a**, **1b** and **1c**; **3a**, **3b** and **3c**; **4a**, **4b** and **4c**; **5a**, **5b** and **5c**; **6a** and **6b**; **7a**, **7b** and **7c**) are virtually identical. Finally, since the values from the *meta*- and *para*-substituted phosphines (**1a**, **1b** and **1c**; **4a**, **4b** and **4c**) are very similar and those from **10b** and **8b** give identical results, the electron-withdrawing effect of the perfluoroalkyl groups on the phosphorus centre is independent of their position in these phosphines. As indicated above, this effect is not apparent from the $^1J_{PtP}$ values for pairs of *cis*-$[PtCl_2L_2]$ complexes, particularly since all attempts at forming *cis*-$[PtCl_2L_2]$ for phosphine **8b** failed, presumably due to steric congestion. However, in direct contrast to the observations of Howell et al., [16] this cannot be extended to the *ortho*-substituted phosphines, **6a** and **6b**, where $|^1J_{SeP}|$ for their selenides are substantially different to those for the selenides of **1a**, **4a**, **1b** and **4b**. This type of effect has, for the *ortho*-methylated triarylphosphine selenides, been attributed to the steric impact of the substituents, [17] and this could equally apply to our fluoroalkylated phosphine selenides. An alternative explanation arises from through space interactions between the phosphorus and fluorine atoms [34]. This is clearly evident in the free phosphines ($R=C_6F_{13}$, $^4J_{PF}=99$ Hz; $R=CF_3$, $^4J_{PF}=53$ Hz) and, although the magnitude of the interaction is reduced in the phosphine selenides ($R=C_6F_{13}$, $^4J_{PF}=10$ Hz; $R=CF_3$, $^4J_{PF}=3$ Hz), its presence is likely to seriously alter the electronic properties of the phosphorus atoms and hence the P–Se interaction.

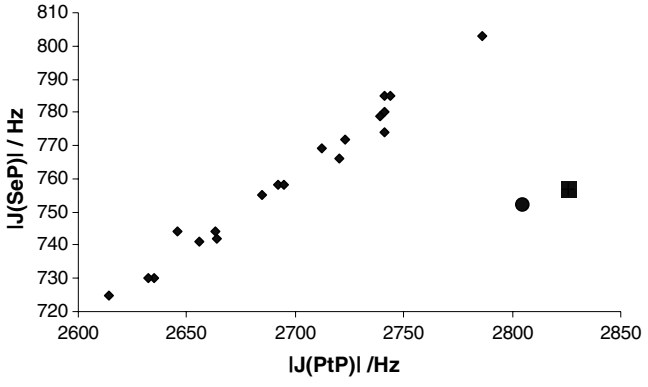
As expected, since both parameters are affected by the electronic environment of the phosphine, there is a linear relationship between $|^1J_{SeP}|$ and $|^1J_{PtP}|$ for both the *cis*-, Fig. 2, and *trans*-$[PtCl_2L_2]$ complexes, Fig. 3. The only data point which does not show the linear correlation in Fig. 2 is that for the *cis*-$[PtCl_2(\mathbf{9a})_2]$ quoted by Alt et al. [22]. However, although ΔJ_{SeP} for the selenide of **9a** is entirely consistent with the presence of six CF_3 groups, we were unable to prepare the *cis*-platinum metal complex to confirm the magnitude of this $^1J_{PtP}$ coupling constant. In contrast, in Fig. 3, the data for *trans*-$[PtCl_2(\mathbf{9a})_2]$ is consistent with the linear correlation. In Fig. 3, the data points associated with phosphines **6a** and **6b** do not follow the linear correlation, which is accounted for by the additional steric and electronic interactions in both their selenides and platinum metal complexes [34].

Many attempts have been made to minimise the electronic effect of fluoroalkyl groups on the donor properties of the



• L = $P\{C_6H_3\text{-}3,5\text{-}(CF_3)_2\}_3$

Fig. 2. Correlation between $|^1J_{SeP}|$ for trisarylphosphine selenides and $|^1J_{PtP}|$ for *cis*-$[PtCl_2L_2]$.



• L = $PPh_2(C_6H_4\text{-}2\text{-}CF_3)$. ■ L = $PPh_2(C_6H_4\text{-}2\text{-}C_6F_{13})$

Fig. 3. Correlation between $|^1J_{SeP}|$ for $Se=PR_3$ and $|^1J_{PtP}|$ for *trans*-$[PtCl_2(PR_3)_2]$.

Table 3
Influence of electronic spacer units on $|^1J_{SeP}|$ coupling constants for $Se = P(4\text{-}C_6H_4R)_3$

R	Label	$\lvert^1J_{SeP}\rvert$ ($CDCl_3$) (Hz)	ΔJ_{SeP} (Hz)[a]
OMe	**3p**	710	−20
Me	**3m**	715	−15
$OCH_2CH_2CH_2C_8F_{17}$	**3h**	715	−15
$CH_2CH_2CH_2C_6F_{13}$	**3e**	725	−5
$OCH_2C_7F_{15}$	**3g**	729	−1
H	**3i**	730	0
$CH_2CH_2C_6F_{13}$	**3d**	733	3
CF_3	**3a**	765	35
C_6F_{13}	**3b**	769	39

[a] $\Delta J_{SeP} = |^1J_{SeP}|(L) - |^1J_{SeP}|(PPh_3)$.

phosphines, which has been achieved by the introduction of spacer groups between the perfluoroalkyl group and the aromatic ring. By examining the $^1J_{SeP}$ data it is possible to determine the efficiency of these groups at insulating the phosphorus centre from the perfluoroalkyl groups and illustrative data are collected in Table 3. It can be seen that, using these different perfluoroalkyl groups, it is possible to generate a range of different electronic environments at the phosphorus atoms. For these triarylphosphines, additional CH_2 spacer units can provide insulation of the phosphorus atom from the perfluoroalkyl groups, but at least two are required for complete insulation. Finally, by using spacer groups incorporating an oxygen atom, it is possible to generate phosphines for use in a perfluorocarbon solvent that are actually electron rich, as illustrated by the data for the $OCH_2CH_2CH_2$ (**3h**) spacer group substituted phosphine that gives the same $^1J_{SeP}$ as tris(4-tolyl)phosphine selenide (**3m**).

4. Conclusions

The $^1J_{SeP}$ coupling constants of a series of trisarylphosphines derivatised with a variety of different perfluoroalkyl groups have been measured, which allow the direct comparison between phosphine ligands that is not possible via other spectroscopic probes. The values have been used to compare a range of different fluorinated groups and to determine the efficiency of a variety of spacer groups at insulating the phosphorus centre from the electron-withdrawing effect of the perfluoroalkyl group. This data illustrates that it is possible to generate phosphines for use in fluorous catalysis that are either electron rich, electron neutral or electron poor with respect to triphenylphosphine.

Acknowledgements

We thank the EPSRC (DJA, JAB, DD, AJW), Merck (JAB, AJW), GSK (DD) and the Royal Society (AMS) for financial support.

References

[1] I.T. Horváth, G. Kiss, R.A. Cook, J.E. Bond, P.A. Stevens, J. Rábai, E.J. Mozeleski, J. Am. Chem. Soc. 120 (1998) 3133.
[2] D. Rutherford, J.J.J. Juliette, C. Rocaboy, I.T. Horváth, J.A. Gladysz, Catal. Today 42 (1998) 381.
[3] E. de Wolf, E.A. Speets, B.-J. Deelman, G. van Koten, Organometallics 20 (2001) 3686.
[4] (a) S. Schneider, W. Bannwarth, Helv. Chim. Acta 84 (2001) 735; (b) C. Markert, W. Bannwarth, Helv. Chim. Acta 85 (2002) 1877; (c) C.C. Tzschucke, W. Bannwarth, Helv. Chim. Acta 87 (2004) 2882.
[5] L.P. Barthel-Rosa, J.A. Gladysz, Coord. Chem. Rev. 190–192 (1999) 587.
[6] (a) D. Sinou, D. Maillard, A. Aghmiz, A.M. Masdeu I-Bultó, Adv. Synth. Catal. 345 (2003) 603; (b) B. Richter, E. de Wolf, G. van Koten, B.-J. Deelman, J. Org. Chem. 65 (2000) 3885; (c) M. Wende, F. Seidel, J.A. Gladysz, J. Fluorine Chem. 124 (2003) 45.
[7] P. Bhattacharyya, D. Gudmunsen, E.G. Hope, R.D.W. Kemmitt, D.R. Paige, A.M. Stuart, J. Chem. Soc., Perkin Trans. I (1997) 3609.
[8] (a) W. Chen, L. Xu, J. Xiao, Org. Lett. 2 (2000) 2675; (b) S. Darses, M. Pucheault, J.-P. Genet, Eur. J. Org. Chem. (2002) 269.
[9] (a) D. Sinou, G. Pozzi, E.G. Hope, A.M. Stuart, Tetrahedron Lett. 40 (1999) 849; (b) D. Sinou, D. Maillard, G. Pozzi, Eur. J. Org. Chem. (2001) 1121.
[10] E. de Wolf, B. Richter, B.-J. Deelman, G. van Koten, J. Org. Chem. 65 (2000) 5424.
[11] H. Jiao, S. Le Stang, T. Soos, R. Meier, K. Kowski, P. Rademacher, L. Jafarpour, J.-B. Hamard, S.P. Nolan, J.A. Gladysz, J. Am. Chem. Soc. 124 (2002) 1516.
[12] T. Soos, B.L. Bennett, D. Rutherford, L.P. Barthel-Rosa, J.A. Gladysz, Organometallics 20 (2001) 3079.
[13] J. Fawcett, E.G. Hope, R.D.W. Kemmitt, D.R. Paige, D.R. Russell, A.M. Stuart, J. Chem. Soc. Dalton Trans. (1998) 3751.
[14] E.G. Hope, R.D.W. Kemmitt, D.R. Paige, A.M. Stuart, D.R.W. Wood, Polyhedron 18 (1999) 2913.
[15] We note that $^1J_{SeP}$ is negative: W. McFarlane, J.A. Nash, J. Chem. Soc. Chem. Commun. (1969) 913.
[16] J.A.S. Howell, N. Fey, J.D. Lovatt, P.C. Yates, P. McArdle, D. Cunningham, E. Sadeh, H.E. Gottlieb, Z. Goldschmidt, M.B. Hursthouse, M.E. Light, J. Chem. Soc. Dalton Trans. (1999) 3015.
[17] R.P. Pinnell, C.A. Megerle, S.L. Manatt, P.A. Kroon, J. Am. Chem. Soc. 95 (1973) 977.
[18] F.R. Hartley, C.A. McAuliffe, Inorg. Chem. 18 (1979) 1394.
[19] R. De Ketelaere, E. Muylle, W. Vanermen, E. Claeys, G.P. Van Der Kelen, Bull. Soc. Chim. Belges 78 (1969) 219.
[20] P.D. Bartlett, G. Meguerian, J. Am. Chem. Soc. 78 (1956) 3710.
[21] V. Ravindar, H. Hemling, H. Schumann, J. Blum, Synth. Commun. 22 (1992) 841.
[22] H.G. Alt, R. Baumgaertner, H.A. Brune, Chem. Ber. 119 (1986) 1694.
[23] J. Porwisick, M. Schlosser, Chem. Ber. 129 (1996) 233.
[24] D.J. Adams, J.A. Bennett, D.J. Cole-Hamilton, E.G. Hope, J. Hopewell, J. Kight, P. Pogorzelec, A.M. Stuart, Dalton Trans. (2005) 3862.
[25] E.G. Hope, A.M. Stuart, A.J. West, Green Chem. 6 (2004) 345.
[26] S.E. Tunney, J.K. Stille, J. Org. Chem. 52 (1987) 748.
[27] S. Schneider, W. Bannwarth, Angew. Chem., Int. Ed. 39 (2000) 4142.
[28] J. Malito, E.C. Alyea, Phosphorus Sulfur Silicon 54 (1990) 95.
[29] R.F. De Ketelaere, G.P. Van Der Kelen, Z. Eeckhaut, Phosphorus 5 (1974) 43.
[30] C.J. Cobley, P.G. Pringle, Inorg. Chim. Acta 265 (1997) 107.
[31] P. Bhattacharyya, B. Croxtall, J. Fawcett, J. Fawcett, D. Gudmunsen, E.G. Hope, R.D.W. Kemmitt, D.R. Paige, D.R. Russell, A.M. Stuart, D.R.W. Wood, J. Fluorine Chem. 101 (2000) 247.
[32] J.P. Farr, F.E. Wood, A.L. Baulch, Inorg. Chem. 22 (1983) 3387.
[33] Q. Zhang, Z. Luo, D.P. Curran, J. Org. Chem. 65 (2000) 8866.
[34] B. Croxtall, J. Fawcett, E.G. Hope, A.M. Stuart, J. Chem. Soc., Dalton Trans. (2002) 491.

($X = Cl^-$, Br^- and CO_3) [11], $[V_{16}O_{38}(X)]$ ($X = Cl^-$, H_2O) [12,8d], $[V_{22}O_{54}(X)]$ $X = (ClO_4^-$, SCN^- and CH_3COO^-) [13] and $[V_{18}O_{42}(X)]$ ($X = H_2O$, Cl^-, Br^-, I^-, SO_4 and VO_4) [14] clusters. The central guest species in the shell exert templating effects on the electronic and framework structures of the host metal-oxide shells [15]. (2) The important family of magnetic polyoxometallates involves the mixed valence $V^{IV/V}$ oxometallates [16]. Magnetic studies performed on the mixed valence vanadium (IV/V) clusters arising from the full or partial deloclization of single 3d electrons of the V^{IV} ions over both V^{IV} and V^{V} have shown antiferromagnetic coupling and a few ferromagnetic coupling [17,14a]. (3) The mixed-valence vanadium oxide clusters have luminescence properties. This class of compounds could be active in photo-oxidation reactions and a potential photocatalyst, which is worth further investigating [9].

Owing to the synergistic interaction between the metal–organic and inorganic components, this class of compounds reveals some remarkable properties. We are currently exploring to design and develop organic–inorganic hybrid materials by the amalgamation of cage-like mixed-valence vanadium clusters with metal–organic complexes. The mixed-valence vanadium clusters that fuse paramagnetic transition metal complexes might be of interest in molecular magnetism [18,8d]. During this ongoing effort, different paramagnetic metal ions have been introduced into the reaction system, such as manganese (II), cobalt (II) and nickel (II). As a result, magnetic materials are obtained through combining paramagnetic metal ions and $[V_7^{IV}V_9^{V}O_{38}X]^{4-}$ clusters. In addition, the significant role of organic components in controlling the inorganic oxide microstructure was investigated by using different organic ligands. In this paper, we describe the synthesis and characterization of hybrid materials **1**–**5**. The magnetic properties of compounds **3**, **4** and **5** are reported as well.

2. Experimental

2.1. General remarks

All reagents were readily available from commercial sources and were used as received without further purification. The IR spectra in KBr pellets were recorded in the range 400–4000 cm^{-1} with an Alpha Centaurt FT/IR Spectrophotometer. Elemental Analyses (C, H and N) were performed with a Perkin–Elmer 2400 CHN Elemental Analyzer. M and V were determined with a PLASMA-SPEC (I) ICP atomic emission spectrometer. X-ray photoelectron spectrometry (XPS) spectra were measured on an ESCALAB spectrometer. Thermogravimetric analyses were carried out using a Pyris Diamond TG/DTA instrument, with a heating rate of 10 °C/min, under a nitrogen atmosphere. Magnetic susceptibility and magnetization data were collected over the temperature range 1.8–300 K in an applied field up to 50 kOe on a Quantum Design MPMS-5 SQUID magnetometer.

2.2. Preparation

2.2.1. Synthesis of $[Ni(4,4'\text{-}bpy)_2]_2[V_7^{IV}V_9^{V}O_{38}F]\cdot(4,4'\text{-}bpy)_{1.5}(H_2O)_3$ (**1**)

A mixture of $NaVO_3$ (122 mg, 1 mmol), Na_2TeO_3 (222 mg, 1 mmol), $Ni(CH_3COO)_2$ (177 mg, 1 mmol), 4,4′-bipyridine (50 mg, 0.38 mmol), HF (40%, 0.2 mL), CH_3CH_2OH (2 mL) and H_2O (5 mL) was stirred for ca. 1 h in air until it was homogeneous, and adjusted by CH_3COOH to pH 4.6, and then transferred and sealed in a 16 mL Teflon-lined stainless steel container. After heated to 170 °C under autogenously pressure for 4d, the bomb was cooled down to room temperature. Black octahedron block crystals of **1** along with an amorphous grey impurity were filtered from the colorless mother liquor, washed by distilled water and air-dried at room temperature. The crystals were mechanically separated from the powdery grey impurity to give a yield of 61% (based on V), and were stable in air and insoluble in water and common organic solvents. IR (KBr, cm^{-1}): $\tilde{\nu} = 3446$ (m), 1601 (m), 1559 (m), 1530 (m), 1487 (m), 1408 (m), 1066 (m), 983 (m), 813 (m), 733 (m), 670 (m), 657 (m), 631 (m), 507 (m), 459 (m), 418 (m), 403 (m). Elemental *Anal.* Calc. for $Ni_2C_{55}H_{50}N_{11}O_{41}V_{16}F$: C, 26.72; H, 2.04; N, 6.23; Ni, 4.75; V, 32.97. Found: C, 27.01; H, 2.27; N, 6.54; Ni, 4.27; V, 32.79%.

2.2.2. Synthesis of $[Ni(4,4'\text{-}bpy)_2]_2[V_7^{IV}V_9^{V}O_{38}Br]\cdot(4,4'\text{-}bpy)_{1.5}(H_2O)_{3.5}$ (**2**)

The reaction was carried out in the same way as for **1** except that HBr (0.25 mL) was used instead of HCl. Yield: 62% based on V. IR (KBr, cm^{-1}): $\tilde{\nu} = 3442$ (m), 1600 (m), 1548 (m), 1516 (m), 1479 (m), 1412 (m), 990 (m), 946 (m), 731 (m), 669 (m), 656 (m), 631 (m), 472 (w), 417 (m). Elemental *Anal.* Calc. for $Ni_2C_{55}H_{51}N_{11}O_{41.5}V_{16}Br$: C, 25.98; H, 2.02; N, 6.06; Ni, 4.62; V, 32.06. Found: C, 26.21; H, 2.19; N, 6.35; Ni, 4.34; V, 29.87%.

2.2.3. Synthesis of $[Co(4,4'\text{-}bpy)_2]_2[V_7^{IV}V_9^{V}O_{38}Cl]\cdot(4,4'\text{-}bpy)_{1.5}(H_2O)_2$ (**3**)

The preparation of **3** was similar to that of **1** except that $Co(CH_3COO)_2$ (177 mg, 1 mmol) was used in place of $Ni(CH_3COO)_2$. Yield: 59% based on V; IR (KBr, cm^{-1}): $\tilde{\nu} = 3680$ (w), 3446 (w), 2360 (m), 1743 (m), 1692 (m), 1646 (m), 1546 m, 1531 (m), 1515 (m), 1482 (m), 1411 (m), 985 (m), 816 (w), 677 (m), 575 (w), 455 (w). Elemental *Anal.* Calc. for $Co_2C_{55}H_{48}N_{11}O_{40}V_{16}Cl$: C, 26.73; H, 1.96; N, 6.23; Co, 4.77; V, 32.98. Found: C, 27.03; H, 2.31; N, 6.44; Co, 4.59; V, 32.65%.

2.2.4. Synthesis of $[Mn(4,4'\text{-}bpy)_2]_2[V_7^{IV}V_9^{V}O_{38}Cl]\cdot(4,4'\text{-}bpy)(H_2O)_{2.5}$ (**4**)

The reaction was carried out in the same way as for **1** except that $MnSO_4$ (151 mg, 1 mmol) was used instead of $Ni(CH_3COO)_2$. Yield: 65% based on V; IR (KBr, cm^{-1}): $\tilde{\nu} = 3740$ (m), 3681 (m), 3416 (w), 2358 (m), 1743 (m), 1688 (m), 1609 (m), 1525 (m), 1514 (m), 1462 (m), 1406

Table 1
Crystal data and structure refinement for **1**–**5**

Compound	**1**	**2**	**3**	**4**	**5**
Formula	$Ni_2C_{55}H_{50}N_{11}O_{41}V_{16}F$	$Ni_2C_{55}H_{51}N_{11}O_{41.5}V_{16}Br$	$Co_2C_{55}H_{48}N_{11}O_{40}V_{16}Cl$	$Mn_2C_{50}H_{45}N_{10}O_{40.5}V_{16}Cl$	$Ni_3C_{90}H_{78}N_{18}O_{39}V_{15}Cl$
Formula weight ($g\ mol^{-1}$)	2472.48	2542.40	2471.40	2394.33	3011.34
T (K)	293(2)	293(2)	293(2)	293(2)	293(2)
Wavelength (Å)	0.71073	0.71073	0.71073	0.71073	0.71073
Crystal system	tetragonal	tetragonal	tetragonal	tetragonal	rhombohedral
Space group	$P\bar{4}n2$	$P\bar{4}n2$	$P\bar{4}n2$	$P\bar{4}n2$	$R\bar{3}c$
a (Å)	17.0616(5)	17.091(2)	17.066(3)	17.266(2)	17.4896(8)
b (Å)	17.0616(5)	17.091(2)	17.066(3)	17.266(2)	17.4896(8)
c (Å)	14.6533(6)	14.611(3)	14.625(3)	14.916(3)	64.058(4)
γ (°)					120
V (Å^3)	4265.5(13)	4268.1(12)	4259.5(14)	4446.5(13)	16969.3(15)
Z	2	2	2	2	6
D_{calc} ($Mg\ m^{-3}$)	1.923	1.976	1.927	1.779	1.750
μ (mm^{-1})	2.185	2.651	2.163	1.980	1.770
$F(000)$	2432	2492	2428	2322	8832
Crystal size (mm)	$0.26\times0.24\times0.18$	$0.241\times0.218\times0.158$	$0.251\times0.218\times0.185$	$0.248\times0.225\times0.172$	$0.26\times0.24\times0.18$
Goodness-of-fit on F^2	1.104	1.080	0.985	1.158	0.954
Final R indices [$I>2\sigma(I)$]	$R_1=0.0532$, $wR_2=0.1679$	$R_1=0.0480$, $wR_2=0.1270$	$R_1=0.0859$, $wR_2=0.2206$	$R_1=0.0615$, $wR_2=0.1821$	$R_1=0.0542$, $wR_2=0.1612$
R indices (all data)	$R_1=0.0685$, $wR_2=0.1775$	$R_1=0.0572$, $wR_2=0.1328$	$R_1=0.1228$, $wR_2=0.2438$	$R_1=0.0646$, $wR_2=0.1841$	$R_1=0.0859$, $wR_2=0.1733$

$R_1 = \sum\|F_o| - |F_c\|/\sum|F_o|$, $wR_2 = \{\sum[w(F_o^2 - F_c^2)^2]/\sum[w(F_o^2)^2]\}^{1/2}$.

(m), 982 (m), 931 (s), 811 (w), 671 (m), 531 (m), 456 (m), 427 (m). Elemental *Anal.* Calc. for $Mn_2C_{50}H_{45}N_{10}O_{40.5}V_{16}Cl$: C, 25.08; H, 1.89; N, 5.85; Mn, 4.59; V, 34.04. Found: C, 25.39; H, 2.27; N, 6.07; Mn, 4.18; V, 33.79%.

2.2.5. Synthesis of $[Ni(2,2'\text{-bpy})_3]_3[V_8^{IV}V_7^{V}O_{36}Cl]\cdot(H_2O)_3$ (**5**)

A mixture of $NaVO_3$ (183 mg, 1.5 mmol), Na_2TeO_3 (220 mg, 1 mmol), $Ni(CH_3COO)_2$ (177 mg, 1 mmol), 2,2′-bipyridine (50 mg, 0.38 mmol), HCl (0.1 mL), CH_3CH_2OH (2 mL) and H_2O (5 mL) was stirred for ca. 45 min in air until it was homogeneous, and adjusted by CH_3COOH to pH 5.5, and then transferred and sealed in a 16 mL Teflon-lined stainless steel container. After heated to 170 °C under autogenously pressure for 4 days, the bomb was cooled down to room temperature. Black block crystals of **5** along with an amorphous grey impurity were filtered from the colorless mother liquor, washed by distilled water and dried at ambient temperature. The crystals were mechanically separated from the grey impurity to give a yield of 51% (based on V), and were stable in air and insoluble in water and common organic solvents. IR (KBr, cm^{-1}): $\tilde{\nu}$ = 3441 (m), 1835 (w), 1741 (m), 1692 (m), 1646 (m), 1565 (m), 1548 (m), 1532 (m), 1516 (m), 1444 (m), 1314 (m), 1162 (m), 980 (m), 767 (m), 664 (m), 477 (m), 429 (m). Elemental *Anal.* Calc. for $Ni_3C_{90}H_{78}N_{18}O_{39}V_{15}Cl$: C, 35.90; H, 2.61; N, 8.37; Ni, 5.85; V, 25.37. Found: C, 36.13; H, 2.87; N, 8.59; Ni, 5.67; V, 25.09%.

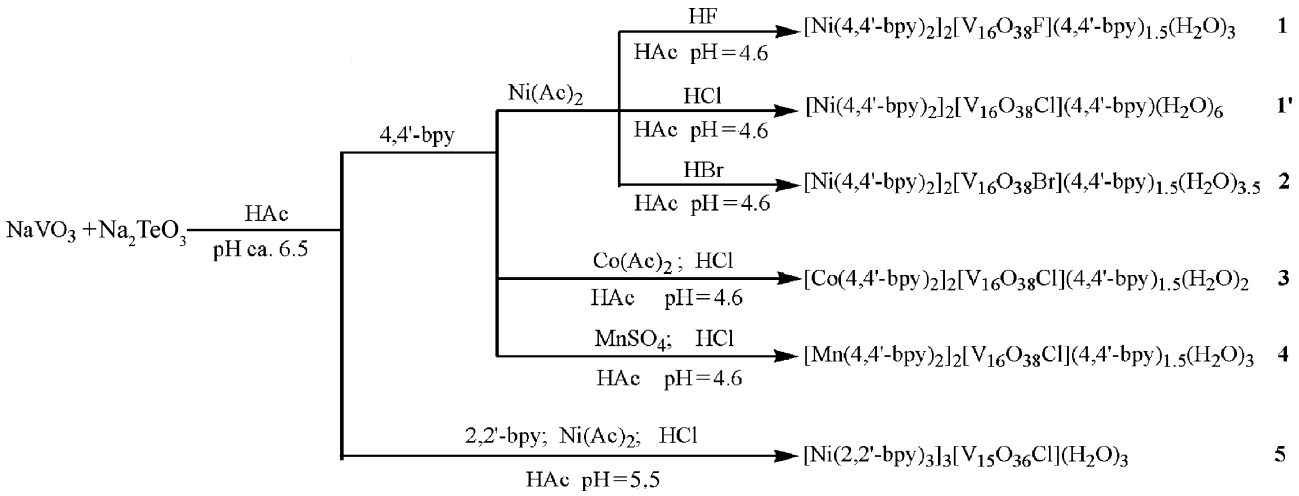
2.3. Crystal structure determination

Black crystals of **1**–**5** were glued on to glass fibers. Data were collected at 298(2) K on a Rigaku R-AXIS RAPID IP diffractometer with Mo Kα monochromated radiation (λ = 0.71073 Å). The structures were solved by direct methods and refined by full-matrix least-squares methods on F^2 with the SHELXTL software package. An empirical absorption correction was applied. All non-hydrogen atoms were refined anisotropically and hydrogen atoms were included at idealized positions and refined by use of the riding model. A summary of the crystallographic data of complexes **1**–**5** is presented in Table 1.

3. Results and discussion

3.1. Synthesis

The syntheses of the compounds **1**, **1′** [19], **2**, **3**, **4** and the spherical mixed-valence host–guest V15 cluster **5** are summarized in Scheme 1. The $\{V_{16}O_{38}\}$ core has been observed in some well characterized compounds containing the same numbers of reduced vanadium (IV) sites [11,8d]. The basic $\{V_{16}O_{38}\}$ shell in all these compounds is built up from 16 VO_5 distorted square pyramids that share edges and corners through two μ_2- and 20 μ_3-oxygen atoms, respectively. The shell could encapsulate Cl^- ions and H_2O molecules that exert templating effects on the electronic and framework structures of the host metal-oxide shells. However,



Scheme 1. Synthetic routes to the isolated compounds **1**–**5**.

we have successfully obtained **1** and **2** with a suitable fluoride and bromide ion source (HF and HBr) in the reaction. Compound **1** is the first example of hybrid materials that contain a $[V_{16}O_{38}F]^{4-}$ cluster and **2** is the first example of hybrid materials that contain a $[V_{16}O_{38}Br]^{4-}$ cluster. Furthermore, the $[V_{16}O_{38}F]^{4-}$ and $[V_{16}O_{38}Br]^{4-}$ clusters present different numbers of reduced vanadium (IV) sites compared to the reported $\{V_{16}O_{38}\}$ core.

Thinking about the comparability of the first-row transition metals, different paramagnetic metal ions Co(II), Ni(II) and Mn(II) were introduced into the reaction system. Compounds **3** and **4** were prepared under similar conditions. In order to study the effect of the organic ligands on the inorganic oxide microstructure, we intended to replace 4,4′-bpy with other organic ligands containing nitrogen (i.e., 2,2′-bpy and en). Based on this thought, compound **5** was obtained by reaction of 2,2′-bpy with $NaVO_3$, Na_2TeO_3 and HCl in acidic aqueous solution (pH 5.5). Though ethanol is not necessary for the formation of compounds **1**–**5**, a large number of parallel experiments indicate that the presence of a small quantity of ethanol could improve the yield and purity of these compounds.

Significantly, the presence of Na_2TeO_3 is necessary for the formation of compounds **1**–**5**. When the reactions were performed in the absence of Na_2TeO_3, nothing could be obtained except for some yellow precipitation, likely corresponding to complexes of V^V. Consequently, it appears that Na_2TeO_3 exerts the role of reducer for V^V. Taking into account the characteristic comparability of identical group elements, we replaced Na_2TeO_3 with an equal amount of Na_2SO_3 or Na_2SeO_3 in the reaction system. When Na_2SO_3 was used, compounds **1**–**5** cannot be obtained. However, compounds **1**–**5** could be obtained when Na_2SeO_3 was used instead of Na_2TeO_3, but at a cost of the yield and crystal quality of these compounds. It can be concluded that the reductive ability of Na_2TeO_3 and Na_2SeO_3 are comparative and both are weaker than that of Na_2SO_3, which indicates that weak reducer is propitious to the formation of **1**–**5**.

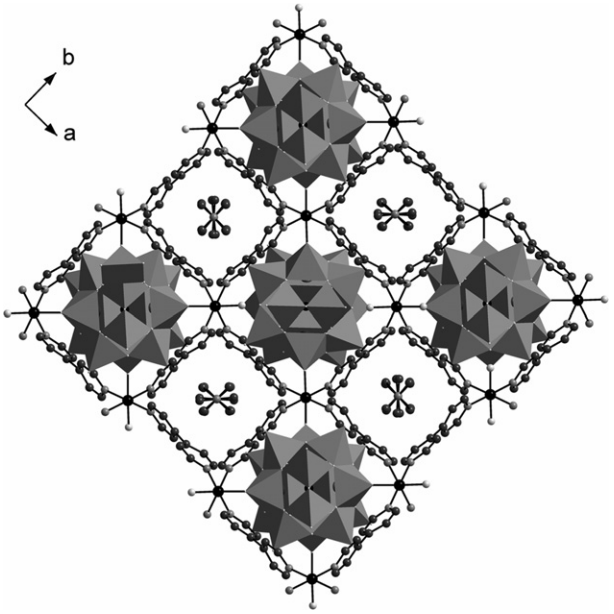


Fig. 1. Simplified schematic representation of the structure of a single crystal of **1**. Color code: $\{V_{16}O_{38}(F)\}^{4-}$ clusters, medium grey; Ni atoms, black; N atoms, medium grey; C atoms, dark grey; O atoms, light grey. All H atoms are omitted for clarity.

During our experiments, we also found that **1**–**5** cannot be obtained when some other common reducers such as oxalic acid, ethylenediamine and hydrazinium sulfate were used instead of Na_2TeO_3.

3.2. Description of the crystal structure

Single crystal X-ray diffraction analysis reveals that compounds **1**–**4** are isomorphous. They have similar molecular formulas and crystal structures, hence only the structure of **1** will be discussed in detail. The crystal structure of **1** can be described as a three-dimensional framework constructed from helical metal–organic coordination polymers $[\{Nibpy\}^{2+}]_n$ cations, $[V_{16}O_{38}(F)]^{4-}$ cluster

anions, guest 4,4′-bpy and water molecules (Fig. 1). The $[V_{16}O_{38}F]^{4-}$ cluster, with S_4 symmetry, is composed of a $\{V_{16}O_{38}\}$ shell with an encapsulated F^- ion in the center. The 16 V atoms are arranged at the surface of the shell with radius of 3.57 ± 0.21 Å from the central haloid ion. The host $\{V_{16}O_{38}\}$ shell consists of 16 VO5 square pyramids by sharing edges and corners with 20 μ_3-O atoms and 2 μ_2-O atoms. The other 16 oxygen atoms are terminal in the polar positions of the 16 VO5 square pyramids. The geometry around vanadium (V1) in the 4 VO5 units is defined by four basal μ_3-O groups and an apical μ-oxygen which in turn is linearly bonded to the Ni(II) center and then {V1–O–Ni–O–V1} bonds, which link $[V_{16}O_{38}F]^{4-}$ clusters, are formed. The square pyramidal geometry around vanadium (V2 and V3) in eight of the 16 VO5 groups is defined by a terminal oxo group and four μ_3-O atoms of the shell. The geometry around vanadium (V4) in the remaining 4 VO5 units is defined by three μ_3-O groups, one μ_2-O group and one terminal oxygen atom.

In the metal–organic coordination polymers, each Ni atom is 6-coordinate and shows a "4+2" distorted octahedron geometry. The equatorial plane is defined by four nitrogen donors of four 4,4′-bpy ligands (Ni–N: 2.141–2.144 Å). The axial positions are occupied by two bridging oxygen atoms coming from two different $[V_{16}O_{38}(F)]^{4-}$ clusters (Ni–O: 2.034 Å). An unusual feature of **1** is that the transition-metal Ni^{2+} and organic 4,4′-bpy are joined by N atoms to generate rectangular left and right-handed helical channels alternately, with N–Ni–N bond angles ranging from 89.38° to 91.2°, and these channels can be seen in a view along the [0 0 1] direction (Fig. 2b). Furthermore, large chiral channels that are suitable for incorporating organic guest molecules exist between the helices, in which disordered 4,4′-bpy as guest molecules reside. Interestingly, each chiral channel is formed by a double-stranded helical chain intertwined by homochiral polymeric chains (Fig. 2a).

In the structure of **1**, the $[V_{16}O_{38}(F)]^{4-}$ cluster acts as a tetradentate ligand coordinating to four Ni^{2+} ions through

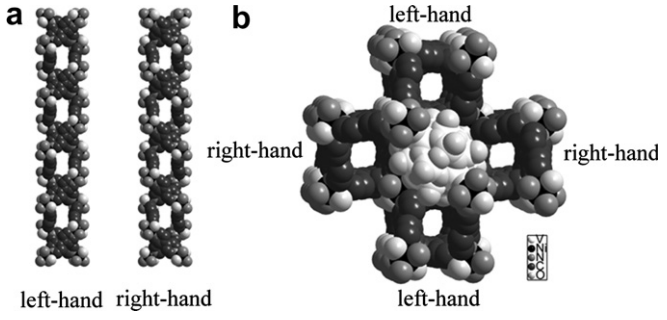


Fig. 2. (a) A space-filling view of the double-stranded left and right-handed helical chains along b exhibited by **1**. (b) The framework viewed along the [0 0 1] direction, showing two types of helical channels and achiral channels which are alternately arranged. All H atoms are omitted for clarity.

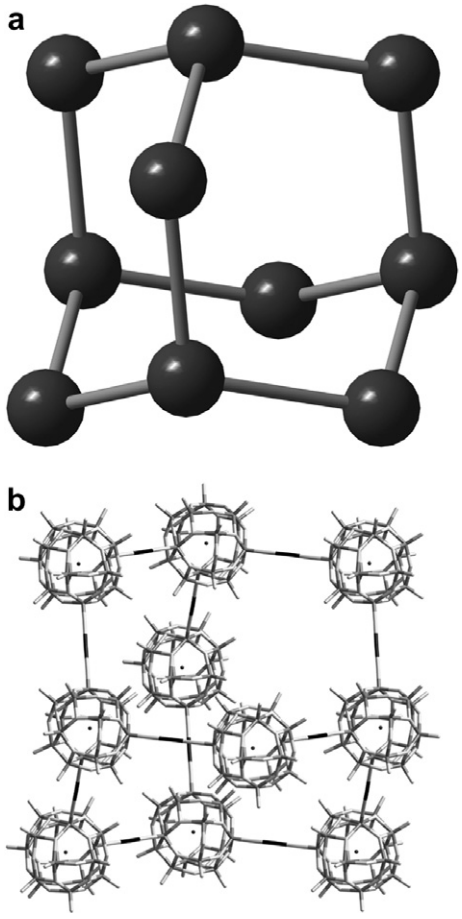


Fig. 3. Schematic illustration presenting the structural analogy recognized between diamond and compound **1**. (a) diamond, (b) compound **1**. Color code: V atoms, medium grey; Ni atoms, black; F atoms, dark grey; O atoms, light grey. All 4,4′-bpy molecules are omitted for clarity.

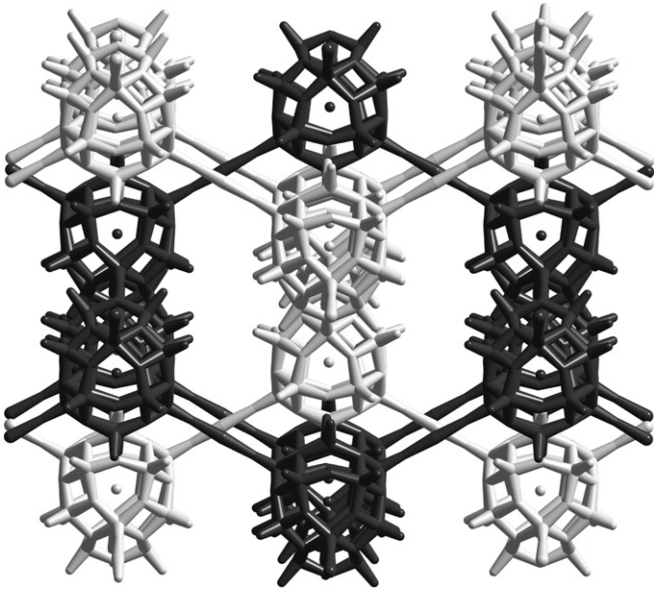


Fig. 4. Simplified schematic representation of the twofold interpenetrating network of **1**. All 4,4′-bpy molecules are omitted for clarity.

the terminal oxo groups of vanadium sites with Ni–O distances ranging from 2.034 to 2.132 Å. The linkage of Ni atoms and $[V_{16}O_{38}(F)]^{4-}$ clusters form a diamond framework by replacing each C in diamond with a $[V_{16}O_{38}(F)]^{4-}$ cluster and each C–C with a Ni(II) center (Fig. 3). This connectivity behavior may enhance the stability of the framework of **1**. Additionally, the metal–organic coordination polymer cations $[\{Nibpy\}^{2+}]_n$ connect with $[V_{16}O_{38}(F)]^{4-}$ clusters to form a twofold interpenetrating three-dimensional structure through the terminal oxo groups of vanadium sites (Fig. 4). Unlike many other solids with interpenetrating networks, the extent of interpenetration in **1** does not fill all the available voids but leaves a significant portion in the form of rectangular extended channels that are occupied by disordered 4,4′-bpy molecules. To the best of our knowledge, the occurrence of this interpenetrating net, composed of large polyoxoanion clusters and a metal–organic coordination polymer, is unprecedented. It shows that the incorporation of large polyoxoanion clusters could provide efficient cation–anion packing to prevent interpenetration of the cationic polymers.

The structure of the $[V_{16}O_{38}Br]^{4-}$ cluster in compound **2** is similar to the $[V_{16}O_{38}F]^{4-}$ cluster, but the bond lengths and bond angles are different, see Figs. S1 and S2. In the case of compounds **1**, **2** and **3**, the polyoxovanadate clusters are composed of a $[V_{16}O_{38}]$ shell with an encapsulated F^-, Br^- or Cl^- ion in the center, respectively. This is confirmed by XPS measurements in the F_{1s}, Br_{3d} and Cl_{2p} energy region, respectively. The XPS spectra of compounds **1**, **2** and **3** show peaks at 684 eV, 70 eV and 198 eV, respectively, attributable to F^-, Br^- and Cl^- (Fig. S3). The host shells are formed by using the template function of the anionic guest and are dependent on its shape and size. The van der Waals radii of the guests must of course be smaller than those of the cavities [20a]. The nearest distance from the center of the $[V_{16}O_{38}F]^{4-}$, $[V_{16}O_{38}Br]^{4-}$ and $[V_{16}O_{38}Cl]^{4-}$ clusters to the O atoms of the periphery is 3.318 Å, 3.358 Å and 3.341Å, and to the 16 V atoms at the surface of the shell is 3.396 Å, 3.397 Å and 3.390 Å, respectively. It is possible that the V16 cluster encapsulates negatively charged halide ions with significant different radii ($F^- = 1.33$ Å, $Br^- = 1.96$ Å, $Cl^- = 1.81$ Å and $O^{2-} = 1.32$ Å). When HCl was replaced with HI, however, the expected product was not obtained. Because the effective ionic radius of the I^- ion (2.20 Å) is larger, the I^- ion cannot be encapsulated by the shell of $[V_{16}O_{38}]$. Also, we have tried to replace halide ions with SO_4^{2-}, CO_3^{2-}, NO_3^- and ClO_4^- in order to study the templating effects of the central ions, but failed. It is due to that the assembly of the host cage is probably determined by the shape and symmetry of the small guest molecule. Additionally the host cage tends to adapt not only to the shape of the guest system, but also to its molecular electrostatic potentials distribution [20b]. So in compounds **1**, **2** and **3**, global halide ions with high symmetry and suited shape, size and molecular electrostatic potential distributions are propitious to form the $\{V_{16}O_{38}\}$ shell.

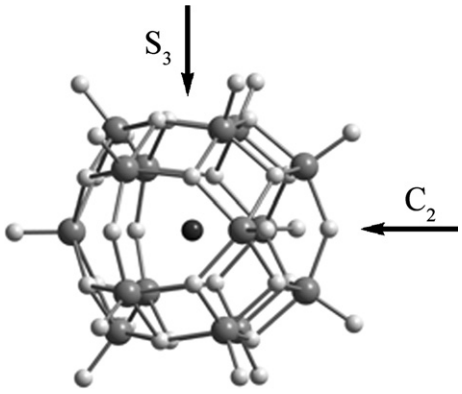


Fig. 5. The structure of $[V_{15}O_{36}Cl]^{6-}$ cluster in **5**. Color code: V atoms, medium grey; Cl atoms, dark grey; O atoms, light grey.

The assignment of the oxidation states of the vanadium atoms in compounds **1**–**4** is based on bond valence sum calculations, which reveal the average value of the V atoms is 4.551 for **1**, 4.555 for **2**, 4.566 for **3** and 4.563 for **4**, very close to the value of 4.562 for $V_7^{IV}V_9^{V}$ [21]. This conclusion and the result of the manganometric titration of V^{IV} sites correspond to the stated formulations of **1**–**4**.

When 2,2′-bpy was used instead of 4,4′-bpy, compound **5** was obtained. Compound **5** is constructed from $[V_{15}O_{36}Cl]^{6-}$ anions and $[Ni(2,2'\text{-bpy})_3]^{2+}$ cations via electrostatic and aryl–aryl interactions (Fig. S4). Each C atom of three 2,2′-bpy coordinating to the Ni(3) atom is disordered over two positions, and the best refinement has been obtained with occupancy factors of about 0.5 and 0.5 (Fig. S5). The spherical cluster $[V_{15}O_{36}Cl]^{6-}$ formally contains 15 V centers arranged on the surface of a sphere at a distance of 3.42 ± 0.11 Å from the center of the cluster in which the Cl^- resides (Fig. 5). For**5**, bond valence sums calculations reveal that the $[V_{15}O_{36}Cl]$ clusters have six negative charges. The average value calculated for the oxidation state of V is 4.423, very close to the value of 4.467 for $V_8^{IV}V_7^{V}$. This conclusion and the result of the manganometric titration of V^{IV} sites correspond to the stated formulation of **5**.

If 4,4′-bpy was substituted by en, compound $[Ni(en)_2][V_6O_{14}]$ was synthesized in our reaction system. The mixed-valence vanadium oxide $[V_6O_{14}]^{2-}$ layers contain infinite zigzag chains composed of edge-sharing VO_5 square pyramids. Adjacent chains are connected through corner-shared VO_4 tetrahedra to form a layer structure. Compound $[Ni(en)_2][V_6O_{14}]$ has been synthesized in our reaction system, though it can be obtained under other conditions [16b]. Several different polyoxovanadate clusters, such as $[V_{16}O_{38}X]^{4-}$, $[V_{15}O_{36}Cl]^{6-}$ and $[V_6O_{14}]^{2-}$, have been obtained by using organic ligands with different functionalities, which indicate that the organic components could modify the inorganic oxide microstructure. So under similar conditions, hybrid materials containing different polyoxometallate clusters are prepared by selecting different organic ligands.

3.3. Thermogravimetric analysis

Thermogravimetric analysis of **1**–**4** reveals a continuous weight loss (36.7% for **1**, 35.5% for **2**, 36.1% for **3** and 35.8% for **4**) until 429 °C, 421 °C, 431 °C and 428 °C, respectively, corresponding to the removal of water molecules, the guest 4,4′-bpy molecule and four coordinated 4,4′-bpy molecules (calc.36.1% for **1**, 36.2% for **2**, 36.9% for **3** and 36.3% for **4**). In compound **5**, the TG curve shows four weight loss steps, which suggests a multiple-stage decomposition process. Heating from about 25 to 130 °C leads to the loss (weight loss of ca. 2.03%) of three crystal H_2O molecules per formula unit (calc. 1.79%). The next three weight loss steps (45.23%), occurring between 180 and 596 °C, correspond to the loss of three 2,2′-bpy molecules per formula unit (calc. 46.68%).

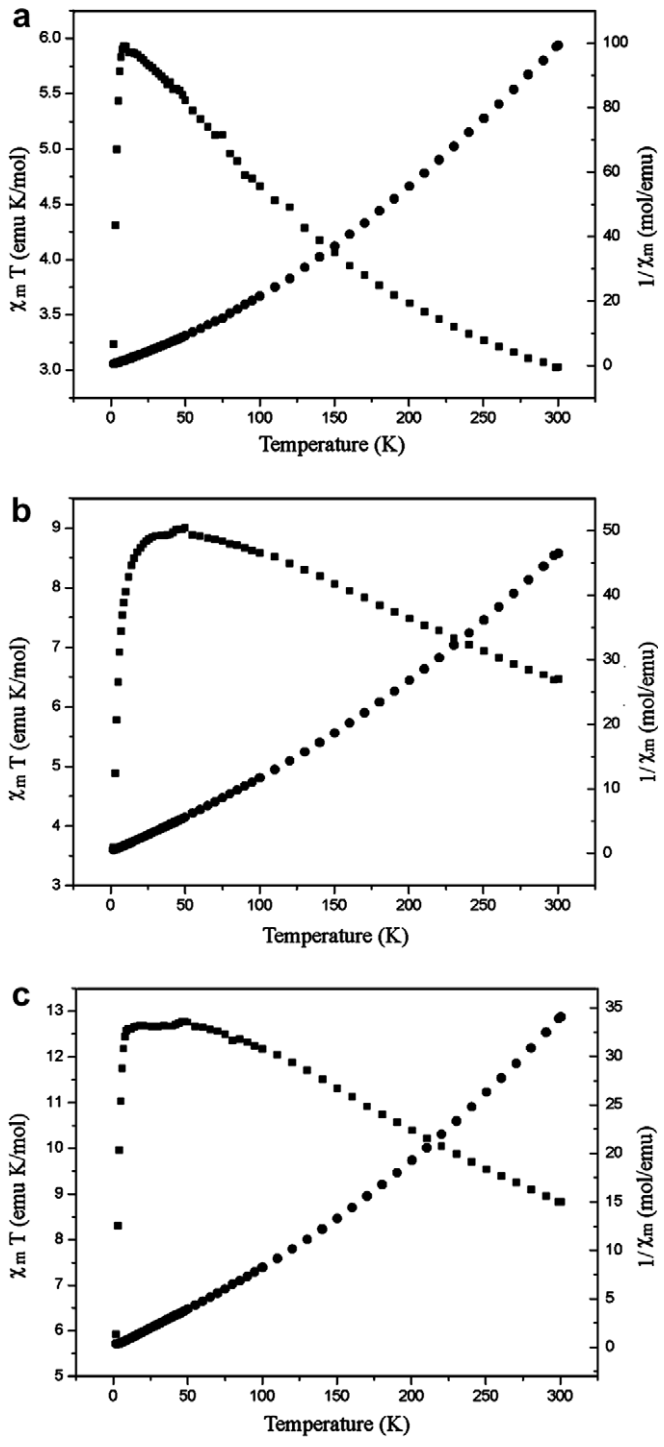


Fig. 6. Thermal variation of $\chi_m T$ and $1/\chi_m$ for compounds **1**′, **3** and **4**. (a) Compound **1**′, (b) compound **3**, and (c) compound **4**.

3.4. Magnetic properties of compounds 3, 4 and 5

The variable-temperature magnetic susceptibilities of **1**′, **3** and **4** were measured between 2 and 300 K at 10000 Oe. The magnetic data of compound **1**′ is included for comparison. The thermal variations of $\chi_m T$ and $1/\chi_m$ are displayed in Fig. 6 (where χ_m is the measured magnetic susceptibility). In the case of compounds **1**′, **3** and **4**, the $\chi_m T$ products at 300 K are 3.02 emu K mol^{-1} (4.92 μ_B), 6.47 emu K mol^{-1} (7.19 μ_B) and 8.82 emu K mol^{-1} (8.40 μ_B), respectively. The $\chi_m T$ values of **1**′ and **4** are smaller than the expected values for two uncorrelated M^{2+} (Ni^{2+}: $S = 1$, Mn^{2+}: $S = 5/2$) and seven V^{4+} ($S = 1/2$) centers per formula unit ($\chi_m T$ (**1**′) = 4.63 emu K mol^{-1}, 6.08 μ_B; $\chi_m T$ (**4**) = 11.38 emu K mol^{-1}, 9.54 μ_B), but the $\chi_m T$ value of **3**(two uncoupled $S = 3/2$ for Co^{2+}, seven uncoupled $S = 1$ for V^{4+}) is higher than the expected value ($\chi_m T$ (**3**) = 6.38 emu K mol^{-1}, 7.14 μ_B). The products $\chi_m T$ increase on cooling to a maximum 5.93 emu K mol^{-1} at 8 K for **1**′, 9.00 emu K mol^{-1} at 50 K for **3** and 12.70 emu K mol^{-1} at 48 K for **4**, which indicates the presence of ferrimagnetic exchange coupling. Subsequently, the curves drop abruptly below 8 K, 50 K and 48 K for **1**′, **3** and **4**, respectively, which may be caused by the zero-field splitting contributions, intercluster magnetic interactions or saturation effects are likely to influence the data in this temperature range. The measured data of **1**′, **3** and **4** were fitted by using the Curie–Weiss equation $\chi_m = C_m/(T - \theta)$

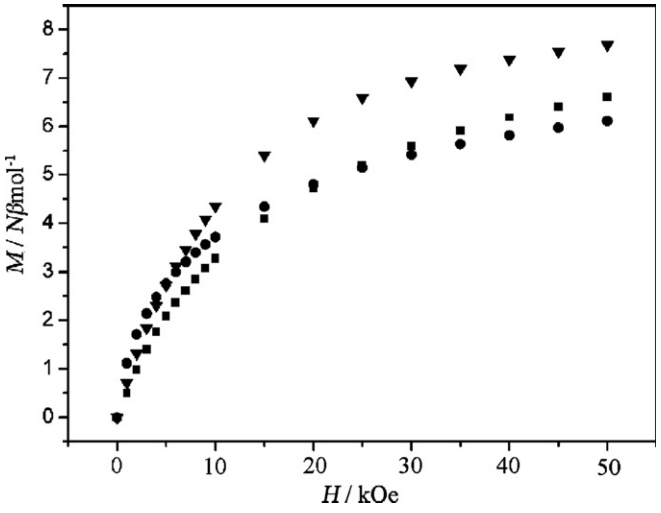


Fig. 7. Field dependence of the magnetizations for complexes **1**′ (■), **3** (●) and **4** (▼).

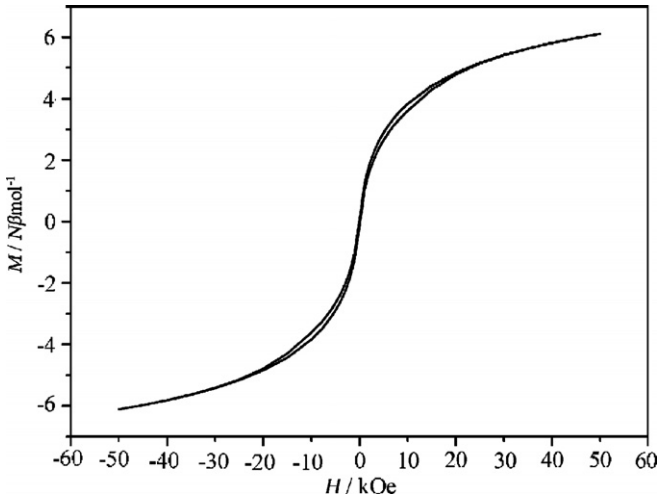


Fig. 8. Hysteresis loop of **3** at 1.8 K.

at $T > 150$ K, where C_m is the Curie constant and θ is the Weiss constant, with $C_m = 2.39$ emu K mol^{-1} and $\theta = 65.85$ K for **1′**, $C_m = 5.32$ emu K mol^{-1} and $\theta = 55.91$ K for **3** and $C_m = 7.16$ emu K mol^{-1} and $\theta = 60.22$ K for **4**.

The variable-temperature magnetic susceptibility of **5** was also measured between 2 and 300 K at 10 000 Oe. $\chi_m T$ versus T shows a value of 6.68 emu K mol^{-1} (7.31 μ_B) at 300 K, higher than the expected total value (6.00 emu K mol^{-1}, 6.93 μ_B) of eight uncoupled $S = 1/2$ spins of V^{4+} atoms and three uncoupled $S = 1$ spins of Ni^{2+} atoms (Fig. S8). The $\chi_m T$ values remain almost constant from 300 K to 18 K, and then decrease on further cooling, reaching a value of 3.74 emu K mol^{-1} at 2 K, which indicates paramagnetic properties in compound **5**. The fit for the curve of the $1/\chi_m$ versus T plot of **5** to the Curie–Weiss law gives a good result in the temperature range 2–300 K with $C_m = 6.66$ emu K mol^{-1} and $\theta = 0.20$ K (see Figs. 7 and 8).

4. Conclusion

In summary, the combination of cage-like polyoxovanadate clusters with metal–organic complexes provides a series of hybrid materials **1**–**5** with different structures and physical properties. Compounds **1**–**4** have 3D coordination complex $[\{Mbpy\}^{2+}]_n$ cationic scaffoldings that incorporate vanadium oxide clusters into their void spaces. The successful preparation of compound **5** and $[Ni(en)_2][V_6O_{14}]$ indicates that organic ligands can dramatically influence the inorganic oxide microstructure. The effects of different reaction factors were discussed in the paper, such as the source of the transition metal salts, organic ligands and central templates, which provide an optional method to design and synthesize novel hybrid materials. Furthermore, the magnetic properties of compounds **3** and **4** could make them excellent candidates for potential applications in magnetic materials.

Acknowledgements

This work was supported by the National Science Foundation of China (Grant No. 20571014) and the Scientific Research Foundation for Returned Overseas Chinese Scholars, the Ministry of Education.

Appendix A. Supplementary material

CCDC 603552, 603553, 603554, 603555, 603556, 603557, 603558, 603559 and 603560 contain the supplementary crystallographic data for this paper. These data can be obtained free of charge via http://www.ccdc.cam.ac.uk/conts/retrieving.html, or from the Cambridge Crystallographic Data Centre, 12 Union Road, Cambridge CB2 1EZ, UK; fax: (+44) 1223-336-033; or e-mail: deposit@ccdc.cam.ac.uk. Supplementary data associated with this article can be found, in the online version, at doi:10.1016/j.poly.2006.11.050.

References

[1] P.J. Hagrman, K. Hagraman, J. Zubieta, Angew. Chem., Int. Ed. 38 (1999) 2638, and references therein.
[2] (a) D. Hagrman, C. Zubieta, D.J. Rose, J. Zubeita, R.C. Haushalter, Angew. Chem., Int. Ed. 36 (1997) 873;
(b) G. Ferey, Chem. Mater. 13 (2001) 3084;
(c) E. Bunkholder, V. Golub, C.J. O'Connor, J. Zubieta, Inorg. Chem. 42 (2003) 6729;
(d) E. Bunkholder, V. Golub, C.J. O'Connor, J. Zubieta, Inorg. Chem. 43 (2004) 7014.
[3] (a) M. Eddaoudi, D. Moler, H. Li, B. Chen, T. Reineke, M. O'Keeffe, O.M. Yaghi, Acc. Chem. Res. 34 (2001) 319, and references therein;
(b) N.L. Rosi, J. Kim, M. Eddaoudi, B. Chen, M. O'Keeffe, O.M. Yaghi, J. Am. Chem. Soc. 127 (2005) 1504;
(c) L. Xie, S. Liu, B. Gao, C. Zhang, C. Sun, D. Li, Z. Su, Chem. Commun. 18 (2005) 2402.
[4] (a) M.I. Khan, E. Yohannes, R.J. Doedens, Inorg. Chem. 42 (2003) 3125;
(b) M.I. Khan, E. Yohannes, R.C. Nome, S. Ayesh, V.O. Golub, C.J. O'Connor, R.J. Doednes, Chem. Mater. 16 (2004) 5273;
(c) L. Chen, F. Jiang, Z. Lin, Y. Zhou, C. Yue, M. Hong, J. Am. Chem. Soc. 127 (2005) 8588.
[5] (a) R.L. LaDuca, R. Finn, J. Zubieta, Chem. Commun. 12 (1999) 1669;
(b) M.I. Khan, J. Solid State Chem. 152 (2000) 105;
(c) L. Zheng, X. Wang, Y. Wang, A.J. Jacobson, J. Mater. Chem. 11 (2001) 1100.
[6] (a) L. Zheng, J. Zhao, K. Lii, L. Zhang, Y. Liu, X. Xin, J. Chem. Soc., Dalton Trans. (1999) 939;
(b) X. Zhang, M. Tong, X. Chen, Chem. Commun. 13 (2000) 1817.
[7] (a) R.L. LaDuca, R.S. Rarig, J. Zubieta, Inorg. Chem. 40 (2001) 607;
(b) P.J. Hagrman, J. Zubieta, Inorg. Chem. 40 (2001) 2800;
(c) C. Liu, Y. Hou, J. Zhang, S. Gao, Inorg. Chem. 41 (2002) 140.
[8] (a) P.J. Hagrman, C. Bridges, J.E. Greedan, J. Zubieta, J. Chem. Soc., Dalton Trans. (1999) 2901;
(b) R.L. LaDuca, C. Brodkin, R.C. Finn, J. Zubieta, Inorg. Chem. Common. 3 (2000) 248;
(c) J. Tao, X. Zhang, M. Tong, X. Chen, J. Chem. Soc., Dalton Trans. (2001) 770;
(d) B. Lin, S. Liu, Chem. Commun. 15 (2002) 2126.
[9] D. Long, D. Orr, G. Seeber, P. Kögerler, L.J. Farrugia, L. Cronin, J. Clust. Sci. 14 (2003) 313.

[10] L. Chen, F. Jiang, Z. Lin, Y. Zhou, C. Yue, M. Hong, J. Am. Chem. Soc. 127 (2005) 8588.
[11] (a) A. Müller, E. Krickemeyer, M. Penk, H.J. Walberg, H. Bögge, Angew. Chem., Int. Ed. 26 (1987) 1045;
(b) A. Müller, M. Penk, R. Rohlfing, E. Krickemeyer, J. Döring, Angew. Chem., Int. Ed. 29 (1990) 926.
[12] (a) C. Pan, J. Xu, G. Li, D. Chu, T. Wang, Eur. J. Inorg. Chem. (2003) 1514;
(b) Y. Chen, X. Gu, J. Peng, Z. Shi, H. Y, E. Wang, N. Hu, Inorg. Chem. Commun. 7 (2004) 705;
(c) Y. Chen, J. Peng, H. Yu, Z. Han, X. Gu, Z. Shi, E. Wang, N. Hu, Inorg. Chim. Acta 358 (2004) 403;
(d) B. Dong, Y. Chen, J. Peng, Y. Kong, Z. Han, J. Mol. Struct. 748 (2005) 171.
[13] (a) A. Müller, E. Krickemeyer, M. Penk, R. Rohlfing, A. Armatage, H. Bögge, Angew. Chem., Int. Ed. 30 (1991) 1674;
(b) A. Müller, R. Rohlfing, E. Krickemeyer, H. Bögge, Angew. Chem., Int. Ed. 32 (1993) 909.
[14] (a) A. Müller, R. Sessoli, E. Krickemeyer, H. Bögge, J. Meyer, D. Gatteschi, L. Pardi, J. Westphal, K. Hovemeier, R. Rohlfing, A. Armatage, J. Döring, F. Hellweg, C. Beugholt, M. Schmidtmann, Inorg. Chem. 36 (1997) 5239;
(b) M.I. Khan, E. Yohannes, D. Powell, Chem. Commun. (1999) 23;
(c) M.I. Khan, E. Yohannes, R.J. Doedens, Angew. Chem., Int. Ed. 38 (1999) 1292.
[15] (a) P.C.H. Mitchell, Nature 348 (1990) 15;
(b) A. Müller, Nature 352 (1991) 115;
(c) M.T. Pope, Nature 355 (1992) 27.
[16] (a) A. Müller, F. Peters, M.T. Pope, D. Gatteschi, Chem. Rev. 98 (1998) 239, and references therein;
(b) J.M. Clemente-Juan, E. Coronado, Coord. Chem. Rev. 193–195 (1999) 361, and references therein.
[17] (a) W. Plass, Angew. Chem., Int. Ed. 35 (1996) 627;
(b) G.B. Karet, Z. Sun, D.D. Heinrich, J.K. McCusker, K. Folting, W.E. Streib, J.C. Huffman, D.N. Hendrickson, G. Christou, Inorg. Chem. 35 (1996) 6450;
(c) M.J. Manos, A.J. Tasiopoulos, E.J. Tolis, N. Lalioti, J.D. Woollins, A.M.Z. Slawin, M.P. Sigalas, T.A. Kabanos, Chem. Eur. J. 9 (2003) 695.
[18] (a) Y. Zhang, J.R.D. DeBord, C.J. O'Connor, R.C. Haushalter, J. Zubieta, Angew. Chem., Int. Ed. 35 (1996) 989;
(b) B. Lin, S. Liu, J. Chem. Soc., Dalton Trans. (2002) 865.
[19] S. Liu, L. Xie, B. Gao, C. Zhang, C. Sun, D. Li, Z. Su, Chem. Commun. (2005) 5023.
[20] (a) A. Müller, H. Reuter, S. Dillinger, Angew. Chem., Int. Ed. 34 (1995) 2328;
(b) M.-M. Rohmer, M. Bénard, J.-P. Blaudeau, J.-M. Maestre, J.-M. Poblet, Coord. Chem. Rev. 178–180 (1998) 1019.
[21] I.D. Brown, D. Altermatt, Acta Crystallogr., Sect. B 41 (1987) 244.

$$g_y = g_e - 2\lambda[4\kappa_y^2/\Delta_y(^3A_g \rightarrow {}^3B_{2g})] \quad (9)$$

$$\chi_{TIP} = N_A\mu_0\mu_B^2(2/3)[4\kappa_x^2/\Delta_x(^3A_g \rightarrow {}^3B_{3g}) + 4\kappa_y^2/\Delta_y(^3A_g \rightarrow {}^3B_{2g}) + 4\kappa_z^2/\Delta_z(^3A_g \rightarrow {}^3B_{1g})] \quad (10)$$

These spin-Hamiltonian parameters are frequently understood as internal characteristics of the complex under study (molecular constants) and fixed by fitting the experimental data (magnetic susceptibility, magnetization, heat capacity, INS, ESR, MCD and FAR-IR spectra). However, all of them originate in the electronic structure of the complex and they can be reconstructed with the help of the more principal electronic-structure parameters [2]: the Racah parameters B and C (electron repulsion), the crystal-field strengths Dq, Ds, ... (or more exactly the crystal-field poles for each ligand F_2(L) and F_4(L)), the spin–orbit coupling constant ξ, and the orbital reduction factors κ (which could be anisotropic, κ_z, κ_x). With a tetragonal compression (negative structural tetragonality), the ground state is the Γ_5-multiplet, and D is negative. On tetragonal elongation (positive structural tetragonality) the ground state is Γ_4-multiplet, and D is positive. Such a general forecast, however, is tuned by the orbital reduction factors κ_z and κ_x.

Three publications preceded the present communication [3–5] where the axial zero-field parameter D (subtracted from the susceptibility and magnetization data sets) has been correlated with the structural anisotropy parameter D_{str} that characterizes the degree of the tetragonality. The complexes involved in such a correlation were either homoleptic (imidazole and its derivative, {NiN_6}-chromophore), N-donor only of the [Ni(base)$_4$(NCS)$_2$] type (possessing the {$NiN_4N'_2$}-chromophore), or heteroleptic complexes of the type [Ni(base)$_2$(carboxylate)$_2$(H_2O)$_2$] having the {$NiN_2O_2O'_2$}-chromophore. We prepared and structurally characterized some more members of the above series with the {NiO_4N_2}, and {NiN_4O_2} chromophores, respectively (three complexes). Five complexes were subjected to magnetochemical studies and involved in the above mentioned correlation.

Because the present paper is, in fact, a continuation of our previous work on heteroleptic Ni(II) complexes [5], we have kept numbering of the previously characterized complexes as follows: [Ni(*Meiz*)$_2$(HCOO)$_2$(H_2O)$_2$] (**1**), [Ni(*Me*$_2$*iz*)$_2$(HCOO)$_2$(H_2O)$_2$] (**2**), [Ni(*iqu*)$_2$(CH_3COO)$_2$(H_2O)$_2$] (**3**), [Ni(*fupy*)$_2$(CH_3COO)$_2$(H_2O)$_2$] (**4**). The new complexes under study are: [Ni(*bzfupy*)$_2$(*ac*)$_2$(H_2O)$_2$] (**5**), [Ni(*Me*$_2$*fupy*)$_2$(H_2O)$_4$](*ac*)$_2$ (**6**), [Ni(*Me*$_2$*iz*)$_4$(H_2O)$_2$]$Cl_2 \cdot 3H_2O$ (**7**), [Ni(*pz*)$_4$(*ac*)$_2$] (**8**) and [Ni(L^{NN})$_2$(H_2O)$_2$] (**9**).

2. Experimental

2.1. Synthesis

The starting materials (1,2-dimethylimidazole, $NiCl_2 \cdot 6H_2O$ and CH_3COOK) were purchased from commercial sources and were used as received. The syntheses of 2,3-dimethylfuro[3,2-*c*]pyridine (abbr. *Me*$_2$*fupy*) and benzo[4,5]furo[3,2-*c*]pyridine (abbr. *bzfupy*) have been conducted in accordance with published recipes [6–9].

Nickel(II) acetate was synthesized by adding potassium acetate to a nickel(II) chloride ethanol solution. Elemental analysis (C, H, N) was performed on an elemental analyzer Eager 300 (Carlo Erba). The nickel content was determined chelatometrically using murexide as indicator.

The two complexes [Ni(*bzfupy*)$_2$(*ac*)$_2$(H_2O)$_2$] (**5**) and [Ni(*Me*$_2$*fupy*)$_2$(H_2O)$_4$](*ac*)$_2$ (**6**) were prepared from nickel acetate. Into the solution of nickel acetate a stoichiometric amount of ligand was added and stirred for half hour. After 2 days the solid complexes were collected. Single crystals were grown from the ethanol solution. The complex [Ni(*Me*$_2$*iz*)$_4$(H_2O)$_2$]$Cl_2 \cdot 3H_2O$ (**7**) was prepared by reacting nickel(II) chloride with a four-fold excess of 1,2-dimethylimidazole in warm ethanol over a 4 h reflux. The single crystals of (**7**) were obtained by slow evaporation at room temperature. Syntheses of compounds **8** and **9** are described elsewhere [11,12].

Anal. Calc. for (**5**) $C_{26}H_{24}N_2NiO_8$: C, 56.66; H, 4.39; N, 5.08. Found: C, 56.09; H, 4.52; N, 5.04%. Calc. for (**6**) $C_{22}H_{32}N_2NiO_{10}$: C, 48.65; H, 5.94; N, 5.16. Found: C, 48.30; H, 6.17; N, 5.47%. Calc. for (**7**) $C_{20}H_{42}Cl_2N_8NiO_5$: C, 39.76; H, 7.01; N, 18.55. Found: C, 40.0; H, 7.05; N, 18.5%.

2.2. Physical measurements

Single-crystal X-ray diffraction experiments for all complexes have been performed using an Xcalibur CCD apparatus (Oxford Diffraction). Data reduction and empirical absorption correction were performed by SHELXS-97.

Electronic spectra were measured using the DRIFT method on a Magna FTIR 750 spectrometer (Nicolet) in the region 5000–11 000 cm^{-1} and in Nujol mull on a Specord 200 (Analytical Jena) in the range 50 000–10 000 cm^{-1}.

Magnetic susceptibility and magnetization measurements were done using a SQUID magnetometer (Quantum Design) between 2 and 300 K at $B = 0.1$ T. The magnetization data until $B = 5.5$ T were taken at $T = 2.0$ and 4.6 K, respectively. Raw susceptibility data were corrected for underlying diamagnetism using a set of Pascal constants [10]. The effective magnetic moment has been calculated as usual: $\mu_{eff}/\mu_B = 798(\chi' T)^{1/2}$ when SI units are employed.

3. Results and discussion

3.1. Molecular and crystal structure

Crystal data for compounds **5** through to **7** are collected in Table 1. The molecular structure is viewed in Fig. 1.

The structure of complex **5** consist of [Ni(*bzfupy*)$_2$(*ac*)$_2$(H_2O)$_2$] monomeric units in which the central Ni(II) atom has a distorted octahedral configuration. The coordination around the Ni(II) atom is defined by two aqua ligands (w), two acetate ligands (a) and two neutral benzo[4,5]furo[3,2-*c*]pyridine (b). The Ni–O(a) distances are 2.060(2) Å, the Ni–O(w) distances are 2.073(2) Å and the Ni–N(b) dis-

Table 1
Summary of X-ray crystallographic data

Compound	**5**	**6**	**7**
Formula	$C_{26}H_{24}N_2NiO_8$	$C_{22}H_{32}N_2NiO_{10}$	$C_{20}H_{42}Cl_2N_8NiO_5$
Formula weight	551.17	543.21	604.23
Crystal system	monoclinic	triclinic	orthorhombic
Space group	$P21/c$	$P\bar{1}$	P_{212121}
Cell parameters			
a (Å)	12.228(4)	7.260(2)	9.387(4)
b (Å)	7.8460(10)	7.679(3)	10.069(4)
c (Å)	12.5980(10)	11.418(2)	29.611(9)
α (°)	90	97.53(2)	90
β (°)	93.75(2)	90.87(2)	90
γ (°)	90	98.08(1)	90
V (Å^3)	1206.1(4)	624.4(3)	2798.8(18)
Z	4	1	4
Density, D_{calc} (g cm^{-3})	1.518	1.445	1.434
Absorption coefficient (mm^{-1})	0.860	0.834	0.929
$F(000)$	572	286	1280
Reflections collected	8272	6496	18 682
Refinement method	full-matrix least-squares on F^2		
Data/restraints/parameters	2430/3/175	2278/6/172	5694/12/424
Final R indices	$R_1 = 0.0297$	$R_1 = 0.0468$	$R_1 = 0.0480$
	$wR_2 = 0.0867$	$wR_2 = 0.1274$	$wR_2 = 0.0951$
CCDC deposit numbers	622567	622568	622569

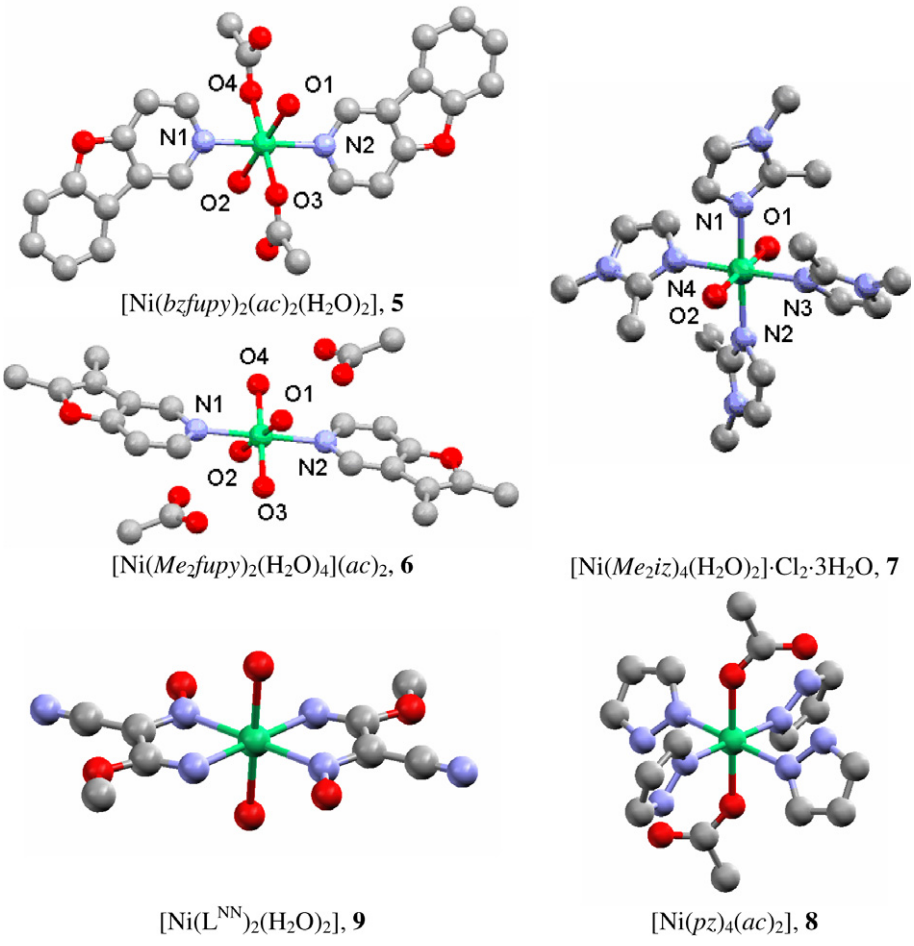


Fig. 1. Molecular structure of complexes **5**–**7**, along with two previously characterized complexes **8** [11] and **9** [12] (hydrogen atoms are deleted for clarity).

Table 2
Selected bond lengths (Å)[a]

Contact	5	6	7
Ni1–N1	2.128	2.168	2.100
Ni1–N2	2.128	2.168	2.065
Ni1–N3			2.077
Ni1–N4			2.063
Ni1–O1	2.073[w]	2.194[w]	2.095[w]
Ni1–O2	2.073[w]	2.194[w]	2.106[w]
Ni1–O3	2.060	2.048[w]	
Ni1–O4	2.060	2.048[w]	

[a] w, the aqua ligand.

tances are 2.128(2) Å (see Table 2). Two oxygen atoms from water molecules and two oxygen atoms from acetate groups form the equatorial plane and two nitrogen atoms from benzo[4,5]furo[3,2-*c*]pyridine are situated in the axial sites.

The molecular structure of complex **6** consists of discrete $[Ni(Me_2fupy)_2(H_2O)_4]^{2+}$ monomeric units with the Ni(II) atom in a distorted octahedral configuration defined by four equatorial aqua (w) ligands and two axial 2,3-dimethylfuro[3,2-*c*]pyridine (b) ligands. The Ni–O(w) distances are 2.194 and 2.048 Å and the Ni–N(b) distances are 2.168(2) Å. Such a geometry predisposes that the usual assumption $|D| > 3E$ is no longer valid for this $\{Ni(O_2O'_2)_{eq}N_2\}$ chromophore.

The $[Ni(Me_2iz)_4(H_2O)_2]^{2+}$ monomeric units represent the structure of compound **7**. The central Ni(II) atom possesses a distorted octahedral configuration formed by two aqua ligands and four neutral 1,2-dimethylimidazole (b) ligands. The distances inside the chromophore are Ni–O(w) 2.095 and 2.106 Å, Ni–N(b) 2.100, 2.065, 2.077 and 2.063 Å, respectively.

For compounds **8** and **9**, whose structures have been published elsewhere, we refer to the original sources [11,12].

The intermolecular O–H···O hydrogen bonds for **5** [H···O = 1.834 and 1.934 Å, and O–H···O = 165 and 163°] are formed through aqua-ligand OH groups to uncoordinated acetate-ligand O-atoms from a neighboring molecule, and they are situated in the equatorial plane. In the crystal structure of this complex, the secondary N-atoms are not involved in the hydrogen bonds; consequently only a two-dimensional network is formed (Fig. 2).

The registered intermolecular contacts for **6** are O–H···O [H···O = 1.683, 1.821, 1.918 and 2.184 Å, O–H···O = 161°, 166°, 171° and 176°]. They are formed by aqua-ligand OH groups to the O atom from an uncoordinated acetate molecule in the equatorial plane. Thus, these hydrogen bonds form a two-dimensional network because the N-atoms are not involved in the hydrogen bonds.

For complex **7** the O–H···O hydrogen bonds [H···O = 2.688, 2.767 and 2.784 Å, Cl···O = 3.146, 3.125, 3.096, 3.142 and 3.110 Å, O–H···O = 161°, 171° and 167° and O–H···Cl = 162°, 170°, 174°, 160° and 167°] are formed through coordinated water OH groups to crystal-water

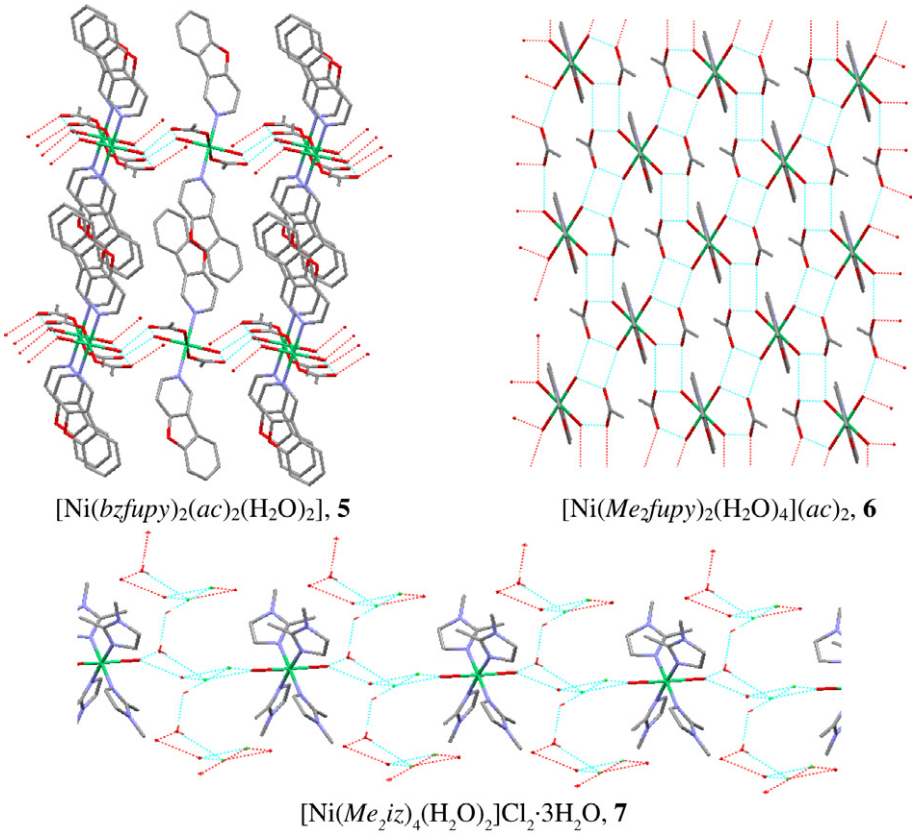


Fig. 2. The hydrogen bonds in complexes **5**, **6** and **7**.

Table 3
Electron spectra for the heteroleptic Ni(II)complexes

Complex	Chromophore, bipyramid[a]	Spin allowed transition, (E/hc) (cm^{-1})		
	Compressed	$^3B_{2g} \leftarrow {}^3B_{1g} = 10Dq$	$^3E_g \leftarrow {}^3B_{1g}$	$^3E_g \leftarrow {}^3B_{1g}$
		$^3E_g \leftarrow {}^3B_{1g}$	$^3A_{2g} \leftarrow {}^3B_{1g}$	$^3A_{2g} \leftarrow {}^3B_{1g}$
	Octahedral	$^3T_{2g} \leftarrow {}^3A_{2g} = 10Dq$	$^3T_{1g}(F) \leftarrow {}^3A_{2g}$[b]	$^3T_{1g}(P) \leftarrow {}^3A_{2g}$
	Elongated	$^3E_g \leftarrow {}^3B_{1g}$	$^3A_{2g} \leftarrow {}^3B_{1g}$	$^3A_{2g} \leftarrow {}^3B_{1g}$
		$^3B_{2g} \leftarrow {}^3B_{1g} = 10Dq$	$^3E_g \leftarrow {}^3B_{1g}$	$^3E_g \leftarrow {}^3B_{1g}$
1, [5]	$\{NiO_2O_2N_2\}$, c	9400	15300 (13531)	26000
2, [5]	$\{NiO_2O_2N_2\}$, c	10893	16207 (13642)	26525
3, [5]	$\{NiO_2O_2N_2\}$, c	9611	15764 (13740)	26000
4, [5]	$\{NiO_2O_2N_2\}$, c	9945	15968 (13800)	26870
5, This work	$\{NiO_2O_2N_2\}$, c	9720	15670 (13673)	26380
6, This work	$\{NiO_4N_2\}$, c	9890	15900 (13878)	26500
7, This work	$\{NiN_4O_2\}$, e	10450	16000 (13696)	25800
8, This work	$\{NiN_4O_2\}$, e	10397	16681 (13603)	27004

[a] Bipyramid: c, compressed; e, elongated; based upon relative structural tetragonality.
[b] Values in parentheses are the positions of the band-arms.

molecules and one of these three hydrogen bonds is formed between two crystal–water molecules. These hydrogen bonds form a two-dimensional network.

3.2. Electron spectra

The electron spectra of the studied complexes show three principal d–d bands ($^3T_{2g} \leftarrow {}^3A_{2g}$, $^3T_{1g}(F) \leftarrow {}^3A_{2g}$ and $^3T_{1g}(P) \leftarrow {}^3A_{2g}$, characteristic for the octahedral geometry) in the region 9400–10893 cm^{-1}, 15300–16681 cm^{-1} and 26000–27004 cm^{-1}, which are split due to the symmetry lowering of the crystal field (Table 3). The splitting is evidenced as an arm and is well visible for the second principal transition; this refers to the transition $^3A_{2g} \leftarrow {}^3B_{1g}$ within the point-group D_{4h}. A weak feature with a maximum at ~13600 cm^{-1} can be assigned to the spin-forbidden transition ($^1A_{1g} \leftarrow {}^3B_{1g}$) arising from the ^1D term.

3.3. Magnetic data

Magnetic data for the complexes under study are shown in Fig. 3. This figure displays the temperature dependence of the effective magnetic moment and the field dependence of the molar magnetization at two temperatures. The effective magnetic moment keeps an almost constant value except at very low temperatures when its decrease reflects a zero-field splitting. The ZFS is also responsible for deviation of the magnetization from the Brillouin-function behaviour.

The experimental data were fit using the spin-Hamiltonian

$$\widehat{H} = \widehat{H}^{\mathrm{zfs}} + \widehat{H}^{\mathrm{Z}} \tag{11}$$

where the first contribution is the zero-field splitting term

$$\widehat{H}^{\mathrm{zfs}} = \hbar^{-2}D(\widehat{S}_z^2 - \widehat{S}^2/3) + \hbar^{-2}E(\widehat{S}_x^2 - \widehat{S}_y^2) \tag{12}$$

describing the axial and rhombic magnetic anisotropy. The Zeeman term entering the spin-Hamiltonian is expressed through the grids of polar angles ϑ_k and φ_l as

$$\widehat{H}^{\mathrm{Z}}(\vartheta_k, \varphi_l) = \mu_{\mathrm{B}} B_m \hbar^{-1}(g_x \sin\vartheta_k \cos\varphi_l \widehat{S}_x + g_y \sin\vartheta_k \times \cos\varphi_l \widehat{S}_y + g_z \cos\vartheta_k \widehat{S}_z) \tag{13}$$

In order to reduce the free parameters, the zero-field splitting parameters were restricted according to the constraints offered by the spin-Hamiltonian formalism

$$D = (\lambda/2)[g_z - (g_x + g_y)/2] \tag{14}$$

$$E = (\lambda/4)(g_x - g_y) \tag{15}$$

Two experimental data-sets (M versus T at 0.1 T, and M versus B at 2.0 and 4.6 K) have been treated simultaneously. The average magnetization data have been calculated as a correct powder average using a random spherical distribution of the magnetic-field vector [13]

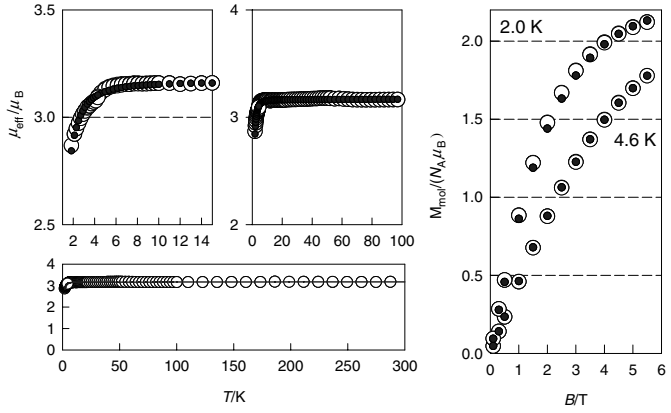
$$M_{\mathrm{av}} = \frac{1}{4\pi}\int_0^{\pi}\int_0^{2\pi} M(\vartheta,\varphi)\sin\vartheta\,\mathrm{d}\vartheta\,\mathrm{d}\varphi \tag{16}$$

The free parameters to be optimized are g_x, g_y, g_z and α_{TIP} (temperature-independent paramagnetism).

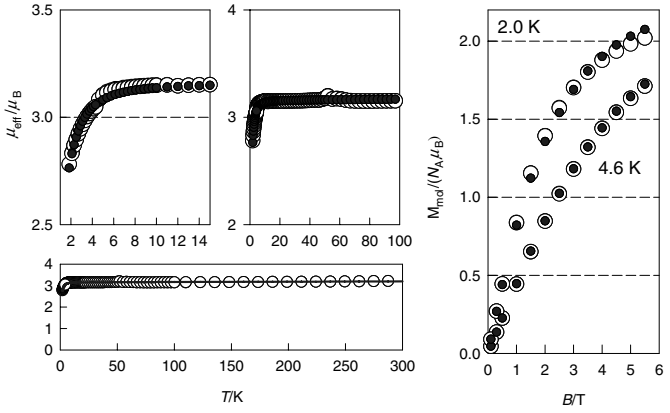
The calculated magnetic parameters are listed in Table 4. The acquired data for compounds **5**–**9** show that the D-parameters adopt values between −3 and +11 cm^{-1}. Enhancement of the magnetic anisotropy in these complexes is caused by the different crystal-field strengths in the axial and equatorial positions.

We also tested the hypothesis about the sign reversal for the D-parameter, since it is problematic to fix the sign of the D-parameter from powder data alone when $|D|$ is small. The sign reversal always led to a worse fit of magnetic data with an enlarged R-factor. Some other techniques could also be applied in detecting the zero-field splitting (e.g., high-field/high-frequency ESR, frequency-domain spectroscopy) but these are less common and hardly accessible for routine usage [1]. Nevertheless, a simultaneous utilization of the susceptibility and magnetization data-sets helps substantially in a reliable determination of the sign of the D-parameter.

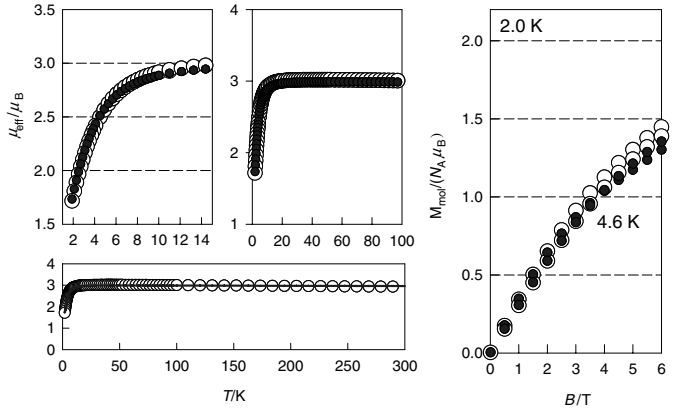
The fitting procedure results in appreciable values of the axial zero-field splitting parameter D. These magnetic data



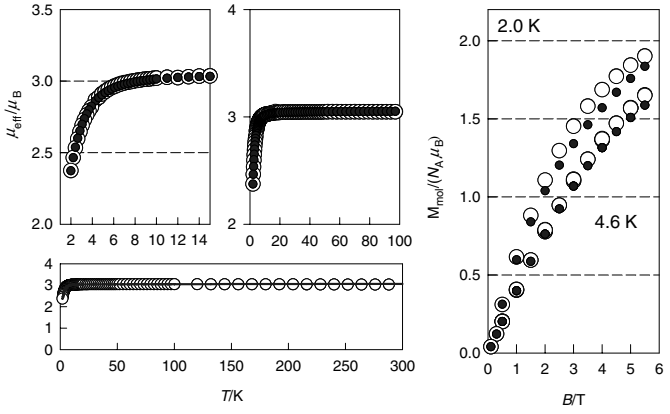
$[Ni(bzfupy)_2(ac)_2(H_2O)_2]$, **5**



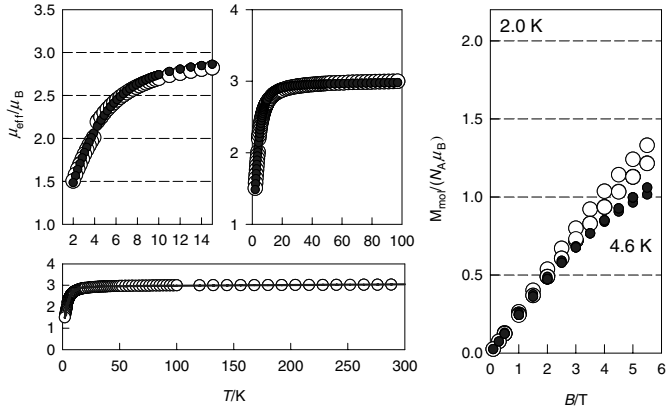
$[Ni(Me_2fupy)_2(H_2O)_4](ac)_2$, **6**



$[Ni(Me_2iz)_4(H_2O)_2]\,Cl_2 \cdot 3H_2O$, **7**



$[Ni(pz)_4(ac)_2]$, **8**



$[Ni(L^{NN})_2(H_2O)]$, **9**

Fig. 3. Temperature dependence of the effective magnetic moment and field dependence of the magnetization (right panel) for **5**–**9**. Filled circles, fitted data.

were used in correlation with the structural D-values subtracted from the X-ray structure data. The latter parameter, in the case of the heteroleptic complexes, is defined as

$$D_{\mathrm{str}} = \Delta_z - (\Delta_y + \Delta_x)/2 \tag{17}$$

where $\Delta_a = (d_a - \bar{d}_i)$ for $a = x, y, z$ is a shift relative to the mean distance $\bar{d}_i$ for a given bond (i = N, O). For the N- and O-donor ligands these values have been taken from complexes containing the $[Ni(NH_3)_6]^{2+}$ and $[Ni(H_2O)_6]^{2+}$ units, respectively; $\bar{d}(\mathrm{Ni–N}) = 2.145$ Å and $\bar{d}(\mathrm{Ni–O}) = 2.055$ Å [14]. As seen from Fig. 4, the correlation of the magnetic D_{mag} values versus the relative structural tetragonality parameters D_{str} is fairly good. However, three notes need to be added: (i) the magnetic as well as structural data bring evidence also for the rhombic anisotropy, which has not been included into the correlation; (ii) the correlation

Table 4
Fitted magnetic parameters for heteroleptic complexes[a]

Compound[b]	g_x	g_y	g_z	D/hc (cm^{-1})[c]	E/hc (cm^{-1})	$\alpha_{TIP}/10^9$ ($m^3\ mol^{-1}$)	R%	D_{str} (pm)	E_{str} (pm)
1, [5]	2.000	2.000	2.038	−6.0	+0.7	+0.49	2.4	−9.9	+1.1
2, [5]	2.139	2.140	2.190	−7.7	+2.0	−1.12	1.8	−6.2	+1.9
3, [5]	2.094	2.104	2.139	−5.3	+1.2	+0.61	0.7	−5.0	+1.4
4, [5]	2.147	2.149	2.179	−5.0	+0.5	−2.25	0.5	−2.25	+1.0
5, This work	2.200	2.203	2.310	−2.85	+0.68	+0.13	0.67	−2.85	+0.7
6, This work	2.218	2.219	2.249	−3.22	+0.74	+1.40	0.91	−8.8	+7.3
7, This work	2.100	2.118	2.079	+7.42	+0.49	−1.08	1.69	+11.45	+0.7
8, This work	2.170	2.181	2.142	+3.88	+0.01	−0.36	1.37	+6.6	+0.4
9, This work	2.103	2.159	2.000	+11.23	+1.46	+3.46	2.89	+15.5	+3.1

[a] Estimated errors: 0.01 for g-factors, 0.1 for ZFS parameters.
[b] Compounds: **1** = [Ni(2-*Meiz*)$_2$(HCOO)$_2$(H$_2$O)$_2$]; **2** = [Ni(1,2-*Me$_2$iz*)$_2$(HCOO)$_2$(H$_2$O)$_2$]; **3** = [Ni(*iqu*)$_2$(*ac*)$_2$(H$_2$O)$_2$]; **4** = [Ni(*fupy*)$_2$(*ac*)$_2$(H$_2$O)$_2$]; **5** = [Ni(*bzfupy*)$_2$(*ac*)$_2$(H$_2$O)$_2$]; **6** = [Ni(*Me$_2$fupy*)$_2$(H$_2$O)$_4$](*ac*)$_2$; **7** = [Ni(*Me$_2$iz*)$_4$(H$_2$O)$_2$] · Cl$_2$ · 3H$_2$O; **8** = [Ni(*pz*)$_4$(*ac*)$_2$]; **9** = [Ni(L^{NN})$_2$(H$_2$O)$_2$].
[c] Fits with a sign-reversed D-value (R-factor/%): **5**, +2.41 cm^{-1} (0.98); **6**, +2.79 cm^{-1} (1.10); **7**, −15.29 cm^{-1} (6.72); **8**, −7.03 cm^{-1} (6.60); **9**, −22.00 cm^{-1} (40.0).

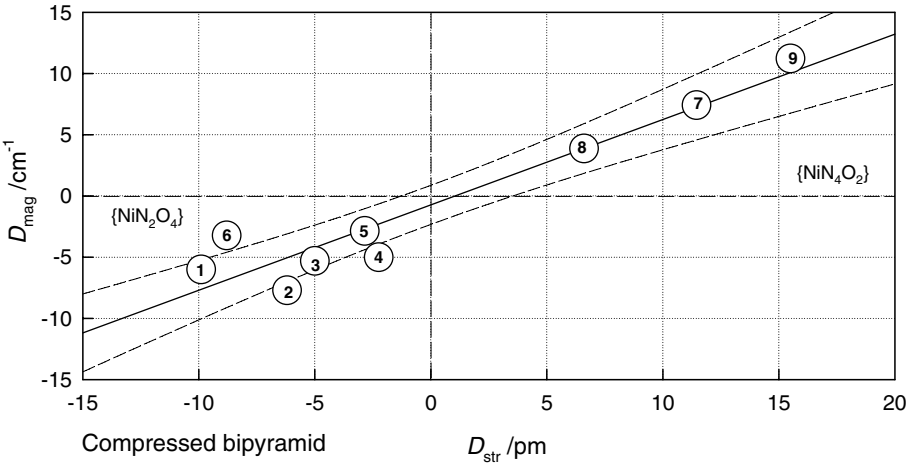


Fig. 4. Correlation of the magnetic vs. structural D-parameters. Broken lines, confidence intervals. **1** = [Ni(2-*Meiz*)$_2$(HCOO)$_2$(H$_2$O)$_2$]; **2** = [Ni(1,2-*Me$_2$iz*)$_2$(HCOO)$_2$(H$_2$O)$_2$]; **3** = [Ni(*iqu*)$_2$(*ac*)$_2$(H$_2$O)$_2$]; **4** = [Ni(*fupy*)$_2$(*ac*)$_2$(H$_2$O)$_2$]; **5** = [Ni(*bzfupy*)$_2$(*ac*)$_2$(H$_2$O)$_2$]; **6** = [Ni(*Me$_2$fupy*)$_2$(H$_2$O)$_4$](*ac*)$_2$; **7** = [Ni(*Me$_2$iz*)$_4$(H$_2$O)$_2$]Cl$_2$ · 3H$_2$O; **8** = [Ni(*pz*)$_4$(*ac*)$_2$]; **9** = [Ni(L^{NN})$_2$(H$_2$O)$_2$].

curve cannot be linear, since the compressed bipyramid cannot be extrapolated to zero metal–ligand distances; (iii) the magnetic parameters (D, E) are influenced by the orbital reduction factors via Eqs. (5) and (6). The last aspect manifests itself in the complex [Ni(imidazole)$_4$](acetate)$_2$: the structural distortion is extremely positive (strongly elongated bipyramid) whereas the axial zero-field splitting parameter, that measures the magnetic anisotropy, is extremely negative, $D/hc = -23\ cm^{-1}$ [15]. This apparent contradiction can be understood by inspecting Eq. (1): the orbital reduction factor for very long axial Ni···O contacts approaches a value of $\kappa_z = 1.0$ whereas that for the equatorial Ni–N bonds adopts normal values of $\kappa_x = 0.7$; this causes the sign reversal of the D-parameter.

It is recapitulated that in the solid state, the magnetic anisotropy for homoleptic Ni(II) complexes adopts small values: $D/hc = -3.5$ to $+2.0\ cm^{-1}$ for [Ni(*iz*)$_6$](*car*)$_2$ type complexes [3] (*car* – carboxylate). In heteroleptic, but "effective octahedral" complexes of the [Ni(*N*-base)$_4$(NCS)$_2$]·*n*H$_2$O type the registered magnetic anisotropy is not enhanced significantly: $D/hc = -3$ to $-1.5\ cm^{-1}$ [4]. On passing to the heteroleptic complexes of the [Ni(*N*-base)$_2$(H$_2$O)$_2$(*car*)$_2$] type the magnetic anisotropy is enhanced substantially: $D/hc = -8$ to $-5\ cm^{-1}$ [5]. Two complexes of the present study (**5** and **6**) span this interval, which is typical for the {NiO$_2$O$_2$N$_2$} chromophore. The remaining complexes (**7**, **8** and **9**) possessing the {NiN$_4$O$_2$} chromophore adopt positive values of $D/hc = +4$ to $+11\ cm^{-1}$.

Acknowledgements

Grant Agencies (Slovakia: VEGA 1/2453/05, APVT 20-005204, VEGA 1/3584/06; Germany: DAAD) are acknowledged for the financial support.

Appendix A. Supplementary material

CCDC 622567, 622568 and 622569 contains the supplementary crystallographic data for **5**, **6** and **7**. These data can be obtained free of charge via http://www.ccdc.ac.uk/

conts/retrieving.html, or from the Cambridge Crystallographic Data Centre, 12 Union Road, Cambridge CB2 1EZ, UK; fax: (+44) 1223-336-033; or e-mail: deposit@ccdc.cam.ac.uk. Calculated magnetic data assuming only the tetragonal distortion are deposited. Supplementary data associated with this article can be found, in the online version, at doi:10.1016/j.poly.2006.11.054.

References

[1] R. Boča, Coord. Chem. Rev. 248 (2004) 757.
[2] R. Boča, Struct. Bonding 117 (2006) 1.
[3] A. Mašlejová, R. Ivaniková, I. Svoboda, B. Papánková, L. Dlháň, D. Mikloš, H. Fuess, R. Boča, Polyhedron 25 (2006) 1823.
[4] P. Baran, M. Boča, R. Boča, A. Krutošíková, J. Miklovič, J. Pelikán, J. Titiš, Polyhedron 24 (2005) 1510.
[5] R. Ivaniková, R. Boča, L. Dlháň, H. Fuess, A. Mašlejová, V. Mrázová, I. Svoboda, J. Titiš, Polyhedron 25 (2006) 3261.
[6] A. Krutošíková, M. Dandárová, Heterocycles 37 (1994) 1695.
[7] M. Bencková, A. Krutošíková, Monatsh. Chem. 126 (1995) 753.
[8] A. Krutošíková, R. Sleziak, Collect. Czech. Chem. Commun. 61 (1996) 1627.
[9] V. Bobošík, A. Krutošíková, U. Jordis, Monatsh. Chem. 126 (1995) 747.
[10] E. König, Magnetic Properties of Coordination and Organo-Metallic Transition Metal Compounds, in: Landolt-Börnstein, Neue Serie, vol. II/2, Springer, Berlin, 1966, p. 1.
[11] B. Papánková, I. Svoboda, H. Fuess, K. Šintálová, Acta Crystallogr., Sect. E 61 (2005) m2036.
[12] M. Hvastijová, J. Kožíšek, J. Kohout, L. Jäger, J. Coord. Chem. 36 (1995) 195.
[13] R. Boča, Theoretical Foundations of Molecular Magnetism, Elsevier, Amsterdam, 1999.
[14] Inorganic Crystal Structure Database, Fachinformationszentrum Karlsruhe, Germany. www: <http://www.fiz-informationsdienste.de/en/DB/icsd/index.html>.
[15] R. Boča, L'. Dlháň, W. Haase, R. Herchel, A. Mašlejová, B. Papánková, Chem. Phys. Lett. 373 (2003) 402.

conditions and we separated complexes of Ca(II), Cd(II) and Mn(II) with the 5-(4-pyridyl)tetrazolato (4-PTZ) anion as ligand [21]. Newly, other Mn(II)-5-pyridyl-tetrazolato (PTZ) complexes were obtained under similar experimental conditions [22].

We now report four new M(II) (M = Cu, Co) complexes obtained by the 1,3-dipolar addition reaction of cyano pyrazine with azide in aqueous solution and analyse their solid state structures using the concept of three-dimensional nets [23].

2. Experimental

2.1. Materials and instrumentation

Infrared spectra were recorded on a Bruker IFS-125 model FT-IR spectrophotometer as KBr pellets [24]. C, H, N analyses were carried out using a Perkin–Elmer analyzer [25], Cu were analysed by a Perkin–Elmer Analyst 300, AAS atomic absorption spectrometer. Raman spectra were recorded on a Bruker IFS 6/s FT-Raman spectrometer with Nd:CYAG laser wavelength (1064 nm) as the light source [26]. Thermogravimetry, TG and differential thermogravimetry, DTG were carried out on a shimadzu DT-50. The measurements were performed by using a dynamic nitrogen atmosphere with a flow rate of 20 ml/min. The heating rate was kept at 10 °C min^{-1} and the sample sizes ranged in mass from 1.45 to 1.66 mg contained in a platinum crucible. Al_2O_3 was used as a reference material. Pyrazine carbonitrile has been purchased from Aldrich Company and other chemicals were of analytical grade quality and used without further purification.

Caution: Metal azide and metal tetrazolate complexes are potentially explosive. Only a small amount of material should be prepared and should be handled with caution.

2.2. Synthesis of copper complexes *1*, *2a*, and *3*

To an ethanolic solution of $Cu(NO_3)_2 \cdot 3H_2O$ (0.48 g, 2 mmol) in 15 cm^3, a (0.42 gm, 4 mmol) of pyrazinecarbonitrile, in 10 cm^3 ethanol were added. Further, (0.65 g, 10 mmol) NaN_3 aqueous solution was added dropwise with continuous stirring. The clear blue solution was allowed to stand at room temperature for a couple of days. Deep blue crystals of (**1**) $[Cu(pyztz)_2(H_2O)]$, green crystals of (**2a**), $[Cu(pyztz)_2(H_2O)_2]$ and blue crystals of (**3**) $[Cu(pyztz)_2(H_2O)_2](H_2O)$ were formed. The three complexes were separated under microscope after filtration, dried in air. The product yielding about ~10% of complex **1**, 20% of complex **2**, and 60% of complex **3**. *Anal.* Calc. for **1**: C, 31.95; H, 2.14; N, 44.72; Cu, 16.91. Found: C, 32.21; H, 2.52; N, 44.85; Cu, 17.23%. *Anal.* Calc. for **2**: C, 30.49; H, 2.55; N, 42.68; Cu, 16.13. Found: C, 30.34; H, 2.34; N, 42.19; Cu, 16.37%. *Anal.* Calc. for **3**: C, 29.16; H, 2.93; N, 40.80; Cu, 15.43. Found: C, 29.06; H, 2.21; N, 40.63; Cu, 15.69%.

2.3. Synthesis of cobalt complex *2b*

To a methanolic solution of $CoCl_2 \cdot 6H_2O$ (0.476 g, 2 mmol) in 15 cm^3, (0.42 gm, 4 mmol) of pyrazinecarbonitrile, in 10 cm^3 methanol was added. Further, (0.65 g, 10 mmol) NaN_3 aqueous solution were added dropwise with continuous stirring. The clear yellow solution was allowed to stand in a refrigerator at around +4 °C for a couple of days. Orange crystals of (**2b**) $[Co(pyztz)_2(H_2O)_2]$ suitable for X-ray measurements were collected by filtration, dried in air. The product yields about ~50%. *Anal.* Calc. for **2b**: C, 30.86; H, 2.59; N, 43.19; Co, 22.08. Found: C, 30.95; H, 2.53; N, 43.35; Co, 22.13%.

2.4. X-ray crystallography

Single crystal X-ray data of **1**, **2a**, and **3** were measured at 100(2) K on a modified STOE four circle diffractometer, of **2b** were collected on a Bruker-AXS SMART APEX CCD diffractometer, using graphite crystal-monochromatized Mo Kα radiation ($\lambda = 0.7107$ Å). The intensities were corrected for Lorentz-polarisation effects and for absorption. Crystallographic data and processing parameters are given in Table 1. The structures were solved by direct methods and subsequent Fourier analyses. The programs DIFABS [27a], SADABS [27b] and SHELXTL/PC program package [28] were used for computations. Analytical expressions of neutral-atom scattering factors were employed, and anomalous dispersion corrections were incorporated. Anisotropic displacement parameters were applied to non-hydrogen atoms in full-matrix least-squares refinements based on F^2. All hydrogen atoms were located from difference Fourier maps assigned with isotropic displacement factors and included in the final refinement cycles as follows: (a) pyrazine hydrogen atoms bonded to carbon by geometrical restraints using the HFIX utility of SHELXTL/PC package; (b) water hydrogen atoms by use of O–H distance restraints. Split occupancy of 0.5 was applied to the disordered lattice water molecule O(2) of **3**. Selected bond distances and bond angles are given in Tables 2–5, for complexes **1**, **2a**, **2b** and **3**, respectively.

2.5. Network analysis

Abbreviations for 3D nets have been taken from M. O'Keeffe and O.M. Yaghi, Reticular Chemistry Structure Resource, 2005, Arizona State University, Tempe, http://okeeffe-ws1.la.asu.edu/rcsr/home.htm where crystallographic coordinates and other useful details for 3D-nets can be obtained. Another source is the EPINET project (http://epinet.anu.edu.au).

3. Results and discussion

In the attempt to prepare $[M(pyrazinecarbonitrile)_2(N_3)_2]_n$, the [2+3] cycloaddition reaction of pyrazinecarbonitrile and sodium azide occurred in the presence of M^{2+} as

Table 1
Crystallographic data and processing parameters

Compound	**1**	**2a**	**2b**	**3**
Empirical formula	$C_{10}H_8CuN_{12}O$	$C_{10}H_{10}CuN_{12}O_2$	$C_{10}H_{10}CoN_{12}O_2$	$C_{10}H_{12}CuN_{12}O_3$
Formula mass	375.83	393.85	389.23	411.87
System	triclinic	monoclinic	monoclinic	monoclinic
Space group	$P\bar{1}$	$P2_1/n$	$P2_1/n$	$C2/c$
a (Å)	6.861(3)	6.294(2)	6.0806(12)	12.947(3)
b (Å)	9.397(3)	11.777(3)	11.396(2)	7.334(2)
c (Å)	11.169(4)	10.017(3)	10.533(2)	16.622(5)
α (°)	72.94(3)	90	90	90
β (°)	79.97(3)	106.24(2)	105.63(3)	101.07(2)
γ (°)	87.75(3)	90	90	90
V (Å^3)	677.8(4)	712.9(3)	702.9(2)	1548.9(7)
Z	2	2	2	4
μ (Mo Kα) (mm^{-1})	1.643	1.571	1.261	1.455
D_{calc} (Mg/m^3)	1.842	1.835	1.839	1.766
Crystal size (mm)	$0.24 \times 0.14 \times 0.08$	$0.25 \times 0.16 \times 0.10$	$0.20 \times 0.16 \times 0.10$	$0.24 \times 0.20 \times 0.12$
θ Range (°)	3.29–26.00	3.44–27.99	2.69–25.80	3.21–26.00
Reflections collected	3035	2152	5198	1927
Independent reflections/R_{int}	2616/0.0963	1724/0.0298	1347/0.0452	1518/0.0365
Parameters	224	122	122	138
Goodness-of-fit on F^2	1.132	1.083	1.328	1.191
R_1/wR_2 (all data)	0.0833/0.2106	0.0400/0.0881	0.0648/0.1330	0.0423/0.1152
Residual extrema (e/Å^3)	0.983/−0.928	0.356/−0.395	0.734/−0.501	0.560/−0.402

Table 2
Selected bond lengths (Å) and angles (°) for (**1**)

Cu(1)–N(13)	1.967(3)	Cu(1)–N(3)	1.975(4)
Cu(1)–N(11)	2.048(4)	Cu(1)–N(1)	2.052(4)
Cu(1)–O(1)	2.219(4)	N(1)–C(1)	1.340(6)
N(1)–C(4)	1.351(5)	C(1)–C(2)	1.407(6)
C(2)–N(2)	1.343(5)	N(2)–C(3)	1.333(6)
C(3)–C(4)	1.402(6)	C(4)–C(5)	1.441(6)
C(5)–N(3)	1.343(6)	C(5)–N(6)	1.350(5)
N(3)–N(4)	1.353(5)	N(4)–N(5)	1.298(5)
N(5)–N(6)	1.377(6)	N(11)–C(11)	1.341(6)
N(11)–C(14)	1.367(5)	C(11)–C(12)	1.388(7)
C(12)–N(12)	1.346(6)	N(12)–C(13)	1.362(6)
C(13)–C(14)	1.390(7)	C(14)–C(15)	1.452(7)
C(15)–N(16)	1.324(5)	C(15)–N(13)	1.346(6)
N(13)–N(14)	1.350(5)	N(14)–N(15)	1.325(5)
N(15)–N(16)	1.357(6)		
N(13)–Cu(1)–N(3)	170.5(2)	N(13)–Cu(1)–N(11)	81.5(2)
N(3)–Cu(1)–N(11)	97.7(2)	N(13)–Cu(1)–N(1)	97.8(2)
N(3)–Cu(1)–N(1)	81.1(2)	N(11)–Cu(1)–N(1)	168.3(2)
N(13)–Cu(1)–O(1)	96.22(14)	N(3)–Cu(1)–O(1)	93.3(2)
N(11)–Cu(1)–O(1)	96.11(14)	N(1)–Cu(1)–O(1)	95.55(14)
C(1)–N(1)–C(4)	118.4(4)	N(1)–C(1)–C(2)	119.4(4)
N(2)–C(2)–C(1)	122.9(4)	C(3)–N(2)–C(2)	116.7(4)
N(2)–C(3)–C(4)	121.7(4)	N(1)–C(4)–C(3)	120.8(4)
N(1)–C(4)–C(5)	113.6(4)	C(3)–C(4)–C(5)	125.5(4)
N(3)–C(5)–N(6)	110.7(4)	N(3)–C(5)–C(4)	118.2(4)
N(6)–C(5)–C(4)	131.1(4)	C(5)–N(3)–N(4)	106.1(3)
N(5)–N(4)–N(3)	109.1(4)	N(4)–N(5)–N(6)	110.2(4)
C(5)–N(6)–N(5)	104.0(3)	C(11)–N(11)–C(14)	117.8(4)
N(11)–C(11)–C(12)	120.9(4)	N(12)–C(12)–C(11)	122.3(5)
C(12)–N(12)–C(13)	117.0(4)	N(12)–C(13)–C(14)	121.1(4)
N(11)–C(14)–C(13)	120.9(4)	N(11)–C(14)–C(15)	113.5(4)
C(13)–C(14)–C(15)	125.5(4)	N(16)–C(15)–N(13)	111.8(4)
N(16)–C(15)–C(14)	130.6(4)	N(13)–C(15)–C(14)	117.5(4)
C(15)–N(13)–N(14)	105.6(3)	N(15)–N(14)–N(13)	107.8(4)
N(14)–N(15)–N(16)	110.4(4)	C(15)–N(16)–N(15)	104.4(4)

Lewis acid catalyst. This gave deep blue crystals of $[Cu(pyztz)_2(H_2O)]$ (**1**), green crystals of $[Cu(pyztz)_2(H_2O_2)]$ (**2a**), orange crystals of $[Co(pyztz)_2(H_2O)_2]$ (**2b**) and blue crystals of $[Cu(pyztz)_2(H_2O)_2](H_2O)$ (**3**).

It is well-known that the tetrazole ring formation via the [2+3] cycloaddition of 4-cyanopyridine and azide takes place under hydrothermal conditions so it is notable that the tetrazole rings were formed at room temperature. The cycloaddition reaction was probably accelerated by the presence of the M(II) salt as a Lewis acid catalyst.

Table 3
Selected bond lengths (Å) and angles (°) for (**2a**)

Cu(1)–N(3)	1.996(2)	Cu(1)–N(1)	2.078(2)
Cu(1)–O(1)	2.316(2)	N(1)–C(1)	1.338(3)
N(1)–C(4)	1.348(3)	C(1)–C(2)	1.403(4)
C(2)–N(2)	1.332(4)	N(2)–C(3)	1.340(4)
C(3)–C(4)	1.395(4)	C(4)–C(5A)	1.459(4)
C(5)–N(6)	1.324(3)	C(5)–N(3)	1.338(3)
N(3)–N(4)	1.348(3)	N(4)–N(5)	1.324(3)
N(5)–N(6)	1.355(3)		
N(3)–Cu(1)–N(1)	98.93(9)	N(1)–Cu(1)–O(1)	92.15(8)
N(3A)–Cu(1)–O(1A)	91.74(9)	C(1)–N(1)–C(4)	117.1(2)
N(1)–C(1)–C(2)	120.9(3)	N(2)–C(2)–C(1)	122.2(3)
C(2)–N(2)–C(3)	116.7(2)	N(2)–C(3)–C(4)	121.7(3)
N(1)–C(4)–C(3)	121.3(3)	N(1)–C(4)–C(5A)	113.7(2)
C(3)–C(4)–C(5A)	125.1(3)	N(6)–C(5)–N(3)	111.8(2)
N(6)–C(5)–C(4A)	129.4(2)	N(3)–C(5)–C(4A)	118.8(2)
C(5)–N(3)–N(4)	105.6(2)	N(5)–N(4)–N(3)	108.2(2)
N(4)–N(5)–N(6)	109.8(2)	C(5)–N(6)–N(5)	104.7(2)

Symmetry code: (A) $-x, -y+1, -z$.

Table 4
Selected bond lengths (Å) and angles (°) for (**2b**)

Co(1)–N(3)	2.103(4)	Co(1)–N(1)	2.180(4)
Co(1)–O(1)	2.059(3)	N(1)–C(1)	1.342(6)
N(1)–C(4)	1.343(6)	C(1)–C(2)	1.384(7)
C(2)–N(2)	1.335(7)	N(2)–C(3)	1.332(6)
C(3)–C(4)	1.384(7)	C(4)–C(5A)	1.469(6)
C(5)–N(6)	1.333(6)	C(5)–N(3)	1.333(6)
N(3)–N(4)	1.345(5)	N(4)–N(5)	1.317(6)
N(5)–N(6)	1.340(6)		
N(3)–Co(1)–N(1)	101.46(15)	N(1A)–Co(1)–O(1)	90.42(14)
N(3)–Co(1)–O(1)	92.14(15)	C(1)–N(1)–C(4)	115.9(4)
N(1)–C(1)–C(2)	121.8(5)	N(2)–C(2)–C(1)	122.1(5)
C(2)–N(2)–C(3)	116.3(5)	N(2)–C(3)–C(4)	122.1(5)
N(1)–C(4)–C(3)	121.8(4)	N(1)–C(4)–C(5A)	114.7(4)
C(3)–C(4)–C(5A)	123.4(4)	N(6)–C(5)–N(3)	111.7(4)
N(6)–C(5)–C(4A)	127.6(4)	N(3)–C(5)–C(4A)	120.6(4)
C(5)–N(3)–N(4)	104.9(4)	N(5)–N(4)–N(3)	108.9(4)
N(4)–N(5)–N(6)	109.8(4)	C(5)–N(6)–N(5)	104.6(4)

Symmetry code: (A) $-x, -y, -z$.

Table 5
Selected bond distances (Å) and angles (°) for (**3**)

Cu(1)–N(3)	1.989(3)	Cu(1)–N(1)	2.044(3)
Cu(1)–O(1A)	2.416(3)	N(1)–C(1)	1.342(5)
N(1)–C(4)	1.356(5)	C(1)–C(2)	1.396(6)
C(2)–N(2)	1.332(5)	N(2)–C(3)	1.346(5)
C(3)–C(4)	1.378(5)	C(4)–C(5)	1.470(5)
C(5)–N(6)	1.329(5)	C(5)–N(3)	1.330(5)
N(3)–N(4)	1.348(4)	N(4)–N(5)	1.320(5)
N(5)–N(6)	1.350(4)		
N(3AS)–Cu(1)–N(1)	98.92(12)	N(3)–Cu(1)–O(1A)	90.21(11)
N(1)–Cu(1)–O(1)	91.74(11)	C(1)–N(1)–C(4)	117.1(3)
C(1)–N(1)–Cu(1)	129.0(3)	C(4)–N(1)–Cu(1)	113.9(2)
N(1)–C(1)–C(2)	120.4(4)	N(2)–C(2)–C(1)	122.9(4)
C(2)–N(2)–C(3)	116.3(4)	N(2)–C(3)–C(4)	121.9(4)
N(1)–C(4)–C(3)	121.5(3)	N(1)–C(4)–C(5)	112.9(3)
C(3)–C(4)–C(5)	125.7(3)	N(6)–C(5)–N(3)	112.7(3)
N(6)–C(5)–C(4)	129.2(3)	N(3)–C(5)–C(4)	118.0(3)
C(5)–N(3)–N(4)	105.2(3)	C(5)–N(3)–Cu(1)	113.9(2)
N(4)–N(3)–Cu(1)	140.9(3)	N(5)–N(4)–N(3)	108.0(3)
N(4)–N(5)–N(6)	110.7(3)	C(5)–N(6)–N(5)	103.5(3)

Symmetry code: (A) $-x+1, -y, -z+1$.

3.1. Structures

A perspective view with atom labelling scheme of complex **1** is given in Fig. 1, selected bond parameters are summarized in Table 2. The copper(II) ions are penta-coordinated by nitrogen atoms N(1), N(3) N(11) and N(13) of two chelating pyztz ligands, which adopt the basal sites, and oxygen atom O(1) of an aqua ligand at apical site. The CuN_4O coordination polyhedron may be described as a slightly distorted tetragonal pyramid ($\tau = 0.04$) [29]. The Cu–N_{pyz} bonds [2.048(4) and 2.052(4) Å] are a little bit longer than the Cu–N_{tet} bonds [1.975(4) and 1.967(3) Å], whereas the Cu(1)–O(1) bond is 2.219(4) Å. Cu(1) is located 0.186 Å above the basal N_4 plane. The chelating N–Cu–N bond angles are 81.1(2)° and 81.5(2)°, the other N–Cu–N bond angles are 97.7(2)°

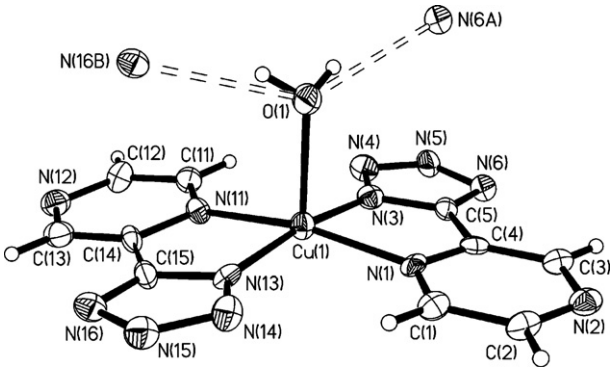


Fig. 1. Perspective view of $[Cu(pyztz)_2(H_2O)]$ (**1**).

and 97.8(2)°, whereas the N–Cu–O bond angles are in the range from 93.3(2)° to 96.22(14)°. The tetrazolato-rings of the pyztz ligands are twisted by 3.2° and 4.2° from their sixmembered pyrazine-rings. The mean planes of the two pyztz ligands have an acute angle of 14.1°. A packing view of **1** is given in Fig. 2. The isolated polyhedra of **1** have a Cu···Cu separation of 6.861(3) Å, and are connected via hydrogen bonds of type O–H···N from O(1) to N(16) $[-x, -y, 1-z]$ and N(6) $[1-x, 1-y, -z]$ to form a 1-D system extented along $[1, 1, -1]$ with O···N separations of 2.841(5) and 2.920(5) Å, respectively. Within these chains adjacent polyhedra are arranged head to tail in order to allow π–π-stacking interactions between neighbouring chelating pyztz ligands.

The molecular structure of **2a**, Fig. 3, has a centrosymmetric configuration, in which the octahedral Cu(II) ion is coordinated by four equatorial nitrogen atoms from two pyztz ligands and axial oxygen atoms of coordinated water molecules. As in **1**, each pyztz ligand chelates to Cu through one tetrazolato-nitrogen atom N1-site of the tetrazolato-ring and through the pyrazine nitrogen atom. The tetrazolato-ring is twisted by 5.1° from the sixmembered ring. Selected bond parameters are listed in Table 3. The

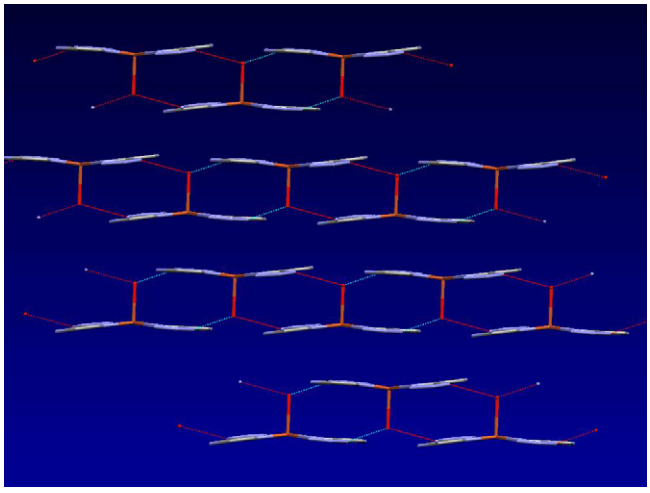


Fig. 2. Packing plot of $[Cu(pyztz)_2(H_2O)]$ (**1**). Broken lines indicate hydrogen bonds.

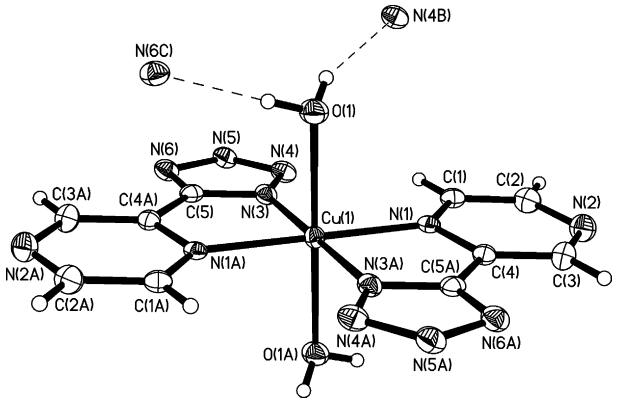


Fig. 3. Perspective view of $[Cu(pyztz)_2(H_2O)_2]$ (**2a**).

distorted CuN_4O_2 octahedron has Cu–N_{pyz} and Cu–N_{tet} bond lengths of 2.078(2) and 1.996(2) Å, respectively, and a Cu–O bond distance of 2.316(2) Å. The water molecule forms hydrogen bonds of type O–H···N from O(1) to N(4) $[1-x, 1-y, -z]$ and N(6) $[-1/2+x,\ 1/2-y,\ -1/2+z]$ with O···N separations of 2.936(4) and 2.816(3) Å, respectively, where two N atoms of the tetrazolato rings in position 1 and 2 act as hydrogen bond acceptors to form cyclic tetrameric subunits. The shortest Cu···Cu separation between Cu(II) polyhedra is 6.294(2) Å, the basal CuN_4 planes form acute angles of 21.6°. Compound **2b** as shown in Fig. 4 is isostructural and selected bond parameters are listed in Table 4. The hydrogen bonding system in **2** differs from that observed in the structure of corresponding $[Mn(2\text{-}PTZ)_2(H_2O)_2]$ complex, (2-PTZ = 5-(2-pyridyl)-tetrazolate anion) [22]. In this latter Mn complex eight intermolecular O–H···N(tetrazole) hydrogen bonds link each Mn complex to four other Mn complexes. In contrast to compounds **2a** and **2b** nitrogen atoms of the 2-PTZ moiety act as acceptors which correspond to N(5) and N(6) atoms of the present tetrazole ligands see Ref [22, Fig. 1b].

A perspective view of compound **3** is given in Fig. 5, selected bond parameters are summarized in Table 5. Although **3** has a similar centrosymmetric configuration as **2a**, in which the octahedral Cu(II) ion is also coordinated by four equatorial nitrogen atoms from two pyztz ligands and axial oxygen atoms of coordinated water molecules, the bond parameters within the CuN_4O_2 coordination polyhedron differ significantly. The Cu–N_{pyz} and Cu–N_{tet} bond lengths are shortened to 2.044(3) and 1.989(3) Å, respectively, whereas the axial Cu–O bond distance is elongated to 2.416(3) Å. The aqua ligands form hydrogen bonds of type O–H···N from O(1) to N(6) $[1-x, 1-y, 1-z]$ and N(5) $[1/2+x, -1/2+y, z]$ to form a supramolecular network, with O···N separations of 2.913(4) and 2.831(3) Å, respectively. In addition, the disordered lattice water molecule with split occupancy 0.5 and related by a diad, form hydrogen bonds of type O–H···O to apical O(1) atoms of adjacent Cu(II) polyhedra. The O···O separations are 2.790(13) and 2.928(13) Å. As a consequence of this additional lattice water molecule the packing of **3** is quite different compared to **2a**. The monomeric polyhedra have a V-type arrangement with acute angles of basal CuN_4 planes of 49.8°. The shortest metal–metal distance is 7.334(2) Å.

Bond lengths and bond angles of the five-membered tetrazolate rings in complexes **1**–**3** are very similar and agree

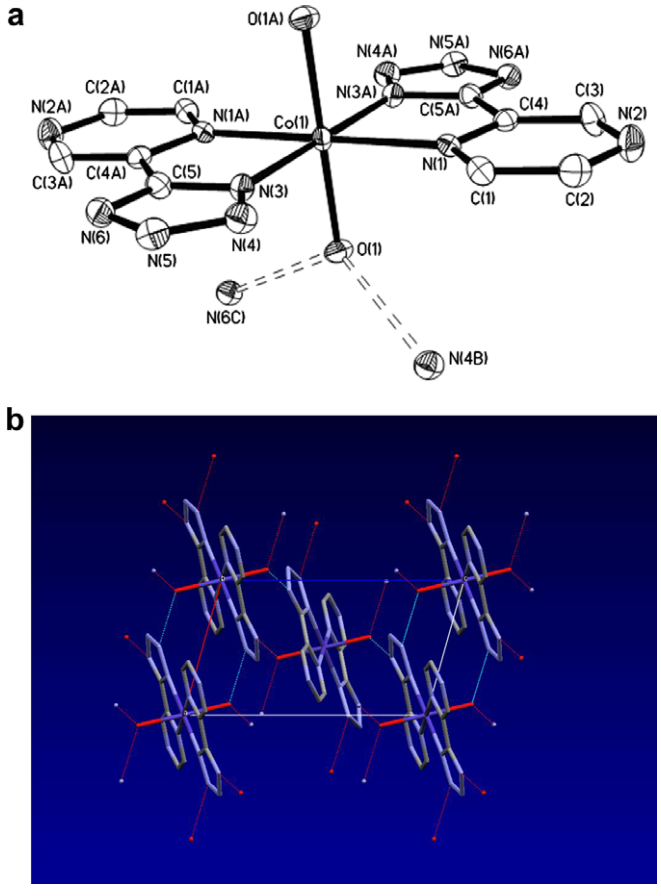


Fig. 4. (a) Perspective view of $[Co(pyztz)_2(H_2O)_2]$ (**2b**). (b) Packing plot of $[Co(pyztz)_2(H_2O)_2]$ (**2b**).

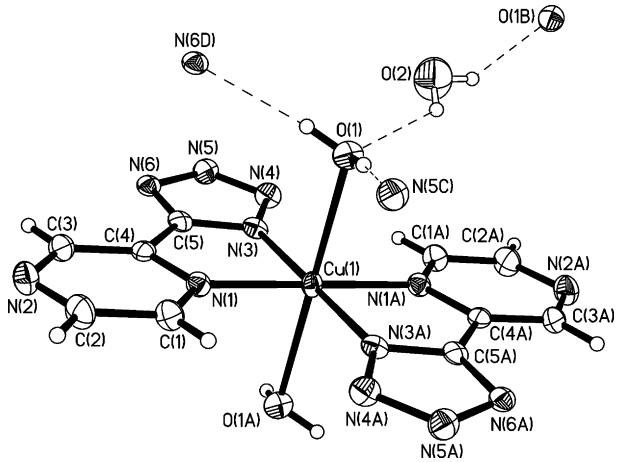


Fig. 5. Perspective view of $[Cu(pyztz)_2(H_2O)_2]\cdot(H_2O)$ (**3**).

well with values reported in a series of bis-tetrazolate-dianions [30]. The N2–N3 bond opposite to C in position 5 is significantly shorter [1.298(5)–1.325(5) Å] than other interatomic distances within the heterocycle despite of the aromatic nature of the five-membered ring. In case of 5-phenyl tetrazolate anion (5-PhTZ) the deprotonation had also led to a noticeable elongation of the N2–N3 bond from 1.247 to 1.307(3) Å, in excellent agreement with *ab initio* calculations [31].

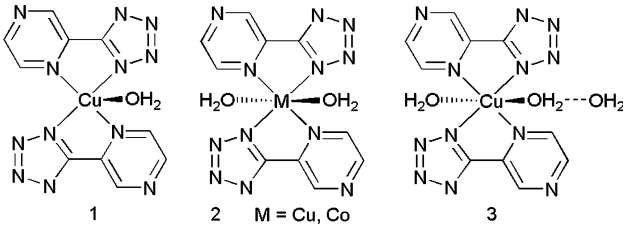
It is interesting to note that in case of the present complexes **1**–**3**, only one (in case of **1**) and two (in case of **2a,b** and **3**) out of four uncoordinated nitrogen donor atoms per pyztz molecule act as hydrogen bond acceptors. In case of previous reported complexes with 5-(4-pyridyl)tetrazolato ligands (4-PTZ) [21] all nitrogen donors are involved in hydrogen bonds. In fact, compound **1** can be described as hydrogen bond mismatched as it has nine possible hydrogen bond acceptors but only two hydrogens can act as classical donors. In **2**, this ratio is 10:4 and in **3** 11:6. Consequently, the most complex hydrogen bond pattern is found in **3**. This fact and the higher nitrogen content compared to the 4-PTZ ligand may also explain the thermal instability of the present compounds.

3.2. Network analysis

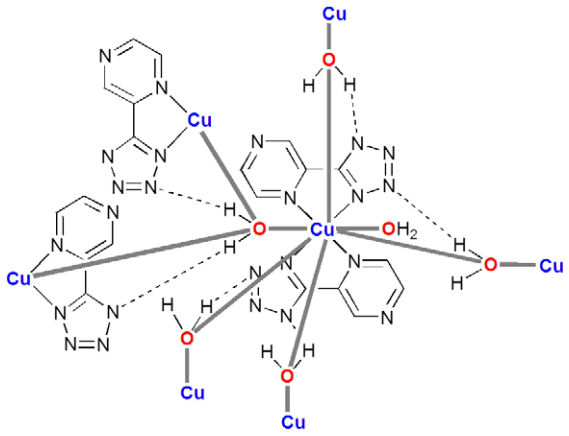
The analysis of network patterns as an aid in the understanding of crystal structures was advocated already in the mid 1950:ies by UK crystallographer Alexander Wells, [32] and recently network analysis of 3D-coordination polymers and Metal–Organic Frameworks have become increasingly important [23,33]. However, as was shown already by Wells, this analysis is relevant also for hydrogen bonded systems [24].

It should be emphasised that all structures do not form 3D-networks, even if hydrogen bonding is considered, so for example is compound **1** clearly well described as the packing of 1D hydrogen bonded chains. Compound **2** on the other hand is clearly hydrogen bonded in all three dimensions, and these bonds are few (compared to the total number of atoms in the molecule) and well defined, thus this structure is probably well described as a 3D-network Scheme 1.

Indeed, when we assign nodes and links in **2** according to Scheme 2 we get a three- and six-connected network, see Fig. 6. Close inspection of this net (visually and by calculating vertex symbols [34]) shows that the net topology is



Scheme 1.



Scheme 2.

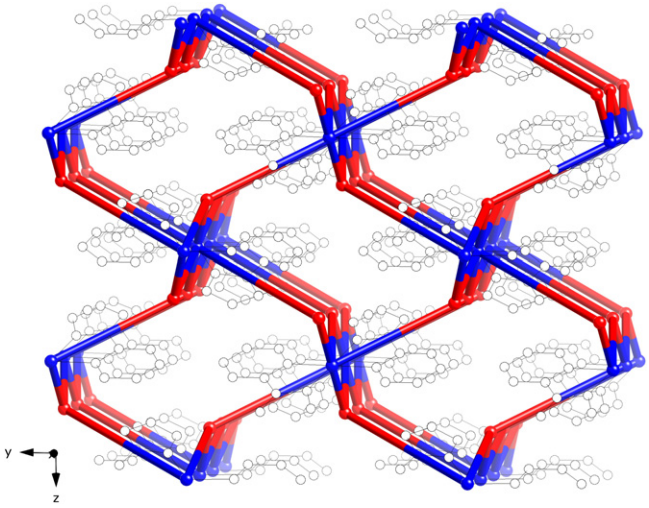
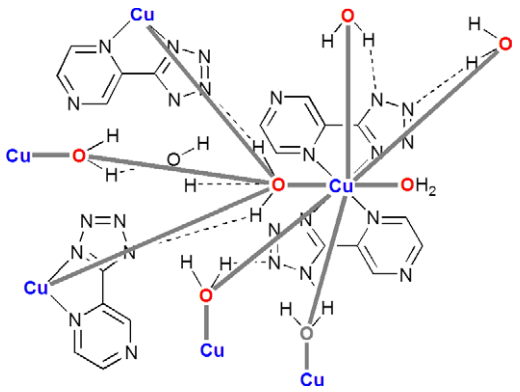


Fig. 6. The three- and six-connected network in **2**, the net topology is a **rtl** or rutile net, the most common of all three- and six-connected nets.

a **rtl**- or rutile net, the most common of all three- and six-connected nets Scheme 3.

The situation in **3** is slightly more complicated as we have introduced more possible hydrogen bond acceptor and donor sites. It appears, however, that this structure can be described by the **fsh**-net, see Fig. 7.



Scheme 3.

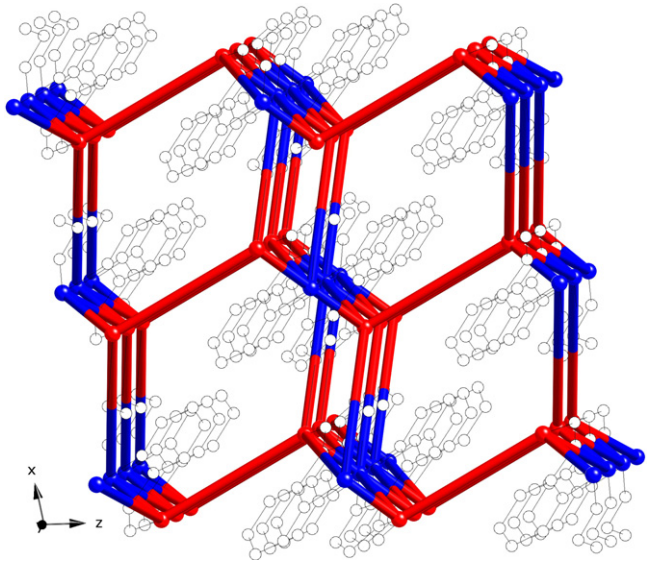


Fig. 7. The four- and six-connected network in **3** has the **fsh** topology.

Note that both nets are somewhat distorted from the ideal nets, but they still have the same topology as the ideal nets as they can be transformed into each other without breaking any bonds.

3.3. Thermal analysis

Thermal decomposition analysis of the given tetrazolate complexes was performed under quite sensitive conditions; very small samples were taken (1.4–1.6 mg.) due to the high explosion properties of such compounds. The only published thermal analysis data for pyridine tetrazolate complexes were performed and tentatively assigned till 250 °C [21]. The DTA and DSC measurements of these complexes failed as the samples were exploding even at low temperatures and lower masses less than 2.0 mg. It also gave some vapors which affects the sensor of the DSC instrument. The stages of decomposition, temperature range, decomposition product losses as well as the found and calculated weight loss% of the complexes are given in Table 6. The TG and DTG curves of complexes **1**, **2a**, **2b** and **3**, Fig. 8, show the decomposition steps.

The first step, almost in all complexes, represents the loss of water content, hydrated and coordinated water molecules in the temperature range 103–280 °C. Although the tetrazolate group is a sensitive exploding group in the complexes, it decomposes slowly over a wide range of temperature, perhaps overlapping with the loss of water molecules or decomposition of the subsequently formed cyano-pyrazine group. Decomposition and liberation of an azido group was found in the temperature range 154–355 °C. The third and fourth steps were generally the decomposition of the cyano-pyrazine group, liberating the pyrazine moiety and leaving the cyano group on the metal atom which was further oxidized to give the final residue as a metal oxide.

3.4. Spectra

In the high energy region the room temperature IR spectra of the crystalline complexes **1**, **2a**, **2b** and **3** exhibit strong broad bands around 3000–3550 cm^{-1} corresponding to the coordinated water molecules to the Cu(II) ro Co(II) ions in the three complexes. Extensive hydrogen bonding of

Table 6
Thermal decomposition of **1**, **2a**, **2b**, and **3**

Complex	DTG peak (°C)	Temperature range (°C)	Decomposition product lost (formula weight)	Weight loss (%)	
				Found (%)	Calculated (%)
$[Cu(Pyztetz)_2(H_2O)]$	121.73	105–127	H_2O	4.63	4.78
	231.67	127–242	$1\frac{1}{2}$ N_2 molecule	10.60	11.23
	303.16	242–468	$1\frac{1}{2}$ N_2 and cyano-pyrazine	37.75	39.14
	584.52	468–650	cyano-pyrazine group	26.14	27.96
			CuO residue	20.19	21.16
$[Cu(Pyrztetz)_2(H_2O)_2]$	120.43	103–159	$2H_2O$	9.50	9.14
	289.26	189–294	$1\frac{1}{2}$ N_2 molecule	9.11	10.71
	300.18	294–355	$1\frac{1}{2}$ N_2 and cyano-pyrazine	36.99	37.35
	421.44	360–476	pyrazine group	19.37	20.10
			CuO residue	22.9	20.19
$[Co(Pyrztetz)_2(H_2O)_2]$	212.82	150–225	$2H_2O$	9.40	9.24
	357.87	225–381	tetrazolate group (in two steps)	17.35	17.74
	399.58	381–427	tetrazolate group	17.41	17.74
	558.97	427–570	2 pyrazine groups	38.80	41.14
			CoO residue	19.86	19.25
$[Cu(Pyrztetz)_2(H_2O)_2]\cdot H_2O$	138.87	106–144	$2H_2O$	8.88	8.74
	221.26	199–287	H_2O	3.96	4.37
	314.72	292–342	2 tetrazolato (3 N_2 and 2 CN^-)	32.99	33.04
	512.65	342–607	2 pyrazine groups	34.07	38.40
			CuO Residue	17.9	19.31

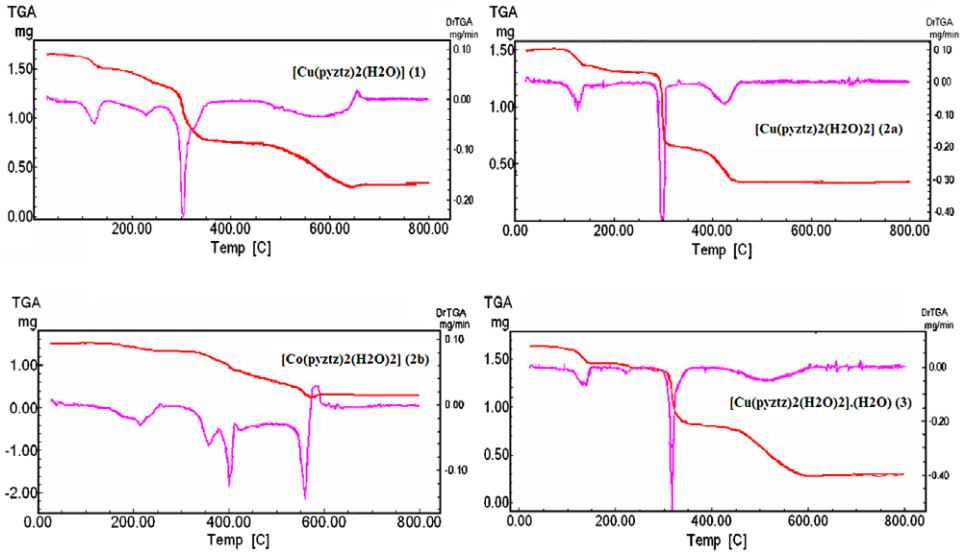


Fig. 8. TG and DTG of complexes **1**, **2a**, **2b** and **3**.

the types O–H···O and N–H···O are indicated by the presence of broad medium strong bands centered around 2400–2600 cm^{-1}. The absence of any bands in the 2200–1750 cm^{-1} region confirms ring formation to the tetrazolate ligand by the 1,3-dipolar reaction of the azide group with the nitrile group on the pyrazine ring. Neither vibrations associated with νCN of the 2-cyanopyrazine (expected week to medium band centered around 2240 cm^{-1}) nor strong bands associated with $\nu_{as}N_3$ in the 2150–2000 cm^{-1} region are present [35]. The vibration frequencies of the coordinated pyrazine tetrazolato ligands could be tentatively assigned in agreement with recently reported metal pyridine tetrazolate [21,22]. In the far region few bands around 296 cm^{-1} could tentatively be

Table 7
Vibrational frequencies (cm^{-1}) in the IR and Raman spectra of complexes **1**, **2a**, **2b** and **3**

Complex **1**		Complex **2a**		Complex **2b**		Complex **3**		Assignment
IR	Raman	IR	Raman	IR	Raman	IR	Raman	
3343 s,b	3466 m	3345 s,b	3301 m	3330 vs,b		3542 s,b		νOH water
3260 s,b			3255 s	3077 vs,b	3075 m	3287 s,b	3262 s	
3089 s	3085 s	3089 s	3090 s	2554 m		3187 s,b	3262 s	νO···H–O
2631 w	2448 m	2605 w	2773 m	2354 m		2630 w	2610 m	νN···H–O
1726 w		1728 w		2328 m		1728 w		
1675 vs		1662 m,b		2063 s				
1631 vs	1608 vs	1635 m,b	1600 vs	1610 m		1616 s	1610 m	
1582 s				1553 m	1597 vs		1585 s	
1534 s	1539 vs	1535 m	1535 vs	1532 m	1532 vs	1534 m	1540 m	
1428 vs	1430 m	1455 s		1447 s	1462 w	1427 vs		
1380 vs	1375 m	1375 s		1371 s		1377 vs		
1299 vs		1300 s	1267 w	1300 m		1301 s		
1235 m		1234 s		1225 s	1373 w	1231 s	1214 m	
1180 vs		1180 vs		1168 vs		1163 vs		
1133 m		1133 s		1134 vs		1130 vs		pyrazine
1071 s		1072 s		1072 vs	1165 w	1070 vs		tetrazolate
1046 vs	1022 s	1046 vs	1019 s	1036 vs		1044 vs		vibrations
954 w		958 w		936 w	1085 m	940 w		
863 s		865 s		864 s	1036 m	866 vs		
769 w		770 s				770 s		
737 m		759 s		759 m		765 s		
627 w,b		625 mb		681 w	755 w	645 w		
593 m		593 s		593 s				
504 m		505 m		478 s	638 w	507 s,b		
418 s		420 s		418 s		417 m		
394 w		396 w		386 s		387 m		
296 w		295 w		293 m		296 w	292 s	M–L vibrations
	126 s		137 s		144 m			
	−126 m		−137 m				−292 m	anti-Stoke

assigned as a M–L vibration. The Raman spectra show some anti-Stokes peaks around −126 m, −137 m and −292 m, cm^{-1} for complexes **1**, **2a** and **3** respectively. Results are summarized in Table 7.

The electronic spectrum of complex **1** exhibits the d–d transitions as a relatively strong broad absorption band around 15000 cm^{-1} suggesting five-coordination geometry around the central copper ion, along with a shoulder on the high frequency side at 24300 cm^{-1} which could be attributed to the LMCT from the pyrazine tetrazolate ligands to the central copper ion [36]. The spectra of penta-amin copper(II) complexes with square pyramidal geometry have been found to exhibit an intense absorption band in the 17000–15000 cm^{-1} range [37]. The complexes **2a** and **3** show the LMCT absorption bands around 26000 cm^{-1} but the d–d transition bands are shifted to higher energy. It is found at 15600 cm^{-1} for complex **2a** and at 16500 cm^{-1} for complex **3**. The cobalt(II) complex **2b** shows the LMCT absorption bands around 26595 cm^{-1} while the d–d transition bands are shifted to higher energy. It is found as a broad band around 20160 cm^{-1}. These shifts could be interpreted as the effect of an increased cf-splitting due to the existence of a sixth ligand and is consistent with the 6-fold coordination field for the copper complexes [38] and the cobalt complex [39].

4. Conclusions

The preparation of 5-(pyridyl)tetrazole M(II) complexes from azide ions and 4-cyanopyridine were achieved under exceptionally mild conditions. The compounds prepared form a series of pseudo-polymorphs with different numbers of water molecules present, going from a system with a massive over-representation of hydrogen bond acceptors through a more balanced system as more water molecules are added. It was shown that the structures showing extended hydrogen bonds in three-dimensions could readily be analysed using the concept of 3D-nets.

5. Supplementary material

CCDC 278952, 278953, 622096 and 278954 contain the supplementary crystallographic data for **1**, **2a**, **2b** and **3**, respectively. These data can be obtained free of charge via http://www.ccdc.ac.uk/conts/retrieving.html, or from the Cambridge Crystallographic Data Centre, 12 Union Road, Cambridge CB2 1EZ, UK; fax: (+44) 1223-336-033; or e-mail: deposit@ccdc.cam.ac.uk.

Ideal form of the **fsh**-net from the RCSR. (http://okeeffe-ws1.la.asu.edu/RCSR/home.htm)

cell: 1.5601, 1.5601, 5.6062, 90, 90, 120
space group: R-3 m
nodes (vertices):
0.0000, 0.0000, 0.4108 (4 connected)
0.0000, 0.0000, 0.0000 (6 connected)

Acknowledgements

M.A.M. Abu-Youssef and A.A. Massoud thank the SIDA-Swedish Research Links program for Grant No. 348-2002-6879. F.A. Mautner thanks Prof. Kratky, Prof. Belaj (Univ. Graz) and Dr. J. Baumgartner (TU-Graz) for assistance.

References

[1] R.N. Butler, in: A.R. Katrizky, C.W. Rees, E.F.V. Scriven (Eds.), Comprehensive Heterocyclic Chemistry, 4, Pergamon, Oxford, UK, 1996.
[2] L. Carlucci, G. Ciani, D.M. Proserpio, Angew. Chem., Int. Ed. Engl. 38 (1999) 3488.
[3] (a) C. Janiak, J. Chem. Soc., Chem. Commun. (1994) 545;
(b) C. Janiak, T.G. Scharmann, W. Gunter, F. Girgsdies, H. Hemling, W. Hinrichs, D. Lentz, Chem. Eur. J. 1 (1995) 637.
[4] G.B. Ansell, J. Chem. Soc., Dalton Trans. (1973) 371.
[5] H. Singh, A.S. Chawla, V.K. Kapoor, D. Paul, R. Malhotra, Prog. Med. Chem. 17 (1980) 151.
[6] (a) V.A. Ostrovskii, M.S. Pevzner, T.P. Kofmna, M.B. Shcherbinin, I.V. Tselinskii, Targets Heterocycl. Syst. 3 (1999) 467;
(b) M. Hiskey, D.E. Chavez, D.L. Naud, S.F. Son, H.L. Berghout, C.A. Bome, Proc. Pyrotech. Semin. 27 (2000) 3.
[7] (a) S. Bhandari, M.F. Mahon, J.G. McGinley, K.C. Molloy, C.E.E. Roper, J. Chem. Soc., Dalton Trans. (1998) 3425;
(b) M. Hill, M.F. Mahon, K.C. Molloy, J. Chem. Soc., Dalton Trans. (1996) 1857;
(c) S. Bhandari, M.F. Mahon, K.C. Molloy, J.S. Palmer, S.F. Sayers, J. Chem. Soc., Dalton Trans. (2000) 1053;
(d) S. Bhandari, C.G. Frost, C.E. Hague, M.F. Mahon, K.C. Molloy, J. Chem. Soc., Dalton Trans. (2000) 663.
[8] D.J. Moderhack, J. Prakt. Chem. 340 (1988) 687.
[9] (a) X. Xue, X.-S. Wang, L.-Z. Wang, R.-G. Xiong, B.F. Abrahams, X.-Z. You, Z.-L. Xue, C.-M. Che, Inorg. Chem. 41 (2002) 6544;
(b) L.-Z. Wang, Z.-R. Qu, H. Zhao, X.-S. Wang, R.-G. Xiong, Z.-L. Xue, Inorg. Chem. 42 (2003) 3969;
(c) J. Tao, Z.-J. Ma, R.-B. Huang, L.-S. Zheng, Inorg. Chem. 43 (2004) 6133;
(d) R.-G. Xiong, X. Xue, H. Zhao, X.-Z. You, B.F. Abrahams, Z. Xue, Angew. Chem., Int. Ed. Engl. 41 (2002) 3800;
(e) X. He, C.Z. Lu, D.Q. Yuan, Inorg. Chem. 45 (2006) 5760;
(f) M. Dinca, A.F. Yu, J.R. Long, J. Am. Chem. Soc. 128 (2006) 8904.
[10] B.B. Straaten, D. Solinger, C. van de Westeringh, H. Veldstra, Rec. Trav. Chim. 77 (1958) 1129.
[11] W.G. Finnegan, R.A. Henry, R. Lofquist, J. Am. Chem. Soc. 80 (1958) 3908.
[12] (a) J.V. Dunica, M.E. Pierce, J.B. Santella III, J. Org. Chem. 56 (1991) 2395;
(b) S.J. Wittenberger, B.G. Donner, J. Org. Chem. 58 (1993) 4139.
[13] (a) A. Kumar, R. Narayanan, H. Shechter, J. Org. Chem. 61 (1996) 4462;
(b) B.E. Huff, M.A. Staszak, Tetrahedron Lett. 34 (1993) 8011.
[14] W.R. Ellis Jr., W.L. Purcell, Inorg. Chem. 21 (1982) 834.
[15] (a) Z.P. Demko, K.B. Sharpless, J. Org. Chem. 66 (2001) 7945;
(b) Z.P. Demko, K.B. Sharpless, Org. Lett. 3 (2001) 4091;
(c) Z.P. Demko, K.B. Sharpless, Org. Lett. 4 (2002) 2525;
(d) Z.P. Demko, K.B. Sharpless, Angew. Chem., Int. Ed. Engl. 41 (2002) 2110;
(e) Z.P. Demko, K.B. Sharpless, Angew. Chem., Int. Ed. Engl. 41 (2002) 2113;
(f) F. Himo, Z.P. Demko, L. Noodleman, K.B. Sharpless, J. Am. Chem. Soc. 125 (2003) 9983.
[16] R. Cortes, L. Lezama, F.A. Mautner, T. Rojo, in: M.M. Turnbull, T. Sugimoto, L.K. Thompson (Eds.), Molecule-Based Magnetic Materials.

Theory, Techniques and Applications, ACS Symposium Series, Vol. 644, ACS, Washington, 1966.
[17] J. Ribas, A. Escuer, M. Monfort, R. Vicente, R. Cortes, L. Lezama, T. Rojo, Coord. Chem. Rev. 193–195 (1999) 1027.
[18] M.A.M. Abu-Youssef, A. Escuer, M.A.S. Goher, F.A. Mautner, G. Reiss, R. Vicente, Angew. Chem., Int. Ed. Engl. 39 (2000) 1624.
[19] A. Escuer, J. Cano, M.A.S. Goher, Y. Journaux, F. Lloret, F.A. Mautner, R. Vicente, Inorg. Chem. 39 (2000) 4688.
[20] A. Escuer, R. Vicente, F.A. Mautner, M.A.S. Goher, M.A.M. Abu-Youssef, J. Chem. Soc., Chem. Commun. (2002) 64.
[21] F.A. Mautner, C. Gspan, K. Gatterer, M.A.S. Goher, M.A.M. Abu-Youssef, E. Bucher, W. Sitte, Polyhedron 23 (2004) 1217.
[22] P. Lin, W. Clegg, R.W. Harrington, R.A. Henderson, J. Chem. Soc., Dalton Trans. (2005) 2388.
[23] (a) L. Öhrström, K. Larsson, Molecule-Based Materials: The Structural Network Approach, Elsevier, Amsterdam, 2005;
(b) M.A.M. Abu-Youssef, V. Langer, L. Öhrström, Chem. Commun. (2006) 1082.
[24] M.A.S. Goher, F.A. Mautner, M.A.M. Abu-Youssef, A.K. Hafez, A.M.A. Badr, J. Chem. Soc., Dalton Trans. (2002) 3309.
[25] M.A.S. Goher, F.A. Mautner, A.K. Hafez, M.A.M. Abu-Youssef, C. Gspan, A.M.A. Badr, Polyhedron 22 (2003) 975.
[26] M.A.M. Abu-Youssef, Polyhedron 24 (2005) 1829.
[27] (a) H. Walker, D. Stuart, Acta Crystallogr., Sect. A 39 (1983) 158;
(b) R.H. Blessing, Acta Crystallogr., Sect. A 51 (1995) 33;
SADABS, Bruker AXS, 1998.
[28] SHELXTL/PC 5.03, Siemens Analytical Automation Inc., Madison, WI, 1995.
[29] A.W. Addison, T.N. Rao, J. Reedijk, J. Chem. Soc., Dalton Trans. (1984) 1349.
[30] A. Hammerl, G. Holl, T.M. Klapötke, P. Mayer, H. Nöth, H. Piotrowski, M. Warchhold, Eur. J. Inorg. Chem. (2002) 834.
[31] I.A. Guzei, G.A. Bikzhanova, Acta Crystallogr., Sect. E 58 (2002) o937.
[32] (a) A.F. Wells, Acta Crystallogr., Sect. 7 (1954) 535, and following papers;
(b) see also A.F. Wells, Three-dimensional nets and polyhedra, Wiley, New York, 1977.
[33] (a) O.M. Yaghi, M. O'Keeffe, N.W. Ockwig, H.K. Chae, M. Eddaoudi, J. Kim, Nature 423 (2003) 705;
(b) N.W. Ockwig, O. Delgado-Friedrichs, M. O'Keeffe, O.M. Yaghi, Acc. Chem. Res. 38 (2005) 176;
(c) M. O'Keeffe, O.M. Yaghi, J. Solid State Chem. 178 (2005) V;
(d) V.A. Blatov, L. Carlucci, G. Ciani, D.M. Proserpio, Crystengcomm 6 (2004) 377.
[34] M. O'Keeffe, M. Eddaoudi, H.L. Li, T. Reineke, O.M. Yaghi, J. Solid State Chem. 152 (2000) 3.
[35] K. Nakamoto, Infrared Spectra of Inorganic and Coordination Compounds, 2nd ed., Wiley, New York, 1978.
[36] M.A.S. Goher, F.A. Mautner, Polyhedron 15 (1996) 1133.
[37] A.G. Tomlinson, B.J. Hathaway, J. Chem. Soc. A 1685 (1968), and 1905.
[38] M.A.S. Goher, F.A. Mautner, Polyhedron 17 (1998) 1561.
[39] M.A.S. Goher, F.A. Mautner, Polyhedron 18 (1999) 2339.

influence of different factors, such as pH, temperature, solvent, catalyst and the steric effects of the substrate, on this hydrolytic reaction were shown to be necessary.

In recent years, the steric influence of the palladium(II) catalyst on the rate of hydrolytic cleavage of the amide bond in histidine- and methionine-containing peptides has been the subject of very broad investigations [3,5,6,8]. It was found that in the reaction between MeCOHis-Gly and different *cis*-$[Pd(L)(H_2O)_2]^{2+}$ complexes (L is ethylenediamine, en; 1,2-propylenediamine, 1,2-pn; *N*-methylethylenediamine, Meen; isobutylenediamine, ibn; or *N*,*N*,*N*′,*N*′-tetramethylethylenediamine, Me_4en, acting as a bidentate ligand) in the pH range 2.0–2.5 and at 60 °C, the rate of the regioselective cleavage of the amide bond involving the carboxylic group of histidine decreases as the steric bulk of the palladium(II) complex increases (en > 1,2-pn > Meen > ibn > Me_4en) [5]. The observed rates of hydrolytic reaction were investigated in terms of steric hindrance of the chelating diamine on the palladium(II) complexes and the results showed that with increasing number of methyl groups at the nitrogen or carbon atom of the chelated diamine ligand, the number of hydrolyzed His-Gly peptide bonds in MeCOHis-Gly decreased. For example, the reaction between *cis*-$[Pd(en)(H_2O)_2]^{2+}$ and this peptide after 48 h at 60 °C was two times faster in comparison with *cis*-$[Pd(Me_4en)(H_2O)_2]^{2+}$, and one and a half times faster in relation to *cis*-$[Pd(ibn)(H_2O)_2]^{2+}$. The results for MeCO-His-Gly peptide are not in accordance with those obtained for MeCOMet-Gly peptide and palladium(II) complexes containing different chelated diamine ligands (en, 1,2-pn, ibn, 1,2-dach, Meen and Me_4en) [8]. The rate of the hydrolysis of the Met-Gly amide bond was approximately the same and the amount of the hydrolyzed MeCOMet-Gly peptide was between 80% and 88% after 4 h. This was explained by the existence of the same catalytically active form in the reaction of *cis*-$[Pd(L)(H_2O)_2]^{2+}$ complexes with MeCOMet-Gly peptide complex obtained by the replacement of the chelated diamine ligand from the initially formed binuclear palladium(II)–peptide complex. Giving importance to recent results with sterically crowded *cis*-$[Pd(L)(H_2O)_2]^{2+}$ complexes and histidine- and methionine-containing peptides and the different effects of these complexes on the rate of hydrolytic cleavage of the amide bonds in these peptides, it seemed reasonable to further investigate the reactions of these peptides with new *cis*-$[Pd(L)(H_2O)_2]^{2+}$ type complexes. The main aim of these investigations was to design a new palladium(II) complex capable of the regioselective cleavage of the amide bond in peptides containing both methionine and histidine amino acids in the side chains.

In the present study, *cis*-$[Pd(dpa)Cl_2]$ and *cis*-$[Pd(dpa)(H_2O)_2]^{2+}$ complexes (dpa is 2,2′-dipyridylamine) were synthesized and employed to investigate their reactions with the dipeptides Met-Gly and His-Gly, and also the reactions of the *cis*-$[Pd(dpa)(H_2O)_2]^{2+}$ complex with the *N*-acetylated derivatives of these peptides, MeCOMet-Gly and MeCOHis-Gly. ^{1}H NMR study of the regioselective hydrolytic cleavage of the amide bond in only the MeCOMet-Gly peptide and the absence of this hydrolytic reaction with the other investigated peptides are promising and may help in the development of new palladium(II) complexes as artificial metallopeptidases.

2. Experimental

2.1. Reagents

Distilled water was demineralized and purified to a resistance greater than 10 MΩ cm^{-1}. The compounds D_2O, DNO_3, NaOD, $(CD_3)_2SO$, 2,2′-dipyridylamine (dpa), K_2PdCl_4 were obtained from the Aldrich Chemical Co. All common chemicals were of reagent grade. The dipeptides methionylglycine (Met-Gly) and histidylglycine (His-Gly) were obtained from the Sigma Chemical Co. The terminal amino group in the peptides was acetylated by standard methods [9].

2.2. Synthesis of cis-dichloro(2,2′-dipyridylamine)palladium(II), cis-[Pd(dpa)Cl$_2$]

The *cis*-$[Pd(dpa)Cl_2]$ complex was prepared by a modification of a method described in the literature [10]. K_2PdCl_4 (0.2000 g, 0.61×10^{-4} mol) was dissolved in 25 cm^3 of water, and to this solution an equivalent amount of 2,2′-dipyridylamine (0.1049 g; 0.61×10^{-4} mol) was added. The pH of the solution was adjusted to ca. 3 by the addition of 1 M HCl, which was followed by refluxing for 5 h. If the pH was carefully controlled, a clear color change from brown to yellow was observed during this time. The obtained yellow solution was left overnight at room temperature. The crystals of *cis*-$[Pd(dpa)Cl_2]$ were removed by filtration, washed with a small amount of water, and air dried. Yield 0.1922 g (90%). *Anal.* Calc. for *cis*-$[Pd(dpa)Cl_2] \equiv C_{10}H_9Cl_2N_3Pd$ (FW = 348.52): C, 34.46; H, 2.60; N, 12.06%. Found: C, 34.35; H, 2.70; N, 12.02%. ^{1}H NMR ($(CD_3)_2SO$, 200 MHz); δ 7.15 (t, H5); δ 7.27 (d, H3); δ 7.96 (t, H4); δ 8.58 (dd, H6); δ 11.12 (s, H–N); ^{13}C NMR ($(CD_3)_2SO$, 200 MHz); δ 114.09 (C4); δ 119.01 (C5); δ 141.33 (C3); δ 149.44 (C6); δ 150.83 (C2).

2.3. Synthesis of cis-diaqua(2,2′-dipyridylamine)palladium(II), cis-[Pd(dpa)(H$_2$O)$_2$]$^{2+}$

Because all the solutions were made in D_2O, all the aqua ligands actually were D_2O. However, for simplicity and consistency with our previous publications, we show the D_2O ligands as H_2O. The *cis*-$[Pd(dpa)(H_2O)_2]^{2+}$ was prepared from the corresponding chloro complex in the same manner as described in the literature for the preparation of similar Pd(II) aqua complexes [11,12]. The *cis*-$[Pd(dpa)Cl_2]$ complex was treated in D_2O solution with the appropriate amount of $AgNO_3$. The Pd(II) complex and $AgNO_3$ were mixed in a molar ratio of 1:1.95. The mixture was stirred at room temperature in the dark for up to 24 h. The precip-

itated AgCl was removed and the filtrate containing *cis*-$[Pd(dpa)(H_2O)_2]^{2+}$ was stored in a refrigerator until used for reaction with the dipeptides.

2.4. Synthesis of bis(2,2′-dipyridylamine)palladium(II) dichloride tetrahydrate, $[Pd(dpa)_2]Cl_2 \cdot 4H_2O$

The schematic presentation of the reaction for the synthesis of the *cis*-$[Pd(dpa)_2]Cl_2 \cdot 4H_2O$ complex is given in Fig. 1. The dipeptide Met-Gly (0.0300 g, 1.45×10^{-4} mol) was dissolved in 4 $cm^3$of water and solid *cis*-$[Pd(dpa)Cl_2]$ (0.0507 g, 1.45×10^{-4} mol) was added to this solution. The pH of the solution was adjusted to ca. 2.4 by the addition of 1 M HCl and then mixture was stirred at 60 °C for 4 h. The precipitate of the unreacted *cis*-$[Pd(dpa)Cl_2]$ was removed, and the filtrate was left in a refrigerator for several days. The light yellow crystals of $[Pd(dpa)_2]Cl_2 \cdot 4H_2O$ were removed by filtration, washed with a small amount of ethanol, and air-dried. Yield 0.0343 g (40%). *Anal.* Calc. for $[Pd(dpa)_2]Cl_2 \cdot 4H_2O = C_{20}H_{26}Cl_2N_6O_4Pd$ (FW = 591.77): C, 40.59; H, 4.43; N, 14.20%. Found: C, 40.06; H, 4.54; N, 14.12%. Spectral characterization: ^{1}H NMR (D_2O, 200 MHz); δ 7.13 (t, H5), δ 7.46 (d, H3); δ 7.61 (d, H4), δ 8.05 (m, H6); ^{13}C NMR (D_2O, 200 MHz); δ 119.41 (C4); δ 125.10 (C5); δ 146.59 (C3); δ 153.48 (C6); δ 155.58 (C2).

2.5. Measurements

All pH measurements were made at 25 °C. The pH meter (Iskra MA 5704) was calibrated with Fischer certified buffer solutions of pH 4.00. The results were not cor-

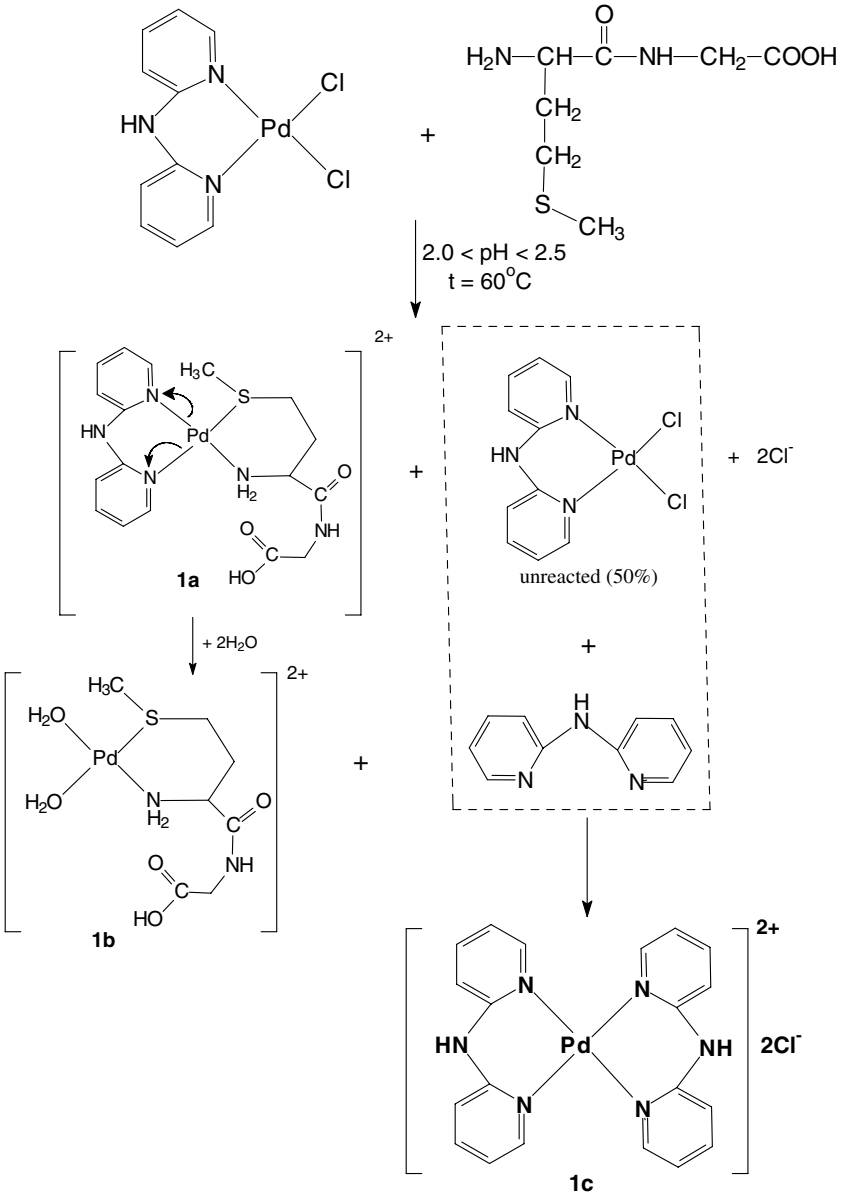


Fig. 1. The reaction scheme between *cis*-$[Pd(dpa)Cl_2]$ and the Met-Gly peptide in the pH range $2.0 < pH < 2.5$ and at 60 °C with the $[Pd(dpa)_2]Cl_2 \cdot 4H_2O$ complex as the final product.

rected for the deuterium isotope effect. The ^{1}H NMR spectra of D_2O solutions containing TSP (3-trimethylsilylpropane-1-sulfonate) as the internal reference were recorded with a Varian Gemini 200 spectrometer. Elemental microanalyses for carbon, hydrogen, and nitrogen were done at the Faculty of Chemistry, University of Belgrade.

2.6. Crystal structure determination of the $[Pd(dpa)_2]Cl_2 \cdot 4H_2O$ complex

The crystal data of the $[Pd(dpa)_2]Cl_2 \cdot 4H_2O$ complex, and the parameters of data collection are summarized in Table 1. The intensity data were measured on a light yellow, plate-like crystal of dimensions $0.25 \times 0.15 \times 0.05$ mm with a KM4CCD kappa-geometry diffractometer [13] using graphite-monochromated Mo Kα radiation ($\lambda = 0.71073$ Å) at ambient temperature, up to the θ value of 25°. The structure was solved by direct methods using SHELXS-86 [14] and refined by least-squares techniques with SHELXL-97 [15]. The intensity data were corrected for Lp effects as well as for absorption. Anisotropic thermal parameters were employed for the non-hydrogen atoms. The hydrogen atoms connected to carbon atoms were placed at the calculated positions while those attached to the water oxygen atoms and the nitrogen atom were located on the subsequent difference Fourier maps. The O–H and N–H bond lengths were standardized to values of 0.85 and 0.90 Å, respectively. All hydrogen atoms were allowed to ride on the atoms to which they were attached and their isotropic displacement parameters were given values 30% higher than the isotropic equivalent for the atom to which the H-atom was bonded. A Siemens Stereochemical Workstation was used to prepare the drawings [16].

Table 1
Crystallographic data collection and structure refinement information

Compound	$[Pd(dpa)_2]Cl_2 \cdot 4H_2O$
Chemical formula	$C_{20}H_{26}Cl_2N_6O_4Pd$
Chemical formula weight	591.77
Crystal system	monoclinic
Space group	$C2/c$
a (Å)	15.8539(11)
b (Å)	7.7580(6)
c (Å)	20.5302(12)
β (°)	107.563(6)
V (Å^3)	2407.4(3)
Z	4
D_{calc} (Mg m^{-3})	1.633
Absorption coefficient (mm^{-1})	1.032
Number of measured reflections	12 500
Number of independent reflections	2137
Number of observed reflections	1705
R [$F^2 > 2\sigma(F_2)$]	0.0360
wR (F^2)	0.0852
S	1.096
$\Delta\rho_{max}$ (e Å^{-3})	1.125
$\Delta\rho_{min}$ (e Å^{-3})	−0.426

3. Results and discussion

^{1}H NMR spectroscopy was applied to study the reactions of the palladium(II) complexes, *cis*-[Pd(dpa)Cl$_2$] and *cis*-[Pd(dpa)(H$_2$O)$_2$]$^{2+}$ (dpa is a bidentate 2,2′-dipyridylamine) with the dipeptides methionylglycine (Met-Gly) and histidylglycine (His-Gly), and the reactions of *cis*-[Pd(dpa)(H$_2$O)$_2$]$^{2+}$ with the *N*-acetylated derivatives of these dipeptides, MeCOMet-Gly and MeCOHis-Gly. All reactions were carried out with equimolar amounts of the palladium(II) complex and the peptide in the pH range 2.0–2.5 and at two different temperatures, 25 and 60 °C. As was shown in previous studies [1–3,17], acidic solutions are needed to suppress the formation of hydroxo-bridged oligomeric palladium(II) complexes, which are catalytically inactive.

3.1. Reactions of the cis-$[Pd(dpa)Cl_2]$ and cis-$[Pd(dpa)(H_2O)_2]^{2+}$ complexes with Met-Gly and His-Gly

In the reactions between *cis*-[Pd(dpa)Cl$_2$] and *cis*-[Pd(dpa)(H$_2$O)$_2$]$^{2+}$ and the peptides Met-Gly or His-Gly, no hydrolysis of the peptide bond was observed in the pH range 2.0–2.5, neither at 25 °C, nor at 60 °C. The signal at 3.80 ppm for the methylene protons of the free glycine did not appear in the ^{1}H NMR spectrum even after the reaction mixture had been kept at 60 °C for 7 days. Upon addition of glycine to the reaction mixture, its resonance at the above mentioned chemical shift appeared immediately. The reaction scheme between *cis*-[Pd(dpa)Cl$_2$] and Met-Gly is given in Fig. 1. A similar reaction pathway can be presumed for the reaction of *cis*-[Pd(dpa)(H$_2$O)$_2$]$^{2+}$ with this peptide, or any of these two palladium(II) complexes with the His-Gly peptide. As can be seen from Fig. 1, one of the final products in these reactions is the square-planar $[Pd(dpa)_2]^{2+}$ complex (**1c**). The preparation of this complex starting from *cis*-[Pd(dpa)Cl$_2$] and the Met-Gly peptide has been described in the experimental part of this paper and the crystal structure of $[Pd(dpa)_2]Cl_2 \cdot 4H_2O$ was confirmed by X-ray diffraction. The absence of hydrolysis of the peptide bond in the reactions between the Pd(II) complexes and Met-Gly, or His-Gly peptides is in accordance with previous results obtained for the Pd(II) complexes and Met-X or His-X peptides (X is an aliphatic amino acid) containing a non-acetylated N-terminal amino group [7]. The final product in these reactions was an extremely stable palladium(II)–peptide complex in which the Pd(II) ion is bound through the sulfur donor atom of methionine, or the N3 imidazole nitrogen atom of histidine, and the nitrogen atom of the N-terminal amino group [18]. This mode of coordination holds the Pd(II) complex away from the downstream peptide bond and prevents its cleavage. It is well established that for the cleavage of the peptide bond involving the carboxylic group of histidine, or methionine, in the His-X and Met-X peptides, it is always necessary to protect their N-terminus amino group [1–3,7].

When an equimolar amount of *cis*-[Pd(dpa)Cl_2] was incubated with Met-Gly at $2.0 < pH < 2.5$ and at 60 °C, the intermediate palladium(II)–peptide complex **1a** was formed (Fig. 1). In this complex, the peptide is bidentate coordinated to the Pd(II) ion via the methionine sulfur atom and the N-terminal amino group. In the reaction with His-Gly, the bidentate coordination of this peptide occurs through the N3 imidazole nitrogen atom and the N-terminal amino group. The coordination of the Pd(II) ion to the methionine sulfur atom can easily be detected in the ^{1}H NMR spectrum. The signal at 2.14 ppm for the CH_3–S protons of the free Met-Gly was decreased, while the signal at 2.54 ppm, corresponding to these protons of the peptide bound to Pd(II) ion through the sulfur atom, appeared in the spectrum. The amount of the palladium(II)–peptide complex **1a** formed in this reaction was calculated by integration of these two signals. This reaction was rather slow, what is opposed to previous results and the well established high affinity of Pt(II) and Pd(II) ions for sulfur-containing ligands [19,20]. The inhibition of this reaction is additionally supported by the steric hindrance between the dpa ligand and the entering Met-Gly peptide in the square-planar [Pd(dpa)(Met-Gly-*S*,*N*)]$^{2+}$ complex **1a**. Approximately 50% of the *cis*-[Pd(dpa)Cl_2] complex had reacted after 2 h at 60 °C. When this reaction was carried out at 25 °C, less than 50% of the complex had reacted after more than 12 h. The next step after the formation of the complex **1a** is the release of the dpa ligand from palladium(II) and its displacement by water molecules, whereby complex **1b** is formed (Fig. 1). The conversion of **1a** into **1b** was very fast and owing to the overlap of the signals corresponding to the protons in free dpa and in the palladium(II)–peptide complex **1a**, multiplet in the region 7.00–8.50 ppm, the displacement of the dpa ligand by water molecules could not be followed by ^{1}H NMR spectroscopy. The fast release of the dpa ligand is also supported by the acidic medium and by the *trans* effect of the coordinated sulfur atom [21]. The liberated dpa ligand further reacts with unreacted *cis*-[Pd(dpa)Cl_2] complex producing the [Pd(dpa)$_2$]$Cl_2 \cdot 4H_2O$ complex **1c**, as one of the final products of the investigated reaction. The latter complex was also obtained in a separate experiment starting from *cis*-[Pd(dpa)Cl_2] and the dpa ligand. The reaction of *cis*-[Pd(dpa)Cl_2] complex with His-Gly was three times slower than that with the Met-Gly peptide, finally resulting in a very small yield of the [Pd(dpa)$_2$]$Cl_2 \cdot 4H_2O$ complex.

3.2. Description of the crystal structure of [Pd(dpa)$_2$]$Cl_2 \cdot 4H_2O$

The title compound consists of a square-planar-coordinated [Pd(dpa)$_2$]$^{2+}$ cation, chloride anions and water molecules (Fig. 2). It represents one of the five Pd(dpa) complexes hitherto investigated by X-ray diffraction [22–24]. The asymmetric unit contains half of the Pd(dpa)$_2$ cation located on an inversion center, two independent Cl^- counterions and two independent solvent water molecules. The Pd(II) ion is four coordinated and bonded in a bidentate fashion to two pyridine rings of the two dpa ligands (Fig. 2). The values of bond lengths and angles, describing the geometry of the complex are presented in Table 2. The distances between the metal center and the N-donor atoms (2.017(3) and 2.024(3) Å) correspond to the mean value of 2.017(4) Å calculated for the variously substituted Pd(dpa) units [23,25–30] (28 observations in the CSD [31]), and the dpa ligand bite angle is 86.16(12)°, rather small in relation to the Pd(II) center, smaller than in the other four Pd(dpa) complexes investigated by X-ray diffraction [22–24], where this value is in the range 87.8–91.8°. The two pyridine rings of the dpa moiety are twisted with respect to each other with a dihedral angle of 42.8(1)°. Again this angle is much larger than the values found in the CSD for Pd(dpa) complexes, which range from 16.2° to 31.3°. There seems to be an inverse relationship between the dpa ligand bite angle and the degree of mutual bending of the pyridine rings of the

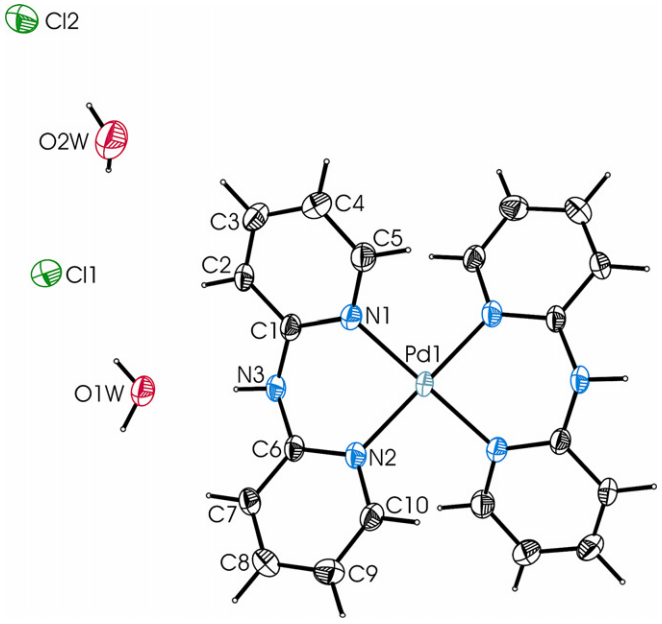


Fig. 2. View of the complex cation with accompanying chloride counterions and water molecules. Displacement ellipsoids for non-H atoms are shown at the 40% probability level. Only symmetry independent atoms are labeled. Generation of the second half of the complex cation requires the symmetry operation $-x, -y, 1-z$.

Table 2
Selected bond distances (Å) and angles (°)

Bond distance (Å)		Bond angle (°)	
Pd(1)–N(2)	2.017(3)	N(2)[a]–Pd(1)–N(1)	93.84(12)
Pd(1)–N(1)	2.024(3)	N(2)–Pd(1)–N(1)	86.16(12)
N(1)–C(1)	1.341(4)	C(1)–N(1)–Pd(1)	121.1(2)
C(1)–N(3)	1.391(4)	N(1)–C(1)–N(3)	119.2(3)
N(2)–C(6)	1.342(4)	C(6)–N(2)–Pd(1)	121.2(2)
C(6)–N(3)	1.391(4)	N(2)–C(6)–N(3)	119.4(3)
		C(1)–N(3)–C(6)	123.4(3)

[a] Atom was generated by inversion.

dpa. The chelate six-membered ring adopts a boat conformation with Pd1 and N3 in the flagpole positions, pointing in the same direction, although the deviation of N3 from the plane of the chelate is smaller than that of Pd1 (0.374(4) versus 0.842(4) Å, respectively). Two chloride anions (Cl2 and its translational equivalent along b) are located above and below the PdN_4 plane but the value of the Pd···Cl^- distance (3.879(2) Å) excludes any bonded interaction.

The solvent water molecules act as double donors to the chloride atoms and either do not accept hydrogen bonds (O2w) or act as single acceptor (O1w) from N–H group of the ligand. Each chloride anion accepts four hydrogen bonds from four neighboring water molecules, with an average O(H)···Cl distance of 3.203(30) Å. The water molecules and the chloride ions form hydrogen bonded tapes oriented along the *c* axis and consisting of $R_4^2(8)$ synthons, as shown in Fig. 3. A search of the CSD [31] affords 534 structures with the water–chloride $R_4^2(8)$ motif, nevertheless, this type of water–chloride cluster seems to have been overlooked in studies on halide ion hydration [32,33]. The hydrogen bond parameters are listed in Table 3. Uninterrupted tapes formed by $R_4^2(8)$ synthons connected in a spiro fashion bind together the columns of Pd(II) cations complexed by the organic ligand. Within the columns, weak off-face stacking interactions between one of the pyridine rings (N2, C6, C7, C8, C9 and C10) and its symmetry equivalent ($-1/2 - x$, $1/2 - y$, $1 - z$) are observed with the distance between the centroids equal to 4.135(3) Å (Fig. 4).

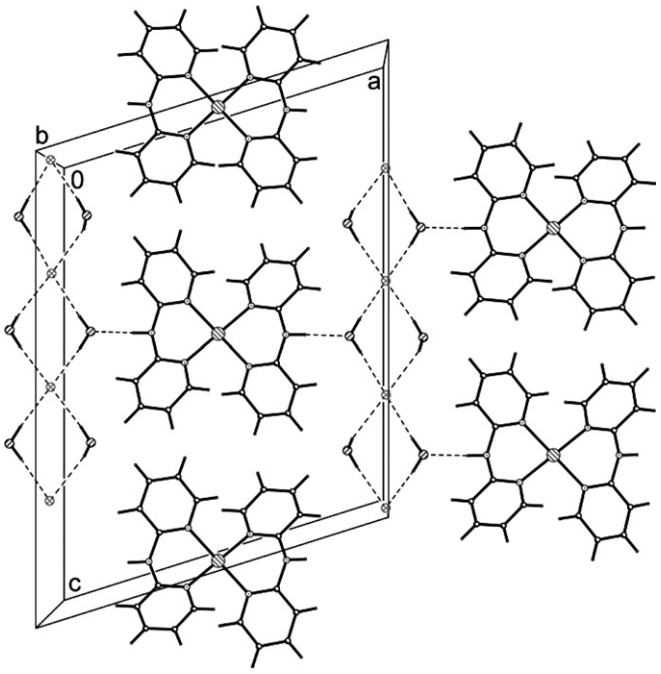


Fig. 3. Supramolecular $R_4^2(8)$ motifs consisting of hydrogen bonded chloride anions and water molecules join together into tapes in a spiro mode. The tapes bind to the metal–organic regions via water molecules acting as acceptors of protons from the N–H groups of the ligand.

3.3. Reactions of *cis*-$[Pd(dpa)(H_2O)_2]^{2+}$ with MeCOMet-Gly and MeCOHis-Gly

The reactions between *cis*-$[Pd(dpa)(H_2O)_2]^{2+}$ and the *N*-acetylated dipeptides, MeCOMet-Gly and MeCOHis-Gly, were carried out at $2.0 < pH < 2.5$ and at two different temperature, 25 and 60 °C. The schematic presentations of the investigated reactions are given in Fig. 5. In the reaction between this Pd(II) complex and the MeCOMet-Gly peptide, regioselective cleavage of the amide bond involving the carboxylic group of methionine was observed. This hydrolytic reaction can be followed successfully using ^1H NMR spectroscopy. The mixing of the palladium(II) complex with an equimolar amount of MeCOMet-Gly resulted in the spontaneous coordination of the palladium(II) com-

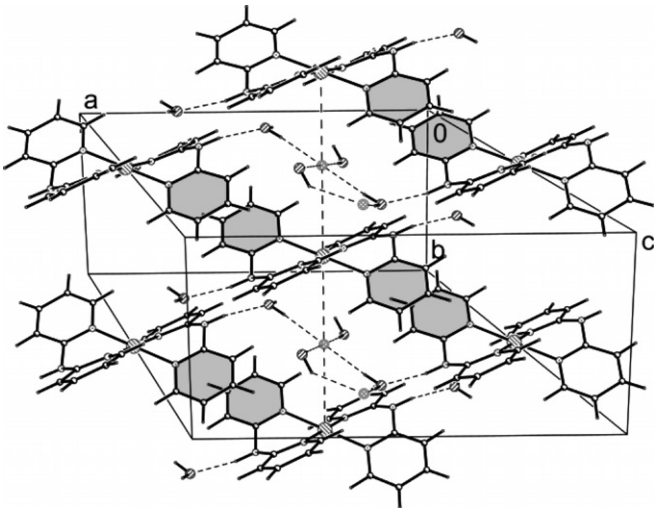


Fig. 4. Off-face stacking of the ligands.

Table 3
Intermolecular hydrogen bond geometry in the crystal of $[Pd(dpa)_2]Cl_2 \cdot 4H_2O$

	D–H (Å)	D···A (Å)	H···A (Å)	D–H···A (°)	Symmetry operations on A
N3–H3N···O1W	0.90	2.901(4)	2.01	168	$-1 - x$, y, $0.5 - z$
O1W–H1W···Cl2	0.85	3.196(3)	2.35	173	
O1W–H2W···Cl1	0.85	3.224(2)	2.38	173	
O2W–H3W···Cl1	0.85	3.237(4)	2.53	141	
O2W–H4W···Cl2	0.85	3.159(3)	2.31	175	

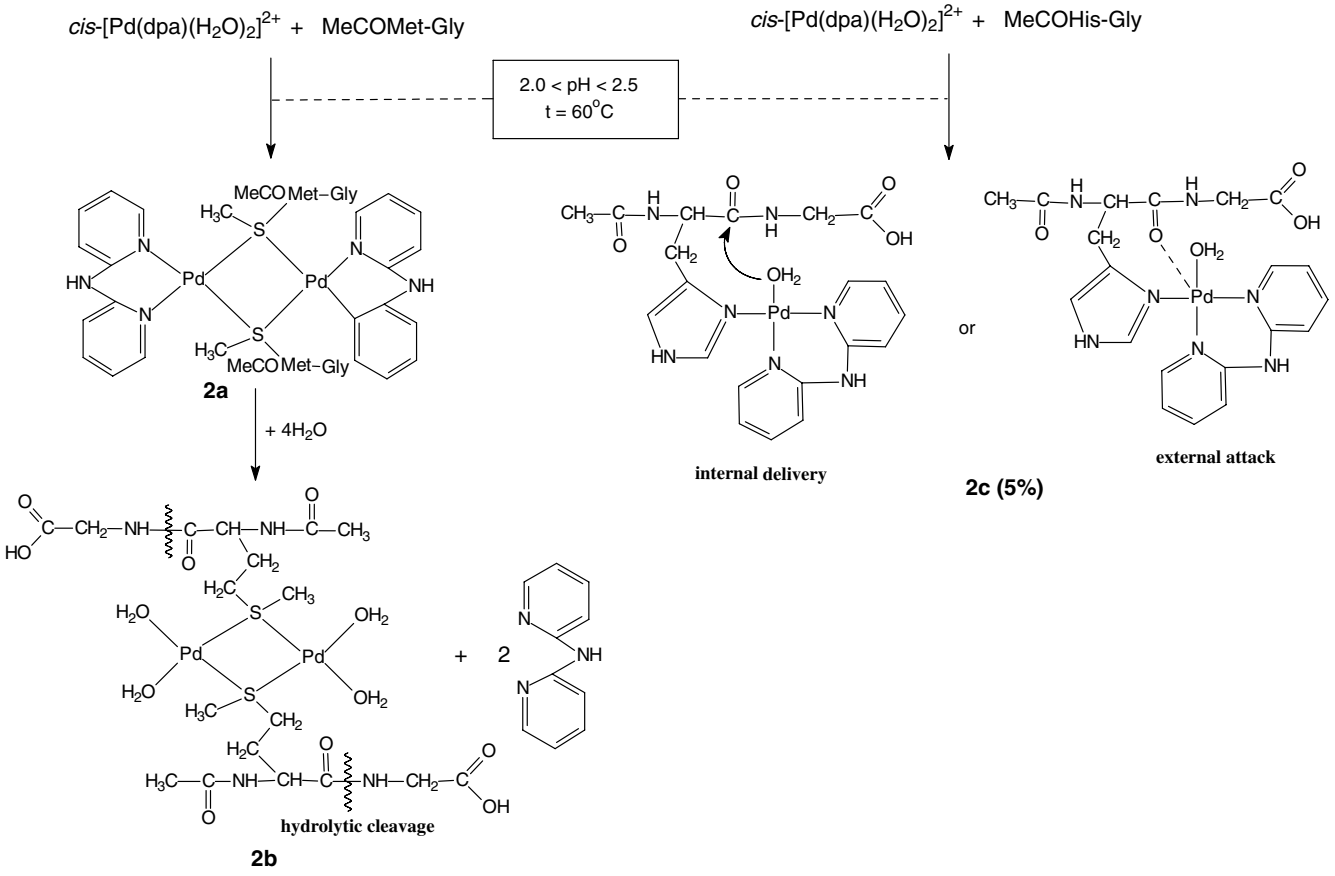


Fig. 5. Different pathways of the hydrolytic reactions between *cis*-$[Pd(dpa)(H_2O)_2]^{2+}$ and the *N*-acetylated dipeptides, MeCOMet-Gly and MeCOHis-Gly, in the pH range $2.0 < pH < 2.5$ and at 60 °C. The regioselective cleavage of the amide bond in the peptide containing a methionine residue.

plex to the sulfur atom of the methionine residue. The binding of palladium(II) to the methionine side chain is very fast and can be easily detected in the ^1H NMR spectrum, as was already explained for the reaction of the Pd(II) complexes with the Met-Gly peptide. The resonance at 3.94 ppm corresponding to the glycine protons of the non-hydrolyzed MeCOMet-Gly decreased while that at 3.60 ppm for free glycine increased. Upon addition of glycine to the reaction mixture, its resonance was enhanced. The amounts of the non-hydrolyzed peptide and the hydrolysis products were determined from the known initial concentration of MeCOMet-Gly and from the integrated resonance of the free glycine. Some of the liberated glycine reacts with the catalyst to form a small amount of the *cis*-$[Pd(dpa)(Gly\text{-}N,O)]^+$ complex, which is easily detected by ^1H NMR spectroscopy by the resonance at 3.52 ppm. Indeed, the same complex is formed upon the mixing of equimolar amounts of *cis*-$[Pd(dpa)(H_2O)_2]^{2+}$ and glycine. The catalytic ability of the *cis*-$[Pd(dpa)(H_2O)_2]^{2+}$ complex in the investigated reaction was determined by measuring the amount of the hydrolyzed MeCOMet-Gly with time under the same experimental conditions. The concentrations of the free and the hydrolyzed MeCOMet-Gly were determined every 30 min and the reaction was followed for 72 h. It was found that 25% of the MeCOMet-Gly had hydrolyzed at 60 °C after 2 h, and 90% when the reaction was carried out for 72 h. When the reaction was performed at 25 °C, only 40% of the MeCOMet-Gly had hydrolyzed after 10 days of reaction.

The hydrolytic reactions of methionine-containing peptides with palladium(II) complexes have been studied in great detail by Milović and Kostić [7]. From the NMR spectra, it was concluded that different promoters produce different hydrolytically active palladium(II)–peptide complexes. When the promoter was $[PdCl_4]^{2-}$, the active form is a mononuclear palladium(II)–peptide complex, whereas with $[Pd(H_2O)_4]^{2+}$ as promoter, a binuclear complex was formed, with the two sulfur atoms of the two methionine side chains as bridges and water molecules in unspecified terminal positions. It was shown that this binuclear complex was more efficient than the corresponding mononuclear complex in promoting the hydrolysis of the scissile amide bond. Additionally, it was found that with methionine-containing peptides and *cis*-$[Pd(en)(H_2O)_2]^{2+}$ (en is ethylenediamine), *cis*-$[Pd(Me_4en)(H_2O)_2]^{2+}$ (Me_4en is *N*,*N*,*N*′,*N*′-tetramethylethylenediamine), and *trans*-$[Pd(py)_2(H_2O)_2]^{2+}$ (py is pyridine) complexes, the nitrogen coordinated ligands were replaced with water molecules, and presumably the same active complex was formed as from $[Pd(H_2O)_4]^{2+}$ [34]. These results are in agreement with results recently obtained in the reactions of MeCOMet-Gly with the series palladium(II) complexes of the type *cis*-

$[Pd(L)(H_2O)_2]^{2+}$ (L is 1,2-propylenediamine, isobutylenediamine, 1,2-diaminocyclohexane, *N*-methylethylenediamine) [8]. As is shown in Fig. 5, from the intermediate binuclear palladium(II)–peptide complex **2a**, the a bidentate dpa ligand had been displaced by water molecules, forming the catalytically active palladium(II)–peptide complex **2b**. The replacement of the chelated dpa ligand by water molecules is very fast and this reaction is additionally supported by the *trans*-effect of the bridged sulfur atom of the methionine side chain and the acidic medium. The binuclear complex **2b** was also observed by Chen et al. in the reaction of *cis*-$[Pd(en)(H_2O)_2]^{2+}$ and *trans*-$[Pd(py)_2(H_2O)_2]^{2+}$ with MeCOMet-Gly [34]. As all the aqua ligands in complex **2b** are in the *cis* position to the substrate, anyone of them can be delivered to the scissile peptide bond.

In the reaction between *cis*-$[Pd(dpa)(H_2O)_2]^{2+}$ and MeCOHis-Gly at $2.0 < pH < 2.5$ and at 60 °C, cleavage the amide bond of neither His-Gly nor MeCO–His was observed. The intensities of the resonances at 3.94 ppm for the glycine protons and 2.00 ppm for the methyl protons of free MeCOHis-Gly remained unchanged under these experimental conditions even when the reaction was prolonged to 7 days. During this time, the resonances at 3.60 ppm for free glycine and 2.08 ppm for the methyl protons of acetic acid, both possible hydrolytic products if cleavage of the amide bonds occurs, did not appear in the ^1H NMR spectrum. The schematic presentation of this reaction is given in Fig. 5. MeCOHis-Gly was used as a model peptide for the study of the mechanism of the regioselective cleavage of the amide bond catalyzed by *cis*-$[Pd(L)(H_2O)_2]^{2+}$ type complexes (L is a bidentate diamine ligand) [1–3,5,7,35]. It was shown that in the reaction between this peptide and *cis*-$[Pd(en)(H_2O)_2]^{2+}$ complexes at $pH < 3$, five palladium(II)–peptide products were formed [1]. These complexes were distinguished on the basis of the chemical shifts of two imidazole protons, H-2 and H-5. Experiments with MeCOHis-Gly selectively methylated at the N-1 or N-3 atom of imidazole and *cis*-$[Pd(en)(H_2O)_2]^{2+}$ showed that only the palladium(II) complex with monodentate coordination to the N-3 atom of imidazole can affect the cleavage of the amide bond involving the carboxylic group of histidine; none of the four other modes of coordination is effective [2]. These findings were explained in terms of two possible limiting mechanisms, external and internal, for the hydrolytic cleavage of the peptide bond promoted by palladium(II) [1–3]. As can be seen from Fig. 5, both of these mechanisms presented for the palladium(II)–peptide complex **2c** require the close approach of the pendant catalyst to the adjacent peptide bond, and in both cases the steric bulk of the palladium(II) complex hinders this crucial interaction. The *cis*-$[Pd(dpa)(H_2O)_2]^{2+}$ complex is sterically very demanding because the two bulky pyridine rings in the dpa ligand, contain a large π-electron density and are close to the palladium(II) center and thus hinder its approach to the MeCOHis-Gly. It has been shown that in the reaction with this peptide in the pH range 2.0–2.5 and at 60 °C only 5% of the *cis*-$[Pd(dpa)(H_2O)_2]^{2+}$ had reacted after 7 days of reaction. The very slow reaction of this complex with the MeCOHis-Gly peptide can be attributed to the large steric hindrance between the dpa ligand of the palladium(II) complex and the entering imidazole ring of the histidine side chain, finally resulting in the total inhibition of the investigated hydrolytic reaction.

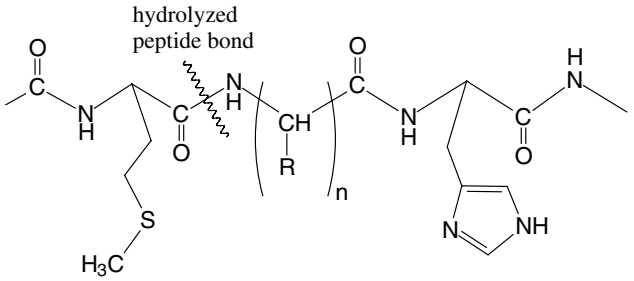


Fig. 6. Schematic presentation of the possible regioselective cleavage of the amide bond involving the carboxylic group of methionine in the proposed polypeptide containing both methionine and histidine residues promoted by the *cis*-$[Pd(dpa)(H_2O)_2]^{2+}$ complex.

4. Conclusions and prospects

Summing up, the sole product of the reaction between *cis*-$[Pd(dpa)Cl_2]$ or *cis*-$[Pd(dpa)(H_2O)_2]^{2+}$ and the peptides Met-Gly or His-Gly is the square-planar $[Pd(dpa)_2]^{2+}$ complex, indicating that no hydrolysis of the peptide bond occurs in the pH range 2.0–2.5, neither at 25 °C nor at 60 °C. On the other hand, the reaction of the *cis*-$[Pd(dpa)(H_2O)_2]^{2+}$ complex with the MeCOHis-Gly or MeCOMet-Gly peptides under the same experimental conditions is remarkably selective in the cleavage of the amide bond involving the carboxylic group of methionine. The schematic representation of the regioselective hydrolytic cleavage of the amide bond in the theoretically proposed polypeptide containing both methionine and histidine residues is given in Fig. 6. The modes of coordination of *cis*-$[Pd(dpa)Cl_2]$ in the reactions with the non-acetylated Met-Gly and His-Gly peptides and the total steric inhibition of the hydrolytic reaction of MeCOHis-Gly peptide with the *cis*-$[Pd(dpa)(H_2O)_2]^{2+}$ complex can be attributed to the steric bulk of the palladium(II) complex. This finding should be taken into consideration in designing new palladium(II) complexes for the regioselective cleavage of peptides and proteins. Studies aimed at investigating these new possible synthetic metalpeptidases are in progress.

5. Supplementary material

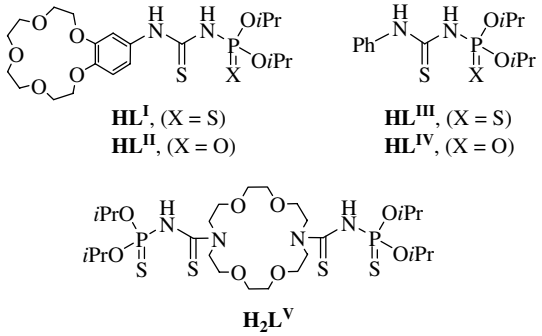
CCDC 622748 contains the supplementary crystallographic data for this paper. These data can be obtained free of charge via http://www.ccdc.cam.ac.uk/conts/retrieving.html, or from the Cambridge Crystallographic Data Centre, 12 Union Road, Cambridge CB2 1EZ, UK; fax: (+44) 1223-336-033; or e-mail: deposit@ccdc.cam.ac.uk.

Acknowledgements

This work was funded in part by the Ministry of Science and Environmental Protection of the Republic of Serbia (Project No. 142008B). Also part of the financial support was obtained from the Polish Ministry of Education and Science Grant 4T09A18525.

References

[1] T.N. Parac, N.M. Kostić, J. Am. Chem. Soc. 118 (1996) 51.
[2] T.N. Parac, N.M. Kostić, J. Am. Chem. Soc. 118 (1996) 5946.
[3] S.U. Milinković, T.N. Parac, M.I. Djuran, N.M. Kostić, J. Chem. Soc., Dalton Trans. (1997) 2771.
[4] X. Chen, L. Zhu, H. Yan, X. You, N.M. Kostić, J. Chem. Soc., Dalton Trans. (1996) 2653.
[5] M.I. Djuran, S.U. Milinković, Polyhedron 19 (2000) 959.
[6] M.I. Djuran, S.U. Milinković, Monatsh. Chem. 130 (1999) 613.
[7] N.M. Milović, N.M. Kostić, in: A. Sigel, H. Sigel (Eds.), Metal Ions in Biological Systems, Palladium(II) and Platinum(II) Complexes as Synthetic Peptidases, vol. XXXVIII, Marcel Dekker, New York, 2001, p. 145.
[8] D.P. Ašanin, S. Rajković, D. Molnar-Gabor, M.I. Djuran, Monatsh. Chem. 135 (2004) 1445.
[9] L. Zhu, N.M. Kostić, Inorg. Chem. 31 (1992) 3994.
[10] M.I. Rauterkus, S. Fakih, C. Mock, I. Puscasu, B. Krebs, Inorg. Chim. Acta 350 (2003) 355.
[11] G. Mehal, R. van Eldik, Inorg. Chem. 24 (1985) 4165.
[12] M.I. Djuran, E.L.M. Lempers, J. Reedijk, Inorg. Chem. 30 (1991) 2648.
[13] CrystAlis CCD software. Version 1.171 Oxford Diffraction, Oxfordshire, England, 2000.
[14] G.M. Sheldrick, Acta Crystallogr., Sect. A 46 (1990) 467.
[15] G.M. Sheldrick, SHELXL-97: Program for the Refinement of Crystal Structures, University of Göttingen, Göttingen, Germany, 1997.
[16] Stereochemical Workstation Operation Manual, Release 3.4. Siemens Analytical X-ray Instruments, Inc., Madison, WI, 1989.
[17] A.F.M. Siebert, Ph.D. Dissertation, University of Bochum, Germany, 1995, p. 166.
[18] S.L. Best, T.K. Chattopadhyay, M.I. Djuran, R.A. Palmer, P.J. Sadler, I. Sovago, K. Varnagy, J. Chem. Soc., Dalton Trans. (1997) 2587.
[19] T.G. Appleton, Coord. Chem. Rev. 166 (1997) 313.
[20] T. Soldatović, Ž.D. Bugarčić, J. Inorg. Biochem. 99 (2005) 1472.
[21] M.L. Tobe, J. Burgess, Inorganic Reaction Mechanisms, Addison-Wesley/Longman, Essex, 1999.
[22] Wen-Rui Yao, Ze-Hua Liu, Qian-Feng Zhang, Acta Crystallogr., Sect. C 59 (2003) m139.
[23] M.J. Rauterkus, S. Fakih, C. Mock, I. Puscasu, B. Krebs, Inorg. Chim. Acta 350 (2003) 355.
[24] Yue Wang, Y. Mizubayashi, M. Odoko, N. Okabe, Acta Crystallogr., Sect. C 61 (2005) m67.
[25] M.R. Buchmeiser, K. Wurst, J. Am. Chem. Soc. 121 (1999) 11101.
[26] C. Seward, Wen-li Jia, Rui-Yao Wang, Suning Wang, Inorg. Chem. 43 (2004) 978.
[27] M.R. Buchmeiser, S. Lubbad, M. Mayr, K. Wurst, Inorg. Chim. Acta 345 (2003) 145.
[28] J. Silberg, T. Schareina, R. Kempe, K. Wurst, M.R. Buchmeiser, J. Organomet. Chem. 622 (2001) 6.
[29] T. Schareina, G. Hillebrand, H. Fuhrmann, R. Kempe, Eur. J. Inorg. Chem. (2001) 2421.
[30] S. Fakih, Wing Chau Tung, D. Eierhoff, C. Mock, B. Krebs, Z. Anorg. Allg. Chem. 631 (2005) 1397.
[31] (a) F.H. Allen, O. Kennard, Chem. Des. Autom. News 8 (1993) 1; (b) F.H. Allen, Acta Crystallogr., Sect. B 58 (2002) 380.
[32] W.H. Robertson, M.A. Johnson, Annu. Rev. Phys. Chem. 54 (2003) 173.
[33] S.S. Xantheas, J. Phys. Chem. 100 (1996) 9703.
[34] X. Chen, X. Luo, Y. Song, S. Zhou, L. Zhu, Polyhedron 17 (1998) 2271.
[35] M.I. Djuran, S.U. Milinković, Polyhedron 18 (1999) 3611.



$\mathbf{HL^{I}}$, (X = S)
$\mathbf{HL^{II}}$, (X = O)
$\mathbf{HL^{III}}$, (X = S)
$\mathbf{HL^{IV}}$, (X = O)

$\mathbf{H_2L^{V}}$

Scheme 1.

$[K(Me_2CO)PhC(S)NP(S)(OiPr)_2]$ [10], $[K(MeOH)PhC(O)NP(S)Ph_2]$ [11] also have polymeric structures in the crystal form. A similar situation is observed for salts of imidodiphosphinate ligands $R_2P(X)NHP(Y)R'_2$ [12,13].

The monomeric structure is characteristic for complexes of alkali salts of *N*-phosphorylamides and thioamides with crown-ether molecules $[M(crown)PhC(Y)NP(X)(OiPr)_2]$, (X, Y = O, S; $M = Na^+$, K^+; crown = 18-crown-6, dibenzo-18-crown-6, 1,10-diaza-18-crown-6). Depending on the nature of the atoms X and Y, the ligand anion in a crystal may have monodentate or bidentate coordination with the cation being situated in a cavity of the macrocycle [6].

It was established that sodium salts of crown-containing thioureas $\mathbf{HL^{I,II}}$ quantitatively precipitate from 96% aqueous ethanol medium and are insoluble in the majority of organic solvents, which allows the separation of Na^+ and K^+ cations. For the other synthesized compounds a similar effect is not displayed.

2. Experimental

2.1. Physical measurements

Infrared spectra (Nujol) were recorded with a Specord M-80 spectrometer in the range 400–3600 cm^{-1}. NMR spectra were obtained on a Varian Unity-300 NMR spectrometer at 25 °C. ^1H and $^{31}P\{^1H\}$ spectra were recorded at 299.948 and 75.429 MHz, respectively. Chemical shifts are reported with reference to $SiMe_4$ (^1H) and H_3PO_4 ($^{31}P\{^1H\}$). Electron ionization high resolution mass spectra of the salts $[\mathbf{NaL^{I,II}}]$ were measured on a TRACE MS Finnigan MAT instrument. The ionization energy was 70 eV. The substance was injected directly into the ion source at 150 °C. Heating was carried out in a programmed mode from 35 to 200 °C at a rate of 35 °C/min. Electrospray ionization mass spectra of the salts $[\mathbf{NaL^{I–IV}}]$, $[\mathbf{KL^{I–IV}}]$, $[\mathbf{Na_2L^{V}}]$, $[\mathbf{K_2L^{V}}]$ were measured with a Thermo Finnigan LCQ mass spectrometer on a 10^{-6} M solution in a $CHCl_3/CH_3OH$ mixture (1:1 v/v). The speed of sample submission was 3 μL/min. The ionization energy was 4.1 kV. The capillary temperature was 210 °C. Electrospray ionization mass spectra of the salts $[\mathbf{LiL^{I,III,IV}}]$, $[\mathbf{BaL_2^{I,III,IV}}]$, $[\mathbf{Li_2L^{V}}]$, $[\mathbf{BaL^{V}}]$ were measured with a Finnigan-Mat TCQ 700 mass spectrometer on a 10^{-6} M solution in CH_3OH. The speed of sample submission was 2 μL/min. The ionization energy was 4.5 kV. The capillary temperature was 200 °C. Elemental analyses were performed with a Perkin–Elmer 2400 CHN microanalyzer. Flame atomic absorption and emission spectrophotometry measurements were performed on a Hitachi Z-6100 Polarized Zeeman Atomic Absorption Spectrophotometer (Hitachi, Japan). An acetylene-air flame and standard 10 cm burner were used for the analyte atomization. For sodium determination a hollow cathode lamp (MITORIKA Co., Japan) was operated at 10 mA; 589.0 nm was selected as the analytical line. Potassium was detected in the emission mode of the spectrophotometer at 766.5 nm. Slit widths were 0.4 and 1.3 nm, respectively. Background correction was used for potassium determination. A stock solution of potassium was prepared from highly pure solid KCl. Working standard solutions were freshly prepared by diluting appropriate aliquots of the stock solution in high-purity water. Quantification of potassium was made from a linear calibration curve.

2.2. Experiment I

Sodium hydroxide was used for the preparation of a Na^+ cation solution. To a solution of $\mathbf{HL^{I}}$ (104.4 mg, 0.2 mmol) in 96% aqueous ethanol (3 mL) a solution of NaOH (8 mg, 0.2 mmol) in 96% aqueous ethanol (3 mL) was added. The initial concentration of Na^+ cations was 33.33 mmol/L (766.67 mg/L). Formation of a white deposit was observed. The solution settled within 15 min. Then 3 mL of solution was taken, the solvent was evaporated and the solid residue was dissolved in the same volume of deionized water. Then the concentration of Na^+ cations was determined. The concentration of Na^+ cations was at the level of the limit of detection of the device, ~0.00044 mmol/L (~0.01 mg/L).

2.3. Experiment II

Sodium and potassium hydroxides were used for preparation of a Na^+ and K^+ cation mixture solution. To a solution of $\mathbf{HL^{I}}$ (104.4 mg, 0.2 mmol) in 96% aqueous ethanol (3 mL) a solution of NaOH (4.0 mg, 0.1 mmol) and KOH (5.6 mg, 0.1 mmol) in 96% aqueous ethanol (3 mL) was added. The initial concentration of Na^+ and K^+ cations was 16.66 mmol/L (383.33 and 650.00 mg/L, respectively). Formation of a white deposit was observed. The solution settled within 15 min. Then 3 mL of solution was taken, the solvent was evaporated and the solid residue was dissolved in the same volume of deionized water. Then the concentration of Na^+ cations was determined. The concentration of Na^+ cations was at the level of the limit of detection of the device, ~0.00044 mmol/L (~0.01 mg/L). For definition of the concentration of K^+ cations 1 mL of a solution was taken and deionized water (249 mL) was added. The concentration of K^+ cations was 16.62 mmol/L (648.05 mg/L).

2.4. Synthesis of HL^{I-IV} (general procedure)

A solution of amine (5.2 mmol) in anhydrous CH_2Cl_2 (15 mL) was treated under vigorous stirring with a solution of $(i\text{PrO})_2\text{P(X)NCS}$ (X = O, S) (5.2 mmol) in anhydrous CH_2Cl_2 (15 mL). The mixture was stirred for an additional 30 min to complete the reaction. The solvent was removed in vacuo, and the product was purified by crystallization from a methylene chloride/*n*-hexane mixture (1:5 v/v).

HL^{I} was prepared using 4′-aminobenzo-15-crown-5 and $(i\text{PrO})_2\text{P(S)NCS}$. M.p. 94 °C. ^{1}H NMR ($CDCl_3$): $\delta = 1.36$ (d, $^3J_{H,H} = 6.2$ Hz, 12H, CH_3), 3.64–4.62 (m, 16H, CH_2), 4.84 (d. sept, $^3J_{POCH} = 10.6$ Hz, $^3J_{H,H} = 6.2$ Hz, 2H, OCH), 6.80–6.83 (m, 1H, H^3, C_6H_3), 6.86–6.60 (m, 1H, H^2, C_6H_3), 7.04 [d, $^2J_{PNH} = 6.1$ Hz, 1H, NHP(S)], 7.23 (s, 1H, H^1, C_6H_3), 9.59 (s, 1H, NH) ppm. $^{31}P\{^1H\}$ NMR ($CDCl_3$): $\delta = 52.8$ ppm. IR: $\tilde{\nu} = 640$ (P═S), 980 (POC), 1140 (COC), 1520, 1556 (S═C–N), 3220, 3280 (NH) cm^{-1}. *Anal.* Calc. for $C_{21}H_{35}N_2O_7PS_2$ (522.16): C, 48.26; H, 6.75; N, 5.36. Found: C, 48.28; H, 6.76; N, 5.34%.

HL^{II} was prepared using 4′-aminobenzo-15-crown-5 and $(i\text{PrO})_2\text{P(O)NCS}$. Yield: 1.394 g (53%). M.p. 120 °C. ^{1}H NMR ($CDCl_3$): $\delta = 1.38$ (d, $^3J_{H,H} = 6.0$ Hz, 6H, CH_3), 1.39 (d, $^3J_{H,H} = 6.1$ Hz, 6H, CH_3), 3.68–4.22 (m, 16H, CH_2), 4.73 (d. sept, $^3J_{POCH} = 7.1$ Hz, $^3J_{H,H} = 6.3$ Hz, 2H, OCH), 6.81 [s, 1H, NHP(O)], 6.82–6.85 (m, 1H, H^3, C_6H_3), 7.01–7.04 (m, 1H, H^2, C_6H_3), 7.32 (s, 1H, H^1, C_6H_3), 10.66 (s, 1H, NH) ppm. $^{31}P\{^1H\}$ NMR ($CDCl_3$): $\delta = -5.8$ ppm. IR: $\tilde{\nu} = 1000$ (POC), 1140 (COC), 1216 (P═O), 1516, 1564 (S═C–N), 3136, 3280 (NH) cm^{-1}. *Anal.* Calc. for $C_{21}H_{35}N_2O_8PS$ (506.19): C, 49.79; H, 6.96; N, 5.53. Found: C, 49.81; H, 6.95; N, 5.56%.

HL^{III} was prepared using aniline and $(i\text{PrO})_2\text{P(S)NCS}$. M.p. 86 °C (85 °C, Ref. [14]). ^{1}H NMR ($CDCl_3$): $\delta = 1.29$ (d, $^3J_{H,H} = 5.9$ Hz, 6H, CH_3), 1.30 (d, $^3J_{H,H} = 6.2$ Hz, 6H, CH_3), 4.78 (d. sept, $^3J_{POCH} = 10.4$ Hz, $^3J_{H,H} = 6.2$ Hz, 2H, OCH), 7.03 [s, 1H, NHP(S)], 7.14–7.17 (m, 1H, *p*-H, C_6H_5), 7.28–7.31 (m, 2H, *m*-H, C_6H_5), 7.43–7.47 (m, 2H, *o*-H, C_6H_5), 9.57 (s, 1H, NH) ppm. $^{31}P\{^1H\}$ NMR ($CDCl_3$): $\delta = 55.1$ ppm. IR: $\tilde{\nu} = 636$ (P═S), 1000 (POC), 1536 (S═C–N), 3063, 3200 (NH) cm^{-1}.

HL^{IV} was prepared using aniline and $(i\text{PrO})_2\text{P(O)NCS}$. M.p. 125 °C (124–125 °C, Ref. [15]) ^{1}H NMR ($CDCl_3$): $\delta = 1.39$ (d, $^3J_{H,H} = 6.0$ Hz, 6H, CH_3), 1.40 (d, $^3J_{H,H} = 6.1$ Hz, 6H, CH_3), 4.75 (d. sept, $^3J_{POCH} = 7.3$ Hz, $^3J_{H,H} = 6.2$ Hz, 2H, OCH), 6.94 [d, $^2J_{PNH} = 6.1$ Hz, 1H, NHP(O)], 7.21–7.24 (m, 1H, *p*-H, C_6H_5), 7.37–7.41 (m, 2H, *m*-H, C_6H_5), 7.58–7.61 (m, 2H, *o*-H, C_6H_5), 10.78 (s, 1H, NH) ppm. $^{31}P\{^1H\}$ NMR ($CDCl_3$): $\delta = -5.3$ ppm. IR: $\tilde{\nu} = 1012$ (POC), 1216, 1244 (P═O), 1508 (S═C–N), 3136, 3304 (NH) cm^{-1}.

2.5. Synthesis of H_2L^V

This was prepared similarly to compounds **HL^{I-IV}** using 1,10-diaza-18-crown-6 and a double amount of $(i\text{PrO})_2$P(S)NCS. M.p. 128 °C (129–132 °C, Ref. [16]). ^{1}H NMR ($CDCl_3$): $\delta = 1.32$ (d, $^3J_{H,H} = 5.9$ Hz, 24H, CH_3), 3.48–4.28 (m, 24H, CH_2), 4.91 (d. sept, $^3J_{POCH} = 10.8$ Hz, $^3J_{H,H} = 6.0$ Hz, 4H, OCH), 8.83 [d, $^2J_{PNH} = 8.1$ Hz, 2H, NHP(S)] ppm. $^{31}P\{^1H\}$ NMR ($CDCl_3$): $\delta = 60.6$ ppm. IR: $\tilde{\nu} = 616$ (P═S), 976 (POC), 1100 (COC), 1520 (S═C–N), 3152 (NH) cm^{-1}.

2.6. Alkali and barium(II) salts of thioureas HL^{I-IV} and H_2L^V

The salts were obtained by a common technique. A suspension of **HL^{I-IV}** (1.2 mmol) in aqueous ethanol (15 mL) was mixed with an ethanol solution (15 mL) of lithium, sodium, potassium hydroxide [1.3 or 2.6 mmol (8% surplus)] or barium hydroxide [0.65 or 1.3 mmol (8% surplus)]. The mixture was stirred at room temperature for a further 1 h. The solvent was then removed in vacuo. A colorless precipitate was recrystallized from an ethanol/*n*-hexane mixture. Compounds [**ML**], [**BaL$_2$**], [**M$_2$L^V**] and [**BaL^V**] were obtained as white powders.

2.6.1. $[LiL^I]$

Yield: 0.393 g (62%). M.p. 87 °C. ^{1}H NMR (D_2O): $\delta = 1.30$ (d, $^3J_{H,H} = 6.1$ Hz, 12H, CH_3), 3.68–4.26 (m, 16H, CH_2), 4.73 (m, 2H, OCH), 6.92–7.02 (m, 2H, H^2+H^3, C_6H_3), 7.18 (s, 1H, H^1, C_6H_3) ppm. $^{31}P\{^1H\}$ NMR (D_2O): $\delta = 64.4$ ppm. IR: $\tilde{\nu} = 616$ (P═S), 1004 (POC), 1120 (COC), 1523 (SCN), 3218 (NH) cm^{-1}. ES-MS (positive ion): *m*/*z* (%) = 529.1 (100) $[LiL+H]^+$, 566.9 (33.9) $[LiL+CH_3OH+Li]^+$, 1081.2 (18.4) $[Li_2L_2+H_2O+Li]^+$, 1609.3 (2.9) $[Li_3L_3+H_2O+Li]^+$. *Anal.* Calc. for $C_{21}H_{34}LiN_2O_7PS_2$ (628.17): C, 47.72; H, 6.48; N, 5.30. Found: C, 47.75; H, 6.50; N, 5.28%.

2.6.2. $[NaL^I]$

Yield: 0.640 g (98%). M.p. 197 °C. ^{1}H NMR (D_2O): $\delta = 1.26$ (d, $^3J_{H,H} = 6.1$ Hz, 12H, CH_3), 3.64–4.18 (m, 16H, CH_2), 4.75 (m, 2H, OCH), 6.87–6.90 (m, 1H, H^2, C_6H_3), 6.93–6.96 (m, 1H, H^3, C_6H_3), 7.13 (s, 1H, H^1, C_6H_3) ppm. $^{31}P\{^1H\}$ NMR (D_2O): $\delta = 65.9$ ppm. IR: $\tilde{\nu} = 610$ (P═S), 1002 (POC), 1133 (COC), 1532 (SCN), 3190 (NH) cm^{-1}. EI-HRMS: *m*/*z* = 463.17945 (exact mass = 463.17936) $[NaL-NaNCS]^+$, 488.17939 (exact mass = 488.17461) $[NaL-NaSH]^+$. ES-MS (positive ion): *m*/*z* (%) = 545.0 (100) $[NaL+H]^+$, 566.9 (5.0) $[NaL+Na]^+$, 1128.9 (5.6) $[Na_2L_2+H_2O+Na]^+$. ES-MS (negative ion): *m*/*z* (%) = 521.0 (41.9) $[L]^-$, 1065.0 (100) $[NaL+L]^-$, 1608.7 (4.4) $[Na_2L_2+L]^-$. *Anal.* Calc. for $C_{21}H_{34}N_2NaO_7PS_2$ (544.14): C, 46.31; H, 6.29; N, 5.14. Found: C, 46.33; H, 6.27; N, 5.15%.

2.6.3. $[KL^I]$

Yield: 0.349 g (52%). M.p. 181 °C. ^{1}H NMR (D_2O): $\delta = 1.24$ (d, $^3J_{H,H} = 6.3$ Hz, 6H, CH_3), 1.25 (d, $^3J_{H,H} = 6.1$ Hz, 6H, CH_3), 3.62–4.24 (m, 16H, CH_2), 4.82 (m, 2H, OCH), 6.86–6.89 (m, 1H, H^2, C_6H_3),

6.91–6.94 (m, 1H, H^3, C_6H_3), 7.13 (s, 1H, H^1, C_6H_3) ppm. $^{31}P\{^1H\}$ NMR (D_2O): $\delta = 64.7$ ppm. IR: $\tilde{\nu} = 608$ (P═S), 1016 (POC), 1128 (COC), 1512 (SCN), 3232 (NH) cm^{-1}. ES-MS (positive ion): m/z (%) = 561.0 (100) $[KL+H]^+$, 679.7 (4.9) $[KL+CHCl_3+K]^+$, 1139.9 (44.4) $[K_2L_2+H_2O+H]^+$, 1683.6 (0.9) $[K_3L_3+H]^+$. ES-MS (negative ion): m/z (%) = 521.0 (76.3) $[L]^-$, 1080.8 (11.9) $[KL+L]^-$, 1099.9 (100) $[KL+H_2O+L]^-$, 1659.7 (6.3) $[K_2L_2+H_2O+L]^-$. *Anal.* Calc. for $C_{21}H_{34}KN_2O_7PS_2$ (560.12): C, 44.98; H, 6.11; N, 5.00. Found: C, 44.95; H, 6.13; N, 5.02%.

2.6.4. [BaL^I_2]

Yield: 0.404 g (57%). M.p. 190 °C. ^1H NMR (D_2O): $\delta = 1.31$ (d, $^3J_{H,H} = 6.2$ Hz, 12H, CH_3), 3.68–4.32 (m, 16H, CH_2), 6.41–6.43 (m, 1H, H^2, C_6H_3), 6.56 (s, 1H, H^1, C_6H_3), 6.89–6.92 (m, 1H, H^3, C_6H_3) ppm. $^{31}P\{^1H\}$ NMR (D_2O): $\delta = 64.5$ ppm. IR: $\tilde{\nu} = 604$ (P═S), 1024 (POC), 1160 (COC), 1533 (SCN), 3384 (NH) cm^{-1}. ES-MS (positive ion): m/z (%) = 545.1 (100) $[NaL+H]^+$, 586.9 (45.5) $[HL+2CH_3OH+H]^+$, 595.1 (86.9) $[NaL+CH_3OH+H_2O+H]^+$, 717.9 (34.5) $[BaL+2CH_3OH]^+$, 1837.0 (6.2) $[Ba_2L_3]^+$. *Anal.* Calc. for $C_{42}H_{68}BaN_4O_{14}P_2S_4$ (1180.21): C, 42.73; H, 5.81; N, 4.75. Found: C, 42.75; H, 5.78; N, 4.77%.

2.6.5. [NaL^{II}]

Yield: 0.596 g (94%). M.p. 183 °C. ^1H NMR (D_2O): $\delta = 1.26$ (d, $^3J_{H,H} = 6.0$ Hz, 6H, CH_3), 1.27 (d, $^3J_{H,H} = 6.2$ Hz, 6H, CH_3), 3.62–4.20 (m, 16H, CH_2), 4.57 (m, 2H, OCH), 6.93 (s, 2H, H^2+H^3, C_6H_3), 7.12 (s, 1H, H^1, C_6H_3) ppm. $^{31}P\{^1H\}$ NMR (D_2O): $\delta = 8.0$ ppm. IR: $\tilde{\nu} = 1020$ (POC), 1216 (P═O), 1132 (COC), 1528 (SCN), 3208 (NH) cm^{-1}. EI-HRMS: $m/z = 447.20059$ (exact mass = 447.20220) $[NaL-NaNCS]^+$, 472.19688 (exact mass = 472.19745) $[NaL-NaSH]^+$. ES-MS (positive ion): m/z (%) = 529.0 (100) $[NaL+H]^+$, 550.9 (21.9) $[NaL+Na]^+$, 1096.9 (8.1) $[Na_2L_2+H_2O+Na]^+$, 1624.9 (0.9) $[Na_3L_3+H_2O+Na]^+$. ES-MS (negative ion): m/z (%) = 505.1 (7.5) $[L]^-$, 1033.1 (100) $[NaL+L]^-$, 1561.1 (10.6) $[Na_2L_2+L]^-$. *Anal.* Calc. for $C_{21}H_{34}N_2NaO_8PS$ (528.17): C, 47.72; H, 6.48; N, 5.30. Found: C, 47.70; H, 6.45; N, 5.32%.

2.6.6. [KL^{II}]

Yield: 0.291 g (43%). M.p. 186 °C. ^1H NMR (D_2O): $\delta = 1.28$ (d, $^3J_{H,H} = 6.1$ Hz, 6H, CH_3), 1.29 (d, $^3J_{H,H} = 6.1$ Hz, 6H, CH_3), 3.60–4.26 (m, 16H, CH_2), 4.58 (d. sept, $^3J_{POCH} \approx {}^3J_{H,H} \approx 6.3$ Hz, 2H, OCH), 6.94 (s, 2H, H^2+H^3, C_6H_3), 7.15 (s, 1H, H^1, C_6H_3) ppm. $^{31}P\{^1H\}$ NMR (D_2O): $\delta = 8.1$ ppm. IR: $\tilde{\nu} = 1024$ (POC), 1196 (P═O),1128 (COC), 1520 (SCN), 3232 (NH) cm^{-1}. ES-MS (positive ion): m/z (%) = 545.0 (100) $[KL+H]^+$, 1107.9 (38.9) $[K_2L_2+H_2O+H]^+$, 1635.6 (1.3) $[K_3L_3+H]^+$. ES-MS (negative ion): m/z (%) = 504.5 (21.3) $[L]^-$, 1067.9 (100) $[KL+H_2O+L]^-$, 1595.9 (18.1) $[K_2L_2+L]^-$, 1612.4 (21.9) $[K_2L_2+H_2O+L]^-$. *Anal.* Calc. for $C_{21}H_{34}KN_2O_8PS$ (544.14): C, 46.31; H, 6.29; N, 5.14. Found: C, 46.33; H, 6.27; N, 5.15%.

2.6.7. [LiL^{III}]

Yield: 0.276 g (68%). M.p. 58 °C. ^1H NMR (D_2O): $\delta = 1.31$ (d, $^3J_{H,H} = 6.0$ Hz, 12H, CH_3), 6.58–7.52 (m, 5H, *o*-H+*m*-H+*p*-H, C_6H_5) ppm. $^{31}P\{^1H\}$ NMR (D_2O): $\delta = 68.4$ ppm. IR: $\tilde{\nu} = 618$ (P═S), 993 (POC), 1536 (SCN), 3328 (NH) cm^{-1}. ES-MS (positive ion): m/z (%) = 339.0 (16.8) $[LiL+H]^+$, 694.9 (100) $[Li_2L_2+H_2O+H]^+$, 683.1 (38.4) $[Li_2L_2+Li]^+$, 1037.0 (29.7) $[Li_3L_3+Na]^+$, 1359.2 (8.3) $[Li_4L_4+Li]^+$, 1375.1 (4.6) $[Li_4L_4+Na]^+$. *Anal.* Calc. for $C_{13}H_{20}LiN_2O_2PS_2$ (338.09): C, 46.15; H, 5.96; N, 8.28. Found: C, 46.18; H, 5.99; N, 8.24%.

2.6.8. [NaL^{III}]

Yield: 0.353 g (83%). M.p. 108 °C. ^1H NMR (D_2O): $\delta = 1.32$ (d, $^3J_{H,H} = 6.0$ Hz, 12H, CH_3), 4.77 (d. sept, $^3J_{POCH} \approx {}^3J_{H,H} \approx 6.3$ Hz, 2H, OCH), 7.15–7.18 (m, 1H, *p*-H, C_6H_5), 7.35–7.39 (m, 2H, *m*-H, C_6H_5), 7.43–7.47 (m, 2H, *o*-H, C_6H_5) ppm. $^{31}P\{^1H\}$ NMR (D_2O): $\delta = 64.3$ ppm. IR: $\tilde{\nu} = 612$ (P═S), 1012 (POC), 1516 (SCN), 3336 (NH) cm^{-1}. ES-MS (positive ion): m/z (%) = 354.9 (38.4) $[NaL+H]^+$, 725.9 (100) $[Na_2L_2+H_2O+H]^+$, 1084.6 (51.6) $[Na_3L_3+Na]^+$, 1100.6 (30.3) $[Na_3L_3+2H_2O+H]^+$, 1438.6 (18.8) $[Na_4L_4+Na]^+$, 1454.5 (15.1) $[Na_4L_4+2H_2O+H]^+$, 1792.4 (11.3) $[Na_5L_5+Na]^+$. ES-MS (negative ion): m/z (%) = 330.8 (17.5) $[L]^-$, 684.7 (100) $[NaL+L]^-$, 1038.5 (29.7) $[Na_2L_2+L]^-$, 1392.2 (5.9) $[Na_3L_3+L]^-$, 1746.1 (1.3) $[Na_4L_4+L]^-$. *Anal.* Calc. for $C_{13}H_{20}N_2NaO_2PS_2$ (354.06): C, 44.06; H, 5.69; N, 7.90. Found: C, 44.08; H, 5.70; N, 7.88%.

2.6.9. [KL^{III}]

Yield: 0.329 g (74%). M.p. 119 °C. ^1H NMR (D_2O): $\delta = 1.30$ (d, $^3J_{H,H} = 6.1$ Hz, 12H, CH_3), 4.77 (m, 2H, OCH), 7.13–7.17 (m, 1H, *p*-H, C_6H_5), 7.34–7.38 (m, 2H, *m*-H, C_6H_5), 7.40–7.44 (m, 2H, *o*-H, C_6H_5) ppm. $^{31}P\{^1H\}$ NMR (D_2O): $\delta = 64.5$ ppm. IR: $\tilde{\nu} = 616$ (P═S), 1004 (POC), 1544 (SCN), 3256 (NH) cm^{-1}. ES-MS (positive ion): m/z (%) = 408.9 (18.1) $[KL+K]^+$, 759.9 (100) $[K_2L_2+H_2O+H]^+$, 778.7 (55.9) $[K_2L_2+K]^+$, 1132.5 (35.3) $[K_3L_3+Na]^+$, 1150.5 (33.8) $[K_3L_3+K]^+$, 1502.1 (10.6) $[K_4L_4+Na]^+$, 1521.3 (13.8) $[K_4L_4+K]^+$, 1877.1 (19.4) $[K_5L_5+K]^+$. ES-MS (negative ion): m/z (%) = 330.9 (29.7) $[L]^-$, 700.7 (100) $[KL+L]^-$, 1070.2 (12.8) $[K_2L_2+L]^-$, 1441.2 (2.8) $[K_3L_3+L]^-$, 1809.9 (1.6) $[K_4L_4+L]^-$. *Anal.* Calc. for $C_{13}H_{20}KN_2O_2PS_2$ (370.03): C, 42.14; H, 5.44; N, 7.56. Found: C, 42.12; H, 5.45; N, 7.60%.

2.6.10. [BaL^{III}_2]

Yield: 0.389 g (81%). M.p. 143 °C. ^1H NMR (D_2O): $\delta = 1.31$ (d, $^3J_{H,H} = 6.2$ Hz, 12H, CH_3), 4.75 (m, 2H, OCH), 7.14–7.18 (m, 1H, *p*-H, C_6H_5), 7.35–7.39 (m, 2H, *m*-H, C_6H_5), 7.42–7.46 (m, 2H, *o*-H, C_6H_5) ppm. $^{31}P\{^1H\}$

NMR (D_2O): $\delta = 64.4$ ppm. IR: $\tilde{\nu} = 615$ (P═S), 1013 (POC), 1540 (SCN), 3320 (NH) cm^{-1}. ES-MS (positive ion): m/z (%) = 334.0 (60.1) $[HL+H]^+$, 470.1 (45.0) $[BaL]^+$, 802.9 (100) $[BaL_2+H]^+$, 1272.3 (14.3) $[Ba_2L_3]^+$. *Anal.* Calc. for $C_{26}H_{40}BaN_4O_4P_2S_4$ (800.05): C, 39.03; H, 5.04; N, 7.00. Found: C, 39.00; H, 5.07; N, 7.02%.

2.6.11. [LiL^{IV}]

Yield: 0.228 g (59%). M.p. 44 °C. ^1H NMR (D_2O): δ = 1.30 (d, $^3J_{H,H} = 6.1$ Hz, 12H, CH_3), 4.62 (m, 2H, OCH), 6.59–7.55 (m, 5H, *o*-H+*m*-H+*p*-H, C_6H_5) ppm. $^{31}P\{^1H\}$ NMR (D_2O): $\delta = 12.1$ ppm. IR: $\tilde{\nu} = 1012$ (POC), 1208 (P═O), 1542 (SCN), 3218 (NH) cm^{-1}. ES-MS (positive ion): m/z (%) = 323.0 (11.5) $[LiL+H]^+$, 663.0 (100) $[Li_2L_2+H_2O+H]^+$, 1003.1 (52.9) $[Li_3L_3+2H_2O+H]^+$, 1307.3 (6.3) $[Li_4L_4+H_2O+H]^+$. *Anal.* Calc. for $C_{13}H_{20}LiN_2O_3PS$ (322.11): C, 48.45; H, 6.25; N, 8.69. Found: C, 48.44; H, 6.27; N, 8.72%.

2.6.12. [NaL^{IV}]

Yield: 0.239 g (59%). M.p. 181 °C. ^1H NMR (D_2O): $\delta = 1.30$ (d, $^3J_{H,H} = 6.3$ Hz, 6H, CH_3), 1.31 (d, $^3J_{H,H}$ = 5.9 Hz, 6H, CH_3), 4.61 (d. sept, $^3J_{POCH} \approx {}^3J_{H,H} \approx 6.2$ Hz, 2H, OCH), 7.13–7.17 (m, 1H, *p*-H, C_6H_5), 7.36–7.40 (m, 2H, *m*-H, C_6H_5), 7.42–7.46 (m, 2H, *o*-H, C_6H_5) ppm. $^{31}P\{^1H\}$ NMR (D_2O): $\delta = 8.1$ ppm. IR: $\tilde{\nu} = 1028$ (POC), 1176 (P═O), 1532 (SCN), 3224 (NH) cm^{-1}. ES-MS (positive ion): m/z (%) = 339.0 (93.1) $[NaL+H]^+$, 694.0 (100) $[Na_2L_2+H_2O+H]^+$, 1049.7 (21.6) $[Na_3L_3+2H_2O+H]^+$, 1387.6 (7.5) $[Na_4L_4+2H_2O+H]^+$. ES-MS (negative ion): m/z (%) = 314.9 (4.4) $[L]^-$, 652.8 (100) $[NaL+L]^-$, 990.6 (41.3) $[Na_2L_2+L]^-$, 1328.6 (19.4) $[Na_3L_3+L]^-$, 1666.1 (1.9) $[Na_4L_4+L]^-$. *Anal.* Calc. for $C_{13}H_{20}N_2NaO_3PS$ (338.08): C, 46.15; H, 5.96; N, 8.28. Found: C, 46.17; H, 5.99; N, 8.27%.

2.6.13. [KL^{IV}]

Yield: 0.285 g (67%). M.p. 122 °C. ^1H NMR (D_2O): $\delta = 1.31$ (d, $^3J_{H,H} = 6.1$ Hz, 6H, CH_3), 1.32 (d, $^3J_{H,H}$ = 6.1 Hz, 6H, CH_3), 4.62 (d. sept, $^3J_{POCH} \approx {}^3J_{H,H} \approx 6.3$ Hz, 2H, OCH), 7.15–7.19 (m, 1H, *p*-H, C_6H_5), 7.36–7.39 (m, 2H, *m*-H, C_6H_5), 7.41–7.46 (m, 2H, *o*-H, C_6H_5) ppm. $^{31}P\{^1H\}$ NMR (D_2O): $\delta = 8.0$ ppm. IR: $\tilde{\nu} = 1008$ (POC), 1184 (P═O), 1536 (SCN), 3248 (NH) cm^{-1}. ES-MS (positive ion): m/z (%) = 538.0 (21.2) $[KL+H+CHCl_3+CH_3CN]^+$, 726.9 (100) $[K_2L_2+H_2O+H]^+$, 1063.7 (8.8) $[K_3L_3+H]^+$, 1459.4 (3.1) $[K_4L_4+CH_3CN+H]^+$, 1854.2 (1.3) $[K_5L_5+2CH_3CN+H]^+$. *Anal.* Calc. for $C_{13}H_{20}KN_2O_3PS$ (354.06): C, 44.05; H, 5.69; N, 7.90. Found: C, 44.03; H, 5.72; N, 7.88%.

2.6.14. [BaL_2^{IV}]

Yield: 0.350 g (76%). M.p. 137 °C. ^1H NMR (D_2O): $\delta = 1.29$ (d, $^3J_{H,H} = 6.1$ Hz, 6H, CH_3), 1.30 (d, $^3J_{H,H}$ = 6.0 Hz, 6H, CH_3), 4.61 (d. sept, $^3J_{POCH} \approx {}^3J_{H,H} \approx 6.3$ Hz, 2H, OCH), 7.13–7.16 (m, 1H, *p*-H, C_6H_5), 7.34–7.38 (m, 2H, *m*-H, C_6H_5), 7.42–7.45 (m, 2H, *o*-H, C_6H_5) ppm. $^{31}P\{^1H\}$ NMR (D_2O): $\delta = 8.2$ ppm. IR: $\tilde{\nu} = 1022$ (POC), 1156 (P═O), 1538 (SCN), 3224 (NH) cm^{-1}. ES-MS (positive ion): m/z (%) = 453.9 (26.0) $[BaL]^+$, 770.7 (100) $[BaL_2+H]^+$, 801.4 (42.7) $[BaL_2+CH_3OH+H]^+$, 1224.3 (14.0) $[Ba_2L_3]^+$. *Anal.* Calc. for $C_{26}H_{40}BaN_4O_6P_2S_2$ (768.09): C, 40.66; H, 5.25; N, 7.29. Found: C, 40.69; H, 5.22; N, 7.28%.

2.6.15. [Li_2L^V]

Yield: 0.749 g (83%). M.p. 98 °C. ^1H NMR (D_2O): δ = 1.31 (d, $^3J_{H,H} = 6.1$ Hz, 24H, CH_3), 3.64–4.20 (m, 24H, CH_2), 4.72 (m, 4H, OCH) ppm. $^{31}P\{^1H\}$ NMR (D_2O): $\delta = 62.1$ ppm. IR: $\tilde{\nu} = 617$ (P═S), 1008 (POC), 1127 (COC), 1556 (SCN) cm^{-1}. ES-MS (positive ion): m/z (%) = 504.4 (21.6) $[H_2L-(iPrO)_2P(S)NCS+H]^+$, 510.5 (41.7) $[LiHL-(iPrO)_2P(S)NCS+H]^+$, 746.9 (37.2) $[LiHL+H]^+$, 770.0 (100) $[Li_2L+H_2O+H]^+$, 1510.5 (3.4) $[Li_4L_2+Li]^+$. *Anal.* Calc. for $C_{26}H_{52}Li_2N_4O_8P_2S_4$ (752.25): C, 41.48; H, 6.96; N, 7.44. Found: C, 41.50; H, 6.98; N, 7.41%.

2.6.16. [Na_2L^V]

Yield: 0.724 g (77%). M.p. 187 °C. ^1H NMR (D_2O): $\delta = 1.29$ (d, $^3J_{H,H} = 6.3$ Hz, 12H, CH_3), 1.30 (d, $^3J_{H,H}$ = 6.2 Hz, 12H, CH_3), 3.60–4.16 (m, 24H, CH_2), 4.69 (d. sept, $^3J_{POCH} = 10.2$ Hz, $^3J_{H,H} = 6.2$ Hz, 4H, OCH) ppm. $^{31}P\{^1H\}$ NMR (D_2O): $\delta = 62.1$ ppm. IR: $\tilde{\nu} = 608$ (P═S), 1004 (POC), 1096 (COC), 1496 (SCN) cm^{-1}. ES-MS (positive ion): m/z (%) = 504.6 (39.1) $[H_2L-(iPrO)_2P(S)NCS+H]^+$, 526.6 (58.2) $[NaHL-(iPrO)_2P(S)NCS+H]^+$, 763.0 (64.4) $[NaHL+H]^+$, 820.0 (100) $[Na_2L+2H_2O+H]^+$, 1590.7 (1.9) $[Na_4L_2+Na]^+$. ES-MS (negative ion): m/z (%) = 500.2 (14.4) $[H_2L-(iPrO)_2P(S)NCS-H]^-$, 738.9 (9.4) $[HL]^-$, 761.0 (100) $[NaL]^-$. *Anal.* Calc. for $C_{26}H_{52}N_4Na_2O_8P_2S_4$ (784.19): C, 39.79; H, 6.68; N, 7.14. Found: C, 39.81; H, 6.65; N, 7.15%.

2.6.17. [K_2L^V]

Yield: 0.862 g (88%). M.p. 120 °C. ^1H NMR (D_2O): $\delta = 1.30$ (d, $^3J_{H,H} = 6.0$ Hz, 24H, CH_3), 3.58–4.18 (m, 24H, CH_2), 4.71 (m, 4H, OCH) ppm. $^{31}P\{^1H\}$ NMR (D_2O): $\delta = 62.2$ ppm. IR: $\tilde{\nu} = 616$ (P═S), 976 (POC), 1108 (COC), 1552 (SCN) cm^{-1}. ES-MS (positive ion): m/z (%) = 504.6 (7.3) $[H_2L-(iPrO)_2P(S)NCS+H]^+$, 542.8 (13.6) $[KHL-(iPrO)_2P(S)NCS+H]^+$, 777.9 (23.8) $[KHL+H]^+$, 820.0 (100) $[K_2L+H]^+$, 838.9 (58.1) $[K_2L+H_2O+H]^+$, 1670.9 (4.4) $[K_4L_2+K]^+$. ES-MS (negative ion): m/z (%) = 500.1 (58.1) $[H_2L-(iPrO)_2P(S)NCS-H]^-$, 738.9 (79.4) $[HL]^-$, 777.0 (100) $[KL]^-$, 808.9 (10.0) $[KL+CH_3OH]^-$. *Anal.* Calc. for $C_{26}H_{52}K_2N_4O_8P_2S_4$ (816.14): C, 38.22; H, 6.41; N, 6.86. Found: C, 38.20; H, 6.38; N, 6.89%.

2.6.18. [BaL^V]

Yield: 0.967 g (92%). M.p. 185 °C. ^1H NMR (D_2O): $\delta = 1.33$ (d, $^3J_{H,H} = 6.2$ Hz, 12H, CH_3), 1.34 (d, $^3J_{H,H}$ = 6.2 Hz, 12H, CH_3), 3.68–4.22 (m, 24H, CH_2), 4.74 (m, 4H,

OCH) ppm. $^{31}P\{^{1}H\}$ NMR (D_2O): $\delta = 62.2$ ppm. IR: $\tilde{\nu} = 612$ (P=S), 996 (POC), 1154 (COC), 1564 (SCN) cm^{-1}. ES-MS (positive ion): m/z (%) = 504.3 (33.1) $[H_2L-(iPrO)_2P(S)NCS+H]^+$, 640.5 (57.2) $[BaL-(iPrO)_2P(S)NCS]^+$, 879.9 (100) $[BaL+H]^+$, 903.3 (14.5) $[BaL+Na]^+$. *Anal.* Calc. for $C_{26}H_{52}BaN_4O_8P_2S_4$ (876.12): C, 35.64; H, 5.98; N, 6.39. Found: C, 35.66; H, 5.97; N, 6.41%.

2.7. Crystal structure determination and refinement

The X-ray diffraction data for the crystals of **[K(Me$_2$CO)L^{III}]** and **HL^{III}** were collected on a CAD4 Enraf-Nonius automatic diffractometer using graphite monochromated Mo Kα (0.71073 Å) and Cu Kα (1.54184 Å) radiation. The crystal data, data collection and the refinement are given in Table 1. The stability of the crystals and the experimental conditions were checked every 2 h using three control reflections, while the orientation was monitored every 200 reflections by centering two standards. No significant decay was observed. An empirical absorption correction based on ψ-scans was applied. The structures were solved by a direct method using the SIR [17] program and refined by full matrix least-squares using SHELXS-97 [18] program. All non-hydrogen atoms were refined anisotropically. The hydrogen atoms were calculated and refined as riding atoms. All calculations were performed on PC using the WinGX [19] program. Cell parameters, data collection and data reduction were performed on an Alpha Station 200 computer using the MolEN [20] program. All figures were made using the program PLATON [21].

Table 1
Crystal data, data collection, and refinement details for **[K(Me$_2$CO)L^{III}]** and **HL^{III}**

	[K(Me$_2$CO)L^{III}]	**HL^{III}**
Empirical formula	$C_{16}H_{26}KN_2O_3PS_2$	$C_{13}H_{21}N_2O_2PS_2$
Formula weight	428.58	332.41
Space group	$P\bar{1}$	$P\bar{1}$
a (Å)	8.115(2)	8.207(3)
b (Å)	10.872(1)	9.850(6)
c (Å)	14.051(3)	12.292(4)
α (°)	69.80(2)	69.62(2)
β (°)	85.81(1)	74.98(3)
γ (°)	67.22(1)	71.69(4)
V (Å^3)	1070.0(4)	871.7(7)
Z	2	2
D_{calc} (Mg m^{-3})	1.33	1.27
$F(000)$	452	352
Crystal color	colorless	colorless
Crystal form	prismatic	prismatic
Crystal size (mm)	0.3 × 0.3 × 0.3	0.3 × 0.2 × 0.2
Radiation (Å)	0.71069	1.54158
Temperature (K)	293	293
Scan mode	$\omega/2\theta$	$\omega/2\theta$
Recording range, θ_{max} (°)	2.73–26.30	3.89–57.2
Absorption correction, μ (cm^{-1})	5.35	3.661
Scan speed (deg min^{-1})	variable, 1–16.4	
Number of recorded reflections	4482	2509
Number of independent reflections	4243	2343
Number of independent reflections with $F^2 \geqslant 2\sigma(F^2)$	2711	2237
R (%)	0.0472	0.0508
R_w (%)	0.1011	0.1308
S	1.031	1.063

3. Results and discussion

3.1. Synthesis

Thioureas **HL$^{I–IV}$** and **H$_2$L^{V}** were synthesized by treatment of 4′-aminobenzo-15-crown-5, aniline, or 1,10-diaza-18-crown-6 with isothiocyanates of diisopropylthiophosphoric and diisopropylphosphoric acids, respectively. The structures of the obtained compounds were confirmed by IR, ^{1}H, and ^{31}P NMR spectroscopy.

Salts of thioureas **HL$^{I–IV}$** and **H$_2$L^{V}** of the formulae **[LiL^{I,III,IV}]**, **[NaL$^{I–IV}$]**, **[KL$^{I–IV}$]**, **[Ba(L^{I,III,IV})$_2$]**, **[M$_2$L^{V}]**, and **[BaL^{V}]** have been obtained by treatment with the hydroxide of the corresponding metal ($M = Li^+$, Na^+, K^+) in 96% aqueous ethanol medium. All salts are solid and stable in air.

Interaction of **HL^{I}** with NaOH in 96% aqueous ethanol medium results in a plentiful precipitate of white color. The same process is observed for thiourea **HL^{II}** but it takes nearly for 15 min under similar conditions. The precipitates are insoluble in the majority of organic solvents (alcohol, acetone, acetonitrile, methylene chloride, benzene, toluene, tetrahydrofuran, dioxane) and slightly soluble in water, dimethylsulfoxide and dimethylformamide. According to the microanalysis they have the composition **[NaL^{I,II}]**.

This phenomenon has induced us to investigate the structures and properties of the proximate analogues of **[NaL^{I,II}]**. Salts of the formulae **[ML$^{I–IV}$]**, **[Ba(L^{I,III,IV})$_2$]**, **[M$_2$L^{V}]**, and **[BaL^{V}]** ($M = Li^+$, Na^+, K^+) were isolated and characterized for the first time. It was established that for none of them was a reduction in solubility observed. On the contrary, there is an expected increase in solubility of the obtained salts in polar organic solvents.

Crystals of the solvate **[K(Me$_2$CO)L^{III}]** were obtained by recrystallization from an acetone/*n*-hexane mixture of **[KL^{III}]**. The structure was investigated by X-ray analysis.

The structures of the obtained compounds were proven by IR, ^{1}H, and ^{31}P NMR spectroscopy, ES-MS experiments (electrospray method) and the composition was confirmed by microanalysis.

3.2. IR and NMR spectroscopy

The IR spectra of **HL$^{I–IV}$** contain two absorption bands for the NH groups in the ranges: 3200–3304 (narrow band) and 3063–3220 (wide intensive band) cm^{-1}. There is only one absorption band for the NH group at 3152 cm^{-1} in the spectrum of **H$_2$L^{V}**.

The P=S group absorption bands for **HL^{I,III}** and **H$_2$L^{V}** are observed in the characteristic area: 616–640 m^{-1} [6,22]. The IR spectra of **HL^{II,IV}** contain strong bands at 1216–

1244 m^{-1} due to the P=O group. Besides very strong absorption bands for the POC group in the region 976–1000 cm^{-1}, there are bands of the COC groups at 1100–1140 m^{-1} in the IR spectra of $\mathbf{HL^{I,II}}$ and $\mathbf{H_2L^V}$, containing crown-ether fragments. Presence of a wide absorption band of the POC fragment in $\mathbf{HL^{III,IV}}$ in the area 1000–1012 cm^{-1} also unequivocally confirms the substituted phosphoric fragment.

The phosphorus atoms of $\mathbf{HL^{I–IV}}$ and $\mathbf{H_2L^V}$ ligands appear as singlet signals at 52.8–60.6 (X = S) and −5.2 to −5.8 (X = O) ppm in the $^{31}P\{^1H\}$ NMR spectra. The observed chemical shift ranges are typical for neutral N-thiophosphorylated and N-phosphorylated thioureas respectively [6,14,23].

Consideration of the ^1H NMR spectra of $\mathbf{HL^{I–IV}}$ and $\mathbf{H_2L^V}$ allows a structure of the obtained compounds to be established definitively and to confirm the fact of interaction of the isothiocyanate with the NH_2 or NH groups of the corresponding amines. In the ^1H NMR spectra of $\mathbf{HL^{I,II}}$ and $\mathbf{H_2L^V}$, containing crown-ether cycles, the signals for the CH_2 protons are at 3.48–4.62 ppm. Integrated intensities of these signals correspond to 16 protons for thioureas $\mathbf{HL^{I,II}}$ and to 24 protons for the thiourea $\mathbf{H_2L^V}$.

The IR spectra of $[\mathbf{ML^{I–IV}}]$ and $[\mathbf{BaL_2}]$ contain the unique absorption band of ArNH groups at 3190–3384 cm^{-1}, whereas no NH group bands are observed for $[\mathbf{M_2L^V}]$ and $[\mathbf{BaL^V}]$. In the spectra of all obtained salts there are intense absorption bands of the conjugated SCN group in the area 1490–1564 cm^{-1} [6]. The absorption bands of the P=S and P=O groups in the IR spectra of the salts are at 604–618 and 1156–1216 cm^{-1}, respectively. They are shifted to low frequencies relative to the band of the parent ligands.

The $^{31}P\{^1H\}$ NMR signals of the obtained salts appear at $\delta = 62.1–68.4$ (X = S) and 8.0–12.1 (X = O) ppm, respectively, with a downfield shift relative to that of the free ligands.

The ^1H NMR spectroscopy unequivocally testifies to the preservation of the ligand structure on deprotonation. In all cases there is a single set of signals for the ligand protons. The integrated intensities of the signals correspond to the offered structure. The signals for the ArNH group protons are absent in the ^1H NMR spectra because of an exchange with the solvent (D_2O).

In the ^1H NMR spectra of the thiourea salts containing crown-ether cycles, the signals for the CH_2 protons are at 3.58–4.32 ppm. Integrated intensities of these signals correspond to the proposed structures.

3.3. EI and ES mass spectrometry

The electron impact mass-spectra (EI-MS) of $[\mathbf{NaL^{I,II}}]$ does not contain the molecular ion peaks, which are unstable under the measurement conditions and undergo rearrangement with exhaust fragments [NaSCN] and [NaSH]. The composition of the formed crown-containing amidophosphates [4′-benzo-15-crown-5]NHP(X)(O*i*Pr)$_2$ and carbodiimides [4′-benzo-15-crown-5]N=C=NP(X)(O*i*Pr)$_2$ is confirmed by high resolution EI-MS.

The ES-MS (electrospray method) of the positive and negative ion area shows propensity of the obtained salts to form dimers and polynuclei associations.

In the ES-MS of $[\mathbf{ML^{III,IV}}]$ the peaks of dimers $[M_2L_2+H_2O+H]^+$ ($M = Li^+$; Na^+; K^+) have maximal intensity. In the salts of $[\mathbf{Ba(L^{III,IV})_2}]$ the peaks with a relative intensity of 100% are fixed for molecular ions of the composition $[BaL_2+H]^+$. The mass spectra also contain peaks of pentanuclei cations of the following composition: $[Na_5L_5+Na]^+$ for $[\mathbf{NaL^{III}}]$, $[K_5L_5+K]^+$ for $[\mathbf{KL^{III}}]$ and $[K_5L_5+2CH_3CN+H]^+$ for $[\mathbf{KL^{IV}}]$. There is a $[Ba_2L_3]^+$ peak in the mass spectrum of $[\mathbf{BaL_2^{III–IV}}]$ with a relative intensity of 14%. Positive ions with a greater weight in the ES-MS of $[\mathbf{BaL_2^{III–IV}}]$ under the measurement conditions were not observed.

ES-MS experiments on $[\mathbf{NaL^{III,IV}}]$ and $[\mathbf{KL^{III}}]$ show peaks for the negative ions. Besides the peaks of $[L]^-$, peaks of the composition $[ML+L]^-$ are fixed with a relative intensity of 100%. There are also peaks of oligomeric composition: $[M_2L_2+L]^-$ (12.9–41.3%), $[M_3L_3+L]^-$ (2.8–19.4%) and $[M_4L_4+L]^-$ (1.3–1.9%).

In the mass spectra of $[\mathbf{ML^{I,II}}]$ salts, in the area of positive ions, the most intense peak belongs to the cation of the composition $[ML+H]^+$. ES-MS of $[\mathbf{LiL^I}]$, $[\mathbf{NaL^{II}}]$ and $[\mathbf{KL^{I,II}}]$ also contain ions of monomer, dimer, and trimer composition, whereas the mass spectrum of $[\mathbf{NaL^I}]$, with the exception of a peak of the composition $[Na_2L_2+H_2O+Na]^+$, does not have peaks of heavier ions. In the mass spectrum of $[\mathbf{Ba(L^I)_2}]$ the peak with the greatest intensity belongs to the cation of composition $[NaL+H]^+$, that, apparently, can indicate the propensity of $\mathbf{HL^I}$ to form the most stable compounds with the sodium cation rather than with the barium one.

In the area of negative ions of $[\mathbf{NaL^{I,II}}]$ and $[\mathbf{KL^{I,II}}]$, besides the peaks of $[L]^-$, the peaks of ions $[NaL+L]^-$ for $[\mathbf{NaL^{I,II}}]$ and $[KL+H_2O+L]^-$ for $[\mathbf{KL^{I,II}}]$, with relative intensity 100%, are observed. Ions of dinuclear composition are also fixed in the ES-MS spectra of these compounds.

The ES-MS spectra of $[\mathbf{M_2L^V}]$ show peaks for cations of dimer composition $[M_2L_4+M]^+$ ($M = Li^+$, Na^+, K^+). In the area of negative ions of $[\mathbf{Na_2L^V}]$ and $[\mathbf{K_2L^V}]$ there are also intensive peaks for the anion $[\mathbf{H_2L^V}–(i\mathrm{PrO})_2\mathrm{P(S)}\text{-}\mathrm{NCS}–\mathrm{H}]^-$ (9.4–58.1%). Mass spectra of $[\mathbf{Na_2L^V}]$ and $[\mathbf{K_2L^V}]$ contain the peaks of composition $[HL]^-$ and $[M_2L–M]^-$, which have maximal intensity.

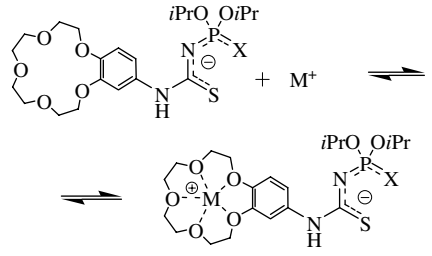
3.4. Flame atomic absorption and emission spectrophotometry research of Na^+ and K^+ cation separation using thiourea HL^I

As it has been noted above, interaction of $\mathbf{HL^I}$ with NaOH in 96% aqueous ethanol medium results in precipitation of $[\mathbf{NaL^I}]$. It was interesting to estimate the degree of Na^+ cation precipitation and also to try and separate Na^+

and K^+ cations from an equimolar solution of NaOH and KOH. For the definition of Na^+ and K^+ concentration, the methods of flame atomic absorption spectrophotometry and flame atomic emission spectrophotometry, respectively, have been used.

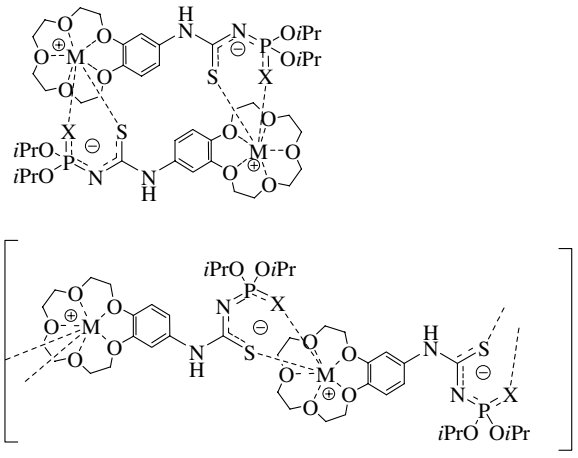
Our research has shown that precipitation of the salt [$\mathbf{NaL^I}$] results in a fall of concentration of Na^+ cations in solution from 766.67 mg/L to the limit of detection of the device: 0.01 mg/L. It was also established that addition of $\mathbf{HL^I}$ to the equal amount solution of Na^+ and K^+ cations leads to precipitation of Na^+ up to the limit of detection of the device while the concentration of K^+ cations remains constant within the limits of experimental error.

We suppose that the effect of solubility reduction, observable for the salts [$\mathbf{NaL^{I,II}}$], can be connected with a distinction in character of the intermolecular association of these compounds in the solid state. The intramolecular interaction of pendant arms with a cation in the macrocyclic cavity is complicated for compounds $\mathbf{HL^{I,II}}$ in comparison with the crown-ethers, modified by flexible exocyclic groups [1]. We assume that the [$\mathbf{ML^{I,II}}$] salt formation in solution leads to zwitter-ionic molecules (Scheme 2), displaying an expressed propensity for self-association.



Scheme 2.

These zwitter-ions can exist in a crystal phase in the form of ''head-to-tail'' type dimers or polymeric chains (Scheme 3). The presence of the Ar–NH–C moiety in a molecule will allow the realization both of types of interaction. Joint participation of a macrocycle and exocyclic group in complexation in such associates leads to 3D cavity formation, that in turn causes an increase of efficiency and selectivity of the interaction with cations of alkali metals.



Scheme 3.

However, it does not explain the remarkable selectivity toward the sodium cation, found in the case of $\mathbf{HL^{I,II}}$. In our opinion, the observed effect can appear by changing the intermolecular assembly type in the case of [$\mathbf{NaL^{I,II}}$], e.g. formation of a dimer instead of a polymeric structure in the other cases. These changes are caused by the affinity of the Na^+ cation to the cavity of 15-crown-5 and the lower coordination number of Na^+ in comparison with the K^+ cation. Cation desolvatation followed by precipitation of the associates from ethanol medium makes this process irreversible.

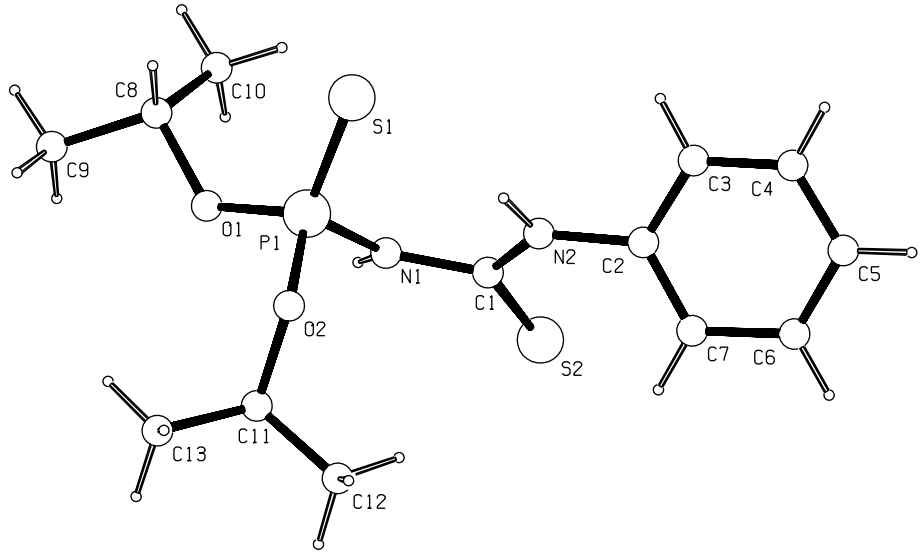


Fig. 1. Molecular structure of $\mathbf{HL^{III}}$.

Additional effective stabilization of di- or polymeric structures can be provided by solid state intermolecular interactions, e.g. intermolecular H-bonding [5]. ArNH-groups could form H-bonds with the sulfur atom of the CS-group – similar to that, found in the crystal of [**K(Me$_2$CO)L^{III}**] (see below) – with oxygen (from the (thio)phosphoryl group or crown-ether moiety), P═S sulfur or P–N nitrogen donor atoms of the neighbor [**ML**] molecule. Obviously, the stabilizing effect of intermolecular hydrogen bonding will strongly differ for different types of the intermolecular assembly. For confirmation of the stated assumptions we are going to carry out additional research, using X-ray diffraction methods and multinuclear NMR spectroscopy in the solid state.

3.5. Crystal structure of *HL^{III}* and *[K(Me$_2$CO)L^{III}]*

Unfortunately, we could not get suitable crystals for structure determination for the salts with crown-containing thioureas. It has induced us to investigate the structure of **HL^{III}** (Fig. 1) and its potassium salt of composition [**K(Me$_2$CO)L^{III}**] (Fig. 2). X-ray data are in Tables 1 and 2.

In a solvate crystal of [**K(Me$_2$CO)L^{III}**] the anion of $[L^{III}]^-$ interacts with the K^+ cation through the sulfur atoms of C═S and P═S groups and an oxygen atom from one *i*PrO group. The coordination number of potassium is supplemented up to six due to interaction with oxygen atoms of two molecules of acetone and a sulfur atom of a P═S group of the neighboring ligand. The coordination environment of potassium can be described as a distorted trigonal prism, on one side of which there are three sulfur atoms, S1, S2, and S2_a, and on the other – oxygen atoms, O1, O40, O40_b (Scheme 4).

Molecules in the crystal form chains due to μ^2-bonds, with participation of POCH oxygen and thiophosphoryl sulfur atoms of the ligands and oxygen atoms of acetone molecules. The chains are parallel to the *oa* plane. The association is similar to the solvate [K(Me$_2$CO)PhC(S)NP(S)(O*i*Pr)$_2$] [10], but in the latter case the ligand forms μ^2-bonds with participation of both sulfur atoms.

Table 2
Selected bond lengths (Å), and bond and torsion angles (°) for [**K(Me$_2$CO)L^{III}**] and **HL^{III}**

	K(Me$_2$CO)L^{III}]	**HL^{III}**
Bond lengths		
S1–P1	1.956(1)	1.920(1)
S2–C1	1.726(3)	1.670(3)
P1–O1	1.591(2)	1.556(2)
P1–O2	1.584(2)	1.555(2)
P1–N1	1.597(2)	1.683(3)
O1–C9	1.460(4)	1.456(4)
O2–C12	1.472(4)	1.478(4)
N1–C1	1.312(4)	1.384(2)
N2–C1	1.367(4)	1.371(4)
N2–C3	1.414(4)	1.417(4)
K1–S1	3.207(1)	–
K1–P1	3.635(2)	–
K1–O2	2.828(2)	–
K1–O20	2.774(3)	–
O20–C20	1.207(5)	–
Bond angles		
S1–P1–O1	110.8(1)	118.78(9)
S1–P1–O2	111.29(9)	111.2(1)
S1–P1–N1	120.5(1)	115.2(1)
O1–P1–O2	100.3(1)	103.9(1)
O1–P1–N1	110.8(1)	106.5(1)
O2–P1–N1	103.4(1)	99.8(1)
P1–O1–C9	124.2(2)	126.1(2)
P1–O2–C12	120.5(2)	123.0(2)
P1–N1–C1	129.1(2)	130.5(2)
S2–C1–N1	127.8(3)	119.3(2)
S2–C1–N2	115.1(2)	124.4(2)
Torsion angles		
C3–N2–C1–S2	−3.4(6)	2.5(5)
P1–N1–C1–S2	−0.4(6)	−163.5(2)

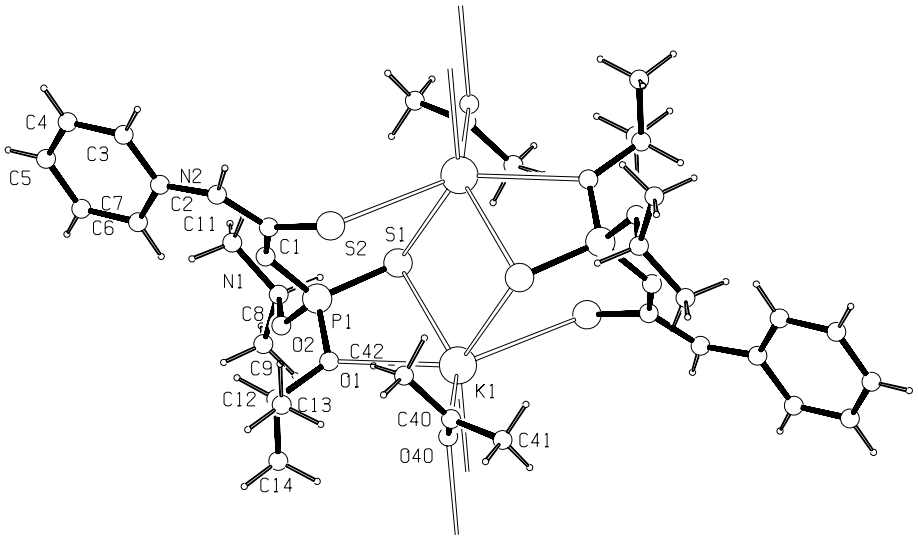
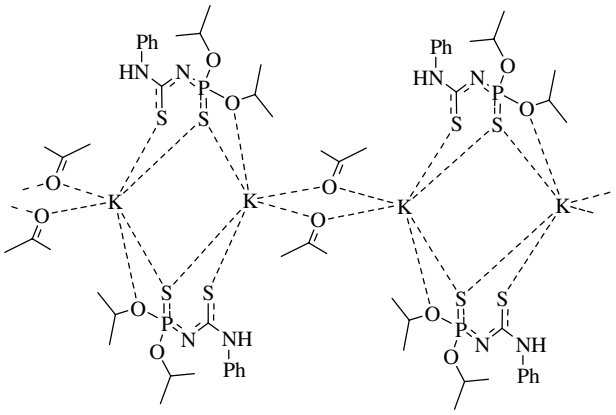


Fig. 2. Molecular structure of [**K(Me$_2$CO)L^{III}**].



Scheme 4.

The negative charge delocalization in the anion $[L^{III}]^-$ results in a characteristic change of bond length in the SCNPS fragment (Table 2) [6]. Bonds C–S and P–S elongate, whereas the C–N and P–N bonds shorten in comparison with a molecule of the neutral ligand $\mathbf{HL^{III}}$. Predictably, the bond N2–C1 increases in length with a reduction of the participation in conjugation of the lone-pair of electrons of N2. In both cases, in a molecule of the ligand it is possible to evolve a planar fragment S2C1N1(N2)P1.

A distinction in the nature of the intermolecular interactions in crystals of $\mathbf{HL^{III}}$ and $[\mathbf{K(Me_2CO)L^{III}}]$ results in the essential distinction of the conformations of the ligand molecules (Table 2). The molecule of $\mathbf{HL^{III}}$ in the crystal has a *syn*-orientation of the bonds C1–S2 and C3–N2 and an *anti*-orientation of the C1–S2 and N1–P1 bonds. The bonds C1–S2 and P1–S1 are in an *anti*-orientation. Such arrangement, apparently, is caused by formation of intramolecular hydrogen bridges N(2)H···S(1) and intermolecular bonds N(1)H···S(2)_a. Parameters for intermolecular hydrogen bonds: N(2)–H(2)···S(1) *d*[N(2)–H(2)] 0.8600, *d*[H(2)···S(1)] 2.47, *d*[N(2)···S(4)] 3.259(4) Å, ∠N(2)H(2)S(4) 152.00°. Parameters for intramolecular hydrogen bonds: N(1)–H(1)···S(2)′ $(2-x, -y, -z)$; *d*[N(1)–H(1)] 0.86, *d*[H(1)···S(2)] 2.60, *d*[N(1)···S(2)]

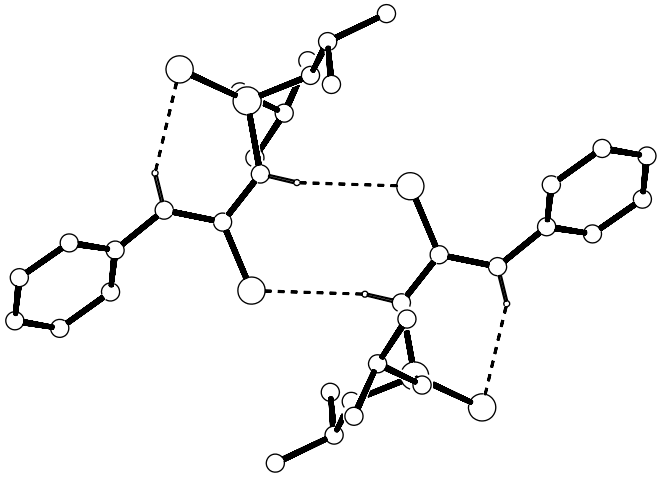


Fig. 3. View of intra- and intermolecular hydrogen bonds NH···S in the crystal of $\mathbf{HL^{III}}$.

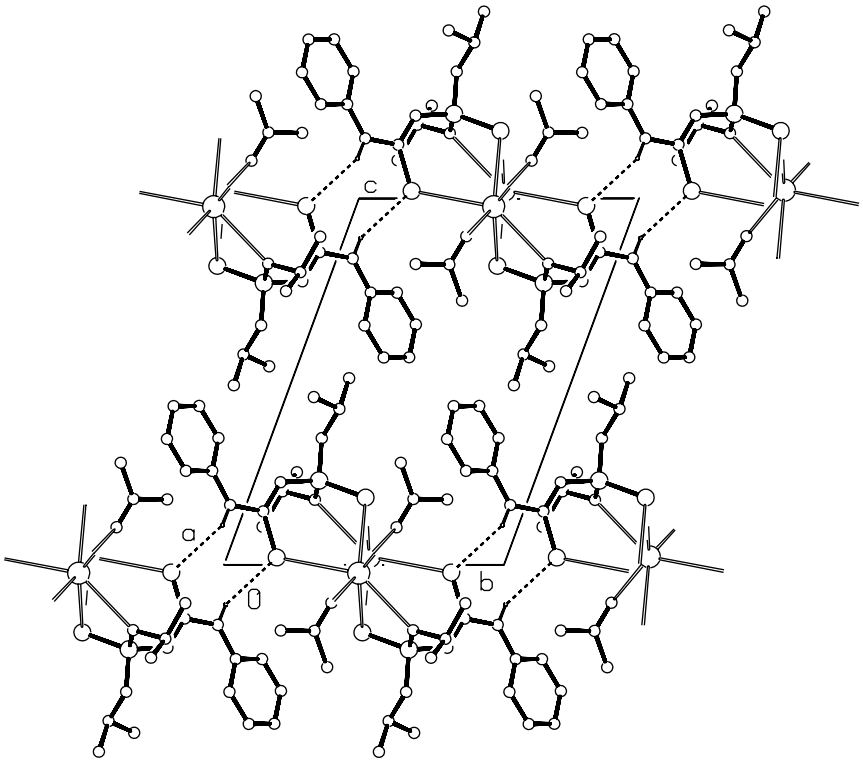


Fig. 4. Structure of molecular layers in a crystal of $[\mathbf{K(Me_2CO)L^{III}}]$.

3.383(3) Å, ∠N(1)H(1)S(2) 151°. As a result of the intermolecular interactions, a centrosymmetric dimer is formed (Fig. 3).

Interaction with the potassium cation results in *gosh*-orientations of the bonds C1–S2 and P1–S1 in the crystal of [**K(Me$_2$CO)L^{III}**]. The geometry of the anion [L^{III}]$^-$ in the crystal is characterized by an *anti*-orientation of the bonds C1–S2 and C3–N2 and a *syn*-orientation of the C1–S2 and N1–P1 bonds.

There are short contacts N(2)H···S(2)_a between molecules of the next polymeric chain in the crystal of [**K(Me$_2$CO)L^{III}**]. The chains, bound by hydrogen bonds, form layers which are parallel to the plane *oab* (Fig. 4). Parameters for intermolecular hydrogen bonds: N(2)–H(2)···S(4)′ (−*x*, −*y*, 2 − *z*) *d*[N(2)–H(2)] 0.9177, *d*[H(2)···S(4)′] 2.7390, *d*[N(2)···S(4)′] 3.597(3) Å, ∠N(2)H(2)S(4)′ 156.04°.

4. Conclusion

The combination of a crown-ether and a negative charged chelating group in a ligand molecule can have unusual consequences. To date we have failed to find another example of alkali ion sedimentation by crown-containing *N*-(thiophosphoryl)thioureas. However we believe that further investigation of the obtained effect would be interesting for the development of new principles of division and concentration of metal ions based on supramolecular interactions of ionic macromolecules.

Well known ways of crown-ether modification are based on intramolecular interactions of additional fragments with a cation in the macrocycle cavity [1], or using additional fragments to form heteronuclei complexes [2,24–26]. However, association in one molecule crown-ether and chelating groups, unable to interact intramolecularly, may be very useful to bind cations of a given type. In this case the effect of recognition can be achieved in two stages: due to selective cation–ligand interaction, and due to interaction of organic molecules after inclusion of the cation in the cavity of the macrocycle.

Acknowledgements

We thank the joint program of CRDF and the Russian Ministry of Education (BHRE 2004 Y2-C-07-02, Grant REC-007) and the Russian Foundation for Basic Research (Grants # 03-03-32372-a, 03-03-96225-r2003tatarstan_a) for financial support. We also thank Mr. Steve Hughes for his help.

Appendix A. Supplementary material

CCDC 613231 and 613232 contain the supplementary crystallographic data for this paper. These data can be obtained free of charge via http://www.ccdc.ac.uk/conts/retrieving.html, or from the Cambridge Crystallographic Data Centre, 12 Union Road, Cambridge CB2 1EZ, UK; fax: (+44) 1223-336-033; or e-mail: deposit@ccdc.cam.ac.uk. Supplementary data associated with this article can be found, in the online version, at doi:10.1016/j.poly.2006.12.024.

References

[1] H. Tsukube, Talanta. 40 (1993) 1313.
[2] F.C.J.M. van Vegel, W. Verboom, D.N. Reinhoudt, Chem. Rev. 94 (1994) 279.
[3] A.E.V. Gorden, J. Xu, K.N. Raymond, P. Durbin, Chem. Rev. 103 (2003) 4207.
[4] M. Ouchi, T. Hakushi, Coord. Chem. Rev. 148 (1996) 171.
[5] J.W. Steed, Coord. Chem. Rev. 215 (2001) 171.
[6] F.D. Sokolov, V.V. Brusko, N.G. Zabirov, R.A. Cherkasov, Curr. Org. Chem. 10 (2006) 27.
[7] L.G. Shaidarova, A.V. Gedmina, V.V. Brusko, N.G. Zabirov, N.A. Ulakhovich, H.K. Budnikov, Russ. J. Appl. Chem. 75 (2002) 919.
[8] M.P. Kutyreva, N.A. Ulakhovich, Yu.I. Salnikov, V.V. Brusko, F.D. Sokolov, N.G. Zabirov, Russ. J. Inorg. Chem. 49 (2004) 1520.
[9] V.A. Trush, K.E. Gubina, V.M. Amirkhanov, J. Swiatek-Kozlowska, K.V. Domasevitch, Polyhedron 24 (2005) 1007.
[10] N.G. Zabirov, F.M. Shamsevaleev, V.A. Shcherbakova, R.A. Cherkasov, V.N. Solovyov, A.N. Chekhlov, G.V. Dmitryeva, I.V. Martynov, J. Gen. Chem. USSR 60 (1990) 1783.
[11] T.Q. Ly, A.M.Z. Slawin, J.D. Woollins, Angew. Chem., Int. Ed. 37 (1998) 2501.
[12] (a) I. Haiduc, Comprehensive Coordination Chemistry II. From Biology to Nanotechnology, vol. 1, 2003, pp. 323–34;
(b) C. Silvestru, J.E. Drake, Coord. Chem. Rev. 223 (2001) 117.
[13] T.Q. Ly, J.D. Woollins, Coord. Chem. Rev. 176 (1998) 451.
[14] M.G. Zimin, R.M. Kamalov, R.A. Cherkasov, A.N. Pudovik, Phosphorus Sulfur 13 (1982) 371.
[15] E.S. Levchenko, I.N. Zhmurova, Ukr. Khim. Zh. (Russ. Ed.) 22 (1956) 623.
[16] N.G. Zabirov, N.I. Galyautdinov, V.A. Sherbakova, R.A. Cherkasov, J. Gen. Chem. USSR 60 (1990) 1112 [Zh. Obshch. Khim. 60 (1990) 1247 (Rus.).
[17] A. Altomare, G. Cascarano, C. Giacovazzo, D. Viterbo, Acta Crystallogr., Sect. A 47 (1991) 744.
[18] G.M. Sheldrick, SHELXS-97, Program for the Solution of Crystal Structures, Unuversity of Göttingen, Göttingen, Germany, 1997.
[19] L.J.J. Farrugia, Appl. Crystallogr. 32 (1999) 837.
[20] L.H. Straver, A.J. Schierbeek, MOLEN. Structure Determination System, vols. 1 and 2, Nonius B.V., Delft, Netherlands, 1994.
[21] A.L. Spek, Acta Crystallogr., Sect. A 46 (1990) 3440.
[22] E.G. Yarkova, N.R. Safiullina, I.G. Chistyakova, N.G. Zabirov, F.M. Shamsevaleev, R.A. Cherkasov, Russ. J. Gen. Chem. 60 (1990) 1790.
[23] N.G. Zabirov, V.V. Brusko, S.V. Kashevarov, F.D. Sokolov, V.A. Sherbakova, A.Yu. Verat, R.A. Cherkasov, Russ. J. Gen. Chem. 70 (2000) 1294.
[24] A.Yu. Verat, F.D. Sokolov, N.G. Zabirov, M.G. Babashkina, D.B. Krivolapov, V.V. Brusko, I.A. Litvinov, Inorg. Chim. Acta 359 (2006) 475.
[25] (a) N.G. Zabirov, F.D. Sokolov, V.V. Brusko, A.K. Tashmukhamedova, N.I. Saifullina, R.A. Cherkasov, Mendeleev Commun. 12 (2002) 154;
(b) F.D. Sokolov, N.G. Zabirov, V.V. Brusko, D.B. Krivolapov, I.A. Litvinov, Mendeleev Commun. 13 (2003) 72.
[26] (a) M. Kemmer, L. Ghys, M. Gielen, M. Biesemans, E.R.T. Tiekink, R.J. Willem, Organomet. Chem. 582 (1999) 195;
(b) C. Sousa, P. Gameiro, C. Freire, B. de Castro, Polyhedron 23 (2004) 1401;
(c) O.P. Kryatova, A.G. Kolchinski, E.V. Rybak-Akimova, Tetrahedron 59 (2003) 231.

studied on the human erythrocyte membrane, which suggested the structural perturbations induced by titanium citrate to human erythrocytes can be extended to the other cells, affecting their functions [21]. Moreover, like some other soluble titanium compounds, titanium citrate exerts effects on the growth of plants [22]. In the form of Ti(III) citrate, it has been used extensively to probe redox reactions involving enzyme catalytic functions [23]. In most of the above cases, the titanium citrate complexes are prepared in situ without rigorous characterization. The compositions, spectroscopic and structural properties of titanium citrate require further attention.

Several important Ti(IV) citrate complexes have been structurally characterized recently. This includes several mononuclear titanium complexes, such as $[Ti(H_2cit)_3]^{2-}$ [24], $[Ti(H_2cit)(Hcit)_2]^{4-}$ [25], $[Ti(Hcit)H(cit)_2]^{6-}$ [26] and $[Ti(cit)_3]^{8-}$ [27] having only citrate ligands with different counterions, an oxo titanium complex with a Ti_8O_{10} structural core [28], two tetranuclear [29] and one dinuclear [30] complex of peroxo citrato titanates(IV). Very recently, a trivalent species $[Ti(H_2cit)_2(Hcit)]^{3-}$ has also been reported [31]. The characterization of these complexes represents important progress towards the structural features of the coordination chemistry of Ti(IV) with citrate. However, there has been no systematical study on the different charges of titanium citrate anions from 2 to 8, in which the citrate binds to the titanium(IV) ion via α-alkoxy and α-carboxy groups in 1:3 Ti:citrate ratio. Moreover, the relationship between the isolated solid complexes and the titanium citrate solutions remains unknown. In this paper, the interaction of Ti(IV) with citrate has been investigated in aqueous solution in detail, including the speciation of the soluble titanium citrate complexes and their related pH-dependent transformations, which contain different counterions at different pH values. At the same time, the ^{13}C NMR studies of a titanium citrate solution in a 1:3 mole ratio were also carried out in the pH ranges 2.0–9.0 for comparison.

2. Experimental

Infrared spectra were recorded as Nujol mulls between KBr plates using a Nicolet 360 FT-IR spectrometer. The pH value was measured by the potentiometric method with a digital pH meter. Elemental analyses were performed using an EA 1110 elemental analyzer. ^1H NMR and ^{13}C NMR spectra were recorded on a Varian UNITY 500 NMR spectrometer using DSS (sodium 2,2-dimethyl-2-silapentane-5-sulfonate) as an internal reference.

2.1. Preparation of $Na_3[Ti(H_2cit)_2(Hcit)]\cdot 9H_2O$ (1) [31], $K_4[Ti(H_2cit)(Hcit)_2]\cdot 4H_2O$ (2) and $K_5[Ti(Hcit)_3]\cdot 4H_2O$ (3)

A typical procedure was used for the preparation of complex **1**. A quantity of citric acid monohydrate (6.30 g, 30 mmol) was placed in a flask and dissolved in 10 mL of water. Subsequently, titanium tetrachloride (1.90 g, 10 mmol) was added slowly under continuous stirring. Aqueous sodium hydroxide (1.0 M) was then added slowly to adjust the pH value to 3.0. The mixture was filtered. Cold ethanol was added to the clear solution, and the resulting solution was placed in a refrigerator at 4 °C. A week later, colorless crystalline material was deposited. The product was isolated by filtration and dried at room temperature. Yield of complex **1**: 4.3 g (50%). C and H elemental *Anal*. Calc. for $C_{18}H_{35}O_{30}Na_3Ti$: C, 25.5; H, 4.2. Found: C, 25.5; H, 3.9%. IR ν_{as}(COOH) 1704_{vs}; $\nu_{as}(CO_2)$ 1624_{vs}, 1557_{vs}; $\nu_s(CO_2)$ 1425_m, 1325_s; ν_s(Ti–O) 671_s, 641_s, 552_m. ^1H NMR δ_H (500 MHz, D_2O) ppm, 2.708 (d, J 14.0 Hz, CH_2), 2.930 (d, J 14.5 Hz, CH_2); ^{13}C NMR δ_C (D_2O) ppm, 186.1 $(CO_2)_\alpha$; 174.8 $(CO_2)_\beta$; 88.7 (=CO); 43.8 (CH_2).

The above procedure for **1** was utilized except the pH value of the mixture was adjusted to 4.0 or 6.0 with aqueous potassium hydroxide (1.0 M), affording the colorless crystals of **2** and **3**. Yield of complex **2**: 4.2 g (50%). C and H elemental *Anal*. Calc. for $C_{18}H_{23}O_{25}K_4Ti$: C, 25.6; H, 3.0. Found: C, 25.5; H, 3.2%. ν_{as}(COOH) 1725_m, 1709_m, 1700_m; $\nu_{as}(CO_2)$ 1648_{vs}, 1627_{vs}, 1526_w; $\nu_s(CO_2)$ 1441_m, 1347_s, 1311_s; ν_s(Ti–O) 662_m, 646_s, 537_m. ^1H NMR δ_H (500 MHz, D_2O) ppm, 2.713 (d, J 14.0 Hz, CH_2), 2.937 (d, J 14.0 Hz, CH_2); ^{13}C NMR δ_C (D_2O) ppm, 189.0 $(CO_2)_\alpha$; 177.5 $(CO_2)_\beta$; 91.6 (=CO); 46.6 (CH_2). Yield of complex **3**: 3.5 g (40%). C and H elemental *Anal*. Calc. for $C_{18}H_{23}O_{25}K_5Ti$: C, 24.5; H, 2.6. Found: C, 24.3; H, 2.8%. IR (KBr, cm^{-1}): ν_{as}(COOH) 1709_m; $\nu_{as}(CO_2)$ 1629_{vs}; $\nu_s(CO_2)$ 1428_w, 1372_m, 1320_m; ν_s(Ti–O) 649_m, 636_s, 543_m. ^1H NMR δ_H (500 MHz, D_2O) ppm, 2.703 (d, J 14.5 Hz, CH_2), 2.926 (d, J 14.0 Hz, CH_2); ^{13}C NMR δ_C (D_2O) ppm, 189.8 $(CO_2)_\alpha$; 180.2 $(CO_2)_\beta$; 92.1 (=CO); 47.6 (CH_2).

2.2. Preparation of $Na_7[Ti(cit)H(cit)(cit)]\cdot 18H_2O$ (4)

A quantity of citric acid monohydrate (6.30 g, 30 mmol) was placed in a flask and dissolved in 10 mL of water. Subsequently, titanium *n*-butoxide (3.40 g, 10 mmol) was added slowly under continuous stirring. The resulting reaction mixture was taken to dryness at 70 °C in a rotary evaporator. The residue was redissolved in 3 mL of water, and the pH value of the solution was raised to 6.5 with 1.0 M sodium hydroxide. The mixture was filtered. Cold ethanol was added to the solution, and the resulting solution was placed in a refrigerator at 4 °C. A week later, colorless crystalline material was deposited. The product was isolated by filtration and dried at room temperature. Yield: 4.4 g (40%). C and H elemental *Anal*. Calc. for $C_{18}H_{49}O_{39}Na_7Ti$: C, 19.7; H, 4.5. Found: C, 19.9; H, 4.3%. IR (KBr, cm^{-1}): ν(COO···H···OOC) 1632_m; $\nu_{as}(CO_2)$ 1578_{vs}; $\nu_s(CO_2)$ 1403_m, 1351_m; ν_s(Ti–O) 647_m, 553_m. ^1H NMR δ_H (500 MHz, D_2O) ppm, 2.723 (d, J 14.5 Hz, CH_2), 2.956 (d, J 14.5 Hz, CH_2); ^{13}C NMR δ_C (D_2O) ppm, 190.0 $(CO_2)_\alpha$; 189.9, 180.4 $(CO_2)_\beta$; 92.3 (=CO); 47.8 (CH_2).

2.3. Interconversion of $K_4[Ti(H_2cit)(Hcit)_2]\cdot 4H_2O$ (2) to $K_5[Ti(Hcit)_3]\cdot 4H_2O$ (3)

$K_4[Ti(H_2cit)(Hcit)_2]\cdot 4H_2O$ (**2**) (1.69 g, 20 mmol) was dissolved in 5 mL of water at 45 °C. The pH value of the solution was adjusted to ~6.0 with an aqueous solution of 1 M potassium hydroxide under continuous stirring. Cold ethanol was added to the solution, and the resulting solution was placed in a refrigerator at 4 °C. A week later, colorless crystalline material was deposited. The product was isolated by filtration and dried at room temperature. Yield: 0.79 g (45%). In a similar procedure, complex **3** was converted to complex **2** in 60% yield. Positive identification of the crystalline material as complexes **2** and **3** came from the IR spectra and the X-ray unit cell determinations.

2.4. Preparations of the solutions a–e (Ti:H_4cit = 1:3) and NMR studies

Citric acid monohydrate (6.30 g, 30 mmol) was placed in a flask and dissolved in 40 mL of water. Titanium *n*-butoxide (3.40 g, 10 mmol) was added slowly under continuous stirring. All of the free solvent was removed on a rotary evaporator, leaving a fine white powder. Distilled water (40 mL) was added, and the mixture was dissolve at 70 °C. Further reduction on the rotary evaporator removed the solvent from the residual before the solution was diluted to 40 mL with water. The resulting solution was divided into five parts (a–e). The pH value of each solution was adjusted to 2.0, 3.5, 5.0, 7.0 and 9.0 with 1.0 M sodium hydroxide. The volume was maintained at 8 mL after evaporation, resulting in approximately a 0.25 M solution based on Ti. The ^{13}C NMR spectra of the solution were recorded in D_2O after 1 h.

2.5. X-ray data collection, structure solution and refinement

Crystals of **1** and **3** were measured on an Enraf-Nonius CAD-4 diffractometer with graphite-monochromated Mo Kα radiation at 296 K. Crystals of **2** and **4** were measured on a Bruker Smart Apex CCD diffractometer with graphite-monochromated Mo Kα radiation ($\lambda = 0.71073$ Å) at 296 K. The data were corrected for Lorentz and polarization effects. An absorption correction was applied using the SADABS program [32]. The structures were primarily solved by direct methods, SHELXS-97 [33], and refined by full-matrix least-squares procedures with anisotropic thermal parameters for all of the non-hydrogen atoms. All calculations were performed on a microcomputer using SHELXL-97 [34]. Hydrogen atoms, except those of O4 and O14 of complex **4** and the disordered water molecules of the four complexes, were calculated geometrically and refined riding on their parent atoms as usual. A summary of the crystallographic data for **1**–**4** is given in Table 1. Selected bond distances and angles of the four complexes are listed in Table 2.

Table 1
Crystal data summary of intensity data collection and structure refinement for $Na_3[Ti(H_2cit)_2(Hcit)]\cdot 9H_2O$ (**1**) [31], $K_4[Ti(H_2cit)(Hcit)_2]\cdot 4H_2O$ (**2**), $K_5[Ti(Hcit)_3]\cdot 4H_2O$ (**3**) and $Na_7[TiH(cit)_3]\cdot 18H_2O$ (**4**)

Compound	**1**	**2**	**3**	**4**
Empirical formula	$C_{18}H_{35}O_{30}Na_3Ti$	$C_{18}H_{24}O_{25}K_4Ti$	$C_{18}H_{23}O_{25}K_5Ti$	$C_{18}H_{49}O_{39}Na_7Ti$
Formula weight	848.33	844.67	882.76	1098.40
Crystal system	monoclinic	monoclinic	triclinic	triclinic
Crystal size (mm)	0.29 × 0.20 × 0.15	0.26 × 0.17 × 0.06	0.15 × 0.12 × 0.09	0.35 × 0.24 × 0.07
Crystal color	colorless	colorless	colorless	colorless
a (Å)	18.922(1)	11.6288(6)	11.1920(3)	9.8486(4)
b (Å)	10.957(1)	15.0989(7)	11.4599(4)	13.6447(6)
c (Å)	31.622(2)	16.9589(8)	12.1981(5)	15.3666(7)
α (°)			88.138(1)	95.971(1)
β (°)	97.50(1)	95.220(1)	85.888(1)	94.933(1)
γ (°)			89.269(1)	94.897(1)
V (Å^3)	6500.3(3)	2965.3(2)	1559.58(9)	2036.9(2)
Space group	$C2_1/c$	$P\,2_1/c$	$P\bar{1}$	$P\bar{1}$
Z	8	4	2	2
D_{calc} (g cm^{-3})	1.734	1.892	1.880	1.791
F(000)	3504	1720	896	1136
Diffractometer/radiation (Å)	0.71073	0.71073	0.71073	0.71073
Reflections collected/unique (R_{int})	5884/5698 (0.0240)	18400/5776 (0.0601)	6423/6095 (0.0523)	12752/9192 (0.0701)
Data/restraints/parameters	5698/26/528	5776/210/466	6095/3/460	9192/54/700
θ Range (°)	1.30–25.00	1.76–26.00	1.67–26.00	1.51–28.44
Goodness-of-fit on F^2	1.038	1.113	1.027	1.026
R_1[a], wR_2[b] [$I > 2\sigma(I)$]	0.074, 0.175	0.067,0.154	0.079, 0.195	0.055, 0.145
R_1, wR_2 (all data)	0.127, 0.208	0.078,0.161	0.135, 0.235	0.064, 0.152
Largest difference in peak and hole (e Å^{-3})	1.414 and −0.817	1.216 and −1.032	1.872 and −0.926	1.200 and −0.892

[a] $R_1 = \sum\|F_o| - |F_c\|/\sum(|F_o|)$.
[b] $wR_2 = \sum[w(F_o^2 - F_c^2)^2]/\sum[w(F_o^2)^2]^{1/2}$.

Table 2
Selected bond distances (Å) and angles (°) for $Na_3[Ti(H_2cit)_2(Hcit)]\cdot 9H_2O$ (**1**) [31], $K_4[Ti(H_2cit)(Hcit)_2]\cdot 4H_2O$ (**2**), $K_5[Ti(Hcit)_3]\cdot 4H_2O$ (**3**) and $Na_7[TiH(cit)_3]\cdot 18H_2O$ (**4**)

Compound	1	2	3	4
Bond distances (Å)				
Ti(1)–O(1)	1.868(4)	1.851(3)	1.882(5)	1.855(2)
Ti(1)–O(2)	2.039(4)	2.039(3)	2.067(5)	2.025(2)
Ti(1)–O(11)	1.854(4)	1.870(3)	1.843(5)	1.857(2)
Ti(1)–O(12)	2.061(4)	2.069(3)	2.049(5)	2.038(2)
Ti(1)–O(21)	1.855(4)	1.850(3)	1.881(5)	1.853(2)
Ti(1)–O(22)	2.056(4)	1.993(3)	2.040(5)	2.008(2)
Bond angles (°)				
O(1)–Ti(1)–O(2)	79.3(2)	79.9(1)	79.0(2)	79.25(7)
O(1)–Ti(1)–O(11)	97.4(2)	97.0(1)	96.2(2)	98.56(7)
O(1)–Ti(1)–O(12)	162.9(2)	161.3(1)	165.0(2)	160.72(7)
O(1)–Ti(1)–O(21)	96.9(2)	94.7(1)	93.6(2)	95.87(7)
O(1)–Ti(1)–O(22)	101.6(2)	100.8(1)	101.4(2)	101.44(7)
O(2)–Ti(1)–O(11)	99.8(2)	98.1(1)	101.9(2)	101.82(7)
O(2)–Ti(1)–O(12)	85.0(2)	82.6 (1)	87.8(2)	82.81(7)
O(2)–Ti(1)–O(21)	160.5(2)	166.3(1)	162.1(2)	157.40(7)
O(2)–Ti(1)–O(22)	83.2(2)	88.5(1)	86.3(2)	80.61(7)
O(11)–Ti(1)–O(12)	78.6(2)	79.1(1)	79.6(2)	78.22(7)
O(11)–Ti(1)–O(21)	99.7(2)	95.1(1)	95.0(2)	100.72(7)
O(11)–Ti(1)–O(22)	161.0(2)	161.9(1)	161.7(2)	159.94(7)
O(12)–Ti(1)–O(21)	100.2(2)	103.8(1)	101.1(2)	103.41(7)
O(12)–Ti(1)–O(22)	83.0(2)	85.1(1)	84.5(2)	82.38(7)
O(21)–Ti(1)–O(22)	78.8(2)	80.1(1)	79.1(2)	78.77(7)
Hydrogen bonds (Å)				
1	O16···O6(a)	2.584(7)	O24···O7(b)	2.605(6)
2	O4···O26(b)	2.525(4)	O6···O12(c)	2.803(4)
	O14···O16	2.479(6)	O24···O17(a)	2.545(5)
3	O24···O6(a)	2.512(9)	O4···O16(b)	2.494(9)
	O14···O26(c)	2.483(8)		
4	O4···O4(a)	2.416(5)	O14···O14(b)	2.423(5)

Symmetric transformations:

(**1**) a: $0.5-x, 0.5-y, 1-z$; b: $-x, -y, 1-z$.
(**2**) a: $-1-x, -0.5-y, 0.5-z$; b: $-x, -y, -z$; c: $x, 0.5-y, -0.5-z$.
(**3**) a: $-x, 1-y, -z$; b: $-1-x, -y, 1-z$; c: $-x, -y, 1-z$.
(**4**) a: $-x, -y, -z$; b: $-x, -y, -1-z$.

3. Results and discussion

3.1. Syntheses and interconversions

Syntheses of complexes **1**–**4** were expediently carried out in aqueous solutions under slightly different conditions. In these reactions, the products do not mainly depend on the ligand-to-metal ratio. Control of the high ratio of titanium(IV) ion and citric acid in the synthetic procedures will drive the reaction completely and lead to the isolation of titanium(IV) citrate complexes in high yield. In the preparation of complex **4**, in order to acquire a good crystal for X-ray structure determination, we choose titanium *n*-butoxide as the titanium source. The procedures for the syntheses of titanium(IV) citrate complexes illustrate the sensitivity of the reactions toward pH and counterions in aqueous solutions containing titanium(IV) ion and citric acid. When the pH is lower than 4.0, solutions containing titanium(IV) ion, sodium ion and citric acid only deposited complex **1**; in contrast, control of pH values in the range of 4.5–6.0, 6.5 and 7.0 results in the formation of $Na_6[Ti(Hcit)H(cit)_2]\cdot 16H_2O$, $Na_7[TiH(cit)_3]\cdot 18H_2O$ and $Na_8[Ti(cit)_3]\cdot 17H_2O$, respectively. When pH is higher than 7.0, no titanium(IV) citrate complexes were isolated from the above solutions. In addition, attempts to isolate the complexes formulated as $Na_2[Ti(H_2cit)_3]\cdot nH_2O$, $Na_4[Ti(H_2cit)(Hcit)_2]\cdot nH_2O$ and $Na_5[Ti(Hcit)_3]\cdot nH_2O$ from the solutions containing titanium(IV) ion, sodium ion and citric acid proved unsuccessful. However, when solutions contain titanium(IV) ion, potassium ion and citric acid, only the complexes formulated as $K_2[Ti(H_2cit)_3]\cdot 4H_2O$, $K_4[Ti(H_2cit)(Hcit)_2]\cdot 4H_2O$ and $K_5[Ti(Hcit)_3]\cdot 4H_2O$ are isolated at the pH values of 2.0, 4.0 and 6.0, respectively. Similarly, no titanium(IV) citrate complex is isolated from solutions containing titanium(IV) ion, potassium ion and citric acid, when the pH is higher than 7.0. These results suggested that the pH values of the solutions containing titanium(IV) and citrate have important effect on the precipitation of titanium citrate complexes.

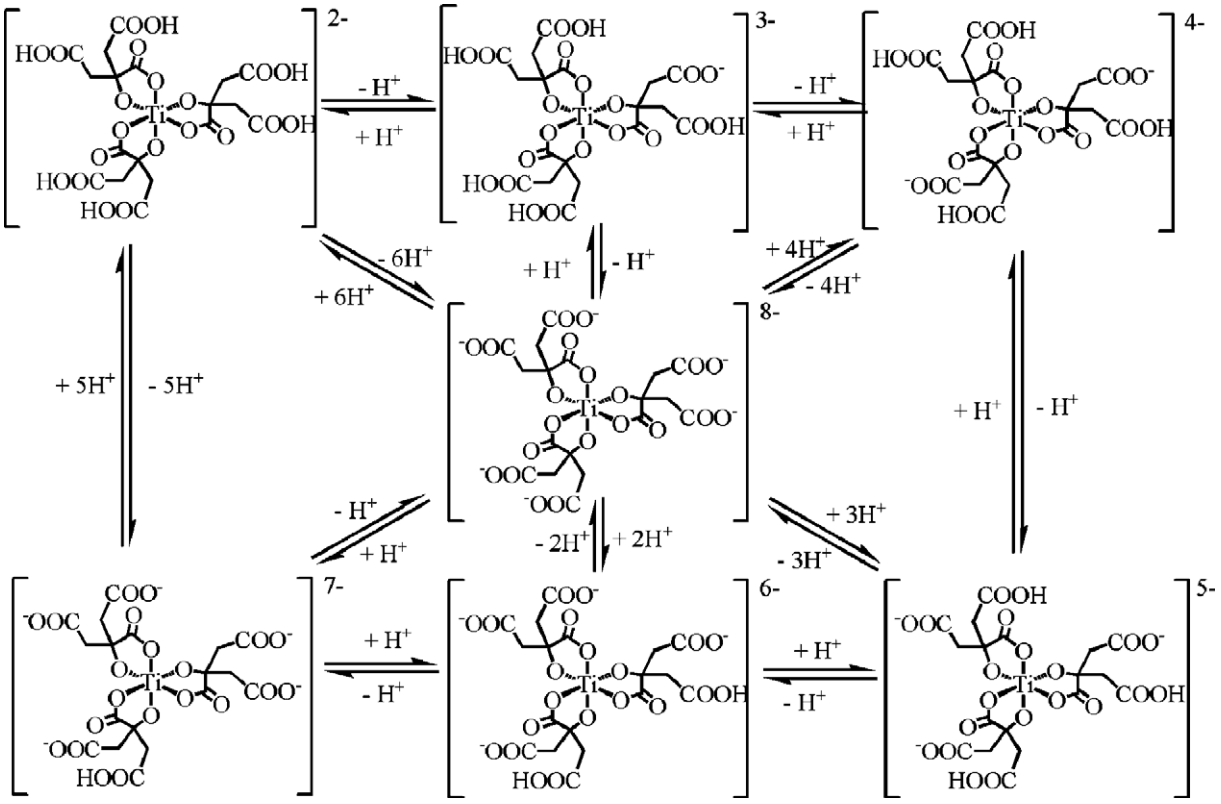
The pH-dependent transformations were carried out between complexes **2** and **3**. The simple dissolution of complex **2** in water and the adjustment of the pH to a final value of ~6.0, with aqueous potassium hydroxide, led to the isolation of complex **3** upon addition of ethanol at 4 °C. Conversely, when complex **3** was dissolved in water and the pH was adjusted to a final value of ~4.0 with aqueous hydrochloric acid, complex **2** could be isolated upon the addition of ethanol at 4 °C. In view of the acid–base reactivity observed between the two mononuclear complexes and a similar result in previously reported literature [24], similar behaviors were envisioned to exist between the two titanium citrate anions which had been synthesized, isolated and characterized crystallographically in the past [24–27]. Based on the interconversions described and all of the seven well characterized titanium species between the charges of 2 and 8, Scheme 1 shows the pH-dependent interconversions of the titanium citrate anions reported.

All the complexes are soluble in water, especially in hot water, and slightly soluble in organic solvents such as ethanol and acetone.

3.2. Description of the crystal structures

The crystal structures of the titanium(IV) citrate complexes **1**–**4** were determined and the ORTEP diagram of complex **3** is given in Fig. 1. The ORTEP diagrams of the other three complexes are given in Figs. S1–S3, respectively.

The titanium atom in all of the complexes is six-coordinated in an octahedral environment by α-alkoxy and α-carboxy groups from three citrate ligands. This geometry is similar to those found in the previously reported titanium citrate complexes [24–27]. But it is different from those of seven-coordinated peroxo titanium(IV) citrate complexes, such as $(NH_4)_8[Ti(O_2)(cit)]_4\cdot 8H_2O$ [29a], $Ba_2(NH_4)_2[Ti_4(O_2)_4(Hcit)_2(cit)_2]\cdot 10H_2O$ [29b] and $(NH_4)_4[Ti(O_2)(cit)]_2\cdot 2H_2O$ [30]. The coordination mode of the titanium atom also argues against the previous models inferred from spectroscopic data, in which the titanium atom is coordinated by α-alkoxy and β-carboxy groups of three citrates



Scheme 1. Transformations of titanium citrate anions in the Ti–citrate–H_2O system.

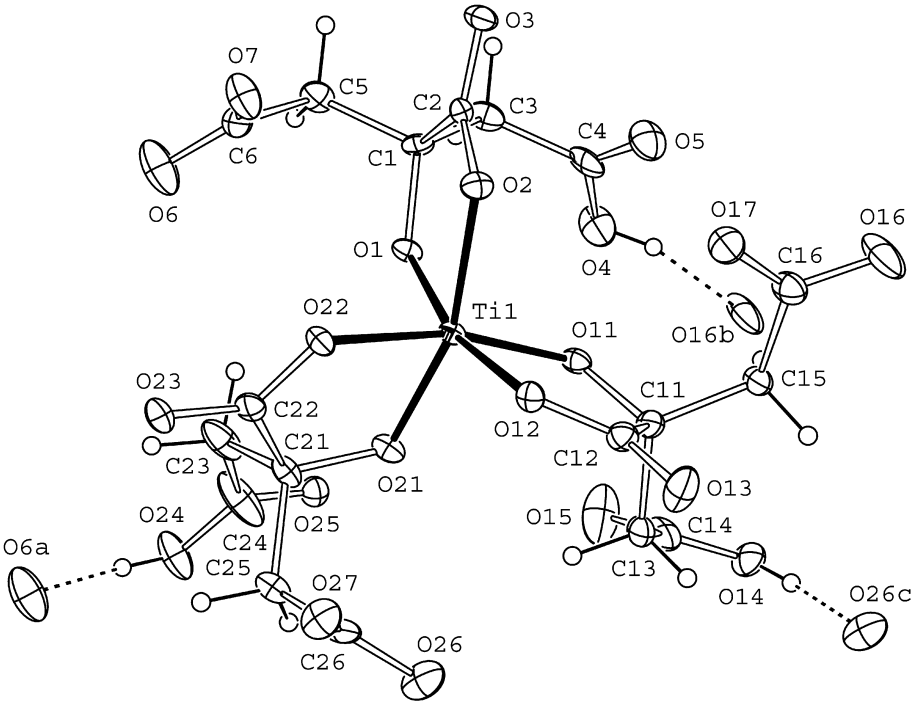


Fig. 1. ORTEP plot of the anion structure of $K_5[Ti(Hcit)_3]\cdot 4H_2O$ (**3**) at the 30% probability level.

[13a,13b], or by three α-alkoxy groups, one α-carboxy group and two β-carboxylic groups [13d]. Bidentate coordination of the citrate ligand through its α-alkoxy group and α-carboxy group with the titanium atom is independent with the pH variations in the pH range 1.0–7.0. Generally, the citrate anion uses its α-hydroxy or α-alkoxy, α- and β-carboxy groups to interact with the metal atom, such as in the complexes $(NH_4)_3[Ga(Hcit)_2]\cdot 4H_2O$ [35],

Table 3
Comparison of the average Ti–O bond distances (Å) in the titanium(IV) citrate complexes

Complex	Anion	Ti–$O_{\alpha\text{-alkoxy}}$	Ti–$O_{\alpha\text{-carboxy}}$	Reference
$K_2[Mg(H_2O)_6][Ti(H_2cit)_3]\cdot 6H_2O$	−2	1.865(1)	2.045(1)	[24]
$(NH_4)_2[Mg(H_2O)_6][Ti(H_2cit)_3]\cdot 6H_2O$	−2	1.866(2)	2.049(2)	[24]
$Na_3[Ti(H_2cit)_2(Hcit)]\cdot 9H_2O$ (**1**)	−3	1.859(4)	2.052(4)	this work
$Na_3[Ti(H_2cit)_2(Hcit)]\cdot 9H_2O$	−3	$1.862(2)_{av}$	$2.055(2)_{av}$	[31]
$K_4[Ti(H_2cit)(Hcit)_2]\cdot 4H_2O$ (**2**)	−4	1.857(3)	2.037(3)	this work
$Ba_2[Ti(H_2cit)(Hcit)_2]\cdot 8H_2O$	−4	1.868(4)	2.007(4)	[25]
$K_5[Ti(Hcit)_3]\cdot 4H_2O$ (**3**)	−5	1.869(4)	2.052(4)	this work
$Na_3(NH_4)_3[Ti(Hcit)_2(cit)]\cdot 9H_2O$	−6	1.868(3)	2.049(4)	[26]
$Na_6[Ti(Hcit)_2(cit)]\cdot 16H_2O$	−6	1.867(2)	2.052(2)	[26]
$Ba_3(NH_4)_7[Ti(Hcit)_3(cit)_3Ti]\cdot 15H_2O$	−6.5	1.871(2)	2.026(2)	[25]
$Na_7[TiH(cit)_3]\cdot 18H_2O$ (**4**)	−7	1.855(2)	2.024(2)	this work
$Na_8[Ti(cit)_3]\cdot 17H_2O$	−8	1.850(2)	2.054(2)	[27]

$(NH_4)_4[M(Hcit)_2]\cdot xH_2O$ [M = Mn(II), Co(II), $x = 0$; M! = Ni(II), $x = 2$] [36] and $(NH_4)_5[M(cit)_2]\cdot 2H_2O$ (M = Mn(III), Fe and Al) [36,37]. A comparable result could be found in vanadate(V) citrate complexes, such as $K_2[V_2O_4(H_2cit)_2]\cdot 4H_2O$, $(NH_4)_2[V_2O_4(H_2cit)_2]\cdot 2H_2O$ [38], $Na_2K_2[V_2O_4(Hcit)_2]\cdot 9H_2O$, $K_4[V_2O_4(Hcit)_2]\cdot 4H_2O$ [39], $(NH_4)_4[V_2O_4(Hcit)_2]\cdot 4H_2O$, $K_2(NH_4)_4[V_2O_4(cit)_2]\cdot 6H_2O$ and $(NH_4)_6[V_2O_4(cit)_2]\cdot 6H_2O$ [40].

The uncoordinated protonated β-carboxylic groups are strongly hydrogen-bonded to the deprotonated β-carboxylate groups of an adjacent molecule, resulting in the polymeric anionic structures of complexes **1**–**4**. The anionic structures of the four titanium citrate complexes through hydrogen-bonding interactions are shown in Figs. S4–S7, respectively. The important hydrogen-bonding interactions of the four complexes are listed in Table 2. Specifically, two of the bound citrate ligands share a hydrogen with their neighbors in complex **4** [O4···O4(a) = 2.416(5), O14···O14(b) = 2.423(5) Å], thus affording the −7 dinuclear citrate ion $[TiH(cit)_3]^{7-}$, which is similar to the centrosymmetric dimer formed through the linear hydrogen bonding of a β-carboxylic acid to a β-carboxy group in the complexes $Ba_3(NH_4)_7[Ti(Hcit)_3(cit)_3Ti]\cdot 15H_2O$ [$O6\cdots O6^i = 2.478(2)$ Å] [25], $Na_6[Ti(Hcit)_2(cit)]\cdot 16H_2O$ [$O7\cdots O7^i = 2.467(2)$ Å; $O17\cdots O17^i = 2.455(2)$ Å] and $Na_3(NH_4)_3[Ti(Hcit)H(cit)_2]\cdot 16H_2O$ [$O7\cdots O7^i = 2.474(2)$ Å; $O17\cdots O17^i = 2.446(2)$ Å] [26]. The hydrogen bond in **4** should be extraordinary strong in view of its intermolecular mode with the consideration of the intramolecular hydrogen bonding distance [O···O = 2.636(7) Å] in salicylic acid [41], and the ordinary OH bond of 0.96 Å.

Comparisons of Ti–O distances for titanium(IV) citrate complexes are given in Table 3. The average Ti–$O_{\alpha\text{-alkoxy}}$ bond distances [1.856(4), 1.856(4), 1.868(3) and 1.871(2) Å for **1**–**4**] are similar to those found in related titanium citrate complexes, or the titanium lactate complex $(NH_4)_2[Ti(lact)_3]$ [1.848(5) Å] [42] (H_2lact = lactic acid). The average Ti–$O_{\alpha\text{-carboxy}}$ distances [2.052(4), 2.037(3), 2.052(4) and 2.024(2) Å for **1**, **2**, **3** and **4**] are normal, the distances also being similar to the reported titanium(IV) complexes. It appears that similar angles are observed in **1**, **2**, **3** and **4** and a number of $Ti^{IV}O_6$-core containing complexes. It is noted that the trends in bond distances of the Ti–O bonds are complicated, which is probably related to the different counterions in the titanium citrate complexes.

3.3. Solution NMR spectroscopy of complexes 1–4

The solution ^{13}C NMR spectra of complexes **1**–**4** were measured in D_2O and the results are listed in Table 4. Owing to obvious dissociation on dissolving in H_2O (D_2O), the solution ^{13}C NMR spectra of **1**–**4** showed some peaks of the free citrate. The observed two sets of resonances were attributed to the free and bound citrate in the titanium citrate complexes. The free citrate could serve as an indicator in the spectra for coordination. There exists an equilibrium between tricitrato titanate(IV) and free citrate ligand. Additional species of titanium citrate are not observed in the ^{13}C NMR spectra.

Fig. 2 illustrates the ^{13}C NMR spectrum of **1**, and the ^{13}C NMR spectra of **3** and **4** are shown in Fig. S8. The results display that the dissociation of the titanium citrate complexes in H_2O (D_2O) changes with the pH value. Specifically, the intensities of free citrate resonances increase with the rise of pH value, while those of peaks belonging to the coordinated titanium citrate complex decrease gradually. Given the similar ^{13}C NMR spectra of **1**–**4**, herein, only the ^{13}C NMR spectrum of complex **1** is discussed. Compared with the corresponding free ligand dissociated from complex **1** [178.2 $(CO_2)_{\alpha\text{-carboxy}}$, 174.8 $(CO_2)_{\beta\text{-carboxy}}$, 74.0 $(C\text{–}O)_{\alpha\text{-hydroxy}}$, 43.8 $(CH_2)_{methylene}$], complex **1** shows large lower field shifts of α-alkoxy and α-carboxy carbons ^{13}C resonances ($\Delta\delta \sim 14.7$ and 7.9 ppm) via coordination.

Table 4
Relevant ^{13}C NMR data, δ/ppm of $Na_3[Ti(H_2cit)_2(Hcit)]\cdot 9H_2O$ (**1**), $K_4[Ti(H_2cit)(Hcit)_2]\cdot 4H_2O$ (**2**), $K_5[Ti(Hcit)_3]\cdot 4H_2O$ (**3**) and $Na_7[TiH(cit)_3]\cdot 18H_2O$ (**4**)

Compound	CH_2	=C–O	$(CO_2)_\alpha$	$(CO_2)_\beta$	C–OH	$(CO_2)_{\alpha\text{-free}}$
1	43.8	88.7	186.1	174.8	74.0	178.2
2	46.6	91.6	189.0	177.5	77.0	181.9
3	47.6	92.1	189.8	180.2	77.4	183.3
4	47.8	92.3	190.0	180.4	77.9	183.7

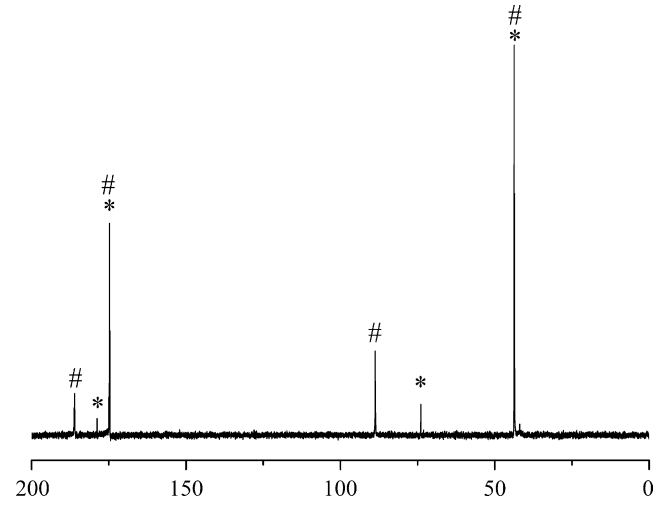


Fig. 2. ^{13}C NMR spectrum of $Na_3[Ti(H_2cit)_2(Hcit)]\cdot 9H_2O$ (**1**) in D_2O. Labels: free citrate (∗); coordinated titanium citrate complex (#).

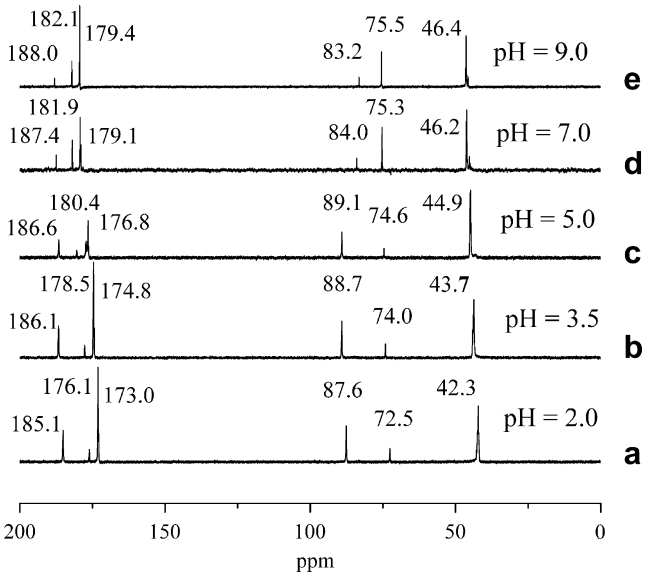


Fig. 3. ^{13}C NMR spectra for the solutions (a–e) with the molar ratio Ti/H_4cit = 1:3 at various pH values.

This indicates that the α-hydroxy and α-carboxylic acid groups in citric acid are fully deprotonated and coordinate to the titanium atom simultaneously. The observation is in agreement with the conclusion derived from the X-ray crystal structure. The ^1H NMR spectrum of complex **1** shows two groups of sharp AB quartets for methylene protons, which also corroborates with the dissociation of the titanium(IV) citrate complex in aqueous solution.

It is worth noting that the previous report showed an undissociated ^{13}C NMR spectrum of complex $Na_6[Ti(Hcit)_2(cit)]\cdot 16H_2O$ [26], in which only one set of resonances were observed. Two peaks in the highfield region were assigned to methylene (47.6 ppm) and α-alkoxy (77.3 ppm) carbon atoms of the bound citrate, while the other two peaks in the downfield region were assigned to the α-carboxy (183.2 ppm) and β-carboxy (180.3 ppm) carbons of the bound citrate. In consideration of the corresponding ^{13}C NMR signals of the bound and dissociated citrate ligands in **3** and **4** at high pH values, it is suggested that full dissociation was observed for the complex of $Na_6[Ti(Hcit)_2(cit)]\cdot 16H_2O$.

3.4. ^{13}C NMR spectroscopy studies of 1:3 Ti:citrate solution

Fig. 3 shows the ^{13}C NMR spectra of 1:3 Ti:citrate solutions of a–e in the region 0–200 ppm, which demonstrates the coordination of the citrate ligand with Ti(IV) ion is consistent with those isolated at the corresponding pH values lower than 7.0. For example, the ^{13}C NMR spectrum of the 1:3 Ti:citrate solution at a pH value of 3.5 reveals two sets of ^{13}C resonances, which is very similar to the ^{13}C NMR spectrum of complex **1** isolated in the pH range 2.0–4.0. The peaks at 186.1, 174.8, 88.7 and 43.7 ppm were assigned to the resonances of α-carboxy, β-carboxy, α-alkoxy and methylene carbons for the coordinated citrate ligands, respectively, and the peaks at 178.5, 174.8, 74.0 and 43.7 ppm were attributed to those of the free citrate ligands. It is noted that the intensities of the free citrate resonances increased with pH, whereas the intensities of those peaks belonging to the coordinated titanium citrate complexes decreased gradually. One of the most striking results is that the ^{13}C NMR spectrum of the 1:3 Ti:citrate solution at a pH value of 7.0 is different from that of the titanium citrate complex $Na_8[Ti(cit)_3]\cdot 17H_2O$ isolated at the corresponding pH value [27], which is attributed to the free citrate ligand. Despite there being two sets of ^{13}C NMR peaks, the peaks at 181.9, 179.1, 75.3 and 46.2 ppm were assigned to the carbons resonances of free citrate, while the peaks at 187.4 and 84.0 ppm were likely attributed to the α-carboxy and α-alkoxy of the bound citrate ligand, respectively. However, the downshift of 8.7 ppm for the α-alkoxy group was less than those in the related titanium citrate complexes. There was not a consistency between the ^{13}C NMR spectra of the 1:3 Ti:citrate solution recorded at pH < 7.0 and those at pH $\geqslant 7.0$. It is probable that the coordinated modes of the citrate ligand with the Ti(IV) ion change when the pH value is higher than 7.0.

4. Biological relevance

Titanium is an essential component of prosthetics used in surgical rectification of human skeletal aberrations or dental fillings [30]. Simultaneously, a series of complexes containing titanium have been used in cancer treatment [43]. Therefore, titanium in one form or another may come in contact with biological fluids such as citric acid. Consequently, it elicits interactions from biological fluids (such as citrate). In so doing, the solubility and bioavailability of the titanium in the relevant fluids are essential for developing these requisite chemistries. The aqueous chemistry of the binary titanium–citrate system shown here has revealed a number of discrete species, all of them reflecting the

solubilization of titanium in the presence of physiological substrate citric acid. Furthermore, in view of the pH-dependent transformations of the titanium citrate complexes in aqueous solutions, it would be reasonable to envision that a pH-dependent chemistry on titanium species with physiological ligands (such as citrate) promotes formation of soluble bioavailable species, which are capable of eliciting interactions from extracellular and intracellular targets. To this end, variable biochemical processes could be influenced. The clearly defined chemical properties of the four mononuclear titanium citrate species reported here constitute a distinct case of species likely to participate in the aqueous speciation of titanium(IV) in the citrate.

The previous works reported titanium citrate can deliver titanium to serum protein transferring in the physiological pH value [16,18,20]. However, titanium nitrilotriacetate does not deliver Ti(IV) to apoprotein. This fact is ascribed to the higher stability of titanium(IV) nitrilotriacetate compared to titanium(IV) citrate [20]. The ^{13}C NMR spectra of the four titanium citrates isolated here and the 1:3 Ti:citrate solutions at different pH suggested the stability of titanium(IV) citrate complexes in aqueous solution decrease with the increase pH value, regardless of the existence of titanium citrate species in solution. In neutral solution, the titanium citrate complex decomposes completely. It probably demonstrates that titanium citrate, as the titanium source, may react easily with apotransferrin in physiological pH value. The structural and spectroscopic characterization of the titanium citrate complexes and the solution behavior of the titanium citrate binary system in different pH values offer a new perspective in pursuit of probing other systems encompassing physiological ligands and metal ions.

5. Conclusions

In summary, the isolated titanium(IV)–citrate complexes $Na_3[Ti(H_2cit)_2(Hcit)]\cdot 9H_2O$ (**1**), $K_4[Ti(H_2cit)(Hcit)_2]\cdot 4H_2O$ (**2**) $K_5[Ti(Hcit)_3]\cdot 4H_2O$ (**3**) and $Na_7[TiH(cit)_3]\cdot 18H_2O$ (**4**) show a similar tricitrato titanium core in different protonated forms, which is not much influenced by the pH values and couterions in the complexes. The aqueous solution ^{13}C NMR spectra of 1:3 Ti:citrate demonstrated the coordination of citrate ligand with Ti(IV) ion is consistent with the titanium citrate complexes isolated when the pH value is lower than 7.0. The dissociation of the citrate ligand increases with the rise in pH values, while the ratios of the bound citrate complexes decrease gradually. The synthetic efforts targeting Ti(IV)–citrate complexes from aqueous solutions have contributed to delineating the nature of a number of such species arising in the course of pH-dependent reactions.

Acknowledgements

We thank the National Science Foundation of China (20571061 and 20423002), and the Ministry of Science and Technology of China (2005CB221408 and 2001CB108906) and the Key Scientific Project of Fujian Province (2005HZ01-3) for the generous support of this research.

Appendix A. Supporting information

CCDC Nos. 289836–289839 contain the supplementary crystallographic data for **1**–**4**. These data can be obtained free of charge via http://www.ccdc.cam.ac.uk/conts/retrieving.html, or from the Cambridge Crystallographic Data Centre, 12 Union Road, Cambridge CB2 1EZ, UK; fax: +44 1223 336 033; or e-mail: deposit@ccdc.cam.ac.uk. Supplementary data associated with this article can be found, in the online version, at doi:10.1016/j.poly. 2006.08.017.

References

[1] (a) J.P. Glusker, Acc. Chem. Res. 13 (1980) 345;
(b) S.B. Etcheverry, M.C. Apella, E.J. Baran, J. Inorg. Biochem. 20 (1984) 269.
[2] S.J. Lippard, J.M. Berg, Principles of Bioinorganic Chemistry, University Science Books, Mil Vallery, CA, 1994, pp. 352–354 (Chapter 12).
[3] J.J.R. Fraústo da Silva, R.J.P. Williams, The Biological Chemistry of the Elements: the Inorganic Chemistry of Life, Oxford University Press, Oxford, 2001.
[4] J. Liang, M. Madden, V.K. Shah, R.H. Burris, Biochemistry 29 (1989) 8577.
[5] S.M. Mayer, C.A. Gormal, B.E. Smith, D.M. Lawson, J. Biol. Chem. 277 (2002) 35263.
[6] M. Kaliva, E. Kyriakakis, A. Salifoglou, Inorg. Chem. 41 (2002) 7015.
[7] Y. Yuan, X. Li, J. Sun, K. Ding, J. Am. Chem. Soc. 124 (2002) 14866.
[8] V. Biehl, T. Wack, S. Winter, U.T. Seyfert, J. Breme, Biomol. Eng. 19 (2002) 97.
[9] D. Bardos, in: D.E. Altobelli, J.D. Gresser, E.R. Schwartz, D.J. Trantolo, D.L. Wise, M.J. Yaszemski (Eds.), Titanium and Zirconium Alloys in Orthopedic Applications, Encyclopedic Handbook of Biomaterials and Bioengineering, Marcel Dekker, New York, 1995, pp. 509–548.
[10] C. Knabe, F. Klar, R. Filtzner, R.J. Radlanski, U. Gross, Biomaterials 23 (2002) 3235.
[11] (a) M.P. Pechini, US Pat. No 3231328, 1966;
(b) M.P. Pechini, US Pat. No 3330697, 1967.
[12] (a) C.D. Chandler, C. Roger, M.J. Hampden-Smith, Chem. Rev. 93 (1993) 1205;
(b) B.L. Cushing, V.L. Kolesnichenko, C.J. O'Connor, Chem. Rev. 104 (2004) 3893.
[13] (a) M. Kakihana, M. Arima, Y. Nakamara, Chem. Matter. 11 (1999) 438;
(b) M. Kakihana, M. Yoshimura, Bull. Chem. Soc. Jpn. 72 (1999) 1427;
(c) J.H. Choy, Y.S. Han, J. Mater. Chem. 7 (1997) 1815;
(d) J.D. Tsay, T.T. Fang, J. Am. Ceram. Soc. 82 (1999) 1409.
[14] C.W. Correns, in: K.H. Wedepohl (Ed.), Handbook of Geochemistry, vol. 2, Springer, Berlin, 1969–1978.
[15] R. Strietzel, A. Hosch, H. kalbfleisch, D. Buch, Biomaterials 19 (1998) 1495.
[16] H.Z. Sun, H.Y. Li, R.A. Weir, P.J. Sadler, Angew. Chem., Int. Ed. Engl. 37 (1998) 1577.
[17] M.L. Guo, H.Z. Sun, H.J. McArdle, L. Gambling, P.J. Sadler, Biochemistry 39 (2000) 10023.

[18] A.D. Tinoco, A.M. Valentine, J. Am. Chem. Soc. 127 (2005) 11218.
[19] O. Aguilera, L.M. Quiros, J.F. Fierro, FEBS Lett. 548 (2003) 5.
[20] L. Messori, P. Orioli, V. Banholzer, I. Pais, P. Zatta, FEBS Lett. 442 (1999) 157.
[21] M. Suwalsky, F. Villena, B. Norris, M.A. Soto, C.P. Sotomayor, L. Messori, P. Zatta, J. Inorg. Biochem. 99 (2005) 764.
[22] (a) M. Hruby, P. Cigler, S. Kuzel, J. Plant Nutr. 25 (2002) 577;
(b) S. Kuzel, M. Hruby, P. Cigler, P. Tlustos, P.N. Van, Biol. Trace Elem. Res. 91 (2003) 179;
(c) X.D. Tang, L. Liu, M.L. Huang, Chin. Pat. No 1052302A, 1994.
[23] (a) K.B. Musgrave, H.C. Angove, B.K. Burgess, B. Hedman, K.O. Hodgson, J. Am. Chem. Soc. 120 (1998) 5325;
(b) A.C. Nyborg, J.A. Erickson, J.L. Johnson, A. Gunn, S.M. Truscott, G.D. Watt, J. Inorg. Biochem. 78 (2000) 371;
(c) R. Uppal, C.D. Incarvito, K.V. Lakshmi, A.M. Valentine, Inorg. Chem. 45 (2006) 1795.
[24] Z.H. Zhou, Y.F. Deng, Y.Q. Jiang, H.L. Wan, S.W. Ng, J. Chem. Soc., Dalton Trans. (2003) 2636.
[25] Z.H. Zhou, Y.F. Deng, H.L. Wan, Inorg. Chem. 43 (2004) 6266.
[26] E.T. Kefalas, P. Panagiotidis, C.P. Raptopoulou, A. Terzis, T. Mavromoustakos, A. Salifoglou, Inorg. Chem. 44 (2005) 2596.
[27] J.M. Collins, R. Uppal, C.D. Incarvito, A.M. Valentine, Inorg. Chem. 44 (2005) 3431.
[28] T. Kemmitt, N.I. Al-Salim, G.J. Gainsford, A. Bubendorfer, M. Waterland, Inorg. Chem. 43 (2004) 6300.
[29] (a) M. Kakihana, M. Tada, M. Shiro, V. Petrykin, M. Osda, Y. Nakamura, Inorg. Chem. 40 (2001) 891;
(b) Y.F. Deng, Z.H. Zhou, H.L. Wan, K.R. Tsai, Inorg. Chem. Commun. 7 (2004) 169.
[30] M. Dakanali, E.T. Kefalas, C.P. Raptopoulou, A. Terzis, G. Voyiatzis, I. Kyrikou, T. Mavromoustakos, A. Salifoglou, Inorg. Chem. 42 (2003) 4632.
[31] J. Paradies, J. Crudass, F. MacKay, L.J. Yellowlees, J. Montgomery, S. Parsons, L. Oswald, N. Robertson, P.J. Sadler, J. Inorg. Biochem. 100 (2006) 1260.
[32] SADABS, University of Göttingen, Göttingen, Germany, 1997.
[33] G.M. Sheldrick, SHELXS-97: Structure Solving Program, University of Göttingen, Göttingen, Germany, 1997.
[34] G.M. Sheldrick, SCHELXL-97: Program for Refinement of Crystal Structure, University of Göttingen, Göttingen, Germany, 1997.
[35] P. O'Brien, H. Salacinski, M. Motevalli, J. Am. Chem. Soc. 119 (1997) 12695.
[36] (a) M. Matzapetakis, N. Karligiano, A. Bino, M. Dakanali, C.P. Raptopoulou, V. Tangoulis, A. Terzis, J. Gapintzakis, A. Salifoglou, Inorg. Chem. 39 (2000) 4044;
(b) M. Matzapetakis, M. Dakanali, C.P. Raptopoulou, V. Tanglouis, A. Terzis, N. Moon, J. Giapintzakis, A. Salifoglou, J. Biol. Inorg. Chem. 5 (2000) 469;
(c) Z.H. Zhou, Y.J. Lin, H.B. Zhang, G.D. Lin, K.R. Tsai, J. Coord. Chem. 42 (1997) 131.
[37] (a) M. Matzapetakis, C.P. Raptopoulou, A. Tsohos, V. Papaefthymiou, N. Moon, A. Salifoglou, J. Am. Chem. Soc. 120 (1998) 13266;
(b) M. Matzapetakis, C.P. Raptopoulou, A. Terzis, A. Lakatos, T. Kiss, A. Salifoglou, Inorg. Chem. 38 (1999) 618.
[38] (a) Z.H. Zhou, W.B. Yan, H.L. Wan, K.R. Tsai, J.Z. Wang, S.Z. Hu, J. Chem. Crystallorgr. 25 (1995) 807;
(b) D.W. Wright, P.A. Humiston, H. Orme-Johnson, W.M. Davis, Inorg. Chem. 34 (1995) 4194;
(c) M. Tsaramysrsi, D. Kavousanak, C.P. Raptopoulou, A. Terzis, A. Salifoglou, Inorg. Chim. Acta 320 (2001) 47.
[39] (a) Z.H. Zhou, H. Zhang, Y.Q. Jiang, D.H. Lin, H.L. Wan, K.R. Tsai, Transition Met. Chem. 24 (1999) 605;
(b) M. Kaliva, T. Giannadaki, A. Salifoglou, C.P. Raptopoulou, A. Terzis, Inorg. Chem. 41 (2002) 3850.
[40] (a) Z.H. Zhou, H.L. Wan, S.Z. Hu, K.R. Tsai, Inorg. Chim. Acta 237 (1995) 193;
(b) M. Kaliva, C.P. Raptopoulou, A. Terzis, A. Salifoglou, J. Inorg. Biochem. 93 (2003) 161.
[41] G.E. Bacon, R.J. Jude, Z. Kristallogr., Kristallgeom. Kristallphys. Kristallchem. 19 (1973) 19.
[42] M. Kakihana, K. Tomita, V. Petrykin, M. Tada, S. Sasaki, Y. Nakamura, Inorg. Chem. 43 (2004) 4546.
[43] E. Meléndez, Crit. Rev. Oncol./Hematol. 42 (2002) 309.

which are normally stable planar chelates, $[M(L)_2]X_2$ [8]. Recently, dach and daco have been alkylated with ethylene sulfide to give a derivative with pendant arms, and then coordinated to the metal [9]. However, the related cyclic diamines have not been studied extensively for mixed chelate complex systems.

In this work, we have obtained new mixed complexes with the medach ligand and some kinds of β-diketonates (dike), Ni(medach)(dike)X, and have determined their crystal structures and the equilibrium constants between a square-planar structure and an octahedral one with coordinated strong donor solvent molecules [10].

2. Experimental

2.1. Materials and instrumentation

Nickel(II) nitrate hexahydrate, nickel(II) sulfate hexahydrate, *N*-methyl-1,4-diazacycloheptane (medach), acetylacetone (Hacac), benzoylacetone (Hbzac), dibenzoylmethane (Hdibm), anhydrous sodium carbonate, sodium tetraphenylborate and *N*,*N*,*N*′,*N*′-tetramethylethylenediamine were purchased from Wako Chemical Co. Ltd. and used without further purification. As the solvents used for spectral measurements 1,2-dichloroethane (DCE), dimethylsulfoxide (DMSO), acetone (ACO) and nitromethane (NM) were used without further purification, all of the solvents were of guaranteed grade for spectral measurements.

Elemental analyses were performed on a Perkin–Elmer 2400 II CHN analyzer. Infrared spectra (400–4000 cm^{-1}) were measured with a Perkin–Elmer FT-IR SPECTRUM 2000 using KBr disks. Electronic spectra of the complexes in solution were observed with Shimadzu UV-3100PC UV–VIS Scanning Spectrophotometer using 10 mm quartz cells and concentrations between 1.0×10^{-3} and 5.0×10^{-3} mol dm^{-3}, except where mentioned differently in the text. Magnetic susceptibility measurements were performed by the Faraday method with a Shimadzu Torsion Magnetometer MB-100 at room temperature. Electric conductances of the solutions were measured with a Conductivity Outfit Model AOC-10 (Denki-Kagaku-Keiki Co. Ltd.) at 25 ± 0.2 °C.

2.2. Syntheses of chelates

2.2.1. Chelates of the nitrate, [Ni(medach)(dike)NO_3]

To an ethanol solution of $Ni(NO_3)_2 \cdot 6H_2O$ (5 mmol in 30 cm^3 of ethanol), a mixture of the appropriate β-diketone (5 mmol) and anhydrous sodium carbonate (2.5 mmol) was added. The ligand, medach (5 mmol in 10 cm^3 of ethanol) was added dropwise to the metal-solution with vigorous stirring. After the reaction was complete, the green solution was filtered and concentrated using a rotary evaporator. The crude crystals obtained were recrystallized from DCE to yield bluish-green crystals. Yield: 70–85%.

Ni(medach)(bzac)NO_3 (**1a**). *Anal*. Calc. for $C_{16}H_{23}N_3O_5Ni$: C, 48.52; H, 5.85; N, 10.61. Found: C, 48.54; H, 5.88; N, 10.62%. μ_{eff}: 3.12 B.M.

Ni(medach)(dibm)NO_3 (**2a**). *Anal*. Calc. for $C_{21}H_{25}N_3O_5Ni$: C, 54.92; H, 5.46; N, 9.14. Found: C, 55.06; H, 5.50; N, 9.17%. μ_{eff}: 3.02 B.M.

2.2.2. Chelates of the tetraphenylborate, [Ni(medach)(dike)]BPh_4

The crude nitrate compounds (1 mmol) were dissolved in DCE, and sodium tetraphenylborate (1.5 mmol) was added with stirring and then filtered. During the procedure, the color of the solution changed from green to reddish-orange. The crude crystals obtained were recrystallized from DCE to yield orange crystals. They were all diamagnetic. Yield: 70–85%.

Ni(medach)(bzac)BPh_4 (**1b**). *Anal*. Calc. for $C_{40}H_{43}N_2O_2BNi$: C, 72.14; H, 6.63; N, 4.33. Found: C, 73.54; H, 6.63; N, 4.29%.

Ni(medach)(dibm)BPh_4 (**2b**). *Anal*. Calc. for $C_{45}H_{45}N_2O_2Ni$: C, 75.51; H, 6.55; N, 3.96. Found: C, 75.55; H, 6.34; N, 3.92%.

2.2.3. Chelates of the ternary bis-diketonate, [Ni(medach)$(dike)_2$]

$NiSO_4 \cdot 6H_2O$ was dissolved in a small amount of water and a chloroform solution containing an equimolar amount of medach and two molar amounts of Hdike was added to it in a separatory funnel. Then sodium carbonate was added to the mixture with shaking. After standing for a minute, the chloroform layer was separated from the aqueous solution and evaporated. The crude crystals obtained were recrystallized from DCE to yield bluish-green crystals. Yield: 70–85%.

Ni(medach)$(bzac)_2$ (**1c**). *Anal*. Calc. for $C_{26}H_{32}N_2O_4Ni$: C, 63.03; H, 6.51; N, 5.66. Found: C, 62.68; H, 6.66; N, 5.63%. μ_{eff} for **1c** · DCE: 2.66 B.M.

Ni(medach)$(dibm)_2$ (**2c**). *Anal*. Calc. for $C_{36}H_{36}N_2O_4Ni$: C, 69.81; H, 5.86; N, 4.52. Found: C, 69.72; H, 5.89; N, 4.39%. μ_{eff}: 3.20 B.M.

2.3. Equilibrium constants

The equilibrium constants (log β) defined by Eq. (1) have been determined by a spectrophotometric method (calculation by a least-square method using the data sets from the electronic spectra at constant temperature, 25 ± 0.2 °C). All spectral data, as a function of the total concentrations of the reactants, were computer-fitted to the appropriate equation, depending on the model to be tested. As a result, the equilibrium constants for each species (log β) and the molar extinction coefficients (ε_{calc}) for each species in the solution were calculated. The number of points used for the calculation of equilibrium constants was 12 from each data set, which were picked up at every 10 nm wavelength in the range of 530–420 nm.

$$[Ni(diam)(dike)]^+ + 2S \xrightarrow{\beta} [Ni(diam)(dike)S_2]^+$$
$$\beta = [Ni(diam)(dike)S_2]^+ / [Ni(diam)(dike)]^+[S]^2 \quad (1)$$

The solvent ligand (S = DMSO) was added to a DCE solution of the respective complex, [Ni(diam)(dike)]BPh_4.

2.4. X-ray crystallography

The measurements for complex **3a** were made on a DIP2030K automated diffractometer with graphite-monochromatic Mo Kα radiation ($\lambda = 0.71073$ Å) at 298 K. The measurements for complexes **1a**, **2a**, **1b**, **3b**, and **2c** were made on a MXC03K automated diffractometer with graphite-monochromatic Mo Kα radiation ($\lambda = 0.71073$ Å) at 298 K. The unit cell parameters were determined by the least square method using 22 well-centered reflections for all the complexes. The reflections were corrected for Lorentz and Polarization effects but not for absorption. Every structure was solved by the direct method SIR92 [11], and was refined by full matrix least-square techniques SHELXS-97 [12]. All non-hydrogen atoms were refined with anisotropic thermal parameters. Hydrogen atoms were included in calculated positions and refined with isotropic thermal parameters. Crystallographic data and refinement parameters are detailed in Table 1.

3. Results and discussion

3.1. Synthesis and structure of the complexes, Ni(medach)(dike)X

We obtained eight mixed ligand complexes of the general formula Ni(medach)(dike)X (X = NO_3^-, BPh_4^- or dike), which are classified into three types: i.e., type **a** = nitrate complexes, type **b** = tetraphenylborate complexes and type **c** = ternary bis-diketonate complexes, and the numbers of the complexes, **1**, **2** and **3**, mean benzoylacetonate, dibenzoylmethanate and acetylacetonate, respectively. Magnetic data of these complexes at room temperature are listed in the experimental section, which show the tetraphenylborate complexes are diamagnetic, and the nitrate and bis-dike complexes have values of nearly 3.0 B.M. These data mean that: (a) the Ni(II) coordination geometry in the tetraphenylborate complexes is square-planar with a N2O2 donor set (type **b**), and (b) those of the nitrate complexes (type **a**) and the ternary bis-dike complexes (type **c**) are octahedral with a N2O4 donor set.

Among these complexes we obtained six good single crystals for X-ray diffraction analysis, complexes **1a**, **2a**, **3a**, **1b**, **3b** and **2c**, whose crystal structures have been determined. For two acac-complexes, **3a** and **3c**, which were previously reported [10], the structures are clarified in this work. The ORTEP plots of complexes **1a**, **1b** and **2c** as examples are depicted in Figs. 1–3, with the atom numbering scheme. Selected bond distances and angles are given in Table 2.

3.1.1. Structure of [Ni(medach)(bzac)NO_3] (*1a*, type *a*)

Complex **1a** crystallizes in the monoclinic space group $P2_1/c$. The nickel atom is coordinated to give an octahedral geometry with two N atoms of the bidentate medach ligand, two O atoms of the bidentate bzac ligand and

Table 1
Crystallographic data

	1a	**2a** · DCE	**3a**	**1b**	**3b** · ACO	**2c**
Empirical formula	$C_{16}H_{23}N_3O_5Ni$	$C_{23}H_{29}N_3O_5NiCl_2$	$C_{11}H_{21}N_3O_5Ni$	$C_{40}H_{43}BN_2O_2Ni$	$C_{38}H_{47}BN_2O_3Ni$	$C_{36}H_{36}N_2O_4Ni$
Formula weight	396.09	557.12	334.02	653.32	649.30	619.40
Crystal dimensions	0.50 × 0.30 × 0.25	0.40 × 0.35 × 0.30	0.35 × 0.25 × 025	0.35 × 0.30 × 0.20	0.35 × 0.30 × 0.20	0.40 × 0.25 × 0.20
Crystal system	monoclinic	triclinic	monoclinic	monoclinic	triclinic	monoclinic
Space group	$P2_1/c$	$P\bar{1}$	$P2_1/c$	$P2_1/c$	$P\bar{1}$	$C2/c$
T (K)	298	298	298	298	298	298
a (Å)	11.026(4)	8.230(4)	13.1740(10)	17.953(7)	9.712(3)	22.920(10)
b (Å)	13.818(5)	11.940(10)	15.3210(10)	10.790(3)	13.411(4)	8.876(5)
c (Å)	14.865(9)	13.54(2)	7.7830(10)	18.666(4)	13.50(2)	18.160(10)
α (°)	90	92.00(10)	90	90	94.23(5)	90
β (°)	127.66(6)	105.71(5)	106.894(3)	109.61(2)	91.37(5)	119.37(5)
γ (°)	90	95.97(5)	90	90	95.31(2)	90
V (Å^3)	1793.0(15)	1271.(2)	1503.1(2)	3406.(2)	1745.(2)	3219.(3)
Z	4	2	4	4	2	4
D_c (Mg m^{-3})	1.467	1.456	1.476	1.274	1.125	1.278
λ (Å)	0.71073	0.71073	0.71073	0.71073	0.71073	0.71073
μ (mm^{-3})	1.11	1.01	1.31	0.61	0.59	0.64
Reflections collected	4475	6090	3344	8501	7699	3932
Independent reflections	3858	5839	3166	8241	7402	2816
Reflections used	3741 ($I > 2\sigma$)	4919 ($I > 3\sigma$)	3043 ($I > 2\sigma$)	5366 ($I > 3\sigma$)	4657 ($I > 3\sigma$)	2256 ($I > 2\sigma$)
R[a]	0.0529	0.070	0.0468	0.064	0.055	0.0901
R_w[b]	0.1559	0.135	0.1349	0.085	0.074	0.2437
S (fit on F)	1.028	1.349	1.038	1.644	1.337	1.097

[a] $R = \sum \| |F_o| - |F_c| \| / \sum |F_o|$.
[b] $R = [(\sum_w (\| |F_o| - |F_c| \|)^2 / \sum |F_o|^2)^{1/2}$.

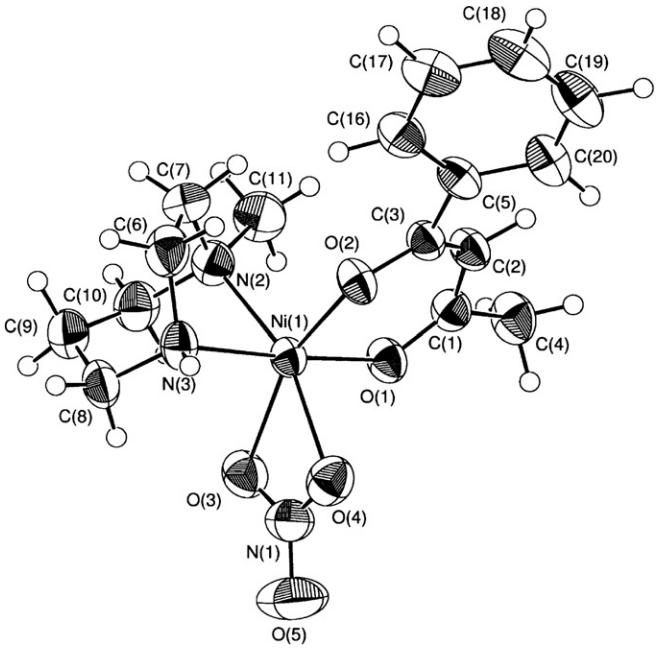


Fig. 1. ORTEP diagram of the complex [Ni(medach)(bzac)NO_3] (**1a**). Thermal ellipsoids are at 50% probability.

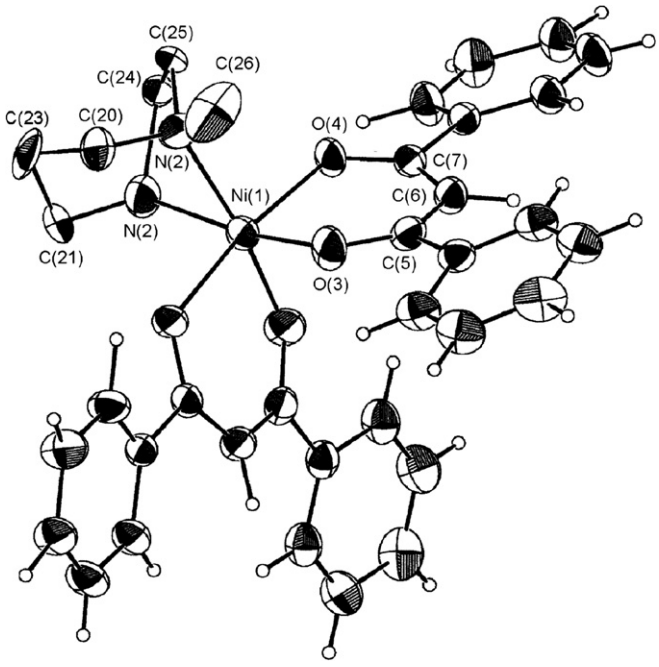


Fig. 3. ORTEP diagram of the complex [Ni(medach)$(dibm)_2$] (**2c**). Thermal ellipsoids are at 50% probability.

two O atoms of the bidentate NO_3 ligand as shown in Fig. 1. The angles O(1)–Ni(1)–N(3), O(2)–Ni(1)–O(3), O(4)–Ni(1)–N(2), O(1)–Ni(1)–O(2), O(3)–Ni(1)–O(4), and N(3)–Ni(1)–N(2) are 173.97°, 158.68°, 160.11°, 91.00°, 59.92° and 76.60°, respectively. The bite angle of the NO_3 ligand to the metal center is too narrow and the bond lengths of Ni(1)–O(3) 2.167 Å and Ni(1)–O(4) 2.173 Å are rather longer than those of the Ni–O(bzac) (Ni(1)–O(1) = 2.009, Ni(1)–O(2) = 2.003 Å). The structural strain of the ligand NO_3 affects the easy dissociation of the NO_3 ligand from the coordination sphere in acceptor or strong donor solvents. Another structural interest is that the axial bonds Ni(1)–O(2) and Ni(1)–O(3) are repelled by the cyclic medach ligand, which means that the angle O(2)–Ni(1)–O(3) 158.68° is smaller than the other equatorial *trans*-bonds. This interligand repulsion between medach and the axial donor atoms (NO_3) may reflect the another reason for the weakened coordination ability of the NO_3 ligand. The structures of **2a** and **3a** show also similar structural properties as explained in this case of **1a**.

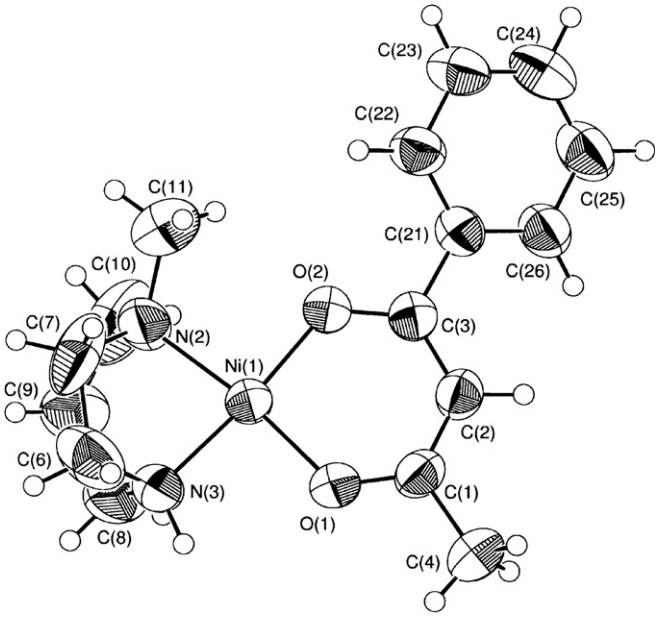


Fig. 2. ORTEP diagram of the complex $[Ni(medach)(bzac)]^+$ (**1b**). Thermal ellipsoids are at 50% probability.

3.1.2. Structure of [Ni(medach)(bzac)]BPh_4 (*1b*, type *b*)

Complex **1b** crystallizes in the monoclinic space group $P2_1/c$. As shown in Fig. 2, the nickel atom is coordinated with medach and bzac to give a square-planar geometry and the uncoordinating anion BPh_4^-. The N2O2 donor set from medach and bzac and the central Ni atom are located on the same plane. If we compare these metal–ligand bond distances and their bite angles with those of

Table 2
Selected bond lengths (Å) and angles (°) for complexes **1a**, **1b** and **2c**

	1a	**1b**		**2c**
Ni(1)–O(1)	2.009(3)	1.819(3)	Ni(1)–O(3)	2.01(14)
Ni(1)–O(2)	2.003(3)	1.831(3)	Ni(1)–O(4)	2.05(14)
Ni(1)–N(2)	2.093(4)	1.936(4)	Ni(1)–N(2)	2.14(14)
Ni(1)–N(3)	2.093(3)	1.887(4)		
Ni(1)–O(3)	2.167(3)			
Ni(1)–O(4)	2.173(3)			
O(1)–Ni(1)–O(2)	91.00(11)	95.80(14)	O(3)–Ni(1)–O(4)	88.(6)
N(2)–Ni(1)–N(3)	76.60(14)	81.3(2)	N(2)–Ni(1)–N′(2)	76.(5)

the corresponding octahedral nitrate complex **1a**, this planar complex has shorter bond lengths Ni–O(bzac) 1.819 and 1.831 Å and Ni–N(medach) 1.936 and 1.887 Å and wider bite angles O(1)–Ni(1)–O(2) 95.80 and N(2)–Ni(1)–N(3) 81.3° than those of the octahedral complex. In this planar complex, the tertiary N-donor of medach coordinates more weakly to the metal center than the secondary N–M bond. The chelate angle of medach in this square-planar mixed complex is almost the same as the angle in the bis-dach square-planar homoleptic complex, $[Ni(dach)_2]Cl_2 \cdot 2H_2O$ 82.2° [13]. It means that the chelate angle of the cyclic dach ligand was determined by the rigid conformation of the ligand and the same metal-ligand bond length. The crystal structure of **3b** show also same geometry as **1b**.

3.1.3. Structure of $[Ni(medach)(dibm)_2]$ (**2c**, type ***c***)

Complex **2c** crystallizes in the monoclinic space group $C2/c$. As shown in Fig. 3, the nickel atom is coordinated to give an octahedral geometry with two N atoms of the bidentate medach ligand and four O-donor atoms from two bidentate dibm ligands, forming the non-charged complex. The medach ligand in the structure is disordered and the structural data is not so well refined. The characteristic properties of this type of complex in the solid state shows the plasticity of the non-charged weak intermolecular interaction in the case of ternary bis-hexafluoroacetylacetonate (hfac), $[M(tmen)(hfac)_2]$ [14]. Due to the very weak intermolecular interaction in this crystal, the diamine (medach) moiety of the complex can easily move position at the temperature for this X-ray crystal determination. Therefore, we could not determine the position of medach ligand with certain accuracy. For the complex **1c**, a good single crystal for X-ray analysis could not be obtained.

3.2. Solvatochromic behavior with the structure change of the complexes in solution

3.2.1. Electric conductivity data of the chelates in various solvents

Table 3 gives the electrical conductivity data at room temperature for the complexes in some organic solvents with different donor numbers (DN) and acceptor numbers (AN) [15]. The standard values of 1:1 electrolytes in the respective solvents are shown in the same table [16]. It can be seen from the table that the ionization of NO_3^- from the complexes in NM is about 10%, which indicates partial dissociation into the NO_3^- anion and the cationic planar complex, $[Ni(medach)(dike)]^+$. In DCE or ACO, the nitrate complexes show almost non-electrolytic behavior, which means that the species in solution is the same as that of the solid state. On the other hand, in a very strong donor solvent like DMSO, the conductivity data show that the nitrate complexes are almost 1:1 electrolytes. Consequently the nitrate complexes are strongly influenced by the respective (donor and acceptor) properties of the solvents for coordination and dissociation of the NO_3^- ion. These data support the following section on spectral chromotropic behaviors (Scheme 1).

Table 3
Molar conductivity ($ohm^{-1}\,cm^2\,mol^{-1}$ at 25 ± 0.2 °C)

	DCE	NM	DMSO	ACO
Ni(medach)(bzac)NO_3 (**1a**)	0.13	7.65	23.43	2.13
Ni(medach)(dibm)NO_3 (**2a**)	0.07	7.55	22.91	1.54
Ni(medach)(acac)NO_3 (**3a**)	0.13	9.26	24.41	1.49
Ni(medach)(azac)BPh_4 (**1b**)	11.91	42.10	11.49	6.31
Ni(medach)(dibm)BPh_4 (**2b**)	11.04	44.08	12.96	7.18
Ni(medach)(acac)BPh_4 (**3b**)	12.95	36.45	10.69	3.89
Ni(medach)$(dibm)_2$ (**2c**)	0.072	2.66	0.96	0.003
1:1 Electrolytes [16]	10–24	75–95	35	100–140

3.2.2. The nitrate complexes $[Ni(medach)(dike)NO_3]$ (type ***a***)

Fig. 4 shows the typical electronic absorption spectra of the nitrate complex **1a** in various organic solvents. These spectra were measured at room temperature in DCE, NM, ACO and DMSO. In Table 4, all of the spectral data for the complexes in these solvents are summarized.

The spectra in DCE and ACO have nearly the same pattern, showing two bands corresponding to the similar spectral pattern of octahedral complexes (Eq. (2)). The anomaly of the spectra is their intensity, which means that the intensity of the first band, at ca. $10 \times 10^3\ cm^{-1}$, is nearly half of that of the second band, $16.5 \times 10^3\ cm^{-1}$. It is probably due to the existence of the bidentate nitrate ion, i.e., the deformation from a regular octahedral structure and the smaller four membered chelate ring of the NO_3 ligand. On the other hand, in the case of DMSO although the spectra also show octahedral bands, the spectral profile is different from that in DCE, especially the intensity profile is drastically changed. The electric conductivity data mentioned above also support that the complexes in DCE or ACO are non-charged octahedral with the coordination of NO_3, while those in DMSO are 1:1 electrolytes and octahedral with the coordination of the solvent molecules (Eq. (3)). In NM, with intermediate acceptor and poor donor properties, the nitrate ion is partially dissociated from the octahedral complex and gives square-planar spectra (Eq. (4)), which shows a new solvatochromism.

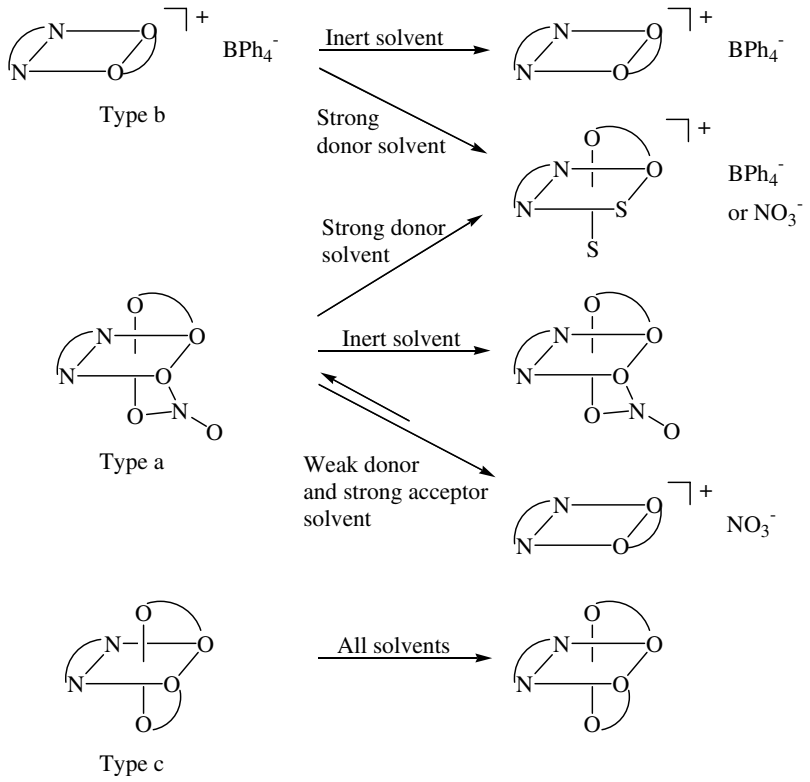
$$[Ni(medach)(dike)(NO_3)] \rightarrow [Ni(medach)(dike)(NO_3)] \quad (2)$$

$$[Ni(medach)(dike)(NO_3)] + 2DMSO \rightarrow [Ni(medach)(dike)(DMSO)_2]^+ + NO_3^- \quad (3)$$

$$[Ni(medach)(dike)(NO_3)] \rightarrow [Ni(medach)(dike)]^+ + NO_3^- \quad (4)$$

3.2.3. The tetraphenylborate complexes $[Ni(medach)(dike)]BPh_4$ (type ***b***)

Fig. 5 shows the typical electronic absorption spectra of the tetraphenylborate complex **1b** in various organic solvents. These spectra were measured at room temperature in DCE, NM, ACO and DMSO. In Table 4, all of the



Scheme 1. Solid structure and solvatochromic behaviors of the complexes in solution.

spectral data for the complexes in these solvents are summarized. In non-coordinated solvents like DCE or NM, the spectra are similar to those of the square-planar species reported earlier [17]. Also in an intermediate coordinating solvent like ACO, they are dissolved as predominantly square-planar species. This is critically different from similar complexes with linear chain diamines, such as tmen, in which the complexes exist as an equilibrium mixture of the square-planar and octahedral species (Eq. (5)). This is a characteristic property of the cyclic diamine. In a strong donor solvent like DMSO, the spectra indicate that the only species in solution is octahedral (Eq. (6)).

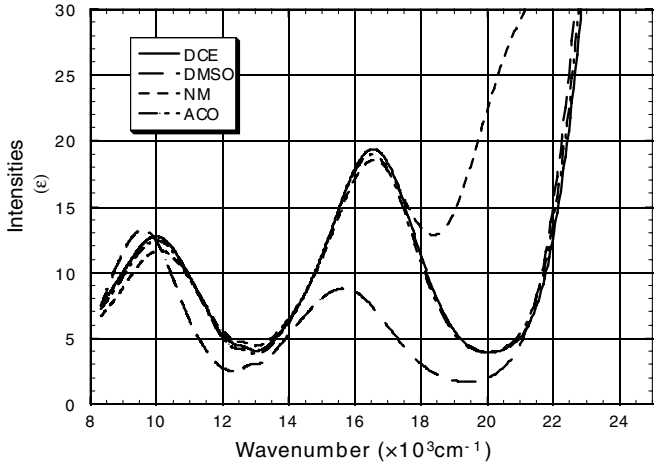


Fig. 4. UV–Vis absorption spectra of [Ni(medach)(bzac)NO_3] (**1a**).

$$2[Ni(medach)(dike)]BPh_4 + 2S \rightarrow [Ni(medach)(dike)(S)_2]^+ + [Ni(medach)(dike)]^+ + 2BPh_4^- \quad (5)$$

$$[Ni(medach)(dike)]BPh_4 + 2DMSO \rightarrow [Ni(medach)(dike)(DMSO)_2]^+ + 2BPh_4^- \quad (6)$$

3.2.4. The ternary bis-diketonato complexes, *[Ni(medach)(dike)$_2$] (type **c**)*

In any kind of solvent, these ternary bis-dike complexes do not show any solvatochromism, which means the spectra in all of the solvents used are similar and any solvent coordination could not be observed.

It is noteworthy that the chelates are very soluble in various organic solvents with high concentrations, which means that there are weak intermolecular interactions in the crystal. As already known for the structure of Ni(acac)$_2$, the chelate is rather insoluble in organic solvents and it is not mononuclear but the trinuclear [Ni_3(acac)$_6$] [18], in which each nickel(II) center is octahedral (other kinds of diketonate chelates also show similar structures). The homoleptic trinuclear, [Ni_3(dike)$_6$] is dissociated into the heteroleptic mononuclear, [Ni(medach)(dike)$_2$], by the addition of the diamine (medach) (Eq. (7)).

$$[Ni_3(dike)_6] + 3medach \rightarrow 3[Ni(medach)(dike)_2] \quad (7)$$

The resultant mononuclear mixed chelates, with very bulky substituent groups on each diamine and diketonate, show very high solubility in various organic solvents, which

Table 4
Wave numbers ($V_{max}/\times10^3$ cm^{-1}) and molar absorption coefficient ($\varepsilon_{max}/\times10^3$ mol^{-1} dm^3 cm^{-1}) of the d–d transition band (at 25 °C)

	DCE	NM	DMSO	ACO
Ni(medach)(acac)NO_3	9.98(12.64) 16.56(18.86)	10.01(10.90) 16.57(16.10) 21.28(21.03)	9.57(12.89) 15.61(7.75)	9.98(12.26) 16.50(17.72)
Ni(medach)(bzac)NO_3	10.00(12.74) 16.57(19.35)	10.10(11.66) 16.58(18.52)	9.60(13.23) 15.63(8.78)	10.05(12.43) 16.52(18.95)
Ni(medach)(dibm)NO_3	10.04(12.71) 16.57(19.83)	10.09(11.54) 16.63(18.05)	9.63(13.37) 15.75(9.59)	10.02(12.21) 16.53(18.61)
Ni(medach)(bzac)BPh_4	21.10(151.7)	21.14(127.9)	9.56(11.15) 15.58(6.33)	21.14(123.9)
Ni(medach)(bzac)BPh_4	21.21(211.0)	21.28(211.7)	9.60(13.18) 15.63(8.26)	21.23(187.2)
Ni(medach)(dibm)BPh_4	21.12(164.4)	21.19(169.6)	9.56(14.13) 15.64(7.94)	21.14(162.1)
Ni(medach)$(dibm)_2$	9.72(15.17) 16.45(18.15)	9.77(14.58) 16.37(16.87)	9.72(14.30) 16.35(17.34)	9.70(14.14) 16.42(17.89)

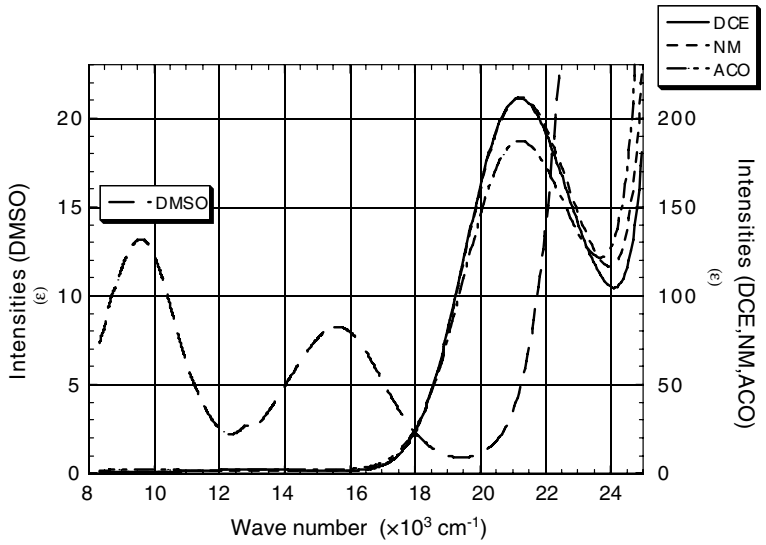


Fig. 5. UV–Vis absorption spectra of [Ni(medach)(bzac)]BPh_4 (**1b**). The left axis is for DMSO solution and the right axis is for DCE, NM and ACO solutions.

means the mixed chelates have hydrophobic properties and weak intermolecular interactions.

3.3. Equilibrium constants

Fig. 6 shows an example of the spectra obtained in the course of the titration procedure of [Ni(medach)(bzac)]-BPh_4 in DCE solution. The absorption maximum of the square-planar species decreases on addition of donor solvent, DMSO, and the absorption band of the octahedral species in the region between 570 and 600 nm increases. A titration procedure can be used to evaluate formation constants. Equilibrium constants ($\log\beta$) according to the reaction are given in Table 5.

The d–d band positions and the corresponding molar absorption coefficients are shifted by a change in the substituents at the diamine ligand. On the other hand, an increase in equilibrium constants of these complexes can be seen with increasing electron-withdrawing and decreasing electron-releasing effects of the substituent group on the β-diketonate ligand; dibm > bzac > acac.

The medach complexes prefer the square-planar geometry to the octahedral geometry. The steric hindrance to axial coordination at the N-donor atoms appears to be much smaller for tmen complexes than the corresponding medach complexes.

4. Conclusion

We have obtained six new mixed chelate complexes with the ligand bzac or dibm as a β-diketonate, medach and three kinds of monoanion, nitrate, tetraphenylborate or

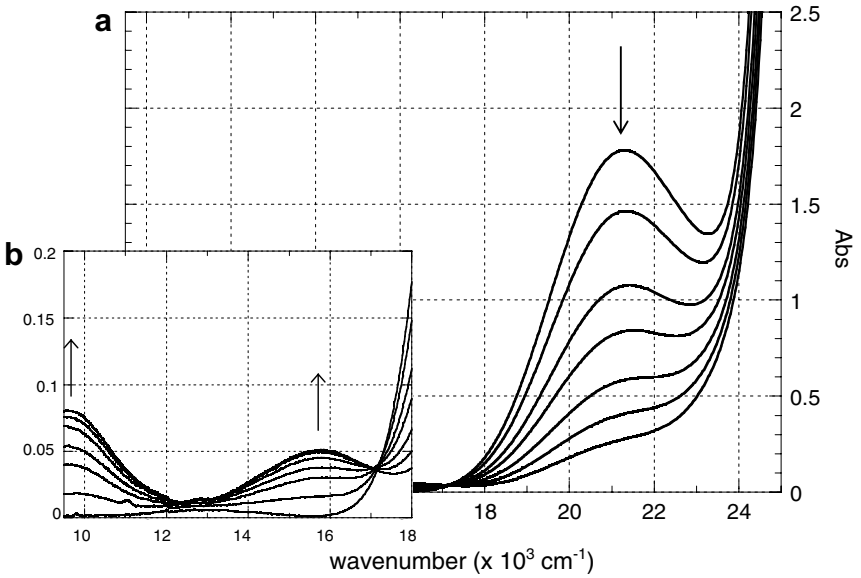


Fig. 6. Spectral changes of [Ni(medach)(bzac)]BPh_4 (**1b**) with the addition of DMSO ligand: (a) square-planar spectral decrease and (b) octahedral spectral increase. The initial concentration of the complex in DCE solution was 8.0×10^{-3} mol dm^{-3} (initial amount of solution: 20 ml) and the light path was 1 cm. The solution was titrated with DMSO–DCE solution (8.0×10^{-1} mol dm^{-3}). Ratios of DMSO/complex are 0, 0.25, 0.50, 0.70, 1.00, 1.35 and 1.85 ((a) spectral curves from top to bottom; (b) those from bottom to top, respectively).

Table 5
Stability constants (log β) (mol^{-1} dm^3)

dike	[Ni(medach)(dike)]BPh_4	[Ni(tmen)(dike)]BPh_4
acac	2.32 ± 0.01	4.50 ± 0.01
bzac	3.04 ± 0.01	5.20 ± 0.02
dibm	3.13 ± 0.02	5.31 ± 0.01

one more β-diketonate, and have determined their crystal structures. These complexes are classified as three categories, type **a** (octahedral with a bidentate nitrate coordination), type **b** (square-planar with tetraphenylborate as a counter anion) and type **c** (octahedral with two β-diketonate ligands). Type **a** complexes show solvatochromic behavior due to the change of acceptor property of the solvents. Type **b** complexes show another type of solvatochromism due to the change of donor properties of the solvents. Type **c** complexes are inert stable octahedral complexes without any chromotropic behavior in various solvents. The medach ligand in the mixed chelate [Ni(dike)(medach)]$^+$ has a much stronger influence on the axial coordination of the donor solvents, which means that the series of the medach mixed ligand system exist as the more stable square-planar structure in comparison to the complexes of the linear *N*-alkylated diamines, such as the tmen analogue.

Acknowledgements

Prof. Hiroshi Miyamae of Josai University in Tokyo is acknowledged for his advice on crystal structure determination. The authors are grateful to Prof. Frank S. Howell of Sophia University in Tokyo for his scientific discussion and also for revising the English of this manuscript.

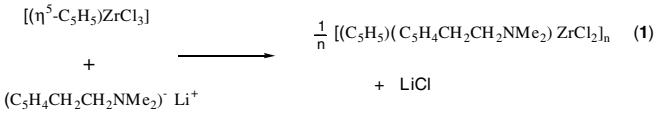
Appendix A. Supplementary material

CCDC 208117, 212342, 207923, 212341, 208119, and 208118 contain the supplementary crystallographic data for **1a**, **2a**, **3a**, **1b**, **3b**, and **2c**. These data can be obtained free of charge via http://www.ccdc.cam.ac.uk/conts/retrieving.html, or from the Cambridge Crystallographic Data Centre, 12 Union Road, Cambridge CB2 1EZ, UK; fax: (+44) 1223-336-033; or e-mail: deposit@ccdc.cam.ac.uk. Supplementary data associated with this article can be found, in the online version, at doi:10.1016/j.poly.2006.11.003.

References

[1] (a) H. Sigel, Metal Ions in Biological Systems, Mix-Ligand Complexes, vol. 2, Marcel Dekker, Basel, 1973;
(b) H. Sigel, Metal Ions in Biological Systems, Properties of Copper, vol. 12, Marcel Dekker, Basel, 1981;
(c) H. Sigel, Metal Ions in Biological Systems, Nickel and Its Role in Biology, vol. 23, Marcel Dekker, Basel, 1988.
[2] (a) S.F. Pavkovic, D.W. Meek, Inorg. Chem. 4 (1965) 20;
(b) D.W. Meek, S.A. Ehrhardt, Inorg. Chem. 4 (1965) 584.
[3] (a) G.A. L'Heureux, A.E. Martell, I. Inorg. Nucl. Chem. 28 (1966) 481;
(b) G.F. Condike, A.E. Martell, J. Inorg. Nucl. Chem. 31 (1969) 2455;
(c) A. Paulovicova, U. El-Ayaan, Y. Fukuda, Inorg. Chim. Acta 321 (2001) 56.
[4] Y. Fukuda, K. Sone, J. Inorg. Nucl. Chem. 34 (1972) 2315.
[5] (a) K. Sone, Y. Fukuda, Inorganic Thermochromism, Inorganic Chemistry Concept, vol. 10, Springer, Heidelberg, 1987;
(b) U. El-Ayaan, F. Murata, Y. Fukuda, Monath. Chem. 132 (2001) 1279;
(c) W. Linert, Y. Fukuda, A. Camard, Coord. Chem. Rev. 218 (2001) 113.
[6] G.A. Melson, Coordination Chemistry of Macrocyclic Compounds, Plenum Press, New York, 1979.

[7] (a) P.J. Hedra, D.B. Powell, J. Chem. Soc. (1960) 5105;
(b) F.G. Mann, H.R. Watson, J. Chem. Soc. (1958) 2772;
(c) N. Iwasaki, K. Sone, Y. Fukuda, Z. Anorg. Allg. Chem. 412 (1975) 170.
[8] (a) J.I. Legg, D.O. Nelson, D.L. Smith, M.L. Larson, J. Am. Chem. Soc. 90 (1968) 5030;
(b) D.O. Nelson, M.L. Larson, R.D. Willett, J.I. Legg, J. Am. Chem. Soc. 93 (1971) 5079;
(c) M. Micheloni, P. Paoletti, S. Burlci, T.A. Kaden, Helv. Chim. Acta 65 (1982) 587;
(d) W.K. Musker, Coord. Chem. Rev. 117 (1992) 133;
(e) N. Hoshino, Y. Fukuda, K. Sone, K. Tanaka, F. Marum, Bull. Chem. Soc. Jpn. 62 (1989) 1822.
[9] (a) Y. Fukuda, K. Yamagata, T.A. Kaden, Bull. Chem. Soc. Jpn. 60 (1987) 3569;
(b) R.D. Hancock, M.P. Ngwenya, A. Evers, W. Wade, J.C.A. Boeyens, S.M. Dobson, Inorg. Chem. 29 (1990) 264;
(c) M. Du, Y. Guo, S. Chen, X. Bu, J. Mol. Struct. 641 (2002) 29;
(d) M.S. Ali, K.H. Whitmire, T. Tyomasu, Z.H. Siddik, A.R. Khokhar, J. Inorg. Biochem. 77 (1999) 231;
(e) J.J. Smee, M.L. Miller, C.A. Grapperhaus, J.H. Reibenspies, M.Y. Darensburg, Inorg. Chem. 40 (2001) 3601;
(f) X. Bu, M. Du, L. Shang, R. Zhang, M. Shionoya, J. Chem. Soc., Dalton Trans. (2001) 729.
[10] Y. Fukuda, Y. Akutagawa, Y. Ihara, K. Sone, Synth. React. Inorg. Met.-Org. Chem. 21 (1991) 313.
[11] A. Atomare, G. Cascarano, C. Giacovazzo, A. Guagliardi, M.C. Burla, G. Polidori, M. Camalli, J. Appl. Crystallogr. 27 (1994) 435.
[12] G.M. Sheldeick, SHELXS97, Program for the Refinement of Crystal Structures, Univ. of Geottingen, Germany, 1997.
[13] M.S. Hussan, Inorg. Chim. Acta 69 (1983) 227.
[14] (a) T. Yoshida, M. Oguni, Y. Mori, Y. Fukuda, Solid State Commun. 93 (1995) 159;
(b) T.M. Yoshida, K. Wada, M. Oguni, T. Chiba, Y. Fukuda, J. Phys. Chem. Solids 60 (1999) 1787.
[15] (a) V. Gutmann, The Donor–Acceptor Approach to Molecular Interactions, Plenum Press, New York, London, 1978;
(b) C. Reichardt, Chem Rev. 94 (1994) 2319;
(c) V. Gutmann, Coord. Chem. Rev. 2 (1967) 239.
[16] W.J. Geary, Coord. Chem. Rev. 7 (1971) 81.
[17] Y. Fukuda, C. Fujita, H. Miyamae, H. Nakagawa, K. Sone, Bull. Chem. Soc. Jpn. 62 (1989) 745.
[18] G.J. Bullen, Nature 189 (1961) 291.



Scheme 1.

The polymerization reaction of monomeric **1** is relatively slow. The deposition of polymeric **1** from a dilute solution takes place after several hours at ambient temperature. Unlike $[Cp_2ZrCl_2]$, **1** is extremely sensitive towards moisture. In contact with atmospheric air **1** turns to a brown slurry in about 10 s.

The examination of a solution of **1** in C_5D_5N by ^1H and ^{13}C NMR indicates some amount (≈20%) of $CpZrCl_3$. The ^1H NMR spectrum displays in the range 3.5–0 ppm strong singlets at 2.54 ppm (broad) and 2.32 ppm, together with three singlets of medium intensity (2.83, 2.51 and 2.18 ppm) and some weak signals. The solution indicates only a very small amount of THF. It seems rather difficult to distinguish between the presence or lack of $Me_2N \rightarrow Zr$ coordination because this solution displays signals which can be attributed to either NMe_2 groups which coordinate to the zirconium centre or to NMe_2 groups which do not coordinate. For compounds which indicate $N \rightarrow Zr$ coordination in the solid state, the NMe_2 resonances are observed near 2.6 ppm, e.g. for $[(C_5H_4CH_2CH_2NMe_2)TiCl_3]$ $\delta(NCH_3) = 2.69$ ppm [3], for $[(C_5H_4CH_2CH_2NMe_2)ZrCl_3 \cdot THF]$ $\delta(NCH_3) = 2.60$ ppm [4] and for $[Cp(C_5H_4CH_2CH_2NMe_2)TiCl_2]$ $\delta(NCH_3) = 2.71$ ppm [8] (no structural data available). For $[(C_5H_4CH_2CH_2NMe_2)Ti(NMe_2)_3]$ without $NMe_2 \rightarrow Ti$ coordination $\delta(NCH_3) = 2.15$ ppm [4] and for $(C_5H_4CH_2CH_2NMe_2)Tl$ $\delta(NCH_3) = 2.21$ ppm [10]. Weak signals in the ^1H NMR spectrum of **1** can be probably be attributed to the $-CH_2CH_2NHMe_2^+$ group, but surely not to $C_5H_4CH_2CH_2NMe_2$. The ^{13}C NMR spectrum of **1** displays sharp singlets in the range for C_5H_5 rings, but the resonances of $CH_2CH_2N(CH_3)_2$ are in the form of broad multiplets which suggests a dynamic equilibrium of oligomeric species in solution.

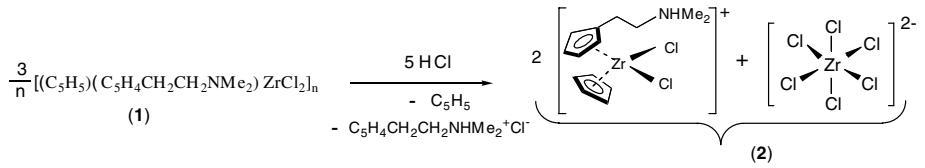
Compound **1** reacts with a methanolic HCl solution (Scheme 2). We have used a solution of monomeric or/and oligomeric **1** in THF for this purpose. Under the applied conditions (1.35 equivalents of HCl) we have isolated pale yellow-green crystals of $[(\eta^5\text{-}C_5H_5)(\eta^5\text{-}C_5H_4CH_2CH_2NHMe_2)ZrCl_2]_2[ZrCl_6]$ (**2**). Recrystallization from CH_3CN solution yields crystals of X-ray quality with the minor formation of a deep green insoluble species. The formation of compound **2** indicates that HCl in polar solvents is able to split off not only $C_5H_4CH_2CH_2NMe_2$ but also the C_5H_5 ligand from $CpZrCl_3$, with the formation of the $[ZrCl_6]^{2-}$ anion. The formation of $C_5H_5CH_2CH_2N^iPr_2 \cdot HCl$ on hydrolysis of polymeric $[(C_5H_4CH_2CH_2N^iPr_2)_2ZrCl_2]_n$ was reported previously [5]. A protonolysis of one Cp group from Cp_2ZrCl_2 was found to be rapid in aqueous KNO_3 solution [11]. Similarly, the splitting of only one Cp group and the formation of tri- or dinuclear OH bridged zirconium complexes were reported in the reaction of Cp_2ZrCl_2 with sodium benzoate in H_2O solution [12], in the reaction of Cp_2ZrCl_2 with nitric acid in $CHCl_3$ solution [13] and in the reaction of Cp_2ZrCl_2 with a THF solution of AgX ($X = CF_3SO_3^-$ or ClO_4^-) followed by subsequent treatment of the reaction solution with water [14].

^1H and ^{13}C NMR spectra of **2** are in agreement with the X-ray structure of this compound. The NMR signals were assigned to **2** according to the literature data for $[(\eta^5\text{-}C_5H_5)(\eta^5\text{-}C_5H_4CH_2CH_2NMe_2)TiCl_2 \cdot HCl]$ [4].

2.2. X-ray crystallographic studies and discussion

The molecular structure of $[(\eta^5\text{-}C_5H_5)(\eta^5\text{-}C_5H_4CH_2CH_2NHMe_2)ZrCl_2]_2[ZrCl_6]$ (**2**) is shown in Fig. 1. Compound **2** crystallizes in the monoclinic space group $P2_1/n$. Its cation is essentially a zirconium chloride sandwich complex which is protonated on the nitrogen atom and occupies a general position in the crystal. The Zirconium Zr2 atom from the $ZrCl_6^{2-}$ anion sits on the symmetry centre at the Wyckoff position *d*. The ions are kept together by additional hydrogen bonds of the $^+N\text{–}H\cdots Cl^-$ type which are both charge-assisted and bifurcated (one donor and two acceptors) at the same time – see Fig. 2.

The surroundings of the Zr1 atom display a distorted pseudotetrahedral geometry. Distances Zr1–Cl1 243.13(12) pm and Zr1–Cl2 244.49(13) pm are typical for pseudotetrahedrally coordinated Zr (IV). For Cp_2ZrCl_2 the related distances are 244.4 and 245.0 pm, and the angle Cl1–Zr1–Cl2 of 95.98(5)° for **2** is similar to the corresponding angle in Cp_2ZrCl_2 (97.04°) [15–17]. The distances to the Cp-plane rings Zr1–Cp^N(C6–C10) of 221.08 pm and Zr1–Cp(C1–C5) of 220.30 pm are similar and in the same range as in Cp_2ZrCl_2 (219.5 and 219.2 pm) [15–17]. Thus, the tethered $CH_2CH_2NHMe_2$ group exerts only minor impact on the geometry of the related zirconocene dichloride skeleton.



Scheme 2.

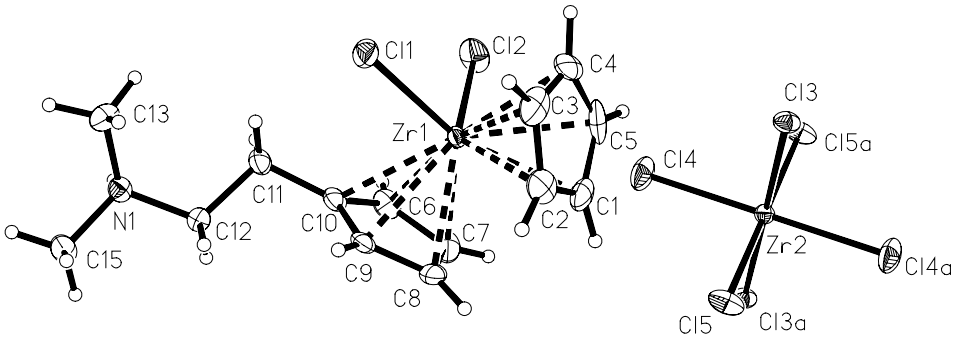


Fig. 1. Molecular structure of $\{2[Cp(Me_2NHC_2H_4C_5H_4)ZrCl_2]^+, ZrCl_6^{2-}\}$, **1**. One cation and one anion are shown. Displacement ellipsoids 50%, symmetry code *a*: $-x+1, -y, -z+2$.

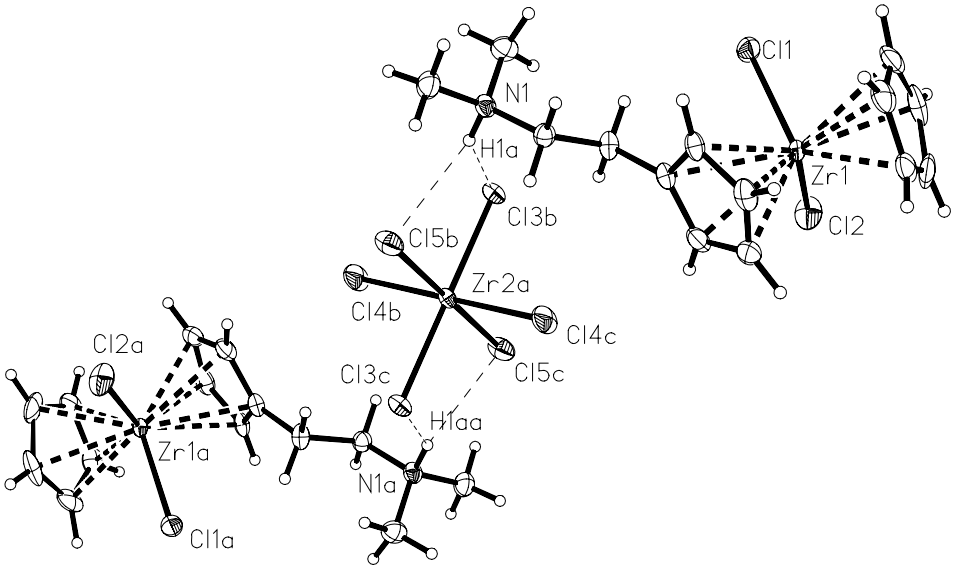


Fig. 2. Hydrogen bonds in the system. N1–H1a 93.0 pm, H1a–Cl3 259.8 pm, H1a–Cl5 259.5 pm, N1–H1a–Cl3 139.97°, N1–H1a–Cl5 135.48°, displacement ellipsoids 50%.

3. Experimental

All manipulations were performed in flame-dried Schlenk type glassware on a vacuum line. THF and toluene were dried over Na/benzophenone and distilled under nitrogen. Pentane was dried over Na/benzophenone/diglyme and distilled under nitrogen. Acetonitrile was distilled under nitrogen over CaH_2 and renewed over P_4O_{10}. ^1H and ^{13}C NMR spectra were recorded on a Varian 500 MHz spectrometer at ambient temperature. $[(\eta^5\text{-}C_5H_5)ZrCl_3]$ [18] and $C_5H_5CH_2CH_2NMe_2$ [19] were prepared by reported methods.

3.1. Synthesis of $(C_5H_4CH_2CH_2NMe_2)Li$

A solution of $C_5H_4CH_2CH_2NMe_2$ (0.48 g, 3.5 mmol) in THF (15 ml) was treated with 1.6 M hexane solution of BuLi (2.2 ml, 3.5 mmol) at 0 °C. The mixture was allowed to warm to room temperature.

3.2. Synthesis of $[(C_5H_5)(C_5H_4CH_2CH_2NMe_2)ZrCl_2]_n$ (*1*)

A solution of $(C_5H_4CH_2CH_2NMe_2)Li$ in THF (3.5 mmol in ≈17.5 ml) was added at −40 °C to solution of $[CpZrCl_3 \cdot DME]$ (1.23 g, 3.5 mmol) in THF (50 ml). The mixture was allowed to warm to room temperature and stirred for 1 day. The colour of the solution turned yellow, then orange and finally brown. After 10 h a brown precipitate was deposited, then filtrated and the solution was evaporated under vacuum (0.001 Torr) for 6 h, yield 0.609 g (48%).

1 ^1H NMR (500 MHz, C_5D_5N, ambient temp.) δ, ppm: several signals were observed in the range 2.1–3.5: 2.83, 2.54 (broad or overlapped), 2.51, 2.32, 2.18; 6.49 (m*, 2.8 Hz, C_5H_4); 6.53 (m*, 2.8 Hz, C_5H_4); 6.58 (s, C_5H_5 of **1**); 6.62 (s, C_5H_5 of $CpZrCl_3$); The weak signals (not listed) might be attributed to the $-CH_2CH_2NHMe_2^+$ group. $^{13}C\{^1H\}$ NMR (89.9 MHz, C_5D_5N, ambient temp.) δ,

ppm: 25.5–28.0 (3 b. m., CpCH_2); 43.0–44.8 (4 b. m., NH(CH_3)$_2$); 57.8–59.8 (3 b. m., NCH_2); 114.32 (s, C_5H_4); 116.34 (s, C_5H_4); 117.20 (s, C_5H_5 of **1**); 118.08 (s, C_5H_5 of $CpZrCl_3$).

We observed several additional weak signals in the range 109.2–120.2 ppm (m* – AA′XX′ pattern, pseudotriplet 2.8 Hz).

We were not able to perform elemental analysis on **1** because of its extreme sensitivity towards atmospheric moisture.

$C_5H_4CH_2CH_2NMe_2$ ^{1}H NMR (500 MHz, C_5D_5N, ambient temp.) δ, ppm: 2.20, s, (CH_3)$_2$N; 2.22, s, (CH_3)$_2$N; 2.44, m; 2.51, m; 2.59, m; 2.93, s; 5.90–6.57 (multiplets).

3.3. Synthesis of $[(\eta^5\text{-}C_5H_5)(\eta^5\text{-}C_5H_4CH_2CH_2NHMe_2)\text{-}ZrCl_2]_2[ZrCl_6]$ (2)

The solution of monomeric or/and oligomeric **1** was prepared according to 3.1 and 3.2 using 0.267 g (1.95 mmol) $C_5H_4CH_2CH_2NMe_2$, 1.2 ml of 1.6 M BuLi solution in hexane (1.95 mmol) and 0.688 g (1.95 mmol) [$CpZrCl_3 \cdot$ DME]. The final solution of **1** was stirred for 2 h at ambient temperature and 15 ml of 0.18 M HCl solution in methanol (2.7 mmol) were dropped in. The brown colour turned rapidly to pale yellow-green. After ca. 1 h the solution was concentrated under vacuum and kept for four days at about +4 °C. 0.419 g of pale yellow-green solid deposited. The precipitate was dissolved in acetonitrile, filtered and the solution was partially evaporated under vacuum and kept at +4 °C. The pale yellow-green crystals of **2** deposited together with a small amount of a deep green oily contamination, insoluble in CH_3CN.

2 ^{1}H NMR (500 MHz, CD_3CN, ambient temp.) δ, ppm: 2.774 {d, 4.9 Hz, (CH_3)$_2$NH}; 3.13 (m, CpCH_2); 3.23 (m, NCH_2); 6.38 (m*, C_5H_4); 6.51 (m*, C_5H_4); 6.56 (s, C_5H_5); ^{13}C{^{1}H} NMR (89.9 MHz, CD_3CN, ambient temp.) δ, ppm: 25.57 CpCH_2; 35.25 weak signal (?); 43.31 NH(CH_3)$_2$; 57.76 NCH_2; 114.52 C_5H_4; 117.37 C_5H_4; 118.30 C_5H_5; 129.94 C_5H_4(*ypso*) (m* – AA′XX′ pattern, pseudotriplet 3.0 Hz).

Elemental analysis (**2**): C, 32.8; H, 3.99, $C_{28}H_{40}Cl_{10}N_2Zr_3$ calc. C, 32.56; H, 3.90%.

3.4. X-ray diffraction structural studies

The structure has been solved by direct methods and refined with the SHELX-97 software package. All non-hydrogen atoms have been refined in anisotropic approximation. H atoms attached to C atoms were positioned geometrically and refined as riding, with methyl C–H = 0.98 Å, methylene C–H 0.99 Å, aromatic C–H = 0.95 Å and $U_{iso}(H) = 1.2\ U_{eq}(C)$ in all cases. The maximum differential electron-density peak is located 0.63 Å from the Zr1 atom and the deepest hole 1.39 Å from the same atom.

Acknowledgements

J.P. and R.G. thank the Polish State Committee of Scientific Research (Project No. 3 T09A 14 628) for financial support.

Appendix A. Supplementary material

CCDC 616901 contains the supplementary crystallographic data for this paper. These data can be obtained free of charge via http://www.ccdc.cam.ac.uk/conts/retrieving.html, or from the Cambridge Crystallographic Data Centre, 12 Union Road, Cambridge CB2 1EZ, UK; fax: (+44) 1223-336-033; or e-mail: deposit@ccdc.cam.ac.uk. Supplementary data associated with this article can be found, in the online version, at doi:10.1016/j.poly.2006.11.007.

References

[1] C. Müller, D. Vos, P. Jutzi, J. Organomet. Chem. 600 (2000) 127.
[2] P. Jutzi, T. Redeker, B. Neumann, H-G. Stammler, J. Organomet. Chem. 533 (1997) 237.
[3] J.C. Flores, J.C.W. Chien, M.D. Rausch, Organometallics 13 (1994) 4140.
[4] P. Jutzi, J. Kleinmeier, J. Organomet. Chem. 486 (1995) 287.
[5] P. Jutzi, T. Redeker, B. Neumann, H-G. Stammler, Organometallics 15 (1996) 4153.
[6] Sai. Nami, Onozawa, Toshiya, Itakura, Toshiyasu, Tanaka, Masato. Jpn. Kokai Tokkyo Koho (1998) Appl. JP 97-230902 19970827, Priority: JP 96-227988 19960829.
[7] Y.L. Qian, R.W. Guo, J.L. Huang, K. Jonas, Chin. Chem. Lett. 7 (1996) 1139.
[8] P.B. Hitchcock, G.J. Leigh, M. Togrou, J. Organomet. Chem. 669 (2003) 101.
[9] P. Jutzi, U. Siemeling, J. Organomet. Chem. 500 (1995) 175.
[10] J. Dahlhaus, M. Bangel, P. Jutzi, J. Organomet. Chem. 474 (1994) 55.
[11] J.M. Toney, T.J. Marks, J. Am. Chem. Soc. 107 (1985) 947.
[12] U. Thewalt, K. Döppert, W. Lasser, J. Organomet. Chem. 308 (1986) 303.
[13] W. Lasser, U. Thewalt, J. Organomet. Chem. 275 (1984) 63.
[14] W. Lasser, U. Thewalt, J. Organomet. Chem. 311 (1986) 69.
[15] K. Prout, T.S. Cameron, R.A. Forder, S.E. Critchley, B. Denton, G.V. Rees, Acta. Cryst. B 30 (1974) 2290.
[16] Recent redeterminations: at room temp. J.Y. Corey, Xiao-Hong Zhu, L. Brammer, N.P. Rath, Acta Cryst. C 51 (1995) 565.
[17] At 193 K: T. Repo, M. Klinga, L. Mutikainen, Y. Su, M. Leskela, M. Polamo, Acta Chem. Scand. 50 (1996) 1116.
[18] E.C. Lund, T. Livinghouse, Organometallics 9 (1990) 2426.
[19] T.F. Wang, T.Y. Lee, J. Organomet. Chem. 423 (1992) 31.

ligands to give a deformed octahedral surrounding. In addition to the structural, electrochemical and spectral study, the interaction of the complexes with the circular and linear forms of p-Bluescript DNA has been reported. The three tested complexes reduce the fluorescence intensity of both circular and linear DNA, but the nature of these interactions remains unknown.

Aoki et al. prepared and studied the zinc supramolecular complex $[(Zn_3L)_4(ttc)_4](NO_3)_{12} \cdot 22H_2O$ (L = 1,3,5-tris-(1,4,7,10-tetraazacyclododecan-1-ylmethyl)benzene), where the ttc anion links three Zn-cyclen moieties through Zn–S coordination bonds [19]. The complex forms a twisted cub-octahedral exterior in which various hydrophobic guest molecules, such as adamantine, can be encapsulated. In another work of this group, zinc supramolecules have been reported with other spacers connecting the cyclene derivatives [20]. In the presented X-ray structure of $[(Zn_3L_1)_3(ttc)_3](NO_3)_9 \cdot 21.5H_2O$, ($L_1$ = tris-cyclen), there are two kinds of ttc bonding i.e. by S atoms only and a tris bidentate chelating mode. In work published by our group we prepared and solved the molecular structure of the complex [Zn(bapen)(ttcH)] · EtOH (bapen = *N*,*N*′-bis(3-amino propyl)ethylenediamine) [21]. The compound is mononuclear only and the zinc atom is coordinated by four N atoms of bapen and by the chelating S, N set of the ttcH dianion.

Many other complexes containing trithiocyanurate anions have been prepared and structurally studied. These complexes can be mononuclear as well as polynuclear, with a chelating S, N donor set or bound by S or N atoms only [22–27]. In our previous works we prepared and structurally characterized a series of nickel(II) and iron(II) complexes containing the trithiocyanurate anion and nitrogen-donor ligands [28–30].

Herein, we present the results of the synthesis and characterization of a series of mixed-ligand complexes involving trithiocyanuric acid and nitrogen-donor ligands of the following composition: [Zn(pmdien)(ttcH)] (**1**), [Zn(taa)-(ttcH)] · H_2O (**2**), $[Fe(nphen)_2(ttcH)] \cdot H_2O$ (**3**), $[Fe(dmbpy)_3](ttcH_2)_2 \cdot 4H_2O$ (**4**), $[Mn(phen)_2(ttcH)] \cdot H_2O$ (**5**), Mn(bpy)(ttcH) · H_2O (**6**), [Ni(taa)(ttcH)] · H_2O (**7**) and $[Ni(phen)_3](ttcH) \cdot 5H_2O$ (**8**), where pmdien = *N*,*N*,*N*′,*N*″,*N*″-pentamethyldiethylenetriamine, $ttcH_3$ = trithiocyanuric acid, taa = tris(2-aminoethyl)amine, nphen = 5-nitro-1,10-phenanthroline, dmbpy = 4,4′-dimethyl-2,2′-bipyridine, phen = 1,10-phenanthroline and bpy = 2,2′-bipyridine. Compounds **3**, [30] **7** [31] and **8** [32] were prepared before by our group and in that work they were tested for biological activity. According to what we know, manganese complexes with a combination of N ligands and the trithiocyanurate anion are reported for the first time. We were also interested in finding out if the newly prepared complexes show any biological activity. In vitro cytotoxic activity of the complexes against G-361 (human malignant melanoma), HOS (human osteogenic sarcoma), K-562 (human chronic myelogenous leukaemia) and MCF-7 (human breast adenocarcinoma) cancer cell lines was determined. Antimicrobial activity was tested on *Escherichia coli* 3954, 3988, 4225, *Pseudomonas aeruginosa* 3955, *Staphylococcus aureus* 3953, 4223 and *Enterococcus faecalis* 4224.

2. Experimental

2.1. Materials and methods

The chemicals and solvents were purchased from Aldrich Co. and Lachema Co. and were used without further purification. The complexes $[Fe(nphen)_2(ttcH)] \cdot H_2O$ (**3**), [Ni(taa)(ttcH)] · H_2O (**7**) and $[Ni(phen)_3](ttcH) \cdot 5H_2O$ (**8**) were prepared according to the literature methods [30–32].

The C, H, N, S analyses were carried out on an EA 1108 instrument (FISONS). IR spectra (400–4000 cm^{-1}) were recorded on a Perkin–Elmer Spectrum One FT-IR spectrometer using KBr pellets. The absorption spectra in MeCN and the diffuse-reflectance spectra in nujol (11 000–40 000 cm^{-1}) were obtained on a Lambda 35 UV/Vis spectrometer (Perkin–Elmer). Magnetochemical data were obtained by the Faraday method at 293 K using a Sartorius M-25D electrobalance. $Hg[Co(SCN)_4]$ was used as a calibrant. The correction for diamagnetism was calculated using Pascal's constants. The transmission Mössbauer spectrum was recorded using a Mössbauer spectrometer in constant acceleration mode with a $^{57}Co(Rh)$ source. Isomer shift parameters are related to metallic iron (with a calibration temperature of 300 K).

2.2. Preparation of the complexes

2.2.1. [Zn(pmdien)(ttcH)] (1)

N,*N*,*N*′,*N*″,*N*″-pentamethyldiethylenetriamine (pmdien) (0.2 ml, 1 mmol) was added to an aqueous solution (70 ml) of $Zn(NO_3)_2 \cdot 6H_2O$ (0.3 g, 1 mmol). The mixture was stirred at room temperature for 30 min. A solution of $ttcNa_3 \cdot 9H_2O$ (0.14 g, 0.33 mmol) in water (5 ml) was added in the form of drops. The formation of a white precipitate was observed. The pH of the solution was adjusted to 8 by addition of aqueous NaOH and the rest of the precipitate was removed by filtration. After a week light yellow crystals were separated by filtration, washed with water and dried under an infrared lamp at 40 °C. Yield: 72%. *Anal.* Calc.: C, 34.8; H, 5.8; N, 20.3; S, 23.2. Found: C, 34.8; H, 6.0; N, 20.5; S, 23.7%. IR (cm^{-1}): 456w, 488m, 750w, 776m, 798m, 857s, 906w, 933m, 984m, 1022m, 1043w, 1120w, 1175m, 1215s, 1243m, 1264w, 1432vs, 1631m, 2897w, 2970w, 3436s.

2.2.2. [Zn(taa)(ttcH)] · H_2O (2)

Tris(2-aminoethyl)amine (taa) (0.15 ml, 1 mmol) was added to an EtOH solution (80 ml) of zinc(II) acetate dihydrate (0.22 g, 1 mmol). The mixture was stirred at room temperature for 30 min. A solution of $ttcNa_3 \cdot 9H_2O$ (0.14 g, 0.33 mmol) in water (5 ml) was added in the form of drops. The white precipitate that formed was dissolved

by addition of aqueous NaOH (resulting pH 11). Light yellow crystals suitable for X-ray analysis were obtained after a week. They were filtered, washed with a small amount of EtOH and dried in air. Yield: 67%. *Anal.* Calc.: C, 26.7; H, 5.2; N, 24.2; S, 23.8. Found: C, 26.9; H, 4.9; N, 24.1; S, 23.0%. IR (cm^{-1}): 422w, 469m, 545w, 632w, 650m, 742m, 781w, 858s, 872s, 978s, 994w, 1072s, 1124m, 1194vs, 1248m, 1283w, 1329s, 1360w, 1435vs, 1489vs, 1576m, 2852w, 2932w, 3297m, 3411m.

2.2.3. $[Fe(dmbpy)_3](ttcH_2)_2 \cdot 4H_2O$ (**4**)

4,4′-Dimethyl-2,2′-bipyridine (dmbpy) (0.36 g, 2 mmol) in EtOH (50 ml) was added with stirring to an aqueous solution (50 ml) of $(NH_4)_2Fe(SO_4)_2 \cdot 6H_2O$ (0.39 g, 1 mmol). The mixture was heated at 60 °C for 45 min. After cooling, a small amount of precipitate was filtered off. Then, $ttcNa_3 \cdot 9H_2O$ (0.4 g, 1 mmol) in water (10 ml) was added dropwise to the solution. A dark red substance, which appeared during addition of the solution of $ttcNa_3$, was filtered off, washed with EtOH and dried under an infrared lamp at 40 °C. Yield: 54%. *Anal.* Calc.: C, 48.8; H, 4.7; N, 16.3; S, 18.6. Found: C, 49.1; H, 4.5; N, 15.9; S, 17.8%. IR (cm^{-1}): 455s, 482m, 530m, 622w, 719w, 824m, 873s, 1038w, 1129vs, 1228vs, 1339m, 1480vs, 1521vs, 1618s, 2888w, 3068m, 3417s. UV–Vis (MeCN/cm^{-1}) ($\varepsilon \times 10^{-4}$/$dm^3\ mol^{-1}\ cm^{-1}$): 18900(1.8), 25200(1.5), 36800(10.3). $\mu_{eff} = 2.44$ BM.

Mössbauer spectrum (300 K): doublet I with isomer shift (i.s.) $= 0.29 \pm 0.01$ mm s^{-1}, quadrupole splitting (q.s.) $= 0.29 \pm 0.01$ mm s^{-1}, half-width of the spectral line (Γ) $= 0.30 \pm 0.01$ mm s^{-1} and relative spectrum area (A) = 61.5%; doublet II with i.s. $= 0.35 \pm 0.01$ mm s^{-1}, q.s. $= 0.81 \pm 0.01$ mm s^{-1}, $\Gamma = 0.43 \pm 0.01$ mm s^{-1}, $A =$ 38.5%.

2.2.4. $[Mn(phen)_2(ttcH)] \cdot H_2O$ (**5**)

1,10-Phenanthroline (phen) (0.4 g, 2 mmol) was added to a water solution (80 ml) of manganese(II) acetate tetrahydrate (0.25 g, 1 mmol). Then $ttcNa_3 \cdot 9H_2O$ (0.4 g, 1 mmol) in water (10 ml) was added in drops to the solution. The yellow precipitate which appeared immediately was filtered off, washed several times with water and EtOH and dried under an infrared lamp at 40 °C. Yield: 76%. *Anal.* Calc.: C, 53.3; H, 3.2; N, 16.1; S, 15.8. Found: C, 53.1; H, 3.0; N, 15.7; S, 15.6%. IR (cm^{-1}): 421w, 639m, 725s, 845s, 865s, 1101m, 1129m, 1206s, 1342s, 1424vs, 1460s, 1516m, 1589w, 1622m, 3429s. UV–Vis (cm^{-1}): 25150, 26200, 29400. $\mu_{eff} = 6.20$ BM.

2.2.5. $Mn(bpy)(ttcH) \cdot H_2O$ (**6**)

A preparation similar to that for the synthesis of (**5**) was applied, only 2,2′-bipyridine (bpy) (0.32 g, 2 mmol) was used instead of 1,10-phenanthroline. The substance is also yellow. Yield: 66%. *Anal.* Calc.: C, 38.6; H, 2.7; N, 17.3; S, 23.8. Found: C, 38.4; H, 2.8; N, 16.9; S, 22.9%. IR (cm^{-1}): 411w, 627m, 649m, 736m, 763s, 873s, 1016m, 1042w, 1059w, 1153 m, 1224s, 1315w, 1439vs, 1473s, 1574w, 1595s, 3090w, 3413s. UV–Vis (cm^{-1}): 25450, 27400, 28900, 36360. $\mu_{eff} = 5.90$ BM.

2.3. X-ray crystallography

X-ray data of (**2**) were collected on a Siemens SMART CCD diffractometer with Mo Kα radiation ($\lambda =$ 0.71073 Å, graphite monochromator). The crystal was cooled to 173(2) K by a flow of nitrogen gas using the LT-2A device. A full sphere of reciprocal space was scanned by 0.3 steps in ω with a crystal-to-detector distance of 3.97 cm. A preliminary orientation matrix was obtained from the first frames using SMART [33]. The collected frames were integrated using the preliminary orientation matrix which was updated every 100 frames. Final cell parameters were obtained by refinement of the positions of reflections with $I > 10\sigma(I)$ after integration of all the frames using the SAINT software [33]. The data were empirically corrected for absorption and other effects using the SADABS program [34]. The structures were solved by direct methods and refined by full-matrix least squares on all $|F^2|$ data using SHELXTL software [35].

The largest peak and hole on the final difference map were 0.427 and −0.251 e $Å^{-3}$. Important crystallographic parameters are as follows: $C_9H_{21}N_7OS_3Zn$, wavelength 0.71073 Å, monoclinic, space group $P2_1/c$, $a =$ 11.8044(3) Å, $b = 12.7373(4)$ Å, $c = 10.7776(3)$ Å, $\beta =$ 95.051(1)°, volume 1614.19(8) $Å^3$, $Z = 4$, density (calc.) 1.666 Mg/m^3, absorption coefficient 1.919 mm^{-1}, $F(000) = 840$, crystal size $0.31 \times 0.19 \times 0.11$ mm, index ranges $-18 \leqslant h \leqslant 17$, $-19 \leqslant k \leqslant 18$, $-16 \leqslant l \leqslant 16$, reflections collected/independent 29364/5883 ($R_{int} = 0.0213$), refinement method full-matrix least-squares on F^2, data/restraints/parameters 5883/0/224, goodness-of-fit on $F^2 = 1.024$, final R_1 (2σ data) = 0.0207, $wR_2 = 0.0550$, final R_1 (all data) = 0.0250, $wR_2 = 0.0571$.

2.4. Biological activity testing

K-562, MCF7, G-361 and HOS were used for a cytotoxicity determination of the complexes by a calcein AM assay. The tumor cells were maintained in 75 ml plastic tissue culture flasks (TPP) and grown on Dulbecco's modified Eagle's cell culture medium (DMEM) containing 1 g l^{-1} glucose, 4 mM glutamine, 100 IU ml^{-1} penicillin, 100 μg ml^{-1} streptomycin, 10% foetal bovine serum and 3.7 g l^{-1} sodium bicarbonate. The cell suspension of approximate density 1.25×10^{-5} cells/ml was redistributed into 96-well microtitre plates (Nunc, 80 μl per well). After preincubation (12 h at 37 °C, 5% CO_2), the test compounds, in sixfold dilutions, were added (20 μl per well). Incubation of the cells with the tested compounds (in the 0.2–100 μM range) lasted for 72 h at 37 °C in 5% CO_2 atmosphere, 100% humidity. At the end of this period, the cells were incubated for 1 h with calcein AM and the fluorescence of the live cells was measured at 485 nm/538 nm (ex/em) with a Fluoroscan Ascent (Labsystems,

Finland). IC_{50} values, the drug concentrations lethal to 50% of the tumor cells, were estimated.

The antimicrobial activities of $ttcNa_3$ and its metal complexes were estimated by MIC ($\mu g\ ml^{-1}$). The bacteria were inoculated into 5 ml of a liquid medium (Mueller-Hinton broth), and cultured for 2 h at 37 °C, then diluted with distilled water in a 1:10 ratio. The cultured fluids were adjusted to the cell concentration of 100 μl and used for inoculation in the MIC test. The test ligand and complexes were dissolved in water. Solutions with concentrations 100 $\mu g\ ml^{-1}$ for $ttcNa_3$ and 357 $\mu g\ ml^{-1}$ for the complexes were prepared. Each 1 ml of culture medium containing various concentrations of the test materials was inoculated with 0.1 ml of the microorganism suspension prepared above. Bacteria were cultured for 18 h at 37 °C, then the growth of microorganisms was observed. When no growth of microorganisms was observed in the medium containing the lowest concentration of the test materials, the MIC of the test material was defined at this point of dilution. All compounds were tested three times and results are given as an average of the three independent experiments.

3. Results and discussion

New Zn(II), Fe(II) and Mn(II) complexes were prepared by the reaction of metal salts with the appropriate amines or imines followed by addition of the sodium salt of trithiocyanuric acid in aqueous or ethanol media. Their composition was proved by elemental analysis and they were characterized by spectroscopic methods and magnetochemical measurements. The results of elemental analysis together with results of physical techniques are given in Section 2. Moreover, our findings dealing with the composition of the complexes were confirmed by complete X-ray analysis of complexes **1**, **2** and **4**. In this work we present the X-ray structure of **2** only, whereas structures of complexes **1** and **4** will be published elsewhere. Briefly, the zinc atom in complex **1** is in a deformed trigonal bipyramidal arrangement formed by three N atoms of pmdien and the N,S donor set of the $ttcH^{2-}$ anion. The structure is similar to that of [Ni(pmdien)(ttcH)], which we reported earlier [29]. The iron atom in **4** is in a deformed octahedral arrangement of three N–N ligands (dmbpy), whereas the $ttcH_2^-$ anions and water molecules are outside the coordination sphere.

3.1. Spectral and magnetochemical study

The vibrational frequencies with their relative intensities are given in the experimental part. In our previous work we used density-functional theory calculations for the geometry optimization and IR frequencies calculations of differently protonated forms of $ttcH_3$ [30]. On the base of DFT calculations, we can assign bands which are connected with the ν(C–N) and ν(C–S) vibrations of the 2,4,6-trimercapto-1,3,5-triazine ring. These are observed in the IR spectra of the complexes in the 1515–1576 and 1175–1264 cm^{-1}, and 845–873 and 411–422 cm^{-1} regions, respectively. The bands observed in the 3068–3436 cm^{-1} region can be attributed to ν(C–H) and ν(N–H) vibrations [36]. In the spectra of complexes **1**, **2** and **4** the bands in the region 2852–2970 cm^{-1} can be connected with $\nu_s(CH_2)$ and $\nu_{as}(CH_2)$ vibrations. IR spectra of complexes **4**–**6**, with coordinated aromatic heterocycles (bpy, phen), contain several bands in the regions 700–900 and 1400–1600 cm^{-1} which are attributed to the ν(C–C) and ν(C–N) ring modes and the ring deformation vibrations, respectively. Most of the peaks of the free ligands are shifted to higher frequencies upon coordination.

There are three bands in the electronic absorption spectrum of **4**. The weak bands at 18 900 and 25 200 cm^{-1} can be attributed to d–d and metal to ligand charge transfer (MLCT) transitions, respectively [37]. The third strong absorption band observed at 36 800 cm^{-1} is probably due to a CT or π–π* transition associated with the ligands. In the spectra of the Mn(II) complexes **5** and **6** we can observe bands expected for octahedral high spin species at 25 150, 26 200 and 29 400 cm^{-1} for **5**, and 25 450, 27 400 and 28 900 cm^{-1} for **6**. These bands can be attributed to the d–d transitions. Very intensive bands in the UV range are probably due to CT or π–π* transitions.

The magnetic moment value for **4** ($\mu_{eff} = 2.44$ BM) is higher than that expected for a low spin deformed octahedral Fe(II) complex. A similar value of magnetic moment ($\mu_{eff} = 2.38$ BM) was calculated for $[Fe(phen)_2(NCS)_2]$ [38]. The authors explained a higher value of magnetic moment by residual paramagnetism due to polymorphism of the complex. Another explanation of a high magnetic moment value is deformation of the octahedral iron environment caused by the presence of methyl groups and the influence of water in the crystal lattice. This suggestion seems to be in agreement with the results of Mössbauer spectroscopy. The room temperature Mössbauer spectrum of **4** is composed of two doublets with the values of isomer shift (0.29 and 0.35 mm s^{-1}) typical for octahedral low-spin iron(II) complexes [39,40]. The doublet I with relative spectrum area $A = 61.5\%$ has a lower value of the quadrupole splitting parameter (q.s. = 0.29 mm s^{-1}) than the doublet II ($A = 38.5\%$, q.s. = 0.81 mm s^{-1}). The two different values of quadrupole splitting show that there are two octahedrally coordinated iron centers with lower and higher distortion from ideal octahedral arrangement found in the polycrystalline material. In our previous work, similar spectra with two doublets were also obtained and interpreted as a result of distortion of the octahedral arrangement of the central atoms in iron(II) complexes [30].

The manganese complexes **5** and **6** have magnetic moments 6.20 and 5.90 μ_{eff}/BM, respectively. These values are very close to the spin only value (5.93 μ_{eff}/BM) expected for five unpaired electrons of high spin deformed octahedrally coordinated manganese(II) atoms. From the composition of **6** we can propose a polymeric structure for the complex, where ttcH can form a bridge between the central atoms.

3.2. X-ray structure of [Zn(taa)(ttcH)] · H_2O (2)

The molecular structure of [Zn(taa)(ttcH)] · H_2O (**2**) is depicted in Fig. 1, while selected bond lengths and angles are listed in Table 1. The crystal structure is stabilized by hydrogen bonds (see Table 2, Fig. 2). The molecular structure of **2** consists of an electroneutral zinc complex and one crystal water molecule, which is hydrogen-bonded to the hydrogen atom of $ttcH^{2-}$. The central zinc atom is coordinated by four N atoms of taa and one N atom of the trithiocyanurate(2^-) dianion. The coordination polyhedron around the zinc atom is deformed trigonal-bipyramid with terminal nitrogen atoms N3A, N3B and N3C of taa in the basal plane while the central (tertiary) nitrogen atom N1 of taa and N2 atom of $ttcH^{2-}$ are coordinated in apical positions. The axial Zn–N1 bond length (2.3490(8) Å) is significantly longer than the equatorial Zn–N bond lengths, which are in the range 2.0618(9)–2.0887(9) Å. The Zn–N2 bond length of 2.1272(8) Å is longer than that found in Ni–N(trithiocyanurate) of [Ni(taa)(ttcH)] (2.040(2) Å),

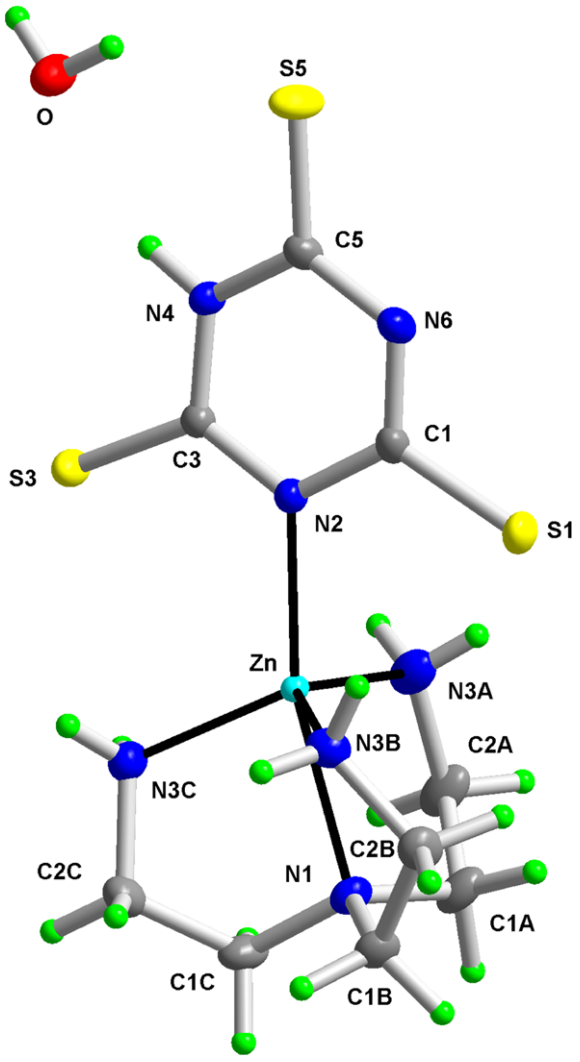


Fig. 1. The molecular structure of **2** with the numbering scheme and atomic displacement ellipsoids drawn at the 50% probability level.

Table 1
Selected bond lengths (Å) and angles (°) for [Zn(taa)(ttcH)] · H_2O (**2**)

Zn–N3C	2.0618(9)
Zn–N3A	2.0689(10)
Zn–N3B	2.0887(9)
Zn–N2	2.1272(8)
Zn–N1	2.3490(8)
N3C–Zn–N3A	110.30(4)
N3C–Zn–N3B	107.82(4)
N3A–Zn–N3B	130.52(4)
N3C–Zn–N2	114.60(3)
N3A–Zn–N2	94.39(4)
N3B–Zn–N2	97.33(3)
N3C–Zn–N1	79.62(3)
N3A–Zn–N1	79.48(3)
N3B–Zn–N1	77.59(3)
N2–Zn–N1	165.77(3)

Table 2
Hydrogen bonds for [Zn(taa)(ttcH)] · H_2O (**2**) (Å, °)

D–H...A	*d*(D–H)	*d*(H...A)	*d*(D...A)	∠(DHA)
O–H1...S5	0.85(2)	2.45(2)	3.1777(10)	144.5(17)
O–H2...S3^{i}	0.785(19)	2.55(2)	3.3361(10)	176.1(18)
N4–H4...O	0.88	2.16	2.9891(12)	157.6
N3A–H31A...S1^{ii}	0.867(19)	2.805(19)	3.5978(10)	152.9(16)
N3A–H31A...N6^{ii}	0.867(19)	2.408(19)	3.1727(14)	147.4(16)
N3A–H32A...S1	0.850(18)	2.878(18)	3.4827(12)	129.7(15)
N3B–H31B...S1	0.839(15)	2.651(15)	3.1906(10)	123.4(13)
N3B–H32B...O^{iii}	0.880(16)	2.449(16)	3.1209(14)	133.6(13)
N3B–H32B...O^{iv}	0.880(16)	2.425(16)	3.1810(14)	144.3(14)
N3C–H31C...S5^{ii}	0.874(17)	2.645(17)	3.4527(10)	154.1(14)
N3C–H32C...S3	0.847(17)	2.853(16)	3.2457(9)	110.3(13)
C2A–H2A1...N6^{v}	0.99	2.55	3.4061(14)	145.3
C2C–H2C1...S3^{vi}	0.99	2.85	3.8339(11)	175.5

Symmetry transformations used to generate equivalent atoms: (i) $-x$, $-y+1$, $-z$, (ii) x, $-y+1/2$, $z-1/2$, (iii) $-x$, $y-1/2$, $-z+1/2$, (iv) x, $-y+1/2$, $z+1/2$, (v) $-x+1$, $y-1/2$, $-z+1/2$, (vi) $-x$, $-y$, $-z$.

whereas other Ni–N(taa) distances are within the range of 2.063(3)–2.109(3) Å, comparable with those found in **2** [31]. In [Zn(bapen)(ttcH)] · EtOH (bapen = *N*,*N*′-bis-(3-aminopropyl)ethylenediamine), where $ttcH^{2-}$ is coordinated in a chelating fashion through N and S atoms, the Zn–N(trithiocyanurate) (2.3132(18) Å) distance is significantly longer in comparison with the Zn–N2 distance in **2** [21].

When we compare the known structures of zinc complexes with the taa ligand [Zn(taa)(H_2O)](ClO_4)$_2$, [Zn(taa)(MeOH)](ClO_4)(BPh_4) and [Zn(taa)(NCS)](SCN) with **2**, we can observe that the equatorial Zn–N bond lengths are very similar, whereas there are big differences in Zn–N(axial) bonds [41–43]. The axial bond lengths are 2.193(4), 2.16(1) and 2.292(4) Å, for the above mentioned complexes, while in **2** the distance is longer (2.3490(8) Å). In comparison with Zn–N(thiocyanate), the distance (2.073(5) Å) in [Zn(taa)(NCS)](SCN) is shorter than that found in **2**, Zn–N(trithiocyanurate) (2.1272(8) Å). We can also mention big differences in the equatorial N–Zn–N angles. In the three complexes mentioned above the

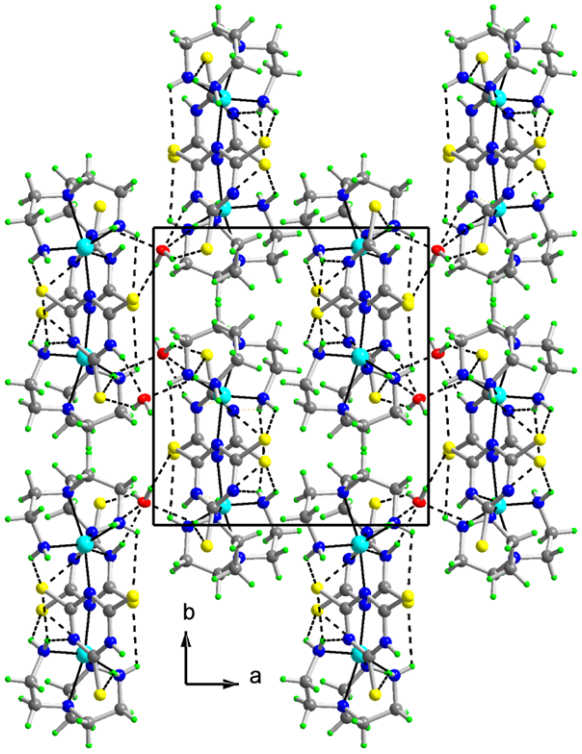


Fig. 2. Hydrogen bonding pattern in projection along the *c*-axis. Hydrogen bonds are shown as broken lines. For geometrical details see Table 2.

equatorial angles are all within an average of 118°, whilst in **2** the angles are in the range 107.82(4)–130.52(4)°.

3.3. In vitro cytotoxicity and antimicrobial activities

The cytotoxic activity of the complexes **1**–**8** and the sodium salt of trithiocyanuric acid ($ttcNa_3$) were studied on G-361, HOS, K-562 and MCF7 cancer cell lines. The results of the study are listed in Table 3. It can be clearly seen that zinc (**1**, **2**) and nickel (**7**, **8**) complexes as well as $ttcNa_3$ show no activity against K-562 and MCF7 in the concentration range used. On the other hand, very promising results were achieved for iron (**3**, **4**) and manganese (**5**, **6**) compounds. The four compounds show activity on K-562 and MCF7 cell lines. Based on average IC_{50} values, in the two cell lines compounds **3** and **5** are the most active ones and the results are comparable or mostly better than those obtained for cisplatin and oxaliplatin. Compound **4** is less active and **6** shows very low activity. The very low activity of **6** can be caused by the possible polymeric structure of the compound. The most active compounds i.e. **3** and **5** were selected for testing on G-361 and HOS cancer cell lines. The compounds are very efficient in inhibiting these cell line growths. They are comparable in activity with cisplatin and are two to four times more effective than oxaliplatin.

A combination of imines and the trithiocyanurate anion is not sufficient in bringing about cytotoxicity. It is seen when complexes **4** and **8** are compared. It can be clearly seen that the metal ion has a big influence on cytotoxicity of the complexes. Zinc and nickel compounds with amines or imines are inactive, whereas those containing iron or manganese ions show cytotoxicity. It seems that it is also important whether the trithiocyanurate anion is coordinated to the central atom or not. It can be demonstrated

Table 3
In vitro cytotoxicity of the complexes

	K-562	MCF7	G361	HOS
(**1**) [Zn(pmdien)(ttcH)]	>25	>25		
(**2**) $[Zn(taa)(ttcH)] \cdot H_2O$	>100	>100		
(**3**) $[Fe(nphen)_2(ttcH)] \cdot H_2O$	5.1	3.9	3.4	3.0
(**4**) $[Fe(dmbpy)_3](ttcH_2)_2 \cdot 4H_2O$	9.8	22.7		
(**5**) $[Mn(phen)_2(ttcH)] \cdot H_2O$	2.7	6.0	3.8	1.6
(**6**) $Mn(bpy)(ttcH) \cdot H_2O$	65.6	45.3		
(**7**) $[Ni(taa)(ttcH)] \cdot H_2O$	>25	>25		
(**8**) $[Ni(phen)_3](ttcH) \cdot 5H_2O$	>25	>25		
$ttcNa_3 \cdot 9H_2O$	>100	>100		
Oxaliplatin	8.8	18.2	7.1	6.8
Cisplatin	4.7	10.9	2.9	3.0

The results are given as IC_{50} values for the compounds (μM) assessed by calcein AM assay of surviving tumor cells. The tumor cell lines (K-562, MCF7, G361, HOS) were treated with a solution of the tested compound in the 0.2–25 μM (**1**, **7**, **8**) and 0.2–100 μM range (for the other compounds) for 72 h at 37 °C, 5% CO_2.

Table 4
Antimicrobial activities of the complexes evaluated by MIC (μg ml^{-1})[a]

	3953[b]	4223[b]	4224[b]	4225[b]	3988[b]	3954[b]	3955[b]
(**1**) [Zn(pmdien)(ttcH)]	>357	>357	>357	>357	>357	>357	>357
(**2**) $[Zn(taa)(ttcH)] \cdot H_2O$	>357	>357	>357	>357	>357	>357	>357
(**3**) $[Fe(nphen)_2(ttcH)] \cdot H_2O$	44.6	44.6	>357	>357	>357	>357	>357
(**4**) $[Fe(dmbpy)_3](ttcH_2)_2 \cdot 4H_2O$	89.3	89.3	>357	89.3	89.3	89.3	89.3
(**5**) $[Mn(phen)_2(ttcH)] \cdot H_2O$	>357	>357	>357	44.6	44.6	89.3	178.5
(**6**) $Mn(bpy)(ttcH) \cdot H_2O$	357	357	>357	357	357	357	357
(**7**) $[Ni(taa)(ttcH)] \cdot H_2O$	>357	>357	>357	>357	>357	>357	>357
(**8**) $[Ni(phen)_3](ttcH) \cdot 5H_2O$	178.5	178.5	>357	357	357	>357	>357
$ttcNa_3 \cdot 9H_2O$	>100	>100	>100	>100	>100	>100	>100

[a] The final concentration was 357 μg ml^{-1} for the complexes and 100 μg ml^{-1} for $ttcNa_3 \cdot 9H_2O$.
[b] The antimicrobial activities were evaluated against *Staphylococcus aureus* 3953, 4223, *Enterococcus faecalis* 4224, *Escherichia coli* 4225, 3988, 3954, *Pseudomonas aeruginosa* 3955.

on complexes **3** and **4**. Complex **3**, where the ttcH anion is coordinated, shows better activity.

The results of antimicrobial activities of $ttcNa_3$ and the complexes, estimated by MIC ($\mu g\ ml^{-1}$), are listed in Table 4. The free salt $ttcNa_3$ and complexes **1**, **2**, **6** and **7** did not inhibit the growth of the test organisms. Compound **3** showed selective and effective antimicrobial activities against Gram-positive bacteria (*S. aureus*); **4** exhibited effective activities against all tested bacteria, except for *E. faecalis*. Complex **5** showed effective activities against *Escherichia coli* and modest activity against *P. aeruginosa*, whereas **8** exhibited modest activities against *S. aureus*. It seems that compounds containing imines are active with the exception of **6**, where a polymeric structure is suggested.

4. Supplementary material

CCDC 610058 contains the supplementary crystallographic data for **2**. These data can be obtained free of charge via http://www.ccdc.cam.ac.uk/conts/retrieving.html, or from the Cambridge Crystallographic Data Centre, 12 Union Road, Cambridge CB2 1EZ, UK; fax: (+44) 1223-336-033; or e-mail: deposit@ccdc.cam.ac.uk.

Acknowledgements

The authors thank the Ministry of Education of the Czech Republic (MSM 6198959218). The authors thank Dr. Zdeněk Šindelář for magnetochemical data collection and Dr. Jitka Frébortová for antimicrobial testing.

References

[1] A.E. Beezer, J.C. Chudy, Thermochim. Acta 6 (1973) 231.
[2] K.R. Henke, D. Robertson, M.K. Krepps, D.A. Atwood, Water Res. 34 (2000) 3005.
[3] J.R. Bailey, M.J. Hatfield, K.R. Henke, M.K. Krepps, J.L. Morris, T. Otieno, K.D. Simonetti, E.A. Wall, D.A. Atwood, J. Organomet. Chem. 623 (2001) 185.
[4] M.M. Matlock, K.R. Henke, D.A. Atwood, J.D. Robertson, Water Res. 35 (2001) 3649.
[5] M.M. Matlock, K.R. Henke, D.A. Atwood, J. Hazardous Mat. B 92 (2002) 129.
[6] V.W. Rosso, D.A. Lust, P.J. Bernot, J.A. Grosso, S.P. Modi, A. Rusowicz, T.C. Sedergran, J.H. Simpson, S.K. Srivastava, M.J. Humora, N.G. Anderson, Org. Process Res. Dev. 1 (1997) 311.
[7] K. Ishihara, M. Nakayama, H. Kurihara, A. Itoh, H. Haraguchi, Chem. Lett. (2000) 1218.
[8] C.E. Garrett, K. Prasad, Adv. Synth. Catal. 346 (2004) 889.
[9] H. Hirahara, K. Mori, Y. Oishi, J. Adhesion Sci. Technol. 11 (1997) 1459.
[10] H. Sasaki, I. Kobayashi, S. Sai, H. Hirahara, Y. Oishi, K. Mori, J. Adhesion Sci. Technol. 13 (1999) 523.
[11] K. Mori, Z. Kang, J. Oravec, Y. Oishi, Mater. Sci. Forum 419 (2003) 921.
[12] H. Hirahara, S. Aisawa, K. Mori, E. Narita, Y. Oishi, Surf. Interface Anal. 35 (2003) 953.
[13] K. Yamada, H. Tabe, J. Electroanal. Chem. 560 (2003) 13.
[14] M. Iltzsch, K.O. Tankersley, Biochem. Pharmacol. 46 (1993) 1849.
[15] M. Iltzsch, K.O. Tankersley, Biochem. Pharmacol. 48 (1994) 781.
[16] Z.Z. Javaid, M.H. el Kouni, M.H. Iltzsch, Biochem. Pharmacol. 58 (1999) 1457.
[17] S. Kar, T.A. Miller, S. Chakraborty, B. Sarkar, B. Pradhan, R. Sinha, T. Kundu, M.D. Ward, G.K. Lahiri, J. Chem. Soc., Dalton Trans. (2003) 2591.
[18] S. Kar, B. Pradhan, R.K. Sinha, T. Kundu, P. Kodgire, K.K. Rao, V.G. Puranik, G.K. Lahiri, J. Chem. Soc., Dalton Trans. (2004) 1752.
[19] S. Aoki, M. Shiro, E. Kimura, Chem. Eur. J. 8 (2002) 929.
[20] S. Aoki, M. Zulkefeli, M. Shiro, E. Kimura, Proc. Natl. Acad. Sci. USA 99 (2002) 4894.
[21] J. Marek, P. Kopel, Z. Trávníček, Acta Crystallogr., Sect. C 59 (2003) m558.
[22] K. Yamanari, Y. Kushi, M. Yamamoto, A. Fuyhiro, S. Kaizaki, T. Kawamoto, Y. Kushi, J. Chem. Soc., Dalton Trans. (1993) 3715.
[23] C.K. Chan, K.K. Cheung, C.M. Che, Chem. Commun. (1996) 227.
[24] I. Haiduc, M.F. Mahon, K.C. Molloy, M.M. Venter, J. Organomet. Chem. 627 (2001) 6.
[25] F. Cecconi, C.A. Ghilardi, S. Midollini, A. Orlandini, J. Organomet. Chem. 645 (2002) 101.
[26] M.F. Mahon, K.C. Molloy, M.M. Venter, I. Haiduc, Inorg. Chim. Acta 348 (2003) 75.
[27] A. Ienco, S. Midollini, A. Orlandini, A. Vacca, Inorg. Chim. Acta 357 (2004) 2615.
[28] P. Kopel, Z. Trávníček, L. Kvítek, R. Panchártková, M. Biler, J. Marek, M. Nádvorník, Polyhedron 18 (1999) 1779.
[29] P. Kopel, Z. Trávníček, L. Kvítek, M. Biler, M. Pavlíček, Z. Šindelář, J. Marek, Transition Met. Chem. 26 (2001) 282, and references therein.
[30] P. Kopel, Z. Trávníček, R. Zbořil, J. Marek, Polyhedron 23 (2004) 2193.
[31] P. Kopel, Z. Trávníček, R. Panchártková, M. Biler, J. Marek, Transition Met. Chem. 24 (1999) 239.
[32] P. Kopel, Z. Trávníček, R. Panchártková, Z. Šindelář, J. Marek, J. Coord. Chem. 44 (1998) 205.
[33] SMART and SAINT: Area Detector Control and Integration Software, Bruker AXS Inc., Madison, WI, USA, 2003.
[34] SADABS: G.M. Sheldrick, Program for Empirical Absorption Correction for Area Detectors (Version 2.10), University of Göttingen, Germany, 2003.
[35] SHELXTL: Structure Determination Programs (Version 6.12), Bruker AXS Inc., Madison, WI, USA, 2001.
[36] C.J. Pouchert, The Aldrich Library of Infrared Spectra, third ed., Aldrich Chemical Company, Milwaukee, WI, 1981.
[37] A.B.P. Lever, Inorganic Electronic Spectroscopy, Elsevier, Amsterdam, 1984.
[38] H.A. Goodwin, Coord. Chem. Rev. 18 (1976) 293.
[39] L.Y. Johansson, R. Larsson, Chem. Phys. Lett. 24 (1974) 508.
[40] H. Sato, T. Tominaga, Bull. Chem. Soc. Jpn. 49 (1976) 697.
[41] M.M. Ibrahim, N. Shimomura, K. Ichikawa, M. Shiro, Inorg. Chim. Acta 313 (2001) 125.
[42] M.M. Ibrahim, K. Ichikawa, M. Shiro, Inorg. Chem. Commun. 6 (2003) 1030.
[43] G.D. Andreetti, P.C. Jain, E.C. Lingafelter, J. Am. Chem. Soc. 91 (1969) 4112.

clear need to synthesize and investigate novel species of this type. What is more, the *fac*-$Re(CO)_3^+$ complexes can be used as diagnostic and therapeutic radiopharmaceuticals. It has resulted in an added increase in the interest of these compounds [13,14].

Here, we present the synthesis, spectroscopic characterization, crystal, molecular and electronic structure of the *fac*-[$Re(CO)_3$(dppt)Cl] tricarbonyl. 5,6-Diphenyl-3-(2-pyridyl)-1,2,4-triazine (dppt) is a bipy-like ligand, but very little is currently know about the binding of this ligand to the rhenium center.

The molecular orbital diagram of the examined complex has been calculated with density functional theory (DFT) calculations, and additional information about binding has been obtained by NBO analysis. Density functional theory (DFT) is commonly used to examine the electronic structure of transition metal complexes. It meets with the requirements of being accurate, easy to use and fast enough to allow the study of relatively large molecules of transition metal complexes [16]. The spin-allowed singlet–singlet electronic transitions of *fac*-[$Re(CO)_3$(dppt)Cl] have been calculated with the time-dependent DFT method (TDDFT method), and a good assignment with the experimental spectrum has been observed.

1. Experimental

1.1. General procedure

All synthetic manipulations were performed under argon atmosphere. The solvents were dried before use, using the appropriate drying reagents. $Re(CO)_5Cl$ and 5,6-diphenyl-3-(2-pyridyl)-1,2,4-triazine were purchased from Aldrich, and they were used as received.

IR spectrum was recorded on a Nicolet Magna 560 spectrophotometer in the spectral range 4000–400 cm^{-1} with the samples in the form of KBr pellets. Electronic spectrum was measured on a spectrophotometer Lab Alliance UV–VIS 8500 in the range 900–200 nm in dichloromethane solution. Elemental analyses (C H N) were performed on a Perkin–Elmer CHN-2400 analyzer.

1.2. Preparation of [$Re(CO)_3$(dppt)Cl]

$Re(CO)_5Cl$ (0.2 g, 0.55 mmol) and dppt (0.18 g, 0.58 mmol) in toluene (50 cm^3) were refluxed for 6 h. After cooling of the reaction mixture to room temperature and slow evaporation of the solvent under reduced pressure, an orange solid was precipitated. The product was further purified by re-crystallization from acetone/hexane. X-ray quality crystals of *fac*-[$Re(CO)_3$(dppt)Cl] were obtained by re-crystallization from a hexane/dichloromethane mixture (Yield 90%).

IR (KBr, cm^{-1}): $\nu_{CO} = 2021$, 1930 and 1891; 1566(w), ν_{CN} and $\nu_{C=C} = 1608$, 1597, 1578 and 1517.

Anal Calc. for $C_{23}H_{14}N_4O_3ClRe$: C, 44.84; H, 2.29; N, 9.09. Found: C, 44.70; H, 2.20; N, 9.20%.

1.3. Crystal structure determination and refinement

A orange crystal of [$Re(CO)_3$(dppt)Cl] was mounted on a KM-4-CCD automatic diffractometer equipped with a CCD detector, and used for data collection. X-ray intensity data were collected with graphite monochromated Mo Kα radiation ($\lambda = 0.71073$ Å) at a temperature of 293.0(2) K. Details concerning crystal data and refinement are given in Table 1. Lorentz, polarization and empirical absorption correction using spherical harmonics implemented in SCALE3 ABSPACK scaling algorithm [17] were applied. The structure was solved by means of the Patterson method and subsequently completed by difference Fourier recycling. All the non-hydrogen atoms were refined anisotropically using the full-matrix, least-squares technique. The hydrogen atoms of the phenyl rings were treated as "riding" on their parent carbon atoms [d(C–H) = 0.96 Å] and assigned isotropic temperature factors equal to 1.2 times the value of the equivalent temperature factor of the parent carbon atom. SHELXS97 [18], SHELXL97 [19] and SHELXTL [20] programs were used for all the calculations. Atomic scattering factors were those incorporated in the computer programs.

Table 1
Crystal data and structure refinement for [$Re(CO)_3$(dppt)Cl]

Empirical formula	$C_{23}H_{14}N_4O_3ClRe$
Formula weight	616.03
Temperature (K)	293(2)
Wavelength (Å)	0.71073
Crystal system	monoclinic
Space group	$C2/c$
Unit cell dimensions	
a (Å)	31.1904(15)
b (Å)	7.6611(2)
c (Å)	23.1612(12)
β (°)	127.211(8)
Volume (Å^3)	4407.7(3)
Z	8
Density (calculated) (Mg/m^3)	1.857
Absorption coefficient (mm^{-1})	5.668
F(000)	2368
Crystal size (mm)	0.34 × 0.10 × 0.03
θ Range for data collection (°)	3.17–32.34
Index ranges	$-46 \leqslant h \leqslant 44$
	$-11 \leqslant k \leqslant 6$
	$-34 \leqslant l \leqslant 33$
Reflections collected	21 175
Independent reflections [R_{int}]	6405 [0.0691]
Maximum and minimum transmission	0.510 and 0.841
Data/restraints/parameters	6405/0/289
Goodness-of-fit on F^2	1.160
Final R indices [$I > 2\sigma(I)$]	$R_1 = 0.0412$,
	$wR_2 = 0.0959$
R indices (all data)	$R_1 = 0.0706$,
	$wR_2 = 0.1161$
Largest difference in peak and hole (e Å^{-3})	1.835 and −1.660

1.4. Computational details

The GAUSSIAN03 program [21] was used in the calculations. The geometry optimization was carried out with the DFT method with the use of the B3LYP functional [22,23]. The electronic spectrum was calculated with the TDDFT method [24]. The calculations were performed by using the ECP basis set on the rhenium atom, the standard 6-31+G** basis for chlorine, oxygen and nitrogen, 6-31+G* for carbon and 6-31G basis for hydrogen atoms. The Xe core electrons of Re were replaced by an effective core potential and the DZ quality Hay and Wadt Los Alamos ECP basis set (LANL2DZ) [25] was used for the valence electrons. An additional *d* function with exponent $\alpha = 0.3811$ and *f* function with exponent $\alpha = 2.033$ on the rhenium atom were added. Natural bond orbital (NBO) calculations were performed with the NBO code [26] included in GAUSSIAN03.

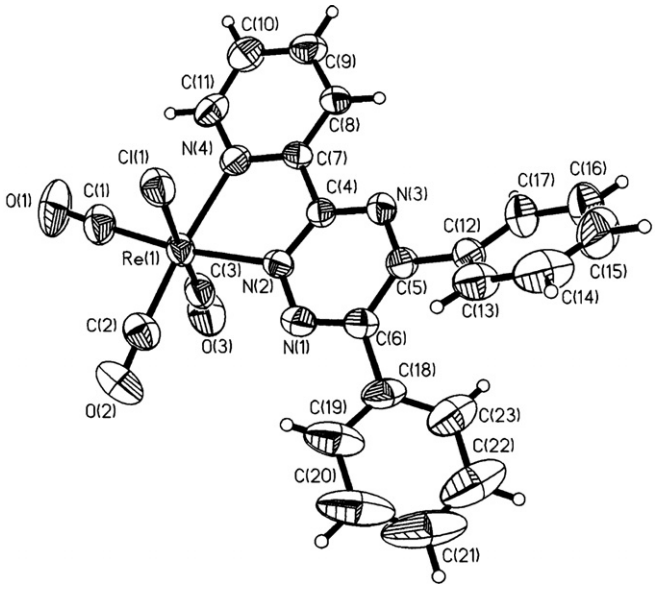


Fig. 1. Plot of $[Re(CO)_3(dppt)Cl]$ showing the atom numbering scheme (50% probability of displacement ellipsoids).

2. Results and discussion

2.1. Preparation and infrared data

The $[Re(CO)_3(dppt)Cl]$ complex was prepared by refluxing the compound $[Re(CO)_5Cl]$ with a small excess of 5,6-diphenyl-3-(2-pyridyl)-1,2,4-triazine (dppt) in toluene. The complex was isolated as an air-stable, microcrystalline solid, soluble in common organic solvents. The infrared spectrum of the complex displays three bands in the carbonyl stretching region: a sharp intense band at 2021 cm^{-1} and two lower-energy bands closely spaced (1930 and 1891 cm^{-1}), typical of Re(I) diimine tricarbonyl complexes [27].

The characteristic bands of the C=C and C=N stretching modes are observed in the range 1616–1510 cm^{-1} [28].

2.2. Crystal structure

The crystallographic data for the title complex are given in Table 1. A perspective drawing of the structure of the complex with the atomic numbering is shown in Fig. 1. The phenyl rings show symptoms of disorder. Detailed examination of difference Fourier maps electron density did not show any abnormal peaks or holes around the disordered atoms, thus it could be supposed that the disorder is dynamic in character. The coordination geometry at the Re atom is a distorted octahedron with the three carbonyl

Table 2
The experimental and optimized bond lengths (Å) and angles (°) for $[Re(CO)_3(dppt)Cl]$

	Bond lengths			Bond angles	
	Experimental	Optimized		Experimental	Optimized
Re(1)–C(1)	1.917(8)	1.934	C(1)–Re(1)–C(2)	91.0(4)	90.60
Re(1)–C(2)	1.924(8)	1.933	C(1)–Re(1)–C(3)	86.4(3)	91.27
Re(1)–C(3)	1.905(7)	1.919	C(3)–Re(1)–C(2)	88.6(3)	90.98
Re(1)–Cl(1)	2.4809(18)	2.533	C(1)–Re(1)–N(2)	172.1(3)	170.78
Re(1)–N(2)	2.147(5)	2.168	C(1)–Re(1)–N(4)	97.7(3)	97.96
Re(1)–N(4)	2.189(6)	2.214	C(1)–Re(1)–Cl(1)	94.6(2)	91.41
C(1)–O(1)	1.139(9)	1.161	C(2)–Re(1)–N(2)	96.2(3)	96.43
C(2)–O(2)	1.148(10)	1.158	C(2)–Re(1)–N(4)	170.3(3)	169.65
C(3)–O(3)	1.148(8)	1.166	C(2)–Re(1)–Cl(1)	93.5(2)	91.43
			C(3)–Re(1)–N(2)	96.8(3)	94.55
			C(3)–Re(1)–N(4)	96.2(3)	94.61
			C(3)–Re(1)–Cl(1)	177.7(2)	176.37
			N(2)–Re(1)–N(4)	74.8(2)	74.47
			N(2)–Re(1)–Cl(1)	81.91(14)	82.49
			N(4)–Re(1)–Cl(1)	81.61(15)	82.60
			O(1)–C(1)–Re(1)	175.9(8)	177.97
			O(2)–C(2)–Re(1)	177.6(8)	178.19
			O(3)–C(3)–Re(1)	175.7(7)	179.52

ligands arranged in a *facial* fashion. The deviation of the rhenium coordination sphere from an ideal octahedron is ascribed to the small bite angle of the five membered chelate ring. Selected bond lengths and angles of $[Re(CO)_3(dppt)Cl]$ are given in Table 2. The Re–C and Re–N bond distances are about the same as those reported for other diimine systems $[Re(CO)_3(diimine)L]$ [15]. A noticeable difference between Re–N(pyridine) and Re–N triazine bond lengths indicates the different donor strength of the two nitrogens donors. The triazine ring favours π-back donation from the rhenium ion to the carbonyl in the *trans* position. Hence, Re–C(1) is shorter in comparison to Re–C(2). In the structure no intermolecular short contacts, which can be considered as classical hydrogen bonds or stacking interactions, were found.

2.3. Optimised geometry

The geometry of $[Re(CO)_3(dppt)Cl]$ was optimised in a singlet state by the DFT method with the B3LYP functional. The optimised geometric parameters are gathered in Table 2. Generally, the calculated bond lengths and angles are in agreement with the values based upon the X-ray crystal structure data.

2.4. Electronic structure and NBO analysis

The $[Re(CO)_3(dppt)Cl]$ complex is a closed-shell structure. Its molecular orbital diagram with several highest HOMO and lowest LUMO contours is presented in Fig. 2. The HOMO–LUMO gap equals 2.67 eV. The low-

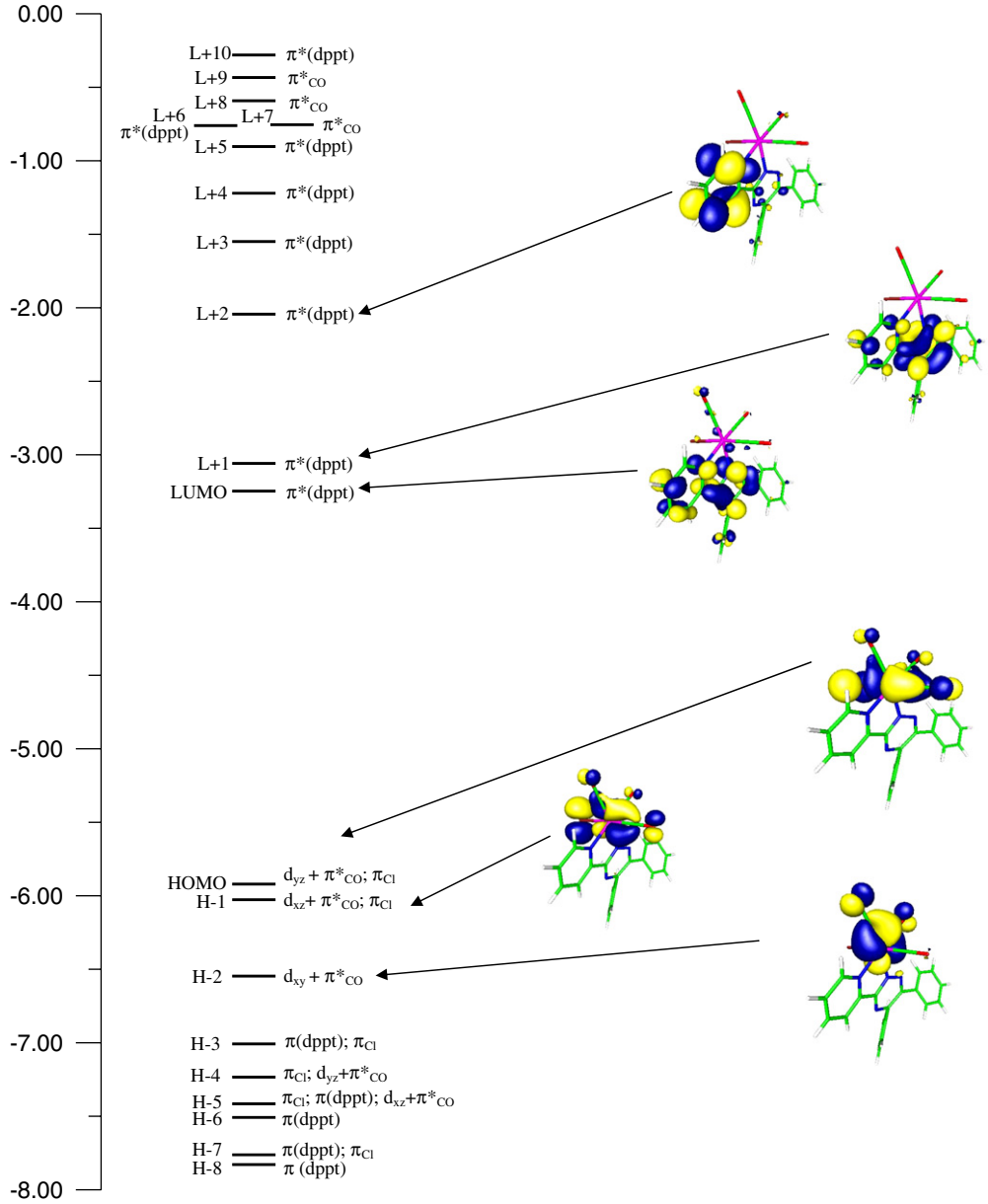


Fig. 2. The energy (eV), character and some contours of the unoccupied molecular orbitals of $[Re(CO)_3(dppt)Cl]$.

lying virtual orbitals correspond to π^*_{dppt} and π^*_{CO}, and energy of the π^*_{dppt} is lower than π^*_{CO} orbitals. The HOMO, HOMO − 1 and HOMO − 2 orbitals are predominantly of d_{Re} orbital character, corresponding to the $(5d_{xy})^2$ $(5d_{\pi})^4$ occupation.

Table 3 presents the occupancies and hybridization of the calculated Re–C and C–O natural bond orbitals (NBOs).

Each natural bond orbital (NBO) σ_{AB} can be written in terms of two directed valence hybrids (HHOs) h_A i h_B on atoms A and B

$$\sigma_{AB} = c_A h_A + c_B h_B$$

where c_A i c_B are polarization coefficients. Each valence bonding NBO must in turn be paired with a corresponding valence *anti*-bonding NBO

$$\sigma^*_{AB} = c_B h_A - c_A h_B$$

to complete the span of the valence space. The Lewis-type (donor) NBOs are thereby complemented by the non-Lewis-type (acceptor) NBOs that are formally empty in an idealized Lewis picture. The interactions between 'filled' Lewis-type NBOs and 'empty' non-Lewis NBOs lead to loss of occupancy from the localized NBOs of the idealized Lewis structure into the empty non-Lewis orbitals, and they are referred to as 'delocalization' corrections to the zeroth-order natural Lewis structure [29].

For each carbonyl group of the $[Re(CO)_3(dppt)Cl]$ complex, three natural bond orbitals were detected for the C–O bond, and one orbital for the Re–C bond. All the Re–C bond orbitals are polarized towards the carbon atom, and the C–O bond orbitals are polarized towards the oxygen end. Each oxygen atom of the carbonyl ligand possesses one lone pair (LP) orbital. The occupancies of the *anti*-bonding NBOs are given in round brackets.

The resonance structure $M-\overset{+}{C}\equiv O:$, which presents the best bonding between the CO ligands and the Re ion in $[Re(CO)_3(dppt)Cl]$, is consistent with the values of the calculated atomic charges. The atomic charges from the Natural Population Analysis (NPA) for $[Re(CO)_3(dppt)Cl]$ are shown in Table 4. The calculated charge on the rhenium atom of $[Re(CO)_3(dppt)Cl]$ is lower than the formal charge +1. The carbon atoms of the carbonyl ligands are positive, whereas the oxygen atoms are negatively charged.

Table 3
The occupancies and hybridization of the calculated Re–C and C–O natural bond orbitals (NBOs) for $[Re(CO)_3(dppt)Cl]$

BD	Occupancy	Hybridization of NBO
Re(1)–C(1)	1.966 (0.299)	$0.563(sd^{2.23})_{Re} + 0.827(sp^{0.55})_C$
Re(1)–C(2)	1.967 (0.299)	$0.569(sd^{2.21})_{Re} + 0.823(sp^{0.55})_C$
Re(1)–C(3)	1.960 (0.356)	$0.568(sd^{2.15})_{Re} + 0.823(sp^{0.56})_C$
C(1)–O(1)	1.998 (0.019)	$0.556(sp^{2.04})_C + 0.832(sp^{1.24})_O$
	1.996 (0.213)	$0.498(p)_C + 0.867(p)_O$
	1.996 (0.197)	$0.497(p)_C + 0.868(p)_O$
C(2)–O(2)	1.998 (0.012)	$0.557(sp^{1.88})_C + 0.831(sp^{1.18})_O$
	1.997 (0.201)	$0.496(p)_C + 0.868(p)_O$
	1.996 (0.190)	$0.498(p)_C + 0.867(p)_O$
C(3)–O(3)	1.999 (0.010)	$0.561(sp^{1.74})_C + 0.828(sp^{1.15})_O$
	1.997 (0.255)	$0.492(p)_C + 0.870(p)_O$
	1.996 (0.228)	$0.496(p)_C + 0.868(p)_O$

BD denotes 2-center bond.

Table 4
Atomic charges and spin densities of $[Re(CO)_3(dppt)Cl]$

Atom	Atomic charge
Re(1)	−0.102
Cl(1)	−0.569
N(1)	−0.181
N(2)	−0.271
N(3)	−0.494
N(4)	−0.458
C(1)	0.605
C(2)	0.634
C(3)	0.546
O(1)	−0.477
O(2)	−0.471
O(3)	−0.495

2.5. Electronic spectrum

The experimental (measured in dichloromethane solution) and calculated electronic spectra of $[Re(CO)_3(dppt)Cl]$ are presented in Fig. 3. Each calculated transition is represented by a gaussian function $y = ce^{-bx^2}$ with the height (c) equal to the oscillator strength and b equal to 0.04 nm^{-2}. In the Fig. 3, the low-energy calculated bands of $[Re(CO)_3(dppt)Cl]$ seems to be somewhat shifted in relation to the longest wavelength experimental band. However, the comparison of the energies in eV for these transitions indicates a satisfactory agreement between the

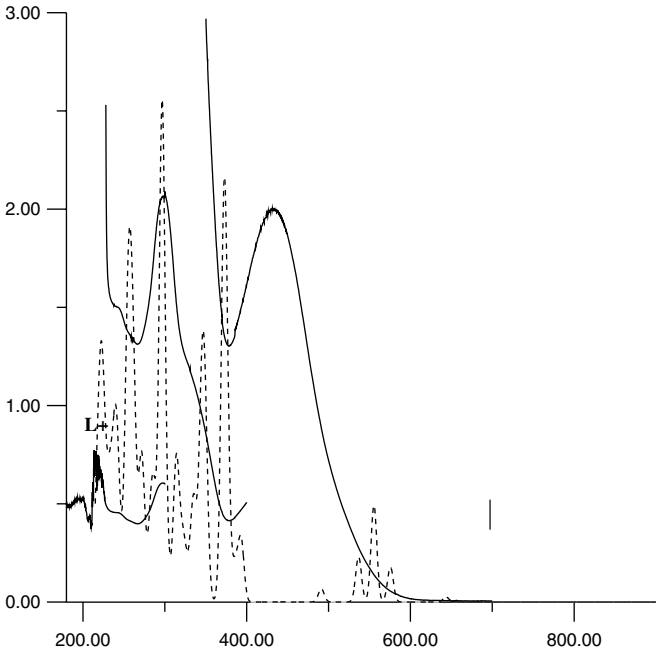


Fig. 3. The experimental (——) and calculated (----) electronic absorption spectra of $[Re(CO)_3(dppt)Cl]$.

experimental and calculated spectra. The spin-allowed singlet–singlet electronic transitions calculated with the TDDFT method for $[Re(CO)_3(dppt)Cl]$ are gathered in Table 5. For the high energy part of the spectrum (below 250 nm), only transitions with oscillator strengths larger than 0.015 are listed in Table 5.

The assignment of the calculated transitions to the experimental bands is based on the criterion of the energy and oscillator strength of the calculated transitions. In the description of the electronic transitions only the main components of the molecular orbital are taken into consideration.

The title complex contains a reducing metal center and an acceptor ligand with low-energy π^* orbitals. Similar to other Re(I) carbonyl-diimine complexes, the UV–Vis spectrum of $[Re(CO)_3(dppt)Cl]$ exhibits a broad low-energy

Table 5
The energy and molar absorption coefficients of experimental absorption bands and the electronic transitions calculated with the TDDFT method for $[Re(CO)_3(dppt)Cl]$

The most important orbital excitations	Character	λ (nm)	E (eV)	f	Experimental λ (nm) (E (eV)) ε
H → L	d → π*(dppt)	643.6	1.93	0.0025	
H − 1 → L	d → π*(dppt)	575.7	2.15	0.0178	
H → L + 1					
H − 1 → L	d → π*(dppt)	555.6	2.23	0.0492	449.4 (2.76) 11700
H → L + 1					
H − 1 → L + 1	d → π*(dppt)	536.7	2.31	0.0230	
H − 2 → L	d → π*(dppt)	491.1	2.52	0.0068	
H − 3 → L	π(dppt)/π_{Cl} → π*(dppt)	393.2	3.15	0.0311	
H → L + 2	d → π*(dppt)	386.1	3.21	0.0183	
H − 4 → L	π_{Cl} → π*(dppt)	377.6	3.28	0.0291	331.0 (3.75) 37800
H − 1 → L + 2	d → π*(dppt)				
H − 3 → L + 1	π(dppt)/π_{Cl} → π*(dppt)	373.3	3.32	0.1455	
H − 1 → L + 2	d → π*(dppt)	370.8	3.34	0.0702	
H − 5 → L	π_{Cl}/π(dppt) → π*(dppt)	349.3	3.55	0.0761	
H − 8 → L	π(dppt) → π*(dppt)	345.0	3.59	0.0890	
H − 5 → L	π_{Cl}/π(dppt) → π*(dppt)				
H − 5 → L + 1	π_{Cl}/π(dppt) → π*(dppt)	336.9	3.68	0.0184	
H − 6 → L	π(dppt) → π*(dppt)	334.3	3.71	0.0370	
H − 6 → L + 1	π(dppt) → π*(dppt)	321.6	3.90	0.0267	
H − 7 → L	π(dppt)/π_{Cl} → π*(dppt)	314.1	3.95	0.0669	
H − 9 → L + 1	σ_{Cl} → π*(dppt)	297.9	4.16	0.0154	300.0 (4.13) 41800
H → L + 7	d→ π^*_{CO}				
H − 10 → L	π/n(dppt) → π*(dppt)	296.7	4.18	0.1959	
H − 1 → L + 7	d→ π^*_{CO}	296.3	4.19	0.0392	
H − 10 → L + 1	π/n(dppt) → π*(dppt)	286.2	4.33	0.0510	
H − 3 → L + 2	π(dppt)/π_{Cl} → π*(dppt)	281.9	4.40	0.0165	
H − 1 → L + 8	d→ π^*_{CO}	271.8	4.56	0.0320	
H − 11 → L	π/n(dppt) → π*(dppt)	271.3	4.57	0.0355	
H − 1 → L + 5	d → π*(dppt)	263.0	4.72	0.0218	
H − 2 → L + 8	d→ π^*_{CO}	261.7	4.74	0.0222	
H → L + 6	d → π*(dppt)	261.4	4.74	0.0195	
H → L + 6	d → π*(dppt)	260.9	4.75	0.0265	
H − 5 → L + 2	π_{Cl}/π(dppt) → π*(dppt)	257.8	4.81	0.0683	
H − 2 → L + 7	d→ π^*_{CO}	254.6	4.87	0.0911	
H − 1 → L + 9	d→ π^*_{CO}	242.7	5.11	0.0215	242.0 (5.12) 44500
H − 9 → L + 2	σ_{Cl} → π*(dppt)	241.2	5.14	0.0155	
H − 8 → L + 2	π(dppt) → π*(dppt)				
H − 1 → L + 10	d → π*(dppt)	240.1	5.16	0.0280	
H − 1 → L + 11	d→ π^*_{CO}/π*(dppt)				
H − 9 → L + 2	σ_{Cl} → π*(dppt)	239.4	5.18	0.0157	
H − 8 → L + 2	π(dppt) → π*(dppt)				
H − 10 → L + 2	π/n(dppt) → π*(dppt)	233.1	5.32	0.0180	
H − 5 → L + 3	π_{Cl}/π(dppt) → π*(dppt)				
H − 7 → L + 2	π(dppt)/π_{Cl} → π*(dppt)	229.0	5.41	0.0162	
H − 6 → L + 3	π(dppt) → π*(dppt)				
H − 6 → L + 3	π(dppt) → π*(dppt)	223.1	5.56	0.0228	216.0 (5.74) 76900
H − 12 → L + 1	π(dppt) → π*(dppt)	221.6	5.59	0.0355	
H − 8 → L + 3	π(dppt) → π*(dppt)				
H − 4 → L + 8	π_{Cl} → π^*_{CO}	218.1	5.69	0.0173	
H − 3 → L + 8	π/n(dppt)→ π^*_{CO}				

absorption band attributed to *MLCT* transitions from the rhenium center to the π-antibonding orbitals of the chelating ligand. The Re → π^*_{dppt} absorption appears at 449.4 nm, and is clearly red shifted in comparison with Re → π^*_{bipy} (370 nm) for [Re(CO)$_3$(bipy)Cl]. The dppt ligand leads to a slight decrease in the HOMO–LUMO energy gap, giving slightly lower energy MLCT transitions.

The experimental absorption bands at 331, 300 and 242 nm result from *Metal–Ligand Charge Transfer* (occurring from the rhenium ion to the π-antibonding orbitals of the N–N ligand or π-antibonding orbitals of the carbonyl group) and *Ligand–Ligand Charge Transfer* transitions. However, the main contribution in these bands can be assigned to the *LLCT* excitations. The oscillator strengths of the *LLCT* transitions are considerable larger than those of *MLCT* transitions.

The intra- and interligand transitions are assigned to the highest energy absorption band at 216 nm.

3. Conclusions

The [Re(CO)$_3$(dppt)Cl] complex has been prepared and structurally as well as spectroscopically characterized. X-ray and IR studies confirm a *facial* geometry of the carbonyl ligands in [Re(CO)$_3$(dppt)Cl]. The molecular orbital diagram of the tricarbonyl has been calculated with the density functional theory (DFT) method. The HOMO, HOMO − 1 and HOMO − 2 orbitals are predominantly of d_{Re} orbital character corresponding to the $(5d_{xy})^2$ $(5d_\pi)^4$ occupation. The low-lying virtual orbitals correspond to π^*_{dppt} and π^*_{CO}. Additional information about binding in [Re(CO)$_3$(dppt)Cl] was obtained by NBO analysis. The resonance structure $\bar{M}-\overset{+}{C}\equiv O:$, represents the best bonding between the CO ligands and the Re ion in [Re(CO)$_3$(dppt)Cl]. The spin-allowed electronic transitions of *fac*-Re(CO)$_3$(dppt)Cl have been calculated with the time-dependent DFT method (TDDFT method), and a good agreement between calculated and experimental spectra is observed.

4. Supplementary material

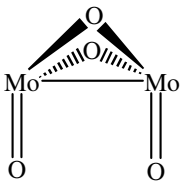
CCDC 623685 contains the supplementary crystallographic data for $C_{23}H_{14}N_4O_3ClRe$. These data can be obtained free of charge via http://www.ccdc.cam.ac.uk/conts/retrieving.html, or from the Cambridge Crystallographic Data Centre, 12 Union Road, Cambridge CB2 1EZ, UK; fax: (+44) 1223-336-033; or e-mail: deposit@ccdc.cam.ac.uk.

Acknowledgement

The GAUSSIAN03 calculations were carried out in the Wrocław Centre for Networking and Supercomputing, WCSS, Wrocław, Poland.

References

[1] A.J. Lees, Chem. Rev. 87 (1987) 711.
[2] A. Juris, V. Balzani, F. Barigelletti, S. Campagna, P. Belser, A. von Zelewsky, Coord. Chem. Rev 84 (1988) 85.
[3] K.S. Schanze, D.B. MacQueen, T.A. Perkins, L.A. Caban, Coord. Chem. Rev. 122 (1993) 63.
[4] V. Balzani, A. Juris, M. Venturi, S. Campagna, S. Serroni, Chem. Rev. 96 (1996) 759.
[5] I.R. Farrell, A. Vlček Jr., Coord. Chem. Rev. 208 (2000) 87.
[6] D.J. Stuffkens, A. Vlček Jr., Coord. Chem. Rev. 177 (1998) 127.
[7] A. Vogler, H. Kunkely, Coord. Chem. Rev 200–202 (2000) 991.
[8] D.R. Striplin, G.A. Crosby, Coord. Chem. Rev (211) (2001) 136.
[9] S. Ranjan, S.-Y. Li, K.-C. Hwang, W.-L. Ching, C.-S. Liu, Y.-T. Tao, C.-H. Chien, S.-M. Peng, G.-H. Lee, Inorg. Chem. 42 (2003) 1248.
[10] F. Li, G. Cheng, Y. Zhao, J. Feng, S. Liu, M. Zhang, Y. Ma, J. Shen, Appl. Phys. Lett. 83 (2003) 4716.
[11] P. Christensen, A. Hamnett, A.V.G. Muir, J.A. Timney, J. Chem. Soc., Dalton Trans. (1992) 1455.
[12] H. Hori, F.P.A. Johnson, K. Koike, K. Takeuchi, T. Ibusuki, O. Ishitani, J. Chem. Soc., Dalton Trans. (1997) 1019.
[13] S.S. Jurisson, J.D. Lydon, Chem. Rev. 99 (1999) 2205.
[14] W.A. Volkert, T.J. Hoffman, Chem. Rev. 99 (1999) 2269.
[15] Cambridge Structural Database, Version 1.8, 2005.
[16] H. Chermette, Coord. Chem. Rev. 178–180 (1998) 699.
[17] CrysAlis RED, Oxford Diffraction Ltd., Version 1.171.29.2.
[18] G.M. Sheldrick, Acta Crystallogr., Sect. A 46 (1990) 467.
[19] G.M. Sheldrick, SHELXL97. Program for the Solution and Refinement of Crystal Structures, University of Göttingen, Germany, 1997.
[20] G.M. Sheldrick, SHELXTL: release 4.1 for Siemens Crystallographic Research Systems, 1990.
[21] M.J. Frisch, G.W. Trucks, H.B. Schlegel, G.E. Scuseria, M.A. Robb, J.R. Cheeseman, J.A. Montgomery Jr., T. Vreven, K.N. Kudin, J.C. Burant, J.M. Millam, S.S. Iyengar, J. Tomasi, V. Barone, B. Mennucci, M. Cossi, G. Scalmani, N. Rega, G.A. Petersson, H. Nakatsuji, M. Hada, M. Ehara, K. Toyota, R. Fukuda, J. Hasegawa, M. Ishida, T. Nakajima, Y. Honda, O. Kitao, H. Nakai, M. Klene, X. Li, J.E. Knox, H.P. Hratchian, J.B. Cross, C. Adamo, J. Jaramillo, R. Gomperts, R.E. Stratmann, O. Yazyev, A.J. Austin, R. Cammi, C. Pomelli, J.W. Ochterski, P.Y. Ayala, K. Morokuma, G.A. Voth, P. Salvador, J.J. Dannenberg, V.G. Zakrzewski, S. Dapprich, A.D. Daniels, M.C. Strain, O. Farkas, D.K. Malick, A.D. Rabuck, K. Raghavachari, J.B. Foresman, J.V. Ortiz, Q. Cui, A.G. Baboul, S. Clifford, J. Cioslowski, B.B. Stefanov, G. Liu, A. Liashenko, P. Piskorz, I. Komaromi, R.L. Martin, D.J. Fox, T. Keith, M.A. Al-Laham, C.Y. Peng, A. Nanayakkara, M. Challacombe, P.M.W. Gill, B. Johnson, W. Chen, M.W. Wong, C. Gonzalez, J.A. Pople, Gaussian 03, Revision B.03, Gaussian, Inc., Pittsburgh PA, 2003.
[22] A.D. Becke, J. Chem. Phys. 98 (1993) 5648.
[23] C. Lee, W. Yang, R.G. Parr, Phys. Rev. B 37 (1988) 785.
[24] M.E. Casida, in: J.M. Seminario (Ed.), Recent Developments and Applications in Modern Density Functional Theory, Theoretical and Computational Chemistry, vol. 4, Elsevier, Amsterdam, 1996.
[25] P.J. Hay, W.R. Wadt, J. Chem. Phys. 82 (1985) 299.
[26] E.D. Glendening, A.E. Reed, J.E. Carpenter, F. Weinhold, NBO (version 3.1).
[27] P.J. Giordano, M.S. Wrighton, J. Am. Chem. Soc. 101 (1979) 2888.
[28] K. Nakamoto, Infrared and Raman Spectra of Inorganic and Coordination Compounds, 4th ed., Wiley-Interscience, New York, 1986.
[29] A.E. Reed, L.A. Curtiss, F. Weinhold, Chem. Rev. 88 (1988) 899.



Scheme 1.

$[n\text{-}Bu_4N]_2[Re_2Cl_8]$ provide a tetramolybdenum cluster consisting of $[Mo_2^{V,V}]$ and $[Mo_2^{V,VI}]$ cores linked through a μ_3-O bridge. X-ray structure of $[Mo_2O_2Cl_2(\mu_2\text{-}O)_2(HprNP)_2]$ (HprNP = 2-(2-pyrrolyl)-1,8-naphthyridine) is also discussed.

2. Results and discussion

Quadruply bonded $[Mo^{II}{\equiv}Mo^{II}]$ complexes undergo aerial oxidation in the presence of π-acid ligands to yield dinuclear polyoxomolybdates. Compounds with neutral and anionic bidentate ligands such as 2,2′-dipyridyls [8], 2-pyridyl(diisopropylphosphino)methane [9a] and 2-mercapto pyrimidines [9b] have been structurally characterized. Our recent interest lies in the 1,8-naphthyridine (NP) based ligands pyNP and HprNP [11]. The reaction of $[Mo_2(OAc)_2(CH_3CN)_6][BF_4]_2$ with HprNP in acetonitrile gave a red solid which was dissolved in dichloromethane and layered with hexane in air yielding red crystals of $[Mo_2O_2Cl_2(\mu_2\text{-}O)_2(HprNP)_2]$ (**1**) at the interface. The IR spectrum of **1** exhibit bands at 968 cm^{-1} assigned to Mo=O and at 724 cm^{-1} assigned to Mo–O_μ stretching vibrations [12].

The X-ray study of **1** reveals the molecular structure to be $[Mo_2O_2Cl_2(\mu_2\text{-}O)_2(HprNP)_2]$. The ORTEP diagram of **1** is shown in Fig. 1 and the structural parameters are given in Table 1. The molecular structure of **1** consists of the $[Mo_2O_2(\mu_2\text{-}O)_2]$ core with the *cisoid* Mo=O bonds [13]. The Mo–Mo bond distance of 2.5707(5) Å is indicative of a Mo–Mo single bond resulting from a d^1–d^1 (Mo^V–Mo^V) interaction [8,14]. The distorted octahedral environment around each Mo atom is completed by one chloride, and one HprNP ligand chelating the metal center through the naphthyridine unit. The N–H hydrogens of the pyrrolyl appendages are engaged in hydrogen bonding interaction with the bridging oxygen atoms (N3···O1 = 2.954(4) Å, angle N3–H3–O1 = 155.9(1)°; N6···O2 = 2.874(4) Å, angle N6–H6–O2 = 177.6(1)°). The two Cl atoms are *trans* to the Mo–Mo single bond with the Mo–Cl distances 2.431(1), 2.448(1) Å and Cl1–Mo1–Mo2–Cl2 dihedral angle 157.9(1)°. The Mo(μ-O)$_2$Mo ring is buckled with the distance between the mid-points of the non-intersecting O···O and Mo···Mo vectors of 0.465 Å. The Mo–O_μ–Mo angles are 82.70(12)° and 83.16(12)° and the O_μ–Mo–O_μ angles are 90.32(13)° and 90.70(13)° reflecting the remarkable symmetry of the bridge. There is a slight twist in the central $[Mo_2O_2]$ core with the O=Mo–Mo=O torsional angle of 8.7(2)°. The Mo–O(bridging) distances are in the range 1.915(3)–1.961(3) Å and the Mo–O(terminal) distances are 1.674(3), 1.680(3) Å. The strong interaction of the Mo atoms with the terminal oxo ligands is demonstrated in an enounced *trans* influence with the Mo–N distances (2.198(4), 2.185(4) Å) *cis* to the Mo=O functionality being shorter than the *trans* Mo–N distances (2.503(4), 2.451(4) Å).

The *cis*-$[Mo_2(OAc)_2(pyNP)_2][BF_4]_2$ exhibits an irreversible metal-based oxidation at +0.86 V. The quadruply bonded $[Re_2Cl_8]^{2-}$ was employed as oxidizing agent ($E_{1/2}$(red) = 1.31 V) yielding the tetranuclear molybdenum cluster $[Mo_4Cl_5O_8(pyNP)_2]$ (**2**). As the reaction was carried out in strict anaerobic condition, the source of oxygens in **2** is possibly the inadvertent water molecules. The use of moist $[n\text{-}Bu_4N]Cl$ failed to yield **2** in any discernable amount implying the essential role of $[Re_2Cl_8]^{2-}$ in the oxi-

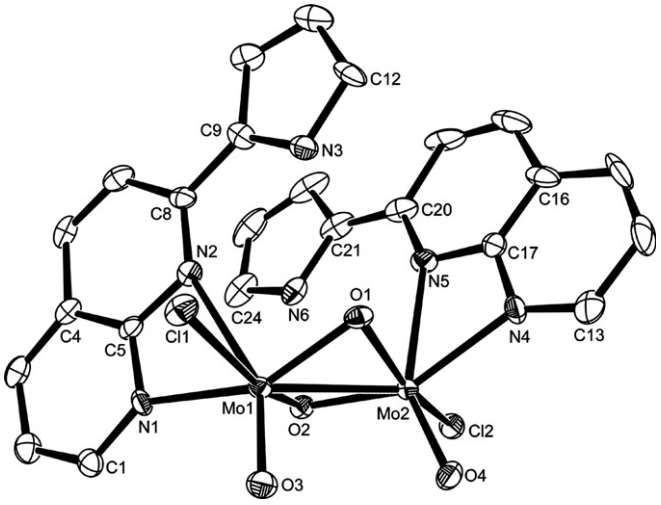


Fig. 1. ORTEP diagram of the molecular structure of $[Mo_2O_2Cl_2(\mu_2\text{-}O)_2(HprNP)_2]$ (**1**) with important atoms labeled. Hydrogen atoms are omitted for the sake of clarity. Thermal ellipsoids are drawn to 50% probability.

Table 1
Selected bond distances (Å) and bond angles (°) for **1**

Mo1–Mo2	2.5707(5)	Mo2–O1	1.961(3)
Mo1–O1	1.930(3)	Mo2–O2	1.915(3)
Mo1–O2	1.958(3)	Mo2–O4	1.680(3)
Mo1–O3	1.674(3)	Mo2–N4	2.185(4)
Mo1–N1	2.198(4)	Mo2–N5	2.451(4)
Mo1–N2	2.503(4)	Mo2–Cl2	2.4482(12)
Mo1–Cl1	2.4310(12)		
N1–Mo1–N2	56.67(13)	O4–Mo2-Mo1	99.75(11)
O2–Mo1–Mo2	47.70(9)	O2–Mo2–Mo1	49.14(9)
N1–Mo1–Mo2	129.23(10)	O1–Mo2–Mo1	48.14(9)
Cl1–Mo1–Mo2	136.24(4)	N4–Mo2–Mo1	130.36(10)
N2–Mo1–Mo2	104.99(9)	Cl2–Mo2–Mo1	132.94(3)
O3–Mo1–Mo2	98.20(11)	O1–Mo2–O2	90.70(13)
O1–Mo1–Mo2	49.16(9)	O1–Mo1–O2	90.32(13)
N4–Mo2–N5	56.81(15)	Mo2–O1–Mo1	82.70(12)
O4–Mo2–Mo1	99.75(11)	Mo2–O2–Mo1	83.16(12)
N5–Mo2–Mo1	107.29(9)		

dation process. The vibrational spectrum is consistent with that of an oxomolybdate. The band at 970 cm^{-1} is assigned to Mo=O stretching vibrations [8]. The EPR spectrum reveals a single electron species with $g = 1.94$ (Fig. 2).

Compound **2** was characterized by X-ray study. The molecular formula of the tetrameric compound may be envisioned as $[Mo_2Cl_3O_2(\mu_2\text{-}O)(\eta^3\text{-}pyNP)][\mu_3\text{-}O][Mo_2Cl_2O_2(\mu_2\text{-}O)_2(\eta^2\text{-}pyNP)]$, the fusion of two oxo-bridged Mo_2 cores bridged through μ_3-oxo linkage. The Mo3 and Mo4 form an ESBO unit involving the $[Mo_2O_2(\mu_2\text{-}O)_2Cl_2]$ core. The Mo_2O_2 four-member ring is puckered and the terminal oxo groups are located in a *cis* arrangement similar to that observed in compound **1**. The distance between the mid points of the non-intersecting O···O and Mo···Mo vectors of 0.431 Å. The eclipsed oxygen atoms form O5–Mo3–Mo4–O8 dihedral angle of 3.1(2)°. The Mo–O (bridged and terminal) distances are typical of those found in other oxomolybdates [13]. The Mo–O_μ–Mo angles are 83.67(17)° and 82.82(17)° and the Oμ–Mo–Oμ angles are 90.5(2)° and 91.8(2)° indicating the remarkable symmetry of the bridge (Table 2). The Cl5–Mo4–Mo3–Cl4 dihedral angle is 10.1(1)° and the Mo–Cl distances are 2.413(2) and 2.441(2) Å. The pyNP ligand caps one end of this Mo_2 core in bypridyl chelating fashion with N4–Mo4–N5 angle 70.1(2)°.

Interestingly, the Mo3 is penta coordinated. Apart from one terminal, two bridging oxo ligands and one chloride, Mo3 is further coordinated to an oxo ligand. The latter oxo ligand, in turn, bridges another Mo_2 unit (Fig. 3). The torsional angle Mo3–O4–Mo2–Mo1 is 173.7(5)°, indicative of almost the planar triply bridging mode of oxygen atom connecting the two Mo_2 cores. The Mo1 and Mo2 form an ESBO structure with both the atoms have in common a μ_3-oxo, μ_2-oxo, one terminal oxo and a chloride ligand. The pyNP ligand bridges the dimetal unit via N–C–N mode and at the same time the pyridyl N-atom binds Mo2 with N3–Mo2–N2 angle of 70.3(2)°. The Mo1 has an additional chloride ligand. The Mo=O distances are 1.666(5) and 1.673(5) Å. The Mo1–O4 and Mo2–O4

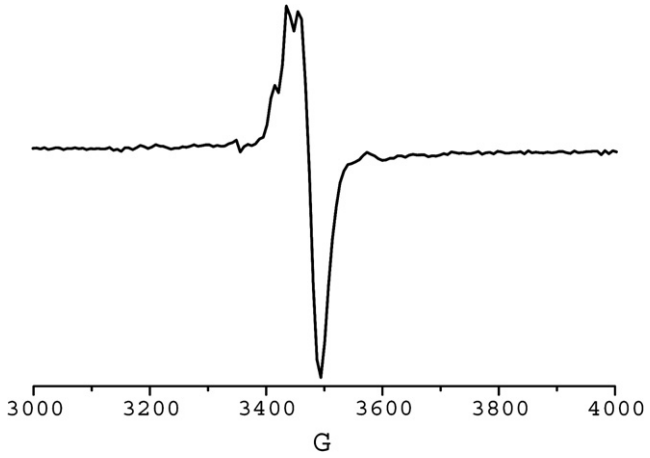


Fig. 2. Solid state EPR of $[Mo_4Cl_5O_8(pyNP)_2]$ (**2**) at 120 K.

Table 2
Selected bond distances (Å) and bond angles (°) for **2**

Mo1–Mo2	2.6015(9)	Mo3–Mo4	2.5685(10)
Mo1–O1	1.666(5)	Mo3–O5	1.679(5)
Mo1–O2	1.942(5)	Mo3–O6	1.913(4)
Mo2–O3	1.673(5)	Mo3–O7	1.933(4)
Mo1–O4	1.958(5)	Mo3–O4	2.065(4)
Mo1–Cl1	2.4135(19)	Mo3–Cl4	2.4134(18)
Mo1–Cl2	2.4457(19)	Mo4–O8	1.687(5)
Mo1–N1	2.529(5)	Mo4–O6	1.938(4)
Mo2–O2	1.925(5)	Mo4–O7	1.950(5)
Mo2–O4	1.982(4)	Mo4–N4	2.213(5)
Mo2–N3	2.241(6)	Mo4–N5	2.408(5)
Mo2–N2	2.302(6)	Mo4–Cl5	2.4405(19)
Mo2–Cl3	2.403(2)		
O1–Mo1–Mo2	101.53(17)	O4–Mo3–Cl4	83.79(13)
O2–Mo1–Mo2	47.45(13)	O5–Mo3–Mo4	97.96(16)
O4–Mo1–Mo2	49.07(13)	O6–Mo3–Mo4	48.58(13)
Cl1–Mo1–Mo2	133.15(5)	O7–Mo3–Mo4	48.89(14)
Cl2–Mo1–Mo2	130.19(5)	O5–Mo3–O4	97.7(2)
N1–Mo1–Mo2	80.75(13)	O6–Mo3–O4	85.87(18)
N3–Mo2–Mo1	141.45(14)	O7–Mo3–O4	152.93(19)
N2–Mo2–Mo1	90.77(14)	O4–Mo3–Mo4	134.42(12)
Cl3–Mo2–Mo1	130.57(5)	Cl4–Mo3–Mo4	135.34(5)
O3–Mo2–Mo1	104.54(17)	O8–Mo4–Mo3	99.23(16)
O2–Mo2–Mo1	48.00(13)	O6–Mo4–Mo3	47.76(13)
O4–Mo2–Mo1	48.29(13)	O7–Mo4–Mo3	48.30(13)
O3–Mo2–O4	103.2(2)	N4–Mo4–Mo3	130.29(14)
O2–Mo2–O4	95.08(19)	N5–Mo4–Mo3	102.33(13)
O4–Mo2–N3	93.64(19)	Cl5–Mo4–Mo3	135.19(5)
N3–Mo2–N2	70.3(2)	O6–Mo3–O7	91.78(18)
O4–Mo2–Cl3	157.11(13)	O6–Mo4–O7	90.50(19)
O2–Mo1–O4	95.30(18)	N4–Mo4–N5	70.1(2)
Mo3–O6–Mo4	83.67(17)	Mo2–O4–Mo1	82.64(17)
Mo3–O7–Mo4	82.82(17)	Mo2–O2–Mo1	84.55(18)

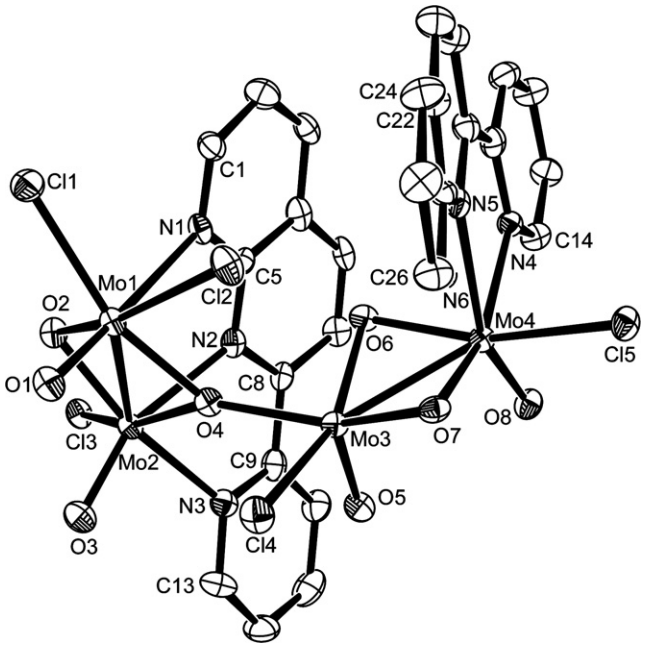
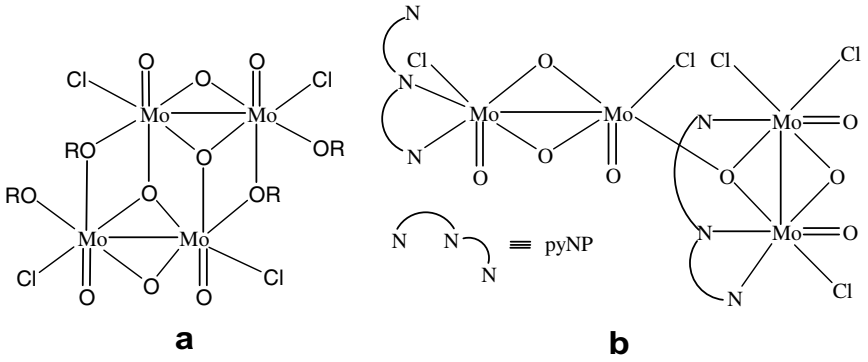


Fig. 3. ORTEP diagram of the molecular structure of $[Mo_4Cl_5O_8(pyNP)_2]$ (**2**) with important atoms labeled. Hydrogen atoms are omitted for the sake of clarity. Thermal ellipsoids are drawn to 30% probability.



Scheme 2.

distances (1.958(5), 1.983(4) Å) are longer in comparison to the doubly bridged Mo–O distances (Mo1–O2 1.942(5) Å, Mo2–O2 1.925(5) Å). The Mo–O_μ–Mo angles are 82.64(17)°, 84.55(18)° and the O_μ–Mo–O_μ angles are 95.08(19)° and 95.30(18)°, once again indicating the remarkable bridge symmetry. The two terminal oxygen atoms are eclipsed with dihedral angle 2.3(2)°. The extent of deviation of the Mo(μ-O)$_2$Mo ring from planarity is significantly less with the distance between the mid-points of the non-intersecting O···O and Mo–Mo being 0.201 Å. Both the molybdenum atoms have terminal chlorine atom with Cl1–Mo1–Mo2–Cl3 torsional angle of 5.1(1)°.

The Mo–Mo distances in compound **2** needs special mention. The Mo1–Mo2 distance of 2.6015(9) Å is longer than the Mo3–Mo4 distance (2.5685(10) Å) despite one pyNP bridging the Mo1–Mo2 whereas the second pyNP chelates the Mo4. It should be noted that pyNP is known to bridge dimetal unit of metal-metal bond order ranging from zero to four and does not influence the metal-metal distance considerably [15]. The electron counting suggests the compound **2** to be a $[Mo_4]^{21+}$ species, a d^3 electron system. The EPR study, however, reveals that compound **2** has one unpaired electron. It is postulated that Mo3–Mo4 utilizes the two d-electrons to form a σ bond of formal bond order 1.0, and the Mo1–Mo2 involves in a 2c–1e bond of formal bond order 0.5 [16].

Dimerization of two Mo_2 cores to a tetranuclear structure has been reported in the literature [5a,17]. The resulted oxochloromolybdates usually are symmetric and posses a combination of oxo and alkoxo bridges [3b]. One such example is shown in Scheme 2a. In compound **2**, however, two Mo_2 units are coupled through one μ_3-oxo link leading to an asymmetric structure (Scheme 2b). Formation of more extended structure is precluded by the pyNP ligand capping the ends of the oligomer.

3. Conclusion

Here we describe the synthesis of polyoxomolybdates incorporating 1,8-napthyridine based ligands. Aerial oxidation of the quadruply bonded $Mo_2(OAc)_4$ in presence of organic ligand and in dichloromethane provides oxochloromolybdates containing the well-characterized $[Mo_2O_2Cl_2(\mu_2\text{-}O)_2]$ core. An alternative route to access high-oxidation state oxomolybdates is to employ suitable oxidizing agent. The quadruply bonded $[Re_2Cl_8]^{2-}$ oxidizes the $Mo_2(OAc)_4$ to oxochlorodimolybdates those subsequently dimerizes to give the tetrameric $[Mo_4Cl_5O_8(pyNP)_2]$. It is our expectation that the *in situ* oxidation of the $[Mo^{II}{\equiv}Mo^{II}]$ core in the presence of suitable peripheral ligands would provide access to polyoxomolybdates of unprecedented topologies.

4. Experimental

4.1. Materials and physical characterizations

The ligands pyNP and HprNP were prepared by the Friedlander condensation of 2-aminonicotinaldehyde with corresponding acyl derivatives [11]. Compounds *cis*-$[Mo_2(pyNP)_2(OAc)_2][BF_4]_2$ and $[n\text{-}Bu_4N]_2[Re_2Cl_8]$ were synthesized according to the literature procedures [10,18]. Infrared spectra were recorded in the range 4000–400 cm^{-1} on a Vertex 70 Bruker spectrophotometer on KBr pellets. EPR spectra were recorded on a Bruker EMX X-band spectrometer. Elemental analyses were performed on a Thermoquest EA1110 CHNS/O analyzer.

4.2. Synthesis

Synthesis of $[Mo_2O_2Cl_2(\mu_2\text{-}O)_2(HprNP)_2]$ (***1***). A sample of $[Mo_2(OAc)_2(CH_3CN)_6][BF_4]_2$ (70.7 mg, 0.097 mmol) dissolved in 20 mL of CH_3CN was treated with HprNP (44 mg, 0.224 mmol), which led to a color change from light pink to dark red. After 8 h stirring at room temperature, red precipitation occurred. The filtrate was discarded; the precipitate was washed with benzene (2 × 10 mL) and isolated. Crystallization was tried in open air by dissolving the precipitate in dichloromethane and layering with hexane in air. Red crystals appeared at the junction of two solvents. Yield: 55 mg (79%). IR (KBr) data (cm^{-1}): ν(Mo=O): 970 cm^{-1}, ν(Mo–O_μ): 724 cm^{-1}. *Anal.* Calc.

Table 3
Crystallographic data and refinement parameters for compounds **1** and **2**

	1	**2**
Empirical formula	$C_{48}H_{36}Cl_4Mo_4N_{12}O_8$	$C_{29}H_{18}Cl_{11}Mo_4N_6O_8$
Formula weight	1434.45	1352.20
Crystal system	monoclinic	monoclinic
Space group	*P*21/*n*	*P*21/*n*
a (Å)	10.8361(7)	10.477(5)
b (Å)	14.6927(10)	18.250(5)
c (Å)	18.4440(13)	24.870(5)
α (°)		
β (°)	105.0400(10)	101.733(5)
γ (°)		
V (Å^3)	2835.9(3)	4656(3)
Z	2	4
ρ_{calcd} (g cm^{-3})	1.680	1.929
μ (mm^{-1})	1.113	1.734
F(000)	1416	2612
Reflections collected	18574	30892
Reflections independent	6967	11499
Reflections observed [$I > 2\sigma(I)$]	5408	8060
Number of variables	346	489
Goodness-of-fit	1.102	1.041
Final *R* indices [$I > 2\sigma(I)$][a]	$R_1 = 0.0461$	$R_1 = 0.0632$
	$wR_2 = 0.0929$	$wR_2 = 0.1639$

[a] $R_1 = \sum\|F_o| - |F_c\|/\sum|F_o|$ with $F_o^2 > 2\sigma(F_o^2)$. $wR_2 = [\sum w(|F_o^2| - |F_c^2|)^2/\sum|F_o^2|^2]^{1/2}$.

for $C_{24}H_{18}N_6Cl_2O_4Mo_2$: C, 40.19; H, 2.53; N, 11.72. Found: C, 40.35; H, 2.71; N, 11.54%.

Synthesis of [*Mo$_4$O$_8$Cl$_5$(pyNP)$_2$*] (**2**). To an acetonitrile solution (20 mL) of *cis*-$[Mo_2(pyNP)_2(OAc)_2][BF_4]_2$ (55 mg, 0.061 mmol) was added $[n\text{-}Bu_4N]_2[Re_2Cl_8]$ (77 mg, 0.068 mmol). The solution was stirred at room temperature for 8 h to give a bright red solution. Stirring was stopped at this point, concentrated, and layered with 15 mL of dichloromethane. The solution was left undisturbed at room temperature, when red-orange single crystals of the title compound appeared at the interface of two solvents within a day in quantitative yield. The crystals were isolated, washed with diethyl ether and dried under vacuum. Yield: 50 mg (74%). IR (KBr) data (cm^{-1}): *ν*(Mo=O): 968 cm^{-1}, *ν*(Mo–O$_μ$): 724 cm^{-1}. *Anal.* Calc. for $C_{26}H_{18}N_6Cl_5O_8Mo_4$: C, 28.30; H, 1.64; N, 7.62. Found: C, 28.45; H, 1.87; N, 7.45%.

4.3. X-ray data collection and refinement

Single-crystal X-ray studies were performed on a CCD Bruker SMART APEX diffractometer equipped with an Oxford Instruments low-temperature attachment. Data were collected at 100(2) K using graphite-monochromated Mo Kα radiation ($\lambda_\alpha = 0.71073$ Å). The frames were integrated in the Bruker SAINT software package, and data were corrected for Lorentz and polarization effects, and an absorption correction was applied. Structures were solved and refined with SHELX suite of programs. Pertinent crystallographic data are provided in Table 3. Hydrogen atoms of the ligands, unless mentioned otherwise, were included in the final stages of the refinement and were refined with a typical riding model. ORTEP-III was used to produce the diagrams. SQUEEZE option was applied for both the compounds to remove severely disordered solvent molecules that could not be modeled. For compound **2**, one of the CH_2Cl_2 was found to be disordered and modeled satisfactorily. All non-H atoms of the CH_2Cl_2 solvates were refined isotropically except C11S and C12S. Hydrogen atoms are not included for solvent molecules. The anisotropic refinement of N4 atom resulted in non-positive definite displacement parameter, and was refined isotropically.

Acknowledgements

Authors thank the CSIR India for the financial support of this research.

Appendix A. Supplementary material

CCDC 624834, 624835 contains the supplementary crystallographic data for (**1**) and (**2**). These data can be obtained free of charge via http://www.ccdc.ac.uk/conts/retrieving.html, or from the Cambridge Crystallographic Data Centre, 12 Union Road, Cambridge CB2 1EZ, UK; fax: (+44) 1223-336-033; or e-mail: deposit@ccdc.cam.ac.uk. Supplementary data associated with this article can be found, in the online version, at doi:10.1016/j.poly.2006.11.042.

References

[1] (a) C.D. Garner, S. Bristow, Molybdenum Enzymes, Wiley, New York, 1985, 343;
(b) C.D. Garner, Comprehensive Coordination Chemistry, Permagon Press, Oxford, 1987, 1421.
[2] V.S. Joshi, M. Nandi, H. Zhang, B.S. Haggerty, A. Sarkar, Inorg. Chem. 32 (1993) 1301.
[3] (a) M.T. Pope, Heteropoly and Isopoly Oxometalates, Springer-Verlag, New York, 1983;
(b) H. Kang, S. Liu, S.N. Shaikh, T. Nicholson, J. Zubieta, Inorg. Chem. 28 (1989) 920;
(c) S. Liu, S.N. Shaikh, J. Zubieta, Inorg. Chem. 26 (1987) 4303;
(d) C.L. Hill, R. Renneke, J. Am. Chem. Soc. 108 (1986) 3528;
(e) I. Ioannidis, E. Papaconstantinou, Inorg. Chem. 24 (1985) 439;
(f) V.W. Day, W.G. Klemperer, Science 228 (1985) 533.
[4] (a) C.L. Hill, Chem. Rev. 98 (1998) 1;
(b) W.G. Klemperer, T.A. Marquart, O.M. Yaghi, Angew. Chem. Int. Ed. Engl. 31 (1992) 49;
(c) I. Matsuura, S. Mizuno, H. Hashiba, Polyhedron 5 (1986) 111.
[5] (a) B. Modec, J.V. Brencic, J. Zubieta, J. Chem. Soc., Dalton Trans. (2002) 1500;
(b) M.I. Khan, J. Zubieta, Prog. Inorg. Chem. 43 (1995) 1;
(c) H.K. Chae, W.G. Klemperer, T.A. Marquart, Coord. Chem. Rev. 128 (1993) 209;
(d) Q. Chen, J. Zubieta, Coord. Chem. Rev. 114 (1992) 107.
[6] J.K. Bera, P.S. Szalay, K.R. Dunbar, Inorg. Chem. 41 (13) (2002) 3429.
[7] M.H. Chisholm, J.C. Huffman, W.G. Van Der Sluys, J. Am. Chem. Soc. 109 (1987) 2514.
[8] J.I. Dulebohn, T.C. Stamatakos, D.L. Ward, D.G. Nocera, Polyhedron 10 (1991) 2813.

[9] (a) H. Lang, P.E. Fanwick, R.A. Walton, Inorg. Chim. Acta. 328 (2002) 232;
(b) F.A. Cotton, W.H. Ilsley, Inorg. Chim. Acta. 59 (1982) 213.
[10] C.S. Campos-Fernandez, L.M. Thomson, J.R. Galan-Mascaros, X. Ouyang, K.R. Dunbar, Inorg. Chem. 41 (2002) 1523.
[11] S.K. Patra, N. Sadhukhan, J.K. Bera, Inorg. Chem. 45 (2006) 4007.
[12] B. Kamenar, B. Korpar-Colig, M. Penavic, J. Chem. Soc., Dalton Trans. (1981) 311.
[13] (a) Y. Lu, E. Wang, M. Yuan, Y. Li, C. Hu, J. Mol. Struct. 649 (2003) 191;
(b) P. Hoffmann, R. Mattes, Inorg. Chem. 28 (1989) 2092;
(c) B.M. Gatehouse, E.K. Nunn, Acta Crystallogr., Sect. B: Struct. Crystallogr. Cryst. Chem. B32 (1976) 2627;
(d) D.R. Staveren, E. Bothe, T. Weyhermuller, N. Metzler-Nolte, Eur. J. Inorg. Chem. (2002) 1518;
(e) I.K. Dhawan, M.A. Bruck, B. Schilling, C. Grittini, J.H. Enemark, Inorg. Chem. 34 (1995) 3801;
(f) K. Wieghardt, M. Hahn, W. Swiridoff, J. Weiss, Angew. Chem. Int. Ed. Engl. 22 (1983) 49;
(g) T.R. Webb, E.S. Talbott, Acta Crystallogr., Sect. C: Cryst. Struct. Commun. 55 (1999) 370;
(h) J. Beck, W. Hiller, E. Schweda, J. Strahle, Z. Naturforsch., B: Chem. Sci. 39 (1984) 1110;
(i) B.S. Lim, M.W. Willer, M. Miao, R.H. Holm, J. Am. Chem. Soc. 123 (2001) 8343;
(j) R. Hazama, K. Umakoshi, A. Ichimura, S. Ikari, Y. Sasaki, T. Ito, Bull. Chem. Soc. Jpn. 68 (1995) 456.
[14] E.I. AStiefel, Prog. Inorg. Chem. 22 (1977) 1.
[15] (a) J.-P. Collin, A. Jouaiti, J.-P. Sauvage, W.C. Kaska, M.A. McLoughlin, N.L. Keder, W.T.A. Harrison, G.D. Stucky, Inorg. Chem. 29 (1990) 2238;
(b) E. Binamira-Soriaga, N.L. Keder, W.C. Kaska, Inorg. Chem. 29 (1990) 3167;
(c) R.P. Thummel, Y. Decloitre, Inorg. Chim. Acta. 128 (1987) 245;
(d) R.P. Thummel, F. Lefoulon, D. Williamson, M. Chavan, Inorg. Chem. 25 (1986) 1675;
(e) E. Binamira-Soriaga, S. D Sprouse, R.J. Watts, W.C. Kaska, Inorg. Chim. Acta. 84 (1984) 135;
(f) W.R. Tikkanen, C. Krüger, K.D. Bomben, W.L. Jolly, W.C. Kaska, P.C. Ford, Inorg. Chem. 23 (1984) 3633;
(g) A.T. Baker, W.R. Tikkanen, W.C. Kaska, P.C. Ford, Inorg. Chem. 23 (1984) 3254;
(h) W.R. Tikkanen, E. Binamira-Soriaga, W.C. Kaska, P.C. Ford, Inorg. Chem. 23 (1984) 141;
(i) W.R. Tikkanen, E. Binamira-Soriaga, W.R. Kaska, P.C. Ford, Inorg. Chem. 22 (1983) 1147;
(j) P. Caluwe, G. Evens, Macromolecules 12 (1979) 803.
[16] J.A. Beaver, M.G.B. Drew, J. Chem. Soc., Dalton Trans. (1973) 1376.
[17] (a) M.F. Belicchi, G.G. Fava, C. Pelizzi, J. Chem. Soc., Dalton Trans. (1983) 65;
(b) B. Modec, J.V. Brencic, L. Golic, L.M. Daniels, Polyhedron 19 (2000) 1407;
(c) C. Limberg, A.J. Downs, A.J. Blake, S. Parsons, Inorg. Chem. 35 (1996) 4439.
[18] (a) T.J. Barder, R.A. Walton, Inorg. Chem. 21 (1982) 2510;
(b) T.J. Barder, R.A. Walton, Inorg. Synth. 23 (1985) 116.

These 1D zincophosphates are synthesized in aqueous medium at various temperatures (from room temperature to 180 °C) using different amines as a template. At the present time their mechanism of formation is not well established.

This paper reports the synthesis and the crystal structure determination of a new 1D zincophosphate $[Zn(H_2PO_4)_2(HPO_4)][C_7H_{17}N_2]$ obtained under hydrothermal conditions using 2-aminomethyl(1-ethyl)pyrrolidine as an organic template.

2. Experimental

2.1. Hydrothermal synthesis

A mixture of 1.18 g (12 mmol) phosphoric acid (Fluka 85 wt% H_3PO_4), 0.51 g (4 mmol) AMEP (Acros), and 0.16 g (2 mmol) zinc oxide (Prolabo) was stirred in 20 mL water (pH ≈ 2) for 20 min. The mixture was then transferred to a Teflon-lined stainless-steel autoclave and kept at 130 °C under autogenous pressure for five days. After cooling to room temperature, transparent prismatic crystals with suitable dimensions for crystallographic study were collected. The crystals were washed several times with distilled water and dried in the open air. They are stable for months under normal conditions of temperature and humidity. Schematically the reaction can be written as follows:

$$ZnO + 3H_3PO_4 + C_7H_{15}N_2 \rightarrow [Zn(H_2PO_4)_2(HPO_4)] \times [C_7N_2H_{17}] + H_2O.$$

2.2. Investigation techniques

The title compound has been studied by various physico-chemical methods: X-ray diffraction, solid state NMR spectroscopy combined with ab initio calculations, infrared spectroscopy and thermal analysis.

2.2.1. X-ray diffraction

The intensity data collection was performed using a MACH3 Enraf Nonius diffractometer. The experimental conditions of data collection, the strategy followed for the structure determination and the final results are given in Table 1. The structure was solved by the SIR 92 [12] program and refined by full-matrix least-squares techniques based on F, using SHELXL 97 [13]. The structure factors were obtained after Lorentz polarization corrections. Analytical empirical absorption corrections were made [14]. The positions of the heavier atoms, including the Zn atom, were located by the direct method. The remaining atoms were found in a series of alternating difference Fourier maps and least-square refinements. The positions of the hydrogen atoms of this hybrid compound were located directly from the difference Fourier maps. The drawings were made with DIAMOND [15].

Table 1
Crystal data and experimental parameters used for the intensity data collection strategy and final results of the structure determination

I. Crystal data	
Formula	$[Zn(H_2PO_4)_2(HPO_4)]$ $[C_7\ N_2H_{17}]$
F_w	392.60
Crystal system	triclinic
Space group	$P\bar{1}$
a (Å)	7.930(3)
b (Å)	8.169(3)
c (Å)	14.795(3)
α (°)	87.22(2)
β (°)	85.35(3)
γ (°)	65.68(3)
V (Å^3)	870.3(4)
Z	2
Refinement of unit-cell parameters with	25 reflections ($7° < \theta < 10°$)
ρ_{calc} (g cm^{-3})	1.882
$F(000) = 410.00$	
Linear absorption factor μ (Ag Kα) (cm^{-1})	1.498
Morphology	prism
Crystal size (mm), $0.35 \times 0.30 \times 0.20$	
Color	transparent
II. Intensity measurements	
Temperature	293.2 K
Wavelength (Å)	Mo Kα (0.7107)
Diffractometer	Enraf-Nonius MACH 3
Scan mode	$\omega - 2\theta$
Monochromator	graphite plate
Θ range (°)	2.74–24.97
Measurement area ($\pm hkl$)	$h_{max} = 9$; $k_{max} = 9$; $l_{max} = 17$
Number of scanned reflections (R_{int})	3077 (0.037)
Number of independent reflections	3018
Orientation and control reflections	−312 and 242
III. Structure determination	
Lorentz and polarization corrections	no absorption correction
Program used	SHELX-97 [36]
All the hydrogen atoms were located from difference Fourier maps. They are not refined	
Determination	direct methods
Unique reflections included	3018($I > 2\sigma$)
Weighting scheme	σ
Refined parameters	249
Residual Fourier density (Å^3 < ρ < 1.34 Å^3): −0.88	$R = 0.048$; $R_w = 0.1304$
Drawings made with DIAMOND	[37]
Goodness-of-fit on F^2	1.081
Largest shift/error	0.000

2.2.2. NMR spectroscopy

All NMR spectra were recorded on a Bruker DSX-300 spectrometer operating at 75.49 MHz for ^{13}C and 121.51 MHz for ^{31}P with a classical 4 mm probehead allowing spinning rates up to 10 kHz. ^{13}C chemical shifts are given relative to tetramethylsilane and ^{31}P ones relative to 85 % H_3PO_4 (external references, precision 0.5 ppm). The phosphorus spectrum was recorded both under classical MAS conditions with high power proton decoupling and

by use of cross-polarization from protons while the carbon one was obtained by use of cross-polarization (contact time 5 ms) and MAS. In all cases it was checked that there was a sufficient delay between the scans allowing a full relaxation of the nuclei. When cross-polarization was used, typically the delay between two consecutive scans was 1 s, while it was 30 s for the classical ^{31}P NMR spectrum.

2.2.3. Ab initio calculations

DFT calculations (at the B3LYP/6-31+G* level) were made to allow the attribution of the ^{31}P and ^{13}C NMR signals to the various crystallographically inequivalent atoms. For phosphorus, the chemical shifts were determined by taking the coordinates of the PO_4 tetrahedra found by X-ray diffraction and calculation of the chemical shifts with the GIAO method. For carbon, the positions of the hydrogen atoms were first optimized at the same level of theory, the carbon and nitrogen atoms being frozen. All calculations were made with the GAUSSIAN 98 software.

2.2.4. Thermal behavior

Thermal analysis was performed using the "multimodule 92 Setaram" analyzer operating from room temperature up to 873 K at an average heating rate of 5 K min^{-1} in a flowing drying argon atmosphere.

2.2.5. IR spectroscopy

Spectra were recorded in the range 4000–400 cm^{-1} with a "Perkin-Elmer FTIR" spectrophotometer 1000 using a sample dispersed in a spectroscopically pure KBr pellet.

3. Results and discussion

3.1. Structure description

Final atomic coordinates and thermal parameters for ZnP-AMEP are given in Table 2. The entities of the main geometrical features are reported in Table 3. All atoms are at general positions. An ORTEP drawing of the asymmetric unit of the compound templated by organic cations is shown in Fig. 1.

The asymmetric unit of ZnP-AMEP contains 25 non-hydrogen atoms. There are one Zn and three crystallographically distinct P atoms present in the asymmetric unit. The Zn atom is tetrahedrally coordinated by four oxygen atom neighbours, with average Zn–O bond lengths of 1.929 Å. The average O–Zn–O bond angle has the expected tetrahedral angle of 109.4°. The Zn atom is connected to four phosphorus atoms through Zn–O–P linkages with an average bond angle of 140.1°. Among the three crytallographically independent phosphorus atoms, P(1) and P(2) are connected to two different Zn atoms via two P–O–Zn linkages. P(1) possesses two terminal P–OH bonds while P(2) has one P–OH and one P–O bond. P(3) exhibits an isolated (H_2PO_4) tetrahedra.

The marginally longer P═O are mainly due to the presence of a large number of hydrogen bond interactions in this compound. As expected, (ZnO)─P═O angles (average 113.7°) as well as the (ZnO)–P–(OZn) angles (average 113.9°) are significantly bigger than O–P–O angles with an OH group involved therein (107.6°). O–P–O angles with two OH residues are again significantly smaller (106.1°).

Table 2
Final atomic coordinates in $[Zn(H_2PO_4)_2(HPO_4)][C_7H_{17}N_2]$

Atoms	x	y	z	$U_{eq.}$
Zn(1)	0.73323(4)	0.76006(4)	0.51942(2)	0.01700(17)
P(1)	0.98283(11)	0.42979(11)	0.65437(5)	0.0188(2)
P(2)	0.70268(11)	1.14011(11)	0.52321(5)	0.0180(2)
P(3)	0.72804(12)	0.54714(12)	0.96124(5)	0.0223(2)
O(1)	1.0478(4)	0.4765(4)	0.74337(16)	0.0290(6)
O(2)	0.9387(4)	0.2650(4)	0.6805(2)	0.0382(7)
O(3)	1.1525(4)	0.3832(4)	0.59071(18)	0.0361(6)
O(4)	0.8129(4)	0.5829(4)	0.62457(18)	0.0326(6)
O(5)	0.8053(3)	0.9376(3)	0.53382(18)	0.0276(5)
O(6)	0.8294(4)	1.2063(4)	0.45652(19)	0.0324(6)
O(7)	0.6701(4)	1.2321(4)	0.61314(18)	0.0333(6)
O(8)	0.5289(3)	1.1941(4)	0.47297(17)	0.0296(6)
O(9)	0.7775(4)	0.5420(4)	1.06202(17)	0.0379(7)
O(10)	0.7302(4)	0.3599(4)	0.9410(2)	0.0390(7)
O(11)	0.8744(4)	0.5718(4)	0.89768(16)	0.0323(6)
O(12)	0.5341(3)	0.6895(3)	0.95618(17)	0.0303(6)
N(1)	0.3818(4)	0.9119(4)	0.81512(19)	0.0246(6)
N(2)	0.3805(5)	0.5365(4)	0.6761(2)	0.0341(7)
C(1)	0.3063(5)	0.8195(5)	0.7528(2)	0.0243(7)
C(2)	0.1080(6)	0.8597(6)	0.7909(3)	0.0398(10)
C(3)	0.0792(6)	0.9635(6)	0.8766(3)	0.0429(10)
C(4)	0.2140(6)	1.0519(5)	0.8639(3)	0.0381(9)
C(5)	0.4353(5)	0.6221(5)	0.7470(2)	0.0283(7)
C(6)	0.5108(7)	0.9830(6)	0.7656(3)	0.0396(10)
C(7)	0.5919(7)	1.0658(7)	0.8294(4)	0.0501(12)

$U_{eq.} = \frac{1}{3}\sum_i\sum_j U_{ij}a_i^*a_j^*(a_i.a_j)$.
Esd are given in parentheses.

The ZnP-AMEP is constructed by the vertex linking of ZnO_4, $PO_3(OH)$ and $PO_2(OH)_2$ tetrahedral units. The connectivity between these tetrahedral units gives rise to one-dimensional chains built from ($Zn_2P_2O_{12}$) four-membered rings sharing their tetrahedral ZnO_4, propagated along $[1\bar{1}0]$ with a general formula of $[Zn(H_2PO_4)(HPO_4)]_n^-$ (Fig. 2). Not only are the individual chain units held together by hydrogen bond interactions and form a sheet-like architecture organization centered by $z = 1/2$ planes, but they are also held with pure phosphate $(H_2PO_4)_n^{n-}$ chains extending along [100] direction at $y = 1/2$ to form finally a 3D anionic network (Fig. 3). To the best of our knowledge, compound ZnP-AMEP represents the first organic templated metallophosphate in which the four-membered rings interact with chains of dihydrogenophosphate. Among the five P–OH entities, two participate in an intra-chain phosphate H bond and three form inter-chain links. This arrangement yields cavities and apertures, wherein the amine molecules reside, this latter has a constraint configuration, confirmed by the short distance (about 6.884 Å) between the sheets of $[Zn(H_2PO_4)(HPO_4)]_n^-$ and chains of $(H_2PO_4)_n^{n-}$. The cavities formed by such interactions (Fig. 4) closely resemble those

Table 3
Interatomic distances (Å) and bond angles (°) in $[Zn(H_2PO_4)_2(HPO_4)][C_7H_{17}N_2]$

ZnO_4 tetrahedron					
Zn		O(3)	O(4)	O(5)	O(8)
O(3)		1.913(3)	3.178(13)	3.163(13)	3.155(13)
O(4)		111.40(13)	1.941(3)	3.113(13)	3.010(13)
O(5)		110.21(12)	106.47(12)	1.947(2)	3.252(13)
O(8)		110.98(11)	102.62(11)	114.86(11)	1.916(2)
Zn–O(3)–P(1) = 142.20(17)			Zn–O(5)–P(2) = 132.60(15)		
Zn–O(4)–P(1) = 138.68(17)			Zn–O(8)–P(2) = 147.17(17)		
$H_2P(1)O_4^-$					
P		O(1)	O(2)	O(3)	O(4)
O(1)		1.570(2)	2.473(3)	2.394(3)	2.522(2)
O(2)		104.90(15)	1.549(3)	2.537(2)	2.439(2)
O(3)		102.24(14)	112.53(18)	1.500(3)	2.529(3)
O(4)		110.86(16)	110.06(16)	115.49(17)	1.493(3)
O(1)–H(2)	0.91		H(1)–O(2)–P(1) 118.22		
O(2)–H(1)	1.02		H(2)–O(1)–P(1) 114.24		
$HP(2)O_4^{2-}$					
P		O(5)	O(6)	O(7)	O(8)
O(5)		1.520(2)	2.495(3)	2.505(3)	2.522(3)
O(6)		106.98(15)	1.585(3)	2.528(3)	2.422(3)
O(7)		111.27(16)	109.13(16)	1.511(3)	2.528(3)
O(8)		112.69(15)	102.75(14)	113.42(16)	1.510(2)
O(6)–H(3)	0.96		H(3)–O(6)–P(2) 119.58		
$H_2P(3)O_4^-$					
P		O(9)	O(10)	O(11)	O(12)
O(9)		1.567(3)	2.522(3)	2.519(3)	2.450(3)
O(10)		107.57(18)	1.566(3)	2.471(3)	2.506(3)
O(11)		110.23(15)	107.23(16)	1.506(3)	2.546(3)
O(12)		106.10(15)	109.37(16)	116.07(16)	1.503(3)
O(9)–H(4)	0.92		H(4)–O(9)–P(3) 114.72		
O(10)–H(5)	0.81		H(5)–O(10)–P(3) 115.72		
Organic group					
N(1)–C(6)		1.499(5)	C(6)–N(1)–C(4)	114.7(3)	
N(1)–C(4)		1.507(5)	C(6)–N(1)–C(1)	112.7(3)	
N(1)–C(1)		1.519(4)	C(4)–N(1)–C(1)	105.5(3)	
N(2)–C(5)		1.474(4)	C(5)–C(1)–N(1)	109.5(3)	
C(7)–C(6)		1.509(6)	C(5)–C(1)–C(2)	115.3(3)	
C(1)–C(5)		1.515(5)	N(1)–C(1)–C(2)	105.9(3)	
C(1)–C(2)		1.532(5)	N(2)–C(5)–C(1)	110.1(3)	
C(2)–C(3)		1.509(6)	C(3)–C(2)–C(1)	106.1(3)	
C(4)–C(3)		1.513(6)	C(3)–C(4)–N(1)	103.4(3)	
			N(1)–C(6)–C(7)	111.8(3)	
			C(2)–C(3)–C(4)	104.9(3)	

Esd are given in parentheses.

in the organic channel structures formed through non-covalent interactions [16].

Assuming the usual valence of Zn, P and O atoms to be +2, +5 and −2, respectively, the framework of $Zn(PO_4)_3$ would result in the highly charged framework of −7. The double protonated AMEP would account for +2. The excess negative charge of −5 then needs to be balanced. Bond valence sum values [17] indicate that P(1)–O(1), P(1)–O(2), P(2)–O(6), P(3)–O(9) and P(3)–O(10) with distances of 1.570(2), 1.549(3), 1.585(3), 1.567(2) and 1.566(3) Å are P–OH units. This assignment is also in agreement with the proton positions observed near the oxygen atoms in the difference Fourier map. The presence of –OH groups in the structure gives rise to an interrupted framework material.

As can be seen, corner-shared chains are indeed rare. The chain of ZnP-AMEP has architectures comparable to similar structures reported in the literature. In the one-dimensional $[Zn_8(HPO_4)_8(H_2PO_4)_8]_8(C_2H_8N)\cdot 4H_2O$ [18] and $RbZn(HPO_4)(H_2PO_4)\cdot H_2O$ [19] , the four-membered rings, forming the corner-shared chains, are made from linkages involving ZnO_4, HPO_4 and H_2PO_4 units. The presence of H_2PO_4 units indicates that the chains can undergo further condensation, giving rise to products with higher dimensional architectures, by deprotonation of terminal –OH groups. This suggestion is validated by the

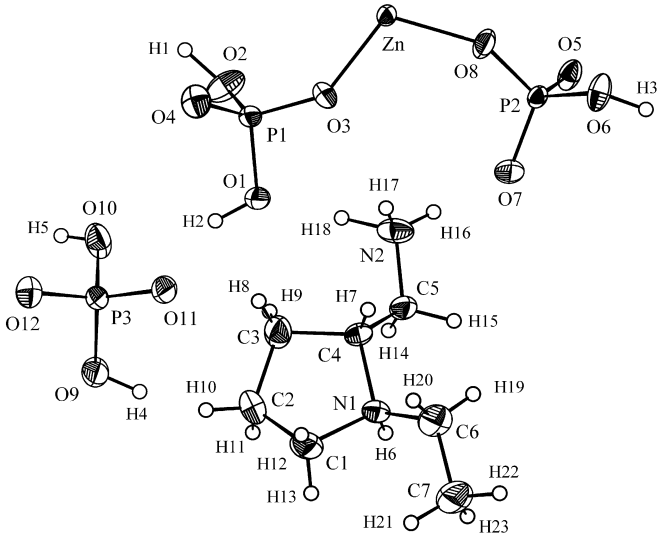


Fig. 1. Asymmetric unit of $[Zn(H_2PO_4)_2(HPO_4)][C_7H_{17}N_2]$. Thermal ellipsoids are shown at 50% probability.

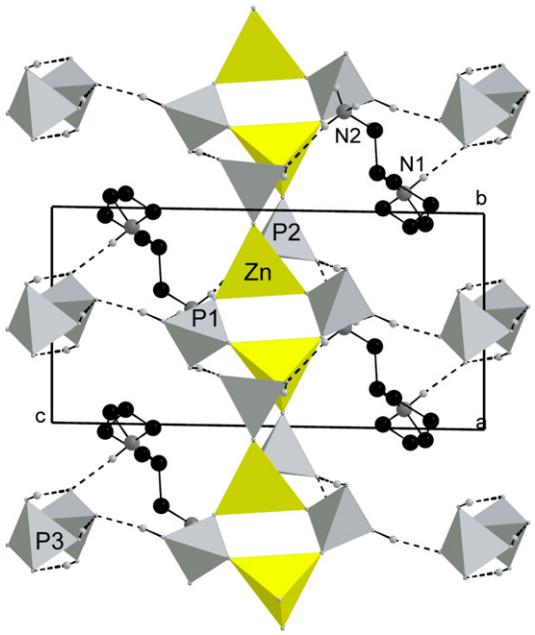


Fig. 3. Projection along the **a** axis of the atomic arrangement in $[Zn(H_2PO_4)_2(HPO_4)][C_7H_{17}N_2]$ showing pure $(H_2PO_4)_n^{n-}$ phosphate chains extending along the [1 0 0] direction at $y = 1/2$.

synthesis of a two-dimensional layer Zn phosphate from the same reaction mixture as employed for the preparation of the one-dimensional chain [20]. The structure of ZnP-AMEP, on the other hand, is closely related to that of $[Zn(HPO_4)_2](C_6H_{14}N_2)$ [21], where the corner-sharing four-membered rings are made only from ZnO_4 and $PO_3(OH)$ tetrahedra. Isolation of an organic templated metallophosphate with a corner-shared chain architecture is important because in one of the mechanisms proposed for the formation of open-framework phosphates the corner-shared chain structure is considered to be the primary building unit [22,23]. A possible reason that such lower dimensional structures are seldom found under conventional hydrothermal conditions may be because they undergo easy transformations to layer and three-dimensional structures.

3.2. NMR spectroscopy and ab initio calculations

The ^{31}P CP-MAS NMR spectrum of ZnP-AMEP is shown in Fig. 5. Three different phosphorus atoms can be seen. As the three signals are enhanced by cross-polarization, it can also be concluded that the three phosphorus atoms are linked to protons, probably via P–O–H bonds. All these features are in full agreement with the X-ray structure. Ab initio calculations can allow the attribution of the three signals to the three crystallographically inequivalent P atoms in the structure. For this purpose, the absolute chemical shifts of the three phosphorus were

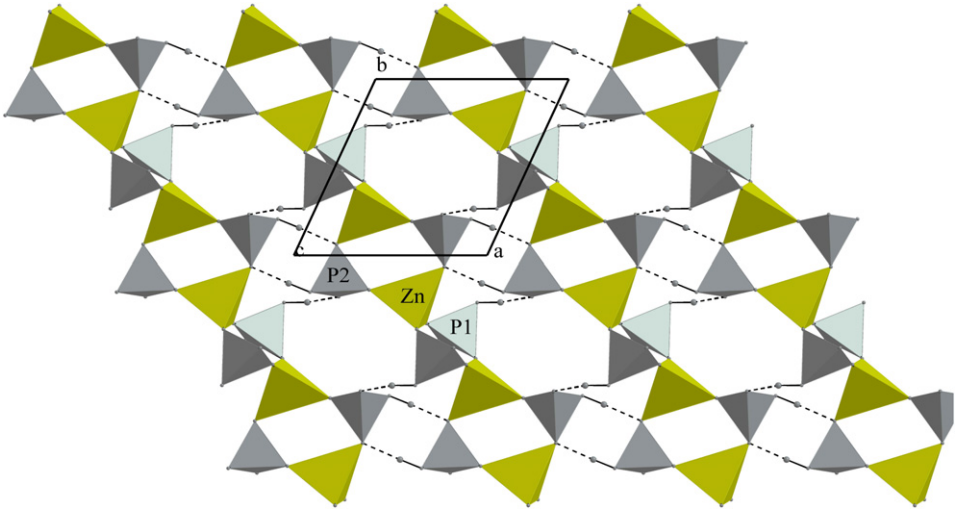


Fig. 2. The atomic arrangement of chains $[Zn(H_2PO_4)(HPO_4)]_n^-$ viewed down the **c** direction.

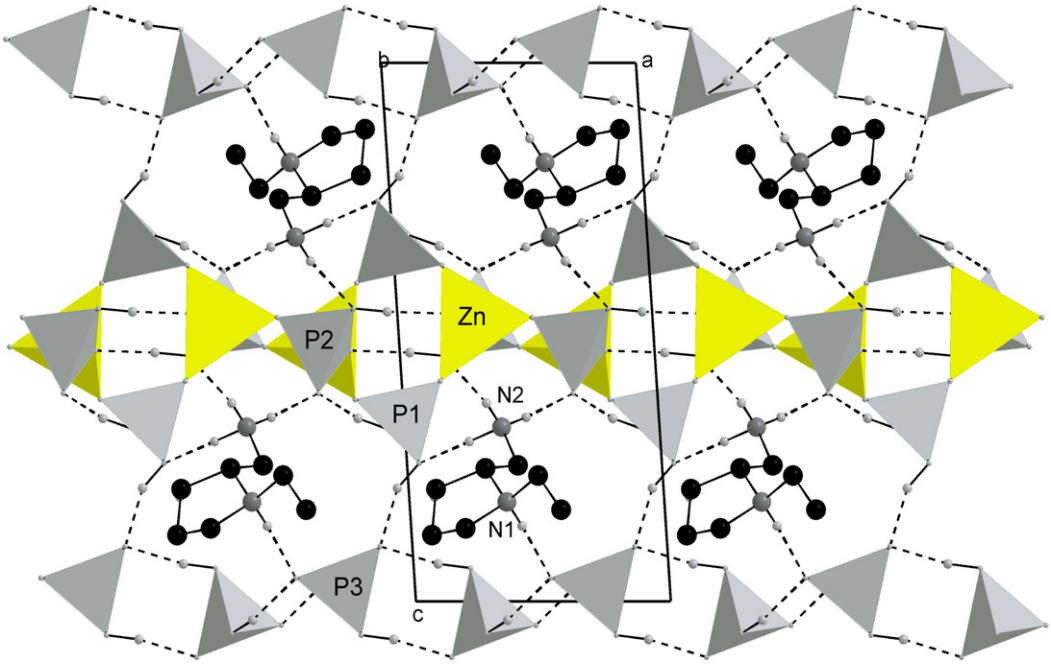


Fig. 4. Structure of $[Zn(H_2PO_4)_2(HPO_4)][C_7H_{17}N_2]$ along the **b** axis showing the position of the amine. Dotted lines represent the various hydrogen bond interactions.

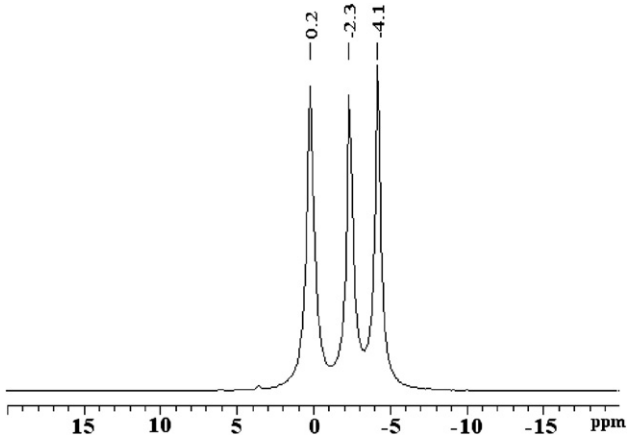


Fig. 5. ^{31}P MAS NMR spectrum of $[Zn(H_2PO_4)_2(HPO_4)][C_7H_{17}N_2]$.

calculated by using the B3LYP/6-31+G* method. The absolute chemical shifts vary in the order P(1) = 362.4 > P(2) = 361.3 > P(3) = 359.5. The same order was also found with other methods and basis sets. As the experimental chemical shifts correspond to the difference between the reference chemical shift and the absolute chemical shift, the experimental chemical shifts should vary in the order P(3) > P(2) > P(1). We can then propose the following attribution:

$P(1)\delta = -4.1$ ppm; $P(2)\delta = -2.3$ ppm; $P(3)\delta = 0.2$ ppm.

These chemical shift values agree well with those of monophosphates (between −10 and +5 ppm), depending on the compound [24–30] (see Table 4).

Table 4
Hydrogen bonds for $[Zn(H_2PO_4)_2(HPO_4)][C_7H_{17}N_2]$ (Å and °)

D–H···A	*d*(D–H)	*d*(H···A)	D(D···A)	∠(DHA)
O(2)–H(1)···O(7)	1.03	1.53	2.540(4)	167
O(1)–H(2)···O(11)	0.92	1.69	2.549(3)	155
O(6)–H(3)···O(5)	0.96	1.69	2.646(4)	176
O(9)–H(4)···O(11)	0.93	1.72	2.640(4)	171
O(10)–H(5)···O(12)	0.82	1.84	2.645(4)	167
N(1)–H(6)···O(12)	0.89	1.83	2.714(3)	176
N(2)–H(16)···O(7)	0.94	1.80	2.738(4)	175
N(2)–H(17)···O(6)	0.86	2.02	2.878(4)	170
N(2)–H(18)···O(1)	1.17	1.80	2.965(4)	179

The ^{13}C CP-MAS NMR spectrum is shown in Fig. 6. It displays seven well-resolved signals which can be attributed to the seven crystallographically inequivalent carbon atoms in the structure. Note that NMR shows that there is only one organic molecule in the asymmetric unit. As for phosphorus, it is possible to attribute the different signals to the various carbon atoms of the structure. For this purpose, the coordinates of C and N atoms of the AMEP molecule were taken from the X-ray structure. The protons were optimized at the B3LYP/6-31+G* level and the chemical shifts were determined. The values were then subtracted from that of C in tetramethyl silane optimized at the same level of theory. The results are depicted in Table 5. There is a relatively good agreement between experimental and theory. More interestingly, the AMEP molecule was also fully optimized and the chemical shifts calculated. The values are also listed in Table 5. The discrepancies between the two sets of theoretical values are a good indication of

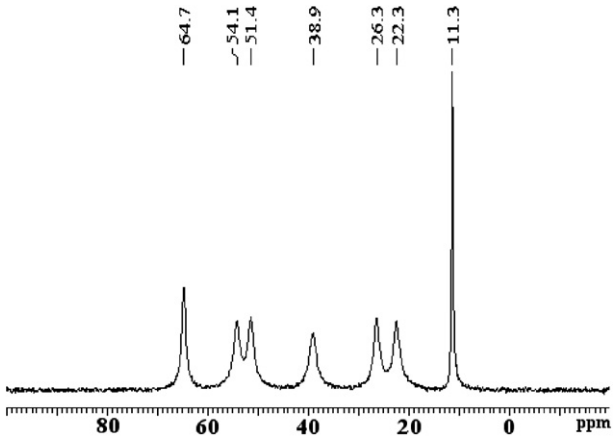


Fig. 6. ^{13}C CP-MAS NMR spectrum of $[Zn(H_2PO_4)_2(HPO_4)][C_7H_{17}N_2]$.

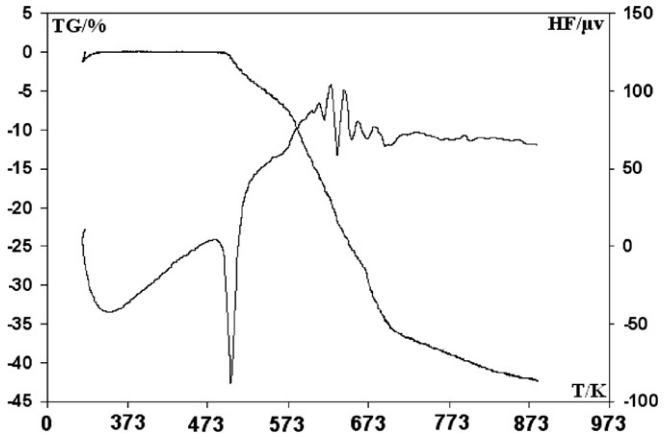


Fig. 7. DTA and TGA curves of $[Zn(H_2PO_4)_2(HPO_4)][C_7H_{17}N_2]$ at the rising temperature.

Table 5
Experimental and theoretical ^{13}C chemical shifts for the AMEP molecule

Carbon	δ experimental (ppm)	δ theory H optimized (ppm)	δ theory fully optimized (ppm)
C1	54.2	57.3	59.3
C2	22.4	23.7	26.1
C3	26.4	26.1	29.4
C4	64.7	65.9	66.8
C5	38.9	42.0	48.3
C6	51.5	56.0	58.7
C7	11.4	13.5	14.4

where constraints are located. The most important constraint is located on C5, the carbon atom linked to the NH_3^+ group. This is probably related to a special position of that chain in the structure. More surprisingly, other constraints exist also on C″, C2 and (less) C1 carbon atoms. These data are in full agreement with the structure as depicted in Fig. 1: the C2 and C3 carbon atoms are located near the $P(3)O_4$ tetrahedra.

3.3. Thermal analysis

Two curves corresponding to differential and thermogravimetric analyses (DTA/TG) under argon flow are given in Fig. 7. The DTA curve shows that the zinc phosphate ZnP-AEMP undertakes at 502 K an endothermic peak which corresponds to the removal of two water molecules arising from the irreversible dehydroxylation reactions due to the presence of terminal P–OH groups and deprotonation of the amine cations, (weight loss calculated 7.43%, experimental 7.41%), according to the following reaction:

$$[Zn(H_2PO_4)_2(HPO_4)][C_7H_{17}N_2] \longrightarrow ZnH_3P_3O_{10} + C_7N_2H_{15} + 2H_2O$$

The simultaneous departure of two water molecules proves the presence of two phosphate chains $[(H_2PO_4)_n^-$, $Zn(H_2PO_4)(HPO_4)_n^-]$ in the compound, which confirms the X-ray diffraction result. Indeed, the removal of two dehydroxylation water molecules of the hydrogenmonophosphates occurs usually at two different temperatures [31] according to the following reactions:

$$2H_3PO_4 \xrightarrow{\approx 473\ K} H_4P_2O_7 + \overset{\uparrow}{H_2O}$$

$$H_4P_2O_7 \xrightarrow{\approx 573\ K} 2HPO_3 + \overset{\uparrow}{H_2O}$$

The weight loss, between 575 K and 694 K, corresponds to the degradation of the template molecule (organic entities), giving the zinc triphosphate $ZnH_3P_3O_{10}$ as the decomposition product. The observed weight loss (26.21%) agrees well with the calculated value (26.65%).

Between 694 K and 873 K, the weight loss corresponds to the condensation of the P–OH groups in $ZnH_3P_3O_{10}$. A grey solid is finally obtained containing probably a carbon residue. This latter can be eliminated by calcination of the sample at 1100 K in air. However, the presence of $ZnH_3P_3O_{10}$ was confirmed by the IR spectrum of the final product. This latter compound exhibits broad bands between 3600 and 3000 cm^{-1} corresponding to the P–OH groups [32]. The stretching vibrations of the PO_2 central groups are observed between 1300 and 1100 cm^{-1}, while those between 1200 and 950 correspond to the stretching vibrations of the PO_3 terminal groups [33,34] and those ranging from 975 to 650 cm^{-1} correspond to the stretching POP modes [35].

3.4. IR spectroscopy

IR spectroscopy is one of the major physical methods for the investigation of molecular structures. Thus, we have studied the IR spectrum of crystalline zinc phosphate, $[Zn(H_2PO_4)_2(HPO_4)][C_7H_{17}N_2]$, which is shown in Fig. 8. To assign the IR peaks to vibrational modes, we examined the modes and frequencies observed in similar compounds [32].

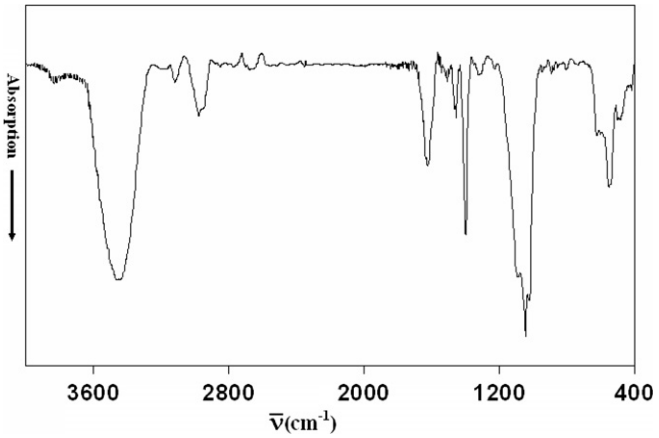


Fig. 8. IR absorption spectrum of $[Zn(H_2PO_4)_2(HPO_4)][C_7H_{17}N_2]$.

- The high-frequency region, between 3400 and 2300 cm^{-1}, is related to the valence vibrations of C–H, N–H and O–H groups interconnected by a system of hydrogen bonds in the crystal [33].
- The vibrations between 1650 and 1200 cm^{-1} are assigned to bending modes (δNH_3^+, δCH_2) [34–37].
- The various vibration bands between 1200 and 400 cm^{-1} are characteristic of monophosphate and correspond to valence and bending modes [38].
- Frequencies in the range 1200–800 cm^{-1} are attributed to the two stretching modes v_s and v_{as} (respectively symmetric and asymmetric) of the PO_4 group [39,40].
- The observed bands between 650 and 400 cm^{-1} can be attributed to the two bending modes δ_s and δ_{as} of the PO_4 group [41–44].

4. Conclusion

A new organic templated metallophosphate, $[Zn(H_2PO_4)_2HPO_4)][C_7H_{17}N_2]$, has been synthesized hydrothermally using 2-aminomethyl,1-ethylpyrrolidine as structure-directing agent. Our investigation shows that it is possible to form 3D open-framework materials containing removable organic templates which might have many potential applications. Further studies are necessary to understand the role of minor compositional changes in yielding different 3D open-framework structures.

Appendix A. Supplementary material

CCDC 622547 contains the supplementary crystallographic data for this paper. These data can be obtained free of charge via http://www.ccdc.cam.ac.uk/conts/retrieving.html, or from the Cambridge Crystallographic Data Centre, 12 Union Road, Cambridge CB2 1EZ, UK; fax: (+44) 1223-336-033; or e-mail: deposit@ccdc.cam.ac.uk. Supplementary data associated with this article can be found, in the online version, at doi:10.1016/j.poly.2006.11.052.

References

[1] R. Masse, M. Bagieu-Beucher, J. Pécault, J.P. Levy, J. Zyss, Nonlin. Opt. 5 (1993) 413.
[2] G. Centi, Catal. Today. 16 (1993) 1.
[3] G.A. Ozin, Adv. Mater. 4 (1992) 612.
[4] D.E.W. Vaughan, (Ed.), Multifunctional Mesoporous Inorganic Solids, vol. 137, NATO ASI Series, Dordrocht, 1993.
[5] G.-Y. Yang, S.C. Sevov, J. Am. Chem. Soc. 121 (1999) 8389.
[6] W.T.A. Harrison, T.M. Nenoff, T.E. Gier, G.D. Stucky, Inorg. Chem. 31 (1992) 5395.
[7] W.T.A. Harrison, M.L.F. Phillips, Chem. Mater. 9 (1997) 1837.
[8] C.N.R. Rao, S. Natarajan, S. Neeraj, J. Am. Chem. Soc. 122 (2000) 569.
[9] W.T.A. Harrison, Z. Biresak, L. Hannooman, J. Solid State Chem. 134 (1997) 148.
[10] D. Chidambaram, S. Neeraj, S. Natarajan, C.N.R. Rao, J. Solid State Chem. 147 (1999) 154.
[11] W.T.A. Harrison, T.M. Nenoff, T.E. Gier, G.D. Stucky, Inorg. Chem. 32 (1993) 2437.
[12] A. Altomare, M. Cascarano, C. Giacovazzo, A. Gualiardi, J. Appl. Cryst. 26 (1993) 343.
[13] G.M. Sheldrick, SHELXS 97 and SHELXL 97. Program for Crystal Structure Solution and Refinement, University of Gottingen, Germany, 1997.
[14] J. Meulenaer, H. Tompa, Acta Cryst. 19 (1965) 1014.
[15] K. Brandenburg, DIAMOND, Version 2.0 Impact GbR, Bonn, Germany, 1998.
[16] V.R. Pedireddi, S. Chatterjee, A. Ranganathan, C.N.R. Rao, J. Am. Chem. Soc. 119 (1997) 10867.
[17] N.E. Brese, M. O'Keeffe, Acta Crystallogr., Sect. B 47 (1991) 192.
[18] P. Reinert, N.Z. Logar, J. Patarin, V. Kaucic, Eur. J. Solid State Inorg. Chem. 35 (1998) 373.
[19] W.T.A. Harrison, Z. Biresak, L. Hannooman, J. Solid State Chem. 134 (1997) 148.
[20] S. Natarajan, L.V. Wullen, W. Klein, M. Jansen, Inorg. Chem. 42 (2003) 6265.
[21] A.V. Chavez, T.M. Nenoff, L. Hannooman, W.T.A. Harrison, J. Solid State Chem. 147 (1999) 584.
[22] S. Oliver, A. Kuperman, A. Lough, G.A. Ozin, Chem. Mater. 8 (1996) 2391.
[23] S. Oliver, A. Kuperman, G.A. Ozin, Angew. Chem., Int. Ed. 37 (1998) 46.
[24] A.R. Grimmer, U. Haubenreisser, Chem. Phys. Lett. 99 (1983) 487.
[25] D. Mûller, E. Jahn, G. Ladwig, U. Haubenreisser, Chem. Phys. Lett. 109 (1984) 332.
[26] A.K. Cheetham, N.J. Clayden, C.M. Dobson, R.J.B. Jakemen, J. Chem. Soc., Chem. Commun. 195 (1986).
[27] L. Mudracovskii, V.P. Shmochkova, N.S. Kentsarenko, V.M. Mastikhin, Phys. Chem. Solids 47 (1986) 335.
[28] G.L. Turner, K.A. Smith, R.J. Kirkpatrick, E.J. Oldfield, Magn. Reson. 70 (1986) 408.
[29] S. Prabhakar, K.J. Rao, C.N.R. Rao, Chem. Phys. Lett. 139 (1987) 96.
[30] P. Hartmann, J. Vogel, B. Schnabel, J. Magn. Reson. 111 (1994) 110.
[31] X.C. Fu, Practical Chemical Handbook, Nanjing University, China, 1989, p. 618.
[32] S. Akriche, M. Zaigui, Mat. Res. Bull. 35 (2000) 2545.
[33] A.N. Lazarev, Vibrational Spectra and Structure of Silicates Consultants Bureau, New York, 1972.
[34] B.C. Cornilson, J. Mol. Struct. 1 (1984) 117.
[35] R.W. Mooney, S.Z. Toma, J. Brunvoll, Spectrochim. Acta A 2 (1967) 1541.
[36] H. Naïli, T. Mhiri, A. Daoud, Int. J. Inorg. Mater. 3 (2001) 393.
[37] I. Nemec, I. Cisarova, Z.J. Micka, J. Solid State Chem. 140 (1998) 71.

[38] S. Skaarup, R.W. Berg, J. Solid State Chem. 26 (1978) 59.
[39] N.B. Colthup, L.H. Daly, S.E. Wiberley, Introduction to Infrared and Raman Spectroscopy, 2nd ed., Academic Press, New York, 1975.
[40] D. Philip, G. Aruldhas, J. Solid Chem. 83 (1981) 198.
[41] Y. Abid, M. Kamoun, A. Daoud, F. Romain, J. Raman Spectrosc. 21 (1991) 709.
[42] S. Kamoun, M. Kamoun, A. Daoud, F. Romain, Spectrochim. Acta A 47 (1991) 1051.
[43] G. Herzberg, Infrared and Raman Spectra of Polyatomic Molecules, Van Nostraand, New York, 1975.
[44] K. Nakamoto, Infrared and Raman Spectra of Inorganic and Coordination Compound, Wiley/Intersciences, New York, 1984.

2. Results and discussion

We have found that the reaction of copper(II) chloride with 4-(4-hydroxyphenyl)-1,2,4-triazole (*L*, $C_8H_7N_3O$, Scheme 1) in EtOH solution with a Cu:*L* molar ratio of 5:1 leads to formation of two crystalline complexes $[Cu_6(\mu_6\text{-Cl})(\mu_3\text{-OH})_2(\mu\text{-}L)_6Cl_9(H_2O)_3]\cdot 3H_2O$ (**1**) and $[Cu(\mu\text{-L})(\mu\text{-OH})(H_2O)_2]Cl$ (**2**). Complex **1** is the main product of the reaction:

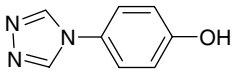
$$6Cu^{2+} + 6L + 12Cl^- + 8H_2O \rightarrow [Cu_6(\mu_6\text{-Cl})(\mu_3\text{-OH})_2(\mu\text{-}L)_6Cl_9(H_2O)_3]\cdot 3H_2O + 2HCl$$

Despite a 1:1 metal-to-ligand stoichiometry in **1** the five times excess of $CuCl_2$ is strongly recommended to avoid precipitating the low soluble ligand.

We found conditions when complex **1** can be prepared pure in high yield, and investigated its magnetic properties. Complex **1** is stable in the ambient air and is readily soluble in water and water–organic mixtures, but poorly soluble in organic solvents (ethanol, MeCN, 2-propanol, $CHCl_3$) and their mixtures. Unfortunately, our attempts to prepare a phase of the individual compound **2** failed.

2.1. Crystal structures

In both compounds the *L* molecules are coordinated to copper ions by N^1 and N^2 atoms in a bidentate-bridging manner. However, the structures of **1** and **2** are different due to the difference in the coordination mode of the hydroxo-group and the role of chloride anion. In compound **1** there are three types of bridging ligands. Three bidentate-bridging 4-(4-hydroxyphenyl)-1,2,4-triazole molecules are coordinated to three copper ions to form Cu_3L_3 triangle. The OH-group caps the Cu_3 triangle, and finally two $Cu_3L_3(OH)$ triangles are joined to one another in quite an unusual way, by the μ_6-Cl ligand (Fig. 1) to form a hexanuclear complex. The distance between Cu_3 planes is 4.21 Å. The coordination polyhedron of the μ_6-Cl ion is trigonal antiprism. The resulting complex molecule lies on the fixed point of the $\bar{3}$ axis of the $R\bar{3}$ space group. Each copper ion has two coordination positions, equatorial and apical, available for terminal ligands. All six equatorial positions are occupied by chloride ions, whereas the apical ones are statistically occupied by three water molecules and three chloride ions. The statistical distribution of H_2O and Cl over the six apical positions is imposed by relatively high crystallographic symmetry. It only became possible to distinguish the positions of Cl ($Cu–Cl_{apical}$, 2.7774(19) Å) and H_2O ($Cu–O_{apical}$, 2.466(7) Å) and to locate H atoms at O of the H_2O molecules due to the low temperature at the diffraction measurements. Thus, the coordination sphere of Cu^{2+} consists of $2N + \mu_3\text{-O(H)} + Cl + \mu_6\text{-Cl} + (Cl \text{ or } H_2O)$. The coordination polyhedron of the copper ion is a distorted octahedron elongated towards μ_6-Cl and $(Cl/H_2O)_{apical}$ positions (Fig. 1).



L

Scheme 1.

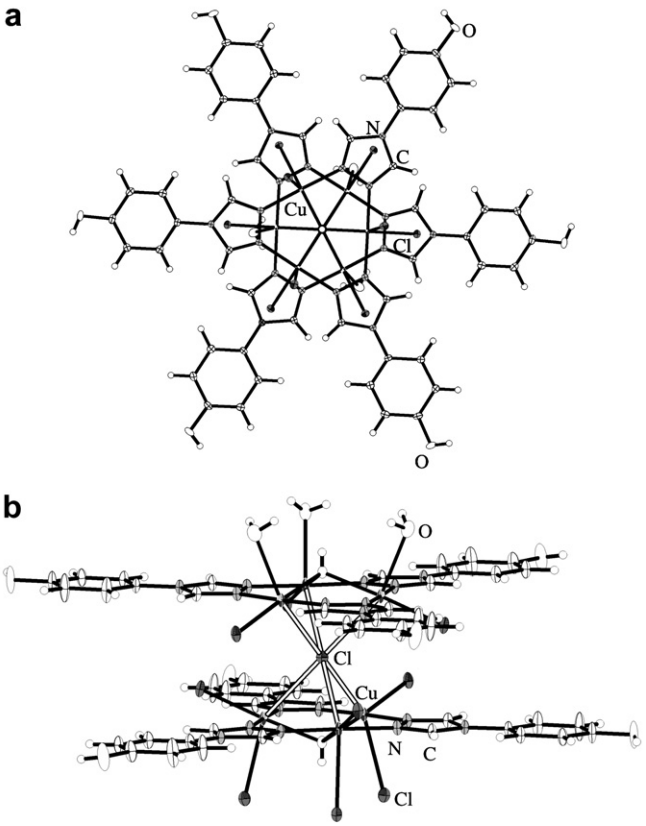
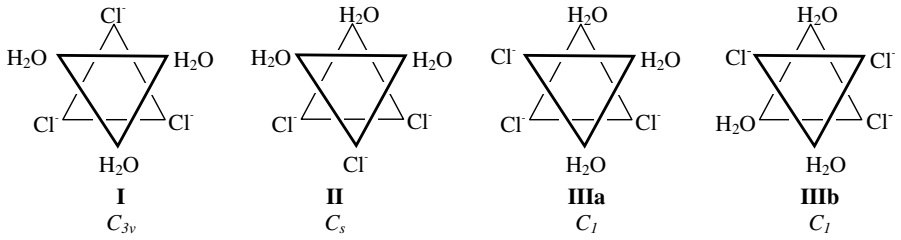


Fig. 1. Molecule of **1**, view along the $\bar{3}$ axis (a) and side-view (b). Main bond distances (Å): Cu ⋯ Cu (within Cu_3), 3.3651(4), Cu–N, 1.9662(17), 1.9632(17), $Cu–\mu_3$-O(H), 2.0681(10), $Cu–\mu_6$-Cl, 2.8397(3), $Cu–Cl_{eq}$, 2.2692(6), $Cu–Cl_{apical}$, 2.7774(19), $Cu–(H_2O)_{apical}$, 2.466(7).

According to the statistical distribution of H_2O and Cl^- over six apical positions, four geometrical and optical isomers of molecule **1** (Scheme 2, view along $\bar{3}$ axis.) may theoretically coexist, but cannot be recognized in the crystal by using X-ray diffraction data.

The most symmetrical isomer, **I**, is shown in Fig. 1, where all "upper" apical positions are occupied by three water molecules and the "lower" ones by chloride ions. It is achiral because of C_{3v} point symmetry. Two isomers with lower symmetry correspond to the combination of $2H_2O + Cl^-$ on one Cu_3 triangle and $H_2O + 2Cl^-$ on the other. One of them, **II**, possesses a mirror plane and therefore is achiral too, while the last, **III**, is asymmetrical and exists as the pair of chiral forms, **IIIa** and **IIIb**. However, the nature of the 6Cu–Cl bonding is unclear, we could even expect free rotation of one $Cu_3L_3(OH)$ triangle with respect to the other. The free rotation might occur, for example, in solution, if the molecule **1** does not dissociate. In this case only two isomers, **I** and **II**, would exist. The existence of an eclipsed conformation in this case might also be possible.



Scheme 2.

The main bond distances are given in Fig. 1 caption. The μ_6-Cl-ligand is equidistant from six copper ions. Relatively large Cu–(μ_6-Cl) distances of 2.8397(3) Å indicate that the two Cu_3 units are weakly joined together. According to the Cambridge Structural Database (release 5.27) [16] the only one copper(II) complex containing μ_6-Cl is known, $[Cu_6(\mu_6\text{-Cl})(\mu_3\text{-OMe})_2(\mu\text{-pz})_9]$ (**3**; pz – pyrazolate anion) [17]. In **3**, in contrast to **1**, two Cu_3 triangles are joined not only by a chloride anion but also by three pyrazolate ligands; all are coordinated to Cu in a bidentate-bridging mode. The resulting coordination environment of the μ_6-Cl^- is trigonal prism, in contrast to trigonal antiprism in **1**. The presence of additional bridging pyrazolate ligands resulted in a shortening of the Cu–Cl bonds to 2.6032(13)–2.623(2) Å. In **3** the chloride ion is "caged" into the molecule while in **1** it binds two parts of the molecule together. Note that in all possible isomers of **1** two Cu_3 triangles are not equivalent but all six (μ_6-Cl)–Cu bonds are of the same length. We carefully checked the residual density around the chloride ion and its a.d.p. ellipsoid shape, and came to the conclusion that it is definitely ordered. It could be an argument *pro* covalent and not electrostatic Cu–Cl bonding.

In the crystal packing, the molecules of **1** are involved in extended network of intermolecular hydrogen bonds between terminal OH-groups of the 4-(4-hydroxyphenyl)-1,2,4-triazole ligand, apical water molecules coordinated to copper and disordered solvent water molecules.

In compound **2** the hydroxo groups together with *L* join copper ions into infinite cationic $\{[Cu(\mu\text{-}L)(\mu\text{-}OH)(H_2O)_2]^+\}_\infty$ polymeric chains (Fig. 2) running along the *b* axis. The chloride anion is in the outer sphere. The coordination environment of Cu^{2+} ions is accomplished by two water molecules and consists of 2N + 2μ-O(H) + 2 elongated $O(H_2)$, thus the coordination polyhedron of the copper ion is a distorted octahedron, as in **1**. There is weak hydrogen bonding between the chloride counter anion and the hydroxo group of *L*, Cl ⋯ O(H), 3.01 Å.

There are about 20 compounds containing the fragment [Cu(μ-*L′*)(μ-OH)], where *L′* is a substituted N-containing heterocycle, coordinated through the N–N bond in a bidentate bridging manner similarly to **2**. All but three of them are molecular, while three chain structures achieve a polymeric motif through neither NO_3 group [18], coordinated to the copper ion, nor through the oxygen atom of an OH-group, being additionally coordinated to one more copper ion [19,20] with an elongated contact Cu–O of about 2.7–2.8 Å. However, most similar to **2**, the compounds contain a cyclic tetranuclear anion $\{Cu_4(\mu\text{-}OH)_2Cl_4(\mu\text{-}pz)_4\}^{2-}$ (**4** [21]) and an octanuclear molecule $\{Cu(\mu\text{-}OH)(\mu\text{-}Me_2pz)\}_8$ (**5** [22,23]). The copper ions in **4**, **5** and **2** are joined through two bridging ligands, N-containing heterocycle and OH-groups, resulting in cyclic species in **4**, **5** and polymeric chains in **2**. The Cu ⋯ Cu distances in **2** are longer by ~0.1 Å and can be compared only with those in the Cu–O(H) ⋯ Cu fragment in **4**, where one of the copper ions weakly coordinates the OH group (Table 1). However, a rather long Cu ⋯ Cu distance leads to Cu–O(H) and Cu–N bonds also becoming longer. Besides, the coordination environment of the copper ions, being distorted octahedral in **2**, also differs from that in **4** and **5**. In **4** there is no additional coordination to the copper ion, the coordination polyhedra of all copper ions are distorted tetrahedra, while in **5** there are copper ions in tetrahedral and in trigonal prismatic environments.

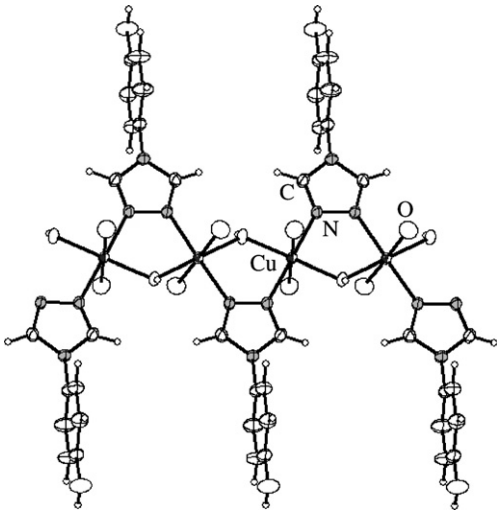


Fig. 2. Fragment of the cationic polymeric chain $\{[Cu(\mu\text{-}L)(\mu\text{-}OH)(H_2O)_2]^+\}_\infty$ in **2**. Main bond distances (Å): Cu ⋯ Cu, 3.3852(3) (*b*/2), Cu–N, 2.0100(17), Cu–μ-O(H), 1.9474(10).

The experimental powder diffraction pattern of **1** (Fig. 3) is in good agreement with that calculated for compound **1**. Some differences between intensity profiles may be accounted for by the texture of the sample.

Table 1
Some distances and bond angles in **1**–**5**

Compound	Formula	Cu ⋯ Cu (Å)	Cu–N (Å)	Cu–O(H) (Å)	Cu–O(H)–Cu (°)	Reference
1	$[Cu_6(\mu_6\text{-}Cl)(\mu_3\text{-}OH)_2(\mu\text{-}L)_6Cl_9(H_2O)_3]\cdot 3H_2O$	3.6660(4)	1.9681(17), 1.9646(17)	2.0639(9)		this work
2	$[Cu(\mu\text{-}L)(\mu\text{-}OH)(H_2O)_2]Cl$	3.3852(3)	2.0100(17)	1.9474(10)	120.72	this work
3	$[Cu_6(\mu_6\text{-}Cl)(\mu_3\text{-}OMe)_2(\mu\text{-}Pz)_9]$	3.209(1)–3.2331(2)	1.931(5)–1.992(7)	2.083(4), 2.085(6)		[17]
4	$(Bu_4N)_2[Cu_4(\mu\text{-}OH)_2Cl_4(\mu\text{-}Pz)_4]$	3.178, 3.194; 3.390, 3.397 (Cu–O(H) ⋯ Cu)	1.938–2.008	1.891–1.949; 2.542, 2.562 (Cu–O(H) ⋯ Cu)	122.69, 125.02; 88.72, 8968	[21]
5	$\{Cu(\mu\text{-}OH)(\mu\text{-}Me_2Pz)\}_8\cdot 2PhNO_3$	3.212–3.267	1.939–1.991	1.912–1.941	111.65–116.68	[22,23]

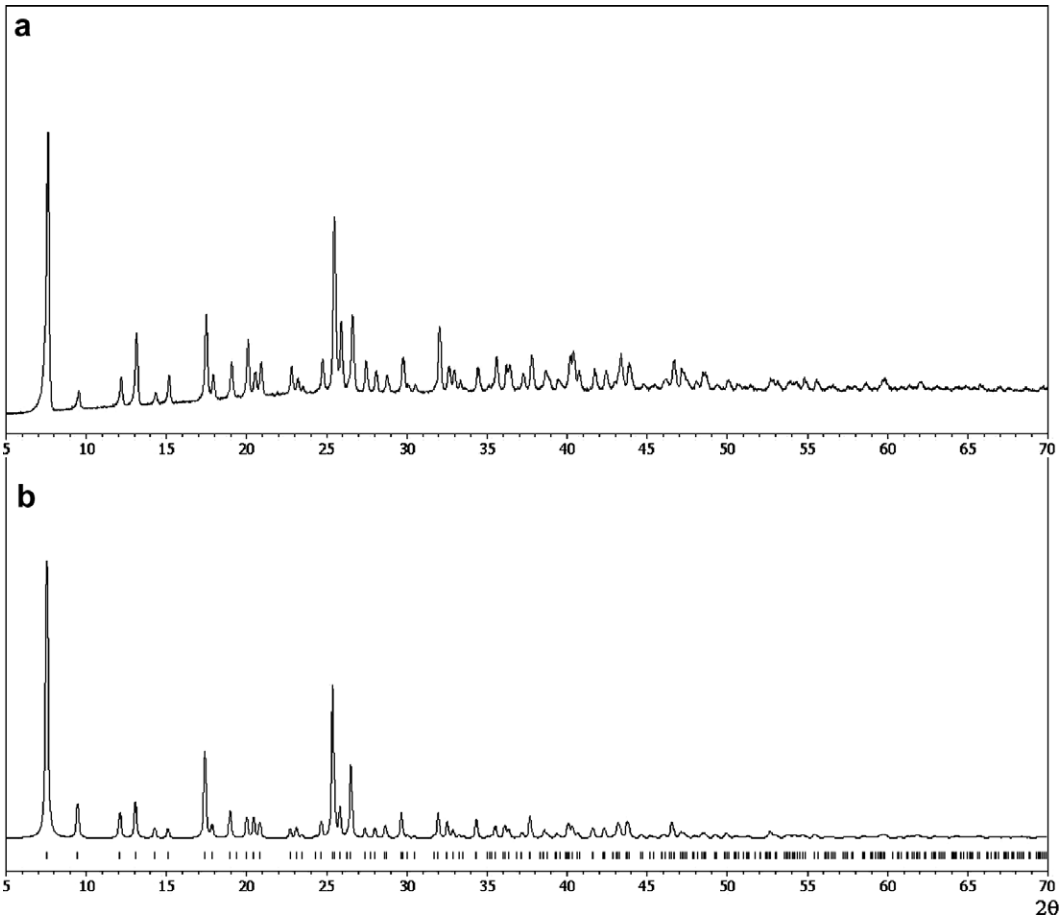


Fig. 3. Observed (a) and calculated (b) X-ray powder diffraction patterns of **1**.

The presence of peaks referring to any additional phase (e.g. phase **2**) is not observed. This fact clearly indicates that the bulk product synthesized corresponds to phase **1** only.

2.2. Magnetic properties

The dependence of the magnetic moment (μ_{eff}) on temperature of **1** is shown in Fig. 4. On decreasing the temperature from 300 K, the μ_{eff} value decreases continuously down to a plateau near 80 K. Further decrease of the temperature causes a decrease of μ_{eff} to 1.75 β at 2 K. Such a behavior points to mainly antiferromagnetic exchange interactions in complex **1**. The structural data shown in Fig. 1 were used to choose a theoretical model for a description of the dependence observed. Thus, we chose the most adequate model for the description of the magnetic properties, consisting of two triangles joined by a μ_6-Cl ion. We considered the model of the exchange cluster consisting of two weakly interacting triangles. The model is valid because the distances between copper(II) ions of different triangles bonded through μ_6-Cl ion are 5.73 Å and are much larger than the distances between copper(II) ions within the same triangle. The model assumes that the value of the exchange interaction parameter J between Cu(II) ions inside triangles is much larger than that of both inter-cluster exchange interactions for the same molecule and other molecules (zJ').

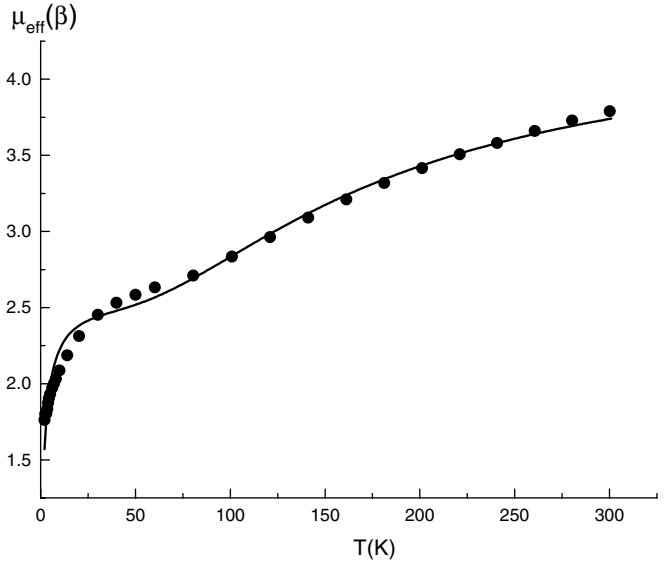


Fig. 4. The dependence of the magnetic moment (μ_{eff}) on the temperature for **1**.

Table 2
Crystallographic data for **1** and **2**

Chemical formula	$C_{48}H_{56}Cl_{10}Cu_6N_{18}O_{14}$	$C_8H_{12}ClCuN_3O_4$
M_r	1844.85	313.20
F(000)	2778	318
Crystal system	trigonal	monoclinic
Space group	$R\bar{3}$	$P2_1/m$
a (Å)	23.4151(4)	6.4942(6)
b (Å)	23.4151(4)	6.7704(5)
c (Å)	10.3131(3)	10.5299(3)
α (°)	90	90
β (°)	90	101.578(3)
γ (°)	120	90
V (Å^3)	4896.79(19)	597.87(9)
Z	3	2
ρ_{calc} (g cm^{-3})	1.877	1.740
μ (mm^{-1})	2.405	2.056
Temperature (K)	90.0(2)	room
Radiation type	Mo Kα	Mo Kα
θ Range (°)	2.5–27.5	2.3–27.5
Crystal colour and shape	green block	blue plate
Crystal size (mm)	0.470 × 0.480 × 0.860	0.190 × 0.081 × 0.076
Diffractometer	Bruker X8APEX CCD diffractometer	
θ_{max} (°)	33.4	27.5
T_{min}/T_{max}	0.745	0.729
No. of measured, unique, observed ($>2\sigma I$) reflections	30043, 3664, 3254	2704, 1400, 1251
No. of parameters	175	102
R_{int}	0.0210	0.0124
h	−33 → 33	−4 → 8
k	−33 → 33	−5 → 8
l	−14 → 15	−18 → 14
$R[F^2 > 2\sigma(F^2)]$, $wR(F^2)$	0.0288, 0.0735	0.0255, 0.0720
Goodness-of-fit	1.293	1.036
$\Delta\rho_{max}$, $\Delta\rho_{min}$ (e Å^{-3})	0.554, −0.567	0.356, −0.255

The theoretical analysis of the magnetic behavior was carried out in cluster approximation with the isotropic spin-Hamiltonian ($\widehat{H} = -2J\sum_i \widehat{S}_i \cdot \widehat{S}_j$) [25]. As the result of optimization the following parameters for the theoretic curve (solid line in Fig. 4) were found: $g_{Cu} = 2.10(5)$, $J = -51.4(3)$ cm^{-1}, $zJ' = -2.3(2)$ cm^{-1}.

A comparison of magnetic properties of complexes **1** and **3** shows that the values of the exchange interaction parameters between Cu(II) ions inside copper triangles for these complexes are comparable ($-51.4(3)$ cm^{-1} in complex **1** (this paper) and $-66.4(1)$ cm^{-1} in complex **3** [17]). However, inter-cluster exchange interactions differ considerably: $zJ' = -2.3(2)$ cm^{-1} (**1**) and $J_2 = -17.1(1)$ cm^{-1} (**3**). This is expected to be due to structural reasons. The Cu_3 units in complex **3** are bonded more strongly than in complex **1** due to the three bridging pyrazolates between them. In **1** only the μ_6-Cl ion bridges similar Cu_3 units.

3. Conclusions

Thus, the reaction between copper(II) chloride and 4-(4-hydroxyphenyl)-1,2,4-triazole leads to the formation of two crystalline complexes, hexanuclear **1** and polymeric **2**. The 1,2,4-triazole ring coordinates in a bidentate-bridging mode. One of complexes, **1**, with an unusual molecular structure is obtained as the bulk product. Two Cu_3 triangles appear to be joined together by six unsupported Cu–Cl bonds of length 2.8397(3) . We think that this crystal structure could be of importance for structural chemistry because it elucidates some aspects of weak chemical bonding between metal and ligand atoms. Traditional structural chemistry treats long interatomic contacts as a sort of non-bonding interaction (specific, electrostatic, *etc.*). In our opinion, we found an example of bonding that lies somewhere between a "normal" covalent bond and specific non-valent bonding. The argument for some covalent nature to this bonding is that the chloride ion symmetrically binds non-equivalent Cu_3 units. The argument for the specific non-bonding nature is that the magnetic exchange between those units is quite small. However, the nature of this bonding is still open. We hope that quantum chemical calculations that we plan in the future will help.

4. Experimental

4.1. General

For the synthesis, we used $CuCl_2 \cdot 3H_2O$ of "p" grade and 4-(4-hydroxyphenyl)-1,2,4-triazole was prepared by the procedure in [24], $T_{m.p.} = 288$–290 °C ($T_{m.p.} = 285$–286 °C [24]).

4.2. Synthesis of $[Cu_6(\mu_6\text{-}Cl)(\mu_3\text{-}OH)_2(\mu\text{-}L)_6Cl_9(H_2O)_3] \cdot 3H_2O$ (1)

A hot solution of L (1 mmol) in 20 ml of ethanol was slowly added with stirring to a hot solution of $CuCl_2 \cdot 2H_2O$ (5 mmol) in 5 ml of water. A green precipitate was formed after a short time (*ca.* 1 min). After stirring for 30 min the precipitate was filtered off, washed with

small amount of ethanol and dried in ambient air. Yield 85%.

Anal. Calcd for $C_{48}H_{56}N_{18}Cl_{10}O_{14}Cu_6$: C, 31.2; H, 3.1; N, 13.7; Cu, 20.7. Found: C, 31.2; H, 3.0; N, 13.3; Cu, 20.6.

Green crystals of **1** suitable for X-ray analysis were obtained by slow evaporation of an ethanol solution of the compound over two weeks.

With a greater excess of copper chloride against *L*, both green crystals of **1** and blue crystals of the complex **2** suitable for X-ray analysis were formed from a solution after leaving in air for two weeks. Unfortunately, we did not succeed in isolating the individual phase of compound **2** without impurities of compound **1**.

4.3. Physical measurements

The copper content was determined by complexonometric titration, the samples being decomposed in a 1:1 mixture of concentrated H_2SO_4 and $HClO_4$. The CHN analyses were performed with a Carlo-Erba analyzer using standard procedures.

4.4. Magnetic measurements

Magnetic susceptibility measurements of polycrystalline samples of the complex were performed on a SQUID magnetometer MPMS-5s (Quantum Design) over the temperature range 2–300 K. The magnitudes of the magnetic field were 5 kOe. Dependence between magnetic susceptibility and intensity of the magnetic field was not found. The effective magnetic moment μ_{eff} was calculated by the formula $\mu_{\text{eff}} = \left(\frac{3k}{N\beta 2}\cdot \chi T\right)^{1/2} \approx (8\chi T)^{1/2}$, where χ is the paramagnetic susceptibility corrected for diamagnetism and is equal to $-870\times10^{-6}\,\text{cm}^3/\text{mol}$, N is Avogadro's number, k is the Boltzsmann constant and β is Bohr's magneton.

4.5. X-ray crystallographic study

Crystallographic data and details of single-crystal diffraction experiments are given in Table 2. X-ray intensity data were collected on a Bruker X8Apex CCD diffractometer at 90 K (**1**) and room temperature (**2**) using standard techniques (ω- and ϕ-scans of narrow frames) and corrected for absorption effects [26]. The structures were solved by direct methods and refined by full-matrix least-squares on F^2 using the SHELXTL program set (version 6.22) [27]. All non-hydrogen atoms were refined anisotropically. Hydrogen atoms at OH-groups and H_2O molecules were refined without geometrical constraints and with thermal parameters related to those of the oxygen atoms. Hydrogen atoms at carbon atoms were refined in calculated positions. In structure **2** the hydrogen atoms of the water molecule coordinated to copper were not located. The solvent water molecule in **1** appeared to be statistically disordered over two symmetrically related positions and refined with s.o.f. = 0.5.

X-ray powder diffraction analysis was performed with a Philips PW1700 automatic diffractometer in Bragg-Brentano geometry with Si as an external standard. Ni-filtered Cu Kα radiation was used. The diffraction pattern was scanned with a step of 0.02° 2θ and in the angular range from 5° to 70° 2θ at room temperature. The PowderCell program set [28] was used to calculate the powder pattern from the single crystal data.

Acknowledgements

The authors acknowledge the financial support of the Russian Foundation for Basic Research (Grant 06-03-32742-a and 05-03-32420a). One of us (E.V.P.) thanks Presidium of the Siberian Branch of the Russian Academy of Sciences for the Lavrentiev Grant for Young Scientists. The authors also thank Prof. G.V. Romanenko (International Tomography Center of SB RAS) for helpful discussions.

Appendix A. Supplementary material

CCDC 607000 and 607001 contain the supplementary crystallographic data for **1** and **2**. These data can be obtained free of charge via http://www.ccdc.cam.ac.uk/conts/retrieving.html, or from the Cambridge Crystallographic Data Centre, 12 Union Road, Cambridge CB2 1EZ, UK; fax: (+44) 1223-336-033; or e-mail: deposit@ccdc.cam.ac.uk. Supplementary data associated with this article can be found, in the online version, at doi:10.1016/j.poly.2006.11.051.

References

[1] J.G. Haasnoot, Coord. Chem. Rev. 200 (2000) 131.
[2] T. Asaji, H. Sakai, D. Nakamura, Inorg. Chem. 22 (1983) 202.
[3] S. Ferrer, J.G. Haasnoot, J. Reedijk, E. Muller, M. Biagini Cindi, M. Lanfranchi, A.M. Manotti Lanfredi, J. Rilas, Inorg. Chem. 39 (2000) 1859.
[4] O.G. Shakirova, A.V. Virovets, D.Yu. Naumov, Yu.G. Shvedenkov, V.N. Elochina, L.G. Lavrenova, Inorg. Chem. Commun. 5 (2002) 690.
[5] L.G. Lavrenova, V.N. Ikorskii, V.A. Varnek, I.M. Oglezneva, Koord. Khim. 16 (1990) 654.
[6] E. König, Structure and Bonding, vol. 76, Springer-Verlag, Berlin, 1991, p 51.
[7] L.G. Lavrenova, S.V. Larionov, Koord. Khim. 24 (1998) 403.
[8] P. Gütlich, Y. Garcia, H.A. Goodwin, Chem. Soc. Rev. 29 (2000) 419.
[9] O. Kahn, C.J. Martinez, Science 279 (1998) 44.
[10] S.C. Bahel, B.L. Dubey, N. Nath, J.K. Srivastava, Inorg. Chim. Acta 43 (1984) 91.
[11] Ch.-Q. Sheng, W.-N. Zhang, M. Zhang, Yu.-L. Song, J. Chen, J. Zhee, H.-T. Ji, J.-Z. Yao, Z.-Yu. Miao, Acta Chim. Sinica 63 (2005) 617.
[12] I.V. Mashevskaya, L.V. Anikina, Yu.B. Vikharev, V.A. Safin, S.V. Koltsova, A.N. Maslivets, Khim.-Farm. Zhurn. 35 (8) (2001) 11.
[13] D.J. Cash, A.N. Ferguson, J. Photogr. Sci. 28 (1980) 121.
[14] P.N. Kulyabko, R.G. Dubenko, P.S. Pelkis, Radiobiologiya 9 (1969) 633.
[15] L.G. Lavrenova, V.N. Ikorskii, L.A. Sheludyakova, D.Yu. Naumov, E.G. Boguslavskii, Koord. Khim. 30 (2004) 442.

[16] F.H. Allen, O. Kennard, Chem. Des. Autom. News 8 (1993) 131.
[17] A. Kamiyama, T. Kajiwara, T. Ito, Chem. Lett. (2002) 980.
[18] M. Zareba, K. Drabent, Z. Ciunik, S. Wolowiec, Inorg. Chem. Commun. (2004) 82.
[19] G.A. Ardizzoia, M.A. Angaroni, G. La Monica, F. Cariati, M. Moret, N. Masciocchi, J. Chem. Soc., Chem. Commun. (1990) 1021.
[20] G.A. Ardizzoia, M.A. Angaroni, G. La Monica, F. Cariati, S. Cenini, M. Moret, N. Masciocchi, Inorg. Chem. 30 (1991) 4347.
[21] G. Mezei, M. Rivera-Carrillo, R.G. Raptis, Inorg. Chim. Acta 357 (2004) 3721.
[22] P. Dapporto, G. De Munno, G. Bruno, M. Romeo, Acta Crystallogr. C 39 (1983) 718.
[23] L.K. Thompson, T.C. Woon, D.B. Murphy, E.J. Gabe, F.L. Lee, Y. Le Page, Inorg. Chem. 24 (1985) 4719.
[24] V.N. Elokhina, A.S. Nakhmanovich, T.I. Yaroshenko, Z.V. Stepanova, L.I. Larina, Zhurn. Obsch. Khim. 76 (2006) 161.
[25] I.V. Ovcharenko, Y.V. Shvedenkov, R.N. Musin, V.N. Ikorskii, J. Struct. Chem. (Russ.) 40 (1999) 29.
[26] G.M. Sheldrick, SADABS, Program for absorption correction with the SMART system, University of Göttingen, Germany, 1996.
[27] Bruker, SHELXTL, Version 6.22, Bruker AXS Inc., Madison, WI, USA, 2003.
[28] W. Kraus, G. Nolze, PowderCell for Windows, version 2.4, Federal Institute for Materials Research and Testing (BAM), Berlin, Germany.

grade and were used as received without further purification.

2.1.1. X-ray crystallography

X-ray crystallographic data were collected using a Bruker SMART APEX-CCD diffractometer with Mo Kα radiation ($\lambda = 0.71073$ Å). The intensity data were corrected for Lorentz and polarization effects and empirical absorption corrections were applied using the SAINT program [20,21]. All the structures were solved by direct methods using SHELXS-97 [22]. Non-hydrogen atoms located from the difference Fourier maps were refined anisotropically by full-matrix least-squares on F^2, using SHELXL-97 [22]. The hydrogen atoms were included in the calculated positions and refined isotropically using a riding model.

2.1.2. Thermal measurements

Thermogravimetry was studied by a computer controlled METTLER TOLEDO STAR^e system of module TGA/SDTA851^e under a static nitrogen atmosphere using a platinum pan at a heating rate of 10 °C min^{-1} in the temperature range 25–700 °C. The instrument was calibrated using a RTypSDTA sensor. The onset temperature obtained from the DTG curve was used to evaluate the onset decomposition temperature of the samples.

2.2. Syntheses

2.2.1. N-(2-Pyridylethyl)pyridine-2-carbaldimine (*L*)

To 2.5 g of anhydrous $MgSO_4$ suspended in 20 mL of CH_2Cl_2, 565 mg (4.62 mmol) of 2-pyridine-2-ylethanamine was added followed by 500 mg (4.62 mmol) of pyridine-2-carbaldehyde. The reaction mixture was refluxed for 1.5 h until a yellowish color appeared and then it was stirred at ambient temperature for another 3 h. The solution was filtered, washed with 2×5 mL portions of CH_2Cl_2, and the volatile components in the combined solution were removed by evaporation in vacuum. The crude product was obtained as a yellowish oil, which was pure enough as inferred from the ^{1}H NMR spectrum, and was used without further purification. Yield: 970 mg (100%). ^{1}H NMR (δ (*J*, Hz), $CDCl_3$): 3.22 (2H, t, 7.2), 4.08 (2H, t, 7.2), 7.08 (1H, t, 6), 7.16 (1H, d, 7.6), 7.26 (1H, t, 6), 7.54 (1H, t, 7.6), 7.69 (1H, t, 7.6), 7.93 (1H, d, 8), 8.31 (1H, s), 8.52 (1H, d, 4.4) and 8.59 (1H, d, 4.4). IR (neat, cm^{-1}): 1648 (C=N_{im}), 1590 (C=N_{py}).

2.2.2. [Co*L*(NO_3)$_2$] (*1*)

To 180 mg (0.85 mmol) of **L** dissolved in 25 mL of methanol, was added 247 mg (0.85 mmol) of $Co(NO_3)_2 \cdot 6H_2O$ dissolved in 20 mL methanol with stirring. After stirring for 4 h, the reaction mixture was left to crystallize. Orange block-like crystals deposited, were collected and washed with ice-cold methanol. Yield: 0.26 g (77%). IR (KBr, cm^{-1}): 1653 (C=N_{im}), 1610 (C=N_{py}). *Anal.* Calc for $C_{13}H_{13}N_5O_6Co$: C, 39.57; H, 3.30; N, 17.76. Found: C, 39.25; H, 3.21; N, 16.50%.

2.2.3. [Ni*L*(NO_3)$_2$] (*2*)

To 180 mg (0.85 mmol) of **L** dissolved in 25 mL of methanol, was added to 250 mg (0.85 mmol) of $Ni(NO_3)_2 \cdot 6H_2O$ dissolved in 20 mL of methanol with stirring, and the stirring was continued overnight. The reaction mixture was kept undisturbed and pale green-colored block-like crystals obtained after few days were collected after washing with ice-cold methanol. Yield: 0.25 g (74%). IR (KBr, cm^{-1}): 1650 (C=N_{im}), 1600 (C=N_{py}). *Anal.* Calc for $C_{13}H_{13}N_5O_6Ni$: C, 39.59; H, 3.30; N, 17.77. Found: C, 39.35; H, 3.19; N, 17.14%.

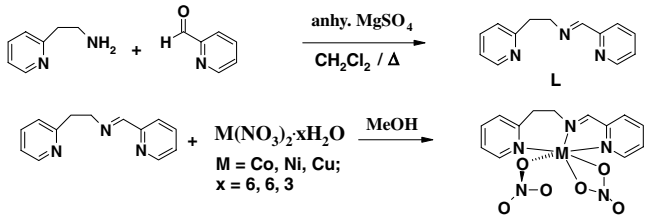
2.2.4. [Cu*L*(NO_3)$_2$] (*3*)

To 180 mg (0.85 mmol) of **L**, dissolved in 25 mL of methanol was added 205 mg (0.85 mmol) of $Cu(NO_3)_2 \cdot 3H_2O$. The reaction mixture was stirred at room temperature overnight and the blue precipitate that deposited was filtered and washed thoroughly with methanol. Dark blue crystals were obtained by slow evaporation of acetonitrile solution. Yield: 0.33 g (97%). IR (KBr, cm^{-1}): 1653 (C=N_{im}), 1602 (C=N_{py}). *Anal.* Calc for $C_{13}H_{13}N_5O_6Cu$: C, 39.11; H, 3.26; N, 17.55. Found: C, 39.18; H, 3.21; N, 17.50%.

3. Results and discussion

3.1. Syntheses

Ligand **L** was synthesized (Scheme 1) in quantitative yield, by refluxing equimolar quantities of pyridine-2-carbaldehyde and 2-aminoethylpyridine in dichloromethane using anhydrous $MgSO_4$ as a Lewis acid as well as a drying agent to absorb the water formed as a product of the condensation. The yellow-oily product obtained after removal of hydrated $MgSO_4$ and other volatile components, does not require further purification and loses its identity on standing, as ascertained from its ^{1}H NMR spectrum. Therefore, freshly prepared **L** was used for the synthesis of the complexes. This method of synthesis is advantageous over the reported procedure, having a shorter reaction time [23]. Complexes of the molecular formula [M**L**(NO_3)$_2$], M = Co(II), Ni(II), and Cu(II) were synthesized in methanol using equimolar quantities each of **L** and the corresponding metal nitrate.



Scheme 1. Synthesis of **L** and complexes.

3.2. Optical properties

UV–Vis spectra of **1**, **2**, and **3** exhibit d–d transitions in acetonitrile solution. The curves were fitted to a Gaussian to obtain λ_{max} and the corresponding molar extinction coefficient values. In complex **1**, two higher energy transitions were observed at 417 nm and as a shoulder at 342 nm with ε values 121 and 200 $M^{-1}\,cm^{-1}$ respectively. Complex **2** shows three transitions at 888, 745, and 590 nm, having the respective molar extinction coefficient values 110, 20, and 46 $M^{-1}\,cm^{-1}$. In the case of **3**, two transitions were observable with λ_{max} at 675 and at 383 nm with ε values 55 and 34 $M^{-1}\,cm^{-1}$ [24,25].

3.3. Magnetism and EPR spectra

The room temperature magnetic moments of **1**, **2**, and **3** are in agreement with the presence of 3 (high-spin Co(II)), 2 and 1 unpaired electrons respectively. The effective magnetic moment, μ_{eff} and molar susceptibility, χ_M of the complexes were determined using a least-square fitting method and are listed in Table 1. In all three cases $\mu_{eff} > \mu_{so}$ is consistent with more than a half-filled configuration for the metal ions. Since $\mu_{S+L} > \mu_{eff} > \mu_{so}$, there is the existence of spin–orbit coupling in the three complexes [26–28]. The X-band (9.44 GHz) EPR pattern of **1** indicates that the complex is high spin in nature.

Table 1
Molar susceptibility and effective magnetic moment

	1	2	3
$\chi_M \times 10^3$ (emu mol^{-1})	6.475	6.372	1.600
μ_{eff} (BM)	3.928	3.897	1.952

The powder EPR spectrum recorded at room temperature exhibits a well-defined $S = 3/2$ $M_s = |\pm 1/2\rangle$ signal indicating a system having modest spin–orbit coupling and a high degree of rhombic distortion of the axial zero-field splitting, with $g_{(x,y)} = 4.25$, $g_z = 2.08$ as well as a signal corresponding to $g_{eff} \sim 10.9$. At 77 K in the X-band (9.12 GHz), the powder EPR spectrum of **1** shows an eight line hyperfine splitting of $g_z(^{59}Co, I = 7/2)$ with $A_z = 91.7 \times 10^{-4}\ cm^{-1}$, whereas in acetonitrile solution an isotropic spectrum with $g_0 = 2.01$ is observed [6–10]. The X-band (9.12 GHz) powder EPR spectrum of **2** at 77 K shows a single-quantum line within the scan range 2000–4000 G having $g_z = 2.16$, $g_x = 2.06$, $g_y = 1.99$ and $g_{ave} = 2.07$, while the acetonitrile solution at 77 K exhibit an isotropic spectrum with $g_0 = 2.01$ [11–13]. The acetonitrile solution as well as polycrystalline sample of **3** at 77 K, exhibits an axial spectrum having $g_\parallel$ and $g_\perp$ values 2.21 and 2.07 respectively and does not show hyperfine splitting. The trend $g_\parallel > g_\perp > 2$, is in agreement with the unpaired electron being in the $d_{x^2-y^2}$ orbital [8–10,14,15].

3.4. Molecular structures

The molecular structures of all three complexes were determined by X-ray crystallography. The crystallographic data and refinement parameters are summarized in Table 2 and selected bond parameters are listed in Table 3. All three complexes are isomorphous and crystallized in the space group *Cc*. In each case, the bivalent metal ion is coordinated by the three nitrogen atoms of the tridentate **L** with two pyridine-N occupying *trans* positions. **L** binds to the metal ions by a near-planar five-membered and a puckered six-membered chelate ring. Of the two nitrate ions, one binds in a bidentate fashion and the other in a monodentate

Table 2
Crystallographic data and refinement parameters

	1	2	3
Empirical formula	$C_{13}H_{13}N_5O_6Co$	$C_{13}H_{13}N_5O_6Ni$	$C_{13}H_{13}N_5O_6Cu$
CCDC number	295199	295200	295198
Formula weight	394.21	393.99	398.82
Temperature (K)	296(2)	296(2)	296(2)
Wavelength (Å)	0.71073	0.71073	0.71073
Crystal system	monoclinic	monoclinic	monoclinic
Space group	*Cc*	*Cc*	*Cc*
a (Å)	8.6093(6)	8.5688(5)	8.5622(16)
b (Å)	14.4532(6)	14.6361(8)	14.747(3)
c (Å)	12.8749(10)	12.5218(7)	12.3162(16)
β (°)	98.314(6)	97.317(3)	96.622(3)
V (Å^3)	1585.21(18)	1557.62(15)	1544.8(5)
Z	4	4	4
D_{calc} (g cm^{-3})	1.652	1.680	1.715
μ (mm^{-1})	1.126	1.289	1.458
Goodness-of-fit (GOF)[a] on F^2	1.032	1.057	1.062
R [$I > 2\sigma(I)$]	R_1[b] = 0.0438, wR_2[c] = 0.1139	R_1[b] = 0.0527, wR_2[c] = 0.1418	R_1[b] = 0.0603, wR_2[c] = 0.1576
R indices (all data)	R_1[b] = 0.0540, wR_2[c] = 0.1234	R_1[b] = 0.0568, wR_2[c] = 0.1467	R_1[b] = 0.0693, wR_2[c] = 0.1703

[a] $GOF = \left[\sum[w(F_o^2 - F_c^2)^2]/M - N\right]^{1/2}$ (M = number of reflections, N = number of parameters refined).
[b] $R_1 = \sum ||F_o| - |F_c|| / \sum |F_o|$.
[c] $wR_2 = \left[\sum[w(F_o^2 - F_c^2)^2] / \sum[w(F_o^2)^2]\right]$.

Table 3
Selected bond distances and angles

Bond distances (Å)				Bond angles (°)			
Bond	**1**	**2**	**3**	Angle	**1**	**2**	**3**
M–N1	2.096(8)	2.039(9)	1.997(9)	O1–M–O2	56.6(3)	58.2(2)	49.6(4)
M–N2	2.094(4)	2.040(4)	1.978(5)	O1–M–O4	122.0(3)	111.8(3)	109.9(3)
M–N3	2.150(8)	2.085(8)	1.988(14)	O1–M–N1	90.2(2)	89.1(2)	86.1(3)
M–O1	2.178(6)	2.167(5)	2.061(6)	O1–M–N2	140.7(3)	146.1(2)	143.4(2)
M–O2	2.159(7)	2.036(7)	2.320(18)	O1–M–N3	97.4(3)	96.2(3)	98.6(5)
M–O4	2.244(9)	2.158(9)	2.538(15)	O2–M–O4	178.5(2)	169.9(2)	159.2(2)
N2–C6	1.403(10)	1.380(14)	1.392(16)	O2–M–N1	91.2(3)	90.9(3)	92.1(5)
N2–C7	1.457(6)	1.456(7)	1.468(10)	O2–M–N2	87.5(2)	91.7(2)	98.6(4)
C5–C6	1.388(16)	1.454(18)	1.322(23)	O2–M–N3	86.9(3)	88.0(3)	88.5(5)
C7–C8	1.281(12)	1.318(13)	1.376(23)	O4–M–N1	89.0(3)	90.0(3)	89.4(3)
C8–C9	1.545(14)	1.497(15)	1.691(27)	O4–M–N2	94.0(2)	98.2(2)	101.9(2)
N1–C5	1.412(10)	1.453(11)	1.462(17)	O4–M–N3	93.1(3)	92.2(3)	92.1(3)
N3–C9	1.274(12)	1.246(12)	1.232(21)	N1–M–N2	73.9(2)	75.1(2)	76.6(3)
O2–N4	1.190(11)	1.213(10)	1.143(15)	N2–M–N3	95.7(3)	98.0(2)	97.7(4)
				N1–M–N3	169.4(3)	172.9(4)	174.3(3)

fashion, giving an overall pseudo-octahedral geometry for the metal center. Therefore, the basal plane contains the three nitrogen (N1, N2, and N3) atoms of **L** and an oxygen (O1) of the bidentate nitrate, the apical positions being occupied by oxygen atoms (O2, O4) from each of the two nitrate ions. In **3**, a long axial Cu1···O4 contact of 2.54(2) Å is present. A perspective view of **1** is shown in Fig. 1. The N1–Co1–N2 angle of the five-membered chelate ring is 73.9(2)°, while N2–Co1–N3 of the six-membered ring is 95.7(3)°. These angles deviate significantly from the ideal value of 90° due to the sizes of the five-membered planar and the six-membered non-planar chelate rings. Average Co1–N lengths are shorter by 0.055(8) Å than that of the Co1–O distances of the bidentate NO_3^-. The bidentate NO_3^- has a shorter contact with Co1 than when it coordinates with one oxygen atom. The chelate bite angle of NO_3^- in **1** is 56.6(3)°. The O1–Co1–N2 angle, 140.7(3)°, deviates considerably from linearity by 39.3° due to the smaller chelate bite of the nitrate group and

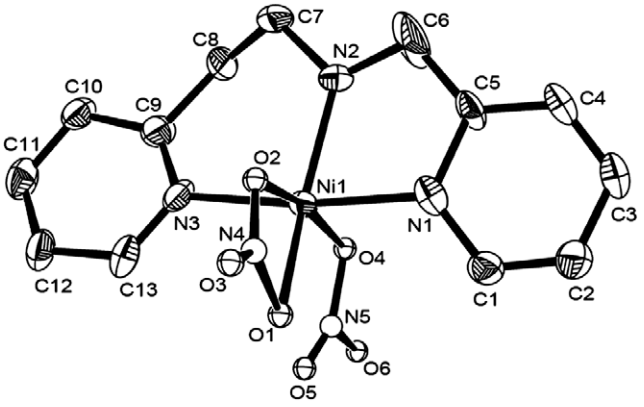


Fig. 2. ORTEP diagram of **2** (30% probability, hydrogens are omitted for clarity).

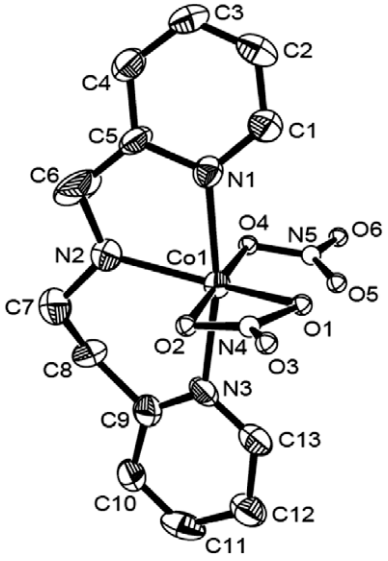


Fig. 1. ORTEP diagram of **1** (30% probability, hydrogens are omitted for clarity).

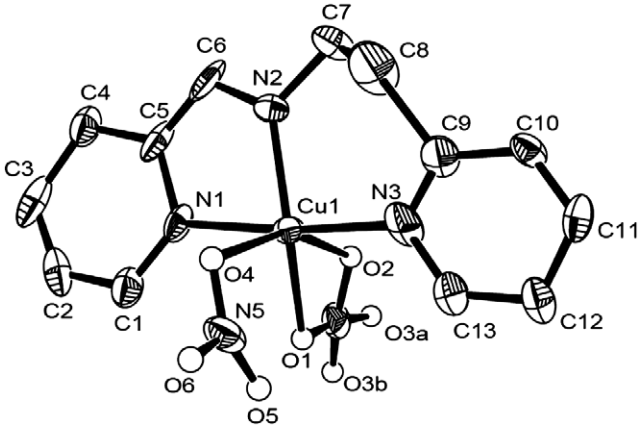


Fig. 3. ORTEP diagram of **3** (30% probability, hydrogens are omitted for clarity). O3a and O3b are disordered entities.

non-bonded O1···O5 interaction of 2.73(2) Å. A perspective views of **2** and **3** are shown in Figs. 2 and 3. Oxygen atoms of the monodentate NO_3^- in **2** are disordered and a reasonable disorder pattern could not be fixed. O3 oxygen atom of the bidentate NO_3^- in **3** is disordered and therefore refined with variable site occupancy factors (O3a, 0.37754; O3b, 0.62246). A non-bonded O1···O5 interaction is present at 2.98(2) Å in **2** and at 3.03 (2) Å in **3**.

On comparison, M–N_{im} and M–N_{py} bond lengths follow the order, Co > Ni > Cu, consistent with the trend in the relative size of the bivalent ions. The six-membered chelate ring has a twisted conformation, N3–M–N2–C7, C9–N3–M–N2, M–N2–C7–C8, and N2–C7–C8–C9 torsional angles respectively lie in the range 0–2°, 10–14°, −(25–36°), and 61–70°. This clearly indicates that C8 and C9 atoms deviate from the plane formed by N3–M–N2–C7 atoms. Twisting about C8 and C9 is more severe in **3** than in **1** and **2**. However, the five-membered chelate ring is closer to planarity as shown by the torsional angles Cu1–N2–C6–C5, N2–C6–C5–N1, and C6–C5–N1–Cu1 respectively being 11.6, −5.2°, and −2.5°. The values of these angles in order in **1** and **2** are 18.5°, −17.0°, 9.3° and 19.6°, −15.9°, 7.4°, respectively suggesting that the deviation is marginal.

3.5. Thermogravimetric (TG) analysis

TG and DTG curves, shown in Fig. 4, (all the temperatures noted in this section are onset mid-point temperatures) of **1** and **2** shows weight loss in two distinct steps: in the first step, loss of the ligand **L** (found 52.9%, 52.7%; *ca.* 53.6%, 53.5%) occurs at 276 and 273 °C respectively and in the second step, loss of two moles of NO_2 and half mole of O_2 gas are at 570 and 482 °C. Whereas, in **3** the loss (84.3%) of ligand **L**, two moles of NO_2 and one mole of O_2 (*ca.* 84.2%) all occur in a single step at 266 °C. This indicates the thermal stability order Co(II) > Ni(II) > Cu(II). The identities of the final residuals were not analyzed.

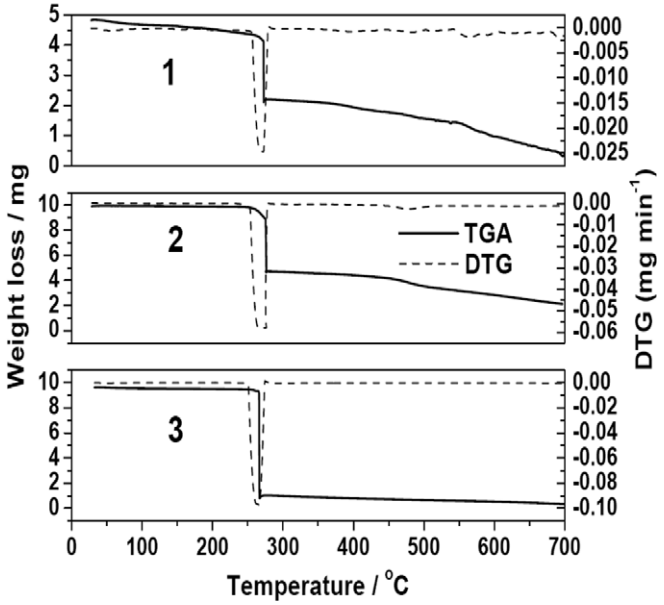


Fig. 4. TG/DTG curve of the complexes **1**, **2**, and **3**.

4. Conclusion

A triad of complexes of the type $[ML(NO_3)_2]$ (M = Co(II), Ni(II), Cu(II)), based on a tridentate N_3–donor ligand, were isolated and characterized using spectral, thermal, and single crystal X-ray studies. Cobalt, nickel, and copper complexes have pseudo-octahedral geometry with a N_3O_3 chromophore. All the complexes exhibit d–d transitions in the visible region. The high-spin Co(II) complex shows modest spin–orbit coupling and a high degree of rhombic distortion of the axial zero-field splitting. The thermal stability order is **1** > **2** > **3**, showing a reverse Irving-Williams trend.

Acknowledgements

We are grateful to the Department of Science and Technology (DST) New Delhi for a financial grant (SR/S1/IC-01/2002) and for establishing the single crystal X-ray diffractometer facility under the FIST scheme. The authors are thankful to Babulal Das for X-ray data, CIF IIT Guwahati for NMR spectrum and SAIF IIT Madras for EPR spectra and VSM data.

Appendix A. Supplementary material

CCDC 295198, 295199 and 295200 contain the supplementary crystallographic data for this paper. These data can be obtained free of charge via http://www.ccdc.ac.uk/conts/retrieving.html, or from the Cambridge Crystallographic Data Centre, 12 Union Road, Cambridge CB2 1EZ, UK; fax: (+44) 1223-336-033; or e-mail: deposit@ccdc.cam.ac.uk. Supplementary data associated with this article can be found, in the online version, at doi:10.1016/j.poly.2006.11.046.

References

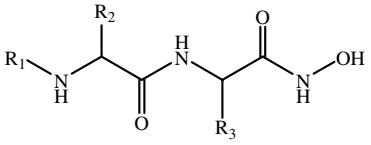
[1] K.D. Karlin, M.S. Haka, R.W. Cruse, G.J. Meyer, A. Faroog, Y. Gultneh, J.C. Hayes, J. Zubieta, J. Am. Chem. Soc. 110 (1988) 1196.
[2] N. Kitajima, K. Fujisawa, Y. Moro-oka, J. Am. Chem. Soc. 111 (1989) 8975.
[3] N. Kitajima, Y. Moro-oka, Chem. Rev. 94 (1994) 737.
[4] S.A. Leaver, M. Palaniandavar, C.A. Kilner, M.A. Halcrow, J. Chem. Soc., Dalton Trans. (2003) 4224.
[5] P. Manikandan, K.R.J. Thomas, P.T. Manoharan, J. Chem. Soc., Dalton Trans. (2000) 2779.
[6] K.J. Tubbs, E. Szajna, B. Bennet, J.A. Halfen, R.W. Watkins, A.M. Arif, L.M. Berreau, J. Chem. Soc., Dalton Trans. (2004) 2398.
[7] S.A. Cockle, J. Biochem. 137 (1974) 587.
[8] S. Chandra, L.K. Gupta, Spectrochim. Acta A 62 (2005) 1102.

[9] S. Chandra, L.K. Gupta, Spectrochim. Acta A 62 (2005) 1125.
[10] K.K. Mothilal, C. Karunakaran, P.S. Rao, R. Murugesan, Spectrochim. Acta A 59 (2003) 3337.
[11] D. Collison, M. Helliwell, V.M. Jones, F.E. Mabbs, E.J.L. McInnes, P.C. Riedi, G.M. Smith, R.G. Pritchard, W.I. Cross, J. Chem. Soc., Faraday Trans. 94 (1998) 3019.
[12] P.J. Van Dam, A.A.K. Klassen, E.J. Reijerse, W.R. Hagen, J. Magn. Reson. 130 (1998) 140.
[13] E. Pereira, L. Gomes, B. de Castro, J. Chem. Soc., Dalton Trans. (1998) 629.
[14] K.J. Tubbs, A.L. Fuller, B. Bennet, A.M. Arif, M.M. Makowska-Grzyska, L.M. Berreau, J. Chem. Soc., Dalton Trans. (2003) 3111.
[15] A.M.F. Benial, V. Ramakrishnan, R. Murugesan, Spectrochim. Acta A 56 (2000) 2775.
[16] P. Manikandan, M. Subramoni, B. Varghese, P.T. Manoharan, J. Chem. Soc., Dalton Trans. (1998) 3219.
[17] M.L. Calatayud, I. Castro, J. Sletten, F. Lloret, M. Julve, Inorg. Chim. Acta 300–302 (2000) 846.
[18] H. Casellas, F. Costantino, A. Mandinnet, A. Caneschi, D. Gatteschi, Inorg. Chim. Acta 358 (2005) 177.
[19] S.K. Padhi, V. Manivannan, Inorg. Chem. 45 (2006) 7994.
[20] G.M. Sheldrick, SADABS, University of Göttingen, Göttingen, Germany, 1996.
[21] SMART and SAINT, Siemens Analytical X-ray Instruments Inc., Madison, WI, 1996.
[22] G.M. Sheldrick, SHELXS-97 and SHELXL-97, University of Göttingen, Göttingen, Germany, 1997.
[23] R.E. Rülke, J.M. Ernsting, A.L. Spek, C.J. Elsevier, Inorg. Chem. 32 (1993) 5769.
[24] A.B.P. Lever, Inorganic Electronic Spectroscopy, Elsevier, Amsterdam, 1986.
[25] K. Nakamoto, Infrared and Raman Spectra of Inorganic and Coordination Compounds. Part B, fifth ed., Wiley, New York, 1997.
[26] C.J. O'Connor, Prog. Inorg. Chem. 29 (1982) 203.
[27] O. Kahn, Molecular Magnetism, Wiley-VCH, 1993.
[28] D. Arcon, K. Prassides, π-Electron magnetism, in: J. Veciana (Ed.), Structure and Bonding, vol. 100, Springer, Berlin, 2001, p. 129.

When entering the body, hydroxamic acid derivatives of peptides as potential drugs may interact with other metal ions, beside the one in the target enzyme, thus the knowledge of their metal ion binding strengths is of particular importance. Furthermore, information about this interaction with metals may aid the design of new chelators specific for a certain metal ion (thus for a given class of enzyme).

Despite the above challenges, only very few papers have been published concerning metal ion peptide hydroxamate interactions in the past two decades. Chang and co-workers studied the Ni^{2+}, Cu^{2+}, Zn^{2+}, UO_2^{2+} and Pb^{2+} complexes of Z-AlaGlyNHOH (Z = benzyloxycarbonyl) and found only the coordination of the hydroxamate group in the complexes [6]. Brown and Mageswaran investigated the Fe^{3+} and Ni^{2+} binding capabilities of GlyGlyNHOH and GlyGlyGlyNHOH [7]. The results obtained at a high excess of ligands indicated again exclusive [O,O] coordination with both metal ions. In a study by Farkas and Kiss the Co^{2+}, Ni^{2+}, Cu^{2+}, Zn^{2+} and Fe^{3+} complexes of ProLeuNHOH and ProLeuGlyNHOH were investigated [8]. While the formation of complexes with moderate stability was found with Co^{2+} and Zn^{2+} in the pH range 6.0–8.5 without the deprotonation of the peptide amides, [NH_2, N_{amid}, $N_{hydrox.}$] coordination of the ligands was suggested above pH 6.0 with Cu^{2+} and Ni^{2+}.

Due to the very limited data and the contradictory results in this field, a systematic investigation was undertaken. In the present paper, we report a detailed solution equilibrium study using combined pH-potentiometric and spectroscopic (UV–Vis, EPR, CD, ^{1}H NMR) methods on the interaction of iron(III), aluminium(III), nickel(II), copper(II) and zinc(II) with simple primary peptide hydroxamic acids, L-Ala-L-AlaNHOH (L^3) or L-Ala-L-SerNHOH (L^4) (Scheme 1). The biological significance of Fe(III), Cu(II) and Zn(II) as constituent of various metalloenzymes is beyond doubt. Ni(II) in ureases and the toxicity of Al(III) make these metal ions also of interest. Since the terminal amino group in oligopeptides has an important role as an anchor in the enhancement of the deprotonation and coordination of the peptide amide group to soft or borderline metal ions [9], for comparative purposes, the Z-protected models, Z-L-Ala-L-AlaNHOH (L^1) and Z-L-Ala-L-Ser-NHOH (L^2) (Scheme 1) were also involved in the work.



R_1	R_2	R_3	Ligand	Abbreviation
$PhCH_2OCO$	CH_3	CH_3	Z-AlaAlaNHOH	L^1
$PhCH_2OCO$	CH_3	CH_2OH	Z-AlaSerNHOH	L^2
H	CH_3	CH_3	AlaAlaNHOH	L^3
H	CH_3	CH_2OH	AlaSerNHOH	L^4

Scheme 1.

2. Experimental

2.1. Materials and stock solutions

Methanol was purified and dried by standard methods [10]. Z-L-Ala-L-Ala-OMe and Z-L-Ala-L-Ser-OMe were purchased from Bachem, hydroxylamine hydrochloride from Fluka, palladium/carbon (10%) from Merck. All chemicals were of the highest purity commercially available and were used without further purification.

The metal ion stock solutions were prepared from $CuCl_2 \cdot 2H_2O$, $NiCl_2 \cdot 5H_2O$, $AlCl_3 \cdot 6H_2O$, $FeCl_3 \cdot 6H_2O$ (Reanal, Hungary) using doubly deionised and ultrafiltered water obtained from a Milli-Q RG (Millipore) water purification system. In the latter two cases the stock solutions also contained hydrochloric acid (~0.1 M). ZnO (Reanal) was dissolved in diluted HCl. The metal ion concentrations were checked gravimetrically via precipitation of the quinolin-8-olate salts; [Fe^{3+}] was determined by a complexometric titration. The acid content of the Al(III) and Fe(III) stock solutions was measured by Gran's method [11]. The purity and the exact concentration of the ligand stock solutions were also determined by Gran's method [11].

2.2. Syntheses of the ligands

2.2.1. Z-L-Ala-L-AlaNHOH (L^1)

To a chilled (0 °C) and stirred solution of $NH_2OH \cdot HCl$ (290 mg, 4.17 mmol) in dry methanol (4 mL), 29%(m/m) NaOMe solution in methanol (1.33 mL, 7.09 mmol) was added under nitrogen. To this mixture, containing solid NaCl, a solution of Z-L-Ala-L-Ala-OMe (1.157 g, 3.75 mmol) in dry methanol (4.5 mL) was added and the mixture was stirred at 0 °C for 5 h. Upon adding water (8 mL) and 1 M HCl (10 ml) to the reaction mixture, a clear solution was obtained which was allowed to stay at 4 °C overnight. The white crystals that separated were filtered off and recrystallised from water/methanol (6/4) affording 577 mg (48%) pure, protected hydroxamic acid. ^{1}H NMR (360 MHz, D_2O/DMSO-d_6 (6/1)) δ: 7.42 (5H, m, C_6H_5); 5.12 (2H, s, $C_6H_5CH_2$); 4.22 (1H, q, CH); 4.10 (1H, q, CH); 1.35 (3H, d, CH_3); 1.32 (3H, d, CH_3). ESI MS, *m/z* (%): 332.133 (100) $[M+Na]^+$ (calc. for $C_{14}H_{19}N_3O_5Na$, 332.122), 641.267 (29) $[2M+Na]^+$.

2.2.2. Z-L-Ala-L-SerNHOH (L^2)

The same procedure was applied using $NH_2OH \cdot HCl$ (472 mg, 6.79 mmol) in methanol (7 mL), 29%(m/m) NaOMe solution in methanol (2.19 mL, 11.5 mmol) and Z-L-Ala-L-Ser-OMe (2.00 g, 6.17 mmol) in methanol (10 mL). Upon adding water (9 mL) and 1 M HCl

(11 ml) to the mixture, a clear solution was obtained. The volume was reduced to half by evaporation and allowed to stay at 4 °C overnight. White crystals were filtered off and recrystallised from water/methanol (6/4) affording 836 mg (42%) pure, protected hydroxamic acid. ^{1}H NMR (360 MHz, D_2O/DMSO-d_6 (6/1)) δ: 7.42 (5H, m, C_6H_5); 5.13 (2H, s, $C_6H_5CH_2$); 4.34 (1H, t, CH); 4.16 (1H, q, CH); 3.79 (2H, d, CH_2); 1.35 (3H, d, CH_3). ESI MS, m/z (%): 348.134 $[M+Na]^+$ (calc. for $C_{14}H_{19}N_3O_6Na$, 348.117), 673.266 (27) $[2M+Na]^+$.

2.2.3. L-Ala-L-AlaNHOH · HCl (*L*^{3} · *HCl*)

Z-L-Ala-L-AlaNHOH (550 mg, 1.78 mmol) was dissolved in a mixture of dry methanol (20 mL) and methanolic HCl solution (1.06 M, 2 mL). Palladium/carbon (10%(m/m), 180 mg) was added and the mixture was hydrogenated for 5 h. The catalyst was removed by filtration and the solution was evaporated to dryness. The fine white, slightly hygroscopic solid was dried in a vacuum at 40 °C. Yield: 335 mg (89%). ^{1}H NMR (360 MHz, D_2O) δ:4.26 (1H, q, CH); 4.08 (1H, q, CH); 1.53 (3H, d, CH_3); 1.39 (3H, d, CH_3). ESI MS, *m/z* (%): 143.094 (99) $[M-NHOH+H]^+$, 176.118 (100) $[M+H]^+$ (calc. for $C_6H_{14}N_3O_3$, 176.103), 198.101 (12) $[M+Na]^+$.

2.2.4. L-Ala-L-SerNHOH · HCl (*L*^{4} · *HCl*)

Z-L-Ala-L-SerNHOH (500 mg, 1.54 mmol) was hydrogenated using the same procedure and conditions as for the AlaAla ligand. Yield: 328 mg (94%). ^{1}H NMR (360 MHz, D_2O) δ:4.40 (1H, t, CH); 4.14 (1H, q, CH); 3.83 (2H, d, CH_2); 1.55 (3H, d, CH_3). ESI MS, m/z (%): 120.075 (40) $[M-COCH(Me)NH_2+H]^+$, 131.090 (61) $[M-CONHOH+H]^+$, 159.086 (100) $[M-NHOH+H]^+$, 192.109 (83) $[M+H]^+$ (calc. for $C_6H_{14}N_3O_4$, 192.098), 214.098 (5) $[M+Na]^+$, 383.199 (19) $[2M+H]^+$.

2.3. Potentiometric and spectroscopic studies

PH-potentiometric and spectrophotometric measurements were carried out at an ionic strength of 0.2 M (KCl) and at 25.0 ± 0.1 °C. Carbonate-free KOH solutions of known concentrations (ca. 0.2 M) were used as titrant. HCl stock solutions were prepared from cc. HCl (both the acid and base were Merck products) and their concentrations were determined by potentiometric titrations. A Radiometer pHM 84 instrument equipped with a Metrohm combined electrode (type 6.0234.100) and Metrohm 715 Dosimat burette were used for the pH-metric measurements. The electrode system was calibrated according to Irving et al. [12], the pH-metric readings could therefore be converted into hydrogen ion concentration. The water ionization constant, pK_w, is 13.76 ± 0.01 under the conditions employed. The titrations were performed in the pH range 2.0–11.0, or until precipitation occurred. The initial volume of the samples was 5.00 mL. The ligand concentrations were varied in the range 0.002–0.004 M and the metal ion to ligand ratios in the range 1:1–1:5. For copper(II) 1.2–1.5:1 metal ion to ligand ratios were also studied. Typically, four or five ratios were measured in each system. The reproducibility of the titration points included in the evaluation was within 0.005 pH unit. Titration points with a waiting time of 10 min or more were omitted from the calculations. About 200 titration points were used for each system. The accepted fitting of the titration curves was always less than 0.006 mL. The samples were in all cases completely deoxygenated by bubbling purified argon for ca. 20 min before the measurements.

An HP 8453 or Perkin–Elmer Lambda 25 spectrophotometer was used to record the UV–Vis spectra over the range 250–900 nm for copper(II), iron(III) and nickel(II) containing systems. The path length was 1 cm. Measurements for the iron(III) containing samples were carried out preparing individual samples in which the 0.2 M KCl was partially or completely replaced by HCl. pH values, varying in the range ca. 0.7–1.6, were calculated from the HCl content. The metal ion concentrations were in the range 0.0004–0.0008 M and the metal ion to ligand ratios were in the range 1:3–1:5. Spectrophotometric titrations were also performed with samples containing Fe(III), Cu(II) or Ni(II) in 0.0004–0.004 M concentrations at metal to ligand ratios ranging from 1.5:1 to 1:5. Spectrophotometric results were utilized to calculate the stability constants for the Fe(III) complexes formed below pH 2.0. Above pH 2.0 potentiometric data were used to find the stoichiometry of the species and calculate their concentration stability constants. The calculations were performed by the PSEQUAD computer program [13] using the literature data ($\log\beta$) for the iron(III) [14] or aluminium(III) [15] hydrolytic species (the Davies equation was used to take the different ionic strengths into account).

^{1}H NMR spectra were recorded on a Bruker AM360 FT NMR instrument at 25 °C. Chemical shifts are reported in ppm (δ_H) from sodium 3-(trimethylsilyl)-propionate (TSP) as internal reference. NMR titrations were carried out in D_2O (99.8%) at $c_{ligand} = 0.025$ M in order to determine the protonation microscopic constants of L-Ala-L-AlaNHOH or L-Ala-L-SerNHOH using the p*D* dependence of the chemical shifts of the CH, CH_2 or CH_3 nuclei. The pH was set up with NaOD or DCl in D_2O. The micro constants were calculated with the aid of PSEQUAD [13] and a MATLAB program [16].

CD spectra of the Cu(II) – L-Ala-L-AlaNHOH or L-Ala-L-SerNHOH systems were taken at different pH values by a JASCO J-810 spectropolarimeter using 1 cm cells in the 300–800 nm range. The temperature was 23 °C. The metal ion to ligand ratios varied in the range 1.5:1–1:2 and c_{ligand} was 0.003 M. The pH was changed by adding small portions of either 0.2 M KOH or HCl solutions to the samples. CD spectra are reported as the difference in molar absorptivity ($\Delta\varepsilon = \varepsilon_l - \varepsilon_r$).

Electrospray ionisation time-of-flight mass spectrometric (ESI-TOF MS) analysis of the ligands was carried out on a Bruker BIOTOF II ESI-TOF instrument using 0.004 M concentration.

Frozen solution EPR spectra in aqueous samples of the copper systems were recorded on a Bruker ER 200D spectrometer equipped with a 3220 data system at 150 K using $^{63}Cu(NO_3)_2$ stock solution. The operating frequency was ~ 9.4 GHz (X-band). The samples for low-temperature measurements contained a few drops of ethylene glycol to ensure good glass formation. The metal ion to ligand ratios varied in the range 1.5:1–1:5 and $c_{Cu(II)}$ was 0.005 M.

3. Results and discussion

3.1. Protonation equilibria of the ligands

The Z-protected ligands L^1 and L^2 can release one proton each, while the fully protonated peptide hydroxamic acids L^3 or L^4 have two deprotonation processes in the measurable pH range. The calculated dissociation constants are listed in Table 1. Taking the different experimental conditions into account the dissociation constants of L^1 and L^2 relating to the hydroxamic group are in reasonable agreement with reported data for Z-AlaGlyNHOH (8.32) [6].

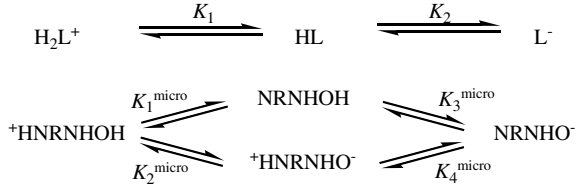
Comparison of the corresponding pK values of L^3 or L^4 with those of H-GlyGlyNHOH (7.52; 8.40) [7] and H-ProLeuNHOH (8.17; 9.11) [8] indicates that the values for L^3 and L^4 fit well in the acidity order of dipeptide hydroxamic acids with increasing electron donating substituents. The values also indicate that the two dissociation processes overlap each other considerably. Therefore, the microscopic protonation processes were also explored from the ^{1}H NMR titration of L^3 and L^4. Chemical shifts of the NMR active nuclei of L^4 in the function of pD are presented in the supplementary material (S1). Calculated values together with the notation of the deprotonation micro processes are summarised in Table 1 (as an example, the distribution of the micro species as a function of pH for L^4 is shown in S2). The data in Table 1 reveal that the $^+NH_3$ groups of L^3 or L^4 are more acidic than the CONHOH functions. This is in accordance with earlier results on α-alanine hydroxamic acid [17]. The overlap between the two dissociation micro processes (see S2) is slightly more considerable for L^4 than L^3: the first proton dissociates to an extent of ca. 78% (L^3: 87) from the $^+NH_3$ group and ca. 22% (L^3: 13) from the CONHOH group.

3.2. Metal complexes of the peptide hydroxamic acids L^3 and L^4

The shape of the corresponding titration curves with L^3 and L^4 is very similar, therefore the curves registered in the Fe(III)-, Al(III)-, Ni(II)-, Cu(II)- and Zn(II)-L^3 systems at 1:2 metal to ligand ratio are only depicted in Fig. 1. As it is seen the complex formation is already significant below pH 2.0 with Fe^{3+}, it starts at 2.5 with Al^{3+}, at 3.0 with Cu^{2+} and at 5.0–5.5 with Zn^{2+} or Ni^{2+}. The best models obtained after the evaluation of the titration curves together with the composition and stability constants of the complexes are summarised in Table 2. All the results on the M^{n+}-L^3 and -L^4 systems indicate that the hydroxyl group of the serine moiety in L^4 has no role in metal binding in the pH range studied.

With iron(III) the complexation starts below pH 2.0 (Fig. 1), therefore this process was also studied quantitatively by UV–Vis. As an example, the absorption spectra of the Fe^{3+}–L^3 system are shown in Fig. 2. It can be seen in Fig. 2 that in the pH range 0.8–1.7 increase of the absorption at $\lambda_{max.} = 494$ nm occurs without any shift. This indicates the formation of a single complexed species. The value of $\lambda_{max.}$ is consistent with the formation of a monohydroxamate complex [18] therefore its composition is most likely to be $[FeHL]^{3+}$. Upon increasing the pH, a continuous shift of the absorption spectra and increase in ε values show unambiguously the formation of bis ($\lambda_{max.} \sim 470$ nm; $\varepsilon \sim 1800\ M^{-1}\ cm^{-1}$) and tris ($\lambda_{max} \sim 425$ nm; $\varepsilon \sim 2500\ M^{-1}\ cm^{-1}$) [18] chelated hydroxamate complexes.

Table 1
Dissociation macro constants (pK_i) and micro constants (pK_i^{micro}) of the ligands at 25.0 °C and at $I = 0.20$ mol/dm^3(KCl)



	L^1	L^2	L^3	L^4
pK_1	8.91(1)	8.69(1)	7.66(1)	7.63(1)
pK_2			8.88(1)	8.73(1)
pK_1^{micro}			7.71(1)	7.73(1)
pK_2^{micro}			8.63(1)	8.32(1)
pK_3^{micro}			8.83(1)	8.63(1)
pK_4^{micro}			7.91(1)	8.04(1)

Standard deviations (3σ values) are in parentheses.

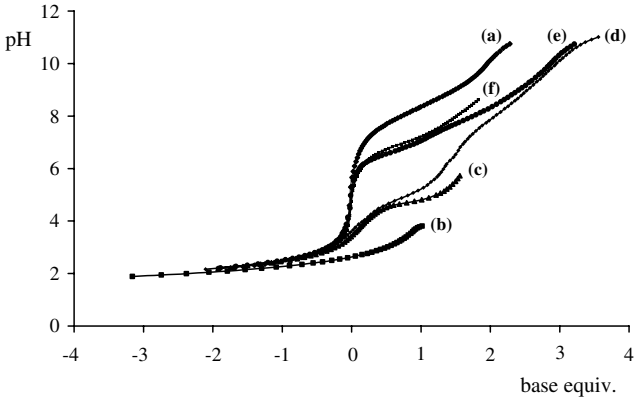


Fig. 1. Representative pH-potentiometric titration curves for L^3 (a) and for metal ion (Fe^{3+} – (b), Al^{3+} – (c), Cu^{2+} – (d), Ni^{2+} – (e) and Zn^{2+} – (f)) – L^3 systems at a 1:2 ratio, $c_M = 0.002$ mol dm^{-3}, $I = 0.2$ mol dm^{-3} and $t = 25.0$ °C.

Table 2
Stability constants ($\log\beta_{pqr}$) for the Fe(III), Al(III), Ni(II), Cu(II) and Zn(II) complexes formed with the peptide hydroxamic acids at 25.0 °C and at $I = 0.20$ mol/dm^3 (KCl)

Metal ion	Complex	p	q	r	$\log\beta_{pqr}$	
					L^3	L^4
Fe(III)	$[FeHL]^{3+}$	1	1	1	17.62(1)[a]	17.39(1)[a]
	$[FeL]^{2+}$	1	0	1	15.09(2)	14.64(3)
	$[FeH_2L_2]^{3+}$	1	2	2	34.57(6)	33.91(7)
					34.00(2)[a]	33.58(3)[a]
	$[FeH_3L_3]^{3+}$	1	3	3	49.40(8)	48.75(11)
					48.61(3)[a]	48.08(4)[a]
Al(III)	$[AlHL]^{3+}$	1	1	1	14.68(4)	14.38(3)
	$[AlL]^{2+}$	1	0	1	9.53(9)	9.63(4)
	$[AlHL_2]^{2+}$	1	1	2	24.20(5)	23.24(6)
	$[AlL_2]^{+}$	1	0	2	17.60(6)	16.48(4)
Ni(II)	$[NiHL]^{2+}$	1	1	1	12.50(9)	12.56(8)
	$[NiL]^{+}$	1	0	1	6.30(3)	5.52(9)
	$[NiH_{-1}L]$	1	−1	1	−1.10(4)	−1.00(5)
	$[NiH_{-2}L]^{-}$	1	−2	1	−9.57(4)	−10.20(6)
Cu(II)	$[CuHL]^{2+}$	1	1	1	14.70(5)	14.46(6)
	$[Cu_2L_2]^{2+}$	2	0	2	23.20(5)	23.28(4)
	$[CuH_{-1}L]$	1	−1	1	4.43(6)	4.68(5)
	$[CuH_{-2}L]^{-}$	1	−2	1	−5.24(8)	−4.73(5)
	$[Cu_3H_{-4}L_2]$	3	−4	2	5.89(6)	6.48(5)
	$[Cu_3H_{-5}L_2]^{-}$	3	−5	2	−3.56(10)	−2.87(9)
	$[Cu_3H_{-6}L_2]^{2-}$	3	−6	2	−14.28(11)	−13.51(10)
Zn(II)	$[ZnHL]^{2+}$	1	1	1	12.35(7)	12.50(6)
	$[ZnL]^{+}$	1	0	1	5.64(4)	5.40(6)
	$[ZnH_{-1}L]$	1	−1	1	−2.58(4)	−2.48(4)
	$[ZnHL_2]^{+}$	1	1	2	17.52(9)	17.49(8)

Standard deviations (3σ values) are in parentheses.
[a] Determined from spectrophotometric titration.

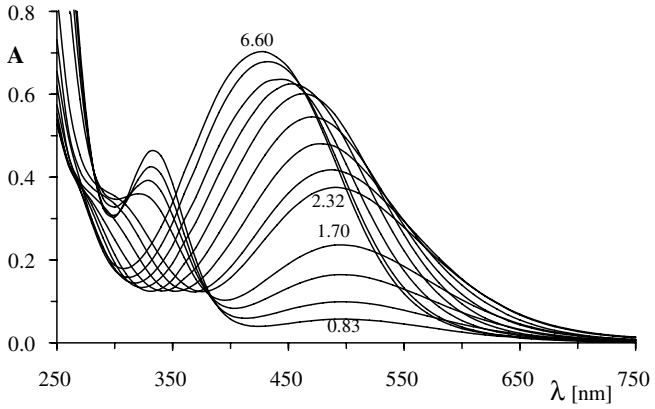


Fig. 2. Representative UV–Vis spectra recorded in the Fe^{3+}– L^3 system at a 1:5 metal to ligand ratio, $c_{Fe(III)} = 0.0003$ mol dm^{-3}, $I = 0.2$ mol dm^{-3} and $t = 25.0$ °C. Numbers indicate selected pH values.

Evaluation of the absorption spectra allowed the calculation of the stability constants of all these major species; the values appear in Table 2. With the fixed constant for $[FeHL]^{3+}$ from spectrophotometry the calculation of the full speciation was possible by treating the pH-potentiometric data. The good agreement between the corresponding values of the major complexes (Table 2) obtained from

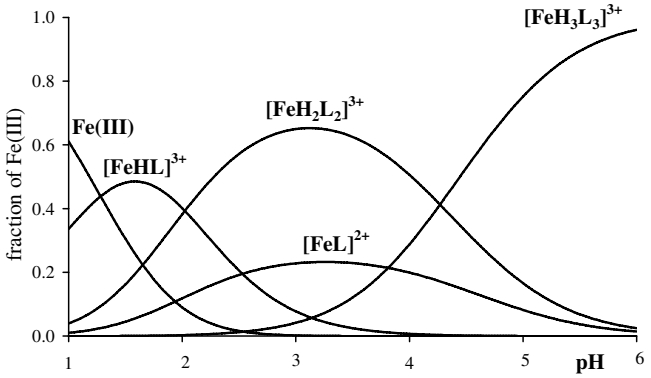


Fig. 3. Concentration distribution curves of the complexes formed in the Fe(III)–L^3 system at a 1:5 metal to ligand ratio, $c_{Fe(III)} = 0.0008$ mol dm^{-3}, $I = 0.2$ mol dm^{-3} and $t = 25.0$ °C.

different techniques also supports the correctness of the model. Representative concentration distribution curves are depicted for the Fe^{3+}– L^3 system in Fig. 3. Above pH 6.0 hydrolysis became significant yielding very slow processes, therefore no attempt was made to evaluate these parts of the titration curves.

In the aluminium(III) containing systems the titration curves can be fitted best with the assumption of mono and binary complexes with a different degree of protonation (Table 2). $[AlHL]^{3+}$ may contain one hydroxamate chelate while the amino group is protonated. Upon increasing the pH, $[AlL]^{2+}$, $[AlHL_2]^{2+}$ and $[AlL_2]^{+}$ are formed. Comparison of the pK values of $[AlHL]^{3+}$ or $[AlHL_2]^{2+}$ (Table 3, rows 8 and 9) with pK_4^{micro} of the free ligands (Table 1), referring to the deprotonation microscopic process of the ammonium group and also with the first hydrolytic constant of Al(III) ($\log\beta_{1-10} = -5.52$) [15], indicates

Table 3
Derived equilibrium constants calculated from the data presented in Tables 2 and 4[a]

Derived equilibrium constant	L^1	L^2	L^3	L^4
$\log K_2$[b]	8.67	8.52	16.38	16.19
$\log K_3$[c]	6.83	6.79	14.61	14.50
$\log(K_1/K_2)$	1.51	1.43	1.24	1.20
$\log(K_2/K_3)$	1.84	1.73	1.77	1.69
$\log K_{FeHL} - pK_4^{micro}$			9.71	9.35
$\log K_{FeH_2L_2} - 2pK_4^{micro}$			18.18	17.50
$\log K_{FeH_3L_3} - 3pK_4^{micro}$			24.88	23.96
pK_{AlL} (L^1, L^2); pK_{AlHL} (L^3, L^4)	5.2	4.66	5.15	4.75
pK_{AlHL_2}			6.60	6.76
$pK_{Cu_3H_{-4}L_2}$			9.45	9.35
$pK_{Cu_3H_{-5}L_2}$			10.7	10.64
$pK_{CuH_{-1}L}$			9.67	9.41
pK_{ZnHL}			6.71	7.10
pK_{ZnL}			8.22	7.88

[a] For Fe(III) species the data obtained from spectrophotometry were used.
[b] Refers to the following equilibria: $FeL + L \rightleftharpoons FeL_2$ (L^1, L^2) or $FeHL + HL \rightleftharpoons FeH_2L_2$ (L^3, L^4).
[c] Refers to the following equilibria: $FeL_2 + L \rightleftharpoons FeL_3$($L^1$, L^2) or $FeH_2L_2 + HL \rightleftharpoons FeH_3L_3$ (L^3, L^4).

that in $[AlHL]^{3+}$ or $[AlHL_2]^{2+}$ deprotonation of the water molecule in the coordination sphere of the metal ion takes place. The formation of mixed hydroxo complexes is further supported by the fact that the formation of tris chelated species cannot be detected and that precipitation occurs above pH 5 even at a 1:5 metal to ligand ratio. Furthermore, it should also be mentioned that pH-potentiometry is not able to distinguish between $[AlH_{-1}L]_n$ type complexes, therefore the formation of oligomeric or polymeric species cannot be ruled out either.

With nickel(II) the complex formation started at pH ~ 5.0 (Fig. 1), above pH 7.0 it became slow and the almost colourless samples turned yellow during the titration. The colour change strongly suggests the formation of square planar complexes [19], yielding a single absorption band ($\lambda_{max.} \sim 450$ nm, $\varepsilon \sim 200\ M^{-1}\ cm^{-1}$) in the visible spectra over the pH range 7–11. Similarly to earlier findings on the ProLeuNHOH system [8], a maximum consumption of four equivalents of base was found in mostly overlapping processes at a 1:1 ratio. Taking into consideration these findings it is reasonable to assume that the two "extra" equivalents of base consumption (promoted by the metal ion) is due to the deprotonation and coordination of the peptide amide and that of the water molecule in the coordination sphere yielding $[NiH_{-2}L]^-$ (more precisely $[NiH_{-1}L(OH)]^-$). Although these processes overlap considerably, the stability constant for $[NiH_{-1}L]$ with [NH_2, N_{amid}, $N_{hydrox.}$] coordination could also be calculated. The model yielding the best fit together with the stability constants is presented in Table 2. As an illustration, the concentration distribution curves obtained in the Ni^{2+}–L^3 system at a 1:1 ratio are shown in Fig. 4.

A strong interaction was also found with copper(II): both L^3 and L^4 were able to keep in solution even 50% Cu^{2+} excess up to pH 11. Depending upon the metal ion to ligand ratio the samples became light green in the pH range 3.5–5.0 and grey to violet above pH 5.0. UV–Vis spectra showed above pH 3.2 a C.T. band at $\lambda \sim 325$ nm, which is characteristic for Cu^{2+}-hydroxamate [O,O] coordination [20]. EPR spectra also indicated clearly the presence of monomeric species with [O,O] coordination up to pH 4.5, but above that a decrease in intensity showed the formation of complexes with higher nuclearity as well (for EPR spectra recorded at a 1:1.1 metal to ligand ratio in the Cu(II)–L^3 system see S3). CD spectra recorded at different metal ion to ligand ratios (Figs. 5 and 6) exhibited two sets of bands in the 300–450 nm region. The series with $\lambda_{max.} \sim 330$ nm may belong to Cu^{2+}-hydroxamate-O^- charge transfer, while the series with $\lambda_{max.} \sim 400$ nm is characteristic for Cu^{2+}-hydroxamate-N^- charge transfer [20]. This is further supported by the CD spectra of the Cu^{2+}-AlaAlaN(Me)OH system (not shown), where only one set of bands with $\lambda_{max.} \sim 350$ nm is observed, which must be characteristic for Cu^{2+}-hydroxamate-O^- charge transfer since hydroxamate-N^- coordination for the secondary hydroxamic acid ligand is not possible [21]. Analysis of the CD spectra in Figs. 5 and 6 indicates therefore that with L^3 (and L^4 too) Cu^{2+}-hydroxamate-O^- interaction takes place up to pH 8 while at more basic conditions the coordination of hydroxamate-N^- is detectable.

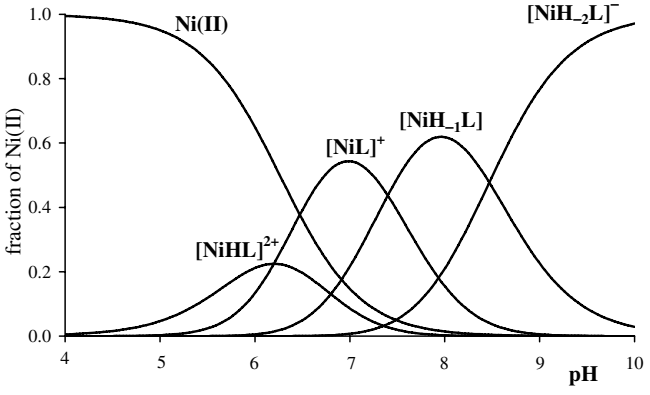


Fig. 4. Concentration distribution curves of the complexes formed in the Ni(II)–L^3 system at a 1:1 metal to ligand ratio, $c_{Ni(II)} = 0.004$ mol dm^{-3}, $I = 0.2$ mol dm^{-3} and $t = 25.0$ °C.

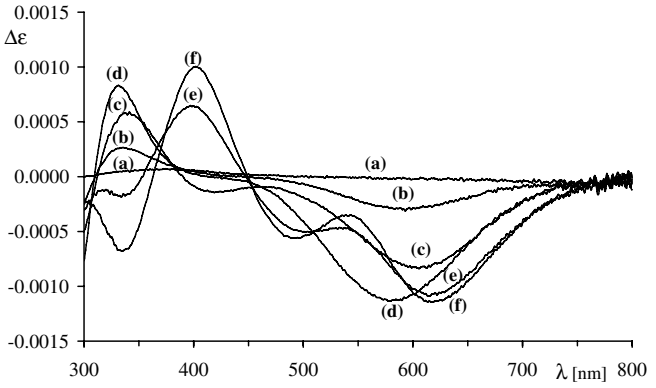


Fig. 5. CD spectra of the Cu(II)–L^3 system at a 1:2 metal to ligand ratio, $c_{Cu(II)} = 0.0015$ mol dm^{-3}, $I = 0.2$ mol dm^{-3} and $t = 25$ °C. The pH values are as follows: 4.33 (a), 4.95 (b), 6.09 (c), 7.93 (d), 10.08 (e), 11.01 (f).

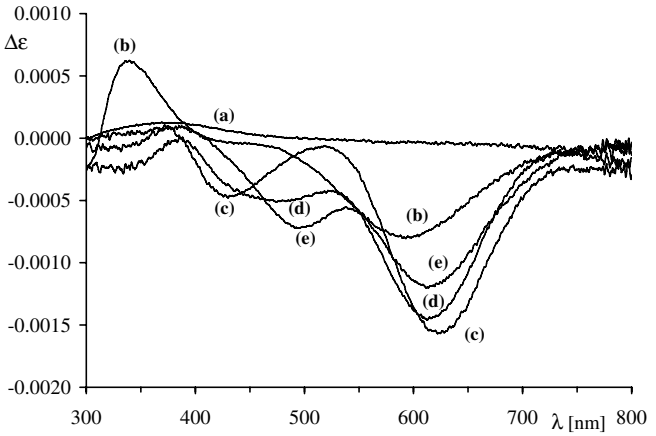


Fig. 6. CD spectra of the Cu(II)–L^3 system at a 1.5:1 metal to ligand ratio, $c_{Cu(II)} = 0.0045$ mol dm^{-3}, $I = 0.2$ mol dm^{-3} and $t = 25$ °C. The pH values are as follows: 4.15 (a), 4.81 (b), 7.00 (c), 9.94 (d), 11.01 (e).

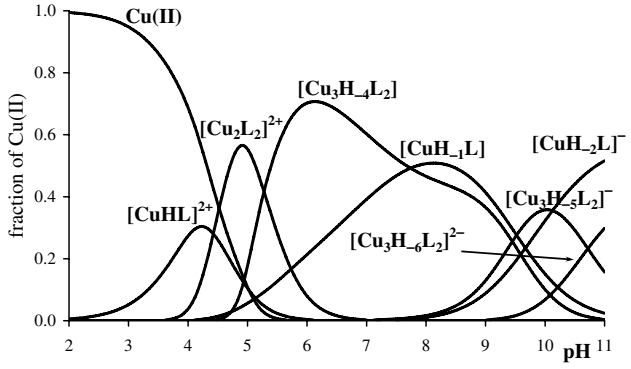
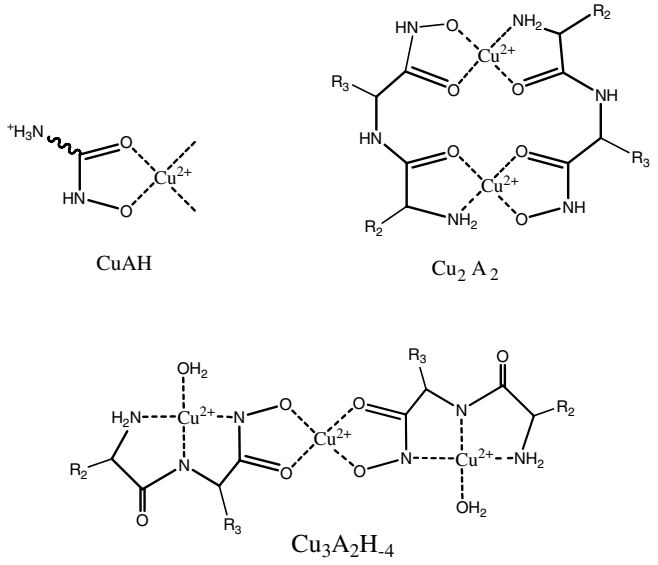


Fig. 7. Concentration distribution curves of the complexes formed in the Cu(II)–L^3 system at a 1:1 metal to ligand ratio, $c_{Cu(II)} = 0.004$ mol dm^{-3}, $I = 0.2$ mol dm^{-3} and $t = 25.0$ °C.



Scheme 2.

Taking into consideration the general spectroscopic information, the best model suitable to fit the potentiometric data is shown in Table 2 while the concentration distribution curves are depicted in Fig. 7. The complexation starts with the formation of $[CuHL]^{2+}$. In this species the ligand coordinates via the [O,O] hydroxamate chelate while the amino group is protonated (Scheme 2). This binding mode is supported by the corresponding VIS and EPR parameters ($CuHL^3$: $\lambda_{max.} \sim 755$ nm, $\varepsilon \sim 15$ M^{-1} cm^{-1}, $g_{\|} = 2.346$, $A_{\|} = 157 \times 10^{-4}$ cm^{-1}; $CuHL^4$: $\lambda_{max.} \sim 760$ nm, $\varepsilon \sim 19$ M^{-1} cm^{-1}, $g_{\|} = 2.338$, $A_{\|} = 160 \times 10^{-4}$ cm^{-1}) which are comparable with those for the mono chelated Cu(II)-hydroxamate species (acetohydroxamate: $g_{\|} = 2.340$, $A_{\|} = 170 \times 10^{-4}$ cm^{-1}, 2,3-diamino-*N*-hydroxypropanamide: $\lambda_{max.} \sim 760$ nm, $g_{\|} = 2.314$, $A_{\|} = 162 \times 10^{-4}$ cm^{-1}) [22,23]. Deprotonation of $[CuHL]^{2+}$ causes considerable change in the spectral parameters and a strong decrease in the intensity of the EPR spectra indicating rearrangement of the binding mode and partial formation of oligonuclear species too. VIS data ($\lambda_{max.} \sim 585$ nm, $\varepsilon \sim 30$–85 M^{-1} cm^{-1}) in the pH range ~4.4–5.0 support the involvement of nitrogen donor(s) in the coordination. Although the pH-metric data could be fitted best with $[Cu_2L_2]^{2+}$ in this range the presence of $[CuL]^{+}$ in the form of different binding isomers cannot be ruled out either. Above pH 6, where the samples still showed decreased EPR activity, a new broad signal with low intensity could be detected which exhibited a continuous shift indicating two EPR active species with very similar structure. VIS spectra ($\lambda_{max.} \sim 585$–575 nm, $\varepsilon \sim 110$ M^{-1} cm^{-1}) in the pH range 4.5–8.5 are supportive for an average of almost 3N coordination [19]. Taking into account these spectral features with the finding that ligands L^3 and L^4 are capable of accommodating up to 50% excess of Cu^{2+}, the potentiometric data could be rationalised with the assumption of trinuclear $[Cu_3H_xL_2]^{x+4}$ type ($x = -4$ to -6) complexes with the parallel presence of monomeric species $[CuH_{-1}L]$ and $[CuH_{-2}L]^{-}$ (Table 2). $[Cu_3H_{-4}L_2]$ most probably consists of two $[CuH_{-1}L]$ units with [NH_2, N_{amide}, $N_{hydrox.}$] coordination of the ligand. Since these units still have uncoordinated hydroxamic chelating groups they may bind a third metal ion with further loss of two protons (Scheme 2). Above pH 8.0 further deprotonation results in the formation of $[Cu_3H_{-5}L_2]^{-}$ and $[Cu_3H_{-6}L_2]^{2-}$. High pK values for $[Cu_3H_{-4}L_2]$ or $[Cu_3H_{-5}L_2]^{-}$ (Table 3, rows 10-11) are consistent with the proton loss from the coordinated water molecules. In the absence of an excess of Cu^{2+} the formation of the EPR silent trinuclear species is slightly less favoured. The base consumption processes above pH 6 can be fitted best with the assumption of $[CuH_{-1}L]$ and $[CuH_{-2}L]^{-}$, beside the trinuclear complexes. The spectral parameters for $[CuH_{-1}L]$ ($\lambda_{max.} \sim 565$ nm, $\varepsilon \sim 130$ M^{-1}cm^{-1}, $g_{\|} = 2.21$, $A_{\|} = 193 \times 10^{-4}$ cm^{-1}) unambiguously supports [NH_2, N_{amide}, $N_{hydrox.}$] coordination, which was found with ProLeuNHOH ($\lambda_{max.} \sim 562$ nm, $g_{\|} = 2.217$, $A_{\|} = 191.3 \times 10^{-4}$ cm^{-1}) [8]. Further deprotonation takes place at the coordinated water molecule as indicated by $pK_{CuH_{-1}L}$ values (Table 3; ProLeuNHOH: 9.92) [8].

For the zinc(II) systems the best models including the refined stability data are presented in Table 2. In order to gain information about the solution structure of the complexes, ^{1}H NMR titrations were also carried out both with L^3 and L^4 at a 1:1 ratio, resulting in identical results. Comparison of the pD dependence of the chemical shifts (δ_H) for the CH, CH_2 or CH_3 protons in the Zn(II)–L^4 system with those of the free ligand (Fig. 8) indicates that at pH = 5.5 where $[ZnHL]^{2+}$ is formed both of the signals belonging to CH(Ala) or CH(Ser) exhibit a shift in the presence of the metal ion. This supports that the ligands are capable of coordinating to Zn(II) either via the hydroxamate group while the amino group is protonated or via the [NH_2, CO] chelating set with the protonated hydroxamic function. Despite the fact that linkage isomers can be formed, attempts to evaluate the potentiometric data of samples having an excess of metal ion always failed. Upon increasing the pH parallel with the formation of

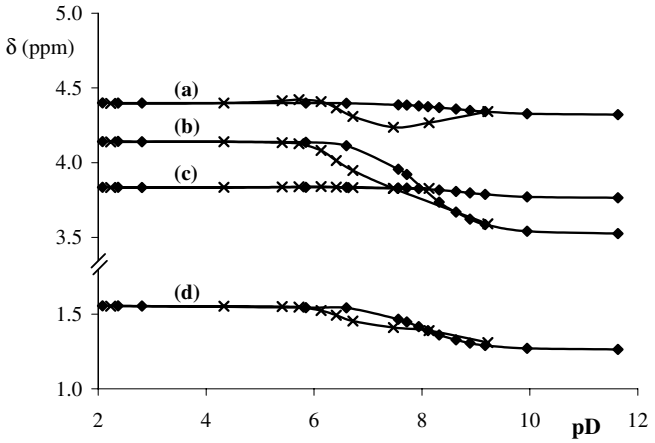


Fig. 8. The pD dependence of the chemical shifts (δ_H) of the CH (a, b), CH_2 (c) and CH_3 (d) protons of the ligand L^4 in the absence (◆) and in the presence of Zn(II) (×) at a 1:1 metal to ligand ratio, $c_{Zn(II)} = 0.02$ mol dm^{-3}, $I = 0.2$ mol dm^{-3} and $t = 25$ °C.

$[ZnHL_2]^+$ mixed hydroxo complexes with a 1:1 stoichiometry, [ZnL] and $[ZnH_{-1}L]^-$, are formed. (Although in the model presented in Table 2, [ZnL] can be replaced by $[Zn_2L_2]$, assumption of the former complex resulted in a slightly better fit and assumption of the parallel formation of them resulted in the rejection of the dimeric species.) The values of pK_{ZnHL} or pK_{ZnL} (Table 3, last two rows) together with the NMR information support hydrolysis and the lack of deprotonation and coordination of the peptide group in these complexes.

3.3. Metal complexes of the Z protected peptide hydroxamic acids L^1 and L^2

The role of the terminal amino group of oligopeptides or aminohydroxamic acids in metal ion binding is well known [9]. The amino group as an anchor facilitates the deprotonation and coordination of the peptide group in oligopeptides or rearrangement from hydroxamate [O,O] binding to N donors in aminohydroxamates yielding stable complexes with soft or borderline metal ions [9].

In order to study the effect of the terminal group on metal ion binding for peptide hydroxamic acids the Z-protected (Z = benzyloxycarbonyl) ligands, L^1 and L^2 were also involved in the work. Similarly to the L^3 and L^4 systems no effect of the hydroxyl group of the serine moiety with any of the metal ions was found.

Depending upon the ligand excess in all systems, precipitation occurred. The useful pH range at a 1:3 metal to ligand ratio was limited to pH = 0.8–4.4 (Fe^{3+}), 2.5–4.7 (Al^{3+}), 5.0–7.0 (Ni^{2+}) and 4.8–7.5 (Zn^{2+}). In the Cu^{2+} containing samples precipitation occurred at a pH as low as 3.6, therefore stability constants could not be determined. However, EPR analysis of the solutions containing the green solid showed the presence of CuL_2 with 2 × [O,O] coordination of the ligand. Stoichiometry and values of the stability constants regarding the other systems are summarised in Table 4.

Table 4
Stability constants ($\log\beta_{pqr}$) for the Fe(III), Al(III), Ni(II) and Zn(II) complexes formed with the Z-protected peptide hydroxamic acids at 25.0 °C and at $I = 0.20$ mol/dm^3(KCl)

Metal ion	Complex	p	q	r	$\log\beta_{pqr}$	
					L^1	L^2
Fe(III)	$[FeL]^{2+}$	1	0	1	10.18(1)[a]	9.95(1)[a]
	$[FeH_{-1}L]^+$	1	−1	1	7.18(2)	7.18(3)
	$[FeL_2]^+$	1	0	2	18.53(9)	19.23(7)
					18.85(2)[a]	18.47(1)[a]
	$[FeL_3]$	1	0	3	25.8(1)	26.6(1)
					25.68(3)[a]	25.26(3)[a]
Al(III)	$[AlL]^{2+}$	1	0	1	7.59(4)	7.07(1)
	$[AlH_{-1}L]^+$	1	−1	1	2.4(2)	2.41(2)
	$[AlH_{-2}L]$	1	−2	1	−2.3(1)	−2.95(6)
Ni(II)	$[NiL]^+$	1	0	1	4.74(4)	4.94(4)
	$[NiH_{-1}L]$	1	−1	1	−3.4(1)	−2.8(2)
Zn(II)	$[ZnL]^+$	1	0	1	4.69(2)	4.67(1)
	$[ZnH_{-1}L]$	1	−1	1	−3.19(3)	−3.09(3)

Standard deviations (3σ values) are in parentheses.
[a] Determined from spectrophotometric titration.

Similarly to L^3 and L^4, with Fe^{3+} complex formation starts well below pH ~ 2.0, therefore spectrophotometric titrations were also carried out. The absorption spectra (not shown) are very similar to those recorded in the presence of L^3 or L^4, indicating unambiguously the formation of 1:1, 1:2 and 1:3 complexes at a 1:5 metal ion to ligand ratio. In the pH range 0.7–1.8 evaluation of the spectra made it possible to calculate the stability constant for the $[FeL]^{2+}$ complexes having one hydroxamate chelate. Keeping this value fixed, computation of the potentiometric data resulted in the model and constants which are presented in Table 4. Upon increasing the pH, 1:2 and 1:3 complexes are present and the formation of $[FeH_{-1}L]^+$, a mixed hydroxo species, can also be detected. At a 1:5 metal ion to ligand ratio the stability constants of the major complexes can be calculated from spectrophotometry too (Table 4). As it is seen in Table 4 the agreement between the corresponding values using different methods is reasonable while the uncertainties of the stability constants from pH-potentiometry are larger than those obtained from spectrophotometry. This difference indicates that at a 1:5 metal ion to ligand ratio (spectrophotometric results) the hydrolysis of Fe^{3+} is no longer significant, whilst at the conditions that the potentiometry was carried out (1:1–1:5 ratios), this process takes place parallel with the coordination of the ligand(s). Therefore, the latter model and values reflect better (although with higher uncertainty) the situation present at a lower excess of ligand.

In order to compare directly the Fe(III) binding strengths of L^3 and L^4 with that of L^1 and L^2, the stepwise formation constants of the iron complexes of L^3 and L^4 corrected by the corresponding protonation microscopic constant (the latter being characteristic for the deprotonation of the non-coordinated ammonium group of the ligand)

($\log K_{FeH_nL_n} - n \times pK_4^{micro}$ values ($n = 1$–3) in Table 3) are calculated. Comparison of them with the corresponding $\log K_{FeL_n}$ values ($n = 1$–3) of L^1 and L^2 (Tables 3 and 4) indicates that the Z protected ligands (L^1 and L^2) form slightly more stable chelates with the metal ion. Comparison of the $\log(K_1/K_2)$ values (Table 3) shows that the preference for the formation of the bis complex is smaller in the case of L^1 or L^2 than L^3 or L^4, most probably due to steric hindrance. However, the corresponding $\log(K_2/K_3)$ values reveal that the preference for the coordination of the third ligand is almost the same in all systems. This suggests that the steric reasons are significantly compensated by charge neutralisation for L^1 and L^2.

With the other metal ions, the formation of 1:1 complexes with different protonation degrees can be detected. In [ML] the ligands L^1 and L^2 most probably coordinate via [O,O] hydroxamate chelation. Upon increasing the pH, the formation of sparingly soluble complexes becomes significant as a consequence of the large Z group and/or hydrolysis of the metal ions. With the "nitrogenophilic" Ni(II) the absence of the amino group decreases dramatically the metal ion binding capabilities of L^1 and L^2 because the rearrangement of the initial [O,O] chelate to the strong [NH_2, N_{amide}, $N_{hydrox.}$] coordination is not possible.

4. Conclusion

Primary dipeptide hydroxamic acids, L^3 and L^4, were found to form stable complexes with hard metal ions, Fe^{3+} and Al^{3+}, at acidic conditions with the exclusive involvement of [O,O] hydroxamate chelates. Due to the stronger interaction with Fe^{3+}, unlike with Al^{3+}, the formation of 1:3 complexes can also be detected in the pH range 4.0–6.5. At physiological conditions, however, with both metals hydrolysis becomes significant. NMR information proved that with Zn^{2+} L^3 and L^4 act as ambidentate ligands, but neither the [O,O] nor the [NH_2, CO] chelates are stable enough to enhance the deprotonation and coordination of the peptide amide group upon increasing the pH. Ni^{2+} and Cu^{2+} form stable complexes with L^3 and L^4 involving the [NH_2, N_{amide}, $N_{hydrox.}$] chelating set after rearrangement of the initial [O,O] or [NH_2, CO] chelation. With Cu^{2+}, the formation of trinuclear species is also significant.

Blocking the terminal amino group in L^1 and L^2 has no major influence on the binding of hard metal ions. The presence of the bulky and hydrophobic Z group, however, results in complexes with less solubility. Furthermore, the effect of charge compensation and therefore enhanced tris complex formation was found with Fe^{3+} compared to the L^3 and L^4 systems. The lack of the NH_2 group as an anchor makes L^1 and L^2 very weak ligands for Ni^{2+} and results in the formation of [O,O] chelated species having partly low solubility with Cu^{2+} and Zn^{2+}.

Acknowledgments

We thank Dr. Katalin Osz for her help in calculating the microscopic protonation constants of the ligands. This work was supported by the Hungarian Scientific Research Fund (OTKA T 046366). P.B. gratefully acknowledges the Hungarian Academy of Sciences for a János Bolyai Research Fellowship.

Appendix A. Supplementary material

Supplementary data associated with this article can be found, in the online version, at doi:10.1016/j.poly.2006.12.014.

References

[1] N. Nishino, J.C. Powers, Peptides 5 (1977) 236.
[2] N. Nishino, J.C. Powers, Biochemistry 17 (1978) 2846.
[3] Y. Inaoka, S. Takahashi, S. Sato, J. Antibiot. 39 (1986) 1382.
[4] S. Parvathy, I. Hussain, E.H. Karran, A.J. Turner, N.M. Hooper, Biochemistry 37 (1998) 1680.
[5] W.M. Moore, C.A. Spilburg, Biochemistry 25 (1986) 5189.
[6] C.A. Chang, V.C. Sekhar, B.S. Garg, F.S. Guziec, T.C. Russo, Inorg. Chim. Acta 135 (1987) 11.
[7] D.A. Brown, R. Mageswaran, Inorg. Chim. Acta 161 (1989) 267.
[8] E. Farkas, I. Kiss, J. Chem. Soc., Dalton Trans. (1990) 749.
[9] I. Sóvágó, in: K. Burger (Ed.), Biocoordination Chemistry, Ellis Horwood, Chichester, 1990, p. 135.
[10] D.D. Perrin, W.L.F. Armarego, Purification of Laboratory Chemicals, third ed., Pergamon, Oxford, 1988.
[11] G. Gran, Acta Chem. Scand. 4 (1950) 559.
[12] H.M. Irving, M.G. Miles, L.D. Pettit, Anal. Chim. Acta 38 (1967) 475.
[13] L. Zékány, I. Nagypál, in: D. Leggett (Ed.), Computational Methods for the Determination of Formation Constants, Plenum Press, New York, 1985, p. 291.
[14] C.F. Baes, R.E. Mesmer, The Hydrolysis of Cations, Wiley, New York, 1976.
[15] L.O. Öhman, W. Forschling, Acta Chem. Scand. A 35 (1981) 795.
[16] K. Osz, G. Lente, C. Kállay, J. Phys. Chem. 109 (2005) 1039.
[17] E. Farkas, T. Kiss, B. Kurzak, J. Chem. Soc., Perkin Trans. 2 (1990) 1255.
[18] E. Farkas, É.A. Enyedy, H. Csóka, Polyhedron 18 (1999) 2391.
[19] H. Sigel, R.B. Martin, Chem. Rev. 82 (1982) 385–426.
[20] E. Farkas, J. Szőke, T. Kiss, H. Kozlowski, W. Bal, J. Chem. Soc., Dalton Trans. (1989) 2247.
[21] P. Buglyó, E.M. Nagy, Á. Seprényi, E. Farkas, D. Sanna, G. Micera (in preparation).
[22] E. Farkas, E. Kozma, M. Pethő, K.M. Herlihy, G. Micera, Polyhedron 17 (1998) 3331.
[23] É.A. Enyedy, H. Csóka, I. Lázár, G. Micera, E. Garribba, E. Farkas, J. Chem. Soc., Dalton Trans. (2002) 2632.

formation of a multisilver complex. For instance, dinuclear (2:2) macrocycles are the most frequently encountered structural motifs for silver(I) salts with oxo-anions when long-chained flexible diphosphanes are used, whereby the rigid bis(diphenylphosphano)acetylene (dppa) selectively forms cationic disilver complexes with triply-bridging diphosphane units [6]. In this context, previous related work from our laboratory has also revealed the variety of structural motifs observed within a series of thione/phosphane ligated derivatives of Ag(I) halides or Ag(I) nitrate to be dependent on the choice of the bidentate phosphane ligand [7].

In the quest for new materials with specialized catalytic properties, investigations are directed at present towards the development of new fine-tuned ligands for catalytic systems with suitable activity and selectivity. For example, the use of sterically demanding diphosphanes as ligands in transition metal catalysed synthesis of chiral organic compounds is becoming a very intense area of study [8]. The P–M–P bite angle has been established to be an important parameter related to the properties of the catalysts. Concerning the later bite angle effect, considerable progress has been made since the development of new diphos ligands based on xanthene-type backbones [9]. In the course of our systematic structural studies on mixed-ligand coordination compounds of group 11 metals, we recently reported on the coordination capability of two sterically demanding and configurationally inflexible diphosphanes, namely 4,5-bis(diphenylphosphano)-9,9-dimethylxanthene (xantphos), the parent member of the extended xantphos ligand family, and 1,2-bis(diphenylphosphano)benzene (dppbz) towards copper(I) halides in the presence of heterocyclic thiones as co-ligands [10]. As these two diphosphanes, based on rigid aromatic backbones, produced different products to those of their extensively studied flexible counterparts, we decided to extend our studies to the analogous silver(I) halide complexes, starting in the present paper with the structural characterization of some derivatives of silver(I) bromide. In addition, these comparative studies could provide useful information regarding the dimerization frequently observed within this class of complexes.

2. Experimental

2.1. Materials and instruments

Commercially available silver bromide, 1,2-bis(diphenylphosphano)benzene (dppbz), 4,5-bis(diphenylphosphano)-9,9-dimethyl-xanthene (xantphos) were used as received while pyridine-2-thione (py2SH) was recrystallized from hot ethanol prior to use (Scheme 1). All the solvents were purified by their respective suitable methods and allowed to stand over molecular sieves. Infra-red spectra in the region of 4000–250 cm^{-1} were obtained in KBr discs with a Perkin-Elmer FT-IR Spectrum 1 spectrophotometer, while a Perkin-Elmer-Hitachi 200 spectrophotometer was used to obtain the electronic absorption spectra. ^1H NMR spectra were recorded on a Brucker AM 300 spectrometer at 25 °C with chemical shifts given in ppm referenced to internal TMS. Melting points were measured in open tubes with a STUART scientific instrument and are uncorrected. Molar conductivities, magnetic susceptibility measurements and elemental analyses for carbon, nitrogen and hydrogen were performed as described previously [11]. Thermogravimetric analyses were performed on a SETSYS-1200 machine with a DTG facility in dry nitrogen atmosphere. Sample sizes were in the range 8–10 mg and open Pt crucibles were used. The heating rate was 10°/min.

2.2. X-ray crystallographic study

Single crystals of **1** and **2** suitable for X-ray crystallographic study were grown by slow concentration over several days at ambient temperature of their acetone and acetonitrile mother liquid, respectively, whereas compound **4** was obtained from an ethanolic solution. X-ray diffraction data were collected on an Enraf-Nonius Kappa CCD area-detector diffractometer.

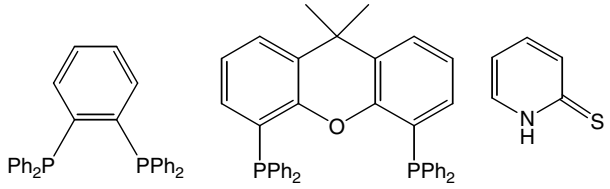
The programs DENZO [12] and COLLECT [13] were used in data collection and cell refinement. Details of crystal and structure refinement are shown in Table 1. The structures were solved using the program SIR 97 [14] and refined with the program SHELX-97 [15]. Molecular plots were obtained with the program ORTEP-3 [16].

2.3. Synthesis of compounds *1* and *2*

The homoleptic complexes were prepared according to the following general procedure. A suspension of silver bromide (47 mg, 0.25 mmol) and 0.25 mmol of the appropriate diphosphane (111.6 mg for dppbz or 144.7 mg for xantphos) in 60 cm^3 acetone or acetonitrile was refluxed for 2 h. The resulting mixture was filtered off and the clear solution was kept at room temperature. Slow evaporation of the solvent at room temperature gave the microcrystalline solid, which was filtered off and dried in vacuo.

2.4. [Ag(μ-Br)(dppbz)]$_2$ (*1*)

Colourless crystals. Yield: 135 mg (85%), m.p. 298 °C; *Anal.* Calc. for $C_{60}H_{48}Ag_2Br_2P_4$: C, 56.81; H, 3.81. Found: C, 56.69; H, 3.91%. IR (cm^{-1}): 3468m, 3051w, 1714s,



dppbz xantphos py2SH

Scheme 1. The diphosphanes and the heterocyclic thione used as ligands, with their abbreviations.

Table 1
Crystal data and structure refinement for **1**, **2** and **4**

	1	**2**	**4**
Chemical formula	$C_{60}H_{48}Ag_2Br_2P_4 \cdot C_3H_6O$	$C_{39}H_{32}AgBrOP_2$	$C_{44}H_{37}AgBrNOP_2S \cdot C_2H_5OH$
Formula weight	1326.50	766.37	923.59
Temperature (K)	120(2)	120(2)	120(2)
Wavelength (Å)	0.71073	0.71073	0.71073
Crystal system	triclinic	monoclinic	monoclinic
Space group	$P\bar{1}$	$P2_1/m$	$P2_1/n$
Unit cell dimensions			
a (Å)	11.4005(2)	8.7806(8)	10.17560(10)
b (Å)	11.9360(2)	18.1236(16)	21.4454(3)
c (Å)	21.4574(4)	12.2833(11)	19.2509(2)
α (°)	105.1170(10)	90	90
β (°)	102.4180(10)	107.589(4)	98.5760(10)
γ (°)	94.61	90	90
Volume (Å^3)	2723.89(8)	1863.3(3)	4153.96(8)
Z	2	2	4
D_{calc} (Mg/m^3)	1.617	1.366	1.477
Absorption coefficient (mm^{-1})	2.346	1.726	1.613
$F(000)$	1328	772	1880
Crystal size (mm^3)	$0.18 \times 0.08 \times 0.06$	$0.36 \times 0.22 \times 0.06$	$0.42 \times 0.28 \times 0.18$
θ Range for data collection (°)	3.04–27.53	3.38–27.49	3.30–27.4
Index ranges	$-14 \leqslant h \leqslant 14$, $-15 \leqslant k \leqslant 15$, $-27 \leqslant l \leqslant 27$	$-11 \leqslant h \leqslant 11$, $-23 \leqslant k \leqslant 22$, $-15 \leqslant l \leqslant 15$	$-13 \leqslant h \leqslant 12$, $-27 \leqslant k \leqslant 27$, $-24 \leqslant l \leqslant 24$
Reflections collected	51314	16003	57932
Independent reflections [R_{int}]	12442 [0.0435]	4357 [0.0455]	9463 [0.0273]
Completeness to $\theta = 27.47°$	99.1%	98.6%	99.6%
Maximum and minimum transmission	0.8721 and 0.6775	0.9035 and 0.5754	0.7600 and 0.5506
Refinement method	full-matrix least square on F^2	full-matrix full-matrix least square on F^2	full-matrix full-matrix least square on F^2
Data /restraints/ parameters	12442/0/652	4357/21/225	9463/21/576
Goodness-of-fit on F^2 (S)	1.011	1.039	1.046
Final R indices [$(I > 2\sigma(I)$]	$R_1 = 0.0302$, $wR_2 = 0.0692$	$R_1 = 0.0652$, $wR_2 = 0.1860$	$R_1 = 0.0268$, $wR_2 = 0.0629$
R indices (all data)	$R_1 = 0.0408$, $wR_2 = 0.0739$	$R_1 = 0.0918$, $wR_2 = 0.1978$	$R_1 = 0.0316$, $wR_2 = 0.0654$
Final weighting scheme	Calc $w = 1/[\sigma^2(F_o^2) + (0.0286P^2) + 2.4902P]$, where $P = (F_o^2 + 2F_c^2)/3)$	Calc $w = (1/[\sigma^2(F_o^2) + (0.1153P)^2 + 3.4918P]$, where $P = (F_o^2 + 2F_c^2)/3)$	Calc $w = (1/\sigma^2(F_o^2) + (0.0263P)^2 + 3.3960P]$, where $P = (F_o^2 + 2F_c^2)/3)$
Extinction coefficient	0.00135(11)		
Largest difference in peak and hole (e Å^{-3})	0.515 and −0.677	2.486 and −1.136	0.442 and −1.365

1479s, 1435vs, 1216s, 1098s, 1026s, 761s, 745vs, 729s, 691vs, 506vs, 495s, 477s; UV–Vis (λ_{max}, $\log\varepsilon$): ($CHCl_3$); 249 (3.77), 269 (3.74), 297 (3.38). ^{1}H NMR ($CDCl_3$, δ ppm): 7.38–7.01 (m, 24H, $4C_6H_5$+C_6H_4).

2.5. [AgBr(xantphos)] · CH_3CN (2)

Colourless crystals. Yield: 186 mg (92%), m.p. 338 °C; *Anal*. Calc. for $C_{41}H_{35}AgBrNOP_2$: C, 60.99; H, 4.37; N, 1.73. Found: C, 60.62; H, 4.23; N, 1.57%. IR (cm^{-1}): 3437m, 3049w, 2975w, 1480m, 1435s, 1405vs, 1238s, 1097m, 1027m, 789s, 746vs, 695vs, 509vs, 457s; UV–Vis (λ_{max}, $\log\varepsilon$): ($CHCl_3$); 253 (3.76). ^{1}H NMR ($CDCl_3$, δ ppm): 7.58 (d, 1H, $H^3_{xantphos}$), 7.30 (m, 8H, PC_6H_5), 7.20 (m, 12H, PC_6H_5), 7.06 (dd, 1H, $H^3_{xantphos}$), 6.58 (d, 1H, $H^1_{xantphos}$), 1.67 (s, 6H, $H_3C_{xantphos}$).

2.6. Synthesis of compounds 3 and 4

The heteroleptic complexes were prepared according to the following general procedure. A suspension of silver bromide (47 mg, 0.25 mmol) and 0.25 mmol of the appropriate diphosphane (111.6 mg for dppbz or 144.7 mg for xantphos) in 40 cm^3 ethanol was refluxed for 2 h until a

white precipitation formed. A solution of pyridine-2-thione (28 mg, 0.25 mmol) in ethanol was treated with a small quantity of pyridine and was then added dropwise to the hot suspension and the reaction mixture was refluxed for an additional 2 h. The resulting solution was filtered off and the clear yellow solution was kept at room temperature. Slow evaporation of the solvent at room temperature gave the microcrystalline solid, which was filtered off and dried in vacuo.

2.7. [AgBr(dppbz)(py2SH)] (3)

Pale yellow crystals. Yield: 158 mg (85%), m.p. 253 °C; *Anal*. Calc. for $C_{35}H_{29}AgBrNP_2S$: C, 56.40; H, 3.92; N, 1.88. Found: C, 55.90; H, 4.20; N, 1.68%. IR (cm^{-1}): 3437m, 3155w, 3047w, 1614s, 1596s, 1556vs, 1479s, 1436vs, 1216m, 1135vs, 1095s, 1025m, 986m, 751vs, 730s, 694vs, 513vs, 488s, 447m; UV–Vis (λ_{max}, $\log\varepsilon$): ($CHCl_3$); 245 (4.31), 274 (4.15), 298 (4.06). ^1H NMR ($CDCl_3$, δ ppm): 7.46 (dd, 1H, H^6_{py2SH}), 7.38–7.06 (m, 24H, $4C_6H_5+C_6H_4$) 7.30 (overlapping t, 1H, H^4_{py2SH}), 6.68 (t, 1H, H^5_{py2SH}).

2.8. [AgBr(xantphos)(py2SH)] · C_2H_5OH (4)

Yellow crystals. Yield: 62 mg (27%), m.p. 279 °C; *Anal*. Calc. for $C_{46}H_{43}AgBrNO_2P_2S$: C, 59.82; H, 4.69; N, 1.51. Found: C, 59.85; H, 4.64; N, 1.41%. IR (cm^{-1}): 3453m, 3148w, 3051w, 2963m, 1617s, 1570vs, 1480m, 1434vs, 1404vs, 1367m, 1230vs, 1134vs, 1094m, 1028m, 991m, 791m, 749vs, 729s, 694vs, 511vs, 484s, 462s; UV–Vis (λ_{max}, $\log\varepsilon$): ($CHCl_3$); 248 (4.43), 281 (4.43), 373 (3.71). ^1H NMR ($CDCl_3$, δ ppm): 7.52 (d, 1H, $H^3_{xantphos}$), 7.49 (dd, 1H, H^6_{py2SH}), 7.40 (m, 8H, PC_6H_5), 7.32 (overlapping t, 1H, H^4_{py2SH}), 7.24 (m, 12H, PC_6H_5), 7.04 (dd, 1H, $H^2_{xantphos}$), 6.72 (d, 1H, $H^1_{xantphos}$), 6.60 (t, 1H, H^5_{py2SH}), 1.63 (s, 6H, $H_3C_{xantphos}$).

3. Results and discussion

3.1. Preparative considerations

The reaction between equimolar quantities of silver(I) bromide and 1,2-bis(diphenylphosphano)benzene (dppbz) or 4,5-bis(diphenyl-phosphano)-9,9-dimethyl-xanthene (xantphos) in dry acetone or acetonitrile afforded microcrystalline solids which, on elemental analysis, were found to be of the composition [AgBr(diphos)] (compounds **1** and **2**, respectively). It should be pointed out that both diphosphanes showed a strong preference for chelation at a single metal centre in their reactions with copper(I) halides [10], despite of the marked difference in their natural bite angles. This coordination behaviour undoubtedly demonstrates their strong chelating power but should be also ascribed, to a significant degree, to the extraordinary versatility of a d^{10} metal ion and therefore chelation was expected to be preferred over bridging also in the case of silver(I). On the other hand, there is a well known tendency for copper(I) and to a lesser extent for silver(I) to achieve the common four-coordination forming dinuclear species involving halide ligands in a μ_2-X bridging mode. Thus, according to our previous experience, particularly with dppbz, compounds **1** and **2** were expected to be halide-bridged dimers of type $[Ag(\mu_2\text{-}Br)(diphos)]_2$. X-ray crystal structure determinations showed, however, that this is the case only for the dppbz derivative, whereas compound **2** is a three-coordinated monomer.

Following the one-pot two-step synthetic procedure that has proven to produce mixed-ligand copper(I) and silver(I) complexes virtually for any heterocyclic thione, we next attempted the preparation of heteroleptic complexes of the type [AgBr(diphos)(thione)]. In particular, we prepared suspensions of compounds **1** and **2** in dry acetonitrile and treated these with an equimolar quantity of a methanolic solution of the appropriate thione. Heating of the mixture at reflux for several hours did not caused, as expected, the disappearance of the white precipitate, indicating the presence of unreacted starting material. Indeed, the white amorphous solid isolated by filtration could be identified as compounds **1** and **2**, respectively. On the other hand, the composition of the microcrystalline solid that was obtained on evaporation of the yellow solution at ambient temperature changed over time as a function of the evaporation state, indicating the presence of a product mixture. Surprisingly, only in the case of py2SH did the reaction proceed towards the expected products, employing an ethanol/pyridine mixture as solvent, which may seem quite unusual and was initially used to possibly favour deprotonation of the thione, thus to increase its coordination capability. It should be, however, anticipated that both [AgBr(dppbz)(py2SH)] (**3**) and [AgBr(xantphos)(py2SH)] (**4**) still contain the thione unit in its neutral (protonated) form.

All the prepared complexes are microcrystalline solids, slightly soluble in acetonitrile and only marginally soluble in chloroform and acetone. They are stable to air and moisture and can be manipulated in air without appreciable decomposition. Their solutions in acetonitrile exhibit no conductivity. Room temperature magnetic measurements confirm the expected diamagnetic nature of the compounds.

3.2. Spectroscopic characterization

The solid state FT-IR spectra of the four compounds, recorded in the range 4000–250 cm^{-1}, show all the expected strong phosphane bands, which remain practically unshifted upon coordination. Moreover the spectra of the mixed-ligand complexes **3** and **4** contain the four characteristic "thioamide bands" required by the presence of the heterocyclic thioamide, with shifts suggestive of its coordination mode. "Thioamide(IV)", for instance, which appears at 742 cm^{-1} in the spectrum of the "free" pyridine-2-thione and mainly involves contribution from the ν(C=S) vibration, undergoes a significant downward shift

(by more than 30 cm^{-1}) upon coordination, indicating M–S bond formation. The thione form of the coordinated heterocyclic thioamide is further established by the presence of the NH stretching vibration at 3159 and 3149 cm^{-1} for **3** and **4**, respectively, in combination with the lack of an S–H stretching band around 2560 cm^{-1}.

The room temperature ^1H NMR spectra of the complexes, recorded in deuterated chloroform, are dominated by the presence of complex multiplets in the 7.20–7.40 ppm region due to phenyl/phenylene resonances, as well as, in the case of compounds **3** and **4**, signals attributable to the aromatic protons of the pyridine-2-thione unit. Upon coordination, the multiplets assigned to the PPh_2 groups of the phosphane ligands undergo splitting due to a small upfield shift of the *ortho*-positioned protons, whereas the signals of the corresponding backbone protons remain practically unshifted.

The electronic absorption spectra of compounds **1** and **2** in chloroform solutions appear to be mainly of intraligand character, consisting of three or one intense sharp band respectively (see Section 2). These bands can be attributed to intraligand $\pi^* \leftarrow \pi$ transitions on the phenyl group of the phosphane ligands, since the uncoordinated 1,2-bis(diphenylphosphano)benzene and 4,5-bis(diphenylphosphano)-9,9-dimethyl-xanthene reveal three or one strong absorptions respectively at 245, 273 and 299 nm or 264 nm, all of them undergoing small shifts upon coordination to Ag(I). The spectra of complexes **3** and **4** show an additional lower energy band that lies in the region where the free thione absorbs, expressing a small red shift as a consequence of the coordination to Ag(I) and should be, therefore, considered as a thione-originating intraligand transition which possesses some MLCT character [17].

3.3. Thermal decomposition

The thermal behaviour of the new compounds was investigated using simultaneous differential thermoanalysis (DTA) and thermogravimetry (TG) in a nitrogen atmosphere. TG and DTA data curves for compounds [AgBr(xantphos)] (**2**) and [AgBr(xantphos)(py2SH)] (**4**) are given in Fig. 1.

Complexes **1** and **2** decompose in one single stage that starts at 330 or 390 °C, respectively and extends over a temperature range of 100 °C. The observed mass loss notified by the TG curve fits in each case perfectly as the loss of the diphosphane, whereby the corresponding DTA curve shows a strong endothermic effect. Complexes **3** and **4** show the typical decomposition pattern observed for the analogous copper(I) halide compounds [10a,10c], generally consisting of two main stages, the low temperature initial stage, observed in the TG curve in the 240–280 °C range, being connected with two endothermic events in the DTA curve and involving overall weight loss indicative of gradual thermal breakdown of the pyridine-2-thione ligand. A very strong endothermic event appears at about 380 °C, which does not affect the consistency of the compounds,

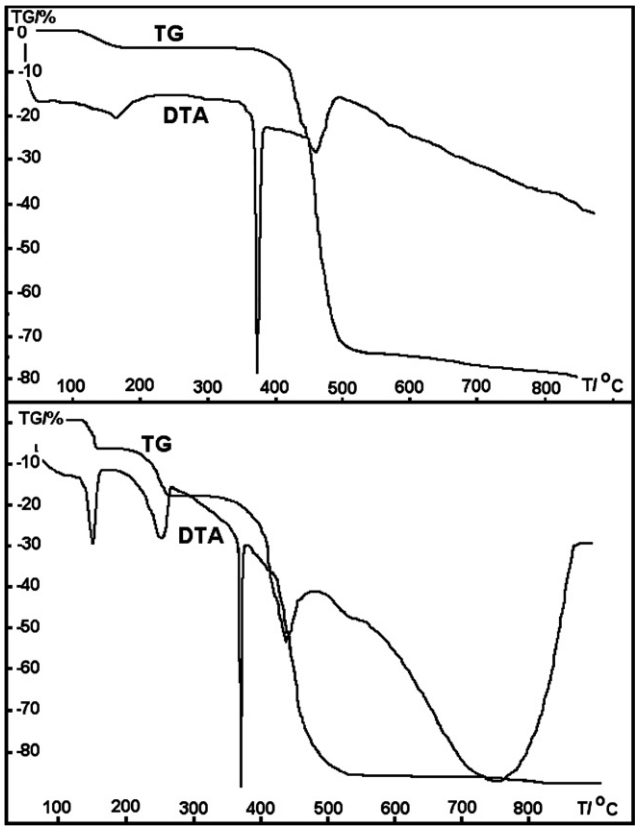


Fig. 1. TG and DTA curves for [AgBr(xantphos)] (**2**) and [AgBr(xantphos)(py2SH)] (**4**).

in any form. In the case of compounds **2** and **4** solvent retention occurs at the temperature 170 °C, indicated by a weak endothermic effect. For all the compounds further heating causes gradual sublimation of the residual AgBr which is almost completely removed at 980 °C.

3.4. Crystal structures

The X-ray crystal structures of $[Ag(\mu_2\text{-}Br)(dppbz)]_2$ (**1**), [AgBr(xantphos)] (**2**) and [AgBr(xantphos)(py2SH)] (**4**) (details of crystal and structure refinement are shown in Table 1) corroborate the spectroscopic results discussed above. Note that many heavy transition metal complexes with xantphos or dppbz have been described in the literature, but no Ag^I complexes are known to be structurally characterized by X-ray crystallography.

Colorless crystals of **1** suitable for X-ray crystallography were grown from its acetone mother liquid by slow evaporation at ambient temperature. The complex crystallizes in the triclinic space group $P\bar{1}$ with two formula units in the unit cell. The asymmetric unit consists of two half-molecules as well as one acetone molecule, which will not be further discussed as there is no evidence of any specific interaction involving this latter solvent molecule. Respective bond lengths and angles within the two half-molecules are slightly different, thus two different centrosymmetric molecules (A and B) result by suitable symmetry transformations.

Fig. 2 depicts a perspective of one of these molecules showing the atom numbering. Bond lengths and angles around the Ag^{I} centre are listed in Table 2.

The crystal structure contains a center of symmetry and features a dinuclear unit in which the two silver(I) centers are joined by two bromine bridges to form a "diamond-shaped" Ag_2Br_2 core with Ag–Br–Ag and Br–Ag–Br bond angles that clearly deviate from the ideal values for symmetric dimers (70.5° and 109.5°) but are very close to the ideal geometry for $Y_2MX_2MY_2$ dimers according to theoretically proposed criteria [18]. The Ag···Ag separation of 3.4985(3) Å is slightly longer than the sum of the van der Waals radii [19], thus excluding any possible metal–metal attractive interaction. It should be noted that, unlike the remarkable non-planarity within the Cu_2Br_2 moiety of the recently reported $[Cu(\mu_2\text{-Br})(dppbz)]_2$ [10b], complex **1** displays a strictly planar central core commonly adopted by halide-bridged dimeric complexes. Another noticeable difference between the two structures arises from the P–M–P intraligand angles, the acute P(1)–Ag(1)–P(2) bite-angle of 79.596(19)° in the present structure being clearly smaller than the corresponding P–Cu–P angles found in the above mentioned copper counterpart, which certainly can be ascribed to the different M–P bond lengths.

As expected, the carbon atoms of the phenylene backbone and the two adjacent phosphorus atoms are nearly coplanar, but the AgPCCP five-membered ring adopts an envelope conformation with the metal atom displaced out of the plane containing the four diphos ligand atoms by 1.2773(15) Å. The two phenyl rings on each phosphorus atom are nearly perpendicular to each other. However, the C(7)–C(12) and C(19)–C(24) phenyl rings have their planes in an almost parallel arrangement as a consequence of a 3.6400(14) Å π-stacking interaction between them. Within the Ag_2Br_2 backbone there are two different Ag–Br bond distances that are somewhat shorter than those found in other tetracoordinate silver(I) phosphane complexes, e.g. in $[Ag(\mu_2\text{-Br})(pymtH)]_2$ [20]. Finally, the two Ag–P distances of 2.5142(6) Å and 2.5260(6) Å are within the limits of the value range expected for tetrahedrally coordinated Ag^{I}.

Table 2
Selected bond lengths (Å) and angles (°) for **1**

Ag(1)–P(1)	2.5142(6)	P(1)–C(7)	1.822(2)
Ag(1)–P(2)	2.5260(6)	P(1)–C(13)	1.819(2)
Ag(1)–Br(1)	2.6343(3)	P(2)–C(2)	1.839(2)
Ag(1)–Br(1)#	2.7521(3)	P(2)–C(19)	1.832(2)
P(1)–C(1)	1.830(2)	P(2)–C(25)	1.826(2)
P(1)–Ag(1)–P(2)	79.596(19)	Ag(1)–Br(1)–Ag(1)#	80.978(8)
P(1)–Ag(1)–Br(1)	121.404(16)	Ag(1)–P(1)–C(1)	101.27(7)
P(2)–Ag(1)–Br(1)	132.078(16)	Ag(1)–P(1)–C(7)	114.08(7)
P(1)–Ag(1)–Br(1)#	113.198(15)	Ag(1)–P(2)–C(2)	100.37(7)
P(2)–Ag(1)–Br(1)#	111.605(15)	Ag(1)–P(2)–C(19)	115.64(8)
Ag(1)–P(2)–C(19)	115.64(8)	P(1)–C(1)–C(2)	119.61(16)
Br(1)–Ag(1)–Br(1)#	99.022(8)	P(2)–C(2)–C(1)	119.30(16)

Symmetry transformations used to generate equivalent atoms: # $-x+1$, $-y+1$, $-z+1$.

Structure refinement for compound **2** was performed in both $P2_1$ and $P2_1/m$ monoclinic space groups and the higher symmetry space group $P2_1/m$ was adopted. However, disorder involving the Br atom position (split over two sites), a poorly defined solvent molecule (occupying

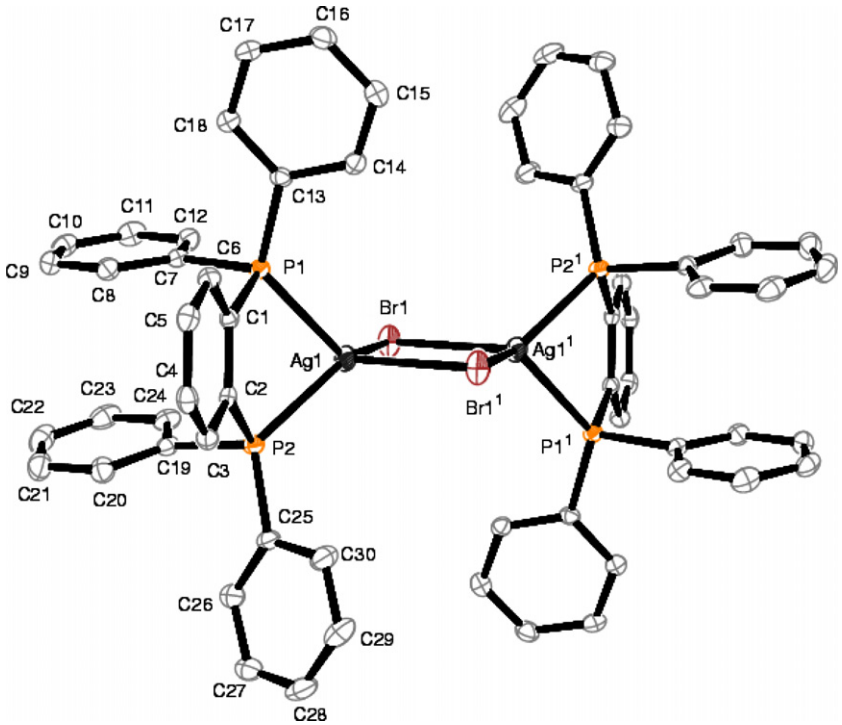


Fig. 2. Molecular structure of complex **1** with atom labels. Displacement ellipsoids are shown at the 50% probability level.

17% of the crystal volume, 18 electrons removed by PLATON [21] and some residual electron density spread along the 2-fold axis led to a structure less well defined than **1** or **4**. Fig. 3 depicts a perspective of the molecule showing the atom labelling scheme. Selected bond lengths and angles are listed in Table 3.

Contrary to the above discussed structure of the silver/dppbz complex, the xantphos derivative is a monomer, the inability for dimerization caused most probably by the marked steric demands of the bulky diphos ligand, expressed by its wide P–Ag–P bite angle versus the corresponding acute bite angle in the structure of **1**. Thus, the silver(I) metal exhibits a distorted trigonal coordination environment surrounded by two phosphorus atoms of the chelating xantphos as well as one bromine atom, with quite small angular deviations from the ideal trigonal value of 120° being mainly directed by the diphosphine bite angle. The crystal structure possess a symmetry plane defined by the C(1), C(8), C(9), O(1), Ag(1) and Br(1a) atoms, which require the P_2AgBr central core to be strictly planar. The smallest angle within this core corresponds to the P(1)–Ag(1)–P(1)# angle, whose value of 109.38(7)° is very close to the ligands calculated "natural" bite angle of 111° [21], indicating the extraordinary versatility of the closed shell central metal ion. Nevertheless, some adjustment on the part of the diphos ligand seems to be unavoidable in order to act as a chelate, which is expressed by the folding of the xanthene unit along its symmetry axis. In fact, the dihedral angle between the planes of the two benzenoid rings form a dihedral angle of 150.3(2)° whereas a value of 156.58° was found for the "free" xanthene molecule [21].

Compound **4** crystallizes in the monoclinic space group $P2_1/n$ with four formula units in the unit cell. Fig. 4 depicts a perspective of the molecule showing the atom numbering.

Table 3
Selected bond lengths (Å) and angles (°) for **2**

Ag(1)–P(1)	2.4478(14)	P(1)–C(6)	1.829(6)
		P(1)–C(10)	1.831(6)
Ag(1)–Br(1a)	2.658(7)		
P(1)–Ag(1)–P(1)#	109.38(7)	C(16)–P(1)–C(6)	104.3(3)
P(1)–Ag(1)–Br(1a)	125.31(4)	C(6)–P(1)–C(10)	103.1(2)
		P(1)–C(6)–C(5)	123.2(4)
Ag(1)–P(1)–C(16)	111.62(19)	P(1)–C(6)–C(7)	118.8(4)

Symmetry transformation used to generate equivalent atoms: $x, -y+0.5, z$.

Bond lengths and angles around the Ag^I are listed in Table 4. Two P donors, one S donor of the heterocyclic thione and the bromine atom form a fairly regular tetrahedron, where the angles around the silver atom vary from 103.300(18)° for S(1)–Ag(1)–Br(1) to 117.13(3)° for P(2)–Ag(1)–S(1). Interestingly, upon chelation the xantphos ligand exactly retains its "natural" bite angle [21].

The geometrical characteristics of the structure under investigation generally refer to those of other silver(I) complexes tetrahedrally coordinated by phosphine and thione ligands. Thus, the two Ag–P distances vary little [Ag(1)–P(1) = 2.4843(5) and Ag(1)–P(2) = 2.4994(5) Å] and lie at the upper limit of values found for a number of complexes containing tetracoordinated silver atoms bonded to two phosphorus atoms [7b]. The Ag–S bond distance of 2.5395(5) Å, coincident with the sum of the corresponding atomic radii, is typical for this bonding arrangement. Finally, hydrogen bonds of type N–H···Br and O–H···Br (from the ethanol molecule) are observed, as well as a weak intramolecular π–π stacking interaction between the C(33) and C(38) phenyl ring of the xantphos unit and the heterocyclic thione ring.

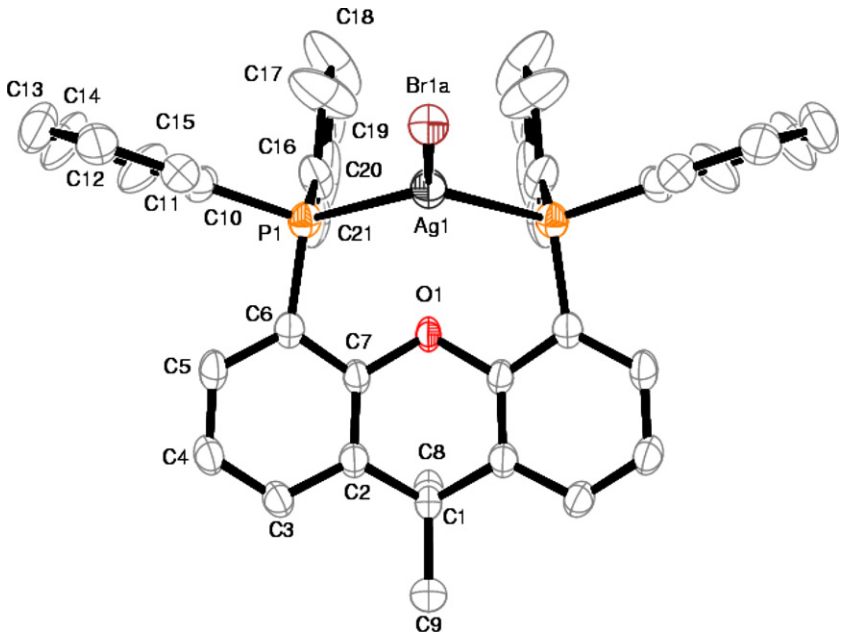


Fig. 3. Molecular structure of complex **2** with disorder removed. Displacement ellipsoids are shown at the 50% probability level.

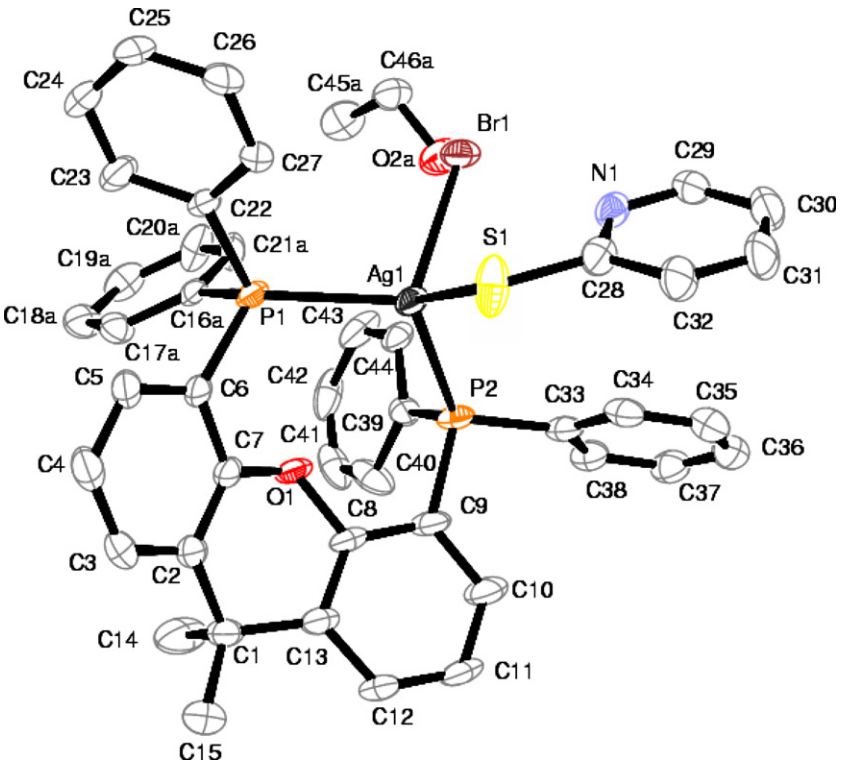


Fig. 4. Molecular structure of complex **4** with atom labels. Displacement ellipsoids are shown at the 50% probability level.

Table 4
Selected bond lengths (Å) and angles (°) for **4**

Bond length			
Ag(1)–P(1)	2.4843(5)	Ag(1)–Br(1)	2.8587(3)
Ag(1)–P(2)	2.4994(5)	S(1)–C(28)	1.703(2)
Ag(1)–S(1)	2.5395(5)		
Bond angle			
P(1)–Ag(1)–P(2)	111.507(17)	P(2)–Ag(1)–Br(1)	104.460(13)
P(1)–Ag(1)–S(1)	112.602(18)	S(1)–Ag(1)–Br(1)	103.300(18)
P(2)–Ag(1)–S(1)	117.13(3)	C(28)–S(1)–Ag(1)	106.16(7)
P(1)–Ag(1)–Br(1)	106.564(13)		
Hydrogen bridges			
N(1)–H(1)	0.8800	N(1)...Br(1)	3.2945(17)
NH(1)–Br(1)	2.4200	Br(1)...H(1)–N(1)	172.0
O(2A)–H(2A)	0.8400	O(2A)...Br(1)	3.577(6)
OH(2A)–Br(1)	2.7400	Br(1)...H(2A)–O(2A)	173

4. Conclusion

The aim of this work was the study of the coordination capability of the diphos ligands 1,2-bis(diphenylphosphano)benzene (dppbz) and 4,5-bis(diphenylphosphano)-9,9-dimethylxanthene (xantphos) toward silver(I) bromide. We have found that, despite the quite different geometrical characteristics of the two diphosphanes, xantphos providing a much larger bite angle than the acute bite angle of dppbz, chelation was observed as the only coordination mode for both diphos ligands. Compounds of the same composition [AgX(diphos)], but of different geometry and nuclearity were formed, namely a halide bridged dimer with tetrahedrally coordinated Ag^I centers for dppbz and monomeric trigonal in the case of xantphos. Both complexes proved to be good precursors for the preparation of mixed ligand monomeric complexes which contain, besides the chelating diphos unit, a heterocyclic thioamide bonded to the metal via the thione-S atom. According to the overall geometries of the structures presented, the xantphos ligand applied can be considered as best tailored for chelation of silver(I) centres.

5. Supplementary material

CCDC 612754, 612755 and 612756 contain the supplementary crystallographic data for **1**, **2** and **4**. These data can be obtained free of charge via http://www.ccdc.cam.ac.uk/conts/retrieving.html, or from the Cambridge Crystallographic Data Centre, 12 Union Road, Cambridge CB2 1EZ, UK; fax: (+44) 1223-336-033; or e-mail: deposit@ccdc.cam.ac.uk.

Acknowledgements

We thank the EPSRC X-ray crystallography service at the University of Southampton for collecting the X-ray data.

References

[1] Effendy, C. di Nicola, M. Fianchini, C. Pettinari, B.W. Skelton, N. Somers, A.H. White, Inorg. Chim. Acta 357 (2004) 1523, and references therein.

[2] M. Sawamura, H. Hamashima, Y. Ito, J. Org. Chem. 55 (1990) 5935.
[3] S.J. Berners-Price, R.K. Johnson, A.J. Giovenella, L.F. Faucette, C.K. Mirabelli, P.J. Sadler, J. Inorg. Biochem. 33 (1988) 285.
[4] C.S.W. Harker, E.R.T. Tiekink, J. Coord. Chem. 21 (1990) 287.
[5] Effendy, C. di Nicola, M. Fianchini, C. Pettinari, B.W. Skelton, N. Somers, A.H. White, Inorg. Chim. Acta 358 (2005) 763.
[6] (a) S.L. James, E. Lozano, M. Nieuwenhuyzen, Chem. Commun. (2000) 617;
(b) E. Lozano, M. Nieuwenhuyzen, S.L. James, Chem. Eur. J. (2001) 2644.
[7] (a) P. Aslanidis, P.J. Cox, S. Divanidis, P. Karagiannidis, Inorg. Chim. Acta 357 (2004) 2677;
(b) P. Aslanidis, S. Divanidis, P.J. Cox, P. Karagiannidis, Polyhedron 24 (2005) 853.
[8] R. Noyori, Asymetric Catalysis in Organic Synthesis, Wiley, New York, 1994.
[9] (a) M. Kranenburg, Y.E.M. van der Burgt, P.C.J. Kamer, P.W.N.M. Leeuwen, Organometallics 14 (1995) 3081;
(b) L.A. van der Veen, M.D.K. Boele, F.R. Bregman, P.C.J. Kamer, P.W.N.M. van Leeuwen, K. Goubitz, J. Fraanje, H. Schenk, C. Bo, J. Am. Chem. Soc. 120 (1998) 11616;
(c) L.A. van der Veen, P.H. Keeven, G.C. Schoemaker, J.N.H. Reek, P.C.J. Kamer, P.W.N.M. van Leeuwen, M. Lutz, A.L. Spek, Organometallics 19 (2000) 872.
[10] (a) A. Kaltzoglou, P.J. Cox, P. Aslanidis, Inorg. Chim. Acta 358 (2005) 3048;
(b) P. Aslanidis, P.J. Cox, A. Kaltzoglou, A.C. Tsipis, Eur. J. Inorg. Chem. (2006) 334;
(c) P.J. Cox, A. Kaltzoglou, P. Aslanidis, Inorg. Chim. Acta 359 (2006) 3183.
[11] P. Karagiannidis, P. Aslanidis, S. Papastefanou, D. Mentzafos, A. Hountas, A. Terzis, Polyhedron 9 (1990) 981.
[12] Z. Otwinowski, W. Minor, in: C.W. CarterJr., R.M. Sweet (Eds.), Methods in Enzymology, Macromolecular Crystallography, vol. 276, Academic Press, 1997, Part A, 307.
[13] R. Hooft, COLLECT Data Collection Software, Nonius B.V, 1998.
[14] A. Altomare, M.C. Burla, M. Camalli, G.L. Cascarano, C. Giacovazzo, A. Guagliardi, A.G.G. Moliterni, G. Polidori, R. Spagna, J. Appl. Cryst. 27 (1994) 434.
[15] G.M. Sheldrick, SHELXL-97. Program for Crystal Structure Analysis (Release 97-2), University of Goettingen, Germany, 1997.
[16] L.J. Farrugia, J. Appl. Crystallogr. 30 (1977) 565.
[17] (a) A.A. Del Paggio, D.R. McMillin, Inorg. Chem. 22 (1983) 691;
(b) C. Kutal, Coord. Chem.Rev. 99 (1990) 213.
[18] R.H. Summerville, R. Hoffmann, J. Am. Chem. Soc. 98 (1976) 7240.
[19] A. Bondi, J. Phys. Chem. 68 (1964) 441.
[20] G.A. Bowmaker, Effendy, J.V. Hanna, P.C. Healy, B.W. Skelton, A.H. White, J. Chem. Soc., Dalton Trans. (1993) 1387.
[21] S. Hildebrand, J. Bruckmann, C. Krűger, M.W. Haenel, Tetrahedron Lett. 36 (1995) 75.

supramolecules *via* intermolecular interactions such as hydrogen bonding, electrostatic and aromatic–aromatic π–π stacking interactions often takes place. Organic counter-cations formed as a result of protonation of pyridine N atom act as templating agents leading to quite unusual crystal structures. The nature of the halogenorhodate(III) or halogenoruthenate(III) species formed is dependent on the size of the counter cation, and the concentration of the halide ion in solution used in the syntheses. In the present paper two new inorganic anions of the type $[(MCl_3M_1Cl_3)^{2-}]_n$, M = Rh, Ru, M_1 = Na, K, have been obtained. Their X-ray structures and IR spectra are presented and discussed.

2. Experimental

2.1. General conditions

Rhodium chloride(III) hydrate, ruthenium chloride(III) hydrate were obtained from Aldrich Chemical Company, 2-amino-6-methylpyridine from Fluka AG.

Infrared spectra were recorded in KBr pellets, as well as in nujol and fluorolube mulls using a Bruker IFS 66/S instrument in the 50–4000 cm^{-1} range.

2.2. Synthesis

All reagents and solvents (except for 2-amino-6-methylpyridine) from commercial sources were used without further purification. 2-Amino-6-methylpyridine was recrystallized from CH_2Cl_2 by addition of petroleum ether.

The complex salt sodium bis(2-amino-6-methyl-pyridinium) heksachlororhodium(III), $Na(C_6H_9N_2)_2[RhCl_6]$ (**1**) is prepared as follow: boiling of hydrochloric acid solution (1 ml of concentrated (36%) HCl and 5 ml of water) of 2-amino-6-methyl-pyridine (0.10814 g, 1 mmol), NaCl (0.02338 g, 0.4 mmol) and rhodium(III) chloride (0.05265 g, 0.2 mmol) (within 10–15 min) gives dark red, clear solution. Slow evaporation (several days) gives red crystals of products **1** adequate for X-ray analysis.

Anal. Calc. for $C_{12}H_{18}N_4NaRhCl_6$: C, 25.88; H, 3.26; N, 10.06; Cl, 38.20. Found: C, 26.01; H, 2.91; N, 10.05; Cl, 38.05%. Selected IR data (KBr pellet, cm^{-1}: 3405vs, 3319vs, 3306shs, 3270 s, 3214vs, 3133vs, 3087s, 3018m, 2992m, 1677shm, 1658vs, 1637s, 1624s, 1550w, 1471w, 1437vw, 1400w, 1377w, 1309w, 1214vw, 1177w, 993w, 948vw, 794m, 715vw, 521w, 454w, 416w. FIR: 319vs, 309shvs, 233w, 176w, 162w, 136vw, 95m.

Potassium bis(2-amino-6-methyl-pyridinium) heksachlororuthenium(III), $K(C_6H_9N_2)_2[RuCl_6]$ (**2**) is prepared in the analogous way as **1** using 2-amino-6-methyl-pyridine (0.10814 g, 1 mmol), KCl (0.02982 g, 0.4 mmol) and ruthenium(III) chloride (0.05229 g, 0.2 mmol).

Anal. Calc. for $C_{12}H_{18}N_4KRuCl_6$: C, 25.31; H, 3.19; N, 9.85; Cl, 36.88. Found: C, 25.74; H, 2.86; N, 9.98; Cl, 37.23%. Selected IR data (KBr pellet, cm^{-1}: 3415vs, 3330vs, 3268s, 3214vs, 3138vs, 3106shs, 3084shs, 2989s, 2921s, 1666shvs, 1658vs, 1635vs, 1621shs, 1554w, 1471w, 1398m, 1377m, 1310m, 1223w, 1177m, 1045w, 993w, 949w, 788vs, 714m, 585w, 562w, 467m, 450m, 417w. FIR: 325vs, 315shvs, 269m, 109bm

2.3. X-ray crystallographic study

X-ray data for both crystals were collected at low temperature using an Oxford Cryosystem device on a Kuma KM4CCD κ-axis diffractometer with graphite-monochromated Mo Kα radiation. The crystals were positioned at 65 mm from the CCD camera. 612 frames were measured at 0.75° intervals with a counting time of 20 s. Accurate cell parameters were determined and refined by least-squares fit of 1150 and 1700 the strongest reflections for **1** and **2**, respectively. The data were corrected for Lorentz and polarization effects. Analytical absorption corrections were applied. Data reduction and analysis were carried out with the Oxford Diffraction (Poland) Sp. z o.o. programs. Both structures were solved by direct methods (program SHELXS97 [25]) and refined by the full-matrix least-squares method on all F^2 data using the SHELXL97 [26] programs. Non-hydrogen atoms were refined with anisotropic displacement parameters; hydrogen atoms were included from geometry of molecules and $\Delta\rho$ maps and were refined as riding groups. Crystal data are given in Table 1, together with the refinement details.

Table 1
Crystal data and structure refinement

Compound	**1**	**2**
Empirical formula	$C_{12}H_{18}N_4NaRhCl_6$	$C_{12}H_{18}N_4KRuCl_6$
Formula weight	556.90	571.17
T (K)	100(2)	100(2)
λ (Å)	0.71073	0.71073
Crystal system	triclinic	triclinic
Space group	$P\bar{1}$	$P\bar{1}$
a (Å)	6.953(1)	7.506(1)
b (Å)	7.883(2)	7.782(1)
c (Å)	9.758(2)	9.837(2)
α (°)	95.20(3)	96.22(2)
β (°)	107.55(3)	112.18(2)
γ (°)	91.77(3)	92.65(1)
V (Å^3)	506.9(2)	526.6(2)
Z	1	1
D_c (Mg m^{-3})	1.824	1.801
μ (mm^{-1})	1.657	1.707
$F(000)$	276	283
Crystal size (mm)	0.18 × 0.14 × 0.12	0.17 × 0.17 × 0.15
θ Range for data collection (°)	3.19–26.00	3.77–27.00
Reflections collected	2060	3510
Independent reflections (R_{int})	1907(0.0793)	2196(0.0580)
Data/parameters	1907/113	2196/113
Absorption coefficients min./max.	0.7546/0.8259	0.7602/0.7839
Goodness-of-fit (F^2)	1.106	1.064
Final R_1/wR_2 indices ($I > 2\sigma_1$)	0.0523/0.1366	0.0403/0.1017
Largest difference in peak/hole (e Å^{-3})	3.048/−1.670	1.160/−1.435

3. Results and discussion

3.1. Crystal structures

Both compounds are isostructural and crystallize in the triclinic space group $P\bar{1}$ – therefore molecular structure with crystallographic numbering and hydrogen bond system (Fig. 1), molecular packing diagram (Fig. 2) as well as perspective view of the layered packing in crystal (Fig. 3) are given for compound **1**. The structure determination shows $[MCl_6]^{3-}$ (M = Rh, Ru), M_1^+ (M_1 = Na, K) and $C_6H_9N_2^+$ ions to be present in the crystal in 1:1:2 ratio.

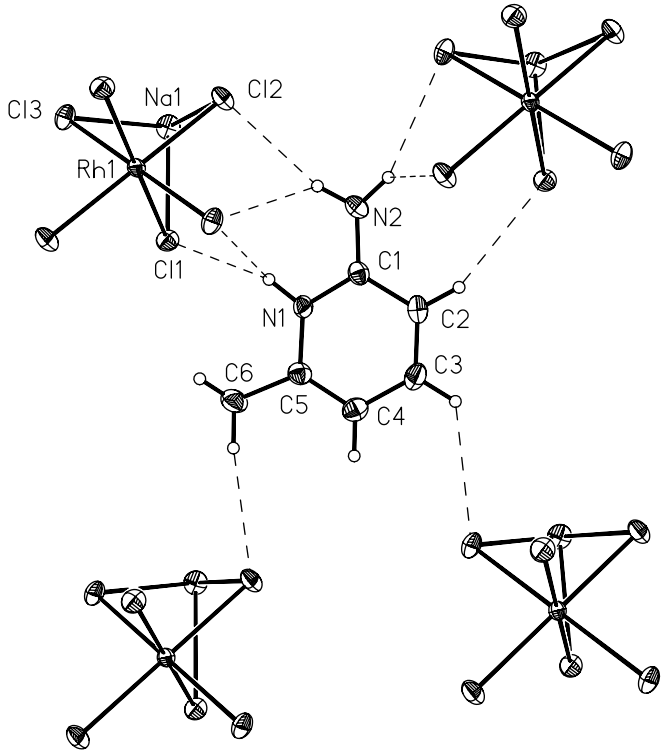


Fig. 1. Molecular structure with crystallographic numbering and hydrogen bond system in **1**.

3.1.1. $NaRhCl_6(2NH_2\text{-}6CH_3\text{-}pyH)_2$ (**1**)

The structure of **1** consists of discrete 2-amino-6-methylpyridinium cations and 1D polymeric $[(RhCl_3NaCl_3)^{2-}]_n$ anions. Both the Rh and Na atoms are situated in symmetry centres with the octahedral environment, and are placed on a line parallel to the [1 0 0] direction (Rh–Na–Rh angle equals 180.0°). Coordination number for both Na and Rh equals 6. The octahedral Rh(III) and Na(I) centers are achieved by means of six bridging chloride atoms. The existence of the triple chloride bridges M–Cl–M_1 makes the polymeric anion more rigid (the same situation occurs in **2**). The resulting infinite linear chain has composition $[(RhCl_3NaCl_3)^{2-}]_n$. $RhCl_6$ and $NaCl_6$ octahedra are sharing only of pair of opposite faces (each octahedron with Rh ion in its center is linked to the two neighboring octahedra with sodium cations in their centers). Similar linking of octahedra have been found in $BaNiO_3$, $CsNiCl_3$ or ZrI_3 [27].

The hexachlororhodate(III) anions exhibit an almost regular octahedral geometry (Table 2), with deviations of the Cl–Rh–Cl angles from the ideal values less than 2.6°. The Rh–Cl bond lengths in $C_{12}H_{18}Cl_6N_4NaRh$ (**1**) in the range 2.3417(12)–2.3545(13) (Table 2) are typical for $[RhCl_6]^{3-}$ anionic octahedra and can be compared with that of 2.302(4)–2.364(4) Å in $K_3RhCl_6 \cdot H_2O$ [28], 2.3415(6)–2.3524(6) Å in $[H_3N(CH_2)_6NH_3]_2[H_9O_4][RhCl_6]Cl_2$ [14],

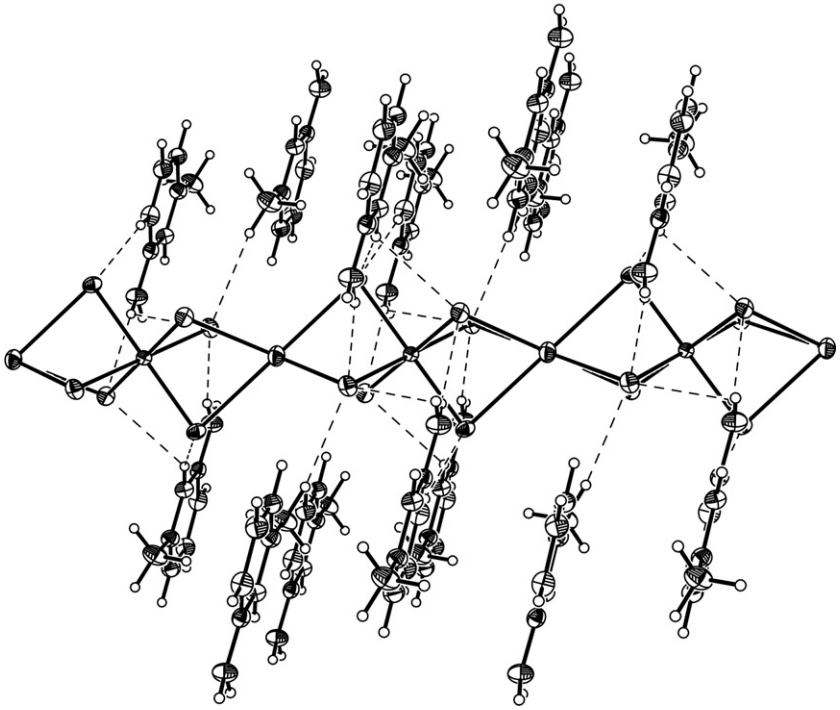


Fig. 2. Molecular packing diagram along [0 1 0] direction for **1**.

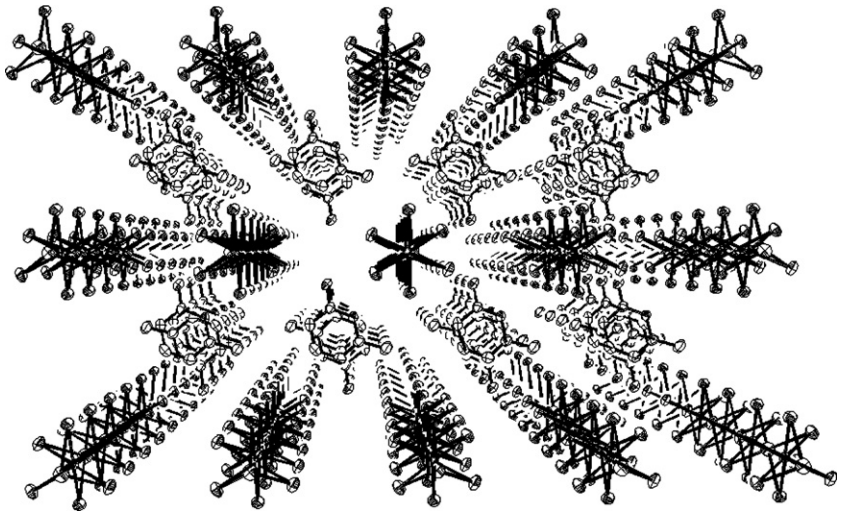


Fig. 3. Perspective view of the layered structure of **1**. Hydrogen atoms have been ommitted for clarity.

Table 2
Selected bond lengths (Å) and angles (°)

Compound	**1**	**2**
M(1)–Cl(1)	2.3545(13)	2.3940(10)
M(1)–Cl(2)	2.3417(12)	2.3736(10)
M(1)–Cl(3)	2.3423(11)	2.3749(9)
M(2)–Cl(1)	2.8458(12)	3.0912(10)
M(2)–Cl(2)	2.8401(14)	3.0859(10)
M(2)–Cl(3)	2.7564(14)	3.0018(11)
N(1)–C(1)	1.331(5)	1.347(5)
N(1)–C(5)	1.366(6)	1.377(5)
N(2)–C(1)	1.334(6)	1.346(5)
C(1)–C(2)	1.401(6)	1.416(6)
C(2)–C(3)	1.361(7)	1.373(6)
C(3)–C(4)	1.412(7)	1.413(6)
C(4)–C(5)	1.349(7)	1.359(6)
C(5)–C(6)	1.490(7)	1.492(6)
Cl(2)–M(1)–Cl(3)	89.80(4)	91.10(3)
Cl(2)–M(1)–Cl(1)	87.49(5)	88.37(4)
Cl(3)–M(1)–Cl(1)	87.91(5)	89.17(3)
Cl(3)–M(2)–Cl(2)	72.41(4)	67.59(3)
Cl(3)–M(2)–Cl(1)	71.15(4)	66.70(3)
Cl(2)–M(2)–Cl(1)	69.66(3)	65.09(3)
M(1)–Cl(1)–M(2)	83.33(3)	85.46(3)
M(1)–Cl(2)–M(2)	83.68(4)	85.68(3)
M(1)–Cl(3)–M(2)	85.57(4)	87.72(3)
C(1)–N(1)–C(5)	124.2(4)	124.2(3)
N(1)–C(1)–N(2)	119.2(4)	118.7(3)
N(1)–C(1)–C(2)	118.2(4)	123.4(4)
N(2)–C(1)–C(2)	122.6(4)	117.9(4)
C(3)–C(2)–C(1)	118.7(4)	118.8(4)
C(2)–C(3)–C(4)	121.5(5)	121.2(4)
C(5)–C(4)–C(3)	118.4(5)	119.1(4)
C(4)–C(5)–N(1)	119.1(4)	118.8(4)
C(4)–C(5)–C(6)	124.6(4)	125.2(4)
N(1)–C(5)–C(6)	116.3(4)	116.0(3)

M(1) and M(2) are Rh/Na atoms for **1**, and Ru/K atoms for **2**, respectively.

2.3473(7)–2.3551(7) Å in $[H_3N(CH_2)_4NH_3]_2[H_5O_2][RhCl_6]$-$Cl_2$ [15], or 2.342(2)–2.356(1) Å in $[H_3N(CH_2)_2NH_3]_2$-$[RhCl_6]Cl$ [11].

Table 3
Lengths (Å) and angles (°) of the hydrogen bonds

D–H···A	H···A	D···A	∠D–H···A
*Compound (**1**)*			
N(1)–H(1N)···Cl(1)	2.41	3.247(4)	156.7
N(1)–H(1N)···Cl(3)#1	2.80	3.309(4)	117.8
N(2)–H(2N)···Cl(2)	2.60	3.470(5)	164.5
N(2)–H(2N)···Cl(3)#1	2.94	3.472(4)	119.5
N(2)–H(3N)···Cl(3)#5	2.72	3.565(4)	157.0
N(2)–H(3N)···Cl(2)#6	2.88	3.424(4)	120.4
C(2)–H(2)···Cl(1)#5	2.73	3.614(5)	155
C(3)–H(3)···Cl(3)#7	2.94	3.603(5)	128
C(6)–H(6A)···Cl(2)#8	2.72	3.685(5)	169
*Compound (**2**)*			
N(1)–H(1N)···Cl(1)	2.29	3.204(3)	151.0
N(1)–H(1N)···Cl(3)#1	2.62	3.230(3)	119.8
N(2)–H(2N)···Cl(2)	2.54	3.499(4)	161.9
N(2)–H(2N)···Cl(3)#1	2.82	3.426(4)	119.8
N(2)–H(3N)···Cl(3)#5	2.66	3.510(4)	161.1
N(2)–H(3N)···Cl(2)#6	2.89	3.435(4)	121.5
C(2)–H(2)···Cl(1)#5	2.73	3.600(4)	152
C(3)–H(3)···Cl(3)#7	3.03	3.638(4)	123
C(6)–H(6A)···Cl(2)#8	2.77	3.752(4)	175

Symmetry transformations used to generate equivalent atoms: #1 $-x, -y, -z$; #2 $x-1, y, z$; #3 $-x+1, -y, -z$; #4 $x+1, y, z$; #5 $x, y+1, z$; #6 $-x, -y+1, -z$; #7 $x, y+1, z+1$; #8 $x, y, z+1$.

The Rh–Na distance is equal half of the ***a*** lattice vector, ie. 3.47 Å and the Rh–Na–Rh units are linear as in $[KAuCl_4(C_{10}H_8N_2)]_n$ ($C_{10}H_8N_2$ = 4,4′-bipyridine) [29] for which Au···K separation is 3.6805 (10) Å. This distance is significantly longer than for Rh–Na (**1**) and Ru–K (**2**) polymers in which Rh–Na and Ru–K are connected via three chlorine bridges.

The inorganic chains are cross-linked by 2-amino-6-methyl-pyridinium cations through bifurcated N–H···Cl hydrogen bonds (Fig. 1) with the N–H···Cl lengths in the range 3.25–3.57 Å (Table 3), indicating rather weak interactions. Both amine hydrogen atoms and protonated pyridine hydrogen take part in the hydrogen bond formation.

There are also some C–H···Cl short contacts (Table 3) which complete the net of hydrogen bonds.

Pyridinium cations are oriented perpendicularly to the anionic polymeric chains and form stacks parallel to [1 0 0] direction. The neighbouring cation molecules are related by centers of symmetry. Alternate perpendicular distances between the aromatic rings are 3.35 and 3.40 Å. These similar distances are typical for π–π stacking interactions. Values of the off set calculated for neighbour aromatic rings equal 0.46 and 1.44 Å show that the column has a *zig-zag* structure. As a result of these interaction cationic column and anionic polymeric chain are packed in a crystal forming a layered structure. The organic cationic layers are separated by anionic inorganic chains (Fig. 3).

The C–N–C angles of pyridine are very sensitive to protonation [30,31]. A pyridinium cation always possesses an expanded angle of C–N–C in comparison with its parent pyridine. The angle of C(1)–N(1)–C(5) [124.2(4)°] in **1** is consistent with the type of pyridinium cation.

In both compounds the N(2)–C(1) bond is slightly but significantly shorter than the N(1)–C(5) bond, which is consistent with the iminium tautomer. Moreover, the existence of the iminium tautomer is supported by the fact that the C(1)–C(2) and C(3)–C(4) bonds are longer than the C(2)–C(3) and C(4)–C(5) bonds [21,22,32–34].

3.1.2. K $RuCl_6(2NH_2\text{-}6CH_3\text{-}pyH)_2$ (2)

The structure of **2** consists of discrete 2-amino-6-methyl-pyridinium cations and 1D polymeric $[(RuCl_3KCl_3)^{2-}]_n$ anions. The asymmetric unit consists of a single $RuCl_3$ moiety, 2-amino-6-methyl-pyridinium cation, and potassium cation. This compound is a 1D coordination polymer isostructural to **1**, with relatively short Ru–K distance of 3.753 Å (half of ***a*** lattice vector). As for **1**, the infinite chains of composition $[(RuCl_3KCl_3)^{2-}]_n$ are linked together *via* hydrogen bonds with 2-amino-6-methyl-pyridinium cations in a way shown in Fig. 1. The hydrogen bonds are rather weak with the N–H···Cl bond lengths in the range 3.20–3.51 Å (Table 3). These interactions are completed by the C–H···Cl contacts as in **1**.

The cation molecules form columns packed in the crystal in a similar fashion as in **1** (Figs. 2 and 3). They involve the π–π stacking interactions. Distances between the aromatic rings are equal 3.35 and 3.48 Å whereas values of the off set are 1.33 and 1.84 Å, respectively. The latter value suggests a smaller overlap between aromatic rings in this cationic column in comparison to **1**.

3.2. IR spectroscopic investigations

The IR spectra of both **1** and **2** in 4000–400 cm^{-1} show bands characteristic for protonated 2-amino-6-methyl-pyridine. Strong bands are observed between 3500 and 2700 cm^{-1} due to the NH_2, NH^+ and CH_3, CH stretching modes, while ring vibrations and NH_2, NH^+ bending and rocking modes occur in the 1670–1600 and 800–600 cm^{-1} regions.

The conclusion derived from X-ray studies concerning symmetry of $[MX_6]^{3-}$ anions in **1** and **2** is confirmed by the FIR spectra where a strong band at ca. 320 cm^{-1} with a shoulder at ca. 310 cm^{-1} due to the M–Cl (M = Rh, Ru) asymmetric stretching mode (ν_3 (F_{1u})) occurs. Fig. 4 compares the FIR spectra obtained for **1** and **2** with that for $K_3RhCl_6 \cdot H_2O$ obtained according to [11] in which the symmetry of $RhCl_6$ octahedron is lower.

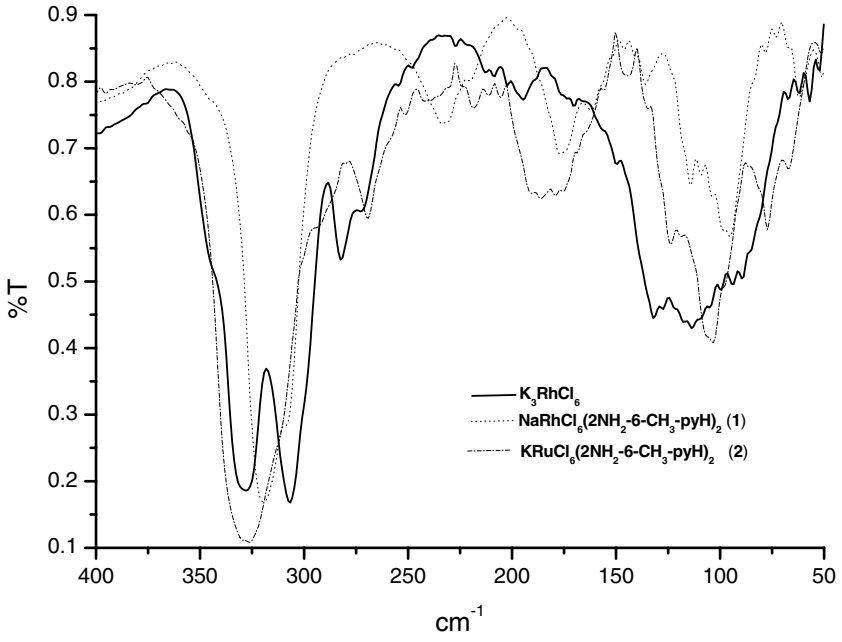


Fig. 4. FIR spectra for **1** and **2**. For comparison the FIR spectrum of K_3RhCl_6 is also given.

4. Conclusion

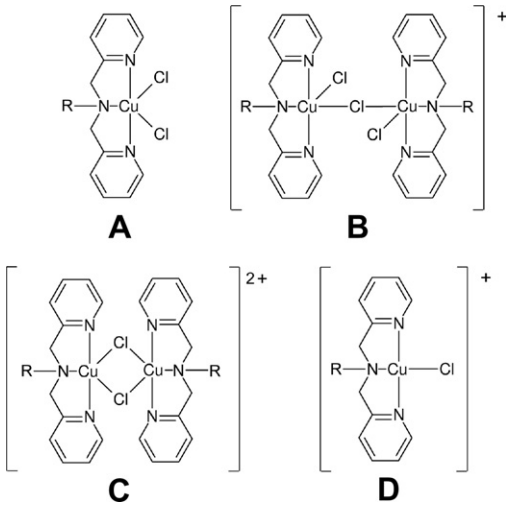
The main feature of the atomic arrangement of both **1** and **2** is the existence of a new kind of 1D linear coordination anionic polymers of the type $-Cl_3MCl_3M_1Cl_3-$ ($M = Rh$ and $M_1 = Na$ or $M = Ru$ and $M_1 = K$). Metal atoms (Rh, Na or Ru, K) in polymeric anions are in octahedral environment. In these polymers all M and M_1 atoms are bonded *via* chloride bridges and M and M_1 atoms are placed in the inversion centers. This is clearly seen in FIR spectra of **1** and **2** where only one strong band (with a shoulder on it) at *ca.* 320 cm^{-1} occurs due to the ν_3 (F_{1u}) mode. Additionally, the existence of chloride bridges makes the polymeric anions more rigid. The polymeric chains are interconnected through hydrogen bonds established between the NH^+ and NH_2 groups of the 2-amino-6-methyl-pyridinium cations as well as *via* C–H···Cl short contacts. All organic cations form columns involving the π–π stacking interactions, and the columns are parallel to the infinite, $[(MCl_3M_1Cl_3)^{2-}]_n$ chains. In the crystal packing columns of organic cations form layers, separated by the layers of inorganic polymeric anions. According to our knowledge these are the first examples of polymeric $[(MCl_3M_1Cl_3)^{2-}]_n$ anions for Rh and Ru.

5. Supplementary material

CCDC 615815 and 615816 contain the supplementary crystallographic data for **1** and **2**. These data can be obtained free of charge via http://www.ccdc.cam.ac.uk/conts/retrieving.html, or from the Cambridge Crystallographic Data Centre, 12 Union Road, Cambridge CB2 1EZ, UK; fax: (+44) 1223-336-033; or e-mail: deposit@ccdc.cam.ac.uk. Supplementary data associated with this article can be found, in the online version, at doi:10.1016/j.poly.2006.11.040.

References

[1] Gmelin, Handbook of Inorganic Chemistry, Rhodium Suppl., 8th ed., B1, Springer-Verlag, Berlin, 1982, p. 87.
[2] M.C. Vincent, M. Friedel, Compt. Rend., Acad. Sci. 101 (1886) 322.
[3] O.V. Fraenkel, Monatsh. Chem. 35 (1914) 119.
[4] A. Gutbier, Z. Anorg. Allgem. Chem. 129 (1923) 67.
[5] A. Werner, Neuere Anschauungen auf dem Gebiet der Anorganischen Chemie, third ed., F. Enke Verlag, 1923.
[6] J. Meyer, M. Kawczyk, K. Hoehne, Z. Anorg. Allg. Chem. 232 (1937) 410.
[7] J. Meyer, H. Kienitz, Z. Anorg. Allg. Chem. 242 (1939) 281.
[8] U. Treiber, M. Zwilling, E. Schweda, J. Strahle, Z. Naturforsch., Sect. B 41 (1986) 1.
[9] A.E. Bukanova, V.S. Sergienko, T.P. Sidorova, V.N. Belan, L.K. Shubochkin, M.A. Porai-Koshits, Russ. J. Inorg. Chem. 33 (1988) 379.
[10] W. Frank, G.J. Reiss, Z. Naturforsch., Sect. B 51 (1996) 1459.
[11] R.D. Gillard, D.E. Hibbs, C. Holland, M.B. Hursthouse, K.M.A. Malik, G. Sykara, Polyhedron 15 (1996) 225.
[12] W. Frank, G.J. Reiss, Z. Naturforsch., Sect. B 51 (1996) 1464.
[13] W. Frank, G.J. Reiss, I. Kleinwachter, Z. Anorg. Allg. Chem. 622 (1996) 729.
[14] W. Frank, G.J. Reiss, Inorg. Chem. 36 (1997) 4593.
[15] W. Frank, G.J. Reiss, Chem. Ber 129 (1996) 1355.
[16] E. Kahrovic, P. Orioli, B. Bruni, M. Di Vaira, L. Messori, Inorg. Chim. Acta 355 (2003) 420.
[17] M. Leduc, A.L. Beauchamp, Acta Cryst. C50 (1994) 1683.
[18] T.A. Balakaeva, A.S. Kanishcheva, Yu.E. Gorbunova, M.G. Ezernitskaya, Yu.N. Mikhailov, N.P. Konovalova, I.A. Efimenko, Russ. J. Coord. Chem. 25 (1999) 118.
[19] I.A. Efimenko, T.A. Balakaeva, A.P. Kurbakova, Yu.E. Gorbunova, Yu.N. Mikhailov, Koord. Khim. 20 (1994) 294.
[20] T.A. Balakaeva, Yu.E. Gorbunova, A.P. Kurbakova, Yu.N. Mikhailov, I.A. Efimenko, Koord. Khim. 20 (1994) 939.
[21] A.S. Albrecht, C.P. Landee, M.M. Turnbull, J. Chem. Crystallogr. 33 (2003) 269.
[22] Z.M. Jin, N. Shun, Y.P. Li, M.L. Hu, L. Shen, Acta. Crystallogr., Sect. C 61 (2005) m43.
[23] H. Place, R.D. Willett, Acta Cryst. C43 (1987) 1497.
[24] H. Place, R.D. Willett, Acta Cryst. C43 (1987) 1050.
[25] G.M. Sheldrick, Acta Crystallogr. A46 (1990) 467.
[26] G.M. Sheldrick, SHELXL97, program for crystal structure refinement, University of Göttingen, 1997.
[27] A.F. Wells, Structural Inorganic Chemistry, Fourth ed., Clarendon Press, Oxford, 1975.
[28] P.J. Cresswell, J.E. Fergusson, B.R. Penfold, D.E. Scaife, J. Chem. Soc., Dalton (1972) 254.
[29] C. Song, Y.Z. Li, Y.Q. Chen, S.J. Xiao, X.Z. You, Acta. Cryst. E60 (2004) m1741.
[30] Z.M. Jin, Y.J. Pan, D.J. Xu, Y.Z. Xu, Acta Crystallogr., Sect. C 56 (2000) e69.
[31] D. Boenigk, D. Mootz, J. Am. Chem. Soc. 110 (1988) 2135.
[32] A. Chtioui, A. Jouini, Mater. Res. Bull. 41 (2006) 569.
[33] Z.M. Jin, Y.J. Pan, M.L. Hu, J.W. Zou, J. Mol. Struct. 609 (2002) 83.
[34] T.J. Coffey, C.P. Landee, W.T. Robinson, M.M. Turnbull, M. Winn, F.M. Woodward, Inorg. Chim. Acta 303 (2000) 54.



Scheme 1. Structural arrangements observed (**A**–**C**) and postulated (**D**) [14] for copper(II) complexes of the N_3-tridentate ligands bpa (R = H), mebpa (R = CH_3) and phbpa (R = C_6H_5).

non-coordinating phenyl substituent in phbpa, coordination oligomerisation to give, for example, the dimeric species $[Cu_2Cl_2(phbpa)_2]^{2+}$ (structure **C** in Scheme 1) seems more likely for this latter complex. We report here structural characterisation of the dinuclear cation type **C**, together with its bpa and mebpa analogues. For phbpa, cation **C** is observed in the solid state in combination with the dinuclear cation **B**, suggesting that an equilibrium exists between the two in solution. In the presence of the coordinating acetate anion, a further variation of the cation type **B** is observed, namely $[CuCl_2(phbpa)_2(CH_3CO_2)]^+$, in which one terminal chloride is replaced by acetate.

2. Experimental

2.1. Synthesis

bis(2-Pyridylmethyl)amine (bpa) was purchased from Aldrich. Mebpa · $2HClO_4$ [15] and phbpa [16] were prepared as described previously. Perchlorate salts of metal complexes are potentially explosive and should be handled with caution in small quantities.

2.1.1. *[$CuCl_2$(phbpa)] (**1**)*

$CuCl_2 \cdot 2H_2O$ (0.1865 g, 1.09 mmol) in 3 ml methanol was added to phbpa (0.3004 g, 1.09 mmol) in 6 ml methanol. After three days, the initial turquoise precipitate redissolved and grass-green rods of **1** were deposited. Yield: 76%.

2.1.2. *[Cu_2Cl_3(phbpa)$_2$]$_2$[Cu_2Cl_2(phbpa)](ClO_4)$_4$ · $2CH_3OH$ (**2a**)*

$CuCl_2 \cdot 2H_2O$ (0.0535 g, 0.31 mmol) in 1 ml methanol and $NaClO_4 \cdot H_2O$ (0.0882 g, 0.62 mmol) in 0.75 ml methanol were added to phbpa (0.0774 g, 0.28 mmol) in 2 ml methanol. After 5–10 min, small dark green crystals of **2a** were deposited. Yield: 63%.

2.1.3. *[Cu_2Cl_3(phbpa)$_2$]$_2$[Cu_2Cl_2(phbpa)](PF_6)$_4$ · $2CH_3OH$ (**2b**)*

Method 1. $CuCl_2 \cdot 2H_2O$ (0.0532 g, 0.31 mmol) in 1 ml methanol and NH_4PF_6 (0.1019 g, 0.63 mmol) in 0.25 ml methanol were added to phbpa (0.0856 g, 0.31 mmol) in 2.25 ml methanol. After 5–10 min, dark green needles of **2b** were deposited. Yield: 81%.

Method 2. NH_4PF_6 (0.0735 g, 0.45 mmol) in 0.5 ml methanol was added to **1** (0.0925 g, 0.23 mmol) in 4 ml hot methanol. After 5–10 min, dark green crystals of **2b** precipitated. Yield: 41%.

2.1.4. *[Cu_2Cl_3(phbpa)$_2$](PF_6) · 0.5CH_3OH (**3**)*

Turquoise crystals of **3** deposited from the filtrate of **2b** (both Method 1 and Method 2 above) in days to weeks. The single crystal used to confirm the structure of **3** was taken from the filtrate of Method 2.

2.1.5. *[Cu_2Cl_2(bpa)$_2$(CH_3OH)$_2$](ClO_4)$_2$ (**4**)*

This complex was isolated as a minor crystalline by-product in an attempt to prepare a more complicated copper complex of an amine-functionalized bpa molecule. Either contaminant bpa was present in the reaction mixture, or it was produced by *N*-dealkylation. We have not optimized this synthesis.

2.1.6. *[Cu_2Cl_2(mebpa)$_2$](ClO_4)$_2$ (**5**)*

Mebpa · $2HClO_4$ (0.0941 g, 0.23 mmol) in 5 ml hot dry methanol was added to $CuCl_2$ (0.0307 g, 0.23 mmol) in 6 ml dry methanol. Dark blue crystals of **5** precipitated at low temperature (−20 °C). Further (polycrystalline) product was obtained by evaporation of the solvent. Total yield: 43%.

2.1.7. *[Cu_2Cl_3(phbpa)$_2$ · 0.5(CH_3OH)]$_{0.85}$ [Cu_2Cl_2(CH_3CO_2)(phbpa)$_2$]$_{0.15}$(PF_6) (**6**) and [Cu_2Cl_2(CH_3CO_2)(phbpa)$_2$](PF_6) · 1.5CH_3OH (**7**)*

Crystals of **6** and **7** were obtained from the same synthesis batch: $Cu(CH_3CO_2)_2 \cdot H_2O$ (0.0131 g, 0.0656 mmol) in 0.75 ml hot methanol, NH_4Cl (0.0035 g, 0.0654 mmol) and NH_4PF_6 (0.0107 g, 0.0656 mmol) were added to phbpa (0.0181 g, 0.0657 mmol) in 0.75 ml methanol. Medium blue crystals precipitated at low temperature (−20°C). The two types of crystals could be distinguished by their habits: crystals of **6** were plates, while those of **7** were blocks.

2.2. Single-crystal X-ray diffraction

X-ray diffraction data were collected at 180(2) K using a Bruker-Nonius X8APEX-II diffractometer (Mo Kα radiation). Selected crystallographic data are summarised in Table 1. The structures were solved by direct methods and refined against F^2 using SHELXTL [17]. H atoms bound to C and N atoms were placed geometrically and refined using a riding model. The H atom of the coordinated methanol molecule in **4** was also placed geometrically and refined in

Table 1
Summary of crystallographic data

	2a	2b	4	5	6	7
Formula	$C_{110}H_{110}C_{112}$-$Cu_6N_{18}O_{18}$	$C_{110}H_{110}Cl_8Cu_6$-$F_{24}N_{18}O_2P_4$	$C_{26}H_{34}Cl_4Cu_2$-N_6O_{10}	$C_{26}H_{30}Cl_4$-$Cu_2N_6O_8$	$C_{36.725}H_{36.15}Cl_{2.85}$-$Cu_2F_6N_6O_{0.725}P$	$C_{39.5}H_{43}Cl_2Cu_2$-$F_6N_6O_{3.5}P$
Formula weight	2778.80	2960.88	859.47	823.46	946.25	1000.75
Crystal system	triclinic	triclinic	triclinic	triclinic	monoclinic	monoclinic
Space group	$P\bar{1}$	$P\bar{1}$	$P\bar{1}$	$P\bar{1}$	$P2_1/n$	$P2_1/c$
a (Å)	12.9998(5)	13.1715(6)	8.8587(3)	8.1461(2)	11.5879(2)	25.500(3)
b (Å)	15.5051(6)	15.6230(7)	9.2217(4)	10.0581(3)	14.3103(3)	14.119(2)
c (Å)	15.6110(7)	15.8596(7)	10.7369(5)	10.8909(3)	23.7622(5)	24.361(3)
α (°)	92.689(2)	92.125(2)	90.340(2)	102.201(1)	90	90
β (°)	110.585(2)	111.580(2)	95.754(2)	101.077(1)	101.521(1)	91.61(1)
γ (°)	94.779(2)	94.086(2)	106.160(1)	107.780(1)	90	90
Volume (Å^3)	2925.6(2)	3020.0(2)	837.69(6)	798.32(4)	3861.01(13)	8767.3(19)
Z	1	1	1	1	4	8
D_{calc} (g cm^{-3})	1.577	1.628	1.704	1.713	1.628	1.516
μ(Mo Kα) (mm^{-1})	1.418	1.362	1.652	1.725	1.409	1.200
Crystal size (mm)	0.10 × 0.10 × 0.06	0.20 × 0.05 × 0.02	0.15 × 0.15 × 0.07	0.40 × 0.30 × 0.20	0.20 × 0.20 × 0.07	0.25 × 0.25 × 0.12
Crystal colour	dark green	dark green	indigo	dark blue	pale blue	pale blue
θ Range	3.53–27.00	3.66–25.03	3.77–23.36	3.53–32.82	3.57–28.28	3.57–25.87
Total data	32221	25851	12841	19543	56091	30549
Unique data	12504	10482	3375	4913	9556	30549[a]
R_{int}	0.061	0.072	0.033	0.020	0.059	
R_1 [$I > 2\sigma(I)$]	0.064	0.053	0.029	0.025	0.046	0.099
wR_2 (all data)	0.190	0.135	0.074	0.069	0.122	0.283
S	1.09	0.96	1.03	1.14	1.08	0.94
ρ_{max}, ρ_{min} (e Å^{-3})	1.85, −1.24	0.89, −0.50	0.41, −0.32	0.52, −0.56	0.72, −0.60	1.58, −1.38
CCDC No.	287934	287935	287936	287937	287938	287939

[a] All data (including Friedel opposites) treated as independent.

the same way. The H atoms of the solvent methanol molecules in **2a**, **2b**, **6** and **7** were placed so as to form a reasonable hydrogen-bond network, at a distance of 0.84 Å along the vectors from the O atom to which they are bound to the nearest H-bond acceptor. They were then allowed to ride on the parent O atom during subsequent refinement.

Refinements of structures **2a**, **2b**, **4** and **5** were straightforward, but structures **6** and **7** presented some difficulties. For **6**, refinement of the complex as $[Cu_2Cl_3(phbpa)_2]$, with the terminal chloride Cl(1) having full site occupancy resulted in an equivalent isotropic displacement parameter (U_{eq}) of 0.0573(3) Å^2 for Cl(1), somewhat larger than 0.0458(2) Å^2 for the other terminal chloride Cl(3). In addition, peaks in the residual electron density of ca. 1 e Å^{-3} were observed in positions close to Cl(1), suggestive of an acetate anion coordinated to Cu(1). Inclusion of this group and refinement of site occupancies (constrained to sum to unity) gave 0.84(1) for Cl(1) and 0.16(1) for the acetate anion. These values were subsequently constrained to be 0.85 and 0.15, respectively. With the chloride/acetate disorder modelled, U_{eq} for Cl(1) refined to 0.0440(3) Å^2 and the highest remaining peak in the residual electron density was 0.70 e Å^{-3}, lying in the vicinity of the PF_6^- anion. Disorder of the substituents bound to Cu(1) has some consequences for the methanol solvent molecule: the intermolecular contact distances suggest that it can only be present when Cl(1) is present. The O atom of this methanol molecule lies on a centre of inversion half-way between two Cl(1) atoms. Thus, there is only one methanol molecule per two $[Cu_2Cl_3(phbpa)_2]$ complexes, and the empirical formula is therefore best written $[Cu_2Cl_3(phbpa)_2 \cdot 0.5(CH_3OH)]_{0.85}$-$[Cu_2Cl_2(CH_3CO_2)(phbpa)_2]_{0.15}(PF_6)$. The X-ray analysis does not distinguish between two discrete crystal domains, i.e. $[Cu_2Cl_3(phbpa)_2 \cdot 0.5(CH_3OH)](PF_6)$ and $[Cu_2Cl_2$-$(CH_3CO_2)(phbpa)_2](PF_6)$, or disorder that is randomly distributed.

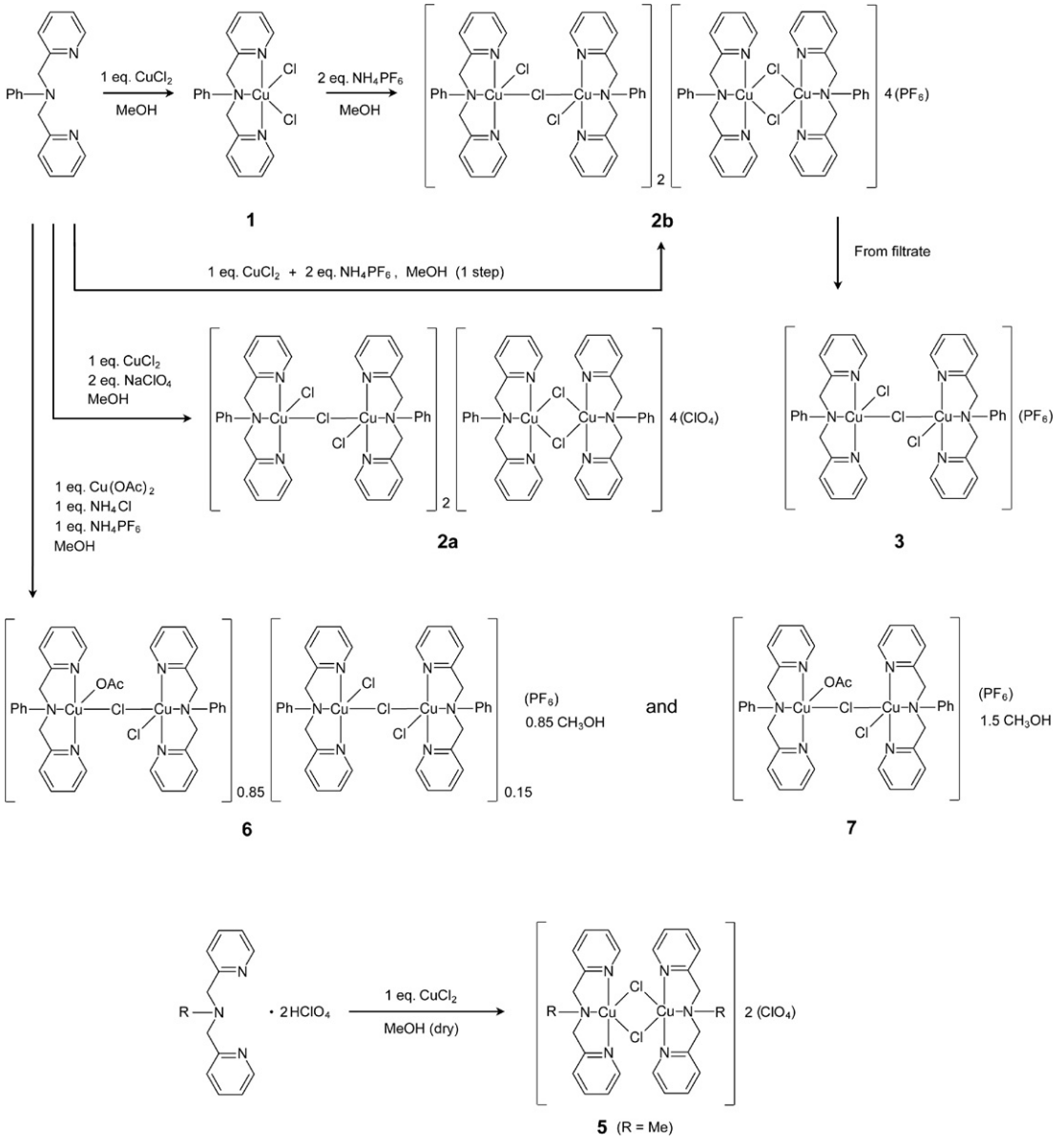
All crystals examined for **7** were twinned by 2-fold rotation about c^*. On account of the β angle that differs only minimally from 90°, the diffraction patterns from the two domains exhibit partial overlap. The measured diffraction pattern was indexed (using the program CELL_NOW [18]) on the basis of two domains, each accounting for ca. 8500 unique discrete reflections, with 14815 unique reflections considered to be overlapped. The frames were integrated using SAINT-PLUS [19] and scaled using TWINABS [19]. The structure was solved with data taken from the major domain (including overlapped reflections), then refined against the two-component data via the HKLF 5 format in SHELXL [17].

3. Results and discussion

3.1. Syntheses

The syntheses and products are summarised in Scheme 2. Mixtures of copper(II) chloride and phbpa crystallize from methanol as the neutral mononuclear complex $[CuCl_2$-(phbpa)] (**1**), identical to that reported previously

[14]. If perchlorate or hexafluorophosphate anions are present in solution, however, crystallisation of chloro-bridged dinuclear cationic species is favoured, presumably driven at least in part by formation of an ionic lattice. Formation of the dichloro-bridged cation **C** or the monochloro-bridged cation **B** is dependent to some degree on the nature of the group R bound to the amine-N atom. For phbpa ($R = C_6H_5$), the dichloro-bridged cation **C** is observed in the double salts, $[Cu_2Cl_3(phbpa)_2]_2[Cu_2Cl_2(phbpa)](ClO_4)_4 \cdot 2CH_3OH$ (**2a**) and $[Cu_2Cl_3(phbpa)_2]_2[Cu_2Cl_2(phbpa)](PF_6)_4 \cdot 2CH_3OH$ (**2b**), in both cases with the monochloro-bridged cation **B** also present in the crystal. The previously characterised **B** salt $[Cu_2Cl_3(phbpa)_2](PF_6) \cdot 0.5CH_3OH$ (**3**) [14] can be isolated by fractional crystallisation after filtration of **2b** from the mother liquor, suggesting that the formation of cation **B** in preference to **C** is favoured by increasing the relative chloride concentration. Conversely, a larger counteranion excess pushes the equilibrium back towards the formation of **C**. Cation **C** also appears to be favoured for both bpa and mebpa, isolated here as the perchlorate salts $[Cu_2Cl_2(bpa)_2(MeOH)_2](ClO_4)_2$ (**4**) and $[Cu_2Cl_2(mebpa)_2](ClO_4)_2$ (**5**). Cation **B** has not been isolated to date for bpa or mebpa. When the coordinating acetate anion is present in the reaction mixture for phbpa, an additional equilibrium exists between cation **B** and the dinuclear cation in which one terminal chloride is replaced by an acetate anion. Two types of crystal have been isolated: **6** exhibits partial replacement of chloride by acetate and **7** exhibits complete replacement.



Scheme 2. Summary of the synthesis conditions and reaction products.

3.2. Crystal structures

The crystal structures of **1** and **3** have been reported previously [14].

3.2.1. Crystal structures of *2a* and *2b*

The structures of the perchlorate salt **2a** and the hexafluorophosphate salt **2b** are essentially identical. The dichloro-bridged cation **C** (Fig. 1) is situated on a centre of inversion, while the monochloro-bridged cation **B** (Fig. 1) lies on a general position. Details of the coordination geometry around the Cu atoms are given in Table 2. The square-pyramidal geometry around Cu is closely comparable in cations **B** and **C** in each of the structures. The τ parameters [20] for each Cu atom (Table 3) indicate that the type **C** cations deviate slightly further from ideal square-pyramidal geometry towards trigonal-bipyramidal geometry, compared to the type **B** cations. The Cu–N and Cu–Cl distances in the basal plane of the square pyramid show no significant differences between the two structures. The axial Cu–Cl distances are elongated in all cases compared to those in the basal plane. These distances are significantly longer in the **B** cations than in the **C** cations. A small concomitant decrease is observed in the Cu–N distance to the amine-N atom in each **B** cation. In the **C** cation of both **2a** and **2b**, the phenyl substituents lie close to co-planar with the Cu_2Cl_2 unit and the shortest contacts to the backside of the Cu square pyramids are made by H atoms in the *ortho*-positions of the phenyl rings. Thus, the phenyl groups partially block any further coordination to Cu(1), and the shortest contacts to Cu(1) are ca. 4 Å, made by an O atom of one (disordered) perchlorate anion in **2a** (ca. 3.9 Å), and by an F atom of one hexafluorophosphate anion in **2b** (ca. 4.07 Å). In the **B** cation of both structures, the Cu_2Cl_3 unit is close to planar, with the terminal Cl atoms lying in an *anti* conformation (the angle between the two terminal Cu–Cl bonds is ca. 180° in projection). One phenyl substituent [C(49)–C(54)] lies close to the plane of the Cu_2Cl_3 unit, again partially blocking any further coordination to Cu(3). The other phenyl substituent [C(31)–C(36)] is twisted from this plane. The principal difference between **2a** and **2b** lies in the magnitude of this twist: the dihedral angle between the least-squares plane through C(31)–C(36) and that defined by the five atoms of the Cu_2Cl_3 unit is 82.0(2) and 50.0(3)° in **2a** and **2b**, respectively. The twist appears to be driven by accommodation of the perchlorate or hexafluorophosphate anions in the vicinity of the phenyl ring. However, peaks in the residual electron density of **2b** suggest a minor rotational disorder component for C(31)–C(36) (which was not modelled), corresponding closely to the ring orientation observed in **2a**.

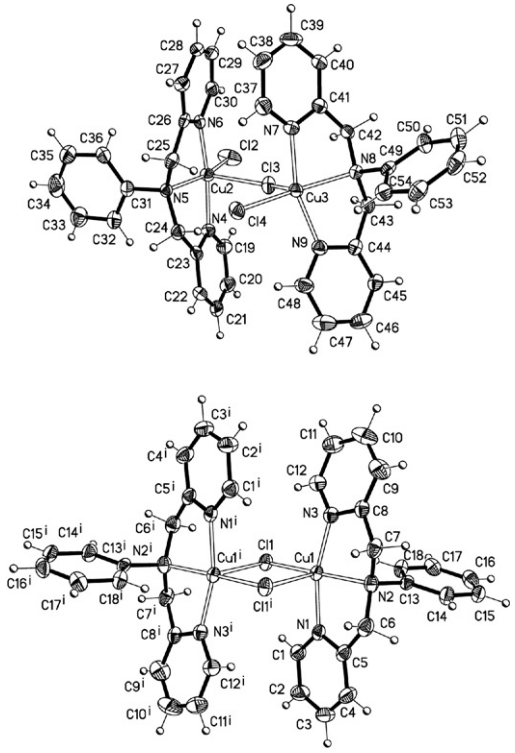


Fig. 1. Type **B** cation (top) and type **C** cation (bottom) in the structure of **2a**, showing displacement ellipsoids at 50% probability for non-H atoms and the atom-labelling scheme. The superscript (i) in the lower figure refers to atoms generated by the symmetry operator $-x, 2-y, -z$. The structure of **2b** is comparable.

3.2.2. Crystal structures of *4* and *5*

In both **4** and **5** (Fig. 2), the dichloro-bridged dinuclear cation (type **C**) lies on a centre of inversion. Details of the coordination geometry around Cu are given in Table 4. The τ parameters (Table 3) indicate that the distortion towards trigonal-bipyramidal geometry is comparable to that of the type **C** cations in **2a** and **2b**, and the Cu–Cl and Cu–N distances in the basal plane are also closely comparable. There are, however, distinct differences in the axial coordination sites. In **4**, the site to the backside of the Cu_2Cl_2 unit is occupied by a methanol molecule, coordinated to Cu with a Cu–O distance of 2.5712(17) Å. The axial Cu–Cl(bridging) distance *trans* to this is 3.1288(7) Å, the longest seen in this series of complexes. The coordination of MeOH to Cu in this complex is facilitated by two features: the N–H group of the bpa ligand provides no steric hindrance to coordination, and furthermore provides an N–H···O hydrogen bond to the perchlorate anion, that is adopted in preference to coordination of ClO_4^- to Cu. The OH group of the coordinated methanol molecule also forms a hydrogen bond to the same O atom of the perchlorate anion, giving rise to a complementary cyclic arrangement of contacts (Fig. 3a). In **5**, the perchlorate anion (modelled as disordered over two closely comparable orientations) is coordinated directly to the Cu atom, with a Cu–O distance of ca. 2.8 Å. This longer Cu–O coordination distance compared to **4**, is coupled with a shorter Cu–Cl(bridging) dis-

Table 2
Details of the coordination geometry (Å, °) of Cu for **2a** and **2b**

Type **C** cation		Type **B** cation			
2a					
Cu(1)–N(1)	1.987(5)	Cu(2)–N(4)	1.982(5)	Cu(3)–N(7)	1.987(5)
Cu(1)–N(2)	2.049(5)	Cu(2)–N(5)	2.090(5)	Cu(3)–N(8)	2.076(5)
Cu(1)–N(3)	1.981(5)	Cu(2)–N(6)	1.973(5)	Cu(3)–N(9)	1.994(5)
Cu(1)–Cl(1)	2.2520(16)	Cu(2)–Cl(2)	2.2368(17)	Cu(3)–Cl(4)	2.2457(15)
Cu(1)–Cl(1)^{i}	2.7074(16)	Cu(2)–Cl(3)	2.6297(16)	Cu(3)–Cl(3)	2.5860(16)
N(1)–Cu(1)–N(2)	82.4(2)	N(4)–Cu(2)–N(5)	82.78(19)	N(7)–Cu(3)–N(8)	80.91(19)
N(1)–Cu(1)–N(3)	163.9(2)	N(4)–Cu(2)–N(6)	164.5(2)	N(7)–Cu(3)–N(9)	162.0(2)
N(2)–Cu(1)–N(3)	82.2(2)	N(5)–Cu(2)–N(6)	82.41(19)	N(8)–Cu(3)–N(9)	82.32(19)
N(1)–Cu(1)–Cl(1)	96.50(15)	N(4)–Cu(2)–Cl(2)	97.71(15)	N(7)–Cu(3)–Cl(4)	96.94(15)
N(2)–Cu(1)–Cl(1)	171.97(15)	N(5)–Cu(2)–Cl(2)	160.16(14)	N(8)–Cu(3)–Cl(4)	164.22(13)
N(3)–Cu(1)–Cl(1)	98.09(15)	N(6)–Cu(2)–Cl(2)	97.77(15)	N(9)–Cu(3)–Cl(4)	97.41(15)
N(1)–Cu(1)–Cl(1)^{i}	87.77(14)	N(4)–Cu(2)–Cl(3)	86.71(14)	N(7)–Cu(3)–Cl(3)	94.45(14)
N(2)–Cu(1)–Cl(1)^{i}	94.28(14)	N(5)–Cu(2)–Cl(3)	92.46(13)	N(8)–Cu(3)–Cl(3)	92.49(13)
N(3)–Cu(1)–Cl(1)^{i}	98.04(14)	N(6)–Cu(2)–Cl(3)	89.37(14)	N(9)–Cu(3)–Cl(3)	92.79(15)
Cl(1)–Cu(1)–Cl(1)^{i}	93.63(5)	Cl(2)–Cu(2)–Cl(3)	107.38(7)	Cl(4)–Cu(3)–Cl(3)	103.28(6)
Cu(1)–Cl(1)–Cu(1)^{i}	86.37(5)	Cu(2)–Cl(3)–Cu(3)	144.57(6)		
2b					
Cu(1)–N(1)	1.993(5)	Cu(2)–N(4)	1.981(4)	Cu(3)–N(7)	1.988(4)
Cu(1)–N(2)	2.057(4)	Cu(2)–N(5)	2.087(4)	Cu(3)–N(8)	2.084(4)
Cu(1)–N(3)	1.975(5)	Cu(2)–N(6)	1.978(4)	Cu(3)–N(9)	1.986(5)
Cu(1)–Cl(1)	2.2536(15)	Cu(2)–Cl(2)	2.2449(16)	Cu(3)–Cl(4)	2.2541(15)
Cu(1)–Cl(1)^{i}	2.7484(16)	Cu(2)–Cl(3)	2.5641(16)	Cu(3)–Cl(3)	2.5772(16)
N(1)–Cu(1)–N(2)	82.29(18)	N(4)–Cu(2)–N(5)	81.19(18)	N(7)–Cu(3)–N(8)	81.33(17)
N(1)–Cu(1)–N(3)	164.62(19)	N(4)–Cu(2)–N(6)	163.89(18)	N(7)–Cu(3)–N(9)	162.15(18)
N(2)–Cu(1)–N(3)	82.69(18)	N(5)–Cu(2)–N(6)	82.91(17)	N(8)–Cu(3)–N(9)	82.10(18)
N(1)–Cu(1)–Cl(1)	96.25(14)	N(4)–Cu(2)–Cl(2)	97.52(14)	N(7)–Cu(3)–Cl(4)	96.66(13)
N(2)–Cu(1)–Cl(1)	172.20(14)	N(5)–Cu(2)–Cl(2)	155.64(14)	N(8)–Cu(3)–Cl(4)	164.74(13)
N(3)–Cu(1)–Cl(1)	98.19(14)	N(6)–Cu(2)–Cl(2)	98.04(13)	N(9)–Cu(3)–Cl(4)	97.57(14)
N(1)–Cu(1)–Cl(1)^{i}	87.33(14)	N(4)–Cu(2)–Cl(3)	89.04(13)	N(7)–Cu(3)–Cl(3)	94.21(13)
N(2)–Cu(1)–Cl(1)^{i}	95.24(13)	N(5)–Cu(2)–Cl(3)	96.32(13)	N(8)–Cu(3)–Cl(3)	92.25(12)
N(3)–Cu(1)–Cl(1)^{i}	97.32(13)	N(6)–Cu(2)–Cl(3)	90.11(13)	N(9)–Cu(3)–Cl(3)	93.03(14)
Cl(1)–Cu(1)–Cl(1)^{i}	92.34(5)	Cl(2)–Cu(2)–Cl(3)	108.00(6)	Cl(4)–Cu(3)–Cl(3)	102.99(6)
Cu(1)–Cl(1)–Cu(1)^{i}	87.66(5)	Cu(2)–Cl(3)–Cu(3)	146.69(6)		

Superscript (i) indicates atoms related by the symmetry operator $-x, 2-y, -z$.

tance of 2.8283(4) Å in the axial site *trans* to O. The methyl substituent of mebpa provides no steric hindrance to coordination of the perchlorate anion, but the absence of the N–H donor in **5** evidently renders this a more stable outcome than incorporation of a MeOH molecule in the sixth coordination site, as seen in **4**.

Table 3
Coordination geometries of the Cu atoms described by the τ parameter

	Atom	τ	Cation type
2a	Cu(1)	0.13	**C**
	Cu(2)	0.07	**B**
	Cu(3)	0.04	**B**
	Cu(1)	0.13	**C**
2b	Cu(2)	0.14	**B**
	Cu(3)	0.04	**B**
4	Cu(1)	0.18	**C**
5	Cu(1)	0.21	**C**
6	Cu(1)[a]	0.24	**B**
	Cu(1)[b]	0.01	**B**
	Cu(2)	0.18	**B**
7 (mol 1)	Cu(1)	0.07	**B**
	Cu(2)	0.15	**B**
7 (mol 2)	Cu(1)	0.03	**B**
	Cu(2)	0.09	**B**

[a] Based on the position of Cl(1).
[b] Based on the position of O(1A).

3.2.3. Crystal structures of **6** and **7**

Details of the coordination geometry around Cu for **6** and **7** are given in Table 5. There are two symmetry-independent molecules in **7**, and the conformation of each is closely comparable to that in **6** (Fig. 4). In all cases, the planes of the phenyl substituents remain aligned with the Cu–N(amine) bonds so that the H atoms in the *ortho*-positions of the phenyl rings partially block further coordination to the Cu atoms. In **7**, one terminal Cl atom is replaced by an acetate anion, displaying an asymmetric μ_2 binding mode in which one O atom lies in a position directly comparable to that adopted by Cl in **2a** and **2b** (Cu–O = 1.927(9) and 1.964(9) Å), and the other O atom forms a significantly longer Cu–O contact (2.774(10) and 2.897(10) Å) towards the backside of the Cu–Cl–Cu bridge. The plane of the acetate anion lies close to that

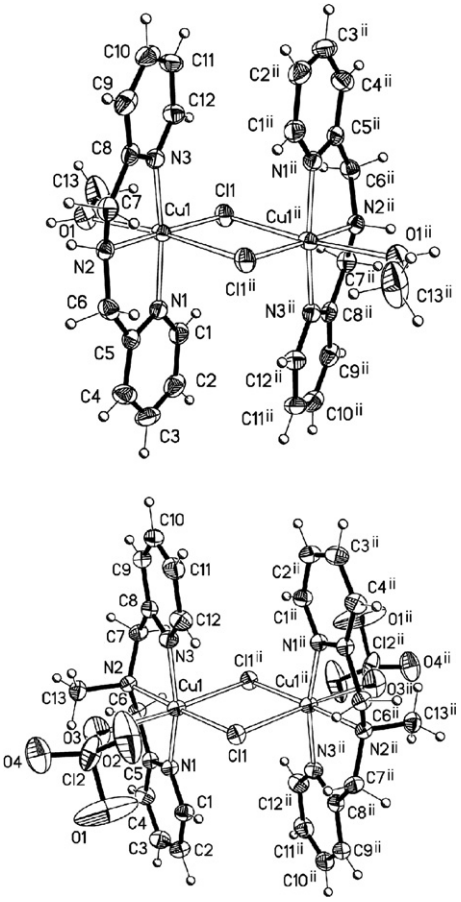


Fig. 2. Type **C** cation in the structure of **4** (top) and **5** (bottom) showing displacement ellipsoids at 50% probability for non-H atoms. The superscript (ii) refers to atoms generated by the symmetry operator $1-x, 1-y, 1-z$.

Table 4
Details of the coordination geometry (Å, °) of Cu for **4** and **5** (type **C** cation)

	4	**5**
Cu(1)–N(1)	1.991(2)	1.9788(12)
Cu(1)–N(2)	1.993(2)	2.0348(12)
Cu(1)–N(3)	1.983(2)	1.9830(13)
Cu(1)–Cl(1)	2.2441(6)	2.2519(4)
Cu(1)–Cl(1)^{ii}	3.1288(7)	2.8283(4)
Cu(1)–O(1)	2.5712(17)	
N(1)–Cu(1)–N(2)	83.15(8)	82.61(5)
N(1)–Cu(1)–N(3)	165.00(8)	164.48(5)
N(2)–Cu(1)–N(3)	82.53(8)	81.94(5)
N(1)–Cu(1)–Cl(1)	96.79(6)	98.03(4)
N(2)–Cu(1)–Cl(1)	175.69(6)	177.37(3)
N(3)–Cu(1)–Cl(1)	97.16(6)	97.47(4)
N(1)–Cu(1)–Cl(1)^{ii}	86.31(6)	88.75(4)
N(2)–Cu(1)–Cl(1)^{ii}	82.10(6)	88.64(3)
N(3)–Cu(1)–Cl(1)^{ii}	87.34(6)	92.46(4)
Cl(1)–Cu(1)–Cl(1)^{ii}	94.60(2)	88.83(1)
O(1)–Cu(1)–Cl(1)^{ii}	168.95(4)	

Superscript (ii) indicates atoms related by the symmetry operator $1-x$, $1-y$, $1-z$.

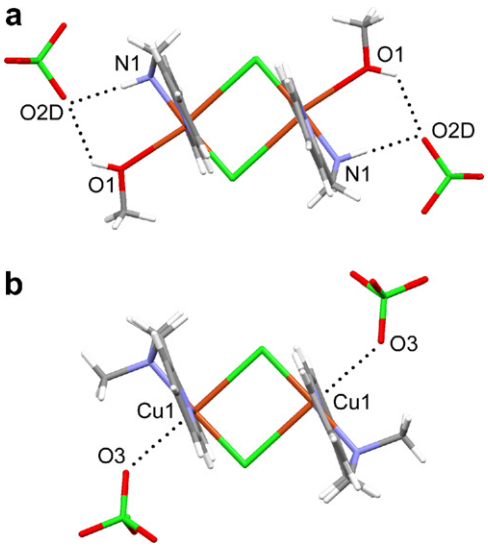


Fig. 3. Location of the perchlorate anions (a) in **4** and (b) in **5**. In **4**, the perchlorate anion accepts hydrogen bonds from the N–H group of bpa and also from a coordinated methanol molecule. In **5**, no comparable hydrogen bond can be formed from mebpa, and the perchlorate anion coordinates directly to Cu.

of the phenyl substituent of the phbpa ligand, and the latter O atom forms a relatively short contact to the *ortho* H atom (C14–H14···O2 = 2.36/2.45 Å), with a linear geometry suggestive of a C–H···O hydrogen bond. This contact may provide a further stabilizing contribution for complexation of the acetate anion. The τ parameters in **7** (Table 3; defined using the O atom of the acetate moiety that forms the shortest Cu–O bond) are comparable to those in **2a** and **2b**, and suggest that there is a slightly greater distortion towards trigonal-bipyramidal geometry for the Cu atoms bearing an acetate anion than for those bearing chloride. In **6**, there appears to be only partial replacement of the terminal chloride by an acetate anion (ca. 15%), and the structure is modelled as disordered. The Cu–O distances in this case are 1.846(16) and 2.932(13) Å. The plane of the acetate anion in **6** forms a dihedral angle of ca. 39° with respect to the plane of the phenyl group in the phbpa moiety [C(13)–C(18)], forming a considerably longer and more bent C–H···O contact compared to that in **7** (C(14)–H(14)···O(2A) = 2.60 Å). Aside from the inclusion or partial inclusion of the acetate anion, a major distinction exists from the planar Cu_2Cl_3 units in the type **B** cations of **2a** and **2b**: the two [(phbpa)Cu(Cl/OAc)] units of the cation in **6** and **7** are rotated with respect to each other so that the terminal Cu–Cl/O bonds form an angle of ca. 110° in projection (torsion angle Cl–Cu···Cu–Cl = 112.7(3)° in **6**, Cl–Cu···Cu–O = 108.6(5)° and 108.0(5)° in **7**). The Cu–Cl–Cu bridge is also marginally closer to linear compared to that in **2a** and **2b**.

Table 5
Details of the coordination geometry (Å, °) of Cu for **6** and **7** (type **B** cation)

	6	7 (mol 1)	7 (mol 2)		6	7 (mol 1)	7 (mol 2)
Cu(1)–N(1)	2.007(2)	2.009(10)	1.969(9)	Cu(2)–N(4)	1.985(2)	2.001(10)	2.003(9)
Cu(1)–N(2)	2.079(2)	2.059(10)	2.043(10)	Cu(2)–N(5)	2.088(2)	2.103(9)	2.079(9)
Cu(1)–N(3)	2.009(2)	2.022(9)	2.019(10)	Cu(2)–N(6)	1.996(3)	1.989(10)	1.968(10)
Cu(1)–Cl(1)	2.2571(14)			Cu(2)–Cl(3)	2.2395(9)	2.210(3)	2.271(3)
Cu(1)–O(1A)	1.846(16)	1.927(9)	1.964(9)	Cu(2)–Cl(2)	2.5545(8)	2.535(3)	2.526(3)
Cu(1)–O(2A)	2.932(13)	2.774(10)	2.897(10)	Cu(1)–Cl(2)	2.4972(8)	2.583(3)	2.592(3)
N(1)–Cu(1)–N(2)	81.29(10)	81.8(4)	83.1(4)	N(4)–Cu(2)–N(5)	82.05(10)	81.0(4)	81.2(4)
N(1)–Cu(1)–N(3)	162.56(10)	164.1(5)	164.6(5)	N(4)–Cu(2)–N(6)	163.94(11)	163.3(5)	162.4(4)
N(2)–Cu(1)–N(3)	81.28(10)	82.5(4)	81.5(4)	N(5)–Cu(2)–N(6)	81.92(10)	82.5(4)	81.3(4)
N(1)–Cu(1)–Cl(1)	96.55(8)			N(4)–Cu(2)–Cl(3)	97.51(8)	98.3(3)	96.9(3)
N(2)–Cu(1)–Cl(1)	148.04(8)			N(5)–Cu(2)–Cl(3)	153.70(7)	154.3(3)	156.9(3)
N(3)–Cu(1)–Cl(1)	97.86(8)			N(6)–Cu(2)–Cl(3)	97.35(8)	95.5(3)	98.6(3)
N(1)–Cu(1)–Cl(2)	92.24(7)	93.9(3)	90.9(3)	N(4)–Cu(2)–Cl(2)	90.56(7)	90.4(3)	94.5(3)
N(2)–Cu(1)–Cl(2)	101.35(7)	98.9(3)	92.3(3)	N(5)–Cu(2)–Cl(2)	96.71(7)	101.6(3)	96.2(3)
N(3)–Cu(1)–Cl(2)	91.84(7)	91.0(3)	90.5(3)	N(6)–Cu(2)–Cl(2)	90.19(7)	95.3(3)	88.8(3)
N(1)–Cu(1)–O(1A)	103.7(5)	100.9(4)	99.2(4)	Cl(2)–Cu(2)–Cl(3)	109.59(3)	104.14(12)	106.94(11)
N(2)–Cu(1)–O(1A)	162.2(5)	168.2(4)	166.3(4)				
N(3)–Cu(1)–O(1A)	92.8(5)	93.9(4)	95.5(4)	Cl(1)–Cu(1)–Cl(2)	110.60(5)		
Cl(2)–Cu(1)–O(1A)	95.5(5)	92.4(3)	101.1(3)	Cu(1)–Cl(2)–Cu(2)	160.14(4)	156.03(13)	158.59(12)

Two symmetry-independent molecules in **7**.

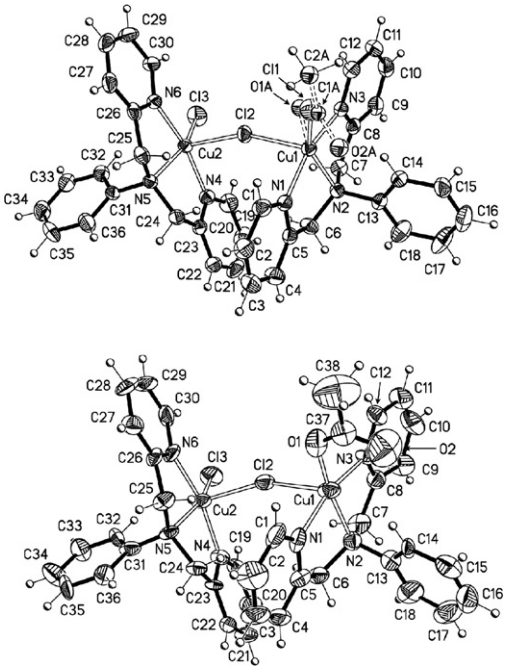


Fig. 4. Type **B** cation in **6** (top) and **7** (bottom) showing displacement ellipsoids at 50% probability for non-H atoms. The minor acetate disorder component in **6** comprises O(1A), O(2A), C(1A) and C(2A). For **7**, only one symmetry independent cation is shown. The other is closely comparable.

Acknowledgements

We are grateful to the Danish Natural Science Research Council (SNF) and Carlsbergfondet for provision of the X-ray equipment. A.D.B. also thanks SNF for funding via a Steno Stipend.

Appendix A. Supplementary material

CCDC 287934, 287935, 287936, 287937, 287938, and 287939 contain the supplementary crystallographic data for **2a**, **2b**, **4**, **5**, **6**, and **7**. These data can be obtained free of charge via http://www.ccdc.cam.ac.uk/conts/retrieving.html, or from the Cambridge Crystallographic Data Centre, 12 Union Road, Cambridge CB2 1EZ, UK; fax: (+44) 1223-336-033; or e-mail: deposit@ccdc.cam.ac.uk. Supplementary data associated with this article can be found, in the online version, at doi:10.1016/j.poly.2006. 12.005.

References

[1] J. Gažo, I.B. Bersuker, J. Garaj, M. Kabešowá, J. Kohout, H. Langfelderová, M. Melnik, M. Serátor, F. Valach, Coord. Chem. Rev. 19 (1976) 253.
[2] R.J.P. Williams, Eur. J. Biochem. 234 (1995) 363.
[3] D.J. White, L. Cronin, S. Parsons, N. Robertson, P.A. Tasker, A.P. Bisson, Chem. Commun. (1999) 1107.
[4] T.C. Higgs, C.J. Carrano, Inorg. Chem. 36 (1997) 291.
[5] J. McMaster, R.L. Beddoes, D. Collison, D.R. Eardley, M. Helliwell, C.D. Garner, Chem. Eur. J. 2 (1996) 685.
[6] B. Murphy, M. Aljabri, A.M. Ahmed, G. Murphy, B.J. Hathaway, M.E. Light, T. Geilbrich, M.B. Hursthouse, Dalton Trans. (2006) 357.
[7] I. Persson, P. Persson, M. Sandström, A.-S. Ullström, J. Chem. Soc., Dalton Trans. (2002) 1256.
[8] H. Stratemeier, B. Wagner, E.R. Krausz, R. Linder, H.-H. Schmidtke, J. Pebler, W.E. Hatfield, L. Haar, D. Reinen, M.A. Hitchmann, Inorg. Chem. 33 (1994) 2320.
[9] G.A. van Albada, W.J.J. Smeets, A.L. Spek, J. Reedijk, Inorg. Chim. Acta 288 (1999) 220.
[10] S.F. Haddad, J. Pickardt, Transition Met. Chem. 18 (1993) 377.
[11] P. Baran, M. Koman, D. Valigura, J. Mroziński, J. Chem. Soc., Dalton Trans. (1991) 1385.

[12] W.G. Haanstra, W.A.J.W. van der Donk, W.L. Driessen, J. Reedijk, J.S. Wood, M.G.B. Drew, J. Chem. Soc., Dalton Trans. (1990) 3123.
[13] K.-Y. Choi, H. Ryu, N.-D. Sung, M. Suh, J. Chem. Cryst. 33 (2003) 947.
[14] F. Ugozzoli, C. Massera, A.M.M. Lanfredi, N. Marsich, A. Camus, Inorg. Chim. Acta 340 (2002) 97.
[15] A. Hazell, K.B. Jensen, C.J. McKenzie, O. Simonsen, H. Toftlund, Inorg. Chim. Acta 257 (1997) 163.
[16] A. Hazell, C.J. McKenzie, L.P. Nielsen, Polyhedron 19 (2000) 133.
[17] G.M. Sheldrick, SHELXTL v. 6.10, Bruker AXS, Madison, WI, USA, 2000.
[18] Bruker Nonius, CELL_NOW, Delft, The Netherlands, 2004.
[19] G.M. Sheldrick, SAINT-PLUS and TWINABS, Bruker AXS, Madison, WI, USA, 2000.
[20] A.W. Addison, T.N. Rao, J. Reedijk, J. van Rijn, G.C. Verschoor, J. Chem. Soc., Dalton, Trans. (1984) 1349.

on two parameters: (a) Cu–N(azide)–Cu angle and (b) Cu–N(azide) bond distance. For example, if the aforesaid angle falls within the range of 96–104° the interaction is ferromagnetic, otherwise it is antiferromagnetic. This is almost in line with Thompson's prediction on the basis of the extrapolation of the magneto-structural correlation found for the μ-1,1 azido complexes [1c]. However, the magnetic character for the end-on azido bridges can be predestined only in the basal-basal linkage. When azido groups bridge Cu(II) centers in a basal-apical fashion, the structural parameters described above do not explain the observed magnetic phenomenon. For asymmetric (basal-apical) end-on azido bridged complexes magnetic interaction is inefficient to exhibit strong ferromagnetic interaction [8]. Various factors like strict and accidental orthogonality of magnetic orbitals [4], spin polarization [4], delocalization of unpaired electrons [4], charge transfer [9], including mean out-of plane deviation of the azido group and hydrogen bonding path way [1c,1g,1h,10a,8a] are found to have considerable influence in determining the characteristic of the magnetic coupling between paramagnetic centers. However, recently the literature has been enriched with asymmetric end-on azido bridged complexes showing antiferromagnetic interactions [10]. It is noteworthy that the copper(II) centers of these dimers are mostly penta-coordinated, whereas dimers with hexa-coordinated copper(II) centers are still very rare [1a,10a,10e].

In earlier attempts, we have succeeded in isolating rare variety of asymmetric μ_2-1,1-azido copper(II) dimers [10c,10d] using (NNO) donor tridentate Schiff bases as co-ligand. The magnetic property of these complexes and other similar μ_2-1,1-azido copper(II) complexes were established by full-structure based DFT calculations [10c]. Further exploration of copper(II) azido systems based on tridentate Schiff base (NNN) donor ligand allowed us to structurally and magnetically characterize a new antiferromagnetic Cu(II) azido system. Here, we report investigation on the synthesis, crystal structure and magnetic properties of a rare asymmetric end-on azido bridged dimer of copper(II) having octahedral coordination environment. The present work constitutes a part of our continuing study on metal-azido complexes of tridentate Schiff base ligands based on diamines.

2. Experimental

2.1. General

All chemicals and solvents used during the synthesis were of AR grade and used as received. Elemental analyses (CHN) were performed using a Perkin Elmer 240 elemental analyzer. IR spectra were recorded on a Nicolate Magna IR 750 Series II FT-IR spectrophotometer. Magnetic measurements were carried out with Quantum Design's SQUID MPMS XL magnetometer. The instruments used for other measurements were reported earlier [11].

2.2. Preparation of $[Cu_2(L)_2(N_3)_2(NO_3)_2]$ (1)

To prepare the complex (**1**), the methanolic solution of 1,3-propanediamine (1 mmol, 0.74 g) was added to a clear solution of $Cu(NO_3)_2 \cdot 3H_2O$ (1 mmol, 0.241 g) dissolved in 25 ml methanol, which immediately produced an intense blue colored solution. This solution was then heated to boil and then a methanolic solution of pyridine-2-aldehyde (1 mmol, 0.107 g) was added with the help of a dropping funnel in 2 h in refluxing condition. After the completion of the addition of pyridine-2-aldehyde the reflux was continued for another 45 min. On cooling the mixture a small amount of green solid was precipitated. The green mass was then filtered out and an excess amount of sodium azide (2 mmol, 0.130 g) dissolved in a minimum volume of water was added to the filtrate. On slow evaporation of the resulting bluish-green solution the light green flaky crystals of (**1**) were separated out in two days. The crystals were filtered out, washed with methanol and dried in air (yield ca. 90%). *Anal.* Calc. for $C_{18}H_{26}N_{14}Cu_2O_6$: C, 32.7; H, 3.9; N, 29.7. Found: C, 32.2; H, 3.8; N, 29.8. IR (KBr): ν_{as} (N_3), 2041 cm^{-1}; ν (NO_3), 1383 cm^{-1}; $\delta(N_3)$, 648 cm^{-1}; ν(C=N), 1597 cm^{-1}. $\lambda_{max} = 285.4$ nm, 383.9 nm and 615.9 nm.

2.3. X-ray crystallography

2.3.1. Crystal data

$C_9H_{13}N_7CuO_3$, $M = 330.8$, triclinic, space group $P\bar{1}$, $a = 7.8396(8)$, $b = 8.6615(9)$, $c = 10.7240(11)$ Å, $\alpha = 69.693(2)$, $\beta = 70.630(2)$, $\gamma = 85.376(3)^\circ$, $V = 643.78(11)$ $Å^3$, $Z = 2$, $R_{int} = 0.18$, $D_{calc} = 1.707$ g cm^{-3} $F_{000} = 338$, $\mu = 1.717$ mm^{-1}, green flaky crystal, dimensions = $0.10 \times 0.40 \times 0.60$ mm, $T = 293$ K.

2.3.2. X-ray single crystal structure determination of (1)

The crystals of the complex were extremely flaky and fragile. A reasonably suitable single crystal was selected and the X-ray diffraction data were collected on a Bruker-Nonius MACH3 diffractometer at room temperature using graphite monochromated Mo Kα radiation ($\lambda = 0.71073$ Å); the intensity data were rather weak possibly owing to the poor quality of the crystals. Of the 2251 reflections that were collected, 2122 ($R_{int} = 0.18$) were unique. The data were corrected for Lorentz, polarization and absorption effects. The structure was solved by direct methods using the program SHELXS-97 [12] and refined on $|F^2|$ by the least-squares method using anisotropic thermal parameters for the non-hydrogen atoms [12]. The final cycle of full-matrix least-squares refinement converged to the unweighted and weighted agreement factors of 0.116 and 0.287, respectively. The hydrogen atoms were placed in idealized geometrical positions and included in the structure factor calculations by being made to 'ride' on the atoms to which they were bonded [12]. Neutral atom scattering factors were taken from Cromer and Weber [13], and anomalous dispersion effects were included in F_{calc} [14].

3. Results and discussion

3.1. Description of structure of the complex (1)

The structure determination reveals that the azido complex consists of a neutral dinuclear entity. It results from the pairing of two mononuclear units related by a crystallographic center of inversion (Fig. 1). Here, two centrosymmetrically related copper(II) centers are bridged by azide ions in an asymmetric end-on fashion leading to a relatively large Cu–Cu distance of 3.317(2) Å. Within this dimeric unit, each of the two octahedrally distorted copper(II) centers is coordinated by four nitrogen atoms: N1, N2, N3 of the tridentate Schiff base ligand, and an end nitrogen atom of the bridging azide ion. This comprises the puckered basal plane. A second nitrogen, N4′ (symmetry = $2-x,-y,-z$) from the centrosymmetrically related bridging azide coordinates axially at a distance of 2.548(13) Å. The sixth coordination site is occupied by the oxygen atom O2 of the nitrate anion through a distal coordination of 2.852(18) Å. The four basal donors N1, N2, N3 and N4 deviate from the least-squares mean plane through them by −0.217(10), 0.263(11), −0.285(12) and 0.321(13) Å, respectively. The copper atom is pulled out of this plane by 0.126(2) Å towards the apical donor atom N4′. The Cu–O2 and Cu–N4′ distances from the basal plane are 2.641(18) and 2.658(13) Å, respectively. The five membered chelate ring Cu–N1–C5–C6–N2 is essentially planar with deviations from planarity lying between −0.032(13) Å for C5 and 0.018(13) Å for C6. The six membered chelate ring Cu–C7–C8–C9–N3–N2 has a chair conformation with the puckering parameters $q_2 = 0.189(12)$, $q_3 = -0.507(13)$, $Q = 0.541(14)$, $\varphi_2 = 15.4(40)^\circ$ and $\theta = 159.5(11)^\circ$ [15].

The bridging Cu_2N_2 network, Cu–N4–Cu′–N4′, is exactly planar as dictated by symmetry. Due to the formation of the basal apical μ_2-1,1-N_3 bridging, the Cu–N bond lengths, Cu–N4 and Cu–N4′, are significantly different ($\Delta d = 0.621$ Å) for the complex. The bridging N_3 anions are quasi-linear; the N4–N5–N6 angle is 173.9(14)°. The crystal structure exhibits the hydrogen bonding pattern

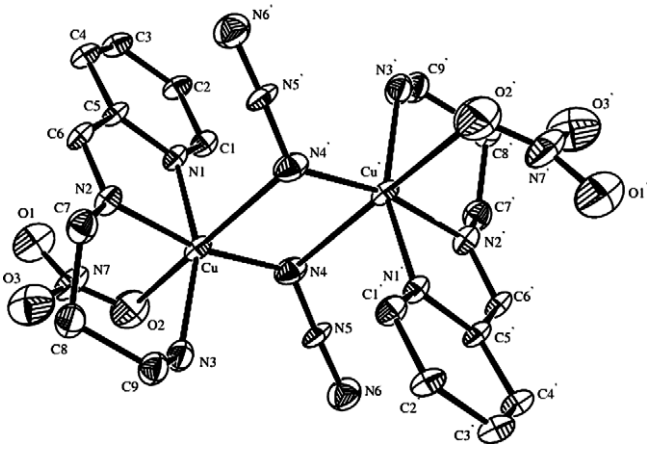


Fig. 1. ORTEP diagram of complex (**1**) showing atom numbering scheme. Symmetry code for the dash marked atoms is $2-x, -y, -z$.

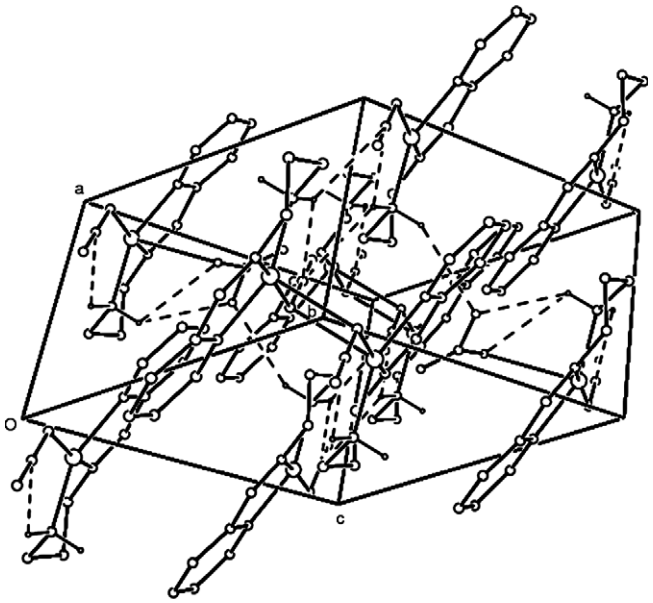


Fig. 2. Diagram showing crystal packing of complex (**1**). The dotted lines denote the intermolecular H-bonding as discussed in the text.

illustrated in Fig. 2; the geometrical details are given in Table 1. The two amino hydrogen atoms, H3A and H3B, are available for hydrogen bond formation, and both of them take part in trifurcated hydrogen bonds with the nitrate oxygen atoms O2 and O3, and the three azide nitrogen atoms N4, N5 and N6 acting as acceptors (Table 2).

3.2. Magnetic properties of $[Cu_2(L)_2(N_3)_2(NO_3)_2]$ (1)

The temperature dependence of the molar magnetic susceptibility, χ_M, for complex (**1**) was measured in 5–300 K temperature range under magnetic field of 1 kOe and is shown in Fig. 3. The $\chi_M T$ value of 0.82 $cm^3\ mol^{-1}$ K at 300 K for complex (**1**) is almost equal to the value expected for two isolated magnetically uncoupled copper(II) ion ($\chi_M T = 0.83\ cm^3\ mol^{-1}$ K for $g = 2.11$). Upon cooling the $\chi_M T$ value for copper(II) ions of complex (**1**) remains almost the same until ca. 60 K and then decreases rapidly

Table 1
Selected bond distances (Å) and bond angles (°) for the complex (**1**)

Bond lengths			
Cu–N(1)	2.004(11)	Cu–N(2)	2.004(11)
Cu–N(3)	1.972(11)	Cu–N(4)	1.927(13)
Cu–N(4′)	2.548(13)	Cu–O(2)	2.852(18)
N(4)–N(5)	1.234(19)	N(5)–N(6)	1.196(20)
Cu–Cu′	3.317(2)		
Bond angles			
N(1)–Cu–N(2)	81.9(4)	N(1)–Cu–N(3)	156.6(5)
N(1)–Cu–N(4)	92.1(5)	N(1)–Cu–N(4′)	93.5(4)
N(2)–Cu–N(3)	91.3(5)	N(2)–Cu–N(4)	167.5(5)
N(2)–Cu–N(4′)	84.1(4)	N(3)–Cu–N(4)	98.4(5)
N(3)–Cu–N(4′)	108.1(5)	N(4)–Cu–N(4′)	85.3(5)
N(1)–Cu–O(2)	75.6(5)	N(2)–Cu–O(2)	106.2(5)
N(3)–Cu–O(2)	75.6(5)	N(4)–Cu–O(2)	82.7(5)
O(2)–Cu–N(4′)	163.5(5)	Cu–N(4)–Cu′	94.7(5)
N(4)–N(5)–N(6)	173.9(14)		

Table 2
Hydrogen bonding distances (Å) and angles (°) of complex (**1**)

D–H···A	D–H	D···A	H ···A	∠D–H···A
N(3)–H(3A)···O(2)	0.90	3.322(24)	2.85	114.5
N(3)–H(3A)···O(3)	0.90	3.362(24)	2.75	126.4
N(3)–H(3B)···N(4)	0.90	2.951(13)	2.75	94.1
N(3)–H(3B)···N(5)	0.90	3.086(14)	2.56	117.8
N(3)–H(3A)···O(3)^{i}	0.90	3.572(18)	2.81	143.9
N(3)–H(3A)···O(3)^{ii}	0.90	3.221(22)	2.47	141.8

Symmetry codes: (i) $-x+1, -y, -z+1$; (ii) $-x+1, -y, -z$.

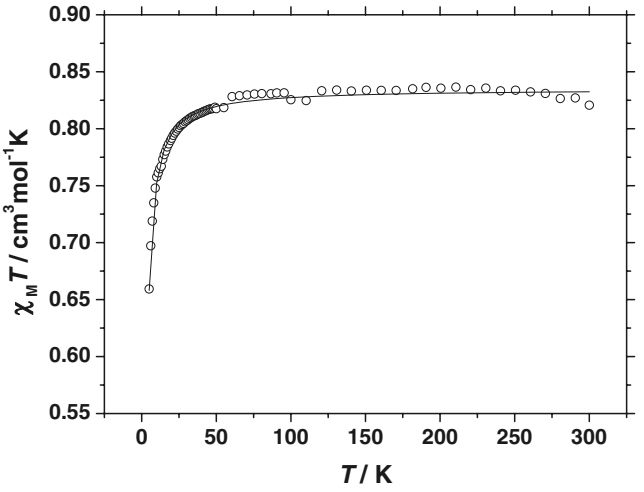


Fig. 3. $\chi_M T$ vs. T (○) plot for complex (**1**). Solid lines represent the best fit of the data with the model described in the text.

to reach a minimum of 0.66 $cm^3\ mol^{-1}$ K at ca. 5 K. The fitting of $1/\chi_M$ versus T with the Curie–Weiss equation yields $C = 0.83$ emu mol^{-1} K and $\theta = -1.29$ K for compound (**1**), which clearly indicates that magnetic interaction between copper(II) ions is antiferromagnetic.

To estimate the magnitude of the antiferromagnetic coupling the magnetic susceptibility data were fitted to the modified Bleaney–Bowers equation for two interacting copper(II) ions ($S = 1/2$) with the Hamiltonian in the form $H = -J\hat{S}_1\hat{S}_2$. The susceptibility equation for such a dimeric system can be written as follows [4a]:

$$\chi = \frac{2Ng^2\beta^2}{kT}[3 + \exp(-J/kT)]^{-1}(1-\rho) + \frac{Ng^2\beta^2}{2kT}\rho \qquad (1)$$

where N, g, β and ρ parameters in the equation bear their usual meaning.

The best fitted parameters obtained were $J = -1.27(1)$ cm^{-1}, $g = 2.11(1)$ and $\rho = 0.0005$. Though it is well established that end-on double azido bridged copper(II) dimers are usually ferromagnetic, the present study clearly indicates that the coupling between two copper(II) ions in this complex is antiferromagnetic.

Generally, the double end-on azido bridging ligands are considered to be capable of inducing a ferromagnetic coupling in copper(II) complexes whereas the double end-toend azido bridging ligands for the antiferromagnetic interactions. However, for asymmetric complexes, experimental results show that there are end-on and end-to-end complexes with the opposite behavior showing antiferromagnetic and ferromagnetic coupling, respectively. In this case it is the Cu–N(azide) distances that are more important than the N(azide)–Cu–N(azide) angles concerning the magnetic interaction. Notably it has been proposed on the basis of DFT study of double end-on azido bridged copper(II) complexes with basal-basal linkage, N(azide)–Cu–N(azide) angles play an important role as regards the nature of the interaction [7]. Recently Triki et al. have reported the DFT calculations of asymmetric end-on azido copper(II) complexes to address this apparently paradoxical nature of magnetic interaction [16]. They have shown for asymmetric end-on azido bridged copper(II) dimers having basal-apical linkage, the magnetic interaction is antiferromagnetic with the Cu–N(azide) distance 2.1–2.8 Å. In complex (**1**) the Cu′–N4 (or Cu–N4′) distances were equal to 2.548(13) Å. This is even significantly longer than the cutoff distance (2.05 Å) for the interaction being ferromagnetic as proposed by Ruiz et al. [7].

Structural and magnetic parameters of the similar other μ_2-1,1 azido bridged octahedral copper(II) complexes are given in Table 3. Even a cursory look at the Table 3 it will be apparent that the J value for complex $[Cu_2(\mu\text{-}N_3)_2(4\text{-Etpy})_4(\mu\text{-}NO_3)_2]$ and $[Cu_2(\mu\text{-}N_3)_2(3\text{-ampy})_4(\mu\text{-}NO_3)_2]\cdot$

Table 3
Structural and magnetic parameters for μ_2-1,1 azido octahedral copper(II) dimers

Compounds	Cu–Cu (Å)	Cu–N (Å)	Cu–N–Cu′ (°)	J (cm^{-1})	Ref.
$[Cu_2(\mu\text{-}N_3)_2(4\text{-Etpy})_4(\mu\text{-}NO_3)_2]$	3.024	1.996 2.004	98.3	230.1	[1a]
$[Cu_2(\mu\text{-}N_3)_2(3\text{-ampy})_4(\mu\text{-}NO_3)_2]\cdot$ EtOH	3.011	2.000 2.006	97.5	223.2	[1a]
$[Cu(L1)(N_3)]_2(ClO_4)_2$	3.452	1.972 2.563	98.3	−3.20	[10e]
$[Cu(terpy)(N_3)(H_2O)]_2[PF_6]_2$	3.60	1.927 2.851	95.7	−2.9	[10a]
$[Cu(L)(N_3)(NO_3)]_2$ (**1**)	3.317	1.927 2.548	94.7	−2.46	this work

4-Etpy = 4-ethylpyridine; 3-ampy = 3-aminopyridine; L1 = *N*,*N*-bis-(2-methylpyridyl) (3,5-dimethyl-2-hydroxybenzyl)-amine; terpy = terpyridine.

EtOH is positive and significantly larger than the other complexes. It is noteworthy that in both these complexes μ_2-1,1 azido ligands connect two copper sites through basal-basal linkage, hence, they show fairly strong ferromagnetic interaction. But for the rest of the complexes including the complex (**1**), which have bridging azido ligands that connect copper sites in basal-apical fashion, magnetic interaction is found to be antiferromagnetic.

4. Conclusion

In summary, we have been succeeded in synthesizing rather a rare variety of azido dimer consisting of octahedral copper(II) sites. In complex (**1**) azido ligands bridged Cu and Cu′ via asymmetric basal-apical linkages. The magnetic interaction in this complex is antiferromagnetic as expected for such type of copper(II) complexes with relatively longer Cu–N(azide) distances.

5. Supplementary material

CCDC 617630 contains the supplementary crystallographic data for this paper. These data can be obtained free of charge via http://www.ccdc.cam.ac.uk/conts/retrieving.html, or from the Cambridge Crystallographic Data Centre, 12 Union Road, Cambridge CB2 1EZ, UK; fax: (+44) 1223-336-033; or e-mail: deposit@ccdc.cam.ac.uk.

Acknowledgements

The work was financially supported by the CSIR, New Delhi, by a Grant (01/(1972)/05/EMR II) to S.K. We are grateful to CDRI, Lucknow for elemental analyses (on a chargeable basis).

References

[1] (a) A. Escuer, M.A.S. Goher, F.A. Mautner, R. Vicente, Inorg. Chem. 39 (2000) 2107;
(b) J. Comarmond, P. Plumerè, J.M. Lehn, Y. Agnus, R. Louis, R. Weiss, O. Kahn, I. Morgensten-Badarau, J. Am. Chem. Soc. 104 (1982) 6330;
(c) S.S. Tandon, L.K. Thompson, M.E. Manuel, J.N. Bridson, Inorg. Chem. 33 (1994) 5555;
(d) S. Sikorav, I. Bkouche-Waksman, O. Kahn, Inorg. Chem. 23 (1984) 490;
(e) M.A. Aebersold, M. Gillon, O. Plantevin, L. Pardi, O. Kahn, P. Bergerat, I. V Seggern, F. Tuczek, L. Öhrström, A. Grand, E. Leliévre-Berna, J. Am. Chem. Soc. 120 (1998) 5238;
(f) G.A. Van Albada, M.T. Lakin, N. Veldman, A.L. Spek, J. Reedjik, Inorg. Chem. 34 (1995) 4910;
(g) L.K. Thompson, S.S. Tandon, M.E. Manuel, J.N. Bridson, Inorg. Chem. 34 (1995) 2356;
(h) C. Adamo, V. Barone, A. Bencini, F. Totti, I. Coifini, Inorg. Chem. 38 (1999) 1996.

[2] (a) Y. Agnus, R. Louis, J.P. Gisselbrecht, R. Weiss, J. Am.Chem. Soc. 106 (1984) 93;
(b) V. McKee, M. Zvagulis, J.V. Dagdigian, M.G. Patch, C.A. Reed, J. Am. Chem. Soc. 106 (1984) 4765.

[3] (a) E.I. Solomon, Metal Clusters in Proteins, in: L. Que (Ed.), ACS Symposium Series, vol. 372, American Chemical Society, Washington, DC, 1998, p. 116;
(b) T.N. Sorrell, C.J. O'Connor, O.P. Anderson, J.H. Reibenspies, J. Am. Chem. Soc. 107 (1985) 4199.

[4] (a) O. Kahn, Molecular Magnetism, VCH, New York, 1993;
(b) O. Kahn, in: R.D. Willett, D. Gatteschi, O. Kahn (Eds.), Magneto-Structural Correlations in Exchange Coupled Systems, D. Reidel, Dordrecht, The Netherlands, 1985;
(c) V.M. Crawford, H.W. Richardson, J.R. Wason, D.J. Hodgson, W.E. Hatfield, Inorg. Chem. 15 (1976) 2107.

[5] L.K. Thompson, S.S. Tandon, Comments Inorg. Chem. 18 (1996) 125, and references therein.

[6] (a) A. Escuer, M. Font-Bardia, E. Peñalba, X. Solans, R. Vicente, Inorg. Chim. Acta 298 (2000) 195;
(b) T.R. Felthouse, D.N. Hendrickson, Inorg. Chem. 17 (1978) 444;
(c) I. Bkouche-Waksman, S. Sikorav, O. Kahn, J. Cryst. Spectrosc. Res. 13 (1983) 303;
(d) A. Escuer, M. Font-Bardia, S.S. Massoud, F.A. Mautner, E. Peñalba, X. Solans, R. Vicente, New J. Chem. 28 (2004) 681;
(e) P.S. Mukherjee, S. Dalai, G. Mostafa, T.-H. Lu, E. Rentschler, N. Ray Chaudhuri, New J. Chem. 25 (2001) 1203;
(f) P. Manikandan, R. Muthukumaran, K.R. Justin, B. Varghese, G.V.R. Chandramouli, P.T. Monoharan, Inorg. Chem. 40 (2001) 2378;
(g) S. Sarkar, A. Mondal, J. Ribas, M.G.B. Drew, K. Pramanik, K.K. Rajak, Inorg. Chim. Acta 358 (2005) 641.

[7] E. Ruiz, J. Cano, S. Alvarez, P. Alemany, J. Am. Chem. Soc. 120 (1998) 11122.

[8] (a) M.S. Ray, A. Ghosh, S. Chaudhuri, M.G.B. Drew, J. Ribas, Eur. J. Inorg. Chem. (2004) 3110;
(b) K. Matsumoto, S. Ooi, K. Nakatsura, W. Mori, S. Suzuki, A. Nakahara, Y. Nakao, J. Chem. Soc., Dalton Trans. (1985) 2095;
(c) L. Li, D. Liao, Z. Jiang, S. Yan, Polyhedron 20 (2001) 681;
(d) S.-Q. Bai, E.-Q. Gao, Z. He, C.-J. Fang, C.-H. Yan, New J. Chem. 29 (2005) 935.

[9] (a) F. Tuczek, E.I. Solomon, Inorg. Chem. 32 (1993) 2850;
(b) F. Tuczek, E.I. Solomon, J. Am. Chem. Soc. 116 (1994) 6916.

[10] (a) R. Cortès, M.K. Urtiaga, L. Lezama, J.I.R. Larramendi, M.I. Arriortua, T. Rojo, J. Chem. Soc., Dalton Trans. (1993) 3685;
(b) Y.S. You, S.H. Chang, K.M. Kim, Polyhedron 24 (2005) 249;
(c) M. Zbiri, S. Saha, C. Adhikary, S. Chaudhuri, C. Daul, S. Koner, Inorg. Chim. Acta 359 (2006) 1193;
(d) S. Koner, S. Saha, T. Mallah, K.-I. Okamoto, Inorg. Chem. 43 (2004) 840;
(e) S. Sarkar, A. Mondal, J. Ribas, M.G.B. Drew, K. Pramanik, K.K. Rajak, Eur. J. Inorg. Chem. (2004) 4633.

[11] S. Koner, S. Saha, K. Okamoto, J.-P. Tuchagues, Inorg. Chem. 42 (2003) 4668.

[12] G.M. Sheldrick, SHELX-97. Program for the Refinement of Crystal Structure, University of Göttingen, Germany, 1997.

[13] D.T. Cromer, J.T. Weber, International Tables for X-ray Crystallography, vol. IV, The Kynoch Press, Birmingham, England, 1974 (Table 2.2A).

[14] J.A. Ibers, W.C. Hamilton, Acta Crystallogr. 17 (1964) 781.

[15] D. Cremer, J. Pople, J. Am. Chem. Soc. 97 (1975) 1354.

[16] S. Triki, C.J. Gómez-García, E. Ruiz, J. Sala-Pala, Inorg. Chem. 44 (2005) 5501.

15-dibenzo-1,4-dioxa-8,12-diazacyclopentadeca-5,14-diene (L) under focused microwave conditions and by conventional thermal reactions either in refluxing ethanol or heating in the solid state. To the best of our knowledge, this is the first example of utilization microwave irradiation to form an alkali metal complex of a macrocyclic compound as well as of sodium macrocyclic complexation in a solid-state reaction. A wide range of coordination compounds, mostly of transition metal ions, have been synthesized by microwave-assisted reactions in solution [10], but among them there are only a few examples of those derived from macrocyclic ligands [11]. In our recent study, we investigated the interactions of a heteromacrocycle L with a series of sodium salts NaX (X = picrate, ClO_4, BF_4, PF_6, SCN, and BPh_4) in methanol and acetonitrile solution [12,13]. Although the hole size of the 15-membered macrocycle would be suitable for complexation of a sodium ion [14], it was shown that in these reactions the sodium complexes were not formed but instead the protonated ligand salts containing the protonated macrocyclic ligand as the cation and the anion from the sodium salt as its counterion were obtained. Crystal structure analyses of these compounds have shown a different mode of ligand protonation and a hydrogen bond network which stabilizes the binding site of the proton. As a continuation of this work herein we report the formation of the sodium complex obtained by the interaction of L with an organophosphorus sodium salt.

2. Experimental

2.1. Materials and instrumentation

5,6,14,15-Dibenzo-1,4-dioxa-8,12-diazacyclopentadeca-5,14-diene (L) was used directly as supplied (Aldrich). The sodium salt of monoethyl [4-α-(benzeneazoanilino)-*N*-benzyl]phosphonic acid ($NaEP \cdot 1.5H_2O$) was prepared and purified as described earlier [15]. Solvents used (AR grade) were purified and dried by standard procedures. Microwave experiments were performed in a microwave oven in an open porcelain vessel at 700 W. The melting point was determined on a hot stage microscope and is uncorrected. FTIR spectra were recorded on an ABB Bomen MB102 spectrometer using KBr pellets. ESI mass measurements were performed on a Finnigan LCQ DECA instrument (ThermoFinnigan, Palo Alto, Ca, USA) operating in the positive ion mode. The compounds were dissolved in methanol (10^{-6} M solutions) and directly injected by a syringe pump at a flow of 5 μL min^{-1}. LDI mass spectra were performed on a Voyager-DE PRO instrument (Applied Biosystems, Foster City, CA, USA) and a Finnigan FT/MS 2001 DD instrument (Finnigan, Madison, Wisconsin, USA), operating in the linear positive ion mode. The one- and two-dimensional ^1H and ^{13}C NMR spectra (in $CDCl_3$), including ^1H, ^{13}C APT, ^1H–^1H COSY, ^1H–^{13}C COSY, HMQC, and HMBC experiments, were recorded with a Bruker XWIN-600 Fourier-transform spectrometer at ambient temperature. The ^1H and ^{13}C chemical shifts (δ) were referred to $SiMe_4$. All two-dimensional experiments were performed by standard pulse sequences, using Bruker XWIN-NMR software Version 3.5. Elemental analyses (CHN) were performed on a Perkin–Elmer Analyser PE 2400 Series 2. The thermogravimetric analyses (TG) were carried out on a Cahn RG electromicrobalance in an air atmosphere at a heating rate of 4 °C min^{-1} up to 850 °C. Differential thermal analyses (DTA) were performed with a Netzsch 406 differential thermal analyzer, applying a heating rate of 5 °C min^{-1} in static air atmosphere. The reference substance was pure alumina.

2.2. Preparations of the complex $[Na(L)(\mu\text{-}EP) \cdot H_2O]_2$

2.2.1. Focused solid-state microwave irradiation

Equimolar amounts of 5,6,14,15-dibenzo-1,4-dioxa-8,12-diazacyclopentadeca-5,14-diene (L) (0.152 g, 0.49 mmol) and the hydrated sodium salt of ethyl [4-α-(benzeneazoanilino)-*N*-benzyl]phosphonic acid ($NaEP \cdot 1.5H_2O$) (0.218 g, 0.49 mmol) in a porcelain mortar were ground together until a fine homogenous powder was obtained. This mixture was then irradiated for 12 min (6 × 2) using a 700 W microwave. After the reaction was completed, the liquefied product was allowed to cool down, washed with diethyl ether and dried *in vacuum* for 24 h giving an orange glassy solid. Yield: 0.337 g, 92%, mp 96–98 °C. *Anal*. Calc. for $C_{40}H_{47}N_5O_5PNa$ (M/2 = 747.79): C, 64.24; H, 6.34; N, 9.37; H_2O, 2.41. Found: C, 64.03; H, 6.10; N, 9.09; H_2O, 2.11%. Selected IR data (KBr, cm^{-1}) 3360 m vbr [ν(NH), ν(OH)], 3060–2825 [ν(aliphCH), ν(ArCH)], 1602 vs, 1512 s [δ(NH),ν(C=C)], 1240 s br, 1220 sh, 1196 sh [$\nu_{as}(PO_2^-)$, ν_{as}(ArCOC), ν(CNC)], 1075 s, 1047 s [$\nu_s(PO_2^-)$, ν(POC)], 941 s [ω, τ, $\rho(CH_2)$, ν(aliphCC)], 795 m, 753 vs, 732 m [δ(NH), δ(ArCH) out-of-plane]. ^1H NMR (600 MHz, $CDCl_3$, δ ppm) L: 1.70 (2H, m, CH_2–CH_2–CH_2), 2.58 (4H, t, J_{HH} = 5.3 Hz, NH–CH_2–CH_2), 2.70 (2H, br s, NH), 3.70 (4H, s, Ar-CH_2–NH), 4.34 (4H, s, O–CH_2), 6.87 (2H, d, J_{HH} = 8.2 Hz, Ar*H*-a), 6.93 (2H, t, J_{HH} = 7.4 Hz, Ar*H*-c), 7.20 (2H, dd, J_{HH} = 7.3; 1,5 Hz, Ar*H*-d), 7.31 (2H, dt, J_{HH} = 8.0; 1.5 Hz, Ar*H*-b), EP: 1.10 (3H, t, J_{HH} = 7.0 Hz, CH_3), 3.76 (2H, m, $POCH_2$), 4.59 (1H, d br, J_{PH} = 23 Hz, PCH), 5.65 (3H, s br, NH, H_2O), 6.55 (2H, d, J_{HH} = 8.1 Hz, H-8,12), 7.15 (1H, t, J_{HH} = 6.8 Hz, H-4), 7.22 (2H, $J_{HH} \sim 7$ Hz, H-3,5), 7.34 (1H, t, J_{HH} = 7.4 Hz, H-16), 7.42 (2H, d, J_{HH} = 7.6 Hz, H-2,6), 7.43 (2H, t, J_{HH} = 7.6 Hz, H-15,17), 7.70 (2H, d, J_{HH} = 7.7 Hz, H-9,11), 7.77 (2H, t, J_{HH} = 8.1 Hz, H-14,18). ^{13}C NMR (150.90 MHz, $CDCl_3$, δ ppm) L: 25.83 (CH_2–*C*H_2–CH_2), 48.50 (NH–*C*H_2–CH_2), 49.58 (Ar-*C*H_2–NH), 65.14 (O–*C*H_2), 109.86 (Ar*C*-a), 120.33 (Ar*C*-c), 127.80 (Ar*C*–CH_2–NH), 129.25 (Ar*C*-b), 131.45 (Ar*C*-d), 156.39 (Ar*C*–O–CH_2), EP: 16.35 ($^3J_{POCC}$ = 6.1 Hz, *C*H_3), 56.38 ($^1J_{PC}$ = 135.1 Hz, P*C*H), 60.74 ($^2J_{POC}$ = 5.6 Hz, P–O*C*H_2), 112.55 (C-8,12), 121.65 (C-14,18), 124.50 (C-9,11), 125.76 (C-4), 127.26

($^3J_{PC} = 3.5$ Hz, C-2,6), 127.44 (C-3,5), 128.36 (C-15,17), 128.63 (C-16), 139.38 (C-1), 144.01 (C-10), 150.25 ($^3J_{PC} = 11.8$ Hz, C-7), 152.74 (C-13). MS (+LDI) *m/z* 1460 ($[(Na(L)EP)_2+H]^+$, 6%), 1275 ($[(NaEP)_3+Na]^+$, 41%), 1170 ($[(NaEP)_2L+Na]^+$, 7%), 1065 ($[Na(L)_2EP+Na]^+$, 6%), 858 ($[(NaEP)_2+Na]^+$, 29%), 441 ($[NaEP+Na]^+$, 78%), 352 ($[L+K]^+$, 9%)$^+$, 335 ($[L+Na]^+$, 10%)$^+$, 313 ($[LH]^+$, 100%), 296 ($[LH-NH_3]^+$, 4%), 284 ($[LH-(CH_2=NH)]^+$, 7%), 256 ($[LH-(CH_3CH_2CH=NH)]^+$, 5%), 241 ($[LH-(NH_2CH_2CH_2CH=NH)]^+$, 7%); MS (+ESI, MeOH/$H_2O$ 1:1) *m/z* 336 ($[L+Na]^+$, 4%)$^+$, 313 ($[LH]^+$, 100%). NaEP: MS (+LDI) *m/z* 1275 ($[(NaEP)_3+Na]^+$, 12%), 858 ($[(NaEP)_2+Na]^+$, 10%), 441 ($[NaEP+Na]^+$, 100%). TG data (temperature range, °C) 40–110 (dehydration), 200–860 (degradation processes). DTA data (exothermic peaks, °C) 310 and 575.

2.2.2. Conventional solid-state thermal method

A homogenous mixture of equimolar amounts of L and NaEP · 1.5H_2O was heated at 190 °C for 6 h giving the liquefied product. The heating was continued for 1 h and the solid obtained after cooling, besides the sodium complex (ca. 70%), contained side products, which could not be completely separated and successfully identified. Heating at lower temperatures or prolonged heating did not give better results. On the other hand, heating over 200 °C initiated a degradation processes of the complex, which was supported by the thermal analyses.

The progress of complex formation in both solid-state reactions was monitored by IR and ^{1}H NMR spectroscopy and the optimal reaction conditions for both methods are reported.

2.2.3. Conventional thermal method in solution

A mixture of L (0.110 g, 0.35 mmol) and NaEP · 1.5H_2O, (0.158 g, 0.40 mmol) in dry EtOH (20 cm^3) was refluxed for 5–6 h with continuous stirring to give a clear solution, which was filtered after cooling and set aside for evaporation. The sodium complex was obtained as a syrup after all the solvent was driven off, and solidified as an orange glassy product on standing under *vacuum* for 24 h. Yield: 0.222 g, 85%; mp 96–98 °C. In reactions carried out in methanol and acetonitrile solutions, the free macrocyclic compound gradually precipitated on cooling and the sodium complex was not isolated.

3. Results and discussion

3.1. Synthesis and properties

The coordination number of the sodium(I) ion varies from five to seven and coordinative forces of macrocyclic ligands play an important role in forming stable metal complexes. It was shown that the type, number, and arrangement of the donor atoms in a macrocyclic cavity have great influence on the cation binding selectivity. An investigation of the interaction of a 15-membered macrocycle containing an O_2N_2-donor set (L) with a number of sodium salts in solution shows that the affinity of this macrocycle for a proton is much larger than for the sodium ion [12,13]. A strong solvation capability of the sodium ion as well as the presence of only two oxygen and two nitrogen donor atoms are in favor of proton binding. The choice of anion in a salt-ligand system along with the choice of solvent (methanol or acetonitrile) is important for the resulting inter- or intra-ligand protonation and hence the different hydrogen bonding networks in various types of protonated macrocyclic salts. The formation of the sodium ethyl benzeneazophosphonate complex of L, containing only four donor atoms, enables additional interactions with the anion phosphonate oxygen atoms. The very low melting point of the complex (96–98 °C), with respect to the high melting point of the free sodium salt (above 220 °C) [15], indicates that the charge of the sodium ion in the complex is extremely delocalized. Some degree of charge transfer between the sodium ion and anion can take place, increasing the stability of the complex. It may be presumed that the sodium ion is bonded to both oxygen and nitrogen donor atoms of the macrocycle and to the two oxygen atoms of the two different molecules of the phosphonic ester, as shown in Fig. 1. The two other oxygen atoms of each molecule of ester are bonded to a second sodium ion and thus form a dinuclear phosphonate-bridged complex in which the sodium ions are hexacoordinated. The same dimeric bridged structure was detected for the corresponding sodium benzeneazophosphonate complex of a 14-membered macrocycle with four oxygen donors, dibenzo-14-crown-4 [16]. The crystal structure determination of this complex, $[Na(DB14C4)(\mu\text{-}EP)]_2$, has shown stronger interactions between the sodium ion and the phosphonate oxygens than with the oxygens in the crown ring. As we could not grow crystals for X-ray analysis, the sodium phosphonate complex of L was identified and characterized on the basis of elemental and thermal (TG and DTA) analyses, and from infrared, ^{1}H and ^{13}C NMR and mass (LDI and ESI) spectroscopic studies.

A comparative study between microwave and conventional heating in ethanol did not reveal significant differences in yields (ca. 7%), while the complexation time was much shorter in the reaction run under microwave irradiation (12 min) compared to that with classical heating (5–7 h). Conventional solid-state heating gave the sodium complex with some impurities (ca. 30%) which could not be successfully separated and identified. It is worth noting that reactions of L with NaEP in methanol and acetonitrile solutions failed to produce either the protonated ligand salt or the sodium complex. It may be presumed that solvent media effects primary arise from the difference in the ion and ligand solvation and the alkali salt solubilization. In addition, it is interesting to note that the solid-state complexation of L also occurred very slowly on irradiation by ultraviolet light in the sun. The reaction was monitored by infrared spectroscopy.

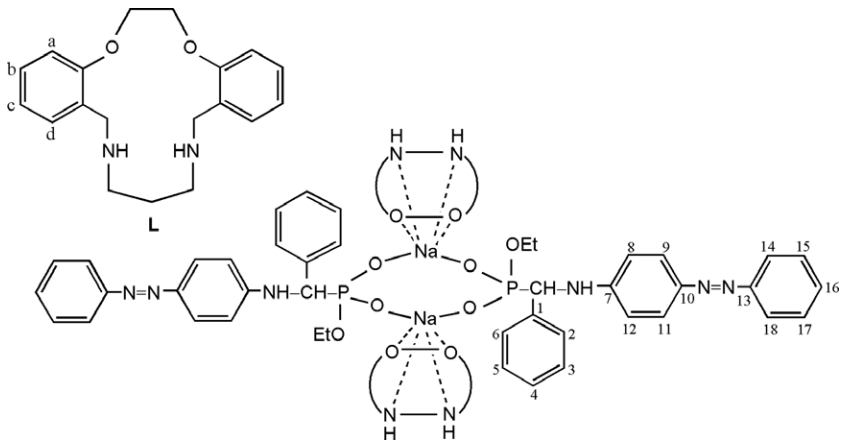


Fig. 1. Schematic molecular structure of the sodium complex.

3.2. Spectroscopic study

The IR spectrum of the complex is very complicated with significant overlapping of absorption bands. However, it is distinctively different from the spectrum of the physical mixture of the sodium salt and the free ligand (Fig. 2), and shows the absence of the uncomplexed constituents [17,18]. Upon complexation the most significant changes may be noticed in the ligand absorptions associated with various stretching and deformation modes of the NH vibrations in the 3400–1500 and 790–730 cm^{-1} regions, as well as within the 2800–2600 cm^{-1} region, where in the free L a series of sharp bands of strong to medium intensity appear, assigned to the perturbed symmetrical stretching vibrations of α-methylene C–H bonds oriented trans to the lone pair of electrons on the nitrogen atoms (Bohlmann bands) [12,19]. These bands are missing in the sodium complex. In addition, marked changes could be observed between 1250 and 1190 cm^{-1} where the stretching ArC–O–C and C–N–C vibrations occur, superimposed on the phosphonate $\nu_{as}(PO_2^-)$ absorption, as well as between 1000 and 900 cm^{-1} where deformation modes of the methylene vibrations are expected to occur [8,13,20]. A very broad absorption around 3360 cm^{-1}, arising from a ν(OH) vibration overlapped with that of a ν(NH) absorption, indicates metal bonding with the macrocyclic amino nitrogens and no interaction with the water oxygens. A broad dehydration step over the range 40–110 °C in the TG curve of the complex supports that the water molecules are lattice-held in this compound. Generally, water in the complex is considered to be metal coordinated if relatively sharp absorption bands appear over 3400 cm^{-1}, especially above 3500 cm^{-1} [21]. The phosphonate bands are broad and complex in structure, confirming bonding of the sodium ion to the phosphonate oxygens.

The ^1H and ^{13}C NMR spectral pattern of the aromatic region of the sodium complex is in general similar to those obtained for the free macrocycle and ethyl benzeneazophosphonate salt [8,22]. As expected, pronounced differences could be observed in the ^1H NMR spectra for the NH protons as well as the methylene macrocyclic and the phosphonate PCH and $POCH_2$ resonances. While the NH absorption broadens and moves to lower field, the methylene protons are shifted upfield by 12–36 Hz with respect to the free macrocycle. These differences may be

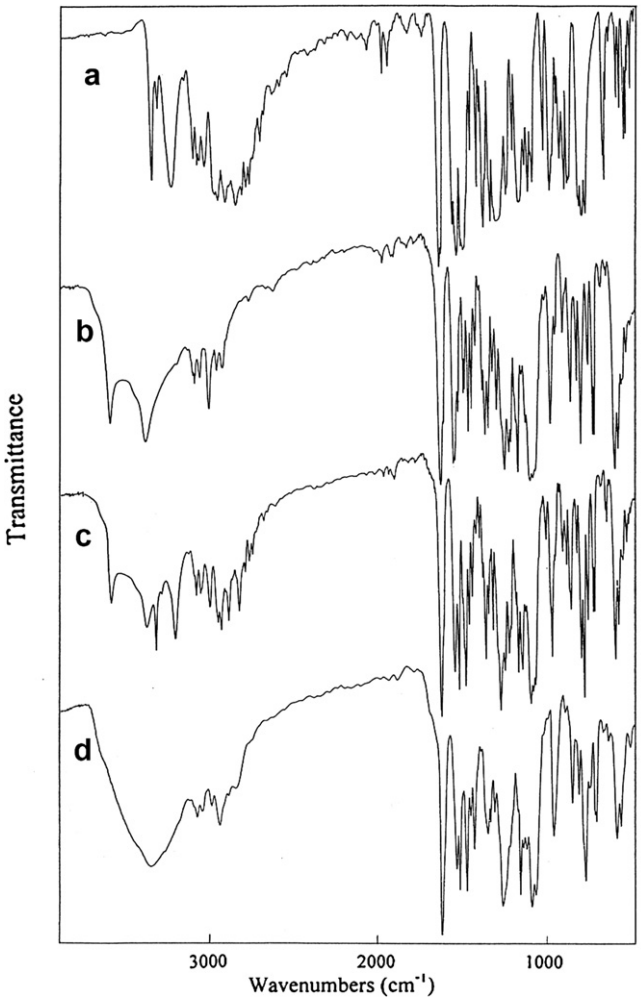


Fig. 2. Infrared spectra of (a) L; (b) $NaEP \cdot 1.5H_2O$; (c) 1:1 mixture of L and $NaEP \cdot 1.5H_2O$; (d) $[Na(L)(\mu\text{-}EP) \cdot H_2O]_2$.

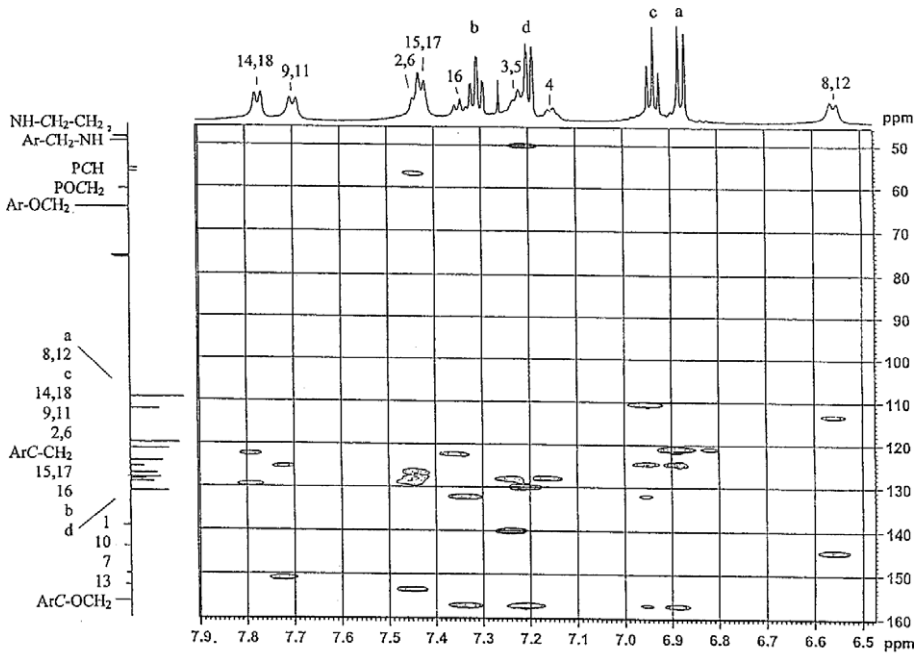


Fig. 3. A part of the long-range ^{1}H–^{13}C HMBC spectrum of the sodium complex.

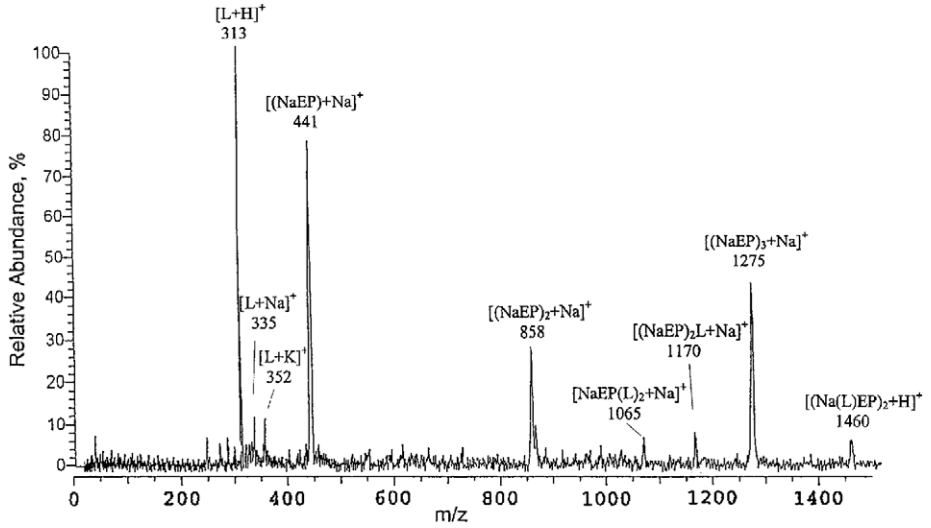


Fig. 4. Positive-ion LDI spectrum of the sodium complex.

explained by the proximity of the macrocycle molecule to the aromatic rings of the phosphonate anion in spite of the complexation with the alkali cation, which in itself would induce a downfield shift due to the increased electronegativity of the donor atoms. In the case of the phosphonate anion, there is an upfield shift for PCH as well as a downfield shift of about 36 Hz ppm for the P–OCH_2 protons. Small changes could also be observed for the corresponding carbon resonances. Various 2D homo- and heteronuclear correlated experiments enabled a complete ^{1}H and ^{13}C signal assignment (Fig. 3).

The MS properties of the sodium complex have been studied by spectrometric measurements carried out under positive-ion ESI and LDI conditions. Both spectra show the base peak at *m*/*z* 313, corresponding to the protonated ligand ion $[LH]^{+}$. While in the ESI spectrum this ion is the only intense fragment ion (the relative abundances of all other fragment ions are very small), the fragmentation pattern is more extensive in the LDI spectra giving relevant structural information about this compound (Fig. 4). The protonated molecular ion, $[(Na(L)EP)_2+H]^{+}$ at *m*/*z* 1460, and the structure-specific fragment ions formed by

decomposition of the complex by the loss of one macrocycle ligand molecule, $[(NaEP)_2L+Na]^+$ at m/z 1170, as well by the loss of one ethyl benzeneazoanilinophosphonate moiety, $[Na(L)_2EP+Na]^+$ at m/z 1065, support the existence of the sodium complex as a dimeric species. Their relative abundance is about 6%. More abundant ions are those containing NaEP molecules $[(NaEP)_3+Na]^+$, $[(NaEP)_2+Na]^+$, and $[(NaEP)+Na]^+$ at m/z 1275 (43%), m/z 858 (29%), and m/z 441 (58%), respectively, indicating strong bonding between the sodium ion and the phosphonate anion. This fact is in accordance with structural data obtained for the sodium benzeneazophosphonate complex of the oxa-macrocycle dibenzo-14-crown-4 [16]. These ions are also dominant in the LDI spectrum of free NaEP.

4. Conclusion

In summary, the first example of supported microwave-assisted synthesis of an alkali complex derived from a heteromacrocyclic compound is described. This simple work-up, eco-friendly solvent free reaction resulted in the formation of a sodium benezeneazophosphonate complex with a 15-membered macrocycle containing an O_2N_2-donor set in a shorter reaction time, with high purity and excellent yield, compared to conventional thermal reactions carried out either in refluxing ethanol or by heating in the solid state.

Acknowledgements

The financial support granted by the Croatian Ministry of Science, Education and Sports is gratefully acknowledged. The authors would like to thank Mr. Ž. Marinić for recording the NMR spectra and Mr. H. Muharemović for some MS measurements.

Appendix A. Supplementary material

Supplementary data associated with this article can be found, in the online version, at doi:10.1016/j.poly.2006.12.012.

References

[1] (a) C.J. Pedersen, J. Am. Chem. Soc. 89 (1967) 7017;
(b) J.-M. Lehn, Angew. Chem., Int. Ed. Engl. 27 (1988) 89;
(c) R.M. Izatt, K. Pawlak, J.S. Bradshaw, Chem. Rev. 95 (1995) 2529;
(d) R. Bergonzi, L. Fabbrizzi, M. Lichelli, C. Mangano, Coord. Chem. Rev. 170 (1998) 31.
[2] (a) B. Dietrich, P. Viout, J.-M. Lehn, Macrocyclic Chemistry, Aspects of Organic and Inorganic Supramolecular Chemistry, VCH Weinheim, New York, 1993;
(b) H.J. Schneider, A. Yatsimirsky, Principles and Methods in Supramolecular Chemistry, Wiley, Chichester, 2000;
(c) Y.A. Zoltov, Macrocyclic Compounds in Analytical Chemistry, Wiley Interscience, New York, 1997;
(d) A. Bianchi, K. Bowman-James, E. Garcia-Espana, Supramolecular Chemistry of Anions, Wiley-VCH, Weinheim, 1997.
[3] (a) A. Bencini, A. Bianci, E. Garcia-Espana, M. Micheloni, J.A. Ramirez, Coord. Chem. Rev. 188 (1999) 97;
(b) S. Balalaie, A. Kunze, R. Gleiter, F. Rominger, S. Geis, T. Oeser, Eur. J. Org. Chem. (2003) 3378.
[4] W.P. Weber, G.W. Gokel (Eds.), Phase Transfer Catalysis in Organic Synthesis, Reactivity and Structure Concepts in Organic Chemistry, vol. 4, Springer-Verlag, New York, 1977.
[5] (a) S. Sasaki, K. Koga, J. Incl. Phenom. 7 (1989) 267;
(b) X.X. Zhang, J.S. Bradshaw, R.M. Izatt, Chem. Rev. 97 (1997) 3313.
[6] (a) M. Pietraszkiewicz, M. Kozbial, O. Pietraszkiewicz, J. Membr. Sci. 138 (1988) 109;
(b) N. Demirel, Y. Bulut, Tetrahedron: Asymmetry 14 (2003) 2633;
(c) M. Togrul, M. Askin, H. Hosgoren, Tetrahedron: Asymmetry 16 (2005) 2771.
[7] C.E. Park, Y.G. Jung, H. Hong, Tetrahedron Lett. 39 (1998) 2353.
[8] (a) Lj. Tušek-Božić, D. Sevdić, Polyhedron 4 (1985) 1959;
(b) Lj. Tušek-Božić, D. Sevdić, Polyhedron 5 (1986) 877;
(c) Lj. Tušek-Božić, J. Coord. Chem. 26 (1992) 345;
(d) Lj. Tušek-Božić, Electrochim. Acta 39 (1994) 471.
[9] (a) L. Tei, A.J. Blake, A. Bencini, B. Valtancoli, C. Wilson, M.J. Schröder, J. Chem. Soc., Dalton Trans. (2000) 4122;
(b) J.G. Mao, Z.K. Wang, A. Clearfield, Inorg. Chem. 41 (2002) 3713.
[10] (a) D.M.P. Mingos, D.R. Baghurst, Chem. Soc. Rev. 20 (1991) 1;
(b) P. Castan, B. Labiad, D. Villemin, F.L. Wimmer, S. Wimmer, J. Organomet. Chem. 479 (1994) 153;
(c) B. Desai, T.N. Danks, G. Wagner, J. Chem. Soc., Dalton Trans. (2004) 166.
[11] (a) D.R. Baghurst, S.R. Cooper, D.L. Greene, D.M.P. Mingos, S.M. Reynolds, Polyhedron 9 (1990) 893;
(b) L.S. Hegedus, M.J. Sundermann, P.K. Dorhout, Inorg. Chem. 42 (2003) 4346.
[12] Lj. Tušek-Božić, A. Višnjevac, E. Marotta, B. Kojić-Prodić, Polyhedron 24 (2005) 97.
[13] Lj. Tušek-Božić, Vibr. Spectrosc. 43 (2) (2007), in press.
[14] P.A. Tasker, J.J. Troter, J. Chem. Res. (1981) 3834.
[15] V. Jagodić, Lj. Tušek, J. Org. Chem. 37 (1972) 1222.
[16] I. Matijašić, Lj. Tušek-Božić, in: Second Croatian-Slovenian-Crystallographic Meeting, Stubičke toplice, Croatia, 1993, p. 19.
[17] P.G. Grimsley, L.F. Lindoy, H.C. Lip, J.T. Smith, J.T. Baker, Aust. J. Chem. 30 (1977) 2095.
[18] (a) Lj. Tušek, V. Jagodić, Croat. Chem. Acta 44 (1972) 445;
(b) Lj. Tušek-Božić, Vibr. Spectrosc. 28 (2002) 235.
[19] B. Jasiewicz, W. Boczon, B. Warzajtis, U. Rychlewska, J. Mol. Struct. 688 (2004) 111.
[20] S.V. Trepalin, A.V. Yarkov, A.F. Solotnov, O.A. Raevsky, Spectrochim. Acta A55 (1999) 1715.
[21] (a) N.S. Poonia, J. Am. Chem. Soc. 96 (1974) 1012;
(b) Lj. Tušek-Božić, Gazz. Chim. Ital. 120 (1990) 775;
(c) P. Dapporto, P. Paoli, I. Matijašić, Lj. Tušek-Božić, Inorg. Chim. Acta 282 (1998) 76;
(d) Lj. Tušek-Božić, R. Trojko, Thermochim. Acta 339 (1999) 41.
[22] Lj. Tušek-Božić, M. Komac, M. Ćurić, A. Lyčka, M. D'Alpaos, V. Scarcia, A. Furlani, Polyhedron 19 (2000) 937.

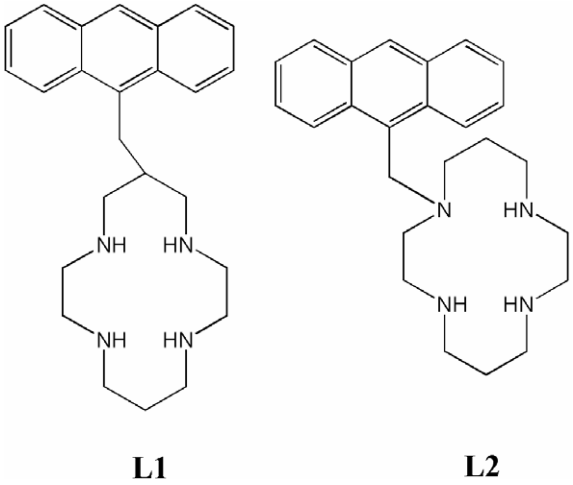


Fig. 1. Structures of the **L1** and **L2** ligands.

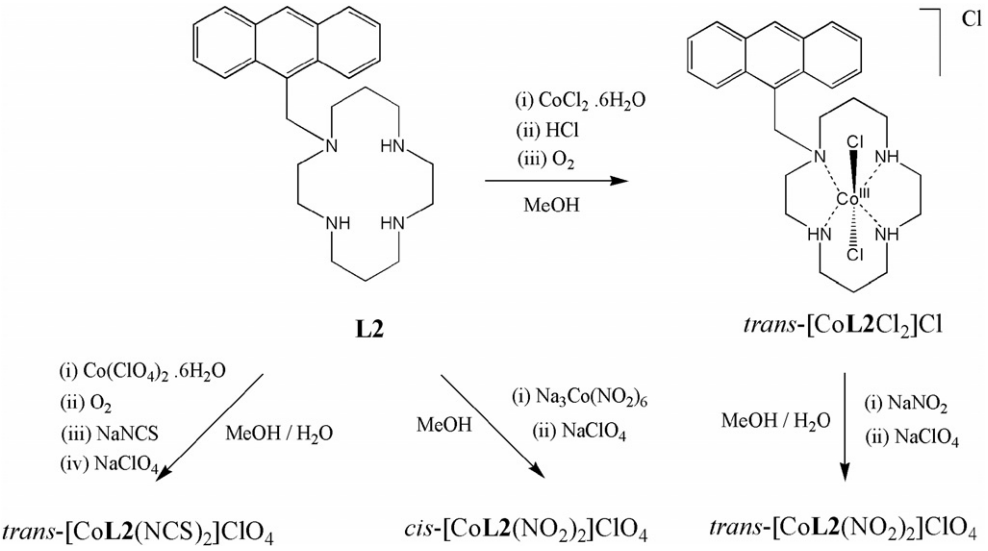
With a view to further developing these ideas, and to better understand the photochemistry of donor–acceptor complexes containing cobalt(III) as the acceptor group, we have prepared a series of cobalt(III) complexes of 1-(anthracen-9-ylmethyl)-1,4,8,11-tetraazacyclotetradecane (hereafter **L2)** in which anthracene (the donor) is appended to a nitrogen atom of the cyclam macrocycle (Fig. 1). The complexes are of the type *trans*-$[Co\mathbf{L2}X_2]^+$ in which $X = Cl^-$, NCS^-, and NO_2^-. These anionic ligands were chosen to cover a broad range of the spectrochemical series and it is these ligands that may be lost following a photo-induced process, with the cobalt atom remaining bound to the cyclam macrocycle. Investigation of complexes of **L2** will also allow comparison of the photochemical properties of these N-appended complexes with those of their C-appended analogues derived from **L1**. In this paper we describe the synthesis and structural characterisation of a series of complexes derived from **L2**. The preparation and structure of the complex *cis*-$[Co\mathbf{L2}(NO_2)_2]^+$, which contains one N-bonded and one O-bonded nitrite ligand is also described.

2. Results and discussion

2.1. Synthesis

The synthesis of **L2** was accomplished by the N-alkylation of cyclam with 9-chloromethyl-anthracene following the method described by Fabrizzi et al. [7]. The synthetic route to the series of complexes *trans*-$[Co\mathbf{L2}X_2]^+$ ($X = Cl^-$, NCS^- and NO_2^-) is summarised in Scheme 1.

The complex *trans*-$[Co\mathbf{L2}Cl_2]^+$ was prepared by the addition of cobalt(II) chloride to **L2** in methanol. Subsequent addition of hydrochloric acid and aerial oxidation led to formation of the *trans*-dichloro cobalt(III) complex which was isolated as its green chloride salt. The complex *trans*-$[Co\mathbf{L2}(NCS)_2]^+$ was prepared by first adding cobalt(II) perchlorate hexahydrate to **L2** in methanol. The resultant complex (presumably with water as the axial ligands) was oxidised to cobalt(III) in air and then an excess of sodium thiocyanate was added. The further addition of excess sodium perchlorate led to the isolation of the complex as its red/brown perchlorate salt. The complex *trans*-$[Co\mathbf{L2}(NO_2)_2]^+$ was prepared via in situ generation of *trans*-$[Co\mathbf{L2}Cl_2]^+$ followed by exchange of the chloride ions with nitrite following the addition of an excess of sodium nitrite. The complex was isolated as its orange perchlorate salt following the addition of $NaClO_4$. The complexes were characterised by elemental analysis, ^1H NMR, ESI-MS and single crystal X-ray diffraction. ESI-MS of each of the complexes discussed in this work clearly displayed M^+ as the most abundant peak with $[M-HX]^+$ and $[M-2(HX)]^+$ peaks ($X = Cl^-$, NCS^- and NO_2^-) also clearly distinguishable. The bridging methylene protons in these complexes



Scheme 1. Reaction scheme for the synthesis of the series of cations *trans*-$[Co\mathbf{L2}X_2]^+$ ($X = Cl^-$, NCS^- and NO_2^-) and the *cis*-$[Co\mathbf{L2}(NO_2)_2]^+$ cation.

were inequivalent and appeared in each case as a single AB quartet [11], within the chemical shift range δ 4.8–6.0 ppm. The presence of a single AB quartet was used to confirm the isomeric purity of the complex.

We were also motivated to explore the synthesis of *trans*-[Co**L2**$(NO_2)_2]^+$ by reaction between **L2** and $Na_3[Co(NO_2)_6]$ rather than by the method described above. In this case the macrocycle **L2** was stirred with $Na_3Co(NO_2)_6$ in a MeOH/H_2O solution for 1 h. Following work up, a red-orange solid was obtained. The ^{1}H NMR spectrum of this material was complex and different from that of *trans*-[Co**L2**$(NO_2)_2]^+$. As indicated above, peaks in the ^{1}H NMR spectrum arising from the bridging methylene protons provide a guide to the isomeric purity of complexes derived from **L2**. The presence in the ^{1}H NMR spectrum of this product of three sets of AB quartets [11] indicated that a mixture of three isomers had resulted from the reaction of **L2** with $Na_3[Co(NO_2)_6]$. The spectrum contained a set of doublets centred at δ 5.2 ppm and the isomer associated with these peaks made up about 70% of the reaction product. Subsequent dissolution of this crude product in chloroform (as the nitrite salt) and slow recrystallisation by diffusion of diethyl ether vapour permitted the isolation of the major product in pure form. ESI-MS and elemental analysis indicated the formation of [Co**L2**$(NO_2)_2]NO_2$. Crystallographic analysis of the perchlorate salt of this complex indicated formation of the *cis*-isomer. The formation of the *cis*-isomer may reflect the kinetic inertness of the cobalt centre which was in a +3 oxidation state before inclusion in the macrocycle. Complexes of the *trans*-[Co**L2**$X_2]^+$ series were formed by reaction with cobalt in its more labile +2 oxidation state, thereby allowing the complex to rearrange to its perhaps more thermodynamically favourable *trans* configuration before being locked in by aerial oxidation to Co(III).

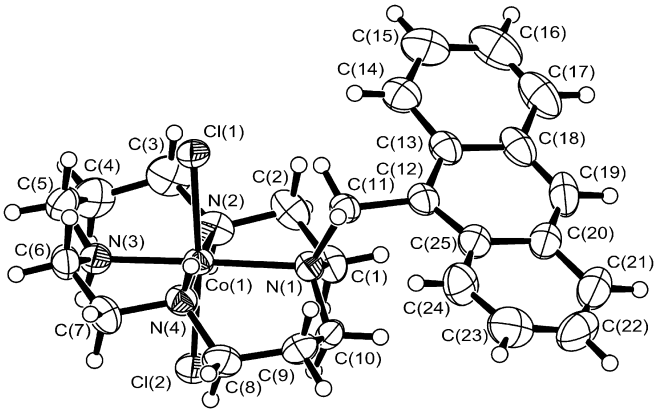


Fig. 2. Crystal structure obtained for the *trans*-[Co**L2**$Cl_2]^+$ cation. Ellipsoids are represented at the 50% probability level.

2.2. Crystal structures

According to Tobe the most thermodynamically favorable configuration of a metal cyclam complex is one where the metal adopts a "*trans(III)*" configuration i.e. two protons on adjacent amines, separated by a C_3 link, point upwards while the other two amine protons are directed downwards [12]. This arrangement is favoured due to a relief of strain in the macrocyclic ring. Accordingly it is reasonable to expect that the complexes, [Co**L2**$Cl_2]^+$, [Co**L2**$(NCS)_2]^+$ and [Co**L2**$(NO_2)_2]^+$ would adopt such a configuration.

The structure of the *trans*-[Co**L2**$Cl_2]^+$ complex is presented in Fig. 2. The metal centre adopts an octahedral geometry with the two *trans* chloro ligands Cl(1) and Cl(2) at distances of 2.25(1) and 2.27(1) Å, respectively, from the cobalt centre. The Cl(1)–Co–Cl(2) bond angle is 173.95(5)°. The macrocycle adopts Tobe's *trans*-(III) configuration. All Co–N bond lengths are typical for cobalt(III)-cyclam complexes (ca. 1.97 Å, Table 1). The N(1)–Co bond is an exception, a longer bond length of 2.123(3) Å perhaps a consequence of the relative steric bulk of the tertiary amino group [13]. All other C–N and non-aromatic C–C bond lengths are typical, as are all bond angles and torsional angles based on a staggered arrangement of the macrocycle about the metal. The relative orientations of the chromophore and macrocycle are presented in Fig. 3a and b. The dihedral angle between the mean planes of the anthracene and the four coordinating nitrogen atoms is 29.75(6)° and the metal is separated by 5.78 Å from the centroid of the anthracene moiety. A slight buckling is observed at one end of the anthracene which may be a result of steric interactions between the chromophore and cyclam ring. Apart from minor distortions associated with this buckling all other C–C bond lengths and

Table 1
Selected bond lengths (Å) and angles (°) for all structure determinations

	trans-[Co**L2**$Cl_2]^+$	*trans*-[Co**L2**$(NCS)_2]^+$	*trans*-[Co**L2**$(NO_2)_2]^+$	*cis*-[Co**L2**$(NO_2)_2]^+$
Co–N(1)	2.123(3)	2.067(5)	2.10(1)	2.115(2)
Co–N(2)	1.973(3)	1.963(5)	1.980(8)	2.011(2)
Co–N(3)	1.979(3)	1.983(5)	1.957(9)	1.978(2)
Co–N(4)	1.978(3)	1.975(5)	2.012(9)	2.007(2)
[a]Co–X(1)	2.247(1); Cl(1)	1.873(5); N(5)	1.93(1); N(5)	1.915(2); O(7)
[a]Co–X(2)	2.271(1); Cl(2)	1.897(6); N(6)	1.94(1); O(3)	1.936(2); N(5)
trans-Angles	173.95(5)–178.9(2)	176.0(2)–179.2(2)	171.5(5)–178.8(4)	173.2(1)–178.8(1)
cis-Angles	85.5(1)–93.2(1)	86.6(2)–93.6(2)	83.8(4)–96.7(5)	84.8(1)–95.2(1)

[a] X(1), X(2) = atoms indicated.

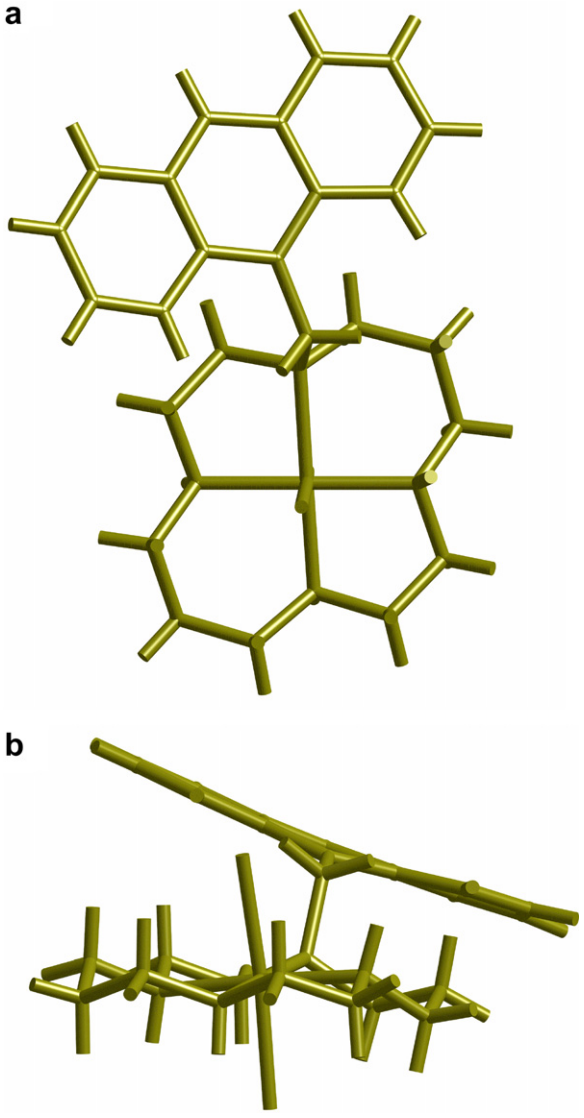


Fig. 3. A view of the *trans*-[Co**L2**Cl_2]$^+$ cation (a) normal to the approximate plane of the macrocycle, (b) parallel to the approximate plane of the macrocycle.

angles are typical for anthracene. While the solid state structure is not necessarily representative of the conformation of the complex in solution, the aforementioned steric interactions with the cyclam may significantly restrict the rotation of the chromophore about the N(1)–C(11) and C(11)–C(12) bonds.

The structure of the thiocyanato complex is presented in Fig. 4 and reveals both axial ligands to be N-bound like the arrangement in the *trans*-[Co(cyc)$(NCS)_2$]$^+$ complex in which the anthracene moiety is absent [14]. The cobalt centre is octahedral with the two nitrogen atoms of the thiocyanato ligands lying at distances of 1.873(5) and 1.897(6) Å from the metal centre (Table 1). The other Co–N bond lengths are in the typical range expected for cobalt(III)-cyclam complexes (ca. 1.97 Å, Table 1) with the exception of the Co–N(1) bond (2.067(5) Å) reflecting the relative steric bulk of the tertiary amino group [13]. A bend is observed at atom N(5) (Co–N(5)–C(26) = 162.8(5)°). As

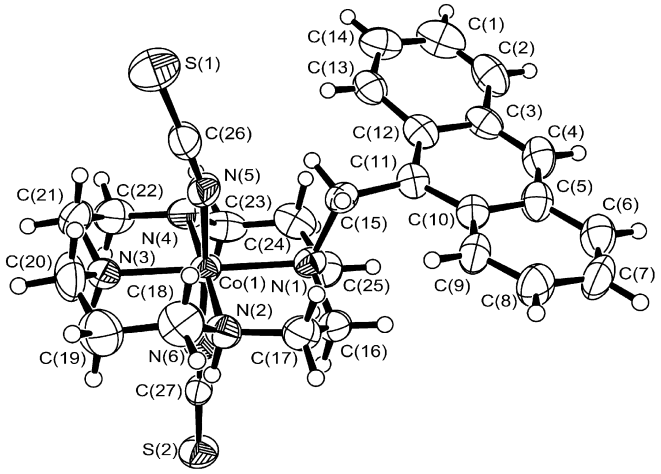


Fig. 4. Crystal structure obtained for the *trans*-[Co**L2**$(NCS)_2$]$^+$ cation. Ellipsoids represented at the 50% probability level.

with the dichloro analogue of the complex, a *trans*-(III) configuration is adopted with the appended chromophore situated well away from the macrocycle. The complex adopts a different conformation to that of the *trans*-[Co**L2**Cl_2]$^+$ complex in which the anthracene moiety is tilted towards a five-membered chelate ring formed by the metal, two amines and a 2-C link of the macrocycle (Fig. 3a). In the *trans*-[Co**L2**$(NCS)_2$]$^+$ complex, the anthracene is tilted towards a six-membered chelate ring. The dihedral angle between the mean planes of the anthracene and the four coordinating nitrogen atoms is 10.6(2)°, and there is a 5.75 Å separation between the cobalt centre and the centroid of the anthracene group. All C–C and C–N bond lengths and bond angles of the macrocycle are unexceptional. Observed torsion angles are as expected based on a staggered arrangement of the macrocycle about the metal centre. Buckling at both ends of the chromophore occurs, which is likely to be a consequence of steric interactions involving the anthracene and cyclam ring. Apart from minor distortions associated with this buckling, all anthracene C–C bond lengths and angles are normal. Like the *trans*-[Co**L2**Cl_2]$^+$ complex, the above-mentioned steric interactions with the cyclam ring are likely to restrict the rotation of the chromophore both in the plane and perpendicular to the plane of the macrocycle.

The structure of the *trans*-[Co**L2**$(NO_2)_2$]$^+$ complex is displayed in Fig. 5 and reveals, quite remarkably, that one of the nitrite ligands is O-bound and the other is N-bound. The metal adopts an octahedral geometry, with the nitro and nitrito donor atoms at distances of 1.93(1) Å and 1.94(1) Å, respectively, from the metal centre. All other Co–N bond lengths are typical for cobalt(III)-cyclam complexes (ca. 1.97 Å, Table 1), the Co–N(1) and Co–N(4) bonds slightly elongated at 2.10(1) and 2.012(9) Å, respectively. All bond lengths, bond angles and torsion angles in the macrocycle are as expected. The N-bound nitro ligand appears to be stabilised by a hydrogen bonding interaction between one of its oxygens and an amine hydrogen of the macrocycle with an O(2)···H–N(2)

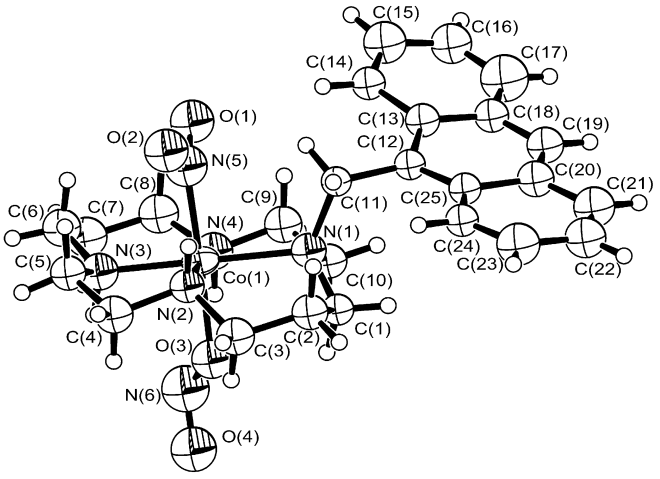


Fig. 5. Crystal structure obtained for the *trans*-[Co**L2**$(NO_2)_2$]$^+$ cation. Ellipsoids represented at the 50% probability level.

separation of 2.72(1) Å. Like the *trans*-[Co**L2**Cl_2]$^+$ complex, the anthracene is situated over a five-membered chelate ring of the macrocycle. The dihedral angle between the mean planes of the anthracene and the four coordinating nitrogen atoms is 26.9(2)° and the metal is separated by 5.73 Å from the centroid of the anthracene moiety. Like the *trans*-[Co**L2**$(NCS)_2$]$^+$ complex, a buckling is observed at both ends of the chromophore. Apart from minor distortions associated with this buckling, all C–C bond lengths and angles are as expected for anthracene.

The structure of the *cis*-[Co**L2**$(NO_2)_2$]$^+$ complex is represented in Fig. 6. The macrocycle wraps itself around the metal centre leaving the two monodentate ligands in a *cis* configuration. This is a remarkable arrangement for a cyclic quadridentate ligand and to the best of our knowledge, the first reported involving cyclam in a *cis*-arrangement about a cobalt centre with two monodentate ligands. Two diagonally opposite amine hydrogen atoms are directed downwards from the plane of the macrocycle while the chromophore and the remaining amine hydrogen are directed upwards i.e. a *cis*-*(V)* configuration according to Tobe's classification [12]. Like the analogous *trans*-[Co**L2**$(NO_2)_2$]$^+$ complex, the structure reveals both a nitro and nitrito ligand in the one complex. The coordination geometry about the cobalt centre is octahedral, the nitro and nitrito donor atoms being at distances of 1.936(2) and 1.915(2) Å, respectively, from the metal centre. All other Co–N bond lengths are slightly longer when compared with the other complexes of the series (Table 1) with the exception of the Co–N(3) bond. All C–N and non-aromatic C–C bond lengths and bond angles are typical as are all torsion angles based on a staggered arrangement of the macrocycle about the metal centre. The structure reveals the anthracene to be situated well away from the macrocycle as one may expect given the steric crowding about the cobalt. The mean plane of the chromophore forms a dihedral angle of 13.95(5)° with the plane formed by nitrogen donor atoms N(1), N(2), N(3) and N(5). The cobalt is a separated by 5.86 Å from the centroid of the anthracene group. Buckling is evident at one end of the chromophore, which is likely to be due to a steric interaction between the anthracene and cyclam ring. Like the complexes of the *trans*-[Co**L2**X_2]$^+$ series, these interactions may well restrict the rotation of the chromophore about both the N(1)–C(11) and C(11)–C(12) bonds. Apart from minor distortions associated with buckling of the chromophore, all aromatic C–C bond lengths and angles are as expected for anthracene.

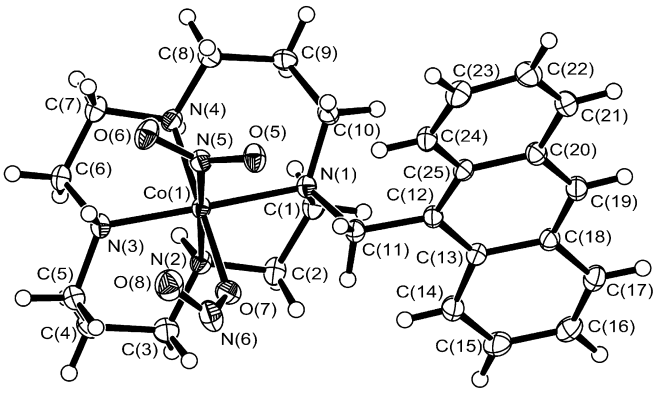


Fig. 6. Solid state structure of the *cis*-[Co**L2**$(NO_2)_2$]$^+$ cation. Thermal ellipsoids represented at the 50% probability level.

3. Conclusion

In this work we have demonstrated the coordinating ability of the ligand **L2** by preparing a series of cobalt(III) complexes of the form [Co**L2**X_2]$^+$. In the 'simple' complex *trans*-[Co(cyc)$(NO_2)_2$]$^+$ both nitro ligands are N-bound [15], so we were somewhat surprised to observe linkage isomerism in the solid state for both the *cis*- and *trans*-isomers of [Co**L2**$(NO_2)_2$]$^+$. There are several examples of mononuclear complexes containing both a nitro and nitrito ligand in the one molecule for complexes of Ni(II) [16–19], Fe(III) [20], Ru(III) [21] and Cu(II) [22], although to our knowledge the complexes *cis*-[Co**L2**$(NO_2)_2$]$^+$ and *trans*-[Co**L2**$(NO_2)_2$]$^+$ are the first examples reported for cobalt(III). The formation of the *cis*- rather than the *trans*-isomer of [Co**L2**$(NO_2)_2$]$^+$ appears to be determined by the oxidation state of the cobalt salt used in the synthesis, with the kinetically inert cobalt(III) favouring the formation of the *cis*-isomer. The photochemistry of these cobalt(III) complexes will be reported in more detail elsewhere [23], however it is worth noting here that the two isomers display marked differences in ground state and excited state behaviour. The *trans*-isomer of [Co**L2**$(NO_2)_2$]$^+$ is labile to ligand exchange in the ground state while, in contrast, the *cis*-isomer is ground state inert but undergoes ligand exchange reactions upon photoexcitation making it a potentially useful photoactivated ligand release system.

4. Experimental

4.1. Instrumentation

ESI-MS experiments were performed using an ion trap (Finnigan Mat) LC-Q spectrometer on dilute solutions of the complexes in methanol. ^{1}H NMR spectra were measured in *d*-chloroform, d_3-acetonitrile and d_4-methanol on a Unity Plus 400 spectrometer. Chemical shifts (δ, positive downfield) are given in ppm (solvent reference) and *J* values in Hz. Aromatic hydrogens are labelled according to IUPAC conventions for anthracene (see supplementary information). Absorption spectra were collected using a Varian Cary 50 Bio ultraviolet–visible spectrophotometer in methanol at 1.0 mM. Elemental analyses were performed by the Microanalytical Laboratory, Department of Chemistry, University of Otago, Dunedin, New Zealand.

4.2. Synthesis

Caution: perchlorate salts of metal complexes with organic ligands are potentially explosive. No problems were encountered with the complexes described below, however, as a precaution, perchlorate salts should never be heated as solids or be handled with metal spatulas.

Reactions were performed in air using as received solvents and AR reagents. Cyclam [24] and 9-chloromethyl-anthracene [25] were prepared by published procedures. 1-(Anthracen-9-ylmethyl)-1,4,8,11-tetraazacyclotetradecane (**L2)** was prepared by the method described by Fabrizzi et al. [7].

4.3. trans-[CoL2Cl$_2$]Cl trans-[1-(anthracen-9-ylmethyl)-1,4,8,11-tetraazacyclotetradecane] dichloro cobalt(III) chloride

A solution of cobalt(II) chloride hexahydrate (0.12 g, 0.52 mmol) in MeOH (15 mL) was added to a solution of **L2** (0.20 g, 0.52 mmol) in MeOH (15 mL). Conc. HCl (1 mL) was added immediately to the brown solution and the mixture was refluxed for 5 min. The solvent and acid were then removed by passage of a stream of air across the mixture. The residue was then stirred with MeOH (15 mL) to yield a green solution and some insoluble material. The mixture was filtered and the filtrate concentrated to 2 mL whereupon a green solid formed. This was collected and recrystallised by infusion of diethyl ether vapour into a concentrated solution of the complex in MeOH to yield small olive green crystals (0.12 g, 0.22 mmol, 42%), m.p. 227–230 °C, ESI-MS data: M^+ *m/z* 519, 521. *Anal.* Calc. for $C_{25}H_{34}N_4Cl_3Co$: C, 54.02; H, 6.17; N, 10.08, Cl, 19.13. Found: C, 53.84; H, 6.29; N, 9.78; Cl, 19.11%. Visible λ_{max}: 618 nm, ε_{max}: 48 L mol^{-1} cm^{-1}. ^{1}H NMR (400 MHz, $CDCl_3$): δ 8.68 (d, *J* 8.8, 1H, Ar-8); 8.61 (br, 1H, Ar-1); 8.53 (s, 1H, Ar-10); 8.35 (br, 1H, NH); 8.04 (d, *J* 8.3, 2H, Ar-4,5); 7.44–7.63 (m, 4H, Ar-2,3,6,7); 5.96 (br, 1H, NH); 5.93 (d, *J* 15.6, 1H, Ar-CH_2-); 5.62 (d, *J* 15.6, 1H, Ar-CH_2-); 4.0–1.0 (many complex multiplets, ~20H, cyclam -CH_2-).

4.4. trans-[CoL2(NCS)$_2$]ClO$_4$ · CH$_3$CN trans-[1-(anthracen-9-ylmethyl)-1,4,8,11-tetraazacyclotetradecane] bis(thiocyanato-N) cobalt(III) perchlorate-CH$_3$CN

A solution of cobalt(II) perchlorate hexahydrate (0.19 g, 0.52 mmol) in MeOH (15 mL) was added to a solution of **L2** (0.20 g, 0.52 mmol) in MeOH (15 mL). Air was bubbled through the brown solution for 4 h and NaNCS (0.13 g, 1.6 mmol) in MeOH (10 mL) was added. The intensely coloured red-brown solution was refluxed for 1 h, then cooled and sodium perchlorate (0.36 g, 2.6 mmol) in H_2O (2 mL) added. The solution was filtered and slowly concentrated to 2 mL by passing a gentle stream of air across the solution whereupon a red-brown solid formed. The solid was collected and recrystallised by the infusion of diethyl ether vapour into a concentrated solution of the complex in acetonitrile yielding intensely coloured red/brown plates (75 mg, 0.11 mmol, 22%), m.p. 205–207 °C, ESI-MS data: M^+*m/z* 565. *Anal.* Calc. for $C_{27}H_{34}N_6O_4S_2ClCo \cdot CH_3CN$: C, 49.33; H, 5.28; N, 13.88; S, 9.08. Found: C, 49.66; H, 5.33; N, 14.19; S, 9.13%. ^{1}H NMR (400 MHz, CD_3CN): δ 8.68 (s, 1H, Ar-10); 8.30 (br, 2H, Ar-1,8); 8.13 (d, *J* 8.4, 2H, Ar-4,5); 7.54–7.63 (m, 4H, Ar-2,3,6,7); 6.37 (br, 1H, NH); 5.60 (br, 1H, NH); 5.23 (br, 1H, NH); 5.11 (d, *J* 15.6, 1H, Ar-CH_2-); 4.89 (d, *J* 15.6, 1H, Ar-CH_2-); 3.8–1.0 (many complex multiplets, ~20H, cyclam -CH_2-).

4.5. trans-[CoL2(NO$_2$)$_2$]ClO$_4$ trans-[1-(anthracen-9-ylmethyl)-1,4,8,11-tetraazacyclotetradecane] (nitrite-N) (nitrito-O) cobalt(III) perchlorate

A solution of cobalt(II) chloride hexahydrate (0.12 g, 0.52 mmol) in MeOH (15 mL) was added to a solution of **L2** (0.20 g, 0.52 mmol) in MeOH (15 mL). Conc. HCl (1 mL) was added immediately to the brown solution and the mixture was refluxed for 5 min. The solvent and acid were then removed by passage of a stream of air across the mixture. The residue was then stirred with MeOH (15 mL) to yield a green solution and some insoluble material. The mixture was filtered and to the filtrate was added $NaNO_2$ (0.11 g, 1.6 mmol) in H_2O (2 mL). The resulting orange/red solution was heated at reflux for 1 h, then cooled and sodium perchlorate (0.36 g, 2.6 mmol) in H_2O (2 mL) was added. The solution was filtered and slowly concentrated to 2 mL by passing a stream of air across the solution whereupon an orange solid formed. This was collected and recrystallised by infusion of diethyl ether vapour into a concentrated solution of the complex in acetonitrile to yield an orange microcrystalline solid (0.11 g, 0.18 mmol, 35%), m.p. 125 °C (dec.), ESI-MS data: M^+ *m/z* 541. *Anal.* Calc. for $C_{25}H_{34}N_6O_8ClCo$: C, 46.85; H, 5.35; N, 13.11; Cl, 5.53. Found: C, 46.85; H, 5.50; N, 13.00; Cl, 5.23%.

^{1}H NMR (400 MHz, CD_3CN): δ 8.68 (s, 1H, Ar-10); 8.21 (br, 2H, Ar-1,8); 8.12 (d, J 8.4, 2H, Ar-4,5); 7.53–7.63 (m, 4H, Ar-2,3,6,7); 6.43 (br, 1H, NH); 5.29 (br, 1H, NH); 5.07 (d, J 15.1, 1H, Ar-CH_2-); 4.88 (d, J 15.1, 1H, Ar-CH_2-); 4.77 (br, 1H, NH); 4.0–1.0 (many complex multiplets, ~20H, cyclam -CH_2-).

4.6. *cis-[CoL2(NO$_2$)$_2$]NO$_2$ cis-[1-(anthracen-9-ylmethyl)-1,4,8,11-tetraazacyclotetradecane] (nitrite-N)-(nitrito-O)-cobalt(III) nitrite*

A solution of trisodium hexanitrocobaltate(III) (0.33 g, 0.57 mmol) in 80:20 MeOH:H_2O (ca. 15 mL) was added to a solution of **L2** (0.20 g, 0.52 mmol) in MeOH (ca. 15 mL) and the pale brown suspension which resulted was stirred at room temperature for 1 h. The resulting blood red solution was filtered and the filtrate taken to dryness under a stream of N_2. The residue was then stirred with chloroform (ca. 15 mL) to yield a red solution and some orange insoluble material (ca. 50 mg). The solid was removed by filtration and the filtrate stirred with the slow addition of diethyl ether (ca. 100 mL) whereupon a red solid formed. This was collected and recrystallised by infusion of diethyl ether vapour into a concentrated solution of the complex in chloroform yielding irregularly-shaped ruby red crystals (54 mg, 0.092 mmol, 18%), m.p. 175 °C (dec.), ESI-MS data: M^+ m/z 541. *Anal*. Calc. for $C_{25}H_{34}N_7O_6Co$: C, 51.11; H, 5.83; N, 16.69. Found: C, 51.28; H, 5.81; N, 16.61%. ^{1}H NMR (400 MHz, $CDCl_3$): δ 8.98 (d, J 9.0, 1 H, Ar-8); 8.46 (s, 1H, Ar-10); 7.93 (m, 3H, Ar-1,4,5); 7.65 (br, 1H, NH); 7.35–7.55 (m, 4H, Ar-2,3,6,7); 7.22 (br, 1H, NH); 6.54 (br, 1H, NH); 5.31 (d, J 15.4, 1H, Ar-CH_2-); 5.13 (d, J 15.4, 1H, Ar-CH_2-); 3.6–1.0 (many complex multiplets, ~20H, cyclam -CH_2-). The ^{1}H NMR spectrum was recorded with the addition of two drops of d_6-DMSO to the $CDCl_3$ solution to aid dissolution of the compound.

4.7. Crystallography

The following is a short summary of the details of the crystal used in each of the structure determinations including the methods employed in their structure determinations. Details of data collection and refinement are summarised in Table 2. Full details, including all bond lengths, angles and atomic coordinates are recorded in cif files on the CCDC database. Structures were refined using a full matrix least squares procedure based on F^2 with all data being used in the refinement. All structures were solved and refined using SHELX-97 [26].

4.8. *trans-[CoL2Cl$_2$]Cl*

Crystals suitable for X-ray crystallography were grown by slow evaporation from a dilute solution of the complex in methanol to produce green rectangular prisms. Data were collected from a single crystal of approximate dimensions $0.27 \times 0.17 \times 0.14$ mm on an Enraf-Nonius CAD4 single crystal X-ray diffractometer using the ω:2θ scan technique.

Table 2
Crystallographic and data collection parameters for all structure determinations

	trans-[Co**L2**Cl$_2$]$^+$	*trans*-[Co**L2**(NCS)$_2$]$^+$	*trans*-[Co**L2**(NO$_2$)$_2$]$^+$	*cis*-[Co**L2**(NO$_2$)$_2$]$^+$
Anion	Cl	[a]ClO_4	ClO_4	ClO_4
Chemical formula	$C_{25}H_{34}Cl_3CoN_4$	$C_{29}H_{37}ClCoN_7O_4S_2$	$C_{25}H_{34}ClCoN_6O_8$	$C_{25}H_{34}ClCoN_6O_8$
Formula weight	555.84	706.16	640.96	640.96
Crystal system	orthorhombic	monoclinic	orthorhombic	orthorhombic
Space group	*Pbca* (no. 61)	$P2_1/c$ (no. 14)	*Pbca* (no. 61)	$Pna2_1$ (no. 33)
a (Å)	9.824(2)	13.227(1)	9.845(3)	14.0908(7)
b (Å)	18.692(4)	11.042(1)	19.230(5)	21.765(1)
c (Å)	27.006(2)	22.369(2)	29.328(8)	8.7994(4)
α (°)	90	90	90	90
β (°)	90	93.555(7)	90	90
γ (°)	90	90	90	90
Volume (Å^3)	4959.2(14)	3260.8(5)	5553(3)	2698.6(2)
Z	8	4	8	4
Temperature (K)	293(2)	293(2)	293(2)	130(2)
λ, D(Mo Kα) (Å)	0.71073	0.71073	0.71073	0.71073
ρ(calc.) (g cm^{-3})	1.489	1.438	1.533	1.578
F(000)	2320	1472	2672	1336
μ (cm^{-1})	1.037	0.782	0.774	0.797
Crystal size (mm)	$0.27 \times 0.17 \times 0.14$	$0.46 \times 0.19 \times 0.04$	$0.25 \times 0.12 \times 0.10$	$0.17 \times 0.17 \times 0.45$
Reflections measured $I > 2\sigma(I)$	4551	6660	21983	16501
Incident reflections [R_{int}]	4351 [0.0194]	5774 [0.0607]	3638 [0.3152]	6067 [0.0195]
wR_2 (all data)	0.1015	0.1462	0.1723	0.0808
$R_1(I > 2\sigma(I))$	0.0462	0.0723	0.0758	0.0317
Completeness of data to 2θ (°)	1.000 to 50	0.998 to 50	1.000 to 45	0.994 to 55

[a] Includes one CH_3CN solvent molecule.

4.9. trans-[CoL2(NCS)$_2$]ClO$_4$ · CH$_3$CN

Crystals suitable for X-ray crystallography were grown by slow evaporation from a dilute solution of the complex in an acetonitrile/water mix to produce dark red/brown rectangular plates. Data were collected from a single crystal of approximate dimensions $0.46 \times 0.19 \times 0.04$ mm on an Enraf-Nonius CAD4 single crystal X-ray diffractometer using the ω:2θ scan technique.

4.10. trans-[CoL2(NO$_2$)$_2$]ClO$_4$

Crystals suitable for X-ray crystallography were grown by H_2O diffusion into a concentrated solution of the complex in acetonitrile to produce irregularly shaped orange/red crystals. Data were collected from a crystal of approximate dimensions $0.25 \times 0.12 \times 0.10$ mm on a Bruker CCD area detector, single crystal X-ray diffractometer. Inspection of the diffraction pattern revealed that the crystal was in fact a multiple crystal. A number of crystals were investigated but all showed significant twinning. Using the program RLATT [27] it was possible to identify reflections belonging to a single crystal. These reflections were indexed in order to obtain a unit cell and an orientation matrix. Since this crystal represented only a small portion of the multiple crystal, the data are very weak and there are very few reflections at high angles. Given the paucity of data only the cobalt and chlorine atoms were refined anisotropically. Despite the difficulties associated with the crystal, the non-hydrogen atoms are clearly defined and the connectivity is beyond doubt.

4.11. cis-[CoL2(NO$_2$)$_2$]ClO$_4$

Crystals suitable for X-ray crystallography were grown from a solution of the perchlorate salt of *cis*-[CoL2(NO$_2$)$_2$]NO$_2$. This was prepared by dissolving *cis*-[CoL2(NO$_2$)$_2$]NO$_2$ (ca. 10 mg) in methanol (ca. 2 mL) and adding $NaClO_4$ (ca. 5 equiv.) in water (0.5 mL) producing an immediate red precipitate. Crystals suitable for X-ray crystallography were grown by diethyl ether diffusion into a dilute solution of the complex in acetonitrile to produce rod-shaped ruby red crystals. Data were collected from a crystal of approximate dimensions $0.17 \times 0.17 \times 0.45$ mm on a Bruker CCD area detector single crystal X-ray diffractometer. The crystal was covered in oil and placed in a stream of cooled nitrogen during the data collection.

Acknowledgement

We thank the Australian Research Council for financial support of this work.

Appendix A. Supplementary material

CCDC 617814, 617813, 617816 and 617815 contain the supplementary crystallographic data for *trans*-[Co**L2**Cl$_2$]$^+$, *trans*-[Co**L2**(NCS)$_2$]$^+$, *trans*-[Co**L2**(NO$_2$)$_2$]$^+$ and *cis*-[Co**L2**(NO$_2$)$_2$]$^+$. These data can be obtained free of charge via http://www.ccdc.cam.ac.uk/conts/retrieving.html, or from the Cambridge Crystallographic Data Centre, 12 Union Road, Cambridge CB2 1EZ, UK; fax: (+44) 1223-336-033; or e-mail: deposit@ccdc.cam.ac.uk. Supplementary data associated with this article can be found, in the online version, at doi:10.1016/j.poly.2006.12.003.

References

[1] M. Engeser, L. Fabbrizzi, M. Licchelli, D. Sacchi, Chem. Commun. (1999) 1191.
[2] R. Bergonzi, L. Fabbrizzi, M. Licchelli, C. Mangano, Coord. Chem. Rev. 170 (1998) 31.
[3] V. Amendola, L. Fabbrizzi, M. Licchelli, C. Mangano, P. Pallavicini, L. Parodi, A. Poggi, Coord. Chem. Rev. 190–192 (1999) 649.
[4] G. De Santis, L. Fabbrizzi, M. Licchelli, N. Sardone, A.H. Velders, Chem. Eur. J. 2 (1996) 1243.
[5] L. Fabbrizzi, M. Licchelli, P. Pallavicini, A. Perotti, D. Sacchi, Angew. Chem. 106 (1994) 2051.
[6] L. Fabbrizzi, M. Licchelli, P. Pallavicini, D. Sacchi, A. Taglietti, Analyst 121 (1996) 1763.
[7] L. Fabbrizzi, M. Licchelli, P. Pallavicini, A. Perotti, A. Taglietti, D. Sacchi, Chem. Eur. J. 2 (1996) 75.
[8] F. DeRosa, X. Bu, K. Pohaku, P.C. Ford, Inorg. Chem. 44 (2005) 4166.
[9] F. DeRosa, X. Bu, P.C. Ford, Inorg. Chem. 44 (2005) 4157.
[10] A.M. Funston, K.P. Ghiggino, M.J. Grannas, W.D. McFadyen, P.A. Tregloan, J. Chem. Soc., Dalton Trans. (2003) 3704.
[11] Assigned as an AX or AB system according to the designation by Silverstein in which $\Delta v/J > 10 = AX$, $\Delta v/J < 10 = AB$; R.M. Silverstein, G.C. Bassler, T.C. Morrill, in: Spectrometric Identification of Organic Compounds, 4th ed., Wiley, 1981, p. 191.
[12] B. Bosnich, C.K. Poon, M.L. Tobe, Inorg. Chem. 4 (1965) 1102.
[13] K.P. Ghiggino, M.J. Grannas, M.S. Koay, A.W.A. Mariotti, W.D. McFadyen, P.A. Tregloan, Aust. J. Chem. 54 (2001) 101.
[14] J. Burgess, J. Fawcett, R.I. Haines, K. Singh, D.R. Russell, Transition Met. Chem. 24 (1999) 355.
[15] S. Ohba, N. Yamada, M. Eishima, Acta Crystallogr., Sect. E: Struct. Rep. Online E57 (2001) m12.
[16] R. Cortes, M.I. Arriortua, T. Rojo, X. Solans, D. Beltran, Polyhedron 5 (1986) 1987.
[17] M.G.B. Drew, S. Hollis, Acta Crystallogr., Sect. B: Struct. Sci. B36 (1980) 1944.
[18] R. Wen, F. Somoza, I. Bernal, F.R. Fronczek, J. Coord. Chem. 48 (1999) 443.
[19] R. Wen, I. Bernal, F. Somoza, W. Li, F.R. Fronczek, Inorg. Chim. Acta 282 (1998) 96.
[20] C. Hauser, T. Glaser, E. Bill, T. Weyhermueller, K. Wieghardt, J. Am. Chem. Soc. 122 (2000) 4352.
[21] D.A. Freedman, D.E. Janzen, J.L. Vreeland, H.M. Tully, K.R. Mann, Inorg. Chem. 41 (2002) 3820.
[22] A. Pajunen, S. Pajunen, Z. Kristallogr. – New Cryst. Struct. 213 (1998) 591.
[23] S. Boyd, K.P. Ghiggino, W.D. McFadyen, in preparation.
[24] E.K. Barefield, F. Wagner, A.W. Herlinger, A.R. Dahl, Inorg. Synth. 16 (1976) 220.
[25] F.H.C. Stewart, Aust. J. Chem. 13 (1960) 478.
[26] G.M. Sheldrick, SHELXL-97, Program for X-ray Crystal Structure Refinement, University of Gottingen, Gottingen, Germany, 1997.
[27] RLATT (reciprocal lattice display program), Bruker Analytical X-ray Instruments Inc., Madison, WI, USA 1998.

as supplied. All the chemicals used were of AR grade. Solvents used in this study were purified following the standard procedures.

2.2. Analysis

Elemental analyses (C, H, N) were performed on a model 2400 Perkin–Elmer elemental analyzer. The vanadium content of each of the complexes was determined volumetrically [13] using decinormal $KMnO_4$ solution as an oxidizing agent in the presence of sulfurous acid. A 100 mg sample of the compound was placed in a silica crucible, decomposed by gentle heating and then adding 1–2 ml of concentrated HNO_3, 2–3 times. An orangish mass (V_2O_5) was obtained after decomposition and complete drying. It was dissolved in the minimum amount of dilute H_2SO_4, and the solution so obtained was diluted with distilled water to 100 ml in a measuring flask. The amount of vanadium in the sample solution was calculated using the standard [13] relationship given below.

One milliliter of 0.1 N $KMnO_4 = 0.005094$ g vanadium.

2.3. Physical measurements

Infrared (IR) spectra were recorded on a Nicolett-400D spectrometer as KBr pellets. NMR spectra were recorded on a model DPX 200 Bruker FT NMR instrument. The electronic spectra were recorded on a model UV160A Shimadzu spectrophotometer. Specific conductivity of the complexes was measured on a model 305 Systronic conductivity bridge. Magnetic moments were measured on a model 7304 Lake Shore Cryotronics vibrating sample magnetometer.

2.4. Synthesis of ligands

The synthesis of ligand is summarized in Scheme 1. However detail procedure is given in the following pages.

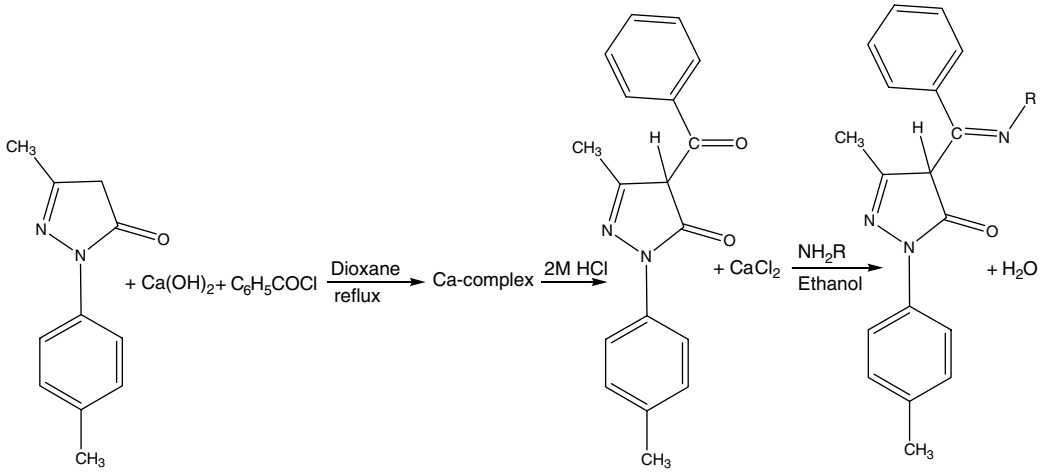
2.4.1. Preparation of 4-benzoyl-3-methyl-1-(4′-methylphenyl)-2-pyrazolin-5-one

3-Methyl-1-(4′-methylphenyl)-2-pyrazolin-5-one (20.1 g, 0.1 mol) was dissolved in hot dioxane (80 cm^3) in a flask equipped with a stirrer, separating funnel and reflux condenser. Calcium hydroxide (14.81 g, 0.2 mol) was added to this solution, followed by benzoyl chloride (18.01 g, 0.1 mol) added dropwise with precaution, as this reaction was exothermic. During this addition the whole mass was converted into a thick paste. After the complete addition, the reaction mixture was refluxed for half an hour and then it was poured into dilute hydrochloric acid (200 cm^3, 2 M). The coloured crystals thus obtained were separated by filtration and recrystallized from an acidified methanol-water mixture ($HCl:MeOH:H_2O = 1:80:19$). Yield 67%. *Anal.* Calc. for $C_{18}H_{15}N_2O_2$: C, 74.21; H, 5.19; N, 9.63. Found: C, 73.43; H, 5.01; N, 9.97%.

2.4.2. General method for the preparation of the ligands

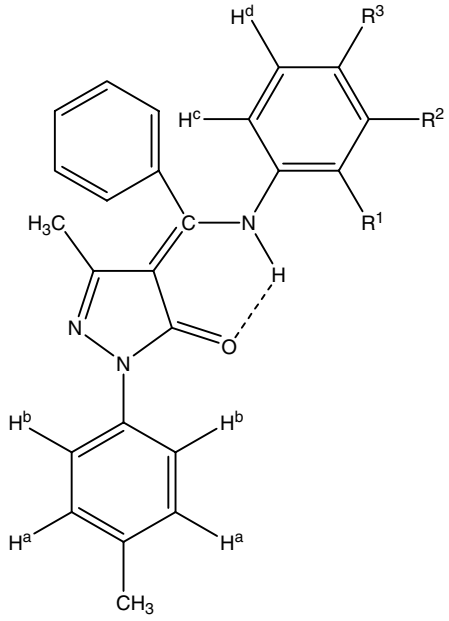
5-methyl-4-(phenyl-phenylamino-methylene)-2-*p*-tolyl-2,4-dihydro-pyrazol-3-one (HL^1)
5-methyl-4-(phenyl-*o*-tolylamino-methylene)-2-*p*-tolyl-2,4-dihydro-pyrazol-3-one (HL^2)
5-methyl-4-(phenyl-*m*-tolylamino-methylene)-2-*p*-tolyl-2,4-dihydro-pyrazol-3-one (HL^3)
5-methyl-4-(phenyl-*p*-tolylamino-methylene)-2-*p*-tolyl-2,4-dihydro-pyrazol-3-one (HL^4)
5-methyl-4-[(2-chloro-pheynylamino)-phenyl-methylene]-2-*p*-tolyl-2,4-dihydro-pyrazol-3-one (HL^5)
5-methyl-4-[(3-chloro-pheynylamino)-phenyl-methylene]-2-*p*-tolyl-2,4-dihydro-pyrazol-3-one (HL^6)
5-methyl-4-[(4-chloro-pheynylamino)-phenyl-methylene]-2-*p*-tolyl-2,4-dihydro-pyrazol-3-one (HL^7)

The compound 4-benzoyl-3-methyl-1-(4′-methylphenyl)-2-pyrazolin-5-one (2.91 g, 0.01 mol) was dissolved in ethanol (20 cm^3) and the appropriate amine (0.01 mol, aniline for HL^1, *ortho*-, *meta*- and *para*-toludine for HL^2–HL^4, respectively, and *ortho*-, *meta*- and *para*-chloroaniline for



Scheme 1.

HL^5–HL^7, respectively) was added to this solution. The reaction mixture was refluxed for 2 h. During the reflux a microcrystalline compound was separated, which was isolated by filtration, washed with ethanol and dried in air. Suitable crystals for single crystal X-ray study were grown from acetonitrile (Fig. 1).



HL^1: $R^1 = H^c$, $R^2 = H^d$, $R^3 = H$

HL^2: $R^1 = CH_3$, $R^2 = H$, $R^3 = H$ HL^5: $R^1 = Cl$, $R^2 = H$, $R^3 = H$

HL^3: $R^1 = H$, $R^2 = CH_3$, $R^3 = H$ HL^6: $R^1 = H$, $R^2 = Cl$, $R^3 = H$

HL^4: $R^1 = H^c$, $R^2 = H^d$, $R^3 = CH_3$ HL^7: $R^1 = H^c$, $R^2 = H^d$, $R^3 = Cl$

Fig. 1. Structural drawing of the ligands with the labeling of the protons.

2.4.3. General method for the preparation of the OV(IV) complexes $[OV(L)_2(H_2O)]$ ($L = L^1$, L^2, L^3, L^4, L^5, L^6 and L^7)

The appropriate ligand (0.01 mol) dissolved in hot DMF (20 cm^3) was added dropwise into an aqueous solution (20 cm^3) of Vanadyl sulfate pentahydrate (0.01 mol, 2.53 g) with stirring. After the complete addition, 2.0 g of sodium acetate was added to the solution and the reaction mixture was refluxed for 2 h. The solution thus obtained was concentrated to half of its original volume by evaporation using a hot plate and allowed to cool to room temperature. During this period, a light greenish microcrystalline solid was separated, which was isolated by filtration, washed with hot water followed by ethanol and dried in air. Yield 50–60%.

2.4.4. X-ray crystallography data collection and processing

Crystallographic data for five of the ligands are summarized in Table 1. The data collections were carried out on a Bruker Mart Apex CCD diffractometer using graphite monochromated Mo Kα ($\lambda = 71\,073$ Å) radiation at 293 K. An absorption correction based on SADABS [14] was also applied. The structures were solved by direct methods (SHELXTL) and refined by least squares methods with atomic anisotropic thermal parameters for all non-hydrogen atoms [15,16]. All hydrogen atoms were either generated geometrically or obtained from the Fourier difference map, and were assigned fixed isotropic thermal parameters in the structure factor calculations. Conformational and H-bonding analysis was performed using PLATON [17].

Table 1
Summary of crystallographic data for the ligands HL^1–HL^5

Compound	HL^1	HL^2	HL^3	HL^4	HL^5
Chemical formula	$C_{24}H_{21}N_3O$	$C_{25}H_{23}N_3O$	$C_{25}H_{23}N_3O$	$C_{25}H_{23}N_3O$	$C_{24}H_{20}ClN_3O$
Formula weight	367.44	381.46	381.46	381.46	401.88
Unit cell dimensions					
a (Å)	10.2619(11)	7.3195(7)	10.179(2)	10.2544(15)	11.425(5)
b (Å)	18.3214(19)	11.1866(11)	19.383(4)	10.5897(15)	11.503(5)
c (Å)	10.5837(11)	13.3163(13)	10.407(2)	11.0504(16)	15.813(8)
α (°)	90.00	103.949(2)	90.00	115.722(3)	90.00
β (°)	99.689(2)	93.793(2)	95.502(4)	101.623(3)	94.854(8)
γ (°)	90.00	92.773(2)	90.00	99.225(3)	90.00
Z	4	2	4	2	4
V (Å^3)	1961.48	1053.54	2043.84	1016.31	2070.72
Crystal system	monoclinic	triclinic	monoclinic	triclinic	monoclinic
Space group	$P21/n$	$P\bar{1}$	$P21/n$	$P\bar{1}$	$P21/c$
Radiation used λ (Å)	0.71073	0.71073	0.71073	0.71073	0.71073
$\rho_{calc.}$ (g cm^{-3})	1.244	1.202	1.240	1.247	1.289
Absolute coefficient, μ (cm^{-1})	0.078	0.075	0.077	0.077	0.204
$F(000)$	776	404	808	404	840
Temperature (°C)	23	23	23	23	23
No. of parameters refined	259	270	269	269	268
Final R	0.0479	0.0471	0.0665	0.0570	0.0721
$wR(F_2)$	0.12970	0.1395	0.1755	0.1296	0.1782
Goodness-of-fit	1.032	1.072	1.024	0.976	1.005

3. Results and discussion

3.1. Characterization of the ligands

All seven ligands, HL^1–HL^7, gave satisfactory elemental analysis (Table 2). The molecular structures of these ligands are such that they can exist in three tautomeric forms as shown in Fig. 2. Detailed solution and solid-state studies of these ligands were carried out to establish their geometry. The IR spectra of these ligands exhibit two characteristic bands in the ranges 3220–3245 and 1610–1630 cm^{-1}, which can either be assigned to $\nu_{(O-H)}$ and $\nu_{(C=N)}$ respectively for the tautomeric imine-ol form (Fig. 2, II) or $\nu_{(N-H)}$ and $\nu_{(C=O)}$ respectively for the amine-one form (Fig. 2, III) of the ligand. We assigned these two peaks to $\nu_{(N-H)}$ and $\nu_{(C=O)}$, respectively for the later form based on the information obtained from crystallographic studies (discussed later).

The ^1H NMR spectra of all the ligands were recorded in $CDCl_3$ at room temperature and the data are presented in Table 3. The signals due to methyl protons appeared as singlets in the range δ 1.56–2.42 ppm. In some cases signals of CH_3 groups are overlapped and all of these signals are so closely spaced that it is difficult to assign each signal to a particular methyl group unambiguously [18]. Moreover, such assignment will not contribute to establish the geometry of the ligands, therefore, no attempt has been made for such assignment. In the aromatic region, a few doublets and in few cases some overlapping doublets/multiplets are observed in the range δ 6.49–7.92 ppm. These doublets/multiplets are due to aryl protons of three benzene rings. Another singlet corresponding to one proton for all compounds is observed in the range δ 12.83–12.99. This signal disappeared when a D_2O exchange experiment was carried out. It can be assigned either to OH or NH, in either case it is strongly deshielded because of hydrogen bonding with the other atom (N/O). It may be noted that the integration of this signal perfectly matches with one proton and there is no other fragment(s) of this signal, which suggests that only one tautomeric form of the ligands exist in solution under the experimental conditions. We have not done any temperature dependent experiments. Comparing with the solid state study, we prefer to assign this signal to NH, however, assignment of this peak to OH cannot be ruled out provided solid state structural evidence is not considered [18].

Table 2
Melting point, elemental analysis (C, H and N)[a] and yield of the ligands

Ligand	Melting point (°C)	% C	% H	% N	Yield (%)
HL^1	154	78.89 (78.44)	5.63 (5.76)	11.01 (11.44)	67
HL^2	165	77.99 (78.70)	6.01 (6.07)	11.10 (11.02)	69
HL^3	173	77.93 (78.70)	6.87 (6.07)	11.35 (11.02)	68
HL^4	184	78.61 (78.70)	6.38 (6.07)	11.37 (11.02)	68
HL^5	144	81.02 (80.10)	5.45 (5.60)	11.51 (11.68)	65
HL^6	153	79.66 (80.10)	5.31 (5.60)	11.44 (11.68)	64
HL^7	161	80.03 (80.10)	5.87 (5.60)	11.74 (11.68)	65

[a] Calculated values are given in the parentheses.

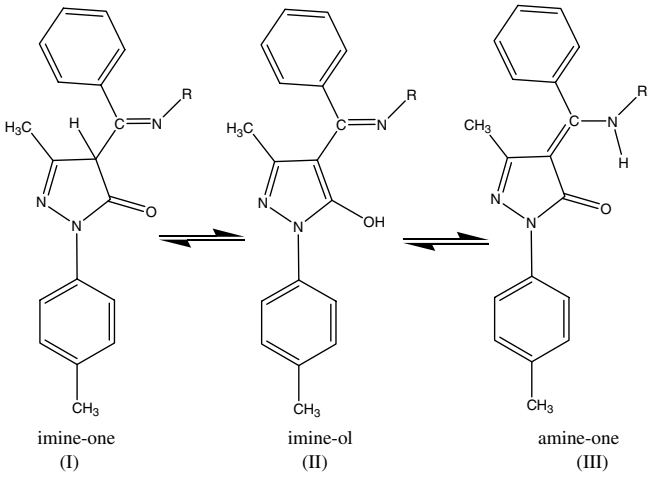


Fig. 2. Tautomeric forms of the ligands.

Table 3
^1H NMR spectral data for the ligands recorded in $CDCl_3$

Ligands	Methyl protons (δ ppm)	Aryl protons (δ ppm)	–NH[a] (δ ppm)
HL^1	[1.56, 2.34] singlet 6H	[7.08–7.90] multiplet 14H	12.98 singlet 1H
HL^2	[1.58, 2.34, 2.42] singlet 9H	[6.56–7.39] multiplet 13H	12.83 singlet 1H
HL^3	[1.56, 2.15, 2.34] singlet 9H	[6.49–7.92] multiplet 13H	12.98 singlet 1H
HL^4	[1.56, 2.21, 2.34] singlet 9H	[6.67–7.91] multiplet 13H	12.93 singlet 1H
HL^5	[1.59, 2.35] singlet 6H	[6.61–7.91] multiplet 13H	12.84 singlet 1H
HL^6	[1.57, 2.36] singlet 6H	[6.70–7.89] multiplet 13H	12.99 singlet 1H
HL^7	[1.58, 2.36] singlet 9H	[6.65–7.89] multiplet 13H	12.99 singlet 1H

[a] Not observed when spectra taken in $CDCl_3 + D_2O$.

3.2. Molecular structures of the ligands

The molecular structures of five ligands (HL^1–HL^5) were determined from single crystal X-ray studies. ORTEP diagrams of compounds HL^1 to HL^5 with the atom numbering schemes are shown in Fig. 3. Important bond lengths and angles for all the compounds are listed in Table 4. The ligand HL^1 crystallizes in the $P\bar{2}1/n$ space group

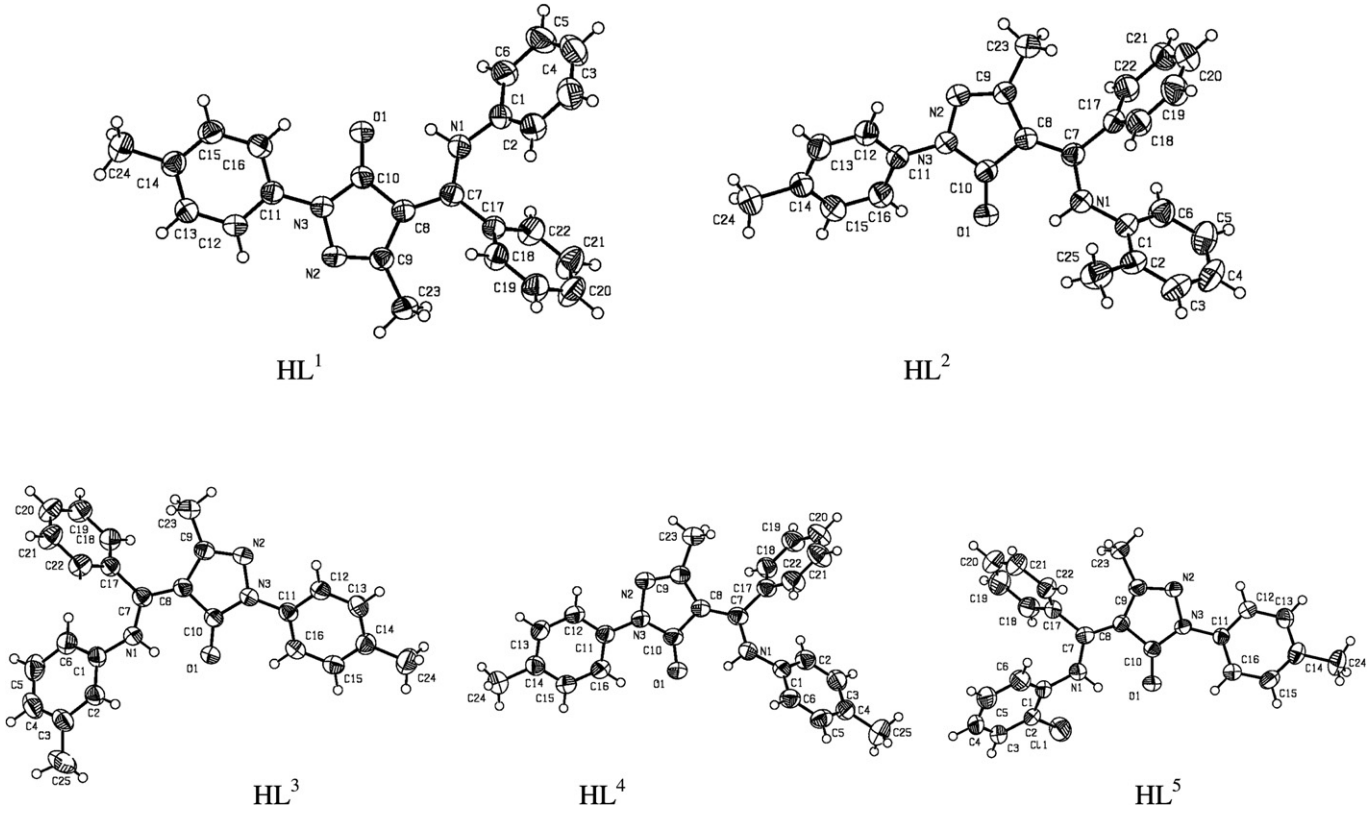


Fig. 3. ORTEP diagram of ligands $HL^{1\text{-}5}$.

Table 4
Selected bond lengths and angles in the ligands HL^1–HL^5

Compounds	HL^1	HL^2	HL^3	HL^4	HL^5
Bond distances (Å) with esd's in parentheses					
N(1)–C(1)	1.4220(18)	1.4260(16)	1.417(3)	1.421(3)	1.414(5)
N(1)–C(7)	1.3419(18)	1.3343(17)	1.338(2)	1.342(2)	1.343(4)
C(7)–C(17)	1.4762(19)	1.4881(18)	1.474(3)	1.483(3)	1.491(5)
C(7)–C(8)	1.3898(19)	1.3903(17)	1.390(3)	1.389(3)	1.381(5)
C(10)–C(8)	1.4464(19)	1.4460(17)	1.442(3)	1.443(3)	1.454(5)
O(1)–C(10)	1.2407(16)	1.2432(15)	1.245(2)	1.246(2)	1.249(4)
N(3)–C(10)	1.3762(17)	1.3780(16)	1.370(2)	1.376(3)	1.371(4)
N(3)-N(2)	1.3963(15)	1.3987(15)	1.397(2)	1.408(2)	1.398(4)
N(2)–C(9)	1.3007(18)	1.3037(16)	1.303(2)	1.300(2)	1.305(4)
C(9)–C(8)	1.4379(18)	1.4374(17)	1.435(3)	1.433(3)	1.432(5)
N(3)–C(11)	1.4159(17)	1.4150(16)	1.410(2)	1.414(2)	1.429(4)
C(7)–C(17)	1.4762(19)	1.4881(18)	1.474(3)	1.483(3)	1.491(5)
Bond angles (°) with esd's in parentheses					
C(7)–N(1)–C(1)	130.48(13)	128.20(12)	131.79(18)	130.51(18)	127.3(3)
N(1)–C(7)–C(17)	120.13(12)	119.20(11)	120.34(17)	119.30(18)	118.1(3)
N(1)–C(7)–C(8)	117.38(12)	118.78(12)	116.53(18)	117.67(17)	119.1(3)
C(8)–C(7)–C(17)	122.50(12)	121.92(11)	123.14(17)	123.03(17)	122.8(3)
C(7)–C(8)–C(10)	122.09(12)	121.94(11)	122.35(17)	121.87(18)	122.4(3)
O(1)–C(10)–C(8)	129.34(12)	129.52(12)	129.33(17)	129.27(19)	128.9(3)
O(1)–C(10)–N(3)	126.08(13)	126.02(12)	125.51(18)	125.67(19)	126.8(3)
C(10)–N(3)–N(2)	111.73(11)	112.04(10)	111.46(16)	111.37(16)	112.4(3)
N(3)–C(10)–C(8)	104.58(11)	104.45(11)	105.16(15)	105.06(16)	104.4(3)
C(9)–N(2)–N(3)	106.91(11)	106.70(10)	106.82(15)	106.31(15)	106.3(3)
N(2)–C(9)–C(8)	111.48(12)	111.49(11)	111.55(16)	112.24(16)	111.9(3)
C(7)–C(8)–C(9)	132.89(13)	132.31(12)	132.97(18)	133.36(18)	132.7(3)
C(9)–C(8)–C(10)	104.89(11)	105.25(11)	104.68(16)	104.72(17)	104.9(3)

with two molecules in the asymmetric unit. The packing diagram of this compound is depicted in Fig. 4.

Existence of acyl pyrazolone derivatives in different tautomeric forms (Fig. 2) in solid state is well known phenomenon and thus many studies have been made to establish the geometry of these derivatives including ours [18–22]. The single crystal X-ray diffraction study on this compound clearly indicates that the present compound exists in amine-one form without any ambiguity. Structural data shows that the C(10)–O(1) distances in the pyrazole moiety of these compounds are in the range 1.240–1.249 Å, which are significantly shorter than the distance found for >C–OH in some pyrazolone derivatives, 1.341, 1.346 Å [23] and 1.331 Å [24]; but well in the range of >C=O distances found similar compounds and 1.254 Å [25]. Significantly longer C(7)–N(1) distances of the imine moiety 1.334–1.343 Å, compared to the C=N in pyrazolone compound, 1.298 Å [26] and 1.292 Å [25], and comparable to >C–N (1.339 Å) distance observed in similar compounds [27], further supports the amine-one from in the present case. The C=O and C–N distances observed in this compound is comparable and well within the range reported by Allen et al. [28] in compilation of CSD data base, which summarizes many bond distances for various types of bonds including required one. The N–H proton is strongly hydrogen bonded with the O(1) atom, the N(1)···O(1) distances are in the range 2.667–2.713 Å and <N(1)–H(1)···O(1) are in the range 135.84–144.28° (Table 5). In addition to the above observations, the location of the hydrogen atom attached to the N1 atom from the difference Fourier map and the geometry around the atom C8 carbon shows the total values of the angle involving the C8 carbon (C(7)–C(8)–C(9) = 132.3–132.9°, C(7)–C(8)–C(10) = 121.9–122.4°, C(9)–C(8)–C(10) = 104.7–105.3° are in the range 358.9–360.6°, which is very close to 360°, expected from the coplanar C(7), C(8), C(9) and C(10) atoms and thus rules out the possibility of imine-ol form with the attachment of hydrogen with C(8). Thus it is clear from the X-ray studies establishing the amine-one form in the present compounds in accordance with the series of similar compounds reported by us recently [18–20].

3.3. Ab initio calculations for HL^1

The full geometry optimization of HL^1 has been carried out in Cartesian coordinates by quasi-Newton–Raphson gradient method using the restricted Hartree–Fock (RHF) approximation with help of Gamess program package [29]. Symmetry restrictions were not applied. The standard basis set of Gauss functions 6-31G [30,31] was used. The choice of basis set was optimal taking into account the computational time required and a reasonable accuracy of the results. The energy corresponds to the minima obtained is −1158.8256151 hartrees. The obtained minimum (Fig. 5) is true minima because it is identical with the crystal structure of the molecule. The same is also confirmed from the conformational analysis. The present compound contains too many hetero atoms. Thus it is interesting to know that out of these which one are the coordinating atoms. The lowdin atomic charges on N1 and O1 are −0.270560, −0.477742, respectively, whereas the lowdin atomic charges on N2 and N3 are −0.141167,

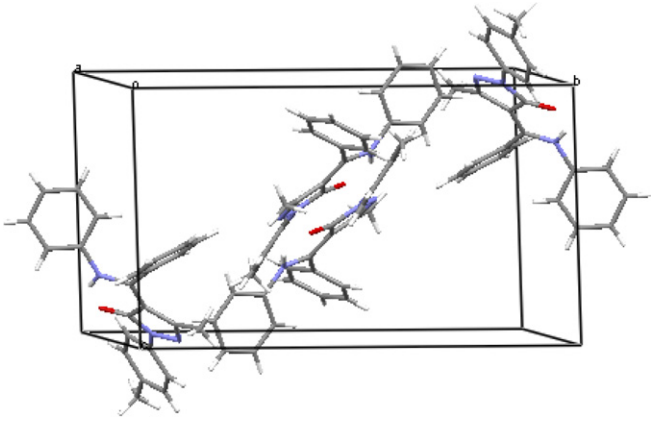


Fig. 4. Packing diagram of HL^1 down the *a*-axis.

Table 5
N–H···O hydrogen bonding distances and angles

Compound	N(1)–H(1)N(1) (Å)	H(1)N(1)···O(1) (Å)	N(1)···O(1) (Å)	<N(1)–H(1)N(1)···O(1) (°)
HL^1	0.919	1.907	2.691	142.04
HL^2	0.915	1.944	2.704	139.37
HL^3	0.890	1.894	2.667	144.28
HL^4	0.922	1.889	2.680	142.42
HL^5	0.936	1.962	2.713	135.84

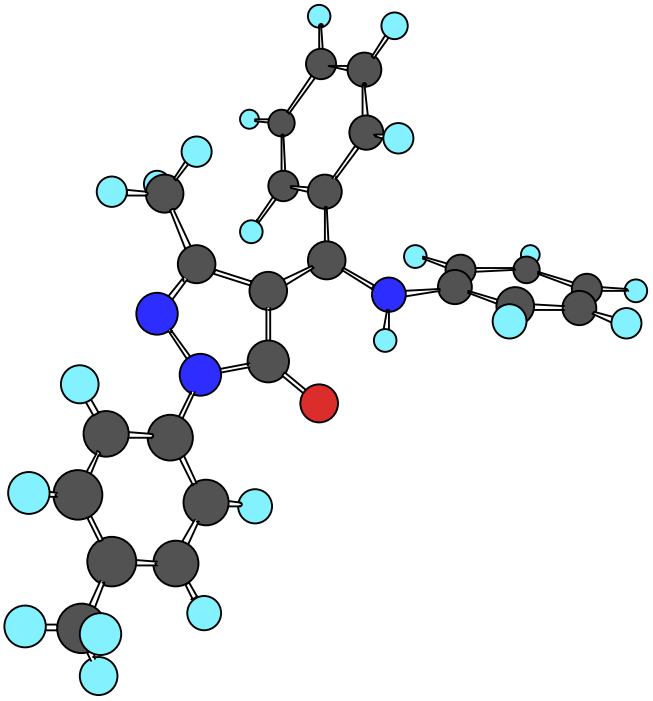


Fig. 5. Minimum energy conformer of the ligand HL^1.

−0.149783, respectively. Thus due to highest electron density available on atoms N1 and O1, these are the atoms which undergo coordination with the metal ions [20].

3.4. Characterization of the metal complexes

OV(IV) complexes of all the seven ligands have been synthesized by the reaction of $VOSO_4 \cdot 5H_2O$ and the respective ligands in water–DMF (1:1) under reflux conditions in the presence of sodium acetate according to following equation:

$$VOSO_4 \cdot 5H_2O + HL^{1\text{–}7} \rightarrow [OV(L^{1\text{–}7})_2(H_2O)] + H_2SO_4$$

where L = deprotonated HL^1, HL^2, HL^3, HL^4, HL^5, HL^6 and HL^7.

The resulting compounds are non-hygroscopic and air-stable solids. The C, H, N and metal percentage along with their conductivity and magnetic moment data of these complexes are presented in Table 6. The analytical data supports the above said molecular composition for these complexes. The observed molar conductance (Table 6) in 10^{-3} M DMF solution of these complexes are consistent with non-electrolytic nature of the complexes. Such a non-zero molar conductance value for each of the complex in the present study is most probably due to the strong donor capacity of DMF, which may lead to the displacement of anionic ligand and change of electrolyte [32] type. The oxovanadium(IV) is a $S = 1/2$ system. The magnetically dilute oxovanadium(IV) complexes usually exhibit magnetic moments to their spin-only value of 1.73 BM. At room temperature, the observed value of the magnetic moments for the present complexes, are in the range 1.63–1.93 BM, as expected for a simple $S = 1/2$ paramagnets with a d_{xy} based ground state [33]. These data suggest that the complexes under this investigation are mononuclear [33]. The IR spectra of the metal complexes exhibit no band for $\nu_{(N\text{–}H)}$ (3228 cm^{-1}) of the ligands, indicating deprotonation of the N–H group in metal complexes. Most of the oxovanadiun(IV) complexes exhibit a strong band near 1000 cm^{-1}, which has been assigned to the $\nu_{(V=O)}$ [34]. In the present work, the $\nu_{(V=O)}$ is found at 900–930 cm^{-1} which suggests the absence of a —V=O—V=O— chain structure [35,36]. To confirm the presence of weakly coordinating H_2O molecules in the complex we carried out thermogravimetric analyses of all the complexes. This study shows loss of weight corresponding to one water molecule in the temperature range 130–170 °C, indicating that the water molecule in these complexes is weakly coordinated to the metal ion. The presence of a H_2O molecule in the complexes is also indicated by IR spectra, which show a broad band centered around 3400 cm^{-1} and two sharp bands at 710 and 420 cm^{-1}, the later two can be assigned to the wagging and rocking modes of vibration of the water molecule, respectively [37]. On the basis of all these data, the molecular geometry assigned to the metal complexes is shown in Fig. 6. Attempts have been made to grow X-ray quality single crystals of these complexes, however, this has been unsuccessful so far.

Table 6
Elemental analysis (M, C, H and N)[a], molar conductance and magnetic moment data of the OV(IV) complexes

Complex	% M	% C	% H	% N	Λ_M[b]	$\mu_{eff.}$ (BM)
$[OV(L^1)_2(H_2O)]$	6.86 (6.90)	70.11 (70.14)	5.59 (5.64)	10.20 (10.22)	5.13	1.85
$[OV(L^2)_2(H_2O)]$	5.95 (5.99)	70.58 (70.65)	5.89 (5.93)	9.86 (9.89)	5.41	1.97
$[OV(L^3)_2(H_2O)]$	5.96 (5.99)	70.53 (70.65)	5.88 (5.93)	9.88 (9.89)	5.39	1.93
$[OV(L^4)_2(H_2O)]$	5.94 (5.99)	70.66 (70.65)	5.90 (5.93)	9.91 (9.89)	5.43	1.92
$[OV(L^5)_2(H_2O)]$	5.69 (5.71)	64.73 (64.71)	4.91 (4.97)	9.40 (9.43)	5.21	1.69
$[OV(L^6)_2(H_2O)]$	5.68 (5.71)	64.74 (64.71)	4.92 (4.97)	9.44 (9.43)	5.20	1.72
$[OV(L^7)_2(H_2O)]$	5.72 (5.71)	64.75 (64.71)	4.95 (4.97)	9.44 (9.43)	5.17	1.63

[a] Calculated values are in parentheses.
[b] Ohm^{-1} cm^2 mol^{-1} in DMF.

3.5. Electronic spectra of the metal complexes

The electronic spectra of all the complexes were recorded in DMF and the data are presented in Table 7. Complexes of oxovanadium(IV) usually show coordination numbers five and six giving tetragonal pyramidal and distorted octahedral structures respectively [38,39]. Because of the presence of a strong axial field, the energy levels associated with these two structures do not differ considerably [40]. Therefore, the same scheme can be used for the interpretation of the spectra of both types of the complexes. The electronic spectra of all complexes show three bands in the region 12 000–26 000 cm^{-1}. These bands may be assigned to three transitions as shown in Table 7, following the "Clustered level" Scheme [41,42]. In addition, all the complexes show a band at ~31 000 cm^{-1}, which may be due to the first spin forbidden charge transfer transition [43]. To support the above assignments, the following study was made for all the complexes. Each complex was dissolved in 2:1:1 ether:toluene:ethanol mixture and allowed to stand

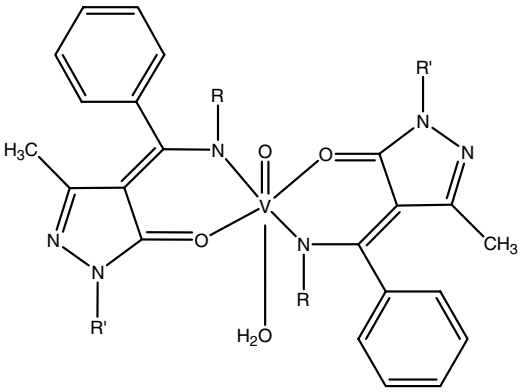


Fig. 6. Structural drawing of the OV(II) complexes.

Table 7
Electronic spectral data (cm^{-1}) of the OV(IV) complexes

Complex	$d_{xy} \rightarrow d_{xz}, d_{yz}$	$d_{xy} \rightarrow d_{x^2-y^2}$	$d_{xy} \rightarrow d_{z^2}$	CT
$[OV(L^1)_2(H_2O)]$	13605 (13698)[a]	17241 (17094)[a]	23866 (24875)[a]	31347 (31645)[a] (30120)[b]
$[OV(L^2)_2(H_2O)]$	12970 (13850)[a]	16447 (17241)[a]	23809 (24390)[a]	31446 (31746)[a] (31055)[b]
$[OV(L^3)_2(H_2O)]$	13386 (13513)[a]	16393 (16611)[a]	25510 (24937)[a]	31055 (31250)[a] (31347)[b]
$[OV(L^4)_2(H_2O)]$	13037 (13698)[a]	16666 (16949)[a]	25510 (24390)[a]	31055 (31746)[a] (31055)[b]
$[OV(L^5)_2(H_2O)]$	13698 (13477)[a]	17241 (17094)[a]	24509 (24813)[a]	31152 (31746)[a] (31152)[b]
$[OV(L^6)_2(H_2O)]$	13175 (13513)[a]	17094 (16556)[a]	24813 (24691)[a]	31746 (31250)[a] (31347)[b]
$[OV(L^7)_2(H_2O)]$	12987 (13440)[a]	16611 (16611)[a]	23866 (24390)[a]	31645 (31055)[a] (31250)[b]

[a] Pyridine spectra.
[b] Oxidation spectra.

to bring the oxidation of OV(IV) to OV(V) [43,44]. The colour of each complex in solution changes rapidly from green to brown. This suggests the change of oxidation state of OV(IV). The solution spectra of the above solutions showed the absence of bands in the region 12000–26000 cm^{-1}. However, only one band ~31000 cm^{-1} appeared in the solution spectra of the all the complexes. The d–d bands are expected to disappear for the OV(V) complexes and therefore, the observed band may be due to charge-transfer process [45]. The vanadyl complexes can usually accept a sixth ligand to vanadium in the axial position trans to the oxygen atom. When this happens, the d-d transition bands will be solvent-dependent. The pyridine spectra of the complexes are very similar to each other and also to those of their electronic spectra. Clearly, there is no significant shift of absorption bands in strong donating solvent, suggesting that it is unlikely that there is any strong interaction between vanadium and the donating molecule. This suggests that, there is no pyridine coordination and no change of the stereochemistry of these complexes in a donor solvent [46,47]. This also confirms the tetragonally distorted octahedral structure for these complexes.

4. Supplementary material

CCDC 617622, 617623, 617624, 617625, and 617626 contain the supplementary crystallographic data for the ligands (HL^1–HL^5). These data can be obtained free of charge via http://www.ccdc.cam.ac.uk/conts/retrieving.html, or from the Cambridge Crystallographic Data Centre, 12 Union Road, Cambridge CB2 1EZ, UK; fax: (+44) 1223-336-033; or e-mail: deposit@ccdc.cam.ac.uk.

Acknowledgement

The authors are thankful to Shree Sidhdhanath Industries, Sachin, Surat, for providing the free gift sample of the pyrazolone.

References

[1] H. Sakurai, A. Tamura, J. Fugono, H. Yasui, T. Kiss, Coord. Chem. Rev. 245 (2003) 31, and reference therein.
[2] H. Sakurai, T. Inohara, Y. Adachi, K. Kawabe, H. Yasui, J. Takada, Bioorg. Med. Chem. Lett. 14 (2004) 1093, and reference therein.
[3] T.S. Smith, R. LoBrutto, V.L. Pecoraro, Coord. Chem. Rev. 228 (2002) 1, and reference therein.
[4] C.E. Holloway, M. Melnik, Rev. Inorg. Chem. 7 (1985) 75.
[5] F.T.G. Hudson, Vanadium Toxicology and Biological Significance, Elsevier, New York, 1996, p. 140.
[6] G. Santoni, D. Rehder, J. Inorg. Biochem. 98 (2004) 758.
[7] S. Liang, D.V. Derveer, S. Qian, B. Sturgeon, X.R. Bu, Polyhedron 21 (2002) 2021.
[8] D.M. Boghaei, S. Mohebi, J. Mol. Catal. A: Chem. 179 (2002) 41.
[9] R.C. Maurya, S. Rajput, J. Mol. Struct. 794 (2006) 24–34.
[10] D.M. Boghaei, A. Bezaatpour, M. Behzad, J. Mol. Catal. A: Chem. 245 (2006) 12.
[11] P. Plitt, H. Pritzkow, T. Oeser, R. Kraemer, J. Inorg. Biochem. 99 (2005) 1230.
[12] D.D. Perrin, W.L.F. Armarego, D.R. Perrin, Purification of Laboratory Chemicals, second ed., Pergamon Press, 1981.
[13] N.H. Furman, Standard Methods of Chemical Analysis, sixth ed., vol. 1, D. Van Nostrand, Princeton, NJ, 1962, p. 1211.
[14] G.M. Sheldrick, SADABS, Universität Göttingen, Germany, 1995.
[15] G.M. Sheldrick, SHELXS-97 Program for X-ray Crystal Structure Solution, Göttingen University, Germany, 1997.
[16] G.M. Sheldrick, SHELXL-97 Program for X-ray Crystal Structure Refinement, Göttingen University, Germany, 1997.
[17] A.L. Spek, J. Appl. Crystallogr. 36 (2003) 7.
[18] R.N. Jadeja, J.R. Shah, E. Suresh, P. Paul, Polyhedron 23 (2004) 2465.
[19] R.N. Jadeja, R.N. Shirsat, E. Suresh, Struct. Chem. 16 (5) (2005) 515.
[20] B.T. Thaker, K.R. Surti, S. Oswal, R.N. Jadeja, V. Gupta, Struc. Chem. (2007) in press, doi:10.1007/s11224-006-9134-x.
[21] Y. Akama, A. Tong, N. Matsumoto, T. Ikeda, S. Tanaka, Vib. Spectrosc. 13 (1996) 113.
[22] G. Cerchiaro, A.M. Da Costa Ferreira, A.B. Teixeira, H.M. Magalhae~s, A.C. Cunha, V.F. Ferreira, L.S. Santos, M.N. Eberlin, J.M.S. Skakle, S.M.S.V. Wardell, J.L. Wardell, Polyhedron 25 (2006) 2055.
[23] F. Bechtel, J. Gaultier, C. Hauw, Cryst. Struct. Commun. 2 (1973) 473.
[24] J. Bechtel, C. Hauw, Cryst. Struct. Commun. 2 (1973) 469.
[25] B. Peng, G. Liu, L. Liu, D. Jia, K. Yu, J. Mol. Struct. 692 (2004) 217.
[26] L. Liu, D.Z. Jia, Y.L. Ji, K.B. Yu, J. Photochem. Photobiol. 154 (2003) 117.
[27] C. Arici, M.N. Tahir, D. Ulku, O. Atakol, Acta Crystallogr. Sect. C 55 (1999) 1961.
[28] F.H. Allen, O. Kennard, G. Watson, L. Brammer, A.G. Orpen, R.J. Taylor, Chem. Soc., Perkin Trans. II (1987) S1, and references cited therein.
[29] M.W. Schmidt, K.K. Baldridge, J.A. Boatz, S.T. Elbert, M.S. Gordon, J.H. Jensen, S. Koseki, N. Matsunaga, K.A. Nguyen, S.J. Su, T.L. Windus, M. Dupuis, J.A. Montgomery, J. Comput. Chem. 14 (1993) 1347.
[30] R. Ditchfield, W.J. Hehre, J.A. Pople, J. Chem. Phys. 54 (1971) 724.
[31] W.J. Hehre, R. Ditchfield, J.A. Pople, J. Chem. Phys. 56 (1971) 724.
[32] W.J. Geary, Coord. Chem. Rev. 7 (1971) 81.
[33] S.K. Dutta, R.T.T. Edward, M. Chaudhury, Polyhedron 16 (1997) 1863.

[34] J. Selbin, Coord. Chem. Rev. 1 (1966) 293.
[35] R.C. Maurya, H. Singh, A. Pandey, T. Singh, Indian J. Chem. 40A (2001) 1053.
[36] L.V. Boas, J.C. Pessoa, in: G. Wilkinson, R.D. Gillard, J.A. McCleverty (Eds.), Comprehensive Coordination Chemistry, first ed., Pergamon Press, Oxford, 1987, p. 540.
[37] H.B. Suthar, U.G. Deshpande, J.R. Shah, Bull. Soc. Chim. Fr. 1 (1986) 55.
[38] J. Selbin, Chem. Rev. 65 (1965) 153.
[39] M. Singh, Synth. React. Inorg. Met.-Org. Chem. 15 (2) (1985) 235.
[40] L. Sacconi, U. Campigli, Inorg. Chem. 5 (1966) 608.
[41] C.J. Ballhausen, B.F. Djurinskij, K.J. Watson, J. Am. Chem. Soc. 90 (1968) 3305.
[42] S.R. Aswale, P.R. Mandlik, A.S. Aswar, J. Indian Chem. Soc. 79 (2002) 722.
[43] J. Selbin, T.R. Ortolano, F.J. Smith, Inorg. Chem. 2 (1963) 1315.
[44] R.N. Jadeja, N.J. Parmar, Synth. React. Inorg. Met.-Org. Nano Met. Chem. 35 (2005) 111.
[45] T.R. Ortolano, J. Selbin, S.P. McGlynn, J. Chem. Phys. 41 (1964) 262.
[46] A.K. Rana, J.R. Shah, J. Indian Chem. Soc. 58 (1981) 1100.
[47] P.M. Parikh, J.R. Shah, Synth. React. Inorg. Met.-Org. Chem. 15 (4) (1985) 493.

1,10-phenanthroline-5,6-dione [11], (IP) and (PIP) [12], $[Co(en)_2phen]Br_3$ [13] *cis*-$[Co(en)_2Cl_2]Cl \cdot 3H_2O$ [14] and $[Co(en)_2L]Br_3$ were prepared by the procedures given below. The structures of the complexes and ligands are shown in Fig. 1. All the experiments involving the interaction of the complexes with DNA were carried out in a buffer (5 mM Tris–HCl, 50 mM NaCl, pH 7.2). A solution of CTDNA in the buffer gave a ratio of UV absorbance at 260 and 280 nm of about 1.90, indicating that the DNA was sufficiently free of protein [15]. The DNA concentration per nucleotide was determined by absorption spectroscopy using the molar absorption coefficient (6600 M^{-1} Cm^{-1}) at 260 nm [16].

2.2. Synthesis of complexes

2.2.1. *[Co(en)$_2$PIP]Br$_3$*

A mixture of *cis*-$[Co(en)_2Cl_2]Cl$ (1.43 g) and phenylimidazo[4,5-f][1,10]-phenanthroline (1 g) was dissolved in EtOH (6 ml), and NaBr (3.0 g) in H_2O (5 ml) was added. The resulting mixture was heated on a water bath until a dark yellow solution was formed. This was then cooled in ice and the thick crystalline precipitate of $[Co(en)_2PIP]^{3+}$ was collected and recrystallized from water (30 ml). The yield by this method was about 80%. (Elemental *Anal.* Calc. for $C_{23}N_8H_{28}Br_3Co$: C, 38.2; H, 3.96; N, 15.7. Found: C, 37.12; H, 3.2; N 14.6%.) IR stretching frequencies: (C=C); 1458, (C=N); 1508, (Co–N (en)); 779, (Co–N(ligand)); 625.5 cm^{-1}.

2.2.2. *[Co(en)$_2$IP]Br$_3$*

The complex $[Co(en)_2IP]^{3+}$ was prepared according to the procedure described above from a mixture of *cis*-$[Co(en)_2Cl_2]Cl$ (1.43 g) and IP (1 g). (Yield: 88%). (Elemental *Anal.* Calc. for $C_{23}N_8H_{28}Br_3Co$: C, 32.08; H, 3.80; N, 17.6. Found: C, 32.28; H, 3.2; N, 16.6%.). IR stretching frequencies: (C=C); 1398, (C=N); 1558, (Co–N (en)); 614, (Co–N(ligand)); 573 cm^{-1}.

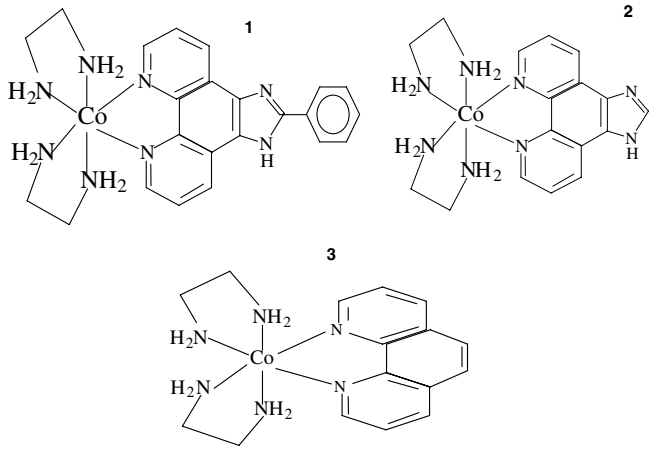


Fig. 1. Chemical structures of the complexes.

2.3. Physical measurements

UV–Vis spectra were recorded with an Elico Bio-spectrophotometer, model BL198. IR spectra were recorded in KBr discs on a Perkin-Elmer FT-IR-1605 spectrometer. ^1H NMR spectra were measured on a Varian XL-300 MHz spectrometer with D_2O as the solvent at room temperature and using tetramethylsilane (TMS) as the internal standard. Magnetic susceptibility measurements for solid samples of the complexes were carried out using a Faraday bakany model. Hg $[Co(CNS)_4]$ was employed as the magnetic susceptibility standard. Microanalyses (C, H and N) were carried out on a Perkin-Elmer 240 elemental analyzer. For the absorption spectra an equal amount of DNA was added to both the complex solution and reference solution to eliminate the absorbance of DNA itself.

Viscosity experiments were carried out using an Ostwald viscometer maintained at a constant temperature of 30.0 ± 0.1 °C in a thermostatic waterbath. Calf thymus DNA samples of approximately 200 bp of average length were prepared by sonicating in order to minimize complexities arising from DNA flexibility [17]. Data were presented as $(\eta/\eta_0)^{1/3}$ versus the concentration of the Co(III) complexes, where η is the viscosity of DNA in the presence of the complex, η_0 is the viscosity of DNA alone. Viscosity values were calculated from the observed flow time of DNA-containing solutions ($t > 100$ s) corrected for the flow time of buffer alone $(t_0)\eta = t - t_0/t_0$, where t is the observed flow time of DNA and t_0 is the flow time of buffer [18]. The DNA melting experiments were carried out by controlling the temperature of the sample cell with a Shimadzu circulating bath while monitoring the absorbance at 260 nm.

For the gel electrophoresis experiments, super coiled pBR 322 DNA (100 μM) was treated with the Co(III) complexes in 50 mM Tris–HCl, 18 mM NaCl buffer, pH 7.2, and the solutions were incubated for 1 h in the dark, then irradiated at room temperature with a UV lamp (302 nm, at 10 W). The samples were analyzed by electrophoresis for 2.5 h at 40 V on a 0.8% agarose gel in tris–acetic acid EDTA buffer; pH 7.2 The gel was stained with 1 μg/ml ethidium bromide and then photographed under UV light.

2.4. Spectroscopic characterization

The IR spectral data for the two complexes were determined, and the complexes clearly exhibit bands at 1450 and 1560–1590 cm^{-1}, corresponding to C=C and C=N of the ring, respectively. Bands at around 626 and 579 cm^{-1} correspond to Co–N(en) and Co–N of L = PIP and IP. NH_2 (en) bending was observed at around 1650 cm^{-1}. The UV–Vis emission maxima were observed at 317, 492 and 347, 437 nm and fluorescence peaks at 408 and 407 for the $[Co(en)_2IP]^{3+}$ and $[Co(en)_2PIP]^{3+}$ complexes, respectively. These bands are due to a MLCT [19]. The electronic environments of the many aromatic hydrogen atoms (PIP and IP) are similar and hence the ^1H NMR spectra appear

in a narrow chemical shift range. In fact the aromatic regions of the spectra of these complexes are complicated due to the overlapping of several signals, which have precluded the identification of individual resonances. In the ^{1}H NMR spectra of the cobalt(III) complexes the peaks due to various H-atoms of PIP and IP were shifted downfield compared to the free ligands, suggesting complexation. As expected the signals for PIP and IP appeared in the range between 7.5 and 9.2 ppm, in agreement with an earlier report [19]. CH_2 groups of the ethylenediamine gave peaks at 2.72 (4H,en-CH_2).

3. Results and discussion

3.1. Absorption spectral studies

The application of electronic absorption spectroscopy is one of the most useful techniques for DNA binding studies [20]. Complex binding with DNA through intercalation usually results in hypochromism and bathochromism, due to the intercalative mode involving a strong stacking interaction between an aromatic chromophore and the base pairs of DNA. The extent of the hypochromism commonly parallels the intercalative binding strength. The absorption spectra of the complexes $[Co(en)_2PIP]^{3+}$ and $[Co(en)_2IP]^{3+}$, in the absence and presence of CT-DNA, are given in Figs. 2 and 3. As the concentration of DNA is increased, it results in hypochromism and a moderate bathochromic shift in the UV spectra of both $[Co(en)_2PIP]^{3+}$ and $[Co(en)_2IP]^{3+}$. According to the data presented in Figs. 2 and 3 it seems that the change in absorption spectra of the two complexes upon addition of DNA follows: $[Co(en)_2PIP]^{3+} > [Co(en)_2IP]^{3+}$. These spectral data may suggest a mode of binding that involves a stacking interaction between the complex and the base pairs of DNA. To compare quantitatively the binding strength of the two complexes, the intrinsic binding constants K of the two complexes with CTDNA were determined according to the following equation [21] through a plot of [DNA]/$(\sum b - \sum f)$ versus [DNA]

$$[\mathrm{DNA}]\Big/\Big(\sum a - \sum f\Big) = [\mathrm{DNA}]\Big/\Big(\sum b - \sum f\Big) + 1\Big/\Big(K\Big(\sum b - \sum f\Big)\Big),$$

where [DNA] is the concentration of DNA in base pairs, the apparent absorption coefficients $\sum a$, $\sum f$ and $\sum b$ correspond to A_{obsd}/[Co], the extinction coefficient for the free cobalt complex and the extinction coefficient for the free cobalt complex in the fully bound form, respectively. In plots of DNA]/$(\sum b - \sum f)$ versus [DNA], K is given by the ratio of the slope to the intercept. Intrinsic binding constants K of $[Co(en)_2PIP]^{3+}$ and $[Co(en)_2IP]^{3+}$ were obtained, the values being $5.34 \pm 0.2 \times 10^4$ and $4.575 \pm 0.3 \times 10^4$ M^{-1}. The binding constants indicate that $[Co(en)_2PIP]^{3+}$ binds more strongly than $[Co(en)_2IP]^{3+}$. This result is expected since PIP possesses a greater planar area and extended π system than that of IP, which would lead to PIP penetrating deeper and stacking more strongly. Hypochromism was indeed observed in the complexes, the order being $[Co(en)_2PIP]^{3+} > [Co(en)_2PIP]^{3+} > [Co(en)_2phen]^{3+}$.

3.2. Fluorescence studies

The complexes $[Co(en)_2PIP]^{3+}$ and $[Co(en)_2IP]^{3+}$ can emit luminescence in Tris buffer (pH 7.0) at ambient temperature with λ maxima at 408 and 407 nm, respectively. Binding of both complexes to DNA was found to increase the fluorescence intensity. The emission spectra of both complexes in the absence and presence of CT DNA are

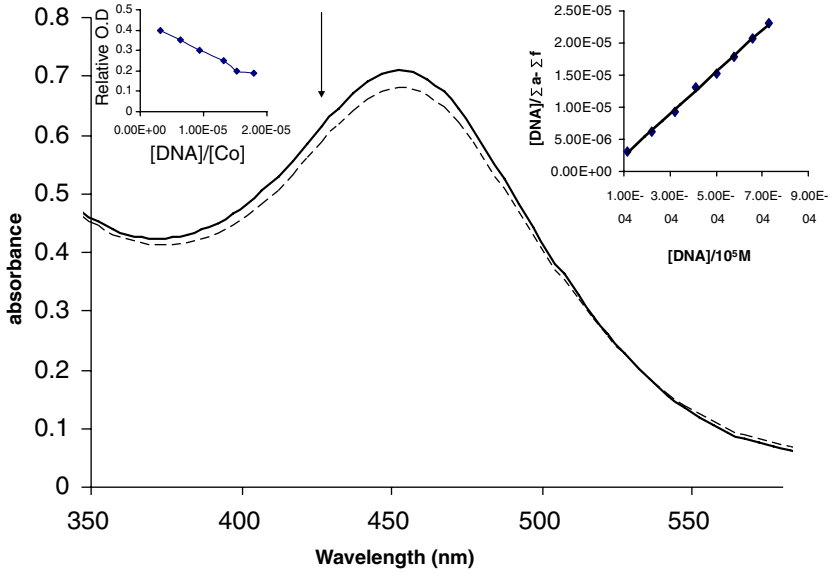


Fig. 2. Absorption spectra of $[Co(en)_2PIP]^{3+}$ (——) in the absence and presence (------) of CT DNA in Tris–HCl buffer; the absorbance changes upon increasing CT DNA concentrations. (10 μl, 20 μl, 30 μl, 40 μl ----- of DNA addition), [Co] = 10 μM, [DNA] = 0–126 μM. The arrow shows the intensity change with increasing DNA concentration. Insert: plots of [DNA]/$(\sum a - \sum f)$ vs. [DNA] for the titration of DNA with the Co(III) complex.

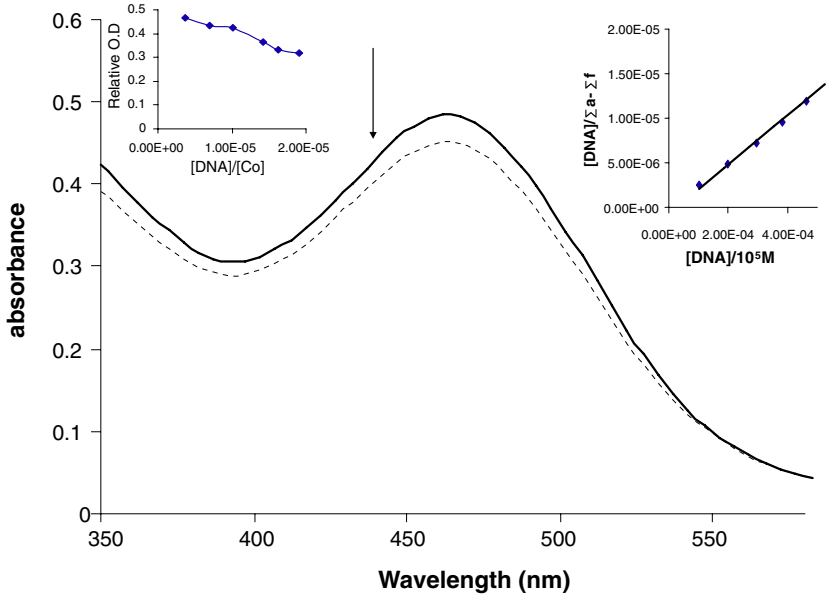


Fig. 3. Absorption spectra of $[Co(en)_2IP]^{3+}$ in the absence (——) and presence (------) of DNA in Tris–HCl buffer. The absorbance changes upon increasing the CT DNA concentration (10 μl, 20 μl, 30 μl, 40 μl ------ of DNA addition), [Co] = 10 μM, [DNA] = 0–126 μM. The arrow shows the intensity change upon increasing the DNA concentration. Insert: plots of $[DNA]/(\sum a - \sum f)$ vs. [DNA] for the titration of DNA with the Co(III) complex.

shown in Figs. 4 and 5. The plots of the relative intensity versus the ratio of [DNA]/[Co] are also indicated in Figs. 4 and 5. Upon addition of CT DNA, the emission intensity increases steadily. The emission intensity difference between absence of CT DNA and presence of CT DNA is greater for the PIP complex than the IP complex, as shown in Figs. 4 and 5. The extent of enhancement increases on going from $[Co(en)_2IP]^{3+}$ to $[Co(en)_2PIP]^{3+}$, which is consistent with the above absorption spectral results. The order of increase in emission intensity of complexes is $[Co(en)_2PIP]^{3+} > [Co(en)_2IP]^{3+} > [Co(en)_2phen]^{3+}$.

This observation is further supported by the emission quenching experiments using $[Fe(CN)_6]^{4-}$ as a quencher. The method essentially consists of titrating a given amount of DNA and DNA binding-metal complexes with an increasing concentration of $[Fe(CN)_6]^{4-}$, and measuring

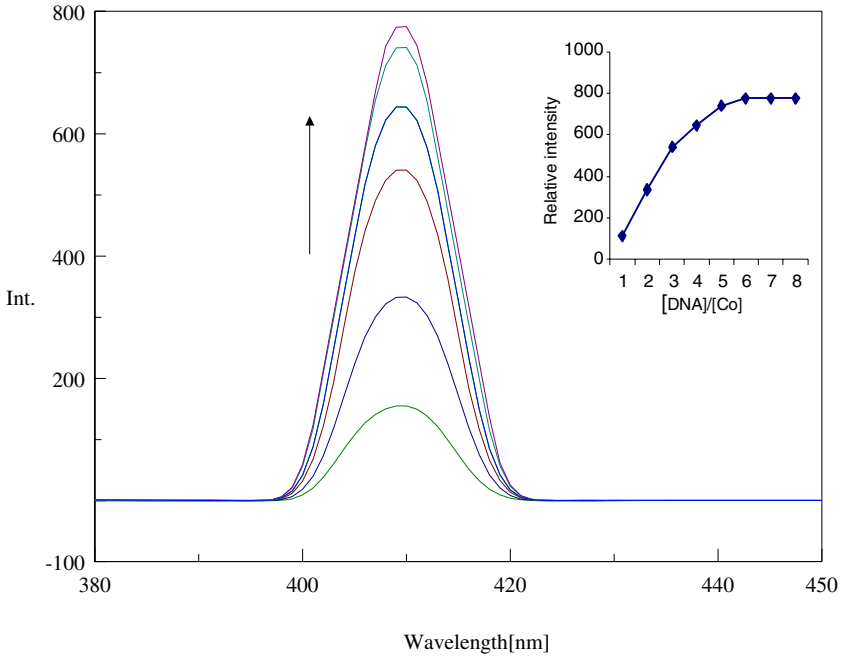


Fig. 4. Emission spectra of complex of $[Co(en)_2PIP]^{3+}$ in aqueous buffer (Tris 5 mM, pH 7.2) at 298 K in the presence of CT DNA, [Co] = 20 μM, [DNA]/[Co] 0, 5, 50, λ_{ex} = 320 nm. The arrow shows the intensity change upon increasing the DNA concentration. Inset: plots of relative integrated emission intensity vs. [DNA]/[Co].

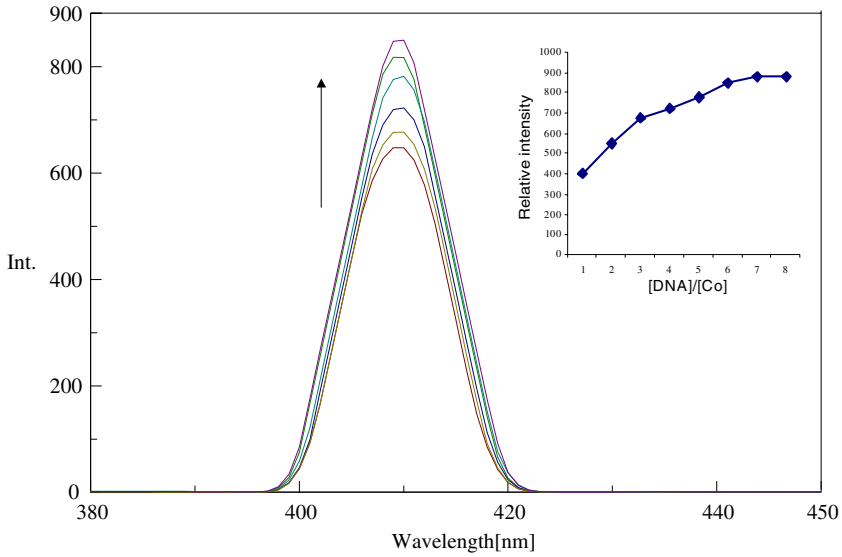


Fig. 5. Emission spectra of complex of $[Co(en)_2IP]^{3+}$ in aqueous buffer (Tris 5 mM, pH 7.2) at 298 K in the presence of CT DNA, [Co] = 20 μM, [DNA]/[Co] 0, 5, 50, λ_{ex} = 320 nm. The arrow shows the intensity change upon increasing the DNA concentration. Insert: plots of relative integrated emission intensity vs. [DNA]/[Co].

the change in fluorescence intensity. The ion $[Fe(CN)_6]^{4-}$ has been shown to be able to distinguish differentially bound cobalt(III) complexes. Positively charged free complex ions would be readily quenched by$[Fe(CN)_6]^{4-}$, whereas a DNA bound complex is protected from the quencher because the highly negatively charged $[Fe(CN)_6]^{4-}$ would be repelled by the negatively charged DNA phosphate backbone, hindering quenching of the bound complex. The ferrocyanide quenching curves for $[Co(en)_2PIP]^{3+}$ and $[Co(en)_2IP]^{3+}$ in the presence and absence of CTDNA are shown in Fig. 6. Obviously the complex $[Co(en)_2PIP]^{3+}$ inserts into DNA much deeper than the complex $[Co(en)_2IP]^{3+}$ Fig. 7.

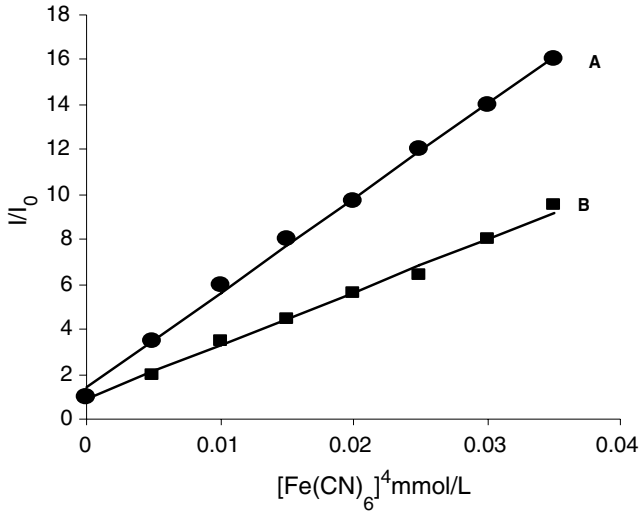


Fig. 6. Emission quenching curves of (A) $[Co(en)_2IP]^{3+}$ (●) and (B) $[Co(en)_2PIP]^{3+}$ (■) in presence of DNA ([Co] = 2 μmol/cm^{-3}, [DNA]/[Co] = 40).

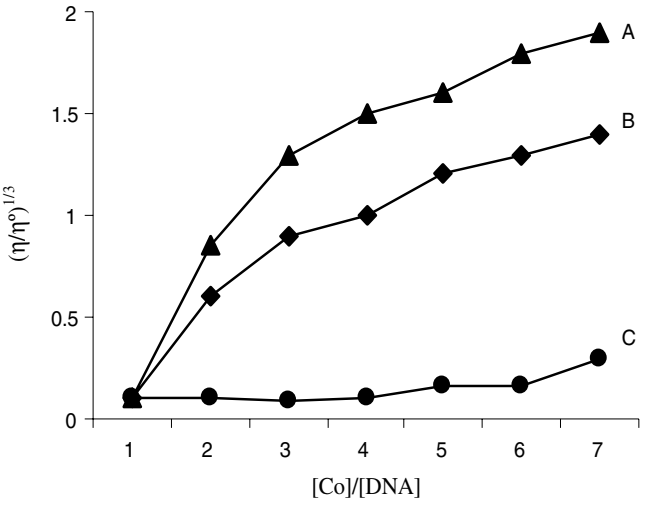


Fig. 7. Effect of increasing the amount of $[Co(en)_2PIP]^{3+}$ (A), $[Co(en)_2IP]^{3+}$ (B) and $[Co(en)_2phen]^{3+}$ (C) on the relative viscosities of CT DNA at 25 ± 0.1 °C.

3.3. Viscosity studies

The mode of the two complexes binding to DNA was explained by viscosity measurements. Optical photo physical probes are necessary, but do not give sufficient clues to support a binding model. Hydrodynamic measurements that are sensitive to length change (i.e. viscosity and sedimentation) are regarded as the least ambiguous [18]. For complexes **2** and **1**, the viscosity of DNA increases greatly with increasing concentration of complex, which is similar to that of the proven intercalator EtBr [22]. Both complexes change the relative viscosity of DNA in a manner consistent with binding by the intercalation mode shown in Fig. 4. This result also parallels the pronounced hypochromism

and spectral red shift and emission enhancement of both complexes, and is comparable with the proven classical intercalator EtBr. The viscosity of DNA increases with the increase of concentration of EtBr. So these two complexes increase the DNA helix length. On the basis of the viscosity results, the complexes bind with DNA through the intercalation mode. The order of increase in viscosity of the complexes follows the order: $[Co(en)_2PIP]^{3+} > [Co(en)_2IP]^{3+} > [Co(en)_2phen]^{3+}$.

3.4. DNA melting studies

Another strong evidence for the binding of the $[Co(en)_2PIP]^{3+}$, $[Co(en)_2IP]^{3+}$ and $[Co(en)_2phen]^{3+}$ complexes to the double helix of DNA is melting temperature T_m. The binding of small molecules into the double helix is known to increase the helix melting temperature. The helix melting temperature is the temperature at which the double helix is denatured into single-stranded DNA. The extinction coefficient of DNA bases at 260 nm in the double-helical form is much less than in the single stranded form. Hence melting of the helix leads to an increase in the absorption at this wavelength. Thus the transition temperature from helix to coil can be determined by monitoring the absorbance of the DNA base at 260 nm as a function of temperature. The melting curves of CT DNA in the absence and presence of $[Co(en)_2PIP]^{3+}$, $[Co(en)_2IP]^{3+}$ and $[Co(en)_2phen]^{3+}$ are presented in Fig. 8. The increase in the melting temperature values of IP and PIP complexes are comparable to the value observed with the classical intercalator EtBr. The values are presented in Table 1. It is clear from these figures that the complexes $[Co(en)_2PIP]^{3+}$ and $[Co(en)_2IP]^{3+}$ are intercalators because the relative absorbance is high compared to that of the pure DNA sample. The increase in absorbance of the complexes follows the order $[Co(en)_2PIP]^{3+} > [Co(en)_2IP]^{3+} > [Co(en)_2phen]^{3+}$.

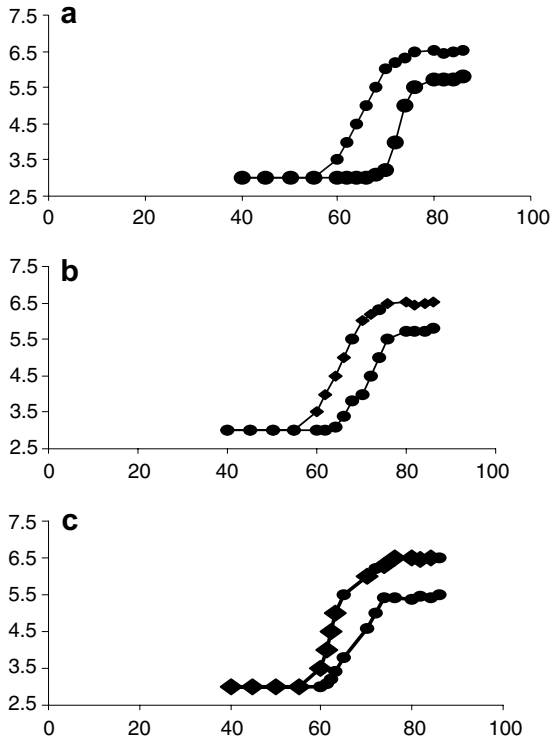


Fig. 8. Thermal melting curves of calf thymus DNA and DNA + Co(III) complexes $[Co(en)_2PIP]^{3+}$ (A), $[Co(en)_2IP]^{3+}$ (B) and $[Co(en)_2phen]^{3+}$ (C).

Table 1
Results of absorption titration and thermal melting experiments

Compound	T_M (°C)
CT DNA	60
$[Co(en)_2phen]^{3+}$	62
$[Co(en)_2IP]^{3+}$	64
$[Co(en)_2PIP]^{3+}$	68

3.5. Photoactivated cleavage of pBR 322 DNA by the Co(III) complexes

There has been considerable interest in DNA endonucleolytic cleavage reactions that are activated by metal ions [23,24]. The delivery of high concentrations of metal ion to the helix, locally generating oxygen or hydroxide radicals, leads to an efficient DNA cleavage reaction. DNA cleavage is monitored by the relation of supercoiled circular pBR 322 (form I) to the nicked circular (form II) and linear (form III) forms. When circular plasimd DNA is subjected to electrophoresis, relatively fast migration will be observed for the supercoiled form (form I). If scission occurs on one strand (nicking), the supercoils will relax to generate a slower-moving open circular form (form II) [25]. If both strands are cleaved, a linear form (form III) will be generated that migrates between forms I and II. Fig. 8 shows the gel electrophoretic separations of plasmid pBR 322 DNA after incubation with Co(III) complexes and irradiation at 302 nm. Fig. 9 reveals the conversion of forms I and II after 60 min irradiation in the presence of varying concentrations of $[Co(en)_2PIP]^{3+}$, $[Co(en)_2IP]^{3+}$ and $[Co(en)_2phen]^{3+}$. It was observed that by increasing the concentration of $[Co(en)_2PIP]^{3+}$, $[Co(en)_2IP]^{3+}$ and $[Co(en)_2phen]^{3+}$ form (I) diminishes gradually. The same has been observed with increasing irradiation time. This is the result of single strand cleavage of pBR322 DNA. It can also be seen in Fig. 8 that neither irradiation of DNA at 302 nm without Co(III) nor incubation with Co(III) without light yields significant strand scission. It is most likely that the reduction of Co(III) is the important step leading to DNA cleavage. Further studies are required to find out the path of the reaction mechanism.

4. Conclusions

The binding behavior of complexes $[Co(en)_2phen]^{3+}$, $[Co(en)_2IP]^{3+}$ and $[Co(en)_2PIP]^{3+}$ with DNA were characterized by absorption titration, fluorescence quenching and viscosity measurements. The results show that the binding

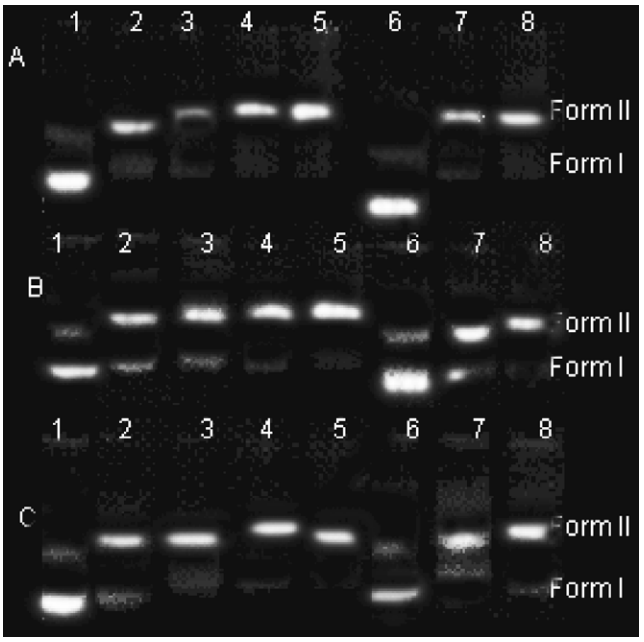


Fig. 9. Photoactivated cleavage of pBR 322 DNA, Lane 1 control plasmid DNA (untreated pBR 322), lanes 2–5 addition of complex 5 μl, 10 μl, 20 μl, 30 μl, and 6th lane +5 μm at 0 time, lanes 7 and 8 +5 μM complex upon irradiation ($\lambda_{irrd} = 302$ nm) at 5 min and 10 min. Complex (A) $[Co(en)_2phen]^{3+}$, (B) $[Co(en)_2IP]^{3+}$ and (C) $[Co(en)_2PIP]^{3+}$.

constants followed the order: $[Co(en)_2PIP]^{3+} > [Co(en)_2PIP]^{3+} > [Co(en)_2phen]^{3+}$, indicating that the PIP ligand, with its large planar surface, is a better intercalating ligand than IP and phen, which interact by electrostatic interactions only.

References

[1] D.S. Sigman, Acc. Chem. Res. 19 (1986) 180.
[2] D.S. Sigman, A. Mazumder, D.M. Perrin, Chem. Rev. 93 (1993) 2295.
[3] Y. Jenkins, A.E. Friedman, N.J. Turro, J.K. Barton, Biochemistry 31 (1992) 10809.
[4] D.L. Carlson, D.H. Huchital, E.J. Mantilla, R.V. Sheardy, W.L. Murphy Jr., J. Am. Chem. Soc 115 (1993) 6424.
[5] J.K. Barton, J. Biomol. Struct. Dyn. 1 (1983) 621.
[6] J.K. Barton, Science 233 (1986) 727.
[7] M. Carter, M. Rodriguez, A.J. Bard, A.J. Bard, J. Am. Chem. Soc. 111 (1989) 8901.
[8] R.J. Morgan, S. Chatterjee, A.D. Baker, T.C. Strekas, Inorg. Chem. 30 (1991) 2687.
[9] A.S. Sitlani, E.C. Long, A.M. Pyle, J.K. Barton, J. Am. Chem. Soc. 114 (1992) 2303.
[10] C. Turro, S.H. Bossman, Y. Jenkins, J.K. Barton, N.J. Turro, J. Am. Chem. Soc. 117 (1995) 9026.
[11] M. Yamada, Y. Tanaka, Y. Yoshimoto, S. Kuroda, I. Shimao, Bull. Chem. Soc. Jpn. 65 (1992) 1006.
[12] J.-Z. Wu, B.-H. Ye, L. Wang, L.-N. Ji, J.-Y. Zhou, R.-H. Li, Z.-Y. Zhou, J. Chem. Soc., Dalton Trans. (1997) 1395.
[13] A. Barve, S. Ghosh, A.A. Kumbhar, A.S. Kumbhar, Trans. Met. Chem. 30 (2005) 312.
[14] J.C. Bailar Jr., in: W. Conard Fernelius (Ed.), *Cis* & *trans* dichlorobis-(ethylenediamine)Co(III)chloride, Inorganic syntheses (II), McGraw-Hill Book Company Inc., London, 1946, pp. 222–224.
[15] J. Marmur, J. Mol. Biol. 3 (1961) 208.
[16] M.F. Reichmann, S.A. Rice, C.A. Thomas, P. Doty, J. Am. Chem. Soc 76 (1954) 3047.
[17] T.B. Chaires, N. Dattagupta, D.M. Crother, Biochemistry 21 (1982) 3933.
[18] S. Satyanaryana, J.C. Dabrowiak, J.B. Chaires, Biochemistry 32 (1993) 2573.
[19] J.K. Barton, Science 233 (1986) 727.
[20] J.K. Barton, J.J. Dannenberg, A.L. Raphael, J. Am. Chem. Soc. 106 (1984) 2172.
[21] A. Wolfe, G.H. Shimer, T. Meehan, Biochemistry 26 (1987) 6392.
[22] Q.-L. Zhang, J.-G. Liu, H. Chao, G.-Q. Xue, L.-N. Ji, J. Inoorg. Biochem. 83 (2001) 49.
[23] R.P. Hertzberg, P.B. Dervam, J. Am. Chem. Soc. 104 (1982) 313.
[24] D.S. Sigman, D.R. Graham, L.E. Marshall, K.A. Reich, J. Am. Chem. Soc. 102 (1980) 5490.
[25] J.K. Barton, A.L. Raphael, J. Am. Chem. Soc 106 (1984) 2466.

Cl^-, N_3^-, NCS^-). In this study, it was observed that the ligand field strengths and redox potentials for the axial ligands reflect the normal spectrochemical series. To date, however, only a few cobalt(III) tetraaza macrocyclic complexes have been isolated and structurally characterized by X-ray crystallography [15–20]. For example, the cyclam and modified cyclam cobalt(III) complexes *trans*-$[Co(cyclam)Cl_2]\,Cl \cdot 4H_2O \cdot 0.47HCl$ [17] and $[Co(H_2ddta)Cl_2](ClO_4)_3 \cdot 2H_2O$ [18] exhibit a low-spin octahedral geometry with four secondary amines of the macrocycle and two axial chloride ligands. However, the coordination environment of $[Co(ddta)](ClO_4)_3$ [18] shows a distorted octahedron with four secondary amines and two pendant amines at the axial positions, in which the maxima in the electronic spectrum is shifted towards higher energy and the redox couple is shifted to a more negative value as compared to $[Co(H_2ddta)Cl_2](ClO_4)_3 \cdot 2H_2O$.

In this paper, we report the synthesis and characterization of $[Co(L)(int)_2]Cl \cdot 3H_2O$ (**1**), $[Co(L)(NCS)_2]NCS \cdot H_2O$ (**2**), $[Co(L)(NCO)_2]NCO \cdot H_2O$ (**3**) (L = 3,14-dimethyl-2,6,13,17-tetraazatricyclo[14,4,$0^{1.18}$,$0^{7.12}$]docosane, int = isonicotinate). To evaluate the effect of the axial groups, we have investigated the X-ray crystal structures, spectroscopic and electrochemical properties of these complexes.

2. Experimental

2.1. Materials and physical methods

All chemicals used in syntheses were of reagent grade and were used without further purification. The macrocycle 3,14-dimethyl-2,6,13,17-tetraazatricyclo[14,4,$0^{1.18}$,$0^{7.12}$]-docosane (L) and $[Co(L)Cl_2]Cl \cdot 4H_2O$ were prepared according to the literature methods [20,21]. Infrared spectra were recorded as KBr pellets on a Perkin–Elmer Paragon 1000 FT-IR spectrometer. Solution electronic spectra were obtained on a Jasco Uvidec 610 spectrophotometer. Solid-state spectra were measured by the diffuse reflectance method on a Shimadzu UV2401 PC/DRS spectrophotometer. Elemental analyses (C, H, N) were performed on a Perkin–Elmer CHN-2400 analyzer. Electrochemical measurements were accomplished with a three-electrode potentiostat BAS-100BW system. A hanging mercury dropping electrode was used as the working electrode. The counter electrode was a coiled Pt wire and a Ag/AgCl electrode was used as a reference electrode. Cyclic voltammetric data were obtained in DMSO solution with 0.10 M Et_4NClO_4 (TEAP) as the supporting electrolyte at 20.0 ± 0.1 °C. The solution was degassed with high purity N_2 prior to carrying out the electrochemical measurements.

2.2. Syntheses of $[Co(L)(int)_2]Cl \cdot 3H_2O$ (1)

To a methanol solution (20 ml) of $[Co(L)Cl_2]Cl \cdot 4H_2O$ (287 mg, 0.5 mmol) was added sodium isonicotinate (145 mg, 1.0 mmol). The mixture was heated to reflux for 1 h and then the color of the solution changed from green to red. The solution was filtered and left at room temperature until red crystals formed. The product was recrystallized from a hot water/acetonitrile (1:1 v/v, 10 ml) mixture. Yield: 73%. *Anal.* Calc. for $C_{32}H_{54}ClCoN_6O_7$: C, 52.71; H, 7.46; N, 11.53. Found: C, 52.63; H, 7.54; N, 11.61%. IR (KBr, cm^{-1}): 3397(s), 3134(m), 3058(m), 2942(m), 2864(m), 1606(s), 1553(s), 1508(w), 1448(w), 1433(w), 1404(m), 1390(m), 1352(s), 1315(m), 1285(w), 1224(w), 1133(m), 1116(m), 1105(m), 1055(m), 1012(m), 998(w), 911(w), 850(w), 846(w), 763(m), 709(m), 695(s), 615(w), 556(w).

2.3. Syntheses of $[Co(L)(NCS)_2]NCS \cdot H_2O$ (2)

This compound was synthesized as red crystals in a reaction similar to that of **1**, except for the use of excess KNCS instead of sodium isonicotinate. The product was recrystallized from a hot water/acetonitrile (1:1 v/v, 10 ml) mixture. Yield: 78%. *Anal.* Calc. for $C_{23}H_{42}CoN_7OS_3$: C, 47.00; H, 7.20; N, 16.68. Found: C, 47.12; H, 7.28; N, 16.56%. IR (KBr, cm^{-1}): 3421(w), 3176(s), 2948(m), 2116(s), 2062(s), 1621(w), 1448(m), 1427(m), 1388(w), 1363(w), 1341(w), 1304(m), 1279(w), 1219(w), 1172(w), 1155(w), 1093(s), 1070(m), 1048(m), 1011(m), 975(m), 906(m), 850(w), 840(w), 798(w), 664(w), 611(w), 555(w).

2.4. Syntheses of $[Co(L)(NCO)_2]NCO \cdot H_2O$ (3)

The red complex was prepared by a method similar to that for **1**, except that excess NaNCO was used instead of sodium isonicotinate. The solid was recrystallized from a hot water/acetonitrile (1:1 v/v, 10 ml) mixture, but unfortunately crystals suitable for X-ray analysis were not obtained. Yield: 67%. *Anal.* Calc. for $C_{23}H_{42}CoN_7O_4$: C, 51.20; H, 7.85; N, 18.17. Found: C, 51.31; H, 7.74; N, 18.06%. IR (KBr, cm^{-1}): 3422(m), 3204(m), 2940(m), 2264(s), 2162(w), 1623(m), 1449(m), 1434(m), 1391(w), 1368(w), 1338(m), 1308(w), 1226(w), 1176(w), 1097(s), 1073(m), 1051(w), 1013(w), 976(m), 909(m), 852(w), 792(w), 662(w), 606(w), 556(w).

2.5. X-ray crystal structure analysis

Intensity data for compounds **1** and **2** were measured on a Bruker SMART 1000 CCD diffractometer using graphite-monochromated Mo Kα radiation ($\lambda = 0.71073$ Å). Accurate cell parameters and an orientation matrix were determined by the least-squares fit of 25 reflections. The intensity data were collected by the ω–2θ technique and corrected for Lorentz and polarization effects. An empirical absorption correction was applied with the SADABS program [22]. The structure was solved by direct methods [23] and the least-squares refinement of the structure was performed by the SHELXL-97 program [24]. For **1**, all atoms except all hydrogen atoms and Ow(3) were refined anisotropically.

Table 1
Crystallographic data

Compound	1	2
Empirical formula	$C_{32}H_{54}ClCoN_6O_7$	$C_{23}H_{42}CoN_7OS_3$
Formula weight	729.19	587.75
Temperature (K)	293(2)	293(2)
Crystal color/habit	block/pink	block/red
Crystal system	triclinic	triclinic
Space group	*P*1	*P*1
Unit cell dimensions		
a (Å)	9.5875(8)	8.5276(6)
b (Å)	10.2985(9)	8.8689(6)
c (Å)	10.9361(9)	10.0137(7)
α (°)	64.004(1)	84.442(1)
β (°)	66.314(1)	82.733(1)
γ (°)	65.613(1)	67.857(1)
V (Å^3)	851.21(12)	694.85(8)
Z	1	1
D_{calc} (Mg m^{-3})	1.423	1.405
Absorption coefficient (mm^{-1})	0.638	0.873
F(000)	388	312
Crystal size (mm)	$0.33 \times 0.28 \times 0.19$	$0.25 \times 0.18 \times 0.10$
θ Range (°)	2.15–28.44	2.05–28.33
Limiting indices	$-12 \leqslant h \leqslant 12$, $-13 \leqslant k \leqslant 13$, $-14 \leqslant l \leqslant 14$	$-11 \leqslant h \leqslant 11$, $-11 \leqslant k \leqslant 11$, $-13 \leqslant l \leqslant 13$
Reflection collected/unique (R_{int})	11 666/8306 (0.0157)	9574/6804 (0.0149)
Absorption correction	SADABS	SADABS
Maximum and minimum transmission	0.8858 and 0.7319	0.9172 and 0.7864
Data/restraints/parameters	8306/3/431	6804/3/328
Goodness-of-fit on F^2	1.066	1.083
Final *R* indices [$I > 2\sigma(I)$]	R_1[a] = 0.0357, wR_2[b] = 0.0886	$R_1 = 0.0442$, $wR_2 = 0.1063$
R indices (all data)	$R_1 = 0.0415$, $wR_2 = 0.0933$	$R_1 = 0.0577$, $wR_2 = 0.1175$
Absolute structure parameter	0.37(2)	0.36(2)
Largest difference peak and hole (e Å^{-3})	0.579 and −0.304	0.739 and −0.696

[a] $R_1 = \sum\|(F_o| - |F_c\|)/\sum|F_o|$.
[b] $wR_2 = \{\sum[w(F_o^2 - F_c^2)^2]/\sum[w(F_o^2)^2]\}^{1/2}$.

Hydrogen atoms were placed in calculated positions, allowing them to ride on their parent C atoms with $U_{iso}(H) = 1.2U_{eq}$(C or N). The hydrogen atoms of Ow(3) were not found. For **2**, the hydrogen atoms of Ow(1) were not found. Crystal parameters and details of the data collections and refinement are summarized in Table 1.

3. Results and discussion

3.1. Crystal structures

An ORTEP drawing of $[Co(L)(int)_2]Cl \cdot 3H_2O$ (**1**) with the atomic numbering scheme is shown in Fig. 1 and selected bond lengths and angles are listed in Table 2. The ligand skeleton of the present compound takes the *trans*-III(*R*,*R*,*S*,*S*) configuration with two chair six-membered and two gauche five-membered chelate rings. The structure of **1** shows that the cobalt(III) ion is coordinated by the secondary amines of the macrocycle and that the axial positions are bonded by the two carboxylate oxygen atoms of the isonicotinate ligands, which is a distorted octahedral environment. The average Co–N (secondary amine) distance of 1.990(2) Å is similar to that found in *cis*-$[Co(cyclam)(en)]Cl_3 \cdot 3H_2O$ [1.996(2) Å] [16] and $[Co(L)Cl_2]Cl \cdot 4H_2O$ [1.999(2) Å] [20]. The N–Co–N angles

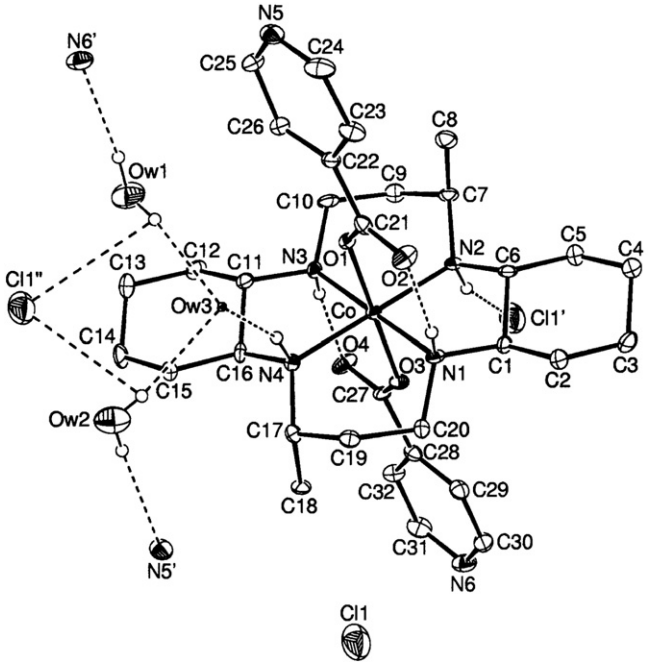


Fig. 1. An ORTEP diagram of $[Co(L)(int)_2]Cl \cdot 3H_2O$ (**1**) with the atom-numbering scheme (30% probability ellipsoids shown). The hydrogen bonds are indicated by dotted lines. The hydrogen atoms except for water molecules are omitted for clarity.

Table 2
Selected bond lengths (Å) and angles (°) for $[Co(L)(int)_2]Cl \cdot 3H_2O$ (**1**)

Bond lengths (Å)			
Co–N(1)	1.981(4)	Co–N(2)	1.995(4)
Co–N(3)	1.983(4)	Co–N(2)	2.002(4)
Co–O(1)	1.921(3)	Co–O(3)	1.929(3)
C(21)–O(1)	1.292(5)	C(21)–O(2)	1.243(6)
C(27)–O(3)	1.289(5)	C(27)–O(4)	1.222(6)
Bond angles (°)			
N(1)–Co–N(2)	84.7(2)	N(1)–Co–N(3)	179.3(2)
N(1)–Co–N(4)	95.2(2)	N(2)–Co–N(3)	94.6(2)
N(2)–Co–N(4)	179.9(3)	N(3)–Co–N(4)	85.5(2)
O(1)–Co–N(1)	94.7(2)	O(1)–Co–N(2)	93.2(2)
O(1)–Co–N(3)	85.6(2)	O(1)–Co–N(4)	86.8(2)
O(3)–Co–N(1)	85.4(2)	O(3)–Co–N(2)	86.5(2)
O(3)–Co–N(3)	94.3(2)	O(3)–Co–N(4)	93.5(2)
O(1)–Co–O(3)	179.7(2)	Co–O(1)–C(21)	133.0(3)
Co–O(3)–C(27)	131.5(3)	O(1)–C(21)–O(2)	125.2(5)
O(3)–C(27)–O(4)	128.5(4)	O(1)–C(21)–C(22)	115.7(4)
O(2)–C(21)–C(22)	119.2(4)	O(3)–C(27)–C(28)	113.4(4)
O(4)–C(27)–C(28)	118.1(4)		

of the six-membered chelate rings are larger than those of the five-membered chelate rings. The dihedral angle (α) between the plane of the carboxylate group and CoN_4 plane is 86.7(4)°. The axial Co–O bonds are not perfectly perpendicular to the CoN_4 plane with the O–Co–N angles ranging from 85.4(2)° to 94.7(2)°. Interestingly, the secondary amines of the macrocycle are hydrogen bonded to the uncoordinated carboxylate oxygen atoms of the isonicotinate [$N(1)\cdots O(2)^{ii}$ 2.717(6) Å, 154.9°; $N(3)\cdots O(4)^{ii}$ 2.726(6) Å, 156.1°; symmetry code: ii: x, y, z], chloride anion [$N(2)\cdots Cl(1)^{iii}$ 3.197(4) Å, 161.9°; symmetry code: iii: x, y, $z+1$] and the water molecule [$N(4)\cdots Ow(3)^{ii}$ 3.256(4) Å, 161.5°]. Furthermore, the water molecules found in the lattice also form hydrogen bonds with the nitrogen atoms of the isonicotinate [$Ow(1)\cdots N(6)^{iv}$ 3.042(7) Å, 151(5)°; $Ow(2)\cdots N(5)^{v}$ 3.066(7) Å, 160(5)°; symmetry codes: iv: $x+1$, $y+1$, $z-1$; v: x, $y-1$, z], with the chloride anion [$Ow(1)\cdots Cl(1)^{i}$ 3.028(6) Å; $Ow(2)\cdots Cl(1)^{i}$ 3.153(6) Å] and with other water inclusions [$Ow(1)\cdots Ow(3)^{ii}$ 3.228(6) Å, 166(4)°; $Ow(2)\cdots Ow(3)^{ii}$ 3.016(6) Å, 172(6)°; $Ow(3)\cdots Ow(2)^{ii}$ 3.016(6) Å; $Ow(3)\cdots Ow(1)^{ii}$ 3.228(6) Å].

An ORTEP drawing of $[Co(L)(NCS)_2]NCS \cdot H_2O$ (**2**) with the atomic numbering scheme is shown in Fig. 2 and selected bond lengths and angles are listed in Table 3. The structure of **2** consists of a $[Co(L)(NCS)_2]^+$ cation, one NCS^- anion and a water molecule. The crystal structure of **2** confirms a six-coordinated octahedral geometry with bonds from the cobalt(III) ion to the secondary amines of the macrocycle and to the two axial thiocyanate ligands. The average Co–N (secondary amines) distance of 1.999(3) Å is significantly longer than the average axial Co–N (thiocyanate) distance [1.886(4) Å], which is similar to that observed for complex **1**. The Co–N (thiocyanate) linkages are bent slightly off perpendicular to the CoN_4 plane by 0.3–2.9°. The two Co–N–C and N–C–S angles coordinated to the thiocynate ligands are 171.4(5)–171.6(5)° and 175.1(10)–177.1(6)°, respectively.

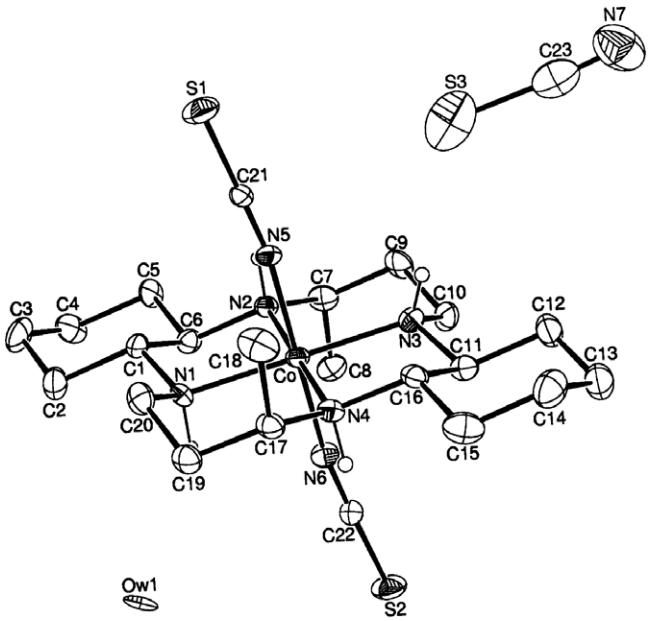


Fig. 2. An ORTEP diagram of $[Co(L)(NCS)_2]NCS \cdot H_2O$ (**2**) with the atom-numbering scheme (30% probability ellipsoids shown). The hydrogen atoms are omitted for clarity.

Table 3
Selected bond lengths (Å) and angles (°) for $[Co(L)(NCS)_2]NCS \cdot H_2O$ (**2**)

Bond lengths (Å)			
Co–N(1)	2.002(5)	Co–N(2)	2.004(5)
Co–N(3)	1.974(6)	Co–N(4)	2.014(5)
Co–N(5)	1.896(5)	Co–N(6)	1.876(5)
C(21)–N(5)	1.129(7)	C(22)–N(6)	1.178(7)
C(23)–N(7)	1.132(13)	C(21)–S(1)	1.640(6)
C(22)–S(2)	1.606(7)	C(23)–S(3)	1.842(8)
Bond angles (°)			
N(1)–Co–N(2)	85.8(2)	N(1)–Co–N(3)	178.9(3)
N(1)–Co–N(4)	94.4(2)	N(2)–Co–N(3)	95.1(2)
N(2)–Co–N(4)	179.6(3)	N(3)–Co–N(4)	84.8(2)
N(5)–Co–N(1)	90.3(2)	N(5)–Co–N(2)	87.1(2)
N(5)–Co–N(3)	89.1(2)	N(5)–Co–N(4)	92.6(2)
N(6)–Co–N(1)	89.7(2)	N(6)–Co–N(2)	92.6(2)
N(6)–Co–N(3)	90.9(2)	N(6)–Co–N(4)	87.7(2)
N(5)–Co–N(6)	179.7(3)	Co–N(5)–C(21)	171.4(5)
Co–N(6)–C(22)	171.6(5)	N(5)–C(21)–S(1)	175.4(6)
N(6)–C(22)–S(2)	177.1(6)	N(7)–C(23)–S(3)	175.1(10)

3.2. Characterization of the complexes

The infrared spectra of these complexes show bands at 3200–3212 cm^{-1}, which are assigned to ν(NH) of the coordinated secondary amines of the macrocycle. That the spectrum of **1** contains two strong ν(COO) bands at 1606 and 1553 cm^{-1} is consistent with the coordinated isonicotinate ligand. Two strong bands at 2116 and 2062 cm^{-1} in **2** are assigned to ν(NCS) stretching of the lattice and coordinated thiocyanate ligands, which are in agreement with

the crystal structure of **2**. For **3** the IR data are in accordance with a N-bonded isocyanato structure, as a strong band at 2264 cm^{-1} is characteristic of Co–N bonding [25]. The spectroscopic data of the complexes are listed in Table 4. The electronic spectra of these complexes in DMSO and in the solid state show bands in the regions 258–264 and 543–583 nm and are attributed to intraligand charge transfer ($n \rightarrow \pi^*$) and d–d transition ($^1A_{1g} \rightarrow {}^1T_{2g}$), respectively, in a low spin d^6 octahedral symmetry [26]. However, the wavelength of the d–d bands of the complexes **1**–**3** is somewhat shorter than that of $[Co(L)Cl_2]\cdot 4H_2O$ [20] in spite of the similar average Co–N(secondary amines) bond distance. Furthermore, the wavelengths of the d–d bands of the complexes increase toward higher energies in the order **1** < **2** < **3**, which is reasonably explained by the spectrochemical series. It was previously observed for cobalt(III) complexes with a tetraaza macrocycle containing various axial ligands that the spectra are affected by the type of the axial ligand [15].

Cyclic voltammetric data for the cobalt(III) complexes in 0.10 M TEAP–DMSO solution are given in Table 5 along with the other macrocyclic cobalt(III) complexes. A typical cyclic voltammogram of **1** is shown in Fig. 3. The complexes exhibit a one-electron wave corresponding to the Co(III)/Co(II) process. It is of interest to compare the redox potentials for the $[Co(L)X_2]^+$ complexes with axial ligands. The reduction potentials for these complexes are considerably more negative than that of *trans*-$[Co(L)Cl_2]Cl\cdot 4H_2O$ [20], indicating that these complexes make reduction more difficult. The reduction potentials of these complexes decrease with the axial ligands in the order **3** > **2** > **1**. That is, the type of axial ligand significantly affects the electrochemical properties of the Co(III) complexes. The above results, together with the crystal structures and spectroscopic data, clearly show that the axial groups of the Co(III) complexes are coordinated to the metal(III) ion.

Table 4
Electronic spectral data[a]

Complex	State	λ_{max}/nm (ε/M^{-1} cm^{-1})
$[Co(cyclam)Cl_2]Cl\cdot H_2O$[b]	MeOH	386 (56), 458 (24), 617 (35)
$[Co(L)Cl_2]\cdot 4H_2O$[c]	DMSO	366 (2.45×10^3), 646 (295)
	Solid	363, 638
$[Co(L)(int)_2]Cl\cdot 3H_2O$ (**1**)	DMSO	264 (1.12×10^3), 583 (109)
	Solid	263, 582
$[Co(L)(NCS)_2]NCS\cdot H_2O$ (**2**)	DMSO	260 (1.15×10^3), 548 (108)
	Solid	259, 548
$[Co(L)(NCO)_2]NCO\cdot H_2O$ (**3**)	DMSO	258 (1.26×10^3), 543 (116)
	Solid	258, 544

[a] Solution = DMSO at 20 ± 0.1 °C; solid = diffuse reflectance.
[b] Ref. [15].
[c] Ref. [20].

Table 5
Cyclic voltammetric data[a]

Complex	Potentials (V) vs. Ag/AgCl
	Co(III)/Co(II)
$[Co(H_2ddta)Cl_2](ClO_4)_3\cdot 2H_2O$[b]	−0.03(i)[d]
$[Co(ddta)](ClO_4)_3$[b]	−0.79
$[Co(L)Cl_2]Cl\cdot 4H_2O$[c]	−0.16
$[Co(L)(int)_2]Cl\cdot 3H_2O$ (**1**)	−0.47
$[Co(L)(NCS)_2]NCS\cdot H_2O$ (**2**)	−0.57(i)[d]
$[Co(L)(NCO)_2]NCO\cdot H_2O$ (**3**)	−0.68(i)[d]

ddta = 6,13-diamino-6,13-dimethyl-1,4,8,11-tetraazacyclotetradecane.
[a] Measured in 0.10 M TEAP–DMSO solution at 20.0 ± 0.1 °C
[b] Ref. [18].
[c] Ref. [20].
[d] i = irreversible.

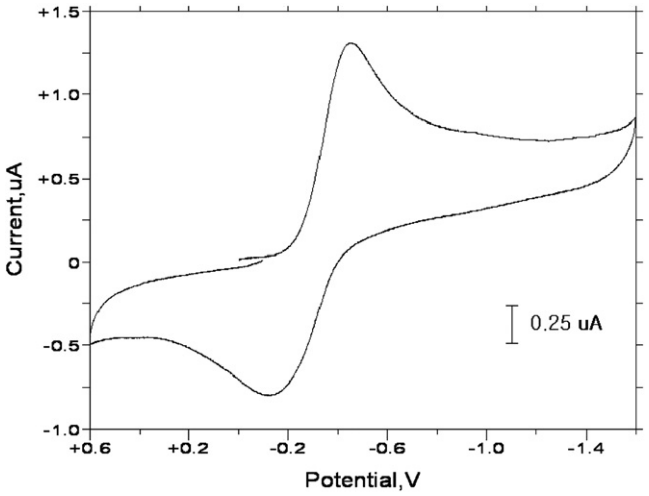


Fig. 3. Cyclic voltammogram of $[Co(L)(int)_2]Cl\cdot 3H_2O$ (**1**) in 0.10 M TEAP–DMSO solution at 20.0 ± 0.1 °C. The scan rate is 100 mV/s.

4. Supplementary material

CCDC 622111 and 622112 contain the supplementary crystallographic data for **1** and **2**. These data can be obtained free of charge via http://www.ccdc.cam.ac.uk/conts/retrieving.html, or from the Cambridge Crystallographic Data Centre, 12 Union Road, Cambridge CB2 1EZ, UK; fax: (+44) 1223-336-033; or e-mail: deposit@ccdc.cam.ac.uk.

Acknowledgement

This work was supported by Grant (No. R05-2003-000-10536-0) from the Basic Research Program of the Korea Science and Engineering Foundation.

References

[1] M.G. Fairbank, P.R. Norman, A. McAuley, Inorg. Chem. 24 (1985) 2639.
[2] R.W. Hay, M.P. Pujari, J. Chem. Soc., Dalton Trans. (1986) 1485.
[3] R.W. Hay, B. Jeragh, G. Ferguson, B. Kaitner, B.L. Ruhl, J. Chem. Soc., Dalton Trans. (1982) 1531.
[4] R. Vicente, A. Escuer, J. Ribas, X. Solans, Inorg. Chem. 31 (1992) 1726.
[5] R. Vicente, A. Escuer, M.S. El Fallah, X. Solans, M.J. Font-Bardia, Inorg. Chim. Acta 261 (1997) 227.

[6] A. Escuer, R. Vicente, M.S. El Fallah, X. Solans, M.J. Font-Bardia, J. Chem. Soc., Dalton Trans. (1993) 2975.
[7] A. Escuer, R. Vicente, J. Ribas, M.S. El Fallah, X. Solans, Inorg. Chem. 32 (1993) 1033.
[8] A. Escuer, R. Vicente, M.S. El Fallah, X. Solans, M.J. Font-Bardia, J. Chem. Soc., Dalton Trans. (1996) 1013.
[9] P.V. Bernhardt, J.C. Hetherington, L.A. Jones, J. Chem. Soc., Dalton Trans. (1996) 4325.
[10] K.-Y. Choi, S.N. Choi, I.-H. Suh, Polyhedron 17 (1998) 1415.
[11] K.-Y. Choi, H. Ryu, I.-H. Suh, Polyhedron 17 (1998) 1241.
[12] K.-Y. Choi, Y.-J. Kim, H. Ryu, I.-H. Suh, Inorg. Chem. Commn. 2 (1999) 176.
[13] K.-Y. Choi, K.M. Chun, I.-H. Suh, Inorg. Chem. Commn. 2 (1999) 210.
[14] L.Y. Martin, C.R. Sperati, D.H. Busch, J. Am. Chem. Soc. 99 (1977) 2968.
[15] Y.H. Ludmila, Y. Martin, S.C. Jackels, M. Tait, D.H. Busch, J. Am. Chem. Soc. 99 (1977) 4029.
[16] T.F. Lai, C.K. Poon, Inorg. Chem. 15 (1976) 1562.
[17] M.E. Sosa-Torres, R.A. Toscano, Acta Crystallogr., Sect. C 53 (1997) 1585.
[18] P.V. Bernhardt, G.A. Lawrance, T.W. Hambley, J. Chem. Soc., Dalton Trans. (1989) 1059.
[19] J. Lichty, S.M. Allen, A.I. Grillo, S.J. Archibald, T.J. Hubin, Inorg. Chim. Acta 357 (2004) 615.
[20] K.-Y. Choi, H.-K. Lee, K.-J. Kim, H. Ryu, K.-C. Lee, J. Ko, M.-J. Kim, Transition Met. Chem. 31 (2006) 1093.
[21] S.-G. Kang, J.K. Kweon, S.-J. Jung, Bull. Korean Chem. Soc. 12 (1991) 483.
[22] A.C.T. North, D.C. Phillips, F.S. Mathews, Acta Crystallogr., Sect. A 24 (1990) 351.
[23] G.M. Sheldrick, Acta Crystallogr., Sect. A 46 (1990) 467.
[24] G.M. Sheldrick, SHELXL-97: Program for the Refinement of Crystal Structures, University of Göttingen, Göttingen, Germany, 1997.
[25] N. Nakamoto, Infrared and Raman Spectra of Inorganic and Coordination Compounds, Wiley, New York, 1997.
[26] N. Saha, A. Saha, S. Chaudhuri, T.C.W. Mak, T. Banerjee, P. Roychowdhury, Polyhedron 11 (1992).

been rarely reported [9]. Our group is interested in the supramolecular coordination chemistry of lanthanide ions with amide-based open-chain crown ethers that have strong coordination capability to the lanthanide ions and terminal group effects [10]. So we have designed a series of multi-functional amide-based open-chain crown ethers having the ability to coordinate lanthanide ions and thus enhance luminescence of lanthanide complexes by providing chromophores suitable for energy transfer, i.e., aryl substitutes.

In this work, we introduced biphenyl groups as the basic molecular frame and obtained a new open-chain crown ether ligand, *N*-phenyl-2-{2′-[(phenyl-ethyl-carbamoyl)-methoxy]-biphenyl-2-yloxy}-*N*-ethyl-acetamide (**L**), and reported the synthesis, luminescent properties of lanthanide complexes with the new ligand and the supramolecular structures of $La(pic)_3L$ and $2[La(NO_3)_3L(H_2O)]\cdot H_2O\cdot 0.5C_2H_5OH$. The results indicate that under excitation, the Eu(III) picrate complex had strong characteristic luminescence whereas the terbium picrate complex showed no luminescence. The lowest triplet state energy level of the ligand in the picrate complex which was calculated from the phosphorescence spectrum of the Gd(III) picrate complex at 77 K, and indicates that the triplet state energy level of the ligand matches better to the resonance level of Eu(III) than Tb(III) ion. The Eu(III) nitrate complex exhibited quite weak characteristic emissions. The $La(Pic)_3L$ crystal structure shows that the La(III) ion could be effectively encapsulated and protected by the coordinated ligand. Furthermore, the $La(Pic)_3L$ complex units are linked by the significant intermolecular π–π interactions between coordinate picrates to form a one-dimensional (1-D) supramolecular zigzag chain. The $2[La(NO_3)_3L(H_2O)]\cdot H_2O\cdot 0.5C_2H_5OH$ crystal structure shows that **L** gives two different arrangements around La(III) ions, and induces axial chirality directed by metal ions in the self-assembly process. Each La(III) ion is coordinated with four oxygen atoms from the ligand **L**, six oxygen atoms from three bidentate nitrate groups and one coordinate water molecule. Furthermore, the $[La(NO_3)_3L(H_2O)]$ complex units are linked by the intermolecular hydrogen bonds and π–π interaction to form a three-dimensional (3-D) netlike supramolecule.

2. Experimental

2.1. Materials

Lanthanide picrate [11] and *N*-ethyl-*N*-phenylchloroacetamide [12] were prepared according to the literature methods. All commercially available chemicals were of A.R. grade and were used without further purification.

2.2. Methods

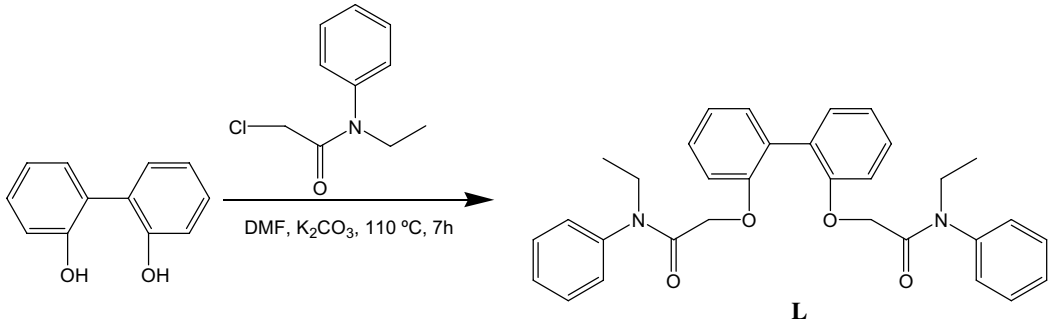
The metal ions were determined by EDTA titration using xylenal orange as indicator. C, H and N were determined using an Elementar Vario EL. Conductivity measurements were carried out with a DDS-307 type conductivity bridge using 10^{-3} mol dm^{-3} solutions at 25 °C. IR spectra were recorded on Nicolet FT-170SX instrument using KBr discs in the 400–4000 cm^{-1} region, ^{1}H NMR spectra were measured on a Varian Mercury plus 300 M spectrometer in $CDCl_3$ solution with TMS as internal standard. Fluorescence and phosphorescence measurements were made on a Hitachi F-4500 spectrophotometer. Mass spectra were obtained on a VG-ZAB-HS mass spectrometer.

2.3. Synthesis of the ligand

The synthetic route for the ligand is shown in Scheme 1. Anhydrous K_2CO_3 (5.6 g, 41 mmol) was added into the 15 mL DMF solution of 2,2′-dihydroxybiphenyl (1.86 g, 10 mmol) at 100 °C. After 1 h, a solution of *N*-ethyl-*N*-phenylchloroacetamide (5.92 g, 30 mmol) in 10 mL DMF was added dropwise to the mixture and maintained at 110 °C for 7 h. When cool, distilled water (60 ml) was added and the turbid solution was extracted with chloroform (3×40 mL). The combined organic phases were washed with water and dried with anhydrous Na_2SO_4. The solvent was removed and the residue was chromatographed to afford the ligand **L**; yield: 85%.

2.4. Synthesis of the lanthanide picrate complexes

To a solution of 0.2 mmol lanthanide picrate in 5 ml of ethanol was added dropwise the solution of 0.2 mmol **L** in



Scheme 1. The synthetic route for the ligand **L**.

10 ml of ethanol. The mixture was stirred at room temperature for 5 h. The precipitated solid complex was filtered, washed with ethanol and dried in vacuum over P_2O_5 for 48 h. All the complexes were obtained as yellow powders in a yield of 80–85%. Slowly evaporating a solution of the lanthanum complex in $CHCl_3/CH_3CH_2OH$ at room temperature, resulted in the formation of block crystals after 2 weeks.

2.5. Synthesis of the lanthanide nitrate complex

To a solution of 0.2 mmol lanthanide lanthanide nitrate in 5 ml of ethanol was added dropwise the solution of 0.2 mmol **L** in 10 ml of ethanol. The mixture was stirred at room temperature for 10 h and a clear solution obtained. The clear solution of lanthanum nitrate complex was filtered and left to crystallise. After about a month, a colorless crystal formed from the solution. After solvent evaporation from the solution of europium nitrate complex in vacuum, a white precipitate obtained, washed with little ethanol and dried in vacuum over P_2O_5 for 72 h.

2.6. Crystal structure determination

X-ray diffraction data of $La(pic)_3L$ and $2[La(NO_3)_3L(H_2O)]\cdot H_2O\cdot 0.5C_2H_5OH$ were collected on a Bruker Smart-1000 CCD area detector diffractometer, using graphite-monochromatized Mo Kα ($\lambda = 0.71073$ Å) at 298(2) K. The structures were solved by direct method and refined by full matrix least-squares techniques on F^2 with all non-hydrogen atoms treated anisotropically. All calculations were performed with the program package SHELXTL. The hydrogen atoms were assigned with common isotropic displacement factors and included in the final refinement by using geometrical restrains.

3. Results and discussion

3.1. Properties of the complexes

Analytical data for the complexes, listed in Table 1, indicate that the seven complexes of rare earth picrates and europium nitrate conform to a 1:1 metal-to-ligand stoichiometry $Ln(pic)_3L$ and $Eu(NO_3)_3L$. All the picrate complexes are soluble in DMF, DMSO, acetonitrile, acetone and $CHCl_3$, but slightly soluble in ethanol. The molar conductances of the picrate complexes in acetone and $Eu(NO_3)_3L$ in DMF (see Table 1) indicate that all the picrate complexes and $Eu(NO_3)_3L$ act as non-electrolytes [13], implying that all the picrate groups and nitrate groups are in the coordination sphere.

3.2. Crystal structure of $La(Pic)_3L$

A summary of crystallographic data and details of the structure refinements are listed in Table 2. The selected bond lengths and bond angles are given in Table 3.

The single-crystal X-ray analysis of the complex $La(Pic)_3L$ reveals that the La(III) ion is coordinated with 10 oxygen donor atoms, six of which belong to three bidentate picrate groups and the remaining four to the tetradentate ligand **L** (Fig. 1). The coordination polyhedron around La(III) ion is a distorted bicapped square antiprism (Fig. 2). The two phenyl rings about the central bond in the molecule have a drastic twisting, with the dihedral angle between them being 62.49°. The La—O (C=O) distances (mean 2.461 Å) are significantly shorter than the La–O (C–O–C) distances (mean 2.701 Å). This suggests that the La—O (C=O) bond is stronger than the La–O (C–O–C) bond.

In the complex, the requirement of high coordination number of the lanthanide ion is satisfied by the tetradentate ligand and three bidentate picrate groups. Due to the space obstacle of coordinated picrates, no coordinated solvent molecules exist in the complex, which can efficiently quench lanthanide luminescence, this is important in the design of supramolecular photonic devices.

Interestingly, the complex has significant intermolecular π–π interaction [14] between two picrates of one complex molecule and equivalent picrates of the adjacent molecules with the dihedral angles between them being 0° and 0°, and the distances between their centroids being 3.774, 4.019 Å, respectively, thus, producing a one-dimensional (1-D) supramolecular zigzag chain (Fig. 3).

3.3. Crystal structure of $2[La(NO_3)_3L(H_2O)]\cdot H_2O\cdot 0.5C_2H_5OH$

A summary of crystallographic data and details of the structure refinements are listed in Table 2. The selected bond lengths and bond angles are given in Table 4.

Table 1
Analytical and molar conductance data for the complexes (calculated values in parentheses)

Complex	Analysis (%)				*Λm* ($cm^2\ \Omega^{-1}\ mol^{-1}$)
	C	H	N	Ln	
$La(pic)_3L$	44.78(45.08)	3.01(2.86)	11.43(11.57)	10.21(10.44)	34.0
$Nd(pic)_3L$	44.63(44.91)	3.04(2.84)	11.38(11.53)	10.53(10.78)	31.7
$Eu(pic)_3L$	44.17(44.64)	2.70(2.83)	11.32(11.46)	11.13(11.31)	29.8
$Gd(pic)_3L$	44.16(44.48)	2.94(2.82)	11.14(11.42)	11.28(11.64)	32.7
$Tb(pic)_3L$	44.12(44.41)	2.72(2.81)	11.26(11.40)	11.32(11.77)	31.2
$Y(pic)_3L$	46.56(46.84)	2.68(2.97)	12.08(12.02)	6.64(6.95)	34.6
$Eu(NO_3)_3L$	45.78(45.39)	3.08(3.78)	8.63(8.27)	17.49(17.97)	50.3

Table 2
Crystal data and structure refinements for lanthanum picrate and lanthanum nitrate complexes

Empirical formula	$C_{50}H_{38}LaN_{11}O_{25}$	$C_{65}H_{73}La_2N_{10}O_{29.50}$
Temperature (K)	298(2)	293(2)
Crystal color	yellow	colourless
Crystal size (mm)	$0.45 \times 0.38 \times 0.19$	$0.53 \times 0.48 \times 0.45$
Formula weight	1331.82	1744.15
Crystal system	triclinic	monoclinic
Space group	$P\bar{1}$	$P2(1)/c$
Unit cell dimensions		
a (Å)	10.9574(18)	25.733(8)
b (Å)	15.381(3)	11.978(4)
c (Å)	16.877(3)	28.383(8)
α (°)	95.734(3)	90
β (°)	90.664(2)	116.452(4)
γ (°)	107.748(2)	90
V (Å^3)	2692.8(8)	7832(4)
Z	2	4
D_{calc} (mg/m^3)	1.643	1.479
$F(000)$	1344	3532
Radiation, graphite-monochromatized, λ (Å)	0.71073	0.71073
Reflections collections	14193	39525
Independent reflection	9335	13698
θ Range for data collection (°)	1.95–25.01	1.92–25.01
Index range	$-13 \leqslant h \leqslant 12$	$-28 \leqslant h \leqslant 30$
	$-9 \leqslant k \leqslant 18$	$-8 \leqslant k \leqslant 14$
	$-20 \leqslant l \leqslant 19$	$-33 \leqslant l \leqslant 33$
Goodness-of-fit on F^2	1.081	1.081
$R[I > 2\sigma(I)]$	$R = 0.0519$, $wR = 0.1132$	$R = 0.0657$, $wR = 0.1641$
R(all data)	$R = 0.0825$, $wR = 0.1327$	$R = 0.1687$, $wR = 0.2313$
Largest difference peak and hole [e Å^{-3}]	1.148, −0.612	1.388, −1.009

Table 3
Selected bond lengths (Å) and bond angles (°) for La(pic)$_3$L

La(1)–O(12)	2.404(4)	La(1)–O(3)	2.700(3)
La(1)–O(5)	2.419(4)	La(1)–O(1)	2.700(3)
La(1)–O(19)	2.423(4)	La(1)–O(20)	2.794(4)
La(1)–O(2)	2.429(3)	La(1)–O(13)	2.842(5)
La(1)–O(4)	2.492(3)	La(1)–O(6)	2.937(5)
O(2)–La(1)–O(4)	124.8(1)	O(3)–La(1)–O(1)	65.9(1)
O(4)–La(1)–O(3)	60.1(1)	O(19)–La(1)–O(20)	60.5(1)
O(2)–La(1)–O(1)	60.1(1)	O(12)–La(1)–O(13)	59.1(1)
O(4)–La(1)–O(1)	73.3(1)	O(5)–La(1)–O(6)	58.4(1)

The $2[La(NO_3)_3L(H_2O)] \cdot H_2O \cdot 0.5C_2H_5OH$ crystal structure reveals that there are two independent molecules in the unit cell. Each La(III) ion is coordinated with 11 oxygen donor atoms. Six of them belong to three bidentate nitrate groups, one of them belongs to one coordinate water molecule, and the remaining four are from the tetradentate ligand **L** (Fig. 4). Upon coordination, **L** gives two different arrangements (A and B) around La(III) ions in the unit cell. In structure A, the two phenyl rings about the central bond in the molecule have a drastic twisting, with the dihedral angle between them being 56.75°. Again, the La(1)—O (C=O) distances (mean 2.512 Å) are shorter than the La–O (C–O–C) distances (mean 2.764 Å), suggesting that La—O (C=O) bond is stronger than the La–O (C–O–C) bond. The same situation occurs in structure B, where the dihedral angle between the two phenyl rings in the molecule is 58.61°, the average distance between La(2) atom and oxygen atoms (C=O) is 2.525 Å and the average distance between La(2) and oxygen atoms (C–O–C) is 2.781 Å. It is interesting that the free ligand is achiral, but upon metal coordination, it induces axial chirality. As shown in Fig. 4, the ligand exhibits (*S*) configuration in structure A and (*R*) configuration in structure B in the unit cell, which is contributed to the metal-directed self-assembly process of the ligands with the metal ions [15].

In structure A, atom O(14) acts as hydrogen bond donor to form O–H···O with the oxygen atom O(12) of the adjacent equivalent molecule [O(12)···H(68), 2.268 Å and O(14)–H(68)···O(12), 144.34°], thus, generating a one-dimensional (1-D) supramolecular zigzag chain along the b axis as shown in Fig. 5a.

In structure B, atom C(51) acts as hydrogen bond donor to form C–H···O with the oxygen atom O(22) of the adjacent equivalent molecule [O(22)···H(51), 2.604 Å and C(51)–H(51)···O(22), 134.33°] [16], thus, generating a dimer as shown in Fig. 5(b); furthermore, the dimeric blocks are linked by the intermolecular hydrogen bond O(28)–H(70)···O(26) [O(26)···H(70), 2.222 Å and O(28)–H(70)···O(26), 150.84°] to form a two-dimensional (2-D) supramolecular layer with hydrogen bonded channels as shown in Fig. 5c and d.

In addition, intermolecular π–π interaction [14] between one phenyl ring of one ligand frame from one chain and another phenyl ring of the adjacent ligand frame from the adjacent layer with the dihedral angle between them being 6.01° and the distance between their centroids being

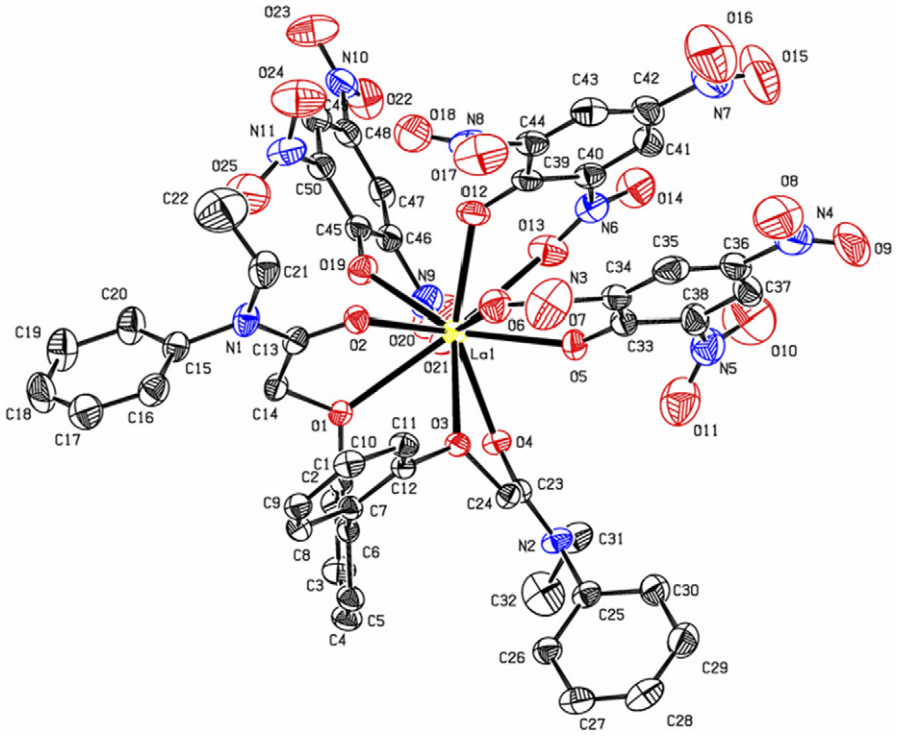


Fig. 1. ORTEP diagram (30% probability ellipsoids) showing the coordination sphere of [La(pic)$_3$L]. Hydrogen atoms are omitted for clarity.

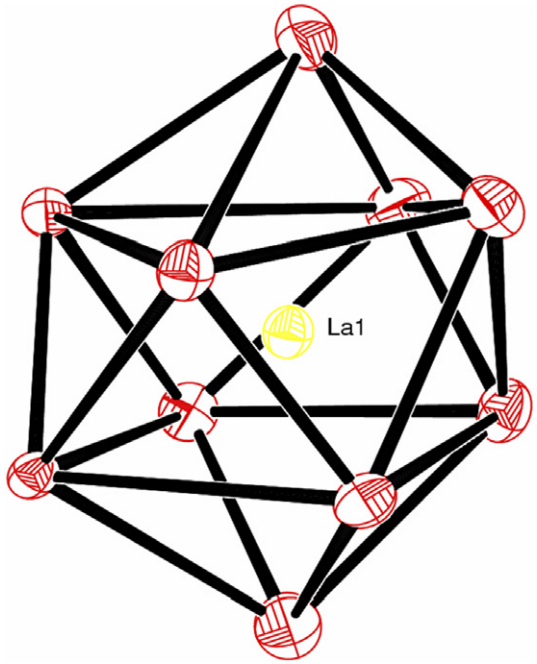


Fig. 2. Coordination polyhedron of La(III) ion in La(pic)$_3$L.

4.058 Å, further produce a three-dimensional (3-D) netlike supramolecule as shown in Fig. 6.

3.4. IR spectra

The main infrared bands of the ligand and their complexes are presented in Tables 5 and 6. The "free" ligand **L** exhibits two absorption bands at 1676 and 1126 cm^{-1} which are assigned to ν(C=O) and ν(C–O–C), respectively.

In picrate complexes, the ν(C=O) and ν(C–O–C) of the free ligand shift by ca. 57 and 46 cm^{-1} towards lower wave numbers, thus indicating that the C=O and ether O-atoms take part in coordination to the metal ions.

The OH out-of-plane bending vibration of the free Hpic at 1151 cm^{-1} disappears in the spectra of the complexes indicating that the H atom of the OH group is replaced by Ln(III) ions. The vibration ν(C–O) at 1265 cm^{-1} is shifted towards higher frequency by ca. 10 cm^{-1} in the complexes. This is due to the following two effects. First, the hydrogen atom of the OH group is replaced by Ln(III), increasing the π-bond character in the C–O bond. Secondly, coordination of the oxygen atom of **L** to Ln(III) causes the π-character to be weakened [10b]. The free Hpic has $\nu_{as}(NO_2)$ and $\nu_s(NO_2)$ at 1555 and 1342 cm^{-1}, respectively, which splits into two bands at 1584, 1545 cm^{-1} and 1352, 1331 cm^{-1} in the complexes. This indicates that some of the O-atoms in the nitro group of Pic$^-$ take part in coordination [17]. On the basis of the similarity of their IR spectra, it may be assumed that the picrate complexes have the similar structures.

In the europium nitrate complex, the ν(C=O) and ν(C–O–C) of the free ligand shift by ca. 50 and 54 cm^{-1} towards lower wave numbers, thus indicating that all the C=O and ether O atoms take part in coordination to the metal ion. The absorption bands assigned to the coordinated nitrate groups (C_{2v}) are observed at about 1495 cm^{-1} (ν_1), 1308 cm^{-1} (ν_4), 1030 cm^{-1} (ν_2) and 815 cm^{-1}(ν_3) [18] for the nitrate complex. In addition, the separation of the

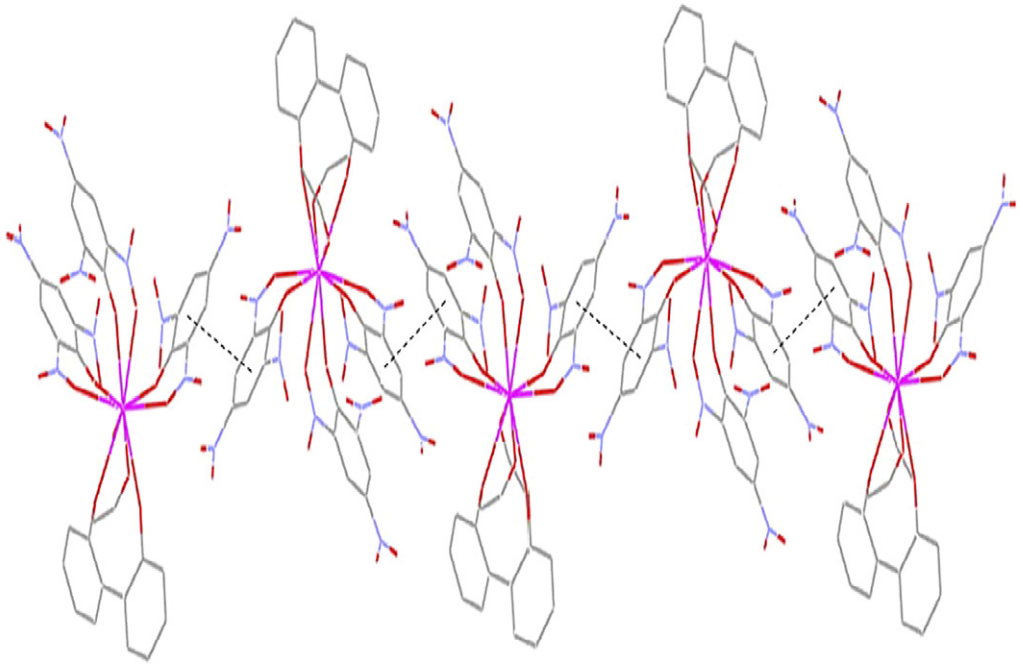


Fig. 3. The zigzag chain of $[La(pic)_3L]$ linked by intermolecular π–π stacking interactions. All the *N*-ethylanilines are omitted for clarity.

Table 4
Selected bond lengths (Å) and bond angles (°) for $2[La(NO_3)_3L(H_2O)]\cdot H_2O\cdot 0.5C_2H_5OH$

La(1)–O(1)	2.492(7)	La(2)–O(15)	2.523(8)
La(1)–O(3)	2.532(7)	La(2)–O(17)	2.527(7)
La(1)–O(14)	2.538(7)	La(2)–O(28)	2.560(7)
La(1)–O(11)	2.636(8)	La(2)–O(22)	2.576(9)
La(1)–O(12)	2.639(7)	La(2)–O(20)	2.623(9)
La(1)–O(8)	2.646(8)	La(2)–O(19)	2.631(8)
La(1)–O(6)	2.649(9)	La(2)–O(26)	2.633(8)
La(1)–O(9)	2.662(8)	La(2)–O(25)	2.690(8)
La(1)–O(5)	2.715(9)	La(2)–O(23)	2.698(9)
La(1)–O(4)	2.722(6)	La(2)–O(18)	2.723(7)
La(1)–O(2)	2.807(7)	La(2)–O(16)	2.839(7)
O(1)–La(1)–O(3)	125.1(2)	O(15)–La(2)–O(17)	128.2(2)
O(1)–La(1)–O(14)	70.0(2)	O(15)–La(2)–O(28)	125.1(3)
O(3)–La(1)–O(14)	123.7(2)	O(17)–La(2)–O(28)	73.1(2)
O(11)–La(1)–O(12)	47.5(2)	O(20)–La(2)–O(19)	47.9(3)
O(8)–La(1)–O(9)	46.6(3)	O(26)–La(2)–O(25)	47.7(3)
O(6)–La(1)–O(5)	46.2(3)	O(22)–La(2)–O(23)	47.3(3)
O(1)–La(1)–O(4)	75.4(2)	O(15)–La(2)–O(18)	81.4(2)
O(3)–La(1)–O(4)	59.3(2)	O(17)–La(2)–O(18)	58.5(2)
O(14)–La(1)–O(4)	79.2(2)	O(28)–La(2)–O(18)	70.1(2)
O(1)–La(1)–O(2)	57.9(2)	O(15)–La(2)–O(16)	57.3(2)
O(3)–La(1)–O(2)	73.0(2)	O(17)–La(2)–O(16)	74.3(2)
O(14)–La(1)–O(2)	119.7(2)	O(28)–La(2)–O(16)	130.7(2)
O(4)–La(1)–O(2)	60.9(2)	O(18)–La(2)–O(16)	61.5(2)

two strongest frequencies $|\nu_1-\nu_4|$ is approximately 187 cm^{-1}, clearly establishing that the NO_3^- groups in the solid complex coordinate to the rare earth ion as bidentate ligands [19]. Also no bands at 1380, 820 and 720 cm^{-1} in the spectrum of complex indicates that free nitrate groups (D_{3h}) are absent, in agreement with the result of the conductivity experiment.

3.5. ^1H NMR spectra and mass spectra

L: ^1H NMR ($CDCl_3$): δ 7.34–7.18(m, 10H, ArH and $C_{12}H_8$–), 7.07(q, $J = 7.8$ Hz, 4H, ArH), 6.96(t, $J = 7.5$ Hz, 2H, ArH), 6.73(d, $J = 7.8$ Hz, 2H, ArH), 4.21(s, 4H, –O–CH_2–CO–), 3.71(q, $J = 7.2$ Hz, 4H, –N–CH_2–), 1.08(t, $J = 7.2$ Hz, 6H, –CH_3).

$[La(pic)_3\cdot L]$: ^1H NMR ($CDCl_3$): δ8.94(s, 6H, pic-), 7.39–7.07(m, 18H, ArH and $C_{12}H_8$–), 4.45(d, $J = 14.7$ Hz, 2H, –O–CH_2–CO–), 4.09(d, $J = 14.7$ Hz, 2H, –O–CH_2–CO–), 3.51(q, $J = 6.9$ Hz, 4H, –N–CH_2–), 0.91(t, $J = 6.9$ Hz, 6H, –CH_3).

$[Y(pic)_3\cdot L]$: ^1H NMR ($CDCl_3$): δ8.84(s, 6H, pic-), 7.42–7.19(m, 18H, ArH and $C_{12}H_8$–), 4.80(d, $J = 15.3$ Hz, 2H, –O–CH_2–CO–), 4.11(d, $J = 15.3$ Hz, 2H, –O–CH_2–CO–), 3.51(q, $J = 6.9$ Hz, 4H, –N–CH_2–), 0.91(t, $J = 6.9$ Hz, 6H, –CH_3).

The ^1H NMR spectra of the "free" ligand **L**, the diamagnetic Ln(III) picrate complexes $La(Pic)_3L$ and $Y(Pic)_3L$ were measured in $CDCl_3$. The spectrum of **L** exhibits a multiplet at ca. 7.26 ppm, a quadruplet at 7.07 ppm ($J = 7.8$ Hz), a triplet at 6.96 ppm ($J = 7.5$ Hz) and a doublet at 6.73 ppm ($J = 7.8$ Hz) assigned to $C_{12}H_8$– and –C_6H_5 protons, a singlet at 4.21 ppm, a quadruplet at 3.71 ppm ($J = 7.2$ Hz), and a triplet at 1.08 ppm ($J = 7.2$ Hz) assigned to –O–CH_2–CO– protons, –N–CH_2– protons, –CH_3 protons, respectively.

Upon coordination, the proton signal of –O–CH_2–CO– in the lanthanum and yttrium complexes split into two doublets at 4.45 ppm ($J = 14.7$ Hz), 4.09 ppm ($J = 14.7$ Hz) and 4.80 ppm ($J = 15.3$ Hz), 4.11 ppm ($J = 15.3$ Hz), respectively. The signal of –N–CH_2– and –CH_3 are shifted to higher field by 0.20 and 0.17 ppm, respectively. The reason is not clear.

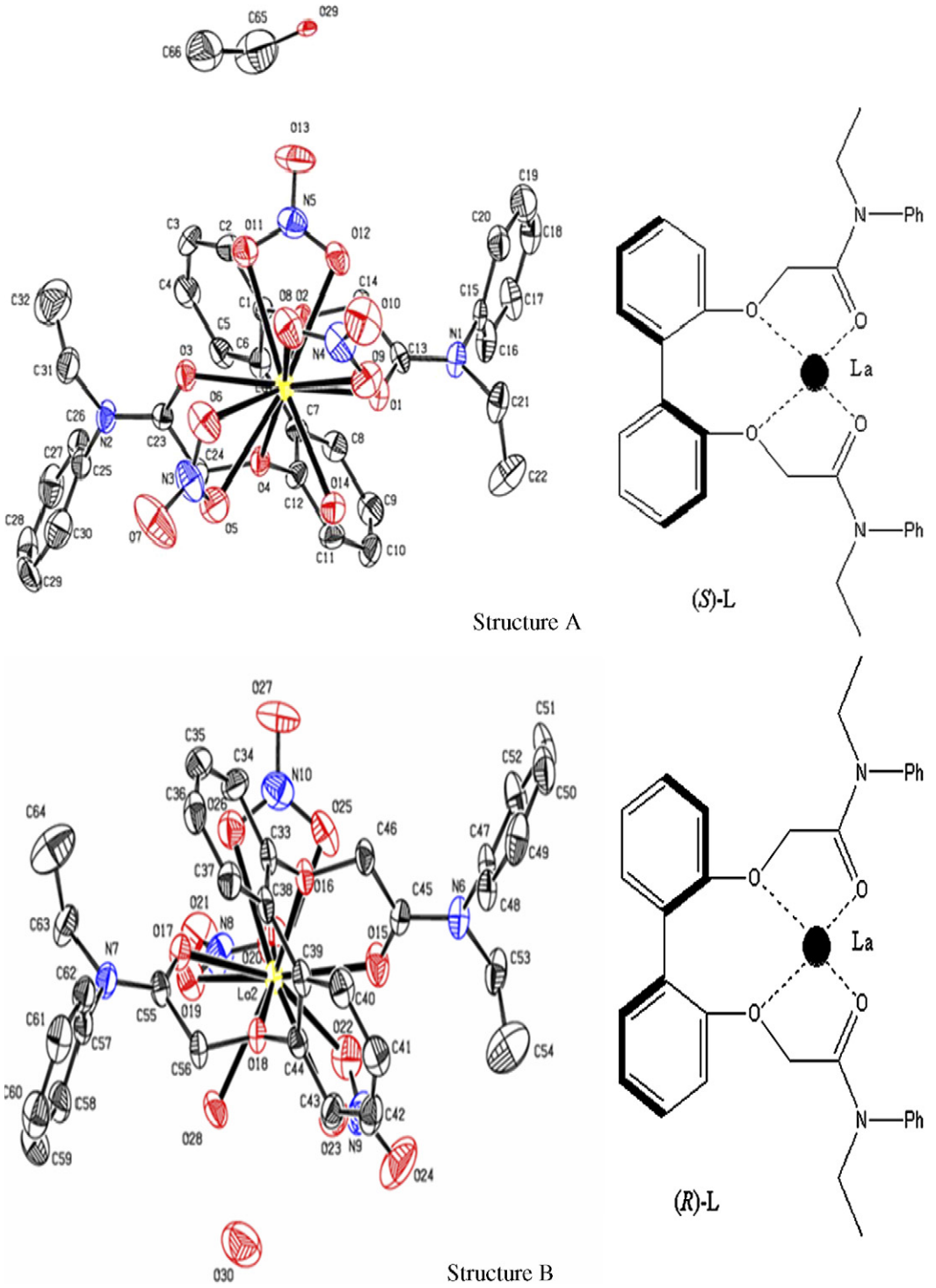


Fig. 4. ORTEP diagram (30% probability ellipsoids) showing the coordination sphere of $[La(NO_3)_3L(H_2O)]$ and coordination modes of L in the nitrate complex.

The proton signal of the OH group in free HPic disappears in the complexes, indicating that the H atom of the OH group is replaced by Ln(III). The benzene ring protons of the free HPic exhibit a singlet at 9.12 ppm. Upon coordination, the signal moves to higher field. Only one singlet is observed for the benzene ring protons of the three coordination picrate groups, indicating fast exchange among the groups in solution [20].

The mass spectrum of **L**shows a molecular ion at $m/z = 509$ (M + H), confirming the molecular formula of **L** as $C_{32}H_{32}N_2O_4$. Above the mass of $C_{12}H_8$ ($m/z = 152$) are observed three major fragment ions at $m/z = 360$ (M−[–CO–$NC_6H_5(C_2H_5)$]), 330 (M−[–O–CH_2–CO–$NC_6H_5(C_2H_5)$]), and 181 (M−[O–CO–$NC_6H_5(C_2H_5)$]–[–O–CH_2–CO–$NC_6H_5(C_2H_5)$]).

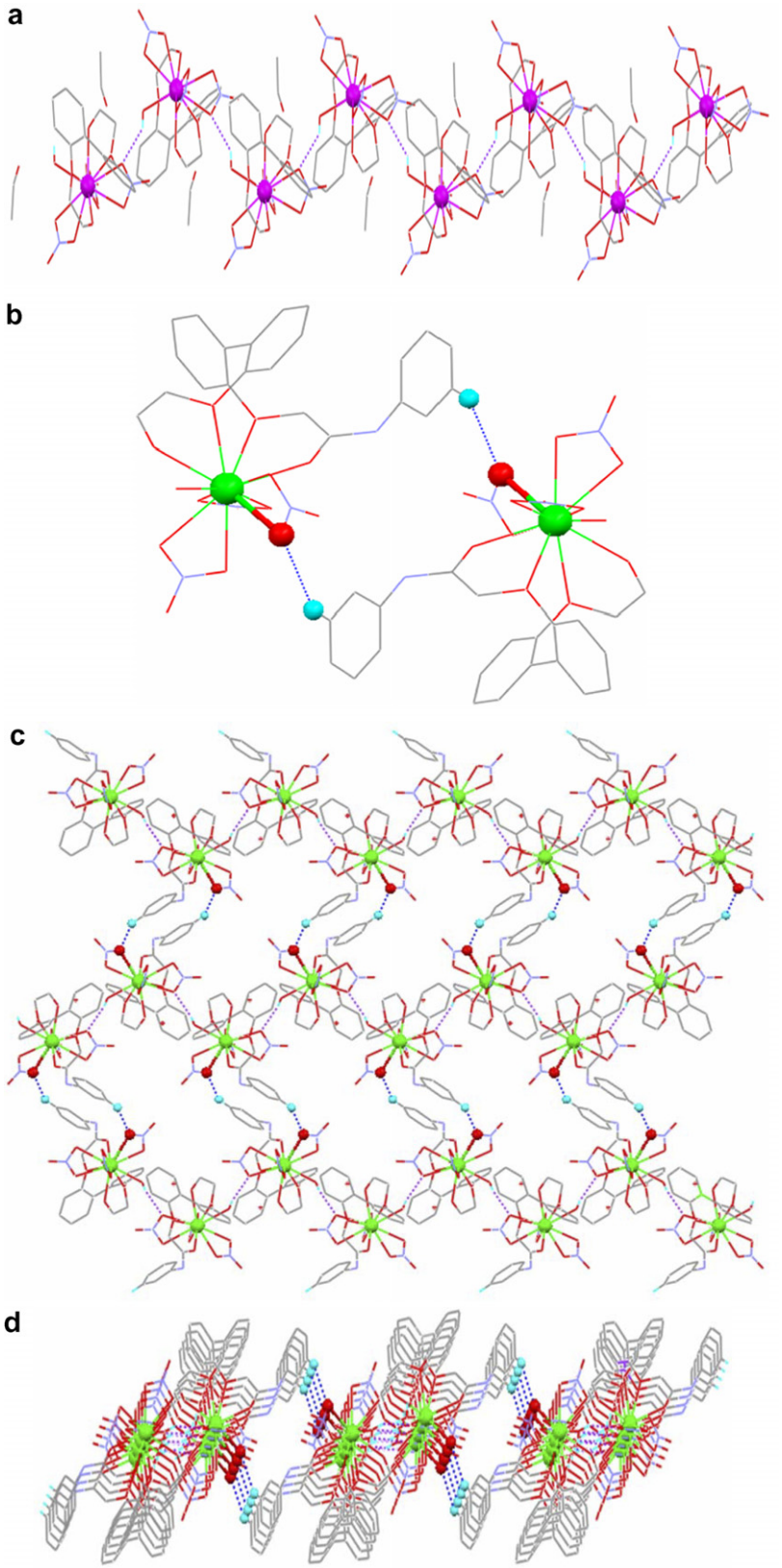


Fig. 5. Hydrogen bonding architecture in lanthanum nitrate complex: (a) 1-D zigzag chain of structure A generated by intermolecular O(14)–H(68) ⋯ O(12) hydrogen bonds [symmetry code is $-x$, $-1/2 + y$, $1/2 - z$; and the hydrogen bonds are indicated by the purple dashed lines]; (b) the dimer of structure B generated by intermolecular C(51)–H(51)⋯O(22) hydrogen bonds [symmetry code is $1 - x$, $2 - y$,$1 - z$; and the hydrogen bonds are indicated by the blue dashed lines]; (c) 2-D layer of structure B generated by intermolecular O(28)–H(70)⋯O(26) hydrogen bonds [symmetry code is $1 - x$, $1/2 + y$, $1/2 - z$; and the hydrogen bonds are indicated by the purple dashed lines] and C(51)–H(51)⋯O(22) hydrogen bonds (the hydrogen bonds are indicated by the blue dashed lines); (d) 2-D layer of structure B viewed down the crystallographic *b*-axis showing the hydrogen bonded channels. Some atoms of the ligand are omitted for clarity.

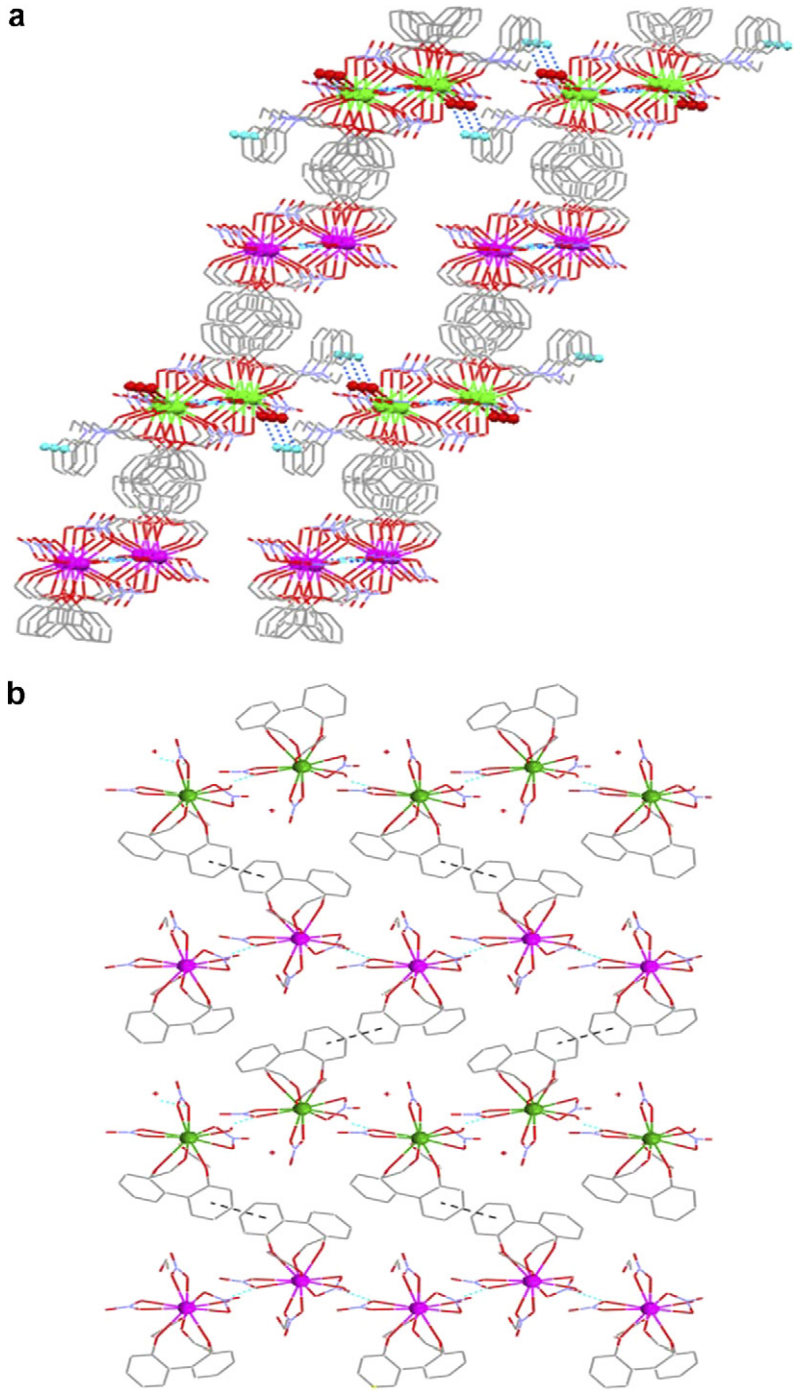


Fig. 6. The intermolecular π–π stacking interactions between the chains and the layers in lanthanum nitrate complex: (a) viewing of the packing diagram of networks along the *b*-axis; (b) packing diagram of the chains and the layers along *a*-axis. Some atoms of the ligand are omitted for clarity.

3.6. Electronic spectra

The electronic spectra in the visible region of the Ln(III) complexes exhibit alternations in intensity and shifts in position of the absorption bands relative to the corresponding Ln(III) aquo ions. The shift has been attributed by Jorgensen to the effect on the crystal field of interelectronic repulsion between the 4f electrons, and is related to the covalent character of the metal–ligand bond, assessed by Sinha's parameter (δ), the nephelauxetic ration (β) and the bonding parameter ($b^{1/2}$) [21]. Absorption spectrum of the Nd(III) complex was recorded in chloroform solution at room temperature and the covalent parameters were calculated (Table 7). The values of β, which are less than unity, and positive values of δ and $b^{1/2}$ support the existence of partial covalent bonding between metal and ligand [22].

Table 5
The most important IR bands of the rare earth picrate complexes (cm^{-1})

Complex	ν(C=O)	ν(C–O–C)	ν(C–O)	ν_{as}(–NO_2)	ν_s(–NO_2)
Hpic			1265	1555	1342
L	1676	1126			
La(pic)$_3$L	1618	1080	1274	1584, 1545	1359, 1330
Nd(pic)$_3$L	1617	1081	1276	1584, 1545	1358, 1329
Eu(pic)$_3$L	1619	1079	1275	1585, 1541	1352, 1331
Gd(pic)$_3$L	1619	1081	1275	1577, 1541	1352, 1332
Tb(pic)$_3$L	1618	1081	1279	1586, 1547	1357, 1328
Y(pic)$_3$L	1620	1080	1274	1578, 1542	1352, 1333

Table 6
The most important IR bands of europium nitrate complexes (cm^{-1})

Complex	ν(C=O)	ν(C–O–C)	$\nu(NO_3^-)$				
			ν_1	ν_2	ν_3	ν_4	$\lvert\nu_1-\nu_4\rvert$
L	1676	1126					
Eu(NO$_3$)$_3$L	1626	1072	1495	1030	815	1308	187

Table 7
Covalent parameters for the neodymium picrate complex

Complex	Frequency (cm^{-1})	Assignment	Covalent parameters
Nd(pic)$_3$L	11429	$^4I_{9/2}$–$^4F_{3/2}$	$\beta = 0.9999$
	12453	$^4F_{5/2}$	$\delta = 0.0100$
	13387	$^4F_{7/2}$	$b^{1/2} = 0.0071$
	13531	$^4S_{3/2}$	
	17182	$^4G_{5/2}$	
	17421	$^2G_{7/2}$	
	19048	$^4G_{7/2}$	

3.7. Fluorescence studies

Monitored by the emission band at 600 nm, the europium picrate complex exhibits broad excitation bands around 450 nm. The luminescence emission spectra of the europium picrate complex in solid state (the excitation and emission slit widths were 1.0 nm, Fig. 7) and in solution (the excitation and emission slit widths were 5.0 nm, Fig. 8) were recorded at room temperature. The luminescence characteristics of the europium picrate complex in solid state and in $CHCl_3$, acetone, acetonitrile, and DMF solutions (concentration: 1.0×10^{-3} mol L^{-1}) are listed in Table 8. It can be seen that the europium picrate complex shows strong emission when excited with 451 nm in the solid state. The highest intensity ratio value $\eta(^5D_0 \rightarrow {}^7F_2/{}^5D_0 \rightarrow {}^7F_1)$ is 7.7, indicative of the Eu(III) ion not lying in a centro-symmetric coordination site [23]. It could also be seen that in DMF solution, the luminescence of europium was quenched which is ascribed to the decomposition of the europium picrate complex in this solvent. In the other three solvents, the europium picrate complex has the similar excitation and emission wavelengths.

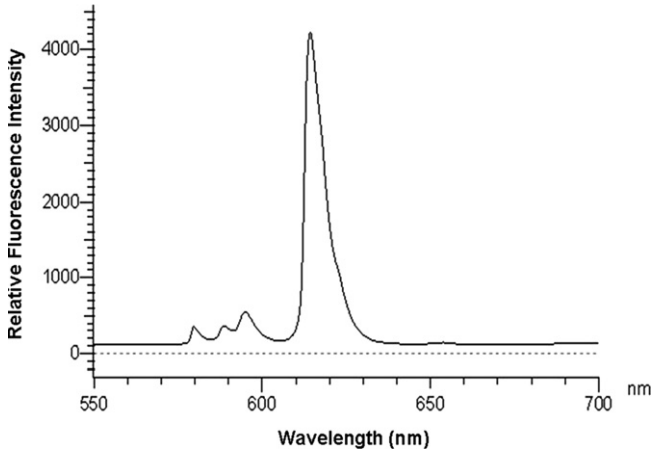


Fig. 7. The emission spectrum of the europium picrate complex in solid state.

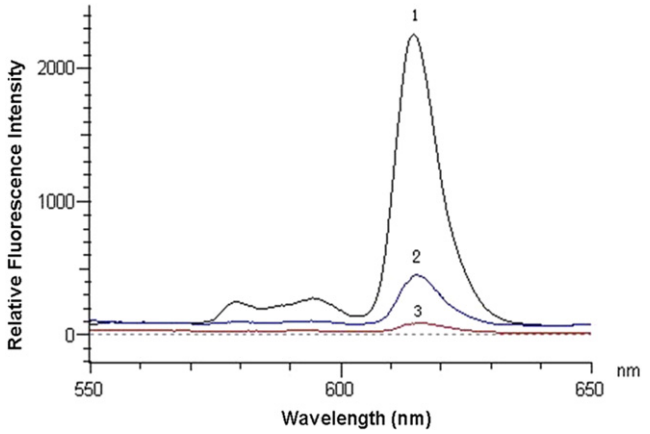


Fig. 8. The emission spectrum of the europium picrate complex in different solutions at room temperature: (1) in $CHCl_3$, (2) in acetone, and (3) in acetonitrile solution.

In $CHCl_3$ solution, the europium picrate complex has the strongest luminescence, followed by acetone and then acetonitrile. This is due to the coordinating effects of the solvents, namely solvate effect [24] where vibrational quenching of the complex excited state may occur through high energy oscillators on the solvent molecule.

The fluorescence quantum yield **Φ** of the europium picrate complex in $CHCl_3$ (concentration: 1.0×10^{-5} mol L^{-1}) was found to be 5.81×10^{-3} with quinine sulfate as Ref. [25].

Table 8
Fluorescence data for the europium picrate complex

Complex	Solvent	λ_{ex} (nm)	λ_{em} (nm)	RFI	assignment
Eu(pic)$_3$L	Solid state	451	595	551	$^5D_0 \rightarrow {}^7F_1$
			614	4233	$^5D_0 \rightarrow {}^7F_2$
	$CHCl_3$	463	594	277	$^5D_0 \rightarrow {}^7F_1$
			615	2260	$^5D_0 \rightarrow {}^7F_2$
	Acetone	463	594	106	$^5D_0 \rightarrow {}^7F_1$
			615	453	$^5D_0 \rightarrow {}^7F_2$
	Acetonitrile	463	594	34	$^5D_0 \rightarrow {}^7F_1$
			615	92	$^5D_0 \rightarrow {}^7F_2$
	DMF				

The characteristic luminescence of the terbium picrate complex was not observed, either in solid state or in solutions. The reason is probably that the energy gap between the triplet state levels of the ligand in picrate complex and the lowest resonance level of the europium favor the energy transfer process for europium. In order to acquire the triplet excited state T_1 of the ligand **L** in the picrate complex, the phosphorescence spectrum of the Gd(III) picrate complex was measured at 77 K in a chloroform–methanol–ethanol mixture (v:v:v, 1:5:5). The triplet state energy levels T_1 of the ligand **L** in picrate complex, which was calculated from the shortest wavelength phosphorescence band [26] of the Gd(III) picrate complex, is 21186 cm^{-1}. This energy level is above the lowest excited resonance level $^5D_0$ of Eu(III) (17300 cm^{-1}) and $^5D_4$ (20500 cm^{-1}) of Tb(III). Thus the absorbed energy could be transferred from ligand to the Eu(III) or Tb(III) ions. The triplet state energy level T_1 of this ligand **L** in picrate complex matches better to the lowest resonance level of Eu(III) ($\Delta v = 3886\ cm^{-1}$) than Tb(III) ($\Delta v = 686\ cm^{-1}$) ion, because such small $\Delta v(T_1 - {}^5D_4)$ could result in a back-energy transfer process from the excited resonance level $^5D_4$ of Tb(III) to the triplet state energy level T_1 of this ligand **L** and quench the luminescence of the Tb(III) picrate complex [27].

In contrast with the strong emission of the europium picrate complex, the europium nitrate complex exhibited weak characteristic emission (the excitation and emission slit widths were 2.5 nm, Fig. 9). The phosphorescence spectrum of the Gd(III) nitrate complex was measured at 77 K in a methanol–ethanol mixture (v:v, 1:1), the triplet state energy levels T_1 of the ligand **L** in the nitrate complex, which was calculated from the shortest wavelength phosphorescence band [26] of the Gd(III) nitrate complex, is 22075 cm^{-1}. The results indicate that the counter anions of complexes hardly influence the triplet state energy level T_1 of this ligand **L**, but notably affect the fluorescence properties of the europium complexes.

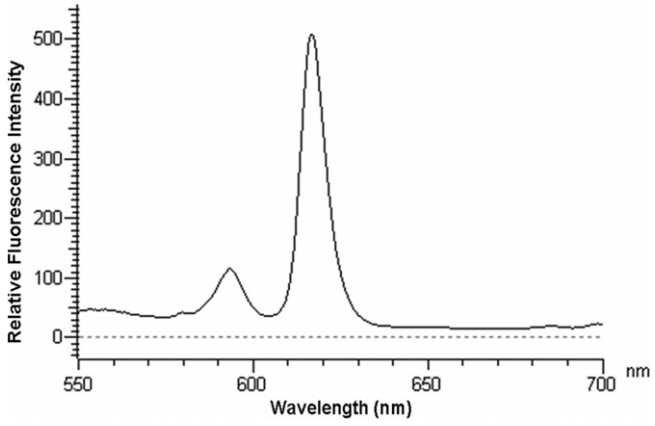


Fig. 9. The emission spectrum of the europium nitrate complex in solid state.

We deduce that this is due to the following three effects. First, the coordinated picrates participate in the energy absorption and transfer process for the Eu(III) ion, make the three-component complex system an optimal state for the luminescence of europium, accordingly enhancing the relative fluorescence intensity of the europium picrate complex. Secondly, the intermolecular π–π stacks between picrates favor to the energy transfer for europium. However, the coordinated nitrates do not play these roles like picrates in the europium complex. Thirdly, the non-radiative deactivation of the europium emitting state could quench the luminescence of the Eu(III) nitrate complex [27].

4. Conclusion

In this paper, we reported the preparation, luminescent properties of *N*-phenyl-2-{2′-[(phenyl-ethyl-carbamoyl)-methoxy]-biphenyl-2-yloxy}-*N*-ethyl-acetamide (**L**) lanthanide complexes and the supramolecular structures of $[La(pic)_3L]$ and $2[La(NO_3)_3L(H_2O)] \cdot H_2O \cdot 0.5C_2H_5OH$ which are the assemblies of the complex units via the intermolecular hydrogen bonds and π–π stacking interactions. The free ligand is achiral, but it induces axial chirality in the lanthanum nitrate complex, which is directed by the metal ions in the assembly process of the organic ligands with the metal ions. The europium picrate complex exhibited strong characteristic fluorescence whereas the terbium picrate complex showed no luminescence. The lowest triplet state energy level of the ligand in the picrate complex matches better to the resonance level of Eu(III) than Tb(III) ion. The Eu(III) nitrate complex exhibited quite weak characteristic fluorescence. So we can see that the counter anion of complexes is very essential in determining the fluorescent properties of the rare earth complexes. Further studies on the ligand and their complexes are in proceeding.

Acknowledgements

We are grateful to the NSFC (Grants 20371022, 20431010 and 20021001), and the Specialized Research Fund for the Doctoral Program of Higher Education (200307300015) for financial support.

Appendix A. Supplementary material

CCDC 622187 and 622188 contain the supplementary crystallographic data for lanthanum picrate complex and lanthanum nitrate complex. These data can be obtained free of charge via http://www.ccdc.cam.ac.uk/conts/retrieving.html, or from the Cambridge Crystallographic Data Centre, 12 Union Road, Cambridge CB2 1EZ, UK; fax: (+44) 1223-336-033; or e-mail: deposit@ccdc.cam.ac.uk. Supplementary data associated with this article can be found, in the online version, at doi:10.1016/j.poly.2006.12.019.

References

[1] S. Faulkner, S.A.P. Pope, J. Am. Chem. Soc. 125 (2003) 10526.
[2] Q. Silvio, M. Giovanni, F. Alessandra, A. Gianluca, B. Francesco, Inorg. Chem. 43 (2004) 1294.
[3] G. Xu, Z.M. Wang, Z. He, Z. Lu, C.S. Liao, C.H. Yan, Inorg. Chem. 41 (2002) 6802.
[4] Q. Li, T. Li, J.G. Wu, J. Phys. Chem. B 105 (2001) 12293.
[5] V. Patroniak, P.N.W. Baxter, J.M. Lehn, Z. Hnatejko, M. Kubicki, Eur. J. Inorg. Chem. (2004) 2379.
[6] B.L. An, M.L. Gong, M.X. Li, J.M. Zhang, J. Mol. Struct. 687 (2004) 1.
[7] Y.-S. Yang, S.-H. Cai, Hua Xue Shi Ji. 6 (1984) 133.
[8] Y.Z. Ding, J.Z. Lu, Y.S. Yang, Hua Xue Shi Ji. 8 (1986) 201.
[9] W. Yang, X.L. Teng, M. Chem, Talanta 46 (1998) 527.
[10] (a) W.S. Liu, X.F. Li, Y.H. Wen, M.Y. Tan, Dalton Trans. (2004) 640;
(b) Y.L. Zhang, W.H. Jiang, W.S. Liu, Y.H. Wen, Polyhedron 22 (2003) 1695;
(c) Y.L. Zhang, W.S. Liu, W. Dou, W.W. Qin, Spectrochim. Acta, Part A 60 (2004) 1707.
[11] Y.C. Tian, Y.Q. Liang, J.Z. Ni, Chem. J. Chin. Univ. 9 (1988) 113.
[12] L.-Y. Fan, W.-S. Liu, X.-M. Gan, N. Tang, M.-Y. Tan, W.-H. Jiang, K.-B. Yu, Polyhedron 19 (2000) 779.
[13] W.J. Gear, Coord. Chem. Rev. 7 (1971) 81.
[14] C. Janiak, Dalton Trans. (2000) 3885.
[15] B. Wu, D. Yuan, F. Jiang, R. Wang, L. Han, Y. Zhou, M. Hong, Eur. J. Inorg. Chem. (2004) 2695.
[16] G.R. Desiraju, Chem. Commun. 24 (2005) 2995.
[17] S.X. Liu, W.S. Liu, M.Y. Tan, K.B. Yu, J. Coord. Chem. 10 (1996) 391.
[18] W. Carnall, S. Siegel, J. Ferrano, B. Tani, E. Gebert, Inorg. Chem. 12 (1973) 560.
[19] K. Nakamoto, Infrared and Raman Spectra of Inorganic and Coordination Compounds, third ed., John Wiley, New York, 1978, p. 227.
[20] X. Mao, L.F. Shen, J.Z. Ni, Bopuxuezazhi 1 (1985) 201.
[21] (a) C.K. Jorgensen, Prog. Inorg. Chem. 4 (1962) 73;
(b) S.P. Sinha, Spectrochim. Acta 22 (1966) 57;
(c) D.E. Henrie, G.R. Choppin, J. Chem. Phys. 49 (1968) 477.
[22] A.K. Solanki, A.M. Bhandaka, J. Inorg. Nucl. Chem. 41 (1979) 1311.
[23] M. Albin, R.R. Wright Jr., W.D. Horrocks, Inorg. Chem. 24 (1985) 2491.
[24] H.Q. Liu, T.C. Cheung, C.M. Che, Chem. Commun. (1996) 1039.
[25] (a) C.A. Parker, W.T. Rees, Analyst 85 (1960) 587;
(b) W. Yang, Z.L. Mo, X.L. Teng, M. Chen, J.Z. Gao, L. Yuan, J.W. Kang, Q.Y. Ou, Analyst 123 (1998) 1745.
[26] W. Dawson, J. Kropp, M. Windsor, J. Chem. Phys. 45 (1966) 2410.
[27] F. Gutierrez, C. Tedeschi, L. Maron, J.-P. Daudey, R. Poteau, J. Azema, P. Tisn‘es, C. Picard, J. Chem. Soc., Dalton Trans. (2004) 1334.

2. Results and discussion

2.1. Chloro- and trifluoroacetato tricarbonylrhenium(I) complexes

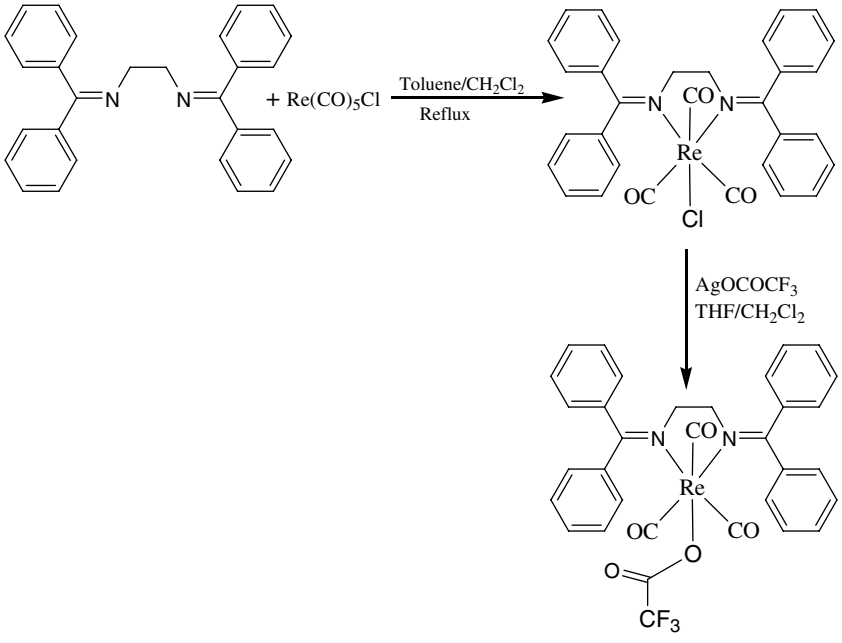
2.1.1. Synthesis and spectroscopic characterization

The new *fac*-[$Re(CO)_3(bz_2en)X$] (X = Cl and $OCOCF_3$), complexes were obtained via substitution reactions, as o utlined in Scheme 1. In the first step (a), the chloride carbonyl, **1**, was prepared in good yield by refluxing equivalent amounts of Re(I) pentacarbonyl chloride and bz_2en in a mixture of toluene/dichloromethane following a previously established method [13]. The trifluoroacetato complex was synthesized by allowing the halide carbonyl, **1**, to react with 1 equiv. of $AgOCOCF_3$ in CH_2Cl_2 in the dark, overnight. After cooling, the AgCl that formed during the reaction was removed by filtration. The partial removal of the solvent and addition of *n*-hexane resulted in the formation of the corresponding complex **2** in good yield.

The new complexes are stable in the solid state and in solution at room temperature, and were characterized by the usual spectroscopic techniques. The IR spectra for complexes exhibit three absorption bands in the carbonyl stretching region, as a sharp intense band at 2017, and two closely spaced bands at 1910 and 1878 cm^{-1} for **1** and about 2024 and 1920 cm^{-1} for **2**, typical of the *fac*-Re(I) α-diimine tricarbonyl complexes [14,15]. The nature of the axial ligand influences to some extent the position and the shape of the absorption bands in the IR spectra. The π-donor character of the Cl ligand and the oxygen atom in the trifluoroacetate group increase the Re → CO back-bonding, which decreases the energy of υ(CO) [15].

The ^1H NMR spectra and peak assignments are presented in the experimental section. For complex **1**, the signal due to the methylene protons of the ethylenediamine chelate appear at 3.72–377 and 4.19–4.24 ppm as two sets of multiplets, and for **2**, at 3.79–3.84 and 3.95–4.00 ppm, respectively. The signal due to the aromatic protons appears at about 7.25–7.62 and 7.22–7.55 ppm for **1** and **2**, respectively. In keeping with the *fac* arrangement of the CO ligands, the $^{13}C\{^1H\}$ NMR spectra show two low-field signals assignable to the CO groups, at about 192.88, 193.93 and 192.46, 197.69 ppm for axial and equatorial carbonyl groups for **1**, and **2**, respectively.

The UV–Vis spectral data of complexes **1** and **2** are presented in Table 1. The absorption spectra of complexes **1** and **2** are dominated in the UV region by ligand-centered π → π* transitions which are qualitatively similar to [$Re(CO)_3$(2-PC)Cl], in which 2-PC is *n*-(2-pyridinylmethylene)cyclohexylamine [16]. The shorter wavelength bands include certainly an intraligand (IL) transition of the



Scheme 1.

Table 1
UV–Vis spectral data of complexes **1** and **2**.

Compound	Concentration (M)	Solvent	UV–Vis λ_{max} (nm) [ε] (M^{-1} cm^{-1})
1	6.25×10^{-5}	CH_2Cl_2	249 [59168], 320 [18727]
2	3.12×10^{-5}	CH_2Cl_2	250 [25488], 323 [8544]

diimine, which absorbs as a free ligand in the same spectral region. The spectral positions of the IL bands are significantly red-shifted in comparison to the free ligand, due to the coordination of the heavy metal core.

The electrochemical behaviour of complexes **1** and **2** was examined by means of cyclic voltammetry (CV) in CH_2Cl_2 (Fig. 1). The ligand bz_2en is electroinactive in the working potential region. Anodic scans reveal a single reversible oxidation at about 1.44 and 1.51 V versus Ag/AgCl for complexes **1** and **2**, respectively. This is assigned to the Re(II)/Re(I) redox couple, which is similar to the anodic peak potential reported for the complexes *fac*-[$Re(CO)_3$(2-PC)Cl] and *fac*-[$Re(CO)_3$(2,2N)Br] [16,17], except that the latter complexes show irreversible behaviour. It is clear from the oxidation potential that complex **2** is more resistant to oxidation than the complex **1** owing to the greater electron-withdrawing property of the trifluoroacetate group. Complexes **1** and **2** show quasireversible redox couples with $E_{1/2}$ values of 1.35 and 1.45 V, respectively. In the cyclic voltammetry, peak-to-peak separations (ΔE_p) of 170 and 100 mV were observed at a scan rate (υ) of 100 mV/s for complexes **1** and **2**, respectively.

2.1.2. X-ray structural study of complexes *1* and *2*

The molecular structure of **1** is shown in Fig. 2, and selected bond lengths and angles are listed in Table 2. The rhenium center is in a distorted octahedral geometry defined by two donors derived from the bz_2en ligand, three carbonyls and one chlorine ligand. The axially disposed chlorine and carbonyl ligands are disordered over two positions and were refined with 53.7% and 46.3% site-occupancy factors. The lengths of the Re–C bond *trans* to the nitrogen atoms range from 1.911(4) to 1.916(4) Å. In the major component of the disorder, due to the π-donor character of the chlorine ligand, the length of the axial Re–C bond is slightly shorter than the values of the equatorial Re–C bonds (see Table 2). The lengths of the two Re–N bonds formed with the bz_2en ligand are equal (2.217(3) Å), and are in the range reported for the *fac*-$Re(CO)_3$(3,2N)Br complex, where 3,2N is the 3,3′-trimethylene-2,2-biquinoline ligand [17]. The X-ray analysis established that the bz_2en ligand in **1** is bound to the rhenium center in a bidentate chelating fashion, leading to five-membered ReN_2C_2 chelate ring with a N(1)–Re(1)–N(2) bite angle of 78.0(1)°. In spite of the sp^2 hybridization of the donor nitrogen atoms of the bz_2en ligand, the ReN_2C_2 five-membered chelate ring is significantly puckered and the mean deviation of the atoms from the least-squares plane is 0.22 Å. The strain in the chelate ring is also reflected in the deviation from the 120° angle about the chelating nitrogen atoms: Re(1)–N(1)–C(1) and Re(1)–N(2)–C(4) angles are 130.8(3) and 129.9(3)°, respectively. The steric requirements of this bidentate ligand cause distortion of the octahedral coordination sphere, which is clearly reflected in the values of the equatorial C(5)–Re(1)–N(1) and C(6)–Re(1)–N(2) bond angles. As can be seen in Table 2, these equatorial bond angles are far from the ideal octahedral value of 90°. In the crystal, the molecules of **1** are linked by C–H ⋯ O hydrogen bonds (Table 3) into infinite chains.

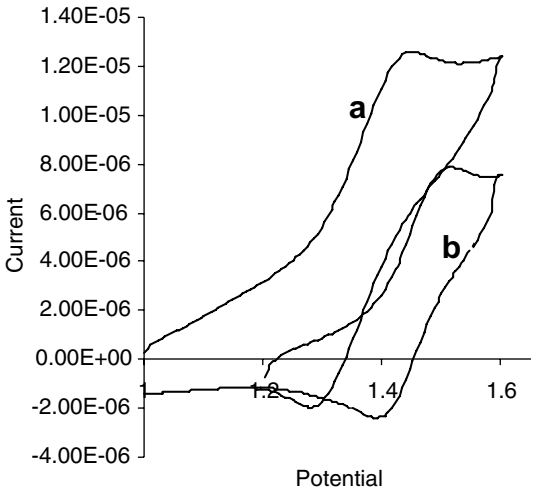


Fig. 1. Cyclic voltammograms of **1** (a) and **2** (b) in CH_2Cl_2 at 293 K (scan rate, 100 mV/s, $C = 2.5 \times 10^{-4}$ M): (a) [$Re(bz_2en)(CO)_3Cl$] (**1**) and (b) [$Re(bz_2en)(CO)_3OCOCF_3$] (**2**).

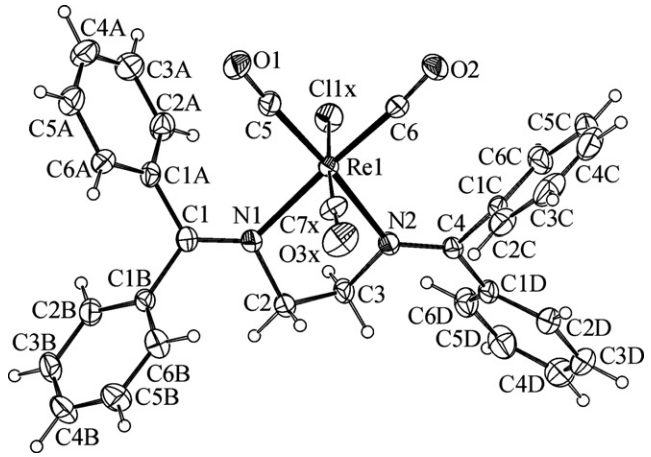


Fig. 2. ORTEP drawing for complex **1**. Non-hydrogen atoms are shown as 30% probability ellipsoids. Only the major component of the disordered axially disposed CO and Cl ligands is shown.

The molecular structure of **2**, established by single-crystal X-ray diffraction, is shown in Fig. 3. The relevant geometric parameters are collected in Table 2. The X-ray data obtained for **2** reveal that there are two structurally similar but symmetry independent molecules (unprimed and primed) in the unit cell. In each molecule, the rhenium center is located in a distorted octahedral coordination environment, with the equatorial plane consisting of two nitrogen atoms of the bidentate bz_2en ligand and two CO ligands, and one CO and the oxygen atom of the trifluoroacetate in the axial positions. The structural similarity between **1** and **2** is reflected in the practically unaltered N–Re–N bite angles (77.5(3)° for the unprimed and 78.1(2)° for the primed molecule) and Re–N distances (Table 2). In a manner similar to **1**, the five-membered ReN_2C_2 chelate rings are significantly puckered and the

Table 2
Crystal data and structure refinement parameters for complexes **1** and **2**

Complex **1**		Complex **2**			
Re(1)–N(1)	2.217(3)	Re(1)–N(1)	2.211(7)	Re(1′)–N(1′)	2.215(7)
Re(1)–N(2)	2.217(3)	Re(1)–N(2)	2.207(7)	Re(1′)–N(2′)	2.218(7)
Re(1)–Cl(1*x*)	2.495(4)	Re(1)–O(4)	2.169(6)	Re(1′)–O(4′)	2.157(6)
Re(1)–Cl(1*y*)	2.513(5)	Re(1)–C(5)	1.911(9)	Re(1′)–C(5′)	1.915(9)
Re(1)–C(5)	1.916(4)	Re(1)–C(6)	1.914(9)	Re(1′)–C(6′)	1.909(9)
Re(1)–C(6)	1.911(4)	Re(1)–C(7)	1.867(9)	Re(1′)–C(7′)	1.892(9)
Re(1)–C(7x)	1.81(2)				
Re(1)–C(7*y*)	1.92(2)				
N(1)–Re(1)–N(2)	78.0(1)	N(1)–Re(1)–N(2)	77.5(3)	N(1′)–Re(1′)–N(2′)	78.1(2)
C(6)–Re(1)–C(5)	84.4(2)	C(6)–Re(1)–C(5)	83.0(4)	C(6′)–Re(1′)–C(5′)	84.5(4)
C(5)–Re(1)–N(1)	97.1(1)	C(5)–Re(1)–N(1)	101.3(3)	C(5′)–Re(1′)–N(1′)	97.0(3)
C(6)–Re(1)–N(2)	100.6(1)	C(6)–Re(1)–N(2)	98.3(4)	C(6′)–Re(1′)–N(2′)	100.2(3)
C(7x)–Re(1)–Cl(1*x*)	174.3(3)	C(7)–Re(1)–O(4)	172.9(4)	C(7′)–Re(1′)–O(4′)	173.3(4)
C(7*y*)–Re(1)–Cl(1*y*)	175.6(6)				

Table 3
Selected bond distances (Å) and angles (°) for compounds **1** and **2**[a]

Complex	D–H ⋯ A	H ⋯ A (Å)	D ⋯ A (Å)	D–H ⋯ A (°)
1	C(5A)–H(5A) ⋯ O(3X)^{i}	2.56	3.23(1)	129
2	C(2D′)–H(2D′) ⋯ O(5)^{ii}	2.38	3.28(1)	164
	C(3′)–H(31′) ⋯ O(5)^{ii}	2.49	3.35(1)	148

[a] Symmetry codes: (i) $-1/2 + x$, y, $1/2 - z$; (ii) x, $1 + y$, z.

mean deviation of the atoms from the least-squares plane is 0.21 Å in both molecules. Owing to the π-donor character of the oxygen atom of the $OCOCF_3$ group, the CO ligand *trans* to the O atom forms shorter Re–C bonds (1.867(9) Å in the unprimed and 1.892(9) Å in the primed molecule) than the other two CO ligands *trans* to the N atoms of the bz_2en ligand (see Table 2). The CF_3 group has high thermal motion consistent with some unresolved rotational disorder, as is often found in other trifluoroacetate compounds [18–20]. In addition, there are some weak C–H ⋯ O interactions (Table 3) in the crystal.

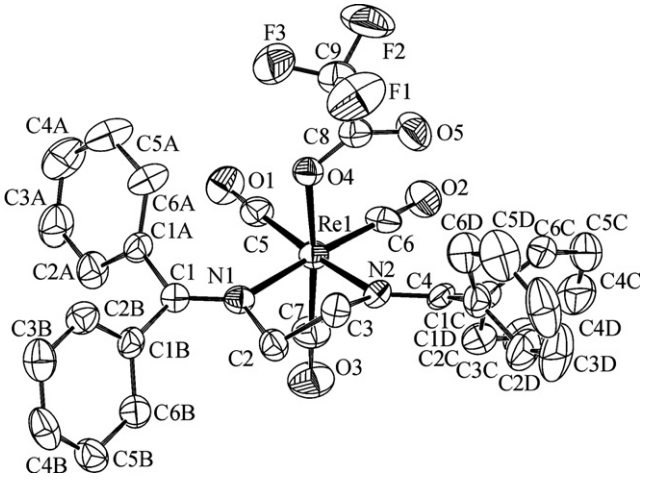


Fig. 3. ORTEP drawing for complex **2**, showing one of the two chemically similar but symmetry independent molecules. Non-hydrogen atoms are shown as 30% probability ellipsoids. Hydrogen atoms have been omitted for clarity.

3. Conclusion

The *fac*-[Re(bz_2en)$(CO)_3X$] (X = Cl and $OCOCF_3$) rhenium(I) complexes have been prepared and characterized by IR, UV–Vis, ^1H, ^{13}C NMR, electrochemical and X-ray diffraction techniques. Variations in the electronic properties related to the rhenium (I), carbonyl and X ligands – such as electronic transition, CO stretching and some crystallographic parameters of the complexes – were interpreted on the basis of the σ- and π-donor character of the X ligand. It is clear from the data that by varying the nature of the X ligand attached to rhenium, the electronic properties of the *fac*-[Re(bz_2en)$(CO)_3X$] complexes could be ''tuned''.

4. Experimental

4.1. Starting materials

All reagents were used as received from Fluka and Merck without further purification. Solvents used for the reactions were purified by literature methods [21]. The ligand *N*,*N*-bis(benzophenone)-1,2-diiminoethane (bz_2en) was synthesized and purified as reported [22].

4.2. Synthesis

4.2.1. [Re(bz_2en)$(CO)_3Cl$] (**1**)

A mixture of $Re(CO)_5Cl$ (181 mg, 0.5 mmol) and bz_2en (118 mg, 0.5 mmol) in 20 ml CH_2Cl_2 and 30 ml of toluene was heated at reflux for 2 h to give a bright yellow solution. The solvent was removed under vacuum and the crude

material recrystallized from CH_2Cl_2/hexane to give $Re(bz_2en)(CO)_3Cl$ as a pure bright yellow powder.

Anal. Calc. for $C_{31}H_{24}ClN_2O_3Re$: C, 53.64; H, 3.48; N, 4.04. Found: C, 53.67; H, 3.50; N, 4.05%.

IR (KBr, cm^{-1}): υ_{max} 3050 (CH); 2017, 1910 and 1878 (CO); 1592 (C=N).

^1H NMR ($CDCl_3$, δ_{ppm}): 3.72–3.76 (m, 2H, $-CH_2-$); 4.20–4.24 (m, 2H, $-CH_2-$); 7.25–7.29 (m, 4H, aromatic hydrogens); 7.39–7.47 (m, 12H, aromatic hydrogens); 7.61–7.62 (m, 4H, aromatic hydrogens).

$^{13}C\{^1H\}$ NMR ($CDCl_3$, δ_{ppm}): 61.25 ($-CH_2-$); 128.27, 128.53, 128.79, 129.47, 130.63, 130.79, 137.55, and 141.93 (aromatic carbons); 183.17 (iminic carbon); 192.88 (CO); 193.93 (2CO).

UV–Vis: λ_{max}, ε (nm, $M^{-1}\,cm^{-1}$): 249 (59 168); 320 (18 727).

4.2.2. $[Re(bz_2en)(CO)_3OCOCF_3]$ (2)

A solution of $AgOCOCF_3$ (55 mg, 0.25 mmol) in 5 ml of THF was added to a solution of $[Re(bz_2en)(CO)_3Cl]$ (166 mg, 0.24 mmol) in 50 ml of CH_2Cl_2 and immediately gave a cloudy yellow mixture. After stirring for 2 h, the precipitate was removed by filtration and the crude material recrystallized from CH_2Cl_2/hexane to give $[Re(bz_2en)(CO)_3OCOCF_3]$ as a pure pale-yellow powder.

Anal. Calc. for $C_{33}H_{27}F_3N_2O_5Re$: C, 51.16; H, 3.51; N, 3.62. Found: C, 51.20; H, 3.50; N, 3.64%.

IR (KBr, cm^{-1}): υ_{max} 3060 (CH); 2024, 1920 (CO); 1592 (C=N).

^1H NMR ($CDCl_3$, δ_{ppm}): 3.79–3.84 (m, 2H, $-CH_2-$); 3.95–4.00 (m, 2H, $-CH_2-$); 7.22–7.24 (m, 4H, aromatic hydrogens); 7.41–7.47 (m, 12H, aromatic hydrogens); 7.51–7.55 (m, 4H, aromatic hydrogens).

$^{13}C\{^1H\}$ NMR ($CDCl_3$, δ_{ppm}): 61.29 ($-CH_2-$); 114.95, 117.26, 128.35, 128.54, 128.86, 128.90, 129.26, 129.37, 130.99, 160.82, 161.10 (aromatic carbons); 184.36 (iminic carbon); 192.46 (CO); 197.69 (2CO).

UV–Vis: λ_{max}, ε (nm, $M^{-1}\,cm^{-1}$): 250 (25 488); 323 (8544).

4.3. Physical measurements

4.3.1. Spectroscopic experiments

NMR spectra were obtained on a Brucker Avance DRX500 (500 MHz) spectrometer. The chemical shifts (δ) are reported in part per million (ppm) relative to an internal standard of Me_4Si. The UV–Vis spectra were recorded on a Shimadzu UV-160 spectrophotometer with quartz cells (1 cm path length). Elemental analyses were performed using a Heraeus elemental analyzer. IR spectra were determined as KBr pellets on a Nicolet Impact 400D spectrophotometer. Electrochemical data were obtained by cyclic voltammetry (CV) with a three-electrode cell containing an Ag/AgCl reference electrode, a Pt wire counter electrode and a Pt working electrode. A Metrohm multipurpose instrument model 757 was used. CV measurements were performed in CH_2Cl_2 with 25 mM of Bu_4NClO_4 (TBAP) as a supporting electrolyte. In all electrochemical experiments, the solutions were purged with Ar gas for at least 5 min.

4.3.2. X-ray crystallography

Suitable single crystals of $[Re(bz_2en)(CO)_3Cl]$ (**1**) and $[Re(bz_2en)(CO)_3OCOCF_3)]$ (**2**) were obtained by diffusion of *n*-hexane vapour into a CH_2Cl_2 solution at −18 °C. Crystal data and refinement parameters for complexes **1** and **2** are summarized in Table 4. Intensity data for complexes **1** and **2** were collected on a Rigaku R-AXIS RAPID image plate diffractometer (λ(Mo Kα radiation) = 0.71070 Å) at 295 ± 2 K. Several scans in the ϕ and ω direction were made to increase the number of redundant reflections, which were averaged over the refinement cycles. The structures were solved by a direct method (SIR92) [23] and refined by full-matrix least-squares (SHELXL-97) [24]. All calculations were carried out using the WINGX package of crystallographic programs [25]. All non-hydrogen atoms were refined anisotropically in the F^2 mode. The water molecule in **2** is disordered and the refined site-occupancy factors of the disordered parts (O1wx/O1wy and associated H atoms) are 0.52(5) and 0.48(5). The water H atoms were found in a difference Fourier map and refined with O–H distances restrained to 0.85(1), $H\cdots H$ distance restrained to 1.37(2) and $U_{iso}(H) = 0.08\ ^2$. Other hydrogen atomic positions were

Table 4
Parameters of hydrogen bonding interactions in complexes **1** and **2**

Complex	**1**	**2**
Empirical formula	$C_{31}H_{24}ClN_2O_3Re$	$2(C_{33}H_{24}F_3N_2O_5Re)$, H_2O
Formula mass	694.17	1561.50
Crystal size (mm)	0.26 × 0.28 × 0.44	0.41 × 0.56 × 0.58
Colour	yellow	yellow
Crystal system	orthorhombic	triclinic
Space group	*Pbca*	$P\bar{1}$
θ Range for data collection (°)	3.0 ⩽ θ ⩽ 27.5	3.0 ⩽ θ ⩽ 25.0
a (Å)	13.582(2)	13.936(3)
b (Å)	17.998(3)	14.360(3)
c (Å)	22.604(4)	18.443(4)
α (°)	90	86.713(8)
β (°)	90	76.169(8)
γ (°)	90	66.793(8)
V (Å^3)	5525.5(16)	3291.0(12)
Z	8	2
d_{calc} (Mg/m^3)	1.669	1.576
μ (mm^{-1})	4.530	3.752
F(000)	2720	1532
Index ranges	−17 ⩽ *h* ⩽ 16 −23 ⩽ *k* ⩽ 23 −29 ⩽ *l* ⩽ 29	−16 ⩽ *h* ⩽ 16 −17 ⩽ *k* ⩽ 17 −21 ⩽ *l* ⩽ 21
No. of collected reflections	79 683	93 505
No. of independent reflections/R_{int}	6322/0.071	11 600/0.108
No. of observed reflections $I > 2\sigma(I)$	4661	8601
No. of parameters	371	825
Goodness-of-fit	1.04	1.059
R_1 (observed data)	0.0284	0.0554
wR_2 (all data)	0.0596	0.1199

generated from assumed geometries and the riding model was applied.

Acknowledgements

R.K. and V.M. thank the University of Isfahan for partial support of this research. Mr. A. Siroueinezhad (Shiraz University) is acknowledged for the CV recordings. Dr. E. Shams is also acknowledged for helpful discussions about the electrochemical data.

Appendix A. Supplementary material

CCDC 622353 and 622354 contain the supplementary crystallographic data for **1** and **2**. These data can be obtained free of charge via http://www.ccdc.cam.ac.uk/conts/retrieving.html, or from the Cambridge Crystallographic Data Centre, 12 Union Road, Cambridge CB2 1EZ, UK; fax: (+44) 1223-336-033; or e-mail: deposit@ccdc.cam.ac.uk. Supplementary data associated with this article can be found, in the online version, at doi:10.1016/j.poly.2006.12.025.

References

[1] A.J. Lee, Chem. Rev. 87 (1987) 711.
[2] I.R. Farrell, A. Vlcek Jr., Coord. Chem. Rev. 211 (2001) 163.
[3] D.R. Striplin, G.A. Crosby, Coord. Chem. Rev. 211 (2001) 163.
[4] J.P. Collin, J.P. sauvage, Coord. Chem. Rev. 93 (1989) 245.
[5] B.R. Rossenaar, F. Hartl, D.J. Stufkens, Inorg. Chem. 35 (1996) 6194.
[6] V. Balzani, A. Juris, M. Venturi, S. Campagna, S. Serroni, Chem. Rev. 96 (1996) 759.
[7] R.V. Slone, J.T. Hupp, Inorg. Chem. 36 (1997) 5422.
[8] S. Nieto, J. Perez, L. Riera, V. Riera, D. Miguel, New. J. Chem. 30 (2006) 838.
[9] E. Hevia, J. Perez, V. Riera, D. Miguel, S. Kassel, A.L. Rheingold, Inorg. Chem. 41 (2002) 838.
[10] J. Hawecker, J.-M. Lehn, R. Ziessel, Helv. Chim. Acta 69 (1986) 1990.
[11] (a) B.P. Sullivan, T.J. Meyer, J. Chem. Soc., Chem. Commun. (1980) 1244;
(b) E. Ioachim, E.A. Medlycott, G.S. Hanan, Inorg. Chim. Acta 359 (2006) 2599.
[12] R. Czerwieniec, A. Kapturkiewicz, J. Lipkowski, J. Nowacki, Inorg. Chim. Acta 358 (2005) 2701.
[13] W. Kaim, H.E.A. Kramer, C. Vogler, J. Rieker, J. Organomet. Chem. 367 (1989) 107.
[14] E. Wolcan, G. Torchia, J. Tocho, O.E. Piro, P. Juliarena, G. Ruiz, M.R. Feliz, J. Chem. Soc., Dalton Trans. (2002) 2194.
[15] A. Klein, C. Vogler, W. Kaim, Organometallics 15 (1996) 236.
[16] R.N. Dominey, B. Hauser, J. Hubbard, J. Dunham, Inorg. Chem. 30 (1998) 4754.
[17] S.A. Moya, J. Guerrero, R. Pastere, R. Schmidt, R. Sariego, R. Sartori, J. Sanz-Aparicio, I. Fonseca, M. Martinez-Ripoll, Inorg. Chem. 33 (1994) 2341.
[18] V.H. Rodrigues, J.A. Paixao, M.M.R.R. Costa, A. Beja Matos, Acta Crystallogr. C 56 (2000) 1053.
[19] V.H. Rodrigues, J.A. Paixao, M.M.R.R. Costa, A. Beja Matos, Acta Crystallogr. C 57 (2001) 417.
[20] R. Kia, V. Mirkhani, A. Deák, A. Kálmán, Acta Crystallogr. E 61 (2005) m566.
[21] D.D. Perrin, W.L. Armarego, D.R. Perrin, Purification of Laboratory Chemicals, 2nd ed., Pergamon, New York, NY, 1990.
[22] S. Chowdhury, G.K. Patra, M.G.B. Drew, N. Chattaopadhyay, D. Data, J. Chem. Soc., Dalton Trans. (2000) 235.
[23] A. Altomare, G. Cascarano, C. Giacovazzo, A. Guagliardi, M.C. Burla, G. Polidori, M. Camalli, J. Appl. Crystallogr. 27 (1994) 435.
[24] G.M. Sheldrick, SHELXL97 – Program for the Refinement of Crystal Structures, University of Göttingen, Germany, 1997.
[25] L.J. Farrugia, J. Appl. Crystallogr. 32 (1999) 837.

Table 1
Crystallographic data collection and structure refinement information for crystals of $[Mg(H_2O)_6][Mg_{0.5}Mn_{0.5}(1,3\text{-pdta})]\cdot 2H_2O$ (**1**), $[Mg(H_2O)_6][Mn(1,3\text{-pdta})(H_2O)]\cdot 2H_2O$ (**2**) and $[Mg(H_2O)_6][Cd(1,3\text{-pdta})(H_2O)]\cdot 2H_2O$ (**3**)

	$[Mg(H_2O)_6][Mg_{0.5}Mn_{0.5}(1,3\text{-pdta})]\cdot 2H_2O$	$[Mg(H_2O)_6][Mn(1,3\text{-pdta})(H_2O)]\cdot 2H_2O$	$[Mg(H_2O)_6][Cd(1,3\text{-pdta})(H_2O)]\cdot 2H_2O$
Crystal data			
Chemical formula	$C_{11}H_{30}Mg_{1.50}Mn_{0.50}N_2O_{16}$	$C_{11}H_{32}MgMnN_2O_{17}$	$C_{11}H_{32}CdMgN_2O_{17}$
M_r	510.29	543.64	601.10
Cell setting, space group	orthorhombic, *Pnna*	orthorhombic, *Pbcn*	orthorhombic, *Pbcn*
Temperature (K)	295(2)	130(2)	130(2)
a (Å)	13.2361(6)	11.6886(5)	11.831(2)
b (Å)	11.7051(6)	9.6970(4),	9.7098(19)
c (Å)	14.0315(7)	19.4488(7)	19.565(4)
V (Å^3)	2173.90(18)	2204.41(15)	2247.6(8)
Z	4	4	4
D_x (Mg m^{-3})	1.553	1.638	1.776
Radiation type	Mo Kα	Mo Kα	Mo Kα
μ (mm^{-1})	0.45	0.71	1.08
Crystal form, colour	prismatic, colourless	prismatic, colourless	cubic, colourless
Crystal size (mm)	$0.4\times0.3\times0.3$	$0.50\times0.40\times0.40$	$0.30\times0.30\times0.30$
Data collection			
Diffractometer	Kuma KM4CCD κ-geometry diffractometer	Kuma KM4CCD κ-geometry diffractometer	Kuma KM4CCD κ-geometry diffractometer
Data collection method	ω scans	ω scans	ω scans
Absorption correction	analytical	analytical	multi-scan (based on symmetry-related measurements)
T_{min}	0.967	0.902	0.878
T_{max}	1.000	1.000	1.000
Number of measured, independent and observed reflections	12443, 1912, 1773	20681, 1944, 1939	24106, 2211, 2054
Criterion for observed reflections	$I > 2\sigma(I)$	$I > 2\sigma(I)$	$I > 2\sigma(I)$
R_{int}	0.020	0.031	0.037
θ_{max} (°)	25.0	25.0	26.1
Refinement			
Refinement on	F^2	F^2	F^2
$R[F^2 > 2\sigma(F^2)]$, $wR(F^2)$, S	0.036, 0.087, 1.14	0.059, 0.134, 1.28	0.041, 0.075, 1.35
Number of reflections	1912	1944	2211
Number of parameters	143	152	152
H-atom treatment	riding	riding	riding
Weighting scheme	calculated $w = 1/[\sigma^2(F_o^2) + (0.0363P)^2 + 1.5542P]$, where $P = (F_o^2 + 2F_c^2)/3$	calculated $w = 1/[\sigma^2(F_o^2) + (0.P)^2 + 17.3742P]$ where $P = (F_o^2 + 2F_c^2)/3$	calculated $w = 1/[\sigma^2(F_o^2) + (0.P)^2 + 8.5789P]$, where $P = (F_o^2 + 2F_c^2)/3$
$(\Delta/\sigma)_{max}$	<0.0001	<0.0001	<0.0001
$\Delta\rho_{max}$, $\Delta\rho_{min}$ (e Å^{-3})	0.55, −0.31	0.42, −0.52	0.38, −0.58

to the selectivity process that is taking place during the crystallization procedure, which results in an exclusive admission of only M(II) ions at the hydrated site [4]. So far the only two complexes that do not conform to the above generalizations are the seven-coordinated $[Cd(1,3\text{-pdta})(H_2O)]^{2-}$ complex, crystallized with the hexaaquamagnesium counter ion in space group *Pbcn* [4], and the eight-coordinated homometallic $[Ca(H_2O)_3Ca(1,3\text{-pdta})(H_2O)]$ complex [3], both reported by us previously. In this paper, we shall illustrate, that depending on the reaction conditions, the Mn(II) ion forms either six- or seven-coordinated complexes with 1,3-pdta ligand by crystallizing with the hexaaquamagnesium counter ion in either *Pnna* or *Pbcn* space groups, respectively. Moreover, by presenting the crystal structure of mixed crystals of the composition $[Mg(H_2O)_6][Mg_{0.5}Mn_{0.5}(1,3\text{-pdta})]\cdot 2H_2O$, we shall demonstrate that the octahedral metal(II) complexes with 1,3-pdta ligand not only form isostructural crystals but also possess the ability to form solid solutions. So far in the heterobimetallic $M[M'(1,3\text{-pdta})]\cdot 8H_2O$ complexes each of the two different metallic ions occupied one of the two types of coordination sites. In this respect, the reported structure of the mixed crystal is unique and can give rise to a new class of materials. A useful by-product of this study is the precise low-temperature crystal structure of the $[Mg(H_2O)_6][Cd(1,3\text{-pdta})(H_2O)]\cdot 2H_2O$ complex, previously investigated at room temperature [4] but now determined at 130 K to allow a direct comparison with the analogous Mn(II) complex and to establish the type of disorder present in its crystal lattice.

2. Experimental

2.1. Compounds preparation

All commercially obtained reagent-grade chemicals were used without further purification. Preparation of barium (1,3-propanediaminetetraacetato)barium(II) dihydrate, $Ba[Ba(1,3\text{-pdta})]\cdot 2H_2O$, has been reported elsewhere [1,8]. The $[Mg(H_2O)_6][Mg_{0.5}Mn_{0.5}(1,3\text{-pdta})]\cdot 2H_2O$ (**1**) and $[Mg(H_2O)_6][Mn(1,3\text{-pdta})(H_2O)]\cdot 2H_2O$ (**2**) complexes have been prepared according to the method described in the literature for preparation of a series of $[M(H_2O)_6][M'(1,3\text{-pdta})]\cdot 2H_2O$ type complexes (M = Co(II), Mg(II), Zn(II); M′ = Co(II), Cu(II), Ni(II), Mg(II), Zn(II)) [1–5].

2.1.1. Preparation of hexaaquamagnesium (1,3-propanediaminetetraacetato)manganese(II)-magnesium(II) dihydrate, $[Mg(H_2O)_6][Mg_{0.5}Mn_{0.5}(1,3\text{-pdta})]\cdot 2H_2O$ (*1*)

$MnSO_4\cdot H_2O$ (0.85 g; 0.005 mol) was dissolved in 25 cm^3 of distilled water at 60 °C. To this solution, solid $Ba[Ba(1,3\text{-pdta})]\cdot 2H_2O$ (6.13 g; 0.01 mol) was added and the reaction mixture was heated at 60 °C with stirring for 20 min. Then, $MgSO_4\cdot 6H_2O$ (3.43 g; 0.015 mol) was added and stirring with heating at 60 °C was continued for next 20 min. The precipitated barium sulphate was filtered out. To the obtained filtrate 5–6 cm^3 of ethanol was added and the solution was left to stand in a refrigerator overnight. The obtained crystals of $[Mg(H_2O)_6][Mg_{0.5}Mn_{0.5}(1,3\text{-pdta})]\cdot 2H_2O$ are colourless in solution, but out of solution they have slightly light-green colour. These crystals were collected, washed with ethanol, and air-dried. The yield was 3.57 g (70%). *Anal.* Calc. for $[Mg(H_2O)_6][Mg_{0.5}Mn_{0.5}(1,3\text{- pdta})]\cdot 2H_2O$, $C_{11}H_{30}Mg_{1.50}Mn_{0.50}N_2O_{16}$ (FW = 510.29): C, 25.89; H, 5.92; N, 5.49. Found: C, 26.00; H, 6.19; N, 5.48%.

2.1.2. Preparation of hexaaquamagnesium aqua(1,3-propanediaminetetraacetato)manganese(II) dihydrate, $[Mg(H_2O)_6][Mn(1,3\text{-pdta})(H_2O)]\cdot 2H_2O$ (*2*)

$MnSO_4\cdot H_2O$ (1.69 g; 0.01 mol) was dissolved in 25 cm^3 of distilled water at 60 °C. To this solution, solid $Ba[Ba(1,3\text{-pdta})]\cdot 2H_2O$ (6.13 g; 0.01 mol) was added and the reaction mixture was heated at 60 °C with stirring for 20 min. The precipitated barium sulphate was filtered out and to the obtained filtrate the solid $MgSO_4\cdot 6H_2O$ (2.28 g; 0.01 mol) was added and stirring with heating at

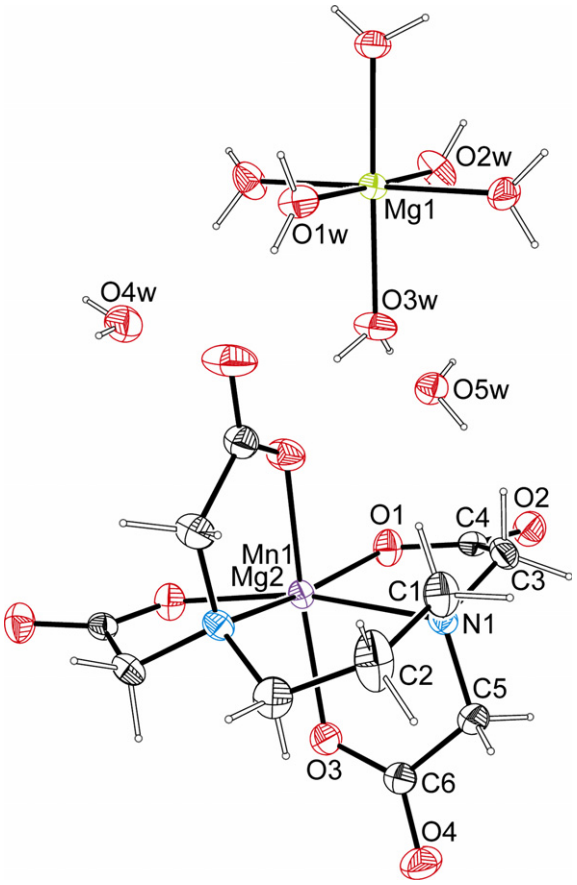


Fig. 1. Perspective drawings of the structural units constituting the crystals of **1**. All molecules occupy twofold symmetry sites. Thermal ellipsoids which are drawn at 40% probability illustrate the displacements of atoms at 295 K. In the anionic complex of **1** both Mn^{II} and Mg^{II} cations occupy the same site, with s.o.f. 0.25.

60 °C was continued for next 20 min. The precipitated barium sulphate was again filtered out. To the obtained filtrate 5–6 cm^3 of ethanol was added and the solution was left to stand in a refrigerator overnight. The light-pink crystals of $[Mg(H_2O)_6][Mn(1,3\text{-pdta})(H_2O)]\cdot 2H_2O$ complex were collected, washed with ethanol, and air-dried. The yield was 3.93 g (75%). The complex was recrystallized from a water solution left to stand in a desiccator over methanol for several days. The recrystallized product was checked by elemental microanalyses and IR spectroscopy, and the obtained results were equal to those for the precipitates obtained before recrystallization. *Anal.* Calc. for $[Mg(H_2O)_6][Mn(1,3\text{-pdta})(H_2O)]\cdot 2H_2O$, $C_{11}H_{32}MgMnN_2O_{17}$ (FW = 543.64): C, 24.30; H, 5.93; N, 5.15. Found: C, 24.24; H, 6.13; N, 5.10%.

2.2. Elemental microanalyses

Elemental microanalyses for carbon, hydrogen, and nitrogen were done by the Faculty of Chemistry, University of Belgrade, Serbia.

2.3. Crystallographic data collection and refinement of the structures

The crystal data of the solid solution of the composition $[Mg(H_2O)_6][Mg_{0.5}Mn_{0.5}(1,3\text{-pdta})]\cdot 2H_2O$ (**1**), $[Mg(H_2O)_6][Mn(1,3\text{-pdta})(H_2O)]\cdot 2H_2O$ (**2**) and $[Mg(H_2O)_6][Cd(1,3\text{-pdta})(H_2O)]\cdot 2H_2O$ (**3**), and the parameters of data collection are summarized in Table 1. The intensity data were measured with a KM4CCD kappa-geometry diffractometer [9] using graphite monochromated Mo Kα radiation ($\lambda = 0.71073$ Å) at 295(2) K for the crystals of **1**, and at 130 K for the crystals of **2** and **3**. The structures were solved by direct methods using SHELXS-97 [10] and refined by least-squares techniques with SHELXL-97 [11]. The intensity data were corrected for Lp effects as well as for absorption. Anisotropic thermal parameters were employed for the non-hydrogen atoms. Hydrogen atoms connected to carbon atoms have been placed at calculated positions, while those attached to the water oxygen atoms have been located on subsequent difference Fourier maps. Although refined at the earlier stages of structure determination, the hydroxyl hydrogens were eventually fixed at a distance of 0.85 Å from their respective oxygen atoms because some of the bond lengths and angles involving these hydrogens as well as their displacement parameters refined to unreasonable values. All hydrogen atoms were allowed to ride on the atoms to which they were attached and their isotropic displacement parameters were given values 20% higher than the isotropic equivalent for the atom to which the H-atom was bonded. Since in the crystals of **1** both the Mn and Mg atoms share the same occupation site 4d [7], the same *x*, *y*, *z* parameters and the same anisotropic displacement parameters were used for both atoms. The occupancy factor refined to 0.25 for both Mn and Mg atoms. In the crystal structures of **2** and **3**, carbon atom C2, as well as hydrogen atoms attached to C1 are disordered and were refined with occupation number 0.5. A Siemens Stereochemical Workstation was used to prepare drawings [12].

Table 2
Bond lengths (Å) and angles (°) in $[Mg_{0.5}Mn_{0.5}(1,3\text{-pdta})]^{2-}$ complex anion of **1**

M(II)–O(1)	2.0530(14)
M(II)–O(3)	2.1480(14)
M(II)–N(1)	2.2526(16)
O(1)–C(4)	1.276(2)
O(2)–C(4)	1.237(2)
O(3)–C(6)	1.265(2)
O(4)–C(6)	1.244(3)
N(1)–C(5)	1.476(3)
N(1)–C(3)	1.481(3)
N(1)–C(1)	1.486(3)
C(1)–C(2)	1.533(3)
C(3)–C(4)	1.526(3)
C(5)–C(6)	1.519(3)
O(1)–M(II)–O(1)#1	110.33(8)
O(1)–M(II)–O(3)#1	92.18(6)
O(1)–M(II)–O(3)	95.65(6)
O(3)#1–M(II)–O(3)	166.28(9)
O(1)–M(II)–N(1)#1	166.26(6)
O(3)–M(II)–N(1)#1	92.85(6)
O(1)–M(II)–N(1)	80.03(6)
O(3)–M(II)–N(1)	77.48(6)
N(1)#1–M(II)–N(1)	91.35(8)
C(4)–O(1)–M(II)	117.30(13)
C(6)–O(3)–M(II)	119.09(13)
C(5)–N(1)–C(3)	110.28(16)
C(5)–N(1)–C(1)	112.53(17)
C(3)–N(1)–C(1)	110.40(16)
C(5)–N(1)–M(II)	109.84(12)
C(3)–N(1)–M(II)	102.73(11)
C(1)–N(1)–M(II)	110.63(12)
N(1)–C(1)–C(2)	115.91(18)
C(1)–C(2)–C(1)#1	120.8(3)
N(1)–C(3)–C(4)	112.59(16)
O(2)–C(4)–O(1)	124.16(19)
O(2)–C(4)–C(3)	119.21(18)
O(1)–C(4)–C(3)	116.52(17)
N(1)–C(5)–C(6)	114.86(17)
O(4)–C(6)–O(3)	125.6(2)
O(4)–C(6)–C(5)	115.88(18)
O(3)–C(6)–C(5)	118.50(18)

In the complex both Mn(1) and Mg(2) cations occupy the same site, so M(II) stands for both Mn(1) and Mg(2). Symmetry transformations used to generate equivalent atoms: #1: x, $-y-1/2$, $-z+1/2$.

3. Results and discussion

3.1. The crystal structure of $[Mg(H_2O)_6][Mg_{0.5}Mn_{0.5}(1,3\text{-pdta})]\cdot 2H_2O$

An ORTEP drawing of $[Mg(H_2O)_6][Mg_{0.5}Mn_{0.5}(1,3\text{-pdta})]\cdot 2H_2O$ is depicted in Fig. 1, where the numbering scheme adopted for the respective atoms is also given. Bond distances and valence angles are listed in Table 2. The investigated crystal structure is a solid solution in

Table 3
Geometry of hexadentate six-coordinated anionic complex $[M'(1,3\text{-pdta})]^{2-}$ as observed in the investigated Mn/Mg mixed crystal **1** and in other homo and heterobimetallic complexes of the type $[M(H_2O)_6][M'(1,3\text{-pdta})]\cdot 2H_2O$

M/M′	M′–N (Å)	M′–O_G (Å)[a]	M′–O_R (Å)[a]	Average ΔO_h (°)[c]	Ref.
Mg(II)/Mn(II)/Mg(II)	2.253	2.053	2.148	8.6	this work
Mg(II)/Mg(II)	2.199	2.015	2.087	7.4	[3]
Mg(II)/Co(II)[b]	2.142	2.054	2.110	5.9	[2]
Co(II)/Co(II)[b]	2.143	2.055	2.112	5.9	[2]
Mg(II)/Zn(II)[b]	2.156	2.037	2.146	5.9	[4]
Zn(II)/Zn(II)[b]	2.153	2.035	2.152	5.8	[4]
Mg(II)/Cu(II)	2.047	1.974	2.272	5.4	[1]
Mn(II)/Cu(II)	2.049	1.974	2.285	5.3	[6]
Mg(II)/Ni(II)	2.073	2.027	2.078	5.2	[5]

[a] M–O_G is the mean in-plane bond length; M–O_R is the mean out-of-plane bond length.
[b] Low temperature data.
[c] The mean deviation from octahedral angles.

which the chelated metal atom site M′ is in 50% occupied by Mn(II) and in 50% by Mg(II) cations. The crystal is isostructural with those of metal(II)-1,3-pdta complexes, namely $[M(H_2O)_6][Cu(1,3\text{-pdta})]\cdot 2H_2O$ (M = Mg(II) [1] or Mn(II) [6]), $[Mg(H_2O)_6][M'(1,3\text{-pdta})]\cdot 2H_2O$ (M′ = Co(II)) [2], Ni(II) [5], Zn(II) [4] and homobimetallic $[Mg(H_2O)_6][Mg(1,3\text{-pdta})]\cdot 2H_2O$ [3], $[Zn(H_2O)_6][Zn(1,3\text{-pdta})]\cdot 2H_2O$ [4] and $[Co(H_2O)_6][Co(1,3\text{-pdta})]\cdot 2H_2O$ [2]. Metal–ligand bond lengths and angles observed in the investigated structure are compared in Table 3 with the corresponding values reported previously for the series of 1,3-pdta structures containing different metal(II) ions.

The structural units consist of a mixture of $[Mn(1,3\text{-pdta})]^{2-}$ and $[Mg(1,3\text{-pdta})]^{2-}$octahedra sharing the same site, and $[Mg(H_2O)_6]^{2+}$ octahedra, as well as two water solvent molecules. All these constituents of the crystal lattice occupy special position sites of twofold symmetry. The twofold axis of the chelated complex anion passes through the M′ metal (which is either Mn(II) or Mg(II)) and C2 atom and bisects the N1–M(II)–N1[a] bond angle ([a] stands for the symmetry operation x, $-0.5-y$, $0.5-z$) making the two glycinate rings of the R type as well as the two glycinate rings of the G type identical.[1] The six-membered (T) ring adopts a symmetrical *twist-boat* conformation with the average torsion angle moduli of 44.7°. The R rings are almost flat, while the G-rings are much more puckered and are halfway between an *envelope* and *twist* conformations. As can be seen from Table 3, the M′–O bond distances are greater in the flat R rings than in the puckered G rings, the difference being 0.095 Å, and the M′–N bonds are by 0.153 Å longer than the average M′–O bond. Examination of the bond angles shows that the reported $[Mg(H_2O)_6][Mg_{0.5}Mn_{0.5}(1,3\text{-pdta})]\cdot 2H_2O$ complex is the most, while the $[Mg(H_2O)_6][Ni(1,3\text{-pdta})]\cdot 2H_2O$ complex is the least distorted from octahedral geometry (compare av. ΔO_h parameters listed in Table 3). The severe distortion from octahedral geometry of Mn(II) and Mg(II) complexes is not unexpected owing to the electronic configuration of the two ions ($3d^0$ and $3d^5$, respectively) and connected with it the lack of crystal field stabilization energy (CFSE) contribution [15].

In the crystal structure of **1**, as in other crystals belonging to the isomorphic series [1–6], the complex cations and anions alternate throughout the entire lattice. This is best viewed along the [0 0 1] direction, as illustrated in Fig. 2. Both "hydrated" and "chelated" complex ions are situated on the twofold axis parallel to *a*-direction. Apart from the electrostatic interactions, the $[M'(1,3\text{-pdta})]^{2-}$ and $[M(H_2O)_6]^{2+}$ octahedra are hydrogen bonded to form a puckered layer parallel to (0 0 1) lattice plane in which the metal aqua ions act solely as donors to carboxylate oxygens [O2, O3 and O4] acting as acceptors. The solvent

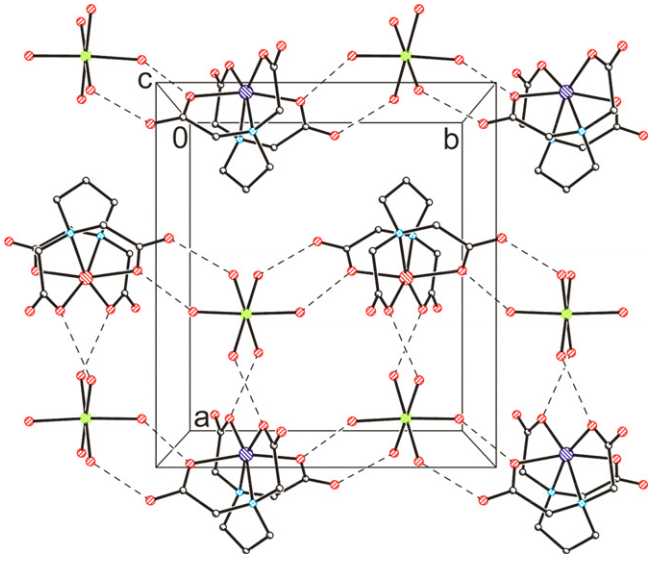


Fig. 2. View of the (0 0 1) layer in the crystal structure of **1**. The layer contains alternating complex cations and anions. The subsequent layers are separated by uncoordinated water molecules.

[1] The convention for describing the various chelate rings formed by edta-type ligands is credited to Weakliem and Hoard [13]. According to the authors, G rings are those whose mean planes are more nearly parallel to the N–M–N plane and R rings are those rings whose mean planes are more nearly perpendicular to the N–M–N plane.

water molecules [O4W and O5W], situated in between the (0 0 1) layers, act as double donors and double acceptors and help to join the neighboring layers. The crystal structure is additionally stabilized by C=O dipolar interactions around the symmetry center at 1/2 1/2 1/2. No carboxylate bridges, commonly present in the crystal structures of $[M(edta\text{-}type)]^{2-}$ and $[M(1,3\text{-}pdta)]^{-}$ complexes [14] are observed.

3.2. Description of the isomorphic crystal structures of $[Mg(H_2O)_6][Mn(1,3\text{-}pdta)(H_2O)]\cdot 2H_2O$ (2) and $[Mg(H_2O)_6][Cd(1,3\text{-}pdta)(H_2O)]\cdot 2H_2O$ (3) at 130 K

An ORTEP drawing of the $[Mg(H_2O)_6][Mn(1,3\text{-}pdta)(H_2O)]\cdot 2H_2O$ (**2**) complex, is depicted in Fig. 3, where the numbering scheme adopted for the respective atoms is also given. As **2** and **3** form isostructural crystals, drawing of the units that constitute complex **3** has not been provided. Metal–ligand bond lengths and valence angles around metal ions are compared in Table 4.

The structural units of **2** and **3** consist of $[Mg(H_2O)_6]^{2+}$ cations, situated at the inversion centers, and either $[Mn(1,3\text{-}pdta)(H_2O)]^{2-}$ or $[Cd(1,3\text{-}pdta)(H_2O)]^{2-}$ complex anions situated on twofold axes of symmetry, and two symmetry related water solvent molecules. The highest symmetry (C_2) axis of both complex anions passes through the metal center and coordinated water molecule O1W making the two out-of-plane glycinate rings (R rings), as well as the two in-plane glycinate rings (G rings), identical. The central carbon atom (C2) of the six-membered 1,3-propanediamine ring and hydrogen atoms attached to C1 are statistically distributed about the twofold symmetry axis. Both transition metals display the sevenfold coordination: with the hexadentate 1,3-pdta ligand and one water molecule O1W, the coordination polyhedron being a C_2 hybrid of the monocapped trigonal prism (CTP) and the pentagonal bipyramid (PB). That the geometry is better described as PB is seen by a detailed examination of Table 4 and Fig. 3. Among in-plane *cis* bond angles, O1–M(II)–O1W (M(II) stands for either Mn(II) or Cd(II)) is the closest to the value of 72° expected for ideal PB structure, while the largest deviation is observed for diamine bite angles (N1–M(II)–N1′) which adopt the values in the range 88.71(19)–90.47(15)°. Conformations of the chelate rings are found to be *envelope* for the glycinates and almost ideal *sofa* (*half boat*) for the six-membered diamine ring in both **2** and **3**, with the out of plane atom C2 disordered over two equally occupied alternative positions. Compared to octahedral complex **1**, the R-rings in **2** and **3** are significantly more puckered. Combined with this is the reverse relationship between M(II)–O_R and M(II)–O_G bond distances: while in octahedral complex **1** the M(II)–O_G bond lengths are significantly shorter than the M(II)–O_R distances, the reverse holds in PB complexes. Hence, we may conclude that a change in coordination number from 6 to 7 mostly affects the conformations of the R- and T-rings, and bond lengths, and angles in the girdle plane. The variation in M(II)–O bond lengths in PB complexes **2** and **3** (0.069 and 0.125 Å, for M(II)–O_G and M(II)–O_R, respectively) corresponds somewhat to the difference in the ionic radii of Cd(II) and Mn(II) ions (0.120 Å) [16] but for M(II)–N bonds the variation is much smaller (0.011 Å) indicating

Table 4
Geometry around metal center in hexadentate seven-coordinated transition metal(II) complexes with 1,3-pdta ligands, $[Mn(1,3\text{-}pdta)(H_2O)]^{2-}$ (**2**) and $[Cd(1,3\text{-}pdta)(H_2O)]^{2-}$ (**3**): bond lengths (Å) and valence angles (°)

	2	3
Mn1(Cd1)–N1	2.429(4)	2.440(3)
Mn1(Cd1)–O1	2.480(3)	2.541(3)
Mn1(Cd1)–O3	2.149(3)	2.270(3)
Mn1(Cd1)–O1W	2.154(5)	2.236(3)
Mg1–O2W	2.046(3)	2.078(2)
Mg1–O3W	2.083(3)	2.050(2)
Mg1–O4W	2.082(3)	2.086(3)
N1–Mn1(Cd1)–N1[a]	88.71(19)	90.47(15)
N1–Mn1(Cd1)–O1	67.26(12)	67.02(9)
N1–Mn1(Cd1)–O1[a]	146.37(12)	146.59(9)
O1–Mn1(Cd1)–O1[a]	143.64(15)	143.23(12)
O3–Mn1(Cd1)–N1	74.14(13)	73.29(10)
O3–Mn1(Cd1)–N1[a]	93.31(13)	94.44(10)
O3–Mn1(Cd1)–O1	101.70(12)	101.68(9)
O3–Mn1(Cd1)–O1[a]	83.75(11)	83.78(9)
O3–Mn1(Cd1)–O3[a]	162.67(18)	162.85(14)
O3–Mn1(Cd1)–O1W	98.67(9)	98.57(7)
O1W–Mn1(Cd1)–N1	135.64(9)	134.77(7)
O1W–Mn1(Cd1)–O1	71.82(8)	71.61(6)

[a] Symmetry code: $-x, y, 0.5-z$ for **2** and $1-x, y, 1.5-z$ for **3**.

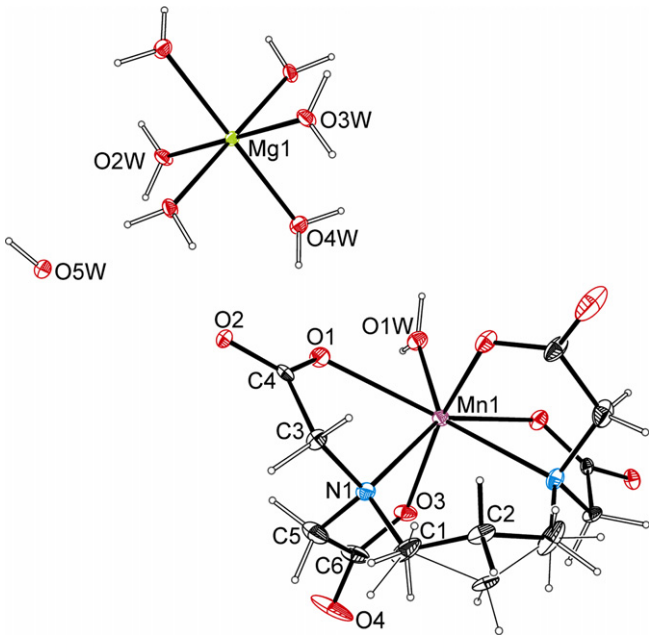


Fig. 3. Perspective drawing of the structural units constituting the crystal of **2.** The symmetry independent parts of the complexed cation and anion are marked by labeled atoms. Thermal ellipsoids which are drawn at 40% probability illustrate the displacements of atoms at 130 K. Within the complex anion, carbon atom C2, as well as hydrogen atoms attached to C1 are statistically distributed over two sites related by a twofold axis. The alternative position is shown by thin lines.

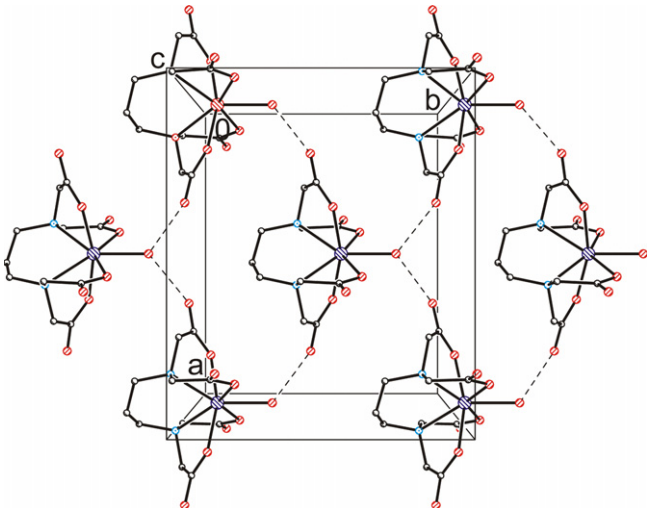


Fig. 4. View of the polar anionic (0 0 1) layer in the crystal structure of **2**. The subsequent anionic layers, separated by the hydrated magnesium cations, are arranged antiparallel.

a marked preference of Cd(II) cation for nitrogen donor atoms.

In the isostructural crystals of **2** and **3**, the complex anions, situated on a twofold *y*-axis, are arranged in (0 0 1) layers (Fig. 4). Within each layer the coordinated water molecules all point in the same direction, demonstrating its polarity. By acting as double hydrogen bond donors these water molecules join together the complex anions within the layer. Anionic layers are loosely packed, thus allowing for static disorder within the 1,3-propanediamine ring (*vide supra*). The type of disorder has been unequivocally established by comparing the previously reported room temperature X-ray results for **3** [4] with those at 130 K, presented in this paper, since lowering the temperature had no effect on the observed disorder. The neighboring anionic layers are arranged antiparallel and are separated by hydrated magnesium cations and solvent water molecules. Apart from electrostatic interactions, the cationic and anionic layers are joined together *via* water/carboxylate type of hydrogen bonds.

4. Conclusions

Isolation and X-ray elucidation of two distictly different Mn(II) complexes with 1,3-pdta ligand confirm our previous observations that 1,3-pdta ligand prefers hexadentate coordination. For metal ions with ionic radii exceeding 0.9 Å, the seven-coordinated hexadentate complex is to be expected. So far we have demonstrated that this is indeed the case for metal ions with d^0 [3], d^5 [this work] and d^{10}[4] configuration, as these ions provide no crystal field stabilization energy (CFSE), so the CFSE confers no advantage on any complex geometry [15]. The Mn(II) cation of the ionic radii 0.97 Å represents most probably the borderline case and, because of its electronic configuration (d^5), is particularly well suited to form complexes with variable geometries. Moreover, the described here solid solution of the composition $Mn_{0.5}Mg_{1.5}$ may be considered as resulting from isomorphic replacement of the Mg(II) ions occupying the "chelate" site by Mn(II) cations. In order to achieve this, the Mn(II) cations, which in general prefer to form seven-coordinated complex anions with 1,3-pdta ligand, readily adjust to the geometrical requirements of the six-coordinate 1,3-pdta complex, however, at the expense of the increased strain of the Mn(II) complex anion. From our previous investigations it follows that metals that can occupy both the "hydrated" and "chelated" site and hence might be expected to form solid solutions of the type described here, are Co(II), Zn(II) and Mg(II). To the best of our knowledge, no solid solution formation in 1,3-pdta complexes have been reported so far.

Acknowledgements

This work was supported by the Polish Ministry of Education and Science Grant 4T09A18525 and by the Ministry of Science and Environmental Protection of the Republic of Serbia Grant No. 142008.

Appendix A. Supplementary material

CCDC 616985, 616986 and 616987 contain the supplementary crystallographic data for **1**, **2** and **3**. These data can be obtained free of charge via http://www.ccdc.cam.ac.uk/conts/retrieving.html, or from the Cambridge Crystallographic Data Centre, 12 Union Road, Cambridge CB2 1EZ, UK; fax: (+44) 1223-336-033; or e-mail: deposit@ccdc.cam.ac.uk. Supplementary data associated with this article can be found, in the online version, at doi:10.1016/j.poly.2006.12.011.

References

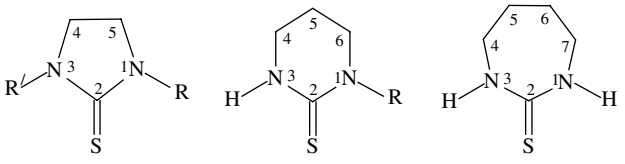
[1] U. Rychlewska, D.D. Radanovic, V.S. Jevtovic, D.J. Radanovic, Polyhedron 19 (2000) 1.
[2] D.D. Radanović, U. Rychlewska, M.I. Djuran, N.S. Drašković, M.M. Vasojević, I.M. Hodžić, D.J. Radanović, Polyhedron 22 (2003) 2745.
[3] D.D. Radanović, U. Rychlewska, M.I. Djuran, B. Warżajtis, N.S. Drašković, D.M. Gurešić, Polyhedron 23 (2004) 2183.
[4] U. Rychlewska, D.M. Gurešić, B. Warżajtis, D.D. Radanović, M.I. Djuran, Polyhedron 24 (2005) 2009.
[5] D.J. Radanovic, T. Ama, H. Kawaguchi, N.S. Draškovic, D.M. Ristanovic, S. Janicijevic, Bull. Chem. Soc. Jpn. 74 (2001) 701.
[6] M. Hernandez-Padilla, E. Chinea, S. Dominguez, A. Mederos, M.C. Munoz, F. Lloret, Polyhedron 19 (2000) 1175.
[7] T. Hahn (Ed.), International Tables for X-ray Crystallography, D. Reidel Publishing Company, Dordrecht, Holland, 1983.
[8] J.A. Weyh, R.E. Hamm, Inorg. Chem. 7 (1968) 2431.
[9] CRYSTALIS CCD software. Version 1.171 Oxford Diffraction, Oxfordshire (England), 2000.
[10] G.M. Sheldrick, Acta Crystallogr., Sect. A 46 (1990) 467.
[11] G.M. Sheldrick, SHELXL 97, Program for the Refinement of Crystal Structures, University of Göttingen, Germany, 1997.

[12] Stereochemical Workstation Operation Manual, Release 3.4. Siemens Analytical X-ray Instruments, Inc., Madison, WI, 1989.
[13] H.A. Weakliem, J.L. Hoard, J. Am. Chem. Soc. 81 (1959) 549.
[14] F.H. Allen, Acta Crystallogr., Sect. B 58 (2002) 380.
[15] N.N. Greenwood, A. Earnshaw, Chemistry of the Elements, Pergamon Press Ltd., Oxford, 1984.
[16] F.A. Cotton, G. Wilkinson, C.A. Murillo, M. Bochmann, Advanced Inorganic Chemistry, Wiley, New York, 1999.

The chemical shift scale of ^{113}Cd covers about 900 ppm and shows a great sensitivity to the environment of Cd, even for complexes with closely related structures. Environments in which ^{113}Cd is completely ligated by oxygen usually give rise to resonances between −100 and +150 ppm. Coordination to nitrogen usually results in a downfield shift with resonances between +200 and +380 ppm, whereas bonding to sulfur causes a further downfield shift to between +350 and +800 ppm [10]. However, within these regions there are relatively few useful correlations with coordination numbers, and so structural predictions from solution chemical shift data are difficult to make. There is the added difficulty that ^{113}Cd chemical shifts in solution are affected by changes in pH and concentration, and there may also be large anion dependences. Further, cadmium complexes in solution are often labile and the chemical exchange behavior of ligands can severely handicap spectral interpretation [9,12–14].

Complexes of heterocyclic ligands such as imidazolidine-2-thione (Imt) and its derivatives with metal ions are of interest in bioinorganic chemistry because of the search for simple model compounds for metal-proteins [5–7]. In view of this, Cu(I), Au(I), Ag(I), Cd(II), Hg(II) and Pd(II) complexes with these ligands have been widely investigated in recent years [15–20]. These penta-atomic ligands exist in the N=C–SH and N–C=S forms, exhibiting a thiol $\Longleftrightarrow$ thione equilibrium [7,21]. However, it has been established that the thione form dominates in the solid state [7]. We have studied extensively the interaction of metal ions with imidazolidine-2-thione (Imt) and its derivatives [19,20,22].

In this paper, we report the solid state, solution NMR as well as X-ray structure studies of $Cd(thione)_2Cl_2$ complexes. Their antimicrobial activities are compared with the corresponding $Zn(thione)_2Cl_2$ complexes (see Scheme 1).



(a-g) (h-i) (j)

(a) R = R′ = H; Imidazolidine-2-thione (Imt)

(b) R = CH_3, R′ = H; N-methylimidazolidine-2-thione (MeImt)

(c) R = C_2H_5, R′ = H; N-ethylimidazolidine-2-thione (EtImt)

(d) R = C_3H_7, R′ = H; N-propylimidazolidine-2-thione (PrImt)

(e) R = *i*-C_3H_7, R′ = H; N-(*i*-propyl)imidazolidine-2-thione (*i*-PrImt)

(f) R = CH_3, R′ = CH_3; N,N′-dimethylimidazolidine-2-thione (Me_2Imt)

(g) R = C_2H_5, R′ = CH_3; N-ethyl-N′-methylimidazolidine-2-thione (EtMeImt)

(h) R = H; 1,3-Diazinane-2-thione (Diaz)

(i) R = C_2H_5; N-ethyl-1,3-Diazinane-2-thione (EtDiaz)

(j) 1,3-Diazipane-2-thione (Diap)

Scheme 1.

2. Experimental

2.1. Chemicals

$CdCl_2$, acetone, acetonitrile and DMSO-d_6 were obtained from Fluka Chemical Co. All the thiones were synthesized according to the procedure described earlier [23].

2.2. Preparation of the complexes

$CdCl_2$ (10 mmol) was dissolved in a minimum amount of water and the ligands (20 mmol) were dissolved in minimum amount of MeOH. In the case of poorly soluble ligands, acetonitrile was added to achieve complete solubility. Both solutions were mixed and stirred for about 30 min. The precipitates were collected and dried under vacuum. Yields of 55–65% were obtained.

The elemental analyses of all the complexes are given in Table 1.

2.3. Spectroscopic measurements

The measurements of solid-state IR and solution NMR were recorded as described in the literature [10a]. The chemical shifts of the ligands along with the corresponding complexes are given in Table 2.

2.4. Solid-state NMR

Natural abundance ^{113}Cd and ^{13}C solid-state NMR spectra were obtained on a JEOL LAMBDA 500 spectrometer operating at 110.85 MHz and 125.65 MHz, respectively, corresponding to a magnetic field of 11.74 T, at an ambient temperature of 25 °C. Samples were packed into 6 mm zirconia rotors. Cross-polarization and high power decoupling were employed. A pulse delay of 7.0 s and a contact time of 5.0 ms were used for cadmium and carbon observations in the CP MAS experiments. The magic angle spinning rates were from 3000 Hz to 5000 Hz. The cadmium chemical shifts were referenced using the secondary reference $Cd(NO_3)_2 \cdot 4H_2O$, by settings the peak to −100 ppm relative to 0.1 M $Cd(ClO_4)_2$ solution. The same $Cd(NO_3)_2 \cdot 4H_2O$ sample was used to set up the Hartmann–Hahn condition for the CPMAS experiments. ^{13}C chemical shifts were referenced to TMS by setting the high frequency isotropic peak of solid adamantine to 38.56 ppm. The isotropic peaks were differentiated from the spinning side-bands by recording the spectra at two different spinning speeds. ^{113}Cd CPMAS spectra for $Cd(EtImt)_2Cl_2$ and $Cd(N,N'DiMeImt)_2Cl_2$ complexes are shown in Figs. 1 and 2, respectively, and the isotropic peaks are indicated by an asterix. The ^{113}Cd and ^{13}C spectra containing spinning side-band manifolds were analyzed using a program based on Maricq and Waugh [24] and developed by Durham University, UK and run on a Unix platform. The calculated ^{113}Cd shielding tensors are shown in Table 3 and the chemical shifts of the thione complexes are given in Table 4.

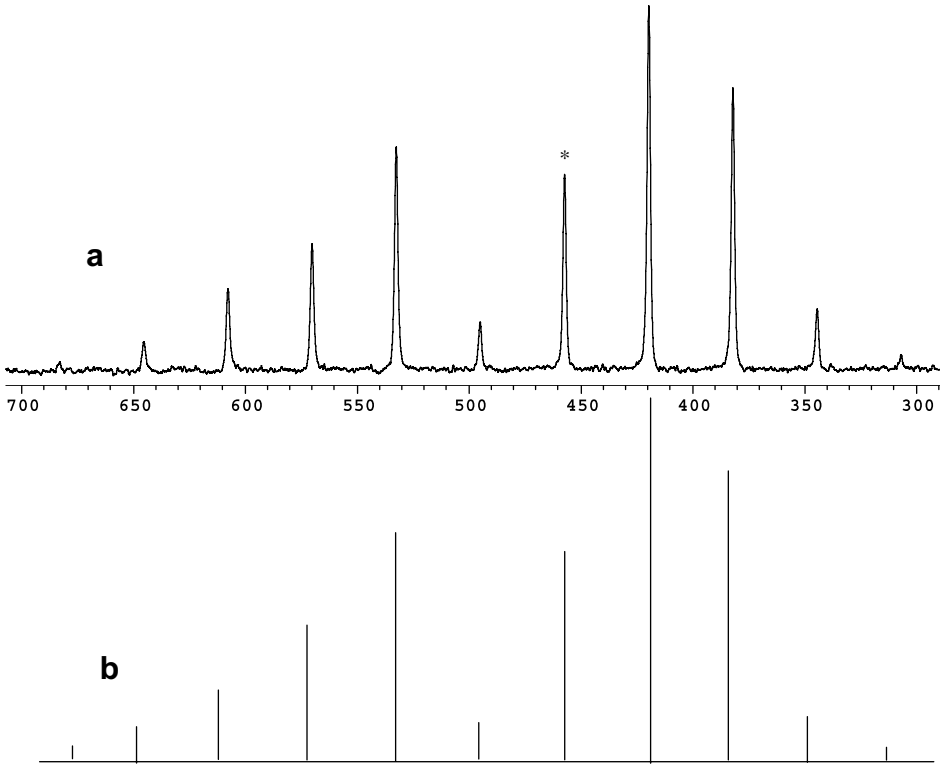


Fig. 1. ^{113}Cd CP MAS spectrum of $Cd(EtImt)_2Cl_2$. (a) Observed (1000 scans) and (b) calculated. * denotes the isotropic peak.

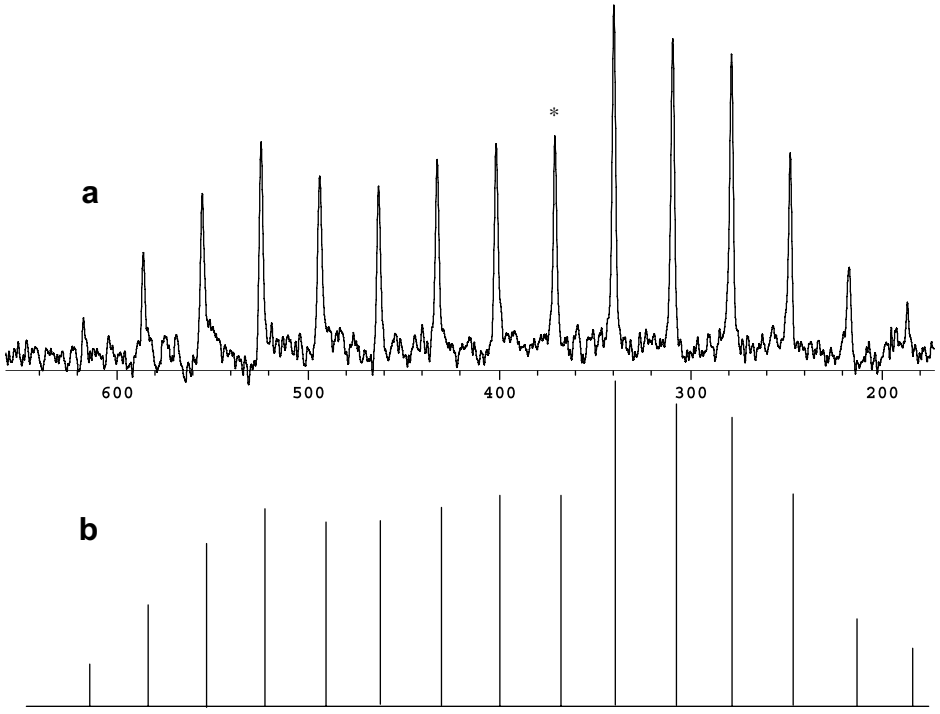


Fig. 2. ^{113}Cd CPMAS spectrum of $Cd(N,N'Me_2Imt)_2Cl_2$. (a) Observed (2000 scans) and (b) calculated. * indicates the isotropic peak.

2.5. Antimicrobial activity

Antimicrobial activity was measured as described in the literature [25]. The data for heterotrotropic plate counts (HPC), *Pseudomonas aeruginosa* (*P. aeruginosa*), Fecal Streptococcus (FS) and *Escherichia coli* (*E. coli*) are given in Table 5.

2.6. X-ray data collection and structure determination

Crystals were mounted on glass fibers. Diffraction data were recorded on a Bruker-Axs Smart Apex system equipped with graphite-monochromatized Mo Kα radiation ($\lambda = 0.71073$ Å). The data were collected using SMART [27]. The data integration was performed using SAINT [28]. An empirical absorption correction was carried out using SADABS [29]. The structure was solved with the direct methods and refined by full-matrix least-square methods based on F^2, using the structure determination and graphics package SHELXTL [30] based on SHELX-97 [31]. Hydrogen atoms were included at calculated positions using a riding model. An sp^2 hybridization was assumed for the nitrogen atoms of the NH groups. Crystallographic data are given in Table 6. Selected bond lengths and angles are given in Table 7. Complete bond lengths and bond angles, anisotropic thermal parameters and calculated hydrogen coordinates are deposited as Supplementary materials. The ORTEP atomic labelling schemes are given in Figs. 3 and 4.

3. Results and discussion

3.1. Solution NMR studies

$CdCl_2$ reacts with Imt and its derivatives in a 1:2 ratio, forming tetrahedral complexes of the general formula CdL_2Cl_2, except for the Diaz ligand. As demonstrated by the ^{13}C NMR (Table 2), the C-2 resonance is shifted by

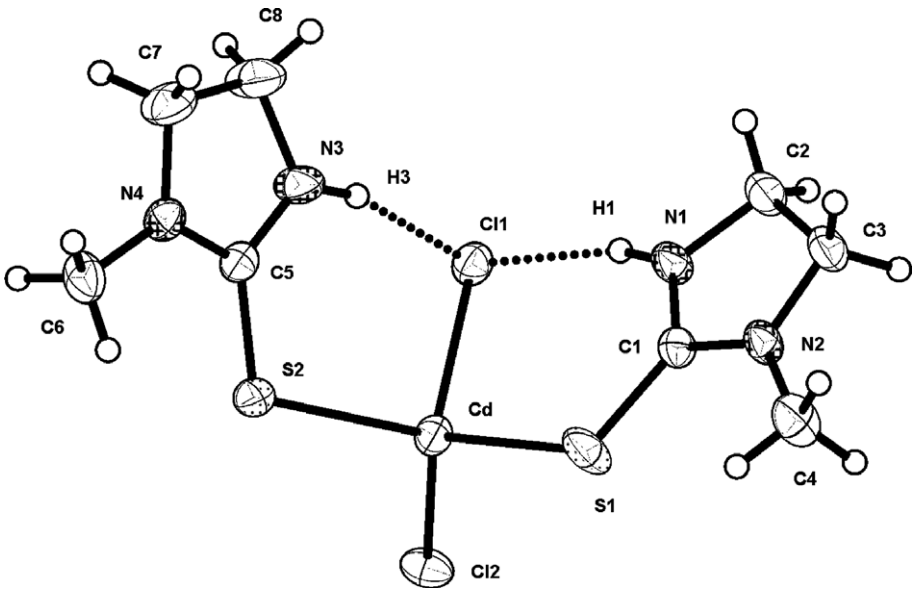


Fig. 3. Molecular structure of $(NMeImt)_2CdCl_2$ (**1**) showing the atomic labelling scheme.

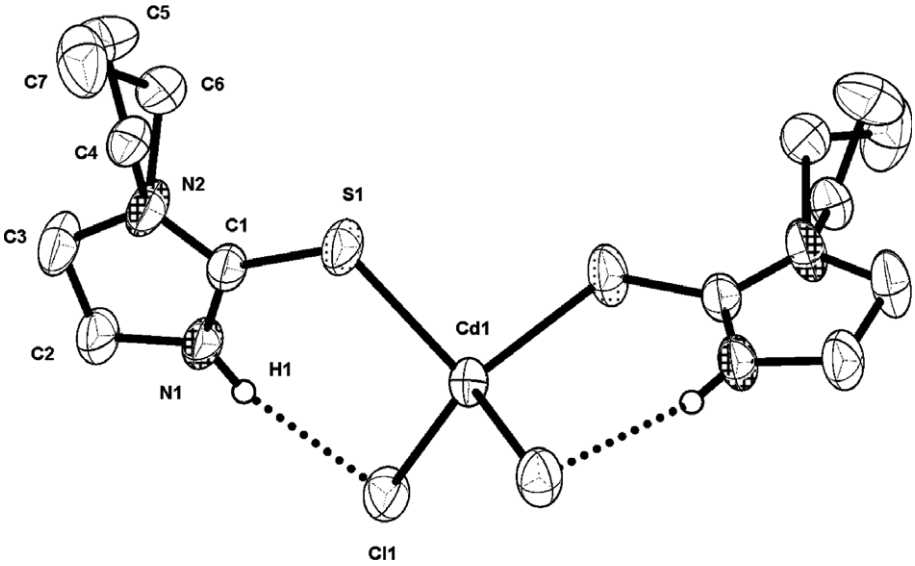


Fig. 4. Molecular structure of $(NEtImt)_2CdCl_2$ (**2**) showing the atomic labelling scheme. Most hydrogen atoms have been omitted for clarity.

2–3 ppm upfield upon complexation. However, similar complexations with HgL_2Cl_2 have shown shifts of more than 5 ppm for the C-2 resonances. All other resonances of the ligands remain unshifted, indicating the thione (>C=S) group of the ligand binding to the $CdCl_2$. Recently, we have reported the complexation of thiourea (TU) with MCl_2 where (M = Zn, Cd and Hg) forming $M(TU)_2Cl_2$ type complexes. The ^{13}C NMR chemical shifts between free and bound TU also show a similar trend, indicating Hg(II) > Cd(II) > Zn(II) [10a]. Lopez-Torres et al. [32] have studied the complexation of benzilbisthiosemicarbazone with Zn(II), Cd(II) and Hg(II) nitrate complexes. They found a similar bonding nature of these metal ions to the thione ligands, where the metal is bonded to the thione group of the ligand along with other binding sites, forming octahedral complexes. Their thione carbon is shifted the highest for the Hg(II) complex. However, selenourea (SeU) complexes with MCl_2 where (M = Zn, Cd and Hg), forming $M(SeU)_2Cl_2$ type complexes, show that the ^{77}Se NMR chemical shift difference between the free and bound SeU in $Cd(SeU)_2Cl_2$ is higher compared to $Zn(SeU)_2Cl_2$ and $Hg(SeU)_2Cl_2$ [10a]. The ^{77}Se NMR nucleus in $Cd(SeU)_2Cl_2$ is deshielded by 87 ppm on coordination relative to the free ligand. In comparison, the analogous Zn(II) and Hg(II) complexes, show deshielding by 33 and 50 ppm, respectively, indicating that the orbital overlap of Se with the second row transition metal is better than that with either the first or third-row metals.

3.2. Solid NMR studies

The cadmium chemical shift tensors, anisotropies and asymmetry factors for the complexes studied are shown in Table 3. Environments in which ^{113}Cd is completely ligated by oxygen usually give rise to resonances between −100 and +150 ppm, coordination to nitrogen results in a high-frequency shift to between +200 and +380 ppm, and bonding to sulfur causes a further high-frequency shift to between +350 and +800 ppm [9]. Among the chalcogens, sulfur is known to be the most deshielding [9].

The ^{113}Cd isotropic shift range observed in the complexes under investigation is +370 to +600 ppm. The cadmium chemical shift anisotropy in half of the complexes studied is negative while that for the other half of complexes are positive. This arises due to apparent swapping of σ_{11} and σ_{33} components in the different complexes. Hence proper care needs to be exercised when comparing individual tensor values. The least shielded tensor element can be aligned nearly orthogonal to the planes containing S ligands, as S would deshield Cd by removing electrons from filled shells in Cd via orbital mixing with outer metal orbitals and ligand orbitals of the appropriate symmetry. The asymmetry factor, η, for the complexes, falls in the full range of 0.0–0.99, indicating that the point symmetry occupied by cadmium in these complexes is very different from one another. This is further supported by the chemical shift anisotropy values showing a wide range. $CdCl_2$(N-Et Diaz)$_2$ and $CdCl_2$(OH Diaz)$_2$ complexes showed two sets of Cd resonances, indicating perhaps the presence of two crystallographically different Cd environments in the unit cell.

The ^{13}C isotropic chemical shifts are given in Table 4. We are able to see two carbon environments for all complexes, except for the Imt, NEtImt, N,N′Me$_2$Imt and N-Et Diaz complexes. Our X-ray study (vide infra) of (NMeImt)$_2CdCl_2$ confirms the presence of two slightly different environments for the two thione ligands, whereas the (NEtImt)$_2CdCl_2$ complex shows a twofold symmetry and hence only one type of thione ligand. However, only two complexes showed two different environments in the Cd spectra. So it may be concluded that most of the complexes studied show two non-equivalent ligands per molecule or two crystallographically inequivalent molecules per unit cell. This can only be resolved by X-ray studies. The thione carbons in the complexes are shielded by about 5 to 9 ppm compared to the free ligands [23] in the solid state.

3.3. Molecular structures of (NMeImt)$_2CdCl_2$ (1) and (NEtImt)$_2CdCl_2$ (2)

In both compounds, the metal ion is bound to the S atoms of two imidazolidine thione ligand molecules, in addition to two chloride ions. The four coordinate complexes have a distorted tetrahedral geometry. The bond angles are in the range 100.77(2)–117.18(3)° and 102.48(5)–111.91(5)° for **1** and **2**, respectively. In compound **1**, the average Cd–S and Cd–Cl bond lengths are 2.5387(7) Å and 2.4999(7) Å, respectively. A pronounced variation of the metal–ligand bond distances is observed in this compound, primarily for Cd–Cl and relatively to a less extent for Cd–S bond distances. In compound **2**, the molecule is located on a twofold rotation axis and due to symmetry considerations the sole bond distances are Cd1–S1: 2.5399(8) Å and Cd1–Cl1: 2.4284(8) Å. The ethyl group was found to be disordered on two positions with 0.5 occupancy each. The observed bond distances of the coordination sphere in the two compounds are in the same range as those found in the complexes $Cd(Imt)_2Cl_2$ [33] and $Cd(thiou)_2Cl_2$ [34]. In compounds **1** and **2**, the ligand molecules have their SCN_2 moieties essentially planar and have similar bond distances. For instance the corresponding bond distances in compound **2** are S1–C1: 1.702(2) Å, N1–C1: 1.312(4) Å and N2–C1: 1.309(3) Å. The bond lengths reported for the free imidazolinethione molecule are d(S–C) = 1.688(3) Å, d(C–N) = 1.330(3) Å and 1.329(4) Å [35]. Intramolecular and intermolecular hydrogen bonding interactions take place in the two compounds between the N-bonded hydrogen atoms and the chloride ions. These are believed to be the main factor at the origin of the distortion of these compounds. The significantly longer bond distance Cd–Cl1: 2.5497(7) Å compared with Cd–Cl2: 2.4501(6) Å in **1** is probably due to the stronger hydrogen bonding interactions of the Cl1 ion, engaged in intramolecular hydrogen bonding with H1 and H3

(Cl1···H1: 2.388 Å and Cl1···H3: 2.379 Å), while the Cl2 ion is involved in relatively weaker intermolecular hydrogen bonding interactions.

3.4. Bioactivity studies

The results of the bioactivity studies are given in Table 5. The Imt free ligand shows significant antimicrobial activity compared to Diaz and Diap. After complexation with Zn(II), the antimicrobial activity is increased [36]. The comparison between the activity of Imt and $Zn(Imt)_2Cl_2$, shows that HPC increased from 650 to 950, *P. aeruginosa* from 250 to 550, FS from 300 to 700, *E. coli* from 250 to 550. However, if we compare Diap and its $CdCl_2$ complex, it is observed that all antimicrobial activities are reduced, indicating the effect of the Cd^{2+} ion. On the other hand, the Zn^{2+} complex of Diap shows no significant effect. These results are important because no bioactivities for any thione ligands are reported in the literature. Since thione and thiol are in equilibrium, the data can be related to thiol containing complexes [25,26].

4. Conclusion

In this study, we have shown that a series of thiones react with $CdCl_2$ to form complexes of the type CdL_2Cl_2, in which the ligands exist in the thione form both in solution as well as in the solid state. The X-ray structures of $(NMeImt)_2CdCl_2$ (**1**) and $(NEtImt)_2CdCl_2$ (**2**) revealed distorted tetrahedral geometries for both complexes. The antimicrobial activity studies show that Imt has the highest activity compared to its six- and seven-membered ring counterparts and their Zn(II) complexes. However, the $Cd(Diap)_2Cl_2$ complex shows significant biological activity.

Acknowledgement

This research was supported by the KFUPM Research Committee under Project No. CY/NMR-STUDY/277.

Appendix A. Supplementary material

CCDC 621823 and 621864 contain the supplementary crystallographic data for **1** and **2**. These data can be obtained free of charge via http://www.ccdc.cam.ac.uk/conts/retrieving.html, or from the Cambridge Crystallographic Data Centre, 12 Union Road, Cambridge CB2 1EZ, UK; fax: (+44) 1223-336-033; or e-mail: deposit @ccdc.cam.ac.uk. Supplementary data associated with this article can be found, in the online version, at doi:10.1016/j.poly.2006.12.022.

References

[1] P.A. Ochoa, M.I. Rodríguez-Tapiador, S.S. Alexandre, C. Pastor F. Zamora, J. Inorg. Biochem. 99 (2005) 1540.
[2] B. Olenyuk, A. Fechtenkotter, P.J. Stang, J. Chem. Soc., Dalton Trans. (1998) 1707.
[3] A. Brydson, Rubbery Materials and Their Compounds, Elsevier, London, 1988.
[4] I.R. McDougall, Thyroid Disease in Clinical Practice, Chapman & Hall, London, 1992.
[5] H. Fleischer, Coord. Chem. Rev. 249 (2005) 799.
[6] S. Ahmad, A.A. Isab, S. Ali, A.R. Al-Arfaj, Polyhedron 25 (2006) 1633.
[7] P.D. Akrivos, Coord. Chem. Rev. 213 (2001) 181.
[8] E. López-Torres, M.A. Mendiola, C.J. Pastor, Polyhedron 25 (2006) 1464.
[9] K. McAteer, A.S. Lipton, P.D. Ellis, in: D.M. Grant, R.K. Harris (Eds.), Encyclopedia of Nuclear Magnetic Resonance, vol. 2, Wiley, New York, 1996, pp. 1085–1091, and reference cited therein.
[10] (a) A.A. Isab, M. I.M. Wazeer, J. Coord. Chem. 58 (2005) 529; (b) D.C. Craig, I.G. Dance, P.A.W. Dean, J.M. Hook, H.A. Jenkins, C.W. Kirby, M.L. Scudder, U. Rajalingam, Can. J. Chem. 83 (2005) 174; (c) A.V. Ivanov, A.V. Gerasimenko, A.A. Konzelko, M.A. Ivanov, O.N. Antzutkin, W. Forsling, Inorg. Chim. Acta 359 (2006) 3855.
[11] A.S. Lipton, G.W. Buchko, J.A. Sears, M.A. Kennedy, P.D. Ellis, J. Am. Chem. Soc. 123 (2001) 992.
[12] A.S. Lipton, S.S. Mason, D.L. Reger, J. Am. Chem. Soc. 116 (1994) 10182.
[13] D.L. Reger, S.M. Myers, S.S. Mason, D.J. Darensbourg, M.W. Holtcamp, J.H. Reibenspies, A.S. Lipton, P.D. Ellis, J. Am. Chem. Soc. 117 (1995) 10998.
[14] C.A. Fyfe, Solid State NMR for Chemists, CFC Press, Ontario, 1983.
[15] G. Stocco, F. Gattuso, A.A. Isab, C.F. Shaw III, Inorg. Chem. Acta 209 (1993) 129, and references cited therein.
[16] F.A. Devillanova, G. Verani, J. Coord. Chem. 7 (1978) 177.
[17] F.A. Devillanova, G. Verani, Transition Met. Chem. 2 (1977) 9.
[18] S. Skoulika, A. Aubry, P. Karagianidis, P. Aslanidis, S. Papastefanou, Inorg. Chem. Acta 183 (1991) 20.
[19] A.A. Isab, Transition Met. Chem. 17 (1992) 374.
[20] A.A. Isab, H.P. Perzanowski, Polyhedron 15 (1996) 2397.
[21] E.S. Raper, Coord. Chem. Rev. 61 (1985) 115.
[22] S. Ahmad, A.A. Isab, H.P. Perzanowski, Can. J. Chem. 80 (2002) 1279.
[23] M.I.M. Wazeer, A.A. Isab, A. El-Rayyes, Spectroscopy 18 (2004) 113.
[24] M. Maricq, J. Waugh, J. Chem. Soc. 70 (1979) 3300.
[25] A.A. Isab, M.I.M. Wazeer, Spectro. Chim. Acta A 65 (2006) 191.
[26] N.C. Kasuga, K. Sekino, M. Ishikawa, A. Honda, M. Yokoyama S. Nakano, N. Shimada, C. Koumo, K. Nomiya, J. Inorg. Biochem. 96 (2003) 298.
[27] SMART APEX software (5.05) for SMART APEX detector, Bruker Axs Inc., Madison, WI, USA.
[28] SAINT software (5.0) for SMART APEX detector, Bruker Axs Inc., Madison, WI, USA.
[29] G.M. Sheldrick, SADABS: Program for Empirical Absorption correction of Area detector Data, University of Göttingen, Göttingen, Germany, 1996.
[30] G.M. Sheldrick, SHELXTL V5.1 Software, Bruker AXS Inc., Madison, WI, USA, 1997.
[31] G.M. Sheldrick, University of Göttingen, Göttingen, Germany, 1997.
[32] E. Lopez-Torres, M.A. Mendiola, J. Rodriguez-Procopio, M.T. Sevilla, E. Colacio, J.M. Moreno, I. Sobrados, Inorg. Chim. Acta 323 (2001) 130.
[33] A.R. Al-Arfaj, J.H. Reibenspies, A.A. Isab, M.S. Hussain, Acta Crystallogr., Sect. C 54 (1998) 51.
[34] C. Marcos, J.M. Alia, V. Adovasio, M. Prieto, S. Garcia-Granda, Acta Crystallogr., Sect. C 54 (1998) 1225.
[35] L.P. Battaglia, A.B. Corradi, M. Nardelli, Croat. Chem. Acta 57 (1984) 545.
[36] M. Fettouhi, M.I.M. Wazeer, A.A. Isab, J. Coord. Chem. (2006) (in press).

attracted considerable interest [7]. Although the mechanism of catalysis depends on the nature of the substrate, the oxidant and experimental conditions, it has been shown [8] that metal ions act as catalysts by one of these different paths such as the formation of complexes with reactants or oxidation of the substrate itself or through the formation of free radicals. Ruthenium(III) catalysis in redox reactions involves several complexes, different oxidation states of ruthenium, etc. The uncatalysed reaction of oxidation of L-leucine by DPA has been studied [9]. We have observed that ruthenium(III) catalyzes the oxidation of L-leucine by DPA in alkaline medium in micro amounts. In order to understand the active species of oxidant and catalyst, and to propose the appropriate mechanism, the title reaction has been investigated in detail. An understanding of the mechanism allows the chemistry to be interpreted, understood and predicted.

2. Experimental

2.1. Materials and reagents

All chemicals used were of reagent grade and double distilled water was used throughout the work. A solution of L-leucine (Sisco – Chem Ltd.) was prepared by dissolving an appropriate amount of recrystallised sample in double distilled water. The required concentration of L-leucine was used from its aqueous stock solution. A stock solution of Ru(III) was prepared by dissolving $RuCl_3$ (S.D. Fine Chemicals) in 0.20 mol dm^{-3} HCl. The concentration was determined [10] by EDTA titration. KNO_3 and KOH (BDH) were used to maintain the ionic strength and alkalinity of the reaction, respectively. An aqueous solution of $AgNO_3$ was used to study the product effect, Ag(I). A stock standard solution of IO_4^- was prepared by dissolving a known weight of KIO_4 (Riedel-de Haen) in hot water and used after keeping for 24 h. Its concentration was ascertained iodometrically [11] at neutral pH maintained using phosphate buffer. KNO_3 and KOH were used to maintain ionic strength and alkalinity of the reaction, respectively. Aqueous solution of $AgNO_3$ was used to study the product effect, Ag(I). The pH of the medium in the solution was measured using a [ELICO (LI613)] pH meter.

2.2. Preparation of DPA

DPA was prepared by oxidizing Ag(I) in the presence of KIO_4 as described elsewhere [12]: the mixture of 28 g of KOH and 23 g of KIO_3 in 100 cm^3 of water along with 8.5 g $AgNO_3$ was heated just to boiling and 20 g of $K_2S_2O_8$ was added in several lots with stirring, the mixture was then allowed to cool. It was filtered through a medium porosity fritted glass filter and 40 g of NaOH was added slowly to the filtrate, whereupon a voluminous orange precipitate agglomerated. The precipitate was filtered as above and washed three to four times with cold water. The pure crystals were dissolved in 50 cm^3 water and warmed to 80 °C with constant stirring, thereby some solid dissolved to give a red solution. The resulting solution was filtered when it was hot, and on cooling at room temperature orange crystals separated out and were recrystallised from water.

The complex was characterized from its UV spectrum, exhibiting three peaks at 216, 255 and 362 nm. These spectral features were identical to those reported earlier for DPA [12]. The magnetic moment study revealed that the complex is diamagnetic. The compound prepared was analysed [13] for silver and periodate by acidifying a solution of the material with HCl, recovering and weighing the AgCl for Ag and titrating the iodine liberated when excess KI was added to the filtrate for IO_4^-. The aqueous solution of DPA was used for the required [DPA] in the reaction mixture. During the kinetics a constant concentration, viz. 1×10^{-4} mol dm^{-3} of KIO_4, was used throughout the study unless otherwise stated. The possibility of oxidation of L-leucine by periodate was tested and found that there was no significant interference due to KIO_4 under the experimental conditions. The effect of dissolved oxygen on the rate of reaction was checked by preparing the reaction mixture and following the reaction in an atmosphere of nitrogen. No significant difference between the results obtained under nitrogen and in the presence of air was observed.

2.3. Kinetic measurements

The kinetic measurements were performed on a Varian CARY 50 Bio UV–Vis spectrophotometer. The kinetics were followed under pseudo-first-order conditions where [L-leu] > [DPA] at 25 ± 0.1 °C, unless specified. The reaction was initiated by mixing DPA with the L-leucine solution which also contained the required concentration of KNO_3, KOH, catalyst Ru(III) and KIO_4. The progress of the reaction was followed spectrophotometrically at 360 nm by monitoring the decrease in absorbance due to DPA with the molar absorbance index, 'ε' being 13 900 ± 100 dm^3 mol^{-1} cm^{-1}. It was verified that there was negligible interference from other species present in the reaction mixture at this wavelength.

The pseudo-first-order rate constants, 'k_C', were determined from the log(absorbance) versus time plots. The plots were linear up to 85% completion of the reaction under the range of [OH^-] used. The orders for various species were determined from the slopes of plots of $\log k_C$ versus respective concentration of species, except for [DPA] in which non-variation of 'k_C' was observed as expected for the reaction conditions. During the kinetic tests, a constant concentration (viz. 1.0×10^{-4} mol dm^{-3}) of KIO_4 was used throughout the study unless otherwise stated. Since periodate is present in excess with DPA, the possibility of oxidation of L-leucine by periodate in alkaline medium at 25 °C was tested. The progress of the reaction was followed iodometrically. However, it was found that there was no

significant reaction under the experimental conditions employed compared to the DPA oxidation of L-leucine. The total periodate concentration was calculated by considering the periodate present in the DPA solution and that was additionally added.

In view of the modest concentration of alkali used in the reaction medium, attention was also directed to the effect of the reaction vessel surface on the kinetics. Use of polythene/acrylic wares and quartz or polyacrylate cells gave the same results, indicating that the surface does not have any significant effect on the reaction rates.

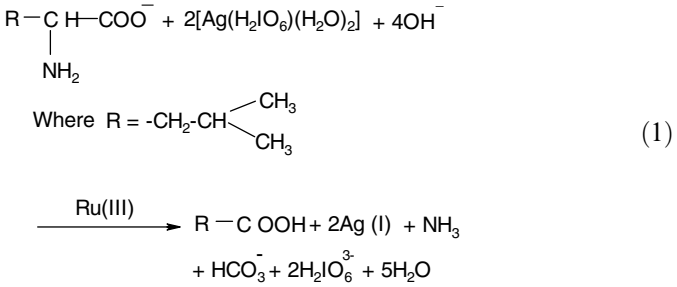
In view of the ubiquitous contamination of carbonate in the basic medium, the effect of carbonate was also studied. Added carbonate had no effect on the reaction rates, however, fresh solutions were nevertheless used for carrying out each kinetic run.

Regression analysis of experimental data to obtain the regression coefficient r and the standard deviation S, of points from the regression line, was performed with the Microsoft office Excel-2003 program.

3. Results and discussion

3.1. Stoichiometry and product analysis

Different sets of reaction mixtures containing varying ratios of DPA to L-leucine in the presence of a constant amount of OH^-, KNO_3 and catalyst, were kept for 3 h in a closed vessel under nitrogen atmosphere. The remaining concentration of DPA was estimated by spectrophotometrically at 360 nm. The results indicate that two moles of DPA consumed one mole of L-leucine, 2:1 stoichiometry, for both catalysts as given in the following equation:



(1)

The main oxidation products were identified as pentanoic acid by a spot test [14], ammonia by Nessler's reagent and the CO_2 was qualitatively detected by bubbling nitrogen gas through the acidified reaction mixture and passing the liberated gas through a tube containing limewater. The nature of the carboxylic acid was confirmed by its IR spectrum, which showed a carbonyl(C=O) stretch at 1708 cm^{-1} and a signal at 3042 cm^{-1} due to the O–H stretching of the acid. The formation of free Ag+ in the solution was detected by adding KCl solution to the reaction mixture, which produced white turbidity due to formation of AgCl. It was observed that pentanoic acid does not undergo further oxidation under the present kinetic conditions. The products obtained are similar to those obtained for the uncatalysed reaction.

3.2. Reaction orders

As the diperiodatoargentate(III) oxidation of L-leucine in alkaline medium proceeds at a measurable rate in the absence of Ru(III), the catalysed reaction is understood to occur in parallel paths with contributions from both the catalysed and uncatalysed paths. Thus, the total rate constant (k_T) is equal to the sum of the rate constants of the catalysed (k_C) and uncatalysed (k_U) reactions, so $k_C = k_T - k_U$. Hence, the reaction orders have been determined from the slopes of $\log k_C$ versus log(concentration) plots by varying the concentrations of L-leucine, IO_4^-, OH^- and catalyst Ru(III), in turn, while keeping the others constant. The DPA concentration was varied in the range of 1.0×10^{-5}–1.0×10^{-4} mol dm^{-3} and the linearity of the plots of log(absorbance) versus time up to 85% completion of the reaction indicates a reaction order of unity in [DPA]. This is also confirmed by varying of [DPA], which did not result in any change in the pseudo-first-order rate constant, k_C (Table 1; Ru(III)). The L-leucine concentration was varied in the range 5.0×10^{-5}–5.0×10^{-4} mol dm^{-3} at 25 °C while keeping other reactant concentrations and conditions constant. The k_C values increased with the increase in concentration of L-leucine, indicating an apparent less than unit order dependence on [L-leu] (Table 1). The effect of alkali on the reaction has been studied in the range of 0.04–0.40 mol dm^{-3} at constant concentrations of L-leucine, DPA, catalyst and a constant ionic strength of 0.60 mol dm^{-3}. The rate constants increased with increasing [alkali] and the order was found to be less than unity (Table 1).

3.3. Effect of [periodate]

Periodate concentration was varied from 8.0×10^{-5} to 8.0×10^{-4} at constant [DPA], [L-leu], [catalyst] and ionic strength. It was observed that the rate constants decreased by increasing $[IO_4^-]$ (Table 1).

3.4. Effect of added products

Initially added products, Ag(I) and pentanoic acid do not affect the rate of reaction.

3.5. Effect of ionic strength (I) and dielectric constant of the medium (D)

The addition of KNO_3, to increase the ionic strength of the reaction, increased the rate of reaction at constant [DPA], [L-leu], $[OH^-]$, $[IO_4^-]$ and [Ru(III)]; the plot of $\log k_C$ versus $\sqrt{I}$ was found to be linear with a negative slope (Fig. 1).

The dielectric constant of the medium, 'D' was varied by varying the t-butyl alcohol and water percentage. The

Table 1
Effect of [DPA], [L-leu], [OH^-] and [IO_4^-] on the ruthenium(III) catalysed oxidation of L-leucine by DPA in alkaline medium at 25 °C, $I = 0.60$ mol dm^{-3}

10^5 [DPA] (mol dm^{-3})	10^4 [L-leu] (mol dm^{-3})	[OH^-] (mol dm^3)	10^4 [IO_4] (mol dm^{-3})	10^6 [Ru(III)] (mol dm^{-3})	10^3 k_T (s^{-1})	10^4 k_U (s^{-1})	10^3 k_C (s^{-1})	
							Found	Calculated
1.0	2.0	0.2	1.0	5.0	4.5	8.8	3.6	3.8
3.0	2.0	0.2	1.0	5.0	4.7	8.7	3.9	3.8
5.0	2.0	0.2	1.0	5.0	4.6	8.9	3.7	3.8
8.0	2.0	0.2	1.0	5.0	4.5	8.9	3.5	3.8
10.0	2.0	0.2	1.0	5.0	4.6	8.9	3.7	3.8
3.0	0.5	0.2	1.0	5.0	3.1	6.5	2.4	2.4
3.0	1.0	0.2	1.0	5.0	3.9	7.9	3.1	3.1
3.0	2.0	0.2	1.0	5.0	4.6	8.9	3.7	3.8
3.0	3.0	0.2	1.0	5.0	5.2	9.2	4.3	4.1
3.0	5.0	0.2	1.0	5.0	5.7	10.2	4.7	4.4
3.0	2.0	0.04	1.0	5.0	3.0	4.8	2.6	2.5
3.0	2.0	0.1	1.0	5.0	3.8	6.5	3.2	3.4
3.0	2.0	0.2	1.0	5.0	4.6	8.9	3.7	3.8
3.0	2.0	0.3	1.0	5.0	5.0	9.6	4.0	4.0
3.0	2.0	0.4	1.0	5.0	5.4	10.1	4.3	4.1
3.0	2.0	0.2	0.8	5.0	5.0	9.4	4.1	3.9
3.0	2.0	0.2	1.0	5.0	4.6	8.9	3.7	3.8
3.0	2.0	0.2	3.0	5.0	4.0	8.4	3.1	3.0
3.0	2.0	0.2	6.0	5.0	3.8	8.1	2.5	2.3
3.0	2.0	0.2	8.0	5.0	2.9	7.7	2.1	2.0
3.0	2.0	0.2	1.0	1.0	2.5	8.9	1.6	1.5
3.0	2.0	0.2	1.0	3.0	3.5	8.9	2.6	2.7
3.0	2.0	0.2	1.0	5.0	4.6	8.9	3.7	3.8
3.0	2.0	0.2	1.0	8.0	11.5	8.9	10.6	10.5
3.0	2.0	0.2	1.0	10.0	15.1	8.9	14.2	14.5

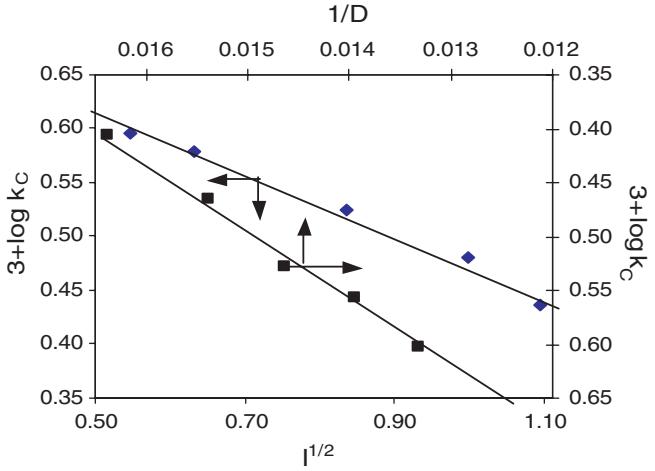


Fig. 1. Effect of ionic strength and dielectric constant of the medium on Ru(III) catalysed oxidation of L-leucine by diperiodatoargentate(III) at 25 °C.

decrease in dielectric constant of the reaction medium increases the rate and the plot of $\log k_C$ versus $1/D$ was linear with a negative slope (Fig. 1).

3.6. Effect of temperature

The influence of temperature on the rate of reaction was studied at 25, 30, 35 and 40 °C. The rate constants (k) of the slow step of Scheme 1 were obtained from the slopes, as were the intercepts of the plots of [Ru(III)]/k_C versus 1/[L-leu], [Ru(III)]/k_C versus 1/[OH] and [Ru(III)]/k_C versus [$H_3IO_6^{2-}$] at four different temperatures. The values are given in Table 2. The activation parameters for the rate determining step were obtained by the least square method of the plot of $\log k$ versus $1/T$ and the results are presented in Table 2.

3.7. Test for free radicals (polymerization study)

The intervention of free radicals was examined as follows, the reaction mixture, to which a known quantity of acrylonitrile scavenger had been added initially, was kept in an inert atmosphere for 1hr. Upon diluting the reaction mixture with methanol, a precipitate resulted, suggesting there is participation of free radicals in the reaction.

3.8. Effect of [Ru(III)]

The [Ru(III)] concentrations were varied from 1.0×10^{-6} to 1.0×10^{-5} mol dm^{-3}, at a constant concentration of diperiodatoargentate(III), L-leucine, alkali and ionic strength. The order in [Ru(III)] was found to be unity from the linearity of the plots of $\log k_C$ versus log[Ru(III)].

3.9. Catalytic activity

It has been pointed out by Moelwyn-Hughes [15] that in the presence of the catalyst, the uncatalysed and catalysed reactions proceed simultaneously, so that

Table 2
Thermodynamic activation parameters for the Ru(III) catalysed oxidation of L-leucine by DPA in alkaline medium with respect to the slow step of Scheme 1

Temperature (K)	$10^{-3}\ k$ (dm^3 mol^{-1} s^{-1})
(A) Effect of temperature	
298	1.00
303	1.08
308	1.17
313	1.25
Parameters	Values
(B) Activation parameters (Scheme 1)	
E_a (kJ mol^{-1})	11.8 ± 0.54
$\Delta H^{\#}$ (kJ mol^{-1})	9.3 ± 0.43
$\Delta S^{\#}$ (J K^{-1} mol^{-1})	-155 ± 7.3
$\Delta G^{\#}$ (kJ mol^{-1})	55 ± 2.3
log A	3.8 ± 0.15

Temperature (K)	K_1 (dm^3 mol^{-1})	$K_2 \times 10^3$ mol dm^{-3}	$K_3 \times 10^{-4}$ (dm^3 mol^{-1})
(C) Effect of temperature to calculate K_1, K_2 and K_3 for the Ru(III) catalysed oxidation of L-leucine by diperiodatoargentate(III) in alkaline medium			
298	0.25 ± 0.01	1.61 ± 0.06	3.64 ± 0.14
303	0.31 ± 0.012	1.05 ± 0.04	4.57 ± 0.20
308	0.38 ± 0.013	0.81 ± 0.03	5.79 ± 0.25
313	0.44 ± 0.02	0.47 ± 0.02	7.47 ± 0.33

Thermodynamic quantities	Values from K_1	Values from K_2	Values from K_3
(D) Thermodynamic quantities using K_1, K_2 and K_3			
ΔH (kJ mol^{-1})	28.2 ± 1.2	-60.7 ± 2.8	37.1 ± 1.5
ΔS (J K^{-1} mol^{-1})	83.7 ± 3.8	-258.3 ± 12.4	212.3 ± 10.2
ΔG_{298} (kJ mol^{-1})	3.3 ± 0.12	15.9 ± 0.84	-26.0 ± 1.0

[DPA] = 3.0×10^{-5}; [L-leu] = 2.0×10^{-4}; [OH$^-$] = 0.20; [Ru(III)] = 5.0×10^{-6} mol dm^{-3}; [IO_4] = 1.0×10^{-4} mol dm^{-3}.

$$k_T = k_U - K_C[\text{catalyst}]^x \quad (2)$$

Here, k_T is the observed pseudo-first-order rate constant in the presence Ru(III) catalyst, k_U the pseudo-first-order rate constant for the uncatalysed reaction, K_C the catalytic constant and 'x' the order of the reaction with respect to [Ru(III)]

$$K_C = \frac{k_T - k_U}{[\text{catalyst}]^x} = \frac{k_C}{[\text{catalyst}]^x} \quad (\text{where, } k_T - k_U = k_C) \quad (3)$$

In the present investigations, x values for the standard run were found to be unity for Ru(III). Then the value of K_C was calculated using Eq. (3). The values of K_C were evaluated for the Ru(III) catalyst at different temperatures and found to vary with temperature. Further, plots of log K_C versus $1/T$ were linear and the values of the energy of activation and other activation parameters with reference to the catalyst were computed. These results are summarized in Table 3. The value of K_C for Ru(III) is 3.6×10^2 at 298 K.

In the later period of the 20th century, the kinetics of oxidation of various organic and inorganic substrates were

Table 3
Values of the catalytic constant (K_C) at different temperatures and activation parameters calculated using K_C values

Temperature (K)	$10^{-2}K_C$
298	3.64
303	4.12
308	4.61
313	5.19
E_a (kJ mol^{-1})	18.1
$\Delta H^{\#}$ (kJ mol^{-1})	15.7
$\Delta S^{\#}$ (J K^{-1} mol^{-1})	−143.0
$\Delta G^{\#}$ (kJ mol^{-1})	58.3
log A	5.75

[DPA] = 3.0×10^{-5}; [L-leu] = 2.0×10^{-4}; [OH$^-$] = 0.20; [IO_4] = 1.0×10^{-4}; $I = 0.60$; [Ru(III)] = 5.0×10^{-6} mol dm^{-3}.

studied by Ag(III) species, which may be due to its strong versatile nature of a two electron oxidant. Among the various species of Ag(III), $Ag(OH)_4^-$, diperiodatoargentate(III) and ethylenebis (biguanide) (EBS) silver(III) were of maximum attention to the researchers due to their relative stability [16]. The stability of $Ag(OH)_4^-$ is very sensitive towards traces of dissolved oxygen and other impurities in the reaction medium whereupon it had not drawn much attention. However, the other two forms of Ag(III) [5,6,17] are considerably stable; DPA is used in highly alkaline medium and EBS is used in highly acidic medium.

The literature survey [12] reveals that the water soluble diperiodatoargentate(III) (DPA) has a formula $[Ag(IO_6)_2]^{7-}$ with the dsp^2 configuration of a square planar structure, similar to the diperiodatocopper(III) complex with two bidentate ligands, periodate, which forms a planar molecule. When the same molecule is used in alkaline medium, it is unlikely to exist as $[Ag(IO_6)_2]^{7-}$ as periodate is known to be in various protonated forms [18] depending on the pH of the solution, as given in the following multiple equilibria (4)–(6):

$$H_5IO_6 \rightleftharpoons H_4IO_6^- + H^+ \quad (4)$$

$$H_4IO_6^- \rightleftharpoons H_3IO_6^{2-} + H^+ \quad (5)$$

$$H_3IO_6^{2-} \rightleftharpoons H_2IO_6^{3-} + H^+ \quad (6)$$

Periodic acid exists as H_5IO_6 in acid medium and as $H_4IO_6^-$ at pH 7. Thus, under the present alkaline conditions, the main species are expected to be $H_3IO_6^{2-}$ and $H_2IO_6^{3-}$. At higher concentrations, periodate also tends to dimerise [3b]. However, formation of this species is negligible under the conditions employed for this kinetic study. On the contrary, the authors [5] in recent past studies have proposed DPA as $[Ag(HL)_2]^{x-}$ in which 'L' is a periodate with an uncertain number of protons and 'HL' is a protonated periodate of an uncertain number of protons. This can be ruled out by considering the alternative form [18] of IO_4^- at pH > 7, which is in the form $H_3IO_6^{2-}$ or $H_2IO_6^{3-}$. Hence, DPA could be $[Ag(H_3IO_6)_2]^-$ or $[Ag(H_2IO_6)_2]^{3-}$ in alkaline medium. Therefore, under the present conditions, diperiodatoargentate(III), may be

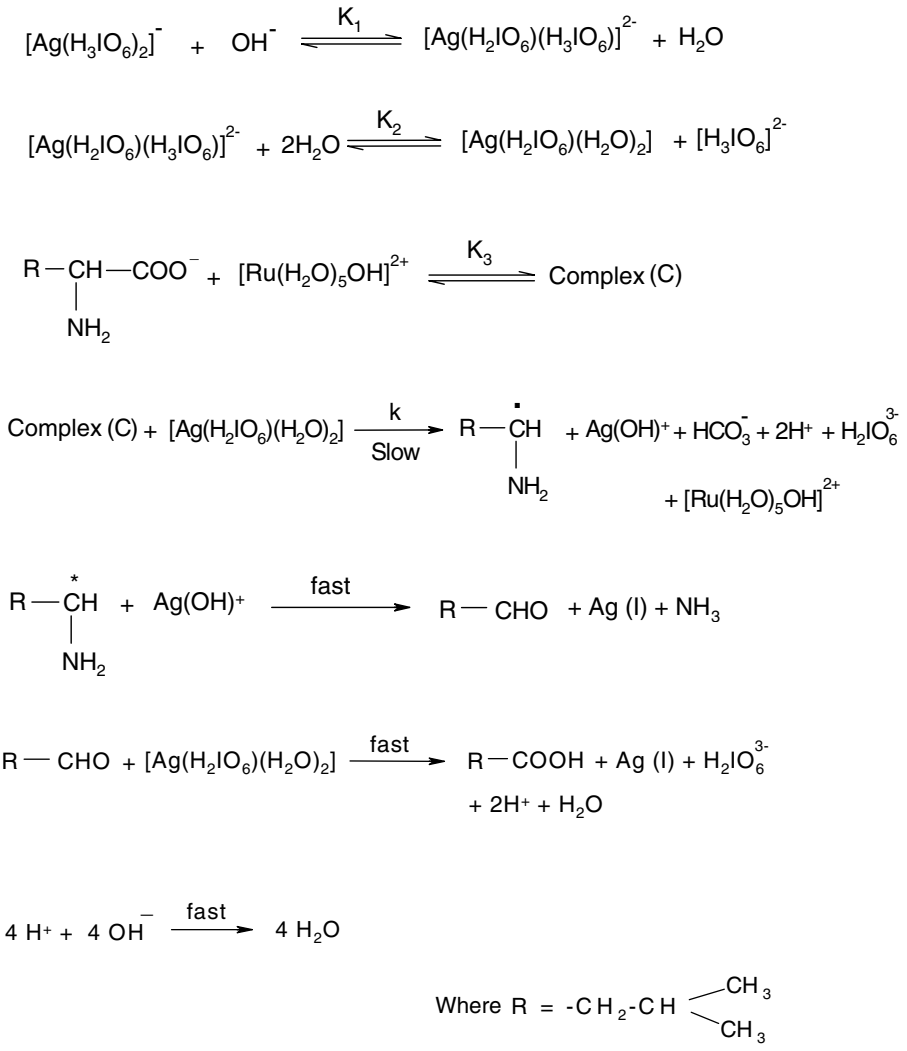
depicted as $[Ag(H_3IO_6)_2]^-$. A similar speciation of periodate in alkali was proposed [19] for diperiodatonickelate(IV).

It is interesting to identify the probable ruthenium(III) chloride species in alkaline media. The added chloride had no effect on the rate of reaction. Electronic spectral studies [20] have confirmed that ruthenium chloride exists in the hydrated form as $[Ru(H_2O)_5OH]^{2+}$. In the present study (at pH 13.3), it is quite probable that for $[Ru(III)(OH)_x]^{3-x}$, the x value would always be less than six because there are no definite reports of any hexahydroxy ruthenium species. The remainder of the coordination sphere would be filled by water molecules. Hence, under the conditions employed, e.g. $[OH^-] \gg [Ru(III)]$, ruthenium(III) is mostly present as the monomerichydroxylated species, $[Ru(H_2O)_5OH]^{2+}$ [21].

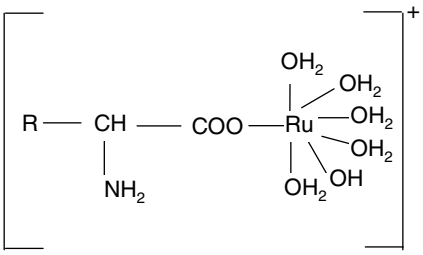
Since, the reaction was enhanced by $[OH^-]$, added periodate retarded the rate and there was first order dependency in [DPA] and catalyst, Ru(III), and fractional order in [L-leu] and $[OH^-]$, Scheme 1 has been proposed by considering L-leu as the anionic form of L-leu in alkaline medium, which also explains all other experimental observations.

In the prior equilibrium step 1, $[OH^-]$ deprotonates the DPA to give a deprotonated diperiodatoargentate(III); in the second step displacement of a periodate ligand takes place to give free periodate, which is evidenced by the decrease in rate with increase in [periodate] (Table 1). It may be expected that lower Ag(III) periodate species such as monoperiodatoargentate(III) (MPA) is a more important active species in the reaction than the DPA. The inverse fractional order in $[H_3IO_6]^{2-}$ might also be due to this reason. In the pre-rate determining stage, the hydroxylated species of Ru(III) combines with a molecule of anionic form of L-leu to give an intermediate complex, which further reacts with one mole of MPA in a rate determining step to give a free radical derived from L-leucine, with regeneration of the ruthenium(III) catalyst. This free radical from L-leucine further reacts with another molecule of MPA species in a fast step to give the products as given in Scheme 1.

The probable structure of complex (C) is given below:



Scheme 1. Detailed scheme for the Ru(III) catalysed oxidation of L-leucine by alkaline diperiodatoargentate(III).



Spectroscopic evidence for complex formation between the catalyst and substrate was obtained from UV–Vis spectra of L-leucine (2.0×10^{-4}), Ru(III) (5.0×10^{-6}, $[OH^-] = 0.2$ mol dm^{-3}) and a mixture of both. A hypsochromic shift of about 4 nm from 511 nm to 507 nm in the spectra of Ru(III) was observed. However, the Michaelis–Menton plot proved the complex formation between the catalyst and the reductant, which explains less than unit order in [L-leu]. Such a complex between a substrate and a catalyst has been observed in other studies. The rate law (8) for Scheme 1 could be derived as

$$\text{Rate} = \frac{-\mathrm{d}[\text{DPA}]}{\mathrm{d}t} = \frac{kK_1K_2K_3[\text{Ag(III)}][\text{L-leu}][OH^-][\text{Ru(III)}]}{[H_3IO_6^{2-}] + K_1[OH^-][H_3IO_6^{2-}] + K_1K_2[OH^-] + K_1K_2K_3[OH^-][\text{L-leu}] + K_3[H_3IO_6^{2-}][\text{L-leu}] + K_1K_3[\text{L-leu}][OH^-][H_3IO_6^{2-}]} \quad (7)$$

The terms $K_3[H_3IO_6^{2-}][\text{L-leu}]$ and $K_1K_3[\text{L-leu}][OH^-][H_3IO_6^{2-}]$ of the denominator of Eq. (7) can be neglected in the view of the low concentrations of L-leucine and periodate used in this study. Therefore, Eq. (7) becomes

$$\frac{\text{Rate}}{[\text{DPA}]} = k_C = k_T - k_U = \frac{kK_1K_2K_3[\text{L-leu}][OH^-][\text{Ru(III)}]}{[H_3IO_6^{2-}] + K_1[OH^-][H_3IO_6^{2-}] + K_1K_2[OH^-] + K_1K_2K_3[OH^-][\text{L-leu}]} \quad (8)$$

Eq. (8) can be rearranged into Eq. (9), which is suitable for verification

$$\frac{[\text{Ru(III)}]}{k_C} = \frac{[H_3IO_6^{2-}]}{kK_1K_2K_3[\text{L-leu}][OH^-]} + \frac{[H_3IO_6^{2-}]}{kK_2K_3[\text{L-leu}]} + \frac{1}{kK_3[\text{L-leu}]} + \frac{1}{k} \quad (9)$$

According to Eq. (9), plots of $[\text{Ru(III)}]/k_C$ versus $[H_3IO_6]^{2-}$, $\text{Ru(III)}]/k_C$ versus $1/[OH^-]$ and $[\text{Ru(III)}]/k_C$ versus $1/[\text{L-leu}]$ should be linear (Fig. 2). From the intercepts and slopes of such plots, the reaction constants K_1, K_2, K_3 and k were calculated as (0.25 ± 0.01) dm^3 mol^{-1}, $(1.61 \pm 0.06) \times 10^{-3}$ mol dm^{-3}, $(3.64 \pm 0.14) \times 10^4$ dm^3 mol^{-1} and $(1.0 \pm 0.03) \times 10^3$ dm^3 mol^{-1} s^{-1}, respectively. These constants were used to calculate the rate constants and were compared with the experimental k_C values, and were found to be in reasonable agreement with each other (Table 1), which fortifies Scheme 1. The equilibrium constant K_1 is far greater than K_2 which may be attributed to the greater tendency of DPA to undergo deprotonation compared to the formation of hydrolysed species in alkaline medium.

The thermodynamic quantities for the different equilibrium steps in Scheme 1 can be evaluated as follows. The L-leucine and hydroxide ion concentrations (Table 1) were varied at different temperatures. The plots of $[\text{Ru(III)}]/k_C$ versus $1/[\text{L-leu}]$ ($r \geqslant 0.9992$, $S \leqslant 0.00131$), $[\text{Ru(III)}]/k_C$ versus $[H_3IO_6^{2-}]$ ($r \geqslant 0.9991$, $S \leqslant 0.00132$), $[\text{Ru(III)}]/k_C$ versus $1/[OH^-]$ ($r \geqslant 0.9994$, $S \leqslant 0.00087$) should be linear as shown in Fig. 2. From the slopes and intercepts, the values of K_1 are calculated at different temperatures. A van't Hoff's plot was made for the variation of K_1 with temperature [i.e., $\log K_1$ versus $1/T$ ($r \geqslant 0.9992$, $S \leqslant 0.1104$)] and the values of the enthalpy of reaction ΔH, entropy of reaction ΔS and free energy of reaction ΔG, were calculated. These values are also given in Table 2. A comparison of the latter values with those obtained for the slow step of the reaction shows that these values mainly refer to the rate limiting step, supporting the fact that the reaction before the rate determining step is fairly slow and involves a high activation energy [22]. In the same manner, K_2 and K_3 values were calculated at different temperatures and the corresponding values of thermodynamic quantities are given in Table 2.

The decrease in the rate with increasing ionic strength is in favour of a reaction between opposite charged species of reactants, as presented in Scheme 1 of the proposed mechanism. The effect of solvent on the reaction rate is described in detail in the literature [23]. For the limiting case of a zero angle approach between two dipoles or anion–dipole system, Amis [23] has shown that a plot of $\log k_C$ versus $1/D$ gives a straight line with a negative slope for a reaction between a negative ion and a dipole or two dipoles, and with a positive slope for positive ion and dipole interaction. In the present study, the plot observed had a negative slope, which is in the right direction as shown in Scheme 1.

The negative value of $\Delta S^{\#}$ suggests that the intermediate complex is more ordered than the reactants [24]. The

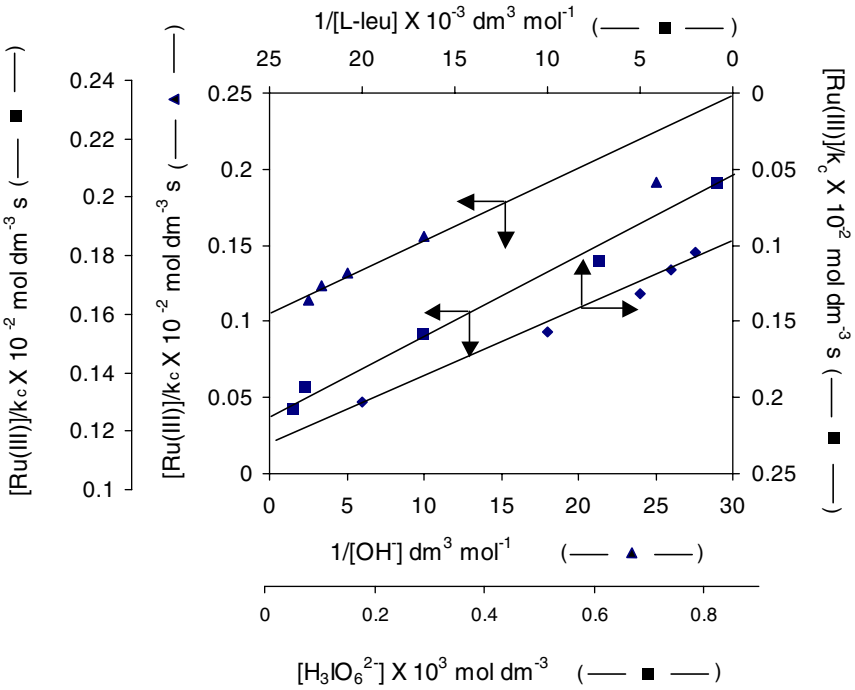


Fig. 2. Verification of rate law (9) of Ru(III) catalysed oxidation of L-leucine by diperiodatoargentate(III) at 25 °C.

observed modest enthalpy of activation and a higher rate constant for the slow step indicates that the oxidation presumably occurs via an inner-sphere mechanism. This conclusion is supported by earlier observations [25]. The activation parameters evaluated for the catalysed and uncatalysed reaction explain the catalytic effect on the reaction. The catalyst Ru(III) form the complex (C) with the substrate, which enhances the reducing property of the substrate than that without the Ru(III) catalyst. Further, the Ru(III) catalyst modifies the reaction path by lowering the energy of activation.

4. Conclusion

The Ru(III) catalysed oxidation of L-leucine by diperiodatoargentate(III) was studied. Oxidation products were identified. Among the various species of Ag(III) in alkaline medium, in earlier reports diperiodatoargentate(III) was the active species, whereas monoperiodatoargentate(III) is considered to be the active species for the title reaction. The active species of Ru(III) was found to be $[Ru(H_2O)_5OH]^{2+}$. Activation parameters were evaluated for both catalysed and uncatalysed reactions. Catalytic constants and the activation parameters with reference to the catalyst were also computed.

References

[1] D. Lalo, M.M. Mahanti, J. Chem. Soc., Dalton Trans. (1990) 311.
[2] K. Bal Reddy, B. Sethuram, T. Navaneeth Rao, Indian J. Chem. A 20 (1981) 395.
[3] (a) B. Sethuram, Some Aspects of Electron Transfer Reactions Involving Organic Molecules, Allied Publishers (P) Ltd., New Delhi, 2003, p. 151;
(b) B. Sethuram, Some Aspects of Electron Transfer Reactions Involving Organic Molecules, Allied Publishers (P) Ltd., New Delhi, 2003, p. 78.
[4] (a) P.K. Jaiswal, K.L. Yadav, Talanta 17 (1970) 236;
(b) P.K. Jaiswal, Analyst 1 (1972) 503.
[5] (a) P. Jayaprakash Rao, B. Sethuram, T. Navaneeth Rao, React. Kinet. Catal. 29 (1985) 289;
(b) K. Venkata Krishna, P. Jayaprakash Rao, Indian J. Chem. A 37 (1998) 1106, references cited therein.
[6] (a) A. Kumar, P. Kumar, P. Ramamurthy, Polyhedron 18 (1999) 773;
(b) A. Kumar, P. Vaishali, P. Ramamurthy, Int. J. Chem. Kinet. 32 (2000) 286.
[7] A.K. Das, Coord. Chem. Rev. 213 (2001) 307.
[8] P. Veerasomaiah, K. Bal Reddy, B. Sethuram, T. Navaneeth Rao, Indian J. Chem. A 26 (1987) 402.
[9] C.V. Hiremath, S.D. Kulkarni, S.T. Nandibewoor, Ind. Eng. Chem. Res. (2006) (in press).
[10] (a) C.S. Reddy, T. Vijaykumar, Indian J. Chem. A 34 (1995) 615;
(b) D.L. Kamble, R.B. Chougale, S.T. Nandibewoor, Indian J. Chem. A 35 (1996) 865.
[11] G.P. Panigrahi, P.K. Misro, Indian J. Chem. A 15 (1977) 1066.
[12] G.L. Cohen, G. Atkinson, Inorg. Chem. 3 (1964) 1741.
[13] G.H. Jeffery, J. Bassett, J. Mendham, R.C. Denney, Vogel's Text Book of Quantitative Chemical Analysis, 5th ed., Longman Singapore Publishers Pte Ltd., Singapore, 1996, p. 467 and p. 391.
[14] F. Fiegl, Spot Tests in Organic Analysis, Elsevier, New York, 1975, p. 212.
[15] E.A. Moelwyn-Hughes, Kinetics of Reaction in Solutions, Oxford University Press, London, 1947, pp. 297–299.
[16] L.J. Krishenbaum, L. Mrozowski, Inorg. Chem. 17 (1978) 3718.
[17] (a) F.A. Cotton, G. Wilkinson, Advanced Inorganic Chemistry, Wiley, New York, 1980, p. 974;
(b) R. Banerjee, R. Das, S. Mukhopadhyay, J. Chem. Soc., Dalton Trans. (1992) 1317.
[18] (a) C.E. Crouthumel, H.V. Meek, D.S. Martin, C.V. Banus, J. Am. Chem. Soc. 71 (1949) 3031;
(b) C.E. Crouthamel, A.M. Hayes, D.S. Martin, J. Am. Chem. Soc. 73 (1951) 82.

[19] (a) S. Bhattacharya, B. Saha, A. Datta, P. Banerjee, Coord. Chem. Rev. 47 (1988) 170;
(b) R.I. Haines, A. McAuley, Coord. Chem. Rev. 39 (1981) 77.
[20] (a) A.M. Balado, B.C. Galan, F.J.PP. Martin, An. Quim. 88 (1992) 170;
(b) F.A. Cotton, G. Wilkinson, Advanced Inorganic Chemistry, Wiley Eastern, New York, 1996.
[21] (a) R.S. Shetter, S.T. Nandibewoor, J. Mol. Catal. A 234 (2005) 137;
(b) T.S. Kiran, C.V. Hiremath, S.T. Nandibewoor, Appl. Catal. A 305 (2006) 79.
[22] K.S. Rangappa, M.P. Raghavendra, D.S. Mahadevappa, D. Channegouda, J. Org. Chem. 63 (1998) 531.
[23] (a) E.A. Moelwyn-Hughes, Physical Chemistry, 2nd ed., Pergamon Press, New York, 1961;
(b) E.S. Amis, Solvent Effects on Reaction Rates and Mechanisms, Academic Press, New York, 1966.
[24] A. Weissberger, in: E.S. Lewis (Ed.), Investigation of Rates and Mechanism of Reactions in Techniques of Chemistry, vol. 4, Wiley, New York, 1974, p. 421.
[25] (a) M. Martinez, M.A. Pitarque, R.V. Eldik, J. Chem. Soc., Dalton Trans. (1996) 2665;
(b) S.A. Farokhi, S.T. Nandibewoor, Tetrahedron 59 (2003) 7595.

2. Experimental

2.1. Materials and measurements

Benzhydrazide, 2-acetylpyridine, copper(II) perchlorate hexahydrate (Fluka), sodium thiocyanate and sodium azide (Aldrich) were used as received. The solvents used were of reagent grade.

Elemental analyses were carried out using a Perkin–Elmer 2400 II elemental analyser. The infrared spectra were recorded on a Perkin–Elmer RX 1 FT-IR spectrophotometer with a KBr disc. The electronic spectra were recorded, in acetonitrile, on a Perkin–Elmer Lambda 40 (UV–Vis) spectrophotometer. Magnetic susceptibility measurements for the complexes **1** and **2** were carried out with a Quantum Design MPMS-5S SQUID magnetometer under an applied magnetic field of 5000 Oe. The temperature dependence of the molar magnetic susceptibility, χ_M, for the complexes **1** and **2** was measured on polycrystalline samples in the temperature range 2–300 K. Diamagnetic corrections were estimated from Pascal tables and magnetic data were corrected for diamagnetic contributions of the sample holder.

2.2. Synthesis of ligand and metal complexes

2.2.1. $[C_6H_5C(O)NHN{=}C(CH_3)C_5H_4N]$ (**LH**)

The ligand **LH** was prepared by the condensation of benzhydrazide (1.36 g, 10 mmol) with 2-acetylpyridine (1.12 ml, 10 mmol) in methanol (50 ml) according to the procedure reported elsewhere [9]. The resulting light yellow liquid was used without further purification.

Caution! Perchlorate salts are potentially explosive and should be used in small quantity and with much care.

2.2.2. $[Cu_2(L)_2(\mu_{1,1}\text{-}N_3)_2]$ (**1**)

To a methanolic solution (20 ml) of copper perchlorate hexahydrate (0.370 g, 1 mmol), the solution of the hydrazone ligand (**LH**) (1 mmol) was added, followed by the addition, with constant stirring, of a solution of sodium azide (0.065 g, 1 mmol) in minimum volume of water–methanol mixture. The final solution was kept at refrigerator temperature yielding dark green, hexagonal crystals suitable for X-ray diffraction after 6 days. Crystals were isolated by filtration and were air-dried. Yield – 61%. *Anal.* Calc. for $C_{14}H_{12}N_6OCu$: C, 48.86; H, 3.52; N, 24.42. Found: C, 48.61; H, 3.32; N, 24.09%.

2.2.3. $[Cu(L)(\mu_{1,3}\text{-}NCS)]_n$ (**2**)

The complex **2** was synthesised in a similar manner as described for **1**, except that sodium thiocyanate was used instead of sodium azide. Dark green, hexagonal crystals suitable for X-ray diffraction were obtained after 7 days. Crystals were collected by filtration and were air-dried. Yield – 53%. *Anal.* Calc. for $C_{15}H_{12}N_4OSCu$: C, 50.01; H, 3.36; N, 15.56. Found: C, 49.00; H, 3.32; N, 14.94%.

2.3. X-ray crystallography

The determination of the unit cell and the data collection for dark green coloured crystals of **1** and **2** was performed on a Bruker-Nonius X8 Apex2 Diffractometer. All data were collected with Mo Kα radiation ($\lambda = 0.71073$ Å). The structures of all the complexes were determined by direct method procedures in SHELXS [10a], and refined by full-matrix least-squares methods in SHELXL [10b]. Carbon-bonded hydrogen atoms were included in idealised positions and set to ride on the parent atoms. The crystallographic data and the refinement results are listed in Table 1.

3. Results and discussion

3.1. Description of the crystal structures

3.1.1. $[Cu(L)_2(\mu_{1,1}\text{-}N_3)_2]$ (**1**)

An ORTEP diagram of **1** with atom numbering scheme is given in Fig. 1. Bond dimensions about the copper atom in **1**, together with those **2**, are in Table 2; dimensions in the main chains of the **L** ligand and in the bridging ligands in both the complexes **1** and **2** are collated in Table 3. The structural study reveals that **1** is a semi-bridging centrosymmetric dimer. The azide ion bridges in an asymmetric (basal-apical) fashion so the bridging Cu–N bond lengths are significantly different ($\Delta d = 0.566$ Å). The copper centres are five-coordinate, bonded to three coordinating

Table 1
Crystallographic and refinement data for complexes **1** and **2**

Complex	**1**	**2**
Chemical formula	$C_{28}H_{24}N_{12}O_2Cu_2$	$C_{15}H_{12}N_4OSCu$
Formula weight	687.68	359.89
Crystal system	triclinic	monoclinic
Space group	$P\bar{1}$	Cc
Z	1	4
a (Å)	7.877(13)	11.424(3)
b (Å)	10.465(7)	11.281(3)
c (Å)	10.616(7)	11.173(3)
α (°)	115.71(2)	90
β (°)	97.73(3)	93.466(4)
γ (°)	103.04(3)	90
V (Å^3)	740.9(14)	1437.3(6)
Temperature (K)	100(2)	100(2)
Density (Mg/m^3)	1.541	1.663
Absorption coefficient (mm^{-1})	1.484	1.671
$F(000)$	350	732
Crystal size (mm)	$0.22 \times 0.12 \times 0.08$	$0.38 \times 0.36 \times 0.04$
θ Range for data collection (°)	2.28–25.36	4.05–37.24
Reflections collected	6690	4456
Independent reflections (R_{int})	1961(0.117)	3387(0.0327)
Number of 'observed' reflections	726	2551
Goodness-of-fit, S	0.788	1.053
R indices (all data)	$R_1 = 0.196$, $wR_2 = 0.187$	$R_1 = 0.0597$, $wR_2 = 0.103$
Final R indices [$I > 2\sigma(I)$]	$R_1 = 0.0719$, $wR_2 = 0.158$	$R_1 = 0.0424$, $wR_2 = 0.0968$
Largest difference in peak and hole (e Å^{-3})	0.88 and −0.98	0.83 and −1.54

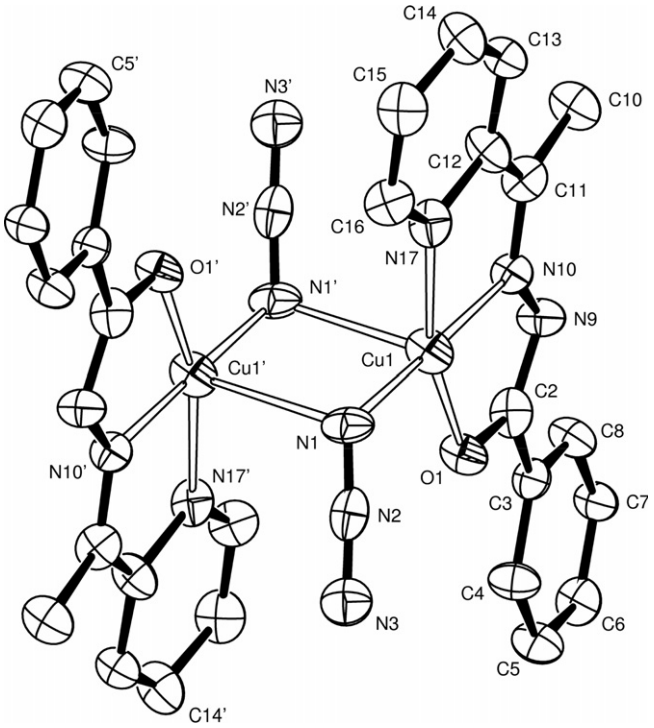


Fig. 1. View of the dimeric unit of **1**, with atom labels. Displacement ellipsoids are shown at 50% probability level. Hydrogen atoms are omitted for clarity.

atoms [N_2O] from the ligand **L** and nitrogen atoms from two bridging azide anions. Both azides bridge in an *end-on* fashion and this leads to a relatively small Cu–Cu (3.205 Å) separation.

The di-$\mu_{1,1}$-azido bridging nitrogen atom is in a planar Cu_2N_2 ring about a crystallographic inversion centre. The azide ions are nearly linear with N–N–N angle of 176.3(11)°. The geometry of the Cu(II) centres is close to square pyramidal with $\tau = 0.268$, [$\tau = |\beta - \alpha|/60°$, where

Table 2
Molecular dimensions (bond lengths in Å and angles in °) about the copper atoms in complexes **1** and **2**

Complex **1**		Complex **2**	
Bond lengths			
Cu1–O4	1.988(7)	Cu1–O1	1.965(3)
N1–Cu1	1.947(8)	Cu1–N10	1.928(3)
Cu1–N2	2.028(9)	Cu1–N17	2.012(3)
Cu1–N21	1.968(9)	Cu1–N1	1.965(4)
Cu1–N21A	2.534(10)	Cu1–S2	2.7110(11)
Bond angles			
N1–Cu1–O4	80.5(3)	N10–Cu1–O1	79.41(13)
O4–Cu1–N2	161.1(3)	O1–Cu1–N17	158.96(13)
N21–Cu1–O4	102.1(3)	O1–Cu1–N1	96.89(14)
O4–Cu1–N21A	92.8(3)	O1–Cu1–S2	102.22(8)
N1–Cu1–N2	81.1(4)	N10–Cu1–N17	80.32(14)
N1–Cu1–N21	177.2(4)	N10–Cu1–N1	159.77(14)
N1–Cu1–N21A	90.9(4)	N10–Cu1–S2	101.29(10)
N21–Cu1–N2	96.2(4)	N1–Cu1–N17	100.17(15)
N2–Cu1–N21A	91.5(4)	N17–Cu1–S2	87.26(9)
N21–Cu1–N21A	90.1(4)	N1–Cu1–S2	98.93(11)

Table 3
Selected bond dimensions (Å and °) in the main chains of the **L** ligand and in the bridging ligands in complexes **1** and **2**

Complex **1**		Complex **2**	
C(29)–O(4)	1.326(11)	O(1)–C(2)	1.295(5)
N(4)–C(29)	1.353(12)	C(2)–N(9)	1.335(5)
N(1)–N(4)	1.424(11)	N(9)–N(10)	1.379(5)
N(1)–C(22)	1.319(13)	N(10)–C(11)	1.303(5)
C(22)–C(6)	1.502(14)	C(11)–C(12)	1.466(6)
N(2)–C(6)	1.421(11)	C(12)–N(17)	1.358(5)
C(29)–O(4)–Cu(1)	108.9(6)	C(2)–O(1)–Cu(1)	110.9(2)
O(4)–C(29)–N(4)	126.8(10)	O(1)–C(2)–N(9)	124.5(4)
C(29)–N(4)–N(1)	105.3(8)	C(2)–N(9)–N(10)	107.1(3)
C(22)–N(1)–N(4)	122.0(8)	C(11)–N(10)–N(9)	123.0(4)
N(1)–C(22)–C(6)	112.5(9)	N(10)–C(11)–C(12)	113.3(4)
N(2)–C(6)–C(22)	113.3(10)	N(17)–C(12)–C(11)	114.2(3)
C(6)–N(2)–Cu(1)	112.4(7)	C(12)–N(17)–Cu(1)	113.0(3)
Complex **1**, azide ligand		Complex **2**, thiocyanate ligand	
N(21)–N(22)	1.209(11)	S(2)–C(1)	1.648(4)
N(23)–N(22)	1.208(12)	C(1)–N(1′)	1.150(6)
N(22)–N(21)–Cu(1)	123.4(8)	C(1)–S(2)–Cu(1)	97.01(13)
N(22)–N(21)–Cu(1′)	109.2(8)	N(1′)–C(1)–S(2)	179.7(4)
Cu(1)–N(21)–Cu(1′)	89.9(4)	C(1″)–N(1)–Cu(1)	160.0(4)
N(23)–N(22)–N(21)	176.3(11)		

E.s.ds are in parentheses.

β and α are the two largest angles around the central atom; $\tau = 0$ and 1 for the perfect square pyramidal and trigonal bipyramidal geometries, respectively] [11]. The square base is formed by pyridyl and imine nitrogen atoms, a benzoyl oxygen atom and the closer of bridging azido nitrogen atoms. The nitrogen atom from the semi-bridging azide group with the longer Cu–N distance is at the apex. The distortion in the geometry is evident from the variation of the basal angles (Table 2) from equivalent *cis* and *trans* values.

3.1.2. [Cu(L)($\mu_{1,3}$-NCS)]$_n$ (2)

An ORTEP representation of **2** with the atom numbering scheme is shown in Fig. 2 and relevant bond dimensions are included in Tables 2 and 3. The structure is made up of infinite chains, in which Cu(II) centres are connected by single *end-to-end* thiocyanate bridges. The copper(II) pentacoordination sphere comprises the N_2O donor atoms from the tridentate deprotonated hydrazone ligand **L**, and a nitrogen and a sulfur atom from two molecules of bridging thiocyanate ligands. The geometry around the copper centre can be described as square pyramidal with $\tau = 0.0135$. The basal plane is formed by the N_2O donor atoms of **L** and the nitrogen atom of a thiocyanate ligand. The sulfur atom from the other thiocyanate ligand is at the apex. The apical Cu–S bond distance is significantly longer [2.7110(1) Å] than the basal bond distances [1.924(4)–2.020(5) Å], even when taking into account the larger covalent radius of sulfur . The bond dimensions around the Cu(II) ion are comparable to those in similar systems [7]. The thiocyanate ligand is almost linear at C1. The intrachain copper–copper separation is

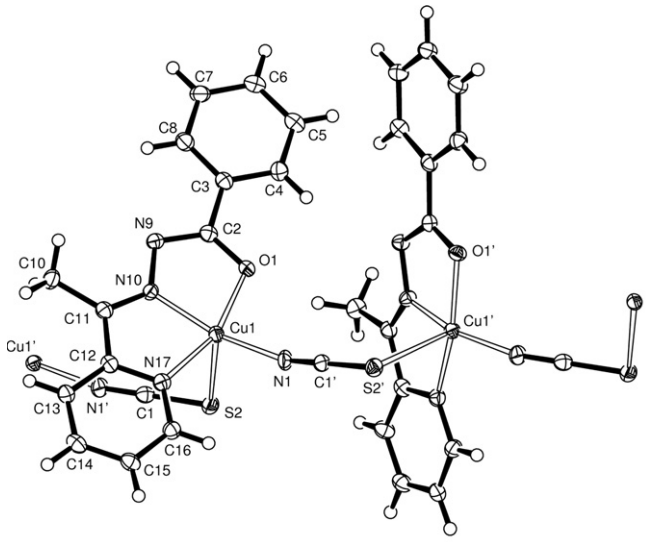


Fig. 2. View of two units in a chain of **2**, with atom labels. Displacement ellipsoids are shown at 50% probability level.

5.806 Å which is comparable to previously reported singly thiocyanate bridged copper complexes [12].

The crystal packing of the complex indicates that adjacent chains have pairwise π–π interactions, by overlap of phenyl with pyridine rings, with four adjacent chains (Fig. 3), thus connecting the chains in a three-dimensional network.

3.2. Infrared spectra

The infrared spectra of the complexes **1** and **2** display absorption bands at *ca.* 1563 cm^{-1} which can be assigned to the C=N stretching frequency of the coordinated ligand **L** [13]. In the spectra of complexes **1** and **2**, strong, well-resolved sharp bands at 2086 and 2028 cm^{-1} are assigned to $\nu_{N=N}$ of the azide (N_3) group and $\nu_{C=N}$ of the NCS group respectively. The ligand coordination to the metal centre is substantiated by two bands appearing for each complex, at 422, 312 (**1**) and 424, 315 (**2**) cm^{-1} attributable to ν_{Cu-N} and ν_{Cu-O} respectively.

3.3. Electronic spectra

The electronic spectral data for the complexes in acetonitrile are in good agreement with their geometries. The UV absorption bands exhibit a charge transfer transition (CT) in the range 350–420 nm for Cu(II) complexes and may be assigned to the ligand-to-metal charge transfer transition for each of the compounds **1** and **2**. The spectra of complexes **1** and **2** each display a broad band at 623 and 635 nm respectively, consistent with the expected five-coordinate geometry.

3.4. Magnetic studies

The temperature dependence of $\chi_M T$ for **1** is depicted in Fig. 4. The curve of $\chi_M T = f(T)$ is almost constant above 60 K with a value near 0.825 cm^3 K mol^{-1}, in good agreement with the expected value for two Cu(II) ions. Below 60 K, $\chi_M T$ slightly increases as T decreases to reach 0.875 cm^3 K mol^{-1} at 4 K. According to the dimeric structure of the complex, the $\chi_M T$ curve has been fitted using a classical Bleaney and Bowers law, using the phenomenological Hamiltonian $\mathbf{H} = -J\mathbf{S}_A\cdot\mathbf{S}_B$. The resulting law has the following form:

$$\chi_M T = \frac{2Ng^2\beta^2}{k[3 + \exp(-J/kT)]}$$

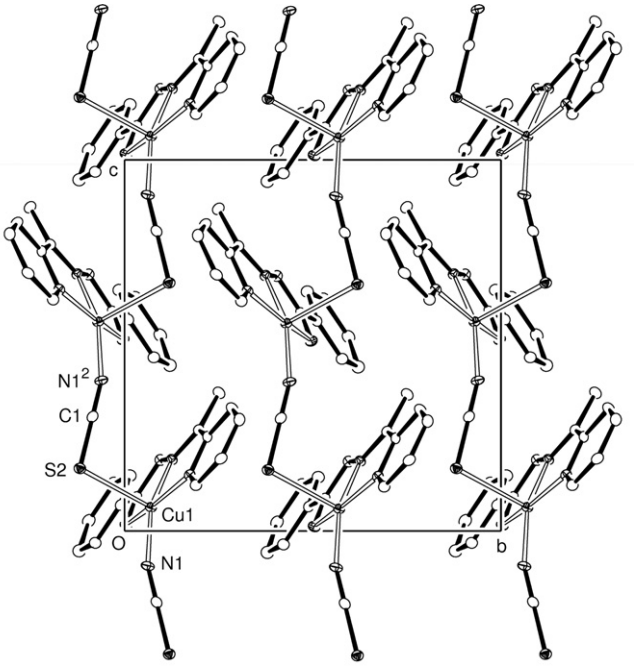


Fig. 3. Crystal packing showing the parallel chains of **2**, and the alignment of overlapping phenyl and pyridine rings.

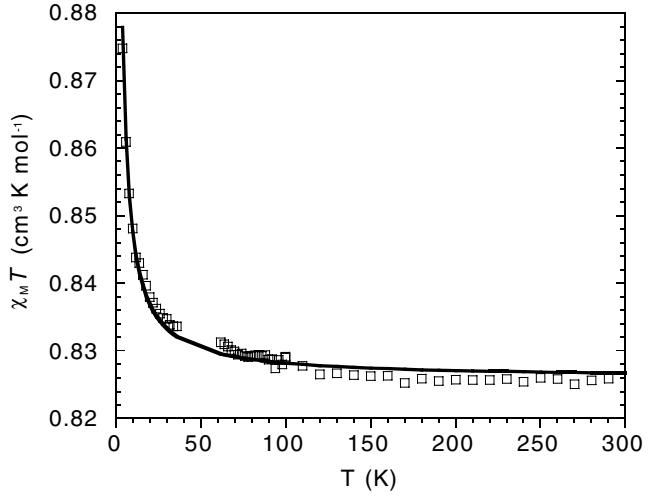


Fig. 4. Experimental (□) and calculated (—) temperature dependence of $\chi_M T$ for **1**.

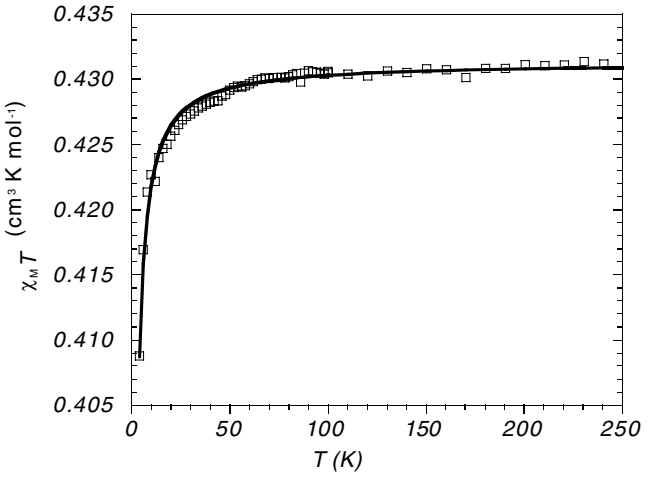


Fig. 5. Experimental (□) and calculated (—) temperature dependence of $\chi_M T$ for **2**.

The best fit was obtained with a Lande factor, g of 2.1, isotropic interaction parameter $J = +0.75\ \text{cm}^{-1}$. The two copper atoms of the dinuclear unit are linked by two azido bridging ligands in an *end-on* fashion. The copper atoms have a square pyramidal geometry and the bridging nitrogen atom of each azido ligand is in a basal position of one copper and the apical position of the second copper.

The temperature dependence of $\chi_M T$ for **2** is shown in Fig. 5. Due to the chain structure of the complexes, the model of equally spaced copper(II) ions has been used. The spin Hamiltonian in zero-field is $H = -J\sum_{i=1}^{n-1} S_{A_i} \cdot S_{A_{i+1}}$ where the summation runs over the n sites of the chain. When n tends to infinity, there is no analytical method to determine the magnetic susceptibility. However, the results can be fitted using the numerical expression for $J < 0$ [14]

$$\chi_M T = \frac{Ng^2\beta^2}{k} \frac{0.25 + 0.074975x + 0.075235x^2}{1.0 + 0.9931x + 0.172135x^2 + 0.757825x^3}$$

with $x = -J/kT$.

For **2**, the best fit was obtained with a Lande factor, g of 2.14 and isotropic interaction parameter $J = -0.23\ \text{cm}^{-1}$. The sulfur atom of the thiocyanate bridge occupies the apical position of the copper cation.

The weak coupling for both the complexes may be explained as follows: the magnetic orbital describing the unpaired electron on a copper(II) ion in square pyramid is of the $d_{x^2-y^2}$ type (the x and y axes being defined by the short basal bonds). The overlap between the magnetic orbitals of two neighbouring coppers is thus very small, and the isotropic interaction parameter (roughly proportional to the square of this overlap) is expected to be small.

4. Conclusion

A double *end-on* azido bridged dinuclear copper(II) hydrazone complex, and a 1D chain copper(II) polymer of the same hydrazone ligand (**L**) with single *end-to-end* thiocyanate bridges have been isolated. Electronic spectra of the complexes support their geometries as established from X-ray analysis. Magnetic studies indicate a weak ferromagnetic interaction operates between the two metal centres in the doubly azido bridged complex **1**, whereas complex **2** exhibits weak antiferromagnetic interactions.

5. Supplementary material

CCDC 615282 and 615283 contain the supplementary crystallographic data for **1** and **2**. These data can be obtained free of charge via http://www.ccdc.cam.ac.uk/conts/retrieving.html, or from the Cambridge Crystallographic Data Centre, 12 Union Road, Cambridge CB2 1EZ, UK; fax: (+44) 1223-336-033; or e-mail: deposit@ccdc.cam.ac.uk.

Acknowledgement

We acknowledge the financial assistance to S. Sen from the CSIR (New Delhi, India).

References

[1] R. Neumann, M. Dahan, Nature 388 (1997) 353.
[2] (a) M. Fujita, Y.J. Kwon, S. Washizu, K. Ogura, J. Am. Chem. Soc. 116 (1994) 1151;
(b) M. Fujita, J. Yazaki, K. Ogura, Tetrahedron Lett. 32 (1991) 5589.
[3] O.M. Yaghi, G.M. Li, H.L. Li, Nature 378 (1995) 703.
[4] J.S. Miller, M. Drillon, Magnetism: Molecules to Materials, Wiley-VCH, Weinheim, 2002.
[5] (a) D. Gatteschi, A. Caneschi, L. Pardi, R. Sessoli, Science 265 (1994) 1054;
(b) A.L. Barra, A. Caneschi, A. Cornia, F.F. Biani, D. Gatteschi, C. Sangregorio, R. Sessoli, L. Sorace, J. Am. Chem. Soc. 121 (1999) 5302;
(c) M. Drillon, in: J.S. Miller (Ed.), Magnetism: Molecules to Materials II; Molecule-Based Magnets, Wiley-VCH, Weinheim, 2001.
[6] S.K. Dey, N. Mondal, M.S. El Fallah, R. Vicente, A. Escuer, X. Solans, M.F. Bardía, T. Matsushita, V. Gramlich, S. Mitra, Inorg. Chem. 43 (2004) 2427.
[7] P. Talukder, A. Dutta, S. Mitra, G. Rosair, M.S. El Fallah, J. Ribas, Dalton Trans. (2004) 4161.
[8] N.K. Karan, S. Mitra, T. Matsushita, V. Gramlich, G. Rosair, Inorg. Chim. Acta 332 (2002) 87.
[9] T.E. Khalil, L. Labib, M.F. Iskander, Polyhedron 13 (1994) 2569.
[10] G.M. Sheldrick, SHELXTL – Programs for Crystal Structure Analysis: (a) Structure Determination (SHELXS) and (b) refinement (SHELXL), University of Göttingen, Germany, 1997.
[11] A.W. Addison, T.N. Rao, J. Reedijk, J. van Rijn, G.C. Verschoor, J. Chem. Soc., Dalton Trans. (1984) 1349.
[12] (a) S. Ferlay, G. Francese, H.W. Schmalle, S. Decurtins, Inorg. Chim. Acta 286 (1999) 108;
(b) Z.E. Serna, R. Cortes, M.K. Urtiaga, M.G. Barandika, L. Lezama, M.I. Arriortua, T. Rojo, Eur. J. Inorg. Chem. (2001) 865.
[13] R.T. Conley, Infrared Spectroscopy, Allyn & Bacon, Boston, 1966.
[14] W.E. Estes, D.P. Gavel, W.E. Hatfield, D. Hodgson, Inorg. Chem. 17 (1978) 1415.

L is hexadentate [10], tridentate [11], bidentate [12] or monodentate [13], respectively. These cationic species show a large variety of SC behaviors, depending on the non-coordinated counter anions and solvent of crystallization. The other family includes neutral compounds $[Fe(L)_y(A)_2]$ where $y = 1$ or 2 when L is tetradentate [14] or bidentate [15], respectively. The monodentate ligands A are most often NCS^- or $NCSe^-$ anions because halides or pseudohalides like N_3^- or NCO^- yield HS compounds (low ligand-field) while LS complexes can be obtained with CN^- (strong ligand field). To our knowledge, very few SC complexes have been prepared with tetradentate ligands [14,16] and an unique example of dissymmetrical ligand is depicted for an Fe^{II} complex [17]. The synthesis of new SC compounds is of utmost importance in this research area, particularly when the synthesis is performed in a controlled manner with the aim of obtaining compounds exhibiting a predictable SC behavior.

In the present contribution, we report an original synthetic route for the synthesis of new SC materials. We first synthesized new Fe^{II} complexes from symmetrical tetradentate Schiff base ligands: $[FeL^A(NCS)_2]$ (**1**) (L^A stands for *N*,*N*′-bis(1-pyridin-2-ylethylidene)-2,2-dimethylpropane-1,3-diamine), and $[FeL^{Bx}(NCS)_2]$ (**2**–**4**) (L^{Bx} stands for *N*,*N*′-bis[(2-R-1*H*-imidazol-4-yl)methylene]-2,2-dimethylpropane-1,3-diamine, with: R = H for L^{B1} in **2**, R = Me for L^{B2} in **3**, and R = Ph for L^{B3} in **4** (Fig. 1)). Complexes **1**–**4** remaining in the same spin-state over the 80–400 K range, dissymmetrical tetradentate Schiff bases L^{Cx} containing both pyridine and imidazole rings (Fig. 1) were then prepared as their $[FeL^{Cx}(NCS)_2]$ complexes, **5**–**10** (L^{Cx} stands for *N*-[(2-R_2-1*H*-imidazol-4-yl)methylene]-*N*′-(1-pyridin-2-ylethylidene)-2,2-R_1-propane-1,3-diamine, with: R_1 = H in **5**–**7**, and Me in **8**–**10**; R_2 = H for L^{C1} in **5** and **8**, R_2 = Me for L^{C2} in **6** and **9**, and R_2 = Ph for L^{C3} in **7** and **10**). Together with the single-crystal X-ray structures of **7** and **9**, variable-temperature magnetic susceptibility and Mössbauer studies of **5**–**10**, showed that it is possible to tune the spin-crossover properties in the $[FeL^{Cx}(NCS)_2]$ series by changing the 2-imidazole and/or C2-propylene substituent of L^{Cx}.

2. Experimental

2.1. Materials

All reagents and solvents were commercially available (Aldrich, Wako) and were used without further purification.

2.2. Syntheses

2.2.1. Ligands

The ligands were characterized by ^1H and in some cases by ^{13}C NMR in $CDCl_3$ (δ, ppm; s, singlet; d, doublet; t, triplet; dt = doublet of triplets; m, multiplet; b, broad).

2.2.1.1. Symmetrical ligands L^A and L^{Bx}. 2,2-Dimethyl-1,3-diaminopropane (0.102 g, 10^{-3} mol) and 2-acetyl-pyridine (0.242 g, 2×10^{-3} mol) for L^A, imidazole-4-carboxaldehyde (0.192 g, 2×10^{-3} mol) for L^{B1}, 2-methylimidazole-4-carboxaldehyde (0.220 g, 2×10^{-3} mol) for L^{B2}, 2-phenylimidazole-4-carboxaldehyde (0.344 g, 2×10^{-3} mol) for L^{B3}, were stirred for 2 h in 20 mL of methanol at room temperature. Slow evaporation of the solvent yielded brown-yellow oils (yield: 0.280 g (90%); 0.210 g (80%); 0.243 g (85%); 0.330 (80%) for L^A, L^{B1}, L^{B2}, and L^{B3},

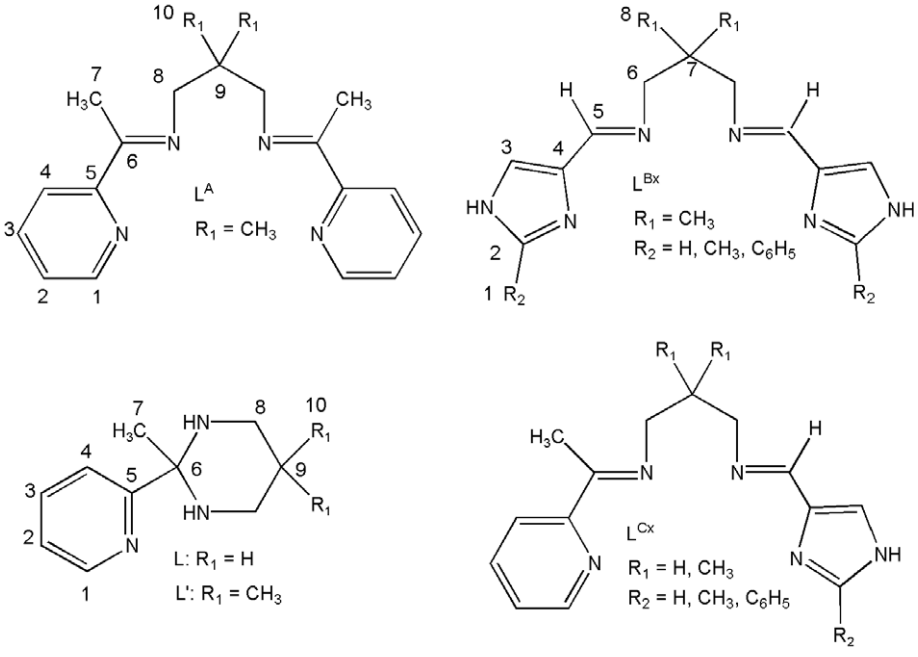


Fig. 1. Schematic representation of ligands L^A, L^{Bx}, L^{Cx} and of the half units L and L′ (R_1 = H, Me; R_2 = H, Me, Ph).

respectively). ^{1}H (250 MHz): L^{B1}, δ 7.91 (s, H5, 2H), δ 7.67–7.65 (sb, H1 and H3, 4H), δ 3.59 (s, H6, 4H), δ 1.06 (s, H8, 6H); L^{B2}, δ 7.98 (s, H5, 2H), δ 7.40 (s, H3, 2H), δ 3.37 (s, H6, 4H), δ 2.40 (s, H1, 6H), δ 0.93 (s, H8, 6H); L^{B3}, δ 7.97 (s, H5, 2H), δ 7.900–7.30 (m, H1, 10H), δ 7.69 (s, H3,2H), 3.42 (s, H6, 4H), δ 1.06 (s, H8, 6H). ^{1}H NMR spectra of L^A could not be assigned due to the presence of a mixture including the aminal resulting from single condensation followed by cyclization, and the Schiff base resulting from the usual bis-condensation [18]. Nevertheless, complexation with $Fe(NCS)_2 \cdot x$solvent led to quantitative formation of the desired symmetrical complex.

2.2.1.2. Synthesis of the half-units L and L′. 2-Acetyl-pyridine (0.121 g, 10^{-3} mol) was added to a solution of 1,3-diaminopropane (0.074 g, 10^{-3} mol) for L or of 2,2-dimethyl-1,3-diaminopropane (0.102 g, 10^{-3} mol) for L′ in 10 mL of CH_2Cl_2. The resulting pale yellow solution was stirred for 30 min and kept undisturbed at room temperature until complete evaporation of the solvent (yield: 0.17 g, 85% for L; 0.15 g, 83% for L′). Colorless crystals and an oil were obtained for L and L′, respectively. Both ligands were characterized by elemental analyses, IR (L), and 2D ^{1}H–^{13}C NMR. Ligand L: *Anal.* Calc. for $C_{10}H_{15}N_3$ (177 g mol^{-1}): C, 67.76; H, 8.53; N, 23.71. Found: C, 66.63; H, 8.25; N, 23.90%. IR (cm^{-1}): 1589, 1558, 1463, 1429, 786. ^{1}H NMR (400 MHz): δ 8.59 (d, H1, $J = 5.5$ Hz, 1H), δ 7.10 (t, H2, $J = 5$ Hz, 1H), δ 7.73 (t, H3, $J = 1.5$ Hz, 1H), δ 7.76 (d, H4, $J = 6$ Hz, 1H), δ 1.35 (s, H7, 3H), δ 2.62 and 2.93 (s, H8, 2H + 2H), δ 1.63 (m, H9, 2H). ^{13}C {^{1}H}NMR (100.6 MHz): δ 164.3 (C5), δ 158.2 (C1), δ 137.2 (C3), δ 121.3 (C2), δ 121.2 (C4), δ 71.7 (C6), δ 41.8 (C8), δ 27.0 (C9). Ligand L′. *Anal.* Calc. for $C_{12}H_{19}N_3$ (205 g mol^{-1}): C, 70.20; H, 9.33; N, 20.47. Found: C, 69.23; H, 9.26; N, 20.54%. ^{1}H (400 MHz): δ 8.61 (d, H1, $J = 5.5$ Hz, 1H), δ 7.77 (d, H4, $J = 7$ Hz, 1H), δ 7.71 (td, H3, $J = 2$ Hz and $J = 7$ Hz, 1H), δ 7.19 (td, H2, $J = 5.5$ Hz and $J = 2$ Hz, 1H), δ 1.41 (s, H7, 3H), δ 2.38 and 2.99 (s, H8, 2H + 2H), δ 0.69 and 1.14 (s, H10, 6H). ^{13}C {^{1}H} NMR (100.6 MHz):δ 164.1 (C5), δ 149.4 (C1), δ 137.1 (C3), δ 122.2 (C2), δ 122.0 (C4), δ 71.3 (C6), δ 53.7 (C8), δ 28.7 (C9), δ 23.3 and 23.88 (C10).

2.2.2. Complexes

All complexation reactions and sample preparations for physical measurements were carried out in a purified nitrogen atmosphere within a glovebox (Vacuum Atmospheres H.E.43.2) equipped with a dry train (Jahan EVAC 7).

2.2.2.1. $Fe(NCS)_2 \cdot xMeOH$. $Fe(ClO_4)_2 \cdot xH_2O$ (10^{-3} mol) was reacted with potassium thiocyanate (0.195 g, 2×10^{-3} mol) in 10 mL of MeOH following a procedure adapted from the preparation of $Fe(py)_4(NCS)_2$ [19]. After removal of potassium perchlorate through filtration, the freshly prepared $Fe(NCS)_2 \cdot x$MeOH was used immediately for the preparation of complexes **1**–**10**.

Caution: Although no such behavior was observed during the present work, perchlorate salts are potentially explosive and should be handled in small quantities and with much care.

*2.2.2.2. General procedure (**1**–**4**).* To a methanolic solution (10^{-3} mol in 10 mL) of the ligand was added slowly a methanolic solution (10^{-3} mol in 10 mL) of $[Fe(NCS)_2] \cdot x$MeOH. The solution immediately changed from pale yellow to dark blue (**1**) or orange–yellow (**2**–**4**) and was left under stirring for 30 min.

$[FeL^A(NCS)_2]$ (**1**): Slow crystallization (over 1 month) yielded dark blue crystals suitable for X-ray analysis. Yield: 0.34 g, 68%. *Anal.* Calc. for $FeC_{21}H_{24}N_6S_2$ (480.4 g mol^{-1}): C, 52.50; H, 5.04; N, 17.49; S, 13.35; Fe, 11.62. Found: C, 52.25; H, 5.05; N, 17.27; S, 13.29; Fe, 11.57%. IR (cm^{-1}): 2110–2090 (NCS); 1600 (imine).

$[FeL^{B1}(NCS)_2]$ (**2**): Orange crystals suitable for X-ray analysis were obtained after addition of Et_2O to the methanolic solution of **2**. Yield: 0.32 g, 75%. *Anal.* Calc. for $FeC_{15}H_{18}N_8S_2$ (430.3 g mol^{-1}): C, 41.87; H, 4.22; N, 26.04; S, 14.90; Fe, 12.98. Found: C, 41.78; H, 3.91; N, 25.88; S, 14.65; Fe, 12.89%. IR (cm^{-1}): 2110–2090 (NCS); 1603 (imine).

$[FeL^{B2}(NCS)_2]$ (**3**): Slow crystallization (over one week) yielded orange crystals suitable for X-ray analysis. Yield: 0.32 g, 70%. *Anal.* Calc. for $FeC_{17}H_{22}N_8S_2$ (458.4 g mol^{-1}): C, 44.55; H, 4.84; N, 24.45; S, 14.00; Fe, 12.20. Found: C, 44.47; H, 4.55; N, 24.44; S, 13.93; Fe, 11.61. IR (cm^{-1}): 2110–2090 (NCS); 1611 (imine).

$[FeL^{B3}(NCS)_2]$ (**4**): Yellow microcrystalline powder. Yield: 0.38 g, 65%. *Anal.* Calc./found for $FeC_{27}H_{27}N_8S_2$ (583.5 g mol^{-1}): C, 55.67; H, 4.50; N, 19.24; S, 11.00; Fe, 9.58. Found: C, 55.60; H, 4.27; N, 19.05; S, 10.29; Fe, 9.20%. IR (cm^{-1}): 2110–2090 (NCS); 1603 (imine).

*2.2.2.3. General procedure (**5**–**10**).* To a pale yellow solution (10^{-3} mol, 10 mL methanol) of the aminal L (**5**–**7**) or L′ (**8**–**10**) the freshly prepared $Fe(NCS)_2$ solution (10^{-3} mol, 10 mL methanol) was slowly added. The color of the reaction mixture immediately turned to dark blue and was stirred for 5 min. The appropriate 2R-imidazole-4-carboxaldehyde (10^{-3} mol, 10 mL methanol) was then added (imidazole-4-carboxaldehyde for **5** and **8**, 2-methylimidazole-4-carboxaldehyde for **6** and **9**, and 2-phenylimidazole-4-carboxaldehyde for **7** and **10**). No further color change was observed; the solution was stirred for 30 more minutes and then left undisturbed until a microcrystalline powder or crystals quantitatively formed.

$[FeL^{C1}(NCS)_2]$ (**5**): Dark blue powder. Yield: 0.32 g, 75%. *Anal.* Calc. for $FeC_{16}H_{17}N_7S_2$ (427.3 g mol^{-1}): C, 44.97; H, 4.01; N, 22.94; S, 15.01; Fe, 13.07. Found: C, 45.15; H, 4.00; N, 22.85; S, 14.67; Fe, 12.72%. IR (cm^{-1}): 2112–2060 (NCS); 1620 (imine).

$[FeL^{C2}(NCS)_2]$ (**6**): Dark blue powder. Yield: 0.32 g, 73%. *Anal.* Calc. for $FeC_{17}H_{19}N_7S_2$ (441.4 g mol^{-1}): C, 46.26; H, 4.34; N, 22.22; S, 14.53; Fe, 12.65. Found: C,

46.33; H, 4.49; N, 20.32; S, 14.39; Fe, 12.50%. IR (cm^{-1}): 2060 (NCS); 1638 (imine).

[$FeL^{C3}(NCS)_2$] (**7**): Dark blue single crystals. Yield: 0.30 g, 60%. *Anal*. Calc. for $FeC_{22}H_{21}N_7S_2$ (503.4 g mol^{-1}): C, 52.49; H, 4.21; N, 19.48; S, 12.74; Fe, 11.09. Found: C, 52.19; H, 3.84; N, 19.09; S, 12.70; Fe, 10.90%. IR (cm^{-1}): 2068 (NCS); 1641 (imine).

[$FeL^{C4}(NCS)_2$] (**8**): Dark blue powder. Yield: m = 0.32 g, 72%. *Anal*. Calc. for $FeC_{18}H_{21}N_7S_2$ (455.4 g mol^{-1}): C, 47.48; H, 4.65; N, 21.53; S, 14.08; Fe, 12.26. Found: C, 47.82; H, 4.47; N, 20.74; S, 13.81; Fe, 11.80%. IR (cm^{-1}): 2108–2058 (NCS); 1618 (imine).

[$FeL^{C5}(NCS)_2]\cdot H_2O$ (**9**): Dark blue single crystals. Yield: 0.35 g, 72%. *Anal*. Calc. for $FeC_{19}H_{23}N_7S_2\cdot H_2O$ (487.4 g mol^{-1}): C, 46.82; H, 5.17; N, 20.12; S, 13.16; Fe, 11.46. Found: C, 47.10; H, 4.52; N, 20.29; S, 12.73; Fe, 11.30%. IR (cm^{-1}): 2058 (NCS); 1634 (imine).

[$FeL^{C6}(NCS)_2$] (**10**): Dark blue microcrystals. Yield: 0.35 g, 66%. *Anal*. Calc. for $FeC_{24}H_{25}N_7S_2$ (531.5 g mol^{-1}): C, 54.24; H, 4.74; N, 18.45; S, 12.06; Fe, 10.51. Found: C, 54.04; H, 4.31; N, 18.16; S, 11.64; Fe, 10.51, 10.37%. IR (cm^{-1}): 2072 (NCS); 1643 (imine).

2.3. Physical measurements

Elemental analyses were carried out on a Perkin–Elmer 2400 series II device (C, H, N) at the Microanalytical Laboratory of the Laboratoire de Chimie de Coordination in Toulouse, and on a Maxim Thermoelectron device (S, Fe) at the Service Central de Microanalyses du CNRS in Vernaison, France. 1D ^1H and 1D ^{13}C NMR spectra were performed on an AC 250 FT spectrometer (Bruker) and 2D $^1H^{13}C$ spectra on an AMX 400 spectrometer (Bruker). Chemical shifts are given in ppm versus TMS (^1H and ^{13}C) using $CDCl_3$ as solvent. IR spectra were measured in the 400–4000 cm^{-1} range on a 9800 FTIR spectrometer (Perkin–Elmer). Samples were run as KBr pellets. Mössbauer spectra were recorded on a constant-acceleration conventional spectrometer with a 50 mCi source of ^{57}Co (Rh matrix). The absorber was a powdered sample enclosed in a 20 mm diameter cylindrical plastic sample holder, the size of which has been determined to optimize the absorption. Spectra were obtained in the 80–400 K range using a MD306 Oxford cryostat (4–293 K) or an home-made vacuum oven (300–500 K), the thermal scanning being monitored by an Oxford ITC4 servo control device (±0.1 K accuracy). A least square computer program [20] was used to fit the Mössbauer parameters and to determine their standard deviations of statistical origin (given in parentheses). Isomer shift values (δ) are relative to iron foil at 293 K. Variable temperature magnetic susceptibility data were collected on powdered samples on a MPMS-55 Quantum Design SQUID magnetometer or a Faraday type susceptometer under applied magnetic fields lower than 0.1 T. Diamagnetic corrections were applied by using Pascal's constants.

2.4. Crystallographic data collection and structure determination for *1*, *2*, *3*, *7* and *9*

The X-ray data for compounds **1**, **2**, **7** and **9** were collected on a Stoe Imaging Plate Diffractometer System (IPDS) equipped with an Oxford Cryosystems cooler device using a graphite monochromator ($\lambda = 0.71073$ Å). Data were collected [21] using φ rotation movement with the crystal-to-detector distance equal to 70 mm ($\varphi = 0.0$-270°, $\Delta\varphi = 1.5°$ for **1**, $\varphi = 0.0$–200°, $\Delta\varphi = 1.5°$ for **2** and **9** and $\varphi = 0.0$–250°, $\Delta\varphi = 1.4°$ for **7**). Diffraction data for **3** were collected using an Oxford-Diffraction XCALIBUR CCD diffractometer equipped with a graphite-monochromated Mo Kα radiation source. The crystal was placed 50 mm from the CCD detector. More than the hemisphere of reciprocal space was covered by combination of four sets of exposures; each set had a different φ-angle (0°, 90°, 180°, 270°) and each exposure of 20 s covered 0.75° in ω. Coverage of the unique set is 99.5% complete up to $2\theta = 63.22°$. The unit cell determination and data integration were carried out using the CrysAlis package of Oxford Diffraction [22]. All structures were solved by direct methods using SHELXS-97 [23] and refined by full-matrix least-squares on F_o^2 with SHELXL-97 [24] with anisotropic displacement parameters for non-hydrogen atoms. The hydrogen atoms were placed in calculated positions (C–H 0.96 Å) and they were included in the refinement in the riding-model approximation with $U_{iso} = 1.1$ U (atom of attachment). Positional parameters of the H(water) atoms in compound **9** were obtained from difference Fourier syntheses and verified by the geometric parameters of the corresponding hydrogen bonds. Scattering factors were taken from the standard compilation [25]. The molecular plots were obtained by using the ZORTEP program [26]. Numerical absorption corrections [27] were applied for **3**, while for compounds **1**, **2**, **7** and **9** the absorption corrections were introduced by semi-empirical methods based on equivalent reflections, using the program MULTISCAN [28]. The final full-matrix least-squares refinement, minimizing $\left[\sum w\left(|F_o^2| - |F_c^2|\right)^2\right]^2$, converged at the values of R and wR listed in Table 1, together with the main crystallographic parameters. The relatively high R-factors for complex **7** are due to the low quality of the crystals: among several sets of diffraction data obtained from different crystals which all diffracted poorly, the best one was used to solve this structure.

3. Results

3.1. Syntheses

While the reaction of 2 equiv of 2R-imidazole-4-carboxaldehyde with 1 equiv of 2,2-dimethyl-1,3-diaminopropane yielded pure samples of the corresponding acyclic tetradentate bis-Schiff bases L^{Bx}, the corresponding condensation reaction carried out with 2-acetyl-pyridine yielded a mixture including the cyclic aminal L′ resulting from single

Table 1
Crystallographic data collection and structure determination for complexes **1**, **2**, **3**, **7** and **9**

Compound	$[FeL^{A}(NCS)_2]$ (**1**)	$[FeL^{B1}(NCS)_2]$ (**2**)	$[FeL^{B2}(NCS)_2]$ (**3**)	$[FeL^{C3}(NCS)_2]$ (**7**)	$[FeL^{C5}(NCS)_2]\cdot H_2O$ (**9**)
Formula	$C_{21}H_{24}FeN_6S_2$	$C_{30}H_{36}Fe_2N_{16}S_4$	$C_{17}H_{22}FeN_8S_2$	$C_{22}H_{21}FeN_7S_2$	$C_{19}H_{25}FeN_7OS_2$
Formula weight	480.43	860.69	458.40	503.43	487.43
Crystal system space group	triclinic $P\bar{1}$ (no. 2)	triclinic $P\bar{1}$ (no. 2)	monoclinic $P2_1/n$ (no. 14)	monoclinic $P2_1/c$ (no. 14)	orthorhombic $Pna2_1$ (no. 33)
a (Å)	8.4584(17)	12.4503(12)	9.3308(5)	12.561(2)	25.719(5)
b (Å)	8.7682(18)	12.7279(13)	13.6987(6)	12.4395(14)	8.0906(16)
c (Å)	16.110(3)	13.5717(13)	16.7115(7)	15.649(3)	11.638(2)
α (°)	98.33(3)	98.289(12)	90	90	90
β (°)	104.53(3)	95.886(12)	90.755(4)	100.047(19)	90
γ (°)	94.39(3)	110.475(11)	90	90	90
V (Å^3)	1136.3(4)	1966.4(3)	2135.89(17)	2407.7(6)	2421.7(8)
Z	2	2	4	4	4
ρ_{calcd} (g cm^{-3})	1.404	1.454	1.426	1.389	1.337
λ (Å)	0.71073	0.71073	0.71073	0.71073	0.71073
Absolute structure parameter					0.30(6)
T (K)	293	200	180	180	293
μ(Mo Kα) (cm^{-1})	0.867	0.996	0.921	0.824	0.819
$R[I > 2\sigma(I)]$[a]	0.0525	0.0375	0.0265	0.1155	0.0446
wR^2[b]	0.0675	0.0741	0.0710	0.2915	0.0780

[a] $R = \sum ||F_o| - |F_c|| / \sum |F_o|$.

[b] $wR = \left[\sum w(|F_o^2| - |F_c^2|)^2 / \sum w|F_o^2|^2\right]^{1/2}$.

condensation, and the Schiff base resulting from the usual bis-condensation. This lower reactivity of ketone compared to aldehyde carbonyl function is well documented [29] but has been scarcely exploited to prepare so-called 'half-unit' synthons through 1:1 condensation with the aim to generate dissymmetrical ligands through opening of the aminal ring and condensation of the amine function with a different carbonyl [30]. One of the reasons is the occurrence of redistribution reactions that yield mixtures of the respective symmetrical bis-Schiff bases corresponding to each carbonyl synthon, including or not a small percentage of the targeted dissymmetrical bis-Schiff base. Using a metal ion in order to favor the acyclic Schiff base versus the cyclic aminal intermediate through complexation, and to subsequently favor formation of the tetracoordinated dissymmetric bis-Schiff base has occasionally allowed avoiding redistribution reactions, and has thus allowed preparing dissymmetric bis-Schiff base cleanly and quantitatively in a very few cases [31].

Based on these results, we explored the 1:1 condensation reactions between 2-acetyl-pyridine and 1,3-diaminopropane or 2,2-dimethyl-1,3-diaminopropane. These reactions yielded the isolated aminal type ligands L: 2-(2-methylhexahydro-2-pyrimidinyl)pyridine and L′: 2-(2-methyl-5-dimethylhexahydro-2-pyrimidinyl)pyridine, respectively (first reaction sketched in Fig. 2).

The NMR spectra clearly showed that, in the case of L and L′, in the absence of metal ion the acyclic single condensation intermediate is not stable and the equilibrium is totally shifted toward the cyclic aminal form. Addition of 2R-imidazole-4-carboxaldehyde to L (L′) yielded mixtures of the respective symmetrical bis-Schiff bases and possibly a small amount of the targeted dissymmetrical bis-Schiff base, as suggested by the NMR spectra that showed a large number of intricated absorption resonances.

Clean and quantitative syntheses of the dissymmetrical ligands L^{Cx} could only be performed in the presence of $Fe(NCS)_2\cdot x$MeOH yielding their $[FeL^{Cx}(NCS)_2]$ (x = 1–6) complexes (Fig. 2). These results suggest that the metal ion displaces totally the equilibrium from the cyclic aminal toward the acyclic Schiff base intermediate through complexation as sketched in the second reaction of Fig. 2. The presence of the pyridine aromatic ring conjugated with Fe^{II} results in a strong MLCT band [32] responsible for the intense blue color of compounds **5**–**10** which are crystals (**7**, **9**), microcrystals (**10**), or more or less microcrystalline powders (**5**, **6**, **8**). The homogeneity (in color and texture) of all samples has been checked by microscopy. Moreover, Mössbauer spectroscopy has confirmed the presence of both HS and LS spin isomers in temperature dependent ratios for all compounds in this series, except for **6** which is 100% HS (see Mössbauer section and Table SM.2). Compounds **5**–**10** are oxidized in aerobic solutions. However, in the solid state, they are reasonably stable in aerobic conditions provided the samples are not exposed to moisture and/or heat. The absence of oxidation for all samples of compounds **1**–**10** in the solid state has been checked by

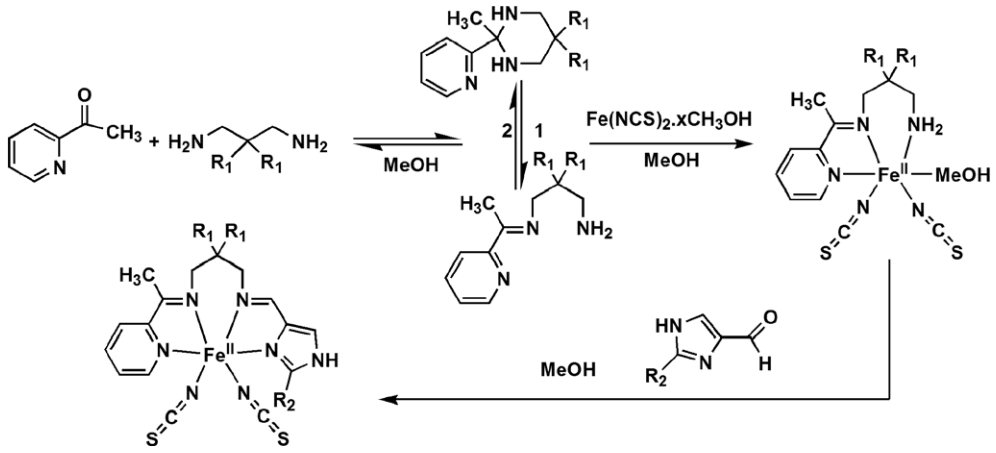


Fig. 2. Synthetic pathway for the family of complexes $[FeL^{Cx}(NCS)_2]$ based on the dissymmetrical tetradentate Schiff base ligands L^{Cx} (R_1 = H, Me; R_2 = H, Me, Ph).

EPR spectroscopy. Formation of the intermediate complexes $FeL(NCS)_2(MeOH)$ and $FeL'(NCS)_2(MeOH)$ sketched in Fig. 2 as resulting from addition of the ferrous salt to L (L′) is assessed on the basis of the color change observed upon addition of $Fe(NCS)_2 \cdot x$MeOH and on the rationale that complexation with the acyclic Schiff base intermediate is more likely due to the entropy gain upon conversion of the bidentate cyclic aminal into the tridentate Schiff base. However, these dark blue intermediate complexes are very soluble and we have not attempted to isolate them.

3.2. Description of the structures

ORTEP plots of complexes **1**, **3**, and **9** are shown in Figs. 3–5, respectively. Selected inter-atomic distances and angles for complexes **1**, **2**, **3**, **7** and **9** are collated in Table 2.

The overall molecular structure of the five complexes is similar: the distorted octahedral $[FeN_6]$ coordination environment includes four nitrogen atoms belonging to the tetradentate Schiff base ligand (L^A (**1**), L^{Bx} (**2** and **3**), and L^{Cx} (**7** and **9**)) in the equatorial positions, while the apical positions are occupied by nitrogen atoms from two NCS^- ligands. Within the estimated standard deviations, the iron atom is in the mean plane of the four equatorial nitrogen donors. However, the tetradentate Schiff base ligands, as a whole, exhibit more or less significant deviations from planarity. This can be due to the steric constraints imposed by the pyridine and/or imidazole moieties upon coordination to the metal center, and results in tilts of the aromatic rings from the mean plane of the tetradentate ligand. The larger tilt is observed for the py–py dihedral angle of **1** (32.6°), and the smaller one for the py–imidazole dihedral angle of **9** (4.8°). The Fe–N bond distances are characteristic of the spin-state of Fe^{II}: the average 1.949 Å value for **1** (293 K) is in good agreement with those observed for similar LS iron(II) complexes, while the average Fe–N bond distances of 2.185 Å (**2**, 200 K), 2.189 Å (**3**, 180 K), 2.196 Å (**7**, 180 K) and 2.150 Å (**9**, 293 K) indicate that the Fe^{II} center is in the HS state at the temperatures of the X-ray data collections for the four remaining compounds that have been structurally characterized [4,18]. In average, in the HS structures the N–Fe–N angles depart more from those expected for a regular octahedron (Table 2). It may thus be concluded that, except for the metric differences resulting from the difference in Fe^{II} spin-state, the complexes based on the L^A, L^{Bx} and L^{Cx} ligands have similar molecular structures.

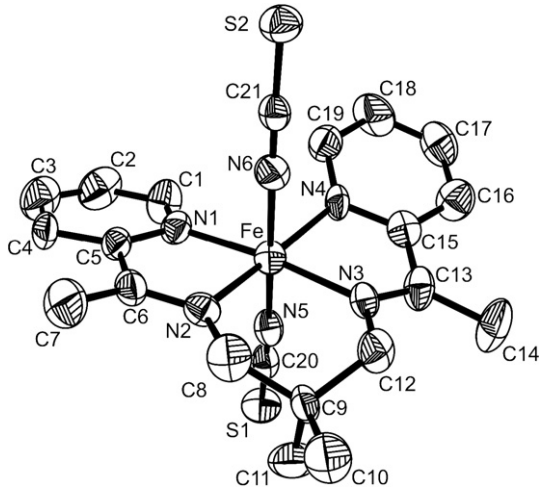


Fig. 3. ORTEP plot of complex **1** at the 40% probability level. H-atoms have been omitted for clarity.

On the other hand, these compounds provide a diversity of crystal packing modes, with a large variety of network topologies and these peculiarities deserve detailed consideration.

The crystal packing of **1** results from an extended 3D network of C–H···S contacts. A fragment of the crystal structure showing five H-bonded molecules is displayed in Fig. 6. The C···S distances between C–H···S bonded molecules are in the 3.59–3.69 Å range, in keeping with previous reports [18,33]. In addition, π–π stacking interactions involving the pyridine rings of molecules related by a crystallographic inversion center participate in the crystal

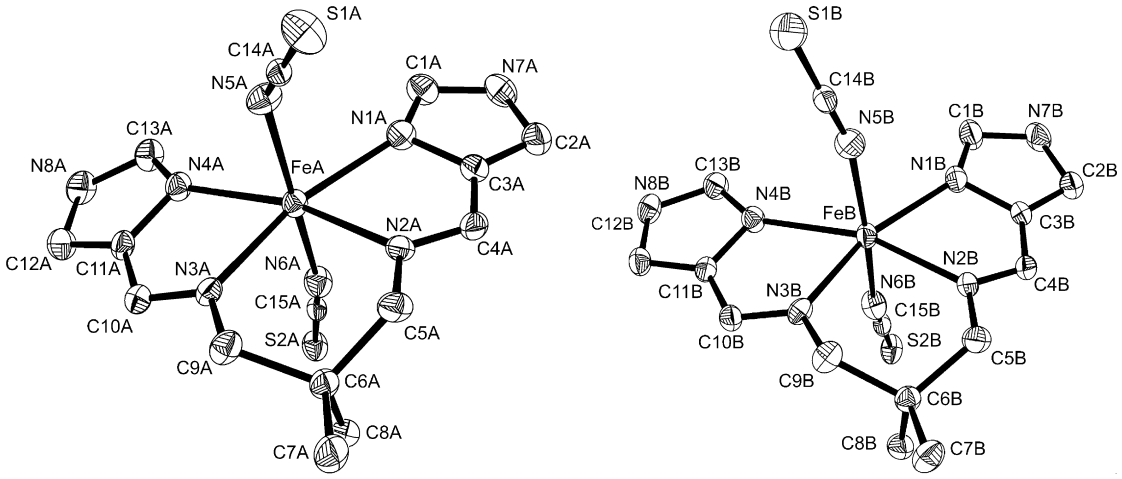


Fig. 4. ORTEP plot of complex **2** at the 50% probability level. H-atoms have been omitted for clarity.

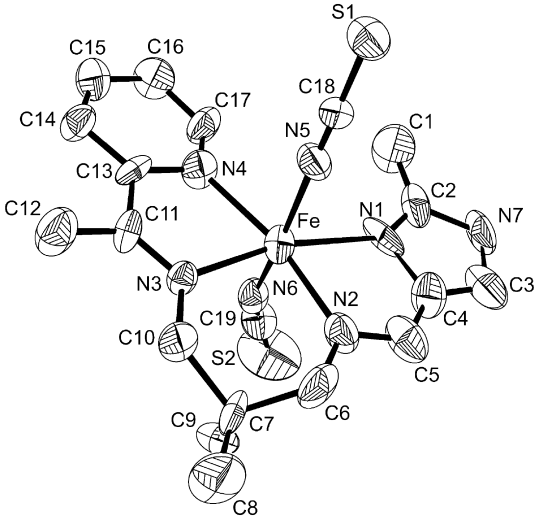


Fig. 5. ORTEP plot of complex **9** at the 30% probability level. H-atoms have been omitted for clarity.

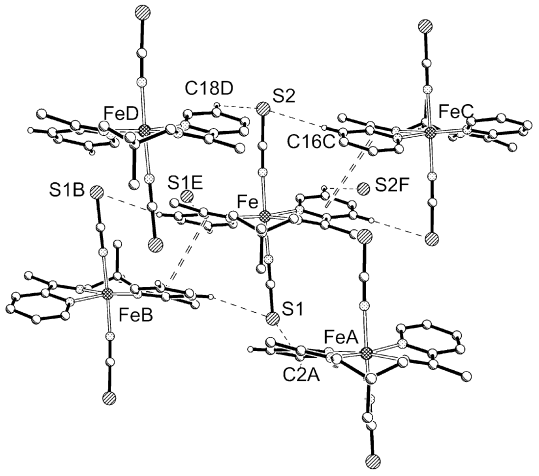


Fig. 6. Intermolecular interactions responsible for the supramolecular structure of $[FeL^{A}(NCS)_2]$ (**1**). π–π stacked pairs of pyridine rings are linked by broken double lines.

packing, as evidenced by the short interplanar (3.64 and 3.93 Å) and centroid to centroid (3.88 and 4.47 Å) distances between interacting pyridine rings.

The asymmetrical unit of **2** contains two crystallographically independent $[FeL^{B1}(NCS)_2]$ complex molecules denoted A and B (Fig. 7). Molecules A and B are linked

Table 2
Selected bond lengths (Å) and angles (°) for complexes **1**, **2**, **3**, **7** and **9**

Compound	$[FeL^{A}(NCS)_2]$ (**1**)	$[FeL^{B1}(NCS)_2]$ (**2**)		$[FeL^{B2}(NCS)_2]$ (**3**)	$[FeL^{C3}(NCS)_2]$ (**7**)	$[FeL^{C5}(NCS)_2]\cdot H_2O$ (**9**)
		Molecule A	Molecule B			
Fe–N1	1.964(5)	2.216(2)	2.241(2)	2.2838(11)	2.28(2)	2.188(17)
Fe–N2	1.953(6)	2.188(2)	2.191(2)	2.1603(11)	2.11(2)	2.158(15)
Fe–N3	1.939(5)	2.180(2)	2.194(2)	2.2170(10)	2.284(15)	2.184(13)
Fe–N4	1.961(6)	2.216(2)	2.245(2)	2.2178(10)	2.31(2)	2.125(15)
Fe–N5	1.938(6)	2.189(3)	2.115(3)	2.1124(12)	2.109(15)	2.135(10)
Fe–N6	1.939(6)	2.121(3)	2.132(3)	2.1409(12)	2.082(16)	2.112(12)
N1–Fe–N2	81.3(3)	77.35(9)	77.03(9)	76.09(4)	79.2(9)	76.3(8)
N1–Fe–N4	102.1(2)	118.05(9)	120.42(9)	120.10(4)	117.3(8)	119.5(8)
N2–Fe–N3	96.8(2)	87.10(8)	86.05(9)	86.58(4)	90.4(9)	88.5(7)
N3–Fe–N4	80.6(2)	77.46(8)	76.43(8)	77.13(4)	73.2(8)	75.6(6)
N5–Fe–N6	173.3(2)	172.36(10)	168.90(11)	166.04(5)	168.8(6)	164.2(5)

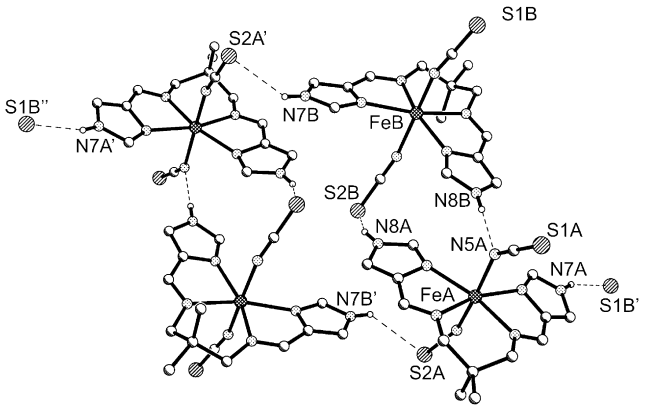


Fig. 7. Intermolecular interactions responsible for the supramolecular structure of $[FeL^{B1}(NCS)_2]$ (**2**). Metric parameters (d, Å; ∠, °): N7A···S1B′, 3.296(3); H···S1B′, 2.48; ∠N7A–H···S1B′, 160.1; N8A···S2B, 3.353(3); H···S2B, 2.62; ∠N8A–H···S2B, 144.4; N8B···N5A, 2.887(4); H···N5A, 2.03; ∠N8B–H···N5A, 172.0; N7B···S2A″, 3.339(2); H···S2A″, 2.70; ∠N7B–H···S2A″, 132.4; symmetry codes: (′) x, $y-1$, z; (″) $-x+1$, $-y+1$, $-z$.

into a 3D supramolecular network via NH···S and NH···N hydrogen bonds, responsible for the crystal packing. A view of this supramolecular network showing four H-bonded molecules is displayed in Fig. 7, along with the hydrogen-bonding parameters. The four non-coordinated nitrogen atoms of molecules A and B act as proton donors, thus fulfilling all H-bonds opportunities in the crystal. The complex molecules inside each [A, B] pair are linked through N8B–H···N5A and N8A–H···S2B hydrogen bonds. It is noteworthy, that one of these hydrogen bonds involves as acceptor the nitrogen atom N7A coordinated to FeA, while the other one involves as acceptor the non-coordinated atom S2B. Further association of the complex molecules results from the N7B–H···S2A short contact which leads to the formation of tetra-molecular centrosymmetrical aggregates and finally to a 3D network through the N7A–H···S1B′ hydrogen bond (Fig. 7).

The crystal packing of **3** results from an extended 3D network of intermolecular interactions. Each $[FeL^{B2}(NCS)_2]$ complex molecule is involved in NH···S hydrogen bonds with its three nearest neighbors. A view of the supramolecular network showing four H-bonded molecules is displayed in Fig. 8, along with the hydrogen-bonding parameters, illustrating how this 3D supramolecular network is generated by two short intermolecular contacts involving the two non-coordinated imidazole nitrogen atoms and both sulfur atoms of the coordinated NCS^- anions. As for compound **2**, all H-bond opportunities are realized.

The molecular structure and crystal packing of **7** are shown in Fig. 9. The latter consists of alternate two-dimensional layers oriented along an *ac* crystallographic plane. Each layer is built from infinite chains connected through short intermolecular contacts (3.797(6) Å) between the S1 and S2 atoms related by translation along *a*. Two types of interactions are responsible for the association of the neutral $[FeL^{C3}(NCS)_2]$ molecules into a chainlike structure:

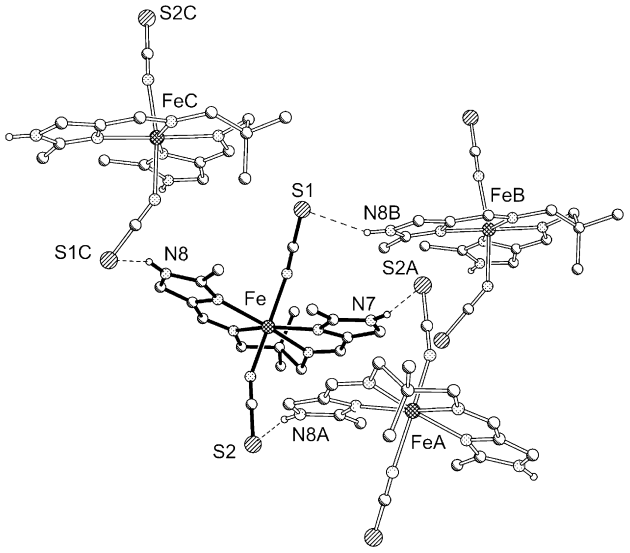


Fig. 8. Intermolecular interactions responsible for the supramolecular structure of $[FeL^{B2}(NCS)_2]$ (**3**). Metric parameters (d, Å; ∠, °): N7···S2′, 3.320(1); H···S2′, 2.457; ∠N7–H···S2′, 146.7°; N8···S1″, 3.340(1); H···S1″, 2.569; ∠N8–H···S1″, 166.7°; symmetry codes: (′) $1-x$, $1-y$, $2-z$; (″) $1.5-x$, $0.5+y$, $1.5-z$.

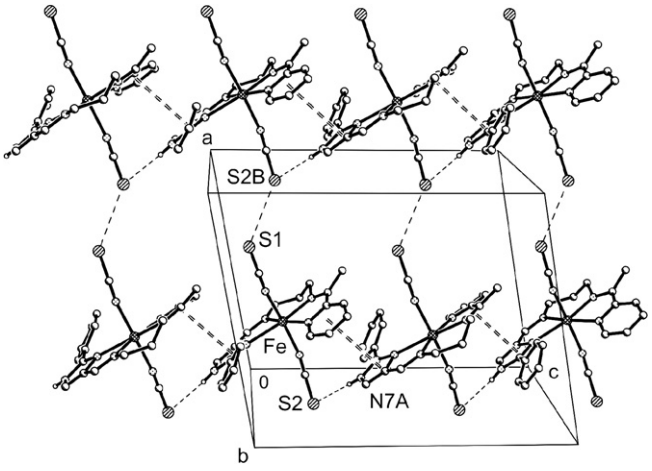


Fig. 9. Projection of the crystal structure of $[FeL^{C3}(NCS)_2]$ (**7**) perpendicularly to an *ac* plane. Centroid to centroid distances between overlapping rings are materialized by broken double lines.

(i) the N7–H···S2′ (x, $0.5-y$, $-0.5+z$) hydrogen bond (N7···S2′, 3.37(2) Å; H···S2′, 2.52 Å; ∠N7–H···S2′, 170.3°); (ii) the π-stacking interaction between the pyridine and imidazole rings of adjacent molecules (centroid to centroid distances of 3.87 Å).

A view of the crystal packing of complex **9** is shown in Fig. 10. The supramolecular network is built from aggregates of complex molecules connected via two intermolecular H-bonds through the solvated water molecules. The water molecule acts as proton acceptor towards the non-coordinated imidazole nitrogen atom (N7···O1w, 2.83(2) Å; H···O1w, 1.97 Å; ∠N7–H···O1w, 173.8°). The water molecule also acts as proton donor towards the sulfur atom S2 of the symmetry related ($0.5-x$, $y-0.5$, $z-0.5$) complex molecule (O1w···S2′, 3.59(2) Å; H···S2′,

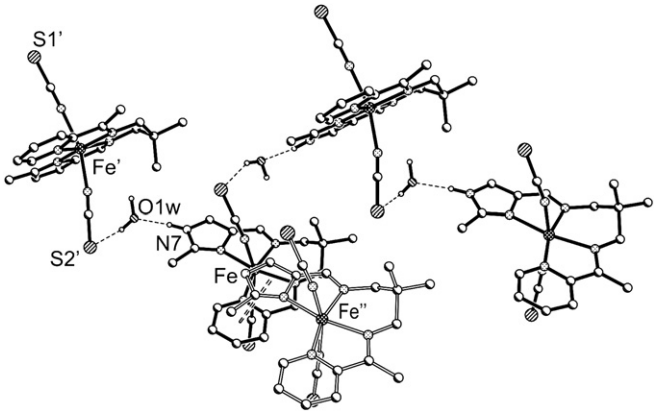


Fig. 10. View of the crystal packing of $FeL^{C5}(NCS)2] \cdot H_2O$ (**9**). Centroid to centroid distances between overlapping rings are materialized by broken double lines.

2.74 Å; ∠O1w–H···S2′, 152.8°). The chains of H-bonded molecules extend into a 3D network through π-stacking interactions between pyridine and imidazole rings belonging to adjacent chains, as evidenced by their centroid to centroid distances of 3.77 Å (Fig. 10). The dihedral angles between π-stacked rings equals 5.3°.

3.3. Magnetic studies

The thermal variation of the magnetic susceptibility χ_M has been explored for complexes **1**–**10** and the $\chi_M T$ data for selected temperatures (T) are collated in Table SM.1. The complete sets of $\chi_M T$ versus T data are shown in Figs. 11 and 12 (**1**–**4**) (**5**–**10**). The $\chi_M T$ product for **1** remains lower than 0.12 $cm^3\ mol^{-1}$ K between 110 and 400 K, indicating that the iron(II) center in this material is LS over the whole temperature range. The $\chi_M T$ product for the $[FeL^{Bx}(NCS)_2]$ complexes **2**–**4** is comprised between 4.12 and 3.70 $cm^3\ mol^{-1}$ K in the 80–300 K temperature range, indicating that the iron(II) center in this series of materials is HS over the whole temperature range. These data agree with the structural studies of complexes **1**–**3** that indicate Fe–N bond lengths characteristic of the LS (**1**, 293 K)

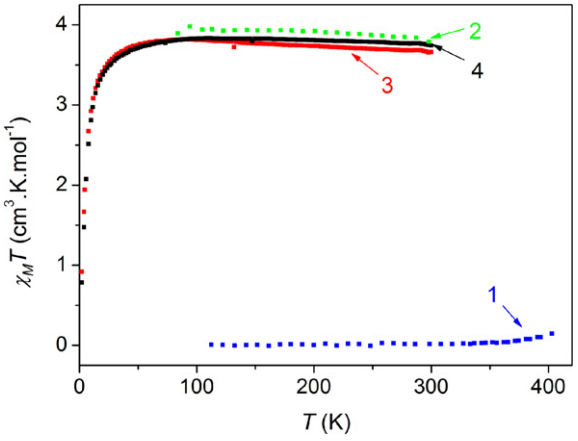


Fig. 11. Thermal variation of the $\chi_M T$ product for $[FeL^{A}(NCS)_2]$ (**1**), and the $[FeL^{Bx}(NCS)_2]$ complexes **2**–**4**.

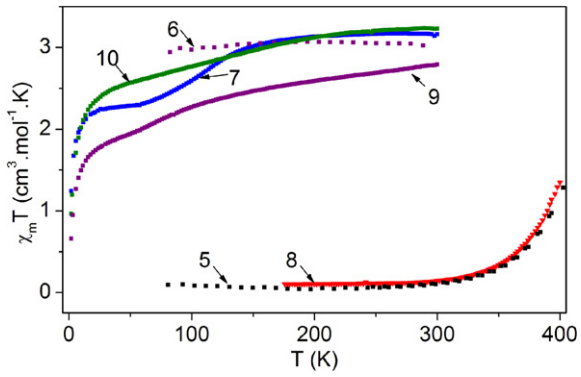


Fig. 12. Thermal variation of the $\chi_M T$ product for the $[FeL^{Cx}(NCS)_2]$ complexes **5**–**10**.

and HS (**2**, 200 K; **3**, 180 K) states, respectively. However, the $\chi_M T$ product at room temperature for **2**–**4**, as well as that for **7** and **10** that will be discussed next, is higher than the spin-only value of ~3 $cm^3\ mol^{-1}$ K expected for $S = 2$ ($g = 2$), as often observed for HS Fe^{II} compounds. The presence of small amounts of HS Fe^{III} (possibly resulting from oxidation of the prepared Fe^{II} materials) being discarded by their Mössbauer spectra (see following subsection), these high $\chi_M T$ values are attributed to operation of spin-orbit coupling (SOC). The $^5T_2$ ground state is split by SOC yielding levels separated by energies on the order of kT (thermally populated in the high temperature range) which results in slightly temperature dependent $\chi_M T$ values above ca. 60 K [34].

With the exception of compound **6**, and at variance with the two previous series, the $\chi_M T$ product for the $[FeL^{Cx}(NCS)_2]$ complexes **5**–**10** is not constant over the explored temperature range (Fig. 12). The $\chi_M T$ product for complexes **7** and **10** (R_2(imidazole) = Ph) is practically constant from 300 to 160 K and characteristic of a large predominance of HS Fe^{II}. Then it decreases between 150 and 50 K: for **7**, $\chi_M T$ decreases from 3.03 to 2.25 $cm^3\ mol^{-1}$ K, indicating a partial HS → LS transition centered around 100 K of ca. 20% Fe^{II} centers. The transition is much more gradual for **10** (Table SM.1). The thermal variation of the $\chi_M T$ product for complex **9** (R_1 = Me, R_2(imidazole) = Me) showing a very gradual and partial SC between 250 and 50 K (ca. 25%) is similar to that described above for **7** and **10** (R_2(imidazole) = Ph). All three compounds exhibit a sharp $\chi_M T$ decrease below 30 K resulting from zero field splitting (ZFS) of HS Fe^{II}. The $\chi_M T$ product for complex **6** (R_1 = H, R_2(imidazole) = Me) is practically constant over the 80–300 K temperature range indicating the absence of SC for Fe^{II} in this material above 80 K.

On the other hand, the magnetic behavior of complexes **5** and **8** (R_2(imidazole) = H) is strikingly different: their $\chi_M T$ product, practically constant and lower than 0.10 (**5**) and 0.13 (**8**) $cm^3\ mol^{-1}$ K from 80 to 300 K, is characteristic of LS Fe^{II}. Then, above 330 K, $\chi_M T$ increases up to 1.29 and 1.37 $cm^3\ mol^{-1}$ K at 400 K for **5** and **8**, respectively, indicating a LS → HS transition centered above

400 K (ca. 30% Fe^{II} centers are involved between 330 and 400 K).

3.4. Mössbauer spectroscopy

Mössbauer spectra have been recorded at selected temperatures in the 20–400 K range for complexes **1**–**10**. Values of the Mössbauer parameters (isomer shift, δ, quadrupole splitting, ΔE_Q, and line width, Γ) resulting from fitting the 80 and 293 K spectra are collated in Table SM.2. The isomer shift values slightly decrease with increasing temperature, indicating operation of second-order Doppler effect [35].

3.4.1. $[FeL^{A}(NCS)_2]$ and $[FeL^{Bx}(NCS)_2]$ complexes

As expected from the structural and magnetic data, the Mössbauer spectrum of **1** at 293 K consists of a unique doublet characteristic of LS Fe^{II} (δ, 0.328(2) mm s^{-1}; ΔE_Q, 0.865(3) mm s^{-1}). In agreement with the structural and magnetic data, Mössbauer spectra of complexes **3** and **4**, recorded between 80 and 293 K, show a unique quadrupole split doublet characteristic of HS Fe^{II} (Table SM.2). At variance with those of **3** and **4**, the Mössbauer spectra of **2** evidence two HS doublets in agreement with the presence of two distinct Fe^{II} sites, Fe^{II}(A) and Fe^{II}(B), in the crystal structure. These doublets present similar isomer shifts (~1.15 mm s^{-1} at 80 K, Table SM.2) as expected for identical N_6 donor sets around the Fe^{II}(A) and Fe^{II}(B) sites and quite different ΔE_Q values (~1.51 and ~2.58 mm s^{-1} at 80 K for Fe^{II}(A) and Fe^{II}(B), respectively), in agreement with different low symmetry environments [36]. The differences in Fe–N bond lengths and N–Fe–N angles associated to the different hydrogen contacts lead to significant differences in symmetry of the ligand environment for the Fe^{II} centers of molecules A and B, see Section 3.2.

3.4.2. $[FeL^{Cx}(NCS)_2]$ complexes

The Mössbauer spectra of complexes **6**–**10** confirm the spin-states deduced from the magnetic data for these materials; however, due to poor counting statistics, the high temperature spectra (350–400 K) of complexes **5** and **8** could not be fitted. As an example, in the following we describe the behavior of complex **7**, $[FeL^{C3}(NCS)_2]$, for which representative Mössbauer spectra recorded in the cooling mode are shown in Fig. 13. These spectra, measured in the 20–293 K range, confirm the partial SC deduced from the magnetic measurements.

The relative area of the HS doublet ($\delta = 1.113(2)$ and $\Delta E_Q = 2.563(4)$ mm s^{-1} at 80 K) slightly decreases from 80% at 293 K to 60% at 20 K, confirming the gradual and incomplete character of the SC in this material. The Mössbauer parameters of the LS doublet ($\delta = 0.439(3)$ and $\Delta E_Q = 0.732(5)$ mm s^{-1} at 80 K) are in agreement with previously reported values [4,18,35].

Comparison of Table SM.1 and Figs. 11 and 12 on the one hand to Table SM.2 and Fig. 13 on the other hand illustrates how important it is to use a local probe like Mössbauer spectroscopy in addition to bulk susceptibility measurements in order to assess the presence or absence of SC, and the relative percentages of spin isomers. Among compounds **6**–**10** for example, **7** shows the second highest $\chi_M T$ product in the high temperature range, suggesting the absence of LS fraction at high temperature. However, Mössbauer spectroscopy evidences a partial SC with ~20% of residual LS fraction at 293 K, the second highest among materials **6**–**10**. On the other hand, **6** shows the lowest $\chi_M T$ product at room temperature while Mössbauer spectroscopy evidences the absence of LS fraction at 293 K.

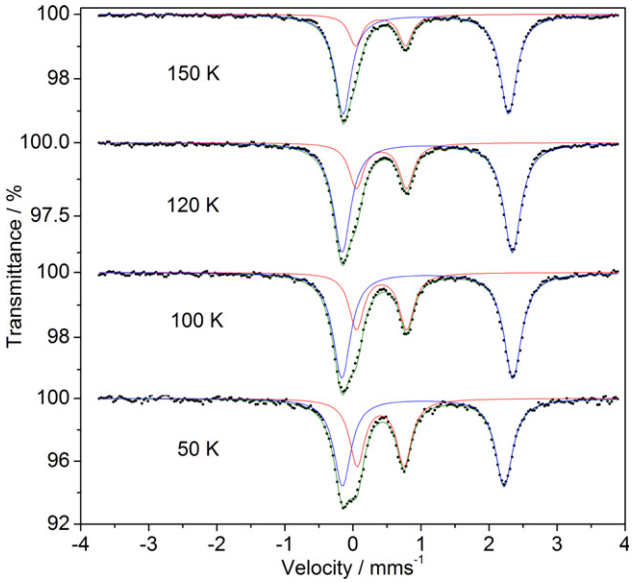


Fig. 13. Selected Mössbauer spectra of $[FeL^{C3}(NCS)_2]$ (**7**).

3.5. IR spectroscopy

The IR study has been focussed on the NCS stretching absorptions (2000–2100 cm^{-1} range) which constitute a good sensor for the *cis* or *trans* conformation of coordinated thiocyanate anions. Usually, *trans* isomers give a single absorption whereas *cis* isomers are characterized by a splitting of the ν_{CN} absorption [15b,37]. However, this criterion must be considered with much caution because the splitting of this band is very sensitive to slight deformations of the coordination sphere (in particular the N–M–N angle between the two thiocyanate ligands coordinated to the metal center). The structural study of complex **3** has evidenced a distorted octahedral geometry around Fe^{II} with a *trans* conformation of the thiocyanate ligands. Two well distinct ν_{CN} absorption bands were observed in the IR spectra at 2093 and 2065 cm^{-1} in compliance with the strong deviation from an ideal *trans* conformation evidenced by the 158.8° (C17–N8–Fe) and 137.5° (C16–N7–Fe) angles. The same conclusion can be drawn from the IR spectra of complexes **2** and **4**, as well as for complexes **5**–**10** ($[FeL^{Cx}(NCS)_2]$ series). The larger splitting (64 cm^{-1})

observed for **4** suggests a larger deformation of the ligand environment symmetry around Fe^{II}, in agreement with the large quadrupole splitting evidenced by Mössbauer spectroscopy. The third band (low intensity) observed for **2** can be explained by the presence of two types of NCS ligands, depending on the atom through which they participate into hydrogen bonds (NH···SCN or NH···NCS that leads to two Fe^{II} sites distinguishable crystallographically and by Mössbauer spectroscopy, see the corresponding subsections above). In line with our previous report on parent iron(II) compounds with related dissymmetric Schiff bases [32], the $\nu_{C=N}$(imine) absorptions observed for compounds **1**–**10** do not seem to depend on the spin-state of iron(II). This is possibly because they are no longer pure $\nu_{C=N}$ (imine) stretches, but correspond to the simultaneous involvement of $\nu_{C=N}$(imine), $\nu_{C=N}$(py) and $\nu_{C=N}$(imidazole) vibrators.

4. Discussion

Tetradentate ligands including exclusively nitrogen donors have been scarcely used in association with coordinating pseudohalide anions to prepare Fe^{II} SC complexes with a N_6 ligand environment. The first examples were reported by Toftlund et al. [14a]. and included tripodal ligands of the tris-pyridylamine (tpa) type associated with two *cis*-coordinated pseudohalide anions: varying the tpa substituents or the pseudohalide yielded different SC behaviors or mixtures of spin isomers. A related type of Fe^{II} SC material, also including a tripodal N_4 ligand (dppa) and two *cis*-coordinated NCS^-, was reported later by Matouzenko et al. [14c]. Finally, Toftlund et al. [14b] also reported a series of Fe^{II} compounds including acyclic Schiff bases resulting from condensation of R-pyridinecarboxaldehydes (R = H, Me) or acetylpyridine with ethylenediamine or propylenediamine (bpn ligand type) associated with two pseudohalide anions: again, depending on the ligand substituents and alkyl bridge, they observed different magnetic behaviors. While the *cis*-coordination mode of NCS anions was imposed by the tpa or the dppa topology, no such constraint was imposed by the bpn ligands; however the NCS anions were also *cis*-coordinated in the bpn series of Fe^{II} compounds [14b]. The diversity of reported SC behaviors in contrast to the scarcity of SC materials built from tetradentate ligands including exclusively nitrogen donors associated with coordinating pseudohalide anions led us to explore the use of such ligand environments with the aim to tune the SC behavior through minute changes in the ligand. An additional incentive to this study was the possibility to benefit from the versatile arrangement of the two pseudohalide ligands: indeed, while the pseudohalide anions are *cis*-coordinated in many SC materials [1,38], a recent work has evidenced that the *trans*-NCS isomer of a Fe^{II} compound including a bidentate triaryltriazole ligand exhibits SC while its *cis*-NCS counterpart is a HS material [15b].

In this study, the 2:1 condensation of acetylpyridine and 2,2-dimethyl-1,3-diaminopropane followed by reaction with ferrous thiocyanate yielded $[FeL^A(NCS)_2]$ (**1**) where the tetradentate ligand is the symmetrical bis-schiff base including two N(pyridine) and two N(imine) donors. This new ferrous material, although based on a tetradentate ligand closely related to bptn [14b] (bptn results from the 2:1 condensation of pyridine carboxaldehyde with 1,3-diaminopropane), is significantly different from $[Fe(bptn)(NCS)_2]$: while the NCS ligands are *cis* in the latter, they are *trans* in compound **1**, and while $[Fe(bptn)(NCS)_2]$ is a SC material, **1** is LS in the 80–400 K temperature range. The differences between **1** and $[Fe(bptn)(NCS)_2]$ are the substituents (Me, H, respectively) on the central carbon atom of the alkyl chain, the substituents (Me, H, respectively) on the imine carbon atoms, and the *trans* versus *cis* arrangement of the NCS ligands. The possible respective roles of these three factors in the difference of electronic behavior between the two materials cannot be untangled yet: it is one of the aims of [32], this report, and a paper in preparation, [40], to independently assess the role of each of these factors.

Condensation of 2R-imidazole-4-carboxaldehyde with the same diamine in the 2:1 ratio followed by reaction with ferrous thiocyanate was expected to yield ferrous complexes with symmetrical tetradentate ligands similar to that in **1**, but better suited to stabilize HS Fe^{II} or to yield Fe^{II} SC materials, depending on the decrease in ligand field on going from L^A to L^{Bx}, and on the *cis* or *trans* arrangement of the thiocyanates ligands. Indeed, compounds **2**–**4** include the expected symmetrical tetradentate ligands L^{Bx} and two *trans*-coordinated thiocyanates. As shown by the results described in the previous section, the ligand field generated by the L^{Bx} ligands associated with two *trans*-NCS stabilizes the HS Fe^{II} state, regardless of the imidazole substituent R_2 (H, Me, Ph). This is in line with the significant difference between L^A and L^{Bx} that results from the replacement of two pyridyl (strong ligand field N donor) by two imidazolyl rings (weaker ligand field N donor).

Considering that the NCS^- ligands are *trans*-coordinated in compounds **1**–**4**, regardless of the tetradentate ligand (L^A or L^{Bx}), it was anticipated that combination of pyridyl and imidazolyl rings to yield a dissymmetrical L^{Cx} bis-Schiff base chelated to Fe^{II} would not affect the *trans*-coordination mode of the NCS^- anions. Then, the only difference in ligand field would result from the change in the tetradentate ligand. Indeed, the results described in the previous section confirm that the NCS^- ligands are *trans*-coordinated in compounds **5**–**10**, allowing us to consider the differences between the tetradentate ligands L^A, L^{Bx} and L^{Cx} as the sole origin of the different electronic behaviors among all materials reported in this study.

Then, comparison of the electronic behavior of **1**–**4** on the one hand to that of **5**–**10** on the other hand evidences that combination of pyridyl and imidazolyl rings to yield a dissymmetrical tetradentate L^{Cx} ligand has indeed

allowed to bring the ligand field from the high (**1**) and low-field (**2**–**4**) ranges to the intermediate SC ligand field range (**5**–**10**).

Within the series, the differences originate from: (i) the substituents on the central carbon atom of the alkyl chain ($R_1 = H$ (**5**–**7**), Me (**8**–**10**)), and (ii) the 2-substituent on the imidazolyl ring ($R_2 = H$ (**5**, **8**), Me (**6**, **9**), Ph (**7**, **10**)). The most important difference in the SC properties within this series is the SC temperature $T_{1/2}$: it is higher than 400 K for **5** and **8**, while it is around 100 K for the remaining compounds. In other words, substitution of the phenyl or methyl group by an hydrogen atom at the C2 imidazolyl shifts the transition temperature $T_{1/2}$ by ~300 K towards higher temperatures.

This result evidences that a prominent electronic effect is exerted by R_2 but not R_1: in other words, the tuning of the ligand field is essentially obtained through modifications of the heterocyclic aromatic rings of the tetradentate ligand. In this report we concentrate on the imidazolyl ring; the effect of pyridyl ring substituents has been described in a previous report [32]. Considering that the ligand fields exerted by L^{C1} (**5**) and L^{C4} (**8**) ($R_2 = H$) are weaker (higher $T_{1/2}$) than those exerted by the remaining L^{Cx} ligands ($R_2 =$ Me or Ph), it may be suggested that the steric effect of the R_2 substituent overpasses its inductive (+I, Me) or mesomeric (+M, Ph) effect. As estimated through roughly approximated $T_{1/2}$ values, the role of R_1 in tuning the ligand field is much more limited. However, although subtle, the trend is the same within the three pairs (**5**, **8**), (**6**, **9**) and (**7**, **10**): the lower $T_{1/2}$ is associated with $R_1 = H$ (**5**–**7**). This seems to indicate that the inductive effect of R_1 (Me for **8**–**10**) slightly lowers the ligand field with regard to its counterpart (**5**–**7**) in each pair. This trend is further substanciated by the results described in [32].

For clarity, only intramolecular effects have been taken into account in the above considerations: this is of course a first approximation because intermolecular effects may also indirectly but significantly contribute to the ligand field onto the Fe^{II} center [39].

Acknowledgements

Financial support by the French Ministry for Education, Research, and Technology, through a doctoral grant to N.B., and by the CNRS-DFG collaborative programme, through a postdoctoral grant to S.S. are gratefully acknowledged.

Appendix A. Supplementary material

CCDC 613879, 613880, 613881, 613882 and 613883 contain the supplementary crystallographic data for **1**, **2**, **3**, **7** and **9**. These data can be obtained free of charge via htpp://www.ccdc.cam.ac.uk/conts/retrieving.html, or from the Cambridge Crystallographic Data Centre, 12 Union Road, Cambridge CB2 1EZ, UK; fax: +(44) 1223-336-033; or e-mail: deposit@ccdc.cam.ac.uk. Supplementary data associated with this article can be found, in the online version, at doi:10.1016/j.poly.2006.12.017.

References

[1] P. Gütlich, H.A. Goodwin, Topics Curr. Chem. 233 (2004) 1–47, and references cited therein.
[2] O. Kahn, J.-P. Launay, Chemtronics 3 (1988) 140.
[3] (a) O. Kahn, J. Krober, C. Jay, Adv. Mater. 4 (1992) 718;
(b) O. Kahn, C. Jay-Martinez, Science 279 (1998) 44.
[4] P. Gütlich, H.A. Goodwin, Topics Curr. Chem. 233–235 (2004).
[5] (a) V. Petrouleas, J.-P. Tuchagues, Chem. Phys. Lett. 137 (1987) 21;
(b) D. Boinnard, A. Bousseksou, A. Dworkin, J.-M. Savariault, F. Varret, J.-P. Tuchagues, Inorg. Chem. 33 (1994) 271;
(c) G. Psomas, N. Bréfuel, F. Dahan, J.-P. Tuchagues, Inorg. Chem. 43 (2004) 4590;
(d) L. Salmon, A. Bousseksou, B. Donnadieu, J.-P. Tuchagues, Inorg. Chem. 44 (2005) 1763.
[6] S.M. Nelson, P.D.A. McLlroy, C.S. Stevenson, E. König, G. Ritter, J. Waigel, J. Chem. Soc., Dalton Trans. (1986) 991.
[7] W.S. Kelly, G.H. Ford, S.M. Nelson, J. Chem. Soc. A (1971) 388.
[8] M. Bacci, C.A. Ghilardi, A. Orlandini, Inorg. Chem. 23 (1984) 388.
[9] (a) W. Levason, C.A. McAuliffe, M.M. Khan, S.M. Nelson, J. Chem. Soc., Dalton. Trans. (1975) 1778;
(b) F. Cecconi, M. Di Varia, S. Midollini, A. Orlandini, L. Sacconi, Inorg. Chem. 20 (1981) 3423;
(c) E. König, G. Ritter, S.K. Kulshreshtha, J. Waigel, L. Sacconi, Inorg. Chem. 23 (1984) 1241;
(d) C.-C. Wu, J. Jung, P.K. Gantzel, P. Gütlich, D.N. Hendrickson, Inorg. Chem. 36 (1997) 5339.
[10] (a) L.J. Wilson, D. Georges, M.A. Hoselton, Inorg. Chem. 14 (1975) 2968;
(b) H. Toftlund, S. Yde-Andersen, Acta. Chem. Scand. A35 (1981) 575;
(c) L.L. Martin, K.S. Hagen, A. Hauser, R.L. Martin, A.M. Sargeson, J. Chem. Soc., Chem. Commun. (1988) 1313;
(d) A.H.R. Obaidi, J.J. McGarvey, K.P. Taylor, S.E.J. Bell, K.B. Jensen, H. Toftlund, J. Chem. Soc., Chem. Commun. (1993) 536;
(e) A.H.R. Al-Obaidi, K.B. Jensen, J.J. McGarvey, H. Toftlund, B. Jensen, S.E.J. Bell, J.G. Carroll, Inorg. Chem. 35 (1996) 5055;
(f) Y. Sunatsuki, Y. Ikuta, N. Matsumoto, H. Ohta, M. Kojima, S. Iijima, S. Hayami, Y. Maeda, S. Kaizaki, F. Dahan, J.-P. Tuchagues, Angew. Chem., Int. Ed. 42 (2003) 1614;
(g) Y. Ikuta, M. Ooidemizu, Y. Yamahata, M. Yamada, S. Osa, N. Matsumoto, S. Iijima, Y. Sunatsuki, M. Kojima, F. Dahan, J.-P. Tuchagues, Inorg. Chem. 42 (2003) 7001;
(h) M. Yamada, M. Ooidemizu, Y. Ikuta, S. Osa, N. Matsumoto, S. Iijima, M. Kojima, F. Dahan, J.-P. Tuchagues, Inorg. Chem. 42 (2003) 8406;
(i) Y. Sunatsuki, H. Ohta, M. Kojima, Y. Ikuta, Y. Goto, N. Matsumoto, S. Iijima, H. Akashi, S. Kaizaki, F. Dahan, J.-P. Tuchagues, Inorg. Chem. 43 (2004) 4154;
(j) S. Arata, H. Torigoe, T. Iihoshi, N. Matsumoto, F. Dahan, J.-P. Tuchagues, Inorg. Chem. 44 (2005) 9288.
[11] (a) R.N. Sylva, H.A. Goodwin, Aust. J. Chem. 20 (1967) 479;
(b) R.N. Sylva, H.A. Goodwin, Aust. J. Chem. 21 (1968) 1081;
(c) E. König, G. Ritter, H.A. Goodwin, Chem. Phys. 1 (1973) 17;
(d) H.A. Goodwin, R.N. Sylva, Aust. J. Chem. 21 (1968) 2881;
(e) H.A. Goodwin, D.W. Mather, Aust. J. Chem. 25 (1972) 715;
(f) K.H. Sugiyarto, D.C. Craig, A.D. Rae, H.A. Goodwin, Aust. J. Chem. 46 (1993) 1269;
(g) B.J. Sugiyarto, D.C. Craig, A.D. Rae, H.A. Goodwin, Aust. J. Chem. 47 (1994) 869;
(h) K.H. Childs, D.C. Craig, K.A. Ross, M.L. Scudder, H.A. Goodwin, Aust. J. Chem. 47 (1994) 891;
(i) G. Lemercier, A. Bousseksou, M. Verelst, J.-P. Tuchagues, F. Varret, J. Magn. Magn. Mater. 150 (1995) 227;

(j) A. Bousseksou, M. Verelst, H. Constant-Machado, G. Lemercier, J.-P. Tuchagues, F. Varret, Inorg. Chem. 35 (1996) 110;
(k) G. Lemercier, M. Verelst, A. Bousseksou, F. Varret, J.-P. Tuchagues, Magnetism: A supramolecular function, in: O. Kahn (Ed.), NATO ASI Series C, Vol. 484, Kluwer Academic Publishers, Dordrecht, 1996, p. 335;
(l) A. Thiel, A. Bousseksou, M. Verelst, F. Varret, J.-P. Tuchagues, Chem. Phys. Lett. 302 (1999) 549.

[12] (a) G.A. Renovitch, W.A. Baker, J. Am. Chem. Soc. 89 (1967) 6377;
(b) M. Sorai, J. Ensling, K.M. Hasselbach, P. Gütlich, Chem. Phys. 20 (1977) 197;
(c) A.M. Greenaway, E. Sinn, J. Am. Chem. Soc. 100 (1978) 8080;
(d) A.M. Greenaway, C.J. O'Connor, A. Schrock, E. Sinn, Inorg. Chem. 18 (1979) 2692;
(e) B.A. Katz, C.E. Strouse, J. Am. Chem. Soc. 101 (1979) 6214;
(f) M. Mikami, M. Konno, Y. Saito, Chem. Phys. Lett. 63 (1979) 566;
(g) H.A. Goodwin, R.N. Sylva, Aust. J. Chem. 21 (1968) 83;
(h) R.J. Dosser, W.J. Eilbeck, A.E. Underhill, J. Chem. Soc. A (1969) 810;
(i) D.M.L. Goodgame, A.A.S.C. Machado, Inorg. Chem. 8 (1969) 2031;
(j) Y. Sasaki, T. Shigematsu, Bull. Chem. Soc. Jpn. 46 (1973) 3438;
(k) Y. Sasaki, T. Shigematsu, Bull. Chem. Soc. Jpn. 47 (1974) 109;
(l) D.M.L. Goodgame, Bull. Soc. Chim. Fr. (1972) 3;
(m) J.R. Sams, J.C. Scott, T.B. Tsin, Chem. Phys. Lett. 18 (1973) 451;
(n) J.R. Sams, T.B. Tsin, J. Chem. Soc., Dalton Trans. (1976) 488;
(o) J.R. Sams, T.B. Tsin, Inorg. Chem. 15 (1976) 1544;
(p) A.T. Baker, H.A. Goodwin, Aust. J. Chem. 30 (1977) 771.

[13] (a) E.W. Müller, J. Ensling, H. Spiering, P. Gutlich, Inorg. Chem. 22 (1983) 2074;
(b) O. Roubeau, A.F. Stassen, I. Ferrero Gramage, E. Codjovi, J. Linares, F. Varret, J.G. Haasnoot, J. Reedjik, Polyhedron 20 (2001) 1709.

[14] (a) F. Hojland, H. Toftlund, S. Yde-Andersen, Acta Chem. Scand. A37 (1983) 251;
(b) H. Toftlund, E. Pedersen, S. Yde-Andersen, Acta Chem. Scand. A38 (1984) 693;
(c) G.S. Matouzenko, A. Bousseksou, S. Lecocq, P.J. van Koningsbruggen, M. Perrin, O. Kahn, A. Collet, Inorg. Chem. 36 (1997) 5869.

[15] (a) J.-F. Létard, P. Guionneau, E. Codjovi, D. Lavastre, G. Bravic, D. Chasseau, O. Kahn, J. Am. Chem. Soc. 119 (1997) 10861;
(b) D. Zhu, Y. Xu, Z. Yu, Z. Guo, H. Sang, T. Liu, X. You, Chem. Mater. 14 (2002) 838, and references cited therein.

[16] (a) A.L. Nivororozhkin, H. Toftlund, M. Nielsen, J. Chem. Soc., Dalton. Trans. (1994) 361;
(b) G. Brewer, J. Jasinski, W. Mahany, L. May, S. Prytkov, Inorg. Chim. Acta 232 (1995) 183.

[17] M.A. Hoselton, L.J. Wilson, R.S. Drago, J. Am. Chem. Soc. 97 (1975) 1722.

[18] N. Bréfuel, C. Lepetit, S. Shova, F. Dahan, J.-P. Tuchagues, Inorg. Chem. 44 (2005) 8916.

[19] N.E. Erikson, N. Sutin, Inorg. Chem. 5 (1966) 1834.

[20] K. Lagarec, Recoil, Mössbauer Analysis Software for windows. <http://www.physics.uottawa.ca/~recoil>.

[21] STOE, IPDS Manual. Version 2.93. Stoe & Cie, Darmstadt, Germany, 1997.

[22] CrysAlis RED, Version 1.170.32, Oxford Diffraction Ltd., Oxford, UK, 2003.

[23] G.M. Sheldrick, SHELXS-97. Program for Crystal Structure Solution. University of Göttingen, Göttingen, Germany, 1990.

[24] G.M. Sheldrick, SHELXL-97. Program for the Refinement of Crystal Structures from Diffraction Data. University of Göttingen, Göttingen, Germany, 1997.

[25] International Tables for Crystallography, Vol. C, Kluwer Academic Publishers, Dordrecht, The Netherlands, 1992.

[26] L. Zsolnai, H. Pritzkow, G. Huttner, ZORTEP. Ortep for PC, Program for Molecular Graphics, University of Heidelberg, Heidelberg, Germany, 1996.

[27] Stoe, X-SHAPE. Crystal Optimisation for Numerical Absorption Corrections, Revision 1.01. Stoe & Cie, Darmstadt, Germany, 1996.

[28] R.H. Blessing, Acta Crystallogr. A 51 (1995) 33.

[29] J.P. Costes, M.I. Fernadez-Garcia, Inorg. Chim. Acta 237 (1995) 57, and references cited therein.

[30] (a) D.E. Fenton, R. Moody, U. Casellato, P.A. Vigato, R.J. Graziani, Heterocycl. Chem. 22 (1985) 1639;
(b) J.P. Costes, F. Dahan, A. Dupuis, J.P. Laurent, New J. Chem. 21 (1997) 1211.

[31] (a) J.P. Costes, F. Dahan, A. Dupuis, J.P. Laurent, Inorg. Chem. 39 (2000) 169;
(b) J.P. Costes, F. Dahan, A. Dupuis, Inorg. Chem. 39 (2000) 5994;
(c) A. Bencini, J.P. Costes, F. Dahan, A. Dupuis, J. Garcia-Tojal, D. Gatteschi, F. Totti, Inorg. Chim. Acta 357 (2004) 2150.

[32] N. Bréfuel, S. Shova, J. Lipkowski, J.-P. Tuchagues, Chem. Mater. 18 (2006) 5467.

[33] (a) G.R. Desiraju, V. Nalini, J. Mater. Chem. 1 (1991) 201;
(b) J.-A. van Derberg, K.R. Seddon, Crystal Growth Design 3 (2003) 643;
(c) G.R. Desiraju, Chem. Commun. (2005) 2995.

[34] F.E. Mabbs, D.J. Machin, Magnetic and Transition Metal Complexes, Chapman and Hall, London, UK, 1973.

[35] N.N. Greenwood, T.C. Gibbs, Mössbauer Spectroscopy, Chapman and Hall, New York, 1971, pp. 9–11, 50–53.

[36] A.K. Boudalis, J.-M. Clemente-Juan, F. Dahan, J.-P. Tuchagues, Inorg. Chem. 43 (2004) 1574, and references cited therein.

[37] K. Nakamoto, Infrared and Raman Spectra of Inorganic and Coordination Compounds, fourh ed., John Wiley & Sons, New York, 1986.

[38] (a) J.A. Real, J. Zarembovitch, O. Kahn, X. Solans, Inorg. Chem. 26 (1987) 2939;
(b) H. Toftlund, Coord. Chem. Rev. 94 (1989) 67.

[39] J.-P. Tuchagues, A. Bousseksou, G. Molnár, J.J. McGarvey, F. Varret, in: P. Gütlich, H.A. Goodwin (Eds.), Topics Curr. Chem. 235 (2004), pp. 85–103, and references cited therein.

[40] N. Bréfuel, S. Shova, C. Duhayon, J.-P. Tuchagues, in preparation.

Compound **2** has been reported previously by Sievers and Morris [12–14]. It is usually described as a green crystalline material [12,14,15], but is evidently dichroic and the crystals also can appear as maroon-colored.

The infrared spectrum of $Cr(hfac)_3$ matches that reported previously [13]. The spectrum of $Cr(hfac)_2(thf)_2$ is very similar to that of $Cr(hfac)_3$ except that it exhibits additional bands at 1029, 916, 872, and 467 cm^{-1} due to the thf ligands.

2.2. Crystal structures of $Cr(hfac)_2(thf)_2$ and $Cr(hfac)_3$

Compound **1** crystallizes in the tetragonal space group $P4_2/mnm$, with two molecules per unit cell. The crystal data are summarized in Table 1, selected distances and angles are given in Table 2, and the molecular geometry of **1** is shown in Fig. 1. The chromium center, which resides on a site of *mmm* symmetry, is trans octahedral, with the two bidentate hfac ligands in the equatorial plane and the two thf molecules in the axial positions. The Cr–O(hfac) distance of 1.936(3) Å is slightly shorter than the two Cr–O distances of 1.984(3) and 1.979(3) Å present in the square-planar acetylacetonate complex $Cr(acac)_2$ [16]. The 92.7° O–Cr–O bite angle of $Cr(hfac)_2(thf)_2$, on the other hand, is greater than the corresponding 90.3(1)° bite angle of $Cr(acac)_2$ [16]. The Cr–O(thf) distance in **1** of 2.019(6) Å is only slightly longer than the Cr–O(hfac) distances. A large tetragonal distortion is not expected in this complex because no Jahn–Teller effect is operative: the axial ligands are chemically different from the equatorial ligands, and, perforce, the electronic symmetry is already broken.

The structure of $Cr(hfac)_2(thf)_2$ is very similar to those of several reported $Mn(hfac)_2L_2$ compounds, the principal difference being that the M–O(hfac) distances are about 0.15–0.2 Å shorter in **1**, as expected for high-spin Cr(II) and Mn(II) species. For example, the Mn–O(hfac) lengths are 2.120(3)–2.145(4) Å in $Mn(hfac)_2(proxyl)_2$ (proxyl = 2,2,5,5-tetramethylpyrrolidinyl-1-oxy) [17], 2.120(4)–2.160(3) Å in $Mn(hfac)_2(tempo)_2$ (tempo = 2,2,6,6-tetramethylpiperidinyl-1-oxy) [17], 2.169(3)–2.212(3) Å in $Mn(hfac)_2(Him)_2$ (Him = imidazole) [18], and 2.171(2)–2.143(3) Å in $Mn(hfac)_2(NOPy)_2$ (NOPy = 4-(*N*-oxy-*N*-*tert*-butylamino)pyridine) [19].

Crystals of the chromium(III) complex **2**, grown by sublimation, conform to the trigonal space group $P\bar{3}c1$ with six molecules per unit cell, but are twinned by merohedry. Because the volumes of the two twin individuals were very nearly equal (volume fractions of 0.547 and 0.453), the diffraction pattern conforms very closely to that expected for hexagonal symmetry under the space group $P6_3/mcm$. Interestingly, the X-ray diffraction pattern of **2** has previously been indexed to the space group $P6_3/mmc$ but with different cell axes ($a = 21.2$ and $c = 12.4$ Å vs. our finding of $a = 18.1$ and $c = 12.1$ Å) [20]. The different apparent space group and cell dimensions probably are consequences

Table 1
Crystallographic data for $Cr(hfac)_2(thf)_2$ and $Cr(hfac)_3$

	$CrC_{18}H_{18}F_{12}O_6$	$CrC_{15}H_3F_{18}O_6$
Space group	$P4_2/mnm$	$P\bar{3}c1$
Unit cell dimensions		
a (Å)	8.5111(7)	18.0862(11)
b (Å)	8.5111(7)	18.0862(11)
c (Å)	16.585(2)	12.0790(11)
α (°)	90	90
β (°)	90	90
γ (°)	90	120
V (Å^3)	1201.4(2)	3421.8(4)
Z	2	6
M_w	610.32	673.17
ρ_{calc} (g cm^{-3})	1.687	1.960
λ (Å)	0.71073	0.71073
μ_{calc} (cm^{-1})	6.01	6.80
R_1	0.1325	0.1388
wR_2	0.1856	0.1610
T (°C)	−75	−75

$R_1 = \sum(||F_o| - |F_c||)/\sum|F_o|$, $wR_2 = [\sum w(F_o^2 - F_c^2)^2/\sum w(F_o^2)^2]^{1/2}$.

Table 2
Selected bond distances (Å) and bond angles (°) for $Cr(hfac)_2(thf)_2$[a]

Distances			
Cr(1)–O(1)	1.936(3)	C(1)–C(2)	1.510(8)
Cr(1)–O(2)	2.019(6)	C(2)–C(3)	1.381(6)
O(1)–C(2)	1.293(6)	O(2)–C(4)	1.438(9)
C(1)–F(1)	1.312(5)	C(4)–C(5)	1.44(2)
C(1)–F(2)	1.327(7)		
Angles			
O(1)–Cr(1)–O(1)′	180.0	F(1)–C(1)–C(2)	111.8(3)
O(1)–Cr(1)–O(1)″	92.7(2)	F(2)–C(1)–C(2)	113.6(6)
O(1)–Cr(1)–O(1)‴	87.3(2)	O(1)–C(2)–C(3)	127.1(5)
O(1)–Cr(1)–O(2)	90.0	O(1)–C(2)–C(1)	111.7(5)
O(2)–Cr(1)–O(2)	180.0	C(3)–C(2)–C(1)	121.1(5)
C(2)–O(1)–Cr(1)	125.2(3)	C(4)–O(2)–Cr(1)	125.4(5)
F(1)–C(1)–F(2)	106.0(4)	C(5)–C(4)–O(2)	107.6(9)

[a] Primed atoms are related to the unprimed atoms by the transformation $(-x, -y, -z)$, doubly primed atoms by $(-x, -y, z)$, and triply primed atoms by $(x, y, -z)$.

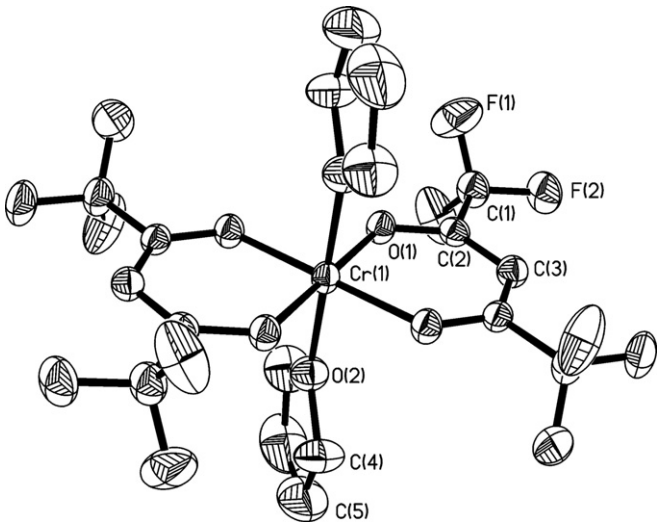


Fig. 1. X-ray crystal structure of $Cr(hfac)_2(thf)_2$ (**1**). The 30% probability density surfaces are shown. Hydrogen atoms have been removed for clarity.

of polymorphism. That polymorphism is likely is shown by the fact that crystals of $Cr(hfac)_3$ are not isomorphous with those of $Fe(hfac)_3$ [21] and $Mn(hfac)_3$ [22]. The latter two complexes crystallize in the monoclinic crystal system, space group $P2_1/c$.

The crystal data for **2** are summarized in Table 1 and the structure is shown in Fig. 2. There are two independent chromium centers in the asymmetric unit, one residing on a site of $\bar{3}$ symmetry and the other on a site of 3 symmetry. We will present the results for the latter molecule, which had the smaller atomic displacement parameters. $Cr(hfac)_3$ is, as expected, an octahedral complex with three equivalent hfac ligands. The two Cr–O distances of 1.943(5) and 1.955(5) Å are very similar to the 1.936(3) Å Cr–O(hfac) distance in the chromium(II) complex **1**; the bite angles of the hfac ligands in **2** are 90.8(2)° (Table 3).

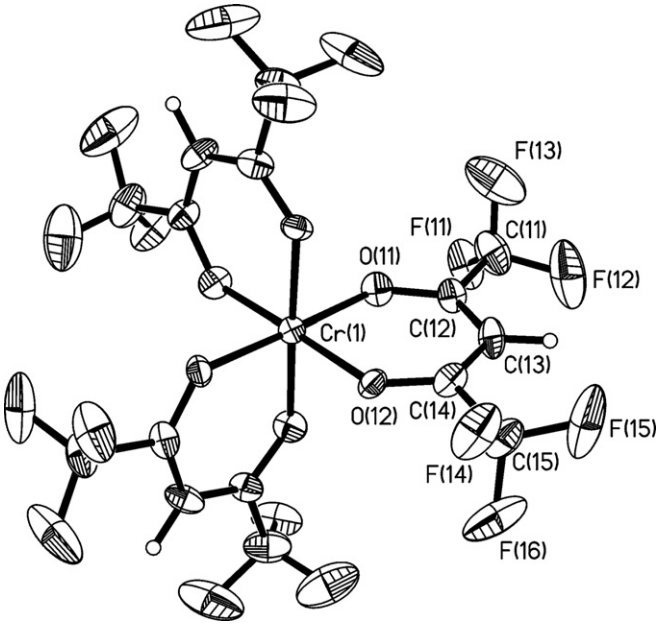


Fig. 2. X-ray crystal structure of $Cr(hfac)_3$ (**2**). The 30% probability density surfaces are shown, except for the hydrogen atoms, which are represented by arbitrarily-sized spheres.

Table 3
Selected bond distances (Å) and bond angles (°) for $Cr(hfac)_3$[a]

Distances			
Cr(1)–O(11)	1.943(5)	C(11)–C(12)	1.483(13)
Cr(1)–O(12)	1.955(5)	C(12)–C(13)	1.373(10)
O(11)–C(12)	1.278(8)	C(13)–C(14)	1.381(10)
O(12)–C(14)	1.249(9)	C(14)–C(15)	1.556(12)
C(11)–F(13)	1.267(12)	C(15)–F(15)	1.295(10)
C(11)–F(11)	1.287(13)	C(15)–F(16)	1.305(10)
C(11)–F(12)	1.347(13)	C(15)–F(14)	1.326(11)
Angles			
O(11)–Cr(1)–O(11)′	90.5(2)	C(12)–C(13)–C(14)	122.2(7)
O(11)–Cr(1)–O(12)	90.8(2)	O(12)–C(14)–C(13)	128.8(7)
O(12)–Cr(1)–O(11)″	178.5(2)	O(12)–C(14)–C(15)	113.2(8)
O(12)–Cr(1)–O(12)′	90.0(2)		

[a] Primed atoms are related to the unprimed atoms by the transformation $(-x+y+1, -x+1, z)$, and doubly primed atoms by $(-y+1, x-y, z)$.

The structure of **2** deduced crystallographically is very similar to that determined previously by electron diffraction. In the gas phase, $Cr(hfac)_3$ adopts a slightly distorted octahedral structure with a Cr–O distance of 1.957(8) Å and an O–Cr–O angle of 87.0° [23]. In the analogous chromium(III) acetylacetonate compound $Cr(acac)_3$ [24], the Cr–O distances lie between 1.942(7) and 1.959(7) Å, and the average bite angle is 91.1°.

The structure is also similar to that of tris(β-diketonate) complexes of other first-row metals. The structure of $Fe(hfac)_3$ exhibits Fe–O lengths of 1.969–2.021(10) Å, and O–Fe–O angles of 86.5–87.6(4)° [21]. In the acetylacetonate derivative $Fe(acac)_3$, the Fe–O distances lie between 1.986 and 2.004(6) Å and the O–Fe–O angles are 86.7–87.3(3)° [25].

Unlike $Cr(hfac)_3$, the manganese complex $Mn(hfac)_3$ is a tetragonally-elongated octahedron owing to a Jahn–Teller effect [22]. The long Mn–O distances are 2.141(3) and 2.147(3) Å whereas the short Mn–O distances are between 1.906(2) and 1.937(3) Å. The average O–Mn–O bite angle is 88.8°. At least two polymorphs of the acetylacetonate analog $Mn(acac)_3$ are known: one in which the molecules are axially compressed [26], and one in which they are axially elongated [27].

3. Experimental

All synthetic procedures were carried out in vacuum or under argon. Tetrahydrofuran, toluene, diethyl ether, and pentane were distilled from sodium/benzophenone. Sodium hydride (Aldrich) was used without further purification. Hexafluoroacetylacetone (Oakwood) was degassed by a freeze-pump-thaw method. The starting materials $CrCl_2(thf)$ [28] and $Cr[N(SiMe_3)_2]_2(thf)_2$ [29] were prepared as previously described. The IR spectra were recorded as Nujol mulls between KBr plates on a Nicolet Impact 410 FTIR instrument. Elemental analyses were performed by the University of Illinois Microanalytical Laboratory. The crystallographic data were collected by the George L. Clark X-ray Laboratory at the University of Illinois. Magnetic moments were determined by the Evans method [30].

3.1. Sodium hexafluoroacetylacetonate

A 60% (w/w) suspension of sodium hydride in mineral oil (5.51 g, 0.138 mol) was washed with toluene (60 mL), and the resulting solid was suspended in tetrahydrofuran (50 mL). To this suspension was added hexafluoroacetylacetone (8.00 mL, 0.0565 mol), and the reaction mixture was stirred at room temperature for 40 min. The yellow-brown solution was filtered, and the solid residue was washed with additional tetrahydrofuran (22 mL). The filtrate and the washings were combined and taken to dryness under vacuum. The yellow-white solid was washed with pentane (100 mL) and dried under vacuum to afford a white solid. Yield: 12.0 g (84%). *Anal.* Calc. for $Na(hfac) \cdot 0.33thf$: C, 29.9; H, 1.46. Found: C, 29.8; H, 1.50%. IR (cm^{-1}): 1672

m, 1556 m, 1533 m, 1514 m, 1488 m, 1318 w, 1261 s, 1202 s, 1144, s, 1079 w, 1046 w, 893 w, 800 m, 795 m, 767 w, 740 w, 665 m, 580 m, 525 w.

3.2. Bis(hexafluoroacetylacetonato)bis(tetrahydrofuran) chromium(II)

To a solution of $CrCl_2$(thf) (2.18 g, 11.2 mmol) in tetrahydrofuran (30 mL) was added a solution of Na(hfac) · 0.33thf (5.55 g, 21.8 mmol) in tetrahydrofuran (30 mL). The initially pale blue solution changed to dark brown. The reaction mixture was stirred overnight at room temperature. The solvent was removed under vacuum, and the resulting residue was extracted with diethyl ether (150 mL). The extract was filtered, and the filtrate was cooled to −20 °C to afford dark brown crystals. Yield: 1.67 g (24%). M.p.: 117–118 °C. *Anal.* Calc. for $CrC_{18}H_{18}F_{12}O_6$: C, 35.4; H, 2.97; Cr, 8.52. Found: C, 35.3; H, 3.60; Cr, 8.46%. IR (cm^{-1}): 1641 m, 1615 m, 1564 w, 1511 w, 1442 s, 1366 w, 1348 w, 1255 s, 1225 s, 1173 s, 1136 s, 1029 m, 916 m, 872 m, 810 m, 742 m, 688 m, 613 w, 580 m, 534 w, 478 sh, 467 m. μ_{eff} (thf): 4.6 μ_B.

3.3. Tris(hexafluoroacetylacetonato)chromium(III)

To a solution of $Cr[N(SiMe_3)_2]_2(thf)_2$ (2.19 g, 4.23 mmol) in diethyl ether (120 mL) at −78 °C was added hexafluoroacetylacetone (1.2 mL, 8.48 mmol) dropwise over 10 min. The initially blue-grey solution turned red-brown. The solution was warmed to room temperature, filtered, concentrated to ~40 mL, and cooled to −20 °C. The resulting red needles were isolated; an additional crop of crystals could be obtained by concentrating and cooling the supernatant. Yield: 0.51 g (26%). M.p.: 92–93 °C. The identity of the product was determined by IR and crystallography. IR (cm^{-1}): 3156 w, 1635 m, 1614 m, 1567 w, 1541 w, 1442 s, 1376 w, 1365 w, 1259 s, 1224 s, 1164 s, 1148 s, 1108 m, 916 w, 872 w, 814 m, 748 m, 678 m, 598 m, 534 w.

3.4. Crystallographic studies [31]

Single crystals of $Cr(hfac)_2(thf)_2$, (**1**), grown from diethyl ether, were mounted on glass fibers with Paratone-N oil (Exxon) and immediately cooled to −75 °C in a cold nitrogen gas stream on the diffractometer. (Single crystals of $Cr(hfac)_3$, (**2**), grown by sublimation in vacuum, were treated similarly. Subsequent comments in parentheses will refer to this compound.) Standard peak search and indexing procedures, followed by least squares refinement, yielded the cell dimensions given in Table 1. The measured intensities were reduced to structure factor amplitudes and their esd's by correction for background and Lorentz and polarization effects. Systematic absences for $0kl$ ($k + l \neq 2n$) were consistent with space groups $P4_2/mnm$, $P4_2nm$, and $P\bar{4}n2$; the centrosymmetric space group $P4_2/mnm$ was chosen and was eventually proven correct upon successful refinement of the proposed model. Systematically absent reflections were deleted and symmetry-equivalent reflections were averaged to yield the data set used to solve the structure. (For **2**, systematic absences for $h\bar{h}0l$ ($l \neq 2n$) were consistent with the trigonal groups $P3c1$ and $P\bar{3}c1$, and the hexagonal groups $P6_3cm$, $P\bar{6}c2$, and $P6_3/mcm$. The diffraction pattern conformed closely to the Laue group $6/mmm$, but no satisfactory solution could be found in any of the hexagonal space groups. Eventually, a satisfactory solution was found in the space group $P\bar{3}c1$.)

The structure of **1** was solved by direct methods, and positions for all the non-hydrogen atoms were deduced from an E-map (SHELXTL). (For **2**, Patterson methods led to a refinable model consisting of two independent chromium atoms. Subsequent least squares refinement and difference Fourier calculations revealed the positions of many of the remaining non-hydrogen atoms. Some of the expected non-hydrogen atoms, however, did not surface in the difference maps, and suitable atoms were added, with bond distance restraints, to complete the molecules.)

The analytical approximations to the scattering factors were used, and all structure factors were corrected for both real and imaginary components of anomalous dispersion. All 832 (2022) unique data were used in the least squares refinement. The quantity minimized by the least squares program was $\sum w(F_o^2 - F_c^2)^2$, where $w = [(\sigma(F_o^2))^2 + (0.0852P)^2 + 0.6505P]^{-1}$ and $P = (F_o^2 + 2F_c^2)/3$. (For **2**, $w = [(\sigma(F_o^2))^2 + (0.0749P)^2]^{-1}$.)

(For **2**, despite the fact that all of the non-hydrogen atoms had been located, wR_2 remained above 0.65 and the "most disagreeable reflections" list was composed entirely of reflections for which $|F_c/F_c(\max)| < 0.03$ and $F_o^2 \gg F_c^2$. This result suggested that the crystal was twinned by merohedry. An investigation of possible twin laws eventually revealed one that led to a substantial reduction in the weighted residual. The twin law relates hkl to $hk\bar{l}$, which corresponds to reflection through the **a*****b*** plane. The intensities were calculated from the expression $F_c^2 = vF_c(hkl)^2 + (1 - v)F_c(hk\bar{l})^2$, where v is the volume fraction of one of the twin individuals. The volume fraction of the major twin individual refined to 0.547(3). At this point, all restraints on atom positions were lifted).

In the final cycle of least squares, independent anisotropic displacement factors were refined for the non-hydrogen atoms. Hydrogen atoms were readily apparent among the largest peaks in the difference maps, and their locations were refined independently. (For **2**, hydrogen atoms were readily apparent among the largest peaks in the difference maps, but they tended to refine to give unreasonable distances, so they were fixed in "idealized" positions with C–H = 0.95 Å.) The isotropic displacement parameters for the hydrogen atoms were set equal to 1.2 times U_{eq} for the attached carbon atom. Although corrections for crystal decay were unnecessary, an empirical absorption correction was applied (SADABS), the maximum and minimum transmission factors being 0.970 and 0.931 (0.998 and 0.937). Successful convergence was indicated by the maximum shift/error of 0.002 (0.001) for the last cycle.

Final refinement parameters are given in Table 1. The largest peak in the final Fourier difference map (0.35 e $Å^{-3}$) was located 0.97 Å from Cr1. (For **2**, the largest peak in the final Fourier difference map (0.39 e $Å^{-3}$) was located 2.1 Å from O21, F23, and C22.) A final analysis of variance between observed and calculated structure factors showed no apparent errors.

Acknowledgements

We thank Rosann Bish for carrying out some of the early stages of the synthetic work, and Dr. Scott Wilson and Ms. Teresa Prussak-Wieckowska for collecting the crystallographic data. We thank the Department of Energy (Grant DEFG02-91-ER45439) for support of this work.

Appendix A. Supplementary material

CCDC 626676 and 626677 contain the supplementary crystallographic data for **1** and **2**. These data can be obtained free of charge via http://www.ccdc.cam.ac.uk/conts/retrieving.html, or from the Cambridge Crystallographic Data Centre, 12 Union Road, Cambridge CB2 1EZ, UK; fax: (+44) 1223-336-033; or e-mail: deposit@ccdc.cam.ac.uk. Supplementary data associated with this article can be found, in the online version, at doi:10.1016/j.poly.2006.12.007.

References

[1] T. Maruyama, H. Akagi, J. Electrochem. Soc. 143 (1996) 1955.
[2] S. Gu, P. Atanasova, M.J. Hampden-Smith, T.T. Kodas, Thin Solid Films 340 (1999) 45.
[3] A. Caneschi, D. Gatteschi, P. Rey, R. Sessoli, Inorg. Chem. 27 (1988) 1756.
[4] A. Caneschi, D. Gatteschi, J.P. Renard, P. Rey, R. Sessoli, Inorg. Chem. 28 (1989) 2940.
[5] D. Luneau, P. Rey, J. Laugier, E. Belorizky, A. Cogne, Inorg. Chem. 31 (1992) 3578.
[6] R.E. Sievers, B.W. Ponders, M.L. Morris, R.W. Moshier, Inorg. Chem. 2 (1963) 693.
[7] W.R. Walker, N.C. Li, J. Inorg. Nucl. Chem. 27 (1965) 2255.
[8] B.D. Fahlman, A.R. Barron, Adv. Mater. Opt. Electron. 10 (2000) 223.
[9] W. Partenheimer, R.S. Drago, Inorg. Chem. 9 (1970) 47.
[10] W. Lin, B.C. Wiegand, R.G. Nuzzo, G.S. Girolami, J. Am. Chem. Soc. 118 (1996) 5977.
[11] W. Lin, R.G. Nuzzo, G.S. Girolami, J. Am. Chem. Soc. 118 (1996) 5988.
[12] R.E. Sievers, R.W. Moshier, M.L. Morris, Inorg. Chem. 1 (1962) 966.
[13] M.L. Morris, R.W. Moshier, R.E. Sievers, Inorg. Chem. 2 (1963) 411.
[14] M.L. Morris, D.A. Aikens, Nature 207 (1965) 631.
[15] P. Mushak, M.T. Glenn, J. Savory, Fluorine Chem. Rev. 6 (1973) 43.
[16] F.A. Cotton, C.E. Rice, G.W. Rice, Inorg. Chim. Acta 24 (1977) 231.
[17] M.H. Dickman, L.C. Porter, R.J. Doedens, Inorg. Chem. 25 (1986) 2595.
[18] G. Mago, M. Hinago, H. Miyasaka, N. Matsumoto, H. Okawa, Inorg. Chim. Acta 254 (1997) 145.
[19] M. Kitano, Y. Ishimaru, K. Inoue, N. Koga, H. Iwamura, Inorg. Chem. 33 (1994) 6012.
[20] H.S. Jarret, J. Chem. Phys. 27 (1957) 1298.
[21] C.E. Pfluger, P.S. Haradem, Inorg. Chim. Acta 69 (1983) 141.
[22] E. Bouwman, K.G. Caulton, G. Christou, K. Folting, C. Gasser, D.N. Hendrickson, J.C. Huffman, E.B. Lobkovsky, J.D. Martin, P. Michel, H.-L. Tsai, Z. Xue, Inorg. Chem. 32 (1993) 3463.
[23] B.G. Thomas, M.L. Morris, R.L. Hilderbrandt, Inorg. Chem. 17 (1978) 2901.
[24] B. Morosin, Acta Crystallogr. 19 (1965) 131.
[25] J. Iball, C.H. Morgan, Acta. Crystallogr. 23 (1967) 239.
[26] J.P. Fackler, A. Avdeef, Inorg. Chem. 13 (1974) 1864.
[27] B.R. Stults, R.S. Marianelli, V.W. Day, Inorg. Chem. 18 (1979) 1853.
[28] L.F. Larkworthy, M.H. Nelson-Richardson, Chem. Ind. (1974) 164.
[29] D.C. Bradley, M.B. Hursthouse, C.W. Newing, A.J. Welch, J. Chem. Soc., Chem. Commun. (1972) 567.
[30] D.F. Evans, G.V. Fazakerley, R.F. Phillips, J. Chem. Soc. A (1971) 1931.
[31] Crystallographic programs and procedures used are described in J.L. Brumaghim, J.G. Priepot, G.S. Girolami, Organometallics 18 (1999) 2139.

Available online at www.sciencedirect.com
ScienceDirect
Polyhedron 26 (2007) 1763
POLYHEDRON
www.elsevier.com/locate/poly

Preface to the proceedings of ICMM 2006

This special issue of Polyhedron is devoted to the proceedings of the 10th International Conference on Molecule-based Magnets, continuing a tradition that has been in place for some time. Hopefully the papers contained in this issue will provide a snapshot of the conference for those in the molecular magnetism community, and also be a stimulating and useful introduction to this exciting area of research to the broader readership.

The 10th ICMM took place from August 13 to 17, 2006 in Victoria, British Columbia, marking the first time this international meeting has been hosted in Canada. 274 delegates from 22 countries gathered in Victoria, and fortunately the weather cooperated, providing a most pleasant setting. Scientifically, the meeting commenced with a new 'keynote' lecture in Olivier Kahn's name, created by the 2006 ICMM Organizing Committee as tribute to a true pioneer and leader in molecular magnetism. Dante Gatteschi, the inaugural ICMM Kahn lecturer, provided an entertaining and outstanding opening to the conference.

The scientific content of the meeting was rich and intense: 65 invited and contributed talks and 235 poster presentations made for a jam-packed program, which also included a wonderful experimental demonstration session on the magic of molecular magnets organized by Michel Verdaguer and Bob Thompson. The program was loosely organized into contemporary themes in molecule-based magnetism. Sunday provided a glimpse of current advances in the magnetism of organic radical-based materials. Monday focused on multifunctional materials, highlighted by an opening plenary lecture by Philipp Gütlich (Mainz) on spin crossover. Tuesday dealt with coordination complexes and materials and was commenced by a plenary lecture on spin glasses by Art Epstein (Ohio State). The plenary given by Juan Novoa (Barcelona) on intermolecular magnetic interactions, marked the beginning of Wednesday's session on physical and computational approaches to understanding molecule-based magnetic materials. Finally, Chris Murray (IBM) introduced the world of magnetic nanoparticles to open Thursday's session on nanomagnetism. It was particularly telling that one of the more difficult tasks facing the organizing committee in assembling the program was deciding where to place many of the presentations, which clearly fell under two or more of these themes. This is a tribute to the truly cross-disciplinary nature of the field.

Organizing a meeting of this size and scope is a hugely time-consuming and, at times, stressful activity. But it is also immensely rewarding too, and it is with pleasure that I have the opportunity to acknowledge the many people who helped make this conference a huge success. First and foremost, I offer my deep gratitude to the members of the ICMM 2006 organizing committee: Natia Frank (University of Victoria), Danny Leznoff (Simon Fraser University), Bob Thompson (University of British Columbia) and Laurie Thompson (Memorial University of Newfoundland). You were a delight to work with and deserve a large portion of the credit for the success of this meeting. I also offer sincere thanks to the student volunteers, essentially the members of my research group as well as Dr. Frank's, for all their hard work behind (and in front of) the scenes. The staff at the Victoria Conference Center also deserves our thanks for their outstanding service in helping the meeting run seamlessly. The efforts of George Christou and Sondra Hayes in assembling this special issue certainly deserve to be recognized. Finally, I wish to acknowledge the sponsors whose contributions made the conference possible. Thanks to Elsevier, the University of Victoria, the American Chemical Society-Petroleum Research Fund, Quantum Design, IQuantum Corporation, Bruker Canada, Rigaku, and the Inorganic and Organic Divisions of the Canadian Society for Chemistry.

Looking forward to an outstanding 11th ICMM in 2008 in Florence!

Robin G. Hicks
Conference Chair,
ICMM 2006
Department of Chemistry,
University of Victoria,
P.O. Box 3065, Victoria,
BC, Canada V8W3V6
E-mail address: rhicks@uvic.ca

Available online 6 December 2006

0277-5387/$ - see front matter © 2007 Elsevier Ltd. All rights reserved.
doi:10.1016/j.poly.2006.12.001

temperature interval between the two-steps [7]. This was also the case in one of the two-step μ-bipyrimidine compound, [Fe(NCS)(bt)]$_2$(μ-bpym) [3]. In contrast, as part of a wide study using different types of bridges [1], some of the present authors have recently described the first 'ordered' [HS–LS] dinuclear molecule containing two bis-bidentate dipyridylamine bridging groups linked, in each ligand, by a pyridyl donor [8]. The term 'ordered', in the present context, means that the dinuclear molecules have a HS Fe(II) end and a LS Fe(II) end when structurally characterised at the [HS–LS] plateau temperature. This is different to the alternative possibility for such an 'intermediate' spin state that contain 50% HS–HS and 50% LS–LS molecules in the crystal lattice, a situation found by Kaizaki et al. in a pyrazolate-bridged complex, [Fe(NCBH$_3$)(4-Ph-py)]$_2$(μ-bpypz)$_2$ [9].

Other key features of interest in solid state dinuclear, and higher nuclearity cluster, SCO systems include their thermal hysteresis (memory/cooperativity) properties, in comparison to related mononuclear Fe(II) compounds [1], and their photomagnetic (LIESST; light induced excited spin state trapping [10]) properties, the latter being investigated, in our case, in collaboration with Letard [11], and, from the Mössbauer spectroscopic perspective, with Gütlich and coworkers [12].

The work reported here focuses on one aspect of covalent bridging in dinuclear Fe(II) crossover compounds. It was aimed at probing the effect upon spin-crossover that the rigidity, ligand field strength and superexchange-coupling properties of two very closely related covalent, bridging ligands produces, in otherwise similar pairs of molecules. The bridges, {N–N}-azolates, are contained in 3,5-bis(2-pyridyl)pyrazolate (bpypz$^-$), used recently, as indicated above, by Kaizaki and coworkers [5,9] and in the triazolate analogue, 3,5-bis(2-pyridyl)-1,2,4-triazolate (bpytz$^-$) (Fig. 1). While 1,2,4(R)-triazole bridging has been incorporated in dinuclear [6,13] and 1D chain iron(II) SCO materials [14,15], the anionic triazolates (trz$^-$) have only been incorporated, along with triazoles, into 1D chain [Fe(Htrz)$_2$(trz)](BF$_4$) species ($T_{1/2} \sim 360$ K, $\Delta T = 60$ K), this occurring [16] as far back as 1977 [14–16]. The general coordinating properties of triazolates, particularly towards 2nd and 3rd row d-block ions, have been reviewed by Haasnoot and reference to the work of his Leiden coworkers is included [16]. A tetranuclear [Cu(I)$_4$(bpytz)$_4$] cluster, and extended [Cu(I)(bpytz)]$_n$ networks have recently been reported [17], in which the bpytz$^-$ ligand bridges adjacent metal centres, and we have recently obtained related Fe$_5$- and Fe$_7$-bpytz clusters as an offshoot of the present work [18].

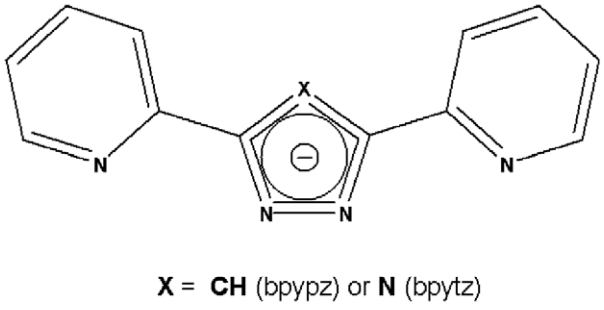


Fig. 1. The *bis*-bidentate bridging ligands 3,5-bis(2-pyridyl)pyrazolate (bpypz$^-$) and 3,5-bis(2-pyridyl)-1,2,4-triazolate (bpytz$^-$).

The present complexes have the general formula [Fe(NCX)(py)]$_2$(μ-L)$_2$. They contain the axial N-donor ligand NCX$^-$, where X = S, Se or BH$_3$, the coplanar equatorial bridging ligand L$^-$ = bpypz$^-$ or bpytz$^-$, and a pyridine (py) in the *trans* axial position. The structural, magnetic and Mössbauer spectral properties are described for representative examples of [Fe(NCS)(py)]$_2$(μ-bpypz)$_2$ (**1**), [Fe(NCSe)(py)]$_2$(μ-bpypz)$_2$ (**2**), [Fe(NCS)(py)]$_2$-(μ-bpytz)$_2$ (**3**), [Fe(NCSe)(py)]$_2$(μ-bpytz)$_2$ (**4**), [Fe(NCBH$_3$)(py)]$_2$(μ-bpytz)$_2$ (**5**). Complex **1** has previously been reported by Kaizaki et al. [5]. We have determined its crystal structure and show that the SCO behaviour previously reported is not exhibited by the crystal phase, but only by precipitated samples.

2. Experimental

Methanol was dried over magnesium turnings while pyridine was used without further purification. Solvents were deoxygenated before use. Iron(II) complexes were synthesised using Schlenk conditions under a nitrogen atmosphere with ~10 mg of ascorbic acid being added to each reaction to prevent oxidation to iron(III). The ligands 3,5-bis(2-pyridyl)pyrazole (Hbpypz) and 3,5-bis(2-pyridyl)-1,2,4-triazole (Hbpytz) were prepared using literature methods [19,20] as were [Fe(NCS)$_2$(py)$_4$] [21] and [Fe(NCS)(py)]$_2$](μ-bpypz)$_2$ (**1**) [5]. Microanalytical data on repeat samples of 'precipitated' **1** [5] were typically as follows: *Anal.* Calc. for $C_{38}H_{28}Fe_2N_{12}S_2$: C, 55.09; H, 3.41; N, 20.29%. *Anal.* Calc. for $C_{38}H_{28}Fe_2N_{12}S_2 \cdot H_2O$: C, 53.91; H, 3.57; N, 19.85; S, 7.58. Found: C, 54.37; H, 3.51; N, 19.54; S, 7.21%. Crystals of **1** were grown as described below. Microanalyses were performed by the Campbell Microanalysis Laboratory, Chemistry Department, University of Otago, Dunedin, New Zealand. Infrared spectra were obtained on a Bruker Opus/IR IFS 55 spectrometer in the range of 4000–400 cm^{-1}. Samples were prepared as a KBr discs (16 scans, resolution ±4 cm^{-1}).

2.1. Syntheses of [(n-Bu$_4$)N](bpypz) and [(n-Bu)$_4$N](bpytz) [5]

Hbpypz and Hbpytz were converted to their respective tetra-*n*-butylammonium salts by dissolving the ligand (3.54×10^{-4} mol) in ~15 ml of methanol followed by the addition of 1 M tetra-*n*-butylammonium hydroxide (0.36 ml). After a period of 15 min, the mixture was condensed to an oily residue in vacuo. The residue was then washed and condensed, repeatedly, with 3 × 20 ml portions of methanol and dried under high vacuum, forming a white to off-white crystalline solid.

2.2. Synthesis of [Fe(NCSe)(py)]$_2$(μ-bpypz)$_2$ (**2**)

$Fe(ClO_4)_2 \cdot 6H_2O$ (0.085 g, 3.3×10^{-4} mol) was dissolved in methanol (5 ml) and, to this solution, was added KNCSe (0.095 g, 6.6×10^{-4} mol). The resulting solution turned a pink colour and $KClO_4$ was deposited. This mixture was filtered and pyridine (5 ml) was added to the clear filtrate, resulting in the precipitation of a yellow solid, $[Fe(NCSe)_2(py)_4]$. To this suspension a solution of [(*n*-Bu$_4$)N](bpypz) (0.153 g, 3.3×10^{-4} mol) in pyridine (5 ml) was added dropwise over a period of 20 min resulting in the initial yellow solid dissolving. The solution was stirred for a further 2 h, with precipitation of a yellow solid observed, which was collected and washed, successively, with methanol and diethyl ether and allowed to dry. Yield: 0.078 g, 51%. *Anal.* Calc. for $C_{38}H_{28}Fe_2N_{12}Se_2$: C, 49.48; H, 3.06; N, 18.22. Found: C, 49.88; H, 3.20; N, 17.72%. IR (KBr disc) cm^{-1}: 2080 *ν*(C≡N).

2.3. Synthesis of [Fe(NCS)(py)]$_2$(μ-bpytz)$_2$ (**3**)

A solution of [(*n*-Bu)$_4$N](bpytz) (0.153 g, 3.3×10^{-4} mol) in pyridine (5 ml) was added dropwise to a stirred methanolic solution of $[Fe(NCS)_2(py)_4]$ (0.161 g, 3.3×10^{-4} mol). The reaction mixture turned a yellow colour with a yellow precipitate being formed. After 2 h, the mixture was filtered to yield a yellow microcrystalline product which was successively washed with methanol and diethyl ether and allowed to dry. Yield: 0.090 g, 66%. *Anal.* Calc. for $C_{36}H_{26}Fe_2N_{14}S_2$: C, 52.06; H, 3.16; N, 23.61. Found: C, 51.47; H, 3.28; N, 22.86%. IR (KBr) cm^{-1}: 2075 *ν*(C≡N).

2.4. Synthesis of [Fe(NCSe)(py)]$_2$(μ-bpytz)$_2$ (**4**)

The same method as for compound **2** was employed. $Fe(ClO_4)_2 \cdot 6H_2O$ (0.085 g, 3.3×10^{-4} mol) was dissolved in methanol (5 ml) to which KNCSe (0.095 g, 6.6×10^{-4} mol) was added. To the resulting clear filtrate was added a pyridine solution of [N(*n*-Bu)$_4$](bpytz) (0.153 g, 3.3×10^{-4} mol), dropwise. This resulted in the formation of a yellow precipitate, which was collected and treated as previously described. Yield: 0.060 g, 39%. *Anal.* Calc. for $C_{36}H_{26}Fe_2N_{14}Se_2$: C, 46.78; H, 2.84; N, 21.22. Found: C, 46.80; H, 2.99; N, 20.60%. IR (KBr) cm^{-1}: 2084 *ν*(C≡N).

2.5. Synthesis of [Fe(NCBH$_3$)(py)]$_2$(μ-bpytz)$_2$ (**5**)

A similar method was again employed, as for compound **2**, but using $Fe(SO_4) \cdot 7H_2O$ (0.092 g, 3.3×10^{-4} mol) and $Na(NCBH_3)$ (0.042 g, 6.8×10^{-4} mol). The methanolic solution (5 ml) of $Fe(SO_4) \cdot 7H_2O$ turned a purple colour upon mixing with $Na(NCBH_3)$ and a precipitate of Na_2SO_4 formed and was removed by filtration. To this clear, methanolic solution, a larger than normal volume of pyridine (15 ml) was added such that the initial yellow precipitate of $[Fe(NCBH_3)_2(py)_4]$ dissolved. To this solution was added, slowly, a solution of [(*n*-Bu)$_4$N](bpytz) (0.153 g, 3.3×10^{-4} mol) in pyridine (5 ml), with the reaction solution turning an orange colour. After 2 h of stirring, and with no precipitation observed, stirring was stopped. The reaction solution was allowed to slowly evaporate by $\sim^2/_3$ of its volume, under a stream of nitrogen, for three days. Fine orange needles of **5** were formed. Yield: 0.055 g, 42%. *Anal.* Calc. for $C_{36}H_{32}B_2Fe_2N_{14}$: C, 54.45; H, 4.06; N, 24.70. Found: C, 55.05; H, 4.47; N, 23.42%. IR (KBr) cm^{-1}: 2356 *ν*(B-H), 2188 *ν*(C≡N).

Single X-ray quality crystals of complexes **1** and **3** grown by slow diffusion methods in H-tubes. One arm of the H-tube contained a solution of NH_4SCN and $Fe(ClO_4)_2 \cdot 6H_2O$, in methanol, and a small amount of ascorbic acid. The other arm contained a solution of [(*n*-Bu)$_4$N](bpypz) (or [(*n*-Bu)$_4$N](bpytz) dissolved in pyridine). Both arms were filled halfway and then layered with a methanol-pyridine (50:50) solution. Crystals formed over 2 weeks.

2.6. Magnetic measurements

Variable temperature DC magnetic susceptibilities of powder samples (~20 mg) were measured on a Quantum Design MPMS 5 SQUID magnetometer with an operating field of 1 Tesla, over a temperature range of 2–300 K. Representative samples were checked for lack of crystallite torquing by dispersal of the powder in a Vaseline mull, and none was present. This is a feature, that can lead to anomalous μ_{eff} ($\chi_M T$) values, and is sometimes observed at low temperatures in orbitally degenerate ($^5T_{2g}$) HS Fe(II) octahedral compounds [22].

2.7. Mössbauer spectral measurements

The spectra were measured using a conventional constant acceleration drive with a symmetrical saw-tooth waveform. The source of ^{57}Co in rhodium was maintained at room temperature. Fresh crystalline samples were loaded into a piston type Perspex holder. The holder was placed in a cold-finger type cryostat in good thermal contact with a reservoir containing liquid nitrogen. The spectra were fitted to Lorentzian lines, with the matching lines of a doublet constrained to have the same intensity and line width. Isomer shifts were calibrated against the spectrum of α-iron.

2.8. X-ray diffraction measurements

Single crystals of **1** and **3** were quench cooled to 123(2) K and mounted on a Bruker Apex-II diffractometer employing graphite monochromated Mo-Kα radiation generated from a fine-focus sealed tube. Cell constants were obtained from a least squares refinement against 4622 reflections located between 0.82 and 56.56° 2*θ*. Data were collected at 123(2) K with scans to 56.46° 2*θ*. Subsequent computations were carried out with the WinGX [23] graphical user interface. An empirical absorption correction determined with SADABS [24] was applied to the data. The structures of **1** and **3** were solved in the space group $P2_1/n$ (#14), by

Table 1
Summary of crystallographic data and refinement details for $[Fe(NCS)(py)]_2(\mu\text{-L})_2$, L = bpypz (**1**) and bpytz (**3**)

Compound	**1**	**1**	**1**	**3**
Formula	$Fe_2S_2C_{38}H_{28}N_{12}$	$Fe_2S_2C_{38}H_{28}N_{12}$	$Fe_2S_2C_{38}H_{28}N_{12}$	$Fe_2S_2C_{36}H_{26}N_{14}$
FW (g mol^{-1})	828.52	828.52	828.52	830.52
T (K)	90(2)	123(2)	200(2)	123(2)
Crystal system	monoclinic	monoclinic	monoclinic	monoclinic
Space group	$P2_1/n$	$P2_1/n$	$P2_1/n$	$P2_1/n$
Z	2	2	2	2
a (Å)	13.1295(7)	13.168(3)	13.1944(13)	13.177(3)
b (Å)	9.3283(6)	9.3384(19)	9.3435(9)	9.3331(19)
c (Å)	14.6500(10)	14.692(3)	14.7453(15)	14.534(3)
β (°)	96.055(4)	95.96(3)	95.994(7)	95.12(3)
V (Å^3)	1784.26(19)	1796.8(6)	1807.9(3)	1780.3(6)
ρ_{calc} (mg m^{-3})	1.542	1.531	1.522	1.549
μ (mm^{-1})	0.979	0.972	0.966	0.983
Reflections collected (R_{int})	12299 (0.0828)	24439 (0.0449)	18513 (0.1618)	29445 (0.0478)
Data/restraints/parameters	4071/0/244	3367/0/244	4139/0/244	4352/0/244
Observed data [$I > 2\sigma(I)$]	2888	2602	2333	3068
R_1, wR_2 [$I > 2\sigma(I)$]	0.0739, 0.1132	0.0447, 0.1113	0.0897, 0.1655	0.0675, 0.1425
R_1, wR_2 (all data)	0.1090, 0.1307	0.0780, 0.1604	0.1583, 0.1956	0.1222, 0.1912
Goodness-of-fit on F^2	1.124	1.199	1.045	1.168

direct methods, with SHELXS-97 [25], and extended and refined with SHELXL-97 [25]. The non-hydrogen atoms in the asymmetric unit were modelled with anisotropic displacement parameters. A riding atom model with group displacement parameters was used for the hydrogen atoms. Crystallographic data are given in Table 1. The structure of **1** was also solved at the temperatures 200(2) K and 90(2) K, the latter by both rapid and slow cooling, to try and obtain the cell volumes and Fe – N distances and angles in the perceived HS–HS and LS–LS regimes, respectively, as judged by the spin transition observed in a bulk sample at 125 K (Fig. 5) and in earlier work [5]. The crystal data, at these temperatures, are given in Table 1 and the bond distances and angles are essentially the same as those given in Table 2. The change in cell volume from 1784.26(19) Å^3 at 90 K, to 1807.9(3) Å^3 at 200 K, is due to normal thermal expansion.

Table 2
Comparisons of bond lengths (Å) and angles (°) for complexes **1** and **3** at 123 K (HS–HS forms)

Bond(s)	**1**	**3**
Lengths (Å)		
N(1)–Fe(1)	2.109(4)	2.087(4)
N(2)–Fe(1)	2.248(3)	2.220(4)
N(3)–Fe(1)	2.296(3)	2.330(3)
N(4)–Fe(1)	2.108(3)	2.119(3)
N(5)–Fe(1)	2.284(3)	2.309(3)
N(6)–Fe(1)	2.114(3)	2.121(4)
Fe(1)–Fe(2)	4.229(3)	4.340(3)
Angles (°)		
N(1)–Fe(1)–N(2)	166.18(13)	165.31(14)
N(1)–Fe(1)–N(3)	87.17(12)	86.81(13)
N(4)–Fe(1)–N(1)	97.80(13)	97.63(14)
N(1)–Fe(1)–N(5)	88.06(12)	88.47(13)
N(1)–Fe(1)–N(6)	99.45(13)	100.01(14)
N(2)–Fe(1)–N(3)	84.42(11)	84.54(12)
N(4)–Fe(1)–N(2)	90.48(12)	91.24(13)
N(2)–Fe(1)–N(5)	85.82(11)	85.00(12)
N(6)–Fe(1)–N(2)	90.92(12)	91.46(13)
N(4)–Fe(1)–N(3)	74.33(11)	73.34(12)
N(5)–Fe(1)–N(3)	116.12(11)	121.63(12)
N(6)–Fe(1)–N(3)	167.53(11)	163.81(13)
N(4)–Fe(1)–N(5)	168.41(12)	164.31(13)
N(4)–Fe(1)–N(6)	94.20(12)	91.12(13)
N(6)–Fe(1)–N(5)	74.92(11)	73.54(13)
Fe(1)–N(1)–C(1)	173.49(11)	169.3(3)
Fe(1)–N(4)–N(6′)	132.61(11)	133.9(3)

Powder X-ray diffraction patterns were obtained by Mr. R. Mackie (School of Physics, Monash University) using a Cu lamp with $\lambda = 1.5405$ Å.

3. Results and discussion

3.1. Syntheses and characterisation

The $[Fe(NCX)(py)]_2(\mu\text{-bpypz})_2$ complexes, **1** (X = S) and **2** (X = Se), were prepared by the route of Kaizaki et al. [5] in which the precursor complexes $[Fe(NCX)_2(py)_4]$ were reacted with $[(n\text{-Bu})_4N](bpypz)$. The new triazolate-bridged analogues $[Fe(NCX)(py)]_2(\mu\text{-bpytz})_2$, **3** (X = S), **4** (X = Se) and **5** (X = BH_3) were likewise made from $[Fe(NCX)_2(py)_4]$, prepared in situ, by reaction with $[(n\text{-Bu})_4N](bpytz)$. Single X-ray quality crystals of **1** and **3** were grown by H-tube methods also. The IR spectra of all the complexes show the presence of a strong C≡N (NCX) stretching band in the range 2075–2188 cm^{-1}. An additional strong band at 2356 cm^{-1} for complex **5** belongs to the ν(B–H) vibration of the cyanoborohydride ligand. The microanalysis data of each complex indicated that the constituent ligands and Fe were present in a ratio of 1:1:1:1. While our early microanalytical results on precipitated samples of **1** were consistent with a monohydrate being formed, and the reported data could likewise be so fitted [5]. Crystal structure analysis did not indicate the presence of water.

3.2. Crystal and molecular structures of *1* and *3*

The structure of $[Fe(NCS)(py)]_2(\mu\text{-bpypz})_2$ (**1**), first synthesised by Kaizaki et al. [5], was solved here, first to confirm the magnetic spin transition reported [5], and also for comparison to the triazolate-bridged analogue, $[Fe(NCS)(py)]_2(\mu\text{-bpytz})_2$ (**3**). The structures and numbering schemes for **1** and **3** are given in Fig. 2. Selected bond lengths and angles are given in Table 2, which were measured at 123 K, a temperature close to the $T_{1/2}$ value. In these isostructural compounds, the two pyrazolate (**1**) or triazolate (**3**) groups bridge Fe(1) and Fe(1′) equatorially to form a rigid, co-planar 6-membered {Fe–N–N–Fe–N–N} ring. The nitrogens of the equatorial pyridyl arms and of the *bis*-azolate core, together with the axial pyridine (py) nitrogen and the NCS^- nitrogen, form the distorted octahedral FeN_6 coordination environments within the centrosymmetric structure. The same coordination sphere about the iron(II) centres, and the same bridge geometry, was observed for the analogous structure of $[Fe(NCBH_3)(py)]_2(\mu\text{-bpypz})_2$ reported by Kaizaki and co-workers [5]. The Fe–N distances in the HS–HS forms of **1** and **3**, given in Table 2, are 2.1–2.2 Å, typical of HS iron(II) and similar to those in the HS–HS form of the $NCBH_3$– derivative [5]. There are some interesting angular distortions, the apical N(1)–Fe(1)–N(2), for example, being 166.2° **1**, 165.3° **3** and Fe(1)–N(1)–C(1) being 173.5° **1**, 169.3° **3**. The outer N(3)–Fe(1)–N(5) angle, 116.1° **1**, 121.6° **3** is more obtuse than the inner N(4)–Fe(1)–N(6) ring angle, 94.2° **1**, 91.2° **3**, as expected. The Fe(1)..Fe(1′) separations are 4.23 Å **1** and 4.34 Å **3**.

From an inter-molecular perspective, there is no solvent molecule present in either crystal lattice and no hydrogen bonding occurs between dinuclear molecules. There are π–π interactions present between dinuclear units in the lattice with the π densities of the pyridyl arm of $bpytz^-$ (or $bpypz^-$) interacting with the azolate ring on the neighbouring dimer, in a slipped π-stacking manner, at a distance of 3.366 Å **1**, 3.353 Å **3**, as shown in Fig. 3 for compound **3**. The π-interactions in the crystal lattice have directed the orientation of the dinuclear molecules into near-perpendicular layers of chains that are connected by the π–π overlap, as shown in Fig. 4. These π interactions and packing orientations are very similar to those observed previously in the complex $[Fe(NCBH_3)(py)]_2(\mu\text{-bpypz})_2$ [5], and also include the bpytz py..py edge-to-edge π–π stacking noted in that case. The intra-dinuclear and inter-dinuclear structural features are very similar for **1** and **3**.

The structure of **1** was also solved at 200 K and 90 K to obtain metrical details on what were expected to be dinuclear Fe(II) molecules existing in the HS–HS and LS–LS spin states (Fig. 5 and Ref. [5]). Surprisingly, the HS–HS

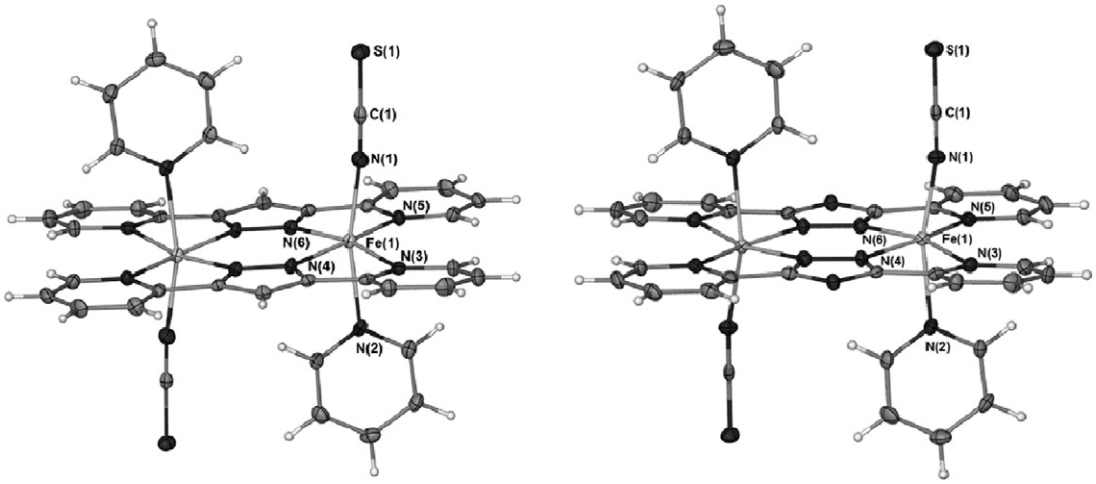


Fig. 2. ORTEP representations (50% probability) of $[Fe(NCS)(py)]_2(\mu\text{-bpypz})_2$ (**1**), left, and $[Fe(NCS)(py)]_2(\mu\text{-bpytz})_2$ (**3**), right, both at 123 K.

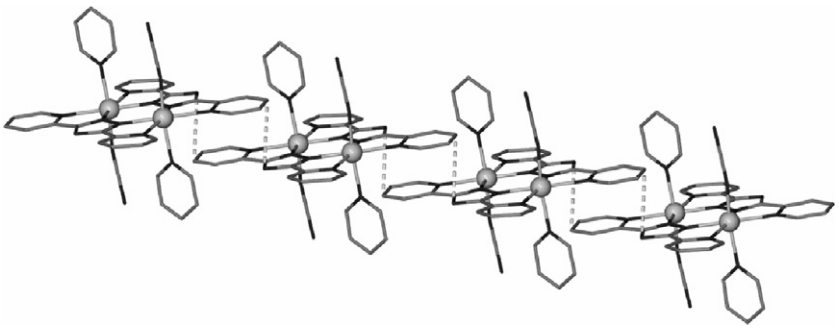


Fig. 3. Stick representation of the inter-ligand π-stacking (dotted lines) in the chains of dinuclear molecules in the μ-bpytz complex, **3**, at 123 K.

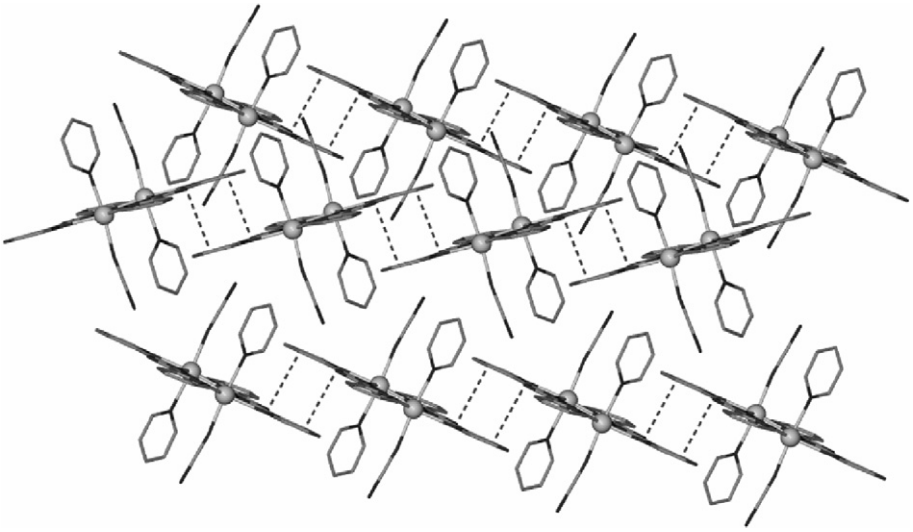


Fig. 4. Stick representation of the inter-dinuclear layer structure of **3**, at 123 K.

form persisted at all temperatures, as did the yellow colour of the crystal, typical of the HS–HS state. We comment further on the crystal and bulk forms of **1** below.

3.3. Magnetic susceptibilities and Mössbauer spectra

The μ_{eff} (per Fe(II)) versus temperature plot for a bulk, powder sample of $[Fe(NCS)(py)]_2(\mu\text{-bpypz})_2$ (**1**), shown in Fig. 5, revealed an abrupt single step spin transition, from HS–HS to LS–LS states, with a $T_{1/2}$ value of 127 K, the same temperature as that reported for this compound by Kaizaki et al. [5]. There was no thermal hysteresis at $T_{1/2}$. The bulk sample of **1** used for the magnetic measurement had a powder X-ray diffraction pattern in which the major crystalline phase appeared to be consistent with that calculated from the crystal structure (*vide infra*).

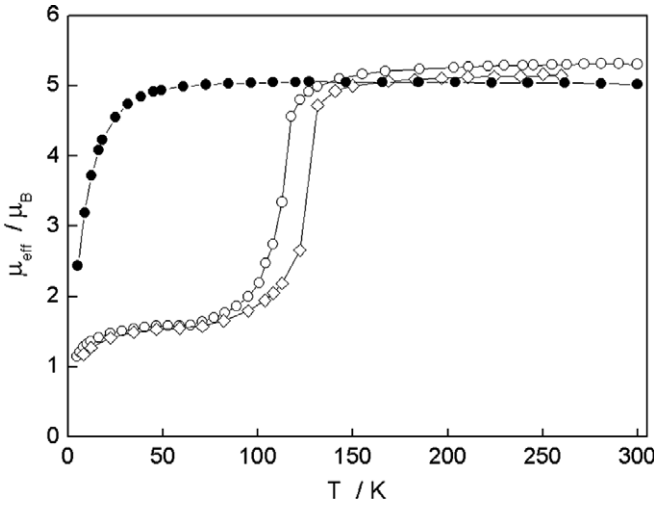


Fig. 5. Plots of magnetic moment, per Fe(II), vs. temperature, for $[Fe(NCX)(py)]_2(\mu\text{-bpypz})_2$, X = S (**1**) and Se (**2**). ● is the sample of identical crystals of **1**; ◇ is the bulk, precipitated powder of **1**; ○ is the bulk powder of **2**. The solid lines join the points.

It can be seen in Fig. 5 that, over the temperature range 300–150 K, the μ_{eff} values plateau at 5.1 μ_B, typical of HS–HS values, and then decrease abruptly to reach a LS–LS plateau value of 1.5 μ_B, a little higher than that reported earlier [5], and somewhat higher than expected for second-order Zeeman effects in t_{2g}^6 Fe(II) centres. Below ~25 K, a small decrease in μ_{eff} is due to a combination of zero-field splitting of remnant Fe(II) $^5T_{2g}$ single-ion states, combined with very weak antiferromagnetic coupling, the latter facilitated by the pyrazolate bridges. The lack of any discernable decrease in μ_{eff}, with decreasing temperature, in the HS–HS region, 150–300 K, supports the antiferromagnetic coupling being very weak. Such decreases were more pronounced in the bipyrimidine bridged SCO compounds of Real et al. [2,3] for which J values of $\sim -4\ cm^{-1}$ were observed.

The crystallography results on **1**, obtained at three temperatures, prompted us to measure the magnetism on single crystals obtained from the same H-tube as the crystallography sample. In contrast to the SCO plot of the precipitated sample, the crystals remain HS–HS over the whole temperature range, with μ_{eff} values constant at 5.0 μ_B (Fig. 5), a decrease towards 2.4 μ_B occurring below ~40 K being due to weak coupling and zero-field splitting effects that are also noted, below, for **3**. The powder XRD data on samples of **1** that display the spin transition at 127 K, described above, suggest that the bulk precipitated powder of **1** is composed, either in part or in its entirety, of a second form, such as a polymorph or solvate.

The new member of the bpypz-bridged family, $[Fe(NCSe)(py)]_2$ μ-$(bpypz)_2$ (**2**), displays an abrupt HS–HS ↔ LS–LS spin transition, without thermal hysteresis, with a $T_{1/2}$ of 109 K.[1] The μ_{eff} values for freshly made, repeat samples are 5.3 μ_B between 300–150 K and they rapidly

[1] Kaizaki et al. have recently observed the same magnetism for crystals of **2** and have solved the structure at 90 K (LS–LS) and at 200 K (HS–HS) [27].

decrease to the LS–LS plateau value of ~1.5 μ_B, per Fe(II) (Fig. 5). For bulk precipitated samples, the $T_{1/2}$ values for the NCSe- and NCS-bpypz compounds appear to be in reverse order to what is commonly expected from the stronger ligand-field strength of $NCSe^-$. Since all other intra-dinuclear constituents of the bpypz compounds are common, we were puzzled by the position of $T_{1/2}$. However, the lack of SCO in crystals of **1**, now of known structure, puts the NCS^- and $NCSe^-$ data in correct order. The Mössbauer spectrum of **2**, at 295 K, shows a single, asymmetric quadrupole doublet due to HS Fe(II) in the HS–HS dinuclear molecules, with parameter values that are typical [5] of this kind of structure; $\delta = 1.00(1)$ mm s^{-1}, $\Delta E_Q = 1.99(1)$ mm s^{-1}. At 79 K, there is a very broad, unusual lineshape that could be fitted to a sum of three static lines, but with line widths (FWHM) of over 1 mm s^{-1}, much bigger than the normal linewidths of 0.3 mm^{-1} found at 295 K (Fig. 6). The three doublets have the following similar sized isomer shifts, probably indicative of one spin state undergoing relaxation effects; (i) $\delta = 0.58(2)$ mm s^{-1}, $\Delta E_Q = 3.71(12)$ mm s^{-1}, area % = 30(11); (ii) $\delta = 0.54(2)$ mm s^{-1}, $\Delta E_Q = 1.15(40)$ mm s^{-1}, area % = 49(33); and (iii) $\delta = 0.49(3)$ mm s^{-1}, $\Delta E_Q = 0.33(12)$ mm s^{-1}, area % = 21(30). Further work is needed to understand the relaxation mechanism. The $NCBH_3^-$ member of the bpypz family had a $T_{1/2}$ of 205 K observed by Kaizaki et al., a position expected from its higher ligand-field strength compared to NCS^- and $NCSe^-$ [5]. Its reported Mössbauer parameters were similar to those of **2** at 295 K, but quite different at 79 K.

In the triazolate-bridged family, prepared here for the first time, a sample of $[Fe(NCS)(py)]_2(\mu\text{-bpytz})_2$ (**3**), that had been checked by powder XRD to be the same as the crystal structure sample, was found to display HS–HS magnetic moment behaviour over the whole temperature range. In Fig. 7, the magnetic moments, μ_{eff}, remain constant at 5.2 μ_B between 300 K and 50 K, as expected for octahedral Fe(II) centres that are showing extremely weak antiferromagnetic coupling across the two, coplanar triazolate bridges. The moments decrease rapidly below 50 K to reach 2.7 μ_B at 2 K. Fitting of these data to a $S = 2$ dimer ($-2J\mathbf{S}_1 \cdot \mathbf{S}_2$) model, assuming zero field splitting (D) to be negligible, gave a best-fit g value of 2.16 and J value of -0.80 cm^{-1}. J values for triazole bridging ligands are known to be small and negative (weakly antiferromagnetic) and those for triazolate bridging are essentially unknown but expected to be even weaker [13,16]. The $NCSe^-$ analogue, **4**, likewise remains HS–HS at all temperatures and shows (Supplementary material) similar magnetism to **3** with best-fit parameters $g = 2.11$ and $J = -0.83$ cm^{-1}.

Only with the stronger field $NCBH_3^-$ ligand in the *trans*-apical positions, does the bpytz family display spin-crossover. Thus, the magnetic moment plot for **5**, in Fig. 8, shows a full spin transition, of the two-step kind, in which the step from the HS–HS state (μ_{eff}, per Fe, $= 5.0$ μ_B), occurring between 210 K and 180 K ($T_1 = 194$ K) is a little more gradual than is the step to the LS–LS state ($\mu_{eff} = 1.8$ μ_B), occurring between 160 K and 120 K ($T_2 =$ 151 K). The plateau of the intermediate "HS–LS" state, with $\mu_{eff} = 3.8$ μ_B, extends over the range 163–188 K. A repeat sample of **5** showed the same two-step transition but with a higher value of μ_{eff} below the transition, the powder XRD patterns of the samples being identical except for the repeat sample lines being a little broader and indicative of a less crystalline sample. Comparison of the powder diffraction pattern and the derived cell constants to those calculated for $[Fe(NCBH_3)(py)]_2(\mu\text{-bpypz})_2$ [5], showed that the two cells were essentially the same. Unfortunately, in the absence of a crystal structure for **5**, it is not possible to unambiguously identify the intermediate spin state, in the plateau region, as a 50:50 HS–HS:LS–LS mixture of dinuclear molecules, as in $[Fe(NCBH_3)(4\text{-Ph-py})]_2(\mu\text{-bpypz})_2$ [3,9], that displayed a rather similar plot to Fig. 6, or as a HS–LS state. Examples of the latter kind have recently been discovered [3,7,8,26].

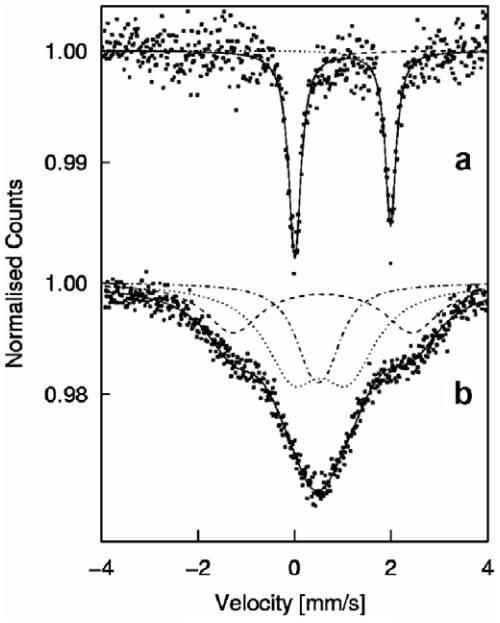


Fig. 6. Mössbauer spectra of compound **2** at (a) 295 K, (b) 79 K, showing the component lines (dots and dashes) used to fit the lineshapes.

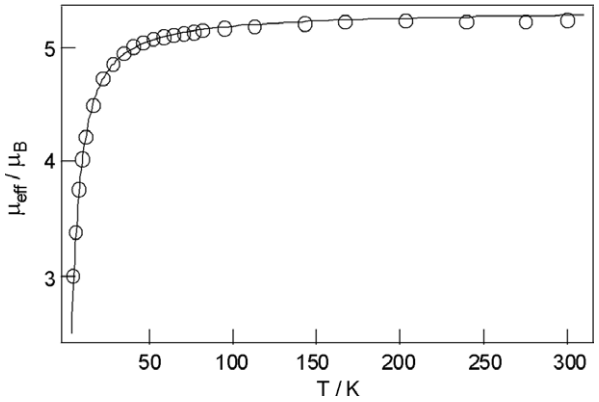


Fig. 7. Plot of magnetic moment, per Fe(II), vs. temperature, for $[Fe(NCS)(py)]_2(\mu\text{-bpytz})_2$ (**3**). The solid line is the best fit to a $S = 2$ dimer model using the g and J parameters given in the text.

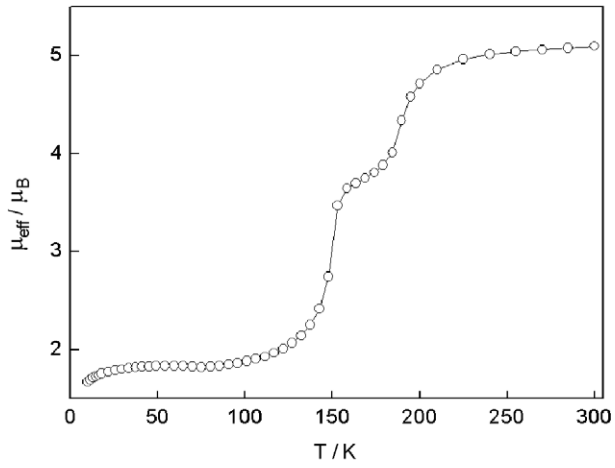


Fig. 8. Plot of the two-step SCO in $[Fe(NCBH_3)(py)]_2(\mu\text{-bpytz})_2$ (**5**).

The variable temperature Mössbauer spectra of **5** are shown in Fig. 9 and the fitted parameters are; (a) 295 K; $\delta = 0.99(1)$ mm s^{-1}, $\Delta E_Q = 1.20(1)$ mm s^{-1}, area % = 100, due to the HS–HS state; (b) 123 K; $\delta = 1.18(2)$ mm s^{-1}, $\Delta E_Q = 2.63(4)$ mm s^{-1}, area % = 9; $\delta = 0.49(1)$ mm s^{-1}, $\Delta E_Q = 0.76(4)$ mm s^{-1}, area % = 51(10); $\delta = 0.51(1)$ mm s^{-1}, $\Delta E_Q = 10.25(3)$ mm s^{-1}, area % = 40; (c) 82 K; $\delta = 1.10(1)$ mm s^{-1}, $\Delta E_Q = 3.07(1)$ mm s^{-1}, area % = 10(1), due to a minor HS species, and $\delta = 0.60(1)$ mm s^{-1}, $\Delta E_Q = 0.55(1)$ mm s^{-1}, area % = 90(1) due to the dominant LS–LS species. The spectra at 295 K and 82 K are as anticipated and like the $[Fe(NCBH_3)(py)]_2(\mu\text{-bpypz})_2$ analogue [5], except for the HS quadrupole splitting at 82 K being much larger than it is at 295 K. In the intermediate region of 123 K, a broad lineshape, quite unlike the spectrum of $[Fe(NCBH_3)(py)]_2(\mu\text{-bpypz})_2$, is observed with a minor

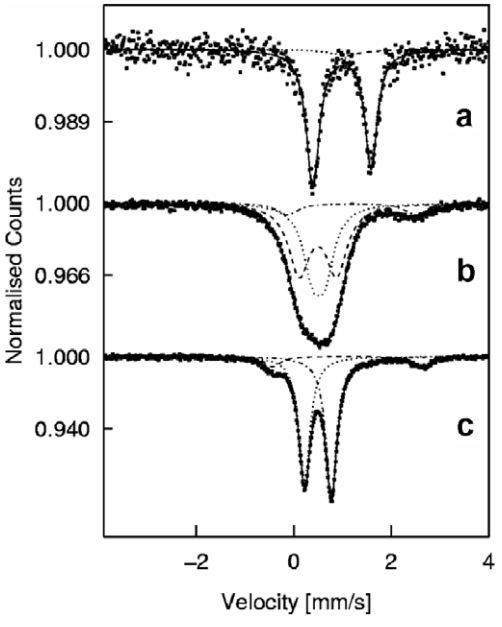


Fig. 9. Mössbauer spectra of compound **5** at (a) 295 K, (b) 123 K, and (c) 82 K, showing the component lines (dots and dashes) used to fit the lineshapes.

HS doublet having splitting of an intermediate magnitude. Inclusion of a third LS-like doublet, with area similar to that of the main LS doublet, was able to reproduce the unusual shape very well. The Mössbauer results suggest two non-identical Fe(II) sites are present with half going LS between 295 K and 82 K, while the other half show dramatic changes in their spectrum that is influenced by the original half. Dynamic processes could also be important. Clearly, when considered with the magnetic data, the spin transition in this bpytz-$NCBH_3$ material, **5**, is different in detail than it is in the corresponding bpypz-$NCBH_3$ species.

3.4. Conclusions

The spin states and spin transitions in structurally similar di-μ-pyrazolate and di-μ-triazolate iron(II) compounds have been probed by means of crystal structures, magnetic susceptibilities and Mössbauer spectral data. New and unexpected observations have emerged in comparison to Kaizaki's earlier, related work [5]. Neither of the examples for which the structures have been solved, $[Fe(NCS)(py)]_2(\mu\text{-bpypz})_2$ (**1**), and $[Fe(NCS)(py)]_2(\mu\text{-bpytz})_2$ (**3**), display a spin crossover transition in their crystalline phases, the compounds remaining HS–HS. The ligand fields provided by the bpypz pyrazolate-nitrogen donor atoms is therefore broadly similar to that of the triazolate-nitrogen donors. Possible reasons have been given to explain a HS–HS to LS–LS transition observed in precipitated samples of **1**. Comparison of the NCSe pair, **2** and **4**, show that $bpypz^-$ provides a stronger ligand field than $bpytz^-$. Only in one di-μ-triazolate example, $[Fe(NCBH_3)(py)]_2(\mu\text{-bpytz})_2$ (**5**), was a spin transition observed in the form of a well resolved 2-step HS–HS to LS–LS crossover, the $NCBH_3^-$ ligand providing a sufficiently strong ligand field contribution in that case. When compared to the di-μ-pyrazolate, $[Fe(NCBH_3)(py)]_2(\mu\text{-bpypz})_2$ [5], with an one-step transition at 205 K, the relative ligand fields are, again, marginally stronger for the pyrazolate bridge. Mössbauer data for **2** and **5** are intriguing and different to those of the pyrazolate analogue.

The synergy between antiferromagnetic coupling across the di-μ-azolate bridges and the spin crossover on each Fe(II) in the dinuclear moieties examined here is probably negligible in view of the very weak spin coupling in comparison, for example, to the well studied bipyrimidine-bridged iron(II) family. The similar crystal packing and intermolecular π-stacking interactions found in **1** and **3** suggest that intermolecular effects play little part in inducing SCO behaviour. The lack of strong cooperativity in **2** and **5**, reflected in a lack of thermal hysteresis, support this conclusion. However, in other dinuclear systems, with different and more flexible bridging ligands, and which display significant molecule–molecule interactions, via enclathrated solvate molecules and/or π–π interactions, the situation is different and observations such as two-step spin transitions have recently been made, as mentioned above [3,8].

Acknowledgement

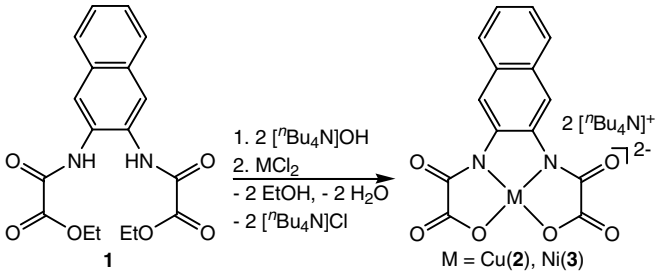
This work was supported by an Australian Research Council Discovery grant to K.S.M. Valuable discussions with Prof. S. Kaizaki are gratefully acknowledged.

Appendix A. Supplementary material

CCDC 617521, 617521, 617521 and 617521 contain the supplementary crystallographic data for this paper. These data can be obtained free of charge via http://www.ccdc.cam.ac.uk/conts/retrieving.html, or from the Cambridge Crystallographic Data Centre, 12 Union Road, Cambridge CB2 1EZ, UK; fax: (+44) 1223-336-033; or e-mail: deposit@ccdc.cam.ac.uk. Supplementary data associated with this article can be found, in the online version, at doi:10.1016/j.poly.2006.09.003.

References

[1] K.S. Murray, C.J. Kepert, Spin crossover in transition metal compounds, in: P. Gütlich, H.A. Goodwin (Eds.), Topics Curr. Chem. 233 (2004) 195.
[2] J.A. Real, A.B. Gaspar, V. Niel, M.C. Muñoz, Coord. Chem. Rev. 236 (2003) 121.
[3] A.B. Gaspar, M.C. Muñoz, J.A. Real, J. Mater. Chem. 16 (2006) 2522.
[4] B.A. Leita, B. Moubaraki, K.S. Murray, J.P. Smith, J.D. Cashion, Chem. Commun. (2004) 156.
[5] K. Nakano, N. Suemura, S. Kawata, A. Fuyuhiro, T. Yagi, S. Nasu, S. Morimoto, S. Kaizaki, Dalton Trans. (2004) 982.
[6] M.H. Klingele, B. Moubaraki, J.D. Cashion, K.S. Murray, S. Brooker, Chem. Commun. (2005) 987.
[7] N. Ortega-Villar, A.L. Thompson, M.C. Muñoz, V.M. Ugalde-Saldívar, A.E. Goeta, R. Moreno-Esparza, J.A. Real, Chem. Eur. J. 11 (2005) 5721.
[8] J.J.M. Amoore, C.J. Kepert, J.D. Cashion, B. Moubaraki, S.M. Neville, K.S. Murray, Chem. Eur. J. (2006), in press.
[9] K. Nakano, S. Kawata, K. Yoneda, A. Fuyuhiro, T. Yagi, S. Nasu, S. Morimoto, S. Kaizaki, Chem. Commun. (2004) 2892.
[10] (a) S. Decurtins, P. Gütlich, K.M. Hasselbach, A. Hauser, H. Spiering, Inorg. Chem. 24 (1985) 2174;
(b) A. Hauser, Spin crossover in transition metal compounds, P. Gütlich, H.A. Goodwin (Eds.), Topics Curr. Chem. 234 (2004) 155.
[11] J.-F. Letard, J. Mater. Chem. 16 (2006) 2550.
[12] J.A. Real, A.B. Gaspar, M.C. Muñoz, P. Gütlich, V. Ksenofontov, H. Spiering, Spin crossover in transition metal compounds, P. Gütlich, H.A. Goodwin (Eds.), Topics Curr. Chem. 233 (2004) 167.
[13] M.H. Klingele, S. Brooker, Coord Chem. Rev. 241 (2003) 119.
[14] O. Kahn, C.J. Martinez, Science 279 (1998) 44.
[15] (a) Y. Garcia, V. Niel, M.C. Muñoz , J.A. Real, Spin Crossover in Transition Metal Compounds'' Eds.P. Gütlich, H.A. Goodwin, Topics Curr. Chem. 233 (2004) 229.;
(b) P.J. van Koningsbruggen, Spin Crossover in Transition Metal Compounds, P. Gütlich, H.A. Goodwin (Eds.), Topics Curr. Chem. 233 (2004) 123.
[16] J.G. Haasnoot, Coord. Chem. Rev. 200–202 (2000) 131.
[17] J.-P. Zhang, Y.-Y. Lin, X.-C. Huang, X.M. Chen, Chem. Commun. (2005) 1258.
[18] C. Schneider, B. Moubaraki, S.M. Neville, K.S. Murray, unpublished work.
[19] P.W. Ball, A.B. Blake, J. Chem. Soc. A (1969) 1415.
[20] F. Lions, J.F. Geldard, J. Org. Chem. 30 (1965) 318.
[21] G.B. Kaufmann, R.A. Alberts, F.L. Harlan, Inorg. Synth. 12 (1970) 251.
[22] B.J. Kennedy, K.S. Murray, Inorg. Chem. 24 (1985) 1557.
[23] WinGX: L.J. Farrugia, J. Appl. Cryst. 32 (1999) 837.
[24] G.M. Sheldrick, SADABS. Empirical absorption correction program for area detector data, University of Gottingen, Germany, 1996.
[25] SHELXTL. Program for crystal structure solution and refinement, Bruker Analytical X-ray Instruments Inc., Madison, Wisconsin, USA, 1997.
[26] S.R. Batten, J. Bjernemose, P. Jensen, B.A. Leita, K.S. Murray, B. Moubaraki, J.P. Smith, H. Toftlund, Dalton Trans. (2004) 3370.
[27] S. Kaizaki, T. Nishikawa, S. Kawata, A. Fuyuhiro, Abstracts ICMM06, Victoria, Canada.



Scheme 1. Synthesis of metal oxamato complexes [5].

was measured by single-crystal rotation in three planes which are perpendicular to each other. Spectra were recorded in 5° intervals. The spectra simulations were performed using the program package SIMFONIA [6].

Quantum chemical calculations were performed with the program package TURBOMOLE [7,8] using methods of density functional theory applying the B3-LYP hybrid functional [9] with def2-TZVP [10] basis sets for all atom types. The two $[^nBu_4N]^+$ counter ions were neglected and the charge of the dianion was compensated by the conductor-like screening model (COSMO) [11], as in previous treatments [12]. This leads to negative energies for all occupied orbitals. All calculations were done with default settings for convergence criteria and with default parameters for the COSMO model. Analysis of the spin density, i.e., the difference of densities of alpha and beta electrons, was done for the optimized geometry.

3. Results and discussion

3.1. EPR spectroscopic investigations

$[^nBu_4N]_2[Cu(dana)]$ **2** was investigated by EPR in single-crystals and powder samples diamagnetically diluted by the corresponding Ni(II) complex **3** as well as in liquid solution using chloroform as solvent. Compound **3** crystallizes monoclinic, space group C2/c, with four molecules in the unit cell [5]. The molecules of the unit cell are magnetically equivalent, therefore, in the single-crystal spectra only one site will be observed. A representative single-crystal EPR spectrum is shown in Fig. 1, together with its simulation. It consists of a quartet ($I(^{63,65}Cu) = 3/2$) of quintets ($I(^{14}N) = 1$) for B_0 field orientations for which both N donor atoms are magnetically equivalent.

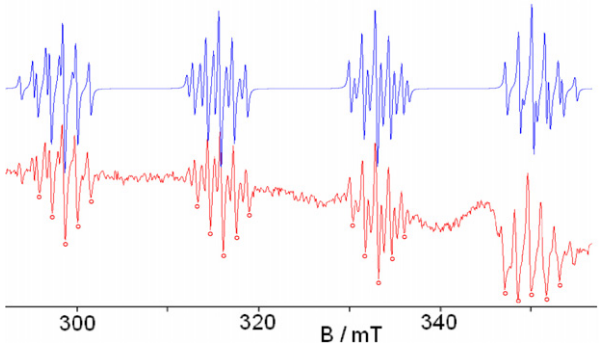


Fig. 1. Simulated (upper graph) and experimental EPR spectrum (lower graph) of single-crystal (0.5% **2** in the crystal lattice of **3**). The peaks resulting from the hyperfine coupling with the isotope ^{63}Cu are marked with circles.

Since the experimental linewidth is small ($\Delta B_{pp} \approx 0.5$–0.6 mT) the individual ^{63}Cu and ^{65}Cu signals which are different in intensity because of their different natural abundances (^{63}Cu (69%), ^{65}Cu (31%), $g_N(^{63}Cu) = 1.4804$, $g_N(^{65}Cu) = 1.5860$) can be observed. For B_0 orientations in the molecular x, y-plane the spectra become more complicated since due to the small $^{63,65}Cu$ hyperfine coupling the ^{14}N quintets overlap each other. In addition, for arbitrary B_0 orientations the nitrogen donor atoms are not magnetically equivalent resulting in more or less resolved triplets of triplets for the ^{14}N hyperfine patterns.

The EPR spectra were analyzed using the following spin-Hamiltonian

$$H_{sp} = \mu_B B_0 \cdot g \cdot S + S \cdot A^{Cu} \cdot I^{Cu} + \sum_{i=1}^{2} S \cdot A^{N_i} \cdot I^{N_i}$$

where all symbols have their usual meaning. The directions of the principal axes within the molecular frame of **2** is shown in Fig. 2. The principal values of g, A^{Cu}, and A^N are given in Table 1, where $g_x = g_y = g_\perp$, $g_z = g_\parallel$, $A_x = A_y = A_\perp$, and $A_z = A_\parallel$ is assumed.

The principal axes of g and A^{Cu} coincide with their maximum components located perpendicular to the molecular plane. The maximum components of the ^{14}N hyperfine tensors, however, were found to lie parallel to the Cu–N bond vectors. Thus, in the parallel part ($B_0 \| z$) of the powder EPR

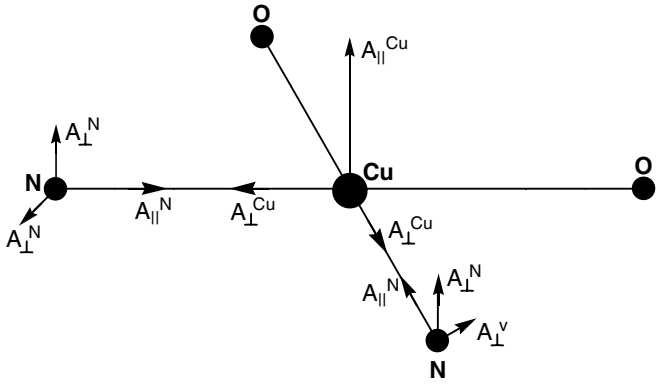


Fig. 2. Principal axis system in **2**.

Table 1
Principal values of g, A^{Cu} and A^N for **2**

g		A^{Cu} ($\times 10^{-4}$ cm^{-1})		A^N ($\times 10^{-4}$ cm^{-1})	
$g_\perp$	2.046 ± 0.003	$A_\perp^{Cu}$	33.4 ± 1.5	$A_\perp^N$	18.7 ± 0.5
$g_\parallel$	2.187 ± 0.002	$A_\parallel^{Cu}$	214.9 ± 1.0	$A_\perp^N$	13.3 ± 0.5
g_{av} [a]	2.093 ± 0.003	A_{av}^{Cu} [a]	91.4 ± 1.5		
g_{iso} [b]	2.094 ± 0.003	A_{iso}^{Cu} [b]	95.6 ± 1.0	A_{iso}^N [b]	15.0 ± 0.5

[a] $g_{av} = (2\,g_\perp + g_\parallel)/3$; $A_{av}^{Cu} = (2A_\perp^{Cu} + A_\parallel^{Cu})/3$.
[b] Liquid solution data.

spectrum the observed ^{14}N hyperfine coupling corresponds to $A_{\perp}^{N}$.

The spin densities in the s and p orbitals (d orbitals for copper) are proportional to the isotropic (A_{iso}) and the dipolar ($A_{dip} = A_{iso} - A_{\perp}$) hyperfine coupling constants, respectively. The procedure for calculating spin densities from experimentally obtained hyperfine coupling constants is given by Morton and Preston [13]. Following this model provided in the literature, the spin densities on the N and Cu atoms were estimated to $(15 \pm 2)\%$ and $(58 \pm 3)\%$, respectively. Thus most of the spin density $(88 \pm 7)\%$ is localized on the N–Cu–N part of the molecule. In the EPR experiment it was not possible to observe ^{17}O hyperfine structure satellites due to the low natural abundance of the ^{17}O isotope (^{17}O, $I = 5/2$, natural abundance 0.04%). To verify the experimentally determined spin density distribution quantum chemical calculations were employed.

3.2. Quantum chemical calculations

For the Ni compound, **3**, a diamagnetic state was found. The spin density, ρ_s, for **2** is plotted in Fig. 3; iso-density surfaces are shown for ρ_s=0.1(0.01) electrons/Bohr^3. One observes a clear localization of the spin-density at the Cu atom and at the N and O atoms. The unpaired electrons occupy the d-orbital pointing to the surrounding N and C atoms and p orbitals of the latter pointing to the central Cu atom.

A Mulliken population analysis was carried out for the spin density in order to quantify the relative distribution of unpaired electrons. Due to the high localization of the spin density this procedure is expected to yield very reliable values. One obtains values of 55.4% at Cu, 14.9% per N, 6.5% per (Cu-bonding) O atom and below 1% for all other atoms, which is in excellent agreement with the values calculated from the experimental data presented above.

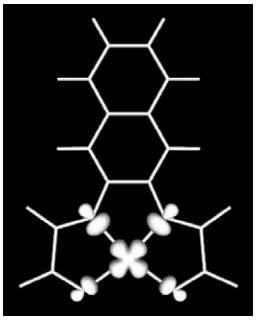


Fig. 3. Spin density of **2**. Iso-surfaces are drawn at 0.01 electrons/Bohr^3.

4. Conclusion

The spin density distribution around the Cu(II) centre in a *N*,*N*′-bis(oxamato) type complex was experimentally determined using EPR spectroscopy in the X-band. The Cu–N bond was found to accommodate a higher spin density compared to the Cu–O bond indicating that the Cu–N bond is more covalent than the Cu–O bond. Quantum chemical calculations using density functional theory provide a spin density distribution very similar to that estimated from the experiment.

N,*N*′-bis(oxamato) type complexes were already used for the synthesis of magnetic molecules whereby the free carbonyl groups coordinate further transition metals (see e.g., [1,2]). In such multimetallic complexes the oxamato-bridge was found to mediate an antiferromagnetic superexchange interaction. The results of this work indicate that the superexchange interaction takes place mainly over the N atoms of the oxamato-bridge.

Acknowledgements

The corresponding author thankfully acknowledges the Fonds der Chemischen Industrie for funding.

References

[1] O. Kahn, Molecular Magnetism, VCH Weinheim, New York, 1993.
[2] R. Costa, A. Garcia, J. Ribas, T. Mallah, Y. Journaux, Inorg. Chem. 32 (1993) 3733.
[3] S. Pillet, M. Souhassou, C. Mathonière, C. Lecomte, J. Am. Chem. Soc. 126 (2004) 1219.
[4] V. Baron, B. Gillon, A. Cousson, C. Mathoniere, O. Kahn, A. Grand, L. Ohrstrom, B. Delley, M. Bonnet, J.X. Boucherle, J. Am. Chem. Soc. 119 (1997) 3500.
[5] T. Rüffer, B. Bräuer, A. Hildebrandt, A. Powell, I. Hewitt, Georgeta Salvan, Eur. J. Inorg. Chem., submitted.
[6] BRUKER Analytik GmbH, Xsophe-Computer Simulation Software, Version 1.0, 1999.
[7] R. Ahlrichs, M. Bär, M. Häser, H. Horn, C. Kölmel, Chem. Phys. Lett. 162 (1989) 165.
[8] TURBOMOLE V5-8, 2005, University of Karlsruhe.
[9] C. Lee, W. Yang, R.G. Parr, Phys. Rev. B 37 (1988) 785.
[10] F. Weigend, R. Ahlrichs, Phys. Chem. Chem. Phys. 7 (2005) 3297.
[11] A. Klamt, G. Schüürmann, J. Chem. Soc. Perkin Trans. 2 (1993) 799.
[12] C. Zimmermann, C.E. Anson, F. Weigend, R. Clérac, S. Dehnen, Inorg. Chem. 44 (2005) 5686.
[13] J.R. Morton, K.F. Preston, J. Magn. Reson. 30 (1978) 577.

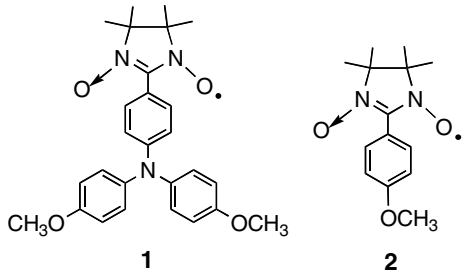


Chart 1.

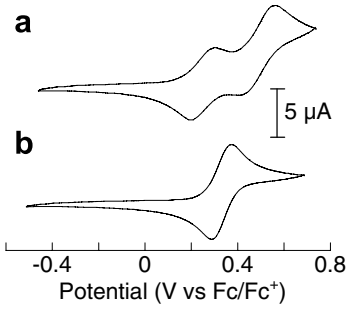


Fig. 1. Cyclic voltammograms of **1** (a) and **2** (b) in a CH_2Cl_2 solution with 0.1 M $(n\text{-}C_4H_9)_4NBF_4$. Scan rate = 0.1 V/s.

describe the synthesis, electronic structure, and hole-transporting property of a nitronyl nitroxide derivative combined with a trialylamine moiety, *N*,*N*-bis(4-methoxyphenyl)-*N*-{4-(1-oxyl-3-oxide-4,4,5,5-tetramethylimidazolin-2-yl)-phenyl}phenylamine (**1**). The redox and hole-transporting property of the control compound, 2-(4-methoxyphenyl)-1-oxyl-3-oxide-4,4,5,5-tetramethylimidazolin-2-yl (**2**), is also described (see Chart 1).

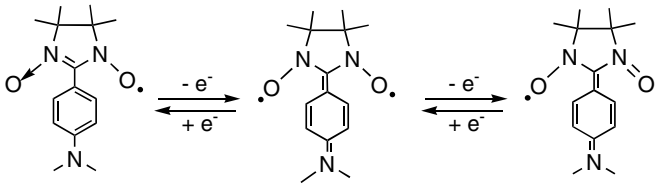


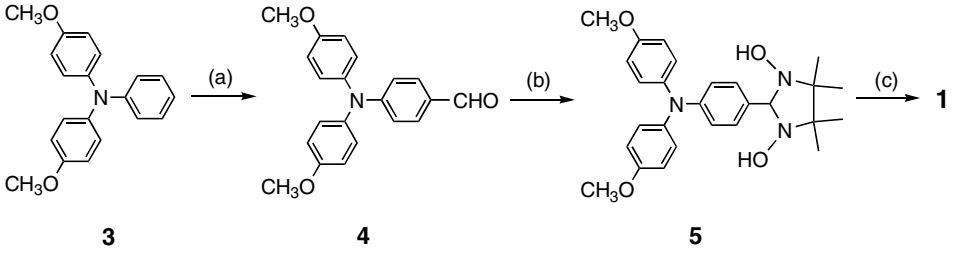
Chart 2.

2. Results and discussion

The synthetic route of the nitronyl nitroxide radical **1** is shown in Scheme 1. The radical **1** was prepared from the corresponding formyl derivative **4** via the Ullman procedure [9]. Bis(4-methoxyphenyl)-4-formylphenylamine **4** was obtained by the Vilsmeier–Haack reaction [10]. 2,3-Bis(hydroxyamino)-2,3-dimethyl-*n*-butane was reacted with **4** to yield the hydroxyamine derivative **5** as the precursor of **1**. Chemical oxidation of **5** with sodium periodate afforded the nitronyl nitroxide **1**. The nitronyl nitroxide bearing the 4-methoxyphenyl moiety, **2**, was also prepared according to the literature [9,11]. The ESR spectrum of **1** in the THF solution gave a five-line signal at $g = 2.006$ with $a_N = 0.78$ mT as the hyperfine coupling constant, which was assigned as a nitronyl nitroxide radical. This hyperfine coupling constant is comparable to 0.75 mT of *N*,*N*-bis[4-(1-oxyl-3-oxide-4,4,5,5-tetramethylimidazolin-2-yl)phenyl]-4-methoxyphenylamine [8a] as a triarylamine-combined nitronyl nitroxide.

Cyclic voltammograms of **1** and **2** are shown in Fig. 1. Two reversible redox couples were observed for **1**, and clearly separated at $E_{1/2} = 0.23$ and 0.49 V with an irreversible reduction wave at −1.2 V. The first reversible redox couple could be attributed to the one-electron oxidation from the triarylamine-moiety to yield the corresponding cationic radical with the quinoid structure, because the oxidation potential of the control triarylamine derivative, *N*,*N*-bis(4-methoxyphenyl)phenylamine **3**, appeared at 0.16 V. The second reversible oxidation of **1** was assigned to the oxidation of the nitronyl nitroxide moiety to afford the corresponding dication, represented in Chart 2. Fig. 2 also shows the reversible redox wave (oxidation potential at $E_{1/2} = 0.33$ V) of **2**, which was slightly lower than the second oxidation potential of **1**. This lower oxidation potential of **2** indicated the electron-donating effect of the methoxy group; on the other hand, the second oxidation of **1** appeared at a higher potential because of the Coulombic interaction between the aminium cation and the nitroxide in $\mathbf{1}^+$. This result also supported the first oxidation of **1** that was ascribed to the oxidation of the triarylamine moiety.

Fig. 2 depicts the UV–Vis absorption spectra during the electrochemical oxidation of **1** in a dichloromethane solution under the potentials up to 0.8 V. The strong absorption bands at 350 nm (π–π*) and 650 nm (n–π*) due to the nitronyl nitroxide moiety [9] gradually disappeared



Scheme 1. Synthesis of **1**. (a) $POCl_3$, DMF, (b) 2,3-bis(hydroxyamino)-2,3-dimethylbutane monosulfate, K_2CO_3, CH_2Cl_2, (c) $NaIO_4$ aq, K_2CO_3, CH_2Cl_2.

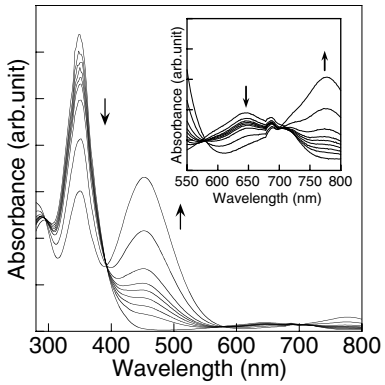


Fig. 2. UV–Vis absorption spectra during electrochemical oxidation of **1** in CH_2Cl_2 with 0.1 M $(n\text{-}C_4H_9)_4NBF_4$ at room temperature (inset: enlarged spectra from 550 to 800 nm).

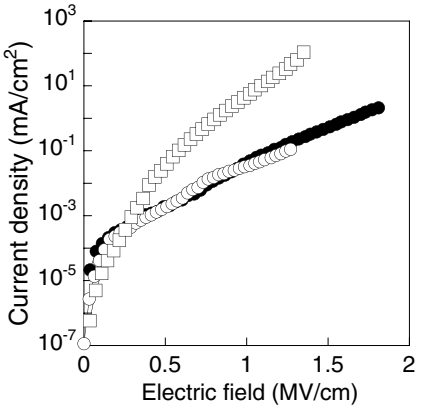


Fig. 3. Current density–electric field characteristics for single-layer devices of **1** (closed circle), **2** (open circle), and TPD (open square) in the device configuration of ITO/hole-transporting molecule:polycarbonate (150 nm)/Al.

during the first oxidation. In contrast, new absorption bands at 780 nm ascribed to the aminium cation moiety and at 450 nm due to the quinoid structure appeared with isosbestic points at 296 and 392 nm. These indicated no subsequent reaction was involved during the one electron oxidation process, which is consistent with the reversible redox couples of **1** observed during the cyclic voltammetry.

A single-layer hole-only device configurated with indium–tin oxide (ITO)/**1**:polycarbonate (150 nm)/Al(150 nm) was fabricated. Compound **1** was dissolved in the THF solution of polycarbonate at a 16 μmol/10 mg ratio, and the resultant solution was spin-coated onto a precleaned ITO substrate. After removal of the solvent under vacuum, aluminum was vapor deposited onto the top of the organic layer as the cathode. Single-layer devices consisting of the polycarbonate layer containing *N*,*N*′-diphenyl-*N*,*N*′-bis(3-methylphenyl)-4,4′-diamine (TPD) or 4-methoxyphenyl nitronyl nitroxide (**2**) were also fabricated as the control.

Current density–electric field plots of the device are shown in Fig. 3. The maximum current density of the **1** device was 0.19 mA/cm^2 at 1.28 MV/cm, which was comparable to that for **2** (0.11 mA/cm^2 at 1.27 MV/cm). The ionization potential of **1** measured by photoelectron spectroscopy was −5.38 eV, which agreed with that of TPD (−5.4 eV) [12]. The hole-injection barrier between the ITO anode (work function = −4.8 eV) and **1** was estimated to be 0.6 eV, which was comparable to that (∼0.6 eV) on the ITO/TPD interface. Therefore, the lower values of the current density for **1** or **2** suggest that the net currents in the radical-containing devices may be dominated by the hole-drift mobility [13] in the radical molecule layer as well as the high hole-injection barrier for the interface between the ITO and the radical layer. The hole-transporting process possibly involves the second redox process due to the localized nitronyl nitroxide moiety or an energetic disorder effect [14] induced by the dipole interaction; These might generate a hole-trapping site, resulting in the lower current density.

Our results concluded that the nitronyl nitroxide combined with the triarylamine moiety possesses a hole-transporting property, which is applicable to a hole-transporting layer. However, the hole-drift mobility would be lower than those of the simple triarylamine derivatives. The drift mobility measurements and further studies to examine the more efficient hole-transporting property by synthesizing other triarylamine-combined nitroxide radical molecules are now underway.

3. Experimental

3.1. *N,N-Bis(4-methoxyphenyl)-4-foymylphenylamine (**4**)*

Compound **4** was synthesized by the Vilsmeier formylation [10]. Phosphoric chloride (10.0 g, 65.2 mmol) was added dropwise into 5.67 ml of DMF at 0 °C under nitrogen, and stirred for 1 h. To the solution was added *N*,*N*-bis(4-methoxyphenyl)-*N*-phenylamine (**3**) (5.00 g, 16.4 mmol) in 20 ml DMF, and the reaction mixture was stirred for 18 h at 100 °C. After cooling to room temperature, the reaction mixture was treated with an aqueous NaCl solution, extracted with CH_2Cl_2, and dried over $MgSO_4$. The solvent was removed under reduced pressure, and the residue was purified by chromatography on silica with the eluent of hexane/dichloromethane (1/4). Recrystallization from ether/hexane afforded greenish-yellow needles. Yield 67%; ^{1}H NMR ($CDCl_3$, 500 MHz) $\delta = 9.75$ (s, 1H), 7.63 (d, $J = 8.8$ Hz, 2H), 7.13 (d, $J = 8.8$ Hz, 4H), 6.89 (d, $J = 9.0$ Hz, 4H), 6.84 (d, $J = 8.8$ Hz, 2H), 3.81 (s, 6H); ^{13}C NMR ($CDCl_3$) $\delta = 190.3$, 157.3, 154.1, 138.8, 131.4, 128.0, 127.8, 116.7, 115.0, 55.5; MS *m*/*z* 333 (M^+). *Anal*. Calc. for $C_{21}H_{19}NO_3$: C, 75.7; H, 5.7; N, 4.2. Found: C, 75.4; H, 5.6; N, 4.1%; mp 102 °C.

3.2. *N,N-Bis(4-methoxyphenyl)-4-(1,3-dihydroxy-4,4,5,5-tetramethylimidazolidin-2-yl)phenylamine (**5**)*

2,3-Bis(hydroxyamino)-2,3-dimethylbutane sulfate (2.95 g, 12.0 mmol) and K_2CO_3 (16.5 g, 120 mmol) were added to 40 ml of ethanol, and stirred for 30 min under nitrogen.

Compound **4** (2.00 g, 6.01 mmol) was added to the reaction mixture and stirred for 48 h at 65 °C. The reaction mixture was concentrated, and the resulting precipitate was filtered and washed with cold methanol and CH_2Cl_2 to give **5** as a white powder (1.73 g). Yield 63%; ^{1}H NMR ($CDCl_3$, 500 MHz) $\delta = 7.27$–7.26 (m, 4H), 7.05–7.03 (m, 4H), 6.91 (d, $J = 8.5$ Hz, 2H), 6.81–6.80 (m, 4H), 4.64 (s, 1H), 3.79 (s, 6H), 1.09 (s, 12H); ^{13}C NMR ($CDCl_3$) $\delta = 155.7$, 148.7, 141.1, 132.2, 129.2, 126.4, 120.6, 114.6, 90.3, 66.9, 55.5, 24.2, 17.0; MS *m*/*z* 461 (M^+).

3.3. N,N-Bis(4-methoxyphenyl)-4-(1-oxyl-3-oxide-4,4,5,5-tetramethylimidazolin-2-yl)phenylamine (*1*)

To the solution of **4** (0.150 g, 0.325 mmol) in CH_2Cl_2 (160 ml) was added a solution of K_2CO_3 (0.454 g, 3.29 mmol) in 5.0 ml of water, and stirred for 5 min under nitrogen. A solution of $NaIO_4$ (83.4 mg, 0.390 mmol) in 5 ml of water was added to the reaction mixture and stirred for 2 h. The reaction mixture was washed with water, dried over Na_2SO_4, and concentrated under reduced pressure. The residue was purified by flash-chromatography on triethylamine-mediated silica gel (hexane/ethylacetate = 3/2) to afford a purple powder (71.8 mg, 0.156 mmol): Yield 48%; FAB MS *m*/*z* 460 (M^+); ESR (in THF): $g = 2.006$, five lines, $|a_N| = 0.78$ mT. *Anal.* Calc. for $C_{27}H_{30}N_3O_4$: C, 70.4; H, 6.6; N, 9.1. Found: C, 70.3; H, 6.8; N, 9.1%.

3.4. Other materials

The other materials, *N*,*N*-bis(4-methoxyphenyl)phenylamine (**3**) [7a], 2,3-bis(hydroxyamino)-2,3-dimethylbutane monosulfate [15], and 2-(4-methoxyphenyl)-4,4,5,5-tetramethylimidazolin-1-oxyl-3-oxide (**2**) [9,11] were prepared according to the literature.

3.5. Measurements

^{1}H and ^{13}C NMR spectra were recorded using a JEOL-Lambda 500 spectrometer. Mass and FAB-Mass spectra were obtained using a Shimadzu GC–MS 17A and a JEOL JMS-SX102A, respectively. UV–Vis spectra were measured with a JASCO V-550. Cyclic voltammetric measurements were carried out with a BAS 100B/W electrochemical analyzer (Bioanalytical Systems, Inc.). The working electrode, the counter electrode, and the reference electrode were a platinum disk, a platinum wire, and a saturated Ag/AgCl, respectively. All cyclic voltammograms were rescaled by the formal redox potential of the ferrocene/ferrocenium couple. ESR spectra were recorded on a JEOL LES-TE200 ESR spectrometer with 100 kHz field modulation. Thin films of the polymers were prepared by spin-coating of a THF solution (1 ml) with radical/polycarbonate = 16 μmol/10 mg on an ITO-glass substrate. The organic solution was filtered through a PTFE filter (pore size ∅ 0.2 μm) before the spin-coating. Thickness of the organic layer was measured with a Dektak surface profilometer. Current–voltage characteristics were measured using a Keithley2400 Source Meter.

Acknowledgements

This work was partially supported by a Grant-in-Aid for the 21COE Program "Practical Nano-Chemistry" from MEXT, Japan. T.K. acknowledges the Research Fellowship of the Japan Society for the Promotion of Science for Young Scientists.

References

[1] (a) C.W. Tang, S.A. VanSlyke, Appl. Phys. Lett. 51 (1987) 913;
(b) J.H. Burroughes, D.D.C. Bradley, A.R. Brown, R.N. Marks, R.H. Friend, P.L. Burn, A.B. Holmes, Nature 347 (1990) 539;
(c) R.H. Friend, R.W. Gymer, A.B. Holmes, J.H. Burroughes, R.N. Marks, C. Taliani, D.D.C. Bradley, D.A. Dos Santos, J.L. Brédas, M. Lögdlund, W.R. Salaneck, Nature 397 (1999) 121;
(d) J. Shinar, Organic Light-emitting Devices: A Survey, Springer, Berlin, 2003.

[2] (a) G. Horowitz, Adv. Mater. 10 (1998) 365;
(b) H.E. Katz, Z.N. Bao, S.L. Gilat, Acc. Chem. Res. 34 (2001) 359;
(c) G. Horowitz, J. Mater. Res. 19 (2004) 1956.

[3] (a) J.J.M. Halls, C.A. Walsh, N.C. Greenham, E.A. Marseglia, R.H. Friend, S.C. Moratti, A.B. Holmes, Nature 376 (1995) 498;
(b) C.J. Brabec, V. Dyakonov, J. Parisi, N.S. Sariciftci, Organic Photovoltaics; Consepts and Realization, Springer, Berlin, 2003;
(c) H. Hoppe, N.S. Sariciftci, J. Mater. Res. 19 (2004) 1974;
(d) S.E. Gledhill, B. Scott, B.A. Gregg, J. Mater. Res. 20 (2005) 3167.

[4] Y. Shirota, J. Mater. Chem. 15 (2003) 75.

[5] (a) T. Kugler, W.R. Salaneck, H. Rost, A.B. Holmes, Chem. Phys. Lett. 310 (1999) 391;
(b) M. Thelakkat, Macromol. Mater. Eng. 287 (2002) 442.

[6] (a) P.M. Lahti, Magnetic Properties of Organic Materials, Marcel Dekker, New York, 1999;
(b) K. Itoh, M. Kinoshita, Molecular Magnetism: New Magnetic Materials, Kohdansha and Gordon & Bsreach, Tokyo and Amsterdam, 2000;
(c) J. Veciana, π-Electron Magnetism From Molecules to Magnetic Materials, Springer, Berlin, 2001;
(d) T. Makarova, F. Palacio, Carbon-Based Magnetism, Elsevier, Amsterdam, 2006.

[7] (a) R.D. Bushby, D.R. McGill, K.M. Ng, N. Taylor, J. Chem. Soc., Perkin Trans. 2 (1997) 1405;
(b) M. Takahashi, T. Nakazawa, E. Tsuchida, H. Nishide, Macromolecules 32 (1999) 6383;
(c) T. Michinobu, J. Inui, H. Nishide, Polyhedron 22 (2003) 1945;
(d) H. Murata, T. Masahiro, K. Namba, N. Takahashi, H. Nishide, J. Org. Chem. 69 (2004) 631;
(e) E. Fukuzaki, H. Nishide, J. Am. Chem. Soc. 128 (2006) 996;
(f) E. Fukuzaki, H. Nishide, Org. Lett. 8 (2006) 1835.

[8] (a) R. Kumai, H. Sakurai, A. Izuoka, T. Sugawara, Mol. Cryst. Liq. Cryst. 279 (1996) 133;
(b) Y. Nakano, T. Yagyu, T. Hirayama, A. Ito, K. Tanaka, Polyhedron 24 (2005) 2141.

[9] E.F. Ullman, J.H. Osiecki, D.G.B. Boocock, R. Darcy, J. Am. Chem. Soc. 94 (1972) 7049.

[10] B.K. Spraul, S. Suresh, T. Sassa, M.Á. Herranz, L. Echegoyen, T. Wada, D. Perahia, D.W. Smith, Tetrahedron Lett. 45 (2004) 3253.

[11] L. Angeloni, A. Caneschi, L. David, A. Fabretti, F. Ferraro, D. Gatteschi, A. le Lirzin, R. Sessoli, J. Mater. Chem. 4 (1994) 1047.

[12] C. Giebeler, H. Antoniadis, D.D.C. Bradley, Y. Shirota, J. Appl. Phys. 85 (1999) 608.
[13] (a) B.K. Crone, P.S. Davids, I.H. Campbell, D.L. Smith, J. Appl. Phys. 84 (1998) 833;
(b) J.C. Scott, G.G. Malliaras, Chem. Phys. Lett. 299 (1999) 115;
(c) Y. Shen, M.W. Klein, D.B. Jacobs, J.C. Scott, G.G. Malliaras, Phys. Rev. Lett. 86 (2001) 3867.
[14] M.V. der Auweraer, F.C. De Schryver, P.M. Bosenberger, H. Bässler, Adv. Mater. 6 (1994) 199.
[15] M. Lamchen, T.W. Mittag, J. Chem. Soc. C (1966) 2300.

common feature for these molecular solids is the system having a quarter-filled π-band, namely, there exists one electron or hole per two molecules.

TCNQ radical (TCNQ = 7,7,8,8-tetracyanoquinodimethanide) possesses a series of variable valences (for example, 0, −0.5 and −1) due to the fine tunable degree of charge transfer and the columnar stack in a donor–acceptor compound, and thus it is possible to obtain the molecular magnets with quasi-1D structure and mixed-valence feature. In this paper, we report the syntheses, crystal structures, IR spectroscopic and magnetic properties of two mixed-valence magnets, $[CNQl]_2[TCNQ]_3$ (**1**) and $[CNPy]_2[TCNQ]_3$ (**2**), where $CNQl^+$ = 1-(4′-cyanobenzyl)quinolinium and $CNPy^+$ = 1-(4′-cyanobenzyl)pyridinium, respectively.

2. Experiments

2.1. Chemicals and reagents

All chemicals and solvents were reagent grade, and were used without further purification. 4-Cyanobenzyl chlorine is the product of Synica Chemicals. 1-(4′-Cyanobenzyl)quinolinium chloride (abbr. as [CNQl]Cl) and 1-(4′-cyanobenzyl)pyridinium chloride (abbr. as [CNPy]Cl) were synthesized following the published procedure [12].

2.2. Physical measurements

Elemental analyses were performed with a Perkin–Elmer 240 analytical instrument. IR spectra were recorded on a Fourier Transform Infrared Spectrometer (170SX) (KBr pellet). Magnetic susceptibility data of **1** and **2** on polycrystalline sample were collected over the temperature range of 2–300 K using a Quantum Design MPMS-5S superconducting quantum interference device (SQUID) magnetometer, and the diamagnetic corrections were made using Pascal's constants ($\chi_0 = 3.3$ emu mol^{-1} for **1** and 2.8 emu mol^{-1} for **2**) [13]. X-band EPR spectra of **1** and **2** were recorded on a Bruker 2000-D-SRC spectrometer on polycrystalline material at room temperature and the microwave frequency is near to 9.7 GHz.

2.3. Syntheses of $[CNQl]_2[TCNQ]_3$ (1) and $[CNPy]_2[TCNQ]_3$ (2)

A modified procedure, described in Ref. [14], was utilized to prepare **1** and **2**. Li(TCNQ) [15] (213 mg, 1.0 mmol) and [CNQl]Cl (283 mg, 1.0 mmol) (1:1 molar ratio) were mixed in water (40 mL) at room temperature, in heterogeneous phase, and stirred for ∼2 h. The black precipitate formed was filtered off, washed with H_2O. The crude product was dissolved in MeOH (∼15 mL) giving a clear solution. The violet-red crystals, which are suitable for X-ray analysis, were obtained after most solvent was evaporated. The crystals of **1** were collected by filtration, washed with Et_2O, and dried in air. Yield: ∼50%. *Anal.* Calc. for $C_{35}H_{19}N_8$: C, 76.2; H, 3.47; N, 20.3. Found: C, 76.0; H, 3.76; N, 20.2%. IR spectra (cm^{-1}): 2227(m) 2199 (m), 2181 (vs), 2174 (vs) and 2156 (sh).

Compound **2** was prepared as that described in **1**, starting from Li(TCNQ) and [CNPy]Cl in water. The yield of final product of crystals is about 52%. *Anal.* Calc. for $C_{31}H_{17}N_8$: C, 74.2; H, 3.42; N, 22.3. Found: C, 73.8; H, 3.68; N, 22.0%. IR spectra (cm^{-1}): 2233 (m), 2185 (vs), 2179 (sh), 2156 (vs).

2.4. X-ray crystallography

Diffraction data of **1** and **2** were collected at 293 K on a Bruker SMART APEX CCD-based diffractometer with graphite-monochromatic Mo Kα radiation. The structures were solved by direct method and refined on F^2 by full-matrix least-squares method using the SHELXTL-PC program package [16]. All non-hydrogen atoms were refined anisotropically. Hydrogen atoms were placed in their calculated positions and refined following the riding model. Crystal data for **1**: $C_{35}H_{19}N_8$, $M = 551.58$, monoclinic, space group $P2(1)/c$, $a = 16.083(3)$ Å, $b = 10.8627(17)$ Å, $c = 17.099(3)$ Å, $\beta = 114.327(3)°$, $V = 2722.0(7)$ Å [3], $Z = 4$, $D_{calc} = 1.346$ g cm^{-3}, $\mu = 0.084$ mm^{-1}, final R, $R_w = 0.0521$, 0.1327. 3856 observed reflections [$I > 2\sigma(I)$] out of 4781 unique ($R_{int} = 0.0534$), GOF = 0.913. Crystal data for **2**: $C_{31}H_{17}N_8$, $M = 501.53$, triclinic, space group $P-1$, $a = 7.314(2)$ Å, $b = 7.659(3)$ Å, $c = 25.131(8)$ Å, $\alpha = 89.900(5)°$, $\beta = 89.450(5)°$, $\gamma = 64.846(5)°$, $V = 1274.2$ (7) Å [3], $Z = 2$, $D_{calc} = 1.307$ g cm^{-3}, $\mu = 0.082$ mm^{-1}, final R, $R_w = 0.0734$, 0.2064. 3556 observed reflections [$I > 2\sigma(I)$] out of 4393 unique ($R_{int} = 0.0511$), GOF = 1.089.

2.5. Details of DFT calculation

The whole non-modelized molecular structure of the real compounds were taken directly from the X-ray crystallography, and the unrestricted density functional theory (DFT) calculations with UB3LYP functional and the 3-21G* basis set are performed using the GAUSSIAN 98 program [17] on the SGI 3800 workstation.

3. Results and discussion

3.1. Descriptions of crystal structures

$[CNQl]_2[TCNQ]_3$ (**1**). Compound **1** crystallizes in a monoclinic system with space group $P2(1)/c$, and an asymmetric unit contains one and half TCNQ entries together with one $[CNQl]^+$ cation (Fig. 1a). For the sake of simple description, two crystallographic independent TCNQ molecules are represented as TCNQ (A) and TCNQ (B). The TCNQ (B) unit containing N(5) atom possesses a inversion centre, while the TCNQ (A) unit containing N(1) atom does not possess any symmetry. The mean molecular planes defined by the corresponding quinodimethane groups between TCNQ (A) and TCNQ (B) make 0.9°

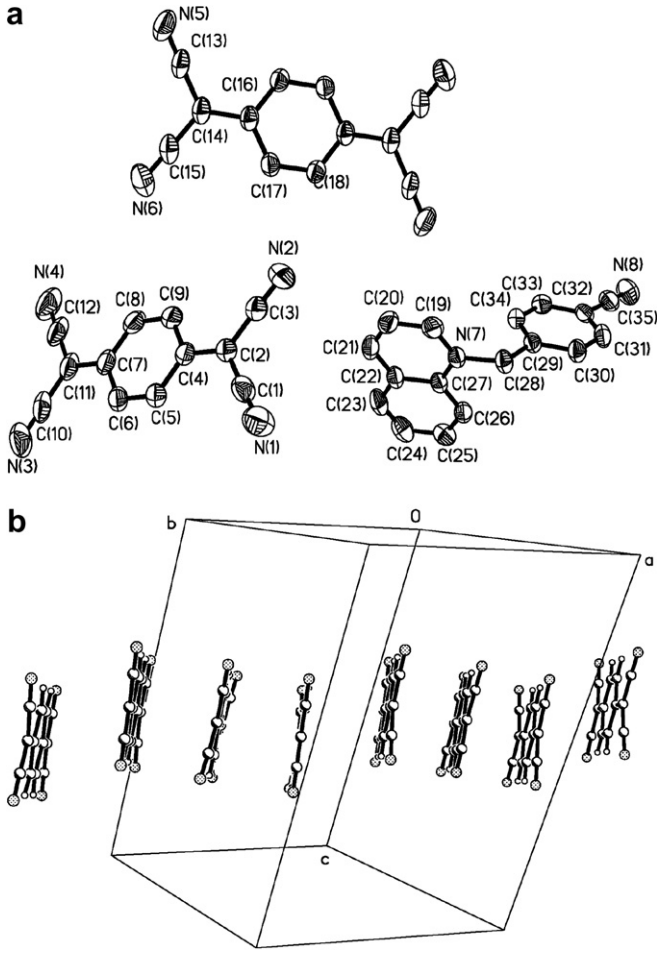


Fig. 1. (a) ORTEP view of **1** at 50% possibility ellipsoids; (b) packing structure of anions showing a triad column in **1**.

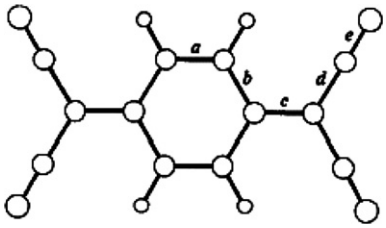
dihedral angle, indicating they are almost parallel to each other. The averaged lengths of chemically similar bonds in TCNQ (A) and TCNQ (B) units, summarized in Table 1, are somewhat different from each other, which are approximately close to $TCNQ^{-1}$ and $TCNQ^{0}$ entries, respectively [18]. Two TCNQ (A) and one TCNQ (B) molecules stack into a triad, and the triads further develop into a column in a pattern …ABA…ABA… along *b*-axis (Fig. 1b). In a TCNQ column, the mean inter-planar separations within three different overlap pairs are 3.207 Å for AA, 3.311 Å for AB and 3.184 Å for BA pairs, respectively.

For the cation, the bond lengths and molecular conformation are in fare agreement with those in $[NO_2Ql]$-$[Ni(mnt)_2]$ [19], and the dihedral angles between aromatic rings and the reference plane, C(28)/C(29)/N(7), are 10.6° for benzene, 73.8° for quinoline, respectively. There exist only van de Waals interactions between the neighboring anions and cations.

[CNPy]$_2$[TCNQ]$_3$ (**2**). Compound **2** crystallizes in a triclinic system with space group $P\bar{1}$, and the asymmetric unit contains one and half TCNQ moieties together with one $CNPy^{+}$ moiety (cf. Fig. 2a). Similar to **1**, one of two crystallographic inequivalence TCNQ molecules possesses an inversion centre (which contains N(5) atom and is labeled as TCNQ (B)), and another does not possess any symmetry (which contains N(1) atom and is labeled as TCNQ (A)). The averaged lengths of chemically similar bonds in TCNQ (A) and TCNQ (B) units are listed in Table 1. It is worthy noting that it is difficult to assign the valence for two crystallographic independent TCNQ species from the metric bond parameters (the averaged bond lengths such as *a*, *b*, *c*, *d* and *e*; cf. Table 1), which is obviously different from that in **1**. Another difference in the aspect of structural feature is the relative arrangement between TCNQ (A) and TCNQ (B) molecules. As shown in Fig. 2b, the mean molecular planes through the corresponding quinodimethane groups in A and B units make a dihedral angle of 68.2°, and TCNQ (A) and TCNQ (B) species form two types of TCNQ columns, respectively.

Table 1
Averaged bond lengths (Å) of the TCNQ molecules in **1** and **2**

The labeling system is illustrated below



	a	*b*	*c*	*d*	*e*
TCNQ in **1** (part A)	1.353	1.412	1.404	1.414	1.140
TCNQ in **1** (part B)	1.344	1.425	1.383	1.421	1.140
TCNQ in **2** (part A)	1.355	1.421	1.405	1.418	1.141
TCNQ in **2** (part B)	1.347	1.418	1.398	1.412	1.142
$TCNQ^{0}$ [18c]	1.346	1.448	1.374	1.440	1.138
$TCNQ^{-1/3}$ [1]	1.350	1.435	1.393	1.430	1.140
$TCNQ^{-1/2}$ [18b]	1.355	1.433	1.396	1.424	1.145
$TCNQ^{-1}$ [18a]	1.362	1.424	1.413	1.417	1.149

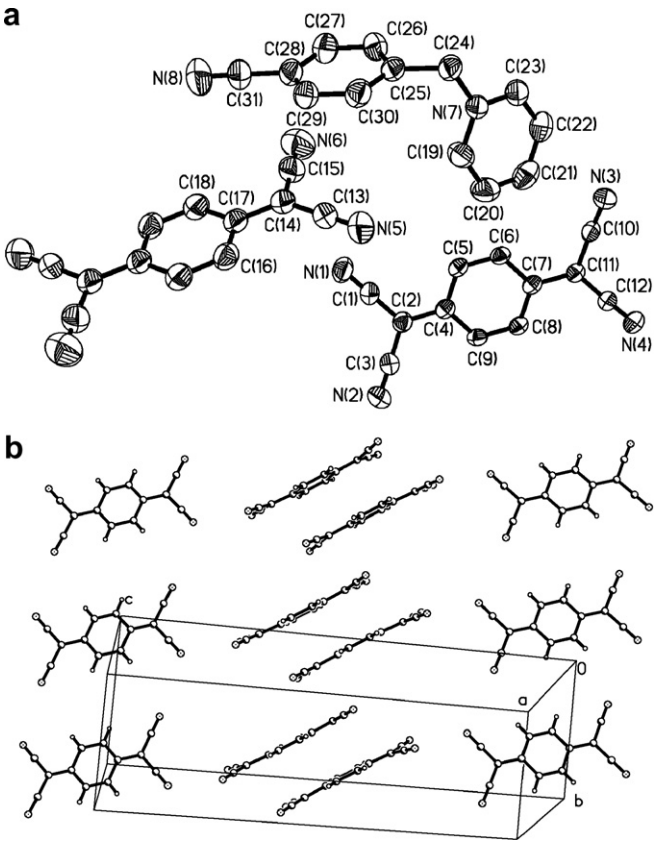


Fig. 2. (a) ORTEP view of **2** at 50% possibility ellipsoids (b) packing structure of anions showing two types of homogeneous columns in **2**.

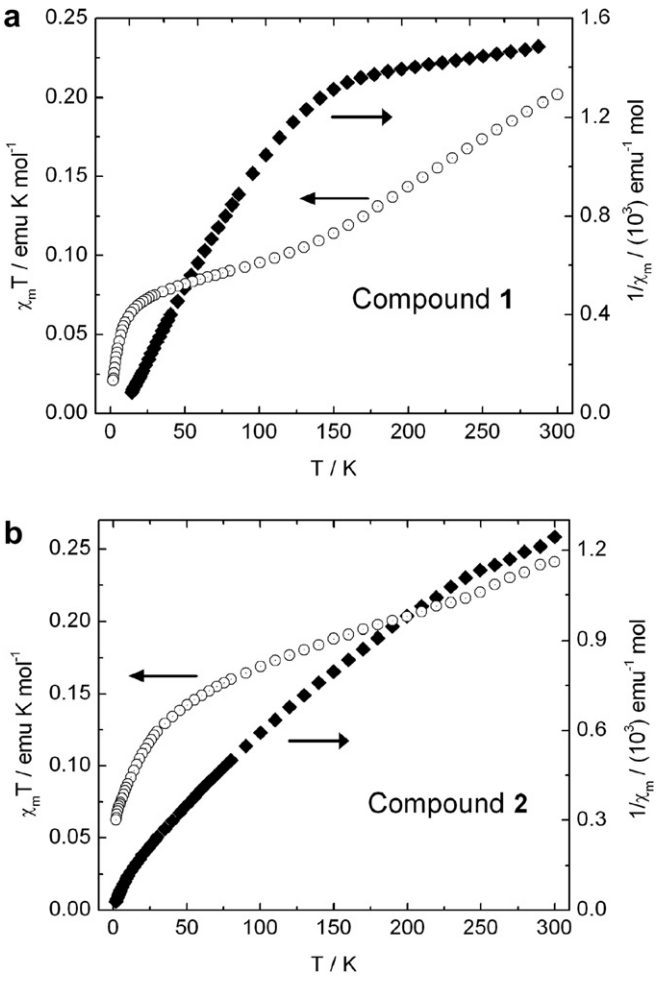


Fig. 3. Temperature dependences of magnetic susceptibility in the forms of $1/\chi_m - T$ and $\chi_m T - T$ for **1** and **2**.

Two different distances between mean-molecular planes are 3.121 and 3.338 Å in TCNQ (A)-type versus 3.771 and 3.771 Å in TCNQ (B)-type columns. Separated by the cations, no short atomic contact is observed between the neighboring TCNQ columns. In $CNPy^+$ moiety, the dihedral angles between aromatic rings and the reference plane, C(24)/C(25)/N(7), are 77.9° for benzene, 129.3° for pyridine, respectively. And there are only weak van de Waals forces between neighboring $CNPy^+$ and TCNQ species.

3.2. Magnetic susceptibilities and EPR spectra

The temperature dependences of magnetic susceptibility are shown as the plots of $1/\chi_m - T$ and $\chi_m T - T$ for **1** and **2** in Fig. 3. To some extent, the magnetic behaviors of both **1** and **2** are similar to each other, and exhibit below features: (1) the $\chi_m T$ values at room temperature are much smaller than expected spin-only values, and upon cooling the $\chi_m T$ values decrease slowly in high temperature range while drop quickly in lower temperature, (2) there is no linear relationship between $1/\chi_m$ and T. These characteristics indicate that there exist strong antiferromagnetic (AFM) coupling interactions within a magnetic TCNQ column and a temperature dependent magnetic coupling behavior. Obviously, the magnetic coupling interaction is stronger in the low temperature range than that in the high temperature range. It is understandable that the temperature dependent magnetic coupling behavior in **1** and **2**. For the planar molecule with extended electric structure, such as TCNQ and M(dithiolene)$_2$ species, spin polarization plays an important role in the intermolecular magnetic coupling interactions, and relatively small adjustments of the intermolecular arrangement (for example, a switch to an eclipsed rather than staggered arrangement) can easily change the magnetic coupling feature. Moreover, a variety of molecular arrangement can be easily reached with temperature change in such molecular crystals, since there are only weak intermolecular interactions. Therefore, the magnetic coupling nature is sensitive to the external perturbations (for example, temperature variation or pressure change) [20,21].

Fig. 4 depicts EPR spectra of **1** and **2** with polycrystalline samples at room temperature. Compound **1** exhibits only one resonance signal even though there exist two types of TCNQ species in solids. The typical radical EPR signal exhibits an isotropic feature without any sizable hyperfine structure observed. The resonance magnetic field, H_r, centered at 3481 Gs with a typical half-width at half-height of

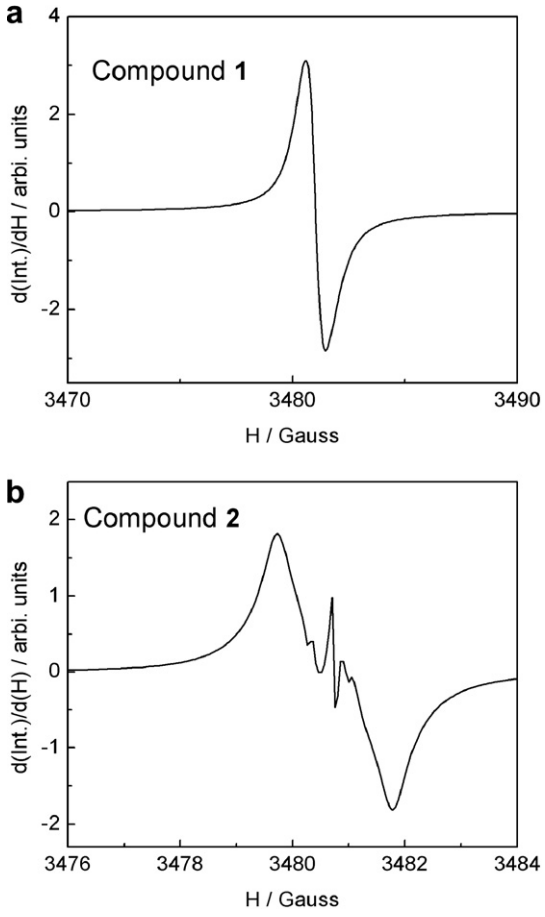


Fig. 4. EPR spectra of **1** and **2** at room temperature.

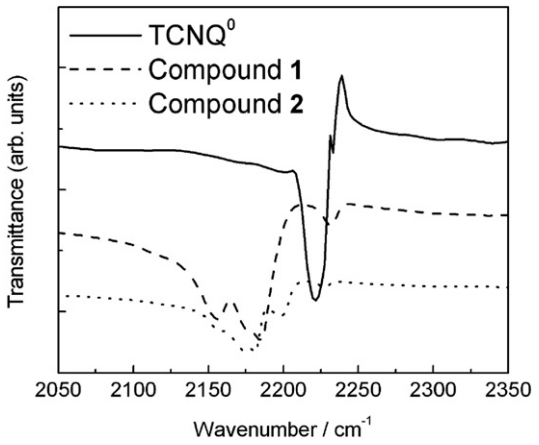


Fig. 5. IR spectra for **1**, **2** and neutral TCNQ in the range of 2050–2350 cm^{-1} at room temperature, and spectra 1 and neutral TCNQ were shifted arbitrarily to transmittance values in order to clarify the figure.

~2 Gs, so the *g*-factors of 2.0066 was obtained. In spectra of **2**, two sets of radical signals are observed. For one set, the resonance field centered at $H_r = 3480$ Gs with a half-width at half-height of ~3 Gs and the corresponding $g = 2.0062$, showing an isotropic characteristic. The other signal exhibits clearly fivefolds hyperfine structure that might arise from the interactions between spins of electron and four equivalent hydrogen atomic nuclear ($I_H = 1/2$) in a quinodimethane group, and the corresponding *g* and *A* values are estimated as 2.0067 and 0.25 Gs, respectively.

3.3. IR spectra and DFT calculations for spin and charge density distribution

For TCNQ species, the geometry varies with the electron population of the MO's, as expected. Thus it is possible to obtain an estimate of the molecular charge from the experimental geometry and IR spectra data. Actually, the relationship between geometric parameters in TCNQ species, IR spectra (especially the intense vibration band *v*(CN) which displays in general no overlap with other vibration models) [22] and the degree of charge transfer has been investigated so far. However, in most cases the different analysis approaches do not consist with each other [18a,18b,18c,18d,22,23]. Fig. 5 shows IR spectra of **1** and **2** which indicate the presence of two types of TCNQ species (*v*(CN) for the neutral TCNQ molecule is usually higher than 2200 cm^{-1}), and one of them seems corresponding to $TCNQ^0$ species. This observation is approximately agreement with the bonding length analyses for **1**, but not for **2** (Ref. Table 1). The reason to cause such a puzzle may arise from that each method is approximate and ignores some other effects, such as the influence of molecular packing on intermolecular geometry [22,23b].

In order to understand the charge distribution of TCNQ species in both **1** and **2**, the DFT calculation for the valence assignment in a $[(TCNQ)_3]^{2-}$ unit was performed at UB3LYP/3-21G* level (one $[(TCNQ)_3]^{2-}$ unit includes two TCNQ (A) moieties and one TCNQ (B) moiety). The calculation results disclosed that two crystallographic independent TCNQ molecules have significantly different charges in **1**. The total charge is −0.8264 for TCNQ (A), −0.8257 for symmetry generated TCNQ (A), and −0.3479 for TCNQ (B) units, that is, the negative charge is mainly localized on TCNQ (A) molecule. For **2**, the total charge is −0.6565 for TCNQ (A), −0.6228 for the symmetry generated TCNQ (A), and −0.7208 for TCNQ (B) units, meaning the negative charges are almost distributed averagely on TCNQ (A) and TCNQ (B) molecules. The above results consist approximately with EPR results of **1** and **2**.

4. Conclusion and remarks

In summary, we have investigated the crystal structural, magnetic property characterizations and theoretic analyses for two radical compounds based on the $[(TCNQ)_3]^{2-}$ unit. In crystals of both **1** and **2**, an asymmetric unit in a cell includes two crystallographic independent TCNQ species (labeled as unit A and B). The unit A and B form a stack in the pattern …ABA…ABA… in **1**, while two types of homogeneous columns (…AA… and …BB…) in **2**, respectively. Temperature dependences of magnetic

susceptibility revealed the magnetic features of strong AFM coupling interaction within a TCNQ stack and temperature dependent magnetic coupling behavior. The IR spectra clearly show the existence of a mixed-valence state in both **1** and **2**, namely, the crystallographic inequivalent TCNQ (A) and TCNQ (B) units possess different negative charge and the values based on the analyses of IR spectra and bond lengths are approximately in agreement with each other for **1** but not for **2**. EPR spectra exhibit two different resonance signals in **2**, however, only one resonance signal in **1** even though **1** and **2** have the same stoichiometry $[cation]_2[TCNQ]_3$. Further, DFT calculation for charge distribution performed in each crystallographic independent TCNQ species disclosed the TCNQ (A) and TCNQ (B) units may be assigned to $TCNQ^{-1}$ and $TCNQ^{0}$ in **1**, and $TCNQ^{-\delta}$ (where partial charge $\delta = 0.62$–0.72) in **2**.

Acknowledgements

This project was financially supported from the National Natural Science Foundation of China (Grant Nos. 20171001 and 20371002), and the Natural Science Foundation of Education Commission of Anhui Province, China (Grant Nos. 044-J-04011, 2005hbz20 and 2006kj042a).

Appendix A. Supplementary materials

CCDC 616746 and 607355 contain the supplementary crystallographic data for **1** and **2**. These data can be obtained free of charge via http://www.ccdc.cam.ac.uk/conts/retrieving.html, or from the Cambridge Crystallographic Data Centre, 12 Union Road, Cambridge CB2 1EZ, UK; fax: (+44) 1223-336-033; or e-mail: deposit@ccdc.cam.ac.uk. Supplementary data associated with this article can be found, in the online version, at doi:10.1016/j.poly.2006.09.028

References

[1] T. Mochida, S. Yamazaki, S. Suzuki, S. Shimizu, H. Mori, Bull. Chem. Soc. Jpn. 76 (2003) 2321, and therein references.
[2] H. Seo, J. Phys. Soc. Jpn. 69 (2000) 805.
[3] H. Seo, H. Fukuyama, Synth. Met. 135–136 (2003) 673.
[4] K. Hiraki, K. Kanoda, Phys. Rev. Lett. 80 (1998) 4737.
[5] M. Mitsumi, K. Kitamura, A. Morinaga, Y. Ozawa, M. Kobayashi, K. Toriumi, Y. Iso, H. Kitagawa, T. Mitani, Angew. Chem., Int. Ed. 41 (2002) 2767.
[6] (a) H. Seo, H. Fukuyama, J. Phys. Soc. Jpn. 66 (1997) 1249;
(b) F. Nad, P. Monceau, J.M. Fabre, Phys. Rev. B 62 (2000) 1753;
(c) D.S. Chow, F. Zamborsky, B. Alavl, D.J. Tantillo, A. Baur, C.A. Merlic, S.E. Brown, Phys. Rev. Lett. 85 (2000) 1698.
[7] M. Sakata, M. Maesato, A. Ota, H. Yamochi, G. Saito, Synth. Met. 153 (2005) 393.
[8] T. Yamamoto, M. Uruichi, K. Yakushi, Phys. Rev. B 73 (2006) 125116.
[9] K. Miyagawa, A. Kawamoto, K. Kanoda, Phys. Rev. B 62 (2000) 7679.
[10] H. Tajima, S. Kyoden, H. Mori, S. Tanaka, Phys. Rev. B 62 (2000) 9378.
[11] K. Yamamoto, K. Yakushi, K. Miyagawa, K. Kanoda, A. Kawamoto, Phys. Rev. B 65 (2002) 085110.
[12] S.B. Bulgarevich, D.V. Bren, D.Y. Movshovic, P. Finocchiaro, S. Failla, J. Mol. Struct. 317 (1994) 147.
[13] R.L. Carlin, Magnetochemistry, Spring, Berlin, 1986, p. 3.
[14] P.F. Wang, G.X. Liu, Y.C. Chen, Acta Crystallogr., Sect. E 62 (2006) O3256.
[15] L.R. Melby, R.J. Harder, W.R. Hertler, W. Mahler, R.E. Benson, W.E. Mochel, J. Am. Chem. Soc. 84 (1962) 3374.
[16] G.M. Sheldrick, SHELXTL, Structure Determination Software Programs, Version 5.10, Bruker Analytical X-ray Systems Inc., Madison, WI, USA, 1997.
[17] M.J. Frisch et al., GAUSSIAN 98, Revision A.11.2, Gaussian, Inc., Pittsburgh, PA, 2001.
[18] (a) G.J. Ashwell, D.D. Eley, A. Harpper, A.C. Torrance, S.C. Wallwork, M.R. Willis, Acta Cryst. B 33 (1977) 2258;
(b) G.J. Ashwell, S.C. Wallwork, S.R. Barker, P.I.C. Bertheir, Acta Cryst. B 31 (1975) 1175;
(c) R.E. Long, R.A. Sparks, K.N. Trueblood, Acta Cryst. 18 (1965) 932;
(d) P.S. Flandrois, D. Chasseau, Acta Crystallogr. Sect. B 33 (1977) 2744;
(e) G.X. Liu, X.M. Ren, R.K. Kremer, Q.J. Meng, J. Mol. Struct. 743 (2005) 125.
[19] X.M. Ren, C.S. Lu, Y.J. Liu, H.Z. Zhu, H.F. Li, C.J. Hu, Q.J. Meng, Trans. Met. Chem. 26 (2001) 136.
[20] A.T. Coomber, D. Beljonne, R.H. Friend, J.L. Brédas, A. Charlton, N. Robertson, P. Underhill, A.E.M. Kurmoo, P. Day, Nature 380 (1996) 144.
[21] Z.P. Ni, X.M. Ren, J. Ma, Z.D. Chen, J.L. Xie, C.L. Ni, Q.J. Meng, J. Am. Chem. Soc. 127 (2005) 14330.
[22] J.S. Chappell, A.N. Bloch, W.A. Bryden, M. Maxfield, T.O. Poehler, D.O. Cowan, J. Am. Chem. Soc. 103 (1981) 2442.
[23] (a) S. Flandrois, D. Chasseau, Acta Crystallogr., Sect. B 833 (1977) 2744;
(b) T.C. Urnland, S. Allie, T. Kuhlmann, P. Coppens, J. Phys. Chem. 92 (1988) 6456.

magnetic building block, $[Ni(mnt)_2]^-$ monoanion, whose syntheses, crystal structures and magnetic susceptibilities are described.

2. Experiment

Disodium maleonitriledithiolate (abbr. as Na_2mnt) were prepared according to the published procedure [9]. [Diprotonated benzene-1,4-diamine][$Ni(mnt)_2$]$_2$ (**1**) and [diprotonated 1,4-diazabicyclo[2.2.2]octane][$Ni(mnt)_2$]$_2 \cdot 3MeCN$ (**2**) were synthesized using a similar procedure described in the literature [8]. *Anal*. Calc. for $C_{11}H_5N_5NiS_4$ (**1**): C, 33.5; N, 17.8; H, 1.28. Found: C, 33.2; N, 17.7; H, 1.47%. *Anal*. Calc. for $C_{28}H_{23}N_{13}Ni_2S_8$ (**2**): C, 36.7; N, 19.9; H, 2.53%. Found: C, 36.2; N, 19.3; H, 2.81%.

The MeCN solution of **1** or **2** was put in a refrigerator at about 0 °C for 24 h, and the block-shaped crystals were obtained which were suitable for X-ray structural analysis and other measurements.

2.1. X-ray crystallography

The diffraction data were collected at 293 K for **1** and 253 K for **2** with graphite-monochromated Mo Kα ($\lambda = 0.71073$ Å) on a Rigaku Raxis-Rapid diffractometer. Structures were solved by direct methods using the SHELXL-97 software package [10]. The non-H atoms were refined anisotropically using the full-matrix least-squares method on F^2. All H atoms were placed at calculated positions and refined riding on the parent atoms. The crystallographic details about data collection and structure refinement are summarized in Table 1.

Table 1
Crystal and structural refinement data of **1** and **2**

	1	**2**
Chemical formula	$C_{11}H_5N_5NiS_4$	$C_{28}H_{23}N_{13}Ni_2S_8$
Formula weight	394.15	915.49
CCDC number	606918	606919
Temperature (K)	293(2)	253(2)
Wavelength (Å)	0.71073	0.71073
Space group	$P\bar{1}$	$P\bar{1}$
a (Å)	6.3306(13)	9.7418(19)
b (Å)	8.7155(17)	12.604(3)
c (Å)	14.334(3)	16.625(3)
α (°)	72.60(3)	101.47(3)
β (°)	78.04(3)	98.26(3)
γ (°)	76.23(3)	101.76(3)
V (Å^3), Z	725.1(3), 2	1922.1(7), 2
D_{calc} (g cm^3)	1.377	1.582
Absorption coefficient (mm^{-1})	0.987	1.455
$F(000)$	304	932
θ Range for data collection	3.01–27.47	2.99–27.48
Index ranges	$-8 \leqslant h \leqslant 8$, $-10 \leqslant k \leqslant 11$, $-18 \leqslant l \leqslant 17$	$-12 \leqslant h \leqslant 12$, $-16 \leqslant k \leqslant 16$, $-21 \leqslant l \leqslant 19$
Reflections collected	12409	18493
Independent reflections [R_{int}]	3299 [0.0193]	8697 [0.0347]
Refinement method on F^2	full-matrix least-squares	
Data/restraints/parameters	3299/0/190	8697/0/460
Goodness-of-fit on F^2	1.082	1.015
Final R indices [$I > 2\sigma(I)$]	$R_1 = 0.0276$, $wR_2 = 0.0803$	$R_1 = 0.0429$, $wR_2 = 0.0962$
R indices (all data)	$R_1 = 0.0338$, $wR_2 = 0.0828$	$R_1 = 0.0953$, $wR_2 = 0.1202$
Residual (e Å^{-3})	0.411 and −0.456	0. 515 and −0.348

$R_1 = \sum(||F_o| - |F_c||)/\sum|F_o|$, $wR_2 = \sum w(|F_o|^2 - |F_c|^2)^2/\sum w(|F_o|^2)^2]^{1/2}$.

2.2. Magnetic susceptibility measurements

Temperature dependent magnetic susceptibilities on polycrystalline samples of **1** and **2** were measured between 2 and 350 K using a Quantum Design MPMS XL superconducting quantum interference device (SQUID) magnetometer.

3. Results and discussion

3.1. Descriptions of crystal structures

*Crystal structure of **1***: An asymmetric unit of **1** consists of one $[Ni(mnt)_2]^-$ anion and a half cation (diprotonated benzene-1,4-diamine), and the centre of benzene ring coincides with an inversion centre, as shown in Fig. 1a. The anion $[Ni(mnt)_2]^-$ possesses an approximately planar geometry. The Ni–S lengths range from 2.1448(8) to 2.1524(8) Å and two S–Ni–S angles in the chelate rings are 92.75(3)° and 92.67(3)°, respectively. These values are in fare agreement with those reported $[Ni(mnt)_2]^-$ compounds [1e,6]. As shown in Fig. 1d, the anions form a π-stacked layer, which is approximately parallel to the *ab*-plane. Two overlap fashions between neighboring anions along the direction of a stack were depicted in Fig. 1b and c. Face-to-face overlap involves anionic pairs containing Ni(1) and Ni(1)^{i} (symmetric code i $= -x+1, -y, -z+1$), in which the distances [Ni(1)...Ni(1)^{i}, 3.717 Å, Ni(1)...S(2)^{i}, 3.887 Å, Ni(1)...S(4)^{i}, 3.872 Å, S(2)...S(3)^{i}, 3.669 Å, and S(1)...S(4)^{i}, 3.698 Å] are comparable to the distance (3.532 Å) between the corresponding mean-molecular-planes (which is defined by the core NiS_4). Longitudinal and transverse offset involve anionic pairs containing Ni(1) and Ni(1)^{ii} (symmetric code ii $= -x+1, -y+1, -z+1$), in which the distances [Ni(1)...Ni(1)^{ii}, 5.829 Å, S(3)...S(4)^{ii}, 4.122 Å, of Ni(1)...S(3)^{ii}, 4.715 Å] are much longer than that of the corresponding mean-molecular-planes (3.685 Å). The interstack Ni...Ni, Ni...S and S...S distances (the shortest distances are 6.331 Å for Ni...Ni, 4.706 Å for Ni...S, and 3.705 Å for S...S) are slight greater than the intrastack distances.

There exist the H-bonding interactions between anions and cations as illustrated in Fig. 2, and geometric parameters, listed in Table 2, are comparable with the values in the literature [1e,11–14]. The adjacent anionic sheets are held together by cations through H-bonding interactions to develop into a 3D network.

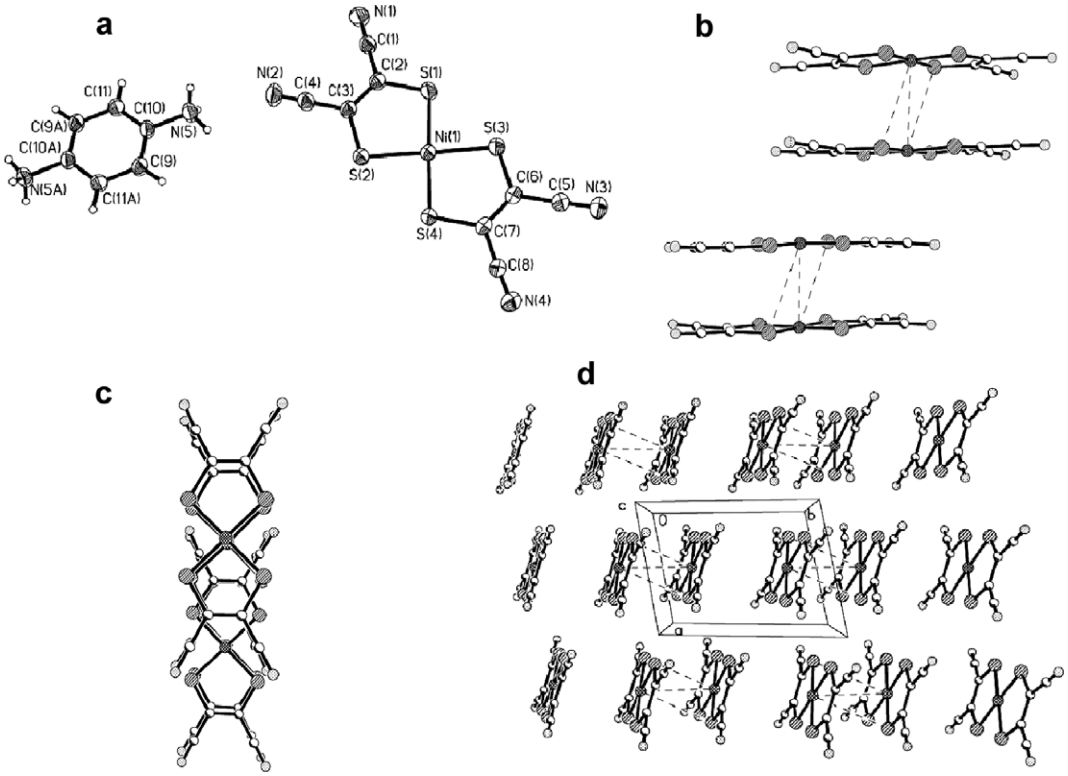


Fig. 1. (a) ORTEP draw (50% probability thermal ellipsoids) of **1**, showing non-hydrogen atomic numbering; (b) side view; (c) top view of anionic stack; (d) anionic layer projected on *ab*-plane.

Crystal structure of **2**: Compound **2** crystallizes in a triclinic system with space group $P\bar{1}$, and an asymmetric unit contains two anions, one cation together with three molecules of solvent MeCN. For a cation, diprotonated 1,4-diazabicyclo[2.2.2]octane, the bond lengths and angles are in good agreement with those reported in the literature [8]. The molecular structures of two crystallographic inequivalent anions rather resemble to **1**, and the Ni–S lengths are in the range 2.1436(11)–2.1472(13) Å and two S–Ni–S angles in the chelate rings are 92.72(4)° and 92.95(4)° in the anion containing Ni(1) [and the corresponding values Ni–S lengths: 2.1450(11)–2.1539(11) Å; S–Ni–S angles in the chelate rings: 92.52(5)° and 92.69(4)° in the anion containing Ni(2)].

As shown in Fig. 3, two adjacent anions stack into a dimer [denoted as Ni(1)Ni(2)], in which the shorter intermolecular separations are 3.802 Å for Ni(1)...Ni(2)^{i}, 3.794 Å for Ni(1)...S(4)^{i} and 3.800 Å for S(1)...S(4)^{i} and 3.807 Å for S(2)...S(3)^{i} (symmetric code i = x, y, $-1+z$). The dimers form a columnar stack in a fashion of

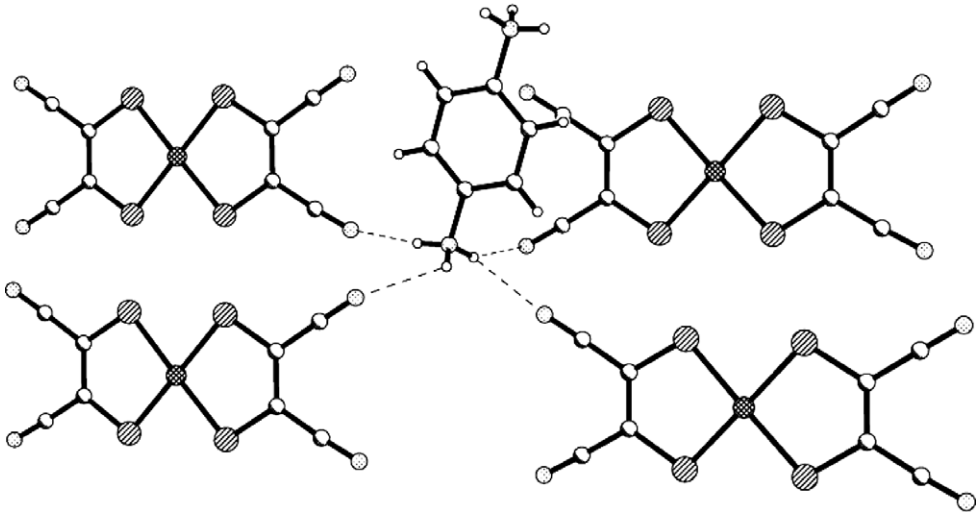


Fig. 2. H-bonding interactions between cation and anions in **1**.

Table 2
Geometric parameters of hydrogen bonds in **1** and **2** (Å and °)

D–H...A	*d*(D–H)	D(H...A)	*d*(D...A)	∠(DHA)
1				
N(5)–H(5A)...N(4)#1	0.89	2.10	2.979(2)	170.8
N(5)–H(5B)...N(3)#2	0.89	2.42	2.954(3)	118.6
N(5)–H(5C)...N(3)#3	0.89	2.32	3.117(3)	149.9
N(5)–H(5C)...N(1)#4	0.89	2.55	2.980(3)	110.6
Symmetric codes: #1 = $-x+2, -y, -z+1$; #2 = $-x+1, -y, -z+1$; #3 = $-x+2, -y, -z$; #4 = $-x+1, -y, -z$				
2				
N(9)–H(9A)...N(1)#1	0.91	2.20	2.931(5)	137.0
N(9)–H(9A)...N(7)#2	0.91	2.45	3.122(4)	130.9
N(10)–H(10A)...N(2)#3	0.91	2.30	3.022(4)	136.7
N(10)–H(10A)...N(13)#3	0.91	2.42	3.116(7)	133.8
Symmetric codes: #1 = $-x, -y-2, -z+1$; #2 = $x+1, y, z$; #3 = $x, y, z-2$				

$\cdots$Ni(2)Ni(1)$\cdots$Ni(1)Ni(2)$\cdots$Ni(2)Ni(1)$\cdots$, and the shorter intermolecular separations are 3.705 Å for Ni(1)...S(2)^{j} and 3.794 Å for Ni(2)...S(6)^{k} Å (symmetric codes: j = $-x, -2-y, 2-z$; k = $-1-x, -3-y, -z$) between the inter-dimers. Further, the anionic stacks arrange into a sheet which is approximately parallel to the crystallographic *ab*-plane. The H-bonding interactions are also observed between cations and anions, as well between cations and solvent molecules (cf. Fig. 4), and their geometric parameters are summarized in Table 2.

In the field of utilizing the crystal-oriented syntheses via non-covalent interactions to generate functional materials, it is important to understand the self-assembly feature of functional molecular building blocks. In our studies, we noted that the countercation, benzylpyridinium derivatives, induces the magnetic molecular building block, $[Ni(mnt)_2]^-$ ion, to form separated stacking columns of cations and anions [6], while the countercation with H-bonding donor nature makes $[Ni(mnt)_2]^-$ ions easily to construct a 2D anionic layer structure [8,14].

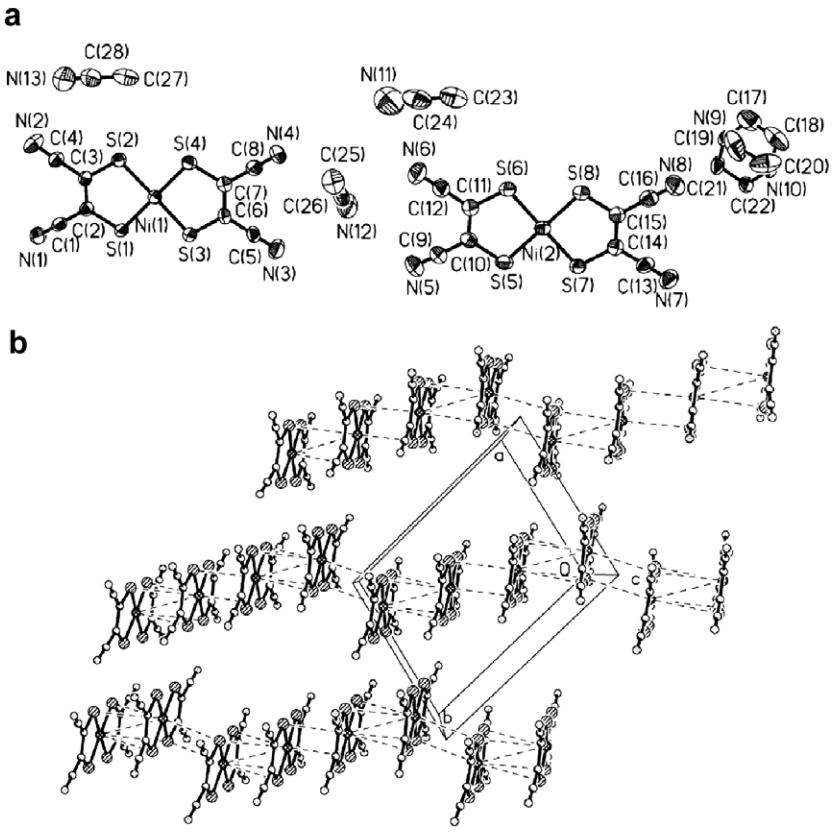


Fig. 3. (a) ORTEP draws of **2** at 50% probability thermal ellipsoids, showing non-hydrogen atomic numbering (H-atoms omitted for clarity). (b) An anionic sheet projected on *ab*-plane.

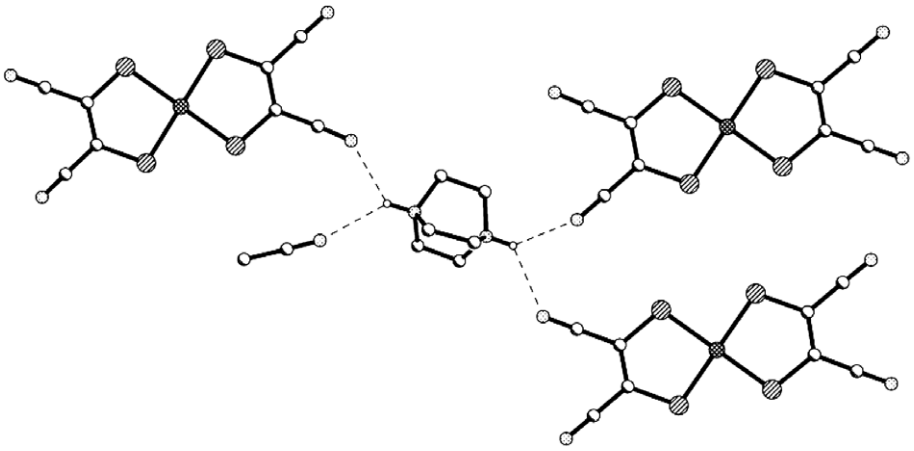


Fig. 4. H-bonding interactions between anions and cation and between solvent molecule MeCN and cation in **2**.

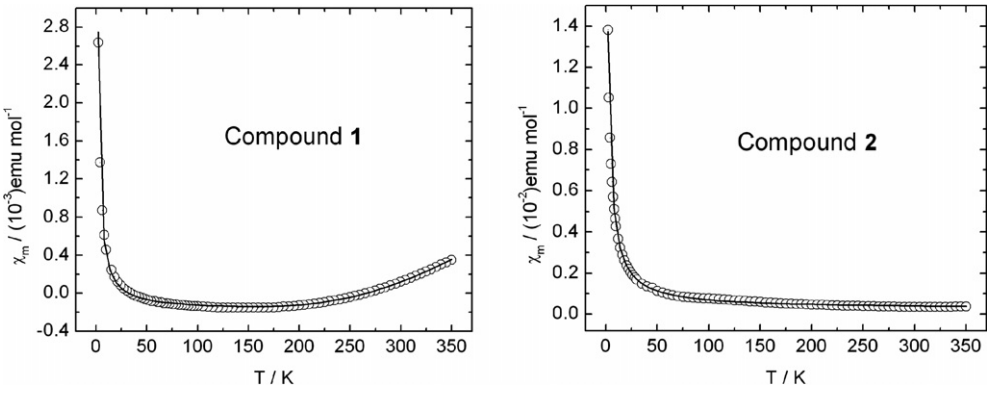


Fig. 5. Temperature dependences of the magnetic susceptibility of **1** and **2**, and the open circles and solid lines are experimental data and fits, respectively (see text).

3.2. Magnetic susceptibilities

Fig. 5 shows the temperature dependences of magnetic susceptibility for **1** and **2**. Compound **1** exhibits an activated magnetic behavior in the high-temperature range together with a Curie tail at the lower temperature range due to magnetic impurities. From the viewpoint of crystal structure, it is possible for **1** to exhibit the magnetic behavior of a spin dimer with $S = 1/2$, however, the temperature dependences of magnetic susceptibility does not follow the Bleaney–Bowers. While Eq. (1) [15] for a dimerized Hubbard spin chain system can be used to fit the magnetic susceptibility data,

$$\chi_m = \frac{\alpha}{T^{\gamma}} \cdot \exp(-\Delta/k_B T) + \frac{C}{T} + \chi_0 \quad (1)$$

where α is a constant corresponding to the dispersion of excitation energy, Δ/k_B is the magnitude of the spin gap, and γ is a constant. The term C/T represents the contributions of the magnetic impurity, χ_0 is the contributions from core diamagnetism and possibly Van Vleck paramagnetism, and other symbols have their usual meanings. The best fits magnetic susceptibility data to Eq. (1) yielded the parameters: $\alpha = 1.76(5)$, $\gamma = 0.65(3)$, $\Delta/k_B = 1504$ (50) K, $C = 5.85(4) \times 10^{-3}$ emu K mol^{-1}, $\chi_0 = -1.8(2) \times 10^{-4}$ emu mol^{-1}. For **2**, the magnetic behavior follows the Curie–Weiss law,

$$\chi_m = \frac{C}{T - \theta} + \chi_0 \quad (2)$$

and fitting the temperature dependence of magnetic susceptibility to Eq. (2) gave the reasonable parameters $C = 4.53(2) \times 10^{-2}$ emu K mol^{-1}, and $\chi_0 = -2.5(1) \times 10^{-4}$ emu mol^{-1}. The smaller Curie constant indicates that the weak paramagnetic interactions maybe originate from the magnetic impurity (lattice defect), and hence the inherent magnetic behaviors of **2** should be diamagnetic due to existence of very strong antiferromagnetic coupling interactions within the eclipsed $[Ni(mnt)_2]^-$ dimers.

4. Conclusions

Summarily, the crystal structures and magnetic properties were presented for two new H-bonding molecular magnets based on molecular building block $[Ni(mnt)_2]^-$. In crystals of both **1** and **2**, the common feature of the crystal

structure is that $[Ni(mnt)_2]^-$ monoanions form π-stacked sheet and the neighboring sheets are held together via H-bonding interactions between anions and cations. The magnetic behavior of **1** deviates from the model of spin dimer with $S = 1/2$ but follows a dimerized Hubbard spin chain model even though its crystal structure reveals the dimer feature. The strongly antiferromagnetic exchange interactions between the nearest spins in **2** make this compound to be nearly diamagnetic. It is very interesting and significant to understand how the geometric nature of a countercation to influence the stacking pattern of $[Ni(mnt)_2]^-$ anions, and how the stacking pattern of $[Ni(mnt)_2]^-$ anions influence on the magnetic coupling feature between anions. To gain more insight into such questions, further experimental and theoretic investigations are in progress [16].

Acknowledgements

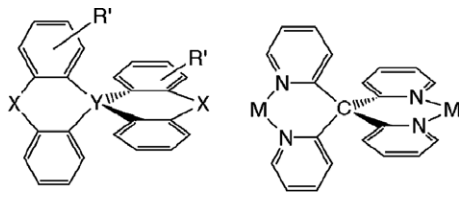
This work was partly supported by a Grant-in-Aid for Science Research from the Ministry of Education, Culture, Sports, Science and Technology of Japan. X.M. Ren thanks National Natural Science Foundation of China for financial support (Projects Nos. 20171001 and 20371002).

Appendix A. Supplementary materials

CCDC 606918 and 606919 contain the supplementary crystallographic data for this paper. These data can be obtained free of charge via http://www.ccdc.cam.ac.uk/conts/retrieving.html, or from the Cambridge Crystallographic Data Centre, 12 Union Road, Cambridge CB2 1EZ, UK; fax: (+44) 1223-336-033; or e-mail: deposit@ccdc.ac.uk. Supplementary data associated with this article can be found, in the online version, at doi:10.1016/j.poly.2006.09.016.

References

[1] (a) D. Braga, L. Maini, M. Polito, F. Grepioni, Struct Bond 111 (2004) 1;
(b) C. Paraschiv, S. Ferlay, Mir W. Hosseini, V. Bulach, J.-M. Planeix, Chem. Commun. (2004) 2270;
(c) T. Akutagawa, S. Takeda, T. Hasegawa, T. Nakamura, J. Am. Chem. Soc. 126 (2004) 291;
(d) M.E. Itkis, X. Chi, A.W. Cordes, R.C. Haddon, Science 296 (2002) 1443;
(e) X.M. Ren, Y.C. Chen, C. He, S. Gao, J.C.S. Dalton Trans. (2002) 3915.
[2] N. Robertson, L. Cronin, Coord. Chem. Rev. 227 (2002) 93.
[3] (a) A.T. Coomber, D. Beljonne, R.H. Friend, J.L. Bredas, A. Charlton, N. Robertson, A.E. Underhill, M. Kurmoo, P. Day, Nature 380 (1996) 144;
(b) I.D. Parker, R.H. Friend, P.I. Clemenson, A.E. Underhill, Nature 324 (1986) 547.
[4] (a) F. Bigoli, P. Deplano, M.L. Mercuri, L. Marchio, L. Pilia, A. Serpe, G. Concas, F. Congiu, S. Sanna, Chem. Phys. Lett. 421 (2006) 361;
(b) R.D. Willett, C.J. Gomez-Garcia, B.L. Ramakrishna, B. Twamley, Polyhedron 24 (2005) 2232;
(c) J. Nishijo, E. Ogura, J. Yamaura, A. Miyazaki, T. Enoki, T. Takano, Y. Kuwatani, M. Iyoda, Solid State Commun. 116 (2000) 661.
[5] S.S. Staniland, W. Fujita, Y. Umezono, K. Awaga, S.J. Clark, H.B. Cui, H. Kobayashid, N. Robertson, Chem. Commun. (2005) 3204.
[6] (a) X.M. Ren, Q.J. Meng, Y. Song, C.S. Lu, C.J. Hu, X.Y. Chen, Inorg. Chem. 41 (2002) 5686;
(b) X.M. Ren, H. Okudera, R.K. Kremer, Y. Song, C. He, Q.J. Meng, P.H. Wu, Inorg. Chem. 43 (2004) 2569;
(c) X.M. Ren, T. Akutagawa, S. Nishihara, T. Nakamura, W. Fujita, K. Awaga, J. Phys. Chem. B 109 (2005) 16610.
[7] (a) O. Kahn, C.J. Martinez, Science 279 (1998) 44;
(b) W. Fujita, K. Awaga, Science 286 (1999) 261.
[8] X.M. Ren, S. Nishihara, T. Akutagawa, S. Noro, T. Nakamura, Inorg. Chem. 45 (2006) 2229.
[9] A. Davison, H.R. Holm, Inorg. Synth. 10 (1967) 8.
[10] G.M. Sheldrick, SHELXL-97, Program for the Refinement of Crystal Structure, University of Göttingen, Germany, 1997.
[11] X.M. Ren, C.S. Lu, P.H. Wu, Q.J. Meng, J. Chem. Crystallogr. 32 (2002) 173.
[12] X.M. Ren, J.L. Xie, Y.C. Chen, R.K. Kremer, J. Mol. Struct. 660 (2003) 139.
[13] M. Fourmigué, C. Mézière, S. Dolou, Crystal Growth Des 3 (2003) 805.
[14] P.C. Crawford, A.L. Gillon, J. Green, A.G. Orpen, T.J. Podesta, S.V. Pritchard, CrystEngComm 6 (2004) 419.
[15] D.C. Johnston, R.K. Kremer, M. Troyer, X. Wang, A. Klümper, S.L. Bud'ko, A.F. Panchula, P.C. Canfield, Phys. Rev. B 61 (2000) 9558.
[16] Z.P. Ni, X.M. Ren, J. Ma, J.L. Xie, C.L. Ni, Q.J. Meng, J. Am. Chem. Soc. 127 (2005) 14330.



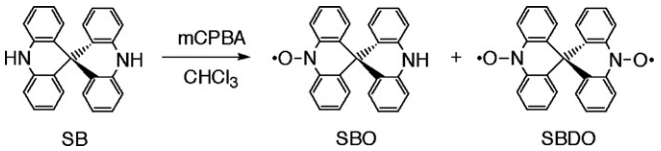
1 : X = N-O• ; Y = C **3** : M = Mn^{II}

2 : X = N•-R ; Y = Si **4** : M = Ni^{II}

Scheme 1. Spiro-type organic biradicals (**1** and **2**) and coordination compounds (**3** and **4**).

2. Experimental

The precursor **SB** [17] prepared from diphenylamine and acridone in three steps [8] was oxidized with *m*-chloroperbenzoic acid (mCPBA) (Scheme 2). To a solution of **SB** (301 mg; 0.87 mmol) in $CHCl_3$ (20 mL) was added a solution of mCPBA (512 mg; 3.0 mmol) in $CHCl_3$ (30 mL) at 0 °C with stirring, and the combined solution was stirred further at 0 °C for 12 h. The color turned dark red. The mixture was passed through a short column (basic alumina) with CH_2Cl_2 as an eluent. A red fraction was collected and concentrated under reduced pressure. The mixture was purified again by HPLC (Japan Analytical Industry 1H + 1H GPC columns; eluted with $CHCl_3$; a flow rate: 3.5 mL min^{-1}). The elution was monitored at UV 254 nm absorption. A red fraction of the retention time of 65 min contained **SBDO** and that of 68 min contained **SBO**, which were assigned by means of ESR and other spectroscopic methods. The yields were 15 mg (0.040 mmol; 5%) and 118 mg (0.33 mmol; 38%) for **SBDO** and **SBO**, respectively. **SBO** · ($CHCl_3$): m.p. 35–36 °C ($CHCl_3$ liberation). *Anal.* Calc. for $C_{26}H_{18}Cl_3N_2O$: C, 64.95; H, 3.77; N, 5.83. Found: C, 65.86; H, 3.90; N, 5.91%. ESI-TOF MS *m*/*z* 384 ($M + Na^+$). IR (KBr disc) 746, 1335, 1373, 1485, 1518, 1608, 3352 cm^{-1}. ESR (9.7 GHz, benzene, room temperature) $g = 2.0082$, $a_N = 8.80$ G, $a_H = 2.35$, 0.72 G. Recrystallization of **SBO** from CH_2Cl_2, $CHCl_3$, CH_3OH, CH_3CN, and C_6H_5Cl gave solvated molecular complexes, **SBO** · (CH_2Cl_2)$_2$, **SBO** · $CHCl_3$, **SBO** · CH_3CN, **SBO** · C_6H_5Cl, and **SBO** · CH_3OH, respectively. **SBDO**: m.p. 226–227 °C (dec). *Anal.* Calc. for $C_{25}H_{16}N_2O_2$: C, 79.77; H, 4.28; N, 7.44. Found: C, 78.06; H, 5.08; N, 7.57%. ESI-TOF MS *m*/*z* 399 ($M + Na^+$). IR (KBr disc) 754, 1373, 1435, 1485, 1610, 1637 cm^{-1}. ESR (9.7 GHz, benzene, room temperature) a broad singlet at $g = 2.008$ with a peak-to-peak line width of ca. 16 G.



Scheme 2. Preparation of **SBO** and **SBDO**.

Diffraction data of single crystals of **SBDO** and solvated **SBO** were collected on a Rigaku R-axis RAPID diffractometer with graphite monochromated Mo Kα or Cu Kα radiation. The structures were directly solved and the parameters were refined in the CrystalStructure program package (version 3.5.1, Rigaku/MSC, The Woodlands, TX 77381, USA (2003)). Numerical absorption correction was used. All of the hydrogen atoms were experimentally found. Selected crystallographic parameters of **SBO** · (CH_2Cl_2)$_2$, **SBO** · CH_3CN and **SBDO** are listed in Table 1. The crystal structures of **SBO** · $CHCl_3$, **SBO** · C_6H_5Cl, and **SBO** · CH_3OH were preliminarily solved.

Magnetic susceptibilities of polycrystalline specimens of **SBDO** and solvated **SBO** were measured on a Quantum Design MPMS SQUID magnetometer equipped with a 7 T coil in a temperature range of 1.8–300 K. The magnetic responses were corrected with diamagnetic blank data of the sample holder measured separately. The diamagnetic contribution of the sample itself was estimated from Pascal's constant.

An ESR spectra were recorded on a Bruker ESP300E X-band (9.7 GHz) spectrometer equipped with an Oxford cryostat for low-temperature measurements. Saturation effects were carefully removed from the spectra by lowering the microwave power. Solid solutions in poly(butyl methacrylate) was obtained from mixing substrate and polymer (the substrate concentration was 10^{-3} to 10^{-5} w/w%) in dichloromethane followed by casting as film on a glass plate. Simulated spectra for the frozen and liquid solutions were calculated in the WinEPR Simfonia program (version 1.25, Bruker Biospin, Rheinstetten, Germany (1996)).

Table 1
Selected crystallographic data for **SBO** · (CH_2Cl_2)$_2$, **SBO** · CH_3CN, and **SBDO**

Compounds	**SBO** · (CH_2Cl_2)$_2$	**SBO** · CH_3CN	**SBDO**
Formula	$C_{27}H_{21}Cl_4N_2O$	$C_{27}H_{20}N_3O$	$C_{25}H_{16}N_2O_2$
Habit	red block	black platelet	brown platelet
Dimension (mm^3)	0.5 × 0.4 × 0.4	0.8 × 0.75 × 0.1	0.7 × 0.6 × 0.1
T (K)	90(1)	100(1)	293(1)
Crystal system	monoclinic	triclinic	triclinic
Space group	*C*2/*c*	$P\bar{1}$	$P\bar{1}$
a (Å)	14.7675(13)	9.203(4)	8.4741(14)
b (Å)	10.0276(6)	14.881(7)	9.0232(17)
c (Å)	16.3530(10)	15.479(8)	13.534(2)
α (°)	90	82.56(4)	96.599(15)
β (°)	97.478(3)	78.05(3)	93.736(14)
γ (°)	90	76.76(4)	115.254(14)
V (Å^3)	2401.0(3)	2011.2(16)	922.2(3)
Z	4	4	2
D_{calc} (g cm^{-3})	1.470	1.329	1.355
Unique data	2733	8986	3185
μ(Mo Kα) (mm^{-1})	0.517	0.082	
μ(Cu Kα) (mm^{-1})			0.697
R_{int}	0.068	0.041	0.064
$R(F)$[a] ($I > 2\sigma(I)$)	0.0524	0.0613	0.0443
$wR(F^2)$[b] (all data)	0.0822	0.0819	0.0614

[a] $R = \sum ||F_o| - |F_c|| / \sum |F_o|$.

[b] $wR = [\sum w(F_o^2 - F_c^2)^2 / \sum w(F_o^2)^2]^{1/2}$.

Molecular orbital calculations were performed on the GAUSSIAN 03 program (Revision C.02, Gaussian Inc., Pittsburgh, PA 15106, USA (2003)). We applied unrestricted density functional (DFT) UB3LYP methods with the Becke exchange functional [18] and the Lee–Yang–Parr correlation functional [19]. The 6-31G** basis set was chosen. The convergence criterion for the energy was set at 10^{-9} a.u. The structural parameters were given from the crystallographic analysis.

3. Results and discussion

Oxidation of **SB** with *m*-chloroperbenzoic acid gave **SBDO** together with a monoradical, **SBO**. Both crystalline radicals are stable in air at room temperature, but **SBDO** in a solution phase was gradually decomposed under ambient conditions. Fig. 1a shows the observed and simulated X-band ESR spectra for **SBO**. The observed coupling pattern is typical of 9,10-dihydroacridin-10-oxyls [14–16]. The hyperfine coupling constants due to the *o*- and *p*-H atoms are close to each other, and those of *m*-H atoms are much smaller than those of *o*- and *p*-H atoms, where *o*-, *m*-, and *p*-positions are defined with respect to the nitroxide group. The simulated curve reproduced well the experimental one with the optimized parameters: $a_{o\text{-H}} = a_{p\text{-H}} = 2.35$ G and $a_{m\text{-H}} = 0.72$ G together with $a_{\text{N}} = 8.80$ G. On the other hand, **SBDO** showed a broad and distorted single signal even in a sufficiently deairated and dilute solution (Fig. 1b). This broadening is owing to intramolecular dipole–dipole and exchange interactions among the unpaired electrons. The presence of monoradical impurities was suggested with the hyperfine structures superposed, indicating that a small portion of **SBDO** is decomposed during these measurements in solutions.

The molecular structures of **SBO** and **SBDO** were unequivocally determined by means of X-ray crystallographic analysis. We found molecular complexes, **SBO** · $(CH_2Cl_2)_2$, **SBO** · $CHCl_3$, **SBO** · CH_3CN, **SBO** · C_6H_5Cl,

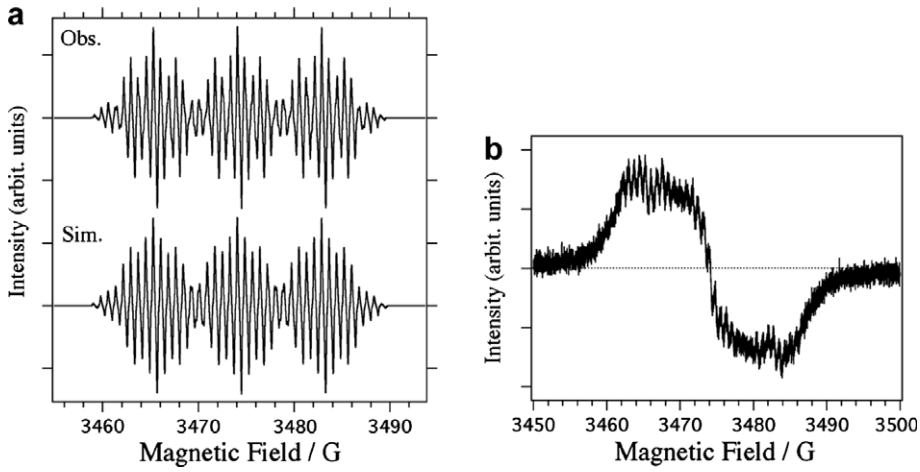


Fig. 1. Solution X-band ESR spectra of (a) **SBD** and (b) **SBDO** in benzene at room temperature.

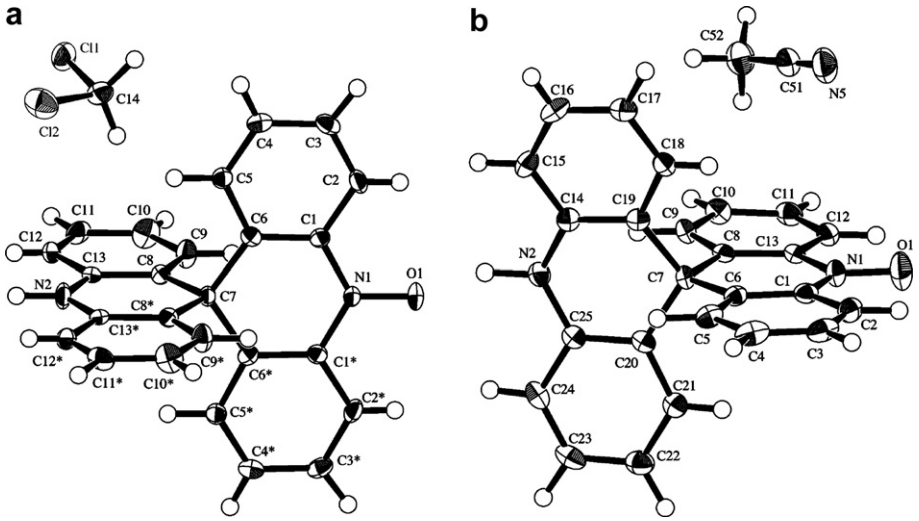


Fig. 2. Ortep drawings of (a) **SBO** · $(CH_2Cl_2)_2$ and (b) **SBO** · CH_3CN with thermal ellipsoids at the 50% probability level for non-hydrogen atoms.

and **SBO** · CH_3OH (Fig. 2 for **SBO** · $(CH_2Cl_2)_2$ and **SBO** · CH_3CN). The solvent molecules are located in a hydrophobic cavity surrounded by the walls of the acridine skeleton. The rigid molecular structure of **SBO** is suitable to form nearly rectangular cavities in the crystal. It has been proved that the a methoxy-derivative of **SB** (abbreviated as **MSB**) can work as a host for conventional organic solvent molecules, affording **MSB** · $(CH_2Cl_2)_2$, **MSB** · $(CHCl_3)_2$, and **MSB** · $CH_2Cl_2 \cdot C_6H_6$ for example [8]. The methoxy group in **MSB** and the oxyl group in **SBO** seem responsible for expansion of the cavity sizes. In the case of **SBO** · $(CH_2Cl_2)_2$, **SBO** · $CHCl_3$, **SBO** · CH_3CN, and **SBO** · C_6H_5Cl, hydrogen-bonding interaction is found between the nitroxide oxygen and amine hydrogen atoms in the crystal packing, while the methanol oxygen atom in **SBO** · CH_3OH interacts with amine hydrogen atoms instead. The nitroxide group in **SBO** has a quite usual geometry as indicated by very planar configuration around the nitrogen atom and the bond lengths of N–O ranges in 1.288(2)–1.292(3) Å being typical of 9,10-dihydroacridin-10-oxyls [14–16].

The crystal structure of **SBDO** was determined, where no solvent molecule was incorporated. Ortep drawing and crystal packing diagram are depicted in Fig. 3a and b. The N–O bond distances are 1.290(1) and 1.283(2) Å, which are also typical of 9,10-dihydroacridin-10-oxyls [14–16]. The intermolecular N–O · · · N–O contacts are found in both sides of the nitroxide groups (Fig. 3b). There is a crystallographical inversion center between two nitroxide groups in neighboring molecules, and two N–O groups form a head-to-tail rectangle. The geometries around N1–O1 · · · $N1^*$–$O1^*$ and around N2–O2 · · · $N2^{\#}$–$O2^{\#}$ are similar to each other. The interatomic distances are 3.176(2) and 3.184(2) Å for O1 · · · $N1^*$ and O2 · · · $N2^{\#}$, respectively, which are only 4% longer than the sum of Van der Waals radii [20]. Recently, very close intermolecular contacts of nitroxide groups are reported to show a practically diamagnetic nature [21,22]. The present compound would exhibit relatively strong antiferromagnetic coupling in an intermolecular manner. Furthermore, this proximity leads to closer packing in the crystal, and purges a guest molecule to give the unsolvated crystal.

We measured the magnetic susceptibility of a randomly oriented polycrystalline sample of **SBDO** to clarify magnetic exchange interaction operative in the crystal. Fig. 4 shows the temperature dependence of the molar magnetic susceptibility χ_{mol} and the product $\chi_{mol}T$ for **SBDO**. The $\chi_{mol}T$ value decreased on lowering temperature, indicating the presence of dominant antiferromagnetic coupling. A step-like behavior was found at 0.1 $cm^3\,K\,mol^{-1}$ due to the almost magnetically isolated monoradical species. The $\chi_{mol}T$ decreased again on further cooling. To estimate the magnitude of magnetic interaction, we applied a singlet–triplet model [23], where the spin-Hamiltonian is defined as $H = -2JS_1 \cdot S_2$. The presence of $S = 1/2$ paramagnetic impurity due to partial decomposition was taken into

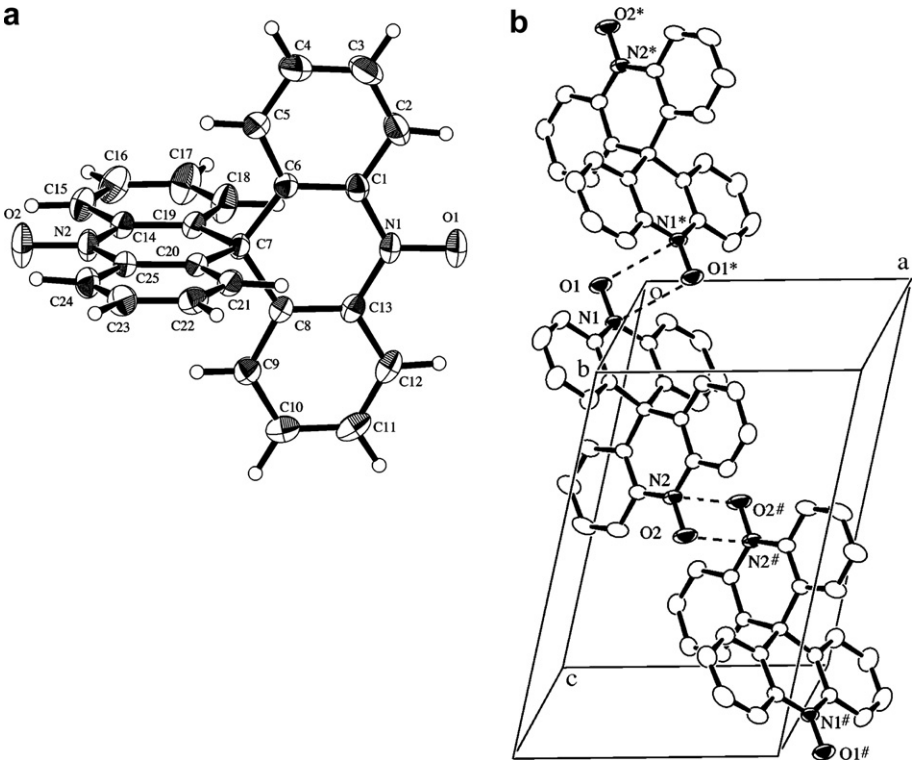


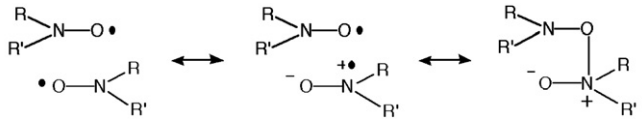
Fig. 3. (a) Ortep drawing of **SBDO** with the thermal ellipsoids at the 30% probability level for non-hydrogen atoms. (b) Molecular arrangement in the crystal of **SBDO**. Three molecules are drawn in a linear array along the $a + b + c$ diagonal direction. Hydrogen atoms are omitted for clarity. Relatively short distances are indicated with dotted lines. Symmetry operation codes for ∗and # are $(-x, -y, -z)$ and $(-x + 1, -y + 1, -z + 1)$, respectively.

consideration, and the molar fraction of the doublet was defined as α. In addition, inter-monomer interaction is included as a Weiss mean field parameter (θ), and Eq. (1) was derived accordingly. We obtained the following optimized parameters: $J/k_B = -70.2(7)$ K, and $\alpha = 0.316(9)$, and $\theta = -2.6(3)$ with $g = 2$ (fixed). The calculated curve well reproduced the experimental data (the solid lines in Fig. 4)

$$\chi_{mol} = (1-\alpha)\frac{Ng^2\mu_B^2}{k_B T}\frac{2}{3+\exp(2J/k_B T)} + \alpha\frac{Ng^2\mu_B^2}{4k_B(T-\theta)} \quad (1)$$

The bulk specimen included a somewhat large quantity of monoradical impurities, which might be decomposed products during the sample preparation. The X-ray diffraction study demonstrated the satisfactory determination of the crystal structure because of the process of manual selection of a well-shaped crystal. Thus, portions of single crystals were sufficiently pure whilst the remainder was not. We found difficulty in preparation of a highly pure bulk specimen, as clarified by the purification and magnetic measurements of **SBDO** several times.

A question arises here: to which the singlet-triplet model should be assigned, a **SBDO** molecule or N–O ··· N-O contacts? In other words, is the ground state of a **SBDO** molecule triplet or singlet? Possible intramolecular magnetic interaction would be clarified by means of a solid solution ESR study and suggested by theoretical calculation (see below). From the results of the X-ray crystallographic analysis of **SBDO**, it is most likely that the observed antiferromagnetic interaction would be ascribed mainly to intermolecular interaction due to a SOMO–SOMO overlap at relatively close contacts. This interaction can be depicted as the following canonical structures; that is, antiferromagnetic coupling appears as a contribution of a very weak covalent bond. There are two independent intermolecular N–O ··· N–O contacts, but both situations are fortunately quite similar to each other. Thus, the coupling constant obtained here implies the average of the two intermolecular interactions.



We attempted ESR measurements of **SBDO** under diluted conditions. Fig. 5a shows the X-band ESR spectrum of **SBDO** solved in a poly(butyl methacrylate) matrix at 20 K. This figure shows a clear fine structure, but additional signals were superposed. Possible origins of the additional signals are hyperfine interaction due to the nitrogen atoms [24] and aggregation of **SBDO** molecules leading to superposition of triplet signals. We supposed that the most outer lines at 3259 and 3437 G were assigned to the **SBDO** $H//z$ signals. The point dipole approximation, $|D'| = |D|/g\mu_B = |-3g\mu_B/2r^3|$, from the zero-field splitting parameter $|D'|$ of 89 G gave a dipole–dipole distance of 6.8 Å. This value is somewhat smaller than the actual distance of

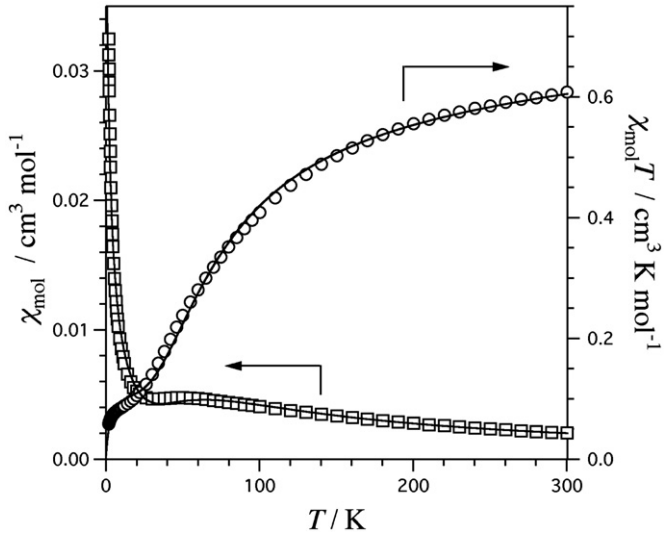


Fig. 4. Temperature dependence of χ_{mol} (squares) and $\chi_{mol}T$ (circles) for **SBDO** measured at 5000 Oe. Solid lines represent a theoretical fit. See the text for the equation and parameters.

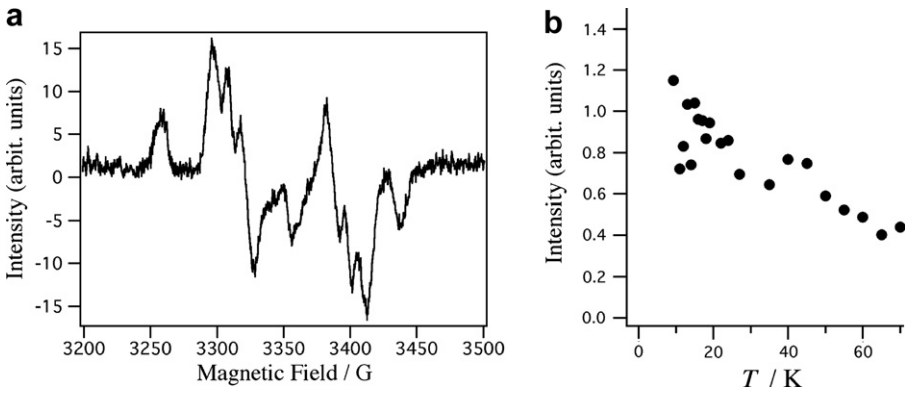


Fig. 5. (a) X-band ESR spectrum of **SBDO** measured in poly(butyl methacrylate) at 20 K. (b) Temperature dependence of the signal intensity of the average of the most outer signals at 3259 and 3437 G.

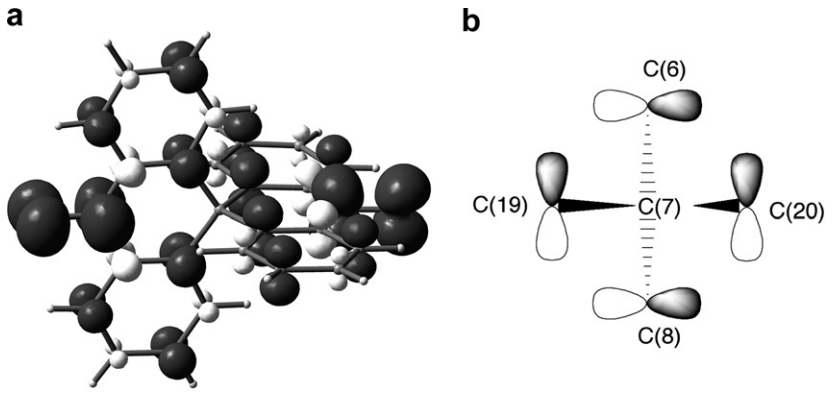


Fig. 6. (a) Spin density distribution at the triplet state of **SBDO** calculated on the UB3LYP/6-31G** level (dark gray: positive spin density; light gray: negative spin density). The geometry was given from the X-ray crystallographic analysis. (b) Orthogonal arrangement between two SOMOs. See Fig. 3 for the atomic numbering.

7.8 Å defined between the centers of the N–O bonds. The calculated distance is rationally acceptable because the spins are delocalized onto the adjacent phenyl rings to approach effectively each other. Another parameter $|E'|$ was 6.7 G, which could not be precisely determined because of the additional lines.

The temperature dependence of the peak heights of the $H//z$ signals approximately obeyed the Curie law (Fig. 5b); the ESR signal intensity increased on lowering temperature. This finding is in sharp contrast to those of the magnetic susceptibility of the bulk **SBDO** solid. The ground spin multiplicity of a free **SBDO** molecule is suggested to be triplet. However, it is not completely eliminated that the singlet and triplet states would be almost degenerate.

We performed theoretical calculation of **SBDO** based on the unrestricted density functional theory (UB3LYP/6-31G**). The distribution of the spin density (2e in total) is drawn in Fig. 6a, which clearly represents the SOMOs carrying a π-character. The alternative spin density throughout the conjugation system is illustrated. We also confirmed orthogonality of the two SOMOs (Fig. 6b), and accordingly ferromagnetic coupling is strongly suggested from this geometry. In this calculation, the SCF energies for the triplet and singlet states were −1221.97118170 and −1221.97110516 a.u., respectively. The calculation indicates that the triplet state is more stable than the singlet state by the energy difference of 7.65×10^{-5} a.u. The energy gap between the $S = 1$ and $S = 0$ states corresponds to $2J_{\text{intra}}$, and accordingly the calculated J_{intra} value was estimated to be 3.83×10^{-5} a.u. $= 1.01 \times 10^{2}$ J mol^{-1}, which is converted to 12 K or 8.4 cm^{-1}.

To evaluate the solid solution data by modeling a free single molecule, the molecular geometry was fully optimized in the calculation of UB3LYP/6-31G** for **SBDO**. We obtained results similar to those of the geometry fixed; the triplet state (−1222.16232761 a.u.) is more stable than the singlet state (−1222.16224543 a.u.) by the energy difference of 8.22×10^{-5} a.u., which gives the calculated J_{intra} value of 13 K. The SOMO lobes and spin density maps were practically identical to those of the single point calculation of the molecular structure determined in the crystal. Thus, the intramolecular ferromagnetic coupling is expected from the DFT calculation. Furthermore, the intramolecular interaction ($J_{\text{intra}}/k_{\text{B}} = 12$–$13$ K) was calculated to be much smaller than the intermolecular antiferromagnetic interaction ($|J_{\text{inter}}/k_{\text{B}}| = 70$ K), and the experimental results on the **SBDO** solid can reasonably be interpreted by the fact that the former is buried by the latter.

It should be noted that **SBDO** has a significant π-spin polarization whilst the dinuclear nickel(II) complex [{Ni(hfac)$_2$}$_2$(py$_4$C)] (**4** in Scheme 1) has a σ-spin superexchange mechanism [12], where Hhfac stands for 1,1,1,5,5,5-hexafluoropentane-2,4-dione. In the case of σ-spin systems, the magnitude of the exchange coupling decays with an increase of the distance between two spins. Actually, the $J_{\text{Ni–Ni}}$ of [{Ni(hfac)$_2$}$_2$(py$_4$C)] was very small (+0.57 K), being consistent with the long distance through the Ni–N–C–C–C–N–Ni skeleton [12]. The calculation on **SBDO** indicates that J_{intra} (12–13 K) is much larger than that of [{Ni(hfac)$_2$}$_2$(py$_4$C)], because the π-spin is ready to be delocalized onto the aromatic rings especially to the *o*- and *p*-positions, and the four carbon atoms surrounding the spiro center possess considerable coefficients of SOMOs. Therefore, the organic free radical systems may have the advantage for development of ground high-spin molecules.

4. Summary

We successfully synthesized and characterized 9,9′(10*H*,10′*H*)-spirobiacridine-10,10′-dioxyl (**SBDO**) as a quite unique molecule symbolized by a point group D_{2d}. Magnetic measurements on the polycrystalline sample of **SBDO** revealed the presence of antiferromagnetic interaction, which can be ascribed mainly to intermolecular interaction due to close contacts between two nitroxide groups. The ESR experiments and DFT calculation indicated the

ground triplet state of **SBDO**. There have been numerous reports on the magnetic properties tunable by mans of supramolecular techniques [25–30]. Possible host-guest molecular complexes from **SBDO** may clarify the intrinsic ground state of **SBDO**, owing to the separation of the radical center and accordingly the absence of intermolecular interactions. To stabilize the nitroxide groups under ambient conditions, introduction of alkoxyl groups to the acridine phenyl rings is now underway.

5. Supporting materials

CCDC 617554, 617555, and 617556 contain the supplementary crystallographic data for the compounds **SBO** · $(CH_2Cl_2)_2$, **SBO** · CH_3CN, and **SBDO**. These data can be obtained free of charge via http://www.ccdc.cam.ac.uk/conts/retrieving.html, or from the Cambridge Crystallographic Data Centre, 12 Union Road, Cambridge CB2 1EZ, UK; fax: (+44) 1223-336-033; or e-mail: deposit@ccdc.cam.ac.uk.

Acknowledgements

This work was supported by Grants-in-Aid for Scientific Research (Nos. 15073101, 16550121, and 15550115) from the Ministry of Education, Culture, Sports, Science and Technology, Japan. The authors thank Dr. Takashi Kawakami for kind instruction of ab initio MO calculation.

References

[1] L. McElwee-White, D.A. Dougherty, J. Am. Chem. Soc. 104 (1982) 4722.
[2] L. McElwee-White, W.A. Goddard III, D.A. Dougherty, J. Am. Chem. Soc. 106 (1984) 3461.
[3] R.M. Dupeyre, A. Rassat, J. Ronzaud, J. Am. Chem. Soc. 96 (1974) 6559.
[4] N.L. Frank, R. Clérac, J.-P. Sutter, N. Daro, O. Kahn, C. Coulon, M.T. Green, S. Golhen, L. Ouahab, J. Am. Chem. Soc. 122 (2000) 2053.
[5] H. Oshio, T. Watanabe, A. Ohto, T. Ito, U. Nagashima, Angew. Chem., Int. Ed. Eng. 33 (1994) 670.
[6] M.E. Itkis, X. Chi, A.W. Cordes, R.C. Haddon, Science 296 (2002) 1443.
[7] X. Chi, M.E. Itkis, B.O. Patrick, T.M. Barclay, R.W. Reed, R.T. Oakley, A.W. Cordes, R.C. Haddon, J. Am. Chem. Soc. 121 (1999) 10395.
[8] M. Ooishi, M. Seino, R. Imachi, T. Ishida, T. Nogami, Tetrahedron Lett. 43 (2002) 5521.
[9] A. Ito, M. Urabe, K. Tanaka, Angew. Chem. Int. Ed. 42 (2003) 921.
[10] A. Okazawa, T. Ishida, T. Nogami, Chem. Lett. 33 (2004) 1478.
[11] A. Okazawa, T. Ishida, T. Nogami, Polyhedron 24 (2005) 2584.
[12] A. Okazawa, T. Nogami, T. Ishida, Chem. Phys. Lett. 427 (2006) 333.
[13] R.S. Mulliken, Phys. Rev. 41 (1932) 751.
[14] M. Seino, Y. Akui, T. Ishida, T. Nogami, Synth. Met. 133–134 (2003) 581.
[15] M. Nakagawa, T. Ishida, M. Suzuki, D. Hashizume, M. Yasui, F. Iwasaki, T. Nogami, Chem. Phys. Lett. 302 (1999) 125.
[16] R. Imachi, T. Ishida, M. Suzuki, M. Yasui, F. Iwasaki, T. Nogami, Chem. Lett. (1997) 743.
[17] W. Trischler, E. Sturm, H. Kiesele, E. Daltrozzo, Chem. Ber. 117 (1984) 2703.
[18] A.D. Becke, J. Chem. Phys. 98 (1993) 5648.
[19] C. Lee, W. Yang, R.G. Parr, Phys. Rev. B 37 (1998) 785.
[20] A. Bondi, J. Phys. Chem. 68 (1964) 441.
[21] G. Kurokawa, T. Ishida, T. Nogami, Chem. Phys. Lett. 392 (2004) 74.
[22] H. Nishimaki, S. Mashiyama, M. Yasui, T. Nogami, T. Ishida, Chem. Mater. 18 (2006) 3602.
[23] B. Bleaney, K.D. Bowers, Proc. R. Soc. Lond., Ser. A 214 (1952) 451.
[24] P. Michon, A. Rassat, J. Am. Chem. Soc. 99 (1977) 2825.
[25] K. Awaga, E. Coronado, M. Drillon, MRS Bull. 25 (2000) 52.
[26] J. Larionova, S.A. Chavan, J.V. Yakhmi, A.G. Froystein, J. Sletten, C. Sourisseau, O. Kahn, Inorg. Chem. 36 (1997) 6374.
[27] A. Rujiwatra, C.J. Kepert, J.B. Claridge, M.J. Rosseinsky, H. Kumagai, M. Kurmoo, J. Am. Chem. Soc. 123 (2001) 10584.
[28] D. Maspoch, D. Ruiz-Molina, K. Wurst, N. Domingo, M. Cavallini, F. Biscarini, J. Tejada, C. Rovira, J. Veciana, Nat. Mater. 2 (2003) 190.
[29] K. Igarashi, T. Nogami, T. Ishida, Chem. Commun. (2006), in press doi:10.1039/b613637k.
[30] T. Ishida, J. Omata, T. Nogami, Polyhedron 22 (2003) 2133.

with the zero-dimensional $FeCl_4^-$ anion a field-induced-superconductivity with π–d interaction was evidenced which is believed to mediate through S···Cl between donor and anion [4,5]. We have been interested in exploring the intermediate dimensionality (1D) by developing methods of obtaining uniform one-dimensional anion with $(C_2O_4)^{2-}$ and Cl^- as charge balancing units with TTF, BEDT-TTF and BEDT-TSF donors, because it is possible to introduce the magnetic interaction by the oxalate bridges between moment-carriers as well as π–d interaction through S···Cl contacts [4] and thus, to produce dual-function molecular materials. This effort resulted in the isolation of charge-transfer salts containing the one-dimensional $[Fe^{III}(C_2O_4)Cl_2^-]_n$ and long range antiferromagnetic ordering at 20 K was observed for the charge-transfer wide-gap semiconductor $TTF[Fe^{III}(C_2O_4)Cl_2]$ and displaying weak-ferromagnetism [6]. In addition, the first weak-ferromagnetic organic conductor κ-$BETS_2[Fe^{III}$-$(C_2O_4)Cl_2]$ was obtained and it has a weakly temperature-dependent metallic conductivity to 4.2 K, [7] and magnetic ordering at 4.5 K. Here, we present a summary of the structural, optical, electrical and magnetic properties of the two above-mentioned charge-transfer salts.

2. Experimental

Charge-transfer complexes of TTF and BETS with the one-dimensional polymeric $[Fe(C_2O_4)Cl_2^-]_n$ anions were obtained by diffusion and electrocrystallization method, respectively. Black small shiny crystals of $TTF[Fe(C_2O_4)Cl_2]$ were obtained by diffusing an acetone solution of $TTF_3[BF_4]_2$ into one of $Me_4NFe(C_2O_4)Cl_2$. Black plate crystals of κ-$BETS_2[Fe(C_2O_4)Cl_2]$ were obtained by electrocrystallization of BETS in the presence of either Me_4N-$Fe(C_2O_4)Cl_2$ or $[Me_4N]_3Fe(C_2O_4)_3$ from C_6H_5Cl and C_2H_5OH. The composition of the crystal was determined on Electron Probe Microanalyzer. Polarized IR reflective spectra, using a Bio-rad FTS6000/UMA500 spectrometer and a gold mirror as reference, were used to identify the different phases.

Single crystal X-ray diffraction data for $TTF[Fe(C_2O_4)Cl_2]$ and κ-$BETS_2[Fe(C_2O_4)Cl_2]$ were collected on a Rigaku AFC7R fine-focus system at room-temperature. The overlap-integrals obtained by extended-Hückel were used to calculate the electronic band-structure by tight-binding method. The conductivity was measured by two-probe or four-probe methods using 20 μm gold wire electrodes attached to the single crystals with gold paste. The magnetic properties were measured by use of a Quantum Design MPMS 7XL system. The magneto-resistance measurements were performed on a PPMS-9 system.

3. Results and discussion

The crystallographic data of the two compounds are listed in Table 1.

Table 1
Crystallographic data for $TTF[Fe(C_2O_4)Cl_2]$ and κ-$BETS_2[Fe(C_2O_4)Cl_2]$

Compound	$TTF[Fe(C_2O_4)Cl_2]$	κ-$BETS_2[Fe(C_2O_4)Cl_2]$
Formula	$C_8H_4Cl_2FeO_4S_8$	$C_{22}H_{16}Cl_2FeO_4S_8Se_8$
Molecular weight	419.10	1359.26
a (Å)	8.858(5)	37.884(5)
b (Å)	11.012(5)	11.258(2)
c (Å)	14.932(9)	8.469(1)
β (°)	103.39(2)	90.573(2)
V (Å^3)	1416.9(13)	3611.8(10)
Space group	$P2_1/c$	$C2/c$
Z	4	4
R_1	0.0667	0.0393
wR_2	0.1702	0.1090
Goodness-of-fit (GOF)	1.132	0.984

For $TTF[Fe(C_2O_4)Cl_2]$, the asymmetric unit contains one TTF and one $[Fe^{III}(C_2O_4)Cl_2^-]$. All the atoms of the TTF cation were found to be coplanar and bond-valence correlation gives it a formal charge of +1. Therefore, it is a half filled system with a spin (1/2) per unit. The structure consists of parallel stacks of donor cations, TTF and $[Fe(C_2O_4)Cl_2^-]_n$ anionic chains along the a-axis (Fig. 1). TTF-pair was formed within the donor stack with short S···S contacts. There are several short contacts between donor and anions as S···Cl, which may be responsible for the π–d interactions in the crystal.

In κ-$BETS_2[Fe(C_2O_4)Cl_2]$ (Fig. 2), the donor molecules stack in two-dimensional κ-phase (Fig. 3) which is slightly different to that of the reported κ-$BETS_2FeCl_4$ and κ-$(BEDT\text{-}TTF)_2Cu[N(CN)_2]_2$. There are Se···Se contacts within the dimers and Se···S, S···S between dimers in one layer where the chain anion fits in the channel between the two donor layers. The formal charge of the donor is assigned by bond-valence correlation to $BETS^{+0.5}$ in κ-$BETS_2$-$[Fe(C_2O_4)Cl_2]$.

The counter-anion of complexes in the one-dimensional chain anion $[Fe(C_2O_4)Cl_2^-]_n$ where the valence of the iron is assigned to Fe^{3+}. Fe(III) is coordinated by oxalate anion in *cis*-position and two terminal chlorine atoms to complete the octahedra. The Fe–O and Fe–Cl bonds lengths in these crystals are listed in Table 2, and lie in the range of those

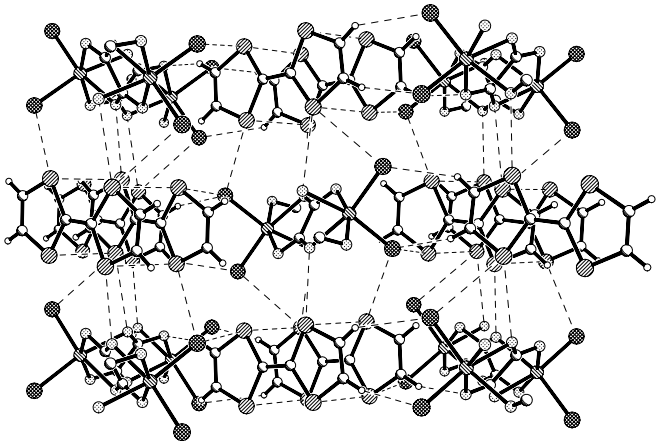


Fig. 1. View of the packing of $TTF[Fe(C_2O_4)Cl_2]$ along a-axis.

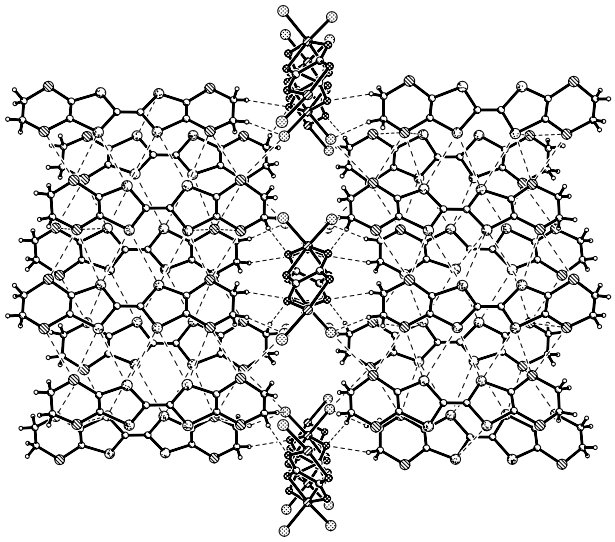


Fig. 2. View of the packing of κ-$BETS_2[Fe(C_2O_4)Cl_2]$ along the *c*-axis.

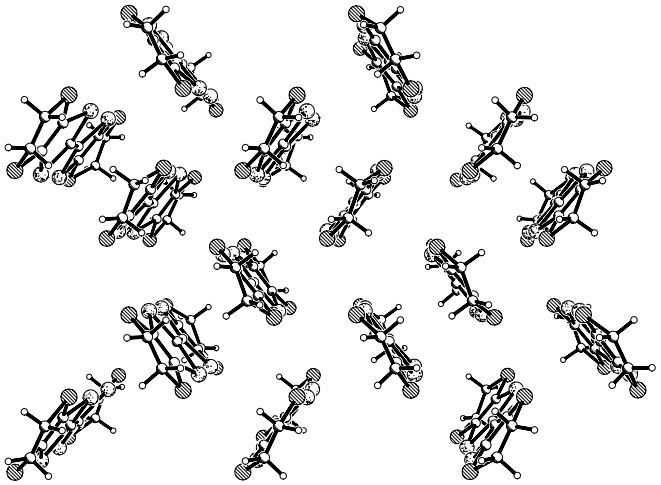


Fig. 3. Donor arrangement in κ-$BETS_2[Fe(C_2O_4)Cl_2]$.

Table 2
Bond lengths and angles of $[Fe(C_2O_4)Cl_2^-]_n$ in $TTF[Fe(C_2O_4)Cl_2]$ and κ-$BETS_2[Fe(C_2O_4)Cl_2]$

Compound	$TTF[Fe(C_2O_4)Cl_2]$		κ-$BETS_2[Fe(C_2O_4)Cl_2]$	
Fe–O (oxalate) (Å)	Fe(1)–O(2)	2.049(3)	Fe(1)–O(1)	2.034(4)
	Fe(1)–O(3)	2.059(3)	Fe(1)–O(2)	2.151(4)
	Fe(1)–O(4)	2.112(3)		
	Fe(1)–O(1)	2.137(3)		
Fe–Cl (Å)	Fe(1)–Cl(1)	2.262(2)	Fe(1)–Cl(1)	2.250(2)
	Fe(1)–Cl(2)	2.259(2)		
Fe···Fe (Å)	5.494		5.447	
Fe···Fe···Fe (°)	108.0		102.0	

reported for Fe–O(oxalate), Fe–Cl bond lengths in charge-transfer complexes and show it can be fit to the different donor arrangements from a one-dimensional column to two-dimensional layer due to its flexibility.

Depending on the formal charge and arrangement of the donor, band structure calculations predict that $TTF[Fe(C_2O_4)Cl_2]$ should be a poor conductor while κ-$BETS_2[Fe(C_2O_4)Cl_2]$ a good conductor.

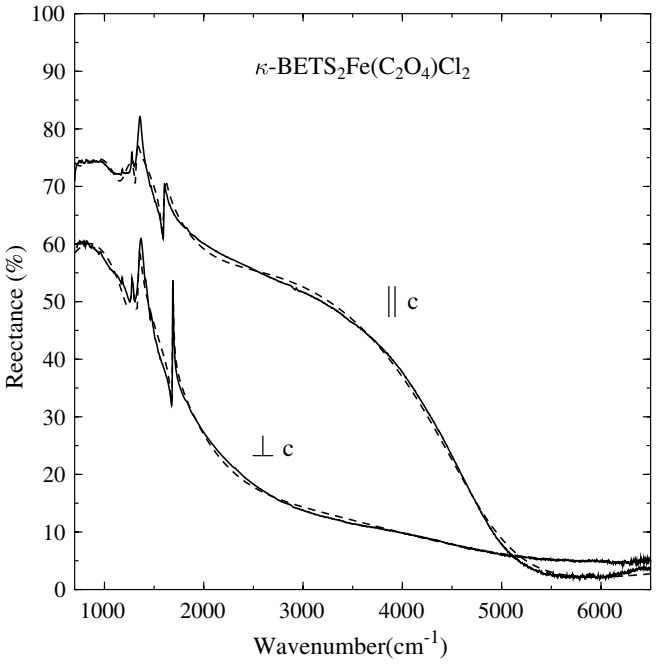


Fig. 4. Polarized IR reflectivity measured at room temperature for κ-$BETS_2[Fe(C_2O_4)Cl_2]$. The dashed lines show the Drude–Lorentz fits.

The IR reflectivity of κ-$BETS_2[Fe(C_2O_4)Cl_2]$ is consistent with those of a conductor (Fig. 4), its band structure and Fermi surface (Fig. 5) [8]. The conductivity was measured on single crystals using 20 μm gold wires attached by gold paste. $TTF[Fe(C_2O_4)Cl_2]$ is a wide-band gap semiconductor with $\sigma_{300\,K} = 10^{-7}$ S cm^{-1} by two-probe methods. κ-$BETS_2[Fe(C_2O_4)Cl_2]$ is a conductor with $\sigma_{300\,K} = 10^2$ S cm^{-1} and retains this state of metallicity down to 2 K. These are in good agreement with the calculated band structures [6,7].

The magnetic properties of the charge-transfer complexes were measured using a Quantum Design MPMS 7XL SQUID. The feature of the temperature dependence of the susceptibility is a broad hump around 50 K that is due to the existence of the one-dimensional antiferromagnetism of the $[Fe(C_2O_4)Cl_2^-]_n$ chain while the most prominent feature is the irreversible ZFC/FC susceptibility below 20 K for $TTF[Fe(C_2O_4)Cl_2]$ (Fig. 6) and 4.5 K for κ-$BETS_2[Fe(C_2O_4)Cl_2]$. The high temperature data above 25 K were fitted to the model of a one-dimensional antiferromagnetic $S = 5/2$ chain and a contribution from Curie impurity as well as a dimer $S = 1/2$ for $TTF[Fe(C_2O_4)Cl_2]$ or a temperature independent term for κ-$BETS_2[Fe(C_2O_4)Cl_2]$. The long-range magnetic ordering can only be ascribed to the presence of π–d interaction between donors and anions because theoretically no long-range ordering is possible at such a high temperature for a 1D-magnetic system. The isothermal magnetization measurement shows a linear dependence above 10 K, a 150 Oe coercive field was observed at 2 K. The magnetization at 70 kOe is lower than that expected if all the moments were aligned parallel. κ-$BETS_2[Fe(C_2O_4)Cl_2]$ is the first organic conductor displaying weak-ferromagnetism deriving from the two-sublattices while κ-$BEDT_2$-

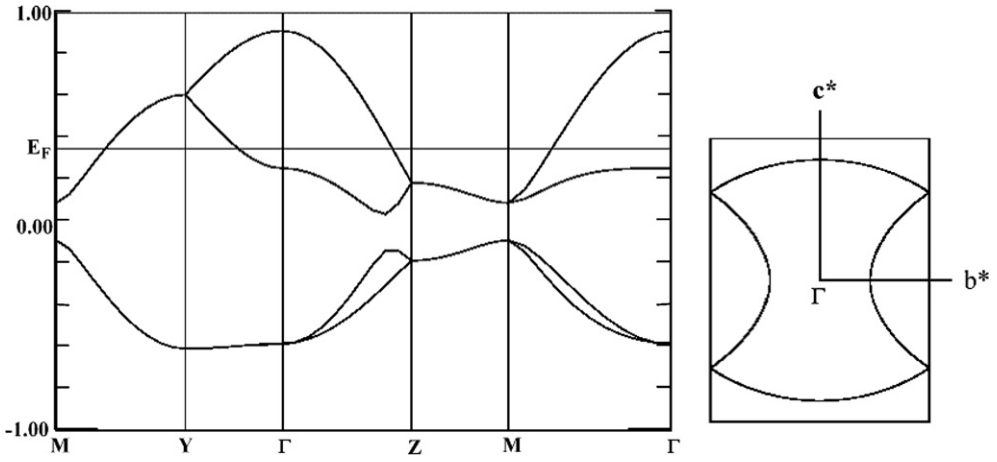


Fig. 5. Band structure and Fermi surface of κ-$BETS_2[Fe(C_2O_4)Cl_2]$.

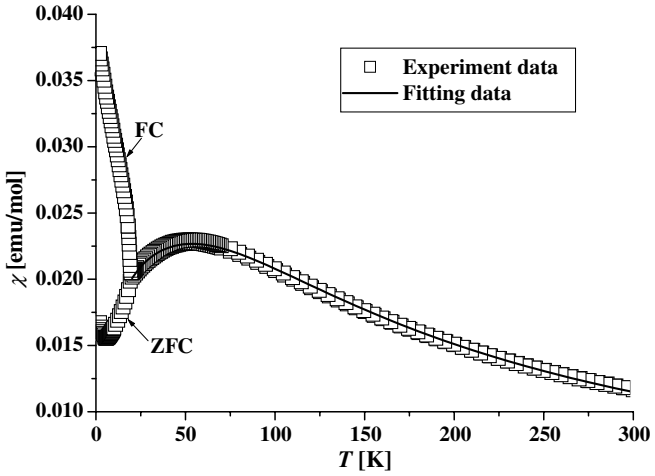


Fig. 6. ZFC and FC-M/H curves in 100 Oe for $TTF[Fe(C_2O_4)Cl_2]$. The black squares are experimental data and the solid line is the calculated susceptibility.

$[Cu\text{-}(N(CN)_2)Cl]$ also exhibits weak-ferromagnetism that, in contrast, is derived from only the π-electrons.

The magneto-resistance measurement of the weak-ferromagnetic organic conductor κ-$BETS_2[Fe(C_2O_4)Cl_2]$ was performed with current flow along the *c*-axis in field of 90 kOe at 2 K. The anisotropic magneto-resistance was observed by rotating the crystal around the *b*-axis. A minimum is observed when the magnetic field is perpendicular to the conduction plane while a maximum value for field parallel to conduction plane. It is different to those of κ-$BETS_2FeBr_4$ and λ-$BETS_2Fe_xGa_{1-x}Cl_4$ where minima were observed when the magnetic fields were parallel to the conduction plane and also where field-induced superconductivity was first observed [9].

4. Conclusion

We have succeeded in preparing the charge-transfer complex containing the magnetic chain anion $[Fe(C_2O_4)Cl_2^-]_n$ [6,7] and have characterized some complexes by single-crystal x-ray, SQUID magnetometry, optical reflectivity and transport measurements as well as calculating their band-structures. The magnetic properties range from paramagnetic, antiferromagnetic to weak-ferromagnetic and conductivity from insulator-like 10^{-7} to 10^2 S/cm. The observation of weak-ferromagnetism suggests the presence of π–d interaction, and proves $[Fe(C_2O_4)Cl_2^-]_n$ is a good anion for dual-function molecular crystals. The search and characterization on new charge-transfer complexes containing the magnetic chain $[Fe(C_2O_4)Cl_2^-]_n$ are in progress.

5. Supplementary material

CCDC 265713 and 280931 contain the supplementary crystallographic data for $TTF[Fe(C_2O_4)Cl_2]$ and κ-$BETS_2[Fe(C_2O_4)Cl_2]$. These data can be obtained free of charge via http://www.ccdc.cam.ac.uk/conts/retrieving.html, or from the Cambridge Crystallographic Data Centre, 12 Union Road, Cambridge CB2 1EZ, UK; fax: (+44) 1223-336-033; or e-mail: deposit@ccdc.cam.ac.uk.

Acknowledgment

This research was supported by NSFC No. 20473095, 20673120 the MOST of China 973 project No. 2006CB601001 and CMS-CX200510, PR China.

References

[1] M. Kurmoo, A.W. Graham, P. Day, S.J. Coles, M.B. Hursthouse, J.L. Caulfield, J. Singleton, F.L. Pratt, W. Hayes, L. Ducasse, P. Guionneau, J. Am. Chem. Soc. 117 (1995) 11209.
[2] H. Kobayashi, H. Tomita, T. Naito, A. Kobayashi, F. Sakai, T. Watanabe, P. Cassoux, J. Am. Chem. Soc. 118 (1996) 368.
[3] E. Coronado, J.R. Galan-Mascaros, C.J. Gomez-Garcia, V.N. Laukhin, Nature 408 (2001) 447.
[4] P. Day, M. Kurmoo, T. Mallah, I.R. Marsden, R.F. Friend, F.L. Pratt, W. Hayes, D. Chasseau, J. Gaultier, G. Bravic, L. Ducasse, J. Am. Chem. Soc. 114 (1992) 10772.
[5] S. Uij, H. Shinagawa, T. Terashima, T. Yakabe, Y. Terai, M. Tokumoto, A. Kobayashi, H. Tanaka, H. Kobayashi, Nature 410 (2001) 908.

[6] B. Zhang, Z.M. Wang, H. Fujiwara, H. Kobayashi, M. Kurmoo, K. Inoue, T. Mori, S. Gao, Y. Zhang, D.B. Zhu, Adv. Mater. 17 (2005) 1988.
[7] B. Zhang, Z.M. Wang, Y. Zhang, K. Takahashi, Y. Okano, H.B. Cui, H. Kobayashi, K. Inoue, M. Kurmoo, F.L. Pratt, D.B. Zhu, Inorg. Chem. 45 (2006) 3275.
[8] A. Kobayashi, M. Sasa, W. Suzuki, E. Fujiwara, H. Tanaka, M. Tokumoto, Y. Okano, H. Fujiwara, H. Kobayashi, J. Am. Chem. Soc. 126 (2004) 426.
[9] H. Kobayashi, H.B. Cui, A. Kobayashi, Chem. Rev. 104 (2004) 5265.

applications. This ligand has been known in organic chemistry for a long time [17], but its uses to date in coordination chemistry have been limited [18]. We used this ligand in the preparation of a new compound: $[Mn_6O_2(O_2CPh)_8L_3]$ (**1**), with an unprecedented hexanuclear Mn_6 topology and structure. The synthesis, structure, and magnetic properties of complex **1** are as follows.

2. Experimental

2.1. Synthesis

All solvents and reagents where used as received, no purification was necessary. All reactions were performed under aerobic conditions. $[Mn_3O(O_2CPh)(py)_2(H_2O)]$ [19] was prepared as described in the literature. The ligand of HL was prepared via a Claisen condensation reaction similar to that previously reported for a similar ligand [17].

2.1.1. $[Mn_6O_2(O_2CPh)_8L_3]$ (**1**)

$[Mn_3O(O_2CPh)_6(py)_2(H_2O)]$ (0.498 g 0.460 mmol) was dissolved in 30.0 ml CH_2Cl_2 and the solid HL (0.169 g, 0.751 mmol) was added. A yellow-brown solution was obtained after stirring for 10 min. The solution was filtered to eliminate any remaining solid and the filtrate was layered with two volumes of a 1:1 hexane/Et_2O solvent to slowly give well-formed brown crystals. The sample for crystallography was maintained in contact with mother liquor to avoid solvent loss and it was identified as $\mathbf{1}\cdot 2CH_2Cl_2$. Yield 40% (based on Mn). *Anal.* Calc. For $[Mn_6O_2(O_2CPh)_8L_3]$ (**1**): C, 59.31; H, 3.75; N, 2.05. Found: C, 59.24; H, 3.99; N, 2.05%. IR data (KBr disk, cm^{-1}): 3062 (w), 2922 (w), 1604 (s), 1561 (s),1499 (s), 1445 (s), 1398 (vs), 1291 (m), 1174 (w), 1068 (w), 1044 (w), 1025 (w), 942 (w), 839 (w), 770 (w), 716 (s), 676 (m), 632 (m), 589 (w), 513 (w).

2.2. X-ray crystallography

Data collation parameters are listed in Table 1. Diffraction measurement for $\mathbf{1}\cdot 2CH_2Cl_2$ was carried out using a Bruker–Nonius Kappa CCD diffractometer with graphite-monochromated Mo Kα radiation ($\lambda = 0.7107$ Å). Cell parameters were retrieved and refined using DENZO-SMN [20] software on all reflections. Data reduction was performed with the DENZO-SMN software. Structure analysis was made by using SHELXTL program on a personal computer. The structure of $\mathbf{1}\cdot 2CH_2Cl_2$ was solved using the SHELXS-86 [21] program and refined using SHELXL-97 [22] program by full-matrix least-squares on F^2 values. All non-hydrogen atoms were refined anisotropically, whereas the hydrogen atoms were placed in ideal, calculated positions, with isotropic thermal parameters riding on their respective carbon atoms. The asymmetric unit of complex $\mathbf{1}\cdot 2CH_2Cl_2$ consists of a Mn_6 molecule and two CH_2Cl_2 molecules. The phenyl rings of one diketonate and one benzoate are disorder as is one pyridine ring of diketonate.

Table 1
Crystallographic data for **1**

	$\mathbf{1}\cdot 2CH_2Cl_2$
Formula	$C_{103}H_{80}Cl_4Mn_6N_3O_{24}$
Formula weight	2215.14
Crystal system	monoclinic
Space group	$P2_1/n$
a (Å)	15.9030(2)
b (Å)	41.1760(5)
c (Å)	17.3400(3)
β (°)	97.8750(10)
V (Å^3)	11247.5(3)
Z	4
T (K)	150(1)
Wavelength (Å)	0.7103
ρ_{calc} (g cm^{-3})	1.308
μ (mm^{-1})	0.815
$(\Delta\rho)_{max}$, $(\Delta\rho)_{min}$ (e Å^{-3})	1.460, −0.760
R_1[a], wR_2[b] (all data)	0.08240, 0.2227
R_1[a], wR_2[b] ($I > 2\sigma(I)$)	0.1303, 0.2481

[a] $R_1 = (\sum\|F_o| - |F_c\|)/\sum|F_o|$.
[b] $wR = [\sum[w(F_o^2 - F_c^2)^2]/\sum[w(F_o^2)^2]]^{1/2}$.

2.3. Physical measurements

Infrared spectra were recorded in the solid state (KBr pellets) on a Nicolet Magna 550 FTIR spectrometer in the 400–4000 cm^{-1} range. ^1H NMR and ^{13}C NMR spectra were measured in d_6-acetone solution on a Bruker AMX-400 (400 MHz) spectrometer with tetramethylsilane (TMS) as the internal standard. The EI-Mass spectrum was recorded on a Bruker APEX II. The melting point was measured using a capillary melting point apparatus. Elemental analyses have been carried out by using an Elementar vario EL III analyzer. Variable temperature dc and ac magnetic susceptibility measurements were collected on a microcrystalline sample, restrained in eicosane to prevent torquing, on a Quantum Design MPMS-XL SQUID magnetometer equipped with a 7.0 T magnet and operating in the range of 1.8–300.0 K. Diamagnetic corrections were estimated from Pascal's constants [23] and subtracted from the experimental susceptibility data to obtain the molar paramagnetic susceptibility of the compound.

3. Results and discussion

3.1. Synthesis

Complex **1** is prepared from a reaction employing the benzoate $Mn^{II}Mn_2^{III}$ complex of $[Mn_3O(O_2CPh)(py)_2(H_2O)]$. Reaction of this complex with ~1.5 equiv. of HL in CH_2Cl_2 followed by filtration and layering the resulting solution with hexane/ether, affords crystalline $[Mn_6O_2(O_2CPh)_8L_3]$ in 40% yield, after one week. The use of more than 2 or less than 1.5 equiv. of HL reduced the yield of the final product. Charge considerations and the inspection of metric parameters indicate that complex **1** is a mixed-valence $Mn_3^{II}Mn_3^{III}$ with a trapped-valence situation (vide infra). The reaction involves reduction state of Mn center

from an average oxidation state of +2.67 in the $Mn^{II}Mn_2^{III}$ starting complex to +2.5 in the $Mn_3^{II}Mn_3^{III}$ product. For **1**, clearly, the overall conversion of $[Mn_3O(O_2CPh)_6(py)_2(H_2O)]$ into the product must involve a complicated mechanism involving the reduction of Mn_3O, fragmentation, and recombination steps.

3.2. Description of structure

Complex $\mathbf{1}\cdot 2CH_2Cl_2$ crystallizes in the monoclinic space group $P2_1/n$. The ORTEP representation of **1** is shown in Fig. 1 and selected interatomic distances and angles are listed in Table 2. The structure of **1** reveals a $[Mn_3^{II}Mn_3^{III}(\mu_4\text{-}O)_2]^{11+}$ core which comprises a central, distorted cubane-like $[Mn_2^{II}Mn_2^{III}O_2(OR)(O_2CR)]$, and either side of which is attached one Mn^{III} [Mn(5)] and one Mn^{II} [Mn(1)] ions by two $\mu_4\text{-}O^{2-}$ ions. The peripheral ligations are provided by eight $PhCO_2^-$ groups and three diketonate ligands. Seven of the eight $PhCO_2^-$ groups are bridging two Mn ions and are in their familiar *syn,syn*-$\eta^1{:}\eta^1{:}\mu_2$ binding mode. The final $PhCO_2^-$ group is in the fairly rare $\eta^1{:}\eta^2{:}\mu_3$ mode, O(10) terminal to Mn(6) and O(9) bridging Mn(4) and Mn(2). The three diketonate groups are categorized into two groups: (i) two diketonate groups behave as $\eta^1{:}\eta^2{:}\eta^1{:}\mu_2$ ligands, where each ligand chelates one metal ion through its nitrogen atom [N(1) and N(3)] and connects this metal ion with a second one through a bridging O atom [O(1) and O(5)] and a terminal O atom [O(2) and O(6)]; and (ii) one diketonate group chelates as a $\eta^1{:}\eta^3{:}\eta^1{:}\mu_3$ bridging type; the coordination of this ligand is similar to (i) by connecting to the metal ion terminally though the N(2) and O(4) atoms, but bridging three Mn ions by O(3) (Scheme 1).

For complex **1**, Mn(1), Mn(2), Mn(3) and Mn(5) are six-coordinate with slightly distorted octahedral geometry, while Mn(4) and Mn(6) are seven-coordinate with distorted pentagonal bipyramidal geometry. In addition, although there is a weak interaction in Mn(6)–O(23) at a distance of 2.870(5), it was considered as the seventh coordination position around Mn(6). Charge considerations require a $3Mn^{II}$, $3Mn^{III}$ oxidation state description, and Mn(1), Mn(4) and Mn(6) are assigned as the Mn^{II} ions on the basis

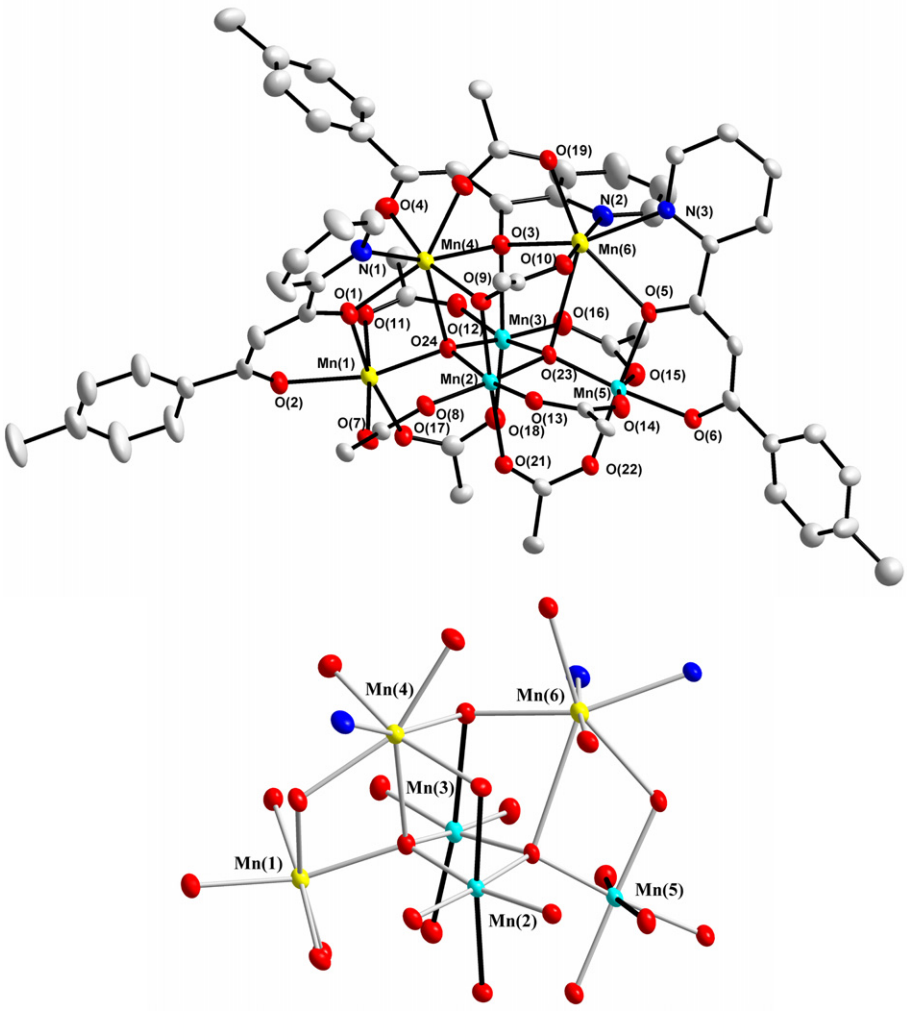
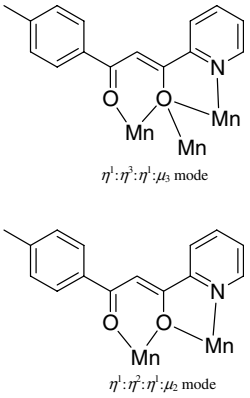


Fig. 1. Crystallographic structure (top) and JT axes orientation (highlight bond) in core structure (bottom) of $[Mn_6O_2(O_2CPh)_8L_3]\cdot 2CH_2Cl_2$ (**1**). Thermal ellipsoids at the 30% probability level. The H atoms and solvated molecules have been omitted for clarity.

Table 2
Selected bond distances (Å) and angles (°) for complex **1** · $2CH_2Cl_2$

1 · $2CH_2Cl_2$			
Mn(1)–O(17)	2.117(5)	Mn(4)–O(9)	2.153(5)
Mn(1)–O(24)	2.152(4)	Mn(4)–O(20)	2.209(5)
Mn(1)–O(11)	2.164(5)	Mn(4)–O(1)	2.255(4)
Mn(1)–O(2)	2.178(4)	Mn(4)–N(1)	2.346(6)
Mn(1)–O(1)	2.187(5)	Mn(4)–O(3)	2.376(4)
Mn(1)–O(7)	2.202(5)	Mn(4)–O(24)	2.414(5)
Mn(2)–O(24)	1.886(4)	Mn(5)–O(23)	1.861(4)
Mn(2)–O(23)	1.920(4)	Mn(5)–O(6)	1.927(4)
Mn(2)–O(8)	1.951(4)	Mn(5)–O(22)	1.994(4)
Mn(2)–O(13)	2.006(4)	Mn(5)–O(5)	2.032(4)
Mn(2)–O(21)	2.126(5)	Mn(5)–O(14)	2.108(5)
Mn(2)–O(9)	2.212(4)	Mn(5)–O(15)	2.116(5)
Mn(3)–O(24)	1.846(4)	Mn(6)–O(10)	2.111(5)
Mn(3)–O(23)	1.928(4)	Mn(6)–O(19)	2.172(5)
Mn(3)–O(16)	1.946(4)	Mn(6)–N(2)	2.259(6)
Mn(3)–O(12)	1.948(5)	Mn(6)–N(3)	2.294(5)
Mn(3)–O(18)	2.120(5)	Mn(6)–O(3)	2.304(4)
Mn(3)–O(3)	2.420(5)	Mn(6)–O(5)	2.365(5)
Mn(4)–O(4)	2.090(5)	Mn(6)–O(23)	2.870(5)
Mn(1)···Mn(3)	3.361(2)	Mn(1)···Mn(2)	3.167(1)
Mn(2)···Mn(3)	2.853(1)	Mn(1)···Mn(4)	3.594(1)
Mn(2)···Mn(5)	3.300(1)	Mn(2)···Mn(4)	3.311(1)
Mn(3)···Mn(4)	3.252(6)	Mn(2)···Mn(6)	4.005(2)
Mn(3)···Mn(6)	3.677(2)	Mn(3)···Mn(5)	3.368(1)
Mn(3)···Mn(6)	3.699(2)	Mn(4)···Mn(6)	3.750(2)
O(17)–Mn(1)–O(24)	95.75(17)	O(23)–Mn(5)–O(22)	95.93(17)
O(17)–Mn(1)–O(11)	91.50(19)	O(6)–Mn(5)–O(22)	89.10(18)
O(24)–Mn(1)–O(11)	95.40(16)	O(23)–Mn(5)–O(5)	85.29(17)
O(17)–Mn(1)–O(2)	109.26(18)	O(6)–Mn(5)–O(5)	89.59(17)
O(11)–Mn(1)–O(2)	89.21(17)	O(23)–Mn(5)–O(14)	95.61(19)
O(24)–Mn(1)–O(1)	74.25(16)	O(6)–Mn(5)–O(14)	81.44(19)
O(11)–Mn(1)–O(1)	90.94(18)	O(22)–Mn(5)–O(14)	90.62(19)
O(2)–Mn(1)–O(1)	80.58(17)	O(5)–Mn(5)–O(14)	87.47(19)
O(17)–Mn(1)–O(7)	89.87(19)	O(23)–Mn(5)–O(15)	96.27(19)
O(24)–Mn(1)–O(7)	88.17(16)	O(6)–Mn(5)–O(15)	86.4(2)
O(2)–Mn(1)–O(7)	86.82(18)	O(22)–Mn(5)–O(15)	91.7(2)
O(1)–Mn(1)–O(7)	88.35(18)	O(5)–Mn(5)–O(15)	89.92(19)
O(24)–Mn(2)–O(23)	80.25(17)	O(10)–Mn(6)–O(19)	88.9(2)
O(24)–Mn(2)–O(8)	94.69(18)	O(19)–Mn(6)–N(2)	90.1(2)
O(23)–Mn(2)–O(13)	99.82(17)	O(10)–Mn(6)–N(3)	91.02(19)
O(8)–Mn(2)–O(13)	85.11(17)	O(19)–Mn(6)–N(3)	87.38(18)
O(24)–Mn(2)–O(21)	105.10(19)	N(2)–Mn(6)–N(3)	85.0(2)
O(23)–Mn(2)–O(21)	91.12(17)	O(19)–Mn(6)–O(3)	80.80(17)
O(8)–Mn(2)–O(21)	90.20(18)	N(2)–Mn(6)–O(3)	71.49(19)
O(13)–Mn(2)–O(21)	87.34(18)	O(10)–Mn(6)–O(5)	92.53(17)
O(24)–Mn(2)–O(9)	85.65(18)	N(2)–Mn(6)–O(5)	86.8(2)
O(23)–Mn(2)–O(9)	93.70(17)	N(3)–Mn(6)–O(5)	68.57(17)
O(8)–Mn(2)–O(9)	85.87(17)	O(4)–Mn(4)–O(20)	86.7(2)
O(13)–Mn(2)–O(9)	81.93(17)	O(9)–Mn(4)–O(20)	82.45(18)
O(24)–Mn(3)–O(23)	81.03(18)	O(4)–Mn(4)–O(1)	83.23(18)
O(23)–Mn(3)–O(16)	96.31(19)	O(9)–Mn(4)–O(1)	110.29(16)
O(24)–Mn(3)–O(12)	98.40(19)	O(4)–Mn(4)–N(1)	98.2(2)
O(16)–Mn(3)–O(12)	83.1(2)	O(9)–Mn(4)–N(1)	88.8(2)
O(24)–Mn(3)–O(18)	97.50(19)	O(20)–Mn(4)–N(1)	83.17(19)
O(23)–Mn(3)–O(18)	102.01(19)	O(1)–Mn(4)–N(1)	68.72(18)
O(16)–Mn(3)–O(18)	87.8(2)	O(4)–Mn(4)–O(3)	80.16(19)
O(12)–Mn(3)–O(18)	91.1(2)	O(9)–Mn(4)–O(3)	89.57(16)
O(24)–Mn(3)–O(3)	81.75(17)	O(20)–Mn(4)–O(3)	78.78(17)
O(23)–Mn(3)–O(3)	85.00(17)	O(4)–Mn(4)–O(24)	109.6(2)
O(16)–Mn(3)–O(3)	93.18(19)	O(9)–Mn(4)–O(24)	75.24(15)
O(12)–Mn(3)–O(3)	81.97(19)	O(1)–Mn(4)–O(24)	68.13(15)



Scheme 1.

Table 3
Bond valence sums of Mn atoms in complex **1**

	Complex **1**					
	Mn(1)	Mn(2)	Mn(3)	Mn(4)	Mn(5)	Mn(6)
Mn(II)	2.174	3.403	3.449	2.039	3.450	1.828
Mn(III)	2.005	3.138	3.180	1.880	3.181	1.686
Mn(IV)	1.967	3.079	3.121	1.845	3.121	1.654

of: (i) the longer average bond lengths compared with those of the other Mn ions. (ii) the clear presence of the Jahn–Teller (JT) axial elongation at Mn(2), Mn(3) and Mn(5), as expected for a high-spin d^4 ion in a near-octahedral geometry; and (iii) bond valence sum calculation (BVS) calculations [24], which give values (Table 3) in good agreement with the above assignments.

3.3. Direct current magnetic susceptibilities and magnetization

Solid-state, variable-temperature magnetic susceptibility measurements were performed on microcrystalline sample of complex **1**, all suspended in eicosane to prevent torquing. The dc magnetic susceptibility data were collected in the 2.0–300 K range in a 1.0 kG magnetic field. In Fig. 2, for complex **1**, the value of $\chi_M T$ gradually decreases from 16.93 emu mol^{-1} K at 300 K to 12.59 emu mol^{-1} K at 30 K. Below this temperature, $\chi_M T$ decreases more rapidly to 5.96 emu mol^{-1} K at 2.0 K. The value of $\chi_M T$ at 300 K is lower than that expected for a cluster of 3 Mn^{II} and 3 Mn^{III} noninteracting ions (22.12 emu mol^{-1} K for $g = 2$), suggesting that antiferromagnetic couplings dominate the overall intramolecular exchange interactions within the complex. The rapid decrease observed for the $\chi_M T$ value for temperatures below 30 K are most likely because of ZFS effects and perhaps weak intermolecular interactions. Because of the topological complexity of the molecule, it is not possible to determine the individual pairwise Mn exchange interactions using the Kambe method [25].

To determine the spin of the ground state, magnetization (M) measurements were performed in the 2.0–4.0 K

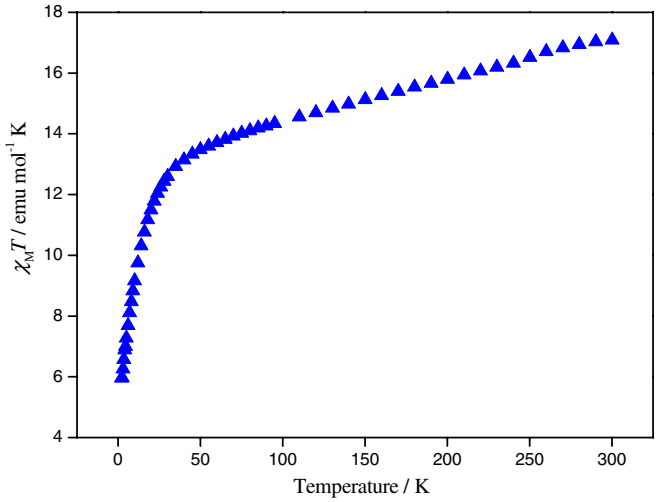


Fig. 2. Plot of $\chi_M T$ vs. temperature for a microcrystalline sample of complex **1**.

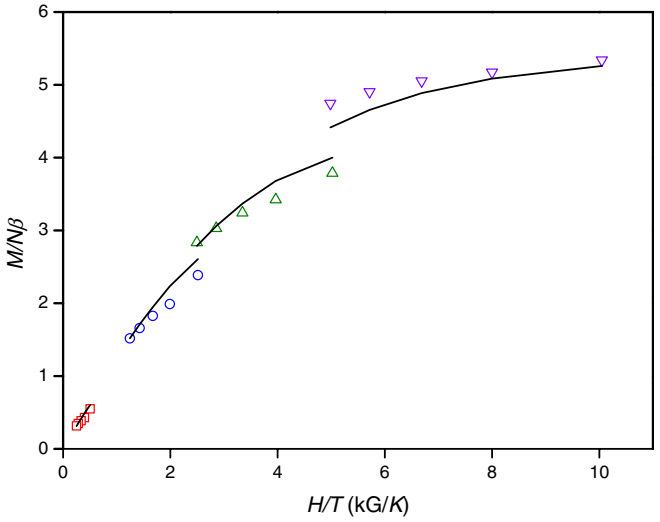


Fig. 3. The reduced magnetization of **1** plotted as $M/N\beta$ vs. H/T at 1 (□), 5 (○), 10 (△), and 20 (▽) kG in eicosane.

temperature range and the 1.0–20 kG dc magnetic field range. The data of complex **1** is plotted as the reduced magnetization ($M/N\beta$) versus H/T in Fig. 3, where N is Avogadro's number, β is Bohr magneton, and H is the applied magnetic field. For a system occupying only the ground state and experiencing no ZFS, the various isofield lines would be superimposed and $M/(N\beta)$ would saturate at a value of gS. The nonsuperposition of the isofield lines in Fig. 3 is indicative of the presence of a significant ZFS. The data were fit using the ANISOFIT [26], which assumes only the spin ground state of the molecule is significantly populated. The best fit for complex **1** was $S = 7/2$, $g = 1.90$, $D = -0.46\ \text{cm}^{-1}$ and $E = -0.003\ \text{cm}^{-1}$ (where D is the axial ZFS parameter and E is the rhombic ZFS parameter).

3.4. Alternating current magnetic susceptibilities

The measurements of the ac magnetic susceptibility were performed on vacuum-dried, microcrystalline sample of complex **1** in the temperature range 1.8–10 K in a zero dc field and a 3.5 G ac field oscillating at frequencies in the 250–1500 Hz range. The results representative of complex **1** are shown in Fig. 4. If the magnetization vector can relax fast enough to keep up with the oscillating field, then there is no imaginary (out-of-phase) susceptibility signal (χ''_M), and the real (in-phase) susceptibility (χ'_M) is equal to the dc susceptibility. However, if the barrier of magnetization relaxation is significant compared to thermal energy (kT), then there is a nonzero χ''_M signal and the in-phase signal decreases. In addition, the χ''_M signal will be frequency-dependent. Such frequency-dependent χ''_M signals are a characteristic signature of the superparamagnetic-like properties of a SMM (but by themselves do not prove the presence of a SMM). The sloping $\chi'_M T$ versus T plot is strongly indicative of a population of low-lying excited states as occupation of only the ground state would give an essentially temperature-independent value. Extrapolation of the plot of $\chi'_M T$ vs. T to 0 K gives a value of ca. 5.2 emu K mol^{-1}, indicative of an $S = 7/2$ ground state and these results are consistent with the fitting of magnetization data. At lower temperatures, the in-phase signal decreases and a frequency-dependent χ''_M signal appears,

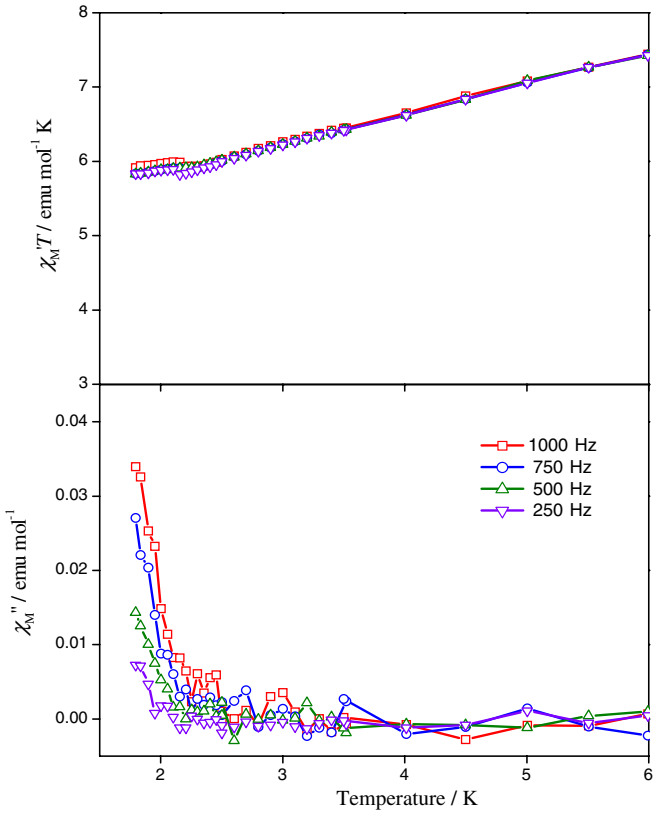


Fig. 4. Plot of $\chi'_M T$ (top) and χ''_M (bottom) vs. temperature for a powder sample of complex **1** in a 3.5 G ac field.

suggestive of the slow relaxation of a single-molecule magnet. However, the peak maxima clearly lie at temperatures below 1.8 K, the operating limit of our instrument. The data thus suggest that complex **1** may exhibit the slow magnetization relaxation of SMMs.

4. Conclusion

The pyridine containing β-diketone of 1-(2-pyridly)-3-(p-tolyl)propane-1,3-dione (HL) has proven to be a bridging ligand and allowed the synthesis a new manganese complex. The reaction of HL with $[Mn_3O(O_2CPh)_6(H_2O)(py)_2]$ yield a hexanuclear of $[Mn_6O_2(O_2CPh)_{10}L_3]$, complex **1**, which represents a new structural topology of $[Mn^{II}_3Mn^{II}_3(\mu_4\text{-}O)_2]^{11+}$ in Mn chemistry. Complex **1** has a ground state spin value of $S = 7/2$, together with a significant magnetoanisotropy as gauged by the D value of $-0.46\ cm^{-1}$, and it shows superparamagnetic behavior in ac susceptibility measurement at low temperature.

Acknowledgements

The magnetic measurements were obtained from SQUID (MPMS XL-7) in NSYSU and we thank the National Science Council of Taiwan (NSC-94-2113-M-006-011) for financial support.

Appendix A. Supplementary material

CCDC 617159 contains the supplementary crystallographic data for this paper. These data can be obtained free of charge via www.ccdc.ac.uk/conts/retrieving.html, or from the Cambridge Crystallographic Data Centre, 12 Union Road, Cambridge CB2 1EZ, UK; fax: (+44) 1223-336-033; or e-mail: deposit@ccdc.cam.ac.uk.

References

[1] D. Gatteschi, R. Sessoli, Angew. Chem., Int. Ed. 42 (2003) 268, and references therein.
[2] A.J. Tasiopoulos, A. Vinslava, W. Wernsdorfer, K.A. Abboud, G. Christou, Angew. Chem., Int. Ed. 43 (2004) 2117.
[3] R. Sessoli, H.-L. Tsai, A.R. Schake, S. Wang, J.B. Vincent, K. Folting, D. Gatteschi, G. Christou, D.N. Hendrickson, J. Am. Chem. Soc. 115 (1993) 1804.
[4] R. Sessoli, D. Gatteschi, A. Caneschi, M.A. Novak, Nature 365 (1993) 141.
[5] D. Gatteschi, A. Caneschi, L. Pardi, R. Sessoli, Science 265 (1994) 1054.
[6] M. Murugesu, M. Habrych, W. Wernsdorfer, K.A. Abboud, G. Christou, J. Am. Chem. Soc. 126 (2004) 4766.
[7] H. Miyasaka, R. Clerac, W. Wernsdorfer, L. Lecren, C. Bonhomme, K. Sugiura, M. Yamashita, Angew. Chem., Int. Ed. 43 (2004) 2801.
[8] M. Soler, W. Wernsdorfer, K. Folting, M. Pink, G. Christou, J. Am. Chem. Soc. 126 (2004) 2156.
[9] (a) J. Villain, F. Hartman-Boutron, R. Sessoli, A. Rettori, Europhys. Lett. 27 (1994) 159;
(b) A.K. Boudalis, B. Donnadieu, V. Nastopoulos, J.M. Clemente-Juan, A. Mari, Y. Sanakis, J.-P. Tuchagues, S.P. Perlepes, Angew. Chem., Int. Ed. 43 (2004) 2266;
(c) H. Oshio, N. Hoshino, T. Ito, M. Nakano, J. Am. Chem. Soc. 126 (2004) 8805.
[10] S.L. Castro, Z. Sun, C.M. Grant, J.C. Bollinger, D.N. Hendrickson, G. Christou, J. Am. Chem. Soc. 120 (1998) 2365.
[11] (a) H.J. Eppley, H.-L. Tsai, N. de Vries, K. Folting, G. Christou, D.N. Hendrickson, J. Am. Chem. Soc. 117 (1995) 301;
(b) D. Ruiz, Z. Sun, B. Albela, K. Folting, J. Ribas, G. Christou, D.N. Hendrickson, Angew. Chem., Int. Ed. 37 (1998) 300;
(c) Z. Sun, D. Ruiz, E. Rumberger, C.D. Incarvito, K. Folting, A.L. Rheingold, G. Christou, D.N. Hendrickson, Inorg. Chem. 37 (1998) 4758.
[12] H.-L. Tsai, D.-M. Chen, C.-I. Yang, T.-J. Jwo, C.-S. Wur, G.-H. Lee, Y. Wang, Inorg. Chem. Commun. 4 (2001) 511.
[13] S.M.J. Aubin, Z. Sun, L. Pardi, J. Krzystek, K. Folting, L.-C. Brunel, A.L. Rheingold, G. Christou, D.N. Hendrickson, Inorg. Chem. 38 (1999) 5329.
[14] H.-L. Tsai, T.-Y. Jwo, G.-H. Lee, Y. Wang, Chem. Lett. (2000) 346.
[15] M. Soler, W. Wernsdorfer, K.A. Abboud, J.C. Huffman, E.R. Davidson, D.N. Hendrickson, G. Christou, J. Am. Chem. Soc. 125 (2003) 3576.
[16] (a) G. Aromi, S.M.J. Aubin, M.A. Bolcar, G. Christou, H.J. Eppley, K. Folting, D.N. Hendrickson, J.C. Huffman, R.C. Squire, H.-L. Tsai, S. Wang, M.W. Wemple, Polyhedron 17 (1998) 3005;
(b) C. Boskovic, W. Wernsdorfer, K.C. Folting, J. Huffman, D.N. Hendrickson, G. Christou, Inorg. Chem. 41 (1992) 5107;
(c) M. Murugesu, J. Raftery, W. Wernsdorfer, G. Christou, E.K. Brechin, Inorg. Chem. 43 (2004) 4203;
(d) E.C. Sa ~nudo, W. Wernsdorfer, W. Abboud, G. Christou, Inorg. Chem. 43 (2004) 4137;
(e) T.C. Stamatatos, D. Foguet-Albiol, C.C. Stoumpos, C.P. Raptopoulou, A. Terzis, W. Wernsdorfer, S.P. Perlepes, G. Christou, J. Am. Chem. Soc. 127 (2005) 15380.
[17] R.L. Levine, J.K. Sneed, J. Am. Chem. Soc. 73 (1951) 5614.
[18] (a) R.W. Saalfrank, A. Dresel, V. Seitz, S. Trummer, F. Hampel, M. Teichert, D. Stalke, C. Stalk, J. Daub, V. Schunemann, A.X. Trautwein, Chem. Eur. J. 3 (1997) 2058;
(b) R.W. Saalfrank, V. Seitz, D.L. Caulder, K.N. Raymond, M. Teichert, G.M. Sheldrick, Eur. J. Inorg. Chem. (1998) 1313;
(c) R.W. Saalfrank, N. Low, S. Trummer, G.M. Sheldrick, M. Teichert, D. Stalke, Eur. J. Inorg. Chem. (1998) 599;
(d) S. Bruck, M. Hider, P.C. Junk, U.H. Kynast, Inorg. Chem. Commun. 3 (2000) 666;
(e) R.W. Saalfrank, V. Seitz, F.W. Heinemann, G. Gobel, R. Herbst-lrmer, J. Chem. Soc. Dalton Trans. (2001) 599.
[19] J.B. Vincent, H.R. Chang, K. Folting, J.C. Huffman, G. Christou, D.N. Hendrickson, J. Am. Chem. Soc. 109 (2002) 5703.
[20] DENZO-SMN: Z. Otwinowsky, W. Minor, Processing of X-ray Diffraction Data Collected in Oscillation Mode, in: C.W. CarterJr. (Ed.), Methods in Enzymology, Macromolecular Crystllography, Part A, Sweet, Vol. 276, Academic Press, New York, 1997, p. 307.
[21] G.M. Sheldrick, SHELXL-86;, University of Gottingen, Gottingen, Germany, 1986.
[22] G.M. Sheldrick, SHELXL-97;, University of Gottingen, Gottingen, Germany, 1997.
[23] E.A. Boudreaux, L.N. Mulay, In Theory and Application of Molecular Paramagnetism, John Wiley & Sons, New York, 1976, p. 491.
[24] (a) I.D. Brown, D. Altermatt, Acta Crystallogr., Sect. B 41 (1985) 244;
(b) I.D. Brown, Solid State Chem. 82 (1989) 122;
(c) H.H. Thorpe, Inorg. Chem. 31 (1992) 1585.
[25] K. Kambe, Phys. Soc. Jpn. 5 (1950) 48.
[26] M.P. Shores, J.J. Sokol, J.R. Long, J. Am. Chem. Soc. 124 (2002) 2279.

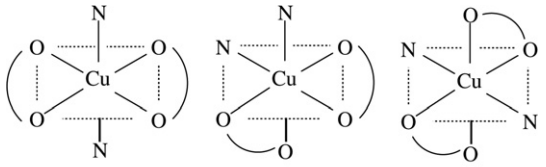


Chart 1. Coordination geometry of a six-coordinated copper ion in polynuclear complexes.

1–**7**, respectively. These polymeric complexes are characterized to be one-dimensional polynuclear compounds and their magnetic properties are investigated on a SQUID magnetometer.

2. Results and discussion

2.1. Preparation and characterization

The products of reaction of [Cu(hfac)$_2$] with diazaaromatic rings are listed in Table 1. All of the products were characterized by means of spectroscopic methods, and the elemental analysis satisfied the 1/1 molar ratio of the Cu/L contents. Molecular structures with the atomic numbering and polymeric molecular arrangement in the crystals of (a) **1**, (b) **2**, (c) **3**, (d) **4**, (e) **5**, (f) **6**, and (g) **7** are shown in Figs. 1 and 2. Selected crystallographic data of the complexes are listed in Table 1 and the Cu–X (X = O, N) bond lengths in Table 2.

2.2. Crystal structures of ax-N_2 Oh type

Complexes **1**, **2**, **4**, **5**, and **6** are polynuclear and the geometry about the copper ion is approximately an Oh structure. The axial positions of the copper ion are occupied by nitrogen atoms of two diazaaromatic rings, and the four equatorial positions are occupied by oxygen atoms from the bidentate hfac ligands (Fig. 1). The coordination geometry of the copper ion belongs to the ax-N_2 Oh type.

Complex **1**. The Cu(1)–N(1) bond (2.543(3) Å) is longer than that of [{Cu(hfac)$_2$(μ-pyz)}$_n$] (2.529(9) Å) [1]. Furthermore, the Cu(1)–N(1)–C(2) bond angle (130.7(2)) is larger than that of Cu(1)–N(1)–C(1) (111.9(2)). Similar bond angles are observed in [{Cu(hfac)$_2$}$_3$(μ-2,3,5-pyz)$_2$] (2,3,5-pyz = 2,3,5-trimethylpyrazine) [2b]. Thus, the neighboring methyl group of the nitrogen atom hinders the approach of the copper ion to the nitrogen atom.

Complex **2**. The Cu(1)–N(1) bond (2.606(2) Å) is longer than the Cu(1)–N(2′) bond (2.408(2) Å). The longer Cu–N bond arises from the steric hindrance of neighboring methyl groups of the 1-nitrogen atom. On the other hand, the 2,6-pyz molecules in **2** are arranged in a head-to-tail fashion. This fashion may result from a mutual repulsion between the hfac ligands coordinated to Cu(1) and the neighboring methyl groups of the 1-nitrogen atom.

Although 2,3,5- and 2,6-pyz molecules have a sterically crowded 2,6-dimethylpyridine-type nitrogen atom [10], the former gave trinuclear complex [{Cu(hfac)$_2$}$_3$(μ-2,3,5-pyz)$_2$] [2b], but the latter gave polynuclear **2**. In [{Cu(hfac)$_2$}$_3$(μ-2,3,5-pyz)$_2$], the geometry about Cu(2) is approximately a trigonal bipyramid with the nitrogen atom N(2) from 2,3,5-pyz molecule at the equatorial position. The Cu(2)–N(2) bond length is 2.030(9) Å. Generally, the coordinating ability of the ligand is affected by steric factors in addition to the electronic effect [11]. In this case, the coordinating ability of the 1-nitrogen atom in 2,6-pyz seems to be weaker than that of the 4-nitrogen atom in 2,3,5-pyz.

Complex **4**. The Cu(2)–N(2) and Cu(2)–N(3) bonds (2.615(7) and 2.657(8) Å, respectively) are somewhat longer than those of [{Cu(hfac)$_2$(μ-pyz)}$_n$] and **1** (Table 2). In addition, the bond angles Cu–N–C are not equal. For example, the Cu(1)–N(1)–C(1) and Cu(1)–N(1)–C(8) bond angles are 116.5(5) and 127.5(5)°, respectively. The *peri*-hydrogen atoms attached to the qxln ring hinder the approach of the chelated copper ion (Fig. 1(d)) [10].

Complex **5**. To our knowledge, the Cu(1)–N(1) bond (2.856(4) Å) is one of the longest Cu–N bonds of [{Cu(hfac)$_2$(μ-L)}$_n$] ever reported [1–7]. On the other hand, Cu(1)–O(1) and Cu(1)–O(2) bonds (1.915(3) and 1.923(3) Å, respectively) are notably shorter than those of [{Cu(hfac)$_2$(μ-L)}$_n$] (Table 2). The bond angles O(1)–Cu(1)–N(1) and O(2)–Cu(1)–N(1) are equal (90.0°), and Cu(1)–N(1)–C(1) and Cu(1)–N(1)–C(1′) are also equal (122.1(2)). Thus the coordination geometry of the copper ion belongs to the extremely elongated ax-N_2 Oh type. It should be noted that the Cu–N distance of 2.856(4) Å is shorter by ca. 0.1 Å than the sum of the van der Waals radii of Cu (1.40 Å) and N (1.55 Å) [12]. Although the Cu–N bond is quite long in **5**, the interaction between the Cu and N atoms seems to be attracting, from the nitrogen atoms located just above the copper center despite of the steric hindrance. The bonding character is also supported by the spectroscopic methods (see the UV–Vis study section).

The steric hindrance of the *peri*-hydrogen atoms attached to the phenazine ring is much larger than that of quinoxaline, which is unhindered on one side of the nitrogen atom described above. Similar steric hindrance of *peri*-hydrogen atoms is observed in the [Cu(acac)$_2$]–acridine complex (Hacac = pentane-2,4-dione) in the ESR measurements [10].

Complex **6**. The Cu(1)–N(2′) bond (2.628(4) Å) is considerably longer than that of **1** (2.543(3) Å), while Cu(1)–N(1) bond (2.505(3) Å) is somewhat shorter. The coordination geometry of Cu(1) belongs to the ax-N_2 Oh type owing to the steric reason. Its structure is rather different from those of [{Cu(hfac)$_2$(μ-pym)}$_n$] (pym = pyrimidine) and [{Cu(hfac)$_2$(μ-4-pym)}$_n$], which have the ax–eq-N_2 Oh structure [5,7].

2.3. Crystal structures of ax-N_2 and trans–eq-N_2 Oh type

Complex **3**. The geometry about Cu(1), Cu(2) and Cu(3) forms approximately an Oh structure. The coordination

Table 1
Crystallographic data and experimental details for complexes **1**–**7**

Complex	**1**	**2**	**3**	**4**	**5**	**6**	**7**
Formula	$C_{16}H_{10}N_2O_4F_{12}Cu$	$C_{16}H_{10}N_2O_4F_{12}Cu$	$C_{17}H_{12}N_2O_4F_{12}Cu$	$C_{18}H_{10}N_2O_4F_{12}Cu$	$C_{22}H_{10}N_2O_4F_{12}Cu$	$C_{16}H_{10}N_2O_4F_{12}Cu$	$C_{22}H_{18}N_2O_4F_{12}Cu$
M	585.79	585.79	599.82	607.80	657.86	585.79	665.92
Crystal system	triclinic	monoclinic	triclinic	monoclinic	monoclinic	orthorhombic	triclinic
Space group	$P\bar{1}$	$C2/c$	$P\bar{1}$	$C2/c$	$C2/m$	$Pbca$	$P\bar{1}$
Color	green	green	green	green	green	green	green
Habit	platelet	block	block	needle	needle	needle	block
Crystal size (mm)	$0.50 \times 0.45 \times 0.20$	$0.80 \times 0.73 \times 0.47$	$0.87 \times 0.67 \times 0.50$	$0.30 \times 0.20 \times 0.20$	$0.25 \times 0.10 \times 0.10$	$1.20 \times 0.80 \times 0.70$	$0.30 \times 0.25 \times 0.15$
T (K)	296	100	103	296	296	296	296
Unit cell dimensions							
a (Å)	8.6584(7)	15.5339(12)	8.660(5)	30.3969(6)	15.660(8)	12.6377(4)	12.2399(5)
b (Å)	8.8051(7)	7.8160(7)	13.717(8)	8.7220(2)	8.565(4)	30.2602(12)	13.9256(7)
c (Å)	7.8486(7)	16.9831(12)	19.526(10)	36.9728(12)	9.003(4)	11.1072(4)	8.4821(3)
α (°)	114.993(4)	90	105.70(4)	90	90	90	98.303(2)
β (°)	99.302(4)	99.674(3)	93.02(4)	114.4706(13)	91.44(3)	90	109.586(2)
γ (°)	94.889(4)	90	99.44(4)	90	90	90	67.7760(13)
V (Å^3)	527.26(8)	2032.6(3)	2191(2)	8921.8(4)	1207.1(11)	4247.6(3)	1260.66(9)
Z	1	4	4	16	2	8	2
D_{calc} (Mg m^{-3})	1.845	1.914	1.818	1.810	1.810	1.832	1.754
μ(Cu Kα) (mm^{-1})	2.743			2.625	2.485	2.723	2.381
μ(Mo Kα) (mm^{-1})		1.212	1.126				
Unique data	1858	2304	9799	7802	1130	3757	4372
R[a]	0.0660	0.0320	0.0420	0.0588	0.0472	0.0630	0.0583
$R_w(F^2)$[b]	0.1260	0.0457	0.0534	0.2269	0.0871	0.1281	0.1246

[a] $R = \sum\|F_o| - |F_c\|/\sum|F_o|$ (unit weights).

[b] $R_w = [\sum w(F_o^2 - F_c^2)^2 / \sum w(F_o^2)^2]^{1/2}$.

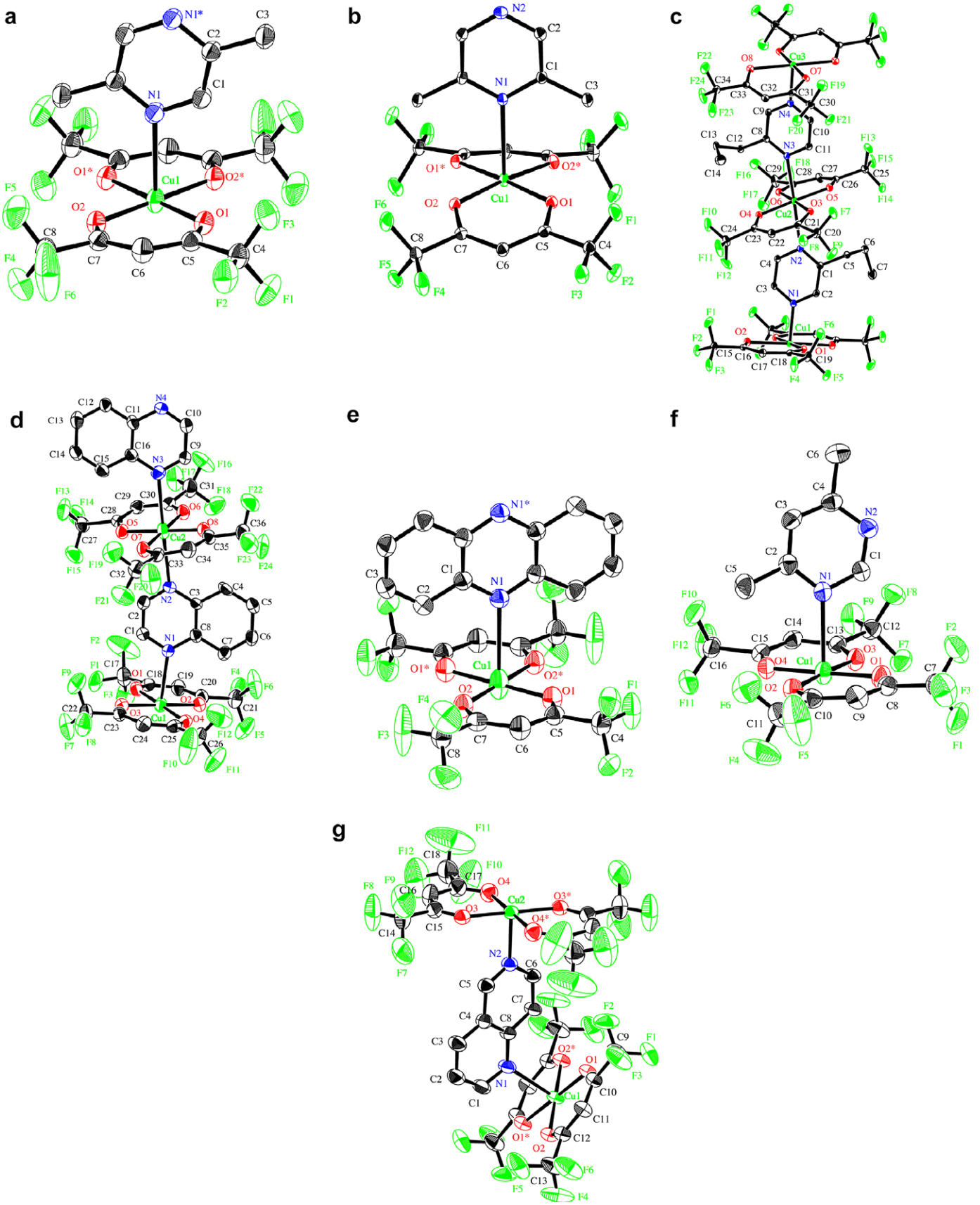


Fig. 1. ORTEP drawings of (a) **1**, (b) **2**, (c) **3**, (d) **4**, (e) **5**, (f) **6**, and (g) **7**. Thermal ellipsoids are drawn at the 30% probability level for (a) and (d)–(g) and the 50% probability level for (b) and (c). Hydrogen atoms are omitted for the sake of clarity.

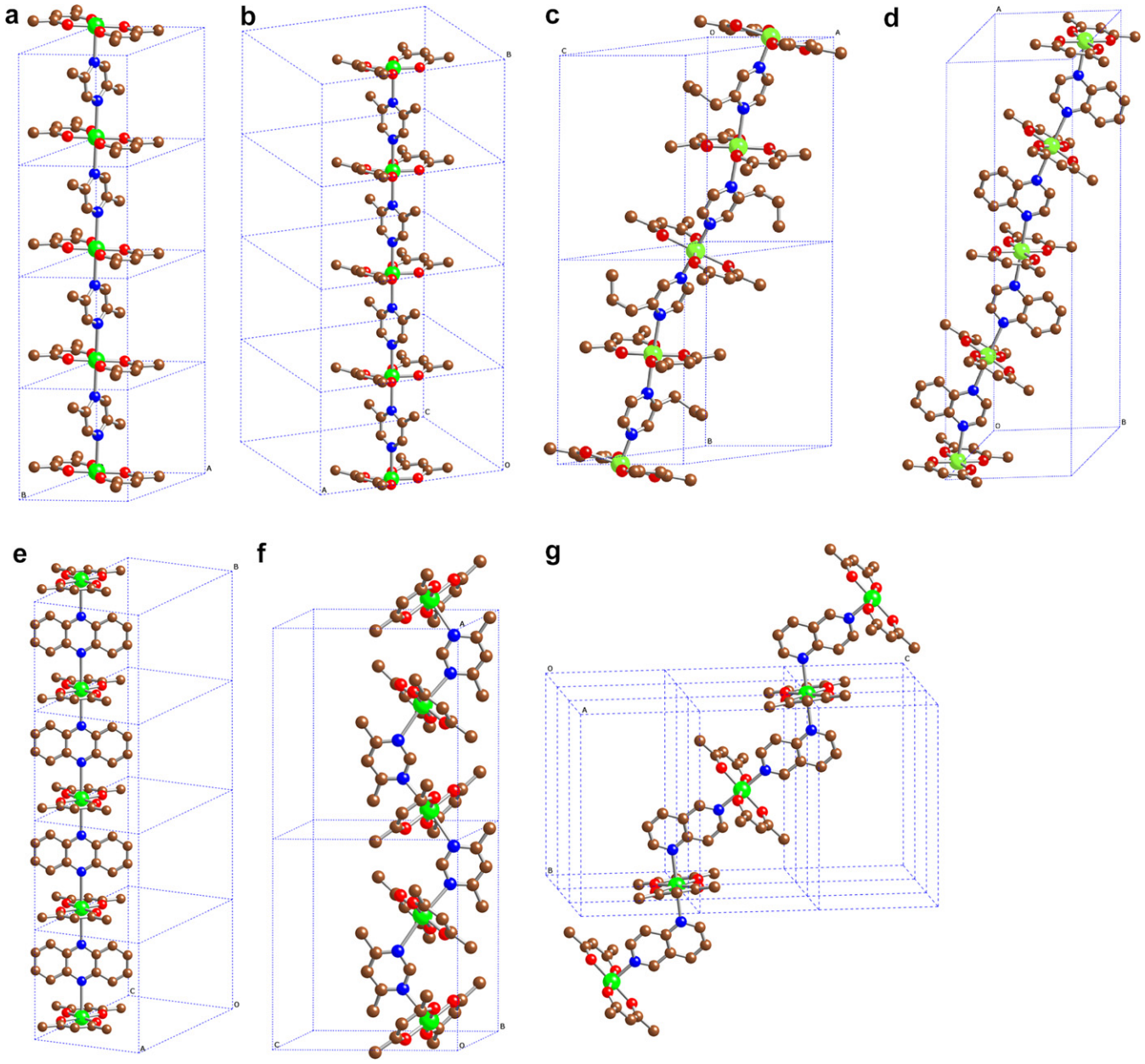


Fig. 2. Polymeric molecular arrangement in the crystals of (a) **1**, (b) **2**, (c) **3**, (d) **4**, (e) **5**, (f) **6**, and (g) **7**. Hydrogen and fluorine atoms are omitted for the sake of clarity.

geometry of Cu(1) and Cu(3) belongs to the *trans*–eq-N_2 Oh type, while that of Cu(2) to the ax-N_2 Oh type (Fig. 1(c)). The equatorial positions of Cu(1) and Cu(3) are occupied by the 4-nitrogen atoms of two prpyz molecules. On the other hand, the 1-nitrogen atoms occupy the two axial positions of Cu(2).

Complex **7**. The coordination type of Cu(1) and Cu(2) is classified into the ax-N_2 and *trans*–eq-N_2 Oh types, respectively. The equatorial positions of Cu(2) are occupied by 6-nitrogen atoms of two 1,6-nprn molecules. The Cu(1)–N(1) and Cu(2)–N(2) bonds (2.444(3) and 2.080(3) Å, respectively) are similar to, or slightly longer than, those of $[\{Cu(hfac)_2(\mu\text{-qzln})\}_n]$ (qzln = quinazoline) (2.439(3) and 2.043(3) Å, in a low-temperature phase) [7].

2.4. Structures of one-dimensional chains

As Fig. 2 shows, all of the present compounds possess the one-dimensional structures consisting of alternating $Cu(hfac)_2$ portions and diazaaromatic bridging ligands (μ-Ls). In the μ-pyrazine series, **2** and **5** show an exactly straight chain structure owing to the symmetry of μ-Ls, while **1** shows a very slight zigzag chain. Complexes **3** and **4** construct a somewhat slant chain against the crystallographic axis (Fig. 2). The linear chain structure of **5** (Fig. 2(e)) is similar to that of $[\{Cu(hfac)_2(\mu\text{-pyz})\}_n]$ [1]. Complex **2** exhibits a head-to-tail arrangements of μ-Ls. On the other hand, complex **3** is a one-dimensional zigzag chain, which has the ax-N_2 and *trans*–eq-N_2 Oh structures.

Table 2
Cu–X (X = O, N) bond lengths (Å) for complexes **1**–**7**

Complex																
1	Cu(1)–O(1)	1.954(2)	Cu(1)–O(2)	1.942(2)					Cu(1)–N(1)	2.543(3)						
2	Cu(1)–O(1)	1.9633(14)	Cu(1)–O(2)	1.9591(12)					Cu(1)–N(1)	2.606(2)	Cu(1)–N(2′)	2.408(2)				
3	Cu(1)–O(1)	1.964(2)	Cu(1)–O(2)	2.2873(18)					Cu(1)–N(1)	2.035(2)						
	Cu(2)–O(3)	1.935(2)	Cu(2)–O(4)	1.951(2)	Cu(2)–O(5)	1.956(2)	Cu(2)–O(6)	1.935(2)			Cu(2)–N(2)	2.584(2)	Cu(2)–N(3)	2.485(2)		
	Cu(3)–O(7)	1.961(2)	Cu(3)–O(8)	2.284(2)											Cu(3)–N(4)	2.033(2)
4	Cu(1)–O(1)	1.970(5)	Cu(1)–O(2)	1.948(5)	Cu(1)–O(3)	1.952(5)	Cu(1)–O(4)	1.955(5)	Cu(1)–N(1)	2.496(7)					Cu(1)–N(4′)	2.549(8)
	Cu(2)–O(5)	1.938(5)	Cu(2)–O(6)	1.944(6)	Cu(2)–O(7)	1.948(6)	Cu(2)–O(8)	1.933(5)			Cu(2)–N(2)	2.615(7)	Cu(2)–N(3)	2.657(8)		
5	Cu(1)–O(1)	1.915(3)	Cu(1)–O(2)	1.923(3)					Cu(1)–N(1)	2.856(4)						
6	Cu(1)–O(1)	1.940(3)	Cu(1)–O(2)	1.953(3)	Cu(1)–O(3)	1.950(3)	Cu(1)–O(4)	1.936(3)	Cu(1)–N(1)	2.505(3)	Cu(1)–N(2′)	2.628(3)				
7	Cu(1)–O(1)	1.972(2)	Cu(1)–O(2)	1.955(3)					Cu(1)–N(1)	2.444(3)						
					Cu(2)–O(3)	1.977(3)	Cu(2)–O(4)	2.288(5)			Cu(2)–N(2)	2.080(3)				

The prpyz molecules are arranged in a head-to-head fashion.

Complexes **6** and **7** exhibit essentially a zigzag chain structure. The one-dimensional chain of **6** (Fig. 2(f)) is rather different from those of $[\{Cu(hfac)_2(\mu\text{-}L)\}_n]$ (L = pym, 4-pym, 5-pym, and qzln) [4,7]. The structural differences among them arise from their Oh structures; **6** has the ax-N_2 Oh structure whereas the pym, 4-pym, 5-pym, and qzln derivatives have the ax–eq-N_2 Oh one, which leads to different magnetic coupling across the μ-Ls (see below). The chain structure of **7** is arranged in a head-to-head fashion (Fig. 2(g)), and is similar to that of $[\{Cu(hfac)_2(\mu\text{-qzln})\}_n]$ [3,7].

2.5. Infrared study

In infrared spectral analysis, the *ν*(C–O) band and the ring deformation band are very useful for prediction of the presence of different hfac ligands, namely different coordination geometry around the copper ion [1,2,9,13]. The spectra of complexes **1**, **2**, **4**–**6** have a single band in the region 1639–1641 cm^{-1}, which is assigned to the vibration of the hfac ligands in the basal plane around the ax-N_2 Oh structures. For complex **3** and **7**, split *ν*(C–O) bands were observed at 1653 and 1641 cm^{-1} for **3**, and 1656 and 1643 cm^{-1} for **7**, respectively (see Section 4). The higher *ν*(C–O) values are assigned to the carbonyl groups in the hfac ligands of *trans*–eq-N_2 Oh copper ion. Similarly split *ν*(C–O) bands were observed at 1654 and 1642 cm^{-1} for $[\{Cu(hfac)_2\}_3(\mu\text{-5-pym})_2]$, which are assigned to the vibration of the hfac ligands around the six-coordinated Cu(1) classified as the *trans*–eq-N_2 Oh type and around the five-coordinated Cu(2), respectively [2].

In the *trans*–eq-N_2 Oh type, the higher *ν*(C–O) band is ascribed to the longer axial Cu–O bond in chelated hfac ligands [2,9]. Actually, the Cu(1)–O(2) and Cu(3)–O(8) bonds (2.287(2) and 2.284(2) Å, respectively) for **3**, and the Cu(2)–O(4) bond (2.288(5) Å) for **7**, are considerably longer than those of the equatorial Cu–O bonds in the complexes.

In addition, the splitting of the ring deformation band of chelated hfac ligand was observed at 681 and 669 cm^{-1} for **3**. The former is assigned to the hfac ligands in the ax-N_2 Oh copper ion, and the latter to those in the *trans*–eq-N_2 Oh copper ion. Similarly the spectrum of **7** showed two ring deformation bands at 680 and 670 cm^{-1}. The lower deformation band is also ascribed to the longer axial Cu–O bond. Thus, the analysis of a pair of the *ν*(C–O) and ring deformation bands is predictable for the presence of the ax-N_2 and *trans*–eq-N_2 Oh types.

2.6. UV–Vis study

For the purpose of assignment of the structures, UV–Vis spectroscopy is very effectively utilized [9]. The diffuse reflectance spectra of the polynuclear complexes **1**, **4** and **6** resemble each other, showing broad maxima at 686,

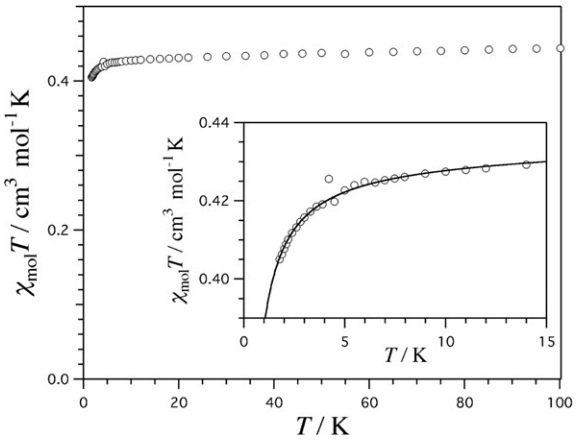


Fig. 3. Temperature dependence of the product $\chi_{mol}T$ for **3**. Inset shows a magnification of a low-temperature region. The solid line represents the theoretical fit. See the text for the equation and optimized parameters.

690 and 694 nm, respectively. On the other hand, the absorption maximum of **5** is observed at 666 nm, which is shifted to lower wavelength than those of them. This may arise from the extremely elongated ax-N_2 Oh structure. One may wonder how can we characterize chemical bonds rather than van der Waals contacts, because the Cu–N distances were sometimes very long. Definite evidence is provided from such UV–Vis absorption measurements. An apparent color of anhydrous [Cu(hfac)$_2$] having a square-planar four-coordinated structure is purple [14], whereas those of [Cu(hfac)$_2$L$_2$] having Oh structures with two N-donor ligands at the axial positions are usually green. All of the present compounds are green. Similarity of the spectra suggests that these complexes have a similar coordination geometry, which is classified as the ax-N_2 Oh structure.

2.7. Magnetic study

The present complexes possess distant axial bonds, which may bring about very weak magnetic channels between the copper(II) spins. Fig. 3 shows the $\chi_{mol}T$ versus T plot for **3**. The magnetic properties in all of the present compounds were found to be almost ideal paramagnetic, and very small antiferromagnetic coupling was observed in some case. Among the pyrazine-bridged series, **3** has the largest interaction, as indicated by the most significant decrease of $\chi_{mol}T$ value on cooling. The other complexes showed practically flat $\chi_{mol}T - T$ profiles (i.e., obeyed the Curie law) after removing the contribution of the temperature independent paramagnetism.

We determine the exchange parameters in **1**–**7** from fitting to a model, where the parameter J is defined with the Heisenberg spin Hamiltonian, $H = -2J\sum S_i \cdot S_j$. Assuming that the chain is equally spaced, we adopted the Bonner–Fisher model [15] to the antiferromagnetic infinite chain structure. Though there are two crystallographically independent Cu—Cu relations in **3** and **4**, they were actually quite similar to each other and this assumption is acceptable. The best fit parameters were: $J/k_B = -0.086(3)$ K and $g = 2.14(7)$ for **3**, and the calculated curve reproduced well the experimental data (Fig. 3, inset). Similar analysis on the plots for other complexes gave the corresponding J and g values, as listed in Table 3.

Table 3
Magnetic coupling parameters (J) and g values for complexes **1**–**7**

Complex	J/k_B	g
1	−0.034(8)	2.2(1)
2	−0.018(2)	2.34(8)
3	−0.086(3)	2.14(7)
4	−0.043(8)	2.1(1)
5	−0.031(6)	2.1(1)
6	−0.10(1)	2.3(2)
7	−0.003(5)	2.1(1)

The simplest pyrazine bridged compound [{Cu(hfac)$_2$-(μ-pyz)}$_n$] with the Cu–N(axial) bond of 2.529(9) Å [1] has been reported to show antiferromagnetic coupling with $\theta = -0.54 \pm 0.5$ K [16] or −0.06 K [5]. We can point out the relationship between the Cu–N distance and exchange coupling. The dibenzo derivative possessed somewhat longer Cu–N(axial) bonds (2.856(4) Å in **5**) due to the steric effect and exhibited smaller magnetic interaction. On the other hand, **3** involves much shorter Cu–N bonds (2.033(2) and 2.035(2) Å), and accordingly **3** showed the largest exchange interaction.

We have already reported several pyrimidine-bridged [Cu(hfac)$_2$] complexes, and many of them showed ferromagnetic couplings [3,6]. We should not overestimate spin-polarization effects [17] onto the heteroaromatic rings, because quite a few compounds containing pyrimidine-bridging ligands did not show ferromagnetic coupling [18]. 4,6-Dimethylpyrimidine in **6** is coordinated to the copper(II) ions at the axial positions on both sides (i.e., ax-N_2 Oh) and transmit no significant exchange interaction, being consistent with our formalism [6,19]. The pyrimidine bridge usually works as a ferromagnetic coupler with an ax–eq-N_2 Oh structure [6,19]. In this sense, **3** raise a question of interest. One nitrogen atom is coordinated to a copper ion at an axial position, and at the same time the other coordinated at an equatorial site, but **3** exhibited antiferromagnetic coupling. This finding may be interpreted partly in terms of spin-polarization on the diazaaromatic rings.

3. Summary

Seven polynuclear complexes of [Cu(hfac)$_2$] with diazaaromatic rings have been prepared and fully characterized. These complexes consist of a one-dimensional chain structure, and the copper centers are six-coordinated. Their magnetic properties were found to be paramagnetic or very weakly antiferromagnetic, which can be ascribed to the somewhat long Cu–N distances due to the steric effect from the bridging ligands. Various diazaaromatic rings play a

role of bridging ligands in spite of sterically bulky substituents (benzo, 2-methyl-, 2-propyl, etc.), which may allow us to develop polynuclear magnetic chains using these bridging ligands with other transition metal ions as a paramagnetic center. More significant magnetic interactions would be available when suitable paramagnetic metal ions are involved, especially metal ions having dπ or dσ(z^2) spins.

4. Experimental

4.1. Materials

Bis(1,1,1,5,5,5-hexafluoropentane-2,4-dionato)copper(II) was purchased from Aldrich Chemical Co. and purified by the reported method [14]. 2,5- and 2,6-Dimethylpyrazines, propylpyrazine, quinoxaline, phenazine, 4,6-dimethylpyrimidine and 1,6-naphthyridine were used without further purification.

[{Cu(hfac)$_2$(μ-2,5-pyz)}$_n$] (**1**). The complex [Cu(hfac)$_2$] (67 mg, 0.14 mmol) was dissolved in a mixture of light petroleum (13 cm^3) and acetone (2 cm^3) with an equimolar quantity of 2,5-dimethylpyrazine (15.2 mg, 0.14 mmol). The solution was refluxed for 1 h. After standing for a few days, light green crystals were formed. They were filtered, washed with a small amount of chilled light petroleum and dried *in vacuo* (51.6 mg, 63% yield). *Anal.* Found: C, 32.55; H, 1.58; N, 4.74%. $C_{16}H_{10}N_2O_4F_{12}Cu$ requires C, 32.81; H, 1.72; N, 4.78%. IR (KBr disk) ν(C–O) 1640, ring def. 681, $\delta_s CF_3$ 597 cm^{-1}.

[{Cu(hfac)$_2$(μ-2,6-pyz)}$_n$] (**2**). This complex was prepared by a similar method to that described above. *Anal.* Found: C, 32.82; H, 1.49; N, 4.76%. $C_{16}H_{10}N_2O_4F_{12}Cu$ requires C, 32.81; H, 1.72; N, 4.78%. IR (KBr disk) ν(C–O) 1639, ring def. 682, $\delta_s CF_3$ 597 cm^{-1}.

[{Cu(hfac)$_2$(μ-prpyz)}$_n$] (**3**). The complex [Cu(hfac)$_2$] (156 mg, 0.327 mmol) was dissolved in pentane with an equimolar quantity of propylpyrazine (40 mg, 0.327 mmol). The solution was refluxed for 1 h. After standing for a few days, light green crystals were formed. They were filtered, washed with a small amount of chilled pentane and dried *in vacuo* (128 mg, 65% yield). *Anal.* Found: C, 33.82; H, 2.24; N, 4.53%. $C_{17}H_{12}N_2O_4F_{12}Cu$ requires C, 34.04; H, 2.02; N, 4.67%. IR (KBr disk) ν(C–O) 1653 and 1641, ring def. 681 and 669, $\delta_s CF_3$ 598 cm^{-1}.

[{Cu(hfac)$_2$(μ-qxln)}$_n$] (**4**) and [{Cu(hfac)$_2$(μ-pnzn)}$_n$] (**5**). These complexes were prepared by a similar method to that described for complex **1**. *Anal.* Found for **4**: C, 35.48; H, 1.21; N, 4.52%. $C_{18}H_8N_2O_4F_{12}Cu$ requires C, 35.57; H, 1.33; N, 4.61%. IR (KBr disk) 1641 ν(C–O), 680 ring def., 596 $\delta_s CF_3$ cm^{-1}. *Anal.* Found for **5**: C, 40.17; H, 1.53; N, 4.26%. $C_{22}H_{10}N_2O_4F_{12}Cu$ requires C, 40.17; H, 1.35; N, 4.25%. IR (KBr disk) ν(C–O) 1639, ring def. 681, $\delta_s CF_3$ 598 cm^{-1}.

[{Cu(hfac)$_2$(μ-4,6-pym)}$_n$] (**6**). The complex [Cu(hfac)$_2$] (45 mg, 0.094 mmol) was dissolved in a mixture of light petroleum (13 cm^3) and acetone (2 cm^3) with an excess of 4,6-dimethylpyrimidine (19.5 mg, 0.18 mmol). The solution was refluxed for 1 h. After standing for a few days, light green needles were formed. They were filtered, washed with a small amount of chilled light petroleum and dried *in vacuo* (26 mg, 47% yield). *Anal.* Found: C, 33.09; H, 1.65; N, 4.93%. $C_{16}H_{10}N_2O_4F_{12}Cu$ requires C, 32.81; H, 1.72; N, 4.78%. IR (KBr disk) ν(C–O) 1641, ring def. 680, $\delta_s CF_3$ 596 cm^{-1}.

[{Cu(hfac)$_2$(μ-1,6-nprn)}$_n$] (**7**). This complex was prepared by a similar method to that described for complex **1**. *Anal.* Found: C, 35.47; H, 1.13; N, 4.66%. $C_{18}H_8N_2O_4F_{12}Cu$ requires C, 35.57; H, 1.33; N, 4.61%. IR (KBr disk) ν(C–O) 1656 and 1643, ring def. 680 and 670, $\delta_s CF_3$ 595 cm^{-1}.

The diffuse reflectance spectra were recorded on a Jasco Ubest V560 spectrophotometer, and IR on a Nicolet 5ZDX Fourier-transform spectrophotometer.

4.2. X-ray crystallographic analysis

X-ray diffraction data of **1**–**7** were collected on a Rigaku R-axis RAPID diffractometer with graphite monochromated Cu Kα ($\lambda = 1.5418$ Å) or Mo Kα ($\lambda = 0.71069$ Å). The structures were directly solved by a heavy-atom Patterson method and expanded using Fourier techniques in the CrystalStructure program package [20]. Numerical absorption correction was used. The parameters of all of the hydrogen atoms were refined as "riding". The thermal displacement parameters of non-hydrogen atoms were refined anisotropically. Full-matrix least-squares methods were applied using all of the unique reflection data. The thermal ellipsoids of these fluorine atoms are somewhat elongated along the motional track. A disorder model was applied for trifluoromethyl groups showing conformational isomerism, but somewhat large thermal displacement parameters of fluorine atoms still remained. Selected crystallographic data are summarized in Table 1.

4.3. Magnetic measurements

Magnetic properties of polycrystalline specimens of **1**–**7** were measured on a Quantum Design MPMS SQUID magnetometer equipped with a 7 T coil in a temperature range 1.8–300 K. The magnetic responses were corrected with diamagnetic blank data of the sample holder measured separately. The diamagnetic contribution of the sample itself was estimated from Pascal's constants.

5. Supplementary material

CCDC 617325, 617326, 617327, 617328, 617329, 617330 and 617331 contain the supplementary crystallographic data for **1**, **2**, **3**, **4**, **5**, **6** and **7**. These data can be obtained free of charge via htpp://www.ccdc.cam.ac.uk/conts/retrieving.html, or from the Cambridge Crystallographic Data Centre, 12 Union Road, Cambridge CB2 1EZ, UK;

fax: (+44) 1223-336-033; or e-mail: deposit@ccdc.cam.ac.uk.

Acknowledgements

One of the authors (T.K.) is grateful to Mr. Masahiko Tohyama of Kanagawa Industrial Research Institute for the elemental analysis, and to Ms. Naoko Masukawa (Juju Cosmetics Co. Ltd.), Ms. Hiroko Ishigami and Mrs. Chinami Kikuchi (nee Arai) of Kanagawa Institute of Technology for their assistance.

References

[1] R.C.E. Belford, D.E. Fenton, M.R. Truter, J. Chem. Soc., Dalton Trans. (1974) 17.
[2] (a) T. Kogane, K. Kobayashi, M. Ishii, R. Hirota, M. Nakahara, Chem. Lett. (1991) 419;
(b) T. Kogane, K. Kobayashi, M. Ishii, R. Hirota, M. Nakahara, J. Chem. Soc., Dalton Trans. (1994) 13.
[3] T. Ishida, S.-i. Mitsubori, T. Nogami, Y. Ishikawa, M. Yasui, F. Iwasaki, H. Iwamura, N. Takeda, M. Ishikawa, Synth. Met. 71 (1995) 1791.
[4] T. Ishida, T. Nogami, M. Yasui, F. Iwasaki, H. Iwamura, N. Takeda, M. Ishikawa, Mol. Cryst. Liq. Cryst. 279 (1996) 87.
[5] M. Nakagawa, Y. Ishikawa, T. Kogane, T. Ishida, M. Yasui, F. Iwasaki, T. Nogami, Mol. Cryst. Liq. Cryst. 286 (1996) 29.
[6] T. Ishida, K. Nakayama, M. Nakagawa, W. Sato, Y. Ishikawa, M. Yasui, F. Iwasaki, T. Nogami, Synth. Met. 85 (1997) 1655.
[7] M. Yasui, Y. Ishikawa, T. Ishida, T. Nogami, F. Iwasaki, Acta Crystallogr., Sect. B 57 (2001) 772.
[8] H.W. Richardson, J.R. Wasson, W.E. Hatfield, Inorg. Chem. 16 (1977) 484.
[9] T. Kogane, M. Ishii, K. Harada, R. Hirota, M. Nakahara, Bull. Chem. Soc. Jpn. 63 (1990) 1005.
[10] T. Kogane, R. Hirota, K. Abe, M. Hirota, J. Chem. Soc., Perkin Trans. 2 (1981) 652.
[11] D.P. Graddon, Coord. Chem. Rev. 4 (1969) 1.
[12] A. Bondi, J. Phys. Chem. 68 (1964) 441.
[13] R.C.E. Belford, D.E. Fenton, M.R. Truter, J. Chem. Soc., Dalton Trans. (1972) 2208.
[14] J.A. Bertrand, R.I. Kaplan, Inorg. Chem. 5 (1966) 489.
[15] J.C. Bonner, M.E. Fisher, Phys. Rev. A 135 (1964) 640.
[16] H.W. Richardson, J.R. Wasson, W.E. Hatfield, Inorg. Chem. 16 (1977) 484.
[17] (a) H. Iwamura, Adv. Phys. Org. Chem. 26 (1990) 179;
(b) A. Rajca, Chem. Rev. 94 (1994) 871.
[18] (a) T. Ishida, T. Kawakami, S.-i. Mistubori, T. Nogami, K. Yamaguchi, H. Iwamura, J. Chem. Soc., Dalton Trans. (2002) 3177;
(b) R. Feyerherm, S. Abens, D. Gunther, T. Ishida, M. Meissner, M. Meschke, T. Nogami, M. Steiner, J. Phys.: Condens. Mat. 12 (2000) 8495.
[19] M. Yasui, Y. Ishikawa, N. Akiyama, T. Ishida, T. Nogami, F. Iwasaki, Acta Crystallogr., Sect. B 57 (2001) 288.
[20] CrystalStructure Version 3.5.1, Single Crystal Structure Analysis Software, Rigaku/MSC, The Woodlands, TX 77381, USA, 2003.

the ratio between the number of molecules in high spin state and the total number of molecules.

For a thermal transition the warming/cooling modes are to be distinguished and there are two different types of FORC experiments, according to the sense of the thermal variations. The measurements start at a sufficiently high/low temperature, such that the high/low temperature (HS/LS) domain structure is saturated. Then temperature is lowered/raised until a given temperature T_b/T_b^*, the reversal temperature, and afterwards raised/lowered, in the warming/cooling mode, respectively, as illustrated in Fig. 1. During the second step of the process, n_{HS}/n_{HS}^* is measured as a function of the actual temperature, T_a/T_a^*. The experiment is repeated for several values of T_b/T_b^*, and the set of $n_{HS}(T_a,T_b)/n_{HS}^*(T_a^*,T_b^*)$ values forms the FORC data.

The FORC distribution is defined as the second mixed derivative of these curves:

$$\rho(T_a,T_b) = -\frac{\partial^2 n_{HS}(T_a,T_b)}{\partial T_a \partial T_b}$$

In the case of non-interacting domains, the FORC distribution $\rho(T_a,T_b)$ is equivalent to the Preisach distribution, e.g. $P(T_{down},T_{up})$ in the warming mode and $P(T_{up},T_{down})$ in the cooling mode. In such a case, the FORC distributions obtained in the cooling and warming modes are expected to be the same, in the limit of inherent experimental errors [4].

Diluted systems are of higher interest for investigating the nature and range of interactions. In the mean-field description, the "effective" interaction in the diluted system is proportional to the number of spin-crossover neighbours, i.e., to the composition parameter x and qualitatively explains why the hysteresis loop collapses bellow a threshold value $x = 0.40$ in the isostructural systems $[Fe_xM_{1-x}(btr)_2(NCS)_2]\cdot H_2O$ where the dilution metal M was Co or Ni [6,7].

In the case of pure and diluted spin transition materials $[Fe_xZn_{1-x}(btr)_2(NCS)_2]\cdot H_2O$, we calculated distributions of internal stresses and domain size, increasing with dilution $(1-x)$. The FORC analysis shows, for increasing dilution parameter an increasing width of the bias distribution, a decreasing width of the coercivity distribution, as well as an increasing correlation between the bias and coercivity distribution. The large variation of the mean transition temperature upon the effect of dilution can be explained by the large ionic radius of the Zn(II) ion, which roughly matches the Fe(II) ion radius in the high spin state.

The representative major thermal hysteresis loops of some Ni diluted compounds are reported in Fig. 2. In Fig. 3, we present the spin state phase diagram for all the three dilutions. A threshold dilution value, which is the limit of the Fe concentration that implies the presence of a hysteresis can be established for every impurity, varying from 0.3 in the case of Zn to about 0.5 for Ni. The large variation of the threshold value, as of the mean transition temperature upon the effect of dilution can be explained by different ionic radius of the impurities. Following the steric arguments used in [6,7], the presence of molecular units with a large radius stabilizes the high spin state of the spin-crossover units, i.e. lowers the equilibrium temperature.

In this paper, we shall present a throughout experimental investigation using the FORC diagram for different dilution metals (Zn, Co and Ni).

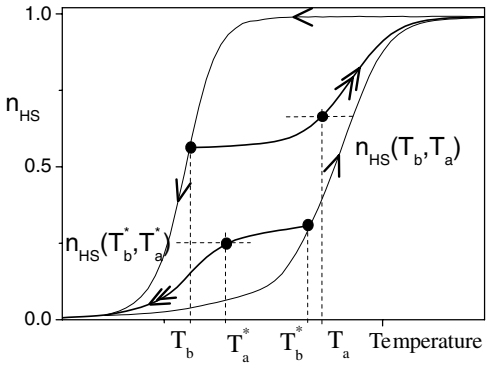


Fig. 1. A FORC in warming and cooling mode.

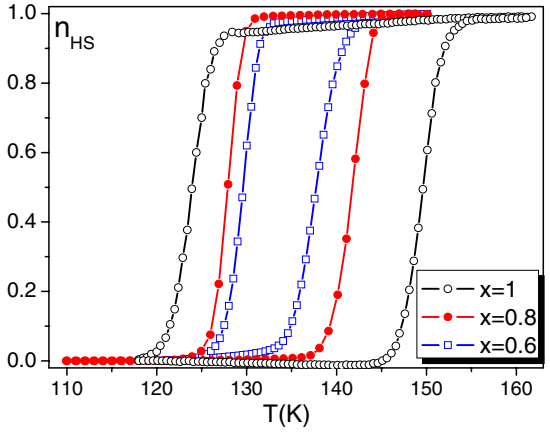


Fig. 2. Thermal hysteresis of $[Fe_xNi_{1-x}(btr)_2(NCS)_2]\cdot H_2O$ for different concentrations.

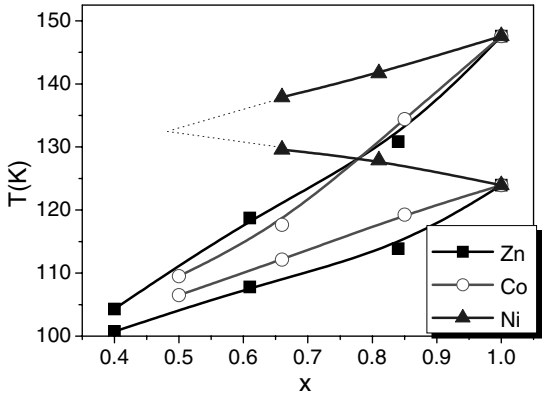


Fig. 3. The dilution phase diagrams of Fe $x = 1$, Zn ($x = 0.8$, 0.6 and 0.4) Co ($x = 0.8$, 0.6 and 0.5) and Ni ($x = 0.8$ and 0.6) taking the switching temperatures corresponding to $n_{HS} = 0.5$.

2. Metal dilution effect investigation with FORC method

We now proceed to a general discussion of the properties induced by dilution of the spin transition complex $[Fe(btr)_2(NCS)_2]\cdot H_2O$ according to the nature of the different diluents: Zn, Co, Ni.

A crucial point is the steric effect induced by the substitution of transition metal in the spin crossover molecular unit. To a first approach, the change in the metal–ligand distance will merely follow the change in the ionic radius, which can be derived from the data listed in Table 1.

Therefore, it can be expected [7] that Ni-dilution will not induce sizeable steric effects, because the Ni(II) radius almost equals the average value of the low-spin and high-spin Fe(II). Consequently, the equilibrium temperature, that is the central temperature of the thermal hysteresis loop is not expect to depend on the dilution factor. On the contrary, Zn-dilution, and to a lesser extent, Co-dilution will induce an increase in the lattice parameter, which favors the Fe(II) high spin state, and finally induce a shift of the thermal hysteresis loop towards the low temperatures.

In our experiments, we used small crystals, in shape of rectangular pellets, slightly coloured (from white to yellow) at room temperature and turning to dark purple at low temperature. We have used magnetization measurements, made with a SQUID magnetometer (MPMS5 Quantum Design) in the RSO (Reciprocating sample option – a more sensitive head) mode. In Fig. 4, we present the experimental FORCs and FORC diagrams of $[Fe_{0.6}Co_{0.4}(btr)_2(NCS)_2]\cdot H_2O$ and $[Fe_{0.6}Ni_{0.4}(btr)_2(NCS)_2]\cdot H_2O$ samples (about 5 mg), derived from the magnetization measurements. Temperature was scanned every 0.5 K for both T_a and T_b and the applied field was 1000Oe. The high spin fraction was derived from the susceptibility value, considering the, respectively, paramagnetic and diamagnetic characters of the high spin and low spin states.

For an easier comparison, we plotted all diagrams on the same graph, in (T_a,T_b) plane (see Fig. 5). It is worth noting that the centres of the FORC distributions are situated along a straight line, which of course is consistent with the phase diagram already shown in Fig. 3. In order to facilitate the discussion of the results in physical terms, we have chosen the $b=(T_a+T_b)/2$, $c=(T_a-T_b)/2$ axes (Fig. 6) which roughly correspond to the energy gap Δ and intra-domain interaction J. The corresponding axes for magnetic systems would be the bias (interactions between domains) and coercivity, respectively.

Table 1
Selected values of ionic radius of divalent 3d transition metals in octahedral symmetry (after [6])

Metal	r (pm)
Zn(II)	96
Fe^{HS}(II)	92
Co(II)	88.5
Ni(II)	83
Fe^{LS}(II)	75

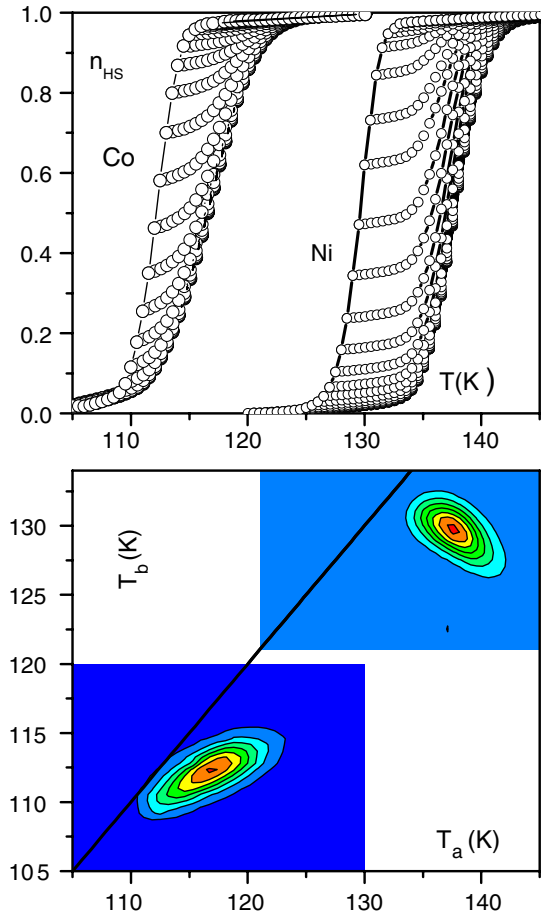


Fig. 4. FORCs and diagram of $[Fe_{0.6}Co_{0.4}(btr)_2(NCS)_2]\cdot H_2O$ and $[Fe_{0.6}Ni_{0.4}(btr)_2(NCS)_2]\cdot H_2O$.

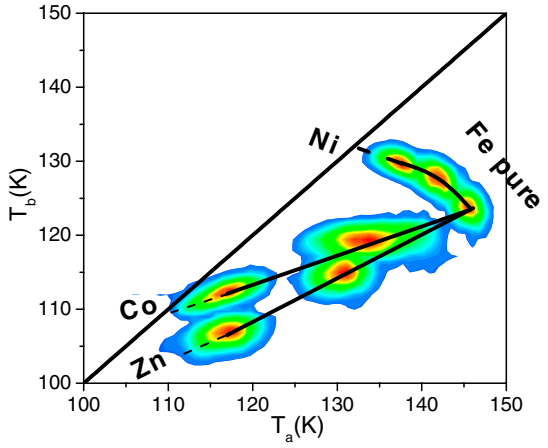


Fig. 5. FORC diagrams of all diluted system in (T_a, T_b) plane.

We also performed the statistical analysis after the procedure described in [4], and we collected in Table 2 the main parameters obtained by this analysis. Following this procedure, we were able to obtain the average values of bias ($\bar{b}$) and coercivity ($\bar{c}$), the dispersion of distributions,

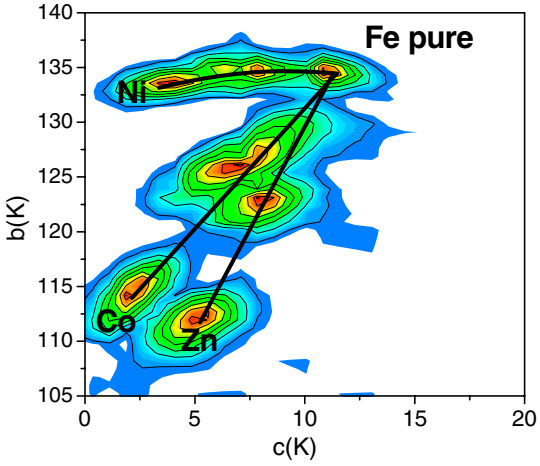


Fig. 6. The diagrams of all diluted systems, in $(b - c)$ plan.

Table 2
The statistical data of (b, c) distributions of diluted $[Fe(btr)_2(NCS)_2] \cdot H_2O$

x		$\bar{c}$ (K)	$\bar{b}$ (K)	σ_c (K)	σ_b (K)	r
Zn	0.61	5.05	111.58	1.28	1.65	0.52
	0.84	7.74	122.61	1.47	1.71	0.25
Co	0.66	1.79	114.4	1.96	1.98	0.76
	0.85	7.47	126.7	2.5	2.57	0.69
Ni	0.66	4.05	133.50	1.77	1.36	0.48
	0.81	7.03	134.61	1.58	1.03	0.11
Fe	pure	10.81	134.56	1.24	1.03	−0.26

σ_b, σ_c, respectively and the factor r which represents the degree of correlation between the joint distributions.

The comparison between the different systems is now made with the help of correlation plots between the bias and coercivity parameters, reported in Figs. 7 and 8. Such plots eliminate the uncertainties or errors which might affect the compositional parameters, and lead to the following observations:

(i) a quasi-linear correlation exists between the $\bar{b}$ and $\bar{c}$ values, for each type of dilution metal, see Fig. 7. This is consistent with the simple idea that both parameters depend linearly on the composition parameter. The plot of course agrees with the phase diagram shown in Fig. 3 since it originates from the same experimental data.

(ii) a similar correlation is suggested between the dispersion width parameters, σ_b and σ_c, with however a larger scatter. This observation supports the idea that the spreading of parameters are also linear functions of the composition parameter.

(iii) the Ni-system, the equilibrium temperature of which little depends on composition, is then expected to exhibit an almost constant dispersion in the bias parameter; this is consistent with Fig. 8.

(iv) the Co-system exhibits very large dispersion width parameters, which have already been assigned to an exceptionally large spreading in composition. The slope of the correlation straight line in Fig. 8 however, is smaller than that of the Zn-system. This can be related to the lesser sensitivity of the equilibrium temperature upon dilution, already illustrated by the phase diagram shown in Fig. 3.

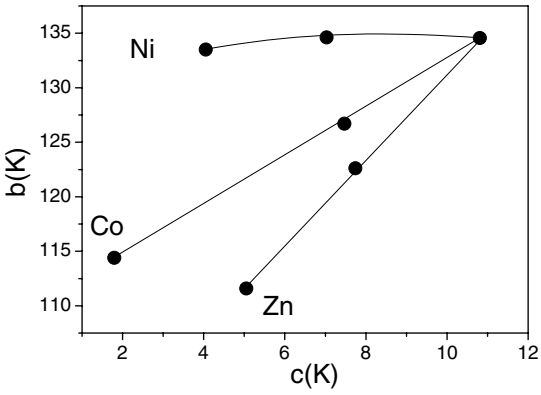


Fig. 7. The average values of the FORC distributions represented in $c - b$ plan.

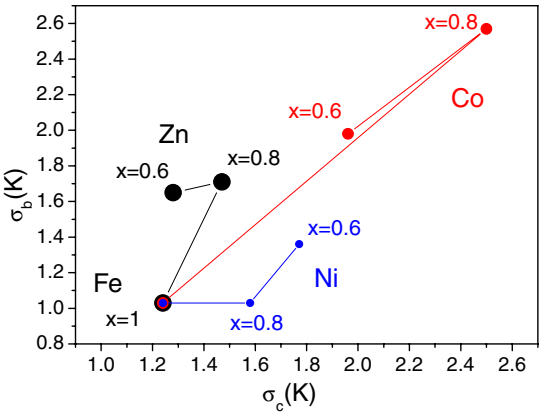


Fig. 8. The coercivity – bias dispersions representation for studied samples.

3. On the squareness of the thermal hysteresis loop

It is known that the ratio between the remanent and saturation magnetization in a magnetic material is an indicator of the importance of the reversible processes. Unfortunately, it is not possible to define a similar parameter in spin transition due to the fact that there is no way to establish in an accurate manner where the origin lies inside the hysteresis loop. We propose here to use the ratio coercivity dispersion/hysteresis width as a general and non-arbitrary procedure to evaluate the reversible component. This statement can be justified by the following observation: when the reversible component is large, the high spin fraction measured on a FORC, will increase right after the returning point thus contributing to a large distribution. If the reversible component is negligible, the variation of the n_{HS} on a FORC will take place in a very small region inside the hysteresis loop, even if the width of the hysteresis is

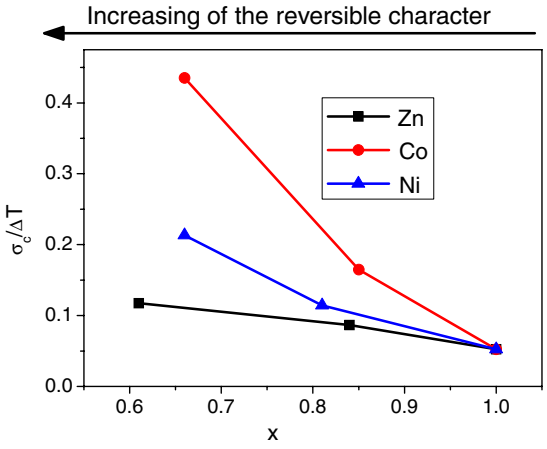


Fig. 9. The plot of relative coercivity dispersion vs. composition parameter of diluted system.

quite big (Fig. 4). The plot of the new parameter values is shown in Fig. 9.

4. Conclusions

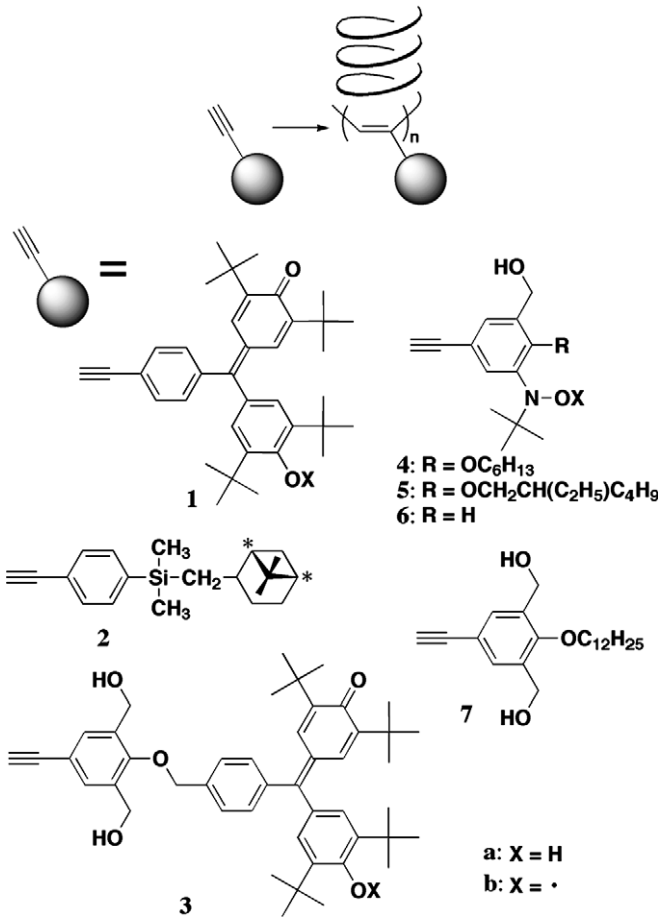
Experimental data on the system under study are consistent with the very simple picture of independent like-spin domains characterized by their equilibrium temperature and internal interaction parameter. In the diluted system, a narrow distribution of composition can explain the observed correlation between equilibrium temperatures and internal interaction parameters.

Acknowledgements

Acknowledgements are due to the MAGMANet Network of Excellence of the European Union (Contract: NMP3-CT-2005-515767-2). CE thanks CNCSIS Romania for a CEEX research Grant.

References

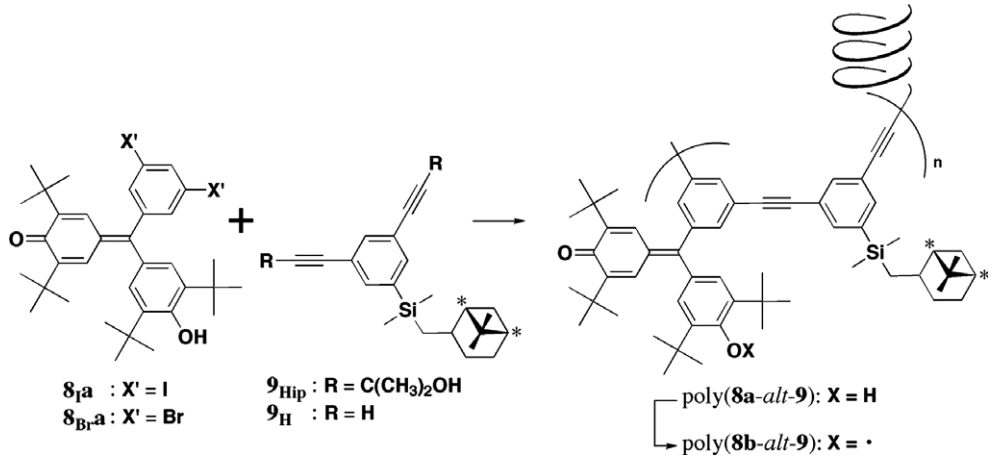
[1] C. Enachescu, H. Constant-Machado, N. Menendez, E. Codjovi, J. Linares, F. Varret, A. Stancu, Physica B 306 (2001) 155.
[2] R. Tanasa, C. Enachescu, A. Stancu, E. Codjovi, J. Linares, F. Varret, J. Opt. Adv. Mater. 6 (2004) 551.
[3] C. Enachescu, R. Tanasa, A. Stancu, E. Codjovi, J. Linares, F. Varret, Physica B 343 (2004) 15.
[4] R. Tanasa, C. Enachescu, A. Stancu, E. Codjovi, J. Linares, F. Varret, J. Haasnoot, Phys. Rev. B 71 (2005) 014431.
[5] K. Boukheddaden, I. Shteto, B. Hoo, F. Varret, Phys. Rev. B 62 (2000) 14806.
[6] J.P. Martin, J. Zarembowitch, A. Bousseksou, A. Dworkin, J.G. Haasnoot, F. Varret, Inorg. Chem. 33 (1994) 6325.
[7] J.P. Martin, J. Zarembowitch, A. Dworkin, J.G. Haasnoot, E. Codjovi, Inorg. Chem. 33 (1994) 2617.



Scheme 1.

(**1a**) and a chiral acetylene monomer **2** using $[Rh(nbd)Cl]_2$ catalyst [14]. The second is the addition of chiral regents leading to interaction or reaction with achiral polymers, which induces a chiral bias between right-handed and left-handed helical conformations. There are no reports about chiral polyradicals using this method, because it is difficult to design polymers which require the ability to form both stable radicals and one-handed helix. The third is the helix-sense-selective polymerization using chiral catalysts or chiral initiators. The helix-sense-selective polymerization is a possible method of obtaining various one-handed helical polymers since the process demands no chiral moiety in the monomer. This fact will give increased flexibility to monomer design, besides obvious economic implications due to using only a catalytic amount of chiral compounds that are often expensive. We have already succeeded in synthesizing optically active helical poly(**1a**) [12,13], poly(**3a**), poly(**4a**), poly(**5a**) and poly(**6a**-*co*-**7**) [15] bearing stable radical precursor by the helix-sense-selective polymerization of the corresponding achiral phenylacetylenes, using the rhodium complex catalyst, in the presence of chiral 1-phenylethylamine. The helical chirality of the polymers was kinetically stabilized by intramolecular hydrogen bonds among hydroxyl groups in the polymer for poly(**3a**), poly(**4a**), poly(**5a**) and poly(**6a**-*co*-**7**), and by the achiral side group's own bulkiness for poly(**1a**) although the obtained polymers possess no chiral moieties except for helicity.

It is well known that poly(phenyleneethynylene)s are obtained from substituted phenylacetylenes by condensation polymerization besides poly(phenylacetylene)s [1,16,17]. In particular, some poly(1,3-phenyleneethynylene)s can form helical foldamer conformation depending on their side groups and/or solvent [18–20], while poly(aryleneethynylene)s have been investigated as a backbone structure of polyradical for magnetic materials [21–28]. Although some poly(1,3-phenyleneethynylene)s bearing stable radicals were also synthesized [29–32], there are no report about optically active helical poly(1,3-phenyleneethynylene)-based polyradicals. In this study, we first synthesized an optically active poly(1,3-phenyleneethynylene) poly(**8b**-*alt*-**9**) bearing galvinoxyl units, which are known as a stable radical, and dimethyl(10-(1*S*)-pinanyl)silyl groups via synthesis of the hydrogalvinoxyl precursor polymer poly(**8a**-*alt*-**9**) by condensation polymerization of (3,5-dihalogenophenyl)hydrogalvinoxyl $\mathbf{8}_{I}\mathbf{a}$ (or $\mathbf{8}_{Br}\mathbf{a}$) and 1,3-diethynylbenzene monomer bearing dimethyl(10-(1*S*)-pinanyl)silyl groups $\mathbf{9}_{H}$ (or $\mathbf{9}_{Hip}$) using $Pd(PPh_3)_4$ catalyst (Scheme 2). The natural optical activity, magnetic optical



Scheme 2.

activity and magnetic interaction of the polymers were discussed in terms of the circular dichroism (CD) spectra, the magneto-circular dichroism (MCD) spectra and SQUID measurements, respectively.

The monomer $\mathbf{8}_{I}\mathbf{a}$ and $\mathbf{8}_{Br}\mathbf{a}$ were synthesized via treatment of 3,5-diiodophenyllithium and 3,5-dibromophenyllithium with 4,4′-diacetoxy-3,3′,5,5′-tetra-*tert*-butylbenzophenone, respectively, followed by elimination of the protecting acetyl groups. 3,5-Dibromophenyllithium was also treated with chlorodimethyl(10-(1*S*)-pinanyl)silane to give 3,5-dibromo-1-(dimethyl(10-(1*S*)-pinanyl)silyl)benzene. The monomer $\mathbf{9}_{Hip}$ was obtained by cross-coupling reaction of 3,5-dibromo-1-(dimethyl(10-(1*S*)-pinanyl)silyl)benzene with twice amount of 2-methyl-3-butyn-2-ol in the presence of a palladium complex catalyst. The monomer $\mathbf{9}_{Hip}$ was converted to the monomer $\mathbf{9}_{H}$ by the elimination reaction of the terminal acetylene-protecting groups.

The polymerization of the monomers was carried out in the presence of $Pd(PPh_3)_4$ catalyst. A yellow solid polymer poly(**8a**-*alt*-**9**) was obtained by precipitation from the polymerization mixtures into methanol. The polymerization data for these resultant polymers are summarized in Table 1. The molecular weight of the polymer was improved by using $\mathbf{8}_{I}\mathbf{a}$ instead of $\mathbf{8}_{Br}\mathbf{a}$. The monomer $\mathbf{8}_{I}\mathbf{a}$ was polymerizable with $\mathbf{9}_{H}$ at lower temperature, i.e. room temperature, in comparison with $\mathbf{8}_{Br}\mathbf{a}$. However, the polymerization of $\mathbf{9}_{Hip}$ with $\mathbf{8}_{I}\mathbf{a}$ required the higher temperature, although this process was expected to circumvent an oxidative coupling side reaction to produce diyne linkage due to combining the deprotection of the ethynyl group and the cross-coupling to the aromatic halide. The polymer was soluble in chloroform, tetrahydrofuran, ethyl acetate, benzene and toluene, but insoluble in acetone, diethyl ether, DMSO, DMF, alcohols and aliphatic hydrocarbons. It was confirmed by IR and ^{1}H NMR spectra of the polymers that polymerization proceeded by cross-coupling reaction between a terminal acetylene and halogeno group of monomers, i.e., the reduction of the peaks assignable to the ethynyl group of $\mathbf{9}_{H}$ at 3302 cm^{-1} ($\nu_{\equiv C-H}$) in IR and δ 3.09 ppm (s, 2H, ≡C–H) in ^{1}H NMR, and the reduction of the peak assignable to the aromatic proton of $\mathbf{8}_{I}\mathbf{a}$ at δ 8.10 ppm (t, 1H, ArH) in ^{1}H NMR. The alternate structure of **8a** and **9** in the polymer was confirmed by ^{1}H NMR; ^{1}H NMR ($CDCl_3$, 270 MHz, ppm) δ 0.29 (s, 3H, $SiCH_3$), 0.30 (s, 3H, $SiCH_3$), 0.65–0.88 (m, 2H, CH or CH_2 in pinanyl), 0.76 (s, 3H, *gem*-CH_3 in pinanyl), 1.13 (s, 3H, *gem*-CH_3 in pinanyl), 1.2–1.3 (m, 1H, CH or CH_2 in pinanyl), 1.25 (s, 9H, *tert*-butyl), 1.28 (s, 9H, *tert*-butyl), 1.34 (d, 1H, $J = 9.9$ Hz, CH or CH_2 in pinanyl), 1.42 (s, 18H, *tert*-butyl), 1.5–1.7 (m, 4H, CH or CH_2 in pinanyl), 1.81 (m, 1H, CH or CH_2 in pinanyl), 1.98 (m, 1H, CH or CH_2 in pinanyl), 2.11 (m, 1H, CH or CH_2 in pinanyl), 5.54 (s, 1H, OH), 7.04 (br, 3H, ArH in **8a**), 7.23 (br, 1H, ArH in **8a**), 7.41 (d, 2H, $J = 1.1$ Hz, ArH in **8a**), 7.60 (d, 2H, $J = 1.1$ Hz, ArH in **9**), 7.63 (t, 1H, $J = 1.1$ Hz, ArH in **9**), 7.78 (t, 1H, $J = 1.1$ Hz, ArH in **8a**).

The polyradical poly(**8b**-*alt*-**9**) was obtained by oxidizing the polymer poly(**8a**-*alt*-**9**) by treatment of the polymer solution in degassed chloroform with fresh PbO_2. The spin concentration of polyradicals were determined by doubly integrating the ESR signal in comparison with that of 2,2,6,6-tetramethyl-1-piperidinyloxyl (TEMPO) solution as a standard. The polyradicals were appropriately stable for maintaining the initial spin concentration under the ESR and SQUID measurement conditions. The ESR spectrum of poly(**8b**-*alt*-**9**) showed a unimodal broad signal at $g = 2.0046$ indicating the formation of the phenoxyl radical, where disappearance of hyperfine structure is attributable to the intramolecular aggregation of radical units along the main chain (Fig. 1).

The CD spectra of poly(**8a**-*alt*-**9**) and poly(**8b**-*alt*-**9**) were measured in various solution. In the CD spectrum of poly(**8a**-*alt*-**9**) taken in ethyl acetate solution, clear Cotton effects were observed in the absorption region of the

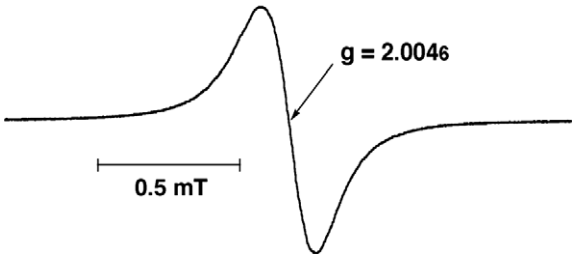


Fig. 1. ESR spectra of poly(**8b**-*alt*-**9**) (0.5 mM, spin conc. = 0.7 spin/phenoxyl unit) in chloroform at room temperature.

Table 1
Polymerization of (3,5-dihalogenophenyl)hydrogalvinoxyl $\mathbf{8}_{I}\mathbf{a}$ (or $\mathbf{8}_{Br}\mathbf{a}$) and 1,3-diethynyl-5-[dimethyl(10-(1*S*)-pinanyl)silyl]benzene monomer $\mathbf{9}_{H}$ (or $\mathbf{9}_{Hip}$) using $Pd(PPh_3)_4$ catalyst

No.	Monomer		Time (h)	Temperature (°C)	Yield[c] (%)	M_w[d] (×10^4)	M_w/M_n[d]	DP[e]
	M_1	M_2						
1[a]	$\mathbf{8}_{I}\mathbf{a}$	$\mathbf{9}_{H}$	24	25	100	17	3.7	417
2[b]	$\mathbf{8}_{I}\mathbf{a}$	$\mathbf{9}_{Hip}$	3	80	90	0.98	1.7	24
3[b]	$\mathbf{8}_{Br}\mathbf{a}$	$\mathbf{9}_{Hip}$	3	110	53	0.65	1.7	16

[a] $[M_1]_0 = [M_2]_0 = 0.25$ M, $[M_1]_0/[Pd(PPh_3)_4]_0 = 20$, $[CuI]_0/[Pd(PPh_3)_4]_0 = 4$, THF/triethylamine (1/1 v/v).
[b] $[M_1]_0 = [M_2]_0 = 0.04$ M, $[M_1]_0/[Pd(PPh_3)_4]_0 = 50$, $[CuI]_0/[Pd(PPh_3)_4]_0 = 1$, 5 M KOH/MeOH, toluene.
[c] Methanol insoluble part. Yield is based on the repeating unit.
[d] Determined by GPC calibrated with polystyrene standard.
[e] Based on the phenyleneethynylene unit, and estimated from M_w.

backbone and hydrogalvinoxyl chromophore, indicating an excess of one-handed helical foldamer conformation (Fig. 2). However, the formation of poly(**8b**-*alt*-**9**) unfortunately became insoluble in ethyl acetate. On the other hand, Cotton effects were hardly observed in chloroform, THF and benzene solution for both poly(**8a**-*alt*-**9**) and poly(**8b**-*alt*-**9**). But the CD signals appeared in CD spectra of the polymer and polyradical by addition of methanol to the chloroform solution, accompanying bathochromic shift of absorption maxima of galvinoxyl chromophore and hypochromic effect of absorption around 300 nm (Fig. 3).

MCD spectra of poly(**8a**-*alt*-**9**) in chloroform are shown in Fig. 4. There, positive and negative Faraday effects are observed for poly(**8a**-*alt*-**9**) in the absorption region of the backbone chromophore (300–350 nm) and of the hydrogalvinoxyl chromophore (420 nm) corresponding to the negative and positive magnetic fields, respectively. On the other hand, the MCD spectrum of poly(**8a**-*alt*-**9**) in ethyl acetate solution shows the Faraday effects overlapping with Cotton effects in the absorption region of the backbone chromophore and of the hydrogalvinoxyl chromophore, and the differential spectrum ($[\theta]_M - [\theta]$) are in agreement with the MCD spectrum of poly(**8a**-*alt*-**9**) in chloroform (Fig. 2). This fact suggests that Faraday effects of poly(**8a**-*alt*-**9**) were independent of the conformation of poly(**8a**-*alt*-**9**). MCD spectra of poly(**8b**-*alt*-**9**) in chloroform are also shown in Fig. 5. The MCD signals, which are mirror images of each other depending on the direction of the magnetic field, appear in the absorption region of the backbone chromophore (300–350 nm) and of the galvinoxyl-radical chromophore (470 nm), although the Cotton effects in the CD spectrum were hardly observed in chloroform.

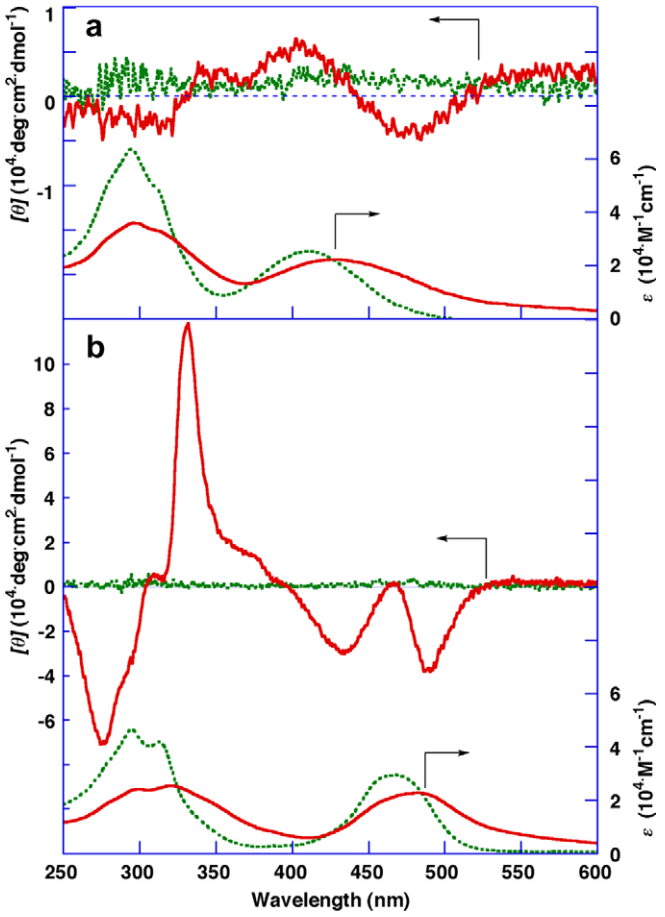


Fig. 3. CD and UV–Vis absorption spectra of (a) poly(**8a**-*alt*-**9**) and (b) poly(**8b**-*alt*-**9**) at 20 °C in chloroform (dashed line) and chloroform/methanol (1/1 (v/v)) (solid line).

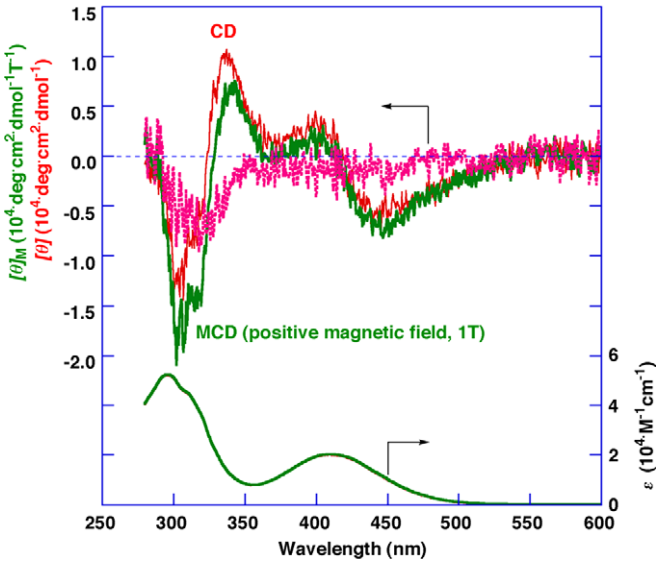


Fig. 2. CD ($[\theta]$), MCD ($[\theta]_M$) and UV–Vis absorption spectra of poly(**8a**-*alt*-**9**) at 20 °C in ethyl acetate. Dashed line: differential spectrum ($[\theta]_M - [\theta]$).

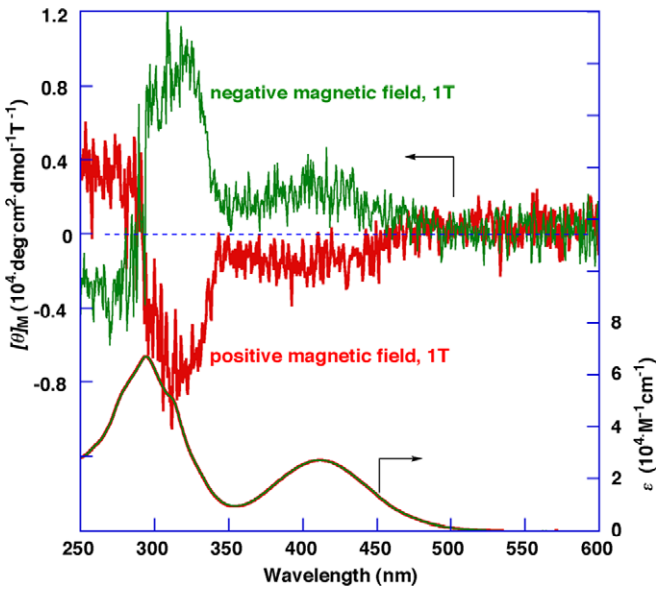


Fig. 4. MCD and UV–Vis absorption spectra of poly(**8a**-*alt*-**9**) at 20 °C in chloroform.

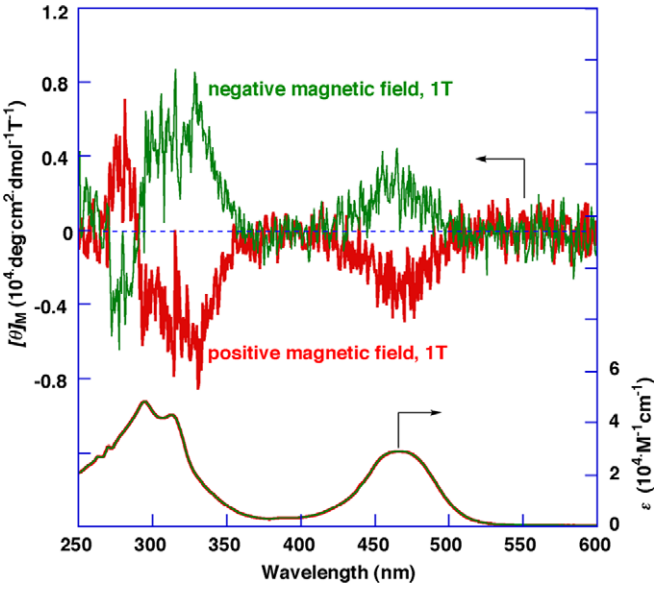


Fig. 5. MCD and UV–Vis absorption spectra of poly(**8b**-*alt*-**9**) at 20 °C in chloroform.

The static magnetic susceptibility (2–300 K at 0.5 T) of poly(**8b**-*alt*-**9**) was measured using a SQUID magnetometer. The powder sample was prepared by evaporating solvent from the chloroform solution of poly(**8b**-*alt*-**9**) and by drying in vacuum. Downward deviation of the χT value of poly(**8b**-*alt*-**9**) at lower temperatures indicated the antiferromagnetic interaction (Weiss const. = −0.7 K, spin conc. = 0.8 spin/unit).

In summary, we have first succeeded in the synthesis of an optically active poly(1,3-phenyleneethynylene)-based polyradical bearing galvinoxyl units, poly(**8b**-*alt*-**9**). The interchain magnetic interaction of helical polyradicals may be modified by the sense of helicity. That is, a one-handed helical polyradical has only interaction between chains of same helical sense, while a racemic helical polyradical has two types of interchain interaction, i.e., interactions between chains of same helical sense and between chains of opposite helical sense. Additionally, magneto-chiral dichroism (MChD) effect is expected in chiral magnetic materials [33–36]. The magnetic and magneto-optical properties of the optically active helical polyradicals will be discussed in more detail in a subsequent paper.

Acknowledgements

This work was partially supported by a Grant-in-Aid for Scientific Research (B) (No. 16350061) from JSPS, by a Grant-in-Aid for Young Scientists (A) (No. 17681010) from Ministry of Education, Culture, Sports, Science and Technology (MEXT), by a Grant for the Promotion of Niigata University Research Projects, and by the Asahi Glass Foundation.

References

[1] T. Aoki, T. Kaneko, M. Teraguchi, Polymer 47 (2006) 4867.
[2] T. Aoki, M. Kokai, K. Shinohara, E. Oikawa, Chem. Lett. (1993) 2009.
[3] K. Shinohara, T. Aoki, E. Oikawa, Polymer 36 (1995) 2403.
[4] T. Aoki, K. Shinohara, T. Kaneko, E. Oikawa, Macromolecules 29 (1996) 4192.
[5] T. Aoki, Y. Kobayashi, T. Kaneko, E. Oikawa, Y. Yamamura, Y. Fujita, M. Teraguchi, R. Nomura, T. Masuda, Macromolecules 32 (1999) 79.
[6] K. Shinohara, T. Aoki, T. Kaneko, J. Polym. Sci. Polym. Chem. Ed. 40 (2002) 1689.
[7] M. Teraguchi, J. Suzuki, T. Kaneko, T. Aoki, T. Masuda, Macromolecules 36 (2003) 9694.
[8] T. Aoki, T. Fukuda, K. Shinohara, T. Kaneko, M. Teraguchi, M. Yagi, J. Polym. Sci. Polym. Chem. Ed. 42 (2004) 4502.
[9] M. Teraguchi, K. Mottate, S.-Y. Kim, T. Aoki, T. Kaneko, S. Hadano, T. Masuda, Macromolecules 38 (2005) 6367.
[10] T. Aoki, T. Kaneko, N. Maruyama, A. Sumi, M. Takahashi, T. Sato, M. Teraguchi, J. Am. Chem. Soc. 125 (2003) 6346.
[11] T. Sato, T. Aoki, M. Teraguchi, T. Kaneko, S.-Y. Kim, Polymer 45 (2004) 8109.
[12] Y. Umeda, T. Kaneko, M. Teraguchi, T. Aoki, Chem. Lett. 34 (2005) 854.
[13] T. Kaneko, Y. Umeda, T. Yamamoto, M. Teraguchi, T. Aoki, Macromolecules 38 (2005) 9420.
[14] T. Kaneko, T. Yamamoto, T. Aoki, E. Oikawa, Chem. Lett. (1999) 623.
[15] T. Kaneko, S. Yoshimoto, S. Hadano, M. Teraguchi, T. Aoki, in preparation.
[16] R. Giesa, J. Macromol. Sci. Rev. Macromol. Chem. Phys. C36 (1996) 631.
[17] U.H.F. Bunz, Chem. Rev. 100 (2000) 1605.
[18] J.C. Nelson, J.G. Saven, J.S. Moore, P.G. Wolynes, Science 277 (1997) 1793.
[19] D.J. Hill, M.J. Mio, R.B. Prince, T.S. Hughes, J.S. Moore, Chem. Rev. 101 (2001) 3893.
[20] M.T. Stone, J.S. Moore, J. Am. Chem. Soc. 127 (2005) 5928.
[21] H. Nishide, T. Maeda, K. Oyaizu, E. Tsuchida, J. Org. Chem. 64 (1999) 7129.
[22] H. Nishide, M. Takahashi, J. Takashima, E. Tsuchida, Polym. J. 31 (1999) 1171.
[23] T. Kaneko, T. Matsubara, T. Aoki, E. Oikawa, Mol. Cryst. Liq. Cryst. 334 (1999) 221.
[24] T. Kaneko, T. Makino, G. Sato, T. Aoki, Polyhedron 20 (2001) 1291.
[25] T. Kaneko, T. Matsubara, T. Aoki, Chem. Mater. 14 (2002) 3898.
[26] T. Kaneko, T. Makino, H. Miyaji, M. Teraguchi, T. Aoki, M. Miyasaka, H. Nishide, J. Am. Chem. Soc. 125 (2003) 3554.
[27] T. Kaneko, T. Makino, H. Miyaji, A. Onuma, M. Teraguchi, T. Aoki, Polyhedron 22 (2003) 1845.
[28] T. Kaneko, A. Onuma, H. Ito, M. Teraguchi, T. Aoki, Polyhedron 24 (2005) 2544.
[29] Y. Miura, Y. Ushitani, Macromolecules 26 (1993) 7079.
[30] Y. Miura, T. Issiki, Y. Ushitani, Y. Teki, K. Itoh, J. Mater. Chem. 6 (1996) 1745.
[31] P. Wautelet, T. Philippe, J. Le Moigne, Synthesis (2002) 1286.
[32] K. Matsuda, M.T. Stone, J.S. Moore, J. Am. Chem. Soc. 124 (2002) 11836.
[33] G. Wagnière, A. Meire, Chem. Phys. Lett. 93 (1982) 78.
[34] G. Wagnière, Chem. Phys. Lett. 110 (1984) 546.
[35] L.D. Barron, J. Vrbancich, Mol. Phys. 51 (1984) 715.
[36] G.L.J.A. Rikken, E. Raupach, Nature 390 (1997) 493.

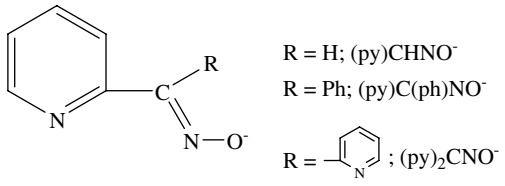


Fig. 1. Formulae and abbreviations of the 2-pyridyloximate(-1) ligands used in this work. The neutral ligands are abbreviated as (py)C(R)NOH.

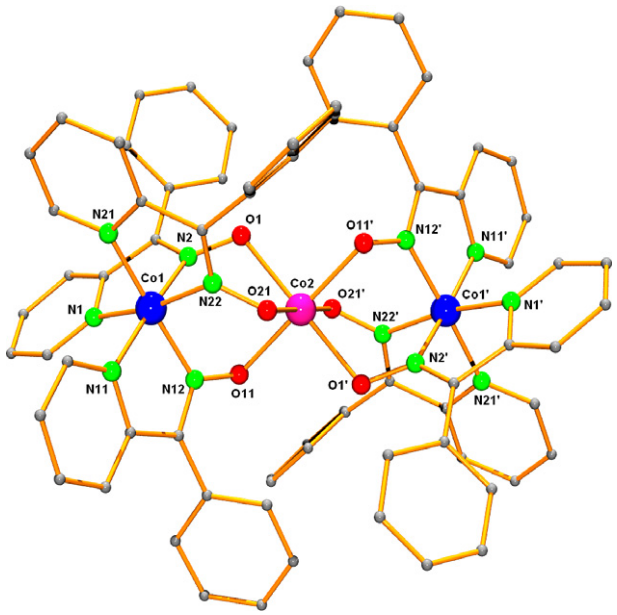


Fig. 2. Molecular structure of the cation $[Co_3^{III,II,III}\{(py)C(ph)NO\}_6]^{2+}$ present in **1** · 6MeCN. Primes are used for the symmetry-related ($-x$, $-y$, $-z$) atoms.

$(py)C(ph)NO^-$ ligands. The six sites on each of the distorted octahedral low-spin, terminal Co^{III} ions are occupied by the nitrogen atoms that belong to the "chelating" part of three $(py)C(ph)NO^-$ ligands, with the three oximate N atoms in the *fac* configuration. Complex **1** can also be obtained by the 2:1 reaction between *mer*-$[Co^{III}\{(py)C(ph)NO\}_3]$ [4] and $Co(PF_6)_2 \cdot 6H_2O$ in MeCN ("metal complexes as ligands" strategy), see Eq. (1). Magnetically, complex **1**

$$2[Co^{III}\{(py)C(ph)NO\}_3] + Co^{II}(PF_6)_2 \cdot 6H_2O \xrightarrow[T]{MeCN} \underset{\mathbf{1}}{[Co_3\{(py)C(ph)NO\}_6](PF_6)_2} + 6H_2O \quad (1)$$

behaves as a monomeric octahedral, high-spin Co(II) complex ($\mu_{eff} = 5.01$ BM per trimer at 22 °C). The Co/(py)CHNOH chemistry [4] is very similar to the Co/(py)C(ph)NOH chemistry.

In order to investigate to what extent the presence of a donor atom on the substituent R of the oxime group of 2-pyridyl oximes might affect the identity of isolated Co products, we studied the Co/$(py)_2$CNOH chemistry. Aerobic reaction of $Co(O_2CMe)_2 \cdot 4H_2O$ with $(py)_2$CNOH, in the presence of $NaClO_4$(1:1:1 reaction ratio), in MeOH/H_2O (5:1, v/v) led to the red cluster $[Co_2^{II}Co_2^{III}(OH)_2(O_2CMe)_2\{(py)_2CNO\}_4(MeOH)_2](ClO_4)_2$ (**2**) in very good yield (>65%), see Eq. (2). The tetranuclear, mixed-valent cation of **2** · 4MeOH · 3.08H_2O (Fig. 3)[2]

$$4Co(O_2CMe)_2 \cdot 4H_2O + 4(py)_2CNOH + O_2 + 2NaClO_4 + 2MeOH \xrightarrow[25\,^\circ C]{MeOH/H_2O} \underset{\mathbf{2}}{[Co_2^{II}Co_2^{III}(OH)_2(O_2CMe)_2\{(py)_2CNO\}_4(MeOH)_2](ClO_4)_2} + 2NaO_2CMe + 4MeCO_2H + H_2O_2 + 14H_2O \quad (2)$$

has the four metal ions in a rectangular arrangement. Based on Co-donor atom bond lengths, Co(1) and its symmetry-related Co(1′) are assigned as the Co^{III} ions. The cobalt centers are bridged along each short edge of the rectangle [Co(1)···Co(2) = 3.213(1) Å] by one hydroxide [O(21), O(21′)], one syn,syn $\eta^1{:}\eta^1{:}\mu_2$-$MeCO_2^-$ group and one oximate group. The bridging along each long side [Co(1)···Co(2′) = 4.441(1) Å] occurs through one oximate group only. Short edge $(py)_2CNO^-$ ligands adopt the $\eta^1{:}\eta^1{:}\eta^1{:}\mu_2$ coordination mode, while long edge $(py)_2CNO^-$ ions function as $\eta^1{:}\eta^1{:}\eta^1{:}\eta^1{:}\mu_2$ ligands. Complex **2** has a novel inverse 12-metallacrown-4 structural motif [5]. Since the paramagnetic, high-spin d^7 Co^{II} ions alternate with the diamagnetic Co^{III} ones in the ring of **2**, superexchange between the former is negligible. The observed decrease of $\chi_M T$ as T is lowered (Fig. S1) can be attributed to the spitting of the $^4T_{1g}$ ground state by low symmetry ligand fields and spin–orbit coupling [6].

Use of 2-pyridyloximate(-1) ligands in nickel(II) chemistry gives different clusters, as expected. The synthetic investigation of the Ni^{II}/(py)CHNOH/OH^- reaction systems in H_2O, H_2O/MeOH or H_2O/MeCN in the presence of coun-

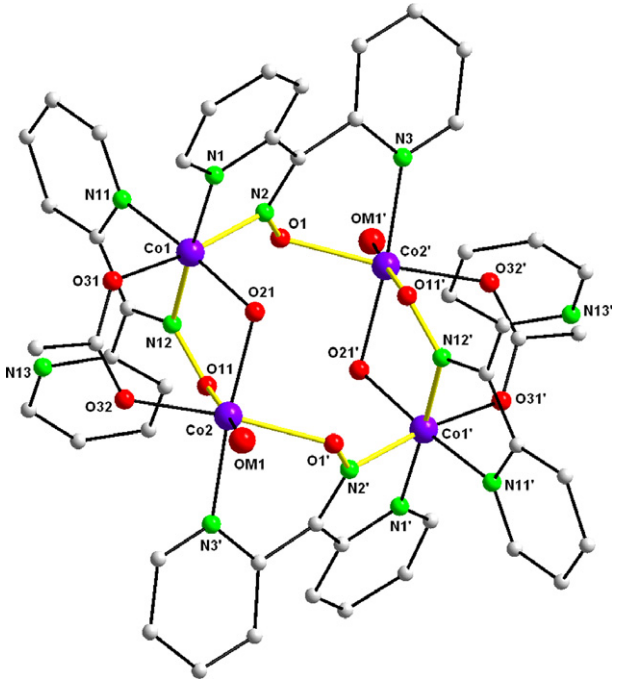


Fig. 3. The molecular structure of the $Co_2^{II}Co_2^{III}$ cation present in complex **2** · 4MeOH · 3.08H_2O. Primed and unprimed atoms are related by the crystallographic inversion center.

terions has led to a variety of salts possessing the thermodynamically stable enneanuclear cation $[Ni_9(\mu_3\text{-}OH)_2(\mu_2\text{-}OH)_2\{\mu_3\text{-}(py)CHNO\}_4\{\mu_2\text{-}(py)CHNO\}_6(\mu_2\text{-}OH_2)_2(H_2O)_6]^{4+}$ ($\mathbf{3}^{4+}$) [7,8]. The preparation of the representative salt **3** $\{N(CN)_2\}_3(ClO_4)$ is summarized in Eq. (3). The cation (Fig. 4)[2] can be described as consisting of two

$$9Ni(ClO_4)_2\cdot 6H_2O + 10(py)CHNOH + 3NaN(CN)_2 + 14NaOH \xrightarrow[\text{“pH”}=7]{H_2O\text{–}MeCN} \underset{\mathbf{3}\{N(CN)_2\}_3(ClO_4)}{[Ni_9(OH)_4\{(py)CHNO\}_{10}(H_2O)_8]\{N(CN)_2\}_3(ClO_4)} + 17NaClO_4 + 56H_2O \quad (3)$$

$[Ni_4(\mu_2\text{-}OH)_2\{\mu_2\text{-}(py)CHNO\}_5(\mu_2\text{-}OH_2)(H_2O)_3]^+$ subunits linked to the central Ni(1) ion through four oximate oxygens and two *trans* disposed bridging OH^- groups; as a result of this association, one OH^- group of each subunit becomes μ_3, and two oximate oxygens of each subunit become μ_2. Six of the $(py)CHNO^-$ ions behave as $\eta^1\text{:}\eta^1\text{:}\eta^1\text{:}\mu_2$ ligands and the remaining four as $\eta^1\text{:}\eta^1\text{:}\eta^2\text{:}\mu_3$ ligands. All the salts of $\mathbf{3}^{4+}$ exhibit a very similar magnetic behaviour. The $\chi_M T$ vs. T plot for the representative cluster $\mathbf{3}(ClO_4)_4\cdot 7.85H_2O\cdot 1.4MeOH$ (2–300 K, 0.1 T), shown in Fig. 5, is indicative of strong antiferromagnetic coupling.

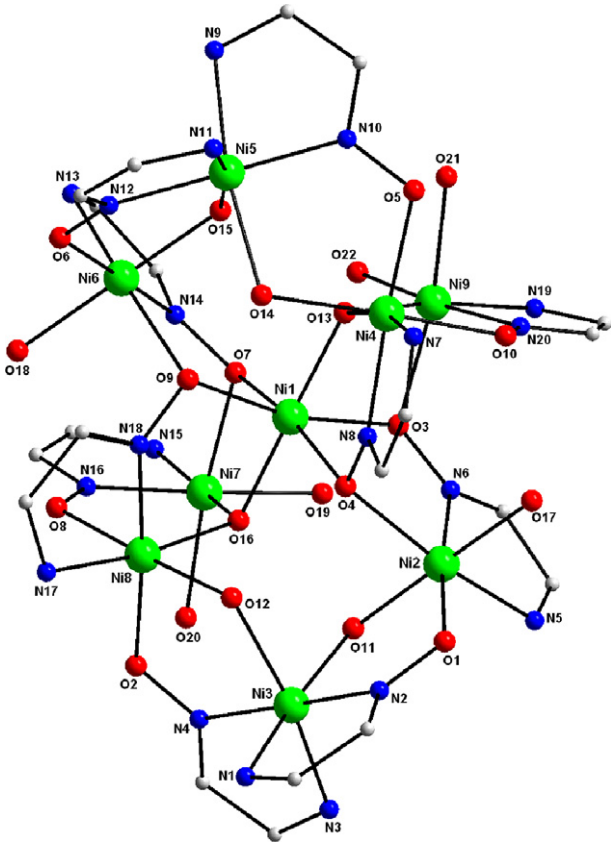


Fig. 4. A plot of the enneanuclear cation present in $\mathbf{3}\{N(CN)_2\}_3(ClO_4)\cdot 11.11H_2O$. Most carbon atoms of the 10 $(py)CHNO^-$ ligands have been omitted. Atoms O(13), O(16) belong to the $\mu_3\text{-}OH^-$ ligands, while atoms O(11) and O(15) to the $\mu_2\text{-}OH^-$ ligands. The $\mu_2\text{-}H_2O$ oxygen atoms are O(12) and O(14), while O(17)–O(22) are the oxygen atoms of the terminal aqua ligands. The rest oxygen atoms belong to the $(py)CHNO^-$ ligands.

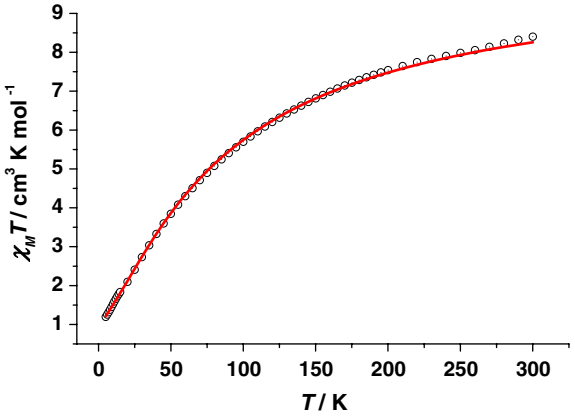


Fig. 5. Plot of the $\chi_M T$ product vs. T for an analytically pure sample of complex $\mathbf{3}(ClO_4)_4\cdot 7.85H_2O\cdot 1.4MeOH$ [6,7]. The solid line is the fit of the data to the appropriate 3-J model (see text).

Magnetization experiments at 2 K (Fig. S2) up to a field of 5 T show a saturation value equivalent to two electrons, indicating an $S_T = 1$ ground state. The susceptibility data were fit to a 3-J model. Best-fit parameters, obtained by means of the program CLUMAG [9], are $J_1 = -16.4\ cm^{-1}$, $J_2 = -8.7\ cm^{-1}$, $J_3 = -27.1\ cm^{-1}$ and $g = 2.079$. The J_1 coupling constant is assigned to Ni···Ni interactions involving a diatomic oximate group and a single O atom that belongs to a $\mu_3\text{-}OH^-$, a $\mu_2\text{-}OH^-$ or to a μ_3-oximate group. The J_2 coupling constant is assigned to Ni···Ni interactions involving two single oxygen atoms, one from a μ_3-oximate group and the second from a $\mu_3\text{-}OH^-$ group, while the J_3 coupling constant is assigned to Ni···Ni interactions through a diatomic oximate group.

Reaction of $Ni(O_2CMe)_2\cdot 4H_2O$ with one equivalent of (py)C(ph)NOH in MeOH and layering of Et_2O onto the resulting red solution gave violet crystals of $[Ni_4(O_2CMe)_4\{(py)C(ph)NO\}_4(MeOH)_2]$ (**4**), see Eq. (4); the yield was 65%.

$$4Ni(O_2CMe)_2\cdot 4H_2O + 4(py)C(ph)NOH + 2MeOH \xrightarrow{MeOH} \underset{\mathbf{4}}{[Ni_4(O_2CMe)_4\{(py)C(ph)NO\}_4(MeOH)_2]} + 4MeCO_2H + 16H_2O \quad (4)$$

The crystal structure of $\mathbf{4}\cdot 2MeOH$[2] reveals the presence of tetranuclear molecules (Fig. 6). The core consists of a tetrahedron of Ni^{II} ions to form a distorted $[Ni_4(NO)_4]^{4+}$ 'cube' (the term '*cubane*' is avoided since it implies the existence of only monoatomic bridges between the metal ions) comprising single (O) and double (N–O) atom edges. Each molecule is held together by two syn,syn $\eta^1\text{:}\eta^1\text{:}\mu_2\text{-}MeCO_2^-$ groups and four $\eta^1\text{:}\eta^1\text{:}\eta^2\text{:}\mu_3$ $(py)C(ph)NO^-$ ligands; the remaining two acetates are monodentate, while one terminal MeOH molecule completes octahedral coordination at Ni(2) and Ni(2′). The terminal acetates can easily be replaced by other monoanionic monodentate ligands providing a family of structurally similar $[Ni_4(O_2CMe)_2X_2\{(py)C(ph)NO\}_4(ROH)_2]$ clusters (X = Cl, Br, NCS, $N(CN)_2^-$, …; R = Me, Et, ^{n}Pr, …). Preliminary variable-

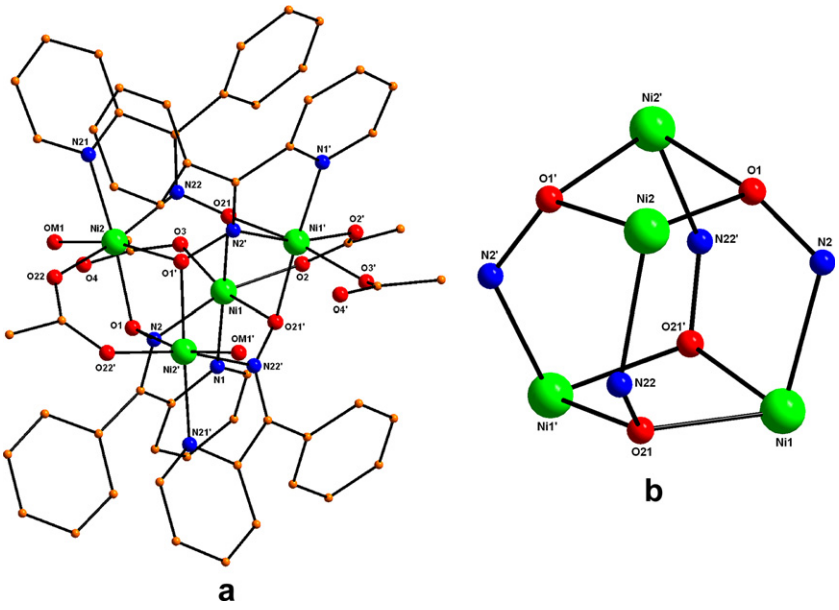


Fig. 6. (a) The molecular structure of the tetranuclear molecule present in complex **4** · 2MeOH, and (b) its core. Primed and unprimed atoms are related by the symmetry operator $x, -y, 1 - z$.

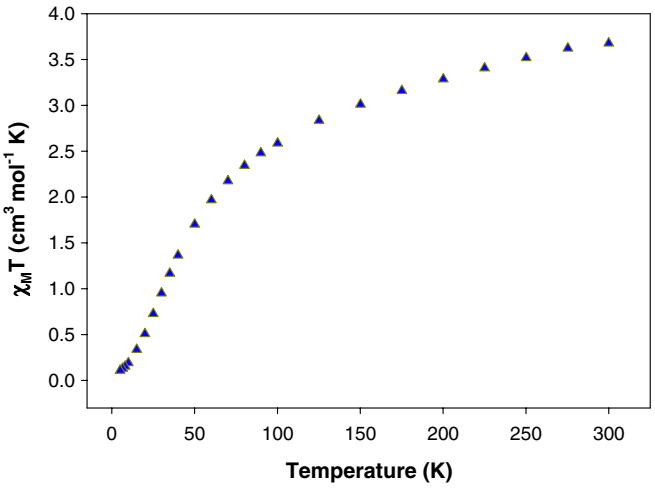


Fig. 7. Plot of the $\chi_M T$ product vs. T for a polycrystalline sample of **4**.

temperature magnetic susceptibility data (Fig. 7) are indicative of antiferromagnetic coupling within the cluster with a resultant $S_T = 0$ ground state.[3]

In conclusion, the present work emphasizes the ability of 2-pyridyloximate ligands to form interesting structural types in 3d-metal cluster chemistry. The great structural diversity of the complexes described stems in part from the ability of the (py)C(R)NO$^-$ ligands to exhibit a variety of distinct coordination modes. Results at the time of writing show that employment of β-diketonates or sulfates in the (py)C(R)NO$^-$ cobalt and nickel chemistry give an extraordinary structural flexibility in the resulting ligand "blends". Reactions are also in progress for the substitution of the hydroxo bridges that are present in **2** and salts of $\mathbf{3}^{4+}$ by end-on azido ligands, in an effort to specifically introduce ferromagnetic components in the superexchange scheme of these clusters.

[3] Details will be provided in the full paper.

Acknowledgements

We thank European Social Fund (ESF), Operational Program for Educational and Vocational Training II (EPEAEK II), and particularly the Program PYTHAGORAS (Grant b. 365.037), for funding the above work. We also thank Profs. Albert Escuer and Ramon Vicente (Departament de Quimica Inorganica, Universitat de Barcelona, Spain) for the magnetic study of the compounds reported in this communication.

Appendix A. Supplementary material

Variable-temperature magnetic susceptibility data for **2** (Fig. S1) and magnetization data at 2 K for $\mathbf{3}(ClO_4)_4$ (Fig. S2).

CCDC 264165, 249267, 602391 and 619211 contain the supplementary crystallographic data for **1**, **2**, **3** and **4**. These data can be obtained free of charge via http://www.ccdc.cam.ac.uk/conts/retrieving.html, or from the Cambridge Crystallographic Data Centre, 12 Union Road, Cambridge CB2 1EZ, UK; fax: (+44) 1223-336-033; or e-mail: deposit@ccdc.cam.ac.uk.

References

[1] (a) A.M. Ako, I.J. Hewitt, V. Mereacre, R. Clerac, W. Wernsdorfer, C.E. Anson, A.K. Powell, Angew. Chem., Int. Ed. 45 (2006) 4926; (b) M. Murugesu, M. Habrych, W. Wernsdorfer, K.A. Abboud, G. Christou, J. Am. Chem. Soc. 126 (2004) 4766.

[2] (a) For reviews, see: G. Aromi, E.K. Brechin, Struct. Bond. 122 (2006) 1;
(b) D. Gatteschi, R. Sessoli, Angew. Chem., Int. Ed. 42 (2003) 268;
(c) G. Christou, D. Gatteschi, D.N. Hendrickson, R. Sessoli, MRS Bull. 25 (2000) 66.
[3] For a review, see: C.J. Milios, Th. C. Stamatatos, S.P. Perlepes, Polyhedron 25 (2006) 134, Polyhedron Report.
[4] Th. C. Stamatatos, A. Bell, P. Cooper, A. Terzis, C.P. Raptopoulou, S.L. Heath, R.E.P. Winpenny, S.P. Perlepes, Inorg. Chem. Commun. 8 (2005) 533.
[5] Th. C. Stamatatos, S. Dionyssopoulou, G. Efthymiou, P. Kyritsis, C.P. Raptopoulou, A. Terzis, R. Vicente, A. Escuer, S.P. Perlepes, Inorg. Chem. 44 (2005) 3374.
[6] O. Kahn, Molecular Magnetism, Wiley–VCH, New York, 1993, p. 38.
[7] S. Khanra, T. Weyhermüller, E. Rentschler, P. Chaudhuri, Inorg. Chem. 44 (2005) 8176.
[8] Th. C. Stamatatos, E. Diamantopoulou, A. Tasiopoulos, V. Psycharis, R. Vicente, C.P. Raptopoulou, V. Nastopoulos, A. Escuer, S.P. Perlepes, Inorg. Chim. Acta 359 (2006) 4149.
[9] D. Gatteschi, L. Pardi, Gazz. Chim. Ital. 123 (1993) 231.

in 1992 [8]. Here, iron nitrate is dissolved in H_2O and the pH of the solution raised to approximately 3.5 through the addition of pyridine. Addition of the polydentate 'H_3metheidi' (*N*-(1-Hydroxymethylethyl)iminodiacetic acid; {$N(CH_2CO_2H)_2(CH(CH_3)CH_2OH)$}) pro-ligand then crystallizes the product within 1 day in yields up to a maximum of approximately 40%. The structure of this complex is related to the $Mg(OH)_2$ brucite lattice.

We recently discovered [9] that the simple dissolution of Fe(III) halides in pyridine leads to the formation of all-ferric pieces of molecular magnetite of formula Hpy-$[Fe_{17}(O)_{16}(OH)_{12}(py)_{12}X_4]X_4$ (X = halide). Here we report an extension of this study by showing that the pyridine – that acts simultaneously as solvent, base and capping ligand – can be replaced with *'similar'* liquid bases such as isoquinoline, 3,5-lutidine, β-picoline, etc. to form analogous heptadecametallic iron clusters of general formula $HL_x[Fe_{17}(O)_{16}(OH)_{12}(L)_{12}Br_4]Br_{3+x}$ (L = isoquinoline, 3,5-lutidine, β-picoline; $x = 0, 1$).

The synthesis is simple – dissolution of anhydrous $FeBr_3$ in L with stirring leads to a dark red solution which, after approximately one hour, is then filtered and allowed to evaporate. Dark red crystals $[Fe_{17}O_{16}(OH)_{12}(\beta\text{-pic})_{12}Br_4]Br_3$ (**1**); Hisoq$[Fe_{17}O_{16}(OH)_{12}(iso\text{-quin})_{12}Br_4]Br_4$ (**2**) and Hlut$[Fe_{17}O_{16}(OH)_{12}(3,5\text{-lut})_{12}Br_4]Br_4$ (**3**) form within 3 days. Their yields can be improved by adding a co-solvent of crystallization such as MeCN, THF or acetone. **1-3** crystallize in the monoclinic space group $P21/c$; the triclinic space group $P\bar{1}$; and the tetragonal space group $I41/a$, respectively. The three complexes (Fig. 1) contain a central tetrahedral Fe(III) ion linked via μ_4-oxo bridges to 12 outer octahedral Fe(III) ions – forming a truncated tetrahedron (Fig. 2). These ions are linked to each other via a combination of μ_3- and μ_4-oxides, and μ_2-hydroxide ligands. The hexagonal faces of the truncated tetrahedron are capped by four further Fe(III) ions each linked via three μ_3-oxo ligands. The inner Fe(III) ion and the four outer Fe(III) ions sit in the tetrahedral sites of the 'lattice' with the others occupying the octahedral sites. The four bromide ions cap the outer tetrahedral Fe(III) ions with the L molecules capping the octahedral Fe(III) ions. The Fe–O–Fe bridges fall into two clear categories (Table 1): those that connect the tetrahedral Fe(III) ions to the octahedral Fe(III) ions are all characterized by angles in the range ~121–127°, whilst those that bridge solely between octahedral Fe(III) ions are characterized by angles in the range ~93–100°. The oxidation states of both Fe and O centres were confirmed by bond length and charge balance considerations, and bond valence sum (BVS) calculations. An inspection of the cores of **1**–**3** reveal that they are fragments of the iron and oxygen positions defined by the magnetite lattice, however their all-ferric nature is in contrast to the situation in magnetite where half the octahedral sites in the lattice are occupied by Fe(II) ions.

Variable temperature magnetic susceptibility data were collected on complex **1** in the temperature range 300–2 K in an applied field of 900 G. The room temperature

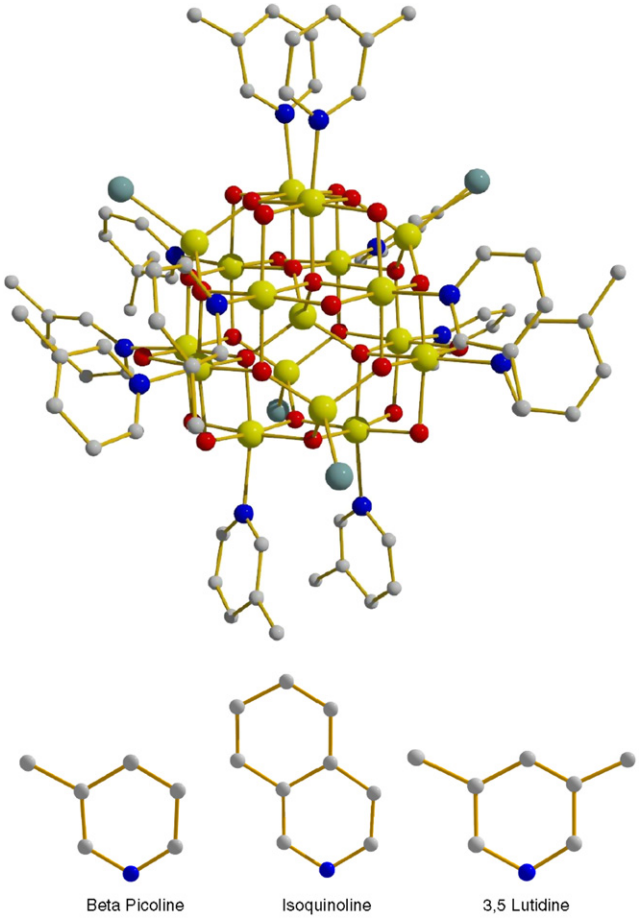


Fig. 1. The molecular structure of complex **1**; colour scheme, Fe = yellow, O = red, N = blue; Br = green, C = grey (top). Structures of β-picoline, isoquinoline and 3,5-lutidine (bottom). (For interpretation of the references in colour in this figure legend, the reader is referred to the web version of this article.)

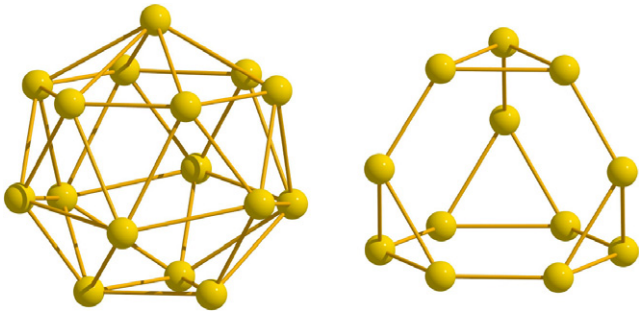


Fig. 2. The metallic core common to complexes **1**–**3**; the central unit is a hexagonal antiprism capped on the upper face by a single Fe ion, and on the lower face by three Fe ions. The truncated tetrahedron formed by the octahedral Fe ions (right). The central tetrahedral Fe ion has been excluded for clarity.

$\chi_M T$ value of approximately 125 cm^3 K mol^{-1} rises constantly as temperature is decreased to a maximum value of approximately 165 cm^3 K mol^{-1} at 75 K, before decreasing to a value of approximately 145 cm^3 K mol^{-1} at 2 K. The spin only ($g = 2$) value for a $[Fe^{III}_{17}]$ unit is approximately 74 cm^3 K mol^{-1}. This behaviour is indicative of

Table 1
Fe–O–Fe angle (°) ranges for complexes **1**–**3**

Complex	Fe–μ_4O–Fe	Fe–μ_3O–Fe	Fe–μ_2OH–Fe
1	93.6–123.3	93.0–127.4	97.4–99.1
2	93.6–123.4	93.8–126.4	93.6–98.7
3	94.0–122.1	93.4–127.3	97.3–100.0

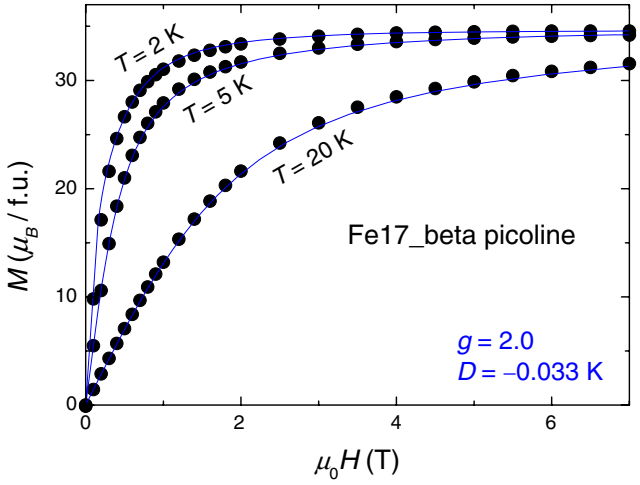


Fig. 3. Isothermal molecular magnetization for complex **1** collected at $T = 2$, 5 and 20 K. The solid lines are a fit of the data – see text for details.

dominant antiferromagnetic exchange between the metal centres with the low temperature maximum indicating an $S \approx 35/2 \pm 1$ spin ground state. The low temperature decrease is likely due to antiferromagnetic inter-molecular interactions. Field-dependencies of the molar magnetization $M(H)$ (Fig. 3) were collected for **1** at $T = 2$, 5 and 20 K. If we consider the single-spin Hamiltonian

$$H = DS_z^2 + g\mu_B \vec{H} \cdot \vec{S},$$

the magnetization in the whole field-range can be fitted with net molecular spin $S = 35/2$, $D = -0.033$ K and $g = 2.00(3)$. This is consistent with the parameters obtained for the analogous pyridine based complex Hpy $[Fe_{17}O_{16}(OH)_{12}(py)_{12}Br_4]Br_4$ (**4**) (Table 2) [10]. The ground state can be rationalized by assuming an antiferromagnetic interaction between the tetrahedral and octahedral Fe(III) sites – consistent with the two distinct categories of Fe–O–Fe bridging angles present in the complex.

In conclusion, simply dissolving $FeBr_3$ in pyridine produces a heptadecametallic cluster that is an all-ferric piece of molecular magnetite. A family of analogous compounds can be made by simply changing the base – that also acts as the solvent and terminal capping ligand. This is therefore a new, simple and extremely attractive methodology for the synthesis of molecular magnetic oxides. Antiferromagnetic exchange between the octahedral and tetrahedral Fe(III) ions, as governed by the Fe–O–Fe bridging angles, leads to the stabilization of an $S = 35/2$ spin ground state.

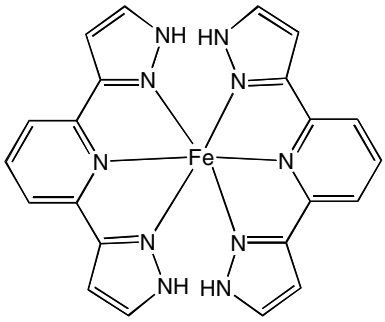
Table 2
Comparison of the magnetic properties of complexes **1** and **4**

Complex	Space group	S	g	D/K
1	$P21/c$	35/2	2.00(3)	−0.033
4a	R-3	35/2	2.06(3)	−0.023
4b	Pa-3	35/2	2.06(3)	−0.023

Details of complex **4** can be found in Ref. 10.

References

[1] (a) C. Theil, Annu. Rev. Biochem. 56 (1987) 289;
(b) S.M. Gorun, G.C. Papaefthymiou, R.B. Frankel, S.J. Lippard, J. Am. Chem. Soc. 109 (1987) 3337.
[2] (a) B. Xu, D.J. Chasteen, J. Biol. Chem. 266 (1991) 19965;
(b) W. Micklitz, S.J. Lippard, J. Am. Chem. Soc. 111 (1989) 6856.
[3] S. Mann, J. Webb, R.J.P. Williams (Eds.), Biomineralization: Chemical and Biochemical Perspectives, VCH, New York, 1988.
[4] (a) D. Gatteschi, R. Sessoli, Angew. Chem., Int. Ed. 42 (2003) 268;
(b) R. Sessoli, D. Gatteschi, D.N. Hendrickson, G. Christou, MRS Bull. 25 (2000) 66;
(c) W. Wernsdorfer, R. Sessoli, Science 284 (1999) 133;
(d) S. Hill, R.S. Edwards, N. Aliaga-Alcalde, G. Christou, Science 302 (2003) 1015.
[5] G. Aromí, E.K. Brechin, Struct. Bonding 122 (2006) 1.
[6] D. Gatteschi, R. Sessoli, A. Cornia, Chem. Commun. (2000) 725.
[7] (a) See for example C. Delfs, D. Gatteschi, L. Pardi, R. Sessoli, K. Wieghardt, D. Hanke, Inorg. Chem. 32 (1993) 3099;
(b) J.C. Goodwin, R. Sessoli, D. Gatteschi, W. Wernsdorfer, A.K. Powell, S.L. Heath, J. Chem. Soc., Dalton Trans. (2000) 1835;
(c) A.L. Barra, A. Caneschi, A. Cornia, F.F. de Biani, D. Gatteschi, C. Sangregorio, R. Sessoli, L. Sorace, J. Am. Chem. Soc. 121 (1999) 5302;
(d) M. Moragues-Canovas, E. Rivière, L. Ricard, C. Paulsen, W. Wernsdorfer, G. Rajaraman, E.K. Brechin, T. Mallah, Adv. Mater. 16 (2004) 1101;
(e) H. Oshio, N. Hoshino, T. Ito, J. Am. Chem. Soc. 122 (2000) 12602;
(f) A.K. Boudalis, B. Donnadieu, V. Nastopoulos, J.M. Clemente-Juan, A. Mari, Y. Sanakis, J.-P. Tuchagues, S.P. Perlepes, Angew. Chem., Int. Ed. 43 (2004) 2266;
(g) L.F. Jones, E.K. Brechin, D. Collison, M. Helliwell, T. Mallah, S. Piligkos, G. Rajaraman, W. Wernsdorfer, Inorg. Chem. 42 (2003) 6601.
[8] S.L. Heath, A.K. Powell, Angew. Chem., Int. Ed. 31 (1992) 191.
[9] G.W. Powell, H.N. Lancashire, E.K. Brechin, D. Collison, S.L. Heath, T. Mallah, W. Wernsdorfer, Angew. Chem., Int. Ed. 43 (2004) 5772.
[10] M. Evangelisti, A. Candini, A. Ghirri, M. Affronte, G.W. Powell, I.A. Gass, E.K. Brechin, D. Collison, S.L. Heath, Phys. Rev. Lett. (2006). arXiv:cond-mat/0602184.



Scheme 1.

of the magnetic orbitals and to larger metal to metal distances. Most of these compounds show Tc's below 3 K, with few exceptions reaching up to 6 K.

The use of "electroactive" cations, instead of the electronically "innocent" ones in the formation of such anionic networks has been one of the most successful approaches to multifunctional materials, where unprecedented multifunctional magnets have been obtained, such as ferromagnetic molecular metals [13,14], chemically-built magnetic multilayers [15], photoactive magnets [16], or chiral magnets [7,8,17]. Most of these examples are built from the hexagonal 2D honeycomb $[M^{II}M^{III}(ox)_3]^-$ networks. The 3D analogs have been much less explored on this regard, probably due to the more synthetically strict conditions needed. Spin crossover complexes [18] and other cations with interesting photophysical properties [19] have been embedded into these 3D systems, but including diamagnetic alkali metals in the network, preventing the appearance of magnetic ordering.

We have been investigating for several years the possibility to use Fe^{II} complexes as templates for oxalate-based magnets. Until now, all our attempts yielded the highly insoluble salts $[A^I][Fe(L)_3][M^{III}(ox)_3]\cdot xH_2O$ (A = Li, Na, K, NH_4^+) [20]. These compounds exhibit indeed spin crossover behavior, but no magnetic ordering is observed, since the paramagnetic centers are isolated from one another in the structure. Here we report how the complex $[Fe(bpp)_2]^{2+}$ (Scheme 1); bpp = 2,6(bis(pyrazol-3-yl)pyridine) that exhibits spin crossover behavior in other simple salts [21] including the LIEST effect [22], is able to be used as cationic guest for bimetallic oxalate-based 3D magnets.

2. Experimental

2.1. Synthesis

All reagents were commercially available and used without further purification The precursor $Ag_3Cr(ox)_3\cdot 3H_2O$ was prepared by metathesis in water from $K_3Cr(ox)_3\cdot 3H_2O\cdot Ag_3Cr(ox)_3\cdot 3H_2O$ (0.098 g, 0.142 mmol) was suspended in 7.5 mL methanol, and then a solution of $MnCl_2\cdot 4H_2O$ (0.042 g, 0.213 mmol) in 7.5 mL methanol was added dropwise. The white AgCl precipitate formed was filtered, and the green solution was added to a red solution of $Fe(ClO_4)_2\cdot H_2O$ (0.090 g, 0.355 mmol) and bpp (0.149 g, 0.71 mmol) in 15 mL of hot MeOH. This solution was refluxed for 2 h. The yellowish precipitate formed was hot filtered, and washed with methanol and acetone. This powder was dissolved in DMF and crystals of $[Fe(bpp)_2][MnCr(ox)_3]_2\cdot bpp\cdot CH_3OH$ (1) were grown from layering this solution with acetone. Yield: 30%. IR (cm^{-1}): 3427, w; 3124, w; 2929, w; 1654, s; 1652, s; 1628, m; 1629, m; 1462, m; 1384, m; 1277, m; 906, w; 811, w; 669, s; 541, m; 478, m; 414, m. $Mn_2N_{15}O_{25}Cr_2FeC_{46}H_{31}$, $M_w = 1463.59$. Elemental *Anal.* Calc.: C, 37.75; H, 2.13; N 14.36. Found: C, 37.12; H, 2.45; N, 15.20%. Desolvation of the sample was carried out by heating the crystals in air at 125 °C for 6 h.

2.2. Structural characterization

A reddish prismatic single crystal of **1** was fixed on a glass fiber and mounted on a Kappa CCD diffractometer equipped with graphite-monochromated Mo Kα radiation ($\lambda = 0.71073$ Å). Cell refinements and data reduction were performed at 150 K using the DENZO and SCALEPACK programs [23]. The structure was solved by direct methods using the SIR97 program [24] and refined on F^2 with the SHELXL-97 program [25]. All atoms belonging to the anionic network were located by successive Fourier transform routines, and refined anisotropically. The cations and solvent molecules, occupying the wholes left in the structure, could no be located due to the presence of severe crystallographic disorder. Two crystallographic independent positions for the Fe centers were found, with partial occupancy. Only the first coordination sphere of N atoms could be located. No good model for these complexes and solvent molecules, including the interstitial bpp moiety could be found due to heavy disorder. Crystal, data collection, and refinement parameters are summarized in Table 1.

Table 1
Crystallographic data and refinement parameters for $[Fe(bpp)_2][MnCr(ox)_3]_2\cdot bpp\cdot CH_3OH$ (**1**)

Space group	monoclinic, $P2_1/n$
a (Å)	21.0100(3)
b (Å)	15.9880(4)
c (Å)	21.9630(6)
β (°)	90.3390(7)
V (Å^3)	7377.4(3)
Z	4
ρ_{calc} ($g\cdot cm^{-3}$)	1.318
T (K)	150(2)
λ (Å)	0.71073
2θ (°) range	$5.88 < 2\theta < 36.08$
Total reflections/unique	19091/4965
parameters	415
$R[I > 2\sigma(I)]$	R_1[a] = 0.1281, wR_2[b] = 0.3350
$\Delta\rho_{max}/\Delta\rho_{min}$ (e Å^3)	0.854/−0.386

[a] $R_1 = \sum(F_o - F_c)/\sum(F_o)$.

[b] $wR_2 = [\sum[w(F_o^2 - F_c^2)]/[\sum[w(F_o^2)^2]]^{1/2}$; $w = 1/[\sigma^2(F_o^2) + (0.2P)^2]$, where $P = (F_o^2 + 2F_c^2)/3$.

Table 2
Estimated parameters for low-spin and high-spin Fe^{II} from the Mössbauer spectra taken at different temperatures of recrystallized $[Fe(bpp)_2][MnCr(ox)_3]_2$ before and after heat treatment

T (K)		Crystals				Desolvated sample			
		IS	QS	Γ	I (%)	IS	QS	Γ	I (%)
297	Fe L.S.	0.39	0.73	0.57	73	0.36	0.78	0.54	80
	Fe H.S.	1.01	2.53	0.39	27	0.97	2.34	0.36	20
120	Fe L.S.	0.49	0.78	0.49	64	0.45	0.77	0.46	73
	Fe H.S.	1.10	3.11	0.33	36	1.11	2.63	0.48	27
4	Fe L.S.	0.50	0.78	0.62	58	0.49	0.74	0.50	67
	Fe H.S.	1.15	3.25	0.35	42	1.20	2.80	0.50	33

IS (mm/s) isomer shift relative to metallic α-Fe at 295 K; QS (mm/s) quadrupole splitting; Γ (mm/s) line-width; I relative area. Estimated errors $\leqslant$0.02 mm/s for IS, QS, Γ, and $< 2\%$ for I.

2.3. Magnetic characterization

Bulk magnetization measurements were carried out on grained polycrystalline samples with a Quantum Design magnetometer with an applied field of 1000 G (0.1 T) in the temperature range 2–300 K, with cooling and warming cycles. AC data was collected in the 2–10 K range with an alternating field of 3.95 G (3.95×10^{-4} T) with frequencies between 1 and 1000 Hz. Hysteresis loops at 2 K were collected between 5 and −5 T. Data were corrected for diamagnetic contributions calculated using the Pascal constants.

2.4. Mössbauer spectroscopy

Mössbauer spectra were collected at different temperatures in transmission mode using a conventional constant-acceleration spectrometer and a 25 mCi ^{57}Co source in a Rh matrix. The velocity scale was calibrated using α-Fe foil. Isomer shifts (IS, Table 2) are given relative to metallic α-Fe at room temperature. Low-temperature spectra were collected using a JANIS bath cryostat. The spectra were fitted to Lorentzian lines using a non-linear least-squares method [26]. The relative areas and widths of both peaks in a quadrupole doublet were kept equal during refinement.

3. Results and discussion

3.1. Synthesis and structure

The insertion of the spin crossover cation $[Fe(bpp)_2]^{2+}$ as guest into oxalate-based bimetallic networks had to start by overcoming the precipitation of the kinetic product $[A^{I}][Fe(bpp)_2][M^{III}(ox)_3] \cdot xH_2O$. This was done following the procedure used in the preparation of other oxalate bimetallic complexes avoiding the presence of any other cations in solution but the transition metal themselves. However, when a solution of $Mn_3[Cr(ox)_3]_2$ is treated with any salt of $[Fe(bpp)_2]^{2+}$, again, an undesired precipitate is obtained. This material could not be structurally characterized. The 2:2:1 ratio found for Fe:Cr:Mn by analysis and the paramagnetic behavior suggest that maybe it is formed by oxalate-bridged trimers [2]. If the same reaction is carried out under reflux conditions for several hours this initial precipitate slowly redisolves to yield a second product, where no traces of this first compound can be found. The main component of this precipitate can be isolated by layering a DMF solution with acetone, to yield a crop of single crystals of $[Fe(bpp)_2][MnCr(ox)_3]_2 \cdot bpp \cdot CH_3OH$ (**1**).

The structure of **1** is built from an anionic 3D polymeric oxalate-bridged bimetallic structure. As in the well-known chiral 3D networks, this anionic structure is formed by bischelating oxalate ligands that connect each divalent metal to three trivalent metals, and vice versa, building ten-membered rings in a (10, 3) topology (Fig. 1). The big difference with the reported chiral 3D networks is that, in this case, the compound is achiral. Actually, it belongs to the centrosymmetric monoclinic $P2_1/n$ space group, with metal centers of both chiralities present. This is somehow surprising because it was discussed in the past that only homochiral networks would be able to adopt such a 3D structure.

In this case, Mn(II) and Cr(III) occupy crystallographically different positions, since they are non-equivalent, and can be clearly distinguished attending to the M–O distances. The metal position with longer distances is assigned to Mn^{II}–O (2.05(3)–2.28(3) Å), and the other to Cr^{III}–O (1.94(3)–2.04(3) Å). There are two crystallographically independent Mn and Cr positions in the asymmetric unit, each one belonging to a different chirality, that are bridged together through heterochiral connections. Thus, if we con-

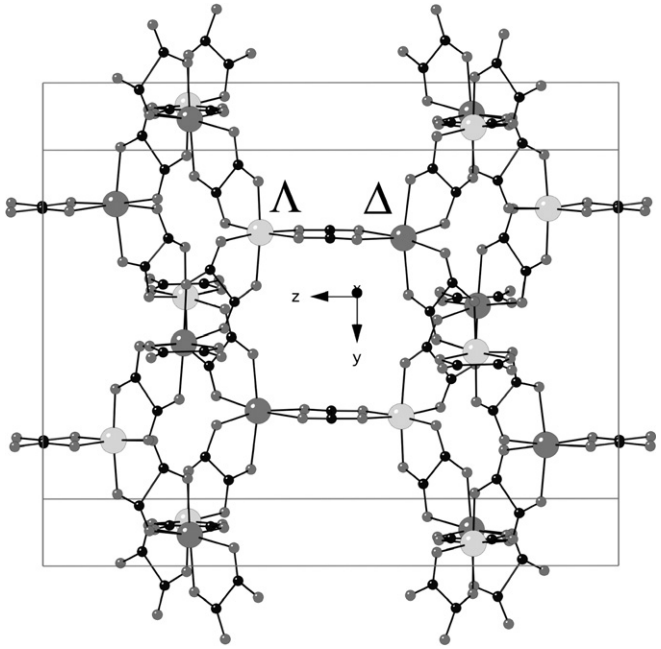


Fig. 1. Two 10-membered rings in the structure of $[Fe(bpp)_2][MnCr(ox)_3]_2 \cdot bpp \cdot CH_3OH$ (**1**) of opposite chirality, connected along the c direction.

sider the rings perpendicular to the *a* and *b* axis, these are formed by five adjacent units of one chirality and opposite to that of the other five. The projections of this achiral 3D structure on the *ac* and *bc* planes are almost identical to those of the well-known chiral 3D analogs (Fig. 2), where all three projections (*ab*, *bc*, and *ac*) are identical. On the contrary, the projection on the *ab* plane for compound **1** now shows an eclipsed disposition of the rings (Fig. 3). This can be understood as a relative movement of the rings on this plane to allow for the heterochiral junctions between homochiral rings.

The electron density inside this 3D network could not be assigned to a good chemical model, due to the presence of important crystallographic disorder. One reason for this, when compared with the chiral 3D analogs, is the much higher present of interstitial solvent molecules, since only one Fe complex is present per MnCr pair, and therefore no extra anions are needed as in those. The cationic complexes occupy analogous positions in the crystal structure, but now with half occupancy, since this positions are shared with disordered solvent and free bpp moieties. With the data obtained, only the position for the Fe atoms, including the first coordination sphere of six N atoms could be located.

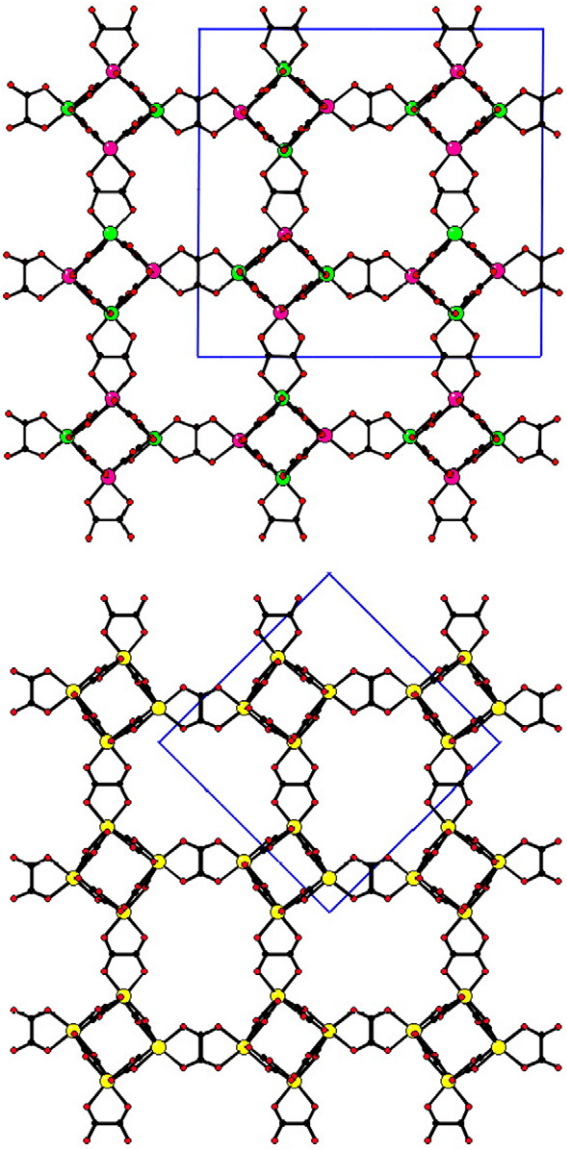


Fig. 2. Projections of the crystal structure of $[Fe(bpp)_2][MnCr(ox)_3]_2 \cdot bpp \cdot CH_3OH$ (top) and $[Ru(bpy)_2][MnCr(ox)_3]_2 \cdot bpp \cdot CH_3OH$ [7] (bottom) on the *bc* plane.

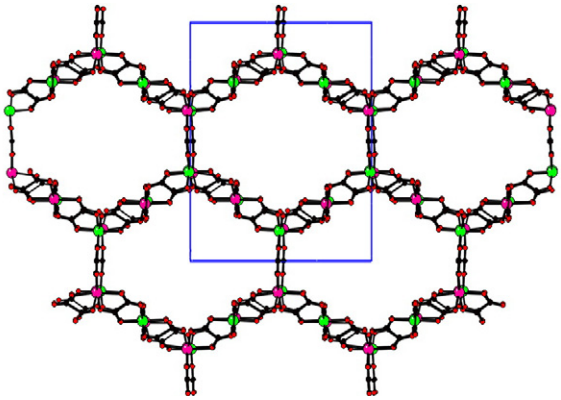


Fig. 3. Projections of the crystal structure of $[Fe(bpp)_2][MnCr(ox)_3]_2 \cdot bpp \cdot CH_3OH$ on the *ab* plane.

3.2. Magnetic properties

With exception of the achiral nature of this network, the connectivity between the metals is identical to that of the chiral 3D bimetallic magnets described before and thus, the magnetic properties were expected to be analogous, with the addition of the magnetic behavior of the embedded Fe^{II} complexes. The thermal dependence of the $\chi_m T$ product (Fig. 4) shows a small but continuous decrease when cooling down the sample. Since the interactions

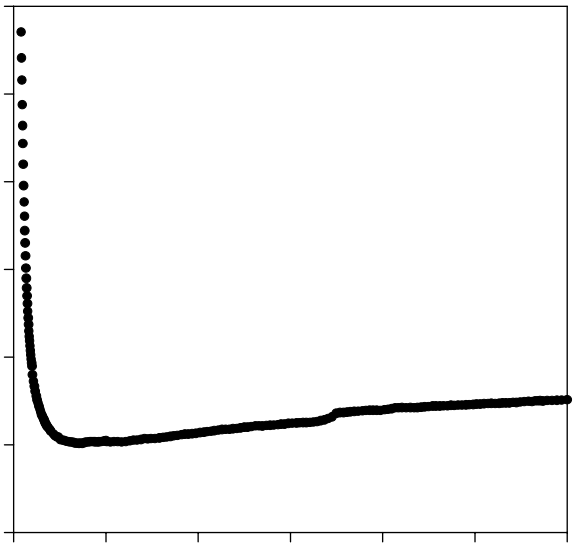


Fig. 4. Thermal dependence of the χT product for $[Fe(bpp)_2][MnCr(ox)_3]_2 \cdot bpp \cdot CH_3OH$.

between Mn^{II} and Cr^{III} centers promoted by the oxalate bridge are expected to be ferromagnetic, this behavior suggests a slow and non-cooperative spin transition for the Fe centers, between high spin (HS) and low spin (LS) configurations. The high temperature regime can be fitted to a Curie Weiss law with a Curie constant of 15.49 emu K mol^{-1}, in perfect agreement with the spin only expected value for a magnetically diluted sample. At 300 K the $\chi_m T$ *is* 15.05 emu K mol^{-1}. This suggests that around 15% of the Fe centers are LS at this temperature. The $\chi_m T$ product reaches a minimum at 35 K (14.03 emu K mol^{-1}) and starts to increase rapidly, due to the ferromagnetic interaction in the network, and suggesting the presence of magnetic ordering at very low temperatures.

AC susceptibility magnetic data (Fig. 5) confirm the onset of ferromagnetic ordering below 3.0 K, with an appearance of a frequency independent out-of-phase signal, accompanying a maximum in the in-phase signal. This temperature is in good agreement with that found for other 3D $[MnCr(ox)_3]^-$ networks, where ferromagnetic ordering is achieved up to 3.9 K [7]. The appearance of ferromagnetic ordering was also confirmed by zero field cooled and field cooled DC measurements at very low applied magnetic fields that deviate from one another at this very same temperature.

The field dependence of the magnetization in the ordered state at 2 K (Fig. 6) shows a very fast increase at low fields and then tends to saturation, although it is not reached even at 5 T, with a value of 15.06μ_B. This is very close to the 16μ_B expected for ferromagnetic alignment of the Mn and Cr centers in the network, and confirms that the magnetic ordering is indeed of ferromagnetic nature. No clear contribution of the Fe centers is found, what suggests that at this temperature most of the Fe centers will be in their LS configuration.

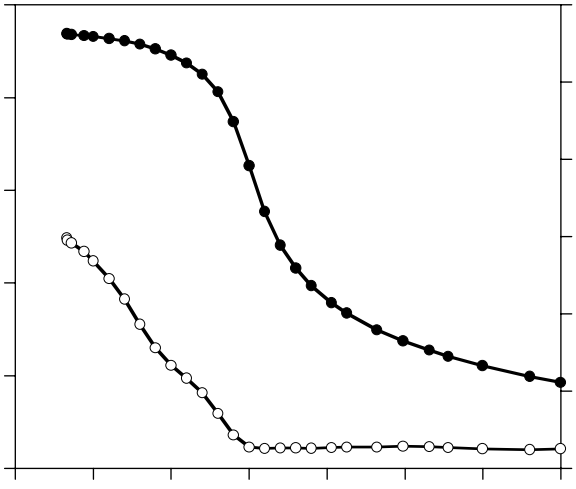


Fig. 5. Thermal dependence of the AC in-phase (χ', full circles) and out-of-phase (χ'', empty circles) magnetic susceptibilities for $[Fe(bpp)_2][MnCr(ox)_3]_2 \cdot bpp \cdot CH_3OH$ at 333 Hz.

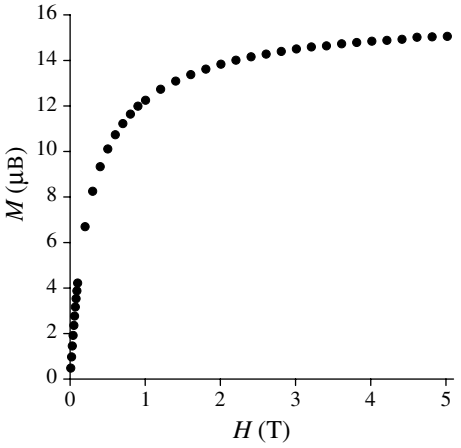


Fig. 6. Field dependence of the magnetization at 2 K for $[Fe(bpp)_2][MnCr(ox)_3]_2 \cdot bpp \cdot CH_3OH$ at 333 Hz.

Since desolvation usually affects the spin crossover behavior, we also performed DC magnetic measurements on desolvated samples. We found that the behavior is essentially identical, while the $\chi_m T$ product is slightly lower, indicating that desolvation increases the population of LS Fe^{II}, but it does not affect qualitatively the thermal magnetic behavior of the sample.

3.3. Mössbauer spectroscopy

All the Mössbauer spectra (Fig. 7) may be fitted with two quadrupole doublets. The estimated parameters (Table 2) for the doublet with the largest quadrupole splitting, QS, are typical of HS Fe^{II} with $S = 2$ [27]. The significantly lower QS and IS as well as the temperature independent

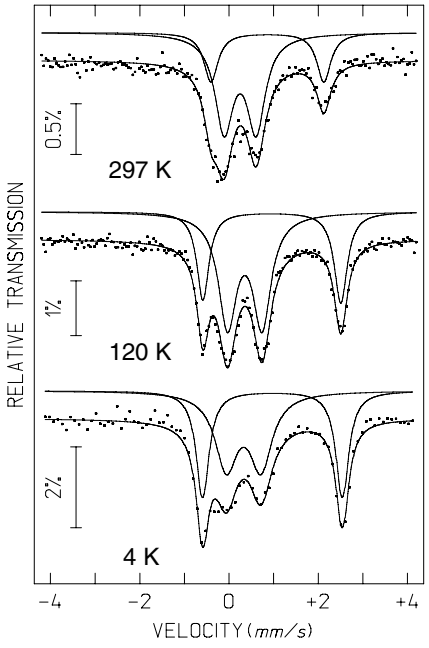


Fig. 7. Mössbauer spectra for $[Fe(bpp)_2][MnCr(ox)_3]_2 \cdot bpp \cdot CH_3OH$ at different temperatures.

QS of the other doublet are consistent with LS Fe^{II}, $S = 0$. After heat treatment, QS and the peak widths estimated for HS Fe^{II} change significantly (Table 2). Furthermore estimated relative areas indicate a stabilization of the LS relative to the HS state after desolvation.

If the recoil-free fractions of both HS and LS Fe^{II} are similar in the measured temperature range a much unexpected conclusion is derived: the fraction of Fe^{II} in the HS state significantly decreases with increasing temperature for both untreated and heat-treated samples. As far as we know, such a result has never been reported. A more detailed investigation is however necessary as the observed difference in the temperature dependencies of the HS and LS Fe^{II} relative areas may be due to much stronger chemical bonds established by HS Fe^{II} than by LS Fe^{II}. This would imply a stronger decrease with increasing temperature of the recoilless factor of the LS Fe^{II} as compared to HS Fe^{II}.

4. Conclusions

We have shown how it is possible to obtain molecule-based magnets based on bimetallic oxalate complexes using as template the spin crossover complex $[Fe(bpp)_2]^{2+}$. The compound $[Fe(bpp)_2][MnCr(ox)_3]_2 \cdot bpp \cdot CH_3OH$ shows ferromagnetic ordering below 3.0 K. From the structural point of view, this is the first achiral polymorph to the well-known chiral 3D cubic structure $[Z(L)_3][ClO_4]$-$[MnCr(ox)_3]$ ($Z = Ru$, Fe; $L = 2,2'$-dipyridyl). It was discussed in the past that the extra perchlorate anions were needed to obtain this type of salts. Now we have also demonstrated that this is not true, and these magnets can also be obtained by substitution of half of the cations by solvent molecules. This lower occupancy of cations and anions inside the anionic network could be responsible for losing the enantiopure character of these systems.

The $[Fe(bpp)_2]^{2+}$ units embedded in this oxalate network are not showing a clear spin transition. Apparently, LS and HS centers co-exist at all temperatures. Magnetic measurements suggest that there is a small decrease in the HS population when the temperature is decreased, that would be responsible for the lowering of the magnetic moment. On the other hand, Mössbauer spectra do not support this hypothesis. They suggest quite the opposite, if recoil-free fractions of LS and HS Fe^{II} are assumed to be similar. At this moment there is no satisfactory explanation for these apparently contradictory data. In any case, although magnetic ordering is achieved, the lack of cooperative spin transition in this compound precludes the study of possible synergy between both processes. Other spin crossover complexes, able to better fill the holes in such structural motif would probably be better candidates in the search for such a material.

Acknowledgements

This work was supported by the European Union (Network of Excellence: MAGMANET). Financial support from the Ministerio de Educación y Ciencia (Projects MAT2004-3849 and BQU2002-01091), and from the Generalitat Valenciana (GV04A/77) is also acknowledged.

Appendix A. Supplementary material

CCDC 618990 contains the supplementary crystallographic data for this paper. These data can be obtained free of charge via http://www.ccdc.cam.ac.uk/conts/retrieving.html, or from the Cambridge Crystallographic Data Centre, 12 Union Road, Cambridge CB2 1EZ, UK; fax: (+44) 1223-336-033; or e-mail: deposit@ccdc.cam.ac.uk. Supplementary data associated with this article can be found, in the online version, at doi:10.1016/j.poly.2006.09.064.

References

[1] S. Triki, F. Berezovsky, J.S. Pala, E. Coronado, C.J. Gómez-Saiz, J.M. Clemente, A. Riou, P. Molinie, Inorg. Chem. 39 (2000) 3771.
[2] E. Coronado, J.R. Galán-Mascarós, C. Giménez-Saiz, C.J. Gómez-García, C. Ruiz-Pérez, Eur. J. Inorg. Chem. (2003) 2290.
[3] E. Coronado, M.C. Giménez, C.J. Gómez-García, F.M. Romero, Polyhedron 22 (2003) 3115.
[4] E. Coronado, J.R. Galán-Mascarós, C.J. Gómez-García, C. Martí-Gastaldo, Inorg. Chem. 44 (2005) 6197.
[5] H. Tamaki, Z.J. Zhong, N. Matsumoto, S. Kida, M. Koikawa, N. Achiwa, Y. Hashimoto, H. Okawa, J. Am. Chem. Soc. 114 (1992) 6974.
[6] R. Pellaux, H. Schmalle, R. Huber, P. Fisher, T. Hauss, B. Ouladdiaf, S. Decurtins, Inorg. Chem. 36 (1997) 2301.
[7] E. Coronado, J.R. Galán-Mascarós, C.J. Gómez-García, J.M. Martínez-Agudo, Inorg. Chem. 40 (2001) 113.
[8] R. Andres, M. Brissard, M. Gruselle, C. Train, J. Vaissermann, B. Malezzieux, J.P. Jamet, M. Verdaguer, Inorg. Chem. 40 (2001) 4633.
[9] E. Coronado, J.R. Galán-Mascarós, C. Martí-Gastaldo, Inorg. Chem. 45 (2005) 1882.
[10] C. Mathonière, S.G. Carling, D. Yusheng, P. Day, Chem. Soc. Chem. Commun. (1994) 1551.
[11] C. Matonière, J. Nutall, S.G. Carling, P. Day, Inorg. Chem. 35 (1996) 1201.
[12] E. Coronado, J.R. Galán-Mascarós, C.J. Gómez-García, J.M. Martínez-Agudo, E. Martínez-Ferrero, J.C. Waerenborgh, M. Almeida, J. Solid State Chem. 150 (2001) 552.
[13] E. Coronado, J.R. Galán-Mascarós, C.J. Gómez-García, V. Laukhin, Nature 408 (2000) 447.
[14] A. Alberola, E. Coronado, J.R. Galán-Mascarós, C. Giménez-Saiz, C.J. Gómez-García, J. Am. Chem. Soc. 125 (2003) 10774.
[15] E. Coronado, J.R. Galán-Mascarós, C.J. Gómez-García, J. Ensling, P. Gütlich, Chem. Eur. J. 6 (2000) 552.
[16] S. Bénard, P. Yu, J.P. Audiére, V. Riviére, R. Clèment, J. Ghilhem, L. Tchertanov, K. Nakatani, J. Am. Chem. Soc. 122 (2000) 9444.
[17] E. Coronado, J.R. Galán-Mascarós, C.J. Gómez-García, E. Martínez-Ferrero, M. Almeida, J.C. Waerenborgh, Eur. J. Inorg. Chem. (2005) 2064.
[18] R. Sieber, S. Decurtins, H. Stoeckli-Evans, C. Wilson, D. Yufit, J.A.K. Howard, S.C. Capelli, A. Hauser, Chem. Eur. J. 6 (2000) 361.
[19] S. Decurtins, H.W. Schmalle, R. Pellaux, P. Schneuwly, A. Hauser, Inorg. Chem. 35 (1996) 1451.
[20] E. Coronado, M.C. Giménez, F.M. Romero., in preparation.
[21] H.A. Goodwin, K.H. Sugiyarto, Chem. Phys. Lett. 139 (1987) 470.
[22] S. Marcen, L. Lecren, L. Capes, H.A. Goodwin, J.F. Letard, Chem. Phys. Lett. 358 (2002) 87.

[23] Z. Otwinowski, W. Minor, in: C.W. CarterJr., R.M. Sweet (Eds.), Methods in Enzymology, vol. 276, Academic Press, New York, 1997, p. 307.
[24] A. Altomare, M.C. Burla, M. Camali, G.L. Cascarano, C. Giacovazzo, A. Guagliardi, A.G.G. Moliterni, G. Polidori, R. Spagna, J. Appl. Crystallogr. 32 (1999) 115.
[25] G.M. Sheldrick, University of Göttingen, Göttingen, Germany, 1997.
[26] J.C. Waerenborgh, M.O. Figueiredo, J.M.P. Cabral, L.C. J. Pereira, J. Solid State Chem. 111 (1994) 300.
[27] T. Buchen, P. Gütlich, K.H. Sugiyarto, H.A. Goodwin, Chem. Eur. J. 2 (1996) 1134.

SMM not simply because of its ease of synthesis and stability in solution but because it displays beautiful hysteresis loops in single crystal *M versus H* studies that possess well defined steps at regular intervals of field indicative of magnetic quantum tunneling [8].

We therefore decided to attempt to make further derivatives of complex **1**, and herein report the syntheses, structures and initial magnetic properties of four such molecules. The complexes $[Mn_9O_7(O_2CMe)_{11}(tmp)(py)_3(H_2O)_2]$ (**2**); $[Mn_9O_7(O_2CMe)_{11}(Hpeol)(py)_3(H_2O)_2]$ (**3**); $[Mn_9O_7(O_2CPh)_{11}(Hpeol)(py)_3(H_2O)_2]$ (**4**); and $[Mn_9O_7(O_2CCMe_3)_{11}(Hpeol)(py)_3(H_2O)_2]$ (**5**) (H_3tmp = 1,1,1-tris(hydroxymethyl)propane; H_4peol = pentaerythritol) are all made in an identical manner, *via* the reaction of the appropriate $[Mn_3O(O_2CR)_6L_3]^{0/+}$ triangle with the appropriate tripodal alcohol in MeCN. All five crystallize in the monoclinic space group $P2(1)/n$.

The metallic skeletons of **2**–**5** (Fig. 1) comprise a series of ten-edge-sharing triangles that describes part of an idealized icosahedron in which three of the twelve vertices are missing. The $[Mn^{IV}_3Mn^{III}_4Mn^{II}_2O_7]^{14+}$ central core can be described as either a series of vertex- and edge-sharing $[Mn_3O]$ units, or perhaps most easily as a $[Mn^{III}_4Mn^{II}_2O_6]^{4+}$ ring on which is sitting a smaller $[Mn^{IV}_3O]^{10+}$ ring. The upper $[Mn_3O]^{10+}$ ring consists only of Mn(IV) ions and is capped on one side by the sole tripodal ligand each O-arm of which acts as a μ-bridge, and on the other side by a μ_3-oxide. The $[Mn^{IV}_3O]^{10+}$ unit is connected to the $[Mn^{III}_4Mn^{II}_2O]^{4+}$ ring *via* six μ_3-oxides within the six-membered wheel and three carboxylates which bridge in their familiar *syn*, *syn*, μ-mode. The remaining carboxylates in the structure bridge between the Mn ions in the $[Mn^{III}_4Mn^{II}_2O_6]^{4+}$ ring in the same manner. The remaining coordination sites are occupied by two water molecules and three pyridines. All the Mn ions are in distorted octahedral geometries, with their oxidation states assigned using charge balance considerations, bond lengths and bond valence sum (BVS) calculations. The Jahn–Teller elongations of the Mn(III) ions all lie approximately perpendicular to the plane of the $[Mn^{III}_4Mn^{II}_2O_6]^{4+}$ ring.

Variable temperature magnetic susceptibility data were collected on **2**–**5** in the temperature range 300–1.8 K in an applied field of 1 kG. For each complex the observed behavior is similar [9]. The room temperature value of $\chi_M T$ of approximately 18 cm^3 K mol^{-1} remains constant until around 200 K where it begins to increase to a maximum value of approximately 37 cm^3 K mol^{-1}at 20 K, before dropping sharply below this temperature. The spin only (g = 2) value for a $[Mn^{IV}_3Mn^{III}_4Mn^{II}_2]$ unit is approximately 30 cm^3K mol^{-1}.The maximum in $\chi_M T$ is indicative of a $S = 17/2 \pm 1$ spin ground state, with the low temperature decrease assigned to zero-field splitting, Zeeman effects and/or intermolecular antiferromagnetic interactions. Magnetization data collected in the ranges 10–70 kG and 1.8–4.0 K for **5** are plotted as reduced magnetization ($M/N\mu_B$) *versus* H/T in Fig. 2. For a complex entirely populating the ground state and experiencing no zero-field splitting, the observed isofield lines should

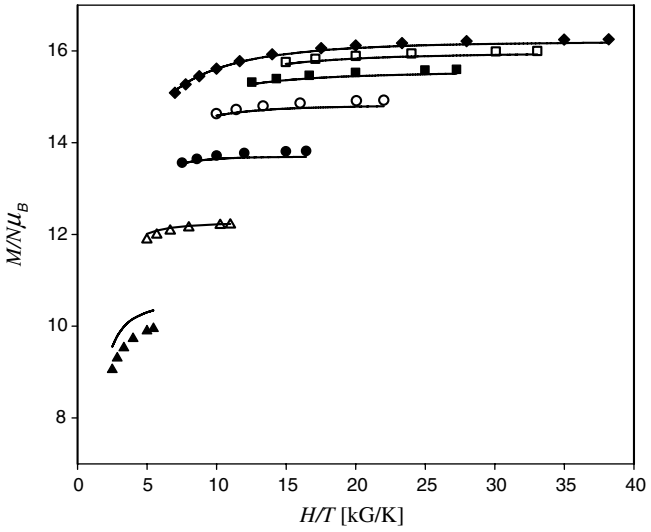


Fig. 2. Plot of reduced magnetization *vs.* H/T for **5**. The solid lines are the fit of the data. See text for details.

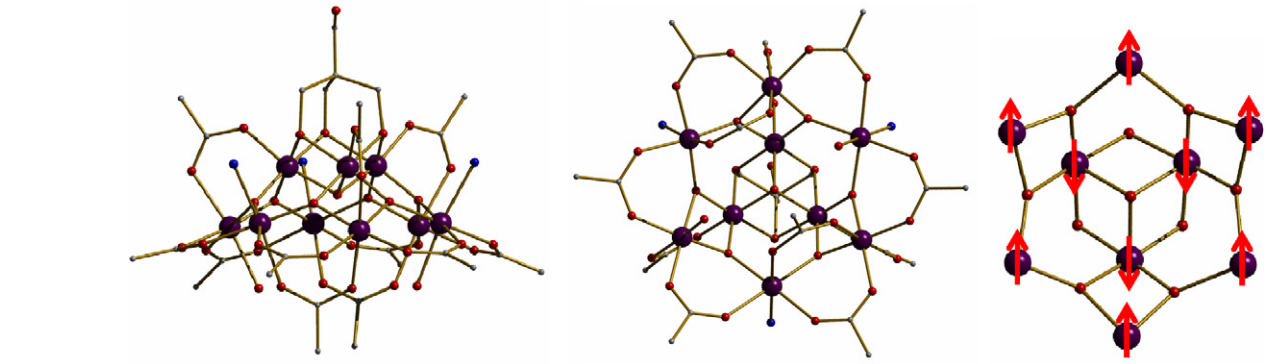


Fig. 1. The molecular structure of complex **5**, viewed parallel (left) and perpendicular (middle) to the $[Mn^{III}_4Mn^{II}_2O_6]^{4+}$ ring; the Me groups of the O_2CCMe_3 ligands and the C atoms of the pyridines have been removed for clarity. The metal–oxygen core common to complexes **1**–**5**, showing the proposed spin topology (right). Colour code: Mn, purple; O, red; N, blue; C, grey. (For interpretation of the references to color in this figure legend, the reader is referred to the web version of this article.)

superimpose and saturate at a value ($M/N\mu_B$) equal to gS. This is clearly not the case and is suggestive of appreciable ZFS. The data were fitted by a matrix-diagonalization method to a model that assumes only the ground state is populated, includes axial zero-field splitting ($D\hat{S}_z^2$), and carries out a full powder average [10]. The best fit gave $S = 17/2$, $g = 1.98$ and $D = -0.27\ cm^{-1}$. The ground state can be rationalized by assuming an antiferromagnetic interaction between the ferromagnetically coupled Mn(IV) ions in the $[Mn_3^{IV}O]^{10+}$ ring and the Mn(III/II) ions in the $[Mn_4^{III}Mn_2^{II}O_6]^{4+}$ ring (Fig. 1).

The in-phase ($\chi'_M T$) and out-of-phase (χ''_M) ac susceptibility signals for **5** are shown in Fig. 3. The in-phase signal shows a plateau above *ca.* 5 K indicative of an isolated spin ground state. Extrapolation of this slope to 0 K gives a value of $\sim 37\ cm^3\ K\ mol^{-1}$ suggesting a spin ground state of $S = 17/2 \pm 1$ in agreement with the dc data. There is a frequency-dependent decrease in the $\chi'_M T$ signal and a frequency-dependent out-of-phase signal at $T < 5$ K. The peak at 1000 Hz occurs at approximately 3.5 K. Both are strong indicators of SMM behavior. The S and D values obtained suggest an upper limit to the potential energy barrier (U) to magnetization reversal ($U = (S^2 - 1/4)|D|$) of ~28 K. This was confirmed by single crystal hysteresis loop and relaxation measurements performed using a micro-SQUID setup [11]. Studies of the magnetization performed at very low temperature and high fields show that all complexes behave as SMMs with long relaxation times. Fig. 4 presents typical magnetization (M) *versus* applied DC field measurements for **5**. Hysteresis loops are observed, whose coercivity is strongly temperature and sweep-rate dependent, increasing with decreasing temperature and increasing field sweep rate, as expected for the superparamagnetic-like behavior of a SMM. The hysteresis

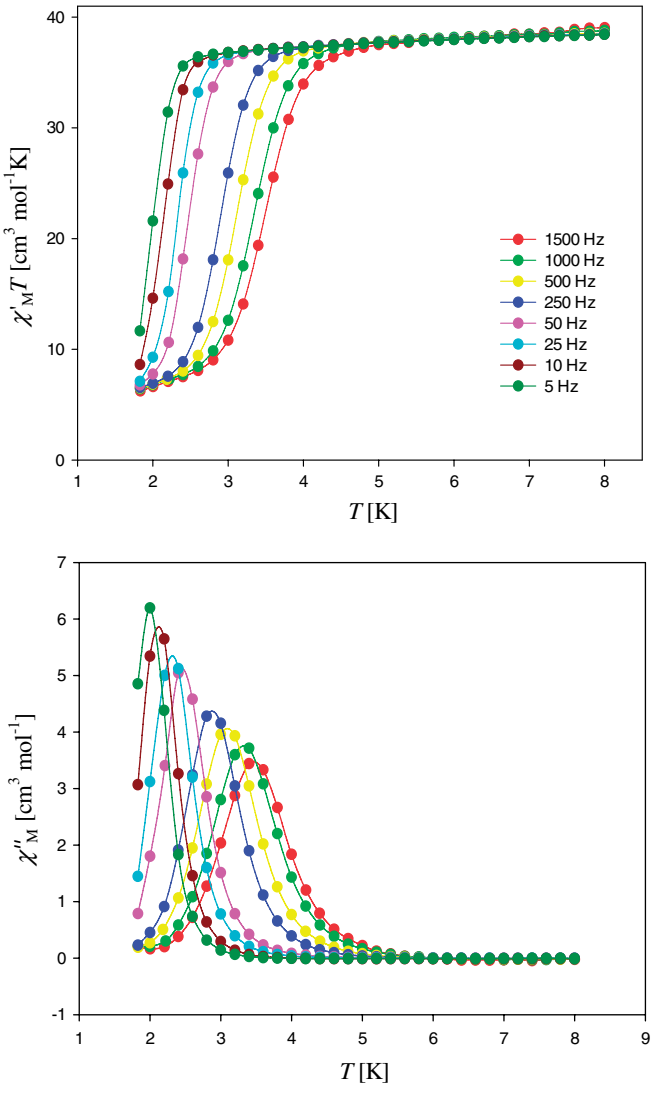


Fig. 3. Plots of the in-phase (χ'_M)) signal as ($\chi'_M T$) and out-of-phase (χ''_M) signal in ac susceptibility studies *vs.* temperature for **5** in a 3.5 G field oscillating at the indicated frequencies.

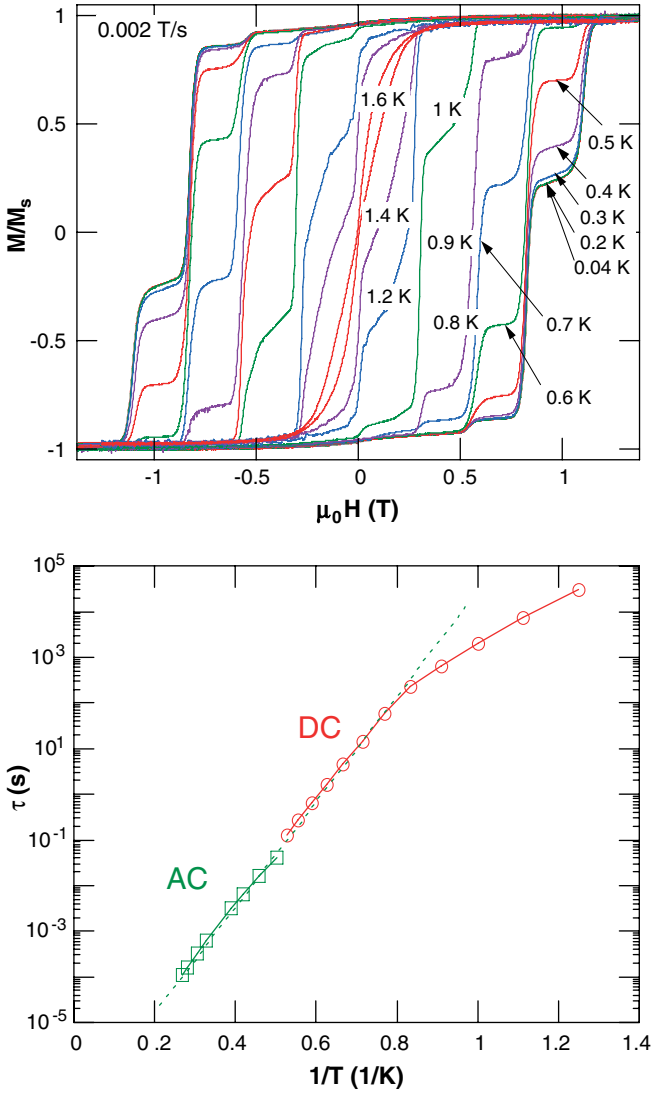


Fig. 4. Single crystal magnetisation (M) *vs.* field (H) hysteresis loops for complex **5** (top) at the indicated field sweep rates and temperatures; the magnetisation is normalised to its saturation value (M_S). Arrhenius plot for **5**; the dashed line is the fit of the thermally-activated region to the Arrhenius equation.

loops show the step-like features indicative of quantum tunneling of magnetization. Relaxation data determined from a combination of single crystal dc relaxation decay measurements and ac measurements on a powdered sample allow the construction of a τ *versus* $1/T$ plot based on the Arrhenius relationship $\tau = \tau_0 \exp(U_{\text{eff}}/kT)$ (Fig. 4). The slope of the thermally-activated region yields an effective energy barrier for the reorientation of the magnetization of 26.5 K with $\tau_0 = 9.6 \times 10^{-8}$ s.

In conclusion, we have successfully made four new analogues of the Mn_9 SMM. These are made *via* analogous reactions choosing the appropriate Mn triangle and the appropriate tripodal ligand in MeCN. Their structures and magnetic properties are similar to the original complex **1** [8]. All display $S = 17/2$ spin ground states and are new examples of high-spin half-integer Mn SMMs. The Mn_9 family have much in common with the prototype Mn SMM $[Mn_{12}O_{12}(O_2CR)_{16}\ (H_2O)_4]^{n-}$ $(n = 1,2)$ family and can be considered their 'baby brothers': not only do they look similar, but in each case the central ferromagnetically coupled Mn(IV) ions couple antiferromagnetically with the surrounding wheel of Mn(III/II) ions, and both have an interchangeable organic 'coat'.

Supplementary material

CCDC 189138 contains the supplementary crystallographic data for **1**–**5**. These data can be obtained free of charge via http://www.ccdc.cam.ac.uk/conts/retrieving.html, or from the Cambridge Crystallographic Data Centre, 12 Union Road, Cambridge CB2 1EZ, UK; fax: (+44) 1223-336-033; or e-mail: deposit@ccdc.cam.ac.uk.

References

[1] G. Aromí, E.K. Brechin, Struct. Bond. 122 (2006) 1.
[2] G. Christou, D. Gatteschi, D.N. Hendrickson, R. Sessoli, MRS Bull. 25 (2000) 66.
[3] G. Christou, Polyhedron 24 (2005) 2065.
[4] (a) See for example: M. Murugesu, M. Habrych, W. Wernsdorfer, K.A. Abboud, G. Christou, J. Am. Chem. Soc. 126 (2004) 4766;
(b) R. Sessoli, H.-L. Tsai, A.R. Schake, S. Wang, J.B. Vincent, K. Folting, D. Gatteschi, G. Christou, D.N. Hendrickson, J. Am. Chem. Soc. 115 (1993) 1804;
(c) D.N. Hendrickson, G. Christou, H. Ishimoto, J. Yoo, E.K. Brechin, A. Yamaguchi, E.M. Rumberger, S.M.J. Aubin, Z. Sun, G. Aromí, Mol. Cryst. Liq. Cryst. 376 (2002) 301;
(d) D.N. Hendrickson, G. Christou, H. Ishimoto, J. Yoo, E.K. Brechin, A. Yamaguchi, E.M. Rumberger, S.M.J. Aubin, Z. Sun, G. Aromí, Polyhedron 20 (2001) 1479.
[5] E.K. Brechin, Chem. Commun. (2005) 5141.
[6] R.T.W. Scott, S. Parsons, M. Murugesu, W. Wernsdorfer, G. Christou, E.K. Brechin, Angew. Chem., Int. Ed. 44 (2005) 6540.
[7] E.K. Brechin, M. Soler, J. Davidson, D.N. Hendrickson, S. Parsons, G. Christou, Chem. Commun. (2002) 2252.
[8] S. Piligkos, G. Rajaraman, M. Soler, N. Kirchner, J. van Slageren, R. Bircher, S. Parsons, H.-U. Güdel, J. Kortus, W. Wernsdorfer, G. Christou, E.K. Brechin, J. Am. Chem. Soc. 127 (2005) 5572.
[9] M. Murugesu, W. Wernsdorfer, G. Christou, E.K. Brechin, in preparation.
[10] E.R. Davidson, MAGNET, Indiana University.
[11] W. Wernsdorfer, Adv. Chem. Phys. 118 (2001) 99.

We chose to synthesize and examine compounds based on copper chloride and phenazine for comparison to the known copper chloride compounds of pyrazine [17] and quinoxaline [18]. Here we report the synthesis and structural analysis of phenazinodichlorocopper(II) [Cu(phz)Cl_2] (**1**) bis(phenazinium) tetrachlorocuprate(II) monohydrate $(phzH)_2$ [$CuCl_4$] · H_2O (**2**) and di[aquaphenazinodichlorocopper(II)] [Cu(phz)(H_2O)Cl_2]$_2$ (**3**) as well as the magnetic properties of compounds **1** and **2**.

2. Experimental

Reagents were purchased from Aldrich or Aesar Chemical Company and used without further purification. Infrared spectra were recorded on a Paragon 500 Spectrophotometer as KBr pellets and referenced to polystyrene.

2.1. Cu(phz)Cl_2 (**1**)

A solution of $CuCl_2$ (anhydrous) (1.34 g, 0.01 moles) dissolved in 40 mL of methanol was added to a stirred solution of phenazine (1.80 g, 0.01 moles) dissolved in 200 mL of methanol. The resulting solution was covered with Parafilm, with a few small holes punched in it, and placed in a fume hood to evaporate. Red crystals grew after several weeks and were recovered by vacuum filtration, 1.66 g (52%). IR data (KBr) ν 1523m, 1473m, 1434m, 1354m, 1151m, 1125s, 839m, 738s, 601m cm^{-1}.

2.2. $(phzH)_2CuCl_4 \cdot H_2O$ (**2**)

Anhydrous $CuCl_2$ (1.34 g, 0.01 moles) was dissolved in 30 mL concentrated HCl and subsequently diluted with 10 mL of water. Phenazine (1.80 g, 0.01 moles) was dissolved in 85 mL concentrated HCl and subsequently diluted with 115 mL of water. The dark green $CuCl_2$ solution was added slowly to the phenazine solution. The beaker was placed in the fume hood for slow evaporation. After several weeks, orange needles of **2** formed and were isolated by vacuum filtration to give 3.31 g (58%) IR data (KBr) ν 3400br m, 2637br m, 1617m, 1518m, 1422s, 1351m, 1129s, 825s, 764s, 753s, 737s, 594s cm^{-1}.

2.3. Cu(phz)$Cl_2 \cdot H_2O$ (**3**)

A phenazine solution (0.097 M) was prepared by mixing 2.18 g phenazine with 125 mL 95% ethanol. A $CuCl_2 \cdot 2H_2O$ (0.1 M) solution was then prepared by mixing 8.5 g $CuCl_2 \cdot 2H_2O$ into 500 mL 95% ethanol. The product was formed via a slow diffusion method in which one container filled with the phenazine solution and one container filled with the copper chloride solution were placed inside a 1 L beaker. The beaker was slowly filled

Table 1
Crystallographic data for compounds **1**–**3**

Compound	**1**	**2**	**3**
Empirical formula	$C_{12}H_8Cl_2CuN_2$	$C_{24}H_{20}Cl_4CuN_4O$	$C_{12}H_{10}Cl_2Cu_1N_2O$
Formula weight	314.64	585.78	665.32
Temperature (K)	295(2)	293(2)	295(2)
Wavelength	0.71073 Å	0.71073 Å	0.71073 Å
Crystal system	orthorhombic	triclinic	triclinic
Space group	*Pbam*	$P\bar{1}$	$P\bar{1}$
a (Å)	12.5363(14)	7.6934(12)	8.4955(11)
b (Å)	6.5036(12)	11.6792(18)	9.2457(19)
c (Å)	6.9356(7)	14.890(2)	9.5011(15)
α (°)	90	71.053(3)	61.199(9)
β (°)	90	75.740(3)	69.793(10)
γ (°)	90	82.200(3)	74.515(13)
V (Å^3)	565.47(13)	1224.2(3)	609.11(18)
Z	2	2	1
D_{calc} (g/cm^3)	1.848	1.589	1.814
Absorption coefficient (mm^{-1})	2.376	1.355	2.217
F(000)	314	594	334
Crystal size (mm)	$0.06 \times 0.22 \times 0.1$	$0.43 \times 0.17 \times 0.15$	$0.05 \times 0.18 \times 0.1$
θ_{min}, θ_{max} (°)	2.94, 25.00	1.48, 25.25	2.53, 25.00
Reflections collected	814	13 714	2512
Independent reflections (R_{int})	545 (0.0405)	4424 (0.0259)	2054 (0.0370)
Completeness to theta = 25.00°	1	0.999	0.956
Absorption correction	empirical	empirical	empirical
Maximum and minimum transmission	0.5794 and 0.4542	0.8226 and 0.5935	0.8183 and 0.7380
Number of refined parameters	43	320	170
Goodness-of-fit on $F2$	1.097	1.128	1.01
Final R_1, wR_2 [$I > 2\sigma(I)$]	0.0344, 0.0782	0.0462, 0.1077	0.0429, 0.0808
All data R_1, wR_2 [$I > 2\sigma(I)$]	0.0510, 0.0869	0.0523, 0.1109	0.0802, 0.0919
Minimum and maximum residual (e Å^{-3})	0.357 and −0.517	0.762 and −0.422	0.357 and −0.382

Table 2
Selected bond lengths (Å) and angles (°) for compounds **1**–**3**

Compound	**1**	**2**		**3**	
Bond lengths					
Cu–N	2.067(4)	Cu1–Cl1	2.2865(11)	Cu1–N1	2.049(3)
Cu–Cl	2.2021(15)	Cu1–Cl2	2.2487(10)	Cu1–O1	2.055(3)
N–C1	1.346(4)	Cu1–Cl3	2.2092(11)	Cu1–Cl1	2.2454(15)
		Cu1–Cl4	2.2167(10)	Cu1–Cl2A	2.2760(14)
		N1–C14	1.339(4)	Cu1–Cl2	2.5951(13)
		N1–C2	1.345(4)	N1–C2	1.351(6)
		N1–H1	0.89(4)	N1–C14	1.353(6)
		N21–C34	1.340(4)	O1–H1A	0.77(4)
		N21–C22	1.342(4)	O1–H1B	0.75(4)
		N21–H21	0.84(4)	C7–N8	1.333(6)
				N8–C9	1.350(6)
Bond angles					
N–Cu–NA	180	Cl3–Cu1–Cl4	99.61(5)	N(1)–Cu(1)–O(1)	149.00(16)
N–Cu–Cl	90	Cl3–Cu1–Cl2	133.38(4)	N1–Cu1–Cl1	90.28(11)
C1A–N–C1	119.1(4)	Cl4–Cu1–Cl2	100.98(4)	O1–Cu1–Cl1	90.59(12)
C1–N–Cu	120.5(2)	Cl3–Cu1–Cl1	100.61(5)	N1–Cu1–Cl2A	89.26(11)
		Cl4–Cu1–Cl1	129.76(4)	O1–Cu1–Cl2A	87.68(12)
		Cl2–Cu1–Cl1	97.46(4)	Cl1–Cu1–Cl2A	175.84(6)
		C14–N1–C2	122.6(3)	N1–Cu1–Cl2	117.97(11)
		C34–N21–C22	123.0(3)	O1–Cu1–Cl2	92.65(11)
				Cl1–Cu1–Cl2	97.07(5)
				Cl2A–Cu1–Cl2	86.79(5)
				Cu1A–Cl2–Cu1	93.21(5)
				C2–N1–C14	117.4(4)
				C2–N1–Cu1	117.5(3)
				C14–N1–Cu1	125.1(3)

with 95% ethanol until the tops of both smaller containers were submerged. This was covered and allowed to sit for several months. Both dark red rods (compound **1**) and yellow/green plates (compound **3**) formed on the sides of the beakers. Small quantities of **3** were manually separated from **1** under a stereomicroscope. No yield was recorded. IR data (KBr) ν 3436br m, 1630br m, 1524m, 1474m, 1434m, 1354m, 1125m, 738s, 601m cm^{-1}.

2.4. X-ray data collection and refinement

Crystals of $Cu(phz)Cl_2$ (**1**) (red), $(phzH)_2CuCl_4 \cdot H_2O$ (**2**) (orange) and $[Cu(phz)Cl_2 \cdot H_2O]_2$ (**3**) (green) resulting from slow evaporation or slow diffusion (see above) were analyzed by single crystal X-ray diffraction. Crystal data and experimental details are reported in Table 1. Selected bond lengths and angles are listed in Table 2.

2.5. Magnetic data collection

Magnetic studies were performed at Clark University on a Quantum Designs MPMS-XL SQUID magnetometer. External field dependent magnetic measurements at 1.8 K were also measured on all three compounds in fields up to 5 T. Compounds **1** and **2** were studied in fields up to 30 T at the National High Magnetic Field Laboratory in Tallahassee, FL. Temperature dependent magnetic susceptibility data were collected in the range 1.8–325 K for compounds **1** and **2**. Corrections were made for diamagnetic contributions (DIA) of the samples according to Pascal's constants and for temperature independent paramagnetism (TIP). Compound **3** was also measured, but the data were not reproducible due to an apparent irreversible, temperature-dependent phase change. Limited amounts of material prevented repeated attempts.

In the discussion below, all data have been interpreted in terms of the single J form of the Heisenberg Hamiltonian

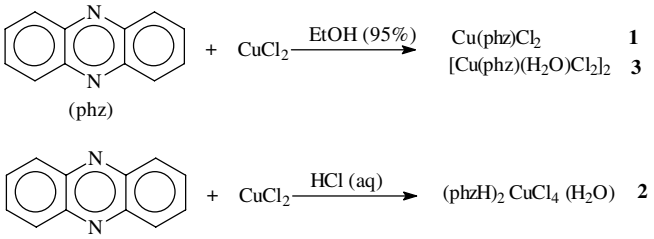
$$H = J\Sigma S_i \cdot S_{I+1}$$

where a positive value of J corresponds to antiferromagnetic interactions.

3. Results and discussion

Reaction of one equivalent of copper (II) chloride with one equivalent of phenazine in 95% ethanol gave red crystals of $Cu(phz)Cl_2$ (**1**) and green crystals of $[Cu(phz)Cl_2 \cdot H_2O]_2$ (**3**) (see Scheme 1). In methanol solution, only red crystals of $Cu(phz)Cl_2$ (**1**) were obtained. $(phzH)_2CuCl_4 \cdot H_2O$ (**2**) was obtained from a 1:1 solution of copper (II) chloride and phenazine in diluted HCl solution (see Scheme 1).

Crystals of $Cu(phz)Cl_2$ (**1**) and $(phzH)_2CuCl_4 \cdot H_2O$ (**2**) suitable for X-ray analysis were obtained through slow evaporation, while single crystals of $Cu(phz)Cl_2 \cdot H_2O$ (**3**) were collected from a slow inter-diffusion of 95% ethanol solutions of Cu(II) chloride dihydrate and phenazine. $Cu(phz)Cl_2$ (**1**) crystallizes in the orthorhombic space



Scheme 1.

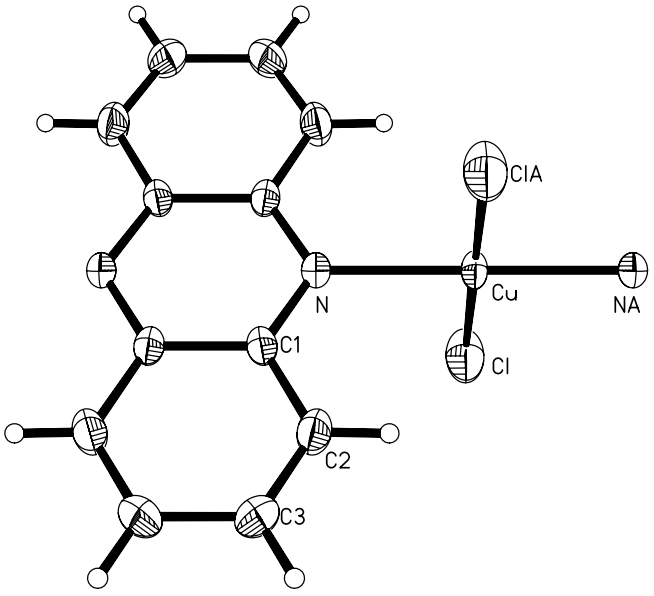


Fig. 1. The molecular structure of $Cu(phz)Cl_2$ (**1**) showing 50% probability thermal ellipsoids. Only the asymmetric unit and the copper coordination sphere have been labeled.

group Pbam (see Fig. 1). The Cu(II) is located in the unit cell at (0,0,0.5) on a two-fold axis and a mirror plane. The local coordination about the Cu ion is square planar with two coordinated phenazine rings and two coordinated chloride ions. The bond angles about the Cu-ion are 90°. The Cu–N bond to the phenazine is 2.067(4) Å which is comparable to the same bond in $Cu(phz)_2Br_2$ and is intermediate in length compared to Cu(I)–N bonds in other phenazine complexes (range 1.977 Å–2.124 Å) [19]. The bond lengths and angles within the phenazine ring are in general unremarkable and compare well with those of phenazine itself [20]. The phenazine ring is planar (mean deviation = 0.0024 Å) and is nearly perpendicular to the Cu coordination plane ($\angle = 89.3°$).

The phenazine ligands link the copper(II) ions into chains parallel to the *c*-axis wherein successive Cu ions are separated by 6.935(1) Å (Fig. 2). Those chains are further linked into sheets along the *b*-axis through π-stacking of the phenazine rings (Fig. 3). The distance between the planes of the phenazine rings is 3.597(1) Å, while the slip angle is 10.6(2)°.

$(phzH)_2CuCl_4 \cdot H_2O$ (**2**) crystallizes in the triclinic space group $P\bar{1}$. The local Cu coordination sphere is a distorted tetrahedron with a mean trans angle of 131.6(1)° (Fig. 4) [21]. The phenazinium ions do not coordinate to the Cu ions through the unprotonated nitrogen atoms as has been observed for some pyrimidine compounds [22]. The Cu–Cl bond lengths range from 2.209(1) Å to 2.286(1) Å. The bond lengths of C(2)–N(1) and C(14)–N(1) are identical to the centro-symmetric structure of the phenazinium

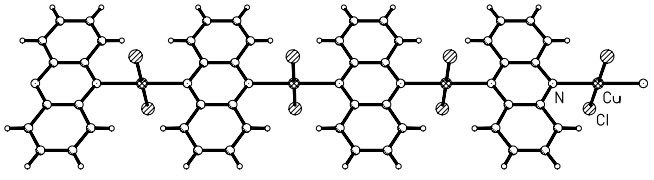


Fig. 2. Detail of the packing diagram for $Cu(phz)Cl_2$ (**1**) showing the chain through the Cu(II) atoms parallel to the *c*-axis.

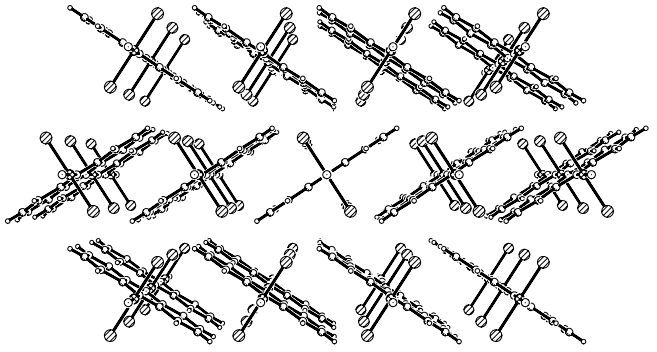


Fig. 3. Packing diagram for $Cu(phz)Cl_2$ (**1**) showing π-stacking of the Cu(phz) chains.

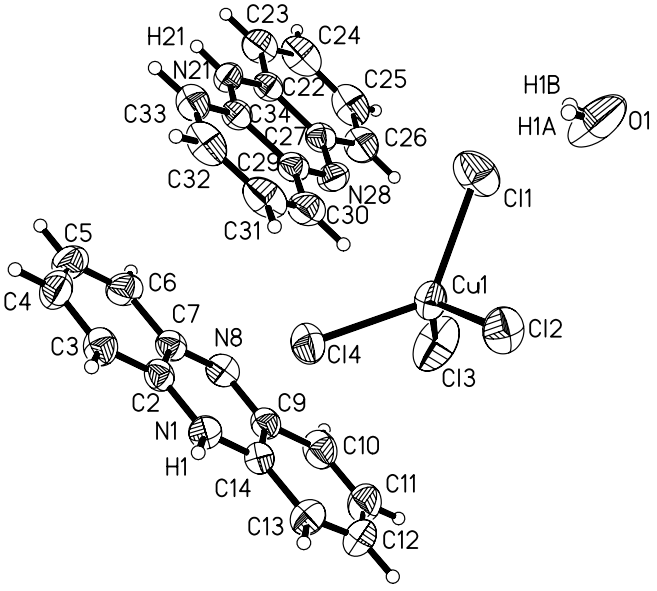


Fig. 4. The molecular unit for $(phzH)_2CuCl_4 \cdot H_2O$ (**2**) showing 50% probability thermal ellipsoids. Only H atoms in refined positions have been labeled.

ligand in (phzH)[Ni(dmit)$_2$]$_3$ [23]; however, the symmetry of the phenazinium ion is reduced in compound **2** as the C(9)–N(8) bond becomes the shortest bond in the central phenazine ring. The N21-containing phenazinium ring exhibits four identical C–N bonds of 1.340(6) Å. Both phenazinium rings are nearly planar with mean deviations of 0.0091 Å (N11) and 0.0426 Å (N21).

Chloride···chloride contacts link the Cu ions into chains parallel to the *a*-axis with successive Cl ions separated by 3.621(1) Å wherein the connection Cu1–Cl1···Cl4A–Cl1A is nearly planar (torsion ∠ = 14.4°) (Fig. 5). Consecutive copper ions are separated by a distance of 7.6934(12) Å. These chains are isolated in the lattice by the phenazinium ions (Fig. 6). The chains are hydrogen bonded to each other by the lattice H_2O molecules to make a ladder motif, but the Cl···Cl distances are too large to support significant magnetic interactions (Fig. 7) (Cl···Cl distance = 4.781 Å; Cu–Cu distance = 7.525 Å). The phenazinium ions in the lattice are nearly coplanar (angle between mean planes = 3.7°) with an interplanar distance of 3.328(1) Å. The phenazinium ions exhibit π-stacking as the C(4) and N(21) ring centroids are separated by a distance of 3.411 Å with alternating slip angles of 12.7° and 9.2°, respectively.

[Cu(phz)Cl$_2$ · H$_2$O]$_2$ (**3**) also crystallizes in the triclinic space group $P\bar{1}$ as a centrosymmetric dimer with the copper ions bridged by chloride ions (Cu–Cu1A = 3.546 Å, see Fig. 8). The Cu ion bonds to the nitrogen in the phenazine ligand with a Cu–N bond length of 2.049(13) Å which is intermediate in length compared to Cu(I)–N bonds in related phenazine complexes [19].

The Cu is bonded to three different Cl atoms (Cl1, Cl2, Cl2A) and a water molecule with bond lengths Cu–Cl = 2.2454(15) Å, 2.2760(14) Å, and 2.5951(13) Å, respectively, and Cu–O = 2.055(3) Å. All bonds, but one, within the central phenazine ring are longer compared to those in phenazine [20]. Using the Continues Symmetry Measure approach [24], the local coordination sphere about the copper is somewhat closer to a square pyramidal configuration with a symmetry factor of 2.183 compared to the 2.601 symmetry factor for a trigonal bipyramid (lower symmetry factors indicate closer agreement with the idealized geometry) [25].

The Cu dimers are linked into layers via hydrogen bonding (see Fig. 9). The dimers are linked into structural ladders due to H-bonding between the coordinated water molecule and the uncoordinated nitrogen on the phenazine ring of the next dimer parallel to the A-face diagonal

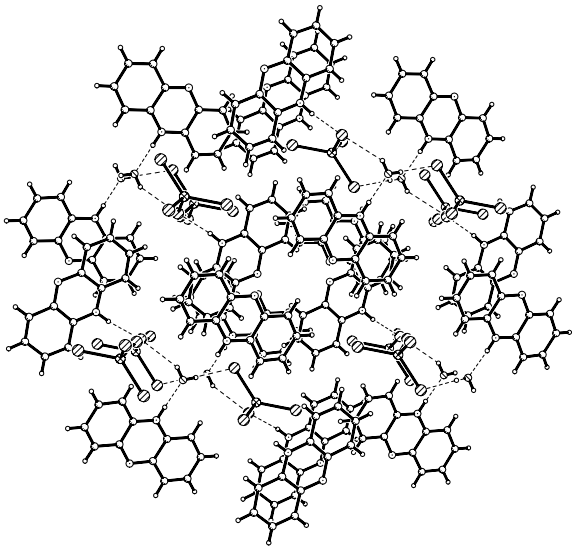


Fig. 6. The packing diagram for (phzH)$_2$CuCl$_4$ · H$_2$O (**2**) showing the alternation of the phenazinium ions through the crystal. Dotted lines represent hydrogen bonds.

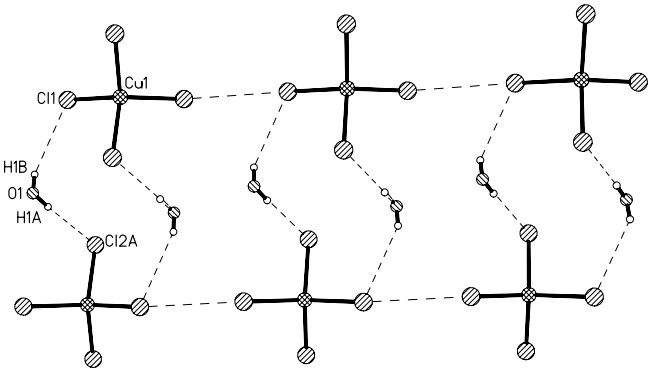


Fig. 7. Detail of chain interactions via hydrogen bonding to the water molecules in the lattice of **2** viewed parallel to the A-face diagonal (the *a*-axis is horizontal) Dotted lines represent hydrogen bonds and close Cl···Cl contacts.

[O1–H1B = 0.75(4) Å, H1B–N = 2.25(4) Å, O1–N = 2.980(5) Å, O–H–N ∠ = 162(5)°]. The ladders are then linked into layers parallel to the *a*-axis via H-bonds between the water molecules and an adjacent Cl1 atom [O1–H1A = 0.77(4) Å, H1A–Cl1 = 2.40(4) Å, O1–Cl1 = 3.136(4) Å, O–H–Cl ∠ = 161(5)°]. π-Stacking between the phenazine ligands also contributes to the layer organization. The distance between adjacent phenazine rings is 3.413(3) Å with a slip angle of 23.9(2)° between the

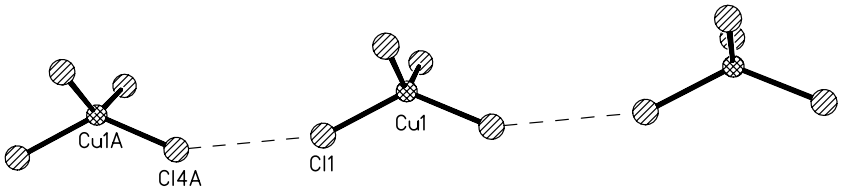


Fig. 5. Detail of the packing of the $CuCl_4^{-2}$ ions in **2** showing the chain formation (parallel to the *a*-axis) through short Cl···Cl contacts.

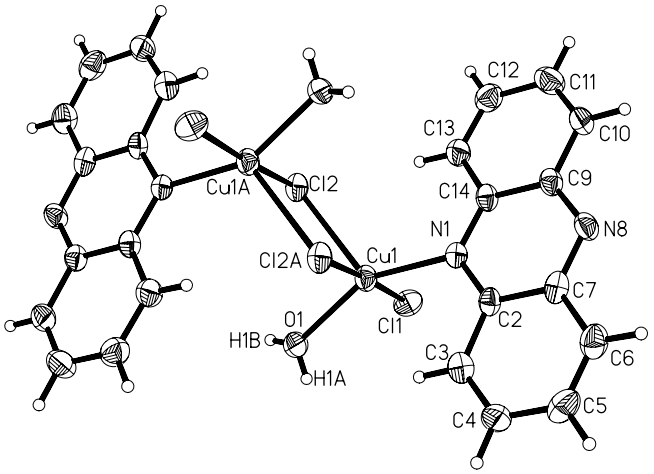


Fig. 8. The molecular unit for $[Cu(phz)Cl_2 \cdot H_2O]_2$ (**3**) showing 50% probability thermal ellipsoids. Only the asymmetric unit and Cu(II) coordination sphere have been labeled.

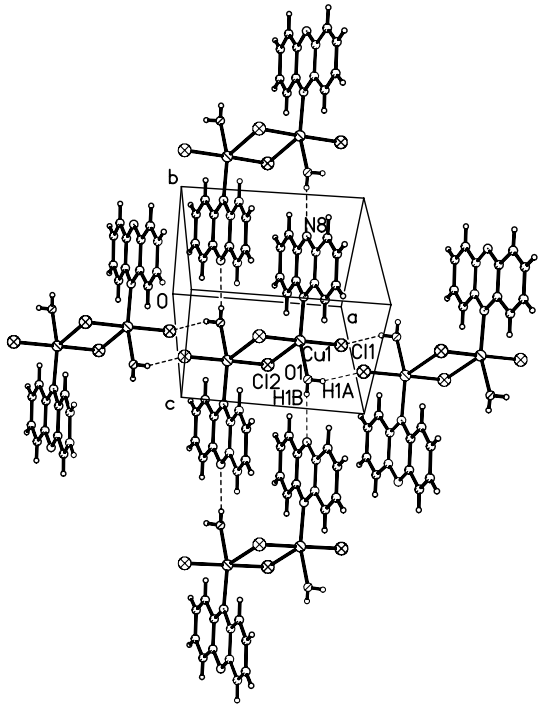


Fig. 9. Detail of the $[Cu(phz)Cl_2 \cdot H_2O]_2$ (**3**) packing diagram showing the unit cell. Dotted lines represent hydrogen bonds.

centroid of the terminal ring and the centroid of the central ring of the successive phenazine. As seen in Fig. 10, the layers are offset parallel to the *a*-axis to minimize the free volume of the crystal.

Infrared data for compounds **1**–**3** are summarized in Table 3. The IR spectrum of the phenazine ligand shows characteristic bands at 1513, 1430, 1359, 1146, 1108, 819, and 742 cm^{-1} which are assigned as previously reported [26]. The expected coordination shifts are observed in **1**–**3** and additional bands are observed in **2** and **3** as a result of the loss of the center of symmetry in the phenazine.

The magnetic susceptibility as a function of temperature between 1.8 K and 325 K of **1** is shown in Fig. 11. The data is characterized by a rounded maximum near 21 K and a local minimum at 6.2 K. This behavior is characteristic of a low-dimensional Heisenberg antiferromagnet with a small paramagnetic contribution that dominates at the lowest temperatures. Considering the linear chain structure of **1**, the data was compared to the theoretical prediction for a $S = 1/2$ Heisenberg antiferromagnetic with a paramagnetic impurity. Three parameters (C, J, and the fraction of paramagnetic impurity) were allowed to the vary and a best fit obtained with values of $C = 0.401(2)$ emu/K-mol, $J/k = 33.8(2)$ K and a paramagnetic impurity fraction of 1.00(5)%. This fit is represented as the solid line in Fig. 11 and is an excellent representation of the data over the entire temperature range.

The molar magnetization of **1** was studied at 1.9 K in fields up to 30 T at the National High Magnetic Field Laboratory. The results are presented in Fig. 12 as the ratio of $M(H/H_{SAT})/M_{SAT}$ versus $H/(H_{SAT})$, where the saturation moment has been calculated from the formula $M_{SAT} = N_A\, g\mu_B/2$ and the value of g (2.07) was obtained from the Curie constant of 0.401(2) emu/K-mol obtained from the fit to the susceptibility data.

The saturation field H_{SAT} was obtained from the molecular-field expression $2H_{SAT} = zk_BJ/(g\mu_B)$ where z is the number of nearest neighbors, using the value of g and J from the susceptibility fit. From these values, $H_{SAT} = 49$ T. As seen in Fig. 12, the magnetization data show the characteristic upward curvature with field, due to the field-induced quenching of the quantum fluctuations in this type of magnetic system.

For this set of experimental data, the ratio of temperature to exchange strength ($T/J = 1.9$ K/33.8 K) equals 0.056. For comparison purposes, the predicted behavior of a $S = 1/2$ Heisenberg antiferromagnetic chain at relative temperatures of 0.05 and 0.10 are shown as well. These two predicted sets only differ by a few percent as the saturation field is approached. The predictions exactly represent the experimental data over the field range measured, confirming both the magnetic one-dimensionality of **1** and the values of C and J obtained from the susceptibility study.

The magnetic susceptibility of **2** as a function of temperature between 1.8 K and 325 K is shown in Fig. 13. The data is also characterized with a rounded maximum, but at a lower temperature, near 5.3 K. This behavior is qualitatively similar to that of **1** and has likewise been compared to the theoretical prediction for an $S = 1/2$ Heisenberg antiferromagnetic chain. Although no low-temperature Curie-like tail is obvious in the data, the best fit was obtained with values of $C = 0.46(1)$ emu/K-mol, $J/k = 8.6(2)$ K and a paramagnetic impurity fraction of 1.23(5) %. This fit is represented as the solid line in Fig. 13 and is an excellent representation of the data over the entire temperature range. The field-dependent magnetization of **2** was measured at 1.8 K in fields up to 5 T. The magnetization is linear up to 1.2 T and shows upward curvature

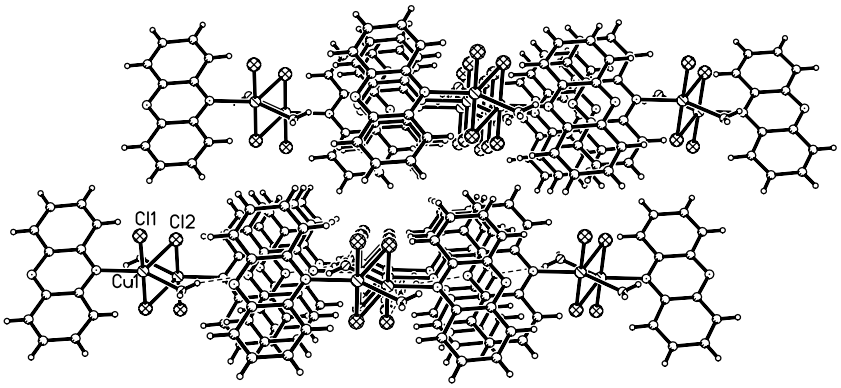


Fig. 10. Packing diagram for $[Cu(phz)Cl_2 \cdot H_2O]_2$ (**3**) viewed parallel to the *a*-axis. Dotted lines represent hydrogen bonds. Only Cu1, Cl1, and Cl2 have been labeled for clarity.

Table 3
Infrared data for compounds **1**–**3**

Compound	Phenazine [a]	1	2	3
Out-of-plane *v*(C–H)	742s	738	753	742
	1108	1125	1130	1111
Skeletal deformation	903	920	915	912
	814	825	840	831
In-plane *v*(C–H)	1209	1219	1227	1214
	1146	1151	1148	1145
	996		1004	
Ring stretch	1514	1524	1617	1518
	1468	1473	1518	1474
	1430	1434	1473	1433
	1359	1354	1422	1364
			1351	

[a] See Ref. [26].

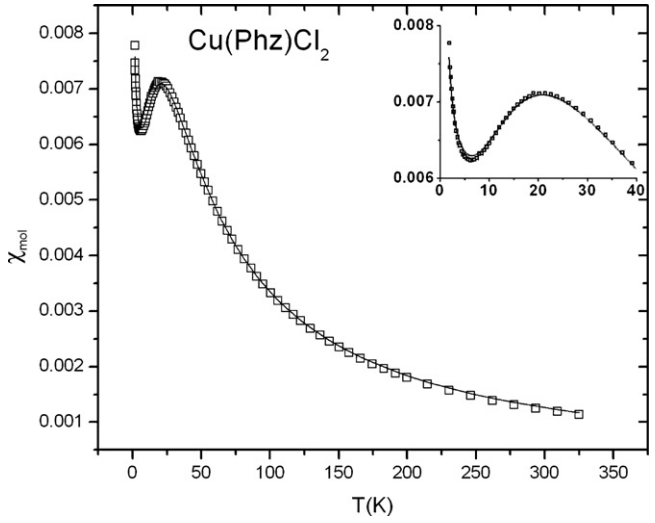


Fig. 11. A plot of χ_{mol} vs temperature for compound **1**. The solid line shows the best fit to the S = 1/2 Heisenberg linear chain model.

at larger fields. Based on the molecular field prediction for saturation field described above, it is anticipated that the moments will reach saturation at a field near 12.5 T.

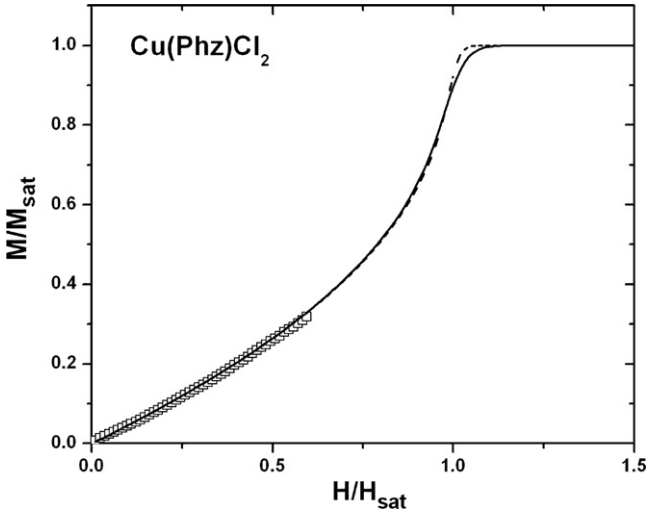


Fig. 12. A plot of moment/saturation moment vs field/saturation field for compound **1**. The squares represent data taken up to 30 T. The dashed and solid lines represent *T*/*J* predictions for 0.05 and 0.1, respectively.

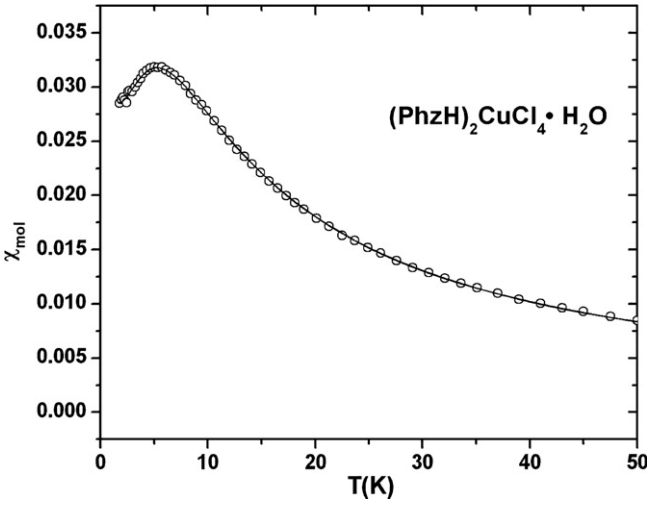


Fig. 13. A plot of χ_{mol} vs temperature for compound **2**. The solid line shows the best fit to the Heisenberg linear chain model.

Attempts to collect magnetic data for **3** were unsuccessful. The sample changed color from green to brown while in the cryostat; different protocols of cooling/heating and application of fields yielded varying and non-reproducible results.

4. Discussion

Compound **3** was a by-product of the synthesis of **1**. During the slow diffusion process in 95% ethanol, both compounds **1** and **3** were produced. Compound **3** was manually isolated from compound **1** under a stereomicroscope. Attempts to prepare compound **3** from aqueous solutions were unsuccessful, most likely due to the insolubility of phenazine in water. We were able to prepare **1** as the sole product**,** however, using absolute methanol as the solvent. The reaction of phenazine and $CuCl_2$ in a concentrated aqueous solution of HCl gave only **2**.

4.1. Structure analysis

The structure of the coordination sphere around the Cu(II) in compound **1** is surprising since it exhibits an idealized square planar geometry with all of the angles 90.00°. The phenazine ligand is also planar (mean deviation = 0.0024 Å) and is nearly perpendicular to the Cu coordination plane ($\angle = 89.3°$). The $\pi - \pi$ stacking of the phenazine rings structurally links the phenazine-bridged chains together along the *b*-axis, but the magnetic interactions are expected to be significantly weaker as evidenced by the excellent fit to the Heisenberg antiferromagnetic chain model, instead of a 2-D model.

In contrast, compound **2**, $(phzH)_2CuCl_4 \cdot H_2O$, contains tetrachlorocuprate(II) anions and discrete phenaznium ions. It is not surprising that this salt forms a magnetic linear chain; such motifs have been observed previously with tetrachlorocuprate systems [27]. As expected, the phenazinium ions are nearly planar and provide the steric bulk and hydrogen bonding which stabilizes the lattice and isolates the chains magnetically. The phenazinium ions are closer together in the lattice than they are in compound **1**, but the π-stacking interactions are still relatively weak.

The dimer, **3**, is unique. No structures for such dimers are reported for any five-coordinate transition metal complexes with water, halides and a coordinated nitrogen, although several related structures with six-coordinate geometries (with the coordinated nitrogen as part of a chelating ligand) have been reported [28]. The coordination sites occupied by the water molecules prevent chain formation as seen in **1** and allow for the structural and magnetic dimer. The symmetry about the inversion center is convenient for the π–π stacking of the phenazine rings and the hydrogen bonding. This allows for the structural layer and ladder motifs to be present within the crystal. The ladder and layer structure might prove to provide interesting magnetic data for this crystal; however, thus far the data has been irreproducible and preliminary results suggest that the coordinated water molecules are easily lost.

4.2. Magnetic data

Pyrazine and substituted pyrazines are well known to provide a superexchange pathway in the range $5 < J < 25$ [1,6–8] while the double halide exchange for chlorides is generally small even though it can be as high as 27 K [29,30]. It is clear from Figs. 11 and 13 that the temperature-dependant magnetic susceptibility data fit very well to a Heisenberg antiferromagnetic linear chain model [31]. Fits to other models (dimers, layers, ...) were also attempted, but the results were clearly poorer.

We have previously reported other S = 1/2 Heisenberg antiferromagnetic linear chains as well with pyrazine, substituted pyrazines, and pyrazine-based ligands such as quinoxaline [32]. The magnetic exchange strengths for these systems differ greatly even though the main superexchange pathway is via a six-membered diazine ring in all cases (see Table 4). The linear chain coordination polymer $Cu(pz)(NO_3)_2$ was originally reported by Santoro et al. [2] and its magnetism studied by Hatfield and coworkers [3] who reported moderate Heisenberg-type exchange ($J/k_B = 10.6$ K).

It appears that as additional rings are added onto the pyrazine ring itself the strength of the exchange increases. The coordination spheres of the compounds are different with the pyrazine and quinoxaline linear chains being nitrate compounds as opposed to chlorides as is the case for **1**. However, the corresponding copper halide compounds of pyrazine [33] and quinoxaline [13] are not linear chains, but rather a layer and a ladder, respectively, and therefore not suitable for direct comparison. Attempts to synthesize $Cu(phz)(NO_3)_2$ have been unsuccessful to date, limiting the usefulness of direct comparison of the magnetic exchange values.

Compound **1**, $Cu(phz)Cl_2$, fits to this linear magnetic chain model ($R^2 = 0.99965$) far better than any other model. This compound has a very strong exchange strength ($|J|/k_B = 33.84(9)$) through the copper, as compared to the other diazine chains [7]. This comparatively strong exchange strength is most likely due to its extremely symmetrical crystallographic structure (Fig. 2).

Compound **2**, $(phzH)_2CuCl_4 \cdot H_2O$, fits almost perfectly to an spin S = 1/2 linear magnetic chain ($R^2 = 0.99973$), even though structurally it is different from compound **1** and the other two diazine-bridged linear chains. $(phzH)_2CuCl_4 \cdot H_2O$ contains its major linear magnetic interactions

Table 4
Comparison of exchange constants

Compound	J/k_B
$Cu(pz)(NO_3)_2$	10.6(2) [8]
$Cu(qnx)(NO_3)_2$	12.82(1) [32]
$Cu(phz)Cl_2$ (**1**)	33.84(9)
$(Phz)_2CuCl_4 \cdot H_2O$ (**2**)	8.59(3)

through the Cl···Cl contacts between adjacent $CuCl_4^{2-}$ groups (Fig. 5). The contact parameters are: $d_{Cl\cdots Cl} = 3.61(1)$ Å, $\angle_{Cu1-Cl1\cdots Cl4A} = 157.78(5)°$, $\angle_{Cu1-Cl4\cdots Cl1B} = 151.56(5)°$, $\tau_{Cu1-Cl1\cdots Cl4A-Cl1A} = 14.4(2)°$. Cu-X···X angles approaching 180° and Cu–X···X–Cu torsion angles near 0° or 180° are correlated with stronger double halide exchange [21] and support the observed exchange strength through the chain of $|J|/k_B = 8.59(3)$ K.

Magnetization as a function of field was also collected for **1** and **2**. Both compounds show the characteristic upward curvature of low-dimensional antiferromagnetic materials (see Fig. 12). Compound **1** was fit to the results of a Quantum Monte Carlo simulation of a 1D chain for a variety of *T*/*J* ratios [34]. Our experimental *T*/*J* ratio was 0.056 and the predictions for ratios of both 0.05 and 0.1 are plotted in Fig. 12. Both values fit the experimental data within the error limit supporting the one-dimensional magnetic nature of the sample.

5. Conclusions

The ability of diazines to provide an effective super exchange pathway has been further demonstrated in the linear chain coordination polymer **1**. The effect of the size and shape of organic cations on the packing of CuX_4^{2-} is shown through the production of the packed linear magnetic system seen in **2**. Regrettably, the instability of **3** prevented the collection of reproducible magnetic data and analysis of the exchange through the bihalide bridge. Further work is in progress on both systems varying the substituents on the phenazine ring and the ancillary ligands on the copper(II).

Acknowledgements

The MPMS-XL SQUID magnetometer was purchased with the assistance of funds from the National Science Foundation (IMR-0314773) and the Kresge Foundation. The Bruker (Siemens) SMART APEX diffraction facility was established at the University of Idaho with the assistance of the NSF-EPSCoR program and the M. J. Murdock Charitable Trust, Vancouver, WA, USA. RTS is grateful for an Albert C. Erickson Summer Fellowship.

Appendix A. Supplementary material

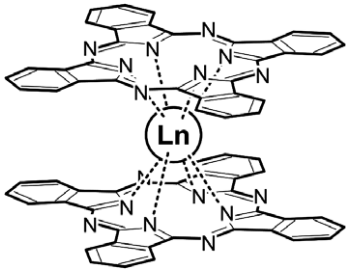
Atomic coordinates and isotropic thermal parameters, a full listing of bond lengths and angles, observed and calculated structure factors and anisotropic thermal parameters are available through the following CCDC numbers. CCDC 603419, 603418 and 603417 contain the supplementary crystallographic data for **1**, **2** and **3**. These data can be obtained free of charge via http://www.ccdc.cam.ac.uk/conts/retrieving.html, or from the Cambridge Crystallographic Data Centre, 12 Union Road, Cambridge CB2 1EZ, UK; fax: (+44) 1223-336-033; or e-mail: deposit@ccdc.cam.ac.uk. Supplementary data associated with this article can be found, in the online version, at doi:10.1016/j.poly.2006.09.019.

References

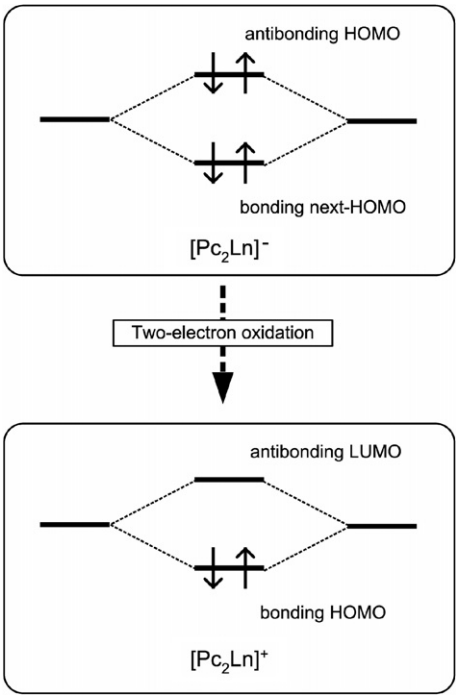
[1] D.N. Hendrickson, in: R.D. Willett, D. Gatteschi, O. Kahn (Eds.), Magneto-Structural Correlations in Exchange Coupled Systems, Reidel Publishers, Dordrecht, 1985, p. 555.
[2] A. Santoro, A.D. Mighell, C.W. Reimann, Acta Cryst. B 26 (1970) 979.
[3] (a) J.F. Villa, W.E. Hatfield, J. Am. Chem. Soc. 93 (1971) 4081; (b) D.B. Losee, H.W. Richardson, W.E. Hatfield, J. Chem. Phys. 59 (1973) 3600.
[4] G. Mennenga, L.J. De Jongh, W.J. Huiskamp, J. Reedjik, J. Mag. Mag. Mat. 44 (1984) 89.
[5] T. Lancaster, S.J. Blundell, M.L. Brooks, P.J. Baker, F.L. Pratt, J.L. Manson, C.P. Landee, C. Baines, Phys. Rev. B 73 (2006) 020410.
[6] W.W. Richardson, W.E. Hatfield, J. Am. Chem. Soc. 98 (1976) 835.
[7] S. Amaral, W.E. Jensen, C.P. Landee, M.M. Turnbull, F.M. Woodward, Polyhedron 20 (2001) 1317.
[8] C.P. Landee, M.M. Turnbull, Mol. Cryst. Liq. Cryst. 335 (1999) 193.
[9] G. Beobide, O. Castillo, U. Garcia-Couceiro, J.P. Garcia-Teran, A. Luque, M. Martinez-Ripoll, P. Roman, Eur. J. Inorg. Chem. (2005) 2586.
[10] L.-G. Zhu, S. Kitagawa, S. Inorg. Chem. Commun. 6 (2003) 1051.
[11] M.M. Turnbull, A.S. Albrecht, G.B. Jameson, C.P. Landee, Mol. Cryst. Liq. Cryst. Sec. A: 335 (1999) 957.
[12] J.L. Manson, M.M. Conner, J.A. Schlueter, T. Lancaster, S.J. Blundell, M.L. Brooks, F.L. Pratt, T. Papageorgiou, A.D. Bianchi, J. Wosnitza and M.-H. Whangbo, Chem. Commun., in press.
[13] C.P. Landee, A. Delcheva, C. Galeriu, G. Pena, M.M. Turnbull, R.D. Willett, Polyhedron 22 (2003) 2325.
[14] W. Maniukiewicz, M. Bukowska-Stzyzewska, M. Sadowska, Acta Crystallogr., Sect. E: Struct. Rep. Online 60 (2004) m73.
[15] D.J. Chesnut, D. Plewak, J. Zubieta, J. Chem. Soc., Dalton Trans. (2001) 2567.
[16] (a) F.A. Cotton, T.R. Felthouse, Inorg. Chem. 20 (1981) 600; (b) H. Miyasaka, R. Clerac, C.S. Campos-Fernandez, K.R. Dunbar, J. Chem. Soc., Dalton Trans. (2001) 858.
[17] J. Pickardt, B. Staub, Z. Naturforsch. B 52 (1997) 1456.
[18] C.P. Landee, M.M. Turnbull, unpublished.
[19] T. Kuroda-Sowa, M. Munakata, H. Matsuda, S. Akiyama, M. Maekawa, J. Chem. Soc., Dalton Trans. (1995) 2201.
[20] K. Wozniak, B. Kariuki, W. Jones, Acta Crystallogr., Sec. C: Cryst. Struct. Commun. 47 (1991) 1113.
[21] M.M. Turnbull, C.P. Landee, B.M. Wells, Coord. Chem. Rev. 249 (2005) 2567.
[22] M.E. Masaki, B.J. Prince, M.M. Turnbull, J. Coord. Chem. 55 (2002) 1337.
[23] Y.S.J. Veldhuizen, W.J. J Smeets, N. Veldman, A.L. Spek, C. Faulmann, P. Auban-Senzier, D. Jerome, P.M. Paulus, J.G. Haasnoot, J. Reedijk, Inorg. Chem. 36 (1997) 4930.
[24] M. Pinsky, D. Avnir, Inorg. Chem. 37 (1998) 5575.
[25] B.R. Landry, M.M. Turnbull, B. Twamley, J. Chem. Cryst., in press.
[26] M.B. Mitchell, G.R. Smith, W.A. Guillory, J. Chem. Phys. 75 (1981) 44.
[27] P.R. Hammar, D.C. Dender, D.H. Reich, A.S. Albrecht, C.P. Landee, J. Appl. Phys. 81 (1997) 8.
[28] (a) S.O. Sommerer, B.L. Westcott, A.J. Jircitano, K.A. Abboud, Inorg. Chim. Acta 238 (1995) 149; (b) A. Garoufis, S. Kasselouri, S. Boyatzis, C.P. Raptopoulou, Polyhedron 18 (1999) 1615.
[29] (a) K. Halvorson, R.D. Willett, Acta Cryst. C 44 (1988) 2071; (b) B.R. Patyel, B.L. Scott, R.D. Willett, Phys. Rev. B 41 (1990) 1657;

(c) F.M. Woodward, C.P. Landee, J. Giantsidis, M.M. Turnbull, C. Richardson, Inorg. Chim. Acta 324 (2001) 324;
(d) B.C. Watson, V.N. Kotov, M.W. Meisel, D.W. Hall, G.E. Granroth, W.T. Montfrooij, S.E. Nagler, D.A. Jensen, R. Backov, M.A. Petruska, G.E. Fanucci, D.R. Talham, Phys. Rev. Lett. 86 (2001) 5168;
(e) F.M. Woodward, A.S. Albrecht, C.M. Wynn, C.P. Landee, M.M. Turnbull, Phys. Rev. B 65 (2002) 144412.

[30] G.S. Long, M. Wei, R.D. Willett, Inorg. Chem. 36 (1997) 3102.
[31] A. Meyer, A. Gleizes, J.J. Girerd, M. Verdaguer, O. Kahn, Inorg. Chem. 21 (1982) 1729.
[32] C.P. Landee and M.M. Turnbull, unpublished.
[33] Th. Fetzer, A. Lentz, T. Debaerdemaeker, Z. Naturfors. B: 44 (1989) 553.
[34] F. Alet, S. Wessel, M. Troyer, Phys. Rev. E. 71 (2005) 036706/1.



Scheme 1.



Scheme 2.

calculation than the previous semi-empirical ones showed the basic picture of the characteristics of the MOs near HOMO–LUMO region is essentially unchanged. More importantly, the calculations predicted that the two-electron oxidation leads to a significantly shortened Pc–Pc distance, which has a effect to strengthen the ligand-field potential under which the lanthanide ion is placed.

2. Theoretical calculation

We have employed model complexes $[Pc_2Y]^-$ and $[Pc_2Y]^+$ with D_{4d} symmetry in which two Pc ligands are in skewed positions made by rotating one Pc by 45° around C_4 axis from an eclipsed position. Y was used in the place of Ln, because the ionic radius of Y^{3+} is among those of trivalent lanthanide ions (more specifically, very close to Ho^{3+}).[1] An X-ray crystal analysis by Koike et al. has shown that the geometric structure of $[Pc_2Ln]^-$ smoothly changes with the atomic number of Ln, and only the size of the lanthanide (and yttrium) ion governs the overall geometric structure of the complexes [4].

The B3LYP theory [5] was employed for obtaining fully optimized molecular structures of both anionic and cationic Pc double-decker complexes. For Y atom, we used the LANL2DZ basis set of valence double-zeta quality [6,7], in which inner core electrons are replaced by an effective core potential (ECP). The triple-zeta type 6-311G(d) basis set, which includes d-type polarization function, was used for H, C and N atoms. Since each Pc ligand in the double-decker complex significantly distorted from planarity, inclusion of the d-polarization function is mandatory in obtaining accurate optimized geometry.

The calculations were carried out using the programs GAMESS [8] on a Pentium-D personal computer and GAUSSIAN-98 [9] on a NEC SX-5 vector supercomputer at Global Scientific Information and Computing Center at Tokyo Institute of Technology, Japan.

3. Results and discussion

Fig. 1 shows energy diagrams of Kohn–Sham orbitals near HOMO–LUMO region obtained for $[Pc_2Y]^-$ and $[Pc_2Y]^+$. The symmetric characters of HOMO, next-HOMO, LUMO, next-LUMO of $[Pc_2Y]^-$ are a_2, b_1, e_3 and e_1, respectively. This is exactly the same as that obtained with the semi-empirical calculations previously reported [3]. In a pictorial view in which two Pc ligands (belonging to D_{4h} point group) make a Pc dimer in face-to-face configuration (D_{4d} point group), the a_2 HOMO and b_1 next-HOMO are obtained by antibonding and bonding linear combination of a_{2u} HOMOs of the two Pc monomers. In the cationic complex $[Pc_2Y]^+$, two electrons are removed from the a_2 orbital (Fig. 1, right), which is now LUMO, and the b_1 orbital becomes HOMO accordingly.

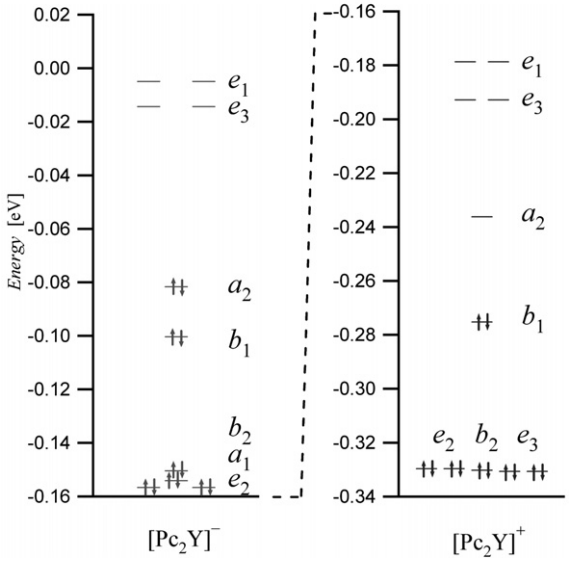


Fig. 1. Energy diagram of Kohn–Sham orbitals of $[Pc_2Y]^-$ and $[Pc_2Y]^+$.

[1] Ionic radius of Ho^{3+} and Y^{3+} are 1.155 Å and 1.159 Å, respectively.

Iso-contour surface of the a_2 HOMO and b_1 next-HOMO of $[Pc_2Y]^-$ are shown in Fig. 2. Inspection of the figure clearly shows the bonding character of the b_1 orbital: the 2p orbitals on the two facing C_α atoms (Fig. 3) on opposite Pc ligands make a bonding linear combination. In contrast, the a_2 HOMO orbital shows anti-bonding linear combination at the same positions. It should be noted that no contribution from Y atom is involved. The ''bond order'' between the C_α atoms in facing Pc ligands has a crucial rule for determining the inter-planar distance since these positions gives the only atom-to-atom contacts (about 3.3 Å) between the two ligands.

Table 1 summarizes theoretical predictions of geometrical changes caused by two-electron oxidation of $[Pc_2Y]^-$. The closest interplanar C_α–C_α distance is predicted to be shortened upon oxidation by ca. 0.10 Å, which is a significant amount. This is a direct effect of the removal of the two electrons in the anti-bonding a_2 HOMO. Since the ''bridges'' connecting two Pc ligands are shortened, the ''Pc–Pc distance'', which can be defined as the distance between the centers of the two Pc ligands, is accordingly decreased by the same degree (bottom, Table 1). The $(N_\alpha)_4$–$(N_\alpha)_4$ distance, which directly affects the LF potential to the lanthanide ion, is shortened by 0.08 Å.

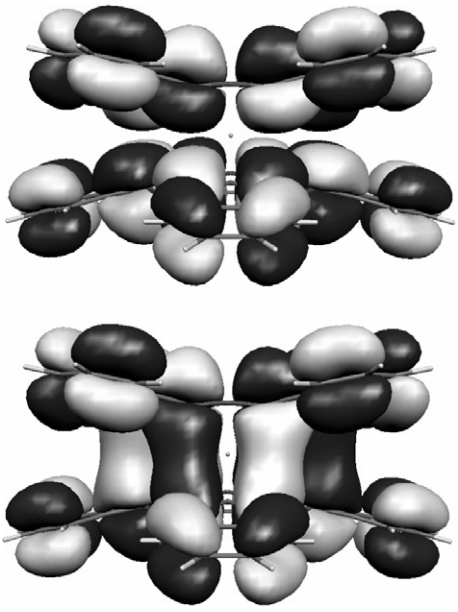


Fig. 2. Iso-contour surface of a_2 HOMO (top) and b_1 next-HOMO (bottom) of $[Pc_2Y]^-$.

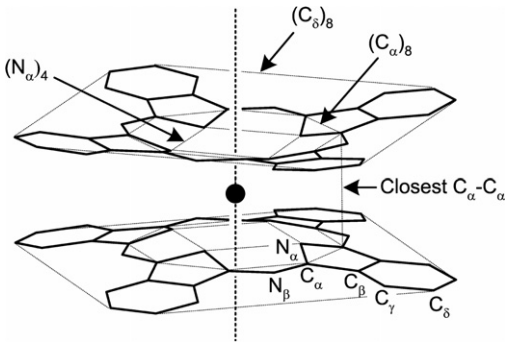


Fig. 3. Planes made by four inner nitrogen atoms, ''$(N_\alpha)_4$'', eight inner carbon atoms, ''$(C_\alpha)_8$'', and eight most-outer carbon C_δ atoms, ''$(C_\delta)_8$''.

Table 1
Closest C_α–C_α and several interplanar distances (Å) of $[Pc_2Y]^-$ and $[Pc_2Y]^+$

	$[Pc_2Y]^-$	$[Pc_2Y]^+$	Difference
Closest C_α–C_α	3.38	3.28	−0.10
$(N_\alpha)_4$–$(N_\alpha)_4$[a]	2.87	2.79	−0.08
$(C_\alpha)_8$–$(C_\alpha)_8$[b]	3.38	3.28	−0.10
$(C_\delta)_8$–$(C_\delta)_8$[c]	5.18	5.15	−0.03
Pc-Pc (C, N)[d]	4.08	4.00	−0.08

[a,b,c] The planes are defined in Fig. 3.
[d] Distance between averaged z coordinates over all C and N atoms in each Pc.

Table 2
Bond lengths and related distances (Å) and angles of $[Pc_2Y]^-$ and $[Pc_2Y]^+$

	$[Pc_2Y]^-$	$[Pc_2Y]^+$	Difference
C_α–N_α	1.368	1.368	0.000
C_α–N_β	1.328	1.328	0.000
C_α–C_β	1.464	1.470	0.006
C_β–C_β	1.404	1.401	−0.003
C_β–C_γ	1.393	1.388	−0.005
C_γ–C_δ	1.392	1.398	0.006
C_δ–C_δ	1.406	1.400	0.006
C_γ–H	1.084	1.084	0.000
C_δ–H	1.086	1.085	−0.001
N_α–Y	2.469	2.440	−0.029
Side of $(N_\alpha)_4$ square	2.840	2.830	−0.010
$\angle(C_\alpha)_8$–(C_α–N_α–C_α)	18.41°	17.73°	−0.68°

Table 2 shows changes of C–C, C–N and C–H bond lengths upon two-electron oxidation. Changes in bond lengths within Pc ligand are not significant compared to the interplanar distances. No bond-length in a Pc ligand is predicted to change by more than 0.006 Å. These results clearly illustrate the effect of the two-electron oxidation to the geometry change of $[Pc_2Ln]^-$: the Pc–Pc distance is significantly shortened while structures of the Pc ligands are essentially unchanged.

The N_α–Y bond length is shortened on the oxidation by ca. 0.03 Å. This is consistent with the decrease of $(N_\alpha)_4$–$(N_\alpha)_4$ length. The side length of the $(N_\alpha)_4$ square is also shortened, as the angle formed by $(N_\alpha)_4$ and C_α–N_α–C_α planes is decreased while keeping N_α–C_α length.

4. Conclusion and perspective

The DFT theoretical calculations predicted that two-electron oxidation of the $[Pc_2Ln]^-$ complexes shortens the interplanar C_α–C_α distance by about 0.1 Å and $(N_\alpha)_4$–$(N_\alpha)_4$ distance by 0.08 Å. This suggests that the ligand field applied to the lanthanide ion is significantly strengthened in the cationic $[Pc_2Ln]^+$ complex. These results gives us expectation that the single-lanthanide-ionic SMM $[Pc_2Tb]^-$ may acquire much larger ligand field splitting, and

accordingly diminished transition rate between "spin-up" and "spin-down" states. We indeed are now undertaking an experimental study, in the light of these interesting results of the theoretical study, towards controlling of dynamic magnetisms of the lanthanide SMMs by ligand oxidation. We have succeeded in establishing preparation methods for two complexes with different oxidation condition in the ligand system, $[(Pc^*)_2Ln]^-N(C_4H_9)_4^+$ and $[(Pc^*)_2Ln]^+(SbCl_6)^-$, where Pc^* is octaethoxyl-Pc. In preliminary AC magnetic susceptibility measurements, we found that the cationic $[(Pc^*)_2Tb]^+$ shows SMM behavior at considerably higher temperature range than the corresponding anionic complex. For example, the χ'' peak for 10^3 Hz AC field was observed at 52 K for the cationic complex which is 12 K higher than the anionic complex. We will report elsewhere the experimental study on the effect of the ligand oxidation to the static and dynamic magnetism of Pc–Tb and Pc–Dy type SMMs.

Acknowledgement

This work was supported by a grant from Tokuyama Science Foundation, by Iketani Science and Technology Foundation, and by Institute of Science and Engineering, Chuo University.

References

[1] (a) N. Ishikawa, M. Sugita, T. Ishikawa, S. Koshihara, Y. Kaizu, J. Am. Chem. Soc. 125 (2003) 8694;
(b) N. Ishikawa, M. Sugita, T. Ishikawa, S. Koshihara, Y. Kaizu, J. Phys. Chem. B 108 (2004) 11265.
[2] N. Ishikawa, M. Sugita, T. Okubo, N. Tanaka, T. Iino, Y. Kaizu, Inorg. Chem. 42 (2003) 2440.
[3] (a) N. Ishikawa, O. Ohno, Y. Kaizu, H. Kobayashi, J. Phys. Chem. 96 (22) (1992) 8832;
(b) N. Ishikawa, O. Ohno, Y. Kaizu, J. Phys. Chem. 97 (5) (1993) 1004;
(c) N. Ishikawa, Y. Kaizu, J. Porphyr. Phthalocya. 3 (1999) 514;
(d) N. Ishikawa, J. Porphyr. Phthalocya. 5 (2001) 87.
[4] N. Koike, H. Uekusa, Y. Ohashi, C. Harnoode, F. Kitamura, T. Ohsaka, K. Tokuda, Inorg. Chem. 35 (1996) 5798.
[5] A.D. Becke, J. Chem. Phys. 98 (1993) 5648.
[6] (a) P.J. Hay, W.R. Wadt, J. Chem. Phys. 82 (1985) 270;
(b) P.J. Hay, W.R. Wadt, J. Chem. Phys. 82 (1985) 284;
(c) P.J. Hay, W.R. Wadt, J. Chem. Phys. 82 (1985) 299.
[7] T.H. Dunning Jr., P.J. Hay, in: H.F. SchaeferIII (Ed.), Modern Theoretical Chemistry, Plenum Press, New York, 1976, p. 1.
[8] M.W. Schmidt, K.K. Baldridge, J.A. Boatz, S.T. Elbert, M.S. Gordon, J.H. Jensen, S. Koseki, N. Matsunaga, K.A. Nguyen, S.J. Su, T.L. Windus, M. Dupuis, J.A. Montgomery, Comput. Chem. 14 (1993) 1347.
[9] M.J. Frisch, G.W. Trucks, H.B. Schlegel, G.E. Scuseria, M.A. Robb, J.R. Cheeseman, V.G. Zakrzewski, J.A. Montgomery Jr., R.E. Stratmann, J.C. Burant, S. Dapprich, J.M. Millam, A.D. Daniels, K.N. Kudin, M.C. Strain, O. Farkas, J. Tomasi, V. Barone, M. Cossi, R. Cammi, B. Mennucci, C. Pomelli, C. Adamo, S. Clifford, J. Ochterski, G.A. Petersson, P.Y. Ayala, Q. Cui, K. Morokuma, D.K. Malick, A.D. Rabuck, K. Raghavachari, B. Foresman, J. Cioslowski, J.B. Foresman, J. Cioslowski, J.V. Ortiz, A.G. Baboul, B.B. Stefanov, G. Liu, A. Liashenko, P. Piskorz, I. Komaromi, R. Gomperts, R.L. Martin, D.J. Fox, T. Keith, M.A. Al-Laham, C.Y. Peng, A. Nanayakkara, C. Gonzalez, M. Challacombe, P.M.W. Gill, B.G. Johnson, W. Chen, M.W. Wong, J.L. Andres, M. Head-Gordon, E.S. Replogle, J.A. Pople, GAUSSIAN-98 (Revision A.11), Gaussian Inc., Pittsburgh, PA, 2001.

super paramagnetic particles. At even lower temperatures the thermal energy cannot overcome the anisotropy energy and the system is said to be in the blocked state

$$E_A = KV \sin^2 \theta. \quad (1)$$

Magnetic properties of nanoparticles dispersed in a non-magnetic matrix have been studied previously. For example, studies of Co [11] and MFe_2O_4 (M = Mn and Co) nanocrystals [12] have shown that interactions are concentration dependent, consistent with dipole–dipole interactions. Several models have been put forth to explain the dependence of the energy barrier on interparticle interactions [9,13]. However, to our knowledge, there has been no study of the interactions in dispersions consisting of mixtures of two types of nanoparticles with distinct superparamagnetic properties.

In this contribution, we study the magnetic behaviour of mixtures of superparamagnetic nanoparticles in the bulk. We take advantage of the synthetic control afforded by the choice of the chemical composition [14] and the size distribution [15] to compare dispersions containing nanoparticles with distinct superparamagnetic properties, but very similar sizes and distributions. The results of this study will be contrasted with those of the study of similar nanoparticles encased within a metal oxide matrix [1].

2. Experimental

2.1. Synthesis of metal oxide nanoparticles

We used previously published methods for the preparation of the metal ferrite nanocrystals [15]. The synthesis of these nanocrystals has been described elsewhere [1].

2.2. Transmission electron microscopy

The nanocrystals were imaged in bright field mode using a FEI Tecnai 20 transmission electron microscope, operating at 200 kV. Nanoparticles were dissolved in hexane, and a drop of the solution was allowed to evaporate on a carbon-coated copper grid.

2.3. SQUID magnetometry

Cobalt ferrite nanoparticles (3.21 mg) were weighed in a polycarbonate capsule. Maghemite nanoparticles (0.67 mg) were added to this capsule. A few drops (~3–4) of hexane were added to the nanocrystals resulting in a solution. A few drops (~1–2) of anhydrous ethanol were added to the solution and a precipitate formed. A strong magnet was placed at the bottom of the capsule and the solvent was decanted. The capsule was then dried for 30 min in a furnace at 100 °C. The capsule was then sealed with Kapton tape and inserted in a diamagnetic plastic straw. This gave a sample consisting of 82.7% (w/w) $CoFe_2O_4$. Samples with 62.5%, 50.5%, 32.9% and 15.8% (w/w) $CoFe_2O_4$ were prepared in a similar fashion. The samples consisting of either of the pure nanoparticles were weighed directly in gelatin capsules.

SQUID magnetometry measurements were carried out using a commercial SQUID magnetometer (Quantum Design MPMS XL-7S). Zero-field cooled (ZFC) and field cooled (FC) measurements were carried out by cooling the samples from 400 to 1.8 K in the absence (ZFC) or presence (FC, $H = 100$ Oe) of an applied magnetic field. A field of 100 Oe was then applied, and the magnetization of the sample measured upon warming from 1.8 to 400 K. Magnetization as a function of field measurements was also carried out.

2.4. Mössbauer spectroscopy

^{57}Fe Mössbauer effect spectra in zero applied magnetic field were measured using a Web Research spectrometer operating in transmission mode. The ^{57}Co in Rh source was mounted on a velocity transducer driven in a constant acceleration mode, using a triangular waveform. Detection of the γ-rays was done using a Reuters–Stoke proportional counter. Spectra were calibrated against a 25 μm Fe foil spectrum obtained at room temperature. The samples were prepared by spreading nanoparticles on Parafilm, and sealed with Kapton tape. Samples were cooled in a Janis Research SHI-850 variable temperature closed cycle refrigerator. WMOSS (v. 2.5) Mössbauer spectral analysis software was used for data analysis and fitting.[1]

3. Results

3.1. Transmission electron microscopy

The nanoparticles were imaged using bright field TEM. The nanoparticles appear spherical, and have narrow size distributions (Figs. 1 and 2). The $CoFe_2O_4$ nanoparticles were found to have an average diameter of 5.1 nm with a standard deviation of 0.7 nm, while the γ-Fe_2O_3 nanocrystals have an average size of 5.0 ± 0.6 nm. The nanoparticles were not agglomerated. In particular, no direct contact between nanoparticles is observed, and we believe this is due to the presence of the oleic acid surfactant at the surface of the nanoparticles. Direct magnetic exchange between nanoparticles is prevented, and the magnetic particles will be coupled primarily via dipole–dipole interactions.

3.2. ^{57}Fe Mössbauer effect spectroscopy

The analysis of low-temperature ^{57}Fe Mössbauer spectra is a useful tool for the differentiation of magnetite (Fe_3O_4) from maghemite (γ-Fe_2O_3) both of which can be formed in this general synthesis [15–17]. These materials

[1] This software may be downloaded for free from http://www.wmoss.org.

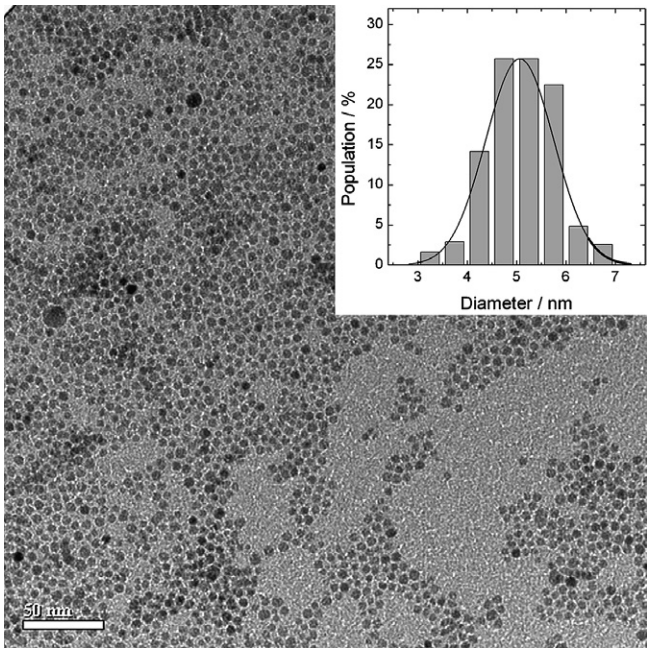


Fig. 1. Bight-field TEM micrograph of cobalt ferrite nanoparticles. Scale bar = 50 nm. Inset: nanoparticle diameter distribution, based on a sample size of 311 nanoparticles. The line represents a normal distribution with an average diameter of 5.1 ± 0.7 nm.

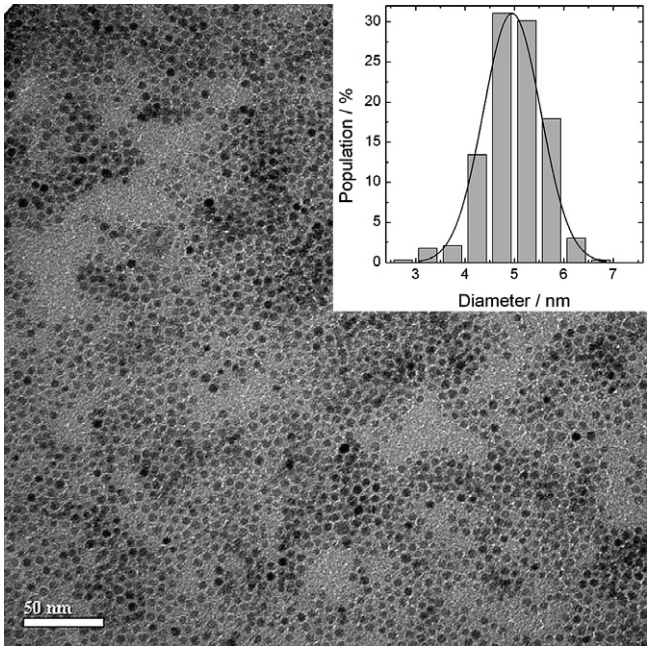


Fig. 2. Bight-field TEM micrograph of maghemite nanoparticles. Scale bar = 50 nm. Inset: nanoparticle diameter distribution, based on a sample size of 335 nanoparticles. The line represents a normal distribution with an average diameter of 5.0 ± 0.6 nm.

are not easily distinguished using diffraction techniques due to their similar lattice parameters and structures [18,19].

The 4.2 K spectrum of the iron oxide nanoparticles used in this study is presented in Fig. 3. The spectrum consists of six lines and the highest velocity line is clearly asymmetric. The spectrum is consistent with being composed of two sextets. The sextet with the smaller isomer shift is responsible for 35.4% of the observed signal. The individual components and the fit line of the two sextets are also shown in Fig. 3. The parameters corresponding to the fit are presented in Table 1.

The values for the isomer shifts suggest that both observed sextets originate from high spin iron(III) [20]. This result also excludes the possibility of the sample consisting of Fe_3O_4, which contains both Fe^{3+} and Fe^{2+} in octahedral sites, which exchange faster than the ^{57}Fe Mössbauer measurement timescale. Consideration of published values [21] indicates that these data are consistent with the assignment of the nanocrystals as maghemite. The structure of maghemite is closely related to that of magnetite (and cobalt ferrite), but contains vacancies on the cation sublattice. As such, γ-Fe_2O_3 may be viewed as $[Fe]^{tet}[Fe_{5/3}\square_{1/3}]^{oct}O_4$, with octahedral (B) and tetrahedral (A) iron sites wherein $\square$ represents a vacant site [19]. The two observed isomer shifts are hence associated with the A and B sites and the assignment given in Table 1 follows the literature assignment.

The 4.2 K spectrum of the $CoFe_2O_4$ nanoparticles is presented in Fig. 4. The spectrum is qualitatively similar

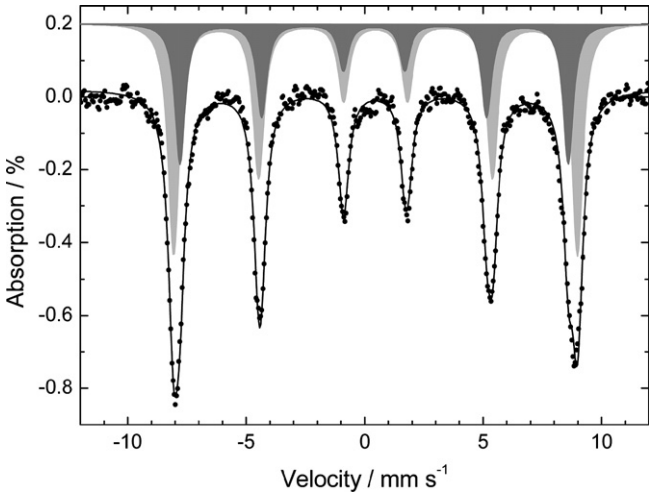


Fig. 3. ^{57}Fe Mössbauer spectrum of γ-Fe_2O_3 nanoparticles at 4.2 K. The solid lines represent the two individual sextets (top, offset for clarity) as well as the envelope obtained from the fit.

Table 1
Isomer shifts δ (mm s^{-1}), hyperfine fields H_{hf} (kOe) and relative areas (%) from 4.2 K ^{57}Fe Mössbauer spectra

Sample	Subspectrum	δ^a	H_{hf}	RA
γ-Fe_2O_3	Site A	0.40	510	35.4
	Site B	0.46	531	64.6
$CoFe_2O_4$	Site A	0.38	518	52.9
	Site B	0.50	545	47.1

[a] Isomer shift relative to Fe foil at 295 K.

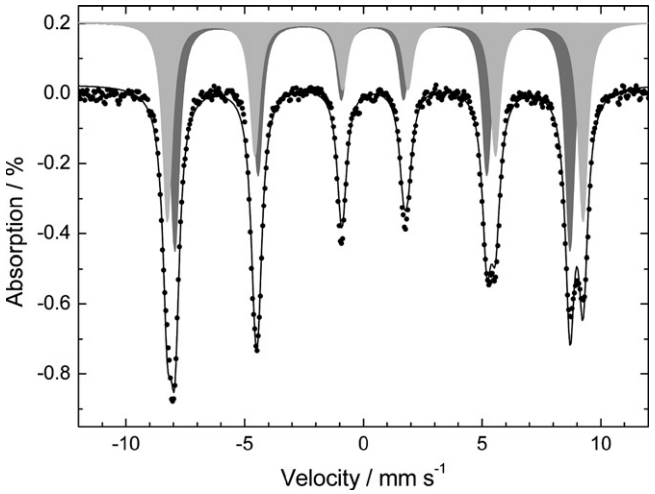


Fig. 4. ^{57}Fe Mössbauer spectrum of $CoFe_2O_4$ nanoparticles at 4.2 K. The solid lines represent the two individual sextets (top, offset for clarity) as well as the envelope obtained from the fit.

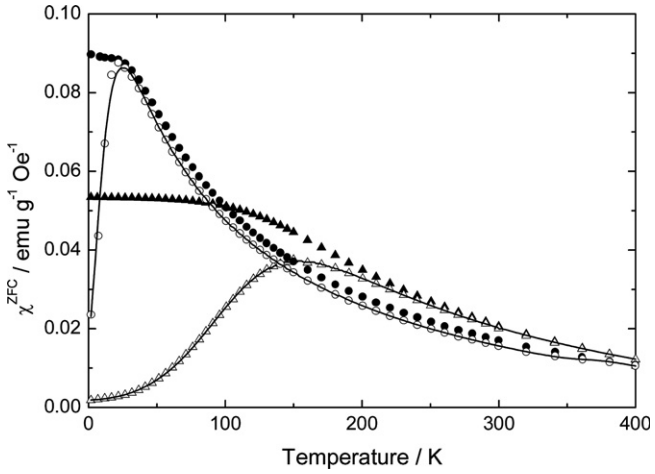


Fig. 5. Magnetization measurements for field-cooled (filled) and zero-field cooled (empty) $CoFe_2O_4$nanoparticles (triangles) and γ-Fe_2O_3 nanoparticles (circles). Solid lines accompanying the ZFC are the best fit obtained using Eqs. (4) and (5).

to the maghemite spectrum and could be fit to two sextets. The relative areas and values of the isomer shifts and hyperfine fields are presented in Table 1.

The two sextets arise from the presence of ferric ions in tetrahedral (A) and octahedral (B) sites in the spinel structure of $CoFe_2O_4$. The degree of inversion x, which represents the fraction of M^{2+} cations in octahedral sites, can be determined from the Mössbauer spectra using

$$\frac{I_A}{I_B} = \frac{f_A}{f_B}\frac{x}{2-x} \tag{2}$$

in which I_A and I_B are the relative intensities due to subspectra due to iron in sites A and B, and f_A/f_B is the recoil-free fraction of ^{57}Fe nuclei in octahedral and tetrahedral sites. We assume the value of f_A/f_B at 4.2 is the same as the fraction estimated at 0 K, at which temperature it is equal to 1 [22]. From the values presented in Table 1 and Eq. (2), we find that our nanoparticles have the inverse spinel structural formula, with a cation distribution of $[Fe]^{tet}[CoFe]^{oct}O_4$.

3.3. SQUID magnetometry

A sample of γ-Fe_2O_3 nanocrystals was cooled in the absence of an applied field and the magnetization measured upon warming in an applied field of 100 Oe. The resultant ZFC measurement is shown in Fig. 5. At low temperature the magnetization is small and increases with increasing temperature. The magnetization reaches a maximum at 22 K. Increasing the temperature results in a loss of magnetization of the sample.

The result can be understood in terms of the forces which act upon the magnetization vector of the individual nanoparticles. When the sample is cooled in the absence of a magnetic field (ZFC) the magnetization vector of each nanoparticle will align with the easy axis of the crystal. Since the nanoparticles are randomly oriented, this results in a random orientation of magnetization vectors, and the observed small magnetization of the sample. As the temperature is increased in the presence of an applied magnetic field, magnetization vectors will align with the poling field, resulting in an increase in magnetization. As temperature is increased, the poling effect of the applied field will be overcome by thermal energy, and the magnetization vectors will start to fluctuate, which will result in a loss in magnetization. The overall effect is a rise and subsequent decay of the magnetization. The blocking temperature is identified as the maximum in the magnetization curve which we observe at 22 K for γ-Fe_2O_3 samples nanocrystals.

A similar experiment was conducted with $CoFe_2O_4$ nanocrystals and the result is shown in Fig. 5. The qualitative features are as was observed for the γ-Fe_2O_3 nanocrystals. The magnetization was minimal at low temperature, reached a maximum, and then decreased as the temperature was increased. The observed blocking temperature for the $CoFe_2O_4$ nanocrystals was 150 K.

The higher blocking temperature observed in cobalt ferrite is consistent with the relative anisotropy constant for the two materials. The anisotropy constant for cobalt ferrite is higher than that of maghemite (18×10^5 vs. 0.47×10^5 erg/cm^3, respectively) [12,23]. In particles of similar volume, this is the dominant contribution which results in a significantly higher anisotropy energy barrier, according to Eq. (1). This barrier is in effect the barrier to changing the orientation of the magnetization vector in the absence of an applied field. When an external field is present the barrier to aligning with that field is reduced. As the temperature is increased, the higher thermal energy results in a greater number of magnetization vectors being able to overcome the barrier. The result is that a greater number of magnetization vectors align with the field, and as such the observed magnetization increases until the blocking temperature is reached [7]. The blocking temperature is hence related to the anisotropy barrier.

The magnetization of the nanocrystals was also measured following cooling of the samples under an applied filed (FC) of 100 Oe. Samples of maghemite nanocrystals had a high magnetization at low temperature which decreased slightly with increasing temperature until the temperature approaches the vicinity of the blocking temperature. Upon farther warming, the magnetization continues to decrease, albeit with a more pronounced temperature dependence. This is the expected behaviour.

When the sample is cooled in the presence of an applied field (FC), the magnetization vectors will be predominantly aligned with the poling field. At low temperature, a high magnetization will be measured. As the temperature is increased the thermal energy overcomes the alignment forces resulting in a decrease in the magnetization which becomes more pronounced above the blocking temperature.

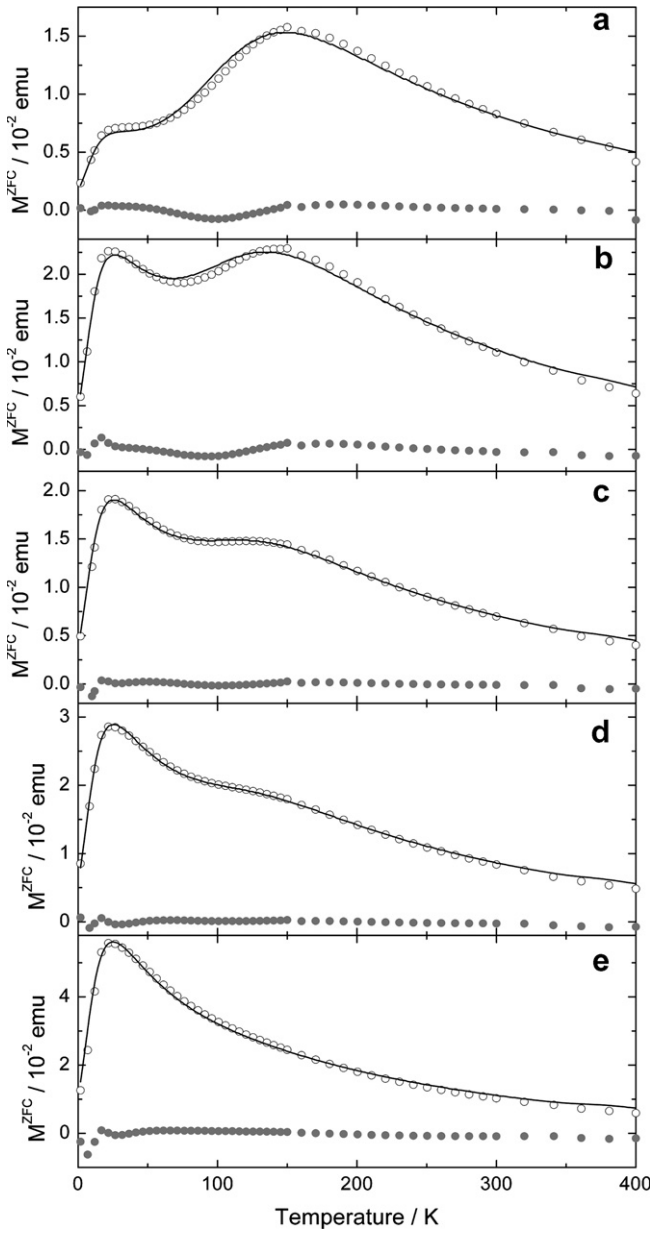


Fig. 6. Experimental (○○○) and fit (—, see text) magnetization curves for zero field cooled mixtures of $CoFe_2O_4$ and γ-Fe_2O_3 nanoparticles consisting of 83 (a), 65 (b), 51 (c), 33 (d), and 16 (e) percent weight $CoFe_2O_4$ measured in a 100 Oe field . Fit residuals are also shown (●●●).

A similar result was obtained for the FC magnetization measurements for cobalt ferrite nanocrystals. A high magnetization is observed at low temperature. As the temperature is increased the magnetization decreases. The loss of magnetization with temperature change increases beyond the blocking temperature of cobalt ferrite at 150 K.

ZFC magnetization measurements were also obtained for mixtures of the $CoFe_2O_4$ and γ-Fe_2O_3 nanoparticles. In Fig. 6a the magnetization curve for a 83% (w/w) $CoFe_2O_4$ nanoparticle mixture is shown. At low temperature, the magnetization is low. As the temperature is raised, the magnetization increases, and then levels off in the region of 20 K. Further increase in temperature results in a further increase in magnetization and a maximum in the magnetization in the region of 150 K. Further increase in the temperature results in a decrease in the observed magnetization.

This behaviour is as anticipated for a non-interacting mixture of two types of nanoparticles. In the zero field cooled experiment the magnetization vectors are aligned with the easy axis of the individual nanocrystals. As the temperature is increased the magnetization vectors of the γ-Fe_2O_3 nanoparticles become free to move and align with the poling field. This results in the initial rise in magnetization which forms a plateau in the region of 20 K. As the temperature is further increased the magnetization of the sample increases as the effect of the poling field overcomes the alignment of the $CoFe_2O_4$ nanoparticles magnetization vector with respect with their easy axis. The magnetization reaches a maximum at 150 K corresponding to the maximal alignment of the $CoFe_2O_4$ nanoparticles.

If there is no interaction between nanoparticles then we may expect that the observed magnetization as a function of temperature, $M^{ZFC}_{total}(T)$, would simply be a weighted average of the magnetization curves (Eq. (3)) of the constituent nanoparticles, $M^{ZFC}_{\gamma\text{-}Fe_2O_3}(T)$ and $M^{ZFC}_{CoFe_2O_4}(T)$, which could be parametrically fit using Eqs (4) and (5):

$$M^{ZFC}_{total}(T) = m_{CoFe_2O_4} \cdot M^{ZFC}_{CoFe_2O_4}(T) + m_{\gamma\text{-}Fe_2O_3} \cdot M^{ZFC}_{\gamma\text{-}Fe_2O_3}(T), \tag{3}$$

$$M^{ZFC}_{CoFe_2O_4}(T) = \frac{a + bT + cT^2 + dT^3 + eT^4}{1 + fT + gT^2 + hT^3 + iT^4 + jT^5}, \tag{4}$$

$$M^{ZFC}_{\gamma\text{-}Fe_2O_3}(T) = \frac{a' + b'T + c'T^2 + d'T^3 + e'T^4 + f'T^5}{1 + g'T + h'T^2 + i'T^3 + j'T^4 + k'T^5}. \tag{5}$$

In these equations, the magnetization is in emu g^{-1}. The best fits are shown as solid lines in Fig. 5.[2]

Using Eqs. (4) and (5), the ZFC magnetization of the cobalt ferrite and maghemite nanoparticle mixture was

[2] See Supplementary Information for parameter values.

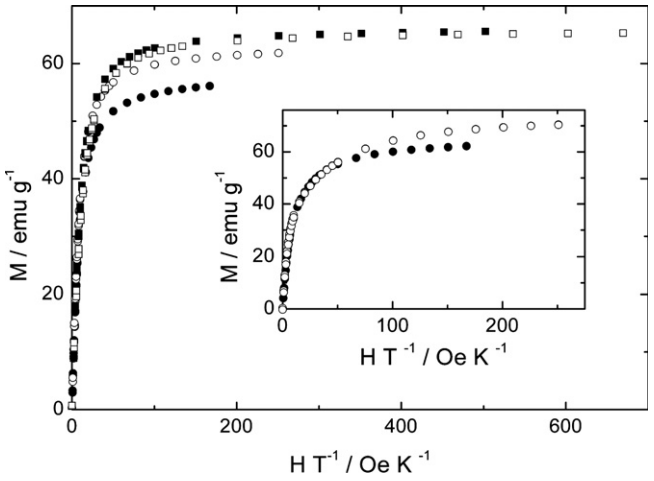


Fig. 7. Magnetization of γ-Fe_2O_3 nanoparticles as a function of field measured at various temperatures above the T_B: 300 (●), 200 (○), 100 (■) and 75 (□) K. The inset figure provides the data for $CoFe_2O_4$ nanoparticles.

fit. The weighting of the contribution from each curve was varied to provide the best fit shown as the solid line in Fig. 6a according to Eq. (3). Using Eq. (3) the mass fraction was determined to be 85%.

Similar results were obtained for each of the nanoparticle mixtures studied. In all cases, two maxima are observed, corresponding to maghemite, at lower temperature, and cobalt ferrite at higher temperature, nanoparticles going through a blocked-superparamagnetic transition. As the amount of cobalt ferrite is decreased in the mixture, the amplitude of the second maximum (cobalt ferrite) decreases with respect to the first (maghemite). The fits obtained from Eqs. (3)–(5) are the solid lines shown in Fig. 6.

Magnetization vs. field measurements were carried out on the γ-Fe_2O_3 nanoparticles at 300 K, in a field of up to 50 kOe. The magnetization increases with applied field and approaches saturation. Upon decreasing the field no hysteresis was observed. The result is shown in Fig. 7 and is as expected for a superparamagnetic sample.

Similar data were obtained at other temperatures above the blocking temperature, and for the cobalt ferrite nanoparticles, also above their blocking temperature. In each case the same behaviour was observed. These results are summarised in Fig. 7. Magnetization versus field curves were also obtained for the nanoparticle mixtures studied here. The results were qualitatively similar.

4. Discussion

The nanoparticles used in this study were prepared by the general method of solvothermal decomposition of metalorganic precursor in the presence of surfactants in a high boiling point solvent. The specific synthesis used here was that of Sun and coworkers who reported the preparation of 6 nm nanoparticles of Fe_3O_4 under these conditions [15]. In our hands the result was the formation of 5 nm nanoparticles of maghemite. This result is not unexpected as previous workers had shown using a similar thermolysis method that the material obtained in the synthesis changed from magnetite to maghemite when the size of the nanoparticle was reduced from 9 to 5 nm [16].

The nanoparticle mixtures were all prepared by forming a solution of both nanoparticles then precipitating the mixture of nanoparticles from this solution. The separation was aided by a strong magnet. The magnet was sufficiently strong that it appeared that all the precipitated material was retained in the capsule as the liquid phase was decanted. Given this observation we do not believe that the reprecipitation altered the size distribution of the sample. Similarly there was no indication that the coprecipitated sample was not intimately mixed and in the discussion of the magnetism we assume intimate mixing was obtained by this procedure.

The magnetization of an ideal superparamagnetic particle with magnetic moment μ_P is described by the Langevin function given as Eq. (6). Acceptable fits were obtained for each of the magnetization versus field measurements indicating that the sample behaved as a superparamagnet. Since the Langevin function depends only on the experimental variable H/T magnetization measurements at various temperatures are expected to scale with H/T [7]. This is clearly not the case, as can be seen in Fig. 7

$$M^{\mathrm{LAN}}(H,T) = M_S\left\{\coth\left(\frac{\mu_P H}{k_B T}\right) - \frac{k_B T}{\mu_P H}\right\}. \quad (6)$$

That the magnetization at various temperatures does not scale as indicates that the system is not a simple superparamagnet. The difference is presumably indicative of a temperature dependent change in the individual magnetic moments, μ_P which comprise the superparamagnet. This behaviour would not be possible if the magnetic moments which form the ensemble were the moments of individual nanoparticles (and hence constant) but are indicative of a cluster contributing the magnetic moment. If the cluster size or internal coupling were a function of temperature then the lack of scaling with H/T would be explained.

Evidence for the cluster interpretation arises from the fits of individual magnetization vs. field measurements. For example magnetization vs. field measurements at 300 K for each of the pure nanoparticles were fit to a Langevin function with additional first and second order terms in the susceptibility [8], in which $M(H,T) = M^{\mathrm{LAN}}(H,T) + \chi^{(1)}H + \chi^{(2)}H^2$. The curves and accompanying best fits are presented in Fig. 8. The magnetic moments μ_P extrapolated from the fits are $3565 \pm 25\ \mu_B$ and $4200 \pm 100\ \mu_B$ for the γ-Fe_2O_3 and $CoFe_2O_4$ nanoparticles, respectively. Fits to the simple Langevin function gave qualitatively similar results but the corrections provided a better fit.

The measured values of μ_P can be compared with calculated values based on the particle size. The expected magnetic moment for a nanoparticle is given by $\mu_P = M_S \rho V$

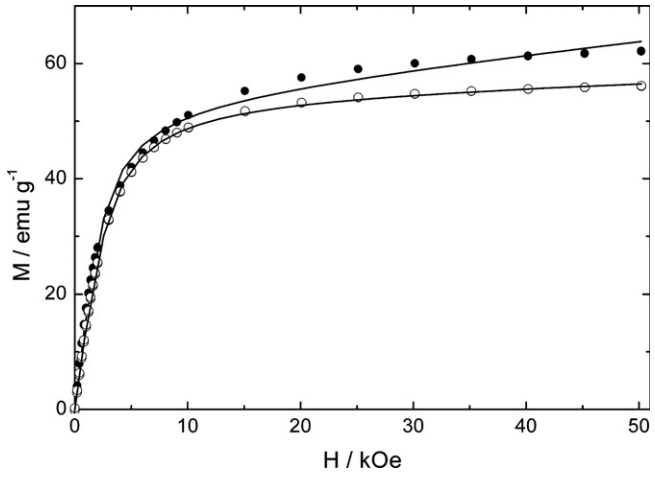


Fig. 8. Magnetization as a function of field measured at 300 K for $CoFe_2O_4$ (●●●) and γ-Fe_2O_3 (○○○) nanoparticles. Lines are best fits obtained using a Langevin with first and second order susceptibility terms model (see text).

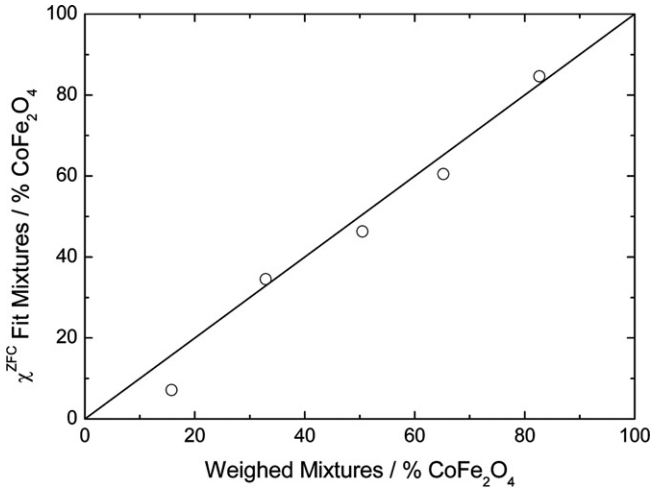


Fig. 9. Comparison between the composition of the samples from weighing and from fitting the ZFC measurements using the Eqs. (3)–(5) described in the text. The solid line represents the identity relationship.

wherein M_S is the saturation magnetization, ρ is the density and V is the volume of the nanoparticle. Using the average sizes determined from the TEM measurements and typical values for M_S and ρ($M_S \sim 80$ and ~ 75 emu g^{-1} and $\rho \sim 4.86$ and 5.3 g cm^{-3} for maghemite and cobalt ferrite, respectively) [24,25], one expects μ_P values of $\sim$2750 and $\sim 3000\mu_B$ for the maghemite and cobalt ferrite nanoparticles. These estimations are in fact upper limits, as it is common for the saturation magnetization of nanoparticles to be below the bulk values used above (see Fig. 8). This is usually attributable to the presence of a magnetically disordered layer at the surface of the nanoparticle [26]. Both of the calculated values of μ_P exceed the measured values substantially.

We believe that these higher than expected magnetic moments are attributable to the presence of clusters of a few correlated nanoparticles, similar to magnetic domains, in which the nanoparticles are coupled in an overall enhanced magnetization state. The mechanism responsible for these clusters is likely to be the same as in two-dimensional assemblies [4,5]. Such nanoparticulate clusters have also been proposed by Zhang in dispersions of $CoFe_2O_4$ nanoparticles [12].

Similar measurement were conducted with the mixtures of nanoparticles. The results are qualitatively similar to the pure nanoparticles. The overall magnetic moments which formed the superparamagnet were larger than the calculated moments of the individual nanoparticles indicating cluster behaviour. The apparent size of the clusters in the mixed nanoparticles was slightly increased over the weighted size from the pure nanoparticles, but it was not clear that this effect was significant.

The ZFC magnetization measurements of the nanoparticle mixtures were fit using Eqs. (3)–(5). The resulting mixtures deduced from this fit can be compared to the measured composition (Fig. 9). In general, this phenomenological model describes fairly well the samples.

This would suggest that the blocking of one species of nanoparticles is not affected by the presence of the other species. If significant magnetic pinning occurred, deviations form the identity relationship would be expected when comparing the measured compositions to the fit compositions. The fact that the behaviour of the mixture is adequately modeled as an algebraic sum of the behaviours of the individual components shows that interactions are not affecting (in any significant way anyways) the relaxation behaviour of the nanoparticles.

We can contrast this behaviour with the magnetic behaviour of $\sim$1:1 mixtures of these nanocrystals, in matrices which we described elsewhere [1]. In that study the nanoparticles were encapsulated in thin films of amorphous aluminium oxide and amorphous titanium dioxide. The results are presented in Fig. 10 for comparison with

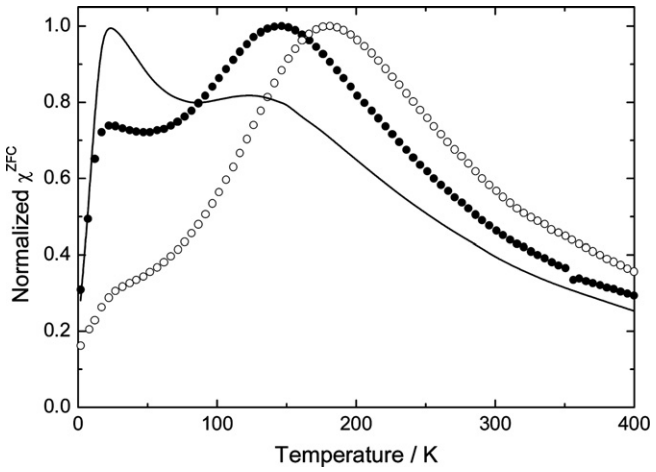


Fig. 10. Experimental magnetization curves for zero field cooled samples consisting of $\sim$1:1 mixtures of γ-Fe_2O_3 and $CoFe_2O_4$ nanoparticles encapsulated in amorphous aluminum oxide (●●●) and amorphous titanium oxide (○○○) (see Ref. [1]). The solid line represents the calculated ZFC curve expected for a 1:1 mixture.

Fig. 6c. The matrix encapsulated sample appears to have a much larger fraction of material behave as if it is blocked at a higher blocking temperature. We tentatively suggested that in a large number of clusters the $CoFe_2O_4$, with a higher T_B, is magnetically pinning the γ-Fe_2O_3 nanoparticles, which then mimic the temperature dependence of the $CoFe_2O_4$ nanoparticles [1].

While this behaviour was observed in clusters encapsulated within the thin films, it is clear that this mechanism is not the prevailing factor in the bulk mixtures presented here. This new result indicates that the behaviour of the encapsulated material may be mediated by the encapsulating material. Support for this interpretation comes from consideration of the difference of the behaviour of the mixture encapsulated in different matrix materials (Fig. 10). In these two samples the deviation from the expected (non-interacting) behaviour is quite different. This is consistent with direct involvement of the matrix material in the behaviour of the magnetization near the blocking temperature.

5. Conclusions

We have studied the magnetic properties of mixtures of $CoFe_2O_4$ and γ-Fe_2O_3 nanoparticles with similar size distributions, but distinct superparamagnetic properties. We find that the zero field cooled magnetization curves can be appropriately modeled as the algebraic sum of the two superparamagnetic contributions. However, magnetization vs. field measurements suggest that the samples do not exhibit ideal superparamagnetism. We find evidence for the presence of magnetic clusters consisting of a few nanoparticles magnetically coupled. In the bulk, the interactions within these clusters must be weak enough as to not influence the relaxation dynamics of ensembles of mixed nanoparticles with distinct superparamagnetic properties. This suggests that the role of the metal oxide matrix in previously studied nanocomposite thin films [1] may go beyond that of an innocent host, and will be addressed in future studies.

Acknowledgements

We thank NSERC of Canada, CFI, BCKDF, and Simon Fraser University for financial support. TEM studies were carried out at the NanoImaging Facility, Simon Fraser University.

Appendix A. Supplementary material

Supplementary information includes parameter values for Eqs. (4) and (5). Supplementary data associated with this article can be found, in the online version, at doi:10.1016/j.poly.2006.09.021.

References

[1] S. Trudel, R.H. Hill, J. Magn. Magn. Mater. (2007) in press.
[2] M.H. Kryder, MRS Bull. 21 (1996) 17.
[3] H. Zeng, C.T. Black, R.L. Sanstorm, P.M. Rice, C.B. Murray, S. Sun, Phys. Rev. B 73 (2006) 020402.
[4] M. Georgescu, M. Klokkenburg, B.H. Erné, P. Liljeroth, D. Vanmaekelbergh, P.A. van Emmichoven, Phys. Rev. B 73 (2006) 184415.
[5] V.F. Puntes, P. Gorostiza, D.M. Aruguete, N.G. Bastus, P.A. Alivisatos, Nat. Mater. 3 (2004) 263.
[6] C. Kittel, Phys. Rev. 70 (1946) 965.
[7] C.P. Bean, J.D. Livingston, J. Appl. Phys. 30 (1959) 120S.
[8] D. Resnick, K. Gilmore, Y.U. Idzerla, M. Klem, E. Smith, T. Douglas, J. Appl. Phys. 95 (2004) 7127.
[9] J.L. Dormann, L. Bessais, D. Fiorani, J. Phys. C 21 (1988) 2015.
[10] E.C. Stoner, E.P. Wohlfarth, Philos. Trans. R. Soc. Lond. A 240 (1948) 599.
[11] G.A. Held, G. Grinstein, H. Doyle, S. Sun, C.B. Murray, Phys. Rev. B 64 (2001) 012408.
[12] C.R. Vestal, Q. Song, Z.J. Zhang, J. Phys. Chem. B 108 (2004) 18222.
[13] J.L. Dormann, D. Fiorani, E. Tronc, J. Magn. Magn. Mater. 202 (1999) 251, and references therein.
[14] C. Liu, B. Zou, A.J. Rondinone, Z.J. Zhang, J. Am. Chem. Soc. 122 (2000) 6263.
[15] S. Sun, H. Zeng, D.B. Robinson, S. Raoux, P.M. Rice, S.X. Wang, G. Li, J. Am. Chem. Soc. 126 (2004) 273.
[16] J. Park, K. An, Y. Hwang, J.-G. Park, H.-J. Noh, J.-Y. Kim, J.-H. Park, N.-M. Hwang, T. Hyeon, Nat. Mater. 3 (2004) 891.
[17] S. Trudel, C.C.W. Jones, R.H. Hill (manuscript in preparation).
[18] V.L. Mazzochi, C.B.R. Parente, J. Appl. Crystallogr. 31 (1998) 718.
[19] A.N. Shmakov, G.N. Kryukova, S.V. Tsybulya, A.L. Chuvilin, L.P. Solovyeva, J. Appl. Crystallogr. 28 (1995) 141.
[20] R.S. Drago, Mössbauer Spectroscopy, second ed., Physical Methods for Chemists, Saunders College Publishing, Ft. Worth, 1992 (Chapter 15).
[21] R. Zboril, M. Mashlan, D. Petridis, Chem. Mater. 14 (2002) 969.
[22] G.A. Sawatzky, F. van der Woude, A.H. Morrish, Phys. Rev. 183 (1969) 383.
[23] J.B. Birks, Proc. Phys. Soc. B 63 (1950) 65.
[24] P. Dutta, A. Manivannan, M.S. Seehra, N. Shah, G.P. Huffman, Phys. Rev. B 70 (2004) 174428.
[25] F. Li, J. Liu, D.G. Evans, X. Duan, Chem. Mater. 16 (2004) 1597.
[26] R.H. Kodama, A.E. Berkovitz, E.J.J. McNiff, S. Foner, J. Appl. Phys. 81 (1997) 5552.

2. Experimental

Non-saturated horse spleen ferritin containing 2200 iron atoms was obtained from Sigma–Aldrich and was exhaustively dialyzed against water using a Spectra/Por Float-A-Lyzer with a molecular weight cut-off (MWCO) of 300 000 Da prior use. EA/SME mixtures in a 1:4 ratio were dissolved in $CHCl_3$ as spreading solution. An appropriate amount of this solution was carefully spread onto an aqueous subphase with 0.01 mg/mL of ferritin at pH 5.7 and 21 °C, and the spreading solvent was allowed to evaporate for 10 min prior to compression. The monolayer was compressed up to a surface pressure of 30 mN/m for transfer. Multilayer LB films were assembled to the substrates by the vertical lifting method. The equipment used for the measurements presented in this communication is described in a previous publication [6].

3. Results and discussion

A commercially available ferritin containing 2200 iron atoms has been used for all the experiments. In our previous work we extended the method developed by Britt et al. to prepare Langmuir monolayers of ferritin at the water–air interface [7] for preparing LB films of four ferritin derivatives with a variable iron content [6]. This method is based on the adsorption of ferritin dissolved in the aqueous subphase, which is negatively charged at the pH of the water subphase (5.5), onto a positively charged monolayer. Britt et al. showed that a higher amount of ferritin is adsorbed using eicosylamine as a cationic surfactant instead of the DODA/SME mixed monolayer [7]. In view of those results we have tried to prepare LB films of ferritin using EA as a cationic surfactant with the aim of increasing the amount of ferritin incorporated within the films. Since transfer onto solid substrates was not possible using pure eicosylamine monolayers, we tried several EA/SME mixtures (EA/SME ratio of 1/1, 1/2 and 1/4). A successful deposition of the monolayers onto solid substrates by the vertical lifting method was achieved for the 1/4 mixture at constant surface pressure of 30 mN/m. Transfer ratios close to unity were obtained giving rise to Y-type and optically defect-free multilayer LB films.

Before the transfer process, the surface pressure–area (π–A) isotherms were recorded. Fig. 1 shows the isotherms corresponding to the mixed EA/SME films fabricated on a subphase in the absence (dashed line) and presence of ferritin (solid line). The area is expressed per surfactant molecule. The presence of ferritin causes an area expansion at low surface pressure, although such a expansion does not correspond to the ferritin area ($d = 120$ Å, $A_{\text{ferritin}} \approx 11\,300$ Å^2/molecule) and thus, it is thought that ferritin molecules are located under the lipid matrix as observed for the DODA/SME mixed monolayer [6].

The mixed monolayers in both the absence and presence of ferritin in the subphase were observed directly by BAM at the air–water interface to obtain information about the morphological properties of the different films. BAM images of the 1/4 EA/SME mixture on pure water, obtained at different surface pressures are shown in Fig. 2a. Thus at a low surface pressure (π) of 0.1 mN/m, a coexistence of gas and liquid expanded phases is observed. Under further compression, when the surface pressure abruptly increases, i.e. around 1 mN/m, a homogeneous monolayer is observed. Further increases of the surface pressure lead to an increase of the reflectivity over the entire surface and to the onset of small brighter points which could correspond to collapse. In the case of the mixed monolayer at the air–water interface with ferritin in the subphase, the morphological characteristics of the film (Fig. 2b) change drastically with respect to the same system in absence of ferritin. At the beginning of the compression process, small irregular domains with higher reflectivity are observed. Under compression, these domains tend to fuse but zones of lower reflectivity remain for all the surface pressures. Reflectivity of these two regions increases continuously under compression. These differences with respect to those recorded without ferritin in the subphase are indicative of the presence of the protein at the interface, probably attached under the lipid matrix. Although these molecules of protein do not seem to form a full monolayer under the mixed film, an increase of the homogeneity is observed with respect to the DODA/SME monolayer [6]. Ellipsometric angle measurements in the zones of different brightness of the mixed monolayer are in progress in order to study the distribution of the protein under the lipid matrix.

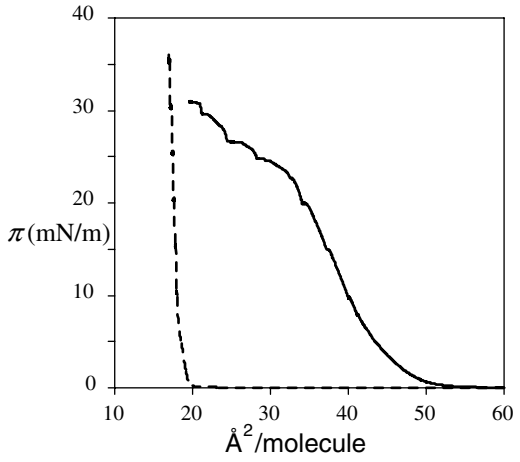


Fig. 1. π–A isotherms of different monolayers prepared at the air–water interface: EA/SME = 1:4 in absence of ferritin (dashed line) and in presence of ferritin, $[\text{ferritin}]_{\text{subphase}} = 0.01$ mg/ml (solid line).

The infrared spectrum of the transferred film (29 monolayers deposited on CaF_2) is shown in Fig. 3. It presents besides the bands at 2916, 2849 and 1456 cm^{-1}, assigned to the CH_2 stretching or scissoring vibrations of EA and SME alkyl chains, and the band at 1738 cm^{-1}, assigned to C=O vibration of SME, two strong bands associated with ferritin at 1653 and 1541 cm^{-1}. These two bands are assigned to the N–H and C=O structural units of the

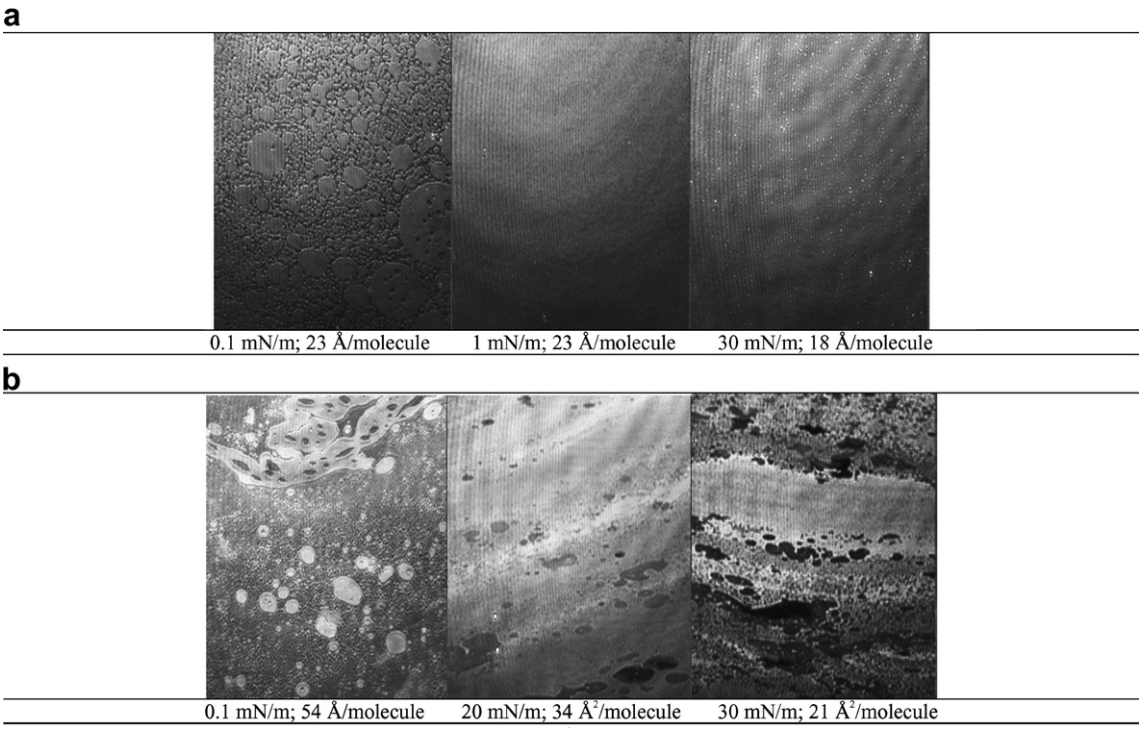


Fig. 2. BAM images of a mixed monolayer of EA/SME = 1:4 on pure water (a) and on a subphase containing ferritin ([ferritin] = 0.01 mg/ml) (b) at several surface pressures. The brightness of each image has been scaled to improve contrast. Width: 430 μm.

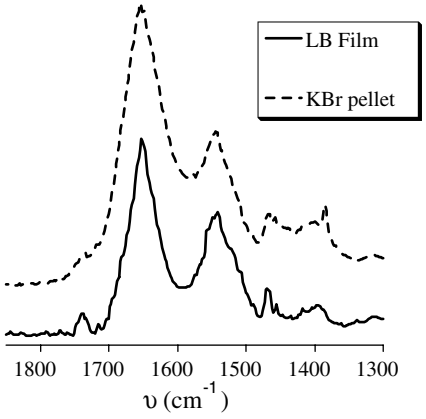


Fig. 3. Infrared spectra of ferritin in KBr pellet and of a LB film of ferritin of 29 monolayers on a CaF_2 substrate.

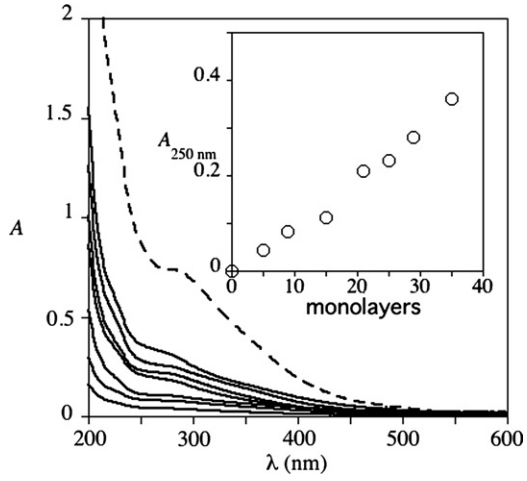


Fig. 4. UV–Vis spectra of LB films of ferritin with 5, 9, 15, 21, 25, 29 and 35 monolayers on a quartz substrate and of a solution of ferritin (dashed line). Inset: Absorbance values at 250 nm of these LB films vs. the number of monolayers.

protein together with the superposition of the –OH bending absorption on the band at 1653 cm^{-1} [8].

The UV–Vis absorption spectra of a LB film of ferritin on quartz substrates shows the typical broad absorption centered below 500 nm of the ferritin iron-core with a shoulder around 280 nm, characteristic of the apoferritin shell (Fig. 4). A linear dependence is found between the absorbance at a given wavelength and the number of monolayers. This indicates that the Langmuir film is transferred in a regular manner after each dipping cycle. Assuming that ferritin molecules are isotropically distributed within the LB films, it is possible to estimate the number of molecules trapped within the LB films. From the absorbance values at 250 nm, a surface concentration of $6.0 \pm 0.5 \times 10^{-13}$ mol/cm^2 per monolayer is calculated for the LB films with 25, 29 and 35 monolayers. This value is higher than that calculated for DODA/SME 1/6 LB films (4×10^{-13} mol/cm^2) [6]. Therefore, these data indicate that the use of a EA/SME mixed monolayer produces an increase of the adsorbed ferritin within the LB films with respect to the DODA/SME mixed monolayer. On the other hand, a mean area per ferritin molecule of 28000 ± 2000 $Å^2$ can be calculated from the inverse of the concentration per

monolayer. This value is higher than the area of the ferritin molecule ($d = 120$ Å, $A_{\text{ferritin}} \approx 11\,300$ Å^2). This indicates that a complete monolayer of ferritin has not been achieved. More measurements with other techniques such as TEM or AFM are in progress to study the arrangement of ferritin molecules in these LB films.

The iron oxohydride core of ferritin is antiferromagnetic below 140 K but possesses a net magnetic moment arising from uncompensated iron spins largely at the surface of the core. It has been shown that ferritin behaves as a superparamagnet above 20 K [9–11]. The magnetic properties of a LB film of ferritin with 260 monolayers deposited onto a diamagnetic mylar substrate were measured. Temperature dependence of the susceptibility of this LB film is very similar to powder measurements (Fig. 5a). The zero-field-cool (ZFC) curve presents a maximum of the susceptibility around 11 K and ZFC and field-cool (FC) curves are superimposed above 20 K (Fig. 5b). This proves clearly that ferritin molecules are present within the LB films. A marked hysteresis loop of magnetisation is obtained with a coercive field of 2400 G (Fig. 6). The shape of the hysteresis loop of magnetisation is again very similar to that of powder measurements. This is an expected result since the magnetic properties of this molecule have a molecular origin and the magnetic isolation provided by the diamagnetic apoferritin shell prevents any magnetic interaction between ferritin molecules.

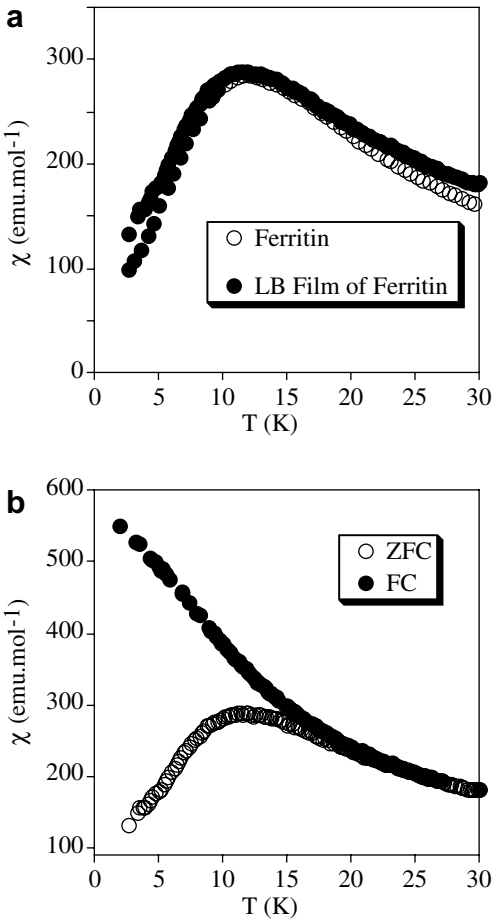


Fig. 5. (a) Thermal dependence of the ZFC susceptibility with an applied field of 50 G of the evaporated sample of ferritin (empty circles) and the LB film of ferritin (full circles) with 260 monolayers deposited on a mylar substrate. (b) Thermal dependence of the ZFC (empty circles) and FC susceptibility (full circles) with an applied field of 50 G of the LB film of ferritin with 260 monolayers deposited on a mylar substrate. The molar susceptibility of the LB film is obtained by normalization to that of the evaporated sample.

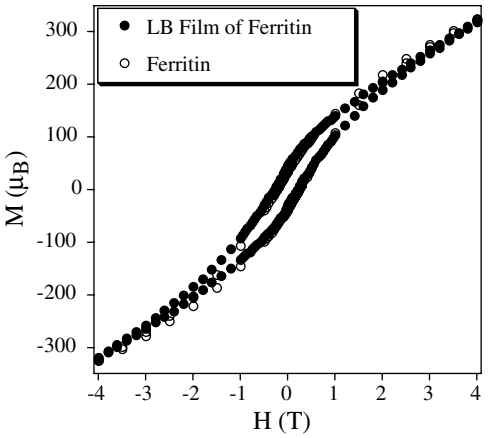


Fig. 6. Hysteresis loop of magnetisation of the evaporated sample of ferritin and the LB film of ferritin with 260 monolayers deposited on a mylar substrate at 2 K. The magnetisation of the LB film was normalized to that of the evaporated sample.

4. Conclusions

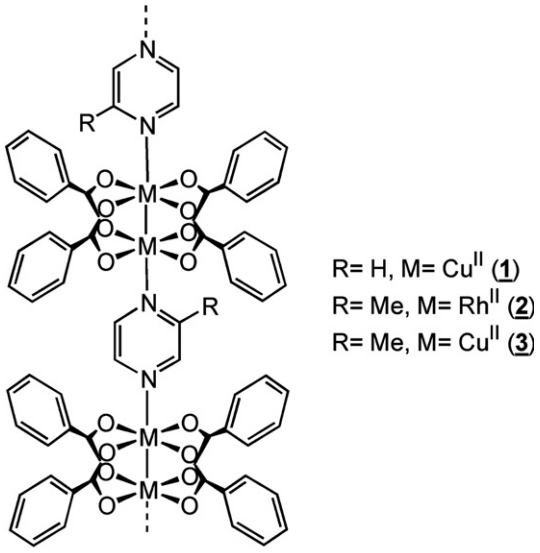
In this communication we have reported the preparation of Langmuir monolayers and LB films of ferritin using a mixed matrix containing EA and SME. These LB films show magnetic memory. The main interest of the LB method is that it permits the preparation of thin films with magnetic memory in a more controlled manner than with other techniques. In this work we have optimized the conditions to obtain LB films of ferritin with a more homogeneous distribution of ferritin, as shown by preliminary BAM measurements at the water–air interface, and with a higher density of the protein, as deduced from UV–Vis data. This may be useful for magnetic recording applications. The next step will be the use of other ferritin derivatives in which the antiferromagnetic iron oxohydride core of natural ferritin has been replaced by other nanoparticles of magnets with higher T_c (metal nanoparticles).

Acknowledgements

Financial support from the European Union (MERG-CT-2004-508033 and MAGMANet network of excellence), the Spanish Ministerio de Educación y Ciencia (projects MAT2004-3849, BQU2002-01091, CTQ2004-03246, CTQ2005-07906 and CTQ2005-09023) and Generalitat Valenciana is gratefully acknowledged. M.C.-L. and N.G. thank the Spanish Ministerio de Educación y Ciencia for a research contract (programa Ramón y Cajal).

References

[1] P.M. Harrison, S.C. Andrews, P.J. Artymuik, G.C. Ford, J.R. Guest, J. Hirzmann, D.M. Lawson, J.C. Livingstone, J.M.A. Smith, A. Treffery, S.J. Yewdall, Adv. Inorg. Chem. 36 (1991) 449.
[2] M.T. Klem, M. Young, T. Douglas, Mater. Today 8 (2005) 28.
[3] J. Hoinville, A. Bewick, D. Gleeson, R. Jones, O. Kasyutich, E. Mayes, A. Nartowski, B. Warne, J. Wiggins, K. Wong, J. Appl. Phys. 93 (2003) 7187.
[4] A. Ulman, Introduction to Ultrathin Organic Films, first ed., Academic Press, Boston, 1991, p. 442.
[5] D.R. Talham, Chem. Rev. 104 (2004) 5479.
[6] M. Clemente-León, E. Coronado, A. Soriano-Portillo, E. Colacio, J.M. Domínguez-Vera, N. Gálvez, R. Madueño, M.T. Martín-Romero, Langmuir 22 (2006) 6993.
[7] D.W. Britt, D. Möbius, V. Hlady, Phys. Chem. Chem. Phys. 2 (2000) 4594.
[8] W. Chua-Anusorn, J. Webb, J. Inorg. Biochem. 79 (2000) 303.
[9] C. Gilles, P. Bonville, K.K. Wong, S. Mann, Eur. Phys. J. B 17 (2000) 417.
[10] S.H. Kilcoyne, R. Cywinski, J. Magn. Magn. Mater. 140–144 (1995) 1466.
[11] F. Luis, E. del Barco, J.M. Hernández, E. Remiro, J. Bartolomé, J. Tejada, Phys. Rev. B 59 (1999) 11837.



Scheme 1.

2. Experimental

Single-crystal hosts **1** and **2** were synthesized as described elsewhere [8,9]. Using the same synthetic procedure performed in **1** and **2**, blue plate crystals of $[Cu_2(bza)_4(2\text{-mpyz})]_n$ (**3**) were obtained by the careful vapor diffusion of 2-methylpyrazine into the methanol solution of copper(II) benzoate in 60% yield. Experimental procedures were performed under strict exclusion of oxygen and water vapor. Careful treatment, especially for NO gas, was taken because of its high degree of reactivity with oxygen.

2.1. Physical measurements

The NO gas used during the physical measurements had a purity of >99.9%. The NO adsorption isotherms for all adsorbents were measured by a volumetric method at 195 K on a Quantachrome Autosorb-1MP instrument (the pressure for the data collections ranged from 0.3 to 800 Torr for all adsorbents). Magnetic susceptibilities of the included NO molecules were measured on a Quantum Design SQUID magnetometer MPMS-XL with an applied magnetic field of 1 T. The crystals were sealed in glass tubes with pressurized NO gas (2.0 MPa for **1**, 2.6 MPa for **2**, and 2.5 MPa for **3**) at 195 K, which can separate from the condensed excess NO at low temperatures. Measurement of the pure NO was performed by using a sample tube containing solid NO, which corresponds to an inner pressure of 7.5 MPa at 298 K. Susceptibility was corrected by the trace background values of the cell and each empty crystal. Calculation of the molar magnetization and susceptibility of the included NO was based on a mass of 1.83 for **1**, 1.00 for **2**, and 1.14 for **3** per M_2 unit, which were estimated by theoretical Bohr magneton numbers applied for the observed maximum values at around 200 K.

3. Results and discussion

3.1. Gas adsorption properties

The NO adsorption isotherm curves of **1**, **2**, and **3** at 195 K are shown in Fig. 1. The sorption curves show a slight curve in **1** and a linear increase to 800 Torr in **2** and **3**; all curves smoothly return reversibly to the starting point without hysteresis. The isotherm curves reach 0.61 for **1**, 0.30 for **2**, and 0.23 for **3** per M_2 unit at 800 Torr. **1** adsorbed more NO molecules than did **2** and **3**. We have reported that, under a saturated inclusion state, the host possesses a one-dimensional channel even if the channel surface is modified by the substituents on the pyrazine linker, such as methyl and ethyl groups, and strong contacts are found between the guests and the substituents on the channel surface [9,25]. Therefore, the observed difference in the NO adsorption property is probably influenced by

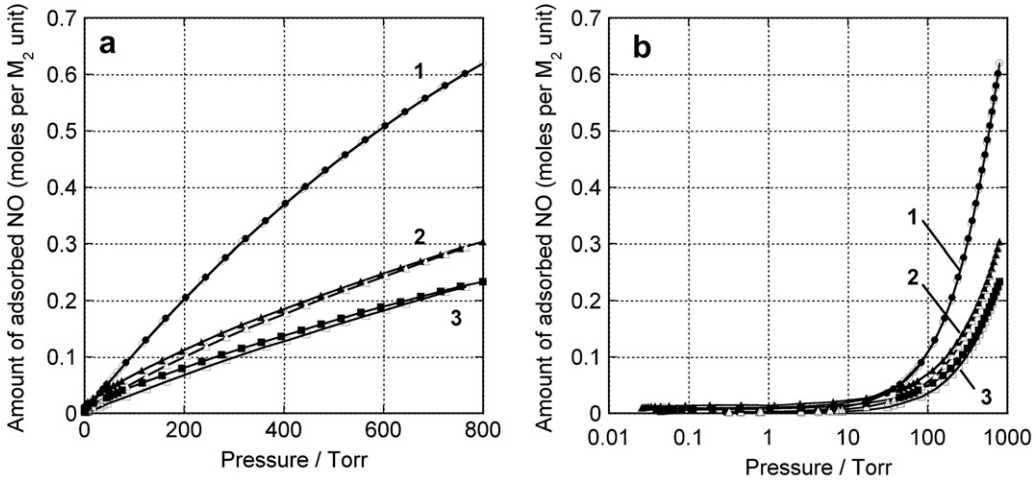


Fig. 1. NO sorption isotherm curves for **1**, **2**, and **3** at 195 K: adsorption process (open point), desorption process (solid point). (a) Linear plot, (b) log plot.

the interference of the channel surface to the adsorbed gas. Cu complex **3** adsorbed a slightly lesser amount of NO molecules than did Rh complex **2**. The difference between the metals might be linked to the flexibility of the host lattice, which is important for the transfer of guests in the process of adsorption, especially for our single-crystal adsorbents, as was described in previous studies [7–19].

We have determined the adsorption properties by sorption isotherm measurement: 2.5(CO_2) for **1** at 195 K [8], 2.4(O_2) for **1** at 77 K [19], 2(CH_4) at 153 K, and 3(N_2O) at 195 K for $[Rh_2(bza)_4(pyz)]_n$ [15,16] per M_2 unit. As compared with these adsorption properties, the amount of NO adsorbed was considerably lower despite its simple molecular structure. This low amount of adsorption might be related to both the shape and dipole moment of the NO molecule within the hydrophobic space, which is reflected in the guest packing, inter-guest interaction, and host–guest interaction.

3.2. Magnetic properties of NO molecule in channel crystals

DC magnetic measurements were conducted on single crystals of **1**, **2**, and **3** under pressurized NO conditions in the temperature range of 2–250 K at an applied field of 1 T. The maximum values of apparent μ_{eff} were obtained based on the compositions estimated from gas adsorption measurements at 195 K at 800 Torr (3.19 μ_B at 212 K for **1**, 3.35 μ_B at 194 K for **2**, and 4.09 μ_B at 174 K for **3**). These apparent μ_{eff} values were extremely high in comparison with the theoretical effective Bohr magneton number of 1.836 for gaseous NO at 293 K [26] because the actual adsorption amounts may increase under the high pressure for the SQUID measurements. The assumption that the observed maximum μ_{eff} values at around 200 K can meet the theoretical value of 1.836 μ_B gave the adsorption amounts of 1.83, 1.00, and 1.14 for **1**, **2**, and **3**, respectively per M_2 unit. The roughly estimated numbers of adsorbed NO molecules for **1**, **2**, and **3** increased 3, 3.3, and 5 times as much as those estimated from the NO adsorption measurements, respectively. The pressure effect on the increase of adsorption amounts was observed more notably in **2** and **3**. Compound **1** adsorbed the NO molecules effectively in comparison with compounds **2** and **3**. This order of the estimated adsorption amounts is in good agreement with that observed in the gas adsorption measurements. A significant increase in the adsorption amount was found in **1**, which is probably influenced by the gas adsorption characteristics of the crystal host with the different bridging ligands of pyz (**1**) and 2-mpyz (**2**, **3**). Fig. 2 shows the converted μ_{eff} versus T plots for **1**, **2**, and **3** with the bulk NO data measured by SQUID methods. With a decrease in temperature, the μ_{eff} value gradually increases and reaches a maximum at around 200 K for **1** and **2**, and at around 175 K for **3**. Below this temperature, the μ_{eff} value decreases rapidly to 0.60 μ_B at 108 K, 0.28 μ_B at 114 K, and 0.60 μ_B at 45 K, for **1**, **2**, and **3**, respectively. With a decrease in temperature, the μ_{eff} value for **1** continuously decreases to reach a minimum of 0.49 μ_B at 30 K. The μ_{eff} values for **1**, **2**, and **3** then increase from their respective minimum values to reach small peaks of 0.55 μ_B at 14 K for **1**, 0.92 μ_B at 8.6 K for **2**, and 0.70 μ_B at 16 K for **3** and finally decrease to 2.0 K (0.34, 0.66, and 0.52 μ_B for **1**, **2**, and **3**, respectively). The increases of μ_{eff} in the high-temperature regions were probably caused by the adsorption of NO into the host as the temperature decreased. The slight difference in magnetic behavior below 110 K between compound **1** and compounds **2** and **3** would be caused by a difference in the guest array because of the substituents on the host lattice of **2** and **3**. These magnetic behaviors of the NO-inclusion crystals are completely different from those of bulk NO. In bulk NO, the spin–orbital contributions of the NO molecule cause the effective magnetic moment to deviate from the Curie law as temperature decreases, and the generation of dimerized NO in solid phase results in very feeble magnetization due to its diamagnetic nature [23,26–28]. In the case of included NO molecules in micropores, two different magnetic properties have been reported. One property is that the dimerized NO molecules generated in the activated carbon fiber exhibit a diamagnetic nature [24]. The other property is that the NO molecules adsorbed on the surface of the silica and alumina gel show magnetization without deviation from the Curie law due to the uncoupling of the spin–orbital interactions [29,30].

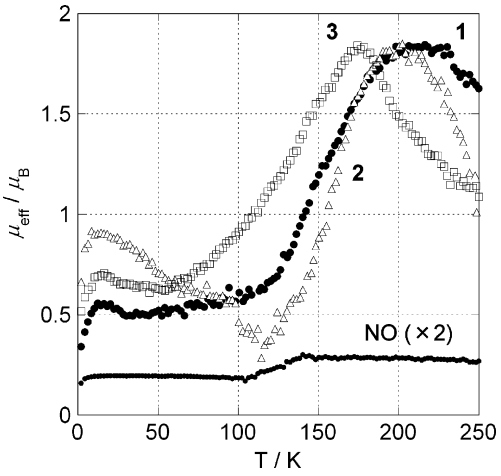


Fig. 2. Temperature dependence of the effective magnetic moment for included NO in **1**, **2**, and **3** at 1 T. Calculation for molar magnetization was based on the mass of NO molecules corrected by the theoretical value and the measured value. The magnetic data of the pure NO was measured by the SQUID method; its intensity was multiplied by 2.

The rapid decrease of μ_{eff} observed in **1**, **2**, and **3** is understood by the antiferromagnetic interaction between the included NO molecules, which is similar to that reported in the oxygen-included crystals of $\mathbf{2}\cdot 3(O_2)$ [9]. We have found one-dimensional arrays of the included oxygen molecules with short inter-guest contacts in both **1** and **2** [9,19]. As shown in Fig. 3, because each chain is separated from the nearest chains with a minimum inter-guest distance of 6.7 Å, the contacts within the channel will mostly contribute to the antiferromagnetic interactions. Based on the reported results, the abrupt decrease of μ_{eff}

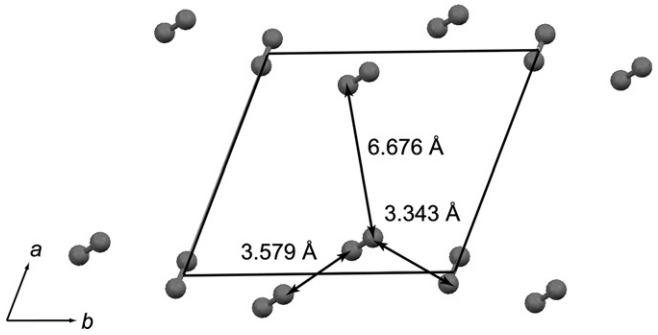


Fig. 3. Ball-and-stick representation of one-dimensional arrays of the included O_2 in the channels of crystal **1** at 90 K (reported in Ref. [19]).

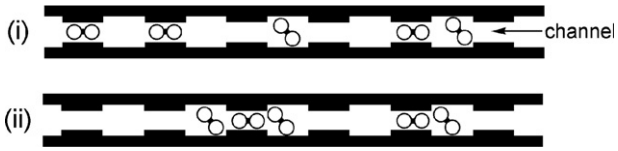


Fig. 4. Schematic views of molecular distributions within the channels under an unsaturated adsorption state: (i) isolated guest molecules; (ii) the aggregated structure.

observed in the included NO molecules indicates that the adsorbed NO molecules generate densely packed structures with short contacts along the channel, which effectively mediate the magnetic interactions.

It was reported that liquid NO exhibits ca. 0.05 μ_B at around 100 K because of a 97% association to N_2O_2 [27,28]. At 90 K, values of μ_{eff} larger than 0.05 μ_B for bulk NO are found with 0.58, 0.58, and 0.83 μ_B for **1**, **2**, and **3**, respectively, which indicate that diamagnetic dimers are not generated in the channels. This is different from that observed in bulk NO. In spite of the relatively strong antiferromagnetic interaction, the μ_{eff} curves showed a gradual decrease for **1** and an increase for **2** and **3**. Because the adsorption amounts of NO are low as compared to the expected value of 3 molecules per dinuclear M_2 unit for the saturated structure, there are two possible methods of distribution of the adsorbed NO in the channels, which could be related to the appearance of magnetic behavior. The first possible method is that the molecules that are located close to each other contribute to antiferromagnetic interactions. The second possible method is that the isolated molecules that are generated by the unsaturated state result in residual paramagnetic contributions (Fig. 4). The observed magnetic behavior of adsorbed NO within the channels of **1**–**3** exhibited antiferromagnetic interaction without residual paramagnetic contributions. This fact confirms that the narrow channels of **1**–**3** include NO molecules with the suppression of N_2O_2 formation and assist in forming NO molecular aggregation even under unsaturated conditions.

4. Conclusion

We have described the NO adsorption properties of a series of single-crystal adsorbents, **1**, **2**, and **3**, and the magnetic properties of the included NO molecules. More NO molecules were adsorbed in compound **1** having no substituent on the host lattice than in compounds **2** and **3** with substituents. Thus, the property of NO gas adsorption probably depends on differences in channel space. The included NO molecules exhibited antiferromagnetic interaction between neighboring guests, which is different from the bulk NO phase. The magnetic behavior of the included NO molecules suggests that the adsorbed NO molecules exist in the monomer NO state without dimerization to N_2O_2, and generate the aggregation fragment of a 1D array within the channel, instead of an isolated array.

Acknowledgements

This work was financially supported by the Ministry of Education, Culture, Sports, Science and Technology, Japan (Nos. 18750051 and 18033043) and a 2006 Strategic Research Project Grant from Yokohama City University (Nos. K18031 and K18032).

References

[1] G.J. Halder, C.J. Kepert, J. Am. Chem. Soc. 127 (2005) 7891.
[2] T.K. Maji, G. Mostafa, R. Matsuda, S. Kitagawa, J. Am. Chem. Soc. 127 (2005) 17152.
[3] E.C. Spencer, J.A.K. Howard, G.J. McIntyre, J.L.C. Rowsell, O.M. Yaghi, Chem. Commun. (2006) 278.
[4] W. Mori, T.C. Kobayashi, J. Kurobe, K. Amaya, Y. Narumi, T. Kumada, K. Kindo, H.A. Katori, T. Goto, N. Miura, S. Takamizawa, H. Nakayama, K. Yamaguchi, Mol. Cryst. Liq. Cryst. 306 (1997) 1.
[5] H. Kanoh, A. Zamma, N. Setoyama, Y. Hanzawa, K. Kaneko, Langmuir 13 (1997) 1047.
[6] R. Kitaura, S. Kitagawa, Y. Kubota, T.C. Kobayashi, K. Kindo, Y. Mita, A. Matsuo, M. Kobayashi, H.-C. Chang, T.C. Ozawa, M. Suzuki, M. Sakata, M. Takata, Science 298 (2002) 2358.
[7] S. Takamizawa, T. Hiroki, E. Nakata, K. Mochizuki, W. Mori, Chem. Lett. 31 (2002) 1208.
[8] S. Takamizawa, E. Nakata, H. Yokoyama, Inorg. Chem. Commun. 6 (2003) 763.
[9] S. Takamizawa, E. Nakata, T. Akatsuka, Angew Chem., Int. Ed. 45 (2006) 2216.
[10] S. Takamizawa, E. Nakata, Cryst. Eng. Commun. 7 (2005) 476.
[11] S. Takamizawa, E. Nakata, T. Saito, Angew. Chem., Int. Ed. 43 (2004) 1368.
[12] S. Takamizawa, E. Nakata, T. Saito, K. Kojima, Cryst. Eng. Commun. 5 (2003) 411.
[13] S. Takamizawa, E. Nakata, T. Saito, Inorg. Chem. Commun. 7 (2004) 1.
[14] S. Takamizawa, E. Nakata, H. Yokoyama, K. Mochizuki, W. Mori, Angew. Chem., Int. Ed. 42 (2003) 4331.
[15] S. Takamizawa, E. Nakata, T. Saito, T. Akatsuka, Inorg. Chem. 44 (2005) 1362.
[16] S. Takamizawa, E. Nakata, T. Saito, Inorg. Chem. Commun. 6 (2003) 1415.
[17] S. Takamizawa, E. Nakata, T. Saito, Chem. Lett. 33 (2004) 538.
[18] S. Takamizawa, T. Saito, T. Akatsuka, E. Nakata, Inorg. Chem. 44 (2005) 1421.
[19] S. Takamizawa, E. Nakata, T. Saito, T. Akatsuka, K. Kojima, Cryst. Eng. Commun. 6 (2004) 197.
[20] S. Kitagawa, Nature 441 (2006) 584.
[21] W.J. Dulmage, E.A. Meyers, M.N. Lipscomb, Acta. Cryst. 6 (1953) 760.

[22] W.N. Lipscomb, F.E. Wang, W.R. May, E.L. Lippert, Acta. Cryst. 14 (1961) 1100.
[23] E. Lips, Helv. Phys. Acta. 8 (1935) 247.
[24] K. Kaneko, N. Fukuzaki, S. Ozeki, J. Chem. Phys. 87 (1987) 776.
[25] S. Takamizawa, K. Kojima, T. Akatsuka, Inorg. Chem. 45 (2006) 4580.
[26] P.W. Selwood, Magnetochemistry, Interscience, New York, 1956.
[27] H. Bizette, Ann. Phys. 1 (1946) 233.
[28] A.L. Smith, H.L. Johnston, J. Am. Chem. Soc. 74 (1952) 4696.
[29] A. Solbakkën, L.H. Reyerson, J. Phys. Chem. 63 (1959) 1622.
[30] A. Solbakkën, L.H. Reyerson, J. Phys. Chem. 64 (1960) 1903.

Calc. for $C_{60}H_{78}N_8O_{33}Mn_5$: C, 42.04; H, 4.59; N, 6.54. Found: C, 41.92; H, 4.46; N, 6.45%. IR (KBr disk): $\nu = 1625.9$, 1591.2 cm^{-1}.

2.3. Synthesis of $[Co_4^{II}Co_2^{III}(fsaea)_2(OMe)_4(NO_3)_2(OAc)_2(MeOH)_2]$ ($[Co_4^{II}Co_2^{III}]$)

To a solution of 3-formylsalicylic acid (498 mg, 3.0 mmol), triethylamine (1212 mg, 12.0 mmol) and 2-ethanolamine (183 mg, 3.0 mmol) in methanol (100 ml) was added a $Mn(OAc)_2 \cdot 4H_2O$ (1471 mg, 6.0 mmol), and the mixture was stirred for several minutes. The resulting solution was diffused with diethyl ether to give brown solid. The brown solid was dissolved in methanol (100 ml), and $Co(NO_3)_2 \cdot 6H_2O$ (1746 mg, 6.0 mmol) was added to the solution. The resulting solution was allowed to stand for several days to give red lozenge crystals of $[Co_4^{II}Co_2^{III}]$. *Anal*. Calc. for $C_{30}H_{42}N_4O_{24}Co_6$: C, 30.12; H, 3.54; N, 4.68; Mn, 0.00, Co, 29.56. Found: C, 30.32; H, 3.56; N, 4.71; Mn, 1.13; Co, 28.72%. IR (KBr disk): $\nu = 1651.0$, 1598.9, 1384.8 cm^{-1}.

2.4. X-ray crystallography

A brown lozenge crystal ($0.30 \times 0.18 \times 0.07$ mm^3) of $[Mn_3^{II}Mn_2^{III}]$, and a red lozenge crystal ($0.17 \times 0.16 \times 0.06$ mm^3) of $[Co_4^{II}Co_2^{III}]$ were mounted with epoxy resin on the tip of a glass fiber. Diffraction data were collected at −70 °C on a Bruker SMART APEX diffractometer fitted with a CCD type area detector, and a full sphere of data were collected using graphite-monochromated Mo Kα radiation ($\lambda = 0.71073$ Å). At the end of data collection, the first 50 frames of data were recollected to establish that the crystal had not deteriorated during the data collection. The data frames were integrated using SAINT and were merged to give a unique data set for structure determination. Total reflections collected were 7939 and 25 546 for $[Mn_3^{II}Mn_2^{III}]$ and $[Co_4^{II}Co_2^{III}]$, respectively, of which independent reflections were 6665 ($R_{int} = 0.0597$) and 9326 ($R_{int} = 0.0487$). The structures were solved by direct methods and refined by the full-matrix least-squares method on all F^2 data using the SHELXTL 5.1 package (Bruker Analytical X-ray Systems). Non-hydrogen atoms were refined with anisotropic thermal parameters. Hydrogen atoms were included in calculated positions and refined with isotropic thermal parameters riding on those of the parent atoms.

Crystal data for $[\{Mn^{II}Mn^{III}(fsatren)\}_2Mn^{II}(H_2O)_4] \cdot 2MeOH \cdot 3H_2O$ ($[Mn_3^{II}Mn_2^{III}]$): $C_{32}H_{32}N_4O_{15}Mn_{2.5}$, F.W. = 849.97; brown lozenge, triclinic, space group $P\bar{1}$, $a = 12.345(2)$ Å, $b = 13.142(2)$ Å, $c = 13.862(3)$ Å, $\alpha = 77.451(4)°$, $\beta = 82.671(4)°$, $\gamma = 65.767(4)°$, $V = 2000.0(6)$ $Å^3$, $Z = 2$, $D_{calc} = 1.411$ Mg m^{-3}, μ(Mo Kα) = 0.850 mm^{-1}, $R_1 = 0.0808$, $wR_2 = 0.2269$ ($I > 2\sigma(I)$).

Crystal data for $[Co_4^{II}Co_2^{III}(fsaea)_2(OMe)_4(NO_3)_2(OAc)_2(MeOH)_2]$ ($[Co_4^{II}Co_2^{III}]$): $C_{30}H_{42}N_4O_{24}Co_6$, F.W. = 1196.26; red lozenge, orthorhombic, space group $P2_12_12_1$, $a = 15.097(3)$ Å, $b = 16.137(3)$ Å, $c = 17.164(3)$ Å, $V = 4181.7(13)$ $Å^3$, $Z = 4$, $D_{calc} = 1.900$ Mg m^{-3}, μ(Mo Kα) = 2.419 mm^{-1}, $R_1 = 0.0696$, $wR_2 = 0.1711$ ($I > 2\sigma(I)$).

3. Result and discussion

3.1. Crystal structures

An ORTEP drawing of $[Mn_3^{II}Mn_2^{III}]$ is shown in Fig. 1. X-ray structure analyses for $[Mn_3^{II}Mn_2^{III}]$ reveals that a $[Mn^{II}(H_2O)_4]$ unit bridges two $[Mn^{II}Mn^{III}(fsatren)]^-$ units to form a linear pentanuclear manganese core. In the $[Mn^{II}Mn^{III}(fsatren)]^-$ unit, a Mn(II) ion has seven-coordinated geometry (monocapped trigonal prism environment)

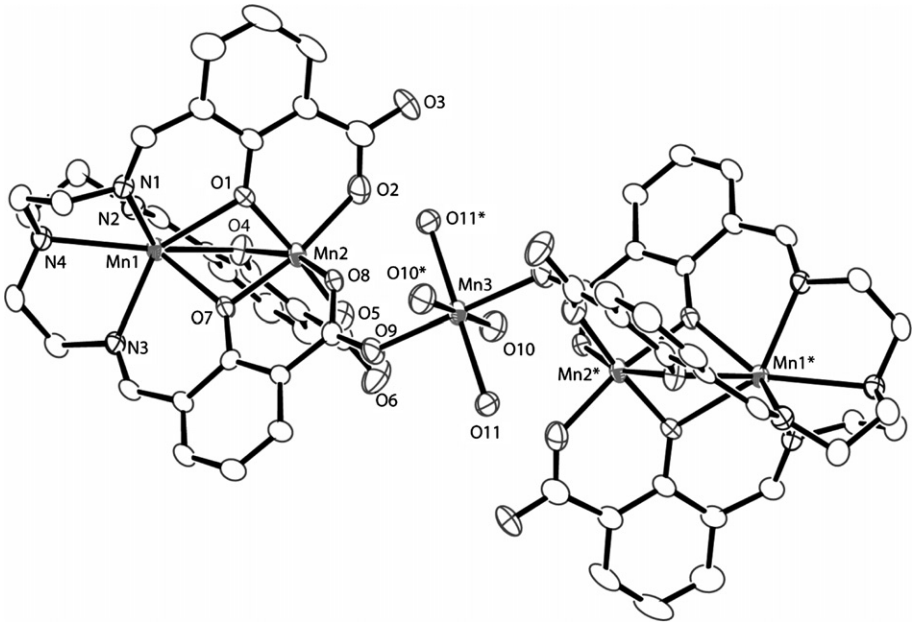


Fig. 1. ORTEP drawing of $[\{Mn^{II}Mn^{III}(fsatren)\}_2Mn^{II}(H_2O)_4] \cdot 2MeOH \cdot 3H_2O$ ($[Mn_3^{II}Mn_2^{III}]$).

and locates at an N_4O_3 site of fsatren^{3-} ligand, whereas a Mn(III) ion has a distorted octahedral environment and locates an O_6 site of fsatren^{3-} ligand. The terminal carboxyl group of $[Mn^{II}Mn^{III}(fsatren)]^-$ unit connects to additional Mn(II) ion with *syn–anti* manner bridge to form a linear pentanuclear manganese core. Coordination bond lengths about Mn1, Mn2 and Mn3 are in the range of 2.245(6)–2.561(7), 1.861(7)–2.059(6) and 2.130(7)–2.220(7) Å, respectively. On the bases of bond valence sum calculations and coordination bond lengths, Mn1 and Mn3 ions are Mn^{II} ions, and Mn2 ions are Mn^{III} ions. Interatomic Mn1···Mn2 and Mn2···Mn3 separations are 3.144(2) and 5.237(2) Å, respectively. The bridging angles of Mn1–O1–Mn2, Mn1–O4–Mn2, and Mn1–O7–Mn2 are 90.9(3)°, 95.2(3)°, and 94.1(3)°, respectively.

An ORTEP drawing for $[Co_4^{II}Co_2^{III}]$ with atom numbering scheme is shown in Fig. 2. The structure of $[Co_4^{II}Co_2^{III}]$ is composed of a face shared incomplete tetra cubane core with four cobalt(II) ions (Co2, Co3, Co5, Co6) and two cobalt(III) ions (Co1, Co4) bridged by μ_3-MeO^-, phenoxo, alkoxo and carboxyl groups. Co1 and Co4 ions have an octahedral coordination geometry and locate at an N_1O_2 site of fsaea^{3-} ligand. Co2 and Co5 ions have an octahedral coordination and locate at an O_2 site of fsaea^{3-} ligand. Co3 and Co6 ions have a distorted octahedral geometry and are coordinated by the oxygen atom of carboxyl group of fsaea^{3-} ligand. Coordination bond lengths are in the range of 1.881(6)–1.942(5), 2.022(5)–2.136(5), 2.009(5)–2.228(6), 1.863(7)–1.950(5), 2.032(5)–2.116(5), 1.995(5)–2.179(6) Å for Co1–Co6, respectively. The assignment of oxidation number was confirmed by the bond distances.

3.2. Magnetic property

Magnetic susceptibilities for $[Mn_3^{II}Mn_2^{III}]$ and $[Co_4^{II}Co_2^{III}]$ were measured in the temperature range of 1.8–300 K. $\chi_m T$ versus T and M versus H plots are given in Figs. 3 and 4, respectively. In the case of $[Mn_3^{II}Mn_2^{III}]$, the $\chi_m T$ value at 300 K is 17.809 emu mol^{-1} K, which is smaller than the expected spin-only value for uncorrelated three Mn(II) ions and two Mn(III) ions (19.125 emu mol^{-1} K, $g = 2$). The $\chi_m T$ value gradually decreased as the temperature was lowered, and reached the value of 6.655 emu mol^{-1} K, which suggests that $[Mn_3^{II}Mn_2^{III}]$ has spin ground states $S = 7/2$ ($g_{ave} = 1.84$). The Curie–Weiss plot gave a negative Weiss constant ($C = 18.939$ emu mol^{-1} K, $\theta = -15.284$ K), which suggested antiferromagnetic interaction between the Mn ions. A magnetization measurement performed at 1.8 K yielded a value of 8.73 $N\beta$ at 5 T, which is still unsaturated. This magnetization behavior suggests the existence of near excited state above a ground spin state $S = 7/2$. In the case of $[Co_4^{II}Co_2^{III}]$, the $\chi_m T$ value at 300 K is 11.978 emu mol^{-1} K, which is larger than the value expected for uncorrelated four Co(II) ions (7.5 emu mol^{-1} K, $g = 2$). As the

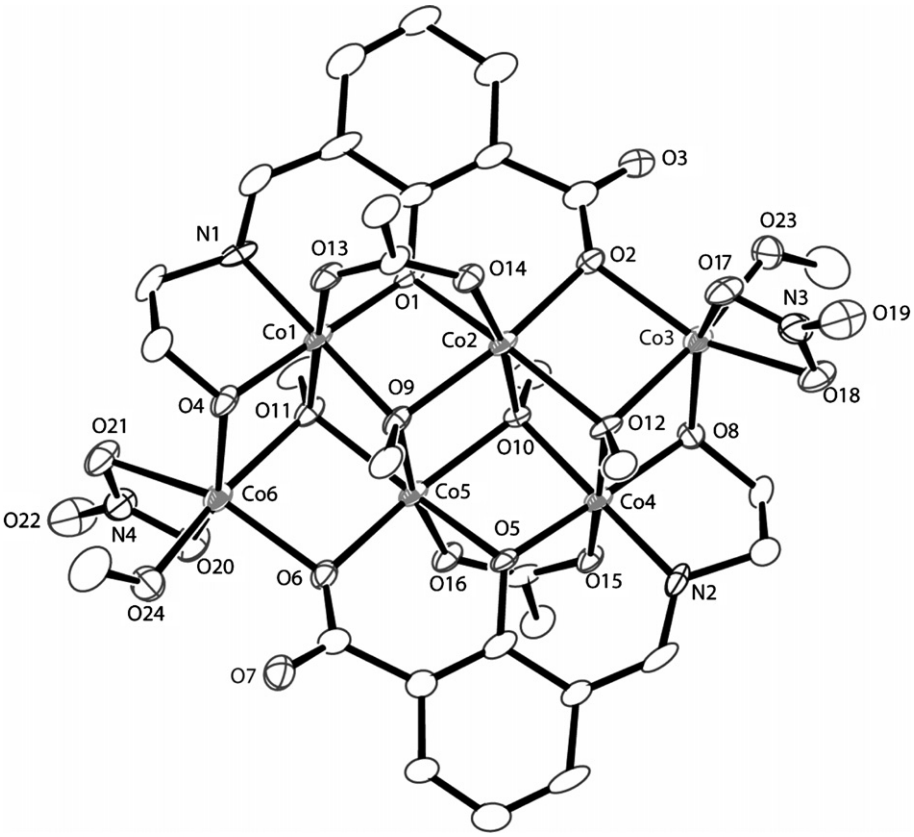


Fig. 2. ORTEP drawing of $[Co_4^{II}Co_2^{III}(fsaea)_2(OMe)_4(NO_3)_2(OAc)_2(MeOH)_2]$ ($[Co_4^{II}Co_2^{III}]$).

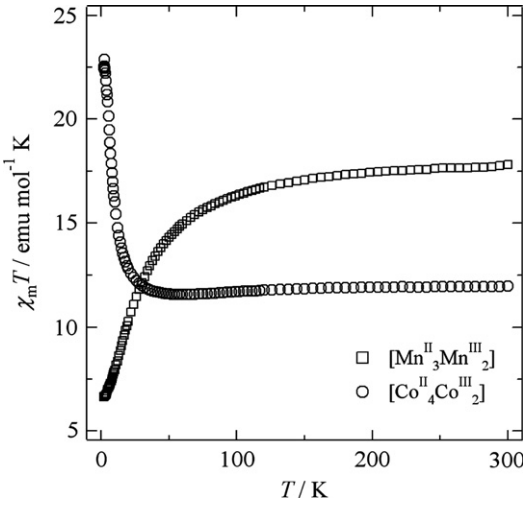


Fig. 3. Plots of $\chi_m T$ vs. T for $[Mn^{II}_3Mn^{III}_2]$ (□), and $[Co^{II}_4Co^{III}_2]$ (○).

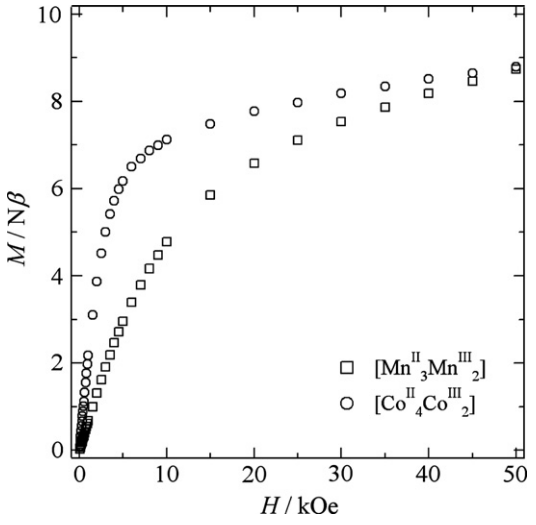


Fig. 4. Plots of M vs. H for $[Mn^{II}_3Mn^{III}_2]$ (□), and $[Co^{II}_4Co^{III}_2]$ (○).

temperature decreased, the $\chi_m T$ value slightly decreased, reaching a minimum value of 11.573 emu mol^{-1} K at 58 K followed by steep increase to 22.877 emu mol^{-1} K at 2.2 K. This magnetic behavior is indicative of ferromagnetic interactions between the Co(II) ions, giving rise to an $S = 6$ ground state. A magnetization measurement performed at 1.8 K yielded a value of 8.80 $N\beta$ at 5 T, which is still unsaturated. The observed magnetization is smaller than the value expected for $S = 6$ ground spin state. This deviation will be brought about by T term contribution of high-spin Co(II). The ferromagnetic behavior can be understood by the accidental orthogonality of magnetic orbitals of Co(II) ions derived from a face shared incomplete tetra cubane core. It is noted that out-of-phase signals in ac magnetic susceptibility measurements were not observed.

4. Conclusion

Mixed-valence pentanuclear manganese complex, $[\{Mn^{II}Mn^{III}(fsatren)\}_2Mn^{II}(H_2O)_4]\cdot n(sol)$, and hexanuclear cobalt complex, $[Co^{II}_4Co^{III}_2(fsaea)_2(OMe)_4(NO_3)_2(OAc)_2(MeOH)_2]$, with Schiff-base ligand derived from 3-formylsalicylic acid have been synthesized. $[Mn^{II}_3Mn^{III}_2]$ complex has a linear pentanuclear core bridged by phenoxo and carboxyl groups, whereas $[Co^{II}_4Co^{III}_2]$ complex has a face shared incomplete tetra cubane core bridged by μ_3-MeO$^-$, phenoxo, alkoxo and carboxyl groups. $[Mn^{II}_3Mn^{III}_2]$ complex shows an antiferromagnetic interaction between the Mn(II) ions, while $[Co^{II}_4Co^{III}_2]$ complex shows a ferromagnetic interaction between Co(II) ions.

5. Supplementary material

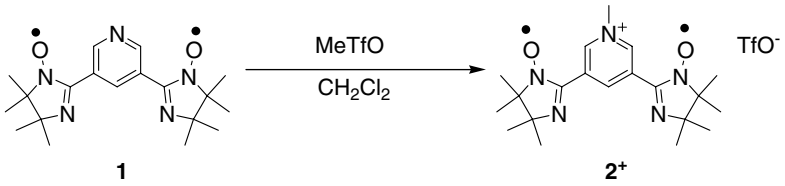
CCDC 617363 and 617364 contain the supplementary crystallographic data for $[Mn^{II}_3Mn^{III}_2]$ and $[Co^{II}_4Co^{III}_2]$. These data can be obtained free of charge via http://www.ccdc.cam.ac.uk/conts/retrieving.html, or from the Cambridge Crystallographic Data Centre, 12 Union Road, Cambridge CB2 1EZ, UK; fax: (+44) 1223-336-033; or e-mail: deposit@ccdc.cam.ac.uk.

Acknowledgements

This work was supported by the COE and TARA projects in the University of Tsukuba and by a Grant-in-Aid for Scientific Research from the Ministry of Education, Culture, Sports, Science and Technology, Japan.

References

[1] G. Christou, D. Gatteschi, D.N. Hendrickson, R. Sessoli, MRS Bulletin 25 (11) (2000) 66.
[2] J. Yoon, L.M. Mirica, T.D.P. Stack, E.I. Solomon, J. Am. Chem. Soc. 126 (2004) 12586.
[3] B. Cage, F.A. Cotton, N.S. Dalal, E.A. Hillard, B. Rakvin, C.M. Ramsey, J. Am. Chem. Soc. 125 (2003) 5270.
[4] (a) H. Okawa, M. Tanaka, S. Kida, Chem. Lett. (1974) 987;
(b) N. Torihara, H. Okawa, S. Kida, Chem. Lett. (1978) 185;
(c) N. Torihara, H. Okawa, S. Kida, Chem. Lett. (1978) 1269;
(d) N. Torihara, H. Okawa, S. Kida, Chem. Lett. (1979) 683;
(e) H. Okawa, W. Kanda, S. Kida, Chem. Lett. (1980) 1281;
(f) J. Zarembowitch, O. Kahn, Inorg. Chem. 23 (1984) 589;
(g) J. Galy, J. Jaud, O. Kahn, P. Tola, Inorg. Chem. 19 (1980) 2945;
(h) O. Kahn, J. Galy, Y. Journaux, J. Jaud, I. Morgenstern-Badarau, J. Am. Chem. Soc. 104 (1982) 2165;
(i) Y. Journaux, O. Kahn, J. Zarembowitch, J. Galy, J. Jaud, J. Am. Chem. Soc. 105 (1983) 7585;
(j) M. Tanaka, M. Kitaoka, H. Okawa, S. Kida, Bull. Chem. Soc. J. 49 (1976) 2469;
(k) H. Okawa, Y. Nishida, M. Tanaka, S. Kida, Bull. Chem. Soc. J. 50 (1977) 127;
(l) N. Torihara, H. Okawa, S. Kida, Bull. Chem. Soc. J. 51 (1978) 3236.
[5] J.C. Duff, E.J. Bills, J. Chem. Soc. (1932) 1987.



Scheme 1. Synthesis of $\mathbf{2}^+ \cdot TfO^-$.

magnetically diluted system in an organic polymer matrix, in which intermolecular exchange interactions are suppressed. The intramolecular ferromagnetic interaction of **1** has been found to be $2J/k_B = 7.0$ K [6]. In this communication, we report ionization of **1**, which gives a cationic biradical, 3,5-bis(1-oxyl-4,4,5,5-tetramethylimidazoline-2-yl)-1-methylpyridinium ($\mathbf{2}^+$) as a trifluoromethanesulfonate salt $\mathbf{2}^+ \cdot TfO^-$ (Scheme 1).

It has been well established that alternant hydrocarbon molecules with two unpaired electrons delocalized in the π-conjugation of *m*-phenylene linkage have a ferromagnetic exchange interaction, giving the energy preference for a triplet ($S = 1$) state [7,8]. Various *m*-phenylene derivatives of nitronylnitroxide and iminonitroxide biradicals have been synthesized and their magnetic properties have been reported [3,9]. Heterocyclic analogues of stable *m*-phenylene biradicals have been found as well in neutral 2,6-pyridine-substituted biradicals [10]. Examples of low-spin species with the *m*-phenylene linkage, however, have been found in heteroatom-substituted oligoradicals [11,12]. An ionic charge in π-conjugated systems is known to affect the high-spin preference [13]. It is shown that a neutral pyridine ring is a ferromagnetic coupling unit, while cationic pyridinium gives both ferromagnetic and antiferromagnetic couplings, depending on substitution at 2,4-, 2,6-, or 3,5-positions [14]. Thus, the preference for a high-spin ground state is not guaranteed for the heteroatom-substituted, charged system of $\mathbf{2}^+$. The ground-state spin multiplicity of $\mathbf{2}^+$ in the salt $\mathbf{2}^+ \cdot TfO^-$ is examined from magnetic susceptibility measurements in both a magnetically diluted system and a neat crystalline solid state. The magnetic susceptibility of the neat crystalline solids of $\mathbf{2}^+ \cdot TfO^-$ is analyzed on the basis of the X-ray crystal structure, supporting the results of the magnetically diluted system.

2. Experimental

2.1. Synthesis

The salt of the biradical cation $\mathbf{2}^+$ was prepared by *N*-alkylation of the neutral precursor **1** with methyl trifluoromethanesulfonate (MeTfO). To MeTfO (0.072 g, 0.439 mmol) in 5 mL of dichloromethane was added the biradical **1** (0.103 g, 0.288 mmol). The solution was stirred at 0 °C for 20 min. Removal of the solvent in vacuo and recrystallization from dichloromethane/hexane gave red needle crystals of the triflate $\mathbf{2}^+ \cdot TfO^-$ (0.102 g, 68%). Elemental analysis (C, H, N) *Anal.* Calc. for $C_{21}H_{30}F_3N_5O_5S$: C: 48.36; H: 5.80; N: 13.43. Found: C: 48.08; H: 5.82; N: 13.40%.

2.2. Crystal structure analysis

Single-crystal X-ray diffraction data of the salt $\mathbf{2}^+ \cdot TfO^-$ were collected on a Rigaku Mercury CCD diffractometer with graphite monochromated Mo Kα radiation at 143 K. The crystal structure was solved by using direct methods in a program package CrystalStructure [15]. Anisotropic thermal parameters analysis was applied for nonhydrogen atoms. Hydrogen atoms with isotropic thermal parameters were refined as riding models.

2.3. Magnetic susceptibility measurements

Magnetic susceptibility was measured on a Quantum Design SQUID magnetometer MPMS-XL under the static magnetic field of 0.1 T in the temperature range down to 1.9 K. The magnetic responses were corrected with diamagnetic blank data of the sample holder obtained separately. The diamagnetic contribution of the sample itself was estimated from Pascal's constants. A polyvinylchloride (PVC) film of the salt was prepared by slow evaporation of dichloromethane solution of PVC and $\mathbf{2}^+ \cdot TfO^-$ (12 wt%), which was used as magnetically diluted samples.

3. Results and discussion

3.1. Crystal structure

The crystallographic data for the salt biradical $\mathbf{2}^+ \cdot TfO^-$ are summarized in Table 1. The unit cell contains two crystallographically independent molecules, $\mathbf{2A}^+ \cdot TfO^-$ and $\mathbf{2B}^+ \cdot TfO^-$.[1] ORTEP drawings of the molecule $\mathbf{2A}^+ \cdot TfO^-$ and $\mathbf{2B}^+ \cdot TfO^-$ are depicted in Fig. 1. The ONCN groups of the iminonitroxide and the pyridinium ring have small dihedral angles (22.11(8)° and 16.23(9)° in $\mathbf{2A}^+$, 5.4(1)° and 24.96(9)° in $\mathbf{2B}^+$) as compared with those of *m*-phenylene bis(iminonitroxide) biradical [9e] and a 2,6-substituted pyridine analogue [10g] of iminonitroxide. The cation molecules $\mathbf{2}^+$ are arranged in a chain structure along the *a*-axis,[1] as shown in Fig. 2. Within

[1] Indexing of observed reflections failed when a lattice of higher symmetry was assumed with one molecule of $\mathbf{2}^+ \cdot TfO^-$ in an asymmetric unit.

Table 1
Selected X-ray crystallographic data of $\mathbf{2}^{+}\cdot TfO^{-}$

Chemical formula	$C_{42}H_{60}F_6N_{10}O_{10}S_2$
Crystal system	monoclinic
Space group	$P2_1/c$
a (Å)	10.963(2)
b (Å)	14.085(3)
c (Å)	32.845(7)
β (°)	89.294(3)
V (Å^3)	5071.3(18)
Z	4
D_{calc} (g cm^{-3})	1.366
T (K)	143
$R(I > 3\sigma(I))$[a]	0.0661
wR (all data)[b]	0.2166
Goodness-of-fit	1.001

[a] $R = \sum \|F_o| - |F_c\| / \sum |F_o|$.

[b] $wR = \left[\sum \left(w\left(F_o^2 - F_c^2\right)^2\right) / \sum w\left(F_o^2\right)^2\right]^{\frac{1}{2}}$, $w = 1/[0.0095F_o^2 + 1.0000\sigma(F_o^2)]/(4F_o^2)$.

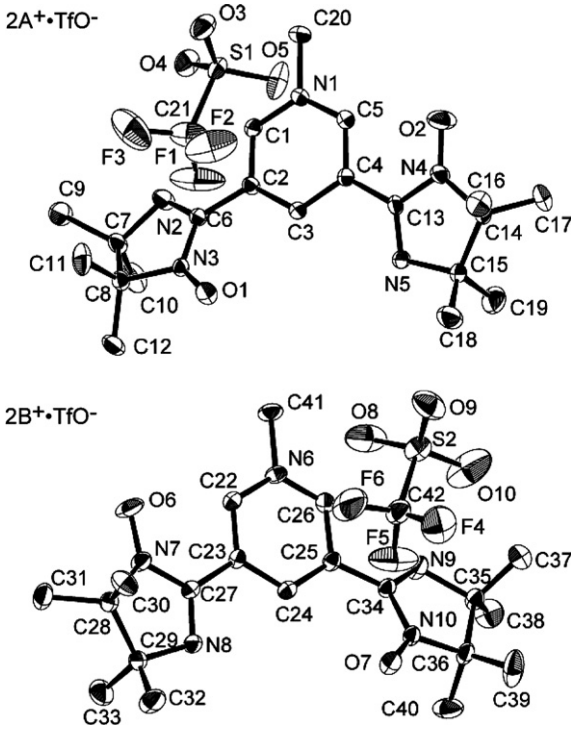


Fig. 1. ORTEP drawings of $\mathbf{2}A^{+}\cdot TfO^{-}$, $\mathbf{2}B^{+}\cdot TfO^{-}$ with the thermal ellipsoids of 50% probability. The hydrogen atoms are omitted for clarity.

the chain, intermolecular short distances close to the Van der Waals contact [16] are found around the nitroxide oxygen atoms with large spin density. Around the O2 atom of $\mathbf{2}A^{+}$, we find (i) O2–N10 = 3.341(3) Å, (ii) O2–O7 = 3.299(3) Å, and (iii) O2–C34 = 3.597(4) Å, while the oxygen atom O6 of $\mathbf{2}B^{+}$ has contacts (iv) O6–O1 = 3.328(3) Å, (v) O6–N2 = 3.575(3) Å, (vi) O6–N3 = 3.051(3) Å, and (vii) O6–C6 = 3.053(3) Å, as depicted in Fig. 3. These contacts are expected to contribute to intermolecular exchange interactions.

3.2. Magnetic susceptibility

The intramolecular exchange interaction in the cation $\mathbf{2}^{+}$ was examined by paramagnetic susceptibility χ_p for the sample of the triflate salt $\mathbf{2}^{+}\cdot TfO^{-}$ dispersed in a polyvinylchloride (PVC) film, in which intermolecular magnetic interactions were suppressed. The χ_pT value of the magnetically diluted system increases as the temperature is lowered, as shown in Fig. 4. This indicates the occurrence of ferromagnetic exchange interaction within the molecule. The temperature dependence of χ_pT is analyzed with the Bleany–Bowers model [17]

$$\chi_p = \frac{2\alpha N_A g^2 \mu_B}{3k_B(T-\theta)} \frac{3}{3+\exp(-2J_F/k_BT)} \quad (1)$$

where the parameter J_F represents the intramolecular ferromagnetic exchange interaction and α denotes the purity of the paramagnetic entity. The mean field θ represents residue of intermolecular exchange interactions due to incomplete dispersion of the molecules in the film, as found in other nitroxide compounds in polymer matrices [18]. The g-factor was fixed as $g = 2.006$ in Eq. (1), which was observed in an ESR spectrum in a dichloromethane solution. The other symbols have their usual meanings. The observed temperature dependence of χ_pT was reproduced by Eq. (1) with the intramolecular exchange interaction of $2J_F/k_B = 7.5 \pm 0.1$ K, the intermolecular mean field of $\theta = -0.50 \pm 0.01$ K, and the purity of $\alpha = 0.880$. The reduced purity is attributed to decomposition during the preparation of the PVC film. It is concluded from the results of magnetic susceptibility for the magnetically diluted system that the ground state of the cation biradical $\mathbf{2}^{+}$ is triplet ($S = 1$).

The temperature dependence of χ_pT measured for neat polycrystalline solid samples of $\mathbf{2}^{+}\cdot TfO^{-}$ is depicted in Fig. 4. With decreasing temperature the χ_pT value increased to reach the maximum of 0.787 emu K mol^{-1} at 17 K. Below this temperature, the χ_pT value decreased down to 0.387 emu K mol^{-1} at the base temperature of 1.9 K. The increase in χ_pT shows that the dominating exchange interaction in the crystalline solid of $\mathbf{2}^{+}\cdot TfO^{-}$ is ferromagnetic, which is assigned to the intramolecular exchange interaction J_F. The decrease in χ_pT below 17 K indicates that additional weak antiferromagnetic interactions are operative between the molecules. The exchange interactions J_F and J_{AF} were estimated by using an antiferromagnetic chain model of arbitrary spin S [19][2]

$$\chi_p = f[2N_A g^2 \mu_B^2/(3k_BT)][(1+u)/(1-u)] \quad (2a)$$

$$u = \coth[2J_{AF}S(S+1)/(k_BT)] - k_BT/[2J_{AF}S(S+1)] \quad (2b)$$

$$f = 3/[3+\exp(-2J_F/k_BT)] \quad (2c)$$

The temperature-dependent population f of the triplet state in the cation molecule $\mathbf{2}^{+}$ is approximated by the simple Boltzmann distribution in Eq. (2c). The observed tempera-

[2] The magnitude alternation of J_{AF} along the chain is neglected.

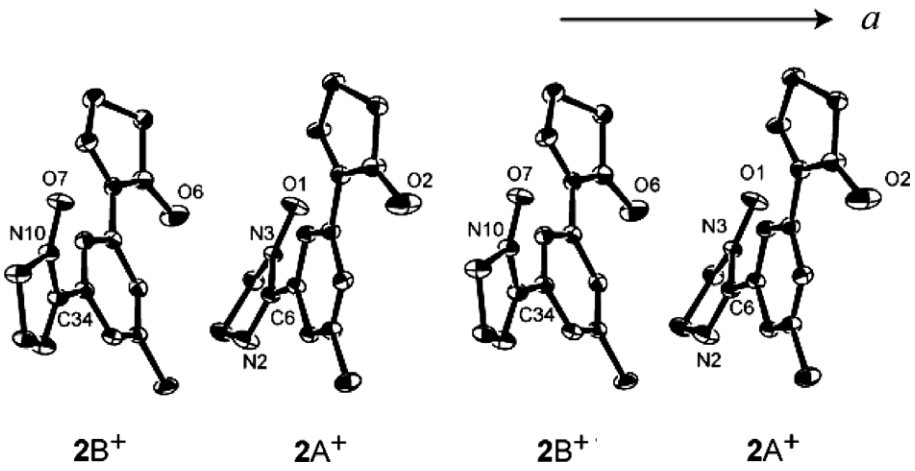


Fig. 2. Molecular chain of the cationic biradical $\mathbf{2}^+$ along the *a*-axis. The methyl groups of the iminonitroxide and the hydrogen atoms are omitted for clarity.

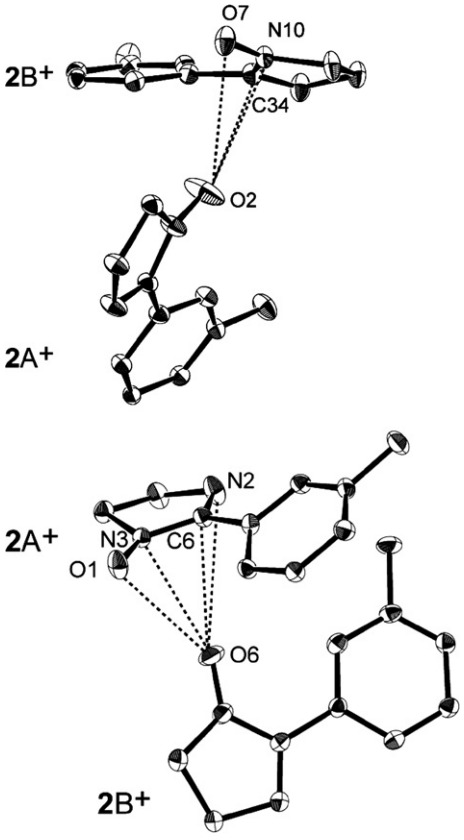


Fig. 3. Intermolecular short contacts of $\mathbf{2}^+ \cdot \mathrm{TfO}^-$ contributing to the intermolecular exchange interactions.

ture dependence of $\chi_p T$ was reproduced by Eq. (2) ($S = 1$) with the intramolecular exchange interaction of $2J_F/k_B = 10.0 \pm 0.1$ K and the intermolecular exchange interaction of $2J_{AF}/k_B = -1.00 \pm 0.01$ K. In the fitting, the *g*-factor was fixed as $g = 2.006$. Fixing the intramolecular ferromagnetic interaction of $2J_F/k_B = 7.5$ K as estimated from the magnetically diluted samples has given a poor fit to the observed temperature dependence of $\chi_p T$. The slightly enhanced interaction of $2J_F/k_B = 10.0$ K suggests a change in the dihedral angles of $\mathbf{2}^+$ in the polymer matrix.

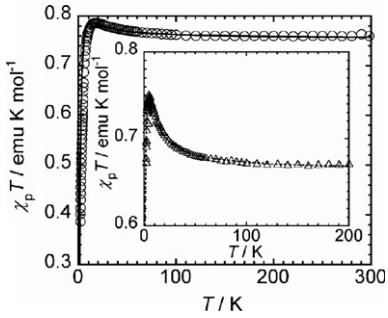


Fig. 4. Temperature dependence of paramagnetic susceptibility χ_p of $\mathbf{2}^+ \cdot \mathrm{TfO}^-$ measured on a SQUID magnetometer with $B = 0.1$ T in the $\chi_p T$ vs. T plots. The solid line denotes the calculated values from Eq. (2). In the inset are shown the $\chi_p T$ values of $\mathbf{2}^+ \cdot \mathrm{TfO}^-$ diluted in the PVC film with $B = 0.1$ T. The dashed line represents the calculated values from Eq. (1).

The magnitude of the intramolecular ferromagnetic exchange interaction in the pyridinium cation $\mathbf{2}^+$, $2J_F/k_B = 7.5 \sim 10$ K, is almost the same as that of the neutral pyridine analogue **1**, $2J_F/k_B = 7$ K [6]. Similar conservation of the intramolecular exchange interactions on *N*-alkylation of the pyridine ring as found in the iminonitroxide biradicals **1** and $\mathbf{2}^+$ has been found in nitronylnitroxide biradicals [20]. Meanwhile, the intramolecular ferromagnetic exchange interaction J_F of $\mathbf{2}^+$ is smaller than that of *m*-phenylene analogues of iminonitroxide [9e]. The heteroatom substitution in the π-conjugated exchange coupler seemingly influences the magnitude of the intramolecular exchange interaction, while we are not allowed to make straightforward comparison of the J values between the related derivatives with differing dihedral angles between the nitroxide and the aryl rings [6,9e,20].

4. Conclusion

The cation biradical of iminonitroxide $\mathbf{2}^+ \cdot \mathrm{TfO}^-$ has been synthesized and isolated in the crystalline solid state. The ground-state spin multiplicity of $\mathbf{2}^+$ has been found to be triplet with the singlet–triplet energy gap of $2J/k_B = 7.5$ K from the magnetic susceptibility of the

magnetically diluted system dispersed in the polymer film. There is little influence of the *N*-methylation for the 3,5-pyridine-substituted iminonitroxide biradicals on the intramolecular exchange interaction. The cation $\mathbf{2}^{+}$ is a building block molecule for ionic crystalline materials, which is stable and, at the same time, carries a ground-state $S = 1$ spin composed of two nitronylnitroxide radical fragments [21]. The ground-state triplet biradical $\mathbf{2}^{+}$ serves as a building block for molecule-based magnets of $S > 1/2$ based on intermolecular noncovalent bonding.

Acknowledgements

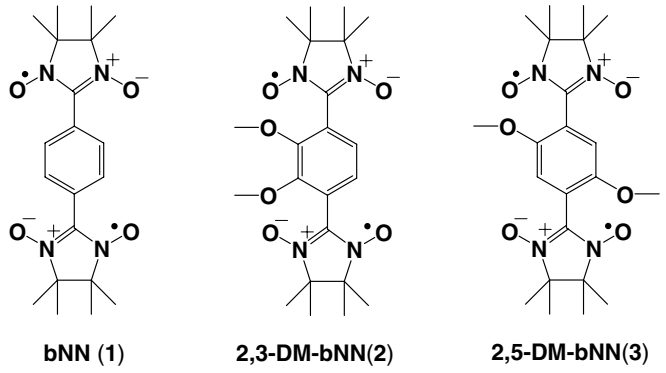
This work has been supported by Grants-in-Aid for Scientific Research from the Ministry of Education, Sports, Culture, Science and Technology, Japan. Financial support from PRESTO of Japan Science and Technology Agency (JST) is also acknowledged. One of the authors (K.H.) acknowledges financial support from Sasakawa Scientific Research Grant of the Japan Science Society.

Appendix A. Supplementary materials

CCDC 617254 contains the supplementary crystallographic data for this paper. These data can be obtained free of charge via http://www.ccdc.cam.ac.uk/conts/retrieving.html, or from the Cambridge Crystallographic Data Centre, 12 Union Road, Cambridge CB2 1EZ, UK; fax: (+44) 1223-336-033; or e-mail: deposit@ccdc.cam.ac.uk.

References

[1] (a) P.M. Lahti (Ed.), Magnetic Properties of Organic Materials, Marcel Dekker, New York, 1999;
(b) K. Itoh, M. Kinoshita (Eds.), Molecular Magnetism, Gordon and Breach, Amsterdam (Kodansha as copublisher: Tokyo), 2000.
[2] K. Awaga, A. Yamaguchi, T. Okuno, T. Inabe, T. Nakamura, M. Matsumoto, Y. Maruyama, J. Mater. Chem. 4 (1994) 1377.
[3] (a) K. Kamiyama, D. Shiomi, S. Hase, M. Nishizawa, K. Sato, M. Kozaki, K. Okada, T. Takui, Appl. Magn. Reson. 19 (2000) 45;
(b) S. Hase, D. Shiomi, K. Sato, T. Takui, J. Mater. Chem. 11 (2001) 756;
(c) S. Hase, D. Shiomi, K. Sato, T. Takui, Polyhedron 20 (2001) 1403.
[4] A. Rajca, M. Pink, T. Rojsajjakul, K. Lu, H. Wang, S. Rajca, J. Am. Chem. Soc. 125 (2003) 8534.
[5] (a) D. Shiomi, M. Nishizawa, K. Sato, T. Takui, K. Itoh, H. Sakurai, A. Izuoka, T. Sugawara, J. Phys. Chem. B 101 (1997) 3342;
(b) M. Nishizawa, D. Shiomi, K. Sato, T. Takui, K. Itoh, H. Sawa, R. Kato, H. Sakurai, A. Izuoka, T. Sugawara, J. Phys. Chem. B 104 (2000) 503;
(c) D. Shiomi, K. Sato, T. Takui, J. Phys. Chem. B 104 (2000) 1961;
(d) D. Shiomi, K. Sato, T. Takui, J. Phys. Chem. B 105 (2001) 2932;
(e) D. Shiomi, K. Sato, T. Takui, J. Phys. Chem. A 106 (2002) 2096;
(f) K. Maekawa, D. Shiomi, T. Ise, K. Sato, T. Takui, J. Phys. Chem. B 109 (2005) 9299;
(g) D. Shiomi, T. Kanaya, K. Sato, M. Mito, K. Takeda, T. Takui, J. Am. Chem. Soc. 123 (2001) 11823;
(h) K. Maekawa, D. Shiomi, T. Ise, K. Sato, T. Takui, J. Phys. Chem. B 109 (2005) 303;
(i) T. Ise, D. Shiomi, K. Sato, T. Takui, Chem. Mater. 17 (2005) 4486;
(j) A. Izuoka, M. Fukada, R. Kumai, M. Itakura, S. Hikami, T. Sugawara, J. Am. Chem. Soc. 116 (1994) 2609;
(k) Y. Hosokoshi, K. Katoh, Y. Nakazawa, H. Nakano, K. Inoue, J. Am. Chem. Soc. 123 (2001) 7921.
[6] K. Hayakawa, T. Ise, D. Shiomi, K. Sato, T. Takui, J. Low Temp. Phys. 142 (2006) 585.
[7] (a) K. Itoh, Pure Appl. Chem. 50 (1978) 1251;
(b) K. Itoh, T. Takui, Proc. Jpn. Acad. Ser. B 80 (2004) 29.
[8] A. Rajca, Chem. Rev. 94 (1994) 871.
[9] (a) D. Shiomi, M. Tamura, H. Sawa, R. Kato, M. Kinoshita, J. Phys. Soc. Jpn. 62 (1993) 289;
(b) A. Caneschi, P. Chiesi, L. David, F. Ferraro, D. Gatteschi, R. Sessoli, Inorg. Chem. 32 (1993) 1445;
(c) A. Izuoka, M. Fukada, T. Sugawara, Mol. Cryst. Liq. Cryst. 232 (1993) 103;
(d) D. Shiomi, M. Tamura, H.A. Katori, T. Goto, A. Hayashi, Y. Ueda, H. Sawa, R. Kato, M. Kinoshita, J. Mater. Chem. 4 (1994) 915;
(e) L. Catala, J.L. Moigne, N. Kyrisakas, P. Rey, J.J. Novoa, P. Turek, Chem. -Eur. J. 7 (2001) 2466.
[10] (a) T. Sugano, M. Tamura, M. Kinoshita, Synth. Met. 56 (1993) 3305;
(b) H. Oshio, A. Ohto, J. Fujisawa, T. Watanabe, T. Ito, K. Isobe, Chem. Lett. 12 (1994) 2353;
(c) G. Ulrich, R. Ziessel, D. Luneau, P. Rey, Tetrahedron Lett. 35 (1994) 1211;
(d) G. Ulrich, R. Ziessel, Tetrahedron Lett. 35 (1994) 1215;
(e) R. Ziessel, G. Ulrich, R.C. Lawson, L. Echegoyen, J. Mater. Chem. 9 (1999) 1435;
(f) G. Francese, F.M. Romero, A. Neels, H. Stoeckli-Evans, S. Decurtins, Inorg. Chem. 39 (2000) 2087;
(g) K. Hayakawa, D. Shiomi, T. Ise, K. Sato, T. Takui, Chem. Lett. 33 (2004) 1494.
[11] W.T. Borden, H. Iwamura, J.A. Berson, Acc. Chem. Res. 27 (1994) 109.
[12] (a) M. Dvolaitzky, R. Chiarelli, A. Rassat, Angew. Chem. Int. Ed. Engl. 104 (1992) 180;
(b) F. Kanno, K. Inoue, N. Koga, H. Iwamura, J. Am. Chem. Soc. 115 (1993) 847;
(c) J. Fujita, M. Tanaka, H. Suemune, N. Koga, K. Matsuda, H. Iwamura, J. Am. Chem. Soc. 118 (1996) 9347.
[13] (a) K. Okada, T. Imakura, M. Oda, A. Kajiwara, M. Kamachi, M. Yamaguchi, J. Am. Chem. Soc. 119 (1997) 5740;
(b) K. Okada, T. Imakura, M. Oda, H. Murai, M. Baumgarten, J. Am. Chem. Soc. 118 (1996) 3047.
[14] A.P. West Jr., S.K. Silverman, D.A. Dougherty, J. Am. Chem. Soc. 118 (1996) 1452.
[15] (a) CrystalStructure (ver.3.7.0): Rigaku and Rigaku/MSC. 9009 New Trails Dr. The Woodlands TX 77381, USA; 2005.;
(b) CRYSTALS (issue 10): D.J. Watkin, C.K. Prout, J.R. Carruthers, P.W. Betteridge, Chemical Crystallography Laboratory, Oxford, UK; 1996.
[16] A. Bondi, J. Phys. Chem. 64 (1964) 441.
[17] B.D. Bleany, K. Bowers, Proc. R. Soc. Lond. Ser. A 214 (1952) 451.
[18] K. Hayakawa, D. Shiomi, T. Ise, K. Sato, T. Takui, J. Phys. Chem. B 109 (2005) 9195.
[19] M.E. Fisher, Am. J. Phys. 32 (1964) 343.
[20] K. Hayakawa, D. Shiomi, T. Ise, K. Sato, T. Takui, J. Mater. Chem., in press.
[21] A dihydrophenazine radical cation substituted with a nitronyl nitroxide group has been synthesized and the triplet ground state has been found: S. Hiraoka, T. Okamoto, M. Kozaki, D. Shiomi, K. Sato, T. Takui, K. Okada, J. Am. Chem. Soc. 126 (2004) 58.



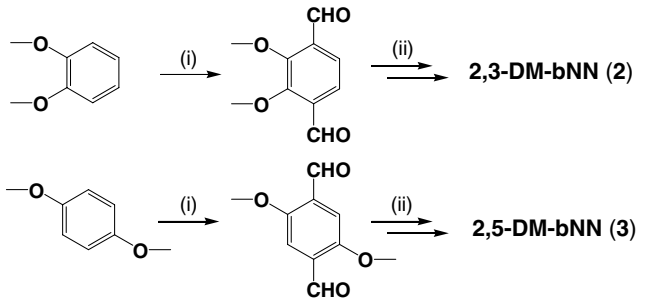
Scheme 1. Biradicals **bNN** (**1**), **2,3-DM-bNN** (**2**) and **2,5-DM-bNN** (**3**).

π-conjugation of *p*-phenylene is discussed from both experiment and DFT molecular orbital calculations. A stable nitronyl nitroxide derivative of *p*-phenylene, **bNN** (**1**, Scheme 1), has an intramolecular antiferromagnetic exchange interaction of $2J/k_B = -104\ \mathrm{K} \sim -106\ \mathrm{K}$ from magnetic susceptibility measurements [9]. In order to clarify effects of torsion angles between the phenyl and the imidazole rings of nitronyl nitroxide, we have designed and synthesized two biradicals **2,3-DM-bNN** (**2**) and **2,5-DM-bNN** (**3**) (Scheme 1). Large torsion angles are expected for **2** and **3** owing to the bulky substituents of the methoxy groups. The intramolecular exchange interactions in **1**, **2**, and **3** are discussed based on magnetic susceptibility, X-ray crystal structures, and DFT molecular orbital calculations. The potentiality of the ground-state singlet biradicals as building blocks for novel exchange-coupled spin systems is discussed.

2. Experimental

2.1. Synthesis

The biradicals **2** and **3** were synthesized from commercial veratrole and 1,4-dimethoxybenzene, respectively, by following the route shown in Scheme 2. The generation of nitronyl nitroxide radicals (Step ii) was carried out by following the conventional method [10]. Elemental analysis (C, H, N) of **2** and **3**. *Anal.* Calc. for $C_{22}H_{32}N_4O_6$: C, 58.91; H, 7.19; N, 12.49. Found for **2**: C, 59.01; H, 7.20; N, 12.45%. Found for **3**: C, 58.98; H, 7.23; N, 12.44%. Single crystals of **2** and **3** suitable for X-ray crystallography experiments were obtained by recrystallization from a mixture of dichloromethane and hexane.



Scheme 2. Synthetic route for **2** and **3**. Reagents: (i) *n*-butyllithium in diethylether; (ii) 2,3-bis(hydroxylamino)-2,3-dimethylbutane in benzene and $NaIO_4$ in CH_2Cl_2/H_2O.

2.2. Crystal structure analysis

Single-crystal diffraction data of **2** and **3** were collected on a Rigaku Mercury CCD diffractometer with graphite monochromated Mo Kα radiation. The crystal structure was solved by using direct methods in a program package *CrystalStructure* [11]. Anisotropic thermal factors were applied for non-hydrogen atoms. Hydrogen atoms with isotropic thermal factors were refined as riding models.

2.3. Magnetic susceptibility measurements

Magnetic susceptibility was measured on a Quantum Design SQUID magnetometer MPMS-XL under the static magnetic field of 0.1 T in the temperature range down to 1.9 K. The magnetic responses were corrected with diamagnetic blank data of the sample holder obtained separately. The diamagnetic contribution of the sample itself was estimated from Pascal's constants.

2.4. DFT molecular orbital calculations

The total electronic energy was calculated for the biradicals **1**, **2**, and **3** by the use of the unrestricted density functional theory (DFT) at UB3LYP/6-31+G(d,p) level with a program package GAUSSIAN98 [12]. The molecular geometries of the biradicals, **1** [9], **2** and **3**, was taken from the X-ray crystal structures.

3. Results and discussion

3.1. Crystal structure

The crystallographic data of **2** and **3** are listed in Table 1. The molecular structures are shown in Fig. 1. A half of the molecule of **3** is crystallographically independent. The common atom numbering was, however, given to **2** and **3** in order to facilitate comparison of the molecular structures. The torsion angles between the phenyl ring and the ONCNO group of nitronyl nitroxide are 66.7° (C2–C1–C7–N2) and 63.8° (C5–C4–C14–N4) for **2** and 70.4° for **3**. The torsion angles of **2** and **3** are much larger than those of **1** (28.5°) [9]. The methoxy groups induce the large dihedral angles, which is likely to weaken the intramolecular exchange interaction through the π-conjugation in **2** and **3** as compared with that in **1**.

No intermolecular short distances close to the van der Waals contact were found around the N–O groups with a large spin density, which would contribute to possible intermolecular exchange interactions.

Table 1
X-ray crystallographic data for **2** and **3**

Compound	**2,3-DM-bNN (2)**	**2,5-DM-bNN (3)**
Formula	$C_{22}H_{32}N_4O_6$	$C_{11}H_{16}N_2O_3$
Crystal system	monoclinic	monoclinic
Space group	$P2_1/a$	$P2_1/c$
a (Å)	11.8145(7)	7.0587(5)
b (Å)	13.6730(7)	10.1562(8)
c (Å)	14.3238(8)	16.0091(14)
β (°)	95.640(3)	94.614(4)
V (Å^3)	2302.7(2)	1143.97(16)
Z	4	4
ρ_{calc} (g cm^{-3})	1.285	1.302
Unique reflections used ($I > 2\sigma(I)$)	4500	2174
$R(I > 2\sigma(I))$[a]	0.0404	0.0761
R_{w2} (all data)[b]	0.1211	0.1207
Goodness-of-fit	1.010	1.047
T (K)	143	133

[a] $R = \sum ||F_o| - |F_c|| / \sum |F_o|$.

[b] $R_{w2} = \left[\sum w(F_o^2 - F_c^2)^2 / \sum w(F_o^2)^2\right]^{0.5}$.

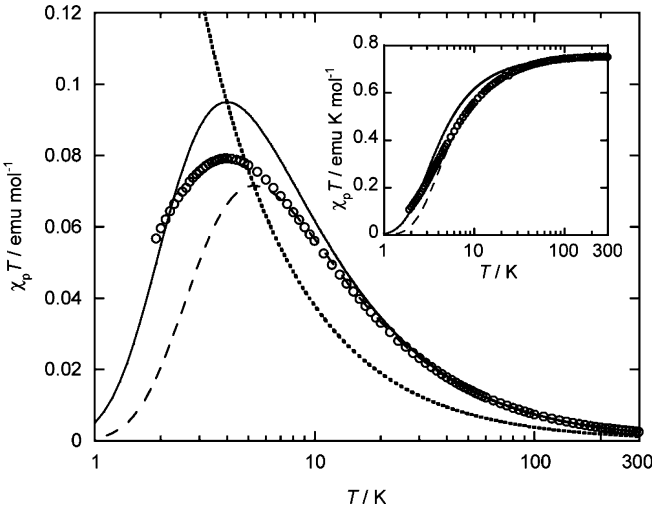


Fig. 2. Temperature dependence of paramagnetic susceptibility χ_p of **2,3-DM-bNN** (**2**) measured for the neat polycrystals. The inset shows the temperature dependence of the product χ_pT. The solid and dashed lines represent the calculation of Eq. (1) with $2J/k_B = -6.4$ K and -8.5 K, respectively. The dotted line shows the trajectory of (T_{max}, χ_{max}) in Eq. (4).

3.2. Magnetic susceptibility

The paramagnetic susceptibility χ_p measured for neat polycrystalline samples of **2** is depicted in Fig. 2. The χ_pT value of 0.75 emu K mol^{-1} at 300 K is consistent with 2 mol of $S = 1/2$ spins with the g-factor of 2.007, which has been determined from an observed ESR spectrum in a solution. The high-temperature limit of χ_pT indicates that the purity is satisfactory.

The magnitude of the intramolecular exchange interaction $2J$ in **2** is estimated using the Bleany–Bowers model [13]

$$\chi_p = \frac{2N_A g^2 \mu_B^2}{k_B T} \times \frac{1}{3 + \exp(-2J/k_B T)} \quad (1)$$

Numerical differentiation of χ_p in Eq. (1) with respect to T gives the temperature T_{max} where χ_p has a maximum

$$T_{max} = 1.247|J|/k_B \quad (2)$$

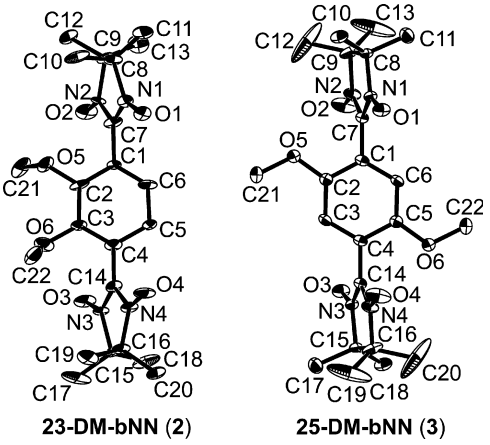


Fig. 1. ORTEP views of **2** and **3** at the 50% probability level. The hydrogen atoms are omitted for the sake of clarity.

as a function of $|J|$. The maximum value of χ_p at T_{max} is given as

$$\chi_{max} = 0.07547g^2/(|J|/k_B) \quad (3)$$

From Eqs. (2) and (3), the trajectory, the locus, of a point (T_{max}, χ_{max}) for the maximum in χ_p is given by

$$\chi_{max} = 0.09413g^2/T_{max} = 0.3792/T_{max} \quad (g = 2.007) \quad (4)$$

The observed maximum in χ_p for **2** is inconsistent with the trajectory Eq. (4), as shown in Fig. 2. The discrepancy is not attributed to impurity of paramagnetic molecules with only one unpaired electron or diamagnetic molecules, since the purity of the polycrystalline sample of **2** has been found to be satisfactory. The biradical **2** has no short contacts giving possible intermolecular exchange interactions,[1] as described above. The dashed line in Fig. 2 shows the best-fit curve calculated with Eq. (1), in which the larger weight is applied for the observed χ_p value at the higher temperature. This gives an estimate for the upper limit of $2|J|$, $2J/k_B = -8.5$ K. A lower limit of $2|J|$ acquired from Eq. (2) is $2J/k_B = -6.4$ K. The estimate of the intramolecular exchange interaction $2J/k_B$ of **2** ranges from -6.4 to -8.5 K.

In the high-temperature range from 300 K down to 10 K, the χ_pT value of **3** is consistent with that of **2** (Fig. 3). This indicates that the magnitude of the intramolecular interaction of **3** is in the same order as that of **2**. The fit with the larger weight at higher temperatures gives an estimate for the upper limit of $2|J|$, $2J/k_B = -8.2$ K for **3**, being comparable to $2J/k_B = -8.5$ K for **2**. The exchange interaction of $2J/k_B = -8.2$ K should give a maximum in χ_p at $T = 6.6$ K. The observed χ_p value of **3** exhibits no maximum in the temperature range examined. A trace of

[1] Trials with a modified Bleany–Bowers model with a mean field θ did not improve the fitting.

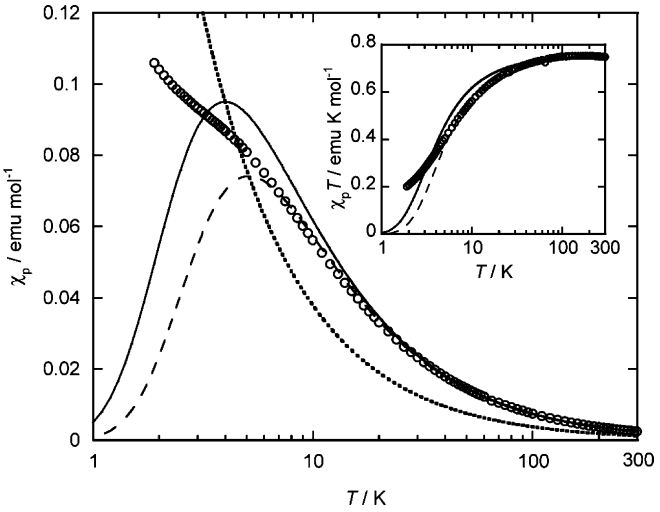


Fig. 3. Temperature dependence of paramagnetic susceptibility χ_p of **2,5-DM-bNN** (**3**) measured for the neat polycrystals. The inset shows the temperature dependence of the product χ_pT. The solid and dashed lines represent the calculation of Eq. (1) with $2J/k_B = -6.4$ K and -8.2 K, respectively. The dotted line shows the trajectory of (T_{max}, χ_{max}) in Eq. (4).

maximum in χ_p is found at $T_{max'} = 4.0$ K, where the second derivative $\partial^2\chi_p/\partial T^2$ is zero, which gives a lower limit of the intramolecular exchange interaction $2J/k_B = -6.4$ K. Thus, the exchange interaction $2J/k_B$ of **3** ranges from -6.4 to -8.3 K.

The growth of χ_p for **3** below 3.5 K is not attributed to any paramagnetic impurity or lattice defects, since the purity is almost 100%, as estimated from the observed χ_pT at 300 K. The growth of χ_p suggests that the magnitude $|J|$ in **3** is reduced at lower temperatures, $2J/k_B \ll -6.4$ K. The temperature-dependent $|J|$ value results from a possible change in the dihedral angle between the phenyl ring and the ONCNO group of nitronyl nitroxide at low temperatures. Similarly, the poor fit for **2** is attributed to the temperature-dependent $|J|$ value as well.

3.3. DFT molecular orbital calculations

It has been established that an energy E_{BS} of a broken-symmetry (BS) state described with an unsymmetrical spin and spatial functions affords a satisfactory estimate for the lowest singlet state [14]. The intramolecular exchange interaction J of a biradical is related to the energy gap between the lowest singlet and the lowest triplet states, $E_{BS} - E_T$, as estimated from DFT-based molecular orbital calculations. The exchange parameter J_{DFT} is expressed as [15]

$$J\mathrm{DFT} = \frac{(E_{BS} - E_T)}{\langle S^2\rangle_T - \langle S^2\rangle_{BS}} \quad (5)$$

where $\langle S^2\rangle$ denotes the spin expectation value for the triplet (T) or the BS singlet state, minimizing spin contamination effects in J_{DFT}. The $2J_{DFT}$ value was calculated for the parent compound **1** with varying torsion angles with increments of 15°, which are compared with those calculated for **2**, and **3**, as listed in Table 2. Although the calculated

Table 2
Torsion angles and intramolecular exchange interactions $2J$

Compound	Torsion angle	$2J_{calc}$[a]	$2J$ (exp.)[b]
1a[c]	15	−421.2	
1[d]	28.5	−306.2	−104 ∼ −106
1b[c]	30	−290.8	
1c[c]	45	−135.8	
1d[c]	60	−33.2	
1e[c]	75	−3.2	
2[d]	63.8 and 66.7	−17.8	−6.4 ∼ −8.5
3[d]	70.4	−8.6	−6.4 ∼ −8.2

[a] Calculated with Eq. (5).
[b] Experimentally estimated from the analysis of magnetic susceptibility.
[c] Molecular geometries are based on the X-ray crystal structure of **1**. Only the torsion angles are altered from those of **1**.
[d] Molecular geometries are taken from the X-ray crystal structure.

$2J_{DFT}$ values are overestimated as compared to the experimental values,[2] the tendency of the $2J$ values *versus* torsion angles is in good agreement with experiment.

4. Conclusion

The new *p*-phenylene-bis(nitronyl nitroxide) biradicals **2** and **3** have been designed and synthesized. The methoxy groups have given rise to the larger torsion angles in **2** and **3** as compared with that in **1**. The large torsion angles should suppress π-conjugation in the *p*-phenylene, providing the smaller intramolecular antiferromagnetic interactions. It is suggested that one of the two biradicals, **2,5-DM-bNN** (**3**), has the temperature-dependent exchange interaction.

In our previous studies, it has been found from theoretical calculations that a one-dimensional alternating chain composed of ground-state singlet biradicals and monoradicals has three kinds of ground states: Two are ferrimagnetic and the other is non-magnetic (spin-less) [16]. The theory indicates that subtle modification of the intra- and intermolecular interactions results in possible switching between the ferrimagnetic high-spin and non-magnetic states [16]. The ground-state singlet biradicals **2** and **3** are potentially suitable building blocks for the theoretical model in which the magnitude of the intramolecular exchange interaction is comparable to those of intermolecular exchange interactions and susceptible to crystal lattice environment.

Acknowledgements

This work has been supported by Grants-in-Aid for Scientific Research from the Ministry of Education, Sports, Culture, Science and Technology, Japan. Financial support from PRESTO of Japan Science, Technology Agency (JST) is also acknowledged. One of the authors (Y.K.) acknowl-

[2] Similar overestimation of intramolecular exchange interactions has been found for *m*-phenylene derivatives of nitronyl nitroxide and iminonitroxide radicals [7].

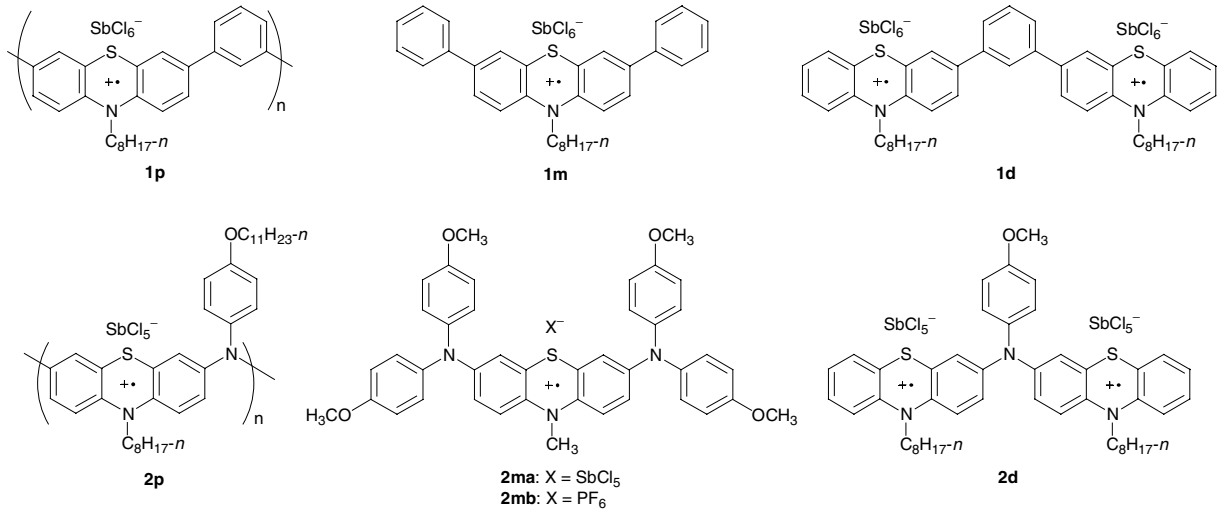
edges Research Fellowships of the Japan Society for the Promotion of Science for Young Scientists.

Appendix A. Supplementary materials

CCDC 615692 and 615693 contain the supplementary crystallographic data for **2,3-DM-bNN** (**2**) and **2,5-DM-bNN** (**3**). These data can be obtained free of charge via http://www.ccdc.cam.ac.uk/conts/retrieving.html, or from the Cambridge Crystallographic Data Centre, 12 Union Road, Cambridge CB2 1EZ, UK; fax: (+44) 1223-336-033; or e-mail: deposit@ccdc.cam.ac.uk. Supplementary data associated with this article can be found, in the online version, at doi:10.1016/j.poly.2006.09.034.

References

[1] (a) For overviews of molecule-based magnetism, see P.M. Lathi (Ed.), Magnetic Properties of Organic Materials, Marcel Dekker, New York, 1999;
(b) K. Itoh, M. Kinoshita (Eds.), Molecular Magnetism: New Magnetic Materials, Gordon & Breach, Amsterdam, (Kodansha as copublisher, Tokyo), 2000;
(c) In: Proceedings of the 9th International Conference on Molecule-Based Magnets, Tsukuba, Japan, 2004;
G. Christou, Polyhedron 24 (2005) 235.
[2] (a) K. Itoh, Chem. Phys. Lett. 1 (1967) 235;
(b) E. Wasserman, R.W. Murray, W.A. Yager, A.M. Torozzolo, G.J. Smolimsky, J. Am. Chem. Soc. 89 (1967) 5076.
[3] (a) K. Itoh, Pure Appl. Chem. 50 (1978) 1251;
(b) K. Itoh, T. Takui, Proc. Jpn. Acad. Ser. B 80 (2004) 29;
(c) A. Rajca, Chem. Rev. 94 (1994) 871.
[4] (a) S. Fang, M.-S. Lee, D.A. Hrovat, W.T. Borden, J. Am. Chem. Soc. 117 (1995) 6727;
(b) W.T. Borden, H. Iwamura, J.A. Berson, Acc. Chem. Res. 27 (1994) 109.
[5] A. Rajca, S. Rajca, J. Chem. Soc., Perkin Trans. 2 (1998) 1077.
[6] (a) M. Dvolaitzky, R. Chiarelli, A. Rassat, Angew. Chem., Int. Ed. Engl. 104 (1992) 180;
(b) F. Kanno, K. Inoue, N. Koga, H. Iwamura, J. Am. Chem. Soc. 115 (1993) 847;
(c) J. Fujita, M. Tanaka, H. Suemune, N. Koga, K. Matsuda, H. Iwamura, J. Am. Chem. Soc. 118 (1996) 9347.
[7] L. Catala, J.L. Moigne, N. Kyritsakas, P. Rey, J.J. Novoa, P. Turek, Chem. Eur. J. 7 (2001) 2466.
[8] M.E. Ali, S.N. Datta, J. Phys. Chem. A 110 (2006) 2776.
[9] (a) D. Shiomi, M. Tamura, H. Sawa, R. Kato, M. Kinoshita, Synth. Met. 56 (1993) 3279;
(b) A. Caneschi, P. Chiesi, L. David, F. Ferraro, D. Gatteschi, R. Sessoli, Inorg. Chem. 32 (1993) 1445.
[10] E.F. Ullman, J.H. Osiecki, D.G.B. Boocock, R. Darcy, J. Am. Chem. Soc. 94 (1972) 7049.
[11] CrystalStructure (ver.3.7.0): Crystal Structure Analysis Package, Rigaku and Rigaku/MSC (2000–2005), 9009 New Trails Dr. The Woodlands, TX 77381, USA.
[12] M.J. Frisch, G.W. Trucks, H.B. Schlegel, G.E. Scuseria, M.A. Robb, J.R. Cheeseman, V.G. Zakrzewski, J.A. Montgomery Jr., R.E. Stratmann, J.C. Burant, S. Dapprich, J.M. Millam, A.D. Daniels, K.N. Kudin, M.C. Strain, O. Farkas, J. Tomasi, V. Barone, M. Cossi, R. Cammi, B. Mennucci, C. Pomelli, C. Adamo, S. Clifford, J. Ochterski, G.A. Petersson, P.Y. Ayala, Q. Cui, K. Morokuma, D.K. Malick, A.D. Rabuck, K. Raghavachari, J.B. Foresman, J. Cioslowski, J.V. Ortiz, B.B. Stefanov, G. Liu, A. Liashenko, P. Piskorz, I. Komaromi, R. Gomperts, R.L. Martin, D.J. Fox, T. Keith, M.A. Al-Laham, C.Y. Peng, A. Nanayakkara, C. Gonzalez, M. Challacombe, P.M.W. Gill, B.G. Johnson, W. Chen, M.W. Wong, J.L. Andres, M. Head-Gordon, E.S. Replogle, J.A. Pople, GAUSSIAN 98, Revision A.9, Gaussian, Inc., Pittsburgh, PA, 1998.
[13] B.D. Bleany, K. Bowers, Proc. R. Soc. London A 214 (1952) 451.
[14] E.R. Davidson, Int. J. Quantum Chem. 69 (1998) 241.
[15] (a) V.H. Smith Jr., H.F. SchaeferIII, K. Morokuma, K. Yamaguchi, Y. Takahara, T. Fueno (Eds.), Applied Quantum Chemistry, D. Reidel publishing company, Boston, 1986, p. 155;
(b) Y. Takano, Y. Kitagawa, T. Onishi, Y. Yoshioka, K. Yamaguchi, N. Koga, H. Iwamura, J. Am. Chem. Soc. 124 (2002) 450;
(c) Y. Takano, S. Kubo, T. Onishi, H. Isobe, Y. Yoshioka, K. Yamaguchi, Chem. Phys. Lett. 335 (2001) 395;
(d) M. Mitani, D. Yamaki, Y. Takano, Y. Kitagawa, Y. Yoshioka, K. Yamaguchi, J. Chem. Phys. 113 (2000) 10486;
(e) T. Soda, Y. Kitagawa, T. Onishi, Y. Takano, Y. Shigeta, H. Nagao, Y. Yoshioka, K. Yamaguchi, Chem. Phys. Lett. 319 (2000) 223;
(f) T. Kawakami, S. Yamanaka, Y. Takano, Y. Yoshioka, K. Yamaguchi, Bull. Chem. Soc. Jpn. 71 (1998) 2097;
(g) S. Yamanaka, T. Kawakami, H. Nagao, K. Yamaguchi, Chem. Phys. Lett. 231 (1994) 25.
[16] (a) D. Shiomi, K. Sato, T. Takui, J. Phys. Chem. B 105 (2001) 2932;
(b) K. Maekawa, D. Shiomi, K. Sato, T. Takui, J. Phys. Chem. B. 109 (2005) 9299.



2. Experimental

2.1. Measurements

The ^{1}H NMR spectra were measured with a JEOL JNM-EX400 spectrometer (400 MHz). Tetramethylsilan was used as an internal standard for chemical shifts. The IR spectra were measured with a JASCO FT/IR-230 spectrometer. Size exclusion chromatography (SEC) was measured with a TOSOH HLC-8020 chromatograph. THF was used as an eluant and the temperature was kept at 40 °C. The ESR spectra were measured with a JEOL JES-RE1X spectrometer (X-band). Mn^{2+} was used as a standard for the g value. The spin concentration of polyradical was determined by using a solution of 1,3,5-triphenylverdazyl in dichloromethane prepared in known concentration. The temperature dependence of the ESR signal intensity was measured in the region of 123–333 K. The magnetization was measured with a Quantum Design MPMS-7T SQUID magnetometer. The external magnetic field dependence of the magnetization was measured in the region of 0–6 T at the constant temperature. The temperature dependence of the magnetic susceptibility was measured in the region of 2–300 K at the constant external magnetic field of 0.5 T. The diamagnetic contribution from a sample holder, poly(vinyl chloride) (PVC) and poly (methyl methacrylate) (PMMA) was previously measured and corrected. The diamagnetic contribution of the paramagnetic sample was estimated with the Pascal's constants and corrected.

2.2. Synthesis of precursors

Precursors **4**, **5**, **9**, and **10** were prepared by the Suzuki-Miyaura coupling and the Pd-catalyzed amination according to Scheme 1. The procedures were similar for preparing precursor polymers **11** and **12** as mentioned below.

2.2.1. Precursor *4*

Yield: 48.3%. Yellow oil. ^{1}H NMR (acetone-d_6) δ 0.85 (t, $J = 7.1$ Hz, 3H), 1.21–1.41 (m, 8H), 1.51 (q, $J = 7.6$ Hz, 2H), 1.86 (q,$J = 7.1$ Hz, 2H), 4.02 (t, $J = 7.1$ Hz, 2H), 7.12 (d, $J = 8.5$ Hz, 2H), 7.32 (tt, $J = 7.3$, 1.2 Hz, 2H), 7.42–7.47 (m, 6H), 7.50 (dd, $J = 8.5$, 2.2 Hz, 2H), 7.63 (dd, $J = 7.3$, 1.2 Hz, 4H).

2.2.2. Precursor *5*

Yield: 58.0%. Yellowish green prisms. ^{1}H NMR (DMSO-d_6) δ 3.21 (s, 3H), 3.71 (s, 12H), 6.60 (d, $J =$ 2.4 Hz, 2H), 6.73 (dd, $J = 8.8$, 2.4 Hz, 2H), 6.75–6.92 (m, 18H).

2.2.3. Precursor *9*

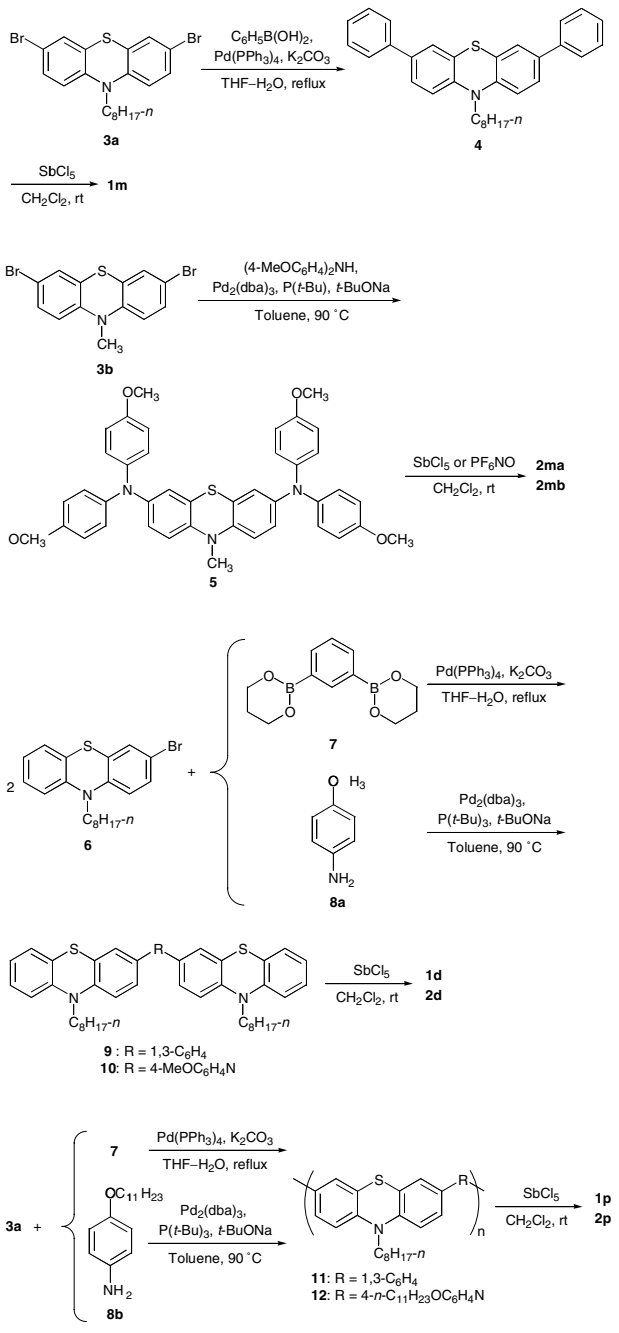
Yield: 34.1%. Yellow oil. ^{1}H NMR (chloroform-d) δ 0.87 (t, $J = 6.8$ Hz, 6H), 1.05–1.51 (m, 20H), 1.84 (q, $J = 6.3$ Hz, 4H), 3.87 (t, $J = 7.1$ Hz, 4H), 6.80–7.02 (m, 6H), 7.08–7.22 (m, 4H), 7.36–7.52 (m, 8H).

2.2.4. Precursor *10*

Yield: 71.0%. Yellowish green oil. ^{1}H NMR (DMSO-d_6) δ 0.83 (t, $J = 6.6$ Hz, 6H), 1.11–1.31 (m, 16H), 1.37 (q, $J = 6.8$ Hz, 4H), 1.66 (q, $J = 6.8$ Hz, 4H), 3.73 (s, 3H), 3.80 (t, $J = 6.8$ Hz, 4H), 6.66 (d, $J = 2.4$ Hz, 2H), (dd, $J = 8.7$, 2.4 Hz, 2H), 6.84–7.01 (m, 10H), 7.09 (d, $J = 7.6$ Hz, 2H), 7.19 (t, $J = 8.3$ Hz, 2H). *Anal.* Calc. for $C_{47}H_{55}N_3OS_2$: C, 76.07; H, 7.47; N, 5.66. Found: C, 76.29; H, 7.67; N, 5.86%.

2.2.5. Precursor *11*

To a solution of **3a** (0.469 g, 1.00 mmol) and **7** (0.246 g, 1.00 mmol) in THF (10 mL) were added a 2M-potassium carbonate aqueous solution (2 mL), tetra-*n*-butylammonium bromide (0.870 g, 2.67 mmol) and $Pd(PPh_3)_4$ (69 mg, 0.06 mmol) and the heterogeneous mixture was refluxed for 24 h under nitrogen. The organic layer was separated and washed with a 5%-sodium cyanide aqueous



Scheme 1. Synthetic route.

solution (3 mL) and brine. After evaporating, the residue was reprecipitated from THF-methanol (7–70 mL) to give **11** in 87.7% yield (0.338 g) as yellow powder. *Anal.* Calcd. for $(C_{26}H_{27}NS)_n$: C, 80.99; H, 7.06; N, 3.63. Found: C, 80.72; H, 7.12; N, 3.54%. The ^{1}H NMR and SEC measurements could not be performed because of the insolubility.

2.2.6. Precursor *12*

To a solution of **3a** (0.704 g, 1.50 mmol) and 4-*n*-undecyloxyaniline (**8b**) (0.395 g, 1.50 mmol) in toluene (15 mL) were added sodium *t*-butoxide (0.432 g, 4.50 mmol), tri-*t*-butylphosphine (36 mg, 0.18 mmol) and $Pd_2(dba)_3$ (82 mg, 0.09 mmol) and the mixture was heated at 90 °C for 12 h under nitrogen. After filtering, the filtrate was washed with a 5%-sodium cyanide aqueous solution (4.4 mL) and brine and dried with anhydrous magnesium sulfate. After evaporating, the residue was reprecipitated from dichloromethane-hexane (5–50 mL) to give **12** in 88.0% yield (0.753 g) as brownish yellow powder. ^{1}H NMR (chloroform-*d*) δ 0.68–0.98 (br s, 6H), 1.09–1.99 (m, 30H), 3.50–4.08 (m, 4H), 6.48–7.18 (m, 10H). *Anal.* Calc. for $(C_{37}H_{50}N_2OS)_n$: C, 77.85; H, 8.83; N, 4.91. Found: C, 65.43; H, 7.18; N, 3.92%. $M_n = 5790$, $M_w = 9640$ (polystyrene standard).

2.3. Formation of cation radicals

To a solution of precursor in dichloromethane was added antimony(V) chloride or nitrosonium hexafluorophosphate. The mixture was stirred for 20 min at room temperature and poured into excess hexane. The precipitate was corrected and recrystallized or reprecipitated.

1m. Recrystallization from dichloromethane-benzene. Yield: 17.4%. Dark green prisms. M.p. 144–145 °C. *Anal.* Calc. for $C_{32}H_{33}Cl_6NSSb$: C, 48.15; H, 4.17; N, 1.75. Found: C, 48.21; H, 4.27; N, 1.64%.

2ma. Reprecipitation from dichloromethane-ether (1:10). Yield: 91.7%. Dark bluish green powder. M.p. 159–160 °C. *Anal.* Calc. for $C_{41}H_{37}Cl_5N_3O_4SSb$: C, 50.93; H, 3.86; N, 4.35. Found: C, 50.22; H, 3.84; N, 4.44%.

2mb. Reprecipitation from THF-ether (1:10). Yield: 58.6%. Dark bluish green powder. M.p. 155–156 °C. *Anal.* Calc. for $C_{41}H_{37}F_6N_3O_4PS$: C, 60.59; H, 4.59; N, 5.17. Found: C, 58.51; H, 4.33; N, 5.76%.

1d. Yield: 22.7%. Reprecipitation from dichloromethane-hexane (1:5). Dark green powder. M.p. 135–136 °C. *Anal.* Calc. for $C_{46}H_{52}Cl_{12}N_2S_2Sb_2$: C, 40.45; H, 3.84; N, 2.05. Found: C, 42.67; H, 4.12; N, 2.08%.

2d. Reprecipitation from dichloromethane-ether (1:10). Yield: 37.7%. Dark bluish green powder. M.p. 129–130 °C. *Anal.* Calc. for $C_{47}H_{55}Cl_{10}N_3OS_2Sb_2$: C, 42.12; H, 4.14; N, 3.14. Found: C, 42.19; H, 4.25; N, 3.38%.

1p. Reprecipitation from dichloromethane-ethyl acetate (1:10). Yield: 85.4%. Dark green powder. *Anal.* Calc. for $(C_{26}H_{27}Cl_6NSSb)_n$: C, 43.37; H, 3.78; N, 1.95. Found: C, 43.17; H, 3.93; N, 1.81%.

2p. Reprecipitation from dichloromethane-ether (1:10). Yield: 79.7%. Dark bluish green powder. *Anal.* Calc. for $(C_{37}H_{50}Cl_5N_2OSSb)_n$: C, 51.09; H, 5.79; N, 3.22. Found: C, 50.88; H, 5.63; N, 3.01%.

3. Results and discussion

3.1. ESR measurement of monomers

The ESR spectra of monomers were measured in dichloromethane (Fig. 1, upper). The spectrum was observed at $g = 2.0055$ for **1m** and 2.0035 for **2ma**. For both **1m** and **2ma**, the signal shape was not a simple triplet line as often observed in the N-centred radicals or cation radicals. The spectrum was then analyzed by the computer-simulation

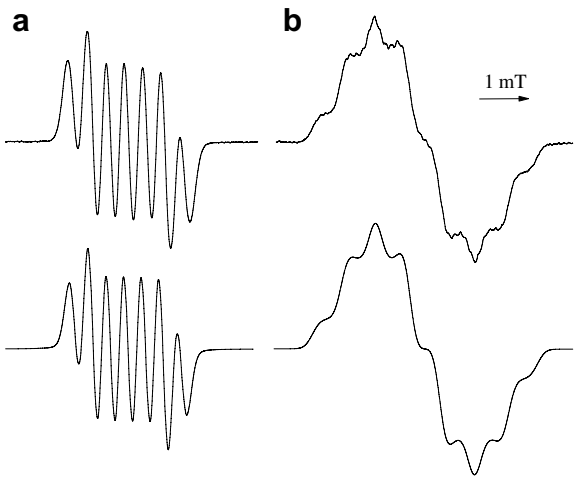


Fig. 1. ESR spectra of (a) **1m** and (b) **2ma** in dichloromethane at room temperature. The upper and bottom spectra are the observed and simulated spectra, respectively.

and the hyperfine coupling (hfc) constants were determined: $a_N = 0.730$ and $a_H = 0.108$ (2H), 0.079 (2H), 0.036 (2H) and 0.362 (2H) mT for **1m** and $a_N = 0.659$ (1N) and 0.234 (2N) and $a_H = 0.118$ (2H), 0.088 (2H), 0.042 (2H) and 0.611 (3H) mT for **2ma**. The simulated spectra reproduced with these hfc constants were in excellent agreement with the observed spectra (Fig. 1, bottom). For **1m**, the delocalization of the spin to two phenyl groups could not be confirmed from this ESR spectrum. Whereas, for **2ma**, the a_N value due to diarylamine nitrogen nuclei suggested the delocalization of the spin to the diarylamine moieties. But, the spin concentration of **2ma** was determined by ESR to be 0.15 spins per molecule, which was unexpectedly low. This would be probably due to another electron transfer shown in Scheme 2. In **2ma**, the electron transfer occurs from not only the phenothiazine moiety but also the diarylamine moiety, resulting in forming dication diradical. Because dication diradical is a singlet specie as shown in the equilibrium with dication, the formation of dication diradical reduces the spin concentration. To improve the spin concentration, the anion part was changed from $SbCl_5$ to PF_6, that is, **2mb** was synthesized (Scheme 1), but the spin concentration was 0.10 spins per molecule, which was similar for **2ma**.

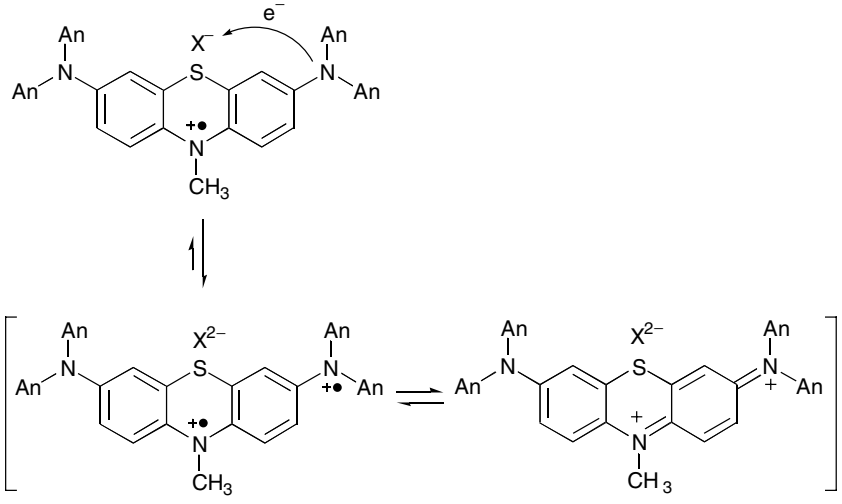
3.2. ESR and magnetization measurements of dimers

The ESR spectra of dimers were measured in dichloromethane and in polymer matrix (Fig. 2). The spectrum was observed in dichloromethane at $g = 2.0051$ for **1d** and 2.0035 for **2d**. For **1d**, the signal shape was a quintet line. Whereas, for **2d**, the signal shape was a singlet line. To confirm the intramolecular spin interaction, the ESR spectra in diluted polymer matrix were measured at 77 K. For **1d** in PMMA matrix, the $\Delta M_S = \pm 2$ transition was observed at ca. 162 mT, indicating of existing the intramolecular spin interaction. The magnetization measurement of **1d** in PMMA matrix was also carried out by a SQUID magnetometer. The external magnetic field dependence of the magnetization is shown in Fig. 3. The experimental data at 2, 4, and 6 K are in accordance with the $S = 1$ line given by the Brillouin function, indicating that **1d** was in the $S = 1$ spin state. This shows that 1,3-phenylene gives the intramolecular ferromagnetic spin interaction as well as polycarbenes and poly(triarylmethine radical)s.

For **2d**, the $\Delta M_S = \pm 2$ transition was not observed in the ESR spectra in PVC matrix. The spin concentration of **2d** was then determined to be 0.34 spins per molecule. Because there are two phenotiazine moieties in **2d**, the percentage of the spin generation was 17%, which was similar for **2ma**. Due to this low spin concentration, **2d** could not be in the triplet state.

3.3. ESR and magnetization measurements of polymers

Because **1p** was insoluble, the ESR spectrum was measured in solid state (Fig. 4a). The spectrum was a singlet



Scheme 2. Potential another electron transfer in **2ma** and **2mb**.

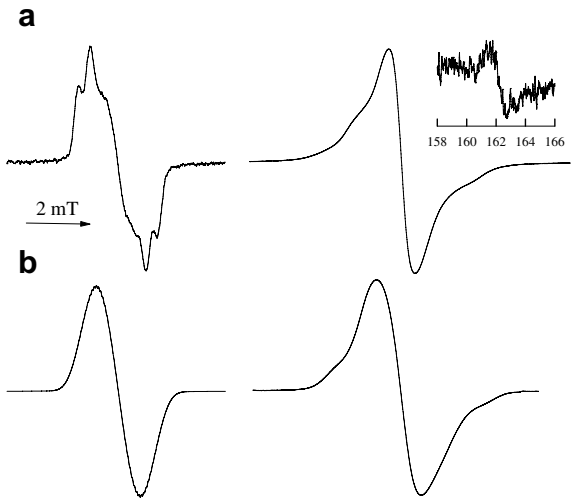


Fig. 2. ESR spectra of (a) **1d** and (b) **2d** at room temperature. The left and right spectra are observed in dichloromethane and in diluted polymer matrix (PMMA for **1d** and PVC for **2d**), respectively. The $\Delta M_S = \pm 2$ transition was observed at ca. 162 mT at 77 K in PMMA matrix in Fig. 2(a).

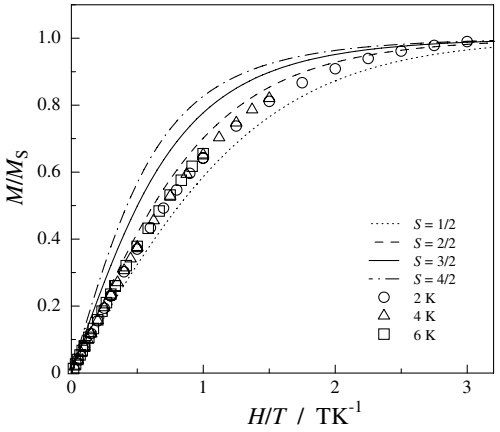


Fig. 3. External magnetic field dependence of the magnetization of **1d** in PMMA matrix (4.7 wt% content). The points are the experimental data at 2, 4, and 6 K. The lines are the theoretical lines for $S = 1/2$, 2/2, 3/2, and 4/2 given by the Brillouin function.

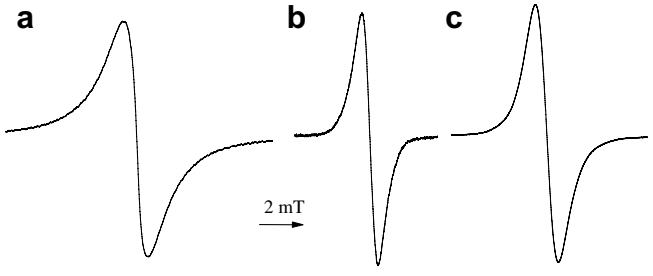


Fig. 4. ESR spectra of **1p** and **2p** at room temperature. (a) **1p** in solid state. (b) **2p** in dichloromethane. (c) **2p** in PVC matrix.

line, indicating that the spin concentration is high. The spin concentration was estimated from the magnetic susceptibility measured by SQUID (Fig. 5). The $\chi_{mol}T$ value is 0.290

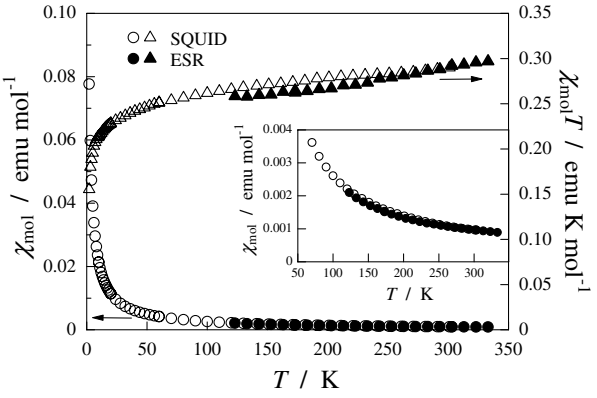


Fig. 5. Temperature dependence of the magnetic susceptibility and the ESR signal intensity of **1p** (bulk solid). The external magnetic field was 0.5 T in the SQUID measurement.

at 300 K, which corresponds to the spin concentration of 0.77 spins per repeating unit. The $\chi_{mol}T$ value already decreases near room temperature region as the temperature decreases. This was also confirmed by ESR [11]. The temperature dependence of the ESR signal intensity is in good accordance with the data obtained by SQUID. The decrease of the $\chi_{mol}T$ value indicates the antiferromagnetic interaction. Because dimer **1d** was in the $S = 1$ spin state (Fig. 3), the intramolecular spin interaction in **1p** was ferromagnetic. Therefore, the antiferromagnetic interaction was due to the intermolecular spin interaction.

The ESR spectra of **2p** were measured in dichloromethane and in PVC matrix (Fig. 2). The spectrum in dichloromethane was observed at $g = 2.0046$ and the signal shape was a singlet line. The spin concentration was determined by ESR to be 0.16 spins per repeating unit. Although the formation percentage of complexes between the phenothiazine moieties in **12** and $SbCl_5$ were estimated to be near 100% from the result of the elemental analysis, the spin concentration was low as well as **2ma** and **2d**. In the ESR

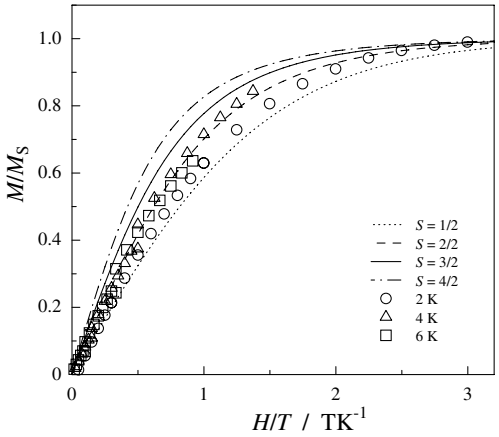


Fig. 6. External magnetic field dependence of the magnetization of **2p** in PVC matrix (4.6 wt% content). The points are the experimental data at 2, 4, and 6 K. The lines are the theoretical lines for $S = 1/2$, 2/2, 3/2, and 4/2 given by the Brillouin function.

spectrum in PVC matrix at 77 K, no $\Delta M_S = \pm 2$ transition was observed, which would be due to the low spin concentration. But, in the magnetization measurement in PVC matrix (Fig. 6), the external magnetic field dependence of the magnetization showed that **2p** was in the $S = 1$ state. In taking into account that the degree of polymerization of **12** was ca. 10 and the spin concentration of **2p** was 0.16 spins per repeating unit, there were two spins per molecule in **2p**. There would be the ferromagnetic interaction between those two spins in the low temperature region.

4. Summary

Two types of organic open-shell polymer containing phenothiazine cation radicals as spin resources were synthesized. The one is the 1,3-phenylene-linked polymer **1p**, and the other is the arylamine nitrogen-linked polymer **2p**. Precursor polymers were prepared by the Suzuki-Miyaura coupling and the Pd-catalyzed amination. The formation of complexes between the phenothiazine moieties in precursor polymers and antimony(V) chloride gave stable open-shell polymers. The magnetic behavior of **1p** was intramolecularly ferromagnetic, but intermolecularly antiferromagnetic. Whereas, **2p** was in the $S = 1$ spin state in spite of low spin concentration of 0.16 spins per repeating unit.

Acknowledgement

We thank the Materials Design and Characterization Laboratory, Institute for Solid State Physics, The University of Tokyo for using a SQUID magnetometer.

References

[1] K. Itoh, M. Kinoshita (Eds.), Molecular Magnetism, Kodansha, Tokyo, 1999.
[2] P.M. Lahti (Ed.), Magnetic Properties of Organic Materials, Marcel Dekker, New York, 1999.
[3] J.A. Crayston, J.N. Devine, J.C. Walton, Tetrahedron 56 (2000) 7829.
[4] (a) T. Michinobu, J. Inui, H. Nishide, Org. Lett. 5 (2003) 2165;
(b) H. Murata, M. Takahashi, K. Namba, N. Takahashi, H. Nishide, J. Org. Chem. 69 (2004) 631;
(c) E. Fukuzaki, H. Nishide, J. Am. Chem. Soc. 128 (2006) 996.
[5] R.J. Bushby, D.R. McGill, K.M. Ng, N. Taylor, J. Mater. Chem. 7 (1997) 2343.
[6] (a) H. Oka, T. Tamura, Y. Miura, Y. Teki, J. Mater. Chem. 9 (1999) 1227;
(b) H. Oka, T. Tamura, Y. Miura, Y. Teki, Polym. J. 31 (1999) 979;
(c) H. Oka, T. Tamura, Y. Miura, Y. Teki, J. Mater. Chem. 11 (2001) 1364.
[7] A.R. Forrester, J.M. Hay, R.H. Thomson, Organic Chemistry of Stable Free Radicals, Academic Press, New York, 1968.
[8] (a) K. Okada, T. Imakura, M. Oda, H. Murai, J. Am. Chem. Soc. 118 (1996) 3047;
(b) K. Okada, T. Imakura, M. Oda, A. Kajiwara, M. Komachi, K. Sato, D. Shiomi, T. Takui, K. Itoh, L. Gherghel, M. Baumgarten, J. Chem. Soc. Perkin Trans. 2 (1997) 1059;
(c) T. Okamoto, M. Kuratsu, M. Kozaki, K. Hirotsu, A. Ichimura, T. Matsushita, K. Okada, Org. Lett. 6 (2004) 3493.
[9] (a) For example Y. Teki, T. Takui, K. Itoh, H. Iwamura, K. Kobayashi, J. Am. Chem. Soc. 108 (1986) 2147;
(b) K. Matsuda, N. Nakamura, K. Takahashi, K. Inoue, N. Koga, H. Iwamura, J. Am. Chem. Soc. 117 (1995) 5550.
[10] (a) For example A. Rajca, Chem. Rev. 94 (1994) 871;
(b) A. Rajca, J. Wongsriratanakul, S. Rajca, Science 294 (2001) 1503;
(c) A. Rajca, J. Wongsriratanakul, S. Rajca, J. Am. Chem. Soc. 126 (2004) 6608.
[11] R. Ziessel, C. Stroh, H. Heise, F.H. Köhler, P. Turek, N. Claiser, M. Souhassou, C. Lecomte, J. Am. Chem. Soc. 126 (2004) 12604.

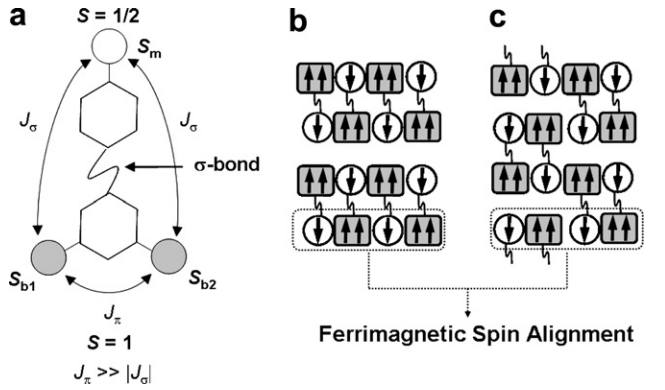
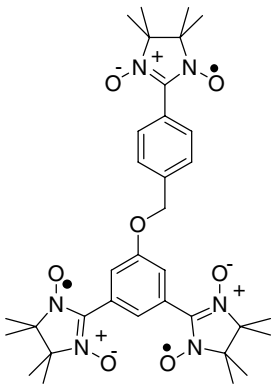


Fig. 1. (a) Triradical consisting of weakly coupled monoradical and biradical moieties. In the three-centered exchange-coupled system, J_σ show the weak exchange interaction through the σ-bonds, while J_π denotes the ferromagnetic exchange interaction through the π-conjugation in the *m*-phenylene-based biradical moiety. (b,c) Head-to-tail packings of triradical molecules leading to the ferrimagnetic spin alignment.

ferrimagnetic spin alignment in a head-to-tail molecular packing of the triradical molecules, as depicted in Fig. 1(b) and (c).

The alternating aggregation of the heterospin entities is achieved by tuning the molecular geometry of the building-block molecules, leading to the close packing of approximately isosceles triangular molecules in a head-to-tail fashion. As building blocks for the head-to-tail packing of the approximately isosceles triangular molecules, we have designed triradicals based on a 1,3,5-triyl benzene framework of 3,5-substituted phenyl benzoate [3]. A close packing of the isosceles triangular molecules has been found to lead to the alternating aggregation of the two kinds of open-shell entities [3]. In the present study, we have designed another type of approximately isosceles triangular molecules; benzyl-phenyl ether derivative of nitronyl nitroxide ***p*-trisNN** (**1**) (Scheme 1). The ether group is expected to truncate the exchange interactions through the π-conjugation. The synthesis of **1** has been reported [4]. Magnetic susceptibility of **1** has been measured for magnetically diluted systems of organic polymer films [4], in which intermolecular exchange interactions are suppressed. From the susceptibility of the isolated molecules, it has been found that the magnitude of $|J_\sigma|$ is much weaker than that of J_π by two orders of magnitude; $J_\pi/k_B = 16.8$ K, $J_\sigma/k_B = -0.27$ K for **1** [4]. Thus, the condition Eq. (2) is fulfilled in **1**, indicating its potential as a building block for single-component ferrimagnetics. In this communication, we report magnetic properties of **1** in the neat crystalline solid state in relation to its crystal structure.



***p*-trisNN (1)**

Scheme 1. Triradical *p*-**trisNN** (**1**).

2. Experimental

2.1. Crystal structure analysis

Single-crystal X-ray diffraction data of **1** were collected on a Rigaku Mercury CCD diffractometer with graphite-monochromated Mo Kα radiation. The crystal structure was solved by using direct methods in a program package CrystalStructure.[1] From powder X-ray diffraction experiments, we have confirmed that the crystal structure of the polycrystalline samples used in magnetic susceptibility measurements is the same as that determined in the single crystal X-ray experiments.

2.2. Magnetic susceptibility measurements

Magnetic susceptibility was measured on a Quantum Design SQUID magnetometer MPMS-XL under the static magnetic field of 0.1 T in the temperature range down to 1.9 K.

3. Results and discussion

3.1. Crystal structure

The crystallographic data of *p*-**trisNN** (**1**) are listed in Table 1. The molecular structure with the atom numbering scheme is given in Fig. 2. The molecules of **1** are arranged in a head-to-tail manner along the *a* axis, as depicted in Fig. 3(a). Intermolecular close contacts shorter than the van der Waals one [5] are found only in pairs of inversion-related nearest-neighboring molecules. Thus, the molecular chain along the *a* axis is regarded as an assemblage of exchange-coupled six $S = 1/2$ spins in the pairs, or dimers, of the triradicals. One of the contacts within the dimer is found between the nitronyl nitroxide group (NN1) of the biradical moiety and the group NN2 of the neighboring inversion-related molecule. The NN1–NN2 contact, termed "Contact A", contains interatomic short distances of O5–C7′ = 3.088(5) Å and O5–C3′ = 3.198 (5) Å, as shown in Fig. 3(b). Another contact occurs between the biradical moiety (NN1) and the phenyl ring (Ph2) with a short distance of O3–C23′ = 3.373(4) Å, as designated "Contact B" in Fig. 3(b). Intermolecular

[1] CrystalStructure (ver.3.7.0): Crystal Structure Analysis Package, Rigaku/Molecular Structure Corporation (2000–2005), 9009 New Trails Dr. The Woodlands, TX 77381, USA.

Table 1
X-ray crystallographic data for **1**

Compound	***p*-trisNN (1)**
Formula	$C_{34}H_{45}N_6O_7$
Crystal system	monoclinic
Space group	$P2_1/a$
a (Å)	12.874(10)
b (Å)	27.517(20)
c (Å)	10.723(8)
β (°)	117.569(9)
V (Å^3)	3367(4)
Z	4
ρ_{calc} (g cm^{-3})	1.282
Unique reflections used ($I > 3\sigma(I)$)	7741
$R(I > 3\sigma(I))$	0.0988[a]
R_{w2} (all data)	0.2799[b]
Goodness-of-fit	1.000
T (K)	143

[a] $R = \sum ||F_o| - |F_c|| / \sum |F_o|$.

[b] $R_{w2} = \left[\sum w(F_o^2 - F_c^2)^2 \Big/ \sum w(F_o^2)^2\right]^{\frac{1}{2}}$, $w = 1/[0.0142F_o^2 + 1.0000\sigma^2(F_o^2)]/(4F_o^2)$.

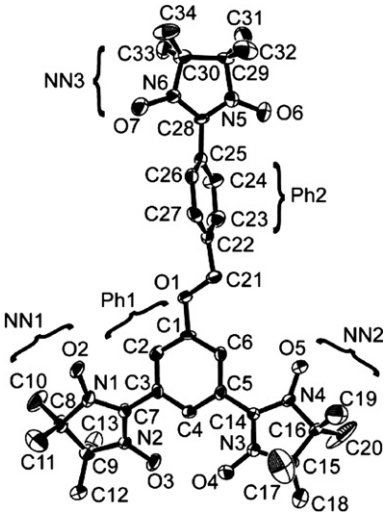


Fig. 2. ORTEP view of **1** at the 50% probability level. The hydrogen atoms are omitted for the sake of clarity.

exchange interactions are expected at Contact A and Contact B, which are designated J_A and J_B, respectively. The possible intermolecular interactions J_A and J_B, together with the intramolecular interactions J_π and J_σ, afford a six-spin cluster in the dimer, as illustrated in Fig. 3(c).

3.2. Magnetic susceptibility

The paramagnetic susceptibility χ_p measured for neat polycrystalline solid samples of ***p*-trisNN (1)** is depicted in Fig. 4 in the χ_pT versus T plots. On lowering the temperature the χ_pT value increases from the high-temperature limit for three moles of $S = 1/2$ spins, indicating the occurrence of a dominating ferromagnetic interaction. It should be noted that the observed χ_pT value is larger than 1.38 emu K mol^{-1}

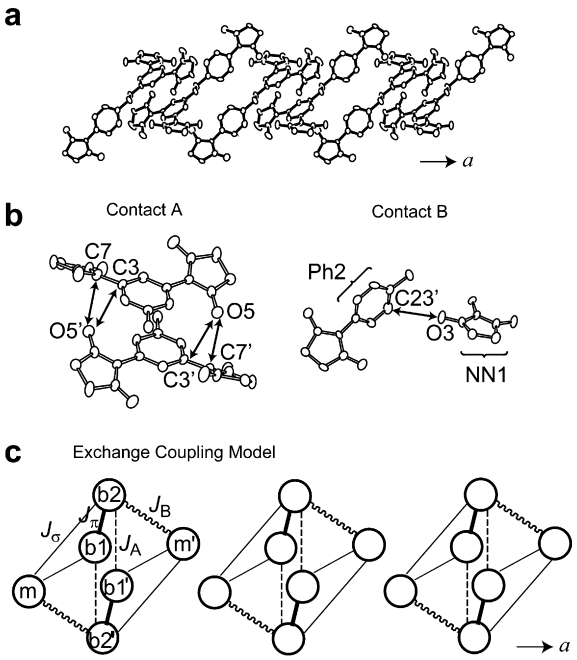


Fig. 3. (a) Molecular packing of ***p*-trisNN (1)** in the head-to-tail alignment along the a-axis. (b) Two types of intermolecular short contacts A, B in the dimer of **1**. (c) Exchange coupling model for the molecular assembly of **1**. The thick and thin solid lines represent the intramolecular exchange interactions J_π and J_σ, respectively. The dashed and wavy lines denote the intermolecular exchange interactions J_A and J_B at the contacts A and B, respectively.

at low temperature, which is expected for a noninteracting pair of $S = 1/2$ and $S = 1$ spins. This indicates that the ferromagnetic interaction is operative between the biradical moieties in the dimer that is ascribed to J_A at Contact A. The χ_pT value has a maximum at 12 K, indicating an antiferromagnetic intermolecular interaction between the monoradical moiety and the ferromagnetically-coupled four $S = 1/2$ spins of the biradical moieties in the dimer, that is J_B of Contact B. The temperature dependence of χ_pT was analyzed with the six-spin cluster model

$$\begin{aligned} H = &-2J_\pi(\mathbf{S}_{b1}\cdot\mathbf{S}_{b2} + \mathbf{S}_{b1'}\cdot\mathbf{S}_{b2'}) \\ &- 2J_\sigma(\mathbf{S}_{b1}\cdot\mathbf{S}_{m} + \mathbf{S}_{b2}\cdot\mathbf{S}_{m} + \mathbf{S}_{b1'}\cdot\mathbf{S}_{m'} + \mathbf{S}_{b2'}\cdot\mathbf{S}_{m'}) \\ &- 2J_A(\mathbf{S}_{b1}\cdot\mathbf{S}_{b2'} + \mathbf{S}_{b2}\cdot\mathbf{S}_{b1'}) - 2J_B(\mathbf{S}_{m}\cdot\mathbf{S}_{b2'} + \mathbf{S}_{b2}\cdot\mathbf{S}_{m'}) \end{aligned} \quad (3)$$

which has been suggested from the X-ray crystal structure analysis [6], as depicted in Fig. 3(c). Numerical diagonalization was applied to Eq. (3), giving energy eigenvalues E_i and spin eigenvalues S_i for the ith eigenstate from which the temperature dependence of χ_pT was calculated as

$$\chi = \frac{N_A g^2 \mu_B^2}{6k_B T} \cdot \frac{\sum_i [S_i(S_i+1)(2S_i+1)\exp(-E_i/k_B T)]}{\sum_i [(2S_i+1)\exp(-E_i/k_B T)]} \quad (4)$$

The intramolecular interactions of $J_\pi/k_B = 16.8$ K and $J_\sigma/k_B = -0.27$ K as obtained from the diluted organic polymer film [4] were assumed to remain unchanged in the crystal in order to avoid overparameterization. The

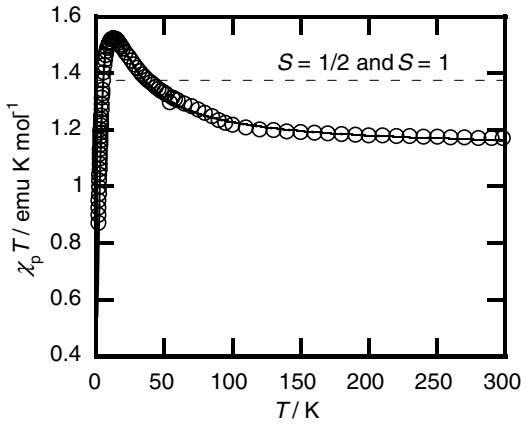


Fig. 4. Temperature dependence of paramagnetic susceptibility χ_p of ***p*-trisNN** (**1**) in the $\chi_p T$ versus T plots. The solid line denotes the calculated values from the six-spin cluster model (Eqs. (3) and (4)). The horizontal dotted lines show the Curie law for a noninteracting pair of $S = 1/2$ and $S = 1$.

g-factor of $g = 2.006$ as observed from the solution ESR spectra of **1** was fixed as well. The independent adjustable parameters J_A and J_B were optimized to be $J_A/k_B = 13 \pm 2$ K, $J_B/k_B = -3.0 \pm 0.4$ K.

An intermolecular short contact between the central carbon atom of nitronyl nitroxide, which is usually negatively spin-polarized, and the nitroxide oxygen with a positive spin density, such as C7 and O5 of contact A in **1**, is expected to give rise to an intermolecular ferromagnetic interaction as found in other nitronyl nitroxide crystals [7]. This is consistent with the positive parameter of $J_A/k_B = 13$ K for **1**.

4. Conclusion

The triradical derivative of nitronyl nitroxide, ***p*-trisNN** (**1**), has been synthesized as a building block molecule for single-component organic molecule-based ferrimagnetics. The crystal structure and the magnetic properties in the solid state have been examined. The alternating arrangement of the $S = 1$ and the $S = 1/2$ moieties has been accomplished by uniting the two open-shell entities in the approximately isosceles triangular geometry. Another triradical derivative (**2**) of benzyl-phenyl ether with the approximately isosceles triangular geometry has been synthesized.[2] The molecular packing of **2** is quite similar to that of **1**, indicating the efficiency of the close packing of isosceles triangular molecules leading to the alternating aggregation of the two kinds of molecular entities. The triradical **1**, however, has been found to possess the intermolecular ferromagnetic interaction which is not suitable for ferrimagnetic spin alignment. The head-to-tail molecular packing of the biradical–monoradical composite molecules is not necessarily compatible with interatomic contacts between the radical fragments leading to intermolecular antiferromagnetic exchange interactions. Further elaborate control for molecular arrangement is necessary for the full control of intermolecular exchange interactions suitable for ferrimagnetic spin alignment.

[2] The monoradical moiety of the isomer **2** is substituted with *m*-benzyl. The magnetic susceptibility of **2** was analyzed with the same model as **1** (Eqs. (3) and (4)) based on the similarity of the crystal structure. The exchange interactions derived from the analysis are $J_\pi/k_B = 16.0$ K, $J_\sigma/k_B = -0.14$ K, $J_A/k_B = 1.5$ K, and $J_B/k_B = -5.2$ K.

Acknowledgements

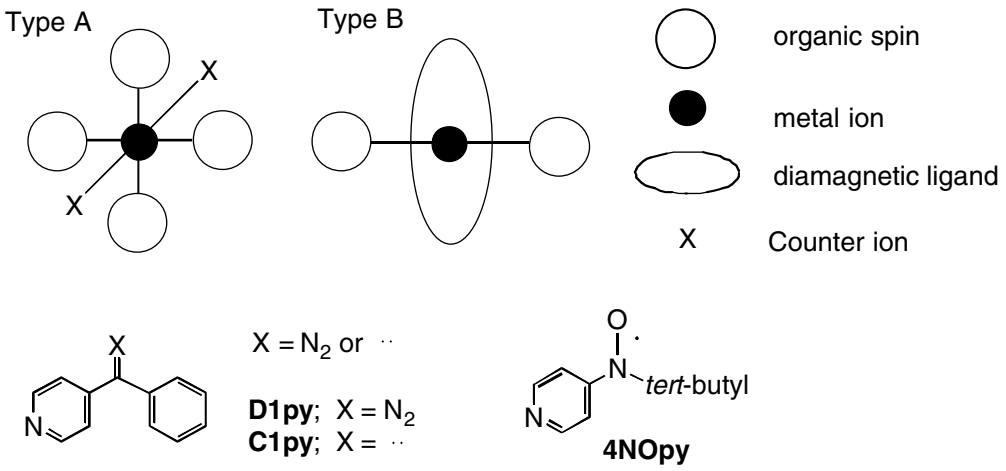
This work has been supported by Grants-in-Aid for Scientific Research from the Ministry of Education, Sports, Culture, Science and Technology, Japan. Financial support from PRESTO of Japan Science, Technology Agency (JST) is also acknowledged. One of the authors (Y.K.) acknowledges Research Fellowships of the Japan Society for the Promotion of Science for Young Scientists.

Appendix A. Supplementary material

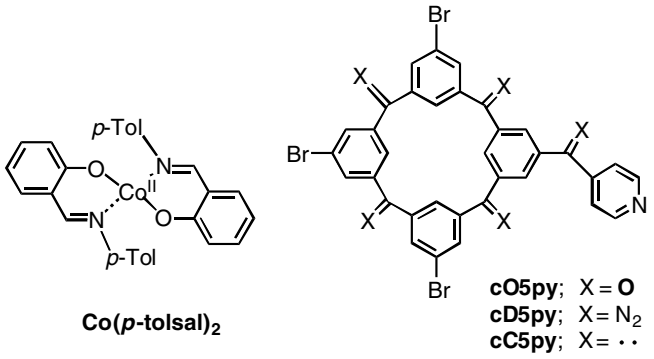
CCDC 615690 and 615691 contain the supplementary crystallographic data for ***p*-trisNN** (**1**) and **2**. These data can be obtained free of charge via http://www.ccdc.cam.ac.uk/conts/retrieving.html, or from the Cambridge Crystallographic Data Centre, 12 Union Road, Cambridge CB2 1EZ, UK; fax: (+44) 1223-336-033; or e-mail: deposit@ccdc.cam.ac.uk. Supplementary data associated with this article can be found, in the online version at doi:10.1016/j.poly.2006.09.035.

References

[1] L. Néel, Ann. Phys. Ser. 12 (3) (1948) 137.
[2] (a) D. Shiomi, T. Kanaya, K. Sato, M. Mito, K. Takeda, T. Takui, J. Am. Chem. Soc. 123 (2001) 11823;
(b) T. Kanaya, D. Shiomi, K. Sato, T. Takui, Polyhedron 20 (2001) 1397;
(c) D. Shiomi, M. Nishizawa, K. Kamiyama, S. Hase, T. Kanaya, K. Sato, T. Takui, Synth. Met. 121 (2001) 1810;
(d) C. Kaneda, D. Shiomi, K. Sato, T. Takui, Polyhedron 22 (2003) 1809;
(e) T. Ise, D. Shiomi, K. Sato, T. Takui, Synth. Met. 154 (2005) 297;
(f) K. Maekawa, D. Shiomi, T. Ise, K. Sato, T. Takui, J. Phys. Chem. B 109 (2005) 3303;
(g) T. Ise, D. Shiomi, K. Sato, T. Takui, Chem. Mater. 17 (2005) 4486;
(h) T. Ise, D. Shiomi, K. Sato, T. Takui, J. Low Temp. Phys. 142 (2006) 589.
[3] Y. Kanzaki, D. Shiomi, C. Kaneda, T. Ise, K. Sato, T. Takui, J. Mater. Chem. 16 (2006) 2064.
[4] Y. Kanzaki, T. Ise, D. Shiomi, K. Sato, T. Takui, J. Low Temp. Phys. 142 (2006) 593.
[5] A. Bondi, J. Phys. Chem. 68 (1964) 441.
[6] A similar model of exchange-coupled systems composed of six $S = 1/2$ spins has been reported: L. Catala, J. Le Moigne, N. Gruber, J.J. Novoa, P. Rabu, E. Belorizky, P. Turek, Chem. Eur. J. 11 (2005) 2440.
[7] (a) For example, see: K. Inoue, H. Iwamura, Chem. Phys. Lett. 207 (1993) 551;
(b) F.L. Panthou, D. Luneau, J. Laugier, P. Rey, J. Am. Chem. Soc. 115 (1993) 9095;
(c) J. Omata, T. Ishida, D. Hashizume, F. Iwasaki, T. Nogami, Inorg. Chem. 40 (2001) 3954;
(d) K. Hayakawa, D. Shiomi, T. Ise, K. Sato, T. Takui, J. Phys. Chem. B 109 (2005) 9195.



ion. Taking the total S value in the hexacoordinate cobalt (II) complex into account, a pyridine ligand having five diazo moieties, **cD5py**, in addition to **D1py**[1] was prepared. The pyridine ligand, **cD5py**, was expected to produce the high-spin carbene, **cC5py**, with $S = 10/2$ after irradiation.



In this work, the magnetic property of 1:2 mixture of Co(*p*-tolsal)$_2$ and cyclic pentadiazo-pyridine ligands, **cD5py**, in dilute frozen solution after irradiation was investigated by SQUID magneto/susceptometry.

2. Experimental

2.1. General

Infrared spectra were recorded on a JASCO 420 FT-IR spectrometer. ^{1}H NMR spectra were measured on a Varian UNITY-400 using $CDCl_3$ as solvent and referenced to TMS. Visible spectra were recorded on a JASCO V570 spectrometer and an NACC cryo-system LTS-22X was attached for the low temperature measurements. The solution samples were placed in separable quartz cells (path length; 1 mm) under helium atmosphere. Photolyses of diazo samples were performed by argon ion laser (514 nm, 200 mW, Omnichrome 543–200 M). Melting points were obtained with a MEL-TEMP heating block and are uncorrected.

2.2. X-ray crystal and molecular structure analyses

Crystallographic data and experimental details for **cD5py** are summarized in Table 1. The selected suitable single crystals were glued on a glass fiber by epoxy resin. All the X-ray data were collected on a Rigaku Raxis-Rapid diffractometer with graphite monochromated Mo Kα radiation ($\lambda = 0.71069$ Å). Reflections were collected at 123 ± 1 K. The structures were solved by direct methods (SIR92) [6]. The refinements were converged using the full-matrix least-squares method of the Crystal Structure software package [7] to give a space group as $P\bar{1}$ (no. 2). All non-hydrogen atoms were refined anisotropically.

Table 1
Crystallographic data of **cD5py**

Formula	$C_{35}H_{18}N_{11}Br_3Cl_2$
Fw	903.22
Crystal system	triclinic
Space group	$P\bar{1}$ (no. 2)
a (Å)	12.415(2)
b (Å)	16.041(2)
c (Å)	8.795(2)
α (°)	99.746(3)
β (°)	97.766(7)
γ (°)	81.759(9)
V (Å^3)	1697.3(4)
Temperature (K)	123
Z	2
D_{calc} (g/cm^3)	1.767
Crystal habit	prism
Color	red
Dimension	$0.25 \times 0.15 \times 0.25$
R_1, wR_2 [$I > 3\sigma(I)$]	0.066, 0.205
Goodness-of-fit	1.003
Number of observations	3810
Number of variables	478

[1] The work using **D1py** in a similar heterospin system will be reported elsewhere.

Hydrogen atoms were found by standard method or from differential electron map and refined isotropically.

2.3. Measurements and analyses of magnetic properties

Ac and dc magnetic susceptibility data were obtained on Quantum Design MPMS2 (0–±10 kOe) and MPMS-5S (0–±50 kOe) SQUID magneto/susceptometers, respectively. Irradiation by the light from an argon ion laser (514 nm, 200 mW, Omnichrome 543–200 M) through a flexible optical fiber (Newport F-MBD; 3 m of length, 1.0 mm of core size, and 1.4 mm of diameter) which passes through the inside of a sample folder for SQUID was performed inside a sample room of SQUID at 7 K. One end of the optical fiber was fixed at 40 mm above the sample cell (capsule) and the other end was attached to a coupler (Body; Newport M-F-916T and lens; M-10X) for the lasers. The bottom part of the capsule (6 mm × 10 mm) without a cap was used as a sample cell. Fifty microlitres of the sample solution (5 mM) in MTHF was placed in the cell held by a straw.

2.4. Materials

2-Methyltetrahydrofuran (MTHF) and ether were distilled from sodium benzophenone ketyl. The cobalt complex, Co(*p*-tolsal)$_2$, was prepared by the procedure reported previously.

cD5py Calix[4]arene derivative which was reported by Rajca [8], was used as the starting compound. A cyclic pentaketone–pyridine derivative, **cO5py**, was prepared by a procedure similar to that for the linear polyketone–pyridine compounds.[1] **cO5py** was converted to the corresponding diazo derivative **cD5py** quantitatively by using a standard procedure reported previously [4]. **cD5py** was crystallized from CH_2Cl_2 at 4 °C and obtained as red needles. Mp: 102 °C (decomp.). IR (KBr disc) ν 2043 cm^{-1}, UV–Vis (CH_2Cl_2, ε) 504 nm (535); ^{1}H NMR (400 MHz, $CDCl_3$): δ 8.51(dd, $J = 1.7$, 4.7 Hz, 2H), 7.13 (d, $J = 1.7$ Hz, 6H), 7.07 (dd, $J = 1.7$, 4.7 Hz, 2H), 6.99 (d,$J = 1.7$ Hz, 2H), 6.95 (s, 4H).

3. Results and discussion

3.1. X-ray molecular structure analysis of *cD5py*

ORTEP drawing of the molecular structure for **cD5py** is shown in Fig. 1. The geometry of the cyclic framework of **cD5py** is similar to that for the calix[4]arene derivatives, in which the phenyl ring directs alternately. The bond angles of the carbon of the diazo moiety inside the ring structure are in the range of 125–129°, which is consistent with that of 127° for the out side the ring structure and for **D1py**, indicating that the carbon of the diazo moieties undergoes no strain caused by the cyclic structure. The dihedral angles between the phenyl rings are in the range of 63–73°. Those values are slightly larger than those (ca. 45°) for linear diphenyldiazo derivatives. The selected bond angles and dihedral angles are given in Table 2.

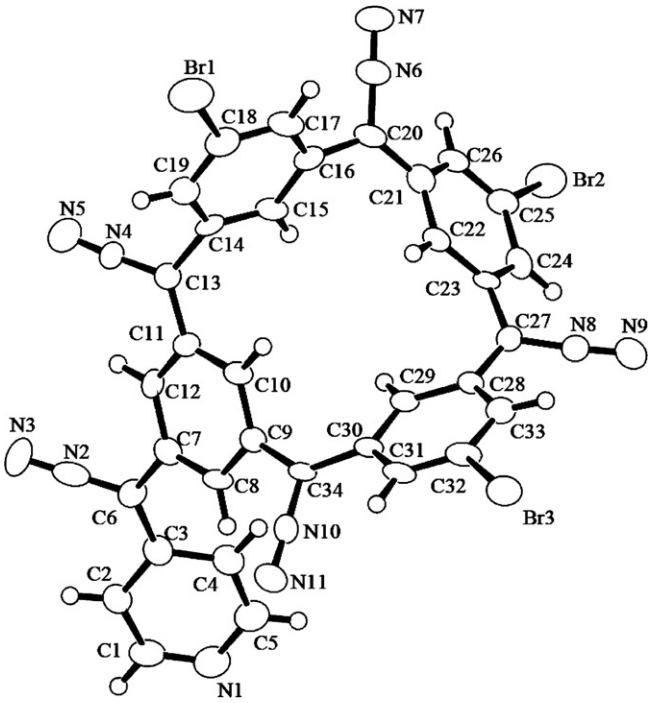


Fig. 1. ORTEP drawing of the molecular structures for **cD5py** showing 50% probabilities ellipsoids, including CH_2Cl_2 are omitted for clarity.

Table 2
Selected bond angles (°), and dihedral angles (°) of **cD5py**

Bond angles (°)		Dihedral angles (°)	
C(11)C(13)C(14)	125.62	C(22)C(24)C(26)–C(15)C(17)C(19)	71.270
C(16)C(20)C(21)	125.19	C(15)C(17)C(19)–C(8)C(10)C(12)	73.220
C(23)C(27)C(28)	128.75	C(8)C(10)C(12)–C(29)C(31)C(33)	62.952
C(30)C(34)C(9)	128.88	C(29)C(31)C(33)–C(22)C(24)C(26)	65.664
C(3)C(6)C(7)	127.26	C(8)C(10)C(12)–N(1)C(2)C(4)	46.617

3.2. Visible spectra of *cD5py* and Co(*p*-tolsal)$_2$-(*cD5py*)$_2$ complex

To confirm the generation of carbene after irradiation and the formation of a six-coordinate structure for **cD5py** and Co(*p*-tolsal)$_2$-(**cD5py**)$_2$ complex, respectively, Visible spectra before and after irradiation were measured at 12 K. The solutions (5 mM) of **cD5py** and Co(*p*-tolsal)$_2$-(**cD5py**)$_2$ complex in MTHF were used as the samples. In the Visible spectrum of **cD5py** at 12 K, the characteristic absorption at 504 nm due to n–π^* transition of the diazo moiety decreased on photolysis ($\lambda = 514$ nm) and a new broad absorption with shoulders in a range of 450–400 nm due to the carbenes appeared. The visible spectrum for a 1:2 mixture of Co(*p*-tolsal)$_2$ and **cD5py** in MTHF at 12 K showed the absorption (shoulder) at ca. 520 nm which is characteristic the d–d transition for an octahedral structure. However, the absorption was overlapped with those

for the diazo moieties with relatively large intensity ($\varepsilon \sim 530$) and could not be clearly assigned as that due to an octahedral structure. A new broad absorption at 650 nm appeared on photolysis at 12 K (Fig. S1), suggesting that **cC5py** coordinates with the cobalt ion. The new absorption disappeared after annealing at 90 K.

3.3. Magnetic properties

3.3.1. *cD5py* in frozen solution after irradiation

In order to determine the ground-state spin multiplicity, S, for **cC5py**, the field dependence of the magnetization after irradiation of **cD5py** was investigated. The solution (4 mM, 50 μl) of **cD5py** in MTHF was used as a sample and the magnetization measurement was carried out under the frozen solution condition. Magnetization data (M_a and M_b; M_a and M_b are magnetization after and before irradiation, respectively,) were collected at 2 and 5 K in the field range of 0–50 kOe. The field dependence of M/M_s; $M = M_a - M_b$ and M_s is a saturation magnetization, for **cC5py** is shown in Fig. 2 together with a theoretical curve with $S = 10/2$. All experimental data at 2 and 5 K traced on the theoretical curve with $S = 10/2$, indicate that five carbene centers generated by photolysis of the diazo units in **cD5py** interact ferromagnetically through the *m*-phenylene ring to produce a high-spin carbene, **cC5py**, with $S = 10/2$.

3.3.2. Co(*p*-tolsal)$_2$-(*cD5py*)$_2$ complex in frozen solution after irradiation

The solution (4 mM, 50 μl) of the 1:2 mixture of Co(*p*-tolsal)$_2$ and **cD5py** in MTHF, was employed as a sample. The ac and dc magnetic susceptibilities of the frozen solution samples were measured before and after irradiation. Photolysis of the sample was performed in SQUID apparatus through an optical fiber and followed by magnetization (M_{mol}) measurements at 5 kOe at 5 K. The magnetization was plotted as the function of the irradiation time (Fig. 3). When the irradiation started, the M_{mol} values gradually developed and leveled off after ca. 1 h. The increase in the M_{mol} values on photolysis results from the generation of carbene.

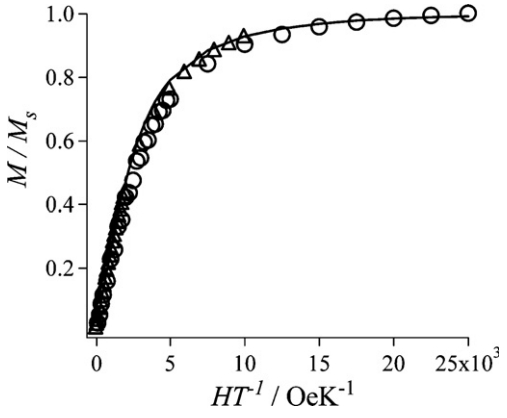


Fig. 2. The plot of M/M_s vs H/T at 2.0 (○) and 5 (△) K for **cC5py** in MTHF frozen solution. The solid curve is theoretical one with $S = 10/2$.

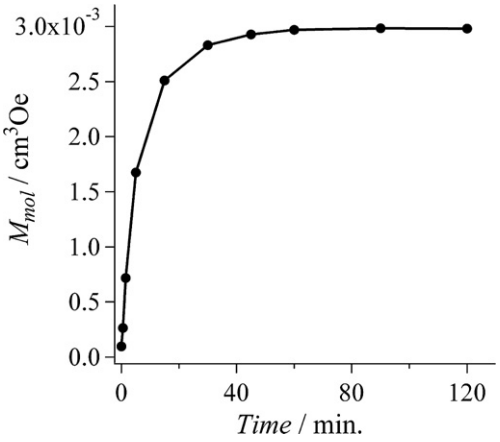


Fig. 3. The plot of M vs. *irradiation time* at 5 kOe at 5 K for the solution sample of 1:2 mixture of Co(*p*-tolsal)$_2$ and **cD5py**.

3.3.2.1. AC magnetic susceptibility measurements. Ac magnetic susceptibility measurements with a 5 Oe ac field oscillating at 997, 499, 99.9, 10, and 1 Hz, for the 1:2 mixture of Co(*p*-tolsal)$_2$ and **cD5py** after irradiation were carried out. The in-phase and out-of phase components (χ' and χ'' signals, respectively) with frequency dependence were observed. The plots of $\chi'T$ versus T and χ'' versus T are shown in Fig. 4a and b, respectively.

In the plot of $\chi'T$ versus T, the in-phase $\chi'T$ value is 37.2 cm^3 K mol^{-1} at 10 K and remains essentially constant on cooling down to 5–7 K. The value (37.2) at 10 K is obviously larger than 31.6 cm^3 K mol^{-1} calculated by a spin-only equation with the isolated carbenes and the cobalt(II) ion (15×2 for carbene and $\chi'T = 1.6$, which is the value before irradiation, for the Co(II) ion), indicating that the carbenes generated by photolysis interact with the cobalt(II) ion ferromagnetically to form a species with $S = 21/2$. Below 5 K, the $\chi'T$ values decreased and the χ'' signals increased depending on the frequency. The peak-top temperature of χ'' signals at each frequency shifted to lower temperature as the frequency increased; 6.3 and 4.1 K at 997 and 1 Hz, respectively. The observation of both signals, χ' and χ'', and their frequency dependence strongly suggest that the 1:2 complex, Co(*p*-tolsal)$_2$-(**cD5py**)$_2$, has slow magnetic relaxation. Since at the peak-top temperature for the χ'' signal, the relaxation rate ($1/\tau$) is equal to the angular frequency ω ($=2\pi\nu$, where ν is the ac field oscillation frequency), the ac data were used for the Arrhenius plot of $\ln(1/\tau)$ versus $1/T$, based on the Arrhenius relationship of equation; $(1/\tau) = (1/\tau_0)\exp(-U_{eff}/k_BT)$, where U_{eff} is the effective activation barrier for the reversal of the magnetism, τ_0 is the pre-exponential factor, and k_B is the Boltzmann constant. The values of U_{eff}/k_B and τ_0 for Co(*p*-tolsal)$_2$-(**cC5py**)$_2$ are 72 K and 2.0×10^{-9} s^{-1}, respectively (see Fig. 4c).

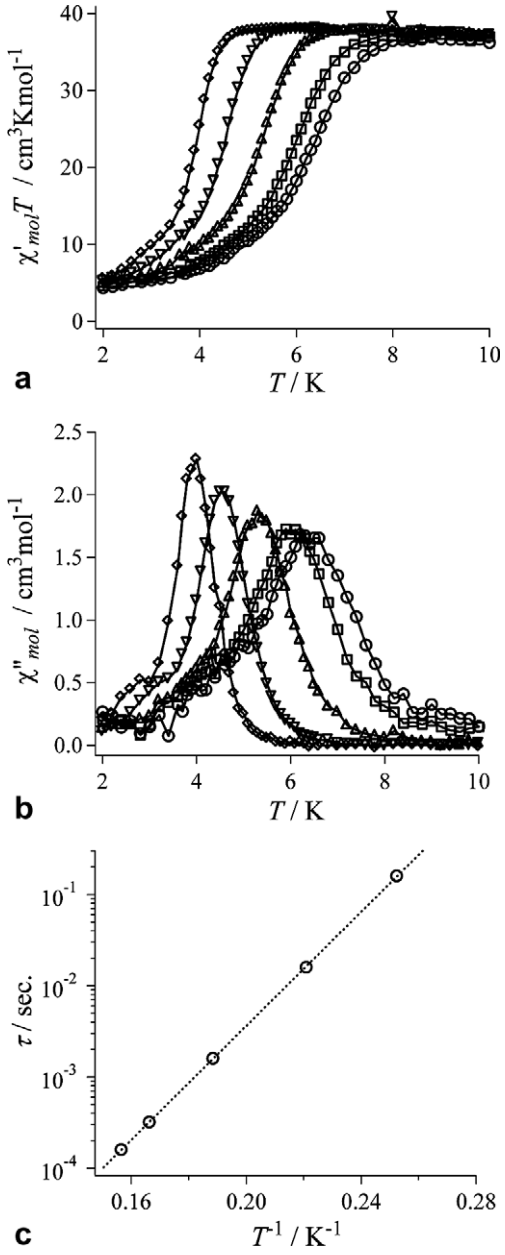


Fig. 4. Plots of (a) $\chi'T$ vs. T and (b) χ'' vs. T after irradiation of the 1:2 mixture of Co(p-tolsal)$_2$ and **cD5Py** in frozen MTHF solution with a 5 Oe ac field oscillating at 997 (○), 499 (□), 99.9 (△), 10 (▽), and 1 (◇) Hz. The solid lines are visual guides; (c) Arrhenius plot.

As observed in Fig. 4b, the signals due to χ'' in the low temperature region at each frequency showed a weak peak (or shoulder), indicating the presence of minor component(s) under the experimental conditions.

*3.3.2.2. Relaxation process of Co(p-tolsal)$_2$-(**cC5py**)$_2$.* In order to investigate the relaxation process due to the cobalt complex in a frozen solution, the ac magnetic susceptibility measurements in more detail were carried out. The ac magnetic susceptibility data after irradiation of the 1:2 mixture, Co(p-tolsal)$_2$-(**cD5py**)$_2$, in frozen MTHF solution were collected by holding the temperature constant and varying the frequency of the ac field (5 Oe) from 997 to 1 Hz. The measurements at two temperatures, 5.5, and 6.0 K, were performed. The plots of χ' versus χ'' (Cole–Cole diagram) at 5.5, and 6.0 K are shown in Fig. 5.

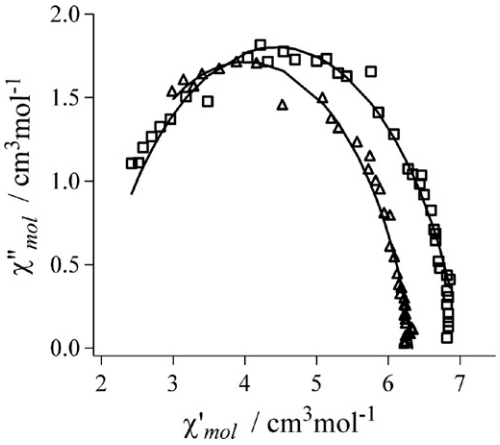


Fig. 5. Plot of χ' vs. χ'' (Cole–Cole plot) at 5.5 (□), and 6.0 (△) K for Co(p-tolsal)$_2$-(**cC5py**)$_2$. Solid lines are a least-square fitting of the data to the distribution of a single relaxation process.

The Cole–Cole plots [9] at 5.5 and 6.0 K, which are nearly symmetric with $\alpha = 0.19$ and 0.23, respectively, also supported that a single relaxation process is present in the Co(p-tolsal)$_2$-(**cC5py**)$_2$. The obtained α value is relatively large, which suggests that there is a distribution in the single relaxation process. This distribution is mainly due to the frozen solution condition used for the formation of SMM. Similar distribution in the relaxation was observed in [CoX$_2$(**4NOpy**)$_4$]; X = NCO and NCS, reported previously [5] and it was elucidated as the distribution in the environment of the metal ion. The distribution in the environment of the cobalt ion–carbene system is more likely in a frozen solution condition than in the microcrystalline state. In a frozen solution, for example, the complex might have various dihedral angles between the N_2O_2 plane for the p-tolsal ligand and the pyridine plane, which leads to the distribution of the zero-field splitting parameters, D and E. The distribution of D and E leads to the distribution in the effective activation barrier, U_{eff}, and in the dc magnetization decay due to a quantum tunneling, respectively. All relaxation fitting parameters obtained from the χ' versus frequency at 5.5 and 6.0 K, are listed in Table 3 and the curves obtained from the least-square fittings of the χ' versus χ'' data are shown as solid lines in Fig. 5.

Table 3
All relaxation fitting parameters obtained from the least-square fitting of the χ' vs. frequency data at 5.5 and 6.0 K for Co(p-tolsal)$_2$-(**cC5py**)$_2$ to a distribution of the single relaxation process

T (K)	χ_0	χ_∞	α
5.5	1.85	7.02	0.23
6.0	1.70	6.33	0.19

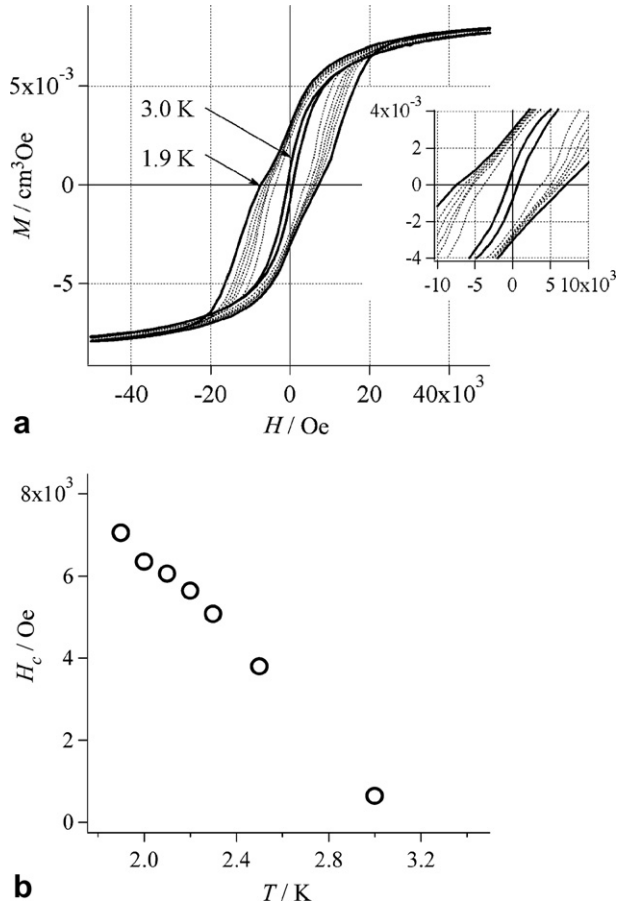


Fig. 6. (a) M vs. H plot at various temperatures below 3.0 K after irradiation of a 1:2 mixture of Co(p-tolsal)$_2$ and **cD5py** in frozen MTHF solution with a sweeping rate of 0.35 kOe/s. The inset shows the magnification of the low field region in M vs. H plot. (b) H_c vs. T plot.

3.3.2.3. Hysteresis loop below 3.0 K. The dc magnetization for the 1:2 complex, Co(p-tolsal)$_2$-(**cC5py**)$_2$, was measured in the range −50 to 50 kOe with a field-sweeping rate of 0.35 kOe/s at seven temperatures in the range 1.9–3.0 K. The cobalt complex showed hysteresis with respect to the applied field below ca. 3.0 K. The hysteresis loops in the temperature range 1.9–3.0 K are shown in Fig. 6a. Coercive force (H_c) and remnant magnetization (M_r) depend on the temperature. On cooling from 3.0 K, both values gradually increased until 1.9 K which is an accessible temperature for our apparatus (Fig. 6b). This temperature dependence of H_c and M_r values is one characteristic of SMM. The values of H_c and M_r at 1.9 K are 7.1 kOe and 3.0×10^4 cm^3 Oe mol^{-1}, respectively.

The strong frequency dependences of the χ'_{mol} and χ''_{mol} signals and the physically reasonable values of τ_0 suggest that these Co(II) complexes in frozen solution function as an SMM rather than a spin glass. The value of $\Delta T_f/T_f(0)\Delta(\log w)$ supports the formation of an SMM, where ΔT_f is the shift of the peak-temperature in χ'_{mol}, $\log w$ is the logarithm of the applied frequency, and $T_f(0)$ is the position of the peak at zero frequency, obtained by the χ'_{mol} versus T plots. The values are 0.21 for Co(p-tolsal)$_2$-(**cC5py**)$_2$. According to Mydosh's work [10], those values are in the region $\Delta T_f/T_f(0)\Delta(\log w) > 0.2$, for an SMM.

4. Conclusion

A cyclic pentadiazo-pyridine derivative, **cD5py**, was prepared as a precursor of a pyridine ligand with $S = 10/2$ for a monometallic SMM in a heterospin system. It was confirmed by the field dependence of magnetization that **cD5py** was photolyzed to form **cC5py** with $S = 10/2$ in frozen solution. The magnetic properties of the 1:2 mixture of Co(p-tolsal)$_2$ and **cC5py** in MTHF frozen solution were investigated by SQUID magneto/susceptometry. Ac and dc magnetic susceptibility experiments indicated that the 1:2 complex, Co(p-tolsal)$_2$-**(cC5py)**$_2$, with $S = 21/2$ formed in frozen solution functions as a monometallic SMM with $U_{eff} = 72$ K and $H_c = 7.1$ kOe at 1.9 K. Similar magnetic behaviors were also observed in the 1:2 complexes using linear polycarbene–pyridine with $S = 2/2$, 4/2, and 6/2 under frozen solution condition.[1]

This time, a cyclic pentadiazo-pyridine derivative **cD5py** was designed and prepared for an SMM in the heterospin system. The framework of **cD5py** still has three positions at which the pyridine units for binding the metal ion can be introduced. Therefore, the use of this framework will be expected as the ligand of an anisotropic metal ion for a higher dimensional spin network. Research work along this line is in progress.

Acknowledgements

This work was supported by a Grant-in-Aid for Scientific Research (B) (No. 17350070) and a Grant-in-Aid for Scientific Research on Priority Areas "Application of Molecular Spin" (No. 15087205) from the Ministry of Education, Science, Sports and Technology (MEXT), Japan. A part of this work was supported by "Nanotechnology Support Project" of the Ministry of Education, Culture, Sports, Science and Technology (MEXT), Japan

Appendix A. Supplementary material

Visible spectra change (Fig. S1) after irradiation of the 1:2 mixture of Co(p-tolsal)$_2$ and **cD5py** in frozen MTHF solution. CCDC 617455 contains the supplementary crystallographic data for **cD5py**. These data can be obtained free of charge via htpp://www.ccdc.cam.ac.uk/conts/retrieving.html, or from the Cambridge Crystallographic Data Centre, 12 Union Road, Cambridge CB2 1EZ, UK; fax: (+44) 1223-336-033; or e-mail: deposit@ccdc.cam.ac.uk. Supplementary data associated with this article can be found, in the online version, at doi:10.1016/j.poly.2006.09.036.

References

[1] D. Gatteschi, R. Sessoli, J. Villain, Molecular Nanomagnets, Oxford University Press, Oxford, 2006.

[2] (a) N.E. Chakov, S.C. Lee, A.G. Harter, P.L. Kuhns, A.P. Reyes, S.Q. Hill, N.S. Dalal, W. Wernsdorfer, K.A. Abbound, G. Christou, J. Am. Chem. Soc. 128 (2006) 6975;
(b) F. Marilena, H. Miyasaka, W. Wernsdorfer, K. Nakata, K. Sugiura, M. Yamashita, C. Coulon, R. Clérac, J. Am. Chem. Soc. 127 (2005) 3090;
(c) H. Oshio, M. Nihei, S. Koizumi, T. Shiga, H. Nojiri, M. Nakano, N. Shirakawa, M. Akatsu, J. Am. Chem. Soc. 127 (2005) 4568.
[3] N. Koga, S. Karasawa, Bull Chem. Soc. Jpn. 78 (2005) 1384.
[4] S. Karasawa, G. Zhou, H. Morikawa, N. Koga, J. Am. Chem. Soc. 125 (2003) 13676.
[5] (a) S. Kanegawa, S. Karasawa, M. Nakano, N. Koga, Bull. Chem. Soc. Jpn. 79 (2006) 1372;
(b) S. Kanegawa, S. Karasawa, M. Nakano, N. Koga, Chem. Commun. (2004) 1750.
[6] SIR92: A. Altomare, G. Cascarano, C. Giacovazzo, A. Guagliardi, M. Burla, G. Polidori, M. Camalli, J. Appl. Cryst. 27 (1994) 435.
[7] CrystalStructure 3.5.1: Crystal Structure Analysis Package, Rigaku and Rigaku/MSC, 9009 New Trails Dr. The Woodlands, TX 77381, USA, 2000–2003.
[8] A. Rajca, R. Padmakumar, D.J. Smithhisler, R.S. Desai, C.R. Ross, J.J. Stezowski, J. Org. Chem. 59 (1994) 7701.
[9] (a) K.S. Cole, R.H. Cole, J. Chem. Phys. 9 (1941) 341;
(b) C. Dekker, A.F. Arts, M.H.W. De Wijn, A.J. Van Duyneveldt, J.A. Mydosh, Phys. Rev. B. 40 (1989) 11243.
[10] J.A. Mydosh, Spin Glasses; An Experimental Introduction, Taylor and Francis, London, 1993.

2. Experimental

2.1. $[Cu(HF_2)(pyz)_2]BF_4$ (1)

The synthesis of **1** has been described previously [5].

2.2. $Cu(ReO_4)_2(H_2O)_2(pyz)$ (2)

Originally, crystals of **2** were obtained as a byproduct in the attempted synthesis of $[Cu(HF_2)(pyz)_2]ReO_4$. Copper(II) chloride dihydrate (341 mg, 2 mmol, Aldrich) was dissolved in 10 ml water. A slurry of silver(I) perrhenate (1432 mg, 4 mmol, Aldrich) in 10 ml water was added. The precipitate of silver chloride was removed from the copper(II) perrhenate solution by filtration. Ammonium hydrogen difluoride (114 mg, 2 mmol, Aldrich) and pyrazine (160 mg, 4 mmol, Aldrich) were placed in a Teflon beaker and dissolved in 20 ml water. The previously prepared copper(II) perrhenate solution was added. After most of the water had slowly evaporated, blue crystals of **2** were found among some unidentified green powder.

In order to prepare **2** in high purity, the following procedure was used. Perrhenic acid solution (70%, 1435 mg, 4 mmol, Aldrich) was added to copper(II) hydroxide (195 mg, 2 mmol, Aldrich) in 10 ml water. When this had dissolved, a 10 ml aqueous solution of pyrazine (144 mg, 2 mmol, Aldrich) was added. The blue crystals of **2**, which began forming after 10 min, were collected by filtration after 2 days. *Anal.* Calc. for $C_4H_8N_2O_{10}CuRe_2$: C. 7.06; H, 1.19; N, 4.12. Found: C, 7.09; H, 1.32; N, 3.98%. IR (cm^{-1}): 3181br, 3135w, 3094m, 3046m, 3009w, 1436s, 1160m, 1126m, 1119w, 1097w, 1074m, 973m, 916sh, 891vs, 836s.

2.3. X-ray data collection and refinement for 2

The crystal structure of **2** was determined by X-ray diffraction using a Siemens SMART single crystal diffractometer equipped with a CCD-based area detector and a sealed-tube Mo Kα source (graphite monochromator). The detector frames were integrated by use of the program SAINT [6] and the intensities corrected for absorption by Gaussian integration based on the measured crystal shape using the program XPREP of SAINT. Other systematic variations were corrected by the analysis of replicate reflections using the program SADABS [7]. The structures were solved by use of direct methods, while full-matrix least-squares refinement on F^2 (including all data) was performed, both using the program package SHELXTL [8]. The electron density difference map shows a large residual peak and hole of 2.96 and −1.15 $e^-/Å^3$, respectively, located 0.86 and 0.66 Å from the Re and Cu atoms. A summary of the crystallographic data is given in Table 1, selected bond lengths and angles are given in Tables 2 and 3. The atomic numbering scheme is illustrated in Fig. 2. Further details of each structure are available in the CIF files also deposited as Electronic supplementary information.

Table 1
Crystal data and structure refinement for $Cu(ReO_4)_2(H_2O)_2(pyz)$ (**2**)

Empirical formula	$C_4H_8CuN_2O_{10}Re_2$
Formula weight	680.06
Temperature (K)	298(2)
Wavelength (Å)	0.71073
Crystal system	monoclinic
Space group	*C*2/*m*
Unit cell dimensions	
a (Å)	13.977(5)
b (Å)	6.816(2)
c (Å)	7.761(3)
α (°)	90
β (°)	123.241(4)
γ (°)	90
Volume ($Å^3$)	618.3(4)
Z	2
Density (calculated) (Mg/m^3)	3.653
Absorption coefficient (mm^{-1})	21.281
F(000)	610
Crystal size (mm^3)	$0.12 \times 0.12 \times 0.38$
Theta range for data collection (°)	3.14–28.28
Index ranges	$-18 \leqslant h \leqslant 17$, $-8 \leqslant k \leqslant 8$, $-10 \leqslant l \leqslant 10$
Reflections collected	2684
Independent reflections (R_{int})	800 (0.0339)
Completeness to theta = 28.28°	95.6%
Refinement method	full-matrix least-squares on F^2
Data/restraints/parameters	800/3/56
Goodness-of-fit on F^2	1.120
Final *R* indices [$I > 2\sigma(I)$]	$R_1 = 0.0235$, $wR_2 = 0.0575$
R indices (all data)	$R_1 = 0.0237$, $wR_2 = 0.0578$
Extinction coefficient	0.0082(5)
Largest difference peak and hole (e $Å^{-3}$)	2.956 and −1.154

Table 2
Selected bond distances (Å) for $Cu(ReO_4)_2(H_2O)_2(pyz)$ (**2**)

Re–O(3)	1.698(6)	Cu–N(1)	2.024(5)
Re–O(2)#1	1.724(4)	Cu–O(1)#2	2.417(6)
Re–O(2)	1.724(4)	N(1)–C(1)	1.337(5)
Re–O(1)	1.727(5)	N(1)–C(1)#3	1.337(5)
O(1)–Cu	2.417(6)	C(1)–C(1)#4	1.388(9)
Cu–O(4)#2	1.963(5)	C(1)–H(1)	0.9300
Cu–O(4)	1.963(5)	O(4)–H(2)	0.818(14)
Cu–N(1)#2	2.024(5)		

Symmetry transformations used to generate equivalent atoms: #1 $x, -y, z$; #2 $-x+1, -y, -z+2$; #3 $-x+1, y, -z+2$; #4 $x, -y-1, z$.

2.4. X-ray powder diffraction

X-ray powder diffraction patterns were collected on a PANalytical X'Pert Pro diffractometer fitted with an X'Celerator detector using Co radiation. Samples were lightly ground in order to reduce preferred orientation and placed on a zero-background Si(5 1 0) substrate sample holder.

2.5. Magnetic measurements

AC susceptibility measurements for both compounds were obtained on a Lakeshore Model 7225 AC susceptometer between 2 and 25 K using a 5 Oe drive field oscillating

Table 3
Selected bond angles (°) for $Cu(ReO_4)_2(H_2O)_2(pyz)$ (**2**)

O(3)–Re–O(2)#1	108.22(18)	O(4)–Cu–O(1)#2	87.96(19)
O(3)–Re–O(2)	108.22(18)	N(1)#2–Cu–O(1)#2	90.000(1)
O(2)#1–Re–O(2)	108.7(3)	N(1)–Cu–O(1)#2	90.000(1)
O(3)–Re–O(1)	109.3(3)	O(4)#2–Cu–O(1)	87.96(19)
O(2)#1–Re–O(1)	111.13(18)	O(4)–Cu–O(1)	92.04(19)
O(2)–Re–O(1)	111.13(18)	N(1)#2–Cu–O(1)	90.000(1)
Re–O(1)–Cu	136.6(3)	N(1)–Cu–O(1)	90.000(1)
O(4)#2–Cu–O(4)	180.0	O(1)#2–Cu–O(1)	180.0
O(4)#2–Cu–N(1)#2	90.000(2)	C(1)–N(1)–C(1)#3	117.9(6)
O(4)–Cu–N(1)#2	90.000(1)	C(1)–N(1)–Cu	121.1(3)
O(4)#2–Cu–N(1)	90.000(1)	C(1)#3–N(1)–Cu	121.1(3)
O(4)–Cu–N(1)	90.000(2)	N(1)–C(1)–C(1)#4	121.1(3)
N(1)#2–Cu–N(1)	180.000(1)	N(1)–C(1)–H(1)	119.5
O(4)#2–Cu–O(1)#2	92.04(19)	Cu–O(4)–H(2)	124(3)

Symmetry transformations used to generate equivalent atoms: #1 $x, -y, z$; #2 $-x+1, -y, -z+2$; #3 $-x+1, y, -z+2$; #4 $x, -y-1, z$.

at 125 Hz. Powder samples with masses of 144 and 200 mg, for **1** and **2**, respectively, were mounted in Delrin® holders and attached to the end of the sample rod. All measurements consisted of zero-field cooling to the lowest temperature and data collected upon warming.

3. Results and discussion

3.1. Crystal structure of $[Cu(HF_2)(pyz)_2]BF_4$ (*1*)

While details of the structure for **1** are given elsewhere [5] we will summarize those results here. At 295 K $[Cu(HF_2)(pyz)_2]BF_4$ crystallizes in the tetragonal space group *P*4/*nbm* with the lattice parameters $a = b = 9.6901(4)$ and $c = 6.6193(4)$ Å. Each Cu^{2+} ion is coordinated to four different pyrazine ligands in the equatorial plane and two F atoms from bifluoride anions along the *c*-direction (Fig. 1). The fourfold rotation symmetry of the Cu site induces counter-rotating pyrazine rings with a twist angle of 59.4(2)° with-respect-to the *ab*-plane. The hydrogen atom of the HF_2^- molecule is symmetrically positioned between the fluorine atoms at a distance of 1.102(4) Å. A 3D coordination polymer results where BF_4^- counterions occupy the interiors of each "cube". The structure of **1** is similar to $[Cu(NO_3)(pyz)_2]PF_6$ where bridging NO_3^- ions link the square layers into a 3D network [9].

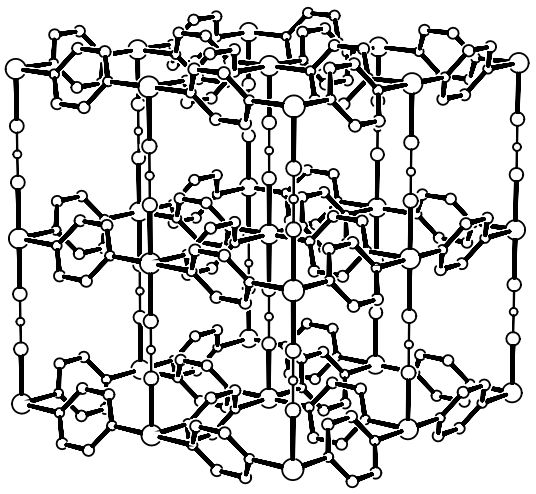


Fig. 1. Crystal structure of **1** showing the μ-bridging HF_2^- and pyrazine linkages. Pyrazine H-atoms and BF_4^- counterions have been omitted for clarity.

3.2. Crystal structure of $Cu(ReO_4)_2(H_2O)_2(pyz)$ (*2*)

Selected bond lengths and angles for **2** are presented in Table 1. As shown in Fig. 2, each Cu^{2+} ion is octahedrally coordinated to two H_2O [Cu–O(4) = 1.963(5) Å], two pyrazine [Cu–N(1) = 2.024(5) Å], and two ReO_4^- [Cu–O(1) = 2.417(6) Å]. Ligands of the same type adopt *trans*-configurations. The geometry of the CuO_4N_2 octahedron deviates slightly from ideal O_h symmetry with largest distortion being the O(1)–Cu–O(4) bond angle that is 92.0(2)°. The ReO_4^- anion adopts a fairly regular tetrahedral geometry with Re–O(1), Re–O(2), and Re–O(4) bond lengths of 1.727(5), 1.724(4), and 1.698(6) Å, respectively. Because the slightly shorter Re–O(3) bond is not affected by additional interactions such as hydrogen bonds, the electron density distribution is more concentrated between those atoms and less withdrawn from the bonding region thus creating a slightly shorter bond. Corresponding bond angles within the perrhenate anion are 108.2(2) [O(2)–Re–O(3)], 109.3(3) [O(1)–Re–O(3)], and 111.1(2)° [O(1)–Re–O(2)]. All bond lengths and angles observed for the pyrazine ligand agree with those previously reported including those found in **1** [2,3,5,9]. Cu(pyzc)(H_2O)(ReO_4)(pyzc = pyrazine-carboxylate) also contains a perrhenate anion however it acts as a bidentate bridge between two different Cu(II) ions [10].

The extended structure of **2** is that of a 1D coordination polymer as shown in Fig. 3. Each octahedron is linked to neighboring octahedra via pyrazine bridges to form linear chains. Pyrazine ligands are uniformly rotated 52.6(3)° out of the equatorial plane defined by Cu, N(1), and O(4). This twist angle is comparable to the 51° observed in the room temperature structure of $Cu(NO_3)_2(pyz)$ [2b]. An extensive hydrogen bonded 3D network (Fig. 3) results

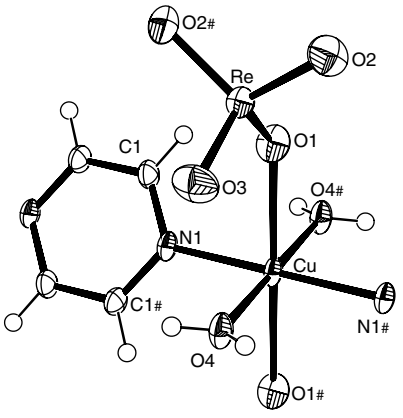


Fig. 2. ORTEP drawing and atom labeling scheme for **2**. Thermal ellipsoids are drawn at the 50% probability level.

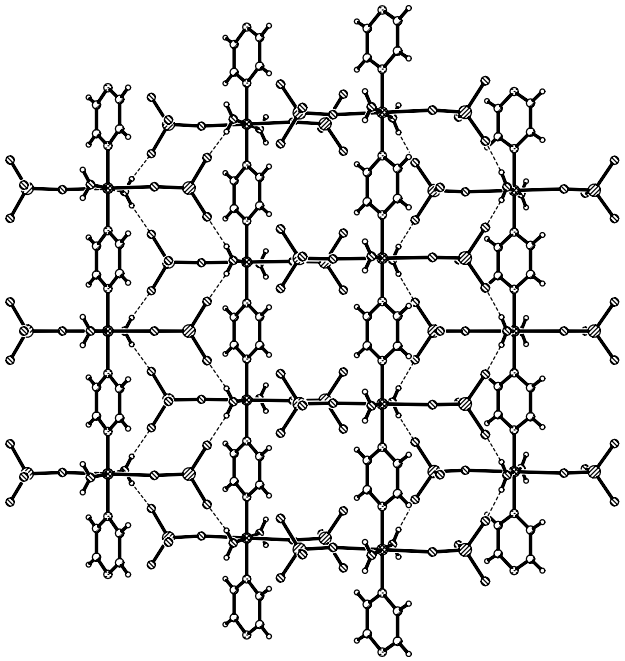


Fig. 3. Chain packing diagram for **2**. Dashed lines delineate hydrogen bonds.

from O(4)–H(2)···O(2) interactions that have an H···O distance of 1.89 Å and a bond angle of 172.5°. Both O(2) and O(2′) participate in hydrogen bonding while O(1) is directly coordinated to the Cu center. The structure of **2** complements that of $Cu(NO_3)_2(pyz)$ in that analogous 1D linear chains are also observed, however **2** features an extensive hydrogen bond network. An X-ray powder diffraction pattern for **2** was also obtained at 295 K and a comparison between the experimental and calculated pattern based on the single crystal structural parameters is shown in Fig. 4.

3.3. Magnetic properties

The temperature-dependence of the real component of the ac susceptibility, χ', for both **1** and **2** are shown in Fig. 5. Each compound shows a broad maximum due to short-range magnetic ordering albeit at somewhat different

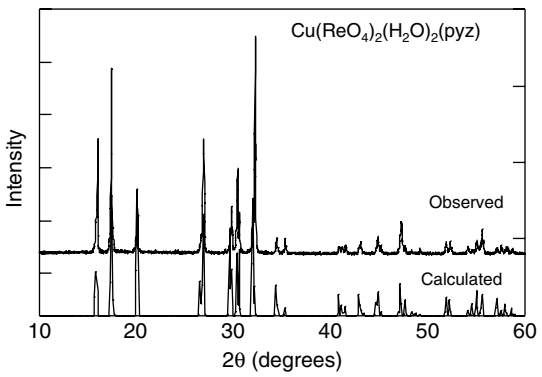


Fig. 4. Comparison of the observed (top) and calculated (bottom) X-ray powder patterns for **2** at 295 K.

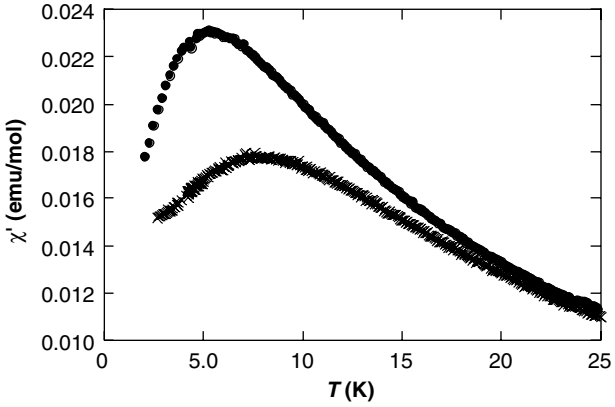


Fig. 5. Temperature-dependence of the real component of the ac susceptibility for **1** (●) and **2** (×) measured between 2 and 25 K.

temperatures; $\chi(T_{max}) = 5.5$ K for **1** and $\chi(T_{max}) = 7.8$ K for **2**. The higher value of $\chi(T_{max})$ for **2** indicates a stronger Cu–pyz–Cu magnetic interaction even though there are twice as many nearest neighbors linked via pyz bridges in **1** than **2**. Below the maximum, the magnetic susceptibility decreases smoothly with no indication for the transition to long-range ordering (LRO) above 2 K. There is no imaginary χ'' component, suggesting a simple collinear antiferromagnetic structure for both **1** and **2**. SQUID magnetic measurements have been reported for **1** [5] and are being conducted on **2**. The full temperature range is needed to fit the data to the appropriate model in order to determine J.

In a previous work [5], **1** was shown by muon-spin relaxation measurements to undergo LRO below $T_N = 1.54(1)$ K. Similar detailed studies are in progress to identify T_N for **2** which we believe may order at a higher temperature due to extensive interchain hydrogen bonding.

The observed antiferromagnetic interactions can be explained in terms of the orientation of the Cu $d_{x^2-y^2}$ magnetic orbital with-respect-to the pyrazine lone-pair orbitals. In the case of **1**, the magnetic orbital lies in the 2D $[Cu(pyz)_2]^{2+}$ plane which places the non-magnetic d_{z^2} orbital along the direction of the bifluoride bridge. For compound **2**, two lobes of the $d_{x^2-y^2}$ magnetic orbital overlap with the nitrogen lone-pair orbitals of the pyrazine ring while the other two lobes overlap lone-pair orbitals of coordinated H_2O ligands. This suggests that there could be an important interchain exchange pathway mediated by the O–H···O–Re hydrogen bonds. Further studies on **2** are in progress to establish the significance of these hydrogen bond interactions.

Acknowledgements

This research was supported by an award from Research Corporation. Work at Argonne National Laboratory was supported by the Office of Basic Energy Sciences, Division of Materials Science of the US Department of Energy under contract W-31-109-ENG-38. J.L.M. gratefully

acknowledges Professor C. Landee (Clark University) and Professor R. Willett (Washington State University) for helpful discussions.

Appendix A. Supplementary material

CCDC 611880 and 285850 contain the supplementary crystallographic data for **1** and **2**. These data can be obtained free of charge via http://www.ccdc.cam.ac.uk/conts/retrieving.html, or from the Cambridge Crystallographic Data Centre, 12 Union Road, Cambridge CB2 1EZ, UK; fax: (+44) 1223-336-033; or e-mail: deposit@ccdc.cam.ac.uk. Supplementary data associated with this article can be found, in the online version, at doi:10.1016/j.poly.2006.09.045.

References

[1] (a) For example, S. Takamizawa, E. Nakata, T. Saito, T. Akatsuka, K. Kojima, Cryst. Eng. Commun. 6 (2004) 197;
(b) S. Takamizawa, E. Nakata, T. Saito, H. Yokoyama, Inorg. Chem. Commun. 6 (2003) 1326;
(c) J.L. Manson, J.A. Schlueter, H.-J. Koo, M.-H. Whangbo, Inorg. Chem. 43 (2004) 4007;
(d) J. Carranza, C. Brennan, J. Sletten, J.M. Clemente-Juan, F. Lloret, M. Julve, Inorg. Chem. 42 (2003) 8716;
(e) C. Nather, J. Greve, Acta Crystallogr., Sect. C 57 (2001) 1388;
(f) T. Otieno, S.J. Rettig, R.C. Thompson, J. Trotter, Inorg. Chem. 32 (1993) 4384;
(g) C.J. O'Connor, C.L. Klein, R.J. Majeste, L.M. Trefonas, Inorg. Chem. 21 (1982) 64.

[2] (a) A. Santoro, A.D. Mighell, C.W. Riemann, Acta Crystallogr., Sect. B 26 (1970) 979;
(b) H.W. Richardson, W.E. Hatfield, J. Am. Chem. Soc. 98 (1976) 835.

[3] J. Darriet, M.S. Haddad, E.N. Duesler, D.N. Hendrickson, Inorg. Chem. 18 (1979) 2679.

[4] C. Yasuda, S. Todo, K. Hukushima, F. Alet, M. Keller, M. Troyer, H. Takayama, Phys. Rev. Lett. 94 (2005) 217201.

[5] J.L. Manson, M.M. Conner, J.A. Schlueter, T. Lancaster, S.J. Blundell, M.L. Brooks, F.L. Pratt, T. Papageorgiou, A.D. Bianchi, J. Wosnitza, M.-H. Whangbo, Chem. Commun. (2006), doi:10.1039/b608791d.

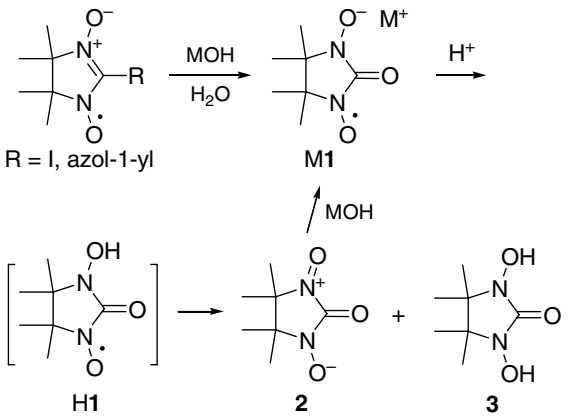
[6] Version 6.28a ed.; Bruker AXS Inc., Madison, WI, USA, 2001.

[7] G.M. Sheldrick, Version 2.03a ed., Bruker AXS Inc., Madison, WI, USA, 2001.

[8] G.M. Sheldrick; Version 6.12 ed.; Bruker AXS Inc., Madison, WI, USA, 2001.

[9] M.M. Turnbull, A.S. Albrecht, G.B. Jameson, C.P. Landee, Mol. Cryst. Liq. Cryst. 335 (1999) 245.

[10] J. Luo, B. Alexander, T.R. Wagner, P.A. Maggard, Inorg. Chem. 43 (2004) 5537.



Scheme 1.

evaporated. The residue was recrystallized with filtration from ethylacetate (80 ml). The resulting rust colored platelets were filtered off, washed with cold ethylacetate, and dried in air. Yield 2.48 g (49%), mp 193–195 °C. IR: $\tilde{\nu}_{max} = 547$, 564, 690, 900, 998, 1133, 1149, 1226, 1375, 1402, 1466, 1761, 2877, 2992 cm^{-1}. Elemental *Anal.* Calc. for $C_7H_{12}N_2O_3$: C, 48.8; H, 7.0; N, 16.3. Found: C, 50.6; H, 7.1; N, 15.8%.

2.1.2. 1,3-Dihydroxy-4,4,5,5-tetramethylimidazolidin-2-one (*3*)

An orange solution of **2** (100 mg, 0.29 mmol) in MeOH (or EtOH) (5 ml) was kept at room temperature for a week. After a week, the solution almost completely decolorized. The solution was evaporated till dry and recrystallized from a mixture of MeOH with toluene. The colorless needles were filtered off. Yield 60 mg (59%). Mp 212–215 °C. IR: $\tilde{\nu}_{max} = 678$, 750, 846, 932, 967, 995, 1052, 1091, 1161, 1213, 1249, 1286, 1362, 1391, 1461, 1692, 2986, 3226 cm^{-1}. Elemental *Anal.* Calc. for $C_7H_{14}N_2O_3 \cdot 0.5H_2O$: C, 45.9; H, 8.3; N, 15.3. Found: C, 45.8; H, 8.3; N, 15.2%.

2.1.3. 2-Methylpropane-2-aminium 3-oxyl-4,4,5,5-tetramethyl-2-oxoimidazolidin-1-olate ((NH_3Bu^t)**1**)

2.1.3.1. Method 1. A suspension of **2** (50 mg, 0.29 mmol) in a mixture of NH_2Bu^t ("Aldrich") (2 ml) and MeOH (2 ml) was kept in a closed vessel at ~5 °C for a week. The resulting blue solution was cooled to −15 °C and stored for another 12 h. The bluish violet thin needles were filtered off and dried in a flow of argon. Yield 20 mg (28%).

2.1.3.2. Method 2. A suspension of **2** (100 mg, 0.58 mmol) in NH_2Bu^t (3 ml) was kept in a closed vessel at ~5 °C for a week. Crystals **2** gradually vanished, and thin violet needle crystals, like "absorbent cotton", filled the bulk of solution. The crystals were quickly transferred to a filter, washed with dry hexane, and dried under argon. Yield 30 mg (42%). When exposed to air, (NH_3Bu^t)**1** crystals transformed into **2** after an hour. When stored under argon, they are stable within a few days. Elemental *Anal.* Calc. for $C_{11}H_{24}N_3O_3$: C, 53.6; H, 9.8; N, 17.1. Found: C, 52.6; H, 9.5; N, 16.7%.

2.1.4. Di-(tert-butylaminopotassium) 3-oxyl-4,4,5,5-tetramethyl-2-oxoimidazolidin-1-olate [$K(NH_2Bu^t)_2$]*1*

Solid KOH (17 mg, 0.30 mmol) was added to a solution of **2** (50 mg, 0.29 mmol) in anhydrous MeOH (5 ml). The reaction mixture was stirred for 10 min, which resulted in a deep blue solution. NH_2Bu^t (50 μl) and toluene (5 ml) were added to the solution, and the mixture was kept for a week in a flask closed with an adapter with $CaCl_2$ at ~5 °C. The resulting navy blue crystals were filtered off and dried on a filter under argon. Yield 20 mg (47%). Elemental *Anal.* Calc. for $C_{15}H_{34}KN_4O_3$: C, 50.4; H, 9.6; N, 15.7. Found: C, 49.2; H, 9.5; N, 15.1%.

2.2. X-ray crystallography and magnetic measurements

Single crystal diffraction data for the compounds were collected on a SMART APEX CCD (Bruker AXS) automatic diffractometer (Mo Kα, $\lambda = 0.71073$ Å, room temperature); an absorption correction was applied using the Bruker SADABS program, version 2.10. The structures were solved by direct methods and refined by the full-matrix least-squares method in an anisotropic approximation for non-hydrogen atoms. The H atoms were located on difference electron density maps and refined together with non-hydrogen atoms in an isotropic approximation. The methyl H atoms were refined as a rigid group with isotropic thermal parameters. All structure solution and refinement calculations were carried out with SHELX-97 and Bruker SHELXTL Version 6.14 program packages.

The magnetochemical experiment was run on an MPMS-5S ("Quantum Design") SQUID magnetometer at temperatures from 2 K to 300 K in a homogeneous external magnetic field of up to 5 kOe. The paramagnetic components of magnetic susceptibility χ were determined with allowance for the diamagnetic term estimated from Pascal's constants. The effective magnetic moment was calculated by the formula $\mu_{eff} = [(3k/N_A\beta^2)\chi T]^{1/2} \approx (8\chi T)^{1/2}$, where k is Boltzmann's constant, N_A is the Avogadro number, and β is the Bohr magneton.

3. Results and discussion

3.1. Synthesis

To have compound **1** stabilized we attempted to use NH_4^+ or its alkyl derivatives for the cation. The initial orange color of the ethanolic solution of zwitterion **2** gradually changed to blue color due to the formation of the ammonium salt (NR_4)**1** after an ethanolic solution of NH_3, NH_2Bu^n, or $NH(Pr^i)_2$ had been added and the reaction mixture had been stored for a month. Similar changes followed after storage of solutions of **2** in pure NH_2Bu^n or $NH(Pr^i)_2$. Evaporation of the resulting solutions, however,

restored the initial color of **2**, and the solid contained the starting compound **2** as the major product. After recrystallization from an ethyl acetate–hexane mixture, the yield of **2** was 80–85%.

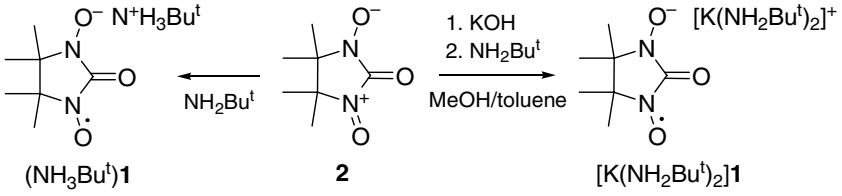
Treatment of **2** with an amine containing a branched hydrocarbon substituent (NH_2Bu^t) and further storage of the reaction mixture in a closed vessel at ~5 °C proved successful. After the reaction mixture had been stored for a week, it was permeated with thin needle crystals of (NH_3Bu^t)**1** throughout (Scheme 2). An X-ray diffraction study of this compound could not be performed because of extremely small crystals of (NH_3Bu^t)**1** and low stability of the salt in air (in contact with air, (NH_3Bu^t)**1** completely converted into the starting compound **2** after an hour). If, however, solid KOH and NH_2Bu^t were added to a solution of **2** in absolute MeOH and the reaction mixture was diluted with toluene, further slow evaporation in dry atmosphere yielded $[K(NH_2Bu^t)_2]$**1** as large navy blue prisms. $[K(NH_2Bu^t)_2]$**1** crystals proved kinetically much more stable than (NH_3Bu^t)**1**. When stored in air, they are slowly covered with an orange film, but are quite stable in an argon atmosphere. It is worth to note, that syntheses of (NH_3Bu^t)**1** and $[K(NH_2Bu^t)_2]$**1** are reproducible but at the moment it is difficult to indicate the possible reducing agent in both cases.

Storage of a MeOH solution of **2** (or of an EtOH suspension of **2**) for a week in the absence of bases led to reduction of **2** to 1,3-dihydroxy-4,4,5,5-tetramethylimidazolidin-2-one (**3**) obtained as colorless needles of a semihydrate $\mathbf{3}\cdot 0.5H_2O$; these crystals, like $[K(NH_2Bu^t)_2]$**1**, are suitable for an X-ray study.

3.2. Structural data

Before discussing the structure of $[K(NH_2Bu^t)_2]$**1** and $\mathbf{3}\cdot 0.5H_2O$, let us recall the structure of compound **2** investigated earlier [2]. Molecule **2** has a twofold symmetry axis through the C7–O3 atoms and the middle of the C1–C4 bond (Fig. 1a). If the methyl substituents are removed from molecule **2**, then all other atoms lie in virtually the same plane. The N–O bond length (1.246 Å) is intermediate between the single and double bond lengths; the C–O bond length (1.204 Å) compares closely with the same bond length in carbonyls [4], and the N1–C7 and N2–C7 distances are equal to 1.368 Å. In the O1–N1–C7(O3)–N2–O2 fragment, high degree of conjugation between atoms is suggested by their coplanarity and interatomic distances, which are markedly smaller than those for single bonds. The torsion angle C1–C4–N1–N2 is 7.4° (Fig. 1a). After sequential reduction of **2** to **1** and then to **3**, this angle opens considerably (to 16.3 and 25.2° (26.0)°, respectively), the symmetry of the O1–N1–C7(O3)–N2–O2 fragment is broken, and the bond lengths in this fragment increase. The general tendencies of variation for parameters are presented in Fig. 1, and it is useful to consider them before discussing the structure of $[K(NH_2Bu^t)_2]$**1** and $\mathbf{3}\cdot 0.5H_2O$.

In the structure of $[K(NH_2Bu^t)_2]$**1**, the five-membered heterocycle is non-planar (Fig. 2a); the deviations of the



Scheme 2.

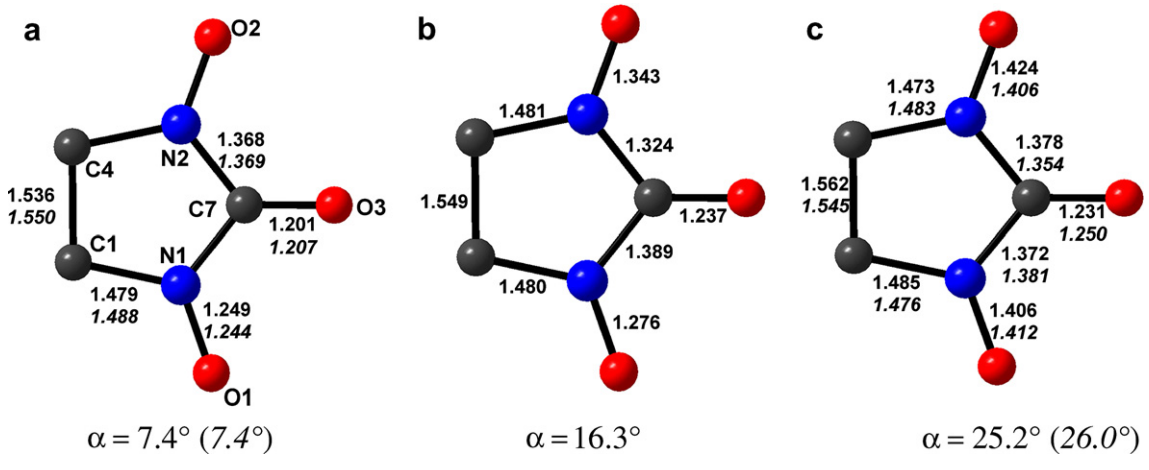


Fig. 1. Atomic numbering scheme (a) and changes in the bond lengths and in the α torsion angle C1–C4–N1–N2 on passing from **2** (a) to **1** (b) and **3** (c) (italicized values are the bond lengths and angles in crystallographically independent molecules).

C1 and C4 atoms from the plane of the CN_2 fragment is, on the average, 0.21 Å, which is much larger than in **2**. The O1A atom of the nitroxyl group lies in the plane of the N1A–C7A–N2A fragment, and the O2A atom of the deprotonated hydroxyl group departs to a distance of 0.150 Å from this plane. Since the N1A–O1A distance (1.276(3) Å) is typical for nitronylnitroxides and the O1A–N1A–C7A–N2A atomic group lies in one plane, the N1A–O1A fragment is reasonably considered to be an >NO nitroxyl group. The N2A–O2A bond length is much larger (1.343(3) Å), which may be attributed to the predominant localization of the negative charge on this group (>N–O$^-$). The C=O distance (1.237(3) Å) is larger than the same distance in **2**, while the N1A–C7A and N2A–C7A distances differ from each other (1.389(3) and 1.324(3) Å).

In solid $[K(NH_2Bu^t)_2]$**1**, the K^+ ions together with H_2NBu^t molecules form centrosymmetric binuclear fragments (Fig. 2b) with K···K distances of 5.029(1) Å and K–N distances of 3.209(3)–3.286(2) Å. This is a unique structure. The Cambridge Crystallographic Database has

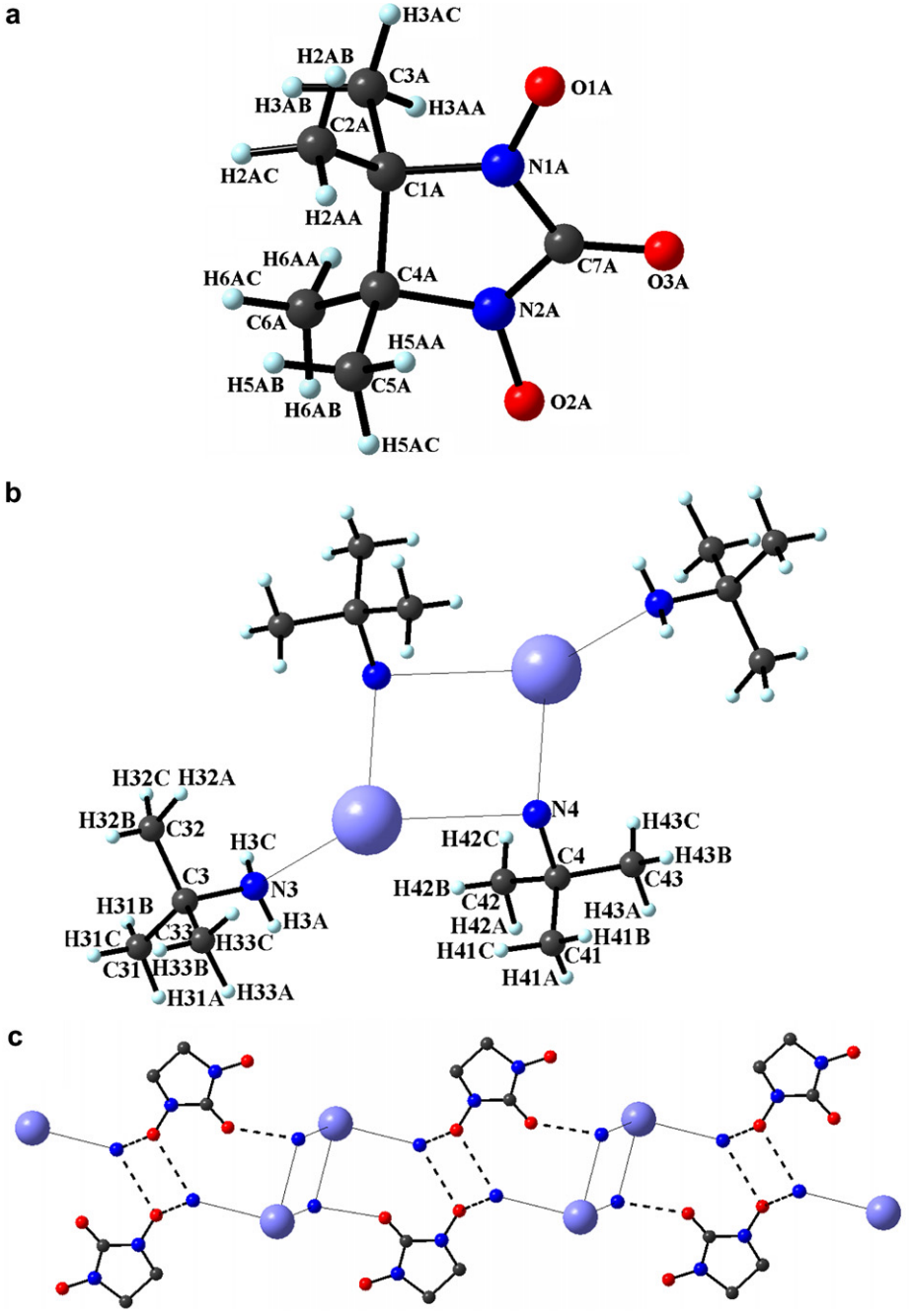


Fig. 2. Structure of anion **1** (a); $\{K_2(NH_2Bu^t)_4\}$ binuclear fragment (b); chain formation in the structure of $[K(NH_2Bu^t)_2]$**1** (c; CH_3 and $(CH_3)_3C$ groups discarded for clarity).

no examples of a binuclear structure of this kind with alkali metal ions surrounded by amine molecules [5]. In the structure, these dimers are hydrogen-bonded with anions, forming infinite chains (Fig. 2c).

According to X-ray diffraction data, in the two crystallographically independent molecules of hydroxyamine derivative **3** (Fig. 3a), the imidazolidine ring is non-planar. The deviations of the C1 and C4 atoms to opposite sides from the plane of the N2C7N1 fragment are, on the average, 0.33 and 0.36 Å. This plane is also flanked by the O1 and O2 atoms of hydroxyl groups, deviating by ~0.66 Å from the plane. The N–O distances vary from 1.406 to 1.424 Å, this variation being typical for the N–O single bond in hydroxyamines [4]. The C7–O3 (1.250(6) and 1.231(6) Å) and N1–C7 and N2–C7 distances (1.354(6)–1.381(6) Å) are virtually the same as in **1**. In solid $\mathbf{3}\cdot 0.5H_2I$, the molecules are bonded by strong H bonds into a framework (Fig. 3b).

Thus structure investigation of $[K(NH_2Bu^t)_2]\mathbf{1}$ and $\mathbf{3}\cdot 0.5H_2O$ and comparison of the resulting data with the structural parameters of **2** have made it possible to trace structure dynamics in the O1–N1–C7(O3)–N2–O2 unit after sequential reduction of zwitterion **2** to the corresponding radical anion **1** and further to dihydroxy derivative **3**.

3.3. Magnetic properties

Magnetic measurements for $(NH_3Bu^t)\mathbf{1}$ showed that the effective magnetic moment $\mu_{eff} \sim 1.73$ B.M. is constant

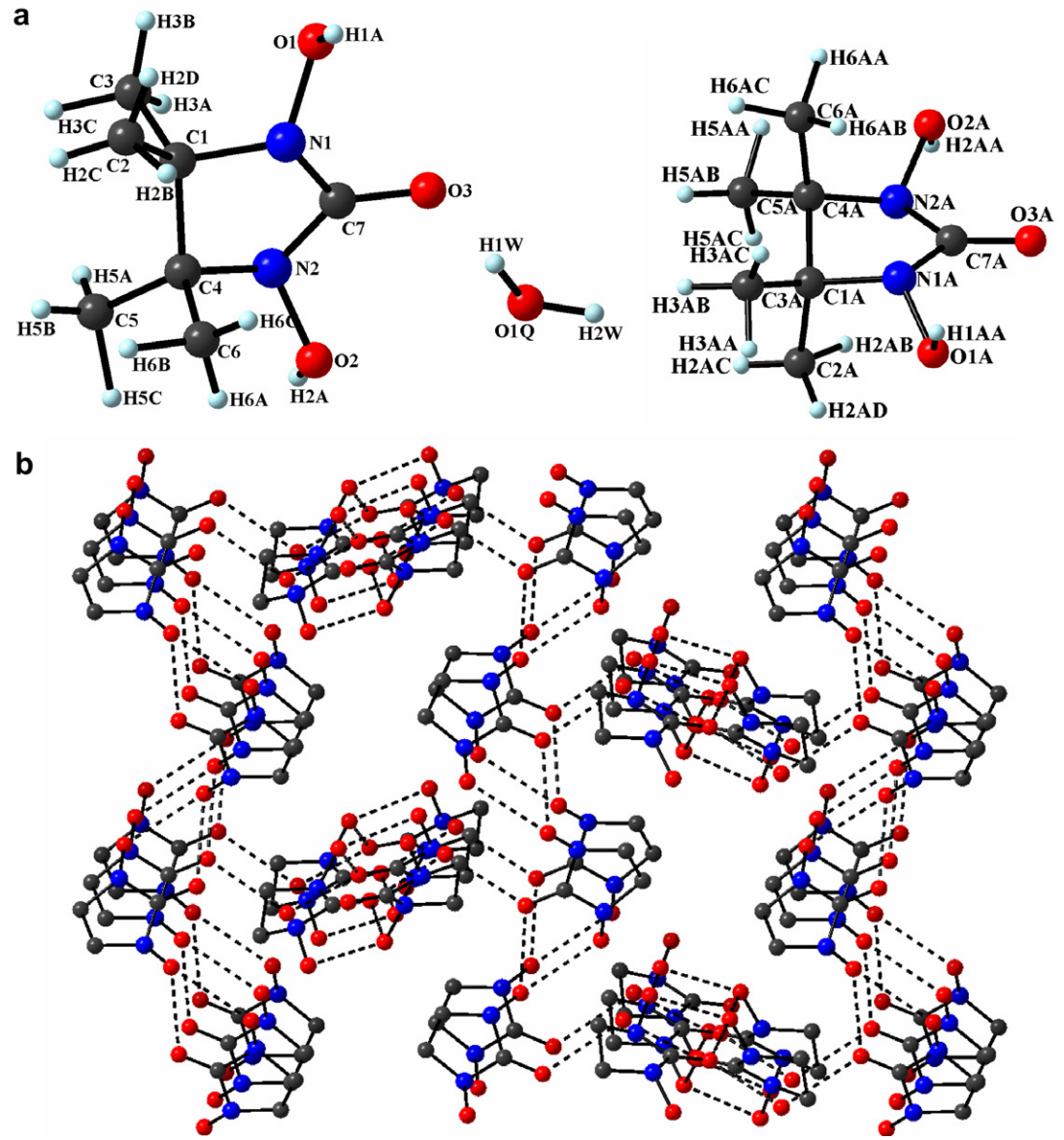


Fig. 3. Structure of crystallographically independent molecules **3** (a) and their packing (b) in the structure of $\mathbf{3}\cdot 0.5H_2I$.

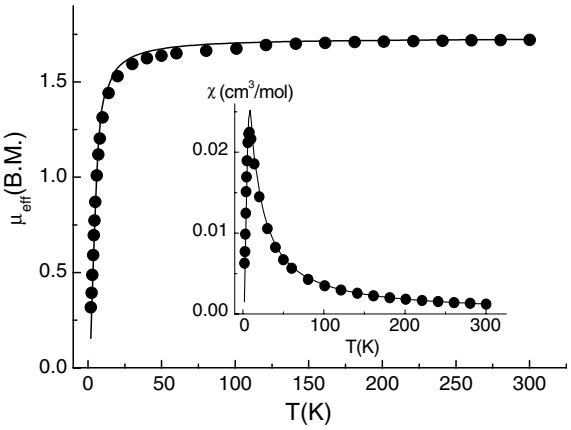


Fig. 4. Temperature dependences of effective magnetic moment and magnetic susceptibility (insert) for $[K(NH_2Bu^t)_2]$**1**.

within the whole temperature range of measurements, indicating that there are very weak exchange interactions between the odd electrons of the paramagnetic anions in solid (NH_3Bu^t)**1**. In polycrystalline $[K(NH_2Bu^t)_2]$**1** (Fig. 4), however, the effective magnetic moment decreases with temperature; the dependence of magnetic susceptibility $\chi(T)$ (insert) has a maximum, which points to dominant antiferromagnetic interactions between the odd electrons of the paramagnetic centers at low temperatures.

As shown by X-ray data, the structure of this complex consists of alternate chains (Fig. 2c) in which the dimers formed by the nitroxyl groups of two radicals bridged by two nitrogen atoms alternate with $[K_2(NH_2Bu^t)_4]^{2+}$ dimer fragments (Fig. 2b). Simulation of experimental data indicated that the most realistic model is the one with isolated dimers weakly interacting with one another via $[K_2(NH_2Bu^t)_4]^{2+}$ fragments. Optimization gave the following parameters of the Bleaney–Bowers equation for dimers with $S = 1/2$ [6]: $g = 2.01$, $-2J = 8.7\ cm^{-1}$. The theoretical curves are shown by solid lines in Fig. 4.

Thus synthetic procedures for **1** and **3** have been developed. In future, these compounds will be introduced in complexation processes with transition metal ions.

4. Supplementary material

CCDC 616899 and 616900 contain the supplementary crystallographic data for $[K(NH_2Bu^t)_2]$**1** and $\mathbf{3}\cdot 0.5H_2O$. These data can be obtained free of charge via htpp://www.ccdc.cam.ac.uk/conts/retrieving.html, or from the Cambridge Crystallographic Data Centre, 12 Union Road, Cambridge CB2 1EZ, UK; fax: (+44) 1223-336-033; or e-mail: deposit@ccdc.cam.ac.uk.

Acknowledgement

Research funded in part by RFBR (grants 05-03-32305, 06-03-08004, 06-03-32157), RAS, SB RAS grants, and the Bruker firm.

References

[1] D.G.B. Boocock, E.F. Ullman, J. Am. Chem. Soc. 90 (1968) 6873.
[2] E.V. Tretyakov, G.V. Romanenko, V.I. Ovcharenko, Tetrahedron 60 (2004) 99.
[3] E.F. Ullman, J.H. Osiecki, D.G.B. Boocock, R. Darcy, J. Am. Chem. Soc. 94 (1972) 7049.
[4] F.H. Allen, O. Kennard, D.G. Watson, L. Brammer, A.G. Orpen, R. Taylor, J. Chem. Soc., Perkin Trans. II (1987) S1.
[5] Cambridge Structural Database, Version 5.27, November 2005 (Updates May 2006).
[6] O. Kahn, Molecular Magnetism, VCH, New York, 1993.

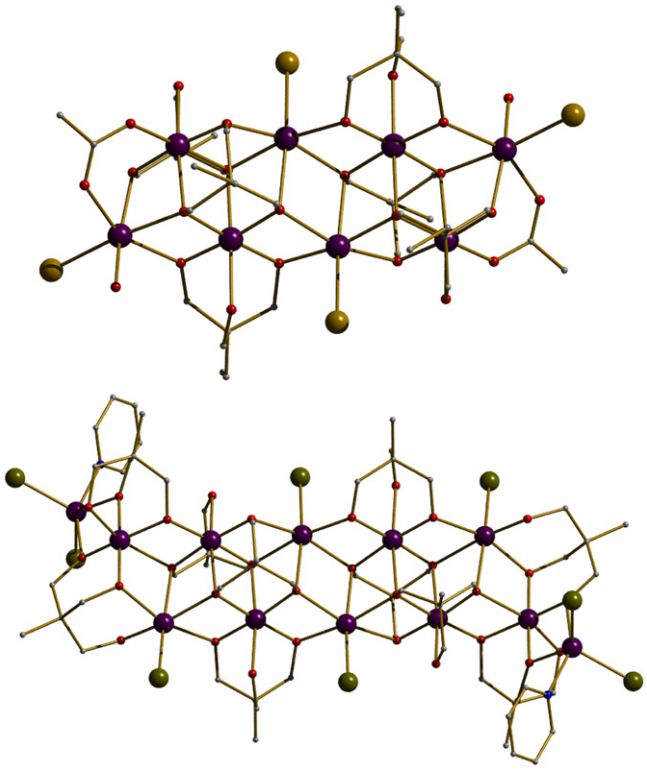


Fig. 1. Molecular structures of complexes **1** (top) and **2** (bottom). Colour code: Mn, purple; O, red; Br, green; C, grey. (For interpretation of the references to color in this figure legend, the reader is referred to the web version of this article.)

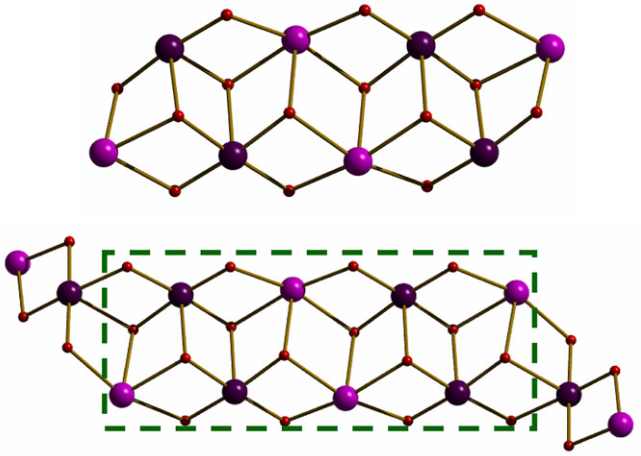


Fig. 2. The Mn–O cores of **1** (top) and **2** (bottom). Colour code: Mn(III), purple; Mn(II), pink; O, red. The $[Mn_4^{III}Mn_4^{II}(\mu_3\text{-}OR)_6(\mu_2\text{-}OR)_8]^{6+}$ unit common to both is highlighted in green. (For interpretation of the references to color in this figure legend, the reader is referred to the web version of this article.)

The core of complex **2** $[Mn_{12}(Hthme)_8(thme)_2(py)_2Br_8]$ is remarkably similar (Figs. 1 and 2). The molecule, made from the reaction of $MnBr_2 \cdot 4H_2O$, H_3thme and H_3tea (triethanolamine) in MeCN/py, consists of a non-planar $[Mn_6^{III}Mn_6^{II}(\mu_2\text{-}OR)_{14}(\mu_3\text{-}OR)_8]^{8+}$ unit, with a trapped-valent core that can be described as consisting of eight edge-sharing $[Mn_3O]$ triangles, or four edge-sharing $[Mn_4O_2]$ butterfly ('planar diamond') units. The 10 central metals this describes are planar with the two outermost (pentagonal bipyramidal) Mn(II) ions above and below that plane, respectively.

The six Mn(III) display Jahn–Teller elongations, all of which are approximately co-parallel at an angle of ~70° with respect to Mn_{10} plane. The two fully deprotonated $thme^{3-}$, ligands are located directly above and below the Mn_{10} plane bridging in a $\eta^3{:}\eta^3{:}\eta^2{:}\mu_5$-fashion to five metal centres that describe three edge-sharing triangles. The other eight tripodal ligands are doubly deprotonated ($Hthme^{2-}$) and coordinate in two different ways: two in a $\eta^3{:}\eta^3{:}\eta^1{:}\mu_5$-fashion linking five metals into three edge-sharing triangles; and six in a $\eta^1{:}\eta^2{:}\eta^2{:}\mu_3$-fashion linking three metals in a near-linear array. Four of the eight bromides are coordinated terminally to the Mn(II) ions in the central Mn_{10} plane, with the remaining four bonded to the peripheral five coordinate Mn(II) ions. The coordination sphere of these ions is completed by two terminal pyridines.

The two complexes are clearly related with the $[Mn_4^{III}Mn_4^{II}(\mu_3\text{-}OR)_6(\mu_2\text{-}OR)_8]^{6+}$ unit present in **1** being replicated exactly in the central section of complex **2** (Fig. 2). The *planar diamond* $[Mn_2^{III}Mn_2^{II}(\mu_3\text{-}OR)_2(\mu_2\text{-}OR)_4]$ moiety seen twice in both complex **1** and complex **2** is well known and has been reported previously in the tetranuclear complexes $[Mn_2^{III}Mn_2^{II}(hmp)_6(NO_3)_2(MeCN)_2]^{2+}$ (**3**), $[Mn_2^{III}Mn_2^{II}(hmp)_6(NO_3)_4]$ (**4**), $[Mn_2^{III}Mn_2^{II}(hmp)_4(acac)_2(MeO)_2]^{2+}$ (**5**), $[Mn_2^{III}Mn_2^{II}(O_2CMe)_2(pdmH)_6]^{2+}$ (**6**), $[Mn_2^{III}Mn_2^{II}Br_2(hmp)_6(H_2O)_2]^{2+}$ (**7**), $[Mn_2^{III}Mn_2^{II}(O_2CMe)_2(teaH)_2(teaH_2)_2(H_2O)_2]^{2+}$ (**8**), $[Mn_2^{III}Mn_2^{II}(O_2CPh)_2(teaH)_2(teaH_2)_2(H_2O)_2]^{2+}$ (**9**), and $[Mn_2^{III}Mn_2^{II}(O_2\,CEt)_2(teaH)_2(teaH_2)_2(H_2\,O)_2]^{2+}$ (**10**) (where hmpH = 2-hydroxymethylpyridine; $pdmH_2$ = pyridine-2,6-dimethanol; $teaH_3$ = triethanolamine) [3–6]. Three '*reverse*' rhomboidal clusters with $[Mn_2^{II}Mn_3^{III}(OR)_6]$ cores in which the metal ions have *swapped* places, i.e. the Mn(III) ions are the 'wing-tips' and the Mn(II) ions are the 'body-ions', have also been reported: $[Mn_2^{III}Mn_2^{II}(O_2CPh)_4(teaH)_2(acac)_2]$ (**11**); $[Mn_2^{III}Mn_2^{II}(teaH)_2(acac)_4(MeOH)_2](ClO_4)_2$ (**12**); $[Mn_2^{III}Mn_2^{II}(bheapH)_2(acac)_4(MeOH)_2](ClO_4)_2$ (**13**) ($bheapH_3$ = 1-[*N*,*N*-bis(2-hydroxyethyl)amino]-2-propanol) [7]. This 'reversed' $[Mn_2^{II}Mn_2^{III}]$ distribution is also found in the hexanuclear cluster $[Mn_2^{III}Mn_4^{II}(teaH)_2(teaH_2)_2(O_2CCH\text{-}Ph_2)_8]$ (**14**) [8].

Both structures are also related to the octa- and dodecanuclear Mn rods $[Mn_8O_4(O_2CCMe)_{10}(py)_2]$ (**15**) and $[Mn_{12}O_4(OH)_2(PhCOO)_{12}(thme)_4(py)_2]$ (**16**) we previously described [2], but here the cores contain bridging O^{2-} ions, and are in different oxidation levels, consisting of a homovalent $[Mn_8^{III}(\mu_3\text{-}O)_4(\mu_3\text{-}OR)_2(\mu_2\text{-}OR)_4]^{10+}$ unit and a $[Mn_{10}^{III}Mn_2^{II}O_4(OH)_2]^{24+}$ unit, respectively.

Solid-state dc magnetic susceptibility (χ_M) measurements were performed on polycrystalline samples of **1** and **2** in a 0.1 T applied dc magnetic field in the 5.00–300 K temperature range. The results are plotted as $\chi_M T$ versus T in Fig. 3. For **1**, the room temperature $\chi_M T$ value

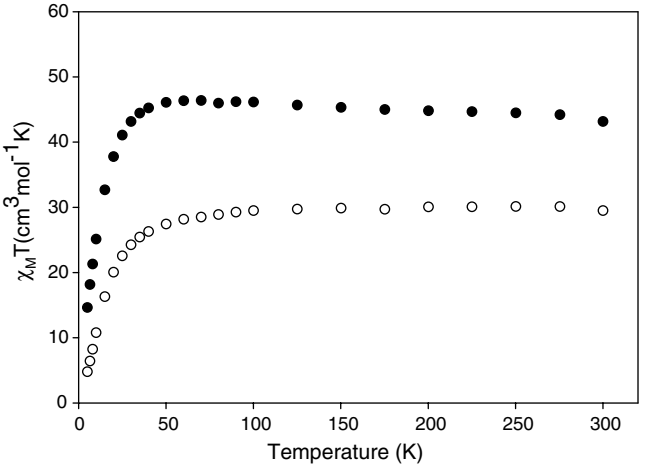


Fig. 3. Plot of $\chi_M T$ versus T for **1** (○) and **2** (●) in an applied field of 0.1 T and the temperature range 300–5 K.

of approximately 29 cm^3 K mol^{-1} (0.1 T) is slightly lower than that expected for a complex comprising four Mn(III) and four Mn(II) ions (29.5 cm^3 K mol^{-1} with $g = 2$). The value of $\chi_M T$ remains almost constant as the temperature is decreased until *ca.* 50 K where it then decreases rapidly to a value of approximately 2 cm^3 K mol^{-1} at 5.0 K. For **2** the behaviour is rather similar: the room temperature $\chi_M T$ value of approximately 43 cm^3 K mol^{-1} (spin only = ~46 cm^3 K mol^{-1}) remains essentially unchanged until *ca.* 50 K where it drops rapidly to a value of 14.6 cm^3 K mol^{-1} at 5 K. This is indicative of dominant (weak) antiferromagnetic exchange between the metal centres with the low temperature values suggesting small spin ground states for both complexes.

In-phase ac susceptibility measurements performed in the temperature range 1.8–10 K support the above assignments: extrapolation of the $\chi'_M T$ signal from values above ~3 K (to avoid decreases due to such effects as intermolecular interactions at lower temperatures) to 0 K gives values of 1 ± 1 cm^3 K mol^{-1} for both. In each case the slope of the $\chi'_M T$ versus T plot decreases rapidly with decreasing temperature revealing the presence of several spin-states of larger S values lying very close to the ground-state. This is to be expected for molecules containing multiple Mn(II) ions that are known to promote weak exchange interactions – the result of which is likely to be a large number of S states with comparable energies to the ground state. This behaviour is consistent with other Mn(III)–Mn(II) systems [3–8].

An attempt to rationalize the $S = 0$ or $S = 1$ ground-states of **1** and **2** (although clearly very difficult) can be made on the basis of the well-known magnetic behaviour of complexes **3**–**13**. The planar diamond $[Mn^{III}_2Mn^{II}_4(OR)_6]$ unit present in complexes **3**–**10** in which the Mn(III) ions occupy the central body positions gives rise to ferromagnetic exchange and $S = 9$ spin ground states. The $[Mn^{II}_2Mn^{III}_2(OR)_6]$ unit in **11**–**13** in which the Mn ions have 'swapped' positions is characterized by antiferromagnetic exchange and results in small ($S = 0$ or 1) spin ground states. The calculated exchange interactions for all are given in Table 1. The majority of the Mn(III)–Mn(III) and Mn(III)–Mn(II) interactions appear to be ferromagnetic (with only J_{wb} in **12** and **13** antiferromagnetic) – but in all cases the interactions are very weak. Both **1** and **2** are linked at their centres by two Mn(II) ions *via* two μ_3-OR bridges. Previous experimental evidence suggests that this interaction is likely to be weak and antiferromagnetic [9–12]. DFT calculations on Mn(II)–O–Mn(II) dimers also suggest an antiferromagnetic interaction with a strong dependence of the strength of coupling as function of the Mn–O–Mn angle. Below angles of ~98° the interaction is weak and antiferromagnetic but becoming increasingly strong and antiferromagnetic for angles in the 98–110° range [13,14]. The Mn(II)–O–Mn(II) angle is 100.3(1)° in **1** and 99.9(1)° in **2** and thus we might expect a reasonably 'strong' antiferromagnetic exchange for both. If we assume that each 'isolated' $[Mn^{III}_2Mn^{II}_2]$ diamond on either side of this central Mn(II)–Mn(II) unit remains ferromagnetically coupled then we can imagine that for complex **1** the two 'halves' of the molecules are "spin-up" and "spin-down" respectively, leading to an $S = 0$ ground state. For **2** we can then simply assume that the two remaining Mn(III)–Mn(II) *dimers* (Mn–O–Mn = ~103–104°) at each end of the same $[Mn_8]$ core 'cancel each other out' either *via* a local antiferromagnetic interaction or one *ferromagnetic dimer* being "spin-up" and the other "spin-down".

All previously characterized Mn rod-like complexes were obtained from reactions involving the oxo-centred metal triangles $[Mn_3O(O_2CR)_6L_3]^{0/+}$. The present work shows that structurally similar complexes but with different levels of oxidation can be made from simple Mn(II) salts like $MnBr_2 \cdot 4H_2O$. Although both complexes **1** and **2** possesses $S = 0$ or $S = 1$ ground states, the magnitude of the exchange interactions present in these types of species suggest that only a very small change in the magnitude of one J-value (e.g. that between the two central Mn(II) ions) could have a pronounced effect on the nature of the ground state. Of course it remains extremely difficult to predict the magnitude and sign of such interactions in complicated molecules, but by synthesizing families of related

Table 1
Exchange interactions calculated for complexes **3**–**13**

Complex	Mn^{III}–Mn^{II}, J_{wb} (cm^{-1})	Mn^{III}–Mn^{III}, J_{bb} (cm^{-1})
3	+1.0	+9.9
4	+4.2	+6.3
5	+0.78	+5.3
6	+0.4	+8.1
7	+0.9	+9.0
8	+1.7	+6.5
9	+0.4	+6.6
10	+0.22	+10.9
11	N/A	N/A
12	−0.7	+0.7
13	−0.8	+2.1

compounds and studying their magnetic properties we can build up some understanding of the correlation between structural and magnetic data which may help us design complexes with predictable, sought-after properties. We hope that chemical/electrochemical oxidation of some of the Mn(II) ions in both **1** and **2** will allow us to further this idea.

1. Supplementary material

CCDC 280380 contains the supplementary crystallographic data for **1** and **2**. These data can be obtained free of charge via http://www.ccdc.cam.ac.uk/conts/retrieving.html, or from the Cambridge Crystallographic Data Centre, 12 Union Road, Cambridge CB2 1EZ, UK; fax: (+44) 1223-336-033; or e-mail: deposit@ccdc.cam.ac.uk.

References

[1] E.K. Brechin, Chem. Commun. (2005) 5141.
[2] G. Rajaraman, M. Murugesu, M. Soler, W. Wernsdorfer, M. Helliwell, S.J. Teat, G. Christou, E.K. Brechin, J. Am. Chem. Soc. 126 (2004) 15445.
[3] E.-C. Yang, N. Harden, W. Wernsdorfer, L. Zakharov, E.K. Brechin, A.L. Rheingold, G. Christou, D.N. Hendrickson, Polyhedron 22 (2003) 1857.
[4] J. Yoo, E.K. Brechin, A. Yamaguchi, M. Nakano, J.C. Huffman, A.L. Maniero, L.-C. Brunel, K. Awaga, H. Ishimoto, G. Christou, D.N. Hendrickson, Inorg. Chem. 39 (2000) 3615.
[5] J. Yoo, A. Yamaguchi, M. Nakano, J. Krzystek, W.E. Streib, L.-C. Brunel, H. Ishimoto, G. Christou, D.N. Hendrickson, Inorg. Chem. 40 (2001) 4604.
[6] L.M. Wittick, K.S. Murray, B. Moubaraki, S.R. Batten, L. Spiccia, J.K. Berry, Dalton Trans. (2004) 1003.
[7] L.M. Wittick, L.F. Jones, P. Jensen, B. Moubaraki, L. Spiccia, K.J. Berry, K.S. Murray, Dalton Trans. (2006) 1534.
[8] M. Murugesu, K.A. Abboud, G. Christou, Angew. Chem., Int. Ed. 44 (2005) 892.
[9] D.P. Kessissoglou, Coord. Chem. Rev. 185–186 (1999) 837, and references therein.
[10] C.J. Milios, E. Kefalloniti, C.P. Raptopoulou, A. Terzis, A. Escuer, R. Vicente, S.P. Perlepes, Polyhedron 23 (2004) 83.
[11] S. Ménage, S.E. Vitols, P. Bergerat, E. Codjovi, O. kahn, J.-J. Girerd, M. Guillot, X. Solans, T. Calvet, Inorg. Chem. 30 (1991) 2666.
[12] S.G. Baca, Y. Sevryugina, R. Clerac, I. Malaestean, N. Gerbeleu, M.A. Petrukhina, Inorg. Chem. Commun. 8 (2005) 474.
[13] E. Ruiz, S. Alvarez, P. Alemany, Chem. Commun. (1998) 2767.
[14] P. Christian, G. Rajaraman, A. Harrison, M. Helliwell, J.J.W. McDouall, J. Raftery, R.E.P. Winpenny, Dalton Trans. (2004) 25.

example), a current will be induced which will travel in phase with the field. If, on the other hand, the charged particles are bound within regions of the material, the electric field component will cause them to move until opposing forces balance the electric force [20,21]. The fundamental difference between microwave heating and conventional heating is that heating under microwave irradiation occurs in an *in–out* fashion, i.e. from the solution to the tube/flask, while with conventional heating energy is transferred *out–in*, i.e. from the flask to the solution. This effect results in superheating phenomena under microwave irradiation. Water, for example, reaches 105 °C before boiling, and acetonitrile makes it to 120–38 °C above its normal boiling point.

In spite of the range of applications and advantages of this heating method, reactions involving liquid phase inorganic syntheses have not yet received great attention. In the area of polymetallic cluster compounds this is hugely surprising since the major problems are often associated with yield and reproducibility. This tends to be especially true as the nuclearity of the product increases and is clearly a stumbling block if detailed physical characterisation is to follow. Coordination chemists attempting to make large polymetallic clusters of paramagnetic transition metals rarely perform syntheses in conditions other than ambient temperature and pressure. The reason is simple – it is not necessary, since the overwhelming majority of polynuclear complexes have been made via simple bench-top methods [22–27]. Only when making complexes of inert ions such as Cr^{3+} have alternative techniques been pursued [28]. Indeed the use of solvothermal synthesis has only recently become 'standard practice' for metal clusters of, for example, Fe, Ni and Mn. Given our recent success in the solvothermal synthesis of large metal clusters [29] we decided to examine whether microwave heating could be used for a similar purpose. In our experience, microwave heating not only provides an alternative synthetic tool, but may help improve the yield and reproducibility of large polymetallic complexes. Moreover, it may lead to novel products, by permitting access to alternative kinetic pathways and stabilizing different energy minima in a reaction system than the conventional methods of heating. This is especially possible when it effects exceptionally rapid heating of the reaction components [30]. Irrespective of the nature of the product, the reduction of reaction times through microwave heating permit a larger number of reaction conditions to be explored more quickly, making exploratory synthetic programs more efficient.

2. Manganese clusters

The first inorganic cluster complex synthesized using microwave heating was $[Mn^{III}_6O_2(sao)_6(O_2CH)_2(CH_3OH)_4]$ (**1**), formed from the reaction of $Mn(ClO_4)_2 \cdot 6H_2O$ with $saoH_2$ (salicylaldoxime) in the presence of NaOMe in MeOH [31]. The reaction mixture was simply placed in a sealed glass tube in the cavity of a microwave reactor and heated at 110 °C under 100 psi pressure for a total of 5 min, with the power of the microwave irradiation kept constant at 200 W. The complex formed immediately upon cooling and after 24 h the yield was approximately 80%. Initially the sample was heated for 10 min but we later found that reducing this to 5 min had no adverse effects on the yield of the product. Complex **1** can be made by repeating the reaction under ambient conditions but crystalline material does not appear immediately – indeed the maximum yield of ~30% is only achieved after a 60 min reaction and a 5 day crystallization period. The complex crystallizes in the triclinic space group $P\bar{1}$ with the molecule lying on an inversion centre. The core of the complex (Fig. 1) contains a non-planar $[Mn^{III}_6(\mu_3\text{-}O^{2-})_2(\mu_3\text{-}O^{1-})_2]^{12+}$ unit of two off-set, stacked $[Mn^{III}_3(\mu_3\text{-}O^{2-})]^{7+}$ triangles linked by two central oximato oxygens. The remaining sao^{2-} ligands bridge in a $\eta^1{:}\eta^1{:}\eta^1{:}\mu$-fashion along the edges of the $[Mn^{III}_3(\mu_3\text{-}O^{2-})]^{7+}$ triangles, with the coordination geometry of the metal ions completed by a combination of terminal methanol and μ-formate groups – the latter derived from the high temperature/pressure assisted oxidation of the solvent. All six Mn ions are in the 3+ oxidation state, as confirmed by a combination of bond length and charge balance considerations and bond valence sum (BVS) calculations. Four are six coordinate and in distorted octahedral geometries displaying the expected Jahn–Teller elongations (Fig. 1), while two are five-coordinate and square-pyramidal. The four Jahn–Teller axes and the apical bond of the five coordinate Mn ions are approximately co-parallel, all perpendicular to the $[Mn_3]$ planes [31].

Magnetization data (Fig. 2), collected in the 1–70 kG and 1.8–6.0 K ranges, were fitted by a matrix-diagonalisation method to a model that assumes only the ground state is populated, includes axial zero-field splitting ($D\hat{S}^2_z$), and carries out a full powder average – the corresponding Hamiltonian is given in the following equation:

$$H = D\hat{S}^2_z + g\mu_B\mu_0\hat{S}\cdot H \quad (1)$$

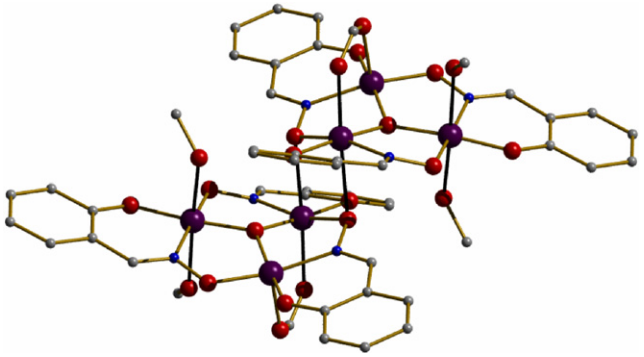


Fig. 1. The molecular structure of complex **1**. The dark bonds highlight the Jahn–Teller axes. Colour code: Mn = purple; O = red; N = blue; C = grey. (For interpretation of the references to colour in this figure legend, the reader is referred to the web version of this article.)

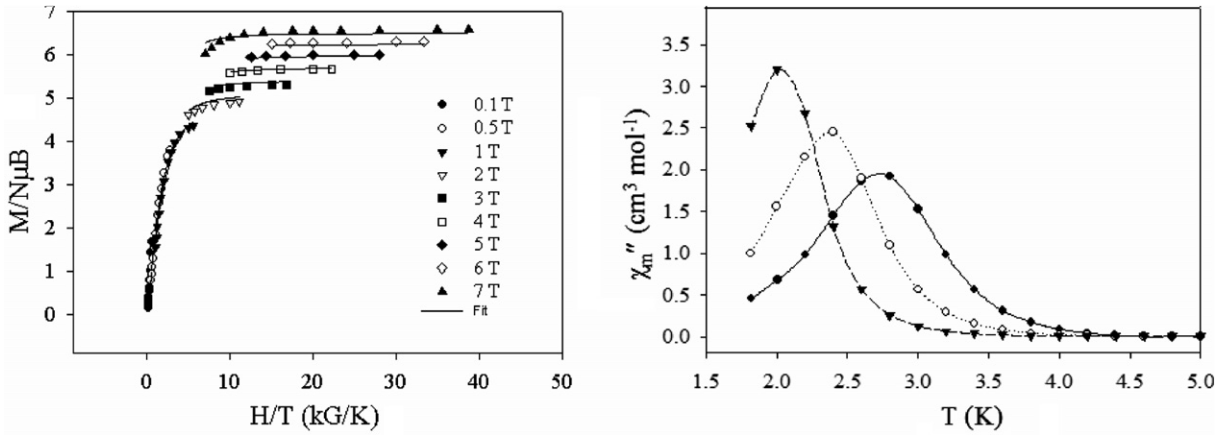


Fig. 2. Plot of reduced magnetization vs. H/T for **1**, the solid lines are the fit of the data (left). Out-of-phase (χ''_M) ac susceptibility measurements for **1** in the temperature range 1.8–5 K and frequencies 50 (▼), 250 (○), 1000 (●) Hz (right).

The best fit parameters were $S = 4$, $g = 1.99(3)$ and $D = -1.39\ \text{cm}^{-1}$. This D value in the largest ever reported for any $[\text{Mn}_x]$ $(x > 3)$ polynuclear complex and is likely the consequence of the parallel alignment of the JT axes of the Mn^{III} ions. Frequency-dependent out-of-phase ac susceptibility signals are observed at $T \leqslant 4$ K. Single-molecule magnetism behaviour was confirmed by the presence of temperature and sweep rate dependent hysteresis loops in single crystal M versus H studies (Fig. 3) performed on an array of micro-SQUIDs [32]. The loops and are not smooth, showing a large step at zero field indicative of quantum tunnelling of the magnetization (QTM). Relaxation data (Fig. 4) determined from a combination of single crystal dc relaxation decay measurements and ac measurements on a powdered sample allow the construction of a τ versus $1/T$ plot based on the Arrhenius relationship of the following equation:

$$\tau = \tau_0 \exp(U_{\text{eff}}/kT), \tag{2}$$

where U_{eff} is the effective relaxation barrier, τ is the relaxation time, and k is the Boltzmann constant. The slope of the thermally activated region yielded an effective energy barrier for the reorientation of the magnetization of $U_{\text{eff}} \approx 28$ K and $\tau_0 = 2 \times 10^{-8}$ s. Below 0.8 K the relaxation rate flattens out suggesting relaxation via ground state quantum tunneling.

The same complex can also be isolated from the reaction of $\text{Mn}(\text{O}_2\text{CH})_2 \cdot 4\text{H}_2\text{O}$ with saoH_2, NaOMe in alcohol, i.e. replacement of $\text{Mn}(\text{ClO}_4)_2 \cdot 4\text{H}_2\text{O}$ with $\text{Mn}(\text{O}_2\text{CH})_2 \cdot 4\text{H}_2\text{O}$ in an otherwise identical reaction. Alternatively **1** can also be made by replacing the NaOMe with TBAMnO_4. By then simply using a different carboxylate a whole family of compounds of general formula $[\text{Mn}^{\text{III}}_6\text{O}_2(\text{sao})_6(\text{O}_2\text{CR})_2(\text{CH}_3\text{OH})_4]$ (R = Me (**2**), Et (**3**), Ph (**4**)) can be isolated. Each displays similar magnetic properties to **1** [33]. Repeating these reactions but in pyridine rather than alcohol results in the formation of the triangular complexes $[\text{Mn}_3\text{O}(\text{sao})_3(\text{O}_2\text{CR})(\text{H}_2\text{O})(\text{py})_3]$ (R = Me (**5**), Ph (**6**), Fig. 5). These have very similar structures to the well-known 'basic carboxylates' of general formula $[\text{Mn}_3\text{O}(\text{O}_2\text{CR})_6\text{L}_3]^{n+}$ (L = py, MeCN, etc.; $n = 0, 1$) and can be regarded as the triangular building blocks of complexes **1**–**4** [33], i.e. **1** contains two such Mn_3 units bridged together via two μ-oximato oxygens. Both **5** and **6** can in fact be isolated under a range of conditions (ambient and solvothermal) but we initially isolated them from

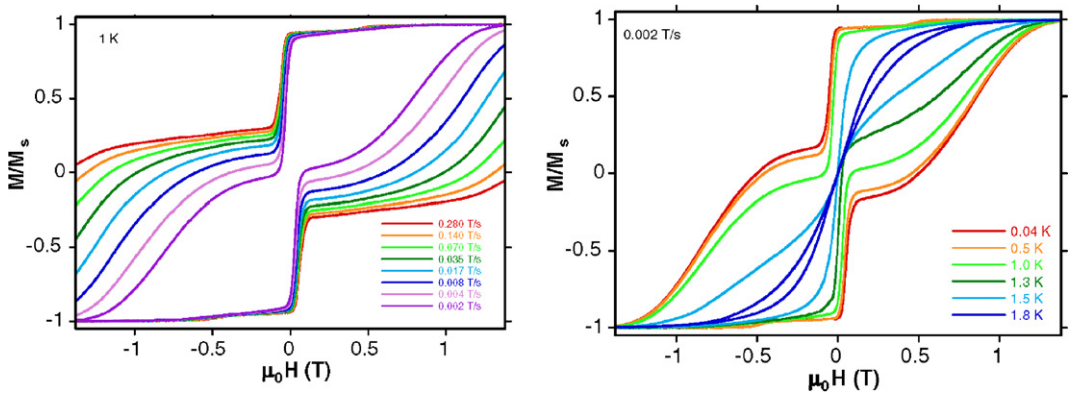


Fig. 3. M vs. H hysteresis loops for a single crystal of **1**. The loops are shown at different field sweep rates (left) and temperatures (right); M is normalized to its saturation value.

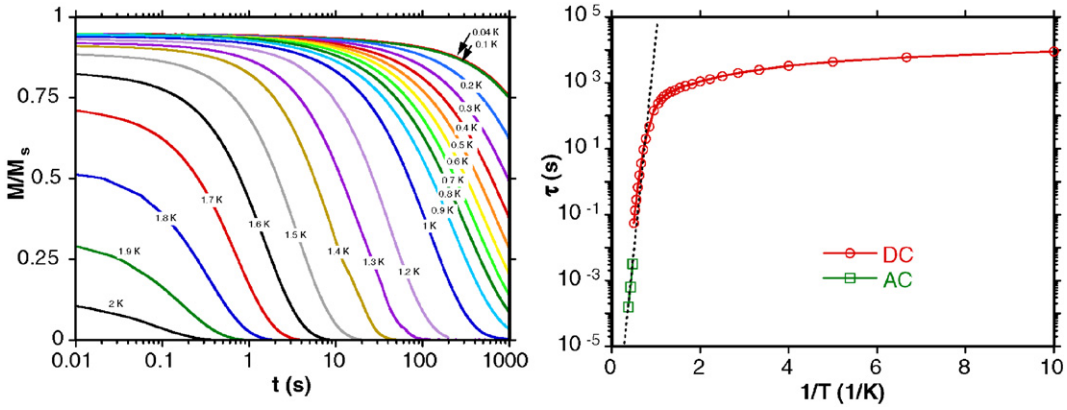


Fig. 4. Single-crystal relaxation data for **1**, plotted as M/M_S vs. time (left). Arrhenius plot using ac and dc data. The dashed line is the fit of the thermally activated region to Eq. (2).

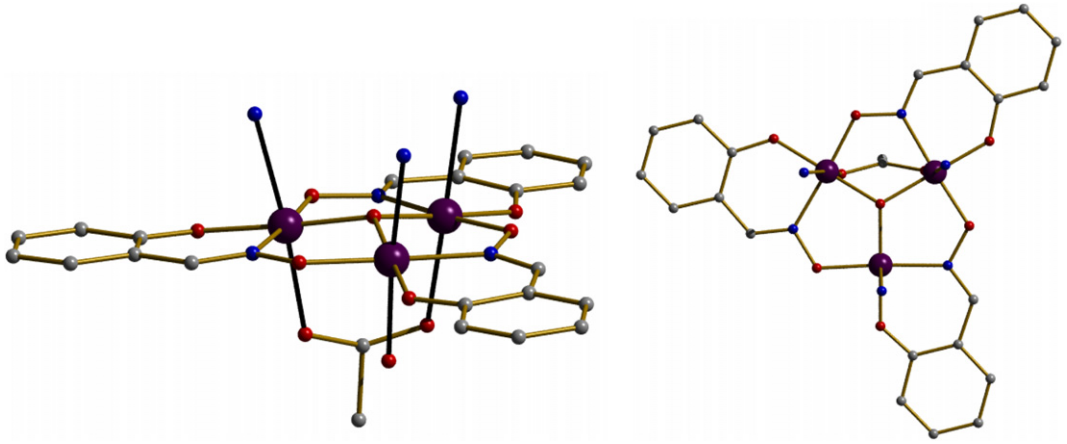


Fig. 5. The molecular structure of complex **5**. The carbon atoms of the pyridine molecules have been omitted for clarity. The solid black lines describe the three Jahn–Teller axes. Colour scheme as for Fig. 1. (For interpretation of the references to colour in this figure legend, the reader is referred to the web version of this article.)

the microwave ($T = 110$ °C; 10 min, 120 psi) and indeed this remains the fastest and most efficient method of synthesis. The structures (Fig. 5) consist of an oxo-centered triangular arrangement of three Mn^{III} ions with each edge bridged by one sao^{2-} ligand. The remaining axial sites on the Mn ions are filled by a combination of terminal pyridine and water molecules and one μ-carboxylate. Magnetic studies reveal that both species display dominant antiferromagnetic exchange interactions between the metal centres with ground states $S = 2 \pm 1$ for **5** and $S = 3 \pm 1$ for **6** [33]. The susceptibility data for **5** were fit to the theoretical expression for an isosceles triangle yielding $J_1 = -6.3$ cm^{-1}, $J_2 = +11.9$ cm^{-1}, but we were unable to fit the data for **6**. In-phase (χ'_M) ac susceptibility measurements taken below 10 K are suggestive the presence of low lying excited states with larger S values for both complexes. Such low-lying excited states are a common feature in many Mn clusters that exhibit relatively weak exchange interactions. The population of excited states even at very low temperatures is difficult to avoid and this clearly complicates the analysis of the data. Frequency-dependent out-of-phase (χ''_M) ac susceptibility signals are seen for complex **6** below approximately 3 K (but no peaks are observed) suggestive of the onset of slow magnetization relaxation. Single crystal hysteresis loop and relaxation measurements are currently underway to see if complex **6** behaves as an SMM.

3. Iron clusters

Heating a mixture of $Fe(O_2CMe)_2$, $saoH_2$ and pyridine at 120 °C, 130 psi and 200 W for a total of 5 min produces the complex $[Fe^{III}_8O_4(sao)_8(py)_4]$ [34] (**7**, Fig. 6), which forms immediately inside the microwave tube in ~70% yield. Complex **2** cannot be made under ambient reaction conditions, nor by refluxing a pyridine solution of $Fe(O_2CMe)_2$ and $saoH_2$. The use of various $Fe^{II/III}$ salts, different solvents or combinations of solvents, and different reaction times did not reproduce **2**. Microcrystalline material displaying a similar IR spectrum to complex **2** can be isolated under solvothermal reaction conditions (sealed Teflon container; 120 °C) using pyridine as solvent but

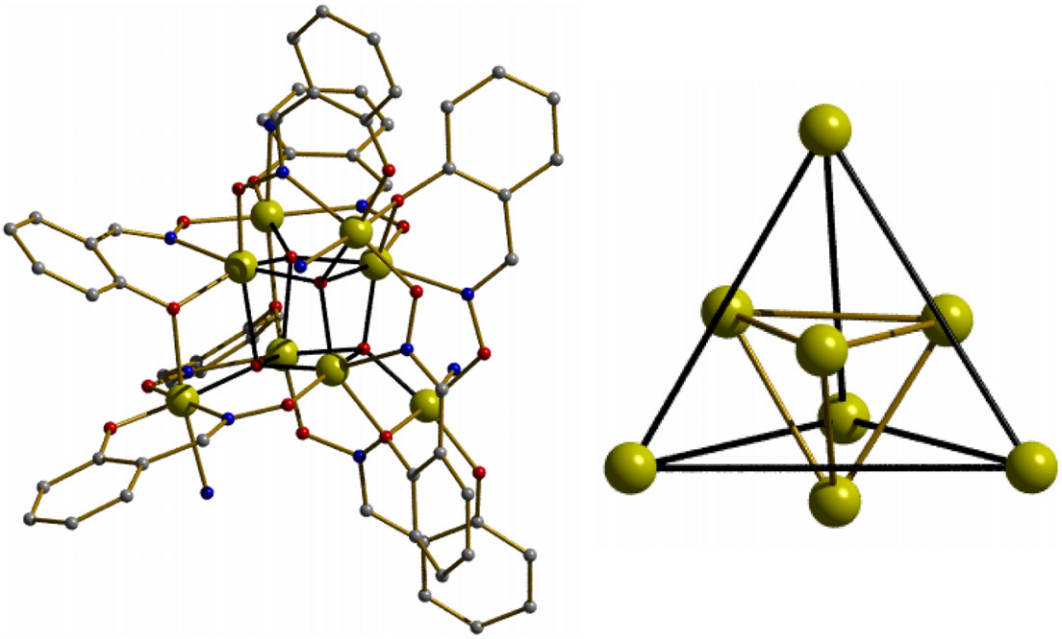


Fig. 6. The molecular structure of complex **7** (left) and its metallic skeleton, showing the tetrahedron inside a tetrahedron (right). The pyridine molecules have been removed for clarity. Colour code: Fe = yellow; O = red; N = blue; C = gold. (For interpretation of the references to colour in this figure legend, the reader is referred to the web version of this article.)

requires a minimum heating/cooling period of 24 h and forms in yields of less than ~10%; this equates to an approximately sevenfold decrease in comparison to the microwave reaction, and suggests the rapid heating and pressure rate employed in the microwave cavity (the reaction reached its maximum temperature/pressure in less than 30 s) plays an important synthetic role.

The complex crystallizes in the tetragonal space group $I4_1/a$. The core of the complex (Fig. 6) contains a central $[Fe^{III}_4O_4]^{4+}$ cubane with each of the four (distorted) tetrahedral μ_4-O^{2-} ions further bridged to a peripheral Fe^{III} ion. The peripheral metal ions themselves form a tetrahedron, encapsulating the cubane such that each face of the tetrahedron is capped. The eight sao^{2-} ligands bridge in two ways: four in a η^2:η^1:η^1:μ_3-fashion along one complete edge of the tetrahedron with the phenolate oxygen atom bridging one Fe ion of the cube and one Fe ion of the tetrahedron; and four in a η^1:η^1:η^1:μ-fashion along half an edge, between an Fe ion in the tetrahedron and a face-capping Fe ion of the central cube. The observed η^2:η^1:η^1:μ_3-coordination mode is unique amongst the structurally characterized metal complexes containing the sao^{2-} ligand [35–37]. A μ_3-behaviour has been observed in sao^{2-} complexes but with the oximate oxygen providing the bridge between metal ions. The coordination sphere of each of the four Fe ions in the outer tetrahedron is completed by a terminal pyridine molecule. Within the $[Fe_4O_4]^{4+}$ cubane there are two small (~96°) and one large Fe–O–Fe (106°) angles suggesting a rather 'twisted' metal cubane. The $[Fe_8O_4]^{4+}$ core is uncommon, observed only in one other complex: $[Fe_8O_4(pz)_{12}Cl_4]$ (pz = pyrazolate anion) reported in 1999 [38] and the central $Fe^{III}_4O_4$ cubane is an extremely rare unit at this oxidation level. Some Fe/O cubanes with Fe^{II} or mixed $Fe^{II/III}$ cores are known, but there are only two $Fe^{III}_4O_4$ cubane units (both inside larger clusters) in the literature [38,39]. Complex **7** has a $S = 0$ ground state, probably due to antiferromagnetic exchange between the peripheral Fe^{III} ions in the tetrahedron and the central Fe^{III} ions in the cubane, mediated by the μ_4-bridging O^{2-} ions that display Fe–O-Fe angles in the range 102.9(1)–124.8(1)°.

4. Nickel and cobalt clusters

The reaction between $Ni(O_2CMe)_2 \cdot 4H_2O$ and one equivalent of NaN_3 in pyridine/MeOH under microwave irradiation ($T = 120$ °C; power = 250 W; pressure = 130 psi) for 4 min produces $[Ni_3(N_3)_3(O_2CMe)_3(py)_5]$ (**8**) in yields of ~55%. The analogous procedure using $Co(O_2CMe)_2 \cdot 4H_2O$ gives pink crystals of $[Co_3(N_3)_3(O_2CMe)_3(py)_5]$ (**9**) in ~40% yield [40]. Neither complex could be produced under ambient reaction conditions despite the use of various solvents and starting materials. The lower yield for **9** can be attributed to the formation of $[Co^{III}(N_3)_3(py)_3]$ which crystallizes upon prolonged standing [41]. Complex **8** crystallizes in the monoclinic space group $P2_1/n$ (Fig. 7). The core of the molecule contains a isosceles triangle of three Ni^{II} ions with Ni···Ni distances of ~3.1 and 3.8 Å. The 'apical' Ni ion is connected to the two basal nickel ions via two end-on, μ-N_3^- ions, two *syn*, *syn*, η^1:η^1:μ-acetates and one end-on μ_3-N_3^- ligand. The basal nickel ions are further bridged by one *syn*, *syn*, η^1:η^1:μ-acetate. The metal coordination environments are completed by five pyridine molecules. All three nickel ions

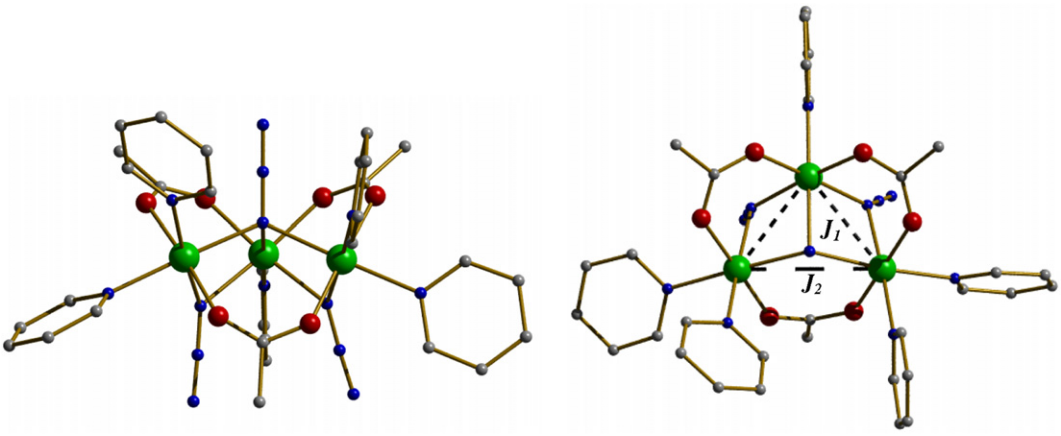


Fig. 7. The molecular structure of complex **3** viewed parallel (left) and perpendicular (right) to the Ni_3 plane. Colour code: Ni = green, O = red, N = blue, C = grey. (For interpretation of the references to colour in this figure legend, the reader is referred to the web version of this article.)

are six-coordinate in slightly distorted octahedral geometry. Complex **9** crystallizes in the monoclinic space group $P2_1/n$ and its structure is analogous to that of **8**, with all three Co ions in the 2+ oxidation state. Both complexes can be considered as M^{II} analogues of the well-known "*M^{III} basic-carboxylates*" of general formula $[M_3O(O_2CR)_6(L)_3]^{n+}$ (M = V, Cr, Mn, Fe, Co; L = py, H_2O, MeCN; $n = 0$, 1) whose structures consist of oxo-centered metal triangles. Here, the compensation of charge is achieved by replacing (a) the central μ_3-O^{2-} ion with a central μ_3-N_3^- ion, and (b) three of the six bridging carboxylates with a combination of two μ-N_3^- ions and two additional terminal pyridines.

Complex **8** has an $S = 3$ ground state as a result of ferromagnetic exchange between the apical and basal Ni ions (Fig. 7). The best-fit parameters obtained by means of the program MAGPACK and employing the spin Hamiltonian $\hat{H} = -2J_1(\hat{S}_1 \cdot \hat{S}_2 + \hat{S}_1 \cdot \hat{S}_3) - 2J_2(\hat{S}_2 \cdot \hat{S}_3)$ were $J_1 = +15.7$ cm^{-1}, $J_2 = -1.2$ cm^{-1} and $g = 2.16$ [40]. Magnetization data collected in the ranges 10–50 kG and 2.0–7.0 K gave best fit parameters of $S = 3$, $g = 2.18$ and $D = +0.67$ cm^{-1}. The exchange in complex **9** is also ferromagnetic. Magnetization data collected in the ranges 10–50 kG and 2.0–7.0 K reveal that saturation is almost reached with a value of $M/N\beta \approx 8.4$ corresponding to an effective $S' = 3/2$ with a large anisotropic g'-value [40].

5. Conclusions

The important chemical message from this preliminary work is that microwave irradiation presents a powerful tool toward the preparation of new polymetallic cluster compounds. It may lead to novel products by permitting access to alternative kinetic pathways and stabilizing different energy minima in a reaction system compared to conventional methods of heating. Here we have shown this to be valid with the synthesis of a host of new metal clusters – many of which have shown interesting magnetic properties. It has also provided a means of improving the yields of known complexes in faster times, and indeed may even be considered a "*green*" approach to the synthesis of polynuclear complexes, since in general, it employs minimal solvent and minimizes energy and heat loss via the *direct* heating of the sample. This all suggests that the future potential of microwave-assisted synthesis to be truly enormous.

Acknowledgements

The work described has been done in collaboration with a number of groups. In particular, the authors thank Prof. George Christou (University of Florida), Dr. Wolfgang Wernsdorfer (Laboratoire Louis Néel), Dr. Mark Murrie (University of Glasgow) and Prof. Spyros Perlepes (University of Patras). Funding for the research was given by The Leverhulme Trust and EPSRC (UK).

References

[1] A.G. Whittaker, D.M.P. Mingos, J. Microwave Power Electromag. Energy 29 (1994) 195.
[2] D. Mingos, Res. Chem. Intermed. 20 (1994) 85.
[3] S. Toma, Chem. Listy 87 (1993) 888.
[4] S. Toma, Chem. Listy 87 (1993) 627.
[5] D.R. Baghurst, D.M.P. Mingos, J. Chem. Soc., Chem. Commun. (1992) 674.
[6] G. Bond, R.B. Moyes, S.D. Pollington, D.A. Whan, Chem. Ind. (1991) 686.
[7] A. Zlotorzynski, Crit. Rev. Anal. Chem. 25 (1995) 43.
[8] K.J. Rao, B. Vaidhyanathan, M. Ganguli, P.A. Ramakrishnan, Chem. Mater. 11 (1999) 882.
[9] A. De La Hoz, A. Diaz-Ortis, A. Moreno, F. Langa, Eur. J. Org. Chem. (2000) 3659.
[10] K. Chatakondu, M. Green, D. Mingos, S.M. Reynolds, J. Chem. Soc., Chem. Commun. (1989) 1515.
[11] K. Olofsson, M. Larhed, A. Hallberg, J. Org. Chem. 63 (1998) 5076.
[12] M. Larhed, G. Lindeberg, A. Hallberg, Tetrahedron Lett. 37 (1996) 8219.
[13] M. Larhed, M. Hoshino, S. Hadida, D.P. Curran, A. Hallberg, J. Org. Chem. 62 (1997) 5583.
[14] U. Bremberg, M. Larhed, C. Moberg, A. Hallberg, J. Org. Chem. 64 (1999) 1082.

[15] K.S.A. Vallin, M. Larhed, K. Johansson, A. Hallberg, J. Org. Chem. 65 (2000) 4537.
[16] B.K. Banik, M.S. Manhas, E.W. Robb, A.K. Bose, Heterocycles 44 (1997) 405.
[17] S. Lutsenko, C. Moberg, Tetrahedron: Asymmetry 12 (2001) 2529.
[18] V. Daniels, Dielectric Relaxation, Academic Press, London, 1967.
[19] N.H. Williams, J. Microwave Power 2 (1967) 123.
[20] W.H. Sutton, Am. Ceram. Soc. Bull. 68 (1989) 376.
[21] V. Kenkre, L. Skala, M. Weiser, J. Katz, J. Mater. Sci. 26 (1991) 2483.
[22] For reviews see: R.E.P. Winpenny, Dalton Trans. (2004) 1.
[23] S. Parsons, R.E.P. Winpenny, Acc. Chem. Res. 30 (1997) 89.
[24] R.E.P. Winpenny, Adv. Inorg. Chem. 52 (2001) 1.
[25] E.K. Brechin, A. Graham, P.E.Y. Milne, M. Murrie, S. Parsons, R.E.P. Winpenny, Philos. Trans. R. Soc. Lond. A 357 (1999) 3119.
[26] E.K. Brechin, Chem. Commun. (2005) 5141.
[27] G.S. Papaefstathiou, S.P. Perlepes, Comments Inorg. Chem. 23 (2002) 249.
[28] E.J.L. McInnes, S. Piligkos, G.A. Timco, R.E.P. Winpenny, Coord. Chem. Rev. 249 (2005) 2577.
[29] D.M. Low, L.F. Jones, A. Bell, E.K. Brechin, T. Mallah, E. Rivière, S.J. Teat, E.J.L. McInnes, Angew. Chem., Int. Ed. 42 (2003) 3781.
[30] D. Stuerga, K. Gonon, M. Lallemant, Tetrahedron 49 (1993) 6229.
[31] C.J. Milios, A. Vinslava, A.G. Whittaker, S. Parsons, W. Wernsdorfer, G. Christou, S.P. Perlepes, E.K. Brechin, Inorg. Chem. 45 (2006) 5272.
[32] W. Wernsdorfer, Adv. Chem. Phys. 118 (2001) 99.
[33] C.J. Milios, G. Christou, S.P. Perlepes, E.K. Brechin, unpublished results.
[34] I.A. Gass, C.J. Milios, A.G. Whittaker, F.P.A. Fabbiani, S. Parsons, M. Murrie, S.P. Perlepes, E.K. Brechin, Inorg. Chem. 45 (2006) 5281.
[35] For a review see: A.G. Smith, P.A. Tasker, D.J. White, Coord. Chem. Rev. 241 (2003) 61.
[36] P. Chaudhuri, Coord. Chem. Rev. 243 (2003) 143.
[37] C.P. Raptopoulou, A.K. Boudalis, Y. Sanakis, V. Psycharis, J.M. Clemente-Juan, M. Fardis, G. Diamantopoulos, G. Papavassiliou, Inorg. Chem. 45 (2006) 2317.
[38] R.G. Raptis, I.P. Georgakaki, D.C.R. Hockless, Angew. Chem., Int. Ed. 38 (1999) 1632.
[39] D. Foguet-Albiol, K.A. Abboud, G. Christou, Chem. Commun. (2005) 4282.
[40] C.J. Milios, A. Prescimone, J. Sanchez-Benitez, S. Parsons, M. Murrie, E.K. Brechin, Inorg. Chem. 45 (2006) 7053.
[41] M.A.S. Goher, R.-J. Wang, T.C.W. Mak, Polyhedron 11 (1992) 829.

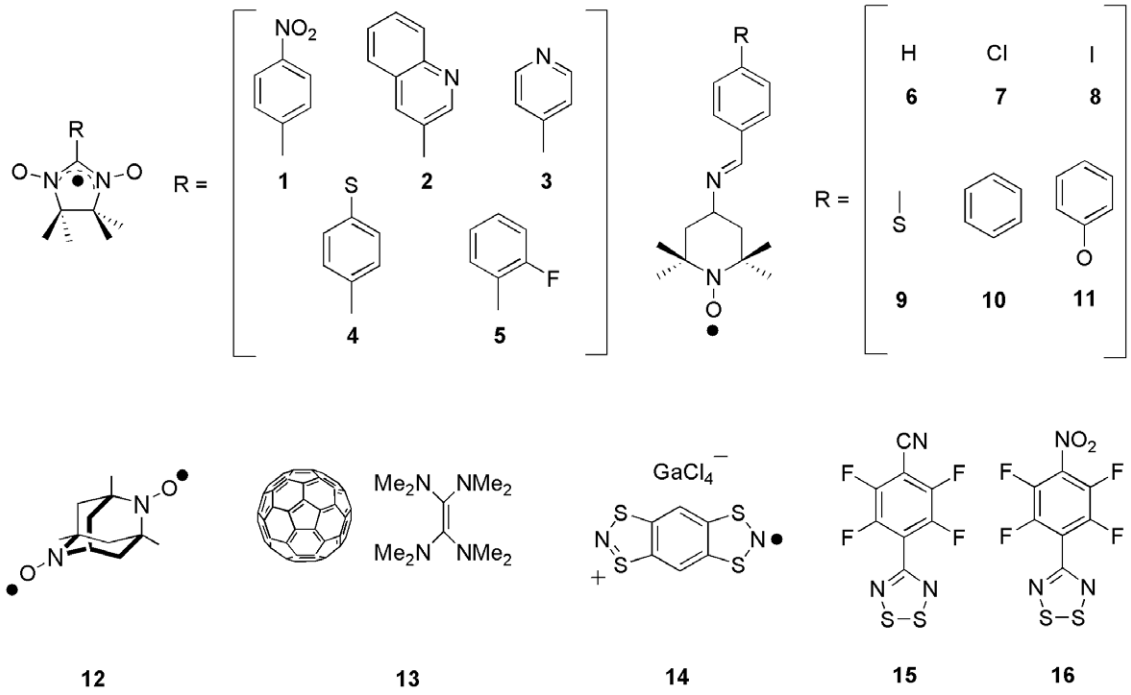


Chart 1.

predilection for antiparallel spin alignments in these molecules. Second, there are complications that usually arise when a transmission of such intermolecular ferromagnetic interactions, along two or three dimensions of the solid and over a long range, is desired. And third, it is impossible to predict the ultimate structure of even the simplest crystalline solids from a knowledge of their chemical composition [9].

In order to minimize these inconveniences, crystal engineering tools are needed. Crystal engineering is the design, construction and study of crystal structures from molecular components built with predesigned intermolecular interactions [10]. Besides π-stacking between verdazyl radicals, that has allowed the transmission of very strong magnetic exchange interactions [11], hydrogen bonds (H-bonds) have been mostly studied because their directional and often predictive nature may allow controlling long-range supramolecular order in solid state [12]. H-bonds are formed by strong donor–acceptor functionalities (OH, NH_2, CO_2H, $CONH_2$) and with weak donors (C≡C–H, C_6H_5, C=C–H, $C(sp^3)$–H) and acceptors (CN, NO_2, halogen, π). In such a context, Veciana and co-workers [13] proposed the idea to use these H-bonds to control the self-assembly of open-shell building-blocks which were used also successfully by Sugawara and co-workers [14]. Such a study was initiated by studying the family of aromatic nitronyl nitroxide derivatives with one or two hydroxylic groups on the aromatic ring as functional groups, susceptible to form hydrogen bond interactions. Success of this approach was reflected in two different organic ferromagnets based on molecules **17** [15] and **18** [16] that are substituted with one and two hydroxylic groups, and which orders at 0.45 and 0.50 K, respectively (Chart 2). Furthermore, additional examples belonging to this family substituted with one or several H-bond donors such as phenol [17], boronic acid [18], imidazole [19], benzimidazole [20], triazole [21], uracil [22], pyrazole [23], phenyl acetylene [24] and benzoic acid [25] have provided an interesting assortment of magnetic behaviours.

In addition to the hydroxylic groups, carboxylic groups are also important for crystal engineering because they also form strong and directional O–H···O hydrogen bonds. H-bonded patterns in carboxylic derivatives in solid state have been described in detail by Leiserowitz [26]. The most frequent and dominant H-bonded motif is the syn–syn centrosymmetric dimer. However, other patterns in the form of infinite non-cyclic H-bonded catemer motifs and more rare cyclic trimeric and tetrameric motifs can also been found [27,28].

Given this background, our group has initiated a new experimental approach based on the synthesis and study of organic/molecular magnetic materials based on the supramolecular arrangement of polychlorotriphenylmethyl

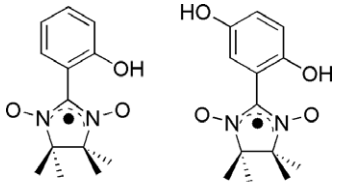


Chart 2.

(PTM) radicals functionalized with carboxylic groups in the *para*- and *meta*-positions of the aromatic rings with respect of the central methyl carbon (Chart 3). The interest for these molecules is multiple according to magnetic, geometrical and structural considerations. First, they exhibit a high thermal and chemical stability thanks to the presence of six bulky chlorine atoms that are shielding the central carbon atom, where the most part of the spin density is localized. Second, from a structural point of view, the rigidity and bulkiness of this family of open-shell molecules [29] was expected not only to prevent close packing and to form robust networks [30], but also to minimize undesired through space magnetic interactions in the solid state. Moreover, for example, PTMTC radical can be considered as an expanded versions of the trimesic acid molecule [31], where the benzene-1,3,5-triyl units has been replaced by an sp^2 hybridized carbon atom decorated with three 4-substituted 2,3,5,6-tetrachlorophenyl rings. Therefore, according to its related trigonal symmetry and functionality and to the molecule rigidity, PTMTC radical was expected to yield a purely organic magnetic open-framework, a goal within the sole crystal engineering field [32]. The last relevant facet of these molecules is related to the possibility to functionalize these radicals with carboxylic acid groups. As has been stated above, among the numerous functional groups used to build self-assembled networks, carboxylic acid groups combine the capability to form strong and directional H-bonds with their ability to promote magnetic interactions between radical species [25]. These functional groups are also particularly appealing in order to use in a further step: PTM radicals as ligands to access to porous and magnetic metal-organic coordination polymers [33], following a strategy combining the so-called ''reticular synthesis'' [34] together with the well-known ''metal-radical approach'' [35].

When we decided to start this work, only three examples of carboxylic substituted PTM radicals were described in the literature [36], and only two of them were characterized magnetically [36b,36c]. They were obtained in low overall yields following multistep synthetic methodologies, and none of them was characterized by X-ray diffraction. As a consequence, the work undertaken was also particularly challenging related to the synthetic and crystal engineering fields.

Here, an overview of the work that has been developed over the last six years in our group on this research line is presented. From the seminal work on the monocarboxylic PTM (Section 2), of great help to determine both the ability of these molecules to form intermolecular H-bonds and the nature of the intermolecular interactions mediated through the resulting supramolecular motifs, we will move to the self-assembly of PTM radicals functionalized with two and three carboxylic groups (Section 3). In both cases, the self-assembly of the paramagnetic units yield robust and porous magnetic organic/molecular structures, associating in some cases magnetic ordering to the latest remarkable characteristics. The last part of the review will present the latest results obtained with the idea to increase both the structural and magnetic dimensionality in purely organic PTM-based materials using a PTM radical functionalized by six carboxylic groups (Section 4). New trends and challenges for this research line, concerning the design and synthesis of new PTM radicals, as well as the obtaining of PTM based sensors or multifunctional materials will be presented in the concluding section (Section 5).

2. The simplest model: self-assembly of monocarboxylic PTMMC radical

The first stage of our study was focused to investigate the capacity of carboxylic acid functions of PTM radicals for the formation of intermolecular H-bonds. Although the ability of carboxylic groups to form H-bonds was widely reported [26,27,31], the neighbouring chlorine atoms located at the aromatic rings of these radicals should cause a high sterical impediment that could frustrate the formation of any direct H-bonds between carboxylic groups. To answer this question, we selected the monocarboxylic PTMMC radical previously synthesized by Ballester et al. in 1982 [36a]. The synthesis, crystallization and structural and magnetic characterization of this simple radical with only one carboxylic moiety would certainly help us to identify the formation of H-bonds as well as the nature and the strength of the expected magnetic exchange interactions mediated through these supramolecular interactions.

PTMMC was obtained following the synthetic procedure that is presented in Scheme 1 [36]. Briefly, this

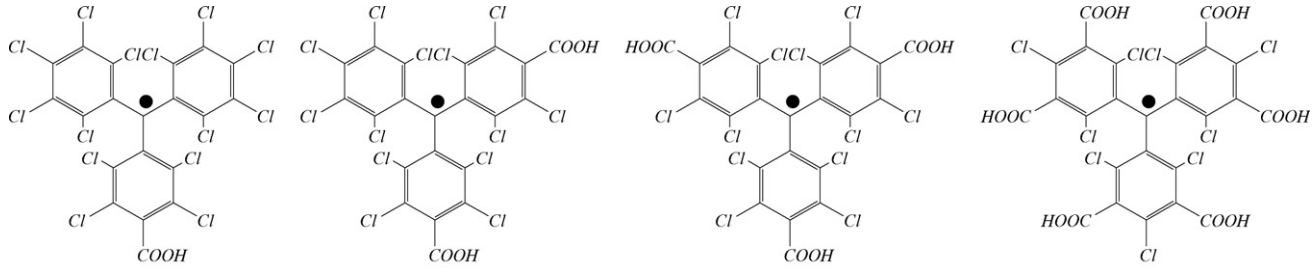


Chart 3.

synthesis involves five crucial points: (i) the formation of the triphenyl methane skeleton (molecule **24**), *via* a Grignard reaction followed by the reduction of the triphenylcarbinol derivative **23** obtained after this reaction; (ii) the chlorination of the methyl group, which is accompanied by the chlorination of the central carbon atom (molecule **25**), that makes necessary an additional step for removing this chlorine; (iii) the chlorination of the three phenyl rings, to obtain the perchlorinated skeleton (molecule **27**); (iv) the conversion of the trichloromethyl group into carboxylic acid (molecule **28**); and finally, (v) the oxidation step to form the PTMMC radical.

The crystallization of this radical was performed by diffusion of hexane into a methylene chloride solution of PTMMC [25e]. This procedure yielded an α-phase of the radical, in which the PTMMC radicals are associated into H-bonded centrosymmetric $[R_2^2(8)]$ dimeric synthons defined by O···O distances of 2.676 Å and O–H···O angles of 144° (Fig. 1) [37,38]. In this synthon, both carboxylate groups of PTMMC are twisted by 88° with respect to the phenyl plane to which they are bonded. We believe that this characteristic is mostly due to the previously predicted steric hindrance from the neighbouring chlorine atoms to the carboxylic groups. Crystal packing of these dimers is then governed by interdimer Cl···Cl short contacts that yield to the formations of tapes running in a plane, while additional Cl···Cl contacts are responsible of the 3-D close packing. A detailed revision of all supramolecular contacts is given in Table 1 (see also Fig. 2a for atom labelling).

Taking into account the basic H-bonded dimeric organization of PTMMC radicals found in α-phase, and that the shortest distance between the central methyl carbons that

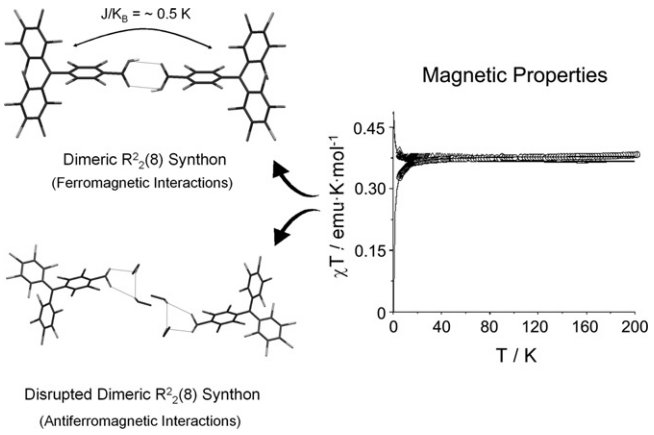
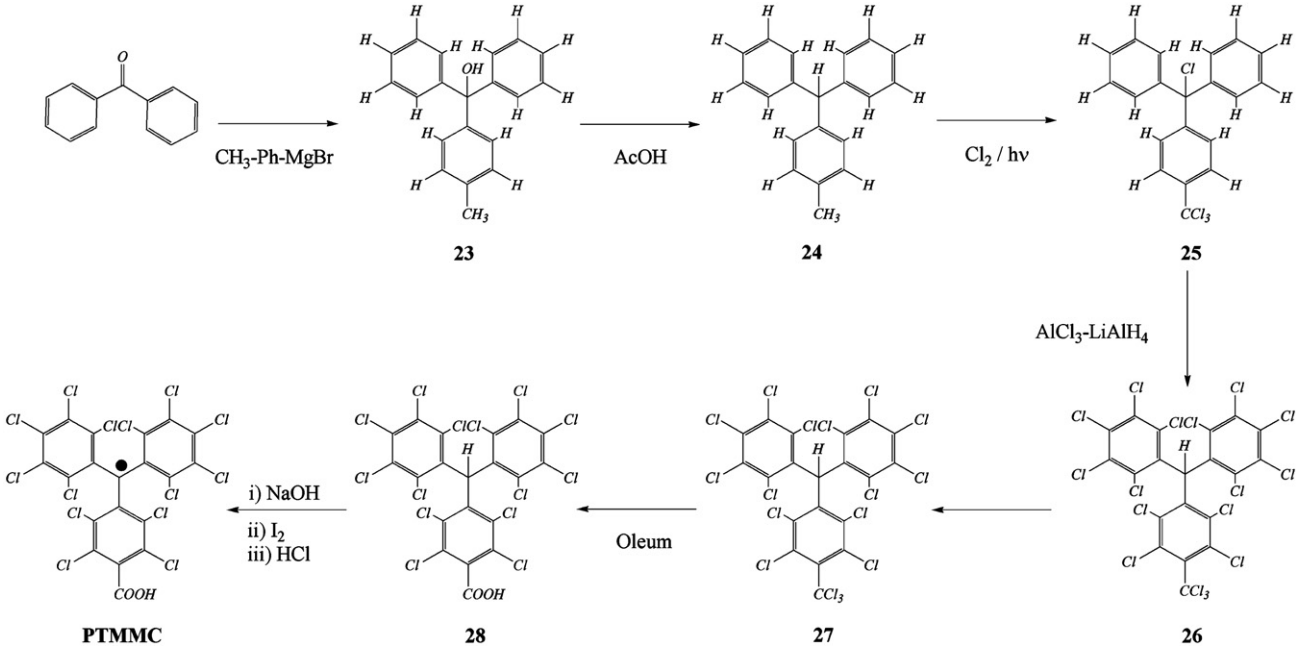


Fig. 1. Temperature dependences of the magnetic susceptibility, χ, of polycrystalline samples of α (Δ) and β (○) phases of radical PTMMC which are plotted as $\chi \cdot T$ vs. T. Solid lines are the best fit of the experimental data. $[R_2^2(8)]$ H-bonded dimers in α phase of PTMMC (top) yield weak ferromagnetic interactions while disruption of this synthon by ethanol molecules in β phase of PTMMC (bottom) is traduced by the onset of weak antiferromagnetic interactions at low temperatures.

bear most of the spin density is just found within these dimers at a length of 15.36 Å, the analysis of the magnetic properties provided the ideal scenario to study the transmission of magnetic exchange interactions between H-bonded PTM radicals. SQUID measurements revealed a paramagnetic behaviour in the 6–200 K temperature range, and the onset of weak ferromagnetic interactions below 6 K (Fig. 1). To confirm this behaviour, ESR measurements were performed on an oriented single crystal of the α phase and revealed the same trend. Hence, weak dominant ferromagnetic interactions are present in this phase.



Scheme 1. Synthesis of PTMMC.

Table 1
Supramolecular interactions and magnetic properties in carboxylic substituted PTM radicals

	α-Phase PTMMC	β-Phase PTMMC	POROF-1	POROF-2	[PTMHC · $(Et_2O)_3$]	[PTMHC · $(THF)_6$]
Primary structure	discrete H-bonded dimers	isolated PTMMC radicals H-bonded through EtOH molecules	2-D H-bonded sheets	2-D H-bonded sheets	2-D H-bonded sheets	isolated PTMHC radicals H-bonded to six THF molecules
H-bonded motifs	$[R_2^2(8)]$	$[R_3^3(8)]$	$[R_2^2(8)]$ and $[R_6^6(24)]$	$[R_6^6(24)]$	$[R_6^6(48)]$	
D···A H-bond distance (Å)	O1···O2 = 2.676	O1···$O_{(EtOH)}$ = 3.070 O2···$O_{(EtOH)}$ = 2.784 $O_{(EtOH)}$···$O_{(EtOH)}$ = 2.837	O3···O4 = 2.677 O3···$Cl11_p$ = 3.092 O1···O2 = 2.692	O1···O2 = 2.657	O1···O4 = 2.696 O2···$O_{(Et_2O)}$ = 2.640	O2···$O_{(THF)}$ = 2.592 O4···$O_{(THF)}$ = 2.598
Cl···Cl contact distance (Å)[a]			$Cl1_m$···$Cl4_m$ = 3.48 $Cl2_o$···$Cl4_m$ = 3.32 $Cl5_o$···$Cl12_m$ = 3.45	$Cl2_o$···$Cl3_o$ = 3.44		
Secondary structure	H-bonded chains connected by Cl···Cl contacts	H-bonded chains connected by Cl···Cl contacts	sheets connected by H-bonds and Cl···Cl contacts	sheets connected by Cl···Cl contacts	sheets isolated by Et_2O layers	weak H-bonds between [PTMHC · $(THF)_6$] supramolecular units
D···A H-bond distance (Å)[a]	O2···$Cl12_p$ = 3.263	O1···$Cl12_p$ = 3.026	O4···$Cl9_o$ = 3.23		Csp_3–$H_{(Et_2O)}$···O1 H-bonds	Csp^3–$H_{(THF)}$···$O_{(PTMHC)}$ H-bonds
Cl···Cl contact distance (Å)[a]	$Cl1_m$···$Cl9_o$ = 3.35 $Cl2_o$···$Cl8_m$ = 3.33 $Cl3_o$···$Cl11_m$ = 3.22 $Cl4_m$···$Cl7_p$ = 3.46 $Cl5_o$···$Cl5_o$ = 3.22 $Cl10_o$···$Cl13_m$ = 3.40	$Cl2_o$···$Cl11_m$ = 3.450 $Cl4_m$···$Cl5_o$ = 3.434 $Cl5_o$···$Cl5_o$ = 3.220 $Cl8_m$···$Cl14_o$ = 3.390 $Cl10_o$···$Cl13_m$ = 3.421	$Cl1_m$···$Cl7_m$ = 3.32 $Cl2_o$···$Cl7_m$ = 3.39 $Cl3_o$···$Cl6_m$ = 3.49	$Cl2_o$···$Cl4_m$ = 3.33		
Magnetic properties	ferromagnetic interactions ($\theta = +0.5$ K)	antiferromagnetic interactions ($\theta = -0.8$ K)	antiferromagnetic interactions ($\theta = -3.1$ K)	ferromagnetic interactions ($\theta = +0.2$ K) and ordering ($T_c \sim 220$ mK)	ferromagnetic interactions ($\theta = +0.3$ K)	antiferromagnetic interactions ($\theta = -0.3$ K)

[a] Abbreviations o (*ortho*), m (*meta*) and p (*para*) positions of the phenyl rings with respect to the central carbon of carboxylic substituted PTM radicals.

The H-bonded dimers could be responsible for the appearance of the ferromagnetic interaction within the dimers. As only Cl···Cl contacts are present between the dimers and the distances between them are quite large, it is possible that the dimers behave as magnetically independent species. Therefore, the Bleaney-Bowers equation was used to fit the magnetic data and gave the following exchange coupling constant, $J/k_B = 0.5 \pm 0.1$ K. This value was later confirmed by fitting single crystal ESR data which gave a similar value, $J/k_B = 1.6 \pm 0.2$ K.

Beside the formation of direct intermolecular H-bonds, a second interesting feature on the crystallization of carboxylic-based PTM radicals was discovered when PTMMC radical was crystallized by slow evaporation of a radical solution in ethanol. From this crystallization, a second β-phase was obtained: the $[R_2^2(8)]$ synthons observed in the α-phase are disrupted by ethanol molecules. Indeed, change in the solvent nature and the possibility offered by ethanol to form H-bonds with carboxylic groups conduces to the disruption of any direct H-bond between PTMMC radicals (Fig. 1). Similar to the first phase, the packing of the PTM units is assumed *via* additional Cl···Cl short contacts that lead to a close packed structure (Table 1 and Fig. 2b).

From a magnetic point of view, the frustration of direct H-bonds between PTMMC radicals allowed us to further investigate the transmission of the magnetic interactions between these radicals. In principle, if H-bonded synthons are mostly responsible for the ferromagnetic interaction measured in α phase, this interaction should not be present in the β-phase. Magnetic measurement on this sample showed a paramagnetic behaviour down to low temperature, where a decrease of the $\chi \cdot T$ value is observed (Fig. 1). This behaviour was fitted to the Curie-Weiss law yielding a Weiss constant of $\theta = -0.80$ K, indicating the presence of dominant antiferromagnetic interactions. Cl···Cl contacts may be responsible for this weak antiferromagnetic interactions, as seen in other chlorinated triphenylmethyl radical derivatives [39]. Hence, the comparison of the solid-state magnetic data of both phases clearly concludes that the propagation of ferromagnetic interactions mostly occurs through the pathways defined by the intermolecular H-bonds between the carboxylic functions of PTM radicals.

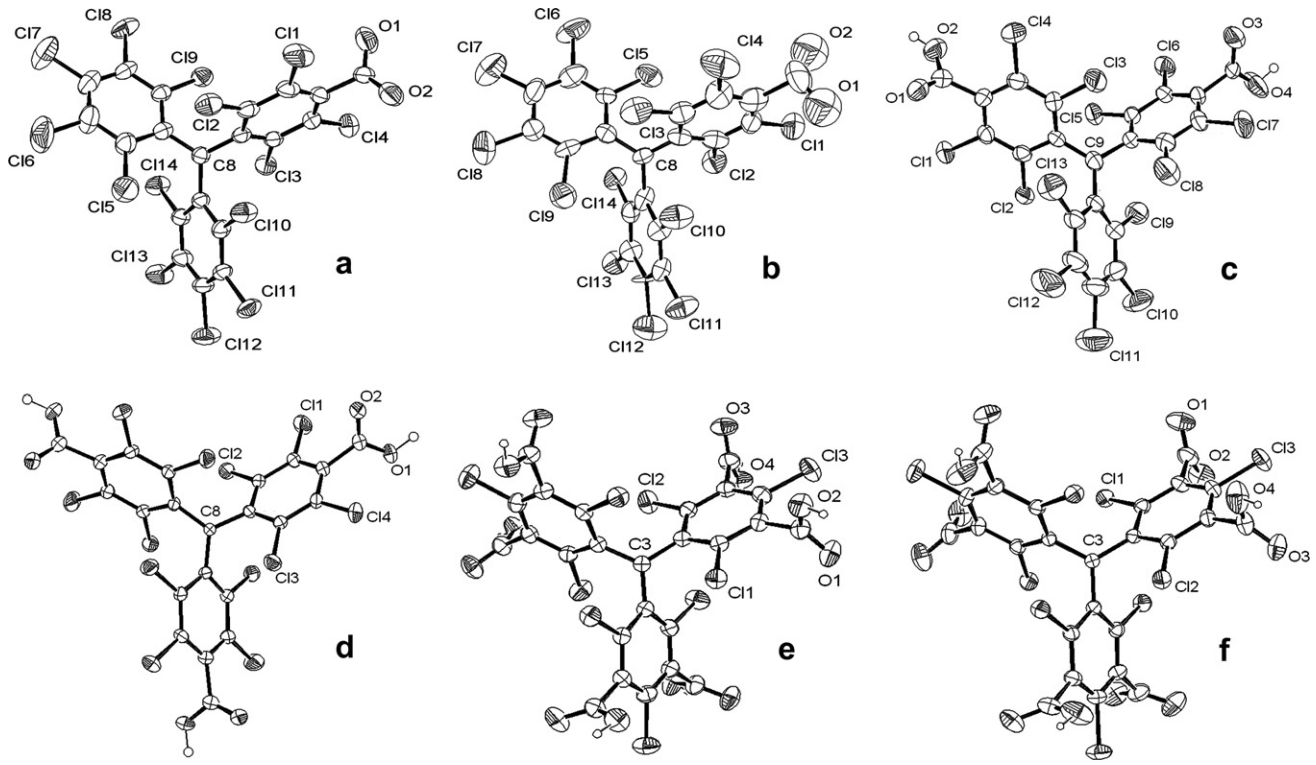


Fig. 2. Representative ORTEP views for the different crystal structures. (a) α phase of PTMMC, (b) β phase of PTMMC, (c) PTMDC (POROF-1), (d) PTMTC (POROF-2), (e) [PTMHC · $(Et_2O)_3$], and (f) [PTMHC · $(THF)_6$]. Thermal ellipsoids are set at 30% of probability and solvates solvent molecules have been omitted for clarity.

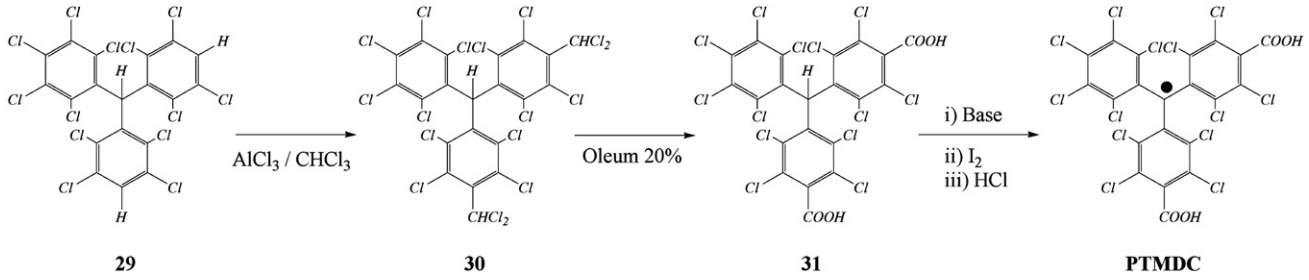
3. Extending the H-bonded dimensionality: self-assembly of di- (PTMDC) and tricarboxylic (PTMTC) radicals

The ability of PTMMC radicals to interact ferromagnetically through H-bonds prompted us to go a step further building extended purely organic/molecular structures, in which the transmission of ferromagnetic interactions could be propagated along the three dimensions and, therefore, induce a long-range magnetic ordering. The natural and rational step to extend the H-bonds in these radicals is the addition of more carboxylic functions to the skeleton of the PTM radicals. Thus, in a first approach, we designed two PTM radicals with two (PTMDC) and three (PTMTC) carboxylic functions to the *para*-positions of the aromatic rings with respect of the central carbon atom (Chart 3). From a structural point of view, both PTMDC and PTMTC radicals can be considered expanded versions of isophtalic and trimesic acids, respectively, where the benzene-1,3-diyl or the benzene-1,3,5-triyl unit has been replaced by an sp^2 hybridized carbon atom decorated with three perchlorophenyl rings substituted with carboxylic groups. And since isophtalic and trimesic acid molecules have been successfully used as building-blocks to create a wide diversity of extended H-bonded organic structures, a similar behaviour could be expected for both radicals [31,40]. Furthermore, the related trigonal symmetries and functionalities of both organic radicals also provides a typical template for getting cavities or channels, which envisions the synthesis of a series of purely organic/molecular magnetic structures with additional porosity characteristics.

A previous synthesis of the PTMDC radical together with preliminary magnetic characterizations was reported in 1994 by Domingo et al. Nevertheless, the overall yield of this multistep synthesis was rather low (12%) and magnetic characterizations, even if showing the onset of weak ferromagnetic interactions at low temperature, were performed on an amorphous sample of the radical [36b].

PTMDC was prepared following a new three-step procedure, starting from compound **29** (Scheme 2). Dichloromethyl groups were introduced by reacting **29** with chloroform following a Friedel–Crafts reaction, using $AlCl_3$ as catalyst (78%), and were subsequently converted to carboxylic groups by a hydrolysis–oxidation reaction using oleum 20% (31%). Finally, the subsequent treatment of the hydrocarbon precursor **31** with excess of NaOH, I_2, and HCl allowed the recovering radical (90%) [41]. Despite the low yield observed for the second step, this straightforward synthetic approach gave a higher overall yield than the synthesis previously reported for the molecule (21%).

With the experience acquired with the crystallization processes of PTMMC radical and in order to avoid any disruption of the expected H-bonded network, the crystallization of PTMDC was carried out without using solvent highly susceptible to generate H-bonds, such as alcohols. Thus, by reproducing the same crystallization conditions



Scheme 2. Synthesis of PTMDC.

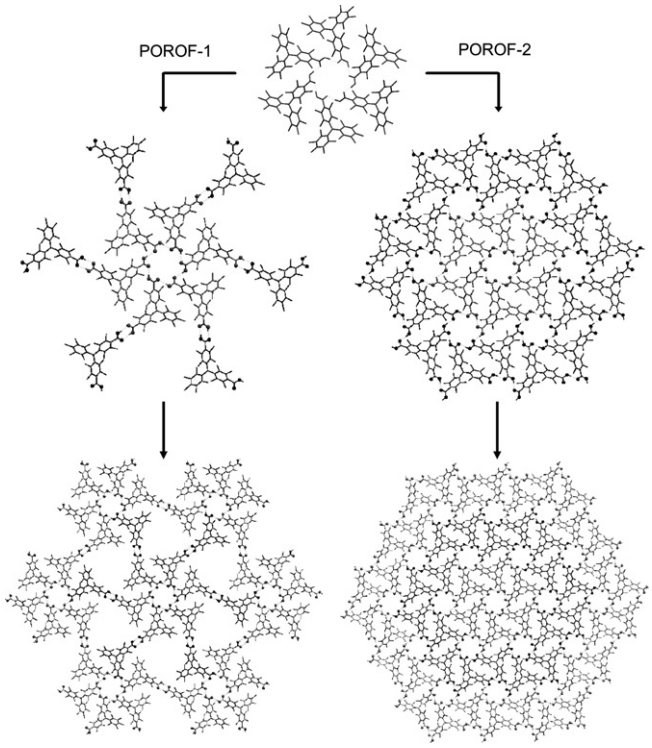


Fig. 3. Crystal structures of POROF-1 and POROF-2. Repetitive $[R_6^6(24)]$ hexamers (center) are connected through $[R_2^2(8)]$ synthon in POROF-1 (left) while this unique motif is responsible of the formation of 2-D porous H-bonded layers in POROF-2.

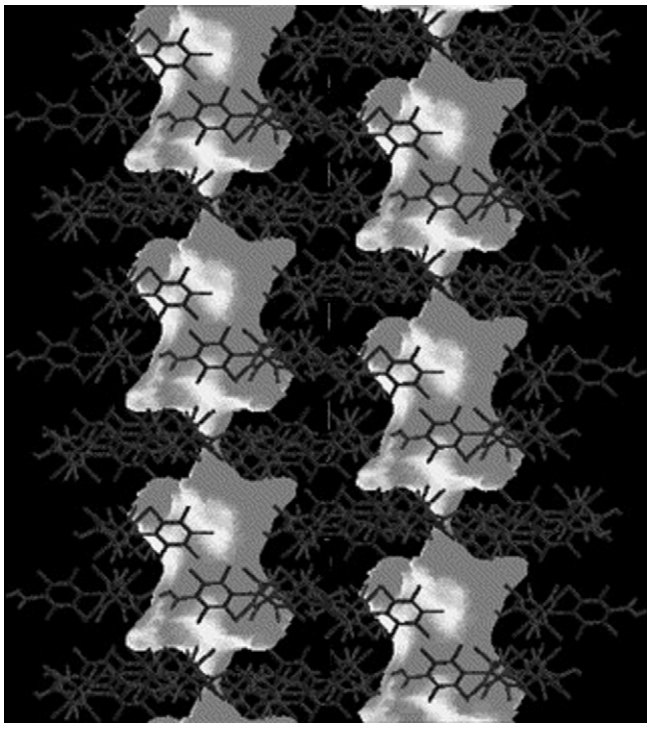


Fig. 4. Space-filling view along the *b* axis of the large nanocontainers formed along the 1-D channels in POROF-1.

that yielded the α-phase of PTMMC, a robust porous extended H-bonded network (POROF-1, where POROF refers to as Pure Organic Radical Open-Framework), that combines the presence of highly non-polar nanocontainers connected by polar narrow windows, was obtained. Thus in the solid state, the intermolecular H-bonded connections between PTMDC radicals create a primary structure consisting of 2-D H-bonded sheets, where each molecule of PTMDC adopts two H-bonded motifs, the expected dimeric $[R_2^2(8)]$ and the unusual hexameric $[R_6^6(24)]$ motifs (Fig. 3)[1] [28]. The first $[R_2^2(8)]$ synthon is almost identical to that observed in the α-phase of PTMMC with O···O distances of 2.677 Å and O–H···O angles of 164°. On the other hand, the new centrosymmetric cyclic $[R_6^6(24)]$ motif is formed by six mutually H-bonded carboxylic groups of PTMDC radicals with O···O distances of 2.692 and O–H···O angles of 169°. Precisely, this hexameric $[R_6^6(24)]$ motif is the repetitive unit in POROF-1, which involves the participation of one of two carboxylic groups of PTMDC radical. The second carboxylic group of each PTMDC radical forms the dimeric motif, which acts as a connecting element. Indeed, the formation of the dimer permits to connect each hexamer with six more identical units in an hexagonal topology, extending the infinitely H-bonded net along the two dimensions (Fig. 3).

These 2-D layers pack together in a shifted manner through several weak Cl···Cl contacts (Table 1 and Fig. 2c), leading an organic/molecular open-framework structure with 1-D channels formed by narrowed polar windows and larger hydrophobic cavities, where a sphere 10 Å in diameter can fit inside them (Fig. 4). The smaller

[1] Cyclic hydrogen bonded supramolecular motifs, as well as polymeric hydrogen bonded catemers, are particularly rare. See Ref. [27].

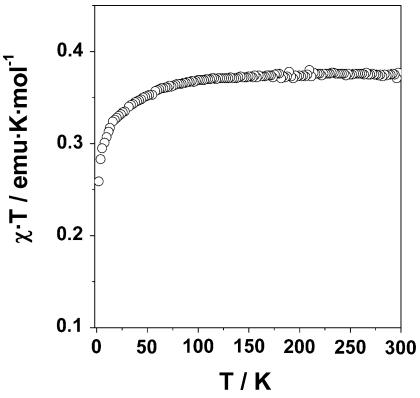


Fig. 5. Temperature-dependence of the magnetic susceptibility of POROF-1.

windows with a highly hydrophilic environment, due to the presence of the carboxylic groups at the inner walls, have a diameter of 5 Å, considering van der Waals radius. The combination of supercages and windows gives way to solvent-accessible voids in the crystal structure that amount up to 31% (5031 $Å^3$ per unit cell) of the total volume (16158 $Å^3$). Furthermore, the fact that POROF-1 is composed of radical tectons leads a magnetic character to this open-framework structure, which exhibits weak antiferromagnetic interactions between radical units at low temperatures (Fig. 5).

The new synthetic approach developed to synthesize PTMDC also allowed the access to the PTM radical with three carboxylic groups at the *para*-positions of phenyl rings. The PTMTC radical was prepared following a similar three-step procedure, starting from compound **32** (Scheme 3), and with a remarkable high overall yield (74%).

The crystallization of this radical was again carried out by diffusing a layer of hexane into a dichloromethane solution of PTMTC. The crystal packing of PTMTC molecules forms a robust porous extended H-bonded 2-D network (POROF-2), which combines the presence of highly polar tubular channels and very interesting magnetic properties, such as long-range magnetic ordering at low temperatures [42]. As shown in Fig. 3, the repetitive unit is the identical cyclic $[R_6^6(24)]$ motif identical to those found in POROF-1, and herein formed by six mutually H-bonded molecules of PTMTC with O···O distances of 2.657 Å and O–H···O angles of 169°. Since every radical unit contains three carboxylic groups, each PTMTC molecule participates in the construction of three identical hexameric units that propagates along a plane (Fig. 3). Remarkable is the fact that the stacking of layers through Cl···Cl contacts (Table 1 and Fig. 2d) occurs in an eclipsed fashion generating a 3-D structure that exhibits regular tubular channels, where a sphere of 5.2 Å in diameter can fit inside them (Fig. 6), without significant constrictions in contrast with POROF-1. In addition, such channels are surrounded by a second set of small pores with a diameter of 3.3 Å. The combination of both originates solvent-accessible voids in the crystal structure that amount up to 15% (450 $Å^3$ per unit cell) of the total volume. Interestingly, the location of carboxylic groups at the inner walls of the largest channels furnishes them with a highly polar and hydrophilic environment. This fact may stand for the lack of guest solvent non-polar molecules within the channels when crystallized from dichloromethane and hexane.

Variable temperature magnetic susceptibility data for a crystalline sample of POROF-2 revealed a paramagnetic behaviour from 300 to 5 K, where the $\chi \cdot T$ value increases on cooling down to 2 K according with the presence of

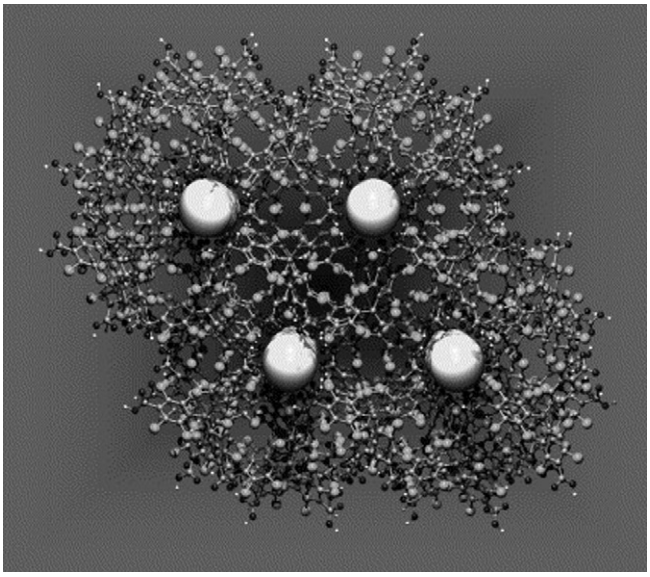
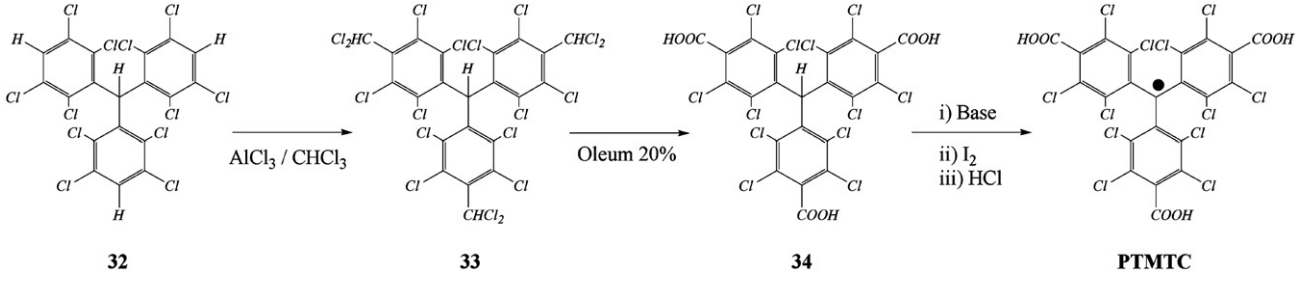


Fig. 6. View of the channel-like system of POROF-2 filled with ideal spheres with 5.2-Å diameter.



Scheme 3. Synthesis of PTMTC.

weak ferromagnetic interactions (Fig. 7). This behaviour was fitted to the Curie–Weiss law with a Weiss constant of $\theta = +0.2$ K. To investigate the existence of a long-range magnetic ordering at very low temperatures, variable temperature magnetic susceptibility experiments down to 70 mK were performed in a dilution cryostat. A considerable increase of the $\chi \cdot T$ value up to a maximum peak around 110 mK was observed on cooling down below 2 K, which reveals the transition to a ferromagnetic ordered state at very low temperatures. The intensity of the peak decreases whereas its maximum shifts slightly to higher temperatures on increasing the external applied magnetic field. For instance, for an applied magnetic field of 20 Oe a value of 2.2 emu K mol^{-1} was obtained, whereas for an external field of 50 Oe the value is reduced to 1.4 emu K mol^{-1}. This behaviour originates in the saturation of magnetization for fields of few hundred Oe. Magnetization curves were measured above and below the critical temperature and are illustrated in Fig. 7b. At 1.35 K, POROF-2 remains in the paramagnetic region, and therefore, the magnetization curve has a slight gradient. On the contrary, the curve at 80 mK, even if it is very close to the critical temperature, traces a hysteretic loop characteristic of a soft ferromagnet. The magnetization is almost saturated at about 400 Oe, and though the coercive force is of the order of 50 Oe (see inset of Fig. 7b) the remanent magnetization at zero field is of about 35% of the saturation value.

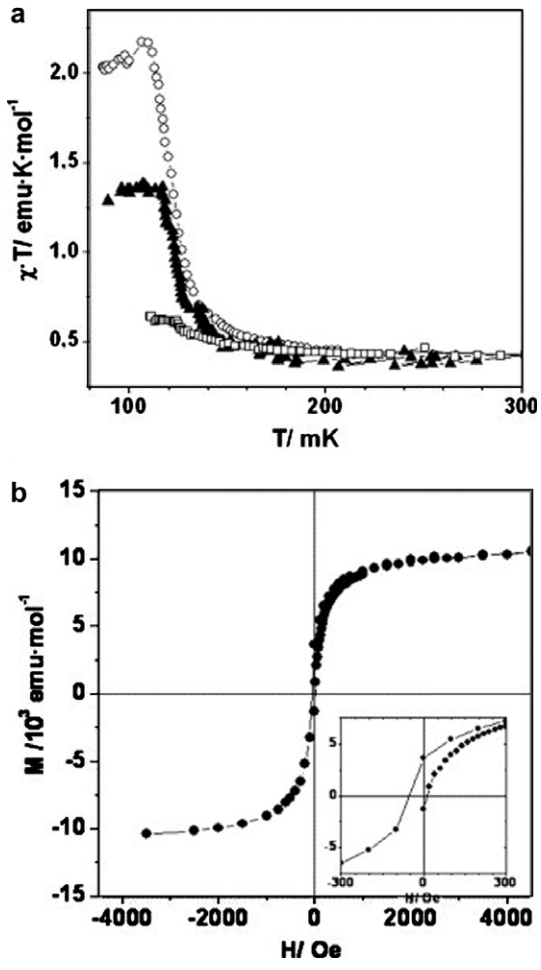


Fig. 7. Magnetic properties of POROF-2. (a) $\chi \cdot T$ as a function of temperature for different applied magnetic fields: empty circles (○), H = 200 Oe; filled triangles (▲), H = 500 Oe; and empty squares (□), H = 1000 Oe. (b) Magnetization curves as a function of the applied magnetic field measured at 80 mK. Inset, detail of the hysteresis curve at 80 mK.

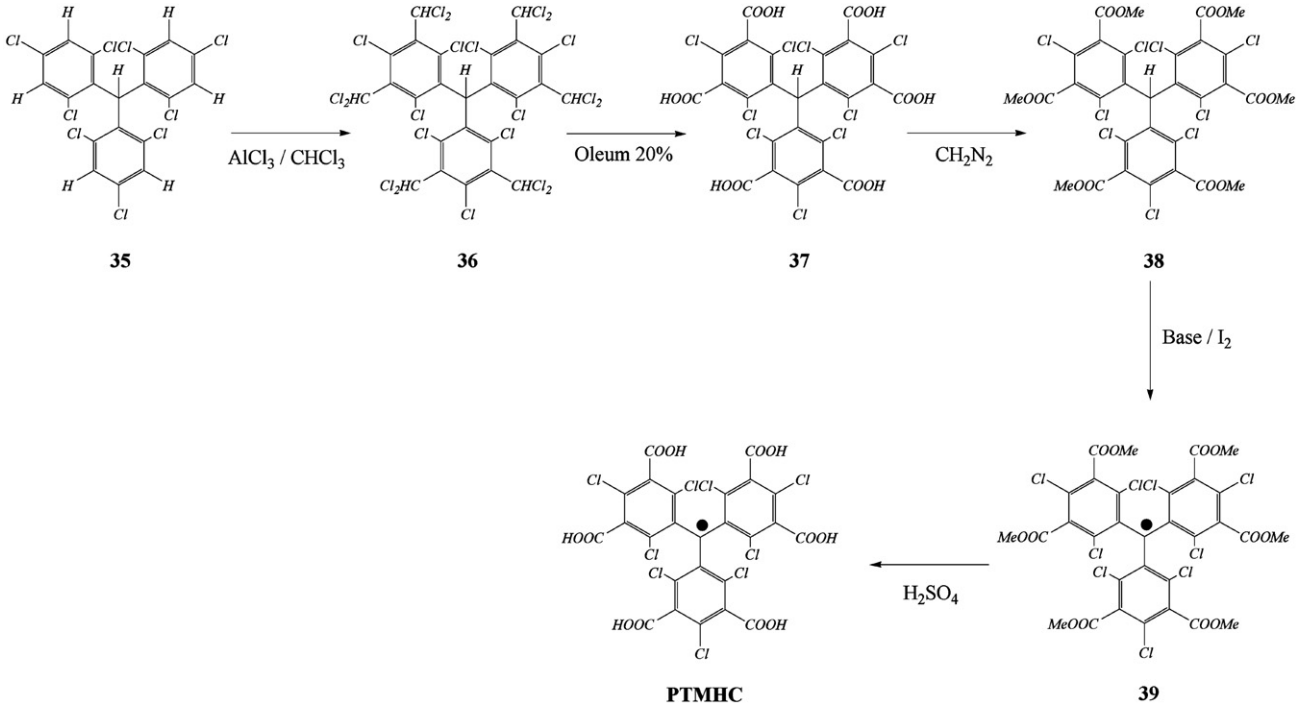
4. A highly carboxylic building-block: self-assembly of hexacarboxylic PTMHC radical

As a natural evolution due to the interest rose up by the work performed on the previous carboxylic substituted radicals, we decided to increase again the number of carboxylic acid functions and prepare a PTM radical with six carboxylic groups in *meta*-positions, studying its supramolecular organization and magnetic properties. In addition to the synthetic challenge that implies the synthesis and characterization of this novel radical [43,44], changes in both the number (six) and location (*meta*-positions) of the carboxylic groups along the PTM moiety was expected to afford new 3-D assemblies, as recently demonstrated in the case of triphenylmethane-based polyphenols [45]. In addition, the presence of six carboxylic groups in PTMHC was also expected to enhance the number of magnetic exchanges pathways between PTM radicals by endorsing the H-bonded network.

PTMHC was prepared following an adaptation of the synthetic methodology used to obtain PTMDC and PTMTC radicals (Scheme 4). While the initial part of this synthetic route was identical, the increase of the number of carboxylic groups in **37** compared to the corresponding di and tri-acid molecules **31** and **34** makes impossible the direct formation of the radical starting from this molecule [46]. To overcome this inconvenience, the hexa-acid **37** was first converted into the corresponding hexa-ester **38**, and then oxidized to give the hexa-ester radical **39**. Methyl groups were finally easily removed to obtain PTMHC with a good overall yield (30%).

The same principles applied for the crystallization of the previous radicals were considered for the crystallization of PTMHC. Multiple attempts of crystallization were performed and different crystallization techniques used in order to disfavour the formation of H-bonds between PTMHC and solvent molecules and, therefore, create a fully 3-D H-bonded organic/molecular material. Thus far, however, all these tries have failed, mainly because of the lack of solubility of the highly polar radical PTMHC in non-oxygenated solvents. Also, other common techniques such as gas phase neutralization, and based on a diffusion of HCl vapours into a saturated solution of the PTMHC hexacarboxylate, did not afford any satisfactory result.

An alternative method for crystallizing highly carboxylic substituted molecules was reported by Darlow in 1961



Scheme 4. Synthesis of PTMHC.

[43a]. By recrystallizing benzene hexacarboxylic acid in concentrated nitric acid, a solvent free structure of this compound was obtained. Following this methodology, we tried the crystallization of the non-radical **37** as a first approach [47]. As expected, the use of this method afforded an organic solid with a formula of $[\mathbf{37}\cdot(H_2O)_{1.5}]$ that shows a fully 3-D H-bonded structure with 1-D channels. Noteworthy is the fact that this H-bonded network is partially disrupted by water molecules, but this disruption is not enough to prevent the formation of a 3-D H-bonded structure. In the structure, the solvent molecules are located in the 1-D channels as isolated water molecules or water tetrahedrons (Fig. 8). Overall, this structure possesses an accessible volume near 8.5% when the water molecules are omitted, that corresponds to a solvent accessible volume of 568.1 $Å^3$ versus the volume of the total unit cell (6564.0 $Å^3$).

If successful with PTMHC, a similar crystallization could lead us to the obtaining of a pure organic/molecular porous material with a 3-D H-bonded structure similar to the water solvate of **37**, with foreseeable magnetic properties. However, and in spite of the fact that the fully chlorinated PTM radical was already shown to be stable in hot concentrated nitric acid during several days [48], PTMHC was oxidized with nitric acid to give the corresponding diamagnetic fuchsone **40**, probably because of the good solubility of this compound in nitric acid at high temperatures which contrasts with the low solubility of the fully chlorinated PTM radical (Scheme 5).

Besides the failures of previous crystallizations, a partial success was later on obtained when a mixture of diethyl ether and *n*-hexane was used. Although diethyl ether molecules can form H-bonds with carboxylic acid groups, the crystallization of PTMHC using these solvents yields an organic/molecular $[\mathrm{PTMHC}\cdot(Et_2O)_3]$ solid with an H-bonded structure that is only partially disrupted by solvent molecules (Table 1 and Fig. 2e). Thus, the primary structure is formed by the H-bonded connections of PTMHC radicals into 2-D H-bonded corrugated layers. As shown in Fig. 9, the repeating unit consists of an unusual

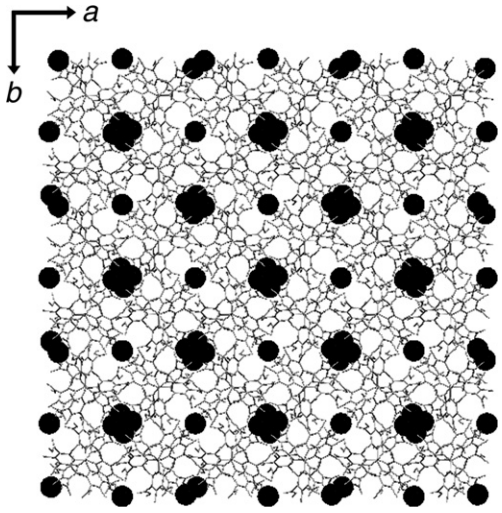
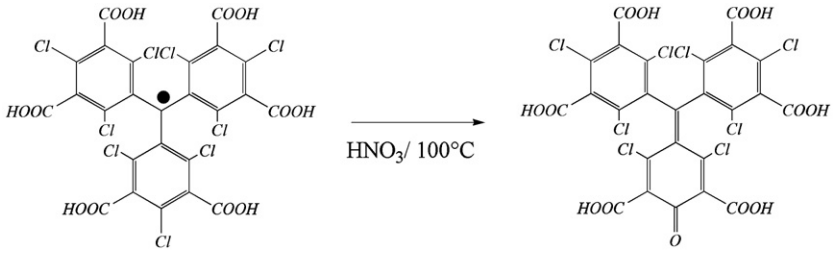


Fig. 8. Crystal structure of $[\mathbf{37}\cdot(H_2O)_{1.5}]$. Packing of molecules of **37** creates a 3-D H-bonded structure that reveals the presence of polar channels in which water molecules are localized. Water molecules are represented as spheres for clarity.



PTMHC 40

Scheme 5. Oxidation of PTMHC to the corresponding fuchsone.

$[R_6^6(48)]$ H-bonded motif formed by six PTMHC molecules (Fig. 9a). In this motif, each radical is H-bonded to two neighbouring radicals through one carboxylic group with O···O distances of 2.696 Å and O–H···O angles of 164°. It is important to note the similarities of these H-bonds with the ones found in POROF-2. The remaining carboxylic group localized in the same phenyl ring is also involved in one H-bond with a diethyl ether molecule. Since every radical unit contains six carboxylic groups (three are involved in H-bonds with PTMHC molecules and three in H-bonds with solvent molecules) each radical molecule participates in the construction of three identical hexameric units, resulting in open polar windows that propagate along the H-bonded layers (Fig. 9b). Three diethyl ether molecules are localized on each side of each polar window contributing to isolate one layer from the two neighbouring ones (the shortest radical-radical interlayer distance is 6.892 Å). Interdigitation of diethyl ether molecules belonging to neighbouring layers avoids then the formation of a fully 3-D H-bonded structure, leading to a ABC arrangement of these layers (Fig. 9c).

The disruption of the direct H-bonds between PTMHC radicals was further confirmed when PTMHC was crystallized from a mixture of THF and *n*-hexane. The higher ability of THF molecules to form H-bonds [27,49] in comparison with diethyl ether yielded a new phase $[PTMHC \cdot (THF)_6]$, in which no direct intermolecular H-bonds between PTMHC radicals can be found (Table 1 and Fig. 2f). Indeed, this crystal shows the particularity that all six carboxylic acid groups of PTMHC radicals are involved in the formation of H-bonds with one THF (Fig. 10a). Consequently, the resulting "supramolecular radical–THF clusters" $[PTMHC \cdot (THF)_6]$, avoid any direct H-bonds between radical molecules pushing them far away. The shortest distance between radical centers, 7.514 Å, is observed in supramolecular columns running along the *c* axis (Fig. 10b). Close packing of supramolecular radical-THF clusters takes place through several weak H-bonds between neighbouring THF molecules leading to a PTMHC-templated honeycomb-like arrangement of the solvent molecules (Fig. 10c).

Variable temperature magnetic susceptibility data for as-synthesized crystalline sample of $[PTMHC \cdot (Et_2O)_3]$ showed a very similar magnetic behaviour than POROF-2 (Fig. 11). At high temperatures (between 20 and 300 K), this compound behaves as a pure paramagnet. However, below 20 K, the $\chi \cdot T$ value smoothly increases upon decreasing temperature to reach a value of 0.395 emu K mol^{-1}at 1.8 K. This result is again in agreement with the presence of very weak intermolecular ferromagnetic interactions between H-bonded radical molecules and, presumably, to the presence of a long-range magnetic ordering at very low temperatures. On the contrary, and also as expected, $[PTMHC \cdot (THF)_6]$ behaves as a paramagnet with only very weak intermolecular antiferromagnetic interactions (through space) at very low temperatures, in agreement with the lack of direct H-bonds between PTMHC radicals in that solvate (Fig. 11).

5. Self-assembly of carboxylic substituted PTM radicals: concluding remarks, new trends and challenges

In this short review, we have demonstrated that polychlorinated triphenylmethyl radicals, properly functionalized with one or more carboxylic functions, are excellent organic building-blocks for the preparation of purely organic/molecular magnetic molecular materials. While the self-assembly of PTMMC yield to the formation of supramolecular dimers and to the onset of weak ferromagnetic interactions between the radical units, increase in the number of carboxylic acid functions in PTMDC and PTMTC has allowed the access to the first examples of purely organic-radical open-frameworks, POROF-1 and POROF-2, that are associating astonishing structural characteristics together with relevant magnetic properties, such as long-range magnetic ordering. Indeed, POROF-1, built by self-assembly of PTMDC molecules, is a paramagnetic material that presents a high porosity, with highly non-polar nanocontainers connected through polar narrow windows. High porosity is also observed in the case of POROF-2, in which the 2-D self-assembly of PTMTC molecules and the packing of the resulting H-bonded layers yield a hydrophilic porous architecture. However, compared to POROF-1, this supramolecular nanoporous purely organic "zeolite-like" material exhibits a long-range ferromagnetic ordering that behaves as a soft-magnet.

Two are the most important features to explain the results obtained for POROFs materials. First, the

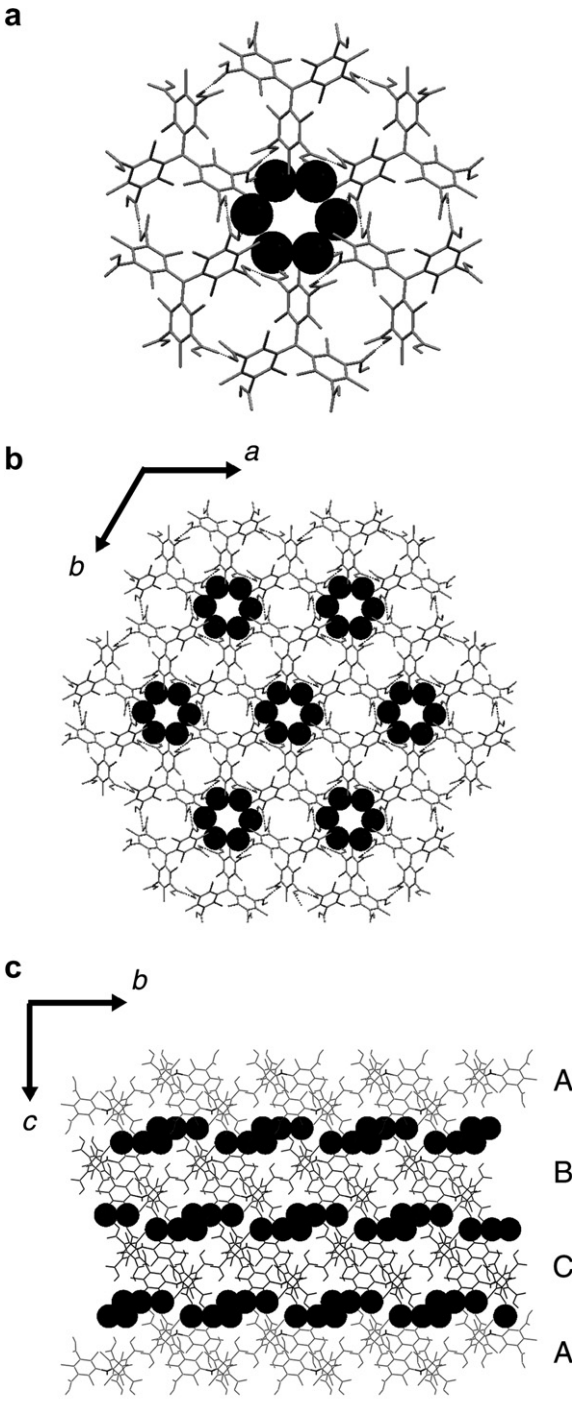


Fig. 9. Crystal structure of [PTMHC · $(Et_2O)_3$]. (a) $R_6^6(48)$ hexamer and (b) extended hydrogen-bonded corrugated layer. (c) ABC arrangement of the layers that are isolated one from each other by solvent molecules. Et_2O molecules are represented as spheres for clarity.

carboxylic groups on these radicals have been shown as good superexchange pathways for attaining magnetic couplings. And second, the geometry and the rigidity of the molecules that together with the paramagnetic character of carboxylic substituted PTM radicals offer magnetic and porous materials with a purely organic nature.

Attempts to take advantage of these characteristics to build a 3-D H-bonded porous and magnetic structure using PTMHC have given interesting results: even if, mainly for solubility problems, the access to a PTM-based 3-D H-bonded structure is still not achieved, the presence of ferromagnetic interactions in the diethyl ether solvate of this radical together with the structural analogy between its structure and the one of POROF-2 are particularly promising. Moreover, two points are particularly relevant for magnetic considerations: (i) increase in the number of carboxylic groups is traduced by the lack of Cl···Cl contacts in the solid state, contacts that are usually responsible for antiferromagnetic interactions in this type of radicals [39]; and (ii) change in the carboxylic groups relative position compared to PTMMC and PTMTC (*meta versus para*) does not modify the nature of the intermolecular magnetic interactions, that are still ferromagnetic. Thus, attempts to crystallize PTMHC are still under progress, but the last point and the possibility to access to new POROFs or new metal-organic materials [33], only changing the relative positions of carboxylic groups, make particularly attractive the synthesis of molecules **41**, **42** and **43** (Chart 4). The later compound, with its distorted tetrahedral geometry, appears also to be a good candidate and a good alternative to PTMHC in order to access to 3-D H-bonded porous and magnetic PTM based materials.

The remarkable properties and characteristics of POROF materials could also be exploited to address several challenging aspects for both crystal engineering and molecular magnetism fields [50]. The synergism of magnetic properties and porous materials together with the molecular characteristics purely organic materials opens a new route to the development of Purely Organic Multifunctional Molecular Materials. For instance, along with the possibility to act as zeolite-like materials, POROFs materials offer excellent conditions to encapsulate different functional systems with conducting, optical, chiral and NLO properties... using, for instance, functional molecules as templates during the crystallization of the radicals [51]. In consequence, the resulting material would combine the magnetic properties of the framework and the inherent properties and applications of the encapsulated functional molecules.

Another field of research for which this type of materials could be particularly interesting is their use as purely organic sensors. For instance, and since the magnetic properties are close dependant to the presence of intermolecular H-bonds between PTM units into the crystal structure, insertion of polar molecules in the solvent-free polar channels of POROF-2 could be expect to yield to weak structural changes (because of the numerous chlorine–chlorine contacts present in the material) and to strong changes in the magnetic properties, by disruption of the H-bonded two dimensional network. In a second time, removal of the solvent molecules only heating the solvated material could be expect to give back the starting

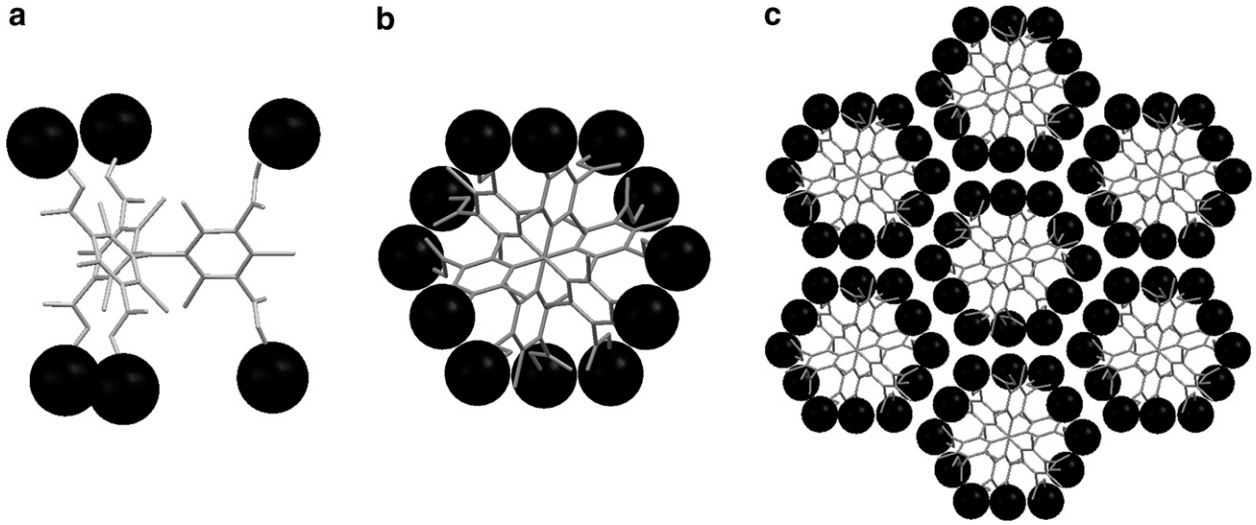


Fig. 10. Crystal structure of [PTMHC · $(THF)_6$]. (a) View of the supramolecular [PTMHC · THF_6] cluster (THF molecules are represented as spheres for clarity). (b) Top view of a supramolecular column resulting from the packing of the supramolecular clusters along the *c* axis. (c) Self-assembly of the columns yield a honeycomb-like arrangement of the THF molecules around the molecules of PTMHC.

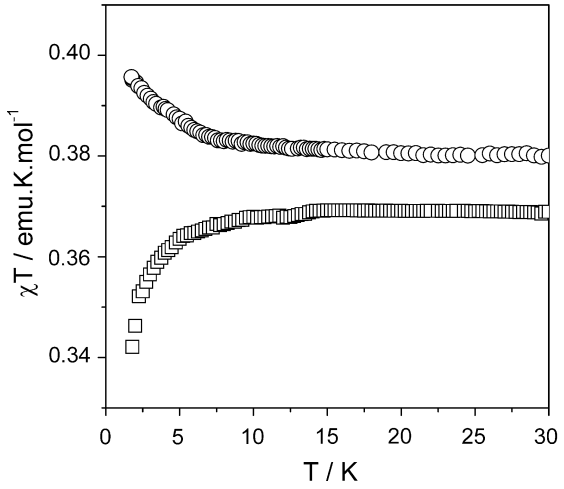


Fig. 11. Magnetic characterization of solvates [PTMHC · $(THF)_6$] (□) and [PTMHC · $(Et_2O)_3$] (○) in the presence of their mother liquors. Product of the magnetic susceptibility with the temperature as a function of the temperature in the lower limit.

POROF-2 material with soft-magnet properties, opening the line towards purely organic magnetic solvent sensors [33c,52].

Actually, work on these two challenging research lines is underway in our laboratory. Further experimentations aimed not only at the generation of new magnetic and porous molecular materials using PTMDC, PTMTC or PTMHC radicals but also at the obtaining of new organic building-blocks by the chemical modification of the polychlorotriphenylmethyl skeleton, such as molecules **41**–**43**, are also in progress. Thus, the use of these radicals as building-blocks is expected to allow the design of novel architectures with interesting porosity characteristics, magnetic properties and surprising topologies. In conclusion, such new radical units, along with PTMDC, PTMTC and PTMHC radicals, are expected to increase the new family of magnetic purely organic/molecular (POROF) radical open-frameworks.

Acknowledgements

This work was supported by the Dirección General de Investigación (Spain) under project EMOCIONa (CTQ2006-06333/BQU), Generalitat de Catalunya (2001SGR00362), EU under a Marie Curie Research Training Network (contract "QuEMolNa" number MCRTN-

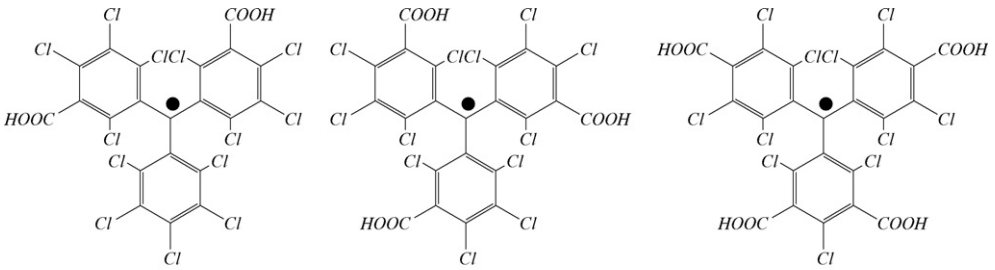


Chart 4.

CT-2003-504880), as well as by NoE MAGMANet (contract 515767-2). D.M. is grateful to the Generalitat de Catalunya for both predoctoral and postdoctoral grants. N.R. thanks the MCRTN for its postdoctoral contract. A.D. is grateful to the MCRTN for a predoctoral grant.

References

[1] (a) P. Lahti (Ed.), Magnetic Properties of Organic Materials, Marcel Dekker, New York, 1999;
(b) J. Miller, M. Drillon (Eds.), Magnetism: Molecules to Materials, vols. 1–3, Wiley-VCS, Weinheim, Germany, 2001;
(c) J. Veciana, H. Iwamura, MRS Bull. 25 (2000) 41.

[2] M. Tamura, Y. Nakazawa, D. Shiomi, K. Nozawa, Y. Hosokoshi, M. Ishikawa, M. Takahashi, M. Kinsohita, Chem. Phys. Lett. 186 (1991) 401.

[3] (a) For examples of aromatic derivatives of nitronyl nitroxides ferromagnets: T. Sugano, M. Tamura, M. Kinoshita, Y. Sakai, Y. Ohashi, Chem. Phys. Lett. 200 (1992) 235;
(b) K. Awaga, T. Inabe, Y. Maruyama, Chem. Phys. Lett. 190 (1992) 349;
(c) A. Caneschi, F. Ferraro, D. Gatteschi, A. Le Lirzin, M.A. Novak, E. Rentscher, R. Sessoli, Adv. Mater. 7 (1995) 476;
(d) S. Nakatsuji, M. Saiga, N. Haga, A. Naito, T. Hirayama, M. Nakagawa, Y. Oda, H. Anzai, K. Suzuki, T. Enoki, M. Mito, K. Takeda, New J. Chem. 22 (1998) 275.

[4] (a) For examples of aromatic derivatives of nitroxides ferromagnets: T. Nogami, K. Tomioka, T. Ishida, H. Yoshikawa, M. Yasui, F. Iwasaki, H. Iwamura, N. Takeda, M. Ishikawa, Chem. Lett. (1994) 29;
(b) T. Nogami, T. Ishida, H. Tsuboi, H. Yoshikawa, H. Yamamoto, M. Yasui, F. Iwasaki, H. Iwamura, N. Takeda, M. Ishikawa, Chem. Lett. (1995) 635;
(c) K. Togashi, R. Imachi, K. Tomioka, H. Tsuboi, T. Ishida, T. Nogami, N. Takeda, M. Ishikawa, Bull. Chem. Soc. Jpn. 69 (1996) 2821.

[5] R. Chiarelli, M.A. Novak, A. Rassat, J.L. Tholance, Nature 363 (1993) 147.

[6] M.P. Allemand, K.C. Khermani, A. Koch, F. Wudl, K. Holczer, S. Donovan, G. Grúner, J.D. Thompson, Science 253 (1991) 301.

[7] (a) W. Fujita, K. Awaga, Chem. Phys. Lett. 357 (2002) 385;
(b) W. Fujita, K. Awaga, Chem. Phys. Lett. 388 (2004) 186.

[8] (a) A.J. Banister, N. Bricklebank, I. Lavender, J.M. Rawson, C.I. Gregory, B.K. Tanner, W. Clegg, R.J. Elsegood, F. Palacio, Angew. Chem., Int. Ed. 35 (1996) 2533;
(b) A. Alberola, R.J. Less, C.M. Pask, J.M. Rawson, F. Palacio, P. Oliete, C. Paulsen, A. Yamaguchi, R.D. Farley, D.M. Murphy, Angew. Chem., Int. Ed. 42 (2003) 4782.

[9] J. Maddox, Nature 335 (1998) 201.

[10] (a) G.R. Desiraju, Crystal Engineering: the Design of Organic Solids, Elsevier, Amsterdam, 1989;
(b) G. Desiraju, Crystal Engineering: The Crystal as a Supramolecular Entity: Perspectives in Supramolecular Chemistry, vol. 2, Wiley, New York, 1996;
(c) J. Bernstein, M. Etter, L. Leiserowitz, Structure Correlation, vol. 2, VCH, New York, 1994, Chapter 11.

[11] R.G. Hicks, M.T. Lemaire, L. Öhrström, J.F. Richardson, L.K. Thompson, Z. Xu, J. Am. Chem. Soc. 123 (2001) 7154.

[12] (a) J.-M. Lehn, Supramolecular Chemistry, VCH, Weiheim, 1995;
(b) C.B. Aakeröy, A.M. Beatty, B.A. Helfrich, Angew. Chem., Int. Ed. 40 (2001) 3240.

[13] (a) J. Cirujeda, C. Hernàndez-Gasió, C. Rovira, J.L. Stanger, P. Turek, J. Veciana, J. Mater. Chem. 5 (1995) 243;
(b) J. Veciana, J. Cirujeda, C. Rovira, J. Vidal-Gancedo, Adv. Mater. 7 (1995) 221.

[14] M.M. Matsushita, A. Izuoka, T. Sugawara, T. Kobayashi, N. Wada, N. Takeda, M. Ishikawa, J. Am. Chem. Soc. 119 (1997) 4369.

[15] J. Cirujeda, M. Mas, E. Molins, F. Lanfranc de Panthou, J. Laugier, J.G. Park, C. Paulsen, P. Rey, C. Rovira, J. Veciana, J. Chem. Soc., Chem. Commun. (1995) 709.

[16] T. Sugawara, M.M. Matsushita, A. Isuoka, N. Wadam, N. Takeda, M. Ishikawa, J. Chem. Soc., Chem. Commun. (1994) 1723.

[17] (a) E. Hernandez, M. Mas, E. Molins, C. Rovira, J. Veciana, Angew. Chem., Int. Ed. 32 (1993) 882;
(b) J. Cirujeda, L. Ochando, J. Amigo, C. Rovira, J. Veciana, Angew. Chem., Int. Ed. 34 (1995) 55;
(c) J. Cirujeda, M. Mas, E. Molins, F. Lanfranc de Panthou, J. Laugier, J. Park, C. Paulsen, P. Rey, C. Rovira, J. Veciana, J. Chem. Soc., Chem. Commun. (1995) 709;
(d) J. Cirujeda, C. Hernandez-Gasio, C. Rovira, J.-L. Stranger, P. Turek, J. Veciana, J. Mater. Chem. 5 (1995) 243;
(e) J. Veciana, J. Cirujeda, C. Rovira, E. Molins, J. Novoa, J. Phys. I (1996) 1967;
(f) T. Sugawara, M. Matsushita, A. Isuoka, N. Wada, N. Takeda, M. Ishikawa, J. Am. Chem. Soc. 119 (1997) 4369.

[18] T. Akita, K. Kobayashi, Adv. Mater. 9 (1997) 346.

[19] (a) N. Yoshioka, M. Irisawa, Y. Mochizuki, K. Tano, H. Inoue, S. Ohba, Chem. Lett. 26 (1997) 251;
(b) N. Yoshioka, M. Irisawa, Y. Mochizuki, T. Aoki, H. Inoue, Mol. Cryst. Liq. Cryst. 306 (1997) 403.

[20] J. Ferrer, P.D. Lahti, C. George, G. Antonerra, F. Palacio, Chem. Mater. 11 (1999) 2205.

[21] A. Lang, Y. Pei, L. Ouahab, O. Khan, Adv. Mater. 8 (1996) 60.

[22] (a) R. Feher, D. Amabilino, K. Wurst, J. Veciana, Mol. Cryst. Liq. Cryst. 334 (1999) 333;
(b) P. Taylor, P.R. Serwinsky, P.M. Lahti, Chem. Commun. (2003) 1400;
(c) D. Shiomi, M. Nozaki, T. Ise, K. Sato, T. Takui, J. Phys. Chem. B 108 (2004) 16606.

[23] (a) L. Catala, R. Feher, D. Amabilino, K. Wurst, J. Veciana, Polyhedron 20 (2001) 1563;
(b) L. Catala, K. Wurst, D. Amabilino, J. Veciana, J. Mater. Chem. 16 (2006) 2736.

[24] (a) F. Romero, R.A. Ziessel, A. De Cian, J. Fischer, P. Turek, New J. Chem. 20 (1996) 919;
(b) F. Romero, R. Ziessel, M. Drillon, J.-L. Tholence, C. Paulsen, N. Kyritsakas, J. Fischer, Adv. Mater. 8 (1996) 826;
(c) F. Romero, R. Ziessel, M. Bonnet, Y. Potillon, E. Ressouche, J. Schweitzer, B. Delley, A. Grand, C. Paulsen, J. Am. Chem. Soc. 122 (2000) 1298.

[25] (a) K. Inoue, H. Iwamura, Chem. Phys. Lett. 207 (1993) 551;
(b) O. Félix, M.W. Hosseini, A. De Cian, J. Fischer, L. Catala, P. Turek, Tetrahedron Lett. 40 (1999) 2943;
(c) C. Stroh, F. Romero, N. Kyritsakas, L. Catala, P. Turek, R. Ziessel, J. Mater. Chem. 9 (1999) 875;
(d) M. Minguet, D. Amabilino, J. Cirujeda, K. Wurst, I. Mata, E. Molins, J. Novoa, J. Veciana, Chem. Eur. J. 6 (2000) 2350;
(e) D. Maspoch, L. Catala, P. Gerbier, D. Ruiz-Molina, J. Vidal-Gancedo, K. Wurst, C. Rovira, J. Veciana, Chem. Eur. J. 8 (2002) 3635;
(f) M. Baskett, P.D. Lahti, Polyhedron 24 (2005) 2645.

[26] L. Leiserowitz, Acta Crystallogr. B 32 (1976) 775.

[27] S.V. Kolotuchin, E.E. Fenlon, S.R. Wilson, C.J. Lowth, S.C. Zimmerman, Angew. Chem., Int. Ed. 34 (1995) 2654, and references therein.

[28] Until we published this work, the highest carboxylic-based cyclic motifs reported in the literature were $R_4^4(16)$. See: (a) J. Cannone, G. Nowogrocki, J.-C. Boivin, D. Thomas, Acta Crystallogr. B 36 (1980) 2664;
(b) J.A. Kanters, G. Roelofsen, Acta Crystallogr. B 32 (1976) 3328.

[29] M. Ballester, Acc. Chem. Res. 18 (1985) 380.

[30] K. Kobayashi, T. Shirasaka, A. Sato, E. Horn, N. Furukawa, Angew. Chem., Int. Ed. 38 (1999) 3483.

[31] S.V. Kolotuchin, P.A. Thiessen, E.E. Fenlon, S.R. Wilson, C.J. Loweth, S.C. Zimmerman, Chem. Eur. J. 5 (1999) 2537, and references therein.
[32] (a) A. Nangia, Curr. Opin. Solid State Mater. Sci. 15 (2001) 115;
(b) M.J. Zaworotko, Angew. Chem., Int. Ed. 39 (2000) 3052;
(c) P.J. Langley, J. Hulliger, Chem. Soc. Rev. 28 (1999) 279;
(d) G.R. Desiraju, Curr. Opin. Solid State Mater. Sci. 2 (1997) 451.
[33] The coordination chemistry of these radicals has also been extensively studied. For examples of PTM based magnetic complexes, see: (a) D. Maspoch, N. Domingo, D. Ruiz-Molina, K. Wurst, J.M. Hernandez, G. Vaughan, C. Rovira, F. Lloret, J. Tejada, J. Veciana, Chem. Commun. 40 (2005) 5035;
(b) D. Maspoch, J. Gomez-Segura, N. Domingo, D. Ruiz-Molina, K. Wurst, C. Rovira, J. Tejada, J. Veciana, Inorg. Chem. 44 (2005) 6936;
(c) D. Maspoch, D. Ruiz-Molina, K. Wurst, N. Domingo, M. Cavallini, F. Biscarini, J. Tejada, C. Rovira, J. Veciana, Nat. Mater. 2 (2003) 190;
(d) D. Maspoch, D. Ruiz-Molina, K. Wurst, C. Rovira, J. Veciana, Chem. Commun. (2004) 1164;
(e) D. Maspoch, D. Ruiz-Molina, K. Wurst, C. Rovira, J. Veciana, Chem. Commun. (2002) 2958;
(f) D. Maspoch, D. Ruiz-Molina, K. Wurst, C. Rovira, J. Veciana, Dalton Trans. (2004) 1073;
(g) D. Maspoch, D. Ruiz-Molina, J. Veciana, J. Mater. Chem. 14 (2004) 2713.
[34] O.M. Yaghi, M. O'Keeffe, N.W. Ockwig, H.K. Chae, M. Eddaoudi, J. Kim, Nature 423 (2003) 705.
[35] A. Caneschi, D. Gatteschi, R. Sessoli, P. Rey, Acc. Chem. Res. 22 (1989) 392.
[36] (a) M. Ballester, J. Castañer, J. Riera, A. Ibáñez, J. Pujades, J. Org. Chem. 47 (1982) 259;
(b) V.M. Domingo, J. Castañer, J. Riera, A. Labarta, J. Org. Chem. 59 (1994) 2604;
(c) S. Lopez, J. Carilla, L. Fajari, L. Julia, E. Brillas, A. Labarta, Tetrahedron 51 (1995) 7301.
[37] M.C. Etter, Acc. Chem. Res. 23 (1990) 120.
[38] S. Kuduva, D.C. Craig, A. Nangia, G.R. Desiraju, J. Am. Chem. Soc. 121 (1999) 1936.
[39] (a) O. Armet, J. Veciana, C. Rovira, J. Riera, J. Castañar, E. Molins, J. Rius, C. Miratvilles, S. Olivilla, J. Brichfeus, J. Phys. Chem. 91 (1987) 5608;
(b) J. Sedo, N. Ventosa, M.A. Molins, M. Pons, C. Rovira, J. Veciana, J. Org. Chem. 66 (2001) 1057.
[40] (a) J.L. Derissen, Acta. Crystallogr. Sect. B: Struct. Crystallogr. Cryst. Chem. 30 (1974) 2764;
(b) R. Alcala, S. Martinez-Carrera, Acta. Crystallogr. Sect. B: Struct. Crystallogr. Cryst. Chem. 28 (1972) 1671.
[41] D. Maspoch, N. Domingo, D. Ruiz-Molina, K. Wurst, Javier Tejada, C. Rovira, Jaume Veciana, J. Am. Chem. Soc. 126 (2004) 730.
[42] D. Maspoch, N. Domingo, D. Ruiz-Molina, K. Wurst, G. Vaughan, J. Tejada, C. Rovira, J. Veciana, Angew. Chem., Int. Ed. 43 (2004) 1828.
[43] Only few examples of hexa-acid molecules have been reported in the literature. See: (a) S. Darlow, Acta Crystallogr. 14 (1961) 159;
(b) J. Podlaha, I. Cisarova, P. Holy, J. Zavada, Z. Kristallograph. – New Cryst. Struct. 214 (1999) 185;
(c) J. Beeson, L. Fitzgerald, J. Gallucci, R. Gerkin, J. Rademacher, A. Czarnick, J. Am. Chem. Soc. 116 (1994) 4621.
[44] To the best of our knowledge, only one example of an octa-acid has been reported. See: P. Holy, P. Sehnal, M. Tichy, J. Zavada, I. Cisarova, Tetrahedron: Asymmetry 15 (2004) 3805.
[45] B. Venkataramanan, W.L.G. James, J.J. Vittal, V. Suresh, Cryst. Growth. Des. 4 (2004) 553.
[46] N. Roques, D. Maspoch, N. Domingo, D. Ruiz-Molina, K. Wurst, J. Tejada, C. Rovira, J. Veciana, Chem. Commun. (2005) 4801.
[47] N. Roques, D. Maspoch, K. Wurst, D. Ruiz-Molina, C. Rovira, J. Veciana, Chem. Eur. J., in press.
[48] M. Ballester, J. Riera, J. Castañer, C. Badia, J. Monso, J. Am. Chem. Soc. 93 (1971) 2215.
[49] (a) Q. Lin, S. Geib, A. Hamilton, J. Chem. Soc., Perkin Trans. 2 (1998) 2109;
(b) R. Kresinki, J. Fackler, Acta Crystallogr. C50 (1994) 2039.
[50] E. Coronado, D. Gatteschi, J. Mater. Chem. 16 (2006) 2513.
[51] N. Kobayashi, T. Naito, T. Inabe, Adv. Mater. 16 (2004) 1803.
[52] To our knowledge, only some examples of dynamic porous coordination polymers with magnetic properties have been so far described. See: (a) G.J. Halder, C.J. Kepert, B. Moubaraki, K.S. Murria, J.D. Cashion, Science 298 (2002) 1762;
(b) Z. Wang, B. Zhang, H. Fujiwara, H. Kobayaschi, M. Kurmoo, Chem. Commun. (2004) 416;
(c) M. Kurmoo, H. Kumagai, K.W. Chapman, C.J. Kepert, Chem. Commun. (2005) 3012;
(d) M. Kurmoo, H. Kumagai, M. Akita-Tanaka, K. Inoue, S. Takagi, Inorg. Chem. 45 (2006) 1627;
(e) O. Kahn, J. Larionova, J.V. Yakhmi, Chem. Eur. J. 5 (1999) 3443;
(f) S.-I. Ohkoshi, K.-I. Arai, Y. Sato, K. Hashimoto, Nat. Mater. 3 (2004) 857;
(g) Y. Sato, S.-i. Ohkoshi, K.-i. Arai, M. Tozawa, K. Hashimoto, J. Am. Chem. Soc. 125 (2003) 14590;
(h) Z. Lu, X. Wang, Z. Liu, F. Liao, S. Gao, R. Xiong, H. Ma, D. Zhang, D. Zhu, Inorg. Chem. 45 (2006) 999.

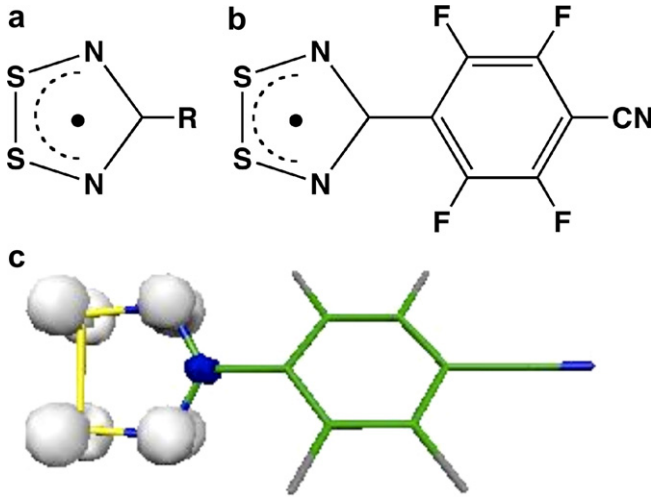


Fig. 1. (a) General formulae of heterocyclic 1,2,3,5-dithiadiazolyl radical (in short, R-CNSSN·). (b) Chemical formulae of cyano-perfluoraryl-dithiadiazolyl, NC-C_6F_4-CNSSN·. (c) Spin density of a NC-C_6F_4-CNSSN· radical at B3LYP/6-31+G(d) level of theory (isodensity surface 0.01 a.u.).

In the α-phase, the interactions are thought to be weaker, leading to a sharp maximum in χ at 10 K indicative of *bulk* antiferromagnetic order. In the β-phase, a broad maximum in χ is observed around 60 K, indicative of short-range ordering, followed by a transition to a canted antiferromagnetic state (critical temperature 36 K). In this first work, we will just focus on the magnetic properties of the α phase (also identified in the literature as α-YOMXUT [9]), given the complexities that it presents. A study of the β phase will form the basis of a future report. In α-YOMXUT, the radicals pack to form chains, which are linked via CN···S interactions, and further connected into planes via additional N···S and S···S interactions (Fig. 2a). These layers stack in a regular ···*AAA*··· disposition (Fig. 2b). However, the experimental magnetic susceptibility curve could not be fitted by any simple magnetic model. Our study will show that this fact is due to the presence of strong ferro and antiferromagnetic interactions whose interplay results in a complex 3D magnetic topology.

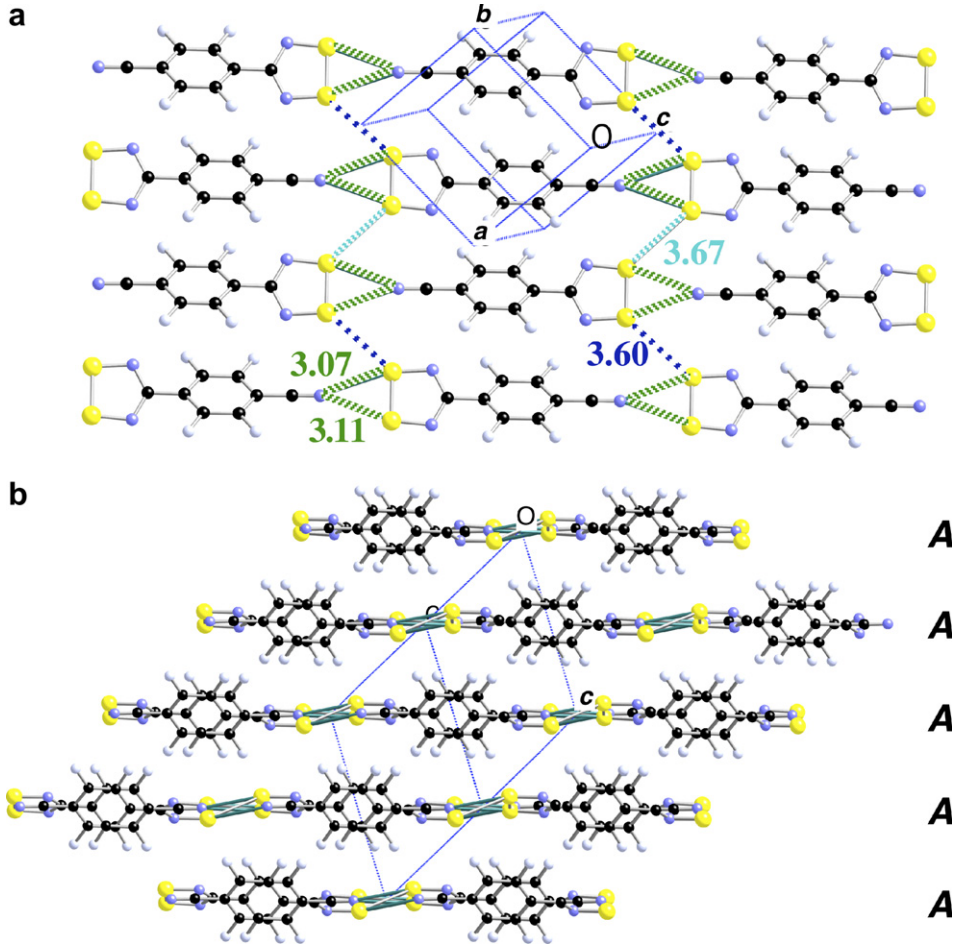


Fig. 2. (a) Crystal packing analyzed in terms of shortest intermolecular distances between NC-C_6F_4-CNSSN· radicals, which form chains in terms of N···S contacts at 3.07 and 3.11 Å that interact with nearby antiparallel chains by means of S···S contacts at 3.60 and 3.67 Å (resulting into *A* sheets). (b) General ···*AAA*··· disposition.

2. Methodology

The theoretical study of the magnetism of α-YOMXUT will be performed applying our first-principles *bottom-up* methodological approach [10], which consists in the sequential application of the following four steps:

(1) Analysis of the crystal structure in order to find all unique A–B radical–radical pairs that might be responsible for the microscopic magnetic interactions.
(2) Computation of the microscopic J_{AB} radical–radical magnetic interactions for all pairs.
(3) Definition of the magnetic topology of the crystal and corresponding minimal magnetic model using the non-negligible J_{AB} values.
(4) Calculation of the macroscopic magnetic properties of the crystal.

In the first step, one selects all unique radical–radical pair candidates (identified as *di*) capable of presenting non-negligible magnetic interaction (identified as $J_{AB}(di)$ and computed in the second step). In practical terms, such selection is done by identifying each unique radical and then choosing all radical–radical pairs whose distance is smaller than a selected cutoff value (that includes all first-nearest neighbors and the closest second-nearest neighbors). Because of the exponential dependence on the distance of the magnetic interactions [11], this was considered to be a safe procedure for selecting all magnetically relevant pairs of radicals. Notice that this procedure is totally unbiased since it does not make any a priori assumptions on the nature or size of the $J_{AB}(di)$ magnetic interactions.

The $J_{AB}(di)$ parameters computed in the second step are defined in terms of the following general Heisenberg Hamiltonian:

$$\widehat{H} = -2\sum J_{AB}\widehat{S}_A \cdot \widehat{S}_B \quad (1)$$

As the *p*-NC-C_6F_4-CNSSN$^{\bullet}$ radicals are doublets, the $J_{AB}(di)$ values can be obtained from the following expression:

$$J_{AB} = E^S_{BS} - E^T \quad (2)$$

where E^T is the energy of the triplet state in the radical–radical pair and E^S_{BS} is the energy of the open-shell singlet state within the broken symmetry approach [12]. Notice that Eq. (2) is obtained after accounting for the zero overlap of the SOMO orbitals of the interacting radicals ($S_{ab} = 0$), that is, by strict application of the broken-symmetry equation for the Heisenberg Hamiltonian (1), whose general expression is:

$$J_{AB} = \frac{E^S_{BS} - E^T}{1 + S^2_{ab}} \quad (3)$$

The values of E^T and E^S_{BS} are computed using the UB3LYP functional [13] and the 6-31+G(d) basis set [14]. These computations were done using the appropriate options in GAUSSIAN-98 [15] to obtain J_{AB} values with an accuracy of $|0.02|$ cm^{-1}. Those *di* pairs whose absolute $J_{AB}(di)$ value is smaller than $|0.05|$ cm^{-1} were discarded (we have previously observed that smaller J_{AB} values are not relevant in the following steps of the first-principles *bottom-up* procedure).

The network of non-negligible $J_{AB}(di)$ magnetic interactions among the radicals define the *magnetic topology* of the crystal. Obviously, such magnetic topology extends over the whole crystal and is infinite. However, for our procedure, we need to find a finite subset of the crystal (the so-called *minimal magnetic model space*) that describes the magnetic interactions of the whole crystal in a balanced way, and whose repetition along the (a,b,c) crystallographic directions regenerates the magnetic topology of the infinite crystal. Then, using the complete set of spin functions of this finite subset, one computes the matrix representation of the Heisenberg Hamiltonian (1). Such matrix representation is diagonalized to obtain the full spectrum of energies. These energies are then used in the appropriate statistical mechanics expressions to obtain the macroscopic magnetic properties in a rigorous way. We stress that the entire procedure is completely unbiased and allows us to connect, in a rational way, the macroscopic magnetic properties with their microscopic $J_{AB}(di)$ origin. As the sign and size of the microscopic $J_{AB}(di)$ parameters depend on the geometry of the radical–radical pairs, the first-principles *bottom-up* procedure is an interesting tool towards a rational design of new materials that could present improved magnetic properties.

3. Results and discussion

The 160 K X-ray structure of the α-phase crystal of the NC-C_6F_4-CNSSN$^{\bullet}$ radical belongs to the triclinic space group $P\bar{1}$, with two radicals per unit cell ($Z = 2$; $a = 7.574$ Å, $b = 8.065$ Å, $c = 9.509$ Å, $\alpha = 65.73°$, $\beta = 69.17°$, $\gamma = 67.52°$ [3]). The crystal packing presents a chain motif with the radicals in a head-to-tail arrangement, in which the shortest S···NC interactions are found at 3.07 and 3.11 Å (see Fig. 2a). Adjacent chains are arranged antiparallel to each other and form planes through S···N and S···S interactions. These planes stack in an $\cdots AAA\cdots$ disposition (see Fig. 2b). The shortest S···S contacts are found at 3.60 and 3.67 Å. The shortness of the in-plane CN···S interactions might indicate a chain-like magnetic topology with one dominant exchange interaction in the crystal.

We now present the results obtained in each step of the first-principles bottom-up theoretical study of the α-YOMXUT crystal.

Step 1: Selection of all unique radical–radical pairs present in the crystal. Theoretical B3LYP/6-31+G(d) calculation on the *p*-NC-C_6F_4-CNSSN$^{\bullet}$ radical indicates that most of the spin density is located on the CNSSN five-membered ring of the radical (see Fig. 1c for 0.01 a.u. isodensity surface). Thus, the CNSSN group is the spin-carrier group of the *p*-NC-C_6F_4-CNSSN$^{\bullet}$ radical. Therefore, it seems appropriate

to select the candidate *di* radical–radical pairs on the basis of the distance between the CNSSN spin-carrier groups, for these pairs that are not symmetry equivalent within the crystal.

In terms of the shortest NSSNC···CNSSN distances, we selected all first nearest-neighbors (cutoff distance of 13 Å) and only the closest next (second) nearest-neighbors. In practice, 16 crystallographically different radical–radical pairs (*d*1–*d*16) were selected in the α-YOMXUT crystal (Fig. 3 shows their geometrical positions within the crystal, while Table 1 collects the value of the NSSNC···CNSSN distances). The geometry of each *di* dimer is fully documented in the supplementary material (Figs. S1–S16, using two different views, depending on whether the dithiadiazolyl ring is parallel or perpendicular to the plane of the figure). Except for the *d*10 and *d*13 pairs, which are second nearest neighbors, all other pairs are first nearest neighbors. Among them, six pairs sit on the same *A* plane (*d*3, *d*4, *d*7–*d*9 and *d*16), and the remaining 10 pairs (*d*1, *d*2, *d*5, *d*6, *d*10–*d*15) are located in adjacent *A*···*A* planes.

Step 2: Evaluation of the microscopic J(di) magnetic interactions. The computed *J*(*di*) values are collected in Table 1. Only six interactions (*d*1–*d*4, *d*7 and *d*8, see Fig. 4 for geometry and also Fig. 3 for their position within the crystal) are non-negligible with two of them (*d*2 and *d*8 with values +10.91 and −10.25 cm^{-1}) much stronger than the remaining four (with values −1.44, +1.02, +0.67, and +0.29 cm^{-1}). It is clear form Table 1 and Fig. 4 that

Table 1
Unrestricted DFT broken symmetry UB3LYP/6-31+G(d) results for the dimeric interaction of all 16 candidates (*d*1–*d*16) listed as NSSNC···CNSSN distance increases for α-YOMXUT crystal

Candidate *di*	Distance (NSSNC···CNSSN) (Å)	$J_{AB}(di)$ (cm^{-1})
*d*1	4.789	+1.02
*d*2	4.990	+10.91
*d*3	6.534	+0.29
*d*4	6.588	+0.67
*d*5	7.574	<|0.05|
*d*6	8.065	<|0.05|
*d*7	8.285	−1.44
*d*8	8.454	−10.25
*d*9	8.700	<|0.05|
*d*10	9.509	<|0.05|
*d*11	9.614	<|0.05|
*d*12	9.785	<|0.05|
*d*13	9.792	<|0.05|
*d*14	9.827	<|0.05|
*d*15	10.482	<|0.05|
*d*16	12.053	<|0.05|

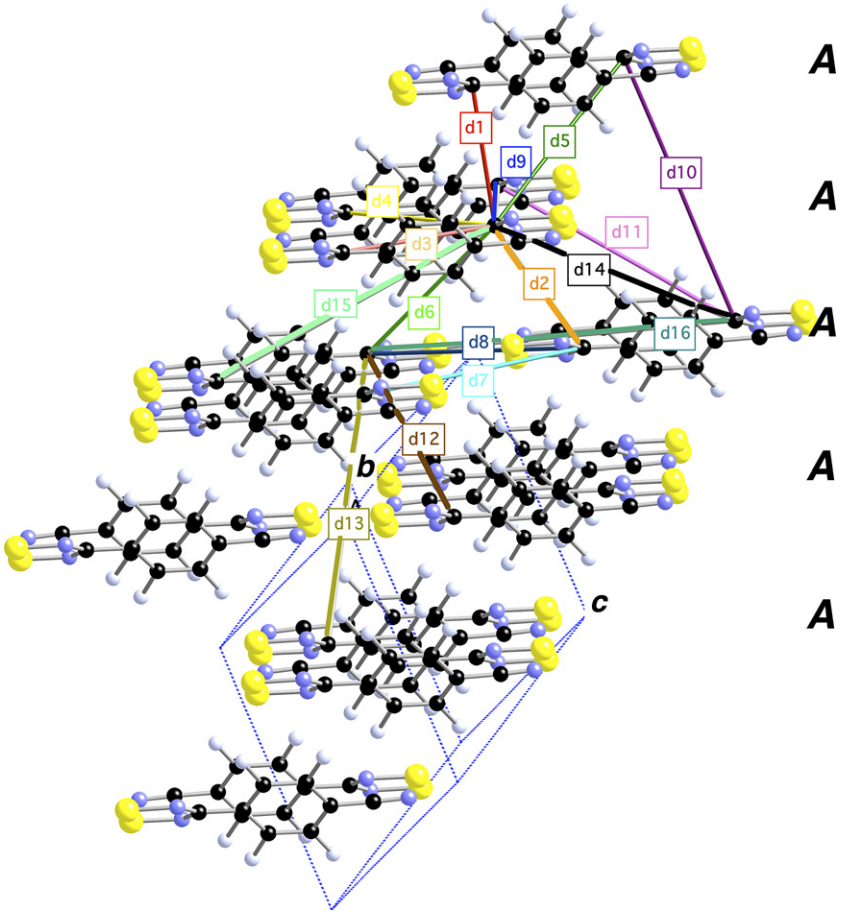


Fig. 3. Representation of all unique *di* pairs of radicals selected in order to compute the corresponding $J_{AB}(di)$ pair interaction.

the $J(di)$ values are sensitive not only to the distance but also to the relative orientation of the *p*-NC-C_6F_4-CNSSN$^{\cdot}$ radicals within the pairs. Among these six non-negligible magnetic interactions, there are some ferromagnetic (FM: $d1$, $d2$, $d3$, $d4$) and some antiferromagnetic (AFM: $d7$, $d8$) interactions. Notably the head-to-tail $d16$ pair, which exhibits the shortest CN···S intermolecular contacts (Fig. 2a), is numerically negligible and consequently cannot contribute to the macroscopic magnetism of α-YOMXUT, i.e. the likely structure-directing influence of this interaction does not influence the magnetic behavior.

Step 3: Definition of the magnetic topology and minimal magnetic model space of the crystal. The magnetic topology is defined in terms of the radicals that are magnetically connected (that is, showing non-negligible magnetic interactions). Fig. 5 shows a diagrammatic representation of Fig. 3, where each radical is replaced by the C-atom of the CNSSN group (the lines represent the non-negligible $J(di)$ magnetic interactions; to improve its clarity, a change in the orientation of the crystallographic axes was done compared to previous figures). The magnetic topology of the α-YOMXUT crystal is clearly three-dimensional (3D) but very complex. The dominant interactions (the ferromagnetic $J(d2) = +10.91\ \mathrm{cm}^{-1}$ and antiferromagnetic $J(d8) = -10.25\ \mathrm{cm}^{-1}$) form alternating FM–AFM zigzag chains, which are connected along the *bc*-plane by adjacent

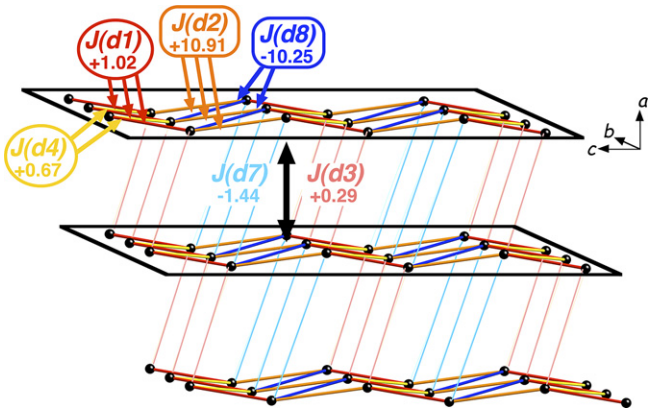


Fig. 5. Magnetic topology of α-YOMXUT crystal. The numerical values of the non-negligible $J_{AB}(di)$ magnetic pair interactions are also given (in cm^{-1}).

alternating FM–FM zigzag chains resulting from the interplay of weaker $J(d1)$ and $J(d4)$ pairs (their values being $+1.02$ and $+0.67\ \mathrm{cm}^{-1}$, respectively). Adjacent *bc*-planes are connected by means of antiferromagnetic ($J(d7) = -1.44\ \mathrm{cm}^{-1}$) and ferromagnetic ($J(d3) = +0.29\ \mathrm{cm}^{-1}$) interactions. This 3D magnetic topology is consistent with the *bulk* antiferromagnetic behavior experimentally reported for α-YOMXUT.

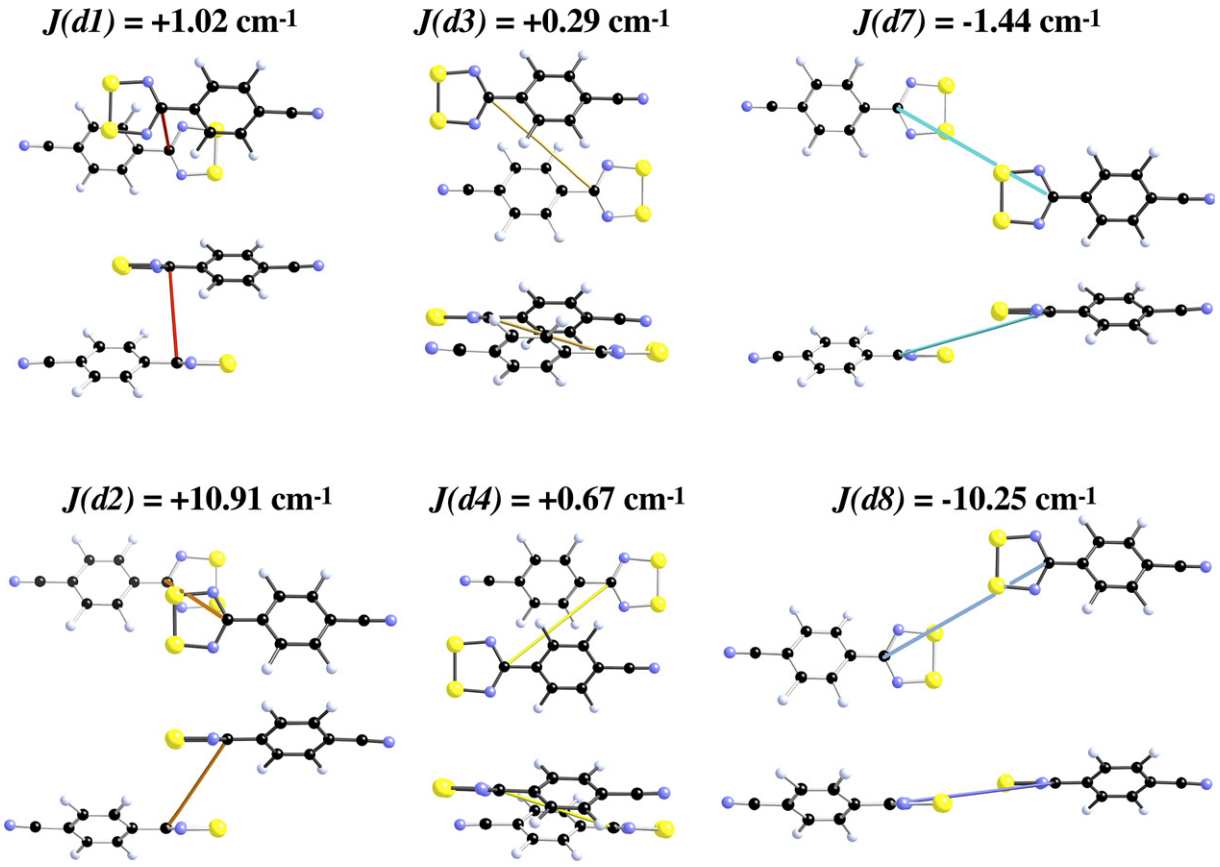


Fig. 4. Pairs of radicals with non-negligible $J_{AB}(di)$ magnetic interaction (see Table 1 for numerical values). For each pair of radicals, the upper and lower views correspond to displaying the dithiadiazolyl rings parallel and perpendicular to the plane of the figure, respectively.

The smallest finite space that can describe the complexities of the previous 3D magnetic topology (the so-called minimal magnetic model space) is the eight-radical model shown in Fig. 6a (we will refer later on to it as the 3d8s model). Fig. 6a also indicates how by extension along the crystallographic axes of this 3d8s minimal model one can generate the infinite crystal.

Step 4: Calculation of the magnetic susceptibility $\chi(T)$. The calculation of the macroscopic magnetic properties of the crystal, such as magnetic susceptibility $\chi(T)$, is carried out using the energy levels obtained from the diagonalization of the matrix representation of the following Heisenberg Hamiltonian:

$$\widehat{H} = -\sum_{A,B} J_{AB}\left(2\widehat{S}_A \cdot \widehat{S}_B + \frac{1}{2}\widehat{I}_{AB}\right) \quad (4)$$

This Hamiltonian provides a spectrum of energies equivalent to that provided by the Heisenberg Hamiltonian of Eq. (1), except for a shift in all energy values; the corresponding energy differences being thus the same. We used Eq. (4) because it is computationally more efficient for our suit of programs. One must be aware of the fact that the matrix representation increases with the number N of doublet radicals as $N!/(N/2)!(N/2)!$. In α-YOMXUT, we have studied the magnetic susceptibility $\chi(T)$ using magnetic models ranging from 8 to 16 radicals (see Fig. 6), with matrix representations of dimensions 70×70 and $12\,870 \times 12\,870$, respectively. The larger models were used to study the convergence of the computed $\chi(T)$ curves when the minimal model space was extended along the crystallographic axes.

The magnetic susceptibility curve for α-YOMXUT was computed from room temperature to nearly 0 K (Fig. 6b and c shows the $\chi T(T)$ and $\chi(T)$ curves, respectively). There is good agreement between the computed and experimental curves, except for some small oscillations found in the experimental data, which have been attributed to the quality of the data acquisition. The computed curves using the 3d8s minimal magnetic model and its extension along (a, b, c)-axes (Fig. 6b and c), are almost identical. Notice that no scaling factor was required to mimic the experimental curves. This possibly could be attributed to the fact that the crystal structure used in our calculations (determined at 160 K, instead of at room temperature [16]) properly reflects the magnetic behavior at lower temperatures. Notice also that the computed $\chi T(T)$ curve shows a

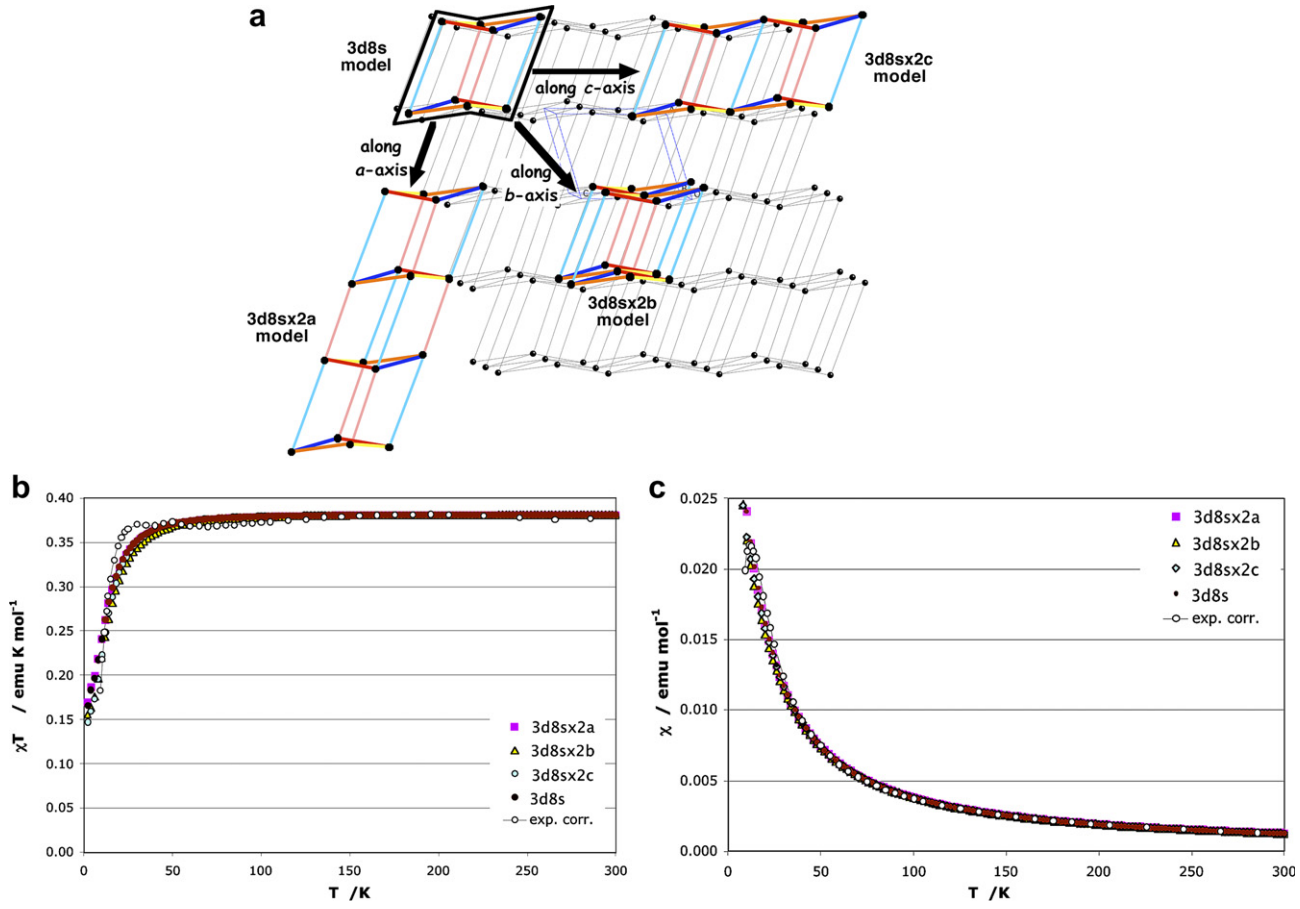


Fig. 6. (a) Representation of the 3d8s (three-dimensional eight-site) minimal magnetic model, and its corresponding extended models along the a, b, c crystallographic axes (3d8sx2a, 3d8sx2b, 3d8sx2c, respectively). (b) Computed and experimental $\chi T(T)$ curves for the α-YOMXUT crystal, obtained using the 3d8s minimal magnetic model and the 3d8sx2a, 3d8sx2b, 3d8sx2c models. (c) Computed and experimental $\chi(T)$ curves for the α-YOMXUT crystal using the same models than in (b).

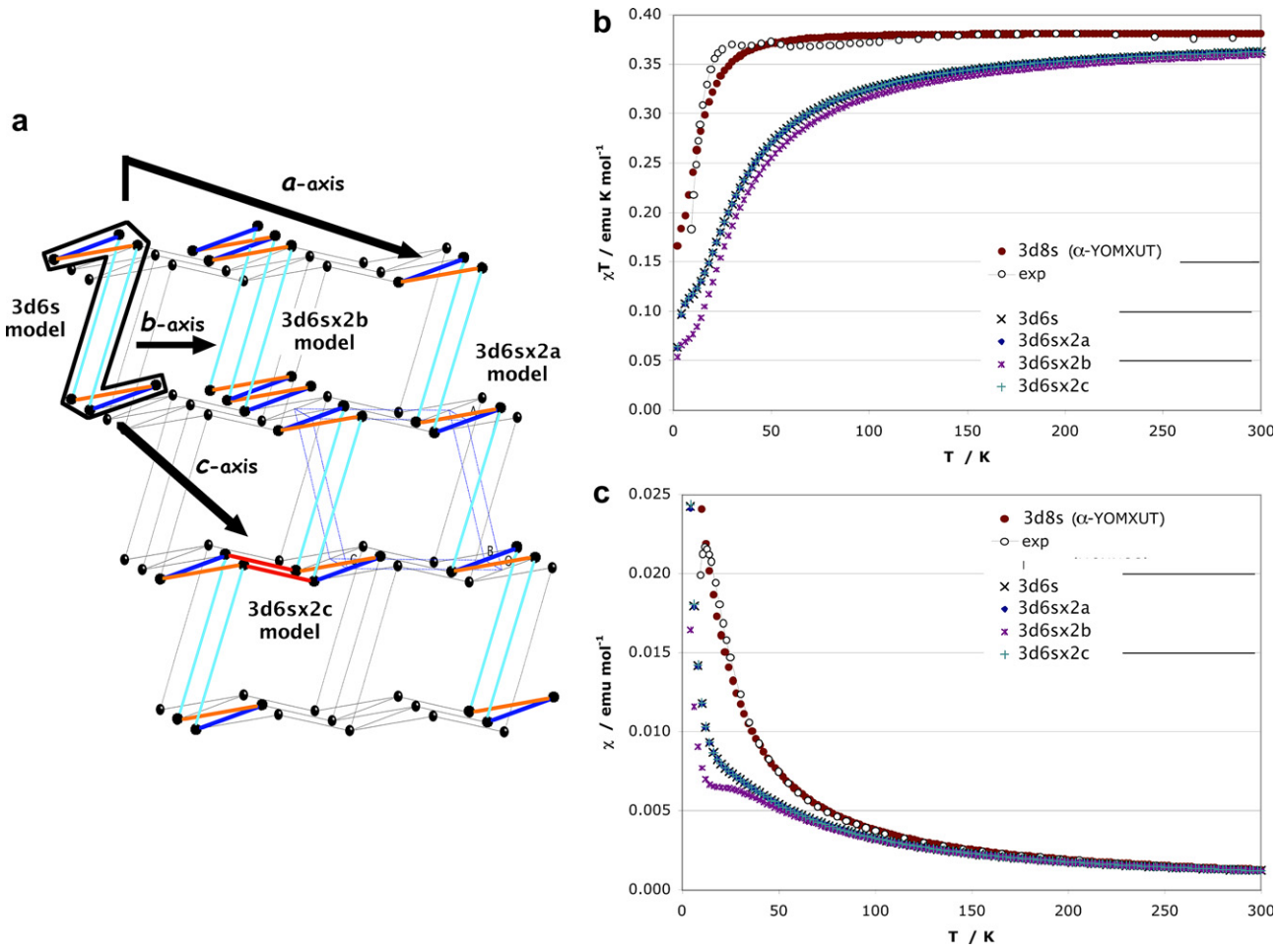


Fig. 7. (a) Representation of the 3d6s (three-dimensional six-site) minimal magnetic model, obtained when α-YOMXUT is truncated to only its five-membered ring, showing also its extended models along the *a*, *b*, *c* crystallographic axes (3d6sx2a, 3d6sx2b, 3d6sx2c, respectively). (b) Computed and experimental $\chi T(T)$ curves using the 3d6s, 3d6sx2a, 3d6sx2b, and 3d6sx2c minimal magnetic models. (c) Computed and experimental $\chi(T)$ curves using the same models than in (b). The curves obtained using the 3d8s model in Fig. 6 are also shown, to allow comparison.

dominating antiferromagnetic behavior, despite the fact that the two dominant $J(di)$ are of similar magnitude but opposite sign. This indicates the key influence of the magnetic topology on the macroscopic magnetic behavior, a fact that cannot be qualitatively evaluated just by looking at the size and sign of the microscopic interactions alone.

At this point, we have completed the first-principles *bottom-up* theoretical description of the α-YOMXUT crystal. The good agreement between the model and the experimental data indicates that the calculated values not only reproduce the experimental results but also provide an unbiased and rigorous microscopic explanation of the origin of the macroscopic behavior. Therefore, we could have ended here our study. However, we decided to pursue carrying out two additional and complementary studies, described in the following two paragraphs.

Our results have shown that the dominant part of the 3D magnetic topology is the alternating FM–AFM zigzag chains that is formed by the propagation of the $J(d2)$ ($+10.91\ cm^{-1}$) and $J(d8)$ ($-10.25\ cm^{-1}$) radical–radical pairs through the structure.[1] In order to test the effect of the smaller exchange interactions, we attempted to model the magnetism based only upon an isolated alternating chain model, excluding the weaker exchange terms. Detailed calculations using a number of alternating chain models (see Fig. S17) indicate that such models cannot reproduce the magnetic properties of α-YOMXUT crystal; the results strongly depend on the number of radicals in the

[1] An infinite alternating chain model would have the same number of FM $J(d2)$ and AFM $J(d8)$ interactions. However, there are two possibilities to build up a finite alternating chain model with an even number of magnetic dithiadiazolyl radical sites to allow both antiferromagnetic and ferromagnetic states depending on the ratio between $J(d2)$ and $J(d8)$ interactions. For instance, the smallest model one can think of is a 4-radical alternating chain model whose $J(d2)$:$J(d8)$ ratio will be either 1:2 or 2:1. We have named AF_F_AF (F_AF_F) the first (second) series of calculations since the number of $J(d8)$ AFM interactions overcomes the number of $J(d2)$ FM interactions (and otherwise). In theory, whenever the model has a large enough number of radical sites, both series will eventually converge.

model space and the ratio between the $J(d2)$ and $J(d8)$ interactions. Thus, we discard a simple chain model to describe the magnetism of this crystal.

Our second test was addressed at evaluating the validity of the common belief that macroscopic magnetic properties can be rationalized only by examining the spin-carrier part of a given radical (in this case, the CNSSN five-membered ring, see Fig. 1c). We thus performed additional calculations for the six non-negligible radical–radical pairs using HCNSSN$^{\bullet}$ radicals instead of *p*-NC-C_6F_4-CNSSN$^{\bullet}$ radicals. In these calculations, each heterocyclic HCNSSN ring adopted the same spatial conformation as in *p*-NC-C_6F_4-CNSSN, just replacing the fluorinated rings by hydrogen atoms. The re-calculated $J(di)$ values (see Table 2) indicate that $J(d1)$, $J(d3)$ and $J(d4)$ are now one order of magnitude smaller than the values obtained with the full-sized *p*-NC-C_6F_4-CNSSN$^{\bullet}$ radicals. The two dominant interactions $J(d2)$ and $J(d8)$ maintain their dominant character, because their shortest contacts are not affected by the absence of the six-membered ring. Even so, the value of $J(d2)$ changes remarkably. Overall, the magnetic topology (Fig. 7) is still 3D, but some significant changes take place. As a consequence, the minimal magnetic model required to compute the magnetic susceptibility is different than the 3d8s model: it is a three-dimensional 6-radical model, referred as the 3d6s model. Not surprisingly, the shape of the $\chi(T)$ and $\chi T(T)$ curves computed using the 3d6s model and the extended models along the crystallographic axis do not agree neither with the experimental magnetic susceptibility curve nor with that computed values using the minimal 3d8s model. Thus, the *p*-NC-C_6F_4-substituent plays an important role in determining the magnetic properties of α-YOMXUT.

Table 2
Study of the effect that the dithiadiazolyl cycle has on the magnetically non-negligible $d1$–$d4$ and $d7$–$d8$ pair interactions using HCNSSN models at the UDFT broken symmetry UB3LYP/6-31+G(d) level. Candidates $d1$–$d4$ and $d7$–$d8$ are listed as (C···C) distance increases

Candidate *di*	Distance (C···C) (Å)	J_{AB} (cm^{-1})
*d*1	4.789	+0.13
*d*2	4.990	+17.65
*d*3	6.534	<|0.05|
*d*4	6.588	<|0.05|
*d*7	8.285	−1.62
*d*8	8.454	−10.04

Finally, we can try to get a deeper insight over the size and sign of the $J(d2)$ and $J(d8)$ through-space magnetic interactions. It has been speculated that $J(d2)$ is a FM interaction due to the almost orthogonality of the SOMO orbitals [17]. UB3LYP/6-31+G(d) calculations show that the SOMO of the *p*-NC-C_6F_4-CNSSN$^{\bullet}$ radical (see Fig. 8) is a π^* orbital localized on the heterocyclic ring in agreement with previous results [18]. However, looking at Fig. 8, the SOMO orthogonality argument does not appear satisfactory. The McConnell-I mechanism [19] also fails to rationalize the sign of the magnetic interaction of *d*2 and *d*8 pairs of *p*-NC-C_6F_4-CNSSN$^{\bullet}$ radicals only in terms of spin densities. According to the common use of the

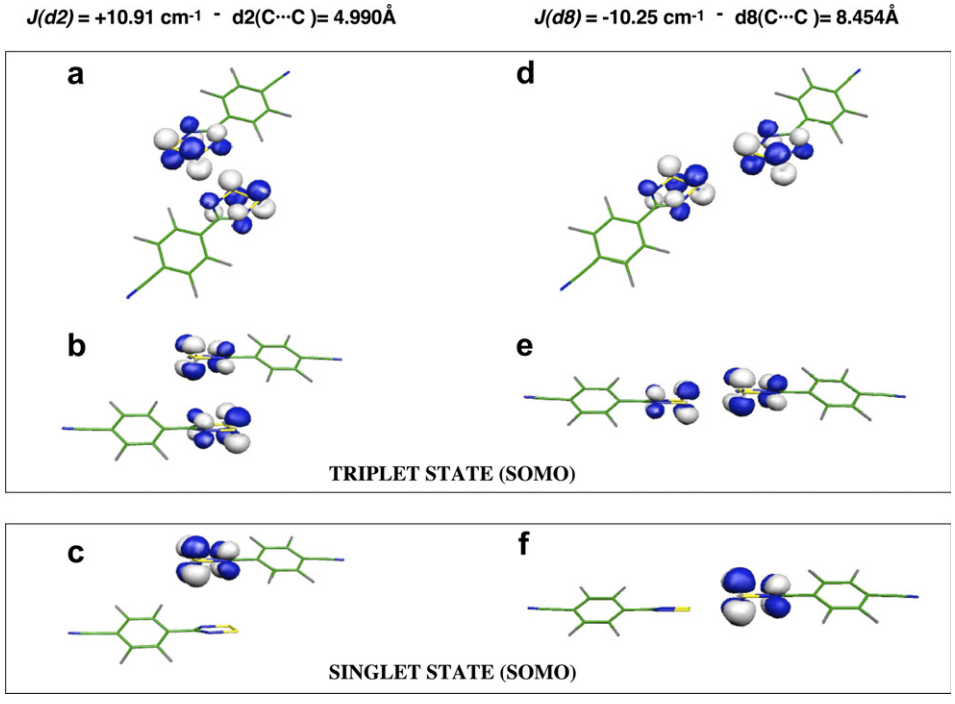


Fig. 8. (a and b) Two different views of the SOMO orbital for the triplet state of the *d*2 pair of NC-C_6F_4-CNNSS radicals ($d2$(C···C) = 4.990 Å, see Fig. 4 for radicals geometry, with $J(d2) = +10.91$ cm^{-1}) for α-YOMXUT at B3LYP/6-31+G(d) level. (c) SOMO orbital for the open-shell singlet state of the *d*2 pair. (d and e) Two different views of the SOMO orbital for the triplet state of the *d*8 pair of NC-C_6F_4-CNNSS radicals ($d8$(C···C) = 8.454 Å, see Fig. 4 for radicals geometry, with $J(d8) = -10.25$ cm^{-1}) for α-YOMXUT. (f) SOMO orbital for the open-shell singlet state of the *d*8 pair.

McConnell-I model, the shortest contacts for *d*2 overlap regions of positive π-spin density of the five-membered rings (see S and N atoms of the two radicals in Fig. 4), and therefore should be antiferromagnetic (whereas it is calculated to be ferromagnetic).

4. Conclusions

A first principles *bottom-up* theoretical study of the magnetism of α-YOMXUT indicates the existence of six non-negligible radical–radical interactions: two interactions of opposite sign (+10.91 and $-10.25\ cm^{-1}$) being one order of magnitude larger than the rest ($\leqslant|1.44|\ cm^{-1}$). The magnetic topology of the crystal has a complex 3D shape, and cannot be inferred from direct observation of the crystal structure. The dominant interactions (+10.91 and $-10.25\ cm^{-1}$) form alternating FM–AFM zigzag chains, which are connected along the *bc*-plane by adjacent FM–FM zigzag chains (+1.02 and $+0.67\ cm^{-1}$). Adjacent *bc*-planes are in turn connected by means of AFM ($-1.44\ cm^{-1}$) and FM ($+0.29\ cm^{-1}$) interactions. The overall antiferromagnetic shape of the experimental magnetic susceptibility is fully reproduced. It is also found that a simple alternating chain motif (in terms of dominating +10.91 and $-10.25\ cm^{-1}$ interactions) does not reproduce the experimental magnetic susceptibility curve. No scaling factor was needed to mimic the experimental curve. When the study was done using only the five-membered HCNSSN ring of the *p*-NC-C_6F_4-CNSSN$^{\bullet}$ radical, the experimental magnetic susceptibility curve was also not properly reproduced.

The sign and magnitude of the *J*(*di*) values has no simple interpretation neither in terms of orthogonality of the SOMOs nor in terms of the standard use of McConnell-I model. The size of the *J*(*di*) values are found to depend on the distance and relative orientation of the *p*-NC-C_6F_4-CNSSN$^{\bullet}$ radicals within each pair.

Acknowledgments

The Barcelona group thanks the support of Spanish "Ministerio de Educación y Ciencia" and the Catalan CIRIT (CTQ2005-02329/BQU2002-04587-C02-02 and 2005-SGR-00036, respectively) and the CESCA and BSC-CNS for the allocation of CPU time in their computers. M.D. thanks the Spanish Science and Education Ministry for the award of a "Ramón y Cajal" Fellowship. S.L. acknowledges the European Union for funding within the 'Transnational Access of HPC-Europe' Program.

Appendix A. Supplementary material

Figs. S1–S16. Candidates *d*1–*d*16: geometry and distances between dithiadiazolyl rings. Fig. S17. Study of the effect of the NC-C_6F_4-substituent of the NC-C_6F_4-CNSSN$^{\bullet}$ radical on the computation of the magnetic susceptibility data. Supplementary data associated with this article can be found, in the online version, at doi:10.1016/j.poly.2006.09.090.

References

[1] (a) D. Gatteschi, O. Kahn, J.S. Miller, F. Palacio (Eds.), Magnetic Molecular Materials, NATO ASI Series, Kluwer, Dordrecht, 1991;
(b) J.S. Miller, A.J. Epstein, Angew. Chem. 106 (1994) 399;
(c) J.S. Miller, A.J. Epstein, Angew. Chem., Int. Ed. Engl. 33 (1994) 385;
(d) O. Kahn, Molecular Magnetism, VCH, New York, 1993;
(e) E. Coronado, P. Delhaès, D. Gatteschi, J.S. Miller (Eds.), Molecular Magnetism: From Molecular Assemblies to the Devices, NATO ASI Series, Kluwer, Dordrecht, 1996;
(f) P.M. Lahti (Ed.), Magnetic Properties of Organic Materials, Marcel Dekker, New York, 1999;
(g) K. Itoh, M. Kinoshita (Eds.), Molecular Magnetism: New Magnetic Materials, Gordon & Breach, Amsterdam, 2000;
(h) J. Veciana (Ed.), π-Electron Magnetism: From Molecules to Magnetic Materials, Structure and Bonding, 100, Springer, 2001;
(i) J.S. Miller, M. Drillon (Eds.), Magnetism: Molecules to Materials (I–IV), Wiley–VCH, Weinheim, 2003.
[2] R. Chiarelli, M.A. Novak, A. Rassat, J.L. Tholence, Nature 363 (1993) 147.
[3] (a) J.M. Rawson, A.J. Banister, I. Lavender, Adv. Heterocycl. Chem. 62 (1995) 137;
(b) J.M. Rawson, F. Palacio, in: J. Veciana (Ed.), π Electron Magnetism: From Molecules to Magnetic Materials, Springer, Berlin, 2001, pp. 94–126.
[4] A.J. Banister, N. Bricklebank, W. Clegg, M.R.J. Elsegood, C.I. Gregory, I. Lavender, J.M. Rawson, B.K. Tanner, J. Chem. Soc., Chem. Commun. 6 (1995) 679.
[5] (a) F. Palacio, G. Antorrena, M. Castro, R. Burriel, J.M. Rawson, J.N.B. Smith, N. Bricklebank, J.J. Novoa, C. Ritter, Phys. Rev. Lett. 79 (1997) 2336;
(b) A.J. Banister, N. Bricklebank, I. Lavender, J.M. Rawson, C.I. Gregory, B.K. Tanner, W. Clegg, M.R.J. Elsegood, F. Palacio, Angew. Chem., Int. Ed. Engl. 35 (1996) 2533.
[6] G. Antorrena, J.E. Davies, M. Hartley, F. Palacio, J.M. Rawson, J.N.B. Smith, A. Steiner, Chem. Commun. (1999) 1393.
[7] C.M. Pask, R.J. Less, J. Rawson, F. Palacio, P. Oliete, Phosphorus Sulfur 168 (2001) 457.
[8] J.M. Rawson, C.M. Pask, F. Palacio, P. Oliete, C. Paulsen, A. Yamaguchi, R.D. Farley, Angew. Chem. Int. Ed. Engl. (submitted for publication).
[9] (a) Refcode according to Cambridge Crystallographic Database (CCSD): F.H. Allen, J.E. Davies, J.J. Galloy, O. Johnson, O. Kennard, C.F. Macrae, D.G. Watson, J. Chem. Inf. Comput. Sci. 31 (1991) 204;
(b) F.H. Allen, O. Kennard, Chem. Des. Automat. News 8 (1993) 31.
[10] M. Deumal, M.J. Bearpark, J.J. Novoa, M.A. Robb, J. Phys. Chem. A 106 (2002) 1299.
[11] C. Herring, in: G.T. Rado, H. Suhl (Eds.), Magnetism, 2, Academic Press, New York, 1966, p. 5.
[12] (a) L. Noodlemann, J. Chem. Phys. 74 (1981) 5737;
(b) L. Noodlemann, E.R. Davidson, Chem. Phys. 109 (1986) 131;
(c) E. Ruiz, S. Alvarez, J. Cano, V. Polo, J. Chem. Phys. 123 (2005) 164110;
(d) C. Adamo, V. Barone, A. Bencini, R. Broer, M. Filatov, N.M. Harrison, F. Illas, J.P. Malrieu, I.P.R. Moreira, J. Chem. Phys. 124 (2006) 107101.
[13] (a) A.D. Becke, Phys. Rev. A 38 (1988) 3098;
(b) C. Lee, W. Yang, R.G. Parr, Phys. Rev. B 37 (1988) 785;
(c) A.D. Becke, J. Chem. Phys. 98 (1993) 5648.
[14] (a) 6-31+G(d) Basis: R.C. Binning Jr., L.A. Curtiss, J. Comput. Chem. 11 (1990) 1206;

(b) , Primitive exponents:T.H. Dunning Jr., J. Chem. Phys. 66 (1977) 1382.

[15] M.J. Frisch, G.W. Trucks, H.B. Schlegel, P.M.W. Gill, B.G. Johnson, M.A. Robb, J.R. Cheeseman, T. Keith, G.A. Petersson, J.A. Montgomery, K. Raghavachari, M.A. Al-Laham, V.G. Zakrzewski, J.V. Ortiz, J.B. Foresman, J. Cioslowski, B.B. Stefanov, A. Nanayakkara, M. Challacombe, C.Y. Peng, P.Y. Ayala, W. Chen, M.W. Wong, J.L. Andres, E.S. Replogle, R. Gomperts, R.L. Martin, D.J. Fox, J.S. Binkley, D.J. Defrees, J. Baker, J.J.P. Stewart, M. Head-Gordon, C. Gonzalez, J.A. Pople, GAUSSIAN-98, Gaussian Inc., Pittsburgh, PA, 1999.

[16] M. Deumal, M.J. Bearpark, M.A. Robb, Y. Pontillon, J.J. Novoa, Chem. Eur. J. 10 (2004) 6422.

[17] J. Luzón, Ph.D. Thesis, Instituto de Ciencia de Materiales de Aragón, CSIC and Universidad de Zaragoza, 2003.

[18] J. Campbell, D. Klapstein, P.F. Bernath, W.M. Davis, R.T. Oakley, J.D. Goddard, Inorg. Chem. 35 (1996) 4264.

[19] H.M. McConnell, J. Chem. Phys. 39 (1963) 1910, The McConnell-I mechanism has been shown to be commonly misused: M. Deumal, J.J. Novoa, M.J. Bearpark, P. Celani, M. Olivucci, M.A. Robb, J. Phys. Chem. A 102 (1998) 8404; J.J. Novoa, M. Deumal, Struct. Bond. 100 (2001) 34.

methanol. 4-Acetamidobenzaldehyde (**pAcB**, Avocado Research Chemicals, 0.326 g, 2.00 mmol) was added and the mixture stirred under nitrogen for 2 days at room temperature. The resulting white precipitate was filtered, washed with water, and dried under vacuum for several hours to give 0.123 g (21%) of a white solid, m.p. 205–208 °C. ^{1}H NMR (DMSO-d_6): δ 1.04 (s, 6H), 1.06 (s, 6H), 2.03 (s, 3H), 4.45 (s, 1H), 7.38 (d, $J = 8.6$ Hz, 2H), 7.49 (d, $J = 8.6$ Hz, 2H), 7.69 (s, 2H), 9.88 (s, 1H).

2.2. 2-(para-Acetamidophenyl)-4,4,5,5-tetramethyl-4,5-dihydro-1H-imidazole-3-oxide-1-oxyl (*pAPNN*)

pAPNNH3 (0.4247 g, 1.448 mmol) in 40 mL of dichloromethane under nitrogen was treated with 33 mL of 0.2 M aq $NaIO_4$ added slowly by syringe, and the reaction mixture stirred for 30 min. The layers were separated and the aqueous layer extracted with 15 mL of dichloromethane. The combined organic layers were washed with 2×15 mL of saturated aq NH_4Cl and dried over anhydrous $MgSO_4$. The solution was filtered and dried under vacuum to yield a blue solid that was recrystallized from dichloromethane:ether to yield 0.345 g (82%) of blue-black solid, m.p. 204–205 °C; *Anal*. Calc. for $C_{15}H_{20}N_3O_3$ requires: C, 62.05; H, 6.94; N, 14.47. Found: C, 61.90; H, 6.91; N, 14.45%. FTIR (KBr, cm^{-1}): 3341, 2992, 1707. ESR (9.65164 GHz, toluene, room temperature): $g = 2.00682$, a(N) = 7.49 gauss (2N).

2.3. 2-para-(tert-Butyloxycarbonyl)aminobenzaldehyde (*pBAB*)

para-Aminobenzyl alcohol (Lancaster Synthesis, 1.0 g, 8.12 mmol) was acetylated to the corresponding "boc" derivative using a literature method [7] to give *para*-(*tert*-butyloxycarbonyl)aminobenzyl alcohol (m.p. 74–76 °C), which was oxidized by stirring at room temperature with solid MnO_2 (10 g, 115 mmol) in 50 mL of dichloromethane for 1 day. Filtration of the reaction and removal of the solvent gave crude product, which was air dried to give 0.569 g (59%) of **pBAB**, a cream-colored solid, m.p. 140–142 °C (lit m.p. 138 °C [7b]). This material was sufficiently pure to use in the next step. ^{1}H NMR (DMSO-d_6): δ 1.49 (s, 9H), 7.67 (d, 2H, $J = 8.0$ Hz), 7.80 (d, 2H, $J = 8.0$ Hz), 9.83 (s, 1H), 9.89 (s, 1H).

2.4. 2-(para-(tert-Butyloxylcarbonyl)aminophenyl)-1,3-dihydroxy-4,4,5,5-tetramethylimidazolidine (*pBPNNH3*)

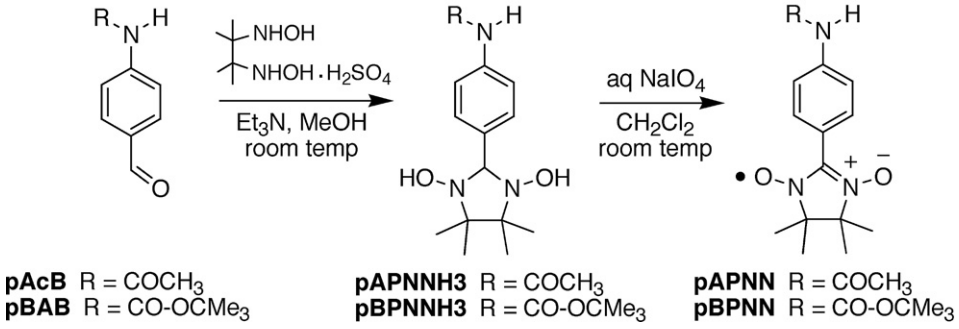
2,3-Bis(hydroxylamino)-2,3-dimethylbutane monosulfate [6] (0.462 g, 1.87 mmol) and 0.3 mL of triethylamine were stirred for 10 min at room temperature in 15 mL of methanol. **pBAB** (0.4145 g, 1.873 mmol) was added and the mixture stirred under nitrogen for 2 days at room temperature. The resultant white precipitate was filtered, washed with cold methanol, and dried under vacuum to give 0.131 g (20%) of white solid, m.p. 180–182 °C, pure enough to use in the next synthetic step. ^{1}H NMR (DMSO-d_6): δ 1.03 (s, 6H), 1.05 (s, 6H), 1.47(s, 9H), 4.43 (s, 1H), 7.32 (d, J 8.6 Hz, 2H), 7.36 (d, J 8.6 Hz, 2H), 7.69 (s, 2H), 9.26 (s, 1H).

2.5. 2-(para-(tert-Butyloxylcarbonyl)aminophenyl)-4,4,5,5-tetramethyl-4,5-dihydro-1H-imidazole-3-oxide-1-oxyl (*pBPNN*)

pBPNNH3 (0.2127 g, 0.605 mmol) was dissolved in 20 mL of dichloromethane under nitrogen and treated with 13.8 mL of 0.2 M $NaIO_4$ added slowly by syringe, and the reaction mixture stirred for 30 min. The layers were separated and the aqueous layer extracted with 10 mL of dichloromethane. The combined organic layers were washed with 2×10 mL of saturated aq NH_4Cl and dried over anhydrous $MgSO_4$. The solution was filtered and the solvent removed under vacuum to yield a blue solid that was recrystallized from dichloromethane:ether to yield. 0.148 g (70 %) of blue-black solid, m.p. 215–218 °C, *Anal*. Calc. for $C_{18}H_{26}N_3O_4$ requires: C, 62.05; H, 7.52; N, 12.06. Found: C, 62.03; H, 7.55; N, 12.04%. FTIR (KBr, cm^{-1}): 3340, 2980, 1728, 1604. ESR (9.65027 GHz, toluene, room temperature): $g = 2.00683$, a(N) = 7.47 gauss (2N).

3. Synthesis and characterization

pAPNN and **pBPNN** were made from the aldehydes shown in Scheme 1. **pAcB** and **pBAB** were each made by functionalizing the $-NH_2$ group of the appropriate aminobenzyl alcohol and oxidizing the alcohol to the corresponding aldehydes. These were then condensed with 2,3-bis(hydroxylamino)-2,3-dimethylbutane monosulfate,



Scheme 1. Synthesis of amide functionalized radicals **pAPNN** and **pBPNN**.

and oxidation to the final NN product. Both the NNs were stable solids at room temperature that were readily characterized by solution ESR, FTIR in KBr matrix, and MS or elemental microanalysis.

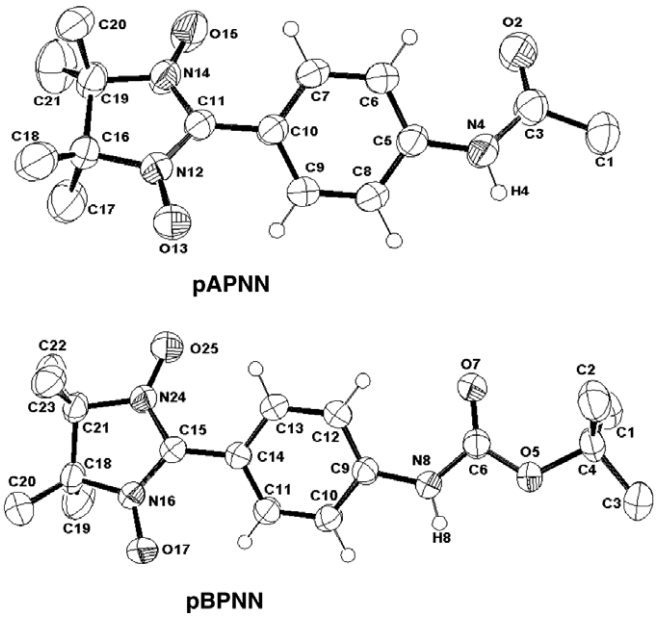


Fig. 1. ORTEP representations of **pAPNN** and **pBPNN**; ellipsoids for non-hydrogen atoms shown at 50% probability limits. Methyl hydrogen atoms omitted for ease of viewing.

4. Crystallography

Diffraction grade single crystals of **pAPNN** and **pBPNN**, were obtained by precipitation from dichloromethane/ether and analyzed [8]. Fig. 1 shows ORTEP style representations of **pAPNN** and **pBPNN**. Structural and crystallographic details are summarized in Tables 1 and 2.

5. Magnetic studies

Measurements for **pAPNN** and **pBPNN** were carried out over 1.8–300 K using a Quantum Design SQUID MPMS5 magnetometer for polycrystalline samples placed in gelatin capsules and held in place with a small plug of cotton. Magnetic susceptibilities were corrected for temperature independent magnetic contributions. Fig. 2 summarizes the results.

6. Results and discussion

The crystallography of **pAPNN** shows antiparallel oriented pairs of molecules held together by amide NH to nitroxide ON hydrogen bonds. For every molecule, only one nitroxide unit, N(12)–O(13), participates in hydrogen bonding, acting as an acceptor to an amide N(4)–H(4) group on another radical, as shown in Fig. 3. The other nitroxide, N(14)–O(15) is stacked almost antiparallel to the N(14′)–O(15′) group in another hydrogen bonded pair, with distance r[N(14)···O(15′)] = 3.931(2) Å (Table 2). The

Table 1
Crystal data for **pAPNN** and **pBPNN**

	pAPNN	**pBPNN**
Empirical formula	$C_{15}H_{20}N_3O_3$	$C_{18}H_{26}N_3O_4$
Formula weight	290.34	348.42
Temperature (K)	293(2)	293(2)
Wavelength (Å)	0.71073	0.71073
Crystal system	monoclinic	monoclinic
Space group	$P2_1/c$	$P2_1/n$
Unit cell dimensions		
a (Å)	11.2200(2)	12.0543(3)
b (Å)	12.4690(2)	9.9704(4)
c (Å)	11.3440(2)	16.3448(7)
β (°)	103.289(1)	105.579(3)
Volume (Å^3)	1544.55(5)	1892.25(12)
Z	4	4
D_{calc} (g/cm^3)	1.249	1.223
Absorption coefficient (mm^{-1})	0.088	0.087
$F(000)$	620	748
Θ Range for data collection (°)	1.86–25.38	3.76–27.48
Index ranges	$-13 \leqslant h \leqslant 13$, $-14 \leqslant k \leqslant 14$, $-13 \leqslant l \leqslant 13$	$-15 \leqslant h \leqslant 15$, $-12 \leqslant k \leqslant 12$, $-20 \leqslant l \leqslant 20$
Reflections collected	10056	8212
Independent reflections [R_{int}]	2823 [0.0207]	4305 [0.0427]
Completeness to θ (%)	99.6	98.3
Refinement method	full-matrix least-squares on F^2	full-matrix least-squares on F^2
Data/restraints/parameters	2823/0/271	4305/0/320
Goodness-of-fit on F^2	0.986	1.00
Final R indices [$I > 2\sigma(I)$]	$R_1 = 0.0461$, $wR_2 = 0.1374$	$R_1 = 0.0490$, $wR_2 = 0.1058$
R indices (all data)	$R_1 = 0.0578$, $wR_2 = 0.1521$	$R_1 = 0.1087$, $wR_2 = 0.1295$
Largest difference in peak and hole (e Å^{-3})	0.224 and −0.202	0.147 and −0.213

Table 2
Selected bonding parameters and intermolecular distances

pAPNN		**pBPNN**	
Parameter	Value	Parameter	Value
N(12)–O(13)	1.285(2)	N(16)–O(17)	1.280(2)
N(14)–O(15)	1.283(2)	N(24)–O(25)	1.280(2)
C(11)–N(12)	1.339(2)	C(15)–N(16)	1.348(2)
C(11)–N(14)	1.350(2)	C(15)–N(24)	1.350(2)
C(3)–O(2)	1.217(2)	C(6)–O(5)	1.341(2)
C(5)–N(4)	1.412(2)	C(6)–N(8)	1.361(2)
		C(6)–O(7)	1.207(2)
C(9)C(10)C(11)N(12)	35.6(2)	C(11)C(14)C(15)N(16)	29.6(2)
C(6)C(5)N(4)C(3)	24.7(2)	C(12)C(9)N(8)C(6)	−15.4(2)
C(5)N(4)C(3)C(1)	0.9(3)	C(9)N(8)C(6)O(5)	172.8(2)
O(13′)···N(4‴)	2.944(2)	O(17)···N′(8)	2.928(2)
O(13′)···H(4‴)	2.06	O(17)···H′(8)	2.12
O(15)···N(14′)	3.931(2)	O(17)···C′(10)	3.243(2)
N(14)···O(15′)	3.931(2)	O(17)···H′(10)	2.53
O(2)···C(20) (NO···methyl)	3.329(3) (not shown)	O(7)···C″(23)	3.396(2)
		O(25)···C″(19)	3.449(2)
		O(25′)···C(12)	3.481(2)
		O(25′)···H(12)	2.81
		O(25′)···C(13)	3.578(2)
		O(25′)···H(13)	3.01
		O(25)···O″(25)	4.839(2) (not shown)

See Figs. 1, 3, and 4 for labelling. Distances in angstroms, angles in degrees, esd in parentheses.

hydrogen bonds and the stacks are the major contacts involving nitronylnitroxide NO groups, and so are likely candidates to provide intermolecular exchange pathways between molecules by spin polarization.

The magnetic susceptibility data for **pAPNN** show a strong low temperature downturn indicating antiferromagnetic (AFM) exchange. Magnetization versus field measurements at 1.8 K (not shown) gave near linear increase from 0 to 50,000 Oe, also consistent with AFM exchange. The near perfect antiparallel alignment of N–O groups in the antiparallel stacks shown in Scheme 2 and Fig. 3 ($\angle$N(14)–O(15)···N(14′) = 91.5°) is ideal [9] to provide antiferromagnetic (AFM) exchange interactions consistent with the observed loss of susceptibility. A nonlinear least squares fit using an equilibrium singlet-triplet (Bleaney–Bowers [10]) model with a mean field term gives an excellent fit to the data as shown in Fig. 2 with $g = 1.998 \pm 0.003$, $2J/k = (-)4.99 \pm 0.02$ K $\theta = (-)0.86 \pm 0.12$ K; uncertainties are statistical 95% confidence limits.

In principle, combination of the hydrogen bonds and nitroxide stacks (involving both NO groups of the nitronylnitroxides) could create chains of **pAPNN** molecules in the lattice. However, a 1D Heisenberg AFM chain model [11] fit to the susceptibility gave poor results. The spin density on the amide NH of **pAPNN** will be quite small [12], so exchange through the hydrogen bond is likely to very weak if present at all. Assuming that there are no gross low temperature crystal lattice changes in **pAPNN**, its AFM exchange appears to be *primarily* due to spin pairing between the close contact N(14)–O(15) nitroxide groups.

pBPNN, unlike **pAPNN**, lacks close direct intermolecular contacts between nitronylnitroxide NO units. There is limited classical hydrogen bonding, despite the presence of the carbamate type HN–CO–O–*t*Bu groups. There is some hydrogen bonding from the nitronylnitroxide O(17) to carbamate H(8′)–N(8)′ unit, but that interaction appears to be assisted by close NO to aryl HC contacts of (N(16))–O(17)···H(10′)–C(10′) – see Fig. 4 and Table 2. There are also some dipolar contacts from the nitronylnitroxide O(25) atoms to nearby aryl C(12′)–H(12′) and C(13′)–H(13′) groups. The NO to aryl HC contacts are possible sources of spin polarized exchange, but are somewhat ambiguous to interpret in magnetostructural terms, because the NO group seems near-equally likely to interact with C–H groups that are both *ortho* and *meta* to a nitronylnitroxide. The signs of the spin density on H(12) and H(13) are expected to be different, so the exchange effects of both interacting with one NO are unlikely to reinforce one another.

The lack of close intermolecular contacts between sites of large spin density is consistent with the essentially isolated paramagnetic behavior shown by the $1/\chi(T)$ (Curie–Weiss) and $\chi T(T)$ plots for **pBPNN** in Fig. 2. The $1/\chi(T)$ linear fit for the data where $T > 100$ K yields a Curie constant of 0.375 ± 0.008 emu K/Oe mol, in excellent agreement with the value expected for $S = 1/2$ spin carriers. The small downturn in the $\chi T(T)$ plot indicates only quite weak AFM interactions that are very difficult to attribute to specific close contacts among any of the intermolecular contacts in **pBPNN**.

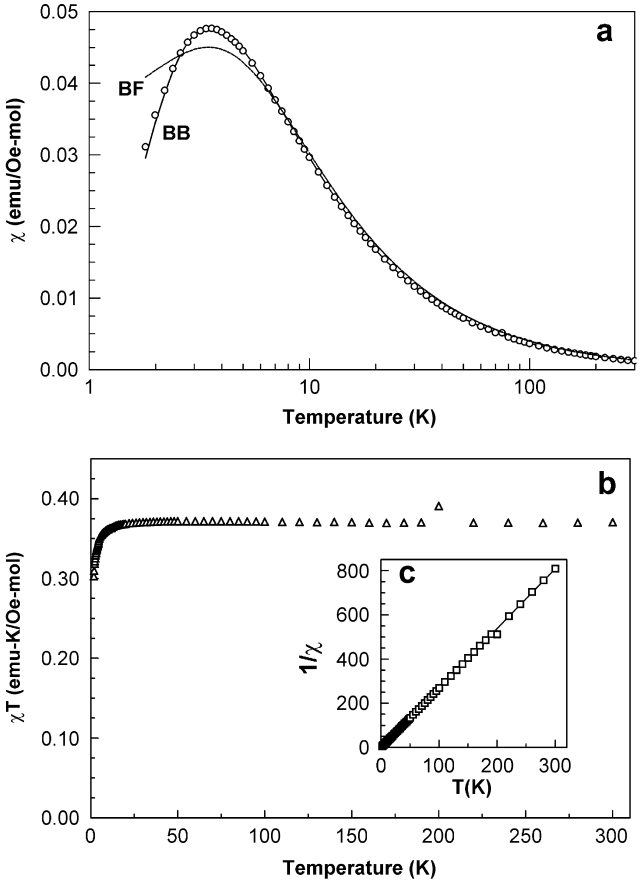


Fig. 2. Magnetic measurements for **pAPNN** (chart a) and **pBPNN** (charts b and c). All data in these charts obtained at 1000 Oe. BF, best fit to Bonner–Fisher 1D AFM chain model; BB, best fit to Bleaney–Bowers spin pairing model with mean field correction. See the text for details. Solid line in chart c is a linear fit to the data for $T > 100$ K.

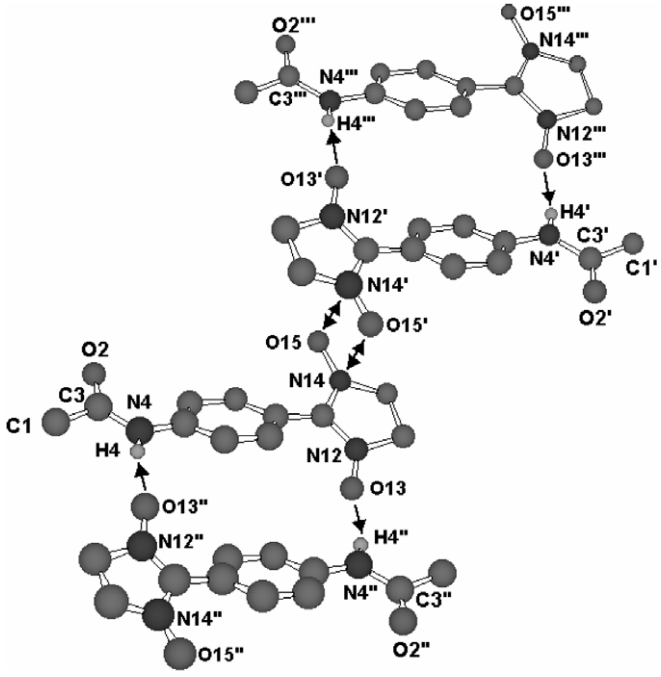
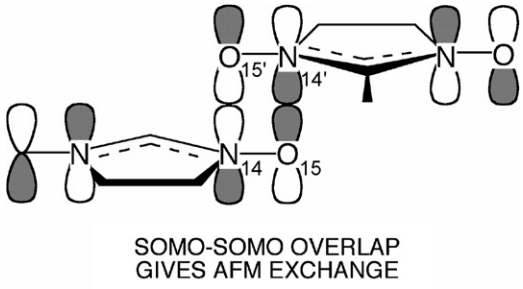


Fig. 3. Selected crystallographic close contacts in **pAPNN**. Numbering derived from Fig. 1. See also Table 2.



Scheme 2. Simplified representation of NO/ON stacking in **pAPNN**.

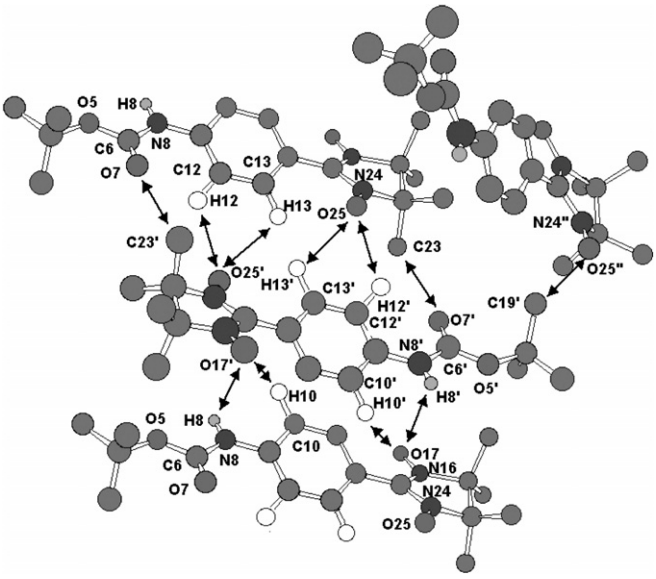


Fig. 4. Selected crystallographic close contacts in **pBPNN**. Numbering derived from Fig. 1. See also Table 2.

7. Conclusions

The amido-substituted radicals **pAPNN** and **pBPNN** differ primarily in that the amido derivative forms pairs due to directional, classic hydrogen bonds between the amide NH and one NO of nitronylnitroxide group, while the boc-derivatized system forms pairs due to a variety of intermolecular contacts in which hydrogen bonds do not necessarily dominate. Spin pairing in **pAPNN** occurs due to a moderately close nitroxide–nitroxide contact. This contact between large spin density sites dominates the magnetic behavior of the amide derivative, although other contact may contribute to a lesser extent to the overall magnetic behavior. By comparison, **pBPNN** shows nearly isolated paramagnetic behavior, with very limited exchange between molecules in the lattice.

The results demonstrate a weakness of the strategy of using hydrogen bonds to bring organic radicals into close proximity in an effort to promote strong exchange interactions: even when the hydrogen bonding is successful, one needs more interactions between sites of significant spin density to promote exchange beyond simple spin pairing

behavior. Further work is ongoing to deprotect the $-NH_2$ groups in these systems and to change from *para* to *meta* connectivity, to try to alter and extend the dimensionality of their exchange interactions in the solid state, by allowing more possibilities for hydrogen bonding.

Acknowledgements

This work was supported by the National Science Foundation under Grant CHE 0415716. We thank Dr. P. Khalifah of the University of Massachusetts Amherst X-ray Structural Characterization Center (NSF CHE-9974648) for assistance with crystallographic analysis. The University of Massachusetts Amherst Nanomagnetics Characterization Facility and Electron Paramagnetic Resonance Facility were supported by National Science Foundation Grants CTS-0116498 and CHE-0443180, respectively.

Appendix A. Supplementary material

CCDC 619976 and 619977 contain the supplementary crystallographic data for **pBPNN** and **pAPNN**. These data can be obtained free of charge via http://www.ccdc.cam.ac.uk/conts/retrieving.html, or from the Cambridge Crystallographic Data Centre, 12 Union Road, Cambridge CB2 1EZ, UK; fax: (+44) 1223-336-033; or e-mail: deposit@ccdc.cam.ac.uk. Supplementary data associated with this article can be found, in the online version, at doi:10.1016/j.poly.2006.09.046.

References

[1] (a) J. Cirujeda, E. Hernàndez-Gasió, C. Rovira, J.-L. Stanger, P. Turek, J. Veciana, J. Mater. Chem. 5 (1995) 243;
(b) E. Hernandez, M. Mas, E. Molins, C. Rovira, J. Veciana, Angew. Chem., Int. Ed. Engl. 32 (1993) 882;
(c) J.L. Garcia-Munoz, J. Cirujeda, J. Veciana, S.F. Cox, J. Chem. Phys. Lett. 293 (1998) 160;
(d) H. Heise, F.H. Koehler, F. Mota, J.J. Novoa, J. Veciana, J. Am. Chem. Soc. 121 (1999) 9659;
(e) J. Cirujeda, J. Vidal-Gancedo, O. Juergens, F. Mota, J.J. Novoa, C. Rovira, J. Veciana, J. Am. Chem. Soc. 122 (2000) 11393;
(f) J. Cirujeda, M. Mas, E. Molins, F. Lanfranc de Panthou, J. Laugier, J.G. Park, C. Paulsen, P. Rey, C. Rovira, J. Veciana, Chem. Commun. (1995) 709;
(g) J. Veciana, J. Cirujeda, C. Rovira, J. Vidal-Gancedo, Adv. Mater. 7 (1995) 221;
(h) J. Cirujeda, C. Rovira, J. Veciana, Synth. Met. 71 (1995) 1799;
(i) J. Cirujeda, E. Hernandez-Gasio, F. Lanfranc de Panthou, J. Laugier, M. Mas, E. Molins, C. Rovira, J.J. Novoa, P. Rey, J. Veciana, Mol. Cryst. Liq. Cryst. Sect. A 271 (1995) 1;
(j) J. Cirujeda, L.E. Ochando, J.M. Amigo, C. Rovira, J. Rius, J. Veciana, Angew. Chem., Int. Ed. Engl. 34 (1995) 55;
(k) T. Sugawara, T. Matsushita, A. Izuoka, N. Wada, N. Takeda, M. Ishikawa, Chem. Commun. (1994) 1723;
(l) M.M. Matsushita, A. Izuoka, T. Sugawara, Mol. Cryst. Liq. Cryst. Sect. A 279 (1996) 139;
(m) M.M. Matsushita, A. Izuoka, T. Sugawara, T. Kobayashi, N. Wada, N. Takeda, M. Ishikawa, J. Am. Chem. Soc. 119 (1997) 4369;
(n) P. Taylor, P.M. Lahti, Chem. Commun. (2004) 2686.

[2] (a) D. Maspoch, D. Ruiz-Molina, K. Wurst, C. Rovira, J. Veciana, Chem. Commun. (2004) 1164;
(b) M. Baskett, P.M. Lahti, Polyhedron 24 (2005) 2645.

[3] R. Feher, D.B. Amabilino, K. Wurst, J. Veciana, Mol. Cryst. Liq. Cryst. Sci. Technol. Sect. A 334 (1999) 333.

[4] (a) P. Taylor, P.R. Serwinski, P.M. Lahti, Chem. Commun. (2003) 1400;
(b) P. Taylor, P.M. Lahti, J.B. Carroll, V.M. Rotello, Chem. Commun. (2005) 895.

[5] (a) M. Aso, T. Ikeno, K. Norihisa, M. Tanaka, N. Koga, H. Suemune, J. Chem. Soc., Perkin Trans. 2 (2000) 1637;
(b) M. Aso, T. Ikeno, K. Norihisa, M. Tanaka, N. Koga, H. Suemune, J. Org. Chem. 66 (2001) 3513;
(c) D. Shiomi, M. Nozaki, T. Ise, K. Sato, T. Takui, J. Phys. Chem. B 108 (2004) 16606;
(d) T. Kaneko, M. Aso, N. Koga, H. Suemune, Org. Lett. 7 (2005) 303.

[6] V. Ovcharenko, S. Fokin, P. Rey, Mol. Cryst. Liq. Cryst. Sci. Technol. Sect. A 334 (1999) 109.

[7] (a) R.E. Swenson, T.J. Sowin, H.Q. Zhang, J. Org. Chem. 67 (2002) 9182;
(b) R. Rai, J. Katzellenbogen, J. Med. Chem. 35 (1992) 4150.

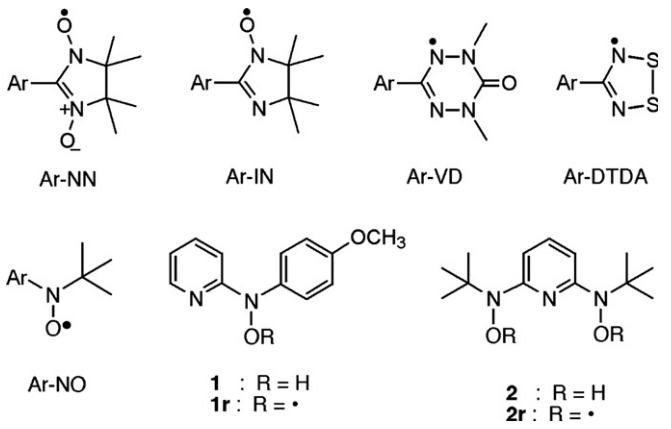
[8] Crystallographic analysis used G.M. Sheldrick, SHELXTL 97 Program for the Refinement of Crystal Structures, University of Göttingen, Germany.

[9] Cf the discussion of exchange as a function of SOMO packing geometries given by K. Yamaguchi, T. Kawakami, A. Oda, Y. Yoshioka, in: P.M. Lahti (Ed.), Magnetic Properties of Organic Materials, Marcel Dekker, New York, NY, 1999, pp. 403–425.

[10] B. Bleaney, K.D. Bowers, Proc. R. Soc. London A (1952) 214, We used the standard hamiltonian; $J < 0$ is antiferromagnetic.

[11] (a) J.C. Bonner, M.E. Fisher, Phys. Rev. A 135 (1964) 650;
(b) J.C. Bonner, Ph.D. Dissertation, University of London, UK, 1968.

[12] UB3LYP/6-31G* computations on the monomeric **pAPNN** (crystallographic fixed geometry) show only (−)0.001([+]0.00006) Mulliken spin populations on the amide N(H) unit, while spin pulations on the phenyl C(H) *ortho* and *meta* to the nitronylnitroxide group are (−)0.027([+]0.001) and (+)0.012([−]0.004–[−]0.005), respectively. Spin population on the nitronylnitroxide nitrogens are (+)0.26–0.27. Computations were carried out using M.J. Frisch, G.W. Trucks, H.B. Schlegel, G.E. Scuseria, M.A. Robb, J.R. Cheeseman, J.A.J. Montgomery, T. Vreven, K.N. Kudin, J.C. Burant, J.M. Millam, S.S. Iyengar, J. Tomasi, V. Barone, B. Mennucci, M. Cossi, G. Scalmani, N. Rega, G.A. Petersson, H. Nakatsuji, M. Hada, M. Ehara, K. Toyota, R. Fukuda, J. Hasegawa, M. Ishida, T. Nakajima, Y. Honda, O. Kitao, H. Nakai, M. Klene, X. Li, J.E. Knox, H.P. Hratchian, J.B. Cross, C. Adamo, J. Jaramillo, R. Gomperts, R.E. Stratmann, O. Yazyev, A.J. Austin, R. Cammi, C. Pomelli, J.W. Ochterski, P.Y. Ayala, K. Morokuma, G.A. Voth, P. Salvador, J.J. Dannenberg, V.G. Zakrzewski, S. Dapprich, A.D. Daniels, M.C. Strain, O. Farkas, D.K. Malick, A.D. Rabuck, K. Raghavachari, J.B. Foresman, J.V. Ortiz, Q. Cui, A.G. Baboul, S. Clifford, J. Cioslowski, B.B. Stefanov, G. Liu, A. Liashenko, P. Piskorz, I. Komaromi, R.L. Martin, D.J. Fox, T. Keith, M.A. Al-Laham, C.Y. Peng, A. Nanayakkara, M. Challacombe, P.M.W. Gill, B. Johnson, W. Chen, M.W. Wong, C. Gonzalez, J.A. Pople, Gaussian 03, Revision B.03, Pittsburgh, PA, 2003.



Scheme 1. Structural formulas.

ethereal solution (25 mL) containing 2-bromopyridine (507 mg; 3.21 mmol) was added a hexane solution (1.57 mol/L) of *n*-butyl lithium (2.1 mL; 3.3 mmol) dropwise at −78 °C under nitrogen atmosphere. The mixture was stirred at −78 °C for 0.5 h. After an ether solution (25 mL) containing *p*-nitrosoanisole (440 mg; 3.21 mmol) was added to the above mixture from a dropping funnel at −78 °C, the mixture was stirred at −78 °C for further 3 h. The reaction mixture was quenched by aqueous $NaHCO_3$ at room temperature, and the organic layer was washed with aqueous $NaHCO_3$ three times. After the mixture was dried over anhydrous $MgSO_4$, the ether solution was filtered and concentrated under reduced pressure. A main product was purified by passing through a short column (silica gel) with ether as an eluent. Recrystallization from ether gave 189 mg of a colorless solid of **1** (0.874 mmol; 27%). M.p. 95–97 °C. ^{1}H NMR (270 MHz, $CDCl_3$) δ 3.81, 6.67, 6.68, 6.89, 7.21, 7.44, 8.13. The OH proton signal was missing. ^{13}C NMR (68 MHz, $CDCl_3$) δ 55.6, 113.7, 114.6, 123.7, 124.6, 127.8, 137.9, 147.5, 157.2, 160.2. MS (EI, 70 eV) *m*/*z* 216.1 (M^+), 199.1, 184.0. IR (KBr disc) 766, 1250, 1431, 1500, 1604, 2656, 3059 cm^{-1}.

2.2. Preparation of 2,6-bis(N-t-butylhydroxylamino)-pyridine (2)

To the ethereal solution (50 mL) containing 2,6-dibromopyridine (1.19 mg; 5.02 mmol) and *N*,*N*,*N*′,*N*′-tetramethylethylenediamine (2.56 g; 22.0 mmol) was added a pentane solution (1.56 mol/L) of *t*-butyl lithium (14 mL; 22 mmol) at −78 °C under nitrogen atmosphere. The mixture was stirred at −30 °C for 0.5 h, and then cooled again to −78 °C. After an ether solution (30 mL) containing 2-methyl-2-nitrosopropane (1.05 g; 12.1 mmol) was added to the above mixture from a dropping funnel, the mixture was stirred at −78 °C for further 5 h. Aqueous work up was done in a manner similar to that of **1**. Recrystallization from ether/hexane gave 0.531 g of a colorless solid of **2** (2.10 mmol; 42%). M.p. 132–134 °C. ^{1}H NMR (270 MHz, $CDCl_3$) δ 1.27, 6.60, 6.89, 7.55. The OH proton signal was missing. ^{13}C NMR (68 MHz, $CDCl_3$) δ 26.6, 619.9, 112.3, 138.0, 159.3. MS (EI, 70 eV) *m*/*z* 253.1 (M^+), 197.1, 141.0. IR (KBr disc) 822, 1203, 1362, 1439, 1576, 2972, 3211 cm^{-1}.

2.3. ESR spectroscopy

ESR spectra were recorded on a Bruker ESP300E X-band (9.7 GHz) spectrometer. The samples of **1** and **2** were oxidized with Ag_2O in toluene at room temperature for 1 h, and the solid was filtered off. After the sample solution was thoroughly purged with nitrogen, the ESR spectra were recorded immediately. Simulated spectra were calculated in the WinEPR Simfonia program (version 1.25, Bruker Biospin, Rheinstetten, Germany (1996)).

2.4. X-ray crystal structure analysis

X-ray diffraction data of single crystals of **1** and **2** were collected on a Rigaku R-axis RAPID diffractometer with graphite monochromated Mo Kα ($\lambda = 0.71069$ Å) radiation at 90 K. The structures were directly solved and the parameters were refined in the CRYSTALSTRUCTURE program package (version 3.5.1, Rigaku/MSC, The Woodlands, TX 77381, USA (2003)). Numerical absorption correction was used. All of the hydrogen atoms were found experimentally. Thermal displacement parameters were refined anisotropically for non-hydrogen atoms and those of hydrogen atoms were treated isotropically. Selected crystallographic data: **1**: $C_{12}H_{12}N_2O_2$, triclinic, $P\bar{1}$, $a = 9.426(2)$ Å, $b = 9.774(3)$ Å, $c = 12.836(4)$ Å, $\alpha = 105.26(3)°$, $\beta = 106.32(2)°$, $\gamma = 91.72(3)°$, $V = 1088.0(6)$ Å^3, $Z = 4$, $d_{calc} = 1.320$ g cm^{-3}, μ(Mo Kα) = 0.092 mm^{-1}, $R(F)(I > 2\sigma(I)) = 0.0393$, and $R_w(F^2)$ (all data) = 0.0503 for 4961 unique reflections. **2**: $C_{13}H_{23}N_3O_2$, monoclinic, $P2_1/c$, $a = 12.41(1)$ Å, $b = 16.828(13)$ Å, $c = 14.131(12)$ Å, $\beta = 92.52(7)°$, $V = 2947(4)$ Å^3, $Z = 8$, $d_{calc} = 1.142$ g cm^{-3}, μ(Mo Kα) = 0.078 mm^{-1}, $R(F)(I > 2\sigma(I)) = 0.0651$, and $R_w(F^2)$ (all data) = 0.0893 for 6493 unique reflections.

2.5. Molecular orbital calculation

Molecular orbital calculations were performed on the GAUSSIAN03 program (Revision C.02, Gaussian Inc., Pittsburgh, PA 15106, USA (2003)). We applied unrestricted density functional (DFT) UB3LYP methods with the Becke exchange functional [11] and the Lee–Yang–Parr correlation functional [12]. The 6-31G** basis set was chosen. The convergence criterion for the energy was set at 10^{-9} a.u.

3. Results and discussion

We have successfully prepared two precursors for paramagnetic chelating ligands, **1** and **2**. They were characterized by means of spectroscopic methods. The X-ray crystallographic analysis revealed the molecular structures as shown in Fig. 1. All of the hydrogen atoms were found

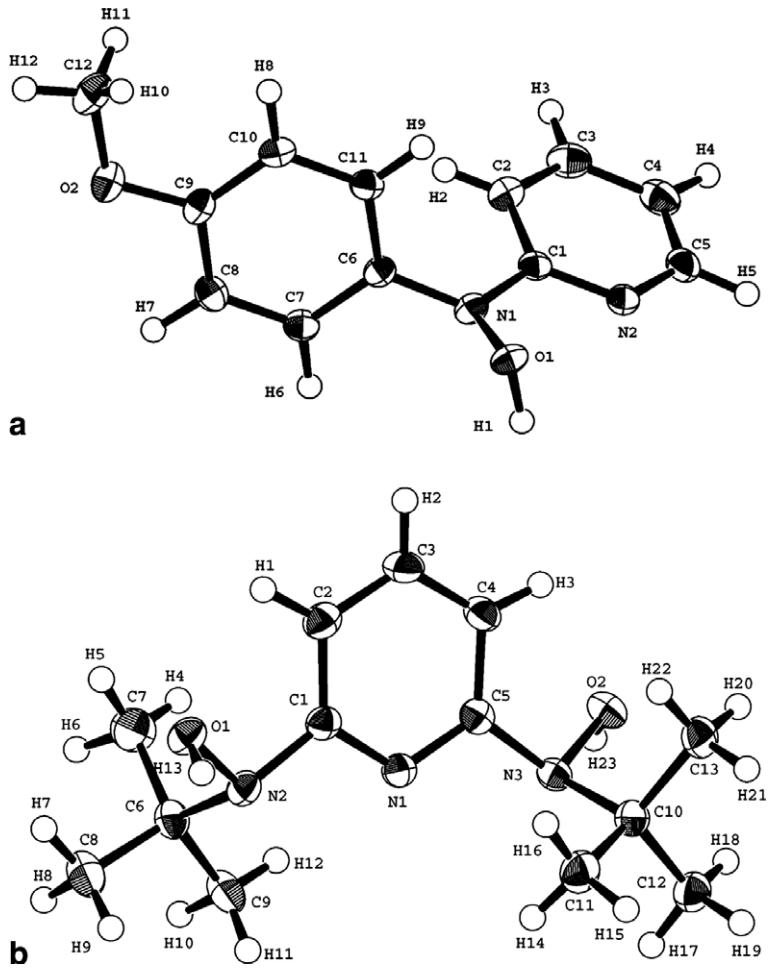
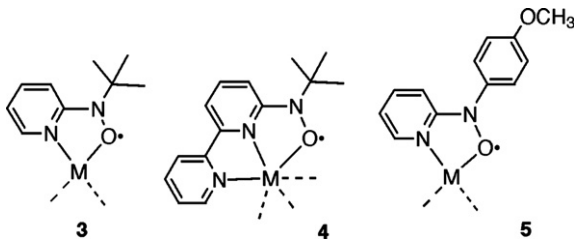


Fig. 1. Ortep drawings of (a) **1** and (b) **2** with the thermal ellipsoids at the 50% probability level for non-hydrogen atoms.

experimentally. As for **2**, there are two crystallographically independent molecules in a unit cell, one of which is shown in Fig. 1(b). The N–O bond distances are 1.420(1) Å for **1** and 1.450(2), 1.449(2), 1.446(2), and 1.450(2) Å for **2**. The latter values are comparable to those of typical *N*-*t*-butyl-*N*-phenylhydroxylamines [13]. The former value is slightly shorter than those of **2**, being compatible with the fact that a slight decrease of electron density at the hydroxylamino nitrogen atom due to the π-conjugation from two aromatic rings. The hydroxylamino nitrogen atom in **1** shows a less pyramidalized geometry than those of **2**.

The successful isolation of **1** is regarded as a rare case, since *N*,*N*-diarylhydroxylamines cannot be isolated in general because of facile autoxidation [14]. The 2-pyridyl group has an intrinsic electron-deficient nature, and may slow down the autoxidation of the hydroxylamino group. After the purification of **1**, the oxidation with silver(I) oxide gave a radical (**1r**) showing an ESR signal at $g = 2.0057$ with $a_N = 9.15$ G (toluene at room temperature), being typical of diaryl nitroxides (Fig. 2a). We have already prepared transition-metal complexes containing *t*-butyl 2-pyridyl nitroxides (**3** and **4**; M = Cu^{II}, Ni^{II}) [7,8]. The *t*-butyl group is useful for kinetically stabilizing nitroxide radicals but, at the same time, has a fatal disadvantage for intermolecular interaction; that is, intermolecular van der Waals contacts keep the spin centers apart from each other owing to the steric bulkiness. When we use the *p*-anisyl group as a stabilizing substituent and the resultant radical (**1r**) is coordinated to a paramagnetic metal ion giving **5**, possible intermolecular interaction would be larger than those of the complexes such as **3** and **4**. It is well known that the *p*-anisyl group has a satisfactorily stabilizing effect on nitroxide radicals [6,15].



Oxidation of **2** gave an unstable radical (**2r**). In sharp contrast to the case of **1r**, the X-band ESR spectrum of **2r** showed an unresolved single line at $g = 2.0060$ even in a dilute and deaerated toluene solution (Fig. 2b). This

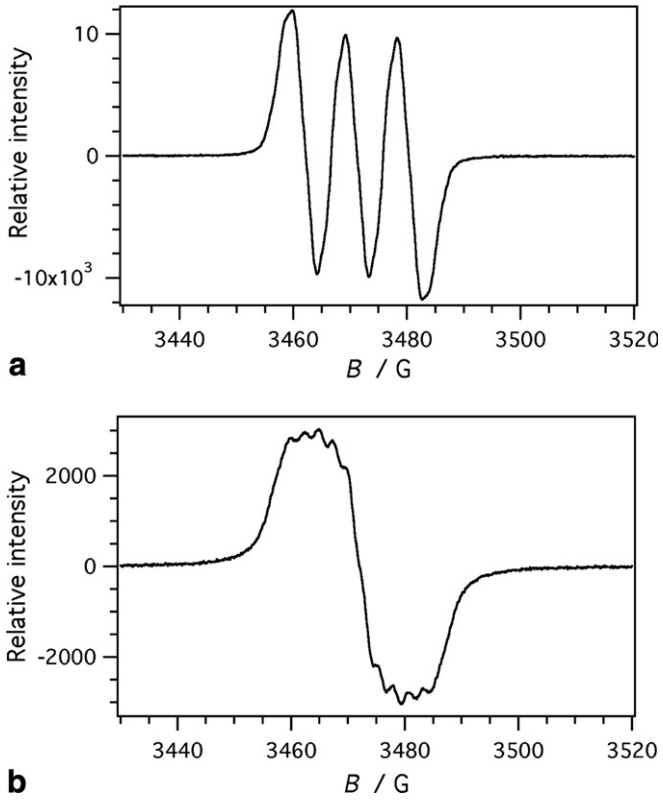
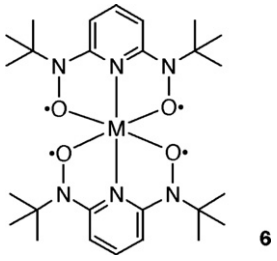


Fig. 2. X-band ESR spectra of **1r** and **2r** in toluene at room temperature.

broadening is due to intramolecular dipole–dipole and exchange interactions among the unpaired electrons and also probably to overlap of different signals and hyperfine structures of conformational isomers like 1,3-phenylene bisnitroxide biradicals [16]. We are now attempting complexation without purification of the corresponding radical (**2r**) to give **6**.



6

Although we could not isolate **2r** so far, we performed theoretical calculation of **2r** based on the unrestricted density functional theory (UB3LYP/6-31G**) with the molecular geometry fully optimized on the same level. The distribution of the spin density (2e in total) is drawn in Fig. 3, which clearly represents the SOMOs carrying a π-character. The alternating spin density on the pyridine ring is illustrated. The SCF energies for the triplet and singlet states were −822.617945729 and −822.616950231 a.u., respectively. The calculation indicates that the triplet state

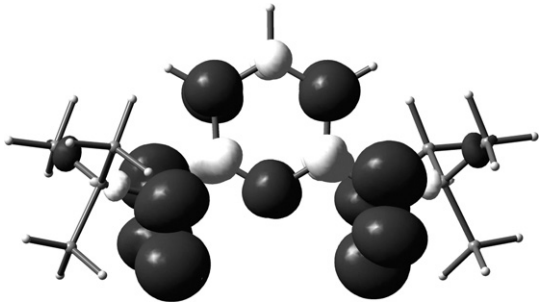


Fig. 3. Spin density distribution at the triplet state of **2r** calculated on the UB3LYP/6-31G**//UB3LYP/6-31G** level (dark gray: positive spin density; light gray: negative spin density).

is more stable than the singlet state by the energy difference of 9.95×10^{-4} a.u., which is converted to 2.61 kJ mol^{-1} or 314 K. This finding is compatible with the fact that 1,3-phenylene bridges work as a ferromagnetic exchange coupler [17], as expected from the spin polarization scheme [18]. Furthermore, the spin polarization mechanism is also applicable to the azabenzene systems. Several magnetic studies involving pyridyl-substituted radical compounds provided ample discussion [19]. Transition-metal complexes containing **2r** would be of great interest for development of ferromagnetic hybrid solids.

4. Conclusion

We successfully synthesized and characterized two precursors for paramagnetic chelating ligands, *N*-*p*-anisyl-*N*-2-pyridylhydroxylamine and 2,6-bis(*N*-*t*-butylhydroxylamino)pyridine. After the purification of the hydroxylamines, oxidation with silver(I) oxide gave radicals showing typical nitroxide ESR signals. Theoretical DFT calculation indicated that the bisnitroxide radical, pyridine-2,6-diyl bis(*t*-butyl nitroxide), had a triplet ground state. Although these radicals are unisolable under ambient conditions, complexation with transition-metal ions would stabilize the radicals [20]. We are now attempting preparation of transition-metal complexes containing **1r** and **2r** by means of in situ trapping of the fragile radicals.

5. Supplementary materials

CCDC 617091 and 617092 contain the supplementary crystallographic data for **1** and **2**. These data can be obtained free of charge via http://www.ccdc.cam.ac.uk/conts/retrieving.html, or from the Cambridge Crystallographic Data Centre, 12 Union Road, Cambridge CB2 1EZ, UK; fax: (+44) 1223-336-033; or e-mail: deposit @ccdc.cam.ac.uk.

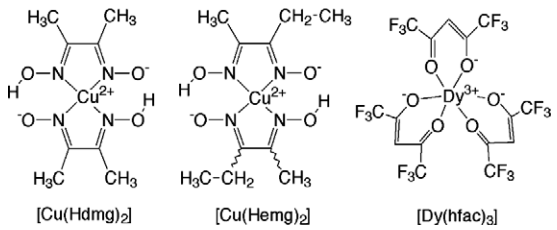
Acknowledgements

This work was supported by Grants-in-Aid for Scientific Research (Nos. 15073101, 16550121, and 15550115) from

the Ministry of Education, Culture, Sports, Science and Technology, Japan.

References

[1] (a) A. Caneschi, D. Gatteschi, R. Sessoli, Acc. Chem. Res. 22 (1989) 392;
(b) J.M. Manriquez, G.T. Yee, R.S. McLean, A.J. Epstein, J.S. Miller, Science 252 (1991) 1415;
(c) K. Inoue, T. Hayamizu, H. Iwamura, D. Hashizume, Y. Ohashi, J. Am. Chem. Soc. 118 (1996) 1803;
(d) M.T. Lamaire, Pure Appl. Chem. 76 (2004) 277.
[2] (a) F.M. Romero, D. Luneau, R. Ziessel, Chem. Commun. (1998) 551;
(b) C. Aoki, T. Ishida, T. Nogami, Inorg. Chem. 42 (2003) 7616.
[3] (a) D. Luneau, P. Rey, J. Laugier, P. Fries, A. Caneschi, D. Gatteschi, R. Sessoli, J. Am. Chem. Soc. 113 (1991) 1245;
(b) D. Luneau, P. Rey, J. Laugier, E. Belorizky, A. Conge, Inorg. Chem. 31 (1992) 3578.
[4] (a) R.G. Hicks, M.T. Lemaire, L.K. Thompson, T.M. Barclay, J. Am. Chem. Soc. 122 (2000) 8077;
(b) T.M. Barclay, R.G. Hicks, M.T. Lemaire, L.K. Thompson, Chem. Commun. (2000) 2141.
[5] (a) N.G.R. Hearns, K.E. Preuss, J.F. Richardson, S. Bin-Salamon, J. Am. Chem. Soc. 126 (2004) 9942;
(b) M. Jennings, K.E. Preuss, J. Wu, Chem. Commun. (2006) 341.
[6] J.F.W. Keana, Chem. Rev. 78 (1978) 37.
[7] A. Okazawa, T. Nogami, T. Ishida (in preparation).
[8] K. Osanai, A. Okazawa, T. Nogami, T. Ishida, J. Am. Chem. Soc. (2006), doi:10.1021/ja065623c.
[9] A. Rising, Ber. 37 (1904) 43.
[10] D. Gallemann, P. Eyer, Biol. Chem. Hoppe-Seyler 374 (1993) 37.
[11] A.D. Becke, J. Chem. Phys. 98 (1993) 5648.
[12] C. Lee, W. Yang, R.G. Parr, Phys. Rev. B 37 (1998) 785.
[13] K. Inoue, H. Iwamura, J. Am. Chem. Soc. 113 (1991) 9803.
[14] K. Maruyama, Bull. Chem. Soc. Jpn. 37 (1964) 1013.
[15] O. Takizawa, Bull. Chem. Soc. Jpn. 49 (1976) 583.
[16] G. Kurokawa, T. Ishida, T. Nogami, Chem. Phys. Lett. 392 (2004) 74.
[17] (a) K. Mukai, H. Nagai, K. Ishizu, Bull. Chem. Soc. Jpn. 48 (1975) 2381;
(b) T. Ishida, H. Iwamura, J. Am. Chem. Soc. 113 (1991) 4238;
(c) H. Nishimaki, S. Mashiyama, M. Yasui, T. Nogami, T. Ishida, Chem. Mater. 18 (2006) 3602.
[18] (a) H. Iwamura, Adv. Phys. Org. Chem. 26 (1990) 179;
(b) A. Rajca, Chem. Rev. 94 (1994) 871;
(c) N. Mataga, Theor. Chim. Acta 10 (1967) 372;
(d) J.C. Longuet-Higgins, J. Chem. Phys. 18 (1950) 265.
[19] (a) H. Kumada, A. Sakane, N. Koga, H. Iwamura, J. Chem. Soc., Dalton Trans. (2000) 911;
(b) T. Shimada, T. Ishida, T. Nogami, T. Polyhedron 24 (2005) 2593.
[20] T. Ise, T. Ishida, D. Hashizume, F. Iwasaki, T. Nogami, Inorg. Chem. 42 (2003) 6106.



Scheme 1. Structural formulas.

$[\{Cu(emg)(Hemg)(ROH)\}_2\{Dy(hfac)_2(ROH)\}_2]$ (R = Me, Et; abbreviated as $[Dy_2Cu_2]$-R hereafter) as Dy analogs of $[Gd_2Cu_2]$. We found that $[Dy_2Cu_2]$-Me and $[Gd_2Cu_2]$ were completely isomorphous to each other. The corresponding polymer $[\{Cu(dmg)(Hdmg)\}_2\{Dy(hfac)_2(CH_3OH)\}_2]_n \cdot 2(MeOH)$ ($[Dy_2Cu_2]_n$) could also be prepared as fine polycrystalline solids, which is isomorphous to the known polymer, $[Gd_2Cu_2]_n$.

2. Experimental

After deprotonation of $[Cu(Hemg)_2]$ in basic media, the resultant anionic oxygen atoms were planned to be trapped with dysprosium(III) hexafluoroacetylacetonate $[Dy(hfac)_3]$ [19]. Practically the same procedure as the preparation of $[Gd_2Cu_2]$ by use of $[Dy(hfac)_3]$ in place of $[Gd(hfac)_3]$ gave $[\{Cu(emg)(Hemg)(ROH)\}_2\{Dy(hfac)_2(ROH)\}_2]$ ($[Dy_2Cu_2]$-Me and $[Dy_2Cu_2]$-Et) in 16% and 26% yields, respectively. Methanol and ethanol molecules from the reaction solvents were incorporated as an O-donor. Polymeric form $[\{Cu(dmg)(Hdmg)\}_2\{Dy(hfac)_2(CH_3OH)\}_2]_n$ was obtained from the reaction of $[Cu(Hdmg)_2]$ and $[Dy(hfac)_3]$ in methanol in 25% yield.

X-ray diffraction data of single crystals of $[Dy_2Cu_2]$-Me and $[Dy_2Cu_2]$-Et were collected on a Rigaku R-axis RAPID diffractometer with graphite monochromated Mo Kα ($\lambda = 0.71069$ Å) radiation at 90 K. The structures were directly solved and the parameters were refined in the CrystalStructure program package (version 3.5.1, Rigaku/MSC, The Woodlands, TX 77381, USA, 2003). Numerical absorption correction was used. All of the hydrogen atoms were located at the calculated position. Thermal displacement parameters were refined anisotropically for non-hydrogen atoms. Owing to the small size of the crystal of $[Dy_2Cu_2]_n$, only the cell parameters of $[Dy_2Cu_2]_n$ were determined. Selected crystallographic parameters are summarized in Table 1.

Magnetic susceptibilities of polycrystalline samples were measured on a Quantum Design MPMS SQUID magnetometer at an applied magnetic field of 500 Oe over a temperature range 1.8–100 K. The magnetic responses were corrected with diamagnetic blank data of the sample holder obtained separately. The diamagnetic contribution of the sample itself was estimated from Pascal's constant. Ac magnetic susceptibilities of polycrystalline samples were measured on a Quantum Design PPMS ac/dc magnetometer down to 1.8 K. Low-temperature magnetizations were measured by using a conventional inductive probe in pulsed magnetic fields, and the temperature was obtained as low as 0.5 K [20].

3. Results and discussion

3.1. Crystal structure analysis

Fig. 1a shows the molecular structure of $[Dy_2Cu_2]$-Me, which is isomorphous to $[Gd_2Cu_2]$ [18], as supported by

Table 1
Selected crystallographic data for $[Dy_2Cu_2]$-Me, $[Dy_2Cu_2]$-Et, and $[Dy_2Cu_2]_n$ together with the known Gd analogs

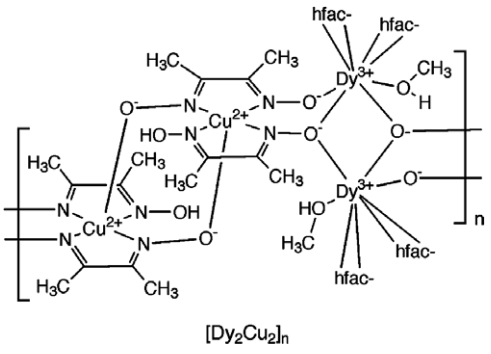
Compounds	$[Dy_2Cu_2]$-Me	$[Gd_2Cu_2]$	$[Dy_2Cu_2]$-Et	$[Dy_2Cu_2]_n$	$[Gd_2Cu_2]_n$
Formula	$C_{44}H_{52}Cu_2Dy_2F_{24}N_8O_{20}$	$C_{44}H_{52}Cu_2F_{24}Gd_2N_8O_{20}$	$C_{48}H_{62}Cu_2Dy_2F_{24}N_8O_{20}$	$C_{20}H_{22}CuF_{12}DyN_4O_{10}$	$C_{20}H_{22}CuF_{12}GdN_4O_{10}$
Habit	black block		black block	brown block	
Dimension (mm^3)	$0.8 \times 0.5 \times 0.1$		$0.4 \times 0.2 \times 0.1$	$0.2 \times 0.02 \times 0.01$	
T (K)	90	105	90	120	95
Crystal system	monoclinic	monoclinic	triclinic	triclinic	triclinic
Space group	$C2/c$	$C2/c$	$P\bar{1}$		$P\bar{1}$
a (Å)	26.231(8)	26.50(1)	13.211(5)	10.566	10.556(7)
b (Å)	11.947(3)	11.984(9)	15.005(7)	11.074	11.115(9)
c (Å)	23.541(9)	23.72(2)	17.632(7)	14.164	14.15(1)
α (°)	90	90	85.67(3)	71.529	71.78(6)
β (°)	115.772(7)°	116.10(4)	84.08(4)	75.831	75.76(6)
γ (°)	90	90	89.06(4)	84.974	84.77(6)
V (Å^3)	6644(4)	6762(7)	3466(3)	1524	1527(1)
Z	4	4	2		2
D_{calc} (g cm^{-3})	1.920	1.876	1.896		2.015
Unique data	4397		15379		
μ(Mo Kα) (mm^{-1})	2.998		2.876		
$R(F)$[a] ($I > 2\sigma(I)$)	0.0908		0.0723		
$R_w(F^2)$[b] (all data)	0.2088		0.0920		
Reference	this work	reference [18]	this work	this work	reference [18]

[a] $R = \sum||F_o| - |F_c||/\sum|F_o|$.
[b] $R_w = [\sum w(F_o^2 - F_c^2)^2 / \sum w(F_o^2)^2]^{1/2}$.

the cell parameters (Table 1). The Gd ions are octacoordinate and a methanol molecule is coordinated in place of an hfac ligand. A lost anion charge is compensated with an oximate oxygen atom (O3). A half of molecule is crystallographically independent and related with the other half by inversion symmetry. The Cu1 ion is coordinated with an additional methanol molecule (C22O10) as a cap. The Dy1–Dy1*, Dy1–Cu1, and Dy1*–Cu separations are 3.919(1), 3.918(2), and 4.730(2) Å, respectively, within a molecule. Though we can expect *cis–trans* isomerism in the [Cu(Hemg)(emg)] moiety, we actually observed solely the *trans*-isomer in the crystal. The ethyl groups in [Cu(Hemg)(emg)] are bent in the same direction with respect to the copper basal plane, and accordingly this steric hindrance disable to dimerize [Cu(Hemg)(emg)] like the starting material [Cu(Hdmg)$_2$] [21]. Instead, a methanol ligand from the solvent occupies the axial position.

Although the space group of [Dy$_2$Cu$_2$]-Et ($P\bar{1}$) (Fig. 1b) is different from that of [Dy$_2$Cu$_2$]-Me ($C2/c$) and accordingly the crystal packing motif is quite different, the core structure of [Dy$_2$Cu$_2$]-Et was practically the same as that of [Dy$_2$Cu$_2$]-Me (Fig. 1c). There are two independent molecules in a unit cell, each of which has an inversion center. The Dy1–Dy1*, Dy1–Cu1, and Dy1*–Cu separations are 3.9549(6), 3.988(1), and 4.699(1) Å, respectively, in a molecule (Fig. 1b) and 3.9380(5), 3.959(1), and 4.724(1) Å, respectively, in the other molecule (not shown). In sharp contrast to the case of [Dy$_2$Cu$_2$]-Me, we observed solely the *cis*-isomer of the [Cu(Hemg)(emg)] moiety in [Dy$_2$Cu$_2$]-Et.

The crystal structure of [Dy$_2$Cu$_2$]$_n$ could not be determined so far, owing to the small size of the crystals, but the cell parameter strongly suggests that [Dy$_2$Cu$_2$]$_n$ and [Gd$_2$Cu$_2$]$_n$ are isomorphous (Table 1). The polymeric complex [Dy$_2$Cu$_2$]$_n$ can be regarded as a polymer form of [Dy$_2$Cu$_2$]-R, just like the Gd version ([Gd$_2$Cu$_2$]$_n$ and [Gd$_2$Cu$_2$]) previously characterized [18]. As the polymer [Gd$_2$Cu$_2$]$_n$–monomer [Gd$_2$Cu$_2$] system shows [18], the polymerization linkage consists of a copper(II)–O (axial) bond formation as a local [Cu(dmg)$_2$]$_2$ dimerization in the absence of alcohol molecules at the axial position of the copper(II) ion. Thus, the proposed structure of [Dy$_2$Cu$_2$]$_n$ is shown below. It should be noted that ferromagnetic coupling takes place between the copper(II) spins within the dimers [18,21].



[Dy$_2$Cu$_2$]$_n$

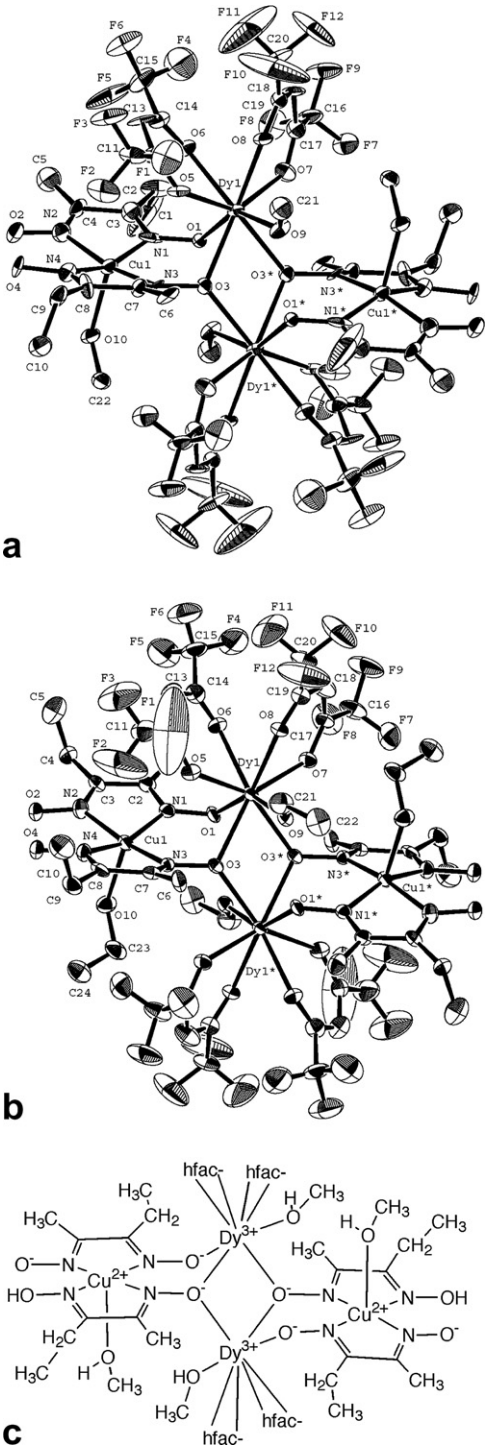


Fig. 1. Ortep drawings of [{Cu(emg)(Hemg)(ROH)}$_2${Dy(hfac)$_2$(ROH)}$_2$] ((a) [Dy$_2$Cu$_2$]-Me for R = Me; (b) [Dy$_2$Cu$_2$]-Et for R = Et) with the thermal ellipsoids at the 50% probability level. Hydrogen atoms are omitted. One of the two crystallographically independent molecules is shown for [Dy$_2$Cu$_2$]-Et. (c) Structural formula of [Dy$_2$Cu$_2$]-Me.

3.2. Magnetic properties

The dc magnetic properties of [Dy$_2$Cu$_2$]-Me were investigated down to 1.8 K (Fig. 2a). The theoretical high-temperature limit of the $\chi_{mol}T$ value should be

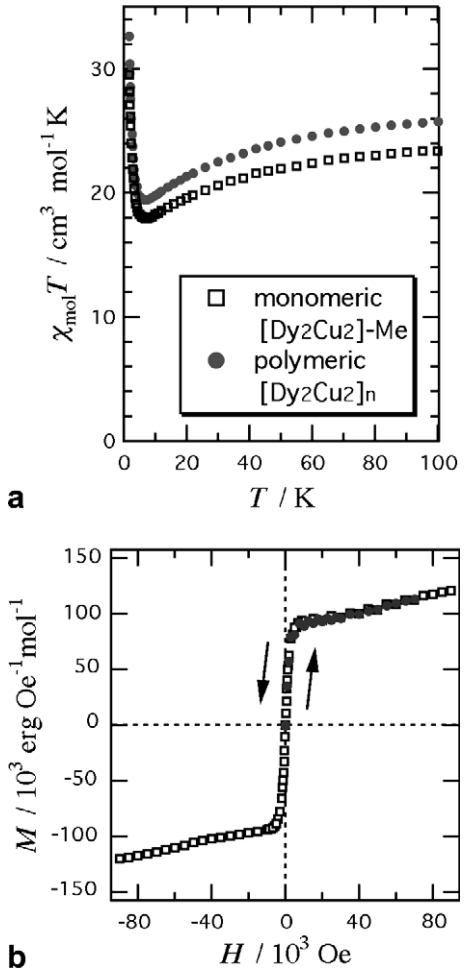


Fig. 2. (a) Temperature dependence of the $\chi_{mol}T$ products for randomly oriented polycrystalline samples of $[Dy_2Cu_2]$-Me and $[Dy_2Cu_2]_n$ measured at 500 Oe. The samples were fixed with a small amount of mineral oil. (b) Magnetization curves for polycrystalline samples of $[Dy_2Cu_2]$-Me (squares) and $[Dy_2Cu_2]_n$ (dark circles) measured at 1.8 K. The field scan rate was 65 Oe s^{-1}.

28.8 cm^3 K mol^{-1} for a Dy_2Cu_2 unit with $J_{Dy} = 15/2$, $g_J = 4/3$, and $S_{Cu} = 1/2$, $g_{Cu} = 2.0$. As Fig. 2a shows, the experimental $\chi_{mol}T$ value (23.4 cm^3 K mol^{-1}) at 100 K are compatible with the calculated one, and the Dy_2Cu_2 spin quantity was verified. Upon cooling, the $\chi_{mol}T$ value once decreased and turned to increase like the $[Gd_2Cu_2]$ case [18]. The decrease of the $\chi_{mol}T$ is presumably caused by the strong anisotropy of Dy ions and the sizable energy gap (see below) between the ground ferrimagnetic state and the excited ferromagnetic state. The sharp increase in lower temperature is due to the evolution of the large ferrimagnetic moment: $\sim 18\mu_B$/$[Dy_2Cu_2]$. The antiferromagnetic coupling between Dy and Cu ions is confirmed by the high-field magnetization measurements shown below. The magnetic couplings between Dy and Cu ions are dominant compared to those between Dy ions, and therefore the present tetranuclear clusters can be regarded as antiferromagnetically correlated four-centered macrocycles, leading to the Dy magnetic moments aligned parallel as schematized like [Cu(↓)Dy(↑)Cu(↓)Dy(↑)].

There have been several reports on the ferromagnetic coupling between Ln^{III} ($4f^n$; $n \geqslant 7$) and Cu^{II} ions so far [22–27], but it has also been pointed out that the coupling is susceptible to the geometry, especially, to the bent structure of the Ln–O–N–Cu bridge [16,28,29]. In the present complex, the torsion angles of Ln–O–N–Cu are considerably large (−60.3(6), 55.1(5), −95.1(4)° in $[Gd_2Cu_2]$ [18]; −58.6(15), 57.0(13), and −94.5(13) in $[Dy_2Cu_2]$-Me). In all cases of our study, the twisted Ln–O–N–Cu bridges play the role of an antiferromagnetic coupler between Ln^{III} and Cu^{II}.

Kahn and co-workers proposed that the ferromagnetic couplings between Ln^{III} and Cu^{II} ions can be explained as follows [27]: when the number of 4f electrons is more than seven, the orbital and spin momenta of Ln^{III} are parallel, and the ferromagnetic spin coupling gives rise to an overall ferromagnetic interaction. In our case, $[Gd_2Cu_2]$ involves the accidentally antiferromagnetic spin coupling between Gd^{III} and Cu^{II} [18], and therefore, in the isomorphous Dy^{III} ($4f^9$) analogue, the spin coupling of Dy^{III} and Cu^{II} is also antiferromagnetic, leading to the overall antiferromagnetic interaction. We have already reported that the pentanuclear $[Gd_4Cu]$ rectangle showed antiferromagnetic coupling between Gd^{III} and Cu^{II} [16,17], and recently we found that the isomorphous $[Tb_4Cu]$ and $[Dy_4Cu]$ rectangles also exhibited antiferromagnetic couplings between Ln^{III} and Cu^{II} [30]. Thus, the Ln^{III}–Cu^{II} interactions have the same sign as that of Gd^{III}–Cu^{II} for the heavier Ln^{III} ions than Gd^{III}, especially for Tb^{III} and Dy^{III}.

We found a stepwise saturation behavior in the M–H curve for $[Dy_2Cu_2]$-Me (Fig. 2b), supporting the ground ferrimagnetic state. The magnetization showed a plateau in 1–4 T and increased again with an increase of the applied field. A plot of dM/dH versus H shows a broad peak around 5 T. The theoretical saturation value should be 1.22×10^5 erg Oe^{-1} mol^{-1} and the experimental value was 1.20×10^5 erg Oe^{-1} mol^{-1} at 9 T. The plateau is located at ca. 1.00×10^5 erg Oe^{-1} mol^{-1}. Therefore, the step is assigned to be a 4-μ_B jump due to the reorientation of two copper(II) spins. The energy-level cross between the ferrimagnetic [Cu(↓)Dy(↑)Cu(↓)Dy(↑)] and the ferromagnetic [Cu(↑)Dy(↑)Cu(↑)Dy(↑)] states occurs here with an aid of the Zeeman energy. The zero field splitting between these two states is evaluated to be 27 K. It is much higher than that observed in the previous $[Dy_2Cu]$ complex [5]. It should be noticed that the ferromagnetic [Cu(↑)Dy(↑)-Cu(↑)Dy(↑)] state is not the first excited state and other states such as [Cu(↑)Dy(↑)Cu(↑)Dy(↓)] are located in between these two states. It means that the energy barrier is much smaller than 27 K.

We performed the χ_{mol}–T and M–H measurements on $[Dy_2Cu_2]_n$ under the same conditions, and clarified that $[Dy_2Cu_2]_n$ exhibited behavior quite similar to that of $[Dy_2Cu_2]$-Me. A $\chi_{mol}T$ minimum around 7 K and an

upsurge on further cooling were found in the $\chi_{mol}T$ versus T plot (Fig. 2a; dark circles). The M–H curve of $[Dy_2Cu_2]_n$ measured at 1.8 K (Fig. 2b; dark circles) was practically identical with that of $[Dy_2Cu_2]$-Me. These findings indicate that the polymer form can be described as an only slightly perturbed system from the monomeric one; i.e., the polymerization linkage Cu–N–O–Cu transmits very small magnetic interaction.

The magnetization jump around 5 T was reproduced in the low-temperature magnetization curve at 0.5 K by means of a pulsed-field technique (Fig. 3a). The jump becomes sharper in lower temperatures because of the suppression of thermal excitations. The magnetization also exhibits a relatively narrow hysteresis within ±0.4 T (Fig. 3b). At beginning, the ferrimagnetic moments of clusters take both parallel and anti-parallel directions to the external magnetic field. The latter group should show the reversal to the parallel at level crossing points. The crossing fields are located in the low field region because the Zeeman energy difference between the ground [Cu(↓)Dy(↑)-Cu(↓)Dy(↑)] state and the excited state [Cu(↑)Dy(↑)-Cu(↑)Dy(↓)] or [Cu(↓)Dy(↑)Cu(↓)Dy(↓)] are large. It is the similar situation as we discussed in the $[Dy_2Cu]$ SMM (see Fig. 3(c) in Ref. [5]). In a small field region, the dM/dH versus H plot (Fig. 3b) clarifies mainly three fine magnetization jumps. Usually this behavior is related with quantum tunneling of magnetization, which is characteristic of a SMM. In the adiabatic limit, the peak positions should be independent of a sweeping rate; however, the small dependence was found here. The reason might be the non-adiabatic feature for the very fast sweeping rate or the mixture of the residual thermal relaxation. The further investigation is needed with a single crystal or oriented crystals to clarify this point.

It is also found that hysteresis curves are asymmetric; in the negative field each step was shifted with respective to the positive one, indicating the presence of a dipolar-coupling bias that affects the field at which magnetization tunneling takes place.

We measured the ac magnetic susceptibility of $[Dy_2Cu_2]$-Me (Fig. 4a). With an increase of frequency, a χ'_{ac} decrease and a concomitant χ''_{ac} increase were clearly observed. We confirmed that the magnetization relaxation became relatively slow, compared with the timescale of these

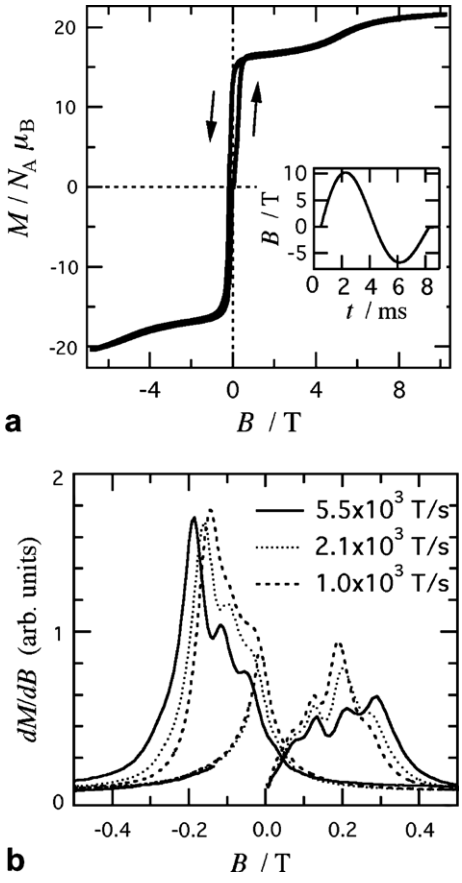


Fig. 3. (a) Magnetization curve of $[Dy_2Cu_2]_n$ measured at 0.5 K. Inset: a field-sweep sequence as a function of time. (b) Differential magnetization curves as a function of a field sweeping rate at 0.5 K.

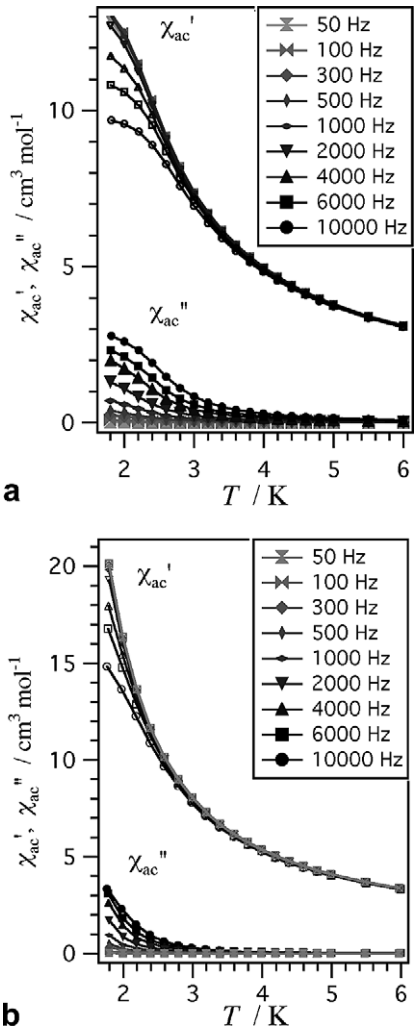


Fig. 4. Ac magnetic susceptibilities (χ'_{ac} and χ''_{ac} for in-phase and out-of-phase parts, respectively) for (a) $[Dy_2Cu_2]$-Me and (b) $[Dy_2Cu_2]_n$ as a function of temperature and frequency. The amplitude of the applied ac magnetic field was 5 Oe.

experiments. However, the χ''_{ac} peak could not be observed above 1.8 K in our apparatus and the activation energy of the magnetization reorientation could not be estimated. We assume that the blocking temperature would be lower than 1.8 K, because no hysteresis was observed in the *M–H* curve measured with a relatively slow field-sweep rate (65 Oe s^{-1}) (Fig. 2b).

Under the same conditions, we measured the ac magnetic susceptibility of $[Dy_2Cu_2]_n$ (Fig. 4b). Similarly, we could observe a χ''_{ac} increase with an increase of frequency. The increase of χ''_{ac} is smaller than that of $[Dy_2Cu_2]$-Me, suggesting that the reorientation rate of $[Dy_2Cu_2]_n$ is faster than that of $[Dy_2Cu_2]$-Me. The polymeric form gives rise to disadvantage in SMM characteristics, which may be caused by acceleration of relaxation due to the presence of spins nearby. On the other hand, Miyasaka and co-workers have reported that the energy barrier for magnetization reorientation of the single-chain magnet (SCM) was larger than that of the precursory SMM for the $[Mn_2Ni]$ and $[Mn_2Fe]$ systems [31]. Here we point out that the present system contains the $S = 1/2$ spins, which may work as the nucleation center of the propagating correlated reversal in SCM. The ESR measurement may be useful to clarify this issue, which shows the collective mode in $[Mn_2Ni]$ system [32].

4. Conclusion

We prepared tetranuclear heterometallic cycles $[Dy_2Cu_2]$-Me and $[Dy_2Cu_2]$-Et, and their polymeric form $[Dy_2Cu_2]_n$. They have isostructures of $[Gd_2Cu_2]$ and $[Gd_2Cu_2]_n$, respectively, which have been fully characterized previously [18]. We clarified that the $[Dy_2Cu_2]$ motif possessed antiferromagnetic coupling between Dy and Cu ions, leading to the ferrimagnetic ground state. Ac magnetic susceptibility measurements of $[Dy_2Cu_2]$-Me and $[Dy_2Cu_2]_n$ exhibited the χ''_{ac} increase with an increase of frequency, indicating the slow magnetization reorientation. Actually, hysteresis curves accompanied by magnetization jumps could be observed at 0.5 K for $[Dy_2Cu_2]_n$ by means of a pulsed-field technique. Their magnetic properties and quantum tunneling mechanism on the single-molecule and single-chain levels are of great interest. Our study demonstrates that the 4f–3d heterometallic approach is a very promising pathway to SMMs and SCMs. Studies on terbium(III) analogs, $[Tb_2Cu_2]$ and $[Tb_2Cu_2]_n$, are currently underway.

5. Supplementary material

CCDC 616904 and 616905 contain the supplementary crystallographic data for $[Dy_2Cu_2]$-Me and $[Dy_2Cu_2]$-Et. These data can be obtained free of charge via http://www.ccdc.cam.ac.uk/conts/retrieving.html, or from the Cambridge Crystallographic Data Centre, 12 Union Road, Cambridge CB2 1EZ, UK; fax: (+44) 1223-336-033; or e-mail: deposit@ccdc.cam.ac.uk.

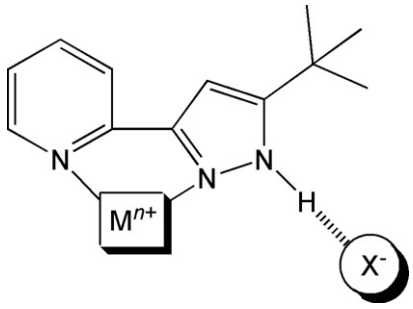
Acknowledgments

This work was supported by Grants-in-Aid for Scientific Research (Nos. 15073101, 16550121, and 15550115) from the Ministry of Education, Culture, Sports, Science and Technology, Japan. A part of this work was performed under the inter-university cooperative research program of the Institute for Materials Research, Tohoku University.

References

[1] O. Kahn, Molecular Magnetism, VCH, New York, 1993.
[2] G. Christou, D. Gatteschi, D.N. Hendrickson, R. Sessoli, MRS Bull. 25 (2000) 66.
[3] F. Lloret, R. Ruiz, B. Cervera, I. Castro, M. Julve, J. Faus, J.A. Real, F. Sapiña, Y. Journaux, J.C. Colin, M. Verdaguer, J. Chem. Soc., Chem. Commun. (1994) 2615.
[4] R. Clérac, H. Miyasaka, M. Yamashita, C. Coulon, J. Am. Chem. Soc. 124 (2002) 12837.
[5] F. Mori, T. Nyui, T. Ishida, T. Nogami, K.-Y. Choi, H. Nojiri, J. Am. Chem. Soc. 128 (2006) 1440.
[6] F. Mori, T. Ishida, T. Nogami, Polyhedron 24 (2005) 2588.
[7] S. Osa, T. Kido, N. Matsumoto, N. Re, A. Pochaba, J. Mrozinski, J. Am. Chem. Soc. 126 (2004) 420.
[8] F.C.M. Zaleski, E.C. Depperman, J.W. Kampf, M.L. Lirk, V.L. Pecoraro, Angew. Chem. Int. Ed. 43 (2004) 3912.
[9] (a) A. Mishra, W. Wernsdorfer, K.A. Abboud, G. Christou, J. Am. Chem. Soc. 126 (2004) 15648;
(b) A. Mishra, W. Wernsdorfer, S. Parsons, G. Christou, E.K. Brechin, Chem. Commun. (2005) 2086.
[10] (a) N. Ishikawa, M. Sugita, T. Ishikawa, S.-y. Koshihara, Y. Kaizu, J. Am. Chem. Soc. 125 (2003) 8694;
(b) N. Ishikawa, M. Sugita, W. Wernsdorfer, J. Am. Chem. Soc. 127 (2005) 3650;
(c) M. Sugita, N. Ishikawa, T. Ishikawa, S.-y. Koshihara, Y. Kaizu, Inorg. Chem. 45 (2006) 1299.
[11] (a) J.P. Costes, F. Dahan, W. Wernsdorfer, Inorg. Chem. 45 (2006) 5;
(b) J.P. Costes, M. Auchel, F. Dahan, V. Peyrou, S. Shova, W. Wernsdorfer, Inorg. Chem. 45 (2006) 1924.
[12] J. Tang, I. Hewitt, N.T. Madhu, G. Chastanet, W. Wernsdorfer, C.E. Ansen, C. Benelli, R. Sessoli, A.K. Powell, Angew. Chem. Int. Ed. 45 (2006) 1729.
[13] (a) K. Bernot, L. Bogani, A. Caneschi, D. Gatteschi, R. Sessoli, J. Am. Chem. Soc. 128 (2006) 7947;
(b) L. Bogani, C. Sangregorio, R. Sessoli, D. Gatteschi, Angew. Chem. Int. Ed. 44 (2005) 5817.
[14] (a) C. Aronica, G. Pilet, G. Chastanet, W. Wernsdorfer, J.-F. Jacquot, D. Luneau, Angew. Chem. Int. Ed. 45 (2006) 4659;
(b) F. He, M.-L. Tong, X.-M. Chen, Inorg. Chem. 44 (2005) 8285.
[15] S. Ueki, T. Ishida, T. Nogami, M. Tamura, Mol. Cryst. Liq. Cryst. 455 (2006) 129.
[16] Y. Kobayashi, S. Ueki, T. Ishida, T. Nogami, Chem. Phys. Lett. 378 (2003) 337.
[17] S. Ueki, M. Sahlan, T. Ishida, T. Nogami, Synth. Met. 154 (2005) 217.
[18] S. Ueki, Y. Kobayashi, T. Ishida, T. Nogami, Chem. Commun. (2005) 5223.
[19] M.F. Richardson, W.F. Wagner, D.E. Sands, J. Inorg. Nucl. Chem. 30 (1968) 1275.
[20] H. Nojiri, T. Taniguchi, Y. Ajiro, A. Müller, B. Brabara, Physica B 346–347 (2004) 216.
[21] J.F. Villa, W.E. Hatfield, J. Chem. Phys. 55 (1971) 4758.
[22] A. Bencini, C. Benelli, A. Caneschi, R.L. Carlin, A. Dei, D. Gatteschi, J. Am. Chem. Soc. 107 (1985) 8128.
[23] N. Matsumoto, M. Sakamoto, H. Tamaki, H. Okawa, S. Kida, Chem. Lett. (1990) 853.

[24] A.J. Blake, P.E.Y. Milne, P. Thornton, R.E.P. Winpenny, Angew. Chem., Int. Ed. Engl. 30 (1991) 1139.
[25] O. Guillow, P. Bergerat, O. Kahn, E. Bakalbassis, K. Boubekeur, P. Batail, M. Guillot, Inorg. Chem. 31 (1992) 110.
[26] M. Andruh, I. Ramade, E. Codjovi, O. Guillou, O. Kahn, J.C. Trombe, J. Am. Chem. Soc. 115 (1993) 1822.
[27] M.L. Kahn, C. Mathonière, O. Kahn, Inorg. Chem. 38 (1999) 3692.
[28] J.-P. Costes, F. Dahan, A. Dupuis, J.-P. Laurent, Inorg. Chem. 39 (2000) 169.
[29] J.-P. Costes, F. Dahan, A. Dupuis, Inorg. Chem. 39 (2000) 5994.
[30] S. Ueki, T. Ishida, T. Nogami, K.-Y. Choi, H. Nojiri, Inorg. Chem., submitted for publication.
[31] (a) M. Ferbinteanu, H. Miyasaka, W. Wernsdorfer, K. Nakata, K.-i. Sugiura, M. Yamashita, C. Coulon, R. Clérac, J. Am. Chem. Soc. 127 (2005) 3090;
(b) H. Miyasaka, T. Nezu, K. Sugimoto, K.-i. Sugiura, M. Yamashita, R. Clérac, Chem. Eur. J. 11 (2005) 1592.
[32] Y. Oshima, H. Nojiri, K. Asakura, T. Sakai, M. Yamashita, H. Miyasaka, Phys. Rev. B 73 (2006) 214435.



Scheme 1. The ditopic nature of ligand L.

supramolecular polymetallic cluster structures [6]. We report here a new tetrameric copper complex of one such ligand, 3{5}-(pyrid-2-yl)-5{3}-*tert*-butylpyrazole ('L', Scheme 1), namely $[Cu_4(\mu_3\text{-}OH)_4(L)_4](ClO_4)_4 \cdot xCH_2Cl_2$ ($\mathbf{1} \cdot xCH_2Cl_2$). The only metal complexes of this ligand to have been reported previously are platinum metal compounds, designed for catalysis [7] or electroluminescence [8] applications, and a pair of isostructural metal carboxylate coordination networks [9].

2. Experimental

5{3}-*tert*-Butyl-3{5}-(pyrid-2-yl)-1*H*-pyrazole (L) was synthesized using a previously reported procedure [10]. Metal salts were obtained commercially while all solvents were used without further purification. *Caution*: Although no difficulties were experienced in handling $\mathbf{1} \cdot xCH_2Cl_2$, metal-organic perchlorates are potentially explosive and should be handled carefully in small quantities.

2.1. Synthesis

$Cu(ClO_4)_2 \cdot 6H_2O$ (400 mg, 1.08 mmol) and 5-*tert*-butyl-3-(pyrid-2-yl)-1*H*-pyrazole (L) (220 mg, 1.08 mmol) were added to 1 equiv. of solid NaOH (86 mg, 1.08 mmol) in 30 cm^3 MeOH and stirred for 24 h. On filtration the green slightly cloudy solution was left to evaporate to dryness. On redissolution in CH_2Cl_2 followed by slow Et_2O diffusion, aqua blue block-like crystals of $\mathbf{1} \cdot xCH_2Cl_2$ were obtained in 20% yield (346 mg). Drying *in vacuo* led to crystal decomposition, affording a material containing 1 mole equiv. of solvent by microanalysis and by NMR. *Anal.* Calc. for $C_{48}H_{60}N_{12}O_{20}Cl_4Cu_4 \cdot CH_2Cl_2$: C, 36.55; H, 4.13; N, 10.44. Found: C, 36.85; H, 4.10; N, 10.55%. Field desorption mass spectrum: *m/z* 627 $[^{63}Cu_4L_4(^{35}ClO_4)_2]^{2+}$, 663 $[^{63}CuL_3\text{–}H]^+$, 527 $[^{63}Cu_4L_4\text{–}2H]^{2+}$, 495 $[^{63}Cu_3L_4\text{–}2H]^{2+}$, 464 $[^{63}Cu_2L_4\text{–}2H]^{2+}$. Selected IR (Nujol): 3485(b), 3236(b), 3131(m), 2725(m), 2670(m), 1619(m), 1574(m), 1561(m), 1303(m), 1269(m), 1218(w), 1204(w), 1141(m), 1113(m), 1041(m), 1000(w), 983(w), 925(w), 828(w), 787(w), 776(w), 722(m) cm^{-1}. ^1H NMR (CD_3NO_2, 298 K): δ, ppm 2.09 (s, 36H, $C(CH_3)_2$), 5.6 (2H, CH_2Cl_2), 13.8 (4H, Py H^4), 25.9 (4H, N*H*), 39.2, 40.2, 43.6 (all 4H, Py H^3 and H^5, and Pz H^4), 119.5 (4H, Py H^6).

2.2. X-ray crystallographic studies

All diffraction measurements were carried out on a Bruker-Nonius Apex X8 diffractometer utilizing a FR591 5 kW X-ray generator, Mo Kα rotating anode X-ray source ($\lambda = 0.71073$) and an Apex II detector. Temperature control was achieved using Oxford Cryosystems 600 and Oxford Helix cryostats to obtain temperatures of 150 and 30 K, respectively. The asymmetric unit of $\mathbf{1} \cdot xCH_2Cl_2$ at 150 and 30 K contains one $[Cu_4(\mu_3\text{-}OH)_4(L)_4](ClO_4)_4$ formula unit, lying on a general position, and four or five partial dichloromethane molecules with occupancies of 0.5 or less. Both structures were solved using direct methods (SHELXS86 [11]) while each of the early refinement models were obtained by least-squares refinement on F^2 (SHELX97 [12]). Figures were produced using XSEED [13], which incorporates POVRAY [14]. Experimental data for the two structure determinations are summarized in Table 1.

The structure of $\mathbf{1} \cdot xCH_2Cl_2$ at 150 K exhibited extensive disorder which was modeled as follows. Three of the four ClO_4^- anions in the asymmetric unit were modeled over two sites in a 50:50 occupancy (labeled A and B). The restraints Cl–O = 1.45(2) and O···O = 2.38(4) Å were applied to these disordered groups. Two of the *tert*-butyl groups of the L ligands were also disordered over two sites and again a 50:50 occupancy proved a suitable model for such disorder. The restraints C–C = 1.55(2) and

Table 1
Experimental data for the crystal structure determinations of $\mathbf{1} \cdot xCH_2Cl_2$

	150 K ($x = 1.75$)	30 K ($x = 1.90$)
Formula	$C_{49.75}H_{67.5}Cl_{7.5}N_{12}O_{20}Cu_4$	$C_{49.9}H_{67.8}Cl_{7.8}N_{12}O_{20}Cu_4$
M_w	1673.69	1686.43
Crystal size (mm)	0.50 × 0.40 × 0.30	0.40 × 0.25 × 0.20
Crystal system	orthorhombic	orthorhombic
Space group	$Pna2_1$	$Pna2_1$
Unit cell dimensions		
a (Å)	15.637(3)	15.4390(12)
b (Å)	17.253(4)	17.0837(12)
c (Å)	26.832(5)	26.5801(18)
V (Å^3)	7239(3)	7010.6(9)
Z	4	4
D_{calc} (g cm^{-3})	1.555	1.597
μ, Mo Kα (mm^{-1})	0.153	0.157
T (K)	150(2)	30(2)
λ (Å)	0.71073	0.71073
Data collected	142 156	43 830
$2\theta_{max}$ (°), completeness (%)	55.0, 99.9	56.6, 99.5
Unique data (R_{int})	16 527 (0.036)	16 532 (0.082)
Observed data [$I > 2\sigma(I)$]	14 375	9904
Parameters/restraints	898/93	866/73
R_1 [$I > 2\sigma(I)$][a], wR_2 [all data][b]	0.042, 0.129	0.067/0.174
S	1.067	1.010
$\Delta\rho$ (maximum/minimum) (e Å^{-3})	0.90/−0.41	1.18/−0.65

1,3-C···C = 2.55(4) Å were used for these moieties. Five partial CH_2Cl_2 solvent molecules also occupy the asymmetric unit, two that are half-occupied and three with occupancies of 0.25. The C–Cl bond lengths in these moieties were all restrained to 1.75(2) Å. All wholly occupied non-H atoms, plus Cl atoms with occupancy $\geqslant 0.5$, were refined anisotropically. No H atoms could be found in the difference map, so these were placed in calculated positions and refined using a riding model.

The structure at 30 K exhibits less disorder than at 150 K. Just two ClO_4^- anions and one *t*-Bu group are now disordered, while five partial CH_2Cl_2 solvent molecules were also located, showing somewhat different positions and occupancies from those at 150 K. The disordered *tert*-butyl group was modeled over two sites using a 50:50 occupancy model. One of the disordered ClO_4^- anions was modeled over two orientations, sharing a common Cl atom, with a 50:50 occupancy, while the second disordered anion was refined over three sites with a 40:30:30 occupancy distribution. The same restraints used at 150 K were applied to all these disordered groups, while other details of the 30 K refinement were also the same as at the higher temperature.

2.3. Other measurements

Elemental analysis was carried out at the University of Leeds School of Chemistry microanalytical service. Infra red spectrum collected as a Nujol mull pressed between NaCl plates in a 600–4000 cm^{-1} frequency range using an Avatar 360 spectrophotometer. Magnetic susceptibility measurements were obtained using a Quantum Design SQUID magnetometer in an applied field of 1000 G. Diamagnetic corrections were estimated from Pascal's constants [15]. Paramagnetic ^1H NMR was carried out using a Bruker ARX 250 MHz instrument, operating at 250.13 MHz. X-band EPR spectra were obtained with a Bruker EMX spectrometer fitted with an ER4119HS resonator and ER4131VT cryostat.

3. Results

Reaction of L [10] with stoichiometric amounts of $Cu(ClO_4)_2 \cdot 6H_2O$ and NaOH in MeOH yielded a blue solution, which was evaporated to dryness. Re-dissolution of the solid residue in the minimum volume of CH_2Cl_2, and slow diffusion of Et_2O vapour into the filtered solution, gives rise to the tetrameric cubane $[Cu_4(\mu_3\text{-}OH)_4(L)_4](ClO_4)_4 \cdot xCH_2Cl_2$ (**1** · xCH_2Cl_2) in 20% recrystallised yield. The crystallographic studies described below implied that x varies between 1.75 and 1.9 in the crystalline material. However, the crystals decompose upon drying *in vacuo*, the resultant powder analysing as the mono-dichloromethane solvate (*i.e.* $x = 1$). The presence of CH_2Cl_2 in the dried material was confirmed by ^1H NMR spectroscopy in CD_3NO_2, which showed a clear singlet peak at 5.6 ppm. Six other contact-shifted peaks of approximately equal integral, and one peak in the diamagnetic region integrating to 9H with respect to the others, were also present in the spectrum. This is the number expected for a single metal-bound L environment, if the pyrazole N–H group is included. The X-band EPR spectrum of solid **1** · xCH_2Cl_2 at 100 K consisted of a single isotropic signal centred at $g = 2.08$, with no detectable half-field resonance.

The room temperature $\chi_m T$ value of 1.66 $cm^3\,mol^{-1}$ K for **1** · xCH_2Cl_2 is that expected from four non-interacting copper(II) centres with a reasonable g value of 2.1–2.2. This value stays essentially constant upon cooling to 100 K, but decreases gradually on further cooling to 1.35 $cm^3\,mol^{-1}$ K at 30 K (Fig. 1). Below this temperature $\chi_m T$ plateaus again at this value, before finally decreasing slightly again below 15 K. The data above 30 K could be well reproduced by treating the cubane core as a pair of non-interacting dimers, through the Bleaney Bowers equation [15] (Fig. 2, $J' = 0$). This afforded the parameters $J = -5.2(1)\ cm^{-1}$ and $g = 2.14(1)$ for the Hamiltonian $H = -2J(S_1 \cdot S_2)$, with a correlation coefficient of 0.980.

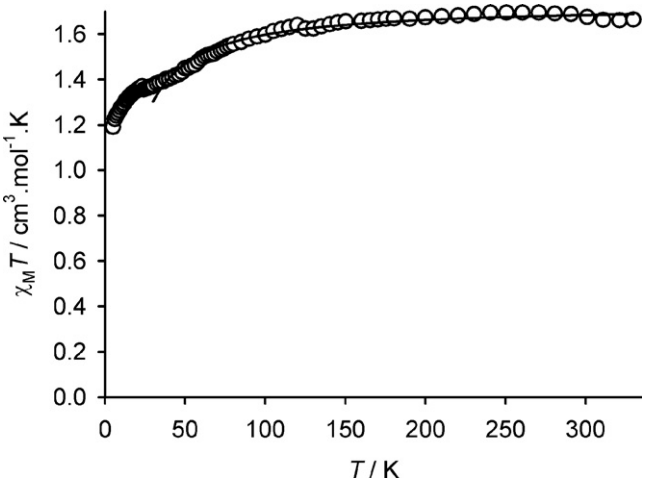


Fig. 1. Observed magnetic susceptibility data (circles) from **1** in the 4–300 K temperature range in a field of 1000 G, and the fit of the data above 30 K to the Bleaney Bowers equation for two dicopper(II) dimers. See text for fitting parameters.

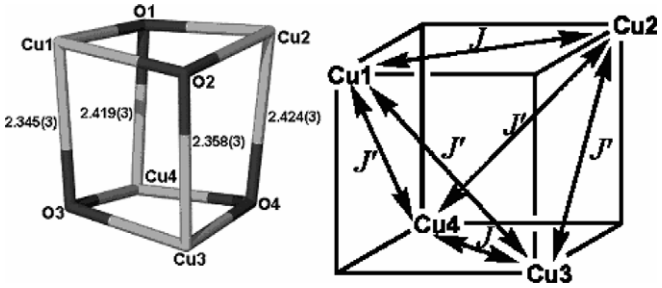


Fig. 2. (left) Cu–O distances (Å) observed in **1** at 150 K illustrating the axial elongation of the distorted cubane along the *z*-axis. Other relevant metric parameters in the cluster core are given in Table 1. (right) Schematic of model used to fit magnetic susceptibility data obtained from **1**.

This approach was necessary because J and J' correlated strongly when refined simultaneously (using the equation in [16]), and is reasonable because the crystal structure of the compound implies that $J \gg J'$ (see below). A paramagnetic impurity term in the fitting equation refined to zero, while no TIP contribution was included. Data below 30 K could not be modeled using the Bleaney Bowers equation, or any other Hamiltonian consistent with the crystal structure, since they all predict an $S = 0$ magnetic ground state for the complex and a steady decrease in $\chi_m T$ towards zero below 30 K, contrary to the observation. Incorporation of a mean field correction into our equations, to model intermolecular interactions [15], was similarly unsuccessful at treating the low-temperature data.

The crystal structure of $\mathbf{1} \cdot x\mathrm{CH_2Cl_2}$ was determined at both 150 K and 30 K, in order to investigate any structural basis for the anomalous low-temperature magnetic behaviour of the compound. It was necessary to use different crystals for these two analyses, which proved to have slightly different solvent contents ($x = 1.75$ at 150 K, $x = 1.90$ at 30 K). The crystals are isostructural at the two temperatures, in the orthorhombic space group

Table 2
Selected bond lengths (Å) and angles (°) for $\mathbf{1} \cdot x\mathrm{CH_2Cl_2}$

	150 K	30 K		150 K	30 K
Cu1–O1	1.943(3)	1.928(5)	Cu3–O2	2.358(3)	2.328(5)
Cu1–O2	1.995(3)	1.993(6)	Cu3–O3	1.953(3)	1.943(5)
Cu1–O3	2.345(3)	2.316(6)	Cu3–O4	1.966(3)	1.969(5)
Cu1–N1	2.005(4)	1.995(6)	Cu3–N7	2.023(5)	2.030(7)
Cu1–N2	2.008(4)	1.989(6)	Cu3–N8	2.015(4)	1.987(7)
Cu2–O1	1.954(3)	1.955(5)	Cu4–O1	2.419(3)	2.407(5)
Cu2–O2	1.970(3)	1.961(5)	Cu4–O3	1.991(3)	1.974(5)
Cu2–O4	2.424(3)	2.418(6)	Cu4–O4	1.962(3)	1.949(6)
Cu2–N4	2.005(4)	1.993(7)	Cu4–N10	2.015(4)	2.013(7)
Cu2–N5	1.991(4)	1.974(7)	Cu4–N11	2.010(4)	1.986(7)
			Cu4–O19A/B/C[i]	2.513(11)/2.596(9)	2.48(2)/2.63(3)/2.51(2)
Cu1···Cu2	2.9853(9)	2.9875(11)	Cu2···Cu3	3.2838(9)	3.2581(14)
Cu1···Cu3	3.2897(9)	3.2560(14)	Cu2···Cu4	3.3025(9)	3.2746(13)
Cu1···Cu4	3.3153(9)	3.2838(13)	Cu3···Cu4	2.9489(8)	2.9367(11)
O1–Cu1–O2	80.17(13)	79.9(2)	O2–Cu3–O3	81.13(13)	81.4(2)
O1–Cu1–O3	81.92(12)	82.29(19)	O2–Cu3–O4	83.21(13)	83.7(2)
O1–Cu1–N1	177.85(16)	177.1(2)	O2–Cu3–N7	98.49(16)	99.3(3)
O1–Cu1–N2	99.67(14)	99.0(2)	O2–Cu3–N8	108.91(15)	109.1(2)
O2–Cu1–O3	80.64(12)	80.67(19)	O3–Cu3–O4	82.56(12)	82.34(19)
O2–Cu1–N1	98.75(15)	98.8(2)	O3–Cu3–N7	177.35(17)	177.3(3)
O2–Cu1–N2	164.09(16)	164.0(2)	O3–Cu3–N8	102.07(16)	102.1(3)
O3–Cu1–N1	99.77(14)	100.1(3)	O4–Cu3–N7	94.79(17)	95.1(3)
O3–Cu1–N2	115.18(15)	115.2(2)	O4–Cu3–N8	167.46(17)	166.8(3)
N1–Cu1–N2	80.85(16)	81.6(3)	N7–Cu3–N8	80.54(17)	80.2(3)
O1–Cu2–O2	80.52(14)	80.0(2)	O1–Cu4–O3	79.10(12)	79.0(2)
O1–Cu2–O4	82.08(12)	82.5(2)	O1–Cu4–O4	82.05(13)	82.9(2)
O1–Cu2–N4	97.77(15)	97.5(2)	O1–Cu4–N10	91.94(14)	91.5(2)
O1–Cu2–N5	169.70(17)	169.9(3)	O1–Cu4–N11	104.28(16)	103.9(3)
O2–Cu2–O4	81.38(13)	81.53(19)	O1–Cu4–O19A/B/C[i]	161.4(2)/163.9(2)	163.1(4)/161.9(5)/157.6(4)
O2–Cu2–N4	178.29(16)	177.5(3)	O3–Cu4–O4	81.68(12)	82.05(18)
O2–Cu2–N5	100.19(16)	100.2(2)	O3–Cu4–N10	99.60(16)	99.1(2)
O4–Cu2–N4	98.50(15)	98.4(2)	O3–Cu4–N11	176.62(18)	177.1(3)
O4–Cu2–N5	108.21(17)	107.6(3)	O3–Cu4–O19A/B/C[i]	83.0(3)/90.4(2)	87.4(5)/88.0(6)/81.8(4)
N4–Cu2–N5	81.48(18)	82.2(3)	O4–Cu4–N10	173.52(16)	174.0(3)
			O4–Cu4–N11	98.76(17)	98.3(3)
			O4–Cu4–O19A/B/C[i]	100.2(3)/108.7(2)	105.4(5)/108.0(6)/83.1(5)
			N10–Cu4–N11	80.33(18)	80.9(3)
			N10–Cu4–O19A/B/C[i]	86.3(3)/77.7(2)	80.6(5)/78.0(6)/102.9(5)
			N11–Cu4–O19A/B/C[i]	93.7(3)/86.3(3)	89.7(5)/89.1(7)/95.3(4)
Cu1–O1–Cu2	100.00(13)	100.6(2)	Cu1–O3–Cu3	99.48(14)	99.4(2)
Cu1–O1–Cu4	98.36(12)	97.9(2)	Cu1–O3–Cu4	99.42(13)	99.6(2)
Cu2–O1–Cu4	97.53(12)	96.8(2)	Cu1–O3–Cu4	96.75(14)	97.1(2)
Cu1–O2–Cu2	97.67(13)	98.17(19)	Cu2–O4–Cu3	96.30(15)	95.4(2)
Cu1–O2–Cu3	97.85(13)	97.5(2)	Cu2–O4–Cu4	97.14(14)	96.6(2)
Cu2–O2–Cu3	98.30(14)	98.5(2)	Cu3–O4–Cu4	97.31(15)	97.1(2)

Atom O19 is part of a perchlorate anion that is disordered over two sites at 150 K and three sites at 30 K, labeled A, B and C. Symmetry code: (i) $1/2 + x$, $3/2 - y$, z.

Pna2_1, although some of the anion and *tert*-butyl group disorder that is present at 150 K has become frozen out at 30 K. A decay in crystal quality as the temperature was lowered means that the 30 K structure is less precise than the 150 K one, despite the reduced disorder present. All the metric parameters quoted in the following paragraph are from the 150 K structure.

The asymmetric unit contains one tetrameric complex and four perchlorate anions, all lying on general positions, and a disordered region containing four or five partial dichloromethane environments. Three of the four copper ions in the cubane complex, Cu1–Cu3, are five-coordinate with one long apical Cu···OH^- bond of 2.328(5)–2.424(3) Å (Table 2 and Fig. 3). The τ parameters for these three copper ions range from 0.11 to 0.26, confirming that their coordination geometry is best described as square pyramidal [17]. The other copper ion, Cu4, is six-coordinate with long axial bonds to one OH^- ligand [2.419(3) Å], and a disordered perchlorate ion [Cu···O = 2.5–2.6 Å] (Table 2). The disposition of elongated Cu···O bonds within the $[Cu_4(OH)_4]^{4+}$ cubane core results in a tetragonal elongation, with two short intermetallic distances of Cu1···Cu2 = 2.9853(9) and Cu3···Cu4 = 2.9489(8) Å spanning opposite faces of the cube. The other four Cu···Cu distances within the cluster core range between 3.2838(9) and 3.3153(9) Å (Fig. 2). Hence, the cubane is best considered as an approximately S_4-symmetric, loosely-associated dimer of $[Cu_2(OH)_2]^{2+}$ dimers. The four basal, apical Cu–O···Cu pathways linking the dimers within the cubane should contribute negligibly to superexchange in the compound, since the apical Cu–O bonds do not overlap with the copper $d_{x^2y^2}$ magnetic orbitals [16,18].

Comparison of the crystal structures at 30 K and 150 K shows that there is a small contraction of the distance between the pair of dimers in the cluster. Two of the apical Cu···O bonds linking the dimers, Cu1···O3 and Cu3···O2, are shorter at 30 K by 0.029(7) Å and 0.030(6) Å, respectively. This leads to a decrease in the four long Cu···Cu distances in the cubane, which are all 0.0257(17)–0.0337(17) Å shorter at 30 K than at 150 K (Table 2). This small perturbation should have no bearing on the magnetochemistry of the compound, since superexchange between the dimers is expected to be very weak [16,18]. Importantly, the Cu–O bonds and Cu–O–Cu angles linking Cu1 and Cu2, and Cu3 and Cu4, are all indistinguishable at the two temperatures, as are the distances between these two pairs of strongly linked copper ions. Hence, the small structural changes in the cubane core observed upon cooling to 30 K cannot be used to rationalise the low-temperature magnetic behaviour of $\mathbf{1} \cdot x CH_2Cl_2$.

Detailed consideration of hydrogen bonding in the compound is hampered by disorder in three of the ClO_4^- anions at 150 K, and in two of them at 30 K. However, it is clear that each of the anions in the structure accepts

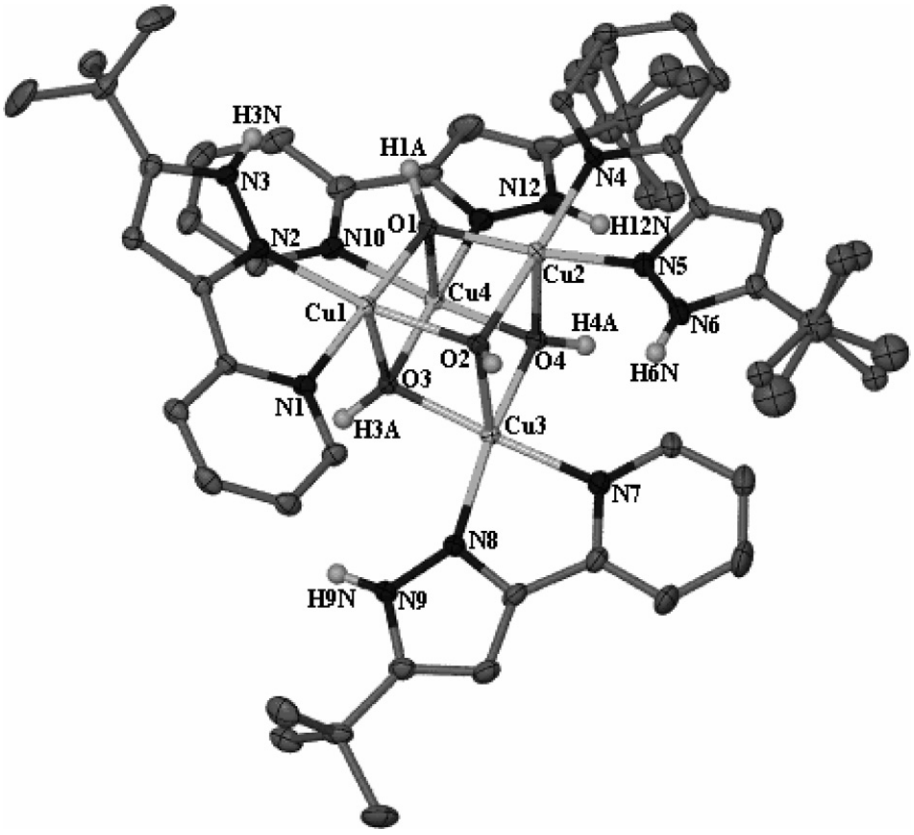


Fig. 3. ORTEP representation of the $[Cu_4(\mu_3\text{-}OH)_4(L)_4]^{4+}$ cations in **1** at 150 K. Thermal ellipsoids are at a 30% probability level and the peripheral H atoms and ClO_4^- counter anions have been omitted for clarity.

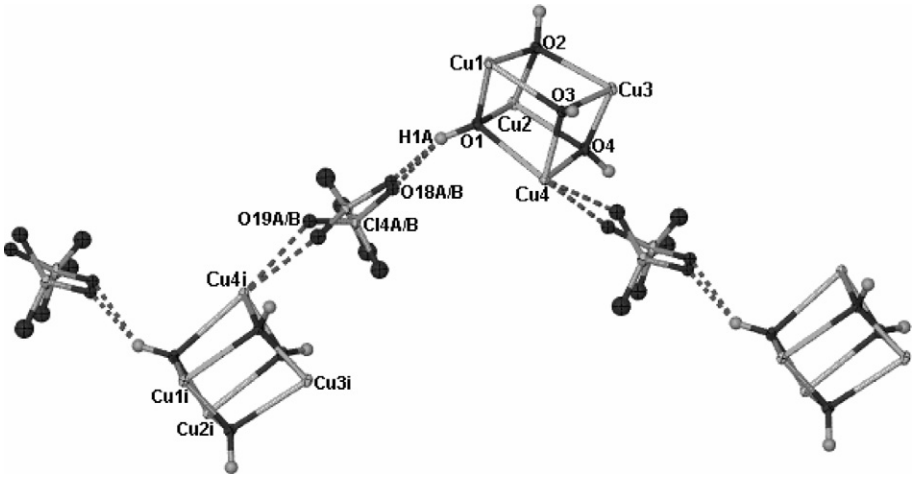


Fig. 4. ORTEP representation at 20% thermal ellipsoids illustrating the intermolecular bonding linking the $[Cu_4(\mu_3\text{-}OH)_4(L)_4]^{4+}$ moieties *via* H-bonding of the disordered O18A/B oxygen donor atom (of the Cl4A/B perchlorate anion) and the axial Cu–O interaction between $Cu4^i$ and O19A/B of the same counter anion.

hydrogen bonds from one OH^- group and from the N–H group of one L ligand, thus occupying alternate corners of the cubane molecule. Importantly, one of the disordered anions also forms the aforementioned weak axial contact, through O19, to Cu4 in a neighbouring molecule related by $-1/2 + x$, $3/2 - y$, z. This bridging interaction associates the cubanes into 1-D chains that zig-zag along the crystallographic *a* direction, that are linked through alternating X–H···O (X = N or O) and Cu···O interactions (Fig. 4). We tentatively attribute the anomalous magnetic behaviour of $\mathbf{1} \cdot x CH_2Cl_2$ below 30 K to weak intermolecular ferromagnetic superexchange mediated by the bridging perchlorate anions.

4. Discussion

Complex $\mathbf{1} \cdot x CH_2Cl_2$ represents only the sixth tetranuclear cupric cluster to exhibit the $[Cu_4(\mu_3\text{-}OH)_4]^{4+}$ distorted cubane core, five of which (including $\mathbf{1} \cdot x CH_2Cl_2$) have been studied magnetically [19–23]. Table 3 contains the structural and magnetic data reported from four previously reported $[Cu_4(\mu_3\text{-}OH)_4(L)_4]^{4+}$ clusters along with data collated in this work. Three of the other complexes have the same approximate S_4 core symmetry found in $\mathbf{1} \cdot x CH_2Cl_2$, and their magnetic susceptibility data were therefore also best fitted using the Bleaney-Bowers dinuclear model. Hatfield and Hodgson's magnetostructural correlation for $[Cu_2(OH)_2]^{2+}$ dimers [24] predict weak ferromagnetic exchange in **3** and strong antiferromagnetic exchange in **5**, due to their Cu–(μ_3-OH)–Cu angles averaging 96.5° and 101.5°, respectively (Table 3). These prediction were proven correct, since these compounds show $J = +12$ and $-207.0\ cm^{-1}$ respectively. Likewise the average Cu–(μ_3-OH)–Cu angle of 98.8° in **4** would impose weaker antiferromagnetic exchange, as proven by the magnetic exchange value of $J = -41.0\ cm^{-1}$. Magnetic susceptibility measurements on **2** were consistent with antiferromagnetic exchange, but no fitting of these data was attempted. Compound $\mathbf{1} \cdot x CH_2Cl_2$ shows comparable Cu···Cu and Cu–O distances with respect to the five previously reported $[Cu_4(\mu_3\text{-}OH)_4(L)_4](X)_4$ systems. Interestingly, the averaged Cu–(μ_3-OH)–Cu angles within each dinuclear unit in **1** at 150 and 30 K range from 96.7° to 99.8°, which lie in the ferromagnetic and antiferromagnetic regions of Hatfield and Hodgson's correlation, respectively. The structure of **1** is therefore in close proximity to the singlet/triplet ground state interface for each strongly coupled dicopper unit, and a very small *J* value would be predicted, as observed.

Table 3
Intradimer structural and magnetic data for $[Cu_4(\mu_3\text{-}OH)_4(L)_4]^{4+}$ cubane clusters[a]

	Cu–O (Å)	Cu···Cu (Å)	Cu–(OH)–Cu (°)	$J\ (cm^{-1})$	Reference
$\mathbf{1} \cdot x CH_2Cl_2$	1.943(3)–1.991(3)	2.9489(8)–2.9853(9)	96.75(14)–100.00(13)	−5.2	this work
$[Cu_4(OH)_4(SO_3CF_3)_2(N(py)_3)_4]$-$(SO_3CF_3)_2 \cdot C_3H_6O$ (**2**)	1.955(7)–1.988(7)	2.967(2)–2.974(2)	97.60(3)–98.40(3)	$S = 0$, J not calculated	[19]
$[Cu_4(OH)_4(bpy)_4](PF_6)_4$ (**3**)	1.947(2)–1.956(2)	2.914	96.60(2), 96.40(2)	+12.0	[20]
$[Cu_4(OH)_4(N\text{-}A)_4](PF_6)_4$ (**4**)	1.930(3)	2.9526(8)	98.84(11)	−41.0	[22]
$[Cu_4(\mu_3\text{-}OH)_4(aib)_4](hfac)_4$ (**5**)	1.942(2)–1.956(2)	3.023(7)	101.33(10), 101.70(10)	−207.0	[23]

Data for $\mathbf{1} \cdot x CH_2Cl_2$ are from the 150 K crystal structure.

[a] Ligand abbreviations: $N(py)_3$ = tri(pyrid-2-yl)amine; N–A = *N*-acylamidine; aib = 2-methyl-2-amino-4-iminopentane; hfac = hexafluoroacetylacetonate.

5. Supplementary material

CCDC 617387 and 617388 contain the supplementary crystallographic data for $\mathbf{1} \cdot x CH_2Cl_2$ at 30 and 150 K. These data can be obtained free of charge via http://www.ccdc.cam.ac.uk/conts/retrieving.html, or from the Cambridge Crystallographic Data Centre, 12 Union Road, Cambridge CB2 1EZ, UK; fax: (+44) 1223-336-033; or e-mail: deposit@ccdc.cam.ac.uk.

Acknowledgements

We thank Dr H. J. Blythe (University of Sheffield, UK) for the magnetic susceptibility measurements. Funding from the Leverhulme Trust is gratefully acknowledged.

References

[1] P.D. Beer, E.J. Hayes, Coord. Chem. Rev. 240 (2003) 167–189.
[2] X. Liu, M.P. de Miranda, E.J.L. McInnes, C.A. Kilner, M.A. Halcrow, Dalton Trans. (2004) 59.
[3] X. Liu, J.A. McAllister, M.P. de Miranda, B.J. Whitaker, C.A. Kilner, M. Thornton-Pett, M.A. Halcrow, Angew. Chem., Int. Ed. 41 (2002) 756.
[4] X. Liu, J.A. McAllister, M.P. de Miranda, E.J.L. McInnes, C.A. Kilner, M.A. Halcrow, Chem. Eur. J. 10 (2004) 1827.
[5] X. Liu, A.C. McLaughlin, M.P. de Miranda, E.J.L. McInnes, C.A. Kilner, M.A. Halcrow, Chem. Commun. (2002) 2978.
[6] (a) C.M. Pask, K.D. Camm, C.A. Kilner, M.A. Halcrow, Tetrahedron Lett. 47 (2006) 2531;
(b) C.M. Pask, K.D. Camm, N.J. Bullen, M.J. Carr, W. Clegg, C.A. Kilner, M.A. Halcrow, Dalton Trans. (2006) 662;
(c) L.F. Jones, K.D. Camm, C.A. Kilner, M.A. Halcrow, Cryst. Eng. Comm. 8 (2006) 719–728.
[7] A. Satake, T. Nakata, J. Am. Chem. Soc. 120 (1998) 10391.
[8] (a) Y.-H. Niu, B. Chen, S. Liu, H. Yip, J. Bardecker, A.K.-Y. Jen, J. Kavitha, Y. Chi, C.-F. Shu, Y.-H. Tseng, C.-H. Chien, Appl. Phys. Lett. 85 (2004) 1619;
(b) Y.-H. Song, S.-J. Yeh, C.-T. Chen, Y. Chi, C.-S. Liu, J.-K. Yu, Y.-H. Hu, P.-T. Chou, S.-M. Peng, G.-H. Lee, Adv. Funct. Mater. 14 (2004) 1221;
(c) F.-M. Hwang, H.-Y. Chen, P.-S. Chen, C.-S. Liu, Y. Chi, C.-F. Shu, F.-I. Wu, P.-T. Chou, S.-M. Peng, G.-H. Lee, Inorg. Chem. 44 (2005) 1344;
(d) S.-Y. Chang, J. Kavitha, S.-W. Li, C.-S. Hsu, Y. Chi, Y.-S. Yeh, P.-T. Chou, G.-H. Lee, A.J. Carty, Y.-T. Tao, C.-H. Chien, Inorg. Chem. 45 (2006) 137.
[9] M.J. Plater, M.R. St. J. Foreman, R.A. Howie, J.M.S. Skakle, E. Coronado, C.J. Gómez-García, T. Gelbrich, M.B. Hursthouse, Inorg. Chim. Acta 319 (2001) 159.
[10] W.-S. Yu, C.-C. Cheng, Y.-M. Cheng, P.-C. Wu, Y.-H. Song, Y. Chi, P.-T. Chou, J. Am. Chem. Soc. 125 (2003) 10800.
[11] G.M. Sheldrick, Acta Crystallogr. A46 (1990) 467.
[12] G.M. Sheldrick, SHELXL97, Program for the Refinement of Crystal Structures, University of Göttingen, Germany, 1997.
[13] L.J. Barbour, J. Supramol. Chem. 1 (2003) 189.
[14] POVRAY v. 3.5, Persistence of Vision Raytracer Pty. Ltd., Williamstown, Victoria, Australia, 2002. Available from: <http://www.povray.org>.
[15] C.J. O'Connor, Prog. Inorg. Chem. 29 (1982) 203.
[16] L. Walz, H. Paulus, W. Haase, H. Langhof, F. Nepveu, J. Chem. Soc., Dalton. Trans. (1983) 657.
[17] A.W. Addison, T.N. Rao, J. Reedijk, J. van Rijn, G.C. Verschoor, J. Chem. Soc., Dalton Trans. (1984) 1349.
[18] (a) H. Alstheimer, F. Nepveu, L. Walz, W. Haase, J. Chem. Soc., Dalton. Trans. (1985) 315;
(b) H. Oshio, Y. Saito, T. Ito, Angew. Chem., Int. Ed. 36 (1997) 2673;
(c) G.D. Fallon, B. Moubaraki, K.S. Murray, A.M. van der Bergen, B.O. West, Polyhedron 12 (1993) 1989.
[19] P.L. Dedert, T. Sorrell, T.J. Marks, J.A. Ibers, Inorg. Chem. 21 (1982) 3506.
[20] J. Sletten, A. Sørensen, M. Julve, Y. Journaux, Inorg. Chem. 29 (1990) 5054.
[21] R.D. Köhn, Z. Pan, M.F. Mahon, G. Kociok-Köhn, Dalton Trans. (2003) 2269.
[22] J.K. Eberhardt, T. Glaser, R.-D. Hoffman, R. Fröhlich, E.-U. Würthwein, Eur. J. Inorg. Chem. (2005) 1175.
[23] N. Lopez, T.E. Vos, A.M. Arif, W.W. Shum, J.C. Noveron, J.S. Miller, Inorg. Chem 45 (2006) 4325.
[24] V.H. Crawford, H.W. Richardson, J.S. Wasson, D.J. Hodgson, W.E. Hatfield, Inorg. Chem. 15 (1976) 2107.

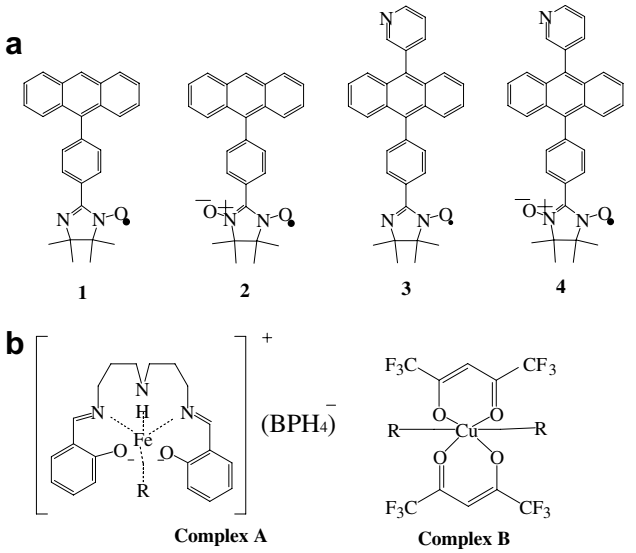
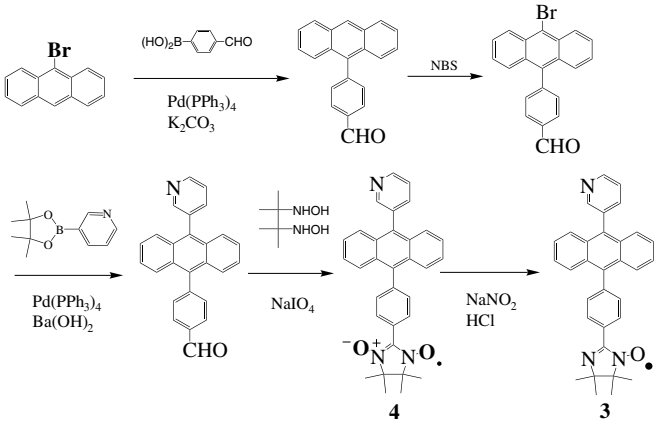


Fig. 1. (a) Molecular structures of the radicals **1**–**4**; (b) structures of the complexes **A** and **B**.



Scheme 1. Synthesis of **3** and **4**.

acetate = 10:1). Recrystallization from ethanol gave **3** as red powders. Mp 205–208 °C. *Anal.* Calc. for $C_{32}H_{28}N_3O$: C, 81.67; H, 6.00; N, 8.83. Found: C, 81.69; H, 5.93; N, 8.93%.

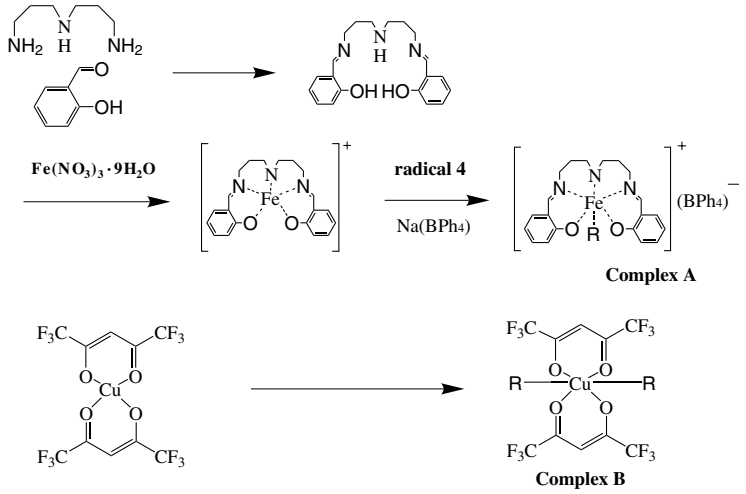
Compound **4** was purified by silica gel column chromatography using mix solvent (dichloroethane:ethyl acetate = 9:1). Recrystallization from toluene gave **4** as blue powders. Mp 224–228 °C. *Anal.* Calc. for $C_{32}H_{28}N_3O_2$: C, 78.99; H, 5.80; N, 8.64%. Found: C, 79.09; H, 5.81; N, 8.39%.

2.2. Synthesis of metal complexes *A* and *B*

Complexes **A** and **B** were synthesized according to Scheme 2. The complex **A** was synthesized according to the similar procedures reported previously [14].

A mixture of 3,3-diaminodipropylamine and salicylaldehyde in methanol solution was stirred for 2 h at room temperature. The solution was fell in drops $Fe(NO_3)_3 \cdot 9H_2O$ methanol solution. To the solution was added a solution of the radical **4**, and the mixture was stirred for 1 h at room temperature. Then, to the solution was added a methanol solution of sodium tetraphenylborate, and stirred for 1 h. The dark purple crystals were collected by filtration and, recrystallized from acetone-ethanol solution, gave the complex A, $[Fe(III)(L)(4)] \cdot (BPh_4)$. ($LH_2$ = *N*,*N*′-bis(1-hydroxy-2-benzyliden)-1,7-diamino-4-azaheptane). *Anal.* Calc. for $C_{76}H_{71}$- $BFeN_6O_4$: C, 76.13; H, 5.97; N, 7.01. Found: C, 76.65; H, 5.49; N, 5.86%.

A solution of $[Cu(hfac)_2 \cdot xH_2O]$ in heptane was concentrated about by distillation. To this solution was added a solution of **4** in toluene. The crystal was collected by filtration, recrystallized from ethanol gave the complex **B**, $Cu(II)(hfac)_2(\mathbf{4})_2$. In the complex using 4-pyridinyl substituted π-radicals as a ligand, it was found by X-ray crystallographic analysis that the complex was contained toluene as crystal solvent. The complex B be expected to contain toluene. *Anal.* Calc. for $C_{76}H_{62}CuF_{12}N_6O_8$: C, 63.46; H, 4.49; N, 5.35. Found: C, 63.86; H, 4.43; N, 5.25%.



Scheme 2. Synthesis of complexes **A** and **B**.

2.3. Measurements

Electro chemical behaviors of **3** and **4** were studied in acetonitrile solution by CV method using a Hokuto Denko HSV-100. The measurements were made with a standard three-electrode configuration: a glassy carbon disk electrode served as the working electrode, a Pt wire and Ag/Ag+ were used as the counter electrode and the reference electrode, respectively. 0.1 M of $(t\text{-Bu})_4NBF_6$ was used as the electrolyte. Ferrocene was used as internal standard.

UV–Vis absorption spectra were obtained with a Hitachi U-3000. Magnetic susceptibility measurements were carried out using a powder samples of **3**, **4**, complexes **A** and **B** on a Quantum Design MPMS2 SQUID magnetometer. Conventional ESR spectra were observed with a JEOL TE300 X-band ESR spectrometer. The ab initio molecular orbital calculations were carried out based on the density functional theory (DFT) using Gaussian 98 [15]. In the ab initio calculations, the STO 6-31G basis sets and UHF Becke 3LYP (UBecke 3LYP) hybrid method were employed. The photo-excited states were investigated by the TRESR measurements. The detail of our experimental setup of the TRESR apparatus was described in our previous paper [3]. The temperature in the ESR and TRESR measurements was controlled using an Oxford ESR 910 cold He gas flow system.

3. Results and discussion

The UV–Vis spectra of the radicals **1**, **3** and **4** are shown in Fig. 2. Peaks of 350–400 nm are assigned to π–π transition of the anthracene moiety. The peak of the radical **3** is red-shifted by about 10 nm relative to **1**. The result shows that energy gap between HOMO and LUMO of the radical **3** decreases by the attachment of the 3-pyridinyl group. Broad peak of 400–500 nm is arising from the $n\pi^*$ transition of the iminonitroxide radical. From this experiment, a laser light of $\lambda = 355$ nm is used for the excitation in the TRESR experiment.

Oxidation potentials of **1**, **3** and **4** are listed in Table 1. First and second oxidation potentials of **3** are larger than the corresponding ones of **1**, showing stabilization both of HOMO and SOMO of **3**.

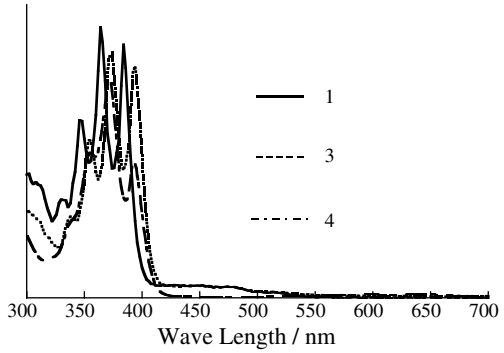


Fig. 2. UV–Vis spectra of **1**, **3** and **4**.

Table 1
Oxidation potentials of **1**, **3** and **4** in acetonitrile

	First oxidation potential (V)	Second oxidation potential (V)
1	0.79	0.91
3	0.81	1.04
Difference	0.02	0.13
4	0.36	0.94

Ferrocene was used as internal standard.

In the ground states, the magnetic properties of the radicals were examined by the susceptibility measurements.

Figs. 3 and 4 are the temperature dependences of $\chi_{mol}T$ for **3** and **4** in the range of 1.7–300 K respectively. Solid lines in these figures are calculated using the Curie–Weiss law. From these fitting, the Weiss constant θ of **3** and **4** were determined to be −1.5 to −0.7 K, respectively, showing inter-molecular interactions of **3** and **4** are weak antiferromagnetic in the ground states. In order to clarify the photo-excited states of the radicals **3** and **4**, TRESR experiments were carried out.

Fig. 6 shows TRESR spectra and spectral simulation [16] of **3** and **4**, respectively. Their TRESR spectra were observed at 30 K in a glass matrix (isopentane:diethylether = 2:3). From the spectral simulation, spin Hamiltonian parameters of **3** were determined to be $S = 3/2$, $g = 2.0043$, $D = 0.0238\ cm^{-1}$ and $E = 0.0004\ cm^{-1}$. For **4**, $S = 3/2$, $g = 2.0045$, $D = 0.0235\ cm^{-1}$ and $E = 0.0004\ cm^{-1}$ were obtained. D of **3** is larger than that of **1** by about 2%. The small difference means that the unpaired electron is almost localized within the phenylanthracene

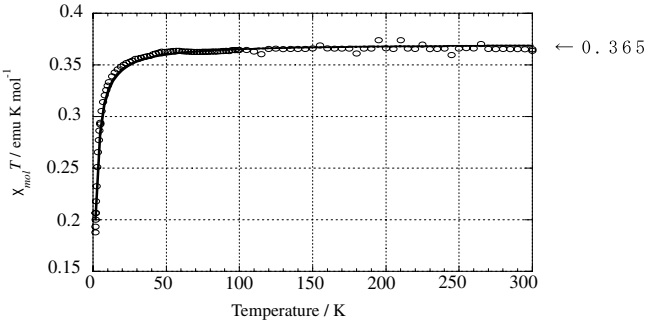


Fig. 3. Temperature dependence of $\chi_{mol}T$ plots for **3**; solid line corresponds to calculation using the Curie–Weiss law.

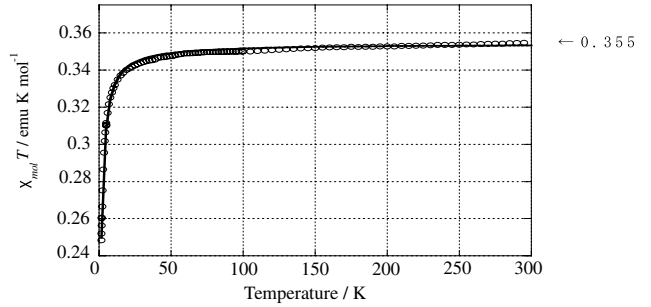


Fig. 4. Temperature dependence of $\chi_{mol}T$ plots for **4**; solid line corresponds to calculation using the Curie–Weiss law.

and the radical moieties and the delocalization toward the 3-pyridinyl group is a little. This result is also supported by the molecular orbital calculation (Fig. 5). Interestingly, spectral intensity of **3** is stronger than that of **1**. The spectral intensity of **4** is also stronger than that of **2** (TRESR signal of **2** was not clearly observed because of the weak intensity). The result shows that the attachment of the 3-pyridinyl group makes the intersystem crossing toward the quartet high-spin state more efficient. TRESR experiments revealed both radicals have the quartet ($S = 3/2$) high-spin photo-excited states.

Therefore, we can conclude that 3-pyridinyl substituted radicals **3** and **4** are used for the candidates of ligands to study the exchange interaction between the photo-excited high-spin state of π-radical and the paramagnetic centers of metal ions.

We have succeeded to synthesize complex **A** and **B**, when we used **4** as the ligand. Unfortunately, the crystals with a suitable size for a X-ray crystallographic analysis were not obtained at the moment.

The temperature dependences of $\chi_{mol}T$ for the complexes **A** and **B** in the range of 1.7–300 K are shown in Figs. 7 and 8, respectively. Solid lines in Figs. 7 and 8 are calculated using the Bleaney–Bowers model

$$\chi T = \frac{Ng^2\beta^2}{k}\frac{1}{3+\exp(-2J/kT)} \tag{1}$$

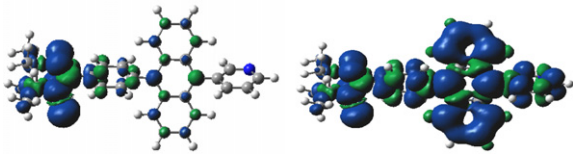


Fig. 5. Spin density of **3** by the molecular orbital calculation (left: ground state, right: excited state).

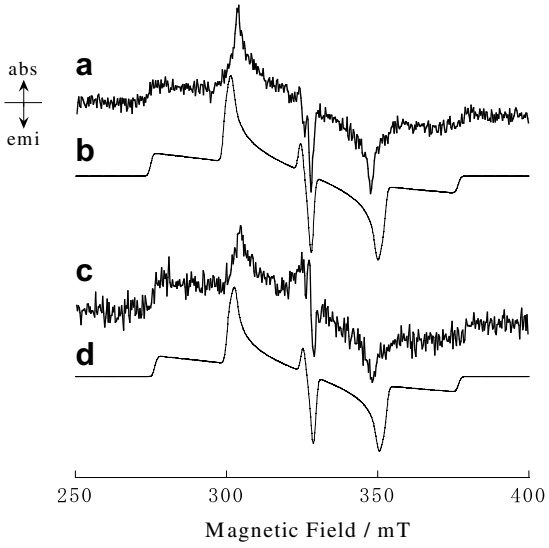


Fig. 6. TRESR spectra and simulations of **3** and **4** (a) spectrum of **3**, (b) simulation of **3**, (c) spectrum of **4**, and (d) simulation of **4**.

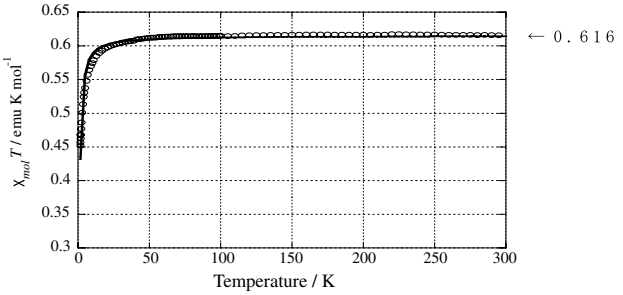


Fig. 7. Temperature dependence of $\chi_{mol}T$ plots for complex **A**; solid line corresponds to calculation using the Bleaney–Bowers model.

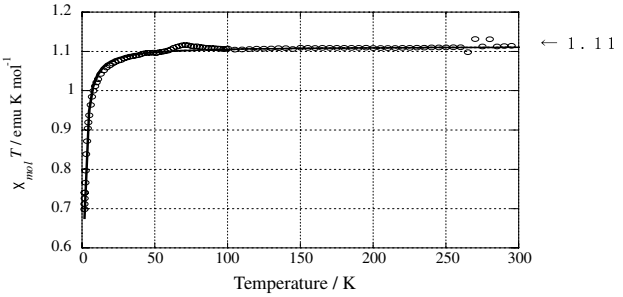


Fig. 8. Temperature dependence of $\chi_{mol}T$ plots for complex **B** (+toluene); solid line corresponds to calculation using three spin cluster model.

and three spin cluster model of S_1–S_M–S_2 ($S_1 = S_M = S_2 = 1/2$).

$$\chi T = \frac{Ng^2\beta^2}{4k}\frac{1+\exp(2J/kT)+10\exp(3J/kT)}{1+\exp(2J/kT)+2\exp(3J/kT)} \tag{2}$$

Here, N is the number of two spin dimmers or three spin clusters.

From the analysis, exchange interaction between the metal ion and the organic ligand of the complexes **A** and **B** were determined to be −0.86 and −1.0 K, respectively, showing weak exchange interactions between them in the ground states. These fitting are not enough accurate because the magnitudes of J values are very small. This is due to a little delocalizaton of the unpaired electron toward the 3-pyridinyl group in their electronic ground states of **4**. In the photo-excited quartet state, the unpaired electrons are expected to be more delocalized to the 3-pyridinyl group as with π-radical **3**. Therefore, the larger exchange interactions and photo-induced spin alignment are predicted between the paramagnetic centers of the metal ions and the photo-excited quartet states of the π-radicals, **3** and **4**. The TRESR experiments are going in progress to clarify the spin alignment in the photo-excited states of the metal complexes.

4. Conclusions

The pyridinyl substituted π-radicals **3** and **4** have the photo-excited quartet states. Their signal intensity of the quartet states become stronger than that of their parent radicals. We have succeeded to synthesize complexes **A**

and **B** using **4** as a ligand. Their magnetic properties were clarified and the exchange interactions between the metal ions and radicals are weak in the ground states.

Acknowledgements

Authors acknowledge to Dr. Masakazu Hirotsu (OCU) for his help in the synthesis of complex A. This work was supported by the Grant-in-Aid for Scientific Research on the general (No. 16350079) and Priority Area "Application of Molecular Spin" (Area No. 769, Proposal No. 15087208) from the Ministry of Education, Culture, Sports, Science and Technology, Japan.

References

[1] G. Christou, Mol. Cryst. Liq. Cryst. 334/335, in: Proceedings of the IXth International Conference on Molecule-based Magnets, Tsukuba, October 4–8, 2004.
[2] Y. Teki, S. Miyamoto, K. Iimura, M. Nakatsuji, Y. Miura, J. Am. Chem. Soc. 122 (2000) 984.
[3] Y. Teki, S. Miyamoto, M. Nakatsuji, Y. Miura, J. Am. Chem. Soc 123 (2001) 294.
[4] Y. Teki, M. Nakatsyuji, Y. Miura, Mol. Phys. 100 (2002) 1385.
[5] Y. Teki, S. Nakajima, Chem. Lett. 33 (2004) 1500.
[6] T. Toichi, Y. Teki, Polyhedron 24 (2005) 2337.
[7] Y. Teki, T. Toichi, S. Nakajima, Chem. Eur. J. 12 (2006) 2329.
[8] Y. Teki, H. Tamekuni, J. Takeuchi, Y. Miura, Angew. Chem., Int. Ed. 45 (2006) 4666.
[9] S.S. Kim, S.I. Weissman, J. Magn. Reson. 24 (1976) 167.
[10] C. Corvaja, M. Maggini, M. Prato, G. Scorrano, M. Venzin, J. Am. Chem. Soc. 117 (1995) 8857.
[11] K. Ishii, J. Fujiwara, Y. Ohba, S. Yamauchi, J. Am. Chem. Soc. 118 (1996) 13079.
[12] K. Ishii, J. Fujisawa, A. Adachi, S. Yamauchi, N. Kobayashi, J. Am. Chem. Soc. 120 (1998) 3152.
[13] N. Mizouchi, Y. Ohba, S. Yamauchi, J. Phys. Chem. 103 (1999) 7749.
[14] S. Hayami, Y. Hosokoshi, K. Inoue, Y. Einaga, O. Sato, Y. Maeda, Bull. Chem. Soc. Jpn. 74 (2001) 2361.
[15] Gaussian 98. Revision A.11. Gaussian. Inc., Pittsburgh, PA, 2001.
[16] The spectral simulation was carried out by the eigenfield [17]/exact-diagonalization hybrid method: Y. Teki, I. Fujita, T. Takui, T. Kinoshita, K. Itoh, J. Am. Chem. Soc. 116 (1994) 11499;
In the spectral simulation of the TRESR spectra, the calculation of ESP has been added as a subroutine to the computer program, and more detailed procedures of the spectral simulation for high spin organic molecules are similar to those described in our previous paper for the perturbation approach:Y. Teki, T. Takui, H. Yagi, K. Itoh, H. Iwamura, J. Chem. Phys. 83 (1985) 539.
[17] G.G. Belford, R.L. Belford, J.F. Burkhalter, J. Magn. Reson. 11 (1973) 251.

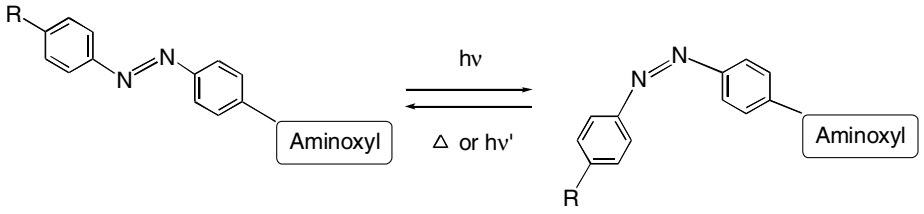
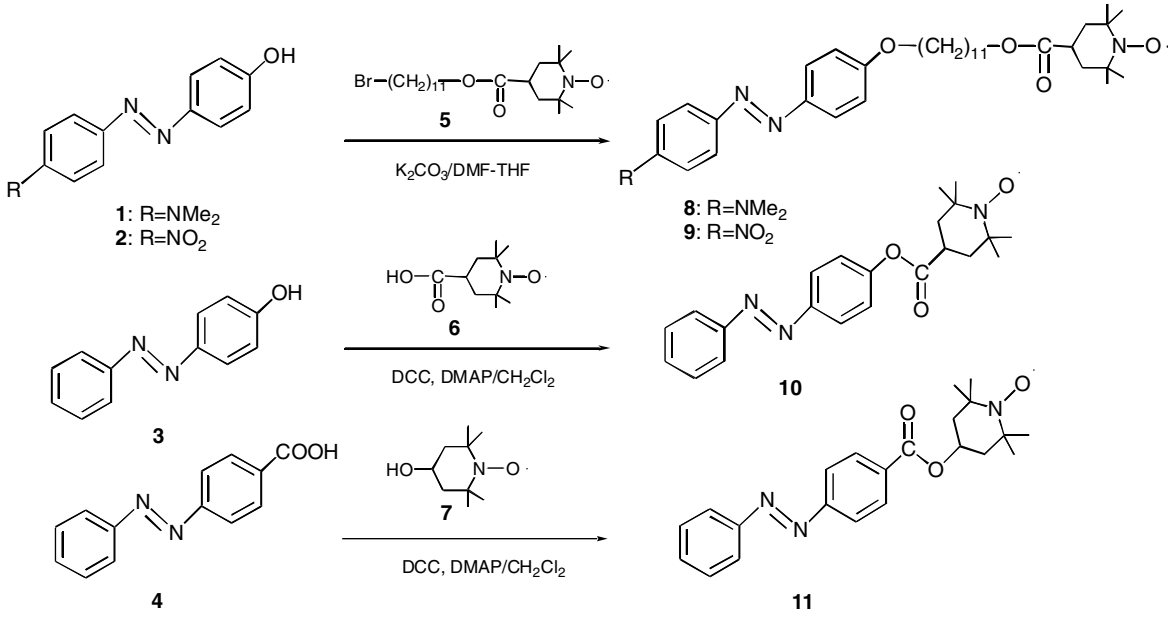
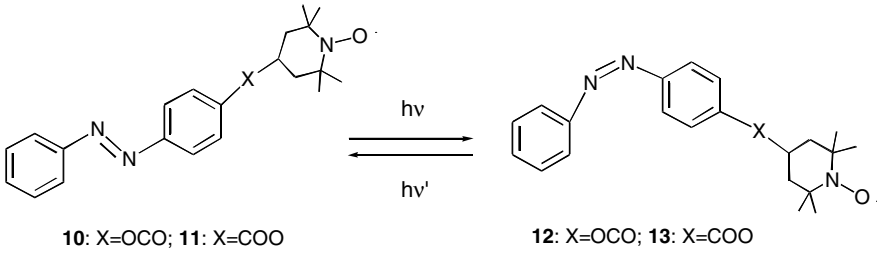


Chart 1.



Scheme 1.



Scheme 2.

4-carboxyazobenzene (**4**) and 4-hydroxy-TEMPO (**7**) by the similar condensation reaction in 66% yield.

2.2. Photo-responsive properties of azobenzene derivatives *8–11*

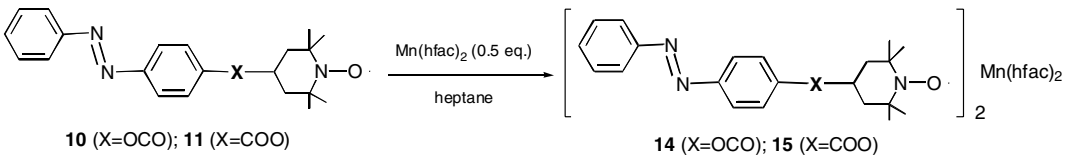
Irradiation of the azobenzene with 4-dimethylamino-substituent (**8**) with an UV light in dichloromethane solution showed an apparent change of its absorption spectrum, suggesting occurrence of the photo-isomerization in the solution but the corresponding *cis*-isomer could not be isolated probably because of unstable nature of the isomer in the solid-state. Similarly, any attempt was failed to isolate the *cis*-isomer of 4-nitroazobenzene derivative (**9**) under the various conditions examined.

Table 1
Magnetic data of azobenzene derivatives **8–13**

Compound	Magnetic interaction	C (emu K mol^{-1})	θ (K)	J (K)
8	antiferromagnetic[a]	0.36	−12.3	
9	ferromagnetic[a]	0.32	0.26	
10	antiferromagnetic[a]	0.37	−3.2	
11	antiferromagnetic[b]			−47.6
12	ferromagnetic[a]	0.38	0.32	
13	ferromagnetic[a]	0.38	0.11	

[a] CW model.
[b] ST model.

On the other hand, the photo-isomerizations of the unsubstituted derivatives with no substituent at 4-position (**10** and **11**) was found to proceed smoothly and the



Scheme 3.

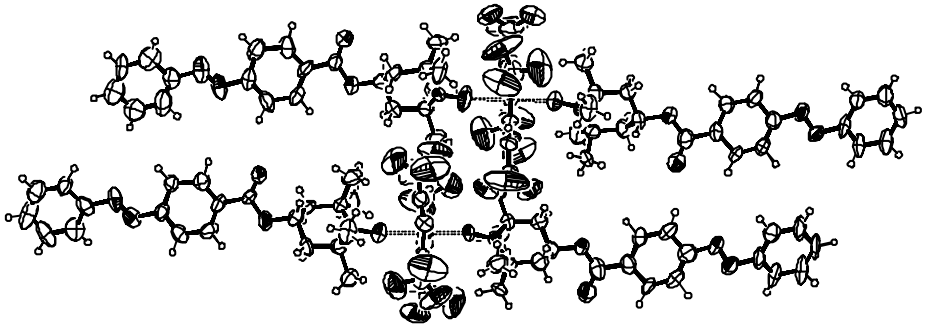


Fig. 1. Crystal structure of complex **15**.

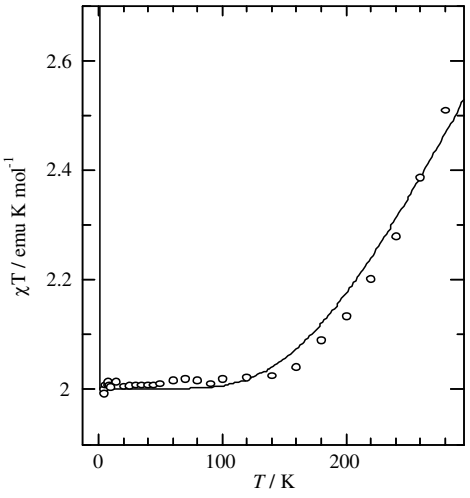


Fig. 2. Temperature dependence of χ_T-values of complex **15**. The theoretical data are shown in a solid line.

corresponding *cis*-isomers (**12** and **13**) could be isolated as relatively stable solid materials.

Thus, irradiation of the *trans*-isomer of an oxocarbonyl-TEMPO-substituent (**10**) with the light of 365 nm in benzene solution showed such an absorption change that a maximum at around 324 nm shifted gradually to a newly developed absorption at around 438 nm with an isosbestic point at 385 nm, while the reverse change was found to occur by irradiation of the latter solution with a fluorescent lamp and hence a reversible system could be constructed in this case (Scheme 2). Moreover, the *cis*-isomer **12** could fortunately be isolated as a relatively stable solid and was found to be durable without appreciable change when kept in the dark and stored in a refrigerator. Similar change was also observed for the isomer **11** to give the corresponding *cis*-isomer **13** as a relatively stable solid material.

2.3. Magnetic properties of azobenzene derivatives 8–13

The magnetic data were obtained by using SQUID susceptometer between the temperature range from 2 K to 300 K and the data for the azobenzenes **8**–**13** are summarized in Table 1. Thus, intermolecular magnetic interactions being based on Curie-Weiss (CW) law were observed in the *trans*-isomers **8** and **9** with relatively large antiferromagnetic interaction in 4-dimethyamino-substituted compound **8** and weak ferromagnetic one in 4-nitro derivative **9**, respectively. While weak antiferromagnetic interaction of CW behavior was apparent in the ester isomer **10**, fairly large exchange interaction ($J = -47.6$ K) of singlet–triplet (ST) model was revealed between the spins in the other ester isomer **11**. Regarding the magnetic properties of the corresponding *cis*-isomers **12** and **13**, both showed weak ferromagnetic interactions of CW behavior and thus, apparent change of intermolecular magnetic interactions could apparently be discerned between both of the photo-isomer couples (**10/12** and **11/13**).

2.4. Preparation and properties of Mn(hfac)$_2$ complexes formed from 10 or 11

When an ester isomer **10** was reacted with 0.5 equiv. of Mn(hfac)$_2$ in heated heptane solution [5], the corresponding Mn(hfac)$_2$ complex **14** was found to form in moderate yields (51%) (Scheme 3). [1]Similarly, a Mn(hfac)$_2$ complex **15** could be prepared from another ester isomer **11** (37%)

[1] Crystal data for **14**: $C_{54}H_{54}N_6O_{10}F_{12}Mn$, $F_W = 1229.97$, monoclinic ($P2_1/n$), $a = 21.7990(6)$ Å, $b = 15.0275(9)$ Å, $c = 35.6207(7)$ Å, $\beta = 96.400(5)°$, $V = 11596.1(6)$ Å^3, $T = 293$ K, $Z = 8$, $D_{calc} = 1.409$ mg cm^{-3}, $R = 0.1046$, $R_W = 0.1049$ [8481 observed reflections and 1603 parameters, $I > 3\sigma(I)$].

and the structure was substantiated by a X-ray analysis obtained by a single crystal of the complex (Fig. 1).

As illustrated in Fig. 1, there are two crystallographically independent complexes in the crystal of the manganese complex **15** and the *trans*-conformation of the azobenzene units are apparently seen for both of them. All of the interatomic distances between the manganese atom and the oxygen atoms of the aminoxyls fall approximately into *ca.* 2.1–2.2 Å [6], suggesting the formation of six-coordinate sphere around the metal centers with oxygen atoms from aminoxyls in *trans* apical fashion.

The magnetic data of the complex **15** are shown in Fig. 2 together with the fitting data as a solid line. The Curie constant at lower temperature region is estimated to be 2.01 emu K mol^{-1} and the gradual increase of the χ_T-values is observed along with the increase of temperatures. Preliminary fitting data shown in Fig. 2 are obtained by using an equation with three spin system of $S = 1/2$, 5/2 and 1/2 [7] and the exchange interaction between the correlating spins is estimated from the data to be $J = -133$ K.

Quite similar magnetic behavior was also observed in the spins of another complex **14** and slightly larger exchange interaction ($J = -147$ K) is suggested in the spins of this complex than that of the complex **15**.

We next tried to isomerize the complexes **14** or **15** photo-chemically under the similar condition with the parent radicals **10** and **11** but the complexes were found to be reluctant to the photo-isomerization and any effort to isolate the corresponding *cis*-isomers has so far been unsuccessful. Nevertheless, we are still making efforts to the possibility under different conditions.

In summary, we have prepared several azobenzene derivatives with a TEMPO radical (**8**–**11**) and explored their photo-responsive as well as magnetic properties. Among them, the *cis*-isomers of unsubstituted derivatives at 4-position and with a TEMPO group at 4′-position (**12** and **13**) could successfully be isolated as relatively stable solid materials showing apparent changes of intermolecular magnetic interactions between the photo-isomer couples. A couple of $Mn(hfac)_2$ complexes derived from isomeric TEMPO-substituted esters (**14** and **15**) were prepared and the magnetic properties of the complexes were investigated but the photo-isomerization but the isolation of the corresponding *cis*-isomers has so far been remained without success.

Acknowledgement

This work was supported by a special grant from University of Hyogo, which is gratefully acknowledged.

References

[1] (a) Cf. K. Hashimoto, S. Ohkoshi, Philos. Trans. Roy. Soc. London, Ser. A 357 (1999) 2977;
(b) R. Mikami, M. Taguchi, K. Yamada, K. Suzuki, O. Satao, Y. Einaga, Angew. Chem. Int. Ed. 43 (2004) 6135;
(c) K. Matsuda, M. Irie, J. Photochem. Photobiol. C: Photochem. Rev. 5 (2004) 169.

[2] S. Nakatsuji, Chem. Soc. Rev. 33 (2004) 348.

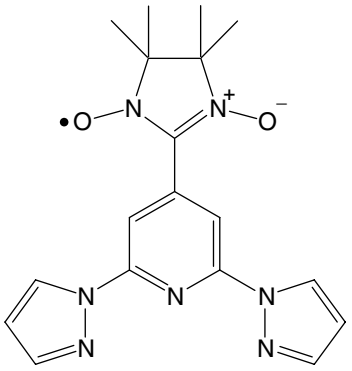
[3] T. Kaneko, T. Amano, H. Akutsu, J. Yamada, S. Nakatsuji, Org. Lett. 5 (2003) 2127.

[4] (a) H. Fujino, T. Amano, H. Akutsu, J. Yamada, S. Nakatsuji, Chem. Commun. (2004) 2310;
(b) T. Amano, H. Fujino, H. Akutsu, J. Yamada, S. Nakatsuji, Polyhedron 24 (2005) 2614.

[5] Cf. K. Griesar, W. Haase, I. Svoboda, H. Fuess, Inorg. Chem. Acta 287 (1999) 181.

[6] (a) M.H. Dickman, L.C. Porter, R.J. Doedens, Inorg. Chem. 25 (1986) 2595;
(b) A. Caneschi, D. Gatteschi, J. Laugier, L. Pardi, P. Ley, C. Zanchini, Inorg. Chem. 27 (1988) 2027.

[7] The following equation is used for the theoretical fitting: $\chi_T = \frac{Ng^2\beta^2}{k}\left[\frac{5(\exp(J/kT))^{-7}+35/2((\exp(J/kT))^{-2}+(\exp(J'/kT))^{-2})+42(\exp(J/kT))^{5}}{4(\exp(J/kT))^{-7}+6((\exp(J/kT))^{-2}+(\exp(J'/kT))^{-2})+8(\exp(J/kT))^{5}}\right]$ where N is the Avogadro's number, β is the Bohr magneton, k is the Boltzmann constant, g is an average g factor and taken here to 2.0, J is the exchange coupling between radical and Mn spins and J' is that between two radicals, which is neglected in this case. Cf. S.J. Gruber, C.H. Harris, E. Sinn, J. Chem. Phys. 49 (1968) 2183, The reason for the deviation of the fitting data around low temperature region from the experimental ones is thought to be due to intermolecular antiferromagnetic interactions between the spin centers..



Scheme 1. Molecular structure of dppNN.

in ethanol (150 ml) and the mixture was refluxed for 6 h. The resulting mixture was evaporated, and 60 ml of water and 23.3 ml of 1 M HCl aq. was added to the residue. The crude product was extracted with dichloromethane and purified by recrystallization from dichloromethane/hexane to yield 1.47 g of **2** (6.09 mmol, 77.7%). *Anal*. Calc. for $C_{12}H_{11}N_5O_1$: C, 59.74; H, 4.60; N, 29.03. Found: C, 59.88; H, 4.66; N, 29.22%. ^{1}H NMR (270 MHz, $CDCl_3$, 25 °C): δ 8.56 (dd, $J = 0.7$, 2.7 Hz, 2H, Pyz), 7.87 (s, 2H, Py), 7.76 (dd, $J = 0.7$, 1.6 Hz, 2H, Pyz), 6.50 (dd, $J = 1.6$, 2.7 Hz 2H, Pyz), 4.86 (d, $J = 5.4$ Hz, 2H, CH_2), 2.51 (t, $J = 5.9$ Hz, 1H, OH).

2.1.2. Dipyrazol-3-yl-4-formylpyridine (*3*)

Dimethylsulfoxide (1.3 ml, 18.3 mmol) in dichloromethane (15 ml) was added to oxalyl dichloride (727 μl, 8.3 mmol) in dichloromethane (35 ml) at −78 °C and the mixture was stirred for 30 min. Compound **2** (1.00 g, 4.15 mmol) in dichloromethane (200 ml) was added drop wise over a period of 1 h to the resulting mixture. After additional stirring for 1 h, triethylamine (5.82 ml, 41.7 mmol) was added to give clear solution, and then allow the temperature increase to rt. The resulting solution was washed with water and extracted with dichloromethane. The crude product was purified by silica-gel column chromatography using ethylacetate/dichloromethane (1/1, v/v) as an eluent to yield 824 mg of **3** (3.44 mmol, 83%). *Anal*. Calc. for $C_{12}H_9N_5O_1$: C, 60.25; H, 3.79; N, 29.27. Found: C, 59.95; H, 3.97; N, 28.99%. ^{1}H NMR (270 MHz, $CDCl_3$, 25 °C): δ 10.16 (s, 1H, CHO), 8.57 (dd, $J = 0.7$, 2.6 Hz, 2H, Pyz), 8.27 (s, 2H, Py), 7.81 (dd, $J = 0.7$, 1.6 Hz, 2H, Pyz), 6.54 (dd, $J = 1.6$, 2.6 Hz, 2H, Pyz).

2.1.3. 2,6-Di(pyrazol-1-yl)-4-(4,4,5,5-tetramethyl-1-oxido-3-ylooxy-4,5-dihydro-3H-imidazol-2′-yl)pyridine (dppNN)

N,*N*′-dihydroxy-2,3-diamino-2,3-dimethylbutane (150 mg, 1.04 mmol) in benzene (6 ml) was added to **3** (750 mg, 1.02 mmol) in benzene (7 ml) and stirred for 2 weeks to obtain white precipitate. The resulting white solid was filtered and dissolved with chloroform (10 ml) and then sodium periodate (215 mg, 1.00 mmol) in water (5 ml) was added. After stirring for 30 min, deep blue solution was obtained and the mixture was washed with water and extracted with dichloromethane. The crude product was purified by silica-gel column chromatography using ethylacetate/dichloromethane (3/1, v/v) as an eluent to yield 90 mg of dppNN (0.25 mmol, 42%). *Anal*. Calc. for $C_{18}H_{20}N_7O_2$: C, 59.01; H, 5.50; N, 26.76. Found: C, 59.21; H, 5.51; N, 26.96%.

2.1.4. [Fe(dppNN$_2$)$_2$](BF$_4$)$_2$ · (CH$_3$COCH$_3$) (*1*)

A solution of $Fe(BF_4)_2 \cdot 6H_2O$ (25 mg, 0.16 mmol) in degassed acetone (5 ml) was added to the blue solution of dppNN (35 mg, 0.06 mmol) in acetone (5 ml) and stirred for 30 min to obtain dark red solution. Diffusion of diethylether to the resulting solution gave dark red crystals of **1**. *Anal*. Calc. for $C_{62}H_{50}B_2F_8Fe_5N_{10} \cdot 4H_2O$: C, 51.00; H, 4.00; N, 9.59. Found: C, 51.18; H, 3.91; N, 9.50%.

2.2. X-ray crystallography

A crystal of **1** was mounted on a glass capillary, and data were collected at −70 °C (Bruker SMART APEX diffractometer coupled with a CCD area detector with graphite monochromated Mo Kα ($\lambda = 0.71073$ Å) radiation). The structure was solved by a direct method and expanded by using Fourier techniques using SHELXTL program. Crystal data of **1** at −73 °C: $C_{39}H_{37}B_2F_8FeN_{14}O_5$, $M = 1011.30$, monoclinic space group $P2_1$, $a = 8.387(2)$, $b = 23.039(4)$, $c = 12.215(2)$ Å, $\beta = 96.587(3)°$, $V = 2346.4(7)$ Å^3, $Z = 2$. A total of 10 549 were collected ($3° < 2\theta < 47°$) of which 5439 unique reflections (R(int) = 0.0379) were measured. Residual R and wR were 0.0739 and 0.1941, respectively, from the refinement on F^2 with $I > 2\sigma(I)$. Empirical absorption corrections by SADABS (G.M. Sheldrick, 1994) were carried out. In the structure analyses, non-hydrogen atoms were refined with anisotropic thermal parameters. Hydrogen atoms were included in calculated positions and refined with isotropic thermal parameters riding on those of the parent atoms.

2.3. Magnetic measurements

DC magnetic susceptibility data of **1** were collected by using a Quantum Design MPMS-XL SQUID magnetometer at temperatures ranging from 5 to 340 K. For the LIESST experiment, Xe lamp was used as light source and 500–600 nm light was isolated by using colour filter and was guided via an optical fiber into the SQUID magnetometer. Irradiation was performed inside the SQUID sample room at 5 K.

3. Results and discussion

3.1. Syntheses of dppNN and [Fe(dppNN)$_2$](BF$_4$)$_2$ · (CH$_3$COCH$_3$) (*1*)

A tridentate ligand of dppNN was synthesized from ethyl 2,6-di(pyrazol-1-yl)isonicotinate[7] by three-step reactions. In

the first step, the carboxyethyl group was reduced by sodium borohydrate affording a hydroxymethyl group, and the hydroxymethyl group was oxidized to a formyl group by the Swern oxidation in the second step. A reaction of formyl compound with *N*,*N*′-dihydroxy-2,3-diamino-2,3-dimethylbutane followed by an oxidation with sodium periodate yielded the ligand dppNN in a moderate yield. An Iron(II) complex of $[Fe(dppNN)_2](BF_4)_2 \cdot (CH_3COCH_3)$ (**1**) was obtained by a reaction of dppNN with $Fe(BF_4)_2 \cdot 6H_2O$. All compounds were characterized by elemental analyses.

3.2. Description of crystal structure: *1*

X-ray crystal structure analysis for **1** was performed at 200 K, and ORTEP diagram of the complex molecule was depicted in Fig. 1. **1** crystallized in monoclinic space group $P2_1$, and the asymmetric unit is composed of one complex cation, two tetrafluoroborate anions, and one acetone molecule. A central iron(II) ion is coordinated by six nitrogen atoms from two tridentate dppNN giving distorted octahedral coordination geometry. Coordination bond lengths of Fe–N1 and Fe–N8 (N1 and N8 are pyridyl nitrogen atoms) are 1.889(6) Å and 1.903(6) Å, respectively, which are shorter than the coordination bond lengths of Fe^{II} ion with pyrazole nitrogen atoms (Fe–N2, N4, N9 and N11: 1.958(6)–1.983(7) Å). The average coordination bond length of 1.948 Å and bite angles (N1–Fe–N2, –N5, N8–Fe–N9, –N12) of 79.7(3)–80.4(3) are typical values for low spin iron(II) ions in the series of this tridentate ligand [9]. Interatomic distances of N–O groups in nitronyl nitroxides are in the range of 1.26(1)–1.28(1) Å for N6–O1, N7–O2, N13–O3 and N14–O4, respectively, which are characteristic of radical centers. It should be mentioned that no significant intermolecular contact between the NO groups of dppNN (>4 Å) was observed and cations are magnetically isolated.

3.3. Magnetic susceptibility measurements of *1*

Magnetic susceptibility measurements for **1** was done in the temperature range of 5–340 K and a $\chi_m T$–T plot was shown in Fig. 2. The $\chi_m T$ values below 130 K are almost constant (0.83 emu mol^{-1} K), which corresponds to the uncorrelated two radical spins. It is pointed out that coordination bond lengths at 200 K are typical values for low-spin iron(II) ions, which magnetically isolate two radicals in the molecule. Sudden decrease of the $\chi_m T$ values below 30 K is due to weak intermolecular antiferromagnetic interactions between dppNN radicals. As the temperature was increased up to 340 K, gradual increase of $\chi_m T$ values was observed and this increase was recovered in the cooling process, suggesting this phenomenon being a reversible thermal spin-crossover phenomenon. A $\chi_m T$ value of 1.21 emu mol^{-1} K at 340 K corresponds to 14% of the central iron(II) ion being in the high spin state. The sum of Curie constants for isolated iron(II) ion and two radicals is 3.75 emu mol^{-1} K, and the critical temperature of the spin transition is higher than 340 K. When the sample was irradiated with 500–600 nm light at 5 K, the $\chi_m T$ values of **1** abruptly increased, suggesting that the metastable HS state was trapped. The $\chi_m T$ values of the light irradiated sample (metastable high-spin state) increased as the temperature was increased, reaching a maximum value of 1.27 emu mol^{-1} K at 26 K. The $\chi_m T$ value is smaller than the value

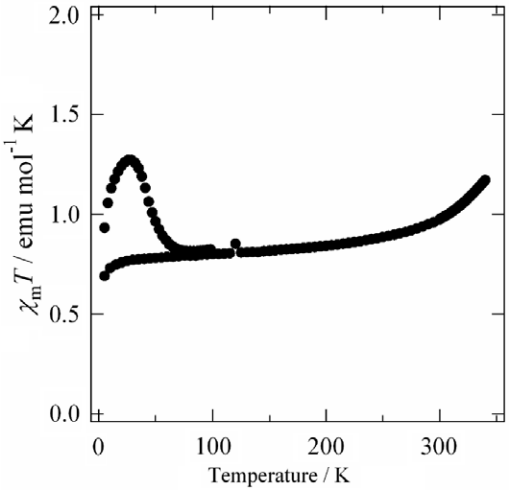


Fig. 2. $\chi_m T$–T plot for **1**.

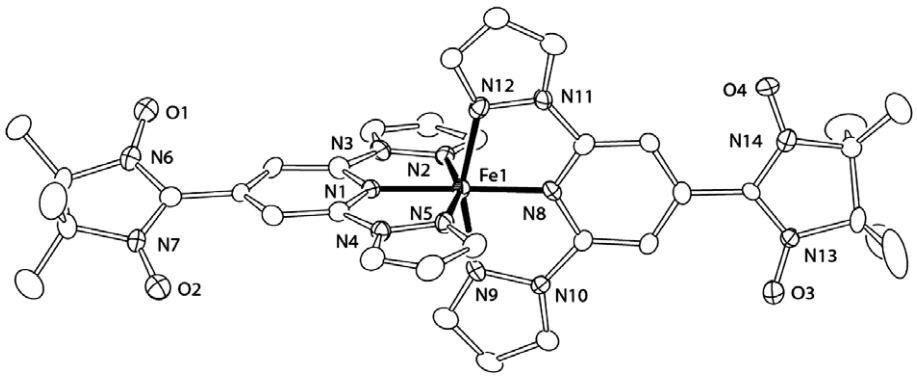


Fig. 1. ORTEP diagram of **1**. Selected interatomic distances (Å) for **1**: Fe1–N1 1.889(6), Fe1–N2 1.974(6), Fe1–N5 1.958(6), Fe1–N8 1.903(6), Fe1–N9 1.983(7), Fe–N12 1.982(8), O1–N6 1.28(1), O2–N7 1.27(1), O3–N13 1.26(1), O4–N14 1.27(1).

(3.75 emu mol^{-1} K) expected for the isolated iron(II) ion and two radicals, and this might be due to the incomplete spin conversion or antiferromagnetic interactions between high spin iron(II) ion and organic radicals. Further increase of temperature resulted in sudden decrease of $\chi_m T$ values, which indicates the occurrence of complete relaxation from the metastable HS state to the LS state.

4. Conclusion

We prepared a novel iron(II) complex with nitronyl nitroxide radicals, and its structure and magnetic property were studied. Magnetic susceptibility measurement suggests central iron(II) ion show the thermal spin transition with a critical temperature higher than 340 K, and LIESST phenomenon was confirmed by light irradiation at 5 K.

Acknowledgements

This work was partially supported by a Grant-in-aid for Scientific Researches from the Ministry of Education, Culture, Sports, Science and Technology, Japan, and by the COE and TARA projects of University of Tsukuaba.

Appendix A. Supplementary material

CCDC 278362 contains the supplementary crystallographic data for this paper. These data can be obtained free of charge via htpp://www.ccdc.cam.ac.uk/conts/retrieving.html, or from the Cambridge Crystallographic Data Centre, 12 Union Road, Cambridge CB2 1EZ, UK; fax: (+44) 1223-336-033; or e-mail: deposit@ccdc.cam.ac.uk. Supplementary data associated with this article can be found, in the online version, at doi:10.1016/j.poly.2006.09.052.

References

[1] (a) M. Kimura, T. Horai, T. Muto, K. Hanabusa, H. Shirai, Chem. Lett. (1999) 1129;
(b) S. Kelch, M. Rehahn, Macromolecules 32 (1999) 5818;
(c) U. Velten, B. Lahn, M. Rehahn, Macromol. Chem. Phys. 198 (1997) 2789;
(d) U.S. Schubert, C. Eschbaumer, Angew. Chem., Int. Ed. 41 (2002) 2892.
[2] U.S. Schubert, C.H. Weidl, C.N. Moorefield, G.R. Baker, G.R. Newkome, Polym. Preprints 40 (1999) 940.
[3] B.J. Holliday, C.A. Mirkin, Angew. Chem., Int. Ed. 40 (2001) 2022.
[4] (a) M. Kinoshita, P. Turek, M. Tamura, K. Nozawa, D. Shiomi, Y. Nakazawa, M. Ichikawa, M. Takahashi, K. Awaga, T. Inabe, Y. Maruyama, Chem. Lett. (1991) 1225;
(b) M. Takahashi, P. Turek, Y. Nakawaza, M. Tamura, K. Nozawa, D. Shiomi, M. Ishikawa, M.M. Kinoishita, Phys. Rev. Lett. 67 (1991) 746;
(c) T. Sugawara, M. Matsushita, A. Izuoka, N. Wada, N. Takeda, M. Ishikawa, J. Chem. Soc., Chem. Commun. (1994) 1723;
(d) M.M. Matsushita, A. Izuoka, T. Sugawara, T. Kobayashi, N. Wada, N. Takeda, M. Ishikawa, J. Am. Chem. Soc. 119 (1997) 4369.
[5] (a) A. Caneschi, D. Gateschi, R. Sessoli, P. Rey, Acc. Chem. Res. 22 (1989) 392;
(b) M. Fettouhi, M. Khaled, A. Waheed, S. Golhen, L. Ouhab, J.P. Sutter, O. Kahn, Inorg. Chem. 38 (1999) 3967;
(c) A. Caneschi, F. Ferrao, D. Gateschi, P. Rey, R. Sessoli, Inorg. Chem. 29 (1990) 4217;
(d) H. Iwamura, K. Inoue, T. Hayamizu, Pure Appl. Chem. 68 (1996) 243.
[6] (a) A. Iino, T. Suzuki, S. Kaizaki, J. Chem. Soc., Dalton. Trans. (2003) 4604;
(b) J.R. Gardinier, R. Clérac, F.P. Gabbaï, J. Chem. Soc., Dalton. Trans. (2001) 3453;
(c) Z. Liu, Z. Lu, D. Zhang, Z. Jiang, L. Li, C. Liu, D. Zhu, Inorg. Chem. 43 (2004) 6620;
(d) M. Fettouhi, B.E. Ali, A.M. EI-Ghanam, S. Golhen, L. Ouahab, N. Daro, J.-P. Sutter, Inorg. Chem. 41 (2002) 3705;
(e) H. Oshio, T. Watanabe, A. Ohto, T. Ito, T. Ikoma, S. Tero-Kubota, Inorg. Chem. 36 (1997) 3014.
[7] C. Stroh, P. Turek, P. Rabu, R. Ziessel, Inorg. Chem. 40 (2001) 5334.
[8] (a) E. Fursova, G. Romanenko, V. Ikorskii, V. Ovcharenko, Polyhedron 22 (2003) 1957;
(b) E. Fursova, V. Ovcharenko, G. Romanenko, E.V. Tretyakov, Tetrahedron Lett. 44 (2003) 6397;
(c) S. Fokin, V. Ovcharenko, G. Romanenko, V. Ikorskii, Inorg. Chem. 43 (2004) 969;
(d) E.V. Tretyakov, S. Fokin, G. Romanenko, V. Ovcharenko, Polyhedron 22 (2003) 1965;
(e) K. Fegy, N. Sanz, D. Luneau, E. Belorizki, P. Rey, Inorg. Chem. 37 (1998) 4518;
(f) C. Lescop, E. Belorizky, D. Luneau, P. Rey, Inorg. Chem. 41 (2002) 3375;
(g) C. Aoki, I. Ishida, T. Nogami, Inorg. Chem. 42 (2003) 7616;
(h) T. Yeltov, V. Ovcharenko, V. Ikorskii, G. Romanenko, S. Vasilevsky, Polyhedron 20 (2001) 1215;
(i) H. Mori, O. Nagano, M. Kozaki, D. Shimoi, K. Sato, T. Takui, K. Okada, Polyhedron 20 (2001) 1663.
[9] A. Caneschi, D. Gateschi, N. Lalioti, C. Sangregorio, R. Sessoli, G. Venturi, A. Vindigni, A. Rettori, M.G. Pini, M.A. Novak, Angew. Chem., Int. Ed. 40 (2001) 1760.
[10] (a) V.A. Money, I.R. Evans, M.A. Halcrow, A.E. Goeta, J.A.K. Howard, Chem. Commun. (2003) 158;
(b) J.M. Holland, J.A. McAllister, Z. Lu, C.A. Kilner, M.T-. Pett, M.A. Halcrow, Chem. Commun. (2001) 577;
(c) V.A. Money, J. Elhaïk, M.A. Halcrow, J.A.K. Howard, J. Chem. Soc., Dalton. Trans. (2004) 1516;
(d) V.A. Money, J. Elhaïk, I.R. Evans, M.A. Halcrow, J.A.K. Howard, J. Chem. Soc., Dalton. Trans. (2004) 65;
(e) V.A. Money, J. Elhaïk, S.A. Barrett, C.A. Kilner, I.R. Evans, M.A. Halcrow, J. Chem. Soc., Dalton. Trans. (2003) 2053.
[11] T. Vermonden, D. Branowska, A.T.M. Marcelis, E.J.R. Sudhölter, Tetrahedron 59 (2003) 5039.
[12] E.F. Ullman, J.H. Osiecki, D.G.B. Boocock, R. Darcy, J. Am. Chem. Soc. 94 (1972) 7049.

2. Experimental

2.1. Syntheses

All reagents were purchased and used without further purification. Schiff base ligands of $H_2$5-Br-sae, $H_2$3-OMe-sap, $H_2$5-Br-sap, and H_2sap were prepared by condensation reactions of corresponding salicylaldehyde with aminoethyl alcohol or aminopropyl alcohol.

*[$Mn^{III}Cu^{II}$(**5**-Br-sap)$_2$Cl(EtOH)] (**1**)*: 5-Br-salicylaldehyde (201 mg, 1.0 mmol), 3-aminopropanol (75 mg, 1.0 mmol) and triethylamine (202 mg, 2.0 mmol) were dissolved in ethanol (20 ml), forming yellow solution. $MnCl_2 \cdot 4H_2O$ (198 mg, 1.0 mmol) in ethanol (10 ml) was added to the yellow solution to obtain dark brown solution, and $CuCl_2 \cdot 2H_2O$ (56 mg, 0.33 mmol) in ethanol (10 ml) was added. The reaction mixture was allowed to stand for overnight to give dark brown crystals of **1**. *Anal.* Calc. for $C_{22}H_{26}N_2Br_2Cl_1Cu_1Mn_1O_5 \cdot C_2H_5OH \cdot H_2O$: C, 37.13; H, 4.41; N, 3.61; Cu, 8.92; Mn, 7.71. Found: C, 37.03; H, 4.22; N, 3.46; Cu, 8.33; Mn, 7.47%.

*[$Mn^{III}Cu^{II}$(5-Cl-sap)$_2$Cl(MeOH)] (**2**)*: Dark brown crystals of **2** were obtained in the same manner as **1** using 5-Cl-salicylaldehyde as a starting material. *Anal.* Calc. for $C_{21}H_{24}N_2Cl_3Cu_1Mn_1O_5 \cdot H_2O$: C, 40.21; H, 4.17; N, 4.46; Cu, 10.43; Mn, 9.02. Found: C, 40.19; H, 3.56; N, 4.47; Cu, 10.29; Mn, 9.21%.

[$Mn^{III}_2Cu^{II}_2$(5-Br-sap)$_4$(H_2O)$_2$](ClO_4)$_2$ (**3**(ClO_4)$_2$): 5-Br-salicylaldehyde (201 mg, 1.0 mmol), 3-aminopropanol (75 mg, 1.0 mmol) and triethylamine (202 mg, 2.0 mmol) were dissolved in acetonitrile (10 ml), forming yellow solution. $Mn(ClO_4)_2 \cdot 6H_2O$ (288 mg, 1.0 mmol) in acetonitrile (10 ml) was added to the yellow solution to give dark brown solution and $Cu(ClO_4)_2 \cdot 6H_2O$ (124 mg, 0.33 mmol) in acetonitrile (10 ml) was added. The reaction mixture was allowed to stand for 3 days to obtain dark brown crystals of **3**$(ClO_4)_2$. *Anal.* Calc. for $C_{40}H_{44}N_4Br_4Cl_2Cu_2Mn_2O_{18} \cdot CH_3CN$: C, 32.81; H, 3.08; N, 4.56; Cu, 8.92; Mn, 7.71. Found: C, 32.61; H, 2.85; N, 4.26; Cu, 7.65; Mn, 7.68.

[$Mn^{III}Cu^{II}_3$(5-Br-sae)$_4$(H_2O)$_2$](PF_6)·2Et_2O (**4**(PF_6) · 2Et_2O): 5-Br-salicylaldehyde (201 mg, 1.0 mmol), 2-aminoethanol (61 mg, 1.0 mmol) and triethylamine (202 mg, 2.0 mmol) were dissolved in methanol (20 ml), forming yellow solution. $MnCl_2 \cdot 4H_2O$ (198 mg, 1.0 mmol) in methanol (10 ml) was added to the yellow solution to give dark brown solution and $CuCl_2 \cdot 2H_2O$ (56 mg, 0.33 mmol) in methanol (10 ml) was added. After stirring for 30 min, $AgPF_6$ was added to the reaction mixture and AgCl was removed by suction. After standing for overnight, resulting precipitate was filtered off and dissolved in acetonitrile. The slow diffusion of diethylether to the acetonitrile solution gave green crystals of **4**$(PF_6) \cdot 2Et_2O$. *Anal.* Calc. for $C_{36}H_{36}N_4Br_4Cu_3F_6Mn_1O_{10}P_1$: C, 31.00; H, 2.60; N, 4.02; Cu, 13.67; Mn, 3.94. Found: C, 31.35; H, 2.55; N, 3.95; Cu, 13.99; Mn, 3.73%.

*[$Mn^{III}_2Mn^{II}_2Cu^{II}_4$(3-OMe-sap)$_4$($\mu_4$-O)$_2$($\mu_2$-OMe)$_2Cl_2$]$Cl_2$ · 2MeOH (**5**Cl_2 · 2MeOH)*: *o*-vaniline (152 mg, 1.0 mmol), 3-amino-1-propanol (75 mg, 1.0 mmol) and triethylamine (202 mg, 2.0 mmol) were dissolved in methanol (20 ml), forming yellow solution. $MnCl_2 \cdot 4H_2O$ (198 mg, 1.0 mmol) in methanol (10 ml) was added to the yellow solution to give dark brown solution, and $CuCl_2 \cdot 2H_2O$ (114 mg, 0.67 mmol) in methanol (10 ml) was added. The reaction mixture was allowed to stand for a week to obtain dark green crystals of **5**$Cl_2 \cdot 2$MeOH. *Anal.* Calc. for $C_{46}H_{58}N_4Cl_4Cu_4Mn_4O_{16} \cdot 2H_2O$: C, 35.08; H, 3.97; N, 3.56; Cu, 16.14; Mn, 13.95. Found: C, 35.20; H, 4.15; N, 3.29; Cu, 16.18; Mn, 13.95%.

[$Mn^{III}_2Ni^{II}_2$(sap)$_2$(sal)$_2$(μ_3-OMe)$_2$(OAc)$_2$] (**6**): Salicylaldehyde (= Hsal, 122 mg, 1.0 mmol), 3-amino-1-propanol (75 mg, 1.0 mmol) and triethylamine (202 mg, 2.0 mmol) were dissolved in methanol (20 ml), forming yellow solution. $Mn(CH_3COO)_2 \cdot 4H_2O$ (246 mg, 1.0 mmol) in methanol (10 ml) was added to the yellow solution to obtain dark brown solution. To the dark brown solution, green mixture of Hsal (122 mg, 1.0 mmol), triethylamine (202 mg, 2.0 mmol), and $Ni(CH_3COO)_2 \cdot 4H_2O$ (248 mg, 1.0 mmol) in methanol (30 ml) was added. The reaction mixture was allowed to stand for one night to give dark green crystals of **6**. *Anal.* Calc. for $C_{40}H_{44}N_2Mn_2Ni_2O_{14} \cdot H_2O$: C, 47.00; H, 4.53; N, 2.74; Mn, 10.75; Ni, 11.48. Found: C, 47.17; H, 4.67; N, 2.67; Mn, 10.69; Ni, 11.88%.

[$Mn^{III}_2Ni^{II}_2$(sap)$_2$(sal)$_2$(μ_3-OMe)$_2$(NO_3)$_2$(MeOH)$_2$] (**7**): Dark green crystals of **7** were obtained in the same manner as **6** using $Mn(NO_3)_2 \cdot 6H_2O$ and $Ni(NO_3)_2 \cdot 6H_2O$ as metal sources. *Anal.* Calc. for $C_{38}H_{46}N_4Mn_2Ni_2O_{19}$: C, 41.87; H, 4.49; N, 5.14; Mn, 10.06; Ni, 10.75. Found: C, 41.96; H, 4.25; N, 5.05; Mn, 9.66; Ni, 10.78%.

2.2. X-ray crystallography

All crystals were mounted on a glass capillary, and data were collected at −70 °C (Bruker SMART APEX diffractometer coupled with a CCD area detector with graphite monochromated Mo Kα ($\lambda = 0.71073$ Å) radiation), respectively. Structures were solved by direct methods and expanded by using Fourier techniques using SHELXTL program. Crystal data for the complexes were summarized in Table 1. Empirical absorption corrections by SADABS (G.M. Sheldrick, 1994) were carried out. In the structure analyses, non-hydrogen atoms were refined with anisotropic thermal parameters. Hydrogen atoms were included in calculated positions and refined with isotropic thermal parameters riding on those of the parent atoms.

2.3. Physical measurements

DC magnetic susceptibility data were collected by using a Quantum Design MPMS-XL SQUID magnetometer at temperatures ranging from 1.8 to 300 K.

Table 1
Crystallographic data for complexes **1**–**7**

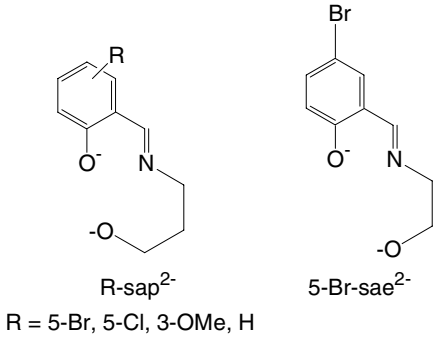
	1	**2**	**3**$(ClO_4)_2$	**4**$(PF_6)\cdot 2Et_2O$	**5**$Cl_2\cdot 2MeOH$	**6**	**7**
Formula	$C_{22}H_{25}Br_2ClCuMnN_2O_5$	$C_{21}H_{23}Cl_3CuMnN_2O_5$	$C_{40}H_{44}Br_4Cl_2Cu_2Mn_2N_2O_{18}$	$C_{44}H_{56}Br_4Cu_3F_6MnN_4O_{12}P$	$C_{48}H_{64}Cl_4Cu_4Mn_4N_4O_{16}$	$C_{40}H_{44}Mn_2N_2Ni_2O_{14}$	$C_{38}H_{44}Mn_2N_4Ni_2O_{20}$
Formula weight ($g\,mol^{-1}$)	711.20	608.27	1468.28	1543.11	1568.80	1004.06	1104.05
Temperature (K)	200	200	200	200	200	200	200
Crystal system	monoclinic	monoclinic	triclinic	monoclinic	monoclinic	triclinic	triclinic
Space group	$P2_1/c$	$P2_1/c$	$P\bar{1}$	$P2/c$	$P2_1/n$	$P\bar{1}$	$P\bar{1}$
a (Å)	11.351(2)	10.7219(19)	9.024(3)	8.764(4)	13.5527(17)	9.159(1)	8.899(2)
b (Å)	17.803(4)	17.738(3)	11.378(3)	14.421(7)	13.4718(18)	11.115(2)	9.637(2)
c (Å)	7.3532(16)	7.2985(13)	13.446(4)	21.802(10)	16.720(2)	11.735(2)	14.929(3)
α (°)			94.809(5)			73.938(3)	84.108(3)
β (°)	92.732(4)	96.290(3)	98.645(6)	92.625(8)	100.626(3)	70.770(3)	86.969(3)
γ (°)			111.246(5)			69.250(3)	65.196(3)
V (Å^3)	1484.3(6)	1379.7(4)	1257.6(6)	2752(2)	3000.4(7)	1037.5(3)	1156.1(4)
Z	2	2	1	2	2	1	1
d_{calc} ($Mg\,m^{-3}$)	1.572	1.482	1.973	1.862	1.774	1.870	1.586
μ (mm^{-1})	3.664	1.239	4.684	4.381	2.451	1.577	1.416
Reflections collected	6495	6148	5470	11 815	14 463	5163	5101
Independent reflections [R_{int}]	2141 [0.0310]	1970 [0.0132]	3541 [0.0235]	3967 [0.0578]	4295 [0.0231]	2963 [0.0154]	3283 [0.0311]
Final R indices[a] [$I > 2\sigma(I)$]	$R_1 = 0.0587$, $wR_2 = 0.2014$	$R_1 = 0.0539$, $wR_2 = 0.1796$	$R_1 = 0.0448$, $wR_2 = 0.1154$	$R_1 = 0.0519$, $wR_2 = 0.1285$	$R_1 = 0.0257$, $wR_2 = 0.0821$	$R_1 = 0.0325$, $wR_2 = 0.0888$	$R_1 = 0.0513$, $wR_2 = 0.1276$

[a] $R_1 = \sum ||F_o| - |F_c|| / \sum |F_o|$. $wR_2 = [\sum[w(F_o^2 - F_c^2)^2]/\sum[w(F_o^2)^2]]^{0.5}$.

3. Results and discussion

3.1. Syntheses of Mn–Cu and Mn–Ni hetero-metal clusters

The Mn–Cu and Mn–Ni hetero-metal clusters, **1**–**7**, were synthesized by simple reactions of multidentate schiff base ligands ($H_2$5-Br-sae, $H_2$3-OMe-sap, $H_2$5-Br-sap, and H_2sap) (Scheme 1), with metal sources and suitable co-ligands (Scheme 2). All reactions possessed good selectivity for the target compounds, and the selectivity can be achieved by optimization of reaction conditions. The dinuclear complex of **1** and **2** were synthesized by the reaction of tridentate Schiff base ligand (5-Br-sap^{2-}) and metal chlorides with a reaction ratio of 3:3:1. The similar reaction in acetonitrile using metal perchlorate gave a tetranuclear complex of **3**$(ClO_4)_2$. The tetranuclear complex of **4**$(PF_6) \cdot 2Et_2O$ was obtained by using metal chloride and 5-Br-sae^{2-} followed by removing chloride ions with $AgPF_6$. On the other hand, octanuclear complex of **5**$Cl_2 \cdot 2MeOH$ was synthesized by employing a quadridentate Schiff base ligand of 3-OMe-sap^{2-}. $Mn^{III}_2Ni^{II}_2$ tetranuclear clusters of **6** and **7** were obtained by the reactions of tridentate Schiff base ligand (sap^{2-}), bidentate co-ligand (sal^{1-}), and metal sources, where **6** and **7** were obtained as acetate and nitrate salts.

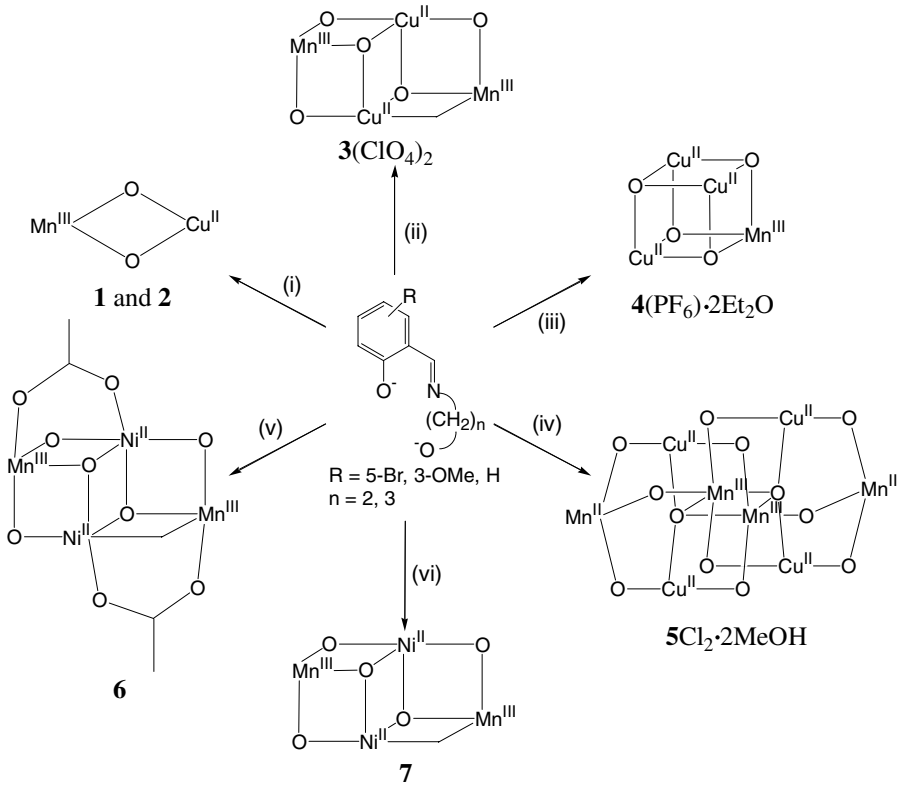


Scheme 1.

3.2. Descriptions of crystal structures

3.2.1. [$Mn^{III}Cu^{II}$(5-Br-sap)$_2$Cl(EtOH)] (**1**) and [$Mn^{III}Cu^{II}$(5-Cl-sap)$_2$Cl(MeOH)] (**2**)

An ORTEP diagram of a Mn–Cu dinuclear complex of **1** is shown in Fig. 1. **1** crystallizes in monoclinic space group $P2_1/c$ with the molecule lying on the crystallographic centre of inversion. The Crystal structure of **1** is isostructural with the previously reported dinuclear complex of [$Mn^{III}Cu^{II}$(5-Br-sap)$_2$Cl(MeOH)] [13], and **1** has a dinu-



(i) $MnCl_24H_2O$, $1/3CuCl_24H_2O$, MeOH, (ii) (1) $MnCl_24H_2O$, $1/3CuCl_24H_2O$, MeOH (2) $AgPF_6$, MeCN, (iii) $Mn(ClO_4)_26H_2O$, $1/3Cu(ClO_4)_26H_2O$, MeCN, (iv) $MnCl_24H_2O$, $2/3CuCl_24H_2O$, MeOH, (v) $Mn(OAc)_24H_2O$, $Ni(OAc)_24H_2O$, sal^{1-}, MeOH, (vi) $Mn(NO_3)_26H_2O$, $Ni(NO_3)_26H_2O$, sal^{1-}, MeOH.

Scheme 2.

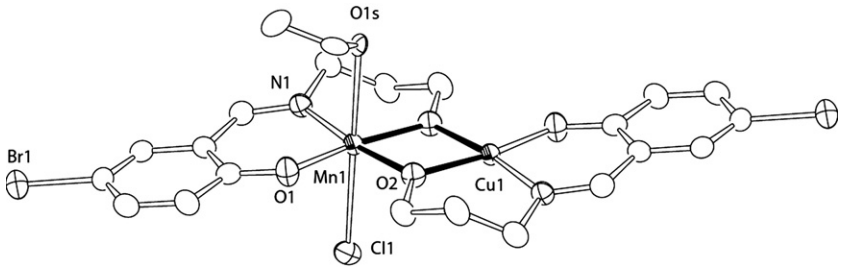


Fig. 1. ORTEP drawing of **1**. Selected bond lengths (Å) and angles (°); Mn(1)–O(1) 1.871(6), Mn(1)–O(2) 1.948(6), Mn(1)–O(2)# 1.928(6), Mn(1)–N(1) 1.959(7), Mn(1)–Cl(1) 2.694(5), Mn(1)–O(1S) 2.477(11), Mn(1)–Mn(1)# 3.013(2), Mn(1)#–O(2)–Mn(1), 102.0(2). Symmetry operation #: $-x+1$, $-y+1$, $-z+2$.

clear structure composed of a Mn^{III} and Cu^{II} core doubly bridged by two alkoxo groups. The dc magnetic susceptibility data and bond valence sum (BVS) considerations (3.05 and 2.02 for Mn^{III} and Cu^{II} ions, respectively) support that **1** is not a 1:1 mixture but a mixed metal system. The dinuclear unit has a crystallographic inversion, and the Mn^{III} and Cu^{II} ion sites are, therefore, positionally disordered. The coordination geometry about Mn^{III} and Cu^{II} ions are presumed to be octahedral and square planar geometry, respectively. Equatorial coordination sites of the Mn^{III} ion are occupied by three oxygen atoms and one nitrogen atom from the tridentate Schiff base ligand, and the axial sites of Mn^{III} ion are occupied by an oxygen atom of coordinating ethanol molecule and a chloride ion. Coordination bond lengths in the equatorial plane are in the range of 1.871(6)–1.959(7) Å, while the axial coordination bonds showed significant elongation (2.477(11) and 2.694(5) Å) which is due to the Jahn–Teller distortion. The coordination bond lengths for Cu^{II} ions are the same as those for the corresponding coordination bonds of Mn^{III} ion due to the crystallographic inversion centre. The Cu^{II} and Mn^{III} ions are bridged by alkoxo groups with bridging angles of 102.0(2)°. The crystallographic data and the molecular structure of **2** were similar to those of **1** except for the coordinating solvent molecule and substituent group on the ligand (Fig. 2). The coordination bond lengths for the equatorial coordination sites of Mn^{III} and Cu^{II} ions are 1.871(6)–1.959(7) Å, and the Jahn–Teller axis of Mn^{III} ion involves an oxygen atom of methanol and a chloride ion with inter-atomic distances of 2.573(7) and 2.662(3) Å, respectively. BVS calculations gave values of 3.00 and 1.99 for Mn^{III} and Cu^{II} ions, respectively. The bridging angle between Mn^{III} and Cu^{II} ions (Mn1–O2–Cu1) are 101.84(15)°.

3.2.2. $[Mn^{III}_2Cu^{II}_2(5\text{-}Br\text{-}sap)_4(H_2O)_2](ClO_4)_2$ (**3**$(ClO_4)_2$)

The tetranuclear complex of **3**$(ClO_4)_2$ crystallizes in triclinic space group $P2_1/c$ and crystallographic inversion centre exists in the middle of the complex cation. The tetranuclear core consists of an incomplete face-sharing double cube composed of two Mn^{III} and two Cu^{II} ions (Fig. 3). Assignments of metal ions were confirmed by the BVS calculations (3.22 and 2.09 for Mn^{III} and Cu^{II} ions, respectively) and the short coordination bond lengths for Mn^{III} ions. The Mn^{III} and Ni^{II} ions are doubly bridged to form a dinuclear unit by two oxygen atoms (O2 and O4), and the symmetrically related dinuclear cores are linked by two phenoxo (O1 and O1$^{\#}$) and two alkoxo groups (O4 and O4$^{\#}$) in μ_2 and μ_3 fashions, respectively. The Mn^{III} ions have N_1O_5 chromophore in which equatorial sites and one of the axial sites are occupied by four oxygen atoms and one nitrogen atom from the Schiff base ligands and remaining axial sites are coordinated by a water molecule, leading to the distorted octahedral coordination geometry. The coordination bond lengths about Mn^{III} ions are in the range of 1.851(4)–2.008(5) Å for the equatorial sites (Mn1–N2, O2, O3, O4), and 2.312(5) and 2.329(4) Å for the axial sites (Mn1–O5, Mn1–O1$^{\#}$). The coordination

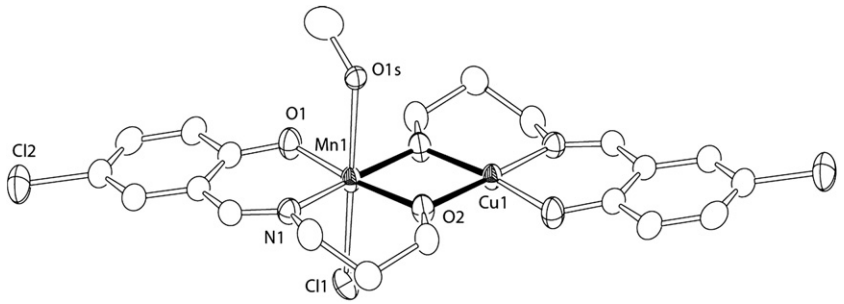


Fig. 2. ORTEP drawing of **2**. Selected bond lengths (Å) and angles (°); Mn(1)–O(1) 1.881(3), Mn(1)–O(2) 1.922(3), Mn(1)–O(2)# 1.948(3), Mn(1)–N(1) 1.977(4), Mn(1)–O(1)S 2.573(7), Mn(1)–Cl(1) 2.662(3), Mn(1)–Mn(1)# 3.0045(12), Mn(1)–O(2)–Mn(1)# 101.84(15). Symmetry operation #: $-x$, $-y+1$, $-z$.

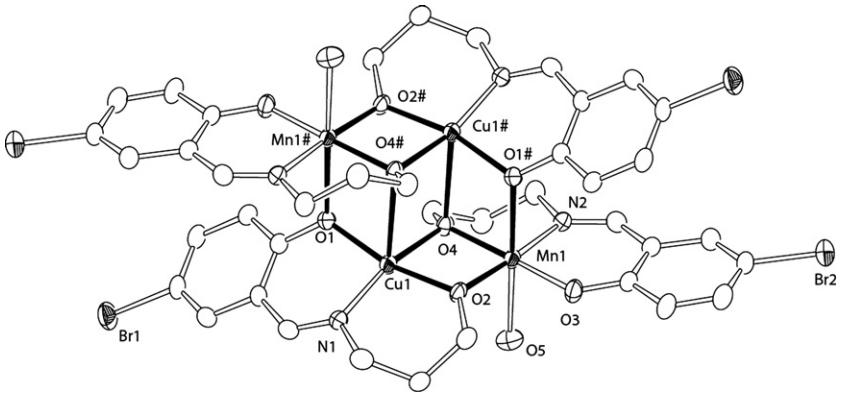


Fig. 3. ORTEP drawing of $\mathbf{3}(ClO_4)_2$. Selected bond lengths (Å) and angles (°); Mn(1)–O(3) 1.851(4), Mn(1)–O(2) 1.898(4), Mn(1)–O(4) 1.901(4), Mn(1)–N(2) 2.008(5), Mn(1)–O(5) 2.312(5), Mn(1)–O(1)# 2.329(4), Cu(1)–O(1) 1.896(4), Cu(1)–O(2) 1.915(4), Cu(1)–N(1) 1.948(5), Cu(1)–O(4) 2.004(4), Cu(1)–O(4)#, 2.585(4), Mn(1)–Cu(1) 2.9613(14), Mn(1)–O(2)–Cu(1), 101.91(18), Mn(1)–O(1)–Cu(1), 105.33(17), Mn(1)–O(4)–Cu(1), 98.62(17), Cu(1)–O(1)–Cu(1)#, 96.94(16), Mn(1)–O(4)–Cu(1)#, 96.17(16). Symmetry operation #: $-x+1$, $-y+1$, $-z+2$.

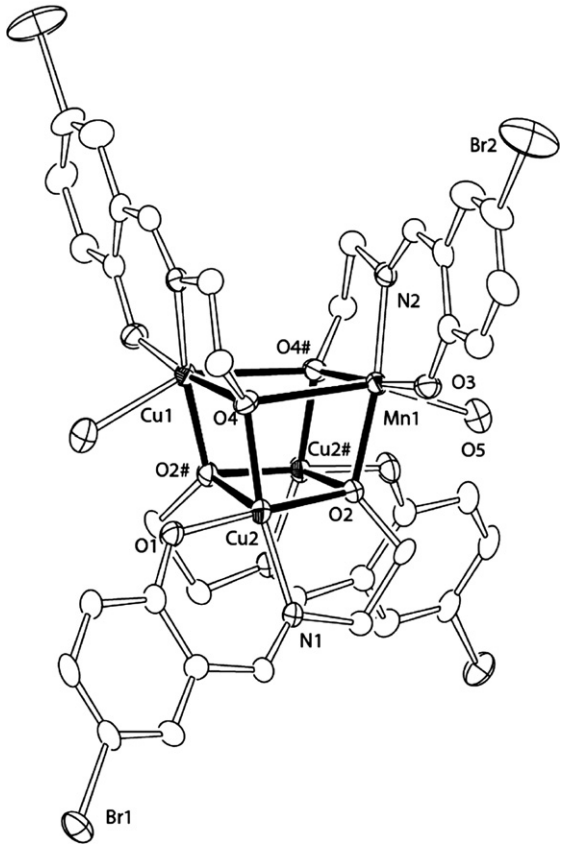


Fig. 4. ORTEP drawing of $\mathbf{4}(PF_6)\cdot 2Et_2O$. Selected bond lengths (Å) and angles (°); Cu(2)–O(1) 1.898(5), Cu(2)–N(1) 1.932(6), Cu(2)–O(4) 1.952(4), Cu(2)–O(2) 1.953(5), Cu(2)–O(2)# 2.511(5), Mn/Cu(1)–N(2) 1.955(6), Mn/Cu(1)–O(2) 1.958(4), Mn/Cu(1)–O(3) 1.901(5), Mn/Cu(1)–O(4)# 1.962(4), Mn/Cu(1)–O(5) 2.319(5), Mn/Cu(1)–O(4) 2.534(5), Cu(2)–O(2)–Mn/Cu(1) 109.7(2), Mn/Cu(1)–O(4)–Mn/Cu(1)# 100.88(19), Cu(2)–O(4)–Mn/Cu(1)# 107.6(2), Cu2(2)–O(4)–Mn/Cu(1) 89.93(16). Symmetry operation #: $-x$, y, $-z+1/2$.

geometry of Cu^{II} ions is square pyramidal, and equatorial positions are occupied by three oxygen atoms (O1, O2, O4) and one nitrogen atom (N1) with coordination bond lengths of 1.896(4)–2.004(4) Å. The apical position of the Cu^{II} ions is weakly coordinated by oxygen atom ($O4^{\#}$) of μ_3-alkoxo group and the bond length of Cu1–$O4^{\#}$ is 2.585(4) Å. The bridging angles between Cu^{II} and Mn^{III} ions are 96.17(16)–105.33(17)°, while Cu1–O4-$Cu1^{\#}$ is 96.94(16)°.

3.2.3. $[Mn^{III}Cu^{II}_3(5\text{-}Br\text{-}sae)_4(H_2O)_2](PF_6)\cdot 2Et_2O$ ($\mathbf{4}(PF_6)\cdot 2Et_2O$)

The ORTEP drawing of **4** is shown in Fig. 4. The crystal of $\mathbf{4}(PF_6)\cdot 2Et_2O$ has monoclinic space group $P2/c$ and the unit cell contains two complex cations, two counter anions, and four diethylether molecules. The complex cation is composed of a tetranuclear cubic core, in which four metal ions are bridged by four μ_3-alkoxo groups from the Schiff base ligands. The cubic core contains two crystallographically independent metal ions with square pyramidal or distorted octahedral coordination geometries, and the two sets of metal ions are related by the crystallographic two-fold axis passing through the centre of the complex cation. The valence sum considerations, elemental analysis, and dc magnetic susceptibilities measurement suggested that the complex cation is constructed by three Cu^{II} ions and one Mn^{III} ion. Consequently, the five-coordinated metal ions are assigned to Cu^{II} ions, while symmetrically related two six-coordinated metal ions can be considered to be positionally disordered Mn^{III} and Cu^{II} ions, respectively. The equatorial coordination bond lengths of the square pyramidal Cu^{II} coordination sites are in the range of 1.898(5)–1.953(5) Å, and the apical position is coordinated by an alkoxo group of the Schiff base ligand with coordination bond length of 2.511(5) Å. The positionally disordered Mn^{III} and Cu^{II} ions have distorted octahedral geometry with elongated axis along O4–Mn1–O5, and the coordination bond lengths with axial atoms are 2.319(5) and 2.534(5) Å for Mn1–O5 and Mn1–O4, respectively. Bridging angles of metal ions with alkoxo groups are in the range of 89.93(16)–109.7(2)°.

3.2.4. $[Mn^{III}_2Mn^{II}_2Cu^{II}_4(3\text{-}OMe\text{-}sap)_4(\mu_4\text{-}O)_2(\mu_2\text{-}OMe)_2Cl_2]Cl_2 \cdot MeOH$ ($\mathbf{5}Cl_2 \cdot 2MeOH$)

$\mathbf{5}Cl_2 \cdot 2MeOH$ crystallizes in monoclinic space group $P2_1/n$ and complex cation situated on the crystallographic inversion centre (Fig. 5). **5** has hexanuclear Mn^{III}_2 Cu^{II}_4 core bridged by μ_4-oxo and μ_2-alkoxo groups, and peripheral Mn^{II} ions are attached to the Cu^{II} and Mn^{III} ions in the core by μ_2-phenoxo- and μ_2-methoxo-bridges, respectively. In **5**, Schiff bases act as quadridentate ligands to construct octanuclear core. The metal assignment and their oxidation states were confirmed by considering coordination bond lengths, existence of Jahn–Teller elongation, and BVS calculations (3.11, 2.06, 1.82 and 1.98 for Mn1, Mn2, Cu1 and Cu2 ions, respectively). Mn^{III} ions have a five-coordinated square pyramidal coordination geometry. The equatorial coordination sites of Mn^{III} ions are occupied by four oxygen atoms (O2, O5, O7, and O8) from two Schiff base ligands, one μ_4-oxo and μ_2-alkoxo groups, respectively, and $O7^{\#}$ ion coordinates from the apical position. The coordination geometries of four-coordinated Cu^{II} ions are square planar with N_1O_3 chromophore and coordination bond lengths are in the range of 1.932(3)–2.036(2) and 1.911(2)–1.959(2) Å for Cu1 and Cu2 ions, respectively. Mn^{II} ions have octahedral coordination geometry, where two Schiff base ligands coordinate to the Mn^{II} ions with phenoxy and methoxy groups acting as bidentate ligands. The remaining coordination sites are occupied by μ_2-alkoxo and chloride ions. The coordination bond lengths of Mn^{II} ions are in the range of 2.119(3)–2.4335(12) Å, which are apparently longer than those of Mn^{III} ions.

3.2.5. $[Mn^{III}_2Ni^{II}_2(sap)_2(sal)_2(\mu_3\text{-}OMe)_2(OAc)_2]$ (**6**) and $[Mn^{III}_2Ni^{II}_2(sap)_2(sal)_2(\mu_3\text{-}OMe)_2(NO_3)_2(MeOH)_2]$ (**7**)

The ORTEP diagrams of tetranuclear complexes **6** and **7** are shown in Figs. 6 and 7. Both complexes crystallized in triclinic space group $P\bar{1}$. The complex **6** has an incomplete face-sharing double cubane core composed of two Mn^{III} and two Ni^{II} ions (Fig. 6). The metal ions were assigned by BVS calculations and observations of Jahn–Teller elongations for the Mn^{III} ions. BVS calculations gave the values of 3.18 and 2.12 for Mn^{III} and Ni^{II} ions, respectively. The Mn^{III} ions are coordinated by tridentate Schiff base ligands forming mononuclear units, while Ni^{II} ion constructs mononuclear unit with bidentate co-ligands (sal^{1-}). These mononuclear units are linked to form a planar Mn^{III}–Ni^{II} dinuclear unit by μ_2-alkoxo and μ_3-methoxo groups, where additional acetate ion bridged the Mn^{III} and Ni^{II} ions from the axial direction supporting dinuclear core. The crystallographically related two dinuclear units are bridged by μ_2-phenoxo and μ_3-methoxo groups to form the tetranuclear core. The equatorial sites of six-coordinated Mn^{III} ions are occupied by N1, O1, O2, O7 atoms with bond lengths of 1.865(2)–2.021(3) Å, and the axial coordination bond lengths are 2.340(2) and 2.198(2) Å, which are significantly elongated due to Jahn–Teller distortions. The Ni^{II} ions

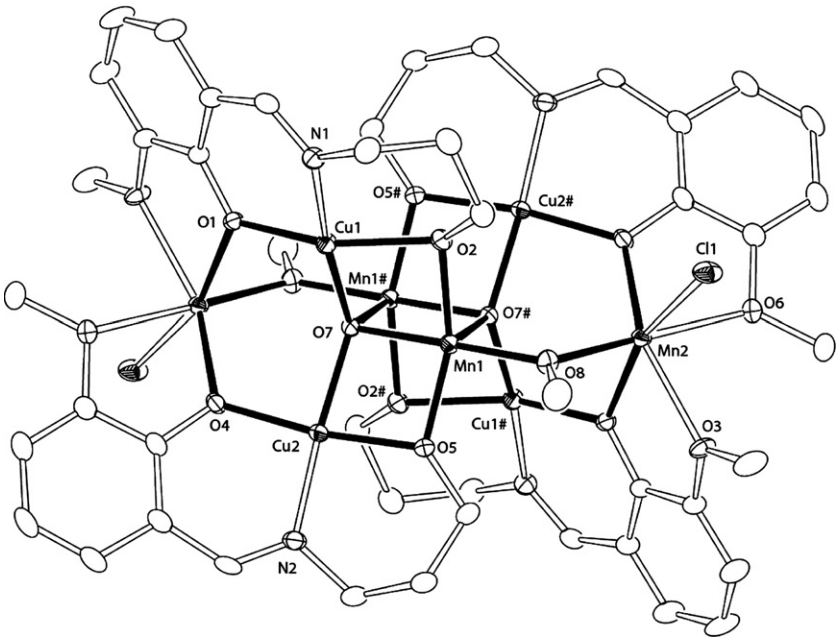


Fig. 5. ORTEP drawing of $\mathbf{5}Cl_2 \cdot 2MeOH$. Selected bond lengths (Å) and angles (°); Mn(1)–O(7) 1.918(2), Mn(1)–O(2) 1.923(3), Mn(1)–O(5) 1.896(3), Mn(1)–O(8) 1.873(3), Mn(1)–O(7)# 2.110(2), Mn(2)–O(3) 2.271(3), Mn(2)–O(6) 2.404(3), Mn(2)–O(1)# 2.195(2), Mn(2)–O(4)# 2.124(3), Mn(2)–O(8) 2.119(3), Mn(2)–Cl(1) 2.4335(12), Cu(1)–O(1) 1.973(2), Cu(1)–O(7) 1.932(2), Cu(1)–N(1) 1.932(3), Cu(1)–O(2) 2.036(2), Cu(2)–O(4) 1.911(2), Cu(2)–O(5) 1.920(3), Cu(2)–N(2) 1.947(3), Cu(2)–O(7) 1.959(2), Cu(2)–Mn(1) 2.8550(7), Cu(1)–Mn(1) 2.8375(7), Mn(1)–Mn(1)# 2.9722(11), Cu(1)–O(1)–Mn(2)# 116.85(11), Cu(1)–O(7)–Cu(2) 127.79(12), Mn(1)–O(2)–Cu(1) 91.52(10), Mn(1)–O(7)–Mn(1)# 94.97(10), Cu(2)–O(4)–Mn(2)# 116.86(12), Cu(1)–O(7)–Mn(1)# 116.86(11), Mn(1)–O(5)–Cu(2) 96.86(11), Cu(2)–O(7)–Mn(1)# 113.14(11), Mn(1)–O(7)–Cu(1) 94.93(10), Mn(1)–O(8)–Mn(2) 118.71(12), Mn(1)–O(7)–Cu(2) 94.83(10). Symmetry operation #: $-x+2$, $-y+1$, $-z$.

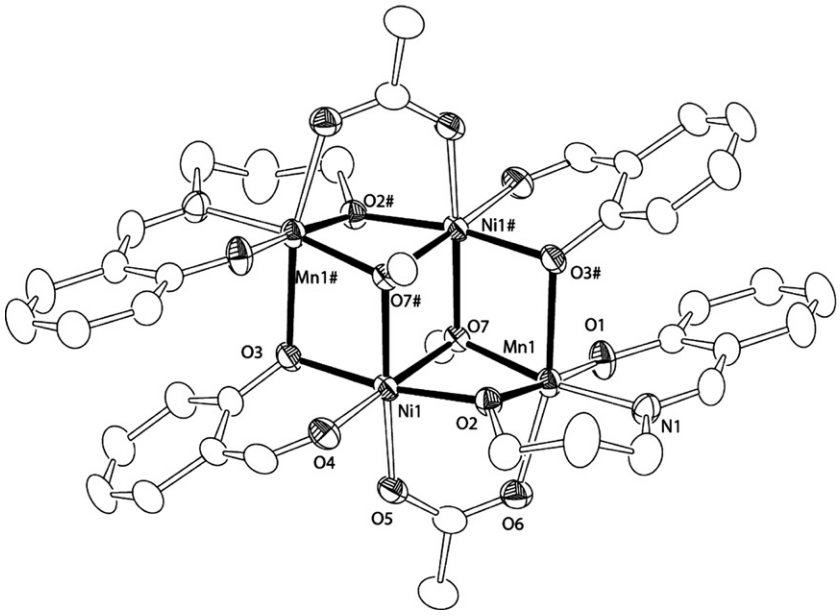


Fig. 6. ORTEP drawing of **6**. Selected bond lengths (Å) and angles (°); Mn(1)–O(1) 1.865(2), Mn(1)–O(2) 1.873(2), Mn(1)–O(7) 1.966(2), Mn(1)–N(1) 2.021(3), Mn(1)–O(6) 2.198(2), Mn(1)–O(3)# 2.340(2), Mn(1)–Ni(1) 2.9614(7), Ni(1)–O(3) 2.006(2), Ni(1)–O(2) 2.027(2), Ni(1)–O(5) 2.032(2), Ni(1)–O(4) 2.044(2), Ni(1)–O(7) 2.0766(19), Ni(1)–O(7)# 2.094(2), Mn(1)–O(2)–Ni(1) 98.74(9), Ni(1)–O(3)–Mn(1)# 94.19(8), Mn(1)–O(7)–Ni(1) 94.16(8), Mn(1)–O(7)–Ni(1)# 103.61(8), Ni(1)–O(7)–Ni(1)# 98.19(8). Symmetry operation #: $-x+1$, $-y+1$, $-z+1$.

with six-coordinated octahedral geometry have coordination bond lengths of 2.027(2)–2.094(2) Å, which are longer than those of Mn^{III} ions. **7** has a similar structural feature as **6** except for the bridging structure between Mn^{III} and Ni^{II} ions (Fig. 7). In the case of **6**, Mn^{III} and Ni^{II} ions in the dinuclear unit were bridged by μ_2-alkoxo, μ_3-methoxo, and μ_2-acetato groups, while in **7** bridging μ_2-acetato groups were replaced with methanol molecules and nitrate ions. It is noted that those different bridging structures lead to the significant difference in the magnetic interactions between Mn^{III} and Ni^{II} ions. The equatorial coordination bond lengths of Mn^{III} ions are in the range of 1.855(4)–

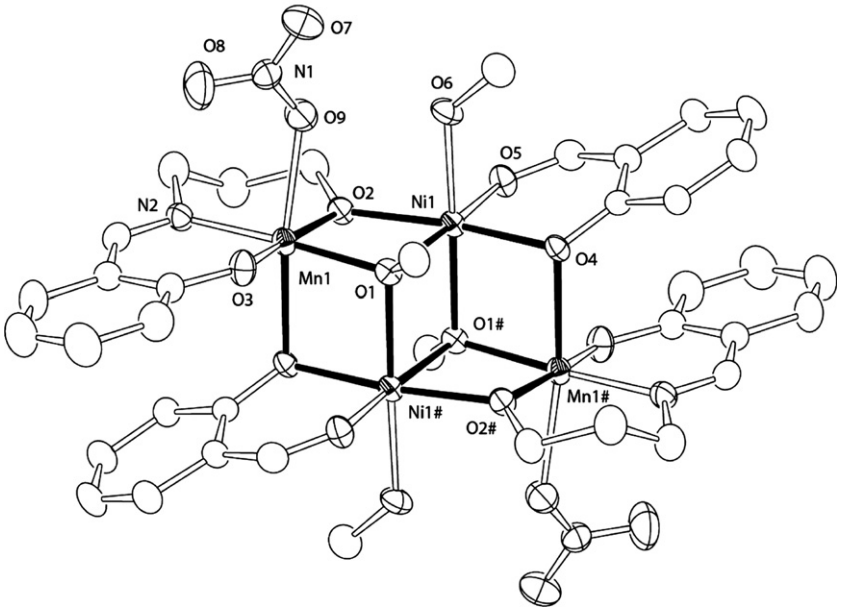


Fig. 7. ORTEP drawing of **7**. Selected bond lengths (Å) and angles (°); Mn(1)–O(3) 1.855(4), Mn(1)–O(2) 1.886(3), Mn(1)–O(1) 1.971(3), Mn(1)–N(2) 2.000(4), Mn(1)–O(4)#1 2.251(3), Mn(1)–O(9) 2.283(4), Ni(1)–O(4) 1.998(3), Ni(1)–O(2) 2.030(3), Ni(1)–O(5) 2.034(4), Ni(1)–O(1) 2.087(3), Ni(1)–O(6) 2.096(4), Ni(1)–O(1)#1 2.109(3), Ni(1)–Mn(1) 3.0758(11), Mn(1)–O(1)–Ni(1) 98.51(14), Mn(1)–O(1)–Ni(1)# 99.95(14), Ni(1)–O(1)–Ni(1)# 97.85(14), Ni(1)–O(4)–Mn(1)# 94.54(13), Mn(1)–O(2)–Ni(1) 103.45(15). Symmetry operation #: $-x$, $-y+2$, $-z+2$.

2.000(4) Å, and the axial coordination bond lengths are 2.251(3) and 2.283(4) Å. The Ni^{II} ions have an O_6 chromophore with bond lengths of 1.998(3)–2.109(4) Å. BVS calculations for Mn^{III} and Ni^{II} ions yielded the values of 3.19 and 2.05, which support the assignment of metal ions. The bridging angles between Ni^{II} and Mn^{III} ions for **6** and **7** are in the range of 94.19(8)–103.61(8)° and 94.54(13)–103.45(15)°, while the crystallographically related two Ni^{II} ions are bridged with the angles of 98.19(8)° and 97.35(14)° for **6** and **7** respectively.

3.3. Magnetic properties of the complexes 1–7

3.3.1. Magnetic properties of 1 and 2

The dc magnetic susceptibility measurements for **1** and **2** were performed in the temperature range of 1.8–300 K (Fig. 8). The $\chi_m T$–T curves for **1** and **2** were very similar to that for the previously reported dinuclear complex of $[Mn^{III}Cu^{II}(5\text{-Br-sap})_2Cl(MeOH)]$ [13], which was proven to be an SMM with $S = 5/2$ and $D = -1.86\ cm^{-1}$. The $\chi_m T$ values at 300 K are 3.91 emu mol^{-1} K and 3.85 emu mol^{-1} K for **1** and **2**, respectively, which is larger than the value (3.375 emu mol^{-1} K with $g = 2$) expected for the uncorrelated Mn^{III} and Cu^{II} ions. The $\chi_m T$ values gradually increased as decreasing the temperature, reaching the plateau values of 4.23 emu mol^{-1} K and 4.03 emu mol^{-1} K for **1** (100 K) and **2** (150 K), respectively. The temperature dependences of $\chi_m T$ values suggested the occurrence of ferromagnetic interactions between Mn^{III} and Cu^{II} ions to give $S = 5/2$ spin ground states in **1** and **2**. The smaller $\chi_m T$ values in the plateau compared with the theoretical value (4.20 emu mol^{-1} K) for the $S = 5/2$ state are due to smaller g value of Mn^{III} ions than 2.0. The sudden decrease of $\chi_m T$ values at lower temperature region is due to intermolecular antiferromagnetic interactions and/or zero-field splitting. The magnetic susceptibility data were analyzed using spin Hamiltonian of $H = -2J_{MnCu}S_{Mn} \cdot S_{Cu}$. The least squares calculations using the data above 24 K (**1**) and 50 K (**2**) gave the best fit parameters of $J_{MnCu} = +64\ cm^{-1}$, $g_{Mn} = 1.93$, $g_{Cu} = 2.10$ for **1**, and $J_{MnCu} = +85\ cm^{-1}$, $g_{Mn} = 1.90$, $g_{Cu} = 2.08$, $\theta = -1.96\ cm^{-1}$ for **2**, where θ is intermolecular magnetic interaction. The preliminary ac magnetic susceptibility measurements for **1** and **2** showed the frequency dependent out-of-phase ac susceptibilities (Figs. S1 and S2), suggesting both complexes being SMMs.

3.3.2. Magnetic properties of $3(ClO_4)_2$, $4(PF_6) \cdot 2Et_2O$, and $5Cl_2 \cdot 2MeOH$

The dc magnetic susceptibility measurements were carried out in the temperature range of 1.8–300 K and the results were depicted in Fig. 9. In $\mathbf{3}(ClO_4)_2$, the $\chi_m T$ value at 300 K is 6.80 emu mol^{-1} K, which is a good agreement with the spin only value for magnetically isolated two Mn^{III} and two Cu^{II} ions (6.75 emu mol^{-1} K, $g = 2$). Upon decreasing the temperature, the $\chi_m T$ value showed gradual increase down to 150 K, followed by the decrease at lower temperature, and this suggested that the ferromagnetic interactions are operative in high temperature region, followed by antiferromagnetic interactions leading to $S = 0$ spin ground state. Analyses of the susceptibility data for $\mathbf{3}(ClO_4)_2$ were carried out by using simple butterfly model, however, curve fitting was inferior, which might be due to the simplified model, and further analysis of the magnetic data has not been done yet. In the $\chi_m T$ versus T plot for $\mathbf{4}(PF_6) \cdot 2Et_2O$, $\chi_m T$ values shows steady decrease upon temperature was lowered, which suggests overall antiferromagnetic couplings among metal ions. The $\chi_m T$ value at 300 K is 3.38 emu mol^{-1} K, which is smaller than the Curie constant (4.13 emu mol^{-1} K) for uncorrelated one Mn^{III} and three Cu^{II} ions. The $\chi_m T$ value reached the minimum value of 0.5 emu mol^{-1} K at 1.8 K. The data was analyzed by using spin Hamiltonian of $H = -2J_{CuCu}(S_{Cu1} \cdot S_{Cu2} + S_{Cu2} \cdot S_{Cu3} + S_{Cu1} \cdot S_{Cu3}) - 2J_{CuMn}S_{Mn1} \cdot (S_{Cu1} + S_{Cu2} + S_{Cu3})$. The least squares calculation gave the best fit parameters of $J_{CuCu} = -12.4\ cm^{-1}$, $J_{MnCu} = -18.0\ cm^{-1}$, $g_{Mn} = 1.98$, and $g_{Cu} = 2.19$, with a spin ground state of $S = 1/2$. The $\chi_m T$ value at 300 K for $\mathbf{5}Cl_2 \cdot 2MeOH$ is 12.38 emu mol^{-1} K and showed constant decrease as temperature was lowered, reaching the value of 2.35 emu mol^{-1} K at

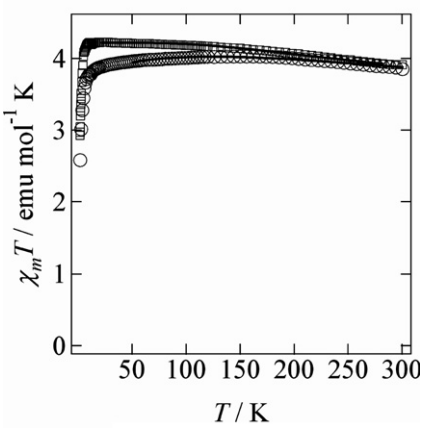


Fig. 8. $\chi_m T$ vs. T plots for **1** (□) and **2** (○).

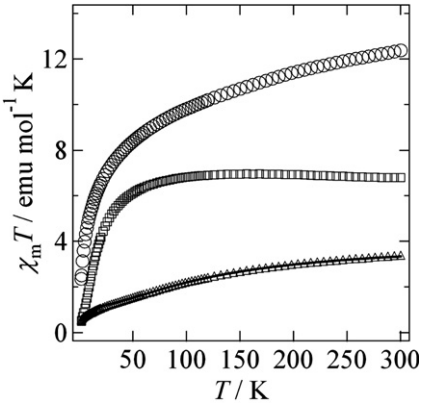


Fig. 9. $\chi_m T$ vs. T plots for $\mathbf{3}(ClO_4)_2$ (□), $\mathbf{4}(PF_6) \cdot 2Et_2O$ (△) and $\mathbf{5}Cl_2 \cdot 2MeOH$ (○).

1.8 K. The theoretical value expected for magnetically isolated four Cu^{II} and two Mn^{III} and Mn^{II} ions is 16.25 emu mol^{-1} K and the smaller value might be due to relatively strong antiferromagnetic interactions. The $\chi_m T$–T plot for **5**$Cl_2 \cdot 2MeOH$ indicated that overall antiferromagnetic interactions are dominant in whole temperature range and further analysis of magnetic data has not been carried out due to complicated magnetic interactions among the metal ions.

3.3.3. Magnetic properties of 6 and 7

DC magnetic susceptibility measurements were performed on **6** and **7** in the temperature range of 1.8–300 K. $\chi_m T$ versus temperature plots for complex **6** and **7** are shown in Fig. 10. In **6**, the $\chi_m T$ value at 300 K is 8.07 emu mol^{-1} K, which is close to the value (8.00 emu mol^{-1} K, $g = 2$) expected for the isolated two Mn^{III} and two Ni^{II} ions. Upon cooling the temperature, the $\chi_m T$ value gradually decreased and reached to 1.97 emu mol^{-1} K at 1.8 K, and this suggested the occurrence of antiferromagnetic interactions among metal centres. The temperature dependence of magnetic data above 20 K was analyzed by using simplified symmetrical butterfly model with spin Hamiltonian of $H = -2J_{MnNi}(S_T^2 - S_A^2 - S_B^2) - 2J_{NiNi}(S_A^2 - S_{Cul}^2 - S_{Cul}^2)$, where $S_A = S_{Ni1} + S_{Ni1\#}$, $S_B = S_{Mn1} + S_{Mn1\#}$, $S_T = S_A + S_B$. The least squares calculation gave the fit parameters of $J_{MnNi} = -1.80$ cm^{-1}, $J_{NiNi} = -3.41$ cm^{-1}, where g_{Ni} and g_{Mn} are fixed to be 2.2 and 1.9, and the spin ground state can be considered to be an $S = 2$. The $\chi_m T$ value at 1.8 K was smaller than the Curie constant (3.00 emu mol^{-1} K, $g = 2$) for an $S = 2$ state, which is due to zero-field splitting and/or intermolecular antiferromagnetic interactions. In complex **7**, the $\chi_m T$ value is 8.93 emu mol^{-1} K at 300 K, which is slightly larger than the spin only value of 8.00 emu mol^{-1} K expected for a complex consisting of two Mn^{III} and two Ni^{II} noninteracting ions. As lowering the temperature, $\chi_m T$ values gradually increased, reaching a maximum value of 17.65 emu mol^{-1} K at 5.00 K, followed by decrease down to 14.83 emu mol^{-1} K at 1.8 K. Based on temperature dependent susceptibility data ferromagnetic interactions were operative between the Mn^{III} and Ni^{II} ions, which is in contrast to **6**. The magnetic data for **7** was fitted by using the data above 20 K and the best fit parameters of $J_{MnNi} = +3.62$ cm^{-1}, $J_{NiNi} = -7.81$ cm^{-1}, $g_{Ni} = 2.2$ (fixed), and $g_{Mn} = 1.9$ (fixed) were obtained. The spin ground state was considered to be $S = 5$. The difference in the magnetic properties between **6** and **7** is originating from the bridging structures of the Mn^{III} and Ni^{II} ions. In **6**, the magnetic paths between Mn^{III} and Ni^{II} ions are through μ_2-alkoxo, μ_3-methoxo and μ_2-acetato bridges, among which antiferromagnetic pathways through acetate bridges might be predominant, leading to the lower spin ground state of $S = 2$. On the other hands, complex **7** has high spin ground state originating from ferromagnetic interactions through μ_2-alkoxo, μ_3-methoxo groups, which might be due to the accidental orthogonality of the magnetic orbitals.

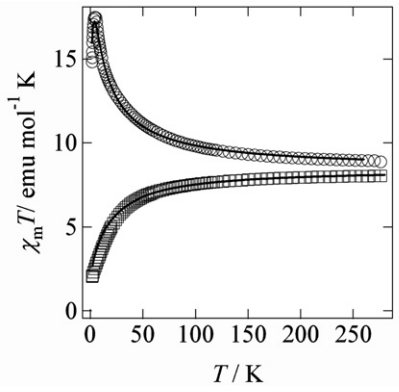


Fig. 10. $\chi_m T$ vs. T plots for **6** (□) and **7** (○).

4. Conclusion

A versatile synthetic method for multi-nuclear hetero-metal clusters has been developed, and a series of Mn–Cu clusters with the core structures of $[Mn^{III}Cu^{II}]$, $[Mn^{III}_2Cu^{II}_2]$, $[Mn^{III}Cu^{II}_3]$, and $[Mn^{III}_2Mn^{II}Cu^{II}_4]$, as well as Mn–Ni clusters with $[Mn^{III}_2Ni^{II}_2]$ cores were synthesized. This strategy might be applicable to prepare various 3d–3d and 3d–4f hetero-metal clusters by changing reaction conditions and slight modifications of bridging ligands. Further studies to obtain larger clusters are in progress.

Acknowledgements

This work was partially supported by a Grant-in-aid for Scientific Researches from the Ministry of Education, Culture, Sports, Science and Technology, Japan, and by the COE and TARA projects of University of Tsukuaba.

Appendix A. Supplementary material

CCDC 617406, 617405, 617409, 617410, 617404, 617407, and 617408 contain the supplementary crystallographic data for **1**, **2**, **3**$(ClO_4)_2$, **4**$(PF_6) \cdot 2Et_2O$, **5**$Cl_2 \cdot 2MeOH$, **6**, and **7**. These data can be obtained free of charge via http://www.ccdc.cam.ac.uk/conts/retrieving.html, or from the Cambridge Crystallographic Data Centre, 12 Union Road, Cambridge CB2 1EZ, UK; fax: (+44) 1223-336-033; or e-mail: deposit@ccdc.cam.ac.uk. Supplementary data associated with this article can be found, in the online version, at doi:10.1016/j.poly.2006.09.053.

References

[1] U. Bossek, T. Weyhermüler, K. Weighardt, B. Nuber, J. Weiss, J. Am. Chem. Soc. 112 (1990) 6387.
[2] C.F. Yocum, V.L. Pecoraro, Curr. Opin. Chem. Biol. 3 (1999) 182.
[3] W. Ruettinger, M. Yagi, K. Wolf, S. Bernasek, G.C. Dismukes, J. Am. Chem. Soc. 122 (2000) 10353.

[4] S. Mukhopadhyay, R.J. Staples, W.H. Armstrong, Chem. Commun. (2002) 664.
[5] S. Bhaduri, M. Pink, G. Christou, Chem. Commun. (2002) 2352.
[6] G. Christou, D. Gatteschi, D.N. Hendrickson, R. Sessoli, MRS Bull. 25 (2000) 66.
[7] H. Oshio, N. Hoshino, T. Ito, J. Am. Chem. Soc. 122 (2000) 12602.
[8] H. Oshio, N. Hoshino, T. Ito, M. Nakano, J. Am. Chem. Soc. 126 (2004) 8805.
[9] S. Koizumi, M. Nihei, M. Nakano, H. Oshio, Inorg. Chem. 44 (2005) 1208.
[10] H. Oshio, M. Nihei, S. Koizumi, T. Shiga, H. Nojiri, M. Nakano, N. Shirakawa, M. Akatsu, J. Am. Chem. Soc. 127 (2005) 4568.
[11] H. Oshio, M. Nakano, Chem. Eur. J. 11 (2005) 5178.
[12] H. Ōkawa, H. Frutachi, D.E. Fenton, Coord. Chem. Rev. 174 (1998) 51.
[13] H. Oshio, M. Nihei, A. Yoshida, H. Nojiri, M. Nakano, A. Yamaguchi, Y. Karaki, H. Ishimoto, Chem. Eur. J. 11 (2004) 843.

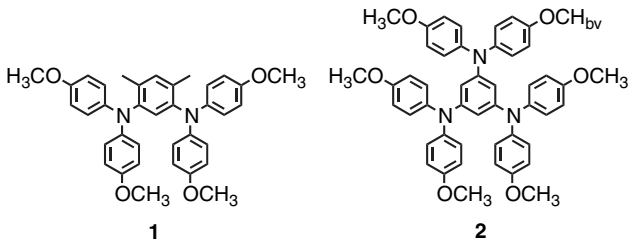
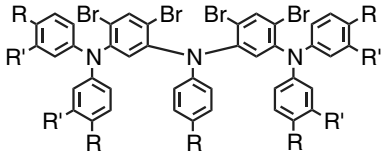


Fig. 1. Structures of *N*,*N*,*N*′,*N*′-tetrakis(4-anisyl)-4,6-dimethyl-1,3-phenylene-diamine (**1**) and *N*,*N*,*N*′,*N*′,*N*″,*N*″-hexakis(4-anisyl)-1,3,5-phenylene-triamine (**2**).

nutation (ESTN) method was applied to the di- and trication, unequivocally identifying the spin multiplicities in their triplet and quartet ground state, respectively. In the designed molecules, four or six methoxy groups, i.e., strong electrodonating groups, are introduced to stabilize the di- or tricationic states, respectively. We have examined the relationship for a number of 1,3-bis(diarylamino)benzenes as exemplified by **1**, establishing the molecular design rules to obtain diamine-based stable triplet dications in the ground state. Thus, an elaborate molecular design for tricationic entities has been challenging issues for us. Although we reported that a two-dimensionally extended triamine gives the corresponding stable trication in solution at low temperature [2b], as one-dimensionally extended triamines, 3,3′-bis(diarylamino)triphenylamines emerge, which allow us to modify molecular structures more easily in terms of synthetic chemistry. Recently, Ito et al. have reported a highly brominated derivative **3** (Fig. 2), which gives the corresponding stable dication upon two electrons oxidation [2h]. However, they failed to detect the corresponding trication with polybromo substitutions. Their results encouraged us to design and synthesize compound **4**, which has five electrodonating methyl groups at the peripheral rings and four bromo groups at the central rings. Compound **4** is expected to yield more thermodynamically stable mono- and oligo-cations than those of **3** [2j]. The CV measurements of **4** showed the generation of both stable dication $\mathbf{4}^{++}$ and moderately stable trication $\mathbf{4}^{+++}$ at ambient temperature. The electron transfer stopped-flow (ETSF) method allowed us to study the spectroscopic properties of the mono-, di- and tricationic states of **4**. These results are the first report on detection of a one-dimensional oligoarylamine-based tricationic state. The enhancement of the thermodynamic and kinetic stability



3: R=Br, R'=H
4: R=CH_3, R'=H
5: R=R'=CH_3

Fig. 2. Structures of 3,3′-bis(diarylamino)triphenylamines (**3**–**5**).

for oligo-cations of **4** is ascribed to the steric as well as electronic effects of the electrodonating methyl groups, which raise the HOMO energy level. The ESR study of the dication $\mathbf{4}^{++}$ showed that the ground state is spin-triplet. The trication $\mathbf{4}^{+++}$ was not stable enough in a time scale for the conventional ESR sampling, indicating that chemical modification was not successful enough to stabilize the tricationic states in solution.

In this study, we have redesigned and synthesized a new alkylated triamine **5** with nine methyl groups at the peripheral aromatic rings, which is expected to give thermodynamically more stable oligocationic states. The stabilities of the corresponding oligo-cationic states have been examined by using the cyclic voltammetry and ETSF method. The electronic states of the oligocationic states have been identified by cw-ESR measurements in rigid glass at low temperature.

2. Results and discussion

2.1. Synthesis of 2,2′,4,4′-tetrabromo-4″-methyl-5,5′-bis(di(3,4-dimethylphenyl)amino)-triphenylamine (5)

As shown in Fig. 3, compound **5** was synthesized and isolated as colorless powder by the similar method reported by Ito et al. [2h]. Benzyltrimethylammonium tribromide (BTMA · Br_3), a mild bromination reagent, has successfully been employed for the regioselective bromination at all *para*-positions of 3,3'-bis(diarylamino)triphenylamines [2h,2k]. As all *para*-positions of the peripheral rings are protected by methyl groups for **7**, only the *para*-positions of the central rings would be brominated. All new compounds were fully characterized by spectroscopic methods. Data only for **5** and **7** are given below. Compound **7**: ^{1}H NMR($CDCl_3$): δ 2.13 (s, 12H), 2.18 (s, 12H), 2.24 (s, 3H), 6.51 (dd, 4H, $J = 8.0$, 1.6 Hz), 6.56 (dd, 4H, $J = 8.0$, 1.6 Hz), 6.75–6.78 (m, 6H), 6.89–7.00 (m, 10H). Compound **5**: In spite of repeated recrystallization, compound **5** exhibited a complicated ^{1}H NMR spectrum probably due to the restricted rotation of the nitrogen–aromatic ring bonds. HRMS: Calc.: 1017.0503 for $C_{51}H_{47}N_3Br_4$. Obsd.: 1017.0498.

2.2. Cyclic voltammetry measurements

For compound **5**, cyclic voltammetry in *n*-butyronitrile at ambient temperature revealed two chemically reversible one-electron transfers, indicating the corresponding stable mono- and dications in solution. However, upon further oxidation, an irreversible oxidation wave was observed, indicating the possible generation of the unstable trication. ($E_1^0 = 0.545$V, $E_2^0 = 0.702$V, $E_3^{ox} = 1.129$V, versus F_c/F_c^+) (Fig. 4). Comparing the first redox potential of **5** and **4** ($E_1^0 = 0.605$V versus F_c/F_c^+) [2k], **5** can be oxidized more easily, suggesting the elevated HOMO level due to polyalkylation. AM1 calculation also indicated that the HOMO energy level of **5** is higher than that of **4**.

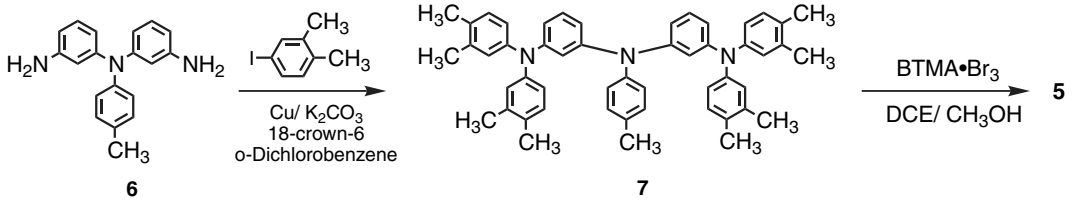


Fig. 3. Synthetic route of **5**.

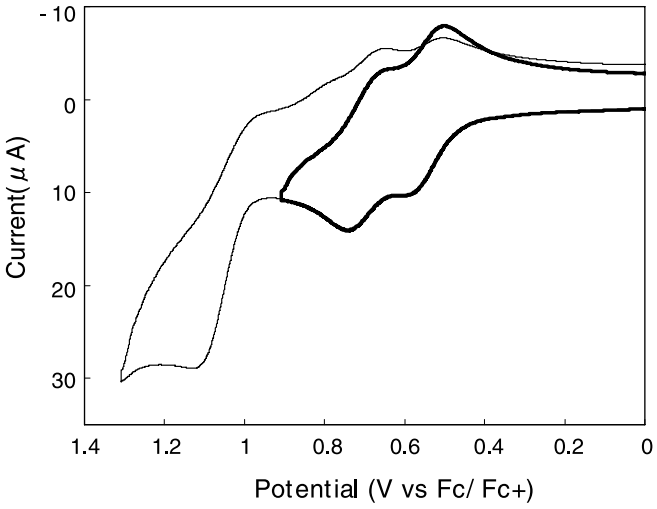


Fig. 4. Cyclic voltammogram of **5** in *n*-butyronitrile at ambient temperature.

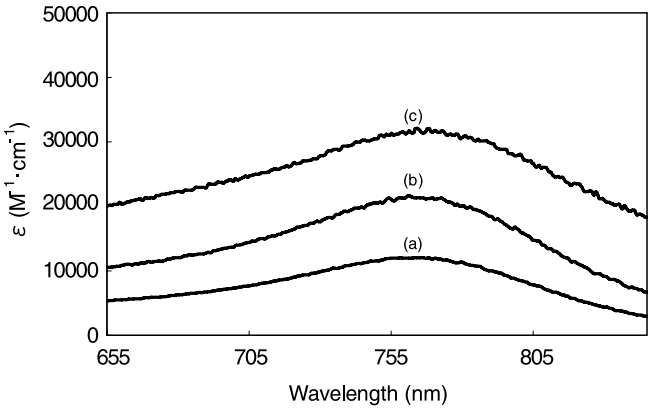


Fig. 5. Absorption spectra observed after mixing of an AN solution of 0.10 mM $TDBPA^{+\cdot}$ with an AN solution of (a) 0.10 mM, (b) 0.050 mM and (c) 0.033 mM of **5**.

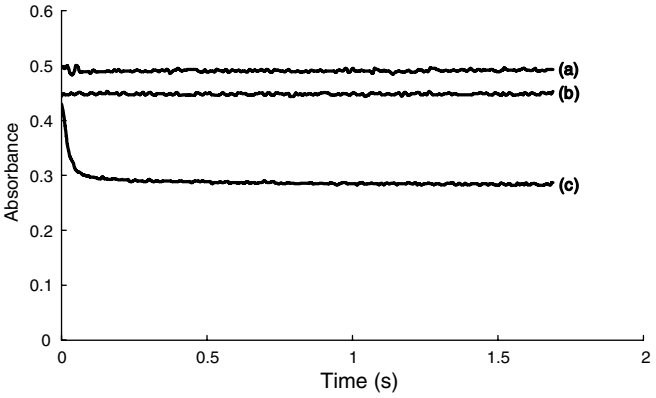


Fig. 6. Time profiles in the absorbance maximum observed after mixing of an AN solution of 0.10 mM $TDBPA^{+\cdot}$ with an AN solution of (a) 0.10 mM, (b) 0.050 mM and (c) 0.033 mM of **5**.

2.3. Electron transfer stopped-flow (ETSF) method

The detail of the ETSF method was described previously [4,5]. The ETSF measurements were carried out in dehydrated acetonitrile (AN) as solvent at ambient temperature. In this study, tris(2,4-dibromophenyl)amine cation radical ($TDBPA^{+\cdot}$)[1] was employed. Compound **5**, upon mixing with 1 equiv. of $TDBPA^{+\cdot}$, exhibited a broad absorption peak at 766 nm, and no decrease in the peak intensity was observed over 1 min, indicating the generation of the stable monocation from **5** (Figs. 5 and 6). The molar absorptivity (ε) of $\mathbf{5}^{+\cdot}$ was determined to be $1.21 \times 10^4\ M^{-1}\ cm^{-1}$ at 766 nm. The ε value of $\mathbf{5}^{+\cdot}$ is smaller than that of $\mathbf{4}^{+\cdot}$ ($\varepsilon = 2.06 \times 10^4\ M^{-1}\ cm^{-1}$), indicating presumably a nonplanar structure for $\mathbf{5}^{+\cdot}$.

Upon mixing with 2 equiv. of $TDBPA^{+\cdot}$, **5** exhibited an absorption peak of the dication $\mathbf{5}^{++}$ at 765 nm. The ε value for $\mathbf{5}^{++}$ was $2.13 \times 10^4\ M^{-1}\ cm^{-1}$ at 765 nm. No decrease in the peak intensity was observed over 1 min, indicating also the stable dication from **5** (Figs. 5 and 6).

On the other hand, upon mixing with 3 equiv. of $TDBPA^{+\cdot}$, **5** exhibited an absorption peak of the trication $\mathbf{5}^{+++}$ at 763 nm ($\varepsilon = 3.18 \times 10^4\ M^{-1}\ cm^{-1}$). Similar to **4**, the ratio of ε for the monocation:dication:trication of **5** was nearly 1:2:3, as expected. Surprisingly, the peak of $\mathbf{5}^{+++}$ completely disappeared in less than 0.2 s, indicating very unstable nature of the trication. As previously reported, $\mathbf{4}^{+++}$ showed the stable trication under the similar condition. The observations suggest that the introduction of extra methyl groups into the *meta*-positions of the peripheral rings results in an unexpectedly large destabilizing effect on the tricationic states. Based on the results of CV, ETSF and ESR measurements of **4** [2k] and the molecular design rules for the stable diamine based dication diradicals, we carefully designed **5**, expecting the trication $\mathbf{5}^{+++}$ to be thermodynamically more stable than $\mathbf{4}^{+++}$. We have claimed that the molecular design guidelines for

[1] TDBPA was synthesized by WAKO Pure Chemicals Ltd. after receiving our special order. See also Ref. [5].

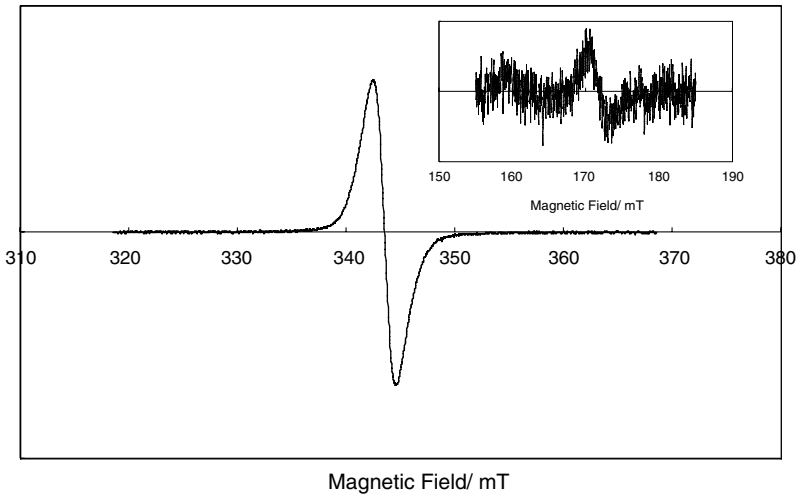


Fig. 7. ESR spectrum observed at 6 K for compound **5** after the oxidation by 3 equiv. of $SbCl_5$, in the allowed ESR transition region (Inset: in the $\Delta M_s = \pm 2$ region). The microwave frequency used was 9.48078 GHz.

the stable monoamine-based cation radicals cannot naively be applied to that for the stable diamine-based dication diradicals. These results suggest that the more sophisticated molecular design rules are required for stabilizing triamine-based trication triradicals. At the present stage, molecular structures of the decomposed products are not identified. Recently, we have found that the ground-state triplet dication $\mathbf{1}^{++}$ slowly decomposes via π-conjugation cleavage [6], suggesting that a similar reaction may have occurred for $\mathbf{5}^{+++}$. Analysis of the decomposed products of $\mathbf{5}^{+++}$ is now in progress.

2.4. ESR measurements

In order to examine the electronic structures of the oligo-cationic states, cw-ESR measurements of chemically oxidized **5** were carried out at liquid-helium temperature. Upon addition of 3 equiv. of $SbCl_5$ into a CH_2Cl_2 solution of **5**, the color of the solution immediately turned blue, indicating the generation of oxidized species. The cw-ESR spectrum observed at 6 K for the oxidized species in the rigid glass is shown in Fig. 7. There appeared a broad line in the allowed ESR transition region. In addition, a weak forbidden transition was observed in the $\Delta M_s = \pm 2$ region, clearly indicating the presence of spin-triplet or quartet species in the ground state (Fig. 7). No signal was observed in the $\Delta M_s = \pm 3$ region. On the other hand, upon addition of a large excess amount of $SbCl_5$, the color of solution containing **5** similarly turned blue immediately, but followed by rapid discoloration to be brown in a few seconds, suggesting the occurrence of rapid decomposition reaction of $\mathbf{5}^{+++}$.

3. Conclusions

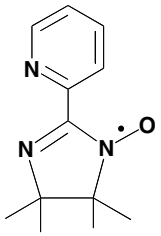
A polyalkylated 3,3′-bis(diarylamino)triphenylamine, (**5**), has been designed and successfully synthesized. Cyclic voltammetry and ETSF measurements have revealed that **5** gives very stable mono- and dicationic states at ambient temperature. However, the corresponding tricationic state was unstable with the lifetime of 0.2 s despite our elaborative molecular design. Conventional continuous-wave ESR study of the chemically oxidized **5** showed that the dication $\mathbf{5}^{++}$ is spin-triplet in the ground state. But the tricationic $\mathbf{5}^{+++}$ may not be stable enough in a time scale for the conventional ESR sampling. Pulse-ESR-based electron nutation spectroscopy at low temperature is applicable to the oxidized states of **5** generated upon addition of 3 equiv. of $SbCl_5$ into a CH_2Cl_2 solution of **5**. Differentiation between the triplet and quartet species is underway by invoking the pulsed-ESR spectroscopy.

References

[1] K. Itoh, M. Kinoshita (Eds.), Molecular magnetism, New Magnetic Materials, Gordon & Breach, Inc., Amsterdam, 2000, Kodansha as copublisher, Tokyo.

[2] (a) P.M. Lahti (Ed.), Magnetic Properties of Organic Materials, Marcel Dekker, Inc., New York, 1999, Chapter 9 and references cited therein;
(b) K. Sato, M. Yano, M. Furuichi, D. Shiomi, K. Abe, T. Takui, K. Itoh, A. Higuchi, K. Katuma, Y. Shirota, J. Am. Chem. Soc. 119 (1997) 6607;
(c) M. Yano, K. Sato, D. Shiomi, A. Ichimura, K. Abe, T. Takui, K. Itoh, Tetrahedron Lett. 37 (1996) 9207;
(d) K.R. Stickley, S.C. Blackstock, J. Am. Chem. Soc. 116 (1994) 11576;
(e) K.R. Stickley, S.C. Blackstock, Tetrahedron Lett. 36 (1995) 1585;
(f) K.R. Stickley, T.D. Selby, S.C. Blackstock, J. Org. Chem. 62 (1994) 448;
(g) T.D. Selby, S.C. Blackstock, J. Am. Chem. Soc. 62 (1997) 448;
(h) A. Ito, H. Ino, K. Tanaka, K. Kanemoto, T. Kato, J. Org. Chem. 67 (2002) 491;
(i) M. Yano, Y. Ishida, K. Aoyama, M. Tatsumi, K. Sato, D. Shiomi, A. Ichimura, T. Takui, Synth. Met. 137 (2003) 1275;
(j) M. Yano, Y. Ishida, M. Tatsumi, K. Sato, D. Shiomi, M. Oyama, T. Takui, J. Phys. Chem. Solids 65 (2004) 733–736;

(k) M. Yano, Y. Nakanishi, K. Matsushita, M. Tatsumi, M. Oyama, K. Sato, T. Takui, Polyhedron 24 (2005) 2116.
[3] (a) E.T. Seo, R.F. Nelson, J.M. Fritsch, L.S. Marcoux, D.W. Leedy, R.N. Adams, J. Am. Chem. Soc. 88 (1966) 3498;
(b) R.F. Nelson, R.N. Adams, J. Am. Chem. Soc. 90 (1968) 3925.
[4] M. Oyama, T. Higuchi, S. Okazaki, J. Chem. Soc., Perkin Trans. 2 (2001) 1287.
[5] M. Oyama, J. Matsui, H. Park, Chem. Commun. (2002) 604.
[6] M. Yano, K. Kitagawa, M. Tatsumi, K. Sato, T. Takui, Polyhedron, in press.



IM-2py

Scheme 1.

to the intraligand IM2py-IM2py magnetic interaction [18]. More definite magnetic information will be afforded from mono (IM2py) complexes without intraligand IM2py–IM2py magnetic interaction. Moreover, IM2py Co(II) complexes are more appropriate to study the magnetic interaction than the NIT2py complexes, because there is a definite antiferromagnetic or ferromagentic interaction of the SOMO π^* with t_{2g} or e_g orbital arising from the orbital overlap or orthogonality, respectively, as found for the Ni(II) and Cr(III) complexes [4–8,12–15].

In this paper, we report a new series of [Co(β-diketonate)$_2$(IM-2py)] with four kinds of β-diketonates; 4,4,4-trifluoro-R-1,3-butanedionates (Rtfc) as shown in Scheme 2, in order to examine the optical and magnetic properties through the substituents effect on the d orbital splitting which are expected from the difference between the electron withdrawing CF_3 and the other substituent groups.

2. Experimental

2.1. Materials

The three 4,4,4-trifluoro-R-1,3-butandiones(HRtfc) of four β-diketones, 4,4,4-trifluoro-1-(trifluoromethyl)-1,3-butanedione(hexafluoroacetylacetone = Hhfac), 4,4,4-trifluoro-1-phenyl-1,3-butanedione(Hphtfc) and 4,4,4-trifluoro-1-(2-naphtyl)-1,3-butanedione(Hnaptfc), were purchased, respectively, from Dojindo Molecular Technologies Inc. and the 4,4,4-trifluoro-1-(2-thienyl)-1,3-butanedione(Hthtfc) from Aldrich.

They were used without further purifications.

2.2. Preparation of IM2py

This was prepared by the literature method [1].

2.3. Preparation of complexes

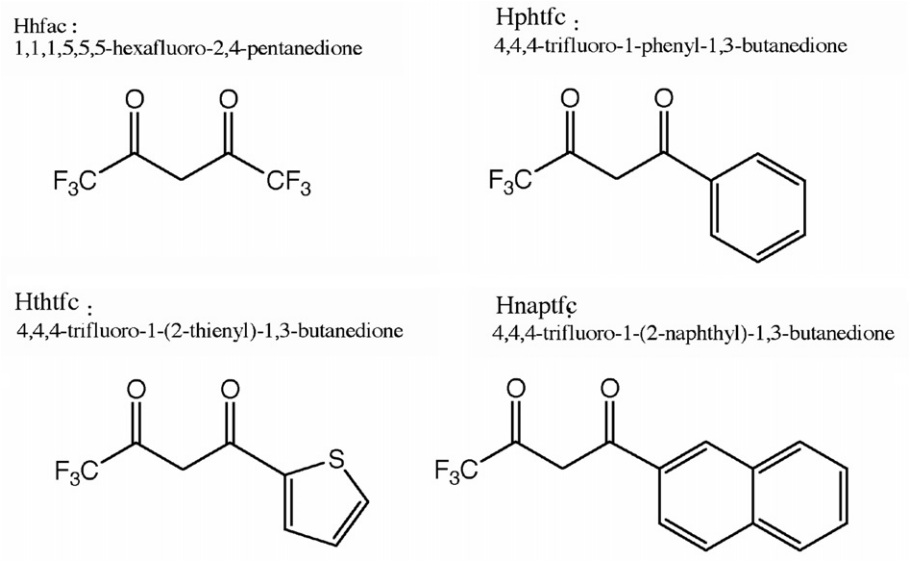
2.3.1. [Co(β-diketonate)$_2$(H$_2$O)$_2$]

The starting complexes [Co(β-diketonate)$_2$(H$_2$O)$_2$] were prepared according to the literature method [2] for the hfac complex by mixing an aqueous solution of $Co(CH_3COO)_2 \cdot 4H_2O$ with twice equimolar amounts of 4,4,4-trifluoro-R-1,3-butandione. The precipitate was filtered, washed with cold water, and dried under vacuum.

2.3.2. [Co(β-diketonate)$_2$(IM2py)]

[Co(β-diketonate)$_2$(H$_2$O)$_2$] (0.10 mmol) was dissolved in hot dry *n*-heptane (50 ml). To this solution was added IM2py (0.10 mmol). After the mixed solution was stirred for 10 min, the precipitate obtained was filtered. Yields were about 60%. The elemental analysis for [Co(hfac)$_2$-(IM2py)] (**1**), [Co(phtfc)$_2$(IM2py)] (**2**), [Co(thtfc)$_2$(IM2py)] (**3**), and [Co(naptfc)$_2$(IM2py)] (**4**) gave the satisfactory results as shown in Table 1.

The identifications for the powdery samples have been confirmed by powder X-ray diffraction patterns (XRD) which were in good agreement with the simulated pattern reproduced from the F_c values of the calculated crystal structures.



Scheme 2.

Table 1
Elemental analysis for a series of [Co(β-diketonato)$_2$(IM2py)]

Complex	Found (calc.) %			
	C	H	N	Colors
[Co(hfac)$_2$(IM2py)] (**1**)	38.45 (38.23)	2.64 (2.60)	6.17 (6.08)	red
[Co(phtfc)$_2$(IM2py)] (**2**)	54.37 (54.34)	3.96 (3.96)	6.05 (5.94)	green
[Co(napfc)$_2$(IM2py)] (**3**)	54.37 (54.34)	3.98 (3.96)	5.25 (5.21)	green
[Co(thtfc)$_2$(IM2py)] (**4**)	46.99 (46.75)	3.30 (3.34)	5.85 (5.84)	green

2.3.3. X-ray crystallography

The crystals suitable for the X-ray analysis were obtained from *n*-heptane solution by a diffused vapor method using ethyl ether.

The X-ray intensities of complex [Co(phtfc)$_2$(IM2py)] (**2**) were measured on a Rigaku automated four-circle diffractometer AFC-5R [graphite monochromated Mo Kα radiation ($\lambda = 0.71073$ Å), ω–2θ scan, $2\theta_{max} = 60°$], and those complexes **3** and **4** on a Rigaku Mercury CCD [graphite monochromated Mo Kα radiation ($\lambda = 0.71073$ Å), $2\theta_{max} = 55°$]. The structures were solved by Rigaku Crystal Structure 3.7.0 [23] and refined on F^2 by full-matrix least squares using SHELXL 97 [24].

The *R* value for the complex **4** is rather large probably owing to a small size of the crystal employed. However, the goodness-of-fit number is not so large as compared with the other complexes as shown in Table 1.

2.3.4. Physical measurements

The magnetic susceptibility data were collected with a SQUID magnetometer on a QUANTUM design model MPMS. Data were corrected for magnetization of the sample holder and for the diamagnetic contributions, which were estimated from Pascal's constants. UV–Vis spectra were measured on a Perkin–Elmer Lambda 19 spectrophotometer. Magnetic circular dichroism (MCD) spectra in CH_3CN were obtained in a magnetic field of 1.5 T ($1\ T = 1.0 \times 10^4$ Gauss) with a Jasco J-720W spectropolarimeter at room temperature. Resonance Raman spectra were measured in solid states on a Jasco NR 1800 spectrophotometer at room temperature using Ar laser lines (514.5 nm), the He–Ne laser line (632.8 nm), and dye laser lines (R6G, 580 nm; DCM, 690, 705 nm) as excitation sources. The Si–O (silicone) stretching at 518 cm^{-1} was used as internal standard.

3. Results and discussion

3.1. Molecular structures

The crystallographic data of the complexes **2**–**4** are given in Table 2.

The ORTEP view of complex [Co(phtfc)$_2$(IM2py)] (**2**) is shown in Fig. 1 and Fig. S1.

The complex has two didentate phtfc other than one chelated IM2py coordinated via the pyridyl and the imidazol nitrogen atoms to a Co(II) center, and forming the six-coordinate octahedron. It is noted that the oxygen atoms close to the trifluoromethyl group in the phtfc ligands are placed at the mutual *trans* position. The other complexes **3** and **4** also take the same *trans*(CF_3) geometrical structure (Figs. S2 and S3). In other words, only the *trans*(CF_3)-isomer among three possible isomeric structures is stereospecifically formed for this kind of complexes. The Co–O bond lengths (2.017(5)–2.089(5) Å) range within those of the hfac Co(II) complex with monodentate NIT radical [20]. There is no systematic tendency in Co–O bond lengths with respect to the substituent positions of the Rftc ligands. The Co–N(py) bond lengths (2.118(8)–2.146(5) Å) are longer than the Co–N(IM) bond lengths (2.082(7)–2.115(8) Å), while this difference is reverse to the case of [MCl_2(IM2py)$_2$](M^{II} = Mn, Co, Ni, Zn); M–N(py) bond lengths are shorter than M–N(IM) ones [18]. Each bond length of Co–N(py) and Co–N(IM) is shorter than those in [$CoCl_2$(IM2py)$_2$]. The averaged N–O bond lengths of IM2py are 1.270(9)–1.252(10) Å, 1.267(8)–1.255(8) Å and 1.281(10)–1.275(8) Å, respectively, in complexes **2**, **3**, and **4**, which are comparable to the reported ones (1.265–1.271 Å) for the IM2py complexes [12,14]. Therefore this

Table 2
Crystallographic data of [Co(β-diketonato)$_2$(IM2py)]

	[Co(phtfc)$_2$-(IM2py)] (**2**)	[Co(thtfc)$_2$-(IM2py)] (**3**)	[Co(naphtfc)$_2$-(IM2py)] (**4**)
Chemical formula	$C_{32}H_{28}N_3O_5F_6Co$	$C_{28}H_{24}N_3O_5F_6S_2Co$	$C_{40}H_{32}N_3O_5F_6Co$
Fw	707.28	719.38	807.36
Crystal system	orthorhombic	orthorhombic	monoclinic
Space group	$Pca2_1$	$Pca2_1$	$P2_1/n$
Z value	8	8	8
a	17.068(4)	17.0726(11)	16.6060(13)
b	11.609(3)	11.5644(8)	14.4493(11)
c	32.911(4)	32.584(2)	31.284(3)
β	90.00	90.0000	92.044(4)
V	6521(2)	6433.1(7)	7501.7(10)
Goodness-of-fit	0.962	1.161	1.164
R^a	0.0480	0.0923	0.1424
$wR_2{}^b$	0.1699	0.2410	0.3908

[a] $R = \sum||F_o| - |F_c||/|F_o|$.
[b] $wR_2 = [\sum(w(F_o^2 - F_c^2)^2)/\sum w(F_o^2)^2]^{1/2}$, where $w = 1/\sigma^2(F_o^2)$.

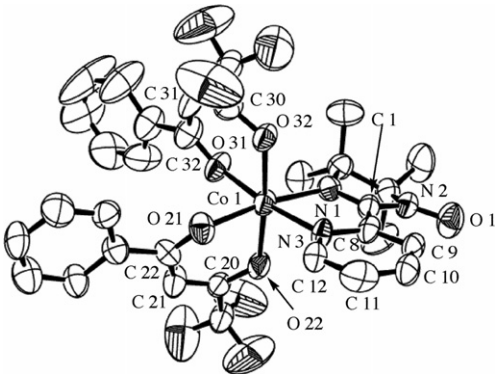


Fig. 1. Ortep drawing of [Co(phtfc)$_2$(IM2py)].

fact supports the existence of the imino niroxide radical in these complexes. The bite angles for the IM2py chelate are 77.3(3)–76.2(3)°, 77.1(2)–76.5(2)°, and 76.0(2)–76.4(2)° for the complexes **2**, **3**, and **4**, which are somewhat larger than that for $[CoCl_2(IM2py)_2]$ [18]. The chelate rings of the IM2py are almost planar, since the averaged dihedral angles between the plane Co–N(py)–N(IM) and the plane N(IM)–C(IM)–C(py)–N(py) are 2.93°, 1.70°, 4.44° for the **2**–**4** complexes, respectively.

3.2. The UV–Vis spectra and magnetic circular dichroism

NIR–UV–Vis spectra of complexes (**1**)–(**4**) in CH_2Cl_2 at room temperature are shown in Fig. 2.

The broad absorption band with similar intensities ($\log\varepsilon \approx 1$) around 9700 cm^{-1} is assigned to the first spin allowed d–d $^4T_1 \rightarrow {}^4T_2$ transition. For the hfac complex (**1**), the d–d band is observed at the lower frequency side than those of the other complexes (**2**)–(**4**). Two intense broad bands are located around 16 500 cm^{-1} and 20 000 cm^{-1} for complexes **2**, **3**, and **4**. For complex **1**, a shoulder and a broad band are observed at 17 500 cm^{-1} and 24 000 cm^{-1}, respectively. The MCD spectra show the similar behavior to the UV–Vis spectra as in Fig. 2. The weak positive MCD band around 17 000 cm^{-1} appears for the phtfc **2** and thtfc **3** complexes, whereas the hfac **1** complex gives a blue-shifted weak positive band with a higher frequency negative component. At the higher frequency side around 20 000–24 000 cm^{-1}, the strong positive MCD band with the lower frequency shoulder is observed for all the complexes, but the difference in peak position between the complex **1** and the Rtfc complexes **2**–**3** is about 2800 cm^{-1}, which is much larger than that (500 cm^{-1}) of the lower frequency one around 17 000 cm^{-1}. Such a similarity in MCD pattern suggests that two absorption bands of the Rtfc complexes (**2**)–(**4**) at 17 000 and 20 000 cm^{-1} arise from the same origins for those of the hfac complex **1** at 17 500 cm^{-1} and 24 000 cm^{-1} , respectively, as inferred from the following resonance Raman spectroscopy.

For $[Co(phtfc)_2(IM2py)]$ (**2**), the resonance Raman spectra gave significant intensity enhancement or the excitation profiles under the visible band around 17 000 cm^{-1}, especially for the Raman peaks due to the stretching vibrations of the O–N–C moiety of the IM2py ligand around 1520, 1468, and those due to the stretching of Co–N(imino) and Co–N(pyridyl) around 443 and 255 cm^{-1} as shown in Fig. 3, as compared from the previous results for the

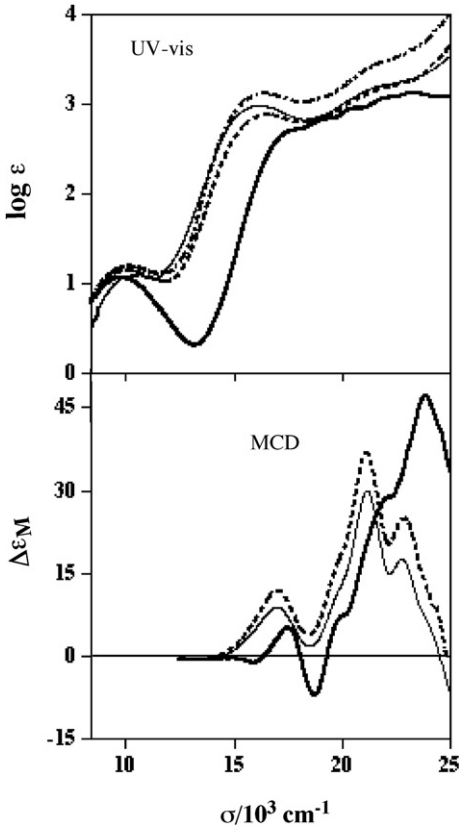


Fig. 2. UV–Vis spectra in CH_2Cl_2 (top) and MCD in CH_3CN (bottom) of $[Co(hfac)_2(IM2py)]$ (—), $[Co(phtfc)_2(IM2py)]$ (—), $[Co(thtfac)_2(IM2py)]$ (----), $[Co(naptfc)_2(IM2py)]$ (—·—).

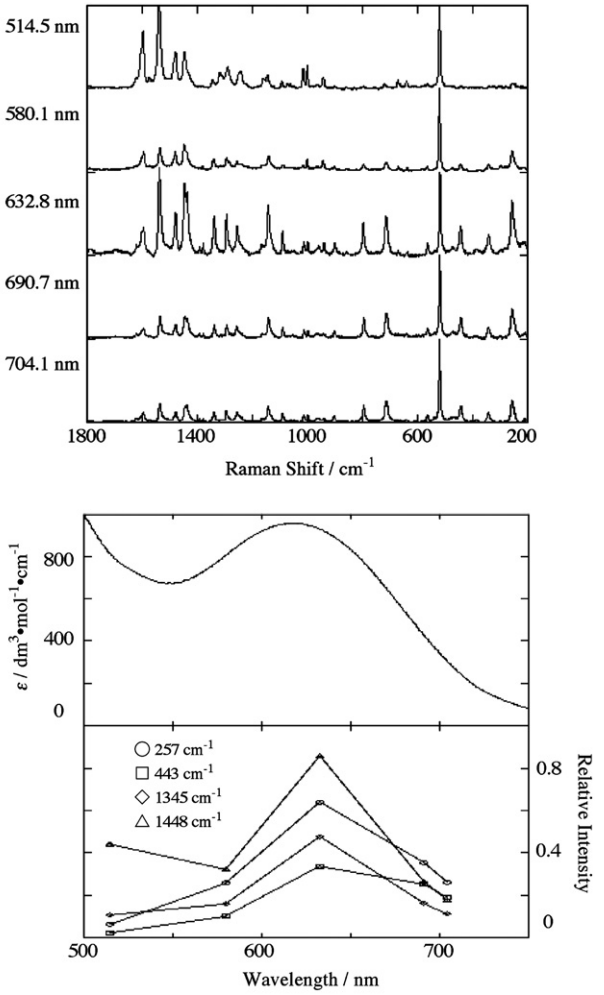


Fig. 3. (Top) Resonance Raman spectra with variation of the excitation lights (bottom) and excitation profile of $[Co(phtfc)_2(IM2py)]$.

Ni(II) and Cr(III) complexes [10–13]. The same behavior for the resonance Raman spectra were observed for the other three complexes **1**, **3**, **4** (Figs. S4–S9). Therefore, the visible band near 17000 cm^{-1} may be assigned to the charge transfer(CT) transition. This CT band is probably due to the metal-to-ligand SOMOπ^*(MLCT) as similarly observed for Ni(II) and Cr(III) complexes [10–13]. For complex **2**, the visible absorption band in dichloromethane or benzene is shifted to longer wavelength side in acetonitrile as shown in Fig. 4. All the complexes have a blue-shifted absorption band with increasing the polarity of the solvents (Figs. S10–S12). These assignments to the MLCT are supported by the similarity of MCD patterns as mentioned above.

3.2.1. Substituents effect on the electronic spectra

The higher energy shifts of the MLCT bands from the Rtfc to the hfac complexes would be elucidated as follows. In the triplet–triplet $t_{2g} \rightarrow \pi^*$ and $e_g \rightarrow \pi^*$ MLCT for octahedral IM2py high spin Co(II) complexes, the transition energy is estimated to be $30(\chi(\mathrm{Co}) - \chi(\mathrm{IM})) + 2D$ for $E(t_{2g} \rightarrow \pi^*)$ with the triplet d^6 excited CT state and $30(\chi(\mathrm{Co}) - \chi(\mathrm{IM})) - \Delta + 2D$ for $E(e_g \rightarrow \pi^*)$, where χ(Co) and χ(IM) refer to the optical electronegativity for Co(II) and the IM2py ligand, respectively and Δ and D are the ligand field splitting and the spin-pairing energy, respectively [25]. The energy difference between two MLCT, $\Delta E = E(e_g \rightarrow \pi^*) - E(t_{2g} \rightarrow \pi^*) = -\Delta$ should be negative. Therefore, the lower energy MLCT component around 17000 cm^{-1} is due to the $e_g \rightarrow$ SOMO MLCT, in accordance with our previous assignment to the d_σ–SOMO transition for the *cis*-[$CoCl_2(IM2py)_2$] [18]. The higher energy shift of the $e_g \rightarrow$ SOMO MLCT for the hfac complex may result from the difference in the ligand field splitting: Δ(hfac) < Δ(Rtfc) being suggested from the lower energy shift of the $^4T_1$–$^4T_2$ d–d band for the hfac complex (Fig. 2). The higher frequency band near 20000 and 24000 cm^{-1} for the Rtfc and hfac complexes, respectively, could be due to the t_{2g}–SOMO MLCT. This assignment is supported by the intensity difference; the $d_{zx}(t_{2g})$–SOMO MLCT intensity with large orbital overlap being stronger than the d_{z^2} (e_g)–SOMOπ^* MLCT one with small overlap. The much higher frequency shift of the $d_{zx}(t_{2g})$–SOMO MLCT for the hfac complex may arise from the spin-pairing energy expense associated with the d_{zx}–SOMO transition from $(d_{yz})^2(d_{zx})^2(d_{xy})^+(d_{z^2})^+(d_{x^2-y^2})^+(\mathrm{SOMO})^-$ to $(d_{yz})^2(d_{zx})^-(d_{xy})^+(d_{z^2})^+(d_{x^2-y^2})^+(\mathrm{SOMO})^2$ or $(d_{xy})^2(d_{zx})^2$-$(d_{yz})^+(d_{z^2})^+(d_{x^2-y^2})^+(\mathrm{SOMO})^-$ to $(d_{xy})^2(d_{zx})^-(d_{yz})^+$ $(d_{z^2})^+$-$(d_{x^2-y^2})^+(\mathrm{SOMO})^2$ for the hfac complex as compared with that from $(d_{yz})^2(d_{xy})^2(d_{zx})^+(d_{z^2})^+(d_{x^2-y^2})^+(\mathrm{SOMO})^-$ to $(d_{yz})^2(d_{xy})^2(d_{z^2})^+(d_{x^2-y^2})^+(\mathrm{SOMO})^2$ as a result of the inversion of the d_{zx} and d_{xy} energy levels (Scheme 3) where the d_{zx}, d_{xy} and d_{yz} are defined according to the Cartesian coordinate in Scheme 4. This inversion of the d orbital orderings is consistent with that inferred from the magnetic properties (vide infra).

3.3. Magnetic properties

The temperature dependences of the $\chi_M \cdot T$ (χ_M = molar magnetic susceptibilities) of [Co(β-diketonato)$_2$(IM2py)] are shown in Fig. 5. The values of $\chi_M \cdot T$ (3.22 for **1**; 3.60 for **2**; 3.49 for **3**; 3.37 $cm^3 \cdot mol^{-1} \cdot K$ for **4**) at 300 K indicate the existence of a high-spin cobalt(II) ion ($S = 3/2$)

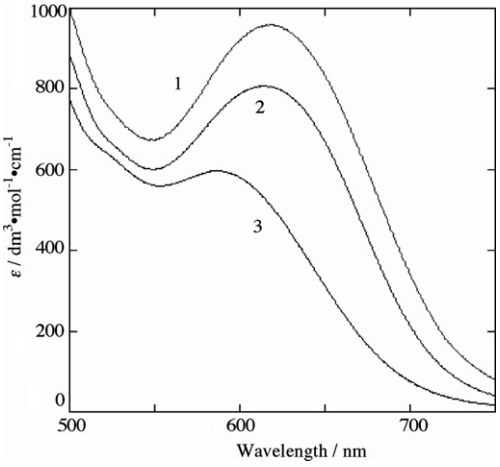
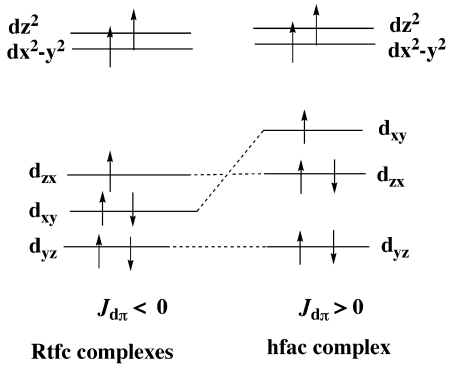
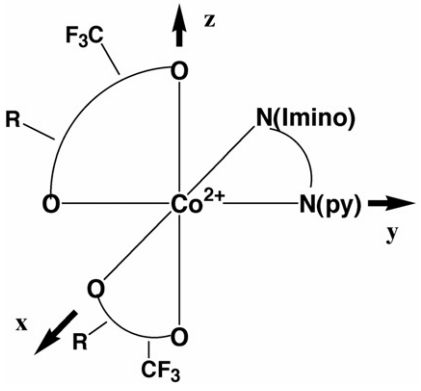


Fig. 4. Solvent dependent UV–Vis spectra of [Co(phtfc)$_2$(IM2py)]: (1) CH_2Cl_2; (2) C_6H_6; (3) CH_3CN.



Scheme 3.



Scheme 4.

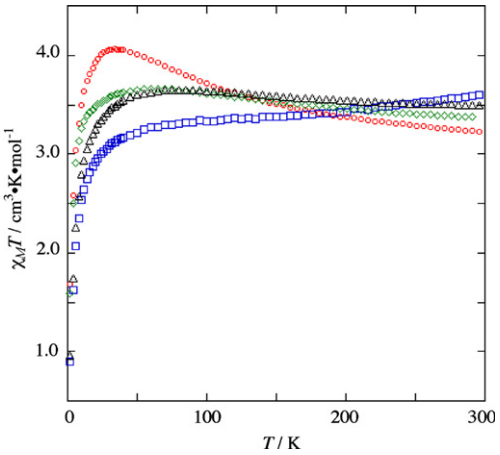


Fig. 5. Temperature dependence of magnetic susceptibilities (χ_M) in the form of $\chi_M \cdot T$. ○ [Co(hfac)$_2$(IM2py)], □ [Co(phtfc)$_2$(IM2py)], ◆ [Co(naptfc)$_2$(IM2py)], △ [Co(thtfc)$_2$(IM2py)].

and an unpaired electron ($S = 1/2$) of IM2py. The magnetic exchange coupling constants J between cobalt(II) and IM2py were estimated by fitting the magnetic susceptibilities using a two-spin system, as employed for a dinuclear Cu(II)–Co(II) complex [26], including the Weiss constant θ. This model gives the spin-Hamiltonian in Eq. (1) and the molar magnetic susceptibility in Eq. (2) as follows:

$$\hat{H} = -2JS_{Co}S_{rad} \tag{1}$$

$$\chi_M = \frac{N\beta^2}{k(T-\theta)}\left\{\frac{10g_2^2 + 2g_1^2\exp(-4J/kT)}{5 + 3\exp(-4J/kT)}\right\} \tag{2}$$

where $g_1 = (5g_{Co} - g_{IMpy})/4$ and $g_2 = (3g_{Co} + g_{IM2py})/4$ (g_{Co} and g_{IM2py} are g value of cobalt(II) and IM2py, respectively). The $\chi_M \cdot T$ curve is almost flat at high temperature. It follows that only one populated level is the ground $S = 2$ level of the complex even at room temperature. It is not easy to analyze the magnetic data, since the ground state of the octahedral cobalt(II) is $^4T_{1g}$ with large anisotropy components. Large depopulation of the lower energy levels or Kramers doublets in the ground state of cobalt(II) makes it difficult to assess the magnetic behavior at low temperature before complete occupation of the lowest level. Therefore, the magnetic exchange coupling constants J between a cobalt(II) and IM2py were estimated between 30 and 300 K, by fitting Eq. (2) (Figs. S13–S16). In Table 3, the best fit results of the coupling constants J, g and θ values are summarized. The g_{Co} values from 2.40 to 2.60 are close to those for the dichloro bis(IM2py) Co(II) complex [18].

It is noted that J values vary with the substituents in the β-diketonate coligand. The hfac complex (**1**) exhibits the fairly large positive J value or ferromagnetic interaction, whereas there are found smaller J values, or weaker antiferromagnetic or ferromagnetic interactions for complexes **2**, **3**, and **4**. Such magnetic behavior is accounted for on the basis of the d orbital energy splitting as previously discussed for the bis(IM2py) Co(II) complexes [18].

3.3.1. The substituent effect on magnetic interactions

The above-mentioned difference in the magnetic properties is considered to be associated with the d orbital splitting: suggesting the substituents effect on going from **1** to **2**, **3**, **4** complexes. The difference in magnetic properties originates from two interactive modes between the magnetic d orbitals of Co(II) and IM2py SOMO; $J_{d\pi}$ and $J_{d\sigma}$ with the $d_\pi(t_{2g})$ and $d_\sigma(e_g)$ orbitals, respectively. The total coupling constant $J(J_{obs})$ is represented as follows:

$$J_{obs} = J_{d\sigma} + J_{d\pi} \tag{3}$$

Since the d_σ orbitals of cobalt(II) ion is orthogonal to the SOMO as found from the X-ray analysis (vide supra), the magnetic interaction of IM2py with the d_σ could be ferromagnetic ($J_{d\sigma} > 0$) [5,12,14]. On the other hand, the interactions of the d_π orbital with the SOMO depend on the splitting patterns of the d_π orbitals. That is, the overlap and orthogolality between the magnetic d_π orbital and the SOMO result in antiferromagnetic ($J_{d\pi} < 0$) [6,12,14] and ferromagnetic interaction ($J_{d\pi} > 0$), respectively. Therefore, it is considered that the substituents effect of the β-diketonate on the magnetic properties originates from the different splitting pattern in d_π orbitals. As assumed from the MLCT band shifts in the previous section, the highest occupied magnetic d_π orbital of the hfac complex **1** is d_{xy}, which is orthogonal with the SOMO (Scheme 3). In this case, both the contributions to the magnetic interaction from the d_σ and d_π are ferromagnetic, so that there may be a fairly large ferromagnetic interaction, $J_{obs} = J_{d\sigma}(F) + J_{d\pi}(F)$. This is the finding just as for the hfac complex **1**. For the complexes **2**, **3** and **4**, on the other hand, the magnetic d_π orbital is d_{zx}, which overlaps with the SOMO. Thus, the total magnetic interaction or $J_{obs} = J_{d\sigma}(F) + J_{d\pi}(ANT)$ would become smaller.This case accords with a weak antiferromagnetic or weak ferromagnetic interaction as observed for complexes **2**, **3**, **4**. It is likely that the inversion of the energy level ordering results from the difference in the electronic properties between the

Table 3
Magnetic data

Complexes	J/cm^{-1}	θ/K	g_{Co}	g_{rad}	χ^2
[Co(hfac)$_2$(IM2py)] (**1**)	21.0 ± 1.10		2.45 ± 0.01	2.0	1.57×10^{-5}
[Co(phtfc)$_2$(IM2py)] (**2**)	−0.81 ± 0.11	−2.93 ± 0.17	2.60 ± 0.01	2.0	1.79×10^{-3}
[Co(thtfc)$_2$(IM2py)] (**3**)	4.47 ± 1.01	−7.89 ± 0.29	2.78 ± 0.05	2.0	1.48×10^{-3}
[Co(naptfc)$_2$(IM2py)] (**4**)	3.14 ± 0.53	−3.90 ± 0.12	2.70 ± 0.03	2.0	1.17×10^{-3}

electron withdrawing CF_3 and the electron donating R groups as examined by the AOM consideration as follows.

The d_π orbital energies are given by the AOM parameters as follows.

$$\varepsilon(d_{xy}) = 2_\pi(O(R))$$
$$\varepsilon(d_{zx}) = e_\pi(N(IM)) + e_\pi(O(CF_3))$$
$$\varepsilon(d_{yz}) = e_\pi(N(py)) + e_\pi(O(CF_3))$$

where the AOM parameters $e_\pi(O(R))$, $e_\pi(O(CF_3))$, $e_\pi(N(IM))$ and $e_\pi(N(py))$ represent the interaction energy between the π orbital of the donor ligand atoms and the dπ orbital orthogonal to the β-diketonate chelate planes: O(R) and $O(CF_3)$ for the oxygen in the O–C–R and O–C–CF_3 of Rtfc, respectively, and N(IM) and N(py) for the nitrogen in the imino radical and the pyridyl group of IM2py, respectively. Assuming the transferability of the AOM parameters among the four complexes, only the d_{xy} orbital energy varies with the substitutents of the Rtfc ligands. The inequality $e_\pi(O(CF_3)) > e_\pi(O(R))$ is required in terms of $\varepsilon(d_{xy}) > \varepsilon(d_{zx})$ for the hfac complex and $\varepsilon(d_{xy}) < \varepsilon(d_{zx})$ for the other Rtfc complexes (Scheme 3). The relation $e_\pi(O(CF_3)) > e_\pi(O(R))$ may reflect the destabilization of the d orbitals by the CF_3 group as inferred from the charge transfer spectra of the β-diketonato Cr(III) complexes [27]. Therefore, the examination in terms of the AOM parametrization supports the inversion of the d orbital energy orderings or the substituents effect on the magnetic properties as well as the MLCT band shifts.

4. Conclusion

The difference in the MLCT band shifts and magnetic interactions among the bis(β-diketonato or Rtfc) IM2py Co(II) complexes can be elucidated on the basis of the d_π orbital energy orderings supported by the AOM parametrization and the ligand field splitting or the spin-paring energy. Thus the present results suggest possibility to regulate magneto-optical properties by changing the electronic properties of the substituents in the β-diketonate coligand.

Acknowledgements

We gratefully acknowledge support of this research by a Grant-in-Aid for Scientific Research (A) (No. 10304056) from the Ministry of Education, Sports, Culture, Science and Technology, Japan.

Appendix A. Supplementary material

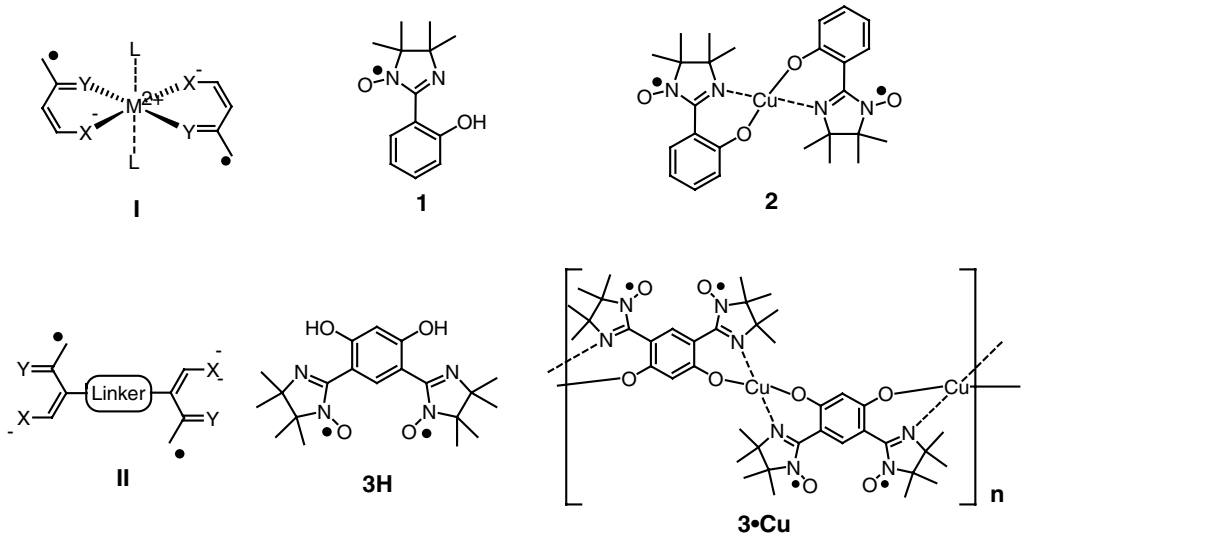
The bond lengths, angles and torsion angles for the complexes **2**, **3**, **4** in Table S1; the ORTEP drawings of two independent complexes of the complexes **2**, **3**, **4** in Figures S1–S3; resonance Raman spectra with variation of excitation lights in Figures S4, S6, S8 for the complexes **1**, **3**, **4** and excitation profiles of resonance Raman spectra in Figs. S5, S7, S9 for the complexes **1**, **3**, **4**; the solvent dependent UV–Vis spectra in Figs. S10, S11, S12 for the complexes **1**, **3**, **4**. A plot of χ_M versus temperature curve with the fitting curve according to Eq. (2) in Figures S13, S14, S15, S16 for the complexes **1**, **2**, **3**, **4**.

CCDC 286098, 286099 and 286100 contain the supplementary crystallographic data for **2**, **3** and **4**. These data can be obtained free of charge via http://www.ccdc.cam.ac.uk/conts/retrieving.html, or from the Cambridge Crystallographic Data Centre, 12 Union Road, Cambridge CB2 1EZ, UK; fax: (+44) 1223-336-033; or e-mail: deposit@ccdc.cam.ac.uk. Supplementary data associated with this article can be found, in the online version, at doi:10.1016/j.poly.2006.09.054.

References

[1] E.F. Ullman, L. Call, J.H. Osiecki, D.G. Boocock, R. Darcy, J. Am. Chem. Soc. 94 (1972) 7049.
[2] A. Caneschi, D. Gatteschi, J. Laugier, P. Rey, R. Sessoli, Inorg. Chem. 27 (1988) 1553.
[3] A. Caneschi, D. Gatteschi, P. Rey, Prog. Inorg. Chem. 39 (1991) 331.
[4] D. Luneau, P. Rey, J. Laugier, E. Belorizky, A. Cogne, Inorg. Chem. 31 (1992) 3578.
[5] D. Luneau, G. Risoan, P. Rey, A. Gramd, A. Caneschi, D. Gatteschi, J. Laugier, Inorg. Chem. 32 (1993) 5616.
[6] (a) D. Luneau, F.M. Romero, R. Ziessel, Inorg. Chem. 37 (1998) 5708;
(b) F.M. Romero, D. Luneau, R. Ziessel, Chem. Commun. (1998) 551.
[7] G. Francese, F.M. Romero, A. Neels, H. Stoeckli-Evans, S. Decurtins, Inorg. Chem. 39 (2000) 2087.
[8] (a) K.E. Vostrikova, D. Luneau, W. Wernsdorfer, P. Rey, M. Verdaguer, J. Am. Chem. Soc. 122 (2000) 718;
(b) A. Marvilliers, Y. Pei, J.C. Bouquera, K.E. Vostrikova, C. Paulsen, E. Rivière, J.-P. Audière, T. Mallah, Chem. Commun. (1999) 1951.
[9] S. Kaizaki, Bull. Chem. Soc. Jpn 76 (2003) 673, and the references therein.
[10] T. Yoshida, T. Suzuki, K. Kanamori, S. Kaizaki, Inorg. Chem. 38 (1999) 1059.
[11] T. Yoshida, T. Suzuki, K. Kanamori, S. Kaizaki, Inorg. Chem. 38 (1999) 5926.
[12] Y. Tsukahara, A. Iino, T. Yoshida, T. Suzuki, S. Kaizaki, J. Chem. Soc. Dalton Trans. (2002) 181.
[13] T. Tsukahara, T. Kamatani, A. Iino, T. Suzuki, S. Kaizaki, Inorg. Chem. 43 (2002) 4363.
[14] Y. Tsukahara, T. Kamatani, T. Suzuki, S. Kaizaki, Dalton Trans. (2003) 1276.
[15] Y. Tsukahara, H. Nakata, S. Kaizaki, Inorg Chem. 43 (2004) 4383.
[16] A. Iino, T. Suzuki, S. Kaizaki, Dalton Trans. (2003) 4604.
[17] H. Kanda, Y. Narumi, Y. Hosokoshi, T. Suzuki, S. Kawata, K. Kindo, K. Inoue, S. Kaizaki, Inorg. Chim. Acta 357 (2004) 3125.
[18] Y. Yamamoto, T. Suzuki, S. Kaizaki, J. Chem. Soc., Dalton Trans. (2001) 1566.
[19] Y. Yamamoto, T. Suzuki, S. Kaizaki, J. Chem. Soc., Dalton Trans. (2001) 2943.
[20] B.-W. Sun, Q.-H. Zhao, D.-Z. Liao, Z.-H. Jiang, S.-P. Yan, G.-L. Wang, X.-K. Yao, H.-G. Wang, Can. J. Chem. 78 (2000) 322.
[21] C.-F. Huang, H.-H. Wei, J. Chin. Chem. 44 (1997) 439.
[22] L.-Y. Wang, B. Zhao, C.-X. Zhang, D.-Z. Liao, Z.-H. Jiang, S.-P. Yan, Inorg. Chem. 42 (2003) 5804.
[23] Rigaku CrystalStructure 3.7.0: Crystal Structure Analysis the first Package, Rigaku and Rigaku/MSC (2000–2005).
[24] G.M. Sheldrick, SHELXS-86, Program for Crystal Structure Determination, University of Göttingen, Göttingen, Germany, 1986.

[25] (a) C.K. Jørgensen, Modern Aspects of Ligand Field Theory, North-Holland Pub. Comp., 1970;
(b) A.B.P. Lever, Inorganic Electronic Spectroscopy, 2nd ed., Elsevier, 1984, p. 209, 224.
[26] H. Okawa, J. Nishino, M. Ohba, M. Tadokoro, N. Mastumoto, M. Koikawa, S. Kida, D.E. Fenton, Inorg. Chem. 32 (1993) 2949.
[27] R.L. Lintvedt, L.K. Kernitsky, Inorg. Chem. 10 (1971) 478.



2. Experimental

2.1. General method

Chemicals were used as received without further purification. Melting points were measured on a Yanako MP-J3 apparatus and are uncorrected. ^{1}H NMR spectra were recorded on JEOL JNM-LA300 (300 MHz) or -LA400 (400 MHz). The chemical shifts were described as values in parts per million relative to tetramethylsilane. MS-spectra were obtained using a JEOL JMS-700T mass spectrometer. ESR spectra were recorded on a JEOL JFS-FE2XG. X-ray data were collected with Rigaku/MSC Mercury CCD system using graphite monochrometer Mo Kα radiation. The magnetic susceptibility measurements were conducted on a Quantum Design SQUID magnetometer MPMS-XL.

2.2. Synthesis of *3H*, *4*, *5*, and the reaction of *3H* with copper acetate in methanolic ammonia solution

2.2.1. Synthesis of 1,3-dihydroxy-4,6-bis(1,3-dihydroxy-4,4,5,5-teramethylimidazolidine-2-yl)benzene (*4*)

A suspension of 4,6-dihydroxyisophthalaldehyde (3.04 g, 24.3 mmol), dry potassium carbonate (8.42 g, 60.9 mmol), and 2,3-dihyroxylamino-2,3-dimethylbutane-H_2SO_4 salt (18.0 g, 73.1 mmol) in dry methanol (300 ml) was refluxed for 24 h under an inert atmosphere. The solvent was partially evaporated under reduced pressure. Then, water (300 ml) was added to the stirred reaction mixture, to give precipitates. The precipitates were filtered and dried over P_2O_5 under reduced pressure, to give almost pure **4** as a pale yellow powder (8.81 g, 20.7 mmol, 85% yield). Compound **4**: HRMS (FAB) *m*/*z* Calc. for $C_{20}H_{34}N_4O_6$: 426.2478; found: 427.2568 (M+H); ^{1}H NMR (300 MHz, DMSO-d_6) δ 1.06 (s, 12H), 1.07 (s, 12H), 4.51 (s, 2H), 5.98 (s, 1H), 6.92 (s, 1H), 8.07 (s, 4H), 11.34 (s, 2H); ^{13}C NMR (100 MHz, DMSO-d_6) δ 17.21, 24.49, 65.87, 88.55, 102.62, 112.66, 132.82, 158.24.

2.2.2. Synthesis 1,3-dihydroxy-4,6-bis(1-hydroxy-4,4,5,5-tetramethylimidazoline-2-yl)benzene (*5*)

A suspension of **4** (2.01 g, 4.72 mmol) and a catalytic amount of selenium dioxide (0.205 g, 1.84 mmol) was stirred at room temperature for 3 days, to give a yellow-colored solution containing a small amount of insoluble materials. The reaction mixture was filtered and concentrated in vacuo. The crude product was purified by a silica gel column eluted with ethyl acetate:methanol = 4:1 (R_f = 0.48) to give a yellowish powder (1.04 g, 2.65 mmol, 56% yield). Recrystallization from ethyl acetate containing a small amount of methanol gave **5** as orange plates (43%). Compound **5**: HRMS (FAB) *m*/*z* Calc. for $C_{20}H_{30}N_4O_4$: 390.2267; found 391.2347 (M+H); ^{1}H NMR (300 MHz, DMSO-d_6) 1.24 (s, 12H), 1.25 (s, 12H), 5.90 (s, 1H), 7.44 (s, 1H); ^{13}C NMR (100 MHz, DMSO-d_6) δ 19.19, 23.30, 62.27, 71.05, 103.64, 107.87, 131.92, 152.14, 168.19.

2.2.3. Synthesis of 1,3-dihydroxy-4,6-bis(4,4,5,5-tetramethylimidazoline-1-oxyl-2-yl)benzene (*3H*)

To a stirred nitrogen-bubbled heterogeneous solution of water (10 ml) and methylene chloride (15 ml) containing **5** (517 mg, 1.32 mmol) was added sodium periodate (561 mg, 2.62 mmol) slowly at 0 °C. The mixture was further stirred at 0 °C for 20 min. The water-layer was removed and the organic layer was washed with water and dried over sodium sulfate under nitrogen. The organic layer was concentrated in vacuo. The resulting solid was recrystallized from ether–hexane in a glove box freezer (−30 °C) to give diradical **3H** (304 mg, 0.779 mmol, 59% yield) as red blocks. Compound **3H**: MS (FAB) *m*/*z* 390 (M+2H); IR (cm^{-1}, KBr) 2986, 2974, 1638, 1605, 1533, 1377, 1331, 1257, 1211, 1180, 1159; *Anal.* Calc. for

$C_{20}H_{28}N_4O_4$: C, 61.84; H, 7.27; N, 14.42. Found: C, 61.91; H, 7.34; N, 14.19%.

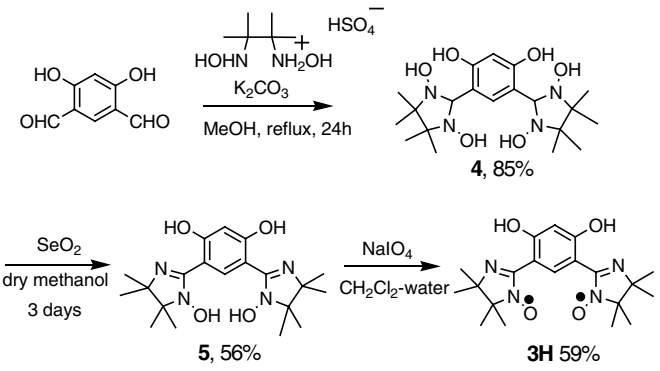
2.2.4. Reaction of *3H* with copper acetate in methanol containing aqueous ammonia

To a solution of copper acetate (64.3 mg, 0.165 mmol) in methanol (6 ml) and aqueous ammonia (25%, 0.2 ml) was slowly added a solution of **3H** (29.0 mg, 0.160 mmol) in methylene chloride (2 ml) in a glove box. Fine precipitates soon appeared and were filtered using a membrane filter with a porous size of 0.2 μm. The collected precipitates were well washed by methanol and methylene chloride to give a blue-green powder (39 mg, 54%). The powder was hardly soluble in various organic solvents. Elementary analysis of the obtained powder: *Anal.* Calc. for $C_{20}H_{26}CuN_4O_4$: C, 53.38; H, 5.82; N, 12.45. Found: C, 53.87; H, 6.11; N, 11.95%; IR (cm^{-1}, KBr) 2980, 2933, 1582, 1516, 1466, 1448, 1433, 1416, 1390, 1369, 1329, 1296, 1265, 1217, 1148, 820, 644.

3. Results and discussion

3.1. Synthesis and structure of *3H*

The synthesis of **3H** is outlined in Scheme 1. 1,3-Dihydroxy-4,6-bis(1,3-dihydroxy-4,4,5,5-tetramethylimidazolidine-2-yl)benzene (**4**) was prepared by the condensation of 4,6-dihydroxylisophthaldehyde with 2,3-dihyroxylamino-2,3-dimethylbutane-H_2SO_4 salt in 85% yield. The conversion of **4** to **5** was conducted by the selenium dioxide oxidation method developed by Ulrich and Ziessel [8]. Oxidation of **5** to **3H** was conducted using periodate oxidation under an inert atmosphere. Diradical **3H** was somewhat unstable in solution even under an inert atmosphere and gradually (with a time scale of days) decomposed into unidentified products. However, this slow decomposition would not be important when one applies **3H** to rapid reactions such as metal complexation at low temperature. Compound **3H** was fairly stable in a solid state. Recrystallization from a mixture of ether–hexane in a freezer of a glove box gave dark-green crystals suitable for X-ray structure analysis.



Scheme 1.

Table 1
Crystallographic data of **3H**

Formula	$C_{20}H_{28}N_4O_4$
Formula weight	388.36
Crystal system	monoclinic
Space group	$P2_1/c$ (#14)
a (Å)	10.6195(11)
b (Å)	11.0214(9)
c (Å)	18.422(2)
α (°)	90.00
β (°)	105.959(4)
γ (°)	90.00
V (Å^3)	2073.1(3)
Z	4
Crystal size (mm)	$0.30 \times 0.20 \times 0.20$
T (K)	173
D_{calc} (g cm^{-3})	1.401
$F(000)$	832.00
μ (Mo Kα) (cm^{-1})	0.88
Unique reflections	4473
Observation	3432 ($I > 2\sigma(I)$)
R_1 [$I > 2\sigma(I)$][a]	0.044
R_w[b]	0.045
Goodness-of-fit	0.91
Largest shift	0.00

[a] $R_1 = \sum ||F_o| - |F_c|| / \sum |F_o|$.
[b] $R_w = [w(F_o^2 - F_c^2)^2 / \sum w(F_o^2)^2]^{1/2}$.

The crystallographic data for **3H** are shown in Table 1. The molecular structure is shown in Fig. 1a. Intramolecular hydrogen bonds between the phenolic hydrogen atoms (H1, H2) and the nitrogen atoms (N1, N2) in the imidazoline rings were clearly seen; the hydrogen atoms H1 and H2 are observed atoms and were refined isotropically with the bond length of H1–N1 = 1.83 Å, H2–N2 = 1.75 Å. As a result, the dihedral angle between the benzene ring and the plane defined by N1–C7–N3 (or N2–C8–N4) is as small as 8.7° (or 4.9°).

Relatively short intermolecular contacts were observed (Fig. 1b). The two benzene rings were aligned almost parallel in anti direction and form a dimer structure with the distance of C2–C6* = C6–C2* = 3.23 Å, which is considerably shorter than the sum (3.54 Å) of the van der Waals radii of aromatic carbon atoms (1.77 Å) [9]. These intermolecular contacts between chemically equivalent carbon atoms should cause an antiferromagnetic interaction between these diradicals. Fig. 1c shows a schematic model (four-spin model) of magnetic interaction based on the X-ray structure considering these intermolecular contacts, where the imino nitroxide radical ($S = 1/2$) is shown as a circle. The model will be discussed in the next section.

3.2. EPR study of *3H*

Fig. 2a shows the EPR spectrum of **3H** measured at 123 K in frozen butyronitrile. High purity of this diradical species is apparent from the spectrum, although a small amount of mono-radical impurities can be observed in the center magnetic field. The spectrum was simulated by using

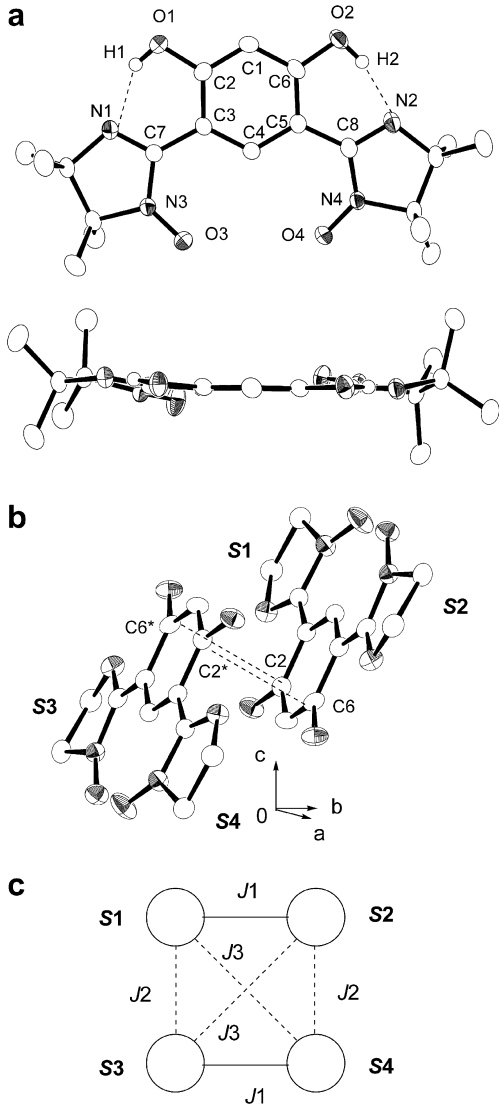


Fig. 1. Molecular structure (a), an intermolecular contact (b), and schematic model (c) for the magnetic interaction of **3H**.

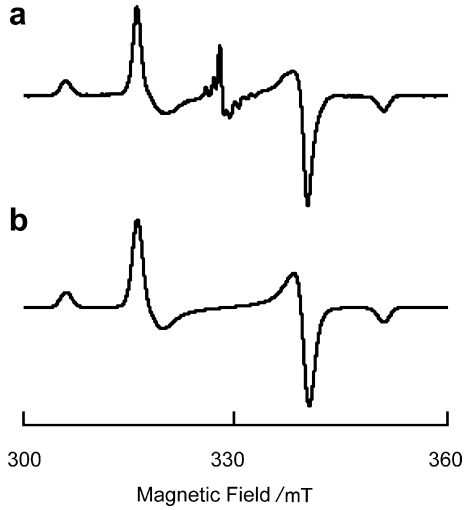


Fig. 2. EPR spectrum of **3H** in butyronitrile at 123 K (a) and a simulated spectrum with the parameters of $D/hc = 0.0211\ \mathrm{cm}^{-1}$ and $E/hc = 0\ \mathrm{cm}^{-1}$ (b).

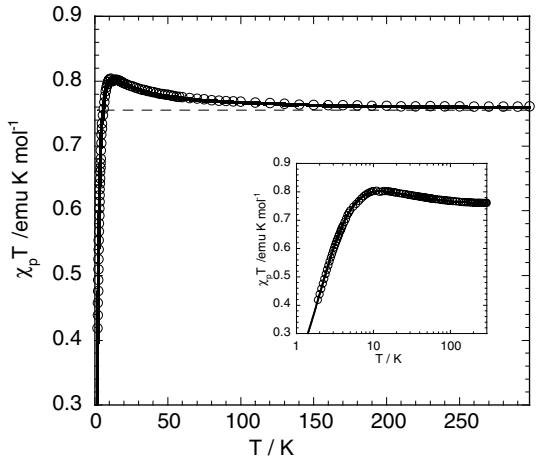


Fig. 3. Magnetic susceptibility of **3H** under magnetic field of 1000 Oe in the $\chi_p T$–T plots; the broken line shows the $\chi_p T$ value corresponding to 2 mol of $S = 1/2$ spins ($\chi_p T = 0.755$ with $g = 2.006$). The solid line shows the simulation curve based on the four spin model with $J_1/k_B = +5.0$ K, $J_2/k_B = J_3/k_B = -0.9$ K. The inset shows the plots in the logarithmic scale of temperature.

the parameters of $D/hc = 0.0211\ \mathrm{cm}^{-1}$ and $E/hc = 0\ \mathrm{cm}^{-1}$ (Fig. 2b). A weak forbidden signal due to $|\Delta m_S| = 2$ was observed in a $g = 4$ region. Linear relationship was observed between the signal intensity of $|\Delta m_S| = 2$ and the reciprocal of temperature, indicating a triplet ground state as expected from the structure of the *m*-phenylene linkage of bis(imino nitroxides) [10]. The singlet–triplet energy gap ($2J$) was estimated from the measurement of magnetic susceptibility of **3H**.

3.3. Magnetic properties of *3H*

Fig. 3 shows the temperature dependence of $\chi_p T$ for **3H**. The $\chi_p T$ value at room temperature was 0.761 emu K mol^{-1}, that is close to 2 mol of $S = 1/2$ spins ($\chi_p T = 0.755$ emu K mol^{-1} with $g = 2.006$ shown as a broken line in Fig. 3). The $\chi_p T$ value increases gradually as temperature decreases (298–10 K) and sharply decreases in lower temperatures. These observations indicate that there are at least two magnetic interactions, which have opposite signs of J, J_1 (ferromagnetic) and J_2 (antiferromagnetic). As shown in the previous section, the intramolecular magnetic interaction through the *m*-phenylene spacer should be responsible to the ferromagnetic interaction J_1. The short contacts between the dimer observed in the crystal structure may cause an intermolecular antiferromagnetic interaction. Another antiferromagnetic interaction may be operative as shown in the diagram of Fig. 1c. We analyzed the temperature dependence of the magnetic susceptibility of **3H** using the four-spin model (Fig. 1c). The spin Hamiltonian of this model is shown in Eq. (1)

$$H = -2J_1(\mathbf{S}_1 \cdot \mathbf{S}_2 + \mathbf{S}_3 \cdot \mathbf{S}_4) - 2J_2(\mathbf{S}_1 \cdot \mathbf{S}_3 + \mathbf{S}_2 \cdot \mathbf{S}_4) - 2J_3(\mathbf{S}_1 \cdot \mathbf{S}_4 + \mathbf{S}_2 \cdot \mathbf{S}_3) \quad (1)$$

One quintet, three triplets, and two singlets are possible for the four-spin model. The energies for these spin-states are given by the following Eqs. (2)–(7):

$$E(S_1 = 2) = -J_1 - J_2 - J_3 \quad (2)$$

$$E(S_2 = 1) = J_1 + J_2 - J_3 \quad (3)$$

$$E(S_3 = 1) = J_1 - J_2 + J_3 \quad (4)$$

$$E(S_4 = 1) = -J_1 + J_2 + J_3 \quad (5)$$

$$E(S_5 = 0) = J_1 + J_2 + J_3 - 2\sqrt{J_1^2 + J_2^2 - J_2J_3 + J_3^2 - J_1(J_2 + J_3)} \quad (6)$$

$$E(S_6 = 0) = J_1 + J_2 + J_3 + 2\sqrt{J_1^2 + J_2^2 - J_2J_3 + J_3^2 - J_1(J_2 + J_3)} \quad (7)$$

The thermal equilibrium between these spin states gives the temperature dependence of magnetic susceptibility as

$$\chi_p = \frac{N_A g^2 \mu_B^2}{3k_B T} \frac{\sum_i S_i(S_i+1)(2S_i+1)\exp(-E(S_i)/k_B T)}{\sum_i (2S_i+1)\exp(-E(S_i)/k_B T)} \quad (8)$$

To avoid over-parameterization, we assumed $J_2 = J_3$. Then, the estimated value is regarded as an average of two magnetic interactions. The observed $\chi_p T$ values are well reproduced using Eq. (8) with $J_1/k_B = +5.0$ K and $J_2/k_B = J_3/k_B = -0.9$ K (solid line in Fig. 3).

3.4. Characterization of a Cu-complex of *3H*

The complex obtained from the reaction of **3H** with copper acetate in methanol containing aqueous ammonia was hardly soluble in various organic solvents. Further purification could not be possible. However, the elementary analysis of this powder showed reasonable values within ±0.5% as a formula of **3 · Cu**. The Cu-complex was stable at room temperature. Because of lack of the structure information for this complex, quantitative argument is not possible. We describe here qualitative characterization including magnetic properties of the obtained powder.

The UV–Vis reflection spectra for solid samples of the obtained Cu-complex **3 · Cu** (Fig. 4a), diradical **3H** (Fig. 4b), Cu-complex **2** (Fig. 4c), and copper(II) acetate (Fig. 4d). A broad absorption extending to 900 nm was observed for **3 · Cu**. The spectrum is similar to that of **2**. The diradical **3H** does not have absorption longer than 700 nm. The longer absorption is obviously due to the Cu(II) species. Furthermore, complex **3 · Cu** showed a very broad EPR spectrum in the region 0–800 mT with the bandwidth of ca. 200 mT at half height. Complex **2** also showed a similar broad EPR signal but with a little narrower bandwidth (ca. 140 mT). The broad signals indicate strong magnetic interactions between the Cu(II) and the radical spins [11].

Fig. 5 shows the $\chi_p T$–T plots for **3 · Cu**. The molecular formula in a magnetic repeating unit was tentatively assumed to be $C_{20}H_{26}CuN_4O_4$ (**3 · Cu**) for the χ_p calculation. One magnetic repeating unit involves 2 mol of imino nitroxide spins and 1 mol of Cu(II) spin. The observed $\chi_p T$ value at room temperature was 1.32 emu K mol^{-1}, which is higher than the value (1.23 emu K mol^{-1}) of magnetically independent 2 mol radical ($S = 1/2$ with a typical value of $g = 2.007$) spins and a one Cu(II) ($S = 1/2$ with a typical value of $g = 2.2$) spin. Decreasing the temperature (298–55 K) increased the $\chi_p T$ values (1.32–1.50 K), indicating the presence of a ferromagnetic interaction between the radical spin and the Cu(II) spin. Further cooling decreased the $\chi_p T$, suggesting a weaker antiferromagnetic interaction. The ferromagnetic interaction observed at high temperature region well accords with our expectation.

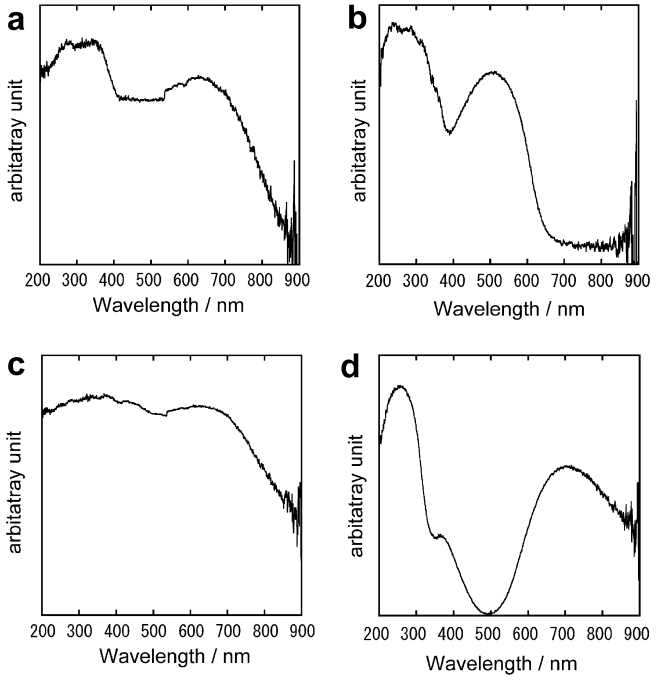


Fig. 4. UV–Vis reflection spectra of Cu-complex **3 · Cu** (a), **3H** (b), **2** (c), and copper acetate (d).

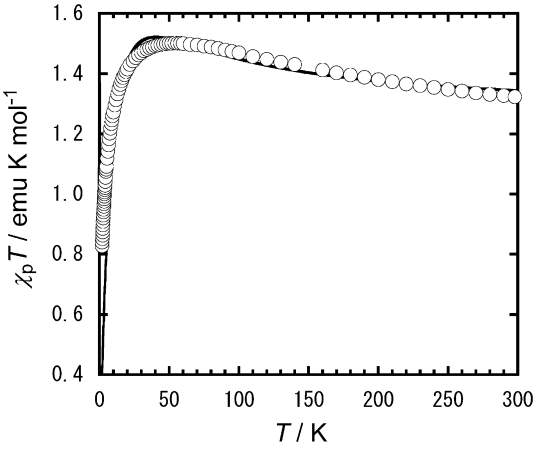


Fig. 5. The $\chi_p T$–T plots of the copper complex of **3H**; the solid line is a simulation line with $J/k_B = +40$ K and $\theta = -8$ K.

Assuming that the ferromagnetic interaction between Cu(II) spin and the radical spins observed at higher temperatures is much stronger than the magnetic interactions through the *m*-phenylene moiety, we may apply the following three-spin model:

$$H = -2J(\mathbf{S}_{IN1} \cdot \mathbf{S}_{Cu} + \mathbf{S}_{Cu} \cdot \mathbf{S}_{IN2}) \quad (9)$$

where the three $S = 1/2$ operators, $\mathbf{S}_{IN1}$, $\mathbf{S}_{IN2}$ on the imino nitroxide moieties and $\mathbf{S}_{Cu}$ on the Cu(II) ion, were coupled by the exchange interaction J. The possible difference in the exchange interactions, J(IN1–Cu) $\neq J$(IN2–Cu), was disregarded. The parameter J in Eq. (9) is regarded as an averaged one. The trimer model affords one quartet ($S = 3/2$) and two doublet ($S = 1/2$) states. The energies of these states are given by

$$E(S_1 = 3/2) = 0 \quad (10)$$

$$E(S_2 = 1/2) = J \quad (11)$$

$$E(S_3 = 1/2) = 3J \quad (12)$$

The thermal equilibrium between these states gives the temperature dependence of susceptibility as

$$\chi_p = \frac{N_A g^2 \mu_B^2}{3k_B(T-\theta)} \frac{15 + \frac{3}{2}e^{-J/kT} + \frac{3}{2}e^{-3J/kT}}{4 + 2e^{-J/kT} + 2e^{-3J/kT}} \quad (13)$$

where θ represents the intermolecular interaction in the mean-field approximation. The observed temperature dependence of $\chi_p T$ was reproduced by Eq. (13) with the parameters $J/k_B = +49$ K and $\theta = -8$ K, as depicted by the solid line in Fig. 5.

The obtained J value is considerably smaller than the value of ferromagnetic interaction ($J/k_B = +250$ K) observed for Cu-complex **2** [7a]. Several explanations are possible; (1) a part of imino nitroxide may not survive under the complexation conditions, so that tight ferromagnetic interaction between imino nitroxide and Cu(II) may be partly lost, (2) only a part of Cu(II) may form the complex. Although these unfavorable reactions should be minor paths judging from the $\chi_p T$ value at room temperature and the elementary analysis, the occurrence of these reactions may seriously affect the overall magnetic behavior of **3 · Cu**.

Appendix A. Supplementary material

CCDC 617391 contains the supplementary crystallographic data for **3H**. These data can be obtained free of charge via http://www.ccdc.cam.ac.uk/conts/retrieving.html, or from the Cambridge Crystallographic Data Centre, 12 Union Road, Cambridge CB2 1EZ, UK; fax: (+44) 1223-336-033; or e-mail: deposit@ccdc.cam.ac.uk. Supplementary data associated with this article can be found, in the online version, at doi:10.1016/j.poly.2006.09.058.

References

[1] (a) O. Kahn, Molecular Magnetism, VCH Publications, Weinheim, 1993;
(b) P.M. Lahti (Ed.), Magnetic Properties of Organic Molecules, Marcell Dekker, New York, 1999;
(c) K. Itoh, M. Kinoshita (Eds.), Molecular Magnetism: New Magnetic Materials, Gordon and Breach, Kodansha, Tokyo, 2000;
(d) J.S. Miller, M. Drillon (Eds.), Magnetism: Molecules to Materials II, Wiley-VCH, Weinheim, 2001;
(e) J.S. Miller, M. Drillon (Eds.), Magnetism: Molecules to Materials III, Wiley-VCH, Weinheim, 2002.
[2] (a) A. Caneschi, D. Gatteschi, J.P. Renard, P. Rey, R. Sessoli, Inorg. Chem. 28 (1989) 3314;
(b) D. Gatteschi, P. Rey, in: P.M. Lahti (Ed.), Magnetic Properties of Organic Materials, Marcel Decker, 1999, pp. 601–625.
[3] (a) K. Inoue, T. Hayamizu, H. Iwamura, D. Hashizume, Y. Ohashi, J. Am. Chem. Soc. 118 (1996) 1803;
(b) M. Kitano, Y. Ishimaru, K. Inoue, N. Koga, H. Iwamura, Inorg. Chem. 33 (1994) 6012.
[4] (a) A. Caneschi, D. Gatteschi, R. Sessoli, P. Rey, Acc. Chem. Res. 22 (1989) 392;
(b) A. Bencini, C. Benelli, D. Gatteschi, C. Zanchini, J. Am. Chem. Soc. 106 (1984) 5818;
(c) A. Caneschi, D. Gatteschi, J. Laugier, P. Rey, J. Am. Chem. Soc. 109 (1987) 2191;
(d) A. Caneschi, D. Gatteschi, A. Grand, J. Laugier, L. Pardi, P. Rey, Inorg. Chem. 27 (1988) 1031;
(e) C.I. Cabello, A. Caneschi, R.L. Carlin, D. Gatteschi, P. Rey, Inorg. Chem. 29 (1990) 2582;
(f) R.N. Musin, P.V. Schastnev, S.A. Mallinovskaya, Inorg. Chem. 31 (1992) 4118.
[5] (a) D. Luneau, P. Rey, J. Laugier, P. Fries, A. Caneschi, D. Gatteschi, R. Sessoli, J. Am. Chem. Soc. 113 (1991) 1245;
(b) A. Cogne, J. Laugier, D. Luneau, P. Rey, Inorg. Chem. 39 (2000) 5510.
[6] (a) Several neutral radicals as chelate-ligands have been reported; For examples, 2-pyridyl or 2-imidazolyl nitronyl nitroxides or imino-nitroxides: P.F. Richardson, R.W. Kreilick, J. Am. Chem. Soc. 99 (1977) 8183;
(b) D. Luneau, C. Risoan, P. Rey, A. Grand, A. Caneschi, D. Gatteschi, J. Laugier, Inorg. Chem. 32 (1993) 5616;
(c) F.L. de Panthou, E. Belorizky, R. Calemzuk, D. Luneau, C. Marcenat, E. Ressouche, P. Turek, P. Rey, J. Am. Chem. Soc. 117 (1995) 11247;
(d) F.L. de Panthou, D. Luneau, R. Musin, L. Öhrström, A. Grannd, P. Turek, P. Rey, Inorg. Chem. 35 (1996) 3484;
(e) K. Fegy, K.E. Vostrikova, D. Luneau, P. Rey, Mol. Cryst. Liq. Cryst. 305 (1997) 69;
(f) K. Fegy, N. Sanz, D. Luneau, E. Belorizky, P. Rey, Inorg. Chem. 37 (1998) 4518;
(g) K. Fegy, D. Luneau, E. Belorizky, M. Novak, J.-L. Tholence, C. Paulsen, T. Ohm, P. Rey, Inorg. Chem. 37 (1998) 4524;
(h) A. Marvillers, Y. Pei, J.C. Boquera, K.E. Vostrikova, C. Paulsen, E. Riviere, J.-P. Audière, T. Mallah, Chem. Commun. (1999) 1951;
(i) T. Yoshida, S. Kaizaki, Inorg. Chem. 38 (1999) 1054;
(j) Y. Yamamoto, T. Suzuki, S. Kaizaki, J. Chem. Soc., Dalton Trans. (2000) 1566.
[7] (a) K. Tanaka, M. Kozaki, D. Shiomi, K. Sato, T. Takui, K. Okada, Polyhedron 22 (2003) 1803;
(b) E.V. Tretyakov, I.V. Eltsov, S.V. Fokin, Y.G. Shvedenkov, G.V. Romanenko, V.I. Ovcharenko, Polyhedron 22 (2003) 2499;
(c) H. Kanda, Y. Narumi, Y. Hosokoshi, T. Suzuki, S. Kawata, K. Kindo, K. Inoue, S. Kaizaki, Inorg. Chim. Acta 357 (2004) 3125.
[8] G. Ulrich, R. Ziessel, Tetrahedron Lett. 35 (1994) 1215.
[9] A. Bondi, J. Phys. Chem. 68 (1964) 441.
[10] (a) L. Catala, J. Le Moigne, N. Kyritsakas, P. Lay, J.J. Novoa, P. Turek, Chem. Eur. J. 7 (2001) 2466;
(b) T. Ichimura, K. Doi, C. Mitsuhashi, T. Ishida, T. Nogami, Polyhedron 22 (2003) 2557.
[11] P.F. Richardson, R.W. Kreilick, J. Phy. Chem. 82 (1978) 1149.

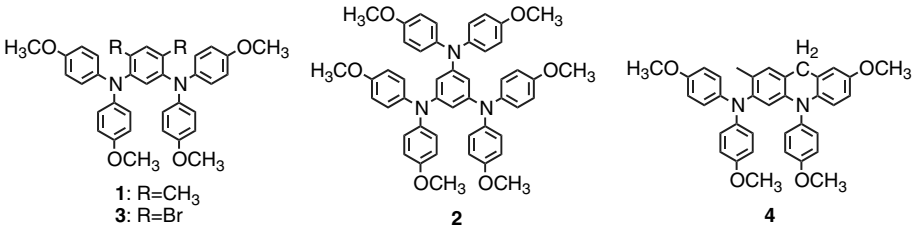


Fig. 1. Structures of compounds **1**–**4**.

states [2k,4]. However, the stabilization mechanism is still not clear. We assumed that the decomposed product was compound **4**, which was generated by intramolecular hydrogen abstraction. Until now, there was no direct evidence for the generation of **4**. Although a number of experimental and theoretical studies have been performed about reaction mechanisms of mono cation radicals [5], triplet dication diradicals have very rarely been dealt with. In this study, we report the generation and decomposition of $\mathbf{1}^{++}$ in preparative scale, and the identification of the structures for the decomposed products.

2. Results and discussion

The diamine **1** was synthesized by the methods reported before [2b]. Compound **3** was synthesized by bromination of *N*,*N*,*N*′,*N*′-tetra(*p*-anisyl)-1,3-phenylenediamine. The synthetic detail of **3** will be reported elsewhere [3]. Fig. 2 shows the NMR spectra of **1** and the corresponding decomposition products. The compound **1** exhibits absorption peaks of the methyl and methoxy groups at 1.97 ppm and 3.75 ppm, respectively (Fig. 2a). The generation of the mono cationic state was conducted as shown below. To the solution of **1** (0.127 g, 0.23 mmol) in dichloromethane (10 ml), 1.5 equiv. of $SbCl_5$ (44.3 μl, 0.35 mmol) in dichloromethane (10 ml) were slowly dropped at 15 °C under nitrogen atmosphere. Upon the addition of $SbCl_5$, the color of the solution immediately turned to blue, indicating the generation of radical species. The solution was stirred for 3 days until no change in solution color was observed. The obtained solution was mixed with aqueous ascorbic acid solution, extracted with chloroform, dried over sodium sulfate, and evaporated under reduced pressure to give pale yellow oil. The NMR spectrum of the product showed approximately quantitative recovery of **1**.

The generation of the dicationic state was conducted similarly. The solution of **1** (0.127 g, 0.23 mmol) in dichloromethane (10 ml) was mixed with 3 equiv. of $SbCl_5$ (87.4 μl, 0.69 mmol) in dichloromethane (10 ml), and allowed to stand for 3 days under the same condition described for the monocation. The color of the solution gradually changed from blue to bluish-purple. The

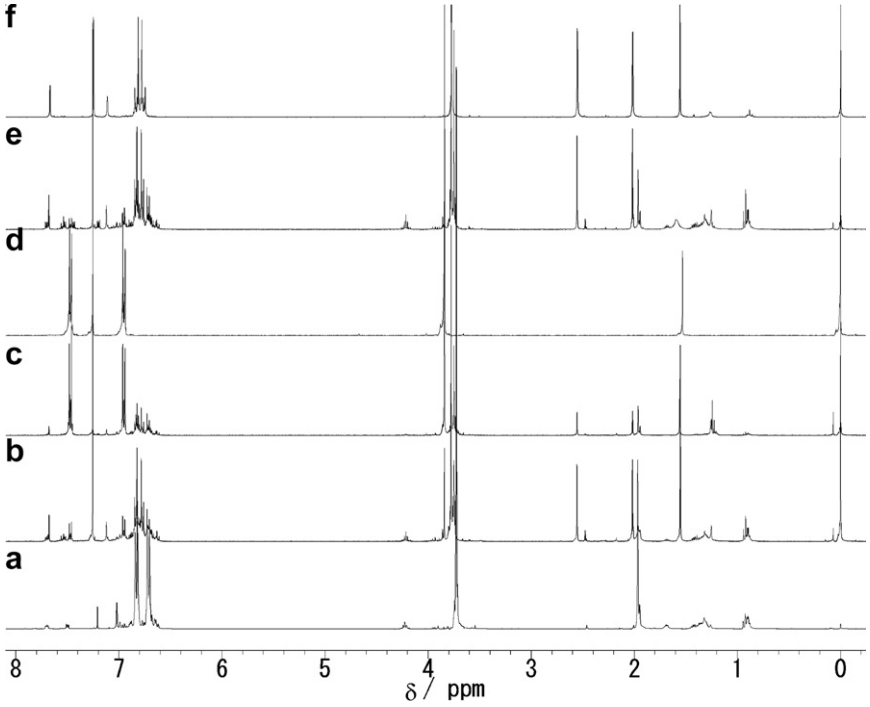


Fig. 2. NMR spectra of **1** and its decomposition products (see the text for details).

obtained solution was treated similarly to give brown oil. As the NMR spectrum of the oil was too complex to identify, short silica gel column chromatography (eluted with chloroform) was conducted to remove minor products with high polarity to give pale yellow oil (0.060 g). The NMR spectrum of the crude product is shown in Fig. 2b. The absorption peaks derived from **1** disappeared almost entirely. Two singlet peaks were observed at 2.0 and 2.5 ppm. Several peaks were observed in the region from 3.6 to 4.0 ppm. Complicated absorption pattern was observed in the aromatic region. The crude oil was recrystallized from ethanol to give pale yellow crystals. The NMR (Fig. 2c) and mass ($m/z = 214.2$) spectra of the main product are consistent with those of commercially available 4,4′-dimethoxybiphenyl (**5**) (Fig. 2d). The absorption peaks derived from anisole (methoxybenzene) were not observed. On the other hand, the filtrate was evaporated and dried in vacuo. The NMR spectrum of the filtrate is shown in Fig. 2e. Some characteristic peaks are completely consistent with that of authentic *N*,*N*-bis(4-methoxyphenyl)-5-nitro-2,4-xylidine (**6**) prepared by us (Fig. 2f) [2b]. UV–Vis MS measurements also supported the formation of **6** ($\lambda_{max} = 284$ nm in $CHCl_3$, $m/z = 378.2$). These results show that the dication $\mathbf{1}^{++}$ decomposed via cleavages of pi-system (Fig. 3). No evidence of the formation of **4** was observed. The other components have not been characterized. The mono- and dicationic states of **3** were generated in the same manner to **1**, and **3** was quantitatively recovered upon reduction by ascorbic acid, indicating surprisingly stable dicationic state on the day time scale. Previously, we examined the stability and absorption spectrum of $\mathbf{1}^{++}$ by ETSF methods [2j]. Dication diradical $\mathbf{1}^{++}$, which was chemically generated by mixing with two equivalents of tris(2,4-dibromophenyl)amine cation radical, gradually decomposed over 10 s. During the process, compound **6** was not observed, showing the generation of **6** after mixing with aqueous ascorbic acid. On the other hand, formation of **5** in the decomposition process was not clear due to the overlapping with other absorption peaks at the shorter wavelength region around 250 nm. Summarizing the experimental results described above, a

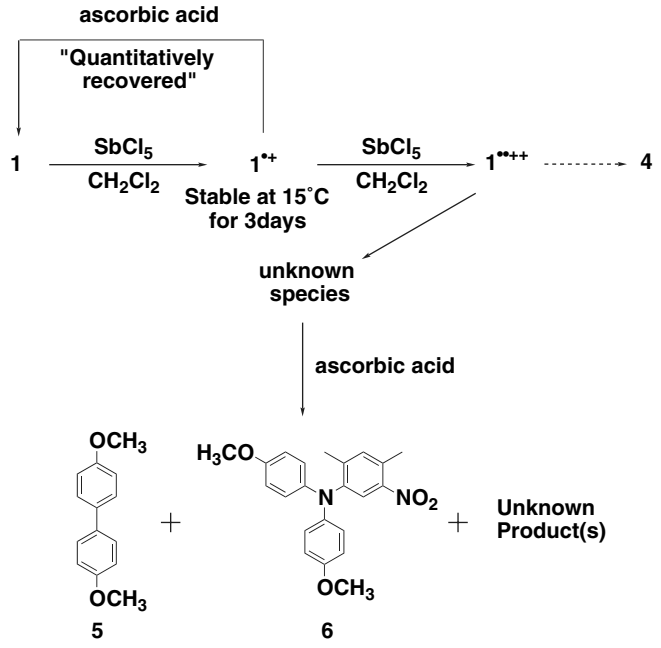


Fig. 3. Decomposition routes of the mono- and dication of **1**.

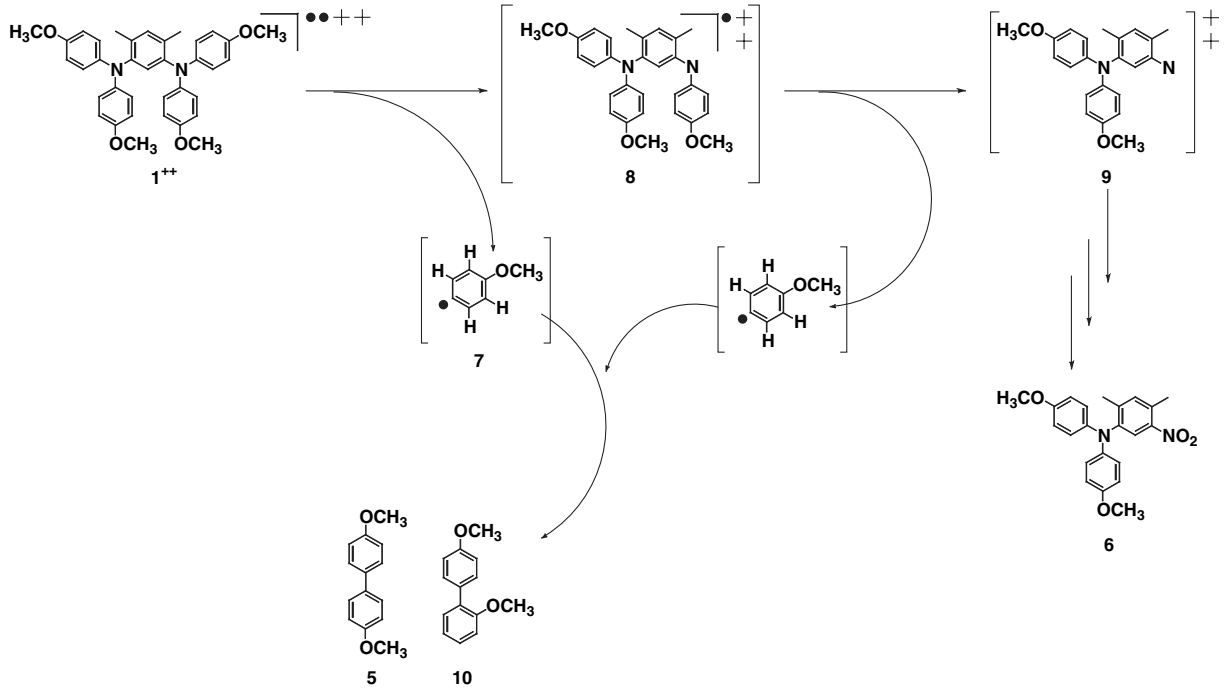


Fig. 4. Proposed decomposition routes of $\mathbf{1}^{++}$.

proposed decomposition route is shown in Fig. 4. Dication diradical $\mathbf{1}^{++}$ decomposes via the cleavage of one nitrogen-aryl bond to give anisyl radical (**7**) and a dication monoradical (**8**). Then **8** decomposes to give one more **7** and a dication (**9**), which was not observed by conventional experimental techniques and suggested to be short-lived. Dimerization of compounds **7** gives **5** via *p–p* coupling reaction. Meanwhile, 2, 4′-dimethoxybiphenyl (**10**), which was not detected in this study, could be formed via *o–p* coupling reaction. In order to examine whether **5** was formed before the addition of ascorbic acid, decomposition of $\mathbf{1}^{++}$ in the presence of radical trapping reagents is underway. Dication **9**, which is tentatively considered to be the precursor of **6**, would be reduced with ascorbic acid and may finally be converted to stable **6** via several steps. At present, the origin of two oxygen atoms in **6** is not clear. Spectroscopic detection of **9** is now in progress

It is widely known that triphenylamine gives the corresponding mono cation radical upon one electron oxidation, which immediately dimerize to give tetraphenylbenzidine [6]. On the other hand, triarylamines with substituents on the *para* positions give very stable mono cation radicals due to the thermodynamic and kinetic stabilization [6]. Based on the knowledge, molecular designs of the oligotriarylamine precursors have been carried out. In other words, the substituents were introduced to avoid rapid follow-up dimerization reactions. We have carefully designed **1** with electrodonating methoxy and methyl groups so that the corresponding mono- and dicationic states could be stabilized. Although $\mathbf{1}^{++}$ is effectively blocked by the substituents from external reagents, it may not be enough for thermodynamic stabilization, leading to the decomposition via the cleavages of the pi-conjugation. In this light, it is crucial to develop a new strategy to stabilize the oligocationic states. To elucidate the role of bromo groups, MO-based theoretical considerations are also underway.

3. Conclusions

In order to clarify the decomposition reaction of ground-state triplet dication diradicals, compound **1** was oxidized with $SbCl_5$ in preparative scale. The mono cation $\mathbf{1}^{+}$ was quantitatively recovered whereas the dication $\mathbf{1}^{++}$ gradually decomposed to give **5** and **6** as the main products, which are considered to be generated via the cleavage of the pi-conjugation. On the other hand, **3** with bromo groups gave extremely stable dication, indicating effectiveness of the bromo groups for the stabilization of the oligoarylamine-based cationic states. Based on the knowledge, studies on brominated 3,3′-bis(diarylamino)triphenylamine trication triradicals in the ground-state quartet are in progress.

References

[1] K. Itoh, M. Kinoshita (Eds.), Molecular Magnetism, New Magnetic Materials, Gordon & Breach, Inc., Amsterdam, 2000 (Kodansha as copublisher, Tokyo).
[2] (a) P.M. Lahti (Ed.), Magnetic Properties of Organic Materials, Marcel Dekker, Inc., New York, 1999 (Chapter 9 and references therein);
(b) K. Sato, M. Yano, M. Furuichi, D. Shiomi, K. Abe, T. Takui, K. Itoh, A. Higuchi, K. Katuma, Y. Shirota, J. Am. Chem. Soc. 119 (1997) 6607;
(c) M. Yano, K. Sato, D. Shiomi, A. Ichimura, K. Abe, T. Takui, K. Itoh, Tetrahedron Lett. 37 (1996) 9207;
(d) K.R. Stickley, S.C. Blackstock, J. Am. Chem. Soc. 116 (1994) 11576;
(e) K.R. Stickley, S.C. Blackstock, Tetrahedron Lett. 36 (1995) 1585;
(f) K.R. Stickley, T.D. Selby, S.C. Blackstock, J. Org. Chem. 62 (1994) 448;
(g) T.D. Selby, S.C. Blackstock, J. Am. Chem. Soc. 62 (1997) 448;
(h) A. Ito, H. Ino, K. Tanaka, K. Kanemoto, T. Kato, J. Org. Chem. 67 (2002) 491;
(i) M. Yano, Y. Ishida, K. Aoyama, M. Tatsumi, K. Sato, D. Shiomi, A. Ichimura, T. Takui, Synth. Met. 137 (2003) 1275;
(j) M. Yano, Y. Ishida, M. Tatsumi, K. Sato, D. Shiomi, M. Oyama, T. Takui, J. Phys. Chem. Solids 65 (2004) 733;
(k) M. Yano, Y. Nakanishi, K. Matsushita, M. Tatsumi, M. Oyama, K. Sato, T. Takui, Polyhedron 24 (2005) 2116.
[3] Unpublished results.
[4] (a) For the details of ETSF measurement see: M. Oyama, T. Higuchi, S. Okazaki, J. Chem. Soc. Perkin Trans. 2 (2001) 1287;
(b) M. Oyama, J. Matsui, H. Park, Chem. Commun. (2002) 604.
[5] J. Fossey, D. Lefort, J. Sorba, Free Radicals in Organic Chemistry, Wiley, 1995 (Chapter 15).
[6] (a) E.T. Seo, R.F. Nelson, J.M. Fritsch, L.S. Marcoux, D.W. Leedy, R.N. Adams, J. Am. Chem. Soc. 88 (1966) 3498;
(b) R.F. Nelson, R.N. Adams, J. Am. Chem. Soc. 90 (1968) 3925.

by adaptation of the procedure of Nakazaki et al. [3] to give a white solid in 60% yield. Mp: 42–47 °C. ^{1}H NMR ($CDCl_3$): δ 6.42 (t, 2H, $J = 2.0$ Hz), 6.93 (t, 2H, $J = 2.0$ Hz).

2.2. 1-(4-[N-tert-Butylhydroxylamino]-2,3,5,6-tetrafluorophenyl)pyrrole (*BNPPF4H*)

A solution of 2.0 M of *n*-BuLi in hexanes (1.37 mL, 2.8 mmol) was slowly added to a solution of **BrPPF4** (0.75 g, 2.5 mmol) in 10 mL of anhydrous THF at −78 °C under nitrogen. After 1 h, a solution of 2-methyl-2-nitrosopropane [4] (0.25 g, 2.8 mmol) in 10 mL of anhydrous THF was added dropwise to the reaction mixture. The reaction was allowed to warm to room temperature while stirring overnight, then was quenched by addition of saturated aqueous ammonium chloride. The layers were separated, and the organic layer was washed with water. The combined aqueous layers were extracted with ether, and the combined organic layers dried over anhydrous magnesium sulfate. The organic solution was reduced in volume *in vacuo*, then the residue was filtered to collect part of the product as white powder; that filtrate was then rotary evaporated and was subjected to column chromatography (silica, dichloromethane) to give additional product (total yield of **BNPPF4H** 0.24 g, 32%). Mp: 128–130 °C. ^{1}H NMR (400 MHz, $CDCl_3$): δ 6.93 (m, 2H, $J = 4$ Hz), 6.40 (m, 2H, $J = 4.4$ Hz), 5.43 (s, 1H); 1.26 (s, 9H).

2.3. 1-(4-[N-tert-Butylaminoxyl]-2,3,5,6-tetrafluorophenyl)pyrrole (*BNPPF4*)

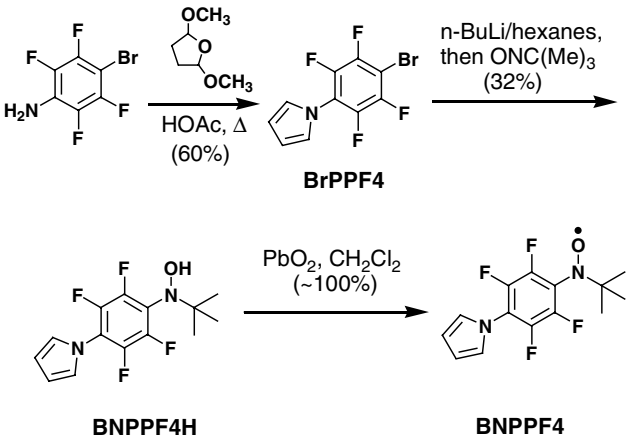
Solid PbO_2 (0.20 g, 0.84 mmol) was added to a solution of **BNPPF4H** (0.103 g, 0.34 mmol) in dichloromethane. The reaction was monitored by TLC and was complete after 1.5 h. The reaction was filtered and evaporated, and the resulting red oil recrystallized from hexanes to give red crystalline product (0.10 g, 100%). Mp: 62–65 °C. *Anal.* Calc. for $C_{14}H_{13}F_4N_2O$: C, 55.82; H, 4.35; N, 9.30. Found: C, 55.94; H, 4.51; N, 9.21%. ESR (9.59 GHz, toluene, 230 K): $g = 2.00780$, $a_N = 12.14$ G.

2.4. Magnetic measurements

Measurements for **BNPPF4** were carried out over 1.8–300 K using a Quantum Design SQUID MPMS5 magnetometer for polycrystalline samples placed in gelatin capsules and held in place with a small plug of cotton. Magnetic susceptibilities were corrected for temperature independent magnetic contributions.

3. Synthesis and characterization

The synthesis of **BNPPF4** is shown in Scheme 1. The radical is red solid that appears to be indefinitely stable under ambient conditions. Its electron spin resonance



Scheme 1. Synthesis of **BNPPF4**.

(ESR) spectrum showed a 1:1:1 hyperfine coupled (hfc) triplet with $a(N) = 12.1 \pm 0.2$ G, somewhat larger than the 11.72 ± 0.02 G nitrogen hfc found [5] for closely related **BNPP** (uncertainties are 95% confidence limits). Steric repulsion between the **BNPPF4** *tert*-butylnitroxide group and its *ortho* C–F units presumably disfavors a conformation where the nitroxide is coplanar or nearly coplanar with the *ortho*-fluorinated arene. The crystallography of **BNPPF4** supports this, as described below.

The limited data available from ESR and NMR studies of aryl-fluorinated, alkyl-arylnitroxides show $a(N) \sim 11$–13 G, and $a(F) \sim 0.6$–1.2 G, with $a(N)$ much affected by steric hindrance (size of the alkyl group on the nitroxide) that interacts with the *ortho* fluorine atoms [2b,2c]. This effect on conformation could lead to unusual delocalization behavior of the radical spin. Torssell and co-workers concluded [2b] that all of the fluorine atoms in 1-(*N*-*tert*-butylnitroxyl)pentafluorobenzene (**PhF5NIT**) surprisingly had the same spin polarization, contrary to the usual expectation of alternant spin density sites. They attributed this to sensitivity of nitroxide delocalization to steric induced twisting of the nitroxide, leading to σ-framework polarization rather than π-spin polarized delocalization. We have not yet obtained $a(F)$ for **BNPPF4** (Torssell and coworkers used perdeuterated *tert*-butyl groups to do this

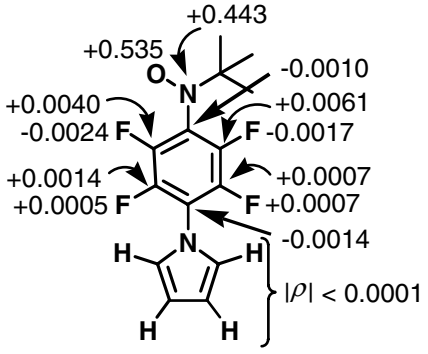


Fig. 1. UB3LYP/EPR-II computed Mulliken spin densities (ρ) for **BNPPF4**, using the geometry of Form A in Fig. 2.

for **PhF5NIT**), but have computed [6] spin densities for **BNPPF4** using the UB3LYP/EPR-II method with Gaussian 03 (Fig. 1). The nonalternant spin polarization found on the aryl carbons is not in accord with a typical π-polarization mechanism, but we did not find the fluorines all to have the same spin polarization sign, unlike the case reported for **PhF5NIT**. Further studies will be needed to determine the hfc of the fluorine atoms in **BNPPF4** and allow further comparisons to the computational results and to **PhF5NIT**.

4. Crystallography

Diffraction grade single crystals of **BNPPF4** were obtained by precipitation from hexanes and analyzed [7]. Fig. 2 shows an ORTEP style representation of the two forms present in the lattice, which have small differences in the nitroxide and pyrrole dihedral torsions relative to the tetrafluoroaryl ring. Structural and crystallographic details are summarized in Tables 1 and 2 for the analysis at room temperature. Analysis of a crystal at 105 K showed little structural change relative to the room temperature structure.

5. Magnetic studies

Fig. 3 shows temperature dependent magnetic susceptibilities and magnetization versus field data for **BNPPF4**. The Curie–Weiss plot shows strong deviation from linearity below about 10 K due to onset of antiferromagnetic (AFM) exchange interactions. A linear fit to the data for $1/\chi(T > 50\ \mathrm{K})$ yielded a Curie constant of 0.362 emu/Oe mol, in good agreement with the expected value for $S = 1/2$ spin carriers; the Weiss constant = (−)1.2 K. The AFM exchange is further shown by the strong downturn in the $\chi(T)$ data below about 7 K. The magnetization plot has inverted curvature consistent with significant AFM exchange, to the point that $M(H)$ does not nearly approach the expected saturation value for $S = 1/2$ at fields up to 50 000 Oe.

Table 1
Crystal data for **BNPPF4** at room temperature

Empirical formula	$C_{14}H_{13}F_4N_2O$
Formula weight	301.27
Temperature (K)	298
Wavelength (Å)	0.71073
Crystal system	monoclinic
Space group	*P2/a*
Unit cell dimensions	
a (Å)	19.0843(7)
b (Å)	5.8566(2)
c (Å)	26.7441(11)
α (°)	90
β (°)	110.6919(17)
γ (°)	90
Volume (Å^3)	2796.35(18)
Z	4
D_{calc} (g/cm^3)	1.4312(1)
Absorption coefficient (mm^{-1})	0.128
F(000)	1240
θ Range for data collection (°)	3.79–25.1
Index ranges	$0 \leqslant h \leqslant 22$, $0 \leqslant k \leqslant 6$, $-31 \leqslant l \leqslant 29$
Reflections collected	5344
Independent reflections (R_{int})	4838 (0.000)
Completeness to θ (%)	97.6
Maximum and minimum transmission	0.889 and 0.615
Refinement method	full-matrix least-squares on F^2
Data/restraints/parameters	4838/0/381
Goodness-of-fit on F^2	0.889
Final *R* indices [$I > 2\sigma(I)$]	$R_1 = 0.0533$, $wR_2 = 0.1480$
R indices (all data)	$R_1 = 0.0823$, $wR_2 = 0.1808$
Largest difference in peak and hole (e Å^{-3})	0.194 and −0.145

6. Results and discussion

The crystallography of **BNPPF4** shows the *tert*-butylnitroxide group to be strongly twisted by dipolar interactions with CF bonds *ortho* to it in the connected aryl ring

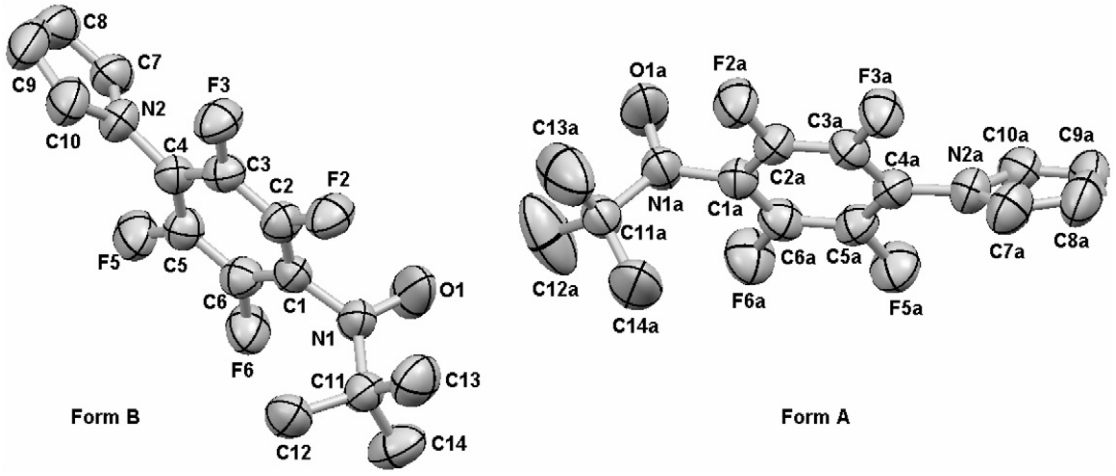


Fig. 2. ORTEP diagram for **BNPPF4**, showing 50% probability ellipsoids.

Table 2
Selected molecular and intermolecular structural parameters for **BNPPF4** at room temperature[a]

Bond lengths					
O(1)	N(1)	1.253(5)	O(1A)	N(1A)	1.268(5)
N(1)	C(1)	1.429(5)	N(1A)	C(1A)	1.432(5)
N(1)	C(11)	1.501(5)	N(1A)	C(11A)	1.487(5)
N(2)	C(4)	1.415(5)	N(2A)	C(4A)	1.410(5)
N(2)	C(7)	1.368(6)	N(2A)	C(10A)	1.360(6)
N(2)	C(10)	1.376(6)	N(2A)	C(7A)	1.370(6)
C(1)	C(2)	1.372(6)	C(1A)	C(6A)	1.390(6)
C(1)	C(6)	1.384(6)	C(1A)	C(2A)	1.358(5)
C(2)	C(3)	1.377(5)	C(6A)	C(5A)	1.371(5)
C(3)	C(4)	1.376(6)	C(5A)	C(4A)	1.370(5)
C(4)	C(5)	1.373(6)	C(4A)	C(3A)	1.389(5)
C(5)	C(6)	1.378(6)	C(3A)	C(2A)	1.376(5)
C(7)	C(8)	1.361(7)	C(10A)	C(9A)	1.343(7)
C(8)	C(9)	1.381(9)	C(9A)	C(8A)	1.404(10)
C(9)	C(10)	1.352(7)	C(8A)	C(7A)	1.354(7)
C(11)	C(12)	1.490(7)	C(11A)	C(14A)	1.524(6)
C(11)	C(13)	1.508(8)	C(11A)	C(13A)	1.515(7)
C(11)	C(14)	1.469(9)	C(11A)	C(12A)	1.505(7)
Selected dihedral torsions					
O(1)	N(1)	C(1)	C(2)		−78.7(5)
O(1)	N(1)	C(1)	C(6)		95.3(5)
O(1)	N(1)	C(11)	C(12)		12.3(6)
O(1)	N(1)	C(11)	C(13)		−104.3(5)
O(1)	N(1)	C(11)	C(14)		−53.7(6)
C(1)	N(1)	C(11)	C(14)		135.5(5)
C(10)	N(2)	C(4)	C(3)		−52.2(6)
C(7)	N(2)	C(4)	C(3)		121.6(5)
C(7)	N(2)	C(4)	C(5)		−56.1(6)
C(10)	N(2)	C(4)	C(5)		130.1(5)
O(1A)	N(1A)	C(1A)	C(2A)		−84.3(5)
O(1A)	N(1A)	C(1A)	C(6A)		−90.9(5)
O(1A)	N(1A)	C(11A)	C(12A)		−54.6(6)
O(1A)	N(1A)	C(11A)	C(13A)		−64.8(5)
O(1A)	N(1A)	C(11A)	C(14A)		−175.7(4)
C(10A)	N(2A)	C(4A)	C(3A)		120.3(4)
C(10A)	N(2A)	C(4A)	C(5A)		−56.1(6)
C(7A)	N(2A)	C(4A)	C(3A)		−54.7(6)
C(7A)	N(2A)	C(4A)	C(5A)		129.0(5)
Selected intermolecular distances					
O(1)···C(13a)		3.508(9)			upper Fig. 4
O(1)···C(12a)		3.673(9)			
O(1a)···C(13)		3.628(9)			
O(1a)···C(14)		4.053(9)			
C(6)···C(8′)		3.392			
C(2a)···C(9a′)		3.423			
O(1)···O(1″)		5.857(5)			lower Fig. 4
O(1)···N(1″)		5.405(5)			
O(1a)···N(1a′)		5.506(5)			
O(1)···N(1a)		5.424(5)			
O(1)···O(1a)		5.949(5)			

All distances in angstroms, all angles in degrees, esd for selected parameters in parentheses. For intermolecular distances, see also Fig. 4 to identify the contact.

[a] See Fig. 2 for atom numbering.

of both forms A and B, consistent with the nitrogen ESR hfc being larger than that for **BNPP** in solution. This implies that the degree of nitroxide spin delocalization onto the aryl ring is small, as mentioned above, and confirmed by the computational investigation.

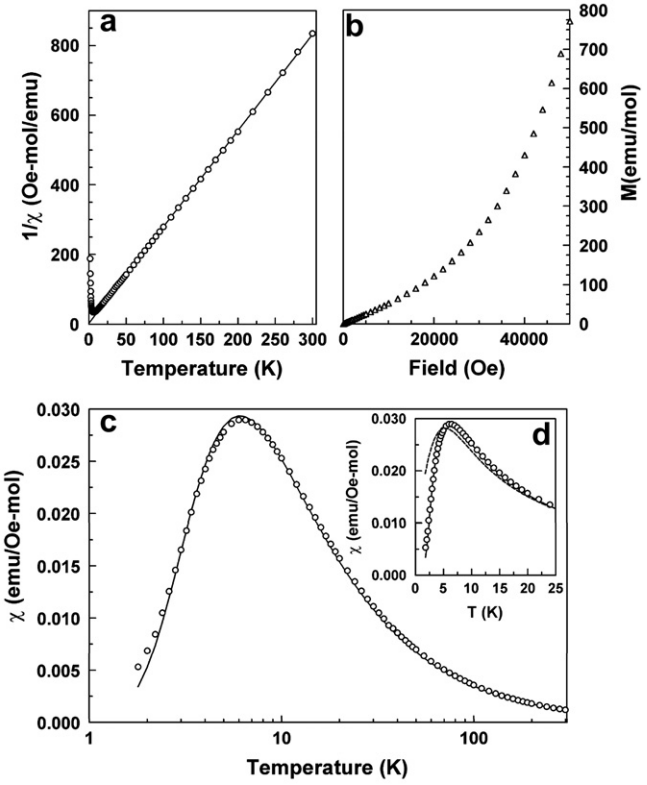


Fig. 3. Magnetic data for **BNPPF4**: (a) Curie–Weiss plot obtained at 1000 Oe, showing a linear fit to the data for $T > 50$ K, (b) magnetization vs. field (M vs. H) plot obtained at 1.8 K, (c) $\chi T(T)$ plot obtained at 1000 Oe, showing spin-pairing fit, (d) expansion of plot (c), comparing a spin-pairing fit (solid black line) to 1D Heisenberg AFM chain fit (gray broken line).

The magnetic exchange behavior of **BNPPF4** was unexpected relative to the room temperature crystal structure. The $\chi(T)$ data show loss of about 90% of paramagnetic susceptibility upon cooling from 8 K to 2 K, suggestive of spin-pairing behavior. An antiferromagnetically coupled singlet–triplet equilibrium model using spin Hamiltonian equation (1) and the Bleaney–Bowers [8] susceptibility equation (2) was applied to the $\chi(T)$ data with inclusion of a mean-field correction θ. For Eq. (2), the constants N, β, and k are Avogadro's number, the Bohr magneton, and the Boltzmann constant, per the usual practice:

$$\hat{H} = -2J\hat{S}_A\hat{S}_B \tag{1}$$

$$\chi = \frac{2Ng^2\beta^2}{k(T-\theta)} \cdot \frac{e^{2J/kT}}{1+3e^{2J/kT}} \tag{2}$$

The fit showed good agreement over the full temperature range studied (Fig. 2c), with $2J/k = (-)8.7 \pm 0.2$ K and $\theta = (-)0.2 \pm 0.2$ K, and $g = 2.017 \pm 0.014$: the uncertainties are 95% confidence limits. However, the only crystallographic dyad motifs are those shown in Fig. 4 relating two molecules of Form A, and two of Form B, both by the symmetry operation $(1/2 - x, y, -1 - z)$. The dyads are head-to-tail π-stacks with the electron poor fluorinated aryl rings interacting with the pyrrole rings. This arrangement

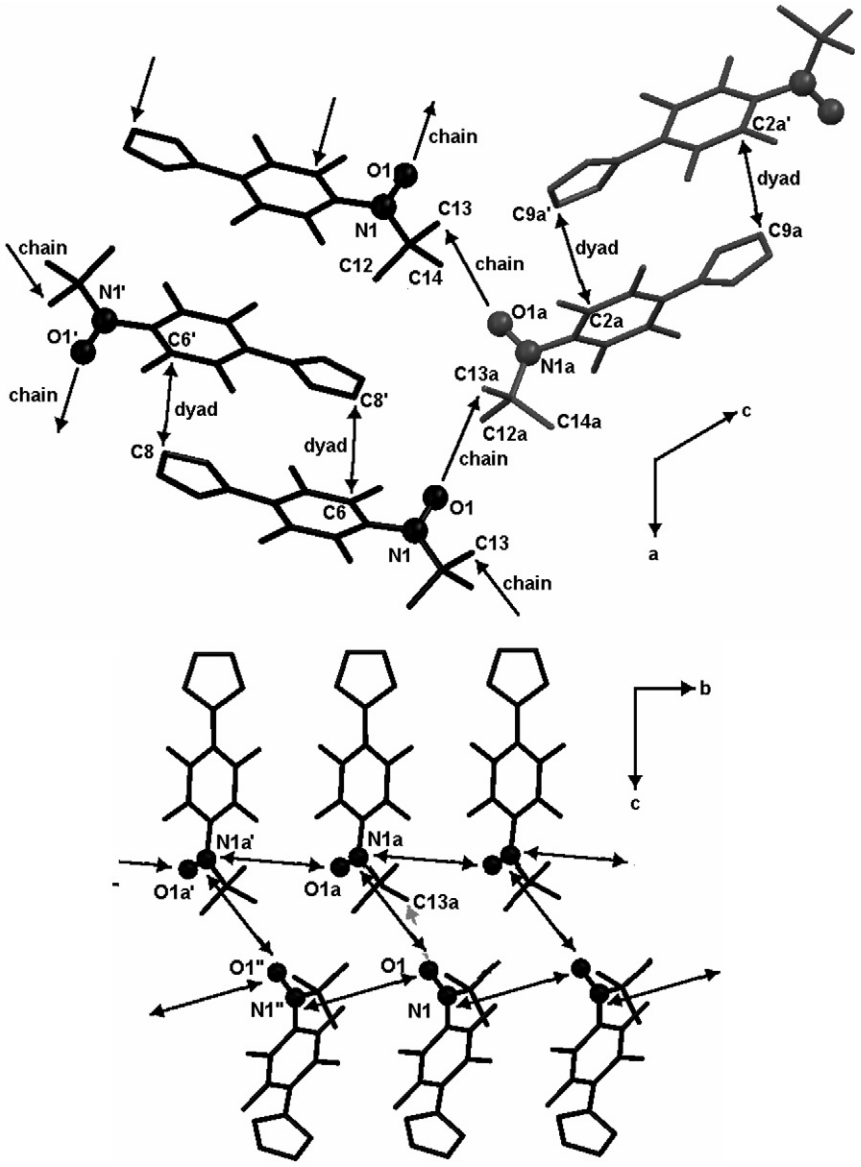


Fig. 4. Crystallographic close contacts in **BNPPF4**. Labeling follows Fig. 2.

brings the large spin density NO sites into contact with pyrrole groups that have virtually no spin density. There are no nitroxide NO–NO contacts at all at distances less than 5.40-5.5 Å. Thus, a simple spin-pairing mechanism between large spin density sites is not easily related to the crystalline packing in **BNPPF4**.

The crystallography suggests the possibility of 1D chain behavior, due to the chains of nitroxide to *tert*-butyl close contacts along the *a*-axis, and of nitroxide to nitroxide contacts along the *b*-axis (Table 2, Fig. 4). Although the *tert*-butyl groups have little unpaired spin density, there might be enough to induce some intermolecular exchange, given the interaction with the large spin density on the nitroxyl oxygen. As mentioned above, the chains of nitroxide NO–NO contacts have large, 5.5 Å distances between large spin density sites, but still should allow for some exchange between nitroxides.

Despite the presence of multiple 1D crystallographic motifs, a 1D AFM Heisenberg chain (Bonner–Fisher) [9] model fit to the $\chi(T)$ data shows poor agreement, even when a mean-field term is included. The nonlinear least squares best fit to this model, shown in Fig. 2d, gives $J/k = (-)3.4 \pm 1.3$ K, and $\theta = (-)0.8 \pm 1.9$ K, with $g = 2.022 \pm 0.014$, and deviates strongly from the data in the lower temperature range.

A tentative explanation for apparent spin-pairing exchange behavior in a nominally chain-like crystal lattice would be if **BNPPF4** undergoes a spin Peierls transition [10] at or somewhat above 8 K from 1D chain to a dimeric or strongly alternating AFM chain behavior. Decreasing temperature could distort the crystal packing in a manner to bring molecules closer together at low temperatures, and favor spin-pairing behavior. No significant change in the crystallography of **BNPPF4** was found down to

105 K, so any spin Peierls transition would have to occur well below this temperature.

Of course, the various close contacts involving C–F bonds may induce unexpected exchange behavior in **BNPPF4**, since that the scarce data to date concerning aryl C–F bond experimental spin polarization and spin density distributions appear to be in some ways anomalous, and sensitive to local environment. Overall, the magnetostructural behavior of **BNPPF4** is not straightforward to interpret, making it a rather interesting though simple molecule.

7. Conclusions

Radical **BNPPF4** is apparently the first heavily ring-fluorinated aryl *tert*-butyl nitroxide to be made by a preparative scale synthetic route, and to be subjected to magnetostructural analysis. Its crystallization behavior is reasonably consistent with interaction between attractive dipoles (nitroxide–HC interactions, fluoroarene–pyrrole π-stack interactions), but its magnetic behavior is not straightforward by comparison to obvious intermolecular close contacts. Neither intramolecular spin density distributions nor their related intermolecular exchange interactions in fluoroarene-substituted *tert*-butylnitroxides have been much explored to date. Further investigation seems warranted for this and related variants to get a better idea of the effect of aryl group fluorination upon organic magnetism of *tert*-butylnitroxides and related systems.

Acknowledgements

This material is based upon work supported by the National Science Foundation under grant CHE-0415716. We thank Dr. P. Khalifah of the University of Massachusetts Amherst X-ray Structural Characterization Center (NSF CHE-9974648) for assistance with crystallographic analysis. The University of Massachusetts Amherst Nanomagnetics Characterization Facility and Electron Paramagnetic Resonance Facility were supported by National Science Foundation grants CTS-0116498 and CHE-0443180, respectively.

Appendix A. Supplementary material

CCDC 620661 and 620662 contain the supplementary crystallographic data for this paper. These data can be obtained free of charge via http://www.ccdc.cam.ac.uk/conts/retrieving.html, or from the Cambridge Crystallographic Data Centre, 12 Union Road, Cambridge CB2 1EZ, UK; fax: (+44) 1223-336-033; or e-mail: deposit@ccdc.cam.ac.uk. Supplementary data associated with this article can be found, in the online version, at doi:10.1016/j.poly.2006.09.066.

References

[1] (a) Cf., for example, J.D. Dunitz, A. Gavezzotti, W.B. Schweizer, Helv. Chim. Acta 86 (2003) 4073;
(b) P. Beier, D. O'Hagan, C. Pearson, M.C. Petty, A.M.Z. Slawin, J. Fluorine Chem. 126 (2005) 673.
[2] (a) J.A. Pedersen, K. Torssell, Acta Chem. Scand. 25 (1971) 3151;
(b) J. Goldman, T.E. Petersen, K. Torrsell, Tetrahedron 29 (1973) 3837;
(c) S. Terabe, K. Kuruma, R. Konaka, J. Chem. Soc., Perkin 2 (1973) 1252.
[3] J. Nakazaki, I. Chung, M. Matsushita, T. Sugawara, R. Watanabe, A. Izuoka, Y. Kawada, J. Mater. Chem. 13 (2003) 1011.
[4] J.C. Stowell, J. Org. Chem. 36 (1971) 3055.
[5] **BNPP** also shows well resolved aryl hfc, *viz.* *a*(*ortho* phenyl CH) = 2.2 G, *a*(*meta* phenyl CH) = 0.9 G: Z. Delen, P.M. Lahti, unpublished results.
[6] M.J. Frisch, G.W. Trucks, H.B. Schlegel, G.E. Scuseria, M.A. Robb, J.R. Cheeseman, J.A.J. Montgomery, T. Vreven, K.N. Kudin, J.C. Burant, J.M. Millam, S.S. Iyengar, J. Tomasi, V. Barone, B. Mennucci, M. Cossi, G. Scalmani, N. Rega, G.A. Petersson, H. Nakatsuji, M. Hada, M. Ehara, K. Toyota, R. Fukuda, J. Hasegawa, M. Ishida, T. Nakajima, Y. Honda, O. Kitao, H. Nakai, M. Klene, X. Li, J.E. Knox, H.P. Hratchian, J.B. Cross, C. Adamo, J. Jaramillo, R. Gomperts, R.E. Stratmann, O. Yazyev, A.J. Austin, R. Cammi, C. Pomelli, J.W. Ochterski, P.Y. Ayala, K. Morokuma, G.A. Voth, P. Salvador, J.J. Dannenberg, V.G. Zakrzewski, S. Dapprich, A.D. Daniels, M.C. Strain, O. Farkas, D.K. Malick, A.D. Rabuck, K. Raghavachari, J.B. Foresman, J.V. Ortiz, Q. Cui, A.G. Baboul, S. Clifford, J. Cioslowski, B.B. Stefanov, G. Liu, A. Liashenko, P. Piskorz, I. Komaromi, R.L. Martin, D.J. Fox, T. Keith, M.A. Al-Laham, C.Y. Peng, A. Nanayakkara, M. Challacombe, P.M.W. Gill, B. Johnson, W. Chen, M.W. Wong, C. Gonzalez, J.A. Pople, Gaussian 03, Revision B.03, Pittsburgh, PA, 2003.
[7] Crystallographic analysis used G.M. Sheldrick, SHELXTL-97 Program for the Refinement of Crystal Structures, University of Göttingen, Germany.
[8] B. Bleaney, K.D. Bowers, Proc. R. Soc. London A (1952) 214.
[9] (a) J.C. Bonner, M.E. Fisher, Phys. Rev. A 135 (1964) 650;
(b) J.C. Bonner, Ph.D. Dissertation, University of London, UK, 1968.
[10] (a) I.S. Jacobs, J.W. Bray Jr., J.R. Hart, L.V. Interrante, J.S. Kasper, G.D. Watkins, D.E. Prober, J.C. Bonner, Phys. Rev. B14 (1976) 3036;
(b) S. Huzinaga, J. Kommandeur, G.A. Swatzky, B.T. Thole, K. Kopinga, W.J.M. de Jonge, J. Roos, Phys. Rev. B19 (1979) 4723.

compound (H_5PTCE, Fig. 1a), whose properties we report here for the first time. Phenyltricyanoethylene reacts with $V(CO)_6$ to yield a material that is magnetically ordered below 215 K. We also report the re-examination of the reaction of $V(CO)_6$ with pentafluorophenyltricyanoethylene (F_5PTCE, Fig. 1b) that, with improved synthesis and handling, gives a material that is attracted to a permanent magnet at room temperature and orders at the highest temperature we have seen for an acceptor other than TCNE, 307 K [8]. On a mass percent basis, this compound has the lowest fraction of transition metal for a material ordered at room temperature (8.6 mass% based on the empirical formula V[acceptor]$_2$).

2. Experimental

2.1. General considerations

Preparations of air sensitive compounds were carried out in a nitrogen-filled Vacuum Atmospheres glovebox. Vanadium hexacarbonyl was made from $[V(CO)_6]^-$-$[(Et)_4N]^+$ according to the literature procedure [10]. Malononitrile, *N*-chlorosuccinimide and piperidine were purchased from Aldrich. Pentafluorobenzaldehyde was purchased from Acros and sublimed prior to use. Reagents were used as received except as noted below. Dichloromethane was distilled from P_2O_5 and degassed with glovebox nitrogen prior to use. Acetonitrile was distilled from P_2O_5 followed by distillation from CaH_2 under argon prior to use. F_5PTCE was synthesized based loosely on the literature procedure and described below [11]. Purity was established by ^{1}H and ^{19}F NMR and by infrared spectroscopy. Elemental analyses were performed by Desert Analytics, Tucson, AZ.

2.2. Magnetic measurements

All magnetic measurements were performed on a 7 T Quantum Design MPMS SQUID magnetometer. Measurements of magnetization as a function of temperature were performed from 5 to 310 or 315 K as indicated. Powder samples were cooled in 100 G applied field and measured upon warming in 5 G applied field. Measurements of magnetization as a function of applied magnetic field were performed at 5 K. The amplitude of the oscillating magnetic field used for ac susceptibility measurements was 3.5 Oe with zero dc bias field and at frequencies of 1, 10 and 100 Hz. Diamagnetic corrections were not applied to the *M* versus *T* or *M* versus *H* data.

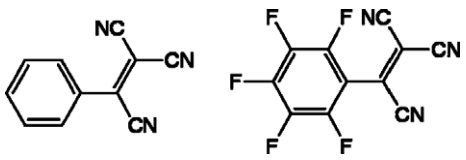


Fig. 1. Structure of (a) phenyltricyanoethylene (H_5PTCE), (b) pentafluorophenyltricyanoethylene (F_5PTCE).

2.3. Electrochemistry measurements

The cyclic voltammogram was recorded using a CH Instruments model 600A potentiostat. Measurements were performed on ~5 mM solutions in CH_3CN/0.1 M [*n*-Bu_4N]-[PF_6] and taken between the potential range of 0 and −400 mV at a scan rate of 100 mV/s using a polished carbon electrode with Ag/AgCl as the reference. Solution resistance was compensated 95% using positive feedback IR compensation for all measurements.

2.4. Powder diffraction measurements

Samples were sealed in 1.0 mm diameter glass capillaries (Blake Industries, Scotch Plains, NJ) inside the glovebox and data were collected in transmission mode on an R-Axis Rapid diffractometer using copper radiation, a graphite-monochromator and a 0.5 mm incident beam collimator.

2.5. Synthesis

2.5.1. 2-(Pentafluorophenyl)-1,1-dicyanoethylene

In a 200 mL beaker, pentafluorobenzaldehyde (6.30 g, 32.1 mmol) and malononitrile (2.15 g, 32.6 mmol) were stirred together and dissolved in 80 mL of 100% ethanol. While stirring, two drops of piperidine were added. The solution was allowed to stir overnight. Afterwards, the solution was diluted with 80 mL of dichloromethane, washed with water (4 × 80 mL), dried with anhydrous sodium sulfate and the solvent removed in vacuo to afford light yellow crystals. Yield: 4.07 g (51.8%). IR (KBr): ν(CN), 2243 cm^{-1}. ^{1}H NMR (400 MHz, $CDCl_3$) δ 7.75 (s, 1H) ppm versus TMS. ^{19}F NMR (376 MHz, $CDCl_3$) δ −132.7 (m, 2F), −143.7 (m, 1F), −158.6 (m, 2F) ppm versus Freon 11 (external standard).

2.5.2. 2-(Pentafluorophenyl)-1,1,2-tricyanoethane

In a 1 L beaker, 2-(pentafluorophenyl)-1,1-dicyanoethylene (3.50 g, 14.3 mmol) was dissolved in 250 mL of 100% ethanol. Separately, potassium cyanide (1.93 g, 29.6 mmol) was dissolved in 150 mL of water and cooled in an ice bath. In quick succession, the cold potassium cyanide solution was added to the ethanol solution followed by 500 mL of ice cold water. After stirring for 45 min, 4 mL of conc. HCl was added to yield a white precipitate. After stirring the solution for another 15 min, the stirbar was removed and the beaker was transferred to the refrigerator overnight to allow the solid to settle. The white crystals were filtered, rinsed thoroughly with water and dried by suction. Yield: 2.68 g (69%). IR (KBr): ν(CN), 2267 cm^{-1} and 2265 cm^{-1} (shoulder). ^{1}H NMR (400 MHz, $CDCl_3$) δ 4.85 (d, 1H), 4.45 (d, 1H) ppm versus TMS. ^{19}F NMR (376 MHz, $CDCl_3$) δ −138.6 (m, 2F),

−145.4 (m, 1F), −156.9 (m, 2F) ppm versus Freon 11 (external standard).

2.5.3. 2-(Pentafluorophenyl)-1,1,2-tricyanoethylene (F_5PTCE)

In a 100 mL round bottom flask equipped with a magnetic stirbar, 2-(pentafluorophenyl)-1,1,2-tricyanoethane (500 mg, 1.84 mmol) was dissolved in ~25 mL of diethyl ether and cooled to 0 °C. *N*-Chlorosuccinimide (260 mg, 1.94 mmol) was then added with rapid stirring. Over the course of 20 min, ~45 mL of ice cold water was also added with vigorous stirring. The mixture was transferred to a separatory funnel; the organic layer was washed with ice cold water (3 × 30 mL) and dried with anhydrous sodium sulfate. Removal of the ether in vacuo left behind a light pink solid which was purified by silica gel column chromatography with dichloromethane as the mobile phase. Yield: 293 mg (59%). IR (KBr): ν(CN), 2248 cm^{-1} and 2238 cm^{-1}. ^{19}F NMR (376 MHz, $CDCl_3$) δ −132.9 (m, 2F), −140.6 (m, 1F), −156.3 (m, 2F) ppm versus Freon 11 (external standard).

2.5.4. Phenyltricyanoethylene (H_5PTCE)

H_5PTCE was prepared by a similar procedure, using benzaldehyde as the starting material. IR (KBr): ν(CN), 2235 cm^{-1}, 2233 cm^{-1} (shoulder). ^1H NMR (400 MHz, $CDCl_3$) δ 8.01 (m, 2H), 7.73 (m, 1H), 7.63 (m, 2H) ppm versus TMS.

2.5.5. $V[F_5PTCE]_2$

Under a nitrogen atmosphere, vanadium hexacarbonyl (21.1 mg, 0.0930 mmol) dissolved in dichloromethane (2 mL) was added dropwise to a solution containing F_5PTCE (77.1 mg, 0.286 mmol) in dichloromethane (2 mL) while stirring. After 15 min, the black precipitate, which adheres to the magnetic stirbar, was collected on a medium frit, rinsed with dichloromethane (3 × 2 mL) and dried in vacuo for 1 h. Yield: 51 mg (93%). IR (KBr): ν(CN), 2140 cm^{-1} and 2101 cm^{-1}. *Anal.* Calc. for $C_{22}F_{10}N_6V \cdot 1/20CH_2Cl_2$: C, 44.63; H, 0.02; N, 14.06. Found: C, 44.69; H, <0.1; N, 13.87%.

2.5.6. $V[H_5PTCE]_2$

$V[H_5PTCE]_2$ was prepared by a similar procedure, using 24.4 mg of $V(CO)_6$ and 54.0 mg of H_5PTCE as the starting materials. Yield: 33 mg (55%). IR (KBr): ν(CN), 2210 cm^{-1} and 2129 cm^{-1}. *Anal.* Calc. for $C_{22}H_{10}N_6V \cdot 3/8CH_2Cl_2$: C, 60.93; H, 2.46; N, 19.05. Found: C, 60.93; H, 2.31; N, 19.14%.

3. Results and discussion

3.1. Synthesis of the coordination polymers

The reaction of either H_5PTCE or F_5PTCE with $V(CO)_6$ in dichloromethane in an inert atmosphere glovebox yields a black air-sensitive solid; in the latter case, the product sticks to the stirbar because it is ordered at room temperature. Based on elemental analyses, the formulas for these compounds are $C_{22}H_{10}N_6V \cdot 3/8CH_2Cl_2$ and $C_{22}F_{10}N_6V \cdot 1/20CH_2Cl_2$, respectively, indicating two acceptors for each vanadium ion. The 2:1 acceptor/V^{2+} ratio has also been established by multiple preparations with different ratios of reactants which yield inferior products (based on lower T_cs) at less than 2:1 and materials with similar T_cs at 2.5:1 and 3:1. Both compounds have been found by powder diffraction to be amorphous, like all of the other examples in this family. The structures are assumed to be a disordered coordination polymer networks of V^{2+} cations bridged through the three nitrile nitrogen atoms by H_5PTCE or F_5PTCE radical anions. In the IR, shifts in the CN stretch to lower wavenumbers in the coordination polymers relative to the free ligands are consistent with reduction of the acceptor to the radical anionic state. H_5PTCE and F_5PTCE have $E_{red} = -0.44$ V and −0.19 V versus Ag/AgCl, respectively. For comparison, the E_{red} for TCNE = +0.25 V.

3.2. Magnetic properties

The magnetic properties of $V[H_5PTCE]_2$ have been determined by SQUID magnetometry on a freshly prepared sample. Magnetization as a function of temperature measured on warming in 5 G applied field (Fig. 2) shows a slow decrease up to about 170 K, followed by a steeper drop, finally going to zero at about 215 K. $V[H_5PTCE]_2$ is a soft ferrimagnet as indicated by the near zero coercivity and a saturation magnetization that is consistent with one unpaired electron per formula unit as would be expected (vide infra, Fig. 3). It is essentially saturated in a field of 100 G. The frequency-independent ac susceptibility (Fig. 4) confirms the onset of order below about 215 K. The corresponding perfluorinated compound, $V[F_5PTCE]_2$ exhibits similar behavior showing a slow decrease in magnetization up to about 250 K, followed by a steeper drop, finally going to zero at 307 K (Fig. 5). This compound is also a soft ferrimagnet (Fig. 6) and shows frequency-independent ac susceptibility with a T_c of 298 K (Fig. 7). The saturation magnetization is slightly below that

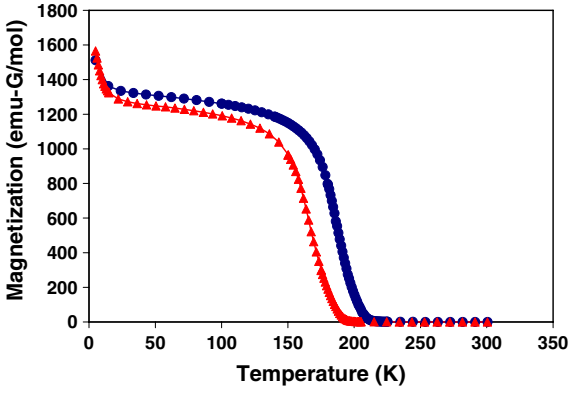


Fig. 2. Magnetization vs. temperature for $V[H_5PTCE]_2$ that has been field cooled in 5 G, measured in 5 G applied field. (●) fresh sample; (▲) sample aged 21 days.

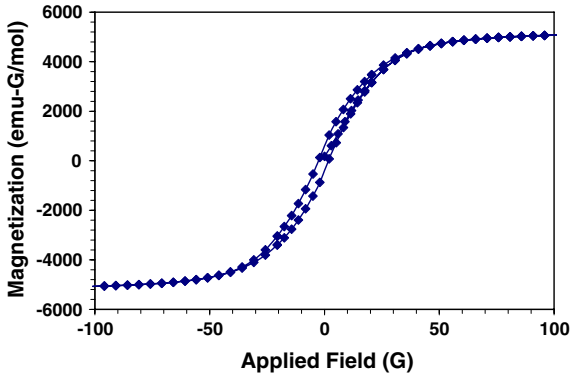


Fig. 3. Magnetization vs. applied field for $V[H_5PTCE]_2$ measured at 5 K.

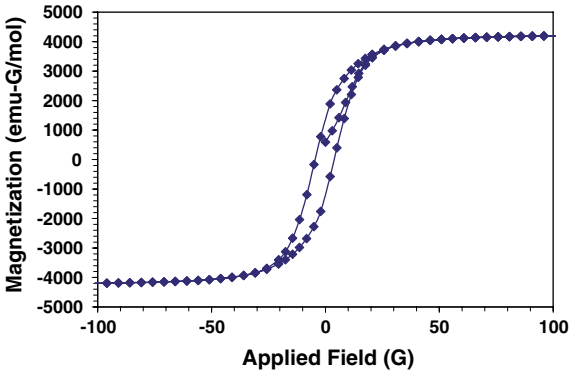


Fig. 6. Magnetization vs. applied field for $V[F_5PTCE]_2$ measured at 5 K.

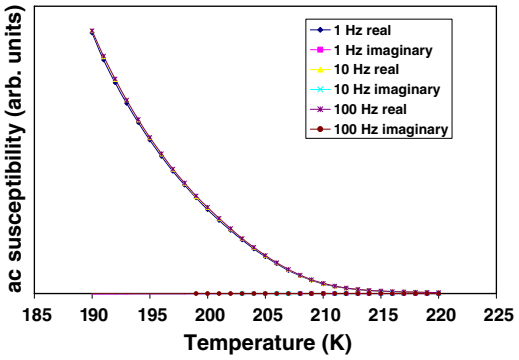


Fig. 4. AC susceptibility for $V[H_5PTCE]_2$.

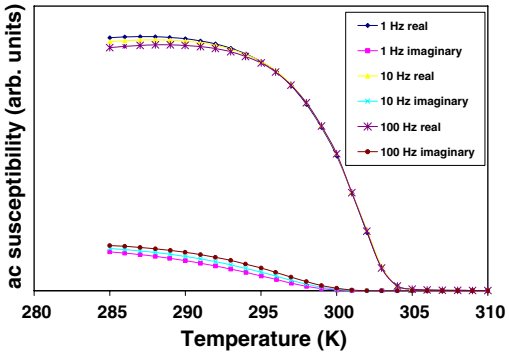


Fig. 7. AC susceptibility for $V[F_5PTCE]_2$.

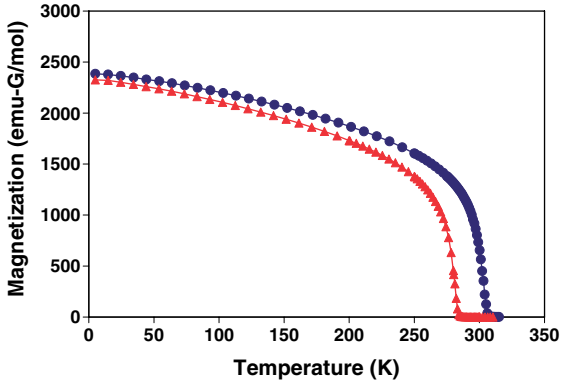


Fig. 5. Magnetization vs. temperature for $V[F_5PTCE]_2$ that has been field cooled in 5 G, measured in 5 G applied field. (●) fresh sample; (▲) sample aged 38 days.

expected for three unpaired electrons on V(II) antiferromagnetically coupled to one unpaired electron on each of two radical anions (5585 emu G/mol, assuming $g = 2.0$). This might reflect some formation of $[TCNE]_2^{2-}$, a diamagnetic structure we have observed in crystal structures of model compounds [12].

The T_cs of both compounds decay over time when the compounds are stored at room temperature, even when under vacuum (Figs. 2 and 5), which provides insight into the slight variability of the T_c from sample to sample. More thorough removal of solvent, more careful handling of these air-sensitive materials and the ability to take magnetic measurements immediately after preparation is credited with the increased T_c for $V[F_5PTCE]_2$ when compared to the previous publication [8]. In a representative experiment, T_c decreased from 305 K to ~295 K after 3 days, but with no significant change in the sharpness of the transition. Even after three months, the sample retains a T_c of ~271 K. The reason for this has not yet been established, but could be the result of a reaction between V^{2+} and carbon–chlorine bonds in the residual solvent, even in the solid state. The causes of variations in T_c have recently been addressed in a publication [2].

4. Conclusions

The phenyltricyanoethylene skeleton clearly supports magnetic order at relatively high temperatures. However, the reasons for the difference in T_c with different acceptors need to be established. One set of experiments that could explore this question is the preparation and reaction of the various mono- and di-fluorine substituted phenyltricyanoethylene derivatives, which we are currently pursuing.

Acknowledgments

We acknowledge the Donors of the Petroleum Research Fund administered by the American Chemical Society for support of this work and the National Science Foundation

and the Virginia Tech ASPIRES program for partially funding the purchase of the SQUID magnetometer. We also thank Professor Ray Butcher for help with powder diffraction.

References

[1] J.M. Manriquez, G.T. Yee, R.S. McLean, A.J. Epstein, J.S. Miller, Science 252 (1991) 1415.
[2] M.S. Thorum, K.I. Pokhodnya, J.S. Miller, Polyhedron 25 (2006) 1927.
[3] E. Dujardin, S. Ferlay, X. Phan, C. Desplanches, C.C. Moulin, P. Sainctavit, F. Baudelet, E. Dartyge, P. Veillet, M. Verdaguer, J. Am. Chem. Soc. 120 (1998) 11347.
[4] S.M. Holmes, G.S. Girolami, J. Am. Chem. Soc. 121 (1999) 5593.
[5] W.R. Entlely, C.R. Treadway, G.S. Girolami, Mol. Cryst. Liq. Cryst. 273 (1995) 153.
[6] J. Zhang, J. Ensling, V. Ksenofontov, P. Gütlich, A.J. Epstein, J.S. Miller, Angew. Chem., Int. Ed. 37 (1998) 657.
[7] J.P. Fitzgerald, B.B. Kaul, G.T. Yee, Chem. Commun. (2000) 49.
[8] B.B. Kaul, G.T. Yee, Inorg. Chim. Acta 326 (2001) 9.
[9] E.B. Vickers, T.D. Selby, J.S. Miller, J. Am. Chem. Soc. 126 (2004) 3716.
[10] X. Liu, J.E. Ellis, T.D. Miller, P. Ghalasi, J.S. Miller, Inorg. Synth. 34 (2004) 96.
[11] B.B. Corson, R.W. Stoughton, J. Am. Chem. Soc. 50 (1928) 2825.
[12] G. Wang, H. Zhu, J. Fan, C. Slebodnick, G.T. Yee, Inorg. Chem. 45 (2006) 1406.

and structure will lead to a high-spin cluster and even more difficult to then synthesize such a species [4]. Moreover, it is also important in this area of chemistry to not only make new examples of high-spin molecules and single-molecule magnets (SMMs), but also to build up families of related compounds so that structure–property relations can be investigated. Towards this end, two successful but opposite strategies have been employed. The first is the use of rigid bridging ligands that impose structural restrictions on the geometry of the resultant cluster [5], and the second is the use of flexible ligands that impose little or no restrictions [6].

In the majority of polynuclear metal complexes, exchange interactions are mainly propagated by bridging OH^-, OR^-, O^{2-}, or RCO_2^- groups (or a combination of these), ligands which usually lead to antiferromagnetic coupling. One approach for increasing the ground state S is the replacement of some or all of these bridges with groups that promote ferromagnetic coupling. One of the best examples of the latter is the azide (N_3^-) group bridging metal ions in the 1,1-fashion (end-on); in this case the exchange coupling is ferromagnetic for a wide range of M–N–M angles [7]. We also have a continuing interest in the usefulness of flexible pyridine-based alkoxide ligands (Fig. 1) in Mn cluster chemistry, and have noticed that the anion of 2-(hydroxymethyl)pyridine (hmp^-) is a versatile N,O-chelating and bridging ligand whose alkoxide arm often supports ferromagnetic coupling between the metal atoms it bridges [8].

In this paper, we describe two mixed-valence Mn_{10} clusters of formula $[Mn^{II}_4Mn^{III}_6O_4(N_3)_4(hmp)_{12}](X)_2$ [$X = N_3^-$ (**1**), ClO_4^- (**2**)] obtained by using a combination of N_3^- and hmp^- groups in certain Mn reactions. They possess very aesthetically pleasing structures of high (T) symmetry, and are completely ferromagnetically coupled with a resulting $S = 22$ ground state, one of the highest yet reported [9]. In addition, the Mn_{10} cation is the first example of μ_3-1,1,1 azido ligands bridging *exclusively* Mn^{3+} ions, and thus presages a potentially rich new area of Mn^{III} clusters with high spin values.

A reaction mixture of $Mn(NO_3)_2$, hmpH, Et_3N and NaN_3 in a 1:1:1:1: ratio in MeCN/MeOH (20:1, v/v) gave a dark brown solution from which was subsequently isolated dark-brown hexagonal crystals of $[Mn_{10}O_4(N_3)_4(hmp)_{12}](N_3)_2$ (**1**) in 20% yield. The use instead of $Mn(ClO_4)_2$ gave the isostructural $[Mn_{10}O_4(N_3)_4(hmp)_{12}](ClO_4)_2 \cdot MeCN$ (**2** · MeCN) in a much higher yield of 75%. The latter reaction but using only MeOH as reaction solvent gave known $[Mn^{II}_2Mn^{III}_2(N_3)_2(hmp)_6]_n(ClO_4)_{2n}$ (**3**), which is a one-dimensional chain [8c].

The cation $[Mn_{10}O_4(N_3)_4(hmp)_{12}]^{2+}$ (Fig. 2) consists of ten Mn ions with a tetra-face-capped octahedral topology (Fig. 3). The central octahedron comprises six Mn^{3+} ions, and the eight faces are bridged by four μ_3-N_3^- ions and four μ_4-O^{2-} ions, with the latter also bridging to four external Mn^{2+} ions that thus cap four non-adjacent faces of the octahedron (Fig. 1). The μ_3-N_3^- ions bind in an η^1:η^1:η^1 (end-on) fashion. The Mn^{II}/Mn^{III} and O oxidation states were assigned using a combination of charge balance, bond length considerations, bond valence sum (BVS) calculations [10], and the presence of the JT distortions expected for octahedral Mn^{3+}. All Mn^{3+} ions (Mn2 and its symmetry related partners) are six-coordinate with near-octahedral geometry and thus display a Jahn–Teller (JT) distortion, which takes the form of an axial elongation of the two *trans* Mn–N_{azide} bonds (2.412(3) Å). The four Mn^{2+} ions (Mn1 and its symmetry related partners) are seven-coordinate with distorted face-capped octahedral geometry, the capping atom being the oxide atom O1 (Mn^{2+}–O^{2-} = 2.304(4) Å). The peripheral ligation about the $[Mn_{10}(\mu_4\text{-}O)_4(\mu_3\text{-}N_3)_4]^{14+}$ core is provided by the twelve hmp^- groups. Three of the latter bind terminally through their N atom to each of the exterior Mn^{2+} ions, with their alkoxide arms bridging this Mn^{2+} ion to a Mn^{3+} ion (Mn2)

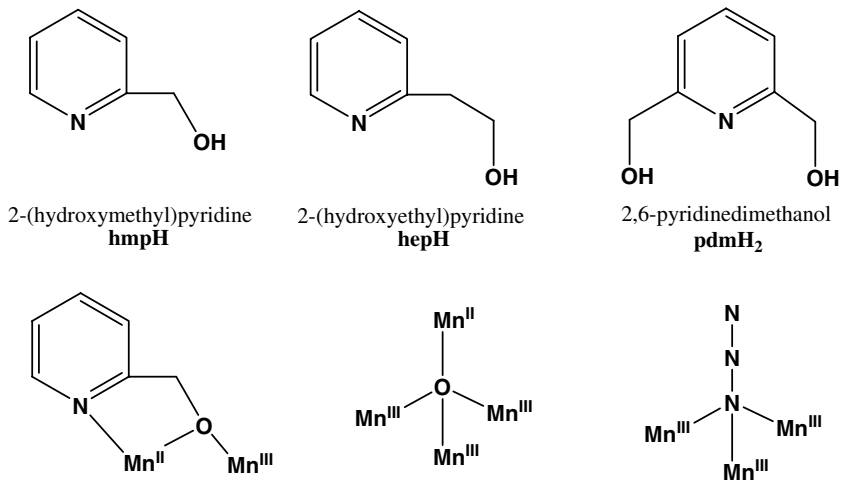


Fig. 1. The pyridyl-alcohol ligands discussed in the text (top), and the crystallographically established coordination modes of the hmp^-, oxo and azido ligands present in complexes **1** and **2** (bottom).

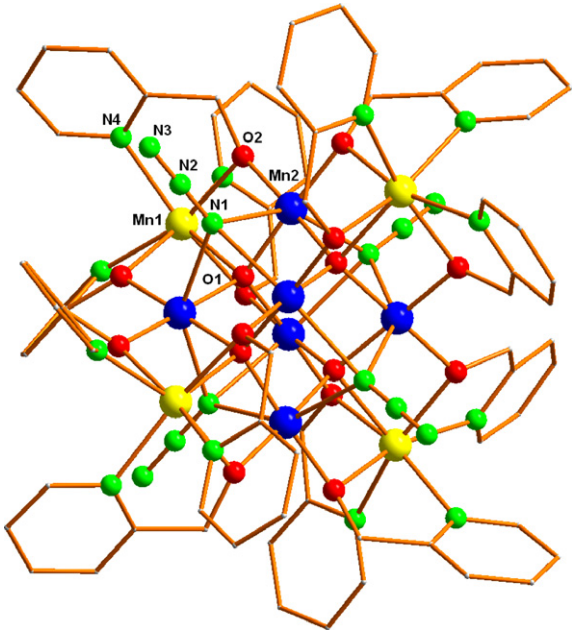


Fig. 2. The structure of the cation of **2**. Color code: Mn^{II} yellow, Mn^{III} blue, O red, N green, C gray. H atoms have been omitted for clarity. Selected interatomic distances (Å) and angles (°): Mn1–O1 2.304(2), Mn1–O2 2.242(3), Mn1–N4 2.288(3), Mn2–O1 1.908(2), Mn2–O2 1.889(3), Mn2–N1 2.412(3), Mn1···Mn1 6.534(1), Mn1···Mn2 3.267(1), Mn2···Mn2 3.239(1), Mn1–O1–Mn2 101.4(1), Mn1–O2–Mn2 104.3(1), Mn2–O1–Mn2 116.2(1), Mn2–N1–Mn2 84.4(9). (For interpretation of the references to colour in this figure legend, the reader is referred to the web version of this article.)

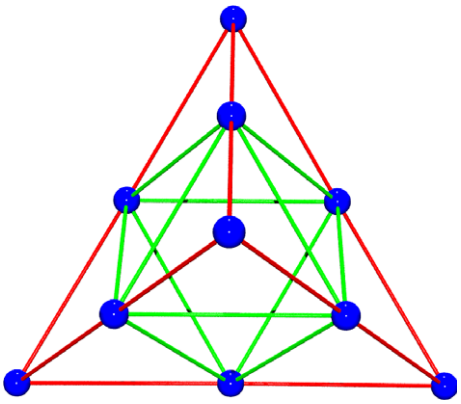


Fig. 3. The Mn_{10} topology, emphasizing the tetra-face-capped octahedral description. Red and green lines indicate the $Mn^{2+}\cdots Mn^{3+}$ and $Mn^{3+}\cdots Mn^{3+}$ vectors, respectively. (For interpretation of the references to colour in this figure legend, the reader is referred to the web version of this article.)

(Fig. 1). There are only weak intermolecular interactions, which involve the hmp phenyl groups.

Complexes **1** and **2** join only a handful of previous mixed-valent Mn_{10} clusters [11], and are the first at the $4Mn^{2+}$, $6Mn^{3+}$ level. The $[Mn_{10}(\mu_4\text{-}O)_4(\mu_3\text{-}N_3)_4]^{14+}$ core has T_d symmetry, but inclusion of the hmp groups removes the σ_d planes and S_4 axes, and the complete $[Mn_4^{II}Mn_6^{III}O_4(N_3)_4(hmp)_{12}]^{2+}$ cation consequently has rare

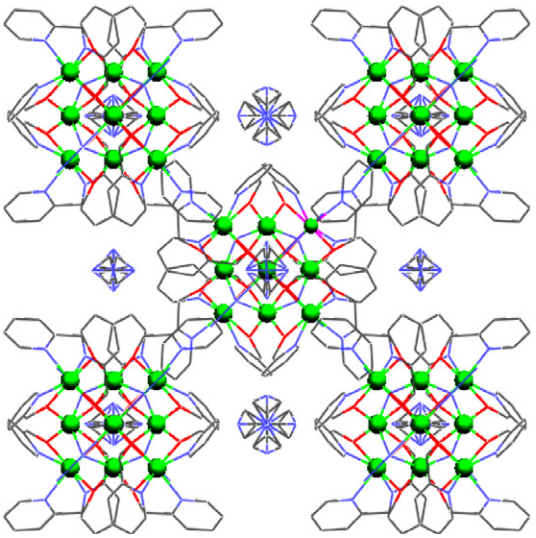


Fig. 4. Packing diagram of **1** along the *a*-axis. N_3^- counter ions are located in the middle of each neighboring Mn_{10} molecules.

T point group symmetry, which is crystallographically imposed; point group T is the rotational sub-group of T_d. This aesthetically pleasing symmetry extends to the packing of the molecules in the crystal, as shown in Fig. 4.

The magnetic behavior of the two complexes is similar. As a result of the high-yield of complex **2** (compared to that of **1**), magnetic data are presented only for the former cluster. Solid-state DC magnetic susceptibility (χ_M) data for complex **2** · MeCN were collected in the temperature range 5.0–300 K in an applied field of 1 kG (0.1 T). The $\chi_M T$ value steadily increases from 53.78 $cm^3\ mol^{-1}$ K at 300 K to a maximum of 231.56 $cm^3\ mol^{-1}$ K at 10 K, before dropping to 220.23 $cm^3\ mol^{-1}$ K at 5.0 K (Fig. 5).

The spin-only ($g = 2$) value for a non-interacting $[Mn_4^{II}Mn_6^{III}]$ unit is 35.5 $cm^3\ mol^{-1}$ K. This indicates ferromagnetic exchange interactions within **2** and the 10 K data strongly suggest a very large ground-state spin (S) value, with the sharp decrease at the lowest temperatures assigned to Zeeman effects, zero-field splitting and/or weak intermo-

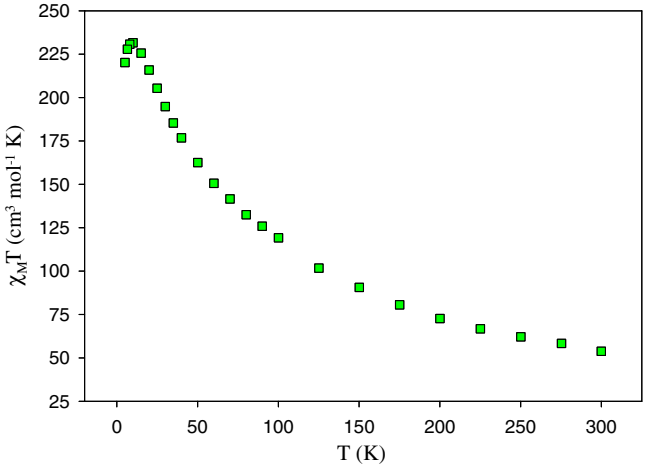


Fig. 5. $\chi_M T$ vs. T plot for complex **2** · MeCN in a 1 kG field.

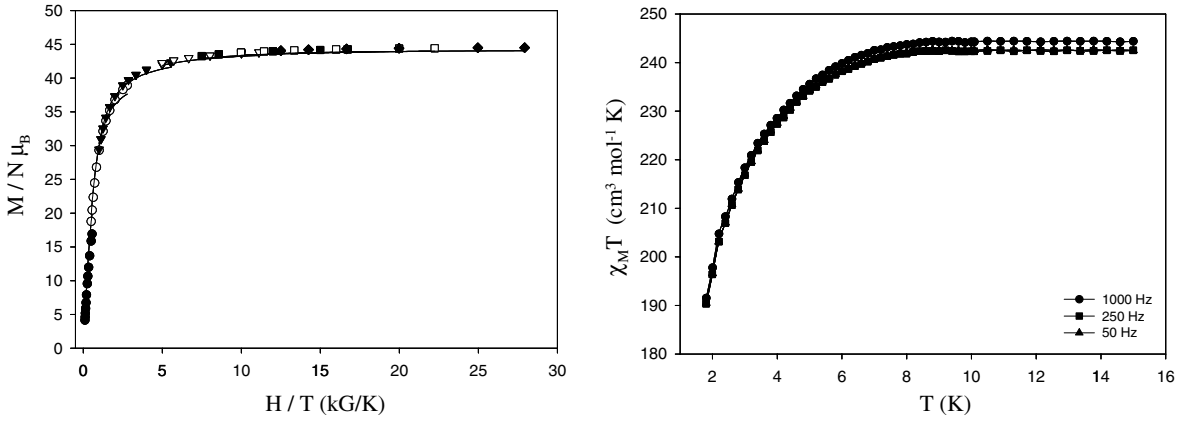


Fig. 6. Plot of reduced magnetization ($M/N\mu_B$) vs. H/T for **2** · MeCN in the temperature range 1.8–10 K and in fields of 0.1 T (●), 0.5 T (○), 1.0 T (▼), 2.0 T (▽), 3.0 T (■), 4.0 T (□), 5.0 T (◆). The solid lines are fits of the data (left). In-phase ac susceptibility ($\chi'_M T$) measurements of complex **2** · MeCN measured below 15.0 K at the indicated frequencies (right).

lecular interactions. The 10 K value is consistent with an $S = 22$ ground state, the maximum possible, and a g value slightly less than 2.0, as expected for a Mn^{II}/Mn^{III} complex; the spin-only ($g = 2$) value for an $S = 22$ state is 253 $cm^3\ mol^{-1}\ K$.

In order to confirm the ground state of **2** · MeCN, magnetization (M) data were collected in the 0.1–5 T and 1.8–10.0 K ranges, and these are plotted as $M/N\mu_B$ versus H/T in Fig. 6. The various isofield lines are virtually superimposed, indicating essentially no zero-field splitting (ZFS) within the ground state, and the saturation value of $M/N\mu_B \approx 44$ is consistent with $S = 22$. The data were fit by matrix-diagonalization to a model that assumes only the ground state is populated, includes axial zero-field splitting ($D\hat{S}_z^2$) and the Zeeman interaction, and carries out a full powder average. The best fit (solid lines in Fig. 4) gave $S = 22$, $g = 2.00(1)$ and $D = -0.011(1)\ cm^{-1}$, confirming a very high-spin ground state with little or no magnetic anisotropy. The $S = 22$ ground state was further supported by alternating current (ac) susceptibility experiments, in which a weak field of 3.5 G oscillating at a particular frequency (ν) was applied to the sample. Ac susceptibility studies use no dc field and thus are an excellent complementary tool for determining S by avoiding potential complications from a large dc field. The in-phase susceptibility (χ'_M) for **2** · MeCN is shown as $\chi'_M T$ versus T in Fig. 6, and $\chi'_M T$ can be seen to be temperature-independent at ~244 $cm^3\ mol^{-1}\ K$ from 15 K down to ~8 K, and this temperature-independent value is consistent with $S = 22$ and $g \sim 1.96$, in satisfying agreement with the dc magnetization fits. The temperature-independent $\chi'_M T$ also indicates no population of excited states in this temperature range. At lower temperatures, $\chi'_M T$ decreases slightly, which we assign to weak intermolecular interactions, both dipolar and superexchange in nature.

There is no out-of-phase (χ''_M) ac susceptibility signal down to 1.8 K, which indicates an insignificant barrier (versus kT) to magnetization relaxation. To explore whether slow relaxation might become apparent at even lower temperatures, magnetization vs dc field scans were performed on a single crystal of **2** · MeCN down to 0.04 K. No hysteresis was observed. The combined results indicate an isotropic crystal and fast magnetization relaxation even at 0.04 K, which are consistent with $D \sim 0$.

In summary, the combination of azide and hmp^- ligands in Mn cluster chemistry has yielded an unusual cation that has both a very high $S = 22$ ground state value and high (T) symmetry. Such a high S value is extremely rare, very similar in magnitude to the $S = 23$ for an Fe_{14} cluster, the largest S in Fe chemistry [1g].

Acknowledgements

The authors thank the US National Science Foundation (Grant CHE-0414155).

Appendix A. Supplementary material

Supplementary data associated with this article can be found, in the online version, at doi:10.1016/j.poly.2006.09.096.

References

[1] For example, see: (a) H.J. Eppley, H.-L. Tsai, N. deVries, K. Folting, G. Christou, D.N. Hendrickson, J. Am. Chem. Soc. 117 (1995) 301;
(b) A.K. Powell, S.L. Heath, D. Gatteschi, L. Pardi, R. Sessoli, G. Spina, F. Del Gialo, F. Pieralli, J. Am. Chem. Soc. 117 (1995) 2491;
(c) M.A. Bolcar, S.M.J. Aubin, K. Folting, D.N. Hendrickson, G. Christou, Chem. Commun. (1997) 1485;
(d) G. Aromi, M.J. Knapp, J.-P. Claude, J.C. Huffman, D.N. Hendrickson, G. Christou, J. Am. Chem. Soc. 121 (1999) 5489;
(e) M. Murugesu, M. Habrych, W. Wernsdorfer, K.A. Abboud, G. Christou, J. Am. Chem. Soc. 126 (2004) 4766;
(f) J. Larionova, M. Gross, M. Pilkington, H. Andres, H. Stoeckli-Evans, H.U. Güdel, S. Decurtins, Angew. Chem., Int. Ed. 39 (2000) 1605;
(g) D.M. Low, L.F. Jones, A. Bell, E.K. Brechin, T. Mallah, E. Riviere, S.J. Teat, E.J.L. McInnes, Angew. Chem., Int. Ed. 42 (2003) 3781;

(h) A.M. Ako, I.J. Hewitt, V. Mereacre, R. Clerac, W. Wernsdorfer, C.E. Anson, A.K. Powell, Angew. Chem., Int. Ed. 45 (2006) 4926.

[2] (a) G. Christou, D. Gatteschi, D.N. Hendrickson, R. Sessoli, MRS Bull. 25 (2000) 66;
(b) D. Gatteschi, R. Sessoli, Angew. Chem., Int. Ed. 42 (2003) 268;
(c) W. Wernsdorfer, N. Aliaga-Alcade, D.N. Hendrickson, G. Christou, Nature 416 (2002) 406;
(d) S. Hill, R.S. Edwards, N. Aliaga-Alcade, G. Christou, Science 302 (2003) 1015;
(e) R. Sessoli, D. Gatteschi, A. Caneschi, M.A. Novak, Nature 365 (1993) 141.

[3] For a mini-review describing the available synthetic procedures to Mn SMMs, see: G. Christou, Polyhedron 24 (2005) 2065, and references therein.

[4] (a) G.S. Papaefstathiou, A. Escuer, R. Vicente, M. Font-Bardia, X. Solans, S.P. Perlepes, Chem. Commun. (2001) 2414;
(b) G.S. Papaefstathiou, S.P. Perlepes, A. Escuer, R. Vicente, M. Font-Bardia, X. Solans, Angew. Chem., Int. Ed. 40 (2001) 884.

[5] (a) J.J. Sokol, A.G. Hee, J.R. Long, J. Am. Chem. Soc. 124 (2002) 7656;
(b) H.J. Choi, J.J. Sokol, J.R. Long, Inorg. Chem. 43 (2004) 1606;
(c) C.P. Berlinguette, D. Vaughn, C. Canada-Vilalta, J.R. Galan-Mascaros, K.M. Dunbar, Angew. Chem., Int. Ed. 42 (2003) 1523.

[6] E.K. Brechin, Chem. Commun. (2005) 5141, and references therein.

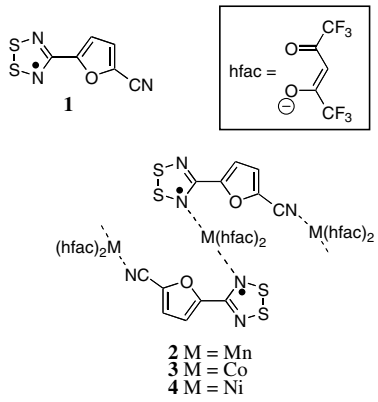
[7] E. Ruiz, J. Cano, S. Alvarez, P. Alemany, J. Am. Chem. Soc. 120 (1998) 11122, and references therein.

[8] (a) E.C. Yang, D.N. Hendrickson, W. Wernsdorfer, M. Nakano, L.N. Zakharov, R.D. Sommer, A.L. Rheingold, M. Ledezma-Gairaud, G. Christou, J. Appl. Phys. 91 (2002) 7382;
(b) N.C. Harden, M.A. Bolcar, W. Wernsdorfer, K.A. Abboud, W.E. Streib, G. Christou, Inorg. Chem. 42 (2003) 7067;
(c) L. Lecren, O. Roubeau, C. Coulon, Y.- G. Li, X.F.L. Goff, W. Wernsdorfer, H. Miyasaka, R. Clerac, J. Am. Chem. Soc. 127 (2005) 17353.

[9] Th.C. Stamatatos, K.A. Abboud, W. Wernsdorfer, G. Christou, Angew. Chem., Int. Ed. 45 (2006) 4134.

[10] (a) Bond-valence sum (BVS) calculations for the Mn ions of **1** and **2** · MeCN gave values of 1.98–2.01 (for Mn1) and 2.97–2.99 (for Mn2);
(b) W. Liu, H.H. Thorp, Inorg. Chem. 32 (1993) 4102.

[11] (a) D.P. Goldberg, A. Caneschi, C.D. Delfs, R. Sessoli, S.J. Lippard, J. Am. Chem. Soc. 117 (1995) 5789;
(b) C. Cavaluzzo, Q. Chen, J. Zubieta, Chem. Commun. (1993) 131.



1

Scheme 1.

mode has the potential to significantly increase the flexibility of design in materials using the DTDA radical (see Scheme 1).

2. Experimental

2.1. General considerations

2,5-Diformylfuran [41], prepared from D-fructose, was used as the starting material for 4-(2′-cyanofuryl-5′)-1,2,3,5-dithiadiazolyl (**1**) [31], following literature procedure. The bis(hexafluoroacetylacetonato) metal starting materials were prepared as dihydrates $M(hfac)_2 \cdot 2H_2O$, according to literature procedure [42], and converted to bis(tetrahydrofuran) adducts $M(hfac)_2 \cdot 2THF$ prior to use; absence of a hydrate O–H stretch at ca. 3400 cm^{-1} in the IR (KBr). THF was dried over Na/benzophenone and distilled under Ar(g). All coordination reactions were performed under Ar(g) atmosphere using standard Schlenk techniques. Infrared spectra were collected using a Nicolet 4700-FTIR spectrometer. Elemental analyses were performed by MHW Labs, Phoenix, AZ, USA. Mass spectra were recorded by Dr. R. Smith at the WATSPEC Facility at the University of Waterloo, Waterloo, Ont., Canada, using a JEOL HX110 double focusing instrument.

2.2. Preparation of Mn complex *2*

Dry THF (45 mL) was added to a solid mixture of **1** (352.2 mg, 1.79 mmol) and $Mn(hfac)_2 \cdot 2THF$ (1.1358 g, 1.85 mmol) and the resulting solution was heated at 60 °C, stirring, for 3.5 h (note that dry 1,2-dichloroethane can be substituted for THF). The solution was allowed to cool to RT whereupon a black precipitate formed. This was recovered by filtration and determined to be uncomplexed **1** (216.1 mg, 1.101 mmol). The solvent was removed *in vacuo* from the remaining filtrate affording a gray-green powder (960.1 mg). This was sublimed under dynamic vacuum (10^{-2} Torr) using a three-stage gradient tube furnace (125, 70, 40 °C) in order to separate complex **2** from the unreacted yellow $Mn(hfac)_2 \cdot 2THF$ and further unreacted **1** starting materials. The recovered complex **2** was then purified by a second sublimation generating dark red block-like crystals. Yield: 133.9 mg (0.2013 mmol, 11.24%). IR (KBr): 3174(w), 3141(w), 2262(m), 1647(s), 1615(w), 1599(w), 1584(w), 1557(m), 1530(m), 1500(s), 1486(s), 1401(w), 1388(w), 1350(m), 1256(s), 1219(s) 1206(s), 1146(s), 1096(w), 1024(m), 986(w), 969(w), 943(w), 860(w), 814(w), 799(s), 780(w), 742(w), 696(w) 665(s), 585(m), 527(w), 517(w) cm^{-1}. Mass spec. (C.I. using NH_3; r.t. = 0.43 min; parent ion assigned as M = $NCC_4H_2OCN_2S_2Mn(O_2C_5F_6)_2$; *m/e*): 944.0 ($[M–NCC_4H_2OCN_2S_2H–S_2–NH_4]^+$, 54.94%), 910.9 ($[M–NCC_4H_2OCN_2S_2–S–NH_4]^+$, 30.02%), 882.9 ($[NCC_4H_2OCN_2S_2Mn(O_2C_5F_5)–Mn–NCC_4H_2OCN_2S–NH_4]^+$, 26.12%), 839.0 ($[M–Mn–NCC_4H_2OCN–H]^+$, 43.64%), 837.0 ($[NCC_4H_2OCN_2S_2Mn(O_2C_5F_6)(O_2C_5F_5)–Mn–NCC_4H_2OCN–NH_4]^+$, 53.77%), 765.0 ($[M–MnO_2C–H]^+$, 100%), 748.0 ($[M–S_2H–NH_4]^+$, 25.40%), 683.0 ($[M–NH_4]^+$, 11.05%), 564.0 ($[Mn(O_2C_5F_6)_2–SSN–NH_3]^+$, 89.40%), 391.9 ($[(NCC_4H_2OCN_2S_2)_2]^+$, 16.17%), 371.0 ($[NCC_4H_2OCN_2S_2–S_2N_2CC_3H_2O–NH_3]^+$, 23.40%), 196.0 ($[NCC_4H_2OCN_2S_2]^+$, 45.32%), 136.1 ($[NCC_4H_2OCN–NH_4]^+$, 2.59%). Elemental *Anal.* Calc. for $C_{16}H_4N_3O_5S_2F_{12}Mn$: C, 28.88; H, 0.61; N, 6.32. Found: C, 29.21; H, 0.71; N, 6.30%.

2.3. Preparation of Co complex *3*

The synthesis of complex **3** is identical to that of complex **2** using $Co(hfac)_2 \cdot 2THF$ as the metal source. Red block-like crystals of **3** were recovered from sublimation. Yield: 6.64%. IR(KBr): 3170(w), 3146(w), 2271(s), 1643(s), 1594(w), 1579(w), 1555(m), 1526(m), 1502(m), 1483(m), 1399(w), 1388(w), 1350(m), 1257(s), 1219(s), 1203(s), 1146(s), 1097(w), 1025(m), 986(w), 970(w), 947(w), 861(w), 813(m), 798(m), 777(w), 743(w), 694(w), 669(s), 590(m), 527(w), 516(m) cm^{-1}. Mass spec. (C.I. using NH_3; r.t. = 1.66 min; parent ion assigned as M = $NCC_4H_2OCN_2S_2Co(O_2C_5F_6)_2$; *m/e*): 687.1 ($[M–NH_4]^+$, 7.39%), 582.1 ($[NCC_4H_2O–Co(O_2C_5F_6)_2–NH_3]^+$, 20.59%), 508.0 ($[Co(O_2C_5F_6)_2–NH_3–NH_4]^+$, 53.68%), 479.0 ($[NCC_4H_2OCN_2S_2CoO_2C_5F_6–NH_3]^+$, 29.38%), 389 ($[NCC_4H_2OCN_2S_2–S_2N_2CC_3H_2–SH–NH_4]^+$, 73.24%), 371.1 ($[NCC_4H_2OCN_2S_2–S_2N_2CC_3H_2O–NH_3]^+$, 83.28%), 317.1 ($[NCC_4H_2OCN_2S_2–S_2N_2C–NH_3]^+$, 51.30%), 300.1 ($[NCC_4H_2OCN_2S_2–S_2N_2C]^+$, 100%), 292.1 ($[NCC_4H_2OCN_2S_2–S_2N–NH_4]^+$, 66.22%), 214.1 ($[NCC_4H_2OCN_2S_2–NH_4]^+$, 40.82%), 196.0 ($[NCC_4H_2OCN_2S_2]^+$, 48.30%), 136.1 ($[NCC_4H_2OCN–NH_4]^+$, 40.79%). Elemental *Anal.* Calc. for $C_{16}H_4N_3O_5S_2F_{12}Co$: C, 28.70; H, 0.60; N, 6.28. Found: C, 29.25; H, 0.66; N, 5.96%.

2.4. Preparation of Ni complex *4*

Complex **4** was prepared in the same manner as complex **2**, using $Ni(hfac)_2 \cdot 2THF$ as the starting material. Red-brown block-like crystals of **4** were recovered from sublimation. Yield: 12.3%. IR(KBr): 3166(w), 3142(w),

2279(s), 1647(s), 1593(w), 1577(w), 1555(w), 1526(m), 1508(m), 1485(m), 1401(m), 1389(m), 1350(m), 1256(s), 1220(m), 1206(m), 1147(s), 1103(w), 1025(m), 988(w), 972(m), 948(w), 862(w), 813(m), 796(m), 777(m), 743(w), 696(w), 675(m), 591(m), 530(w), 517(w) cm^{-1}. Mass spec. (C.I. using NH_3; r.t. = 0.70 min; parent ion assigned as $M = NCC_4H_2OCN_2S_2Ni(O_2C_5F_6)_2$; *m/e*): 788.1 ($[M–NiO_2C–NH_4]^+$, 100%, isotope pattern for 2 Ni), 686.1 ($[M–NH_4]^+$, 54.69%, isotope pattern for 1 Ni), 507.1 ($[Ni(O_2C_5F_6)_2–NH_3–NH_4]^+$, 75.49%, isotope pattern for 1 Ni), 196.0 ($[NCC_4H_2OCN_2S_2]^+$, 57.81%), 136.1 ($[NCC_4H_2OCN–NH_4]^+$, 19.38%). Elemental *Anal.* Calc. for $C_{16}H_4N_3O_5S_2F_{12}Ni$: C, 28.72; H, 0.60; N, 6.28. Found: C, 29.00; H, 0.50; N, 6.38%.

2.5. Crystallographic details

Crystals of $[Mn(C_5HF_6O_2)_2(\mu\text{-}C_6H_2N_3O_1S_2)]$ (**2**) arrived at U.W.O. from the University of Guelph. The red plate was mounted on a goniometer head. Data were collected at low temperature (−173 °C) on a Nonius Kappa-CCD area detector diffractometer with COLLECT [43]. The unit cell parameters were calculated and refined from the full data set. Crystal cell refinement and data reduction were carried out using HKL2000 DENZO-SMN [44]. The absorption correction was applied using HKL2000 DENZO-SMN (SCALEPACK). The reflection data were consistent with a triclinic space group: $P\bar{1}$. The SHELXTL/PC V6.14 for Windows NT suite of programs [45] was used to solve the structure by direct methods. The complex consisted of a linear chain of $Mn(hfac)_2$ units bridged by the ligand. Most of the atoms were well ordered, however, one of the perfluoro butyl groups showed some disorder. The disorder was modeled as a staggered configuration with the occupancies set at 0.71 and 0.29. All of the non-hydrogen atoms were refined with anisotropic thermal parameters. The hydrogen atom positions were calculated geometrically and were included as riding on their respective carbon atoms. The largest residue electron density peak (0.368 e/Å^3) was associated with one of the sulfur atoms. Full-matrix least squares refinement on F^2 gave $R_1 = 5.96$ for 2σ data and $wR_2 = 16.20$ for all data (goodness-of-fit = 1.049).

Crystals of $[Co(C_5HF_6O_2)_2(\mu\text{-}C_6H_2N_3O_1S_2)]$ (**3**) arrived at U.W.O. from the University of Guelph. The red shoebox was mounted on a goniometer head. Data were collected at low temperature (−173 °C) on a Nonius Kappa-CCD area detector diffractometer with COLLECT [43]. The unit cell parameters were calculated and refined from the full data set. Crystal cell refinement and data reduction were carried out using HKL2000 DENZO-SMN [44]. The absorption correction was applied using HKL2000 DENZO-SMN (SCALEPACK). The reflection data were consistent with a triclinic space group: $P\bar{1}$. The SHELXTL/PC V6.14 for Windows NT suite of programs [45] was used to solve the structure by direct methods. The complex consisted of a linear chain of $Co(hfac)_2$ units bridged by the ligand. The molecule was very well ordered. All of the non-hydrogen atoms were refined with anisotropic thermal parameters. The hydrogen atom positions were calculated geometrically and were included as riding on their respective carbon atoms. The largest residue electron density peak (0.446 e/Å^3) was associated with one of the trifluoro moieties. Full-matrix least squares refinement on F^2 gave $R_1 = 4.27$ for 2σ data and $wR_2 = 10.01$ for all data (goodness-of-fit = 1.012).

Crystals of $[Ni(C_5HF_6O_2)_2(\mu\text{-}C_6H_2N_3O_1S_2)]$ (**4**) arrived at U.W.O. from the University of Guelph. The dark, red block was mounted on a goniometer head. Data were collected at low temperature (−173 °C) on a Nonius Kappa-CCD area detector diffractometer with COLLECT [43]. The unit cell parameters were calculated and refined from the full data set. Crystal cell refinement and data reduction were carried out using HKL2000 DENZO-SMN [44]. The absorption correction was applied using HKL2000 DENZO-SMN (SCALEPACK). The reflection data were consistent with a triclinic space group: $P\bar{1}$. The SHELXTL/PC V6.14 for Windows NT suite of programs [45] was used to solve the structure by direct methods. The complex consisted of a linear chain of $Ni(hfac)_2$ units bridged by the ligand. The molecules were well ordered. All of the non-hydrogen atoms were refined with anisotropic thermal parameters. The hydrogen atom positions were calculated geometrically and were included as riding on their respective carbon atoms. The largest residue electron density peak (0.531 e/Å^3) was associated with the furan ring. Full-matrix least squares refinement on F^2 gave $R_1 = 5.47$ for 2σ data and $wR_2 = 12.69$ for all data (goodness-of-fit = 1.089).

3. Results

The single crystal X-ray structural determinations of complexes **2**–**4** reveal identical chain-like complexes in the solid state. These chains are characterized by three important interactions. The $M(hfac)_2$ unit bridges two ligands (**1**) via coordination with one nitrogen atom of the DTDA ring

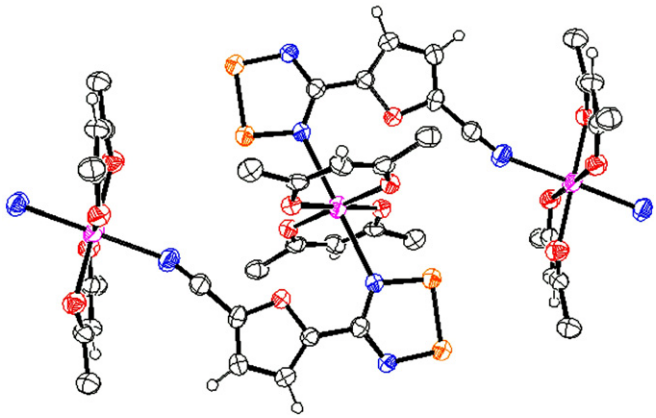


Fig. 1. Single crystal X-ray structure of Mn complex **2** showing the monodentate N-coordination of the two DTDA rings to a Mn(II) ion. Color scheme: C, H: black; O: red; N: blue; S: orange; Mn: magenta. F atoms omitted for clarity. (For interpretation of the references to colour in this figure legend, the reader is referred to the web version of this article.)

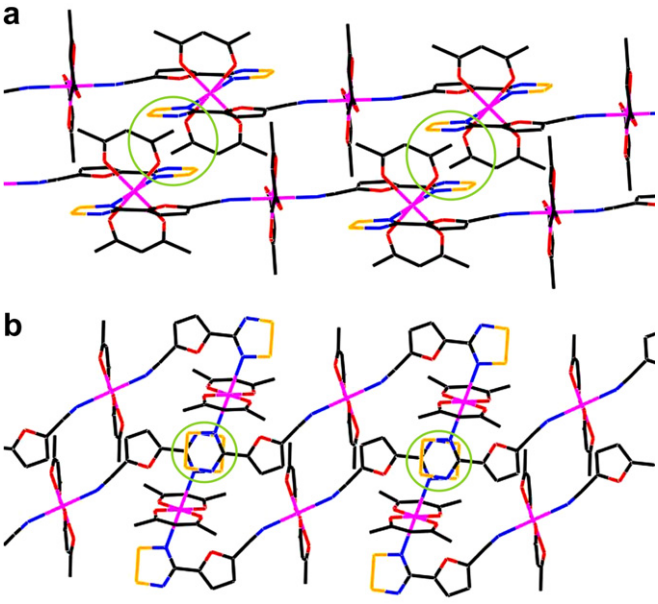


Fig. 2. Single crystal X-ray structure of Mn complex **2** showing: (a) side view of DTDA dimers (green circles) and (b) top view of DTDA dimers (green circles). H and F atoms omitted for clarity. (For interpretation of the references to colour in this figure legend, the reader is referred to the web version of this article.)

of each. The hexafluoroacetylacetonato-ligands are in the equatorial plane while the nitrogen atoms of the DTDA rings are in the axial positions of a pseudo-octahedral coordination sphere about the metal center (Fig. 1). A second bridging interaction of the $M(hfac)_2$ unit with one nitrogen atom of the pendant nitrile group of each of two ligands (**1**) is also present. Again the hfac-ligands are in the equatorial plane while the nitrile groups complete the pseudo-octahedral coordination sphere at the axial positions. The third important interaction is the interchain dimerization of the ligands through a cofacial interaction of the DTDA rings. This dimerization is highlighted by circles in Fig. 2.

Table 1 provides a summary of the important crystallographic features of all three complexes. The only notable differences in structure are the changes in M–N bond lengths about the metal sites depending on the nature of the metal ion. In all important respects, the three complexes are crystallographically equivalent. The DTDA nitrogen to metal bond distances are of particular interest. They range from 2.459(5) to 2.309(5) Å, depending on the nature of the metal ion. These are longer than the $M–N_{(DTDA)}$ contacts for the chelated Mn(II)–, Co(II)– and Ni(II)– $(hfac)_2$ complexes with 4-(2′-pyridyl)-1,2,3,5-dithiadiazolyl, which range from 2.288(6) to 2.082(15) Å [39,40,46]. Nevertheless, they are reasonable metal to nitrogen bond distances. It is tempting to suggest that there is some contribution from the furyl oxygen atom, given that it is oriented toward the metal center. It should be noted, however, that the furyl oxygen to metal distances range from 3.160(4) to 3.285(4) Å and are, therefore, significantly longer than would normally be assigned as a bond.

The intermolecular sulfur to sulfur atom contacts are longer than ca. 3.1 Å, the typical distance for most known DTDA dimers in the solid state [31]. Nevertheless, the DTDA rings are dimerized in the solid state through what has been referred to as a *trans*-cofacial interaction [30,47] that suffices to render the DTDA dimer unit diamagnetic. In order to confirm that there is no significant contribution from the DTDA units to the magnetic properties of these materials, the magnetic susceptibility measurements for complex **2** (Fig. 3) were obtained by DC-SQUID. These indicate a room temperature $\chi_{para}T$ value of ca. 4.7 emu K mol^{-1} that decreases only slightly with decreasing temperature until ca. 20 K. This is consistent with isolated Mn(II) ions ($S = 5/2$). The decrease in $\chi_{para}T$ below 20 K suggests the onset of weak intermolecular

Table 1
Selected crystallographic information for complexes **2**–**4**

	Complex **2** (Mn)	Complex **3** (Co)	Complex **4** (Ni)
Space group	triclinic $P\bar{1}$	triclinic $P\bar{1}$	triclinic $P\bar{1}$
Cell length (Å)			
a	8.3865(15)	8.2712(6)	8.1940(5)
b	12.287(2)	12.2510(7)	12.3523(8)
c	12.323(3)	12.3309(9)	12.3523(8)
Cell angle (°)			
α	110.936(8)	108.765(4)	108.909(2)
β	91.253(10)	108.701(3)	109.258(3)
γ	107.040(10)	91.269(4)	89.216(3)
Bond distances (Å)			
$M–N_{(NC–)}$	2.281(5)	2.140(3)	2.074(5)
$M–N_{(DTDA)}$	2.459(5)	2.375(3)	2.309(5)
$M–O_{(furyl)}$	3.160(4) (no bond)	3.273(4) (no bond)	3.285(4) (no bond)
S–S	2.092(2)	2.0843(12)	2.079(2)
Intermolecular contacts (Å)			
S–S	3.653(2)	3.629(2)	3.625(2)
$S–N_{(DTDA)}$	3.054(3), 3.125(3)	3.025(3), 3.121(3)	3.022(3), 3.131(3)

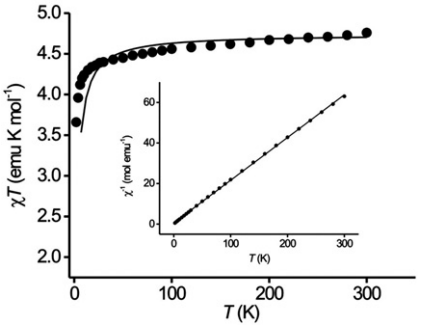


Fig. 3. Magnetic susceptibility measurements of **2** as a microcrystalline solid (●) performed using DC-SQUID at a field of 100 Oe. Diamagnetic contributions subtracted using Pascal's constants. Curie–Wiess fit (−) of $1/\chi$ as a function of temperature; $C = 4.74 \pm 0.01$ emu K mol^{-1}, $\theta = -2.4 \pm 0.4$ K.

antiferromagnetic exchange interactions, possibly between manganese centers mediated through the dimerized DTDA ligands. A Curie–Wiess fit was optimized for a plot of $1/\chi$ as a function of temperature (Fig. 3, inset) generating a Curie constant C of 4.74 ± 0.01 emu K mol^{-1} and a Wiess constant θ of -2.4 ± 0.4 K. These fitting parameters were then used to generate a $\chi_{para}T$ curve as a function of temperature, shown as a solid line in Fig. 3. Clearly, the data is adequately fit using a Curie–Wiess function, supporting the hypothesis that the dimerized DTDA moieties do not contribute to the magnetic properties of these complexes in the solid state to any significant degree.

4. Discussion

In order to ascertain at which point in the preparatory procedure the chain-like complexes identified in the crystal structures of **2**–**4** are, in fact, formed, we have monitored the C ≡ N stretch in the IR absorption spectrum. In the free ligand **1**, the CN stretch occurs at 2234 cm^{-1}. In the Mn, Co and Ni complexes, the absorption occurs at 2261, 2271 and 2279 cm^{-1}, respectively. Using the Mn complex **2** as a representative case, the IR spectrum of the grayish powder recovered after removal of the solvent reveals a new CN stretch at 2254 cm^{-1} in addition to the absorption at 2234 cm^{-1} for the free ligand **1**, in a roughly 1:10 ratio with respect to peak area. This stretch is neither free ligand nor the chain-like complex. Our hypothesis is that it is representative of some intermediate coordination mode that is formed in solution, perhaps involving only one nitrile group coordinated to a Mn(hfac)$_2$ unit. Only after sublimation of this gray solid (under dynamic vacuum) did the IR spectrum of the recovered dark red crystals show evidence of the chain-like complex. In light of this discovery, we have attempted the synthesis of **2** by grinding the solid starting materials, under inert atmosphere, to homogeneity with a mortar and pestle and submitting this mixture to sublimation under dynamic vacuum at the same conditions. The result was quantitative recovery of the free ligand **1** and the unreacted Mn(hfac)$_2 \cdot$ 2THF starting materials from different zones of the three-stage sublimation tube furnace. The procedure was repeated using static vacuum at the same temperature, and again only starting materials were recovered. Thus, it appears that formation of an intermediate *in solvo* is a necessary step in the preparatory procedure, perhaps to generate monomeric units from which the chain is ultimately comprised. It is worth noting that, once formed in the crystalline state, these chain-like structures can be re-sublimed and recovered quantitatively. This supports the idea that the structure may be comprised of preformed, volatile monomeric or oligomeric units. Further evidence is provided by the mass spectra of the complexes wherein m/e values consistent with fragmentation of oligomeric units are detected.

The relatively low yield of **2**–**4** is likely a reflection of the equilibrium between free starting materials and some initial coordination complex in solution. For this reason, we attempted the synthesis in THF, 1,2-dichoroethane, dichloromethane and acetonitrile. The highest yields were obtained from sublimation of the gray product formed in THF, but reasonable quantities were also obtained from dichloroethane. No product was obtained from dichloromethane or acetonitrile, probably owing to the insolubility of the starting materials at achievable temperatures in the former and competing nitrile moieties of the solvent in the latter. It should be noted, however, that the red crystalline product, once formed, is sparingly soluble in warm dichloromethane or dichloroethane such that it will slightly colour the solvent. IR spectra of very dilute warm solutions in either solvent (1.0 mm CaF_2 cell) show a CN stretch at 2262 cm^{-1} for **2**, indicating that the coordination of the nitrile moieties to the metal remains intact. Furthermore, when **2** is heated vigourously into a large volume of dichloroethane, red crystals form upon cooling, again suggesting that once the oligomeric units are formed, the chain-like complexes can be reformed nearly quantitatively.

Although we have successfully obtained IR spectra in very dilute warm solutions, the relatively low solubility of these complexes has inhibited other solution state analyses. We have attempted to collect solution magnetometry data in toluene and dichloroethane by Evans' NMR method, but the achievable concentration is too low to have a measurable impact on the shifting of the solvent signal, even at higher temperatures (ca. 60 °C). We have also attempted to collect solution EPR data of the Mn(II) complex at room temperature and at higher temperatures (ca. 60 °C) but have been unable to resolve a signal. The concentration of the complex is likely too low to observed the manganese-centered unpaired electrons, however, it is not unreasonable to expect to observe the ligand-centered unpaired electrons at very low concentration. There are three possible explanations for the lack of signal, then. The first is that the dimers persist in solution. We feel this is unlikely given that the intermolecular interaction between DTDA rings is generally considered to be weak and therefore there should be at least a monomer–dimer equilibrium. The second explanation is that coordination of Mn(II) to the DTDA

affects the relaxation properties of the ligand centered spin such that the intensity of the absorption is lowered and the solution's concentration is too low for the signal to be observed. The third possible explanation is that solution state oligomeric units have integer ground state S values and sufficient zero-field splitting that they are EPR silent (e.g., for one Mn(II) coordinated to one DTDA, $S = 2$ for AFM coupling). In any case, we are unable to make any comment regarding spin distribution or the magnetic nature of these complexes in solution.

5. Conclusions

Ligand **1** reacts with $M(hfac)_2 \cdot 2THF$ (M = Mn, Co, Ni) generating chain-like complexes **2**–**4** in the solid state. Although the yields of purified material are relatively low (ca. 10%), the syntheses are reproducible and complexes of all three metal ions have the same crystalline motif. The most interesting feature of these complexes is the unprecedented monodentate N-coordination of the DTDA moiety to the metal ion. This new coordination mode has the potential to significantly increase the design flexibility of materials incorporating DTDA-based radicals as spin-bearing ligands.

Acknowledgements

K.E.P. gratefully acknowledges the Natural Sciences and Engineering Research Council (NSERC) of Canada for a Discovery Grant (DG) and a Research Tools and Instruments Grant (RT). N.G.R.H. thanks the Government of Ontario for an Ontario Graduate Scholarship (OGS). C.S.S. thanks the University of Guelph Co-op program. J.L.K. thanks NSERC for an Undergraduate Student Research Award (USRA). The authors thank the University of Guelph for additional funding and Prof. L.K. Thompson at Memorial University, NFLD who performed the DC-SQUID measurements.

Appendix A. Supplementary material

CCDC 622093, 622094 and 622095 contain the supplementary crystallographic data for **1**, **2** and **3**. These data can be obtained free of charge via http://www.ccdc.cam.ac.uk/conts/retrieving.html, or from the Cambridge Crystallographic Data Centre, 12 Union Road, Cambridge CB2 1EZ, UK; fax: (+44) 1223-336-033; or e-mail: deposit@ccdc.cam.ac.uk. Supplementary data associated with this article can be found, in the online version, at doi:10.1016/j.poly.2006.09.078.

References

[1] J.S. Miller, Dalton Trans. (2006) 2742.
[2] S.J. Blundell, F.L. Pratt, J. Phys.: Condens. Matter 16 (2004) R771.
[3] J.V. Yakhmi, Macromol. Symp. 212 (2004) 141.
[4] A. Caneschi, D. Gatteschi, R. Sessoli, Acc. Chem. Res. 22 (1989) 392.
[5] A. Caneschi, D. Gatteschi, P. Rey, R. Sessoli, Inorg. Chem. 27 (1988) 1756.
[6] D. Luneau, G. Risoan, P. Rey, A. Grand, A. Caneschi, D. Gatteschi, J. Laugier, Inorg. Chem. 32 (1993) 5616.
[7] K. Inoue, H. Iwamura, J. Am. Chem. Soc. 116 (1994) 3173.
[8] K. Inoue, T. Hayamizu, H. Iwamura, D. Hashizume, Y. Ohashi, J. Am. Chem. Soc. 118 (1996) 1803.
[9] S. Zheng, J. Lan, S.I. Khan, Y. Rubin, J. Am. Chem. Soc. 125 (2003) 5786.
[10] Y. Morita, S. Suzuki, K. Fukui, S. Nakazawa, K. Sato, D. Shiomi, T. Takui, D. Nakasuji, Polyhedron 22 (2003) 2215.
[11] S. Yamada, M. Yasui, T. Nogami, T. Ishida, Dalton Trans. (2006) 1622.
[12] R.G. Hicks, M.T. Lemaire, L.K. Thompson, T.M. Barclay, J. Am. Chem. Soc. 122 (2000) 8077.
[13] T.M. Barclay, R.G. Hicks, M.T. Lemaire, L.K. Thompson, Inorg. Chem. 40 (2001) 5581.
[14] T.M. Barclay, R.G. Hicks, M.T. Lemaire, L.K. Thompson, Inorg. Chem. 42 (2003) 2261.
[15] D. Maspoch, J. Gómez-Segura, N. Domingo, D. Ruiz-Molina, K. Wurst, C. Rovira, J. Tejada, J. Veciana, Inorg. Chem. 44 (2005) 6936.
[16] Y. Miura, I. Kato, Y. Teki, Dalton Trans. (2006) 961.
[17] G. Wang, H. Zhu, J. Fan, C. Slebodnick, G.T. Yee, Inorg. Chem. 45 (2006) 1406.
[18] W. Fujita, K. Awaga, J. Am. Chem. Soc. 123 (2001) 3601.
[19] S.A. Fairhurst, K.M. Johnson, L.H. Sutcliffe, K.F. Preston, A.J. Banister, Z. Hauptman, J. Passmore, J. Chem. Soc., Dalton Trans. (1986) 1465.
[20] H.-U. Höfs, J.W. Bats, R. Gleiter, G. Hartmann, R. Mews, M. Eckart-Maksić, H. Oberhammer, G.M. Sheldrick, Chem. Ber. (1985) 3781.
[21] A.D. Bond, D.A. Haynes, C.M. Pask, J.M. Rawson, J. Chem. Soc., Dalton Trans. (2002) 2522.
[22] A.J. Banister, M.I. Hansford, Z.V. Hauptman, S.T. Wait, W. Clegg, J. Chem. Soc., Dalton Trans. (1989) 1705.
[23] W.V.F. Brooks, N. Burford, J. Passmore, M.J. Schriver, L.H. Sutcliffe, J. Chem. Soc., Chem. Commun. (1987) 69.
[24] A. Vegas, A. Pérez-Salazar, A.J. Banister, R.G. Hey, J. Chem. Soc., Dalton Trans. (1980) 1812.
[25] A.W. Cordes, R.C. Haddon, C.D. MacKinnon, R.T. Oakley, G.W. Patenaude, R.W. Reed, T. Rietveld, K.E. Vajda, Inorg. Chem. 35 (1996) 7626.
[26] A.J. Banister, N. Bricklebank, I. Lavender, J.M. Rawson, C.I. Gregory, B.K. Tanner, W. Clegg, M.R.J. Elsegood, F. Palacio, Angew. Chem., Int. Ed. Engl. 35 (1996) 2533.
[27] F. Palacio, G. Antorrena, M. Castro, R. Burriel, J. Rawson, J.N.B. Smith, N. Bricklebank, J. Novoa, C. Ritter, Phys. Rev. Lett. 79 (1997) 2336.
[28] R.A. Beekman, R.T. Boeré, K.H. Moock, M. Parvez, Can. J. Chem. 76 (1998) 85.
[29] C.M. Aherne, A.J. Banister, T.G. Hibbert, A.W. Luke, J.M. Rawson, Polyhedron 24 (1997) 4239.
[30] A. Alberola, C.S. Clarke, D.A. Haynes, S.I. Pascu, J.M. Rawson, Chem. Commun. (2005) 4726.
[31] A.W. Cordes, C.M. Chamchoumis, R.G. Hicks, R.T. Oakley, K.M. Young, R.C. Haddon, Can. J. Chem. 70 (1992) 919.
[32] A.W. Cordes, J.D. Goddard, R.T. Oakley, N.P.C. Westwood, J. Am. Chem. Soc. 111 (1989) 6147.
[33] A.J. Banister, I.B. Gorrell, W. Clegg, K.A. Jørgensen, J. Chem. Soc., Dalton Trans. (1989) 2229.
[34] A.J. Banister, I.B. Gorrell, W. Clegg, K.A. Jørgensen, J. Chem. Soc., Dalton Trans. (1991) 1105.
[35] A.J. Banister, I.B. Gorrell, S.E. Lawrence, C.W. Lehmann, I. May, G. Tate, A.J. Blake, J.M. Rawson, J. Chem. Soc., Chem. Commun. (1994) 1779.
[36] A.J. Banister, J.A.K. Howard, I. May, J.M. Rawson, Chem. Commun. (1997) 1763.

[37] A.J. Banister, I. May, J.M. Rawson, J.N.B. Smith, J. Organomet. Chem. 550 (1998) 241.
[38] H.F. Lau, V.W.L. Ng, L.L. Koh, G.K. Tan, L.Y. Goh, T.L. Roemmele, S.D. Seagrave, R.T. Boeré, Angew. Chem., Int. Ed. 45 (2006), doi:10.1002/anie.200600724.
[39] N.G.R. Hearns, K.E. Preuss, J.F. Richardson, S. Bin-Salamon, J. Am. Chem. Soc. 126 (2004) 9942.
[40] M. Jennings, K.E. Preuss, J. Wu, Chem. Commun. (2006) 341.
[41] G.A. Halliday, R.J. Young Jr., V.V. Grushin, Org. Lett. 5 (2003) 2003.
[42] F. Izumi, R. Kurosawa, H. Kawamoto, H. Akaiwa, Bull. Chem. Soc. Jpn. 48 (1975) 3188.
[43] COLLECT, Nonius, B.V., Delft, The Netherlands, 2001.
[44] Z. Otwinowski, W. Minor, in: C.W. Carter, R.M. Sweet (Eds.), Methods in Enzymology, Macromolecular Crystallography, Part A, vol. 276, Academic Press, London, 1997, pp. 307–326.
[45] G.M. Sheldrick, SHELXTL/PC. Version 6.14 for Windows NT, Bruker AXS Inc., Madison, Wisconsin, USA, 2001.
[46] Unpublished results from the Preuss lab.
[47] T.M. Barclay, A.W. Cordes, N.A. George, R.C. Haddon, M.E. Itkis, R.T. Oakley, Chem. Commun. (1999) 2269.

reversible magnetic switching. Then Kawamoto et al. [27] calculated the band structure of Co–Fe cyanide using full-potential linearized augmented planewave method (FLAPW). Their calculated results indicated that the interaction between the d electrons of the Co^{III} ion and surrounding crystal field might conduce metal–metal charge transfer. Further Kawamoto et al. [27,28] performed ab initio quantum chemical cluster computations and concluded that the existence of vacancies for absent Fe^{II} ions is essential for the bidirectional photoinduced magnetic phase transition in Co–Fe Prussian blue analogues. In the meantime, their studies [29] showed that the light excitation could induce the local structures of the crystal to be changed forward and backward. All the theoretical works mentioned obviously indicate that it is necessary to exist a meta-stable intermediate structure in the photoinduced magnetization process. As a matter of fact, both experimentally and theoretically there is yet a lack of explicit detailed evidence of the meta-stable intermediate structure in the reversible photoinduced magnetization.

The photoinduced high-spin molecule, $[Mo^{IV}(CN)_2(CN\text{-}CuL)_6]^{8+}$ with perchlorate was synthesized and structurally characterized in 2004 [14], where the terminal ligand L is tris(3-aminoehtylamine). Its geometry structure is depicted in Fig. 1. It should be said that this experimentally isolated molecule is of great advantage to theoretical study on the meta-stable intermediate structure, thereby opens the door of the theoretical study on photoinduced magnetization in chemical detail. The experimentally measured $\chi_M T$ value for the molecule is a constant (2.5 cm^3 K mol^{-1} down to 20 K), which indicates that each $[Mo^{IV}(CN)_2(CN\text{-}CuL)_6]^{8+}$ cation is constituted with a diamagnetic Mo^{IV} surrounded by six $S = 1/2$ paramagnetic Cu^{II} cations in the ground state. Thus the magnetic property of the ground state molecule behaves like a system with six isolated spin 1/2 ions. Once irradiated with blue light (406–415 nm) at 10 K for 10 h, the magnetic behaviors changed drastically, with the $\chi_M T$ value of 4.8 cm^3 K mol^{-1}, which reveals a high-spin ferromagnetic molecule with total spin $S = 3$. Experimentally it is also shown that when turning off the light and heating up the system to 300 K, the change process of the magnetic properties is totally reversible. Herrera et al. [14] attributed the change of magnetic properties to MMCT between the Mo^{IV} and one Cu^{II} cations induced by the light irradiation, thus yielding the $Mo^{V}Cu^{I}Cu^{II}_5$ electronic configuration, which implies ferromagnetic interaction between the $S = 1/2$ Mo^{V} ion and five $S = 1/2$ Cu^{II} ions. After 1 h at room temperature, the $\chi_M T$ values measured in the cooling process indicate the compound almost completely relaxed back to the initial state. Herrera et al. ascribed the high relaxation temperature to the photoinduced metastable state related to significant change of the coordination sphere around the Cu^{I} ion. Thus the structure and the properties of the metastable state are the most important thing to explain the micromechanism of the reversible photoinduced magnetization. Unfortunately, there is no direct experimental verity of the metastable structure till now. In this communication, we shall focus on calculations of the structure and magnetic properties of the possible metastable state to understand micromechanism of the photoinduced magnetization phenomenon of $[Mo^{IV}(CN)_2(CN\text{-}CuL)_6]^{8+}$. Both density functional theory and ab initio multireference configuration interaction [30,31] methods are used in geometry optimization and exchange coupling constant calculations.

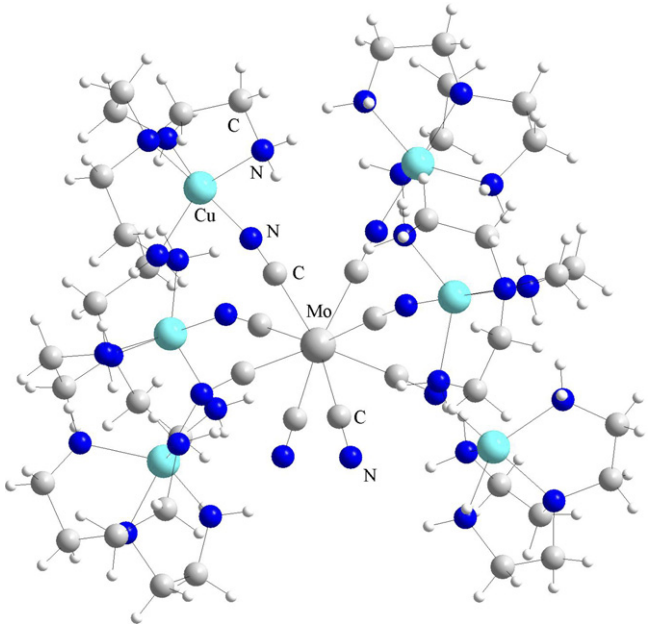
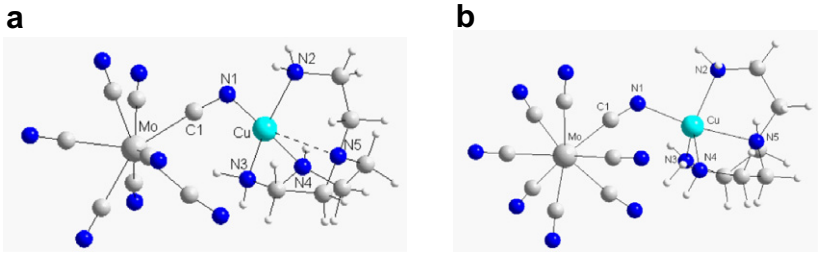


Fig. 1. X-ray crystal structure of the $[Mo^{IV}(CN)_2(CN\text{-}CuL)_6]^{8+}$ cation [14].

As shown in the previous theoretical studies [27,28], the local structure or composition around transition metal cations might be changed with the light irradiation. For the $[Mo^{IV}(CN)_2(CN\text{-}CuL)_6]^{8+}$ cation, the change might occur around the Mo^{IV} and Cu^{II} ions. Except for outer anions, each $[Mo^{IV}(CN)_2(CN\text{-}CuL)_6]^{8+}$ entity has 191 atoms, it is too large to directly calculate the geometry structure optimization and the magnetic properties for the whole cation. Considering the six $(Cu–L)^{2+}$ parts have nearly same geometry structures, it is a reasonable choice to reserve only one and omit all the other five $(Cu–L)^{2+}$ groups, then the left calculated model is the $[Mo(CN)_8CuL]^{2-}$ anion. After the MMCT from the Mo^{IV} to a Cu^{II} with light irradiation, there exist one $[Mo^{V}(CN)_8Cu^{I}L]^{2-}$ (abbreviated to Mo^{V}-Cu^{I}) and five $[Mo^{V}(CN)_8Cu^{II}L]^{-}$ (abbreviated to Mo^{V}-Cu^{II}) fragments in the photoinduced molecule at the same time. The Fig. 2 displays the optimized local geometry structures and selected bond distances of these two fragments by using density functional theory with ADF software package [32].

Comparing the bond distances calculated in Fig. 2, the distance of Cu–N5 is 2.24 Å in the fragment **B**, but 2.71 Å in the fragment **A**, lengthened by 0.47 Å, which likely further leads the Cu–N5 bond to be broken. The change for all the other bond distances is so few as to be



A $[Mo^{V}(CN)_8Cu^{I}L]^{2-}$

Cu–N1	2.04Å	Cu–N2	2.24Å
Cu–N3	2.13Å	Cu–N4	2.28Å
Cu–N5	2.71Å		
Mo–C1	2.20Å	C1–N1	1.18Å

B $[Mo^{V}(CN)_8Cu^{II}L]^{-}$

Cu–N1	2.02Å	Cu–N2	2.16Å
Cu–N3	2.13Å	Cu–N4	2.17Å
Cu–N5	2.24Å		
Mo–C1	2.19Å	C1–N1	1.18Å

Fig. 2. Optimized geometry structures and selected bond distances for the fragments **A** $[Mo^{V}(CN)_8Cu^{I}L]^{2-}$ (a) and **B** $[Mo^{V}(CN)_8Cu^{II}L]^{-}$ (b).

negligible effect on the coordination properties of the Cu and Mo atoms. It seems that the light irradiation induces the reducing of one copper cation from Cu^{II} to Cu^{I}, and simultaneously the change of its coordination environment from five- to four-coordination. The tetrahedral Cu^{I} ion coordinated by four nitrogen atoms holds the one electron originating from the Mo^{IV} ion and this electron does not be relaxed back spontaneously to the Mo^{IV} ion. The other five Cu^{II} cations have little structure changes and are still coordinated by five nitrogen atoms in an ordinary trigonal-bipyramid manner. It is interesting to note that the two optimized local geometry structures mentioned above consist well with the previous proposal experimentally on the local reorganization of the coordination sphere around Cu^{I} [14].

Because the Cu^{I} ion is a diamagnetic center, the magnetic behavior of the photoinduced molecule is determined by the magnetic coupling interactions between the paramagnetic Mo^{V} ion and five Cu^{II} ions. Following the above modelling, we calculated the magnetic coupling properties of the $Mo^{V}Cu^{II}$ fragment by using the density functional theory combined with broken symmetry approach (DFT-BS) [33] and the ab initio complete active space self-consistent-field (CASSCF) [34,35], as well as multireference configuration interaction (MRCI) methods [30,31], respectively. In general, the magnetic coupling between two magnetic centers is usually described in term Heisenberg spin Hamiltonian:

$$H = -JS_A \cdot S_B, \tag{1}$$

where S_A and S_B are electron spin operators at the magnetic centers A and B, respectively; J stands for the spin coupling constant, which magnitude and sign character the magnetic exchange interaction in the magnetic molecule. A positive J predicts the ferromagnetic interaction between the magnetic centers A and B.

In the calculations with DFT-BS method [36], spin Hamiltonian (1) is relative to the calculated energy difference $E_{HS} - E_{BS}$:

$$\frac{1}{2}S_{max}J_{AB} = E_{BS} - E_{HS}, \tag{2}$$

where S_{max} is the highest spin multiplet of the $Mo^{V}Cu^{II}$ fragment studied; E_{BS} and E_{HS} are the energy expecting value of the broken symmetry state (BS) and the energy eigenvalue of the highest spin state (HS), respectively. The calculated J value is 89.7 cm^{-1} when using the general gradient approximation (Becke and Perdew exchange correlation functional [37–39]). The calculated positive J value indicates that the magnetic interaction is ferromagnetic between the Mo^{V} and Cu^{II} cations. As reported in the literature [40], the DFT-BS approach can give a reasonable evaluation of the magnetic exchange interaction qualitatively for large binuclear transition metal systems. Meanwhile, the CASSCF and MRCI methods, under the active space and active electrons referring to CAS(2,2), are further used to calculate the exchange coupling constant in the fragment $[Mo^{V}(CN)_8Cu^{II}L]^{-}$. The calculated J values are 6.2 and 7.4 cm^{-1} at CASSCF and MRCI levels of theory, respectively. Due to existing such five magnetic interactions between the Mo^{V} and Cu^{II} cations for the whole cation studied, we can conclude that the photoinduced metastable state of the $[Mo^{V}(CN)_2(CN\text{-}Cu^{I}L)(CN\text{-}Cu^{II}L)_5]^{8+}$ cation is a high-spin molecule with strong ferromagnetic properties. It is evident that the DFT-BS calculated J value, 89.7 cm^{-1}, is closer to the experimental evaluation ($J > 100$ cm^{-1}) [14] than that of CASSCF (6.2 cm^{-1}) and MRCI (7.4 cm^{-1}). Herein, the calculated results from the different methods reproduce well the high-spin magnetic properties of the photoinduced intermediate, though there is discrepancy of the magnitude of the calculated J values for the different methods.

Spin density distribution can experimentally be observed by the neutron scattering experiment, and gives valuable information for the magnetic exchange mechanism. For further confirming the spin density distribution of Mo^{V}, Cu^{I} and Cu^{II} ions in the fragments **A** and **B**, the Mulliken spin populations are calculated using DFT method. Because the spin population of the copper cation tends to

delocalize unduly in the DFT calculations, the population analyses based on the CASSCF method are also carried out for the purpose of comparison. Calculated spin populations of the metal ions and the bridge ligand atom C1, N1 are listed in Table 1, where all the other nonmetal atoms are not shown for simplify.

From Table 1, the calculated spin populations on the Mo^{V}, Cu^{I} and Cu^{II} cations are approximately in accord with the electronic configuration of $Mo^{V}Cu^{I}$ and $Mo^{V}Cu^{II}$. In the DFT calculations, for the fragment $Mo^{V}Cu^{I}$, the spin population value 0.035 on the Cu^{I} ion indicates that it is a diamagnetic ion and no magnetic coupling with the Mo^{V} center might occur. The results of CASSCF calculations for the Cu^{I} ion confirm its diamagnetic character. On the contrary, for the fragment $Mo^{V}Cu^{II}$, the spin population values on the Mo^{V} and Cu^{II} ions are as large as 0.877 and 0.410, respectively. While in the CASSCF calculations the spin population values on the Mo^{V} and Cu^{II} ions for the fragment $Mo^{V}Cu^{II}$ are 0.940 and 0.888, respectively. The latter is close to one formal unpaired electron on the Mo^{V} and Cu^{II} ions, respectively. It is evident that both the Mo^{V} and Cu^{II} ions for the fragment $Mo^{V}Cu^{II}$ are the paramagnetic ions. Combined with the calculated exchange coupling constant *J*, it could conclude that the Mo^{V} ion interacts with the Cu^{II} ion by means of ferromagnetic coupling through the superexchange pathway of the cyano ligand. Just this magnetic coupling determines the magnetic properties of the whole system.

In summary, there are two key reasons of photoinduced magnetization. The first one is changes of bonding and the structure with light induced, which could produce a metastable state. And this metastable state could not be relaxed back to initial state fast and spontaneously. The second one is that the part or whole structure of the metastable state has appropriate magnetic properties. In our calculations, the local geometry structure of the possible metastable state for the $[Mo^{IV}(CN)_2(CN\text{-}CuL)_6]^{8+}$ cation is optimized with the DFT method. The calculation results indicate that the trigonal-bipyramid coordination environment surrounding one Cu^{II} ion has been changed to the tetrahedral coordination around the Cu^{I} ion after the light irradiation. The magnetic properties calculated by using different levels of theory reveal the high-spin ground state, which are also consistent with the experimental results. The spin population analyses confirm the validity of the calculated models. These calculations will help to understand photoinduced magnetization phenomenon and provide a clue for the synthesization of new reversible photoinduced magnetic compounds.

Table 1
Spin populations on the Mo, Cu ions for $[Mo^{V}(CN)_8Cu^{I}L]^{2-}$ and $[Mo^{V}(CN)_8Cu^{II}L]^{-}$ fragments

Atom	DFT-BS		CASSCF	
	$Mo^{V}Cu^{I}$	$Mo^{V}Cu^{II}$	$Mo^{V}Cu^{I}$	$Mo^{V}Cu^{II}$
Mo	0.907	0.877	0.949	0.940
Cu	0.035	0.410	0.001	0.888
C1	0.048	0.009	−0.002	0.007
N1	−0.041	0.085	0.008	0.042

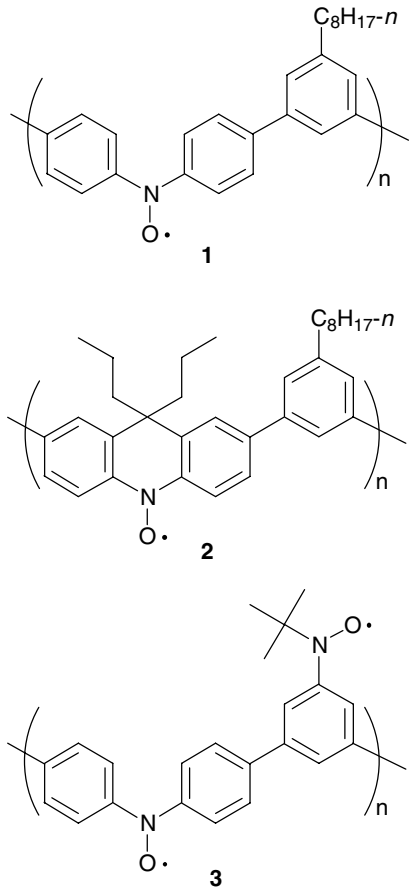
Acknowledgements

This work is supported by National Basic Research Program of China (2006CB601102), the National Natural Science Foundation of China (Nos. 20503001 and 20490210), Doctoral Program Foundation of Education Minister (No. 20030001066). The computer resources and softwares are supported by "Virtual Laboratory for Computational Chemistry of CNIC and Supercomputing Center of CNIC, Chinese Academy of Sciences".

References

[1] O. Sato, T. Iyoda, A. Fujishima, K. Hashimoto, Science 272 (1996) 704.
[2] M. Verdaguer, Science 272 (1996) 698.
[3] O. Sato, Acc. Chem. Res. 36 (2003) 692.
[4] O. Sato, Y. Einaga, T. Iyoda, A. Fujishima, K. Hashimoto, Inorg. Chem. 38 (1999) 4405.
[5] S. Ohkoshi, K. Hashimoto, J. Photochem. Photobiol. C 2 (2001) 71.
[6] N. Shimamoto, S. Ohkoshi, O. Sato, K. Hashimoto, Inorg. Chem. 41 (2002) 678.
[7] A. Bleuzen, C. Lomenech, V. Escax, F. Villain, F. Varret, C. Cartier, dit Moulin, M. Verdaguer, J. Am. Chem. Soc. 122 (2000) 6648.
[8] C. Cartier dit Moulin, F. Villain, A. Bleuzen, M.-A. Arrio, P. Sainctavit, C. Lomenech, V. Escax, F. Baudelet, E. Dartyge, J.-J. Gallet, M. Verdaguer, J. Am. Chem. Soc. 122 (2000) 6653.
[9] V. Escax, A. Bleuzen, C. Cartier dit Moulin, F. Villain, A. Goujon, F. Varret, M. Verdaguer, J. Am. Chem. Soc. 123 (2001) 12536.
[10] G. Champion, V. Escax, C. Cartier dit Moulin, A. Bleuzen, F. Villain, F. Baudelet, E. Dartyge, M. Verdaguer, J. Am. Chem. Soc. 123 (2001) 12544.
[11] A. Goujon, F. Varret, V. Escax, A. Bleuzen, M. Verdaguer, Polyhedron 20 (2001) 1339.
[12] A. Goujon, F. Varret, V. Escax, A. Bleuzen, M. Verdaguer, Polyhedron 20 (2001) 1347.
[13] D.A. Pejaković, J.L. Manson, J.S. Miller, A.J. Epstein, Synth. Met. 122 (2001) 529.
[14] J.M. Herrera, V. Marvaud, M. Verdaguer, J. Marrot, M. Kalisz, C. Mathniere, Angew. Chem., Int. Ed. 43 (2004) 5467.
[15] M. Bal, J.R. Friedman, Y. Suzuki, K.M. Mertes, E.M. Rumberger, D.N. Hendrickson, Y. Myasoedov, H. Shtrikman, N. Avraham, E. Zeldov, Phys. Rev. B 70 (2004) 100408.
[16] Y. Arimoto, S. Ohkoshi, Z.J. Zhang, H. Seino, Y. Mizobe, K. Hashimoto, J. Am. Chem. Soc. 125 (2003) 9240.
[17] S. Ohkoshi, N. Machida, Y. Abe, Z.J. Zhong, K. Hashimoto, Chem. Lett. 4 (2001) 312.
[18] G. Rombaut, M. Verelst, S. Golhen, L. Ouahab, C. Mathonière, O. Kahn, Inorg. Chem. 40 (2001) 1151.
[19] Z.-Z. Gu, O. Sato, T. Iyoda, K. Hashimoto, A. Fujishima, J. Phys. Chem. 100 (1996) 18289.
[20] G. Li, T. Akitsu, O. Sato, Y. Einaga, J. Am. Chem. Soc. 125 (2003) 12396.
[21] G. Li, P. Yan, O. Sato, Y. Einaga, J. Solid State Chem. 178 (2004) 6.
[22] D.A. Pejaković, C. Kitamura, J.S. Miller, A.J. Epstein, Phys. Rev. Lett. 88 (2002) 57202.
[23] K. Nagau, T. Iyoda, A. Fujishima, K. Hashimoto, Solid State Commun. 201 (1997) 809.
[24] Y. Sano, M. Tanaka, N. Koga, K. Matsuda, H. Iwamura, P. Rabu, M. Drillon, J. Am. Chem. Soc. 119 (1997) 8246.
[25] T. Yokoyama, T. Ohta, O. Sato, K. Hashimoto, Phys. Rev. B 58 (1998) 8257.

[26] M. Nishino, K. Yamaguchi, S. Miyashita, Phys. Rev. B 58 (1998) 9303.
[27] T. Kawamoto, Y. Asai, S. Abe, Phys. Rev. B 60 (1999) 12990.
[28] T. Kawamoto, Y. Asai, S. Abe, J. Lumin. 87 (2000) 658.
[29] T. Kawamoto, Y. Asai, S. Abe, Phys. Rev. Lett. 86 (2001) 348.
[30] H.-J. Werner, P.J. Knowles, J. Chem. Phys. 89 (1988) 5803.
[31] P.J. Knowles, H.-J. Werner, Chem. Phys. Lett. 145 (1988) 514.
[32] Amsterdam Density Functional (ADF), version 2004.01, Scientific Computing and Modelling, Theoretical Chemistry, Vrije Universiteit, Amsterdam, 2004.
[33] L. Noodleman, D.A. Case, A.J. Aizman, J. Am. Chem. Soc. 110 (1988) 1001.
[34] H.-J. Werner, P.J. Knowles, J. Chem. Phys. 82 (1985) 5053.
[35] P.J. Knowles, H.-J. Werner, Chem. Phys. Lett. 115 (1985) 259.
[36] L. Noodleman, J. Chem. Phys. 74 (1981) 5737.
[37] S.H. Vosko, L. Wilk, M. Nusair, Can. J. Phys. 58 (1980) 1200.
[38] A.D. Becke, Phys. Rev. A 38 (1988) 3098.
[39] J.P. Perdew, Y. Wang, Phys. Rev. B 33 (1986) 8822.
[40] B.W. Wang, H.Y. Wei, M.W. Wang, Z.D. Chen, J. Chem. Phys. 122 (2005) 204310.



2. Experimental

2.1. Measurements

The ^{1}H NMR spectra were measured with a JEOL JNM-EX400 spectrometer (400 MHz). Tetramethylsilan was used as an internal standard for chemical shifts. The IR spectra were measured with a JASCO FT/IR-230 spectrometer. Size exclusion chromatography (SEC) was measured with a TOSOH HLC-8020 chromatograph. THF was used as an eluant and the temperature was kept at 40 °C. The ESR spectra were measured with a JEOL JES-RE1X spectrometer (X-band). Mn^{2+} was used as a standard for the *g* value. The spin concentration of polyradical was determined by using a solution of 1,3,5-triphenylverdazyl in dichloromethane prepared in known concentration. The magnetization was measured with a Quantum Design MPMS-7T SQUID magnetometer. The external magnetic field dependence of the magnetization was measured in the region of 0–6 T at the constant temperature. The temperature dependence of the magnetic susceptibility was measured in the region of 2–300 K at the constant external magnetic field of 0.5 T. The diamagnetic contribution from a sample holder and poly(vinyl chloride) (PVC) was previously measured and corrected. The diamagnetic contribution of the paramagnetic sample was estimated with the Pascal's constants and corrected.

2.2. Suzuki–Miyaura coupling between dibromo- and diboron monomers

To a solution of dibromo- (1.50 mmol) and diboron monomes (1.50 mmol) in THF (15 mL) were added a 2 M-pottasium carbonate aqueous solution (3 mL), TBA Br (1.29 g, 4.00 mmol) and $Pd(PPh_3)_4$ (0.104 g, 0.09 mmol) and the heterogeneous mixture was refluxed for 24 h under nitrogen. The organic layer was separated, washed with a 5%-sodium cyanide aqueous solution (4.5 mL) and brine and dried with anhydrous magnesium sulfate. After evaporating, the residue was reprecipitated from THF–methanol (7 mL–70 mL) to give polymers **6** or **10**.

*Polymer **6***. Yield: 85.6%. ^{1}H NMR (chloroform-*d*): 0.87 (t, $J = 6.8$ Hz, 3H), 1.15–1.43 (m, 10H), 1.50 (s, 9H), 1.60–1.76 (m, 2H), 2.62–2.77 (m, 2H), 7.28–7.41 (m, 6H), 7.50–7.63 (m, 5H).

*Polymer **10***. Yield: 50.3%. ^{1}H NMR (chloroform-*d*): 1.41 (s, 9H), 1.49 (s, 9H), 3.70 (s, 1H), 6.91 (br s, 2H), 7.14 (br s, 1H), 7.24–7.37 (m, 4H), 7.50–7.61 (m, 4H).

2.3. BOC deprotection

To a solution of **6** or **10** (0.480 mmol) in dichloromethane (8 mL) was added trifluoroacetic acid (2.75 g, 24.1 mmol). The mixture was stirred for 1h at room temperature and poured into water (30 mL). The organic layer was separated, washed with 1 N-sodium hydroxide aqueous solution and brine and dried with anhydrous magnesium sulfate. After evaporating, the residue was reprecipitated from dichloromethane–hexane (5 mL–50 mL) or THF–hexane (5 mL–50 mL) to give polymers **7** or **11**, respectively.

Polymer 7. Yield: 60.4%. ^{1}H NMR (chloroform-*d*): 0.88 (t, $J = 6.6$ Hz, 3H), 1.10–1.49 (m, 10H), 1.56–1.83 (m, 2H), 2.50–2.82 (m, 2H), 5.89 (br s, 1H), 7.09–7.24 (m, 4H), 7.30–7.44 (m, 2H), 7.49–7.74 (m, 5H). *Anal*. Calc. for $(C_{26}H_{29}N)_n$: C, 87.84; H, 8.22; N, 3.94. Found: C, 83.73; H, 8.17; N, 3.62%.

*Polymer **11***. Yield: 66.0%. ^{1}H NMR (chloroform-*d*): 1.43 (s, 9H), 5.87 (br s, 1H), 6.84–6.92 (m, 2H), 7.06–7.23 (m, 5H), 7.47–7.60 (m, 4H). *Anal*. Calc. for $(C_{22}H_{22}N_2)_n$: C, 84.04; H, 7.05; N, 8.91. Found: C, 78.80; H, 6.73; N, 8.05%.

2.4. Oxidation of the precursor polymer

To a solution of **7** (70 mg) in dichloromethane (4 mL) was added 3-chloroperoxybenzoic acid (80 mg) and the mixture was stirred for 20 min at room temperature. After a 10%-sodium carbonate aqueous solution (5 mL) was added, the organic layer was separated, washed with brine and dried with anhydrous magnesium sulfate. After evaporating, the residue was reprecipitated from dichlorometh-

ane–methanol (3 mL–30 mL) to give **1** as brownish red powder in 26.0% yield (19 mg). The spin concentration determined by ESR was 0.57 spins per repeating unit.

To a solution of **11** (72 mg) in dichloromethane (10 mL) was added 3-chloroperoxybenzoic acid (178 mg) and the mixture was stirred for 20 min at room temperature. After a 10%-sodium carbonate aqueous solution (5 mL) was added, the organic layer was separated, washed with brine and dried with anhydrous magnesium sulfate. After filtering, the filtrate was directly used in the ESR measurement and in the preparation of the poly(vinyl chloride) (PVC) matrix sample. The spin concentration determined by ESR was 0.93 spins per repeating unit.

3. Results and discussion

3.1. Synthesis

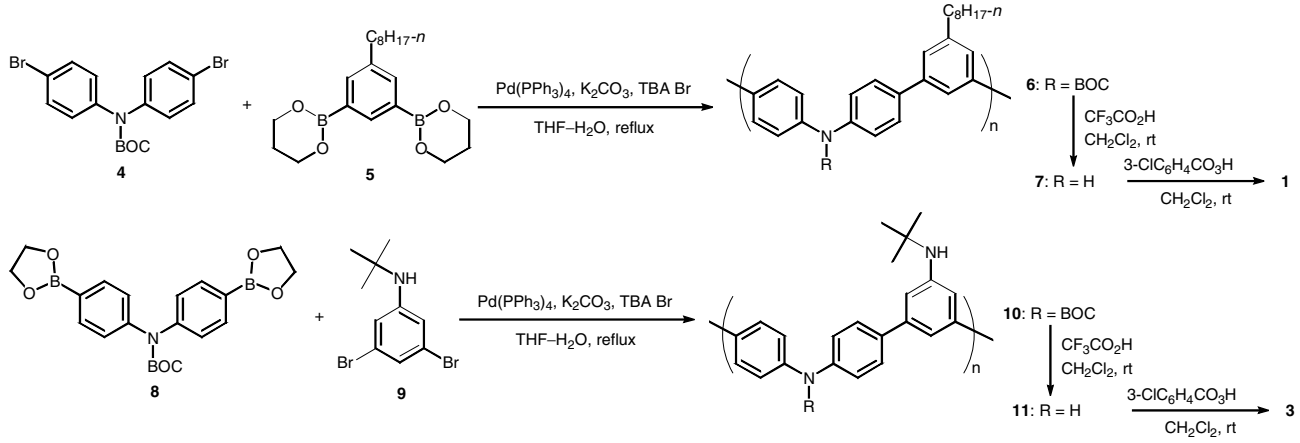
Polyradicals **1** and **3** were synthesized according to Scheme 1. The precursor polymers were prepared by the Miyaura–Suzuki coupling between dibromo- and diboron monomers and the following BOC deprotection. In the Suzuki–Miyaura coupling, the amino group of diphenylamine moiety was protected by the *t*-butoxycarbonyl (BOC) group to make the coupling proceed efficiently. The yields of **6** and **10** were 86 and 50%, respectively. The BOC deprotection was carried out by using trifluoroacetic acid. The deprotection proceeded completely, which was confirmed by the disappearance of the carbonyl group of BOC in the IR spectra. The yields of **7** and **11** were 60 and 66%, respectively. The molecular weights of **7** and **11** were determined by SEC. The number-averaged molecular weight (M_n) was 3010 for **7** and 1570 for **11**. From these values, the degree of polymerization (n) was estimated to be 6.6 for **7** and 5.0 for **11**. The degree of polymerization was also estimated from the result of the elemental analysis. The found elemental analysis values of **7** were C = 83.73, H = 8.17 and N, 3.62%. When it is assumed that the end groups of **7** are Br and $B(OH)_2$, the calculated elemental analysis values are C = 83.65, H = 7.91 and N = 3.75% for $n = 7$ and C = 84.15, H = 7.94 and N = 3.77% for $n = 8$. These values are in good agreement with the found values. Similarly, the degree of polymerization of **11** was estimated to be 5–6 (Found: C = 78.80; H = 6.73; N = 8.05%. Calc.: C = 77.86, H = 6.65 and N = 8.25% for $n = 5$ and C = 78.83, H = 6.72 and N = 8.36% for $n = 6$). From these results, the degree of polymerization was ca. 7 for **7** and ca. 5 for **11**.

The oxidation of precursor polymers was carried out by using 3-chloroperoxybenzoic acid. Radical **1** was very stable both in solution and in solid state in the atmosphere. The spin concentration was determined by ESR to be 0.57 spins per repeating unit. Whereas, **3** was stable in solution, but decomposed when the solvent was removed. Therefore, as soon as the oxidation was carried out, the dichloromethane solution was used in the ESR measurement and in the preparation of the PVC matrix sample. The spin concentration determined by ESR was 0.93 spins per repeating unit. Because there is two spin generation sites per repeating unit in **11**, the spin concentration per spin generation site was 0.47.

3.2. ESR spectra of polyradicals

The ESR spectra of polyradical **1** were measured in dichloromethane, in PVC matrix and in powder solid state at room temperature (Fig. 1a). The spectrum in dichloromethane was observed at $g = 2.0060$, which is typical for nitroxides. The signal was split five lines, showing that the spin concentration is low because the spectrum of a polyradical is a singlet line in the case of the high spin concentration. The spectrum in PVC matrix was neither a singlet line. The shape was similar for the anisotropic spectrum of mononitroxides [8]. These ESR spectra suggests that there is no intramolecular spin interaction, but the $\Delta M_S = \pm 2$ transition was observed in the $g = 4$ region at 103 K.

The ESR spectra of **3** were measured in dichloromethane and in PVC matrix (Fig. 1b). The spectrum in dichloromethane was observed at $g = 2.0058$. The shape was a



Scheme 1. Synthetic route of **1** and **3**.

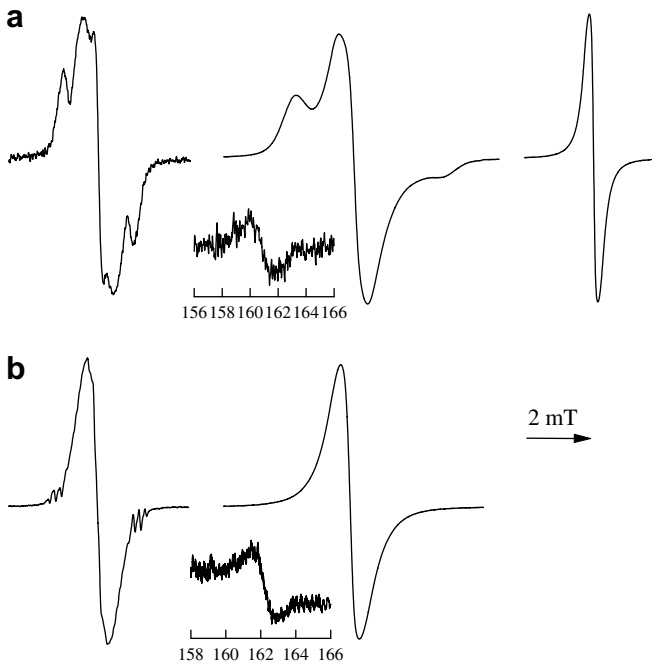


Fig. 1. ESR spectra of (a) **1** and (b) **3** at room temperature. The spectra were measured in dichloromethane (left), PVC matrix (center) and powder solid state (right, only **1**). The spin concentration was 0.57 for **1** and 0.93 spins per repeating unit for **3**. The $\Delta M_S = \pm 2$ transition was observed in the $g = 4$ region in PVC matrix at 103 K for **1** and at 77 K for **3**.

singlet line with small finely splitting lines at the foot. Although the spin concentration of **3** was low, the exchanging narrowing would occur because the distance between spins is close. The spectrum in PVC matrix was also a singlet line. At 77 K, the $\Delta M_S = \pm 2$ transition was observed in the $g = 4$ region as well as **1**. This indicates that there is the intramolecular spin interaction.

3.3. Magnetization measurement

The magnetization of polyradicals **1** and **3** was measured by a SQUID magnetometer. To investigate the intramolecular spin interaction, the external magnetic field dependence of the magnetization of polyradicals in diluted PVC matrix was measured (Fig. 2). The experimental data at 2, 4 and 8 K for **1** were in accordance with the $S = 2/2$ theoretical line given by the Brillouin function, indicating that **1** was in the $S = 2/2$ spin state. From the degree of polymerization of ca. 7 and the spin concentration of 0.57 spins per repeating unit, there were of ca. 4 spins (ca. 7×0.57) per molecule, that is, 2 spins out of 4 spins were aligned in **1**. Whereas, for **3**, the experimental data at 2, 4 and 6 K were in accordance with the $S = 3/2$ theoretical line, indicating that **3** was in the $S = 3/2$ spin state. From the degree of polymerization of ca. 5 and the spin concentration of 0.93 spins per repeating unit, there were ca. 5 spins (ca. 5×0.93) per molecule, that is, 3 spins out of 5 spins were aligned in **3**. The spin sate of **2** was 3/2 and 3 spins out of 8 spins were aligned because there were 8 spins per molecule from the degree of polymerization of

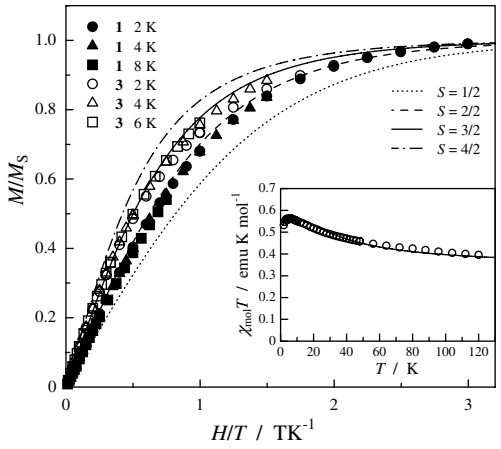


Fig. 2. External magnetic field dependence of the magnetization of **1** and **3** in PVC matrix. The spin concentration was 0.57 for **1** and 0.93 spins per repeating unit for **3**. The points are the experimental data at the constant temperature. The lines are the theoretical lines for $S = 1/2$, 2/2, 3/2 and 4/2 given by the Brillouin function. Inset: the temperature dependence of the magnetic susceptibility of **3** in PVC matrix. The line is the least-square fit with Eq. (2).

ca. 11 and the spin concentration of 0.71 spins per repeating unit [7]. Therefore, the intramolecular spin interaction in **3** occurs more efficiently than in **2**.

To examine the intramolecular spin interaction in **1**–**3**, the S values were numerically calculated. The spin concentration of polyradical can be expressed as 4/7 (=0.57) for **1**, 8/11 (=0.73) for **2** and 5/10 (=0.50) for **3** based on the degree of polymerization and the spin concentration. Because there are 4 spins (and 3 spin defects) on 7 repeating units in **1**, the number of spin arrangement patterns is calculated to be 35 (=7!/4!3!). Similarly, the numbers of spin arrangement patterns in **2** and **3** are calculated to be 165 (=11!/8!3!) [7] and 252 (=10!/5!5!), respectively. Some spin arrangement patterns in **1** are shown in Table 2. When it is assumed that the intramolecular spin interaction between two neighboring spins is ferromagnetic and the spin defect intercepts the spin interaction, which are expressed as $J_0 > 0$ and $J_1 = 0$ in Fig. 3, respectively, there are one $S = 1/2$ and one $S = 3/2$ states in entry 2 in Table 1. In this way, when the number of the spin states in all entries are counted, the total number and the percentage in each spin state are 38% and 49% for $S = 1/2$, 22% and 28% for $S = 2/2$, 18% and 18% for $S = 3/2$ and 4% and 5% for $S = 4/2$ as shown in Tables 1 and 2. Because many spin states are intermingled in open-shell polymers, except for

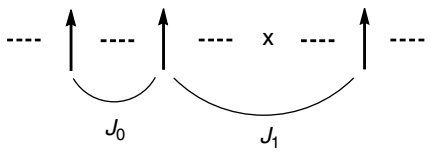


Fig. 3. Intramolecular exchange interaction J_0 and J_1. The subscript denotes the number of spin defects between spins. ↑ and × denote the spin and the spin defect, respectively.

Table 1
Spin arrangement pattern for 4 spins on 7 repeating units

Entry	Spin arrangement pattern[a]	Exchange interaction[b]	Number of the spin states			
			1/2	2/2	3/2	4/2
1	↑↑↑↑×××	$J_0 > 0, J_1 = 0$	0	0	0	1
		$J_0 > 0, J_1 > 0$	0	0	0	1
2	↑↑↑×↑××	$J_0 > 0, J_1 = 0$	1	0	1	0
		$J_0 > 0, J_1 > 0$	0	0	0	1
⋮	⋮	⋮			⋮	
35	↑×↑×↑×↑	$J_0 > 0, J_1 = 0$	4	0	0	0
		$J_0 > 0, J_1 > 0$	0	0	0	1
	Total number	$J_0 > 0, J_1 = 0$	38	22	18	4
		$J_0 > 0, J_1 > 0$	12	10	12	18

[a] ↑ and × denote the spin and the spin defect, respectively.
[b] J_0 and J_1 are defined in Fig. 3.

the cases of the spin generation percentage near 100%, the external magnetic field dependence of the magnetization is expressed as follows:

$$\frac{M}{M_S} = p_{1/2}B_{1/2} + p_{2/2}B_{2/2} + \cdots + p_{n/2}B_{n/2} = \sum p_S B_S, \qquad (1)$$

where p_S is the percentage of the spin state S in the spin states intermingling and B_S is the Brillouin function for the spin state S. The external magnetic field dependence of the magnetization calculated with Eq. (1) is shown as open circles ($J_0 > 0$ and $J_1 = 0$) in Fig. 4. The curve drawn by open circles in Fig. 4a corresponds to the line given by the Brillouin function for $S = 0.86$, that is, the calculated S value for **1** was 0.86. This is in good agreement with the experimental value. Similarly, the percentages of the spin states intermingling in **2** and **3** are calculated as shown in Table 2 and the calculated S value for **2** was 1.23 as shown in Fig. 4b, which is also in good agreement with the experimental value. But, for **3**, the calculated S value was 0.80, which is much lower than the experimental value. Then, the S value in the case of $J_0 > 0$ and $J_1 > 0$ was calculated. The result is shown as open triangles in Fig. 4c. From the curve drawn by open triangles, the calculated S value was 1.21, which is in good agreement with the experimental value. The calculated S values in the case of $J_0 > 0$ and $J_1 > 0$ for **1** and **2** were 1.27 and 2.56, respectively, which are

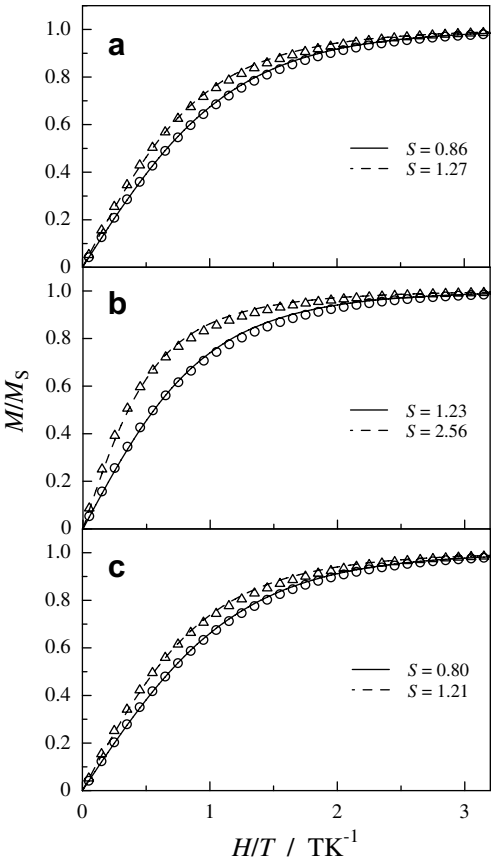


Fig. 4. External magnetic field dependence of the calculated normalized magnetization for (a) **1**, (b) **2** and (c) **3**. The points are the calculated normalized magnetization: open circle, $J_0 > 0$ and $J_1 = 0$; open triangle, $J_0 > 0$ and $J_1 > 0$. The lines are the theoretical lines given by the Brillouin function.

larger than the experimental values. These results indicate that the spin defect intercepts the intramolecular spin interaction in **1** and **2**, but there is the spin interaction across the spin defect in **3**.

The inset in Fig. 2 is the temperature dependence of the magnetic susceptibility of **3** in PVC matrix. The $\chi_{mol}T$ value increases as the temperature decreases. The behavior was analyzed by using Eq. (2) which is often used as the doublet–quartet model for analyzing the intramolecular spin interaction in triangle triradicals [9,10]:

Table 2
Percentage of the spin state in polyradical

Polyradical[a]	Exchange interaction[b]	Percentage of the spin state in polyradical (%)							
		1/2	2/2	3/2	4/2	5/2	6/2	7/2	8/2
1	$J_0 > 0, J_1 = 0$	49	28	18	5				
(4/7)	$J_0 > 0, J_1 > 0$	23	19	23	35				
2	$J_0 > 0, J_1 = 0$	29	25	18	13	7	5	2	1
(8/11)	$J_0 > 0, J_1 > 0$	8	8	8	8	8	8	8	44
3	$J_0 > 0, J_1 = 0$	55	27	13	4	1			
(5/10)	$J_0 > 0, J_1 > 0$	28	22	21	16	13			

[a] The number in parenthesis is the spin concentration.
[b] J_0 and J_1 are defined in Fig. 3.

$$\chi_{\mathrm{mol}}T = f\frac{2Ng^2\mu_{\mathrm{B}}^2}{4k_{\mathrm{B}}}\frac{1+5\exp(3J/k_{\mathrm{B}}T)}{1+\exp(3J/k_{\mathrm{B}}T)}\frac{T}{T-\theta}. \quad (2)$$

The least-square fit gave $J/k_{\mathrm{B}} = +17.7$ K. This value is larger than that of **2** ($J/k_{\mathrm{B}} = +4.2$ K) [7]. This is due to that the distance between spins is closer in **3** than in **2**.

4. Summary

Stable 1,3-phenylene linked polyradicals **1** and **3** were synthesized. Compound **1** was stable both in solution and in solid state, whereas **3** was stable only in diluted solution or PVC matrix. The comparison of the experimental S values with the values numerically calculated based on the degree of polymerization and the spin concentration showed that there is the intramolecular spin interaction across the spin defect in **3**.

Acknowledgment

We thank the Materials Design and Characterization Laboratory, Institute for Solid State Physics, The University of Tokyo for using a SQUID magnetometer.

References

[1] K. Itoh, M. Kinoshita (Eds.), Molecular Magnetism, Kodansha, Tokyo, 1999.
[2] P.M. Lahti (Ed.), Magnetic Properties of Organic Materials, Marcel Dekker, New York, 1999.
[3] J.A. Crayston, J.N. Devine, J.C. Walton, Tetrahedron 56 (2000) 7829.
[4] (a) For example, Y. Teki, T. Takui, K. Itoh, H. Iwamura, K. Kobayashi, J. Am. Chem. Soc. 108 (1986) 2147;
(b) K. Matsuda, N. Nakamura, K. Takahashi, K. Inoue, N. Koga, H. Iwamura, J. Am. Chem. Soc. 117 (1995) 5550.
[5] (a) For example, A. Rajca, Chem. Rev. 94 (1994) 871;
(b) S. Rajca, A. Rajca, J. Solid State Chem. 159 (2001) 460;
(c) A. Rajca, J. Wongsriratanakul, S. Rajca, Science 294 (2001) 1503;
(d) A. Rajca, J. Wongsriratanakul, S. Rajca, J. Am. Chem. Soc. 126 (2004) 6608.
[6] (a) H. Oka, T. Tamura, Y. Miura, Y. Teki, J. Mater. Chem. 9 (1999) 1227;
(b) H. Oka, T. Tamura, Y. Miura, Y. Teki, Polym. J. 31 (1999) 979;
(c) H. Oka, T. Tamura, Y. Miura, Y. Teki, J. Mater. Chem. 11 (2001) 1364.
[7] H. Oka, H. Kouno, H. Tanaka, J. Mater. Chem., in preparation.
[8] A. Ito, M. Urabe, K. Tanaka, Curr. Appl. Chem. 3 (2003) 149.
[9] F. Kanno, K. Inoue, N. Koga, H. Iwamura, J. Phys. Chem. 97 (1993) 13267.
[10] P.M. Lahti, Y. Liao, M. Julier, F. Palacio, Synth. Met. 122 (2001) 485.

Generally speaking, an $\widehat{O}_x^y$ Stevens operator utilizes xth order spin operators to create energy biases having y-fold rotational symmetry as the applied magnetic field rotates about the quantization (z)-axis. Here, a zero-fold pattern indicates contributions to the zfs. As one moves to the right along the terms in Eq. (1), ignoring the Zeeman interaction for the moment, contributions to the energies diminish, making it more difficult to detect the presence of higher order terms in experiment. The sum as a whole then parameterizes the spin–orbit coupling in a SMM.

Out of necessity, the giant spin model ignores the fact that large numbers of exchange-coupled ions contribute to the magnetism in a SMM, and the parameters associated with the Stevens operators have little physical significance. In reality, each of these linked ions has its own spin–orbit parameterization. We set out to explore the relationships between the local and molecular anisotropies and also to address whether higher order terms in the giant spin Hamiltonian could arise from a simple isotropic Heisenberg exchange interaction.

One interesting compound, $[Ni(hmp)(dmb)Cl]_4$ and referred to as Ni_4 hereafter, falls into a regime where it may be studied numerically as either a giant spin or as four spins coupled through Heisenberg exchange [3]. The magnetic core is composed of four $S = 1$, Ni^{2+} ions, which couple ferromagnetically to form a spin $S = 4$ ground state. Hilbert spaces span 9 and 81 dimensions for the giant spin and exchange models, respectively. High frequency EPR experiments have determined giant spin parameters up to fourth order with non-zero D, B_4^0 and B_4^4 [3,4]. Thermodynamic measurements have also determined a value for the exchange coupling constant J [5,6]. Additionally, single-ion anisotropy parameters and alignments with respect to crystallographic axes have been found through synthesis and experiment on an isostructural form, $[Zn_{3.91}Ni_{0.09}(hmp)_4(dmb)_4Cl_4]$ or NiZn for short [7]. These studies found non-zero d and e values for the single ions. With this significant base of experimental data one may begin to piece together an exchange coupled Hamiltonian with a general expectation as to what parameters should fit the model.

$$\widehat{H} = \sum_{i=1}^{4}\left[d\widehat{O}_2^0(i) + e\widehat{O}_2^2(i) + g\mu_B\vec{B}\cdot\widehat{S}_i\right] + \sum_{i=1}^{4}\sum_{j>i} J\widehat{S}_i\cdot\widehat{S}_j \tag{2}$$

A four-ion Hamiltonian is written in Eq. (2), where $\widehat{O}_2^0(i)$ and $\widehat{O}_2^2(i)$ represent Stevens operators for the ith particle, scaled by d and e. Lower case indicates parameters for the four-ion model to prevent confusion with the giant spin Hamiltonian. The Hamiltonian matrices for the individual ions have dimensions 3×3. Consequently, the second order Stevens operators completely account for the local anisotropy. The four ions are each coupled to the others netting six interactions with identical J values. A more precise model would include two values of J, due to the axial distortion of the cubic core of the molecule (having S_4 symmetry). However, the use of a single J value does not have any significant effect on the analysis below, where the discussion is of a more qualitative nature. In addition, fits to magnetic susceptibility data using a two-J model suggest that the values are quite similar [6].

The four-ion model is evaluated in two ways. The first part involves the zfs, i.e. the energy differences between adjacent m_s states at $B = 0$. The second part involves fitting oscillations of the ground state splitting as a function of the applied field orientation within the hard plane. The latter provides the most straightforward measurement of the off-diagonal (transverse) anisotropy parameters via an EPR experiment [8]. We then compare the data generated via the four-ion model with those from the giant spin Hamiltonian. In looking at the ground state multiplet for the four-ion Hamiltonian, one would expect to find d to be the primary contributor to the zfs, and e to dictate the behavior when the field is in the hard plane. This is indeed the case. However, as we shall see, J does play an important role for both regimes. Furthermore, due to its S_4 symmetry, the molecular E parameter is necessarily zero. It is, therefore, interesting to see how e influences the transverse anisotropy in the giant spin Hamiltonian, and what role (if any) J plays in the correspondence between the anisotropy parameters in the two models.

2. Data and discussion

Fig. 1 compares the zfs for both the giant spin and four-ion models. Black data points in Fig. 1a represent the lowest nine zero field energies for the four-ion model with their shape indicating the spin projection within the $S = 4$ state,

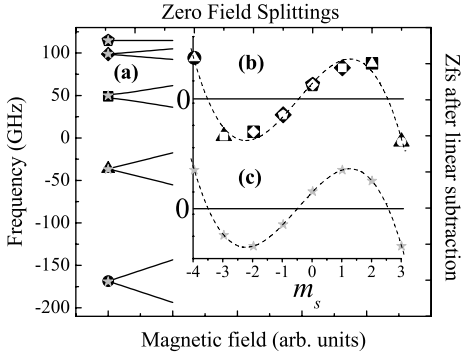


Fig. 1. (a) The lowest nine energy levels (black shapes) are plotted for the four-ion model with the full set of corresponding energies from the giant spin model (grey stars), superimposed with lines proceeding to higher field representing the Zeeman splitting brought on by a longitudinal field. (b) The energy differences between consecutive projections, m_s (horizontal axis), are plotted for the four-ion model after subtraction of the linear dependence. This is necessary to graphically represent the differences between the two models. A cubic polynomial fit to the eight data points is included to provide a guide to the eye. (c) The energy differences between consecutive m_s states are plotted for the giant spin model after subtraction of the linear dependence. In (c), the data points all fall onto the fit whereas, in (b), points fall away from the fit indicating a subtle difference between the two models.

where projections of equal magnitude are essentially degenerate. Lines emerging to the right of the data points indicate the energy splitting arising from an applied longitudinal field. The grey stars are the energies calculated from the giant spin model using parameters which are published elsewhere [3,4]. At first glance this comparison shows that one may indeed model zero field data using a four-ion model, i.e. there is no visible difference between the two sets of data points.

A subtle contrast appears only upon closer inspection of the differences between the zfs energies predicted in either model. As previously discussed, the dominant second order axial anisotropy results in a linear dependence of the zfs on m_s, where m_s represents the lower of the values for the two levels in question, i.e. the zfs are numbered from -4 to $+3$ (see Fig. 1b). Plotting the eight zfs versus m_s (not shown) reveals a slight deviation from linearity [5]. This shift is small enough that, in order to make comparison between models graphically, the linear component must be subtracted. This allows emphasis to be placed on the curvature (non-linearity, or higher-order zfs) with the results shown in Fig. 1b for the four-ion model, and Fig. 1c for the giant spin model. Cubic polynomial fits overlay the two sets of data points. The discrepancy between the two models reveals itself as points in Fig. 1b that fall away from the cubic fit. In other words, higher order polynomial components are required to fit the data points for the four-ion model.

The analysis to this point reveals several very important results. The cubic behavior seen in Fig. 1c is a direct consequence of $\widehat{O}_4^0$, and the cubic term in the polynomial fit provides a direct measure of the B_4^0 parameter in the giant spin model. However, when one applies the four-ion model to the same data set, higher-order corrections to the cubic behavior automatically appear. The experimental accuracy of the data is insufficient to determine which model is correct. However, one can directly compare the two models. In doing so, it seems that one must include terms of order higher than four in the giant spin model in order to force it into agreement with the four-ion model. Indeed, there is no physical reason for truncating the giant spin Hamiltonian (Eq. (1)) at fourth order, whereas local anisotropy terms in Eq. (2) of order higher than two are completely unphysical. In this sense, although both approaches already involve approximation, Eq. (2) is somehow complete, whereas Eq. (1) is further approximated by limiting it to 4th order.

Nevertheless, there is a more important conclusion that can be drawn from comparison between the two models. Namely, that the non-linearities in Fig. 1b depend explicitly on the isotropic Heisenberg interaction parameter J. This dependence is discussed at greater length in a separate paper [5]. For infinite coupling, the curvature goes to zero. In other words, one necessarily requires a finite J to account for the cubic behavior observed in the experimental data and, therefore, the B_4^0 term deduced on the basis of the giant spin model. Thus, a combination of d and J is required to account for the non-linear dependence of the zfs on m_s in the four-ion model. What is more, the resultant non-linearities produce fourth and higher-order terms in the giant spin model. The effect of a finite J is to generate mixing between spin multiplets with different S quantum numbers. This mixing leads to a breakdown of the giant spin approximation.

Fig. 2 illustrates the oscillation of the ground state splitting as a transverse field sweeps through 360° within the hard plane. Here, the ground state splitting indicates the energy difference between the two lowest levels at 5 T. In the main part of the figure, eigenvalues are plotted as a function of magnetic field for two orientations, with arrows indicating the maximum (grey) and minimum (black) magnitudes of the splitting. An oscillation in the splitting occurs when operators, $\widehat{O}_x^{2n}$ with $n > 0$, appear in either Hamiltonian. Tracing this magnitude over 360° yields a four-fold oscillatory pattern shown in the lower left inset, which represents both the giant spin and four ion models, i.e. they are indistinguishable on this scale. Here the four-ion model replicates the effect of the B_4^4 term in the giant spin model. Precisely as noted above for the zfs above, a combination of both the exchange interaction parameter J, and the e term in Eq. (2) is required to produce the desired result; the magnitude of the oscillation scales inversely with J. Although each of the ions has an e term, the molecular S_4 symmetry guarantees cancellation of the second order (two-fold) behavior plotted in the upper right inset for comparison. Were one to break the S_4 symmetry of the Ni_4 molecule, such an angle dependence would naturally arise, even for infinite J. In the strictly S_4 case, no oscillation (transverse anisotropy) is observed for infinite

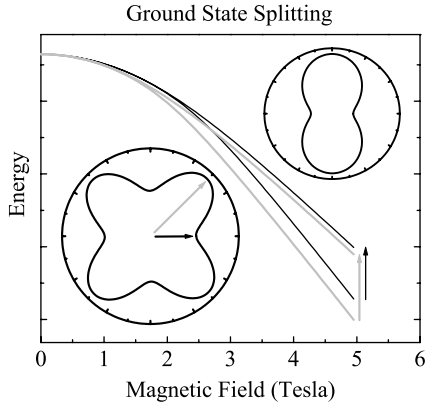


Fig. 2. The ground state energy splitting is plotted for increasing values of transverse magnetic field for two angles within the hard plane. The grey traces indicate field orientations which yield maximum splitting, while the black traces show minimal splitting. The arrows indicate the energy differences (ground state splitting) which are plotted as insets in the lower-left and upper-right portions of the figure for a full rotation of a 5 T field within the hard plane. The combination of an e term and the exchange parameter J in the four-ion model replicates the effect of a B_4^4 term in the giant spin model. By contrast, a similar plot for a single particle with an e term (or an E term for a giant spin) is plotted in the upper right inset.

J. For a finite J, the effect of the second order e term shows up again at higher orders in the giant spin model.

3. Conclusion

Heisenberg exchange coupling does indeed introduce apparent effects attributed to higher-order anisotropic interactions in the giant spin Hamiltonian. Non-linear zfs attributed to the B_4^0 term in the giant spin model appears to result from the interaction between energy levels belonging to higher-lying spin multiplets [5]. A similar behavior was recently noted in an Fe_4 complex [9]. Although the mapping is not exact, the similarity is striking. The difference between models indicates a shift in an EPR peak of close to 0.03 T, which in many cases is difficult to measure because of peak broadening brought on by D- and g-strain within a typical crystal. As the giant spin model is an expansion of terms that leads into higher orders, it seems reasonable that the models should come into better agreement as more terms such as B_6^0 and B_8^0 are added into the giant spin parameterization. But that discussion diverts from the main point. The apparent B_4^0 and B_4^4 terms measured under the giant spin Hamiltonian are actually artifacts of exchange, which in turn convolutes the physical meaning of a giant spin Hamiltonian. The series of terms no longer parameterizes spin–orbit coupling but instead measures a combination of interactions, which are impossible to extract from the model. While the giant spin model will work in the simulation of experimental data, it does not do an ideal job of explaining the physical processes within a SMM. The above calculations were made using the Hamiltonian parameters, $d = -141.8$ GHz, $e = -35.6$ GHz, $J = -178$ GHz, $g = 2.25$, including a dipolar interaction as well as a 15° tilt of the Ni ion easy axes away from the molecular easy axes [5,7].

Acknowledgement

This work was supported by the US National Science Foundation under Grant numbers DMR-0239481, DMR-0414809 and DMR-0506946.

References

[1] D. Gatteschi, R. Sessoli, Angew. Chem. 42 (2003) 268.
[2] M.I. Katsnelson, V.V. Dobrovitski, B.N. Harmon, Phys. Rev. B 59 (1999) 6919.
[3] E.-C. Yang, W. Wernsdorfer, S.O. Hill, R.S. Edwards, M. Nakano, S. Maccagnano, L.N. Zakharov, A.L. Rheingold, G. Christou, D.N. Hendrickson, Polyhedron 22 (2003) 1727.
[4] C. Kirman, J. Lawrence, S. Hill, E.C. Yang, D.N. Hendrickson, J. Appl. Phys. 97 (2005) 10M501.
[5] A. Wilson, J. Lawrence, E.-C. Yang, M. Nakano, D.N. Hendrickson, S. Hill, Phys. Rev. B 74 (2006) R140403.
[6] E.-C. Yang, W. Wernsdorfer, L.N. Zakharov, Y. Karaki, A. Yamaguchi, R.M. Isidro, G.-D. Lu, S.A. Wilson, A.L. Rheingold, H. Ishimoto, D.N. Hendrickson, Inorg. Chem. 45 (2006) 529.
[7] E.-C. Yang, C. Kirman, J. Lawrence, L.N. Zakharov, A.L. Rheingold, S. Hill, D.N. Hendrickson, Inorg. Chem. 44 (2005) 3827.
[8] E. del Barco, A.D. Kent, S. Hill, J.M. North, N.S. Dalal, E.M. Rumberger, D.N. Hendrickson, N. Chakov, G. Christou, J. Low Temp. Phys. 140 (2005) 119–174.
[9] S. Accorsi, A.-L. Barra, A. Caneschi, G. Chastanet, A. Cornia, A.C. Fabretti, D. Gatteschi, C. Mortalo, E. Olivieri, F. Parenti, P. Rosa, R. Sessoli, L. Sorace, W. Wernsdorfer, L. Zobbi, J. Am. Chem. Soc. 128 (2006) 4742.

chain taken from experimental structure. The theoretical methodology was developed in our recent works [5a,6], the new results proving its reliability in tackling the realistic description of real chemical systems and physical problems.

2. Experimental

All chemicals and solvents were used as received and no purification was needed. The complex $[Fe(bpca)_2][Er(NO_3)_3(H_2O)_4]\cdot NO_3\cdot H_2O$ (**1**) was obtained by adding a solution of $Er(NO_3)_3\cdot 6H_2O$ (0.05 mmol) in methanol (2 mL) to an equimolar solution of $[Fe(bpca)_2]NO_3$ (synthesized as described elsewhere [7]) in nitromethane (2 mL). After 30 min stirring at room temperature, the solution was left undisturbed. Well formed orange crystals resulted in several days (yield 83%). Crystals were used for X-ray and magnetic measurements. *Anal*. Calc. for $C_{24}H_{18}ErFeN_{10}O_{21}$ (**1**): C, 28.67; N, 13.93; H, 1.80. Found: C, 28.54; N, 13.71, H, 2.20%.

The diffraction data were collected on SMART-1000/CCDD (Bruker AXS) area detector using the standard procedure (Mo Kα radiation). The data integration and reduction were undertaken with SAINT and XPREP [8]. The intensity data were empirically corrected for absorption using the program SADABS [9]. The structures were solved by direct methods and refined using least-squares methods on F^2 with SHELXL-97 [10]. Non-hydrogen atoms were modeled with anisotropic displacement parameters, and hydrogen atoms were placed by difference Fourier syntheses and refined isotropically. $\lambda(\text{Mo K}\alpha) = 0.71073$ Å, $T = 100$ K, orange blocks, formula $C_{24}H_{16.33}ErFeN_{10}O_{21}$, MW = 1003.91, $0.80\times0.65\times0.60$ mm, triclinic, $P\bar{1}$, $a = 13.4837(15)$ Å, $b = 19.766(3)$ Å, $c = 20.801(2)$ Å, $\alpha = 85.321(4)°$, $\beta = 85.321(4)°$, $\gamma = 85.321(4)°$, $Z = 6$, $V = 5182.0(11)$ Å^3, $R_1 = 0.0411$, $wR_2 = 0.0979$, GOF = 1.012.

Magnetic measurements for **1** were carried out on a Quantum Design SQUID MPMS 5S magnetometer on polycrystalline samples. The dc measurements were made using an external magnetic field of 1000 Oe over a temperature range of 1.8–300 K and ac measurements using a 3 Oe magnetic field oscillating at 10–1400 Hz. Diamagnetic corrections were estimated from Pascal constants.

3. Results and discussion

The network of compound **1** contains the $[Fe(bpca)_2]^+$ distinct cations and 1-D assembled $[Er(NO_3)_3(H_2O)_4]$ neutral units, the d and f nodes being weakly connected by hydrogen bonding. The non-coordinated nitrate ions play a role in the hydrogen bond bridging of neighbor lanthanide complex units. The $[Fe(bpca)_2]^+$ cation is a compressed octadedron (see Fig. 1), made of tris-dentate mononegative ligands $bpca^-$ and Fe(III). As expected for a system consisting in floppy components (lanthanide coordination spheres and the intermolecular connections), the crystal structure show disordering promoted by the hydrogen bond dynamics.

The disorder brings slight differences between the lanthanide molecular moieties (belonging to three species in the crystal). These are, however, roughly similar, differing in rather small tilts of the chelate NO_3^- groups. A description that match the common features of $[Er(NO_3)_3(H_2O)_4]$ units is the 10 vertex topology established by the three NO_3^- chelates and the four monodentate H_2O ligands. In each case, two NO_3^- groups are coordinated symmetrically, with Er–O bond lengths in the 2.30–2.58 Å range, while another group coordinates asymmetrically, with one bond elongated at 3.2–3.6 Å. The four water ligands are situated approximately in the same plane, in a sequence of *cis* mutual positions. The average planes of $\{(H_2O)_4Er\}$ and $\{Er(NO_3)_3\}$ molecular halves are mutually perpendicular. It is worth noting the dipolar structure of the neutral $[Er(NO_3)_3(H_2O)_4]$ complexes, with the negative ligands placed in one hemisphere. The $\{(H_2O)_4Er\}$ molecular half shows, in counterpart, positive polarization and outer protons as vectors for hydrogen bonding. The dipolar nature and hydrogen bonding capabilities are the factors determining the 1-D assembling of the lanthanide units. The

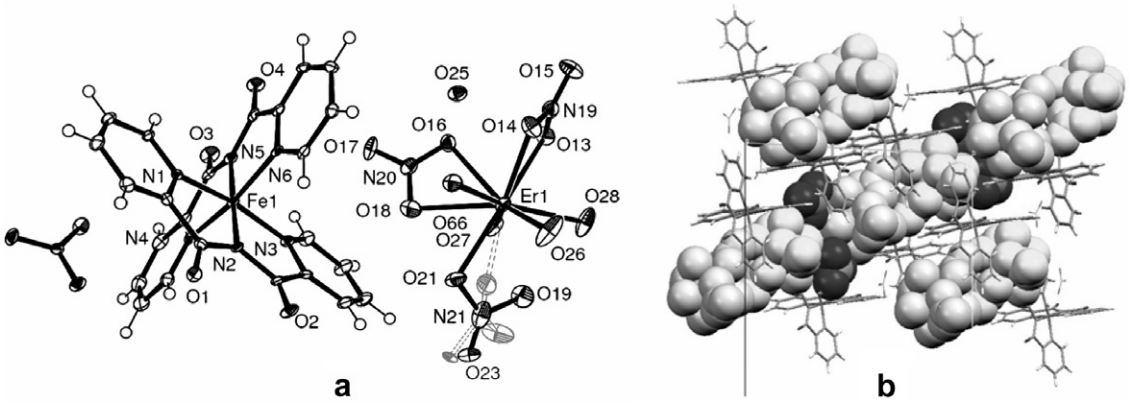


Fig. 1. (a) ORTEP view of complex $[Fe(bpca)_2][Er(NO_3)_3(H_2O)_4]\cdot NO_3\cdot H_2O$ (**1**) with 50% thermal probability ellipsoids and selected atom labeling scheme. (b) Packing diagram of the crystal structure **1**, showing the chain arrangement of the lanthanide units (light grey spheres) including the non-coordinated NO_3^- groups (dark grey spheres), while the $[Fe(bpca)_2]^+$ complexes are drawn with sticks.

qualitatively estimated electric dipole orientations of individual complexes are tilted with respect of the chain averaged direction. The symmetry along the chain involves inversion operations. Therefore the crystal is, as sum, non-polar. At the point where the inversion of sequences occurs, the lattice NO_3^- groups are intervening to establish hydrogen bond bridges with ligands from $\{(H_2O)_4Er\}$ molecular sides of neighbour units. The described features can be visualized in Fig. 2.

The magnetic properties of the complex **1** were studied using a polycrystalline sample in the 1.8–300 K temperature range. The χT product (Fig. 3) at room temperature is 12.03 $cm^3 \cdot K/mol$, in line with an effective $^4I_{15/2}$ ground state on Er(III) plus the uncoupled $S = 1/2$ Fe(III) center. Treated with a simplistic Curie–Weiss linearization, $\chi^{-1} = (T - \theta)/C$, the parameters are $C = 12.23\ cm^3 \cdot K/mol$ and $\theta = -9.75$ K. The C value is close to the paramagnetic summation equated using the ideal values $g_J = 1.2$, $J = 15/2$ for Er(III) component and $g_S = 2$, $S = 1/2$ for Fe(III). The θ parameter is similar with the values reported in comparable cases [11]. However, this cannot be assigned, as attempted in the above cited work, to some antiferromagnetic coupling, the Er(III) single ion anisotropy being likely the origin of the χT function of temperature. The χT increasing from 6.02 $cm^3 \cdot K/mol$ at 1.8 K occurs on a large temperature domain, a fact that implies statistics over energy gaps larger that those conceivable to d–f or f–f exchange coupling. The magnetization versus field measurements shows the highest value of the magnetization at about 5.62 μ_B at 50 kOe at 1.8 K. The magnetization curve does not correspond to a regular Langevin pattern, but is in line with an effective moment lower than the maximal one, as suggested also by the χT value at the lowest temperature.

Zero field cooled and field cooled (ZFC-FC) dependences were recorded on the polycrystalline sample and no difference was observed between the two curves down to 1.8 K. The temperature dependence of the ac magnetic susceptibilities of the polycrystalline sample of **1** measured in zero magnetic field is shown in Fig. 4a. In a field oscillating at 1400 Hz, the complex shows no out-of-phase component of ac magnetic susceptibility χ'' above 1.8 K, while the in-phase component χ' decreases monotonically with the increasing of the temperature. This behavior suggests that

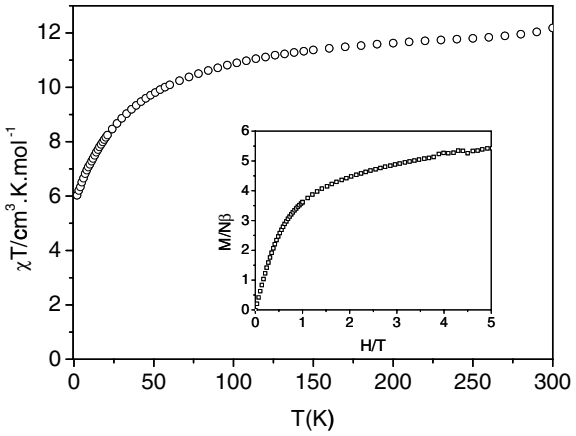


Fig. 3. Temperature dependence of the χT product for **1**. Inset the magnetization vs. field (1.8 K).

the magnetic moments follow the ac magnetic field. In the presence of a static magnetic field (Fig. 4b) the complex shows a significant decrease in χ' from the corresponding zero dc field values and, for χ'', peaks depending on the ac frequency, suggesting a lag in the response of the magnetic moment to the ac magnetic field.

The ac susceptibility for **1** was measured down to 1.8 K and in the frequency range 10–1400 Hz (Fig. 4c and d). Such behavior is similar to the other several systems containing lanthanide ions [12] and this procedure avoids fast tunneling regime of the Kramer type systems at zero static field. The explanation for the origin of dc field-induced relaxation as the lifting of the Kramer degeneracy by magnetic field is valid merely for "isolated ion-like" systems [13]. Even having a presumable small role in the χT function, the long range couplings, dipolar, or even exchange mediated through hydrogen bonds, can play decisively in assisting the dynamic magnetic behavior. Considering the Er···Er separation in the chain, around 7.7 Å, one may estimate, with dipolar formulas, energies in a 0.26 cm^{-1} range, suggesting that such effects can intervene in the intricate phenomena related with the magnetization relaxation.

An interesting view to the magnetic anisotropy was added with the help of the ab initio calculations. As described elsewhere [5a,6], the calculation of lanthanide systems is a non-routine task, for which we developed spe-

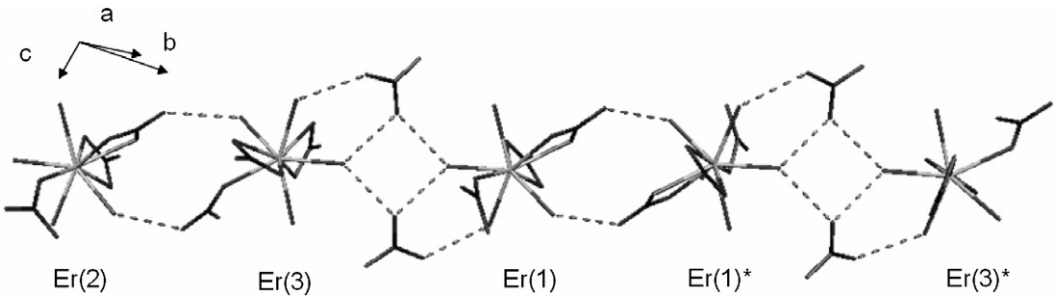


Fig. 2. The hydrogen-bonded chain structure formed by $[Er(NO_3)_3(H_2O)_4]$ units. Selected lengths: Er(1)–Er(3) 8.419 Å, Er(3)–Er(2) 7.732 Å. The symmetry operation for the (*) atoms: $-x$, $-y$, $-z$.

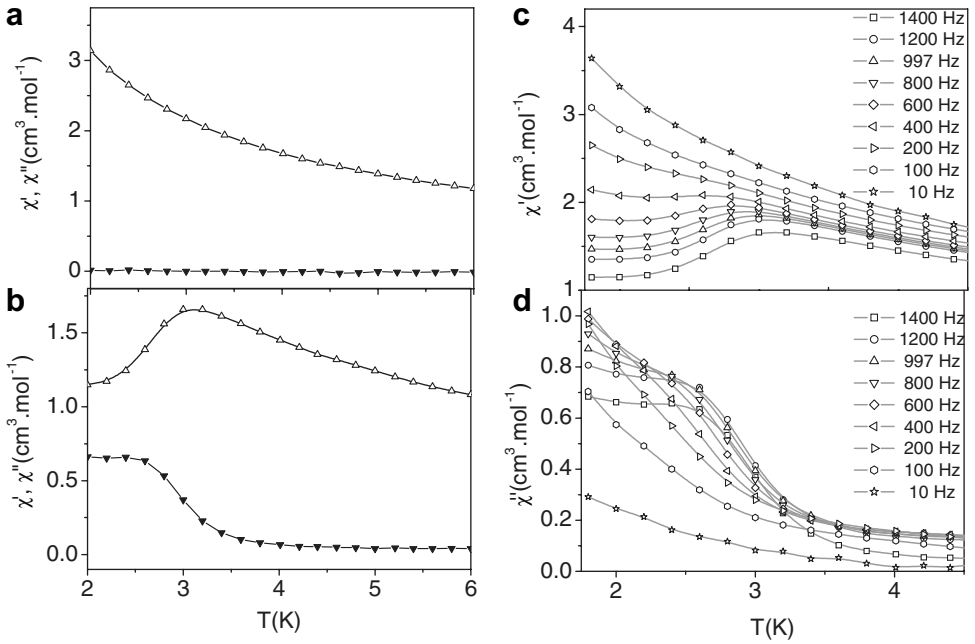


Fig. 4. (a) Temperature dependence of in-phase ac χ' (△) and out-of-phase ac χ'' (▼) magnetic susceptibilities for $[Fe(bpca)_2][Er(NO_3)_3(H_2O)_4]\cdot NO_3\cdot H_2O$ (**1**), performed in a 3 Oe ac magnetic field oscillating at 1400 Hz with the absence of the dc component and (b) in a dc field of 1000 Oe. (c and d) Temperature dependence of the real χ' and imaginary χ'' components of the ac susceptibility measured in 0.1 T applied field (lines are guides to the eye).

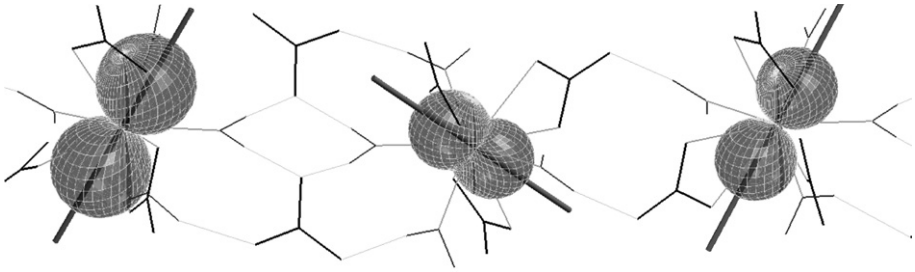


Fig. 5. The magnetization tensors for the groundstates of the $[Er(NO_3)_3(H_2O)_4]$ units, obtained via CASSCF+SO ab initio calculations including subsequently the modeling of magnetic field effects. The axes drawn with the origin in each center correspond to a -10 μ_B to $+10$ μ_B scale. Note the tilt of the easy magnetization axis resulted on centers related by inversion operations (the two nodes from the right side sequence).

cial procedures. The calculations were performed with the GAMESS program [14], the further handling using original codes. The calculation were performed on three individual $[Er(NO_3)_3(H_2O)_4]$ complex units as depicted in Fig. 5. The position of hydrogen atoms was fixed with the help of geometry optimization considered for a $\{[Lu(NO_3)_3(H_2O)_4]_5(NO_3)_4\}^{(-4)}$ sequence (similar to those depicted in Fig. 2), where Lu(III) was used as surrogate to avoid at this step the open shell intricacies. The next calculations consisted in CASSCF(11,7) procedures (i.e. 11 electrons in 7 orbitals) corresponding to the f^{11} configuration of the Er(III) in the $[Er(NO_3)_3(H_2O)_4]$ complexes. A state-averaging regime (on 13 levels) was employed, accounting in balanced manner for the ^4I multiplet.[3] Afterwards, the spin orbit (SO) calculations were done, incorporating as result all the ^4I_J sets with J between 15/2 and 9/2 (totally, 52 microstates). The CASSCF calculations accounted well for the ligand field regime, yielding a total gap about 400 cm^{-1}on the ^4I term, with SO ignored. The subsequent SO computation yielded for the groundstate sequence a series of 16 states grouped in doubly degenerate pairs, whose full gap falls in the 300 cm^{-1} range. The spacing between successive sublevels are in the 20–60 cm^{-1} range. This interplay between ligand field and spin orbit effects is somewhat similar to the ZFS effect, but in a more complex fashion. The doubly degenerate companions formally correspond to $\pm J_z$ pairs, but one may take the precaution to consider that, in principle, the J_z labels may loose their effective quantum number qualities, due to the imbrications with the ligand field part.

The full output from CASSCF+SO calculations afforded the supplementary information needed to build the

[3] The SBKJC effective potential and basis set were used on the Er atom and 6-31G* basis sets for O, N, and H atoms.

orbital part of the Zeeman Hamiltonian, aside to the obvious spin type Zeeman part. Taking this advent and having all the necessary ingredients, we modeled the further splitting in magnetic field with a separate original code. Performing the corresponding derivatives with the field, the magnetization tensors became available. The computed polar diagrams for the ground state magnetization of the selected centers are depicted in Fig. 5.

The maximal extension along the easy magnetization axis is at one center about 7 μ_B (left side in Fig. 5). This would correspond to a certain reduction of the $g_z J_z \mu_B$ amount taken with respect of the ideal $J_z = \pm 15/2$ projections. The other centers show advanced reduction, about 5 μ_B in the magnitude of magnetic anisotropy. Keeping a semi-quantitative use of ab initio results, one may suggest a rather significant dependence of magnetic properties as function of slight geometry changes. The noticed reduction can be assimilated to a non-monotonous J_z type ordering or a J_z projection-admixed nature of levels, once the J_z labels cease to be rigorous quantum numbers. A certain reduction of effective magnetization of the ground state (as compared to the ideal maximal 15/2 component), while, in counterpart, the next levels bear higher moments, would be in line with the observed χT increase with T, as such sequences are progressively populated. The intermediate effective J_z is also in line with lower plateau trend in magnetization taken at small temperatures. Though too complex yet for the full understanding, the magnetic properties due to intrinsic anisotropy and complicate dependence on ligand field can be gradually decrypted, taking different structural case studies and complementing them with theoretical insight, as we attempted here. The ab initio approach, reliable for accounting the main ligand field and spin orbit mechanisms, at least qualitatively, helps encompassing parametric uncertainties and algebraic complications that affect traditional ligand field model approaches on lanthanide systems. The investigation of lanthanide complexes with different symmetries and ligand fields can provide rationalization for the dynamical magnetism of lanthanide complexes. Further systems and structural correlations in this line are in the progress and our current focus.

Acknowledgements

This work was supported by Japan Society for Promotion Science post-doctoral fellowship program (P04390-MF) and COE program (F.C.). M.F. and F.C. also thank to CNCSIS/RO (886 and 1422/2005).

Appendix A. Supplementary material

CCDC 617390 contains the supplementary crystallographic data for this paper. These data can be obtained free of charge via http://www.ccdc.cam.ac.uk/conts/retrieving.html, or from the Cambridge Crystallographic Data Centre, 12 Union Road, Cambridge CB2 1EZ, UK; fax: (+44) 1223-336-033; or e-mail: deposit@ccdc.cam.ac.uk. Supplementary data associated with this article can be found, in the online version, at doi:10.1016/j.poly.2006.10.003.

References

[1] (a) G. Christou, D. Gatteschi, D.N. Hendrickson, R. Sessoli, MRS Bull. 25 (2000) 66;
(b) D. Gatteschi, R. Sessoli, Angew. Chem., Int. Ed. 42 (2003) 268.
[2] (a) N. Ishikawa, M. Sugita, W. Wernsdorfer, J. Am. Chem. Soc. 127 (2005) 3650;
(b) N. Ishikawa, M. Sugita, W. Wernsdorfer, Angew. Chem., Int. Ed. 44 (2005) 2931.
[3] (a) L. Bogani, C. Sangregorio, R. Sessoli, D. Gatteschi, Angew. Chem., Int. Ed. 44 (2005) 5817;
(b) K. Bernot, L. Bogani, A. Caneschi, D. Gatteschi, R. Sessoli, J. Am. Chem. Soc. 128 (2006) 7947.
[4] (a) C.M. Zaleski, E.C. Depperman, J.W. Kampf, M.L. Kirk, V.L. Pecoraro, Angew. Chem., Int. Ed. 43 (2004) 3912;
(b) A. Mishra, W. Wernsdorfer, K.A. Abboud, G. Christou, J. Am. Chem. Soc. 126 (2004) 15648.
[5] (a) M. Ferbinteanu, T. Kajiwara, K.-Y. Choi, H. Nojiri, A. Nakamoto, N. Kojima, F. Cimpoesu, Y. Fujimura, S. Takaishi, M. Yamashita, J. Am. Chem. Soc. 128 (2006) 9008;
(b) J.-P. Costes, F. Dahan, W. Wernsdorfer, Inorg. Chem. 45 (2006) 5.
[6] J. Paulovic, F. Cimpoesu, M. Ferbinteanu, K. Hirao, J. Am. Chem. Soc. 126 (2004) 3321.
[7] S. Wocadlo, W. Massa, J.V. Folgado, Inorg. Chim. Acta 207 (1993) 199.
[8] SMART, SAINT and XPREP, Area detector control and data integration and reduction software, Bruker Analytical X-ray Instruments Inc., Madison, WI, 1995.
[9] G.M. Sheldrick, SADABS: Program for Empirical Absorption Correction of Area Detector Data, University of Göttingen, Göttingen, Germany, 1996.
[10] G.M. Sheldrick, SHELX-97: Programs for Crystal Structure Analysis, University of Göttingen, Göttingen, Germany, 1998.
[11] H. Cui, T. Otsuka, A. Kobayashi, N. Takeda, M. Ishikawa, Y. Misaki, H. Kobayashi, Inorg. Chem. 42 (2003) 6114.
[12] Y.-Z. Zhang, G.-P. Duan, O. Sato, S. Gao, J. Mater Chem. 16 (2006) 2625.
[13] M. Sugita, N. Ishikawa, T. Ishikawa, S. Koshihara, Y. Kaizu, Inorg. Chem. 45 (2006) 1299.
[14] M.W. Schmidt, K.K. Baldridge, J.A. Boatz, S.T. Elbert, M.S. Gordon, J.H. Jensen, S. Koseki, N. Matsunaga, K.A. Nguyen, S.J. Su, T.L. Windus, M. Dupuis, J.A. Montgomery, J. Comput. Chem. 14 (1993) 1347.

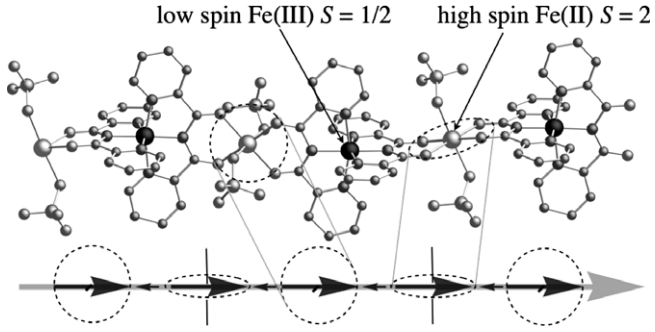


Fig. 1. Crystal structure and spin arrangement of **1**.

the formula of $\mathbf{1}\cdot 3CH_3NO_2$.[1] Each chain is directing along crystallographic a–c vector, and cylindrical pores are formed along this axis surrounded by four chains (Fig. 2a). The crystal of **1** contains three molecules CH_3NO_2 molecules per a Fe(II)–Fe(III) unit as crystallization solvent which occupy the pores. These CH_3NO_2 molecules can be released gradually at room temperature and the crystal breaks into fragments. Thermogravimetry analysis for the fresh crystals of **1** was carried out to show 19% decrease of weight at 30 °C, which corresponds to the loss of three CH_3NO_2 molecules from the solvated crystal (17.5%) (Fig. 2b). Here after, we called the crystal which contains three CH_3NO_2 molecules as solvated sample ($\mathbf{1}\cdot 3CH_3NO_2$), and the crystal which released all CH_3NO_2 molecules as dried sample (**1**).

Although the completely dried sample does not maintain its quality for the single crystal X-ray diffraction, a partially dried crystal of **1** keeps enough quality for single crystal X-ray analysis. To investigate the structure of dried sample, we first revealed the X-ray structure for partially dried single crystal of **1**. A freshly prepared single crystal was covered with grease and dried under vacuum for 1 h. The partially dried **1** has the similar structure with the solvated crystals, however, the space group was changed from $P2_1/n$ to $C2/c$, with the formula changing to $\mathbf{1}\cdot 2.5CH_3NO_2$.[2] The unit cell volume is decreased (from 3966 Å^3 to 3910 Å^3) along with the decrease of the number of CH_3NO_2 (from 3 to 2.5). Intra and inter-chain Fe–Fe distances are maintained during the changing of the volume.

To confirm the structure of the completely dried sample, an X-ray powder diffraction (XRD) analysis was carried out

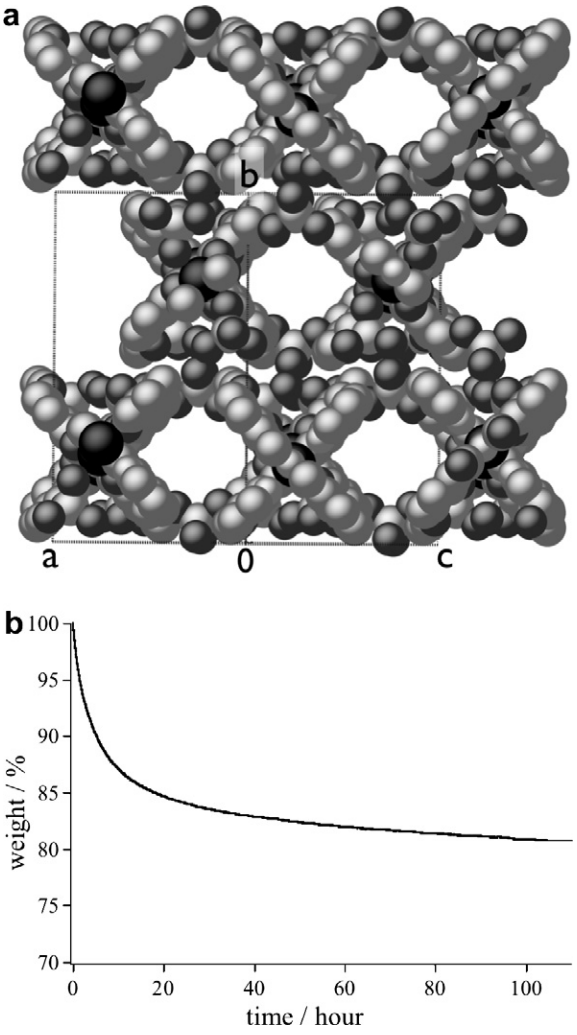


Fig. 2. (a) The packing diagram of **1** viewed from the chain direction. (b) Plot of weight vs. time at 30 °C for fresh prepared solvated sample.

on the powdered **1** of which crystals were mashed under N_2 and dried for 1 h, and compared with the simulated XRD pattern on the basis of the crystal data for the partially dried single crystal with the $C2/c$ space group mentioned above (Fig. 3a upper and Fig. 3b). Compound **1** keeps its crystal character under a completely dried condition and does not change to the amorphous phase. Both the diffraction pattern for the completely dried sample and the simulation pattern for the partially dried crystal are very similar to each other and a slight difference was found from the simulation pattern of solvated $\mathbf{1}\cdot 3CH_3NO_2$ crystallized in $P2_1/n$ (Fig. 3a lower). A Rietvelt analysis, based on the parameter of partially dried single crystal structural data with $C2/c$, resulted to give a smaller unit cell volume of 3815 Å^3 for the former, which is consistent with the complete loss of solvent molecules [7].[3]

[1] Crystallographic data for the fresh prepared solvated **1**: Dark red bar, fomula $C_{27}H_{16}Cl_3\,Fe_2N_9O_{22}$, MW = 1036.54, 0.5 mm × 0.2 mm × 0.1 mm, monoclinic, space group $P2_1/n$, $a = 13.818(9)$ Å, $b = 18.549(1)$ Å, $c = 15.474(1)$ Å, $\beta = 90.268(4)°$, $V = 3966.1(5)$ Å^3, $T = 293(2)$ K, $Z = 4$, $D_{calc} = 1.736$ g/cm^3, 22978 reflections were observed, of which 6231 were independent, $R_1 = 0.0681$ ($I > 2\sigma(I)$) and $wR_2 = 0.1769$ (all data) for 508 parameters, GOF = 0.913.

[2] Crystallographic data for the partially dried **1**: Dark red bar, formula $C_{26.5}H_{16}Cl_3Fe_2N_{8.5}O_{21}$, MW = 1007.54, 0.5 mm × 0.2 mm × 0.1 mm, monoclinic, space group $C2/c$, $a = 13.795(1)$ Å, $b = 18.509(2)$ Å, $c = 15.316(2)$ Å, $\beta = 90.317(4)°$, $V = 3910.6(7)$ Å^3, $T = 293(2)$ K, $Z = 4$, $D_{calc} = 1.711$ g/cm^3, 11161 reflections were observed, of which 3054 were independent, $R_1 = 0.0681$ ($I > 2\sigma(I)$) and $wR_2 = 0.1839$ (all data) for 257 parameters, GOF = 1.099.

[3] Cell parameters from Rietvelt analysis: dried: $C2/c$, $a = 13.748(4)$ Å, $b = 18.528(3)$ Å, $c = 14.992(4)$ Å, $\beta = 92.27(2)°$, $V = 3815(2)$ Å^3. Solvated: $P2_1/n$, $a = 13.884(3)$ Å, $b = 18.651(4)$ Å, $c = 15.600(3)$ Å, $\beta = 90.36(1)°$, $V = 4039(2)$ Å^3.

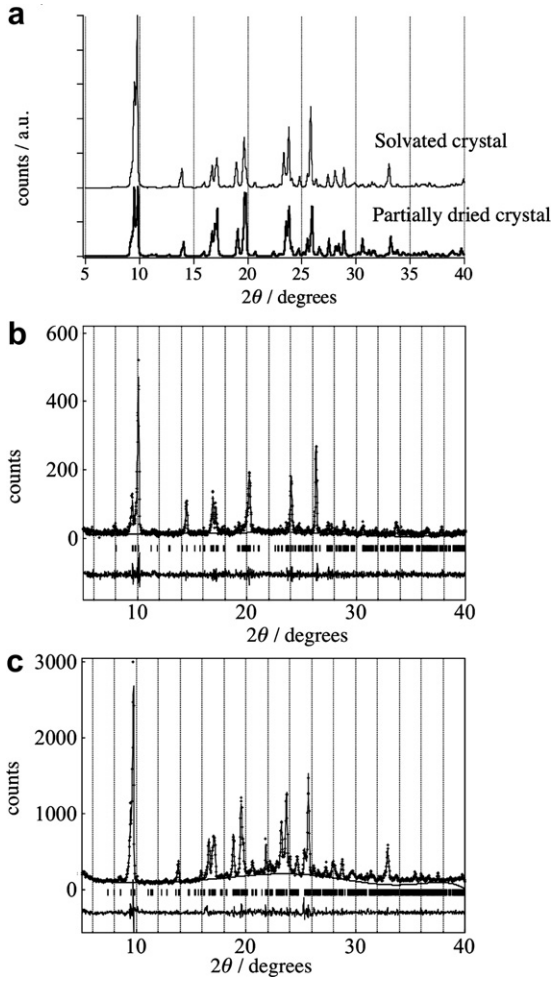


Fig. 3. X-ray powder diffraction patterns. (a) Simulated patterns based on the single crystal diffraction data of the freshly prepared sample (solvated sample; upper) and partially dried sample (lower). (b) Comparison between the observed and calculated patterns of dried sample. From top to bottom: dotted line, observed intensity; solid line, calculated intensity; vertical short lines, position of reflections; solid line, difference between observed and calculated intensity. (c) Comparison between the observed and calculated patterns of solvated **1**. From top to bottom: dotted line, observed intensity; solid line, calculated intensity; vertical short lines, position of reflections; solid line, difference between observed and calculated intensity.

Interestingly, dried sample reabsorbs CH_3NO_2 and reproduce the similar condition of the initial solvated sample. The 20 mg of completely dried sample was added about 0.1 ml of CH_3NO_2 and kept for 2 h, then XRD measurement is carried out (Fig. 3c). The XRD pattern is different from dried one, and very similar to the simulation XRD pattern obtained from structural data of the initial single crystal. The Rietvelt analysis shows the reversion of unit cell volume 4039 Å^3 which indicates that dried crystal reabsorb CH_3NO_2 molecules and return to the solvated condition.

The crystal of **1** can release or reabsorb $MeNO_2$ molecules reversibly like "sponges", possessing the chain structure of **1**.

Magnetic properties of the freshly prepared solvated sample ($\mathbf{1}\cdot 3CH_3NO_2$) and dried sample (**1**) are shown in Fig. 4. The solvated sample was dried under N_2 for 48 h to give the dried sample. DC magnetic susceptibilities for both samples at room temperature are equal to 4.40 cm^3 K mol^{-1} which is corresponding to the expected spin-only value of 4.275 cm^3 K mol^{-1} for a high-spin Fe(II) ($S = 2$) and a low-spin Fe(III) ($S = 1/2$). The χT value remains constant down to about 20 K for both solvated and dried samples. Under 20 K, the χT value of dried sample rapidly increased to a maximum value of 58.7 cm^3 K mol^{-1} around 3 K. On the other hand, the χT value of solvated sample starts increasing at lower temperature (13 K) and does not show a peak down to 1.8 K (Fig. 4a). Fig. 4b shows the frequency dependence of the out-of-phase AC magnetic susceptibility (χ'') of the solvated and dried samples. The temperature, at which χ'' has the maximum value, corresponds to blocking temperature (T_B) for each frequency. With the crystal condition changed from the solvated to the dried, the peak top for each frequency shifts toward higher temperature. The increase of T_B is 21% for the dried sample compared with the solvated sample. By analyzing T_B versus $\ln(2\pi f)$ using Arrhenius equation, $1/T_B = -(k_B/\Delta)\{\ln(2\pi f) + \ln\tau_0\}$, the values of Δ/k_B were estimated as 21.9(3) K for solvated condition, 26.0(9) K for dried condition, respectively. Similar to the change of T_B, Δ/k_B increases when the crystal state changes from the solvated condition to the dried condition. At some fixed temperatures, semicircle Cole–Cole diagrams were obtained with small α values both for the solvated and dried samples (0.24 and 0.14, respectively), as expected for a Debye model with a single relaxation time [8].

This changing of magnetic properties is reversible. Fig. 5 shows the reversible changing of Arrhenius plot of **1**. The Δ/k_B value obtained for each condition remains almost unchanged for three drying and CH_3NO_2 addition cycles. This result is consistent with the reversible changing of the crystal structure.

We can point out the possible structural distortion of Fe(II)–Fe(III) chain which is increasing when changing from the solvated to the dried. Since the easy-axis of this SCM arises from the strict orthogonal arrangement of each easy-plane of Fe(II) ion along chain, slight deviation of the easy-plane from the ideal position might strongly affects the magnetic property of the whole chain.[4] Moreover, neighboring Fe(II)–Fe(III) ions present a moderate antiferromagnetic interaction through a long Fe(II)–Fe(III) distance (longer than 5 Å), and during the condition changing,

[4] Partially dried single crystal of **1** shows slightly different magnetization behavior from that of the freshly prepared single crystal of **1**. The latter only shows a very weak magnetization when the external magnetic filed was applied perpendicular to the chain, whereas, the former shows a considerable magnetization even in a weak magnetic field perpendicular to the chain. This indicates that a slight structural distortion occurs on the alignment of the magnetic easy-plane along the chain axis during the process of the solvent removal.

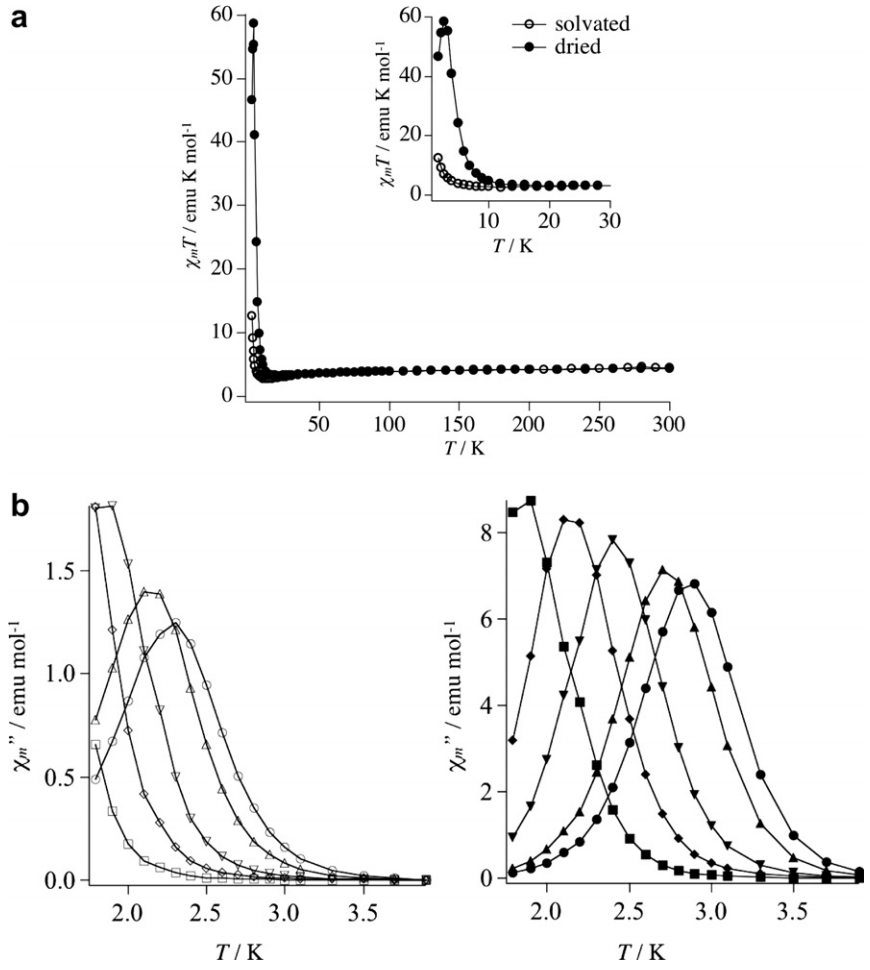


Fig. 4. (a) Plot of χT vs. T under 0.01 T for solvated and dried samples. Solid lines are guides. (b) Plot of χ'' vs. T under zero dc field for the solvated (left) and the dried (right) samples (○, ●: 1000 Hz, △, ▲: 500 Hz, ▽, ▼: 100 Hz, ◇, ◆: 25 Hz, and □, ■: 5 Hz, respectively). Solid lines are guides.

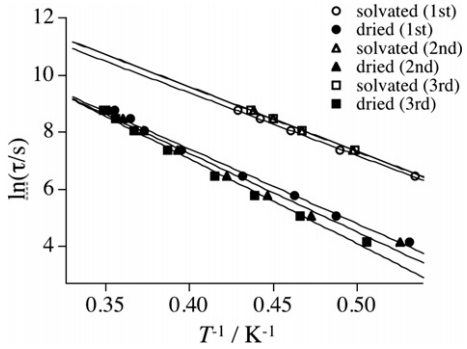


Fig. 5. The reversible changing of Arrhenius plot for the sample under dried/moistened cycles with CH_3NO_2. Open and closed makers represent the solvated and dry conditions, respectively.

it may be shortened with the decreasing of cell parameters to enhance the magnetic interaction. To reveal the small structural changes, more detailed XRD analyses for both samples should be needed. The high-field magnetization study for the dried sample will give the information both for intra-chain magnetic interaction J and magnetic anisotropy of Fe(II) ion D, and detailed studies for these phenomena are now ongoing.

In summary, the crystal of **1** can release and reabsorb CH_3NO_2 molecules reversibly like "sponges" maintaining the structure of the Fe(II)–Fe(III) chain, and simultaneously, its magnetic properties changes significantly. Compound **1** is the first nano-magnet, which shows the solvent induced reversible change of magnetic properties.

Supplementary material

CCDC 619557 and 619558 contain the supplementary crystallographic data for this paper. These data can be obtained free of charge via http://www.ccdc.cam.ac.uk/conts/retrieving.html, or from the Cambridge Crystallographic Data Centre, 12 Union Road, Cambridge CB2 1EZ, UK; fax: (+44) 1223-336-033; or e-mail: deposit@ccdc.cam.ac.uk.

Acknowledgements

This work was supported by a Grant-in-Aid for Young Scientists from the Ministry of Education, Culture, Science, Sports, and Technology, Japan, as well as the Mitsubishi Chemical Corporation Fund.

References

[1] (a) S. Ohkoshi, K. Arai, Y. Sato, K. Hashimoto, Nat. Mater. 3 (2004) 857;
(b) S. Ohkoshi, S. Yorozu, O. Sato, T. Iyoda, A. Fujushima, K. Hashimoto, Appl. Phys. Lett. 70 (1997) 1040;
(c) L. Egan, K. Kamenev, D. Papanikolaou, Y. Takabayashi, S. Margadonna, J. Am. Chem. Soc. 128 (2006) 6034.

[2] (a) O. Kahn, J. Larionova, J.V. Yakhmi, Chem. Eur. J. 5 (1999) 3443;
(b) D. Maspoch, D. Ruiz-Molina, K. Wurst, N. Domingo, M. Cavallini, F. Biscarini, J. Tejada, C. Rovira, J. Veciana, Nat. Mater. 2 (2003) 190.

[3] (a) D. Thomas, F. Lionti, R. Ballou, D. Gatteschi, R. Sessoli, B. Barbara, Nature 383 (1996) 145;
(b) D. Gatteschi, R. Sessoli, Angew. Chem., Int. Ed. 42 (2003) 268;
(c) W. Wernsdorfer, R. Sessoli, Science 284 (1999) 133;
(d) S.M.J. Aubin, Z. Sun, L. Pardi, J. Krzystek, K. Folting, L.-C. Brunel, A.L. Rheingold, G. Christou, D.N. Hendrickson, Inorg. Chem. 38 (1999) 5329.

[4] (a) A. Caneschi, D. Gatteschi, N. Lalioti, C. Sangregorio, R. Sessoli, G. Venture, A. Vindigni, A. Rettori, M.G. Pini, M.A. Novak, Angew. Chem., Int. Ed. 40 (2001) 1760;
(b) R. Clérac, H. Miyasaka, M. Yamashita, C. Coulon, J. Am. Chem. Soc. 124 (2002) 12837;
(c) R. Lescouëzec, J. Vaissermann, C. Ruiz-Pérez, F. Lloret, R. Carrasco, M. Julve, M. Verdaguer, Y. Dromzee, D. Gatteschi, W. Wernsdorfer, Angew. Chem., Int. Ed. 42 (2003) 1483;
(d) T.-F. Liu, D. Fu, S. Gao, Y.-Z. Zhang, H.-L. Sun, G. Su, Y.-J. Liu, J. Am. Chem. Soc. 125 (2003) 13976.

[5] T. Kajiwara, M. Nakano, Y. Kaneko, S. Takaishi, T. Ito, M. Yamashita, A. Igashira-Kamiyama, H. Nojiri, Y. Ono, N. Kojima, J. Am. Chem. Soc. 127 (2005) 10150.

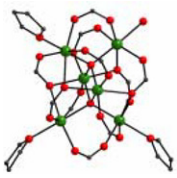
[6] A. Kamiyama, T. Noguchi, T. Kajiwara, T. Ito, Inorg. Chem. 41 (2002) 507.

[7] The Rietvelt method was performed using RIETAN-2000 F. Izumi, T. Ikeda, Mater. Sci. Forum 198 (2000) 321.

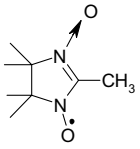
[8] (a) K.S. Cole, R.H. Cole, J. Chem. Phys. 9 (1941) 341;
(b) C.J.F. Boettcher, Theory of Electric Polarization, Elsevier, Amsterdam, 1952;
(c) S.M. Aubin, Z. Sun, L. Pardi, J. Krzysteck, K. Folting, L.-J. Brunel, A.L. Rheingold, G. Christou, D.N. Hendrickson, Inorg. Chem. 38 (1999) 5329.

1. Introduction

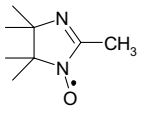
Reactions of polynuclear pivalates of paramagnetic metal ions with nitroxides are capable of triggering self-assembly of highly dimensional magnetic heterospin structures [1]. High solubility of the polynuclear pivalate in low-polar organic solvents is an important factor that favors effective interaction of this compound with organic paramagnets. The symmetric structure of the nitronyl nitroxide molecule, in turn, favors bridging coordination of the latter (formation of polymer structures), although co-existence of bulky substituents "on the periphery" of the polynuclear molecule and in the structure of the organic paramagnet does not always favor spatial complementarity of reactant molecules [2].



$[Co_6(O)_2Piv_{10}Thf_3H_2O]$



NIT-Me



Im-Me

Recently, it was demonstrated that the $[Mn_6(O)_2Piv_{10}Thf_4]$ hexanuclear matrix (Piv is trimethylacetate and Thf is tetrahydrofuran) shows high efficiency in reactions with nitronyl nitroxides containing alkyl or heterocyclic substituents in the side chain, leading to heterospin compounds [1–3], including compounds capable of cooperative magnetic ordering. Therefore, it was interesting to investigate $[Co_6(O)_2Piv_{10}Thf_3H_2O]$, whose molecular structure is similar to that of the hexanuclear Mn pivalate. For the starting nitronyl nitroxide we chose 2,4,4,5,5-pentamethyl-4,5-dihydro-1*H*-imidazole-3-oxide-1-oxyl (NIT-Me), which does not create steric hindrances to highly dimensional structures formed in the reaction with the hexanuclear Mn pivalate [1–3]. All this gave us reason to hope that the reaction of $[Co_6(O)_2Piv_{10}Thf_3H_2O]$ with NIT-Me would also provide a convenient route to new heterospin systems with a $\{Co_6(O)_2Piv_{10}\}$ cluster nucleus and coordinated NIT-Me molecules. As in the case of $[Mn_6(O)_2Piv_{10}Thf_4]$, the interaction of $[Co_6(O)_2Piv_{10}Thf_3H_2O]$ with NIT-Me was expected to lead to substitution of the monodentate Thf molecules and probably to replacement of the water molecule by nitroxide. Our study, however, revealed that the reaction of $[Co_6(O)_2Piv_{10}Thf_3H_2O]$ with NIT-Me and/or 2,4,4,5,5-pentamethyl-4,5-dihydro-1*H*-imidazole-1-oxyl (Im-Me) occurs with simultaneous transformation of both the polymetallic nucleus and nitroxides. This conclusion was made from X-ray crystallographic analysis of the reaction products isolated as single crystals. This paper describes the procedures that gave single crystal products of the interaction of $[Co_6(O)_2Piv_{10}Thf_3H_2O]$ with NIT-Me and/or Im-Me and reports structural data for the complex products.

2. Experimental

2.1. Synthesis

All solvents were commercially available and used as received. 2,4,4,5,5-Pentamethyl-4,5-dihydro-1*H*-imidazole-3-oxide-1-oxyl (NIT-Me) and 2,4,4,5,5-pentamethyl-4,5-dihydro-1*H*-imidazole-1-oxyl (Im-Me) nitroxides were prepared according to the literature [4–6]. To synthesize $[Co_6(O)_2Piv_{10}Thf_3H_2O]\cdot 1.5Thf$ according to the known procedure [7] for the starting compound we used the $[Co(OH)_x(OOCCMe_3)_{2-x}]_n$ polymer obtained by the known procedure [8], as well as purified [9] Thf, which was then intentionally kept exposed to light and air for a month in order to generate organic peroxides for mild oxidation of Co^{II} into Co^{III} (Thf was not used in syntheses of heterospin complexes with nitroxides).

2.1.1. $[Co_9Piv_{12}(OH)_2L^1_2]\cdot n0.5C_7H_{16}$ $(n = 0.5, 1, 2)$

NIT-Me (0.06 g, 0.35 mmol) dissolved in a mixture of heptane (1 ml) and CH_2Cl_2 (1 ml) was added at room temperature to a solution of $[Co_6(O)_2Piv_{10}Thf_3H_2O]\cdot 1.5Thf$ (0.15 g, 0.089 mmol) in a mixture of heptane (2 ml) and CH_2Cl_2 (1 ml). The resulting reaction mixture was passed through a paper filter, and heptane (5 ml) was then added through the filter. After 24 h, fine dark red crystals of the complex formed in the filtrate, and after another six or seven days the crystals were filtered off and washed with MeCN. The crystal surface generally contained a minor blue gel impurity, which was separated mechanically. The yield of $[Co_9Piv_{12}(OH)_2L^1_2]\cdot 0.5C_7H_{16}$ was 0.006 g (2–3%). *Anal.* Calc. for $Co_{18}C_{159}H_{288}N_8O_{68}$: C, 43.8; H, 6.5; N, 2.5. Found: C, 42.7; H, 6.9; N, 2.5%. Single crystals of the same complex more highly saturated with heptane solvate molecules ($[Co_9Piv_{12}(OH)_2L^1_2]\cdot C_7H_{16}$ and $[Co_9Piv_{12}(OH)_2L^1_2]\cdot 2C_7H_{16}$) are formed when synthesis is carried out in heptane (without a CH_2Cl_2 addition). Since the starting polynuclear Co compound has better solubility in a heptane/CH_2Cl_2 mixture than in pure heptane, more heptane is needed for the same initial amounts of reagents. A typical procedure for the preparation of $[Co_9Piv_{12}(OH)_2L^1_2]\cdot C_7H_{16}$ and $[Co_9Piv_{12}(OH)_2L^1_2]\cdot 2C_7H_{16}$ is given below. To a solution of $[Co_6(O)_2Piv_{10}Thf_3H_2O]\cdot 1.5Thf$ (0.15 g, 0.089 mmol) in heptane (5 ml) was added NIT-Me (0.06 g, 0.35 mmol) in heptane (10 ml). The resulting dark claret red solution was filtered through a paper filter, and another portion of heptane (5 ml) was then added to the reaction mixture through this filter. The reaction mixture was kept for three or four days in an open flask. The solvent gradually evaporated, and a thin layer of blue gel settled at the bottom of the flask. Fine dark red crystals of $[Co_9Piv_{12}(OH)_2L^1_2]\cdot C_7H_{16}$ and $[Co_9Piv_{12}(OH)_2L^1_2]\cdot 2C_7H_{16}$ suitable for an X-ray analysis formed under the gel layer; they were filtered off together with gel and then separated from gel mechanically. The total mass of the crystals was up to 5–6 mg. A similar process of crystal growth from gel is described elsewhere [10].

2.1.2. $[Co_8Piv_8(OH)_6(HPiv)_4(H_2O)_2L^4_2]$

A solution of iminonitroxide Im-Me (0.018 g, 0.12 mmol) in heptane (3 ml) and a solution of nitronylnitroxide NIT-Me (0.02 g, 0.12 mmol) in heptane (3–4 ml) were added to the solution of $[Co_6(O)_2Piv_{10}Thf_3H_2O]\cdot 1.5Thf$ (0.1 g, 0.059 mmol) in heptane (3 ml). The resulting claret red mixture was filtered, and the filtrate was diluted with heptane (5–6 ml) and kept in an open flask at room temperature. Dark red crystals formed in three or four days; after another three or four days they were filtered off, washed with cooled heptane, and separated mechanically from the minor gel impurity. The mass of the crystals formed was up to 0.007 g. *Anal.* Calc. for $Co_8C_{92}H_{174}N_8O_{42}$: H, 6.9; N, 4.4. Found: H, 6.8; N, 4.3%.

2.1.3. $L^6[Co_6(O)_4Piv_9(H_2O)_2]\cdot 2HPiv$, $[Co_6Piv_8(HPiv)_2L^5_2]\cdot nC_6H_6$ $(n = 0, 1)$, $[Co_6Piv_8(HPiv)_2L^5_2][Co_{10}Piv_{14}(HPiv)_2L^2_2L^3_2]\cdot C_7H_{16}$, and $[Co_{10}Piv_{14}(HPiv)_2L^2_2L^3_2]\cdot C_6H_{14}$

Im-Me (0.038 g, 0.238 mmol) in hexane (or heptane) (2–3 ml) was added to the solution of $[Co_6(O)_2Piv_{10}Thf_3H_2O]\cdot 1.5Thf$ (0.1 g, 0.059 mmol) in hexane (or heptane) (2 ml) and CH_2Cl_2 (1 ml). The resulting brown solution was filtered and another (8 ml) portion of hexane was added through the same filter. After two or three days, dark green crystals formed in the solution; they were separated by decanting and recrystallized from CH_3CN. $L^6[Co_6(O)_4Piv_9(H_2O)_2]\cdot 2HPiv$ crystals suitable for an X-ray analysis formed. Yield 0.018 g (10%). *Anal.* Calc. for $Co_6C_{63}H_{122}N_2O_{28}$: C, 44.3; H, 7.2; N, 1.6. Found: C, 44.4; H, 7.2; N, 1.7%. Storage of the mother solution obtained by decanting for another two days led to red crystals of $[Co_6Piv_8(HPiv)_2L^5_2]$. *Anal.* Calc. for $Co_6C_{82}H_{144}N_8O_{30}$: C, 47.5; H, 7.0; N, 5.4. Found: C, 48.0; H, 7.6; N, 5.1%. In some experiments, brown crystals of $[Co_6Piv_8(HPiv)_2L^5_2][Co_{10}Piv_{14}(HPiv)_2L^2_2L^3_2]\cdot C_7H_{16}$ were isolated in small amounts along with the crystals of the given complex. *Anal.* Calc. for $Co_{16}C_{201}H_{358}N_{16}O_{72}$: C, 47.4; H, 7.1; N, 4.4. Found: C, 47.1; H, 7.2; N, 4.2%. Also, thin pale green platelets with a composition $[Co_{10}Piv_{14}(HPiv)_2L^2_2L^3_2]\cdot C_6H_{14}$ (XRD data) were occasionally found among the crystalline products. The total mass of the crystals isolated in different experiments was up to 5 mg. For an X-ray investigation, the single crystals of the compounds were selected mechanically. When benzene was used as a solvent, only $[Co_6Piv_8(HPiv)_2L^5_2]\cdot C_6H_6$ solvate crystals formed in very small amounts; their structure and composition were determined by X-ray diffraction analysis. Further analysis for $[Co_{10}Piv_{14}(HPiv)_2L^2_2L^3_2]\cdot C_6H_{14}$ and $[Co_6Piv_8(HPiv)_2L^5_2]\cdot C_6H_6$ was not possible because of the low yields of these compounds.

2.2. X-ray crystallography and magnetic measurements

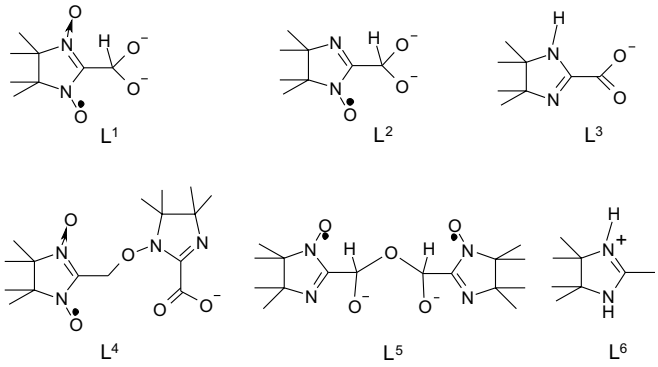
For all compounds, data were collected on a Smart Apex diffractometer (λMo Kα, graphite monochromator). The structures were solved by direct methods and refined by full-matrix least-squares (SHELX97 program complex). Some of the hydrogen atoms were localized in a difference electron density map; the remaining hydrogen atoms were placed geometrically and refined as a rigid group. Crystal data for the complexes and selected bond lengths and angles in the structures are listed in Tables 1 and 2.

Magnetic measurements for the polycrystalline samples were carried out on an MPMS-5 s Quantum Design SQUID magnetometer in the temperature range from 2 to 300 K and in magnetic fields of up to 4.5 O. The paramagnetic components of magnetic susceptibility χ were determined with allowance for the diamagnetic contribution estimated from Pascal's constants. The effective magnetic moment was calculated by the formula $\mu_{\text{eff}} = (\frac{3k}{N_A\beta^2}\cdot\chi T)^{1/2} \approx (8\chi T)^{1/2}$, where N_A is the Avogadro number, β is the Bohr magneton, and k is Boltzmann's constant.

3. Results and discussion

3.1. Synthesis of compounds

Investigation of the products of interaction of $[Co_6(O)_2Piv_{10}Thf_3H_2O]\cdot 1.5Thf$ with NIT-Me and/or Im-Me showed that the ensuing redox processes transform both the $\{Co_6(O)_2Piv_{10}\}$ polymetallic matrix and the starting nitroxide. In nitroxide molecules, the methyl substituent in the 2nd position of the 2-imidazoline ring is oxidized, leading to complexes with ligands L^1-L^5 shown below.



Special attention should be paid to the spin-labeled anions L^1, L^2, L^4, and L^5 fixed in the polynuclear matrix. Simple salts and organic derivatives of these anions are unknown, and it is now difficult to suggest pure organic approaches to their synthesis. The starting nitroxide molecule is transformed on the coordinating polymetallic matrix; for L^4 and L^5, this transformation is a variety of template synthesis. In this case, the polymetallic matrix serves for fixation and kinetic stabilization of the resulting organic substrate molecules.

Oxidation of NIT-Me and/or Im-Me is accompanied by reduction of Co^{III} to Co^{II} and transformation of the polymetallic matrix. It seems that Co^{III} plays an important role

Table 1
Crystallographic data and selected bond lengths (Å) for $[Co_6Piv_8L_2^5(HPiv)_2]$, $[Co_6Piv_8(HPiv)_2L_2^5] \cdot C_6H_6$, $[Co_{10}Piv_{14}(HPiv)_2L_2^2L_2^3] \cdot C_6H_{14}$, and $[Co_6Piv_8(HPiv)_2L_2^5][Co_{10}Piv_{14}(HPiv)_2L_2^2L_2^3] \cdot C_7H_{16}$

Compound	$[Co_6Piv_8(HPiv)_2L_2^5]$	$[Co_6Piv_8(HPiv)_2L_2^5]\cdot C_6H_6$,	$[Co_{10}Piv_{14}(HPiv)_2L_2^2L_2^3]\cdot C_6H_{14}$	$[Co_6Piv_8(HPiv)_2L_2^5][Co_{10}Piv_{14}(HPiv)_2L_2^2L_2^3] \cdot C_7H_{16}$
Formula	$C_{82}H_{144}Co_6N_8O_{30}$	$C_{88}H_{150}Co_6N_8O_{30}$	$C_{124}H_{226}Co_{10}N_8O_{42}$	$C_{208}H_{374}Co_{16}N_{16}O_{72}$
F_w	2075.63	2153.74	3090.43	5194.12
T (K)	295	295	295	295
Sp. gr., Z	$P\bar{1}$, 1	$P\bar{1}$, 1	$P\bar{1}$, 1	$P2_1/c$, 2
a (Å)	14.026(5)	13.9027(15)	14.1298(9)	13.9938(13)
b (Å)	14.321(5)	15.4360(16)	15.3960(11)	26.966(3)
c (Å)	15.287(6)	15.9063(17)	20.9470(14)	35.465(3)
α (°)	88.461(7)	81.670(2)	75.733(2)	
β (°)	69.887(6)	64.834(2)	78.106(2)	92.306(2)
γ (°)	66.290(6)	63.255(2)	65.033(2)	
V (Å^3)	2617.8(17)	2754.4(5)	3976.5(5)	13372(2)
D_{calc} (g/cm^3)	1.317	1.298	1.291	1.290
μ (mm^{-1})	1.002	0.955	1.086	1.039
Total/uniq/Number of reflections	30524/13221/647	20666/7958/671	17465/11390/924	103075/19274/1596
R_{int}	0.1240	0.0815	0.1367	0.0964
θ_{max} (°)	1.70–29.60	1.80–23.35	1.70–23.29	1.62–23.33
Goodness-of-fit	0.868	0.930	0.967	0.898
$R1$ ($I > 2\sigma_I$)	0.0719	0.0546	0.0984	0.0627
wR_2	0.1608	0.1113	0.1906	0.1685
R_1	0.1456	0.0871	0.2268	0.0986
wR_2	0.1881	0.1205	0.2684	0.1888
Co···Co	2.963–3.624	2.979–3.336	3.030–3.637	2.984–3.690
Co–O_L	2.112(3)–2.193(3)	2.114(3)–2.192(3)	2.069(8)–2.188(10)	2.059(4)–2.316(3)
Co–N_L	2.098(4)–2.126(4)	2.128(4)–2.087(4)	2.087(11)–2.056(14)	2.070(6)–2.111(5)
N–O	1.312(9)–1.317(6)	1.343(6)–1.279(7)	1.243(13)	1.320(9) 1.288(11)–1.277(6)

Table 2
Crystallographic data and selected bond lengths (Å) for $[Co_8Piv_8(OH)_6(HPiv)_4(H_2O)_2L^4_2]$, $[Co_9Piv_{12}(OH)_2L^1_2]\cdot 0.5C_7H_{16}$, $[Co_9Piv_{12}(OH)_2L^1_2]\cdot C_7H_{16}$, $[Co_9Piv_{12}(OH)_2L^1_2]\cdot 2C_7H_{16}$, and $L^6[Co_6(O)_4Piv_9(H_2O)_2]\cdot 2HPiv$

Compound	$[Co_8Piv_8(OH)_6(HPiv)_4(H_2O)_2L^4_2]$	$[Co_9Piv_{12}(OH)_2L^1_2]\cdot 0.5C_7H_{16}$	$[Co_9Piv_{12}(OH)_2L^1_2]\cdot C_7H_{16}$	$[Co_9Piv_{12}(OH)_2L^1_2]\cdot 2C_7H_{16}$	$L^6[Co_6(O)_4Piv_9\ (H_2O)_2]\cdot 2HPiv$
Formula	$C_{92}H_{174}Co_8N_8O_{42}$	$C_{79.\ 50}H_{144}Co_9N_4O_{34}$	$C_{83}H_{152}Co_9N_4O_{34}$	$C_{90}H_{168}Co_9N_4O_{34}$	$C_{63}H_{122}Co_6N_2O_{28}$
F_w	2535.83	2230.36	2280.46	2380.65	1709.21
T (K)	298	298	100	200	293
Sp. gr., Z	$P\bar{1}$, 1	$C2/c$, 4	$P2_1/c$, 8	$P\bar{1}$, 1	$P2_1/n$, 4
a (Å)	14.745(2)	30.866(4)	41.759(10)	14.662(3)	16.208(2)
b (Å)	16.029(2)	17.029(2)	16.982(4)	15.474(3)	20.649(3)
c (Å)	16.198(2)	22.369(3)	31.187(7)	15.951(3)	27.548(3)
α (°)	67.922(3)			61.355(3)	
β (°)	63.958(2)	110.169(3)	108.514(4)	64.514(3)	90.380(2)
Γ (°)	82.901(3)			65.571(3)	
V (Å^3)	3183.7(6)	11 036(3)	20 972(8)	2767.1(9)	9219(2)
D_{calc} (g/cm^3)	1.323	1.342	1.445	1.429	1.231
μ (mm^{-1})	1.092	1.387	1.462	1.388	1.120
Total/uniq/ number of reflections	13 867/9065/769	23 049/7938/657	89 786/30 204/2610	11 523/7785/691	54 112/13 225/1039
R_{int}	0.0956	0.0350	0.1047	0.0392	0.1377
θ_{max} (°)	2.11–23.31	1.94–23.40	1.38–23.31	1.91–23.29	1.46–23.25
Goodness-of-fit	0.970	1.053	0.845	1.047	0.683
$R1$ ($I > 2\sigma_I$)	0.0865	0.0421	0.0505	0.0646	0.0544
wR_2	0.1469	0.1122	0.1283	0.1757	0.1249
R_1	0.1707	0.0577	0.0768	0.0945	0.1246
wR_2	0.1785	0.1202	0.1475	0.2178	0.1594
Co···Co	3.097–3.446	3.016–3.427	2.986–3.417	2.993–3.356	2.704–2.867
Co–O_L	2.100(6)–2.228(6)	1.994(2)–2.043(3)	1.990(3)–2.100(4)	1.988(5)–2.090(6)	
Co–N_L	2.067(9)				
N–O	1.269(11)–1.309(12)	1.292(4)–1.289(4)	1.285(5)–1.298(5)	1.262(8)–1.291(8)	

in these processes. It is not ruled out that the presence of Co^{III} is just responsible for the oxidation of the organic substrate. This is supported by the fact that oxidation of an organic substrate was not previously recorded in reactions of NIT-R (including NIT-Me) with $[Mn^{III}_2Mn^{II}_4(O)_2Piv_{10}Thf_4]$. The $[Mn^{III}_2Mn^{II}_4(O)_2Piv_{10}Thf_4]$ polymetallic nucleus always remained unchanged [1–3].

The reactions leading to L^1–L^6 are essentially multistep transformations accompanied not only by the rearrangement of the starting hexanuclear framework, but also, in many cases, by a change in the nuclearity of the polymetallic fragment. Therefore at the initial stage, it was difficult to suggest a reasonable scheme for the transformation of nitroxide molecules, especially because these processes can form by-products. Moreover, investigation was complicated by the fact that the starting components and reaction products have high solubility in organic solvents [10] so that single crystals had to be grown from small volumes of rather concentrated solutions. Fast removal of the minor residue of the solvent from the reaction system had to be avoided because it ended in the formation of a lacquer film. Growth of single crystals of the complexes was also hindered by the fact that concentration of the reaction mixture led to the formation of an amorphous gel. Moreover, some compounds ($[Co_{10}Piv_{14}(HPiv)_2L^2_2L^3_2]\cdot C_6H_{14}$ and $[Co_6Piv_8(HPiv)_2L^5_2]\cdot C_6H_6$) could only be obtained as unit crystals. Further analysis, therefore, was not possible because of the small yields of these compounds; according to Christou [11], this is a frequent occurrence in studies on compounds of this type. Nevertheless, structural analysis of all isolated single crystals convinced us that interaction of $[Co_6(O)_2Piv_{10}Thf_3H_2O]\cdot 1.5Thf$ with NIT-Me and/or Im-Me leads to simultaneous transformation of both the polymetallic nucleus and the nitroxides.

All synthetic procedures given in Section 2 are well reproducible, despite the low yields of the products. The compounds were obtained as single crystals mostly suitable for an X-ray crystal structure analysis. The quality of the crystals was higher if they were separated as early as possible after they appeared in solution. Naturally, the product yield was extremely low in this situation. Numerous attempts were made to raise the yield. As mentioned above, these complexes, which are well soluble in organic solvents, had to be grown from very small volumes of solutions. Attempts to raise the yield led to the formation of large amounts of increasingly small crystals of the complex, from which we had to separate larger crystals for X-ray analysis. Moreover, when the volume of the solution became very small, dark blue gel formed at the bottom of the flask. The gel not only covered the single crystals and retarded their growth, but also provoked complex formation in the form of numerous fine crystals. The composition of the gel was not determined because it quickly dried into finely disperse powder after the mother solution was separated. No compounds other than the complexes described in the present work and amorphous gel have been recorded.

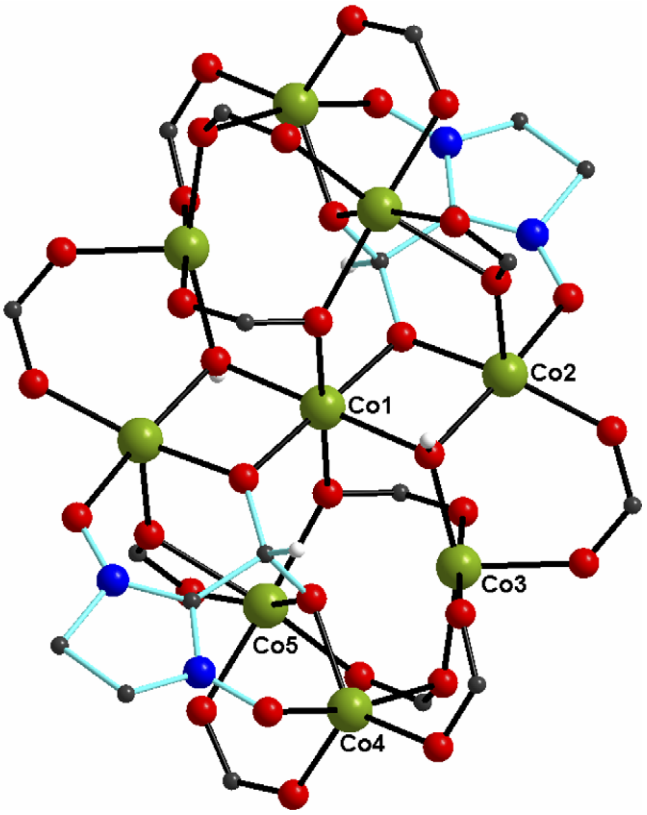


Fig. 1. Nonanuclear molecule $Co_9Piv_{12}(OH)_2L^1_2$. The $(CH_3)_3C$ groups of pivalates and the CH_3 groups of the 2-imidazoline cycles are omitted for clarity. (Co: green ball; O: red ball; N: navy ball; C: small black ball; H: small white ball. Blue bonds highlight the atom connectivity in L^1).

3.2. Structural data

Interaction of $[Co_6(O)_2Piv_{10}Thf_3H_2O]\cdot 1.5Thf$ with thoroughly purified NIT-Me always led to the formation of $[Co_9Piv_{12}(OH)_2L^1_2]\cdot nC_7H_{16}$ crystals, where $n = 0.5$, 1, or 2. The number of solvate molecules in $[Co_9Piv_{12}(OH)_2L^1_2]\cdot nC_7H_{16}$ depends on synthetic conditions, although the $[Co_9Piv_{12}(OH)_2L^1_2]$ hexanuclear molecules proper (Fig. 1) are identical in all solvates. The $Co_9Piv_{12}(OH)_2L^1_2$ molecule is centrosymmetric relative to the Co1 atom. The polyhedron is a distorted octahedron for Co1 and Co5, square pyramid for Co2, and elongated distorted trigonal bipyramid for Co3 and Co4. The O atom of the OH group links three Co atoms (Co1, Co2, and Co3; d_{Co-O} 2.040(5), 1.991(5), and 2.048(5) Å). The sum of the CoOCo angles in this unit is ~315°, indicating that the bridging O atom of the OH group lies inside the Co1Co2Co3H pyramid.

In the NO groups of L^1, the distances are virtually identical: 1.289(4) and 1.292(4) Å. In the $C2—C\begin{smallmatrix}H\\<\\O\end{smallmatrix}$ fragment, where C2 is the C atom in the 2nd position of the imidazoline ring, the C–O bond lengths are 1.361(4) and 1.406(5) Å. The C2–C–O angles are 111.1(3) and 111.3(3)°. These parameters confirm that the structure has a methanediolate substituent in the 2nd position of the imidazoline ring. As

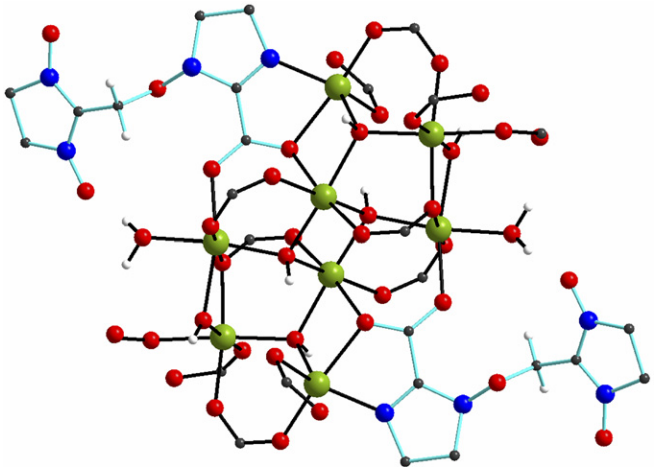
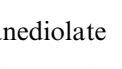


Fig. 2. Octanuclear molecule $[Co_8Piv_8(OH)_6(HPiv)_4(H_2O)_2L^4_2]$. The $(CH_3)_3C$ groups of pivalates and the CH_3 groups of the 2-imidazoline cycles are omitted for clarity. (Co: green ball; O: red ball; N: navy ball; C: small black ball; H: white ball. Blue bonds highlight the atom connectivity in L^4).

shown in Fig. 1, all four O atoms of the bridging L^1 ligand are coordinated to the Co1, Co2, Co4, and Co5 atoms. In this case, L^1 is a hexadentate ligand because one of the O atoms of the deprotonated methanediolate fragment is a bridge between Co1 and Co2 (d_{Co-O} 1.994(2) and 2.001(3) Å), and another O atom links Co4 and Co5 (d_{Co-O} = 1.999(2) and 2.043(3) Å). The NO groups are coordinated by the Co4 and Co2 atoms (d_{Co-O} = 2.085(3) and 2.117(3), respectively), forming two six-membered metallocycles involving the Co2 and Co4 atoms.

The reaction of $[Co_6(O)_2Piv_{10}Thf_3H_2O]\cdot 1.5Thf$ with a specially prepared mixture of NIT-Me and Im-Me led to crystals of the octanuclear $[Co_8Piv_8(OH)_6(HPiv)_4(H_2O)_2L^4_2]$ complex containing a spin-labeled anion L^4 (the product of complex transformation of NIT-Me and Im-Me on the polynuclear matrix). The $[Co_8Piv_8(OH)_6(HPiv)_4(H_2O)_2L^4_2]$ molecule is centrosymmetric (Fig. 2). All Co atoms bonded to only O atoms have a distorted octahedral environment. Two Co atoms bonded to the imine N atom of the imidazoline ring are surrounded by a distorted trigonal bipyramid. The Co–O and Co–N distances are in the range 2.003(7)–2.231(11) Å.

All atoms of the conjugated O˙–N–C=N → O nitronyl nitroxide fragment of the coordinated L^4 ligand lie in one plane, which is typical for nitronyl nitroxides. The distances in the NO groups are 1.266(11) and 1.312(12) Å. In the alkoxy imine fragment between the nitronyl nitroxide fragment and the coordinated 2-carboxy derivative of 2-imidazoline, the N–O bond length is much larger, 1.423(8) Å. In contrast to the atoms of the above-discussed methanediolate fragment L^1, in the  fragment (CO_2 is a carboxylate fragment and C2 is the C atom in the 2nd position of the coordinated imidazoline ring) all atoms lie in one plane. In the carboxylate fragment of L^4 (1.251(11) and 1.262(10) Å), the C–O distances are much shorter than the C–O distances in the methanediolate fragment L^1 (1.361(4) and 1.406(5) Å). The coordinated L^4 molecules generally perform the bridging tridentate function. One of the O atoms, together with the imine N atom of the 2-imidazoline heterocycle, forms a five-membered chelate ring. In the $[Co_8Piv_8(OH)_6(HPiv)_4(H_2O)_2L^4_2]$ molecule, the central $\{Co_4O_2\}$ fragment (Fig. 3a) is identical in structure to the same fragment analyzed in detail by Winpenny [10], who constructed integral topology of polynuclear frameworks for the cobalt-pivalate system.

Investigation of the single crystals resulting from the reaction of $[Co_6(O)_2Piv_{10}Thf_3H_2O]\cdot 1.5Thf$ with Im-Me revealed the following. The reaction primarily formed dark green crystals of $L^6[Co_6(O)_4Piv_9(H_2O)_2]\cdot 2HPiv$. In this compound, the $[Co_6(O)_4Piv_9(H_2O)_2]^-$ anion has exactly the same structure as in the previously described compound $[(C_4H_9)_4N][Co_6(O)_4Piv_9(H_2O)_2]$ [10], also dark green in color. This anion has a $[Co^{III}_4O_4]$ heterocubane fragment bonded to two terminal Co^{II} ions [10] in the $\{Co_6O_4\}$ hexanuclear unit (Fig. 3b). The role of the cation is performed by L^6, which is protonated 2,4,4,5,5-pentamethyl-4,5-dihydro-1*H*-imidazole (Fig. 3c).

The L^6 cation is not likely to be the product of Im-Me transformation; rather, this is a minor admixture of 2,4,4,5,5-pentamethyl-4,5-dihydro-1*H*-imidazole, which was present from the start. This is indicated by well-known data of classical studies [5,6], stating that Im-Me is very difficult to be isolated as an individual compound. Moreover, because of its ion associate nature and hence low solubility in organic solvents, $L^6[Co_6(O)_4Piv_9(H_2O)_2]\cdot 2HPiv$ is always the first compound to be isolated as a solid after consolidation of the solutions of $[Co_6(O)_2Piv_{10}Thf_3H_2O]\cdot 1.5Thf$ and Im-Me. After $L^6[Co_6(O)_4Piv_9(H_2O)_2]\cdot 2HPiv$ crystals have been separated, new crystals of this

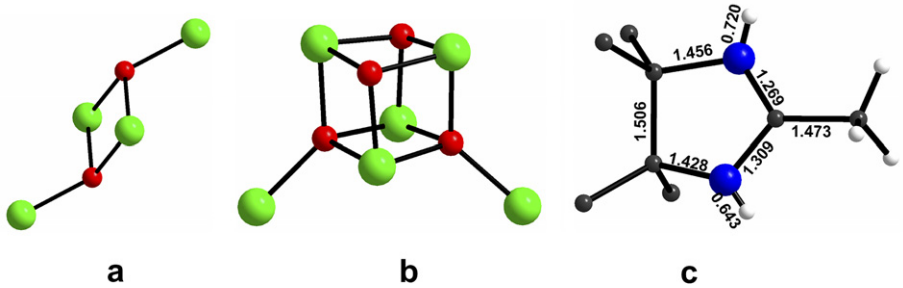


Fig. 3. Fragments of $[Co_8Piv_8(OH)_6(HPiv)_4(H_2O)_2L^4_2]$ and $L^6[Co_6(O)_4Piv_9(H_2O)_2]\cdot 2HPiv$: $\{Co_4O_2\}$ (a); $\{Co_6O_4\}$ (b), and L^6 cation (c).

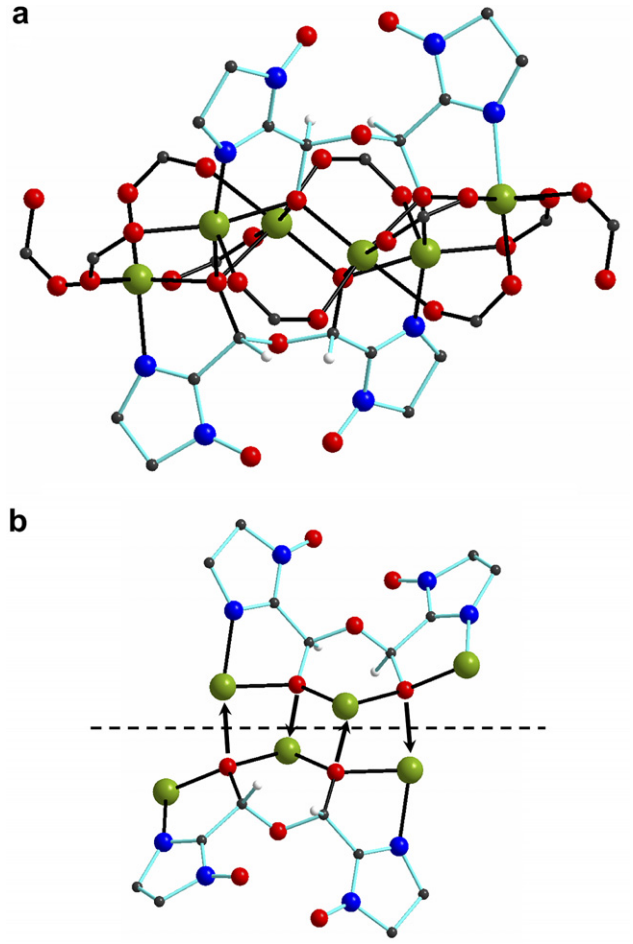


Fig. 4. Hexanuclear molecule $[Co_6Piv_8(HPiv)_2L^5_2]$ (a). Fragment of the molecule containing L^5s and Co atoms (b). The $(CH_3)_3C$ groups of pivalates and the CH_3 groups of the 2-imidazoline cycles are omitted for clarity. (Co: green ball; O: red ball; N: navy ball; C: small black ball; H: white ball. Blue bonds highlight the atom connectivity in L^5).

compound are no longer formed in the mother solution even when stored for arbitrarily prolonged periods of time.

After $L^6[Co_6(O)_4Piv_9(H_2O)_2]\cdot 2HPiv$ crystals have been separated, further storage of the mother solution leads to crystallization of $[Co_6Piv_8(HPiv)_2L^5_2]$ (sometimes with a minor admixture of $[Co_6Piv_8(HPiv)_2L^5_2][Co_{10}Piv_{14}(HPiv)_2L^2_2L^3_2]\cdot C_7H_{16}$ crystals and, more rarely, with a still smaller admixture of $[Co_{10}Piv_{14}(HPiv)_2L^2_2L^3_2]\cdot C_6H_{14}$ crystals). Structure analysis indicated that these are structurally related compounds that form a single group of reaction products.

Fig. 4a shows the structure of the centrosymmetric hexanuclear molecule of $[Co_6Piv_8(HPiv)_2L^5_2]$. The structure is quite simple – it does not contain any bridging OH groups, and all cobalt atoms are bonded to the L^5 paramagnetic ligand, which is the major distinction of the compound. L^5 is formally the product of condensation of two imino nitroxides with a methanediolate substituent in the 2nd position of the imidazoline ring. It is certainly formed on the polynuclear matrix because pure organic approaches to synthesis of such compounds are unknown. In Fig. 4b, all Piv and HPiv are discarded, and the remaining fragment is conventionally halved by a dashed line; it can be seen that each L^5 forms three metallocycles with three Co atoms of the isolated half. Furthermore, each of the oxygen donor bridging atoms is coordinated to the Co atom from the other half of the polynuclear fragment (these bonds are indicated by alternant arrows). As a result, L^5 serves as a bridging octadentate ligand because each of the bridging O atoms is coordinated to three different Co atoms. Also note that the geometrical characteristics of the complex molecule in the structure of the $[Co_6Piv_8(HPiv)_2L^5_2]\cdot C_6H_6$ solvate obtained from benzene are nearly identical to those in $[Co_6Piv_8(HPiv)_2L^5_2]$.

Let us consider the structure of the $[Co_{10}Piv_{14}(HPiv)_2L^2_2L^3_2]$ polynuclear molecule (Fig. 5a) in the isolated $[Co_{10}Piv_{14}(HPiv)_2L^2_2L^3_2]\cdot C_6H_{14}$ solvate. Like $[Co_6Piv_8(HPiv)_2L^5_2]$, this molecule does not contain any bridging OH groups, and all cobalt atoms are bonded to L^2 and/or L^3, which together with Piv serve as bridges in the Co_{10} metal core. If the monodentate HPiv and bridging Piv ligands are removed (Fig. 5b), one can see that each bridging L^3 ligand is bonded to three Co atoms. With one of them L^3 forms a chelate ring. Each L^2 ligand is bonded to five Co atoms enclosed in a dashed ellipse in Fig. 5b. With two of these Co atoms L^2 forms chelate cycles.

All atoms of L^3 depicted in Fig. 5b lie in the same plane. The C–O bond lengths are 1.18(2) and 1.29(2) Å. This shows that L^3 is the 2-carboxy derivative of 4,5-dihydro-1*H*-imidazole. In the L^2 methanediolate fragment, the C–O bond lengths are much larger (1.35(1) and 1.39(1) Å), and the O atoms of the C2—C(H)(O)O fragment, where C2 is a C atom in the 2nd position of the imidazoline ring, are not coplanar with the C2 and C atoms of this fragment.

From synthetic viewpoint, it is important that the L^2 ligands fixed in the structure of $[Co_{10}Piv_{14}(HPiv)_2L^2_2L^3_2]$ are precursors of L^5 found in the structure of $[Co_6Piv_8(HPiv)_2L^5_2]$. L^5 is formally the product of condensation of two L^2. It is not surprising, therefore, that we succeeded in isolating only unit crystals of $[Co_{10}Piv_{14}(HPiv)_2L^2_2L^3_2]\cdot C_6H_{14}$. It is not ruled out that the decanuclear $[Co_{10}Piv_{14}(HPiv)_2L^2_2L^3_2]$ is constantly transformed into the hexanuclear $[Co_6Piv_8(HPiv)_2L^5_2]$, which is much easier to crystallize. Apart from being itself isolated as a solid, the $[Co_6Piv_8(HPiv)_2L^5_2]$ product brings out of solution some part of $[Co_{10}Piv_{14}(HPiv)_2L^2_2L^3_2]$ (see Section 2) in the form of a pair cluster of mixed nuclearity $[Co_6Piv_8(HPiv)_2L^5_2][Co_{10}Piv_{14}(HPiv)_2L^2_2L^3_2]\cdot C_7H_{16}$. The structure of the latter does not require special discussion because the structure of separate components of the $[Co_6Piv_8(HPiv)_2L^5_2][Co_{10}Piv_{14}(HPiv)_2L^2_2L^3_2]$ pair cluster coincides with the structure of $[Co_6Piv_8(HPiv)_2L^5_2]$ and $[Co_{10}Piv_{14}(HPiv)_2L^2_2L^3_2]$ examined in a separate study. Therefore, Fig. 6 shows only a fragment of the packing

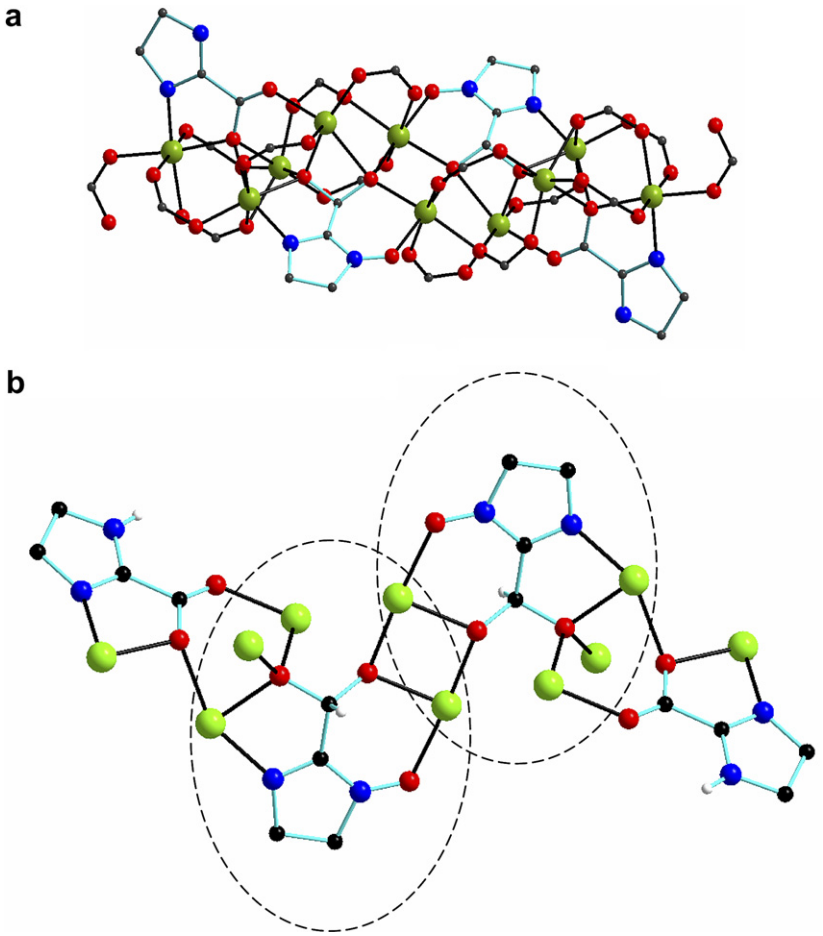


Fig. 5. Decanuclear molecule $[Co_{10}Piv_{14}(HPiv)_2L^2_2L^3_2]$ (a). Fragment of the molecule containing L^2s, L^3s, and Co atoms (b). The $(CH_3)_3C$ groups of pivalates and the CH_3 groups of the 2-imidazoline cycles are omitted for clarity. (Co: green ball; O: red ball; N: navy ball; C: small black ball; H: white ball. Blue bonds highlight the atom connectivity in L^2 and L^3).

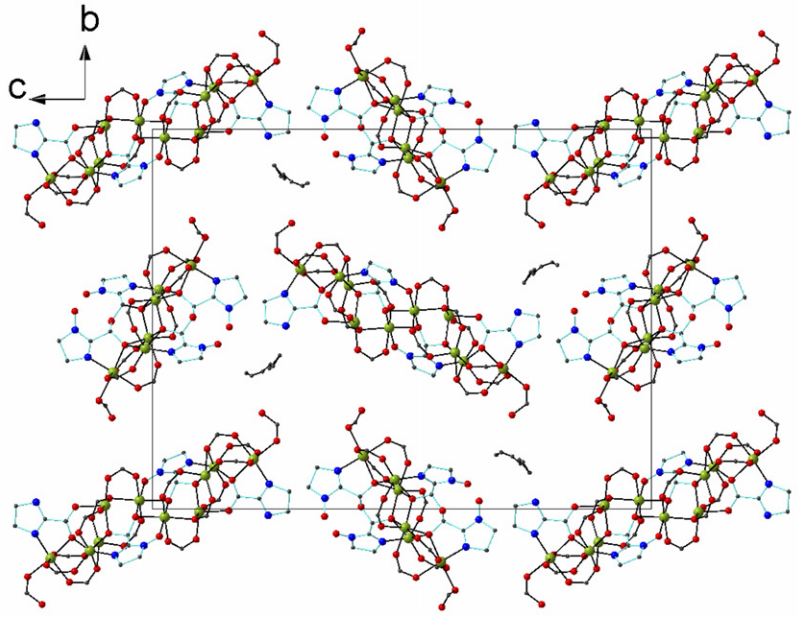


Fig. 6. Packing of clusters in $[Co_6Piv_8(HPiv)_2L^5_2][Co_{10}Piv_{14}(HPiv)_2L^2_2L^3_2] \cdot C_7H_{16}$.

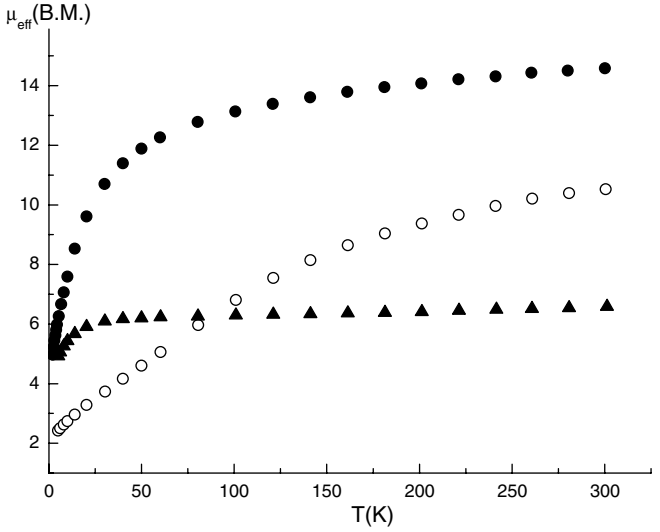


Fig. 7. Temperature dependences of μ_{eff} for $[Co_9Piv_{12}(OH)_2L^1_2]\cdot 0.5C_7H_{16}$ (●), $[Co_6Piv_8(HPiv)_2L^5_2]$ (○), and $L^6[Co_6(O)_4Piv_9(H_2O)_2]\cdot 2HPiv$ (▲).

of the $[Co_6Piv_8(HPiv)_2L^5_2][Co_{10}Piv_{14}(HPiv)_2L^2_2L^3_2]$ pair cluster.

Magnetic measurements did not reveal any specific effects for the compounds under study. No dependence of magnetic susceptibility on the magnetic field has been found over the whole range of measurements (2–300 K). Fig. 7 shows the experimental dependences $\mu_{eff}(T)$ for $[Co_9Piv_{12}(OH)_2L^1_2]\cdot 0.5C_7H_{16}$, $[Co_6Piv_8(HPiv)_2L^5_2]$, and $L^6[Co_6(O)_4Piv_9(H_2O)_2]\cdot 2$ HPiv. All of them belong to the same type of dependence. At reduced temperatures, μ_{eff} decreases, suggesting that antiferromagnetic exchange interactions dominate inside the polynuclear clusters. At 300 K, μ_{eff} is 14.6, 10.5, and 6.6 B.M. for $[Co_9Piv_{12}(OH)_2L^1_2]\cdot 0.5C_7H_{16}$, $[Co_6Piv_8(HPiv)_2L^5_2]$, and $L^6[Co_6(O)_4Piv_9(H_2O)_2]\cdot 2HPiv$, respectively. For the first two complexes, these values correspond to the effective magnetic moments for the sum of contributions from nine and six Co(II) atoms, respectively. In view of the difficulty of theoretical analysis of magnetic properties for Co^{II} compounds, one can only state that the high-temperature asymptotics of μ_{eff} lie in the range of expected values for all compounds under study. For $L^6[Co_6(O)_4Piv_9(H_2O)_2]\cdot 2$ HPiv, μ_{eff} is much smaller than for other complexes because of all compounds we studied this is the only compound containing Co^{III} ions. As is known [10], the diamagnetic Co^{III} ions form a cubane fragment $[Co^{III}_4O_4]$ (Fig. 3b). Therefore, the contribution to magnetic susceptibility of $L^6[Co_6(O)_4Piv_9(H_2O)_2]\cdot 2HPiv$ is made by only two of the remaining terminal Co^{II} ions.

Thus our study gave a new group of heterospin complexes based on polynuclear cobalt pivalates with nitroxides $[Co_9Piv_{12}(OH)_2L^1_2]\cdot 0.5C_7H_{16}$, $[Co_9Piv_{12}(OH)_2L^1_2]\cdot C_7H_{16}$, $[Co_9Piv_{12}(OH)_2L^1_2]\cdot 2C_7H_{16}$, $[Co_8Piv_8(OH)_6(HPiv)_4(H_2O)_2L^4_2]$, $[Co_6Piv_8(HPiv)_2L^5_2]$, $[Co_6Piv_8(HPiv)_2L^5_2]\cdot C_6H_6$, $[Co_6Piv_8(HPiv)_2L^5_2][Co_{10}Piv_{14}(HPiv)_2L^2_2L^3_2]\cdot C_7H_{16}$, $[Co_{10}Piv_{14}(HPiv)_2L^2_2L^3_2]\cdot C_6H_{14}$, where L^1– L^5 are modified molecules of the starting 2,4,4,5,5-pentamethyl-4,5-dihydro-1*H*-imidazole-(3-oxide)-1-oxyl. It has been found that the reaction of $[Co_6(O)_2\text{-}Piv_{10}Thf_3H_2O]\cdot 1.5Thf$ with NIT-Me and/or Im-Me occurs with simultaneous transformation of both the starting polynuclear fragment and the starting nitroxide (nitroxides). The possibility of this transformation should be taken into account in design of heterospin systems based on polynuclear metal-containing matrices and nitroxides.

Acknowledgements

Research funded in part by US Civilian Research and Development Foundation (Y2-C-08-01), RFBR (Grants 05-03-32095, 05-03-32305, 06-03-08004, 06-03-32157), RAS and SB RAS Grants, and the Bruker firm.

Appendix A. Supplementary material

CCDC 616890, 616891, 616892, 616893, 616894, 616895, 616896, 616897 and 616898 contain the supplementary crystallographic data for $[Co_9Piv_{12}(OH)_2L^1_2]\cdot 0.5C_7H_{16}$, $[Co_9Piv_{12}(OH)_2L^1_2]\cdot C_7H_{16}$, $[Co_9Piv_{12}(OH)_2L^1_2]\cdot 2C_7H_{16}$, $[Co_8Piv_8(OH)_6(HPiv)_4(H_2O)_2L^4_2]$, $L^6[Co_6(O)_4Piv_9(H_2O)_2]\cdot 2HPiv$, $[Co_6Piv_8(HPiv)_2L^5_2]$, $[Co_6Piv_8(HPiv)_2L^5_2]\cdot C_6H_6$, $[Co_6Piv_8(HPiv)_2L^5_2][Co_{10}Piv_{14}(HPiv)_2L^2_2L^3_2]\cdot C_7H_{16}$ and $[Co_{10}Piv_{14}(HPiv)_2L^2_2L^3_2]\cdot C_6H_{14}$. These data can be obtained free of charge via http://www.ccdc. ac.uk/conts/retrieving.html, or from the Cambridge Crystallographic Data Centre, 12 Union Road, Cambridge CB2 1EZ, UK; fax: (+44) 1223-336-033; or e-mail: deposit @ccdc.cam.ac.uk. Supplementary data associated with this article can be found, in the online version, at doi:10.1016/j.poly.2006.10.010.

References

[1] V. Ovcharenko, E. Fursova, G. Romanenko, V. Ikorskii, Inorg. Chem. 43 (2004) 3332.
[2] E. Fursova, V. Ovcharenko, K. Nosova, G. Romanenko, V. Ikorskii, Polyhedron 24 (2005) 2084.
[3] K. Nakata, H. Miyasaka, F. Iwahori, K. Sugiura, M. Yamashita, Polyhedron 24 (2005) 2250.
[4] D.G.B. Boocock, R. Darcy, E.F. Ullman, J. Am. Chem. Soc. 90 (1968) 5945.
[5] E.F. Ullman, J.H. Osiecki, D.G.B. Boocock, R. Darcy, J. Am. Chem. Soc. 94 (1972) 7049.
[6] E.F. Ullman, L. Call, J.H. Osiecki, J. Org. Chem. 35 (11) (1970) 3623.
[7] A.A. Sidorov, M.E. Nikiforova, E.V. Pakhmutova, G.G. Alexandrov, V.N. Ikorskii, V.M. Novotortsev, I.L. Eremenko, I.I. Moiseev, Russ. Chem. Bull. (Engl. Transl.) 55 (2006) 1456.
[8] M.A. Golubnichaya, I.G. Fomina, M.O. Ponina, S.M. Deomidov, S.E. Nefedov, I.L. Eremenko, I.I. Moiseev, Russ. Chem. Bull. (Engl. Transl.) 48 (1999) 1751.
[9] A.J. Gordon, R.A. Ford, The Chemist's Companion, Wiley, New York, London, Sydne, Toronto, 1972.
[10] G. Aromí, A.S. Batsanov, P. Christian, M. Helliwell, A. Parkin, S. Parsons, A.A. Smith, G.A. Timco, R.E.P. Winpenny, Chem. Eur. J. 9 (2003) 5142.
[11] P. King, W. Wernsdorfer, K.A. Abboud, G. Christou, Inorg. Chem. 44 (2005) 8659.

total spin value of 3d-metal clusters [7–9]. We herein report examples of this approach.

2. Experimental

2.1. General and physical measurements

All manipulations were performed under aerobic conditions using materials (reagent grade) and solvents as received. Microanalyses (C, H, N) were performed by the University of Ioannina (Greece) Microanalytical Laboratory using an EA 1108 Carlo Erba analyser. IR spectra (4000–500 cm^{-1}) were recorded on Perkin–Elmer 16 PC and Nicolet 520 FTIR spectrometers with samples prepared as KBr pellets. Magnetic susceptibility measurements under magnetic fields of approximately 0.1 T in the range 2–300 K and magnetisation measurements (only for complexes **2** and **4**) in the field range of 1–5 T were performed with a Quantum Design MPMS-XL SQUID magnetometer at the Magnetochemistry Service of the University of Barcelona. All measurements were performed on polycrystalline samples. Pascal's constants were used to estimate the diamagnetic corrections which were subtracted from the experimental susceptibilities to give the corrected molar magnetic susceptibilities.

2.2. Compound preparation

2.2.1. $[Co_9(OH)_2(O_2CMe)_8\{(py)_2CO_2\}_4]\cdot 14.6H_2O$ ($\mathbf{1}\cdot 14.6H_2O$)

MeCN (45 mL) was added to a mixture of $Co(O_2CMe)_2\cdot 4H_2O$ (0.27 g, 1.08 mmol) and $(py)_2CO$ (0.10 g, 0.54 mmol). The solids dissolved on stirring under reflux for 2 h to give a pale purple solution, which was allowed to stand undisturbed at room temperature overnight. Well-formed, X-ray quality crystals of $\mathbf{1}\cdot 14.6H_2O$ appeared slowly. The purple crystals were collected by filtration, washed with a little cold EtOH, and dried in air. Yield: 30%. *Anal.* Calc. for $C_{60}H_{87.2}Co_9N_8O_{40.6}$: C, 34.31; H, 4.18; N, 5.33; Co, 25.25. Found: C, 34.42; H, 4.13; N, 5.51; Co, 25.74%. IR (KBr, cm^{-1}): 3589s, 3434s, 2927w, 1675s, 1584s, 1476m, 1431s, 1352w, 1293w, 1232m, 1155w, 1123m, 1097m, 1031s, 976m, 890w, 805m, 784m, 754m, 690m, 675m, 646m, 621m, 542w, 485w, 445w, 416w.

2.2.2. $[Co_9(N_3)_2(O_2CMe)_8\{(py)_2CO_2\}_4]\cdot 4DMF\cdot 2.5H_2O$ ($\mathbf{2}\cdot 4DMF\cdot 2.5H_2O$)

DMF (25 mL) was added to a mixture of $Co(O_2CMe)_2\cdot 4H_2O$ (0.17 g, 0.60 mmol), $(py)_2CO$ (0.06 g, 0.32 mmol) and NaN_3 (0.02 g, 0.30 mmol). The solids dissolved on stirring under heating to give a dark blue solution, which was allowed to stand undisturbed at room temperature for 3 days. Well-formed, X-ray quality pink-red crystals of $\mathbf{2}\cdot 4DMF\cdot 2.5H_2O$ appeared, which were isolated by filtration, washed with DMF and Et_2O, and dried in air. Yield: 60%. *Anal.* Calc. for $C_{72}H_{89}Co_9N_{18}O_{30.5}$: C, 38.87; H, 4.03; N, 11.33. Found: C, 38.24; H, 4.05; N, 11.65%. IR (KBr, cm^{-1}): 3446m, 3070w, 3025w, 2928w, 2802w, 2504w, 2073s, 1669s, 1583s, 1475m, 1430s, 1346w, 1294w, 1254w, 1229m, 1155w, 1119m, 1092m, 1057s, 1041s, 1020m, 973m, 962m, 890w, 806m, 780m, 757m, 686m, 664m, 617w, 529w, 475w, 442w, 421w.

2.2.3. $[Ni_9(OH)_2(O_2CMe)_8\{(py)_2CO_2\}_4]\cdot 19H_2O$ ($\mathbf{3}\cdot 19H_2O$)

DMF (25 mL) was added to a mixture of $Ni(O_2CMe)_2\cdot 4H_2O$ (0.15 g, 0.60 mmol) and $(py)_2CO$ (0.06 g, 0.32 mmol). The solids dissolved on stirring under heating to give a green solution, which was allowed to stand undisturbed at room temperature for 4 days. Well-formed, X-ray quality green crystals of $\mathbf{3}\cdot 19H_2O$ appeared, which were isolated by filtration, washed with DMF and Et_2O, and dried in air. Yield: 60%. *Anal.* Calc. for $C_{60}H_{96}Ni_9N_8O_{45}$: C, 33.09; H, 4.44; N, 5.15. Found: C, 33.41; H, 4.48; N, 5.03%. IR (KBr, cm^{-1}): 3591s, 3441s, 2930w, 1678s, 1588s, 1477m, 1431s, 1353w, 1293w, 1232m, 1157w, 1125m, 1098m, 1030s, 975m, 891w, 807m, 782m, 756m, 691m, 676m, 648m, 620m, 540w, 484w, 445w, 416w.

2.2.4. $[Ni_9(N_3)_2(O_2CMe)_8\{(py)_2CO_2\}_4]\cdot 4DMF\cdot 4.5H_2O$ ($\mathbf{4}\cdot 4DMF\cdot 4.5H_2O$)

Method A. DMF (25 mL) was added to a mixture of $Ni(O_2CMe)_2\cdot 4H_2O$ (0.15 g, 0.6 mmol), $(py)_2CO$ (0.06 g, 0.32 mmol) and NaN_3 (0.02 g, 0.30 mmol). The solids dissolved on stirring under heating to give a green solution, which was allowed to stand undisturbed at room temperature for 7 days. Well-formed, X-ray quality green crystals of $\mathbf{4}\cdot 4DMF\cdot 4.5H_2O$ appeared, which were isolated by filtration, washed with DMF and Et_2O, and dried in air. Yield: 60%. *Anal.* Calc. for $C_{72}H_{93}Ni_9N_{18}O_{32.5}$: C, 38.28; H, 4.15; N, 11.16. Found: C, 38.50; H, 4.19; N, 11.25%. IR (KBr, cm^{-1}): 3436s, 3070w, 2929w, 2085s, 1652s, 1587s, 1477m, 1431s, 1348w, 1293w, 1232m, 1156w, 1123m, 1099m, 1039s, 976m, 891w, 807m, 782m, 757m, 691m, 675m, 648m, 620w, 537w, 486w, 445w, 420w.

Method B. DMF (15 mL) and MeOH (10 mL) were added to a mixture of $\mathbf{3}\cdot 19H_2O$ (0.15 g, 0.6 mmol) and NaN_3 (0.08 g, 1.20 mmol). The solids dissolved on stirring under heating to give a green solution, which was allowed to stand undisturbed at room temperature for 5 days. Well-formed, X-ray quality green crystals of $\mathbf{4}\cdot 4DMF\cdot 4.5H_2O$ appeared, which were isolated by filtration, washed with DMF and Et_2O, and dried in air. Yield: 80%. IR data and elemental analyses (C, H, N) were similar to the data obtained for the product prepared by Method A.

2.3. Single-crystal X-ray crystallography

Crystals of $\mathbf{2}\cdot 4DMF\cdot 2.5H_2O$, $\mathbf{3}\cdot 19H_2O$ and $\mathbf{4}\cdot 4DMF\cdot 4.5H_2O$ were mounted in air, while crystals of $\mathbf{1}\cdot 14.6H_2O$ were mounted in capillary. Diffraction measurements for $\mathbf{1}\cdot 14.6H_2O$ were made on a Crystal Logic Dual Goniometer diffractometer using graphite-monochromated Mo

Table 1
Brief crystallographic data for complexes $\mathbf{1}\cdot 14.6H_2O$, $\mathbf{2}\cdot 4DMF\cdot 2.5H_2O$, $\mathbf{3}\cdot 19H_2O$ and $\mathbf{4}\cdot 4DMF\cdot 4.5H_2O$

Parameter	$\mathbf{1}\cdot 14.6H_2O$	$\mathbf{2}\cdot 4DMF\cdot 2.5H_2O$	$\mathbf{3}\cdot 19H_2O$	$\mathbf{4}\cdot 4DMF\cdot 4.5H_2O$
Formula	$C_{60}H_{87.2}Co_9N_8O_{40.6}$	$C_{72}H_{89}Co_9N_{18}O_{30.5}$	$C_{60}H_{96}Ni_9N_8O_{45}$	$C_{72}H_{93}Ni_9N_{18}O_{32.5}$
Formula weight	2114.58	2224.99	2177.67	2258.75
Crystal system	monoclinic	tetragonal	tetragonal	tetragonal
Space group	*C*2/*c*	*P*4/*n*	*P*4/*ncc* (no.130)	*P*4/*n* (no. 85)
Unit cell dimensions				
a (Å)	14.37(1)	17.762(1)	17.785(8)	17.841(8)
b (Å)	39.28(3)	17.762(1)	17.785(8)	17.841(8)
c (Å)	16.62(1)	14.203(1)	27.313(3)	14.008(3)
β (°)	115.69(3)			
V (Å^3)	8451(1)	4480.9(5)	8639(6)	4459(3)
Z	4	2	4	2
ρ_{calc} (g cm^{-3})	1.651	1.652	1.643	1.676
Radiation, *λ* (Å)	Mo Kα, 0.71073	Mo Kα, 0.71069	Mo Kα, 0.71069	Mo Kα, 0.71069
Temperature (K)	298	298	293	293
μ (mm^{-1})	1.814	1.710	2.013	1.947
Reflections collected/unique (R_{int})	7637/7369 (0.0384)	18191/4761 (0.0531)	37752/7038 (0.082)	24451/5241 (0.038)
Data with $I > 2\sigma(I)$	5734	2950	4166	3417
$R_1(I > 2\sigma(I))$[a]	0.0642	0.0365	0.0630	0.0375
$wR_2(I > 2\sigma(I))$[b]	0.1712	0.1037	0.1703	0.1052

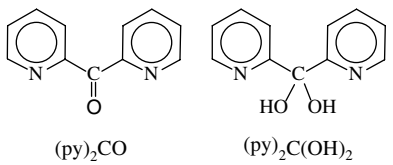
[a] $R_1 = \sum(|F_o| - |F_c|)/\sum(|F_o|)$.
[b] $wR_2 = \{\sum[w(F_o^2 - F_c^2)^2]/\sum[w(F_o^2)^2]\}^{1/2}$.

radiation. Analyses on $\mathbf{2}\cdot 4DMF\cdot 2.5H_2O$, $\mathbf{3}\cdot 19H_2O$ and $\mathbf{4}\cdot 4DMF\cdot 4.5H_2O$ were carried out with a MAR345 diffractometer with an image plate detector; intensities were collected with graphite-monochromated Mo radiation. Crystal data and parameters for data collection and processing are reported in Table 1.

The structures were solved by direct methods (SHELXS-86, SHELXS-97) and refined by full-matrix least squares techniques on F^2 (SHELXL-97). For the four structures, almost all non-hydrogen atoms were refined using anisotropic thermal parameters. Almost all hydrogen atoms were introduced at calculated positions as riding on their respective bonded atoms.

3. Results and discussion

The reaction of an excess of $Co(O_2CMe)_2\cdot 4H_2O$ with di-2-pyridyl ketone, $(py)_2CO$ (Fig. 1), in MeCN under reflux for 2 h gave the enneanuclear cluster $[Co_9(OH)_2(O_2CMe)_8\{(py)_2CO_2\}_4]$ (**1**), see Eq. (1). The complex contains the doubly deprotonated form, $(py)_2CO_2^{2-}$, of the *gem*-diol form of di-2-pyridyl ketone, $(py)_2C(OH)_2$ (Fig. 1) [10]; this is a consequence of the excess of acetates in the reaction mixture. The structure of $\mathbf{1}\cdot 14.6H_2O$ consists of



$(py)_2CO$ $(py)_2C(OH)_2$

Fig. 1. Structural formulae and abbreviations of di-2-pyridyl ketone (left) and its *gem*-diol form (right). The ligand $(py)_2C(OH)_2$ does not exist as a free species, but only in the presence of metal ions.

enneanuclear molecules (Fig. 2, top). The complex has a crystallographic twofold axis passing through Co(1) and bisecting the angles around this metal ion, i.e. O(1)–Co(1)–O(1), O(2)–Co(1)–O(2), O(3)–Co(1)–O(3) and O(4)–Co(1)–O(4),

$$9Co(O_2CMe)_2\cdot 4H_2O + 4(py)_2CO \xrightarrow[T]{MeCN} \underset{\mathbf{1}}{[Co_9(OH)_2(O_2CMe)_8\{(py)_2CO_2\}_4]} + 10MeCO_2H + 30H_2O \quad (1)$$

which is the shared apex of two square pyramids. The most characteristic feature of the structure is the coordination number 8 for Co(1), which is extremely rare in cobalt(II) chemistry. The dianion $(py)_2CO_2^{2-}$ bridges five metal ions (Fig. 3) with the simultaneous formation of three chelate rings per ligand (coordination mode $\eta^1{:}\eta^3{:}\eta^3{:}\eta^1{:}\mu_5$). Each of the two hydroxides bridges four metal ions and all $MeCO_2^-$ groups are in the familiar *syn*,*syn*-$\eta^1{:}\eta^1{:}\mu_2$ mode. The complex has an overall antiferromagnetic behaviour; the antiferromagnetic interactions are due to the $\eta^4{:}\mu_4$ OH^- ligands [11]. It is self-evident that we could not predict the structure of **1**; clearly it was obtained by serendipity [12].

At this point we started thinking in a more rational way. We decided to perform the same reaction that leads to **1**, but in the presence of N_3^- ions. The choice of the latter was based on established magnetostructural correlations which had shown that the end-on N_3^- ligand is an effective ferromagnetic coupler [13]. We hoped that the end-on azido ligands would be incorporated into the enneanuclear skeleton, instead of the hydroxo ligands which mediate a strong antiferromagnetic interaction. This substitution would lead to an increase of the total spin in the ground state.

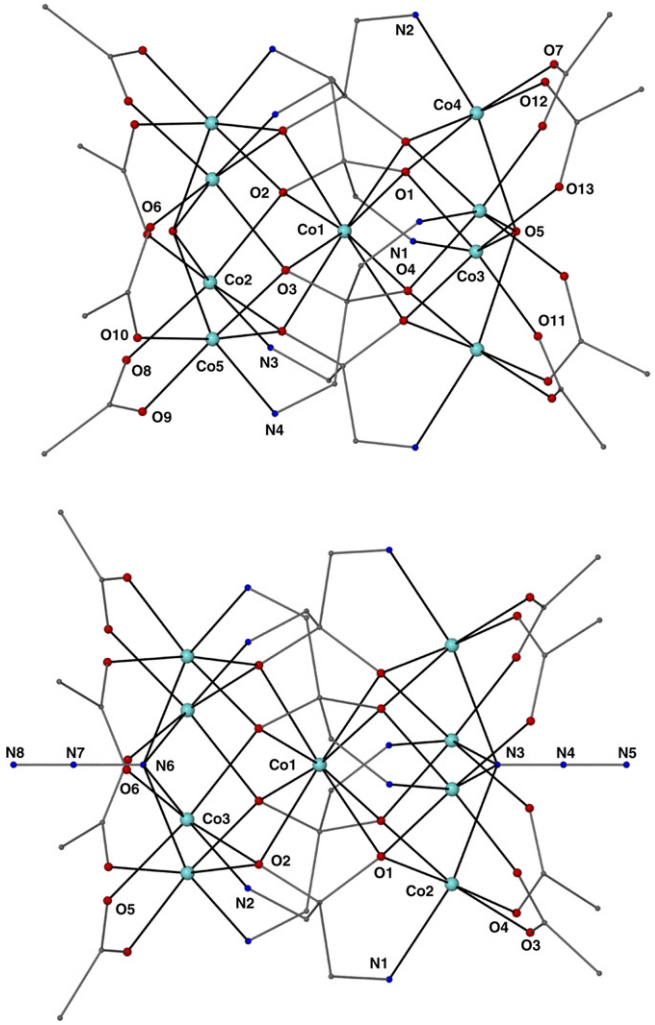


Fig. 2. Partially labeled plots of $[Co_9(OH)_2(O_2CMe)_8\{(py)_2CO_2\}_4]$ (**1**, top) and $[Co_9(N_3)_2(O_2CMe)_8\{(py)_2CO_2\}_4]$ (**2**, bottom). All H atoms and most C atoms of the $(py)_2CO_2^{2-}$ ligands have been omitted for clarity.

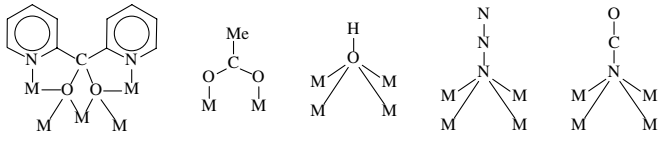


Fig. 3. The crystallographically established coordination modes of the ligands present in the complexes discussed in this work.

This has, indeed, turned out to be the case. The reaction represented by Eq. (2) in hot DMF (to keep the produced NaO_2CMe soluble) gave a dark blue solution from which the enneanuclear cage $[Co_9(N_3)_2(O_2CMe)_8\{(py)_2CO_2\}_4]$ (**2**) was isolated in 60% yield. Complex **2** · 4DMF · 2.5H_2O (Fig. 2, bottom) bears striking structural similarity

$$9Co(O_2CMe)_2\cdot 4H_2O + 4(py)_2CO + 2NaN_3 \xrightarrow{DMF} \underset{\mathbf{2}}{[Co_9(N_3)_2(O_2CMe)_8\{(py)_2CO_2\}_4]} + 8MeCO_2H + 2NaO_2CMe + 32H_2O \quad (2)$$

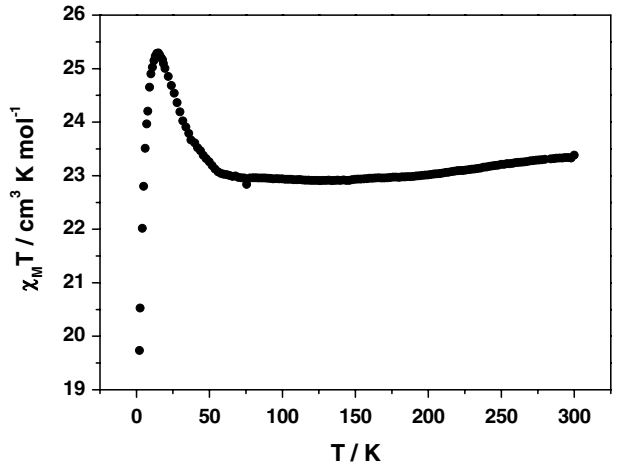


Fig. 4. Plot of the $\chi_M T$ vs. T product for **2**.

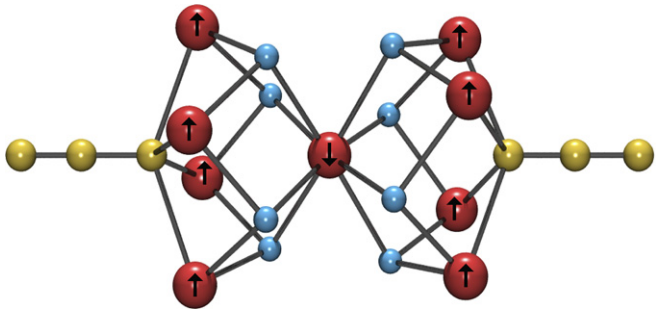


Fig. 5. The ferrimagnetic "structure" of complex **2**.

with the hydroxo cluster, the only difference being the presence of the novel quadruply bridging end-on azido ligands (η^4:μ_4, Fig. 3) instead of the quadruply bridging hydroxo ligands. The complex has a crystallographic fourfold axis passing through Co(1) and the azido nitrogen atoms N(3), N(4), N(5), N(6), N(7) and N(8), thus bisecting the angles around this metal ion, i.e O(1)–Co(1)–O(1′) [1.5 − x, 1.5 − y, z] and O(2)–Co(1)–O(2′) [1.5 − x, 1.5 − y, z].

The weak minimum in the $\chi_M T$ vs. T plot at 116 K for **2** (Fig. 4) is the ferrimagnetic signature of the antiferromagnetic coupling between the central Co^{II} ion and the two ferromagnetically-coupled squares in the bases of the cage (Fig. 5). The ferromagnetic coupling in the square bases of the double square pyramid is mediated by the end-on μ_4-N_3^- ligands [7].

A similar reaction performed by using NaOCN instead of NaN_3 yielded the cyanate analogue of **2** containing novel μ_4 end-on (through the single N atom) OCN^- ligands (Fig. 3).[1]

Using procedures similar to those described in Eqs. (1) and (2), the nickel(II) analogues of **1** and **2**, i.e. complexes $[Ni_9(OH)_2(O_2CMe)_8\{(py)_2CO_2\}_4]$ (**3**) and $[Ni_9(N_3)_2$-

[1] Details will be given in another paper.

$(O_2CMe)_8\{(py)_2CO_2\}_4]$ (**4**), respectively, were prepared in very good yields and structurally characterized. Their molecular structures (Figs. 6 and 7) are very similar to those of the analogous Co_9^{II}/OH^- and Co_9^{II}/N_3^- clusters. Complex **4** can also be prepared by the reaction of the pre-formed hydroxo cluster **3** with a slight excess of N_3^- ions in DMF–MeOH (2:1 v/v) in ~80% yield.

$$[Ni_9(OH)_2(O_2CMe)_8\{(py)_2CO_2\}_4] + 2NaN_3 \underset{\mathbf{3}}{} \xrightarrow{\text{DMF–MeOH}} [Ni_9(N_3)_2(O_2CMe)_8\{(py)_2CO_2\}_4] + 2NaOH \quad (3)$$
$$\mathbf{4}$$

Variable temperature (300–2.0 K) dc magnetic susceptibility data for **3** (Fig. 8) indicate a dominant antiferromagnetic superexchange pattern. Full analysis of the data [8] shows that the antiferromagnetic behaviour is due to the OH^- bridges and that the ground-state total spin is 1.

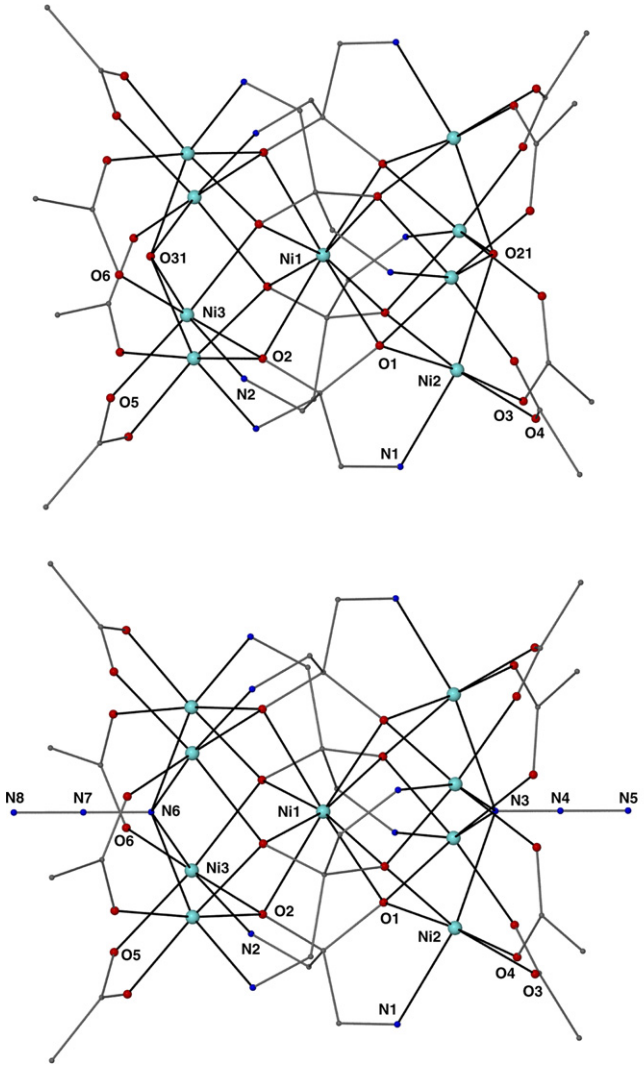


Fig. 6. Partially labeled plots of $[Ni_9(OH)_2(O_2CMe)_8\{(py)_2CO_2\}_4]$ (**3**, top) and $[Ni_9(N_3)_2(O_2CMe)_8\{(py)_2CO_2\}_4]$ (**4**, bottom). Both complexes have a fourfold axis. All H atoms and most C atoms of the $(py)_2CO_2^{2-}$ ligands have been omitted for clarity.

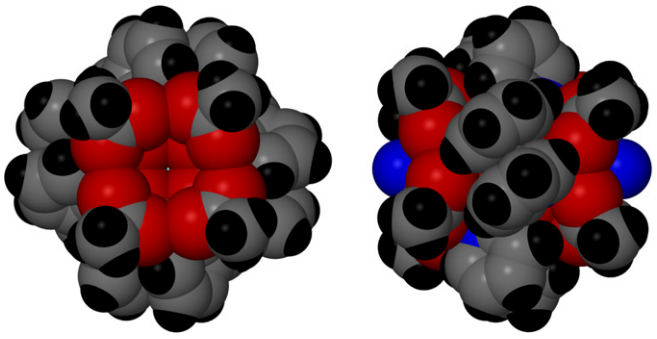


Fig. 7. Space filling models of $[Ni_9(N_3)_2(O_2CMe)_8\{(py)_2CO_2\}_4]$ (**4**); a view perpendicular to the base of the double square pyramid showing the N_3^--trapping cavity (left) and a view showing the azides within the cavities (right).

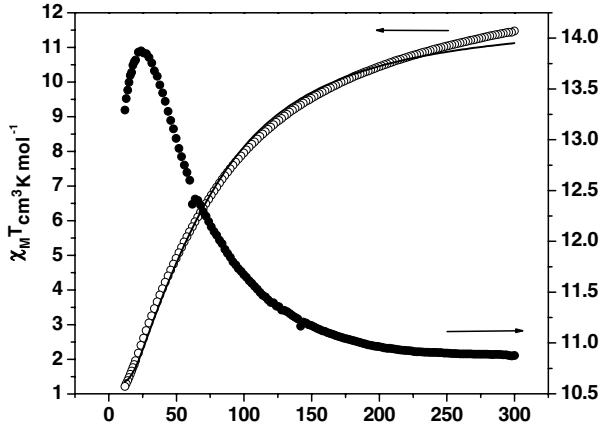


Fig. 8. Plots of the $\chi_M T$ vs. T products for **3** (left y axis, open circles) and **4** (right y axis, solid circles). The solid line is fit of the data to the appropriate 3-**J** model [8].

The dc $\chi_M T$ product of **4** increases from the 300 K value of 10.87 cm^3 mol^{-1} K to a maximum of 13.88 cm^3 mol^{-1} K at 24 K, and then decreases continuously down to 2.0 K (Fig. 8). This behaviour is compatible with moderate ferromagnetic coupling. Full analysis of the data shows that the ferromagnetic behaviour is due to the end-on azido bridges and that the ground-state total spin of the cluster is probably 9 (Fig. 9).

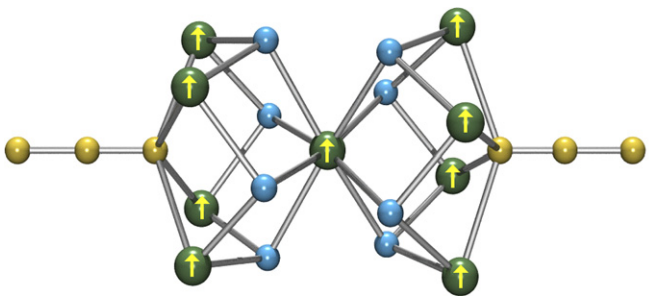


Fig. 9. The ferromagnetic "structure" of complex **4**.

The pivalate analogues of **1**–**4** have also been prepared.[1] These clusters have very similar molecular structures and magnetic properties with their corresponding acetate clusters. Similar chemistry occurs also with iron(II). Reactions of the initially isolated OH^--bridged cluster $[Fe_9(OH)_2(O_2CMe)_8\{(py)_2CO_2\}_4]$ with N_3^- and OCN^- ions in refluxing MeCN under an inert atmosphere yielded complexes $[Fe_9(N_3)_2(O_2CMe)_8\{(py)_2CO_2\}_4]$ and $[Fe_9(NCO)_2(O_2CMe)_8\{(py)_2CO_2\}_4]$, respectively, that contain quadruply bridging pseudohalogeno ligands. Not only the N_3^-- and OCN^--bridged clusters are ferromagnetic in nature, but these also display SMM behaviour [9].

4. Conclusions and perspectives

In summary, the end-on azido (and probably N-cyanato ligands) are good substitutes for hydroxo bridges in 3d-metal clusters to increase the *S* value of the ground state. The described N_3^- or OCN^- for OH^- substitution has the potential for wide application in the area of high-spin molecules. Often this approach involves ''true'' reactivity chemistry on pre-isolated clusters. Results at the time of writing reveal that application of the described strategy in at least 10 different hydroxo and alkoxo clusters leads to the retainment of the core and the introduction of specific ferromagnetic components in the superexchange scheme.

Acknowledgements

We thank European Social Fund (ESF), Operational Program for Educational and Vocational Training II (EPEAEK II) and particularly the Program PYTHAGORAS (Grant b.365.037), for funding the above work.

Appendix A. Supplementary material

CCDCs 102038, 147542, 169287 and 169286 contain the supplementary crystallographic data for $(\mathbf{1}\cdot 14.6H_2O)$, $(\mathbf{2}\cdot 4DMF\cdot 2.5H_2O)$, $(\mathbf{3}\cdot 19H_2O)$ and $(\mathbf{4}\cdot 4DMF\cdot 4.5H_2O)$. These data can be obtained free of charge via http://www.ccdc.cam.ac.uk/conts/retrieving.html, or from the Cambridge Crystallographic Data Centre, 12 Union Road, Cambridge CB2 1EZ, UK; fax: (+44) 1223-336-033; or e-mail: deposit@ccdc.cam.ac.uk. Supplementary data associated with this article can be found, in the online version, at doi:10.1016/j.poly.2006.10.009.

References

[1] (a) For excellent reviews, see: G. Aromi, E.K. Brechin, Struct. Bond. 122 (2006) 1;
(b) R. Bircher, G. Chaboussant, C. Dobe, H. Güdel, S.T. Ochsenbein, A. Sieber, O. Waldmann, Adv. Funct. Mater. 16 (2006) 209;
(c) D. Gatteschi, R. Sessoli, Angew. Chem., Int. Ed. 42 (2003) 268;
(d) G. Christou, D. Gatteschi, D.N. Hendrickson, R. Sessoli, MRS Bull. 25 (2000) 66.
[2] For example, see: G. Aromi, J.-P. Claude, M.J. Knapp, J.C. Huffman, D.N. Hendrickson, G. Christou, J. Am. Chem. Soc. 120 (1998) 2977.
[3] A.M. Ako, I.J. Hewitt, V. Mereacre, R. Clérac, W. Wernsdorfer, C.E. Anson, A.K. Powell, Angew. Chem., Int. Ed. 45 (2006) 4926.
[4] M. Murugesu, M. Habrych, W. Wernsdorfer, K.A. Abboud, G. Christou, J. Am. Chem. Soc. 126 (2004) 4766.
[5] J. Larionova, M. Gross, M. Pilkington, H. Andres, H. Stoeckli-Evans, H.U. Güdel, S. Decurtins, Angew. Chem., Int. Ed. 39 (2000) 1605.
[6] Th.C. Stamatatos, K.A. Abboud, W. Wernsdorfer, G. Christou, Angew. Chem., Int. Ed. 45 (2006) 4134.
[7] G.S. Papaefstathiou, S.P. Perlepes, A. Escuer, R. Vicente, M. Font-Bardia, X. Solans, Angew. Chem., Int. Ed. 40 (2001) 884.
[8] G.S. Papaefstathiou, A. Escuer, R. Vicente, M. Font-Bardia, X. Solans, S.P. Perlepes, Chem. Commun. (2001) 2414.
[9] A.K. Boudalis, B. Donnadieu, V. Nastopoulos, J.M. Clemente-Juan, A. Mari, Y. Sanakis, J.-P. Tuchagues, S.P. Perlepes, Angew. Chem., Int. Ed. 43 (2004) 2266.
[10] For a review concerning the coordination chemistry of the various forms of di-2-pyridyl ketone, see: G.S. Papaefstathiou, S.P. Perlepes, Comments Inorg. Chem. 23 (2002) 249.
[11] A. Tsohos, S. Dionyssopoulou, C.P. Raptopoulou, A. Terzis, E.G. Bakalbassis, S.P. Perlepes, Angew. Chem., Int. Ed. 38 (1999) 983.
[12] For an excellent perspective, see: R.E.P. Winpenny, J. Chem. Soc., Dalton Trans. (2002) 1.
[13] J. Ribas, A. Escuer, M. Monfort, R. Vicente, R. Cortes, L. Lezama, T. Rojo, Coord. Chem. Rev. 193–5 (1999) 1027.

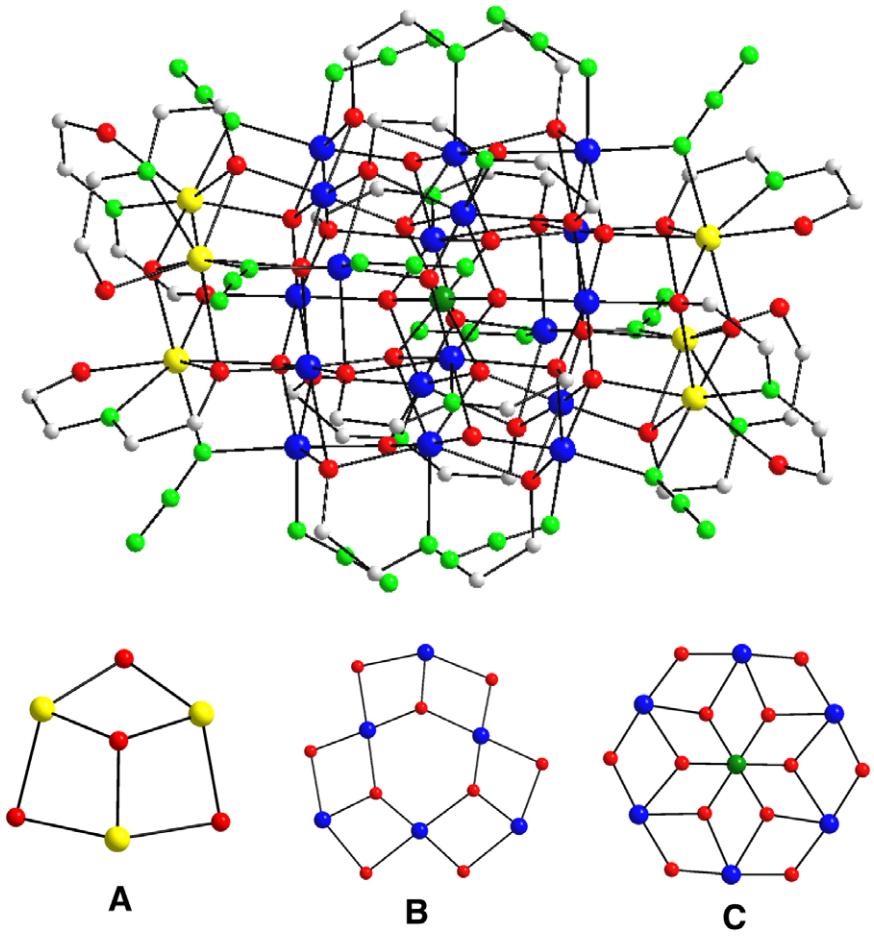
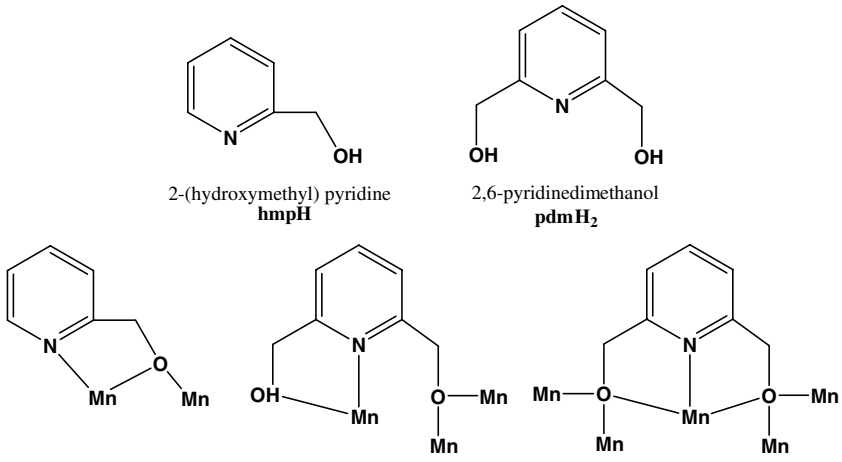


Fig. 1. Structure of the cation of **1** (top) and the three types of constituent layers of its core (bottom). Color code: Mn^{II} yellow, Mn^{III} blue, Mn^{IV} olive, O red, N green, C gray. H atoms have been omitted for clarity. (For interpretation of the references in colour in this figure legend, the reader is referred to the web version of this article.)

An alternative approach to new high-spin molecules pertinent to the present report is to start with a preformed, high-spin molecule and then perturb it in some way, without major structural change, in order to modify the constituent exchange parameters and possibly alter the ground state (hopefully to a larger value rather than a smaller one). While this is often stated in the literature as an objective, it has yet to be realized. In the present work, we show that it is indeed possible to significantly modify the ground state spin of a complicated, already high-spin molecule without significant core structural change by controlled ligand substitution within the peripheral ligation about the magnetic core. Specifically, we show that ligand-induced tweaking of a SMM with $S = 51/2$ causes the ground state to increase to $S = 61/2$ without unduly affecting the anisotropy. As a result, the product is a new SMM.

The present Short Communication deals with the Mn_{25} SMM complex of full formula $[Mn^{II}_6Mn^{III}_{18}Mn^{IV}O_{18}(OH)_2(N_3)_{12}(pdm)_6(pdmH)_6]X_2$ [(**1**); X = Cl or N_3; $pdmH_2$ is 2,6-pyridinedimethanol]. The $X = Cl^-$ salt was the original one prepared [5a] but the present work has been carried with the $X = N_3^-$ salt, available in a much better yield of 75% from a related procedure. The Mn_{25} cation of **1**[1] has a barrel-like cage structure with twelve μ_4-O^{2-}, six μ_3-O^{2-}, and two μ_3-OH^- ions holding the core together (Fig. 1, top). The peripheral ligation is provided by chelating/bridging pdm^{2-}/$pdmH^-$ and both terminal and end-on bridging N_3^- groups. The core may be dissected into five layers of three types with an ABCBA arrangement (Fig. 1, bottom). Layer A is a Mn^{II}_3 triangular unit with a capping μ_3-OH^- ion; layer B is a Mn^{III}_6 triangle comprising three corner-sharing Mn^{III}_3 triangles; and layer C is an Anderson-type Mn^{III}_6 hexagon with a central Mn^{IV} ion. Each layer is held together and linked to its neighboring layers by a combination of O^{2-}, OR^-, and/or N_3^- bridges.

[1] Crystal structure data for $\mathbf{1}\cdot 10MeCN$: $C_{104}H_{122}Mn_{25}N_{64}O_{44}$, $M_r = 4345.98$, triclinic, space group $P\bar{1}$, $a = 15.9646(12)$, $b = 16.5361(13)$, $c = 17.3483(14)$ Å, $\alpha = 97.895(2)$, $\beta = 101.094(1)$, $\gamma = 117.345(1)°$, $V = 3855.8(5)$ Å^3, $Z = 1$, $\rho_{calcd} = 2.085$ g cm^{-3}, $T = 173(2)$ K, 21329 reflections collected, 13437 unique ($R_{int} = 0.0335$), $R_1 = 0.0519$ and $wR_2 = 0.1546$, using 13437 reflections with $I > 2\sigma(I)$. Crystal structure data for $\mathbf{2}\cdot x$MeCN$\cdot y$MeOH: $C_{121}H_{130}Mn_{25}N_{24}O_{74}Cl_6$, $M_r = 4690.67$, rhombohedral, space group $R\bar{3}c$, $a = 22.0975(9)$, $c = 69.811(5)$ Å, $V = 29522(3)$ Å^3, $Z = 6$, $\rho_{calcd} = 1.495$ g cm^{-3}, $T = 173(2)$ K, 16378 reflections collected, 4080 unique ($R_{int} = 0.0756$), $R_1 = 0.0674$ and $wR_2 = 0.1860$, using 4080 reflections with $I > 2\sigma(I)$.



Scheme 1. The pyridyl–alcohol ligands discussed in the text (top), and the crystallographically established coordination modes of the hmp^-, $pdmH^-$, and pdm^{2-} ligands present in complexes **1** and **2** (bottom).

The $[Mn_{25}O_{18}(OH)_2(N_3)_{12}(pdm)_6(pdmH)_6]^{2+}$ cation has an $S = 51/2$ ground state, and we undertook the challenge of tweaking this spin value without core structural change.

We have extensive experience with pyridine-based alkoxide ligands in Mn cluster chemistry, and have seen that the anion of 2-(hydroxymethyl)pyridine (hmp^-), like $pdmH^-$ and pdm^{2-} (Scheme 1), is a versatile N,O-chelating and bridging ligand that often yields ferromagnetic coupling between metal atoms [5b,6]. We thus targeted replacement of the twelve azide ions of **1** by six hmp^- groups, and this ultimately proved successful.

The reaction of **1** ($X = N_3^-$), Na(hmp), and $NaClO_4 \cdot H_2O$ in a 1:6:6 molar ratio in MeCN/MeOH[2] gave a dark brown solution from which were subsequently isolated crystals of $[Mn_{25}O_{18}(OH)(OMe)(hmp)_6(pdm)_6(pdmH)_6](N_3)_2(ClO_4)_6 \cdot x\text{MeCN} \cdot y\text{MeOH}$ ($\mathbf{2} \cdot x\text{MeCN} \cdot y\text{MeOH}$) in 63% yield. The crystal structure[1] shows the core of **2** to be isostructural with that in **1**; Mn oxidation states and the protonation levels of all O atoms in the molecule were established by Mn and O bond valence sum (BVS) calculations [7],[3] inspection of metric parameters, and detection of Mn^{III} Jahn-Teller (JT) elongation axes. The main difference is that the twelve bound azides of **1** are now replaced by six $\eta^1{:}\eta^2{:}\mu_2$ hmp^- ligands in **2** and also a μ_3-OH^- group of **1** is substituted by a μ_3-MeO^- ligand in **2** (Fig. 2). As a result, all intra- and inter-layer bridges, as well as all M_2 pairwise exchange interactions, are now through oxo-atoms, and there are consequently small metric differences between the cores of **1** and **2**.[4] There will thus some changes expected to many of the exchange interactions in the molecule. Considering that the ground state of such a large molecule consisting of both ferro- and antiferromagnetic interactions will be acutely sensitive to the relative magnitudes of the multiple exchange interactions, many of them competing, it was considered likely that the ground state S value might change, and this was therefore explored by detailed magnetochemical measurements.

Solid-state DC magnetic susceptibility (χ_M) data for dried $\mathbf{2} \cdot 4\text{MeCN}$ were collected in the temperature range 5.0–300 K in an applied field of 1 kG (0.1 T). $\chi_M T$ steadily increases from 120.20 $cm^3\,mol^{-1}\,K$ at 300 K to a maximum of 457.42 $cm^3\,mol^{-1}\,K$ at 20 K, before dropping to 401.94 $cm^3\,mol^{-1}\,K$ at 5.0 K (Fig. 3). The spin-only ($g = 2$) value for a non-interacting $[Mn^{II}_6Mn^{III}_{18}Mn^{IV}]$ unit is 82.125 $cm^3\,mol^{-1}\,K$, indicating at least some ferromagnetic exchange interactions within **2**, and the 20 K data strongly suggest a very large ground-state spin (S) value. The low temperature data are consistent with an S in the 59/2 to 65/2 range, depending on the g value, significantly greater than the $S = 51/2$ of **1**.

In order to determine the ground state of $\mathbf{2} \cdot 4\text{MeCN}$, magnetization ($M$) data were collected in the 0.1–1.0 T and 1.8–10.0 K ranges, and these are plotted as $M/N\mu_B$ versus H/T in Fig. 4. We used only low field data ($\leqslant$1.0 T), as we previously did for **1**, to avoid problems associated with M_s levels from excited states with higher S values crossing with the ground state, which would lead to an erroneously high value for the ground-state S. The data were fit by matrix-diagonalization to a model that

[2] It is pertinent to ask whether the Mn_{25} core structure stays intact in the MeCN/MeOH solvent used for the ligand substitution. Although we cannot answer this directly on the present system because of its complexity, we know from experience on related, higher symmetry Mn clusters (e.g. Mn_{12}, Mn_4, etc.), which we can study by NMR, that systems with higher average oxidation states and lots of oxide bridges retain their structures in solution. Compound **2** is one such molecule. Also the fact that the product is indeed of the same core structure as the starting material supports this in the present case.

[3] Bond-valence sum (BVS) calculations for Mn^{II}, Mn^{III} and Mn^{IV} ions of **2** gave oxidation state values of 1.94 (Mn^{II}), 2.88–2.99 (Mn^{III}) and 4.18 (Mn^{IV}) and for the oxygen atoms of O^{2-}, OH^-, hmp^-, $pdmH^-$, pdm^{2-} values of 1.84–2.03 (O^{2-}), 1.16–1.17 (OH^-, OMe^-, OR^-).

[4] A detailed comparison will be provided in the full paper of this work.

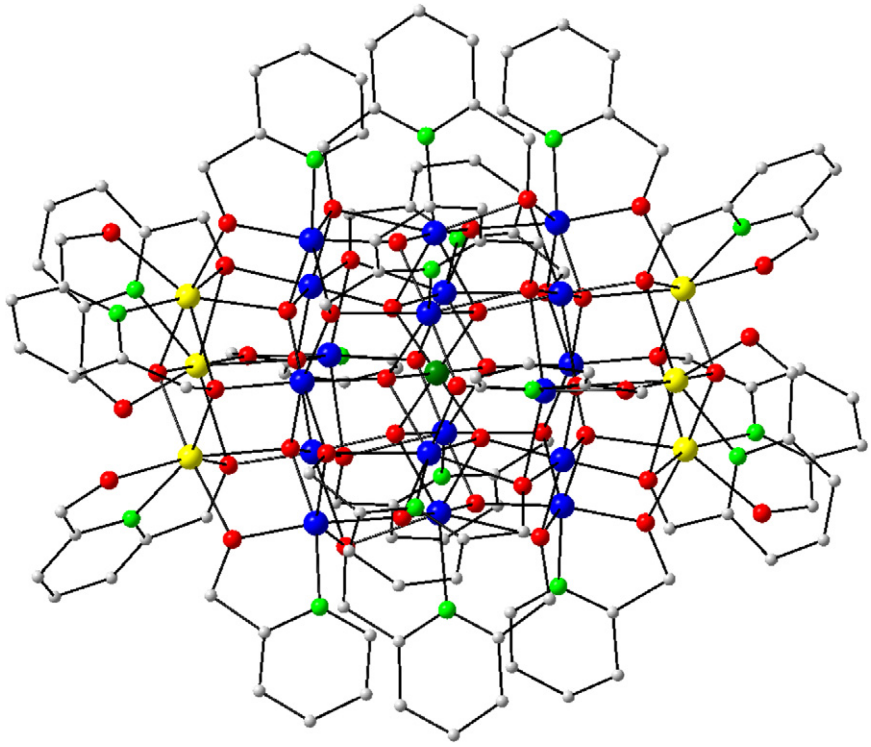


Fig. 2. Structure of the cation of **2**. Color code: Mn^{II} yellow, Mn^{III} blue, Mn^{IV} olive, O red, N green, C gray. H atoms have been omitted for clarity. (For interpretation of the references in colour in this figure legend, the reader is referred to the web version of this article.)

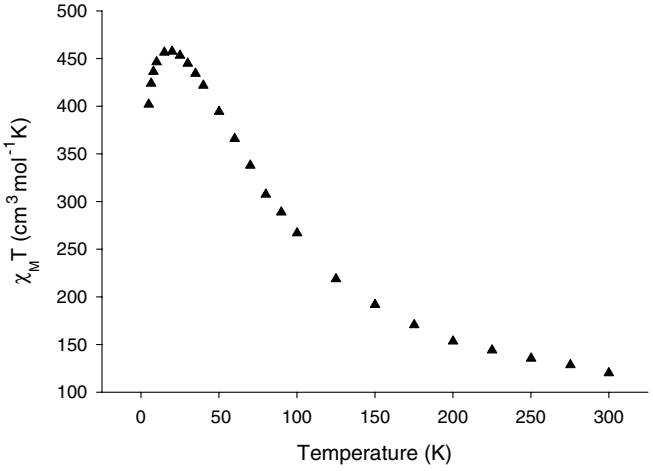


Fig. 3. $\chi_M T$ vs. T plot for complex **2** · 4MeCN in a 1 kG field.

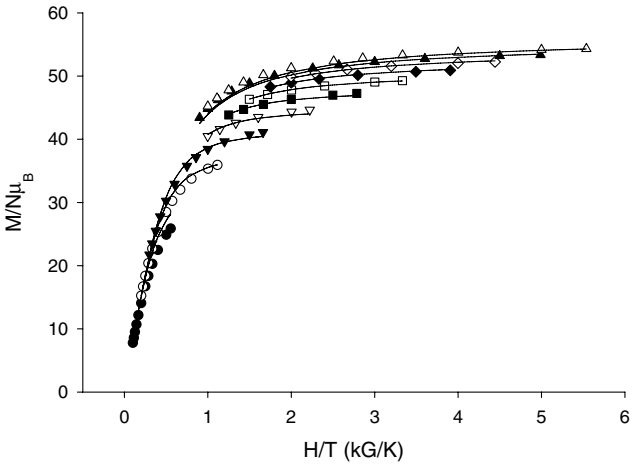


Fig. 4. Plot of reduced magnetization ($M/N\mu_B$) vs. H/T for **2** · 4MeCN in the temperature range 1.8–10 K and in fields of 0.1 T (●), 0.2 T (○), 0.3 T (▼), 0.4 T (▽), 0.5 T (■), 0.6 T (□), 0.7 T (◆), 0.8 T (◇), 0.9 T (▲), and 1.0 T (△). Solid lines are the fit; see the text for the fitting parameters.

assumes only the ground state is populated, includes axial zero-field splitting ($D\widehat{S}_z^2$) and the Zeeman interaction, and carries out a full powder average. The best fit (solid lines in Fig. 4) gave $S = 61/2$, $g = 1.92(1)$ and $D = -0.0120(1)\ cm^{-1}$. The fits for $S = 59/2$, 63/2, and 65/2 were inferior, with best-fit parameters of $g = 1.98(1)/D = -0.0128(1)\ cm^{-1}$, $g = 1.86(1)/D = -0.0113(1)\ cm^{-1}$, and $g = 1.79(1)/D = -0.0106(1)\ cm^{-1}$, respectively. We conclude that **2** has a ground state of $S = 61/2 \pm 1$.

Confirmation of the ground state S of **2** · 4MeCN was obtained by alternating current (ac) susceptibility experiments. Ac susceptibility studies use no dc field and thus are an excellent complementary tool for determining S by avoiding potential complications from a large dc field. The in-phase susceptibility (χ'_M) for **2** · 4MeCN is shown as $\chi'_M T$ versus T in Fig. 5, and extrapolation of the $\chi'_M T$ signal to 0 K from above ~8 K (to avoid the effects of intermolecular interactions at lower temperatures) gives a value of 440–470 $cm^3\ mol^{-1}$ K, consistent with the dc data

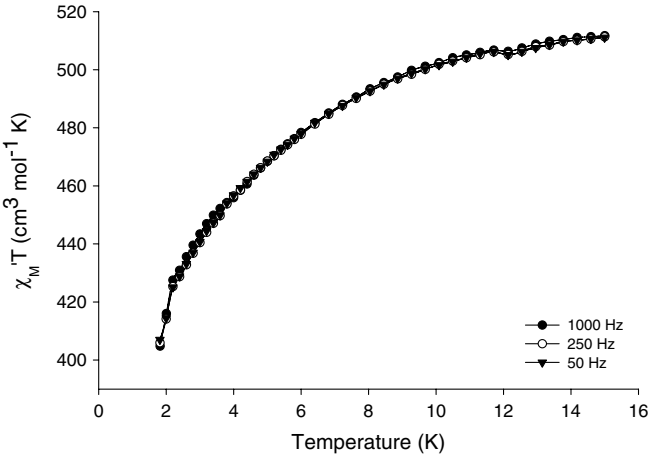


Fig. 5. In-phase ac susceptibility ($\chi'_M T$) measurements of complex **2** · 4MeCN measured below 15.0 K at the indicated frequencies.

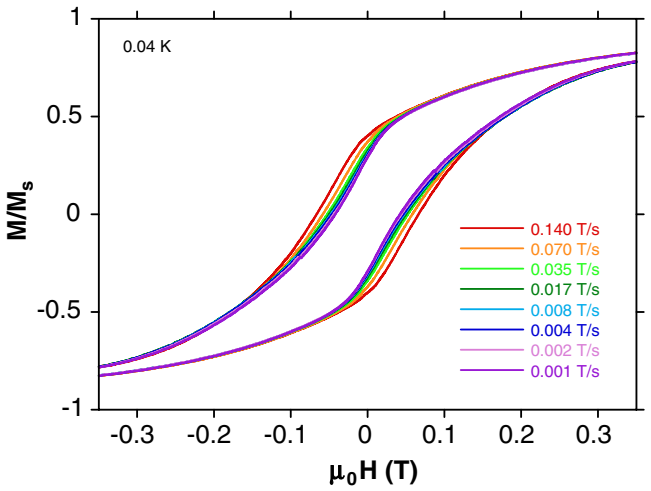


Fig. 6. Magnetization (M) vs field (H) hysteresis loops for a single-crystal of complex **2** · 4MeCN at the indicated field sweep. The magnetization is normalized to its saturation value (M_s).

of Fig. 3. A value of 455 $cm^3\ mol^{-1}$ K is consistent with: (i) $S = 59/2$ and $g = 2.01$, (ii) $S = 61/2$ and $g = 1.95$, and (iii) $S = 63/2$ and $g = 1.89$. The AC data thus confirm a high ground state spin of $S = 61/2 \pm 1$.

The $S = 61/2$ ground state and the negative D value suggested that **2** might be an SMM. Indeed, at temperatures <4.0 K, frequency-dependent tails were seen in the out-of-phase (χ''_M) ac susceptibility signals for **2** · 4MeCN whose maxima lie below the operating minimum temperature of our SQUID instrument (1.8 K). Such signals are an indication of the superparamagnetic-like slow relaxation of a SMM, although they do not prove an SMM because intermolecular interactions and phonon bottlenecks can also lead to such signals. The upper limit to the relaxation barrier is $U = (S^2 - 1/4)|D|$ for a half-integer spin, or only 11.2 cm^{-1} (=16.20 K) for **2** · 4MeCN, but the actual (or effective) barrier (U_{eff}) will be significantly less due to magnetization quantum tunneling through the barrier. In order to confirm whether **2** is an SMM, magnetization versus applied dc field data down to 0.04 K were collected on single-crystals using a micro-SQUID apparatus [8]. The resulting magnetization responses at different field sweep rates and a constant temperature of 0.04 K are shown in Fig. 6. The corresponding magnetization responses at different temperatures and a fixed field sweep rate of 0.14 T/s. Hysteresis loops are seen below ~1.0 K whose coercivities increase with increasing sweep rate and with decreasing temperature, as expected for the superparamagnet-like properties of a SMM. This confirms **2** to be an SMM. An Arrhenius plot, constructed from magnetization decay data, gave $U_{eff} = 6.43\ cm^{-1} = 9.3$ K and $\tau_0 = 5 \times 10^{-11}$, where τ_0 is the pre-exponential factor.

In summary, we have shown that it really is possible to significantly adjust, or tweak, the spin of an already high-spin molecule by altering the peripheral ligation in a way that does not alter the core structure but nevertheless perturbs the exchange coupling. The spin-tweaking is accomplished in this prototypical case by replacement of a bridging and terminal pair of azides with a chelating/bridging hmp^- group, the chelate ring introducing new types of bridging atoms and also some structural restrictions. As a result, the ground state spin increases from $S = 51/2$ to $61/2$.

Acknowledgement

The authors thank the U.S. National Science Foundation (Grant CHE-0414155).

Appendix A. Supplementary material

CCDC 617249 and 617248 contain the supplementary crystallographic data for this paper. These data can be obtained free of charge via http://www.ccdc.cam.ac.uk/conts/retrieving.html, or from the Cambridge Crystallographic Data Centre, 12 Union Road, Cambridge CB2 1EZ, UK; fax: (+44) 1223-336-033; or e-mail: deposit@ccdc.cam.ac.uk).

Supplementary data associated with this article can be found, in the online version, at doi:10.1016/j.poly.2006.10.011.

References

[1] (a) R. Sessoli, D. Gatteschi, D.N. Hendrickson, G. Christou, MRS Bull. 25 (2000) 66;
(b) S.M.J. Aubin, N.R. Gilley, L. Pardi, J. Krzystek, M.W. Wemple, L.-C. Brunel, M.B. Maple, G. Christou, D.N. Hendrickson, J. Am. Chem. Soc. 120 (1998) 4991;
(c) H. Oshio, M. Nakano, Chem. Eur. J. 11 (2005) 5178.
[2] J.R. Friedman, M.P. Sarachik, J. Tejada, R. Ziolo, Phys. Rev. Lett. 76 (1996) 3830.
[3] (a) W. Wernsdorfer, R. Sessoli, Science 284 (1999) 133;
(b) W. Wernsdorfer, M. Soler, G. Christou, D.N. Hendrickson, J. Appl. Phys. 91 (2002) 7164.
[4] (a) G. Christou, Polyhedron 24 (2005) 2065;
(b) G. Aromi, E.K. Brechin, Struct. Bond. 122 (2006) 1.

[5] (a) M. Murugesu, M. Habrych, W. Wernsdorfer, K.A. Abboud, G. Christou, J. Am. Chem. Soc. 126 (2004) 4766;
(b) Th.C. Stamatatos, K.A. Abboud, W. Wernsdorfer, G. Christou, Angew. Chem., Int. Ed. 45 (2006) 4134;
(c) A.M. Ako, I.J. Hewitt, V. Mereacre, R. Clerac, W. Wernsdorfer, C.E. Anson, A.K. Powell, Angew. Chem., Int. Ed. 45 (2006) 4926.
[6] (a) N.C. Harden, M.A. Bolcar, W. Wernsdorfer, K.A. Abboud, W.E. Streib, G. Christou, Inorg. Chem. 42 (2003) 7067;
(b) L. Lecren, O. Roubeau, C. Coulon, Y.-G. Li, X.F.L. Goff, W. Wernsdorfer, H. Miyasaka, R. Clerac, J. Am. Chem. Soc. 127 (2005) 17353;
(c) E.C. Yang, D.N. Hendrickson, W. Wernsdorfer, M. Nakano, L.N. Zakharov, R.D. Sommer, A.L. Rheingold, M. Ledezma-Gairaud, G. Christou, J. Appl. Phys. 91 (2002) 7382.
[7] W. Liu, H.H. Thorp, Inorg. Chem. 32 (1993) 4102.
[8] W. Wernsdorfer, Adv. Chem. Phys. 118 (2001) 99.

ity of these oxalate complexes from 1D chains [13] to 2D honeycomb-like layers [14]. All these examples behave as ferromagnets with critical temperatures below 3.5 K. Even in the chain compound {[K(18-crown-6)][$Mn(H_2O)_2$-$Cr(ox)_3$]0.5(18-crown-6) [13] magnetic ordering is observed due to the presence of weak ferromagnetic interchain interactions. This is favored by the short contacts between chains, that appear strongly related by hydrogen bond interactions between the water molecules that act as ligands. Attending to the interest in the magnetic behavior of chain compounds, particularly since the discovery of the so-called "single-chain-magnets", we have used organic chelating ligands, such as 2,2′-dipyridyl, to substitute the water molecules in order to enlarge the interchain distance, and to decrease the interchain magnetic interactions.

Crystals of [K(18-crown-6)][$Mn(bpy)Cr(ox)_3$] (**1**) were obtained by slow diffusion of a methanolic solution of [K(18-crown-6)]$_3$[$Cr(ox)_3$] into an aqueous solution of $Mn(bpy)Cl_2$.[1] It is important to point out that this compound can only be obtained by slow reaction. Analogous bulk reactions yielded rapid precipitation of insoluble products different from **1**, kinetic products that have to be characterized yet.

[K(18-crown-6)][$Mn(bpy)Cr(ox)_3$] crystallizes in the $P2_12_12_1$ orthorhombic space group.[2] It is built by neutral layers formed by anionic $[Mn(bpy)Cr(ox)_3]^-$ oxalate-bridged bimetallic chains and cationic $[K(18\text{-crown-6})]^+$ complexes (Fig. 1). The bimetallic chains are composed by $[Cr(ox)_3]^{3-}$ complexes and Mn^{II} ions bridged through bidentate oxalate ligands. Each Cr^{III} center presents regular octahedral coordination geometry, with all Cr–O distances within a 0.01 Å range of each other. The octahedral Mn^{II}centers are chelated by two oxalate bridging units and one 2,2′-dipyridyl molecule. There is also little distortion from perfect octahedra, with slightly longer Mn–N distances (2.224 Å for 2.155(3) Å for the shortest M–O distance) and bite angles close to 73° for the chelating bpy. The metal centers along a chain possess opposite chirality, with Cr centers adopting Λ configuration, and all Mn centers adopting Δ configuration. Since there is only one crystallographically independent position for the Mn and Cr centers, this means that all Cr and Mn centers in a single crystal possess identical configuration, since **1** crystallizes in a chiral space group.

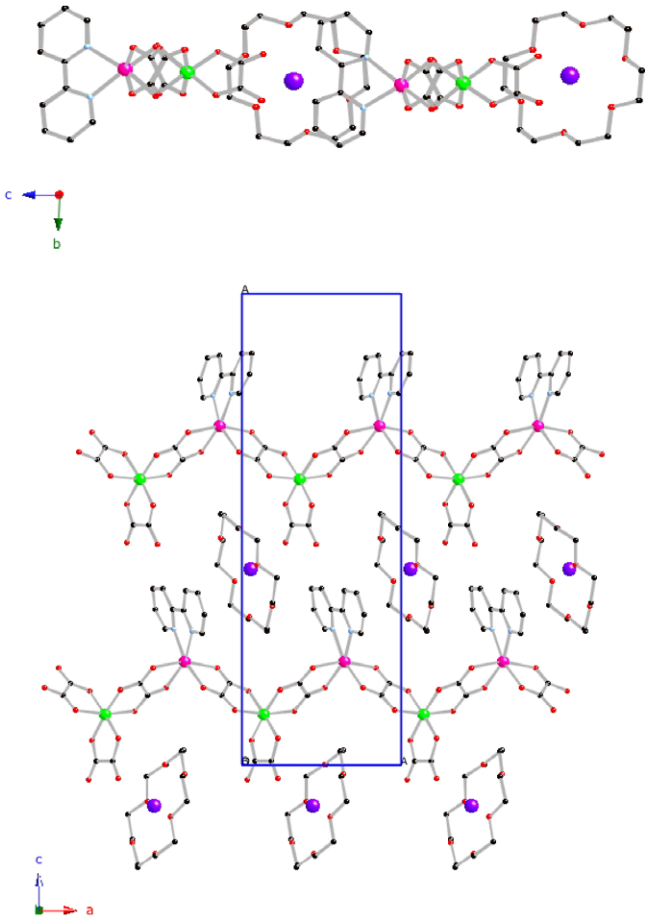


Fig. 1. View of the structural units packing of **1** along the *a* axis (top) and of the structure of the anionic chains in the *ac* plane (down): Cr, green; Mn, pink; K, purple; O, red; C, black. (For interpretation of the references in colour in this figure legend, the reader is referred to the web verison of this article.)

This natural resolution has to be related to the special packing of these chains in the crystal (Fig. 1). Given one chain, all bpy ligands point towards the same direction, with the cations located on the opposite side of the chain, at an intermediate distance to two terminal adjacent oxalate groups, and occupying the holes left by these two oxalate ligands and two bpy ligands from the adjacent chain. The potassium atoms slightly deviate from the crown ether mean plane, as a result of a stronger electrostatic interaction to one of the terminal oxalate ligands (O_{ox}–K = 2.687 Å). For this effective packing all chains need to adopt the same configuration.

There are important differences in comparison to the analogous $[Mn(H_2O)_2Cr(ox)_3]^-$ chain [13], where both enantiomers present show alternating chirality by pairs (–ΔΔΛΛ–) along the chain. The strong hydrogen bonding between chains in the latter compound has been destroyed in this new case by the inclusion of the bpy ligand

[1] Single dark blue crystals were prepared by the slow layering of a 10 mL water solution of $MnCl_2 \cdot 4H_2O$ (0.198 g; 1 mmol) and 2,2′-dipyridyl (0.156 g; 1 mmol) into a 15 mL methanolic solution of [K(18-crown-6)]$_3$-[$Cr(ox)_3$] (0.751 g; 1 mmol). After a few days the prismatic crystals which grew in the interphase were hand collected, washed thoroughly with methanol and dried in air. $KMnN_2O_{18}CrC_{28}H_{32}$ (M_W = 830.6) *Anal.* Calc. (found) for **1**: C, 30.95 (40.49); H, 3.85 (3.88).

[2] Crystal data for **1**. Data were collected with a Nonius KappaCCD diffractometer using graphite monochromatic Mo Kα radiation (λ = 0.71073 Å) at 293 K. The structure was solved by direct method (SIR97) followed by Fourier synthesis, and refined on F^2 (SHELXL-97). The non-hydrogen atoms were refined anisotropically. $KMnN_2O_{18}CrC_{28}H_{32}$, M_W = 830.6, orthorombic, $P2_12_12_1$, a = 9.0510(2) Å, b = 14.4710(3) Å, c = 26.8060(8) Å, V = 3510.97(1) Å^3, T = 293(1) K, Z = 4, ρ_{calc} = 1.571 g/cm^3, $F(000)$ = 1704, μ = 0.868 mm^{-1}, 6328 reflections (R_{int} = 0.000), 2θ max = 54.96°, $R(F)$ = 0.0505 and $Rw(F^2)$ = 0.1073 for 4575 reflections [$I > 2\sigma(I)$].

occupying the position of water molecules. Now the shortest M–M distance is 7.847(1) Å, instead of 6.897(1) Å. The absence of H bonding and longer interchain distances provides better magnetic isolation of the chains in the crystal.

DC magnetic measurements were performed on hand collected grained single crystals between 2 and 300 K under an applied field of 100 G. The $\chi_m T$ product value at 300 K is 6.04 emu K mol^{-1} (Fig. 2), it remains almost constant while the sample is cooled from room temperature down to 150 K, and then it starts to increase exponentially, going over 35 emu K mol^{-1}at 2 K. This fast increase corresponds to an abrupt jump in the $\chi_m$versus T plot. Experimental data in the 50–300 K interval can be fitted to a Curie–Weiss law, with a Curie constant of 5.95 emu K mol^{-1}, in good agreement with the expected spin-only value of 6.25 emu K mol^{-1} ($g \approx 1.95$) corresponding to the sum of the contributions of a Cr^{III} ($S = 3/2$) and a Mn^{II} ($S = 5/2$) ion. The sign of the θ value (+3.78 K) is indicative of the presence of ferromagnetic interactions between the metallic centers through the oxalate bridging ligands. There is no sign of magnetic ordering for **1** above 2 K. The data can be fitted in the 2–300 K range to the equation developed for a Heisenberg 1D chain with alternating spins (a mean g value for both the ions was used for the model) [15]. The obtained results are very satisfactory (Fig. 2) giving a g value of 2.08(2) and a J constant equal to +7.8(7) cm^{-1}. The sign and order of this constant corresponds fairly well with previously reported values in other oxalate-bridged Mn–Cr compounds [16]. As previously observed, the nature of the magnetic exchange involving Mn–Cr ions bridged through an oxalate ligand in its bis-chelating form is ferromagnetic.

The field dependent magnetization of **1** at 2 K (Fig. 3) confirms the ferromagnetic exchange between metallic centers along the chain. The M value increases rapidly at very low fields reaching a 7.73 μ_B value at 5 T, in excellent agreement with the expected value for a parallel alignment of the two interacting spins (8 μ_B).

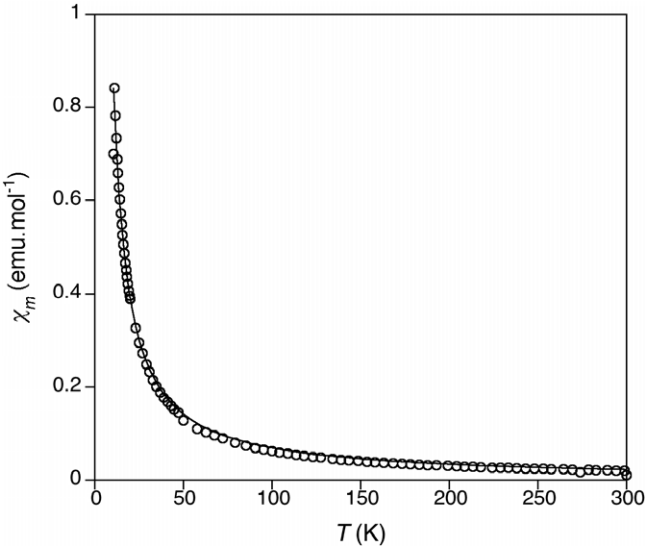


Fig. 2. Thermal dependence of the χ_m value for **1** with the best fitting to a 1D bimetallic Heisenberg chain model in the 2–300 K range.

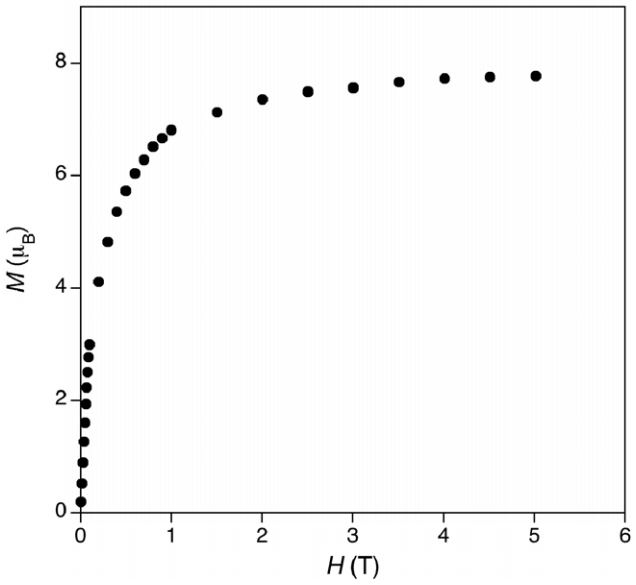


Fig. 3. Field dependence of the magnetization at 2 K for **1**.

In conclusion, we have prepared and characterized the oxalate bridged bimetallic chain [K(18-crown-6)][Mn(bpy)-Cr(ox)$_3$] (**1**). Magnetically, it behaves as a quasi-1D Heisenberg system because, structurally, the introduction of organic capping ligand leads to a good enough magnetic isolation. Nevertheless, the ferromagnetic chains do not show "single-chain magnet" behavior, [17] but rather behave as a ferromagnetic chain, down to 2 K. This same strategy can now be extended to other metals to increase the magnetic exchange and the magnetic anisotropy, both key parameters for the appearance of relaxation phenomena.

Acknowledgments

This work was supported by the Ministerio de Educación y Ciencia (Projects MAT2004-3849 and BQU2002-191) and the Generalitat Valenciana (GV04A/77). C.M-G. thanks the Ministerio de Educación y Ciencia for a predoctoral fellowship.

Appendix A. Supplementary material

CCDC 616683 contains the supplementary crystallographic data for this paper. These data can be obtained free of charge via htpp://www.ccdc.cam.ac.uk/conts/retrieving.html, or from the Cambridge Crystallographic Data Centre, 12 Union Road, Cambridge CB2 1EZ, UK; fax: (+44) 1223-336-033; or e-mail: deposit@ccdc.cam.ac.uk. Supplementary data associated with this article can be found, in the online version, at doi:10.1016/j.poly.2006.10.024.

References

[1] H. Tamaki, Z.J. Zhong, N. Matsumoto, S. Kida, M. Koikawa, N. Achiwa, Y. Hashimoto, H. Okawa, J. Am. Chem. Soc. 114 (1992) 6974.

[2] R. Pellaux, H. Schmalle, R. Hubber, P. Fischer, T. Hauss, B. Ouladiaff, S. Decurtins, Inorg. Chem. 36 (1997) 2301.

[3] (a) H. Tamaki, M. Mitsumi, N. Nakamura, N. Matsumoto, S. Kida, H. Okawa, S. Ijima, Chem. Lett. (1992) 1975;
(b) (b) H. Okawa, N. Matsumoto, H. Tamaki, N. Ohba, M. Mol. Cryst. Liq. Cryst. 232 (1993) 617.

[4] (a) C. Mathonière, S.G. Carling, P.J. Day, J. Chem. Soc., Chem. Commun. (1994) 1551;
(b) C. Mathonière, J. Nutall, S.G. Carling, P.J. Day, Inorg. Chem. 35 (1996) 1201.

[5] E. Coronado, J.R. Galán-Mascarós, C.J. Gómez-García, J.M. Martínez-Agudo, E. Martínez-Ferrero, J.C. Waerenborgh, M. Almeida, J. Solid. State. Chem. 159 (2001) 391.

[6] K.S. Min, J.S. Millar, Dalton. Trans. 20 (2006) 2463.

[7] E. Coronado, J.R. Galán-Mascarós, C. Martí-Gastaldo, J. Mater. Chem. 16 (2006) 2685.

[8] (a) E. Coronado, J.R. Galán-Mascarós, C.J. Gómez-García, J. Ensling, P. Gütlich, Chem. Eur. J. 6 (2000) 552;
(b) E. Coronado, J.R. Galán-Mascarós, C.J. Gómez-García, J.M. Martínez-Agudo, Adv. Mater. 11 (1999) 558;
(c) M. Clemente-León, E. Coronado, J.R. Galán-Mascarós, C.J. Gómez-García, Chem. Commun. (1997) 1727.

[9] (a) S. Bénard, P. Yu, J.P. Audière, E. Rivière, R. Clèment, J. Ghilhem, L. Tchertanov, K. Nakatani, J. Am. Chem. Soc. 122 (2000) 9444;
(b) S. Bénard, E. Rivière, P. Yu, K. Nakatani, J.F. Delouis, Chem. Mater. 13 (2001) 159.

[10] E. Coronado, J.R. Galán-Mascarós, C.J. Gómez-García, V. Laukhin, Nature 408 (2000) 447.

[11] E. Coronado, J.R. Galán-Mascarós, C.J. Gómez-García, J.M. Martínez-Agudo, Inorg. Chem. 40 (2001) 4633.

[12] G. Ballester, E. Coronado, C. Giménez-Saiz, F.M. Romero, Angew. Chem., Int. Ed. 40 (2001) 792.

[13] E. Coronado, J.R. Galán-Mascarós, C.J. Gómez-García, C. Martí-Gastaldo, Inorg. Chem. 44 (2005) 6197.

[14] E. Coronado, J.R. Galán-Mascarós, C. Martí-Gastaldo, Inorg. Chem. 45 (2006) 1882.

[15] A. Mosset, J. Galy, E. Coronado, M. Drillon, D. Beltrán, J. Am. Chem. Soc. 106 (1984) 2864.

[16] E. Coronado, J.R. Galán-Mascarós, C. Giménez-Saiz, C.J. Gómez-García, C. Ruiz-Pérez, Eur. J. Inorg. Chem. (2003) 2290.

[17] (a) A. Caneschi, D. Gatteschi, N. Lalioti, C. Sangregorio, R. Sessoli, G. Venturi, A. Vindigni, A. Rettori, M.G. Pini, M. Novak, Angew. Chem., Int. Ed. 40 (2001) 1760;
(b) R. Clerac, H. Miyasaka, M. Yamashita, C. Coulon, J. Am. Chem. Soc. 124 (2002) 12837;
(c) R. Lescouezec, J. Vaisserman, C. Ruiz-Perez, F. Lloret, R. Carrarasco, M. Julve, M. Verdaguer, Y. Dromzee, D. Gatteschi, W. Wernsdorfer, Angew. Chem., Int. Ed. 42 (2003) 1483;
(d) E. Pardo, R. Ruiz-García, F. Lloret, J. Faus, M. Julve, Y. Journaux, F. Delgado, C. Ruiz-Pérez, Adv. Mater. 16 (2004) 1597;
(e) L. Toma, R. Lescouezec, J. Pasan, C. Ruiz-Pérez, J. Vaisserman, J. Cano, R. Carrasco, W. Wernsdorfer, F. Lloret, M. Julve, J. Am. Chem. Soc. 128 (2006) 4842.

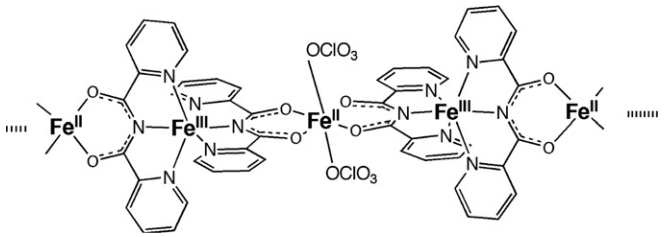


Fig. 1. Structure of high-spin Fe(II)/low-spin Fe(III) alternate single chain magnet **1**.

[7,8]. Hence it was desired to develop a synthetic method for derivatives of Hbpca ligand. To realize the fine-tuning of the complex ligand $[M(bpca)_2]$ and $[M'(bpca)_2]^+$, introduction of alkyl group(s) on the pyridyl rings bound to metal ion would be effective. Here, we will report the synthesis, structure, and magnetic property of the second example of high-spin Fe^{II} and low-spin Fe^{III} alternate SCM, *catena*-$[Fe^{II}(ClO_4)(H_2O)\{Fe^{III}(bmpca)_2\}](ClO_4)_2$ (**2**), which is constructed by the use of methyl-substituted Hbpca ligand, Hbmpca (bis(4-methyl-2-pyridylcarbonyl)amine).

Scheme 1 shows the synthetic scheme of complex **2**. The common synthetic procedure for Hbpca and Hbpmca (bis(2-pyrimidylcarbonyl)amine [6]) adopts the hydrolysis reaction of appropriate tris-2-pyridyltriazine or tris-2-pyrimidyltriazine under the presence of Cu(II) ions [6,9,10a]. The resulting $bpca^-$ and $bpmca^-$ ligands are obtained as copper(II) complexes formulated as $\{Cu(bpca)\}^+$ or $\{Cu(bpmca)\}^+$. Along this line, we first synthesized the 1,3,5-tris(4-methyl-2-pyridyl)triazine according to the reported method with a slight modification [10b]. 4-Methyl-2-cyanopydine was obtained by the reaction of 4-methylpridine N-oxide and trimethylsilylcyanide according to the reported procedure [10c], then the cyanopyridine was heated up to 125 °C for 24 h with the presence of a catalytic amount of sodium hydorate to form 1,3,5-tris(4-methyl-2-pyridyl)triazine by the trimerization reaction. The crude product was purified by alumina chromatography using chloroform as an eluent and yellow oil was obtained. The further purification was performed by recrystallization from heptane/dichloromethane (1:1) and nearly pure triazine was obtained as yellow crystal. The triazine was reacted with an excess amount of copper nitrate in water/EtOH solution to afford the hydrolysis reaction, and copper complex of $[Cu(bmpca)(H_2O)_2]NO_3$ (**3**) was crystallized as blue plates.[1] The free organic ligand was obtained by the treatment of **3** with an excess amount of Na_4edta in the water/chloroform mixture, and Hbmpca was obtained as pale yellow crystals. Overall yield from 4-methylpyridine was about 10%.

Mononuclear Fe(III) complex $[Fe(bmpca)_2]ClO_4$ (**4**) was formed by the reaction of iron(III) nitrate, Hbmpca and $Et_4N(ClO_4)$ in 1:2:5 reaction ratio from water/acetone solution. Fig. 2 shows the crystal structures of mononuclear complex **4**.[2] The whole structure was very similar with the reported complex $[Fe(bpca)_2]ClO_4$ (**5**) [9]. The iron(III) ion in **4** takes low-spin state in a strong ligand-field with the short Fe–N bonding of 1.955(4)–1.971(4) Å for pyridyl nitrogen atoms and 1.894(4)–1.924(4) Å for imide nitrogen atoms, respectively, showing the similar bond distances with $bpca^-$ compound (1.960(3)–1.980(3) Å for pyridyl nitrogens and 1.908(3) Å imide nitrogens, respectively). The introduction of the methyl group on pyridyl ring does not affect on the coordination of $bpca^-$ ligand.

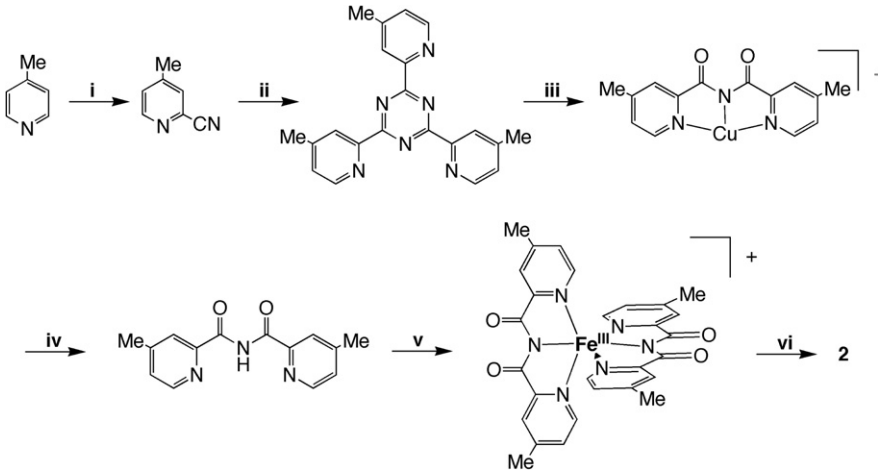
Electrochemical properties of **4** and **5** were investigated by means of cyclicvoltammetry in nitromethane solutions (Fig. 3). Both complexes show reversible redox waves assigned to Fe(II)/Fe(III) couples. The redox potential of **4** is more positive than **5**. The presence of an electron donating methyl group at 4-position on the pyridyl ring stabilizes the trivalent iron ion. This indicates that we can control the electronic state of the central Fe(III) ion by the introduction of one or more substitutional group(s) on the coordinating pyridyl ring.

The alternating Fe(II)–Fe(III) chain complex **2** was synthesized by the reaction of **4** and $Fe(H_2O)_6(ClO_4)_2$ in nitromethane solution under nitrogen atmosphere. Black rod-like crystals were afforded for X-ray analysis, and the resulting structure of cationic part of **2** is shown in Fig. 4.[3] Complex **2** is composed of an alternating arrangement of $\{Fe(bmpca)_2\}^+$ units and$\{Fe(ClO_4)(H_2O)\}^+$ units to form infinite chains. The crystal involves two independent pairs of $\{Fe(bmpca)_2\}^+$ and $\{Fe(ClO_4)(H_2O)\}^+$ units with the similar structures. High-spin Fe(II) ion in the $\{Fe^{II}(ClO_4)(H_2O)\}$ unit is in an elongated octahedoral geometry with four equatorial carbonyl oxygen atoms (Fe–O = 2.059(3)–2.075(2) Å) and two axial oxygen atoms from one perchlorate anion and a water molecule with a distances of 2.144(3) Å and 2.154(3) Å for the former and 2.123(3) Å and 2.131(3) Å for the later, respectively. The π-donor character of $O_{carbonyl}$ splits the t_{2g} orbitals into e_g and b_{2g} orbitals, and therefore the orbital angular momentum should be quenched as found in **1**. The ground state of the Fe(II) ions is $^5B_{2g}$ rather than $^5T_{2g}$. This coordination geometry again leads to a uniaxial zero-field splitting parameter of $D > 0$. Thus the $S = 2$ spin on the Fe(II) ions would have a hard-axis type anisotropy along the

[1] Crystallographic data for **3**: triclinic, space group $P\bar{1}$, $a = 6.6921(7)$ Å, $b = 15.6931(17)$ Å, $c = 18.756(2)$ Å, $\alpha = 84.596(3)°$, $\beta = 85.398(3)°$, $\gamma = 80.204(3)$ °, $V = 1928.2(4)$ Å^3, $T = 100$ K, $Z = 2$, 19366 reflections were observed, of which 8827 were independent, $R_1 = 0.0463$ ($I > 2\sigma(I)$) and $wR_2 = 0.1223$ (all data) for 527 parameters.

[2] Crystallographic data for **4**: monoclinic, space group $P2_1/c$, $a = 20.762(21)$ Å, $b = 14.7262(14)$ Å, $c = 20.5139(23)$ Å, $\beta = 94.925(4)°$, $V = 6248.87(112)$ Å^3, $T = 100$ K, $Z = 8$, 38834 reflections were observed, of which 12204 were independent, $R_1 = 0.0608$ ($I > 2\sigma(I)$) and $wR_2 = 0.1444$ (all data) for 872 parameters.

[3] Crystallographic data for **2**: triclinic, space group $P\bar{1}$, $a = 13.7728(16)$ Å, $b = 16.1281(19)$ Å, $c = 19.790(2)$ Å, $\alpha = 109.849(3)°$, $\beta = 91.070(3)°$, $\gamma = 90.302(3)°$, $V = 4133.8$ (8) Å^3, $T = 100$ K, $Z = 2$, 41998 reflections were observed, of which 18983 were independent, $R_1 = 0.0488$ ($I > 2\sigma$(I)) and $wR_2 = 0.1002$ (all data) for 1212 parameters.



Scheme 1. (i) a, H_2O_2; b, Me_3SiCN. (ii) NaH. (iii) Excess $CuSO_4$. (iv) Excess Na_4edta. (v) $Fe^{III}(NO_3)_3 \cdot 9\,H_2O$, $Et_4N(ClO_4)$. (vi) $Fe^{II}(ClO_4)_2 \cdot 6H_2O$.

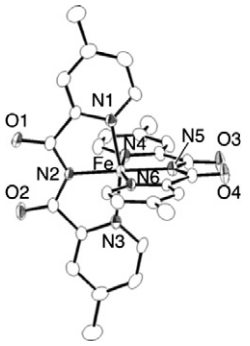


Fig. 2. Ortep diagram of cationic part of complex **4**.

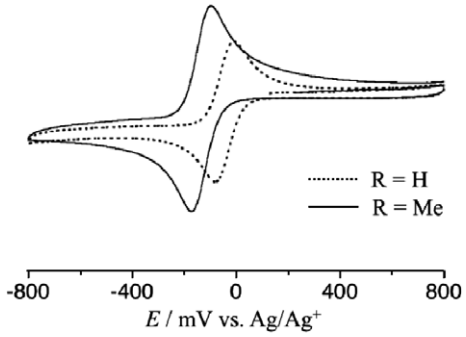


Fig. 3. Cyclic voltammogram of complexes **4** and **5** (1 mM) in $MeNO_2$. Potentials are vs. Ag/Ag^+, with scan rate 100 mV s^{-1}, glassy carbon working electrode, and 0.1 M nBu_4NPF_6.

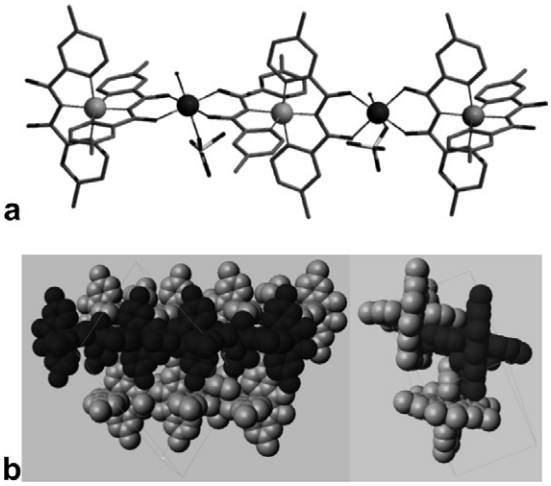


Fig. 4. (a) Crystal structure of the chain complex **2**. Black and gray spheres represent Fe(II) and Fe(III) ions, respectively. Packing diagram of **2**.

O_B–Fe–O_B axis, or easy-plane type. The shortest intra- and inter chain Fe–Fe distances were estimated as 5.2161(9) Å (Fe(II)–Fe(III)) for the former and 10.6468(12) Å (Fe(II)–Fe(III)) for the later, respectively.

The magnetic properties of complex **2** were studied using a polycrystalline sample. The temperature dependence of $\chi_m T$ for **2** is clearly consistent with the presence of ferrimagnetic interactions (Fig. 5). As the temperature was lowered, $\chi_m T$ gradually decreased to a minimum value at 18 K (2.79 emu K mol^{-1}), and then abruptly increased to a maximum value at 1.8 K (19.1 emu K mol^{-1}). The temperature at which the $\chi_m T$ reaches the minimum is slightly lower than that of **1** (22 K), indicating that the magnetic interaction between adjoining Fe(II)–Fe(III) ions would be weaker than **1**. No evidence for long-range ordering was observed even at the lowest temperatures studied.

Ac magnetic susceptibility measurements were performed to observe the frequency dependence of χ''_m (Fig. 5b). Complex **2** shows a typical SCM behavior below 3 K; with cooling, the in-phase signal χ'_m increased in accordance with the Curie law to a maximum value and then decreased, eventually approaching zero, with the corresponding appearance of the out-of-phase signal χ''_m. As the frequency was swept from 1000 Hz to 5 Hz, the temperature of maximum χ''_m shifted from 2.3 K

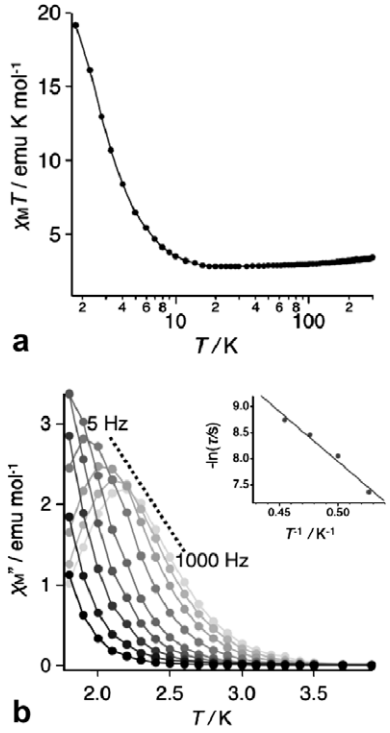


Fig. 5. (a) Temperature dependence of $\chi_m T$ for **2**. (b) Temperature dependence of χ''_m. inset: Arrhenius plot.

(1000 Hz) to 1.9 K (50 Hz). The temperature for the maximum χ''_m in the lower frequency fields were lower than this temperature range. At fixed temperatures between 1.8 and 1.9 K, semicircle Cole–Cole plots were obtained with small α parameters in the range of 0.24(7)–0.26(1), which indicates that relaxation occurs via a single process. This typical SCM behavior is again attributed to a mutually orthogonal arrangement of the Fe(II) molecular axes inducing Ising interactions along the chain observed in **1** [3]. The relaxation times $\tau(T)$ extracted from the ac susceptibility were used to construct an Arrhenius plot, giving an estimated activation energy Δ of 19(1) K. This Δ value is smaller than that of **1** reported as 27(1) K, reflecting the smaller Fe(II)–Fe(III) interaction suggested by the temperature dependence of dc susceptibility. The detailed investigation of magnetic interactions is now on undergoing.

In conclusion, we developed a synthetic route for substituted bpca$^-$ ligands and synthesized the second example of Fe(II)–Fe(III) alternate single chain magnet by the introduction of methyl group on the coordinating pyridyl rings. This twisting easy-plane system is unique since which exhibits easy-axis anisotropy over the whole chain, giving rise to slow magnetization reversal despite single-ion anisotropy of the constituent Fe(II) ions with easy-plane [4,11]. The substitution of alkyl group on bpca$^-$ ligand is very effective to control the SCM behavior since the introduction of methyl group affects on the dc susceptibility as well as the activation energy Δ.

Supplementary material

CCDC 622578, 622579 and 622580 contain the supplementary crystallographic data for this paper. These data can be obtained free of charge via http://www.ccdc.cam.ac.uk/conts/retrieving.html, or from the Cambridge Crystallographic Data Centre, 12 Union Road, Cambridge CB2 1EZ, UK; fax: (+44) 1223-336-033; or e-mail: deposit@ccdc.cam.ac.uk.

Acknowledgements

This work was supported by a Grant-in-Aid for Young Scientists from the Ministry of Education, Culture, Science, Sports, and Technology, Japan, as well as the Mitsubishi Chemical Corporation Fund.

References

[1] (a) L. Thomas, F. Lionti, R. Ballou, D. Gatteschi, R. Sessoli, B. Barbara, Nature 383 (1996) 145;
(b) D. Gatteschi, R. Sessoli, Angew. Chem., Int. Ed. 42 (2003) 268;
(c) W. Wernsdorfer, R. Sessoli, Science 284 (1999) 133;
(d) S.M.J. Aubin, Z. Sun, L. Pardi, J. Krzystek, K. Folting, L.-C. Brunel, A.L. Rheingold, G. Christou, D.N. Hendrickson, Inorg. Chem. 38 (1999) 5329.

[2] (a) A. Caneschi, D. Gatteschi, N. Lalioti, C. Sangregorio, R. Sessoli, G. Venture, A. Vindigni, A. Rettori, M.G. Pini, M.A. Novak, Angew. Chem., Int. Ed. 40 (2001) 1760;
(b) R. Clérac, H. Miyasaka, M. Yamashita, C. Coulon, J. Am. Chem. Soc. 124 (2002) 12837;
(c) R. Lescouëzec, J. Vaissermann, C. Ruiz-Pérez, F. Lloret, R. Carrasco, M. Julve, M. Verdaguer, Y. Dromzee, D. Gatteschi, W. Wernsdorfer, Angew. Chem., Int. Ed. 42 (2003) 1483;
(d) T.-F. Liu, D. Fu, S. Gao, Y.-Z. Zhang, H.-L. Sun, G. Su, Y.-J. Liu, J. Am. Chem. Soc. 125 (2003) 13976;
(e) M. Ferbinteanu, H. Miyasaka, W. Wernsdorfer, K. Nakata, K.-i. Sugiura, M. Yamashita, C. Coulon, R. Clérac, J. Am. Chem. Soc. 127 (2005) 3090;
(f) K. Bernot, L. Bogani, A. Caneschi, D. Gatteschi, R. Sessoli, J. Am. Chem. Soc. 128 (2006) 7947.

[3] T. Kajiwara, M. Nakano, Y. Kaneko, S. Takaishi, T. Ito, M. Yamashita, A. Igashira-Kamiyama, H. Nojiri, Y. Ono, N. Kojima, J. Am. Chem. Soc. 127 (2005) 10150.

[4] (a) R.J. Glauber, J. Math. Phys. 4 (1963) 294;
(b) C. Coulon, R. Clérac, L. Lecren, W. Wernsdorfer, H. Miyasaka, Phys. Rev. B69 (2004) 132408.

[5] (a) A. Kamiyama, T. Noguchi, T. Kajiwara, T. Ito, Angew. Chem., Int. Ed. 39 (2000) 3130;
(b) A. Kamiyama, T. Noguchi, T. Kajiwara, T. Ito, Inorg. Chem. 41 (2002) 507;
(c) A. Kamiyama, T. Noguchi, T. Kajiwara, T. Ito, Cryst. Eng. Comm. 5 (2003) 231;
(d) T. Kajiwara, R. Sensui, T. Noguchi, A. Kamiyama, T. Ito, Inorg. Chim. Acta 337 (2002) 299;
(e) T. Kajiwara, T. Ito, Mol. Cryst. Liq. Cryst. 335 (1999) 73.

[6] D.C. de, C. Gomes, H.O. Stumpf, F. Lloret, M. Julve, V. González, H. Adams, J.A. Thomas, Inorg. Chim. Acta 358 (2005) 1113.

[7] (a) T. Kajiwara, A. Kamiyama, T. Ito, Chem. Commun. (2002) 1256;
(b) T. Glaser, H. Theil, I. Liratzis, T. Weyhermüller, E. Bill, Inorg. Chem. 45 (2006) 4889.

[8] (a) A. Igashira-Kamiyama, T. Kajiwara, T. Konno, T. Ito, Inorg. Chem. 45 (2006) 6460;

(b) M.-L. Tong, Y.-M. Wu, Y.-X. Tong, X.-M. Chen, H.-C. Chang, S. Kitagawa, Eur. J. Inorg. Chem. (2003) 2385.
[9] S. Wocadlo, W. Massa, J.-V. Folgado, Inorg. Chim. Acta 207 (1993) 199.
[10] (a) D. Marcos, R. Martinez-Mañez, J.V. Folgado, A. Beltran-Porter, D.B.-P. Corresponding, A. Fuertes, Inorg. Chim. Acta 159 (1989) 11;
(b) H.C. Francis, K. Emil, J. Am. Chem. Soc. 81 (1959) 905;
(c) P.G. Theobald, W.H. Okamura, J. Org. Chem. 55 (1990) 741.
[11] M. Nakano, G. Matsubayashi, T. Muramatsu, T.C. Kobayashi, K. Amaya, J. Yoo, G. Christou, D.N. Hendrickson, Mol. Cryst. Liq. Cryst. 376 (2002) 405.

than benzoic acid which was added slowly into 30 mL of a toluene suspension of $Mn(O_2CCH_3)_2$ (1.00 g, 5.78 mmol) with constant stirring. The solution changed from yellow to dark brown after 5 h reaction at elevated temperature. The pale pink product was washed with toluene and dried under vacuum (yield, 1.64 g). Elemental analysis (duplicate) was performed at Galbraith Laboratories, Inc. (Knoxville, TN). *Anal.* Calc for $C_9H_8O_{4.1}Mn_1$: C, 45.67; H, 3.41. Found: C, 44.12; H, 3.26%.

2.2. Crystallography

The structure was examined by X-ray powder diffraction collected using a Phillips PW3040 X'pert-MPD Multipurpose Diffractometer in Bragg–Brentano geometry (Cu Kα radiation) with a Cu monochromator, programmable divergence, scatter and receiving slits, and soller slits on both incident and diffracted beams.

2.3. XANES

X-ray absorption near edge structure (XANES) data were collected at the Center for Advanced Microstructures and Devices synchrotron radiation facility using the X-ray microprobe double crystal monochromator beamline. The monochromator is of the Lemonnier type equipped with a pair of Ge(220) crystals [12]. Mn(0) foil was used to calibrate the energy scale of the monochromator. The energy threshold E_0 of the Mn(0) metal foil was determined from the first inflection point in the XANES spectrum (6539 eV). XANES spectra of MnO and Mn_2O_3 powders were measured to place the K edge positions and to determine the chemical shift of these oxides relative to Mn(0) foil in order to explore the valency of compound **1**. A thin powder layer of these oxide powders and compound **1** were prepared on a piece of Kapton tape for the XANES measurement. All measurements were performed in a transmission mode by using an ionization chamber filled with 1 atm. air for MnO and Mn_2O_3 samples. XANES spectra of the pristine form of **1** was acquired while holding the sample in a dry nitrogen purged sample container and later was exposed to atmosphere for periods of 10 min and 2 days to explore the effect of ambient background. A linear background was subtracted and normalization of spectra to **1** at 6640 eV photon energy was performed using commercially available Athena software [13]. XANES spectra were scanned with −100; −20; +40; +200 eV intervals relative to Mn K edge with a step of 2, 0.4, 1 eV per respective energy interval and an integration time of 1 sec. per step.

2.4. Magnetometry

The magnetic data were collected with a Quantum Design PPMS using the VSM option for M(H,T) measurements and the ACMS option for the in and out-of-phase susceptibility determinations. Calibrations were competed using DyO and Pd references. Custom nylon sample holders and pharmaceutical gel caps used for holding sample powders demonstrated less than 10^{-8} emu diamagnetic background; the data presented are without diamagnetic correction.

3. Results and discussion

3.1. Physical structure

Powder diffraction of **1** (Fig. 1) is found to superpose on the powder diffractogram of **2**, the single crystal reported in [11], with additional peaks whose origin remains under investigation. A paper detailing the synthesis and complete structure of **1** is forthcoming. Because of the good diffraction fit, we propose and will assume through the remainder of this paper that the honeycomb structure solved by Liu et al. (Fig. 2) is the foundational structure with additional coordinates (e.g., H_2O, μ-O) causing the extraneous peaks. Such extra peaks do not fit with any known manganese or manganese oxide impurity like phase; also, background magnetization and NMR studies of the starting materials showed paramagnetic behavior with coercive crossings of less than one oersted indicating clean starting materials.

With regard to explaining the low temperature magnetic behavior, it is important to note certain key features of the structure: (1) the Mn_{12} hexagon rings with carboxylate bridging; (2) the two-dimensional honeycomb sheets built from the edge sharing Mn_{12} hexagons; and, (3) the benzyl, methyl and possible water positions between neighboring sheets. Such structural information combined with the valency is critical in explaining the subtle differences between static and dynamic structural reorientations that form the basis for each magnetic transition. An example of a subtle structural change can be the temperature dependence of the bond angles between two manganese through oxygen. This effect, supported in general by Goodenough–Kanamori theory [14], has been shown to invert the exchange interaction from ferromagnetic to antiferromagnetic with as little as a 10° angle change [9].

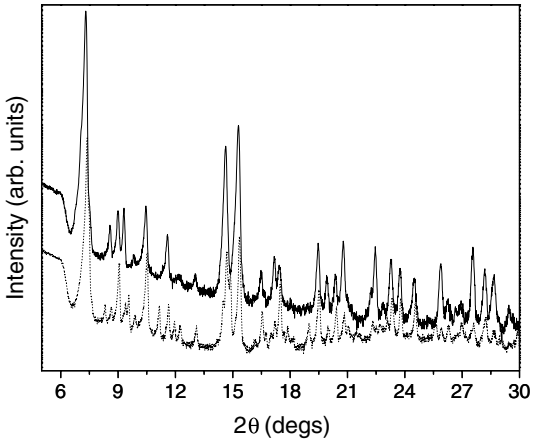


Fig. 1. Powder diffraction of **1** (---) and **2** (—) demonstrating the superposition of **1** on **2** plus extraneous peaks.

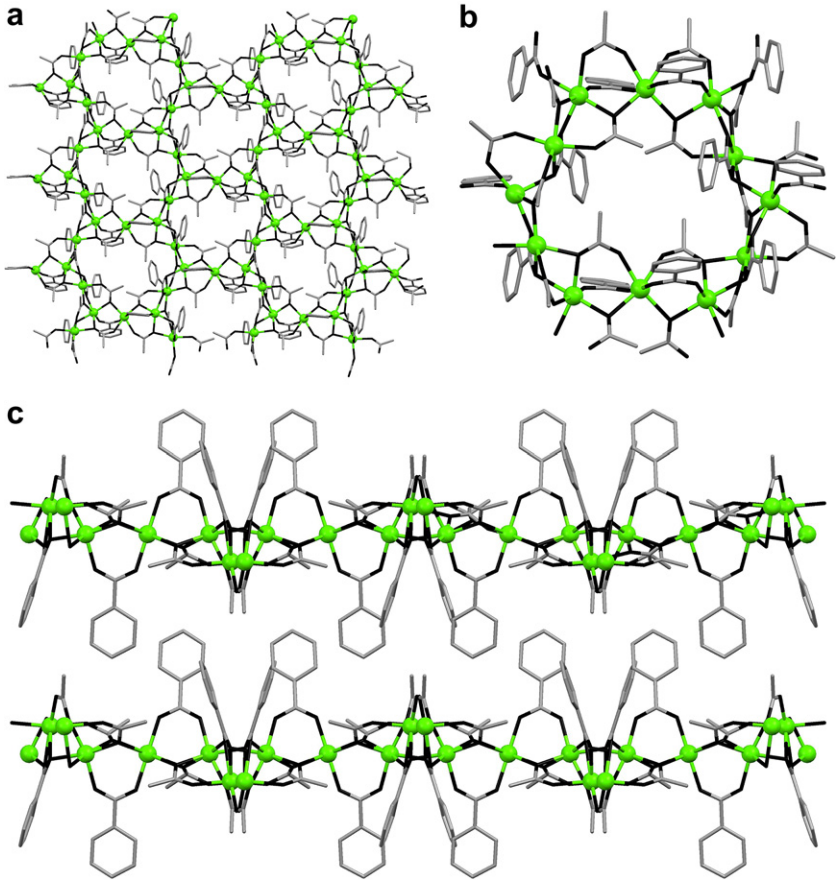


Fig. 2. Nominal structure of **1** showing the (a) top view of the edge sharing hexagon rings; (b) top view detail of one ring; and (c) side view showing layering, alignment and interplane ligands. *Note*: the benzyl rings in (c) are more than 10 Å apart and do not π-stack.

3.2. Oxidation state

XANES spectroscopy, which is highly sensitive to local chemical and thus the electronic environment of the excited atom, has been used to determine the formal oxidation state of compound **1** (pristine form). The XANES data, shown in Fig. 3, present spectra from compound **1** (pristine form) relative to the Mn(II) and Mn(III) standards. It is qualitatively obvious that the K-edge of compound **1**, located at 6548 eV, lies between the 2+ (6544 eV) and 3+ (6552 eV) states, indicating a mixed valence state. Exposure of **1** to atmosphere did not significantly change its valence states (not shown) as determined by the superposition of K edges at 6548 eV. The attempt to reproduce the compound **1** spectra by a linear combination fit of references spectra MnO (II) and Mn_2O_3 (III), using standard fitting procedures in Athena [13], reveals a quantitative valence split of 71 ± 12% Mn(II) and 29 ± 12% Mn(III). 13 eV below and 10 eV above the K edge of compound **1** were chosen as a fitting range in the fitting procedure. Given this result and the chemical anaylsis (vide supra), it is speculated that the complex has the following nominal formula "$Mn(II)_{0.8}Mn(III)_{0.2}(OAc)(OBz)(\mu\text{-}O)_{0.1}$" whereby oxygen reacts with neighboring Mn(II) metal centers to give Mn(III)-O-Mn(III) μ-oxo bridges.

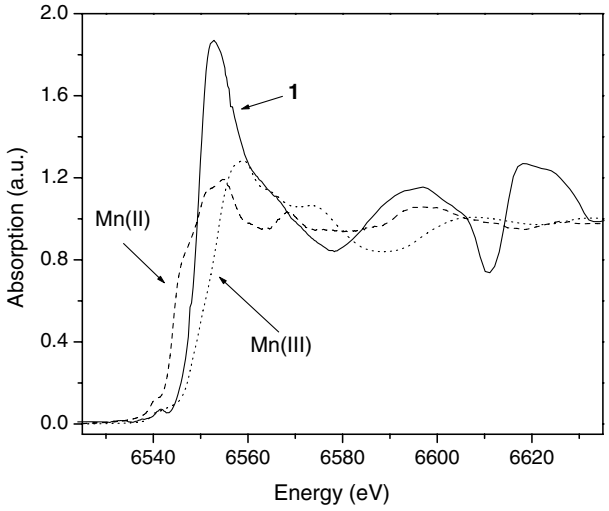


Fig. 3. XANES spectra of MnO, Mn_2O_3 and 1. K edge position of 1 (—) located between the K edge positions of MnO (– – –), and Mn_2O_3 (----) indicates a mixed valence state.

3.3. Magnetic structure

The low temperature magnetic behavior of **1** contains various transitions that exist as a function of the manganese valency, the intramolecular exchange due to the

honeycomb structure with carboxylate mediation and the interplanar exchange mediated by the benzyl, methyl, hydrogen and possible H_2O pathways. We discuss the exchange type and assign the magnetic character in various temperature and applied field regions from ac and dc extraction methods.

3.3.1. Temperature dependent magnetization and susceptibility

The magnetization (M), in-phase susceptibility (χ') and out-of-phase susceptibility (χ'') of **1** (Fig. 4) demonstrate three distinct magnetic states; the first from 1.9 to 2.1 K is labeled A; the second from 2.1 to 7.9 K denoted B; and 7.9 K onward labeled C. Also shown is the inverse susceptibility $\chi^{-1}(T)$ and susceptibility temperature product $\chi T(T)$ in Fig. 5 which reveal Weiss constants which reverse sign at $T = 2.3$ and 11 K as well as respective slope changes $d(\chi T)/dT$ between the regions A, B and C. In regions B and C, the Weiss constants are $\theta = +7$ and -50 Oe. Such combined pieces of evidence, along with the mixed Mn(II)/Mn(III) valency, lead to suggest that the low temperature regions A, B and C are represented by ferrimagnetic ordering (AFM exchange), ferromagnetic ordering and back to ferrimagnetic ordering. Further support for this conjecture is demonstrated in Fig. 6 where the coercivity versus temperature is shown to approach zero at 10 K, representative of the ferromagnetic to ferrimagnetic transition point (7.9 K). Low temperature transition behavior of this kind is common among the Mn-carboxylate systems where the interplanar ligand mediated exchange can play a vital role [7]. In addition to the ferrimagnetic ordering could be antiferromagnetic spin canting as observed by Price et al. [3] and/or an order/disorder transition that will be discussed further with regard to applied field measurements.

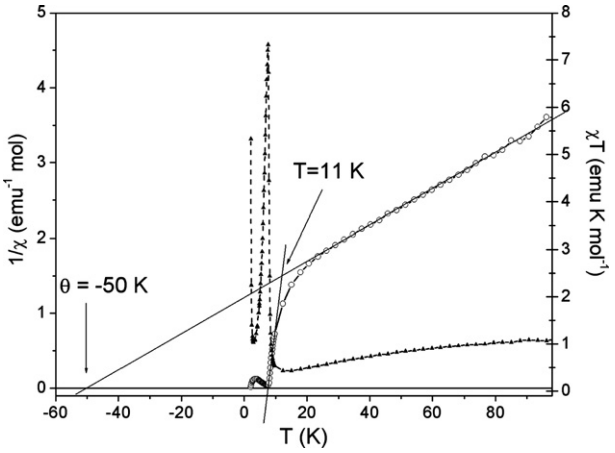


Fig. 5. Inverse susceptibility (○) and the susceptibility temperature product (▲) are shown as a function of temperature for **1** with an applied field of 10 Oe, in the non-field cooled configuration at $v = 7919$ Hz.

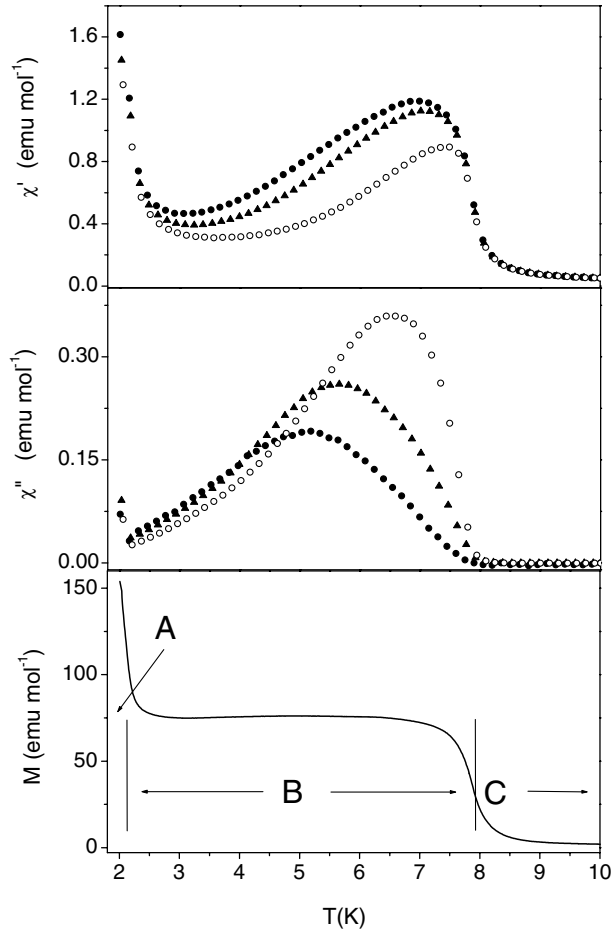


Fig. 4. Temperature and frequency dependence of the (top) in-phase susceptibility and (middle) out-of-phase susceptibility and (bottom) magnetization of **1**. The three frequencies are represented as (●), (▲) and (○) for $v = 17$, 727 and 7919 Hz. All measurements were completed with $H_{dc} = 0$ Oe and the susceptibility at $H_{ac} = 3$ Oe.

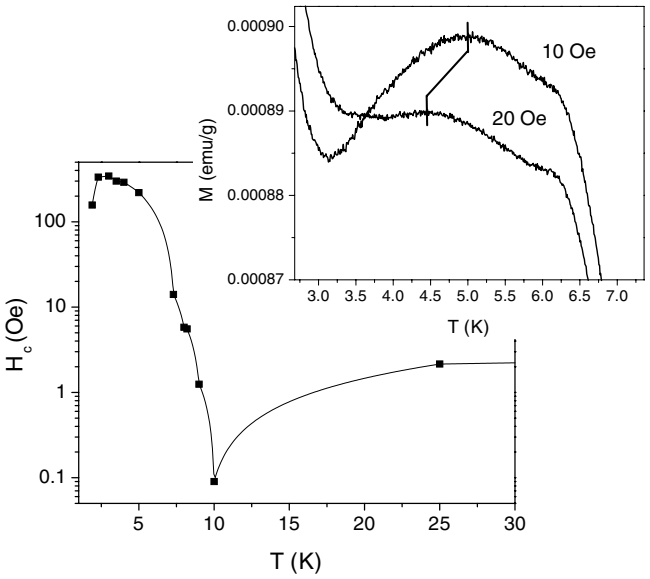


Fig. 6. Coercivity and (inset) magnetization as a function of temperature. Both measurements were completed under non-field cooled conditions. It is interesting to note the trend in coercivity with the magnetization in Fig. 4 and exchange field in Fig. 8.

3.3.2. Spin-glass behavior

The inset to Fig. 6 demonstrates a shift in the peak position in the ferromagnetic region B, where the zero-field-cooled (ZFC) magnetization was measured as a function of temperature and applied field. The peak shift with applied field is similar to the results found for spin glasses, wherein the glass transition temperature decreases as higher fields are applied. Fig. 8 shows a concavity change in the FC data through the temperature range of 6–8 K, that is not observed in the ZFC curve, and inflection in either susceptibility component is absent as well. Such behavior is indicative of an unthawing glass or superparamagnetic transition wherein the magnetocrystalline anisotropy is lifted [15]. Lastly, both the real and imaginary components of the susceptibility in the 2.1–7.9 K range are frequency dependent wherein as the applied field frequency increases, so does the transition temperature indicating glass like behavior [15]. The general superparamagnetic or glassy behavior has been observed by others for the Mn-carboxylate based complexes [3,4]. It is because of the combined frequency dependence (Fig. 4) and field dependence (Fig. 6 inset) that we attribute glass or superparamagnetic behavior rather than domain wall motion for frequency dependence only.

3.3.3. Metamagnetic transition

Metamagnetism is a transition phenomena that can occur by application of field, temperature or pressure and is usually recognized by dramatic changes in the magnetization or susceptibility [16e]. Fig. 7 demonstrates the magnetization and susceptibility components as a function of applied field at 1.7 K; from Section 3.3.1 the zero-field ordering was found to be ferrimagnetic up to 2.3 K, where indeed the step behavior of M(H) vanishes. In the low field isothermal (1.7 K) region (Fig. 7a) an abrupt increase in the magnetization is observed at ~200 Oe and continues to saturation at 4 T. We posit that this field value marks an intramolecular transition from ferrimagnetic to weak-ferromagnetic or spin-canted ferrimagnetic order. However, a lack of either susceptibility component in this 200–40000 Oe range does not directly support the above claim, raising even more questions as to the exact nature and type of transition. A similar metamagnetic effect was observed by Price et al. [3] for $\{[Mn(\mu\text{-}OH)(\mu\text{-}OAc)_2]\cdot HOAc\cdot H_2O\}_n$ linear chains wherein the transition was assigned as antiferromagnetic to spin-canted antiferromagnetic and that a ferromagnetic alignment was not observed below 5 T, helping to support the above postulate.

With respect to the magnetization climb from 6 to 9 T we can only remark that this response is rigorously unexplainable, especially given the negative concavity. Even grossly speculative arguments such as lifting of interlayer anisotropy [4] or quenched angular momentum are difficult to invoke, although we should expect that a transition from canted ferrimagnetic to ferromagnetic will be convoluted at high field due to their superposition. One qualitative

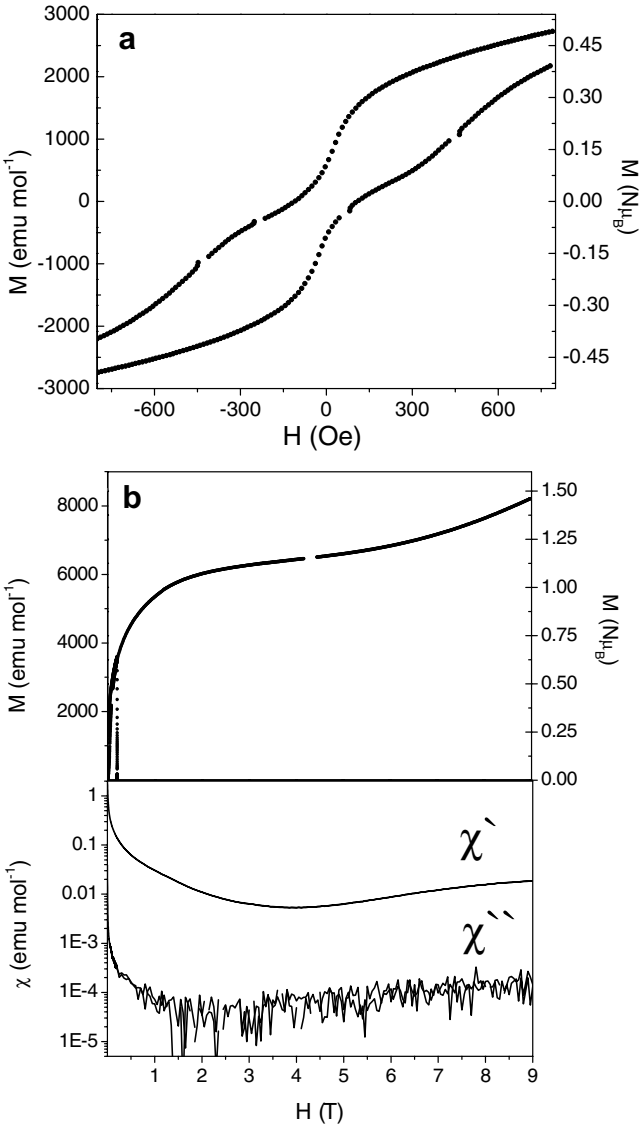


Fig. 7. Magnetic field dependence of the magnetization, in-phase and out-of-phase susceptibility of **1** completed at $T = 1.7$ K. (a) Shows the low field dependent metamagnetic transitions and (b) the high field.

observation from this work, is an inflection point at 6 T, which in previous work on the canted antiferromagnet $[Mn(bipyridine)(N_3)_2]_n$ [17] was attributed to the beginning of a spin flop transition, but is still not enough to account for such a high moment above manganese. This inflection point is also supported by the rise in susceptibility beginning at 4 T (Fig. 7). Furthermore, in such two-dimensional systems and especially in the manganese carboxylate based materials, canted antiferromagnetism at low temperatures is common. Lastly, it is interesting to note the difference in the minimum observed at 2 versus 4 T for the out-of-phase versus in-phase susceptibility components, which may suggest frustration is further complicating these magnetization dynamics. Higher fields, lower temperatures and varying transition metal types, may help understand this rather unusual transition.

3.3.4. Exchange anisotropy

Exchange anisotropy was first reported in 1956 [18] when the field dependent magnetization of ferromagnetic cobalt covered by a thin antiferromagnetic cobalt oxide, demonstrated a non-symmetric hysteresis loop about zero field. Since then, an entire sub-field of magnetism has been devoted to understanding this rather elusive effect [19]. The root of exchange anisotropy is not yet fully understood; the present and most simple theory holds that exchange anisotropy is a phenomenon induced by interfacial pinning, typically between a ferromagnet and antiferromagnet or by a ferromagnet and some structural defect [19]. For organic-based magnets, this phenomenon has rarely been reported and is attributed to intermolecular ferromagnetic exchange between two intramolecular antiferromagnetic Ni or Mn single molecular magnets [20]. The evidence which led to a determination of exchange anisotropy in the single molecular magnets was a non-symmetric field dependence of the resonant quantum tunneling of the magnetization.

In the present work, we indeed find a hysteresis loop whose center is shifted from zero and whose magnitude (H_{ex}) is temperature dependent (Fig. 8). Because exchange anisotropy exists due to ferromagnetic/antiferromagnetic interaction, the value of H_{ex} should provide a means by which to measure the interlayer exchange. From Section 3.3.1, we know above 7.9 K, that the intrasheet exchange is antiferromagnetic with the intersheet exchange being ferromagnetic at all temperatures. The enhanced exchange bias or anisotropy field H_{ex} as observed in Fig. 8 follows the temperature trend of the magnetization. Although this response is rather crude and weak, compared with standard inorganic exchange anisotropy, it nevertheless does provide a means by which to gauge intersheet exchange coupling and is worth further measurement and consideration.

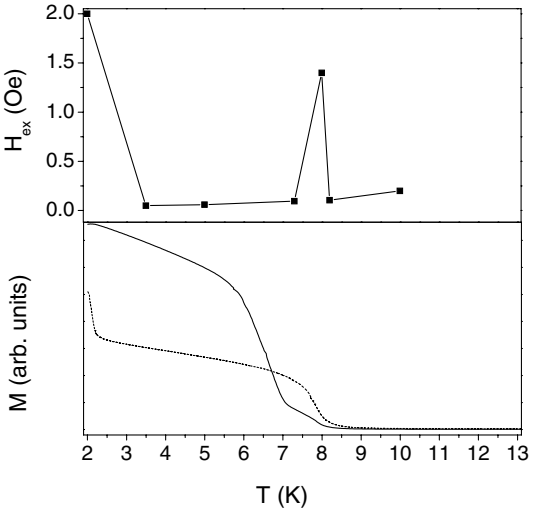


Fig. 8. Exchange bias (H_{ex}) and magnetization as a function of temperature. The dashed curve (---) represents the non-field cooled while the solid line (—) is the field cooled magnetization. *Note*: the concavity change between 6 and 8 K in the field cooled data which is not observed in the non-field cooled curve is attributed to a thawing (magnetocrystalline anisotropy lifting) of the moments rather than an exchange transition.

3.3.5. Magnetic properties of other honeycomb systems

A number of different honeycomb structures have been reported that contain 6 [21] or 12 [22] atoms per edge sharing hexagon as well as lower symmetry sheet structures [16]. A general trend in the low temperature region is the ferromagnetic to antiferromagnetic exchange transition (positive to negative Weiss behavior) which for single valency result in a finite moments by canted antiferromagnetic ordering. Other trends include quick rises to saturation (within tens of oersted), strong communication within the layers and weak interlayer exchange. Such strong antiferromagnetic exchange due to the increased dimensionality was highlighted by Kahn [22a] and encouraged as a means by which higher ordering temperatures and technologically relevant materials might succeed. It is therefore our intention to endeavor to understand how the intra and interlayer exchange may be enhanced so that high temperature remnant behavior may be applied.

4. Conclusions

Three distinct temperature transitions and three applied field dependent transitions have been shown to occur in the low temperature region of a manganese mixed carboxylate complex we are speculating as "$Mn(OAc)(OBz)(\mu\text{-}O)_{0.1}$". XANES K edge determination finds a mixed valence of 71% Mn(II) and 29% Mn(III). Explicity, transitions from ferrimagnetic to ferromagnetic to ferrimagnetic are observed in the region from 1.9 to 8.5 K as observed by temperature dependent magnetization and susceptibility. Frequency dependence of the susceptibility reveals relaxation effects typically attributed to glass like behavior. Metamagnetic behavior was also seen at 2.3 K and below as is explainable within a field dependent transition model where the ferrimagnetic moments rotate at a strong enough field to align parallel, although field greater than 6 T result in an unexplainable 7.3 μ_B moment. Lastly, a crude trend is found in the coercivity offset with temperature that is attributed to exchange anisotropy and assigned as a monitor of the interlayer exchange which will be further investigated. Overall, this carboxylate-mediated layered system opens the door for systematic synthesis to help understand antiferromagnetic intralayer exchange and interlayer ligand-mediated exchange through variation of the transition metal types, valencies and ligands to vary the spin–orbit coupling, number of available ground states and nearest-neighbor spacing. Polaronic incorporation to enhance the state of metallicity [22d,23] may provide application enhancement in addition to the physical structure (two-dimensionality) and will be a focus of future research.

Acknowledgements

This work was supported by the Defense Microelectronics Activity (DMEA) under agreement DMEA 90-02-2-0218 and the NSF through ND EPSCoR grant EPS-0447679.

References

[1] (a) D.A. Ewards, R.N. Hayeard, Can. J. Chem. 46 (1968) 3443;
(b) T.E. Wood, G. Kokaszka, P. Day, Inorg. Chem. 18 (1979) 2936.
[2] (a) James D. Martin, Ryan F. Ness, Chem Commun. (1996) 2419;
(b) Hui-Juan Yang, Hui-Zhong Kou, Zhong-Hai Ni, Ai-Li Cui, Ru-Ji Wang, Inor. Chem. Comm. 8 (2005) 846.
[3] David J. Price, Stuart R. Batten, Boujemaa Moubaraki, Keith S. Murray, Polyhedron 22 (2003) 2161.
[4] Anastasios J. Taskiopoluos, Wolfgang Wernsdorfer, Khalil A. Abboud, George Christou, Polyhedron 24 (2005) 2505.
[5] (a) R.B. Flippen, S.A. Friedberg, Phys. Rev. 121 (1961) 1591;
(b) J.H. Schelleng, C.A. Raquet, S.A. Friedberg, Phys. Rev. 176 (1968) 708;
(c) V.A. Schmidt, S.A. Friedberg, Phys. Rev. 188 (1969) 809;
(d) Yuichi Okuda, Motohiro Matsuura, Taiichiro Haseda, J. Phys. Soc. Jpn. 44 (1978) 371;
(e) Motohiro Matsuura, Yuchi Okuda, Masaki Morotomi, Hiroshi Mollymoto, Muneyuki Date, J. Phys. Soc. Jpn. 46 (1979) 1031;
(f) Shigeru Takatori, Keisuke Kimura, Yuichi Okuda, Kazuko Motizuiki, J. Phys. Soc. Jpn. 49 (1980) 136;
(g) Anastasios J. Taskopolous, Nicholas C. Harden, Khalil A. Abboud, George Christou, Polyhedron 22 (2003) 133.
[6] G.R. Wagner, S.A. Friedberg, Phys. Lett. 9 (1964) 11.
[7] D.M. Aranaz, T.R. Lomer, J. Phys. C: Solid State Phys. 2 (1969) 2431.
[8] Jinkwon Kim, Jin Mook Lim, Man Cheol Suh, Hoseop Yun, Polyhedron 20 (2001) 1947.
[9] Zheming Wang, Bin Zhang, Hideki Fujiwara, Hayao Kobayashi, Mohamedally Kurmoo, Chem. Commun. (2004) 416.
[10] E.Y. Tsymbal, O.N. Mryasov, P.R. LeClair, J. Phys. Cond. Matt. 15 (2003) R109.
[11] Shengming Liu, P. Jeppson, J. Sandstrom, A.N. Caruso, D.L. Schulz, Polyhedron (2007), in press.
[12] B.C. Craft, M. Feldman, E. Morikawa, E.D. Poliakoff, V. Saile, J.D. Scott, R.L. Stockbauer, Rev. Sci. Instrum. 63 (1992) 1561.
[13] B. Ravel, M. Newville, J. Synch. Rad. 12 (2005) 537.
[14] J.B. Goodenough, Magnetism and the Chemical Bond, Wiley, New York, 1963.
[15] J.A. Mydosh, Spin Glasses: An Experimental Introduction, Taylor & Francis, London, 1993.
[16] (a) J.N. McElearney, L.L. Balagot, J.A. Muir, R.D. Spence, Phys. Rev. B 19 (1979) 306;
(b) Marla Lorente, Jean-Pierre Tuchagues, Vasili Petrouleas, Jean-Michel Savariault, Richard Poinsot, Marc Drillon, Inorg. Chem. 30 (1991) 3587;
(c) Simon G. Carling, Peter Day, Dick Visser, R.K. Kremer, J. Solid State Chem. 106 (1993) 111;
(d) Qihua Zhao, Haifang Li, Ruibin Fang, Trans. Metal Chem. 28 (2003) 220;
(e) Peter Day, J. Chem. Soc., Dalton. Trans. (1997) 701;
(f) E. Stryjewski, N. Giordano, Adv. Phys. 26 (1977) 487.
[17] Sujin Han, Jami L. Manson, Jinwon Kim, Joel S. Miller, Inorg. Chem. 39 (2000) 4182.
[18] W.H. Meiklejohn, C.P. Bean, Phys. Rev. 102 (1956) 1413.
[19] A.E. Berkowitz, Kentaro Takano, J. Mag. Mag. Mat. 200 (1999) 552.
[20] (a) Wolfgang Wersdorfer, Nurla Allaga-Alcade, David N. Hendrickson, George Christou, Nature 416 (2002) 406;
(b) W. Wernsdorfer, S. Bhaduri, R. Tiron, D.N. Hendrickson, G. Christou, Phys. Rev. Lett. 89 (2002) 197201;
(c) S. Hill, R.S. Edwards, N. Aliaga-Alcalde, G. Christou, Science 302 (2003) 1015;
(d) En-Che Yang, Wolfgang Wernsdorfer, Stephen Hill, Rachel S. Edwards, Motohiro Nakano, S. Maccagnano, Lev N. Zakharov, Arnold L. Rheingold, George Christou, David N. Hendrickson, Polyhedron 22 (2003) 1727;
(e) R. Tiron, W. Wernsdorfer, N. Aliaga-Alcalde, G. Christou, Phys. Rev. B 68 (2003) 140407R;
(f) R. Tiron, W. Wernsdorfer, D. Foguet-Albiol, N. Aliaga-Alcalde, G. Christou, Phys. Rev. Lett. 91 (2003) 227203.
[21] (a) Karine Fegy, Dominique Luneau, Thorsten Ohm, Carely Paulsen, Paul. Rey, Angew. Chem., Intl. Ed. 37 (1998) 1270;
(b) Corine Mathoniere, Christopher J. Nuttall, Simon G. Carling, Peter Day, Inorg. Chem. 35 (1996) 1201;
(c) Talal Mallah, Arnaud Marvilliers, Eric Riviere, Phil. Trans. R. Soc. Lond. A 357 (1999) 3139;
(d) Siegfried O.H. Gutschke, Daniel J. Price, Annie K. Powell, Paul T. Wood, Angew. Chem., Intl. Ed. 38 (1999) 1088;
(e) Roberto Cortes, Luis Lezama, J. Luis Pizarro, M. Isabel Arriortua, Teofilo. Rojo, Angew. Chem., Intl. Ed. Engl. 35 (1996) 1810.
[22] (a) Homberto O. Stumpf, Yu Pei, Olivier Kahn, Jorunn Sletten, Jean Pierre Renard, J. Am. Chem. Soc. 115 (1993) 6738;
(b) Humberto O Stumpf, Lahcene Ouahab, Yu Pei, Pierre Bergerat, Olivier Kahn, J. Am. Chem. Soc. 116 (1994) 3866;
(c) Olivier Kahn, Adv. Inorg. Chem. 43 (1995) 179;
(d) Humberto O. Stumpf, Lahcene Ouhab, Yu Pei, Daniel Grandjean, Olivier Kahn, Science 261 (1993) 447.
[23] Eugenio Coronado, Jose R. Galan-Mascaros, Carlos J. Gomez-Garcia, Vladimir Laukhin, Nature 408 (2000) 447.

$$\mathscr{H}_{\mathrm{U}} = J_1 \sum_i^6 (\mathbf{s}_{2i-1}\cdot\mathbf{S}_{2i} + \mathbf{S}_{2i}\cdot\mathbf{s}_{2i+1}) + D\sum_i^6 (\mathbf{S}_{2i}^z)^2$$

$$\begin{aligned}\mathscr{H}_{\mathrm{T}} = \mathscr{H}_{\mathrm{U}} + J_3 \sum_i^3 [\{&(1-\alpha)(\mathbf{s}_{4i-3}\cdot\mathbf{S}_{4i-2})(\mathbf{S}_{4i-2}\cdot\mathbf{s}_{4i-1}) \\ &+(1-\alpha)(\mathbf{s}_{4i-1}\cdot\mathbf{S}_{4i-2})(\mathbf{S}_{4i-2}\cdot\mathbf{s}_{4i-3})\} \\ &+\{(\mathbf{s}_{4i-1}\cdot\mathbf{S}_{4i})(\mathbf{S}_{4i}\cdot\mathbf{s}_{4i+1}) + (\mathbf{s}_{4i+1}\cdot\mathbf{S}_{4i})(\mathbf{S}_{4i}\cdot\mathbf{s}_{4i-1})\}\end{aligned}$$

$$\mathscr{H}_{\mathrm{F}} = \mathscr{H}_{\mathrm{U}} + J_2 \sum_i^3 \{(1-\alpha)\mathbf{s}_{4i-3}\cdot\mathbf{s}_{4i-1} + \mathbf{s}_{4i-1}\cdot\mathbf{s}_{4i+1}\}$$

Here $\mathbf{S}_i$ ($\mathbf{s}_i$) represents the spin operator at an $S = 5/2$ ($S = 1/2$) spin site. The periodic boundary condition, $\mathbf{s}_{13} = \mathbf{s}_1$, is imposed in these models because of the ring structure of Mn_6R_6. Although $\mathscr{H}_{\mathrm{U}}$ with $D = 0$ was proposed by Caneschi et al. [4], the single-ion anisotropy exists at $S = 5/2$ sites in general. $\mathscr{H}_{\mathrm{T}}$ contains the three-spin interaction and the bond alternation of J_3. Kostyuchenko et al. proposed $\mathscr{H}_{\mathrm{T}}$ with $D = 0$ and $\alpha = 0$ [5]. The third one contains the interaction between NN radicals J_2 and the bond alternation of J_2. $\mathscr{H}_{\mathrm{F}}$ with $D = 0$ and $\alpha = 0$ was proposed by present authors [7–9].

In spite of the zero-point spin deviation, the local spin density in the ferrimagnetic spin system usually remains to be finite. To determine the effective spin model for such a system, we propose a new criterion that the model should reproduce the spatial configuration of the local spin densities as well as the low-energy excitation spectrum. The spin densities are integrated in a separated area and assigned to "a magnetic unit" in a reference calculation. We call this method the spin density reference (SDR) method. The reference is given by the hybrid density-functional-theory calculation (UB3LYP) in this work. This technique is sufficiently accurate for calculating the spin density of NN-radicals [11,12]. The computation is performed by the GAUSSIAN-03 program packages [13]. The spin density of the spin model is calculated by the exact diagonalization based on the householder method.

To reduce the computational cost in the ab initio calculations, we consider three types of cut molecules terminated by hydrogen atoms hereafter rather than Mn_6R_6. Since the cut molecule has open ends, we adopt the open boundary condition for the corresponding spin models. The schematic pictures of these molecules are depicted in Fig. 1. The first molecule which is called MOL1 contains two NN radicals and a manganese atom. The manganese unit is determined to be a manganese atom with two hfac ligands, hereafter. The second MOL2 contains three NN radicals and two manganese units. The third MOL3 contains four NN radicals and three manganese units. Applying the SDR method to cut molecules, the spin density profile is modified depending on the shape and the size of the molecule. The obtained spin model should be valid for a rather general condition, if we can determine the effective interaction valid for cut molecules and Mn_6R_6. Actually, our result suggests that spin interactions are almost the same for MOL2 and MOL3 as shown below.

Now, we examine the validity of hydrogen termination. The terminated hydrogen atom (H0) connects to an oxygen atom (O1) in NN radical. The O1 connects to a nitrogen atom (N2) and the N2 connects to a carbon atom (C3). N2 and C3 form a pentagon on NN radical. Thus there are three parameters specifying the termination. The variable r represents the bond distance between H0 and O1. The variable a represents the bond angle formed by H0–O1–N2. The variable d represents the dihedral angle formed by H0–O1–N2–C3. We confirm the validity of hydrogen termination using the result of MOL1. The way of the termination is adjusted with respect to these parameters so that the energy minimum point is well realized.

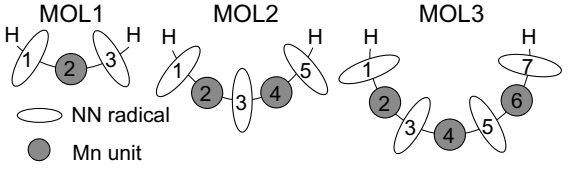


Fig. 1. Schematic pictures of cut molecules of Mn_6R_6. Gray circles represent manganese units. White ellipses represent NN radicals. The numbers written in circles or ellipses show indexes of the spin site. Each of the two ends of a molecule is terminated by a hydrogen atom.

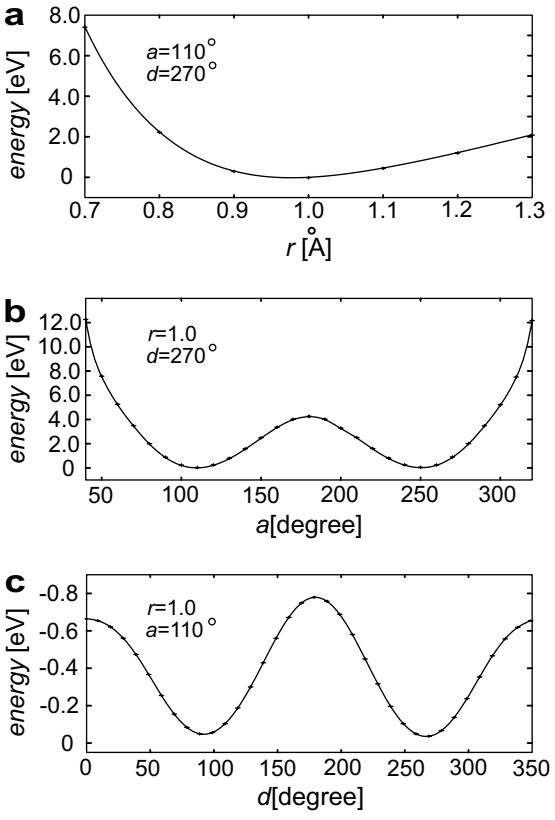


Fig. 2. The total energy of MOL1 obtained by the hybrid density-functional-theory calculation with the 6-31G(d,p) basis set. Three parameters a, r, and d are changed to find the minimum. In all figures, the energy of a configuration with $r = 1.0$ Å, $a = 110°$, $d = 270°$ is taken to be 0 eV.

Fig. 2 shows the total energy of MOL1. Fig. 2a is the result of the calculation when $a = 110°$ and $d = 270°$. In this situation, the energy minimum point exists at $r = 1.0$ Å. Fig. 2b is the result for $r = 1.0$ Å and $d = 270°$. In this situation, the energy minimum point exists at $a = 110°$. Fig. 2c is the result for $r = 1.0$ Å and $a = 110°$. In this situation, the energy minimum point exists at $d = 270°$. These results indicate that the condition of ($r = 1.0$ Å, $a = 110°$, $d = 270°$) is the most stable condition of hydrogen termination. Recall that the condition in which O2 for real Mn_6R_6 connects to the manganese atom is ($r \sim 2.1$ Å, $a \sim 129°$, $d \sim 278°$). The direction toward manganese atom from O2 is approximately the same as that given by the optimized two angles a and d. Therefore, we calculate the spin density at the condition of ($r = 1.0$ Å, $a = 110°$, $d = 270°$).

Results of the spin density obtained by ab initio calculation are shown in Table 1. In these calculations, we consider states with $S = 3/2$, $S = 7/2$ and $S = 11/2$ as the relevant spin states displaying ferrimagnetic spin configuration for MOL1, MOL2 and MOL3, respectively. The spin density at each magnetic site is calculated as the sum of the spin densities of all the atoms in each magnetic unit. The 6-31G basis sets are selected for all the atomic species. We test the effect of the polarization function included for light atoms. The 6-31G(d,p) basis and 6-31G(d) basis give approximately the same result and the polarization does not affect the spin density drastically. Now the z-component of the spin at an NN radical and that at a manganese unit are deviated from 1/2 and 5/2, respectively. The origin of this deviation is considered to be the quantum effect detected in the reference calculation. Since the molecules are finite size systems, it is reasonable that the spin density at NN radical site is shrinked from 1/2 and that the spin density of manganese unit is shrinked from 5/2.

Results of the spin densities obtained by the exact diagonalization of the effective spin model are shown in Fig. 3 and fitted to the reference calculation of UB3LYP/6-31G(d,p). D and α are fixed at ($D = -0.01$, $\alpha = 0.3$), respectively. The spin densities of each model are not drastically affected by D and α. On the contrary, the configuration of the spin densities is very sensitive to the change of the variables J_3/J_1 and J_2/J_1. This means that the configuration of the spin densities gives an essential knowledge for construction of the effective spin model.

In order to detect the optimum condition, we define the following parameter Y:

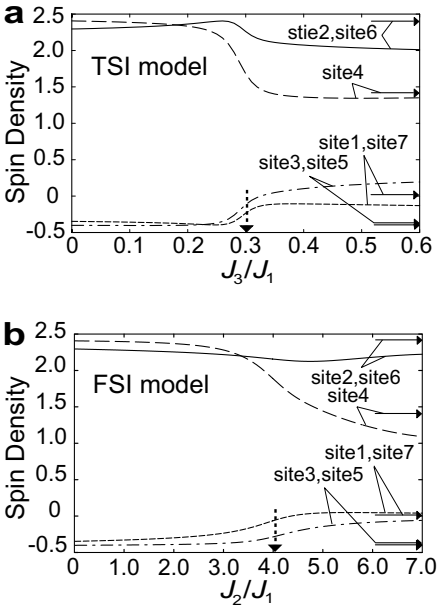


Fig. 3. The result of the spin density calculated by the exact diagonalization of the TSI model and the FSI model. The conditions, $D = -0.01$, $\alpha = 0.3$, are imposed in each model.

$$Y = Y_{5/2} + Y_{1/2}$$

$$Y_{5/2} = \sum_i \left(\frac{\langle S_i^z \rangle_G}{2.5} - \frac{\langle S_i^z \rangle_M}{2.5} \right)^2$$

$$Y_{1/2} = \sum_i \left(\frac{\langle S_i^z \rangle_G}{0.5} - \frac{\langle S_i^z \rangle_M}{0.5} \right)^2$$

Here, $\langle S_i^z \rangle_G$ and $\langle S_i^z \rangle_M$ represent the spin densities obtained by the ab initio calculation and that of the effective spin model, respectively. Y is minimized at the optimized parameters of J_3/J_1 and J_2/J_1. The optimum conditions for MOL3 are shown by dotted arrows in Fig. 3. There is qualitative difference between the TSI model and the FSI model at the optimum condition. In the FSI model, the order of the magnitude of the spin density at site 1 (site 7) and site 3 (site 5) obtained by the exact diagonalization is consistent with the result of the ab initio calculation. On the contrary, the TSI model does not show this consistency. Optimum conditions are summarized in Table 2. These results clearly show the following two facts. Firstly, the USI model can never reproduce the reference. Secondly, the results of MOL2 and MOL3 show that Y_{min} of FSI model is

Table 1
Results of the integrated spin density at each magnetic site obtained by *ab-initio* calculation with $r = 1.0$ Å, $a = 110°$, $d = 270°$

	Site 1	Site 2	Site 3	Site 4	Site 5	Site 6	Site 7
MOL1 (UB3LYP/6-31G(d,p))	−0.00386	1.47974	0.02245				
MOL1 (UB3LYP/6-31G(d))	−0.00383	1.47969	0.02192				
MOL2 (UB3LYP/6-31G(d,p))	0.01632	2.42441	−0.35835	1.42416	−0.00767		
MOL2 (UB3LYP/6-31G(d))	0.01622	2.42357	−0.36105	1.41687	0.00260		
MOL3 (UB3LYP/6-31G(d,p))	0.01559	2.41665	−0.37206	1.41554	−0.40604	2.40976	0.01870
MOL3 (UB3LYP/6-31G(d))	0.01557	2.41663	−0.37200	1.41542	−0.40587	2.40972	0.01896

Table 2
Determined optimum conditions of interaction strength and Y_{min} of each model. The USI model is given by $J_2 = J_3 = 0$

	Optimum	Y_{min}
MOL1		
USI model		0.8283
TSI model	$J_3/J_1 > 0.24$	0.0001
FSI model	$J_2/J_1 > 3.61$	0.0001
MOL2		
USI model		1.1050
TSI model	$J_3/J_1 = 0.31$	0.6536
FSI model	$J_2/J_1 = 4.09$	0.3311
MOL3		
USI model		2.0671
TSI model	$J_3/J_1 = 0.30$	1.9304
FSI model	$J_2/J_1 = 4.05$	0.1950

The exact diagonalization of the Hamiltonian for MOL1 shows that the wave function of each ground state of TSI model and FSI model does not change in each region shown by the inequality.

getting smaller for a larger molecule. On the contrary, Y_{min} of TSI model is getting larger for a larger molecule. Approaching to Mn_6R_6, FSI model fits well the ab initio calculation. Hence one can say that the FSI model is more appropriate model for Mn_6R_6 than the TSI model and the USI one.

In concluding the present work, the SDR method clearly shows that the FSI model is the suitable model for the nano scale ferrimagnetic ring Mn_6R_6. The main point in this study is that the configuration of the spin densities is an essential quantity for determination of the effective spin model. Of course, one can also determine the model from the spin density obtained by the precise experimental observation. As a final point, we should emphasize that the SDR method is a powerful method for determination of the effective spin model for a nano scale magnet which has a finite magnetization.

Acknowledgements

This work was partly supported by a Grand-in-Aid for scientific research in a priority area No. 17064006, the 21st COE Program supported by the Japan Society for the Promotion of Science, NEDO under the Materials and Nano-technology Program and ACT-JST. Numerical calculations have been done using the computer facilities of the Institute for Molecular Science and the Tohoku University.

References

[1] J.R. Friedman, M.P. Sarachik, J. Tejeda, R. Siolo, Phys. Rev. Lett. 76 (1996) 3830.
[2] T. Sakai, K. Okamoto, Phys. Rev. B 65 (2002) 214403.
[3] S. Tonooka, H. Nakano, K. Kusakabe, N. Suzuki, Prog. Theor. Phys. Suppl. 159 (2005) 148.
[4] A. Caneschi, D. Gatteshi, J. Laugier, P. Rey, R. Sessoli, C. Zanchini, J. Am. Chem. Soc. 110 (1988) 2795.
[5] V.V. Kostyuchenko, I.M. Markevtsev, A.V. Philoppov, V.V. Platonov, V.D. Selemir, O.M. Tatsenko, A.K. Zvezdin, A. Caneschi, Phys. Rev. B 67 (2003) 184412.
[6] H. Hori, S. Yamamoto, Phys. Rev. B 68 (2003) 054409.
[7] S. Tonooka, H. Nakano, K. Kusakabe, N. Suzuki, J. Phys. Soc. Jpn. 73 (2004) 1597.
[8] S. Tonooka, K. Kusakabe, N. Suzuki, H. Nakano, J. Phys. 16 (2004) S5739.
[9] S. Tonooka, K. Kusakabe, H. Nakano, N. Suzuki, Polyhedron 24 (2005) 2396.
[10] S. Funabashi, T. Itou, A. Oyamada, S. Maegawa, K. Fujita, K. Amezawa, R. Yamaguchi, Abstracts the Meeting of the Physical Society of Japan (Sectional Meeting, Kyoto, September, 2005) Pt. 3, 21pPSB-21.
[11] A. Zheludev, V. Barone, M. Bonnet, B. Delley, A. Grand, E. Ressouche, P. Rey, R. Subra, J. Schweizer, J. Am. Chem. Soc. 116 (1994) 2019.
[12] N.L. Frank, R. Clérac, J. Sutter, N. Daro, O. Kahn, C. Coulon, M.T. Green, S. Golhen, L. Ouahab, J. Am. Chem. Soc. 122 (2000) 2053.
[13] M.J. Frisch et al., Gaussian 03, Rivision C002 Gaussian, Inc., Wallingford CT, 2004.

present in $[Cu_4(bipy)_4V_4O_{11}(PO_4)_2]nH_2O$ ($n \sim 5$) (**1**), for which the used analytical models did not give a good fit of the experimental magnetic data. The theoretical methods used in the present work are based on density functional theory [12–14].

In the present work, we will discuss the magnetic behaviour of three hybrid organo-inorganic compounds which present different bridging forms of the phosphate/phosphonate/oxovanadium groups, showing different bulk magnetic properties. Compounds (**2**) and (**3**) correspond to $[Cu_2(phen)_2(PO_4)(H_2PO_4)_2(VO_2) \cdot 2H_2O]$ and $[Cu_2(phen)_2(O_3PCH_2PO_3)(V_2O_5)(H_2O)]H_2O$, respectively.

2. Experimental

The syntheses of compounds (**1**), (**2**) and (**3**) were previously reported [9,15,10].

3. Computational details

All the calculations for compound (**1**) were performed using the crystal structure of the molecule [10]. Single point calculations were performed with the GAUSSIAN03 code [16] using the quadratic convergence approach (convergence criteria 0.02 cm^{-1}) with the hybrid B3LYP functional [17] and a guess function generated with the JAGUAR 5.5 code [18]. We have employed a triple-ζ all electron Gaussian basis set for all atoms [19]. Since the crystal structure corresponds to an extended system which contains tetranuclear copper cores connected by phosphovanadates moieties, a tetranuclear unit was used for the calculations, see Fig. 1. This tetranuclear unit was obtained using four pentacoordinated copper(II) centres, each metal centre bonded to a bipyridine and to three oxygen atoms from phosphate and oxovanadium groups. In the case of an oxo-vanadium group bridging in a 1,1 form, hydrogen atoms were added to the two oxygen atoms which were originally bonded to a phosphate group. In the case of a phosphovanadate group bridging in a 1,3 form, one hydrogen atom was added to a oxygen atom originally bonded to a phosphate group. The hydrogen atoms added to the structure were optimized with MM+ molecular mechanics force field using the TITAN package [20]. The fragment has four different Cu–Cu distances (3.19; 4.10; 5.38 and 5.01 Å), and therefore four different exchange coupling constants (J_1, J_2, J_3 and J_4) are expected. Therefore, the studied system can be described with the phenomenological Hamiltonian

$$\hat{H} = -J_1[\hat{S}_1\hat{S}_2 + \hat{S}_3\hat{S}_4] - J_2[\hat{S}_1\hat{S}_3 + \hat{S}_2\hat{S}_4] - J_3[\hat{S}_2\hat{S}_3] - J_4[\hat{S}_1\hat{S}_4]$$

In order to obtain the four different J values, five calculations are needed: a high spin solution ($S = 2$), three solutions with $S = 0$, and one solution with $S = 1$. The calculated temperature dependence of the magnetic susceptibility was obtained with the MAGPACK code [21] using $g = 2.00$.

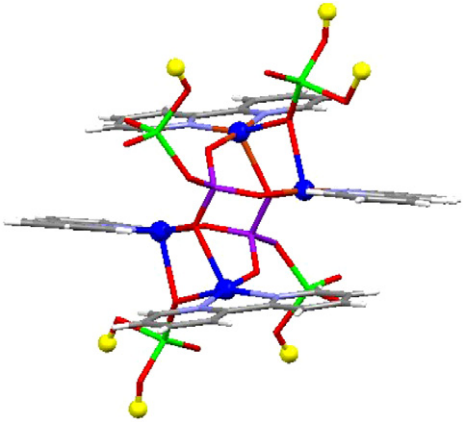


Fig. 1. Tetranuclear copper(II) model of compound (**1**) used for the calculations. The four central deep blue spheres correspond to copper atoms. The six peripherical yellow spheres correspond to added hydrogen atoms. Phosphorous, purple; vanadium, green; oxygen, red; nitrogen, light blue; carbon, grey. (For interpretation of the references to color in this figure legend, the reader is referred to the web version of this article.)

4. Results and discussion

4.1. Structural description

The three reported hybrid organo-inorganic copper(II) compounds, based on the vanadium(V)/phosphorus/oxygen substructure (VPO) have different extended structures. In compound (**1**), the existing tetranuclear copper(II) species are connected by the $V_4P_2O_{19}$ chain-like fragments to form infinite chains running parallel [1 0 0] [9]. In compound (**2**), the vanadium octahedral and phosphorous tetrahedra share common corners to form infinite chains based on the VP_2O_{12}. An extra phosphorous tetrahedron acts as a single bridge between two copper(II) centres, giving rise to the existence of $Cu_2(phen)_2(PO_4)^+$ species. These cationic species are interconnected by μ_2-oxo bridges of phosphorous and vanadium forming infinite chains, which propagate along the a direction [15]. In compound (**3**), the vanadium tetrahedra and diphosphonate groups share common corners to give infinite zig-zag chains, $[V_2O_5O_3PCH_2PO_3]$ running along the [1 0 0] direction. The infinite chains are connected by the tetrameric units to form layers [10].

In all the reported copper(II) compounds, the metal centres present a square pyramidal geometry. However, different type of bridges between the copper(II) centres are observed in each case. The copper(II) tetranuclear unit present in compound (**1**) is the most complex, in relation to the bridges that exist between the metal centres. The two nearest copper(II) centres (d_{Cu-Cu} 3.19 Å) are linked by three bridges: a 1,1-oxo-vanadium group, a 1,1-phosphate group, and a 1,3-phosphate group. These dinuclear species are interconnected by two 1,3-phosphate group, thus giving rise to a rhombohedral tetranuclear unit (d_{Cu-Cu} 4.10 Å). The internal diagonals of this rhombohedral struc-

ture correspond to two 1,3-phosphate bridges each, with distances of 5.03 and 5.38 Å (Fig. 2).

In compound (**2**), the dinuclear copper(II) unit is formed with the presence of one 1,3-phosphate bridge ($d_{Cu–Cu}$ 3.46 Å) (Fig. 3). In compound (**3**), the tetranuclear species is formed by the central bis 1,1-oxo bridged dimer ($d_{Cu–Cu}$ 3.25 Å) and the two external copper(II) atoms with 1,3-bis phosphate bridges ($d_{Cu–Cu}$ 5.13 Å) (Fig. 4).

5. Magnetic behaviour

Only compound (**2**) presents Curie–Weiss behaviour in the whole temperature range (3–300 K), while all three compound show this behaviour for the high temperature region (>100 K). The magnetic behaviour of compound (**3**) has been analyzed elsewhere; the obtained J values being $J_{intra} = -30\ cm^{-1}$ and $J_{inter} = -8.5\ cm^{-1}$ [10].

For compound (**1**) the magnetic behaviour below 60 K is complex, and the analytical expression used did not give a good fit of the experimental magnetic data. A theoretical model with four exchange pathways was used in order to describe the magnetic behaviour of the rhombohedral tetranuclear species. The experimental magnetic data for compound (**1**) (Fig. 5a) is well described with the following calculated J parameters: $J_1 = +3.29$, $J_2 = -0.63$, $J_3 = -2.23$ and $J_4 = -46.14\ cm^{-1}$ (Fig. 5b). The overall antiferromagnetic behaviour at low temperatures is due mainly to a inter-dimer exchange interaction, while the intra-dimer exchange interaction due to the existence of the three bridges results slightly ferromagnetic. Therefore, the 1,1-oxo-vanadium bridge present in the dinuclear unit may be acting counter complementary in relation to the two phosphate bridges. The Cu_2–Cu_3 diagonal ($d_{Cu–Cu}$ 5.01 Å) presents the phosphate ligands with the most symmetrical copper–oxygen distances (Cu_2O: 1.92; Cu_3O: 1.95; Cu_2O': 1.95 and Cu_3O': 1.92 Å). This fact may influence the magnitude of the J value ($J_4 = -46.14\ cm^{-1}$), in comparison to the much smaller obtained J values ($J_2 = -0.63$, $J_3 = -2.23\ cm^{-1}$). For this latter exchange pathways greater differences in the Cu–O distances are observed, ranging from 1.89 Å (shortest) to 2.29 Å (longest). It is known that geometrical factors greatly influence the magnitude of the magnetic exchange coupling between paramagnetic metal centres.

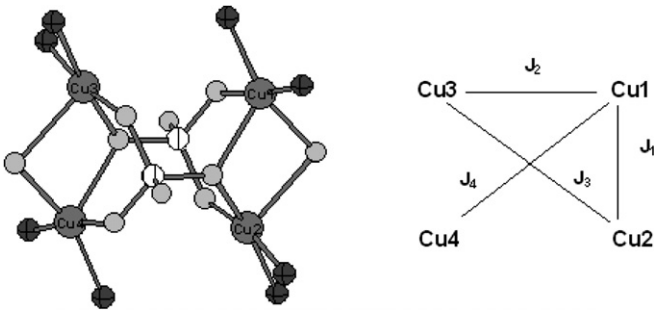


Fig. 2. Tetranuclear copper(II) core of compound (**1**) with all the oxygen atoms involved in the magnetic exchange phenomenon. Dark gray, nitrogen; light gray, oxygen; dashed, phosphorus. Schematic diagram of the four different magnetic exchange pathways.

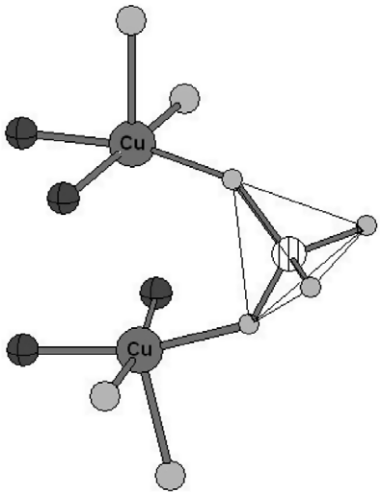


Fig. 3. Binuclear copper(II) core of compound (**2**) showing the 1,3-phosphato bridge. Dark gray, nitrogen; light gray, oxygen; dashed, phosphorus.

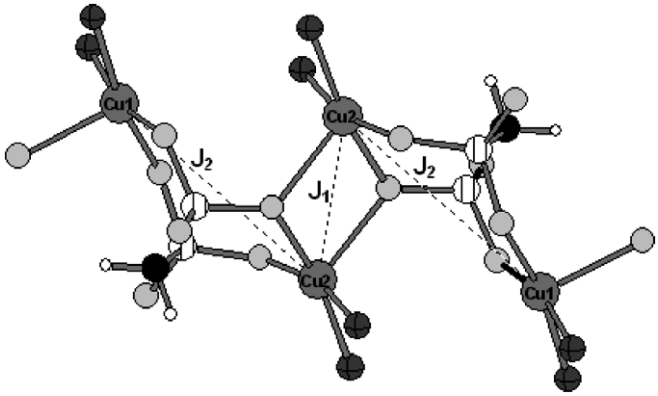


Fig. 4. Tetranuclear copper(II) core of compound (**3**) showing all the phosphate bridges involved in the magnetic exchange phenomenon. Dark gray, nitrogen; light gray, oxygen; dashed, phosphorus. J_1, J_2: magnetic exchange constants.

When a simpler model was used to describe the tetranuclear unit of compound (**1**) in which the two diagonals are taken as equal, assuming a perfect rectangular geometry for the species, the following j values were obtained: $J_1 = +4.93$, $J_2 = -0.63$, $J_3 = -24.2\ cm^{-1}$ [11]. Even though the same trend is obtained in the sign of the j values, these do not reproduce the low temperature behaviour of compound (**1**) as can be seen in Fig. 5c. It is interesting to point out that the J_3 value of the rectangular model corresponds to the mean value of the J_3 and J_4 values of the rhombohedral model.

The fact that compound (**2**) does not show antiferromagnetism in the whole temperature range, may be due to the fact that the bridged copper(II) centres of the

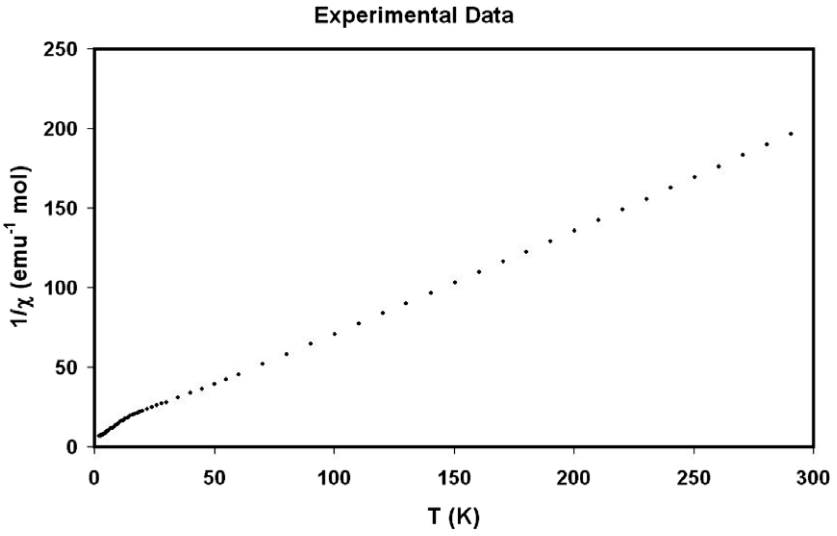


Fig. 5a. Experimental magnetic data of compound (**1**). $1/\chi$ vs. T.

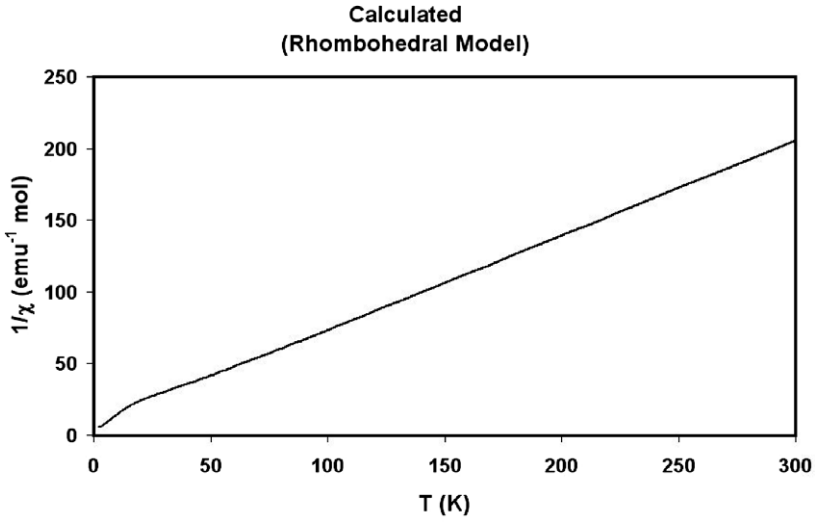


Fig. 5b. Calculated magnetic data of compound (**1**) using the rhombohedral model. $1/\chi$ vs. T.

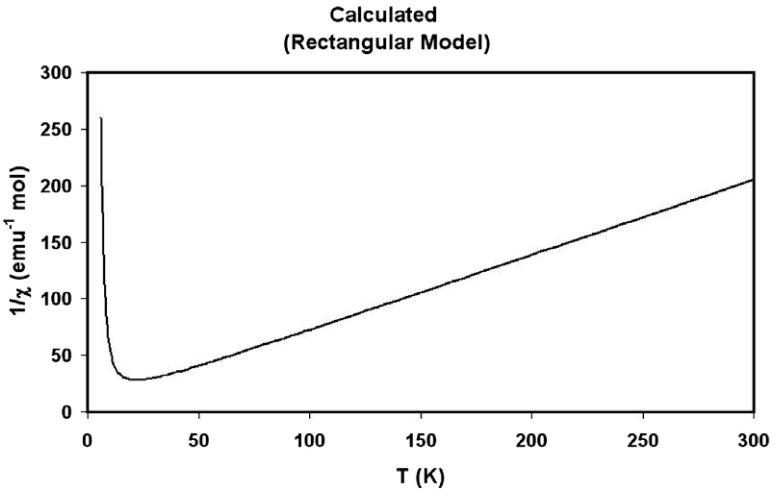


Fig. 5c. Calculated magnetic data of compound (**1**) using the rectangular model. $1/\chi$ vs. T.

$Cu_2(phen)_2(PO_4)^+$ fragment are located on different planes, and present only one chelate phosphate bridge. Thus the only possible pathway for the magnetic exchange interaction is not adequately located to be effective.

Compound (**3**) presents a typical antiferromagnetic behaviour with a maximum at 64 K. The two 1,1-phosphate bridges link the two copper(II) centres at a short distance of 3.25 Å, and represent adequate magnetic exchange pathways ($J_1 = -30.0\ cm^{-1}$). The 1,3 mode of bridging of the two phosphate groups of the phosphonate ligands assure an inter-dimer antiferromagnetic exchange interaction with $J_2 = -8.5\ cm^{-1}$.

6. Conclusions

The different modes of bridging of the phosphate and oxo-vanadium ligands give rise to completely different magnetic behaviour of the three hybrid organo-inorganic copper(II) compounds.

Phosphates bridges permit the existence of antiferromagnetic exchange coupling between the copper(II) centres. The exchange interaction being stronger when the copper(II) oxygen distances involved are similar in length giving a more symmetrical structure.

Acknowledgements

Financial support for this work provided by FONDAP 11980002, ECOS–CONICYT C02E01 and Dirección de Investigación de la Universidad de Chile grants is gratefully acknowledged. S.U. thank DAAD for a Doctoral scholarship.

References

[1] S. Boudin, A. Guesdon, A. Leclaire, M-M. Borel, Int. J. Inorg. Mater. 2 (2000) 561, and references therein.
[2] R.C. Finn, J. Zubieta, J. Chem. Soc., Dalton Trans. (2000) 1821.
[3] R.C. Finn, J. Zubieta, Inorg. Chim. Acta 332 (2002) 191.
[4] R.C. Finn, J. Zubieta, Inorg. Chim. Acta 335 (2002) 131.
[5] G. Yucesan, V. Golub, Ch. J. O'Connor, J. Zubieta, Solid State Sci. 7 (2005) 133.
[6] R.C. Finn, R. Lam, J.E. Greedan, J. Zubieta, Inorg. Chem. 40 (2001) 3745.
[7] R.B. Fu, X.T. Wu, S.M. Hu, W.X. Du, J.J. Zhang, Z.Y. Fu, Inorg. Chem. Com. 6 (2003) 694.
[8] Y. Moreno, A. Vega, S. Ushak, R. Baggio, O. Pena, E. Le Fur, J.Y. Pivan, E. Spodine, J. Mater. Chem. 13 (2003) 2381.
[9] S. Ushak, E. Spodine, D. Venegas-Yazigi, E. Le Fur, J.Y. Pivan, O. Pena, R. Cardoso-Gil, R. Kniep, J. Mater. Chem. 15 (2005) 4529.
[10] S. Ushak, E. Spodine, E. Le Fur, D. Venegas-Yazigi, J.Y. Pivan, W. Schnelle, R. Cardoso-Gil, R. Kniep, Inorg. Chem. 45 (2006) 5393.
[11] E. Spodine, D. Venegas-Yazigi, S. Ushak, E. Le Fur, J.Y. Pivan, Physica B 384 (2006) 120.
[12] E. Ruiz, P. Alemany, S. Alvarez, J. Cano, J. Am. Chem. Soc. 119 (1997) 1297.
[13] E. Ruiz, S. Alvarez, A. Rodríguez-Fortea, P. Alemany, Y. Pouillon, C. Massobrio, in: J.S. Miller, M. Drillon (Eds.), Electronic Structure and Magnetic Behavior in Polynuclear Transition-metal Compounds, Weinheim, 2001.
[14] E. Ruiz, Struct. Bond. 113 (2004) 71.
[15] S. Ushak, Doctoral Thesis, University of Chile, 2006.
[16] M.J. Frisch et al., GAUSSIAN 03 (Revision B.4), Gaussian, Inc., Pittsburgh, PA, 2003.
[17] A.D. Becke, J. Chem. Phys. 98 (1993) 5648.
[18] Jaguar 5.5, Schrödinger, Inc., Portland, 2003.
[19] A. Schaefer, C. Huber, R. Ahlrichs, J. Chem. Phys. 100 (1994) 5829.
[20] Titan, V.1.08, Wavefunction Inc. and Schrodinger Inc. Von Karman Av., Suite 370, Irvine, CA, USA.
[21] MAGPACK Software: J.J. Borrás-Almenar, J.M. Clemente-Juan, E. Coronado, B.S. Tsukerblat, J. Comp. Chem. 22 (2001) 985.

basis functions were also considered for Cu. We enabled and disabled use of integral symmetry corresponding to the standard orientation and in the specified *Z*-matrix orientation for **1**. For the calculation of original singly occupied molecular orbitals (SOMOs) of investigated complex, the geometries revealed by X-ray crystal structure analyses were used without any reduction of size for **1**.

3. Calculated results and discussion

For open-shell system, correct SOMOs for high-spin states those show the nature of ferro- or antiferromagnetic coupling for investigated complexes are the most interested calculated results. Because the restricted open-shell DFT calculation (RO-DFT) prevents the spin contamination, we will investigate the dependence of SOMO distribution with various calculation techniques, for comparison, the unrestricted DFT calculation (U-DFT) are also involved. For U-DFT calculation, one of the most important parameters obtained is the total angular momentum of each state ($\langle S^2 \rangle$), by which the spin contamination can be determined compared with the expected one. Our previous calculation [7] suggests that U-DFT calculation usually results in serious spin contamination for low-spin states. Herein, we only pay more attention to the calculated $\langle S^2 \rangle$ for high-spin (quartet) state.

Among the U-DFT calculations with various functionals, basis sets, orientation of geometry, and symmetry constraints, the obtained smallest $\langle S^2 \rangle$ value for quartet high-spin state of complex **1** is 3.772 (expected value 3.750). Where UB3LYP calculation are performed with 6-31G(d) basis sets for C, H, O, N, F and pure LanL2DZ for Cu, under disabled use of integral symmetry. The corresponding SOMO distribution for high-spin state with smallest $\langle S^2 \rangle$ value is shown in Fig. 1. Where three SOMOs are consisting of one $d_{x^2-y^2}$ from Cu^{II} (1a) and two sets of p orbitals (1b, 1c) on organic radicals, respectively. UB3LYP/6-31G(d) calculation under disabled use of integral symmetry suggests the $d_{x^2-y^2}$ lies in the plane of hfac [8]. It is found

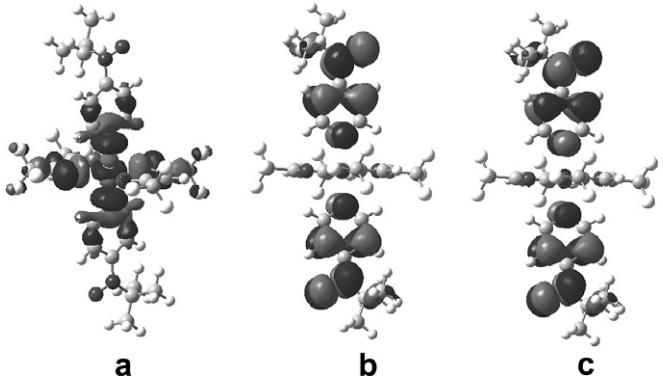


Fig. 1. SOMO distribution of complex **1** by UB3LYP with 6-31G(d) basis sets for C, H, O, N, F and pure LanL2DZ for Cu^{II}, under disabled use of integral symmetry.

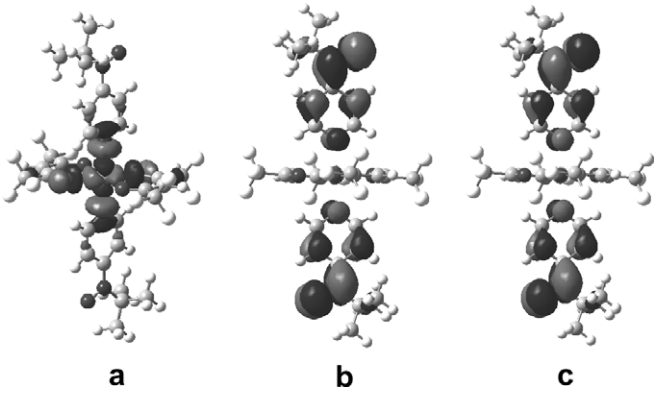


Fig. 2. SOMO distribution of complex **1** by ROB3LYP approach.

that UB3LYP calculations are sensitive to the basis sets and orientation of investigation system. All UBLYP, UPBE, and UPBE0 calculations failed to give reasonable SOMO distribution. Therefore unrestricted DFT calculation is a plausible approach for the SOMO distribution of investigated complex **1**.

RO-B3LYP calculations are tolerant for the different basis sets and orientation of investigation system, except for the Cartesian LanL2DZ for Cu^{II} with standard orientation for the complex **1**. All RO-PBE, RO-PBE0, RO-BLYP, and most of the RO-B3LYP calculation can offer reasonable SOMO distribution for complex **1** as shown in Fig. 2. It is shown in Fig. 2 that the magnetic orbitals are consisting of three near-degenerate MOs. 2a is formed by d_σ type atomic orbital (AO), i.e. $d_{x^2-y^2}$ from Cu^{II}, the σ AOs from two oxygens of hfac forming *X*-axis and σ AOs from two nitrogens of pyridine rings forming *Y*-axis. 2b and 2c are from p AOs of organic radical parts, which is alternatively distributed on 4NOPY, i.e. there are nodes between neighboring p orbitals. Moreover, according to the coefficients of AOs for three SOMOs, they are orthogonal to each other. Therefore, near degenerate and orthogonal SOMOs in **1** contribute to form the ferromagnetic coupling between three hetero-spin centers. RO-BLYP, RO-PBE, and ROPBE0 calculations can give same SOMOs for **1** when LanL2DZ is used for Cu^{II}. It is worth to note that the approaches mentioned above are also valid for other complexes consisting with aminoxyl radicals possessing bipyridyl ligands and $Cu(hfac)_2$.

4. Conclusion

In summary the calculations presented here reveal that the SOMOs for complex **1** is calculation technique dependent, and RO-B3LYP, RO-BLYP, RO-PBE, and RO-PBE0 in combination with LANL2DZ basis set are promising approaches for offering correct SOMOs of investigated system, which can offer a visible image for the magnetic orbitals. It can be expected that our findings may give a general method for further investigation of SOMOs of other hetero-spin systems.

Acknowledgement

This work has been supported by National Natural Science Foundation of China (Grant No. 20274006).

References

[1] O. Kahn, Ed. Mol. Cryst. Liq. Cryst. (1999) 334.
[2] P.M. Lahti (Ed.), Magnetic Properties of Organic Materials, Marcel Dekker, New York, 1999.
[3] K. Itoh, M. Kinoshita (Eds.), Molecular Magnetism, Gordon and Breach, Amsterdam (Kodansha: Tokyo), 2000.
[4] Y. Ishimaru, M. Kitano, N. Koga, H. Iwamura, Inorg. Chem. 37 (1998) 2273.
[5] E.A.A. Noh, J. Zhang, Chem. Phys. 330 (2006) 82.
[6] J.M. Seminario (Ed.), Density Functional Theory, Adv. Quantum Chem, vol. 33, Academic, San Diego, 1998, and references therein.
[7] GAUSSIAN 98 (A.3), Gaussian, Inc., Pittsburgh PA, 1998.
[8] J. Zhang, L. Wang, R. Wang, N. Koga, Synth. Met. 137 (2003) 1355.

parallel. This group has not previously been used in manganese chemistry, but we have found that it yields interesting products. We herein report two mixed-valent (Mn^{II}_6, Mn^{III}_6, Mn^{IV}) tridecanuclear Mn clusters obtained using the ndc^{2-} ligand. In addition, a route has been found to an analogous Mn_{13} species with only monocarboxylate groups. The magnetic properties vary significantly within this family, and a qualitative magnetostructural correlation has provided some insight into the influence on the observed properties of the mono- versus dicarboxylate ligation.

The reaction of $Mn(O_2CMe)_2 \cdot 4H_2O$ in DMF with 1,8-naphthalic anhydride and NEt_3 led to subsequent isolation, on layering with Et_2O, of $[Mn_{13}O_8(OH)_6(ndc)_6] \cdot 8DMF \cdot H_2O$ (**1**) in ~70% yield. When the same reaction solution was layered with EtOH, the product was $[Mn_{13}O_8(EtO)_{5.5}(OH)_{0.5}(ndc)_6] \cdot 6MeCN \cdot 2H_2O$ (**2**) in similar yield. Finally, reaction of preformed $[Mn_3O(O_2CPh)_6(pyr)_2(H_2O)]$ [5] with NEt_3 in EtOH produced $[Mn_{13}O_8(EtO)_6(O_2CPh)_{12}] \cdot 7H_2O$ (**3**) in ~80% yield. Fuller details of the syntheses will be provided in the full paper [6].

Complex **1** crystallizes in the triclinic space group $P\bar{1}$ with the molecule on an inversion center. The core of the cluster (Fig. 1) contains one Mn^{IV}, six Mn^{II}, and six Mn^{III} ions held together by six μ_5-O^{2-}, two μ_3-O^{2-}, and six μ_3-OH^- ions. Peripheral ligation is provided by six ndc^{2-} groups whose carboxylate arms each bridge two Mn atoms. The only Mn^{IV} atom (Mn6) is located at the center of the cluster, surrounded by a nearly planar ring of six Mn^{II} atoms (Mn3, Mn4, Mn7, and their symmetry equivalents). The six Mn^{III} atoms (Mn1, Mn2, Mn5, and their symmetry equivalents) form two equilateral triangles, one above and one below the nearly planar Mn^{II}_6 ring. The OH^- groups are O atoms O14, O15, O17, and their symmetry partners. Alternatively, the $[Mn_{13}O_{14}]$ core can be described as eight face-fused $[Mn_4O_4]$ cubane units with a common vertex at the central Mn^{IV} atom (Mn6). Each cubane shares three of its faces with its neighbors, creating a larger cubane-like unit whose eight vertices are all O atoms; in this description, the Mn atoms each lie at the mid-point of an edge and at the center of the larger cubane. The thirteen Mn ions in **1** are all six-coordinate with near-octahedral geometry, and their assigned oxidation states were established by charge considerations, bond valence sum calculations [6], and the clear Jahn–Teller (JT) distortions (elongations) at the Mn^{III} ions.

Complex **2** crystallizes in the triclinic space group $P\bar{1}$. The core of the cluster again contains one Mn^{IV}, six Mn^{II}, and six Mn^{III} ions, but now held together by six μ_5-O^{2-}, two μ_3-O^{2-}, and six μ_3-OEt^- ions. Thus, the six OH^- groups in **1** are now EtO^- groups in **2**; however, one EtO^- group is disordered with a OH^- group, with ~50:50% relative occupancies. Peripheral ligation is again by six ndc^{2-} groups. Complex **2** is thus structurally very similar to **1**, with small differences as summarized in Table 1.

Complex **3** crystallizes in the monoclinic space group $C2/c$. The core of the cluster again contains one Mn^{IV}, six Mn^{II}, and six Mn^{III} ions, held together as in **2** by six μ_5-O^{2-}, two μ_3-O^{2-}, and six μ_3-OEt^- ions (with no disorder in the occupancies of the latter). However, the peripheral ligation is now provided by 12 benzoate groups, each bridging two Mn atoms (Fig. 2). The core is thus very similar with those of **1** and **2**, with various small differences as summarized in Table 1. Note that complex **3** has also been previously obtained by others from a very different procedure [7].

The cores of the structures of **1**–**3** are thus overall very similar to each other, except for the OH^- versus EtO^- difference (Figs. 1–3). Closer inspection of the structures and the metric parameters in Table 1 reveal few major differences. The biggest, of course, is the C···C separation between two adjacent carboxylate groups. In **1** and **2**, this is only 2.899 ± 0.042 and 2.909 ± 0.017 Å, respectively, since the two carboxylate groups are attached to the

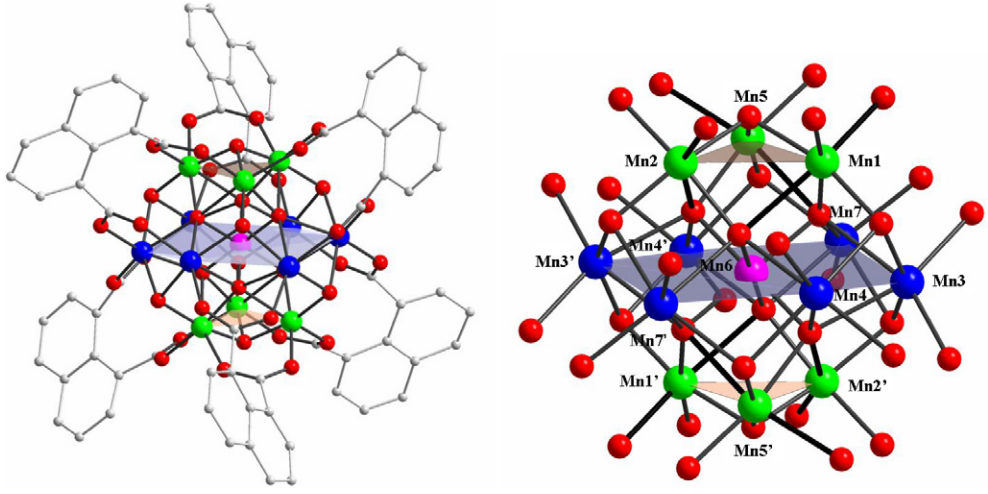


Fig. 1. The structure of complex **1** (left) and its partially labeled core (right). Color code: Mn^{II} blue, Mn^{III} green, Mn^{IV} purple, O red, C grey. (For interpretation of the references in color in this figure legend, the reader is referred to the web version of this article.)

Table 1
Structural comparisons between complexes **1**, **2**, and **3**

Parameter[a]	1	2	3
C···C (Å)	2.899 ± 0.042	2.909 ± 0.017	3.434 ± 0.043
$Mn^{III}\cdots Mn^{III}$ (Å)	2.945 ± 0.004	2.987 ± 0.010	2.952 ± 0.003
$Mn^{II}\cdots Mn^{III}$ (Å)	3.186 ± 0.013	3.177 ± 0.038	3.202 ± 0.043
$Mn^{II}\cdots Mn^{IV}$ (Å)	3.239 ± 0.021	3.195 ± 0.007	3.206 ± 0.008
$Mn^{II}\cdots Mn^{II}$ (Å)	3.250 ± 0.031	3.208 ± 0.041	3.207 ± 0.020
$Mn^{III}\cdots Mn^{IV}$ (Å)	3.018 ± 0.008	3.054 ± 0.010	3.061 ± 0.008
Mn^{III}–μ_5O^{2-}–Mn^{III} (°)	86.17 ± 0.18	86.43 ± 0.19	84.35 ± 0.35
Mn^{III}–μ_3O^{2-}–Mn^{III} (°)	103.85 ± 0.75	102.25 ± 0.45	104.20 ± 0.40
Mn^{II}–O^{2-}–Mn^{IV} (°)	99.93 ± 1.08	98.54 ± 1.30	98.85 ± 2.75
Mn^{III}–O^{2-}–Mn^{IV} (°)	97.16 ± 6.94	97.42 ± 6.78	97.40 ± 7.80
Mn^{II}–O^{2-}–Mn^{II} (°)	88.18 ± 0.53	88.15 ± 1.70	88.41 ± 0.50
trans Mn^{II}–μ_5-O^{2-}–Mn^{III} (°)	162.15 ± 7.65	162.60 ± 7.90	161.85 ± 6.55
cis Mn^{II}–μ_5O^{2-}–Mn^{III} (°)	90.66 ± 5.03	90.41 ± 5.20	91.55 ± 6.65
Mn^{II}–RO^{-}–Mn^{III} (°)	102.30 ± 1.60	101.11 ± 1.26	100.80 ± 1.60
Mn^{II}–RO^{-}–Mn^{II} (°)	96.49 ± 0.02	94.66 ± 0.54	92.30 ± 0.30
$O^{2-}\cdots Mn^{III}_3$ plane (Å)	0.782	0.837	0.769
$Mn^{IV}\cdots Mn^{III}_3$ plane (Å)	2.492	2.520	2.543

[a] Average values; indicated are the ranges in that parameter.

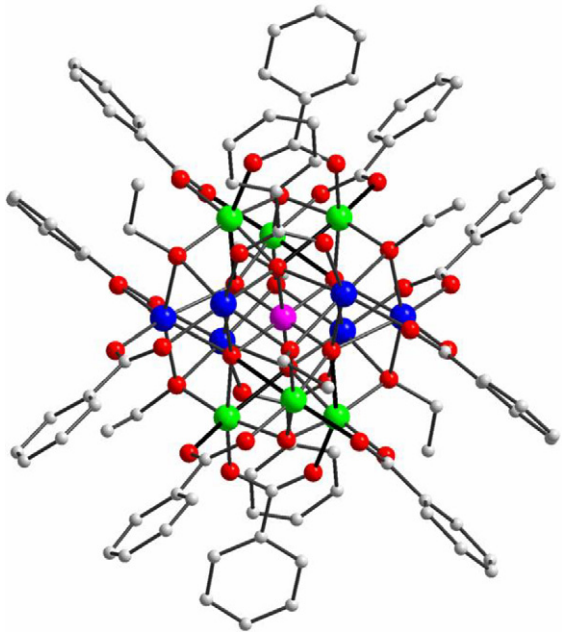


Fig. 2. The structure of complex **3**. Color code: Mn^{II} blue, Mn^{III} green, Mn^{IV} purple, O red, C grey. (For interpretation of the references in color in this figure legend, the reader is referred to the web version of this article.)

naphthalene backbone, and these are much shorter than the 3.434 ± 0.043 Å between two separate benzoate groups in **3**. However, this strain imposed on the disposition of the peripheral carboxylate ligands does not appear to have a significant effect on the distances and angles within the $[Mn_{13}O_{14}]$ core. The metric parameters of benzoate complex **3** are essentially all within the ranges of the corresponding values of either **1** or **2**, or both. In approximately half the entries in Table 1, there are no differences between the three complexes. Among the remainder, it is interesting to note that for some parameters ($Mn^{III}\cdots Mn^{III}$, $Mn^{II}\cdots Mn^{III}$ distances, and Mn^{III}–μ_3-O^{2-}–Mn^{III} angles), the values for **1** are closer to those **3** than those for **2**. This suggests that for many of the metric parameters, changes caused by the HO^{-}-to-EtO^{-} substitution (**1** to **2**) are essentially equal and opposite to those due to the ndc^{2-}-to-$PhCO_2^{-}$ substitution (**2** to **3**), resulting in some parameters for **1** being the same as those for **3**. In other cases, the values for **2** are closest to those for **3** (e.g. $Mn^{II}\cdots Mn^{II}$, $Mn^{II}\cdots Mn^{IV}$, and $Mn^{III}\cdots Mn^{IV}$ distances, Mn^{II}–O^{2-}–Mn^{IV} angles) showing the values are dominated by the EtO^{-} versus OH^{-} difference.

With respect to the magnetic properties to be discussed below, a probably significant difference within Table 1 is found in the Mn^{II}–RO^{-}–Mn^{II} angles, where R = H (**1**) or Et (**2**, **3**). In this case, the values for the latter two are both smaller than that of **1**. This is likely a contributory factor in the observed differences in magnetic properties to be discussed below, because it is well known that even very small changes in the angles at monoatomic bridges between two metal atoms can have a significant effect on the magnitude of the resulting superexchange interaction [8]; this was first demonstrated in the classic work on bis-hydroxo-bridged Cu(II) dimers [9].

Solid state, variable-temperature magnetic susceptibility measurements were performed on vacuum-dried microcrystalline samples of complexes **1**, **2**, and **3** suspended in eicosane to prevent torquing. The dc magnetic susceptibility (χ_M) data were collected in the 5.0–300 K range in a 0.1 Tesla (T) (1000 Oe) magnetic field. The obtained data are plotted as $\chi_M T$ versus T in Fig. 4, and it can be seen that the overall profiles are very similar for the three complexes, $\chi_M T$ steadily decreasing with decreasing temperature and thus suggesting dominant antiferromagnetic interactions between the metal centers in the molecule. However, the plots for **1** and **3** are the most similar, which

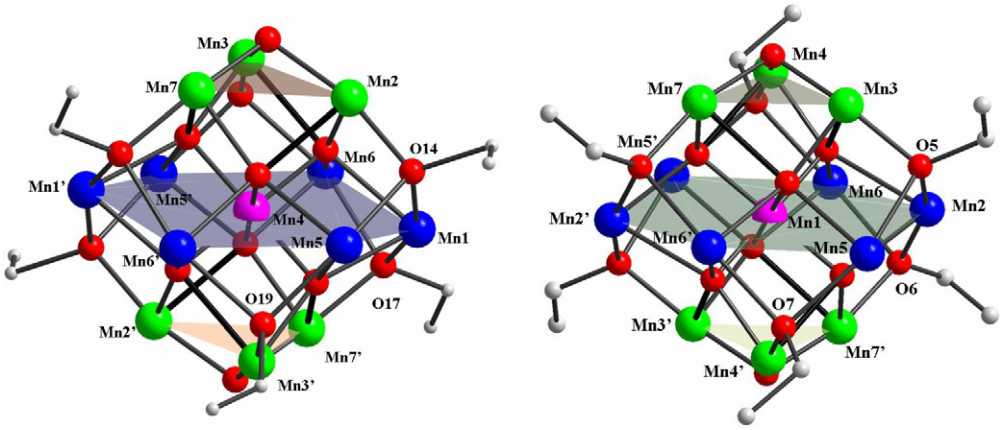


Fig. 3. Partially labeled cores of complexes **2** (left) and **3** (right). Color code: Mn^{II} blue, Mn^{III} green, Mn^{IV} purple, O red, C grey. (For interpretation of the references in color in this figure legend, the reader is referred to the web version of this article.)

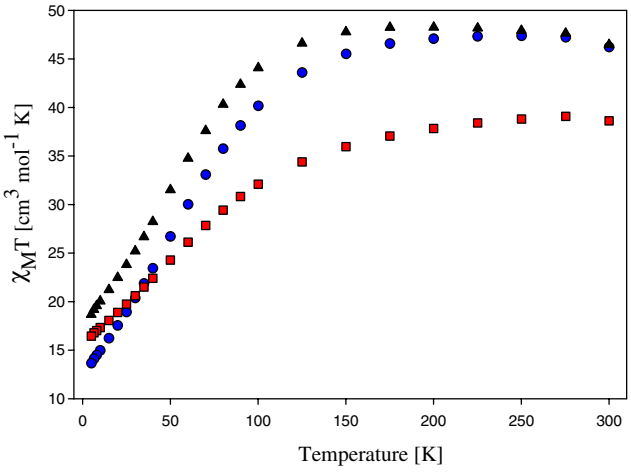


Fig. 4. $\chi_M T$ vs. T for complexes **1** (●), **2** (■), and **3** (▲) in a 0.1 T applied dc field.

likely reflects the fact that these two complexes have several similar core metric parameters, as described above.

For all three compounds, the 5.0 K data suggest that the complexes all possess ground states with significant S values. This would not be unexpected for such a complicated Mn_{13} topology with multiple inequivalent exchange parameters, most of which, if not all, being almost certainly antiferromagnetic. This is because of the spin frustration effects expected within the many Mn_3 triangular units within the Mn_{13} structure. We define spin frustration here in its more general form as competing exchange interactions of comparable magnitude that prevent (frustrate) the preferred pairwise antiparallel spin alignments that would give small (0 or 1/2) ground states.

In order to determine the ground states of complexes **1**, **2**, and **3**, magnetization (M) data were collected in the magnetic field and temperature ranges of 0.1–7 T and 1.8–10 K, respectively. Attempts to fit the resulting data using the program MAGNET [10], which assumes that only the ground state is populated at these temperatures, includes axial zero-field splitting (ZFS) and the Zeeman interaction with the applied field, and carries out a full powder average, did not lead to satisfactory fits. In our experience, this is the case when there are low-lying excited states that are consequently populated even at these relatively low temperatures and/or excited states that are more separated from the ground state but have S values greater than that of the ground state and thus their larger M_S levels rapidly decrease in energy due to the applied magnetic field and approach (or even cross) those of the ground state. Such situations are expected for **1**–**3** because of their high Mn^{II} content (exchange interactions involving Mn^{II} are known to be very weak and almost always antiferromagnetic, yielding small energy separations between the ground state and many nearby excited states with larger S values), and will lead to poor fits of the magnetization data since the fitting program assumes population of only the ground state levels. As we have described elsewhere on multiple occasions [11], these complications can sometimes be avoided by using only data collected at the lowest fields. For complex **1**, a satisfactory fit was obtained using data collected in the field range 0.1–0.8 T, as shown in Fig. 5, with fit parameters $S = 9/2$, $g = 2.00(1)$ and $D = -0.14(1)\ cm^{-1}$. However, attempts to fit the magnetization data for complexes **2** and **3** collected at only the lower fields still did not lead to acceptable fits. Therefore, we turned to the use of more reliable methods based on ac magnetic susceptibility measurements [12], which do not employ a dc field, to identify the ground state spins of **2** and **3**, and also confirm (or otherwise) our initial conclusion of an $S = 9/2$ ground state for **1**.

Alternating-current magnetic susceptibility studies were performed on vacuum-dried microcrystalline samples of **1**–**3** in the temperature range 1.8–15 K in a zero dc field and a 3.5 Oe ac field oscillating at frequencies between 250 and 1000 Hz. The resulting data are plotted as $\chi'_M T$ versus T in Fig. 6, where χ'_M is the in-phase component of the ac susceptibility. For all three complexes, $\chi'_M T$ decreases essentially linearly with decreasing temperature, this downward slope supporting a decreasing population of excited

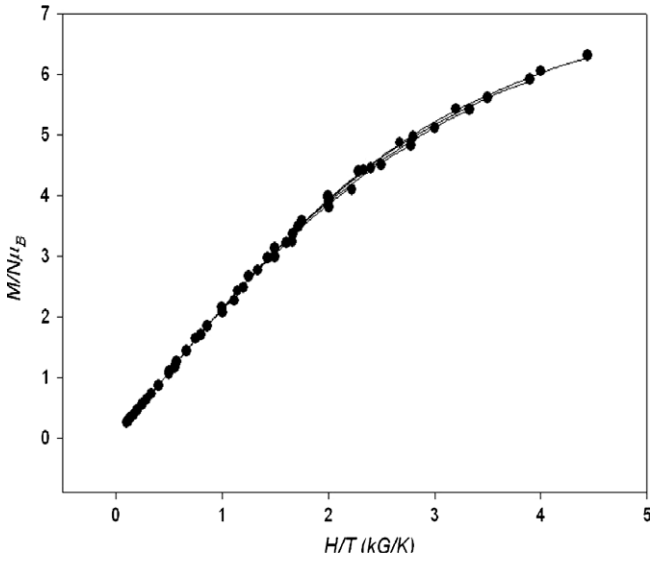


Fig. 5. Plot of the reduced magnetization, $M/N\mu_B$, vs. H/T for complex **1**; the solid line is the fit of the data (see the text for the fitting parameters and the fields used).

states with a larger S than the ground state, in agreement with the statements above re the dc magnetization fitting problems. A linear extrapolation of the data for **1** to 0 K, where only the ground state will be populated, gives an approximate $\chi'_M T$ of $\sim$13 $cm^3\,mol^{-1}$ K, indicating an $S = 9/2$ ground state (expected spin-only ($g = 2.0$) value for $S = 9/2$ is 12.4 $cm^3\,mol^{-1}$ K). This is satisfyingly consistent with the conclusion from the dc magnetization fit in Fig. 5. For complexes **2** and **3**, the $\chi'_M T$ values are significantly higher, and extrapolations to 0 K give approximate values of $\chi'_M T$ of $\sim$16.2 and $\sim$17 $cm^3\,mol^{-1}$ K, respectively, consistent with a $S = 11/2$ ground states for these complexes (spin-only value for $S = 11/2$ is 17.88 $cm^3\,mol^{-1}$ K).

It is interesting that complexes **1** and **3** have the overall more similar $\chi_M T$ versus T behavior up to 300 K (Fig. 4) but that **2** and **3** are the more similar at very low temperatures and in their ground states (Figs. 4 and 6). The former observation is consistent with the several structural similarities between **1** and **3** seen in Table 1, even though they differ in both the EtO^- versus OH^- and benzoate versus ndc^{2-} identities, whereas the difference in ground state is perhaps due to the significantly different $Mn^{II}Mn^{II}$ exchange interactions via the Mn^{II}–RO^-–Mn^{II} superexchange pathways. These are likely the weakest interactions in the molecule, their impact thus becoming evident only at the lowest temperatures, and given the significant difference in the angles at the bridging HO^- or EtO^- atoms mentioned earlier, it seems reasonable that differences in this exchange parameter could cause a flip in the relative energies of some of the closely separated, lowest-lying spin states, causing a change in the ground state.

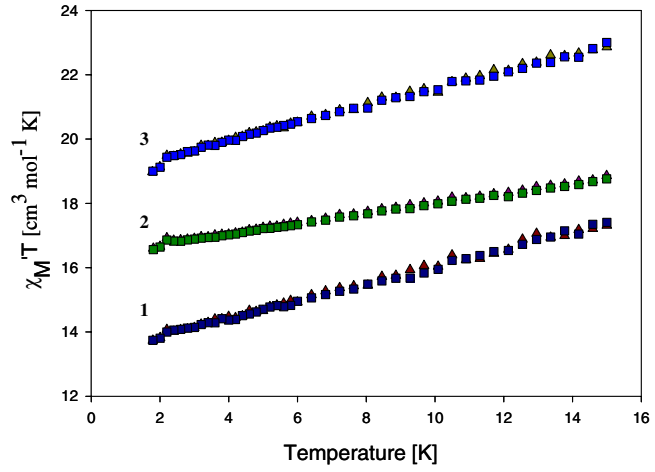


Fig. 6. Plot of the in-phase (χ'_M) ac magnetic susceptobility (as $\chi'_M T$) vs. T for complexes **1**, **2**, and **3** in a 3.5 Oe field oscillating at 250 (▲) and 1000 (■) Hz. The blips at 2.2 K are instrumental artifacts.

In summary, the initial use of the ndc^{2-} group in Mn chemistry has led to two mixed-valent Mn_{13} clusters containing three different oxidation states of this metal and differing only in the HO^- versus EtO^- identity of some of the bridging ligands. In addition, a rational and convenient synthesis has been developed for the corresponding benzoate version, which was already known in the literature. The unusual $\eta^1{:}\eta^1{:}\eta^1{:}\eta^1{:}\mu_4$ coordination mode adopted by the ndc^{2-} group suggests that it may prove a route to a variety of new metal clusters with other transition metals or lanthanides. Examination of the structural parameters of the three complexes **1**, **2**, and **3** led to the conclusion that the inflexible ndc^{2-} group actually imposes little significant structural change on the core of the molecule, and what is seen appears comparable with the HO^- versus EtO^- effect. Complexes **1**–**3** were determined to have $S = 9/2$, 11/2, and 11/2 ground states, respectively; a fuller rationalization of this difference will be provided in the full report of this work.

Acknowledgement

This work was supported by the National Science Foundation.

Appendix A. Supplementary material

CCDC 617346, 617347 and 617348 contain the supplementary crystallographic data for this paper. These data can be obtained free of charge via http://www.ccdc.cam.ac.uk/conts/retrieving.html, or from the Cambridge Crystallographic Data Centre, 12 Union Road, Cambridge CB2 1EZ, UK; fax: (+44) 1223-336-033; or e-mail: deposit@ccdc.cam.ac.uk. Supplementary data associated with this article can be found, in the online version, at doi:10.1016/j.poly.2006.10.038.

References

[1] (a) G. Christou, D. Gatteschi, D.N. Hendrickson, R. Sessoli, MRS Bull. 25 (2000) 66;

(b) R. Sessoli, H.-L. Tsai, A.R. Schake, S. Wang, J.B. Vincent, K. Folting, D. Gatteschi, G. Christou, D.N. Hendrickson, J. Am. Chem. Soc. 115 (1993) 1804;
(c) R. Sessoli, D. Gatteschi, A. Caneschi, M.A. Novak, Nature 365 (1993) 141;
(d) G. Christou, Polyhedron 24 (2005) 2065;
(e) W. Wernsdorfer, N. Aliaga-Alcalde, D.N. Hendrickson, G. Christou, Nature 416 (2002) 406;
(f) M. Soler, W. Wernsdorfer, K.A. Abboud, D.N. Hendrickson, G. Christou, Polyhedron 22 (2003) 1777;
(g) M. Soler, W. Wernsdorfer, K.A. Abboud, J.C. Huffman, E.R. Davidson, D.N. Hendrickson, G. Christou, J. Am. Chem. Soc. 125 (2003) 3576;
(h) H. Andres, R. Basler, A.J. Blake, C. Cadiou, G. Chaboussant, C.M. Grant, H.-U. Güdel, M. Murrie, S. Parsons, C. Paulsen, F. Semadini, V. Villar, W. Wernsdorfer, R.E.P. Winpenny, Chem. Eur. J. 8 (2002) 4867;
(i) E.K. Brechin, M. Soler, G. Christou, M. Helliwell, S.J. Teat, W. Wernsdorfer, Chem. Commun. (2003) 1276;
(j) D.J. Price, S.R. Batten, B. Moubaraki, K.S. Murray, Chem. Commun. (2002) 762.
[2] J.R. Friedman, M.P. Sarachik, J. Tejada, R. Ziolo, Phys. Rev. Lett. 76 (1996) 3830.
[3] (a) W. Wernsdorfer, R. Sessoli, Science (2000) 2417;
(b) W. Wernsdorfer, M. Soler, G. Christou, D.N. Hendrickson, J. Appl. Phys. 91 (2002) 7164;
(c) W. Wernsdorfer, N.E. Chakov, G. Christou, Phys. Rev. Lett. 95 (1–4) (2005) 037203.
[4] (a) R.C. Squire, S.M.J. Aubin, K. Folting, W.E. Streib, G. Christou, D.N. Hendrickson, Inorg. Chem. 34 (1995) 6463;
(b) M.W. Wemple, H.L. Tsai, S. Wang, J.P. Claude, W.E. Streib, J.C. Huffman, D.N. Hendrickson, G. Christou, Inorg. Chem. 35 (1996) 6437;
(c) C. Canada-Vilalta, W.E. Streib, J.C. Huffman, T.A. O'Brien, E.R. Davidson, G. Christou, Inorg. Chem. 43 (2004) 101.
[5] J.B. Vincent, H.R. Chang, K. Folting, J.C. Huffman, G. Christou, D.N. Hendrickson, J. Am. Chem. Soc. 109 (1987) 5703.
[6] Details will be given in the full paper.
[7] Z. Sun, P.K. Gantzel, D.N. Hendrickson, Inorg. Chem. 35 (1996) 6640.
[8] O. Kahn, Molecular Magnetism, VCH, New York, 1993.
[9] W.H. Crawford, H.W. Richardson, J.R. Wasson, D.J. Hodgson, W.E. Hartfield, Inorg. Chem. 15 (1976) 2107.
[10] E.R. Davidson, MAGNET, Indiana University, Bloomington, IN, 1999.
[11] (a) M. Soler, W. Wernsdorfer, K. Folting, M. Pink, G. Christou, J. Am. Chem. Soc. 126 (2004) 2156;
(b) E.C. Sanudo, W. Wernsdorfer, K.A. Abboud, G. Christou, Inorg. Chem. 43 (2004) 4137;
(c) M. Murugesu, J. Raftery, W. Wernsdorfer, G. Christou, E.K. Brechin, Inorg. Chem. 43 (2004) 4203.
[12] (a) E.K. Brechin, C. Boskovic, W. Wernsdorfer, J. Yoo, A. Yamaguchi, E.C. Sanudo, T.R. Concolino, A.L. Rheingold, H. Ishimoto, D.N. Hendrickson, G. Christou, J. Am. Chem. Soc. 124 (2002) 9710;
(b) E.C. Sanudo, W. Wernsdorfer, K.A. Abboud, G. Christou, Inorg. Chem. 43 (2004) 4137;
(c) M. Soler, E. Rumberger, K. Folting, D.N. Hendrickson, G. Christou, Polyhedron 20 (2001) 1365.

also reported the ferromagnetism of $[Mn(C_5Me_5)_2]^+$-$[TCNE]^-$ and $[Cr(C_5Me_5)_2]^+[TCNE]^-$ systems [9,10]. Because Cr(III) has a d^3 (a_{1g}^1 e_{2g}^2) electronic configuration and Mn(III) has d^6 (a_{1g}^2 e_{2g}^2), they should exhibit antiferromagnetic coupling if forward-charge-transfer mechanism was appropriate.

Tchougreeff et al. presented another charge transfer mechanism, namely back-charge-transfer. In this mechanism, up-spin in π^* orbital on acceptor (A^-) back transferred to the e_{1g}^* orbitals in metal site resulting in A^0D^0 state [11,12].

Kollmar et al. notified that the sign of spin population on the cyclopentadienyl ring was a keypoint to determine which mechanism were appropriate [13]. The back-charge-transfer put an up-spin in e_{1g}^* orbitals which are mixed with π-orbitals in cyclopentadienyl rings therefore, the sign of the spin density on cyclopentadienyl rings is positive. On the other hand, spin-polarization mechanism cause negative spin density on the carbon ring.

Yamaguchi et al. reported spin densities on the cyclopentadienyl ring by UHF calculation of $[Fe(C_5Me_5)_2]^+$, $[Cr(C_5Me_5)_2]^+$, $[Mn(C_5Me_5)_2]^+$ and $[Ni(C_5Me_5)_2]^+$ [14]. Their results showed the negative spin densities on the carbon ring in case of $[Fe(C_5Me_5)_2]^+$, $[Cr(C_5Me_5)_2]^+$, and $[Mn(C_5Me_5)_2]^+$. Otherwise, in case of $[Ni(C_5Me_5)_2]^+$, the positive spin densities were appeared on the cyclopentadienyl ring. Ni(III) had one electron in e_{1g}^* orbitals therefore, this result seemed to be reasonable.

In our previous paper, we demonstrated the calculated results of the broken-symmetry hybrid DFT methods on the reduced model complex of $[Fe(C_5Me_5)_2]^+[TCNE]^-$ system [15]. The calculated effective exchange integrals reproduced the experimental result and we concluded that McConnell I mechanism via spin polarization of cyclopentadienyl ring could explain the ferromagnetism.

In this study, we applied hybrid-DFT calculation to the reduced model complex of $[Cr(C_5(CH_3)_5)_2]^+[TCNE]^-$(**1**) and $[Mn(C_5(CH_3)_5)_2]^+[TCNQ]^-$ (**2**) systems by using available structures of X-ray crystallographic data. The effective exchange integrals of 3-site chain reduced model of realistic 3D systems were calculated by using broken-symmetry method. The spin density distributions were also examined for both model complexes. From those calculated results, the effectiveness of McConnell I mechanism (spin-polarization mechanism) was demonstrated. In addition, the way of orbital interaction between metal site and accepter molecule ($TCNE^-$ or $TCNQ^-$) was discussed by using natural orbital analysis of the broken-symmetry hybrid-DFT solutions.

2. Theoretical background and computational details

2.1. Effective exchange integrals

To describe the magnetic interaction between the magnetic sites, Heisenberg Hamiltonian was employed

$$\widehat{H} = -2\sum_{ab} J_{ab} S_a S_b \tag{1}$$

Recent computational developments of ab initio calculation and the density functional theory enable us to calculate the effective exchange integral for transition metal complexes. The details about a derivation of the effective exchange integral were described in elsewhere [16]. J_{ab} value can be calculated as follows:

$$J = \frac{E_{LS} - E_{HS}}{\langle S^2 \rangle_{HS} - \langle S^2 \rangle_{LS}} \tag{2}$$

E_X and $\langle S^2 \rangle_X$ denote the total energy and the total spin angular momentum, respectively. The structure of the reduced model complex is shown in Fig. 1. Fig. 2(a) shows the spin aliment of high-spin (HS) and low-spin (LS) states and site number.

In order to apply Eq. (2) to this model, we used simple assumption that we only considered magnetic interactions between the sites 1 and 2 (J_{12}) and between sites 2 and 3 (J_{23}). The magnetic interaction between site 1 and site 3 (J_{13}) were neglected. Therefore, calculated effective exchange integral was single $J = J_{12} = J_{23}$.

2.2. Computational methods

The Kohn–Sham (KS) density functional theory [17] is one of the most popular approaches in computational chemistry. The energy expression is given by

$$E = T_0[\{\psi_i\}] + V_{Ne}[\rho] + V_{clumb}[\rho] + E_{xc}[\rho] \tag{3}$$

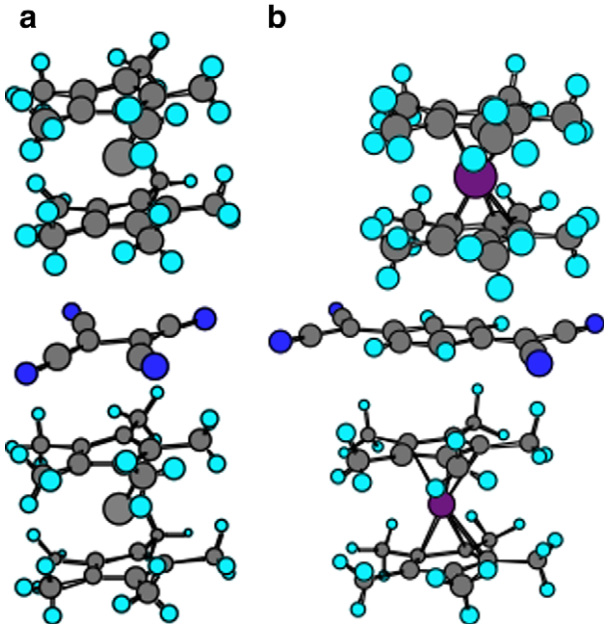


Fig. 1. (a) The reduced model complexes of $[Cr(C_5(CH_3)_5)_2]^+[TCNE]^-$ system (model **1**) and (b) is the reduced model of $[Mn(C_5(CH_3)_5)_2]^+$-$[TCNQ]^-$ system (model **2**). Each model have three spin sites.

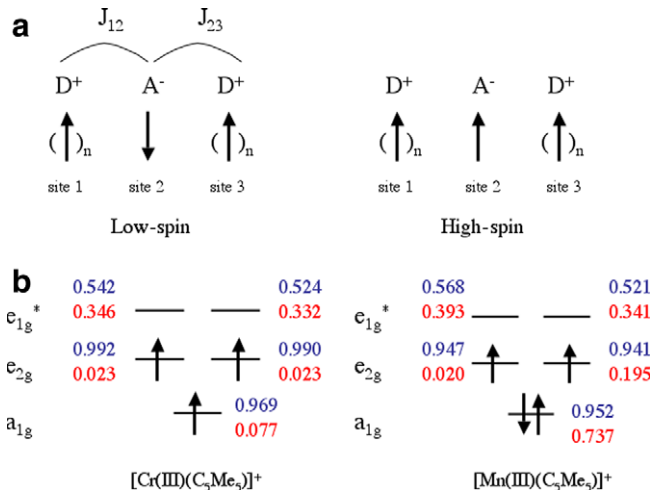


Fig. 2. (a) The spin alignments of high-spin (HS) and low-spin (LS) states. J_{12} means the interaction between spin site 1 and site 2. D^+ indicates the transition metal (=Cr(III) or Mn(III)) and A^- indicate the acceptor (=$TCNE^-$ or $TCNQ^-$). The n is 3 in case of Cr(III) and 2 in case of Mn(III), respectively. (b) Schematic views of electron configurations in 3d-orbital in Cr(III) and Mn(III) in reduced model complexes. The values in upper row (blue) indicates the population of α electron and values in lower row (red) indicates the population of β electron. The values indicate the one of two transition metals. The values of the other metal show same tendency.

where T_0, V_{Ne} and V_{clumb} are the kinetic energy of electron, nuclear attraction energy and classical coulomb term respectively. E_{xc} is the exchange-correlation term [18]. In hybrid-DFT [19], the exchange-correlation term is described as

$$E_{xc} = C_1 E_x^{HF} + C_2 E_x^{Slater} + C_3 E_x^{Becke88} + C_4 E_c^{VWN} + C_5 E_c^{LYP} \quad (4)$$

where E_x^{HF}, E_x^{Slater}, and $E_x^{Becke88}$ denote the Hartree–Fock, Slater and Becke's exchange functionals, respectively. E_c^{VWN} and E_c^{LYP} denote the Vosko, Wilk and Nusair (VWN) [20] and Lee, Yang and Parr (LYP) [21] correlation functionals, respectively. c_i ($i = 1$–5) are the mixing parameters. They are (0.5, 0.5, 0.5, 1.0, and 1.0) and (0.2, 0.8, 0.72, 1.0, and 0.81) for B2LYP (Becke's half and half LYP) and UB3LYP, respectively [22–24].

All calculations were performed by using GAUSSIAN 98 program package [25] and geometries of model complexes were prepared using X-ray crystallographic data from Cambridge Structural Data-base (CSD). Huzinaga's MIDI+p basis set (533(21)/53(21)/(41)) is employed for Mn and Cr [26]. 6-31G* basis sets are adopted for C and N atoms. For all H atoms, we used 4-31G level basis sets.

2.3. Natural orbital and occupation number

Although the broken-symmetry (BS) hybrid-DFT method could approximately include the static electron correlation, the obtained orbitals are often different from familiar MOs, namely symmetry-adapted (SA) MOs. In order to obtain the SA MO picture from the broken-symmetry (BS) solutions, the natural orbital (NO) analysis has been carried out. The NOs of broken-symmetry solution is determined by diagonalizing first-order density matrices [27] as

$$\rho(r, r') = \sum n_i \phi_i(r) \phi_i(r')^* \quad (5)$$

where n_i and ϕ_i denote the occupation number and natural orbital, respectively. The occupation numbers of bonding and antibonding NOs are almost 2.0 and 0.0, respectively. Occupation numbers of magnetic orbitals are usually close to 1.0 occupation number. These orbitals are also called as singly occupied natural orbitals (SONO). The spin-polarized MOs ψ^+ and ψ^- for up and down spins can be connected with the in- and out-of phase combinations of the bonding and antibonding natural orbitals:

$$\psi_i^{\pm} = \cos\theta_i \phi_i \pm \sin\theta_i \phi_i \quad (i = 1, 2, 3, \ldots, N) \quad (6)$$

where θ_i the orbital mixing parameter and N is the number of bonding natural orbitals. The occupation numbers of the bonding and antibonding natural orbitals are expressed by using T_i value

$$n_i = 1 + T_i, \quad n_i^* = 1 - T_i \quad (7)$$

where T_i values are orbital overlap which are expressed as

$$T_i = \langle \psi_i^+ | \psi_i^- \rangle \quad (8)$$

3. Results and discussions

3.1. Electronic structure of $[Cr(C_5Me_5)_2]^+[TCNE^-]^-[Cr(C_5Me_5)_2]^+$ and $[Mn(C_5Me_5)_2]^+[TCNQ^-]^-[Mn(C_5Me_5)_2]^+$

In Fig. 2(b), gross orbital populations in 3d-orbitals of Cr and Mn in reduced model complex were summarized. This tables only presented the UB3LYP results. UB2LYP results were same tendency.

Table 1 summarized the spin density distributions on the both type of model complexes. The magnitude for α spin ($s = 1/2$) and β spin ($s = -1/2$) were defined to be 1.0 and −1.0, respectively. In case of UB3LYP calculation, the spin densities on two Cr and Mn were about 3.3 and 2.3, respectively.

Table 1 also showed NBO (natural bond orbital) natural charge distribution of metal and TCNE sites. The charge populations on TCNE and TCNQ were close to their formal charges i.e. −1.0 in both cases of model **1** and model **2**. However, the charge populations on Cr site were about 1.1 and 1.3 in case of UB3LYP and UB2LYP, respectively and populations on Mn site were about 1.1 and 1.2. These results showed the strong donation from cyclopentadienyl rings to a metal center.

3.2. Effective exchange integrals

Table 2 summarized calculated effective exchange integrals (J values). Both UB3LYP and UB2LYP calculations

Table 1
Spin density and NBO natural charge distributions

	Spin density		Charge density	
	High-spin	Low-spin	High-spin	Low-spin
UB3LYP				
Cr(1)	3.32	3.32	1.11 (0.399)	1.11 (0.399)
Cr(2)	3.32	3.32	1.11 (0.400)	1.11 (0.400)
TCNE	0.994	−1.00	−0.978 (−0.899)	−0.979 (−0.899)
Mn(1)	2.28	2.28	1.06 (0.514)	1.06 (0.514)
Mn(2)	2.28	2.28	1.06 (0.513)	1.06 (0.513)
TCNQ	0.924	−0.999	−0.976 (−0.880)	−0.976 (−0.880)
UB2LYP				
Cr(1)	3.41	3.41	1.25 (0.576)	1.25 (0.576)
Cr(2)	3.41	3.41	1.25 (0.576)	1.25 (0.576)
TCNE	0.999	−1.00	−0.934 (−0.918)	−0.985 (−0.917)
Mn(1)	2.41	2.41	1.18 (0.635)	1.18 (0.635)
Mn(2)	2.41	2.41	1.18 (0.634)	1.18 (0.634)
TCNQ	0.924	−1.00	−0.983 (−0.902)	−0.983 (−0.902)

Mulliken charges are presented in parentheses. The spin density and charges on TCNE and TCNQ are the sum of the values on each atoms which compose the molecule.

Table 2
The total energies, $\langle S^2 \rangle$ and effective exchange integrals of UB3LYP and UB2LYP calculations

Method	HS state		LS state		J_{ab} (cm^{-1})
	Energy (a.u.)	$\langle S^2 \rangle$	Energy (a.u.)	$\langle S^2 \rangle$	
(a)					
UB3LYP	−4095.24345015	15.9413	−4095.24335908	9.9421	+3.33
UB2LYP	−4093.91700600	16.0235	−4093.91697150	10.0244	+1.26
Experimental					+6.3
(b)					
UB3LYP	−4539.43737105	8.9137	−4539.43727291	4.9123	+5.38
UB2LYP	−4537.93029313	9.0167	−4537.93017681	5.0171	+6.38
Experimental					+ 9.7

(a) and (b) are results of **1** and **2**, respectively.

have reproduced positive J values, which correspond to ferromagnetic interactions of experimental results. The experimental values of model **1** and model **2** were 6.3 cm^{-1} [28] and 9.7 cm^{-1} [7], respectively. Calculated results are qualitatively consistent with the experimental results. Comparing the results of UB3LYP with those of UB2LYP, it was clear that both methods showed close results. So, differences from functionals used in hybrid-DFT calculations could not be detected. Because effective exchange integral is sensitive to electronic structure we could conclude that the calculated electronic structures were sufficient and reliable for further discussions.

3.3. Spin density and McConnell mechanisms

As was discussed in introduction of this paper, charge transfer mechanism (McConnell II mechanism) causes positive spin densities on cyclopentadienyl rings. Otherwise, spin-polarization mechanism (McConnell I mechanism) causes negative spin densities on the ring. In Figs. 3 and 4, we presented the spin densities on cyclopentadienyl rings in case of model **1** and model **2**, respectively. In

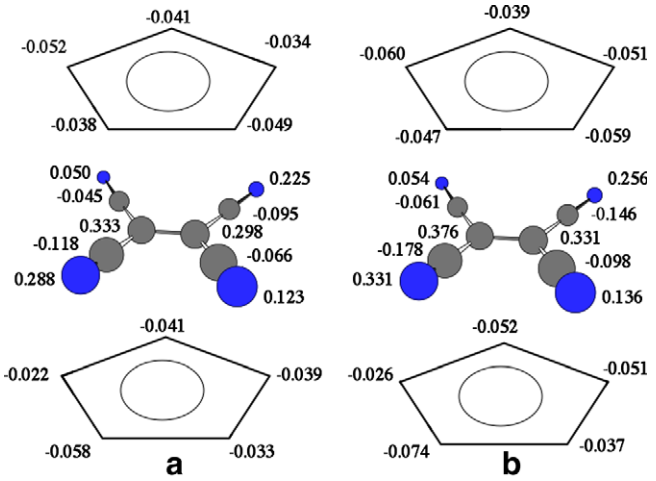


Fig. 3. Spin density distributions in case of **1**. (a) The result of UB3LYP and (b) is the result of UB2LYP.

Fig. 4 we neglected the hydrogen atoms in TCNQ for simplicity. The calculated results in both case of UB3LYP and UB2LYP calculations showed that the sign of spin

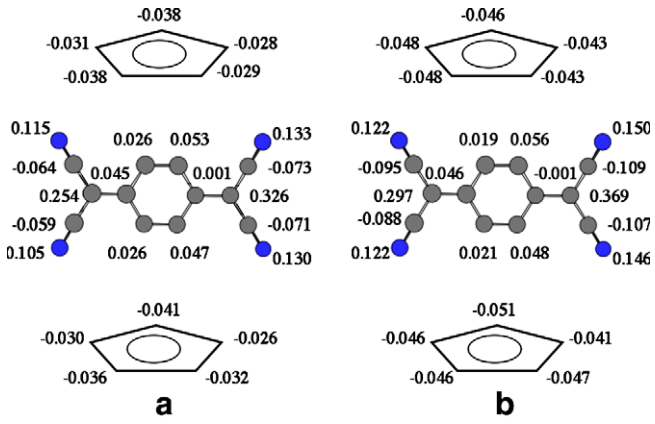


Fig. 4. Spin density distributions in case of **2**. (a) The result of UB3LYP and (b) is the result of UB2LYP. Hydrogen atoms in TCNQ are neglected for simplicity.

densities on the rings was negative, therefore these results supported the spin-polarization mechanism proposed by C.Kollmar et al [3,13].

3.4. Natural orbital analysis, occupation numbers and effective exchange integral

We have confirmed that spin-polarization effect has some contribution to the ferromagnetism of these systems. However, the orbital interactions of these systems have not been discussed yet. In order to consider the relation between magnetic property and electronic structure, we performed natural orbital analysis. Figs. 5 and 6 presented the natural orbitals (NOs) and their occupation numbers. These figures indicated the NOs whose occupation numbers were close to 1.0, therefore other NOs had about 2.0 or 0.0 in occupation numbers. The singly occupied NOs (SONO) were degenerated. From the figures of NOs, it was clear that NOs whose orbital numbers are (203) and (209) represented the interaction between d-orbital in Cr

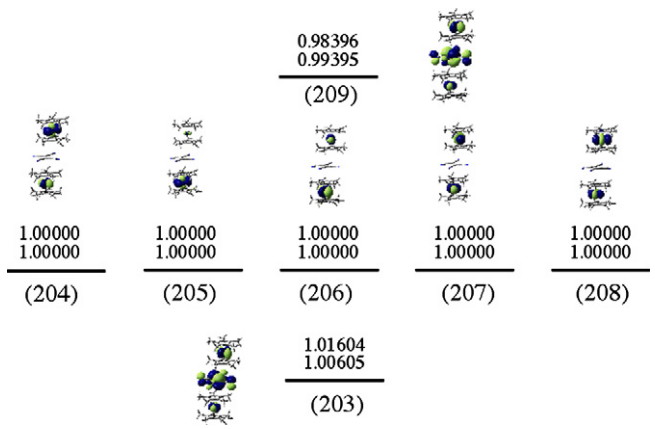


Fig. 5. Singly occupied natural orbitals (SONOs) and occupation numbers of **1**. The numbers in parentheses indicate orbital numbers. Occupation numbers in upper row indicate the results of UB3LYP and occupation numbers in lower row indicate the results of UB2LYP.

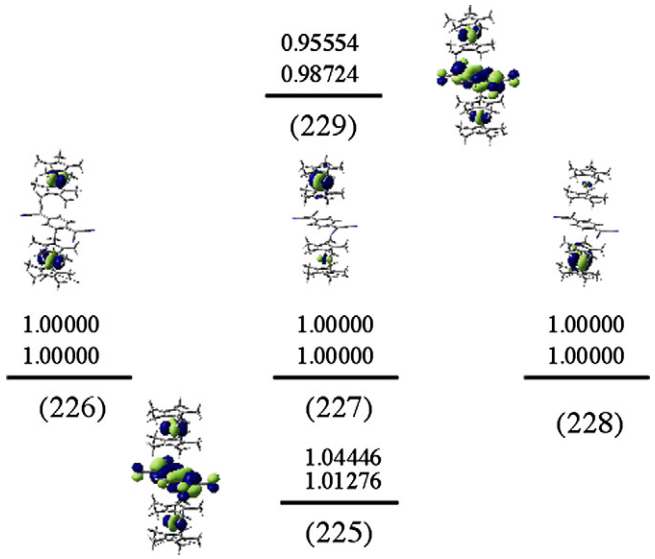


Fig. 6. Singly occupied natural orbitals (SONOs) and occupation numbers of **2**. The numbers in parentheses indicate orbital numbers. Occupation numbers in upper row indicate the results of UB3LYP and occupation numbers in lower row indicate the results of UB2LYP.

and HOMO of $TCNE^{-}$ anion in case of **1**. The other NOs represented SONOs which localized only on metal site. In case of **2**, NOs of number 225 and 229 represented the interaction between d-orbital in manganese and HOMO of TCNE anion.

In Table 3, T_i of each SONO were summarized. In case of **1**, NO of orbital number 203 had almost no orbital overlap (T). This result indicated that SOMO on Cr and SOMO on TCNE anion were orthogonal. The same discussion could be applicable to the orbital number 225 in **2**. According to the Kanamori–Goodenough rule [28–30], ferromagnetic interaction could be expected if SOMO–SOMO overlap was zero.

Previously, we have discussed on the ferrimagnetic behavior of charge transfer manganese porphyrin and TCNE system [16]. The T value of NO which represented the SOMO–SOMO interaction between d-orbital in manganese and TCNE anion was 0.30. This result showed the large overlap of SOMO–SOMO caused the antiferromagnetic interaction.

Table 3
Orbital overlap T_i (i = orbital number)

	203	204	205	206	207	208	209
(a)							
T_i(UB3LYP)	0.01604	0.00	0.00	0.00			
T_i(UB2LYP)	0.00605	0.00	0.00	0.00			

	225	226	227	228	229
(b)					
T_i(UB3LYP)	0.04446	0.00	0.00		
T_i(UB2LYP)	0.01276	0.00	0.00		

(a) is the results of **1** and (b) is the results of **2**.

3.5. Decomposition of J value and ferromagnetism

In unrestricted Hartree–Fock approximation scheme, effective exchange integral is generally expressed by different terms as

$$J_{ab} = J_{ab}(\mathrm{KE}) + J_{ab}(\mathrm{PE}) + J_{ab}(\mathrm{SP}) \quad (9)$$

$$J(\mathrm{KE}) = -cS_{ab} \quad (10)$$

$$J(\mathrm{PE}) = K_{ab} \quad (11)$$

$$J(\mathrm{SP}) = -\sum A\rho_a\rho_b \quad (12)$$

where kinetic (KE) and potential (PE) terms are represented by SOMO–SOMO orbital overlap S_{ab} (T value in formula Eq. (8)) and exchange integral K_{ab}, respectively [31,32]. c and A are parameters determined by ab initio calculation. Spin-polarization (SP) term was given by the product of spin densities ρ. In DFT scheme, it is unclear how to express the exchange (J(PE)) term explicitly, however this type of decomposition could be available on assumption that J(PE) is always positive considering the Hund rule. Considering the orbital overlap was almost zero, calculation results could be explained that negative J(KE) was nearly zero and J(PE) was positive therefore, the net magnetic interaction by J(PE) plus J(KE) contributed to positive J_{ab}.

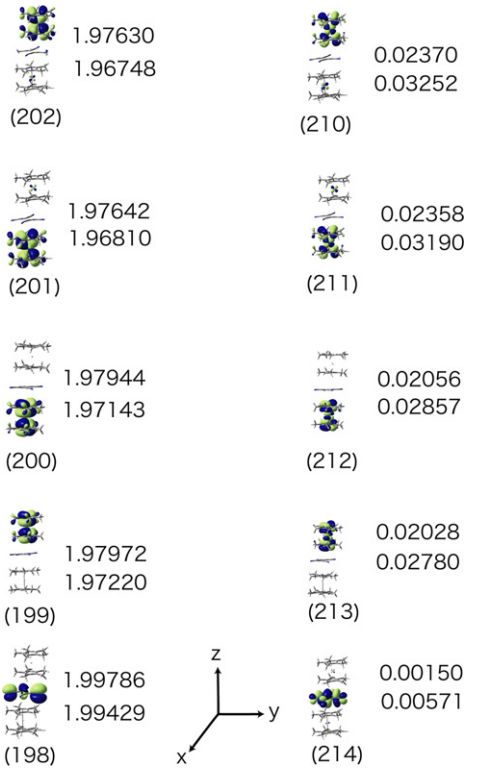


Fig. 7. Natural orbitals around SONOs and their occupation numbers in case of **1**. The numbers in parentheses are orbital numbers. NOs of orbital numbers 198 and 214 are bonding and anti-bonding pair, and so on. Occupation numbers in upper row indicate the results of UB3LYP and those in lower row indicate the results of UB2LYP.

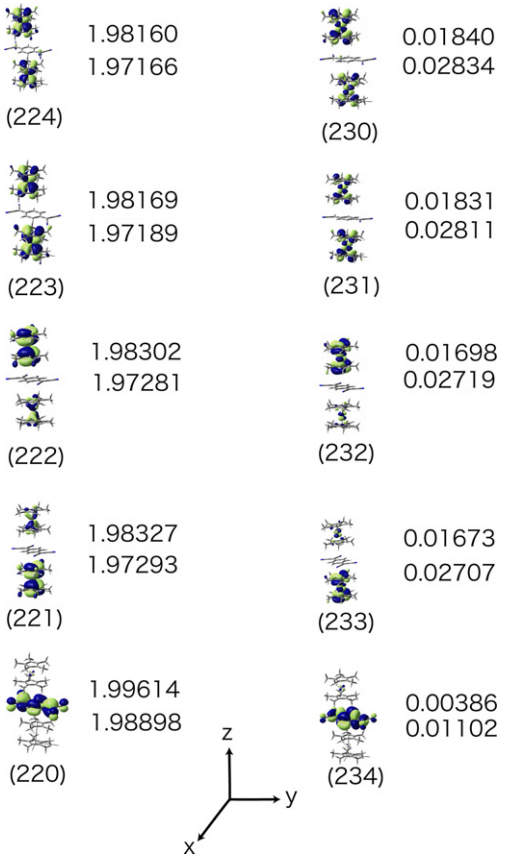


Fig. 8. Natural orbitals around SONOs and their occupation numbers in case of **2**. The numbers in parentheses are orbital numbers. NOs of orbital numbers 220 and 234 are bonding and anti-bonding pair, and so on. Occupation numbers in upper row indicate the results of UB3LYP and those in lower row indicate the results of UB2LYP.

To estimate the effect of spin polarization, occupation numbers around singly occupied natural orbitals (SONOs) and shapes of these NOs were depicted in Figs. 7 and 8. From Fig. 7, NOs of number 199–202 of **1** whose occupation numbers were about 1.97 showed localization on cyclopentadienyl ring. These results suggested the existence of spin-polarization effect of the ring, because the NOs of occupation number 2.0 were described as RHF like picture, which showed no spin-polarization. The same discussion could be applied to **2**. Therefore, it might be suggesting that spin-polarization effect had some contribution to positive J_{ab} value. To examine the effect of J(SP) term quantitatively, we need to perform multi-reference calculations beyond single reference broken-symmetry method.

4. Conclusion

To explain the ferromagnetism of donor–acceptor systems of $[Cr(C_5Me_5)_2]^+[TCNE^-]^-$ and $[Mn(C_5Me_5)_2]^+[TCNQ^-]^-$, hybrid-DFT calculation of reduced model complexes was performed. By using broken-symmetry hybrid-DFT method, effective exchange integrals were calculated. Those effective exchange integrals reproduced the experimental values well. Therefore, electronic structures

of model complexes could be considered as good models of real systems. The results of spin density distributions showed the spin-polarization and the sign of spin densities on cyclopentadienyl rings was negative. These results supported the so-called McConnell I mechanism. On the other hand, natural orbital analysis made it clear that the SOMO–SOMO overlap between metal site and TCNE or TCNQ anion site were almost zero. Therefore orbital orthogonality might be the important key point for explaining the ferromagnetism of these systems. By using decomposition of effective exchange integral, effects by both exchange term and spin-polarization term for ferromagnetism was explained well. To estimate the spin-polarization effect for ferromagnetism quantitatively, multi-reference methods are necessary, however it is impossible because of computing cost at this stage. Therefore, broken-symmetry hybrid-DFT was powerful method to analyze those electronic structures.

Acknowledgements

This work has been supported by Grants-in-Aid for Scientific Research on Priority Areas (Nos. 16750049 and 18350008) from Ministry of Education, Culture, Sports, Science and Technology, Japan. K.K is also supported by Research Fellowships of the Japan Society for the Promotion of Science for Young Scientists.

References

[1] K. Itoh, M. Kinoshita (Eds.), Molecular Magnetism, Kodansha Gordon and Breach Science Publishers, 2000.
[2] J.S. Miller, J.C. Calabrese, H. Rommelmann, S.R. Chittipeddi, J.H. Zhang, W.M. Reiff, A.J. Epstein, J. Am. Chem. Soc. 109 (1987) 769.
[3] C. Kollmar, M. Couty, O. Kahn, J. Am. Chem. Soc 113 (1991) 7994.
[4] H.M. McConnell, Robert. A. Welch, Proc. Found. Conf. Chem. Res 11 (1967) 144.
[5] R. Breslow, Pure Appl. Chem 54 (1982) 927.
[6] H.M. McConnell, J. Chem. Phys 39 (1963) 1910.
[7] W.E. Broderick, A. Thompson, E.P. Day, B.M. Hoffman, Science 249 (1990) 401.
[8] W.E. Broderick, B.M. Hoffman, J. Am. Chem. Soc 113 (1991) 6334.
[9] G.T. Yee, J.M. Manriquez, D.A. Dixon, R.S. McLean, D.M. Groski, R.B. Flippen, K.S. Narayan, A.J. Epstein, J.S. Miller, Adv. Mater 3 (1991) 309.
[10] J.S. Miller, R.S. Mclean, C. Vazquez, J.C. Calabrese, F. Zuo, A.J. Epstein, J. Matter Chem. 3 (1993) 215.
[11] A.L. Tchougreeff, I.A. Misurkin, Phys. Rev. B 46 (1992) 5357.
[12] A.L. Tchougreeff, J. Chem. Phys. 96 (1992) 6026.
[13] C. Kollmar, O. Kahn, Acc. Chem. Res. 26 (1993) 259.
[14] K. Yamaguchi, M. Okumura, T. Kawamura, T. Noro, K. Nakasuji, Mol. Cryst. Liq. Cryst. 218 (1992) 229.
[15] K. Koizumi, M. Takenaka, M. Shoji, Y. Kitagawa, T. Kawakami, M. Okumura, K. Yamaguchi, To be published.
[16] K. Koizumi, M. Shoji, Y. Kitagawa, T. Taniguchi, T. Kawakami, M. Okumura, K. Yamaguchi, Polyhedron 24 (2005) 2720.
[17] R.G. Parr, W. Yang, Density Functional Theory of Atoms and Molecules, Oxford University Press, 1989.
[18] W. Kohn, L.J. Sham, Phys. Rev. 140 (1965) A1133.
[19] W. Koch, M.C. Holthausen, A Chemist's Guide to Density Functional Theory, Willy-VCH, 2001.
[20] S.H. Vosko, L. Wilk, M. Nusair, Can. J. Phys. 58 (1980) 1200.
[21] C. Lee, W. Wang, R.G. Parr, Phys. Rev. B 37 (1988) 785.
[22] A.D. Becke, J. Chem. Phys. 98 (1993) 5648.
[23] Y. Kitagawa, T. Soda, Y. Shigeta, S. Yamanaka, Y. Yoshioka, K. Yamaguchi, Int. J. Quant. Chem. 84 (2001) 592.
[24] Y. Kitagawa, T. Kawakami, K. Yamaguchi, Mol. Phys. 100 (2002) 1829.
[25] M.J. Frisch, G.W. Trucks, H.B. Schlegel, G.E. Scuseria, M.A. Robb, J.R. Cheeseman, V.G. Zakrzewski, J.A. Montgomery Jr, R.E. Stratmann, J.C. Burant, S. Dapprich, J.M. Millam, A.D. Daniels, K.N. Kudin, M.C. Strain, O. Farkas, J. Tomasi, V. Barone, M. Cossi, R. Cammi, B. Mennucci, C. Pomelli, C. Adamo, S. Clifford, J. Ochterski, G.A. Petersson, P.Y. Ayala, Q. Cui, K. Morokuma, D.K. Malick, A.D. Rabuck, K. Raghavachari, J.B. Foresman, J. Cioslowski, J.V. Ortiz, B.B. Stefanov, G. Liu, A. Liashenko, P. Piskorz, I. Komaromi, R. Gompert, R.L. Martin, D.J. Fox, T. Keith, M.A. Al-Laham, C.Y. Peng, A. Nanayakkara, C. Gonzalez, M. Challacombe, P.M.W. Gill, B. Johnson, W. Chen, M.W. Wong, J.L. Andres, M. Head-Gordon, E.S. Replogle, J.A. Pople, GAUSSIAN 98, Gaussian, Inc., Pittsburgh, PA, 1998.
[26] H. Tatewaki, S. Huzinaga, J. Chem. Phys. 71 (1979) 4339.
[27] K. Yamaguchi, M. Okumura, K. Takeda, S. Yamanaka, Int. J. Quant. Chem. 27 (1993) 501.
[28] P. Zhou, M. Makivic, F. Zuo, S. Zane, J.S. Miller, A.J. Epstein, Phys. Rev. B 49 (1994) 4364.
[29] J. Kanamori, J. Phys. Chem. Solids 10 (1959) 87.
[30] J.B. Goodenough, J. Phys. Chem. Solids 6 (1958) 287.
[31] T. Kawakami, S. Yamanaka, W. Mori, K. Yamaguchi, A. Kajiwara, M. Kamachi, Chem. Phys. Lett. 235 (1995) 414.
[32] K. Yamaguchi, T. Fueno, Chem. Phys. Lett. 159 (1989) 465.

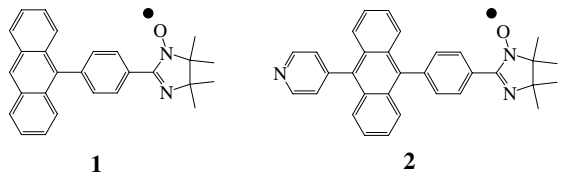


Fig. 1. Molecular structures of organic radicals which has photo-excited quartet state.

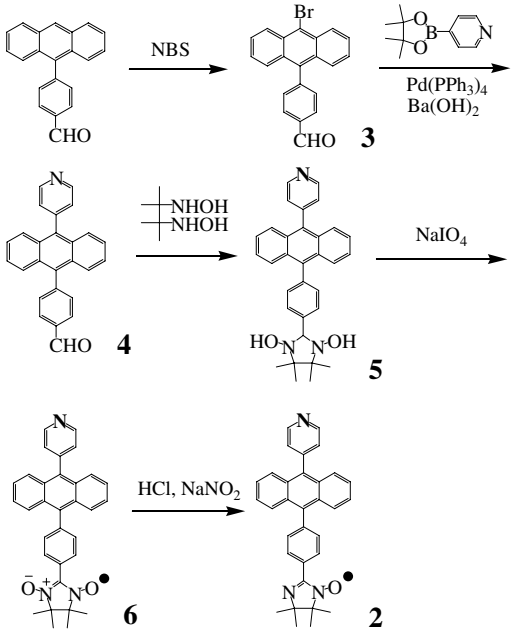
2. Experimental

2.1. Materials

2,3-Bis(hydroxyamino)-2,3-dimethylbutane [7] and 9-(4-formylphenyl)anthracene [1] were prepared according to the literature methods. **2** was synthesized according to Scheme 1.

2.1.1. 9-(4-Formylphenyl)-10-bromoanthracene (3)

A mixture of 4.23 g (15 mmol) of 9-(4-formylphenyl)-anthracene and 2.67 g (15 mmol) of NBS in DMF anhydrous (180 ml) was stirred at room temperature for 24 h. After toluene was added, the organic layer was extracted, washed with brine, and dried ($MgSO_4$). After filtration, evaporation, and recrystallization from toluene gave **3** in 73% yield as yellow prisms: mp 225–226 °C; ^1H NMR ($CDCl_3$) δ 7.40 (dd, $J = 8.7$, 6.3 Hz, 2H, ArH), 7.53–7.63 (m, 6H, ArH), 8.12 (d, $J = 7.9$ Hz, 2H, ArH), 8.64 (d, $J = 9.0$ Hz, 2H, ArH), 10.20 (s, 1H, CHO); *Anal.* Calc. for $C_{21}H_{13}OBr$: C, 69.82; H, 3.63. Found: C, 70.03; H, 3.63%.



Scheme 1. Synthesis of 4-pyridinyl-phenylanthracene-stable radicals **2**.

2.1.2. 9-(4-Formylphenyl)-10-(4-pridyl)anthracene (4)

A mixture of 3.61 g (10.0 mmol) of **3**, 2.05 g (10.0 mmol) of 4-(4,4,5,5-tetramethyl-1,3,2-dioxa-borolan-2-yl)pyridine, 5 mol% of $Pd(PPh_3)_4$, 9.5 g of $Ba(OH)_2 \cdot 8H_2O$ in 1,4-dioxane (350 ml)-H_2O (100 ml) was refluxed under Ar for 72 h. After ethylacetate was added, the organic layer was extracted, washed with brine, and dried ($MgSO_4$). After filtration and evaporation, chromatography (silica-gel, the first developing solvent was toluene, the second one is toluene:ethyl acetate = 2:1) and recrystallization from toluene gave **4** in 30% yield as yellow powder: mp > 300 °C; ^1H NMR ($CDCl_3$) δ 7.36–7.43 (m, 4H, ArH), 7.50 (d, $J = 6.0$ Hz, 2H, ArH), 7.59–7.69 (m, 6H, ArH), 8.16 (d, $J = 7.9$ Hz, 2H, ArH), 8.90 (d, $J = 6.1$ Hz, 2H, ArH), 10.22 (s, 1H, CHO); *Anal.* Calc. for $C_{26}H_{17}NO$: C, 86.88; H, 4.77; N, 3.90. Found: C, 87.11; H, 4.87; N, 3.72%.

2.1.3. 9-[4-(4,4,5,5-Tetramethyl-1,3-dihydroxyimidazolidin-2-yl)phenyl]-10-(4-pyridyl)anthracene (5)

A mixture of 0.84 g (2.3 mmol) of **4**, 0.83 g (5.6 mmol) of 2,3-bis(hydroxyamino)-2,3-dimethylbutane, 0.14 g of 2,3-bis(hydroxyamino)-2,3-dimethylbutane dihydrogen sulfate in MeOH (50 ml)–$CHCl_3$ (50 ml) was refluxed under Ar for 24 h. After filtration, the deposit was washed with MeOH and H_2O to give **5** in 68% yield as white powder (crude).

2.1.4. 9-[4-(4,4,5,5-Tetramethyl-4,5-dihydro-1H-imidazolidin-1-oxyl-3-oxide)phenyl]-10-(4-pyridyl)anthracene (6)

A suspension of 0.94 g (1.9 mmol) of **5** in 100 ml of toluene was added a solution of 1.5 g of $NaIO_4$ in 50 ml of H_2O, and for 3 h. The organic layer was separated, washed with brine, dried ($MgSO_4$). After filtration and evaporation, recrystallization from MeOH gave **5** in 79% yield as blue powder: *Anal.* Calc. for $C_{32}H_{28}N_3O_2$: C, 78.99; H, 5.80; N, 8.64. Found: C, 78.95; H, 5.83; N, 8.36%.

2.1.5. 9-[4-(4,4,5,5-Tetramethyl-1-yl-oxyimidazolidin-2-yl)-phenyl]-10-(4-pyridyl)anthracene (2)

The mixture of 0.70 g (1.44 mmol) of **5** and 2.07 g of $NaNO_2$ in CH_2Cl_2 (80 ml)–H_2O (30 ml). 18 ml of 0.1 M HCl was added dropwise to the mixture at 0 °C. The organic layer separated, washed with brine, dride ($MgSO_4$). After filtration and evaporation, the residue was purified by chromatography (silicagel, dichloromethane:ethyl acetate = 5:1) and recrystallization from hexane/toluene gave **2** in 88% yield as orange powder: mp 263–264 °C (decomp.); *Anal.* Calc. for $C_{32}H_{28}N_3O$: C, 81.67; H, 6.00; N, 8.93. Found: C, 81.55; H, 5.94; N, 8.83%.

2.1.6. Cu(II)(hfac)$_2$(2)$_2$ and Mn(II)(hfac)$_2$(2)$_2$

In order to remove the water of crystallization, the solution of $M(hfac)_2 \cdot xH_2O$ (M = Cu(II) or Mn(II)) in heptane was dried by concentration at 100 °C. To the solution was added a toluene solution of **2** and the mixture was stirred

1 h. After cooling, the deposit was corrected by filtration. Recrystallization from hexane/toluene gave Cu(II)-(hfac)$_2$(**2**)$_2$ as orange prisms: *Anal*. Calc. for $C_{74}H_{58}F_{12}N_6O_6Cu \cdot 0.5C_7H_8$ (toluene): C, 63.54; H, 4.27; N, 5.74. Found: C, 63.67; H, 4.28; N, 5.71%. (The existence of toluene of crystallization was confirmed by a X-ray crystallographical analysis described later.) Repeating recrystallization from hexane/toluene and from hexane/dichloromethane gave Mn(II)(hfac)$_2$(**2**)$_2$ as red prisms: *Anal*. Calc. for $C_{74}H_{58}F_{12}N_6O_6Mn \cdot 0.5C_6H_{14}$ (hexane): C, 63.64; H, 4.51; N, 5.78. For $C_{74}H_{58}F_{12}N_6O_6Mn \cdot 0.5\,C_7H_8$ (toluene): C, 63.92; H, 4.30; N, 5.71. Found: C, 63.76; H, 4.30; N, 5.71%. (The existence of toluene or hexane of crystallization was suggested by elemental analysis.)

2.2. Measurements

TRESR spectra were measured with a JEOL TE300 X-Band ESR spectrometer modified to the TRESR measurements and a Nd:YAG pulse laser was used for a excitation ($\lambda = 355$ nm, pulse width <7 ns). The temperature was controlled by Oxford ESR 910 He gas flow system. The details of TRESR setup were described in our previous paper [1]. Magnetic susceptibility measurement were carried out with a SUQID magnetometer (Quantum Design MPMS2). The X-ray crystallographic data of the metal complexes were collected on a Rigaku/MSC Mercury CCD diffractometer with graphite-monocromated Mo Kα radiation. The structure was solved by a direct method (SIR 97) and expanded using Fourier techniques DIRDIF 99 [8,9].

2.3. Molecular orbital calculations

Molecular orbital calculations were performed based on the density functional theory (UHF Becke 3LYP hybrid method) by GAUSSIAN 98 program using 6-311G^{++} basis set [10].

3. Results and discussion

Fig. 2 shows the TRESR spectrum of **2** in isopentane/dietylether 2:3 glass matrix at 30 K. The spectral simulation was carried out with the eigenfield [11]/exact-diagonalization hybrid method taking dynamic electron polarization into account [1]. The TRESR spectrum is assigned to a photo-excited quartet state. The spin Hamiltonian parameters were determined to be $S = 3/2$, $g = 2.0043$, $D = 0.0220\ \text{cm}^{-1}$, $E = 0.0004\ \text{cm}^{-1}$ for **2**. The D value of **2** is about 6% smaller than that of **1**. The decrease of D shows that the unpaired electrons are delocalized slightly to the 4-pyridyl group. It was interesting to note that 3-pyridyl group shows an opposite effect to that of 4-pridyl group [12]. Thus in 3-pyridyl substituted phenylanthracene-iminonitroxide radical, D value is slightly bigger than that of **1** [1]. This difference comes from the position of a nitrogen atom in the pyridyl group, suggesting a difference of the electronic effect.

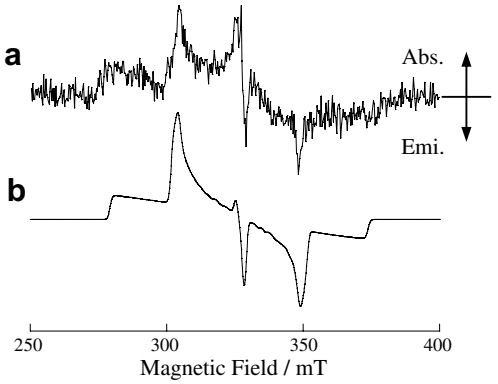


Fig. 2. Typical TRESR spectra and simulations. (a) Observed spectrum of **2** at 0.76 μs after LASER pulse, 280 times accumulated, (b) spectral simulation.

Fig. 3 shows electron spin density distributions of **2** in the doublet ground state and the lowest excited quartet spin state obtained by the ab-initio molecular orbital calculations. As shown in Fig. 3(a), the unpaired electron of **2** distributed in almost only the iminonitroxide radical moiety in the doublet ground state. In contrast, in the excited quartet state, the spin densities were distributed in whole of molecule **2** as shown in Fig. 3(b). By looking the coefficients of each one-electron molecular orbitals, it has been clarified that the α spin densities in the pyridyl moiety are arising from the delocalization of the unpaired spins of the triplet state of the anthracene moiety. The unpaired electrons of the anthracene moiety is strongly coupled to the radical spin [1,2]. Therefore, if **2** is used as a ligand of the metal complex, a strong exchange interaction between paramagnetic center of the metal ion and the photo-excited quartet spin state of π-radical is expected upon photo-excitation.

Crystallographic data of Cu(II)(hfac)$_2$(**2**)$_2$ are shown in Table 1. Fig. 4 shows an ORTEP drawing of Cu(II)-(hfac)$_2$(**2**)$_2$. Two radicals are coordinated symmetrically with the Cu(II) ion in a trans configuration from both side of Cu(II)(hfac)$_2$ plane. The bond distance of Cu–N3 is 1.99 Å. As shown in Fig. 4, a toluene molecule is incorporated into the crystal, which has supported the result of the elemental analysis. For Mn(II)(hfac)$_2$(**2**)$_2$, the single crystals with a suitable size for the X-ray analysis was not obtained at the moment, and only fine crystals were obtained.

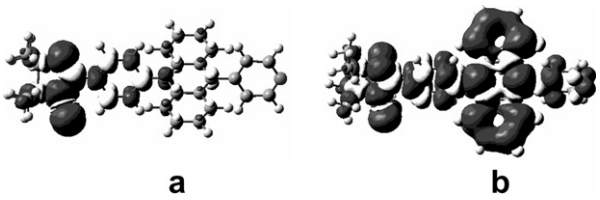


Fig. 3. Calculated spin density of **2**, dark: α spin, light: β spin. (a) Doublet ground state, (b) lowest excited quartet state.

Table 1
X-ray crystallographic data of Cu(II)(hfac)$_2$(**2**)$_2$

Chemical formula	$C_{74}H_{58}F_{12}N_6O_6Cu$
Crystal systems	triclinic
Space group	$P\bar{1}$ (#2)
a (Å)	9.6531(18)
b (Å)	10.674(2)
c (Å)	19.613(4)
α (°)	90.985(4)
β (°)	92.143(4)
γ (°)	103.389(5)
V (Å^3)	1963.8(7)
Z	1
D (g/cm^3)	1.200
T (K)	223 ± 1
R_1 ($I > 2\sigma(I)$)	0.0685
wR_2 (all reflections)	0.2061
GOF	1.004

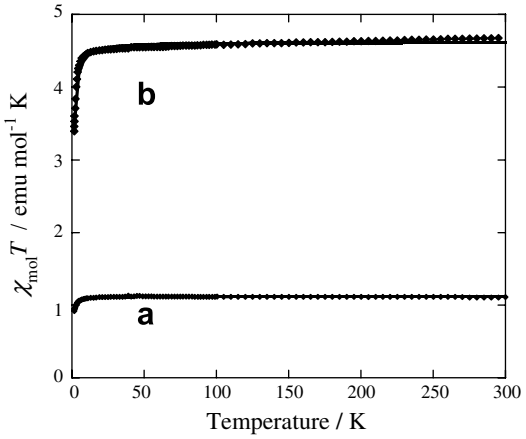


Fig. 5. Temperature dependences of magnetic susceptibility and fitting curve based on Eq. (1) or (2). (a) Cu(II)(hfac)$_2$(**2**)$_2$, (b) Mn(II)(hfac)$_2$(**2**)$_2$.

Fig. 5 shows the temperature dependences of the magnetic susceptibilities of Cu(II)(hfac)$_2$(**2**)$_2$ and Mn(II)-(hfac)$_2$(**2**)$_2$. The temperature dependence of the molar magnetic susceptibility of Cu(II)(hfac)$_2$(**2**)$_2$ shown in Fig. 5(a) was analyzed by three-spin cluster model $S_1 - S_{Cu} - S_2$ ($S_1 = S_2 = S_{Cu} = 1/2$) given by

$$\chi = \frac{N_A g^2 \beta^2}{4k_B(T-\theta)} \times \frac{1 + \exp(2J/k_BT) + 10\exp(3J/k_BT)}{1 + \exp(2J/k_BT) + 2\exp(3J/k_BT)} \quad (1)$$

Here, J is intramolecular exchange interaction between the metal ion and π-radical **2** in ground states, and θ is Weiss constant, $g = 2.006$ was used (the g value of **1** which similar to **2** [1]). $J/k_B = 1.0$ K, $\theta = -0.6$ K were estimated with for Cu(II)(hfac)$_2$(**2**)$_2$ in the ground states. The exchange interaction between Cu(II) ion and **2** was a weak ferromagnetic. The magnitude of J/k_B was estimated from the fitting using the data in high-temperature region, 50–300 K. The slight decrease observed lower than 10 K in Fig. 5(a) is due to the intermolecular antiferromagnetic exchange.

The temperature dependence of the molar magnetic susceptibility of Mn(II)(hfac)$_2$(**2**)$_2$ was well analyzed by three-spin cluster model $S_1 - S_{Mn} - S_2$ ($S_1 = S_2 = 1/2$, $S_{Mn} = 5/2$) given by

$$\chi = \frac{N_A g^2 \beta^2}{4k_B(T-\theta)} \times \left[\frac{10 + 35\exp(5J/k_BT) + 84\exp(12J/k_BT) + 35\exp(7J/k_BT)}{2 + 3\exp(5J/k_BT) + 4\exp(12J/k_BT) + 3\exp(7J/k_BT)}\right] \quad (2)$$

Here, $g = 2.006$ was used. The exchange interaction between Mn(II) and **2** is determined to be $J/k_B = -0.2$ K, and $\theta = -0.1$ K. The intramolecular exchange interaction is antiferromagnetic in this case. The sign change between the Cu(II) and Mn(II) complexes is a well known phenomena which is originated from the nature of the molecular orbitals coordinated by the pyridyl group. It was clarified that the spin exchange interactions between metal ion and ligand **2** were weak in the ground states. This result was supported by the molecular orbital calculations for ligand **2** in the doublet ground state, in which the unpaired electron is almost localized in the radical moiety of **2** in the ground state.

4. Conclusions

In this work, we synthesized 4-pyridyl-phenylanthracene-iminonitroxide radical **2**, which can make the coordination to metal ion by a pyridyl group. We confirmed by

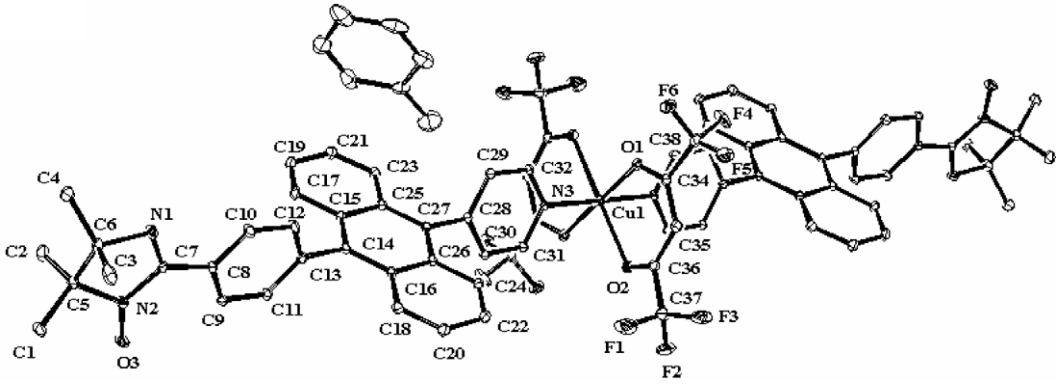


Fig. 4. ORTEP drawing of Cu(II)(hfac)$_2$(**2**)$_2$. A toluene molecule is incorporated into the crystal.

TRESR that **2**, has a photo-excited quartet ($S = 3/2$) state. Calculated spin density is very small in the N atom of the 4-pyridyl group, leading to a weak exchange interaction between the radical **2** and Cu(II) or Mn(II) in the electronic ground state. In contact, it is expected that the exchange interaction in photo-excited state becomes stronger because of the delocalization of the unpaired electrons.

To clarify the interaction between the paramagnetic center of the metal ions and the photo-excited quartet spin state of the π-radical **2**, trials to detect the photo-excited states of the metal complexes are in progress.

Acknowledgements

This work was supported by the Grant-in-Aid for Scientific Research on the general (No. 16350079) and Priority Area "Application of Molecular Spin" (Area No. 769, Proposal No. 15087208) from the Ministry of Education, Culture, Sports, Science and Technology, Japan.

References

[1] Y. Teki, S. Miyamoto, M. Nakatsuji, Y. Miura, J. Am. Chem. Soc. 123 (2001) 294.
[2] Y. Teki, T. Toichi, S. Nakajima, Chem. Eur. J. 12 (2006) 2329 and references cited therein.
[3] Y. Teki, H. Tamekuni, J. Takeuchi, Y. Miura, Angew. Chem., Int. Ed. 45 (2006) 4666.
[4] (a) C. Corvaja, M. Maggini, M. Prato, G. Scorrano, M. Venzin, J. Am. Chem. Soc. 117 (1995) 8857;
(b) F. Arena, F. Bullo, F. Conti, C. Corvaja, M. Maggini, M. Prato, G. Scorrano, J. Am. Chem. Soc. 119 (1997) 789.
[5] (a) K. Ishii, J. Fujisawa, Y. Ohba, S. Yamauchi, J. Am. Chem. Soc. 118 (1996) 13079;
(b) K. Ishii, J. Fujiwara, A. Adachi, S. Yamauchi, N. Kobayashi, . J. Am. Chem. Soc. 120 (1998) 3152.
[6] K. Ishii, Y. Hirose, N. Kabayashi, J. Am. Chem. Soc. 120 (1998) 10551.
[7] C. Hirel, E. Kira, J. Pécant, V.I. Ovcharenko, Chem. Eur. J. 7 (2001) 2007.
[8] A. Altomare, M. Burla, M. Camalli, G. Cascarano, C. Giacovazzo, A. Guagliardi, A. Moliterni, G. Polidori, R. Spagna, J. Appl. Cryst. 32 (1999) 115, SIR97.
[9] P.T. Beurskens, G. Admiraal, G. Beurskens, W.P. Bosman, R. de Gelder, R. Israel, J.M.M. Smits, The DIRDIF-99 program system, Technical Report of the Crystallography Laboratory, University of Nijmegen, The Netherlands, 1999, DIRDIF99.
[10] The DFT calculations were performed by using GAUSSIAN 98, Revision A.ll, Gaussian, Inc., Pittsburgh, PA, 1998.
[11] G.G. Belford, R.L. Belford, J.F. Burkhalter, J. Magn. Reson. 11 (1973) 251.
[12] H. Tamekuni, Y. Teki, Polyhedron, in press.

although the details about them have not still been understood well.

Our group has been studying about magnetic interactions between metal ions in 1-D complexes by theoretical calculations of the effective exchange integrals (J_{ab}) [10–13], in addition to a development of unrestricted hybrid density functional theory (DFT) method for quantitative calculations of J_{ab} values [15,16]. Understanding of the magnetic interactions is a very effective way to study their electronic structures because the magnetic properties in those complexes are easily affected by their ligand-effects and so on.

In this study, we focused on the variety of the structural phases in $Ni_2(dta)_4I$ and $Pt_2(dta)_4I$ complexes explained above. In order to elucidate the relation among structures, electronic states and magnetic interactions, we carried out the unrestricted hybrid DFT (UHDFT) calculations by using reduced model clusters of those complexes. As a first step, we verified basic information about their electronic structures by using experimental structures. Next, potential and J_{ab} surfaces were examined by using theoretical calculations in order to explain structural phases of those complexes.

2. Theoretical background

2.1. Effective exchange integrals (J_{ab})

The magnetic properties of transition metal complexes were usually investigated by the use of Heisenberg–Dirac–van Vleck spin Hamiltonian [17–19]. For example, the effective exchange interaction between localized spins is described by the total spin form of the spin-coupling Hamiltonian,

$$H = -2\sum J_{ab}\mathbf{S}_a \cdot \mathbf{S}_b, \tag{1}$$

where J_{ab} is the orbital-averaged effective exchange integrals between the spin site a and b with total spin operators $\mathbf{S}_a$ and $\mathbf{S}_b$, respectively. J_{ab} values are usually determined by experiments such as magnetic susceptibility. Recent developments in computational quantum chemistry enabled us not only estimations of molecular structure of large polymetal complexes [20,21] but also the quantitative estimation of J_{ab} values by using broken-symmetry (BS) ab initio and DFT methods [10–16].

The BS approach can be performed at a low computing cost. In singlet biradicals and low-spin (LS) species, however, it suffers from the spin contamination of high-spin (HS) states. Our group proposed spin projection scheme as follows:

$$J_{ab} = \frac{E(\mathrm{LS}) - E(\mathrm{HS})}{\langle S^2\rangle(\mathrm{HS}) - \langle S^2\rangle(\mathrm{LS})}, \tag{2}$$

where $E(X)$ and $\langle S^2\rangle(X)$ denote the total energy and total spin angular momentum for the spin state X (X = LS and HS), respectively [22,23]. In this paper, the magnetic interactions between MM units were discussed J_{ab} values calculated by using the equation.

2.2. Natural orbital analyses

Usual orbital-correlation diagram, which helps us to understand orbital interactions, is not obtained by the BS calculation because of 'different orbitals for different spins (DODS)' approach. In order to clarify the effective exchange interactions in the complexes by using expression like closed-shell MOs, we introduced natural orbitals (NOs), which were determined by diagonalizing their first order density matrices as

$$\rho(r, r') = \sum n_i \{\phi_i(r)\}^* \phi_i(r') \tag{3}$$

where n_i denoted the occupation number of NO ϕ_i [24,25]. If an occupation number of a magnetic orbital is close to 1.0, then two electrons in the orbital are almost localized on each spin site. On the other hand, n_i should be equal to 2.0 if stable chemical bond exists. In other words, the occupation numbers of the BS method contain an important information to understand the nature of chemical bonds and electron localizations in MMX complexes.

To assess a degree of spin localization, instability value (y_i) for a magnetic orbital i (i expresses such as σ, π, δ orbitals) is introduced here as follows:

$$y_i = 2W_D^2 = \frac{n_i^2 - 4n_i + 4}{n_i^2 - 2n_i + 2}, \tag{4}$$

where n_i and n_i^* are occupation numbers of bonding and anti-bonding NO, respectively and W_D denotes a weight of double excitation for orbital i [26]. If a chemical bond (or interaction between spin orbitals) of orbital i is stable, y_i is close to zero. On the other hand, if chemical bond of orbital $i$is unstable and spins are localized like radicals, then y_i is close to unity. Especially, $y_i/2$ is consistent to a weight of the doubly exited configuration in the MCSCF theory [25,26]. In this way, bond natures and degrees of spin-localization can be discussed by using the index.

2.3. Construction of two unit model

In order to analyze a spin–spin interaction in detail from a viewpoint of molecular orbital and to reduce computing costs, we construct two MM units models, namely model complex **1-Ni** and **2-Pt** for $Ni_2(dta)_4I$ and $Pt_2(dta)_4I$, respectively, as illustrated in Fig. 1a. Initial atomic coordinates of **1-Ni** and **2-Pt** were constructed from data of X-ray crystal structure analyses that were available in the Cambridge Structural Database (CSD). The structural parameters used in this study are summarized in Table 1. The definition of metal–iodine distance (d(M–In) ($n = 1,2,\ldots,4$)) is depicted in Fig. 2b.

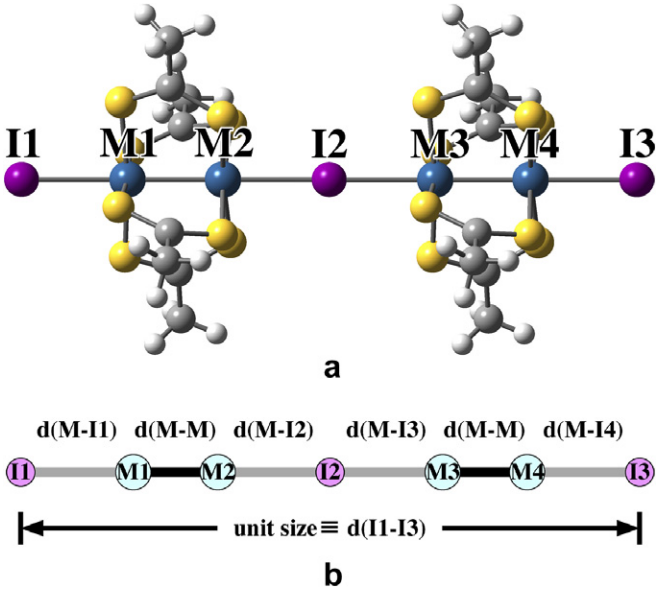


Fig. 1. (a) Illustration of calculated model complex, which is constructed by two MM units. (b) Definition of d(M–In) ($n = 1,2,\ldots,4$), which is expressing a metal–iodine distance. External point charges were added for model complex **1** (see text).

Table 1
Experimental structural parameters[a] of $Ni_2(dta)_4I$ and $Pt_2(dta)_4I$ complexes

Complex	d(M–M) (Å)	d(M–I1) (=d(M–I3)) (Å)	d(M–I2) (=d(M–I4)) (Å)	Ref.
$Ni_2(dta)_4I$	2.514	2.928	2.940	[2]
$Ni_2(dta)_4I$	2.538	2.920	2.923	[3]
$Pt_2(dta)_4I$	2.677	2.975	2.981	[4]

[a] Notations of d(M–M), d(M–In) ($n = 1,2,\ldots,4$) in the table are explained in Fig. 1.

2.4. Computational details

All calculations were performed by use of Tatewaki–Huzinaga MIDI plus p (533(21)/53(21)/(41)) basis set [27] for Ni atoms, LANL2DZ [28] basis set for Pt atoms and 4-31G basis sets for dta^- ligand. For axial iodide ions, MIDI plus d (3333(21)/333(21)/331) basis set and LANL2DZ basis set were used for **1-Ni** and **2-Pt**, respectively. Unrestricted hybrid DFT methods (UB3LYP [29]) were applied for all calculations on GAUSSIAN98 [30].

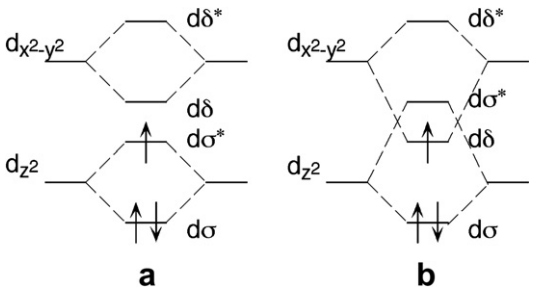


Fig. 2. Two possible electron (spin) configurations in MM unit: (a) the σ spin model and (b) δ spin model, respectively.

3. Calculated results and discussion

3.1. Calculated results of Ni and Pt model complexes by using X-ray structure

In order to elucidate fundamental information about those complexes in terms of magnetic interactions, their electronic structures were examined using experimental (X-ray) structure. The MM unit has a spin because formal charge of metal ion is +2.5 [9]. As already pointed out, there were two possible electron (spin) configurations in those complexes [10]. One is σ spin model and another is δ spin model as illustrated in Figs. 2a and b, respectively. In this study, σ spin model was adopted because our previous calculated results suggested a possibility of σ spin model [10].

The magnetic coupling of two spins causes an energy gap between singlet and triplet spin states. In order to calculate the magnetic coupling parameter (J_{ab}), singlet and triplet spin states were calculated for **1-Ni** and **2-Pt**. The calculated negative J_{ab} values indicated that antiferromagnetic spin coupling between neighboring MM unit for both **1-Ni** and **2-Pt** (see Table 2). J_{ab} value of **1-Ni** was $-488\ cm^{-1}$ and in good agreement with our previous data calculated by the use of rich basis sets ($-403\ cm^{-1}$) [10]. The results showed that the basis sets used here were appropriate to estimate electronic structure of **1-Ni** even if they were small in comparison with previous ones. The absolute values of J_{ab}s were considerably large, especially for **2-Pt**. Such a strong antiferromagnetic interaction might not be recognized as magnetic material but diamagnetic material by experimental [9]. Because there were no bridge ligands except for halogen ion, the origin of strong antiferromagnetic interaction must be a super-exchange interaction between MM units through halogen ion.

In order to make sure whether calculated results were appropriate ones, Mulliken spin densities of singlet state are summarized in Table 3. One electron spin was equally distributed to two metal ions in MM unit. Each spin was found in each MM unit and they coupled antiferromagnetically. Spin densities on MM units of **2-Pt** decreased in comparison with ones of **1-Ni**. It suggested that large spin orbital overlap interaction through iodide ion between Pt dimer units existed in **2-Pt**. Because larger overlap usually induced larger antiferromagnetic interaction [26], the results explained stronger antiferromagnetism in **2-Pt**. Spin densities of terminal iodide ions could not be negligible for **2-Pt**, while very small spin densities on terminal iodide ions for **1-Ni**. This problem strongly related to model structure.

Table 2
Calculated J_{ab} values of model complexes **1-Ni** and **2-Pt**

Models	J_{ab} (cm^{-1})
1-Ni	−488 (−403)[a]
2-Pt	−1274

[a] In Ref. [10].

Table 3
Calculated Mulliken spin densities on atoms of one-dimensional axis[a]

Atoms	Models	
	1–Ni	2–Pt
I1	0.061	−0.199
M1	0.469	−0.174
M2	0.373	−0.132
I2	−0.005	−0.001
M3	−0.396	0.121
M4	−0.445	0.182
I3	−0.057	0.205

[a] Notations of atom numbers in the table are explained in Fig. 1.

Here, infinite MMX chain was reduced into two MM-unit models for a reduction of computing costs. For the construction of the model complexes, we tested several model structures in order to obtain appropriate electronic configuration. The result showed us that positive point charges at locations of neighboring Ni ions were effective for **1-Ni**. Because the terminal positive charges attracted the valence electrons in iodide ions, iodide ions could remain closed shell type (I^{2-}) structures. On the other hand, the point charges easily changed σ spin configuration into δ spin configuration for **2-Pt**. For that reason, the terminal point charges could not be used in order to keep σ spin structure. The lacking of positive charges on terminal position made valence electrons of edge iodide ions delocalizing into MM units. Therefore, edge iodide ions could not keep their closed shell type electron structure because of strong on-site Coulomb repulsion.

In order to examine details about spin–spin interaction between MM units, natural orbital (NO) analyses were carried out for both model complexes **1-Ni** and **2-Pt**. NOs of magnetic orbitals of **1-Ni** and **2-Pt** are depicted in Fig. 3. The NOs were obviously showing that magnetic orbitals were σ orbitals of MM units. The highest occupied NO (HONO) and lowest unoccupied NO (LUNO) were results of 'in phase' and 'out of phase' interactions between two dσ orbitals of MM units, respectively, for both **1-Ni** and **2-Pt**. The figure suggested larger delocalization of NOs in **2-Pt** in comparison with ones of **1-Ni**. Occupation numbers of NOs and instability values summarized in Table 4 clearly indicated it. Calculated y value of **1-Ni** was 50%, while y value of **2-Pt** was only 8%. The results indicated that orbital overlap between two spins on MM units were very large in **2-Pt**. On the other hand, two spins had almost localized at each MM units in **1-Ni**. The delocalized spin orbitals of **2-Pt** made interactions between MM units easier. The difference between **1-Ni** and **2-Pt** seemed to reflect the difference in the nature of 3d and 5d electrons directly, because 3s orbitals usually shrank although 4d and 5d electrons tended to delocalize. Originally σ orbitals in 1-D complexes tend to delocalize along its 1-D axis [10,11]. Such strong delocalizing nature of 5d electrons seems to enhance the overlapping between MM units through iodide anion. Our previous results suggested that four MM units model was preferable for the quantitative study. In order to relieve the influence of spin densities of terminal iodide anion, four MM units model seemed to be necessary. However, two MM units model, which used here is enough for semi-quantitative discussion from the calculated results.

3.2. Potential and J_{ab} surfaces

Finally, potential and J_{ab} surfaces with relative position of metal and iodide ions were examined by using model structures. In pure AVSDW state, all metal–iodine (M–I) bond-length should be same i.e. d(M–I1) = d(M–I2) = d(M–I3) = d(M–I4) [3], where d(M–In) was defined in Fig. 2b. Experimental data summarized in Table 1, how-

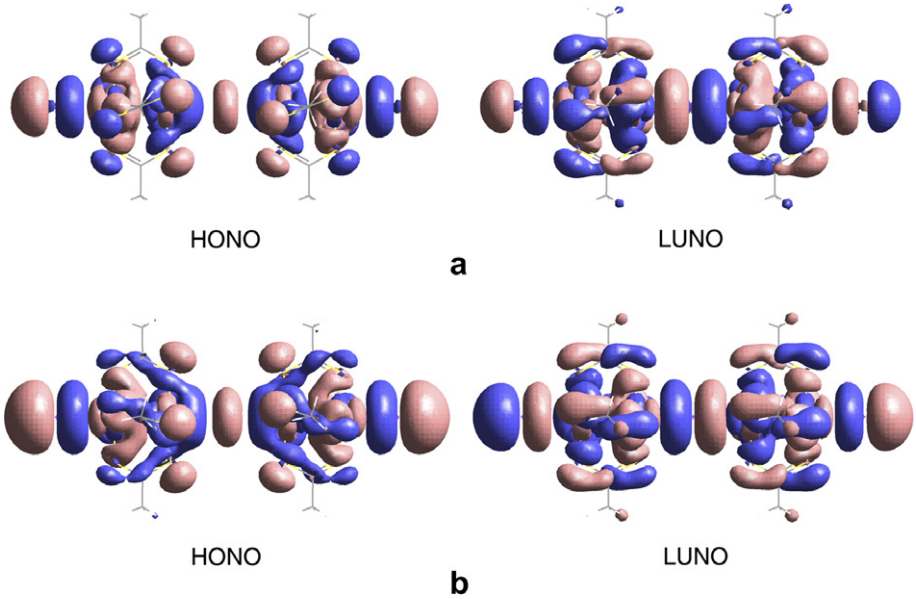


Fig. 3. The highest occupied NO (HONO) and lowest unoccupied NO (LUNO) of **1-Ni** and **2-Pt**: (a) **1-Ni** and (b) **2-Pt**, respectively.

Table 4
Calculated occupation numbers of HONO, LUNO and y values

Models	HONO	LUNO	y Value (%)
1-Ni	1.268	0.732	50.0
2-Pt	1.661	0.339	8.0

ever, were indicating that the complexes were not pure AVSDW structure but rather CP structure. In other words, the M–I bonds were classified into two types i.e shorter d(M–I2), d(M–I3) and longer d(M–I1), d(M–I3). In order to focus on a relation among stability, magnetic interaction, metal–metal distance and metal–halogen distance, we assumed model displacement as illustrated in Fig. 4. Starting from the pure AVSDW structure, artificial structural distortions were added in the model complexes. The added distortions were symmetric and anti-symmetric ones. The anti-symmetric distortion leads the complex to CP-type structure, while symmetric distortion leads the complex to ACP-type structure. Because the position of iodide ion was fixed during the procedure, unit size (d(I1–I3)) was constant.

Calculated results of **1-Ni** are depicted in Fig. 5. Oblique dash lines expressed the points of d(M–I1) = d(M–I2) = d(M–I3) = d(M–I4). In other words, the line meant the point, where the model complex was pure AVSDW structure. Within surveyed area, shape of potential surfaces of singlet and triplet state were, roughly, similar each other

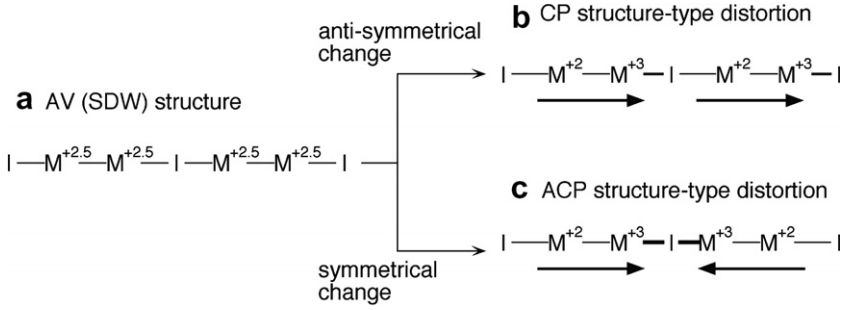


Fig. 4. Illustration of model displacement added to model complexes **1-Ni** and **2-Pt**. Starting from the formal AVSDW structure (a), symmetric and anti-symmetric artificial structural distortions were added to metal ions in the complexes, but position of iodide ion was fixed. The anti-symmetric distortion leads the complex to CP type structure (b), while symmetric distortion leads the complex to ACP type structure (c).

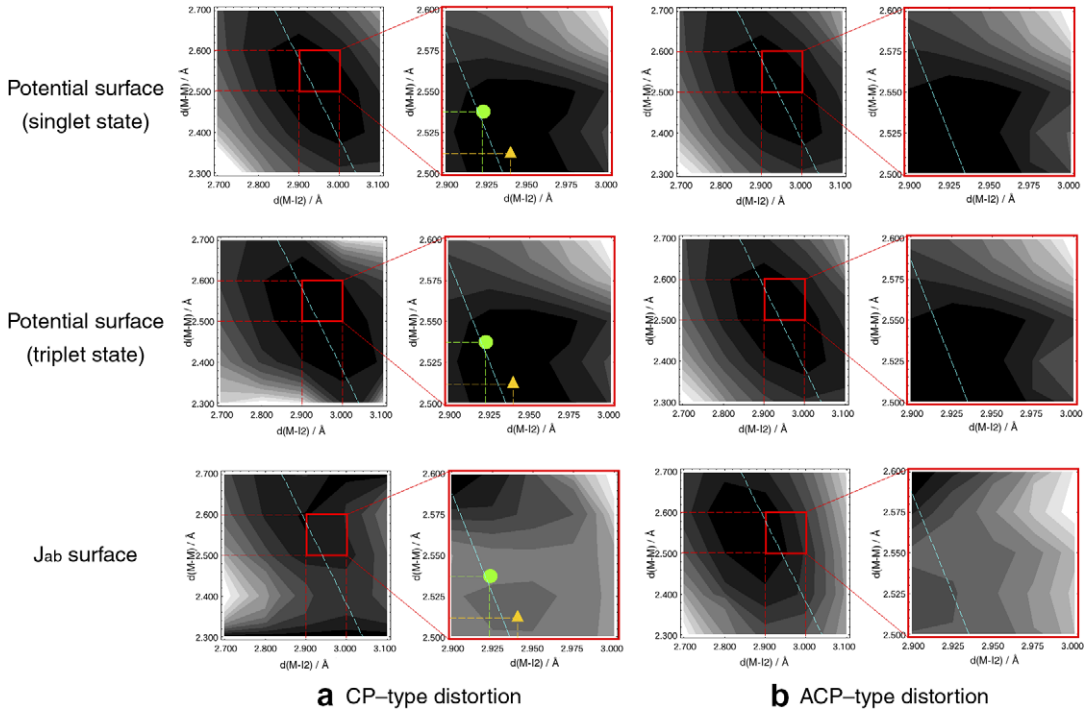


Fig. 5. Potential surfaces and J_{ab} surfaces of **1-Ni**. (a) and (b) are surfaces when CP-type and ACP-type distortion were added to AVSDW structure, respectively. Darker area indicated more stable area in potential surfaces (or more negative J_{ab} values). Oblique dash lines expressed the points that AVSDW structure (see text). ▲ and ● expressed experimental structure in Refs. [2,3], respectively. Left pictures on each group were enlarged ones.

in regard to both CP- and ACP-type structural changes. In addition, J_{ab} values were negative in all area, so the singlet state was stable in whole area. Although CP surface was slightly stable in comparison with ACP surface, the only one stable area, which was very close to the oblique dash lines, was found. It indicated that stable structure had the only minimum and AVSDW structure was the only possible structure. The result was consistent with experimental ones [2,3]. Two experimental structures mapped in the figures (▲ [2] and ● [3]) were located on the broad and most stable region along oblique dash lines.

On the other hand, two minima were observed in **2-Pt** as illustrated in Fig. 6. One stable minimum was located along AVSDW oblique dash lines on surface of ACP-type structure. Another meta-stable minimum was found in CP-type surface. This meta-stable minimum was energetically unstable in comparison with global minimum on ACP-type surface at least 0.6 eV within the calculated model. Of course, the energy difference between global minimum and meta-stable minimum must be smaller if rearrangement of ligands' structure was taken into account. As mentioned before, experimental results indicated that $Pt_2(dta)_4I$ complex as classified into AVSDW structure at higher temperature ($T > 300$ K), however CP structure and ACP structure were observed at lower temperature, $300 > T > 80$ K and $T < 80$ K, respectively [9]. The calculated results supported such experimental results at lower temperature.

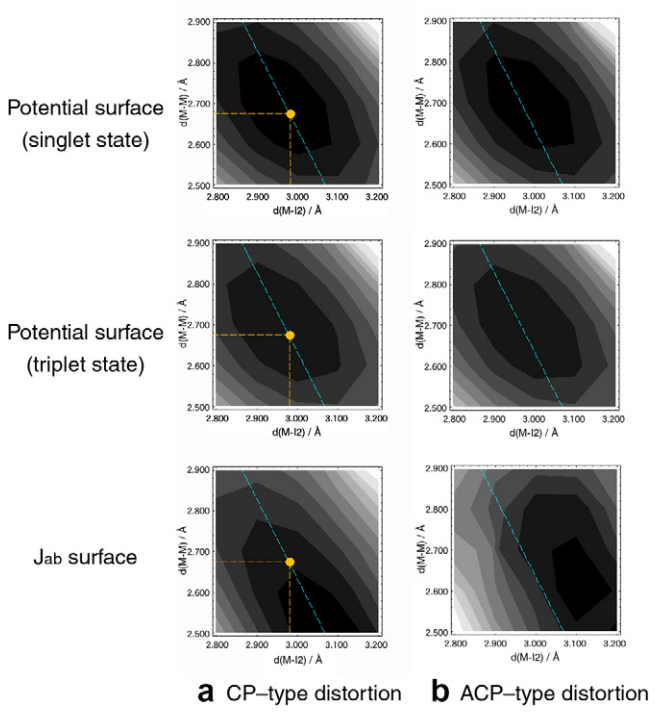


Fig. 6. Potential surfaces and J_{ab} surfaces of **2-Pt**. (a) and (b) are surfaces when CP-type and ACP-type distortion were added to AVSDW structure, respectively. Darker area indicated more stable area in potential surfaces (or more negative J_{ab} values). Oblique dash lines expressed the points that AVSDW structure (see text). ● expressed experimental structure in Ref. [4].

Unfortunately, we could not compare those obtained structures (minima) with experimental structures because there were no available data of X-ray structural analyses for CP and ACP structure. Interestingly, experimental structure [4], which was indicated by orange circle in the figure, was not classified into both minima, but located at intermediate position between both minima. The result of X-ray crystallography analysis might be an averaged structure of both CP and ACP structure.

4. Conclusion

The electronic structures of model clusters of $Ni_2(dta)_4I$ and $Pt_2(dta)_2I$ complexes were examined by using UB3LYP calculations. The calculated results indicated strong antiferromagnetic interactions between spins on MM units. Estimated orbital overlap between two spin orbitals on MM units indicated that spins were delocalized along 1-D chain in $Pt_2(dta)_2I$, while they were almost localized on MM units in $Ni_2(dta)_4I$. Calculated potential surfaces of **1-Ni** that had the only minimum at AVSDW structure supported the experimental results that no other phases except for AVSDW were reported. On the other hand, two minima were found in **2-Pt**. The global minimum located on ACP surface but it was very close to AVSDW structure. The meta-stable minimum was on CP surface. The results were supporting that existence of stable and meta-stable phases i.e. CP and ACP structure in $Pt_2(dta)_2I$. Those calculations were carried out under an approximation of fixed ligands. In real systems, ligands must rearrange in order to stabilize a total energy of the crystal. For the further quantitative analyses, the effects of those rearrangements should be taken into account.

Although Heisenberg Hamiltonian was used here to estimate magnetic interactions between MM units, it is desirable to use Peierls–Hubbard Hamiltonian in order to consider the physical meanings of calculated results in detail. Yamamoto [31] has reported calculated phase diagrams by using Peierls–Hubbard Hamiltonian for 5/6-filled one-dimensional two-band three-orbital systems,

$$\begin{aligned} H = & \sum_{m,s}\sum_{j=1,2}\left(\varepsilon_M - \beta l_{j:n}\right)n_{j:m,s} + \sum_{m,s}\varepsilon_X n_{3:m,s} \\ & - \sum_{m,s}\sum_{j=1,2}\left(t_{MX} - \alpha l_{j:n}\right)\left(a^{\dagger}_{j:n,s}a_{3:n,s} + a^{\dagger}_{3:n,s}a_{j:n,s}\right) \\ & - \sum_{m,s} t_{MM}\left(a^{\dagger}_{1:n,s}a_{2:n-1,s} + a^{\dagger}_{2:n-1,s}a_{1:n,s}\right) \\ & + \sum_{m}\sum_{j=1,2} U_M n_{j:m,+}n_{1:m,-} + \sum_{m} U_X n_{3:n,+}n_{3:n,-} \\ & + \sum_{m,s,s'}\sum_{j=1,2} V_{MX} n_{j:m,s}n_{3:m,s'} + \sum_{m,s,s'} V_{MM} n_{1:m,s}n_{2:m-1,s'} \\ & + \sum_{m}\sum_{j=1,2}\frac{K}{2} l^2_{j:m}, \end{aligned} \tag{5}$$

where $n_{j:m,s} = a^{\dagger}_{j:m,s}a_{j:m,s}$ with $a^{\dagger}_{j:m,s}$ being the creation operator of an electron with spin $s = \pm$ (up and down) for the M

d_{z^2} ($J = 1,2$) or X p_z ($j = 3$) in the mth MXM unit, and $l_{j:m} = (-1)^j(u_{j:m} - u_{3:m})$ with $u_{j:m}$ being the chain-direction displacement of a metal ($j = 1,2$) or halogen ($j = 3$) in the mth MXM unit from its equilibrium position. α and β are the inter-site and intra-site electron-lattice coupling constants, respectively, while K is the metal–halogen spring constant. For further investigation of physical properties using ab initio or DFT calculations, projection of calculated results onto such Hamiltonian is necessary.

Up to now, many kinds of MMX complexes consist of Pt such as $R[Pt_2(pop)_4I]\cdot nH_2O$ (R = counter ion, pop = $P_2O_5H_2^{2-}$) has been reported [5,8,32]. The complexes take several phases as their ligands. Those ligands seem to control not only relative stability of potential minima but also their properties [32,33]. The existence of two minima would be useful for material design because it is meaning that physical properties of the complexes could be controlled by external fields such as photon, magnetic fields and so on, if intra-chain structure could be controlled by them. In fact, photo-induced phase transition from CDW to CP state was reported in $R[Pt_2(pop)_4I]\cdot nH_2O$ [32]. In this sense, it is meaningful to examine relation between structure of bridging ligands and potential surfaces by theoretical calculations.

Acknowledgment

This work has been supported by Grant-in-Aid for Scientific Research (KAKENHI) (Nos. 16750049 and 18350008) from Japan Society for the Promotion of Science (JSPS).

References

[1] J.K. Bera, K.R. Dunbar, Angew. Chem. Int. Ed. 41 (2002) 23.
[2] C. Bellitto, G. Dessy, U. Fares, Inorg. Chem. 24 (1985) 2815.
[3] M. Yamashita, Y. Wada, K. Toriumi, T. Mitani, Mol. Cryst. Liq. Cryst. 216 (1992) 207.
[4] C. Bellitto, A. Flamini, L. Gastaldi, L. Scaramuzza, Inorg. Chem. 24 (1983) 444.
[5] M. Yamashita, S. Miya, T. Kawashima, T. Manabe, T. Sonoyama, H. Kitagawa, T. Mitani, H. Okamoto, R. Ikeda, J. Am. Chem. Soc. 121 (1999) 2321.
[6] M. Mitsumi, T. Murase, H. Kishida, T. Yoshinari, Y. Ozawa, K. Toriumi, T. Sonoyama, H. Kitagawa, T. Mitani, J. Am. Chem. Soc. 123 (2001) 11179.
[7] A. Kobayashi, H. Kitagawa, R. Ikeda, S. Kitao, M. Seto, M. Mitsumi, K. Toriumi, Synth. Met. 135–136 (2003) 405.
[8] M. Yamashita, T. Toriumi, Inorg. Chem. Acta 178 (1990) 143.
[9] H. Kitagawa, N. Onodera, T. Sonoyama, M. Yamamoto, M. Fukawa, T. Mitani, M. Seto, Y. Maeda, J. Am. Chem. Soc. 121 (1999) 10068.
[10] S. Nakano, Y. Kitagawa, T. Kawakami, K. Yamaguchi, Polyhedron 22 (2003) 2027.
[11] Y. Kitagawa, M. Shoji, K. Koizumi, T. Kawakami, M. Okumura, K. Yamaguchi, Polyhedron 24 (2005) 2751.
[12] Y. Kitagawa, S. Nakano, T. Kawakami, K. Mashima, K. Yamaguchi, Polyhedron 22 (2003) 2019.
[13] Y. Kitagawa, S. Nakano, T. Kawakami, K. Mashima, K. Tani, K. Yamaguchi, Mol. Cryst. Liq. Cryst. 379 (2002) 525.
[14] Y. Kitagawa, T. Kawakami, Y. Yoshioka, K. Yamaguchi, Polyhedron 20 (2001) 1189.
[15] Y. Kitagawa, T. Soda, Y. Shigeta, S. Yamanaka, Y. Yoshioka, K. Yamaguchi, Int. J. Quantum Chem. 84 (2001) 592.
[16] Y. Kitagawa, T. Kawakami, K. Yamaguchi, Mol. Phys. 100 (2002) 1829.
[17] D. Gatteschi, O. Kahn, J.S. Miller, F. Palacio (Eds.), Magnetic Molecular Materials, Kluwer Academic Publishers, Dordrecht, 1991.
[18] O. Kahn (Ed.), Magnetism: A Supermolecular Function, NATO ASI Series C, vol. 484, Kluwer Academic Publishers, Dordrecht, 1996.
[19] E. Coronado, P. Dekhais, D. Gatteschi, J.S. Miller (Eds.), Molecular Magnetism: From Molecular Assemblies to the Devices, NATO ASI Series E, vol. 321, Kluwer Academic Publishers, Dordrecht, 1996.
[20] P. Kiehl, M.M. Rohmer, M. Bénard, Inorg. Chem. 43 (2004) 3151.
[21] M. Bénard, J.F. Berry, F.A. Cotton, C. Gaudin, X. Lopez, C.A. Murillo, M.M. Rohmer, Inorg. Chem. 45 (2006) 3932.
[22] T. Kawakami, S. Yamanaka, S. Yamada, W. Mori, K. Yamaguchi, in: M.M. Turnbull, T. Sugimoto, L.K. Thompson (Eds.), Molecular-Based Magnetic Materials, Theory, Technique and Applications, ACS Symposium Series, vol. 644, American Chemical Society, Washington, DC, 1996, p. 30.
[23] K. Yamaguchi, in: R. Carbeó, M. Klobukowski (Eds.), Self-Consistent Field, Theory and Applications, Studies in Physical and Theoretical Chemistry, vol. 70, Elsevier, Amsterdam–Oxford–New York–Tokyo, 1990, p. 727.
[24] K. Takatsuka, T. Fueno, K. Yamaguchi, Theoret. Chem. Acta 48 (1978) 175.
[25] K. Yamaguchi, M. Okumura, K. Takada, S. Yamanaka, Int. J. Quantum Chem. Symp. 27 (1993) 501.
[26] K. Yamaguchi, T. Kawakami, Y. Takano, Y. Kitagawa, Y. Yamashita, H. Fujita, Int. J. Quantum Chem. 90 (2002) 370.
[27] H. Tatewaki, S. Huzinaga, J. Chem. Phys. 71 (1979) 4339.
[28] W.R. Wadt, P.J. Hay, J. Chem. Phys. 82 (1985) 299.
[29] A.D. Becke, J. Chem. Phys. 98 (1993) 5648.
[30] M.J. Frisch, G.W. Trucks, H.B. Schlegel, G.E. Scuseria, M.A. Robb, J.R. Cheeseman, V.G. Zakrzewski, J.A. Montgomery Jr., R.E. Stratmann, J.C. Burant, S. Dapprich, J.M. Millam, A.D. Daniels, K.N. Kudin, M.C. Strain, O. Farkas, J. Tomasi, V. Barone, M. Cossi, R. Cammi, B. Mennucci, C. Pomelli, C. Adamo, S. Clifford, J. Ochterski, G.A. Petersson, P.Y. Ayala, Q. Cui, K. Morokuma, N. Rega, P. Salvador, J.J. Dannenberg, D.K. Malick, A.D. Rabuck, K. Raghavachari, J.B. Foresman, J. Cioslowski, J.V. Ortiz, A.G. Baboul, B.B. Stefanov, G. Liu, A. Liashenko, P. Piskorz, I. Komaromi, R. Gomperts, R.L. Martin, D.J. Fox, T. Keith, M.A. Al-Laham, C.Y. Peng, A. Nanayakkara, M. Challacombe, P.M.W. Gill, B. Johnson, W. Chen, M.W. Wong, J.L. Andres, C. Gonzalez, M. Head-Gordon, E.S. Replogle, J.A. Pople, GAUSSIAN 98, Gaussian, Inc., Pittsburgh, PA, 2002.
[31] S. Yamamoto, J. Phys. Soc. Jpn. 70 (2001) 1198.
[32] H. Matsuzaki, H. Kishida, K. Takizawa, M. Yamashita, H. Okamoto, Synth. Met. 135–136 (2003) 607.
[33] S. Ikeuchi, K. Saito, Y. Nakazawa, A. Sato, M. Mitsumi, K. Toriumi, M. Sorai, Phys. Rev. B 66 (2002) 115110.

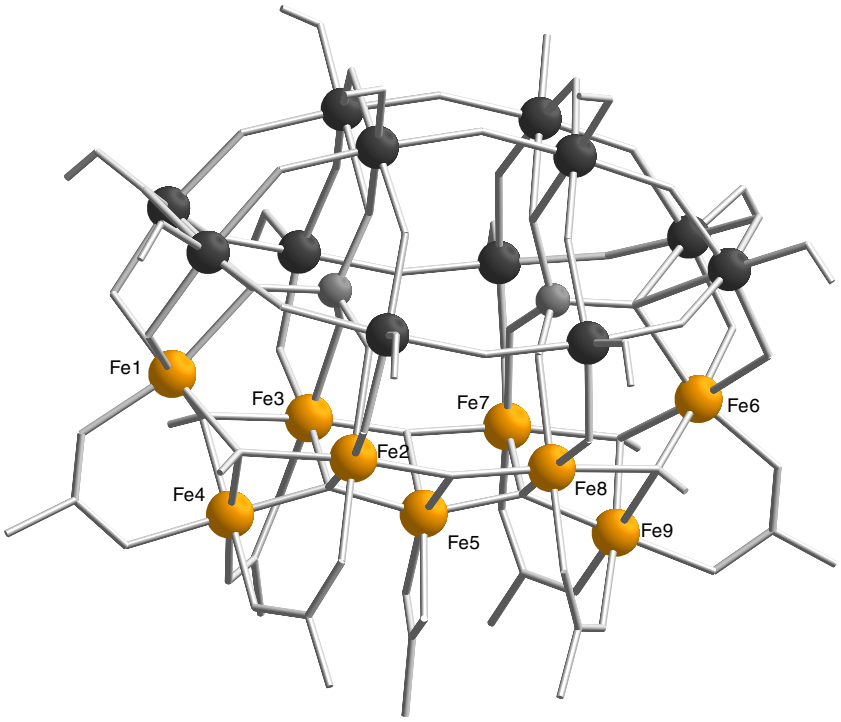


Fig. 1. Representation of the molecular structure of the $[H_4P_2W_{12}Fe_9O_{56}(OAc)_7]^{6-}$ anion. The iron, phosphorus and tungsten atoms are represented as orange, gray and black spheres, respectively. (For interpretation of the references in colour in this figure legend, the reader is referred to the web version of this article.)

theory provide an accurate description of the exchange interaction present in such systems [12]. In all cases, there is a clear relationship between the exchange coupling constants and the kind of bridging ligand present in the exchange pathway. Thus, the exchange interactions are usually antiferromagnetic, with the strongest interactions being mediated by μ_3-oxo bridging ligands, although a double bridging ligand present in an Fe_8 complex favors ferromagnetic coupling [9]. Hence, the aim of this communication is to report a study of the J values in this Fe_9W_{12} complex using methods based on density functional theory.

2. Results and discussion

The analysis of the structure (see Fig. 1) indicates that seven different exchange coupling constants must be considered. Hence, the spin Hamiltonian, considering only the exchange coupling terms, can be expressed as:

$$\begin{aligned}\hat{H} = &-J_1[\hat{S}_3\hat{S}_7 + \hat{S}_2\hat{S}_8] - J_2[\hat{S}_2\hat{S}_5 + \hat{S}_3\hat{S}_5 + \hat{S}_7\hat{S}_5 \\ &+ \hat{S}_8\hat{S}_5] - J_3[\hat{S}_2\hat{S}_3 + \hat{S}_7\hat{S}_8] - J_4[\hat{S}_1\hat{S}_4 + \hat{S}_6\hat{S}_9] \\ &- J_5[\hat{S}_1\hat{S}_3 + \hat{S}_1\hat{S}_2 + \hat{S}_6\hat{S}_7 + \hat{S}_6\hat{S}_8] - J_6[\hat{S}_2\hat{S}_4 \\ &+ \hat{S}_3\hat{S}_4 + \hat{S}_7\hat{S}_9 + \hat{S}_8\hat{S}_9] - J_7[\hat{S}_4\hat{S}_5 + \hat{S}_5\hat{S}_9] \qquad (1)\end{aligned}$$

where $\hat{S}_i$ are the spin operators of each paramagnetic Fe^{III} center (see Fig. 2). A detailed description of the procedure used to obtain the exchange coupling constants can be found in previous papers [13–15] and a summary is provided in the Computational Details section. Despite that hybrid functionals provide a better description of the exchange interaction than generalized gradient approximation (GGA) ones, we have found for Fe^{III} polynuclear complexes that the results obtained with the numerical code SIESTA and a GGA functional reproduce very well experimental J values [16]. Taking into account this fact and due to the large size of the Fe_9W_{12} complex, we have employed such less CPU time consuming approach instead of the usual calculations with Gaussian functions and hybrid functionals. Due to the high sensitivity of the exchange coupling constants to small structural changes, we have employed the crystallographic structure, to include also the packing effects present in solid state to be closer to the experimental measurement conditions.

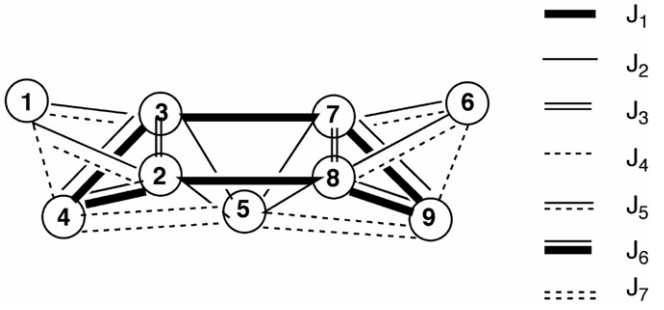


Fig. 2. Scheme showing the topology of the seven exchange interaction.

The calculated exchange coupling constants are presented in Table 1. They show similar trends than previously

Table 1
Description of the bridging ligands, average metal–metal and metal–oxygen distances (Å), Fe–O–Fe bond angles (°) and calculated exchange coupling constants J (cm^{-1}) for the Fe_9W_{12} complex

	Bridging ligands	Fe···Fe	Fe–O	Fe–O–Fe	J_{PBE}
J_1	μ_3-O	3.762	1.895	166.3	−73.9
J_2	μ_3-O, μ_4-O	2.925	2.044, 1.949	90.0, 96.7	−3.1
J_3	μ_4-O, μ_2-O_2P	3.588	2.002, 2.105	127.3	−42.0
J_4	μ_2-OH, μ_2-OH, μ_2-O_2CMe	2.913	2.115, 2.030	87.1	+26.9
J_5	μ_3-OH, μ_2-O_2P	3.733	2.097, 2.029	125.8	+3.0
J_6	μ_4-O, μ_3-OH, μ_2-O_2CMe	2.948	1.963, 2.020, 2.048	97.4, 88.0	−3.9
J_7	μ_4-O	3.659	1.910	146.6	−59.8

found for other polynuclear Fe^{III} complexes [6–10]: (i) The single μ_3-O bridges provide the strongest antiferromagnetic coupling (J_1) even larger than the μ_4-O bridges (J_7), probably due to the large Fe–O–Fe bond angle; (ii) the simultaneous presence of the μ_4-O and μ_3-O bridges between two iron atoms with relatively small Fe–O–Fe bond angles, as in the case of the J_2 interaction results in a weak antiferromagnetic coupling; (iii) a μ_4-O bridge combined with a μ_2-O_2P one yields significantly antiferromagnetic coupling (J_3); (iv) a double hydroxo bridge together with a μ-acetato bridge (J_4) produce a ferromagnetic coupling, probably favored by the small Fe–O–Fe bond angle (87.1°) and the large out-of-plane shift of the hydrogen atoms (O···O–H angle of 140.4°) [10,11]; and (v) the coupling through a μ_3-OH bridging ligand is weak and the sign of the interaction depends on the other bridging ligands present in the exchange pathway (J_5 and J_6).

The exact diagonalization of the Hamiltonian matrix is computationally very demanding due to the large number of states involved, more than 1×10^7. We would need around 30 GB of memory to store the largest block (88 900 states) corresponding the $S = 9/2$ states. Thus, we have carried out a study of the single determinant state energies, and found that the ground state corresponds to an $S = 15/2$ situation with all iron atoms having spin up, except for Fe3, Fe5 and Fe8 (or the equivalent Fe2, Fe5 and Fe7) atoms. The lowest excited single determinants, 403.5 cm^{-1} above the ground state, are four degenerate $S = 5/2$ solutions with four spin-down iron atoms {Fe1, Fe2, Fe5, Fe7}, {Fe1, Fe3, Fe5, Fe8}, {Fe2, Fe5, Fe6, Fe7} and {Fe3, Fe5, Fe6, Fe8}.

Finally, we have analyzed the distribution of the spin density in the Fe_9W_{12} complex in its $S = 15/2$ single determinant ground state (see Fig. 3). The spin density is mostly localized at the Fe^{III} cations, even if the GGA functionals used here provide a more delocalized picture than the hybrid ones [17,18], with local magnetic moments of around 4.3 e^-. Significant spin delocalization towards donor atoms is observed from the outermost iron cations, especially to oxygen atoms even toward the polyoxometalate part of the molecule and also to the two phosphorus atoms. It is worth noting that there is no spin density at the tungsten atoms, which suggests that the role of these metal atoms is only to provide a scaffold for the arrangement of the magnetic iron atoms.

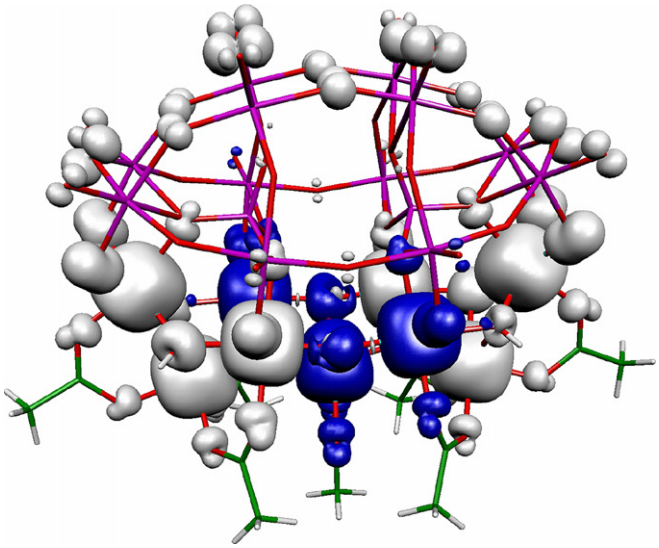


Fig. 3. Representation of the spin density map for the single-determinant ground state $S = 15/2$ of the Fe_9W_{12} complex. The isodensity surface represented corresponds to a value of 0.05 $e^-/bohr^3$ (clear and dark regions indicate positive and negative spin populations, respectively).

3. Computational details

All calculations have been carried out using the version 1.3 of the SIESTA program (Spanish Initiative for Electronic Simulations with Thousands of Atoms) [19]. This computer code has been developed for efficient calculations in large low-symmetry systems [20]. As exchange-correlation functional, we have employed the generalized-gradient approximation one proposed by Perdew et al. (PBE) [21]. Only valence electrons are included in the calculations, the cores are replaced by norm-conserving scalar relativistic pseudopotentials factorized in the Kleinman–Bylander form [22]. These pseudopotentials are generated following to the procedure proposed by Trouiller and Martins [23] from the ground state atomic configurations for all the atoms except for Fe, for which the $[Ar]3d^74s^1$ configuration was employed. The core radii for the s, p and d components of Fe are all 2.00 a.u. while 2.74, 2.24 and 2.24 were employed for tungsten atoms and we have included partial-core corrections for a better description of the core regions [24]. The cutoff radii were 1.15 for oxygen and

hydrogen atoms, 1.25 for carbon and 1.83 for phosphorus atoms, respectively.

We have employed a numerical basis set of triple-ζ quality with polarization functions for the iron and tungsten atoms and a double-ζ one with polarization functions for the main group elements. In this kind of calculations, there are two fundamental parameters that control the accuracy of the numerical calculation [20]. The numerical wavefunction is zero at distances larger than the chosen confinement radius r_c, whose value is different for each atomic orbital. The energy radii of different orbitals is determined by a single parameter, *the energy shift*, that corresponds to the energy increase of the atomic eigenstate due to the confinement. The integrals of the self-consistent terms are calculated with the help of a regular real space grid in which the electron density is projected. The grid spacing is determined by the *maximum kinetic energy* of the plane waves that can be represented in that grid. We have studied the influence of these two parameters on the calculated J values in many transition metal complexes. Thus, the values of 50 meV for the energy shift and 250 Ry for mesh cutoff provide a good compromise between accuracy and computer time needed to calculate the exchange coupling constants [16].

Twelve calculations were performed on the $[H_4P_2W_{12}Fe_9O_{56}(OAc)_7]^{6-}$ complex in order to obtain by least-squares fitting the seven exchange coupling constant, solutions corresponding to the high spin solution ($S = 45/2$), three solutions with $S = 15/2$ {Fe1, Fe5, Fe6}, {Fe4, Fe5, Fe9} and {Fe3, Fe5, Fe8} and eight calculations with $S = 5/2$ {Fe1, Fe2, Fe6, Fe7}, {Fe1, Fe3, Fe6, Fe7}, {Fe1, Fe2, Fe3, Fe4}, {Fe2, Fe3, Fe7, Fe8}, {Fe1, Fe4, Fe6, Fe9}, {Fe2, Fe4, Fe7, Fe9}, {Fe3, Fe4, Fe8, Fe9} and {Fe2, Fe6, Fe7, Fe9}, where the indicated iron atoms are those with spin down.

4. Conclusions

Due to the problems to obtain of a proper experimental magnetic susceptibility curve and the large number of exchange interactions, the use of theoretical methods seems to be the only way to obtain a detailed description of the exchange interactions present in a polyoxometalate Fe_9W_{12} complex. We have found for those interactions the same trends and values than for other polynuclear Fe^{III} complexes, with the μ_3-O bridging ligands mediating the strongest antiferromagnetic coupling. The strength of the antiferromagnetic interactions through oxo-bridging ligands seems to be related with the Fe–O–Fe bond angles. The presence of hydroxo bridging ligands favors the presence of ferromagnetic or very weak antiferromagnetic interactions. Our calculations predict an $S = 15/2$ single determinant ground state, and a four-degenerate first excited state with $S = 5/2$.

Acknowledgements

The research has been supported by the *Dirección General de Investigación del Ministerio de Educación y Ciencia* and *Comissió Interdepartamental de Ciència i Tecnologia* (CIRIT) through grants CTQ2005-08123-C02-02/BQU and 2005SGR-00036, respectively. The computing resources were generously made available in *the Centre de Supercomputació de Catalunya* (CESCA) with a grant provided *by Fundació Catalana per a la Recerca* (FCR) and the *Universitat de Barcelona*.

References

[1] D. Gatteschi, Angew. Chem. Int. Ed. 42 (2003) 246.
[2] J.S. Miller, M. Drillon (Eds.), Magnetism: Molecules to Materials I–V, Wiley-VCH, Weinheim, 2001–2005.
[3] B. Godin, Y.-G. Chen, J. Vaissermann, L. Ruhlmann, M. Verdaguer, P. Gouzerh, Angew. Chem. Int. Ed. 44 (2005) 3072.
[4] E. Ruiz, Struct. Bond. 113 (2004) 71.
[5] E. Ruiz, S. Alvarez, A. Rodríguez-Fortea, P. Alemany, Y. Pouillon, C. Massobrio, in: J.S. Miller, M. Drillon (Eds.), Magnetism: Molecules to Materials II, Wiley-VCH, Weinheim, 2001, p. 227.
[6] E. Ruiz, A. Rodríguez-Fortea, J. Cano, S. Alvarez, J. Phys. Chem. Solids 65 (2003) 799.
[7] E. Ruiz, J. Cano, S. Alvarez, Polyhedron 24 (2005) 2364.
[8] G. Rajaraman, E. Ruiz, J. Cano, S. Alvarez, Chem. Phys. Lett. 415 (2005) 6.
[9] E. Ruiz, J. Cano, S. Alvarez, Chem. Eur. J. 11 (2005) 4767.
[10] T. Cauchy, E. Ruiz, S. Alvarez, Phys. B 384 (2006) 123.
[11] E. Ruiz, S. Alvarez, ChemPhysChem 6 (2005) 1094.
[12] E. Ruiz, P. Alemany, S. Alvarez, J. Cano, J. Am. Chem. Soc. 119 (1997) 1297.
[13] E. Ruiz, S. Alvarez, J. Cano, V. Polo, J. Chem. Phys. 123 (2005) 164110.
[14] E. Ruiz, J. Cano, S. Alvarez, P. Alemany, J. Comp. Chem. 20 (1999) 1391.
[15] E. Ruiz, A. Rodríguez-Fortea, J. Cano, S. Alvarez, P. Alemany, J. Comp. Chem. 24 (2003) 982.
[16] E. Ruiz, A. Rodríguez-Fortea, J. Tercero, T. Cauchy, C. Massobrio, J. Chem. Phys. 123 (2005) 074102.
[17] J. Cano, E. Ruiz, S. Alvarez, M. Verdaguer, Comment Inorg. Chem. 20 (1998) 27.
[18] E. Ruiz, J. Cirera, S. Alvarez, Coord. Chem. Rev. 249 (2005) 2649.
[19] E. Artacho, J.D. Gale, A. García, J. Junquera, R.M. Martin, P. Ordejón, D. Sánchez-Portal, J.M. Soler, SIESTA v. 1.3, 2001.
[20] J.M. Soler, E. Artacho, J.D. Gale, A. García, J. Junquera, P. Ordejón, D. Sánchez-Portal, J. Phys.: Condens. Mat. 14 (2002) 2745.
[21] J. Perdew, K. Burke, M. Ernzerhof, Phys. Rev. Lett. 77 (1996) 3865.
[22] L. Kleinman, D.M. Bylander, Phys. Rev. Lett. 48 (1982) 1425.
[23] N. Trouiller, J.L. Martins, Phys. Rev. B 43 (1991) 1993.
[24] S.G. Louie, S. Froyen, M.L. Cohen, Phys. Rev. B 26 (1982) 1982.

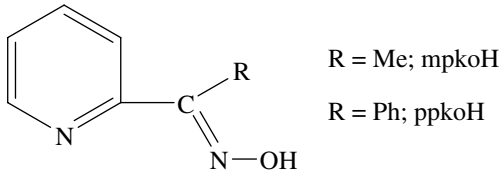


Fig. 1. The general formula of the 2-pyridyl oximes used in this work.

[1b]. The metal ions are antiferromagnetically coupled, and these complexes are not therefore SMMs. We are now pleased to report that the reactions of $[Mn_3^{III}O(O_2CR)_6(py)_3](ClO_4)$, where py is pyridine, with 2-pyridyl oximes (L′H) [5] give a family of oxide-centered triangular, ferromagnetically coupled $[Mn_3^{III}O(O_2CR)_3L'_3](ClO_4)$ complexes [6], which are the first triangular Mn SMMs. The ligands used are methyl 2-pyridyl ketone oxime (mpkoH) and phenyl 2-pyridyl ketone oxime (ppkoH); see Fig. 1.

Reactions of $[Mn_3O(O_2CMe)_6(py)_3](ClO_4)$ (**1**) with mpkoH, $[Mn_3O(O_2CEt)_6(py)_3](ClO_4)$ (**2**) with mpkoH, and $[Mn_3O(O_2CMe)_6(py)_3](ClO_4)$ (**1**) with ppkoH, in a 1:3 ratio in MeOH/MeCN gave dark brown solutions. These were evaporated to dryness under reduced pressure at room temperature, and the residues dissolved in CH_2Cl_2 and layered with *n*-hexane to slowly give dark brown crystals of $[Mn_3O(O_2CMe)_3(mpko)_3](ClO_4)\cdot 3CH_2Cl_2$ (**3**$\cdot 3CH_2Cl_2$), $[Mn_3O(O_2CEt)_3(mpko)_3](ClO_4)\cdot 1.2CH_2Cl_2\cdot 1.4H_2O$ (**4**$\cdot 1.2CH_2Cl_2\cdot 1.4H_2O$) and $[Mn_3O(O_2CMe)_3(ppko)_3](ClO_4)\cdot 2CH_2Cl_2$ (**5**$\cdot 2CH_2Cl_2$) in very good isolated yields (>70%). All three complexes gave very good analytical results.[1] The formation of the representative complex **4** can be summarized in the following balanced equation:

$$\underset{\mathbf{2}}{[Mn_3O(O_2CEt)_6(py)_3](ClO_4)} + 3mpkoH \xrightarrow{MeCN/MeOH/CH_2Cl_2} \underset{\mathbf{4}}{[Mn_3O(O_2CEt)_3(mpko)_3](ClO_4)} + 3EtCO_2H + 3py \quad (1)$$

The structure[2] of the cation of **3** (Fig. 2a) consists of an almost equilateral Mn_3^{III} triangle capped by the central oxide ion, O(61). Each edge of the triangle is bridged by a diatomic oximate group and an $\eta^1:\eta^1:\mu$-$MeCO_2^-$ group. The $mpko^-$ anions behave as $\eta^1{:}\eta^1{:}\eta^1{:}\mu$-ligands forming five-membered chelate rings. The oxide ion lies 0.295 Å above the plane defined by the three Mn^{III} ions. The coordination geometry of the metal ions is distorted octahedral. The O^{2-} character of O(61) and the Mn^{III} oxidation states were confirmed by charge considerations, bond lengths, bond valence sum (BVS) calculations [7] and the presence of Mn^{III} Jahn–Teller elongation axes [O(1)–Mn(1)–O(31), O(11)–Mn(2)–O(51), O(21)–Mn(3)–O(42)]. The trinuclear cations of complexes **4**$\cdot 1.2CH_2Cl_2\cdot 1.4H_2O$ (Fig. 2b) and **5**$\cdot 2CH_2Cl_2$ (Fig. S1) have very similar structures; their capping oxide ion lies 0.308 and 0.313 Å above the Mn_3^{III} plane, respectively.

Solid-state, direct current (DC) magnetic susceptibility (χ_M) data for dried **3**–**5** were collected in the temperature range 5.0–300 K in an applied field of 1 kG (0.1 T).[3] The $\chi_M T$ of **3** steadily increases from 13.01 $cm^3\,mol^{-1}\,K$ at 300 K to a maximum of 19.39 $cm^3\,mol^{-1}\,K$ at 30 K, before dropping to 17.41 $cm^3\,mol^{-1}\,K$ at 5.00 K (Fig. 3). This behaviour is indicative of ferromagnetic exchange between the metal centers resulting in an $S = 6$ ground state, with the low temperature decrease assigned to zero-field splitting, Zeeman effects and/or intermolecular antiferromagnetic interactions. The theoretical $\chi_M T$ (spin-only, $g = 2$) for $S = 6$ is 21 $cm^3\,mol^{-1}\,K$, close to the experimental value at 30.0 K. The data were fit to the theoretical expression for a Mn_3^{III} isosceles triangle [8]. The fit gave $J = +14.1\ cm^{-1}$, $J' = +3.8\ cm^{-1}$, $g = 1.91$, and 0.9% paramagnetic impurity term, assumed to be Mn^{II}. The corresponding fit values for **5** are $J = +31.1\ cm^{-1}$, $J' = +6.7\ cm^{-1}$, $g = 1.91$, and 1.5% paramagnetic impurity term.

In order to confirm the spin ground states of the complexes, magnetization data were collected in the ranges 1–70 kG and 1.8–10.0 K, and these are plotted as reduced magnetization ($M/N\mu_B$) versus H/T for **3** in Fig. 4. For a cluster entirely populating the ground state and experiencing no zero-field splitting, the isofield lines should superimpose and saturate at a $M/N\mu_B$ value equal to gS. The data were fit by matrix diagonalization to a model that assumes only the ground state is populated, includes axial zero-field splitting ($D\widehat{S}_z^2$) and the Zeeman interaction, and carries out a full powder average. The best fit (solid lines in Fig. 4) gave $S = 6$, $g = 1.92$ and $D = -0.34\ cm^{-1}$. The corresponding data for the other two complexes are $S = 6$, $g = 1.93$, $D = -0.34\ cm^{-1}$ for **4**, and $S = 6$, $g = 1.91$, $D = -0.36\ cm^{-1}$ for **5**.

The magnitude of S and sign of D suggested these complexes might be SMMs, and AC susceptibility studies were therefore carried out in the 1.8–10.0 K range in a 3.5 G field oscillating at frequencies up to 500 Hz. Frequency-dependent out-of-phase AC susceptibility signals were seen

[1] Elemental analyses: *Anal.* Calc. for $C_{27}H_{30}N_6O_{14}ClMn_3$ (**3**): C, 37.59; H, 3.50; N, 9.74. Found: C, 37.32; H, 3.49; N, 9.54%. *Anal.* Calc. for $C_{30}H_{38}N_6O_{15}ClMn_3$ (**4**$\cdot H_2O$): C, 39.04; H, 4.15; N, 9.11. Found: C, 39.24; H, 3.82; N, 9.07%. The dried complex **5**$\cdot 2CH_2Cl_2$ is hygroscopic and was analyzed as **5**$\cdot 3H_2O$. *Anal.* Calc. for $C_{42}H_{42}N_6O_{17}ClMn_3$ (**5**$\cdot 3H_2O$): C, 45.73; H, 3.84; N, 7.62. Found: C, 45.67; H, 3.26; N, 7.49%.

[2] Crystallographic data in brief: For complex **3**$\cdot 3CH_2Cl_2$: $C_{30}H_{36}N_6O_{14}Cl_7Mn_3$, 1117.64 g mol^{-1}, monoclinic, $P2_1/c$, $a = 12.986(5)$ Å, $b = 14.978(6)$ Å, $c = 23.150(10)$ Å, $\beta = 93.82(2)°$, $Z = 4$, $V = 4493(3)$ Å^3, $\rho_{calc} = 1.492$ g cm^{-3}, $T = 293(2)$ K, R_1 (on F) = 0.0696, wR_2 (on F^2) = 0.1936. For complex **4**$\cdot 1.2CH_2Cl_2\cdot 1.4H_2O$: $C_{31.2}H_{41.2}N_6O_{15.4}Cl_{3.4}Mn_3$, 1032.06 g mol^{-1}, monoclinic, $P2_1/c$, $a = 12.988(5)$ Å, $b = 15.111(6)$ Å, $c = 27.740(10)$ Å, $\beta = 94.82(1)°$, $Z = 4$, $V = 5425(4)$ Å^3, $\rho_{calc} = 1.264$ g cm^{-3}, $T = 293(2)$ K, R_1 (on F) = 0.0738, wR_2 (on F^2) = 0.2065. For complex **5**$\cdot 2CH_2Cl_2$: $C_{44}H_{40}N_6O_{14}Cl_5Mn_3$, 1218.92 g mol^{-1}, monoclinic, $P2_1/c$, $a = 13.566(2)$ Å, $b = 29.859(2)$ Å, $c = 26.085(3)$ Å, $\beta = 98.87(1)°$, $Z = 4$, $V = 10439.72(16)$ Å^3, $\rho_{calc} = 1.341$ g cm^{-3}, $T = 100(2)$ K.

[3] The magnetic behaviour of the three complexes is similar; detailed magnetic data are presented only for cluster **3**.

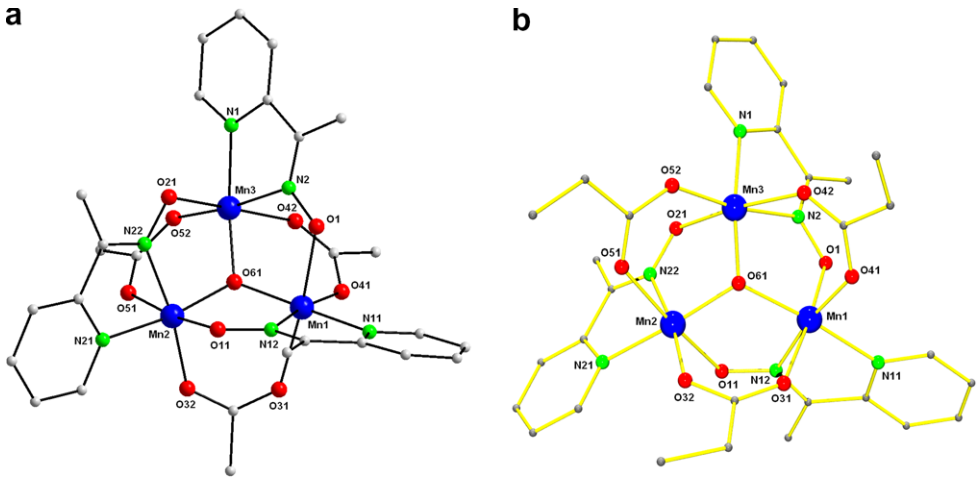


Fig. 2. Partially labeled plots of the trinuclear cations of (a) $\mathbf{3}\cdot 3CH_2Cl_2$ and (b) $\mathbf{4}\cdot 1.2CH_2Cl_2\cdot 1.4H_2O$.

for the three complexes below 3 K (but no peaks were observed) along with a concomitant decrease in the in-phase signal, indicative of SMM behaviour. The data for **4** are shown in Fig. 5.

In order to probe the possible SMM behaviour further, single-crystal hysteresis loop and relaxation measurements were performed for $\mathbf{3}\cdot 3CH_2Cl_2$ and $\mathbf{5}\cdot 2CH_2Cl_2$ using a micro-SQUID apparatus [9]. Fig. 6 presents typical magnetization (M) versus applied DC field measurements at 0.04 K for $\mathbf{3}\cdot 3CH_2Cl_2$. A hysteresis loop, the diagnostic property of a magnet, was observed below 1 K, whose coercivity increases with decreasing temperature and increasing field sweep rate, as expected for the superparamagnetic-like behaviour of an SMM. The loops show the step-like features indicative of quantum tunneling of magnetization (QTM) between M_s levels of the $S = 6$ ground state; the temperature-independent coercivity below 0.3 K indicates ground-state QTM. Magnetization decay versus time data and AC data to lower T were collected on

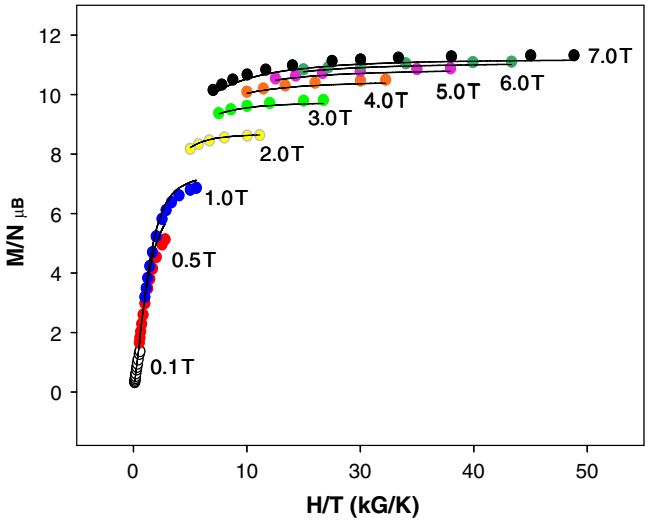


Fig. 4. Plot of the reduced magnetization, $M/N\mu_B$, vs. H/T for complex **3** at the indicated fields. The solid lines are the fit of the data; see the text for the fit parameters.

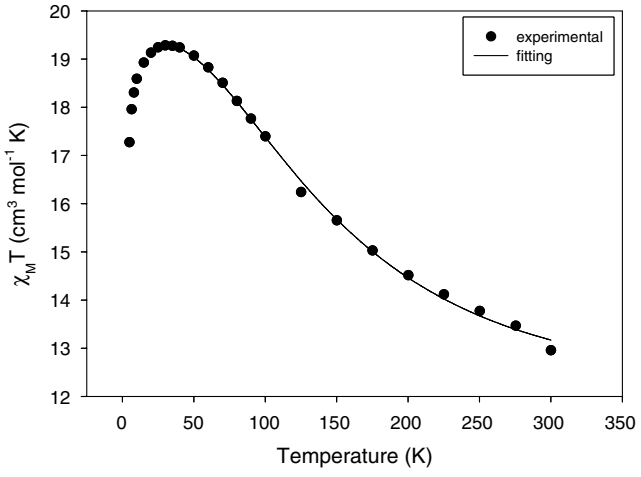


Fig. 3. $\chi_M T$ vs. T plot for complex **3** in the temperature range 5.0–300 K in a 1000 G (0.1 T) applied DC field; the solid line is the fit of the data (see the text for details).

$\mathbf{3}\cdot 3CH_2Cl_2$ and used to construct an Arrhenius plot (Fig. S2); fitting of the thermally activated region to the equation $\tau = \tau_0 \exp(U_{eff}/kT)$ gave $U_{eff} = 10.9$ K and $\tau_0 = 5.7\times 10^{-8}$ s, where U_{eff} is the effective magnetization relaxation barrier. Below 0.3 K, the relaxation is temperature-independent, consistent with relaxation by ground-state QTM. Slightly different SMM properties are observed for $\mathbf{5}\cdot 2CH_2Cl_2$ due to the presence of two crystallographically independent trinuclear cations in the crystal.[4]

An important question is the following: why are **3**–**5** ferromagnetically coupled and SMMs, whereas **1** and **2** (and many similar $[Mn_3O(O_2CR)_6L_3]^+$ complexes) are antiferromagnetically coupled and are not SMMs? A probable contributory factor is that **3**–**5** have their central oxide ligand ~0.3 Å above the Mn_3 plane due to the tridentate

[4] Details will be given in the full paper.

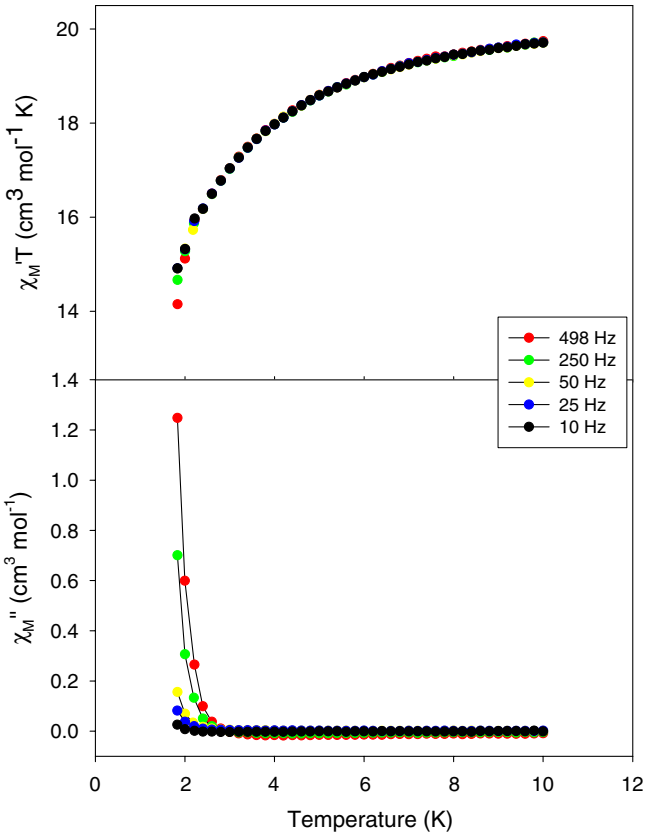


Fig. 5. Plots of the in-phase (χ'_M) as $\chi'_M T$ (top), and out-of-phase (χ''_M) (bottom) AC magnetic susceptibilities vs. T in a 3.5 G field oscillating at the indicated frequencies for complex **4**. The solid lines are visual aids.

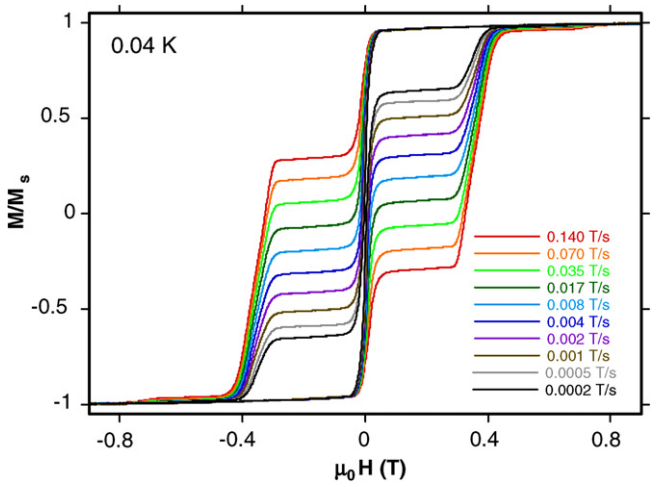


Fig. 6. Magnetization (M) vs. DC field hysteresis loops for a single crystal of $\mathbf{3} \cdot 3CH_2Cl_2$ at 0.04 K at the indicated field scan rates. The magnetization is normalized to its saturation value, M_s.

coordination of mpko$^-$ or ppko$^-$. In contrast, the oxide ion in **1**, **2** and related species is coplanar with the three metal ions. This distortion from planarity in **3**–**5** weakens the antiferromagnetic contributions (via $Mn^{III}_{d\pi}$–$O^{2-}_{p\pi}$–$Mn^{III}_{d\pi}$ orbital overlap) to the observed exchange between two Mn^{III} ions, and the latter (which is the sum of ferro- and antiferromagnetic contributions) becomes ferromagnetic leading to $S = 6$ ground states.

In summary, reactivity studies of the well known and well studied antiferromagnetically coupled $[Mn_3O(O_2CR)_6(py)_3](ClO_4)$ "starting materials" with 2-pyridyl oximes have led to a new family of triangular, oxide-centered, mixed carboxylate/2-pyridyloximate Mn(III) complexes that are ferromagnetically coupled with an $S = 6$ ground state. Complexes **3**–**5** are SMMs, the first for 3d metal complexes with a triangular topology. Given this success, the use of 2-pyridyl oxime ligands in Mn carboxylate chemistry continues to be investigated.

Acknowledgements

Th.C.S. and S.P.P. thank ESF, EPEAEK II, and particularly the Program PYTHAGORAS (Grant b.365.037), for funding the above work. G.C. thanks the NSF for support.

Appendix A. Supplementary material

CCDC 291916, 622143 and 623023 contain the supplementary crystallographic data in CIF format for $\mathbf{3} \cdot 3CH_2Cl_2$, $\mathbf{4} \cdot 1.2CH_2Cl_2 \cdot 1.4H_2O$ and $\mathbf{5} \cdot 2CH_2Cl_2$. These data can be obtained free of charge via http://www.ccdc.cam.ac.uk/conts/retrieving.html, or from the Cambridge Crystallographic Data Centre, 12 Union Road, Cambridge CB2 1EZ, UK; fax: (+44) 1223-336-033; or e-mail: deposit@ccdc.cam.ac.uk. Supplementary data associated with this article can be found, in the online version, at doi:10.1016/j.poly.2006.10.025.

References

[1] (a) For reviews, see: G. Christou, D. Gatteschi, D.N. Hendrickson, R. Sessoli, MRS Bull. 25 (2000) 66;
(b) G. Aromi, E.K. Brechin, Struct. Bond. 122 (2006) 1;
(c) R. Bircher, G. Chaboussant, C. Dobe, H.U. Güdel, S.T. Oshsenbein, A. Sieber, O. Waldmann, Adv. Funct. Mater. 16 (2006) 209;
(d) D. Gatteschi, R. Sessoli, Angew. Chem., Int. Ed. 42 (2003) 268.
[2] J.R. Friedman, M.P. Sarachik, J. Tejada, R. Ziolo, Phys. Rev. Lett. 76 (1996) 3830.
[3] W. Wernsdorfer, R. Sessoli, Science 284 (1999) 133.
[4] J.B. Vincent, H.-R. Chang, K. Folting, J.C. Huffman, G. Christou, D.N. Hendrickson, J. Am. Chem. Soc. 109 (1987) 5703.
[5] For a review, see: C.J. Milios, Th.C. Stamatatos, S.P. Perlepes, Polyhedron 25 (2006) 134, polyhedron report.
[6] Th.C. Stamatatos, D. Foguet-Albiol, C.C. Stoumpos, C.P. Raptopoulou, A. Terzis, W. Wernsdorfer, S.P. Perlepes, G. Christou, J. Am. Chem. Soc. 127 (2005) 15380.
[7] W. Liu, H.H. Thorp, Inorg. Chem. 32 (1993) 4102.
[8] R.D. Cannon, U.A. Jayasooriya, R. Wu, S.K. arapKoske, J.A. Stride, O.F. Nielsen, R.P. White, G.J. Kearley, D. Summerfields, J. Am. Chem. Soc. 116 (1994) 11869.
[9] W. Wernsdorfer, Adv. Chem. Phys. 118 (2001) 99.

2. Experimental

2.1. Materials and instrumentation

$[Cr_3O(CO_2Me)_6(MeOH)_3]Cl$ was prepared as previous literature [9]. All manipulations were performed under aerobic conditions using materials (reagent grade) and solvents as received without further purification. X-ray diffraction data were collected using a Siemens SMART APEX CCD diffractometer with Mo Kα radiation and a graphite monochromator. Magnetic measurement was performed in the range of 2–300 K with a Quantum Design MPMS-XL SQUID magnetometer at an applied field of 100 Oe. Elemental analyses (C, H) were performed on a Vario EL CHN Elementar Analyzer.

2.2. Preparation of complex $[Cr_{10}(\mu\text{-}O_2CMe)_{10}(\mu\text{-}OMe)_{10}(\mu\text{-}OEt)_{10}]$ (1)

$[Cr_3O(CO_2Me)_6(MeOH)_3]Cl$ (100 mg) in EtOH (10 ml) was placed in a Teflon-lined autoclave and heated to 413 K for 3 d, and then cooled at 6 K h^{-1} to room temperature, dark-green crystals of **1** deposited on the walls of container, were collected and air-dried. Yield: ~60%. $C_{50}H_{110}Cr_{10}O_{40}$ (Fw: 1871.38) *Anal.* Calc. C, 32.06; H, 5.92. Found: C, 32.70; H, 5.73%.

2.3. Single-crystal structure determination for complex 1

Single crystal X-ray diffraction was performed on a CCD area detector with graphite monochromated Mo Kα radiation ($\lambda = 0.71073$ Å) [10] in the range of $0.915 < \theta < 28.65°$. The structure was solved in $P2_1/n$ by the direct method and refined by the Full-matrix least squares on F^2 using the SHELXTL-97 software [11]. 10 (O)Me groups those located inside of the 'wheel' **1** showed twofold disorder. Crystal data for **1** are shown in Tables 1 and 2.

2.4. Magnetic measurement of complex 1

Magnetic susceptibility measurement on complex **1** was obtained on a finely ground polycrystalline sample with the use of a Quantum Design SQUID magnetometer MPMS-XL. The direct current measurements were collected from 2.0 to 300 K under 100 Oe. Experimental data were also corrected for the sample holder and for the diamagnetic contribution calculated from Pascal constants [12].

3. Results and discussion

3.1. Structural data for complex 1

The ORTEP drawing for complex **1** presented in Figs. 1–3 presents the packing diagram of **1** viewed down the crystallographic *a*-axis and crystallographic *b*-axis, respectively. As shown in Fig. 1, the complex $[Cr_{10}(\mu\text{-}O_2CMe)_{10}(\mu\text{-}OMe)_{10}(\mu\text{-}OEt)_{10}]$, consists of 10 Cr(III) ions forming a ring structure. Each of the two neighboring metal atoms are bridged by one μ-acetate, one μ-ethoxide, and one μ-methoxide ligands, with a Cr···Cr average distance of 2.995(6) Å, this distance is similar to 2.995(2) Å reported in the $[Cr_{10}(\mu\text{-}O_2CMe)_{10}(\mu\text{-}OEt)_{20}]$, while that of complex bridged by methoxide was 2.990(8) Å [3b]. The Cr atom adopts a distorted octahedral coordination geometry. It is bonded to two neighboring bidentate acetate anions pointing to the outside of the "wheel" through two of their oxygen atoms, two neighboring methoxide anions pointing to the inside of the "wheel" through two of their oxygen atoms, and two neighboring ethoxide anions pointing to the outside of the "wheel" through two of their oxygen atoms in *trans* position. Therefore, all the methoxide ligands line in the cavity pointing to the inside of the "wheel" alternately above and below the Cr_{10} ring. All the ethoxide ligands bridge Cr atoms around the outside of the "wheel", alternately above and below the ring. The oxygen atoms of acetato ligands are in the *trans* positions to those methoxide groups, hence, all the acetato ligands are pointing to the outside of the "wheel" alternately above and below the Cr_{10} ring. The distances for Cr···Cr in *trans* position in the ring are in the range 9.664–9.748 Å. The average value of the bond angle Cr–O(Et)–Cr of **1** is 99.64°, which is 99.30° in $[Cr_{10}(\mu\text{-}O_2CMe)_{10}(\mu\text{-}OEt)_{20}]$ [3b]. The average value of the bond angle Cr–O(Me)–Cr of **1** is 98.67°, while it is 99.34° in $[Cr_{10}(\mu\text{-}O_2CMe)_{10}(\mu\text{-}OMe)_{20}]$ [3b].

The unit cell parameters of complex **1** are *a* 9.4752(18) Å, *b* 16.056(3) Å, *c* 28.627(5) Å, *β* 90.921(4)°, which are almost the same as those of $[Cr_{10}$-

Table 1
Crystal data and structure refinement for complex **1**

Empirical formula	$C_{50}H_{110}Cr_{10}O_{40}$
Formula weight	1871.38
Temperature (K)	293(2)
Radiation, wavelength (Mo Kα) (Å)	0.71073
Crystal system	monoclinic
Space group	$P2_1/n$
a (Å)	9.4752(18)
b (Å)	16.056(3)
c (Å)	28.627(5)
α (°)	90
β (°)	90.921 (4)
γ (°)	90
V (Å)^3	4354.5(14)
Z	2
ρ (Mg m^{-3})	1.427
μ (mm^{-1})	1.274
F(000)	1940
Crystal size (mm)	$0.22 \times 0.16 \times 0.06$
Reflections collected	27120
Independent reflections	10246
Refinement method	full-matrix least-squares on F^2
Goodness-of-fit	1.007
Final *R* indices [$I > 2\sigma(I)$]	$R_1 = 0.0626$, $wR_2 = 0.1381$
R indices	$R_1 = 0.1542$, $wR_2 = 0.1590$

Table 2
Selected bond lengths (Å) and angles (°) for complex **1**

Cr(1)–O(16)	1.958(4)	O(16)–Cr(1)–O(11)	78.12(15)
Cr(1)–O(20)	1.962(4)	O(20)–Cr(1)–O(11)	97.73(16)
Cr(1)–O(15)	1.972(4)	O(15)–Cr(1)–O(11)	95.88(15)
Cr(1)–O(1)	1.982(4)	O(1)–Cr(1)–O(11)	89.81(16)
Cr(1)–O(11)	1.983(4)	O(16)–Cr(1)–O(10)	92.73(16)
Cr(1)–O(10)	1.984(4)	O(20)–Cr(1)–O(10)	91.66(16)
Cr(2)–O(17)	1.967(4)	O(15)–Cr(1)–O(10)	89.05(16)
Cr(2)–O(16)	1.965(4)	O(1)–Cr(1)–O(10)	86.70(17)
Cr(2)–O(11)	1.976(4)	O(11)–Cr(1)–O(10)	170.12(16)
Cr(2)–O(12)	1.983(4)	O(17)–Cr(2)–O(16)	172.89(16)
Cr(2)–O(2)	1.997(4)	O(17)–Cr(2)–O(11)	96.99(15)
Cr(2)–O(3)	1.998(4)	O(16)–Cr(2)–O(11)	78.12(15)
Cr(3)–O(12)	1.960(4)	O(17)–Cr(2)–O(12)	78.42(15)
Cr(3)–O(18)	1.963(4)	O(16)–Cr(2)–O(12)	96.77(15)
Cr(3)–O(13)	1.972(4)	O(11)–Cr(2)–O(12)	95.28(15)
Cr(3)–O(17)	1.975(4)	O(17)–Cr(2)–O(2)	93.44(16)
Cr(3)–O(4)	1.977(4)	O(16)–Cr(2)–O(2)	91.72(16)
Cr(3)–O(5)	1.995(4)	O(11)–Cr(2)–O(2)	89.89(16)
Cr(4)–O(19)	1.953(4)	O(12)–Cr(2)–O(2)	170.81(16)
Cr(4)–O(18)	1.960(4)	O(17)–Cr(2)–O(3)	92.21(16)
Cr(4)–O(13)	1.972(3)	O(16)–Cr(2)–O(3)	92.90(17)
Cr(4)–O(14)	1.985(4)	O(11)–Cr(2)–O(3)	170.57(16)
Cr(4)–O(6)	1.985(4)	O(12)–Cr(2)–O(3)	88.58(15)
Cr(4)–O(7)	2.000(4)	O(2)–Cr(2)–O(3)	87.48(17)
Cr(5)–O(19)	1.947(4)	O(12)–Cr(3)–O(18)	97.35(16)
Cr(5)–O(9)	1.971(4)	O(12)–Cr(3)–O(13)	95.55(15)
Cr(5)–O(14)	1.982(4)	O(18)–Cr(3)–O(13)	77.92(15)
Cr(5)–O(8)	1.990(4)	O(12)–Cr(3)–O(17)	78.76(15)
O(13)–Cr(4)–O(6)	88.95(16)	O(18)–Cr(3)–O(17)	174.68(16)
O(14)–Cr(4)–O(6)	169.71(17)	O(13)–Cr(3)–O(17)	98.73(15)
O(19)–Cr(4)–O(7)	91.06(17)	O(12)–Cr(3)–O(4)	89.69(16)
O(18)–Cr(4)–O(7)	93.38(17)	O(18)–Cr(3)–O(4)	92.76(16)
O(13)–Cr(4)–O(7)	170.53(17)	O(13)–Cr(3)–O(4)	169.80(15)
O(14)–Cr(4)–O(7)	88.88(16)	O(17)–Cr(3)–O(4)	90.86(16)
O(6)–Cr(4)–O(7)	87.40(17)	O(12)–Cr(3)–O(5)	170.71(16)
O(19)–Cr(5)–O(9)	92.64(17)	O(18)–Cr(3)–O(5)	91.38(16)
O(19)–Cr(5)–O(14)	78.09(16)	O(13)–Cr(3)–O(5)	89.37(16)
O(9)–Cr(5)–O(14)	169.76(16)	O(17)–Cr(3)–O(5)	92.73(16)
O(19)–Cr(5)–O(8)	90.84(17)	O(4)–Cr(3)–O(5)	86.70(17)
O(9)–Cr(5)–O(8)	86.49(18)	O(19)–Cr(4)–O(18)	173.87(16)
O(14)–Cr(5)–O(8)	89.29(16)	O(19)–Cr(4)–O(13)	97.83(15)
O(16)–Cr(1)–O(20)	174.27(17)	O(18)–Cr(4)–O(13)	78.00(15)
O(16)–Cr(1)–O(15)	98.34(15)	O(19)–Cr(4)–O(14)	77.89(16)
O(20)–Cr(1)–O(15)	78.04(15)	O(18)–Cr(4)–O(14)	97.96(16)
O(16)–Cr(1)–O(1)	91.47(16)	O(13)–Cr(4)–O(14)	96.14(15)
O(20)–Cr(1)–O(1)	92.46(17)	O(19)–Cr(4)–O(6)	92.59(17)
O(15)–Cr(1)–O(1)	169.48(15)	O(18)–Cr(4)–O(6)	91.83(17)

(μ-$O_2CMe)_{10}(\mu$-$OEt)_{20}$], and different from those of [$Cr_{10}(\mu$-$O_2CMe)_{10}(\mu$-$OMe)_{20}$] [3b]. This is may ascribed to the bridged ligands around the outside of the "wheel" being the main factors for molecular stacking in this series.

3.2. Magnetic properties for complex *1*

Fig. 4 shows the magnetic behavior of **1** at an applied field of 100 Oe in the form of $\chi_M T$ vs T plot. The $\chi_M T$ value of 10 Cr(III) at 300 K is 15.6 emu K mol^{-1}, lower than the spin-only value (18.4 emu K mol^{-1}) expected for a magnetically isolated high-spin Cr(III) ion with $g = 2.00$. As the sample is cooled from room temperature, the $\chi_M T$ first keeps constant in the temperature range 150–300 K, then

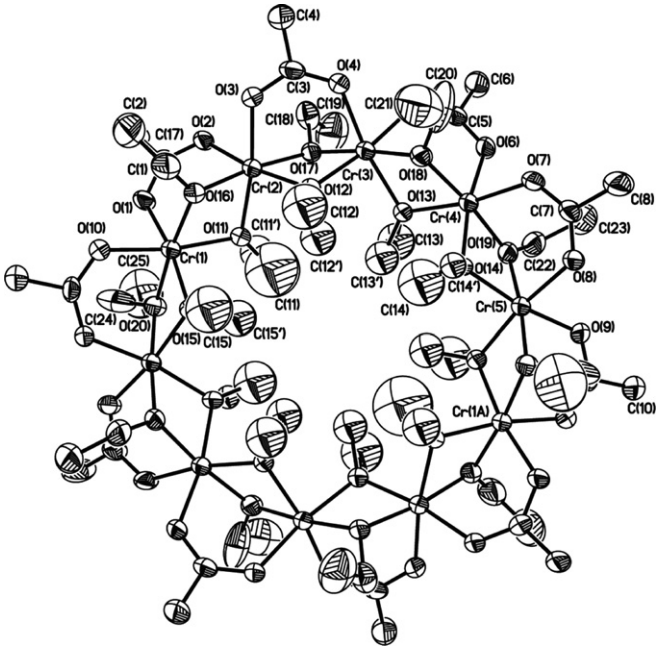


Fig. 1. Molecular structure (30% thermal ellipsoids) of complex **1**. The 10 (O)Me groups in **1** showed twofold disorder. Bond length ranges: Cr–O(Me) 1.960(4)–1.985(4) Å, Cr–O(Et) 1.953(4) –1.975(4) Å, Cr–O(acetate) 1.971(4)–2.000(4) Å. Bond angle ranges: Cr–O(Me)–Cr 98.28(17)–99.05(16)°, Cr–O(Et)–Cr 98.69(17)–100.58(19)°.

decreases slowly from 150 to 50 K, and finally more quickly to a value of 9.25 emu K mol^{-1} at 2 K. The $1/\chi_M$ vs T plot is almost linear in the entire temperature range (not shown here), and the data (above 4 K) can be fitted to the Curie–Weiss law with $C = 15.79$ cm^3 mol^{-1} K and $\Theta = -1.33$ K. The Cr $\cdots$ Cr exchange can then be calculated from Θ [13], giving $J = +0.37$ cm^{-1}.

The magnetic behavior of **1** indicates the presence of very weak intra-molecular antiferromagnetic exchange interactions between Cr(III) ions. The magnetic behavior of **1** may be ascribed to the fact that the mixing methoxide and ethoxide ligand in **1** results in the mixing magnetic

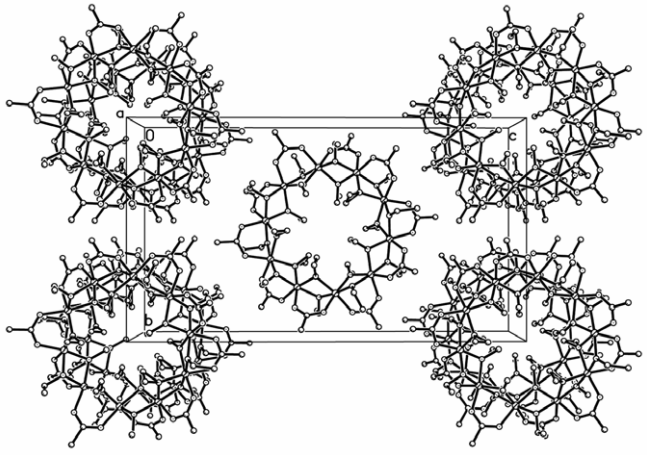


Fig. 2. Packing diagram of **1** viewed down the crystallographic *a*-axis. All hydrogen atoms are omitted for clarity.

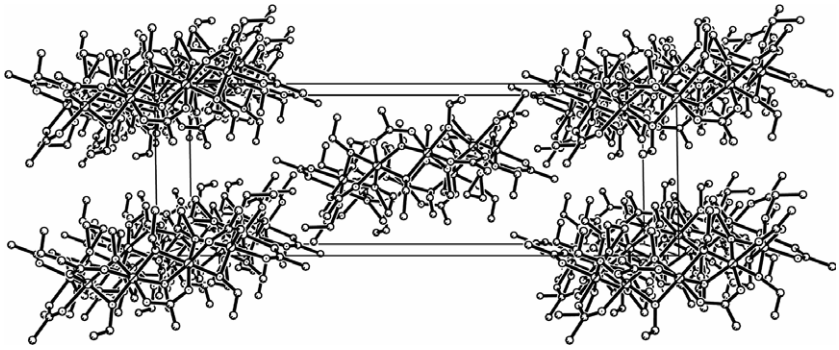


Fig. 3. Packing diagram of **1** viewed down the crystallographic *b*-axis. All hydrogen atoms are omitted for clarity.

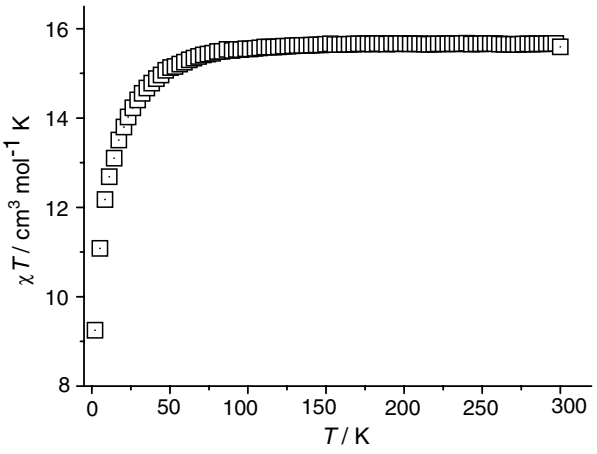


Fig. 4. Temperature dependence of $\chi_M T$ for **1**.

properties for pure methoxide (ferromagnetic) and ethoxide (antiferromagnetic) ligand, respectively.

4. Conclusions

In summary, we have described a new nano-decanuclear cyclic Cr(III) complex, $[Cr_{10}(\mu\text{-}O_2CMe)_{10}(\mu\text{-}OMe)_{10}(\mu\text{-}OEt)_{10}]$ (**1**), bridged by ethoxide, methoxide, and acetate ligands under solvothermal conditions. Structural and the unit cell parameters of complex **1** are more similar to those of $[Cr_{10}(\mu\text{-}O_2CMe)_{10}(\mu\text{-}OEt)_{20}]$, possibly due to ethoxide ligand outside of the "wheel" is the main factor for molecular stacking. The complex **1** shows more weak antiferromagnetic exchange interaction than that of $[Cr_{10}(\mu\text{-}O_2CMe)_{10}(\mu\text{-}OEt)_{20}]$ due to the mixing ethoxide and methoxide ligands.

Acknowledgement

We gratefully acknowledge the financial support received from the Natural Science Foundation of China (Grant No. 20274006).

Appendix A. Supplementary material

CCDC 615739 contains the supplementary crystallographic data for **1**. These data can be obtained free of charge via http://www.ccdc.cam.ac.uk/conts/retrieving.html, or from the Cambridge Crystallographic Data Centre, 12 Union Road, Cambridge CB2 1EZ, UK; fax: (+44) 1223-336-033; or e-mail: deposit@ccdc.cam.ac.uk. Supplementary data associated with this article can be found, in the online version, at doi:10.1016/j.poly.2006.10.027.

References

[1] (a) A. Caneschi, D. Gatteschi, C. Sangregorio, R. Sessoli, L. Sorace, A. Cornia, M.A. Novak, C. Paulsen, W. Wernsdorfer, J. Magn. Magn. Mater. 200 (1999) 182;
(b) D. Gatteschi, R. Sessoli, A. Cornia, Chem. Commun. (2000) 725.

[2] A.J. Tassiopoulos, A. Vinslave, W. Wernsdorfer, K.A. Abboud, G. Christou, Angew. Chem., Int. Ed. 43 (2004) 2117.

[3] (a) I.M. Atkinson, C. Benelli, M. Murrie, S. Parsons, R.E.P. Winpenny, Chem. Commun. (1999) 285;
(b) E.J.L. McInnes, C. Anson, A.K. Powell, A.J. Thomson, S. Poussereau, R. Sessoli, Chem. Commun. (2001) 89;
(c) D.M. Low, G. Rajaraman, E.J.L. McInnes, Chem. Eur. J. 12 (2006) 1385.

[4] (a) S.X. Liu, S. Lin, B.Z. Lin, C.C. Lin, J.Q. Huang, Angew. Chem., Int. Ed. 40 (2001) 1084;
(b) D. Fenske, A. Fischer, Angew. Chem. 107 (1995) 340;
Angew. Chem., Int. Ed. Engl. 34 (1995) 307;
(c) K.L. Taft, C.D. Delfs, G.C. Papaefthymiou, S. Foner, D. Gatteschi, S.J. Lippard, J. Am. Chem. Soc. 116 (1994) 823;
(d) C. Benelli, S. Parsons, G.A. Solan, R.E.P. Winpenny, Angew. Chem., Int. Ed. 35 (1996) 1825;
(e) M. Frey, S.G. Harris, J.M. Holmes, D.A. Nation, S. Parsons, P.A. Tasker, R.E.P. Winpenny, Chem. Eur. J. 6 (2000) 1407;
(f) A. Caneschi, A. Cornia, A.C. Fabretti, D. Gatteschi, Angew. Chem., Int. Ed. 38 (1999) 1295;
(g) S.P. Watton, R. Fuhrmann, L.E. Pence, A. Caneschi, A. Cornia, G.L. Abbati, S.J. Lippard, Angew. Chem., Int. Ed. 36 (1997) 2774.

[5] P.L. Jones, K.J. Byrom, J.C. Jeffery, J.A. McCleverty, M.D. Ward, Chem. Commun. (1997) 1361.

[6] (a) A.L. Dearden, S. Parsons, R.E.P. Winpenny, Angew. Chem., Int. Ed. 40 (2001) 151;
(b) A.J. Blake, C.M. Grant, S. Parsons, J.M. Rawson, R.E.P. Winpenny, Chem. Commun. (1994) 2363;
(c) H. Andres, R. Basler, R.E.P. Winpenny, Chem. Eur. J. 8 (2002) 4867.

[7] (a) G.A. Ardizzoia, M.A. Angaroni, G.L. Monica, F. Cariati, S. Cenini, M. Moret, N. Masciocchi, Inorg. Chem. 30 (1991) 4347;
(b) C.H. Chang, K.C. Hwang, C.S. Liu, Y. Chi, A.J. Carty, L. Scoles,

S.M. Peng, G.H. Lee, J. Reedijk, Angew. Chem., Int. Ed. 40 (2001) 4651.
[8] P.A. Lay, A. Levina, in: J.A. McCleverty, T.J. Meyer (Eds.), Comprehensive Coordination Chemistry II, vol. 4, Elsevier, Oxford, UK, 2004, p. 373.
[9] S. Uemura, A. Spencer, G. Wilkinson, J. Chem. Soc., Dalton Trans. (1973) 2565.
[10] Siemens, SMART. Version. 5.05, Siemens Analytical X-ray Instruments Inc., Madison, WI, USA, 1995.
[11] G.M. Sheldrick, SHELXS97 and SHELXL97, University of Göttingen, Germany, 1997.
[12] O. Khan, Molecular Magnetism, VCH, New York, 1993.
[13] M. Eshel, A. Bino, I. Felner, D.C. Johnston, M. Luban, L.L. Miller, Inorg. Chem. 39 (2000) 1376.

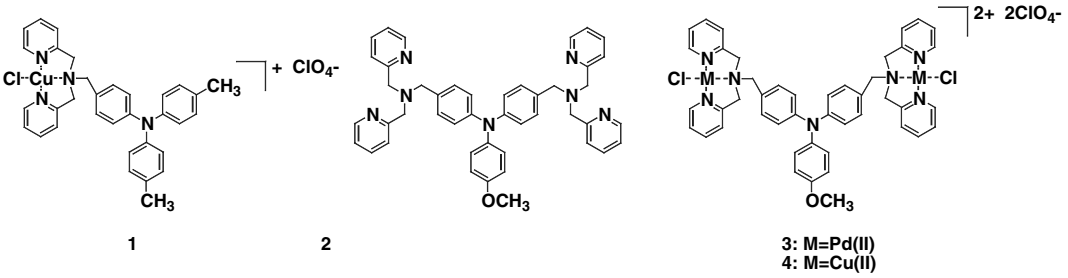


Fig. 1. Structures of compounds **1**–**4**.

[4]. CV measurements of **1** showed reversible Cu^{I}/Cu^{II} and TPA/TPA^{+} redox couples. The spin–spin interaction of the copper complex with pendant TAA cation radical, generated upon one electron oxidation of **1**, was examined by ESR measurements. This result encouraged us to examine more complicated systems.

In this study, we report on a novel ligand (**2**) and its dinuclear palladium (**3**) and copper (**4**) complexes. The ligand is expected to be a promising redox-active building unit of supramolecular transition metal clusters. The methoxy group was introduced to improve the stability of the TAA cation radical (see Fig. 1).

2. Experimental

Synthetic detail will be reported elsewhere. All new compounds were fully characterized by spectroscopic methods. Data only for **3** and **4** are given below.

Compound **3**: pale yellow powder, ^{1}H NMR (CD_3CN); 3.78 (s, 3H), 4.10 (s, 4H), 4.51 (d, 4H, $J = 16$ Hz), 5.26 (d, 4H, $J = 16$ Hz), 6.44 (d, 4H, $J = 7.6$ Hz), 6.67 (d, 2H, $J = 7.6$ Hz), 6.96 (d, 2H, $J = 7.6$ Hz), 7.47 (d, 4H, $J = 5.1$ Hz,), 7.50 (t, 4H, $J = 8.2$ Hz), 7.69 (d, 4H, $J = 7.6$ Hz), 8.05 (dt, 4H, $J = 8.2$ Hz, 1.5 Hz), 8.56 (d, 4H, $J = 5.1$ Hz,), **4**; blue crystals, HRMS: Calcd.: 893.1698 for $C_{45}H_{43}Cl_2N_7OCu_2$, obsd.: 893.1477.

Caution: Although no problem was encountered in the preparation of the perchlorate salts, suitable care should be taken when handling such potentially hazardous compounds.

3. Results and discussion

3.1. Synthesis of the ligand, and the Pd(II) and Cu(II) dinuclear complexes

The ligand, 4-methoxy-4′,4″-bis[*N*,*N*-bis(2-pyridylmethyl)aminomethyl]triphenyl-amine (**2**), was synthesized as shown in Fig. 2. Ullmann coupling reaction of diphenylamine with iodoanisole gave 4-methoxytriphenylamine in 75% yield. This compound in turn was transformed into 4,4′-diformyl-4″-methoxytriphenylamine by the reaction with phosphoryl chloride in 82% yield. The formylation occurred regiospecifically and successfully at the two *para* positions of triarylamine, and no mono-substituted derivative was found. Treatment of 4,4′-diformyl-4″-methoxytriphenylamine with 2-picolylamine and sodium borohydride gave the secondary amine, 4-methoxy-4′,4″-bis[*N*-(2-pyridylmethyl)]aminomethyltriphenyl-amine. This compound then was reacted with 2-(bromomethyl)pyridine hydrobromide under a basic condition to give the target compound, **2**, in excellent isolated yield (67%). The complex **3** and **4** were prepared by reacting **2** with palladium (II) chloride and copper (II) chloride in the presence of sodium perchrolate, respectively.

3.2. UV/Vis spectrum measurements

In order to examine the spectroscopic properties of the metal complexes, UV/Vis absorption-spectrum measurements were examined. The spectra of those compounds are shown in Fig. 3. In acetonitrile solution, **3** and **4** exhibited a strong absorption around 300 nm, which is characteristic for triarylamine chromophores [5]. In addition, **4** exhibited a weak absorption at 623nm ($\varepsilon = 280^{-1}\ cm^{-1}$). This peak can be assigned to the d-d transition of the copper (II) ion.

3.3. Cyclic voltammetric measurements

Electrochemical behavior of **3** and **4** was studied by cyclic voltammetry in *n*-butyronitrile at ambient temperature. Upon sweeping anodically, **3** exhibited reversible redox waves ($E^0 = 0.473$ V versus Fc/Fc^{+}) as shown in Fig. 4, which can be assigned to the one electron oxidation process of the triarylamine unit. Compound **4** also showed similar redox couple ($E^0 = 0.477$ V versus Fc/Fc^{+}). On the other hand, upon sweeping cathodically, the copper complex exhibited one set of quasi-reversible redox waves ($E^0 = -0.690$ V versus Fc/Fc^{+}). Upon repeating sweeps several times in potential ranging from 1.0 to −1.0 (V versus Fc/Fc^{+}), no decrease in the current peak intensity was observed, indicating the three possible species ($Cu(I)_2$–TAA, $Cu(II)_2$–TAA and $Cu(II)_2$–TAA^{+}) are stable in terms of the time scale of cyclic voltammetry.

3.4. Electron transfer stopped-flow (ETSF) method

The detail of the ETSF method was described previously [6]. The ETSF measurements were carried out in dehydrated acetonitrile as solvent at ambient temperature. In this study,

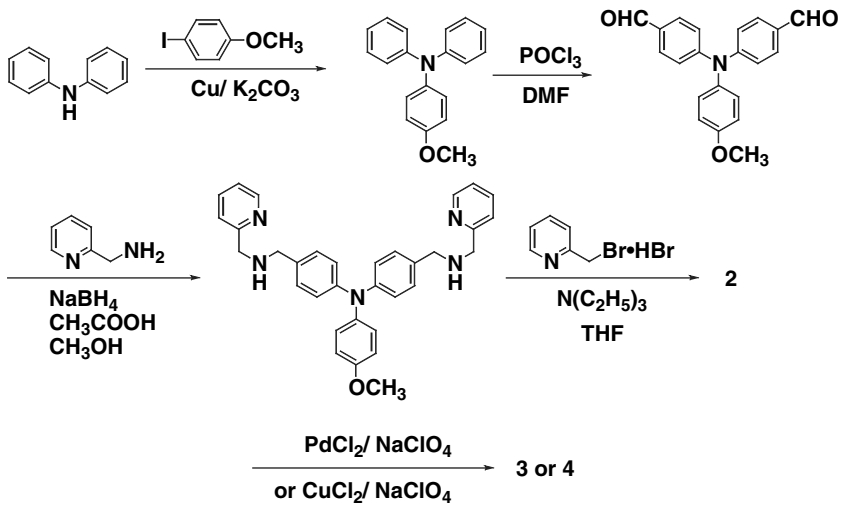


Fig. 2. Synthetic route of **3** and **4.**

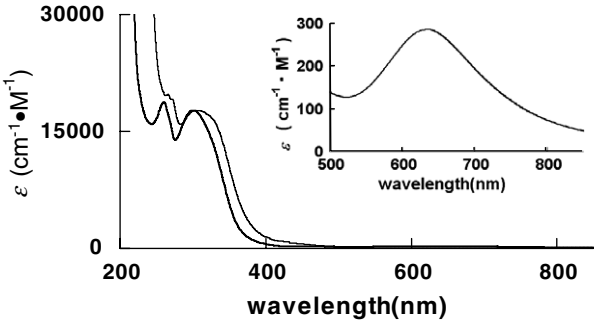


Fig. 3. UV/Vis spectra of **3** (plain), **4** (bold) in acetonitrile. Inset: UV/Vis spectra of **4** in acetonitrile (expanded around 650 nm).

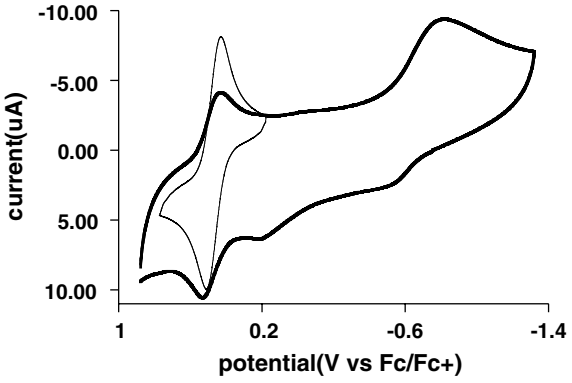


Fig. 4. The cyclic voltammogram of **3** (plain), **4** (bold) in *n*-butyronitrile.

tris(2,4-dibromophenyl)amine cation radical ($TDBPA^{+\cdot}$)[1] was employed. Complex **3**, upon mixing with one equivalent of $TDBPA^{+\cdot}$, exhibited a broad absorption peak at 718 nm ($\varepsilon = 1.56 \times 10^4\ M^{-1}\ cm^{-1}$), and no significant decrease in the peak intensity was observed over 100 s, indicating the generation of the stable monocation. Similarly, complex **4** exhibited a peak at 718 nm ($\varepsilon = 1.51 \times 10^4\ M^{-1}\ cm^{-1}$), and no decrease in the peak intensity was observed.

3.5. Two-dimensional NMR measurements

COSY (correlated spectroscopy) and NOESY (nuclear Overhauser effect spectroscopy) are widely employed powerful NMR techniques in the field of organic chemistry. COSY and NOESY can observe through-bond and through space dipolar H–H interaction, respectively. NOESY cross peaks can be observed only for nuclei that are proximate in space (<3.5 Å), which enables the determination of the geometrical structure of molecules in solution. COSY and NOESY measurements were applied to **3** to examine its conformation in CD_3CN solution. In the NOESY spectrum of **3** at 25 °C, correlations were seen between the Ha, Hb, Hc peaks and Hd peak. Similar correlations were also seen between the Ha, Hb, Hc peaks and He peak. These results indicate that Hd and He are proximate to the pyridine rings in space, respectively. The data clearly show that **3** prefers a "folded conformation" (Fig. 5) due to intramolecular stacking interactions. Upon heating to 75 °C, The cross peaks described above

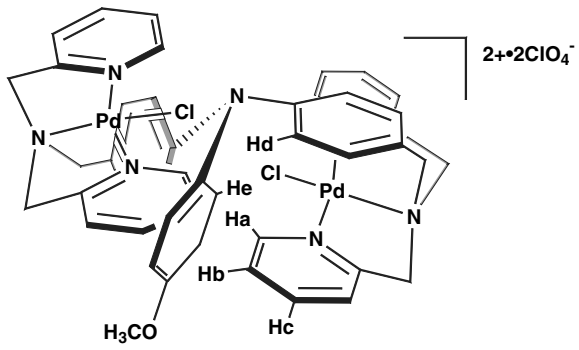


Fig. 5. An estimated conformation of **3** in CD_3CN solution.

[1] TDBPA was synthesized by WAKO Pure Chemicals Ltd. after receiving our special order. See also Ref. [6].

disappeared completely, indicating the preference of "opened conformation" at this condition. The detail will be reported elsewhere.

3.6. ESR measurements

The magnetic properties of **4** and its oxidized species were examined by cw-ESR measurements in propionitrile at 77 K. Tri(*p*-tolyl)amine cation radical (**5**) and a copper complex (**6**) without the triarylamine unit (Fig. 6), were also examined under the same conditions for comparison (Fig. 7). Compound **6** gave an ESR Cu-hyperfine structure ($S = 1/2$) shown in Fig. 7b, which is characteristic of copper bis(2-picolyl)amine complexes with $S = 1/2$. On the other hand, compound **4** exhibited a broad ESR spectrum with a similar Cu-hyperfine splittings to that of **6** except their reduced intensity (Fig. 7c), indicating that the broadened ESR spectrum is due to the intramolecular exchange-coupled dinuclear copper system with the total spin quantum number $S = 1$. The Cu-hyperfine tensor $\boldsymbol{A}$ for the dinuclear copper complex **4** is described as $\boldsymbol{A} = (\boldsymbol{A}_1 + \boldsymbol{A}_2)/2$ with $S = 1$ in the strong exchange limit, where $\boldsymbol{A}_i$ ($i = 1, 2$) denotes the Cu-hyperfine tensor of the local Cu site i of **4**. We safely assume that the component Cu-hyperfine $\boldsymbol{A}_i$ is similar to that of **6**. Considering the molecular symmetry of **4**, we obtain the structural relationship between the tensor $\boldsymbol{A}_1$ and $\boldsymbol{A}_2$. In compound **4**, $\boldsymbol{A}_1 \cong \boldsymbol{A}_2$ interprets the triplet Cu-hyperfine structure with $\boldsymbol{A}_1 \cong \boldsymbol{A}_2$ for 4 as well as $\mathbf{g} \cong \mathbf{g}_1$. Upon addition of one equivalent of cerium ammonium nitrate (CAN), the color of the solution immediately changed from light blue to deep purple, which revealed the generation of the TAA cation radical chromophore. The ESR spectrum of the oxidized species is shown in Fig. 7d, indicating the occurrence of an intramolecularly exchanged system in which the two local Cu site is bridged by the open-shell ligand **5**. In the oxidized **4**, exchange-coupled doublet and quartet states with reduced anisotropy for the resultant $\boldsymbol{g}$ and $\boldsymbol{A}$ tensors, which is due to the isotropic g-value of **5** and no contribution to the Cu-hyperfine structure from **5**, are anticipated. The observed Cu-hyperfine splittings with the reduction factor of 2/3 (Fig. 7d), as well as the reduction of the observed $\boldsymbol{g}$-anisotropy, are strongly indicative that the observed ESR spectrum arises from an exchange-coupled quartet state. Only the cw-ESR spectrum observed at 77 K (Fig. 7d) does not give straightforward information on the location of the exchange-coupled doublet states. For complete analyses of the ESR spectra, pulse-based electron spin transient nutation spectroscopy for the oxidized copper complex is underway.

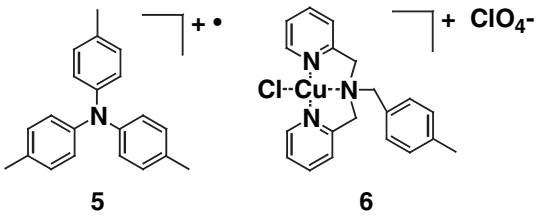


Fig. 6. Structures of compounds **5** and **6**.

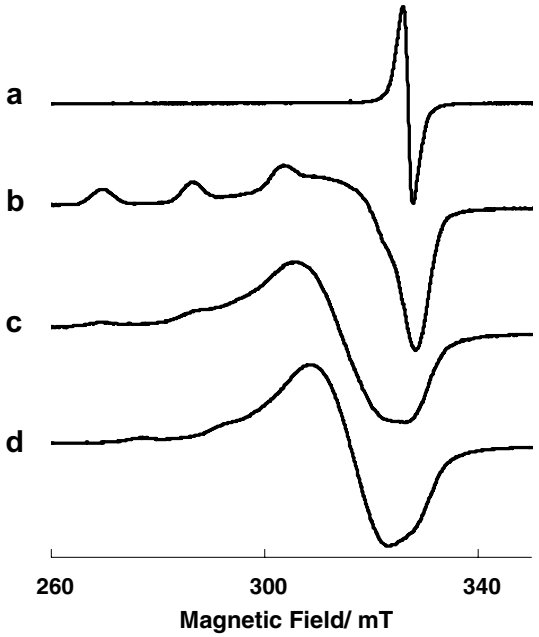


Fig. 7. ESR spectra of: (a) **5**, (b) **6**, (c) **4** and (d) **4** oxidized with CAN in C_2H_5CN at 77 K.

4. Conclusions

A novel ligand having a redox active triarylamine group and two coordinating groups was designed and synthesized. The corresponding palladium and copper complex were also successfully prepared. The cyclic voltammetry and ETSF study revealed that the complexes gave novel stable complexes with a pendent radical, respectively. The COSY and NOESY studies revealed that the palladium complex prefers the "folded conformation" in solution at ambient temperature. The ESR study of the oxidized dinuclear copper complex showed that the exchange-coupled high-spin entity in the quartet ground state is generated by the oxidation of the central ligand, triaryamine.

References

[1] (a) E.T. Seo, R.F. Nelson, J.M. Fritsch, L.S. Marcoux, D.W. Leedy, R.N. Adams, J. Am. Chem. Soc. 88 (1966) 3498;
(b) R.F. Nelson, R.N. Adams, J. Am. Chem. Soc. 90 (1968) 3925.
[2] (a) K. Itoh, M. Kinoshita (Eds.), Molecular Magnetism New Magnetic Materials, Gordon & Breach, Inc./Kodansha, Amsterdam/Tokyo, 2000;
(b) P.M. Lahti (Ed.), Magnetic Properties of Organic Materials, Marcel Dekker, Inc., New York, 1999 (Chapter 9 and references therein);
(c) K. Sato, M. Yano, M. Furuichi, D. Shiomi, K. Abe, T. Takui, K. Itoh, A. Higuchi, K. Katuma, Y. Shirota, J. Am. Chem. Soc. 119 (1997) 6607;
(d) M. Yano, K. Sato, D. Shiomi, A. Ichimura, K. Abe, T. Takui, K. Itoh, Tetrahedron Lett. 37 (1996) 9207;
(e) K.R. Stickley, S.C. Blackstock, J. Am. Chem. Soc. 116 (1994) 11576;

(f) K.R. Stickley, S.C. Blackstock, Tetrahedron Lett. 36 (1995) 1585;
(g) K.R. Stickley, T.D. Selby, S.C. Blackstock, J. Org. Chem. 62 (1994) 448;
(h) T.D. Selby, S.C. Blackstock, J. Am. Chem. Soc. 62 (1997) 448;
(i) A. Ito, H. Ino, K. Tanaka, K. Kanemoto, T. Kato, J. Org. Chem. 67 (2002) 491;
(j) M. Yano, Y. Ishida, K. Aoyama, M. Tatsumi, K. Sato, D. Shiomi, A. Ichimura, T. Takui, Synth. Met. 137 (2003) 1275;
(k) M. Yano, Y. Ishida, M. Tatsumi, K. Sato, D. Shiomi, M. Oyama, T. Takui, J. Phys. Chem. Solids 65 (2004) 733;
(l) M. Yano, Y. Nakanishi, K. Matsushita, M. Tatsumi, M. Oyama, K. Sato, T. Takui, Polyhedron 24 (2005) 2116.

[3] (a) J. Bonvoisin, J.P. Launay, M.V. Auweraer, F.C.D. Schryver, J. Phys. Chem. 98 (1994) 5052;
(b) J. Bonvoisin, J.P. Launay, W. Verbouwe, M.V. Auweraer, F.C.D. Schryver, J. Phys. Chem. 100 (1996) 17079;
(c) C. Lambert, G. Nöll, J. Am. Chem. Soc. 121 (1999) 8434;
(d) C. Lambert, G. Nöll, Angew. Chem., Int. Ed. Engl. 37 (1998) 2107.

[4] M. Yano, K. Inoue, T. Motoyama, Y. Azuma, M. Tatsumi, O. Yamauchi, M. Oyama, K. Sato, T. Takui, Polyhedron 24 (2005) 2112.

[5] (a) F.A. Neugebauer, S. Bamberger, W.R. Groh, Chem. Ber. 108 (1975) 2406;
(b) W. Schmidt, E. Steckhan, Chem. Ber. 113 (1980) 577.

[6] (a) M. Oyama, T. Higuchi, S. Okazaki, J. Chem. Soc., Perkin Trans. 2 (2001) 1287;
(b) M. Oyama, J. Matsui, H. Park, Chem. Commun. (2002) 604.

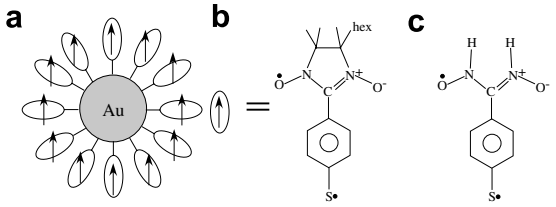


Fig. 1. The schematic diagrams of (a) SPN-hex@Au system, (b) structure of SPN-hex, and (c) the structure of organic radical molecule used for the model systems.

large cluster, it is important to elucidate the magnetic interaction between the organic stable radicals grafted on the same aspect of a cluster. Therefore, the stable nitroxide molecules grafted onto Au slab type cluster models (Au_{10} slab–nitroxide hybrid model systems) were investigated as it is difficult to investigate the large Au clusters, such as Au_{38}, Au_{55} and etc., due to the limit of the computer resources. Moreover, the electronic state of Au clusters could be modified by the surrounding environment, such as support materials. This is mainly due to the charge polarization effect. In order to investigate this effect, the background charges were induced instead of the support materials for Au cluster models.

The present theoretical study has been undertaken to investigate the magnetic interaction of Au slab–nitroxide hybrid model systems as a first step for understanding the magnetic interaction of radical molecules grafted on a same aspect of Au cluster. Hybrid density functional theory (HDFT) calculations have been carried out for Au slab–nitroxide hybrid model systems.

2. Calculation method and models

2.1. Calculation method

All the computations were performed by GAUSSIAN 03 program packages [12]. Unrestricted hybrid DFT (UB3LYP) calculation was used for the model systems computations using D95** basis set for C, N, O, and H and the LANL2DZ basis set for Au. The LS–HS energy gap of the system was calculated by the spin-polarized DFT expression.

In the case of organic radical molecules, the spin polarization and the spin delocalization of the π-electrons are the dominant factors to determine the spin alignment between the localized radical spins while the spin polarization of the conduction electrons are also the important factor for the spin alignment in the case of metal clusters. In order to investigate the magnetic interaction in the model system, the effective exchange integral of Heisenberg model was calculated using Noodleman–Yamguchi equation [13,14]. Natural orbital analysis was also carried to examine these features for the investigated model systems.

2.2. Calculated models

The schematic illustrations of SPN-hex and SPN-hex grafted Au cluster are shown in Fig. 1(a) and (b). This illustration shows that many organic radicals are densely grafted on a surface of a large cluster. Therefore, it is important to elucidate the magnetic interaction between the organic stable radicals grafted on the same aspect of a cluster. The model systems that the model nitroxide molecules (Fig. 1(c)) were grafted onto Au_{10} slab type cluster as shown in Fig. 2(a) and (b) were investigated as it is difficult

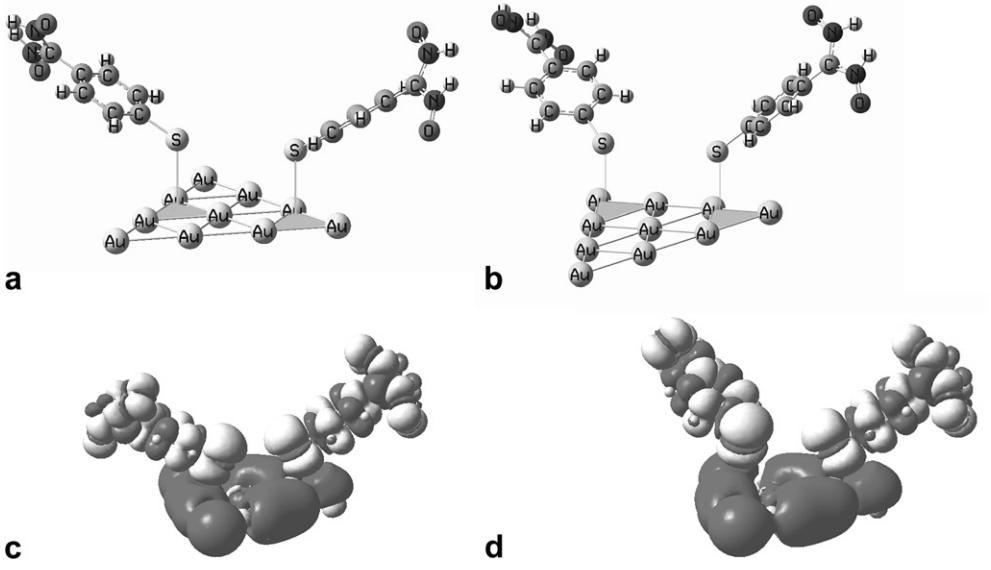


Fig. 2. The illustrations of the Au_{10}–organic spin molecule model system: (a) type I, (b) type II, (c) spin density of type I (triplet state) and (d) spin density of type II (triplet state).

to investigate the large Au clusters, such as Au_{38}, Au_{55} and etc., due to the limit of the computer resources. The model systems depicted in Fig. 2(a) and (b) were named type I and type II, respectively. The geometry of the organic spin molecule was based on the geometry of NPNN molecule.

3. Results and discussion

3.1. Au_{10} model system

As shown in Table 1, it was found that the triplet state was the ground state in Au_{10} slab cluster, while the energy gap between the triplet and singlet states is very small. Mulliken spin densities of the perimeter Au atoms and the center Au atom in Au_{10} slab cluster were 0.23 (average) and −0.06 and the Mulliken charge densities of the center atom, the side atoms and the vertex atoms were 0.42, 0.04 (average) and −0.22 (average), respectively. Therefore, it shows that the perimeter Au atoms have the homogeneous spin densities and the vertex Au atoms are only negatively charged in this cluster. The energy levels of HOMOs in α and β orbitals and LUMOs in α and β orbitals of this cluster were −0.23053, −0.22984, −0.12892 and −0.19310, respectively. As the small energy gaps are existed in this cluster, Au_{10} slab cluster has a semiconducting feature.

From the calculation results shown in Table 1, it was found that the triplet state was the ground state in these systems. The triplet states of spin densities of these two models shown in Fig. 2(a) and (b) were also depicted in Fig. 2(c) and (d), respectively. The results showed that the parallel spin moments were presented on the S atoms and nitroxide groups in the organic radical fragments and the magnetic interaction between two organic radical molecules were ferromagnetic in these model systems. Natural orbital analysis for the triplet states of the type I model system was carried out in order to understand the electronic state of this model system. The schematic diagrams of the two natural orbitals whose occupation numbers are 1.0 are shown in Fig. 3. These natural orbitals are localized onto the nitronyl nitroxide group. Therefore, they are the radical orbitals (SOMOs) of the organic radical molecules. From these results it was found that the ferromagnetic interaction between the stable organic radicals through Au slab cluster could be possible.

Table 1
Total energies and total spin angular momenta of the Au_{10} model systems

Model	Spin state	Energy[a]/h	S^2	ΔE[b]/h	J/cm^{-1}
Au_{10}	singlet	−1354.92628			
	triplet	−1354.92854		−0.00226	
Type I	singlet	−3211.67650	2.984		
	quintet	−3211.68371	6.634		
	triplet	−3211.68390	3.877	−0.00740	1820
Type II	singlet	−3211.66823	1.630		
	quintet	−3211.67879	7.036		
	triplet	−3211.68102	4.068	−0.01279	1151

[a] UB3LYP/LANL2DZ for Au and D95** for the others is used.
[b] $\Delta E = E(\text{triplet}) - E(\text{singlet})$.

3.2. Spin crossover of Au_{10} model system

The present work showed that the ground states of both of the Au_{10} model systems were triplet. It is well known that the electronic state of Au cluster deposited on a support was polarized by the hetero-junction with a support in Au catalysts [15]. Moreover, it might be possible to

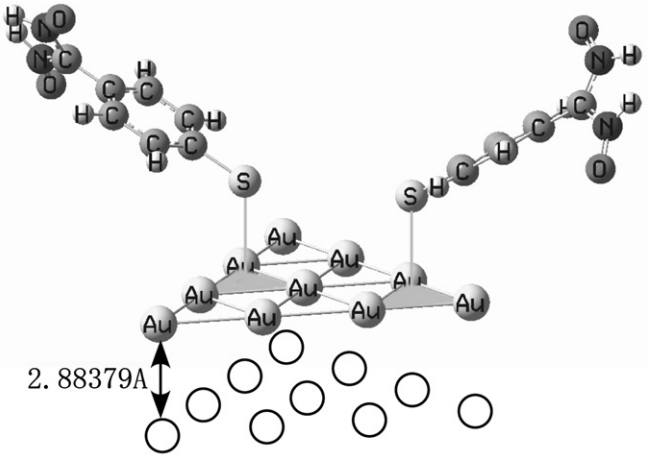


Fig. 4. The schematic diagram of Au_{10} model system with the point charges. Circles indicate the positions of the point charges.

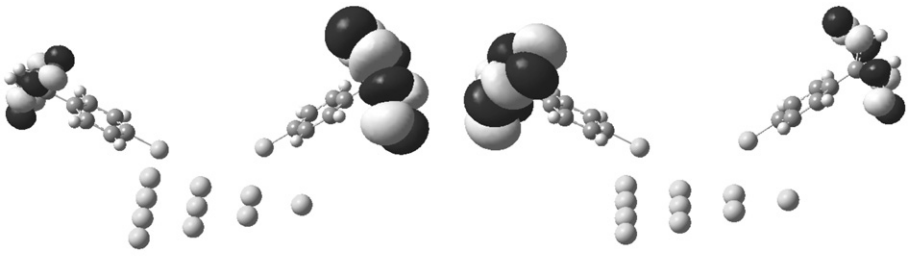


Fig. 3. (a) and (b) The singly occupied natural orbitals of the type I model system.

Table 2
Total energies and total spin angular momenta for Au_{10} model hybrid system (type I) with the background charge

Charge	Spin state	Energy[a]/h	S^{**2}	ΔE[b]/h	J/cm^{-1}
0.0	singlet	−3211.67650	2.984		
	quintet	−3211.68371	6.634		
	triplet	−3211.68390	3.877	−0.00740	1820
0.1	singlet	−3211.65548	2.654		
	quintet	−3211.65744	6.591		
	triplet	−3211.65610	3.840	−0.00620	940
0.2	singlet	−3211.55596	2.165		
	quintet	−3211.55357	6.591		
	triplet	−3211.55486	2.980	0.00110	−296

[a] UB3LYP/LANL2DZ for Au and D95** for the others is used.
[b] $\Delta E = E(\text{triplet}) - E(\text{singlet})$.

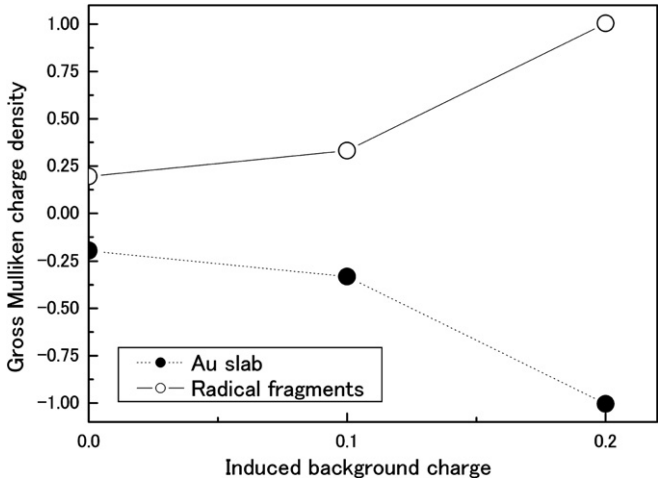


Fig. 5. Variation of gross Mulliken charges in Au_{10} slab and radical fragments for different point charges.

modulate the electronic state of Au cluster by induced external field. As an addition of artificial point charges to the theoretical calculation model also makes such polarizations in the model systems, the model systems with point charges instead of a support are examined in order to investigate the polarization effect for the magnetic interactions in the model systems.

The spin crossover in Au_{10} model system (type I) is examined using the point charges in order to consider the polarization of the Au clusters. The positive point charges ranging from 0.1 to 0.2 were placed under the Au_{10} slab as shown in Fig. 4. The calculation results are summarized in Table 2. The results showed that quintet state was the ground sate in the case of the model with the point charge (0.1) and singlet state was the ground sate in the case of the model with the point charge (0.2). In Fig. 5, the gross Mulliken charges of Au_{10} slab and organic radical fragments were depicted. This shows that the induction of point charges boosts the charge transfer from organic radical fragments to Au_{10} slab. These results suggest that the modulation of Au_{10} slab by the point charge greatly affects the magnetic interaction between the organic radical molecules grafted on Au cluster.

3.3. Rational design of molecular magnet

From these results, it was found that the point charge introduction into this model system could modulate the magnetic interaction of the model system. Therefore, it could be presumed that the hetero-junction with the support materials and Au–organic spin molecule system and/or the induction of the electric field to Au–organic spin molecule system might be practical for the modulation of the magnetic interaction in the real system.

4. Conclusions

From the calculation results, it was found that the Au_{10} model systems have the ferromagnetic interaction between the organic radical molecules grafted on Au slab and the magnetic interactions of them were dramatically changed depending on the addition of the point charges.

Acknowledgement

This work has been supported by a Grant-in-Aid for Scientific Research on Priority Areas from the Ministry of Education, Culture, Sports, Science and Technology, Japan.

References

[1] M. Haruta, N. Yamanaka, T. Kobayashi, S. Iijima, J. Catal. 115 (1989) 301.
[2] M. Okumura, K. Tanaka, A. Ueda, M. Haruta, Solid State Ionics 95 (1997) 143.
[3] M. Okumura, S. Tsubota, M. Haruta, Catal. Lett. 51 (1998) 53.
[4] M. Okumura, S. Tsubota, M. Iwamoto, M. Haruta, Chem. Lett. 315 (1998).
[5] M. Okumura, M. Haruta, Chem. Lett. 396 (2000).
[6] M. Okumura, S. Tsubota, M. Haruta, J. Mol. Catal. A-Chem. 199 (2003) 73.
[7] M. Okumura, Y. Kitagawa, M. Haruta, K. Yamaguchi, Chem. Phys. Lett. 346 (2001) 163.
[8] Y. Maeda, M. Okumura, S. Tsubota, M. Kohyama, M. Haruta, Appl. Surf. Sci. 222 (2004) 409.
[9] G. Harada, H. Sakurai, M. Matsushita, A. Izuoka, T. Sugawara, Chem. Lett. (2002) 1030.
[10] M. Okumura, Y. Kitagawa, T. Kawakami, T. Taniguchi, K. Yamaguchi, Synth. Metals 154 (2005) 313.
[11] M. Okumura, Y. Kitagawa, T. Kawakami, T. Taniguchi, K. Yamaguchi, Polyhedron 24 (2005) 2330.
[12] M.J. Frisch, et al., Gaussian Inc., Pittsburgh, PA, 1998.
[13] K. Yamaguchi, Y. Takahara, T. Fueno, in: V.H. Smith, et al. (Eds.), Applied Quantum Chem. (Eds.), D. Reidel Pub. Com., Lancaster, 1986, p. 155.
[14] S. Yamanaka, T. Kawakami, H. Nagao, K. Yamaguchi, Chem. Phys. Lett. 231 (1994) 25.
[15] Y. Maeda, M. Okumura, S. Tsubota, M. Kohyama, M. Haruta, Appl. Surf. Sci. 222 (2004) 409.

and its incorporation into a Mn cluster does not complicate the magnetic analysis. The investigated reactions have resulted in the isolation of a number of Mn–Ce compounds that can be divided into three general types on the basis of the Mn and Ce oxidation states, Mn^{IV}–Ce^{IV}, Mn^{III}–Ce^{IV}, and Mn^{III}–$Ce^{III/IV}$ [8,9]. These results will be described in this paper.

2. Mn^{IV}–Ce^{IV} compounds

Six Mn^{IV}–Ce^{IV}compounds have been prepared and crystallographically characterized [8]. These were the first Mn–Ce compounds to be discovered, and they possess three different types of aesthetically pleasing structural motifs. They were all prepared by addition of Ce^{IV} to a solution of a Mn^{II} salt in aqueous acetic acid. This reaction system was a modification of the comproportionation reaction between $[Mn(O_2CMe)_2]\cdot 4H_2O$ and $KMnO_4$ (in a Mn^{II}:Mn^{VII} ratio giving an average of $Mn^{3.33+}$) in concentrated aqueous acetic acid that is the well known procedure for the preparation of $[Mn_{12}O_{12}(O_2CMe)_{16}(H_2O)_4]$ [10]. Our modification involved substituting $(NH_4)_2[Ce(NO_3)_6]$ as the oxidant in place of $KMnO_4$, hoping for mixed-metal products, and this was indeed what was observed. In addition, we also explored a range of Mn:Ce ratios, the use of other Mn^{II} reagents, and the effect of the presence of chelate groups. Selected results will be presented below.

The reaction of $Mn(NO_3)_2\cdot xH_2O$ and bpy with $(NH_4)_2Ce(NO_3)_6$ in a 1:1:2 molar ratio in 25% aqueous acetic acid gave $[Mn_2CeO_3(O_2CMe)(NO_3)_4(H_2O)_2(bpy)_2](NO_3)$ (**1**) in 40% yield. The structure of the cation of **1** (Fig. 1) comprises a familiar $[Mn^{IV}_2(\mu\text{-}O)_2(\mu\text{-}O_2CMe)]^{3+}$ unit linked to a Ce^{IV} ion through a linear oxide bridge.

In contrast, the reaction of $[Mn(O_2CMe)_2]\cdot 4H_2O$ and $(NH_4)_2[Ce(NO_3)_6]$ in a 2:3 molar ratio in concentrated (50%) aqueous acetic acid gave $[Mn_6CeO_9(O_2CMe)_9(NO_3)(H_2O)_2]$ (**2**). When this was repeated but with a 0.5 M solution of $Ce(ClO_4)_4$ in aqueous $HClO_4$ as the oxidizing agent in place of $(NH_4)_2[Ce(NO_3)_6]$, and with a few drops of methanol to help solubility, the product was now $[Mn_6CeO_9(O_2CMe)_9(H_2O)_2(MeOH)](ClO_4)$ (**3**), which is structurally very similar to **2**.

The structures of **2** (Fig. 2) and **3** consist of an unprecedented Mn^{IV}_6 wheel. Its edges are bridged alternately by $(\mu_2\text{-}O)(\mu_3\text{-}O)(\mu\text{-}O_2CMe)$ and $(\mu_3\text{-}O)(\mu\text{-}O_2CMe)_2$ ligand sets. The six $\mu_3\text{-}O^{2-}$ ions are those bound to, and thus holding in place, the central Ce^{IV} ion, which lies slightly out of the almost planar Mn_6 ring. Apart from being the first Mn^{IV}_6 wheels, complexes **2** and **3** are also the first wholly Mn^{IV} complexes with only oxide and carboxylate ligands, and their $[M_7O_9]$ core is of a structural type never seen before for any metal.

Further mixed-metal Mn–Ce products were obtained from reactions performed in the presence of 2-hydroxy-6-methylpyridine (mhpH). The addition of potentially chelating mhpH was based on the observation that it had been successfully employed by others for the synthesis of mixed metal 3d-4f complexes [11]. Indeed, the reaction of $Mn(O_2CMe)_2\cdot 4H_2O$, $(NH_4)_2[Ce(NO_3)_6]$ and mhpH in a 2:3; ~4.4 ratio in 30% aqueous acetic acid gave $[Mn_2Ce_3O_6(O_2CMe)_6(NO_3)_2(mhpH)_4]$ (**4**) (Fig. 3).

The $[Ce_3Mn_2O_6]^{8+}$ core consists of a Ce^{IV}_3 isosceles triangle, each edge of which is bridged by two $\mu_3\text{-}O^{2-}$ ions that also bridge to the two Mn^{IV} ions lying one each above and below the Ce^{IV}_3 plane forming an M_5 trigonal bipyramid. Peripheral ligation is completed by bridging acetate, chelating nitrate and terminal mhpH groups, the latter

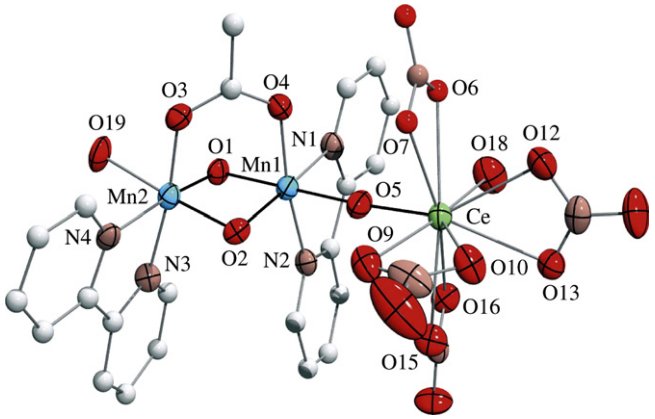


Fig. 1. Labelled ORTEP plot (at the 50% probability level) of the anion of **1**. Color scheme: Mn (blue), Ce (green), O (red), N (brown), C (grey). (For interpretation of the references to colour in this figure legend, the reader is referred to the web version of this article.)

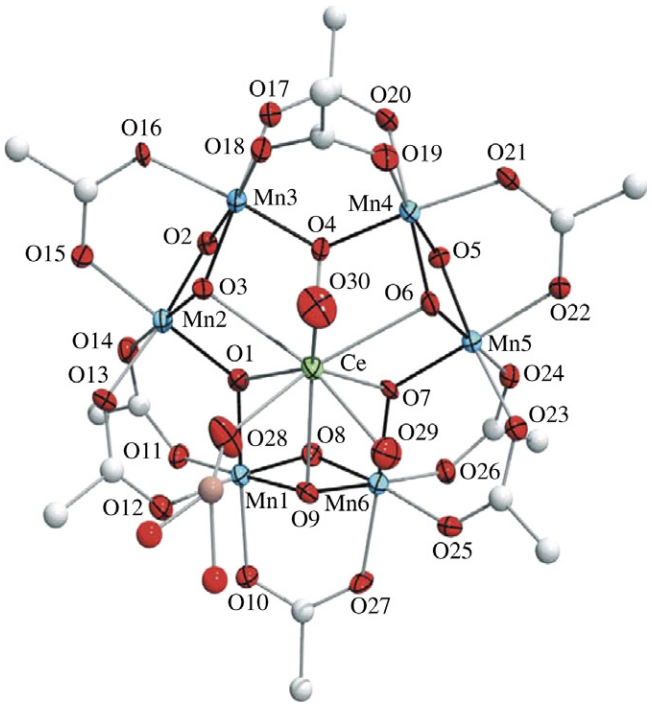


Fig. 2. Labelled ORTEP plot (at the 50% probability level) of **2**. Color scheme: Mn (blue), Ce (green), O (red), N (brown), C (grey). (For interpretation of the references to colour in this figure legend, the reader is referred to the web version of this article.)

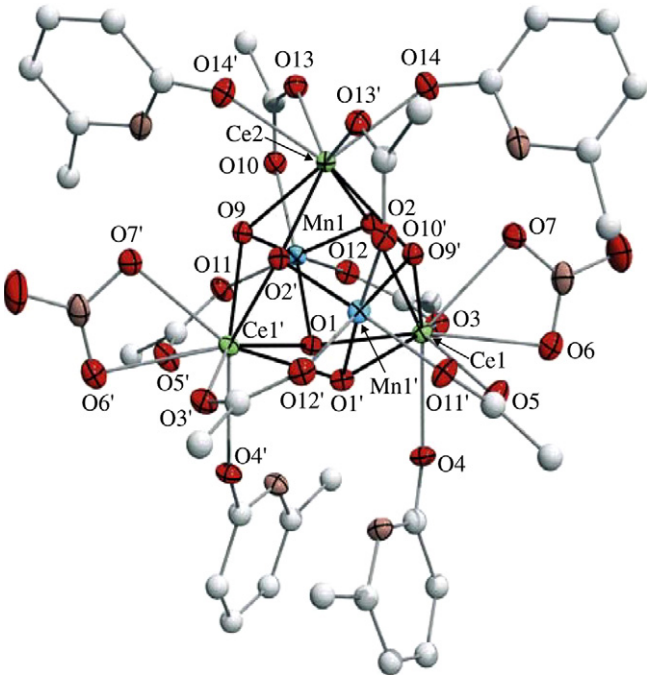


Fig. 3. Labelled ORTEP plot (at the 50% probability level) of **4**. Color scheme: Mn (blue), Ce (green), O (red), N (brown), C (grey). (For interpretation of the references to colour in this figure legend, the reader is referred to the web version of this article.)

protonated at their N atoms and binding only through their O atoms (O4 and O14). The Ce_3Mn_2 trigonal bipyramidal topology has been observed in mixed 4f/3d chemistry only once before, in a $Nd^{III}_3Cr^{III}_2$ complex that contains hydroxide bridges, rather than oxide ones as in **4** [12].

We found it interesting that the mhpH stayed protonated and bound in a monodentate fashion (*vide infra*), and the reaction was thus repeated with a similar organic molecule, 2-pyrrolidinone (pyroH) [13], instead of mhpH; clean product was obtained using a slightly more concentrated (37%) aqueous acetic solution, and it was identified as $[Mn_2Ce_3O_6(O_2CMe)_6(NO_3)_2(pyroH)_2(H_2O)_3]$ (**5**). Compound **5** is very similar to **4** in that it contains the same $[Mn_2Ce_3(\mu_3\text{-}O)_6]^{8+}$ core. The main differences between the two compounds are: (i) the pyroH vs mhpH terminal ligands, and (ii) all three Ce ions in **5** are nine-coordinate, whereas only two of those in **4** are nine-coordinate, the other being eight-coordinate.

Finally, the procedure was repeated but with an excess of pyridine instead of mhpH or pyroH, and the same Mn_2Ce_3 core was again obtained, but this time within the polymer $\{\{(pyrH)_3[Mn_2Ce_3O_6(O_2CMe)_{7.5}(NO_3)_3]\cdot(HO_2CMe)_{0.5}\cdot(H_2O)_2\}_2(NO_3)\}_n$ (**6**). The structure can be alternatively described as a dimer of $[Mn_2Ce_3(\mu_3\text{-}O)_6]^{8+}$ units linked by two acetate bridging ligands, which is connected to the other dimer units by an acetate group to form a polymer of dimers.

Solid-state, magnetic susceptibility measurements were carried out on vacuum-dried, microcrystalline samples of complexes **1**–**6** in the temperature range 5.0–300 K in a 0.5 T field. All paramagnetism of the Mn^{IV}–Ce^{IV} compounds is associated with the Mn^{IV} ions, since Ce^{IV} is diamagnetic (f^0). The $\chi_M T$ values at 300 K of all compounds decreases rapidly with decreasing temperature reaching values close to zero at 5 K. This behavior suggests the existence of antiferromagnetic interactions resulting in an $S_T = 0$ ground state.

The various products described span a wide range of Mn:Ce ratios, from Mn_2Ce_3 in **4**–**6**, Mn_2Ce in **1**, to Mn_6Ce in **2** and **3**. Other combinations are no doubt also possible as this work is extended.

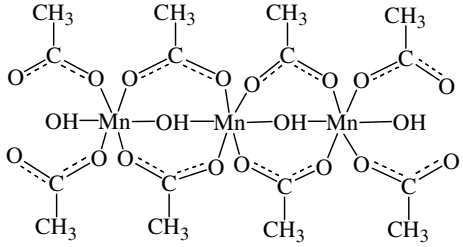
3. Mn^{III}–Ce^{IV} compounds

Four enneanuclear $Mn^{III}_8Ce^{IV}$ clusters $[Mn_8CeO_8(O_2CMe)_{12}(H_2O)_4]$ (**7**), $[Mn_8CeO_8(O_2CMe)_{12}(py)_4]$ (**8**), $[Mn_8CeO_8(O_2CPh)_{12}(MeCN)_4]$ $[Mn_8CeO_8(O_2CPh)_{12}(dioxane)_4]$ (**9**) and $[Mn_8CeO_8(O_2CCHPh_2)_{12}(H_2O)_4]$ (**10**) have been isolated.

Compound **7** was the first Mn^{III}–Ce^{IV} cluster to be isolated. It was originally obtained by accident in low yield from a solution of **2** in $MeCN/Et_2O$ that had stood for a long time. With the identity and properties of **7** established, it was clear that a rational synthesis was crucial and this was developed using an oxophilic Ce^{4+} ion as the template around which wrapped the linear Mn^{III} polymer $\{[Mn^{III}(OH)(O_2CMe)_2]\cdot(MeCO_2H)\cdot(H_2O)\}_n$ (**11**) as Ce^{4+}–OH^- contacts developed. With a Ce:Mn ratio of 1:8, this reaction caused all the very insoluble polymer **11** (Scheme 1) to dissolve as the reaction proceeded to yield **7**, which was obtained in 55% isolated yield.

The structure of **7** (Fig. 4) consists of a non-planar, saddle-like $[Mn_8O_8]^{8+}$ loop attached to the central Ce^{4+} via the O^{2-} ions (Fig. 5). Eight μ- and four μ_3-acetate groups and four terminal water molecules provide the peripheral ligation. The $[Mn_8O_8]$ loop is the same as that found in $[Mn_{12}O_{12}(O_2CMe)_{16}(H_2O)_4]$ (**12**), where

there is a central $[Mn_4O_4]$ cubane instead of the smaller Ce atom. The eight Ce–O^{2-}bonds are undoubtedly crucial to the formation of **7**, and cause a greater folding of the $[Mn_8O_8]$ ring than in **12**. Another important difference between **12** and **7** is that the Mn^{III} Jahn–Teller (JT) elongation axes of **7** divide into groups that are nearly perpendicular to each other, in contrast to the situation in **12**. A close examination of the packing of **7** revealed the existence of



Scheme 1. A representation of the linear Mn^{III} polymer **11** employed as starting material for the rational synthesis of **7**.

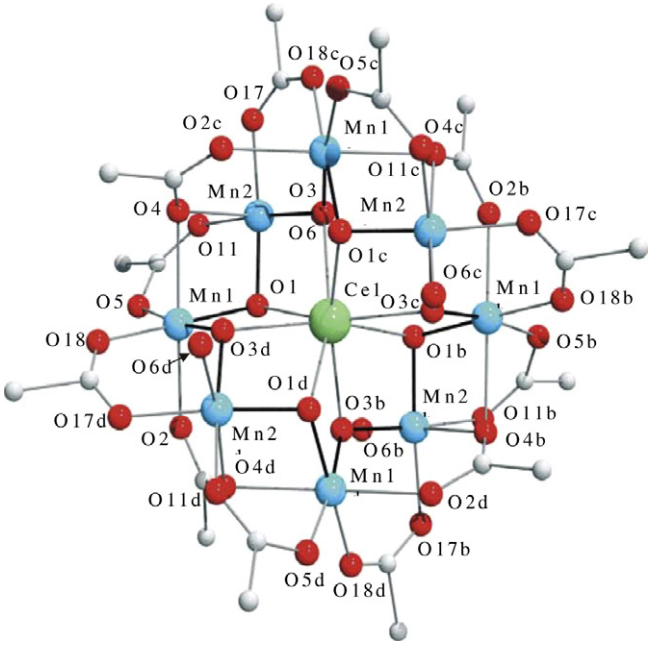


Fig. 4. Labeled PovRay plot of **7**. Color scheme: Mn (blue), Ce (green), O (red), C (grey). (For interpretation of the references to colour in this figure legend, the reader is referred to the web version of this article.)

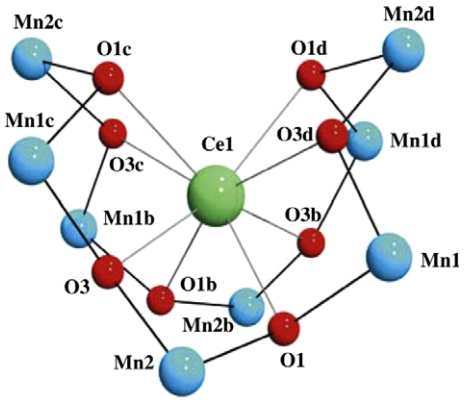


Fig. 5. Labeled PovRay plot of the $[CeMn_8O_8]^{12+}$ core of **7** emphasizing the saddle-like folding of the $[Mn_8O_8]$ ring. Color scheme: Mn (blue), Ce (green), O (red). (For interpretation of the references to colour in this figure legend, the reader is referred to the web version of this article.)

intermolecular hydrogen-bonding interactions involving the Mn-bound as well as the lattice H_2O molecules.

Solid-state dc magnetic susceptibility studies on **7** showed that the $\chi_M T$ value at 300 K increases rapidly with decreasing temperature suggesting the existence of ferromagnetic interactions. This was confirmed by variable field magnetization studies where the fit of the data gave $S = 16$, $D = -0.10(1)\ cm^{-1}$, and $g = 1.98(1)$. An $S = 16$ ground state and a negative D value for **7** suggested that it might have a sufficient barrier to magnetization relaxation to be a single-molecule magnet. The existence of hysteresis loops below ~0.6 K with coercivities that increase with decreasing temperature confirmed that **7** is a new SMM. The hysteresis loops do not show the steps that are characteristic of quantum tunneling of magnetization, probably due to the existence of intermolecular interactions mediated by the hydrogen-bonds and dipolar interactions. The low temperature at which **7** is a SMM is clearly due to the small D value, which is consistent with some of the Mn^{III} JT axes being nearly perpendicular. We thus, also prepared Mn_8Ce derivatives with bulky carboxylates in an attempt to minimize the intermolecular interactions, and which might also lead to a flattening of the Mn_8O_8 loop to a more planar configuration thereby increasing the D value. We initially performed reactions between $(NH_4)_2Ce(NO_3)_6$ and preformed Mn^{III}-containing carboxylate clusters such as $[Mn_3O(O_2CMe)_6(py)_3]$ ($2Mn^{III}$, $1Mn^{II}$) (**13**) and $(NBu^n_4)[Mn_4O_2(O_2CPh)_9(H_2O)]$ (**14**) ($4Mn^{III}$), common stepping-stones to higher nuclearity complexes [3,7e,14].

The reaction of **13** with Ce^{4+} in MeCN in an approximately 3:1 ratio gave $[Mn_8CeO_8(O_2CMe)_{12}(py)_4]$ (**8**) in 60% yield. This is structurally similar to **7**, except that the four terminal water molecules have been replaced by pyridine (py) molecules, thereby eliminating intermolecular interactions via hydrogen-bonding at these positions. Similarly, reaction of **14** with Ce^{IV} in a 1:2 ratio in MeCN with subsequent employment of dioxane to obtain crystals gave $\{[Mn_8CeO_8(O_2CPh)_{12}(MeCN)_4]\,[Mn_8CeO_8(O_2CPh)_{12}(dioxane)_4]\}$ (**9**) in 45% yield. Complex **9** is again structurally very similar to **7** (and **8**), with the unit cell containing two separate Mn_8Ce complexes with either MeCN or dioxane terminal ligands.

A further derivative of **7** possessing an even bulkier carboxylate group was prepared using diphenylacetic acid (Ph_2CHCO_2H) in a carboxylate substitution reaction with **7**; such ligand substitution methods are a common way of derivatizing Mn carboxylate clusters [1,3c,4a,5a]. Hence, complex **7** was treated with an excess (20 equiv.) of diphenylacetic acid and the free acetic acid removed under vacuum as its toluene azeotrope. This successfully gave $[Mn_8CeO_8(O_2CCHPh_2)_{12}(H_2O)_4]$ (**10**) in 60% isolated yield.

The magnetic properties of compounds **8** and **10** were investigated by both dc and ac methods. These studies revealed that the small structural perturbations resulting from the modifications to the nature of the carboxylate ligands and the water vs pyridine terminal ligation significantly affected the exchange interactions within the Mn_8Ce core, these no longer being all ferromagnetic as in **7**. Thus, the ground states spin values of **8** and **10** are $S = 5$ and 6, respectively, with the D values of both compounds being $\sim -0.3\ cm^{-1}$. Nevertheless, ac magnetic susceptibility studies of **8** and **10** revealed the presence of out-of-phase signals at low temperatures (close to 2 K) suggesting SMM behavior. Single-crystal hysteresis studies are in progress.

4. Mn^{III}–$Ce^{III/IV}$ compounds

Addition of $(NBu^n_4)_2Ce(NO_3)_6$ to an MeCN solution of **14** followed by filtration and layering of the filtrate with

MeOH gave the unusual complex $[Mn_{10}Ce_4O_{10}(OMe)_6(O_2CPh)_{16}(NO_3)_2(MeOH)_2(H_2O)_2]\cdot 4H_2O$ (**15**) (Fig. 6 top).

This is the only member of this family of Mn–Ce compounds with mixed valency in its Ce component. In fact, **15** is the first 3d/4f cluster of any type with mixed-valency in the lanthanide component. The $[Mn_{10}Ce_4O_{10}(OMe)_6]^{18+}$ core of **15** (Fig. 6, bottom) consists of a central $[Mn^{III}_4Ce^{IV}_2O_6(OMe)_2]$ unit attached at either end to a $[Mn^{III}_3Ce^{III}O_2(OMe)_2]$ distorted-cubane unit, giving a tubular structure.

The magnetic properties of **15** were studied by employing both dc and ac methods. The dc magnetic studies revealed the existence of antiferromagnetic interactions within the structure of **15** resulting in an $S = 4$ ground state. Out-of-phase ac magnetic susceptibility studies showed the existence of a signal at low temperatures suggesting SMM behavior. However, single-crystal micro-SQUID measurements revealed only very little hysteresis, and whose coercivity did not increase with either decreasing T or increasing scan rate. This is not the behavior expected for a SMM, and the small coercivity is probably mainly due to a phonon bottleneck rather than a real barrier to magnetization relaxation. This result thus represents an important caveat against taking such out-of-phase ac magnetic susceptibility signals in molecular species as proof of the presence of a SMM.

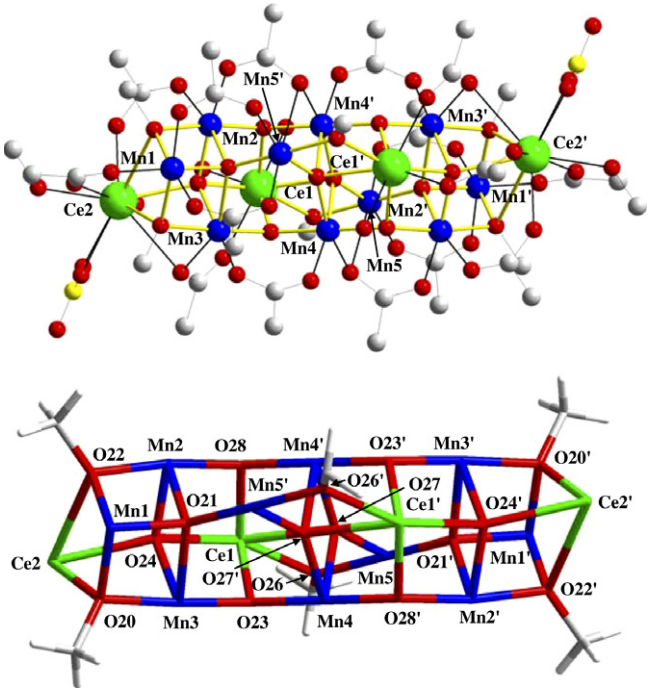


Fig. 6. (top) The structure of centrosymmetric **15** with the benzoate rings removed for clarity, except for the *ipso* C atom. (bottom) The tube-like core of **15**, emphasizing the position of the bridging MeO^- groups. Color scheme: Mn (blue), Ce (green), O (red), C (grey). (For interpretation of the references to colour in this figure legend, the reader is referred to the web version of this article.)

5. Conclusions

We have described a powerful synthetic method for the preparation of new heterometallic Mn–Ce clusters. This method involves addition of Ce^{IV} to various Mn sources and has so far resulted in the isolation of eleven new compounds. These compounds have been divided in three categories (Mn^{IV}–Ce^{IV}, Mn^{III}–Ce^{IV} and Mn^{III}–$Ce^{III/IV}$) on the basis of the oxidation states of the constituent metal ions. All the compounds have aesthetically pleasing structures and some of them interesting magnetic properties. Further exploration of this area is expected to result in the isolation of further Mn–Ce species. In addition, we have recently shown that the method can also be extended to actinides, and have reported the preparation of the first Mn/Th complex [15]. Further extension of this strategy is currently under exploration.

Acknowledgement

This work was supported by the National Science Foundation.

References

[1] (a) R. Sessoli, H.-L. Tsai, A.R. Schake, S. Wang, J.B. Vincent, K. Folting, D. Gatteschi, G. Christou, D.N. Hendrickson, J. Am. Chem. Soc. 115 (1993) 1804;
(b) R. Sessoli, D. Gatteschi, A. Ganeschi, M.A. Novak, Nature 365 (1993) 141.
[2] S.M.J. Aubin, M.W. Wemple, D.M. Adams, H.-L. Tsai, G. Christou, D.N. Hendrickson, J. Am. Chem. Soc. 118 (1996) 7746.
[3] (a) G. Christou, D. Gatteschi, D.N. Hendrickson, R. Sessoli, MRS Bull. 25 (2000) 66;
(b) D. Gatteschi, R. Sessoli, Angew. Chem. Int. Ed. 42 (2003) 268;
(c) G. Christou, Polyhedron 24 (2005) 2065;
(d) E.K. Brechin, Chem. Commun. (2005) 5141.
[4] (a) H.J. Eppley, H.-L. Tsai, N. de Vries, K. Folting, G. Christou, D.N. Hendrickson, J. Am. Chem. Soc. 117 (1995) 301;
(b) M. Soler, S.K. Chandra, D. Ruiz, E.R. Davidson, D.N. Hendrickson, G. Christou, Chem. Commun. (2000) 2417;
(c) M. Soler, W. Wernsdorfer, K.A. Abboud, J.C. Huffman, E.R. Davidson, D.N. Hendrickson, G. Christou, J. Am. Chem. Soc. 125 (2003) 3576;
(d) S.M.J. Aubin, Z. Sun, L. Pardi, J. Krzystek, K. Folting, L.-C. Brunel, A.L. Rheingold, G. Christou, D.N. Hendrickson, Inorg. Chem. 38 (1999) 5329.
[5] (a) M. Soler, P. Artus, K. Folting, J.C. Huffman, D.N. Hendrickson, G. Christou, Inorg. Chem. 40 (2001) 4902;
(b) P. Artus, C. Boskovic, J. Yoo, W.E. Streib, L.-C. Brunel, D.N. Hendrickson, G. Christou, Inorg. Chem. 40 (2001) 4199;
(c) C. Boskovic, M. Pink, J.C. Huffman, D.N. Hendrickson, G. Christou, J. Am. Chem. Soc. 123 (2001) 9914.
[6] (a) S.M.J. Aubin, Z. Sun, H.J. Eppley, E.M. Rumberger, I.A. Guzei, K. Folting, P.K. Gantzel, A.L. Rheingold, G. Christou, D.N. Hendrickson, Inorg. Chem. 40 (2001) 2127;
(b) M. Soler, W. Wernsdorfer, Z. Sun, J.C. Huffman, D.N. Hendrickson, G. Christou, Chem. Commun. (2003) 2672;
(c) N.E. Chakov, S.C. Lee, A.G. Harter, P.L. Kuhns, A.P. Reyes, S.O. Hill, N.S. Dalal, W. Wernsdorfer, K.A. Abboud, G. Christou, J. Am. Chem. Soc. 128 (2006) 6975.

[7] (a) A.J. Tasiopoulos, A. Vinslava, W. Wernsdorfer, K.A. Abboud, G. Christou, Angew. Chem. Int. Ed. 43 (2004) 2117;
(b) A.J. Tasiopoulos, W. Wernsdorfer, K.A. Abboud, G. Christou, Angew. Chem. Int. Ed. 43 (2004) 6338;
(c) D.J. Price, S.R. Batten, B. Moubaraki, K.S. Murray, Chem. Commun. (2002) 762;
(d) M. Soler, W. Wernsdorfer, K. Folting, M. Pink, G. Christou, J. Am. Chem. Soc. 126 (2004) 2156;
(e) E.K. Brechin, M. Soler, G. Christou, M. Helliwell, S.J. Teat, W. Wernsdorfer, Chem. Commun. (2003) 1276;
(f) R.T.W. Scott, S. Parsons, M. Murugesu, W. Wernsdorfer, G. Christou, E.K. Brechin, Angew. Chem. Int. Ed. 44 (2005) 6540;
(g) C.J. Milios, C.P. Raptopoulou, A. Terzis, F. Lloret, R. Vicente, S.P. Perlepes, A. Escuer, Angew. Chem. Int. Ed. 43 (2004) 210;
(h) C.J. Milios, T.C. Stamatatos, S.P. Perlepes, Polyhedron 25 (2006) 134;
(i) T.C. Stamatatos, D. Foguet-Albiol, C.C. Stoumpos, C.P. Raptopoulou, A. Terzis, W. Wernsdorfer, S.P. Perlepes, G. Christou, J. Am. Chem. Soc. 127 (2005) 15380;
(j) S. Maheswaran, G. Chastanet, S.J. Teat, T. Mallah, R. Sessoli, W. Wernsdorfer, R.E.P. Winpenny, Angew. Chem. Int. Ed. 44 (2005) 5044;
(k) A.M. Ako, I.J. Hewitt, V. Mereacre, R. Clérac, W. Wernsdorfer, Christopher E. Anson, A.K. Powell, Angew. Chem. Int. Ed. 45 (2006) 4926.

[8] A.J. Tasiopoulos, T.A. O'Brien, K.A. Abboud, G. Christou Angew, Chem. Int. Ed. 43 (2004) 345.

[9] A.J. Tasiopoulos, W. Wernsdorfer, B. Moulton, M.J. Zaworotko, G. Christou, J. Am. Chem. Soc. 125 (2003) 15274.

[10] T. Lis, Acta Crystallogr., Sect. B 36 (1980) 2042.

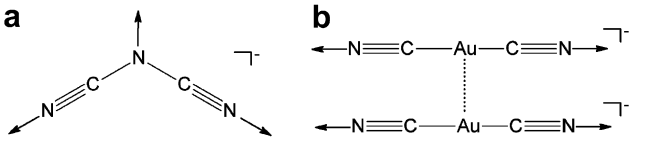
[11] R.E.P. Winpenny, Chem. Soc. Rev. 27 (1998) 447.

[12] N. Sakagami, M. Tsunekawa, T. Konno, K. Okamoto, Chem. Lett. (1997) 575.

[13] (a) The ligand Hpyro has also been successfully employed in the past for the synthesis of mixed metal 3d–4f complexes [13b];
(b) X.-R. Sun, Z.-D. Chen, F. Yan, S. Gao, K.-K. Cheung, C.M. Che, X.-X.J. Zhang, J. Cluster Sci. 13 (2002) 103.

[14] M. Murugesu, A. Mishra, W. Wernsdorfer, K.A. Abboud, G. Christou, Polyhedron 25 (2006) 613.

[15] A. Mishra, K.A. Abboud, G. Christou, Inorg. Chem. 45 (2006) 2364.



Scheme 1.

physical (e.g. shape) and chemical (e.g. hydrogen-bonding) properties to influence or ideally, to template structures has been a subject of considerable interest [19–21]. For example, counterions that contain phenyl-groups often assemble using ''phenyl embraces'' of π–π stacking interactions that influence the accompanying coordination polymer geometry [22]. In anionic metal oxalate networks the choice of cation influences the formation of 2-D (6, 3) sheets or 3-D chiral (10, 3) networks [23,24].

The structural effect of such cations in metal dicyanamide (dca) polymers of the form [cation]{M(dca)$_3$} has been particularly well-studied, yielding a wide range of different structural motifs as a function of the size and shape of the cations [20,25–28]. For example, increasing the size and π–π stacking ability of the cations in 3-D systems such as [EtPh$_3$P]{Ni(dca)$_3$} to larger ones such as $[Ph_4P]^+$ induces a reduction in structural dimensionality as the 3-D system cannot flex to accommodate the cation bulk [27,28]. The dca anion is a divergent, bent bridging unit that can also bind metals via the central nitrogen donor (Scheme 1a); the five-atom bridge is not linear but subtends *c.a.* 120–125° angles through the central nitrogen and M–M distances range from 7 to 8 Å when only the ends are bound ($\mu_{1,5}$-binding) [29]. In comparison, the cyanometallate $[Au(CN)_2]^-$ also contains a five-atom bridging unit but is essentially linear (C–Au–C angles are generally >175°), leading to M–M distances of 10–11 Å through the dicyanoaurate. Also, while the central Au-atom cannot bind to other transition metals, it can readily form attractive aurophilic interactions that can increase the structural dimensionality of the polymer (Scheme 1b) [30]. As part of our investigations into coordination polymers containing the $[Au(CN)_2]^-$ building block [12,13,31–33], and given the diverse structural motifs generated by modifying countercations in the related dca-based systems, we initiated an examination of the analogous [organic cation]{M[Au(CN)$_2$]$_3$} system. We hereby report the first structures of metal tris-cyanoaurate systems with organic cations and their magnetic properties.

2. Experimental

2.1. Reagents and general procedures

All reagents were purchased from commercial sources and used as received. Infrared spectra were recorded on a Thermo Nicolet Nexus 670 FT-IR spectrometer with samples prepared as KBr pressed pellets. Microanalyses (C, H, N) were performed by Miki Yang using a computer-controlled Carlo Erba (Model 1106) CHN analyzer. Thermogravimetric analyses (TGA) were performed in an air atmosphere on a Shimadzu TGA-50 instrument at a rate of 5 °C per minute.

Solid-state UV–Vis–NIR absorption spectra of **1**–**5** were measured by reflectance using an Ocean Optics SD2000 spectrophotometer equipped with tungsten halogen and deuterium lamps. Prior to analysis, the samples were ground into fine powders, dispersed in water, deposited on a glass plate and left to dry completely. Magnesium oxide powder, prepared in the same fashion, was used as a reference.

2.2. Synthesis of $^nBu_4N[Au(CN)_2]\cdot 0.5H_2O$

A 30 mL aqueous solution of $^nBu_4NBr$ (2.325 g, 7.21 mmol) was added to a 30 mL aqueous solution of $KAu(CN)_2$ (2.002 g, 6.95 mmol) while stirring. A white solid immediately precipitated and was stirred for 30 min. The powder of $^nBu_4N[Au(CN)_2]\cdot 0.5H_2O$ was isolated by filtration and dried overnight. Yield: 3.409 g (97%). *Anal.* Calc. for $C_{18}H_{37}N_3AuO_{0.5}$: C, 43.20; H, 7.45; N, 8.40. Found: C, 43.24; H, 7.48; N, 8.11%. IR (KBr, cm^{-1}): 2962 (s), 2932 (s), 2875 (m), 2865 (sh), *ν*(CN) 2146 (s), 1630 (w), 1488 (m), 1463 (m), 1384 (w), 1156 (w), 1111 (w), 1054 (w), 1030 (w), 882 (m), 805 (w), 740 (m), 490 (s).

2.3. Synthesis of $^nBu_4N\{Ni[Au(CN)_2]_3\}$ (*1*)

A 5 mL ethanolic solution of $Ni(NO_3)_2\cdot 6H_2O$ (28 mg, 0.096 mmol) was added to a 5 mL ethanolic solution of $^nBu_4N[Au(CN)_2]\cdot 0.5\ H_2O$ (153 mg, 0.31 mmol). The solution was left to evaporate for several days. When *c.a.* 5 mL of solvent were left, a purple powder of $^nBu_4N\{Ni[Au(CN)_2]_3\}$ (**1**) was collected by filtration and air dried. Yield: 44 mg (44%). *Anal.* Calc. for $C_{22}H_{36}N_7Au_3Ni$: C, 25.21; H, 3.46; N, 9.35. Found: C, 25.52; H, 3.59; N, 9.62%. IR (KBr, cm^{-1}): 2961 (s), 2933 (s), 2887 (m), *ν*(CN) 2195 (s), 1479 (m), 1377 (m), 1150 (w), 1106 (w), 1051(w), 1024 (w), 880 (m), 800 (w), 736 (m), 491 (s). UV–Vis–NIR (nm): 305, 355, 564 (broad) and 910 (broad).

Crystals of **1** suitable for single crystal X-ray diffraction analysis were obtained by recrystallization of the purple powder under hydrothermal conditions in a sealed glass ampoule inserted into a stainless steel vessel and heated in a Lindberg Heavy-Duty furnace equipped with a programmable temperature controller. Specifically, a sample of $^nBu_4N\{Ni[Au(CN)_2]_3\}$ (90 mg in 3 mL of water) was heated to 125 °C over a period of 2 h, maintained at this temperature for 6 h, and slowly cooled to 25 °C at a rate of 1 °C per hour. The crystals and the powder had identical powder X-ray diffractograms and IR spectra.

2.4. Synthesis of $Co[Au(CN)_2]_2(H_2O)_2$

A 5 mL acetonitrile solution of $^nBu_4N[Au(CN)_2]\cdot 0.5\ H_2O$ (98 mg, 0.20 mmol) was added to a 5 mL acetonitrile

solution of $Co(ClO_4)_2 \cdot 6H_2O$ (38 mg, 0.10 mmol). An immediate pink precipitate was obtained but was left covered overnight. The powder of $Co[Au(CN)_2]_2(H_2O)_2$ was then collected by filtration and air dried. Yield: 44 mg (38%). *Anal.* Calc. for $C_4H_4N_4Au_2CoO_2$: C, 8.10; H, 0.68; N, 9.45. Found: C, 8.37; H, 0.77; N, 9.33%. IR (KBr, cm^{-1}): 3143 (b), ν(CN) 2204 (s), ν(CN) 2168 (s), $\nu(^{13}CN)$ 2118 (w), 1530 (m), 886 (w), 755 (w), 542 (w), 467 (m).

2.5. Synthesis of $^nBu_4N\{Co[Au(CN)_2]_3\}$ (2)

$^nBu_4N[Au(CN)_2] \cdot 0.5H_2O$ (40 mg, 0.080 mmol) and $Co[Au(CN)_2]_2(H_2O)_2$ (31 mg, 0.052 mmol) were dissolved completely in 15 mL of ethanol by stirring for 10 min. Once dissolved, the stirring was discontinued and the peach solution was left to evaporate to dryness at room temperature, yielding peach crystals covered with white precipitate. To this mixture 3 mL of ethanol was added and the solution was lightly stirred and then filtered after 3 min. The filtrate was separated and the pink precipitate of $^nBu_4N\{Co[Au(CN)_2]_3\}$ (**2**) was washed with 3 mL of water and 3 mL of cold ethanol. The separated filtrate was evaporated to dryness and subjected to the same treatment to increase the yield. Yield: 29 mg (52%). *Anal.* Calc. for $C_{22}H_{36}N_7Au_3Co$: C, 25.20; H, 3.46; N, 9.35. Found: C, 25.42; H, 3.54; N, 9.39%. IR (KBr, cm^{-1}): 2960 (s), 2933 (m), 2873 (m), ν(CN) 2189 (s), $\nu(^{13}CN)$ 2157 (vw), 1479 (m), 1462 (w), 1377 (w), 1175 (vw), 1149 (w), 1104 (vw), 1053 (vw), 1024 (w), 879 (w), 800 (vw), 734 (w), 484 (w). UV–Vis–NIR (nm): 470 (broad), 490 (sh), 515 (sh), 1030.

2.6. Synthesis of $\{Co[Au(CN)_2]_2(H_2O)_2\} \cdot {}^nBu_4N[Au(CN)_2]$ (3)

$^nBu_4N[Au(CN)_2] \cdot 0.5H_2O$ (40 mg, 0.080 mmol) and $Co[Au(CN)_2]_2(H_2O)_2$ (35 mg, 0.059 mmol) powders were mixed together, suspended in a 1 mL mixture of ethanol/water (9:1, v/v) and sealed with parafilm. The precipitate slowly turned pink, and formed small pink rectangular prism crystals of $\{Co[Au(CN)_2]_2(H_2O)_2\} \cdot {}^nBu_4N[Au(CN)_2]$ (**3**) after three days. The solution was then filtered and the crystals isolated. Yield: 49 mg (77%). *Anal.* Calc. for $C_{22}H_{38}N_7O_2Au_3Co$: C, 24.37; H, 3.72; N, 9.04. Found: C, 24.55; H, 3.79; N, 9.26%. IR (KBr, cm^{-1}): 3454 (b), 3207 (m), 2960 (s), 2930(m), 2872 (m), ν(CN) 2183 (s), ν(CN) 2147 (s), 2108 (vw), 1600 (m), 1469 (m), 1380 (w), 1164 (vw), 1104 (vw), 1068 (vw), 1032 (vw), 926 (vw), 881 (w), 731 (vw), 490 (m). UV–Vis–NIR (nm): 470, 500, 1040.

Crystals of **3** suitable for single crystal X-ray diffraction analysis were obtained by a different route: A 5 mL ethanol/water (1:1 v/v) solution of $^nBu_4N[Au(CN)_2] \cdot 0.5H_2O$ (105 mg, 0.210 mmol) was added slowly to a 5 mL ethanol/water solution of $Co(ClO_4)_2 \cdot 6H_2O$ (26 mg, 0.071 mmol). The pink solution immediately became peach colored, and was left to slowly evaporate. Pink/red rectangular prism crystals of **3** and white $^nBu_4N(ClO_4)$ crystals formed as the ethanol evaporated. The solution was then filtered, and the crystals of **3** were separated by hand; they can be cleaned with ethanol, but are somewhat soluble. Yield: 25 mg (33%). The crystals and the powder had identical powder X-ray diffractograms and IR spectra.

2.7. Synthesis of $PPN[Au(CN)_2]$

A 10 mL aqueous solution of $KAu(CN)_2$ (251 mg, 0.872 mmol) was added to a 20 mL mixture of ethanol/water (1:1 v/v) solution of bis(triphenylphosphoranylidene)ammonium chloride (PPNCl) (525 mg, 0.915 mmol) while stirring. An immediate white precipitate formed. After standing for 30 min, the solid of $PPN[Au(CN)_2]$ was filtered, washed with water and air-dried overnight. Yield: 666 mg (97%). *Anal.* Calc. for $C_{38}H_{30}N_3AuP_2$: C, 57.95; H, 3.84; N, 5.38. Found: C, 57.71; H, 3.86; N, 5.17%. IR (KBr, cm^{-1}): 3088 (vw), 3075 (w), 3055 (m),3038 (w), 3022 (w), 3008 (vw), 2990 (vw), ν(CN) 2145 (s), 1589 (m), 1483 (m), 1456 (m), 1439 (s), 1434 (s), 1285 (s), 1267 (s), 1180 (m), 1160 (w), 1116 (s), 997 (m), 796 (m), 743 (s), 726 (s), 690 (s), 548 (s), 531 (s), 496 (s). A different preparation of this salt, via $[AuCl_2]^-$, has previously been reported [34].

2.8. Synthesis of $PPN\{Ni[Au(CN)_2]_3\}$ (4)

A 5 mL ethanolic solution of $PPN[Au(CN)_2]$ (100 mg, 0.127 mmol) was added slowly to a 5 mL ethanolic solution of $Ni(NO_3)_2 \cdot 6H_2O$ (13 mg, 0.044 mmol). A solid immediately precipitated from the solution, which changed from blue to completely colorless. A very fine pale blue powder of $PPN\{Ni[Au(CN)_2]_3\}$ (**4**) was obtained upon filtration. Yield: 39 mg (69%). *Anal.* Calc. for $C_{42}H_{30}N_7Au_3NiP_2$: C, 37.53; H, 2.25; N, 7.29. Found: C, 37.30; H, 2.34; N, 7.19%. IR (KBr, cm^{-1}): 3076 (w), 3055 (m), 3021 (w), 3009 (w), 2998 (vw), 2971 (vw), ν(CN) 2192 (s), ν(CN) 2151 (vw), 1588 (w), 1476 (w), 1436 (m), 1383 (s), 1330 (m), 1302 (w), 1272 (w), 1186 (w), 1160 (vw), 1117 (s), 1026 (w), 997 (w), 738 (w), 723 (s), 688 (w), 550 (m), 531 (s), 499 (m). UV–Vis–NIR (nm): 335, 562 (broad) and 895 (broad).

Crystals suitable for X-ray crystallography were obtained using an H-tube technique. On one side of a 55 mL H-shaped tube filled with ethanol, a 2 mL ethanolic solution of $PPN[Au(CN)_2]$ (96 mg, 0.121 mmol) was deposited at the bottom. On the other side, a 0.5 mL ethanolic solution of $Ni(NO_3)_2 \cdot 6H_2O$ (15 mg, 0,052 mmol) was deposited. The H-shaped tube was sealed, and after 10 days, light purple cubic crystals of **4** formed. The crystals and the powder had identical powder X-ray diffractograms and IR spectra.

2.9. Synthesis of $PPN\{Co[Au(CN)_2]_3\}$ (5)

A 7 mL ethanolic solution of $PPN[Au(CN)_2]$ (150 mg, 0.190 mmol) was added slowly to a 7 mL ethanolic solution of $Co(ClO_4)_2 \cdot 6H_2O$ (23 mg, 0.060 mmol). A peach powder

immediately precipitated from the solution, which changed from pink to completely colorless. A very fine peach powder of PPN{Co[Au(CN)$_2$]$_3$} (**5**) was obtained upon filtration. Yield: 40 mg (71%). *Anal.* Calc. for $C_{42}H_{30}N_7Au_3CoP_2$: C, 37.52; H, 2.25; N, 7.29. Found: C, 37.77; H, 2.15; N, 7.47%. IR (KBr, cm^{-1}): 3145 (vw), 3076 (w), 3055 (m), 3021 (w), 3009 (w), 2989 (vw), ν(CN) 2187 (s), ν(CN) 2175 (sh), 1588 (w), 1476 (w), 1438 (m), 1384 (s), 1330 (m), 1320 (m), 1302 (w), 1272 (w), 1186 (w), 1160 (vw), 1117 (s), 1026 (w), 997 (w), 881 (vw), 840 (vw), 800 (vw), 738 (w), 723 (s), 690 (w), 550 (m), 531 (s), 499 (m). UV–Vis–NIR (nm): 475 (broad), 490 (sh), 510 (sh) and 990.

2.10. X-ray crystallographic analysis

Powder X-ray diffractograms of all compounds were measured on a Rigaku RAXIS-Rapid Auto diffractometer equipped with a Cu Kα source ($\lambda = 1.54056$ Å). Samples were mounted on a glass fiber using grease and were exposed, as the phi axis was spun (10° s^{-1}), for a period of 40–60 min.

Single crystals of **1**, **3** and **4** were mounted on glass fibers using epoxy adhesive. Single crystal X-ray diffraction data for **1**, **3** and **4** were recorded on an Enraf Nonius CAD4F diffractometer equipped with a Mo Kα source ($\lambda = 0.71073$ Å) and controlled by the DIFRAC program [35] in the following ranges: **1**, $4° < 2\theta < 51°$; **3**, $4° < 2\theta < 48°$; **4**, $4° < 2\theta < 55°$. The NRCVAX Crystal Structure System was used to perform a psi-scan absorption correction (in the transmission range 0.0135–0.0409 for **1**, 0.1068–0.1707 for **3** and 0.0303–0.1154 for **4**) and data reduction, including Lorentz and polarization corrections. The crystal structure of each compound was solved using the Sir 92 routine and refined through Fourier techniques using the CRYSTALS software package [36].

Crystallographic data for compounds **1**, **3** and **4** are collected in Table 1. For **1**, the Ni and Au atoms were refined anisotropically while the C and N atoms were kept isotropic due to the limited number of observed data. Full matrix least-squares refinement for **1** (1540 reflections included) on F (156 parameters) converged to $R_1 = 0.0483$, $wR_2 = 0.0529$ ($I_o > 2.5\sigma(I_o)$). For **3**, all non-hydrogen atoms were refined anisotropically except for the C atoms of the ^{n}Bu-groups that were kept isotropic due to their very large thermal motion. Full matrix least-squares refinement for **3** (689 reflections included) on F (87 parameters) converged to $R_1 = 0.0406$, $wR_2 = 0.0469$ ($I_o > 2.5\sigma(I_o)$). For **4**, all non-hydrogen atoms were refined anisotropically. Full matrix least-squares refinement for **4** (1172 reflections included) on F (87 parameters) converged to $R_1 = 0.0303$, $wR_2 = 0.0411$ ($I_o > 2.5\sigma(I_o)$). Hydrogen atoms were placed in geometric positions in all compounds and their coordinates allowed to ride with their associated atoms.

Diagrams were prepared using ORTEP-3 (version 1.076) [37] and POV-RAY (version 3.6.0) [38]. Selected bond lengths and angles for **1**, **3** and **4** are reported, respectively, in Tables 2–4.

Table 1
Crystallographic data and structural refinement details for **1**, **3** and **4**

Compound	**1**	**3**	**4**
Formula	$C_{22}H_{36}N_7Au_3Ni$	$C_{22}H_{40}N_7Au_3CoO_2$	$C_{42}H_{30}N_7Au_3NiP_2$
fw	1048.19	1095.52	1344.30
Colour	purple	red/dark pink	pale purple
Shape	block	rectangular prism	cube
Dimension (mm^3)	$0.42 \times 0.42 \times 0.28$	$0.22 \times 0.20 \times 0.14$	$0.34 \times 0.31 \times 0.17$
Crystal system	tetragonal	tetragonal	rhombohedral
Space group	$I4_1c$ d	$P4_2/mnm$	$R\bar{3}c$
Z	16	4	6
Unit cell dimensions			
a (Å)	23.532(4)	14.444(2)	15.284(3)
b (Å)	23.532	14.444	15.284
c (Å)	23.181(3)	15.453(2)	31.530(10)
α (°)	90	90	90
β (°)	90	90	90
γ (°)	90	90	120
V (Å^3)	12,837(3)	3223.9(6)	6379(2)
ρ_{calc} (g cm^{-3})	2.169	2.232	2.100
μ (mm^{-1})	14.270	14.143	10.867
R_1 ($I > 2.5\sigma(I)$)	0.0483	0.0420	0.0303
wR_2 ($I > 2.5\sigma(I)$)	0.0529	0.0351	0.0411
Goodness-of-fit	1.3778	1.4542	1.888

$R_1 = \sum|(|F_o| - |F_c|)|/\sum|F_o|$, for observed data ($I_o > 2.5\sigma(I)$), $wR_2 = [\sum(w(|F_o| - |F_c|)^2)/\sum(wF_o)^2]^{1/2}$, for observed data ($I_o > 2.5\sigma(I)$), GOF = $[\sum(w(|F_o| - |F_c|)^2)/\text{degrees of freedom}]^{1/2}$.

2.11. Magnetometry

Magnetization measurements were performed with a Quantum Design MPMS-XL-7S SQUID magnetometer with an Evercool-equipped liquid helium dewar. Microcrystalline samples of **1**–**5** were packed in gelatin capsules and mounted in diamagnetic plastic straws. Direct current (dc) magnetization was measured for all samples upon

Table 2
Selected bond lengths (Å) and angles (°) for ^{n}Bu$_4$N{Ni[Au(CN)$_2$]$_3$} (**1**)

Bond lengths			
Ni(1)–N(1)	2.02(3)	Ni(1)–N(4)	2.07(3)
Ni(1)–N(2)	2.07(3)	Ni(1)–N(5)	2.04(3)
Ni(1)–N(3)	2.07(3)	Ni(1)–N(6)	2.00(3)
Angles			
N(1)–Ni(1)–N(3)	85.1(10)	N(2)–Ni(1)–N(3)	92.4(12)
N(1)–Ni(1)–N(4)	94.0(12)	N(2)–Ni(1)–N(4)	88.4(12)
N(1)–Ni(1)–N(5)	90.9(11)	N(2)–Ni(1)–N(5)	88.8(11)
N(1)–Ni(1)–N(6)	92.8(11)	N(2)–Ni(1)–N(6)	87.5(12)
N(3)–Ni(1)–N(5)	93.1(10)	N(4)–Ni(1)–N(5)	86.9(12)
N(3)–Ni(1)–N(6)	85.9(11)	N(4)–Ni(1)–N(6)	94.1(13)
C(1)–Au(1)–C(6′)	173.1(16)	C(3)–Au(3)–C(4*)	175.0(16)
C(2)–Au(2)–C(5″)	173.5(14)		

Symmetry transformation: (′) y, $-x-1/2$, $z+1/4$; (″) $y+1/2$, $-x$, $z-1/4$; (*) y, $x-1/2$, $z-1/4$.

Table 3
Selected bond lengths (Å) and angles (°) for $\{Co(H_2O)_2[Au(CN)_2]_2\}\cdot {}^nBu_4N[Au(CN)_2]$ (**3**)

Bond lengths			
Co(1)–N(1)	2.096(12)	Au(1)–Au(2)	3.4250(13)
Co(1)–O(1)	2.089(16)	O(1)···N(2)	2.898
Angles			
O(1)–Co(1)–N(1)	85.1(4)	C(1)–Au(1)–C(1*)	171.5(10)
N(1)–Co(1)–N(1′)	90.42(7)	C(2)–Au(2)–C(2″)	179.7(13)
Au(1)–Au(2)–Au(1‡)	163.30(6)		

Symmetry transformation: (′) $y+1/2, -x+1/2, -z+5/2$; (*) $-y, -x, z$; (″) $-y, -x, -z+3$; (‡) $x, y, -z+3$.

Table 4
Selected bond lengths (Å) and angles (°) for $PPN\{Ni[Au(CN)_2]_3\}$ (**4**)

Bond lengths			
Ni(1)–N(1)	2.072(5)	P(1)–N(2)	1.548(3)
Au(1)–C(1)	1.988(6)	C(1)–N(1)	1.114(8)
Angles			
N(1)–Ni(1)–N(1′)	88.9(2)	N(1)–Ni(1)–N(″)	91.1(2)
C(1)–Au(1)–C(1*)	177.3(4)		

Symmetry transformation: (*) $x-y, -y, -z+1/2$; (′) $x-y+1/3, x+1/3, -z+2/3$; (″) $-y+1, x-y, z$.

cooling from 300 to 1.8 K under an applied dc field of 1 kOe. Measurements for all compounds were also performed under an applied field of 100 Oe and no field dependency was observed. The magnetic susceptibility of each compound was corrected for the diamagnetic contribution of the constituent atoms using Pascal's constants [39].

3. Results

3.1. Synthesis and structural characterization of $^nBu_4N\{Ni[Au(CN)_2]_3\}$ (1) and $^nBu_4N\{Co[Au(CN)_2]_3\}$-(2)

The reaction of Ni(II) with $^nBu_4N[Au(CN)_2]\cdot 0.5H_2O$ in ethanol afforded, over a period of several hours, a purple precipitate whose composition was consistent with $^nBu_4N\{Ni[Au(CN)_2]_3\}$ (**1**) by elemental analysis. When the same reaction was performed with Co(II), a mixture of $^nBu_4N$-salts and Co-containing products were obtained, probably due to the higher solubility of the Co-analogue. To eliminate the resulting separation problem, $Co[Au(CN)_2]_2(H_2O)_2$ was dissolved in ethanol and used as the Co(II) source, to which was added one equivalent of $^nBu_4N[Au(CN)_2]\cdot 0.5H_2O$, thereby yielding the byproduct-free $^nBu_4N\{Co[Au(CN)_2]_3\}$ (**2**). The FT-IR spectra of **1** and **2** show only one cyanide vibration frequency at 2195 and 2189 cm^{-1}, respectively, blue-shifted with respect to the ν_{CN} frequency of 2146 cm^{-1} for $^nBu_4N[Au(CN)_2]\cdot 0.5\ H_2O$, consistent with all *N*-cyano groups binding to the transition metal [9].

Dark blue crystals of $^nBu_4N\{Ni[Au(CN)_2]_3\}$ (**1**) suitable for single crystal X-ray diffraction analysis were obtained by hydrothermal recrystallization. The solid-state structure determined for $^nBu_4N\{Ni[Au(CN)_2]_3\}$ (**1**) is shown in Fig. 1. The Ni(II) centers are coordinated to six *N*-cyano groups, with an average bond length of 2.04(3) Å (Fig. 1a, Table 2), yielding a distorted octahedral geometry. Each $[Au(CN)_2]^-$ unit in **1** bridges two Ni(II) centers, generating a three dimensional network (Fig. 1). The structure is built up by a series of two-dimensional (4, 4) rectangular grids, each oriented in a different direction. Each rectangular unit in each grid contains six Ni(II) centers connected by $[Au(CN)_2]^-$ units: one Ni(II) center at each corner and two Ni(II) centers along one pair of opposite edges (Fig. 1b). Each Ni(II) center occupies the edge position on three intersecting fused grids (shown in black in Fig. 1c). Additional $[Au(CN)_2]^-$ units allow the formation of another set of three grids that intersect at the same Ni(II) center (edge-position of the first set of grids) which now occupies the corner position in each of this latter set of grids (shown in grey in Fig. 1c). In other words, six rectangular grids intersect at one Ni center: each Ni center occupies an edge position on three grids and a corner position on the other three grids. No interpenetration of additional networks occurs.

The pores generated by this network accommodate the $^nBu_4N^+$ cations. The central *N* atom lies above an $[Au(CN)_2]^-$ unit while the *n*-butyl groups spread on both sides to occupy the empty space. Thus, the structure of $^nBu_4N\{Ni[Au(CN)_2]_3\}$ (**1**) does not contain any empty pores. In addition, no Au–Au (aurophilic) interactions are present in this system, perhaps a result of the ''insulating'' *n*-butyl groups that surround the $[Au(CN)_2]$ units.

Although no crystal of **2** suitable for single crystal X-ray diffraction analysis could be obtained, the powder diffractogram of **2** was found to be superimposable to that generated from the single-crystal structure of **1** (Fig. 2); this is excellent evidence to suggest that **2** is isostructural with **1**.

The solid state UV–Vis–NIR absorption spectra of **1** and **2** (Figure S1) show maxima attributable to $d-d$ transitions at 305, 355, 564 (br) and 910 nm for **1** and 470 (with shoulder peaks at 490 and 515 nm) and 1030 nm for **2**. These spectra are as expected for octahedral Ni(II) and Co(II) systems with moderate ligand fields [40].

3.2. Synthesis and structural characterization of $\{Co(H_2O)_2[Au(CN)_2]_2\}\cdot {}^nBu_4N[Au(CN)_2]$ (3)

When water was added to the reaction of pale pink $Co[Au(CN)_2]_2(H_2O)_2$ with $^nBu_4N[Au(CN)_2]$ in ethanol, a product with a different colour was obtained. The composition of this dark red-pink product was consistent with $\{Co(H_2O)_2[Au(CN)_2]_2\}\cdot {}^nBu_4N[Au(CN)_2]$ (**3**) by elemental analysis; hence, it was different than **2**, which is anhydrous. The FT-IR spectrum of $\{Co(H_2O)_2[Au(CN)_2]_2\}\cdot {}^nBu_4N[Au(CN)_2]$ (**3**) shows two different cyanide vibration frequencies, 2182 and 2147 cm^{-1}, which suggests the presence

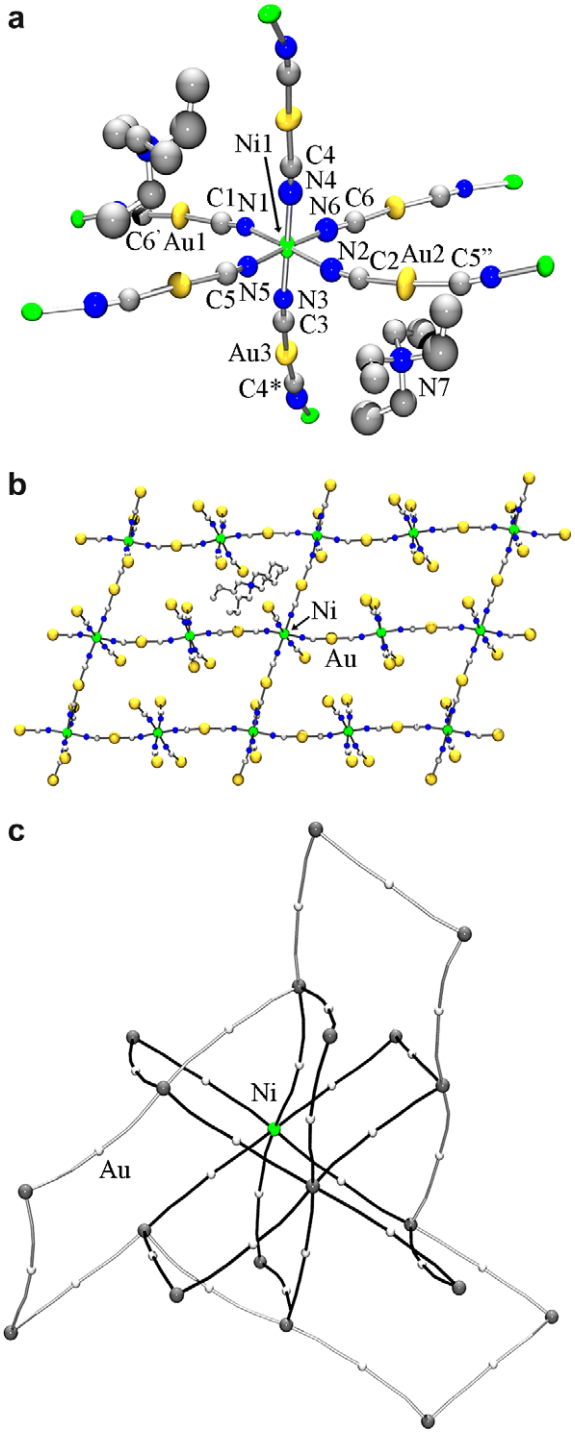


Fig. 1. (a) Coordination sphere around the Ni(II) center (only two cations are shown; butyl groups were simplified for clarity); (b) Extended network showing a two dimensional rectangular (4, 4) grid and the position of one $^{n}Bu_4N^+$ cation; (c) Six rectangular grids intersecting at one Ni(II) center (labelled): the Ni center occupies an edge position on three grids (shown in black) and a corner position on the other three grids (shown in grey) (C and N atoms were removed for clarity and Au atoms are shown smaller and pale grey).

of bound *N*-cyano groups as well as free or weakly interacting *N*-cyano groups; complex **2** had only one ν_{CN} band at 2189 cm^{-1}.

The structure of $\{Co(H_2O)_2[Au(CN)_2]_2\}\cdot{}^{n}Bu_4N[Au(CN)_2]$ (**3**) contains octahedral Co(II) centers that are coordinated to four *N*-cyano groups in the equatorial plane (Co–N = 2.096(12) Å) and two water molecules (Co–O = 2.089(16) Å) in the axial sites (Fig. 3, Table 3); thus, **3** is not a true polymorph of **2** but rather a pseudo-polymorph [41] or, more appropriately, a solvent adduct. A 2-D square grid is formed through the cobalt-bridging $[Au(CN)_2]$ units with the water molecules lying above and below the grid (Fig. 3a). Free $[Au(CN)_2]$ units are also present and lie above and parallel to opposing edges of the $Co[Au(CN)_2]_2$ square array. Each free $[Au(CN)_2]$ unit interacts with the underlying grid both through hydrogen-bonding between the terminal *N*-cyano atoms and the hydrogen of the water molecules, and also through aurophilic (Au–Au) interactions (Au1–Au2 = 3.4250(13) Å, Fig. 3b). Aurophilic interactions are considered to exist when the distance between two Au atoms is smaller than the sum of the van der Waals radii, 3.6 Å [42–44]. The alignment of each layer of free $[Au(CN)_2]$ units alternates 90° with the two pairs of parallel edges of the square arrays. Hence, through aurophilic interactions and hydrogen-bonding, a 3-D network is obtained. The $^{n}Bu_4N^+$ cations occupy the empty sites in the layer of unbound $[Au(CN)_2]$ units. Overall, $\{Co(H_2O)_2[Au(CN)_2]_2\}\cdot{}^{n}Bu_4N[Au(CN)_2]$ (**3**) can be considered to be a layered polymer that contains neutral sheets of $\{Co(H_2O)_2[Au(CN)_2]_2\}$ which are separated by $^{n}Bu_4N[Au(CN)_2]$ layers.

The geometry around the Au atom in the bridging $[Au(CN)_2]$ unit (C(1)–Au(1)–C(1*) = 171.5(10)°) differs from that observed in the free unit (C(2)–Au(2)–C(2″) = 179.7(13)°): a clear bending of the $[Au(CN)_2]$ units within the 2-D grid can be observed (Fig. 3). Theoretically, an angle of 173.6° was calculated for an anionic dimer of $[Au(CN)_2]$ units, with a Au–Au interaction of 3.742 Å and a torsion angle of 90° [45]. Hence, the experimentally observed acute C–Au–C angle could reflect the presence of Au–Au interactions, even though the torsion angle is different, or this unusually large distortion from linearity around the Au atom could reflect the need to accommodate the large $^{n}Bu_4N^+$ cation incorporated between the grids.

The basic 2-D grid structure of $\{Co(H_2O)_2[Au(CN)_2]_2\}\cdot{}^{n}Bu_4N[Au(CN)_2]$ (**3**) is similar to that reported for other solvent adducts, such as $\{Co(dmf)_2[Au(CN)_2]_2\}$ [45], $\{Mn(H_2O)_2[Au(CN)_2]_2\}$ [46] and $\{Cu(pyridine)_2[Au(CN)_2]_2\}$ [12]. In these polymers, no extra $^{n}Bu_4N[Au(CN)_2]$ layer is present and the solvent molecules, binding through their donor atom, replace the water molecules in **3**. The packing of the 2-D square grids is different in these other systems as the grids are offset to allow direct aurophilic interactions of ~3.1 Å between two grids [45,46] or π–π interactions between the pyridine rings [12].

Interestingly, heating a sample of **3** at 150 °C for 90 min to remove the bound water molecules cleanly generated the dehydrated 3-D array of **2** as indicated by X-ray diffractograms and FT-IR spectra that were superimposable with those of independently synthesized **2**. This significant

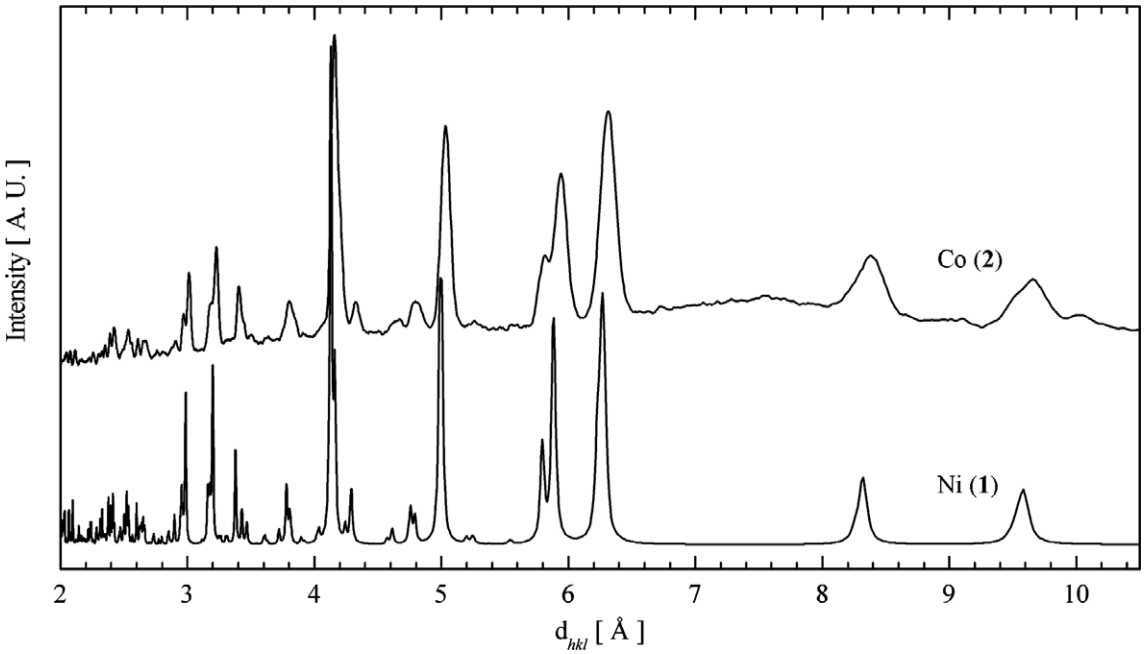


Fig. 2. Powder X-ray diffractograms generated for $^{n}Bu_4N\{Ni[Au(CN)_2]_3\}$ (**1**) from the single crystal diffraction data and measured for $^{n}Bu_4N\{Co[Au(CN)_2]_3\}$ (**2**).

structural rearrangement in the solid state is a strong indication of the flexible nature of cyanoaurate-based coordination polymers [12]. Note that **3** is not regenerated in the solid state by exposure to water vapour.

3.3. Synthesis and structural characterization of *PPN{Ni[Au(CN)$_2$]$_3$}* (*4*) and *PPN{Co[Au(CN)$_2$]$_3$}* (*5*)

The reaction of $PPN[Au(CN)_2]$ with M(II) salts (M = Ni and Co) in ethanol immediately yielded very fine precipitates. Elemental analysis confirmed that the product compositions were consistent with $PPN\{M[Au(CN)_2]_3\}$ (M = Ni (**4**); Co (**5**)). FT-IR spectroscopy showed one cyanide vibration frequency for **4** at 2192 cm^{-1} and two barely resolved frequencies for **5** at 2187 and 2175 cm^{-1}. This suggests that all the cyanide groups are in a similar environment in **4** while a slight structural difference among the cyanide groups exists in **5**, likely due to broken symmetry. No ν_{CN} band corresponding to free $[Au(CN)_2]$ (~2140 cm^{-1}) could be observed in the FT-IR spectrum of either **4** or **5**, suggesting that all *N*-cyano units are coordinated to the metal centers.

Pale purple crystals of $PPN\{Ni[Au(CN)_2]_3\}$ (**4**) were obtained through slow diffusion of reagents in an H-shaped tube. The structure determined for **4** is shown in Fig. 4. As for **1**, the Ni(II) centers have an octahedral geometry and coordinate to six *N*-cyano groups (Table 4). Each $[Au(CN)_2]$ unit bridges two Ni(II) centers to create a 3-D Prussian-Blue-type pseudo-cubic array. The PPN^+ cation occupies the space in the center of each cube, preventing the interpenetration of a second network. This "expanded Prussian Blue" analogue, with 10.269 Å edges (Ni–Ni), can be compared with other examples such as $Fe_4[Re_6Te_8(CN)_6]_3 \cdot xH_2O$ [47] and $[Ni(en)_2]_3[Fe(CN)_6](PF_6)_2$ [48] which have edges of 14.1285 and 9.908 Å, respectively.

The powder X-ray diffractograms of **4** and **5** are nearly superimposable (Fig. 5), which indicates that an identical arrangement of the building blocks is present in the two polymers. This is also consistent with the FT-IR spectra; the small difference in cyanide vibration frequency can be attributed to the difference between *N*-cyano group binding to Ni or Co.

The solid-state UV–Vis–NIR absorption spectra of **4** and **5** (Figure S1) were found to have two *d–d* maxima at 562 and 895 nm for **4** and 475 nm (with shoulder peaks at 490 and 510 nm) and 990 nm for **5**; absorptions below 400 nm are obscured by strong PPN-based peaks. The absorption spectra of the $PPN\{M[Au(CN)_2]_3\}$ polymers are very similar to those of their respective $^{n}Bu_4N\{M[Au(CN)_2]_3\}$ analogues, consistent with the observation that the geometry and coordination sphere of the metal centers are similar in both pairs of compounds.

3.4. Templating effects of the cation

The structures of **1**–**5** can be contrasted with the related $K\{Fe[Au(CN)_2]_3\}$ [46], $K\{Co[Au(CN)_2]_3\}$ [49] and $K\{Mn[Ag(CN)_2]_3\}$ [50] structures, which contain triply interpenetrated pseudo-cubic 3-D cyanometallate arrays. The switch of the non-steric K^+ cation for the $^{n}Bu_4N^+$ cation has eliminated the interpenetration and modified the form of the 3-D network, but has not caused a reduction in dimensionality. Hydration of the Co(II) in **3** does, however, cause a reduction in dimensionality in terms of the coordinate bond network. Finally, the PPN^+ cation rather surprisingly also does not force any reduction in

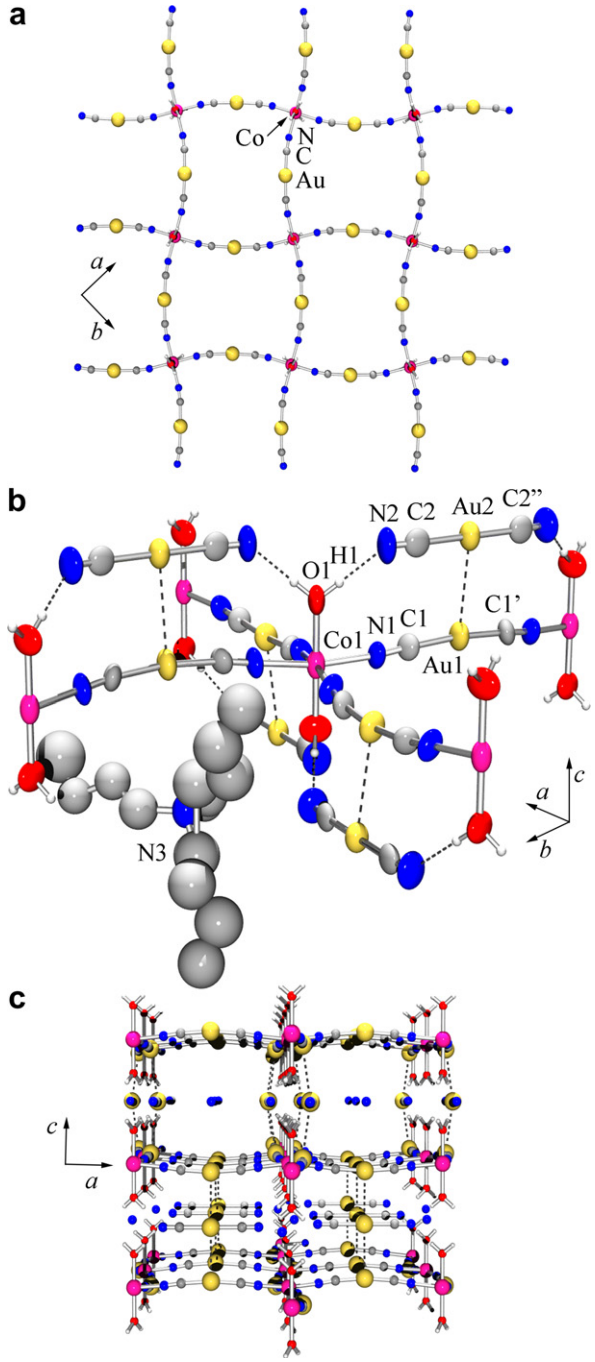


Fig. 3. (a) 2-D square grid of $\{Co(H_2O)_2[Au(CN)_2]_2\} \cdot {}^nBu_4N[Au(CN)_2]$ (**3**) showing the 2-D square grids viewed down the *c*-axis; (b) Coordination sphere around a Co(II) center in **3**; (c) Interactions between the grids and the free $[Au(CN)_2]$ units along the *c*-axis. ^{n}Bu groups were omitted for clarity.

dimensionality; indeed, this non-interpenetrated structures is strain-free and nearly identical to a single pseudo-cubic network found in the K^+-analogues.

3.5. Thermal stability

Thermogravimetric analysis data from 25 to 500 °C were collected for **1**, **2**, **3** and up to 820 °C for **4** and **5**.

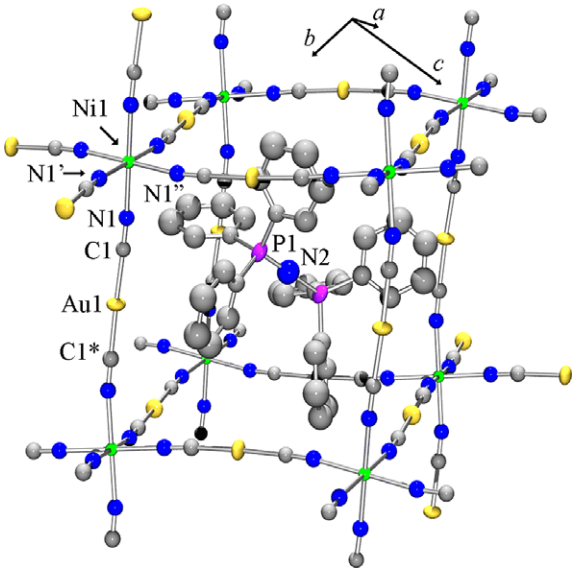


Fig. 4. Extended structure of $PPN\{Ni[Au(CN)_2]_3\}$ showing the coordination sphere around the Ni(II) centers and the Prussian-Blue-type pseudo-cubic array.

Compounds **1**–**3** decompose within the same narrow temperature range, losing the six cyanide groups and the cation all at once. The nickel compounds have slightly higher decomposition temperatures, with **1** being stable until 295 °C, then losing cyanides and the $^nBu_4N^+$ cation, leaving gold and nickel oxide at 330 °C (observed: 64.0%; calculated: 63.5%). Complex **4** starts decomposing at 325 °C, with a slow decomposition of the PPN^+ cation occurring up to 750 °C, obtaining $Ni(P_2O_3)$ and gold (final mass observed: 55.0%; calculated: 56.5%). In the case of the cobalt compounds, **2** is stable until to 260 °C, and then loses the cyanides and $^nBu_4N^+$ cation until 338 °C, leaving gold and cobalt oxide (observed: 62.5%; calculated: 63.9%). Hydrated **3** first loses its two water molecules between 100 °C and 120°C (observed: 4.0%; calculated: 3.3%) then further decomposes along the same path as **2**, losing all cyanides and $^nBu_4N^+$ in the same 260–338 °C temperature range (observed: 60.3%; calculated: 61.8%). Complex **5** follow the same pattern as **4**, slowly decomposing after 275 °C up until 730 °C, forming $Co(P_2O_3)$ and gold as the end products (final mass observed: 56.7%; calculated: 56.5%).

Thus, the tris-cyanoaurate frameworks are in general stable until 260–325 °C. These decomposition temperatures are typical for cyanometallate systems [51] but lower than for cyanoaurate arrays that show substantial aurophilic interactions such as $M(pyrazine)[Au(CN)_2]_2$, which loses its cyanides at a remarkable 406 °C for M = Ni and 360 °C for Co [32].

3.6. Magnetic properties of $^nBu_4N\{M[Au(CN)_2]_3\}$ (Ni, **1**; Co, **2**)

The magnetization of $^nBu_4N\{M[Au(CN)_2]_3\}$ (M = Ni (**1**); Co (**2**)) was measured upon cooling from 300 to

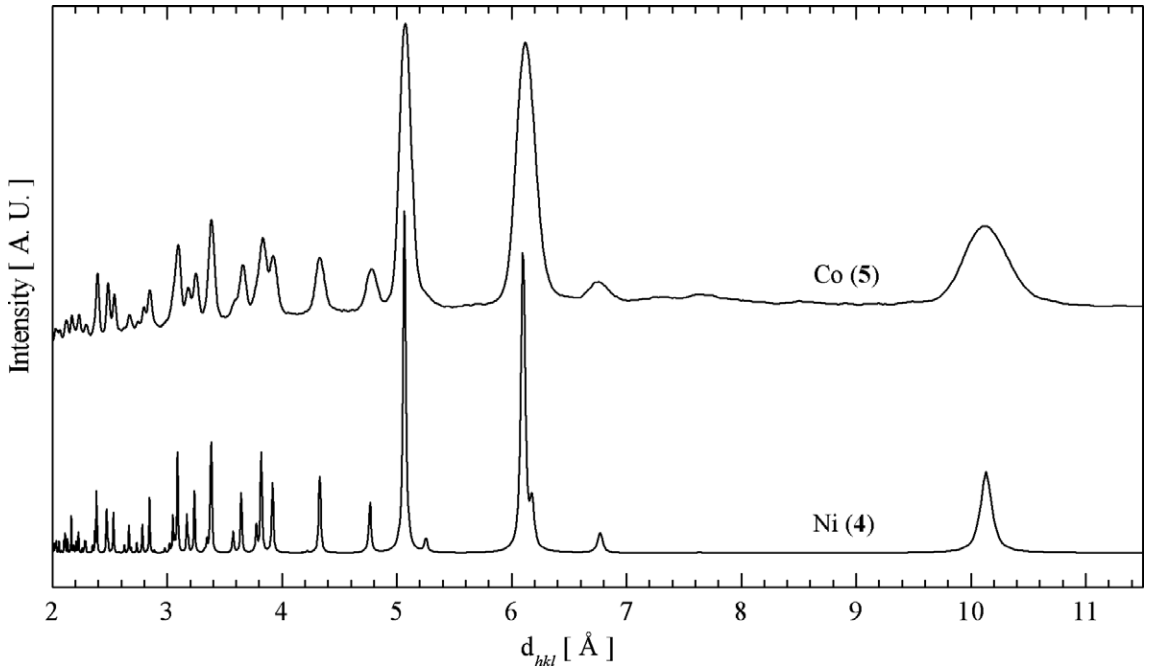


Fig. 5. Comparison between the powder X-ray diffractogram of PPN{Co[Au(CN)$_2$]$_3$} (**5**) and the diffractogram predicted from the single-crystal structure of PPN{Ni[Au(CN)$_2$]$_3$} (**4**).

1.8 K in a 1 kOe applied magnetic field. The calculated effective magnetic moments ($\mu_{\text{eff}} = 2.828\sqrt{\chi_{\text{M}}T}$) of **1** and **2** as a function of temperature are shown in Fig. 6. At 300 K, a value of 3.03 μ_{B} is observed for **1**, which is consistent with isolated spin-only $S = 1$ Ni(II) centers.[52] As the temperature is lowered, the μ_{eff} of **1** remains constant until 30 K and then decreases to reach 2.22 μ_{B} at 1.8 K. The inverse of the susceptibility χ_{M}^{-1} of **1** can be fit to the Curie–Weiss expression, [52] yielding a g of 2.166(2) and a θ value of −1.27(5) K.

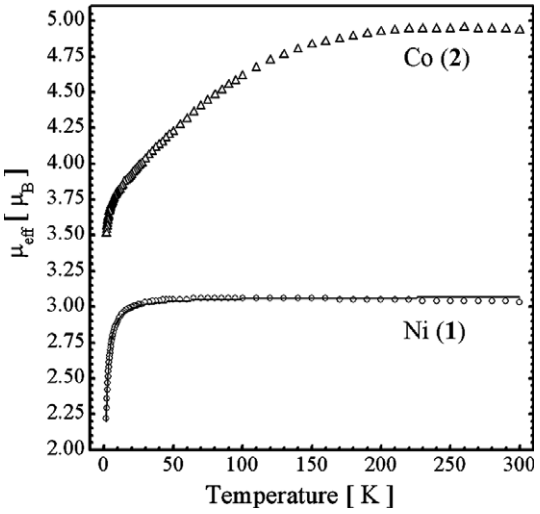


Fig. 6. Temperature dependence of the effective magnetic moment (μ_{eff}) for ^{n}Bu$_4$N{Ni[Au(CN)$_2$]$_3$} (**1**, ○) and ^{n}Bu$_4$N{Co[Au(CN)$_2$]$_3$} (**2**, Δ). The solid line represents the theoretical fit to the zfs expression with a molecular field approximation for the Ni(II) analogue (see text).

The drop in the μ_{eff} of **1** at low temperature could be due to either zero field splitting (zfs) or weak antiferromagnetic interactions mediated through the [Au(CN)$_2$]-units or a combination of both. The product of the susceptibility by the temperature ($\chi_{\text{M}}T$) for **1** can be fitted to the zfs expression for an $S = 1$ system, [52] yielding a D of 5.4(1) cm^{-1} and a g of 2.13(1). The fit of $\chi_{\text{M}}T$ for **1** was improved by introducing a molecular field approximation to estimate the magnetic coupling between the Ni(II) centers:

$$\chi_{\text{mf}} = \frac{\chi_{\text{zfs}}}{\left(1 - \frac{2zJ}{Ng^2\mu_{\text{B}}^2}\chi_{\text{zfs}}\right)} \quad (1)$$

where zJ is the exchange coupling constant with the neighboring Ni(II) centers. This second fit yielded a D of 2.7(1) cm^{-1}, a g of 2.173(2) and zJ/k_{B} of −0.85(2) cm^{-1}. Values of D for related octahedral Ni(II) centers, such as in Ni(tren)[Au(CN)$_2$]$_2$, range from 1 to 4 cm^{-1} [53]. The value for a symmetric octahedral Ni(II) center such as that found in **1** should be on the low side of this range. Hence, these values are reasonable and suggest very weak interactions between the Ni(II) centers may be present at best.

For **2**, an effective moment of 4.93 μ_{B} is observed at 300 K (Fig. 6), which is larger than the spin-only value of an $S = 3/2$ system, but is in the range expected for an octahedral high-spin Co(II) center (4.1–5.2 μ_{B}), [40] for which a large first-order orbital contribution is present. As the temperature decreases, the μ_{eff} remains constant down to 175 K, after which it decreases steadily and reaches 3.51 μ_{B} at 1.8 K. The decrease in the μ_{eff} of **2** can be due to a

combination of single-ion effects and very weak antiferromagnetic interactions; no maximum was observed in the magnetic susceptibility (χ_M) versus temperature plot. No attempt was made to model this behaviour as any coupling through the $[Au(CN)_2]$ units would have a very small magnitude and would be difficult to distinguish from the single-ion effects. In related Co(II) dicyanamide complexes with $\mu_{1,5}$-bridging dca units, any coupling was shown to be below 1 cm^{-1}, with single-ion effects dominating [29].

3.7. Magnetic properties of $\{Co(H_2O)_2[Au(CN)_2]_2\} \cdot {}^nBu_4N[Au(CN)_2]$ (3)

Despite the different structural arrangement described for **2** and **3**, the temperature dependence of the effective magnetic moment of both compounds is nearly identical: **3** has an effective moment of 4.88 μ_B at 300 K and 3.57 μ_B at 1.8 K (not shown).

The magnetic behaviour of $\{Co(H_2O)_2[Au(CN)_2]_2\} \cdot {}^nBu_4N[Au(CN)_2]$ (**3**) is similar to that reported for other coordination polymers containing Co(II) centers linked via $[Au(CN)_2]$-units in a 2-D grid array. $\{Co(dmf)_2[Au(CN)_2]_2\}$ [45] and $\{Co(pyrazine)_2[Au(CN)_2]_2\}$ [32] have effective moments of 4.92 and 5.21 μ_B, respectively, at 300 K, which decrease to reach 3.79 and 3.64 μ_B at 1.8 K.

3.8. Magnetic properties of $PPN\{M[Au(CN)_2]_3\}$ (M = Ni (4), Co (5))

The magnetization of **4** and **5** was also measured upon cooling from 300 to 1.8 K in a 1 kOe external magnetic field and the temperature dependence of the effective magnetic moments are shown in Fig. 7. At 300 K, a value of 3.05 μ_B is observed for **4**, as expected for an $S = 1$ Ni(II) center. The μ_{eff} remains constant until 20 K and then decreases slightly to a value of 2.22 μ_B at 1.8 K. The inverse of the susceptibility of **4** was fitted to the Curie–Weiss expression and yielded a g of 2.173(1) and a θ of −1.11(4) K. As for **1**, the $\chi_M T$ of **4** could be fitted to the zfs expression and yielded a D of 5.0(1) cm^{-1} and a g of 2.145(4). When a molecular field approximation was added to the fit (Eq. (1)), a D of 2.6(1) cm^{-1}, a g of 2.180(2) and a zJ/k_B of −0.75(2) cm^{-1} were obtained. As for **1**, these values indicate the presence of very weak interactions between the Ni(II) centers. Similarly, the effective moment of 5.06 μ_B determined for **5** at 300 K, which is consistent with an octahedral Co(II) center, drops to 3.69 μ_B at 1.8 K. As for **2** and **3**, the behaviour of **5** is dominated by Co(II) single-ion effects.

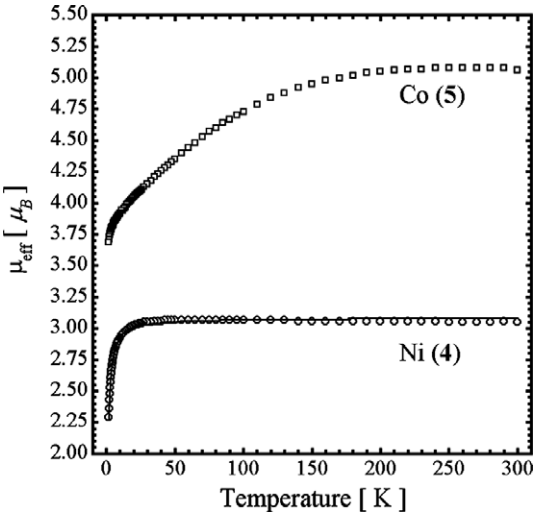


Fig. 7. Temperature dependence of the effective magnetic moment of $PPN\{M[Au(CN)_2]_3$ (M = Ni (**4**, ○) and Co (**5**, □)) with a 1 kOe applied magnetic field.

3.9. Magneto-structural conclusions and comparison with other complexes

To summarize, these results indicate that $[Au(CN)_2]$ is a poor mediator of magnetic exchange in these 2-D and 3-D systems, although in other reported $[Au(CN)_2]$-based coordination polymers, significant coupling can be observed [31,54]. It is possible that, in these high dimensionality/high symmetry systems, competing ferromagnetic and antiferromagnetic interactions might contribute to cancel out the overall coupling. The lack of any significant magnetic interactions, even in the structurally cohesive, pseudo-cubic 3-D cyanoaurate polymers **4** and **5** is comparable to the observation that magnetic coupling through $\mu_{1,5}$-dca bridges is generally very weak [18,19,29].

4. Conclusion

This preliminary study has shown that 3-D $\{M[Au(CN)_2]_3\}^-$ coordination polymers can be readily prepared. The structures of ${}^nBu_4N\{M[Au(CN)_2]_3\}$ and $PPN\{M[Au(CN)_2]_3\}$ (M = Ni and Co) contain two distinct 3-D anionic frameworks of $\{M[Au(CN)_2]_3\}^-$, thus the framework was sensitive to the cation, but not to the identity of the metal center. Despite using large cations such as ${}^nBu_4N^+$ or PPN^+, a 3-D structure is maintained (except when the metal remains solvated), contrary to the reduction in structural dimensionality observed in dicyanamide (dca) systems [18,19]. The longer reach of linear $[Au(CN)_2]^-$ compared to bent dca may account for this difference. A further increase in cation bulkiness or the introduction of hydrogen-bonding moieties into the cations is likely to eventually result in a significant superstructure rearrangement [55,56] and we are pursuing these avenues.

Unfortunately, despite the presence of 2-D and 3-D networks with strongly N-bound cyanoaurates, including a pseudo-cubic Prussian Blue-type array, no magnetic ordering was detected above 1.8 K; indeed, almost no significant coupling through the $[Au(CN)_2]$ units was observed, indicating that the linear d^{10}-$Au(CN)_2$ bridge is a very weak mediator of magnetic exchange in these systems.

Acknowledgements

We thank NSERC of Canada, CFI, BCKDF and Simon Fraser University for financial support and Dr. Raymond J. Batchelor (Simon Fraser University) for assistance with the X-ray structural determinations.

Appendix A. Supplementary material

CCDC 619401, 619402 and 619403 contain the supplementary crystallographic data for **1**, **3** and **4**. These data can be obtained free of charge via http://www.ccdc.cam.ac.uk/conts/retrieving.html, or from the Cambridge Crystallographic Data Centre, 12 Union Road, Cambridge CB2 1EZ, UK; fax: (+44) 1223-336-033; or e-mail: deposit@ccdc.cam.ac.uk. Supplementary data associated with this article can be found, in the online version, at doi:10.1016/j.poly.2006.10.045.

References

[1] S.R. Batten, R. Robson, Angew. Chem., Int. Ed. Engl. 37 (1998) 1460.
[2] B. Moulton, M.J. Zaworotko, Chem. Rev. 101 (2001) 1629.
[3] S.L. James, Chem. Soc. Rev. 32 (2003) 276.
[4] C. Janiak, J. Chem. Soc., Dalton Trans. (2003) 2781.
[5] S. Kitagawa, R. Kitaura, S.-I. Noro, Angew. Chem., Int. Ed. Engl. 43 (2004) 2334.
[6] J.S. Miller, Inorg. Chem. 39 (2000) 4392.
[7] O. Kahn, Magnetism; A supramolecular Function, Kluwer Academic Publisher, Dordrecht, The Netherlands, 1996.
[8] S. Decurtins, R. Pellaux, G. Antorrena, F. Palacio, Coord. Chem. Rev. 190–192 (1999) 841.
[9] K.R. Dunbar, R.A. Heintz, Prog. Inorg. Chem. 45 (1997) 283.
[10] M. Verdaguer, A. Bleuzen, V. Marvaud, J. Vaissermann, M. Seuleiman, C. Desplanches, A. Scuiller, C. Train, R. Garde, G. Gelly, C. Lomenech, I. Rosenman, P. Veillet, C. Cartier, F. Villain, Coord. Chem. Rev. 190–192 (1999) 1023.
[11] M. Verdaguer, G.S. Girolami, Magnetic prussian blue analogs, in: J.S. Miller, M. Drillon (Eds.), Magnetism: Molecules to Materials V, vol. 5, Wiley–VCH, Weinheim, 2005, pp. 283–346.
[12] J. Lefebvre, R.J. Batchelor, D.B. Leznoff, J. Am. Chem. Soc. 126 (2004) 16117.
[13] M.J. Katz, P.M. Aguiar, R.J. Batchelor, A.A. Bokov, Z.-G. Ye, S. Kroeker, D.B. Leznoff, J. Am. Chem. Soc. 128 (2006) 3669.
[14] L.G. Beauvais, M.P. Shores, J.R. Long, J. Am. Chem. Soc. 122 (2000) 2763.
[15] T. Iwamoto, Supramolecular chemistry in cyanometallate systems, in: J.L. Atwood, J.M. Lehn, J.E.D. Davies, D.D. MacNicol, F. Vogtle, G.T.B. Alberti (Eds.), Comprehensive Supramolecular Chemistry, vol. 6, 1996, pp. 643–690.
[16] J. Lefebvre, D.B. Leznoff, in: A.S. Abd-El-Aziz, C.E. Carraher Jr., C.U. Pittman Jr., M. Zeldin (Eds.), Macromolecules Containing Metal and Metal-Like Elements, vol. 5, Wiley-Interscience, 2005, pp. 155–208 (Chapter 7).
[17] M. Pilkington, S. Decurtins, A rational approach for the self-assembly of molecular building blocks in the field of molecule-based magnetism, in: G.R. Desiraju (Ed.), Crystal Design: Structure and Function, John Wiley & Sons Ltd, 2003.
[18] S.R. Batten, K.S. Murray, Coord. Chem. Rev. 246 (2003) 103.
[19] S.R. Batten, K.S. Murray, Aust. J. Chem. 54 (2001) 605.
[20] J.A. Schlueter, J.L. Manson, U. Geiser, Inorg. Chem. 44 (2005) 3194.
[21] A. Yuan, J. Zou, B. Li, Z. Zha, C. Duan, Y. Liu, Z. Xu, Chem. Commun. (2000) 1297.
[22] M. Scudder, I. Dance, J. Chem. Soc., Dalton Trans. (1998) 3155.
[23] P. Day, J. Chem. Soc., Dalton Trans. (1997) 701.
[24] S. Decurtins, H. Schmalle, R. Pellaux, New J. Chem. 22 (1998) 117.
[25] S.R. Batten, P. Jensen, B. Moubaraki, K.S. Murray, Chem. Commun. (2000) 2331.
[26] P.M. Van der Werff, E. Martinez-Ferrero, S.R. Batten, P. Jensen, C. Ruiz-Perez, M. Almeida, J.C. Waerenborgh, J.D. Cashion, B. Moubaraki, J.R. Galan-Mascaros, J.M. Martinez-Agudo, E. Coronado, K.S. Murray, Dalton Trans. (2005) 285.
[27] P.M. van der Werff, S.R. Batten, P. Jensen, B. Moubaraki, K.S. Murray, J.D. Cashion, Cryst. Growth Des. 4 (2003) 503.
[28] P.M. van der Werff, S.R. Batten, P. Jensen, B. Moubaraki, K.S. Murray, Inorg. Chem. 40 (2001) 1718.
[29] D. Armentano, G. De Munno, F. Guerra, M. Julve, F. Lloret, Inorg. Chem. 45 (2006) 4626.
[30] D.B. Leznoff, J. Lefebvre, Gold Bull. 38 (2005) 47.
[31] D.B. Leznoff, B.-Y. Xue, B.O. Patrick, V. Sanchez, R.C. Thompson, Chem. Commun. (2001) 259.
[32] D.B. Leznoff, B.Y. Xue, C.L. Stevens, A. Storr, R.C. Thompson, B.O. Patrick, Polyhedron 20 (2001) 1247.
[33] D.B. Leznoff, B.-Y. Xue, R.J. Batchelor, F.W.B. Einstein, B.O. Patrick, Inorg. Chem. 40 (2001) 6026.
[34] R.-Y. Liau, H. Ehlich, A. Schier, H. Schmidbaur, Z. Naturforsch. 57b (2002) 1085.
[35] E.J. Gabe, P.S. White, G.D. Enright, DIFRAC A Fortran 77 Control Routine for 4-Circle Diffractometers, N.R.C., Ottawa, 1995.
[36] P.W. Betteridge, J.R. Carruthers, R.I. Cooper, K. Prout, D.J. Watkin, J. Appl. Crystallogr. 36 (2003) 1487.
[37] L.J. Farrugia, J. Appl. Crystallogr. 30 (1997) 565.
[38] T.D. Fenn, D. Ringe, G.A. Petsko, J. Appl. Crystallogr. 36 (2003) 944, Persistence of Vision Raytracing: <http://www.povray.org>.
[39] O. Kahn, Molecular Magnetism, VCH, Weinheim, 1993.
[40] F.A. Cotton, G. Wilkinson, Advanced Inorganic Chemistry: A Comprehensive Text, Interscience Publishers, New York, 1972.
[41] J.L. Bernstein, Polymorphism in Molecular Crystals, Oxford University Press, Oxford, 2002.
[42] H. Schmidbaur, Chem. Soc. Rev. 24 (1995) 391, and references therein.
[43] P. Pyykkö, Angew. Chem., Int. Ed. Engl. 43 (2004) 4412, and references therein.
[44] M. Bardaji, A. Laguna, J. Chem. Educ. 76 (1999) 201.
[45] E. Colacio, F. Lloret, R. Kivekaes, J. Ruiz, J. Suarez-Varela, M.R. Sundberg, Chem. Commun. (2002) 592.
[46] W. Dong, L.-N. Zhu, Y.-Q. Sun, M. Liang, Z.-Q. Liu, D.-Z. Liao, Z.-H. Jiang, S.-P. Yan, P. Cheng, Chem. Commun. (2003) 2544.
[47] M.P. Shores, L.G. Beauvais, J.R. Long, J. Am. Chem. Soc. 121 (1999) 775.
[48] N. Fukita, M. Ohba, H. Okawa, K. Matsuda, H. Iwamura, Inorg. Chem. 37 (1998) 842.
[49] S.C. Abrahams, J.L. Bernstein, R. Liminga, J. Chem. Phys. 73 (1980) 4585.
[50] W. Dong, Q.-L. Wang, S.-F. Si, D.-Z. Liao, Z.-H. Jiang, S.-P. Yan, P. Cheng, Inorg. Chem. Commun. 6 (2003) 873.
[51] J. Chomic, J. Cernak, Thermochim. Acta 93 (1985) 93.
[52] R.L. Carlin, Magnetochemistry, Springer-Verlag, Berlin Heidelberg, Germany, 1986.
[53] C.J. Shorrock, B.-Y. Xue, P.B. Kim, R.J. Batchelor, B.O. Patrick, D.B. Leznoff, Inorg. Chem. 41 (2002) 6743.
[54] J. Lefebvre, F. Callaghan, M.J. Katz, J.E. Sonier, D.B. Leznoff, Chem. Eur. J., 2006.
[55] N.D. Draper, R.J. Batchelor, P.M. Aguiar, S. Kroeker, D.B. Leznoff, Inorg. Chem. 43 (2004) 6557.
[56] N.D. Draper, R.J. Batchelor, D.B. Leznoff, Cryst. Growth Des. 4 (2004) 621.

sized by the reaction of a known "butterfly" complex with a $[Mn_4^{III}(\mu_3\text{-}O_2)]^{8+}$ core, with the tripodal ligand triethanolamine (H_3tea). The small $Mn_2^{III}Mn_2^{II}$ core allows us to use a full Hamiltonian matrix diagonalization approach, in addition to the simple Kambe approach, to fit the magnetic susceptibility data for complex **1**. The full Hamiltonian matrix is 900×900 and includes Zeeman, zero-field and magnetic (both isotropic and antisymmetric) interactions.

2. Experimental

2.1. Materials

All reactions were performed under aerobic conditions. The ligands 9-anthracenecarboxylic acid (Hanca), dibenzoylmethane (Hdbm), triethylamine (Et_3N) and triethanolamine (H_3tea) were purchased from Sigma–Aldrich and used without further purification.

2.2. Synthesis

*$[Mn_4(anca)_4(Htea)_2(dbm)_2] \cdot 2.5Et_2O$ (**1**).* (0.25 g, 0.124 mmol) $[Mn_4O_2(anca)_6(dbm)_2] \cdot 3CH_2Cl_2$ [10] was added to a solution of Et_3N (0.075 g, 0.740 mmol) in methanol (30 mL) and then was allowed to stir for 30 min. H_3tea (0.11 g, 0.740 mmol) was added to the resulting opaque, brown solution dropwise over 5 min. The solution was allowed to stir for 1 h followed by gravity filtration to remove unreacted starting material. Layering of the filtrate with 50 mL of a 1:1 mixture of diethyl ether and hexanes produced red-brown analytically pure crystals (**1**) suitable for X-ray diffraction studies after 30 days. *Anal.* Calc. for $C_{102}H_{84}Mn_4N_2O_{18}$ (**1**): C, 66.36; H, 4.59; N, 1.51. Found: C, 66.64; H, 4.21; N, 1.69%. Yield: 5% based on manganese. Selected FT-IR data (KBr, cm^{-1}): 3418(m,b), 2923(s), 2825(m), 1574(s), 1524(s), 1479(m), 1440(m), 1384(s), 1348(m), 1320(s), 1277(w), 1068(m), 1025(w), 885(w), 761(w), 733(m), 686(w), 649(w), 559(w), 474(w,b), 421(w).

2.3. Physical techniques

FT-IR spectra were collected using a Thermo-Nicolet Avatar series spectrometer. Elemental analysis was performed by NuMega Resonance Labs (San Diego, CA). *Note*: The formula listed for the elemental analysis of complex **1** does not include ether solvent molecules as they are lost upon removal from the mother liquor. The dc magnetic susceptibility data were collected on a Quantum Design MPMS-5 magnetometer with a 5.5 T magnet. Microcrystalline samples were restrained with eicosane to prevent torquing. Diamagnetic corrections of magnetic susceptibility data were made employing Pascal's constants.

2.4. Crystal structure determination

Mo $K\alpha = 0.71073$ Å; crystal system, triclinic; space group, $P\bar{1}$; $Z = 1$, $Z' = 0.5$; unit cell dimensions: $a = 12.8242(17)$ Å, $b = 13.2663(17)$ Å, $c = 14.3325(19)$ Å, $\alpha = 80.355(2)°$, $\beta = 82.983(2)°$, $\gamma = 85.730(2)°$, and $V = 2382.3(5)$ Å^3; temperature = −173 °C; total reflections measured = 20 310 [10 365 independent, $R_{int} = 0.0313$]; completeness to θ [25.00°] = 98.9%. A red plate-shaped crystal ($0.30 \times 0.20 \times 0.08$) was mounted on a Bruker Smart Apex CCD diffractometer, integrated using Bruker SAINT software program, and corrected for absorption using the Bruker SADABS program. Electron density associated with a hydrogen atom H9B attached to oxygen O9 (distance 1.288 Å) was allowed to refine. Unresolved solvent were accounted for by using the PLATON program SQUEEZE which found 106 electrons or 2.5 molecules of diethyl ether (42 electrons/molecule). All other hydrogen atoms were placed using a riding model and their positions constrained relative to their parent atom using the appropriate HFIX command in SHELXL-97. Full-matrix least-squares refinement on F^2 for 10 365 data and 572 parameters gave final R indicies of $R(F) = 0.0522$ and $R_w(F^2) = 0.0883$ (where $R = \sum\|F_o| - |F_c\|/\sum|F_o|$ and $R(wF^2) = \{\sum[w(F_o^2 - F_c^2)^2]/\sum[w(F_o^2)^2]\}^{1/2}$) [11–13].

3. Results and discussion

3.1. Synthesis

In this study a $[Mn^{III}O_2]^{8+}$ "butterfly" complex was reacted with a 1:1 molar ratio of Et_3N and the tetradentate ligand H_3tea yielding the solvent dependent, mixed-valent wheel, complex **1**. In the absence of a base to deprotonate the H_3tea ligand, reaction conditions favored formation of the mono-nuclear species $[Mn(dbm)_3]$. Conversely, if an excess of base is used, no product was obtained. Under the reaction conditions used in this study, yields for complex **1** were very low (5% by manganese); however, low product yields have been previously reported and are not uncommon in polynuclear transition metal complexes. This is due to a number of factors inherent in the synthetic process that include solubility, pH control and competing products.

3.2. Crystal structure

$[Mn_4(anca)_4(Htea)_2(dbm)_2] \cdot 2.5Et_2O$ (**1**) crystallizes in the triclinic $P\bar{1}$ space group (ORTEP and Mn_4 core shown in Figs. 1 and 2, respectively). Table 1 gives selected bond distances and angles for complex **1**. Since the molecule sits on an inversion center, the symmetry transformations of $-x + 2$, $-y + 2$, and $-z + 1$ were used in order to generate the equivalent atoms in the target complex. The $[Mn_4O_4]$ core consists of two 6-coordinate Mn^{III} atoms in the wing positions and two 6-coordinate Mn^{II} atoms in the body positions, all of which are nearly coplanar. Each Mn^{II} atom interacts with two neighboring Mn^{III} atoms via a μ_2-alkoxide group from the $Htea^{2-}$ ligand and a bridging $anca^-$ ligand. The structure is capped by two dbm^- ligands, filling the remaining two coordination sites of the

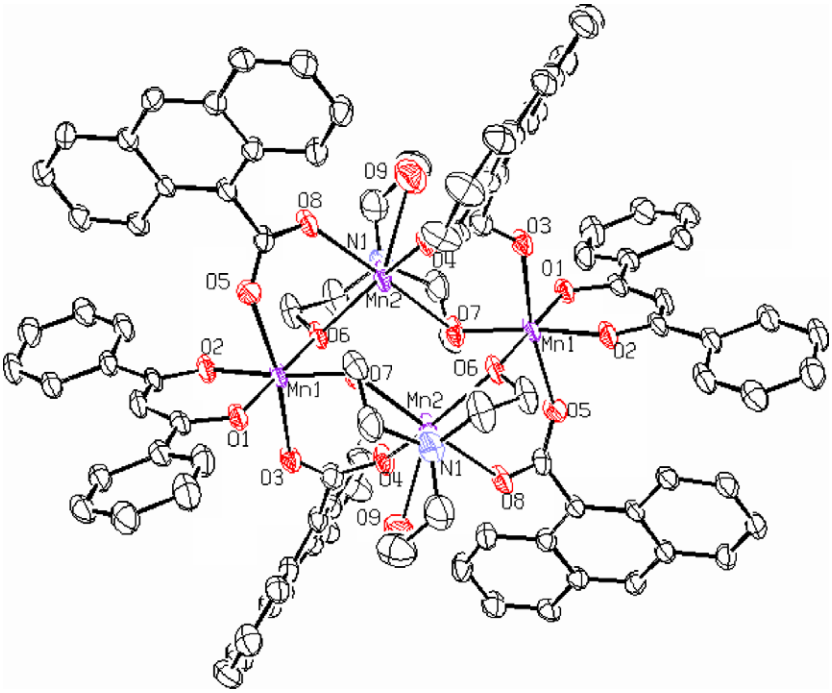


Fig. 1. ORTEP of $[Mn_4(anca)_4(Htea)_2(dbm)_2]\cdot 2.5Et_2O$ (**1**) showing 50% probability of thermal ellipsoids. The ether solvate molecules were not refined.

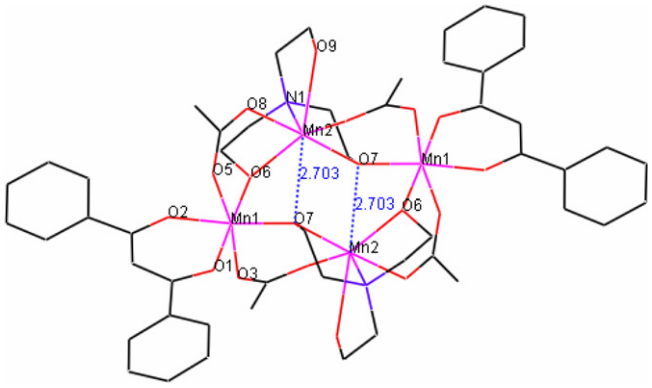


Fig. 2. Mn_4 core of $[Mn_4(anca)_4(Htea)_2(dbm)_2]\cdot 2.5Et_2O$ (**1**) (anthracene rings omitted for clarity) illustrating the magnetic exchange pathways and across-wheel $Mn^{II}\cdots O$ distance of 2.703 Å.

Table 1
Selected interatomic distances (Å) and angles (°) for $[Mn_4(anca)_4(Htea)_2(dbm)_2]\cdot 2.5Et_2O$ (**1**)

Mn(1)–O(1)	1.9375(19)	Mn(2)–O(8)	2.1852(18)
Mn(1)–O(2)	1.9226(19)	Mn(2)–O(9)	2.474(3)
Mn(1)–O(3)	**2.1591(18)**	Mn(2)–N(1)	2.389(3)
Mn(1)–O(5)	**2.2255(18)**	***Mn(2)–O(7)***	**~2.703(5)**
Mn(1)–O(6)	1.8742(18)	O(7)–Mn(1)–O(6)	84.24(8)
Mn(1)–O(7)	1.9228(18)	O6–Mn(2)–O(7)#1	92.91(6)
Mn(2)–O(4)	2.1104(18)	Mn(1)–O(6)–Mn(2)	110.01(8)
Mn(2)–O(6)	2.1659(17)	Mn(1)–O(7)–Mn(2)	122.00(8)
Mn(2)–O(7)#1	2.2030(18)	Mn(2)–O(7)–Mn(2)#1	~97.24(8)

Jahn–Teller axes and through-wheel $Mn^{II}\cdots O$ distance highlighted.

Mn^{III} atoms. All three arms of the $Htea^{2-}$ ligands are coordinated to the body Mn^{II} atoms, although one of the arms (O(9)) remains protonated.

The valency of the Mn atoms was confirmed by the presence of Jahn–Teller distortion around the Mn(1) atom. The Mn(1)–O(3) and Mn(1)–O(5) bonds (2.1591(18) Å and 2.2255(18) Å, respectively) are significantly longer than the Mn(1)–O bonds making up the square planar portion of the distorted octahedron (1.87–1.94 Å). The Jahn–Teller axes are oriented orthogonal to the plane of the dbm ligands which deviate slightly from planarity.

The crystal data for this complex give some evidence for the presence of a wheel-shaped molecule as opposed to a pseudo-dicubane structure. The Mn(2)···O(7) body–body distance of 2.703 Å (Fig. 2) is ~0.4–0.8 Å longer than the corresponding bond in known dicubanes [14–18]. This distance is also considerably longer than the sum of the ionic radii of Mn^{2+} and O^{2-} (~2.2 Å) [19]. Since the molecule is a wheel, the interaction between the two Mn^{II} ions in the body positions (body–body coupling constant, J_{bb}) is negligible and the complex can be assumed to have only one exchange pathway between the Mn atoms (wing–body, J_{wb}), as established further by the fitting of the susceptibility data (vide infra).

3.3. Magnetic measurements

Variable-temperature dc magnetization data were collected for complex **1** at 0.1 T from 300 K to 1.8 K. A maximum molar susceptibility of ~10.6 $cm^3\,mol^{-1}\,K$ is observed at 300 K (Fig. 3), which gradually decreases when the temperature is decreased to 50 K. A decline in susceptibility with decreasing temperature results from intramolecular antiferromagnetic exchange interactions. The observed $\chi_m T$ value of ~10.6 $cm^3\,mol^{-1}\,K$ at 300 K is

smaller than the theoretical spin-only value of 14.8 cm^3 K mol^{-1} calculated for two Mn^{II} and two Mn^{III} non-interacting ions. The rapid decline in magnetic susceptibility at temperatures below ~20 K is due to zero-field splitting and Zeeman interactions. The $\chi_m T$ values determined below 5 K plateau at a value of approximately ~0.8 cm^3 K mol^{-1}.

Two approaches were used in the fitting of dc molar magnetic susceptibility data: the simple Kambe approach [20] that only accounts for Heisenberg isotropic magnetic exchange between pairs of Mn atoms, and a full Hamiltonian matrix diagonalization approach. In the latter approach, the Zeeman interaction, single-ion zero-field and even antisymmetry in the exchange interactions are explicitly included.

3.3.1. Fitting of susceptibility by the Kambe approach

Scheme 1 illustrates the one J-value Kambe vector coupling scheme used to model the magnetic exchange pathways in complex **1**, assuming there are no across-wheel exchange interactions. The model incorporates a single coupling constant (J) which represents exchange coupling between Mn^{II} and Mn^{III} atoms, where Mn(1) and Mn(3) are Mn^{III} atoms, and Mn(2) and Mn(4) are Mn^{II} atoms

$$\widehat{H} = -2J\left[\widehat{S}_1\widehat{S}_2 + \widehat{S}_2\widehat{S}_3 + \widehat{S}_3\widehat{S}_4 + \widehat{S}_4\widehat{S}_1\right] \quad (1)$$

$$\widehat{S}_A = \widehat{S}_1 + \widehat{S}_3; \quad \widehat{S}_B = \widehat{S}_2 + \widehat{S}_4; \quad \widehat{S}_T = \widehat{S}_A + \widehat{S}_B \quad (2)$$

$$E(S_T) = -J[S_T(S_T+1) - S_A(S_A+1) - S_B(S_B+1)] \quad (3)$$

The Heisenberg spin Hamiltonian for complex **1** is given in Eq. (1). Application of the appropriate Kambe vector coupling scheme (Eq. (2)) and substitution of equivalent terms into Eq. (1) leads to Eq. (3). Least squares analysis of the observed molar magnetic susceptibility, in conjunction with the Van Vleck equation [21], produced a good theoretical fit as illustrated by the solid line in Fig. 3. Theoretical fitting parameters were calculated to be $g = 1.8$ and $J = -2.1$ cm^{-1} with a spin ground state of $S = 1$.

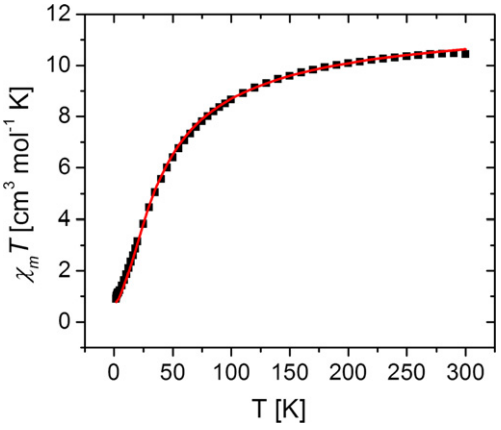
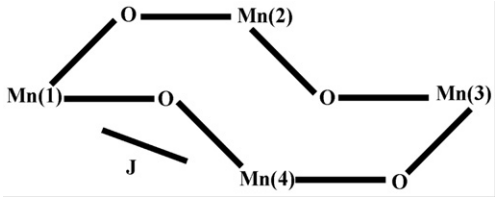


Fig. 3. DC magnetic susceptibility vs. temperature data for $[Mn_4(anca)_4(Htea)_2(dbm)_2]\cdot 2.5Et_2O$ (**1**) collected from 300 K to 1.8 K in an applied field of 0.1 T. (■ observed). The solid line represents the best theoretical fit obtained through least squares fitting employing one J-value as depicted in Scheme 1.



Scheme 1. Kambe exchange model illustrating magnetic exchange pathways for $[Mn_4(anca)_4(Htea)_2(dbm)_2]\cdot 2.5Et_2O$ (**1**), where Mn(1) and Mn(3) represent Mn^{III} ions and Mn(2) and Mn(4) represent Mn^{II} ions.

Theoretical fits of the magnetic susceptibility data were also carried out employing the same Kambe strategy (Scheme 2) that has been applied to previously reported Mn_4 "dicubane" and "butterfly" complexes with two coupling constants (J_{wb} and J_{bb}) [22,23]

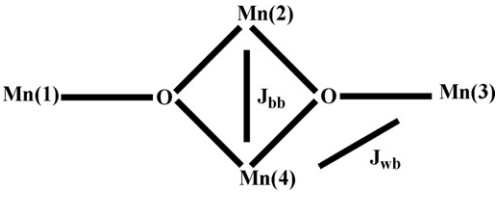
$$\widehat{H} = -2\left[J_{12}\left(\widehat{S}_1\cdot\widehat{S}_2\right) + J_{23}\left(\widehat{S}_2\cdot\widehat{S}_3\right) + J_{24}\left(\widehat{S}_2\cdot\widehat{S}_4\right) + J_{34}\left(\widehat{S}_3\cdot\widehat{S}_4\right) + J_{41}\left(\widehat{S}_4\cdot\widehat{S}_1\right)\right] \quad (4)$$

$$E(S_T) = -J_{wb}[S_T(S_T+1) - S_A(S_A+1) - S_B(S_B+1)] - J_{bb}[S_A(S_A+1)] \quad (5)$$

The Heisenberg spin Hamiltonian that represents the spin-coupling for the two-J model (J_{wb} and J_{bb}), as previously reported, is given in Eq. (4), and the resulting eigenvalue equation (5). Theoretical fitting parameters for g, J_{wb}, and J_{bb}, and were calculated to be 1.8, -2.2 cm^{-1} and -0.7 cm^{-1}, respectively. The fitting incorporating two J-values, one for the across-wheel $Mn^{II}\cdots Mn^{II}$ interaction, is **not** better than the fit for one J-value. The two theoretical fits are essentially identical. Furthermore, when we examined the change in error of fitting as J_{bb} is changed from -0.7 cm^{-1}, we find there is little response and $J_{bb} = 0$ is just as good as $J_{bb} = -0.7$ cm^{-1}. We conclude that only one J-value (J_{wb}) is needed to fit the data for complex **1** and, thus, complex **1** is a wheel complex.

3.3.2. Fitting of susceptibility by full matrix diagonalization approach

It has been shown that the simple Kambe approach does not fully describe systems where there exist low-lying



Scheme 2. The Kambe coupling model illustrating magnetic exchange pathways for $[Mn_4(anca)_4(Htea)_2(dbm)_2]\cdot 2.5Et_2O$, where Mn(1) and Mn(3) represent Mn^{III} ions and Mn(2) and Mn(4) represent Mn^{II} ions. In this case it is assumed that there is an across-wheel exchange interaction between the two Mn^{II} ions.

excited states [24]. In addition to the HDVV type (isotropic) of super-exchange discussed in Section 3.3.1, the Dzialoshinsky–Moriya type antisymmetric exchange interactions [25,26], zero-field splitting, and Zeeman interactions were also factored in order to fully model the spin Hamiltonian of the system (Eq. (6)):

$$\widehat{H} = \widehat{H}_{\mathrm{ex}} + \widehat{H}_{\mathrm{DM}} + \widehat{H}_{\mathrm{zfs}} + \widehat{H}_{\mathrm{Zeeman}} \tag{6}$$

$$\widehat{H}_{\mathrm{ex}} = -2J_{\mathrm{wb}}\left(\widehat{S}_1 + \widehat{S}_3\right)\cdot\left(\widehat{S}_2 + \widehat{S}_4\right) - 2J_{\mathrm{bb}}\widehat{S}_2\widehat{S}_4 = J_{\mathrm{wb}}\left(\widehat{S}_{13}^2 + \widehat{S}_{24}^2 - \widehat{S}_{\mathrm{T}}^2\right) + J_{\mathrm{bb}}\left(\widehat{S}_2^2 + \widehat{S}_4^2 - \widehat{S}_{24}^2\right) \tag{7}$$

$$\widehat{H}_{\mathrm{DM}} = d_{12}\cdot\widehat{S}_1\times\widehat{S}_2 + d_{23}\cdot\widehat{S}_2\times\widehat{S}_3 + d_{34}\cdot\widehat{S}_3\times\widehat{S}_4 + d_{41}\cdot\widehat{S}_4\times\widehat{S}_1 \tag{8}$$

$$\widehat{H}_{\mathrm{zfs}} = \sum_{j=1,3} D\left(\widehat{S}_{j\zeta}^2 - \frac{1}{3}\widehat{S}_j^2\right) = \sum_{j=1,3} D\left[\left(\widehat{S}_j^x\cos\phi_j\sin\theta_j + \widehat{S}_j^y\sin\phi_j\sin\theta_j + \widehat{S}_j^z\cos\theta_j\right)^2 - \frac{1}{3}\widehat{S}_j^2\right] = \sum_{j=1,3} D\left[\left(\frac{\sin\theta_j}{2}\mathrm{e}^{-\mathrm{i}\phi_j}\widehat{S}_j^+ + \frac{\sin\theta_j}{2}\mathrm{e}^{+\mathrm{i}\phi_j}\widehat{S}_j^- + \widehat{S}_j^z\cos\theta_j\right)^2 - \frac{1}{3}S_j(S_j+1)\right] \tag{9}$$

$$\widehat{H}_{\mathrm{Zeeman}} = -g\beta\sum_{j=1}^{4}\left(H_x\widehat{S}_j^x + H_y\widehat{S}_j^y + H_z\widehat{S}_j^z\right) \tag{10}$$

where $\widehat{S}_j$ stands for the spin operator of j-th spin ($S = 5/2$ for Mn^{II} and $S = 2$ for Mn^{III}), $\widehat{S}_{13} \equiv \widehat{S}_1 + \widehat{S}_3$, $\widehat{S}_{24} \equiv \widehat{S}_2 + \widehat{S}_4$ and $\widehat{S}_{\mathrm{T}} \equiv \widehat{S}_{13} + \widehat{S}_{24}$ are the partial-sum and the resultant spin operators, respectively, J_{wb} and J_{bb} are defined as in Eq. (4), $\boldsymbol{d}_{ij}$ is the Dzialoshinsky–Moriya vector for the interaction between i-th and j-th ions (Eq. (8)), D is the uniaxial zero-field splitting parameter for each ion, (ϕ_j, θ_j) are the azimuthal and polar angles of single-ion anisotropy axis ζ for j-th ion (Eq. (9)), g is the Landé g factor, β is the Bohr magneton, and H_α is α-component of external magnetic field $\boldsymbol{H}$ (Eq. (10)).

Due to the symmetry of the $Mn_2^{III}Mn_2^{II}$ cluster, the quantization axes in the anisotropy term $\widehat{H}_{\mathrm{zfs}}$ were aligned in the same direction, and were taken as parallel, i.e. $(\phi_1, \theta_1) = (\phi_3, \theta_3) = (0°, 0°)$. The Jahn–Teller elongation axes for the two Mn^{III} ions in complex **1** are parallel. In order to avoid over-parameterization, the Dzialoshinsky–Moriya vectors for the Mn–O–Mn interaction pathways were taken to be identical, and perpendicular to the molecular plane [2], i.e. $\boldsymbol{d}_{12} = \boldsymbol{d}_{23} = \boldsymbol{d}_{34} = \boldsymbol{d}_{41} = (0, 0, d)$. Other interactions, such as biquadratic exchange interaction, were omitted in the present treatment since their contribution to thermodynamic quantities is not dominant.

Based on this spin Hamiltonian, magnetization values $M(H, T)$ are evaluated by the conventional way as given in the following equation:

$$M(H,T) = \frac{Ng\mu_{\mathrm{B}}}{4\pi}\int \mathrm{d}\cos\theta\int \mathrm{d}\phi\,\frac{\langle \boldsymbol{S}_{\mathrm{T}}\rangle\cdot\boldsymbol{H}}{H} \tag{11}$$

where

$$\langle \boldsymbol{S}_{\mathrm{T}}\rangle = Tr\left[\widehat{S}_{\mathrm{T}}\exp(-\widehat{H}(\boldsymbol{H})/k_{\mathrm{B}}T)\right]\Big/Z(\boldsymbol{H}) \tag{12}$$

and

$$Z(\boldsymbol{H}) \equiv Tr\left[\exp\left(-\widehat{H}(\boldsymbol{H})/k_{\mathrm{B}}T\right)\right] \tag{13}$$

where N is Avogadro's number, and (θ, ϕ) are polar and azimuthal angles of the external field $\boldsymbol{H}$, k_{B} is the Boltzmann constant, T is the temperature, and the trace is evaluated using a set of energy eigenvectors $|E_i\rangle$, i.e. $\mathrm{Tr}[A] = \sum_i \langle E_i|A|E_i\rangle$, following the full-matrix diagonalization of the spin Hamiltonian by an LAPACK subroutine ZHEEV [27]. The powder average procedure over (θ, ϕ) is approximated by spherical gaussian quadrature using 43-point Lebedev grid on a hemisphere [28]. Temperature-independent contribution from the Van Vleck paramagnetism χ_{TIP}, was also considered. The optimized parameter set (g, J_{wb}, J_{bb}, d, D, χ_{TIP}) for complex **1** is obtained by minimizing a square deviation sum of effective magnetic moment, $\sum[\mu_{\mathrm{eff}}(\mathrm{obs}) - \mu_{\mathrm{eff}}(\mathrm{calc})]^2$ ($\mu_{\mathrm{eff}} = \sqrt{3Mk_{\mathrm{B}}T/NH}$), using a downhill simplex algorithm [29–32].

Fig. 4 illustrates a plot of the reduced magnetization ($M/N\beta$) versus H/T data for complex **1** employing the full-matrix diagonalization approach. Data were collected at 5, 4, 3, 2, 1, 0.5 and 0.1 T in the temperature range of 1.8–4 K. The solid lines represent a theoretical fit the of data that gave fitting values of $S = 1$, $g = 2.2$, $D = -9.2\ \mathrm{cm}^{-1}$, and $J = -2.8\ \mathrm{cm}^{-1}$. It should be noted that theoretical fit depicted in Fig. 4 (solid lines) is based on a model employing a single J-value (Scheme 1) and is preliminary, however, it can be seen in Fig. 4 that the fit is quite good. It is not possible to fit these magnetization

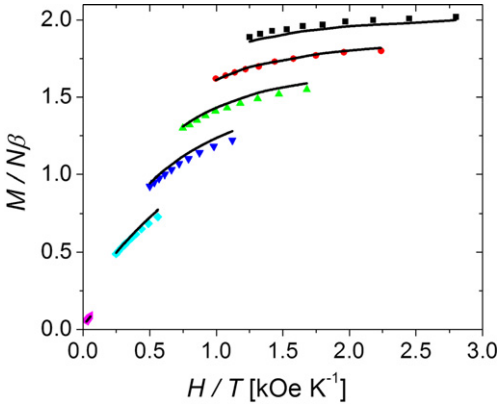
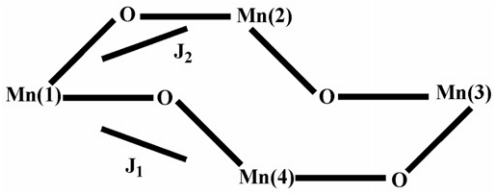


Fig. 4. Plot of reduced magnetization ($M/N\beta$) vs. H/T data for complex **1**, where M is the molar magnetization, N is Avogadro's number, and β is the Bohr magneton. Data were collected at 5 (■), 4 (●), 3 (▲), 2 (▼), 1 (◆) and 0.1 T (◀) in the temperature range of 1.8–4 K. The solid lines represent a theoretical fit of the data employing the full (900 × 900) Hamiltonian matrix diagonalization on each iteration. This gave preliminary fitting values of $S = 1$, $g = 2.2$, $D = -9.2\ \mathrm{cm}^{-1}$, and $J = -2.8\ \mathrm{cm}^{-1}$. See text for details of analysis.



Scheme 3. Illustration of an exchange model with two J-values as dictated by the symmetry of complex **1**. It is not possible to use the Kambe approach to simplify the spin Hamiltonian for this case. The full matrix diagonalization approach is required.

data assuming only an isolated $S = 1$ ground state. A full matrix diagonalization approach is needed and it shows that there is considerable mixing of excited spin states.

4. Conclusion

A new Mn_4 complex has been prepared that appears to be a wheel complex. This is supported by the relatively long Mn–O contact distances across the wheel and by the success of fitting the susceptibility data with only one J-value. Since there are low-lying excited states, the Kambe approach is a simplified method. The full Hilbert space (900×900) Hamiltonian matrix (set up in the uncoupled basis set and incorporating single-ion zero-field and Zeeman interactions) has to be diagonalized on fitting iterations. Preliminary results from the full-matrix diagonalization approach (Fig. 4) show that the reduced magnetization data for both complexes can be fit employing only one J-value. However, the value of $g = 2.2$ calculated in preliminary fits of magnetization data employing a full matrix diagonalization approach is larger than the expected value of $g \leqslant 2.0$ reported for similar mixed-valent polynuclear manganese complexes. Furthermore, the value of $g = 2.2$ calculated using a full matrix diagonalization approach is not in agreement with $g = 1.8$ calculated employing the Kambe model, suggesting the need for further investigation. Additional full-matrix diagonalization calculations are in progress for both variable temperature dc susceptibility data and reduced magnetization data employing a two J-value model (Scheme 1) and a symmetry dictated two J-value model (Scheme 3) where there are alternating coupling constants around the periphery of the wheel. These calculations will be fully described in a later paper.

Acknowledgement

This work was funded by the National Science Foundation.

Appendix A. Supplementary material

CCDC 624505 contains the supplementary crystallographic data for this paper. These data can be obtained free of charge via http://www.ccdc.cam.ac.uk/conts/retrieving.html, or from the Cambridge Crystallographic Data Centre, 12 Union Road, Cambridge CB2 1EZ, UK; fax: (+44) 1223-336-033; or e-mail: deposit@ccdc.cam.ac.uk. Supplementary data associated with this article can be found, in the online version, at doi:10.1016/j.poly.2006.10.036.

References

[1] S.M.J. Aubin, M.W. Wemple, D.M. Adams, H.-L. Tsai, G. Christou, D.N. Hendrickson, J. Am. Chem. Soc. 118 (1996) 7746.
[2] R. Sessoli, D. Gatteschi, A. Caneschi, M.A. Novak, Nature 365 (6442) (1993) 141.
[3] R. Sessoli, H.L. Tsai, A.R. Schake, S.Y. Wang, J.B. Vincent, K. Folting, D. Gatteschi, G. Christou, D.N. Hendrickson, J. Am. Chem. Soc. 115 (5) (1993) 1804.
[4] M. Murugesu, W. Wernsdorfer, K.A. Abboud, G. Christou, Angew. Chem., Int. Ed. 44 (2005) 892.
[5] X.S. Liu, S. Lin, B.Z. Lin, C.C. Lin, J.Q. Huang, Angew. Chem., Int. Ed. 40 (2001) 1084.
[6] E.M. Rumberger, S.J. Shah, C.C. Beedle, L.N. Zakharov, A.L. Rheingold, D.N. Hendrickson, Inorg. Chem. 44 (2005) 2742.
[7] E.M. Rumberger, L.N. Zakharov, A.L. Rheingold, D.N. Hendrickson, Inorg. Chem. 43 (2005) 6531.
[8] M. Murugesu, J. Raftery, W. Wernsdorfer, G. Christou, E.K. Brechin, Inorg. Chem. 43 (2004) 4203.
[9] A.J. Tasiopoulos, A. Vinslava, W. Wernsdorfer, K.A. Abboud, G. Christou, Angew. Chem., Int. Ed. 43 (2004) 2117.
[10] C.C. Beedle, D.N. Hendrickson, unpublished.
[11] SMART, SAINT, SADABS and SHELXTL programs obtained Bruker AXS Madison, WI.
[12] A.L. Spek, PLATON: A Multipurpose Crystallographic Tool, Utrecht University, Utrecht, The Netherlands, 1998.
[13] P. Sluis, A.L. Spek SQUEEZE, Acta Crystallogr., Sect. A 46 (1990) 194.
[14] L.M. Wittick, K.S. Murray, B. Moubaraki, S.R. Batten, L. Spicca, K.J. Berry, Dalton Trans. (2004) 1003.
[15] D. Foguet-Albiol, T.A. O'Brien, W. Wernsdorfer, B. Moulton, M.J. Zaworotko, K.A. Abboud, G. Christou, Angew. Chem., Int. Ed. 44 (2005) 897.
[16] J. Yoo, E.K. Brechin, A. Yamaguchi, M. Nakano, J.C. Huffman, A.L. Maniero, L.C. Brunel, K. Awaga, H. Ishimoto, G. Christou, D.N. Hendrickson, Inorg. Chem. 39 (2000) 3615.
[17] S. Wang, K. Folting, W.E. Streib, E.A. Schmitt, J.K. McCusker, D.N. Hendrickson, G. Christou, Angew. Chem., Int. Ed. Engl. 30 (3) (1991) 305.
[18] E.C. Yang, N. Harden, W. Wernsdorfer, L. Zakharov, E.K. Brechin, A.L. Rheingold, G. Christou, D.N. Hendrickson, Polyhedron 22 (2003) 1857.
[19] G.L. Miessler, D.A. Tarr, Inorganic Chemistry, 3rd ed., Pearson Prentice-Hall, Englewood Cliffs, NJ, 2004.
[20] K. Kambe, J. Phys. Soc. Jpn. 5 (1950) 48.
[21] J.H. Van Vleck, The Theory of Electric and Magnetic Susceptibilities, Oxford University Press, London, 1932.
[22] J.B. Vincent, C. Christmas, H.-R. Chang, Q. Li, P.D.W. Boyd, J.C. Huffman, D.N. Hendrickson, G. Christou, J. Am. Chem. Soc. 111 (1989) 2086.
[23] E. Libby, J.K. McCusker, E.A. Schmitt, K. Folting, D.N. Hendrickson, G. Christou, Inorg. Chem. 30 (1991) 3486.
[24] A. Wilson, J. Lawrence, E-C. Yang, M. Nakano, D.N. Hendrickson, S. Hill, Phys. Rev. B 74, 1 (R) (2006).
[25] M. Honda, J. Phys. Soc. Jpn. 62 (1993) 704.
[26] M. Honda, J. Phys. Soc. Jpn. 62 (1993) 1818.
[27] E. Anderson et al., LAPACK Users' Guide, Software, Environments and Tools, 3rd ed., vol. 9, Society for Industrial and Applied Mathematics, Philadelphia, PA, 1999. Available from: <http://www.netlib.org/lapack/>.

[28] M. Edén, M.H. Levitt, J. Magn. Reson. 132 (1998) 220. Available from: <http://www.mhl.soton.ac.uk/research/software/orientations/>.
[29] R. Mead, J.A. Nelder, Comput. J. 7 (1965) 308.
[30] J.M. Parkinson, D. Hutchinson, in: F.A. Lootsma (Ed.), Numerical Methods for Non-linear Optimization, Academic Press, London, 1972, p. 115.
[31] W.H. Press, S.A. Teukolsky, W.T. Vetterling, B.P. Flannery, Numerical Recipes, Cambridge University Press, Cambridge, 1986.
[32] C.T. Kelly, SIAM J. Optimiz. 10 (1999) 43.

employing short bridging ligands having not more than three bridging diamagnetic atoms is important in constructing porous magnets [8–10]. In last two years we and other authors [11–16] have reported a novel porous family of $[M_3(HCOO)_6]$ constructed by the smallest and shortest carboxylate connector, $HCOO^-$. They show permanent porosity, thermal stability, a wide spectrum of guest inclusion and interesting guest-sensitive magnetism. In this paper we summarize the achievement and report briefly recent develop on the study of this porous magnet family based on our own work.

2. Synthesis

The novel family of porous $[M_3(HCOO)_6]$, where M = Mn, Fe, Co, Ni, Zn and Mg, has been recently discovered by us and other groups independently employing different synthetic methods. Albeit the compounds have been synthesized through solvo-thermal methods by other authors [13–15], we have developed a simple solution chemistry method at ambient temperature [11,12,16–19]. The compounds of this series, Mn, Fe, Co, Ni, and Zn, can be easily prepared with satisfactory yield by the reaction of the common divalent metal salt hydrate with formic acid neutralized by triethylamine in methanol at room temperature, though we have not test the Mg salt. For Mn and Zn, simply mixing the methanol solution of metal salt with that of formic acid and triethylamine produces good quality crystals of the porous frameworks with guest of methanol and water, while for Fe and Co diffusion methods are needed for obtaining crystals of good quality, and for the Ni compound good crystals have not been obtained but the phase is proved by powder X-ray diffraction (PXRD, Fig. 1). Carefully applied diffusion method should be further tested to obtain good crystals of Ni compound. In our approach, the usage of bulky triethylamine and non-coordinating solvent such as methanol are the two key requirements for producing these porous framework compounds, because the former inhibits the formation of anionic frameworks, as what observed for the small amine cations as templates [20], and the later avoids the formation of metal-formates with coordinating solvent as co-ligands [21]. The de-solvated $[M_3(HCOO)_6]$ samples with empty channels could be easily obtained by treating the samples of the parent compound under dynamic vacuum at ca. 90 °C to remove the guests, and the de-solvated samples still show good crystallinity, which is important for further study of guest-inclusion by single crystal X-ray diffraction method (SXRD). By exposing samples of de-solvated $[M_3(HCOO)_6]$ to the vapor of guests used, a series of guest-inclusion compounds could be prepared. Compared to the solvo-thermal techniques employed by other groups, our approach seems to be milder, easier, and beneficial for guest inclusion or exchange study. Finally, the mixed-metal frameworks with different ratio and kind of metal could be prepared by our method.

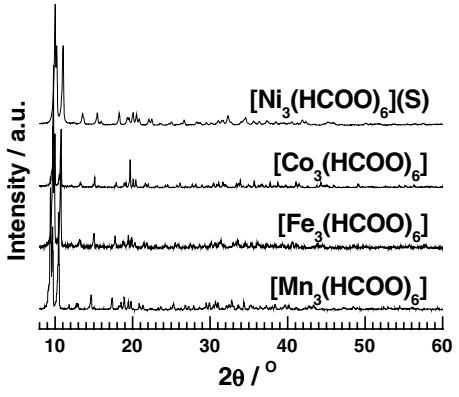


Fig. 1. PXRD patterns of $[M_3(HCOO)_6]$ for M = Mn, Fe, Co, and $[Ni_3(HCOO)_6](S)$ where S is presumed to be one CH_3OH by TGA (not presented here). Peak shift to higher two theta from M = Mn to Ni indicated the lattice shrinkage.

3. Thermal property, permanent porosity and guest inclusion behavior

The $[M_3(HCOO)_6]$ porous frameworks are thermally stable. This has been proved by both thermal analyses (TGA/DSC) and PXRD study (Fig. 2). For $[Mn_3(HCOO)_6]$, the framework was found to keep the porous phase up to 220 °C, then a phase transition, probably a collapse of the porous framework, occurred with energy release of 11 $kJmol^{-1}$, and it finally decomposed around 260 °C. Other members, Fe [19], Co [12] and Ni, seem to be thermally stable up to 270 °C, without any phase transition before the framework decomposition. The stability is clearly related to the diamond structure and further contribution of concerted C–H···O hydrogen bonds in the structure. The permanent porosity of $[M_3(HCOO)_6]$ has also been proved by gas (N_2/H_2) adsorption experimental [12,13,15,19]. Regarding currently great interest in H_2 storage [22] the $[M_3(HCOO)_6]$ family is a class of H_2 storage materials of middle capacity of ca. 1% wt.

The study on the guest inclusion chemistry of the $[M_3(HCOO)_6]$ family [11,15–19] revealed that the porous frameworks are robust as well as flexible for guest inclusion/exchange, and they display a wide spectrum of guest absorption. Our investigation on the Mn [11,17,18] and Fe [19] (and non-magnetic Zn [16]) compounds demonstrated that both can absorb various guests and the possible limitation for guest inclusion is the size of the guests. Especially, $[Mn_3(HCOO)_6]$ has undergone an extended investigation on its guest inclusion chemistry performed by us, and over 40 kinds of guests have been successfully inserted into the pores. The guests can be liquid or volatile solid, polar as carboxylic acids and alcohols or non-polar as alkanes and benzene, small as acetonitrile and formic acid and large as tetrathiafulvalene, and enantiomer-pure guests and the racemic mixture. Although guest-inclusion behaviors of many porous metal-organic framework systems [5–10,23] have been investigated, it is the present

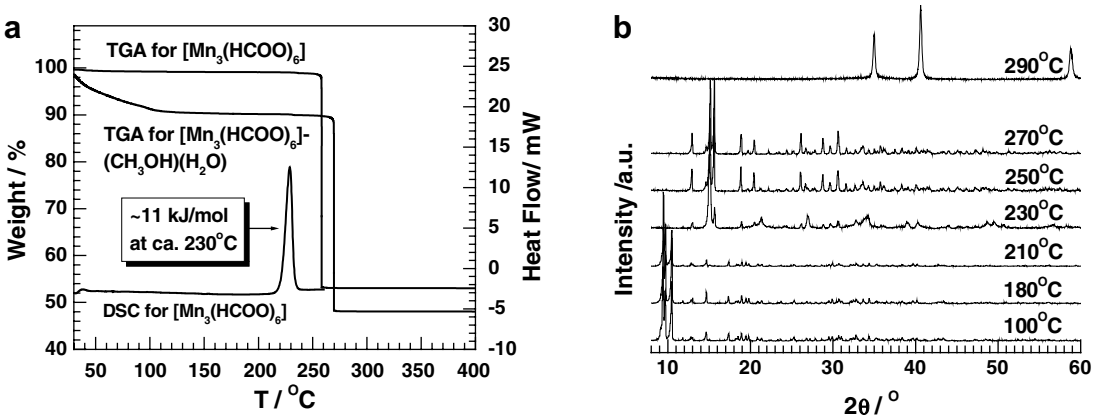


Fig. 2. (a) TGA and DSC runs for $[Mn_3(HCOO)_6]$ parent compound and its de-solvated form. For Fe, Co, and Ni compounds similar traces were observed except that they showed no phase transition before the framework decomposition. (b) PXRD patterns for $[Mn_3(HCOO)_6]$ samples pretreated at different temperatures. The structure of the phase after collapse is still unknown.

family of porous $[M_3(HCOO)_6]$ frameworks that shows such widest spectrum of guest inclusion.

4. Structures

4.1. The structure of $[M_3(HCOO)_6]$ framework

The compounds of the $[M_3(HCOO)_6]$ family are isostructural (Table 1 and Fig. 1). The porous framework (Fig. 3) is a diamond net consisting of the apex-sharing M-centered MM_4 tetrahedron nodes, in which all metal atoms possess octahedral coordination geometry, a striking feature of the family because it is usually known that most diamondoid coordination frameworks have metal atoms in tetrahedral coordination geometry [24]. The MM_4 tetrahedron node has one central M^{2+} ion, four apical M^{2+} ions, and six edges of $HCOO^-$ groups, which link the metal ions in *syn–syn/anti* mode (Fig. 3a). The four central to apical M–M linkages are two with one pair of M–O–M bridge and one *syn–syn* M–O–C–O–M bridge, and two with one M–O–M bridge and one pair of *syn–syn* M–O–C–O–M bridge, and the six apical to apical M–M linkages are all single *syn–anti* M–O–C–O–M bridge. It worth noting that due to the complicated metal–metal linkages described above giving rise to multiple super-exchange pathways and competition between them might be possible. M–O bond distances are in good agreement with the ionic radii of the divalent ions (Table 1), and this results in the size sequence of the frameworks from largest Mn to probably smallest Ni. The important M–O–M angles are around 97° for the double M–O–M connections, and around 112° for the single M–O–M ones. The framework is further strengthened by C–H···O hydrogen bonds [25] involving all $HCOO^-$ ligands.

The openness of the framework is shown by the empty channels running along the *b* direction and in an

Table 1
Cell parameters, void space and M–O distances of de-solvated $[M_3(HCOO)_6]$ of M[a] = Mn, Fe, Co, Zn and Mg in space group $P2_1/c$ around 100 K

Compound	$[Mn_3(HCOO)_6]$	$[Fe_3(HCOO)_6]$	$[Co_3(HCOO)_6]$	$[Zn_3(HCOO)_6]$[c]	$[Mg_3(HCOO)_6]$[c]
a (Å)	11.726(1)	11.4702(2)	11.2783(4)	11.3376(2)	11.324(2)
b (Å)	10.176(1)	9.9598(2)	9.8567(4)	9.8429(2)	9.847(2)
c (Å)	18.724(3)	18.3735(4)	18.1630(6)	18.1765(4)	18.314(2)
β (°)	127.190(3)	127.443(2)	127.204(2)	127.266(1)	127.03(2)
V (Å^3)	1779.9(4)	1666.52(6)	1608.2(1)	1614.27(6)	1630.2(6)
Void space per cell/% (Å^3)	32.8, 584	30.4, 507	29.8, 479	29.8, 480	30.9, 504
M–O distances (Å)	2.105–2.233	2.065–2.161	2.043–2.119	2.033–2.147	2.020–2.114
Ionic radius of M^{2+} (Å)	0.97	0.92	0.89	0.88	0.86
Reference	[17]	[19]	[12][b]	[16]	[15]

[a] Data for the Ni analogue without guest is currently not available. The cell parameters (at 300 K) for Ni analogue with guests of formic acid and water, reported by Powell et al. [14] and transformed according to space group setting $P2_1/c$, are: $a = 11.1586$, $b = 9.7789$, $c = 17.9410$ Å, $\beta = 126.998°$, $V = 1563.53$ Å^3. The temporary cell parameters obtained from the PXRD data (Fig. 1) for $[Ni_3(HCOO)_6](S)$ are $a = 11.117$, $b = 9.741$, $c = 17.834$ Å, $\beta = 127.4°$, $V = 1534$ Å^3. The Ni framework should be the smallest one in the series regarding the smallest radius of Ni^{2+} (0.83 Å).

[b] Data available from the supporting information of [12].

[c] Data of $[Zn_3(HCOO)_6]$ and $[Mg_3(HCOO)_6]$ are for the purpose of comparison. For $[Mg_3(HCOO)_6]$ the cell parameters have been transformed according to space group setting $P2_1/c$, with the same e.s.d.'s we presumed.

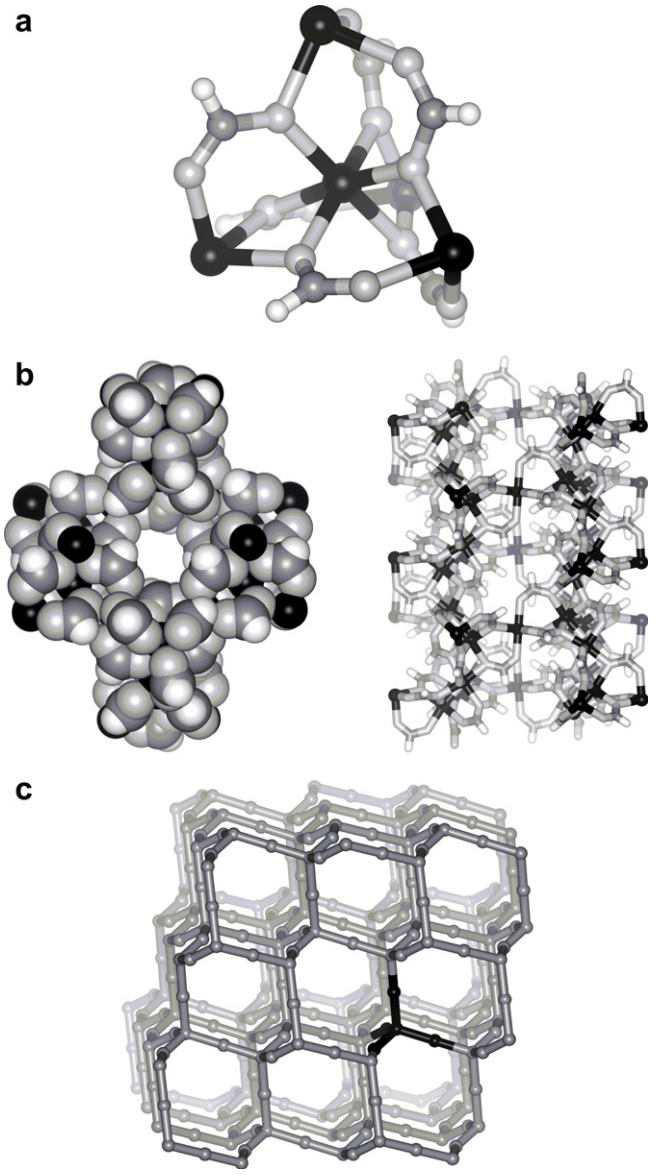


Fig. 3. The structure of the porous diamond framework of $[M_3(HCOO)_6]$ formed by the M-centred MM_4 tetrahedra as nodes sharing apices and showing open channels. (a) The MM_4 tetrahedron unit, (b) the top, space filling view and side view of one channel and (c) the diamond framework with one tetrahedral node highlighted in black. Atomic scheme is M black, C grey, O light grey and H white, in (a) and (b).

approximately honeycomb arrangement (Fig. 3b and c), with cross-section of ca. 4×5 Å. It is apparent that the large nodes or thick walls prohibit the interpenetration thus result in the permanent porosity of the framework. The void spaces are ca. 30%, depending on the kind of metal. It is worth noting that for the available de-solvated $[M_3(HCOO)_6]$ the frameworks change from the smallest $[Co_3(HCOO)_6]$ with the cell volume of 1608.2 $Å^3$ to the largest one for $[Mn_3(HCOO)_6]$ of 1779.9 $Å^3$ (Table 1), therefore the framework has ca. 20% lattice volume change by using the metal ions of different ionic radii. Due to the different orientations of the $HCOO^-$ groups the channel is zigzag like. It is lined by alternate arrays of C–H groups and oxygen atoms thus shows an amphiphilic character. The framework is flexible and it could breath to accommodate guests of different size. Finally, the channel is chiral because it lies at the 2_1-axis. These are the structural basis for the experimental observations of the wide and interesting guest inclusion behavior of the porous materials.

4.2. The structure of guest inclusion compounds of $[M_3(HCOO)_6](G)$ (G = guest)

As mentioned above, the $[M_3(HCOO)_6]$ frameworks can absorb guests of wide range. Due to the robust and flexible character of the porous framework, the guest inclusion compounds have good crystallinity in most cases, therefore the structures of guest inclusion compounds of $[M_3(HCOO)_6](G)$ can be determined by SXRD. Four representatives of $[Mn_3(HCOO)_6](CH_3CN)$ (acetonitrile), $[Mn_3(HCOO)_6](C_3H_4N_2)$ (imidazole), $[Mn_3(HCOO)_6]$-$(C_6H_5NO_2)$ (nitrobenzene) and $[Mn_3(HCOO)_6](R\text{-}CH_3\text{-}C^*HClCH_2OH)$ (*R*-chloropropan-1-ol), which have not been published yet, are shown in Fig. 4. The host framework displays considerable flexibility for accommodating guests of different size, where small guests like acetonitrile made the host framework shrink while large ones such as nitrobenzene expand it (notes in Fig. 4). For the Mn framework the volume of the lattice can be modulated by as much as 11%, and still retains crystalline, while for Fe framework a lattice volume change of 8.3% has been observed upon guest inclusion [19]. The guest molecules form zigzag array (Fig. 4) in the confined space of the zigzag like channel, and the host–guest interaction are mainly the weak hydrogen bonds [25] between hydrogen bond donors/acceptors of guest molecule and acceptors/donors of framework. Guests can have possible interaction between themselves. For example, imidazole molecules in the channel form $(imidazole)_n$ chain *via* N–H···N hydrogen bonds (Fig. 4b, N–H···N geometry: 3.04 Å, 163°) between them and the chain can be considered as proton wire [26]. It merits to point out that the polar guests form polar molecular array in one channel, indicating the uniaxial or chiral character of the channel, and the channel is wide enough for guests molecules of not so large size to rotate to find their energetically favorable positions and orientations in the channel. The larger or longer guests such as nitrobenzene (Fig. 4c) are unable to rotate freely in the channel, consequently, they are found to display two orientations in one channel. Finally, it has been observed that the chirality of the channel results in some selectivity for chiral guests upon their inclusion as found in compound of $[Mn_3(HCOO)_6](R\text{-}CH_3C^*HClCH_2OH)$ (Fig. 4d) [17].

The effect of guest-inclusion upon the molecular geometries of the host framework is subtle and complicated, and regular changes are mainly observed for the important M–O–M angles and the M···M distances that show increasing tendency with the size of the guest, and this

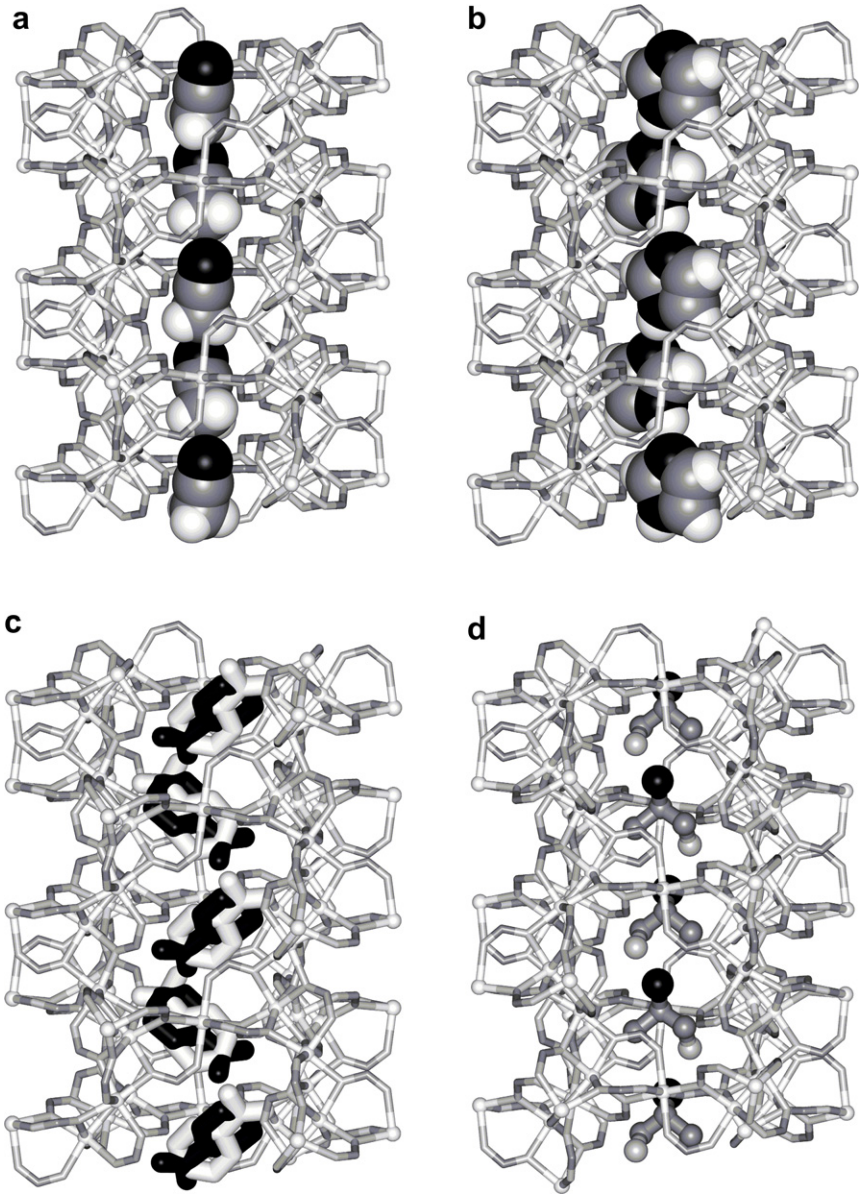


Fig. 4. Four representative structures guest-inclusion compounds of $[Mn_3(HCOO)_6](G)$: (a) $[Mn_3(HCOO)_6](CH_3CN)$ (acetonitrile), (b) $[Mn_3(HCOO)_6](C_3H_4N_2)$ (imidazole), (c) $[Mn_3(HCOO)_6](C_6H_5NO_2)$ (nitrobenzene) and (d) $[Mn_3(HCOO)_6](R\text{-}CH_3C^*HClCH_2OH)$ (*R*-chloropropan-1-ol). Atomic scheme for frameworks (without H) is Mn white, C grey, O light grey, and different styles for guests, CPK for acetonitrile and imidazole with C grey, N black and H white in (a) and (b), thick stick for nitrobenzene in (c) with black and white indicating two orientations of the guest molecule, and ball and stick for *R*-chloropropan-1-ol with C grey, O light grey, and Cl black in (d). Noting in (d) the R-guest is order in the channel of one handedness (in this case the *M*-channel) while disordered in the channel of opposite handedness (the *P*-channel, not shown here). Lattice volumes are (a) 1681.3(4), (b) 1718.0(6), (c) 1886.0(1) and (d) 1792.1(1) $Å^3$.

reflects the host framework expansion from small to large guests, and reveals the flexibility or breathing character of the host framework upon guest inclusion. The difference in the lattices of $[M_3(HCOO)_6]$ due to the metal ion arise subtle effect on the guest-inclusion behavior and host–guest interaction. For instance, it is found that included iodine molecules shows different host–guest and guest–guest interaction in $[Mn_3(HCOO)_6]$ compared to $[Fe_3(HCOO)_6]$ probably due to the size effect of the void space [11,19].

5. Magnetism

5.1. Magnetism of $[M_3(HCOO)_6]$

The magnetic properties of the $[M_3(HCOO)_6]$ series have been investigated [11,12,14,17–19]. The compounds display different magnetic behaviors (Fig. 5) depending on the kind of metal ion, that is the spin state. While Mn and Fe compounds are considered as ferrimagnets with critical temperatures of 8.0 K and 16.1 K, respectively,

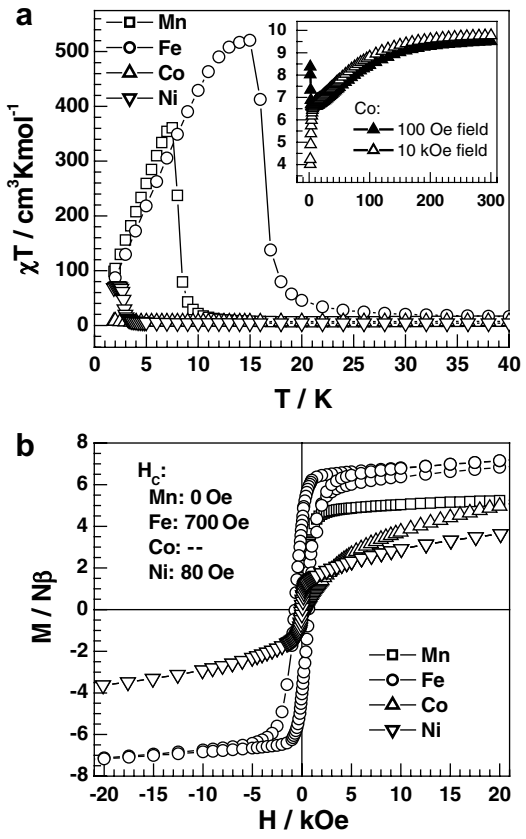


Fig. 5. Temperature dependence of susceptibility for $[M_3(HCOO)_6]$ of M = Mn, Fe, Co, and $[Ni_3(HCOO)_6](S)$ under 100 Oe field. Inset is detail for $[Co_3(HCOO)_6]$. (b) Field dependent magnetizations of the compounds at ca. 2 K.

the Co analogue is probably an antiferromagnet with a spin canting arrangement below 2 K, and the Ni compound might show 3D long-range ferrimagnetic ordering at 2.7 K. Mn and Ni compounds are soft magnets while the Fe compound is quite hard magnet. Detailed investigation on the magnetism of Mn and Fe compounds at low fields (Fig. 6) revealed that there should be a second magnetic transition below the critical temperature, indicating possible spin re-orientation [11,17–19]. It is merit to point out that the framework is closely related to the pyrochlore structure [27] except for the presence of the central metal site of the corner-shared tetrahedral nodes. This similarity might provide possible geometrical frustration. On the other hand, the diamond framework has several superexchange pathways between the metal sites and the possible competition among them due to the similar coupling strengths [28]. Consequently the frameworks of $[Mn_3(HCOO)_6]$ and $[Fe_3(HCOO)_6]$ should be magnetic competition systems [29]. Based on these observations we think that the magnetic structures might not be simply collinear and non-collinear spin arrangement is possible. The possible spin re-orientation or multiple magnetic transitions might result from these magnetically structural features. It is apparent that more investigations will be needed to elucidate the nature of the magnetism for these compounds.

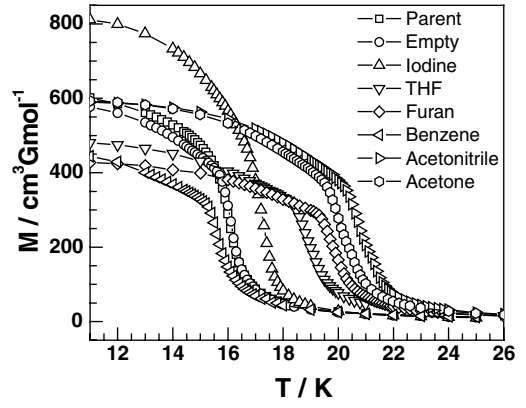


Fig. 6. FC measurements of $[Fe_3(HCOO)_6]$ and its guest-inclusion compound series with the guest names shown under an applied field of 10 Oe. Parent is the parent compound with guests of methanol and water and Empty is the framework without guest.

5.2. Guest-modulated magnetism of $[M_3(HCOO)_6](G)$ (M = Mn, Fe)

Guest-dependent magnetism has been observed and investigated for Mn and Fe frameworks [11,17–19]. The main effect of guest inclusion on the magnetic property of the framework is the change of the critical temperature. For $[Mn_3(HCOO)_6](G)$, T_C were modulated by guests in range of 4.8–9.7 K [11], compared with 8.0 K for $[Mn_3(HCOO)_6]$ without guest. While for $[Fe_3(HCOO)_6](G)$, T_C changes from 15.6 to 20.7 K compared to 16.1 K for the guest-free $[Fe_3(HCOO)_6]$ (Fig. 6), together with higher coercive fields (H_C) and remanant magnetizations (R_M) for $[Fe_3(HCOO)_6](G)$ materials with higher T_C [19]. The guest-sensitive magnetism might come from (a) the subtle changes in the important M–O–M angles of the host framework, where materials with larger M–O–M angles have lower T_C, and (b) host–guest interactions, mainly the H-bonds, where the existence of more strong host–guest H-bonds seems to favor high T_C. Finally, enantiomer pure and racemic guest have small but significant different influence on the magnetism [17]. The guest inclusion does not change the framework structure much more, but modifies the key structural parameters thus the coupling strengths therefore finally change the magnetic behavior. However, more detailed studies are needed to reveal the nature of guest-dependent magnetism for these porous magnets of $[M_3(HCOO)_6]$.

5.3. Magnetism of mixed-metal porous magnets of $[Fe_xZn_{3-x}(HCOO)_6]$

Finally, we briefly present here recent results on the series of mixed-metal porous magnet of $[Fe_xZn_{3-x}(HCOO)_6]$.

Table 2
Cell parameters and M–O distances of de-solvated $[Fe_xZn_{3-x}(HCOO)_6]$[a] series in space group $P2_1/c$ around 100 K, showing lattice shrinkage upon increasing Zn component

x	2.43	2.22	1.78	1.03	0.26
a (Å)	11.4504(2)	11.4421(2)	11.4258(2)	11.4058(3)	11.3581(2)
b (Å)	9.9391(2)	9.9248(2)	9.9042(2)	9.8909(2)	9.8589(2)
c (Å)	18.3326(5)	18.3270(4)	18.2786(5)	18.2691(5)	18.2017(5)
β (°)	127.393(1)	127.340(2)	127.377(1)	127.341(2)	127.259(1)
V (Å^3)	1657.60(6)	1654.68(6)	1643.72(6)	1638.58(7)	1622.21(6)
M–O distances (Å)	2.055–2.164	2.052–2.157	2.042–2.157	2.040–2.148	2.031–2.147

[a] The x values were calculated by comparing the Curie constants of the mixed-metal compounds to that of $[Fe_3(HCOO)_6]$. The x values from ICP analysis are 2.38, 2.15, 1.64, 0.92 and 0.25, slightly lower than but agreeable to that obtained from magnetic measurement.

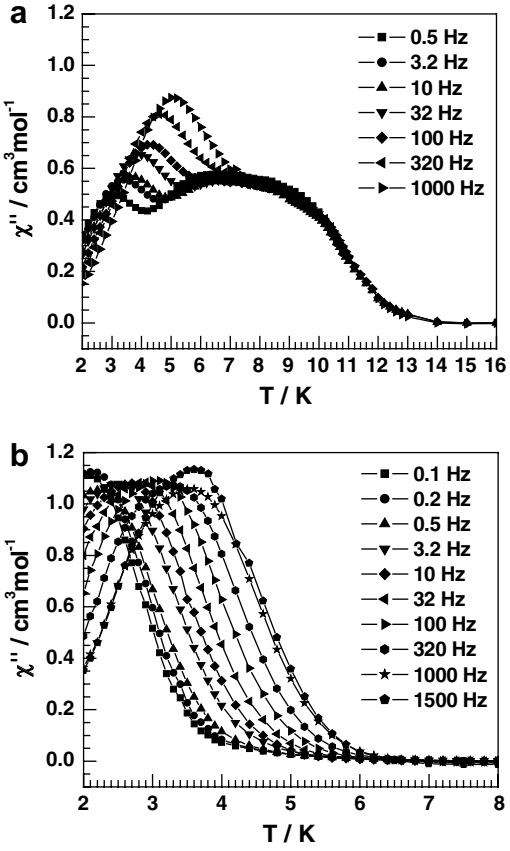


Fig. 7. The ac susceptibilities (out of phase components presented here only) measured with amplitude of 1 Oe and different oscillating frequencies in zero dc-field for two $[Fe_xZn_{3-x}(HCOO)_6]$ compounds with $x = 2.22$ (a) and 1.78 (b). For $x = 2.43$ the system displays mainly the high temperature broad peaks at ca. 11 K showing small frequency dependence with ϕ (defined as $\Delta T_p/[T_p\Delta(\log f)]$) [30] of 0.015, indicating spin glass behavior (not shown here). For $x = 2.22$, the high temperature broad peaks at ca. 9 K characterize spin glassy components in the system with a $\phi = 0.033$ while the low temperature peaks at ca. 4 K characterize superparamagnetic components (or single molecular magnet) with ϕ of 0.194. For $x = 1.78$ of further dilution, only low temperature peaks at ca. 3 K, showing strong frequency-dependence, with $\phi = 0.125$, were observed. For $x = 1.03$ the low temperature peaks have $\phi = 0.222$ (no shown here). And finally for $x = 0.26$, only paramagnetism was observed.

The isomorphs nature of the $[M_3(HCOO)_6]$ family allow the possibility to prepare the mixed metal frameworks with different ratio and kind of metal, thus the continuous change in lattice volume as well as pore size, and modulation of the magnetic property, can be expected. Indeed, for the $[Fe_xZn_{3-x}(HCOO)_6]$ series this has been realized (Table 2 and Fig. 7). When x decreases from 3 for the pure $[Fe_3(HCOO)_6]$ by increasing the component of diamagnetic and smaller Zn^{2+} in the framework, the lattice shrinks, and most interesting, the series undergoes systematic change from 3D long-range-ordering *via* spin glass (small frequency dependence in ac susceptibility) [30] to superparamagnetic behavior or possible single molecule magnet (SMM) (large frequency dependence in ac susceptibility) [31] and finally to paramagnet. This could be expected for the continuous dilution of the 3D magnetic system by diamagnetic component. However, it now occurs in porous materials. This will be of much interesting in view of creating and understanding different magnetic behaviors and possible guest-sensitive character in different magnetic materials such as porous SMM and porous spin glass. The study is going further and details will be reported in near future.

6. Conclusion

In summary, the family of porous magnets of $[M_3(HCOO)_6]$ can be easily prepared by a mild solution chemistry method. The frameworks exhibit permanent porosity, thermal stability, a wide spectrum of guest inclusion behavior and 3D long-range magnetic ordering. The robust but still flexible porous diamond frameworks allowed the successful preparation of guest-inclusion compounds as well as their structural characterization by SXRD. The guest molecules form zigzag molecular arrays in the channels of host framework, and the host–guest H-bonding provides the main host–guest interaction. These guest-inclusion compounds exhibit guest-modulated magnetism, which might be due to the guest induced subtle changes of the molecular geometry of the framework and the nature of host–guest interaction. The mixed-metal $[Fe_xZn_{3-x}(HCOO)_6]$ series exhibits systematic change from 3D long-range ordering to spin glass to superparamagnet and finally to paramagnet upon the increase of diamagnetic component of zinc in the series. Future study on this interesting porous magnet family will be (a) elucidating the real magnetic structure by neutron diffraction and detailed specific heat studies, (b) exploring

more guests to reveal the nature of guest-dependent magnetism, (c) studying mixed metal systems with different magnetism, and (d) combining functional guests such as organic radical, optical, photoactive or conductive units within the porous magnetic framework to explore multi-functionality. These researches are in progress.

Acknowledgements

This work was supported by the National Natural Science Foundation of China (No. 20571005, 20473095, 20221101, 20490210, 20673120), the Chinese Academy of Sciences, CMS-CX200510, the National Basic Research Program of China (2006CB601102), CREST, Japan Science and Technology Coorporation, and CNRS, France.

References

[1] (a) E. Coronado, F. Palacio, J. Veciana, Angew. Chem. Int. Ed. 42 (2003) 2570;
(b) T. Sugawara, H. Oshio, K. Awaga, Proceeding of the International Conference of Molecule-based Magnets, Polyhedron 24 (2005) 2063.

[2] For example, (a) E. Coronado, J.R. Galán-Máscarós, C.J. Gómez-García, V. Laukhin, Nature 408 (2000) 447;
(b) E. Coronado, P. Day, Chem. Rev. 104 (2004) 5419;
(c) S. Uji, H. Shinagawa, T. Terashima, T. Yakabe, Y. Terai, M. Tokumoto, A. Kobayashi, H. Tanaka, H. Kobayashi, Nature 410 (2001) 908;
(d) H. Kobayashi, H.-B. Cui, A. Kobayashi, Chem. Rev. 104 (2004) 5265.

[3] For example, (a) O. Sato, Acc. Chem. Res. 36 (2003) 692;
(b) Y. Sunatsuki, Y. Ikuta, N. Matsumoto, H. Ohta, M. Kojima, S. Iijima, S. Hayami, Y. Maeda, S. Kaizaki, F. Dahan, J.P. Tuchagues, Angew. Chem. Int. Ed. 42 (2003) 1614;
(c) J.S.O. Evans, S. Bénard, P. Yu, R. Clément, Chem. Mater. 13 (2001) 3813.

[4] For example, (a) K. Inoue, S.-i. Ohkoshi, H. Imai, in: J.S. Miller, M. Drillon (Eds.), Magnetism: Molecules to Materials V, WILEY-VCH Verlag GmbH & Co. KgaA, Weinheim, Germany, 2005, chapter 2;
(b) E. Coronado, J.R. Galán-Mascarós, C.J. Gómez-García, M. Martínez-Ferrero, M. Almeida, J.C. Waerenborgh, Eur. J. Inorg. Chem. (2005) 2064;
(c) R. Clément, S. Decurtins, M. Gruselle, C. Train, Monatshefte für Chemie 134 (2003) 117;
(d) E.-Q. Gao, Y.-F. Yue, S.-Q. Bai, Z. He, C.-H. Yan, J. Am. Chem. Soc. 126 (2004) 1419.

[5] (a) D. Maspoch, D. Ruiz-Molina, J. Veciana, J. Mater. Chem. (2004) 2713, and references cited in;
(b) C.J. Kepert, Chem. Commun. (2006) 695, and references therein.

[6] (a) G.J. Halder, C.J. Kepert, B. Moubaraki, K.S. Murray, J.D. Cashion, Science 298 (2002) 1762;
(b) V. Niel, A.L. Thompson, M.C. Muñoz, A. Galet, A.E. Goeta, J.A. Real, Angew. Chem. Int. Ed. 42 (2003) 3759;
(c) T. Glaser, Angew. Chem. Int. Ed. 42 (2003) 5668.

[7] (a) D. Maspoch, D. Ruiz-Molina, K. Wurst, N. Domingo, M. Cavallini, F. Biscarini, J. Tejada, C. Rovira, J. Veciana, Nat. Mater. 2 (2003) 190;
(b) D. Maspoch, N. Domingo, D. Ruiz-Molina, K. Wurst, J. Tejada, C. Rovira, J. Veciana, C.R. Chimie 8 (2005) 1213, and references cited in.

[8] (a) A. Rujiwatra, C.J. Kepert, J.B. Claridge, M.J. Rosseinsky, H. Kumagai, M. Kurmoo, J. Am. Chem. Soc. 123 (2001) 10584;
(b) M. Kurmoo, H. Kumagai, S.M. Hughes, C.J. Kepert, Inorg. Chem. 42 (2003) 6709.

[9] (a) M. Kurmoo, H. Kumagai, K.W. Chapman, C.J. Kepert, Chem. Commun. (2005) 3012;
(b) M. Kurmoo, H. Kumagai, M. Akita-Tanaka, K. Inoue, Inorg. Chem. 45 (2006) 1627.

[10] (a) L.G. Beauvais, J.R. Long, J. Am. Chem. Soc. 124 (2002) 12096;
(b) S.-I. Ohkoshi, K.-I. Arai, Y. Sato, K. Hashimoto, Nat. Mater. 3 (2004) 857.

[11] Z.-M. Wang, B. Zhang, H. Fujiwara, H. Kobayashi, M. Kurmoo, Chem. Commun. (2004) 416.

[12] Z.-M. Wang, B. Zhang, M. Kurmoo, M.A. Green, H. Fujiwara, T. Otsuka, H. Kobayashi, Inorg. Chem. 44 (2005) 1230.

[13] D.N. Dybtsev, H. Chun, S.H. Yoon, D. Kim, K. Kim, J. Am. Chem. Soc. 126 (2004) 32.

[14] M. Viertelhaus, P. Adler, R. Clérac, C.E. Anson, A.K. Powell, Eur. J. Inorg. Chem. (2005) 692.

[15] J.A. Rood, B.C. Noll, K.W. Henderson, Inorg. Chem. 45 (2006) 5521.

[16] Z.-M. Wang, Y.-J. Zhang, M. Kurmoo, T. Liu, S. Vilminot, B. Zhao, S. Gao, Aust. J. Chem. 59 (2006) 617.

[17] B. Zhang, Z.-M. Wang, M. Kurmoo, S. Gao, K. Inoue, H. Kobayashi, Adv. Funct. Mater., in press.

[18] Z.-M. Wang, B. Zhang, H. Fujiwara, T. Otsuka, H. Kobayashi, M. Kurmoo, 3D porous magnets of $M_3(HCOO)_6$ (M = Mn and Co), presentation on AsCA04, in: The 6th Conference of the Asian Crystallographic Association, Hong Kong, China, June 27–30, 2004.

[19] (a) Z.-M. Wang, Synthesis, Structure and Guest-modulated Magnetism of Guest Inclusion Compounds Based on a 3D Permanently Porous Magnetic Framework of $[Fe_3(HCOO)_6]$, presentation on ICMM2006, Victoria, B.C., Canada, August 13–17, 2006;
(b) Z.-M. Wang, Y.-J. Zhang, T. Liu, M. Kurmoo, S. Gao, Adv. Funct. Mater., in press.

[20] (a) Z.-M. Wang, B. Zhang, T. Otsuka, K. Inoue, H. Kobayashi, M. Kurmoo, Dalton Trans. (2004) 2209;
(b) X.-Y. Wang, L. Gan, S.-W. Zhang, S. Gao, Inorg. Chem. 43 (2004) 4615.

[21] See for example, the references 7–12 cited in [20(a)].

[22] For example, see (a) X. Zhao, B. Xiao, A.J. Fletcher, K.M. Thomas, D. Bradshaw, M.J. Rosseinsky, Science 306 (2004) 1012;
(b) J.L.C. Rowsell, O.M. Yaghi, Angew. Chem. Int. Ed. 44 (2005) 4670, and references cited in.

[23] For some recent reviews, see (a) S. Kitagawa, R. Kitaura, S. Noro, Angew. Chem., Int. Ed. 43 (2004) 2334;
(b) M. O'Keeffe, O.M. Yaghi (Eds.), Special issue on Reticular Chemistry, J. Solid. State Chem 178 (2005) 2409;
(c) C.A. Reed (Ed.), Special issue on Molecular Architectures, Acc. Chem. Res. 38 (2005) 215;
(d) S. Kitagawa, K. Uemura, Chem. Soc. Rev. 34 (2005) 109, and references cited in.

[24] S.R. Batten, R. Robson, Angew. Chem. Int. Ed. 37 (1998) 1460.

[25] (a) T. Steiner, Angew. Chem., Int. Ed. 41 (2002) 48;
(b) G.R. Desiraju, T. Steiner, The Weak Hydrogen Bond In Structural Chemistry and Biology, Oxford University Press, New York, USA, 1999.

[26] J.-M. Lehn, Supramolecular Chemistry, Concepts and Perspectives, VCH, Weinheim, Germany, 1995, p. 121.

[27] For example, (a) S.T. Bramwell, M.J.P. Gingras, Science 294 (2001) 1495;
(b) A.P. Ramirez, A. Hayashi, R.J. Cava, R. Siddharthan, B.S. Shastry, Nature 399 (1999) 333.

[28] A survey on many related literatures about the magnetic study of the three kinds of metal-metal (Mn and Fe) linkages by carboxylates similar to that observed in the $[M_3(HCOO)_6]$ framework revealed that the couplings have strengths of a few reciprocal centimeters or less, thus they are comparable.

[29] J.C. Bonner, in: R.D. Willett, D. Gatteschi, O. Kahn (Eds.), Magneto-Structural Correlations in Exchange Coupled Systems, D. Reidel Publishing Company, Dordrecht, Holland, 1985, p. 161.

[30] J.A. Mydosh, Spin Glass: An Experimental Introduction, Taylor & Francis, London · Washington, DC, 1993, pp. 63–76.
[31] For example, (a) S.K. Ritter, C&EN News 82 (2004) 29;
(b) D. Gatteschi, R. Sessoli, Angew. Chem., Int. Ed. 42 (2003) 268;
(c) A.J. Tasiopoulos, A. Vinslava, W. Wernsdorfer, A. Abboud, G. Christou, Angew. Chem., Int. Ed. 43 (2004) 2117;
(d) W. Wernsdorfer, N. Aliaga-Alcaide, D.N. Hendrickson, G. Christou, Nature 416 (2002) 406.

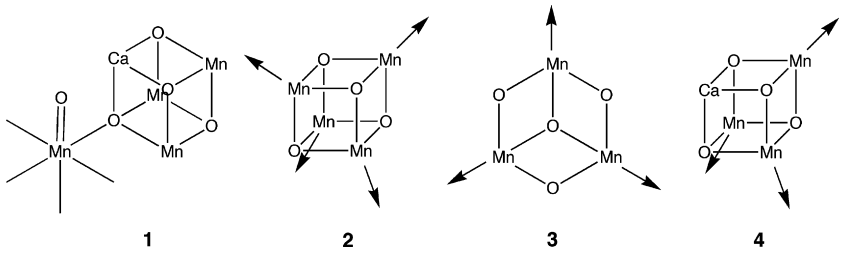


Fig. 1. $CaMn_4O_5$ cluster (**1**) in the photosynthesis II and related cubane Mn_4O_4 (**2**), triangular Mn_3O_4 (**3**), and cubane $CaMn_3$ (**4**) clusters. **2** and **3** exhibit the tetrahedral and triangular (antiferromagnetic) spin alignments, respectively, at the low-spin state.

tetranuclear manganese complex $Mn(IV)Mn(III)_3Cl_7(O_2CCCH_3)_3]^{3-}$, a cubane complex, has been carried out to elucidate its electronic and spin states [16]. Belinskii [18] has carried out the theoretical studies on the mixed-valence $Mn(III)_3Mn(IV)$ and $Mn(IV)_3Mn(III)$ clusters on the basis of the quantum Heisenberg models, assuming trapezoid, butterfly, bent, T-type and distorted tetrahedron structures. Possible ground spin states for these five structures have been elucidated, changing effective exchange interactions between manganese ions.

We have examined possible spin structures of tetranuclear (**2**) [19] and trinuclear (**3**,**4**) [20] manganese clusters in Fig. 1 on the basis of the spin vector model [21]. The strong spin frustration [15] in **3** and **4** [20] has provided non-collinear spin structures such as triangular spin structure in Fig. 1, on the assumption of the experimentally determined effective exchange integrals (J_{ij}). The J_{ij} values for the binuclear manganese complexes [22,23] have been calculated using the hybrid DFT method to elucidate the mechanisms for effective exchange interactions between Mn ions [24]

$$J_{ij} = \frac{^{LS}E(X) - {}^{HS}E(X)}{^{HS}\langle \widehat{S}^2\rangle(X) - {}^{LS}\langle \widehat{S}^2\rangle(X)}, \quad (2)$$

where $^{Y}E(X)$ and $^{Y}\langle \widehat{S}^2\rangle(X)$ are the total energy and total angular momentum for the state Y(= LS; the lowest spin state, HS; the highest spin state) by the method X (= UHF, UMPn, UDFT, etc.). It was shown that the sign of J_{ij} is negative because of the greater stability of LS than HS, and the magnitude of J_{ij} values is variable with the oxidation numbers of Mn ion. The calculated J_{ij} values have been consistent with the experiments available. Very recently, Yamanaka et al. [25] have performed the DFT calculation of cubane-type $Mn(II)_4$ cluster (**2**) using the general spin orbitals (GSO), namely, two component spinor. The resulted spin structure of **2** was consistent with the tetrahedral type in Fig. 1.

The variations of charge and spin populations of manganese oxo (MnO) bonds with the oxidation number of Mn ion were also examined by the unrestricted Hartree–Fock (UHF) method [24]. It was concluded that the nature of oxygen atom in the manganese oxo bond (X = O in **5**) varies from nucleophilic to electrophilic with the change of formal charge of Mn ion from low (II) to high (V) valent as illustrated in Fig. 2. The oxygen atom in the Mn(V)O core exhibited the radical character responsible for the radical reactivity for water [24–28]. These results enabled us to propose three possible models of oxygenation reactions of substrates by metal–oxo species: (1) SE_2 model, (2) ^{1}O-model and (3) ^{3}O-model as shown in Fig. 3 [25,26]: note that singlet and triplet states of atomic oxygen undergoes, respectively, insertion and abstraction reactions with X–H bonds (X = CH_3, OH, etc.). Similar situations are expected for low-spin (LS) and high-spin (HS) metal-oxo species.

As a first step toward theoretical approaches to water oxidation in OEC, Isobe et al. [28] have performed the DFT calculation of the model compound $XH_3Mn(IV)O_2Mn(IV)H_3Y$ (X,Y = O, H) (**6**) for the Limburg compound $[(terpy)(H_2O)Mn(\mu\text{-}O)_2Mn(terpy)(H_2O)]^{3+}$ (**7**) [29] as shown in Fig. 2. It was found that electron correlation plays a crucial role to determine the nature of manganese–oxygen bonds in **7**. Diradical or nonradical mechanism is found to be feasible for the oxygen atom transfer from water to high-valent manganese–oxo bond Mn(V)=O

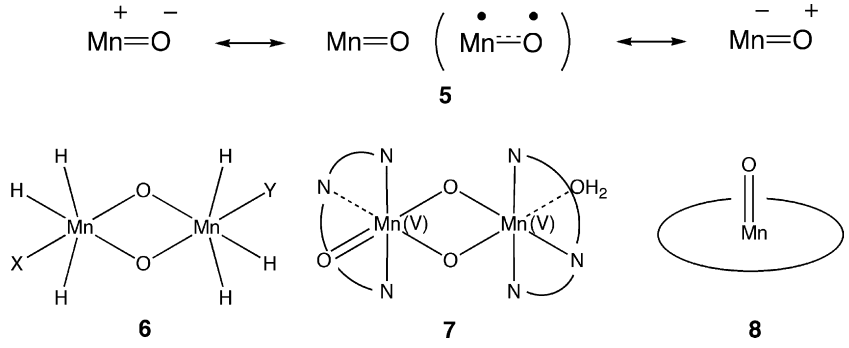


Fig. 2. Variations of electronic structures of the manganese–oxo bond (**5**), and Mn–oxo model complexes (**6**, **7**, and **8**) for oxygen evolution center (OEC).

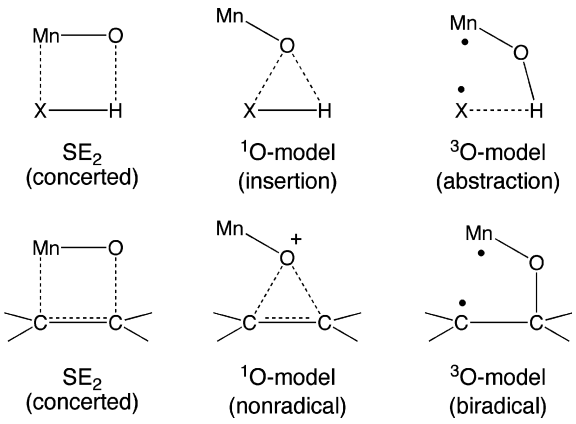


Fig. 3. SE_2, ^1O- and ^3O-models for oxygenation reactions of X–H ($X = CH_3$, OH, etc.), bonds and expoxidation reactions of C–C double bonds in Refs. [24,28]. The discrete radicals are generated in the ^3O-model, though such species are hardly detectable in the ^1O-model because of rapid recombination (or insertion).

in **7**. The environmental effects such as solvent are considered to play an important role for control of the mechanism. The electronic and spin structure of the $CaMn_3O_4$ cluster **4** in **1** have been elucidated on the basis of both classical (spin vector) and quantum Heisenberg models [30]. The GSO DFT calculations of the cluster **4** were also performed to elucidate charge and spin populations and non-collinear spin structure (see **4** in Fig. 1). Possible reaction mechanisms of **1** have been proposed on the theoretical and experimental grounds [30]. However, the detailed computations of the metal–oxo part in **1** have not been performed yet.

As a continuation of previous work [24–28,30], we here perform theoretical studies on the high-valent Mn–O bonds in OEC and porphyrin model complexes **8**. The electronic structures of these species are investigated from the viewpoint of charge and spin populations, and diradical character. The strong diradical character of the Mn(V)=O bonds in the model complexes is consistent with the ^1O- and/or ^3O-models for oxygenations of X–H bonds. The SE_2 mechanism in Fig. 3 is also examined as a possible model of the transition state of the O–O bond formation process. Implications of the calculated results are discussed in relation to possible mechanisms of oxygen evolution in OEC. Our previous [22–28,30] and present calculations conclude that Mn(V)=O (**5a**) or Mn(IV)=O (**5b**) plays a crucial role in both native (**1**) and artificial (**8**) OEC systems.

2. Theoretical background and computational details

Electronic structures of Mn–oxo model complexes of OEC and Mn–oxo porphyrine complex were investigated using the unrestricted B3LYP (UB3LYP) method [31,32] with the Huzinaga's MIDI+F basis set (533(21)/53(21)/(41)) [33] for Mn ion and the 6-31G* basis set [34] for other atoms [35]. The coordinates of model complexes of OEC were taken from the X-ray crystallographic structure in Protein Data Bank (PDB code 1S5L) [1]. All calculations were performed with the Gaussian 98 program package [34].

To obtain the symmetry-adapted (SA) picture for the broken-symmetry (BS) UB3LYP calculations, we have used the natural orbitals, which are determined by diagonalizing their spin-traced first-order density matrices γ [23–28] as

$$\gamma(\mathbf{r},\mathbf{r}') = \sum_i n_i \phi_i(\mathbf{r})\phi_i^*(\mathbf{r}'), \tag{3}$$

where n_i denotes the occupation number of a natural orbital ϕ_i, ranging from 0 to 2. The spin-polarized BS molecular orbitals ($\psi_i^{\pm}$) for the up-spin and down-spin states are derived by bonding (ϕ_i) and antibonding (ϕ_i^*) natural orbitals as

$$\psi_i^{\pm} = \cos\theta_i\phi_i \pm \sin\theta_i\phi_i^* \quad (i = 1,2,\ldots,N), \tag{4}$$

where θ_i is the orbital mixing parameter and N is the number of bonding natural orbitals. The orbital overlap T_i between the up-spin and down-spin orbitals is defined as a measure of orbital splitting by

$$T_i = \langle\psi_i^+|\psi_i^-\rangle = \cos 2\theta_i. \tag{5}$$

T_i is unity for closed-shell systems ($\theta_i = 0$) and $0 \leqslant T_i < 1$ for open-shell systems ($0 < \theta_i \leqslant \pi/4$). The occupation numbers of the bonding and antibonding natural orbitals are expressed by the orbital overlap T_i as

$$n_i = 1 + T_i, \quad n_i^* = 1 - T_i. \tag{6}$$

This means that contribution of doubly excited configuration $\left|\phi_i^*\overline{\phi_i^*}\right|$ is significant because of small orbital-energy gap and strong electron repulsion (correlation). The diradical character y is defined with the weight (W_D) of the contribution of doubly excited configuration [23–28] as

$$y_i = 2W_D = 1 - \frac{2T_i}{1+T_i^2}. \tag{7}$$

In the extreme case of BS solutions ($\theta_i = \pi/4$, $T_i = 0$, and $n_i = n_i^* = 1$), the up- and down-spin orbitals are simply in- and out-of phase combinations of bonding and antibonding natural orbitals, respectively, as shown in Eq. (8), showing strong electron localizations at different fragments A and B

$$\psi_i^{\pm} = \frac{1}{\sqrt{2}}\phi_i \pm \frac{1}{\sqrt{2}}\phi_i^* \quad (\psi_A \equiv \psi_i^+ \quad \text{and } \psi_B \equiv \psi_i^-). \tag{8}$$

3. Results and discussion

3.1. The nature of metal–oxo bonds in OEC

The models 1, 2 and 3 with and without extra two waters are examined as the active site of **1** in OEC. As a continuation of previous work [30], we examine the high-valent Mn(V)=O cores with the ligand fields revealed by the X-ray diffraction method [1]. In the model 1, three waters and two CH_3COO anions were employed as the ligands,

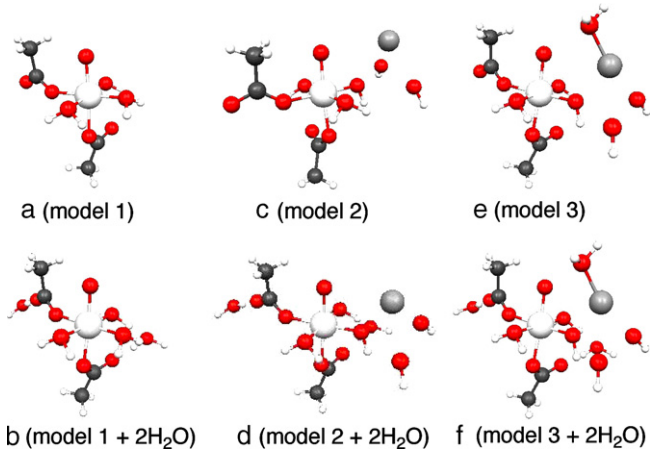


Fig. 4. Computational model 1: $[Mn(V)=O\ (CH_3CO_2)_2\ (H_2O)_3]^{+1}$ without (a) and with (b) extra $2H_2O$, model 2: $[Mn(V)=O\ (CH_3CO_2)_2(H_2O)_2(OHCa(OH)_2)]^0$ without (c) and with (d) extra $2H_2O$, and model 3: $[Mn(V)=O\ (CH_3CO_2)_2(H_2O)_2(OHCa(OH)_2)(H_2O)]^0$ without (e) and with (f) extra $2H_2O$.

while one water in model 1 is replaced with the $(OH)Ca(OH)_2$ anion in the model 2 as shown in Fig. 4. Further one water is added to the Ca(II) ion in model 3. As shown previously [24], the Mn(V)=O core has the so-called oxene structure $(\sigma)^2(d\pi_x–p\pi_x)^2(d\pi_y–p\pi_y)^2$ with one $d\sigma–p\sigma$ and two $d\pi–p\pi$ bonds.

However, the $d\pi–p\pi$ bonds are usually spin-polarized because of strong electron correlation, and the resulting magnetic orbitals (ψ_i) in Eq. (4) are more or less localized on the Mn and O sites, respectively. Here, ligand field effects on the Mn–O bonding are examined by our methods described in Section 2.

Table 1 summarizes spin densities (Mulliken charge) on Mn, O, and ligand obtained by the UB3LYP calculations. The negative spin densities are populated on the O-site, in accord with the diradical character ($\cdot\uparrow$Mn–O$\cdot\downarrow$) of the Mn=O bond. Interestingly, the negative spin densities also appear on the ligands, namely CH_3COO ligands in model 1 and $Ca(OH)_2$ part in models 2 and 3, respectively. This means that the charge transfer (CT) from ligands (L) to the $d\pi_y–p\pi_y$ antibonding orbital is not negligible, showing a contribution of the $[\cdot\uparrow Mn(IV)=OL^{\cdot+}\downarrow]$ structure. Thus, the situation in the Mn(V)=O bond is similar to that of the high-valent Fe(V)=O and Mn(V)=O cores in porphyrine complex: $[\cdot\uparrow Fe(IV)=OPor^{\cdot+}\downarrow]$ and $[\cdot\uparrow Mn(IV)=OPor^{\cdot+}\downarrow]$.

However, the CT from ligands to Mn(V)=O is a little suppressed by addition of two extra waters as shown in the model 1 with $2H_2O$. The diradical character of the $d\pi_x–p\pi_x$ bond is also decreased with change of the ligand field. For example, coordination of water to the Ca(II) ion largely reduced the spin density on the O-atom of MnO. The CT diradical character is rather significant in the models 2 and 3 with extra $2H_2O$. This implies that the cubane unit $CaMn_3O_4$ (**4**) in **1** play important roles in regulation of the nature of chemical bonds of the Mn–oxo part in **1**. The present results indicate that the electrophilic character of the high-valent Mn(V)=O bond should be enhanced with suppression of the CT biradical character with $CaMn_3O_4$ in **1**. This entails a possibility of the SE_2 mechanism instead of the ^{1}O- and/or ^{3}O-models for oxygen evolution from waters, though the latter(s) are rather conceivable from strong diradical character of the Mn=O bonds in models 1 and 2, which can be regarded as models for synthetic manganese–oxo complexes [12–16,29].

The natural orbital analysis of the broken-symmetry (BS) UB3LYP solutions for the six models in Fig. 4 have been performed to obtain the natural orbitals and their occupation numbers, which are also available by the symmetry-adapted (SA) CASSCF procedure. Table 2 summarizes the occupation numbers of bonding (antibonding) $d\sigma–p\sigma$ and $d\pi_x–p\pi_x$ orbitals, together with those of the ligand orbital (L) and $d\pi_y–p\pi_y$ antibonding orbitals. The $d\sigma–p\sigma$ orbitals are almost doubly occupied, showing the nonradical character. While, the occupation numbers of the antibonding $d\pi_x–p\pi_x$ orbitals are 0.602 (model 1), 0.562 (model $1 + 2H_2O$), 0.831 (model 2), 0.423 (model $2 + 2H_2O$), 0.748 (model 3), and 0.336 (model $3 + 2H_2O$), respectively. This in turn means that the orbital overlaps (T_i) between the magnetic $d\pi_x–p\pi_x$ orbitals ($\psi_i^{\pm}$) are 0.398, 0.438, 0.169, 0.577, 0.252, and 0.664, respectively. Thus the diradical character of the $d\pi_x–p\pi_x$ bond is sensitive to the ligand fields. On the other hand, the orbital overlaps (T_i) between the magnetic CT ($d\pi_y–\pi_y$) orbitals are 0.113, 0.324, 0.002, 0.171, 0.210, and 0.184, respectively, indicating the strong CT diradical character. This indicates that contribution of the $[Mn(IV)=OL^{\cdot+}]$ structure is significant in the model complexes 1, 2, and 3.

Judging from the occupation numbers in Table 2, the four active orbitals and four active electrons [4,4] are at least crucial for the complete active space (CAS) for SA CASCI treatment of the models 1, 2, and 3. However, inclusion of the bonding and antibonding $d\sigma–p\sigma$ orbitals

Table 1
Spin densities (Mulliken charge) of the model complexes **1**, **2** and **3** by UB3LYP

Models	Mn	O	Ligands
Model 1	1.881 (1.884)	−1.048 (−0.509)	−0.833 (−1.375)
Model 1 ($2H_2O$)	1.396 (1.942)	−0.771 (−0.529)	−0.625 (−1.413)
Model 2	1.681 (1.886)	−0.816 (−0.665)	−0.865 (−1.221)
Model 2 ($2H_2O$)	1.701 (1.878)	−0.458 (−0.762)	−1.243 (−1.116)
Model 3	1.455 (1.906)	−0.449 (−0.751)	−1.006 (−1.155)
Model 3 ($2H_2O$)	1.457 (1.900)	−0.368 (−0.765)	−1.089 (−1.135)

Table 2
Occupation numbers of natural orbitals for models **1**, **2** and **3** by UB3LYP

Models	σ (σ*)	π (π*)	L ($\pi_\perp$*)
Model 1	1.986 (0.014)	1.398 (0.602)	1.183 (0.817)
Model 1 ($2H_2O$)	1.984 (0.016)	1.438 (0.562)	1.324 (0.676)
Model 2	1.971 (0.029)	1.121 (0.831)	1.002 (0.998)
Model 2 ($2H_2O$)	1.928 (0.072)	1.577 (0.423)	1.171 (0.829)
Model 3	1.977 (0.023)	1.252 (0.748)	1.210 (0.790)
Model 3 ($2H_2O$)	1.920 (0.080)	1.664 (0.336)	1.184 (0.816)

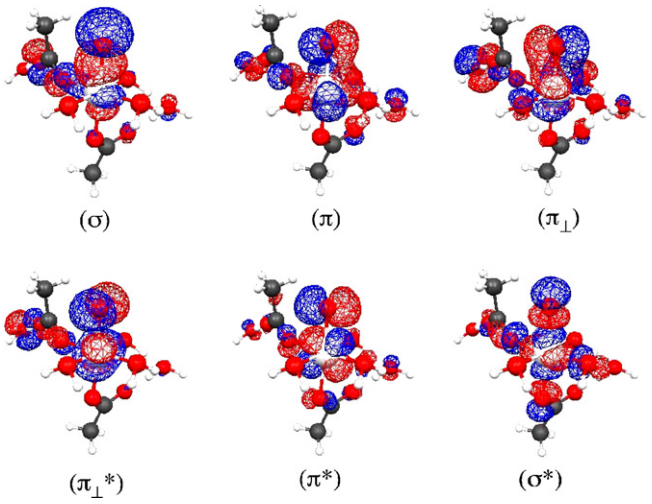


Fig. 5. Graphic drawings of the bonding and antibonding pairs of dσ–pσ(σ), $d\pi_x$–$p\pi_x(\pi)$, and $d\pi_y$–$p\pi_y(\pi)$ type natural orbitals of MnO in the model 1 with extra $2H_2O$ (b in Fig. 4).

becomes essential for MO-theoretical tracing of the dissociation process of the Mn=O bond. The six natural orbitals for the model complex **1** with $2H_2O$ are depicted in Fig. 5

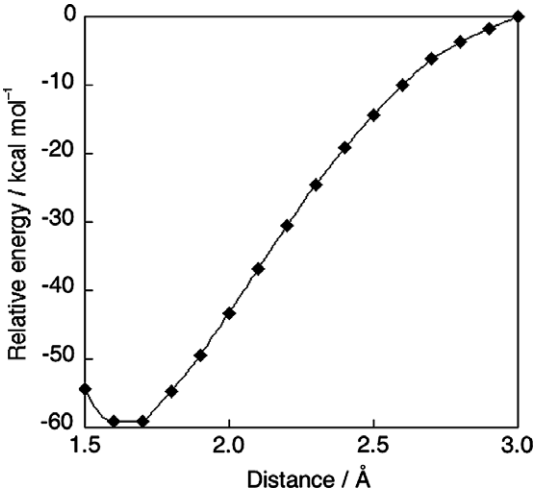


Fig. 6. Potential curve of the Mn(V)=O porphyrine complex (**7**) with change of the Mn–O distance.

as an example. These natural orbitals are utilized for successive SA computations of the complexes, 1, 2, and 3. The CASCI results will be published elsewhere.

3.2. Electronic structures of Mn–oxo porphyrine complex

Here, a manganese–oxo porphyrin complex (**8**), [Mn(V)=OPor](H_2O) is examined as an example of artificial high-valent manganese–oxo species. Fig. 6 shows variations of the potential curve of **8** with changing the Mn–O bond distance (R). At the dissociation limit ($R = \infty$), **8** is regarded as the exchange-coupled low-spin (LS) state constructed of the triplet state of [Mn(III)Por](H_2O) and triplet atomic oxygen (^3O) as illustrated in Fig. 7. This characteristic property remains even at $R \ll \infty$. For example, the spin density (Mulliken charge) of Mn and porphyrine of **8** at $R = 3.0$ Å, namely [Mn(III)Por](H_2O) fragment, are 2.57 (1.22) and −0.63 (−0.38), respectively. Then the π-electron of porphyrine is spin-polarized because of the internal magnetic field of triplet Mn(III) ion. The net charge of Mn(III) is largely reduced by the coordination of porphyrine dianion. The oxygen site of **8** is regarded as triplet oxygen with negative spin density (−1.94). These results are consistent with the triplet O (^3O) model in Fig. 3.

The Mn–O distance at the equilibrium geometry of **8** is calculated to be 1.6 Å and the binding energy is 59.12 kcal/mol. The spin density (Mulliken charge) of Mn, O and porphyrine are 1.53 (1.42), −0.47 (−0.43) and −1.06 (−0.15), respectively. Judging from the orbital spin densities, the $d\pi_x$–$p\pi_x$ covalent bond is considerably spin-polarized, namely $[\uparrow\delta\cdot\mathrm{Mn}(0.47)\text{–}\mathrm{O}(-0.47)\delta\cdot\downarrow]$ (where spin densities are given in parentheses), because of strong electron correlation. On the other hand, the charge transfer from the π-bonding closed-shell orbital of porphyrine to the $d\pi_y$–$p\pi_y$ antibonding orbital of the MnO site occurs at the geometry, giving rise to the porphyrine π-cation radical, which is responsible for the CT biradical structure: $[\uparrow\cdot\mathrm{Mn(IV)}\text{–}\mathrm{O}(1.06)\mathrm{Por}^{\cdot+}(-1.06)\downarrow](H_2O)$. This behavior is similar to that of the models 1, 2, and 3 for the Mn=O bond in OEC.

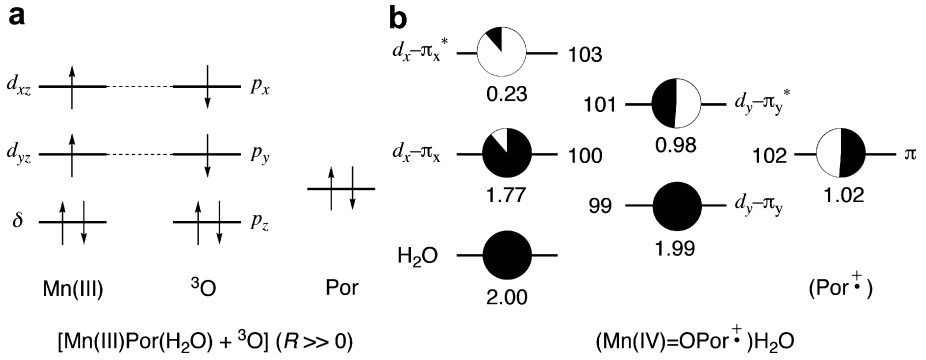


Fig. 7. (a) The exchange-coupled low-spin (singlet) state between triplet Mn(III) and triplet oxygen atom (^3O) with the closed-shell porphyrine at a dissociated ($R = 3.0$ Å) manganese–oxo porphyrine complex. (b) Schematic illustrations of the occupation numbers of natural orbitals for the charge transfer (CT) diradical (singlet) state constructed of doublet Mn(IV)=O and doublet cation radical of porphyrine.

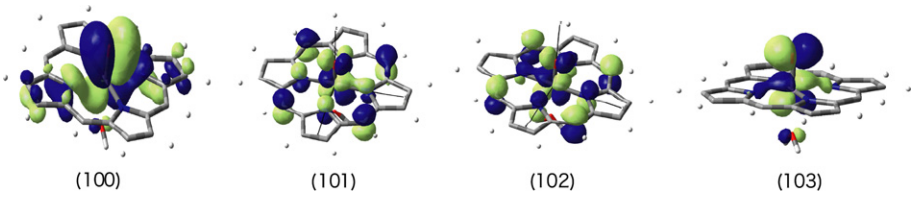


Fig. 8. Graphical drawings of the bonding (100) and antibonding (103) pairs of the $d\pi_y$–$p\pi_y$ type natural orbital and those (101 and 102) of the CT type orbitals, which are constructed of the porphyrine π- and $d\pi_y$–$p\pi_y$ antibonding orbitals. The CT diradical property is variable with Mn–O distance.

The natural orbital analysis of the broken-symmetry (BS) UB3LYP solution of **8** at the equilibrium geometry has been performed to elucidate symmetry-adapted (SA) CASSCF picture. Figs. 7 and 8 illustrate, respectively, populations of occupation numbers and shapes of natural orbitals. From Fig. 8, the natural orbitals (ϕ_i) 101 and 102 are delocalized over both Mn=O and porphyrine groups, and their occupation numbers are almost 1.0. Then the magnetic orbitals ($\psi_i^{\pm}$) given by the mixing of them are localized on the Mn=O group ($\psi_i^{+} = \psi_A$) and porphyrine group ($\psi_i^{-} = \psi_B$), respectively, leading to the singlet biradical configuration. On the other hand, the natural orbitals 100 and 103 are the bonding and antibonding $d\pi_x$–$p\pi_x$ orbitals. The occupation number of the antibonding orbital is 0.23, indicating a homolytic diradical character. However, this small number does not suppress significantly the electron accepting property of this LUMO. This is compatible with the electrophilic property of MnO. Thus the high-valent Mn–O bond in porphyrine complex exhibits similar characteristic to that of the model complexes 1 and 2 for OEC in Fig. 4.

4. Possible mechanisms of oxygen evolution

4.1. Importance of the Mn(V)=O bond

Past two decades [22–28], Yamaguchi et al. elucidated electronic structures and spin states of transition-metal oxides on the basis of ab initio broken-symmetry (BS) (UHF UDFT, GHF and GDFT) calculations followed by the approximate spin projection. It was found that the oxygen atom in the metal-oxo species MO (M = Cr, Mn, Fe) exhibits the nucleophilic character $M^{+}O^{-}$ in the case of the lower-valent stage of M^{+}; M(II) and Mn(III). For example, the Mn(III) ion forms an ionic bond with hydroxide anion, $[Mn(III)–OH]^{2+}$, as shown in Fig. 2. On the other hand, the oxygen atom in the high-valent metal-oxo species such as Mn(V)=O may have singlet or triplet oxygen atom (O) character, showing an electrophilic property to many substrates as illustrated in Fig. 3, for example:

$$Mn(V)=O + {}^{-}OH \rightarrow Mn(IV)—OOH \quad (9a)$$

$$Mn(V)=O + H—OH \rightarrow Mn(IV)—OH + \cdot OH \quad (9b)$$

$$Mn(V)=O + H—OH \rightarrow Mn(III) + HOOH \quad (9c)$$

The reaction (9a) may be operative in ion reactions to generate the O–O bond. The hydrogen abstraction from water by Mn(V)=O in (9b) is also conceivable for high-spin states of manganese–oxo species, though the insertion (or very fast rebound mechanism) is more reasonable in the low-spin (LS) state of them (in Eq. (9c)).

Isobe et al. [28] have performed the DFT calculations of the model compound (**6**) for the Limburg compound (**7**). They have found that the metal–oxo bonds (Mn(V)=O) in **6** show the diradical character ·Mn–O· (see Fig. 2), and therefore the oxygen atom in Mn(V)=O in **7** may undergo electrophilic reactions with substrates in Eq. (9): note that singlet biradical character of the low-spin (LS) Mn(V)=O bond decrease significantly in the case of insertion-type reaction in Fig. 3. Several evidence [29] suggests that chloride anion plays an important role for oxygen evolution in Limburg reaction systems (**7**) like native OEC (**1**) in Fig. 1. This implies that SE_2-like mechanism is also conceivable as discussed later (see Fig. 10).

Koizumi et al. [35] have carried out the DFT calculations of dimer of manganese–oxo (MnO) porphyrin (PO) synthesized and characterized by Naruta's group [36]. They have investigated variations of the electronic structures of POMn(X)=O with the change of oxidation number (X) of the Mn ion. It was found that the Mn(V)=O bond in Naruta's oxygen evolution system has the oxygen-diradical character, which may entail the oxygen-atom radical coupling as follows:

$$(POMn(V)=O)_2 \rightarrow POMn(IV)—O—O—Mn(IV)PO \rightarrow (POMn(III))_2 + O_2 \quad (9d)$$

However, more complex mechanisms involving ionic processes are conceivable even in this case. For example, Fig. 9a illustrates the radical coupling mechanism for the formation of molecular oxygen in Eq. (9d), which is theoretically feasible because of the biradical nature of the Mn=O bond as shown in Figs. 7 and 8. On the other hand, strong electrophilic nature of the high-valent [Mn(V)=O^{+} Por] and/or [Mn(IV)=O Por $^{\cdot+}$] bonds indicates a possibility of the ionic (SE_2) process [24] in Fig. 9b, where electrophilic attack of the oxygen of MnO to the lone pair of water is a key step for the O–O bond formation in oxygen evolution. Thus our theoretical studies on native OEC and artificial OEC [28,30,35] systems have revealed the crucial role of the high-valent Mn(V)=O and/or Mn(IV)=O bonds.

4.2. SE_2 mechanism of oxygen evolution

The present computational results indicate that the insertion (or rapid rebound) mechanism, ^{1}O-model [24], is

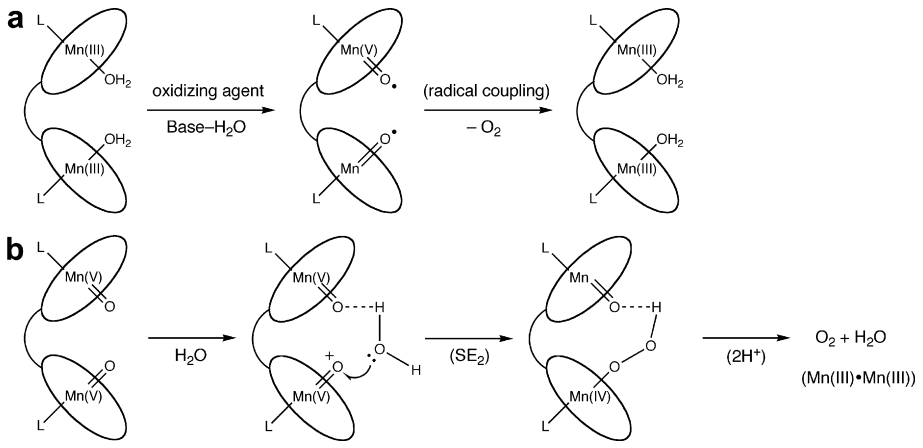


Fig. 9. (a) Radical coupling mechanism of the O–O bond formation in the artificial OEC system and (b) ionic (SE_2) mechanism of the O–O bond formation. The latter mechanism is closely related to that of OEC in Fig. 10.

applicable to the oxygenation by high-valent Mn–oxo species examined here because of strong diradical characters. However, the diradical character of the Mn–O bond is found to be sensitive to environmental effects such as hydrogen bonding and clustering of waters (see Tables 1 and 2). This in turn indicates that the nature of Mn=O bonds in **1** is variable depending on the electronic states of the cubane unit $CaMn_3O_4$. Therefore, three mechanisms in Fig. 3 are conceivable theoretically.

Present computational results indicate a possibility of our previous bimolecular electrophilic substitution (SE_2) mechanism (see Fig. 3) for oxygen evolution reaction in OEC as illustrated in Fig. 10. From Fig. 10, the oxygen site of the high valent manganese–oxo bonds [Mn(V)=O$^+$ **4**] and/or [Mn(IV)=O **4** $^{\cdot+}$] in OEC undergoes the electrophilic attack of lone pair of water molecule, followed by the concerted proton migration with base (for example hydrogen-bonding networks involving protein side chains within local environment). This SE_2 reaction produces the Mn(IV)–hydroperoxide anion complex, which undergoes second proton migration to afford the low-spin Mn(IV)–superoxide anion complex. The regulation of charge on O_2 fragment by $CaMn_3O_4$ (**4**)part is feasible in the case of **1**. The back electron transfer from superoxide anion to Mn(IV) generates triplet molecular oxygen and triplet Mn(III) complex as follows:

$$^1[\mathrm{Mn(IV)O_2^-}] \rightarrow {}^1[{}^3\mathrm{Mn(III)}{}^3\mathrm{O_2}] \rightarrow {}^3\mathrm{Mn(III)} + {}^3\mathrm{O_2} \qquad (9e)$$

It is noteworthy that $^3O_2$ is generated without spin inversion via spin–orbit interaction. The key point of the SE_2 mechanism is the electrophilic nature of oxygen site in the high-valent manganese–oxo bonds [24]. The SE_2 mechanism in Fig. 10 is consistent with the proposal by Iwata and Barber on the experimental ground [37,38]. The reaction scheme in Fig. 10 is now under further investigation in our laboratory.

4.3. Implications to related oxygenation reactions

Finally, implications of the previous [24–28] and present computational results are briefly discussed in relation to other oxygenation reactions by metal–oxo species. For

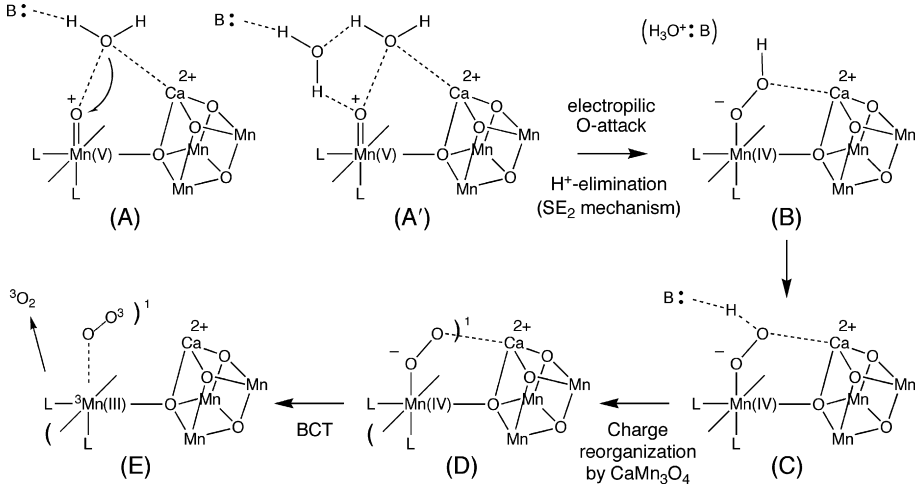


Fig. 10. Possibility of the bimolecular electrophic substitution (SE_2) mechanism of oxygen evolution reaction from water in OEC of the photosynthesis II. The SE_2 mechanism is a direct extension of that in Fig. 3 (see text). It does not entail the formation of hydroxyl radical as in the case of the ^3O-model.

example, the conversion of methane to methanol is catalyzed at the active site of a metalloenzyme known as methane monooxygenase (MMO) (Mn ions in **6** and **7** are replaced with Fe ions in MMO)

$$CH_4 + NADH + H^+ + O_2 \rightarrow CH_3OH + NAD^+ + H_2O \quad (10)$$

Both cationic and radical intermediates (or transition structures) have been proposed for this reaction on the experimental grounds [39]. Past decade, several computations have been performed to elucidate the nature of the intermediate in MMO. According to our previous proposal [24], computational results on the iron–oxo (Fe(IV)=O) species in MMO are classified into three categories illustrated in Fig. 3.

Yoshizawa et al. [40,41] have proposed a concerted (four-centered) mechanism between Fe=O and H–CH_3 fragments on the basis of the spin-restricted (RHF) calculations. Their mechanism is similar to the SE_2 (concerted) mechanism in Fig. 3, though our SE_2 mechanism is based on the high-spin configuration of the Fe(IV) center instead of their closed-shell (RHF) configuration. On the other hand, Basch, Morokuma and co-workers [42,43] have been proposed a hydrogen-abstraction mechanism for hydroxylation reaction by MMO, assuming the four unpaired spins at each Fe(IV) center of **Q** (namely the high-spin ^{9}A dimer) in the spin-unrestricted DFT (UDFT) calculations. The hydrogen-abstraction mechanism in the ^{9}A dimer model is similar to the ^{3}O (abstraction)-model in Fig. 3 since the reaction site is regarded as the ^{3}O plus H–CH_3 system. Siegbahn et al. [44,45] have proposed a hydrogen abstraction model in the high-spin mixed-valence (MV) state: **Q** = [Fe(II)(S = 5/2) Fe(IV)(S = 2/2)O-radical]. Siegbahn model is regarded as a high-spin (^{3}O) model in our terminology (Fig. 3) [24]. Friesner, Lippard and their co-workers [46,47] proposed a bound-radical pair model, assuming the low-spin (antiferromagnetic) dimer state of the high-spin iron (Fe(IV)) centers. Friesner–Lippard model is similar to the ^{1}O (insertion)-model, where both insertion and rapid recombination between the singlet radical pair (·OH plus ·CH_3) are feasible, depending on the reaction conditions [24,26].

Table 3 summarizes the proposed reaction mechanisms of methane monooxygenation (MMO) by several theoretical groups. The conclusions are dependent on the assumed anti (AF) and ferro (F) magnetic spin couplings of the iron oxo cores (Fe_2O_2) in MMO. However, the low-spin (LS) AF broken-symmetry usually involves the high-spin (HS) component. Therefore use of an approximate spin projected (AP) BS solution [23–28] is desirable for location of transition structure on the pure LS surface. This situation clearly indicates necessity of further theoretical investigations based on more realistic reaction-site and spin-state models including protein environments. Both radical and ionic mechanisms are also proposed for hydroxylation reactions of P450 with the active site: [Fe(IV)=O·Por$^{\cdot+}$] [48]. The situation is quite similar to those of MMO and OEC in the photosynthesis II system.

Table 3
Classifications of the reaction mechanisms of methane monooxygenation by several theoretical groups

Our proposals[a]	Recent computational results	Methods
SE_2 model	Yoshizawa (concerted) model[b]	RHF
^{1}O-model	Friesner–Lippard (bound-radical) model[c]	^{1}UDFT
^{3}O-model	Morokuma–Basch (hydrogen abstraction) model[d]	^{9}A by UDFT
	Siegbahn (hydrogen abstraction) model[e]	high spin MV by UDFT

[a] Refs. [24,26].
[b] Refs. [40,41].
[c] Refs. [46,47].
[d] Refs. [42,43].
[e] Refs. [44,45].

This in turn indicates that theoretical and computational efforts may provide a unified picture and key concepts for understanding of oxygenation reactions in general [24,26].

5. Concluding remarks

The nature of high-valent manganese–oxo (Mn(V)=O) bonds has been investigated on the basis of the hybrid DFT calculations of the model complexes 1, 2, and 3 for oxygen evolution center (OEC) and the Mn–oxo prophyrine complex (**8**). It is found that charge transfer from ligands to Mn(V)=O occur to indicate significant contribution of the [Mn(IV)=O L$^{\cdot+}$] configuration. Therefore the high-valent (HV) Mn–O bond is regarded as the superposed state of these two configurations in general,

$$\Psi(\mathrm{Mn(HV)}{=}\mathrm{O}) = C_1\Psi_1(\mathrm{Mn(V)}{=}\mathrm{O}\cdot\mathrm{L}) + C_2\Psi_2(\mathrm{Mn(IV)}{=}\mathrm{O}\cdot\mathrm{L}^{\cdot+}), \quad (11)$$

where C_i denotes the mixing coefficients, which are variable with ligands and environmental effects as shown in this paper. The dual character of the HV Mn–O bond would be a key factor for theoretical understanding of complex behaviors of chemical reactions by HV Mn–O compounds. Similar situations are also found in HV iron–oxo species in MMO and P450. The hybrid DFT (HDFT) followed by the natural orbital analysis is a useful and practical method for theoretical investigations of metalloenzymes as shown in this series of papers [49].

Acknowledgement

This work has been supported by a Grant-in-Aid for Scientific Research on Priority Areas (Nos. 18350008 and 18205023) from Ministry of Education, Science, Sports and Culture, Japan.

References

[1] K.N. Ferreira, T.M. Iversion, K. Maghlaoui, J. Barber, S. Iwata, Science 303 (2004) 1831.
[2] B. Kok, B. Forbush, M. McGloin, Photochem. Photobiol. 11 (1970) 457.

[3] G.C. Dismulces, Photochem. Photobiol. 43 (1986) 99.
[4] G. Renger, Angew. Chem., Int. Ed. 26 (1987) 643.
[5] V.L. Pecoraro, Photochem. Photobiol. 48 (1988) 249.
[6] R.J. Debus, Biochimi. Biophys. Acta 1102 (1992) 269.
[7] V.K. Yachandra, K. Sauer, M.P. Klein, Chem. Rev. 96 (1996) 2927.
[8] G.C. Dismulces, Chem. Rev. 96 (1996) 2909.
[9] W. Ruttinger, G.C. Dismulces, Chem. Rev. 97 (1997) 1.
[10] J. Stubbe, W.A. v.d. Donk, Chem. Rev. 98 (1998) 705.
[11] M. Yagi, M. Kaneko, Chem. Rev. 101 (2001) 21.
[12] V.K. Yachandra, V.J. DeRose, M.J. Latimer, I. Mukerji, K. Sauer, M.P. Klein, Science 260 (1993) 675.
[13] C. Philouze, G. Blondin, J.-J. Gired, J. Guilhem, C. Pascard, D. Lexa, J. Am. Chem. Soc. 116 (1994) 8557.
[14] J.B. Vincent, C. Christmas, H.R. Chang, Q. Li, P.D.W. Boyd, J.C. Huffman, D.N. Hendrickson, G. Christou, J. Am. Chem. Soc. 111 (1989) 2086.
[15] N. Hendrickson, G. Christou, E.A. Schmitt, E. Libby, J.S. Bashkin, S. Wang, H.L. Tsai, J.B. Vincent, P.D.W. Boyd, J.C. Huffman, K. Folting, Q. Li, W.E. Streib, J. Am. Chem. Soc. 114 (1992) 2455.
[16] E.A. Schmitt, L. Noodleman, E.J. Baerends, D.N. Hendrickson, J. Am. Chem. Soc. 114 (1992) 6109.
[17] M.R.A. Blomberg, P.E.M. Siegbahn, S. Styring, G.T. Babcock, B. Åkermark, P. Korall, J. Am. Chem. Soc. 119 (1997) 8285.
[18] B.I. Belinskii, Chem. Phys. 179 (1994) 1.
[19] Y. Yoshioka et al., Bull. Chem. Soc. Jpn 78 (2001) 1231.
[20] K. Yamaguchi, S. Yamanaka, M. Nishino, Y. Takano, Y. Kitagawa, H. Nagao, Y. Yoshioka, Theoret. Chem. Acc. 102 (1999) 328.
[21] K. Yamaguchi, Chem. Phys. Lett. 30 (1975) 288.
[22] T. Soda, Y. Kitagawa, T. Onishi, Y. Takano, Y. Shigeta, H. Nagao, Y. Yoshioka, K. Yamaguchi, Chem. Phys. Lett. 319 (2000) 223.
[23] T. Soda, Y. Kitagawa, T. Onishi, Y. Takano, Y. Yoshioka, K. Yamaguchi, Mol. Cryst. Liq. Cryst. 343 (2000) 157.
[24] K. Yamaguchi, Y. Takahara, T. Fueno, Appl. Quant. Chem. (V.H. Smith, Reidel, 1986) 155.
[25] S. Yamanaka, R. Takeda, K. Yamaguchi, Polyhedron 22 (2003) 2013.
[26] K. Yamaguchi, in: A.A. Frimer (Ed.), Singlet Oxygen, vol. III, CRC Press, 1985.
[27] S. Yamanaka, K. Yamaguchi, Bull. Chem. Soc. Jpn. 77 (2004) 1269.
[28] H. Isobe, T. Soda, Y. Kitagawa, Y. Takano, T. Kawakami, Y. Yoshioka, K. Yamaguchi, Int. J. Quant. Chem. 85 (2001) 34.
[29] J. Limburg, J.S. Vrettos, L.M. Liable-Sands, A.L. Rheingold, R.H. Crabtree, G.W. Brudvig, Science 283 (1999) 1524.
[30] H. Isobe, M. Shoji, K. Koizumi, Y. Kitagawa, S. Yamanaka, S. Kuramitsu, K. Yamaguchi, Polyhedron 24 (2005) 2767.
[31] A.D. Becke, Phys. Rev. A 38 (1988) 3098.
[32] S.H. Vosko, L. Wilk, M. Nusair, Can. J. Phys. 58 (1980) 1200.
[33] H. Tatewaki, S. Huzinaga, J. Chem. Phys. 71 (1979) 4339.
[34] M.J. Frisch, G.W. Trucks, H.B. Schlegel, G.E. Scuseria, M.A. Robb, J.R. Cheeseman, J.A. Montgomery, Jr., T. Vreven, K.N. Kudin, J.C. Burant, J.M. Millam, S.S. Iyengar, J. Tomasi, V. Barone, B. Mennucci, M. Cossi, G. Scalmani, N. Rega, G.A. Petersson, H. Nakatsuji, M. Hada, M. Ehara, K. Toyota, R. Fukuda, J. Hasegawa, M. Ishida, T. Nakajima, Y. Honda, O. Kitao, H. Nakai, M. Klene, X. Li, J.E. Knox, H.P. Hratchian, J.B. Cross, V. Bakken, C. Adamo, J. Jaramillo, R. Gomperts, R.E. Stratmann, O. Yazyev, A.J. Austin, R. Cammi, C. Pomelli, J.W. Ochterski, P.Y. Ayala, K. Morokuma, G.A. Voth, P. Salvador, J.J. Dannenberg, V.G. Zakrzewski, S. Dapprich, A.D. Daniels, M.C. Strain, O. Farkas, D.K. Malick, A.D. Rabuck, K. Raghavachari, J.B. Foresman, J.V. Ortiz, Q. Cui, A.G. Baboul, S. Clifford, J. Cioslowski, B.B. Stefanov, G. Liu, A. Liashenko, P. Piskorz, I. Komaromi, R.L. Martin, D.J. Fox, T. Keith, M.A. Al-Laham, C.Y. Peng, A. Nanayakkara, M. Challacombe, P.M. W. Gill, B. Johnson, W. Chen, M.W. Wong, C. Gonzalez, J.A. Pople, Gaussian, Inc., Wallingford CT, 2004.
[35] K. Koizumi, M. Shoji, Y. Nishiyama, Y. Maruno, Y. Kitagawa, T. Soda, S. Yamanaka, M. Okumura, K. Yamaguchi, Int. J. Quant. Chem. 100 (2004) 943.
[36] Y. Naruta, M. Sasayama, K. Ichihara, J. Mol. Catal A 117 (1997) 115.
[37] J. Barber, K. Ferreira, K. Maghlaoui, S. Iwata, Phys. Chem. Chem. Phys. 6 (2004) 4737.
[38] S. Iwata, J. Baber, Curr. Opin. Struct. Biol. 14 (2004) 447.
[39] M.H. Baik, N. Newcomb, R.A. Friesner, S.J. Lippard, Chem. Rev. 103 (2003) 2385.
[40] K. Yoshizawa, Y. Shiota, T. Yamabe, Chem. Eur. J. 3 (1997) 1160.
[41] Y. Shiota, Y. Yoshizawa, J. Am. Chem. Soc. 122 (2000) 12317.
[42] H. Basch, K. Mogi, D.G. Musaev, K. Morokuma, J. Am. Chem. Soc. 121 (1999) 7249.
[43] D.G. Musaev, H. Basch, K. Morokuma, J. Am. Chem. Soc. 124 (2002) 4135.
[44] P.E.M. Siegbahn, R.H. Crabtree, J. Am. Chem. Soc. 119 (1997) 3103.
[45] P.E.M. Siegbahn, M.R.A. Blomberg, Chem. Rev. 100 (2000) 421.
[46] B.F. Gherman, B.D. Dunietz, D.A. Whittingtom, S.J. Lippard, R.A. Friesner, J. Am. Chem. Soc. 123 (2001) 3836.
[47] V. Guallar, B.F. Gherman, W.H. Miller, S.J. Lippard, R.A. Friesner, J. Am. Chem. Soc. 124 (2002) 3377.
[48] S. Shaik, M. Falitov, D. Schröder, H. Schwarz, Chem. Eur. J. 4 (1998) 193.
[49] M. Shoji, K. Koizumi, Y. Kitagawa, S. Yamanaka, M. Okumura, K. Yamaguchi, Y. Ohki, Y. Sunada, M. Honda, K. Tatsumi, Int. J. Quant. Chem. 106 (2006) 3288.

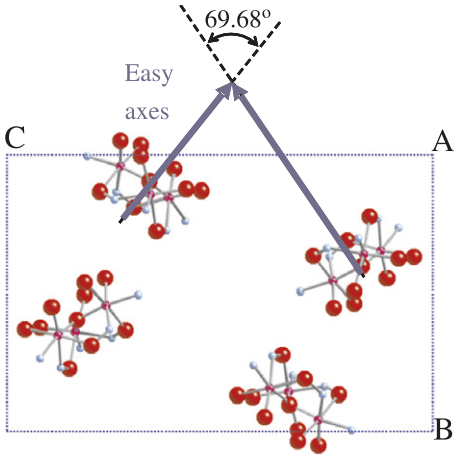


Fig. 1. Crystal structure showing the two sites in the lattice with differently oriented magnetic axes.

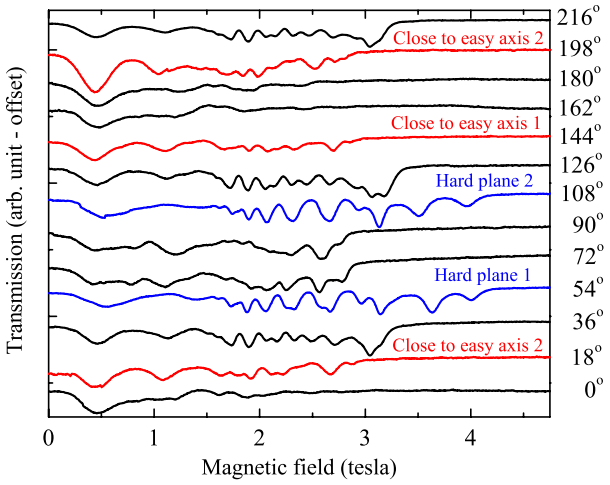


Fig. 2. Angle-dependent spectra taken at 62 GHz and 5 K; the angles are given on the right hand side. The blue curves correspond to the directions of the two hard planes. The red curves correspond to the closest approaches to the two easy axes. (For interpretation of the references in color in this figure legend, the reader is referred to the web version of this article.)

In this work, we perform high-frequency electron paramagnetic resonance (HFEPR) measurements to quantitatively determine the zero-field-splitting (zfs) parameters in the spin Hamiltonian based on the giant spin approximation [4]. HFEPR measurements were performed at various temperatures and frequencies from 60 to 170 GHz, with magnetic fields applied at different orientations relative to a single crystal. The HFEPR spectra were obtained at fixed frequencies and temperatures while varying the DC magnetic field strength. Details of the experiments can be found elsewhere [5]. These studies allow us to identify the ground state spin quantum number and to construct the Zeeman diagram associated with this state. By comparing the experimentally constructed Zeeman diagram to simulations obtained via exact diagonalization of the spin Hamiltonian, the zfs parameters can be determined quantitatively.

3. Data and discussion

The HFEPR study of this complex is complicated due to the existence the two inequivalent sites in the lattice, with differently oriented magnetic axes, neither of which align with the principal crystallographic axes (see Fig. 1). Shown in Fig. 2 are the angle-dependent spectra taken at 62 GHz and 5 K. The appearance of multiple peaks spanning a wide field range is indicative of a molecular species with an appreciable spin quantum number and significant anisotropy [6]. If one assumes an easy axis type of anisotropy (negative D value), then one expects to see the strongest peaks appearing at low fields when the field is aligned near to the easy axis, while the strongest peaks should appear at high fields when the field is in the hard plane. Clearly, the data in Fig. 2 exhibit both of these behaviors.

Since the orientation of the crystal was not known a priori, we do not know the exact plane of rotation relative to either the crystallographic axes or the magnetic axes associated with the two sites in the lattice. However, for rotation over more than a 180° angle range, we are guaranteed to pass through the hard planes associated with both sites (not necessarily coincidentally); we are also likely to pass close to the easy axes, but it is not guaranteed that we will hit those directions exactly. As can be seen from the coloring of the curves in Fig. 2, there exist two field orientations (54° and 108°, colored blue) exhibiting essentially identical spectra, with strong EPR peaks extending to the highest fields. These orientations, which are separated by about 50° (see Fig. 4 below), correspond to the two hard planes associated with each lattice site. The fact that the obtained separation is less than the ~70° separation of the easy axes confirms that the plane of field rotation is inclined relative to the plane containing the two easy axes. Nevertheless, we do expect to pass close to the easy axes for field orientations 90° away from the hard planes, i.e. 18°, 144° and 198°. One can indeed see from these traces (colored in red) that the spectra do resemble easy axis data at low fields, i.e. broader, well spaced peaks decreasing in strength with increasing field [7]; the cluster of small peaks at higher fields originate from the other species.

Fig. 3 shows an expanded view of the 54° data in Fig. 2. At high fields, one clearly sees two series of more-or-less evenly spaced peaks marked by blue squares and red arrows. The highest field series (blue squares) correspond to the main peaks associated with one of the hard planes; the field is exactly in the hard plane for these sites (species 1). Meanwhile, the field is ~50° from the other hard plane, i.e. ~40° from the easy axis associated with the other sites (species 2). For such an orientation, one expects to observe remanences of both the easy axis spectrum (strong low-field peaks) and the hard plane spectrum (strong peaks at moderately high fields). The second series of closely spaced high-field peaks (marked by red arrows) and the two broad peaks at low fields (marked by black dots) correspond to the second species. The peaks marked by the red arrows

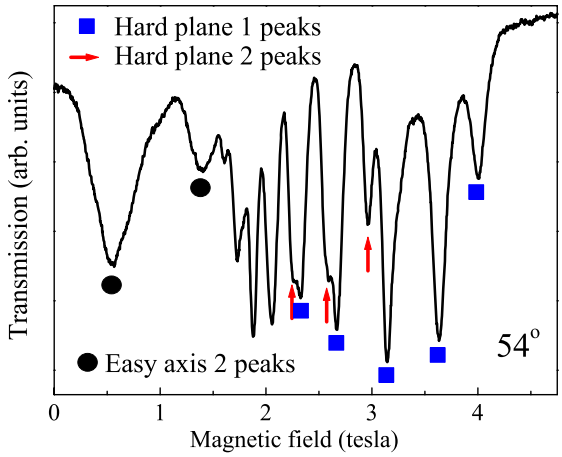


Fig. 3. An expanded view of the 54° data from Fig. 2 (field ‖ hard plane 1). The blue squares mark the resonances corresponding to the field parallel to hard plane 1 (species 1). The remaining resonances are due to the second species: the low-field peaks marked with black dots are remnants of the easy axis spectra, while the higher field peaks marked with red arrows are remnants of the hard plane spectra (see text). The field is oriented approximately 42° away from the easy axis of the second species. (For interpretation of the references in color in this figure legend, the reader is referred to the web version of this article.)

occur at lower fields than those marked by the blue squares because the field is significantly out of the hard plane for the second species.

Angle dependent measurements were also performed at a frequency of 129 GHz. Fig. 4 displays the angle dependence of the strongest peak positions. For a uniaxial system (easy axis or easy plane) in the high-field limit, $g\mu_B B \gg DS$ (= 2 T), one expects each peak to approximately follow a $(1 - 3\cos^2\theta)$ angle dependence about the isotropic position ($g = 2$ line), where θ is the orientation of the field relative to the principal (z-) axis (not the experimental angle from Fig. 4). As can be seen from the figure, each peak does

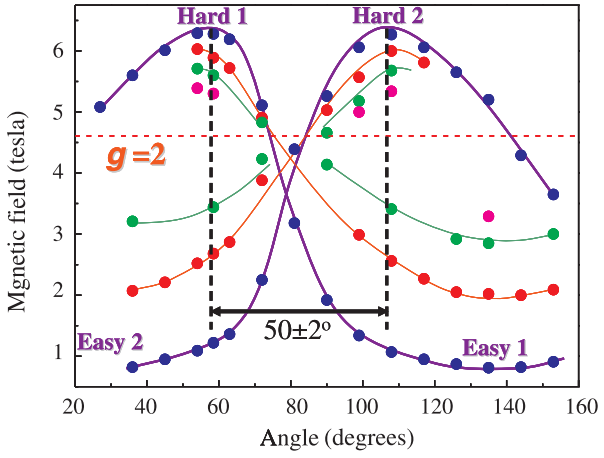


Fig. 4. EPR peak positions plotted vs. angle extracted from data obtained at a higher frequency of 129 GHz; the temperature is 5 K. Each peak exhibits an asymmetric twofold pattern (180° periodicity). The hard and easy directions are indicated in the figure for each species. The $g = 2$ line for a frequency of 129 GHz is also shown as a guide.

oscillate about $g = 2$. Furthermore, as expected, the deviation to the low-field side (field close to z-direction) of $g = 2$ is roughly twice the deviation to the high field side (field ‖ xy-plane) for each transition. The solid curves through the data points were generated by hand. Assuming D to be negative (see below), the locations of the two hard planes (dashed vertical lines) were estimated from the maxima of the blue curves.

There are multiple reasons for the departure from a perfect $(1 - 3\cos^2\theta)$ angle dependence seen in Fig. 4. First, when the field is near to the easy axis, the $g\mu_B B \gg DS$ condition is not satisfied; this causes sharper maxima and broader minima. Second, the field rotation plane is not orthogonal to the two hard planes, i.e. it does not coincide with the two easy axes. Consequently, there is a variation in the in-plane field component for each species as the magnetic field is rotated. Thus, the data in Fig. 4 provide the first evidence for transverse (in-plane) anisotropy. If there was no in-plane anisotropy, one would expect the angle dependence to be symmetric about the hard plane directions. This is clearly not the case, i.e. for hard plane 1, the fall off in the position of the peak is much sharper to the right of the hard plane than to the left (vice versa for hard plane 2). Consequently, there must be two anisotropies at play, one which depends only on the out-of-plane field component which is symmetric about the hard plane, and another that depends only on the in-plane field component, which need not necessarily be symmetric about the hard plane (this depends on the orientations of the hard and medium axes relative to the intersection between the hard plane and the field rotation plane).

In order to quantify the zfs parameters, frequency dependent measurements were performed with the magnetic field applied within the hard plane of one of the species of molecules, corresponding to 54° in Fig. 2 (hard plane 1). The positions of the observed resonances are plotted in the frequency versus field plot displayed in Fig. 5. We limited this analysis to the highest field series of evenly spaced peaks which we associate with the hard plane of one of the species (1), i.e. those marked by blue squares in Fig. 3, together with the strongest low-field peaks which we associate with the other species (2). We then simultaneously fit each series of peak positions to the usual spin Hamiltonian [4], using identical zfs parameters, since the two lattice sites are related by a simple rotation. We made the assumption that $S = 6$. However, similar attempts to fit the data were made with larger and smaller S values, and the quality of the best fits were significantly worse. In other words, the data plotted in Fig. 5 appear to confirm the spin quantum number of $S = 6$ deduced from magnetic measurements [1].

The red and blue curves in Fig. 5 correspond to the frequency differences between Zeeman split levels which differ in m_s by ±1, i.e. levels between which there are allowed magnetic dipole transitions. The red curves were fit to the red low-field data points and the blue curves to the high-field blue data points. We made the assumption that the

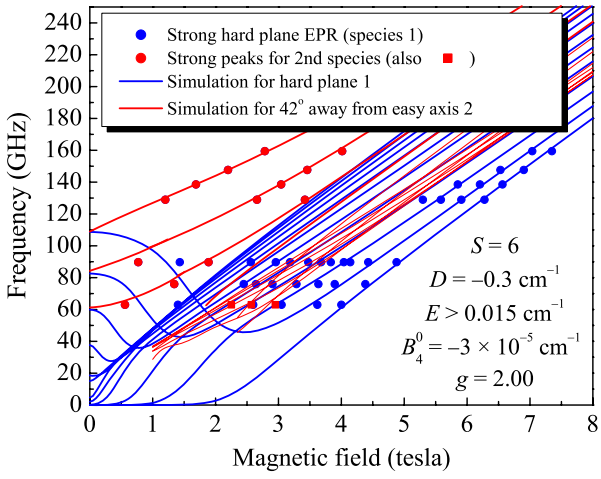


Fig. 5. Frequency dependence of the main EPR peaks observed at 5 K for the field applied parallel to hard plane 1 (54°). The solid blue circles correspond to species 1 and the solid red circles to the low-field peaks associated with species 2; the solid red squares correspond to the peaks marked by red arrows in Fig. 3. The curves represent the best fit to both data sets, yielding the zfs parameters given in the figure. The blue curves correspond DC fields applied in the hard plane for species 1, and red curves for fields applied 42° away from the easy axis associated with species 2. (For interpretation of the references in color in this figure legend, the reader is referred to the web version of this article.)

field was exactly in the hard plane for the blue curves, while the orientation of the field was adjusted for the red curves. The red data place the strongest constraint on the axial D and B_4^0 parameters, as well as determining the orientation of the field relative to the easy axis of the second species. In order to maintain a good fit to the low-field data, whilst simultaneously fitting the blue data points, we found it necessary to include a significant transverse anisotropy. Since we do not know the exact plane of rotation, we cannot determine the precise value of the transverse anisotropy parameter. Furthermore, we cannot determine its symmetry, as has been done for other SMMs via field rotation studies within the hard plane [8,9]. Nevertheless, to get some idea of the degree of transverse anisotropy, we use the standard rhombic interaction of the form $E(\hat{S}_x^2 - \hat{S}_y^2)$ [4].

The optimum fits to the data in Fig. 5 yield: $S = 6$, $D = -0.3\ \mathrm{cm}^{-1}$, $B_4^0 = -3 \times 10^{-5}\ \mathrm{cm}^{-1}$, $g = 2.00$ and a significant $E \geqslant 0.015\ \mathrm{cm}^{-1}$. For the second species, the field is found to be $42° \pm 2°$ away from the easy axis ($48° \pm 2°$ away from the hard plane), which agrees with the angle dependent measurements. The reason for the lower bound on E is because our fits assumed that the field was precisely along the hard axis for the high field data points (species 1, blue data points). One could include a larger E value and rotate the field slightly towards the medium axis (within the hard plane) and obtain an equally good fit. To place this in context, an E/D ratio of 0.05 is about a quarter of that found for the biaxial Fe_8 SMM [7,10]. Therefore, the transverse anisotropy is fairly significant.

Also seen in Fig. 5 are a series of thinner red curves which overlap the lower field blue curves. These red lines correspond to the higher field peaks expected of the second species (marked by red arrows in Fig. 3). We did not consider these peaks when fitting the data. However, three data points (red squares) are included in Fig. 5 corresponding to the peaks marked by red arrows for the 62 GHz data in Fig. 3. As can be seen, the locations of these peaks agree reasonably well with the thinner red curves in Fig. 5. Thus, the earlier explanation for these peaks appears to be sound. The slight deviations between the red square positions and the thin red curves may be attributed to the fact that we do not know the precise orientation of the field within the hard plane, i.e. one does not expect perfect agreement due to the uncertainty in the E value.

Finally, Fig 6 displays 129 GHz data obtained at 10 K and 5 K with the field parallel to the hard plane of species 1. The two insets display the Zeeman diagrams generated using the obtained zfs parameters for two field orientations: 42° away from the easy axis (left) and parallel to the hard plane (right). The red bars in these insets represent the observed EPR transitions. As can be seen from the figure, the EPR intensity transfers to the lowest and highest field peaks upon lowering the temperature, i.e. the transitions from the lowest lying levels in the two Zeeman diagrams. This behavior can only be explained assuming a negative D value. We note that changing the sign of D would not affect the fits displayed in Fig. 5. However, changing the sign of D would invert the Zeeman diagrams. Were this the case, one would expect the EPR intensity to shift to intermediate fields (around $g = 2$) upon lowering the temperature. Consequently, the temperature depen-

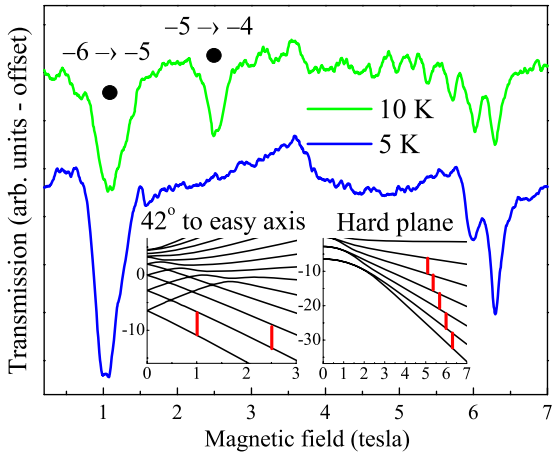


Fig. 6. Temperature dependence of the 129 GHz spectra obtained with the field parallel to hard plane 1 (54°). The two insets display the Zeeman diagrams generated using the obtained zfs parameters for two field orientations: 42° away from the easy axis (left) and parallel to the hard plane (right). The red bars in these insets represent the observed EPR transitions. The low-field transitions have been labeled according to the m_s values involved in the transitions. (For interpretation of the references in color in this figure legend, the reader is referred to the web version of this article.)

dence provides spectroscopic confirmation of a negative D value, thereby verifying that Mn_3 is in fact a SMM.

4. Summary

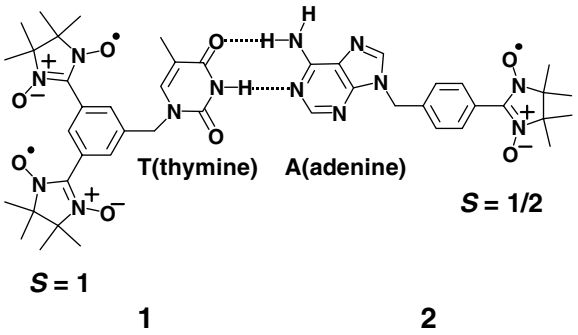
Multi-high-frequency single-crystal EPR measurements have enabled a quantitative determination of the zfs parameters of the first triangular Mn SMM. The obtained parameters are in good agreement with previously published values deduced from thermodynamic measurements, thereby providing spectroscopic evidence that Mn_3 is indeed a SMM.

Acknowledgement

This work was supported by the US National Science Foundation under grant numbers DMR-0239481 and DMR-0506946.

References

[1] Theocharis C. Stamatatos et al., J. Am. Chem. Soc. 127 (2005) 15380.
[2] J.B. Vincent, H.-R. Chang, K. Folting, J.C. Huffman, G. Christou, D.N. Hendrickson, J. Am. Chem. Soc. 109 (1987) 5703.
[3] G. Rajaraman, J. Brockman, M. Murugesu, C.E. Sanudo, J. Raftery, S.J. Teat, W. Wernsdorfer, G. Christou, E.K. Brechin, D. Collison, Chem.-Eur. J. 10 (2004) 5180.
[4] D. Gatteschi, R. Sessoli, Angew. Chem. 42 (2003) 268.
[5] S. Takahashi, S. Hill, Rev. Sci. Instrum. 76 (2005) 023114.
[6] S. Hill, J.A.A.J. Perenboom, N.S. Dalal, T. Hathaway, T. Stalcup, J.S. Brooks, Phys. Rev. Lett. 80 (1998) 2453.
[7] S. Hill, S. Maccagnano, K. Park, R.M. Achey, J.M. North, N.S. Dalal, Phys. Rev. B 65 (2002) 224410.
[8] S. Hill, R.S. Edwards, S.I. Jones, J.M. North, N.S. Dalal, Phys. Rev. Lett. 90 (2003) 17204.
[9] E. del Barco, A.D. Kent, S. Hill, J.M. North, N.S. Dalal, E.M. Rumberger, D.N. Hendrickson, N. Chakov, G. Christou, J. Low Temp. Phys. 140 (2005) 119.
[10] A.L. Barra, D. Gatteschi, R. Sessoli, Chem. Eur. J 6 (2000) 1608.



Scheme 1. Heterospin nucleobase pair composed of thymine-substituted biradical T-bisNN **1** ($S = 1$) and adenine-substituted monoradical **2** ($S = 1/2$).

ferrimagnets, we have proposed a bio-inspired scheme in which the hydrogen bonding between the nucleobase substituents serves to assemble organic radicals in a controllable manner [5]. Two kinds of nucleobases with different spin quantum numbers should be connected by complementary hydrogen bonds to give a two-component heteromolecular assemblage suitable for a ferrimagnetic spin alignment. An example of the hydrogen-bonded aggregation is shown in Scheme 1. In this communication, we report synthesis and characterization of a thymine-substituted nitronyl nitroxide biradical T-bisNN (**1**) as a building block of heterospin nucleobase pairing of thymine and adenine. We examine X-ray crystallography and magnetic properties of the biradical **1**. Intermolecular hydrogen bonding motifs and the ground-state spin multiplicity of **1** are presented. Potentiality of **1** as a building block for bio-inspired ferrimagnet is discussed.

2. Experimental

2.1. Synthesis

The thymine-substituted biradical **1** was synthesized by a direct coupling of thymine with a 5-chloromethylphenyl derivative of nitronyl nitroxide **3**, as shown in Scheme 2. The precursor **3** has been prepared from hexatriene [6] according to the literature procedures [7,8]. The precursor **3** (100 mg, 0.23 mmol) was added to a suspension of thymine (43.9 mg, 0.35 mmol), K_2CO_3 (46.8 g, 0.34 mmol), and KI (53.6 mg, 0.32 mmol) in CH_3CN (6 ml). The reaction mixture was stirred at 80 °C for 18 h. After filtration, the reaction solution was concentrated and chromatographed on silicagel using CH_2Cl_2/acetone (4/1 in volume) as an eluent to yield a blue solid of **1** (61.7 mg, 50.9%). A polyvinylchloride (PVC) film, used as magnetically diluted samples, was prepared by slow evaporation of a dichloromethane solution of PVC and **1** (26.9 wt%).

2.2. Crystal structure analysis

Single crystals of T-bisNN (**1**) were obtained by recrystallization from a mixed solution of dichloromethane and hexane. Single crystal diffraction data of **1** were collected on a Rigaku Mercury CCD diffractometer with graphite monochromated Mo Kα radiation at 193 K. The crystal structure was solved by using direct methods in a program package CRYSTALSTRUCTURE[1]. Anisotropic thermal parameters analysis was applied for non-hydrogen atoms. Hydrogen atoms with isotropic thermal parameters were refined as riding models.

2.3. Magnetic susceptibility measurements

The static paramagnetic susceptibility χ_p was measured for polycrystals and diluted samples in the PVC films on a SQUID magnetometer with an applied magnetic field of 0.1 T in the temperature range of 1.9–300 K. The magnetic responses were corrected with diamagnetic blank data of the sample holder obtained separately. The diamagnetic contribution of the sample itself was estimated from Pascal's constants.

3. Results and discussion

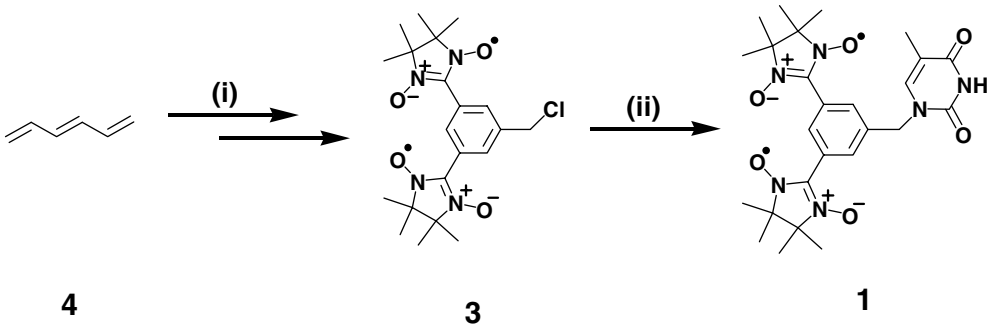
3.1. Crystal structure

The crystalline solid of **1** was stable under aerated conditions at room temperature. The crystallographic data for **1** are listed in Table 1. The crystal contains one mole of dichloromethane as crystal solvent. The molecular structure is shown in Fig. 1 with the atom numbering. The phenyl and the thymine rings have a large dihedral angle of 81.0° around the methylene bridge. It is expected that the delocalization of unpaired electron spin in **1** is truncated at the methylene bridge. It was found from molecular orbital calculations that the thymine moiety has little spin density[2]. Thus, the thymine group in **1** should play a role primarily in determining the molecular packing instead of propagating intermolecular magnetic interactions.

Twofold hydrogen bonds are found between the thymine substituents of inversion-related nearest-neighbor molecules, as shown in Fig. 2(a). The length of the hydrogen bond is N6H30–O5 = 2.863(4) Å. This is very close to those of pristine thymine [9]. In another pair of molecules related by an inversion center, a short contact of 3.222(5) Å is found between the nitronyl nitroxide oxygen atom (O4) and the central carbon atom (C7), as depicted in Fig. 2b. This kind of oxygen–carbon contact for nitronyl nitroxide radicals is expected to have a contribution to intermolecular ferromagnetic interaction, as found in other nitronyl nitroxide derivatives [10].

[1] CRYSTALSTRUCTURE (ver.3.6.0): Rigaku/Molecular Structure Corporation (2000–2004), 9009 New Trails Dr. The Woodlands, TX 77381, USA.

[2] Molecular orbitals and spin density distribution of **1** have been calculated with the density functional theory. The molecular geometry of **1** was taken from the X-ray crystal structure. The results of the spin density calculations are given in Supporting Information.



Scheme 2. Synthesis of T-bisNN (**1**): (i) procedures reported in Ref. [6] and (ii) thymine, K_2CO_3, KI in CH_3CN.

Table 1
Selected X-ray crystallographic data of **1**

Chemical formula	$C_{27}H_{36}N_6O_6Cl_2$
Crystal systems	triclinic
Space system	$P\bar{1}$
Unit cell dimensions	
a (Å)	10.7859(2)
b (Å)	12.118(3)
c (Å)	12.522(4)
α (°)	78.150(2)
β (°)	69.167(2)
γ (°)	75.158(2)
V (Å^3)	1466.8(5)
Z	2
D_{calc} (g cm^{-3})	1.385
T (K)	193
$R(I > 3\sigma(I))$[a]	0.068
R_w (all data)[b]	0.187
Goodness-of-fit	1.001

[a] $R = \sum \|\|F_o\| - |F_c\|\| / \sum |F_o|$.

[b] $R_w = \sqrt{\sum w(|F_o| - |F_c|)^2 / \sum w(F_c)^2}$.

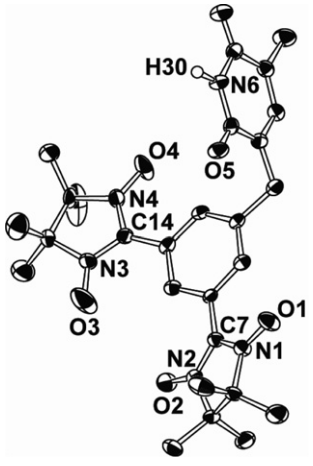


Fig. 1. ORTEP view of the asymmetric unit of T-bisNN (**1**) with the thermal ellipsoids at the 50% probability level. The hydrogen atoms are omitted for clarity except those in the hydrogen bonding moiety.

3.2. Magnetic susceptibility

The intramolecular exchange interaction in **1** is examined by paramagnetic susceptibility χ_p for the sample dispersed in the PVC film, in which the radical molecules are diluted and the intermolecular magnetic interactions are suppressed. The χ_pT value of the magnetically diluted system increases as the temperature is lowered, as shown in Fig. 3. This indicates the occurrence of ferromagnetic interactions within the molecule. A decrease in χ_pT is ascribed to residue of intermolecular exchange interactions due to incomplete dispersion of the molecules in the film, as found in other nitroxide compounds in organic polymer matrices [10d,11]. The temperature dependence of χ_pT is analyzed by assuming the thermal equilibrium of the singlet and triplet states [12]:

$$\chi_p = \frac{\alpha N_A g^2 \mu_B^2}{k_B(T-\theta)} \frac{2}{3+\exp(-2J(\pi)/k_BT)} \quad (1)$$

where the singlet–triplet energy gap is denoted by $2J(\pi)$. The mean field θ in Eq. (1) represents the residue of intermolecular interactions. The purity of the sample is designated by α. The observed χ_pT was reproduced by Eq. (1) with the parameters $2J(\pi)/k_B = 21.4 \pm 0.2$ K, $\theta = -0.8 \pm 0.1$ K, $\alpha = 0.88$ and the g-factor of $g = 2.006$, which was observed from the ESR spectrum of **1**. The reduced purity of 88% is attributed to decomposition of **1** during the preparation of the PVC film, as found in other radical compounds in PVC matrices [10d,11]. From the susceptibility measurements, the intramolecular exchange interaction of **1** has been found to be ferromagnetic, which gives a triplet ground state.

The magnetic susceptibility of **1** measured for the neat polycrystals is compared with that of the diluted sample in Fig. 3. With decreasing temperature the χ_pT value of the polycrystal increased and reached a rounded maximum at 13 K. The increase in χ_pT indicates that the dominating exchange interaction is ferromagnetic in the crystalline solid of **1**, which is attributed to the intramolecular interaction $J(\pi)$ or to the intermolecular interaction originating from the short contact at O4–C7 in the dimeric structure shown in Fig. 2b. The decrease in χ_pT at lower temperature tells us that additional weak antiferromagnetic interactions occur between the dimers. The magnetic coupling of **1** in the dimeric structure is approximated by a spin cluster consisting of four $S = 1/2$ spins, as described by a Heisenberg Hamiltonian:

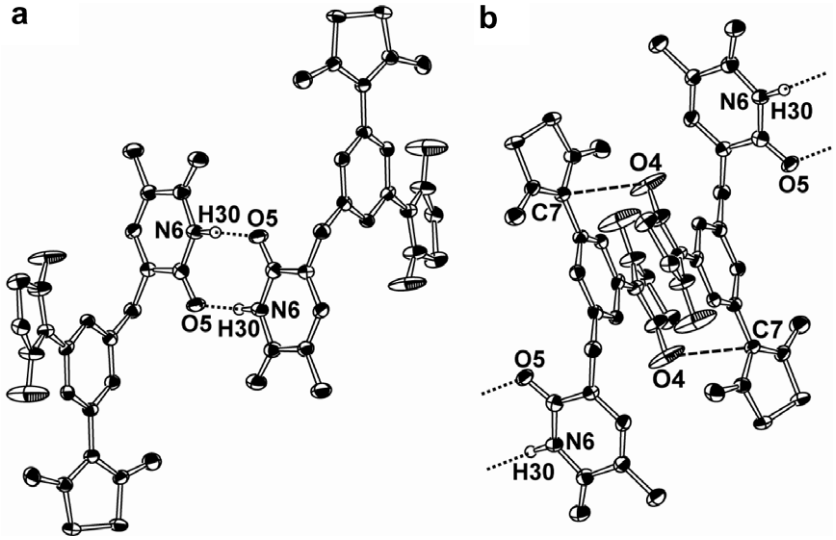


Fig. 2. (a) Hydrogen-bonded pair of inversion-related molecules. (b) Intermolecular contacts in the dimer. The methyl groups are omitted for clarity.

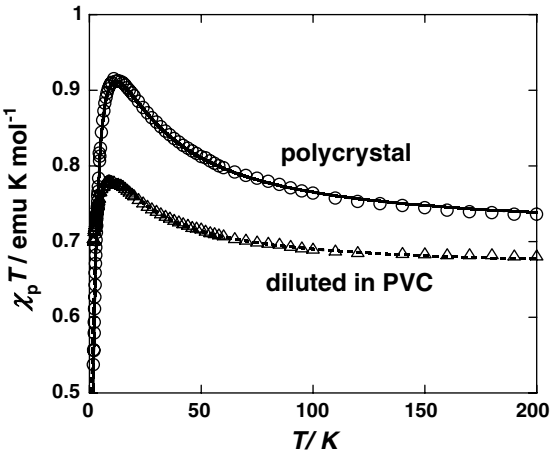


Fig. 3. Magnetic susceptibility χ_p of the T-bisNN (**1**) in the χ_pT vs. T plots. The circles represent the χ_pT value of the randomly oriented polycrystals. The solid line is calculated from Eq. (2) and Eq. (3). The triangles denote the χ_pT value of the diluted sample in the PVC film. The dashed line indicates the calculation from Eq. (1).

$$H = -2J_1(\mathbf{S}_1 \cdot \mathbf{S}_2 + \mathbf{S}_3 \cdot \mathbf{S}_4) - 2J_2(\mathbf{S}_1 \cdot \mathbf{S}_3 + \mathbf{S}_2 \cdot \mathbf{S}_4) \qquad (2)$$

where J_1 and J_2 represent the intra- and intermolecular interactions, respectively. The Hamiltonian equation (2) retains the inversion symmetry of the dimeric structure of **1**. The spin Hamiltonian was numerically diagonalized to give energy eigenvalues E_i and spin eigenvalues S_i for the ith eigenstate [13], from which the temperature dependence of χ_pT was calculated as

$$\chi = \frac{N_A g^2 \mu_B^2}{6k_B(T-\theta)} \cdot \frac{\sum_i [S_i(S_i+1)(2S_i+1)\exp(-E_i/k_BT)]}{\sum_i [(2S_i+1)\exp(-E_i/k_BT)]} \qquad (3)$$

The parameter θ represents the weak interdimer interaction in the mean field approximation. The observed temperature dependence of χ_pT was reproduced by the parameters $2J_1/k_B = 36.8 \pm 0.4$ K, $2J_2/k_B = 10.2 \pm 0.1$ K, $\theta = -3.1 \pm 0.1$ K and $\alpha = 0.94$. In the model of Eq. (2), we are not allowed to distinguish between the intra- and the intermolecular interactions within the dimer. Both $2J_1/k_B = 36.8$ K and $2J_2/k_B = 10.2$ K are different from $2J/k_B = 21.4$ K estimated from the magnetically diluted system[3]. The discrepancy of the magnitude of the intramolecular exchange interaction results from a possible change in the dihedral angles of the molecule **1** in the crystalline solid and the organic matrix of the polymer film. The range of the amplitude of the intramolecular ferromagnetic interaction, $2J/k_B = 20$–40 K, is consistent with 1,3-diyl phenyl nitronyl nitroxide biradicals with 5-alkyl substituents [6,14].

4. Conclusion

The biradical **1** with a thymine substituent has been synthesized. The ground state spin multiplicity of **1** has been found to be triplet ($S = 1$) from the magnetic susceptibility measurements. It has been found from the X-ray crystallographic analysis that the thymine substituents of **1** form aggregates based on intermolecular hydrogen bonds. The hydrogen bonding motif of **1** is the same as that of pristine thymine. Thus, introduction of the radical substituent into the nucleobase results in little disturbance to the molecular arrangement usually found in nucleobase molecules or intermolecular hydrogen bonding motifs. Thymine has been found to be an efficient element for molecular assembly of bio-inspired molecule-based magnets in terms of crystal engineering for nucleobase-substituted radicals. The present results indicate that the biradical **1** serves as

[3] Fixing one of the two adjustable parameters in Eq. (2) as estimated from the magnetically diluted samples ($2J_1/k_B = 21.4$ K) has resulted in a poor fit to the observed temperature dependence of χ_pT, which has not been repaired by reoptimization of the other parameter J_2.

an $S = 1$ component of the bio-inspired molecule-based ferrimagnets. Complexation of **1** with an adenine-substituted monoradical **2** is in progress.

Acknowledgements

This work has been supported by Grants-in-Aid for Scientific Research from the Ministry of Education, Sports, Culture, Science and Technology, Japan. Financial support from PRESTO of Japan Science and Technology Agency (JST) is also acknowledged.

Appendix A. Supplementary material

CCDC 613290 contains the supplementary crystallographic data for this material. These data can be obtained free of charge via http://www.ccdc.cam.ac.uk/conts/retrieving.html, or from the Cambridge Crystallographic Data Centre, 12 Union Road, Cambridge CB2 1EZ, UK; fax: (+44) 1223-336-033; or e-mail: deposit@ccdc.cam.ac.uk. Supplementary data associated with this article can be found, in the online version, at doi:10.1016/j.poly.2006.10.044.

References

[1] (a) M. Tamura, Y. Nakazawa, D. Shiomi, K. Nozawa, Y. Hosokoshi, M. Ishikawa, M. Takahashi, M. Kinoshita, Chem. Phys. Lett. 186 (1991) 401;
(b) Y. Nakazawa, M. Tamura, N. Shirakawa, D. Shiomi, M. Takahashi, M. Kinoshita, M. Ishikawa, Phys. Rev. B 46 (1992) 8906.

[2] (a) For overviews of molecule-based magnetism, see P.M. Lathi (Ed.), Magnetic Properties of Organic Materials, Marcel Dekker, New York, 1999;
(b) K. Itoh, M. Kinoshita (Eds.), Molecular Magnetism: New Magnetic Materials, Gordon & Breach, Amsterdam, 2000 (Kodansha as copublisher, Tokyo);
(c) Proceedings of the Ninth International Conference on Molecule-based Magnets, Tsukuba, Japan, 2004; G. Christou (Ed.), Polyhedron 24 (2005).

[3] (a) There are several examples in which stable radicals of nitroxide are introduced to nucleobase in crystalline solid state: R. Feher, D.B. Amabilino, K. Wurst, J. Veciana, J. Mol. Cryst. Liq. Cryst. 334 (1999) 333;
(b) P. Taylor, P.R. Serwinski, P.M. Lahti, Chem. Commun. (2003) 1400;
(c) P. Taylor, P.M. Lahti, J.B. Carroll, V.M. Rotello, Chem. Commun. (2005) 895;
(d) K. Das, M. Pink, S. Rajca, A. Rajca, J. Am. Chem. Soc. 128 (2006) 5334.

[4] (a) For recent examples of stable nitroxide-labeled nucleosides and nucleotides, see: T. Kaneko, M. Aso, N. Koga, H. Suemune, Org. Lett. 7 (2005) 303;
(b) A. Okamoto, T. Inasaki, I. Saito, Tetrahedron Lett. 46 (2005) 791.

[5] D. Shiomi, M. Nozaki, T. Ise, K. Sato, T. Takui, J. Phys. Chem. B 108 (2004) 16606.

[6] H. Tanaka, T. Ise, D. Shiomi, K. Sato, T. Takui, J. Low Temp. Phys., in press.

[7] P.S. Traas, H.J. Takken, H. Boelens, Tetrahedron Lett. (1977) 2129.

[8] E.F. Ullman, J.H. Osiecki, D.G.B. Boocock, R. Darcy, J. Am. Chem. Soc. 94 (1972) 7049.

[9] R. Gerdil, Acta Crystallogr. 14 (1961) 333.

[10] (a) For example, see: K. Inoue, H. Iwamura, Chem. Phys. Lett. 207 (1993) 551;
(b) F.L. Panthou, D. Luneau, J. Laugier, P. Rey, J. Am. Chem. Soc. 115 (1993) 9095;
(c) J. Omata, T. Ishida, D. Hashizume, F. Iwasaki, T. Nogami, Inorg. Chem. 40 (2001) 3954;
(d) K. Hayakawa, D. Shiomi, T. Ise, K. Sato, T. Takui, J. Phys. Chem. B 109 (2005) 9195.

[11] Y. Kanzaki, D. Shiomi, C. Kaneda, T. Ise, K. Sato, T. Takui, J. Mater. Chem. 16 (2006) 2064.

[12] B.D. Bleany, K. Bowers, Proc. R. Soc. Lond. A 214 (1952) 451.

[13] K. Kamiyama, D. Shiomi, S. Hase, M. Nishizawa, K. Sato, M. Kozaki, K. Okada, T. Takui, Appl. Magn. Reson. 19 (2000) 45.

[14] L. Catala, J.L. Moigne, N. Kyrisakas, P. Rey, J.J. Novoa, P. Turek, Chem. Eur. J. 7 (2001) 2466.

single crystal that would afford structural determination by X-rays. The results of this paper speak to the isolation of a crystalline material, $\{Mn_5(OC(O)CH_3)_6(OC(O)C_6H_5)_4\}_\infty$ or ($\{Mn_5(OAc)_6(OBz)_4\}_\infty$), that we anticipate is directly related to the aforementioned room-temperature metal-organic ferromagnet.

2. Experimental

2.1. Preparation of $\{Mn_5(OAc)_6(OBz)_4\}_\infty$ (1)

Single crystals of **1** ($\{Mn_5(OAc)_6(OBz)_4\}_\infty$) were prepared by solvothermal reaction with all manipulations performed under anaerobic conditions using an N_2-filled Innovative Technologies (IT) glovebox and standard Schlenk techniques. Dried, deoxygenated toluene was collected from an IT solvent treatment system and degassed with N_2 for 10 min prior to introduction into the glovebox. Anhydrous Mn(acetate)$_2$ (98%) and benzoic acid (99.5%) were used as received from Aldrich. A typical procedure for the isolation of **1** consisted of loading Mn(OAc)$_2$ (0.210 g, 1.21 mmol) and benzoic acid (0.150 g, 1.23 mmol) into a 120 mL PTFE-lined Parr autoclave reactor with three mL toluene added as a crystallization solvent. After appropriate sealing in the glovebox, the bombs were introduced into an oven with temperature controlled via an Omega CN9600. The thermal profile that resulted in the formation of **1** was heating from room temperature to 110 °C at 20 °C/h with a 36 h soak followed by cooling to 30 °C at a rate of 4 °C/h. *Warning:* these reaction conditions are above the flash point of the toluene solvent and appropriate consideration should be made to safely manage thermal runaway and reactor rupture.

The Parr reactors were then loaded back into the glovebox with single crystals being stored under Fomblin oil and samples for analysis washed with 3 × 5 mL aliquots of dry toluene prior to being dried under vacuum. The total yield for this reaction was 0.251 g (93% based on Mn). Sealed capillary melting point data was measured with an Electrothermal melting point apparatus, m.p. 260–264 °C (dec.). Elemental analysis was performed at Galbraith Laboratories, Inc. (Knoxville, TN). *Anal.* Calc. for $C_{40}H_{38}O_{20}Mn_5$: C, 43.10; H, 3.40. Found: C, 42.56; H, 3.36%. IR spectra were recorded on KBr pellets using a Bruker FT-IR Vertex 70 spectrophotometer. Selected IR data (KBr, cm^{-1}): 3069 (m), 3015 (w) 2935 (w), 1591 (vs), 1554 (s), 1504 (s), 1494 (s, sh), 1409 (vs), 1342 (s), 1310 (m), 1284 (w), 1181 (w), 1159 (w), 1103 (vw), 1070 (m), 1049 (m), 1025 (s), 944 (m), 859 (m), 839 (m), 824 (w), 724 (s), 674 (s, sh), 663 (s), 614 (m), 573 (w), 534 (w), 511 (w), 461 (m), 429 (m).

2.2. X-ray crystallographic studies

Data for complex **1** was collected at 150 K on a Nonius Kappa CCD diffractometer with a graphite monochromator utilizing Mo Kα radiation (0.71073 Å, λ). Data collection parameters are listed in Table 1. Cell parameters were refined using up to 8182 reflections. An absorption correction by integration was applied, based on the measured indexed crystal faces. The structure was solved by direct methods using SHELX 97 [3] and refined using full-matrix least squares on F^2_{obs}. Non-hydrogen atoms were refined anisotropically, whereas the hydrogen atoms were placed in ideal, calculated positions with isotropic thermal parameters residing on their respective carbon atoms. Some disorder was observed in **1** (see Supporting Information) for one of three acetate ligands. In this instance, the acetate was refined anisotropically in two parts using respective site occupancy factors. The acetate ligand adopts two sets of alternate positions related by a 54° rotation of the acetate ligand with two components being defined as follows: component 1 – C41, C42, O41, O42; and component 2 – C41, C42a, O41a O42a. Each component exhibits a site occupancy factor of 50%.

Table 1
Crystal data and structure refinement for **1**

Empirical formula	C_{40} $H_{38}Mn_5O_{20}$
Formula weight	1113.40
Crystal system	orthorhombic
Space group	*Aba2* (41)
a (Å)	19.643(4)
b (Å)	24.014(5)
c (Å)	10.173(2)
Volume (Å^3)	4798.6(16)
Z	4
D_{calc} (mg/m^3)	1.541
Color of crystal	colorless
Crystal size (mm)	0.23 × 0.15 × 0.03
T (°C)	−123
Radiation (λ, Å)	Mo Kα (0.71073)
μ (mm^{-1})	1.353
Maximum and minimum transmission	0.9605 and 0.7460
Scan mode	ω at 55/−55
2θ Limits (°)	3.98–50.04
$\pm h$	23
$\pm k$	28
$\pm l$	12
Number of reflections measured	8182
Number of unique reflections	4176
Restraints	7
Number of variables	323
R_1 [$I > 2\sigma(I)$]	0.0599
wR_2 (all data)	0.1538
R_{int}	0.0386
Goodness-of-fit	1.055

2.3. Other measurements

The magnetic data of powdered, microcrystalline samples were collected with a 9 T Quantum Design PPMS using the VSM option for M(H) measurements and the ACMS option for the in-phase and out-of-phase susceptibility determinations. Calibrations were competed using DyO and Pd references. Nylon sample holders and pharmaceutical gel caps showed less than 10^{-7} emu diamagnetic background.

3. Results and discussion

3.1. Synthesis

Previous reports teach the utility of ligand exchange reactions for the formation of mixed carboxylate manganese complexes [2,4,5]. An excellent description of the equilibria involved has been provided by Christou et al. who find that while mixed ligand complexes are readily observed, complete ligand substitution typically require either: (i) isolation of a mixed ligand complex followed by further treatment in the presence of excess carboxylic acid or (ii) azeotropic removal of acetic aced when an acetate-containing Mn complex is used as a starting material [5]. It is almost certain that the product reported in this work is the consequence of an equilibrium ligand exchange where the reaction of manganese acetate and benzoic acid in toluene under solvothermal conditions results in the isolation of **1** (Eq. 1). It seems plausible that there are several $Mn_x(OAc)_y(OBz)_z$ species present in the reaction mixture with the kinetics of crystallization favoring the formation of **1** under these conditions (i.e., ratio of reagents, dielectric properties of the solvent, etc.). It might be noted that excessive quantities of solvent give microcrystalline products but diffraction-quality crystals of **1** are observed after a reaction time of 36 h and a slow cooling to room temperature.

$$5Mn(OC(O)CH_3)_2 + 4HOC(O)C_6H_5 \xrightarrow[\text{Toluene}]{\Delta} \{Mn_5(OC(O)CH_3)_6(OC(O)C_6H_5)_4\}_\infty + 4CH_3CO_2H \quad (1)$$

It is noteworthy that $Mn(OAc)_2$ is not freely soluble in refluxing toluene but ^1H NMR control experiments show it to be at least slightly soluble at room temperature. While manganous acetate appears to be freely soluble in alcohols (e.g., MeOH and EtOH), these solvents were avoided given their propensity to co-crystallize with manganese carboxylates (e.g., $[Mn_4(OAc)_8(MeOH)_2]_n$ [6]). It seems reasonable to speculate that under the solvothermal conditions employed in this study, both the $Mn(OAc)_2$ starting reagent and the equilibrium products are soluble in toluene and that **1** crystallizes during the cooling period of the thermal treatment. Further experimentation toward understanding the kinetics of crystallization are ongoing.

3.2. Structure of $\{Mn_5(OAc)_6(OBz)_4\}_\infty$ (1)

Crystals of $\{Mn_5(OAc)_6(OBz)_4\}_\infty$ (**1**) are colorless with hexagonal thin plate-shape. A single crystal with the size of $0.03 \times 0.15 \times 0.23$ mm^3 was utilized for structural analysis. Crystallographic data and selected bond lengths/angles for **1** are listed in Tables 1 and 2, respectively. Compound **1** crystallizes in the orthorhombic *Aba2* space group and the asymmetric unit (Fig. 1) has the nominal formula $Mn_{2.5}(OC(O)CH_3)_3(OC(O)C_6H_5)_2$. Mn1, Mn2 and Mn3 are linked together through three acetate and two benzoate ligand bridges with Mn3 located on a C_2 axis special position. All of the Mn atoms maintain sixfold distorted octahedral coordination via acetate and benzoate ligands (Fig. 2). One benzoate and four acetate ligands are bonded to Mn1 (Fig. 2a) while Mn2 is bound by three benzoates and three acetates (Fig. 2b). Mn3 exhibits the least distorted O_h geometry with the two benzoate ligands occupying axial positions and four different acetate groups located along the equatorial plane.

Table 2
Selected bond lengths (Å) and bond angles (°) for **1**

Bond lengths			
Mn(1)–O(42)	2.058(9)	Mn(2)–O(12)	2.225(5)
Mn(1)–O(51)	2.082(5)	Mn(2)–O(52)	2.246(5)
Mn(3)–O(21)	2.093(5)	Mn(1)–O(12)	2.239(5)
Mn(1)–O(11)	2.352(4)	Mn(2)–O(22)	2.085(4)
Mn(3)–O(31)	2.242(5)	Mn(2)–O(41)	2.196(9)
Mn(3)–O(41)	2.328(8)	Mn(2)–O(31)	2.205(4)
O(11)–C(11)	1.269(8)	O(12)–C(11)	1.285(8)
C(11)–C(12)	1.471(9)	C(12)–C(17)	1.366(10)
C(12)–C(13)	1.397(10)	C(13)–C(14)	1.361(11)
C(14)–C(15)	1.350(14)	C(15)–C(16)	1.384(14)
C(16)–C(17)	1.391(10)	O(31)–C(31)	1.282(9)
O(32)–C(31)	1.232(9)	C(31)–C(32)	1.50(2)
Bond angles			
O(51)–Mn(1)–O(32)#1	93.0(2)	O(42)–Mn(1)–O(51)	87.6(3)
O(42)–Mn(1)–O(12)	103.3(3)	O(51)–Mn(1)–O(12)	105.8(2)
O(32)#1–Mn(1)–O(12)	92.1(2)	O(42)–Mn(1)–O(11)	96.0(3)
O(32)#1–Mn(1)–O(11)	88.2(2)	O(51)–Mn(1)–O(11)	162.7(2)
O(52)#1–Mn(1)–O(11)	80.5(2)	O(12)–Mn(1)–O(11)	56.9(2)

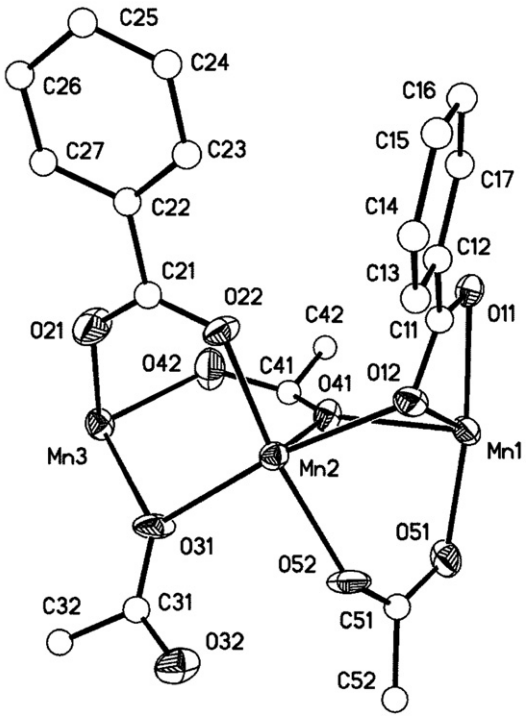


Fig. 1. ORTEP representation of the asymmetric unit of **1** with 50% probability thermal ellipsoids for Mn and O.

Acetate and benzoate ligands connect manganese atoms through four bridging modes which are shown in Fig. 3. All acetate ligands bridge three metal centers in a 3.21 (Harris notation) mode (Fig. 3a) or a disordered 3.21 mode (Fig. 3b). Benzoate ligands exhibit symmetric coordination and adopt either the 3.22 mode (Fig. 3c) or 2.11 mode (Fig. 3d). Overall, Mn-O distances range from 2.058 to 2.328 Å in this mixed ligand complex with mono-coordinating oxygen bonds always shorter than bridging carboxylates.

Fig. 4 shows ball-and-stick representations of manganese carboxylates that exhibit the rare 3.22 (or μ_3-symmetric) bridging mode. While the acetate ligand has been observed to bridge in this manner in both anhydrous γ-$Mn(OAc)_2$ (Fig. 4b) and $[Mn_4(OAc)_8 \cdot 2MeOH]_n$ (Fig. 4c), the observation of a 3.22 bridging mode for a benzoate ligand (Fig. 4a) appears to be unprecedented. It is interesting to note that for these μ_3-symmetric bridges, the distances between manganese atoms in **1** (3.317 and 3.405 Å in Fig. 4a) are shorter than those reported for both γ-$Mn(OAc)_2$ (3.840 Å in Fig. 4b) and $[Mn_4(OAc)_8 \cdot 2\ MeOH]_n$ (3.887 Å in Fig. 4c) presumably due to a strong coordination behavior of benzoate ligand.

Compound $\{Mn_5(OAc)_6(OBz)_4\}_\infty$ (**1**) has a unique two-dimensional structure as shown in Fig. 5. The sheets are defined as the *ac*-plane and consist of Mn_{12} loops as the basic units arranged in a honeycomb-like pattern. The symmetry relations of the metal centers within the 2D sheet is shown schematically in Fig. 6. The sheet may be described by defining an asymmetric unit (Mn3–Mn2–Mn1) as subunit a_1. A C_2 operation on a_1 generates subunit a_2 (Mn1–Mn2–Mn3). The sum of these two subunits (i.e., a_1 and a_2) defines block A. Next, a symmetric operation $(0.5 + X, 0.5 - Y, Z)$ on a_1 gives b_1 (Mn1–Mn2–Mn3) with

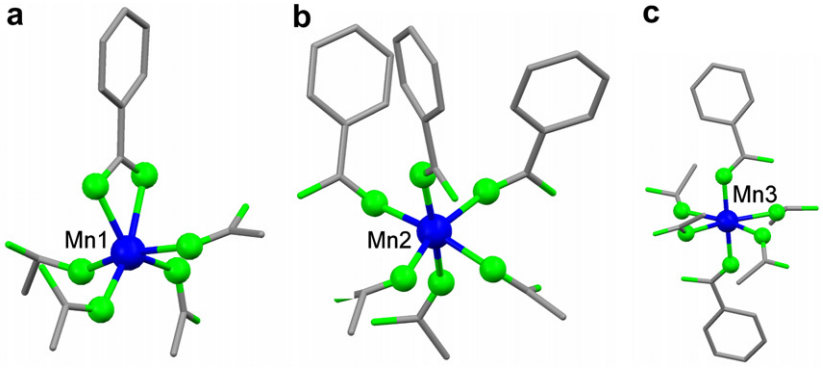


Fig. 2. Local coordination environments in **1** for: (a) Mn1, (b) Mn2 and (c) Mn3.

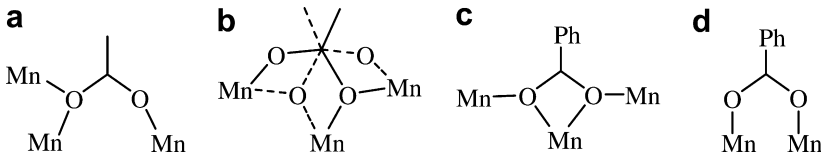


Fig. 3. The four types of bridging modes observed in the mixed carboxylate complex **1** with Harris notation of: (a) 3.21 acetate, (b) 3.21 acetate (disordered), (c) 3.22 benzoate and (d) 2.11 benzoate.

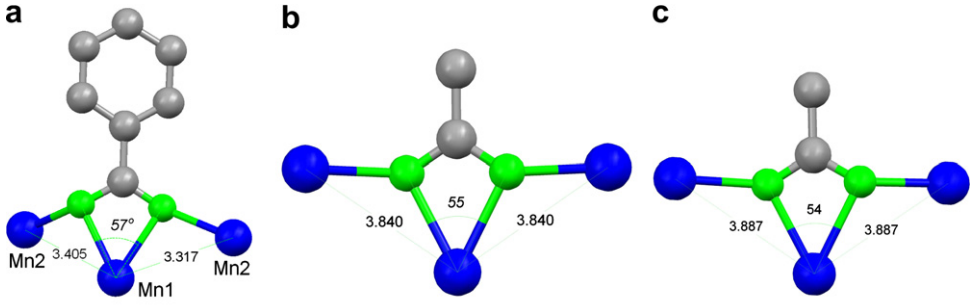


Fig. 4. Ball-and-stick rendering of the rare μ_3-symmetric (or 3.22) bridging mode in: (a) **1**, (b) γ-$Mn(OAc)_2$ (from Ref. [13]) and (c) $[Mn_4(OAc)_8 \cdot 2MeOH]_n$ (from Ref. [6]).

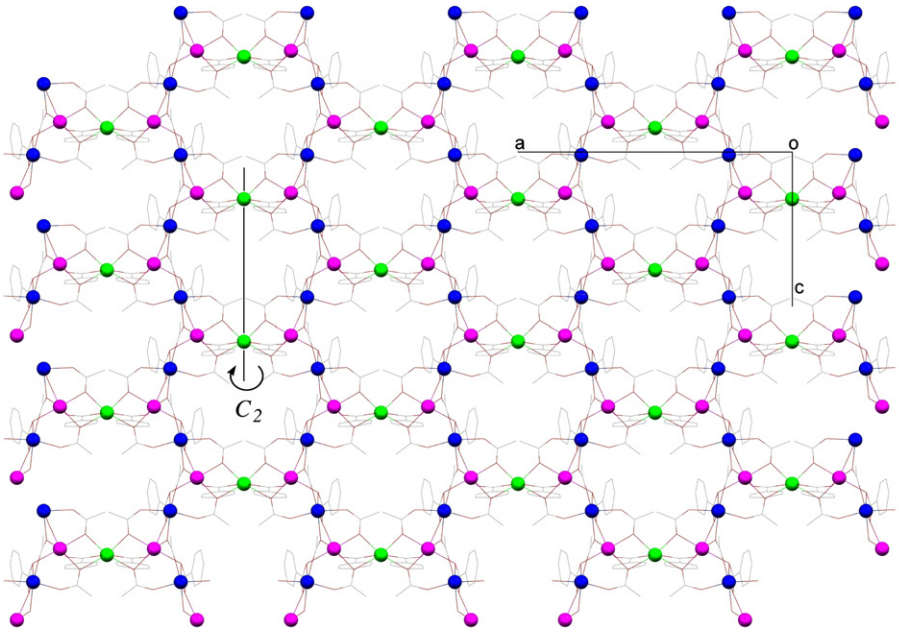


Fig. 5. A 2D sheet of **1** described in terms of a Mn2–Mn3–Mn2–$(Mn1)_2$ motif and a C_2 symmetry operation viewed along the *b*-axis. Mn atoms are drawn as balls (Mn3 in green, Mn2 in magenta and Mn1 in blue). Carbon and oxygen atoms are drawn as grey and red wire frames, respectively, and hydrogen atoms are omitted for clarity.

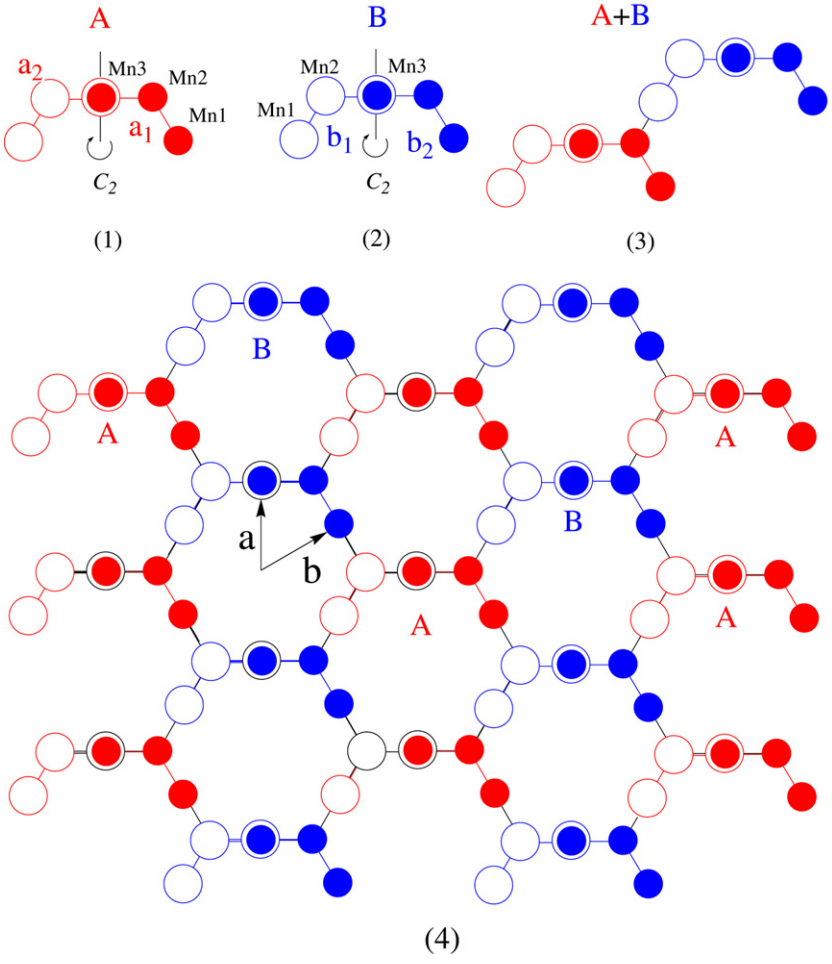


Fig. 6. Schematic diagram illustrating symmetry relations of metal centers in **1**. Red and blue parts are the two different repeating units $A + B$.

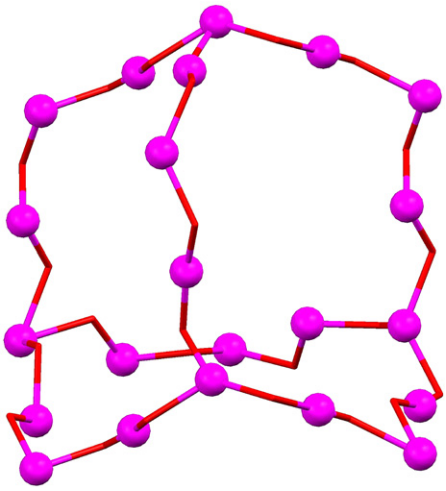


Fig. 7. Diamond-like structural arrangement of Mn_{12} loops observed in β- and γ-$Mn(OAc)_2$.

b_2 (Mn3–Mn2–Mn1) generated through a C_2 rotation on Mn3. The sum of these two units defines the second block, B ($B = b_1 + b_2$). $A + B$ is the basic repeating unit with hexagonal Mn_{12} loops generated through translations of $A + B$. A two-dimensional sheet emerges from the further extension of the structure through the same operation repeating in an ABA fashion as shown in Fig. 6. The crystal structure of $[Mn_{12}(OAc)_{14}(mda)_8] \cdot CH_3CN$ (where mda = methyldiethanolamine) was recently determined and Mn_{12} loops are reported [7]. However, $[Mn_{12}(OAc)_{14}(mda)_8] \cdot CH_3CN$ is different from **1** in that the Mn_{12} loops comprising the former exist as discrete molecules in the solid state whereas the loops in the latter are joined in a two-dimensional infinite array.

It is interesting to note that while both the β- and γ-phases of $Mn(OAc)_2$ are comprised of Mn_{12} loops, a diamond-like structure is observed (Fig. 7) versus a 2D sheet as in **1**. Two kinds of Mn atoms are reported with Mn–Mn distances of 3.283 and 3.840 Å. If other atoms are omitted, Mn1 is surrounded by four Mn2 atoms and Mn2 is connected to two Mn1 atoms. By way of comparison, the distances between Mn atoms in **1** are shorter at 3.317, 3.405 and 3.398 Å.

Fig. 8 shows a ball-and-stick representation of two layers of **1** viewed down the *ac*-plane. The distance between adjacent layers is 12.007 Å which is equivalent to one half the *b*-axis. It is shown that the Mn2 and Mn3 atoms are located in a plane with Mn1 atoms dispose slightly above and below the plane in a periodic fashion. The differential orientations of benzoate ligands led to different environments for the Mn_{12}-based hexagons that exist in a chair configuration akin to cyclohexane. It is interesting to note that there is no π–π overlap between the phenyl rings of adjacent sheets with the closest C—C distance being 3.740 Å. In addition, there is only one C—C contact between adjacent phenyl rings and the dihedral angle is nearly 90°. This is similar to the structure of $\{Mn(OBz)_2 \cdot 2H_2O\}_\infty$ where Mn_4 squares are arranged in 2D sheets that also exhibit no intersheet π–π interactions [8]. By way of comparison, π-stacking is observed between neighboring benzoate groups in the one-dimensional chain polymer $[Mn(OMe)(OBz)_2]_n$ where an average interchain phenyl-to-phenyl C—C distance of 3.719 Å was reported [9]. The authors report the π-interactions could be responsible for weak ferromagnetism observed at $T < 8$ K where the antiferromagnetically coupled chains presumably begin to align with neighboring chains through the benzoate linkages. A related 1D chain compound (i.e., $[Mn(OMe)(OAc)_2]_n$) contains no phenyl groups for such π interactions but exhibits nearly identical magnetic behavior at low temperature (i.e., weak ferromagnetic interaction between chains) [10]. A similar, yet more pronounced effect has been reported for $\{[Mn(OH)(OAc)_2] \cdot H_2O \cdot HOAc\}_n$ where stronger interchain interactions are presumably mediated via hydrogen-bonding [6,11].

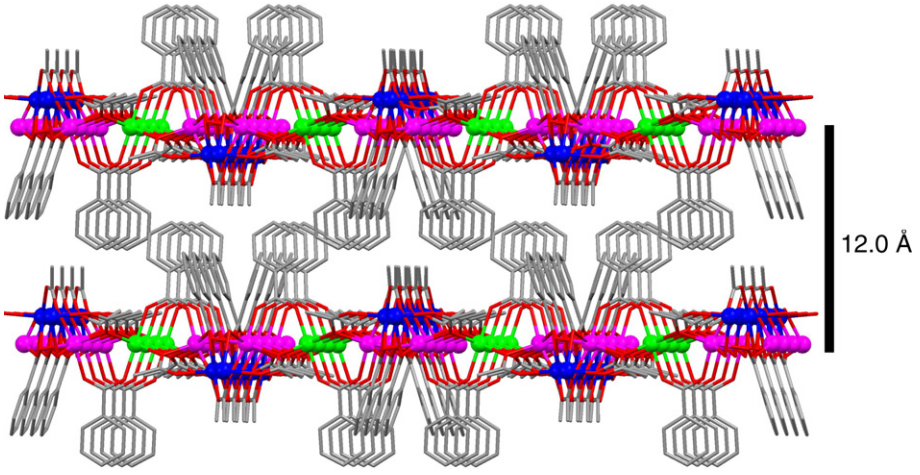


Fig. 8. The molecular structure of **1** viewed along the *c*-axis illustrating interplanar interaction. Mn atoms are drawn as balls (Mn3 in green, Mn2 in magenta and Mn1 in blue). Carbon and oxygen atoms are drawn as grey and red wire frames, respectively, and hydrogen atoms are omitted for clarity.

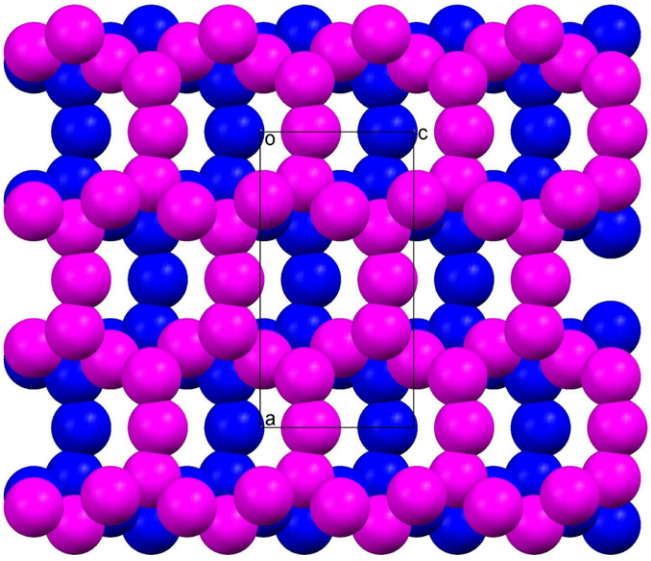


Fig. 9. Spacefill packing diagram of Mn atoms in **1** viewed along the *b*-axis illustrating the eclipsed packing of a first layer (magenta) and second layer (blue).

The stacking of the sheets in **1** is illustrated in Fig. 9 where two layers of the Mn atoms are viewed along the *b*-axis. The honeycomb-like sheets are again apparent with the first layer shown in magenta. The second layer (blue) lies below the first and is translated by one-half the *c*-axis with no translation along the *a*-direction (implicit in this figure is a translation of one-half the *b*-axis).

3.3. Magnetic properties of *1*

Thermomagnetic ac and dc characterization were completed on the title compound as represented by Fig. 10. Although single crystals were available for XRD, they were too small in volume and mass for individual magnetic measurements such that the following results represent a collection of single crystals packed into a holder with isotropic axis orientation. A ferromagnetic to antiferromagnetic transition is observed at 9.5 K as evidenced by the following: Curie-Weiss temperature transition from $\theta = +4$ K to $\theta = -53$ K at $T = 10$ K; a finite value of the out of phase susceptibility $\chi'' > 0$ and coercivity $H_c > 0$ for $T < 9.5$ K; a $d(\chi T)/dT$ sign change at $T = 12$ K; and, a reduction in the saturation moment above $T = 10$ K. Although each of the magnetic observations alone could constitute some other type of magnetic exchange and response, the combined pieces of evidence led to suggest that a FM to AFM exchange occurs. Similar magnetic transition behavior has been observed for various phases of anhydrous manganese (II) acetate where the low temperature magnetic behavior is described in terms of canted antiferromagnetism with transition temperatures of 4.5, 15 and 40 K for the α-, β- and γ-phases, respectively [12,13]. In addition, $\{Mn(OBz)_2 \cdot 2H_2O\}_\infty$ is also a canted antiferromagnet with $T_c \sim 3.5$ K [8].

From the inverse susceptibility curve (Fig. 10a) it is interesting to note a transition to stronger antiferromagnetic exchange with increasing temperature where the Weiss temperature increases from $\theta = -53$ K to $\theta = -165$ K at $T = 159$ K. Future directions will include

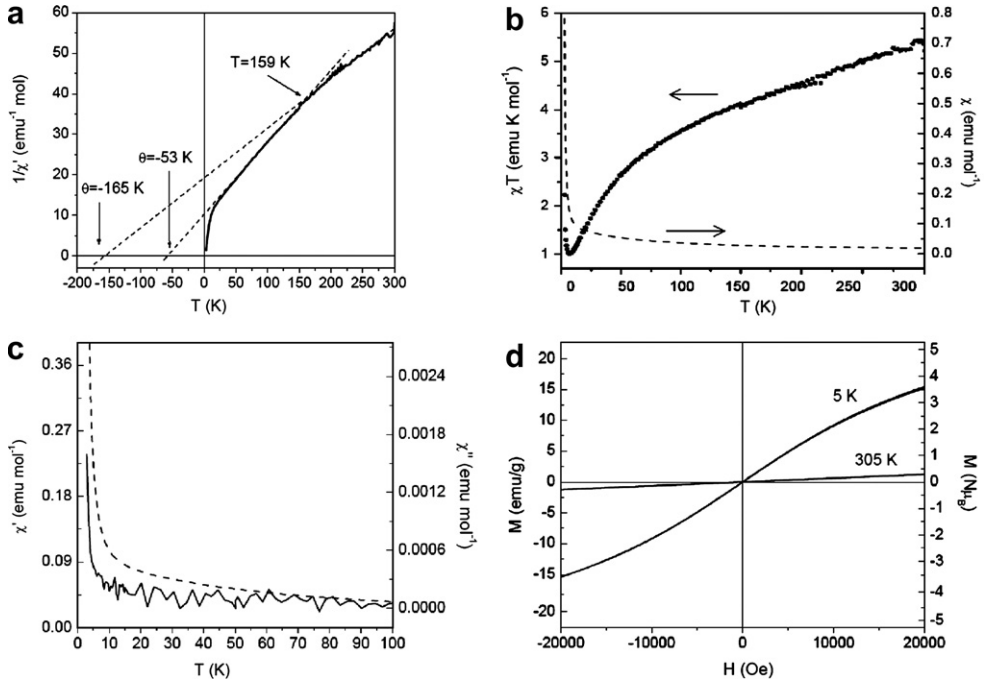


Fig. 10. Magnetic characterization of **1** showing: (a) inverse susceptibility; (b) susceptibility temperature product (•) and susceptibility (---) vs. temperature; (c) low temperature region of real (---) and imaginary (—) susceptibility components; and (d) magnetization as a function of applied field.

growth of larger single crystals that will allow for separation of $\chi_{\perp}$ from $\chi_{\parallel}$ to compare with the expected result for non-interacting high spin Mn(II) as well as any information regarding the role played by intersheet exchange.

4. Conclusions

A new mixed carboxylate manganese (II) complex is reported. $\{Mn_5(OAc)_6(OBz)_4\}_{\infty}$ (**1**) has a 2D structure that consists of Mn_{12} loops arranged in a honeycomb-like fashion. The structure is related to another manganese (II) carboxylate, $\{Mn(OBz)_2 \cdot 2H_2O\}_{\infty}$, and both 2D complexes exhibit little or no π-π overlap between phenyl groups of adjacent sheets. In addition, both complexes are canted antiferromagnets with transition temperatures of 9.5 and ~3.5 K for **1** and $\{Mn(OBz)_2 \cdot 2H_2O\}_{\infty}$, respectively. Future synthetic efforts will be aimed at the formation of single crystals with targeted *x*:*y*:*z* ratio (i.e., for $Mn_x(OAc)_y(OBz)_z$) as a means of proving the structure of a related complex that exhibits remnant moment at room temperature. In order to allow application of **1** in magnetoelectronics, control over thin film formation and an increase in the state of metallicity will need to be realized. These needs are being addressed via vapor deposition/ligand exchange and ligand replacement by radical (polaron) ligands, respectively.

Acknowledgements

This work was supported by the DoD Defense Microelectronics Activity (DMEA) under agreement DMEA90-02-2-0218 and the NSF through ND EPSCoR grant EP-0132289.

Appendix A. Supplementary material

CCDC 618053 contains the supplementary crystallographic data for **1**. These data can be obtained free of charge via http://www.ccdc.cam.ac.uk/conts/retrieving.html, or from the Cambridge Crystallographic Data Centre, 12 Union Road, Cambridge CB2 1EZ, UK; fax: (+44) 1223-336-033; or e-mail: deposit@ccdc.cam.ac.uk. Supplementary data associated with this article can be found, in the online version, at doi:10.1016/j.poly.2006.11.040.

References

[1] G. Christou, Acc. Chem. Res. 22 (1989) 328.
[2] R. Sessoli, H.-L. Tsai, A.R. Schake, S. Wang, J.B. Vincent, K. Folting, D. Gatteschi, G. Christou, D.N. Hendrickson, J. Am. Chem. Soc. 115 (1993) 1804.
[3] G.M. Sheldrick, SHELX 97, Program for Crystal Structure Refinement, University of Göttingen, Göttingen, Germany, 1997.
[4] H.J. Eppley, H.-L. Tsai, N. deVries, K. Folting, G. Christou, D.N. Hendrickson, J. Am. Chem. Soc. 117 (1995) 301.
[5] M. Soler, P. Artus, K. Folting, J.C. Huffman, D.N. Hendrickson, G. Christou, Inorg. Chem. 40 (2001) 4902.
[6] A.J. Tasiopoulos, N.C. Harden, K.A. Abboud, G. Christou, Polyhedron 22 (2003) 133.
[7] D. Foguet-Albiol, T.A. O'Brien, W. Wernsdorfer, B. Moulton, M.J. Zaworotko, K.A.A.G. Christou, Angew. Chem., Int. Ed. 44 (2005) 897.
[8] J.L. Manson, J.A. Schlueter, personal communication, August 17, 2006.
[9] A.J. Tasiopoulos, W. Wernsdorfer, K.A. Abboud, G. Christou, Polyhedron 24 (2005) 2505.
[10] D.J. Price, S.R. Batten, B. Moubaraki, K.S. Murray, Polyhedron (2006), doi:10.1016/j.poly.2006.05.044.
[11] D.J. Price, S.R. Batten, B. Moubaraki, K.S. Murray, Polyhedron 22 (2003) 2161.
[12] J.D. Martin, R.F. Hess, Chem. Commun. (1996) 2419.
[13] H.-J. Yang, H.-Z. Kou, Z.-H. Ni, A.-L. Cui, R.-J. Wang, Inorg. Chem. Commun. 8 (2005) 846.

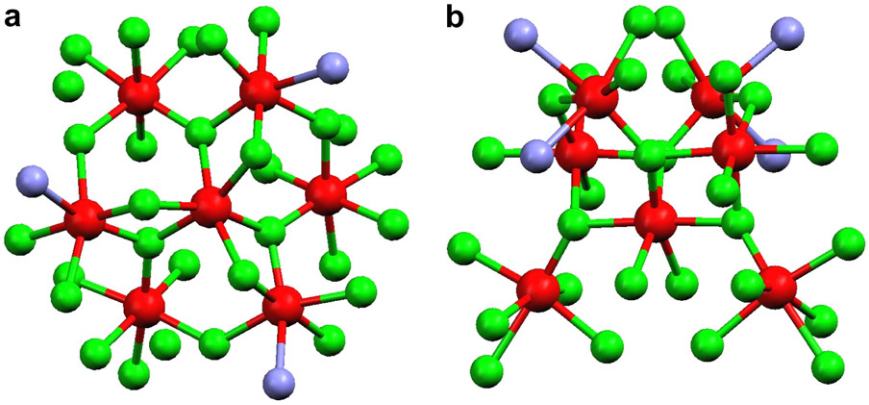


Fig. 1. (a) Structure of complex **1**; hydrogen atoms and t-butyl groups have been omitted for clarity. The C_3 symmetry axis is out of the page. Color code: Fe^{III} – red; O – green; N – blue. (b) Structure of complex **2**; hydrogen atoms and phenyl rings have been omitted for clarity. Color code: Fe^{III} – red; O – green; N – blue. (For interpretation of the references in color in this figure legend, the reader is referred to the web version of this article.)

grease to prevent solvent loss during cooling in helium gas at atmospheric pressure. A sensitive cavity-perturbation technique and a millimeter-wave vector network analyzer (MVNA) were used to detect the EPR signals (details are given elsewhere [8,9]). The spectra were obtained at fixed microwave frequencies and temperatures while sweeping the DC magnetic field.

3. Data and discussion

The magnetic axial direction of complex **2** was hard to determine due to its low symmetry. Therefore, single-axis angle-dependent HFEPR studies only allow us to locate the plane perpendicular to the axial direction. Extensive measurements at various temperatures and frequencies were then performed with DC fields applied in this plane to determine the ground state transitions and zero-field splitting (zfs) parameters in the spin Hamiltonian, $\widehat{H} = D\widehat{S}_z^2 + E(\widehat{S}_x^2 - \widehat{S}_y^2) + g\mu_B\vec{B}\cdot\widehat{S}$.

Fig. 2 shows temperature-dependent spectra for complex **2** taken at 197 GHz, with the field in the (xy-) plane perpendicular to the axial (z-) direction. A total of five main peaks are observed, thus confirming the $S = 5/2$ ground state of the molecule. Each peak exhibits fine structures which are most probably caused by weak disorder, which leads to distributions in the zfs parameters. The lowest field peak (labeled a) corresponds to the excitation from the ground state within the $S = 5/2$ multiplet, since it clearly becomes stronger upon lowering the temperature. Based upon this observation, we conclude that the magnetic anisotropy of complex **2** is of the easy-plane type, i.e. it possesses a positive D value. The inset to Fig. 2 displays the Zeeman diagram for a spin $S = 5/2$ system with a positive D value and the field applied within the easy plane. The five observed transitions (a–e) are indicated in the inset.

We note that it is possible to fit the spectra in Fig. 2 assuming a negative D value. However, we cannot account for the angle dependence on the basis of such an assignment. Consequently, it is clear that D must be positive. Further frequency dependent studies were subsequently performed with the magnetic field applied within the easy plane in order to quantify the zfs parameters for complex **2**. Fig. 3 displays the positions of the observed EPR peaks plotted versus frequency. Superimposed on the data is the best fit to the above Hamiltonian; the curves correspond to the energy differences between levels connected by the arrows in the Zeeman diagram in Fig. 2. The obtained zfs parameters are: $D = +0.62\ \mathrm{cm}^{-1}$, $g_{xy} = 2.00$ and a significant rhombic anisotropy, $|E| \geqslant 0.067\ \mathrm{cm}^{-1}$. The obtained value of E is a lower limit, as the orientation of the field within the easy plane is not exactly known. In order to determine the precise value of E, angle-dependent studies would have to be performed within the easy plane. However, since this complex does not appear to be a SMM, such studies were not performed.

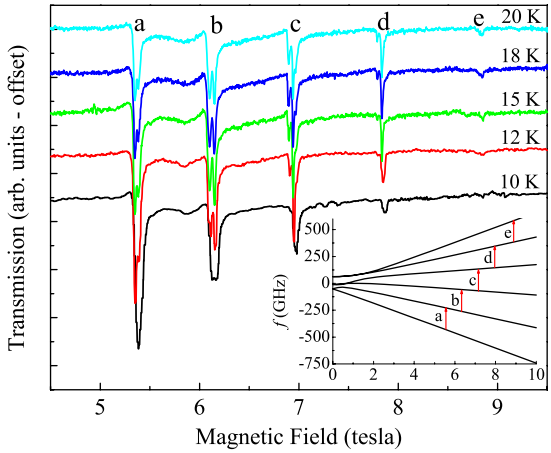


Fig. 2. Temperature-dependent EPR spectra of complex **2** taken at 197 GHz with the DC magnetic field applied within the easy plane. The inset shows the simulated Zeeman diagram for a positive D system. Transitions labeled 'a' (ground state transition) to 'e' in the spectra are also indicated in the inset. For the negative D case (see Fig. 3), the ground state transition would appear at the highest fields.

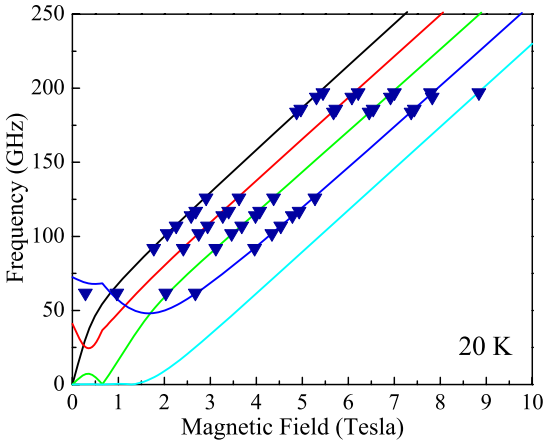


Fig. 3. Easy plane EPR peak positions for complex **2** plotted versus frequency. The solid lines are simulations using the zfs parameters given in the text.

On the other hand, complex **1** exhibits SMM-like EPR spectra. Fig. 4 shows single crystal data obtained at 51.8 GHz and at different temperatures, with the DC magnetic field applied within the hard-plane. Once again, five EPR peaks are observed (labeled 1–5), confirming the $S = 5/2$ ground state of this molecule. The fact that the strongest peak is seen at the highest field (opposite to what was observed for complex **2**) indicates that D is negative. Another set of three weaker peaks can be seen as shoulders on three of the main peaks (labeled with subscripts x). There are several possible explanations for these weaker peaks, including: a low lying $S = 3/2$ excited state; intermolecular exchange interactions; or disorder-induced strains in the sample leading to different molecular species [10]. Recent calculations seem to exclude the possibility of low lying excited states [6]. However, further studies are required for precise determination of the origin of the weaker EPR peaks.

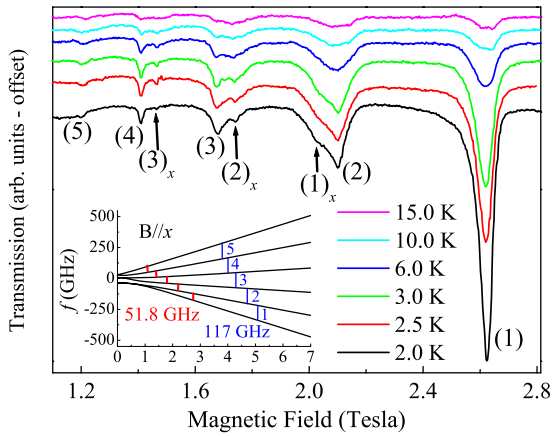


Fig. 4. HFEPR spectra of complex **1** taken at 51.8 GHz, at temperatures from 2 to 15 K. The inset shows the simulated Zeeman diagram for a negative D system. Transitions labeled (1) (ground state transition) to (5) in the spectra are also indicated in the inset for two different frequencies.

The inset to Fig. 4 shows the Zeeman diagram for a spin $S = 5/2$ system with a negative D value and the field applied within the hard plane. The five observed transitions (1–5) are shown for two different EPR frequencies (51.8 and 117 GHz). Because the energy differences between Zeeman-split levels are much smaller at lower fields, less thermal energy is required to populate the higher-lying levels within the $S = 5/2$ state. Higher frequency EPR

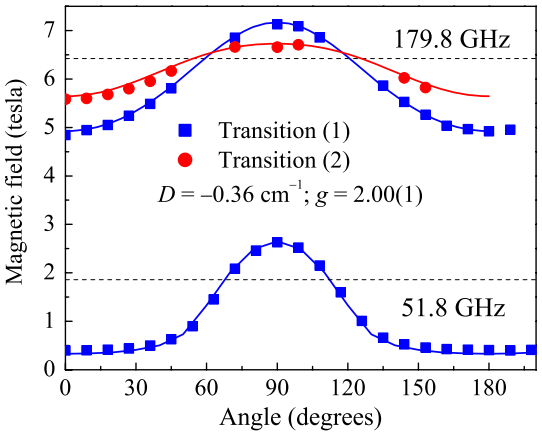


Fig. 5. Plot of the HFEPR peak positions for complex **1** obtained from angle-dependent measurements at 51.8 and 179.8 GHz, while rotating the field from the c-axis (0°) to the ab-plane (90°). The dashed lines represent the $g = 2.00$ references for each frequency, and the solid lines are simulations with the given parameters.

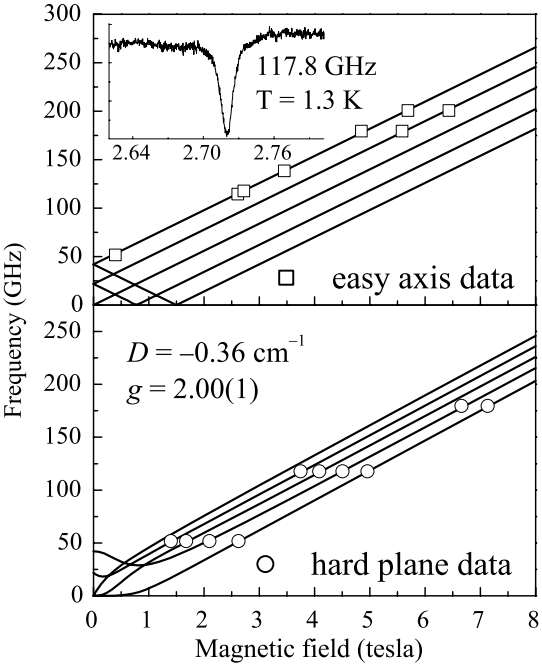


Fig. 6. Energy difference diagrams for complex **1** constructed from frequency-dependent measurements with the field along both the easy-axis and within the hard-plane. The solid lines are simulations with the given parameters. The inset shows a typical easy-axis EPR peak for a crystal of complex **1**, with a line width of about a hundred gauss.

spectra (not shown here) taken at 117.8 GHz show only peak (1) at 1.3 K.

Angle-dependent measurements from the *c*-axis to *ab*-plane were performed at 6 K, and frequencies of 51.8 and 179.8 GHz, as shown in Fig. 5. Superimposed on the data points are simulations using the following simple Hamiltonian (the parameters are listed in the figure): $\widehat{H} = D\widehat{S}_z^2 + g\mu_B\vec{B}\cdot\widehat{S}$. The solid blue squares represent the transition from the ground state [labeled (1) in Fig. 4]; the red circles correspond to transition (2). The two dashed lines indicate the isotropic positions ($D = 0$, $g = 2.00$). The fact that the peaks shift approximately twice as far to the low field side of the $g = 2.00$ reference, as compared to the high field side, implies a uniaxial anisotropy with a negative D parameter. Indeed, the high frequency data fit very well to a $(1 - 3\cos^2\theta)$ angle dependence, which is expected for a SMM in the high field limit. The angle corresponding to $\theta = 0°$ marks the easy axis orientation.

Precise determination of the spin Hamiltonian parameters D and g is achieved through EPR spectra taken at various frequencies (50–200 GHz) for both the easy-axis and hard-plane orientations, as shown in Fig. 6. Simulations for both the easy-axis and hard-plane diagrams suggest that the system is best described with $D = -0.36\ \text{cm}^{-1}$ and $g = 2.00(1)$. These parameters were used to simulate the angle-dependent EPR peak positions at 179.8 and 51.8 GHz, as shown in Fig. 5.

It is worth noting that the line width of the easy-axis EPR peak (inset of Fig. 6) is much sharper than the hard-plane ones. Further study is required to identify the cause of this difference. The easy-axis line width for complex **1** is ~0.01 T, which is considerably narrower than other well studied SMMs [10,11]. The extraordinary sharpness of the EPR spectra seems to confirm the reduced decoherence in this system ($T_2 \approx 3$ ns) relative to other known SMMs, thus making it an interesting candidate for studies of coherent quantum magnetization dynamics.

4. Summary and conclusions

On the basis of detailed frequency and field orientation dependent HFEPR studies, we show that $[Fe_7O_3(O_2CBu^t)_9(mda)_3(H_2O)_3]$ (**1**) represents a rare example of a half-integer-spin ($S = 5/2$) iron SMM, having a negative uniaxial zero-field-splitting parameter $D = -0.36\ \text{cm}^{-1}$. Meanwhile, $[Fe_7O_4(O_2CPh)_{11}(dmem)_2]$ (**2**) is not a SMM. The EPR linewidth for complex **1** is considerably narrower in comparison to spectra obtained for other SMMs, making it an interesting candidate for studies of coherent quantum magnetization dynamics.

Acknowledgement

This work was supported by the US National Science Foundation under Grant numbers DMR-0239481, DMR-0414809 and DMR-0506946.

References

[1] J.R. Friedman, M.P. Sarachik, J. Tejada, R. Ziolo, Phys. Rev. Lett. 76 (1996) 3830.
[2] L. Thomas, F. Lionti, R. Ballou, D. Gatteschi, R. Sessoli, B. Barbara, Nature 383 (1996) 145.
[3] R. Sessoli, A. Caneschi, D. Gatteschi, L. Sorace, A. Cornia, W. Wernsdorfer, J. Magn. Magn. Mater. 226 (2001) 1954.
[4] S. Hill, R.S. Edwards, N. Aliaga-Alcalde, G. Christou, Science 302 (2003) 1015.
[5] N. Aliaga-Alcalde, R. Edwards, S. Hill, W. Wernsdorfer, K. Foelting, G. Christou, J. Am. Chem. Soc. 126 (2004) 12503.
[6] D. Foguet-Albiol, T.A. O'Brien, W. Wernsdorfer, S.C. Lee, S. Hill, K.A. Abboud, G. Christou, in preparation.
[7] R. Bagai, S. Datta, A. Betancur Rodriguez, S. Hill, K.A. Abboud, G. Christou, in preparation.
[8] M. Mola, S. Hill, P. Goy, M. Gross, Rev. Sci. Instrum. 71 (2000) 186.
[9] S. Takahashi, S. Hill, Rev. Sci. Instrum. 76 (2005) 023114.
[10] S. Hill, S. Maccagnano, K. Park, R.M. Achey, J.M. North, N.S. Dalal, Phys. Rev. B 65 (2002) 224410.
[11] J. Lawrence, S. Hill, C. Kirman, E.-C. Yang, D. Hendrickson, R. Edwards, A. Yamaguchi, H. Ishimoto, W. Wernsdorfer, C. Ramsey, N.S. Dalal, M. Olmstead, in preparation.

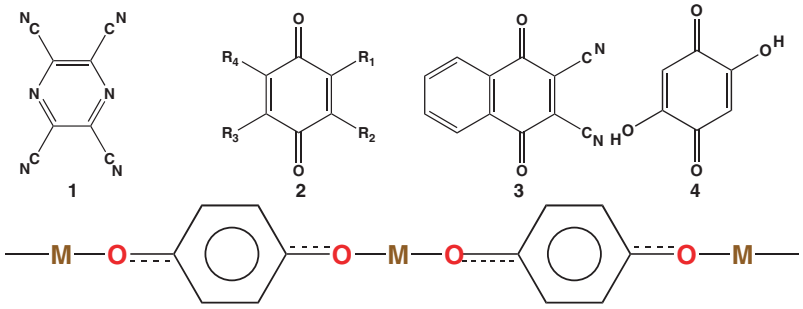


Fig. 1. Schematic illustration of $2^{\cdot-}$ bridging two M sites.

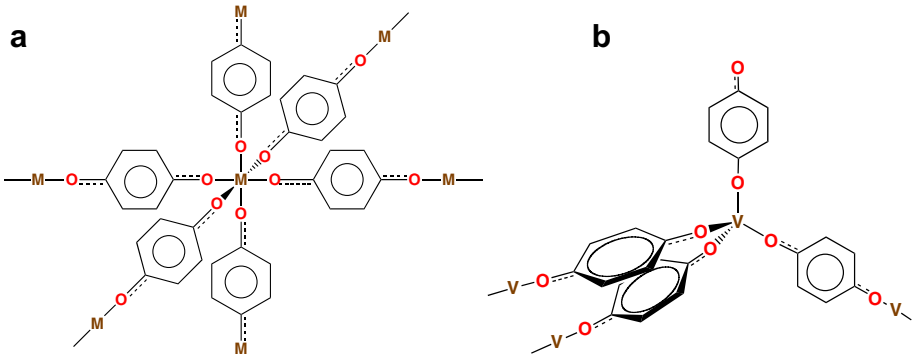


Fig. 2. Schematic illustration of a cubic extended 3-D network structure if M is octahedrally coordinated (a) or tetrahedral if M is tetrahedrally coordinated (b). Either of these motifs may possess interpenetrating lattices.

(CH_2Cl_2)] [24]. Nonetheless, immediate reactions occur for A = BQ, CA, DCNQ, and $BQ(OH)_2$ forming a dark, amorphous product of nominal $VA_2 \cdot zCH_2Cl_2$ composition (Eq. (1)).

In addition we report on the precipitates formed from the reaction of $[V(NCMe)_6][BF_4]_2$ with both $[CA]^{\cdot-}$ and $[DDQ]^{\cdot-}$ (Eq. (2)). This latter route has been successful in preparing magnets of nominal $M[TCNQ]_2$ composition, albeit the T_c for magnets prepared via this route are typically reduced with respect to those of similar composition prepared via other routes [9,25].

$$V(CO)_6 + 2A \rightarrow VA_2 \cdot zCH_2Cl_2 + 6CO \quad (1)$$

$$[V^{II}(NCMe)_6]^{2+} + xA^- \rightarrow VA_x \quad (2)$$

2. Experimental

All manipulations involving the use of vanadium compounds were performed under a nitrogen atmosphere (<1 ppm O_2 and <1 ppm H_2O) using standard Schlenk techniques and Vacuum Atmospheres DriLab gloveboxes. CH_2Cl_2 was sparged with nitrogen and passed through two columns of activated alumina prior to use [26]. $V(CO)_6$ was prepared from $[NEt_4][V(CO)_6]$ and phosphoric acid and purified by sublimation at 25° C and 0.05 Torr [27]. $[V(NCMe)_6][BF_4]_2$ [28,29] and $[NEt_4][DDQ]$ [13,30] were prepared by a literature method. $[NEt_4][CA]$ was prepared by a modified literature method [31], as $[NEt_4]Cl$ was slowly added to an acetone solution of NaCA in a dry-ice bath under N_2(g) atmosphere. After stirring for 1 h, the white precipitate was filtered, and the filtrate was concentrated *in vacuo* to ca. one fifth, and the dark red solid was collected, and recrystallized from a CH_2Cl_2/hexane mixture. The benzoquinones were purchased from Acros or Aldrich and purified by sublimation or recrystallization from toluene except for 2,3-dicyano-1,4-naphthoquinone (DCNQ) that was prepared according to a published procedure [32].

V[BQ]$_2$. $V(CO)_6$ (50.9 mg, 0.232 mmol) was dissolved in ~5 mL of CH_2Cl_2 and the bright yellow solution was added dropwise to a stirred yellow solution of 1,4-benzoquinone (BQ) (50.2 mg, 0.464 mmol) dissolved in ~2 mL of CH_2Cl_2. A rapid reaction occurred and the mixture became black and CO evolved. After the evolution of CO had ceased the vial containing the mixture was closed and allowed to stand for 12 h before the black solids were collected by suction filtration (Yield: 60.0 mg; 98%). IR(KBr, cm^{-1}): 1570, 1482(s), 1194(s), 831(s). *Anal.* Cal. for $V[BQ]_2$, $C_{12}H_8O_4V$: C, 53.95; H, 3.02; N, 0.00. Found: 54.16, 2.93, <0.2%.

V[CA]$_2$. $V(CO)_6$ (26.0 mg, 0.119 mmol) was dissolved in ~5 mL of CH_2Cl_2 and the bright yellow solution was added dropwise to a stirred suspension of *p*-chloranil (CA) (58.1 mg, 0.236 mmol) in ~10 mL of CH_2Cl_2. A rapid reaction occurred and the mixture became black and CO was evolved. After the evolution of CO had ceased the vial containing the mixture was closed and allowed to stand for

12 h before the black solids were collected by suction filtration (Yield: 55.5 mg: 84%). IR(KBr, cm^{-1}): 1528, 1391(s), 1170, 931(s), 721, 581. Anal. Calc. for $V[CA]_2 \cdot 0.15CH_2Cl_2$, $C_{12.15}H_{0.3}Cl_{8.3}O_4V$: C, 26.28; H, 0.05; N, 0.00; V, 9.17. Found: 26.52, <0.2, <0.2, 8.90%.

V[DCNQ]$_2$. $V(CO)_6$ (28.4 mg, 0.130 mmol) was dissolved in ~5 mL of CH_2Cl_2 and the bright yellow solution was added dropwise to a stirred yellow solution of 2,3-dicyano-1,4-naphthoquinone (DCNQ) (53.4 mg, 0.257 mmol) dissolved in ~10 mL of CH_2Cl_2. A rapid reaction occurred and the mixture became black and CO was evolved. After the evolution of CO had ceased the vial containing the mixture was closed and allowed to stand for 12 h before the black solids were collected by suction filtration (Yield: 65.7 mg: 99%). IR(KBr, cm^{-1}): 2223, 1385(s), 1015, 896. *Anal.* Calc. for $V[DCNQ]_2 \cdot 0.10CH_2Cl_2$, $C_{24.1}H_{8.2}Cl_{0.2}N_4O_4V$: C, 60.84; H, 1.74; N, 11.78. Found: 61.09, 1.70, 11.38%.

V[BQ(OH)$_2$]$_2$. $V(CO)_6$ (39.4 mg, 0.180 mmol) was dissolved in about 5 mL of CH_2Cl_2 and the bright yellow solution was added dropwise to a stirred suspension of 2,5-dihydroxy-1,4-benzoquinone ($BQ(OH)_2$) (49.9 mg, 0.356 mmol) in about 10 mL of CH_2Cl_2. A slower reaction occurred and the mixture gradually became black over a period of about 30 min. The vial containing the mixture was then closed and allowed to stand for 6 h before the black solids were collected by suction filtration. Yield: 59.5 mg. The product was visibly contaminated with unreacted $BQ(OH)_2$. IR(KBr, cm^{-1}): 1502(s, br), 1360, 1248, 1159, 878. *Anal.* Calc. for $V[BQ(OH)_2]_2$: $C_{12}H_8O_8V$: C, 43.53; H, 2.44; N, 0.00. Found: 43.43, 2.25, <0.2%.

[NBu$_4$]$_{0.5}$V[CA]$_{2.5}$ · 0.34MeCN. $[V(NCMe)_6][BF_4]_2$ (32 mg, 0.068 mmol) was dissolved in 10 mL of CH_2Cl_2 to which $[NBu_4][CA]$ (102 mg, 0.21 mmol) dissolved in CH_2Cl_2/MeCN (10 mL, v/v, 9.5:0.5) was added at room temperature, and a black precipitate slowly formed. After stirring for 2 h the black solid was isolated by suction filtration, washed with CH_2Cl_2, and dried *in vacuo* (Yield: 42 mg: 77%). IR(KBr, cm^{-1}): 2964, 2876, 1532, 1401(s), 1170, 920(s), 717, 554. *Anal.* Calc. for $[NBu_4]_{0.5}V[CA]_{2.5} \cdot 0.34MeCN$, $C_{23.68}H_{19.02}Cl_{10}N_{0.84}O_5V$: C, 35.52; H, 2.39; N, 1.47. Found: 35.73, 2.82, 1.27%.

[NBu$_4$]V[DDQ]$_3$ · 0.1MeCN. $[V(NCMe)_6][BF_4]_2$ (39 mg, 0.083 mmol) was dissolved in 10 mL of CH_2Cl_2 to which $[NBu_4][DDQ]$ (118 mg, 0.25 mmol) dissolved in CH_2Cl_2/MeCN (10 mL, v/v, 9.5:0.5) was added at room temperature, and a dark green precipitate slowly formed. After stirring for 2 h the dark green solid was isolated by suction filtration, washed with CH_2Cl_2, and dried *in vacuo* (Yield: 51 mg: 63%). IR(KBr, cm^{-1}): 2964, 2878, 2250(sh), 2226, 1542, 1408(s), 1235, 1093, 1001, 908, 575. *Anal.* Calc. for $[NBu_4]V[DDQ]_3 \cdot 0.1MeCN$, $C_{40.2}H_{36.3}Cl_6N_{7.1}O_6V$: C, 49.94; H, 3.75; N, 9.90. Found: 49.35, 3.74, 10.16%.

Infrared spectra were taken from 400 to 4000 cm^{-1} using a Bruker Tensor 37 FTIR spectrometer (±1 cm^{-1}). Samples were prepared as KBr pellets under an inert atmosphere. Magnetic susceptibility measurements were made between 5 and 300 K using a Quantum Design MPMS-5XL 5 T SQUID magnetometer equipped with a reciprocating sample measurement system as previously described [33]. Measurements were made on powders contained in airtight Delrin holders packed with quartz wool to prevent sample movement in the holder. The data were corrected for the diamagnetism of the holders.

3. Results and discussion

Hexacarbonylvanadium(0) readily reacts with benzoquinone (BQ) and three related compounds: CA, $BQ(OH)_2$, and DCNQ, to form materials of $V^{II}(A)_2 \cdot zCH_2Cl_2$ ($z \leqslant 0.1$) composition. During the reaction the quinone likely forms a coordination complex with vanadium, followed by the release of CO and electron transfer in which V(0) ultimately undergoes a two electron oxidation to vanadium(II) and two quinones, A, are reduced to semiquinones, $A^{\cdot -}$. In all cases the major ν_{CO} features of the IR spectra of the benzoquinones are broadened and shifted to lower energy consistent with the formation of coordination to vanadium and the formation of radical anions, and formation of V=O, as evidenced by a new absorption ~1000 cm^{-1}, does not occur. For example, $[NBu_4][CA]$ and $[NBu_4][DDQ]$ have strong ν_{CO} absorptions at 1523 and 1570 cm^{-1} that upon coordination to V(II) ions are shifted to lower frequencies, i.e. 1401 cm^{-1} for $(NBu_4)_{0.5}V[CA]_{2.5}$ and 1408 cm^{-1} for $(NBu_4)V[DDQ]_3$. Likewise, when nitriles are present, the ν_{CN} is shifted to lower energy.

In contrast, the metathesis reaction of $[V(NCMe)_6][BF_4]_2$ with $[CA]^{\cdot -}$ and $[DDQ]^{\cdot -}$ forms precipitates of different composition, namely, $(NBu_4)_{0.5}V[CA]_{2.5}$ and $(NBu_4)V[DDQ]_3$, respectively. Both compounds show split absorptions at 2964 and 2876 cm^{-1} for $(NBu_4)_{0.5}V[CA]_{2.5}$ and at 2964 and 2878 cm^{-1} for $(NBu_4)V[DDQ]_3$, indicative of $[NBu_4]^+$ cation. In the IR spectrum of $(NBu_4)_{0.5}V[CA]_{2.5}$, the strong, single absorptions characteristic of coordinated $[CA]^{\cdot -}$ are observed at 1401 and 920 cm^{-1}. These peaks are slightly different to those of $V[CA]_2$ that made from $V(CO)_6$ that occur at 1391 and 931 cm^{-1}. In the IR spectrum of $(NBu_4)V[DDQ]_3$, the strong peak characteristic of coordinated DDQ is appeared at 1408 cm^{-1}. Additionally, the ν_{CN} peak shows at 2250 and 2226 cm^{-1}, indicative of the coordination of cyano group.

Powder diffraction data, like those observed for $V[TCNE]_x$ [6a], indicate that each of these materials is amorphous. Unlike $V^{II}[A]_2 \cdot zCH_2Cl_2$ (A = BQ, CA) have semiquinones that can solely bridge between two V^{II}s and these materials are proposed to nominally have the structure illustrated in Fig. 2b. For A = DCNQ, DDQ, and $BQ(OH)_2$ the nitrile nitrogens for the former, and chelating nature of the latter's oxygens can lead to an extended structure with octahedral V(II) sites. Further studies are in progress to elucidate the structure.

The 5–300 K magnetic susceptibility, $\chi(T)$, reported as $\chi T(T)$ and $\chi^{-1}(T)$ was determined for **V[BQ(OH)$_2$]$_2$**, **V[BQ]$_2$**, **V[DCNQ]$_2$**, and **V[CA]$_2$**. The room temperature

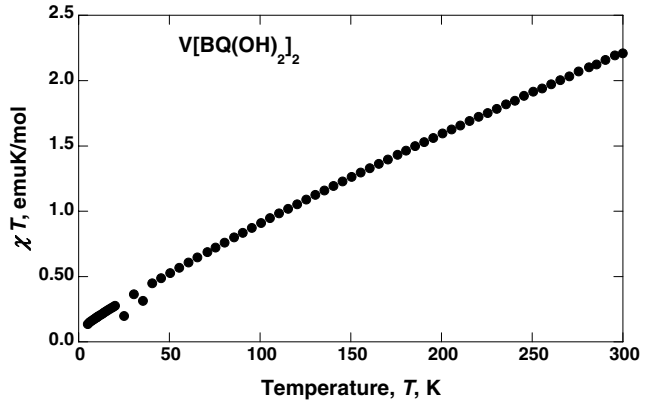


Fig. 3. The 5–300 K $\chi T(T)$ for **V[BQ(OH)$_2$]$_2$**.

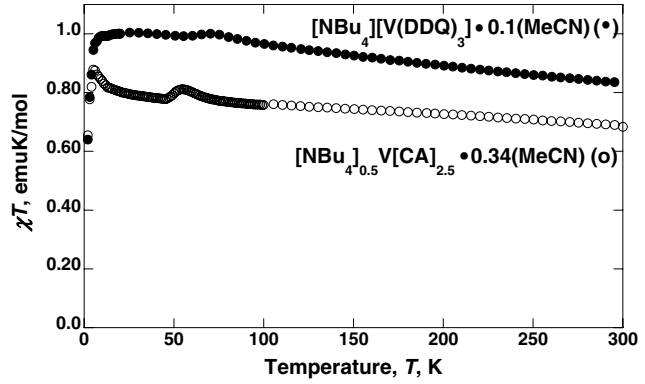


Fig. 4. The 5–300 K $\chi T(T)$ for $[NBu_4]V[DDQ]_3 \cdot 0.1(MeCN)$ (●) and $[NBu_4]_{0.5}V[CA]_{2.5} \cdot 0.34(MeCN)$ (○).

χT value for **V[BQ(OH)$_2$]$_2$** is 2.20 emuOe/mol, which is less than the expected spin-only value of 2.63 emuOe/mol, indicative of antiferromagnetic coupling, Fig. 3. Strong antiferromagnetic coupling is observed from the $\chi T(T)$ data that decreases almost linearly with decreasing temperature down to 5 K. The same trend of strong antiferromagnetic coupling with the lack of evidence for magnetic ordering is also observed for **V[BQ]$_2$**, **V[DCNQ]$_2$**, and **V[CA]$_2$**.

$[NBu_4]V[DDQ]_3 \cdot 0.1MeCN$ and **$[NBu_4]_{0.5}V[CA]_{2.5} \cdot 0.34MeCN$** have reduced room temperature χT values 0.83 and 0.68 emuOe/mol (Fig. 4), respectively, that suggests stronger antiferromagnetic coupling than observed for **V[BQ(OH)$_2$]$_2$**, **V[BQ]$_2$**, **V[DCNQ]$_2$**, and **V[CA]$_2$**. However, $\chi T(T)$ increases with decreasing temperature until below 8 K when it drops in value, This suggests ferromagnetic coupling, albeit weak, is present; however, magnetic ordering does not occur. Due to the lack of magnetic ordering, ferro-, ferri-, or antiferro-magnetic, further detailed studies were not execute.

4. Conclusion

The reaction of either quinones with $V^o(CO)_6$ or $[quinones]^{\cdot -}$ with $[V^{II}(NCMe)_6]^{2+}$ forms materials, albeit of differing compositions, possessing $[quinones]^{\cdot -}$ bonded to V(II). The $S = 1/2$ $[quinones]^{\cdot -}$ antiferromagnetically coupling to the $S = 3/2$, but do not yield magnetically ordered materials. This is in contrast to $S = 1/2$ cyanocarbons radical anions, and is attributed to the greater number of V(II) sites that can magnetically couple to a cyanocarbon with respect to the two for a $[quinones]^{\cdot -}$.

Acknowledgement

We thank Øyvind Hatlevik for preliminary studies, and the continued partial support by the Department of Energy Division of Materials Science (Grant No. DE-FG03-93ER45504) is gratefully appreciated.

References

[1] (a) Reviews: J.S. Miller, A.J. Epstein, Chem. Commun. (1998) 1319;
(b) V.I. Ovcharenko, R.Z. Sagdeev, Russ. Chem. Rev. 68 (1999) 345;
(c) W. Plass, Chem. Zeit 32 (1998) 323;
(d) J.S. Miller, A.J. Epstein, Chem. Eng. News 73 (40) (1995) 30;
(e) J.S. Miller, A.J. Epstein, Angew. Chem., Int. Ed. Engl. 33 (1994) 385;
(f) M. Kinoshita, Jpn. J. Appl. Phys. 33 (1994) 5718;
(g) J.S. Miller, A.J. Epstein, Adv. Chem. Ser. 245 (1995) 161;
(h) A. Caneschi, D. Gatteschi, Progr. Inorg. Chem. 37 (1991) 331;
(i) A.L. Buchachenko, Russ. Chem. Rev. 59 (1990) 307;
(j) J.A. Crayson, J.N. Devine, J.C. Walton, Tetrahedron 56 (2000) 7829;
(k) S.J. Blundell, F.L. Pratt, J. Phys.: Condens. Mat. 16 (2004) R771.
[2] (a) Conference proceedings: P. Day, A.E. Underhill, Metal-organic and organic molecular magnets, Phil. Trans. R. Soc. Lond. (A) 357 (1999) 2849;
(b) P. Day, A.E. Underhill, in: O. Kahn (Ed.), Proceedings of the 6th International Conference on Molecule-based Based Materials, Mol. Cryst., Liq. Cryst., 1999, p. 334/335;
(c) P. Day, A.E. Underhill, in: K. Itoh, J.S. Miller, T. Takui (Eds.),Proceedings of the Conference on Molecular-Based Magnets, Mol. Cryst., Liq. Cryst., 1997, pp. 305;
(d) P. Day, A.E. Underhill, in: G. Christou (Ed.), Proceedings of the 7th International Conference on Molecule-based Magnets, Polyhedron, 2001, p. 20;
(e) P. Day, A.E. Underhill, in: G. Christou (Ed.), Proceedings of the 8th International Conference onMolecule-based Magnets, Polyhed., 2003, p. 22(#14–17).
[3] J.S. Miller, J.C. Calabrese, A.J. Epstein, R.W. Bigelow, J.H. Zhang, W.M. Reiff, J. Chem. Soc. Chem. Commun. (1986) 1026.
[4] J.S. Miller, J.C. Calabrese, H. Rommelmann, S. Chittipeddi, J.H. Zhang, W.M. Reiff, A.J. Epstein, J. Am. Chem. Soc. 109 (1987) 1769.
[5] S. Chittipeddi, K.R. Cromack, J.S. Miller, A.J. Epstein, Phys. Rev. Lett. 58 (1987) 2695.
[6] (a) J.M. Manriquez, G.T. Yee, R.S. McLean, A.J. Epstein, J.S. Miller, Science 252 (1991) 1415;
(b) J.S. Miller, G.T. Yee, J.M. Manriquez, A.J. Epstein, in: Proceedings of Nobel Symposium #NS-81 Conjugated Polymers and Related Materials: The Interconnection of Chemical and Electronic Structure, Oxford University Press, 1993, p. 461;
(c) J.S. Miller, G.T. Yee, J.M. Manriquez, A.J. Epstein, La Chim. La Ind. 74 (1992) 845.
[7] J. Zhang, P. Zhou, W.B. Brinckerhoff, A.J. Epstein, C. Vazquez, R.S. McLean, J.S. Miller, A.C.S. Sym. Ser. 644 (1996) 311.
[8] K.I. Pokhodnya, A.J. Epstein, J.S. Miller, Adv. Mater. 12 (2000) 410.
[9] E.B. Vickers, T.D. Selby, M.S. Thorum, M.L. Taliaferro, J.S. Miller, Inorg. Chem. 43 (2004) 6414.
[10] E.B. Vickers, T.D. Selby, J.S. Miller, J. Am. Chem. Soc. 126 (2004) 3716.

[11] M.L. Taliaferro, M.S. Thorum, J.S. Miller, Angew. Chem. 45 (2006) 5326.
[12] J.P. Fitzgerald, B.B. Kaul, G.T. Yee, Chem. Commun. 49 (2000).
[13] J.S. Miller, P.J. Krusic, D.A. Dixon, W.M. Reiff, J.H. Zhang, E.C. Anderson, A.J. Epstein, J. Am. Chem. Soc. 108 (1986) 4459.
[14] G. Zanotti, Acta Crystallogr. B38 (1982) 1225.
[15] C. Vazquez, J.C. Calabrese, D.A. Dixon, J.S. Miller, J. Org. Chem. 58 (1993) 65.
[16] A. Zheludev, A. Grand, E. Ressouche, J. Schweizer, B. Morin, A.J. Epstein, D.A. Dixon, J.S. Miller, J. Am. Chem. Soc. 116 (1994) 7243.
[17] J.S. Miller, Adv. Mater. 14 (2001) 525.
[18] J.S. Miller, T.E. Vos, W.W. Shum, Adv. Mater. 17 (2005) 2251.
[19] D.A. Shultz, in: J.S. Miller, M. Drillon (Eds.), Magnetism – Molecules to Materials, vol. 2, Wiley-VCH, Mannheim, 2001, p. 281.
[20] G.C. Pierpont, R.M. Buchanan, Coord. Chem. Rev. 38 (1981) 45.
[21] E.J. Brandon, B.M. Burkhart, R.D. Rogers, J.S. Miller, Chem. Eur. J. 4 (1998) 1938.
[22] A. Anmüller, S. Hünig, Lieb. Ann. 142 (1986).
[23] M.R. Bryce, S.R. Davies, M. Hasan, G.J. Ashwell, M. Szablewski, M.G.B. Drew, M.R. Short, M.B. Hursthouse, J. Chem. Soc., Perkin Trans. 2 (1989) 1285.
[24] A.M. Bond, F.A. Cotton, Inorg. Chem. 15 (1976) 2036.
[25] E.B. Vickers, I.D. Giles, J.S. Miller, Chem. Mater. 17 (2005) 1667.
[26] A.B. Pangborn, M.A. Giardello, R.H. Grubbs, R.K. Rosen, F.J. Timmers, Organometallics 15 (1996) 1518.
[27] X. Liu, X.J.E. Ellis, T.D. Selby, P. Ghalsasi, J.S. Miller, Inorg. Synth. 34 (2004) 68.
[28] S.J. Anderson, F.J. Wells, G. Wilkinson, B. Hussain, M.B. Hursthouse, Polyhedron 7 (1988) 2615.
[29] P. Ghosh, H. Taube, T. Hasegawa, R. Kuroda, Inorg. Chem. 34 (1995) 5761.
[30] D. Gordon, M.J. Hove, J. Chem. Phys. 59 (1973) 3419.
[31] V. Ganesan, S.V. Rosokha, J.K. Kochi, J. Am. Chem. Soc. 125 (2003) 2559.
[32] G.A. Reynolds, J.A. Van Allan, J. Org. Chem. 29 (1964) 3591.
[33] E.J. Brandon, D.K. Rittenberg, A.M. Arif, J.S. Miller, Inorg. Chem. 37 (1998) 3376.

were carried out under anaerobic conditions using standard Schlenk apparatus and degassed solvents to avoid oxidation by atmospheric dioxygen. $MnCl_2 \cdot 4H_2O$ (59 mg, 0.3 mmol) was dissolved in a deoxygenated water (ca. 10 cm^3) in a 50 ml Schlenk apparatus. To this solution were added an aqueous solution (ca. 10 cm^3 each) of diethylenetriamine (21 mg, 0.2 mmol) and that of $K_3[Cr(CN)_6]$ (65 mg, 0.2 mmol) in turn. Resulting mixture was allowed to stand for several hours to give pale green plates of **1**. These crystals were collected, washed with water and dried in vacuo. In the atmosphere, **1** rapidly effloresced and changed to a dehydrated form $[Mn_3(dien)_2(H_2O)_2][Cr(CN)_6]_2$ (**1a**). Compound **1a** did not adsorb water and not recover the initial hydrated form **1**. When the molar ratio of Mn^{2+}:dien was 1:1 and water–ethanol (2:1) mixture was used as solvent, crystals of **1** were obtained with yellow cubic crystals of $[Mn(dien)]_3[Cr(CN)_6]_2 \cdot 2H_2O$ (**2**).[1] Elemental analysis (%): *Anal*. Calc. for $[Mn_3(dien)_2(H_2O)_2][Cr(CN)_6]_2$ (**1a**), $C_{20}H_{30}N_{18}Cr_2Mn_3O_2$: C, 29.17; H, 3.67; N, 30.62. Found: C, 29.09; H, 3.70; N, 30.50%. As the efflorescent nature of **1**, the dehydrated form **1a** was basically used for physical measurements.

2.2. X-ray crystallography

X-ray diffraction data of **1** were collected at −30 °C on Rigaku Mercury CCD diffractometer with graphite-monochromated Mo Kα radiation ($\lambda = 0.71070$ Å). The maximum 2θ value is 55.0°. A total of 1240 oscillation images were collected on five sweep setting. The structure was solved by direct methods (SIR-92) and followed successive Fourier and difference Fourier syntheses and refined by full-matrix least-squares on *F*. All nonhydrogen atoms were refined anisotropically. All hydrogen atoms were added geometrically and refined by using a riding model. All calculations were performed using the teXsan crystallographic software package of MSC. Crystal data for **1**: $C_{20}H_{38}N_{18}O_6Cr_2Mn_3$, FW = 895.44; pale green plate, crystal dimensions $0.08 \times 0.08 \times 0.02$ mm^3, triclinic, space group $P\bar{1}$, $a = 7.755(5)$ Å, $b = 10.939(7)$ Å, $c = 12.544(8)$ Å, $\alpha = 71.92(3)°$, $\beta = 71.26(3)°$, $\gamma = 61.71(3)°$, $V = 930.5(1)$ $Å^3$, $Z = 1$, $D_{calc} = 1.598$ g cm^{-3}, μ(Mo Kα) = 16.15 cm^{-1}, $T = -30$ °C, $R = 0.126$, $R_w = 0.155$ [$I > 0.00\sigma(I)$], GOF = 1.50.[2] The structure was not completely refined, because the crystals were very thin and gave poor diffraction data. Reproducibility of the structure was confirmed by single crystal and powder X-ray diffraction, many times. The structure of the dehydrated form **1a** was tentatively solved based on poor diffraction data. Crystal data for **1a**: $C_{20}H_{30}N_{18}O_2Cr_2Mn_3$, FW = 823.38; green plate, crystal dimensions $0.12 \times 0.12 \times 0.04$ mm^3, triclinic, space group $P\bar{1}$, $a = 7.9263(2)$ Å, $b = 10.606(2)$ Å, $c = 11.317(3)$ Å, $\alpha = 87.99(6)°$, $\beta = 73.07(5)°$, $\gamma = 69.70(5)°$, $V = 851.2994$ $Å^3$, $Z = 1$, $D_{calc} = 1.606$ g cm^{-3}, μ(Mo Kα) = 17.49 cm^{-1}, $T = -30$ °C, $R = 0.167$, $R_w = 0.253$ [$I > 0.00\sigma(I)$].

2.3. Magnetic measurements

DC and ac magnetic measurements of polycrystalline hydrated form **1** and dehydrated form **1a** were performed on a Quantum Design MPMS-5XL SQUID magnetometer in the temperatures range of 2–300 K under applied dc field of 500 G and 2–300 K under ac field of 3 G with oscillation 1–100 Hz, respectively. Field-dependences of magnetization were measured under the field range of 0–50 kG. All data were corrected for the magnetization of the sample holder and capsule used. Diamagnetic corrections for the constituting atoms were made using Pascal's constants. During the magnetic measurements, **1** was partially dehydrated in SQUID.

2.4. MCD spectra

Magnetic circular dichroism (MCD) of **1a** was measured as Faraday ellipticity using KBr disks under an applied field parallel to the incident light in the temperature range of 6–300 K. A circular dichroism spectrometer (JASCO J-820) equipped an electromagnet ($H = -15$ to $+15$ kG) and a cryostat, was used for the actual measurements. KBr disks containing ca. 1% of sample were prepared by applying a pressure of 8000 kg/cm^2.

3. Results and discussion

3.1. IR spectrum

Infrared spectra were measured using a KBr disk with a Perkin–Elemer Spectrum BX FT-IR system. IR spectrum of **1a** shows an intense ν(C≡N) band at 2156, 2147 and 2139 cm^{-1}. The IR bands at 2156 and 2147 cm^{-1} and 2131 cm^{-1} are attributed to the bridging and non-bridging cyanide groups, respectively.

3.2. TG analyses

In order to confirm the stability of compounds **1** and **1a** the thermal gravimetry (TG) were carried out under nitrogen atmosphere with a Rigaku Instrument TG8120 (Fig. 1). TGA curve of the as-synthesized sample **1** shows a decrease with ca. 8% weight loss from RT to 70 °C, which suggests that efflorescence starts from RT and all lattice water molecules are removed until 70 °C. Above 70 °C, **1** shows an additional decrease with ca. 2% weight loss corresponding to two water molecules coordinated to Mn^{II}. On the other hand, **1a** does not show any weight loss until 100 °C, which means **1a** does not adsorb moisture in the atmosphere. Then it shows one step decrease with ca.

[1] Details about compound **2** are omitted, because the structure was not solved.

[2] CCDC-623090 contains the supplementary crystallographic data for this paper.

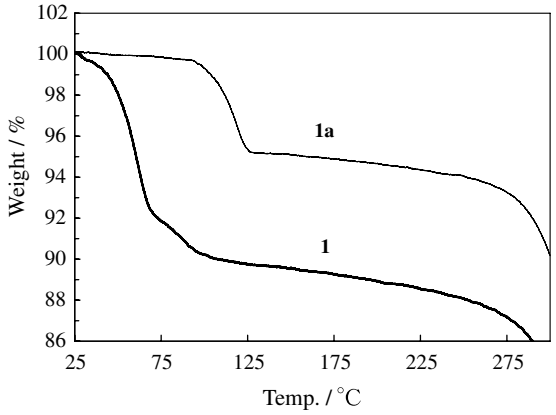


Fig. 1. TGA curves of **1** (thick line) and **1a** (thin line).

4.5% weight loss corresponding to two coordinated water molecules, and decomposition above 250 °C.

3.3. Crystal structures

The asymmetric unit of $[Mn_3(dien)_2(H_2O)_2][Cr(CN)_6]_2 \cdot 4H_2O$ (**1**) consists of one Mn1, one $[Mn2(dien)(H_2O)]^{2+}$ cation and one $[Cr(CN)_6]^{3-}$ anion (Fig. 2). Five cyanide groups of $[Cr(CN)_6]^{3-}$ are involved in the coordination to adjacent Mn ions. The co-ligand of triamine dien acts as a {bidentate + monodentate} ligand and bridges between Mn1 and Mn2. Mn1 resides at the inversion center and is in a pseudo-octahedral geometry with four cyano nitrogen atoms (N1, $N1^{\#1}$, $N3^{\#2}$ and $N3^{\#3}$; #1, #2 and #3 indicate symmetry operations of $(-x, -y, -z)$, $(x-1, y, z)$ and $(-x+1, -y, -z)$) on the equatorial positions and two monodentate-sites of dien (N7 and $N7^{\#1}$) at the axial positions. On the other hand, Mn2 has a pseudo-octahedral geometry with a bidentate-site of dien (N8 and N9) and three cyano nitrogen atoms (N2, $N4^{\#4}$ and $N6^{\#5}$; #4 and #5 indicate symmetry operations of $(-x, -y, -z+1)$ and $(-x+1, -y, -z+1)$) and one water oxygen atom (O1). The dien bridges between Mn1 and Mn2, and forms a Mn2–Mn1–$Mn2^{\#1}$ trinuclear unit, $[Mn_3(dien)_2(H_2O)_2]^{6+}$. In the lattice, 1-D zigzag chains are formed along the *a*-axis by alternate array of $[Mn2(dien)(H_2O)]^{2+}$ and $[Cr(CN)_6]^{3-}$ through Cr–C4N4–Mn2 and Cr–C6N6–Mn2 linkages. The chains are combined by Mn1 through two Cr–C1N1–Mn1 and two Cr–C3N3–Mn1 bridges. All the above-mentioned cyanide bridges are in the same plane and forms a 1-D ribbon structure along the *a*-axis. Furthermore, the ribbons are interlocked by complementary Cr–C2N2–Mn2 bridges where N2 coordinate to the apical position of Mn2 atom in the next ribbon. Also Mn1–dien–Mn2 linkage connects the ribbons and finally a unique 2-D hollow sheet structure comprising defective cubes with three Cr, one Mn1, and three Mn2 atoms at the seven corners and nine Cr–CN–Mn edges, is formed on the *ac*-plane (Fig. 3). Lattice water molecules are located in the defective cubes and form hydrogen bonds with coordinated water (O1···O2 and O1···O3 separations are 3.309 and 2.883 Å, respectively).

Although the quality was not sufficient, the crystal structure of the dehydrated form **1a** was tentatively determined (Fig. 4). The asymmetric unit and the 2-D sheet structure of **1a** is essentially same as **1**. However, the bridging dien of **1a** is remarkably bended toward inside of the defective cube and the hollow sheet structure is shrunk by the lost of the lattice water molecules. With the bend of dien, C1–N1–Mn1 and C3–N3–Mn1 bond angles in **1a** (157(1)° and 150(1)°, respectively) notably decrease compared to those of **1** (164.7(8)° and 171.9(8)°, respectively).

3.4. Magnetic properties

The temperature dependences of χ_M for **1** and **1a** are shown in Fig. 5. At room temperature, the μ_{eff} value of the dehydrated form **1a** per $Mn_3^{II}Cr_2^{III}$ unit is 8.91 μ_B, which is smaller than the spin-only value, 11.6 μ_B, expected for magnetically isolated three Mn^{II} ($S = 5/2$) and two Cr^{III} ($S = 3/2$) ions. The μ_{eff} value gradually decreases upon cooling down to a minimum value of 8.16 μ_B at 115 K, suggesting an antiferromagnetic interaction between Mn^{II} and Cr^{III} ions through cyanide bridges. The μ_{eff} value increases gradually upon further cooling, then shows an abrupt

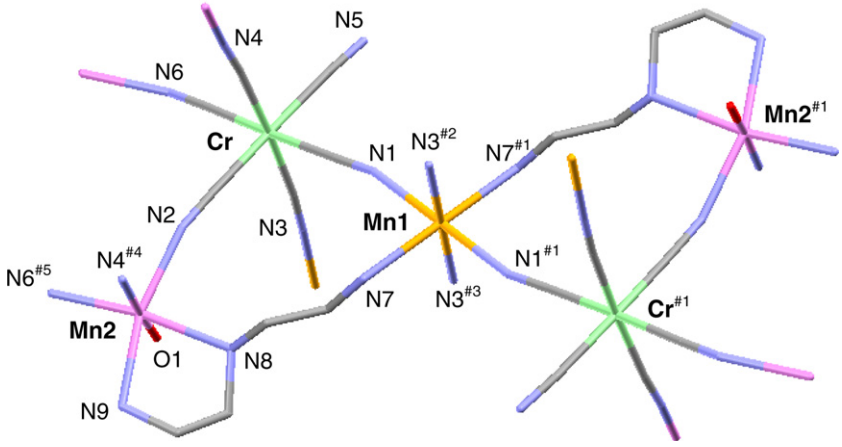


Fig. 2. Structure of **1** with atom numbering scheme (omitted lattice water).

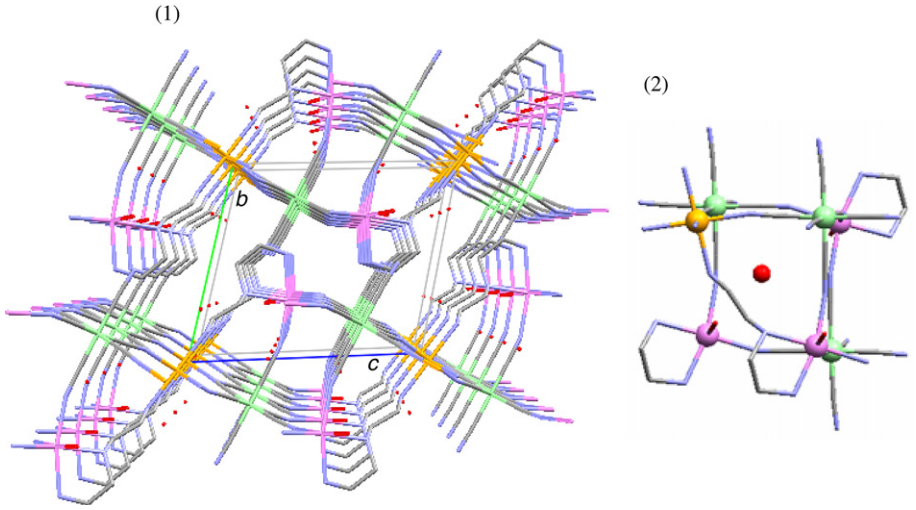


Fig. 3. Projection of the 2-D hollow sheet structure of **1** onto the *bc*-plane (1) and the Cr_3Mn_4 defective cube (2). Atoms: Mn1 (orange) Mn2 (pink), Cr (green), N (blue), O (red), C (gray). (For interpretation of the references to colour in this figure legend, the reader is referred to the web version of this article.)

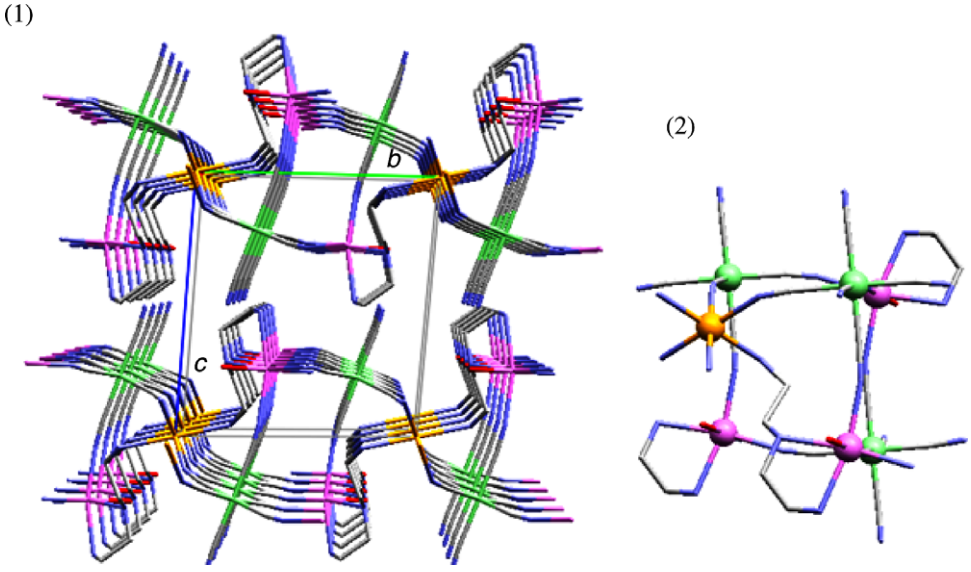


Fig. 4. Structure of **1a** onto the *bc*-plane (1) and the Cr_3Mn_4 defective cube (2). Atoms: Mn1 (orange) Mn2 (pink), Cr (green), N (blue), O (red), C (gray). (For interpretation of the references to colour in this figure legend, the reader is referred to the web version of this article.)

increase below 60 K up to a maximum value of 89.0 μ_B at 32 K. Below 32 K, the μ_{eff} decreases down to 28.1 μ_B at 2 K because of the saturation of the magnetization. Compound **1** also shows essentially the same behaviour as **1a**. The dM/dT vs. T plots of **1a** shows a minimum at 40 K with very small minima around 34 and 50 K, while that of **1** shows a minimum at 34 K with small minima around 40 and 48 K (Fig. 5, inset). The magnetic phase transition temperature (T_C) is determined to be 30 K for **1** and 40 K for **1a** by the weak-field magnetization measurement under 5 G, the dM/dT differential plot and the ac magnetic susceptibility. It means that the ferrimagnetic ordering temperature increases by 10 K with the compression of the hollow sheet by dehydration. Temperature-dependences of the χ'_M and χ''_M of **1a** and **1** are shown in Figs. 6 and 7. The χ'_M versus T plot of **1a** shows a gradual increase below 54 K, an abrupt increase below 40 K, a gradual decrease below 38 K, and a subtle frequency-dependence around 10 K. The χ''_M of **1a** slightly increases below 54 K, then suddenly increase below 40 K, and shows three round peaks around 35, 30 and 10 K. These dc and ac magnetic results suggest that the dehydrated form **1a** changes the magnetic phases at least twice below T_C. The multi-step magnetic phase change would be concerned with the ferrimagnetic ordering over the lattice originated from the complicated 2-D network structure based on the 1-D ferrimagnetic ribbons. The 1-D ribbon consists of Cr–CN–Mn1, Cr–CN–Mn2, and Mn1–dien–Mn2 bridges. From the X-ray crystallographic results, it is sure that comparable antiferromagnetic interaction operates between Cr and each Mn ion (J_{CrMn}). The Mn1···Mn2

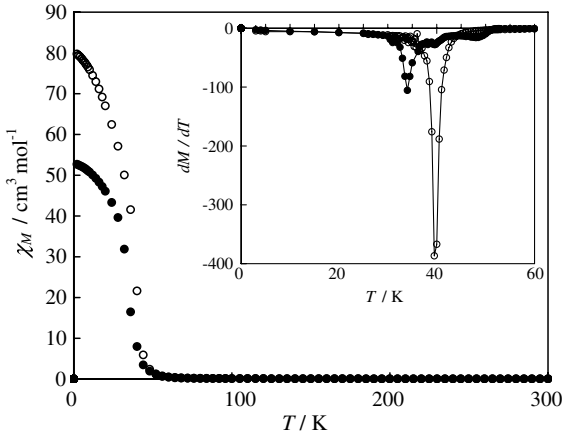


Fig. 5. χ_M vs. T plots of **1** (closed circle) and **1a** (open circle) under an applied dc field of 500 G. Inset: dM/dT vs. T plots of **1** (closed circle) and **1a** (open circle) calculated by field-cooled magnetization data under dc 5 G.

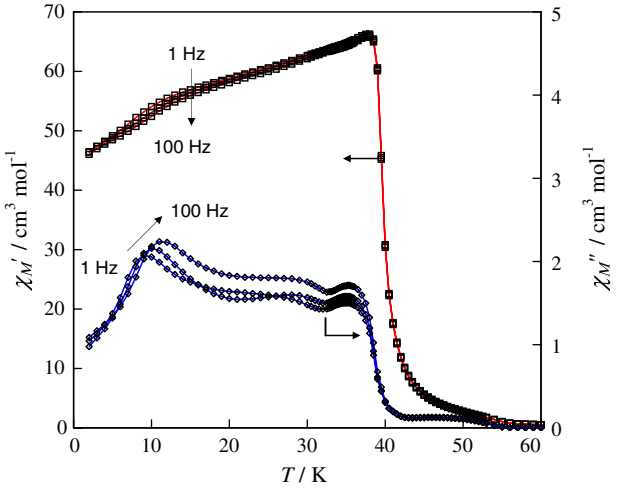


Fig. 6. χ' and χ'' vs. T plots for **1a** under an applied ac magnetic field of 3 G.

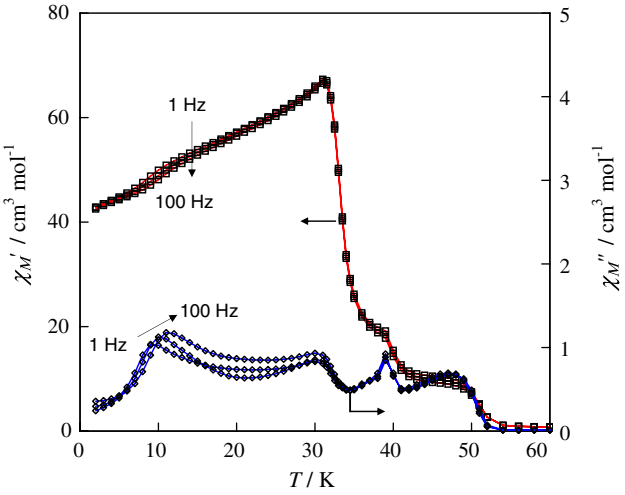


Fig. 7. χ' and χ'' vs. T plots for **1** under an applied ac magnetic field of 3 G.

distance through dien-bridge is about 6.369(5) Å, in which a through-space antiferromagnetic interaction (J_{Mn1Mn2}) will operate and make an antiferromagnetic triangle spin arrangement in CrMn1Mn2 unit. Of course the J_{CrMn} is dominant within the sheet (average intrasheet Cr···Mn1 and Cr···Mn2 separation through the cyanide-bridge are 5.310(5) and 5.393(7) Å, respectively), however, the effect of J_{Mn1Mn2} cannot be neglected in the low temperature region. Also, the nearest intersheet Cr···Mn2 and Mn2···Mn2 separation are, respectively, 6.412(7) and 5.952(7) Å, in which an intersheet antiferromagnetic interaction will operate. Such complicated magnetic interactions would cause a spin re-orientation and be the origin of the unusual magnetic behaviour. In the case of **1**, the χ_M'' versus T plot shows four round peaks around 10, 30, 40 and 48 K. As **1** was partially dehydrated during the measurement, the peak around 40 K would be attributed to contamination of the dehydrated form **1a**. The peak around 48 K was almost vanished after dehydration. However, the multi-step magnetic phase change below T_C is common between **1** and **1a**. The magnetic behaviour was confirmed by other samples prepared in different batches many times. However, the exact reason of the magnetic anomaly of **1** and **1a** are unclear at this time. Compound **1** which was heated at 400 K for 3 h in SQUID also shows the same magnetic behaviour to **1a**. Judged from the reproducibility, co-existence of any by-products is unlikely (T_C of the by-product **2** is 63 K). We need to carry out more detailed measurements using single crystals.

The field-dependence of the magnetization of **1a** measured at 2 K. The saturation magnetization value per $Mn_3^{II}Cr_2^{III}$ unit at 50 kG is 9.64$N\beta$ which corresponds to the value expected for antiferromagnetically coupled three Mn^{II} ($S = 5/2$) and two Cr^{III} ($S = 3/2$) ions. The theoretical curve based on the Brillouin function for $S = 9/2$ is shown as the solid line in Fig. 8, where $g = 2.16$ is used. The shape of M versus H curve strongly supports the ferrimagnetic ordering of **1a** in the bulk. The magnetic hysteresis loop of **1a** at 2 K is given in Fig. 8. The hysteresis curve shows a typical shape of soft ferrimagnet with a small remnant magnetization of 0.487$N\beta$ and a small coercive field of 20 G. The small coercive field must be associated with the isotropic electronic configuration of high-spin Mn^{II} ($S = 5/2$) and Cr^{III} ($S = 3/2$).

3.5. Magneto-optical properties

MCD spectra for **1a** at 6 K under ±15 kG are given in Fig. 9 as Faraday spectra. The spectrum shows peaks at 243 (−), 253 (−), 268 (+), 288 (−), 314 (−), 350 (−), 388 (−) and 430 (−) nm under the applied field of +15 kG, and the spectral pattern is inverted by the change of the direction of the external magnetic field. The intense band around 300 nm would be associated with the allowed transition of $t_{2u}(\sigma) \rightarrow t_{2g}(\pi)$, which is experimentally and theoretically assigned based on the spectrum of $[Cr(CN)_6]^{3-}$ ion [14,15]. The temperature dependence of the molar Faraday

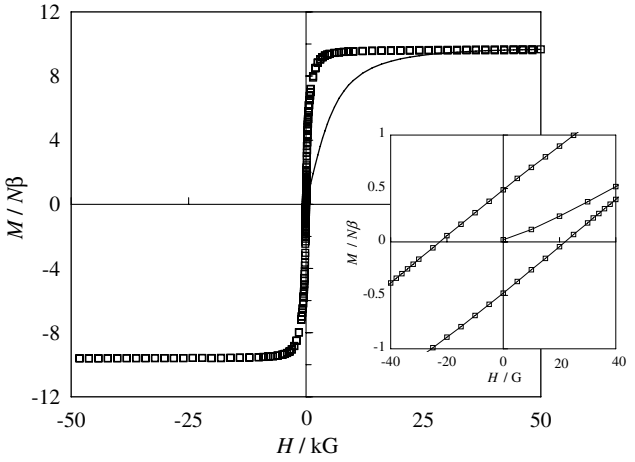


Fig. 8. Magnetic hysteresis loop for **1a** at 2 K. Solid line expresses Brillouin function for $S = 9/2$ with $g = 2.16$. The inset is an expansion in the range of −40 to +40 G.

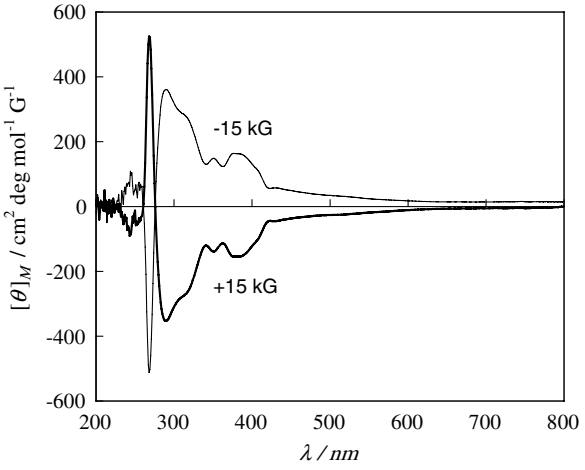


Fig. 9. MCD spectra for **1a** at 6 K under ±1 5 kG.

ellipticity $[\theta]_M$ in the region of 250–500 nm was measured in the temperature range of 6–60 K under an applied magnetic field of 250 G (Fig. 10). Faraday ellipticity increased

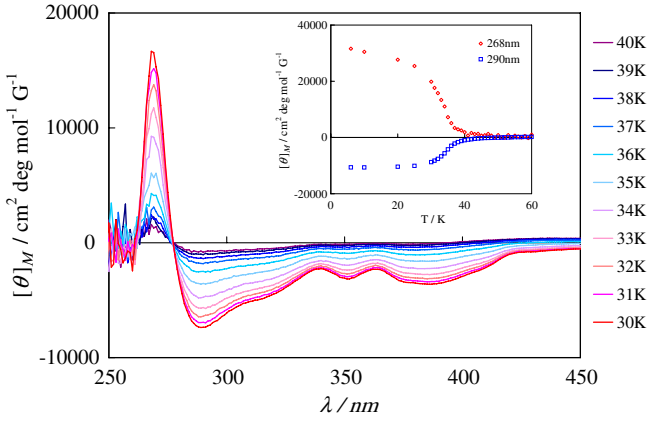


Fig. 10. Temperature dependence of Faraday ellipticity for **1a** under an applied field of 250 G. Inset $[\theta]_M$ vs. T plots at 268 (red) and 290 (blue) nm. (For interpretation of the references to colour in this figure legend, the reader is referred to the web version of this article.)

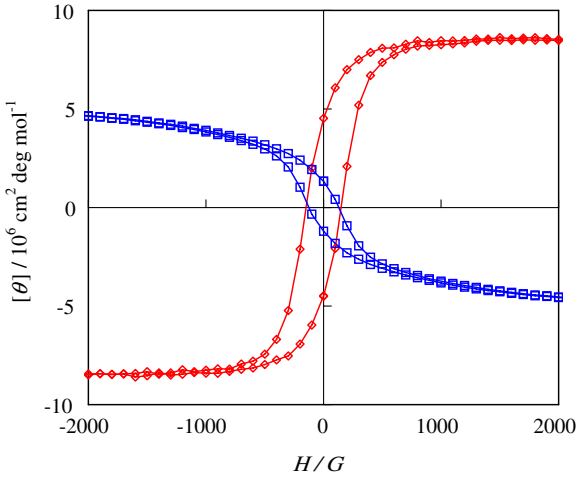


Fig. 11. MCD hysteresis loops for **1a** measured at 6 K and at 268 (red), and 290 (blue) nm. (For interpretation of the references to colour in this figure legend, the reader is referred to the web version of this article.)

on decreasing temperature and reached a maximum value, ca. 100 times as large as the values above T_C, at 6 K. The $[\theta]_M$ versus T plots at 268 and 290 nm are given in the inset of Fig. 10. The shapes of $[\theta]_M$ versus T curves have a marked resemblance to that of χ_M versus T curve (see Fig. 5) with two-step like increase on decreasing temperature. This result demonstrates that the large enhancement of Faraday ellipticity is strongly associated with the magnetic ordering. The field dependence of the Faraday ellipticity at 268 and 290 nm are shown in Fig. 11. The $[\theta]$ versus H plots show a hysteresis with a small remnant $[\theta]$ and a small coercive field as well as the magnetic hysteresis.

4. Conclusion

A new $Mn^{II}Cr^{III}$ bimetallic assembly, $[Mn_3(dien)_2(H_2O)_2][Cr(CN)_6]_2 \cdot 4H_2O$ (**1**), has been prepared and evaluated its structural and magnetic changes associated with dehydration. This compound formed a unique 2-D cyanide-bridged hollow sheet constructed by the 1-D ribbon networks which contain dien-bridged Mn^{II} trimer units and μ_5-$[Cr(CN)_6]^{3-}$ bridges. Compound **1** was efflorescent and irreversibly changed to the dehydrated form **1a**. Magnetic results revealed that **1** and **1a** are ferrimagnets below 30 K and 40 K, respectively, and provides unusual magnetic behavior with a tendency of multiple magnetic phase changes until 2 K owing to the complicated intra- and inter-sheet structure. MCD spectra of **1a** demonstrated a large Faraday ellipticity around 300 nm with a characteristic spectrum pattern. The Faraday ellipticity was remarkably enhanced below T_C in line with the long-range ferrimagnetic ordering. These results suggest compound **1** potentially can act as a humidity-reactive colored-transparent magnet.

Acknowledgements

This work was supported by a Grant-in-aid for Science Research in a Priority Area "Chemistry of Coordination

Space" (16074209) from the Ministry of Education, Science, Sports and Culture of Japan, Core Research for Evolutional Science and Technology (CREST), Japan Science and Technology Corporation (JST), Japan. W.K. is grateful to JSPS Research Fellowships for Young Scientists.

Appendix A. Supplementary material

CCDC 623090 contains the supplementary crystallographic data for this paper. These data can be obtained free of charge via http://www.ccdc.cam.ac.uk/conts/retrieving.html, or from the Cambridge Crystallographic Data Centre, 12 Union Road, Cambridge CB2 1EZ, UK; fax: (+44) 1223-336-033; or e-mail: deposit@ccdc.cam.ac.uk. Supplementary data associated with this article can be found, in the online version, at doi:10.1016/j.poly.2006.11.037.

References

[1] O. Kahn, Molecular Magnetism, VCH, New York, 1993.
[2] S. Kitagawa, R. Kitaura, S. Noro, Angew. Chem., Int. Ed. 43 (2004) 2334.
[3] M. Yamashita, S. Takaishi, A. Kobayashi, H. Kitagawa, H. Matsuzaki, H. Okamoto, Coord. Chem. Rev. 250 (2006) 2335.
[4] M. Ohba, H. Ōkawa, Coord. Chem. Rev. 198 (2000) 313.
[5] H. Ōkawa, M. Ohba, Bull. Chem. Soc. Jpn. 75 (2002) 1191.
[6] W. Kaneko, M. Ohba, H. Ōkawa, S. Kitagwa, Inorg. Chem. 45 (2006) 7191.
[7] N. Usuki, M. Ohba, H. Ōkawa, Bull. Chem. Soc. Jpn. 75 (2002) 1693.
[8] T. Maeda, M. Mito, H. Deguchi, S. Takagi, W. Kaneko, M. Ohba, H. Ōkawa, Polyhedron 24 (2005) 2497.
[9] T. Nuida, T. Matsuda, H. Tokoro, S. Sakurai, K. Hashimoto, S.-i. Ohkoshi, J. Am. Chem. Soc. 127 (2005) 11604.
[10] O. Sato, T. Kawakami, M. Kimura, S. Hishiya, S. Kubo, Y. Einaga, J. Am. Chem. Soc. 126 (2004) 13176.
[11] Z. Wang, B. Zhang, H. Fujiwara, H. Kobayashi, M. Kurmoo, Chem. Commun. 416 (2004).
[12] T. Kimura, T. Goto, H. Shintani, K. Ishizaka, T. Arima, Y. Tokura, Nature 426 (2003) 55.
[13] S.-i. Ohkoshi, K.-i. Arai, Y. Sato, K. Hashimoto, Nat. Mater. 3 (2004) 857.
[14] E. Wasielewska, Inorg. Chim. Acta 122 (1986) L1.
[15] M.F.A. Hendrickx, V.S. Mironov, L.F. Chibotaru, A.J. Ceulemans, J. Am. Chem. Soc. 125 (2003) 3694.

synthesis and characterization of these new materials. Lattice dynamics have been preliminarily probed in the HS and LS states using ^{57}Fe Mössbauer spectroscopy.

2. Experimental

2.1. Materials

All syntheses were carried out in solution and in air. Chemicals were commercially available and solvents were not dried prior to use.

2.2. Synthesis of $[Fe(NH_2trz)_3](AF_6)\cdot nH_2O$

Iron salts were prepared in situ by stirring iron powder and the respective acids at room temperature for 30 min, the solution of which was filtered leading to a green solution. This procedure was not carried out for the tin salt which was directly obtained from aqueous solutions of $FeCl_2\cdot 4H_2O$ and $(NH_4)_2SnF_6$. The coordination polymers were obtained as follows: 15 ml of a methanolic or ethanolic solution of 1 mmol of the iron(II) salts and ascorbic acid (0.1 g), to prevent oxidation to iron(III), were added to a hot alcoholic solution (15 ml) (methanol or ethanol) of 3 mmol of NH_2trz. The complexes precipitated immediately as white powders which were stirred for ~1 h, filtered off, washed with a 5–10 ml of water and dried in air.

C1. $[Fe(NH_2trz)_3](TiF_6)\cdot 0.5H_2O$ (from MeOH). Yield: 0.61 g, 83%. *Anal.* Calc for $FeC_6H_{13}N_{12}O_{0.5}TiF_6$: C, 15.05; H, 2.74; N, 35.09; Fe, 11.66. Found: C, 15.51; H, 2.80; N, 35.54; Fe, 10.14%. IR (cm^{-1}): $\upsilon(NH_2)$ ~3305 (s), υ(N–N) ~1217 (s), υ(C–H out of plane) ~1027 (m), υ(C–H ring torsion) = 621 (vs), υ(Ti–F) ~569 (m).

C2. $[Fe(NH_2trz)_3](TiF_6)\cdot H_2O$ (from EtOH). Yield: 0.43 g, 86.5 %. *Anal*. Calc. for $FeC_6H_{14}N_{12}OTiF_6$: C, 14.77; H, 2.89; N, 34.44; Fe, 11.44. Found: C, 15.26; H, 2.59; N, 34.87; Fe, 12.57%. IR (cm^{-1}): $\upsilon(NH_2)$ ~3318 (s), υ(N–N) ~1218 (s), υ(C–H out of plane) ~1031 (m), υ(C–H ringtorsion) = 624 (vs), υ(Ti–F) ~567 (m).

C3. $[Fe(NH_2trz)_3](ZrF_6)\cdot 0.5H_2O$ (from MeOH). Yield: 0.94 g, 66.4 %. *Anal*. Calc. for $FeC_6H_{13}N_{12}O_{0,5}ZrF_6$: C, 13.80; H, 2.51; N, 32.18; Fe, 10.69. Found: C, 14.36; H, 2.47; N, 32.81; Fe, 9.96%. IR (cm^{-1}): $\upsilon(NH_2)$ ~3308 (s), υ(N–N) ~1218 (s), υ(C–H out of plane) ~997 (m), υ(C–H ring torsion) = 625 (vs), υ_1(Zr–F) ~590 (m).

C4. $[Fe(NH_2trz)_3](ZrF_6)$ (from EtOH). Yield: 0.64 g, 50%. *Anal.* Calc. for $FeC_6H_{12}N_{12}ZrF_6$: C, 14.04; H, 2.36; N, 32.75; Fe, 10.88. Found: C, 14.80; H, 2.49; N, 33.03; Fe, 9.65%. IR (cm^{-1}): $\upsilon(NH_2)$ ~3226 (m), υ(N–N) ~1218 (s), υ(C–H out of plane) ~997 (m), υ(C–H ring torsion) = 624 (vs), υ_1(Zr–F) ~590 (m).

C5. $[Fe(NH_2trz)_3](SnF_6)\cdot 0.5H_2O$ (from MeOH). Yield: 0.38 g, 76%. *Anal.* Calc. for $FeC_6H_{13}N_{12}O_{0,5}SnF_6$: C, 13.11; H, 2.38; N, 30.57; Fe, 10.16. Found: C, 13.31; H, 2.31; N, 29.84; Fe, 9.80%. IR (cm^{-1}): $\upsilon(NH_2)$ ~3215 (s), υ(N–N) ~1217 (s), υ(C–H out of plane) ~1000 (m), υ(C–H ring torsion) = 612 (s), υ(Sn–F) ~601 (m).

C6. $[Fe(NH_2trz)_3](SnF_6)\cdot H_2O$ (from EtOH). Yield: 0.4 g, 80%. *Anal.* Calc. for $FeC_6H_{14}N_{12}OSnF_6$: C, 12.90; H, 2.53; N, 30.08; Fe, 9.99. Found: C, 13.04; H, 2.27; N, 29.80; Fe, 9.17%. IR (cm^{-1}): $\upsilon(NH_2)$ ~3225 (s), υ(N–N) ~1217 (s), υ(C–H out of plane) ~998 (m), υ(C–H ring torsion) = 610 (s), υ(Sn–F) ~600 (m).

2.3. Physical techniques

Elemental analyses were performed at University College London (UK). Atomic absorption analyses were carried out on a Perkin–Elmer 3110 spectrometer. Sampling was carried out in aqueous solutions containing nitric acid (65%). Standard solutions were prepared with Mohr's salt. IR spectra were collected on a BioRad FTS-135 spectrometer on KBr pellets. Thermogravimetric analyses were performed in air from 293 K to 400 K at a heating rate of 1 °C/min using a Mettler Toledo TGA/SDTA851^e analyzer. UV–Vis solid-state spectra were recorded with a CARY 5E Varian spectrophotometer using the diffuse reflectance technique with polytetrafluoroethylene as a reference. Powder X-ray diffraction patterns were recorded on a Siemens D5000 counter diffractometer working with Cu Kα radiation and operating at room temperature. The samples were mounted on the support with silicon grease. ^{57}Fe Mössbauer spectra were recorded in transmission geometry over the temperature range (78–300 K) with conventional Mössbauer spectrometers equipped with a ^{57}Co(Rh) radioactive source operating at room temperature. The samples were sealed in aluminum foil and mounted on a nitrogen cryostat. The spectra were fitted to the sum of Lorentzians by a least-squares refinement using Mossfit [6] or Recoil 1.05 Mössbauer Analysis Software [7]. All isomer shifts refer to α-Fe at room temperature. Magnetic susceptibilities were measured in the temperature range 50–300 K using a MPMS-5 SQUID magnetometer. Data were corrected for magnetization of the sample holder and diamagnetic contributions, which were estimated from the Pascal constants.

3. Results and discussion

3.1. Synthesis and characterization

The coordination compounds were precipitated as powders from MeOH or EtOH media, and successfully characterized by CHN and TGA analyses, atomic absorption, X-ray powder diffraction, infrared, UV–Vis and ^{57}Fe Mössbauer spectroscopies. Thermogravimetric and elemental analyses did not show the presence of alcoholic solvents but instead revealed non-coordinated water molecules, allowing us to derive the general formula $[Fe(NH_2trz)_3]AF_6\cdot nH_2O$. Syntheses carried out in MeOH or EtOH lead to hemihydrates or monohydrates, respectively, except for the zirconium derivative. This series of materials have essentially identical infrared and X-ray powder diffraction patterns. At room temperature, the compounds appear as

white powders and present a reversible thermochromism to pink on cooling. These colors depend on the spin state of the iron(II) centers. The white color is due to the fact that the spin-allowed lowest energy d–d transition, $^5T_{2g} \rightarrow {}^5E_g$, for the HS sites occurs in the near infrared region ($\sim$11 800 cm^{-1}) [2b]. The pink color is due to the $^1A_{1g} \rightarrow {}^1T_{1g}$ d–d transition of LS iron(II) sites occurring at $\sim$520 nm. Mössbauer spectroscopy revealed the absence of oxidation and confirmed the presence of only one FeN_6 site undergoing spin crossover behavior on cooling. ^{57}Fe Mössbauer parameters are typical of coordination polymeric chains with 4-amino-1,2,4-triazole as ligand [8].

3.2. Magnetic susceptibility measurements and Mössbauer spectroscopy

The magnetic properties of $[Fe(NH_2trz)_3]TiF_6 \cdot nH_2O$ (**C1**, **C2**) and $[Fe(NH_2trz)_3]SnF_6 \cdot 0.5H_2O$ (**C5**) were recorded on cooling and warming over the temperature range (300–70 K) (Fig. 1). At room temperature, $\chi_M T$ is equal to 3.64 $cm^3\,K\,mol^{-1}$ for **C1**, which coincides with the expected value for a HS iron(II) ion, as confirmed by Mössbauer spectroscopy ($\delta^{HS} = 1.047(1)$ mm s^{-1} and $\Delta E_Q^{HS} = 2.782(1)$ mm s^{-1}). $\chi_M T$ decreases slightly down to $\sim$235 K and quite abruptly down to $\sim$140 K. Below this temperature, $\chi_M T$ decreases smoothly down to $\sim$0.54 $cm^3\,K\,mol^{-1}$ at 90 K, indicating an incomplete ST. This incomplete character was confirmed by Mössbauer spectroscopy at 78 K which revealed the presence of HS and LS iron(II) ions ($\delta^{LS} = 0.531(1)$ mm s^{-1} and $\Delta E_Q^{LS} = 0.297(1)$ mm s^{-1}, $A_{HS}/A_{tot} = 0.16$). As the temperature is increased, similar behavior is observed, with a thermal hysteresis width of 6 K. The transition temperatures on cooling and warming are $T_{1/2}\downarrow = 194$ K and $T_{1/2}\uparrow = 200$ K, respectively. The ST behavior of **C2** is similar with a hysteresis loop of width 7 K, shifted to lower temperatures ($T_{1/2}\downarrow = 189$ K and $T_{1/2}\uparrow = 196$ K). The ST is complete at 300 K and incomplete at low temperature, as confirmed by Mössbauer spectroscopy at 78 K ($A_{HS}/A_{tot} = 0.27$). The ST behavior of $[Fe(NH_2trz)_3]SnF_6 \cdot 0.5H_2O$ is somewhat different. On cooling, $\chi_M T$ remains constant at 3.02 $cm^3\,K\,mol^{-1}$ down to $\sim$ 230 K, after which $\chi_M T$ decreases abruptly at $T_{1/2}\downarrow = 211$ K and then smoothly down to 0.64 $cm^3\,K\,mol^{-1}$ at 70 K indicating an incomplete ST which is also confirmed by Mössbauer at 78 K ($A_{HS}/A_{tot} = 0.20$). This lower $\chi_M T$ value at room temperature compared to that of **C1**–**2** indicates the presence of LS iron(II) ions which are also probed by Mössbauer. It can be noted that the ST proceeds more smoothly on warming with $T_{1/2}\uparrow = 223$ K.

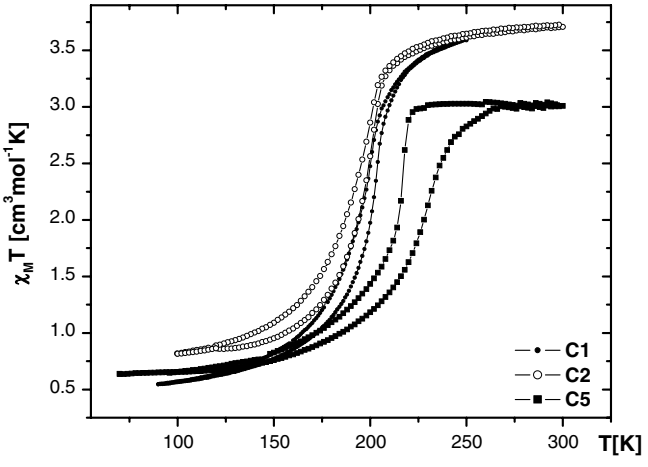


Fig. 1. $\chi_M T$ vs. T on cooling and warming modes for $[Fe(NH_2trz)_3]TiF_6 \cdot nH_2O$ ($n = 0.5$ (●); $n = 1$, (○)) and $[Fe(NH_2trz)_3]SnF_6 \cdot 0.5H_2O$ (■).

The ST of these materials range around 200 K which nicely fit with the relation between the transition temperatures and the anions radii suggested by Lavrenova for the $[Fe(NH_2trz)_3]A_2$ series [8] since the radii of AF_6 anions are found above 2.5 Å [9].

The origin of the incomplete ST at low temperature can be addressed. It could be due to crystal defects, HS FeN_6-sites or end of chains coordinated to water molecules. A closer look at the Mössbauer spectra of **C1**–**6** at 78 K reveals only one iron(II) site being in the LS and HS states. Thus, there is no indication of an FeN_3O_3 environment which would be characteristic of three terminal coordinated water molecules [10] provided these are present in enough concentration. Nevertheless, ends of chains with two coordinated water molecules may not be detected by Mössbauer [11] and thus cannot be excluded. Interestingly, the addition of half a water molecule per iron(II) has a noticeable effect on the ST behavior of **C1**–**2** since a shift of the curve of $\sim$4 K downwards is observed and the HS plateau at 78 K increases. This shift has been confirmed by tracking the ST by Mössbauer spectroscopy thanks to the A_{HS}/A_{tot} ratio recorded over the whole temperature range of investigation. The increase of water molecules per formula unit could be attributed to the increase in the number of terminal coordinated solvent molecules setting a lower ligand field strength and thus preventing a spin state change. This hypothesis is validated by the fact that the abrupt character of the ST of **C1**–**2** is not affected by this incorporation which could lead to chains of different lengths that would show different cooperative behaviors [12].

At room temperature, ΔE_Q^{HS} remains constant at $\sim$2.78(1) mm s^{-1} whatever the inserted anion (Table 1). This indicates that the local distortion around the HS iron(II) ions is not modified by the position of the non-coordinated anions in the crystal lattice. This result suggests the location of these anionic species in the external coordination sphere. This was observed in the crystal structure of $[Cu(NH_2trz)_3](ZrF_6) \cdot H_2O$ where the hexafluorozirconate anion is connected to the amino groups of the NH_2trz ligand through hydrogen bonding. The anion as well as a non-coordinated water molecule, which are situated in the interchain space whose dimension is 10.997(4) Å, are part of a dense hydrogen bonding network establishing supramolecular bridges between copper(II) chains [13]. At 78 K where all

Table 1
Selection of Mössbauer parameters for $[Fe(NH_2trz)_3](AF_6)\cdot nH_2O$

Chain	A	n	ΔE_Q^{HS} (295(5) K) (mm s^{-1})	ΔE_Q^{LS} (78 K) (mm s^{-1})	A_{HS}/A_{tot} (78 K)	$\theta_D^{(HS)}$ (K)	$\theta_D^{(LS)}$ (K)	$\Delta\theta_D$ (K)
C1	Ti	0.5	2.782(1)	0.297(1)	0.16	218(5)	244(5)	26(10)
C2	Ti	1	2.785(1)	0.306(1)	0.27	188(5)	209(5)	21(10)
C3	Zr	0.5	2.790(2)	0.292(1)	0.08	122 (5)	148(5)	26(10)
C4	Zr	0	2.795(3)	0.291(1)	0.07	151(5)	171(5)	20(10)
C5	Sn	0.5	2.781(4)	0.318(2)	0.20	132(5)	149(5)	17(10)
C6	Sn	1	2.784(3)	0.317(1)	0.19	167(5)	184(5)	17(10)

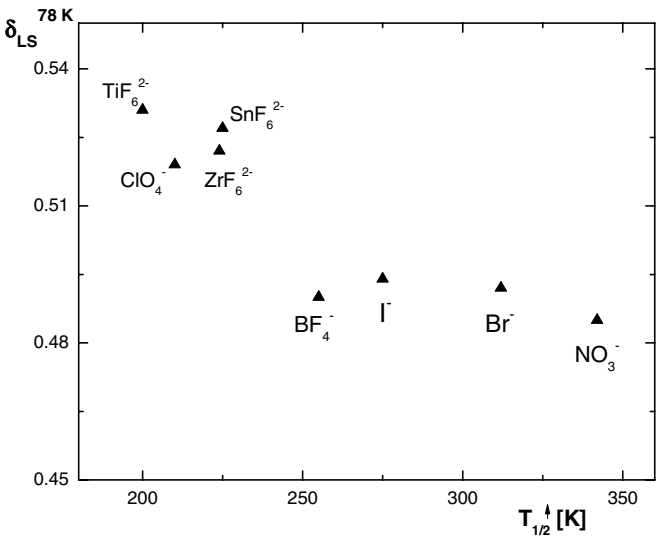


Fig. 2. $\delta_{LS}^{(78\ K)}$ *vs.* $T_{1/2}^{\uparrow}$ for $[Fe(NH_2trz)_3]A_{x(x=1,2)}$ prepared in MeOH. The data for monovalent anions are from [8].

compounds are in the LS state, ΔE_Q^{LS} also remains constant at 0.30(1) mm s^{-1} (Table 1). The lattice contribution to the quadrupole splitting thus indicates that the iron(II) sites are distorted, as expected for these metal centers connected within a chain by three *N*1,*N*2-1,2,4-triazole bridges.

Fig. 2 shows the evolution of $\delta_{LS}^{(78\ K)}$ versus $T_{1/2}^{\uparrow}$ for cationic chains $[Fe(NH_2trz)_3]^{2+}$ incorporating monovalent [8] and divalent anions, prepared in MeOH. The isomer shift decreases when the transition temperature increases which necessarily implies an increase in the degree of Fe–N bond covalency.

The Debye temperature, θ_D, was preliminarily determined for **C1-6** in the HS and LS states in order to investigate the rigidity of these switchable networks. To derive these terms, we have recorded several spectra at various temperatures. The Debye temperatures are listed in Table 1.

The LS lattice is more rigid than the HS one since the vibrational frequencies decrease during the LS to HS transition, as a result of the increase in the Fe–N bond lengths. For comparison, the Debye temperatures in the HS state of **C1**–**2** are similar for $[Fe(NH_2trz)_3](ClO_4)_2$ with $\theta_D^{(HS)} = 188(12)$ K [8]. Overall, the variation of the lattice rigidity, $\Delta\theta_D = \theta_D^{(LS)} - \theta_D^{(HS)}$, accompanying the ST is on the same order of magnitude (~21 K). The present θ_D values are however overestimated since thickness corrections were neglected [14] and for a careful evaluation, effective mass variation during the ST must be considered. Such investigations are in progress.

4. Conclusion

In this work, new 1D ST chain compounds including novel fluorinated counteranions have been investigated. Lattice dynamics were preliminarily evaluated in the LS and HS states using the Debye Model. Insertion of novel inorganic counteranions in iron(II) ST coordination polymers is continuing in our laboratories.

Acknowledgements

This work was partly funded by the Agence Universitaire de la Francophonie (Ref. 6313PS668), the Fonds Special de Recherche de l'Université Catholique de Louvain, the Fonds National de la Rercherche Scientifique (Crédit aux Chercheurs), the CGRI (Tournesol 2006) and the CNRS (Centre National de la Recherche Scientifique). We also thank Prof. E. Gaigneaux for providing access to a X-ray diffractometer.

References

[1] (a) P. Gütlich, A. Hauser, H. Spiering, Angew. Chem., Int. Ed. Engl. 33 (1994) 2024;
(b) P. Gütlich, Y. Garcia, H.A. Goodwin, Chem. Soc. Rev. 29 (2000) 419;
(c) P. Gütlich, Y. Garcia, H. Spiering, From Molecules to Materials IV, vol. 8, WileyVCH, 2003, pp. 271.
[2] (a) O. Kahn, E. Codjovi, Y. Garcia, P.J. van Koningsbruggen, R. Lapouyade, L. Sommier, in: M.M. Turnbull, T. Sugimoto, L.K. Thompson (Eds.), Molecule-Based Magnetic Materials, ACS Symposium Series, vol. 644, American Chemical Society, Washington, 1996, p. 298;
(b) O. Kahn, J. Kröber, C. Jay, Adv. Mater. 4 (1992) 718;
(c) O. Kahn, C. Jay-Martinez, Science 279 (1998) 44.
[3] Y. Garcia, V. Niel, M.C. Muñoz, J.A. Real, Top. Curr. Chem. 233 (2004) 229.
[4] (a) A. Michalowicz, J. Moscovici, B. Ducourant, D. Cracco, O. Kahn, Chem. Mater. 7 (1995) 833;
(b) Y. Garcia, J. Moscovici, A. Michalowicz, V. Ksenofontov, G. Levchenko, G. Bravic, D. Chasseau, P. Gütlich, Chem. Eur. J. 8 (2002) 4992.
[5] Y. Garcia, P.J. van Koningsbruggen, G. Bravic, P. Guionneau, D. Chasseau, G.L. Cascarano, J. Moscovici, K. Lambert, A. Michalowicz, O. Kahn, Inorg. Chem. 36 (1997) 6357.
[6] Mossfit, J. Teillet, F. Varret, unpublished work.

[7] K. Lagarec, D.G. Rancourt, Recoil, Mössbauer Spectral Analysis Software for Windows 1.0, Department of Physics, University of Ottawa, Canada, 1998.
[8] V.A. Varnek, L.G. Lavrenova, J. Struct. Chem. 36 (1995) 104.
[9] H.K. Roobottom, H.D.B. Jenkins, J. Passmore, L. Glasser, J. Chem. Ed. 76 (1999) 1570.
[10] Y. Garcia, P. Guionneau, G. Bravic, D. Chasseau, J.A.K. Howard, O. Kahn, V. Ksenofontov, S. Reiman, P. Gütlich, Eur. J. Inorg. Chem. (2000) 1531.
[11] M. Thomman, O. Kahn, J. Guilhem, F. Varret, Inorg. Chem. 33 (1994) 6029.
[12] Y. Garcia, P.J. van Koningsbruggen, R. Lapouyade, L. Fournès, L. Rabardel, O. Kahn, V. Ksenofontov, G. Levchenko, P. Gütlich, Chem. Mater. 10 (1998) 2426.
[13] M.M. Dîrtu, Y. Garcia, B. Tinant, in: Conference Proceedings ECM, vol. 23, 2006, m41.p07.
[14] K. Boukheddaden, F. Varret, Hyperfine Interact. 72 (1992) 349.

where the ladder rungs are constructed of double $\mu_{1,5}$-dca bridges and the legs with single $\mu_{1,5}$-dca bridges [15]. These ladders are linked into a two-dimensional array through hydrogen bonding interactions between terminal dicyanamide and water molecules that are coordinated to the periphery of the ladder. We have recently reported that the $(PPh_4)_3[Cu_4(dca)_{11}]$ salt possesses a novel triple ladder structure in which the rungs are comprised of single $\mu_{1,5}$-dca bridges while the sides are constructed of double $\mu_{1,5}$-dca bridges. No terminal ligands are attached to these triple ladders, resulting in close, through space metal separations of 4.003(1) Å [16].

Square, two-dimensional anionic frameworks are formed through the infinite coupling of ladders. This is observed in the $(PPh_4)M(dca)_3$ (M = Mn and Co) and $(AsPh_4)M(dca)_3$ (M = Mn, Co and Ni) structures [11,14,17]. The $(Et_4N)[Cd(dca)_3]\cdot 3/4H_2O$ structure contains the same two-dimensional anionic topology [18]. Two-dimensional hexagonal honeycomb sheets with double $\mu_{1,5}$-dca bridges result when cations such as $[M(bipy)_3]^{2+}$ (M = Fe and Ni; bipy = 2,2′-bipyridine) are used as templates [19]. We have recently found that when partially oxidized bis(ethylenedithio)tetrathiafulvalene (BEDT-TTF) is used as the templating cation, a novel triangular anionic layer with single $\mu_{1,5}$-dca bridges is formed [20].

Several three-dimensional motifs are also known in (cation)$M(dca)_3$ salts. Superlattices of a simple cubelike (also called perovskite, α-polonium, or ReO_3) structure with single $\mu_{1,5}$-dca bridges form through use of the $(BzR_3N)^+$ (Bz = benzyl, R = Bu and Et) [21], $(SPh_3)^+$ [22], $[N(C_3H_7)_4]^+$ [23], and $(Cp^*_2M)^+$ [24] counter ions. A triple-rutile type structure is found in the salts with $[N(C_4H_9)_4]^+$ [23] and $[RPh_3P]^+$ (R = Me and Et) [17,25] cations. Although in both of these salts, the metal centers are five-connecting (each end of a $\mu_{1,5}$-dca doubly bridged unit is linked to four equivalent units through single $\mu_{1,5}$-dca bridges), the anionic lattice topologies are different. Finally, we have found that the $[N(C_5H_{11})_4]^+$ templates a lithium antimonate structure which is formed by linking *cis* bibridged $\mu_{1,5}$-dca chains through single $\mu_{1,5}$-dca bridges [23].

Clearly, very small differences in the coordination geometry of divalent first row transition elements and crystallization conditions can affect the identity of the crystallized product. Taking, for example, the very similar EPh_4^+ (E = P and As) cations, three different anionic cobalt(II) dicyanamide structural motifs have been reported: chains, ladders, and sheets. When copper(II) is substituted for cobalt(II), a triple ladder structure results.

Almost all of the anionic dicyanamide complexes that have been reported contain divalent manganese, iron, cobalt, or nickel. A couple of structures contain divalent cadmium and there is one lone example of an anionic divalent copper salt. Anionic copper(I) dca salts have only been studied to a slightly greater extent: the $[Rb(18\text{-crown-}6)]_3Cu_2(dca)_5$ salt contains both tetrahedrally and triangularly coordinated copper, while $[Tl(18\text{-crown-}6)]Cu(dca)_2$ contains only tetrahedrally coordinated copper [26]. Anionic copper(I) dicyanamide anions are also important for the preparation of superconducting charge transfer salts in the $(BEDT\text{-}TTF)_2Cu(dca)X$ (X = Br and Cl) [27,28].

2. Experimental

2.1. Synthesis

2.1.1. $(PPh_4)(dca)$

Tetraphenylphosphonium bromide (22.674 g, 54.07 mmol, Aldrich) was dissolved in 400 ml water. Sodium dicyanamide (4.813 g, 54.07 mmol, Lonza) was dissolved in 200 ml water. These two solutions were combined and stirred thoroughly. The heavy white precipitate of $(PPh_4)(dca)$ was collected by suction filtration, rinsed with deionized water, and dried with diethyl ether. This product was recrystallized from hot ethanol: $(PPh_4)(dca)$ (14.3 g, 35.27 mmol) was dissolved in 50 ml hot ethanol, filtered, and slowly cooled to yield colorless crystals. *Anal.* Calc. for $C_{26}H_{20}N_3P$: C, 77.02; H, 4.97; N, 10.37. Found: C, 77.04; H, 5.00; N, 10.40%. Mp: 215–217 °C. IR (cm^{-1}): 2228m, 2189 m, 2129vs, 2100w, 1585w, 1482m, 1438s, 1307s, 1189w, 1163w, 1106vs, 1074w, 1028w, 996m, 932w, 901w, 862w, 760m, 753m, 722vs, 690s.

2.1.2. $(PPh_4)Cu(dca)_3(H_2O)$ (**1**)

$(PPh_4)(dca)$ (811 mg, 2 mmol) was dissolved in 25 ml ethanol (Aaper, 200 proof). Copper(II) tetrafluoroborate hydrate (118 mg, 0.5 mmol, Aldrich) was dissolved in 10 ml water. The precipitate that formed immediately when these two solutions were combined was removed by filtration. The filtrate was allowed to slowly evaporate. After 2 days, some green crystals of the title compound formed. *Anal.* Calc. for $C_{30}H_{22}N_9OPCu$: C, 58.20; H, 3.58; N, 20.37. Found: C, 58.72; H, 4.29; N, 19.77%. IR (cm^{-1}): 2349w, 2309m, 2252m, 2237m, 2177m, 2169vs, 1484w, 1436m, 1376m, 1364m, 1338w, 1313w, 1189w, 1163w, 1109s, 1052w, 995m, 758m, 722s, 687s.

2.1.3. $(PPh_3Bu)_2Cu(dca)_4$ (**2**)

Butyltriphenylphosphonium bromide (399 mg, 1 mmol, Aldrich) was dissolved in 10 ml of ethanol and combined with a solution of sodium dicyanamide (208 mg, 2 mmol, Lonza) in 10 ml of water. This mixture was layered on top of a solution of copper(II) tetrafluoroborate hydrate (237 mg, 1 mmol, Aldrich) in 10 ml of water. After 1 month, green, rod shaped crystals were collected by filtration. Mp: 109 °C. *Anal.* Calc. for $C_{52}H_{48}P_2N_{12}Cu$: C, 64.62; H, 5.01; N, 17.39. Found: C, 64.78; H, 5.20; N, 17.26%. IR (cm^{-1}): 2967w, 2930w, 2906w, 2870w, 2289m, 2245m, 2238m, 2167vs, 1441m, 1437m, 1352m, 1228w, 1184w, 1160w, 1114m, 1091w, 996w, 961w, 918w, 905w, 803w, 769w, 753m, 738m, 721m, 712w, 687m.

2.1.4. Synthesis of $Cu(dca)_2$

$Cu(dca)_2$ was prepared according to the literature procedure [5]. Aqueous solutions of copper(II) nitrate hydrate

(1396 mg, 6 mmol, Aldrich) and sodium dicyanamide (1068 mg, 12 mmol, Lonza) were combined and the precipitate collected by filtration and dried in air. IR (cm^{-1}): 2417w, 2328m, 2272s, 2194vs, 1356s, 1061w, 1006w, 956m, 678m.

2.2. Single crystal X-ray diffraction

The crystal structures of **1** and **2** were determined by X-ray diffraction using a Siemens SMART single crystal diffractometer equipped with a CCD-based area detector and a sealed-tube Mo Kα source (graphite monochromator). The detector frames were integrated by use of the program SAINT [29] and the intensities corrected for absorption by Gaussian integration based on the measured crystal shape using the program XPREP of SAINT. Other systematic variations were corrected by the analysis of replicate reflections using the program SADABS [30]. The structures were solved by use of direct methods, while full-matrix least-squares refinement on F^2 (including all data) was performed, both using the program package SHELXTL [31]. A summary of the crystallographic data is given in Table 1, while selected bond lengths and angles are listed in Tables 2 and 3 for the two compounds, respectively. The atomic numbering schemes are illustrated in Figs. 1 and 5 (anions) and in the Supporting information Figs. S1 and S2 (cations), and further details of each structure are available in the CIF files also deposited as electronic Supplementary information.

2.3. X-ray powder diffraction

X-ray powder diffraction patterns were collected on a PANalytical X'Pert Pro diffractometer fitted with an X'Celerator detector using Co radiation. Samples were lightly ground in order to reduce preferred orientation and placed on a zero-background Si(5 1 0) substrate sample holder. Powder patterns were calculated from single crystal data through use of the program CrystalDiffract (CrystalMaker software, version 1.0.3).

2.4. Magnetic measurements

The direct current (dc) magnetizations of **1** and **2** were measured between 5 and 300 K and 3.25 and 240 K, respectively, using a Quantum Design (San Diego, CA) MPMS-7 SQUID magnetometer. A collection of crystals of each compound was tightly packed in gelatin capsules, mounted in a plastic straw and affixed to the end of the sample rod. Sample masses were 23.1 mg and 75.4 mg for **1** and **2**,

Table 1
Crystal data, data collection, and structure refinement for **1** and **2**

	1	**2**	
Empirical formula	$C_{30}H_{22}N_9OPCu$	$C_{52}H_{48}N_{12}P_2Cu$	
Formula weight	619.08	966.50	
Temperature (K)	296(2)	296(2)	150(2)
Wavelength (Å)	0.71073		
Crystal system	monoclinic		
Space group	$P2_1$	$P2_1/n$	$P2_1/n$
Unit cell dimensions			
a (Å)	7.4094(11)	15.541(2)	15.466(10)
b (Å)	23.526(4)	7.5256(10)	7.460(5)
c (Å)	8.9951(13)	21.261(3)	21.153(14)
β (°)	111.938(6)	101.810(6)	102.079(10)
V (Å^3)	1454.4(6)	2433.9(9)	2387(4)
Z	2	2	2
Reflections for cell determination	1775	2011	1960
D_{calc} (Mg m^{-3})	1.414	1.319	1.345
Absorption coefficient (mm^{-1})	0.85	0.56	0.575
Transmission T_{min}, T_{max}	0.813, 0.895	0.813, 0.932	0.812, 0.930
F(0 0 0)	634	1006	
Crystal size (mm)	0.14 × 0.18 × 0.30	0.14 × 0.22 × 0.44	
Reflections collected	13 880	21 818	20 057
Coverage (%)			
0.75 Å ($\theta = 28.28°$)	96.3	95.6	95.8
0.80 Å ($\theta = 26.37°$)	100	99.9	99.9
Independent, allowed reflections	6693	5780	5661
$I > 2\sigma(I)$	5767	4200	4720
R_{int}	0.0331	0.0360	0.0315
Data/restraints/parameters	6693/4/385	5780/0/304	5661/0/304
Goodness-of-fit on F^2	1.039	1.054	1.036
Final R indices			
R_1 [$I > 2\sigma(I)$]	0.0357	0.0380	0.0340
wR_2 (all data)	0.0837	0.1103	0.0928
Largest difference in peak, hole (e Å^{-3})	0.25, −0.36	0.37, −0.27	0.41, −0.34

Table 2
Selected bond lengths (Å) and angles (°) for **1**

Bond lengths			
Cu–N(4)	1.961(3)	N(4)–C(4)	1.130(4)
Cu–N(1)	1.968(2)	N(5)–C(5)	1.122(4)
Cu–N(7)	1.984(3)	N(6)–C(5)	1.282(5)
Cu–O	1.987(2)	N(6)–C(4)	1.289(5)
Cu–N(8)[a]	2.263(3)	N(7)–C(7)	1.129(4)
N(1)–C(1)	1.140(4)	N(8)–C(8)	1.140(4)
N(2)–C(2)	1.133(5)	N(9)–C(7)	1.293(4)
N(3)–C(1)	1.283(4)	N(9)–C(8)	1.299(4)
N(3)–C(2)	1.314(5)		
Bond angles			
N(4)–Cu–N(1)	164.75(12)	C(4)–N(4)–Cu	169.7(3)
N(4)–Cu–N(7)	90.58(11)	C(5)–N(6)–C(4)	123.6(4)
N(1)–Cu–N(7)	91.94(12)	C(7)–N(7)–Cu	170.8(3)
N(4)–Cu–O	84.10(11)	C(8)–N(8)–Cu[b]	139.6(2)
N(1)–Cu–O	90.39(11)	C(7)–N(9)–C(8)	121.4(3)
N(7)–Cu–O	167.67(11)	N(1)–C(1)–N(3)	172.2(4)
N(4)–Cu–N(8)[a]	97.51(12)	N(2)–C(2)–N(3)	172.4(4)
N(1)–Cu–N(8)[a]	96.92(12)	N(4)–C(4)–N(6)	173.3(4)
N(7)–Cu–N(8)[a]	99.26(10)	N(5)–C(5)–N(6)	171.8(4)
O–Cu–N(8)[a]	92.47(10)	N(7)–C(7)–N(9)	171.8(3)
C(1)–N(1)–Cu	172.3(3)	N(8)–C(8)–N(9)	173.5(3)
C(1)–N(3)–C(2)	125.5(3)		

[a] $x+1, y, z$.
[b] $x-1, y, z$.

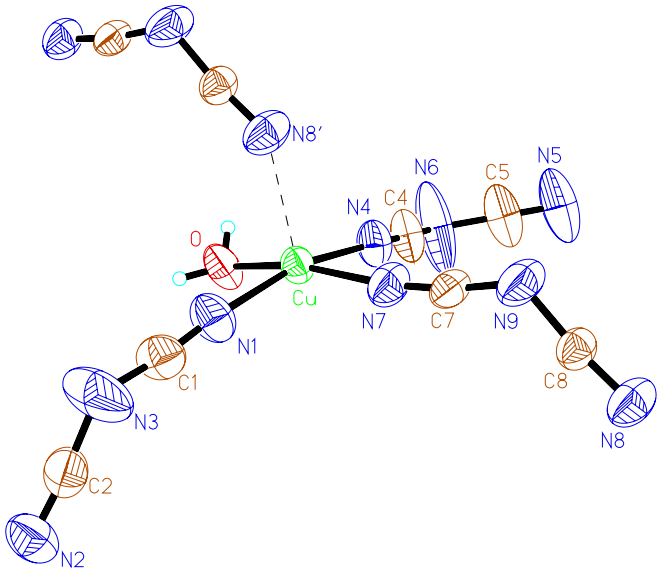


Fig. 1. Atomic numbering scheme of the $[Cu(dca)_3(H_2O)]^-$ anion in the $PPh_4[Cu(dca)_3(H_2O)]$ salt. Displacement ellipsoids are drawn at the 50% probability level.

respectively. Samples were cooled in zero magnetic field to the lowest temperature. As shown in Fig. S3, the magnetization was measured as a function of field up to 7 T at 2 K. The magnetizations approach the expected value of 5585 emu Oe/mol at 7 T. The dc field was then changed to 1 T, which is within the linear portion of the magnetization versus field curve, and the magnetization data were recorded upon warming. All magnetic data were corrected for core diamagnetism using Pascal's constants.

2.5. Fourier transform infrared spectroscopy (FTIR)

FTIR spectra were collected using a Bruker Vertex 70 spectrometer equipped with a mercury cadmium telluride (MCT) detector and a Pike ATR accessory.

3. Results

3.1. Crystal structures

The crystal structure of **1** was determined at room temperature (RT). As illustrated in Fig. 1, the coordination

Table 3
Selected bond lengths (Å) and angles (°) for **2**

	RT	150 K		RT	150 K
Bond lengths					
Cu–N(1)	1.959(2)	1.963(2)	C(2)–N(3)	1.296(3)	1.312(2)
Cu–N(11)[b]	1.991(2)	1.996(2)	C(11)–N(11)	1.137(2)	1.148(2)
Cu–N(12)	2.569(2)	2.504(2)	C(11)–N(13)	1.285(3)	1.298(2)
C(1)–N(1)	1.137(3)	1.143(2)	C(12)–N(12)	1.129(3)	1.149(2)
C(1)–N(3)	1.296(3)	1.301(2)	C(12)–N(13)	1.304(3)	1.310(2)
C(2)–N(2)	1.129(3)	1.144(2)			
Bond angles					
N(1)–Cu–N(1)[a]	180.0	180.0	N(2)–C(2)–N(3)	172.3(3)	172.8(2)
N(1)–Cu–N(11)[b]	89.19(7)	89.40(7)	C(1)–N(1)–Cu	173.23(17)	174.03(14)
N(11)[b]–Cu–N(11)[c]	180.0	180.0	C(2)–N(3)–C(1)	122.77(19)	121.86(16)
N(1)–Cu–N(12)[a]	88.93(7)	89.11(7)	N(11)–C(11)–N(13)	171.9(2)	172.0(2)
N(11)[b]–Cu–N(12)[a]	93.14(6)	92.64(7)	N(12)–C(12)–N(13)	174.0(2)	173.9(2)
N(1)–Cu–N(12)	91.07(7)	90.89(7)	C(11)–N(11)–Cu[d]	173.69(18)	175.36(15)
N(11)[b]–Cu–N(12)	86.86(6)	87.36(7)	C(12)–N(12)–Cu	135.84(17)	133.93(13)
N(12)[a]–Cu–N(12)	180.00(8)	180.00(7)	C(11)–N(13)–C(12)	123.5(2)	121.9(2)
N(1)–C(1)–N(3)	172.0(2)	172.4(2)			

[a] $-x+2, -y+2, -z$.
[b] $-x+2, -y+1, -z$.
[c] $x, y+1, z$.
[d] $x, y-1, z$.

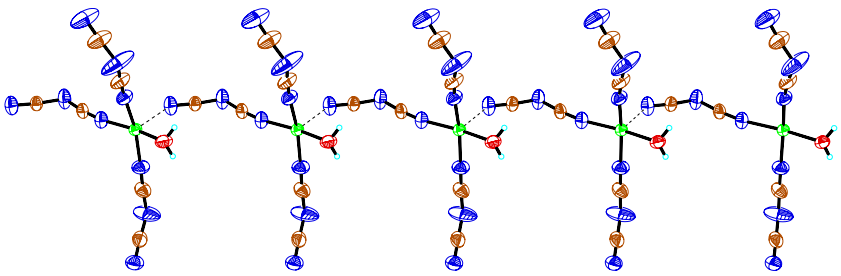


Fig. 2. The anionic one-dimensional chain motif in **1** lies parallel to the *a*-axis. Thermal ellipsoids are drawn at the 50% probability level.

geometry of the Cu^{2+} is distorted square pyramidal. The basal plane consists of three dicyanamide anions and one water molecule. These equatorial Cu–N bonds range from 1.961(3) to 1.984(3) Å, with the Cu–O bond length of 1.987(2) Å. A nitrile nitrogen atom of a bridging dca anion occupies the axial site with a Cu–N bond distance of 2.263(3) Å. Within the equatorial plane, the N–Cu–N′ bond angles are 91.94(12)°, 90.58(11)°, and 164.75(12)°, whereas the N–Cu–O bond angles are 90.39(11)°, 84.10(11)°, and 167.67(11)°. The N(8)–Cu–N/O bond angles involving the axial nitrogen atom range from 92.47(10)° to 99.26(10)°. The equatorial Cu–N–C bond angles are relatively linear, with angles ranging from 169.7(3)° to 172.3(3)°, while the axially coordinated ligand is considerably more bent, with a bond angle of 139.6(3)°. The average nitrile bond length is 1.132(7) Å, while the average amide bond length is 1.293(12) Å, indicating that these bonds have triple and single bond character, respectively. The average amide C–N–C bond angle is 123(2)°, which is typical for the dicyanamide anion. Due to thermal effects, there is clearly some 'wagging' of the dca ligands, as is evident in the elongated atomic displacement ellipsoids perpendicular to the ligand molecular plane at room temperature. This effect is especially noticeable in the amide nitrogen atoms of the mono-coordinated dca ligands.

As illustrated in Fig. 2, the $[Cu(dca)_3(H_2O)]^-$ anions form a one-dimensional chain along the *a*-axis. The Cu···Cu separation through the *cis* singly bridged $\mu_{1,5}$-dca chains corresponds to the *a*-axis length, which is 7.409(1) Å. This separation is significantly shorter than the 8.159(1)–8.352(1) Å intrachain separation in *trans* singly bridged $\mu_{1,5}$-dca chains in the previously reported $(PPh_4)_3Cu_4(dca)_{11}$ salt [16].

As illustrated in Fig. 3, the anionic $[Cu(dca)_3(H_2O)]^-$ chains are linked together through hydrogen bonding interactions to form two-dimensional sheets parallel to the *ac*-plane. Specifically, the two hydrogen atoms of the coordinated water molecule form hydrogen bonds to the two non-coordinated nitrile nitrogen atoms. The O–H(1)···N(5) distance is 2.727 Å and the angle 164.6°, while the O–H(2)···N(2) distance is 2.845 Å with an angle of 177.4°. The closest interchain Cu···Cu separations are 8.995(1) and 9.274(1) Å, while the closest interlayer Cu···Cu separations are 12.459(2) Å. It is noted that **1** crystallizes in the non-centrosymmetric space group $P2_1$, and all the coordinated water molecules lie on the same side of each anionic sheet.

The packing of the PPh_4^+ cations is shown in Fig. 4. As they are given by unit cell translations, the P···P separations mirror those of Cu···Cu: 7.409(1) Å along the *a*-axis cationic PPh_4^+ chain and interchain separations of 8.995(1) and 9.274(1) Å along the *c*-axis and *ac*-diagonal. It is likely that concerted phenyl embraces [32] are responsible for the templating effect for the anion.

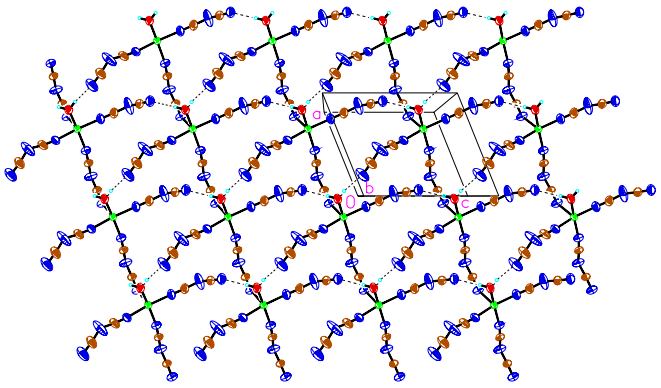


Fig. 3. The one-dimensional chains in **1** are linked into a two-dimensional sheet through hydrogen bonding interactions. These anionic sheets lie in the *ac*-plane. Atomic displacement ellipsoids are drawn at the 50% probability level.

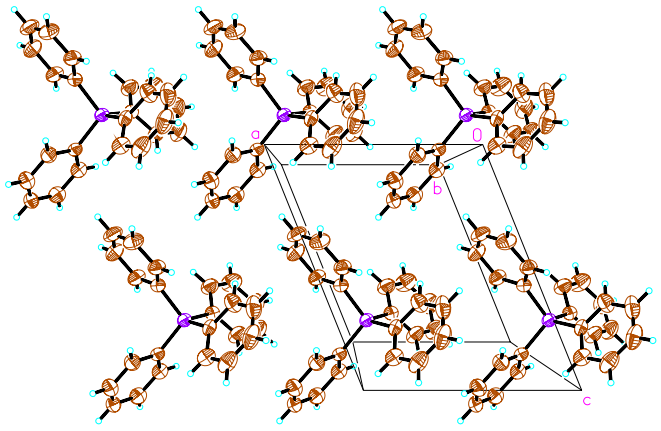


Fig. 4. One-dimensional chains of the PPh_4^+ cations in **1** lie along the *a*-axis. These chains are packed into a two-dimensional motif within the *ac*-plane. Atomic displacement ellipsoids are drawn at the 50% probability level.

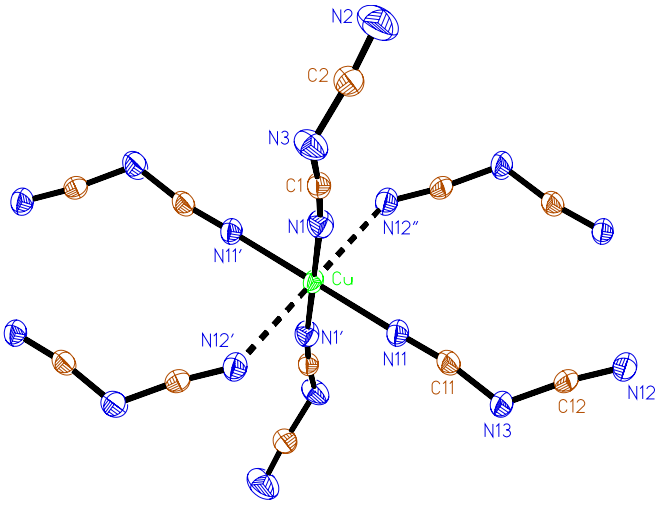


Fig. 5. Atomic numbering scheme of the $[Cu(dca)_4]^{2-}$ anion in the $(PPhBu)_2[Cu(dca)_4]$ salt at 150 K. Displacement ellipsoids are drawn at the 50% probability level.

The crystal structure of **2** was determined at both RT and 150 K. As illustrated in Fig. 5, the coordination geometry of the Cu^{2+} is a Jahn–Teller distorted octahedron with equatorial Cu–N bonds of 1.963(2) and 1.996(2) Å with the axial bond 2.504(2) Å at 150 K. At RT, the equatorial bonds shorten to 1.959(2) and 1.991(2) Å while the axial bond expands to 2.569(2) Å. This coordination geometry is similar to that observed in $Cu(dca)_2$, where the average equatorial distance is 1.975(1) Å and the average axial distance is 2.478(2) Å at 293 K [33]. The N–Cu–N′ bond angles are only slightly distorted from ideal, with the largest discrepancy being 93.14(6)° at RT and 92.64(7)° at 150 K. The equatorial Cu–N(1)–C(1) and Cu–N(11)–C(11) bond angles of 174.0(1)° and 175.4(2)° at 150 K [173.2(2)° and 173.7(2)° at RT] are only slightly non-linear, while the axial Cu–N(12)–C(12) bond angle of 133.9(2) at 150 K [135.8(2)° at RT] is significantly bent. The average cyanide and amide bond distances are both slightly longer at 150 K than RT: the C≡N bonds increase from 1.133(5) Å at RT to 1.146(3) Å at 150 K, while the C–N bonds increase from 1.295(5) to 1.305(7) Å upon cooling. This observation is likely due to foreshortening of the apparent interatomic distances compared to the true distances due to librational thermal motion at the higher temperature.

As illustrated in Fig. 6, the $[Cu(dca)_4]^{2-}$ anions form a one-dimensional chain along the *b*-axis. The Cu···Cu separation through the doubly bridged $\mu_{1,5}$-dca chains (corresponding to the *b*-axis length) is 7.526(1) Å at RT and contracts to 7.460(5) Å at 150 K. This separation is slightly longer than the 7.1911(4) Å intrachain separation for doubly bridged $\mu_{1,5}$-dca chains in the previously reported $(PPh_4)_3Cu_4(dca)_{11}$ salt [16]. The shortest interchain Cu···Cu separation of 12.399(1) Å shortens to 12.302(6) Å at 150 K.

The PPh_3Bu^+ cations are similarly packed into chains, as illustrated in Fig. 7. It is likely that concerted phenyl embraces [32] are responsible for the templating effect of this cation, which dictates a chain type packing motif for the anion. Note that the P···P separation is also equivalent to the *b*-axis length.

The cyano stretching region of the infrared spectra for **1** and **2** is compared to that of $PPh_4(dca)$ and $Cu(dca)_2$ in Fig. 8. As compared to the non-coordinated dca^- anion in the $PPh_4(dca)$ salt, the absorption bands are shifted to higher wavenumbers in the metal complexes. The bands below 2250 cm^{-1} have been assigned to $(\nu_{as})_{C\equiv N}$ and $(\nu_s)_{C\equiv N}$ modes, while those at higher wavenumbers have been assigned to $(\nu_{as}+\nu_s)_{C\equiv N}$ combination modes [6]. The spectra of **1** and **2** in this region are similar to the

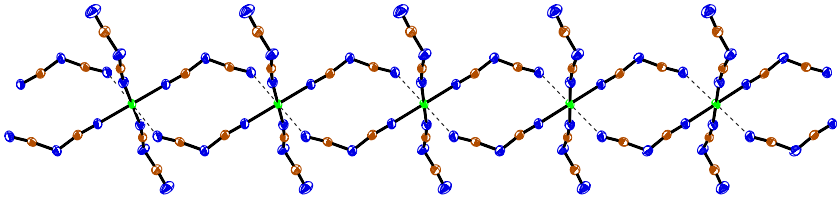


Fig. 6. The one-dimensional polymeric chain motif of the $[Cu(dca)_4]^{2-}$ anion in the $(PPh_3Bu)_2[Cu(dca)_4]$ salt at 150 K. Thermal ellipsoids are drawn at the 50% probability level.

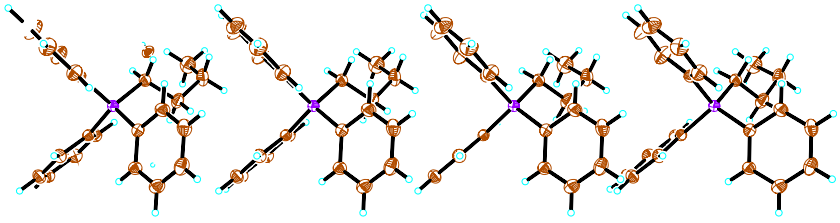


Fig. 7. The one-dimensional chain motif of the PPh_3Bu^+ cation in the $(PPh_3Bu)_2[Cu(dca)_4]$ salt at 150 K. The P···P separation coincides with the Cu···Cu separation in the anion layer, and is equivalent to the *b*-axis length. Atomic displacement ellipsoids are drawn at the 50% probability level.

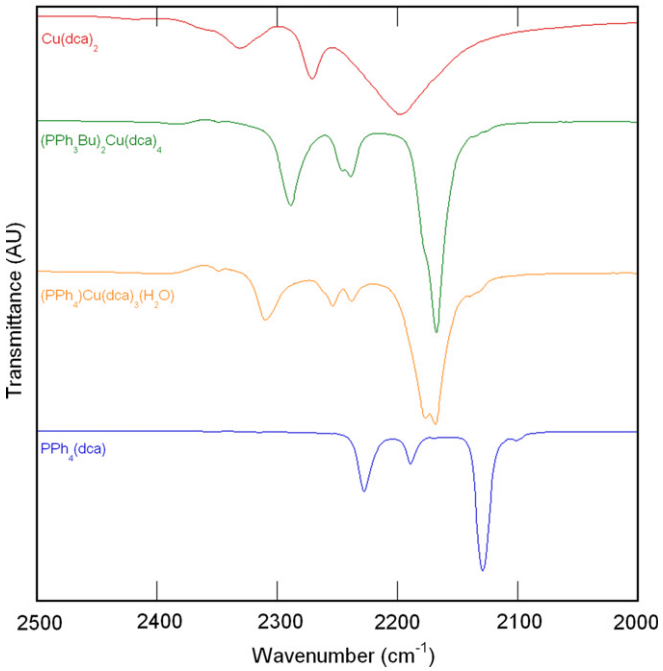


Fig. 8. Comparison of the cyano stretching region of the infrared spectrum of **1** and **2** as compared to the model compounds $Cu(dca)_2$ and $PPh_4(dca)$. Spectra are offset for clarity.

$(NR_4)[M(dca)_3]$ ($R = C_3H_7$, C_4H_9 and C_5H_{11}; M = Mn and Ni) salts [23].

3.2. Magnetic properties

The temperature-dependent magnetic susceptibility for **1** and **2** is illustrated in Fig. 9. From the data it can be seen that there is no maximum observed for either compound down to the lowest measured temperature suggesting the presence of only weak magnetic interactions. This is not surprising in that all of the reported Cu-dicyanamide compounds show negligible exchange along Cu–N≡C–N–C≡N–Cu pathways.

The magnetic data for **1** and **2** were fitted to the Curie–Weiss expression, $\chi = 0.125g^2S(S+1)/(T-\theta)$(emu/mol), yielding good agreement for $g = 2.123(1)$ and $\theta = -0.063(4)$ K and $g = 2.081(1)$ and $\theta = -0.063(5)$ K. The very small θ-values confirm the negligibly small interaction mediated by the dca ligands. Landé g-values expectedly exceed the free electron value of 2.0023 due to anisotropy of the g-tensor which is not a result of single-ion effects but rather due to the structural distortion of the Cu chromophores.

4. Discussion

It is often not appreciated how subtle changes in crystallization conditions can result in the formation of entirely different crystalline structures. We recently reported the synthesis of $(PPh_4)_3[Cu_4(dca)_{11}]$ [16], but had difficulty producing this material in pure form. To grow crystals of $(PPh_4)_3[Cu_4(dca)_{11}]$, ethanolic solutions of $(PPh_4)(dca)$ and $Cu(NO_3)_2 \cdot xH_2O$ were combined. Although small amounts of water were in the crystallization solution from the hydrated copper salt and exposure to atmospheric moisture, there was apparently not enough water present to preferentially crystallize the hydrated $(PPh_4)Cu(dca)_3H_2O$ complex **1** described in this paper. However, under the synthetic conditions reported in this paper, in which the $Cu(BF_4)_2 \cdot xH_2O$ was dissolved in water prior to mixing with an ethanolic solution of $(PPh_4)(dca)$, the hydrated phase crystallized in high purity. Ethanol has a higher vapor pressure than water, and thus the crystallization solution was mostly water when the $(PPh_4)Cu(dca)_3H_2O$ complex crystallized. We are confident that the crystalline material reported in this paper is of high purity, because no sign of impurities such as $(PPh_4)_3[Cu_4(dca)_{11}]$, $Cu(dca)_2$, or $(PPh_4)(dca)$ were observed in the X-ray powder diffraction pattern shown in Fig. 10.

Small differences in the coordination environment of the metal atom can entirely change the topology of the anion framework, even with the same templating cation. When EPh_4^+ (E = P and As) is used as a templating cation with the divalent first row transition elements Co(II), Mn(II), and Ni(II), the two-dimensional square lattice motif is commonly observed. A ladder structure has also been observed in the $(AsPh_4)_2[M_2(dca)_6(H_2O)] \cdot H_2O \cdot xCH_3OH$ (M = Co and Ni) salts, and a chain structure only for the cobalt derivative, $(PPh_4)_2Co(dca)_4$. Perhaps due to the Jahn–Teller distortion of the Cu^{2+} ion, these structural types have not yet been observed for that metal. Instead,

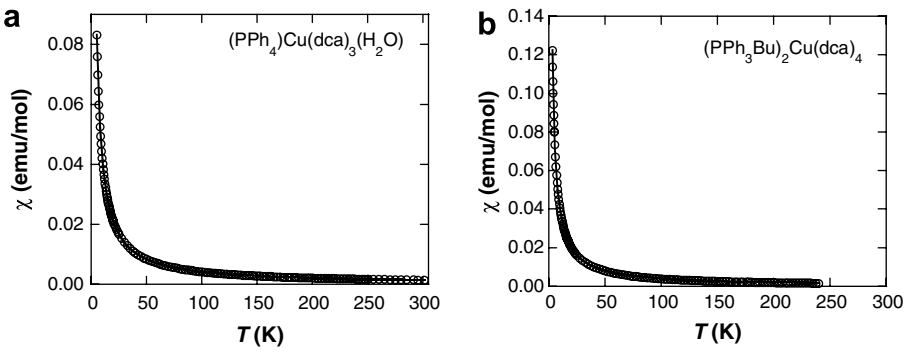


Fig. 9. Plots of the magnetic susceptibility (χ) vs. temperature (T) for **1** and **2**. Solid lines represent fits to the Curie–Weiss law as described in the text.

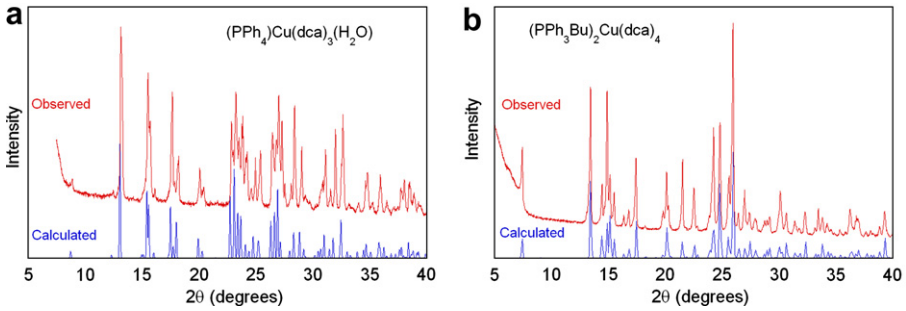


Fig. 10. The X-ray powder diffraction pattern of **1** (left) and **2** (right). The observed patterns (top) are compared to the calculated pattern (bottom).

two new anionic topologies have now been discovered in $(PPh)_3Cu_4(dca)_{11}$ and $PPh_4Cu(dca)_3H_2O$.

It has previously been shown that replacing one of the four phenyl groups of PPh_4^+ with methyl or ethyl results a breakdown of the lower dimensional lattice types and the formation of a three-dimensional distorted triple-rutile structural motif in the $(PPh_3R)M(dca)_3$ (R = Me and Et, M = Fe, Co, Ni and Mn) salts. The related $(NBzR_3)$-$M(dca)_3$ (R = Bu and Et; M = Mn, Co and Fe) structures, in which three of the phenyl groups have been replaced with small alkyl groups, also results in the formation of a three-dimensional structural motif: perovskite. We have also found three-dimensional structural motifs for the $[N(C_nH_{2n+1})_4]M(dca)_3$ salts ($n = 3$–5; M = Mn and Ni). It is interesting that no three-dimensional anionic structures of Cu^{+2} have yet been observed.

The $PPh_4Cu(dca)_3(H_2O)$ salt is chiral and crystallizes in a non-centrosymmetric space group. Such salts are of interest for possible non-linear optical behavior. Because the $Cu(dca)_3(H_2O)^-$ anion can crystallize in a non-centrosymmetric space group, it will be of interest to attempt to incorporate this anion into salts containing non-centrosymmetric cations with large β values which would enhance the non-linear optical properties.

5. Conclusion

Cationic templation often determines the anionic structural motif in dicyanomidometallate salts. These salts provide model compounds and precursor materials for the possible synthesis of hybrid materials that combine various properties such as magnetism, conductivity, non-linear optical behavior, etc. Among the dicyanamide salts, anionic coordination polymers containing divalent copper have rarely been studied. We have crystallized and magnetically characterized the $(PPh_4)Cu(dca)_3H_2O$ and $(PPh_3Bu)_2Cu(dca)_4$ salts. The former crystallizes in a chiral structure that contains singly bridged *cis* $\mu_{1,5}$-dca chains that are linked into a two-dimensional network through hydrogen bonding through coordinated water molecules. An entirely different structural motif, a triple ladder, forms when the crystallization occurs under anhydrous conditions. Replacement of one of the cation's phenyl groups with a butyl group results in the formation of the $(PPh_3Bu)_2Cu(dca)_4$ salt, which contains doubly bridged $\mu_{1,5}$-dca chains. Because the copper ions are bridged through long $\mu_{1,5}$-dca linkages, only negligibly weak magnetic interactions were observed in both compounds.

Acknowledgement

Work at Argonne National Laboratory was supported by the Office of Basic Energy Sciences, Division of Materials Science, US Department of Energy under Contract No. W-31-109-ENG-38.

Appendix A. Supplementary material

CCDC 618796, 618797 and 618798 contain the supplementary crystallographic data for this paper. These data can be obtained free of charge via http://www.ccdc.cam.ac.uk/conts/retrieving.html, or from the Cambridge Crystallographic Data Centre, 12 Union Road, Cambridge CB2 1EZ, UK; fax: (+44) 1223-336-033; or e-mail: deposit@ccdc.cam.ac.uk.

References

[1] J.S. Miller, J.L. Manson, Acc. Chem. Res. 34 (2001) 563.
[2] S.R. Batten, K.S. Murray, Coord. Chem. Rev. 246 (2003) 103.
[3] J.L. Manson, in: J.S. Miller, M. Drillon (Eds.), Magnetism: Molecules to Materials V, Wiley-VCH, Weinheim, 2005, p 71.
[4] J.L. Manson, C.R. Kmety, Q.Z. Huang, J.W. Lynn, G.M. Bendele, S. Pagola, P.W. Stephens, L.M. Liable-Sands, A.L. Rheingold, A.J. Epstein, J.S. Miller, Chem. Mater. 10 (1998) 2552.
[5] M. Kurmoo, C. Kepert, New J. Chem. 22 (1998) 1515.
[6] J.L. Manson, C.R. Kmety, A.J. Epstein, J.S. Miller, Inorg. Chem. 38 (1999) 2552.
[7] C.R. Kmety, Q. Huang, J.W. Lynn, R.W. Erwin, J.L. Manson, S. McCall, J.E. Crow, K.L. Stevenson, J.S. Miller, A.J. Epstein, Phys. Rev. B 62 (2000) 5576.
[8] J.L. Manson, C.R. Kmety, F. Palacio, A.J. Epstein, J.S. Miller, Chem. Mater. 13 (2001) 1068.
[9] S.R. Batten, P. Jensen, C.J. Kepert, M. Kurmoo, B. Moubaraki, K.S. Murray, D.J. Price, J. Chem. Soc., Dalton Trans. (1999) 2987.
[10] M. Kurmoo, C.J. Kepert, Mol. Cryst. Liq. Cryst. 334 (1999) 693.
[11] J.W. Raebiger, J.L. Manson, R.D. Sommer, U. Geiser, A.L. Rheingold, J.S. Miller, Inorg. Chem. 40 (2001) 2578.
[12] L. Jager, C. Wagner, M. Korabik, A. Zygmunt, J. Mrozinski, J. Mol. Struct. 570 (2001) 159.
[13] Z.M. Wang, B.W. Sun, J. Luo, S. Gao, C.S. Liao, C.H. Yan, Y. Li, Inorg. Chim. Acta 332 (2002) 127.

[14] P. van der Werff, S.R. Batten, P. Jensen, B. Moubaraki, K.S. Murray, E.H.K. Tan, Polyhedron 20 (2001) 1129.
[15] Z.-M. Wang, B.-W. Sun, J. Luo, S. Gao, C.-S. Liao, C.-H. Yan, Y. Li, Polyhedron 22 (2003) 433.
[16] J.A. Schlueter, J.L. Manson, U. Geiser, C.R. Chim. (2006), doi:10.1016/j.crci.2006.06.011.
[17] P. van der Werff, S.R. Batten, P. Jensen, B. Moubaraki, K.S. Murray, Inorg. Chem. 40 (2001) 1718.
[18] M. Biswas, S.R. Batten, P. Jensen, S. Mitra, Aust. J. Chem. 59 (2006) 115.
[19] S.R. Batten, P. Jensen, B. Moubaraki, K.S. Murray, J. Chem. Soc., Chem. Commun. (2000) 2331.
[20] J.A. Schlueter, U. Geiser, J.L. Manson, J. Phys. IV France 114 (2004) 475.
[21] M.L. Tong, J. Ru, Y.M. Wu, X.M. Chen, H.C. Chang, K. Mochizuki, S. Kitagawa, New J. Chem. 27 (2003) 779.
[22] J.A. Schlueter, J.L. Manson, K.A. Hyzer, U. Geiser, Inorg. Chem. 43 (2004) 4100.
[23] J.A. Schlueter, J.L. Manson, U. Geiser, Inorg. Chem. 44 (2005) 3194.
[24] P.M. van der Werff, E. Martinez-Ferrero, S.R. Batten, P. Jensen, C. Ruiz-Perez, M. Almeida, J.C. Waerenborgh, J.D. Cashion, B. Moubaraki, J.R. Galan-Mascaros, J.M. Martinez-Agudo, E. Coronado, K.S. Murray, Dalton Trans. (2005) 285.
[25] P. van der Werff, S.R. Batten, P. Jensen, B. Moubaraki, K.S. Murray, J.D. Cashion, Cryst. Growth Des. 4 (2004) 503.
[26] Y.A. Manskaya, K.V. Domasevich, V.R. Polyakov, V.N. Kokozei, O.Y. Vasil'eva, Russ. J. Gen. Chem. 69 (1999) 101.
[27] J.M. Williams, A.M. Kini, H.H. Wang, K.D. Carlson, U. Geiser, L.K. Montgomery, G.J. Pyrka, D.M. Watkins, J.M. Kommers, S.J. Boryschuk, A.V. Strieby Crouch, W.K. Kwok, J.E. Schirber, D.L. Overmyer, D. Jung, M.-H. Whangbo, Inorg. Chem. 29 (1990) 3272.
[28] A.M. Kini, U. Geiser, H.H. Wang, K.D. Carlson, J.M. Williams, W.K. Kwok, K.G. Vandervoort, J.E. Thompson, D.L. Stupka, D. Jung, M.-H. Whangbo, Inorg. Chem. 29 (1990) 2555.
[29] Version 6.28a ed., Bruker AXS, Inc., Madison, WI, USA, 2001.
[30] G.M. Sheldrick, Version 2.03a ed., Bruker AXS, Inc., Madison, WI, USA, 2001.
[31] G.M. Sheldrick, Version 6.12 ed., Bruker AXS Inc., Madison, WI, USA, 2001.
[32] M. Scudder, I. Dance, J. Chem. Soc., Dalton Trans. (1998) 3155.
[33] S.R. Batten, P. Jensen, B. Moubaraki, K.S. Murray, R. Robson, Chem. Commun. (1998) 439.

TEM grid. A representative image is shown in Fig. 1. In addition, selected area electron diffraction was compared to published powder X-ray diffraction patterns to confirm the structure (Fig. 2). Using Image J imaging software [19], the TEM images were analyzed to obtain the particle size distribution, and these data were fit to a log-normal distribution that yielded a characteristic diameter of 10 (±2) nm, Fig. 3.

To isolate particles, three volumes of acetone were added to the synthesis solution, which was centrifuged, and then further washed with acetone and dried under vacuum. Chemical analysis was obtained from a combination of CHN combustion analysis and ICP-MS. The formula was determined to be $Rb_{1.8}Co_4[Fe(CN)_6]_{3.2}$ and the ratio of PVP repeat unit to cobalt was found to be 55. The formula corresponds to a bulk composition known to show photoinduced magnetism [3]. The room temperature IR characterization of the sample of nanoparticles revealed one peak in the cyanide stretching region at 2124 cm^{-1}, and the result is consistent with a Fe^{II}–Co^{III} (ls) pair [4].

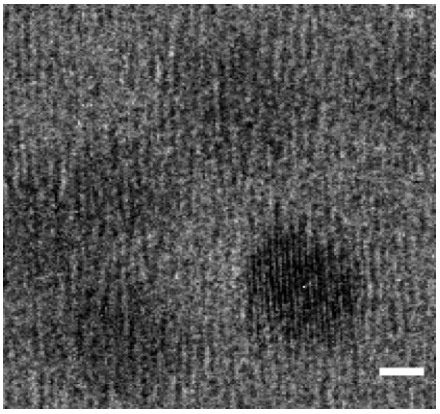


Fig. 1. HRTEM image of one Co–Fe Prussian blue nanoparticle. A 5 nm scale bar is shown.

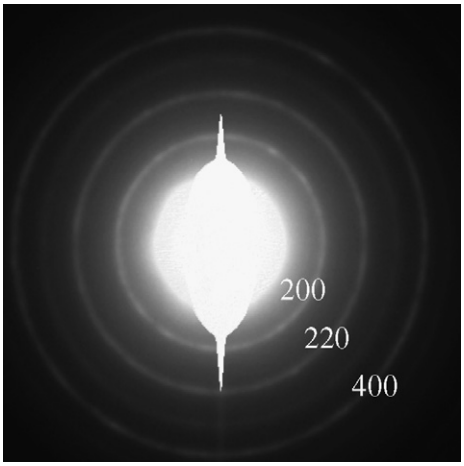


Fig. 2. Nanoparticle selected area electron diffraction pattern of a large agglomerate consisting of over 100 particles with the 200, 220 and 400 reflections identified.

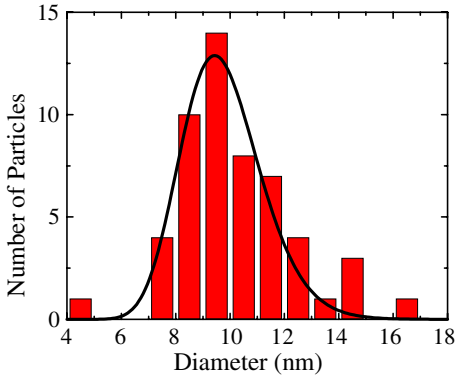


Fig. 3. Histogram of the nanoparticle size measured from HRTEM. The result of a log-normal fit is shown by the solid line.

3. Magnetic behavior

Samples were mounted to commercial transparent tape for magneto-optical measurements. A bundle of optical fibers, connected to a room temperature halogen light source, were introduced to the sample [20], and magnetic measurements were performed using a commercial SQUID magnetometer. The temperature dependent DC magnetic susceptibility of the particles in the light and dark states is shown in Fig. 4. Upon irradiation with light at 5 K, the nanoparticles show an increase in the field-cooled (FC) susceptibility. The difference between the FC susceptibilities of the light and dark states, i.e. $\Delta\chi$ plotted in the inset of Fig. 4, can only arise from the photoinduced magnetism. The nanoparticle FC magnetism increased by 40% when photoexcited at 5 K.

There is an increase in T_C from 15 K to 17 K and an increase in T_B (defined as the peak in ZFC magnetization) from 8 K to 10 K. Similar shifts are known for bulk

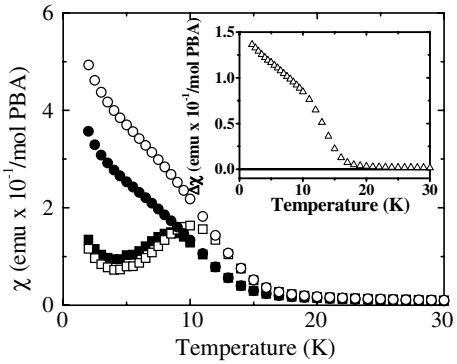


Fig. 4. Zero-field-cooled (ZFC) and field-cooled (FC) magnetic susceptibility versus temperature measured in a 100 G DC magnetic field for dark and light states. Dark state ZFC data (filled squares, ■) were obtained after cooling in zero applied field from 300 K, and dark state FC data (filled circles, ●) were taken after cooling in 100 G from 300 K. The light state was established after field cooling the samples from 300 K to 5 K in 100 G and subsequently illuminating with white light for 5 h. Light state FC data (open circles, ○) were obtained after cooling from 30 K in 100 G, and light state ZFC data (open squares, □) were taken after cooling from 30 K in zero applied field. The inset displays the difference between the light state FC data and dark state FC data.

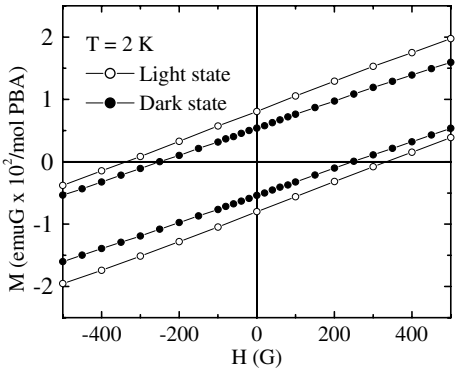


Fig. 5. Magnetization vs. field at 2 K. A coercive field of 250 G is present for the particles in the dark state (●) that increases to 330 G for the particles after 5 h of illumination (○).

material and are attributed to increased interaction lengths when the spins generated by the photoswitchable pairs increase the magnetic domain size.[1] There is a related increase in coercive field from 250 G in the dark state to 330 G in the light state (Fig. 5). The corresponding bulk material had a coercive field increase from 700 G to 1000 G.[1] The Co–Fe PBAs are characterized by glassy behavior that manifests itself in the DC data as a bifurcation in the FC and ZFC susceptibility plots below the blocking temperature. A similar response is observed for the nanoparticle sample (Fig. 4) in both light and dark states.

The data presented in Fig. 4 suggest that the nanoparticle sample possesses a distribution of particle sizes. This range of sizes leads to a distribution of transition temperatures, the highest being 15 K similar to the ferrimagnetic ordering temperature of the bulk, and is responsible for the gradual increase in susceptibility as the temperature is decreased. In contrast, the temperature dependence of the increase in the FC susceptibility weakens below T_B for bulk powder samples of the same formula [3]. In the nanoparticle sample with a range of particle diameters, smaller particles order at lower temperatures due to their restricted domain size. The particle size distribution is also reflected in the temperature dependent difference between FC light and dark susceptibilities, which increases with a steady slope as temperature is lowered.

4. Conclusion

Cobalt iron Prussian blue analogue nanoparticles have been synthesized and characterized. The nanoparticles have chemical formulas and structures consistent with the bulk material of the same composition. Analysis of TEM images shows the particles have an average size of 10 ± 2 nm. The ferrimagnetism observed in the bulk material is also seen in the nanoparticles, although the DC magnetization is altered by the reduced particle size and dispersion in particle diameter. Like the bulk, the nanoparticles are capable of exhibiting long-lived photoinduced magnetism. There is an effect of size on the magnetic behavior. A detailed study of the magnetic properties of nanoparticles of different sizes will be reported elsewhere.

Acknowledgements

This work was supported, in part, by NSF DMR-0305371 (MWM) and NSF DMR-0543362 (DRT). HRTEM image was obtained at the Major Analytical Instrumentation Center, Department of Materials Science and Engineering, University of Florida. ICP-MS measurements were conducted at the Department of Geology, University of Florida.

References

[1] O. Sato, T. Iyoda, A. Fujishima, K. Hashimoto, Science 272 (1996) 704.
[2] O. Sato, Y. Einaga, A. Fujishima, K. Hashimoto, Inorg. Chem. 38 (1999) 4405.
[3] A. Bleuzen, C. Lomenech, V. Escax, F. Villain, F. Varret, C. Cartier dit Moulin, M. Verdaguer, J. Am. Chem. Soc. 122 (2000) 6648.
[4] V. Escax, A. Bleuzen, C. Cartier dit Moulin, F. Villain, A. Goujon, F. Varret, M. Verdaguer, J. Am. Chem. Soc. 123 (2001) 12536.
[5] D. Pejaković, J. Manson, J. Miller, A. Epstein, Phys. Rev. Lett. 85 (2000) 1994.
[6] K. Yoshizawa, F. Mohri, G. Nuspl, T. Yamabe, Phys. Chem. B 102 (1998) 5432.
[7] T. Kawamoto, Y. Asai, S. Abe, Phys. Rev. Lett. 86 (2001) 348.
[8] N. Shimamoto, S. Ohkoshi, O. Sato, K. Hashimoto, Inorg. Chem. 41 (2002) 678.
[9] S. Gawali-Salunke, F. Varret, I. Maurin, C. Enachescu, M. Malarova, K. Boukheddanden, E. Codjovi, H. Tokoro, S. Ohkoshi, K. Hashimoto, J. Phys. Chem. B 109 (2005) 8251.
[10] M. Kamiya, M. Hananwa, Y. Moritomo, Y. Isobe, J. Tateishi, K. Kato, A. Nakamura, Phys. Rev. B 69 (2004) 052102.
[11] H. Liu, K. Matsuda, Z. Gu, K. Takahashi, A. Cui, R. Nakajima, A. Fujishima, O. Sato, Phys. Rev. Lett. 90 (2003) 167403.
[12] A. Bleuzen, V. Excax, A. Ferrier, F. Villain, M. Verdaguer, P. Munsch, J.-P. Itie, Angew. Chem. Int. Ed. 43 (2004) 3728.
[13] K. Boukheddanden, M. Nishino, S. Miyashita, F. Varret, Phys. Rev. B 72 (2005) 014467.
[14] S. Vaucher, J. Fielden, M. Li, E. Dujardin, S. Mann, NanoLetter 2 (2002) 225.
[15] M. Yamada, M. Arai, M. Kurihara, M. Sakamoto, M. Miyake, J. Am. Chem. Soc. 126 (2004) 9482.
[16] J.G. Moore, E.J. Lochner, C. Ramsey, N.S. Dalal, A.E. Stiegman, Angew. Chem. 115 (2003) 2847.
[17] T. Uemura, S. Kitagawa, J. Am. Chem. Soc 125 (2003) 7814.
[18] T. Uemura, M. Ohba, S. Kitagawa, Inorg. Chem. 43 (2004) 7339.
[19] ImageJ. http://rsb.info.nih.gov/ij/. Online available 09/08/2006.
[20] J.-H. Park, Ph.D. Thesis, University of Florida, 2006, unpublished.

[1] Unpublished results of Co–Fe PBA powder prepared without PVP using the same solution concentrations as the nanoparticles.

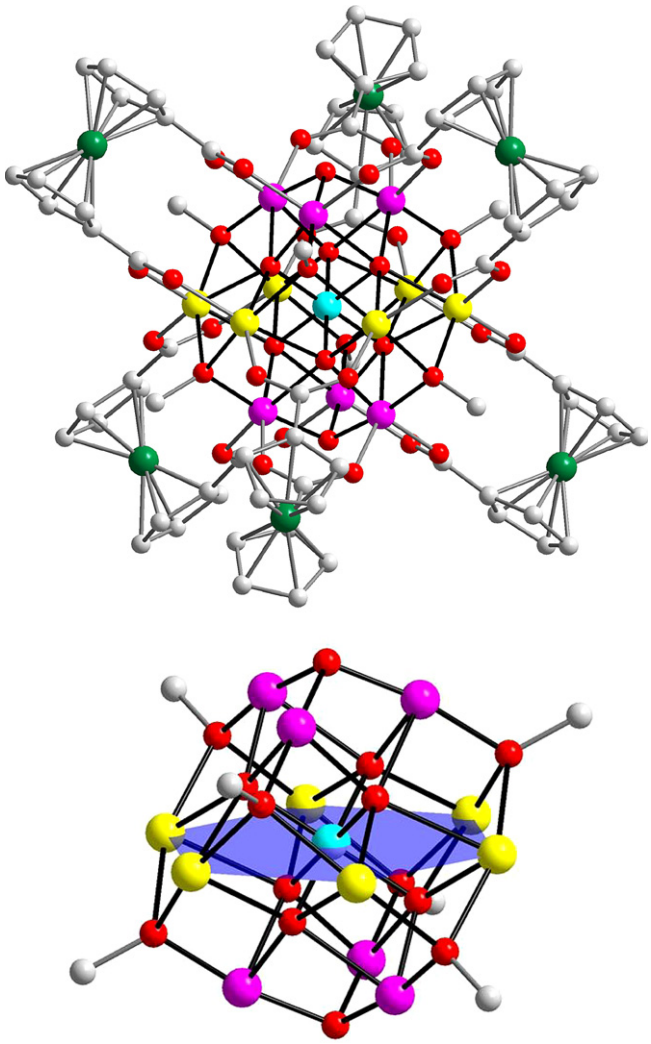


Fig. 1. Pov-Ray representation of **1** (top) and its core (bottom): Mn^{IV} (cyan), Mn^{III} (purple), Mn^{II} (yellow), O (red), Fe (green). Hydrogen atoms have been omitted for clarity. (For interpretation of the references to color in this figure legend, the reader is referred to the web version of this article.)

The reaction between $[Mn_{12}O_{12}(O_2CMe)_{16}(H_2O)_4]\cdot 2MeCOOH\cdot 4H_2O$ and $fdcH_2$ in a 1:4 molar ratio in CH_2Cl_2/MeOH (1:1) gave a dark brown suspension, which was filtered. The filtrate slowly forms dark brown needles of $[Mn_{13}O_8(OMe)_6(fdc)_6]\cdot 8CH_2Cl_2$ (**1** · $8CH_2Cl_2$) suitable for X-ray crystallography.[1] The same product resulted from reactions in different solvent mixtures such as MeCN/MeOH. The core can be described as consisting of three layers: there is a central layer comprising a Mn^{II}_6 hexagon with a central Mn^{IV} atom, and a Mn^{III}_3 triangular unit above and below this (Fig. 1). The core is held together by bridging O^{2-} and MeO^- groups, and the peripheral ligation is provided by six μ_4-fdc^{2-} groups. Complex **1** is a known compound, having been obtained previously by Horiba et al. using a different procedure [3], and the same Mn_{13} core has also been observed with benzoate ligation by Sun et al. [6]. We have also prepared the ethoxide analogue of **1** by repeating the reaction in CH_2Cl_2/EtOH, which gave $[Mn_{13}O_8(OEt)_6(fdc)_6]\cdot 7EtOH$ (**2** · 7EtOH). The complex was not structurally characterized by X-ray crystallography, but instead it was identified by the similarity of its IR spectrum and magnetic properties with those of **1**, and by its elemental analysis. The procedure to complex **2** is actually superior to that for **1** in that it gives a cleaner reaction and a higher yield of product. In particular, the crystallization solutions show no sign of minor side-products, as sometimes plagues the preparation of **1**.

The filtration residue from the reaction that gives **1** or **2** was treated with DMF resulting in a dark brown suspension. This was filtered and the filtrate left undisturbed to slowly yield dark brown needles of the novel complex $[Mn_8O_4(fdc)_6(DMF)_2(H_2O)_2]\cdot 4DMF\cdot 4H_2O$ (**3** · 4DMF · $4H_2O$) suitable for X-ray crystallography.[2] Complex **2** contains a core comprising a central $[Mn^{III}_4(\mu_4\text{-}O)_4]^{4+}$ cubane to each O^{2-} ion of which is attached a Mn^{II} atom (Fig. 2). The Mn_8 topology is thus two concentric Mn_4 tetrahedra. There are six fdc^{2-} groups, each carboxylate group of which bridges a Mn^{II}/Mn^{III} pair in the same *syn*, *syn* $\eta^1{:}\eta^1{:}\mu_2$-mode seen in **1**. The peripheral ligation is completed by a terminal DMF ligand on two of the Mn^{II} atoms, and a terminal H_2O ligand on the remaining two. As a result, the Mn^{III} and Mn^{II} atoms are six- and five-coordinate with near-octahedral and trigonal bipyramidal geometries, respectively. The metal oxidation states were again confirmed by charge considerations, bond valence sum (BVS) calculations [7,8], and the observation of Mn^{III} Jahn–Teller distortions. The torsion angles between the two carboxylate groups of the fdc^{2-} ligands vary: four fdc^{2-} groups have torsion angles of $<30°$ (synperiplanar configuration) and the other two have angles between 30° and 90° (synclinal configuration) [9].

Since $fdcH_2$ had given two interesting complexes from its reactions with $[Mn_{12}O_{12}(O_2CMe)_{16}(H_2O)_4]\cdot 2MeCOOH\cdot 4H_2O$, we also explored other reactions with various Mn^{II} starting materials. The reaction of $Mn(ClO_4)_2\cdot 6H_2O$ and $fdcH_2$ in a 1:1 molar ratio in DMF/MeOH (ratio 1:1) formed an orange suspension. This was filtered and the filtrate layered with Et_2O. Dark brown crystals of $[Mn_7O_3(OMe)(fdc)_6(H_2O)_3]\cdot 3DMF\cdot 3MeOH$ (**4** · 3DMF · 3MeOH) slowly grew as hexagonal plates that were suitable for X-ray crystallography.[3] The structure of **4** is somewhat

[1] *Crystal data for* **1** · $8CH_2Cl_2$: $C_{86}H_{82}Cl_{16}Mn_{13}Fe_6O_{38}$, $M_r = 3340.10$, triclinic, $P\bar{1}$, $a = 14.1308(12)$ Å, $b = 15.1738(12)$ Å, $c = 15.3656(13)$ Å, $\alpha = 119.4700(10)°$, $\beta = 91.4320(10)°$, $\gamma = 100.339(2)°$, $V = 2797.0(4)$ Å^3, $Z = 1$, $T = 173(2)$ K, $R_1 = 0.0479$, $wR_2 = 0.1190$ (F^2 all data), 18 432 reflections.

[2] *Crystal data for* **3** · 4DMF · $4H_2O$: $C_{90}H_{102}N_6Mn_8Fe_6O_{40}$, $M_r = 2682.40$, monoclinic, $C2/c$, $a = 23.282(3)$, $b = 19.331(3)$, $c = 22.198(3)$ Å, $\alpha = 90°$, $\beta = 97.885(3)°$, $\gamma = 90°$, $V = 9896(3)$ Å^3, $Z = 4$, $T = 173(2)$ K, $R_1 = 0.0934$, $wR_2 = 0.1117$ (F^2 all data), 32 126 reflections.

[3] *Crystal data for* **4** · 6MeOH: $C_{85}H_{90}N_3Mn_7Fe_6O_{37}$, $M_r = 2465.30$, rhombohedral, $R3$, $a = 15.8534(6)$, $b = 15.8534(6)$, $c = 64.090(5)$ Å, $\alpha = 90°$, $\beta = 90°$, $\gamma = 120°$, $V = 13949(13)$ Å^3, $Z = 6$, $T = 173(2)$ K, $R_1 = 0.0566$, $wR_2 = 0.1016$ (F^2 all data), 21 258 reflections.

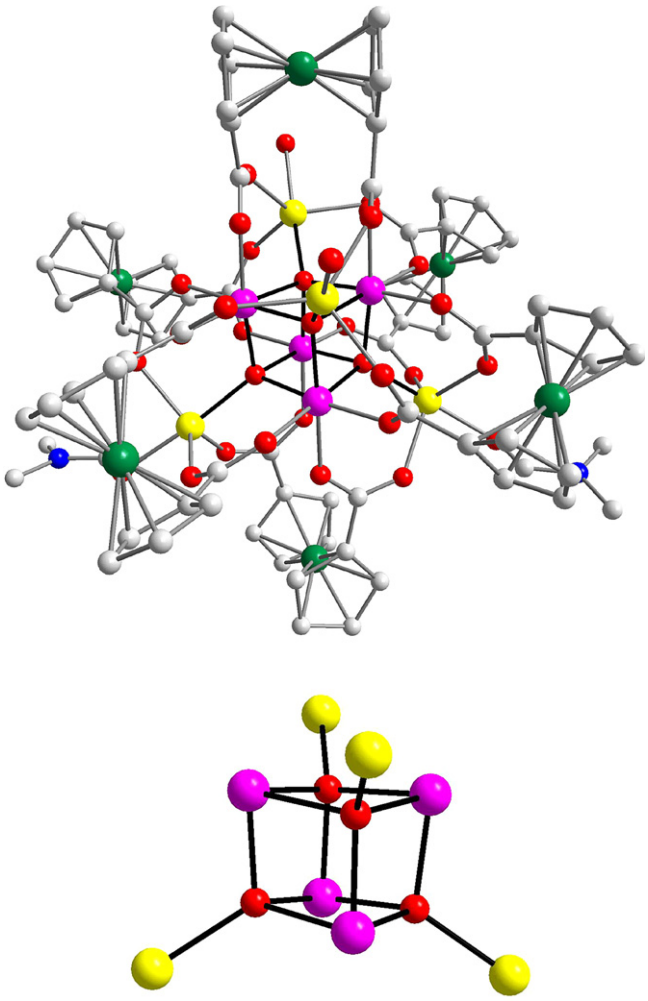


Fig. 2. Pov-Ray representation of **3** (top) and its core (bottom): Mn^{III} (purple), Mn^{II} (yellow), O (red), N (blue), Fe (green). Hydrogen atoms have been omitted for clarity. (For interpretation of the references to color in this figure legend, the reader is referred to the web version of this article.)

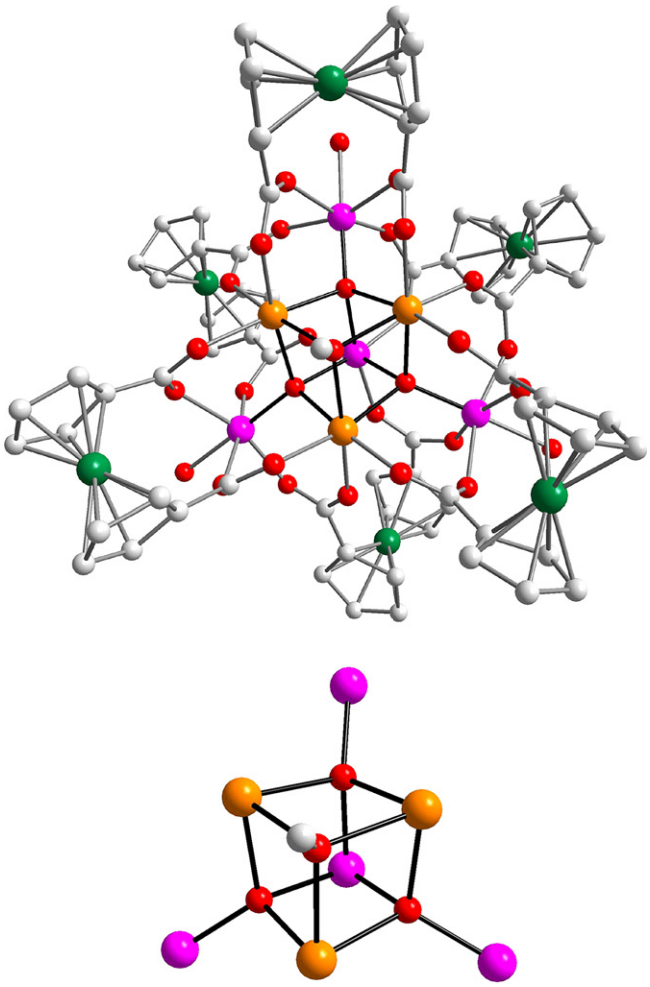


Fig. 3. Pov-Ray representation of complex **4** (top) and its core (bottom). Mn^{III} (purple), disordered $2Mn^{II}$ plus Mn^{III} (orange), O (red), Fe (green). Hydrogen atoms have been omitted for clarity. (For interpretation of the references to color in this figure legend, the reader is referred to the web version of this article.)

similar to that of **3** in that there is a central Mn_4O_4 cubane, but one of the O atoms is now part of a MeO^- group, rather than an O^{2-} ion, and thus there are only a total of three additional Mn atoms, each attached to one of the three O^{2-} ions of the central cubane (Fig. 3). The overall $[Mn_7(\mu_4\text{-}O)_3(\mu_3\text{-}OMe)]$ core is unprecedented.

The Mn oxidation states of **4** are not analogous to those in **3**, and this represents another major difference between the two structures. The oxidation states have been probed by BVS calculations, and the results were overall consistent with charge balance considerations based on the electroneutrality of the complex, and assuming none of the ferrocene groups are in the oxidized form, but with a few uncertainties in the precise details. The following preliminary conclusions have been reached: the three exterior Mn atoms attached to the cubane are all clearly Mn^{III}. The three Mn atoms in the central cubane core bridged by the MeO^- group are related by the crystallographic C_3-axis and thus give the same BVS value, which is characteristic of an average oxidation state less than 2.5+. We thus conclude that these three Mn atoms comprise one Mn^{III} and two Mn^{II} that are statically disordered by the symmetry axis. In other words, their Mn–O bond lengths are in-between those typical for true Mn^{III}–O and Mn^{II}–O bonds. The remaining Mn atom in the cubane and diagonally opposite the MeO^- group (Fig. 3) was expected, on the basis of charge neutrality, to be Mn^{III} but had a BVS lower than expected, and we believe this may be due to a Mn^{III}/ferrocene versus Mn^{II}/ferrocenium static disorder, i.e. one of the ferrocenes may be oxidized. At this time, we cannot unequivocally conclude anything more definite, but this point is currently under further investigation and will be discussed in more detail in the full paper.

There are again six fdc^{2-} groups providing the peripheral ligation about the core, which can be divided into two sets with equivalent torsion angles and binding modes within each set. In fact, this is the first case in this work where we have seen the fdc^{2-} groups to adopt different binding conformations, and no doubt this is due to the

lower symmetry of **4** compared to **1** and **3**. The three Mn^{III} atoms outside the cubane define a plane that divides the two sets of fdc^{2-} groups; the set lying on the opposite to the methoxide has the same kind of binding mode as in **1** and **3**, i.e. each fdc^{2-} attaches to a total of four Mn atoms in an $\eta^1{:}\eta^1{:}\eta^1{:}\eta^1{:}\mu_4$ bridging mode with a torsion angle of 6.48°. In contrast, the other set of fdc^{2-} groups bind to a total of three Mn atoms in an $\eta^1{:}\eta^1{:}\eta^1{:}\eta^1{:}\mu_3$-mode with a torsion angle of 26.67°. Thus, each carboxylate O atom is still attached to only a single Mn atom, but two of them are now attached to the same Mn^{III} atom, the one external to the cubane. Finally, there is a terminal H_2O group bound to each external Mn^{III} atom, and all Mn atoms are consequently six-coordinate with near-octahedral geometries.

Magnetic susceptibility (χ_M) data were collected for complexes **1**–**4** on polycrystalline samples in a 0.1 T DC field in the 5.00–300.00 K temperature range. The data for **1** and **2** were essentially superimposable, and thus we report here only the data for complexes **2**, **3** and **4** (Fig. 4). $\chi_M T$ for **2** is almost constant at ~47 cm^3 K mol^{-1} from 300 to 150 K and then decreases steadily to 11.54 cm^3 K mol^{-1} at 5.00 K. This suggests the presence of dominant antiferromagnetic exchange interactions within the cluster. $\chi_M T$ for **3** remains almost constant with decreasing temperature, with a value close to ~15 cm^3 K mol^{-1} for the entire temperature range. It fluctuates with decreasing temperature before reaching a value of 13.64 cm^3 K mol^{-1} at 5.00 K. $\chi_M T$ for **4** decreases steadily from 12.00 cm^3 K mol^{-1} at 300 K to 2.43 cm^3 K mol^{-1} at 5.00 K, again indicating dominant antiferromagnetic interactions within the molecule.

Complexes **2**, **3** and **4** are too large and/or too low symmetry for easy determination of the various pairwise exchange parameters J_{ij} between two Mn atoms Mn_i and Mn_j, and we therefore concentrated instead on determining their ground state spin (S) values. This was carried out by two independent methods, fitting of their variable-temperature (T) and -field (H) DC magnetization data, and AC susceptibility measurements. DC magnetization (M) data were collected in the 1.8–10.0 K range in fields varying between 0.1 and 7 T, and fit to a model that assumes only the ground state is populated, includes axial zero-field splitting ($\widehat{S}_z^2 D$) and the Zeeman interaction ($g\mu_B\mu_0\widehat{S}\cdot H$), and incorporates a full powder average. The obtained best-fit S, g and D values for complexes **2**–**4** are listed in Table 1. In order to avoid complications from low-lying excited states, data collected in very high DC fields were not employed. For **2** and **4**, we could only get good fits by using data collected only in fields up to 0.8 T. For **3**, data up to higher field values could be employed.

The ground state S values for **2**–**4** were confirmed by AC susceptibility measurements in the temperature range 1.8–15 K using a 3.5 G AC field oscillating at a frequency of 50, 250 and 997 Hz. AC susceptibility studies are performed in the absence of a DC field and therefore avoid the problems caused by low-lying excited states. The real, or in-phase, AC susceptibility (χ'_M) of complexes **2**–**4** is plotted as $\chi'_M T$ versus T in Fig. 5. Extrapolation of the plots to 0 K, from temperatures above ~4 K to avoid the effects of weak intermolecular interactions (dipolar and superexchange), gives values of ~11, ~13 and ~2.5 cm^3

Table 1
The g and D values obtained from fits of magnetization data for complexes **2**–**4**

Complex	Fields (T)	S	g[a]	D (cm^{-1})[b]
2	0.1–0.8	9/2	1.91	−0.23
3	0.1–4	5	1.97	−0.32
4	0.1–0.8	2	1.81	−0.93

[a] ±0.01.
[b] ±0.05 cm^{-1}.

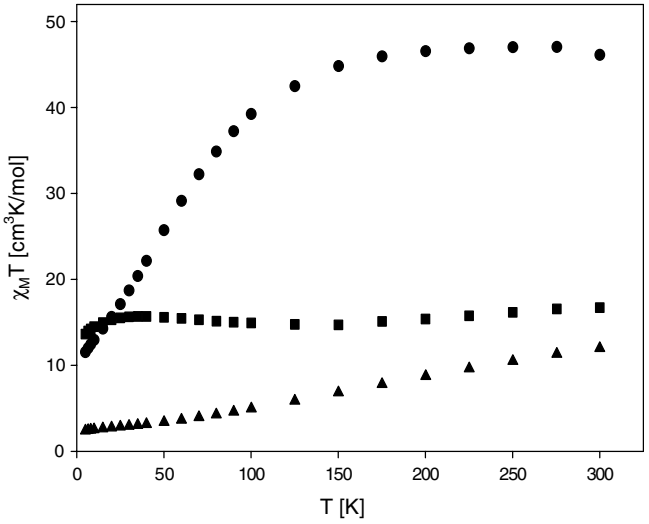


Fig. 4. Plot of $\chi_M T$ vs. T for complexes **2** (●), **3** (■) and **4** (▲).

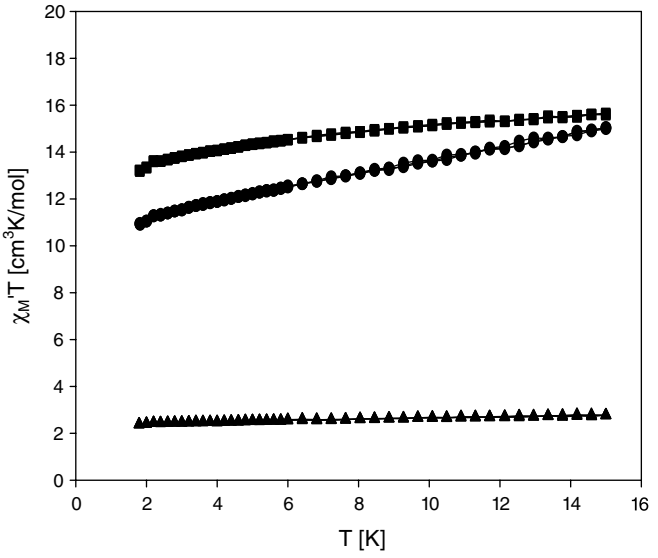


Fig. 5. Plot of $\chi'_M T$ vs. T for complexes **2** (●), **3** (■) and **4** (▲); the signals at 50, 250 and 997 Hz are essentially superimposed.

K mol^{-1}, confirming ground state S values of 9/2, 5 and 2, respectively (with $g < 2$, as expected for Mn), in satisfying agreement with the DC magnetization fits. None of the complexes displayed out-of-phase (χ''_M) AC susceptibility peaks above 1.8 K, the operating limit of our SQUID magnetometer. There were some signs of the beginnings of signals whose peaks lie below 1.8 K, and these may correspond to the very small dips in the $\chi'_M T$ plots of Fig. 5 at $T < 2$ K. Studies at temperatures below 1.8 K are in progress to explore this point further.

In summary, the use of $fdcH_2$ in Mn cluster chemistry has led to an interesting family of ferrocene-rich Mn_7, Mn_8 and Mn_{13} complexes. The latter two were obtained by a carboxylate substitution reaction on $[Mn_{12}O_{12}(O_2CMe)_{16}(H_2O)_4] \cdot 2MeCOOH \cdot 4H_2O$, which caused structural changes to the core. Although the core of Mn_{13} has been seen before, the present work has provided both a convenient synthetic route and also a means to prepare the previously unknown ethoxide analogue. All three structural types possess non-zero ground state spin values, although they do not seem to be new examples of single-molecule magnets, at least based on data collected at >1.8 K. The described work represents the desired synthetic breakthrough into this area of ferrocene-rich Mn clusters, and work is currently in progress to investigate the electrochemical properties of these clusters. Indeed, preliminary results on **4**, the easiest to study because of its high solubility, show rich redox behavior with multiple reversible processes.

Acknowledgement

We thank the National Science Foundation for supporting this work.

Appendix A. Supplementary material

CCDC 622659, 622660 and 622661 contain the supplementary crystallographic data for this paper. These data can be obtained free of charge via http://www.ccdc.cam.ac.uk/conts/retrieving.html, or from the Cambridge Crystallographic Data Centre, 12 Union Road, Cambridge CB2 1EZ, UK; fax: (+44) 1223-336-033; or e-mail: deposit@ccdc.cam.ac.uk. Supplementary data associated with this article can be found, in the online version, at doi:10.1016/j.poly.2006.11.014.

References

[1] (a) D.M. Kurtz, Chem. Rev. 90 (1990) 585;
(b) E.J.M. Hensen, J.A.R. van Veen, Catal. Today 86 (2003) 87.
[2] (a) For reviews, see: G. Christou, D. Gatteschi, D.N. Hendrickson, R. Sessoli, MRS Bull. 25 (2000) 66;
(b) G. Aromi, E.K. Brechin, Struct. Bond. 122 (2006) 1;
(c) R. Bircher, G. Chaboussant, C. Dobe, H.U. Güdel, S.T. Oshsenbein, A. Sieber, O. Waldmann, Adv. Funct. Mater. 16 (2006) 209;
(d) D. Gatteschi, R. Sessoli, Angew. Chem., Int. Ed. 42 (2003) 268.
[3] M. Kondo, R. Shinagawa, M. Miyazawa, M. Kabir, Y. Irie, T. Horiba, T. Naito, K. Maeda, S. Utsuno, F. Uchida, Dalton Trans. (2003) 515.
[4] (a) J.A. Mata, E. Peris, R. Llusar, S. Uriel, M.P. Cifuentes, M.G. Humphrey, M. Samoc, B. Luter-Davies, Eur. J. Inorg. Chem. (2001) 2113;
(b) U. Löffler, W. Göpel, B. Speiser, Electroanalysis 3 (9) (1991) 917.
[5] M. Soler, W. Wernsdorfer, K.A. Abboud, J.C. Huffman, E.R. Davidson, D.N. Hendrickson, G. Christou, J. Am. Chem. Soc. 135 (2003) 3576.
[6] Z. Sun, P. Gantzel, D. Hendrickson, Inorg. Chem. 35 (1996) 6640.
[7] I.D. Brown, D. Altermatt, Acta Crystallogr. B41 (1985) 244.
[8] W. Liu, H.H. Thorp, Inorg. Chem. 32 (1993) 4102.
[9] IUPAC, Compendium of Chemical Terminology, 2nd ed., 1997.

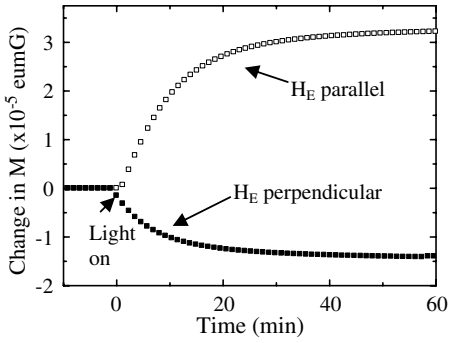


Fig. 1. Anisotropy in the photoinduced magnetism of a 75 nm film of Co–Fe PBA, measured at 5 K with the measuring field of 200 G oriented parallel (□) and perpendicular (■) to the film.

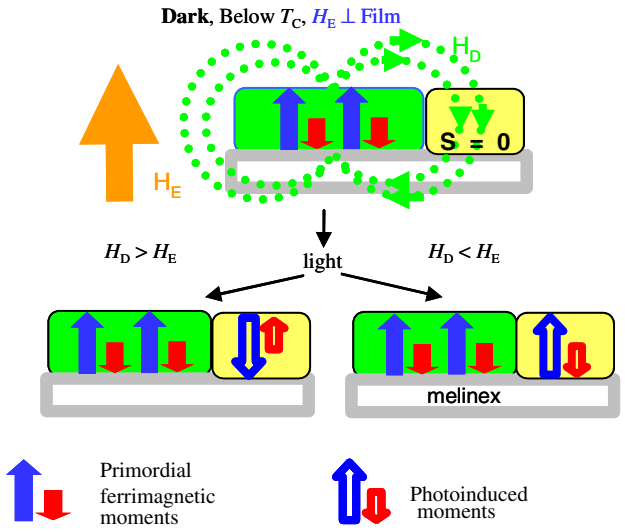


Fig. 2. The photoinduced magnetism in a quasi-two-dimensional film of Co–Fe PBA. The direction of the induced moments will depend on the vector sum of the dipolar field (H_D) from the primordial moments and the applied magnetic field (H_E).

nature of the thin film. If correct, then the anisotropic response should be influenced by the film thickness. In order to investigate this conjecture, a method of generating continuous, thickness-controlled films of the Co–Fe PBA is needed. This fabrication protocol would allow the generation of progressively thicker films possessing an evolution of photomagnetic behavior.

Methods of generating Prussian blue films and their analogues include electrochemical methods [17–23], which are the most common, dip-coating or spin casting of colloidal solutions [20,24], adsorption onto sol–gel films [25,26], adsorption at Langmuir monolayers [27–34], and multiple sequential adsorptions (MSA) [14–16,35–39] at modified surfaces. The MSA method offers the advantages of homogeneous film generation, availability of different substrates, fine thickness control, and the ability to easily tailor the composition of the generated film. We have adapted the MSA methods to prepared photoactive Co–Fe PBA thin films possessing a range of thickness. In this article, we investigate the influence of film thickness on the anisotropic photoinduced magnetism in Co–Fe PBA thin films. Whereas thinner films (<~200 nm) show the anisotropic behavior previously reported, we show here that the magnitude of the photoinduced decrease diminishes as the film thickness increases until the film behaves like the three-dimensional powder with a photoinduced increase in magnetism in all orientations.

2. Experimental

2.1. Sample preparation of $Rb_{0.7}Co_4[Fe(CN)_6]_{3.0} \cdot nH_2O$ thin films

Method 1, fast growth [15]. A hydrophilic solid support such as silicon or Melinex® was used as a substrate. The substrate was quickly immersed five times in a 5 mM aqueous solution of cobalt(II) nitrate over 3 s. The excess solution was drained and the substrate was quickly immersed five times in an aqueous solution of 20 mM potassium ferricyanide and 12.5 mM rubidium nitrate over 3 s. The substrate was then rinsed with deionized water for 5 s. This process was repeated 1, 5, 10, 20 or 40 times to generate films increasing in thickness (Films 1a–e). After deposition, the film was rinsed with methanol and dried under vacuum.

Method 2, slow growth [37]. A sheet of Melinex® was placed in a 5 mM aqueous solution of cobalt nitrate for 60 s. The film was rinsed with DI water for 10 s then rinsed with methanol for 2 s and dried with a stream of N_2. The film was then placed in a solution containing 20 mM potassium ferricyanide and 0.125 mM rubidium nitrate for 60 s. The film was rinsed with DI water for 10 s then rinsed with methanol for 2 s and dried with a stream of N_2 to complete one cycle. The process was repeated for 5, 10, 20, 40, and 75 cycles (Films 2a–e) to generate films of varied thickness.

2.2. Instrumentation

The elemental analyses were performed by inductively coupled plasma mass spectrometry (ICP-MS) on a Thermo-Finnigan Element-2 spectrometer. FTIR spectra were recorded using a Bruker Vector 22 spectrometer. Atomic force microscopy (AFM) measurements were performed using a Digital Instruments multimode scanning probe microscope. Scanning electron microscopy (SEM) images were obtained using a Hitachi S-4000 FE-SEM. Magnetic measurements were made using a Quantum design MPMS XL superconducting quantum interference device (SQUID) magnetometer. A bundle of 10 optical fibers, 270 μm OD (Ocean Optics Model 200), was used to introduce a room temperature halogen light source of 1–2 mW power into the SQUID magnetometer.

2.3. Analysis preparations

Solid supports were cut to 8 cm × 2.5 cm and cleaned. Silicon wafers, used for transmission FT-IR experiments,

were cleaned using the RCA procedure [40] and 20 cycles of material using Method 1 was deposited. Melinex® 535/380 gauge obtained from DuPont Teijin films was cleaned using methanol and used for all other processes. ICP-MS samples of the 40 cycle films from both methods were prepared by digesting the film and substrate in 2 mL of 100 °C concentrated sulfuric acid for 4 h, resulting in a black liquid. Concentrated nitric acid (0.5 mL) was then added dropwise, before diluting the mixture to 100 mL with DI water. The samples were compared to matrix matched metal blends between 1 ppm and 1 ppb. For magnetic measurements the samples were cut into squares $\sim$10.5 mm^2 and stacked, with the surfaces parallel, into a polycarbonate sample holder. Background contributions of the container and Melinex were measured separately and subtracted from the signals obtained from the samples.

3. Results and discussion

3.1. Film generation and characterization

As described in the preceding section, the solid support was first immersed in a solution containing Co^{II} ions followed by immersion in a solution containing Rb^+ and $[Fe(CN)_6]^{-3}$. For Method 1, substrates were immersed in both solutions before rinsing, resulting in a film that developed quickly. In Method 2, the substrate was rinsed between changing solutions, limiting the amount of material deposited during each cycle. Thickness and roughness data were obtained by averaging the measurements of five different 4 μm^2 AFM scans. Both methods display a linear increase of thickness with number of cycles (Fig. 3). Although the slow growth Method 2 affords finer control of the film thickness, the roughness of films generated by the two methods are comparable at similar thickness, as indicated in Table 1.

The homogeneity of the films prepared by each method can be compared by SEM, Figs. 4 and 5. After only one cycle of Method 1 (Fig. 4a) the substrate is still visible, indicating that uniform coverage is not yet achieved. After 5 cycles, Film 1b, the substrate is completely covered with

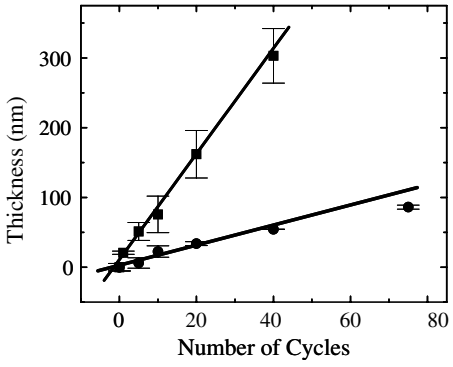


Fig. 3. Thickness vs. number of cycles for the fast growth, Method 1 (■), and slow growth, Method 2 (●), using multiple sequential adsorption deposition to generate thin films of the Co–Fe PBA.

Table 1
Thickness and roughness data for MSA films of Co–Fe PBA

Film	Number of cycles	Thickness (nm)	RMS roughness (nm)
Fast growth			
1a	1	21 ± 3.2	11
1b	5	51 ± 7.5	17
1c	10	75 ± 21	23
1d	20	160 ± 29	62
1e	40	300 ± 34	100
Slow growth			
2a	5	6.1 ± 2.1	2.0
2b	10	22 ± 2.7	8.8
2c	20	34 ± 2.7	12
2d	40	71 ± 14	22
2e	75	86 ± 2.6	37

powder-like features. The surface morphology is retained as the film develops beyond 5 cycles (Fig. 4). Films generated using Method 2 deposit more slowly. The average thickness of a 20 cycle Film 2 is 34 nm in contrast to the 20 cycle film from Method 1 which has an average thickness of 160 nm. The SEM images for Method 2 confirm the slower deposition rate (Fig. 5). Complete coverage is not obtained until 20 cycles, at which point the films show similar morphology to those generated using Method 1. After 75 cycles of Method 2 the morphology changes with larger blocks taking form.

All films are a light pink with uniform coloration over the surface of the substrate. The room temperature IR spectra of a 20 cycle fast growth film (Fig. 6) shows two peaks in the cyanide stretching range, a sharp peak at 2169 cm^{-1} attributed to the Fe^{III}–Co^{II}(hs) bridging cyanide and a broad peak centered at 2103 cm^{-1} that is attributed to the Fe^{II}–Co^{II}(hs) bridging cyanide stretch. The energy of these stretches agrees with previously reported powder samples [2].

3.2. Magnetic behavior of Films 1b–e

The photomagnetic response of four films, 1b–e, with nominal thicknesses of 51, 75, 160 and 300 nm were measured at $T = 5$ K using dc magnetometry with $H_E =$ 200 G applied perpendicular to the plane of the films, Fig. 7. Only Method 1 films are described because we were interested in monitoring changes in behavior as a function of film thickness, and significant changes were only realized for thicker films. The 51, 75, and 160 nm thick films all show a decrease in magnetization upon illumination. The magnitude of the effect (not corrected for the film thickness) increases as the thickness increases from 51 to 75 nm, but then diminishes for the 160 nm thick film. For the 300 nm film, illumination increases the magnetization, as is known for bulk samples.

The magnetic behavior confirms that the thin-film geometry is necessary to observe the photoinduced decrease in magnetization. The result is consistent with the proposed mechanism whereby the photoswitchable

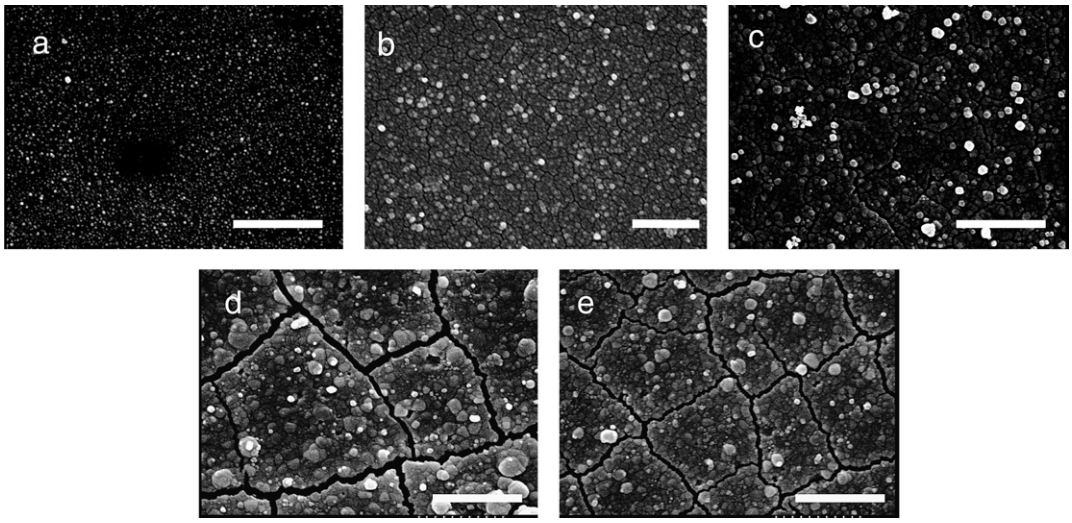


Fig. 4. SEM images of Method 1 Films, 1a–e, with thicknesses of 21, 51, 75, 160, and 300 nm, respectively. A 1 μm scale bar is shown for each. The MSA method develops a homogeneous film after 5 cycles. The surface morphology is retained as the film develops beyond 5 cycles.

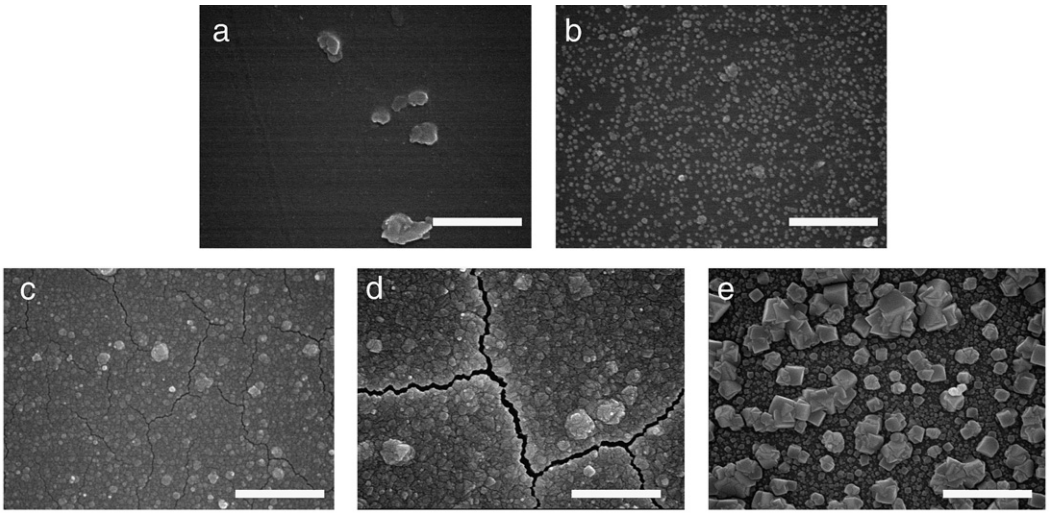


Fig. 5. SEM images of Method 2 Films, 2a–e, with thicknesses of 6.1, 22, 34, 71, and 86 nm, respectively. A 1 μm scale bar is shown for each. Uniform coverage is achieved after 20 cycles; less material is deposited by Method 2 when compared to Method 1. Method 2 films show roughness and surface coverage similar to Method 1 images of similar thicknesses.

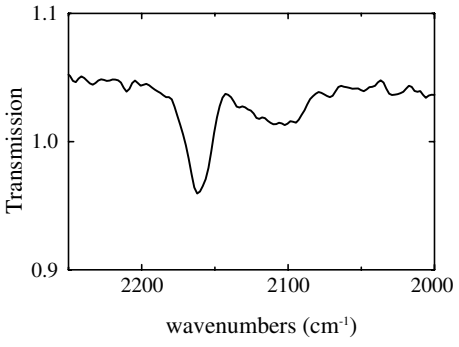


Fig. 6. FT-IR of a 20 cycle fast growth film on silica at room temperature. IR bands are similar to those found in powder samples of the same composition. A sharp peak at 2169 cm^{-1} is attributed to the Fe^{III}–Co^{II}(hs) bridging cyanide stretch and the broad peak centered at 2103 cm^{-1} is attributed to the Fe^{II}–Co^{II}(hs) bridging cyanide stretch.

moments are influenced by the dipolar field generated by the primordial ferrimagnetic domains. For thin films, the photoswitchable moments are only influenced by neighbors within the plane of the film, and so these dipolar fields orient perpendicular to the film, opposing the applied field. As the film grows into a random three-dimensional powder, the neighboring moments become more random, losing the directional influence. For the films studied here, the transition to three-dimensional behavior begins for thicknesses greater than 75 nm, suggesting that the important interaction length is of this order. By 300 nm, bulk-like behavior is seen.

It was previously observed that the influence of the internal dipolar field can be cancelled with a sufficiently strong external field causing the photoinduced moments to increase the overall magnetization instead of decreasing

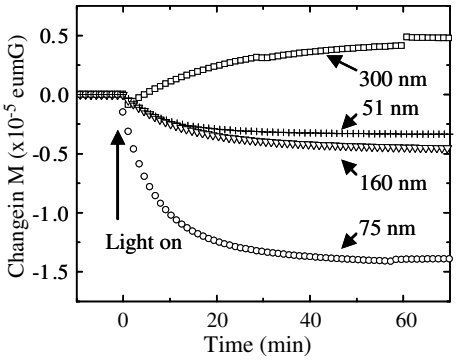


Fig. 7. Thickness dependence of the photoinduced magnetization in Co–Fe PBA thin films with H_E perpendicular to the film plane, Film 1b (+) 51 nm, 1c (○) 75 nm, 1d (△) 160 nm, and 1e (□) 300 nm. The films less than 200 nm thick show a decrease in magnetization upon illumination. As the film thickness increases further the photoinduced increase in magnetization becomes similar to that of bulk powder samples.

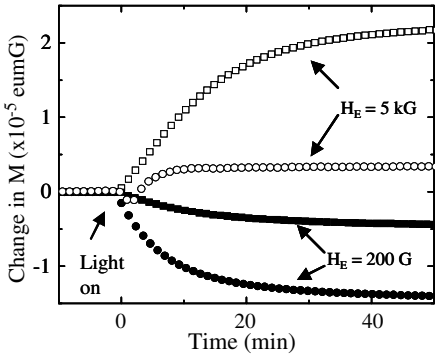


Fig. 8. Applied field dependence of the photoinduced magnetism with H_E perpendicular to the plane of the film. The 75 nm Film 1c measured with $H_E = 200$ G (●) and 5 kG (○) and the 160 nm Film 1d with $H_E = 200$ G (■) and 5 kG (□).

it. To confirm this behavior, the 75 and 160 nm films were measured in $H_E = 5$ kG oriented perpendicular to the films (Fig. 8), and both samples show a photoinduced increase in magnetization in this higher field, consistent with the mechanism illustrated in Fig. 2.

4. Conclusions

The anisotropy in the photoinduced magnetism of thin films of Co–Fe PBA is dependent on several factors. There must be residual ferrimagnetic moments present in the film to align with H_E, generating an internal dipolar field that influences the surrounding photoswitchable moments. The film geometry needs to be quasi-two-dimensional so that the overlapping dipolar fields do not cancel. In this paper, the effect of film thickness on the quasi-two-dimensional character of the film was explored. The photoinduced decrease in magnetism is maintained for films ~100 nm and less, but the effect diminishes for thicker films and is eliminated for films greater than ~200 nm. The MSA method provides sufficient thickness control and film homogeneity to easily generate Prussian blue analogue thin films that meet the requirements for observing this phenomenon unique to continuous thin films.

Acknowledgements

This work was supported, in part, by NSF DMR-0305371 (MWM) and NSF DMR-0543362 (DRT). SEM images were obtained at the University of Florida electron microscopy core laboratory. ICP-MS data were collected at the Department of Geology, University of Florida.

References

[1] O. Sato, T. Iyoda, A. Fujishima, K. Hashimoto, Science 272 (1996) 704.
[2] O. Sato, Y. Einaga, A. Fujishima, K. Hashimoto, Inorg. Chem. 38 (1999) 4405.
[3] A. Bleuzen, C. Lomenech, V. Escax, F. Villain, F. Varret, C. Cartier dit Moulin, M. Verdaguer, J. Am. Chem. Soc. 122 (2000) 6648.
[4] V. Escax, A. Bleuzen, C. Cartier dit Moulin, F. Villain, A. Goujon, F. Varret, M. Verdaguer, J. Am. Chem. Soc. 123 (2001) 12536.
[5] D. Pejaković, J. Manson, J. Miller, A. Epstein, Phys. Rev. Lett. 85 (2000) 1994.
[6] K. Yoshizawa, F. Mohri, G. Nuspl, T. Yamabe, Phys. Chem. B 102 (1998) 5432.
[7] T. Kawamoto, Y. Asai, S. Abe, Phys. Rev. Lett. 86 (2001) 348.
[8] N. Shimamoto, S. Ohkoshi, O. Sato, K. Hashimoto, Inorg. Chem. 41 (2002) 678.
[9] S. Gawali-Salunke, F. Varret, I. Maurin, C. Enachescu, M. Malarova, K. Boukheddanden, E. Codjovi, H. Tokoro, S. Ohkoshi, K. Hashimoto, J. Phys. Chem. B 109 (2005) 8251.
[10] M. Kamiya, M. Hananwa, Y. Moritomo, Y. Isobe, J. Tateishi, K. Kato, A. Nakamura, Phys. Rev. B 69 (2004) 052102.
[11] H. Liu, K. Matsuda, Z. Gu, K. Takahashi, A. Cui, R. Nakajima, A. Fujishima, O. Sato, Phys. Rev. Lett. 90 (2003) 167403.
[12] A. Bleuzen, V. Excax, A. Ferrier, F. Villain, M. Verdaguer, P. Munsch, J.-P. Itie, Angew. Chem., Int. Ed. 43 (2004).
[13] K. Boukheddanden, M. Nishino, S. Miyashita, F. Varret, Phys. Rev. B 72 (2005) 014467.
[14] J.-H. Park, Y.-H. Huh, E. Čižmár, S. Gamble, D.R. Talham, M.W. Meisel, J. Magn. Magn. Mater. 272–276 (2004) 1116.
[15] J.-H. Park, E. Čižmár, M.W. Meisel, Y.-D. Huh, F. Frye, S. Lane, D.R. Talham, Appl. Phys. Lett. 85 (2004) 3797.
[16] J. Culp, J.-H. Park, F. Frye, Y.-H. Huh, M.W. Meisel, D.R. Talham, Coord. Chem. Rev. 249 (2005) 2642.
[17] S. Ohkoshi, Y. Einaga, A. Fujishima, K. Hashimoto, J. Electroanal. Chem. 473 (1999) 245.
[18] K. Itaya, T. Ataka, S. Toshima, J. Am. Chem. Soc. 104 (1982) 4767.
[19] W. Buschmann, S. Paulson, C. Wynn, M. Girtu, A. Epstien, A. White, J. Miller, Chem. Mater. 10 (1988) 1386.
[20] V. Neff, J. Electrochem. Soc. 125 (1978) 886.
[21] V. Ivanov, M. Kaplun, V. Kondrat'ev, A. Tikhomirova, V. Zigel', S. Yakovleva, N. Malev, Russ. J. Electrochem. 38 (2002) 200.
[22] N. Tacconi, K. Rajeshwar, Chem. Mater. 15 (2003) 3046.
[23] C. Lundgren, R. Murray, Inorg. Chem. 27 (1988) 933.
[24] N. Toshima, K. Liu, M. Kaneko, Chem. Lett. (1990) 485.
[25] Y. Guo, A. Guadalupe, O. Resto, L. Fonseca, S. Weisz, Chem. Mater. 11 (1999) 135.
[26] K. Honda, H. Hayashi, K. Chiba, Chem. Lett. (1988) 191.
[27] G.R. Torres, B. Agricole, P. Delhaes, C. Mingotaud, Chem. Mater. 14 (2002) 4012.
[28] T. Yamamoto, Y. Umemura, O. Sato, Y. Einaga, Chem. Lett. 33 (2004) 500.
[29] T. Yamamoto, Y. Umemura, O. Sato, Y. Einaga, Chem. Mater. 16 (2004) 1195.

[30] T. Yamamoto, Y. Umemura, O. Sato, Y. Einaga, J. Am. Chem. Soc. 127 (2005) 16065.
[31] T. Yamamoto, Y. Umemura, O. Sato, Y. Einaga, Sci. Technol. Adv. Mater. 7 (2006) 134.
[32] S. Ravaine, C. Lafuente, C. Mingotaud, Langmuir 14 (1998) 6347.
[33] C. Mingotaud, C. Lafuente, J. Amiell, P. Delhaes, Langmuir 15 (1999) 289.
[34] G. Romualdo-Torres, B. Agricole, C. Mingotaud, S. Ravaine, P. Delhaes, Langmuir 19 (2003) 4688.
[35] R. Millward, C. Madden, I. Suther, R. Mortimer, S. Fletcher, F. Marken, Chem. Commun. (2001) 1994.
[36] M. Pyrasch, B. Tieke, Langmuir 117 (2001) 7706.
[37] W. Jin, A. Toutianoush, M. Pyrasch, J. Schnepf, H. Gottschalk, W. Rammensee, B. Tieke, J. Phys. Chem. B 107 (2003) 12062.
[38] J. Culp, J.-H. Park, I. Benitez, Y.-D. Huh, M. Meisel, D. Talham, Chem. Mater. 15 (2003) 3431.
[39] J.-H. Park, F. Frye, S. Lane, E. Čižmár, Y.-D. Huh, D.R. Talham, M.W. Meisel, Polyhedron 24 (2005).
[40] W. Kern, J. Electrochem. Soc. 137 (1990) 1887.

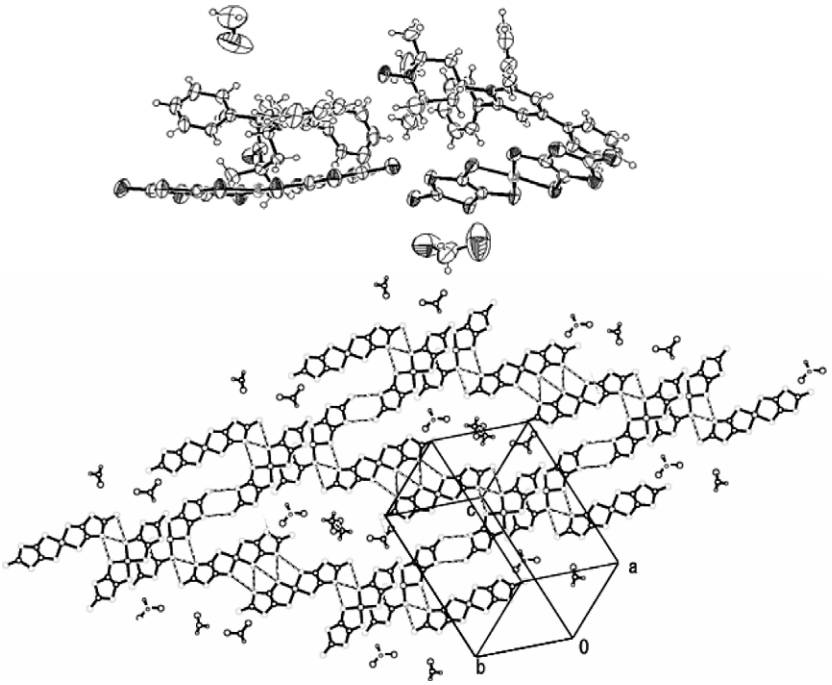


Fig. 1. (Upper) Crystal structure of **III** · $[Ni(dmit)_2](CH_2Cl_2)_{0.75}$ salt. (Lower) 2D structural feature of the anion layer in the same salt.

amount of $[n\text{-}Bu_4N]^+[Ni(dmit)_2]^-$ in a mixed solution of acetone–dichloromethane (1:1), dark greenish solid was precipitated, which then was filtered to give a radical salt. The single crystal grown from dichloromethane solution was then analyzed by X-ray crystallography to reveal that the cation-to-anion ration is 1:1 with incorporation of dichloromethane in a ratio of 0.75 in the crystal (Fig. 1, upper).[1] There exist a couple of crystallographically independent ion pairs being composed of the pyridinium and the anion and no close contact is seen between the spins on aminoxyls and also between the oxygen atoms and neighboring $[Ni(dmit)_2]$ anions, suggesting the paramagnetic behavior of isolated aminoxyl spins of $S = 1/2$. However, several S–S contacts are observed between the $[Ni(dmit)_2]$ anions as shown in Fig. 1(lower) to propagate in the crystal forming sheet-like structures in two-dimensional manner and inferring significant magnetic interactions between the spins on the nickel atoms.

The magnetic data of the salt are shown in Fig. 2(left). Weak antiferromagnetic interaction is discerned in the lower temperature region with the values of Curie constant of 0.66 emu K mol^{-1} and Weiss temperature −0.68 K, respectively. Its larger value than that of isolated $S = 1/2$ spin (0.375 emu K mol^{-1}) suggests the contribution χ–χ_{TEMPO} from the spins on $[Ni(dmit)_2]$ anions to the total χ-values. The χ-χ_{TEMPO} values can be well expressed by 2D Heisenberg model [4] as indicated in Fig. 2 (right), thus reflecting 2D structural feature found in the crystal (*vide supra*). However, the exchange interactions are estimated to be rather weak ($J = -3.11$ K) from the data.

The air oxidation of the **III** · $[Ni(dmit)_2]$ (1:1) salt in an acetone solution containing acetic acid and acetic anhydride yielded black powdery solid and the results of the elemental analyses indicate the formation of a 1:6 salt with somewhat larger anion ratio than that of most salts previously reported [1]. The magnetic data of the salt showed CW behavior with Curie constant of 0.67 emu K mol^{-1} and Weiss temperature 1.87 K, respectively. The resistivity measurement was performed for the compressed pellet of the salt, using the standard four-probe method and the data of Arrhenius plot are shown in Fig. 3. Thus, the salt shows semi-conducting behavior with room temperature conductivity of 1.55 S cm^{-1} and relatively small activation energy E_A of 85 meV.

2.2. *Pd(dmit)$_2$ complexes and Ni(mnt)$_2$ complexes of* ***III***

The $\mathbf{III}_2$ · $[Pd(dmit)_2]$ (2:1) salt was prepared by the reaction of **III** with 0.5 molecular amount of $[n-Bu_4N]_2^+[Pd(dmit)_2]^{2-}$ in an acetone solution and the cation-to-anion ration is substantiated from the crystal structure obtained by the X-ray analysis of a single crystal of the salt.[2] Very weak antiferromagnetic interaction of CW behavior is observed in the salt between the aminoxyl spins with Curie constant of 0.37 emu K mol^{-1} and Weiss

[1] Crystal data for **III** · $[Ni(dmit)_2]_2$ (1:1) salt: $C_{38}H_{34}N_2OCl_2NiS_{10}$, $F_W = 984.91$, triclinic ($P-1$), $a = 14.813(3)$ Å, $b = 16.499(2)$ Å, $c = 19.430(4)$ Å, $\alpha = 76.226(5)°$, $\beta = 73.446(2)°$, $\gamma = 78.889(2)°$, $V = 4380.8(12)$ $Å^3$, $T = 296$ K, $Z = 4$, $D_{calc} = 1.493$ mg cm^{-3}, $R = 0.1052$, $R_W = 0.1050$ [9175 observed reflections and 982 parameters, $I > 3\sigma(I)$].

[2] Details of the crystal data will be reported in a full paper.

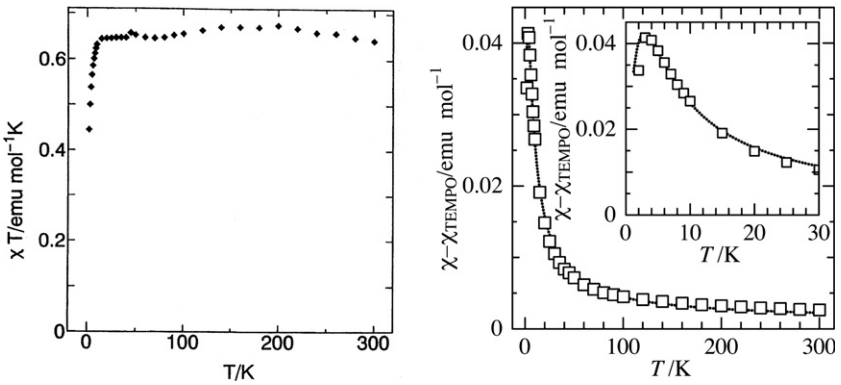


Fig. 2. (Left) The χT–T data of **III** · $[Ni(dmit)_2](CH_2Cl_2)_{0.75}$ salt. (Right) Contribution from χ–χ_{TEMPO} data and an enlarged figure at lower temperature region is inserted as inset. The solid line indicates the theoretical one calculated by 2D Heisenberg model.

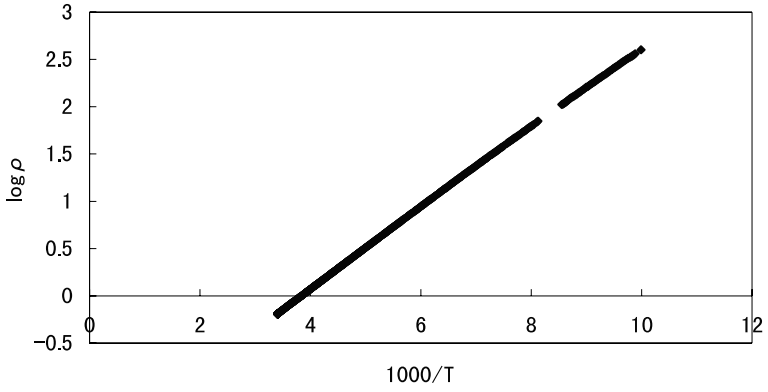


Fig. 3. The Arrhenius plot of resistivity data for the oxidized salt of **III** · $[Ni(dmit)_2]_6$.

temperature of −0.13 K. Air oxidation of the salt yielded the corresponding oxidized salt again with the cation-to-anion ratio of 1:6 and the semi-conducting property is also observed in the salt with room temperature conductivity of 6.44 S cm^{-1} and activation energy E_A of 85 meV.

Similar treatment of the pyridinium tetrafluoroborate (**III**) with either $[n-Bu_4N]_2^+[Ni(mnt)_2]^{2-}$ or $[n\text{-}Bu_4N]^+$-$[Ni(mnt)_2]^-$ gave the corresponding salts and their crystal structure analyses on the single crystals obtained from acetonitrile revealed that the cation-to-anion ratio of the former salt is 2:1 with inclusion of one acetonitrile molecule in the unit cell and the latter salt has the ratio of 4:5 with two acetonitrile molecules.[2] Only weak antiferromagnetic interactions are observed in the spins of both salts with CW behavior ($C = 0.39$ emu K mol^{-1} and $\theta = -0.80$ K for the former salt and $C = 0.37$ emu K mol^{-1} and $\theta = -0.96$ K for the latter salt), indicating absence of significant interactions between the spin centers in both salts and the room temperature conductivity measurements of both salts reveal them to be almost insulating. Although the oxidation by using iodine is so far unsuccessful for both salts, we are still trying to prepare the oxidized species by other conditions and/or methods such as electrocrystallization with regulated current.

In summary, we have prepared several magnetic salts derived from a TEMPO-substituted 2,4,6-triphenyl pyridinium (**III**) with $Ni(dmit)_2$, $Pd(dmit)_2$ or $Ni(mnt)_2$ as counter anions and the structures and magnetic properties of the salts have been investigated. While only weak antiferromagnetic interaction of CW behavior derived from $S = 1/2$ spin is predominantly observed in the salts of **III**$_2$ · [Pd-$(dmit)_2$], **III**$_2$ · $[Ni(mnt)_2]$, and **III** · $[Ni(mnt)_2]$, the magnetic behavior of **III** · $[Ni(dmit)_2]$ can be explained by the summation of $S = 1/2$ spin and the contribution from the spins on $[Ni(dmit)_2]$ anions (χ–χ_{TEMPO}), which obeys 2D Heisenberg model and reflects its crystal structure with 2-D structural feature. The electrical conductivities of **III** · $[Ni(dmit)_2]$, **III**$_2$ · $[Pd(dmit)_2]$, and a couple of $Ni(mnt)_2$ salts are less than 10^{-6} S cm^{-1} but the oxidized salts of the $Ni(dmit)_2$ as well as $Pd(dmit)_2$ salts show semi-conducting properties with relatively high conductivities and low activation energies.

3. Supplementary material

CCDC 624575 contains the supplementary crystallographic data for **III** · $[Ni(dmit)_2]_2$. These data can be obtained free of charge via http://www.ccdc.cam.ac.uk/conts/retrieving.html, or from the Cambridge Crystallographic Data Centre, 12 Union Road, Cambridge CB2 1EZ, UK; fax: (+44) 1223-336-033; or e-mail: deposit@ccdc.cam.ac.uk.

Acknowledgement

A financial support from Kawanishi Memorial Shinmeiwa Foundation to B.R. is gratefully acknowledged.

References

[1] (a) Cf. H. Imai, H. Otsuka, T. Naito, K. Awaga, T. Inabe, J. Am. Chem. Soc. 121 (1999) 8098;
(b) S. Aonuma, H. Casellas, C. Faulmann, B. Garreau de Bonneval, I. Malfant, P. Cassoux, P.G. Lacroix, Y. Hosokoshi, K. Inoue, J. Mater. Chem. 11 (2001) 337;
(c) K. Mukai, T. Hatanaka, N. Senba, T. Nakayashiki, H. Minakuchi, Y. Misaki, K. Tanaka, K. Ueda, T. Sugimoto, N. Azuma, Inorg. Chem. 41 (2002) 5066;
(d) K. Mukai, N. Senba, T. Hatanaka, H. Minakuchi, K. Ohara, M. Taniguchi, Y. Misaki, Y. Hosokushi, K. Inoue, N. Azuma, Inorg. Chem. 43 (2004) 566;
(e) K. Mukai, D. Shiba, K. Yoshida, K. Mukai, H. Hisatou, K. Ohara, Y. Hosokushi, N. Azuma, Bull. Chem. Soc. Jpn. 78 (2005) 2114.

[2] (a) H. Akutsu, J. Yamada, S. Nakatsuji, Chem. Lett. (2001) 208;
(b) H. Akutsu, J. Yamada, S. Nakatsuji, Syn. Met. 120 (2001) 871;
(c) H. Akutsu, J. Yamada, S. Nakatsuji, Chem. Lett. 32 (2003) 1118;
(d) H. Akutsu, K. Masaki, K. Mori, J. Yamada, S. Nakatsuji, Polyhedron 24 (2005) 2126;
(e) A. Yamashita, H. Akutsu, J. Yamada, S. Nakatsuji, Polyhedron 24 (2005) 2614.

[3] K. Kanbara, H. Akutsu, J. Yamada, S. Nakatsuji, Chem. Lett. 34 (2005) 306.

[4] M.E. Lines, J. Phys. Chem. Solids 31 (1970) 101.

CN linker, and those attached to the nitrogen end. The superexchange mechanism in these solids involves delocalization of spin density via π backbonding of unpaired t_{2g} electrons from the metals in the carbon sites into the bridging cyanide π^* orbitals; more efficient delocalization typically leads to larger exchange couplings (J) and higher magnetic ordering temperatures (T_C or T_N). The magnetic ordering temperatures of Prussian blue analogues can be maximized by constructing them from metal centers bearing electrons in high-energy d-orbitals: such centers are capable of back bonding strongly into the cyanide π^* orbitals and maximizing the extent of spin delocalization [7–9].

For hexacyanometalate ions of first-row transition metals, the energies of the d-electrons depend on two parameters. The first of these parameters is the oxidation state of the metal. Metals in lower oxidation states have more electrons to screen the nuclear charge, and the increased screening leads to an increase in the energies of all the valence electrons. Although hexacyanometalates are known in the +1 oxidation state, all are diamagnetic and thus ill-suited for preparing Prussian blue magnets; the lowest oxidation state accessible for paramagnetic hexacyanometalate ions is +2. The second parameter that controls the energies of the d-electrons is the position of the metal in the first-row of the periodic table. Other things being equal, metals early in the d-block have higher-energy d-electrons because they have lower nuclear charges. This fact explains why the highest ordering temperatures seen to date are for Prussian blue analogues that contain vanadium(II) centers: early transition metal ions in low oxidation states have electrons in high-energy, radially expanded d-orbitals, and these electrons delocalize quite readily into the cyanide π^* orbitals, thus increasing the exchange coupling between adjacent spin centers, and affording magnetic materials with higher magnetic ordering temperatures.

Because substitution of early transition metals into the Prussian blue structure gives magnets with unusually high ordering temperatures, we have long been interested in preparing a Prussian blue analogue that contains the earliest first-row transition metal, titanium. In 1997, we described the synthesis of the hexacyanotitanate(III) ion, and had high hopes for preparing new magnets from this building block in which the Ti^{III} center occupied the carbon sites of the Prussian blue structure [10]. Unfortunately, all attempts to prepare magnetic phases from this starting material have been unsuccessful. The $[Ti^{III}(CN)_6]^{3-}$ ion is instantly hydrolyzed in water, so this medium cannot be used for the synthesis of Prussian blue analogues from this starting material. Although the $[Ti^{III}(CN)_6]^{3-}$ ion is soluble in acetonitrile, and its solutions afford precipitates upon the addition of transition metal cations such as V^{II}, Cr^{II}, or Mn^{II}, the solids obtained are non-crystalline and non-magnetic, probably because the precipitation is rapid and irreversible in this poorly coordinating solvent, so that there is no opportunity for an ordered Prussian blue structure to form [6].

In the present study, we report our attempts to prepare Prussian blues in which the titanium(III) center is not in the carbon site, but rather in the nitrogen site of the PB structure. Despite the fact that the titanium(III) center carries only one unpaired electron, so that few spin exchange pathways are available, the low value of the effective nuclear charge of the titanium(III) ion means that this electron will reside in a very high energy d-orbital. As a result, incorporating Ti^{III} into a PB should afford solids with high magnetic ordering temperatures because the one d-electron should delocalize significantly into the cyanide π^* orbital.

The high energy of the d-orbitals on titanium(III) ion means that it is a strong reductant, a fact that is well known from its electrochemistry and solution reaction chemistry. Thus, in order to use this cation as a starting material for the synthesis of Prussian blues, we chose to investigate its reactions with an anion that is relatively difficult to reduce: the hexacyanochromate(III) ion $[Cr(CN)_6]^{3-}$. The redox potentials suggest that these two reactants should not undergo a redox reaction. We find that these two building blocks do react to generate a Prussian blue phase, but not one containing both titanium and chromium. Instead, the product has been identified as a nanocomposite of titanium dioxide with an all-chromium Prussian blue. Such nanocomposites have recently been shown to be useful in the construction of photoelectrodes [11].

2. Results and discussion

2.1. Attempts to synthesize titanium(III) hexacyanochromate(III) in water

We began our investigations with the reaction of titanium(III) ions with hexacyanometalates in aqueous solutions. The hexaaquotitanium(III) ion is known to be stable in water only if the pH is kept below ~1 [12]. At higher pH values, the hexaaqua ion undergoes ionization reactions to produce $[Ti^{III}(OH)(OH_2)_5]^{2+}$ and other, more highly condensed species. Therefore, we dissolved titanium(III) *p*-toluenesulfonate in water that had been acidified to pH ~2 with *p*-toluenesulfonic acid, and to this solution we added $[NEt_4]_3[Cr(CN)_6]$. From the mixture, we isolated a gray solid, which was isolated by centrifugation, washing, and drying; we will refer to this product as **1**. The metal weight percentages (Cr, 19.4; Ti, 17.4) were consistent with those calculated (Cr, 19.0; Ti, 17.5) for the molecular formula "$Ti[Cr(CN)_6]\cdot H_2O$".

The X-ray powder diffraction pattern of **1** contains several peaks, all of which can be indexed to a face-centered cubic cell with a lattice constant of 10.36 Å (Fig. 1). The symmetry of the cell and its cell parameters are strongly indicative of the presence of a Prussian blue phase. The average crystallite size, which was estimated from the widths of the diffraction peaks using the Debye–Scheerer equation [13], is 224 Å.

The infrared spectrum of **1** features a single intense cyanide stretching absorption at 2181 cm^{-1}. The shifting

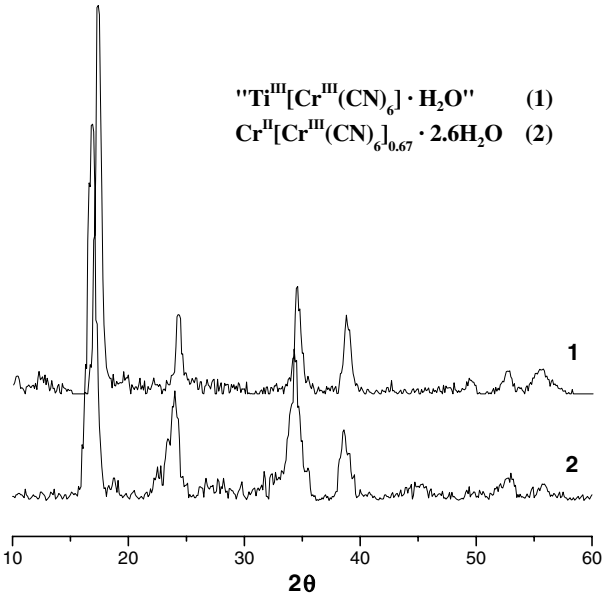


Fig. 1. Base-line-corrected powder X-ray diffraction patterns of **1** (top) and **2** (bottom). The seven main peaks are the 200, 220, 400, 420, 440, 442, and 620 reflections (left–right).

of the ν_{CN} stretching absorption to higher energies relative to that of 2112 cm^{-1} in $[NEt_4]_3[Cr(CN)_6]$ is diagnostic for the formation of cyanide groups that bridge between two metal centers. The frequency lowering is the consequence of the depopulation of the cyanide 5σ orbital upon formation of a bond between the nitrogen atom and a second metal center [14].

For Prussian blue analogues, (and other magnetic solids constructed from two interpenetrating lattices), the sign of the local exchange interactions can usually be determined from the shape of the μ_{eff} versus T curve: for ferrimagnetic solids there is a minimum in μ_{eff} above the ordering temperature owing to the effects of short-range antiferromagnetic correlations that cancel spins [15–19]. Such a minimum is observed in **1** and thus it is clearly a ferrimagnet (Fig. 2). The minimum is rather shallow and appears at *ca.* 325 K. At lower temperatures, the magnetic moment increases dramatically as the magnetic ordering temperature is approached Fig. 2.

The magnetic ordering temperature can be deduced from plots of χ^{-1} versus T (Fig. 3). The curve can be fit to Néel's hyperbolic equation, $1/\chi = (T-\theta)/C - \zeta/(T-\theta')$, where θ and C are the Weiss and Curie constants, and θ' and are ζ are proportional to $\eta_A\eta_B\, C[\eta_A - \eta_B]$ and $\eta_A\eta_B C$, where η_i is the fractional occupancy of each sublattice site [20,21]. The sign of the Weiss constant is negative; this feature is characteristic of ferrimagnets. The intersection of the hyperbola with the temperature axis gives the magnetic ordering temperature (T_N). The derived value for **1** is 265 K, although a slightly different value was determined from the magnetization curves (see below), and the Weiss and Curie constants are provided in Table 1.

At 350 K, the magnetic moment per formula unit (reckoned according to the formula given above) is 4.50 μ_B and this value suggests that **1** is composed of $S = {}^3/_2$ Cr^{III} and $S = {}^1/_2$ Ti^{III} metal centers in a 1:1 ratio: the value of μ_{eff} calculated for randomized Ti^{III} and Cr^{III} spins with $g = 2$ is 4.52 μ_B.

The temperature dependence of the field-cooled, zero-field cooled, and remnant magnetization for **1** clearly show the onset on long-range magnetic order at 255 K (Fig. 4); the ordering temperature is the point at which the field-cooled and zero-field curves diverge, and also the point at which the magnetization goes to zero. The magnetic ordering temperature defined in this way is more accurate than that deduced from the χ^{-1} versus T curve.

The magnetization value of **1** (Table 1) at 5 K is 5.0 kG cm^3 mol^{-1} (again, for the formula unit given above) at an applied magnetic field of 70 kG (Fig. 5). The magnetization has not saturated even at 70 kG, but if we extrapolate to large fields, we can estimate that the saturation magnetization should be near 11 kG cm^3 mol^{-1}. For the formula "$Ti[Cr(CN)_6]\cdot H_2O$," the calculated saturation magnetization for antiferromagnetically coupled Ti^{III} and Cr^{III} centers is 11.2 kG cm^3 mol^{-1}. Compound **1**

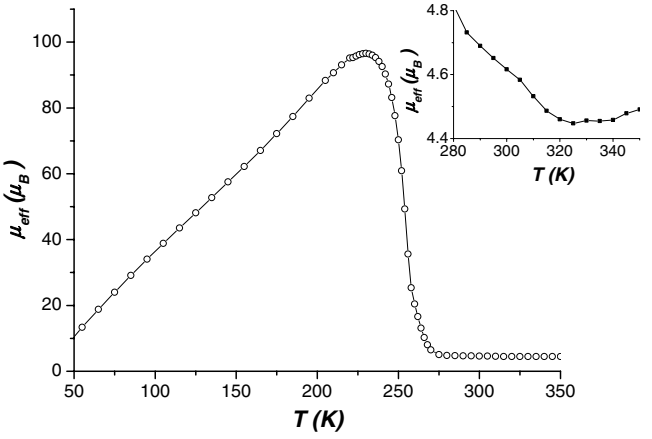


Fig. 2. Temperature dependence of the effective moment per formula unit for **1** at $H_{dc} = 25$ G. Inset: μ_{eff} vs. T plot near *ca.* 325 K.

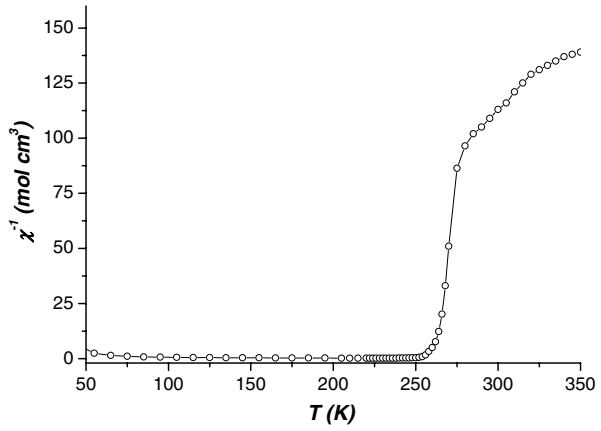


Fig. 3. Temperature dependence of the reciprocal susceptibility of **1** at $H_{dc} = 25$ G.

Table 1
Structural and magnetic data for the new hexacyanochromates

Compound	a (Å)	T_N (K)	C[a]	θ (K)	M_{sat}[b]
"$Ti^{III}[Cr^{III}(CN)_6]\cdot H_2O$ (**1**)"	10.36	255	3.95	−240	5.00
$Cr^{II}[Cr^{III}(CN)_6]_{0.66}\cdot 2.6H_2O$ (**2**)	10.44	242	2.76	−100	5.17

[a] $cm^3\ K\ mol^{-1}$.
[b] $kG\ cm^3\ mol^{-1}$ at 5 K.

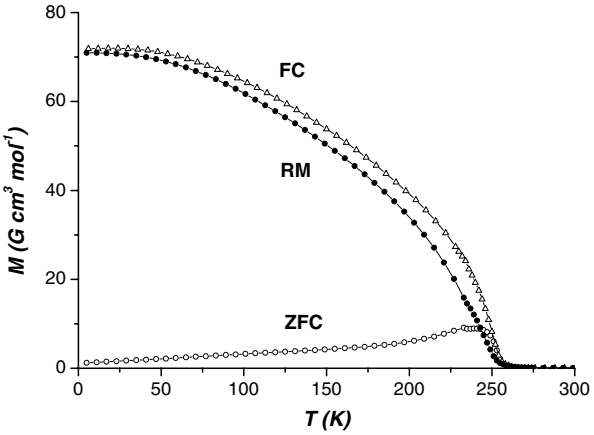


Fig. 4. Temperature dependence of the zero-field cooled (ZFC, ○), field-cooled (FC, △) and remnant magnetization (RM, ●) curves for **1** at $H_{dc} = 1$, 1, and 0 G, respectively.

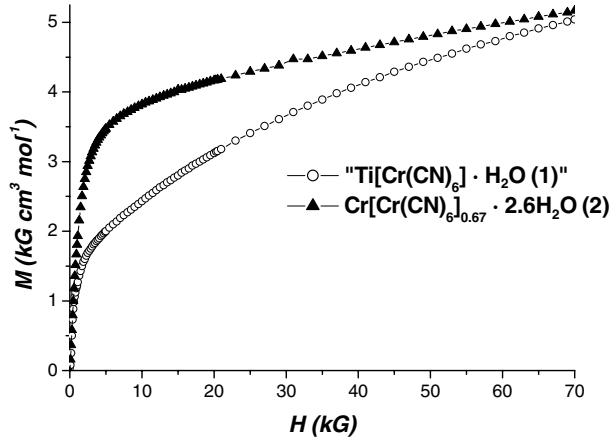


Fig. 5. Field dependence of the magnetization for **1** (○) and **2** (▲) at 5 K.

also exhibits hysteresis below its magnetic ordering temperature (Fig. 6). The coercive field measured at 5 K is 260 G (Table 2).

To summarize the results above, the metal content and all the spectroscopic data suggested that **1** was the first Prussian blue magnet containing Ti^{III}. One measurement was inconsistent with this conclusion, however: the experimentally determined carbon, hydrogen, and nitrogen analyses (C, 8.75; H, 2.49; N, 14.0) disagreed with those calculated for the formula "$Ti[Cr(CN)_6]\cdot H_2O$" (C, 26.3; H, 0.74; N, 30.7). We, therefore, were forced to reconsider

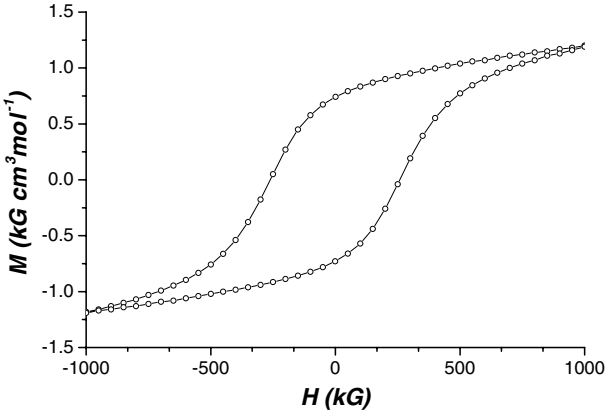


Fig. 6. Hysteresis of **1** at 5 K.

our findings about the nature of **1**. Before we discuss our conclusions, we describe a related Prussian blue compound that will be relevant to this discussion.

2.2. Synthesis and characterization of a chromium(II) hexacyanochromate(III)

Combining aqueous solutions of chromium(II) *p*-toluenesulfonate and $[NEt_4]_3[Cr(CN)_6]$ immediately affords a red-brown suspension from which an air sensitive red-brown solid of stoichiometry $Cr^{II}[Cr^{III}(CN)_6]_{0.67}\cdot xH_2O$ (**2**) can be isolated ($x \sim 2.6$).

The infrared spectrum of **2** exhibits an intense cyanide stretching band at 2180 cm^{-1}, and the high frequency of this band clearly suggests that the bridging cyanide ligands are C-bound to Cr^{III} centers. A weaker low frequency band at 2075 cm^{-1} is most likely due to cyanide groups C-bound to Cr^{II}. The powder X-ray diffraction pattern can be indexed to a face-centered cubic cell having a cell constant of 10.44(4) Å (Fig. 1). The average crystallite size, which was estimated using the Debye–Scheerer equation [13], is 102 Å.

As judged from the temperature dependence of the magnetization of **2** in an applied field of 1 G, the magnetic ordering temperature is 242 K (Figs. 7 and 8). At this temperature, the field-cooled (1 G) and zero-field-cooled (1 G) curves diverge and the remnant magnetization curve goes to zero. A fit of the χ^{-1} versus T plot (25 G) to Néel's hyperbolic function gives an essentially identical value for the magnetic ordering temperature of 237 K. The hysteresis curve for **2** is shown in Fig. 9.

Table 2
Remnant magnetizations and coercive fields for the new molecular magnets at 5 K; estimation of exchange coupling parameters (J) from the observed magnetic ordering temperatures

Compound	M_r (G cm^3 mol^{-1})	H_C (G)	J (cm^{-1})	T_N (K)
"$Ti^{III}[Cr^{III}(CN)_6]\cdot H_2O$ (**1**)"	753	260	−57	255
$Cr^{II}[Cr^{III}(CN)_6]_{0.66}\cdot 2.6H_2O$ (**2**)	760	275	−36	242

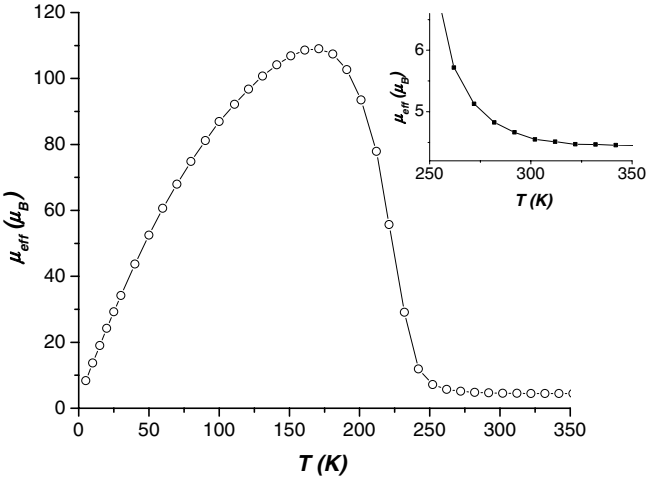


Fig. 7. Temperature dependence of **2** at $H_{dc} = 25$ G. Inset: minimum observed at *ca.* 300 K. on cooling from the high temperature limit.

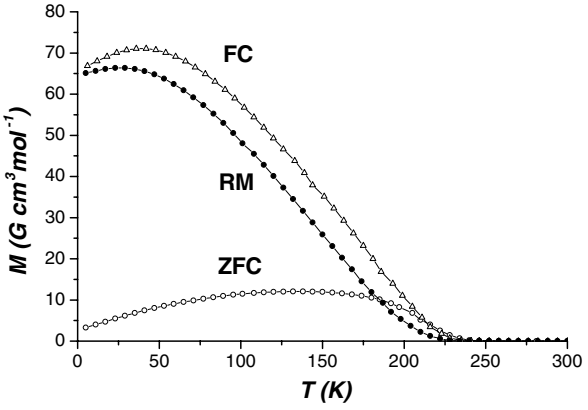


Fig. 8. Temperature dependence of the zero-field cooled (ZFC, ○), field-cooled (FC, △), and remnant magnetization (RM, ●) for **2** at $H_{dc} = 1$, 1, and 0 G, respectively.

The measured saturation magnetization of 5.17 kG cm^3 mol^{-1} (5 K, 70 kG) suggests that about half of the Cr^{II} ions are low spin and the other half are high spin, but that both types of Cr^{II} centers are coupled antiferromagnetically to the Cr^{III} center (Fig. 5). Specifically, if all of the low-spin Cr^{II} ions were low spin, then the saturation magnetization would be 0.056 kG cm^3 mol^{-1}, whereas if all of the Cr^{II} ions were high spin, then the saturation magnetization would be 11.1 kG cm^3 mol^{-1}. The slow approach to saturation could mean that **2** is a canted antiferromagnet or that it has some spin glass character [22,23]. Verdaguer has reported a similar distribution of both low and high

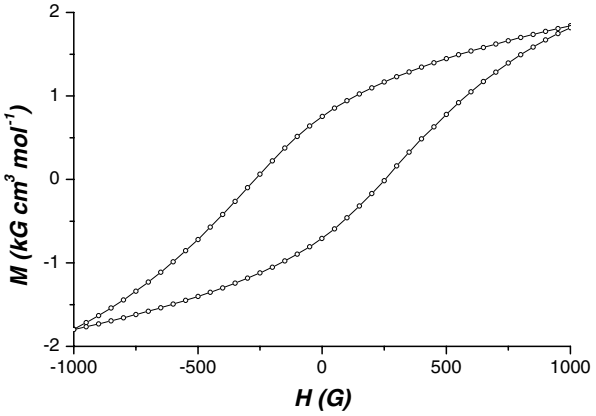


Fig. 9. Hysteresis for **2** at 5 K.

spin Cr^{II} centers in the solid $Cs_{0.75}Cr_{1.025}[Cr(CN)_6]\cdot 5H_2O$ [24].

The plot of the magnetic moment versus temperature (μ_{eff} versus T) at 25 G does not exhibit the shallow minimum just above T_N that is expected for a ferrimagnetic material (Fig. 7). It is possible that this minimum is located above 350 K, the upper limit of our data set. The observed value of the magnetic moment at room temperature (4.66 μ_B at 292 K and 4.547 μ_B at 320 K) again suggests that both low- and high-spin Cr^{II} centers are present: if all had been low-spin, then μ_{eff} should be ~4.25 μ_B, whereas if all had been high-spin, then μ_{eff} should be ~5.84 μ_B.

Verdaguer has described a similar reaction, using $CrCl_2$ as the Cr^{II} source, and has formulated the gray product as $Cr_5(CN)_{12}\cdot 10H_2O$ (or, equivalently, $Cr[Cr(CN)_6]_{0.67}\cdot 3.3H_2O$) [24]. In addition, Miller and Hashimoto have reported that thin films of mixed Cr^{II}/Cr^{III} cyanometalates, can be prepared from $CrCl_3$ and $K_3[Cr(CN)]_6$ at negative applied potentials [25–28]. Also described by Verdaguer is the green all-Cr^{II} compound $Cs_{0.75}Cr_{1.025}[Cr(CN)_6]\cdot 5H_2O$, which exhibits IR absorptions at 2187 and 2069 cm^{-1}, and is ferromagnetic below $T = 190$ K [24].

2.3. Reformulation of *1*

As mentioned above, treatment of $[Ti(OH_2)_6]^{3+}$ with $[Cr(CN)_6]^{3-}$ in water affords a gray solid whose spectroscopic properties and metal content were entirely consistent with it being a Prussian blue analog of stoichiometry $Ti[Cr(CN)_6]\cdot H_2O$. However, this formulation is inconsistent with elemental analysis carbon, hydrogen, and nitrogen values expected for **1**; several lines of evidence suggest that it is not a Prussian blue analogue containing

Ti^{III}. (1) The XRD pattern of **1** (which can be indexed to a fcc cell with a cell constant of 10.36 Å) is almost identical to the 10.44 Å value seen for $Cr^{II}[Cr^{III}(CN)_6]_{0.67} \cdot xH_2O$. The absence of peaks due to the TiO_2 component is consistent with the known behavior of nanophase titania, which generally remains amorphous until heated to temperatures above 250 °C [29]. (2) The infrared spectrum of **1** (which contains a strong absorption at 2180 cm^{-1} and a weaker broad absorption at 2075 cm^{-1}) closely resembles that of the all-chromium complex $Cr^{II}[Cr^{III}(CN)_6]_{0.67} \cdot xH_2O$. The presence of TiO_2 is signaled by the IR band at 800 cm^{-1}, which is assigned to the longitudinal optical (LO) mode of the Ti-O bonds in rutile, which appears at 806 cm^{-1} [30]. (3) The magnetic ordering temperature ($T_N = 255$ K) for **1** is close to the magnetic phase transition temperature ($T_N = 242$ K) for $Cr^{II}[Cr^{III}(CN)_6]_{0.67} \cdot xH_2O$.

These facts strongly suggest that **1** is a mixture of $Cr^{II}[Cr^{III}(CN)_6]_{0.67} \cdot xH_2O$ and some other titanium-containing phase. In fact, all the properties of **1**, including the microanalytical data, are consistent with the conclusion that it is a mixture of $Cr^{II}[Cr^{III}(CN)_6]_{0.67} \cdot xH_2O$ and $TiO_2 \cdot nH_2O$ in the ratio of 1–1.6.

These results suggest that Ti^{III} reduces $[Cr^{III}(CN)_6]^{3-}$ to generate Ti^{IV} and Cr^{II}. The electrochemical potentials for $[Cr(CN)_6]^{3/4-}$ (−1.140 V versus SHE) [31], and Ti^{3+}/TiO^{2+} (0.008 V versus NHE) [32,33] suggest that the $[Cr^{III}(CN)_6]^{3-}$ ion should not be reduced by Ti^{III}. Of course, there will be some equilibrium concentration of the redox products of this reduction; we hypothesize that the hexaquotitanium(III) ion reduces some of the $[Cr^{III}(CN)_6]^{3-}$ ions to Cr^{II}; the latter ion is kinetically labile and will lose its CN ligands, thus providing the source of aquated Cr^{II} ions necessary to produce $Cr^{II}[Cr^{III}(CN)_6]_{0.67} \cdot x\ H_2O$. In this process the Ti^{3+} ions are oxidized to Ti^{4+}, which in aqueous solutions at low pH will generate hydrated $TiO_2 \cdot nH_2O$ [33].

2.4. Attempts to synthesize titanium(III) hexacyanochromate(III) in methanol

Treatment of $[NEt_4]_3[Cr(CN)_6]$ with $Ti(OTs)_3$ in methanol affords a dark purple suspension which slowly becomes a gel over 24 hours. The solid was collected after 3 days by centrifugation and washed with methanol to afford a dark blue solid. Consistent with the results described above, our characterization of this solid strongly suggests that it is best formulated not as a mixed Ti–Cr Prussian blue, but rather as the biphasic material $Cr[Cr(CN)_6]_{0.67} \cdot 7MeOH \cdot 1.67TiO_2$, **3**. Its XRD pattern is consistent with a fcc unit cell with a cell constant essentially identical to that described above for **1**, but the material is less crystalline, as judged from the widths of its diffraction peaks. This difference is not unexpected, because water is a better solvent than methanol, and should better facilitate the annealing out of defects in the structure as it is assembled from solution during the synthesis. The infrared spectrum of **3** exhibits an intense cyanide stretching absorption at 2168 cm^{-1} that is lower than that of 2181 cm^{-1} observed for **1**, but still consistent with the presence of $[Cr^{III}(CN)_6]^{3-}$ centers in which the CN ligands bridge to another metal center. The magnetic ordering temperature for **3** (54 K; Fig. 10) is lower than the ordering temperature observed for **1**, probably because the PB component is less crystalline.

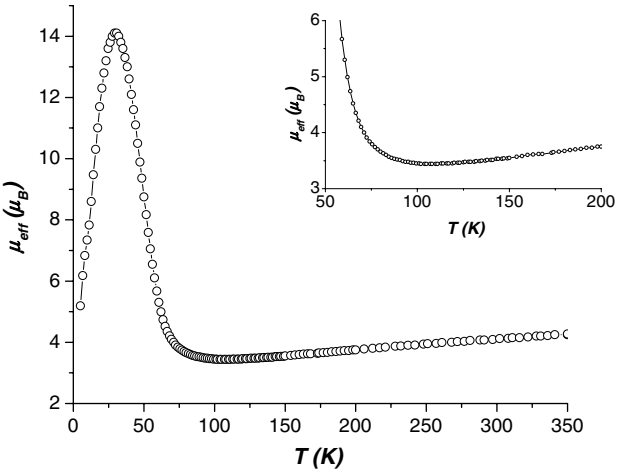


Fig. 10. Temperature dependence of the effective moment per formula unit for $Cr^{II}[Cr^{III}(CN)_6]_{0.67} \cdot 7MeOH \cdot 1.67TiO_2$ (**3**) in an applied field of 25 G. The inset shows the minimum observed near 80 K on cooling from the high temperature limit.

3. Experimental

3.1. General considerations

All operations were conducted in vacuum or under an argon atmosphere by using standard Schlenk techniques. Transfers of solutions containing cyanide were carried out through teflon cannulas. Solvents were distilled under dinitrogen from CaH_2 (acetonitrile), Mg turnings (methanol), or sodium-benzophenone (diethyl ether) and sparged with argon before use. Deionized water was sparged with argon. The salts $Cr(OTs)_2$, $Ti(OTs)_3$, and $[NEt_4]_3[Cr(CN)_6]$ are described elsewhere [34,35]. The IR spectra were recorded as Nujol mulls between KBr plates on a Perkin–Elmer 1600 FTIR instrument. Magnetic measurements were conducted on Quantum Design MPMS and MPMS^2 SQUID magnetometers. Diamagnetic corrections were estimated using Pascal's constants [36]: $\chi_{dia} = -150 \times 10^{-6}$ cm^3 mol^{-1} for **1** and -108×10^{-6} cm^3 mol^{-1} for **2**. Microanalyses were performed by the University of Illinois Microanalytical Laboratory. Powder diffraction measurements were carried out on a Bruker P4RA/GADDS wide angle diffractometer using a Cu Kα radiation source.

3.2. $Ti[Cr(CN)_6] \cdot H_2O$ (1)

To a solution of $Ti(OTs)_3$ (0.51 g, 0.908 mmol) and $HOTs \cdot H_2O$ (0.06 g, 0.315 mmol) in water (20 mL) was

added a solution of $[NEt_4]_3[Cr(CN)_6]$ (0.50 g, 0.835 mmol) in water (20 mL) over 10 s, affording an orange solution. After 10 min, a gray solid precipitated and the mixture was centrifuged at 3000 r.p.m. for 10 min. The supernatant was discarded and the gray solid was washed with water (2×40 mL), centrifuging and discarding the supernatant each time. The gray solid was washed with acetonitrile (15 mL) and was dried under vacuum at room temperature overnight. Yield: 0.094 g (34%). *Anal.* Calc. for $Ti[Cr(CN)_6] \cdot H_2O$ ($C_6H_2N_6OCrTi$): Cr, 19.0; Ti, 17.5. Found: C, 8.75; H, 2.49; N, 14.0; Cr, 19.4; Ti, 17.4%. *Anal.* Calc. for $Cr[Cr(CN)_6]_{0.67} \cdot 7H_2O \cdot 1.67TiO_2$ ($C_4H_{12}N_4O_{9.33}Cr_{1.67}Ti_{1.67}$): Cr, 19.2; Ti, 17.8. IR (cm^{-1}): 3270 (vs), 2181 (s), 2069 (w), 1614 (w), 1305 (w), 1261 (m), 1151 (m), 1074 (m), 1023 (m), 800 (vs), 525 (vs, br).

3.3. $Cr[Cr(CN)_6]_{0.67} \cdot 2.6H_2O$ (2)

To a solution of $[NEt_4]_3[Cr(CN)_6]$ (0.30 g, 0.501 mmol) in water (20 mL) was added a solution of $Cr(OTs)_2 \cdot 3.2H_2O$ (0.39 g, 0.863 mmol) in water (10 mL) over 25 s to afford a fine red-brown suspension. The mixture was transferred to an argon-filled centrifuge bottle and was centrifuged at 3000 r.p.m. for 10 min. The pale red supernatant was discarded and the brown solid was washed with water (2×50 mL), centrifuging and discarding the supernatant each time. The solid was then suspended in acetonitrile (20 mL) and the slurry was transferred to a flask. The solvent was removed in vacuum and the red-brown solid was dried for 10 h in vacuum at room temperature. Yield: 0.068 g (38%). *Anal.* Calc. for $Cr[Cr(CN)_6]_{0.67} \cdot 2.6H_2O$: C, 20.3; H, 2.20; N, 23.6; Cr, 36.5. Found: C, 20.8; H, 2.56; N, 18.1; Cr, 36.5%. IR (cm^{-1}): 3606 (s, br), 3302 (s, br), 3192 (s, br), 2180 (s), 2075 (w), 1623 (w), 530 (s).

3.4. Attempts to synthesize titanium(III) hexacyanochromate(III) in methanol

To a solution of $[NEt_4]_3[Cr(CN)_6]$ (0.30 g, 0.501 mmol) in methanol (10 mL) was added a solution of $Ti(OTs)_3$ (0.31 g, 0.561 mmol) in methanol (10 mL). The initially dark purple suspension slowly became a gel over the course of one day. After 3 days, the dark blue solid was transferred to an argon-filled centrifuge bottle washing with methanol (5 mL) and centrifuged. The clear supernatant was discarded and the blue solid was washed with xmethanol (2×35 mL), centrifuging and discarding the clear supernatant each time. The solid was transferred to a flask by washing with methanol (25 mL). The solvent was removed under vacuum and the blue solid was dried under vacuum overnight. Yield: 0.127 g (89%). *Anal.* Calc. for $Cr[Cr(CN)_6]_{0.67} \cdot 7MeOH \cdot 1.67TiO_2$; $C_{11}H_{28}N_4O_{10.34}Cr_{1.67}Ti_{1.67}$: C, 24.0; H, 5.09; N, 10.2; Cr, 15.8; Ti, 14.9. Found: C, 27.0; H, 3.88; N, 12.8; Cr, 16.7; Ti, 14.9. IR (cm^{-1}): 2168 (vs), 1121 (s), 1078 (s), 1033 (s), 605 (s, sh), 504 (vs, br).

Acknowledgements

We thank the Department of Energy (Grant DEFG02-96-ER45439) for support of this research through the Frederick Seitz Materials Research Laboratory at the University of Illinois at Urbana-Champaign.

References

[1] S. Ferlay, T. Mallah, R. Ouahes, P. Viellet, M. Verdaguer, Nature 378 (1995) 701.
[2] S.M. Holmes, G.S. Girolami, J. Am Chem. Soc. 121 (1999) 5593.
[3] O. Hatlevik, W.E. Buschmann, J. Zhang, J.L. Manson, J.S. Miller, Adv. Mater. 11 (1999) 914.
[4] J.M. Manriquez, G.T. Yee, R.S. McLean, A.J. Epstein, J.S. Miller, Science 252 (1991) 1415.
[5] By varying the synthetic procedure, samples of vanadium(II) pentafluorotricyanoethylene can be isolated that order as high as 307 K, and vanadium(II) 2,6-difluorophenyltricyanoethylene is magnetically ordered up to 293 K. M.D. Harvey, G.T. Yee, Abstr. Pap. Am. Chem. Soc. 232 (2006) INOR 810.
[6] M. Verdaguer, G.S. Girolami, Magnetism: Mol. Mater. V (2005) 283.
[7] W.R. Entley, G.S. Girolami, Science 268 (1995) 397.
[8] W.R. Entley, G.S. Girolami, Mol. Cryst. Liq. Cryst. 273 (1995) 153.
[9] S.M. Holmes, G.S. Girolami, Mol. Cryst. Liq. Cryst. 305 (1997) 279.
[10] W.R. Entley, C.R. Treadway, S.R. Wilson, G.S. Girolami, J. Am. Chem. Soc. 119 (1997) 6251.
[11] K. Szaciłowski, W. Macyk, G. Stochel, J. Mater. Chem. 16 (2006) 4603.
[12] F.A. Cotton, G. Wilkinson, C.A. Murillo, M. Bochmann, Advanced Inorganic Chemistry, sixth ed., Wiley, New York, 1999.
[13] L.V. Azaroff, Elements of X-ray Crystallography, McGraw-Hill, New York, 1968.
[14] K. Nakamoto, Infrared and Raman Spectra of Inorganic and Coordination Compounds, fourth ed., Wiley, New York, 1986, p. 272.
[15] A. Caneschi, D. Gatteschi, A.L. Lirzin, J. Mater. Chem. 4 (1994) 319.
[16] A. Caneschi, D. Gatteschi, J.P. Renard, P. Rey, R. Sessoli, J. Am. Chem. Soc. 111 (1989) 785.
[17] A. Caneschi, D. Gatteschi, P. Rey, R. Sessoli, Inorg. Chem. 27 (1988) 1756.
[18] H.O. Stumpf, L. Ouahab, Y. Pey, D. Grandjean, O. Kahn, Science 261 (1993) 447.
[19] M. Hitzfield, P. Ziemann, W. Buckel, H. Claus, Phys. Rev. B 29 (1984) 5023.
[20] L. Néel, Ann. Phys (Paris) 3 (1948) 37.
[21] J.S. Smart, Am. J. Phys. 23 (1955) 356.
[22] A.H. Morrish, The Physical Principles of Magnetism, Wiley, New York, 1965.
[23] B.D. Cullity, Introduction to Magnetic Materials, Addison-Wesley, Reading, MA, 1972.
[24] T. Mallah, S. Thiébaut, M. Verdaguer, P. Veillet, Science 262 (1993) 1554.
[25] W.E. Buschmann, S.C. Paulson, C.M. Wynn, M.A. Girtu, A.J. Epstein, H.S. White, J.S. Miller, Adv. Mater. 9 (1997) 645.
[26] W.E. Buschmann, S.C. Paulson, C.M. Wynn, M.A. Girtu, A.J. Epstein, H.S. White, J.S. Miller, Chem. Mater. 10 (1998) 1386.
[27] O. Sato, T. Iyoda, A. Fujishima, K. Hashimoto, Science 271 (1996) 49.
[28] O. Sato, Z. Gu, H. Etoh, J. Ichiyanagi, T. Iyoda, A. Fujishima, K. Hashimoto, Chem. Lett. (1997) 37.
[29] A.G. Gaynor, R.J. Gonzalez, R.M. Davis, R. Zallen, J. Mater. Res. 12 (1997) 1755.
[30] D.M. Eagles, Phys. Chem. Solids 25 (1964) 1243.
[31] A. Dostal, F. Scholz, Angew. Chem., Int. Ed. Engl. 34 (1996) 2685.

[32] B. Diethelm, F. Forster, Z. Phys. Chem. 62 (1908) 129.
[33] L. Ciavatta, D. Ferri, G. Riccio, Polyhedron 4 (1985) 15.
[34] S.M. Holmes, G.S. Girolami, Inorg. Synth. 33 (2002) 91.
[35] S.M. Holmes, Molecule-Based Magnets Constructed From Hexacyanometalates, Ph.D. Thesis, University of Illinois, 1999.
[36] O. Kahn, Molecular Magnetism, VCH Publishers, New York, 1993.

spin-orbit coupling in the former [13]. Therefore, the usual giant spin approximation must be modified to account for the orbital contribution to the magnetic properties. However, as we shall see, only the lowest Kramers' doublet contributes to the low-temperature (<20 K) HFEPR spectrum of complex **1**, thus reducing the problem to that of an effective spin $S' = 1/2$. The magnetic properties can then be simulated in terms of a simple Zeeman Hamiltonian, $\widehat{H} = \mu_B \widehat{S}' \cdot \overleftrightarrow{g}' \cdot \vec{B}$, where $\overleftrightarrow{g}'$ represents an effective Landé g-tensor associated with the effective spin $S' = 1/2$. We also show from angle-dependent single-crystal HFEPR measurements that the easy-axis associated with each Co^{2+} ion is significantly tilted away from the c-axis of the crystal. More detailed studies of both complexes will be discussed in a future paper [14].

2. Experimental details

Single-crystal HFEPR measurements were carried out using a sensitive cavity perturbation technique. A millimeter-wave vector network analyzer (MVNA) acted as both a continuously tunable microwave source and phase sensitive detector covering a broad frequency range (8–700+ GHz). Detailed descriptions of the instrumentation can be found in the literature [15,16]. A detailed account of the synthesis of complex **1** will be published elsewhere; we note that the procedure is similar to the previously reported synthesis of a related Co_4 complex [17]. The unit cell details are found in Table 1. Crystals with dimensions on the order of a few millimeters on a side, having the shape of a square based pyramid with four clean sides forming a sharp apex, were carefully selected so that the principal crystallographic axes could be aligned with respect to the applied magnetic field.

The ratio of Zn to Co in the crystals employed in this investigation was 0.995:0.005. As long as there is little difference in the heats of formation for complex **1** and the analogous Co_4 complex, the Co^{2+} ions should be randomly distributed throughout complex **1**. For the 0.995:0.005 Zn to Co ratio, the Zn_4 and Zn_3Co species respectively make up 98% and 1.97% of the molecules in the crystal, while the remaining species (Zn_2Co_2, $ZnCo_3$, Co_4) account for the remaining .03%. Therefore, the overwhelming contribution to the HFEPR spectra will come from the Zn_3Co molecules.

Table 1
Crystallographic data for $[Zn_{3.98}Co_{0.02}(hmp)_4(dmb)_4Cl_4]$

Formula	$C_{48}H_{80}Cl_4N_4O_8Zn_4$
Formula weight	1245.55
Temperature (K)	100(2)
Wavelength (Å)	0.71073
Crystal system	tetragonal
Space group	$I41/a$
Unit cell dimensions	
a (Å)	12.9141(7)
b (Å)	12.9141
c (Å)	35.001(2)
α (°)	90
β (°)	90
γ (°)	90
Volume (Å^3)	5837.3(5)
Z, Z'	4, 0.25
Density (calculated) (g/cm^3)	1.411
Crystal size (mm^3)	$0.29 \times 0.17 \times 0.15$

X-ray crystallographic data taken for a single crystal of complex **1**.

Analogous to the Ni complexes, the core of each molecule forms a distorted cube (the c direction being slightly longer than the equivalent a and b directions, see Table 1) with pseudo S_4 site symmetry about the crystallographic c-axis, with metal atoms (Zn or Co) and oxo-atoms from the alkoxy-arm of the deprotonated Hhmp ligand occupying alternate vertices. Each of the four metal centers is additionally coordinated to an hmp nitrogen atom, a chloride ion and a dmb ligand in a distorted 6-coordinate octahedral geometry. The oxygens of the dmb ligands remain protonated. For each molecule, there are four possible sites for the Co^{2+} ion to reside, related by the S_4 symmetry operation.

3. Results and discussion

At the lowest temperatures, one can make the assumption that only the ground state for each Co^{2+} ion is populated. Furthermore, as we shall see below, the ground state is a well isolated Kramers' doublet. Thus, each Co^{2+} ion may be expected to contribute only one peak to the HFEPR spectrum (containing some fine structure due to disorder-induced strain). Thus, assuming the magnetic axes associated with the four possible Co^{2+} sites on the Zn_3Co molecule are non-collinear, one should observe four separate HFEPR peaks for arbitrary field orientations (one for each Co^{2+} site). For field orientations along certain symmetry directions, two or more of these transitions may become degenerate, thus reducing the number of peaks.

Fig. 1 displays frequency-dependent data for complex **1** obtained at 2 K, with the field tilted 32° away from the c-axis of the crystal in the (1 0 0) plane (vide infra, see Fig. 3). The inset to Fig. 1 shows a typical spectrum obtained at a frequency of 51.8 GHz. As can be seen, absorptions are grouped into three clusters. The position of each peak is plotted versus frequency in the main part of the figure for measurements performed on higher-order cavity modes. As can be seen, each peak lies on an absolutely straight line which passes exactly through the origin. Landé g-factors have been assigned to each of the peaks based on the slope of the straight line through each set of data points. The shapes of the data points (solid and open circles and squares) have been chosen for comparison with Fig. 3 below. We believe the fine structures are caused by disorder induced g-strain (as was found from similar studies of the Ni/Zn analog [8,10]).

Based on the angle-dependent studies discussed below, we find that the $g = 4.2$ branch in Fig. 1 is in fact degenerate, consisting of two HFEPR transitions. This explains the observation of only three peaks. The relative intensities of

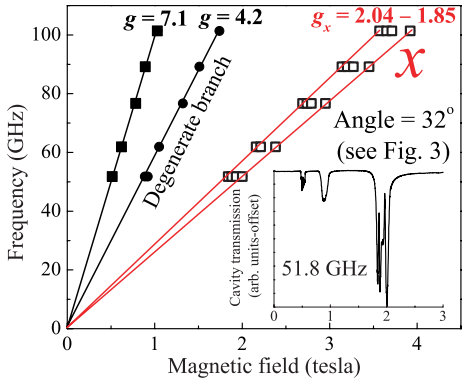


Fig. 1. Frequency-dependent data for complex **1** obtained at 2 K, with the field tilted ~32° away from the *c*-axis (see also Fig. 3). The inset shows a typical spectrum obtained at a frequency of 51.8 GHz. The positions of each of the three main peaks are plotted versus frequency in the main part of the figure. Landé *g*-factors have been assigned to each of the peaks based on the slope of the straight line through each set of data points; the field is oriented such that the highest field peak corresponds approximately to the *x*-component of the *g*-tensor. The shapes of the data points (solid and open circles and squares) have been chosen for comparison with Fig. 3.

the peaks may be understood in terms of the transition rates [18], which depend on the respective Landé *g*-factors (smaller *g*-factor, larger transition rate). The fact that each resonance lies on a perfectly straight line is a clear indication that the transitions occur within a very well isolated effective spin $S' = 1/2$ Kramers' doublet. The anisotropy is contained entirely within the effective Landé *g*-tensor. Further confirmation comes from the temperature dependence in Fig. 2. These data were obtained for the same frequency and field orientation as the data in Fig. 1; one can see that the field alignment is not precisely the same due to the slight splitting of the degenerate branch. Nevertheless, all peaks increase in intensity upon lowering the temperature, thus confirming the assignment of the ground state as a spin $S' = 1/2$ Kramers' doublet.

By far the most detailed information comes from angle-dependent studies. For an arbitrary rotation plane each spectrum should consist of four peaks. However, for high symmetry rotation planes there will be degeneracies and some resonance peaks will superimpose upon one another. The highest symmetry direction corresponds to a magnetic field applied along the *c*-axis of the crystal, where only one peak should be seen. A magnetic field applied at an arbitrary angle within the *ab*-plane of the crystal will give rise to two peaks. Any misalignments of the sample with respect to the applied field will lift this degeneracy and give rise to up to four major peaks.

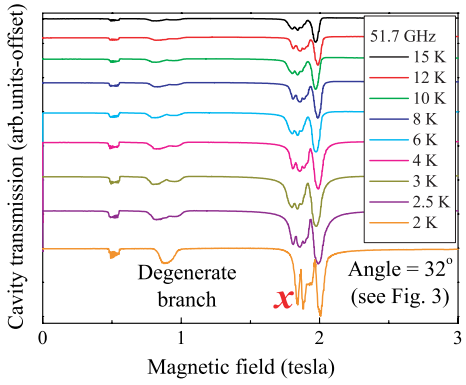


Fig. 2. Temperature dependence of the HFEPR spectra for approximately the same frequency and field orientation as the data in Fig. 1.

The first experiment (rotation **1**) involved rotating the magnetic field in the (1 1 0) plane from the *c*-axis to the *ab*-plane (Fig. 3a). The second experiment (rotation **2**) involved rotating the magnetic field within the *ab*-plane (Fig. 3b). For rotation **1** we observe three resonance branches, which collapse into approximately 1 peak for $\theta = 0°$ (field//*c*-axis) and approximately two peaks for $\theta = 90°$ (field//*ab*-plane, 45° from *a* and *b*). Since only three branches are observed in Fig. 3a, we must assume that one of them is degenerate (solid circles).

Based on simple geometrical considerations, we can immediately determine the nature of the anisotropy at the individual Co^{2+} sites. Due to the octahedral coordination, we assume the anisotropy will be approximately axial (easy-plane or easy-axis [19]). First of all, it is clear from Fig. 3a that the local magnetic axes are tilted with respect to the crystallographic axes (and, therefore, with respect to each other). Starting with the field along *c* (Fig. 3a): when one tilts the field away from this symmetry direction, it necessarily tilts away from three of the local *z*-axes and towards three of the *xy*-planes; conversely, it tilts towards one of the *z*-axes and away from one of the *xy*-planes. Considering the two-fold degeneracy of the branch represented

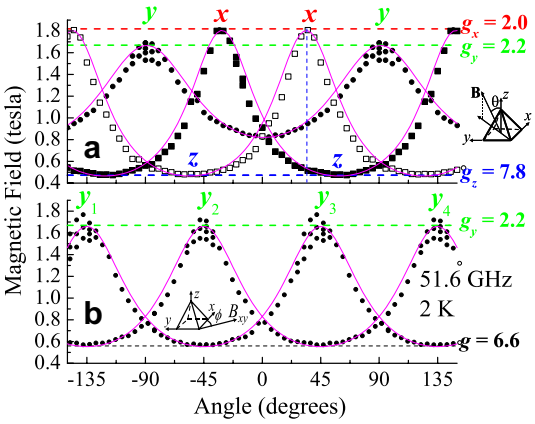


Fig. 3. Angle dependence of the HFEPR peak positions observed for a frequency of 51.6 GHz and a temperature of 3 K, for field rotation in (a) the (1 1 0) plane, and (b) the *ab*-plane. In (a), the angle is referenced to the crystallographic *c*-axis while, in (b), the angle is referenced to either the *a* or *b* axes. In (a), the degenerate branch is indicated by the solid circles, while the squares denote rotations along a plane intersecting two of the easy-axes (labeled *z*). The schematic insets illustrate the two field rotation planes relative to the pyramid shaped single crystal. The *g*-values associated with the extreme positions in the angle-dependence are indicated on the right. The magenta curves are simulations based on the obtained extreme *g*-values for each plane of rotation. The directions of the local magnetic axes (*x*, *y*, *z*) are indicated in the figure.

by the solid circles, upon tilting the field away from c one sees that three of the branches move to higher fields (they become harder), whereas only one moves to lower field (it becomes easier). Therefore, based on the above geometrical consideration, one can conclude that the planes are hard, while the axes are easy, i.e. the anisotropy is of the easy-axis type.

Upon rotating the field over a 180° interval, one is guaranteed to find all four hard planes. These directions correspond to the maxima at −90° (two planes), −32° and +32° (the peak at +90° is equivalent to the one at −90°) in Fig. 3a, and the maxima at $[(n \times 90°) + 45°]$ in Fig. 3b, where n is an integer. Since we observe a degenerate branch in Fig. 3a, this implies that orientation of the field, as it rotates, is the same for both ions contributing to the branch. Thus, the field rotation plane must be perpendicular to the easy-axis tilt plane for these two ions and, therefore by symmetry, it must be parallel to the easy axis tilt plane for the other two ions. Therefore, we conclude that the two minima labeled z correspond precisely to the easy axes. One can then immediately determine that $g_z = 7.80$ (indicated by blue dashed line). The minimum at 0° in Fig. 3a corresponds to the point of closes approach of the field to the other two easy axes. From the positions of the maxima and minima, we determine that the easy axes (hard planes) are tilted about 58° (32°) away from the crystallographic c-axis, and the easy axes are tilted in the $(1\,1\,0)$ and $(1\,\bar{1}\,0)$ planes.

It is notable in Fig. 3a that the heights of the maxima at ±90° and ±32° are slightly different, corresponding to g-values close to 2.00 and 2.20. This observation implies weak in-plane anisotropy, suggesting a weak orthorhombic distortion at the individual Co^{2+} sites. The lesser of the two g-values corresponds to $g_x \approx 2.00$ (the hard axis, red dashed line) and the intermediate value to $g_y \approx 2.20$ (the medium axis, green dashed line).[1] From the hard-plane rotations (Fig. 3b), we see that the maxima coincide with $g_y \approx 2.20$ in Fig. 3a. Therefore, we can conclude that the medium axes lie along the intersections of the four hard planes, within the ab-plane of the crystal [along $(1\,1\,0)$ and $(1\,\bar{1}\,0)$]. The hard axes are, therefore, directed maximally out of the ab-plane [with projections also along $(1\,1\,0)$ and $(1\,\bar{1}\,0)$], tilted 32° away from c. The minima in Fig. 3b correspond to the projection of the easy axis anisotropy onto the ab-plane, i.e. $g = g_z \times \cos 32° = 6.61$ (marked by horizontal black dashed line). Finally, the vertical dashed line in Fig. 3a denotes the orientation of the data presented in Figs. 2 and 3. As can be seen, the data points are coded similarly to the corresponding 51.8 GHz data in Fig. 1.

As already discussed, the Hamiltonian for a well isolated effective spin $S' = 1/2$ Kramers' doublet takes the form $\widehat{H} = \mu_B \widehat{S}' \cdot \overleftrightarrow{g}' \cdot \vec{B}$, where $\overleftrightarrow{g}'$ represents an effective Landé g-tensor that parameterizes all of the anisotropy associated with the spin-orbit coupling. The resulting relation between the measurement frequency, f, and the resonance field, B_{res}, is then $hf = g(\theta)\mu_B B_{res}$. Thus, for a fixed frequency measurement, $B_{res} = hf/g(\theta)\mu_B$. One can therefore attempt to fit the data in Fig. 3 assuming a simple angle dependence of the form $g(\theta) = g_{min} + \delta g \cos^2(\theta - \theta_o)$, where g_{min} is the minimum g-value for a particular plane of rotation, δg is the difference between the minimum and maximum g-values, and θ_o is the angle corresponding to g_{min}. The magenta curves in Fig. 3 correspond to such fits. As can be seen, the agreement is quite good.

4. Conclusions

The orientations of the magnetic axes, with respect to the crystal lattice, were determined for single Co^{2+} ions doped into a nonmagnetic Zn_4 complex. Frequency and temperature dependence studies confirm the ground state to be an effective spin $S' = 1/2$ Kramers' doublet with a highly anisotropic g-factor. The anisotropy is found to be of the easy-axis type, with the single-ion easy axis directions tilted away from the crystallographic c direction by 58°. The g-factor anisotropy ($g_z = 7.8$ and $g_x \approx 2.0$) is close to the maximum expected for an octahedral Co^{2+} complex [19], suggesting a huge axial zero-field-splitting. It is presently unclear how the Kramers ions could combine into a Co_4 complex to give rise to SMM behavior.

Acknowledgement

This work was supported by the US National Science Foundation under Grant numbers DMR-0239481, DMR-0414809 and DMR-0506946.

Appendix A. Supplementary material

CCDC 627008 contains the supplementary crystallographic data for the compound referred in this paper. These data can be obtained free of charge via http://www.ccdc.cam.ac.uk/conts/retrieving.html, or from the Cambridge Crystallographic Data Centre, 12 Union Road, Cambridge CB2 1EZ, UK; fax: +(44) 1223-336-033; or e-mail: deposit@ccdc.cam.ac.uk. Supplementary data associated with this article can be found, in the online version, at doi:10.1016/j.poly.2006.11.018.

References

[1] R. Sessoli et al., Nature 365 (6442) (1993) 141.
[2] R. Sessoli et al., J. Am. Chem. Soc. 115 (5) (1993) 1804.
[3] G. Christou et al., MRS Bull. 25 (11) (2000) 66.
[4] S. Hill et al., Science 302 (5647) (2003) 1015.
[5] J.R. Friedman et al., Phys. Rev. Lett. 76 (20) (1996) 3830.
[6] L. Thomas et al., Nature 383 (6596) (1996) 145.
[7] W. Wernsdorfer, R. Sessoli, Science 284 (5411) (1999) 133.
[8] E.-C. Yang et al., Inorg. Chem. 44 (2005) 3827.
[9] S. Hill et al., J. Appl. Phys. 97 (2005) 10M501.

[1] For interpretation of references in color, the reader is referred to the web version of this article.

[10] R. Edwards et al., J. Appl. Phys. 93 (2003) 7807.
[11] E.-C. Yang, Doctoral thesis.
[12] A. Wilson et al., Phys. Rev. B 74 (2006) 140403.
[13] O. Kahn, Molecular Magnetism, Wiley, 1993.
[14] J. Lawrence, C. Beedle, J. Ma, S. Hill, D.N. Hendrickson, Unpublished.
[15] M. Mola et al., Rev. Sci. Instrum. 71 (1) (2000) 186.
[16] S. Takahashi, S. Hill, Rev. Sci. Instrum. 76 (2005) 023114.
[17] E.-C. Yang et al., J. Appl. Phys. 91 (2002) 7382.
[18] A. Abragam, B. Bleaney, Electron Paramagnetic Resonance of Transition Metal Ions, Oxford University Press, 1970.
[19] L.L. Lohr, J.C. Miller, R.R. Sharp, J. Chem. Phys. 111 (1999) 10148.

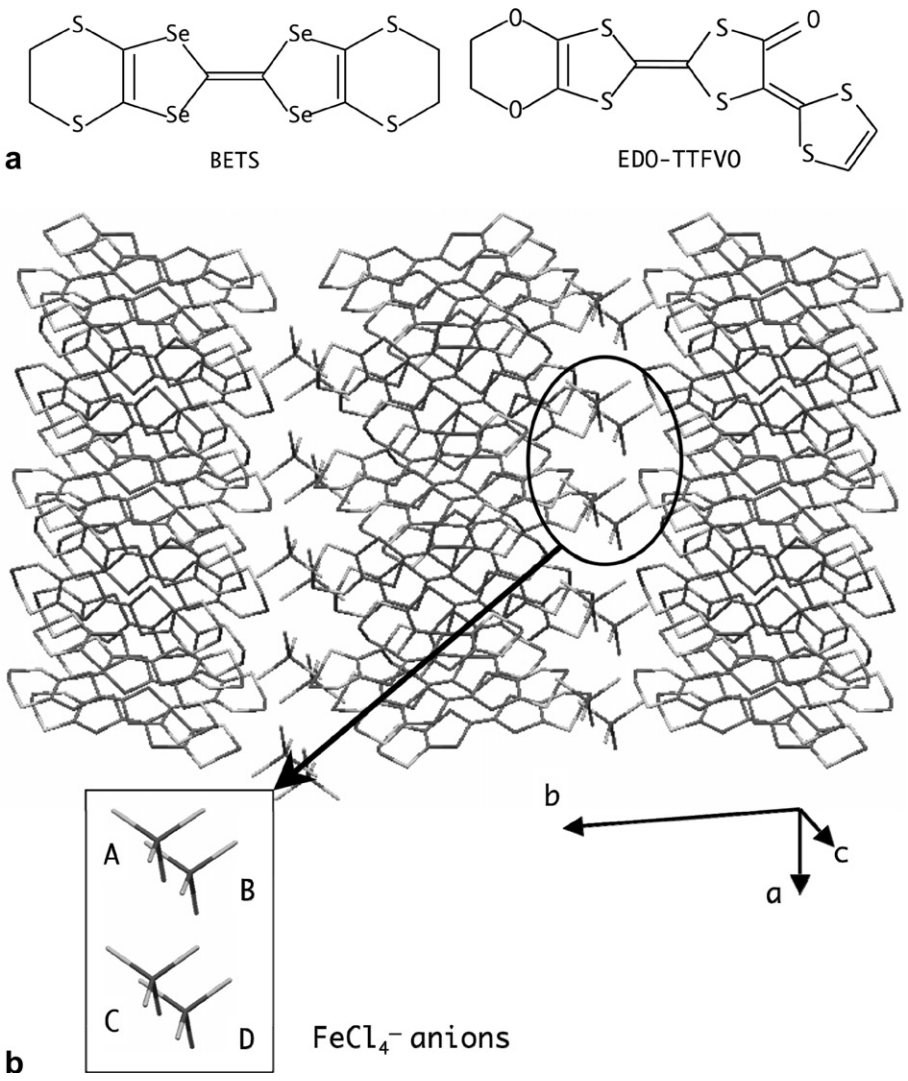


Fig. 1. (a) Molecular structures of BETS EDO-TTFVO. (b) Crystal structure of κ-$(BETS)_2FeCl_4$ and $FeCl_4^-$ pairs.

MO methods. The relations between magnetic interaction and configurations were discussed.

2. Theoretical background

As well known, the Heisenberg spin model is useful to describe magnetic interaction between spins. The J values based on Heisenberg Hamiltonian can indicate magnitude of magnetic interaction. The spin–Hamiltonian is defined as

$$\mathbf{H} = \sum -2J_{ij}\mathbf{s}_i \cdot \mathbf{s}_j, \tag{1}$$

where $\mathbf{s}_i$ is total spin operator at ith site, and J_{ij} is the effective exchange integral between ith and jth sites. The physical meaning of J_{ij} is energy difference between lower spin state (LS) and higher spin state (HS) in systems. The positive value of J_{ij} means ferromagnetic interaction in the ground state, while the negative value of J_{ij} means antiferromagnetic interaction in the ground state.

By using *ab initio* MO computational techniques, J_{ij} values can be estimated quantitatively. For unrestricted calculations, broken-symmetry approach with our spin projected scheme [7], which eliminates spin contamination, can calculate the J_{ij} with the following equation:

$$J_{ij} = -\frac{^{HS}E(X) - {}^{LS}E(X)}{^{HS}\langle S^2\rangle - {}^{LS}\langle S^2\rangle}, \tag{2}$$

where $E(X)$ and $\langle S^2\rangle$ denote, respectively, total energy and total spin angular momentum.

In series of our studies, theoretical calculations by using the KS-DFT (Kohn–Sham hybrid density functional theory) methods were carried out [8]. The UB3LYP method has been employed to elucidate electronic properties. Here, Becke's three parameter exchange [9], and Lee, Yang, and Parr's correlation functionals were chosen for our calculations [10]. Our calculations were carried out by Gaussian98 program packages [11], and SCF conversion were controlled in 10^{-8} a.u. level.

3. Crystal structure and model preparation

The crystal structure of κ-$(BETS)_2FeCl_4$ were illustrated in Fig. 1b. The X-ray crystallographic data in Cambridge Structural Database (CSD) were employed. It is found that both layers of BETS donors and $FeCl_4^-$ anions are stacked alternatively. The complexes of **1** have unit cells classified by the space group *Pnma* and the cell parameter sets are $a = 11.483(4)$ Å, $b = 35.720(15)$ Å, and $c = 8.383(3)$ Å. The bond lengths of all Fe–Cl bonds in $FeCl_4^-$ anion are 2.178, 2.198, 2.198, and 2.205 Å. The average of bond lengths of Fe–Cl bonds is 2.195 Å.

The four $FeCl_4^-$ anions (A, B, C, and D) from crystal structure were extracted. The three pairs (A–B, A–C, and A–D) were proposed. The distances of Fe–Fe in A–B pair, A–C pair, and A–D pair were 8.383, 5.775, and 9.658 Å, respectively. In the following section, we proposed dimer models, which were based on these pairs.

4. Computational results

4.1. The geometry optimization of monomer model

First, let us investigate the most suitable basis sets for both Fe and Cl atoms in $FeCl_4^-$ monomer. With the various basis functions, ionization potential (IP) for Fe atom and electron affinity (EA) for Cl atom were calculated by the UB3LYP method. The following basis functions were employed: STO-3G, 6-31G, 6-31G*, 6-31+G, 6-31+G*, 6-311G, 6-311G*, 6-311+G, and 6-311+G* in the GAUSSIAN program packages. As shown in Table 1, the calculated first, second, and third IPs with 6-31G basis sets for Fe atom were 7.72, 16.08, and 31.31 eV, respectively. The calculated EA with 6-31+G basis sets for the Cl atom were 3.751 eV. As optimum basis functions, 6-31G and 6-31+G basis sets for Fe and Cl atoms were employed, respectively. Our calculated results could denote the near tendency of reference data [12].

Next, structure of $FeCl_4^-$ monomer with regular tetrahedron was optimized by using of UB3LYP method. All the bond lengths of Fe–Cl bonds (R_{Fe-Cl}) in $FeCl_4^-$ anion were varied, though all angles and dihedral angles were fixed to regular tetrahedron structure. The obtained value of R_{Fe-Cl} was 2.27 Å, which was 0.075 Å longer than numerical average of Fe–Cl lengths in the $FeCl_4^-$ anion in crystal **1**. In the following, the optimized structure was successfully used.

Table 1
Calculated IPs for the Fe atom and EA for the Cl atom by using UB3LYP method

	Fe atom/eV			Cl atom/eV
	First	Second	Third	
STO-3G	4.91	16.95	24.43	−0.586
6-31G	7.72	16.08	31.31	3.194
6-31G*	7.72	16.08	31.32	3.155
6-31+G	8.07	16.43	31.65	3.751
6-31+G*	8.07	16.43	31.66	3.712
6-311G	7.74	16.26	31.37	3.699
6-311G*	7.74	16.26	31.39	3.661
6-311+G	8.00	16.48	31.56	3.762
6-311+G*	8.00	16.48	31.57	3.724
Ref. [12]	7.87	16.18	30.651	3.615

4.2. The J values in simple dimer models

In this section, simple dimer models of $FeCl_4^-$ anion were assembled by using the previous optimized monomer model in order to examine various magnetic *d–d* interactions. As shown in Fig. 2, the following three types of dimer models were proposed: 1–1 model, 1–2 model, and 1-3 model. The 1–1 model denoted that Cl(A) in $FeCl_4$(A) came close to Cl(B) in $FeCl_4$(B).

First, magnetic *d–d* interactions dependency on rotation angles were evaluated. For 1–1 model, $FeCl_4$(A) was fixed and $FeCl_4$(B) was rotated θ degrees clockwise on this paper as shown in Fig. 2a. The distance of Fe(A) to Fe(B) (R_{Fe-Fe}) was fixed to be 7.0 Å. As the results of rotation, ferromagnetic structures ($\theta = 70°$ (inset in Fig. 3) and 180°) were found and the J values were 0.04 cm^{-1}. These

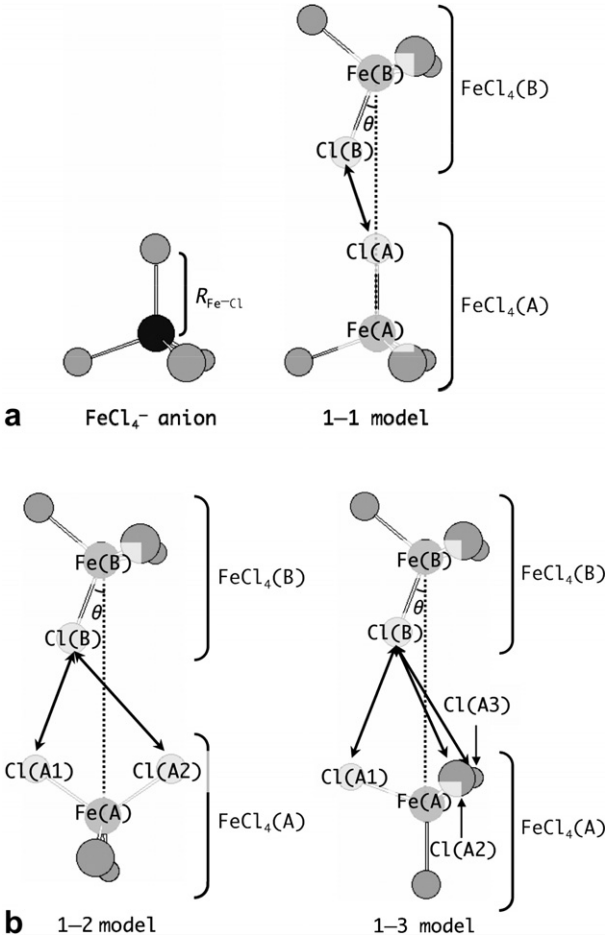


Fig. 2. Dimer models of $FeCl_4^-$ anion: (a) 1–1 model and (b) 1–2 and 1–3 models.

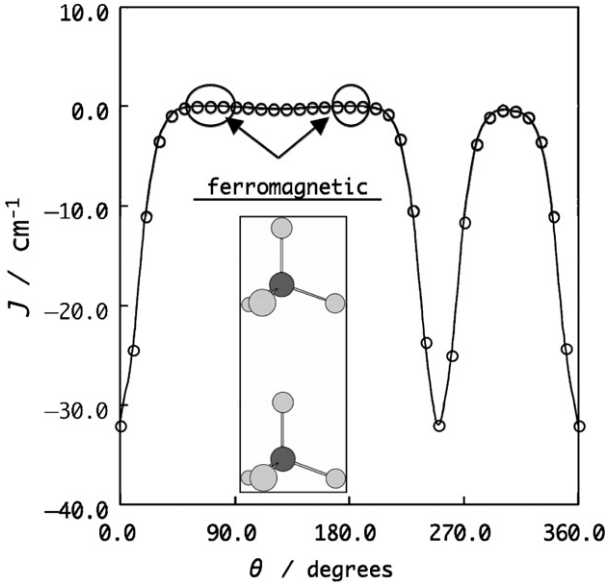


Fig. 3. Calculated J values in 1–1 model by using UB3LYP method were plotted against rotation angle θ. Inset illustrated the interesting structure where the evaluated magnetic interaction is ferromagnetic.

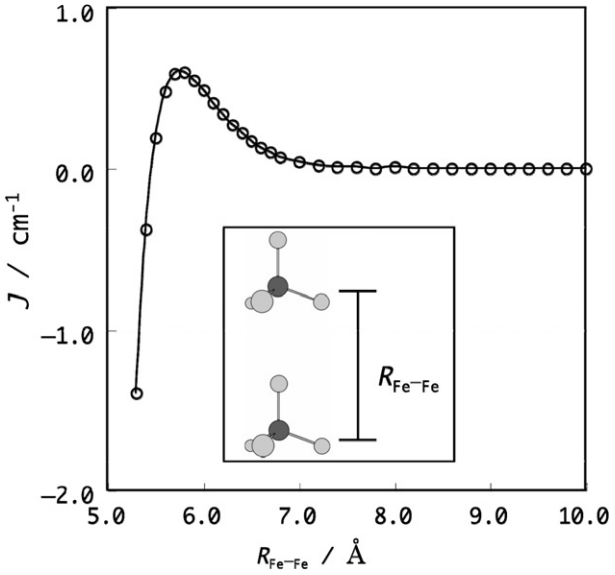


Fig. 5. Calculated J values in ferromagnetic structure in 1–1 model by using UB3LYP method were plotted against interatomic distance R_{Fe-Fe}.

ferromagnetic structure denoted that Cl(A) of $FeCl_4$(A) came close to three Cl atoms of $FeCl_4$(B). On the other hand, magnetic interactions in almost all configurations were antiferromagnetic.

In a similar way, magnetic d–d interaction dependency on rotation angles for both 1–2 model and 1–3 model were investigated as shown in Fig. 2b. The 1–2 model denoted that Cl(A1) and Cl(A2) in $FeCl_4$(A) came close to Cl(B) in $FeCl_4$(B). The 1–3 model denoted that Cl(A1), Cl(A2), and Cl(A3) in $FeCl_4$(A) came close to Cl(B) in $FeCl_4$(B). The value of R_{Fe-Fe} was also fixed to be 7.0 Å. In 1–2 model, magnetic interactions in all configurations were antiferromagnetic. As shown in Fig. 4, ferromagnetic structures ($\theta = 0°$ and 250°) were found in 1–3 model and the J values were 0.04 cm^{-1}. These ferromagnetic structure was the same as the ferromagnetic structure in 1–1 model. Magnetic interactions in almost all configurations in 1–3 model were antiferromagnetic.

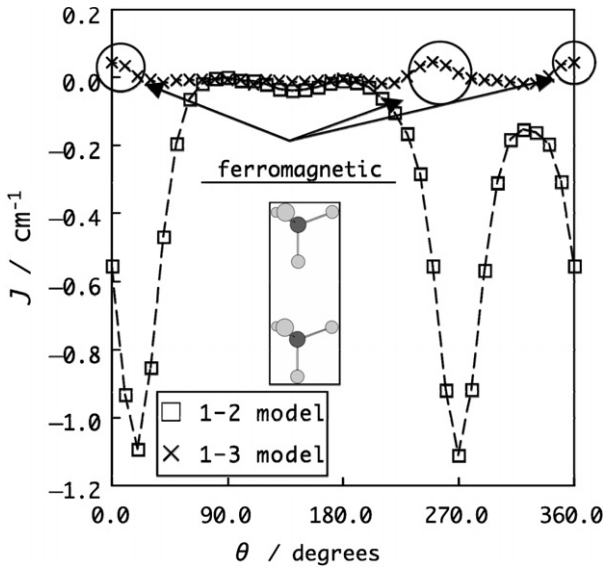


Fig. 4. Calculated J values in 1–2 and 1–3 models by using UB3LYP method were plotted against rotation angle θ.

Next, in order to evaluate d–d interaction dependency on distance, the value of R_{Fe-Fe} was varied from 5.3 to 10.0 Å in the ferromagnetic structure in 1–1 model. As shown in Fig. 5, the largest ferromagnetic interaction can be yielded in the structure with $R_{Fe-Fe} = 5.8$ Å and J value was 0.60 cm^{-1}. On the other hand, when $FeCl_4$(B) was brought too close to $FeCl_4$(A), magnetic interactions turned to be antiferromagnetic. There was no interaction when the value of R_{Fe-Fe} was from 8.0 to 10.0 Å.

5. Conclusion

In our studies, the ferromagnetic conformations between $FeCl_4^-$ anions were found. This configuration denoted that one Cl atom of $FeCl_4$(A) came close to three Cl atoms of $FeCl_4$(B). It seemed that this structure was feasible for crystal structure. The largest J value was 0.6 cm^{-1} when the value of R_{Fe-Fe} was 5.8 Å. Unfortunately, these magnetic interactions were relatively small.

In addition to these calculations for simple model systems, we investigated magnetic d–d interactions of $FeCl_4^-$ anion pairs in the real crystal of **1**. The evaluated J values of A–B pair, A–C pair, and A–D pair in Fig. 1b were −0.05, −0.05, and 0.00 cm^{-1}, respectively.

In a similar way, dimer models of $FeBr_4^-$ anion were also assembled in order to check difference between Cl and Br atoms to magnetic d–d interaction. The structure of $FeBr_4^-$ monomer with regular tetrahedron was optimized by using UB3LYP method with 6-31G and 6-311G

basis set for Fe and Br atoms, respectively. The obtained value of the Fe–Br bond length was 2.42 Å. To evaluate magnetic *d–d* interaction dependency on rotation angle and distance, the dimer models were used: 1–1, 1–2, and 1–3 models. As a result of rotation, the ferromagnetic interaction was found in a certain structure. In 1–1 model, the J value in ferromagnetic structure ($\theta = 70°$ and 180°) was 0.13 cm^{-1}. In 1–3 model, the J value of ferromagnetic structure ($\theta = 0°$ and 250°) was 0.13 cm^{-1}. These structure were very resembled to ferromagnetic structure of $FeCl_4^-$ anion dimer. As a result of variation of distance, when the distance between Fe(A) in $FeBr_4$(A) and Fe(B) in $FeBr_4$(B) was 6.1 Å, where the J value was 0.77 cm^{-1}.

Acknowledgement

This work has been supported by a Grant–in–Aid for Scientific Research on Priority Areas (Nos. 18350008 and 18205023) from Ministry of Education, Science, Sports and Culture, Japan.

References

[1] H. Kobayashi, H. Tomita, T. Naito, A. Kobayashi, F. Sakai, T. Watanabe, P. Cassoux, J. Am. Chem. Soc. 118 (1996) 368.
[2] T. Otsuka, A. Kobayashi, Y. Miyamoto, J. Kiuchi, N. Wada, E. Ojima, H. Fujiwara, H. Kobayashi, Chem. Lett. (2000) 732.
[3] E. Ojima, H. Fujiwara, K. Kato, H. Kobayashi, H. Tanaka, A. Kobayashi, M. Tokumoto, P. Cassoux, J. Am. Chem. Soc. 121 (1999) 5581.
[4] H. Kobayashi, H. Tanaka, H. Fujiwara, I. Tamura, V. Gritsenko, T. Otsuka, E. Fujiwara, A. Kobayashi, M. Tokumoto, P. Cassoux, Synth. Met. 133 (2003) 477.
[5] H. Fujiwara, K. Wada, T. Hiraoka, T. Hayashi, T. Sugimoto, H. Nakazumi, K. Yokogawa, M. Teramura, S. Yasuzuka, K. Murata, T. Mori, J. Am. Chem. Soc. 127 (2005) 14166.
[6] T. Kawakami, T. Taniguchi, M. Shoji, Y. Kitagawa, M. Okumura, K. Yamaguchi, Polyhedron 24 (2005) 2382.
[7] T. Soda, Y. Kitagawa, T. Onishi, Y. Takano, Y. Shigeta, H. Nagao, Y. Yoshioka, K. Yamaguchi, Chem. Phys. Lett. 319 (2000) 223.
[8] R.G. Parr, W. Young, Density-functional Theory of Atoms and Molecules, Springer, Berlin, 1996.
[9] D. Becke, J. Am. Chem. Soc. 98 (1993) 5648.
[10] C. Lee, W. Yang, R.G. Parr, Phys. Rev. B 37 (1988) 785.
[11] M.J. Frisch, G.W. Trucks, H.B. Schlegel, G.E. Scuseria, M.A. Robb, J.R. Cheeseman, V.G. Zakrzewski, J.A. Montgomery Jr., R.E. Stratmann, J.C. Burant, S. Dapprich, J.M. Millam, A.D. Daniels, K.N. Kudin, M.C. Strain, O. Farkas, J. Tomasi, V. Barone, M. Cossi, R. Cammi, B. Mennucci, C. Pomelli, C. Adamo, S. Clifford, J. Ochterski, G.A. Petersson, P.Y. Ayala, Q. Cui, K. Morokuma, D.K. Malick, A.D. Rabuck, K. Raghavachari, J.B. Foresman, J. Cioslowski, J.V. Ortiz, A.G. Baboul, B.B. Stefanov, G. Liu, A. Liashenko, P. Piskorz, I. Komaromi, R. Gomperts, R.L. Martin, D.J. Fox, T. Keith, M.A. Al-Laham, C.Y. Peng, A. Nanayakkara, C. Gonzalez, M. Challacombe, P.M.W. Gill, B.G. Johnson, W. Chen, M.W. Wong, J.L. Andres, M. Head-Gordon, E.S. Replogle, J.A. Pople, Gaussian 98, Gaussian, Inc., Pittsburgh, PA, 1998.
[12] Chemical Handbook (Kagaku Binran), 3th ed., The Chemical Society of Japan (Eds.), Maruzen, Tokyo (in Japanese), 1984.

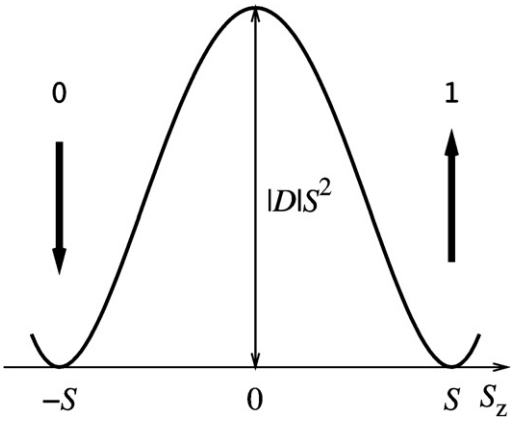


Fig. 1. Energy diagram of the ZFS Hamiltonian when $D < 0$. The height of the energy barrier between the ground states is $|D|S^2$. The pair of states can be taken as a memory bit for the use of data storage.

2. Computational scheme to calculate ZFS parameters

The one-center spin–orbit coupling (SOC1) mainly causes the ZFS of transition metal complexes. The SOC1 Hamiltonian is

$$\hat{H}_{\mathrm{SOC1}} = \frac{1}{i}\sum_j \hat{\mathbf{V}}(\mathbf{r}_j)\cdot\hat{\mathbf{s}}_j, \quad \hat{\mathbf{V}}(\mathbf{r}) \equiv -\frac{1}{2c^2}\nabla\times\mathbf{E}(\mathbf{r}), \tag{2}$$

where $\mathbf{r}_j$ and $\hat{\mathbf{s}}_j$ are coordinates and spin operator of jth electron, c is the speed of light, and $\mathbf{E}(\mathbf{r})$ is the electric field of the nuclei. The ZFS parameters can be calculated with the second order perturbation theory of the SOC1 energy with non-relativistic broken-symmetry mean-field theories taken as the zeroth-order description [10]. The perturbation energy is

$$E_{\mathrm{SOPT2}} = {}^t\mathbf{SDS}, \tag{3}$$

$$\mathbf{D} = \frac{1}{4S^2}\begin{pmatrix} N_{xx}+N'_{yy}+N'_{zz} & N_{xy}+N'_{xy} & N_{zx}+N'_{zx} \\ N_{xy}+N'_{xy} & N'_{xx}+N_{yy}+N'_{zz} & N_{yz}+N'_{yz} \\ N_{zx}+N'_{zx} & N_{yz}+N'_{yz} & N'_{xx}+N'_{yy}+N_{zz} \end{pmatrix}, \tag{4}$$

$$N_{pq} \equiv M^{\alpha\alpha}_{pq} + M^{\beta\beta}_{pq}, \quad N'_{pq} \equiv M^{\alpha\beta}_{pq} + M^{\beta\alpha}_{pq}, \tag{5}$$

$$M^{\sigma\tau}_{pq} \equiv \sum_a^{\sigma\text{-occupied}} \sum_s^{\tau\text{-virtual}} \frac{\langle\psi^\sigma_a|\hat{V}_p|\psi^\tau_s\rangle\langle\psi^\tau_s|\hat{V}_q|\psi^\sigma_a\rangle}{\varepsilon^\tau_s - \varepsilon^\sigma_a}, \tag{6}$$

where $\mathbf{S}$ is the total spin vector, and $|\psi^\sigma_a\rangle$ and ε^σ_a are the ath σ-spin molecular orbital and the orbital energy, respectively. We could find the ZFS parameters by diagonalizing the $\mathbf{D}$ tensor.

$$E_{\mathrm{SOPT2}} = {}^t\mathbf{S}'\mathbf{d}\mathbf{S}', \tag{7}$$

$$\mathbf{d} = \mathbf{U}\mathbf{D}'^t\mathbf{U}, \quad \mathbf{S}' = \mathbf{U}\mathbf{S}, \tag{8}$$

$$D = d_z - \frac{d_x+d_y}{2}, \quad E = \frac{d_x-d_y}{2}, \tag{9}$$

and the primary axis is $\mathbf{u}_z$ of $\mathbf{U} = (\mathbf{u}_x\mathbf{u}_y\mathbf{u}_z)$. Here, the coordinates are chosen so that $|D| > 2|E|$.

3. Calculations, results, and discussion

3.1. Manganese porphyrin complex $[MnP]^+$

We performed ab initio calculations of a manganese porphyrin complex $[MnP]^+$ (Fig. 2). $[MnP]^+$ was used as a model complex of $[MnTBrPP]^+$, which is the main source of spin of $[MnTBrPP]^+[TCNE]^-$. The X-ray crystal structure of $[MnTBrPP]^+[TCNE]^-$ was used, and hydrogen atoms were substituted for TBrP. We used the UDFT (UBLYP) and hybrid UDFT (UB3LYP, UB2LYP [11]) for the calculations. We employed Huzinaga's MIDI+P basis sets (533(21)/53(21)/(41)) for the transition metals [12] and 6-31G* basis sets by Pople et al. for the other atoms.

Table 1 shows the computational results. The spin magnitude S of the ground state is 2. All the D values are negative, and the magnetic easy axes are perpendicular to the porphyrin plane. In fact, the real $[MnP]^+$ has a negative D value as shown in the Refs. [13,14]. The calculated D values are in good agreement with $[MnP]^+$ quantitatively. Since the real $[MnP]^+$ has the uniaxial symmetry, the E value is zero. However, all the calculated E values are much smaller than the D values but not zero because of the slight distortion of the porphyrin in the $[MnTBrPP]^+[TCNE]^-$ X-ray crystal structure.

3.2. $[MnP]^+[TCNE]^-[MnP]^+$

Next, we performed calculations of a manganese porphyrin dimer linked by TCNE, $[MnP]^+[TCNE]^-[MnP]^+$ (MTM) (Fig. 3). The same computational methods, basis sets, and scheme of getting the geometry as the previous subsection were employed.

Table 1 shows the results. The low spin state ($\uparrow\downarrow\uparrow$) is preferred rather than the high spin state ($\uparrow\uparrow\uparrow$), and the spin magnitude S is 7/2. Although the uniaxial symmetry is

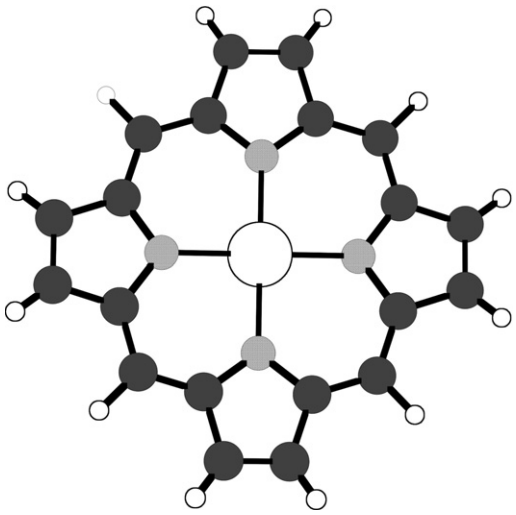


Fig. 2. Structure of the manganese porphyrin complex.

Table 1
ZFS parameters and energy barriers $|D|S^2$ of the model molecules in cm^{-1}

Methods	$[MnP]^+$			MTM			TMT		
	D	E	$\|D\|S^2$	D	E	$\|D\|S^2$	D	E	$\|D\|S^2$
UBLYP	−3.35	0.022	13.4	−2.06	0.047	25.2	–	–	–
UB3LYP	−1.55	0.009	06.2	−1.01	0.022	12.4	−6.43	0.058	06.4
UB2LYP	−0.88	0.004	03.5	−0.59	0.002	07.2	−3.31	0.048	03.3
Exp.[a]	−2.30	0.000	09.2						

[a] Refs. [13,14].

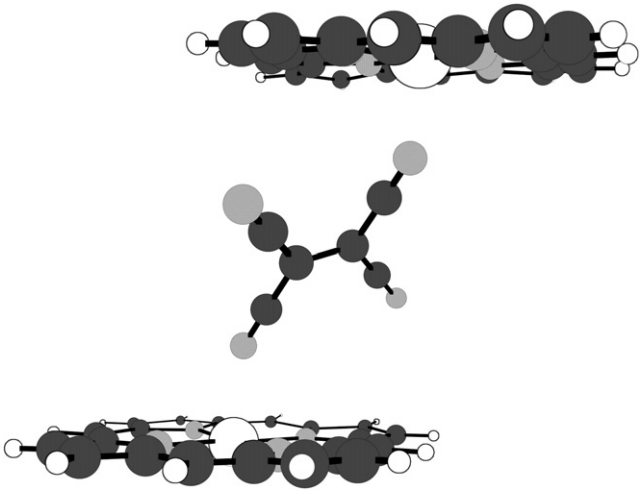


Fig. 3. Structure of $[MnP]^+[TCNE]^-[MnP]^+$.

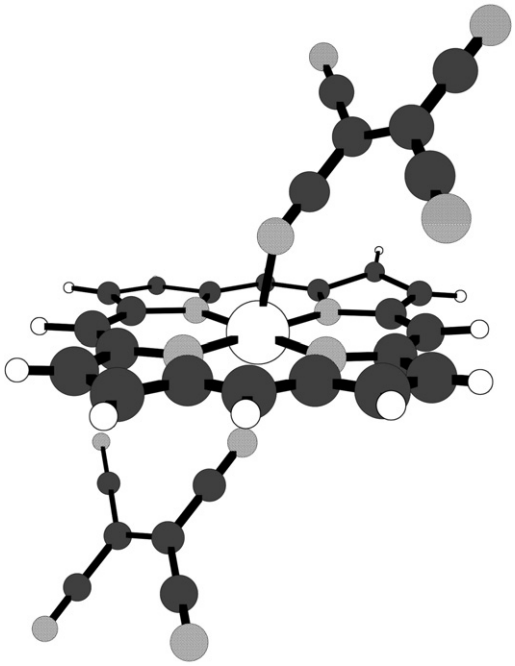


Fig. 4. Structure of $[TCNE]^-[MnP]^+[TCNE]^-$.

broken, all the E values are very small and the easy axes are almost the same as that of $[MnP]^+$. The D values become smaller than those of $[MnP]^+$, but the energy barriers $|D|S^2$ become larger. The energy barriers are twice as large as those of $[MnP]^+$. Therefore, the coordination of $[TCNE]^-$ hardly affect the magnetic anisotropy of $[MnP]^+$.

3.3. $[TCNE]^-[MnP]^+[TCNE]^-$

Finally, we performed calculations of manganese porphyrin with two $[TCNE]^-$, $[TCNE]^-[MnP]^+[TCNE]^-$ (TMT) (Fig. 4). The same conditions as above were employed.

Table 1 shows the results. The UBLYP calculation was failed. The low spin state ($\downarrow\uparrow\downarrow$) is preferred rather than the high spin state ($\uparrow\uparrow\uparrow$), and the spin magnitude S is 1. The D values are negative, and the E values are very small. The easy axes are almost the same as that of $[MnP]^+$. The energy barriers $|D|S^2$ are almost the same as that of $[MnP]^+$. Also in this case, the $[TCNE]^-$ ligands play almost no role in the magnetic anisotropy.

3.4. Minimal model

The bridging ligands TCNEs are important to the ferrimagnetic alignment of the SCM [4,6]. The exchange interaction between MnTBrPP and TCNE is antiferromagnetic, and the effective exchange integral J is $-178\ cm^{-1}$ [4]. However, it is found from the present model calculations that coordinating TCNEs is not important to the magnetic anisotropy of the manganese porphyrin complexes. The contribution of the spin–spin dipole coupling to the ZFS, which is important to the organic radicals as TCNE, is not considered in the present paper. However, it is ignorable, since the D values of organic radicals are normally one order less than those of the transition metal complexes and the spin magnitude S of TCNE is also small.

These results can be summarized as the following minimal model Hamiltonian is

$$H = -|J_{\mathrm{MnTXPP-TCNE}}| \sum_{\langle i,j\rangle}^{\langle \mathrm{MnTXPP,TCNE}\rangle} \mathbf{S}_i \cdot \mathbf{S}_j - |D_{\mathrm{MnTXPP}}| \sum_i^{\mathrm{MnTXPP}} S_i^2, \quad (10)$$

where $\langle i,j\rangle$ runs over all the nearest-neighbor pairs.

4. Concluding remarks

We investigated the magnetic anisotropy of $[MnTXPP]^{+}[TCNE]^{-}$, which is a SCM, with ab initio calculations. MnTXPP was reduced to MnP for reducing the computational cost. The ZFS parameters of the MnP were in good agreement with the experimental values quantitatively. From the calculations of the model complexes, we found that TCNE hardly affect the magnetic anisotropy of MnP. Therefore, the TCNEs are important only to the ferrimagnetic alignment.

Acknowledgements

R. Takeda thanks the financial support for Research Fellowships of the Japan Society for the Promotion of Science for Young Scientists. This work has been supported by Grants-in-Aid for Scientific Research (16750049, 18350008, 18205023) from Japan Society for the Promotion of Science (JSPS).

References

[1] A. Caneschi, D. Gatteschi, R. Sessoli, J. Am. Chem. Soc. 113 (1991) 5873.
[2] S.M.J. Aubin, M.W. Wemple, D.M. Adams, H.-L. Tsai, G. Christou, D.N. Hendrickson, J. Am. Chem. Soc. 118 (1996) 7746.
[3] D. Gatteschi, R. Sessoli, Angew. Chem., Int. Ed. 42 (2003) 268.
[4] D.K. Rittenberg, A.M. Arif, J.S. Miller, J. Chem. Soc., Dalton Trans. (2000) 3939.
[5] H. Miyasaka, T. Madanbashi, K. Sugimoto, Y. Nakazawa, W. Wernsdorfer, K. Sugiura, M. Yamashita, C. Coulon, R. Clérac, Chem. Eur. J. 12 (2006) 7028.
[6] K. Koizumi, M. Shoji, Y. Kitagawa, T. Taniguchi, T. Kawakami, M. Okumura, K. Yamaguchi, Polyhedron 24 (2005) 2720.
[7] M.J. Frisch, G.W. Trucks, H.B. Schlegel, G.E. Scuseria, M.A. Robb, J.R. Cheeseman, V.G. Zakrzewski, J.A. Montgomery Jr., R.E. Stratmann, J.C. Burant, S. Dapprich, J.M. Millam, A.D. Daniels, K.N. Kudin, M.C. Strain, O. Farkas, J. Tomasi, V. Barone, M. Cossi, R. Cammi, B. Mennucci, C. Pomelli, C. Adamo, S. Clifford, J. Ochterski, G.A. Petersson, P.Y. Ayala, Q. Cui, K. Morokuma, D.K. Malick, A.D. Rabuck, K. Raghavachari, J.B. Foresman, J. Cioslowski, J.V. Ortiz, B.B. Stefanov, G. Liu, A. Liashenko, P. Piskorz, I. Komaromi, R. Gompert, R.L. Martin, D.J. Fox, T. Keith, M.A. Al-Laham, C.Y. Peng, A. Nanayakkara, C. Gonzalez, M. Challacombe, P.M.W. Gill, B. Johnson, W. Chen, M.W. Wong, J.L. Andres, M. Head-Gordon, E.S. Replogle, J.A. Pople, GAUSSIAN 98, Gaussian, Inc., Pittsburgh, PA, 1998.
[8] M.R. Pederson, S.N. Khanna, Phys. Rev. B 60 (1999) 9566.
[9] J. Kortus, M.R. Pederson, T. Baruah, N. Bernstein, C.S. Hellberg, Polyhedron 22 (2003) 1871.
[10] R. Takeda, S. Mitsuo, S. Yamanaka, K. Yamaguchi, Polyhedron 24 (2005) 2238.
[11] Y. Kitagawa, T. Soda, Y. Shigeta, S. Yamanaka, Y. Yoshioka, K. Yamaguchi, Int. J. Quant. Chem. 84 (2001) 592.
[12] H. Tatewaki, S. Huzinaga, J. Chem. Phys. 71 (1979) 4339.
[13] D.P. Goldberg, J. Telser, J. Krzystek, A.G. Montalban, L.-C. Brunel, A.G.M. Barrett, B.M. Hoffman, J. Am. Chem. Soc. 119 (1997) 8722.
[14] J. Krzystek, J. Telser, L.A. Pardi, D.P. Goldberg, B.M. Hoffman, L.-C. Brunel, Inorg. Chem. 38 (1999) 6121.

complete-active-space self-consistent field (CASSCF) results [11,12]. They performed CAS computations using up to the [6,6] active space, and discussed that the [26,26] active space is required for discussions of magnetic interaction in various general stacking modes of the phenalenyl radical dimer. It is not feasible from the viewpoint of the present computational resource. On the other hand, the multistate MR second-order perturbation (MRMP2) calculations using perfect pairing type of two-configuration MR reference [13,14] have been performed for modeled phenalenyl dimers with omitting *tert*-butyl groups by Head-Gordon and his co-workers [13]. They have showed a reasonable potential curve, of which binding energy, 11 kcal/mol, is consistent with the experimental enthalpy in CH_2Cl_2 solution (−9.5 kcal/mol).

As an alternative MR theory, the multireference version of DFT has been recently developed [18–20]. We also have developed some versions of multireference DFT approaches [18,19]. In this theory, electrons exhibiting quantum spin behaviors are treated by an MR wavefunction, while remaining correlation effects by DFT. In this study, we present the CASCI[2,2]-DFT study of phenalenyl dimeric systems. This is a minimum treatment for multireference wavefunction part that is compatible with the MRMP2 based on 2×2 VB configurations in Ref. [13]. We examine the antistacking 2,5,8-tri-*tert*-butyl-phenalenyl dimer [1] and its simplified model as a though-space interacted phenalenyl radical. The recently synthesized di-phenyl-IDPL [1] is also examined as a through-bond interacted model compound. The computational results are discussed in relation to the experimental ones, hybrid DFTs' [21] results, and physics behind the CASCI[2,2]-DFT treatment for phenalenyl radical systems.

2. Complete-active-space (CAS) DFT method

We briefly describe the theoretical background of our approach, CAS-DFT. A starting point is the Hohenberg–Kohn theorem [16] that states the ground-state energy for the system under the external potential $V_{\text{ext}}(\mathbf{r})$ is determined by density:

$$E_0 = \text{Min}_{\rho(\mathbf{r})\to N}[F[\rho(\mathbf{r})] + \int \mathrm{d}\mathbf{r}\rho(\mathbf{r})V_{\text{ext}}(\mathbf{r})]. \tag{1}$$

In the usual Kohn–Sham DFT, the universal functional,

$$F[\rho(\mathbf{r})] = \text{Min}_{\Psi\to\rho(\mathbf{r})}\langle\Psi|\hat{T} + \hat{V}_{\text{ee}}|\Psi\rangle, \tag{2}$$

is divided into noninteracting kinetic term, classical Coulomb, and exchange correlation terms,

$$F[\rho(\mathbf{r})] = \text{Min}_{\Phi\to\rho(\mathbf{r})}\langle\Phi|\hat{T}|\Phi\rangle + \frac{1}{2}\int\frac{\rho(\mathbf{r}_1)\rho(\mathbf{r}_2)}{r_{12}}\mathrm{d}\mathbf{r}_1\,\mathrm{d}\mathbf{r}_2 + E_{\text{XC}}[\rho(\mathbf{r})]. \tag{3}$$

Note that the constrained search region for the first term is limited to the single-determinant wavefunctions, leading to the effective one electron problem, i.e. the Kohn–Sham equation.

In the CAS-DFT, the universal functional is divided into the modified universal functional, $F^{\text{CAS}}[\rho(\mathbf{r})]$ and the residual correlation (RC) functional, $E_{\text{RC}}^{\text{CAS}}[\rho(\mathbf{r})]$, as

$$F[\rho(\mathbf{r})] = F^{\text{CAS}}[\rho(\mathbf{r})] + E_{\text{RC}}^{\text{CAS}}[\rho(\mathbf{r})]. \tag{4}$$

Here $F^{\text{CAS}}[\rho(\mathbf{r})]$ is defined as

$$F^{\text{CAS}}[\rho(\mathbf{r})] = \text{Min}_{\Psi\to\rho(\mathbf{r})}^{\text{CAS}}\langle\Psi|\hat{T} + \hat{V}_{\text{ee}}|\Psi\rangle. \tag{5}$$

The point to note is that the constrained search region denoted as $\text{Min}_{\Psi\to\rho(\mathbf{r})}^{\text{CAS}}$, is that of the CAS type of the wavefunction expansion. All of classical Coulomb, exchange, and correlation parts of CAS wavefunction are covered by the modified universal functional given by Eq. (5). The remaining RC term then covers correlations beyond the CAS wavefunction

$$E_{\text{RC}}^{\text{CAS}}[\rho(\mathbf{r})] = \int \mathrm{d}\mathbf{r}\rho(\mathbf{r})\varepsilon_{\text{RC}}^{\text{CAS}}[\rho(\mathbf{r})]. \tag{6}$$

In order to construct the residual correlation energy $\varepsilon_{\text{RC}}^{\text{CAS}}[\rho(\mathbf{r})]$ from the usual DFT correlation energy, the portion of correlation effects covered by CAS wavefunction must be projected out from the original DFT correlation functional. For this purpose, we employed the Lee–Yang–Parr correlation functional with Miehlich–Stoll–Savin–Gräfenstein–Cremer (MSS–GC) prescription. For details, please refer Refs. [18–20].

A remarkable point of CAS-DFT is that the working equation is not for one-electron orbital, but for many-body wavefunction given by

$$(\hat{T} + \hat{V}_{\text{ee}} + \hat{V}_{\text{ext}} + \hat{V}_{\text{RC}}^{\text{CAS}})|\Psi\rangle = E_{\text{CAS-DFT}p}|\Psi\rangle. \tag{7}$$

Here the coordination representation of the RC potential operator, $\hat{V}_{\text{RC}}^{\text{CAS}}$ is

$$V_{\text{RC}}^{\text{CAS}}(\mathbf{r}) = \frac{\delta E_{\text{RC}}^{\text{CAS}}[\rho(\mathbf{r})]}{\delta\rho(\mathbf{r})} = \varepsilon_{\text{RC}}^{\text{CAS}}[\rho(\mathbf{r})] + \rho(\mathbf{r})\frac{\delta\varepsilon_{\text{RC}}^{\text{CAS}}[\rho(\mathbf{r})]}{\delta\rho(\mathbf{r})}. \tag{8}$$

Since the RC potential depends on the CAS solution itself, Eq. (7) must be solved by a self-consistent manner. Another noteworthy point is that the approximated excited state can also be obtained by solving Eq. (7).

In the context of CAS-DFT, we assume that there are two types of electron: first one is so-called "active electrons", i.e., explicitly interacting electrons that occupy valence orbitals with fractional occupation numbers. In molecular magnetic systems, these electrons are responsible for magnetic properties. Other electrons do not play a primary role for any spin property, but affect on the properties via the effective correlation potential field given by Eq. (8). We call these electrons as "inactive electrons". This is the physical picture behind the application of CAS-DFT approach.

3. Results and discussions

In this section, we present the computational results. All of CAS-DFT calculations are performed using our original code, while the usual Kohn–Sham DFT computations by

Gaussian 03 [22]. The 6-31G** basis is employed for all calculations.

3.1. Monomer

We consider the 2,5,8-tri-*tert*-butyl-phenalenyl monomer (**1**) illustrated in Fig. 1(a). The geometry is fixed to be that of the reported X-ray structure [1]. Carbon sites that are mainly responsible for magnetic properties are C_1–C_{13} in this figure. As is already reported [7], a simple molecular orbital calculation like the Hückel approximation yields the orbital energy spectrum and the single-occupied molecular orbital (SOMO), shown in Fig. 1(b) and (c), respectively. The ability to three-redox states is obviously due to this orbital energy spectrum: both of removal and addition of one-electron lead to stable configurations.

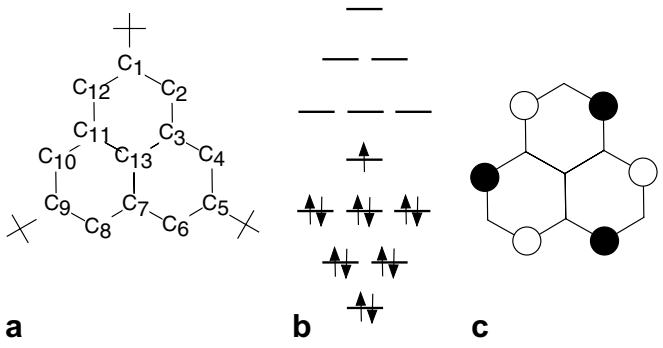


Fig. 1. (a) A schematic illustration of 2,5,8-tri-*tert*-butyl-phenalenyl monomer (**1**). (b) Orbital energy diagram of the phenalenyl radical. The horizontal axis denotes occupation numbers for the case of UHF natural orbitals. (c) Schematic illustration of singly occupied molecular orbital of the phenalenyl radical.

In the neutral state, a main radical source is the electron occupied in SOMO that is schematically illustrated in Fig. 1(c). Thus, the spin densities of phenalenyl radical also appear on C_2, C_4, C_6, C_8, C_{10}, C_{12}. Morita and his co-workers have determined the spin density population of phenalenyl monomer using ENDOR spectra with McConnel, Heller, Fraenkel–Karplus equations [5]. We can see from their data shown in Fig. 2(a) that the primary part of the unpaired electron populates over C_2, C_4, C_6, C_8, C_{10}, C_{12}. But note that the spin populations on other sites are not negligible. This might result, in part, from the experimental condition of ESR: since the local magnetic fields for all carbon sites exist during the ESR experimental process, the observed population might deviate from that of the (nonrelativistic) quantum solution. The spin-unrestricted

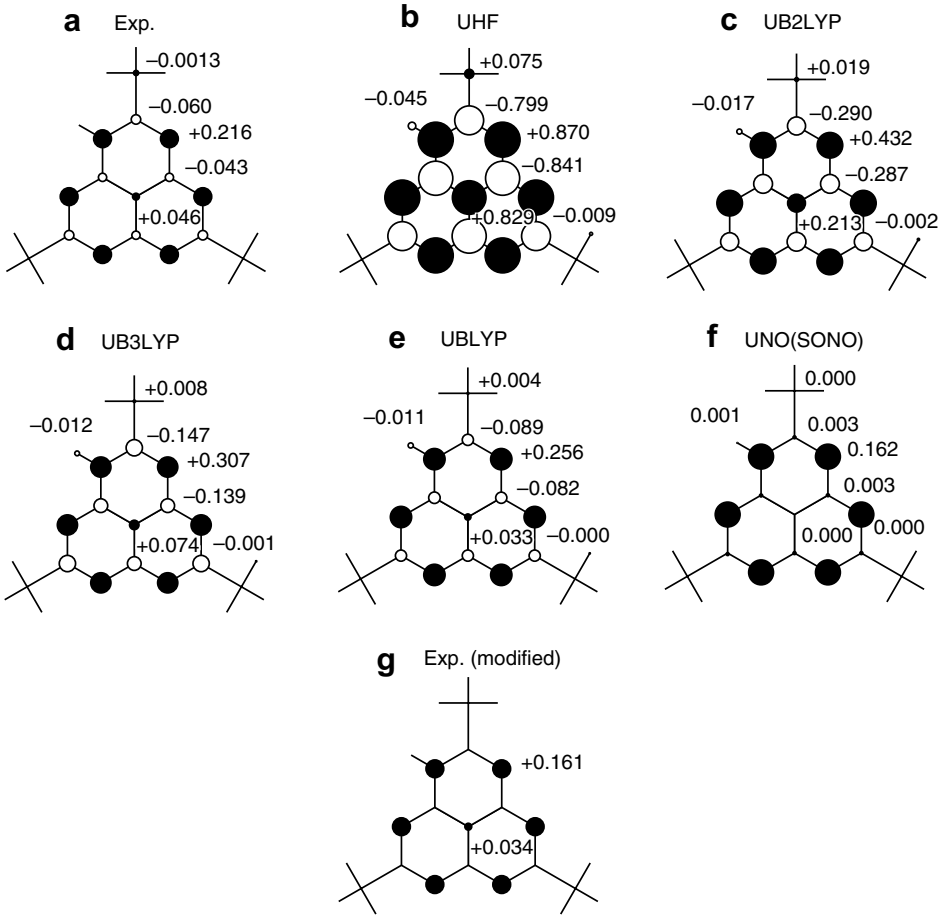


Fig. 2. Spin-density distribution of **1** estimated by (a) the ENDOR experiment [5], (b) UHF, (c) UB2LYP, (d) UB3LYP, (e) UBLYP solutions, (f) singly occupied UHF natural orbital(UNO). (g) A spin-density distribution modified by removing negative spin density of the ENDOR result.

DFT and hybrid DFT results, on the other hand, involve the artificial effective exchange-correlation (XC) magnetic field. Indeed, UHF, UB2LYP, UB3LYP, and UBLYP results show nonzero spin populations on sites besides C_2, C_4, C_6, C_8, C_{10}, C_{12} as shown in Fig. 2(b)–(e). Since the magnitude of XC magnetic field varies with the individual's XC functional, the magnitudes of spin populations are different each other as we can see from Fig. 2(b)–(e). Judging from these results, the artificial XC magnetic fields yielded in UHF and Hybrid DFT (UB2LYP and UB3LYP) calculations are too large to mimic the local magnetic field of the ESR experiment, while the XC term of pure DFT (UBLYP) provides the field comparable with the experimental one. This is consistent with the previous computational results obtained by Morita et al. [5].

Next, we computed UHF natural orbitals (UNO) of phenalenyl monomer. The UNO's spectrum ordered by their occupation numbers is similar to Fig. 1(b). The spin density of singly occupied UNO (SONO) presented in Fig. 2(f) is similar to that of experimental one, but missed the negative populations on C_1, C_3, C_5, C_7, C_9, C_{11}, C_{13} and underestimated the spin-magnitudes on other sites slightly. Indeed, if we remove the negative spin density population in Fig. 1(a) and then scale the positive spin densities to conserve S_z value (+1/2), we obtain the spin population presented in Fig. 1(g). The spin population calculated using SONO is very similar to this modified spin population. Based on this fact, we assume that the active electron responsible for magnetic properties of phenalenyl radical species is the SONO electron. In other words, "one active electron per one phenalenyl radical picture" is employed throughout this paper.

3.2. Phenalenyl dimer

Now, we proceed to phenalenyl radical dimers that are illustrated in Fig. 3.

At first, the face-to-face antistacking dimer of 2,5,8-tri-*tert*-butyl-phenalenyl radicals (**2**: Fig. 3(a)) is considered. This is a fundamental dimeric unit in the solid state, of which geometry has been observed by the X-ray analysis [1]. The geometry of monomer is slightly distorted from a plane with D_{3h} symmetry. So we examined the dimer of simplified monomer illustrated in Fig. 3(b) (**3**), of which geometry is determined in the previous study [11] by averaging the atomic distances and fixing the intermolecular distance to that of experimental value (3.3 Å).

The inspection of spin population of monomer discussed above leads to the physical picture of CASCI-DFT illustrated in Fig. 4. We select the bonding-and-antibonding MOs pair as the active space, which is indicated by the dotted square in this figure. So two electrons occupied in these MOs are "active electrons". The gray arrow from the bonding MO to the antibonding MO denotes quantum fluctuation effects covered by the CASCI[2,2] wavefunction, which is just the origin of the quantum biradical character of this species. Two striped arrows, denoted as (2a) and (2b), are DFT correlation effects from active electrons themselves (2a), and from inactive electrons (2b), respectively. This is a minimum treatment of CASCI-DFT, in which all correlations besides the biradical character are covered by DFT correlation.

Judging from the intermolecular distance ($R = 3.3$ Å) that is determined by the solid-state X-ray observation, the intermolecular bond of **2** is expected to exhibit an intermediate character between covalent bond and pure

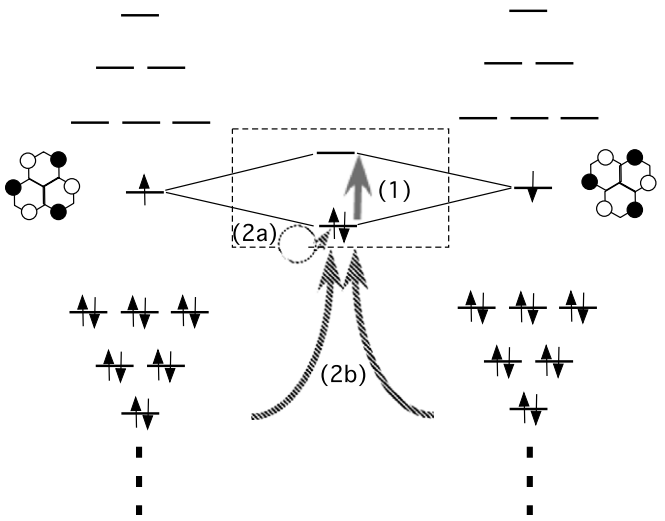


Fig. 4. Schematic illustration of CASCI-DFT solution of **2** and **3**. The dotted square is the active space (CASCI[2,2]) we employed. The gray arrow indicates the explicit quantum correlation effects covered by CASCI[2,2], while the remaining DFT correlation effects are denoted as striped arrows.

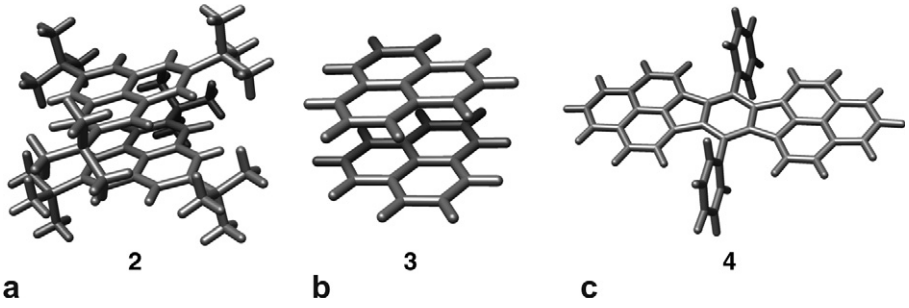


Fig. 3. Phenalenyl dimer (a and b) and carbon radicals containing two phenalenyl moieties (c). (a) 2-5-8 tri-*tert*-butyl-phenalenyl radical dimer [1], (b) a simplified model of (a) [11,12], (c) di-phenyl-IDPL [9].

biradical. Indeed, the occupation number of bonding natural orbital of UNO-CASCI[2,2]-DFT solution becomes approximately 1.7, implying that this dimer shows the weak covalent bonding with the biradical character. We computed the effective exchange interaction (J_{ab}) of the Heisenberg model

$$\hat{H} = -2J_{ab}\hat{\mathbf{S}}_a \cdot \hat{\mathbf{S}}_b. \tag{9}$$

via the expression,

$$J_{ab} = \frac{^{\mathrm{LS}}E_X - {}^{\mathrm{HS}}E_X}{^{\mathrm{HS}}\langle\hat{\mathbf{S}}^2\rangle_X - {}^{\mathrm{LS}}\langle\hat{\mathbf{S}}^2\rangle_X}, \tag{10}$$

using energies (E_X) and spin expectation values ($\langle\hat{S}^2\rangle$) of low-spin (LS) and high-spin (HS) states calculated by ab initio method (X). The computational values of UHF, UDFT, Hybrid DFT, CASCI-DFT, together with the experimental value [2,3] are listed in Table 1. The values in parentheses are of the simplified model (Fig. 3(b)). CASCI[2,2]-DFT computations using two types of molecular orbitals, UHF natural orbitals (UNO) and canonical Hartree–Fock orbitals (RHF), yield similar results each other. However these $|J_{ab}|$ values ($\sim$2253 cm^{-1}) are larger than the experimental one (1318 cm^{-1}). On the other hand, the UHF and hybrid DFT (B2LYP and B3LYP) results yield good estimation of J value, being consistent with the previous report [11]. This difference is attributable to the description of the high-spin (HS) state, rather than of the low-spin state. That is, the UHF exchange term, which is known to cause the spin-polarization of the inner shells in a high-spin case, results in over-stabilization of the HS state. Indeed, the J value of UHF result is less antiferromagnetic than that of experimental one, while $|J_{ab}|$ value of UBLYP, in which UHF exchange effect is not included, is larger than that of CASCI[2,2]-DFT. The $|J_{ab}|$ of CASCI[2,2]-DFT is also attributable to its description of HS state: it is noteworthy that the CASCI[2,2]-DFT for the HS state reduces to an usual open-shell HF plus DFT correlation method.

The first excited energy is also calculated by CASCI[2,2]-DFT. In contrast to J value, the molecular orbitals employed in CASCI-DFT computations affect the results: the RHF-CASCI-DFT value is smaller than the UNO-CASCI-DFT value. The reason is that since UNO is obtained by the variational UHF procedure with succeeding natural orbital analysis for the singlet-biradical state it is appropriate for the ground-state but not for the singlet excited state involving an ionic character. The RHF orbitals do not show the diradical character, so improve the excited energy slightly. However, compared with the experimental one, the excited energy calculated by RHF-CASCI-DFT is still larger than the experimental one, indicating that there is room for improvement of CASCI[2,2]-DFT approach.

Table 1
Effective exchange integral values and lowest-lying excited energies for **2**

Method	J (cm^{-1})	First excitation energy (eV)
UHF	−1212.22 (−1085.00)	
UB2LYP	−1361.82 (−1413.20)	
UB3LYP	−1496.12 (−1827.10)	
UBLYP	−2332.79 (−2256.80)	
UNO-CASCI[2,2]-DFT	−2253.33 (−2032.00)	3.312
RHF-CASCI[2,2]-DFT	−2253.49 (−2417.95)	3.190
Experiment	−1318	2.065

The corresponding values for **3** are in parentheses.

3.3. Di-phenyl-IDPL

Next, we consider the di-phenyl-IDPL (**4** in Fig. 3) [9]. For this system, we also assume that the two-electrons in two-orbitals play essential role for the magnetic interaction. However, the two-orbitals are newly formed HOMO and LUMO as shown in Fig. 5. This set of HOMO and LUMO that is reported in Ref. [9] is consistent with our UHF natural orbitals (UNOs). The active space is circled by the dotted square. The HOMO constitutes from LUMO of benzene and antibonding type of two phenalenyl HOMOs. On the other hand, the LUMO is the antibonding type of MO constructed from the second HOMO of benzene and the bonding MO of two-phenalenyl HOMOs. The occupation number of the natural orbital of UNO-CASCI[2,2]-DFT solution is 1.43, which exhibits the stronger biradical character than that of **2**. The computational J values are presented in Table 2. All of $|J_{ab}|$ values calculated by UHF, UB2LYP, UB3LYP, and UB3LYP are larger than the experimental one. One possible reason is the well-known over-stabilization of the LS state of diradical molecules by the symmetry-broken feature and the approximated XC functional [23]. On the other hand, the UNO-CASCI[2,2]-DFT result shows the excellent agreement with the experimental one. This might be because the LUMO of **4** is not a straightforward antibonding type

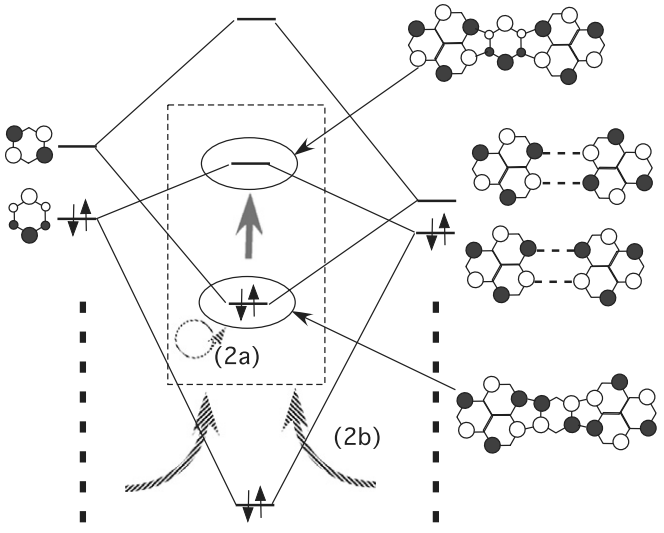


Fig. 5. Schematic illustration of CASCI-DFT solution of **4**. The dotted square is the active space (CASCI[2,2]) we employed. The gray arrow indicates the explicit quantum correlation effects covered by CASCI[2,2], while the remaining DFT correlation effects are denoted as striped arrows.

Table 2
Effective exchange integral values and lowest-lying excited energies for **4**

Method	J (cm^{-1})	First excitation energy (eV)
UHF	−967.70	
UB2LYP	−993.37	
UB3LYP	−1117.39	
UBLYP	−1515.74	
UNO-CASCI[2,2]-DFT	−770.55	3.905
Experiment	−764.5	1.661

of MO. However, the first excited energy calculated by UNO-CASDFT is much larger than the experimental one, implying that the points to be improved remain besides the reference MOs for well-balanced description among the ground and excited states.

4. Discussion and concluding remarks

So far, we present a CASCI-DFT study of phenalenyl dimeric systems based on a modest active space (CAS[2,2]). We found that this CASCI-DFT treatment works well at the quality level for J values, but that there remain slight deviations from the experimental values, in particular, of the excited spectrum.

There are several ways to improve our approach. First one is the bull force computation by increasing the size of the active space. This is a most straightforward way to cover the many-body quantum effects explicitly, but is not feasible at present. For instance, CASCI[14,14]-DFT and CASCI[20,20]-DFT are required for **2** and **3**, respectively if we intend all of π electrons. Such CAS spaces are too large to compute large molecular systems. The ad hoc CI-DFT treatment with selecting important configurations is a second idea. When the resonating valence bond (VB) picture is more effective than molecular orbital picture, the VB-CI-DFT with essential VB configurations becomes better than the present CASCI-DFT approach based on molecular orbitals. In these, we intend to improve the wavefunction part of multireference DFT, i.e. $F^{\mathrm{CAS}}[\rho(\mathbf{r})]$ in Eq. (4). Another way is to refine the DFT correlation part of CAS-DFT, i.e., $E_{\mathrm{RC}}^{\mathrm{CAS}}[\rho(\mathbf{r})]$ in Eq. (4) without changing the wavefunction part. Indeed, the RC term used in this study is originally designed for the ground-state. This is a possible reason why the excited energies of CASCI[2,2]-DFT are not so good. For better description of the excited states, the state-specific correlation terms might be needed. For such a purpose, we have recently proposed an orbital-dependent correlation correction for CAS-DFT [19]. Using this alternative CAS-DFT, the computational results of excited states of phenalenyl systems are expected to be improved further.

Acknowledgement

We are grateful to Dr. Y. Takano and Dr. T. Taniguchi for their helpful discussions.

References

[1] K. Goto, T. Kubo, K. Yamamoto, K. Nakasuji, K. Sato, D. Shiomi, T. Takui, M. Kubota, T. Kobayashi, K. Yakusi, J. Ouyang, J. Am. Chem. Soc. 121 (1999) 1619.
[2] K. Fukui, K. Sato, D. Shiomi, T. Takui, K. Itoh, K. Goto, T. Kubo, K. Yamamoto, K. Nakasuji, A. Naito, Synth. Met. 103 (1999) 2257.
[3] K. Fukui, K. Sato, D. Shiomi, T. Takui, K. Itoh, T. Kubo, K. Goto, K. Yamamoto, K. Nakasuji, A. Naito, Mol. Cryst. Liq. Cryst. 334 (1999) 49.
[4] Y. Morita, S. Nishida, J. Kawai, K. Fukui, S. Nakazawa, K. Sato, D. Shiomi, T. Takui, K. Nakasuji, Org. Lett. 4 (2002) 1985.
[5] Y. Morita, K. Fukui, S. Suzuki, T. Aoki, S. Nakazawa, K. Tamaki, A. Fuyuhiro, K. Yamamoto, K. Sato, D. Shiomi, A. Naito, T. Takui, K. Nakasuji, Polyhedron 22 (2003) 2199.
[6] Y. Morita, J. Kawai, K. Fukui, S. Nakazawa, K. Sato, D. Shiomi, T. Takui, K. Nakasuji, Org. Lett. 5 (2003) 3289.
[7] K. Nakasuji, T. Kubo, Bull. Chem. Soc. Jpn. 77 (2004) 1791.
[8] T. Kubo, M. Sakamoto, K. Nakasuji, Polyhedron 24 (2005) 2522;
S. Suzuki, Y. Morita, K. Fukui, K. Sato, D. Shiomi, T. Takui, K. Nakasuji, Polyhedron 24 (2005) 2618.
[9] T. Kubo, A. Shimizu, M. Sakamoto, M. Uruichi, K. Yakushi, M. Nakano, D. Shiomi, K. Sato, T. Takui, Y. Morita, K. Nakasuji, Angew. Chem., Int. Ed. 44 (2005) 6564.
[10] S. Suzuki, Y. Morita, K. Fukui, K. Sato, D. Shiomi, T. Takui, K. Nakasuji, J. Am. Chem. Soc. 128 (2006) 2530.
[11] Y. Takano, T. Taniguchi, H. Isobe, T. Kubo, Y. Morita, K. Yamamoto, K. Nakasuji, T. Takui, K. Yamaguchi, Chem. Phys. Lett. 358 (2002) 17.
[12] Y. Takano, T. Taniguchi, H. Isobe, T. Kubo, Y. Morita, K. Yamamoto, K. Nakasuji, T. Takui, K. Yamaguchi, J. Am. Chem. Soc. 124 (2002) 11122.
[13] D. Small, V. Zaitsev, Y. Jung, S.V. Rosokha, M. Head-Gordon, J.K. Kochi, J. Am. Chem. Soc. 126 (2004) 13850.
[14] H. Nakano, J. Chem. Phys. 99 (1993) 7983;
W.A. Goddard, L.B. Harding, Ann. Rev. Phys. Chem. 29 (1978) 363.
[15] W. Kohn, L.J. Sham, Phys. Rev. 140 (1964) A1131.
[16] R.G. Parr, W. Yang, Density Functional Theory of Atoms and Molecules, Oxford University Press, 1989.
[17] K. Yoshida, Theory of Magnetism, Springer, Berlin, 1996.
[18] R. Takeda, S. Yamanaka, K. Yamaguchi, Chem. Phys. Lett. 366 (2002) 321;
S. Yamanaka, T. Ohsaku, D. Yamaki, K. Yamaguchi, Int. J. Quantum Chem. 91 (2003) 376;
R. Takeda, S. Yamanaka, K. Yamaguchi, Int. J. Quantum Chem. 96 (2004) 463.
[19] (a) S. Yamanaka, K. Nakata, T. Takada, K. Kusakabe, J.M. Ugalde, K. Yamaguchi, Chem. Lett. 35 (2006) 242;
(b) K. Nakata, T. Ukai, S. Yamanaka, T. Takada, K. Yamaguchi, Int. J. Quantum Chem. 106 (2006) 3325;
(c) S. Yamanaka, K. Nakata, T. Ukai, T. Takada, K. Yamaguchi, Int. J. Quantum Chem. 106 (2006) 3312.
[20] B. Miehlich, H. Stoll, A. Savin, Mol. Phys. 91 (1997) 527;
J. Gräfenstein, D. Cremer, Chem. Phys. Lett. 316 (2000) 569.
[21] S. Yamanaka, R. Takeda, M. Shoji, Y. Kitagawa, H. Honda, K. Yamaguchi, Int. J. Quantum Chem. 105 (2005) 605.
[22] M.J. Frisch, G.W. Trucks, H.B. Schlegel, G.E. Scuseria, M.A. Robb, J.R. Cheeseman, J.A. Montgomery, Jr., T. Vreven, K.N. Kudin, J.C. Burant, J.M. Millam, S.S. Iyengar, J. Tomasi, V. Barone, B. Mennucci, M. Cossi, G. Scalmani, N. Rega, G.A. Petersson, H. Nakatsuji, M. Hada, M. Ehara, K. Toyota, R. Fukuda, J. Hasegawa, M. Ishida, T. Nakajima, Y. Honda, O. Kitao, H. Nakai, M. Klene, X. Li, J.E. Knox, H.P. Hratchian, J.B. Cross, V. Bakken, C. Adamo, J. Jaramillo, R. Gomperts, R.E. Stratmann, O. Yazyev, A.J. Austin, R. Cammi, C. Pomelli, J.W. Ochterski, P.Y. Ayala, K. Morokuma, G.A. Voth, P. Salvador, J.J. Dannenberg, V.G. Zakrzewski, S. Dapprich, A.D. Daniels, M.C. Strain, O. Farkas, D.K. Malick, A.D. Rabuck,

K. Raghavachari, J.B. Foresman, J.V. Ortiz, Q. Cui, A.G. Baboul, S. Clifford, J. Cioslowski, B.B. Stefanov, G. Liu, A. Liashenko, P. Piskorz, I. Komaromi, R.L. Martin, D.J. Fox, T. Keith, M.A. Al-Laham, C.Y. Peng, A. Nanayakkara, M. Challacombe, P.M.W. Gill, B. Johnson, W. Chen, M.W. Wong, C. Gonzalez, J.A. Pople, Gaussian, Inc., Wallingford, CT, 2004.

[23] S. Yamanaka, T. Kawakami, H. Nagao, K. Yamaguchi, Chem. Phys. Lett. 231 (1994) 25.

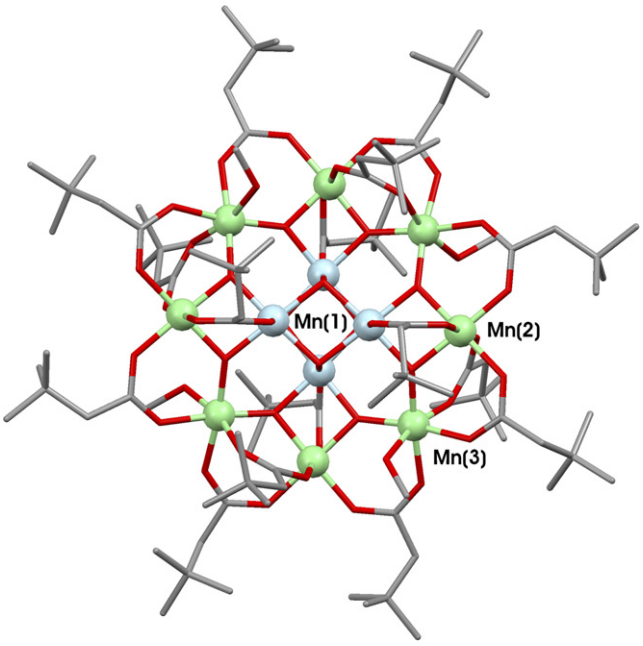


Fig. 1. Mn_{12}-*t*-Bu crystal structure.

Mn^{3+} ions are ferromagnetically coupled to each other and form a ring around the cubane-like (Mn_4O_4) structure of the Mn^{4+} ions, which are also ferromagnetically coupled. The interaction between the Mn^{3+} and Mn^{4+} ions, however, is antiferromagnetic, giving a total spin, $S_T = 10$. The electronic Hamiltonian representing this system is then given (assuming a giant spin model) as

$$\mathscr{H} = \mu_B H \cdot g \cdot S + DS_z^2 + B_4^0 O_4^0 + B_4^4 O_4^4 + \mathscr{H}',$$

where the first term represents the Zeeman interaction, and for our purposes is zero (because we apply no external field). D is the axially anisotropic zero-field splitting parameter and is followed by higher order crystal field terms; the last term representing rather small perturbations. For the case of Mn_{12}-*t*-Bu: $D = -0.665$ K, $B_4^0 = -0.036$ mK, and $B_4^4 = -0.062$ mK, as established by EPR [11]. The negative axial anisotropy makes the $m_S = \pm 10$ levels the ground state and can be thought of as a type of double potential well. Because our experiments are performed at 3 K and below, our only excitations occur in the ground state of the system, which is where we would like to probe the QTM mechanism. The nuclei at these temperatures are relaxed through the coupling of the electrons to the phonons, thus, nuclear relaxation measurements give insight into the dynamics of the electronic system, which is why this technique has been chosen. To this end we have measured the spectrum and spin–lattice relaxation (T_1) of Mn_{12}-*t*-Bu and show that, in zero external field, the electron relaxation from 700 mK to 400 mK does not occur dominantly through a tunneling mechanism.

2. Synthesis and crystal growth

Mn_{12}-*t*-Bu is synthesized by a carboxylate substitution of Mn_{12}-Ac followed by re-crystallization with CH_3OH/Et_2O, as described elsewhere [8b]. The crystals were dark with a brick shape and had dimensions of 1 mm × 1 mm × 2 mm.

3. NMR experimental details

^{55}Mn NMR measurements were made using a locally developed MAGRes2000 Integrated Wideband NMR spectrometer with quadruture detection and a home built high frequency probe [12,13]. For the measurement of the spectrum, samples were prepared by removing the crystal from its mother liquor and immediately covering in 5-min epoxy to prevent crystal fractures after thermal cycling. Immediately after the epoxy was set, the sample was mounted into the coil and cooled in a dewar of liquid Helium. The spectrum was acquired at 1.45 K, below the blocking temperature, T_B, of ~3 K because of fast T_2 times above this temperature. A Hahn echo pulse sequence was used while the frequency was scanned from 220 MHz to 400 MHz, usually taking 0.25 MHz steps. Frequency scans were necessary because of the large peak widths (~5–20 MHz). Pulse lengths were of the order of 500 ns.

Preparation of the sample for He-3 measurements consists of surrounding the crystal with N-grease before placing into a coil. He-3 experiments were performed in a Janis cryostat. The system is capable of maintaining ~380 mK for 12 h with the heat load from the NMR probe and pulses. After that time, the He-3 is re-condensed. T_1 measurements were conducted on the Mn^{4+}, Mn(1) peak, down to 390 mK. In order to saturate any quadrupole split peaks, we apply a frequency hopping comb pulse, discussed in a previous publication [9]. This comb pulse is repeated up to 20 times to ensure the spins are perturbed from equilibrium. Evidence for this is seen in the good fits of the relaxation data to a single exponential function. Any deviation from exponential is due to the fact that we are unable to achieve full saturation. The T_1 data are fit to the following exponential, as reported earlier [9]: $M(t) = (M_\infty - M_0)[1 - \exp(-t/T_1)] + M_0$, where $M(t)$ is the time dependent nuclear magnetization, M_∞ is the equilibrium magnetization, t is the time between the saturation sequence and the observation spin-echo, M_0 is the remnant magnetization immediately following the saturation comb, and T_1 is the longitudinal (spin–lattice) relaxation time.

4. Results

As shown in Fig. 2, the ^{55}Mn NMR spectrum of Mn_{12}-*t*-Bu exhibits three sets of peaks, the two Mn^{3+} ion environments and the Mn^{4+} ion environment, essentially similar to those for Mn_{12}-Ac and Mn_{12}-BrAc [9,10,14,15]. Peaks are assigned by considering the number of unpaired electrons at each Mn site, along with any Jahn–Teller distortion

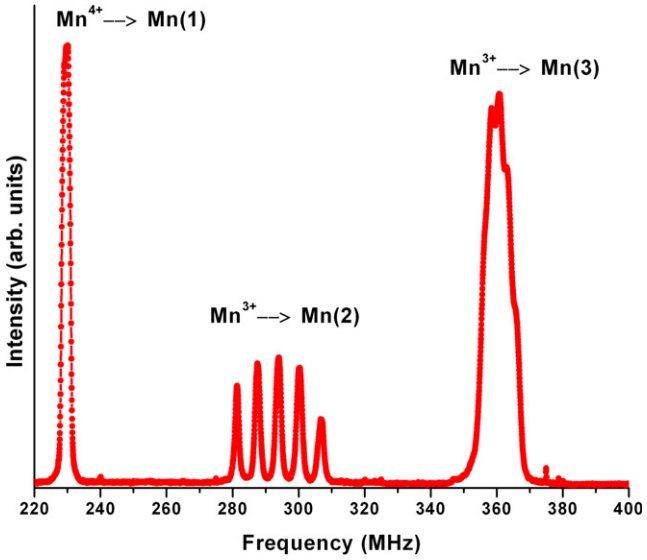


Fig. 2. Single crystal ^{55}Mn NMR spectrum of Mn_{12}-*t*-Bu.

[14]. Because the Mn^{4+} ions have one less electron than the Mn^{3+} ions, it is expected that the Mn^{4+} Fermi Contact hyperfine field will be smaller, thus resulting in a lower resonance frequency. Also, because the Mn^{4+} ion is in an environment of electron distribution which is close to cubic, we do not expect there to be a large quadrupole splitting. The Mn(1) peak at 230.1 MHz (21.91 T) can then be assigned to the Mn^{4+} ions. The full width at half maximum (FWHM) is 2.8 MHz, which is broad when compared against the Mn(2) peaks FWHM of 1.9 MHz. A closer examination of the Mn(1) peak shows structure at the apex, indicating the presence of quadrupolar interactions, which would result in a broadened peak. Isomers could also increase the peak width, similar to that seen in Mn_{12}-Ac [10], however, there is no clear evidence for isomers after examination of the Mn(2) peak. If in fact the Mn(1) peak is split by quadrupole effects, then the Mn^{4+} ions no longer exist in a cubic environment.

The Mn(2) and Mn(3) peaks are assigned by considering their X-ray structure (Fig. 1). The angle the local Jahn–Teller axis makes with the molecular *c*-axis governs the strength of the quadrupole and dipolar interaction. The smaller the angle, the larger the quadrupole splitting and dipolar contribution will be. Because the dipolar hyperfine term is opposite in sign to the Fermi contact term (the main contributor to the hyperfine field), a larger dipole interaction will result in a smaller effective hyperfine field (lower resonant frequency) felt at the nuclear site [14].

The Mn(2) peak, with the largest quadrupole frequency and lower resonant frequency, can then be assigned to the four Mn^{3+} ions which are slightly tilted away from the *c*-axis with an angle of ~13.7°. The central peak for the quadrupolar split resonance is located at 294.0 MHz, has an internal field of 28.00 T, and a FWHM of 1.9 MHz. The separation between each resonance, $\Delta\nu_Q \sim 6.4$ MHz, results in $e^2qQ \sim 46.6$ MHz; with the quadrupole energies being obtained from the following equation:

$$E_m = -\gamma_n \hbar H_0 m_n + \frac{e^2qQ}{4I(2I-1)}\left(\frac{3\cos^2\theta - 1}{2}\right)[3m_n^2 - I(I+1)]$$

The first term is a result of the effective hyperfine splitting and the second term is the quadrupole perturbation. eQ is the electric quadrupole moment, eq is the gradient of the electric field along the *z*-axis, and θ is the angle the Jahn–Teller axis makes with the crystallographic *c*-axis. Taking the energy difference between two neighboring m_n levels allows the calculation of e^2qQ.

The Mn(3) peak has a central frequency of 360.8 MHz resulting in an internal field of 34.36 T. It is also split by quadrupole interactions as a result of its 36.6° tilt of the local Jahn–Teller axis with respect to the molecular *c*-axis. Because of the larger angle, the quadrupolar and dipole terms are smaller, making assignment of this peak straight forward. For Mn(3), $e^2qQ \sim 36.1$ MHz is calculated taking the separation between each resonance, $\Delta\nu_Q \sim 2.5$ MHz.

While the bulkier ligands provide a greater separation among Mn_{12} molecules, diminishing intercluster dipolar effects, they also provide a small distortion in the local electron symmetry, evidenced by the quadrupole splitting of the Mn(1) peak. Although isomers do not appear to be present in this system, the loss of local symmetry gives Mn_{12}-BrAc the advantage of a being the model system for SMMs. However, in terms of sample stability, it seems that Mn_{12}-*t*-Bu is superior, as no asymmetry is seen in any of the resonance signals. Previous studies on Mn_{12}-BrAc do show asymmetry in the first and third peaks and are thought to be a result of sample degradation [10,11]. Even the freshest crystals of Mn_{12}-BrAc exhibit this behavior. Thus, the bulkier ligands in Mn_{12}-*t*-Bu seem to protect the core molecule from the effects that interstitial solvent loss may have on smaller systems.

T_1 measurements of the Mn(1) peak show very similar behavior to the two previously studied Mn_{12} compounds (Mn_{12}-Ac and Mn_{12}-BrAc) in the high temperature limit (Fig. 3) and are fit in a similar manner to that previously reported [9,16] (solid line in Fig. 3) using,

$$T_1^{-1} \approx C\exp(-\Delta E/T), \text{ with } C \approx \frac{\gamma_N^2\langle h_\perp^2\rangle}{\omega_N^2\tau_0},$$

resulting in a pre-exponential factor of $C \sim 1.64 \times 10^5\ s^{-1}$ and a activation energy of $\Delta E = 13.1$ K, corresponding well with the separation between the $m_S = \pm 10$ and $m_S = \pm 9$ states.

Upon reducing the temperature below 0.8 K, we see a dramatic increase in the spin–lattice relaxation time. In fact, at 400 mK $T_1 \sim 1000$ s, roughly three times as long as Mn_{12}-BrAc and an order of magnitude longer than Mn_{12}-Ac, partly a result of the bulkier ligands. The data at these temperatures follows either a T^2 or exponential type of dependence (Fig. 4). It is obvious that QTM is not the dominant relaxation mechanism in this temperature range as this would produce a temperature-independent relaxation region.

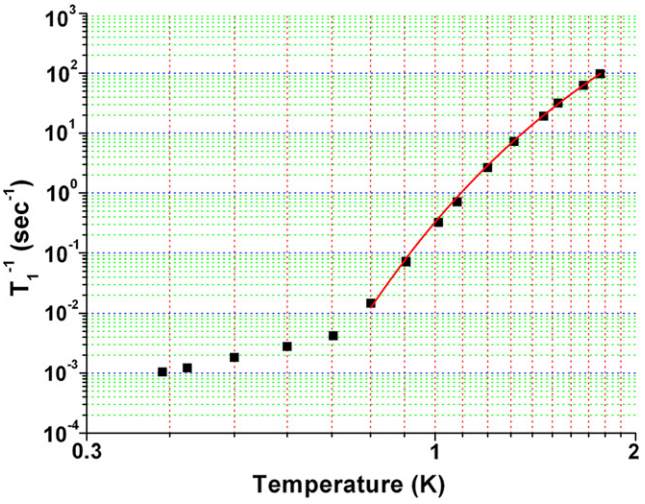


Fig. 3. Inverse T_1 of the Mn(1) peak of Mn_{12}-*t*-Bu single crystal.

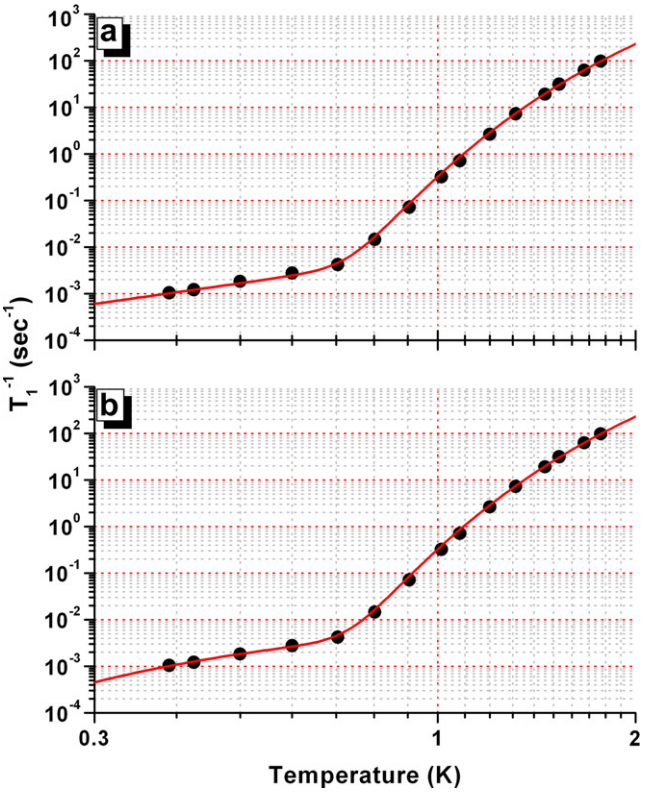


Fig. 4. Inverse T_1 of the Mn(1) peak of Mn_{12}-*t*-Bu single crystal with high and low temperature fit: (a) low temperature fit is a T^2 dependence and (b) low temperature fit is exponential in temperature.

5. Discussion and conclusion

This study again shows that ^{55}Mn NMR using single crystals consistently provides higher resolution data than crushed aligned powders. Of the high symmetry molecules, Mn_{12}-BrAc and Mn_{12}-*t*-Bu, both offer impressive potential for investigation as new model SMM compounds. While Mn_{12}-*t*-Bu shows evidence for the loss of cubic symmetry at the Mn^{4+} site, the sample shows no asymmetry in its peaks, in contrast to Mn_{12}-Ac and Mn_{12}-BrAc, thus attesting to be a more solvate-tough lattice.

The bulky ligands of the Mn_{12}-*t*-Bu also reduce intercluster interactions, greatly increasing the length of T_1 for this compound in the low temperature limit ($T_1 \sim 1000$ s at 400 mK). The data also clearly show a temperature dependence over the entire range studied, indicating that tunneling is not the dominant mechanism by which the nuclei are relaxed. The low temperature (below 0.7 K) thermally-activated nuclear T_1 observed for Mn_{12}-*t*-Bu here, and earlier for Mn_{12}-BrAc [9] is in sharp contrast to the temperature-independent behavior reported for Mn_{12}-Ac by Morello et al. [16], and ascribed to the relaxation caused by the so-called 'fast relaxing' isomers (estimated to be present in 5–8% concentration in crystals of Mn_{12}-Ac). These fast-relaxing isomers have a much lower anisotropy barrier, and lower symmetry (Jahn–Teller axes deviating from their easy axes), and they exhibit tunneling in zero field. On the other hand, the standard Mn_{12}-Ac molecules have their Jahn–Teller axes parallel to the easy (*c*-axis), including the solvent isomers [1,17]. Since no such fast-relaxing species are present in Mn_{12}-*t*-Bu, one may surmise that this compound should show a different nuclear relaxation behavior than Mn_{12}-Ac. Nevertheless, both Mn_{12}-BrAc and Mn_{12}-*t*-Bu show a definitive change in the slope of their nuclear T_1 below about 0.8 K.

Above 0.8 K, the T_1 follows the model of nuclear relaxation via electronic spin fluctuations between the $M_S = \pm 10$ and $M_S = \pm 9$ states. Clearly, once nuclear relaxation by spin fluctuations freezes out below ~0.8 K, some other relaxation process takes over. The details of this new process remain unclear at this point, although the exponential fit to the data between 0.39 K and 0.70 K reveals that there might be a lower temperature barrier of about 1.1 K. Further studies using Mn_{12}-Ac, and at temperatures lower than 0.39 K should prove helpful to understand this process, and are being contemplated.

Acknowledgement

This work was supported by the NSF-DMR Grant # DMR 0506946.

References

[1] (a) D. Gatteschi, R. Sessoli, J. Villain, Molecular Nanomagnets, Oxford University Press, 2006;
(b) G. Christou, Polyhedron 24 (2005) 2065;
(c) D. Gatteschi, R. Sessoli, J. Mag. Mag. Mater. 272-276 (2004) 1030;
(d) D. Gatteschi, R. Sessoli, Angew. Chem., Int. Ed. 42 (2003) 268.
[2] M.N. Leunberger, D. Loss, Nature (London) 410 (2001) 789.
[3] S. Hill, R.S. Edwards, N. Aliagga-Alcade, G. Christou, Science 302 (2003) 1015.
[4] T. Lis, Acta Crystallogr. B36 (1980) 2042.
[5] (a) J.R. Friedman, M.P. Sarachik, J. Tejada, R. Ziolo, Phys. Rev. Lett. 76 (1996) 3830;

(b) L. Thomas, P. Lionti, R. Ballou, D. Gatteschi, R. Sessoli, B. Barbara, Nature (London) 383 (1996) 145;
(c) A.L. Barra, D. Gatteschi, R. Sessoli, Phys. Rev. B 56 (1997) 8192;
(d) M. Hennion, L. Pardi, I. Mirebeau, E. Suard, R. Sessoli, A. Canneschi, Phys. Rev. B 56 (1997) 8819;
(e) J.A.A.J. Perenboom, J.S. Brooks, S. Hill, T. Hathaway, N.S. Dalal, Phys. Rev. B 58 (1998) 330;
(f) S. Hill, J.A.A.J. Perenboom, N.S. Dalal, T. Hathaway, T. Stalcup, J.S. Brooks, Phys. Rev. Lett. 80 (1998) 2453;
(g) Z. Kutnjak, C. Filipic, A. Levstik, R.M. Achey, N.S. Dalal, Phys. Rev. B 59 (1999) 11147;
(h) A.B. Sushkov, B.R. Jones, J.L. Musfeldt, Y.J. Wang, R.M. Achey, N.S. Dalal, Phys. Rev. B 63 (2001) 214408;
(i) W. Wernsdorfer, M. Soler, G. Christou, D.N. Hendrickson, J. Appl. Phys. 91 (2002) 7164;
(j) S. Hill, S. Maccagnano, K. Park, R.M. Achey, J.M. North, N.S. Dalal, Phys. Rev. B 65 (2002) 224410;
(k) K. Park, M.A. Novotny, N.S. Dalal, S. Hill, P.A. Rikvold, Phys. Rev. B 65 (2002) 014426;
(l) Y. Furukawa, K. Watanabe, K. Kumagai, F. Borsa, T. Sasaki, N. Kobayashi, D. Gatteschi, Phys. Rev. B 67 (2003) 064426;
(m) S. Hill, R.S. Edwards, S.I. Jones, N.S. Dalal, J.M. North, Phys. Rev. Lett. 90 (2003) 217204;
(n) E. del Barco, A.D. Kent, E.M. Rumberger, D.N. Hendrickson, G. Christou, Phys. Rev. Lett. 91 (2003) 047203;
(o) S. Takahashi, R.S. Edwards, J.M. North, S. Hill, N.S. Dalal, Phys. Rev. B 70 (2004) 094429.

[6] A. Cornia, R. Sessoli, L. Sorace, D. Gatteschi, A.L. Barra, C. Daiguebonne, Phys. Rev. Lett. 89 (2002) 257201.

[7] (a) K. Petukhov, S. Hill, N.E. Chakov, K.A. Abboud, G. Christou, Phys. Rev. B 70 (2004) 054426;
(b) W. Wensdorfer, M. Murugesu, G. Christou, Phys. Rev. Lett. 96 (2006) 057208.

[8] (a) J. An, Z.-D. Chen, X.-X. Zhang, H.G. Raubenheimer, C. Esterhuysen, S. Gao, G.-X. Xu, Dalton Trans. 22 (2001) 3352;
(b) M. Soler, P. Artus, K. Folting, J.C. Huffman, D.N. Hendrickson, G. Christou, Inorg. Chem. 40 (2001) 4902.

[9] N.E. Chakov, S.-C. Lee, A.G. Harter, P.L. Kuhns, A.P. Reyes, S.O. Hill, N.S. Dalal, W. Wernsdorfer, K.A. Abboud, G. Christou, J. Am. Chem. Soc. 128 (2006) 6975.

[10] A.G. Harter, N.E. Chakov, B. Roberts, R. Achey, A. Reyes, P. Kuhns, G. Christou, N.S. Dalal, Inorg. Chem. 44 (2005) 2122.

[11] S. Hill, N. Anderson, A. Wilson, S. Takahashi, N.E. Chakov, M. Murugesu, J.M. North, N.S. Dalal, G. Christou, J. Appl. Phys. 97 (2005) 10M510.

[12] R.M. Achey, P.L. Kuhns, A.P. Reyes, W.G. Moulton, N.S. Dalal, Phys. Rev. B 64 (2001) 064420.

[13] R.M. Achey, P.L. Kuhns, A.P. Reyes, W.G. Moulton, N.S. Dalal, Solid State Commun. 121 (2002) 107.

[14] T. Kubo, T. Goto, T. Koshiba, K. Takeda, K. Awaga, Phys. Rev. B 65 (2002) 224425.

[15] A.G. Harter, N.E. Chakov, R. Achey, A. Reyes, P. Kuhns, G. Christou, N.S. Dalal, Polyhedron 24 (2005) 2346.

[16] A. Morello, O.N. Bakharev, H.B. Brom, R. Sessoli, L.J. de Jongh, Phys. Rev. Lett. 93 (2004) 197202.

[17] W. Wernsdorfer, R. Sessoli, D. Gatteschi, Europhys. Lett. 47 (1999) 254.

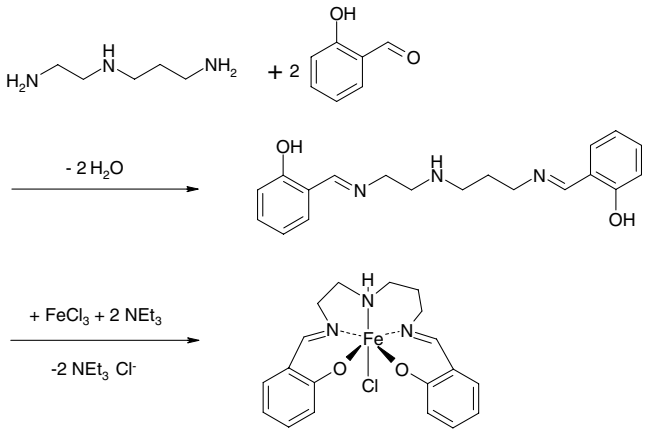


Fig. 1. Synthesis of the [Fe(^{5X}L)Cl] precursor (with X = N).

butterfly''). Molecular dynamic as well as Monte Carlo simulations, both on an empirical level, confirm this modality.

Fig. 5 and Table 1 show results of temperature-dependent Mössbauer spectroscopy of the dodecanuclear star compounds. At 300 K, the spectra indicates a quadrupole splitted doublet which is common for Fe(III) in the high-spin state. For the N-star this signal has been assigned to two positions with only weak deviations. One explanation may be a *cis–trans* isomerisation within the ligand around the Fe(III) centers (as seen above). Beside that, there certainly exists a distribution of the anions. There is no evidence for Fe(III) in the low-spin state. The Mössbauer parameters of N-star and the S-star in comparison with the mononuclear precursor clearly indicate coordination. Apparently the N-star deviates much stronger in isomer shift and quadrupol splitting then the S-star. This can be understood on the basis of the HSAB concept: the hard N-donor suits better to the Fe(III) compared to the soft S-donor (see Fig. 6).

Beside the Fe(III)-HS, the spectra indicates another small quadrupole splitted doublet which is characteristic for an Fe(II) in the low-spin state. This signal is characteristic and expected for the $[Fe(II)(CN)_6]^{4-}$core. The area fraction in the N-star at 20 K accounts well for the expected 1/11, i.e. 9%. The S-star overshoots with 15%. This may be due to low Debeye–Waller factor in the soft Fe(III)–S coordination.

The dodecanuclear star-cluster have been characterized by IR spectrum. The characteristic splitting of the C–N stretching vibration band support the octahedral symmetry around the Fe(II) and Co(III) centers and their CN bridge. Evidently three types are expected Fe–CN, Co–CN, and the Fe–CN–Co bridge. The splitting was absent for the hepta and nonanuclear clusters as only M–CN–Fe was present. The shift of the CN-band varies within the N-star and the S-star: 2123; 2054 cm^{-1} and 2128; 2070; 2051 cm^{-1}. The S-star shows an resolved additional peak while the N-star shows only a shoulder in that region. This

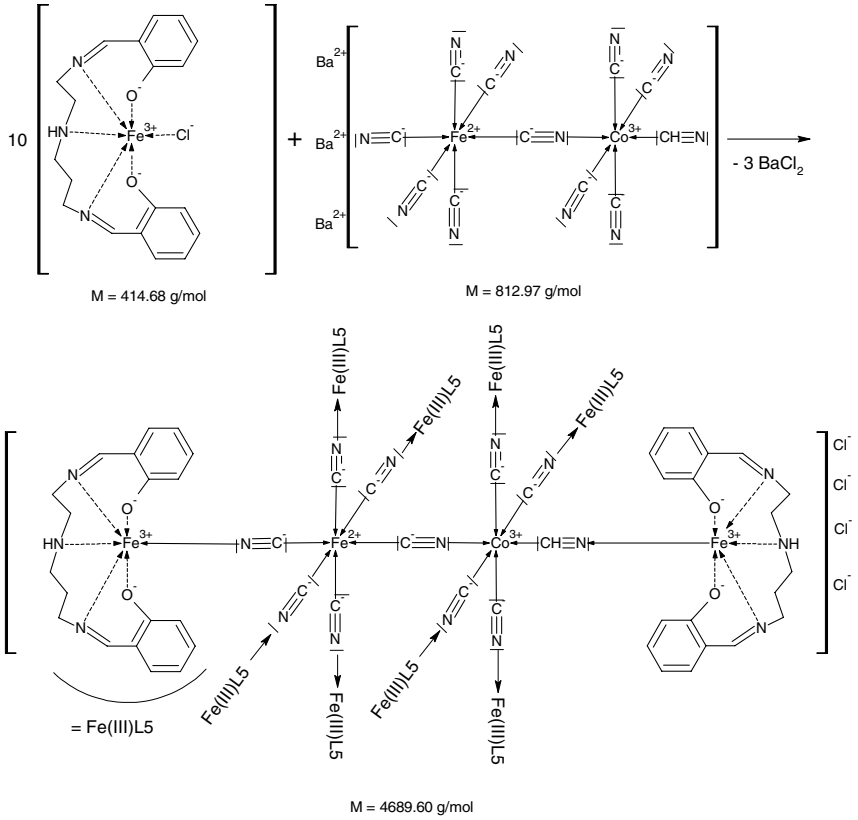


Fig. 2. Synthesis of the [(^{5X}LFe(III)-NC)$_5$Fe(II)-CN-Co(III)(CN-Fe(III)^{5X}L)$_5$]Cl$_4$ cluster (with X = N).

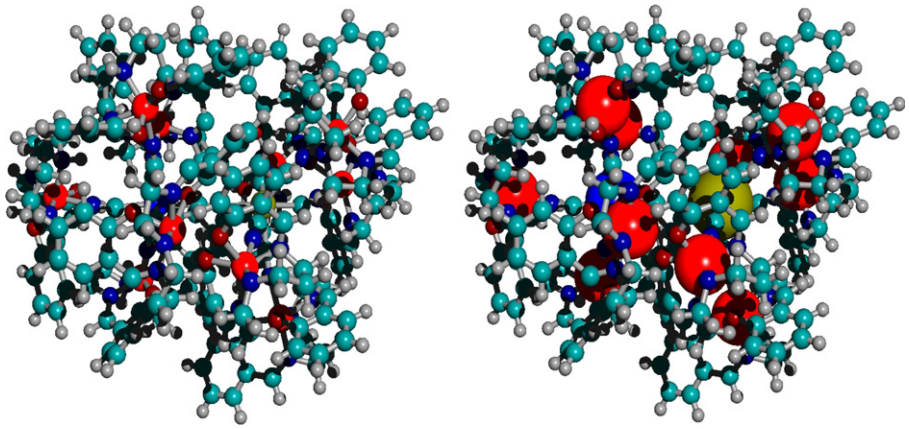


Fig. 3. MM+ model of the $[(^{5N}LFe(III)\text{-}NC)_5Fe(II)\text{-}CN\text{-}Co(III)(CN\text{-}Fe(III)^{5N}L)_5]Cl_4$ cluster (normal and enlarged metal centers).

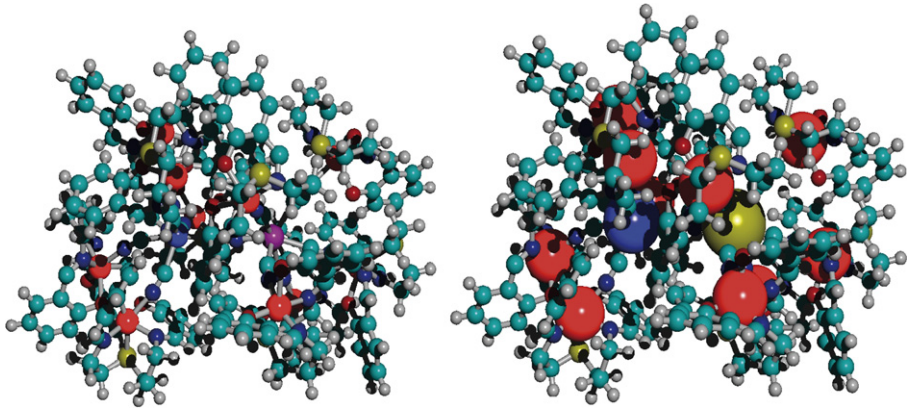


Fig. 4. MM+ model of the $[(^{5S}LFe(III)\text{-}NC)_5Fe(II)\text{-}CN\text{-}Co(III)(CN\text{-}Fe(III)^{5S}L)_5]Cl_4$ cluster (normal and enlarged metal centers).

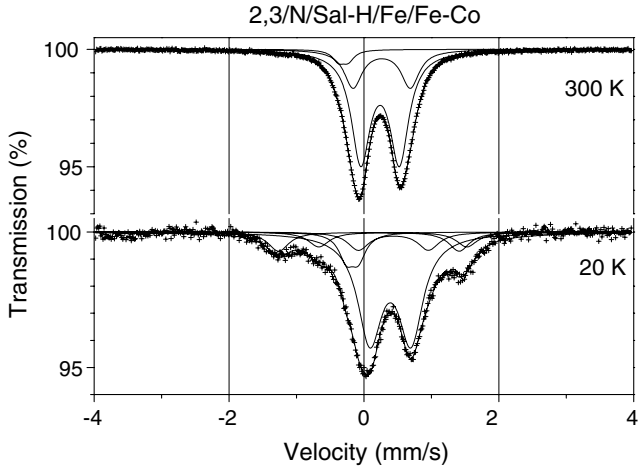


Fig. 5. Mössbauer spectra of the dodecanuclear $[(^{5X}LFe(III)\text{-}NC)_5Fe(II)\text{-}CN\text{-}Co(III)(CN\text{-}Fe(III)^{5X}L)_5]Cl_4$ cluster (with X = N) at 300 K and 20 K.

supports the conclusion indicated by Mössbauer spectroscopy.

At 20 K the Mössbauer spectra of the S-star conserves the same features (Fe(III)-HS and Fe(II)-LS) as at room temperature beside some HS–HS transitions within the distribution. However, the N-star exhibits two additional doublets characteristic for Fe(III) in the low-spin state [2,3].

This indicates that in the dodecanuclear complex $[(^{5N}LFe(III)\text{-}NC)_5Fe(II)\text{-}CN\text{-}Co(III)(CN\text{-}Fe(III)^{5N}L)_5]Cl_4$ a thermally induced transition between an HS to LS state exists. The area fraction of the respective doublets $A(Fe^{III}\text{-high-spin}):A(Fe^{III}\text{-low-spin})$ is 72.8:17.7. This accounts for 19.5% in the LS state.

In the N-star case several Fe(III) centres exhibit electronic switching. This enables us to talk about a multiple electronic transition. This is the first example for electronic switching in a dodecanuclear complex compound. On the other hand, the S-star remains in the HS state between 20 and 300 K.

Magnetic investigation are in progress and will further resolve the switching in our stars. The difficulties in the evaluation of the magnetic properties, such as coupling, in pure high-spin compounds usually rises, at least exponentially, with the number of spin centers in the molecule. Now the dodecanuclear stars are orders of magnitude higher in complexity compare to the hepta- and nonanuclear-stars. On top of the usual high-spin problems they change to different total high-spin states, i.e. spin transition, as a function of temperature.

Table 1
Mössbauer parameter of the dodecanuclear $[(^{5X}LFe(III)\text{-}NC)_5Fe(II)\text{-}CN\text{-}Co(III)(CN\text{-}Fe(III)^{5X}L)_5]Cl_4$ clusters (with X = N, S) at 300 K and 20 K

Temperature (K)	HS state					LS state			
		δ (mm/s)	Δ (mm/s)	$W+$ (mm/s)	Fraction (%)	δ (mm/s)	Δ (mm/s)	$w+$ (mm/s)	Fraction
[2,3/N/Sal-H/Fe/Fe-Co]									
300	Fe(III)	0.239	0.573	0.168	71.90				
	Fe(III)	0.263	0.846	0.160	23.70				
	Fe(II)					−0.307	0.142	0.108	4.48
20	Fe(III)	0.391	0.608	0.219	63.40	0.073	2.677	0.185	9.90
	Fe(III)	0.438	1.040	0.190	9.40	0.429	2.195	0.189	7.80
	Fe(II)					−0.173	0.178	0.135	9.40
[2,3/S/Sal-H/Fe/Fe-Co]									
300	Fe(III)	0.204	0.801	0.265	82.2				
	Fe(II)					−0.28	0.00	0.12	17.0
20	Fe(III)	0.362	0.839	0.283	80.3				
	Fe(II)					−0.172	0.000	0.215	19.7

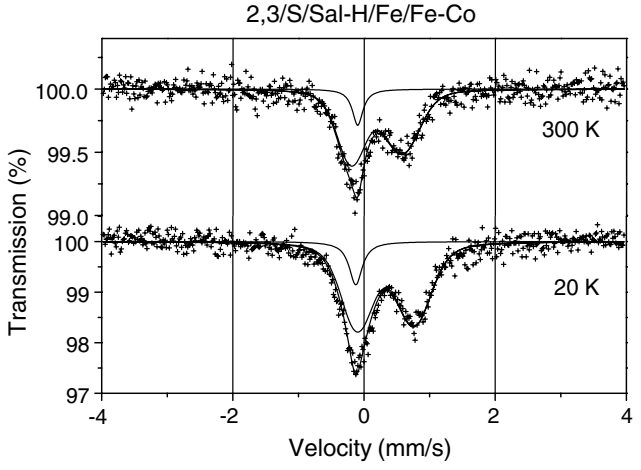


Fig. 6. Mössbauer spectra of the dodecanuclear $[(^{5X}LFe(III)\text{-}NC)_5Fe(II)\text{-}CN\text{-}Co(III)(CN\text{-}Fe(III)^{5X}L)_5]Cl_4$ cluster (with X = S) at 300 K and 20 K.

The technological transfer from the molecular switchability in mononuclear spin transition to multinuclear systems has been achieved. The dodecanuclear star-shaped compounds open a new dimension of switching between 10 and 50 unpaired electrons per star ontop of novel synergysms.

2. Experimental

2.1. Ligand $^{5N}LFeCl$

Partly prepared in analogy to the literature [4]. The pentadentate ligand $L_1 = N,N'$-bis (1-hydroxy-2-benzyliden) 1,6-diamino-3-azahexane has been prepared by a Schiff base condensation between N^1-(2-amino-ethyl)-propan-1,3-diamine and salicylaldehyde at a ratio of 1:2. A mixture of the salicylaldeyde (0.2 mol) and 1,6-diamino-3-azahexane (0.1 mol) in methanol (100 cm^3) was boiled for 10 min and the solution subjected to crowding. The yellow oily material resulted and used without any purification. NMR spectra agree with the expected structure.

A solution of anhydrous iron(III) chloride (10 mmol) in methanol (50 cm^3) was added to a solution of the pentadentate ligand ^{5N}L (10 mmol) in methanol (40 cm^3). The mixture was stirred at 50 °C for 10 min and then triethylamine (20 mmol) was added. The resulting solution was stirred at 50 °C for 1 h and after cooling until black crystals precipitated. These were collected, washed with methanol and diethyl ether, and dried in vacuum.

2.2. Ligand $^{5S}LFeCl$

Partly prepared in analogy to the literature [4]. The pentadentate ligand $^{5S}L = N,N'$-bis (1-hydroxy-2-benzyliden) 2-aminoethyl-3-aminopropylsulfide has been prepared by a Schiff base condensation between 2-aminoethyl-3-aminopropylsulfide and salicylaldehyde at a ratio of 1:2. A mixture of the salicylaldeyde (0.2 mol) and 2-aminoethyl-3-aminopropylsulfide (0.1 mol) in methanol (100 cm^3) was boiled for 10 min and the solution subjected to crowding. The yellow oily material resulted and used without any purification. NMR spectra agree with the expected structure.

A solution of anhydrous iron(III) chloride (10 mmol) in methanol (50 cm^3) was added to a solution of the pentadentate ligand ^{5S}L (10 mmol) in methanol (40 cm^3). The mixture was stirred at 50 °C for 10 min and then triethylamine (20 mmol) was added. The resulting solution was stirred at 50 °C for 1 h and after cooling until black crystals precipitated. These were collected, washed with methanol and diethyl ether, and dried in vacuum.

2.3. Binuclear complexes $Ba_3[(NC)_5Fe(II)\text{-}CN\text{-}Co(III)(CN)_5]$

Partly prepared in analogy to the literature [5]. $K_6[(NC)_5Fe(II)\text{-}CN\text{-}Co(III)(CN)_5]$ has been prepared with 4.8g (0.02 mol) $CoCl_2 \cdot 6H_2O$ in 200 cm^3 H_2O. 6.5 g (0.1 mol) KCN in 100 cm^3 H_2O were added under nitrogen atmosphere.

The well stirred mixture has been cooled down to 0 °C and 6.6 g (0.02 mol) $K_3[Fe(III)(CN)_6]$ in 300 cm^3 H_2O were added drop wise. The mixture is stirred for further 5–10 min and 1000 cm^3 ethanol has been added. The precipitated crystals were collected. It is a mixture K_6 $[(NC)_5Fe(II)\text{-}CN\text{-}Co(III)(CN)_5]$ and K_3 $[Fe(II)(CN)_6]$. Yield: 13.89 g of the mixture.

13.77 g of the mixture has been solved in 23 cm^3 water and 16.7 g (0.069 mol) $BaCl_2 \cdot 2H_2O$ in 23 cm^3 water has been added. The solution has been cooled down to 0 °C. After adding 150 cm^3 of ethanol light yellow crystals of Ba_3 $[(NC)_5Fe(II)\text{-}CN\text{-}Co(III)(CN)_5]$, were collected from the solution. Yield: 4.13 g (0.005 mol) ≈ 25%.

2.4. Dodecanuclear complexes $[(^{5N}LFe(III)\text{-}NC)_5Fe(II)\text{-}CN\text{-}Co(III)(CN\text{-}Fe(III)^{5N}L)_5]Cl_4$

Partly prepared in analogy to the literature [3,4]. A methanol solution (50 cm^3) of $[L_1FeCl]$ (2 mmol) was combined with (20 cm^3) aqueous–methanol solution (1:1) of Ba_3 $[(NC)_5Fe(II)\text{-}CN\text{-}Co(III)(CN)_5]$ (0.2 mmol). The dark-black precipitate was stirred for 30 min. About 60% of the solvent was evaporated using a rotary evaporator at temperatures never higher than 35 °C. Approximately 50 ml of water were then added in order to precipitate the complex. It was cooled in order to enhance the yield. The complexes were filtered using a Fritta IV filter and cleaned with cold water and diethylether and dried under vacuum for 24 h, the filtered off on the Frita funnel, washed twice with methanol and dryed under argon. Yield: −79%.

IR (KBr): ν (cm^{-1}) = 3384 (NH, val.), 2945 (CH_2, val.), 2123, 2054 cm^{-1} (C≡N, val. splitted), 1620 cm^{-1} (C=N, val.), 1600–1500 cm^{-1} (aromat. C=C, val.), 790–750 cm^{-1} (C–H, o. o. p.). Cyanide valence band splitted in fact of the different coordination between iron and cobalt.

2.5. Dodecanuclear complexes $[(^{5S}LFe(III)\text{-}NC)_5Fe(II)\text{-}CN\text{-}Co(III)(CN\text{-}Fe(III)^{5S}L)_5]Cl_4$

Partly prepared in analogy to the literature [3,4]. A methanol solution (50 cm^3) of $[L_2FeCl]$ (2 mmol) was combined with (20 cm^3)g aqueous-methanol solution (1:1) of Ba_3 $[(NC)_5Fe(II)\text{-}CN\text{-}Co(III)(CN)_5]$ (0.2 mmol). The dark-black precipitate was stirred for 30 min. About 60% of the solvent was evaporated using a rotary evaporator at temperatures never higher than 35 °C. Approximately 50 ml of water were then added in order to precipitate the complex. It was cooled in order to enhance the yield. The complexes were filtered using a Fritta IV filter and cleaned with cold water and diethylether and dried under vacuum for 24 h, the filtered off on the Frita funnel, washed twice with methanol and dried under argon.

Yield: 71.1%; reaction time: 30 min;

IR (KBr): ν (cm^{-1}) = 2917 (CH_2, val.), 2128, 2070, 2051 cm^{-1} (C≡N, val.), 1615 cm^{-1} (C=N, val. splitted), 1600–1500 cm^{-1} (aromat. C=C, val.), 760–750 cm^{-1} (C–H, o. o. p.). Cyanide valence band splitted in fact of the different coordination between iron and cobalt.

2.6. Mössbauer spectroscopy

Mössbauer spectroscopy is performed in a conventional spectrometer in scanning the Mössbauer spectra at 20 K and room temperature (^{57}Co/Rh source kept at room temperature; isomeric shifts are relative to the source).

Acknowledgements

This work was partly funded by the DFG (SPP 1136 "Molecular Magnetism"; Re1627/1–3), the "Fonds der chemischen Industrie", the University of Mainz "Forschungsfond" and the "Material-Wissenschaftliches Forschungs-Zentrum" (MWFZ).

References

[1] P. Gütlich, P. van Koningsbruggen, F. Renz, Optical Spectra and Chemical Bonding in Transition Metal Complexes, Structure and Bonding, vol. 107, Springer, 2004, pp. 27–75.
[2] F. Renz, P. Kerep, Hyperfine Interactions 156/157 (2004) 371.
[3] F. Renz, P. Kerep, Polyhedron 24 (2005) 2849.
[4] M. Gembický, R. Boča, F. Renz, Inorg. Chem. Commun. 3 (2000) 662.
[5] A. Haim et al., J. Am. Chem. Soc. 83 (1961) 83.

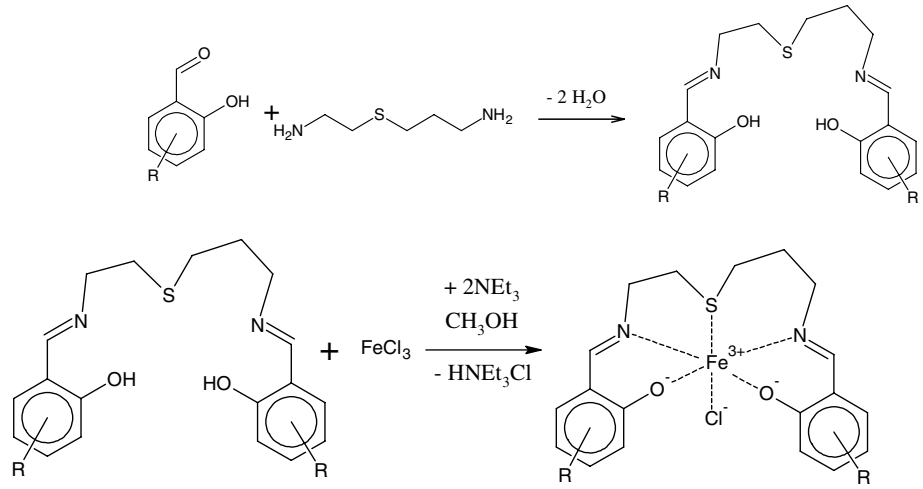


Fig. 1. Synthesis of the [Fe(^{SY}L)Cl] (=[2,3/S/Sal-Y/Fe/Cl]) precursor (with Y = H, 3EtO, 5Me).

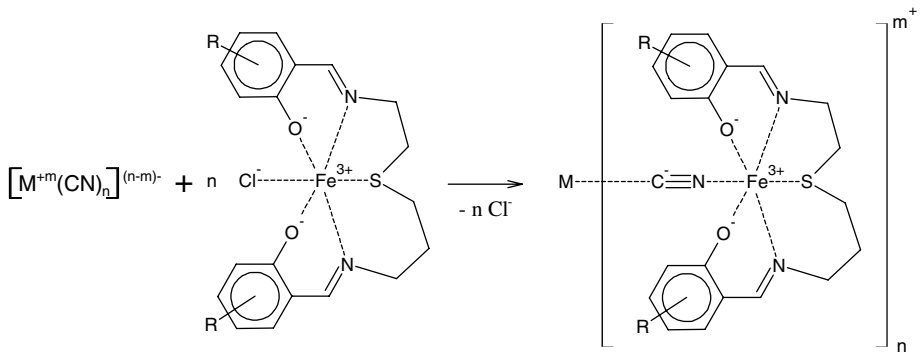


Fig. 2. Synthesis of the heptanuclear star [M(z)(CN–Fe^{SY}L)$_6$]Cl$_z$ (=[2,3/S/Sal-Y/Fe/M]) (with M = Fe(II), Co(III); Y = H, 3EtO, 5Me).

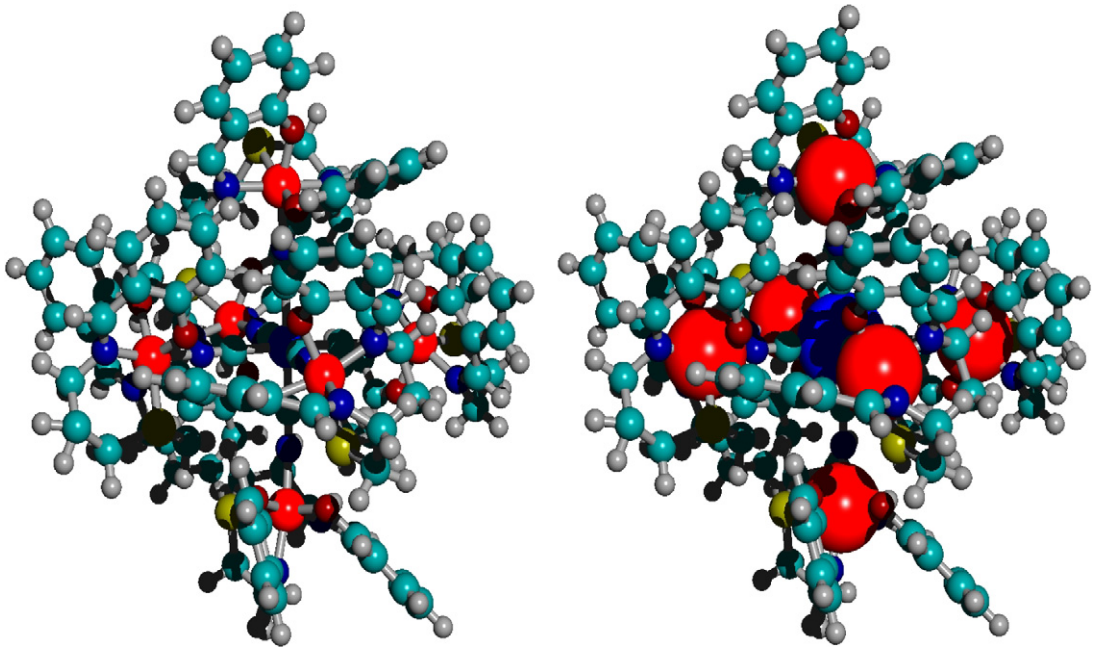


Fig. 3. MM+ model of the [Fe(II)(CN–Fe(III)^{SH}L)$_6$]$^{2+}$ cluster (normal and enlarged metal centers).

isomerization has been observed. This allows the pentadentate to adapt. Molecular dynamics as well as Monte Carlo simulations, both on an empirical level, confirm this modality.

Fig. 4 and Table 1 show results of temperature-dependent Mössbauer spectroscopy of the heptanuclear S-star compounds. At 300 K the spectra indicates a quadrupole split doublet which is common for Fe(III) ions in the high-spin state. For both S–Co-stars the signal has been assigned to two positions with only weak deviations. One explanation may be a *cis–trans* isomerization within the ligand around the Fe(III) centers (as seen above). There is no evidence for Fe(III) in the low-spin state. The Mössbauer parameters of the S-stars in comparison with the mononuclear precursors clearly indicate coordination.

Beside the Fe(III)-HS, the spectra of the S–Fe-stars indicate another small quadrupole split doublet which is characteristic for an Fe(II) in the low-spin state. This signal is characteristic and expected for the $[Fe(II)(CN)_6]^{4-}$ core. The area fraction in the 3EtO–S–Fe-star at 20 K accounts well for the expected 1:7, i.e. 15%. The H–S–Fe-star overshoots that ratio. This may be due to deviations in the Debye–Waller factor.

The heptanuclear star-cluster have been characterized by IR spectrum. The characteristic non-split band of the C–N stretching vibration supports the octahedral symmetry around the Fe(II) or Co(III) centers and their CN bridge. No splitting was observed for the heptanuclear clusters.

At 20 K the Mössbauer spectra of the S-stars conserves the same features (two Fe(III)-HS and one Fe(II)-LS) as at room temperature beside an altered area ratio among the two HS signals within the distribution. In both S–Co-star cases, the HS–Fe(III)-position with the wider quadrupol splitting gained area-fraction on cooling. This indicates a multiple HS–HS transition. Such transitions have not been detected in both S–Fe-star compounds.

Magnetic investigation are in progress and will further resolve the switching in our stars. The difficulties in the evaluation of the magnetic properties, such as coupling, in pure high-spin compounds usually rises, at least exponentially, with the number of spin centers in the molecule.

2. Experimental

2.1. 2-Aminoethyl-3-aminopropylsulfid (aeaps)

Aeaps was prepared as described in the literature [8]. The colorless liquid was characterized by ^{1}H NMR (400 MHz, CD_3OD): 4.73 ppm (s, 4H, NH_2); 2.80–2.78

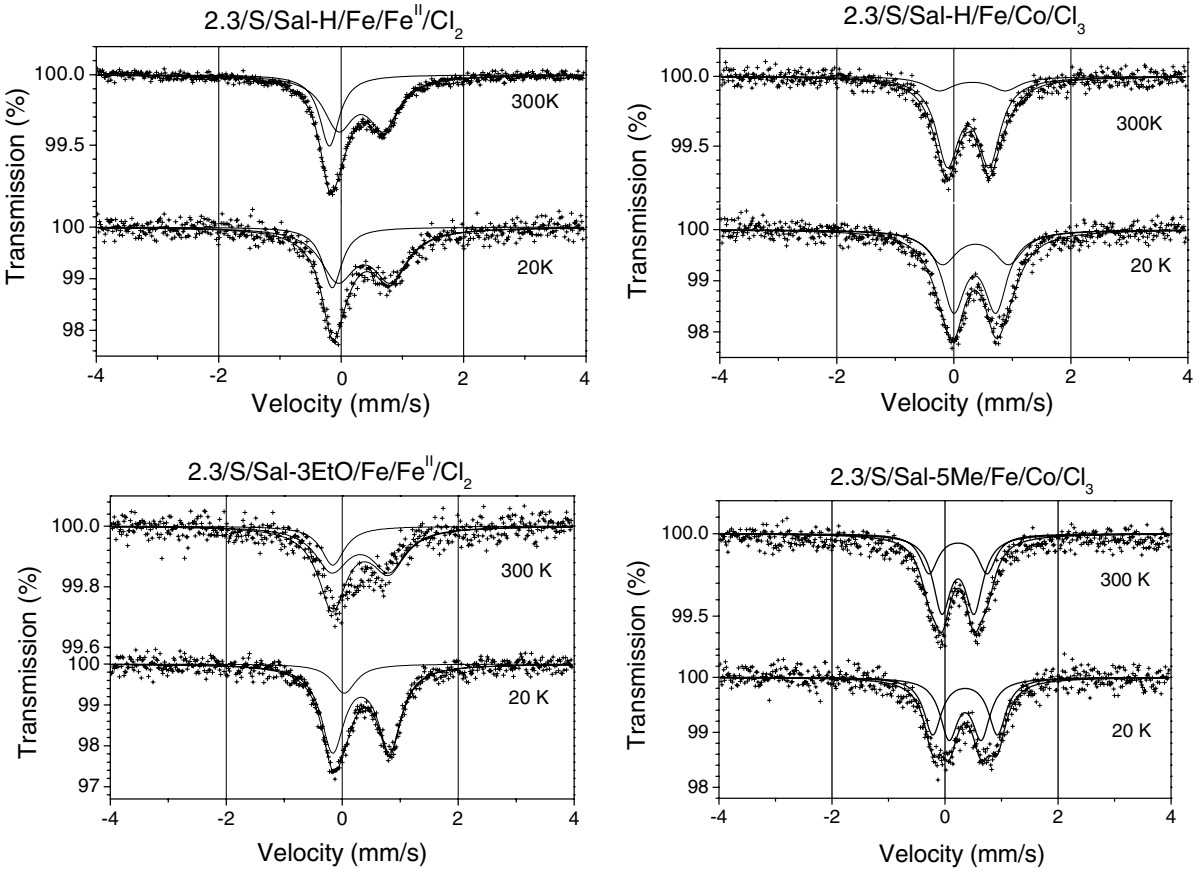


Fig. 4. Mössbauer spectra of the heptanuclear (from top): [2,3/S/Sal-H/Fe/Fe(II)/Cl_2], [2,3/S/Sal-3EtO/Fe/Fe(II)/Cl_2], [2,3/S/Sal-H/Fe/Co/Cl_3], and [2,3/S/Sal-5Me/Fe/Co/Cl_3].

Table 1
Mössbauer parameter of the heptanuclear star $[M(z)(CN–Fe^{SY}L)_6]Cl_z$ (=[2,3/S/Sal-Y/Fe/M(z)/Cl_z]) (with M = Fe(II), Co(III); Y = H, 3EtO, 5Me) clusters at 300 K and 20 K

Temperature (K)	Fe(III) HS state				Fe(II)LS state			
	δ (m/s)	Δ (mm/s)	w_+ (mm/s)	Fraction (%)	δ (m/s)	Δ (mm/s)	w_+ (mm/s)	Fraction (%)
[2,3/S/Sal-H/Fe/Fe(II)/Cl_2]								
300	0.324	0.736	0.299	68	−0.191	0	0.196	32
20	0.375	0.864	0.340	74	−0.145	0	0.192	26
[2,3/S/Sal-3EtO/Fe/Fe(II)/Cl_2]								
300	0.310	0.980	0.35	76	−0.162	0	0.244	24
20	0.327	0.981	0.243	85	0.035	0	0.244	15
	Fe(III) HS state				Fe(III) HS state			
[2,3/S/Sal-H/Fe/Co/Cl_3]								
300	0.247	0.712	0.232	83	0.315	1.13	0.30	17
20	0.356	0.72	0.238	65	0.371	1.13	0.302	35
[2,3/S/Sal-5Me/Fe/Co/Cl_3]								
300	0.230	0.57	0.19	65	0.231	1.025	0.19	35
20	0.355	0.57	0.19	51	0.355	1.143	0.19	49

ppm (t, 2H, –CH_2–S–); 2.74–2.71 ppm (t, 2H, S–CH_2–); 2.64–2.56 ppm (quin, 4H, NH_2–CH_2–); 1.78–1.71 ppm (quin, 2H, –CH_2–CH_2–CH_2–). Yield: 50%.

2.2. Precursor

The precursors were prepared as described in the literature [7]. The dark red-brown powders were characterized by IR and mass spectroscopy and by elemental analysis.

2.2.1. [2,3/S/Sal-H/Fe/Cl]

Yield: 72.8%. *Anal.* Calc. for $C_{19}H_{20}N_2SO_2FeCl$: C, 52.8; N, 6.5; H, 4.6; S, 7.4. Found: C, 51.4; N, 6.7; H, 5.8; S, 6.3%. EI MS $m/z = 396.3$ (100%, $[2,3/S/Sal\text{-}H/Fe]^+$).

2.2.2. [2,3/S/Sal-3EtO/Fe/Cl]

Yield: 90.0%. *Anal.* Calc. for $C_{23}H_{28}N_2SO_4FeCl$: C, 53.1; N, 5.4; H, 5.4; S, 6.2. Found: C, 53.7; N, 5.6; H, 5.8; S, 6.1%. EI MS $m/z = 484.4$ (100%, $[2,3/S/Sal\text{-}3EtO/Fe]^+$).

2.2.3. [2,3/S/Sal-5Me/Fe/Cl]

Yield: 95.4%. *Anal.* Calc. for $C_{21}H_{24}N_2SO_2FeCl$: C, 54.9; N, 6.1; H, 5.3; S, 7.0. Found: C, 51.5; N, 5.9; H, 5.7; S, 6.1%. EI MS $m/z = 424.4$ (100%, $[2,3/S/Sal\text{-}5Me/Fe]^+$).

2.3. Heptanuclear complexes

The heptanuclear complexes were prepared in analogy to the literature [5–7] except for the reaction time which was increased from 30 min to seven days. The products were characterized by IR-, ESI- and Mössbauer spectroscopy.

2.3.1. [2,3/S/Sal-H/Fe/Fe(II)/Cl_2]

Yield: 78.4%; reaction time: 30 min; ESI MS $m/z = 1294.5$ (85.5%, $[2,3/S/Sal\text{-}H/Fe/Fe(II)]^{2+}$]).

IR (KBr): ν (cm^{-1}) = 2916 (CH_2, val.), 2068 cm^{-1} (C≡N, val.), 1616 cm^{-1} (C=N, val.), 1600–1500 cm^{-1} (aromat. C=C, val.), 760–750 cm^{-1} (C–H, o. o. p.).

2.3.2. [2,3/S/Sal-3EtO/Fe/Fe(II)/Cl_2]

Yield: 95.6%; reaction time: 10 d; ESI MS $m/z = 1558.9$ (0.3%, $[2,3/S/Sal\text{-}3EtO/Fe/Fe(II)]^{2+}$]).

IR (KBr): ν (cm^{-1}) = 2903 (CH_2, val.), 2073 cm^{-1} (C≡N, val.), 1616 cm^{-1} (C=N, val.), 1600–1500 cm^{-1} (aromat. C=C, val.), 760–750 cm^{-1} (C–H, o. o. p.).

2.3.3. [2,3/S/Sal-H/Fe/Co/Cl_3]

Yield: 71.1%; reaction time: 30 min;

IR (KBr): ν (cm^{-1}) = 2919 (CH_2, val.), 2128 cm^{-1} (C≡N, val.), 1615 cm^{-1} (C=N, val.), 1600–1500 cm^{-1} (aromat. C=C, val.), 760–750 cm^{-1} (C–H, o. o. p.).

2.3.4. [2,3/S/Sal-5Me/Fe/Co/Cl_3]

Yield: 48.5%; reaction time: 7 d;

IR (KBr): ν (cm^{-1}) = 2919 (CH_2, val.), 2129 cm^{-1} (C≡N, val.), 1621 cm^{-1} (C=N, val.), 1600–1500 cm^{-1} (aromat. C=C, val.), 760–750 cm^{-1} (C–H, o. o. p.).

2.4. Mössbauer spectroscopy

Mössbauer spectroscopy was performed in a conventional spectrometer in scanning the Mössbauer spectra at 20 K and room temperature (300 K) (^{57}Co/Rh source kept at room temperature; isomeric shifts are relative to the source).

Acknowledgements

This work was partly funded by the DFG (SPP 1136 "Molecular Magnetism"; Re1627/1-3), the "Fonds der chemischen Industrie", the University of Mainz "Forschungsfond" and the "Material-Wissenschaftliches Forschungs-Zentrum" (MWFZ).

References

[1] J.K. McCusker, E.A. Schmitt, D.N. Hendrickson, in: D. Gatteschi, O. Kahn, J.S. Miller, F. Palacio (Eds.), Magnetic Molecular Materials, NATO ASI Series, vol. 198, Kluwer, Dordrecht, 1991, p. 297.
[2] O. Kahn, Molecular Magnetism, VCH, New York, 1993.
[3] D. Gatteschi, in: E. Coronado, P. Delhaes, D. Gatteschi, J.S. Miller (Eds.), Molecular Magnetism: From Molecular Assemblies to the Devices, NATO ASI Series, vol. 321, Kluwer, Dordrecht, 1996, p. 141, 289.
[4] P. Gütlich, P. van Koningsbruggen, F. Renz, in: Optical Spectra and Chemical Bonding in Transition Metal Complexes, Structure and Bonding, 107, Springer-Verlag, 2004, pp. 27–75.
[5] F. Renz, P. Kerep, Hyperfine Interactions 156/157 (2004) 371.
[6] F. Renz, P. Kerep, Polyhedron 24 (2005) 2849.
[7] M. Gembický, R. Boča, F. Renz, Inorganic Chemistry Communications 3 (2000) 662.
[8] M.J. Bjerrum, T. Laier, E. Larsen, Inorganic Chemistry 25 (1986) 816.

(GSO) descriptions are inevitable [9]. A number of theoretical and experimental studies were reported for the series of the iron–sulfur clusters, however, the first principle calculations for the noncollinear spin structures have not been reported, to our knowledge.

At the reduced form the [2Fe–2S] cluster has one odd electron which could delocalize over iron centers [5,6,10]. The formal charge can be either $Fe^{3+}Fe^{2+}$ or $Fe^{2.5+}Fe^{2.5+}$. The former state is a trapped valence (TV) state, where the odd electron is localized at one iron center. On the other hand, the latter state is a mixed valence (MV) state, where the electron is delocalized over the iron centers. The BS approach has been successfully applied to the study of the electronic structures of these transition metal complexes, however, for the incomplete treatment of the non-dynamical correlation, the MV state could not be described. So, only the electronic structure of the TV state has been investigated by BS methods.

In this study, the spin structures and magnetic orbitals of [2Fe–2S] clusters at the GSO spin states are investigated using the GSO–DFT methods. The orbital interactions and noncollinear spin structures are characterized by natural orbitals.

2. Theoretical backgrounds

2.1. Generalized spin orbital (GSO) method

The unrestricted method based on the different orbitals for different spins is inappropriate to describe the helical or the noncollinear spin structures [11–13]. For such cases, the generalized spin orbital (GSO) description is necessary to expand the spin space of the wavefunctions. The GSO $\{\varphi_i\}$ is defined as

$$\varphi_i(\mathbf{x}) = \chi_i^{\alpha}(\mathbf{r})\alpha(\varpi) + \chi_i^{\beta}(\mathbf{r})\beta(\varpi), \tag{1}$$

which can take both alpha and beta spin spaces with different spatial orbitals $\{\chi_i^{\omega}\}$. Unrestricted wavefunctions are only one case of Eq. (1) that the orbital is in either alpha or beta spin. The special orbitals are expressed as a linear combinations of atomic orbitals

$$\chi_i^{\omega}(\mathbf{x}) = \sum_{\lambda}^{K} C_{\lambda i}^{\omega}\phi_{\lambda}, \tag{2}$$

where K is a number of orbitals. The expansion coefficients $C_{\lambda i}^{\omega}$ are complex numbers. Density matrix ($\mathbf{P}$) is a $2K\times 2K$ matrix defined by

$$\mathbf{P}_{\lambda\sigma} = \sum_{a}^{N} C_{\lambda a}C_{\sigma a}^{*}. \tag{3}$$

The $\mathbf{P}_{\lambda\sigma}$ is expressed by a 2×2 matrix in terms of the spin space

$$P_{\lambda\sigma} = \begin{pmatrix} P^{\alpha\alpha} & P^{\alpha\beta} \\ P^{\beta\alpha} & P^{\beta\beta} \end{pmatrix}_{\lambda\sigma} \tag{4}$$

Charge density matrix ($\mathbf{D}$) is obtained from the density matrixes as

$$\mathbf{D}_{\lambda\sigma} = \sum_{i=j}^{\alpha,\beta} \mathbf{P}_{\lambda\sigma}^{ij} = \mathbf{P}_{\lambda\sigma}^{\alpha\alpha} + \mathbf{P}_{\lambda\sigma}^{\beta\beta}. \tag{5}$$

The SCF equation of the GSO is given as

$$\mathbf{FC} = \mathbf{SC}\boldsymbol{\varepsilon}, \tag{6}$$

where $\mathbf{F}$, $\mathbf{S}$ and $\boldsymbol{\varepsilon}$ are a Fock matrix, an orbital overlap matrix and an orbital energy matrix, respectively. The $2K\times 2K$ matrix equation of Eq. (6) becomes

$$\begin{pmatrix} \mathbf{F}^{\alpha\alpha} & \mathbf{F}^{\alpha\beta} \\ \mathbf{F}^{\beta\alpha} & \mathbf{F}^{\beta\beta} \end{pmatrix}\begin{pmatrix} \mathbf{C}^{\alpha} \\ \mathbf{C}^{\beta} \end{pmatrix} = \varepsilon\begin{pmatrix} \mathbf{S}^{\alpha\alpha} & \mathbf{0} \\ \mathbf{0} & \mathbf{S}^{\beta\beta} \end{pmatrix}\begin{pmatrix} \mathbf{C}^{\alpha} \\ \mathbf{C}^{\beta} \end{pmatrix}. \tag{7}$$

The difference between the GSO equation and unrestricted equation is only the off-diagonal terms: $F_{\mu\nu}^{\alpha\beta}$ and $F_{\mu\nu}^{\beta\alpha}$. The Fock matrix $\mathbf{F}$ of the GSO–HF method is given by

$$\begin{aligned}\mathbf{F}_{\lambda\sigma} =& \begin{pmatrix} \mathbf{h}_{\lambda\sigma}^{\alpha\alpha} & \mathbf{0} \\ \mathbf{0} & \mathbf{h}_{\lambda\sigma}^{\beta\beta} \end{pmatrix} + \mathbf{D}_{\lambda\sigma}^{ii}\begin{pmatrix} \left(\begin{matrix}\alpha\alpha \\ \mu\nu\end{matrix}\middle|\begin{matrix} ii \\ \sigma\lambda\end{matrix}\right) & 0 \\ 0 & \left(\begin{matrix}\beta\beta \\ \mu\nu\end{matrix}\middle|\begin{matrix} ii \\ \sigma\lambda\end{matrix}\right) \end{pmatrix} \\ & - \begin{pmatrix} \mathbf{P}_{\lambda\sigma}^{\alpha\alpha}\left(\begin{matrix}\alpha\alpha \\ \mu\lambda\end{matrix}\middle|\begin{matrix}\alpha\alpha \\ \sigma\nu\end{matrix}\right) & \mathbf{P}_{\lambda\sigma}^{\alpha\beta}\left(\begin{matrix}\alpha\alpha \\ \mu\lambda\end{matrix}\middle|\begin{matrix}\beta\beta \\ \sigma\nu\end{matrix}\right) \\ \mathbf{P}_{\lambda\sigma}^{\beta\alpha}\left(\begin{matrix}\beta\beta \\ \mu\lambda\end{matrix}\middle|\begin{matrix}\alpha\alpha \\ \sigma\nu\end{matrix}\right) & \mathbf{P}_{\lambda\sigma}^{\beta\beta}\left(\begin{matrix}\beta\beta \\ \mu\lambda\end{matrix}\middle|\begin{matrix}\alpha\alpha \\ \sigma\nu\end{matrix}\right) \end{pmatrix},\end{aligned} \tag{8}$$

where $\mathbf{h}$ is one-electron operator given by the kinetic term and the potential energy term of electronic field from nucleuses

$$h = -\frac{1}{2}\nabla^2 - \sum_{A}\frac{Z_A}{r_A}. \tag{9}$$

The two-electron integrals is defined as

$$\left(\begin{matrix}\omega_i & \omega_j \\ i & j\end{matrix}\middle|\begin{matrix}\omega_k & \omega_l \\ k & l\end{matrix}\right) = \int d\mathbf{x}_1 d\mathbf{x}_2 \phi_i^{\omega_i *}(\mathbf{x}_1)\phi_j^{\omega_j *}(\mathbf{x}_1)\mathbf{r}_{12}^{-1}\phi_k^{\omega_k}(\mathbf{x}_2)\phi_l^{\omega_l}(\mathbf{x}_2). \tag{10}$$

The Fock matrix of the GSO–DFT method is given by

$$\mathbf{F} = \begin{pmatrix} \mathbf{h}^{\alpha\alpha} & 0 \\ 0 & \mathbf{h}^{\beta\beta} \end{pmatrix} + \begin{pmatrix} \mathbf{V}_{\mathrm{ee}} & 0 \\ 0 & \mathbf{V}_{\mathrm{ee}} \end{pmatrix} + \begin{pmatrix} \mathbf{V}_{\mathrm{XC}}^{\alpha\alpha} & \mathbf{V}_{\mathrm{XC}}^{\alpha\beta} \\ \mathbf{V}_{\mathrm{XC}}^{\beta\alpha} & \mathbf{V}_{\mathrm{XC}}^{\beta\beta} \end{pmatrix}, \tag{11}$$

where $\boldsymbol{V}_{\mathrm{ee}}$ and $\boldsymbol{V}_{\mathrm{XC}}$ are the classical Coulomb term and an exchange correlation potential.

Tilted spins is expressed by spinor

$$|\theta,\phi\rangle = \begin{pmatrix} \cos\frac{\theta}{2}\mathrm{e}^{-\mathrm{i}\frac{\phi}{2}} \\ \sin\frac{\theta}{2}\mathrm{e}^{\mathrm{i}\frac{\phi}{2}} \end{pmatrix}, \tag{12}$$

where θ is a direction angle and ϕ is a oblique angle in the spin space. For example, alpha ($S_z = 1/2$), beta ($S_z = -1/2$), S_x, $-S_x$, S_y, $-S_y$ spins are given by

$$\left\{\begin{matrix} |\alpha\rangle = \frac{1}{2}\begin{pmatrix}1\\0\end{pmatrix} \\ |\beta\rangle = \frac{1}{2}\begin{pmatrix}0\\1\end{pmatrix}\end{matrix}\right., \quad \left\{\begin{matrix} |x\rangle = \frac{1}{\sqrt{2}}\begin{pmatrix}1\\1\end{pmatrix} \\ |-x\rangle = \frac{1}{\sqrt{2}}\begin{pmatrix}-\mathrm{i}\\ \mathrm{i}\end{pmatrix}\end{matrix}\right., \quad \left\{\begin{matrix} |y\rangle = \frac{1}{2}\begin{pmatrix}1-\mathrm{i}\\ \mathrm{i}+\mathrm{i}\end{pmatrix} \\ |-y\rangle = \frac{1}{2}\begin{pmatrix}1+\mathrm{i}\\ 1-i\end{pmatrix}\end{matrix}\right.. \tag{13}$$

Note that the phase factor of the spin states does not change the expected values

$$|\text{state}\rangle' = e^{i\phi}|\text{state}\rangle. \tag{14}$$

Thus, the spin density matrices for S_x, S_y and S_z are given by

$$P^{Sx} = P^{\alpha\beta} + P^{\beta\alpha}, \tag{15a}$$

$$P^{Sy} = i(P^{\alpha\beta} - P^{\beta\alpha}), \tag{15b}$$

$$P^{S_z} = (P^{\alpha\alpha} - P^{\beta\beta}), \tag{15c}$$

respectively. The expectation value of total squared-magnitude of the spin, S^2, can be written as

$$S^2 = \sum_{I}^{x,y,z}\sum_{i}^{N}\sum_{j}^{N} s_I(i)s_I(j) = S_- \cdot S_+ + S_z + S_z^2. \tag{16}$$

The first term of Eq. (16) simplifies to

$$\begin{aligned} S_- \cdot S_+ &= \sum_{i}^{N}\sum_{j}^{N} s_-(i)s_+(i) \\ &= \sum_{i}^{N} s_-(i)s_+(j) + \sum_{i\neq j}^{N} s_-(i)s_+(j) \\ &= N_\beta + \sum_{i\neq j}^{N} s_-(i)s_+(j). \end{aligned} \tag{17}$$

These terms of Eq. (17) can be written in terms of $P^{\beta\beta}$, **S** and **C** as

$$N_\beta = \sum_{i}^{N}\sum_{j}^{N} P_{ij}^{\beta\beta}\cdot S_{ij}, \tag{18a}$$

$$\sum_{i\neq j}^{N} s_-(i)s_+(j) = \sum_{i\neq j}^{N,N}\left\{\sum_{k,l}(C_{ik}^{\beta *}\cdot C_{il}^{\alpha} S_{k,l})\cdot\sum_{k,l}(C_{jk}^{\beta}\cdot C_{jl}^{\alpha *} S_{k,l})\right\}. \tag{18b}$$

Natural orbitals are evaluated by solving the generalized eigenvalue equation of the charge density matrix:

$$\mathbf{DSf} = \mathbf{nf}, \tag{19}$$

where **f**, **n** and **S** are $K\times K$ matrices for natural orbitals, occupation numbers and orbital overlaps, respectively.

2.2. Spin Hamiltonian of mixed valence states

The broken-symmetry (BS) approach has been a practical first principle method for strongly correlated electron systems such as multinuclear transition metal complexes [1–8,10]. However, one of the problems for the BS method is an incomplete treatment of the nondynamical correlations. In fact, a BS solution is not a pure spin state and the total energy is slightly higher for the spin contamination. For the strongly correlated systems composed of localized spins, the Heisenberg spin Hamiltonian has been applied to the BS states. The spin Hamiltonian is defined by

$$H = -2\sum_{\langle i,j\rangle} J_{ij} S_i \cdot S_j, \tag{20}$$

where J_{ij} is an exchange interaction between the ith spin (S_i) and the jth spin (S_j). The energy levels and the magnetic properties could be evaluated by solving the spin Hamiltonian [1,2]. On the other hand for delocalized systems, the adequate model Hamiltonian is the Heisenberg exchange term and the double exchange term, like t–J model as

$$H = -2\sum_{\langle i,j\rangle} J_{ij} S_i \cdot S_j + b_{ij}\cos\frac{\theta_{ij}}{2}, \tag{21}$$

where b_{ij} and θ_{ij} is a transfer integral and an angle between vector spin S_i and S_j, respectively [4,5]. The second term of Eq. (21) is for the electron delocalization between spin centers. The electron delocalization occurs with a $\theta/2$ rotation for the spinor nature of the spin. For two spin sites systems, the energy levels are given by

$$E = -JS(S+1) \pm \sqrt{\frac{\Delta^2}{4} + B^2\left(S+\frac{1}{2}\right)^2}, \tag{22}$$

where B, Δ and S are resonance parameter, potential energy difference between spin sites and total spin state, respectively. The B is given in terms of b and S as

$$B = \frac{b}{2S+1}. \tag{23}$$

The tilt angle θ depends on the total spin state S as

$$\cos\frac{\theta}{2} = \frac{S+1/2}{S_{\max}+1/2}, \tag{24}$$

where $S_{\max}$ is a total spin at the ferromagnetic coupling state ($\theta = 0$).

On the approximation of neglecting the overlaps (T) between spin orbitals, expected S^2 values at the TV state and MV state are given by

$$S_{\text{TV}}^2 = \frac{5}{4}\cos^2(\theta) + 10\cos(\theta) + \frac{27}{2}, \tag{25a}$$

$$S_{\text{MV}}^2 = \frac{9}{8}(\cos^2(\theta) + 9\cos(\theta) + 12), \tag{25b}$$

respectively. At the ferromagnetic state ($\theta = 0$), both Eqs. (25a) and (25b) give $S^2 = 99/4$ values. At the antiferromagnetic state ($\theta = 180°$), these are $S_{\text{TV}}^2 = 4.75$ and $S_{\text{MV}}^2 = 4.5$. The S_{TV}^2 is slightly larger than S_{MV}^2 as θ increase, though the difference between S_{TV}^2 and S_{MV}^2 is very small. The spin orbital overlap (T) effect has greater influence on the S^2 value than these charge state differences. S^2 value decreases as the T value increases.

3. Computational procedures

GSO and unrestricted calculations were carried out by employing the GSO-X program package, which is developed by Yamanaka et al. [11–13]. The B3LYP exchange-correlation functional was used and a Huzinaga's MINI basis set [14] and STO-3G basis sets were used for iron and other atoms, respectively. These basis sets were

single-ζ quality (SZ). A pruned (75, 305) integral grid, having 75 radial shells and 305 angular points per shell was used. The total SCF energy was converged to a threshold of 10^{-6} a.u. For a geometry optimization, unrestricted method was carried out using the Gaussina98 program package [15]. The BLYP functional with a Huzinaga's MIDI basis set and 6-31G* basis sets was employed for the optimization calculation. These basis sets were valence double-ζ quality (VDZ).

4. Calculated results

Two theoretical models for a ferredoxin-type [2Fe–2S] cluster are examined (Fig. 1). One is a symmetrical [2Fe–2S] model (**1a**) whose geometrical parameters were taken based on native ferredoxin-type clusters. The potential energy difference of **1a** is zero ($\Delta = 0$) for the symmetrical core. The other model (**1b**) is an optimized structure performed by the BS-BLYP/VDZ method. The geometrical core structure of **1b** is asymmetrical by the electron localization of the BS state. The structural parameters are summarized in Table 1. It is clear that the asymmetrical distortion of **1b** is very small.

Using these models (**1a** and **1b**), three spin states are investigated. They are ferromagnetic spin state (F), antiferromagnetic spin state (AF) and generalized spin state (G). These spin states are shown in Fig. 2. The initial θ values of G states was 170°. The F and AF spin states are in the collinear spin states. The S_z values of F and AF are $S_F = 9/2$ and $S_{AF} = 1/2$, respectively. Calculated total energies and S^2 results are summarized in Table 2. By the structure optimization, all the spin states of **1b** are stabilized in energies by about 0.021 hartree (13 kcal mol^{-1}) in comparison with **1a**. The energy gaps between F and AF spin states (ΔE_{F-AF}) are in the 10^{-3} hartree orders and **1b** has larger ΔE_{F-AF} value than **1a**. It is because the electron delocalization at the F state is more stabilized for **1a**. The energy gaps between G and AF states were almost zero for **1a** and **1b**. Thus the energy stabilization by an odd electron delocalization is little at the ground state. It is shown that the energy stabilization of exchange interactions is stronger than that of the electron delocalization mechanism in the [2Fe–2S] cluster.

The S^2 values at the F state are close to the ideal $S^2 = 24.75$. For the AF states, the S^2 values are smaller than the $S^2_{TV} = 4.75$ values. The S^2 values at G states are larger than those of AF states for the tilted spin structures. $S^2_{MV} = 6.48$ and $S^2_{TV} = 4.77$ values are expected by Eq. (25) for **1a** and **1b** using calculated angle $\theta = 139.2°$ and $\theta = 176.2°$, respectively. The calculated S^2 values for **1a** and **1b** are 6.01 and 4.505. The decrease of the calculated S^2 values are ascribed for the T effects as discussed in later.

The charge and spin density distributions of **1a** and **1b** are summarized in Table 3. The F and G state of **1a** show the MV state, where the charge and spin densities are

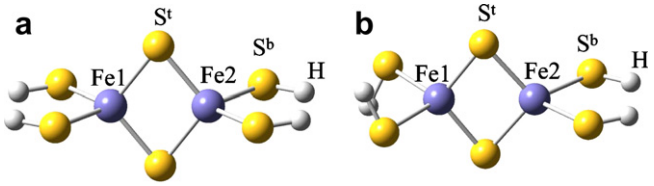


Fig. 1. Molecular structure of the [2Fe–2S] cluster ($Fe_2S_2(SH)_4^{3-}$) used in this study. Compound **1a** is a theoretical model with a symmetrical [2Fe–2S] core. Compound **1b** is an optimized structure obtained by the BS-BLYP/VDZ method. The core is slightly asymmetrical.

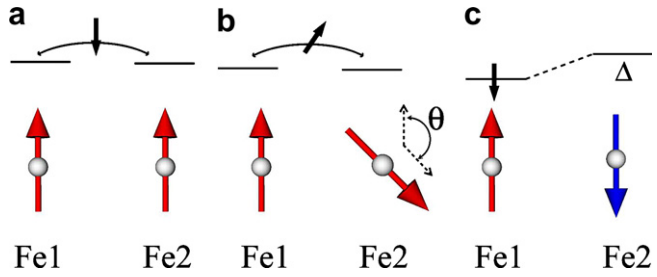


Fig. 2. Schematic representations of the electron delocalizations and the spin states. (a) At the ferromagnetic (F) spin state, the odd electron delocalizes over spin centers. (b) At the generalized (G) spin state, the odd electron delocalizes over spin centers with rotation. (c) At the antiferromagnetic (AF) spin state with potential energy difference such as the asymmetrical core structures or asymmetrical ligand termination, the odd electron is localized at one spin center.

Table 1
Structural parameters[a] of $Fe_2S_2(SH)_4^{3-}$ molecules (**1a** and **1b**)

Molecule	Distance (Å)					Angle (°)
	Fe–S^b	Fe–S^t	Fe···Fe	S^b···S^b	S^t···S^t	Fe–S^b–Fe
1a[b]	2.26	2.38	2.77	2.56	3.72	75.66
1b[c]	2.26	2.52	2.86	3.60	3.93	76.93
	(2.34)	(2.50)			(3.74)	

[a] b, bridging; t, terminal.
[b] Parameters are taken from the ferredoxin-type [2Fe–2S] cluster [4,5]. The [2Fe–2S] core is symmetrical.
[c] An optimized structure calculated by the BS-BLYP/VDZ method. In parentheses, parameters of the Fe(II) center, Fe2, are given. The [2Fe–2S] core is asymmetrical.

Table 2
Calculated total energy (E), energy difference (ΔE)[a] and S^2 values at the F, AF, G spin states[a] of the $Fe_2S_2(SH)_4^{3-}$ molecules (**1a** and **1b**) by the GB3LYP/SZ method

Molecule	Spin state	Total energy (a.u.)	ΔE (cm^{-1})	S^2
1a	F	−4890.2691636	1.01×10^3	24.751
	AF	−4890.2737439	0	4.46
	G	−4890.2737267	4.	6.01
1b	F	−4890.2913205	2.55×10^3	24.751
	AF	−4890.3029449	0	4.484
	G	−4890.3029289	4.	4.505

[a] ΔE: energy difference from the most stable spin state; F: ferromagnetic spin state ($S_z = 9/2$); AF: antiferromagnetic spin state ($S_z = 1/2$), which is same as a broken-symmetry solution of the spin-unrestricted method; G: generalized spin state with a noncollinear spin structure.

Table 3
Calculated charge (spin) densities and relative angles (θ) between spin sites at the F, AF, G spin states[a] of the $Fe_2S_2(SH)_4^{3-}$ molecules (**1a** and **1b**) by GB3LYP/SZ methods

Molecule	Spin state	Löwdin atomic charge (spin) population				θ (°)
		Fe1	Fe2	S^b	S^tH	
1a	F	0.443	0.443	−0.667	−0.638	0
		(1.742)	(1.742)	(0.370)	(0.069)	
	AF	0.444	0.415	−0.668	−0.616	180
		(1.727)	(−1.647)	(0.184)	(0.081)	
	G[a]	0.430	0.4230	−0.662	−0.634	139.2
		(1.691)	(1.691)	(0.177)	(0.067)	
1b	F	0.416	0.398	−0.635	−0.631	0
		(1.747)	(1.745)	(0.371)	(0.074)	
	AF	0.423	0.369	−0.638	−0.611	180
		(1.744)	(−1.688)	(0.185)	(0.088)	
	G[a]	0.424	0.369	−0.638	−0.611	176.2
		(1.744)	(1.688)	(0.185)	(0.088)	

[a] Magnitudes of the spins at atomic centers are listed for the G state.

approximately equal at two Fe centers. The AF state of **1a** show a typical electronic structure of a TV state despite the symmetrical core model. At the AF state, the odd electron is mainly localized at the one iron center: Fe2. The atomic spin distribution (S_x, S_y, S_z) of G state are (0.712, 0.0000, 1.5386) and (0.9693, 0.0000, −1.3905) for Fe1 and Fe2 centers, respectively, indicating that the spins are slightly tilt to the S_x direction. The angle θ between the spins is 139.2°. The noncollinear spin structure of the G state is the MV state at the antiferromagnetically coupled spin state. It is noteworthy that the θ is decreased from the initial spin state, indicating that the spins rotated by the double exchange interaction. On the other hand for **1b**, both the AF and G states show the TV state. The atomic spin distributions of the G state are (−0.0807, 0.0000, 1.7420) and (0.1903, 0.0000, −1.6777) for Fe1 and Fe2 centers. The angle θ between the spins is 176.2°. Atomic charges and spin population at the G state show that the electronic structure is very close to those of the AF state ($\theta = 180°$). For the asymmetrical core geometry of **1b**, the double exchange interaction is suppressed and the electron localization is stabilized by the geometrical reorientation. The odd electron mainly localizes at the Fe2 center at the AF state. The F state shows more delocalized structures. Thus the electronic structure of GSO solution is largely influenced by the geometrical asymmetry.

The natural orbitals (NO) can clearly show the magnetic orbital interactions between the antiferromagnetically coupled spin centers. For each coupling pair, bonding and antibonding NOs are obtained in pairs. According to the occupation number of these NOs, they are classified into highest occupied natural orbitals (HONOs) and lowest unoccupied natural orbitals (LUNO). Non-pairing orbital is single occupied natural orbital (SONO). The occupation numbers of the HONO and LUNO pears satisfy the following relations:

$$2 = n(\mathrm{HONO}) + n(\mathrm{LUNO}), \tag{26}$$

where n is the occupation number. In general, using the orbital overlap T between site orbitals and angle θ between spin directions, the n are given by

$$n(\mathrm{HONO}) = \frac{(1+T)\left(1 - T\cos^2\frac{\theta}{2}\right)}{1 - T^2\cos^2\frac{\theta}{2}}, \tag{27a}$$

$$n(\mathrm{LUNO}) = \frac{(1-T)\left(1 + T\cos^2\frac{\theta}{2}\right)}{1 - T^2\cos^2\frac{\theta}{2}}. \tag{27b}$$

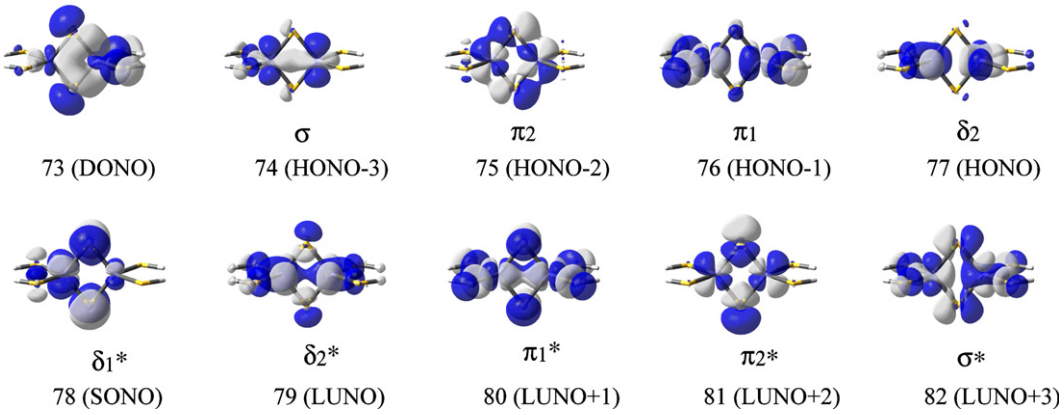


Fig. 3. Natural orbitals of **1a** at the antiferromagnetic spin (AF) state.

Table 4
Calculated occupation numbers of natural orbitals at the AF and G spin states[a] of the $Fe_2S_2(SH)_4^{3-}$ molecules (**1a** and **1b**) by GB3LYP/SZ methods

No.	Molecule and spin state			
	1a AF	**1a** G	**1b** AF	**1b** G
73	1.9997	1.9245	1.9990	1.9947
74	1.3771	1.3374	1.3329	1.3174
75	1.3762	1.3362	1.3069	1.2909
76	1.0900	1.0755	1.2382	1.1937
77	1.0577	1.0633	1.0829	1.0831
78	1.0000	1.0509	1.0000	1.0001
79	0.9423	0.9493	0.9171	0. 9169
80	0. 9100	0.9384	0.7618	0. 8064
81	0. 6238	0.6641	0.6931	0.7092
82	0. 6229	0.6627	0.6671	0.6836

[a] AF: antiferromagnetic spin state ($S_z = 1/2$); G: generalized spin state.

As the θ decreases from 180° to 0°, the difference of the occupation numbers (n(HONO) − n(LUNO)) decrease. The bond order is given by

$$b = \frac{n(\mathrm{HONO}) - n(\mathrm{LUNO})}{2}. \quad (28)$$

It is reasonable that the b value decrease as the θ decreases.

The NOs of **1a** at the AF state are shown in Fig. 3. SONO is an δ_1 type NO(78), which are mainly populated on the Fe1 and bridging sulfur centers. HONOs and LUNOs are pairing with each other for σ, π_1, π_2 and δ_2 type interactions in order of the occupation numbers (Table 4). NO(73) is double occupied natural orbital (DONO). Thus it is clearly shown that the AF state is an δ_1 doped TV state. The NOs of **1a** at the G state are shown in Fig. 4. These NOs are also pairing. The pairing HONO and LUNO can be classified as δ_1, σ, π_1, π_2, δ_2 type interactions in order of occupation numbers. The DONO is an δ_1 type NO(73), which are pairing to the NO(76). It is noteworthy that these NOs are symmetric. Thus it is clear that the G state is δ_1 doped MV state. By Eq. (27a), the occupation number (n) at the G state can be estimated from those at AF state. The n(HONO) values for π_1, σ, δ_1 and π_2 type HONOs are 1.3371, 1.3363, 1.0791 and 1.0507, respectively. These values are close to those of the SCF results. The AF and G states are both δ_1 doped states and the spin orbitals have σ, π_1, π_2 and δ_2 type interactions in the same order. The NOs at AF state of **1b** are shown in Fig. 5. These NOs are very similar to those of G state (not shown). The SONO is an δ_1 type NO(78), which is localized at the Fe1 side. HONOs and LUNOs are π_1, σ, π_2 and δ_2 in order of the orbital interactions. The n(HONO) values at AF state are larger than those of G state. The estimated n(HONO) values for G state from the n(HONO) values at AF state by Eq. (27a) are 1.3326, 1.3066, 1.2380 and 1.0828, respectively. These n(HONO) values become slightly smaller than those of AF state, because the angle θ of the G state is near to 180°. The SCF calculated

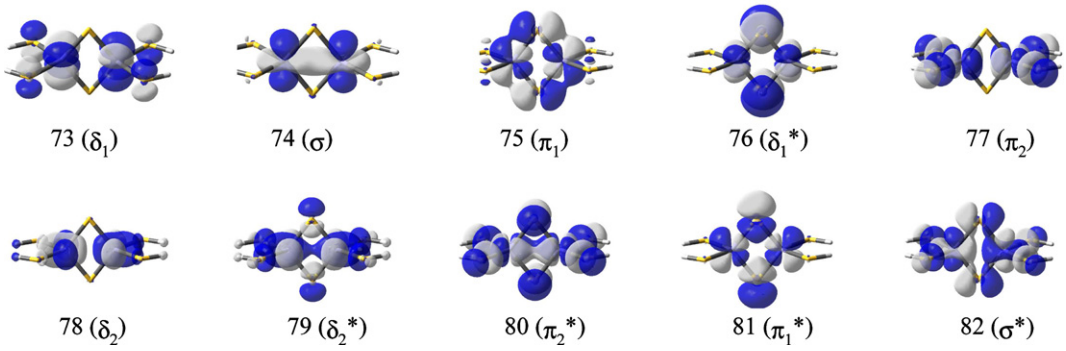


Fig. 4. Natural orbitals of **1a** at the generalized spin (G) state.

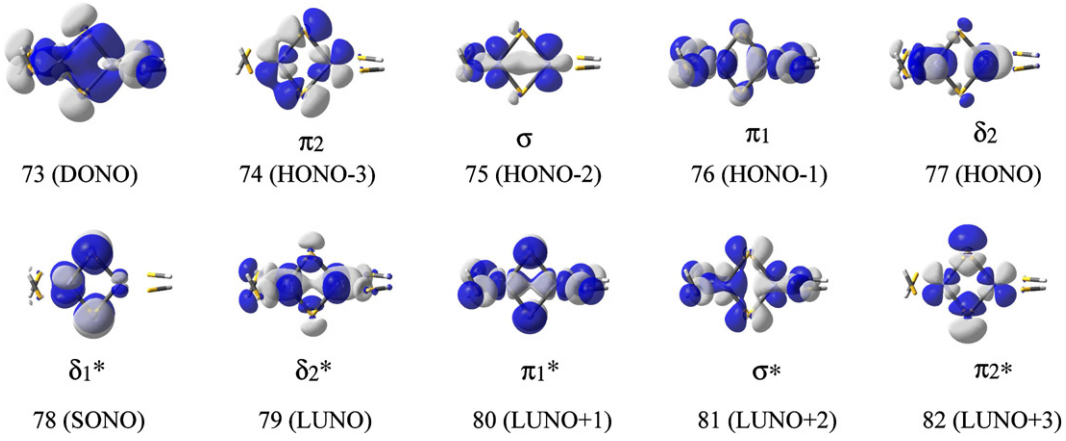


Fig. 5. Natural orbitals (NOs) of **1b** at the antiferromagnetic spin (AF) state. These NOs are indistinguishable from those of the generalized spin (G) state.

n(HONO) values at the G state are smaller than those of the estimated *n*(HONO) values, indicating that the electronic structure is slightly changed during the spin rotations. It is shown that the AF and G states are both in the δ_1 doped states.

5. Conclusion

Using the generalized spin orbital (GSO) approach, the electronic and spin structure of the reduced form of the [2Fe–2S] clusters were examined. Ferromagnetic (F), antiferromagnetic (AF), and generalized (G) spin states were calculated for the symmetrical and asymmetrical [2Fe–2S] core models (**1a** and **1b**). It was found that the delocalization of the odd electron highly depends on the core structure. For **1a**, the G state was in the mixed valence (MV) state. For **1b**, the G state was in the trapped valence (TV) state. On the other hand for the AF state, TV states are only evaluated for both **1a** and **1b**. The MV state of the **1a**-G state had a tilted spin structure for the double exchange interaction and the TV state of the 1b-G state was very close to the electronic structure of the AF state. Natural orbitals (NOs) clearly showed the electronic structures. Magnetic orbital interactions are discussed from the NOs and the occupation numbers. It was found that the energy differences between the G and AF states are very small. However, it is shown the GSO approach can describe more flexible spin and charge states.

Acknowledgements

M.S. thanks the financial support for Research Fellowships of the Japan Society for the Promotion of Science for Young Scientists. This work has been supported by Grant-in-Aid for Scientific Research (16750049, 1835008, 18205023) from Japan Society for the promotion of Science (JSPS).

References

[1] M. Shoji, K. Koizumi, T. Hamamoto, Y. Kitagawa, S. Yamanaka, M. Okumura, K. Yamaguchi, Chem. Phys. Lett. 421 (2006) 483.
[2] M. Shoji, K. Koizumi, Y. Kitagawa, T. Kawakami, S. Yamanaka, M. Okumura, K. Yamaguchi, Chem. Phys. Lett. 432 (2006) 343.
[3] M. Shoji, Y. Nishiyama, Y. Maruno, K. Koizumi, Y. Kitagawa, S. Yamanaka, T. Kawakami, M. Okumura, K. Yamaguchi, Int. J. Quantum Chem. 100 (2004) 887.
[4] M. Shoji, K. Koizumi, Y. Kitagawa, S. Yamanaka, T. Kawakami, M. Okumura, K. Yamaguchi, Int. J. Quantum Chem. 105 (2005) 628.
[5] M. Shoji, K. Koizumi, Y. Kitagawa, S. Yamanaka, T. Kawakami, M. Okumura, K. Yamaguchi, Int. J. Quantum Chem. 107 (2006) 116.
[6] M. Shoji, K. Koizumi, Y. Kitagawa, S. Yamanaka, T. Kawakami, M. Okumura, K. Yamaguchi, Int. J. Quantum Chem., in press.
[7] M. Shoji, K. Koizumi, Y. Kitagawa, S. Yamanaka, T. Kawakami, M. Okumura, K. Yamaguchi, Int. J. Quantum Chem. 106 (2006) 3288.
[8] M. Shoji, K. Koizumi, Y. Kitagawa, T. Kawakami, S. Yamanaka, M. Okumura, K. Yamaguchi, Lecture Series on Computer and Computational Sciences, vol. 7, Brill Academic Publishers, Netherlands, 2006, p. 499.
[9] K. Yamaguchi, T. Fueno, N. Ueyama, A. Nakamura, M. Ozaki, Chem. Phys. Lett. 164 (1989) 210.
[10] L. Noodelman et al., Adv. Inorg. Chem. 38 (1992) 423.
[11] S. Yamanaka, D. Yamaki, Y. Shigeta, H. Nagao, Y. Yoshioka, N. Suzuki, K. Yamaguchi, Int. J. Quantum Chem. 80 (2000) 664.
[12] S. Yamanaka, T. Ohsaku, D. Yamaki, K. Yamaguchi, Int. J. Quantum Chem. 91 (2003) 376.
[13] S. Yamanaka, Ryo Takeda, K. Yamaguchi, Polyhedron 22 (2003) 2013.
[14] S. Huzinaga, Gaussian Basis Sets for Molecular Calculations, Elsevier, Amsterdam, Oxford, New York, Tokyo, 1984.
[15] M.J. Frisch, G.W. Trucks, H.B. Schlegel, G.E. Scuseria, M.A. Robb, J.R. Cheeseman, V.G. Zakrzewski, J.A. Montgomery Jr., R.E. Stratmann, J.C. Burant, S. Dapprich, J.M. Millam, A.D. Daniels, K.N. Kudin, M.C. Strain, O. Farkas, J. Tomasi, V. Barone, M. Cossi, R. Cammi, B. Mennucci, C. Pomelli, C. Adamo, S. Clifford, J. Ochterski, G.A. Petersson, P.Y. Ayala, Q. Cui, K. Morokuma, N. Rega, P. Salvador, J.J. Dannenberg, D.K. Malick, A.D. Rabuck, K. Raghavachari, J.B. Foresman, J. Cioslowski, J.V. Ortiz, A.G. Baboul, B.B. Stefanov, G. Liu, A. Liashenko, P. Piskorz, I. Komaromi, R. Gomperts, R.L. Martin, D.J. Fox, T. Keith, M.A. Al-Laham, C.Y. Peng, A. Nanayakkara, M. Challacombe, P.M.W. Gill, B. Johnson, W. Chen, M.W. Wong, J.L. Andres, C. Gonzalez, M. Head-Gordon, E.S. Replogle, J.A. Pople, Gaussian 98, Revision A. 11.3, Gaussian, Inc., Pittsburgh, PA, 2002.

NMR spectrum over the wide temperature region revealed the microscopic picture of this conversion between the low-spin and high-spin states. The result indicated a rapid electron exchange between SQ and Cat in the low-spin state. We measured dielectric constant in the cryogenic temperature region to characterize a fluctuation of molecular dipole moment due to an electron exchange between SQ and Cat.

2. Experiment

[Co(3,5-di-*t*-butyl-1,2-benzoquinone)$_2$(2,2′-bipyridine)] (**1**) was prepared from a tetramer [Co^{II}(3,5-di-*t*-butyl-1,2-benzoquinone)$_2$]$_4$ according to the procedure reported previously [2,7]. The specimen was once heated up to 390 K to remove crystal solvent molecules and to obtain the stable crystalline phase. Valence tautomerism did not occur for the virgin sample recrystallized from toluene solution but occurred in the stable crystalline phase [7].

[Co(3,6-di-*t*-butyl-1,2-benzoquinone)$_2$(2,2′-bipyridine)] (**2**) was prepared according to a similar method for manganese complex [8]. Three reactants, i.e. 3,6-di-*t*-butyl-1,2-benzoquinone, $Co_2(CO)_8$, and 2,2′-bipyridine, were treated in toluene for 5 h under Argon atmosphere. Evaporation of the solvent gave black powder. Powder X-ray diffraction confirmed the reported structure of **2**. Since fractional coordinates in the crystal of this compound are not reported in Ref. [9], we used the fractional coordinate of isomorphic crystal of manganese complex to estimate the powder X-ray diffraction pattern [8,9]. 3,6-Di-*t*-butyl-1,2-catechol was prepared by a reaction of catechol and isobutene under Ti/Cat catalyst in an autoclave at 140 °C. This catechol was oxidized with Ag_2O to obtain 3,6-di-*t*-butyl-1,2-benzoquinone.

Sample **1** was characterized by thermogravimetry combined with differential thermal analysis (TG–DTA) with TG/DTA 220 U (Seiko Epson) under argon gas flow to confirm the stable phase [7]. Direct current magnetic susceptibility was measured at an external magnetic field of 1 T with SQUID magnetometer (Quantum Design MPMS 5). The solid-state high-resolution ^{13}C NMR spectra were measured for polycrystalline sample at a magic angle spinning (MAS) speed of ca. 9 kHz and at a resonance frequency of 75.4 MHz, with a Bruker DSX300 spectrometer. Polycrystalline sample was packed into a center of a zirconia rotor of 4 mm diameter within a length of ca. 5 mm to minimize the temperature gradient of the sample. The thermometer of the MAS NMR probe was carefully calibrated [10,11]. The shifts of ^{13}C NMR spectra were measured from an external second reference of hexamethylbenzene (CH_3: 17.17 ppm). Dielectric constant was measured for a disk of compressed powder crystals by four terminals method with HP-4824A Precision LCR Meter between 10 and 295 K in a frequency region between 1 and 100 kHz. The size of the disk was 10 mm diameter and 0.3 mm thickness. Temperature was kept constant for each measurement.

3. Results and discussion

Thermal hysteresis of magnetic susceptibility of **1** is shown in Fig. 1. After the virgin sample was cooled down to 6 K, three runs of the measurements were continued. In the first run (step 1 in Fig. 1), the magnetic susceptibility was measured on heating up to 390 K. Then, two successive measurements were continued on cooling down to 6 K (step 2) and on heating up to 390 K (step 3). The first run (step 1) for the virgin sample indicated a sharp increase of χT value around 360 K due to a phase change from the meta-stable to the stable phase. After the phase change occurred, a reversible temperature dependence of the χT value was observed in the steps 2 and 3. This result shows the valence tautomeric interconversion between low-spin-[Co^{III}(SQ)(Cat)(bpy)] and high-spin-[Co^{II}(SQ)$_2$(bpy)] in the stable phase [7]. Almost only the low-spin state exists at 186 K both for the meta-stable and stable phases. It can be determined by ^{13}C NMR spectrum whether an electron exchange occurs or not between SQ and Cat in the low-spin state. Solid-state magic angle spinning (MAS) ^{13}C NMR spectra of the meta-stable and stable phases are compared at 186 K in Fig. 2. For meta-stable phase, relatively sharp and temperature independent peak (γ) was observed at 30 ppm. Since this shift is typical for methyl carbon of diamagnetic 3,5-di-*t*-butyl-1,2-benzoquinone [12], the peak γ was assigned to the diamagnetic Cat ligand. Broad peaks (α and β) around 100–150 ppm were assigned to methyl carbons of SQ. Shifts of peaks α and β were temperature dependent due to an electron spin of SQ, while the shift of peak γ

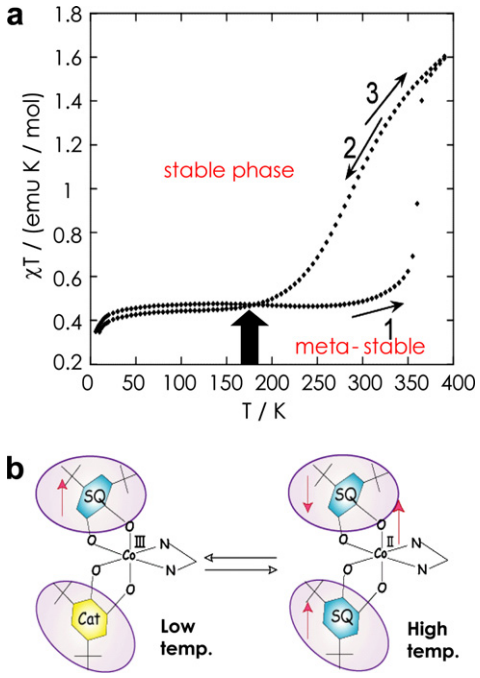


Fig. 1. (a) Magnetic susceptibility of [Co(3,5-di-*t*-butyl-1,2-benzoquinone)$_2$(2,2′-bipyridine)] in the meta-stable and stable phases. Three successive runs for the measurements were continued, step 1: from 6 to 390 K, step 2: from 390 to 6 K, and step 3: from 6 to 390 K. (b) A schematic view of valence tautomerism in the stable phase.

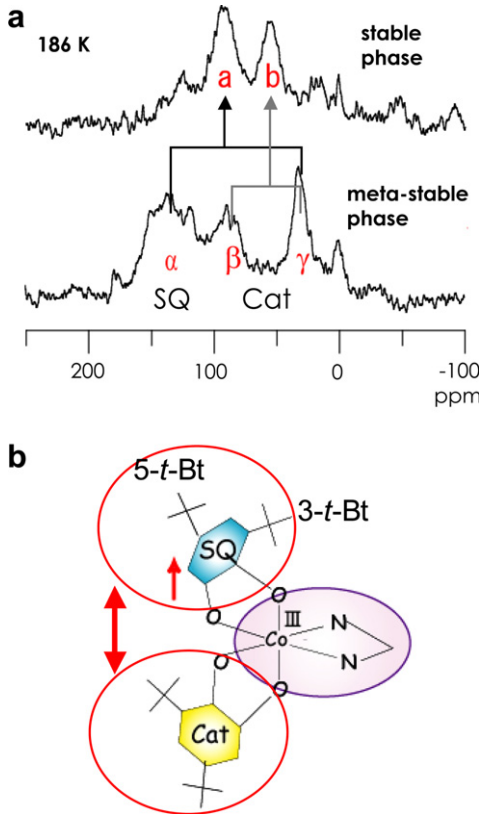


Fig. 2. (a) Magic angle spinning ^{13}C NMR spectrum of methyl carbon of 3 and 5-*t*-butyl groups of [Co(3,5-di-*t*-butyl-1,2-benzoquinone)$_2$(2,2′-bipyridine)] measured at 186 K in the meta-stable and stable phases. (b) A schematic view of rapid averaging between semiquinoate (SQ) and catecholate (Cat) in the low-spin state.

was almost independent of temperature. Since SQ and Cat were distinguished, no electron exchange occurred between SQ and Cat in the meta-stable phase. In contrast to the meta-stable phase, ^{13}C MAS NMR signals of the stable phase were observed near 55 (b) and 95 ppm (a), where the peak at 55 ppm (b) is an average of the two peaks at 30 (Cat, γ) and 90 (SQ, β) ppm in the meta-stable phase and the peak at 95 ppm (a) is an average of the two peaks at 30 (Cat, γ) and 150 (SQ, α) ppm. Both the shifts of 55 and 95 ppm signals were temperature dependent. This result clearly indicates that an exchange of electron spin between SQ and Cat states was directly detected by the NMR spectrum. The exchange rate is much larger than the NMR time scale of ca. $5\times10^4\ s^{-1}$ at 186 K.

Temperature dependence of magnetic susceptibility of **1** and **2** is shown in Fig. 3. For a random equilibrium between the high-spin (HS) and low-spin (LS) states, the observed magnetic susceptibility χ can be expressed by magnetic susceptibility of HS state (χ_{HS}) and LS state (χ_{LS}) as follows,

$$\chi = \chi_{HS}\cdot f_{HS} + \chi_{LS}\cdot f_{LS} = \frac{C_{HS}}{T}\cdot f_{HS} + \frac{C_{LS}}{T}\cdot f_{LS},$$
$$\chi T = 0.125\left(\frac{\mu_{eff}}{\mu_B}\right)^2 = C_{HS}\cdot f_{HS} + C_{LS}\cdot f_{LS}, \quad (1)$$

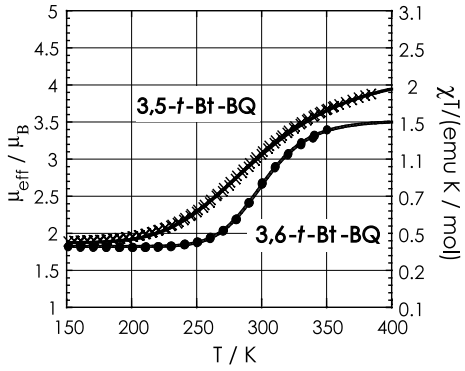


Fig. 3. Effective magnetic moment of [Co(3,5-di-*t*-butyl-1,2-benzoquinone)$_2$(2,2′-bipyridine)] (3,5-*t*-Bt-BQ) and [Co(3,6-di-*t*-butyl-1,2-benzoquinone)$_2$(2,2′-bipyridine)] (3,6-*t*-Bt-BQ) plotted as a function of temperature.

where C_{HS} and C_{LS} are Currie constants for HS state and LS state, respectively, and the fractions of HS state (f_{HS}) and LS state (f_{LS}) can be written by

$$f_{LS} = \frac{\exp\left(-\frac{\Delta S}{R}+\frac{\Delta H}{RT}\right)}{1+\exp\left(-\frac{\Delta S}{R}+\frac{\Delta H}{RT}\right)}, \quad f_{HS} = \frac{1}{1+\exp\left(-\frac{\Delta S}{R}+\frac{\Delta H}{RT}\right)}. \quad (2)$$

The observed χT value of **1** was fitted by Eq. (1) and values of entropy and enthalpy change between HS and LS states were estimated to be $\Delta S = 53\ J\ K^{-1}\ mol^{-1}$ and $\Delta H = 17\ kJ\ mol^{-1}$ [7]. The same procedure gave very large thermodynamic parameters of $\Delta S = 145\ J\ K^{-1}\ mol^{-1}$ and $\Delta H = 44\ kJ\ mol^{-1}$ for **2**. These values are very different from the reported values of $\Delta S_{trs} = 48\ J\ K^{-1}\ mol^{-1}$ and $\Delta H_{trs} = 15\ kJ\ mol^{-1}$, which were estimated from an excess heat capacity of this compound [13]. This result indicates that Eq. (1) for random equilibrium of non-interacting molecules cannot be applied to the crystalline phase of **2**. Then we assumed domain or cluster formation due to a cooperative effect for the isomer conversion of **2** in the crystalline phase. Sorai et al. proposed a domain model for spin crossover transition [14–16]. One domain contains n molecules and they changes spin state cooperatively. In this model, fraction of the high-spin state can be described by,

$$f_{HS} = \frac{1}{1+\exp[n\Delta H_{trs}/R\cdot(1/T-1/T_{1/2})]}, \quad (3)$$

where $T_{1/2}$ is the center of the temperature region of transition. When the number n becomes infinite, transition is the first order phase transition with a definite transition temperature. The number n of molecules in a domain was estimated to be 3.6 from reported excess heat capacity [13]. Three or four molecules change their spin state cooperatively in average. In a framework of this domain model, thermodynamic parameters of $\Delta S_{trs} = 40\ J\ K^{-1}\ mol^{-1}$ and $\Delta H_{trs} = 12\ kJ\ mol^{-1}$ were estimated from the temperature dependence of χT value shown in Fig. 3. These values are almost consistent with those estimated from the excess heat capacity, $\Delta S_{trs} = 48\ J\ K^{-1}\ mol^{-1}$ and $\Delta H_{trs} = 15\ kJ\ mol^{-1}$

[13]. Magnitude of the spin was estimated to be $S = 3/2$ from the high temperature limiting value of the effective moment both for **1** and **2**. Assuming an isotropic g tensor ($g = 2$), effective moment (μ_{eff}/μ_B) is 1.7, 3.9 and 5.9 for $S = 1/2$, 3/2 and 5/2, respectively. Therefore a strong antiferromagnetic coupling exists in the high temperature region. Entropy difference estimated from the change of spin multiplicity is 11.5 J K^{-1} mol^{-1}, which is much smaller than the observed value. The large entropy change may be ascribed to a change of vibrational density of state, since metal ligand coordination bond length of high-spin Co(II) form is longer than that of low-pin Co(III) form by ca. 0.02 nm in general, and vibrational frequencies become lower for the high-spin Co(II) form [2,6,17,18].

Since averaging process between SQ and Cat in the low-spin sate may be detected by solid-state high-resolution ^{13}C NMR spectrum, temperature variation of ^{13}C MAS NMR spectrum of **2** was measured. The spectrum at 293 K is shown in Fig. 4. We found two large signals (peaks 1 and 2) and two small signals (peaks 3 and 4). Large signals were assigned to methyl carbons of *t*-butyl groups at 3 and 6 positions, while small signals to the center carbon of the two *t*-butyl groups. SQ and Cat states are averaged by rapid exchange of electron spin. This behavior is similar to the stable phase of **1**. Spectral region of **2** is narrow compared with **1**, since electron spin density is smaller at the substitution position 6 compared with the position 5 for SQ in general [19]. Only the four signals were observed in the temperature region investigated as shown in Fig. 5. This result indicates that the exchange of electron spin between SQ and Cat is rapid even at 200 K. The domain model used for the χT values in Fig. 3 could be also applied for the temperature variation of the sift of NMR signals

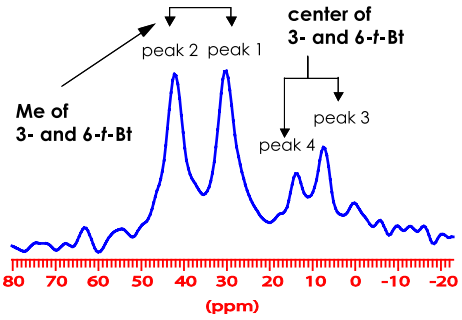


Fig. 4. Magic angle spinning ^{13}C NMR spectrum of methyl carbon of 3 and 6-*t*-butyl groups of [Co(3,6-di-*t*-butyl-1,2-benzoquinone)$_2$(2,2′-bipyridine)] measured at 293 K. A group of large peaks 1 and 2 was assigned to the methyl carbons of two *t*-butyl groups, whereas a group of small peaks was assigned to the center carbons of two *t*-butyl groups.

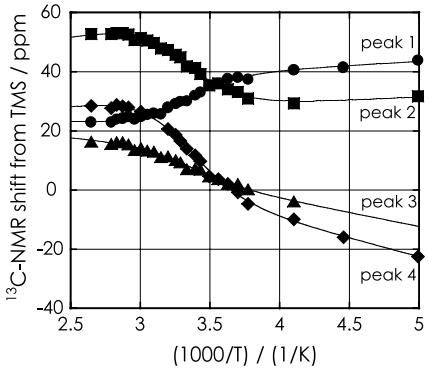


Fig. 5. Temperature variation of shifts of magic angle spinning ^{13}C NMR spectrum of [Co(3,6-di-*t*-butyl-1,2-benzoquinone)$_2$(2,2′-bipyridine)]. Solid curves were obtained by fitting a model equation, in which strong antiferromagnetic interaction between the two semiquinoate ligands in the high-spin state was assumed.

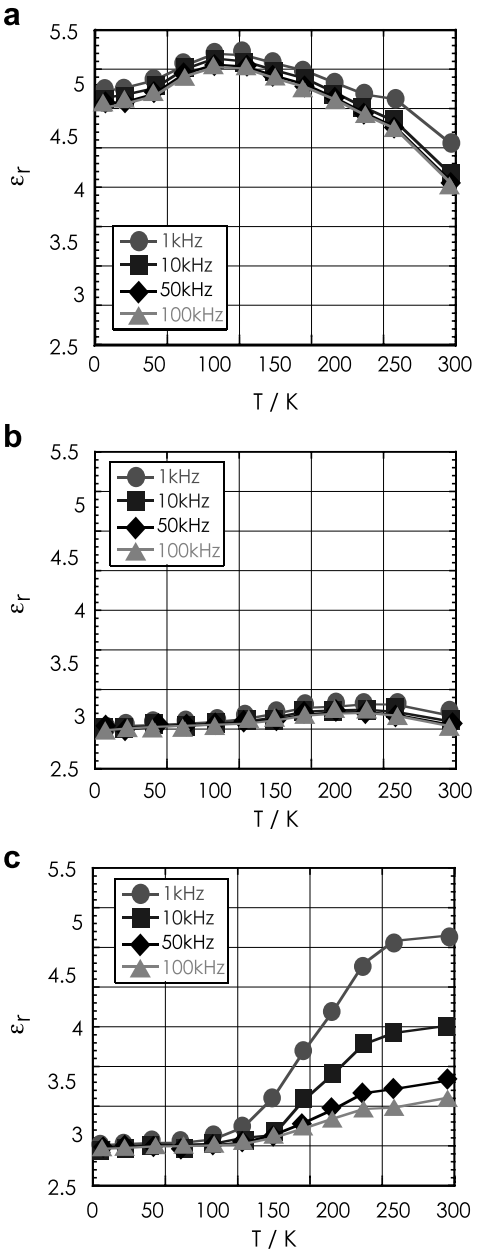


Fig. 6. Temperature and frequency dependence of dielectric constant.(a) [Co(3,6-di-*t*-butyl-1,2-benzoquinone)$_2$(2,2′-bipyridine)], (b) stable phase of [Co(3,5-di-*t*-butyl-1,2-benzoquinone)$_2$(2,2′-bipyridine)], (c) virgin metastable phase of [Co(3,5-di-*t*-butyl-1,2-benzoquinone)$_2$(2,2′-bipyridine)]·$x(C_6H_5CH_3)$.

and almost the same values were obtained for ΔS_{trs} and ΔH_{trs} of transition from low-spin to high-spin state.

It may be obtained from dielectric measurements whether the electron exchange between SQ and Cat freezes or not as the temperature is decreased into cryogenic temperature region, since the electron exchange between SQ and Cat states induces a fluctuation of molecular dipole moment. Observed dependence of dielectric constant on frequency and on temperature is shown in Fig. 6 for **1** and **2**. No significant anomaly was observed both for the stable phase of **1** (Fig. 6b) and **2** (Fig. 6a), both of which exhibited valence tautomerism. The spin and charge exchanges between SQ and Cat are considered to be much faster than 100 kHz at 10 K. Meta-stable phase of **1** showed a remarkable frequency dependence of dielectric constant in the high temperature region as shown in Fig. 6c. However, this anomaly was attributed to molecular motion of toluene in the crystalline lattice.

In conclusion, [Co(3,6-di-*t*-butyl-1,2-benzoquinone)$_2$-(2,2′-bipyridine)] showed a cooperative effect for valence tautomerism in the crystalline phase, whereas the cooperative effect is small in the case of the stable phase of a similar compound [Co(3,5-di-*t*-butyl-1,2-benzoquinone)$_2$(2,2′-bipyridine)]. The origin of the cooperative effect is not clear at present. The spin and charge exchange between SQ and Cat in the low-spin state was clarified by solid-state high-resolution ^{13}C NMR spectrum. This exchange did not freeze above 10 K.

Acknowledgments

This research was supported by Grant-in-Aid for Scientific Research on Priority Areas "Application of Molecular Spins" Area No. 769, Proposal No. 15087201 from the Ministry of Education, Culture, Sports, Science and Technology of Japan.

References

[1] C.G. Pierpont, Coord. Chem. Rev. 216–217 (2001) 99.
[2] R.M. Buchanan, C.G. Pierpont, J. Am. Chem. Soc. 102 (1980) 4951.
[3] O.S. Jun, C.G. Pierpont, Inorg. Chem. 33 (1994) 2227.
[4] G.A. Abakumov, V.K. Cherkasov, M.P. Bubnov, O.G. Ellert, Z.B. Dobrokhotova, L.N. Zarkharov, Y.T. Struchovkov, Dokl. Akad. Nauk. 328 (1993) 12.
[5] D.M. Adams, A. Dei, A.L. Rheingold, D.N. Hendrickson, Angew. Chem., Int. Ed. Engl. 32 (1993) 880.
[6] D.M. Adams, A. Dei, A.L. Rheingold, D.N. Hendrickson, J. Am. Chem. Soc. 115 (1993) 8221.
[7] K. Morii, G. Maruta, S. Takeda, Polyhedron 24 (2005) 2607.
[8] A.S. Attia, C.G. Pierpont, Inorg. Chem. 34 (1995) 1172.
[9] G.A. Abakumov, V.K. Cherkasov, M.P. Bubnov, O.G. Ellert, Z.V. Dobrokhotova, L.N. Zakharov, Y.T. Struchkov, Dokl. Akad. Nauk. 328 (1993) 332.
[10] G. Maruta, S. Takeda, R. Imachi, T. Ishida, T. Nogami, K. Yamaguchi, J. Am. Chem. Soc. 121 (1999) 424.
[11] P.A. Beckmann, C. Dybowski, J. Magn. Reson. 146 (2000) 379.
[12] Integrated Spectral Data Base System for Organic Compounds, SDBSWeb: <http://www.aist.go.jp/RIODB/SDBS/>.
[13] B.V. Lebedev, N.N. Smirnova, G.A. Abakumov, V.K. Cherkasov, M.P. Bubnov, J. Chem. Thermodyn. 34 (2002) 2093.
[14] T. Nakano, Z. Tan, M. Sorai, Inorg. Chem. 40 (2001) 3805.
[15] M. Sorai, Bull. Chem. Soc. Jpn. 74 (2001) 2223.
[16] M. Sorai, M. Nakano, Y. Miyazaki, Chem. Rev. 106 (2006) 976.
[17] D.M. Adams, D.N. Hendrickson, J. Am. Chem. Soc. 118 (1996) 11515.
[18] C.G. Pierpont, R.M. Buchanan, Coord. Chem. Rev. 38 (1981) 45.
[19] S. Patai (Ed.), The Chemistry of the Quinonid Compounds, Part 1, Willy, New York, 1974.

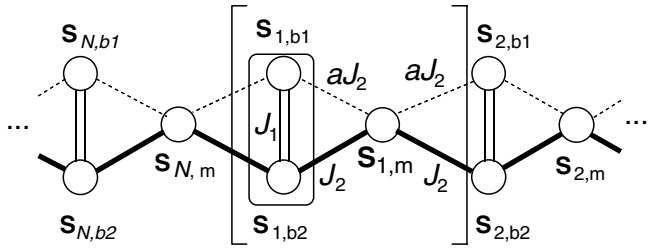


Fig. 1. Schematic view of the Heisenberg spin Hamiltonian (Eq. (1)). The rounded rectangle represents the biradical molecule with two unpaired electron spins ($\mathbf{S}_{i,b1} = 1/2$ and $\mathbf{S}_{i,b2} = 1/2$) interacting with the adjacent monoradicals with $\mathbf{S}_{i,m} = 1/2$. The intramolecular exchange interaction in the biradical is defined as J_1. The solid and dashed lines denote the intermolecular interactions J_2 and aJ_2 ($0 < a < 1$), respectively.

A problem in constructing molecule-based heterospin systems such as generalized ferrimagnetics is co-crystallization of two kinds of open-shell molecules. We have proposed several approaches [2] to attain co-crystallization in purely organic heteromolecular systems, one of which employs nucleobases (nucleic acid bases) such as guanine, cytosine, adenine, and thymine [2b]. Multiple-point hydrogen bonds feature in the nucleobases, which are superior to conventional hydrogen-bonding compounds such as phenols, carboxylic acids, and pyridines with respect to selectivity and directionality of hydrogen bonding as found in a DNA duplex. Hydrogen-bonded pairs of nucleobases substituted with open-shell groups can be a building block for bio-inspired heterospin assembly, as shown in Scheme 1.

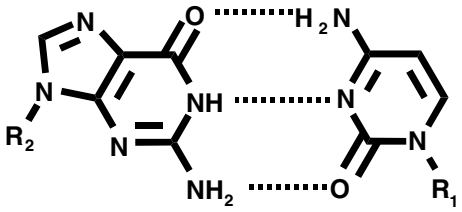
In this communication, we report on syntheses of building block molecules for generalized ferrimagnets based on the nucleobase pairing approach. Syntheses, crystal structures, and magnetic properties are described for a cytosine-substituted nitronyl nitroxide monoradical **1** and a biradical **2** in a singlet ($S = 0$) ground state. The radicals **1** and **2** are expected to form a hydrogen-bonded pair with guanine-substituted radicals,[1] leading to a heterospin, heteromolecular system consisting of the ground-state singlet biradicals and monoradicals.

2. Experimental

2.1. Synthesis

The synthetic routes for the monoradical **1** and the biradical **2** are shown in Scheme 2.

*Monoradical **1***. A suspension of 4-(2-bromoethoxy)-benzaldehyde **3** [3] (480 mg, 2.10 mmol) and 2,3-dimethyl-2,3-dihydroxylaminobutane (313 mg, 2.11 mmol) in dry benzene (30 ml) was refluxed under Ar atmosphere for 21.5 h to give a colorless powder of an adduct. The precipitate was filtered and washed with benzene, and then dried. An aqueous solution of $NaIO_4$ (278 mg, 1.30 mmol) was added to a suspension of the adduct (467 mg, 1.30 mmol) in a mixed solution of CH_2Cl_2 (30 mL) and H_2O (10 mL). The reaction mixture was stirred for 40 min to give a blue solution. The aqueous phase was extracted with CH_2Cl_2. The combined organic phase was dried over $MgSO_4$. The solvent was evaporated under reduced pressure, and the residue was chromatographed on silica gel. The elution with CH_2Cl_2/acetone (6: 1) gave **4** as a blue solid (380 mg, 1.06 mmol, 50.5%). A mixture of **4** (381 mg, 1.31 mmol), cytosine (217 mg, 1.96 mmol), K_2CO_3 (271 mg 1.96 mmol) and KI (325 mg, 1.96 mmol) in dry MeCN (50 ml) was stirred for 43 h at 90 °C. After the precipitate was filtered, the solvent was evaporated under reduced pressure, and then the residue was purified on silica gel. The elution with CH_2Cl_2/MeOH (9: 1) gave **1** as a blue solid (147 mg, 0.381 mmol, 29.1%). Elemental *Anal.* Calc. for $C_{19}H_{24}N_5O_4$: C, 59.06; H, 6.26; N, 18.12. Found: C, 58.79; H, 6.28; N, 17.85%. ESI-MS *m*/*z* 385.4 (M^-).



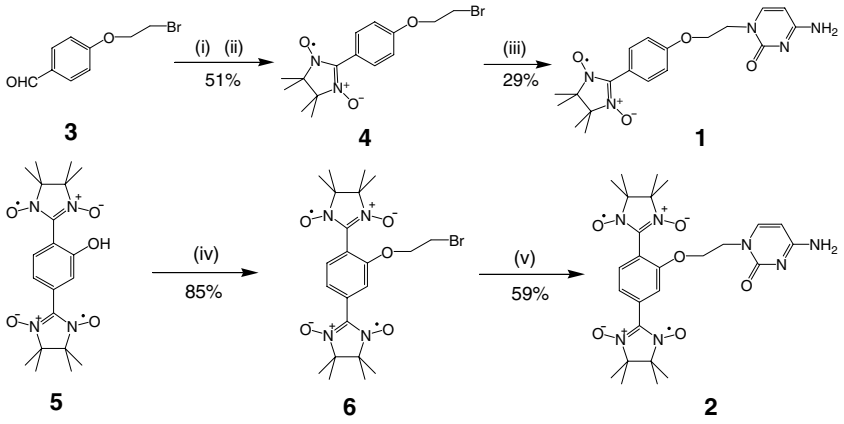
Scheme 1. Hydrogen-bonded Watson–Crick pair of nucleobases substituted with radical groups R_1 and R_2.

*Biradical **2***. Phenolic biradical **5** was prepared according to the procedure reported previously [4]. A mixture of 5 (207 mg, 0.511 mmol) and K_2CO_3 (271 mg 0.759 mmol) in dry DMF (8 ml) was stirred for 35 min at 60 °C. To the mixture was added 1,2-dibromoethane. After the mixture was stirred for 6.5 h at 60 °C, the precipitate was filtered. To the filtrate were added CH_2Cl_2 and a small amount of hexane, and the solution was washed with brine. The solvent was evaporated under reduced pressure, and the residue was purified on silica gel. The elution with CH_2Cl_2/acetone (4:1) gave **6** as a purple solid (240 mg, 0.468 mmol, 91.6%). A mixture of **6** (1.44 g, 2.80 mmol), cytosine (477 mg, 4.31 mmol) and *t*-BuOK (491 mg 4.38 mmol) in dry DMF (56 ml) was stirred for 24 h at 55 °C. After the precipitate was filtered, the solvent was evaporated under reduced pressure, and the residue was purified on silica gel. The elution with CH_2Cl_2/MeOH (10:1) and CH_2Cl_2/MeOH (7:1) gave **2** as a purple solid (891 mg, 1.65 mmol, 58.7%). Elemental *Anal.* Calc. for $C_{26}H_{35}N_7O_6CH_3OH$: C, 55.71; H, 6.85; N, 16.24. Found: C, 55.61; H, 6.47; N, 16.86%. *m*/*z* (FAB^+) (NBA): 542.3 $[M+H]^+$.

2.2. Crystal structure analysis

The X-ray diffraction measurements of **1** were made on a Rigaku Mercury CCD diffractometer at 193 K with graphite monochromated Mo Kα radiation up to $2\theta_{max} = 55°$. The crystal structure was solved by direct methods (SIR92) [5] and succeeding Fourier syntheses fol-

[1] A guanine-substituted nitronyl nitroxide radical has been synthesized as a counterpart of **1** and **2**. Full characterization of the radical is under way and will be reported in a separate paper.



Scheme 2. Synthesis of cytosine-substituted nitronyl nitroxide monoradical **1** and biradical **2**: (i) 2,3-bis(hydroxyamino)-2,3-dimethylbutane, benzene; (ii) $NaIO_4$, CH_2Cl_2, H_2O; (iii) cytosine, K_2CO_3, KI, MeCN. (iv) 1,2-dibromo-ethane, K_2CO_3, DMF; (v) cytosine, *t*-BuOK, DMF.

lowed by the full-matrix least-squares refinement with the anisotropic approximation for non-hydrogen atoms. Positions of the hydrogen atoms were calculated and included in the final refinement. All the calculations were made using a program package CRYSTALSTRUCTURE by Rigaku/Molecular Structure Corporation [6].

2.3. Magnetic susceptibility measurements

The magnetic susceptibilities of **1** and **2** were measured for randomly oriented polycrystalline samples on a Quantum Design SQUID magnetometer MPMS-XL with an applied magnetic field of 0.1 T in the temperature range of 1.9–298 K.

3. Results and discussion

3.1. Crystal structure

The crystallographic data for **1** are listed in Table 1. Neighboring cytosine moieties in **1** related by an inversion center form two-fold hydrogen bonds of N5H–N4 = 3.013(3) Å, as shown in Fig. 2a. The hydrogen bond length is close to that in pristine cytosine [7] and an analogous cytosine derivative [2b].

Table 1
X-ray crystallographic data for **1**

Formula	$C_{19}H_{24}N_5O_4$
Crystal system	triclinic
Space group	$P\bar{1}$
a (Å)	8.647(3)
b (Å)	9.378(3)
c (Å)	13.052(4)
α (°)	106.748(6)
β (°)	92.677(5)
γ (°)	105.587(6)
V (Å^3)	967.2(5)
Z	2
D_{calc} (g cm^{-3})	1.327
T (K)	193
Unique reflections used ($I > 3\sigma(I)$)	2907
R_1[a], R_w[b]	0.056, 0.134
Goodness-of-fit	1.108

[a] $R = \sum||F_o| - |F_c||/\sum|F_o|$.
[b] $R_w = (\sum w(|F_o| - |F_c|)^2/\sum wF_o^2)^{1/2}$, $w = 1/[0.0010F_o^2 + 3\sigma(F_o^2) + 0.5000]/(4F_o^2)$.

Between the nitronyl nitroxide moieties are found two kinds of short contacts close to sum of van der Waals radii [8]. One is found between the carbon atom C10 on the phenyl ring and the nitroxide oxygen atom O2 with the length of C10–O2 = 3.438(3) Å. The other contact is between C12 and O1 (3.544(3) Å). These contacts lead to a ladder structure of $S = 1/2$ spins, as schematically shown in Figs. 2b and c.

3.2. Magnetic susceptibility

3.2.1. Monoradical *1*

The temperature dependence of paramagnetic susceptibility χ_p for a randomly oriented polycrystalline sample of **1** is shown in Fig. 3a in the χ_pT versus T plots. The χ_pT value of 0.37 emu K mol^{-1} at room temperature corresponds to 1 mol of $S = 1/2$ spins. The χ_pT value decreases as the temperature is lowered, indicating that antiferromagnetic interactions are dominating in the crystalline solid state.

The temperature dependence of χ_pT was analyzed using the two-leg ladder model in Fig. 2c

$$H = \sum_{i=1}^{N}[-2J_1\mathbf{S}_{i,1}\cdot\mathbf{S}_{i,2} - 2J_2(\mathbf{S}_{i,1}\cdot\mathbf{S}_{i+1,1} + \mathbf{S}_{i,2}\cdot S_{i+1,2})], \qquad (2)$$

where $\mathbf{S}_{i,1}$ and $\mathbf{S}_{i,2}$ denote the spin-1/2 operators in the *i*th unit cell and N is the number of unit cells. The Hamiltonian was numerically diagonalized to give an eigenenergy E_j, and an eigenvalue S_j for the *j*th eigenstate, from which the temperature dependence of χ_pT was calculated as

$$\chi_p = \frac{1}{2N}\cdot\frac{N_A g^2\mu_B^2}{3k_BT}\cdot\frac{\sum_j\left[S_j(S_j+1)(2S_j+1)\exp\left(-\frac{E_j}{k_BT}\right)\right]}{\sum_j\left[(2S_j+1)\exp\left(-\frac{E_j}{k_BT}\right)\right]}. \qquad (3)$$

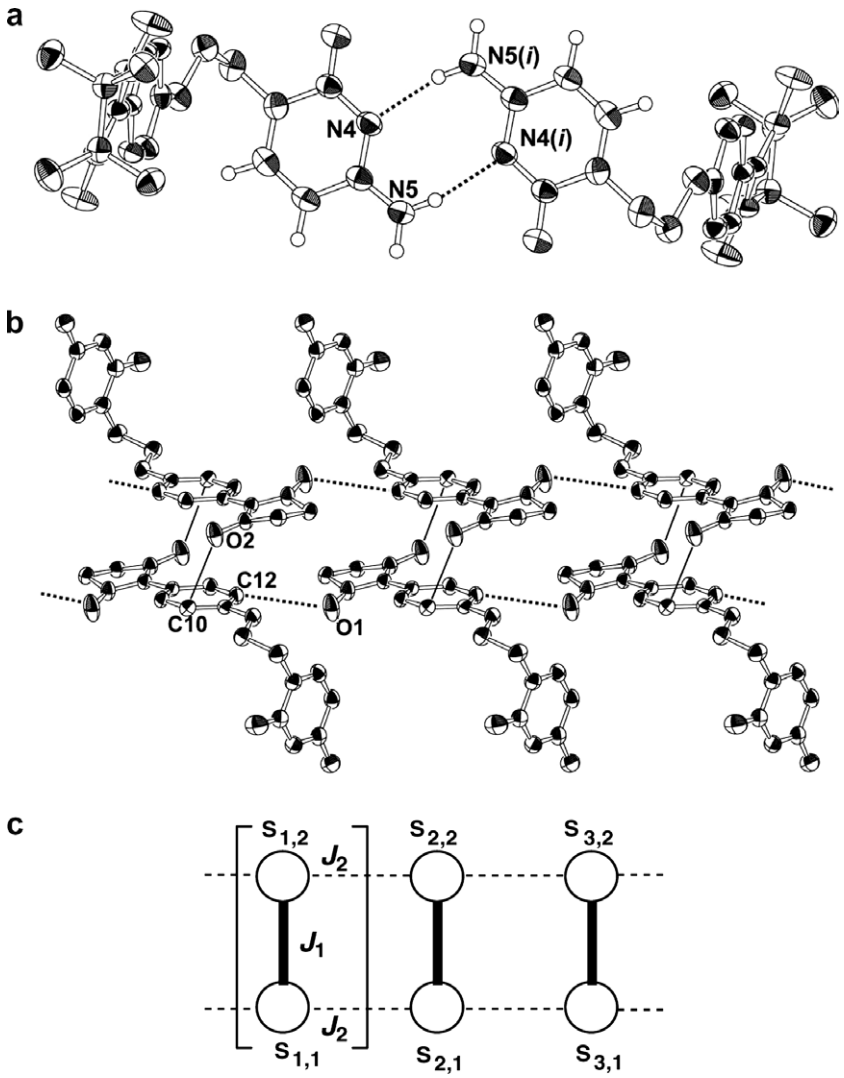


Fig. 2. (a) Hydrogen-bonded pair of **1**. (b) Molecular chain of **1** along the *a*-axis. Two kinds of short contacts are depicted by the dotted and solid lines. (c) Schematic view of the exchange pathway in the molecular chain. The exchange couplings J_1 and J_2 are attributed to the contact C10–O2 and C12–O1 in (b), respectively. The bracket represents the repeating unit of the chain.

The symbols N_A, g, μ_B and k_B stand for Avogadro constant, the g-factor, Bohr magneton and Boltzmann constant, respectively. In the calculations of Eqs. (2) and (3), periodic boundary condition is imposed for $N = 6$ repeating units with twelve $S = 1/2$ spins.[2] The model, however, provided unsatisfactory fit to the observed temperature dependence of $\chi_p T$. The poor fitting implies the presence of weak exchange interactions between the ladder chains. A dimer model with the singlet–triplet energy gap of $2J_1$ plus an interdimer mean field failed to improve the fitting as well.

To obtain an estimate for the intermolecular exchange interactions for **1**, the temperature dependence of $\chi_p T$ was fitted to the Curie–Weiss law

$$\chi = \frac{C}{(T-\theta)}. \tag{4}$$

Optimized parameters of $C = 0.37$ emu K mol^{-1} and $\theta = -1.4$ K were obtained from the fitting in which the larger weight was applied for the observed χ_p value at the higher temperature, as depicted in the inset of Fig. 3a. The Curie constant of $C = 0.37$ emu K mol^{-1} indicates a satisfactory purity of 100%, which is consistent with the chemical analysis. The mean field of $\theta = -1.4$ K is an estimate for the average of the interactions J_1, J_2, and possible interchain interactions in the high-temperature approximation.

3.2.2. Biradical **2**

Fig. 3b shows the temperature dependence of paramagnetic susceptibility χ_p measured for randomly oriented polycrystalline sample of **2**. A maximum in χ_p is found at 6.5 K, indicating that antiferromagnetic interactions

[2] For even number N of unit cells, the spin chain of $N = 6$ gives the largest dimension of the spin Hamiltonian, for which we are allowed to diagonalize numerically the Hamiltonian matrix. Hamiltonian matrices for $N > 8$ are too large to diagonalize numerically giving all eigenenergies.

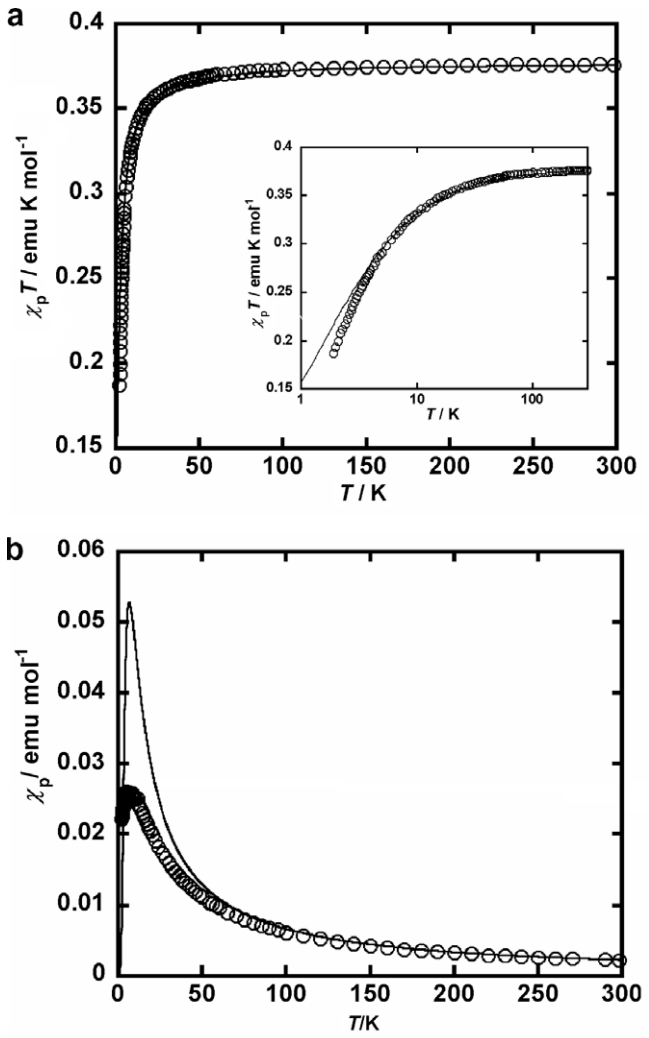


Fig. 3. Temperature dependence of magnetic susceptibility χ_p. (a) The $\chi_p T$ vs. T plots of **1**. The solid line depicts the calculated curve based on the Curie–Weiss law. The inset shows the logarithmic plot. (b) The χ_p vs. T plots of **2**. The solid line depicts the theoretical curve from Eq. (5).

are operative in a dimer, a one-dimensional chain, or other low-dimensional lattices of $S = 1/2$ spins. Singlet ground states with intramolecular antiferromagnetic interactions have been found in *p*-phenylene-based biradicals substituted with nitronyl nitroxide radical groups [4,9,10] having molecular structures similar to that of **2**. Thus, the biradical **2** is likely to have an intramolecular antiferromagnetic exchange interaction. The temperature dependence of χ_p was analyzed by using the singlet–triplet model

$$\chi_p = \frac{N_A g^2 \mu_B^2}{3k_B T} \frac{2}{3 + \exp(-2J/k_B T)}, \quad (5)$$

where J represents the exchange parameter. Numerical differentiation of χ_p in Eq. (5) with respect to T gives the temperature T_{max} where χ_p has a maximum

$$T_{max} = 1.247|J|/k_B \quad (6)$$

as a function of $|J|$. The observed $T_{max} = 6.5$ K gives the exchange parameter of $J/k_B = -5.2$ K. The solid line in Fig. 3 is calculated with the exchange parameter of $J/k_B = -5.2$ K and the purity of 93.9%. The model of Eq. (5) gives χ_p values larger than the observed one around T_{max}. The discrepancy is not attributed to the unsatisfactory purity, i.e., impurities of paramagnetic molecules with only one unpaired electron or diamagnetic molecules considering the χ_p values at higher temperatures. This indicates the presence of additional antiferromagnetic interactions. Introduction of an intermolecular mean field into Eq. (5) did not improve the fitting. It is premature that the coupling constant $J/k_B = -5.2$ K is assigned solely to the intramolecular interaction within the biradical. X-ray single crystal structure analyses are underway to improve the exchange coupling model. The exchange interaction of $J/k_B = -5.2$ K is an estimate for the intramolecular exchange interaction.

4. Conclusion

The cytosine derivatives of nitronyl nitroxide monoradical **1** and biradical **2** have been prepared and isolated as stable crystalline solids under ambient atmosphere. The molecular packing of **1** features in intermolecular hydrogen bonding of the cytosine moiety, giving a spin ladder chain structure based on nitronyl nitroxide radical moieties. For the biradical **2**, the magnetic susceptibility suggests the singlet ground state with an estimated intramolecular antiferromagnetic exchange interaction of $J/k_B \sim -5$ K. These radicals can be components for the Watson–Crick base pairing, leading to hydrogen bonding-based heteromolecular assembly.

Acknowledgments

This work has been supported by Grants-in-Aid for Scientific Research from the Ministry of Education, Sports, Culture, Science and Technology, Japan. Financial support from PRESTO of Japan Science and Technology Agency (JST) is also acknowledged. One of the authors (M.K.) acknowledges Research Fellowships of the Japan Society for the Promotion of Science for Young Scientists.

Appendix A. Supplementary material

CCDC 617516 contains the supplementary crystallographic data, excluding structure factors, for this paper. These data can be obtained free of charge via http://www.ccdc.cam.ac.uk/conts/retrieving.html, or from the Cambridge Crystallographic Data Centre, 12 Union Road, Cambridge CB2 1EZ, UK; fax: (+44) 1223-336-033; or e-mail: deposit@ccdc.cam.ac.uk. Supplementary data associated with this article can be found, in the online version, at doi:10.1016/j.poly.2007.01.004.

References

[1] (a) D. Shiomi, K. Sato, T. Takui, J. Phys. Chem. B 105 (2001) 2932;
(b) K. Maekawa, D. Shiomi, K. Sato, T. Takui, J. Phys. Chem. B. 109 (2005) 9299.

[2] (a) D. Shiomi, T. Kanaya, K. Sato, M. Mito, K. Takeda, T. Takui, J. Am. Chem. Soc. 123 (2001) 11823;
(b) D. Shiomi, M. Nozaki, T. Ise, K. Sato, T. Takui, J. Phys. Chem. B 108 (2004) 16604;
(c) K. Hayakawa, D. Shiomi, T. Ise, K. Sato, T. Takui, J. Phys. Chem. B 109 (2005) 9195.

[3] V. Biji, P.K. Sudeep, K.G. Thomas, M.V. George, Langmuir 18 (2002) 1831.

[4] T. Ise, D. Shiomi, K. Sato, T. Takui, Chem. Mater. 17 (2005) 4786.

[5] A. Altomare, M.C. Burlea, M. Camalli, M. Cascarano, C. Giacovazzo, A. Guagliardi, G. Polidre, J. Appl. Crystallogr. 27 (1994) 435.

[6] CRYSTALSTRUCTURE (ver.3.6.0), Rigaku/Molecular Structure Corporation (2000–2004), 9009 New Trails Dr. The Woodlands, TX 77381, USA.

[7] (a) G.A. Jeffrey, Y. Kinoshita, Acta Crystallogr. 16 (1963) 20;
(b) R.J. McClure, B.M. Craven, Acta Crystallogr., Sect. B 29 (1973) 1234;
(c) S. Neidle, A. Achari, M. Rabinovitch, Acta Crystallogr., Sect. B 32 (1976) 2050;
(d) D.L. Barker, R.E. Marsh, Acta Crystallogr. 17 (1964) 1581;
(e) R.J. McClure, B.M. Craven, Acta Crystallogr., Sect. B 29 (1973) 1234;
(f) M. Eisenstein, Acta Crystallogr., Sect. B 44 (1988) 412.

[8] A. Bondi, J. Phys. Chem. 68 (1964) 441.

[9] (a) D. Shiomi, M. Tamura, H. Sawa, R. Kato, M. Kinoshita, Synth. Met. 56 (1993) 3279;
(b) A. Caneschi, P. Chiesi, L. David, F. Ferraro, D. Gatteschi, R. Sessoli, Inorg. Chem. 32 (1993) 1445.

[10] Y. Kanzaki, D. Shiomi, T. Ise, K. Sato, T. Takui, in: The 10th International Conference on Molecule-Based Magnets, Victoria, Canada, 2006, Polyhedron, 2006. doi:10.1016/j.poly.2006.09.034.

building blocks are allowed to self-assemble into a common structural archetype, thus allowing for the systematic tuning of the optical and magnetic properties of the resulting reaction products, and accurate magneto-structural correlations to be described; examples include photomagnetic lattices [10–14], room temperature magnets [3–5], and polynuclear complexes [8] and low-dimensional chains that exhibit slow relaxation of the magnetization [9].

The radial extent and diffuseness of second- and third-row transition metal centers present in $[M^n(CN)_8]^{(n-8)}$ anions (Mo, W) are expected to exhibit enhanced π-backbonding, charge delocalization, and efficient superexchange interactions between metal centers in networks and clusters constructed from M(μ-CN)M′ units [22]. Octacyanometalate anions generally adopt square antiprismatic, bicapped trigonal prismatic, or dodecahedral structures and are capable of forming up to eight cyanide bridges to adjacent metal centers. These factors are expected to afford cyanometalate materials that exhibit markedly different magnetic and optical properties than hexa- and heptacyanometalate derivatives. Octacyanometalates are also attractive building blocks because they undergo facile photoejection of electrons and often form lattices and clusters that exhibit long-lived photo-induced magnetization changes, with several reports indicating that $Cu^{II}/[Mo(CN)_8]^{n-}$ and $Co^{II/III}/[W(CN)_8]^{n-}$ units being the most useful for constructing such photoresponsive networks and clusters [10–14]. While the first examples of lattices containing octacyanometalate anions, $M^{II}_2[Mo^{IV}(CN)_8]\cdot nH_2O$ $(2 \leqslant n \leqslant 9)$ $(M^{II} = Mn, Fe, Co, Ni, Cu, and Zn)$, were reported in 1927 relatively few octacyanometalate clusters and networks have been reported, in comparison to better known hexacyanometalate analogues [15–21].

Recently pentadecanuclear octacyanometalate(V) clusters of $Co^{II}[Co^{II}(MeOH)_3]_8[M^V(CN)_8]_6\cdot n$MeOH stoichiometry ($M^V = Mo$, W) were reported to exhibit slow relaxation of the magnetization that is characteristic of superparamagnetic compounds [22a]. These cyanide-bridged polynuclear complexes are typically prepared in alcoholic media and are often prone to rapid desolvation and aggregation under mild conditions [22]; we rationalized that DMF might be a more suitable donor ligand than alcohols for stabilizing the cluster framework. Methanolic mixtures of these clusters treated with DMF rapidly afforded precipitates while combination of divalent 3d tosylates with octacyanometalate(V) salts in DMF give a series of structurally related one-dimensional chains that are essentially isostructural to "glassy" networks reported by Tang et al. [23,24]. We rationalized that substitution of Mn^{II} for more anisotropic metal centers (e.g. Ni^{II}) might afford magnetic chain analogues that exhibit higher blocking temperatures than Mn^{II} analogues, assuming that efficient superexchange interactions are maintained. Moreover, we rationalized that octacyanometalates may be promising building blocks for constructing polynuclear complexes and lattices that exhibit markedly different and/or enhanced properties (e.g. photomagnetism, magnetism) relative to 3d hexa- and heptacyanometalate analogues [1–5,13–15]. In the present contribution we describe the syntheses, crystallographic, spectroscopic, and magnetic details of several one- and two-dimensional octacyanometalate(V) networks containing a series of paramagnetic 3d transition metal centers.

2. Experimental

2.1. General considerations

All operations were conducted while dark in a vacuum or under an argon atmosphere by using standard Schlenk and drybox techniques. Transfers of solutions containing cyanides were carried out through stainless steel cannulas. The salts Cs(OTs), $Mn(OTs)_2$, $Co(OTs)_2$, $Ni(OTs)_2$, $[NBu_3H]_3[Mo(CN)_8]$, and $[NBu_3H]_3[W(CN)_8]$ were prepared according to modified literature methods [16,17,25–28]. Solvents were distilled under dinitrogen from sodium-benzophenone (diethyl ether) or Mg turnings (methanol and ethanol) and were sparged with argon prior to use. DMF (Baker) was dried over activated Linde 13-X molecular sieves and sparged with argon prior to use. $FeCl_3$ (Cerac), nitric acid (Baker), tributylamine (Aldrich), Celite (Aldrich), and deionized water were used as received.

The IR spectra were recorded as Nujol mulls between KBr plates on a Mattson Galaxy 5200 FTIR instrument. Room temperature powder susceptibility measurements were collected on a Johnson–Matthey magnetic susceptibility balance. Variable temperature and magnetic field measurements were performed at the Frederick Seitz Materials Research Laboratory at the University of Illinois at Urbana-Champaign (U.I.) and Virginia Tech University (V.T.) on Quantum Design MPMS (U.I. and V.T.) and MPMS2 (U.I.) SQUID magnetometers. Diamagnetic corrections were estimated using Pascal's constants [29,30]: $\chi_{dia} = -771.36\times10^{-6}\,cm^3\,mol^{-1}$ for **5**, $\chi_{dia} = -771.36\times10^{-6}\,cm^3\,mol^{-1}$ for **6**, $\chi_{dia} = -827.36\times10^{-6}\,cm^3\,mol^{-1}$ for **5**, $\chi_{dia} = -749.36\times10^{-6}\,cm^3\,mol^{-1}$ for **7**, and $\chi_{dia} = -827.36\times10^{-6}\,cm^3\,mol^{-1}$ for **8**. Microanalyses were performed by the University of Illinois Microanalysis Laboratory.

2.2. Preparation of complexes and networks

2.2.1. $[HBu_3N]_3[Mo(CN)_8]$ (1)

Treatment of aqueous (80 mL) $K_4[Mo(CN)_8]\cdot 2H_2O$ (25.04 g, 50.4 mmol) with concentrated HNO_3 (110 mL) over 5 min. affords a brown solution. Subsequent addition of water (200 ml) followed by tributylamine (40 mL, 168 mmol) while stirring affords a pale brown suspension over 10 min; water (1200 mL) was added and the mixture was allowed to stir an additional 30 min. The crude product was isolated by suction filtration and washed with water (3×50 mL) followed by Et_2O (50 mL). The remaining yellow solid was dissolved into absolute EtOH (250 mL), filtered through Celite, and the pale yellow

filtrate was concentrated under vacuum (60 °C) to *ca.* 100 mL volume. Addition of Et_2O (200 mL) afforded a pale yellow solid that was isolated by suction filtration, washed with Et_2O (2 × 20 mL), and dried under vacuum for 2 h at room temperature (29 °C). Yield: 24.51 g (56.3%). *Anal.* Calc. for $C_{44}H_{84}N_{11}Mo$: C, 61.17; H, 9.83; N, 17.84; Mo, 11.11. Found: C, 61.51; H, 9.70; N, 17.82; Mo, 10.89%. IR (Nujol, cm^{-1}): 3027 (vs, br), 2962 (vs, br), 2935 (vs), 2871 (vs), 2853 (vs), 2798 (vs), 2141 (s), 2114 (w), 1224 (w), 1156 (w), 1107 (w), 1066 (w), 1035 (w), 984 (vw), 931 (w), 902 (vw), 802 (vw), 741 (w), 499 (vw), 487 (vw), 451 (vw).

2.2.2. $[HBu_3N]_3[W(CN)_8]$ (**2**)

Treatment of aqueous (120 mL) $K_4[W(CN)_8]\cdot 2H_2O$ (24.98 g, 42.7 mmol) with concentrated HNO_3 (120 mL) over 3 min. affords a dark purple solution. Subsequent addition of water (200 ml) followed by tributylamine (40 mL, 168 mmol) with stirring gradually affords a pale purple suspension over 10 min; addition of water (750 mL) gradually afforded a pale purple suspension over 30 min. The crude product was isolated via suction filtration and was washed with water (3 × 50 mL) followed by Et_2O (50 mL). The remaining pale purple solid was dissolved into anhydrous EtOH (300 mL) and the mixture was filtered through Celite. The pale purple filtrate was concentrated under vacuum (60 °C) to *ca.* 100 mL volume and Et_2O (100 mL) was added. The precipitated white solid was isolated via suction filtration, washed with Et_2O (3 × 50 mL), and dried under vacuum for 2 h at room temperature (29 °C). Yield: 30.43 g (74.9%). *Anal.* Calc. for $C_{44}H_{84}N_{11}W$: C, 55.52; H, 8.92; N, 16.19. Found: C, 55.57; H, 8.8; N, 16.07%. IR (Nujol, cm^{-1}): 3343 (w), 3321 (w), 3298 (w), 3027 (vs), 2936 (vs), 2871 (vs), 2854 (vs), 2798 (vs), 2748 (s), 2663 (m), 2548 (w), 2144 (m), 2120 (w), 1277 (w), 1224 (w), 1156 (w), 1107 (w), 1066 (w), 1034 (w), 985 (w), 931 (w), 902 (vw), 803 (w), 741 (w), 440 (w).

2.2.3. $Cs_3[Mo(CN)_8]$ (**3**)

Treatment of **1** (5.14 g, 5.95 mmol) in MeOH (50 mL) with methanolic (125 mL) CsOTs (4.94 g, 18.2 mmol) rapidly precipitated a yellow solid. The mixture was allowed to stir for 5 min and the yellow solid was isolated via suction filtration, washed with EtOH (2 × 25 mL) and Et_2O (30 mL), and dried under vacuum for 2 h at room temperature (29 °C). Yield: 4.04 g (91.8%). *Anal.* Calc. for $C_8N_8Cs_3Mo$: C, 13.66; H, 0; N, 15.94; Cs, 56.73; Mo, 13.65. Found: C, 13.72; H, 0; N, 15.31; Cs, 55.98; Mo, 13.22%. IR (Nujol, cm^{-1}): 3615 (w), 3480 (w, br), 3348 (w), 3321 (w), 3298 (w), 2143 (vs), 2135 (s, sh), 2114 (w), 1606 (vw), 505 (w), 471 (w).

2.2.4. $Cs_3[W(CN)_8]$ (**4**)

Treatment of CsOTs (6.11 g, 22.5 mmol) in MeOH (50 mL) with methanolic **2** (7.24 g, 7.61 mmol) rapidly affords a pale yellow suspension. The mixture was allowed to stir for 15 min. and subsequently filtered via suction filtration. The yellow precipitate was washed with EtOH (2 × 10 mL) and Et_2O (2 × 15 mL) and dried for 2 h under vacuum at room temperature (30 °C). Yield: 5.18 g (86.0%). *Anal.* Calc. for $C_8H_8N_8Cs_3W$: C, 12.14; H, 0; N, 14.16; Cs, 50.43; W, 23.25. Found: C, 12.31; H, 0.03; N, 13.6; Cs, 48.57; W, 20.19%. IR (Nujol, cm^{-1}): 3603 (w), 3532 (w), 2144 (m), 2131 (m), 1619 (w), 446 (w), 420 (w).

2.2.5. $\{[trans\text{-}Mn^{II}(DMF)_4][cis\text{-}Mn^{II}(DMF)_4]_2[W^{V}(CN)_8]_2\}_n$ (**5**)

Treatment of a DMF (20 mL) solution of $Mn(OTs)_2$ (1.25 g, 3.15 mmol) with **2** (1.98 g, 2.08 mmol) in DMF (20 mL) afforded an amber solution that was allowed to stand for 4 d at room temperature (20 °C). The brown crystals were isolated via filtration, washed with DMF (2 × 5 mL) and Et_2O (3 × 5 mL), and dried under vacuum for 2 min at room temperature (20 °C). Yield: 1.25 g, (65.8%). *Anal.* Calc. for $C_{52}H_{84}N_{28}O_{12}Mn_3W_2$: C, 34.21; H, 4.64; N, 21.48; Mn, 9.03; W, 20.14. Found: C, 34.02; H, 4.11; N, 20.87%. IR (Nujol, cm^{-1}): 3144 (s), 3062 (s), 2157 (vs), 2130 (m, sh), 2114 (w), 1645 (vs), 1560 (s), 1540 (s), 1496 (vs), 1454 (vs), 1421 (vs), 1251 (vs), 1154 (m), 1110 (vs), 1062 (s), 1016 (m), 865 (m), 678 (s), 675 (s), 439 (s), 421 (s).

2.2.6. $\{[trans\text{-}Mn^{II}(DMF)_4][cis\text{-}Mn^{II}(DMF)_4]_2[W^{V}(CN)_8]_2\}_n$ (**6**)

Treatment of a DMF (20 mL) solution of $Mn(OTs)_2$ (1.17 g, 2.94 mmol) with **2** (2.59 g, 2.72 mmol) in DMF (20 mL) afforded an amber solution that was allowed to stand for 4 d at room temperature (28 °C). The brown crystals were isolated by filtration, washed with DMF (2 × 5 mL) and Et_2O (3 × 5 mL), and dried under vacuum for 2 min at room temperature (28 °C). Yield: 1.51 g, (84.4%). *Anal.* Calc. for $C_{52}H_{84}N_{28}O_{12}Mn_3W_2$: C, 34.21; H, 4.64; N, 21.48; Mn, 9.03; W, 20.14. Found: C, 34.05; H, 4.31; N, 20.83%. IR (Nujol, cm^{-1}): 3143 (s), 3060 (s), 2156 (vs), 2129 (m, sh), 2113 (w, sh), 2029 (w), 2016 (w, sh), 1645 (vs), 1559 (s), 1540 (s), 1496 (vs), 1456 (vs), 1420, (vs), 1252 (vs), 1152 (m), 1110 (vs), 1062 (s), 1017 (m), 865 (m), 678 (s), 674 (s), 439 (s), 421 (s), and 403 (s).

2.2.7. $\{[trans\text{-}Ni^{II}(DMF)_4][cis\text{-}Ni^{II}(DMF)_4]_2[Mo^{V}(CN)_8]_2\}_n$ (**7**)

Treatment of a DMF (20 mL) solution of $Ni(OTs)_2$ (1.25 g, 3.12 mmol) with **1** (1.95 g, 2.25 mmol) in DMF (20 mL) afforded a lime-green solution that was allowed to stand for 4 d at room temperature (26 °C). The pale green crystals were isolated by filtration, washed with DMF (2 × 5 mL) and Et_2O (3 × 5 mL), and dried under vacuum for 2 min. at room temperature (26 °C). Yield: 1.07 g, (62.1%). *Anal.* Calc. for $C_{52}H_{84}N_{28}O_{12}Mo_2Ni_3$: C, 37.58; H, 5.09; N, 23.60; Ni, 23.61; Mo, 11.55. Found: C, 36.98; H, 4.85; N, 22.91%. IR (Nujol, cm^{-1}): 3140 (m), 3055 (m, sh), 2193 (m, sh), 2183 (m), 2138 (w), 1672 (vs), 1643 (vs), 1548 (w), 1499 (s), 1456 (vs), 1439 (vs), 1422

(vs), 1378 (vs), 1254 (s), 1151 (m), 1114 (vs), 1096 (s), 1063 (s), 1011 (m), 869 (w), 685 (s), 658 (m), 520 (w), 487 (m).

2.2.8. {[*trans*-$Ni^{II}(DMF)_4$][*cis*-$Ni^{II}(DMF)_4$]$_2$-[$W^V(CN)_8$]$_2$}$_n$ (**8**)

Treatment of a DMF (20 mL) solution of $Ni(OTs)_2$ (1.25 g, 3.12 mmol) with **2** (2.16 g, 2.27 mmol) in DMF (20 mL) afforded a lime-green solution that was allowed to stand for 4 d at room temperature (26 °C). The pale green crystals were isolated by filtration, washed with DMF (2 × 5 mL) and Et_2O (3 × 5 mL), and dried under vacuum for 2 min at room temperature (26 °C). Yield: 1.21 g, (63.3%). *Anal.* Calc. for $C_{52}H_{84}N_{28}O_{12}Ni_3W_2$: C, 33.99; H, 4.61; N, 21.35; Ni, 9.58; W, 20.01. Found: C, 33.54; H, 3.96; N, 20.54%. IR (Nujol, cm^{-1}): 3142 (w), 3052 (m, sh), 2186 (m), 2170 (m, sh), 2137 (w), 1671 (vs), 1643 (vs), 1548 (m), 1499 (s), 1454 (vs, sh), 1440 (vs), 1422 (vs), 1378 (vs), 1255 (s), 1150 (m, sh), 1114 (vs), 1096 (s, sh), 1063 (s), 1017 (m), 869 (w), 816 (w, sh), 693 (s, sh), 684 (s), 658 (w), 478 (w), 454 (m).

2.2.9. [$Fe^{II}(DMF)_6$]$_2$[$W^{IV}(CN)_8$] (**9**)

Treatment of a DMF (15 mL) solution of $FeCl_3$ (0.17 g, 1.05 mmol) with **2** (1.01 g, 1.06 mmol) in DMF (15 mL) afforded a dark orange solution; after 3 d (20 °C) Et_2O (20 mL) was layered on top of the yellow mixture forming yellow crystals within 1 week. The crystals were isolated via filtration, washed with DMF (3 × 5 mL) and Et_2O (3 × 5 mL), and dried under vacuum for 16 h at room temperature (20 °C). Yield: 0.86 g (60.9%). *Anal.* Calc. for $C_{44}H_{84}N_{20}O_{12}Fe_2W$: C, 38.24; H, 6.14; N, 20.28. Found: C, 37.88; H, 5.75; N, 19.69%. IR (Nujol, cm^{-1}): 3142 (w), 3053 (vs), 2923 (vs), 2854 (vs), 2181 (w), 2164 (w), 2151 (w), 2121 (w), 1683 (vs, sh), 1671 (vs, sh), 1645 (vs), 1496 (m), 1455 (s), 1439 (s), 1378 (vs), 1254 (m), 1152 (w), 1117 (s), 1094 (m), 1064 (m), 1019 (m), 685 (m), 671 (m, sh), 661 (w), 447 (m), 403 (s). μ_{eff} (μ_B) = 6.79. Upon standing several months DMF/Et_2O mixtures of **9** afford small quantities of {[*trans*-$Fe^{II}(DMF)_4$][*cis*-$Fe^{II}(DMF)_4$]$_2$-[$W^V(CN)_8$]$_2$}$_n$ (**10**) as brown crystals. IR (Nujol, cm^{-1}): 3144 (m), 3056 (m), 2280 (w, sh), 2155 (m, sh), 2145 (m), 2127 (m), 2116 (m), 2029 (w), 1658 (vs), 1642 (vs), 1495 (s), 1456 (vs), 1439 (vs), 1253 (s), 1150 (w), 1115 (vs), 1064 (s), 866 (w), 805 (w), 683 (vs), 441 (m), 417 (s).

2.3. Structure determinations and refinements

Crystals of **5**–**8** were grown from DMF solutions of either $Mn(OTs)_2$ (**5**, **6**), $Ni(OTs)_2$ (**7**, **8**), or $FeCl_3$ (**9**, **10**) treated with **1** or **2**. X-ray diffraction data were collected at 90.0(2) K on a Nonius kappaCCD diffractometer from irregular shaped crystals, mounted in Paratone-N oil on glass fibers. Initial cell parameters were obtained (DENZO) [31] from ten 1° frames and were refined via a least-squares scheme using all data-collection frames (SCALEPACK) [31]. Lorentz/polarization corrections were applied during data reduction. The structures were solved by direct methods (SHELXS97) [32] and completed by difference Fourier methods (SHELXL97) [32]. Refinement was performed against F^2 by weighted full-matrix least-squares (SHELXL97) [32] and empirical absorption corrections (either SCALEPACK [31] or SADABS [32]) were applied. Hydrogen atoms were found in difference maps and subsequently placed at calculated posi-

Table 1
Crystallographic data for {[*trans*-$Mn^{II}(DMF)_4$][*cis*-$Mn^{II}(DMF)_4$]$_2$[$W^V(CN)_8$]$_2$}$_n$ (**5**), {[*trans*-$Mn^{II}(DMF)_4$][*cis*-$Mn^{II}(DMF)_4$]$_2$[$W^V(CN)_8$]$_2$} $_n$ (**6**), {[*trans*-$Ni^{II}(DMF)_4$][*cis*-$Ni^{II}(DMF)_4$]$_2$[$W^V(CN)_8$]$_2$}$_n$ (**8**), [$Fe^{II}(DMF)_6$]$_2$[$W^{IV}(CN)_8$] (**9**), and {[*trans*-$Fe^{II}(DMF)_4$][*cis*-$Fe^{II}(DMF)_4$]$_2$[$W^V(CN)_8$]$_2$}$_n$ (**10**)

	5	**6**	**8**	**9**	**10**
Chemical formula	$C_{52}H_{84}Mn_3N_{28}O_{12}W_2$	$C_{52}H_{84}Mn_3N_{28}O_{12}W_2$	$C_{52}H_{84}N_{28}Ni_3O_{12}W_2$	$C_{44}H_{84}Fe_2N_{20}O_{12}W$	$C_{52}H_{84}N_{28}Fe_3O_{12}W_2$
Formula weight	1826.00	1826.00	1837.30	1380.82	1828.72
Temperature (K)	90.0(2)	90.0(2)	90.0(2)	90.0(2)	90.0(2)
λ (Å)	0.71073	0.71073	0.71073	0.71073	0.71073
Crystal size (mm)	0.25 × 0.20 × 0.20	0.28 × 0.22 × 0.20	0.15 × 0.15 × 0.15	0.20 × 0.20 × 0.15	0.38 × 0.32 × 0.25
Space group	$P2_1/n$	$P2_1/n$	$P\bar{1}$	$P2_1/c$	$P2_1/c$
Crystal system	monoclinic	monoclinic	triclinic	monoclinic	monoclinic
a (Å)	17.6370(2)	11.0050(1)	11.5800(1)	9.9660(1)	11.0030(1)
b (Å)	12.0850(1)	20.6320(2)	12.5510(1)	19.3100(2)	20.5090(3)
c (Å)	18.5330(2)	16.7420(2)	13.4950(1)	19.4650(3)	18.0580(3)
V (Å^3)	3740.81(7)	3725.69(7)	1834.63(3)	3698.94(8)	3695.28(9)
α (°)			86.6240(4)		
β (°)	108.7380(5)	101.4510(5)	73.8650(4)	99.0830(6)	114.9301(5)
γ (°)			76.8430(4)		
ρ (g cm^{-3})	1.621	1.796	1.663	1.592	1.644
Z	4	4	2	4	2
μ (mm^{-1})	3.628	3.503	3.952	3.556	3.749
Final R indices	$R_1 = 0.0203$,	$R_1 = 0.0177$,	$R_1 = 0.0224$,	$R_1 = 0.0240$,	$R_1 = 0.0349$,
$[I > 2\sigma(I)]$[a]	$wR_2 = 0.0401$	$wR_2 = 0.0359$	$wR_2 = 0.0546$	$wR_2 = 0.0520$	$wR_2 = 0.0615$
R indices (for all data)	$R_1 = 0.0288$,	$R_1 = 0.0236$,	$R_1 = 0.0261$,	$R_1 = 0.0305$,	$R_1 = 0.0657$,
	$wR_2 = 0.0419$	$wR_2 = 0.0373$	$wR_2 = 0.0566$	$wR_2 = 0.0541$	$wR_2 = 0.0693$

[a] $R = \sigma||F_o| - |F_o||\sum|F_o|$. $wR = \left[\left(\sum w(|F_o| - |F_c|)^2 / \sum wF_o^2\right)\right]^{1/2}$.

tions using suitable riding models with isotropic displacement parameters derived from their carrier atoms. Non-hydrogen atoms were refined with anisotropic displacement parameters. Atomic scattering factors were taken from the International Tables for Crystallography vol. C.3 [33]. Crystal data, relevant details of the structure determinations, and selected geometrical parameters are provided in Tables 1–3.

Table 2
Selected bond distances (Å) for {[*trans*-$Mn^{II}(DMF)_4$][*cis*-$Mn^{II}(DMF)_4$]$_2$[$W^{V}(CN)_8$]$_2$}$_n$ (**5**), {[*trans*-$Mn^{II}(DMF)_4$][*cis*-$Mn^{II}(DMF)_4$]$_2$[$W^{V}(CN)_8$]$_2$}$_n$ (**6**), {[*trans*-$Ni^{II}(DMF)_4$][*cis*-$Ni^{II}(DMF)_4$]$_2$[$W^{V}(CN)_8$]$_2$}$_n$ (**8**), [$Fe^{II}(DMF)_6$]$_2$[$W^{IV}(CN)_8$] (**9**), and {[*trans*-$Fe^{II}(DMF)_4$][*cis*-$Fe^{II}(DMF)_4$]$_2$[$W^{V}(CN)_8$]$_2$}$_n$ (**10**)

5		**6**		**8**		**9**		**10**	
W1–C1	2.184(2)	W1–C1	2.161(2)	W1–C1	2.167(3)	W1–C1	2.168(3)	W1–C1	2.155(6)
W1–C2	2.168(2)	W1–C2	2.170(3)	W1–C2	2.175(3)	W1–C2	2.181(3)	W1–C2	2.177(6)
W1–C3	2.173(2)	W1–C3	2.172(3)	W1–C3	2.161(3)	W1–C3	2.172(3)	W1–C3	2.155(6)
W1–C4	2.168(2)	W1–C4	2.160(3)	W1–C4	2.161(3)	W1–C4	2.186(3)	W1–C4	2.156(6)
W1–C5	2.162(2)	W1–C5	2.169(2)	W1–C5	2.159(3)	W1–C5	2.167(3)	W1–C5	2.174(5)
W1–C6	2.171(2)	W1–C6	2.177(3)	W1–C6	2.168(3)	W1–C6	2.179(3)	W1–C6	2.177(5)
W1–C7	2.162(2)	W1–C7	2.158(3)	W1–C7	2.169(3)	W1–C7	2.172(3)	W1–C7	2.175(6)
W1–C8	2.157(2)	W1–C8	2.179(3)	W1–C8	2.167(3)	W1–C8	2.168(3)	W1–C8	2.172(6)
C1–N1	1.146(3)	C1–N1	1.141(3)	C1–N1	1.146(4)	C1–N1	1.139(4)	C1–N1	1.160(6)
C2–N2	1.149(3)	C2–N2	1.142(3)	C2–N2	1.149(4)	C2–N2	1.147(4)	Fe1–N1	2.137(5)
C6–N6	1.147(3)	C4–N4	1.153(3)	C6–N6	1.141(4)	C3–N3	1.145(4)	Fe1–N4A	2.170(4)
Mn1–N1	2.261(2)	Mn1–N1	2.245(2)	Ni1–N1	2.044(3)	Fe1–O1A	1.975(2)	Fe1–O1	2.108(3)
Mn1–O1A	2.162(2)	Mn1–O1	2.164(2)	Ni1–O1A	2.063(2)	Fe1–O1B	1.984(2)	Fe1–O2	2.148(3)
Mn1–O1AA	2.162(2)	Mn1–O2	2.172(2)	Ni1–O1AA	2.063(2)	Fe1–O1C	2.006(2)	Fe1–O3	2.155(3)
Mn1–O1B	2.167(2)	Mn1–O3	2.158(2)	Ni1–O1B	2.057(2)	Fe2–O1D	2.008(2)	Fe1–O4	2.100(4)
Mn1–O1BA	2.168(2)	Mn1–O4	2.176(2)	Ni1–O1BA	2.057(2)	Fe2–O1E	2.000(2)	Fe2–O5	2.095(3)
Mn2–O1C	2.174(2)	Mn2–O5	2.10(1)	Ni2–O1C	2.057(2)	Fe2–O1F	2.196(2)	Fe2–O6	2.123(4)
Mn2–O1D	2.134(2)	Mn2–O6	2.158(2)	Ni2–O1D	2.047(2)			Fe2–N7	2.154(4)
Mn2–O1E	2.126(2)	Mn2–N2	2.232(2)	Ni2–O1E	2.070(2)			Fe1···Fe1A	8.576(5)
Mn2–O1F	2.172(2)	Mn1–N4A	2.217(2)	Ni2–O1F	2.064(2)			W1···W1B	10.809(5)
Mn2–N6	2.258(2)	Mn1···Mn1E	8.535(3)	Ni2–N6	2.073(5)			W1B···W1BA	23.462(5)
N2–Mn2	2.245(2)	Mn2···Mn2A	18.118(3)	N2–Ni2	2.064(5)			Fe2···Fe2A	18.058(5)
Mn2···Mn2B	6.590(3)	W1···W1A	10.925(3)	W1···Ni1	5.313(4)				
W1···W1B	8.644(3)	W1···Mn1	5.472(3)	W1···Ni2	5.267(4)				
W1···Mn1	5.562(3)	W1A···W1AB	23.629(3)	W1···W1A	8.394(4)				
W1···Mn2	5.452(3)			Ni2···Ni2A	6.382(4)				

Table 3
Selected bond angles (°) for {[*trans*-$Mn^{II}(DMF)_4$][*cis*-$Mn^{II}(DMF)_4$]$_2$[$W^{V}(CN)_8$]$_2$}$_n$ (**5**), {[*trans*-$Mn^{II}(DMF)_4$][*cis*-$Mn^{II}(DMF)_4$]$_2$[$W^{V}(CN)_8$]$_2$}$_n$ (**6**), {[*trans*-$Ni^{II}(DMF)_4$][*cis*-$Ni^{II}(DMF)_4$]$_2$[$W^{V}(CN)_8$]$_2$}$_n$ (**8**), [$Fe^{II}(DMF)_6$]$_2$[$W^{IV}(CN)_8$] (**9**), and {[*trans*-$Fe^{II}(DMF)_4$][*cis*-$Fe^{II}(DMF)_4$]$_2$[$W^{V}(CN)_8$]$_2$}$_n$ (**10**)

(**5**)		(**6**)		(**8**)		(**9**)		(**10**)	
C1–W1–C2	131.81(8)	C1–W1–C2	87.48(9)	C1–W1–C2	130.8(1)	C1–W1–C2	70.9(2)	C1–W1–C2	76.1(2)
C1–W1–C3	72.38(8)	C1–W1–C3	79.31(9)	C1–W1–C3	72.0(1)	C1–W1–C3	94.9(1)	C1–W1–C3	90.2(2)
C1–W1–C4	75.93(8)	C1–W1–C4	148.13(9)	C1–W1–C4	73.6(1)	C1–W1–C4	142.8(1)	C1–W1–C4	148.0(2)
C1–W1–C5	142.88(8)	C1–W1–C5	141.34(9)	C1–W1–C5	140.1(1)	C1–W1–C5	145.3(1)	C1–W1–C5	141.0(2)
C1–W1–C6	130.53(8)	C1–W1–C6	76.40(9)	C1–W1–C6	137.4(1)	C1–W1–C6	76.4(1)	C1–W1–C6	70.5(2)
C1–W1–C7	71.47(8)	C1–W1–C7	96.62(9)	C1–W1–C7	73.0(1)	C1–W1–C7	75.9(1)	C1–W1–C7	102.5(2)
C1–W1–C8	76.69(8)	C1–W1–C8	70.60(9)	C1–W1–C8	74.5(1)	C1–W1–C8	94.1(1)	C1–W1–C8	77.0(2)
N1–C1–W1	178.7(2)	N1–C1–W1	176.2(2)	N1–C1–W1	176.9(3)	N1–C1–W1	179.3(3)	N1–C1–W1	177.1(5)
N2–C2–W1	175.7(2)	N2–C2–W1	179.1(2)	N2–C2–W1	176.0(3)	N2–C2–W1	178.9(3)	N4–C4–W1	174.9(4)
N6–C6–W1	179.1(2)	N4–C4–W1	178.3(2)	N6–C6–W1	175.8(3)	N3–C3–W1	178.7(3)	N7–C7–W1	179.7(5)
C2–W1–C6	70.64(8)	C2–W1–C6	140.01(9)	C2–W1–C6	71.6(1)	O1A–Fe1–O1B	93.05(9)	C4–W1–C7	88.2(2)
Mn1–N1–C1	168.5(2)	Mn1–N1–C1	157.7(2)	Ni1–N1–C1	167.0(3)	O1A–Fe1–O1C	91.8(1)	Fe1–N1–C1	163.6(4)
N1–Mn1–O1A	92.24(6)	N1–Mn1–O1	91.25(7)	N1–Ni1–O1A	92.1(1)	O1D–Fe2–O1E	87.81(9)	N1–Fe1–O1	95.4(2)
N1–Mn1–O1AA	87.76(6)	N1–Mn1–O2	83.62(7)	N1–Ni1–O1AA	87.9(1)	O1D–Fe2–O1F	87.49(9)	N1–Fe1–O2	173.2(2)
N1–Mn1–O1B	85.90(6)	N1–Mn1–O3	173.42(7)	N1–Ni1–O1B	91.9(1)			N1–Fe1–O3	87.0(2)
N1–Mn1–O1BA	94.10(6)	N1–Mn1–O4	169.66(6)	N1–Ni1–O1BA	88.1(1)			N1–Fe1–O4	88.6(2)
Mn2–N2–C2	159.5(2)	Mn2–N2–C2	160.2(2)	Ni2–N2–C2	157.4(2)			N1–Fe1–N4A	97.5(2)
Mn2–N6A–C6A	152.7(2)	Mn1–N4–C4	164.2(2)	Ni2–N6A–C6A	93.7(1)			Fe2–N7–C7	161.9(4)
N2–Mn2–O1C	92.28(6)	N2–Mn2–O5	95.9(3)	N2–Ni2–O1C	88.58(9)			N7–Fe2–O5	88.3(1)
N2–Mn2–O1D	87.32(6)	N2–Mn2–O6	92.78(7)	N2–Ni2–O1D	93.97(9)			N7–Fe2–O5B	91.7(1)
N2–Mn2–O1E	178.93(6)			N2–Ni2–O1E	177.65(9)			N7–Fe2–O6	85.0(2)
N2–Mn2–O1F	89.48(6)			N2–Ni2–O1F	88.99(9)			N7–Fe2–O6B	95.1(2)
N2–Mn2–N6A	91.34(7)			N2–Ni2–N6A	93.7(1)				

3. Results and discussion

3.1. Syntheses and infrared characterization

We had initially anticipated that a series of isostructural clusters of $M^{II}[M^{II}(DMF)_3]_8[M^{V}(CN)_8]_6 \cdot n$DMF stoichiometry, would be obtained upon treatment of binary transition metal *p*-toluenesulfonates with tri(butyl)ammonium octacyanometalates in DMF at room temperature. Instead of clusters several networks are obtained, suggesting that solvent choice is a critical factor in preparing octacyanometalate materials. Treatment of several binary transition metal *p*-toluenesulfonates $[M^{II}(OTs)_2]$ with **1** or **2** in DMF readily affords one- and two-dimensional crystalline octacyanometalate networks of $[M^{II}(DMF)_4]_3[M^{V}(CN)_8]_2$ (M^{V} = Mo, W; M^{II} = Mn, **5**, **6**; Ni, **7**, **8**) stoichiometry [23,24]; Attempts to prepare iron(II) analogues from $Fe^{II}(OTs)_2$ salts consistently afford intractable amorphous precipitates while iron(III) chloride initially affords a trimetallic salt $[Fe^{II}(DMF)_6]_2[W^{IV}(CN)_8]$ (**9**), and small crystalline quantities of $\{[Fe^{II}(DMF)_6]_3[W^{V}(CN)_8]_2\}_n$ (**10**) after standing for several months.

The infrared spectra of **1**–**4** exhibit several high-energy cyano stretching absorptions (ν_{CN}) that are characteristic of octacyanometalate(V) salts. The ν_{CN} stretches are found between 2114 and 2144 cm^{-1} for tributylammonium salts (**1** and **2**) while cesium analogues range from 2131 to 2143 cm^{-1} (**3** and **4**). The energies of the ν_{CN} absorptions fall within expected value ranges and elemental analysis data support their formulation as octacyanometalate(V) salts [20,45].

Likewise, compounds **5**–**8** and **10** exhibit several intense, high-energy ν_{CN} absorptions in their infrared spectra. The highest energy cyano stretching absorptions are shifted to higher energies in comparison to those seen in **1** and **2**, and appear to scale as a function of divalent metal center electronegativity, consistent with the presence of $M^{II}(\mu\text{-NC})M^{V}$ units in **5**–**8**. Generally, the ν_{CN} absorptions range from 2129 to 2193 cm^{-1} suggesting that both bridging and terminal cyanides are present. The Mn^{II} analogues (**5** and **6**) exhibit low-energy ν_{CN} absorptions near 2156 cm^{-1}, while the Ni^{II} derivatives (**7**, **8**) have absorptions that are shifted to much higher energies (2183–2193 cm^{-1}), suggesting that these modes are due to bridging cyanides; this trend is generally consistent with increasing π backbonding and decreasing depopulation of the cyanide 5σ orbital within the $M^{II}(\mu\text{-NC})M^{V}$ unit progressing from Ni^{II} to Mn^{II} [20,36–45]. Additional ν_{CN} stretches are also present at lower energies in the infrared spectra of **5**–**8** and **10** being close in energy to those found for **1** and **2**; we tentatively assign these as terminal cyanide ν_{CN} absorptions. For **10**, ν_{CN} stretching absorptions are found at 2155, 2127, and 2116 cm^{-1}, suggesting that bridging and terminal cyanides are also present. Assuming that kinematic effects [46] are absent in **5**–**8** and **10** we conclude that the bridging and terminal cyano stretching absorptions are those between *ca.* 2156–2193 cm^{-1} and 2129–2138 cm^{-1}, respectively [10b,18a,20–22,36–47].

For **9**, the infrared spectrum exhibits cyano stretching absorptions that are comparable in energy to ionic octacyanotungstate(IV) salts that are absent of μ-CN linkages. Octacyanometalate(IV) compounds generally exhibit ν_{CN} stretches that range from 2060 to 2160 cm^{-1} and 2085 to 2141 cm^{-1} for terminal and bridging cyanides, respectively [20,34–47]. In the infrared spectrum of **9** three medium intensity cyano stretching absorptions [2145, 2127, 2116 cm^{-1}] are found, in addition to a weak ν_{CN} at 2029 cm^{-1}, suggesting that $[M^{IV}(CN)_8]^{4-}$ centers are present. The energy of the ν_{CN} absorptions found for **9** are markedly different than those observed for $K_4[W^{IV}(CN)_8] \cdot 2H_2O$ (2125, 2095, and 2056 cm^{-1}) and bi- and trimetallic clusters of $[M^{II}(en)_3][cis\text{-}M^{II}(en)_2(OH_2)(\mu\text{-NC})M^{IV}(CN)_7] \cdot 2H_2O$ and $[M^{II}(en)_2(OH_2)]_2[(\mu\text{-NC})_2M^{IV}(CN)_6] \cdot 6H_2O$ stoichiometry (2142–2062 cm^{-1}) [20x,44].

3.2. Crystallographic studies: one-dimensional chains

Compounds **5** and **8** crystallize in the monoclinic ($P2_1/n$) and triclinic ($P\bar{1}$) space groups, respectively (Table 1). The neutral networks consist of an alternating array of distorted $\{[cis\text{-}M^{II}(DMF)_4(\mu\text{-NC})_2M^{V}(CN)_5(\mu\text{-CN})]_2\}^{2-}$ squares that are linked via bridging cyanides to adjacent $[trans\text{-}(\mu\text{-CN})M^{II}(DMF)_4(\mu\text{-NC})]^{2+}$ units, leaving five terminal cyanides per three-connected $[W^{V}(CN)_8]^{3-}$ center. The one-dimensional $\{[trans\text{-}M^{II}(DMF)_4][cis\text{-}M^{II}(DMF)_4]_2[(\mu\text{-NC})_3W^{V}(CN)_5]_2\}_n$ chains (Figs. 1 and 2) are separated by coordinated DMF ligands and have closest $M^{II}\cdots M^{II}$ interchain contacts of *ca.* 7.61(3) and 8.43(3) Å for **5** and **8**, respectively [23,24]; this structural motif has been previously reported by Shore, Tang, and Colacio for "expanded Prussian blues" and a few octacyanometalate(V) lattices [15,20–24,48].

For the octacyanotungstate(V) centers the W–C bond lengths differ slightly, ranging from 2.157(2) to 2.184(2) Å and 2.159(3) to 2.169(3) Å for **5** and **8**, respectively (Table 2). For **5**, the C–W–C bond angles range from 70.64(8) to 142.88(8)° while the W–C–N bond angles are nearly linear, ranging from 175.7(2) to 179.1(2)° (Table 3). For **8**, the C–W–C bond angles range from 72.0(1) to 140.1(1)° and nearly linear W–C–N bond angles are again found (Table 3); the bridging cyanide C2–W1–C6 and C1–W1–C2 angles are 70.64(8) and 131.81(8)° for **5** and 71.6(1) and 130.8(1)° for **8**. The coordination geometries of the $[W^{V}(CN)_8]^{3-}$ centers are best described as distorted square antiprismatic (Fig. 1) [20–24,34–47].

The $\{M^{V}_2(\mu\text{-CN})_4M^{II}_2\}$ fragments in each chain appear to distort as a function of the divalent center present. The M^{II}–N bond distances present in the $[cis\text{-}M^{II}(DMF)_4(\mu\text{-NC})_2]^{2+}$ units contained within the $\{M^{V}_2(\mu\text{-CN})_4M^{II}_2\}$ fragments appear to scale as a function of divalent metal center ionic radii, with the longest M^{II}–N distances found in **5** [2.245(2) and 2.258(2) Å], while those in **8** [2.064(3) and 2.073(3) Å] are shorter. The M^{II}–

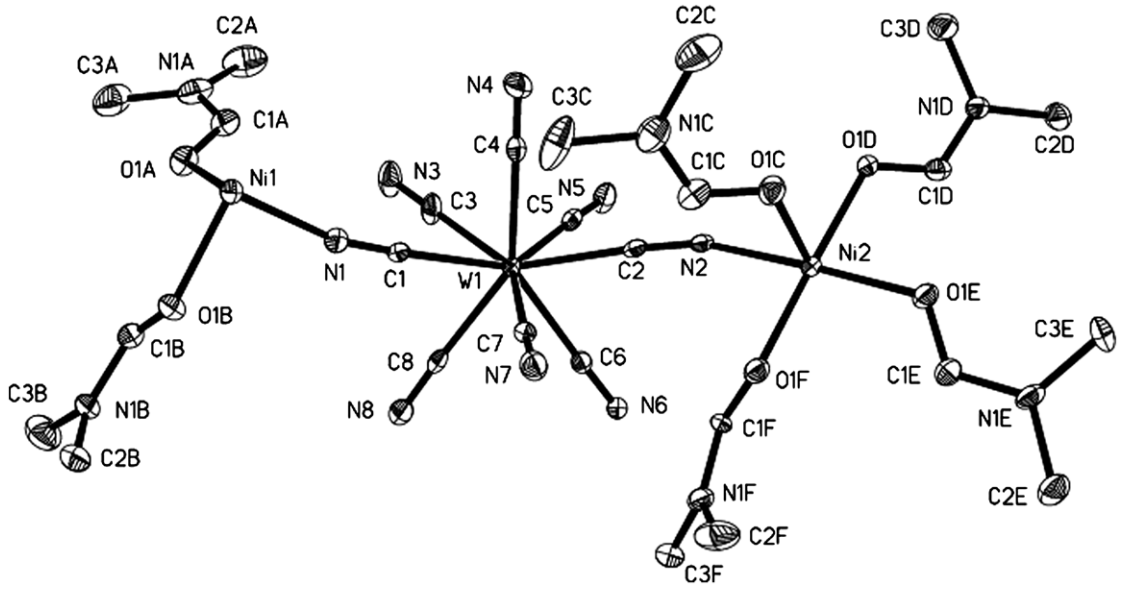


Fig. 1. Asymmetric unit of **8**. Thermal ellipsoids are at the 50% level and all hydrogen atoms are removed for clarity.

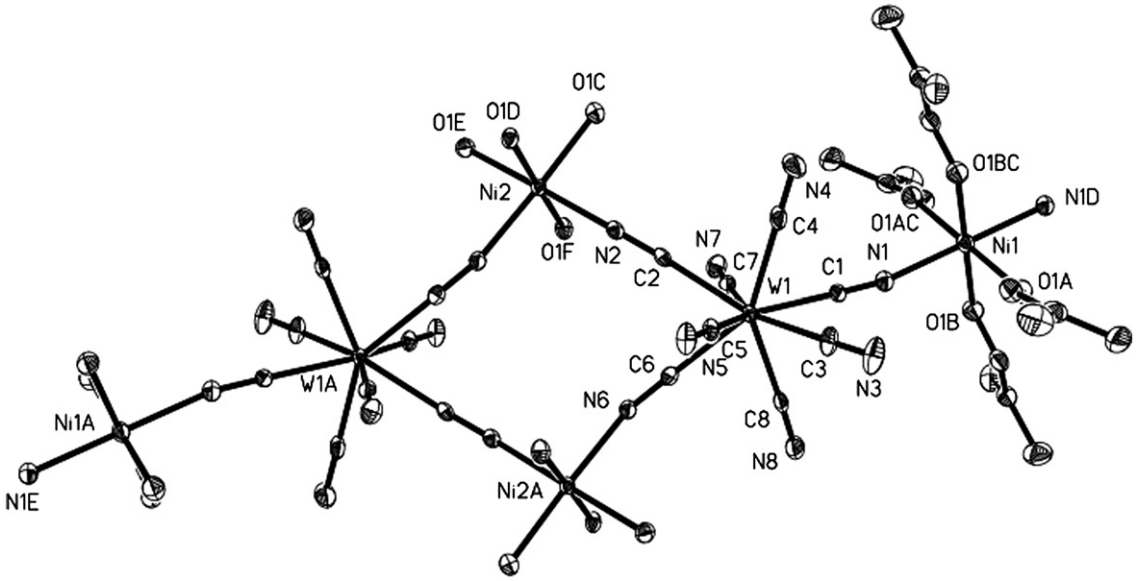


Fig. 2. X-ray structure of **8** illustrating the one-dimensional chain of squares motif present. Thermal ellipsoids are at the 50% probability level and all hydrogen atoms and selected carbon and nitrogen atoms are removed for clarity.

O_{DMF} bond distances range from 2.156(2) to 2.172(2) Å and 2.047(2) to 2.064(2) Å for **5** and **8**, with no discernable trends regarding their relationship to the coordinated cyanides (Table 2). The twisting of the imbedded tetranuclear fragments can be described via the distance of the metal centers from a mean plane defined the atoms present within the $\{M^{V}_{2}(\mu\text{-}CN)_{4}M^{II}_{2}\}$ fragment; the tungsten and manganese centers in **5** are *ca.* ±0.27(1) and ±0.23(2) Å from this plane, while the tungsten and nickel centers in **8** are located at slightly larger and smaller distances [*ca.* ±0.41(2) and ±0.05(4) Å], respectively. As a final means of comparison, the $M^{II}\cdots M^{II}$ and W···W contacts are slightly larger in **5** [6.59(2) and 8.64(2) Å], while those in **8** [6.39(3) and 8.39(2) Å] are smaller, suggesting that the $\{M^{V}_{2}(\mu\text{-}CN)_{4}\text{-}M^{II}_{2}\}$ fragment size depends on the divalent metal centers present.

Significant distortion of the $\{M^{V}_{2}(\mu\text{-}CN)_{4}M^{II}_{2}\}$ fragments is also apparent in the N–M^{II}–N and N–M^{II}–O bond angles present in **5** and **8**. The smallest N–M^{II}–N and largest N–M^{II}–O bond angles are found for **5**, suggesting that M^{II}–N bond distances are related to the electronegativity and radius of the divalent centers present, affording highly distorted $\{M^{V}_{2}(\mu\text{-}CN)_{4}M^{II}_{2}\}$ fragments within the one-dimensional chains (Table 3). The N–M^{II}–N bond angles are more acute in **5** [91.34(7)°] in comparison to those seen for **8** [93.7(1)°], while larger N2–M2–O1C and N2–M2–

O1E bond angles are found for **5** [92.28(6) and 178.93(6)°]. Consistent with expected periodic trends compound **8** has slightly smaller N2–M2–O1C and N2–M2–O1E angles [88.99(9) and 177.65(9)°] in comparison to those seen in **5**.

The remaining [*trans*-$M^{II}(\mu\text{-}NC)_2(DMF)_4]^{2+}$ units in **5** and **8** have M^{II}–N and M^{II}–O bond distances that are comparable to those seen in the $\{M^{V}_2(\mu\text{-}CN)_4M^{II}_2\}$ units. The average M^{II}–N and M^{II}–O bond distances are 2.252(2) and 2.165(2) Å for **5**, while **8** exhibits smaller distances [2.069(3) and 2.060(2) Å] (Table 2). The shortest M^{II}–N bonds are again found for the most electronegative analogues (**8**, Ni^{II}) with larger values found for early metal derivatives (**5**, Mn^{II}). The N1–M1–N1A bond angles are linear while the N1–M1–O bond angles range from 85.90(6) to 94.10(6)° and 87.9(1) to 92.1(1)° for **5** and **8**, respectively (Table 3) [20g,45]. The W(1)···W1A and M2···M2A contacts are 8.644(3) and 6.590(3) Å for **5** while comparatively smaller values [8.394(3) and 6.382(3) Å] are found for **8**.

3.3. Crystallographic studies: two-dimensional sheets

Crystals of **6** and **10** crystallize in the monoclinic $P2_1/n$ and $P2_1/c$ space groups, respectively (Table 1). The neutral, corrugated two-dimensional sheets contain [*cis*-$M^{II}(DMF)_4(\mu\text{-}NC)_2]^{2+}$, [*trans*-$M^{II}(DMF)_4(\mu\text{-}NC)_2]^{2+}$, and three-connected $[M^{V}(CN)_5(\mu\text{-}CN)_3]^{3-}$ units that are linked via cyanides into 12-membered rings in a 4:2:6 ratio (Fig. 2), respectively; the asymmetric unit and 12-membered ring fragments present in **6** are illustrated in Figs. 3 and 4. The 12-membered rings are the basic building units of the corrugated two-dimensional sheets (Fig. 3), with each offset by *ca.* 5 Å and linked via shared [*trans*-$M^{II}(\mu\text{-}NC)_2(DMF)_4]^{2+}$ units to adjacent $[M^{V}(CN)_8]^{3-}$ centers. The ruffled sheets are separated by *ca.* 6.8 [Mn···Mn] and 7.0 Å [Fe···Fe] for **6** and **10**, respectively, and are comparable to those reported (*ca.* 7.0 Å) for structurally related two-dimensional $Mn^{II}_3Mo^{V}_2$ lattices (**11**) [20g,45]. The ring dimensions are *ca.* 10 [W1A···W1E] × 18 Å [W1A···W1B] and 11 [W1···W1A] × 18 [W1···W1E] for **6** and **10**, respectively, being slightly smaller than reported for 2-D $Mn^{II}_3Mo^{V}_2$ (**11**) analogues (*ca.* 9 × 24 Å) [45].

The W–C bond distances and C–W–C angles are within the ranges expected for octacyanometalate networks (Table 2). The W–C bonds vary from 2.158(3) to 2.179(3) Å for **6** and 2.155(6) and 2.177(6) Å for **10**, while the C–W–C bond angles range from 70.60(9) to 148.13(9)° and 70.5(2) to 148.0(2)° for **6** and **10**, respectively; again the tungsten centers have distorted square antiprismatic coordination geometries. The terminal and bridging cyanide W–C–N angles are also nearly linear ranging from 176.2(2) to 179.1(2) and 174.9(4) to 179.7(5)° for **6** and **10**, respectively (Table 3).

In **6** and **10** the two-dimensional lattices consist of 12-membered rings that are composed of [*trans*-$M^{II}(\mu\text{-}NC)_2(DMF)_4]^{2+}$ and [*cis*-$M^{II}(\mu\text{-}NC)_2(DMF)_4]^{2+}$ units. The [*trans*-$M^{II}(\mu\text{-}NC)_2(DMF)_4]^{2+}$ units have M–N and M–O bond distances that are slightly longer than those seen in the [*cis*-$M^{II}(\mu\text{-}NC)_2(DMF)_4]^{2+}$ fragments (Table 2). The M–N and M–O bond distances in the [*trans*-$M^{II}(\mu\text{-}NC)_2(DMF)_4]^{2+}$ fragments are 2.232(2) and 2.154(4) Å, while those for the [*cis*-$M^{II}(\mu\text{-}NC)_2(DMF)_4]^{2+}$ units are slightly shorter, being 2.217(2) and 2.170(4) Å for **6** and **10**, respectively; similar bond distance trends are observed in **5**, **7**, and **8**.

The N–M–N and O–M–O bond angles also exhibit structure-dependent changes depending on their location within the 2-D sheets (Table 3). For [*trans*-$M^{II}(\mu\text{-}NC)_2(DMF)_4]^{2+}$ fragments, the symmetry related N–M–N angles are 180°, while the O–M–O angles range from 87.4(3) to 180° for **6** and 88.6(1) to 180° for **10**. In comparison, the N–M–N and O–M–O angles for the [*cis*-$M^{II}(\mu\text{-}NC)_2(DMF)_4]^{2+}$ fragments range between 88.57(7) and 169.66(6)° and 86.8(1) and 173.2(2)° for **6** and **10**, respectively, being close to those seen for structurally related $Mn^{II}_3Mo^{V}_2$ (**11**) lattices [20g,45].

3.4. Crystallographic studies of 9

Crystals of **9** are in the monoclinic $P2_1/c$ space group and crystallize as trimetallic salts of $[Fe^{II}(DMF)_6]_2[W^{IV}(CN)_8]$ stoichiometry (Table 1). The W–C bond distances range from 2.167(3) to 2.181(3) Å while the C–W–C bond angles are between 70.9(2) and 145.3(1)°; the W–C–N angles are nearly linear, ranging from 178.7(3) to 179.3(3)° (Fig. 5). The Fe–O lengths are all slightly different, ranging from 1.975(2) [Fe1–O1A] to 2.196(2) Å [Fe2–O1F], while the O–Fe–O bond angles are nearly octahedral, ranging from 87.49(9) to 93.05(9)° [O1D–Fe2–O1F and O1A–Fe1–O1B]. The $[Fe^{II}(DMF)_6]^{2+}$ and $[W^{IV}(CN)_8]^{4-}$ ions are well-separated and are not related by rotational symmetry; the Fe1···Fe2, Fe1···W1, and Fe2···W1 contacts are 9.66(2), 7.16(3), and 8.88(3) Å, respectively (see Fig. 6).

3.5. Magnetic studies

Magnetic studies of suggest that the magnetic exchange interactions present in the $Mn^{II}(\mu\text{-}NC)W^{V}$ units of **5** and **6** are antiferromagnetic [20g]. The room temperature χT values for **5** and **6** [13.73 and 14.15 emu K mol^{-1}] are close to the spin-only value (13.88 emu K mol^{-1}) expected for a 3:2 ratio of non-interacting W^{V} ($S = 1/2$; $g = 2$) and Mn^{II} ($S = 1/2$; $g = 2$) centers. The sign of the local exchange interactions can often be predicted from the shape of the χT versus T curve. A shallow minimum is often found when short-range antiferromagnetic correlations compensate spins [49] and such minima are observed at *ca.* 75 and 200 K for **5** and **6**, respectively. At lower temperatures the χT product monotonically increases reaching maximum values of 24.82 and 151.2 emu K mol^{-1} at 3.7 and 10.0 K, with χT again decreasing towards minimum values of 23.41 and 99.7 emu K mol^{-1} at 1.8 and 5 K, for **5** and **6**, respectively. Fitting of the χ^{-1} versus T data (at $H_{dc} = 1$ kG) with the Curie–Weiss expression affords negative Weiss constants (−0.66 K for **5** and −4.78 K for **6**) ver-

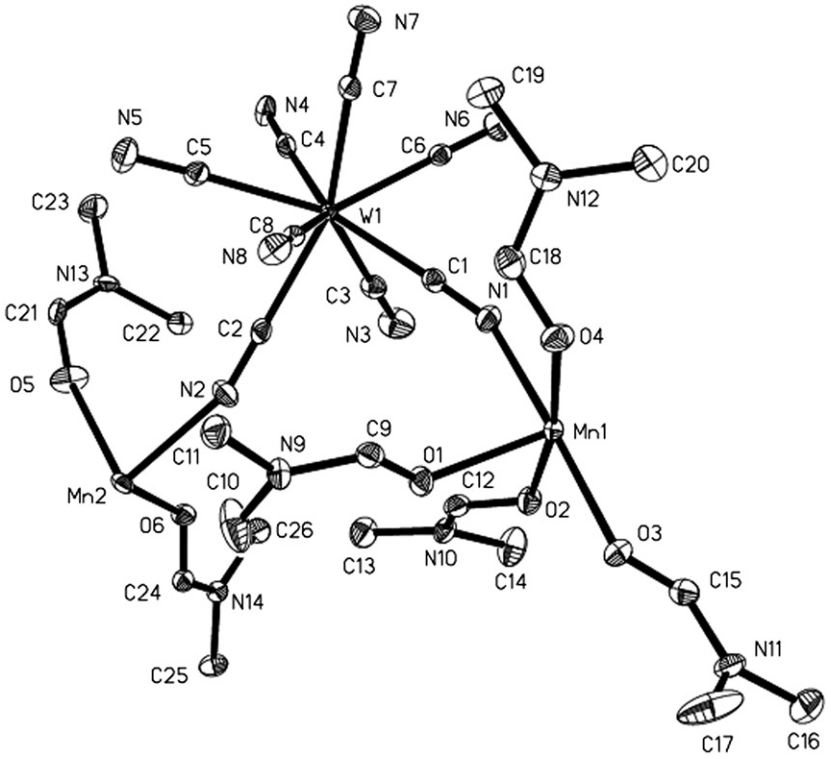


Fig. 3. Asymmetric unit of **6**. Thermal ellipsoids are at the 50% level and all hydrogen atoms are removed for clarity.

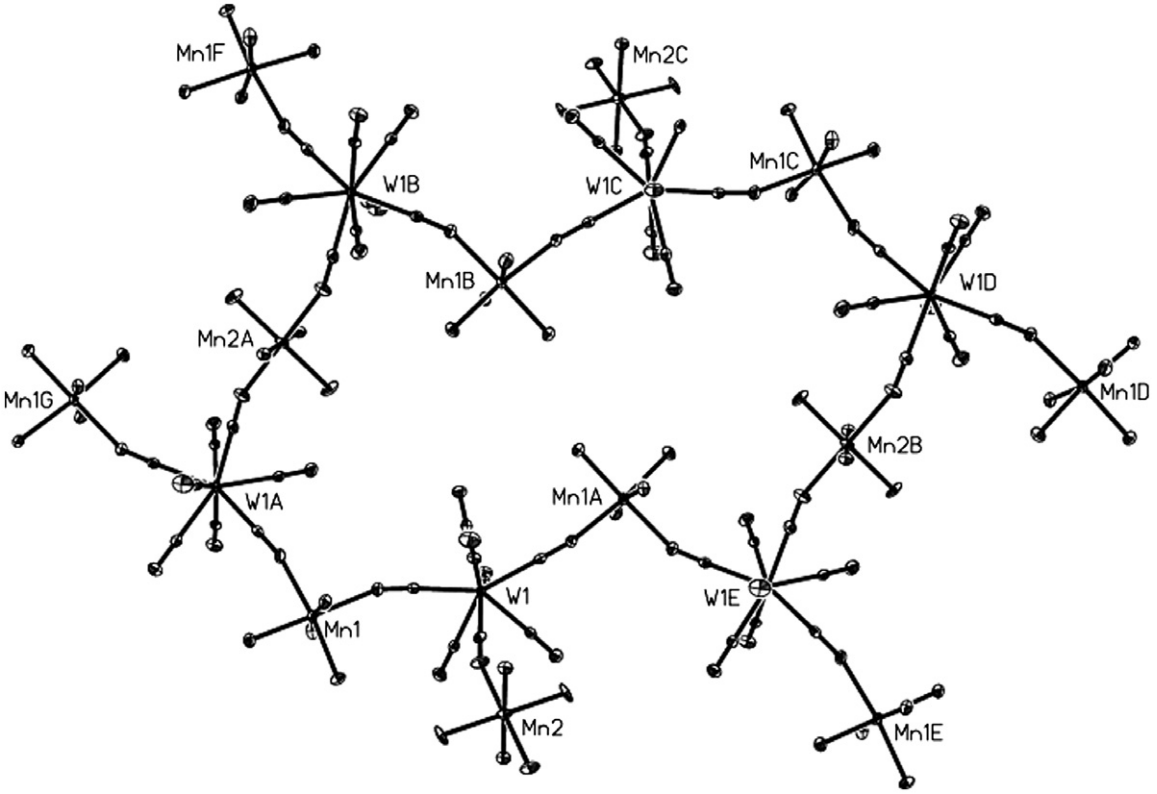


Fig. 4. X-ray structure of **6** illustrating the 12-membered rings present. Thermal ellipsoids are at the 50% level, DMF ligands are truncated, and all hydrogen atoms are removed for clarity.

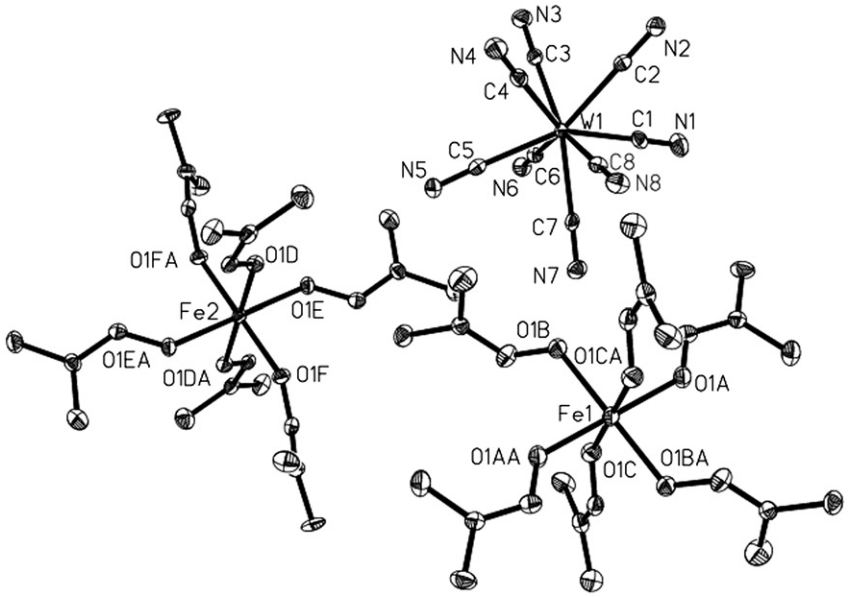


Fig. 5. X-ray structure of **9**. Thermal ellipsoids are at the 50% probability level and all hydrogen atoms are removed for clarity.

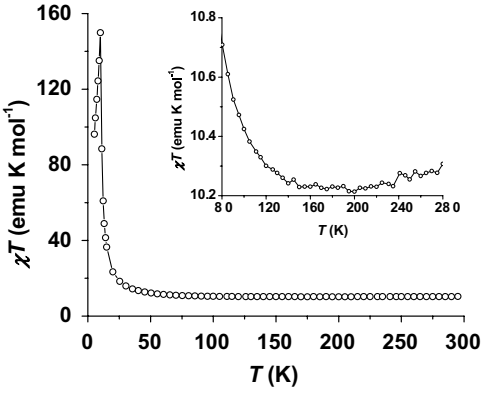


Fig. 6. Temperature dependence of χT for **6** at $H_{dc} = 1$ kG.

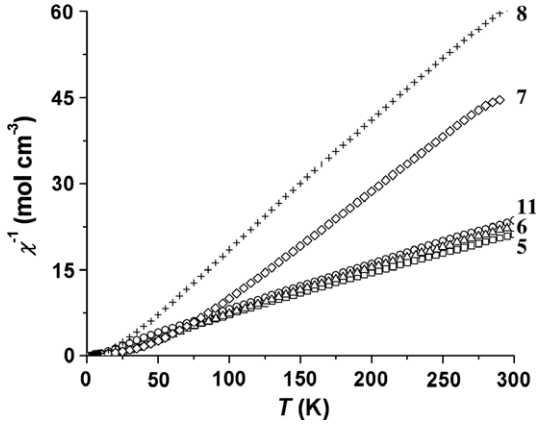


Fig. 7. Temperature dependence of the reciprocal susceptibility for **5**–**8** and **11** at $H_{dc} = 1$ kG.

ifying that local antiferromagnetic interactions are present. As judged from the divergence of the zero-field-cooled and field-cooled magnetization curves ($H_{dc} = 2$ G) we conclude that $T_N = 8$ K for **6** (Fig. 8), while **5** does not appear to exhibit long-range magnetic ordering above 1.8 K.

The field dependence of the magnetization at 2 K further indicates that the Mn^{II} and W^{V} ions in **5** and **6** engage in antiferromagnetic exchange interactions. The experimental saturation magnetization values ($H_{dc} = 70$ kG) for **5** and **6** are 72.3 and 73.4 kG cm^3 mol^{-1} and are close to the expected value of 72.61 kG cm^3 mol^{-1} assuming that $g = 2$. Both **5** and **6** exhibit closed hysteresis loops and small coercive fields (Fig. 9) consistent with the presence of isotropic metal ions.

For **7** and **8** cyanide-mediated superexchange within the $Ni^{II}(\mu\text{-NC})M^{V}$ units is expected to be ferromagnetic (Ni^{II}, $S = 1$) assuming that the magnetic orbitals are orthogonal and that Goodenough–Kanamori rules are applicable [1–8h,50]. Using crushed single crystals of **7** and **8** the room-

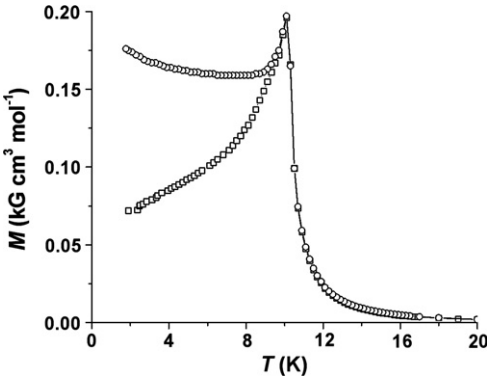


Fig. 8. Temperature dependence of zero-field-cooled (□) and field-cooled (○) magnetization for **6** ($H_{dc} = 2$ G).

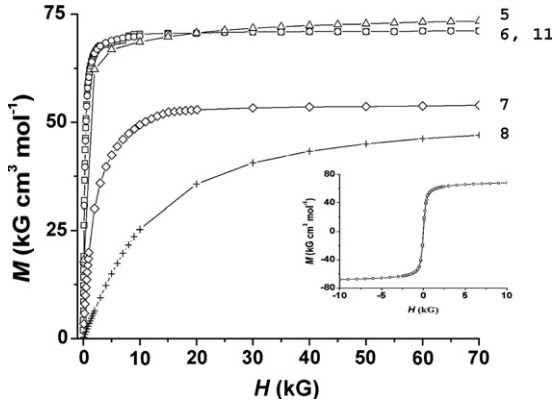


Fig. 9. Field dependence of the magnetization for **5**–**8** and **11** at 2 K. Inset: Hysteresis of **6** at 2 K.

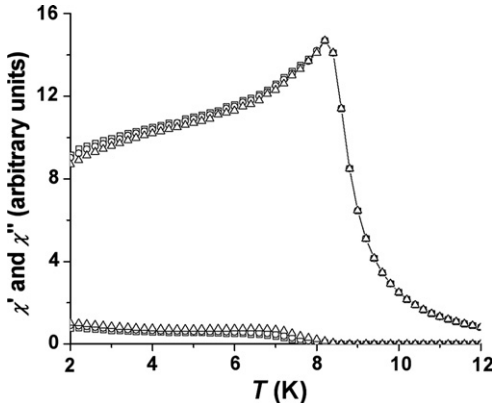


Fig. 10. Temperature dependence of the real (χ', top) and imaginary components (χ'', bottom) of the ac susceptibility for **6** ($H_{dc} = 0$ Oe; $H_{ac} = 3$ Oe) at 1 (○), 10 (△), and 100 (□) Hz.

temperature χT values [6.43 and 5.32 emu K mol^{-1}] are near the expected (5.92 emu K mol^{-1}, $g_{Ni} = 2.2$ assumed) value for a 3:2 ratio of non-interacting Ni^{II} ($S = 1$) and M^{V} ($S = 1/2$; Mo, W) spin centers. The temperature dependence of the χT product ($H_{dc} = 1$ kG) suggests that the Ni^{II} and M^{V} (Mo^{V} and W^{V}) centers undergo short-range ferromagnetic exchange interactions, with χT increasing as a function of decreasing temperature, reaching maximum values [36.72 emu K mol^{-1} for **7** and 50.03 emu K mol^{-1} for **8**] at 19 and 3.8 K for **7** and **8**, respectively. Fitting the χ^{-1} versus T data via the Curie-Weiss expression affords positive Weiss constants (47.56 K for **7** and 11.87 K for **8**) verifying that local ferromagnetic interactions are present (Fig. 7) [20g].

The field dependence of the magnetization data suggests that the cyanide-bridged transition metal centers present in **7** and **8** are ferromagnetically coupled at 1.8 K and large H_{dc} (Fig. 9). Assuming that $g = 2$ the expected saturation magnetization value is 48.03 kG cm^3 mol^{-1} and is between the experimental values found for **7** and **8** [53.9 and 47.0 kG cm^3 mol^{-1}]. Lastly the field dependence of the magnetization indicates that **7** and **8** exhibit closed hysteresis loops with negligible coercive fields at 1.8 K [20g].

ac susceptibility measurements suggest that χ'' is frequency-dependent for **6** despite the presence of isotropic metal ions, while **5**, **7**, and **8** exhibit no frequency-dependent behavior ($H_{dc} = 0$ G; $H_{ac} = 3.5$ G). Using freshly-prepared, crushed crystals of **5**, we find that χ'' is invariant with respect to changing frequency, in stark contrast to reports claiming that structurally-related 1-D $[Mn^{II}(bpy)_2]_3[W^{V}(CN)_8]_2$ lattices exhibit frequency-dependent χ'' maxima [23,24]. However for samples of **5** (*ca.* 2 weeks) unsymmetrical and broad frequency-dependent maxima (Fig. 10) are observed in plots of χ'' versus T, that appear to increase in intensity with respect to time and increasing temperature; the frequency-dependent peaks in χ'' are qualitatively similar to those found for Tang's 1-D chains, **6**, and a recently reported 2-D $[Mn^{II}(DMF)_4]_3[Mo^{V}(CN)_8]_2$ lattice (**11**) [23,24,45]. The unsymmetrical χ'' peak is suggestive of multiple relaxation processes, the presence of multiple magnetic phases, and/or that **5**, **6**, and $[Mn^{II}(DMF)_4]_3[Mo^{V}(CN)_8]_2$ are unstable under the conditions of the ac susceptibility measurements [20g]. For freshly prepared samples of **5**, **7**, and **8** we tentatively propose that they exhibit incipient magnetic ordering in the presence of large H_{dc} fields.

3.6. Chemical and thermal stability of networks

Heating crystalline samples of **5** and **6** decreases the intensity of the DMF $\nu_{C=O}$ stretching absorption while the energies and intensities of the ν_{CN} absorptions remain unchanged. We previously reported that heated samples of **11** afford additional magnetic phases ($T_N \sim 21$ K), that are not due to linkage isomerism [2c,51], but rather desolvation followed by aggregation [20h,45]. Unfortunately all attempts to structurally characterize the microcrystalline and amorphous solids precipitated from hot reaction mixtures containing crystals of **5**–**8** or **11** have consistently met with failure.

Furthermore, the isolation of one- and two-dimensional phases (**5** and **6**) from essentially the same reaction conditions (at or near 300 K) suggests that the M^{II}(μ-NC)M^{V} linkages can be ruptured to form a variety of aggregated products under relatively mild conditions. At lower reaction temperatures (20 °C) and short reaction times a 1-D chain of squares lattice (**5**) is obtained, while longer reaction times and higher temperatures (28 °C) appear to afford 2-D phases (**6**); to date only 2-D lattices have been obtained when using **1** as a starting material. In the absence of counterions ($HNBu_3^+$ and OTs^-) crystals of **5** do not transform into **6** when stored at room temperature (28 °C) in DMF over 3 weeks, in addition to small quantities of DMF-insoluble amorphous precipitates. However, in the presence of counterions (DMF solution, 28 °C) **5** transforms into **6** over a period of weeks, as judged via indexing several crystals removed from the reaction mixture. In addition, wet DMF mixtures of **1** or **2** in the pres-

ence of manganese(II) tosylate exclusively affords 2-D phases in addition to amorphous precipitates. Apparently wet DMF accelerates the transformation of **5** into **6** and attempts to insert other metal centers (e.g. Fe^{II}, Co^{II}, Ni^{II}) into the lattice affords intractable precipitates. To date only Mn^{II} analogues appear to undergo slow one- to two-dimensional phase changes. We propose that formation **5** precedes **6**, being highly dependent on the quantity of water and counterions present. In the presence of counterions we presume that for **5**, labilization of coordinated DMF and rupture of the $Mn^{II}(\mu\text{-NC})M^{V}$ linkages afford soluble species that undergo aggregation, gradually transforming the chains into the two-dimensional corrugated sheets found in **6** [46e].

4. Conclusions

We have described the synthesis, structural, infrared, and magnetic characterization of a trimetallic salt and several one- and two-dimensional networks derived from octacyanometalate(V) centers. Coordinated DMF appears to limit the number of cyano linkages formed and the dimensionality of the resulting lattices. The one-dimensional chains appear to exhibit short-range magnetic interactions but no spontaneous magnetic ordering above 1.8 K. Surprisingly, conversion of one- to two-dimensional crystalline phases in the presence of counterions occurs in solution, while heating of crystalline samples introduces an additional magnetic phases without linkage isomerism. Two-dimensional phases containing Mn^{II} centers appear to be the sole product when wet DMF is used as a reaction solvent. The experimental evidence suggests that coordinated DMF ligands are labile and the $M^{II}(\mu\text{-NC})M^{V}$ linkages are susceptible to fragmentation.

Acknowledgements

S.M.H. gratefully acknowledges the donors of the American Chemical Society Petroleum Research Fund (PRF 38388-G3), the University of Kentucky Summer Faculty Research Fellow, and the National Science Foundation Research Experience for Undergraduates (CHE-0097668) programs for financial support. We are indebted to the Frederick Seitz Materials Research Laboratory at the University of Illinois at Urbana-Champaign for access to their Magnetometer facility. G.T.Y. thanks the National Science Foundation (CHE-0210395) for partial financial support.

Appendix A. Supplementary material

CCDC 621773, 621774, 621775, 621776 and 621777 contain the supplementary crystallographic data for this paper. These data can be obtained free of charge via http://www.ccdc.cam.ac.uk/conts/retrieving.html, or from the Cambridge Crystallographic Data Centre, 12 Union Road, Cambridge CB2 1EZ, UK; fax: (+44) 1223-336-033; or e-mail: deposit@ccdc.cam.ac.uk. Supplementary data associated with this article can be found, in the online version, at doi:10.1016/j.poly.2007.01.049.

References

[1] W.R. Entley, G.S. Girolami, Science 268 (1995) 397.
[2] (a) M. Verdaguer, A. Bleuzen, V. Marvaud, J. Vaissermann, M. Seuleiman, C. Desplanches, A. Scuiller, C. Train, R. Garde, G. Gelly, C. Lomenech, I. Rosenman, P. Veillet, C. Cartier, F. Villain, Coord. Chem. Rev. 190–192 (1999) 1023;
(b) K.R. Dunbar, R.A. Heintz, Prog. Inorg. Chem. 45 (1997) 283;
(c) A.G. Sharpe, The Chemistry of Cyano Complexes of the Transition Metals, Academic Press, New York, 1976.
[3] S. Ferlay, T. Mallah, R. Ouahès, P. Veillet, M. Verdaguer, Nature 378 (1995) 701.
[4] S.M. Holmes, G.S. Girolami, J. Am. Chem. Soc. 121 (1999) 5593.
[5] Ø. Hatlevik, W.E. Buschmann, J. Zhang, J.L. Manson, J.S. Miller, Adv. Mater. 11 (1999) 914.
[6] D. Gatteschi, O. Kahn, J.S. Miller, F. Palacio (Eds.), Magnetic Molecular Materials, Kluwer, Dordrecht, 1991.
[7] C.P. Landee, D. Melville, J.S. Miller, in: D. Gatteschi, O. Kahn, J.S. Miller, F. Palacio (Eds.), Magnetic Molecular Materials, NATO ASI Series E, vol. 198, Plenum, New York, 1991.
[8] (a) L.M.C. Beltran, J.R. Long, Acc. Chem. Res. 38 (2005) 325;
(b) J.J. Sokol, A.G. Hee, J.R. Long, J. Am. Chem. Soc. 124 (2002) 7656;
(c) C.P. Berlinguette, D. Vaughn, C. Cañada-Vilalta, J.R. Galán-Mascarós, K.R. Dunbar, Angew. Chem., Int. Ed. 42 (2003) 1523;
(d) A.V. Palii, S.M. Ostrovsky, S.I. Klokishner, B.S. Tsukerblat, C.P. Berlinguette, K.R. Dunbar, J.R. Galán-Mascarós, J. Am. Chem. Soc. 126 (2004) 16860;
(e) E.J. Schelter, A.V. Prosvirin, K.R. Dunbar, J. Am. Chem. Soc. 126 (2004) 15004;
(f) S. Wang, J.-L. Zuo, H.-C. Zhou, H.J. Choi, Y. Ke, J.R. Long, X.-Z. You, Angew Chem., Int. Ed. 43 (2004) 5940;
(g) K.R. Dunbar, E.J. Schelter, A.V. Palii, S.M. Ostrovsky, V.Y. Mirovitski, J.M. Hudson, M.A. Omary, S.I. Klokishner, B.S. Tsukerblat, J. Phys. Chem. A 107 (2003) 11102;
(h) E.J. Schelter, A.V. Prosvirin, W.M. Reiff, K.R. Dunbar, Angew. Chem., Int. Ed. 42 (2004) 4912;
(i) H. Miyasaka, H. Takahashi, T. Madanbashi, K.-I. Sugiura, R. Clérac, H. Nojiri, Inorg. Chem. 44 (2005) 5969;
(j) M. Ferbinteanu, H. Miyasaka, W. Wernsdorfer, K. Nakata, K.-I. Sugiura, M. Yamashita, C. Coulon, R. Clérac, J. Am. Chem. Soc. 127 (2005) 3090;
(k) D. Li, S. Parkin, G. Wang, G.T. Yee, A.V. Prosvirin, S.M. Holmes, Inorg. Chem. 44 (2005) 4903;
(l) D. Li, R. Clérac, S. Parkin, G. Wang, G.T. Yee, S.M. Holmes, Inorg. Chem. 45 (2006) 5251;
(m) D. Li, R. Clérac, S. Parkin, G. Wang, G.T. Yee, S.M. Holmes, Inorg. Chem. 45 (2006) 7569;
(n) D. Li, S. Parkin, G. Wang, G.T. Yee, R. Clérac, W. Wernsdorfer, S.M. Holmes, J. Am. Chem. Soc. 128 (2006) 4214;
(o) K. Park, S.M. Holmes, Phys. Rev. B (in press);
(p) D. Li, S. Parkin, R. Clérac, G. Wang, G.T. Yee, S.M. Holmes, Eur. J. Inorg. Chem., doi:10.1002/ejic.200600819;
(q) D. Li, C. Ruschman, S. Parkin, R. Clérac, S.M. Holmes, Chem. Commun. 4036 (2006);
(r) D. Li, S. Parkin, G. Wang, G.T. Yee, S.M. Holmes, Inorg. Chem. 45 (2006) 1951.
[9] (a) L.M. Toma, R. Lescouëzec, F. Lloret, M. Julve, M. Verdaguer, Inorg. Chem. 41 (2002) 818;
(b) R. Lescouëzec, J. Vaissermann, C. Ruiz-Pérez, F. Lloret, R. Carrasco, M. Julve, M. Verdaguer, Y. Dromzee, D. Gatteschi, W.

Wernsdorfer, Angew. Chem., Int. Ed. 42 (2003) 1483;
(c) S. Wang, J.-L. Zho, S. Gao, Y. Song, H.-C. Zhou, Y.-Z. Zhang, X.-Z. You, J. Am. Chem. Soc. 126 (2004) 8900.
[10] (a) O. Sato, Acc. Chem. Res. 36 (2003) 692, and references therein;
(b) Y. Arimoto, S. Ohkoshi, Z.J. Zhong, H. Seino, Y. Mizobe, K. Hashimoto, J. Am. Chem. Soc. 125 (2003) 9240;
(c) T. Yokoyama, K. Okamoto, T. Ohta, S.-I. Ohkoshi, K. Hashimoto, Phys. Rev. 65B (2001) 1;
(d) S. Ohkoshi, K. Hashimoto, J. Am. Chem. Soc. 121 (1999) 10591;
(e) O. Sato, T. Iyoda, A. Fujishima, K. Hashimoto, Science 272 (1996) 704;
(f) O. Sato, Y. Einaga, T. Iyoda, A. Fujishima, K. Hashimoto, Inorg. Chem. 38 (1999) 4405;
(g) N. Shimamoto, S.-I. Ohkoshi, O. Sato, K. Hashimoto, Inorg. Chem. 41 (2002) 678;
(h) A. Bleuzen, C. Lomenech, V. Escax, F. Villain, F. Varret, C. Cartier dit Moulin, M. Verdaguer, J. Am. Chem. Soc. 122 (2000) 6648;
(i) C. Cartier dit Moulin, F. Villain, A. Bleuzen, M. Arrio, P. Sainctavit, C. Lomenech, V. Escax, F. Baudelet, E. Dartyge, M. Verdaguer, J. Am. Chem. Soc. 122 (2000) 6653;
(j) S. Ohkoshi, S. Yorozu, O. Sato, T. Iyoda, A. Fujishima, K. Hashimoto, Appl. Phys. Lett. 70 (1977) 1040;
(k) S. Ohkoshi, Y. Einaga, A. Fujishima, K. Hashimoto, J. Electroanal. Chem. 473 (1999) 245;
(l) S. Ohkoshi, M. Mizuno, G. Hung, K. Hashimoto, J. Phys. Chem. 40 (2000) 9365;
(m) Z.-Z. Gu, O. Sato, T. Iyoda, K. Hashimoto, A. Fujishima, J. Phys. Chem. 100 (1996) 18289;
(n) Z.-Z. Gu, O. Sato, T. Iyoda, K. Hashimoto, A. Fujishima, Chem. Mater. 9 (1997) 1092;
(o) S.-I. Ohkoshi, K. Hashimoto, J. Photochem. Photobiol. C: Photochem. Rev. 2 (2001) 71;
(p) S. Ohkoshi, N. Machida, J. Zhong, Z.J. Hashimoto, Synth. Met. 122 (2001) 523;
(q) G. Rombaut, M. Verelst, S. Golhen, L. Ouahab, C. Mathonière, O. Kahn, Inorg. Chem. 40 (2001) 1151.
[11] R. Billing, A.J. Vogler, J. Photochem. Photobiol. A: Chem. 103 (1997) 239.
[12] S.I. Ali, K. Majid, Thermochim. Acta 317 (1998) 141.
[13] A.K. Sra, M. Andruh, O. Kahn, S. Golhen, L. Ouahab, J.V. Yakhmi, Angew. Chem., Int. Ed. 38 (1999) 2606.
[14] G. Rombaut, S. Golhen, L. Ouahab, C. Mathonière, O. Kahn, J. Chem. Soc., Dalton Trans. 3609 (2000).
[15] (a) A. Yuan, J. Zou, B. Li, Z. Zha, C. Duan, Y. Liu, Z. Xu, S. Keizer, Chem. Commun. 1297 (2000);
(b) M. Ohba, N. Fukita, H. Ōkawa, J. Chem. Soc., Dalton Trans. 1733 (1997);
(c) H. Kou, W. Bu, D. Liao, Z. Jiang, S. Yan, Y. Fan, G. Wang, J. Chem. Soc., Dalton Trans. 4161 (1998);
(d) M. Ohba, N. Usuki, N. Fukita, H. Ōkawa, Inorg. Chem. 37 (1998) 3349;
(e) N. Fukita, M. Ohba, H. Ōkawa, K. Matsuda, H. Iwamura, Inorg. Chem. 37 (1998) 842;
(f) S. Zhang, D. Fu, W. Sun, Z. Hu, K. Yu, W. Tang, Inorg. Chem. 39 (2000) 1142;
(g) N. Usuki, M. Yamada, M. Ohba, H. Ōkawa, J. Solid St. Chem. 159 (2001) 328;
(h) M. Ohba, H. Ōkawa, N. Fukita, Y. Mashimoto, J. Am. Chem. Soc. 119 (1997) 1011;
(i) F. Thétiot, S. Triki, J.S. Pala, New J. Chem. 26 (2002) 196;
(j) H.-Z. Kou, J.-K. Tang, D.-Z. Liao, S. Gao, P. Cheng, Z.-H. Jiang, S.-P. Yan, G.-L. Wang, B. Chansou, J. Tuchagues, Inorg. Chem. 40 (2001) 4839.
[16] (a) W.R. Bucknall, W. Wardlaw, J. Chem. Soc. 2981 (1927);
(b) W.U. Malik, S.I. Ali, Bull. Chem. Soc. Jpn. 1306 (1961);
(c) W.U. Malik, S.I. Ali, Bull. Chem. Soc. Jpn. 1310 (1961);
(d) G.F. McKnight, G.P. Haight, Inorg. Chem. 12 (1973) 3007.
[17] J.M. Herrera, D. Armentano, G. de Munno, F. Lloret, M. Julve, M. Verdaguer, New J. Chem. 27 (2003) 128.
[18] (a) J.M. Herrera, A. Bleuzen, Y. Dromzée, M. Julve, F. Lloret, M. Verdaguer, Inorg. Chem. 42 (2003) 7052;
(b) S. Willemin, J. Larionova, R. Clérac, B. Donnadieu, B. Henner, X.F. Le Goff, C. Guérin, Eur. J. Inorg. Chem. 1866 (2003).
[19] A.K. Sra, G. Rombaut, F. Lahitête, S. Golhen, L. Ouahab, C. Mathonière, J.V. Yakhmi, O. Kahn, New J. Chem. 24 (2000) 871.
[20] (a) Y. Arimoto, S. Ohkoshi, Z.J. Zhong, H. Sieno, Y. Mizobe, K. Hashimoto, J. Am. Chem. Soc. 125 (2003) 9240;
(b) A. Bleuzen, C. Lomenech, V. Escax, F. Villain, F. Varret, C. Cartier dit Moulin, M. Verdaguer, J. Am. Chem. Soc. 122 (2000) 6648;
(c) D. Li, L. Zheng, X. Wang, J. Huang, S. Gao, W. Tang, Chem. Mater. 15 (2003) 2094;
(d) D. Li, T. Okamura, W. Sun, N. Ueyama, W. Tang, Cryst. Struct. Commun. C58 (2002) m280;
(e) D. Li, D. Yang, S. Li, W. Tang, Inorg. Chem. Commun. 5 (2002) 791;
(f) R. Podgajny, Y. Dromzée, K. Kruczała, B. Sieklucka, Polyhedron 20 (2001) 685;
(g) F. Chang, H.-L. Sun, H.-Z. Kou, S. Gao, Inorg. Chem. Commun. 5 (2002) 660;
(h) W. Meske, D.Z. Babel, Anorg. Allg. Chem. 625 (1999) 51;
(i) A.K. Sra, G. Rombaut, F. Lahitête, S. Golhen, L. Ouahab, C. Mathonière, J.V. Yakhmi, O. Kahn, New J. Chem. 24 (2000) 871;
(j) R. Billing, A.J. Vogler, J. Photochem. Photobiol. A: Chem. 103 (1997) 239;
(k) S.I. Ali, K. Majid, Thermochim. Acta 317 (1998) 141;
(l) A.K. Sra, M. Andruh, O. Kahn, S. Golhen, L. Ouahab, J.V. Yakhmi, Angew. Chem., Int. Ed. 38 (1999) 2606;
(m) G. Rombaut, S. Golhen, L. Ouahab, C. Mathonière, O. Kahn, J. Chem. Soc., Dalton Trans. (2000) 3609;
(n) R. Kania, K. Lewinski, B. Sieklucka, Dalton Trans. (2003) 1033;
(o) J.M. Herrera, V. Marvaud, M. Verdaguer, J. Marrot, M. Kalisz, C. Mathonière, Angew. Chem., Int. Ed. 43 (2004) 5467;
(p) J.R. Withers, C. Ruschman, P. Bojang, S. Parkin, S.M. Holmes, Inorg. Chem. 44 (2005) 352;
(q) S.-I. Ohkoshi, Y. Einaga, A. Fujishima, K. Hashimoto, J. Electroanal. Chem. 473 (1999) 245;
(r) S.-I. Ohkoshi, M. Mizuno, G. Hung, K. Hashimoto, J. Phys. Chem. 40 (2000) 9365;
(s) Z.-Z. Gu, O. Sato, T. Iyoda, K. Hashimoto, A. Fujishima, J. Phys. Chem. 100 (1996) 18289;
(t) Z.-Z. Gu, O. Sato, T. Iyoda, K. Hashimoto, A. Fujishima, Chem. Mater. 9 (1997) 1092;
(u) S.-I. Ohkoshi, K. Hashimoto, J. Photochem. Photobiol. C: Photochem. Rev. 2 (2001) 71;
(v) S.-I. Ohkoshi, N. Machida, Z.J. Zhong, K. Hasimoto, Synth. Met. 122 (2001) 523;
(w) G. Rombaut, M. Verelst, S. Golhen, L. Ouahab, C. Mathonière, O. Kahn, Inorg. Chem. 40 (2001) 1151;
(x) J.R. Withers, C. Ruschman, S. Parkin, S.M. Holmes, Polyhedron 24 (2005) 1845.
[21] (a) S. Willemin, J. Larionova, R. Clérac, B. Donnadieu, B. Henner, X.F. Le Goff, C. Guérin, Eur. J. Inorg. Chem. (2003) 1866;
(b) B. Sieklucka, J. Szklarzewicz, T.J. Kemp, W. Errington, Inorg. Chem. 39 (2000) 5156;
(c) J. Larionova, R. Clérac, B. Donnadieu, S. Willemin, C. Guérin, Cryst. Growth Des. 3 (2003) 267.
[22] (a) Y. Song, P. Zhang, X.-M. Ren, X.-F. Shen, Y.-Z. Li, X.-Z. You, J. Am. Chem. Soc. 127 (2005) 3708;
(b) Z.J. Zhong, H. Seino, Y. Mizobe, M. Hidai, A. Fujishima, S. Ohkoshi, K. Hashimoto, J. Am. Chem. Soc. 122 (2000) 2952;
(c) J. Larionova, M. Gross, H.A. Pilkington, H. Stoeckli-Evans, H.U. Güdel, S. Decurtins, Angew. Chem., Int. Ed. 39 (2000) 1605;
(d) F. Bonadio, M. Gross, H. Stoeckli-Evans, S. Decurtins, Inorg. Chem. 41 (2002) 5891;

(e) Z.J. Zhong, H. Seino, Y. Mizobe, M. Hidai, M. Verdaguer, S. Ohkoshi, K. Hashimoto, Inorg. Chem. 39 (2000) 5095;
(f) Unpublished results;
(g) See the Supporting Section;
(h) E. Ruiz, G. Rajaraman, S. Alvarez, B. Gillon, J. Stride, R. Clérac, J. Larionova, S. Decurtins, Angew. Chem., Int. Ed. 44 (2005) 2711.
[23] D. Li, L. Zheng, Y. Zhang, J. Huang, S. Gao, W. Tang, Inorg. Chem. 42 (2003) 6123.
[24] D. Li, S. Gao, L. Zhong, W. Tang, J. Chem. Soc., Dalton Trans. 2805 (2002).
[25] S.M. Holmes, S.G. McKinley, G.S. Girolami, P.S. Szalay, K.R. Dunbar, Inorg. Synth. 33 (2002) 91.
[26] J.G. Leipoldt, L.D. Bok, P.J. Cilliers, Z. Anorg. Allg. Chem. 409 (1974) 343.
[27] N.H. Furman, C.O. Miller, P.G. Arvan, L.F. Audrieth, Inorg. Synth. 3 (1950) 160.
[28] L.D. Bok, J.D. Leipoldt, S.S. Basson, Z. Anorg. Allg. Chem. 415 (1975) 81.
[29] R.L. Carlin, Magnetochemistry, Springer-Verlag, New York, 1986.
[30] O. Kahn, Molecular Magnetism, VCH, New York, 1993.
[31] Z. Otwinowski, W. Minor, Methods Enzymol. 276 (1997) 307.
[32] (a) G.M. Sheldrick, SADABS – An Empirical Absorption Correction Program. Bruker Analytical X-Ray Systems; Madison, Wisconsin, 1996;
(b) G.M. Sheldrick, SHELX-97. Programs for Crystal Structure Solution and Refinement, University of Gottingen, Germany, 1997.
[33] International Tables for Crystallography vol. C: Kluwer Academic Publishers, Dordrecht, The Netherlands, 1992.
[34] (a) M. Bogdanov, R. Grybos, A. Samotus, K. Bogolitsyn, Trans. Met. Chem. Dordrecht 18 (1993) 599;
(b) C.R. Dennis, S.S. Basson, J.G. Leipoldt, Polyhedron 2 (1983) 1357;
(c) D. Li, S. Gao, L. Zheng, K. Yu, W. Tang, New. J. Chem. 26 (2002) 1190;
(d) A. Marchaj, A. Plesinski, Z. Stasicka, Rocz. Chem. 50 (1976) 1239.
[35] (a) W.L. Waltz, A.W. Adamson, P.D. Fleischauer, J. Am. Chem. Soc. 89 (1967) 3923;
(b) K.R. Butter, T.J. Kemp, B. Sieklucka, A. Samotus, J. Chem. Soc., Dalton Trans. 1217 (1986);
(c) S. Zofia, B. Hanna, Rocz. Chem. 48 (1974) 389;
(d) S.I. Zofia, Rocz. Chem. 47 (1973) 1993;
(e) G.W. Gray, J.T. Spence, Inorg. Chem. 10 (1971) 2751;
(f) Unpublished results.
[36] K. Nakamoto, Infrared and Raman Spectra of Inorganic and Coordination Compounds, Part B, Fifth ed., Wiley, New York, 1997, pp. 54–58 and 105–116.
[37] (a) Y. Arimoto, S. Ohkoshi, Z.J. Zhong, H. Seino, Y. Mizobe, K. Hashimoto, Chem. Lett. 832 (2002);
(b) Y. Song, S. Ohkoshi, Y. Arimoto, H. Seino, Y. Mizobe, K. Hashimoto, Inorg. Chem. 42 (2003) 1848;
(c) T. Korzeniak, R. Podgajny, N.W. Alcock, K. Lewiński, M. Bałanda, T. Wasiutyński, B. Sieklucka, Polyhedron 22 (2003) 2183;
(d) D. Li, L. Zheng, X. Wang, J. Huang, S. Gao, W. Tang, Chem. Mater. 15 (2003) 2094;
(e) D. Li, S. Gao, L. Zheng, W. Sun, T. Okamura, N. Ueyama, W. Tang, New J. Chem. 26 (2002) 485.
[38] (a) B. Sieklucka, J. Szklarzewicz, T.J. Kemp, W. Errington, Inorg. Chem. 39 (2000) 5156;
(b) T. Kashiwagi, S.-I. Ohkoshi, H. Seino, Y. Mizobe, K. Hashimoto, J. Am. Chem. Soc. 126 (2004) 5024.
[39] T.V. Long, G.A. Vernon, J. Am. Chem. Soc. 93 (1971) 1919.
[40] K.O. Hartman, F.A. Miller, Spectrochim. Acta 24A (1968) 669.
[41] E.G. Brame, F.A. Johnson, E.M. Larsen, V.W. Meloche, J. Inorg. Nucl. Chem. 2 (1958) 99.
[42] (a) R. Podgajny, B. Sieklucka, W. Łasocha, J. Chem. Soc., Dalton Trans. 1799 (2000);
(b) W.P. Griffith, J. Chem. Soc., Dalton Trans. 2489 (1975).
[43] W. Meske, D. Babel, Z. Anorg. Allg. Chem. 625 (1999) 51.
[44] F. Chang, H.-L. Sun, H.-Z. Kou, S. Gao, Inorg. Chem. Commun. 5 (2002) 660.
[45] J.R. Withers, D. Li, J. Triplet, C. Ruschman, S. Parkin, G. Wang, G.T. Yee, S.M. Holmes, Inorg. Chem. 45 (2006) 4307.
[46] (a) C.A. Bignozzi, R. Argazzi, J.R. Schoonover, K.C. Gordon, R.B. Dyer, F. Scandola, Inorg. Chem. 31 (1992) 5260;
(b) M.A. Watzky, J.F. Endicott, X. Song, Y. Lei, A. Mccatangay, Inorg. Chem. 35 (1996) 3463;
(c) K.F. Purcell, S.M. Yeh, J.S. Eck, Inorg. Chem. 16 (1977) 1708;
(d) M.Y. Darensbourg, H.L.C. Barros, Inorg. Chem. 18 (1979) 3286;
(e) M.J. Scott, R.H. Holm, J. Am. Chem. Soc. 116 (1994) 11357;
(f) H. Vahrenkamp, A. Geiss, G.N. Richardson, J. Chem. Soc., Dalton Trans. 3643 (1997);
(g) B.S. Lim, R.H. Holm, Inorg. Chem. 37 (1998) 4898;
(h) G.N. Richardson, U. Brand, H. Vahrenkamp, Inorg. Chem. 38 (1999) 3070;
(i) A. Geiss, H. Vahrenkamp, Eur. J. Inorg. Chem. 1793 (1999);
(j) A. Geiss, H. Vahrenkamp, Inorg. Chem. 39 (2000) 4029;
(k) R. Podgajny, C. Desplanches, B. Sieklucka, R. Sessoli, V. Villar, C. Paulsen, W. Wernsdorfer, Y. Dromzée, M. Verdaguer, Inorg. Chem. 41 (2002) 1323;
(l) C.A. Bignozzi, F. Scandola, Inorg. Chem. 23 (1984) 1540;
(m) K.F. Purcell, J. Am. Chem. Soc. 89 (1967) 247;
(n) K.F. Purcell, Inorg. Chem. 89 (1967) 6139.
[47] P.M. Kiernan, W.P. Griffith, J. Chem. Soc., Dalton Trans. 2489 (1975).
[48] (a) E. Colacio, J.M. Domínguez-Vera, F. Lloret, A. Rodriguez, H. Stoeckli-Evans, Inorg. Chem. 42 (2003) 6962;
(b) D.W. Knoeppel, J. Liu, F.A. Meyers, S.G. Shore, Inorg. Chem. 37 (1998) 4828;
(c) D.W. Knoeppel, S.G. Shore, Inorg. Chem. 35 (1996) 1747;
(d) J.A. Smith, J.-R. Galán-Mascarós, R. Clérac, J.-S. Sun, X. Quyang, K.R. Dunbar, Polyhedron 20 (2001) 1727;
(e) C.P. Berlinguette, J.A. Smith, J.-R. Galán-Mascarós, K.R. Dunbar, CR Acad. Sci., Ser. IIc: Chim. 5 (2002) 665;
(f) C.P. Berlinguette, J.-R. Galán-Mascarós, K.R. Dunbar, Inorg. Chem. 42 (2003) 3416.
[49] (a) A. Caneschi, D. Gatteschi, A.L. Lirzin, J. Mater. Chem. 4 (1994) 319;
(b) A. Caneschi, D. Gatteschi, J.P. Renard, P. Rey, R. Sessoli, J. Am. Chem. Soc. 111 (1989) 785;
(c) A. Caneschi, D. Gatteschi, P. Rey, R. Sessoli, Inorg. Chem. 27 (1988) 1756;
(d) H.O. Stumpf, L. Ouahab, Y. Pey, D. Grandjean, O. Kahn, Science 261 (1993) 447;
(e) M. Hitzfield, P. Ziemann, W. Buckel, H. Claus, Phys. Rev. B 29 (1984) 5023.
[50] (a) J.B. Goodenough, J. Appl. Phys. 39 (1968) 403;
(b) J.P. Goodenough, Phys. Rev. 164 (1967) 785;
(c) J.B. Goodenough, Magnetism and the Chemical Bond, Interscience, New York, 1953;
(d) J.B. Goodenough, Phys. Rev. 100 (1955) 564;
(e) J.B. Goodenough, J. Phys. Chem. Solids 6 (1958) 287;
(f) J. Manamori, J. Phys. Chem. Solids 10 (1959) 87.
[51] (a) D.B. Brown, D.F. Shriver, Inorg. Chem. 8 (1969) 37;
(b) E. Reguera, J.F. Bertrán, L. Nuñez, Polyhedron 13 (1994) 1619;
(c) D.B. Brown, D.F. Shriver, L.H. Schwartz, Inorg. Chem. 7 (1968) 77;
(d) J.E. House, J.C. Bailar Jr., Inorg. Chem. 8 (1969) 672;
(e) D.B. Brown, D.F. Shriver, S.E. Anderson, Inorg. Chem. 4 (1965) 725.

and pyrazine groups (pyz) (or 2-methylpyrazin groups (2-mpyz)). The nano-pores were shown as zigzag-type one-dimensional channels. The X-ray structural studies for single crystals showed both position and orientation of O_2 molecules in nano-pores. In this study, we especially employed the crystal **2** in order to investigate crystal constructions and magnetic properties by using of theoretical treatments.

Magnetic measurement also has been carried out for each crystal and interesting magnetization with stable spins in O_2 molecules was found. It was expected that magnetic interactions between O_2 pairs existed and these cooperation might run in the nano-porous cavity. These results will lead new approach to arrangement of spin sources in organic radicals. Thus, several *ab initio* molecular orbital (MO) methods were employed in order to evaluate magnetic interaction quantitatively.

In addition, structure–function relationships were theoretically elucidated by using of molecular dynamics (MD), MO and statistical mechanics theories [11–15]. For example, the Monte Carlo (MC) procedures in MD simulation enable–us to evaluate number of adsorbed molecules. The Hartree–Fock (HF) and density functional (DFT) methods as MO-based methods can give us information of both position and orientation of guest molecules.

2. Crystal structure and model preparation

Takamizawa, Mori and their co-workers have been reported the series of nano-porous crystals of organometallic conjugation complexes. These solids of dinuclear transition-metal carboxylates can be constructed by using of dicarboxylates (M = Cu(II), Mo(II), Ru(II, III) and so on) or monocarboxylates (M = Rh(II), Cu(II) and so on). In addition, physical adsorption of small size molecules into such organometallic conjugation complexes can be achieved. Reversibly adsorption of a large number of gases such as N_2, O_2, Ar and Xe were reported. Especially, the crystal **2** with adsorption of O_2 molecules will be studies in this paper.

Building units of the organometallic conjugation compound **2** were $Rh_2(bza)_4(pyz)_2$ molecules. According to their experiments, coordination of both four benzoate and two pyrazine ligands in equatorial and axial direction, respectively, are illustrated in Fig. 1a. Pairing of two Rh atoms can be achieved with multiple binding between two metal atoms and indirect binding with coordination of these ligands. As mentioned in our previous paper [11–15], di-carboxylates can elongate building units with coordination in both ends of carboxyl groups as shown in the crystal **1**. On the other hand, in mono-carboxylate systems such bridges between two building units can not be achieved. Thus, construction is made by face-to-face contact between two phenyl groups. Takamizawa and his coworkers reported that they could make single crystals of **2** with adsorption of O_2 molecules. The obtained crystal in $T = 10$ K are illustrated in Fig. 1b, though structural analysis by their X-ray diffraction studies successfully carried out in various temperatures ($T = 10$ K, 90 K and 190 K).

Four fragments in a white circle in the left figure indicate adsorbed O_2 molecules. Such alignment of O_2 molecules indicates existence of one-dimensional channels. We can find two-dimensional arrangements of such channels. The right figure indicates another view of the left figure and two unit cells are shown. It is found that zigzag alignment of adsorbed O_2 molecules. We can find three O_2 molecules in a white square, though each structural disorder causes fluctuation of spatial positions for oxygen atoms. The disorder is much remarkable when experimental temperature is made higher. They studied structural measurement for $T = 10$ K, 90 K and 190 K, though uncertainty of oxygen atoms much increased at $T = 190$ K. Apart from the effects of kinetic motion of O_2 molecules, three O_2 molecules per one unit cell occupy nano-porous cavity.

In the following section, let us employ this structure for our studies. Throughout the MD simulation, this experimental structure in $T = 10$ K was employed, though already adsorbed O_2 molecules were removed. For the evaluation of magnetic interaction between adsorbed O_2 molecules, alignment of O_2 molecules was extracted for our studies as shown in Fig. 1c, though structural disorder was inherent for this crystal. In this figure, each O_2 molecule is indicated O_2(A), O_2(B) and O_2(C) in one unit cell and O_2(A′) is equivalent to O_2(A) in the next cell. Bond lengths in each O_2 molecules are 1.184 (average) and 1.179 Å and intermolecular distances are 3.130 and 3.354 Å. Zigzag orientation between O_2 molecules was expected, though angles and dihedral angles between two O_2 molecules were not described in this figure. The spatial relation between the pairs O_2(A)–O_2(B) and O_2(A′)–O_2(C) are equivalent, since the unit cell has symmetry operation (inverse). In addition, periodic condition for the unit cell requires repeating of two types of magnetic interaction along O_2 chains.

3. Magnetic interactions in spin arrangements of triplet oxygen molecules

First, we investigated magnetic interactions among radical spins on the adsorbed O_2 molecules. Theoretical schemes for magnetic parameter have been highly progressed and *ab initio* MO methods can evaluate magnetic interaction quantitatively. Thus, the effective exchange integrals between radical spins were theoretically evaluated with unrestricted(U)-HF, post-HF and DFT computational methods. It is well known that the energy gaps between both higher (quintet) and lower (singlet) spin states can be well reproduced by these methods. The unrestricted-based methods can cause broken-symmetry (BS) solutions for each spin state [16]. However, such solutions are permitted to involve spin contamination. Thus, the spin projection were applied to the results, which reduced the spin contamination including higher-order spin states.

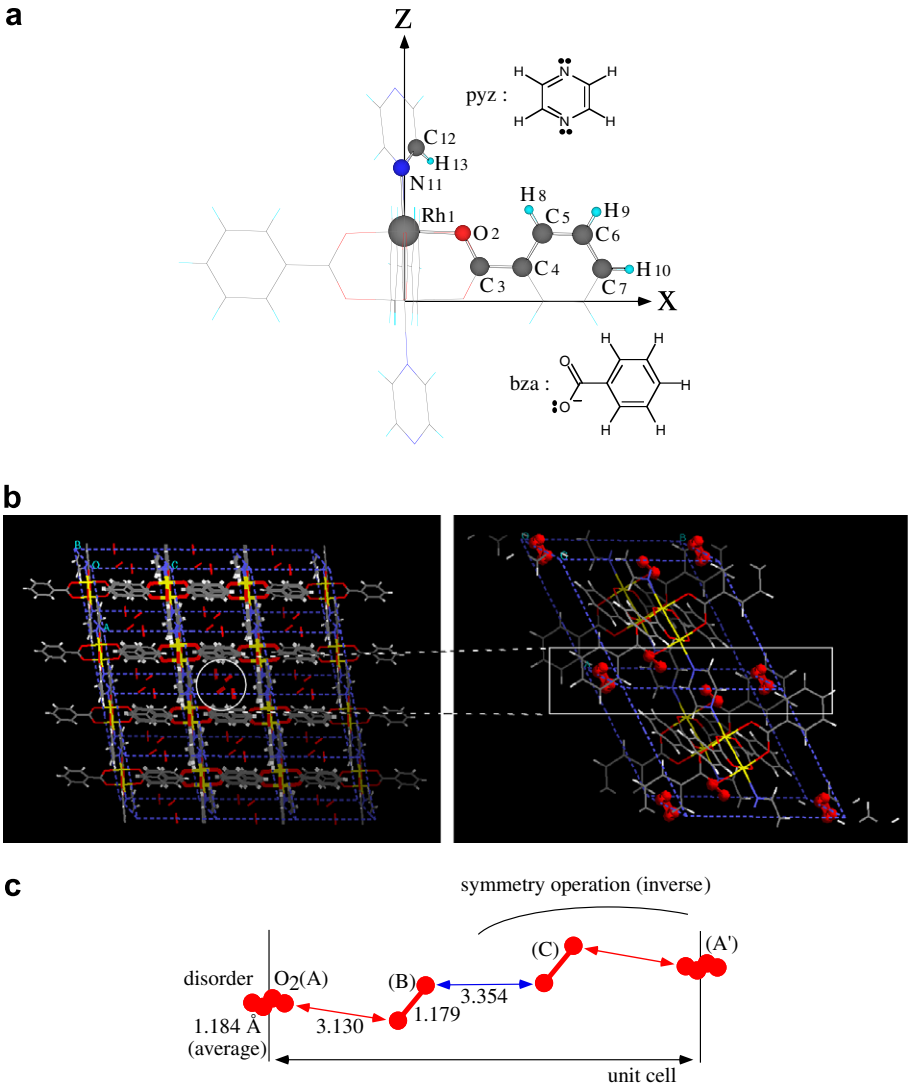


Fig. 1. (a) Building units $Rh_2(bza)_4(pyz)_2$ for the organometallic conjugation compounds $[Rh_2(bza)_4(pyz)]_n$ (**2**). Indices for each atom were referred in Table 2. (b) Alignment of the adsorbed O_2 molecules in cavities, which was reported in experimental studies in $T = 10$ K by Mori, Takamiza and their co-workers. (c) Spatial relations between each O_2 molecule. Structural disorder was reported in O_2(A) molecule.

Here, two types of magnetic interaction were expected, that is, direct and indirect ones. The former was the intermolecular interaction between two O_2 molecules in one-dimensional cavities, though the latter was more complex by use of indirect paths through frame atoms. First, we considered only the former, because two Rh^{2+} metal ions had no magnetic spins, which will be made sure in the following section in this paper. For the latter effect, more extended studies will be done in our following studies.

The O_2(A) molecule had structural disorder and we employed three types of structure: disorder 1, disorder 2 and average. All the calculated results were summarized in Table 1. The evaluate values by the UHF, UCCSD(T) and UB3LYP methods for the pair O_2(A:average)–O_2(B) were small plus and indicated weak ferromagnetic interaction. On the other hand, the values by UCCSD(T) and UB3LYP methods but the UHF methods for the pair O_2(B)–O_2(C) indicated weak antiferromagnetic interaction. Judging from the obtained values and crystal structure in Fig. 1c, only two types of magnetic parameters can deduce the style of spin arrangement in the infinite O_2 chains i.e., $\ldots O_2(A) = O_2(B) - O_2(C) = O_2(A') = O_2(B') - O_2(C') \ldots$ (=: +0.78 cm^{-1} (ferromagnetic); –: −0.29 cm^{-1} antiferromagnetic) by UCCSD(T) methods. Spin arrangement –

Table 1
Evaluated magnetic interactions by HF (UHF/4-31G), post-HF (UCCSD(T)/4-31G) and DFT (UB3LYP/4-31G) methods for all pairs in one unit cell of O_2 molecular chain

Pair	J_{ab} (cm^{-1})		
	UHF	UCCSD(T)	UB3LYP
O_2(A:average) – O_2(B)	1.06	0.78	0.41
O_2(A:disorder 1) – O_2(B)		0.37	
O_2(A:disorder 2) – O_2(B)		1.53	
O_2(B) – O_2(C)	0.08	−0.29	−1.46

$[\uparrow\uparrow\uparrow-\downarrow\downarrow\downarrow-]_\infty$ ($\uparrow$: $S = 1$) was expected and ferromagnetic trimer clusters were coupled with antiferromagnetic interaction, though the implied trimer was not so clear. Anyhow, it was expected that magnetic behaviour from only direct interaction between O_2 molecules will be not remarkable, since magnitude of the all evaluated magnetic interactions was very small. On the other hand, the experimental studies had reported interesting magnetic behaviour at about $T = 60$ K. We could not explain such the experimental results. Indirect interaction between metal complex (host) and O_2 molecules (guest) will be worth considering and it will be mentioned in our following studies.

4. Position of oxygen molecules in cavity of crystals

4.1. The details for molecular simulations

In addition to development of synthetic technique, theoretical calculation methods have also progressed and they enable us to evaluate number of adsorbed molecules with MD simulation methods. In addition, position of each O_2 molecule can be calculated. Furthermore, MO methods can give us information of orientation of molecules by using geometry optimization technique. Our calculations in this paper will give a theoretical insight of gas-adsorption behaviour. Our systematic procedures have the following two steps: (Step 1) Decision of parameters for MD. simulations (Step 2) Execute MD simulation.

Here, let us start Step 1 and this step is important to the following steps. A series of grand canonical Monte Carlo (GCMC) simulations of single-gas adsorption were performed in order to elucidate the experimental results. For reliable simulation, force-field (FF) condition must be decided carefully. Suitable FF types on each atom in both frameworks and adsorbed molecules were assigned manually. Through this simulation a general FF parameter sets of "UNIVERSE_OFF 1.02" in the CERIUS2 program package were employed. The parameter sets include a set of hybridization atomic bond radii, a set of hybridization angles, van der Waals (VDW) parameters, torsional and inversion barriers and a set of effective nuclear charges.

For charge densities on each atom in both frame and adsorbed molecules, additional computations were performed with the UHF and UB3LYP methods. During our calculations LanL2DZ and 4-31G basis sets for metal complex and O_2 molecules were employed, respectively. The broken-symmetry procedure were used in order to realize spin polarized states. GAUSSIAN 98 program package was used for these calculations [17]. The evaluated charge densities for metal complex were summarized in Table 2, where indices for each atom were already defined in Fig. 1a. In addition, the obtained spin densities by UHF and UB3LYP methods were illustrated in Fig. 2a and b, respectively. Here, total spin states were fixed to singlet ($\uparrow$–$\downarrow$). In the results by the UHF method, spin densities on two pyrazine groups were overestimated by huge spin contamination. Thus, we concluded that the UHF method without post-HF procedures was not suitable. On the other hand, only small spin densities on Rh atoms were given by the UB3LYP method and decreased according to requiring of more severe SCF conversion In this system metal complex will tend to get non-magnetic spin distribution. In the following simulation, we employed charge densities by the UB3LYP methods in order to account Coulomb interaction.

Table 2
Calculated charge densities in each atoms in $Rh_2(bza)_4(pyz)_2$ molecules by UB3LYP methods. Summations to Rh, bza and pyz group were also listed

Atom	Number	Charge densities
Rh	1	0.369
O	2	−0.368
C	3	0.402
C	4	0.213
C	5	−0.401
C	6	−0.293
C	7	−0.285
H	8	0.332
H	9	0.297
H	10	0.297
N	11	−0.078
C	12	−0.256
H	13	0.323
Rh		0.369
bza		−0.241
pyz		0.113

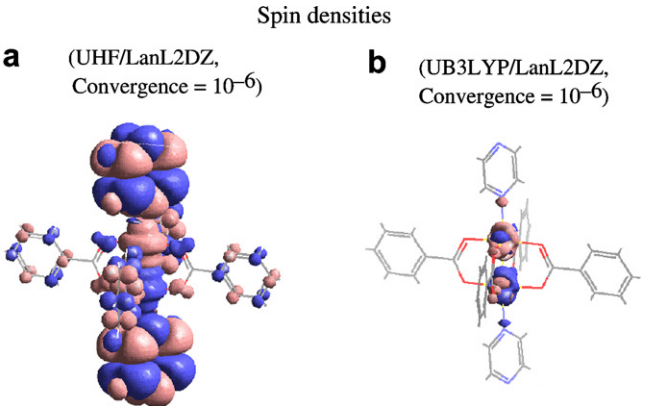


Fig. 2. (a) The evaluated spin densities by using UHF/LanL2DZ (a) and UB3LYP/LanL2DZ (b) methods.

A series of the MC simulation of single-gas adsorption was performed and we employed CERIUS2 program packages for this purpose. Next step was equivalent to Step 2. We have to employ many trial and dispose some initial samplings in order to improve the precision, because MC steps progress by random samplings. Thus, in this study our sampling number is 6000000 and the first 1000000 cycles are discarded.

For guest molecules, a O_2 molecule was employed as radical species with $S = 1$ spin per one molecule. In addition, a carbon dioxide molecule (CO_2) was also focused, since detailed experimental data were also reported by Takamizawa and his co-worker.

4.2. The results for molecular simulations

The MC simulation was carried out in the condition of P (external pressure) = 1 atm and T = 77 K, which is boiling temperature of liquid nitrogen. In Fig. 3a the obtained simulation results were described with cloud of mass density of O_2 molecules. From the results, alignment of O_2 molecules in channels was found. The obtained distribution of O_2 molecules showed structural interaction between host frames and guest molecules. The some experimental studies in the condition of several temperatures were already reported: T = 10 K, 90 K and 190 K. It was reported that uncertainty of spatial position of O atoms turned to be more small in the lower temperature. The simulation results in these temperatures were obtained and their mass cloud of O_2 molecules were illustrated in this figure. Distribution of mass center of O_2 molecules was shrunk and position got more sharp in lower temperature. On the other hand, in higher temperature kinetic motion of O_2 molecules got large. In this simulation temperature dependency of mass distribution is very reasonable.

In order to study the temperature dependence, not only mass distribution but also the number of adsorbed O_2 molecules was also simulated. Schematic calculations in all range of temperature as shown in Fig. 3b, where left and right scales indicated converted values to number (mole-

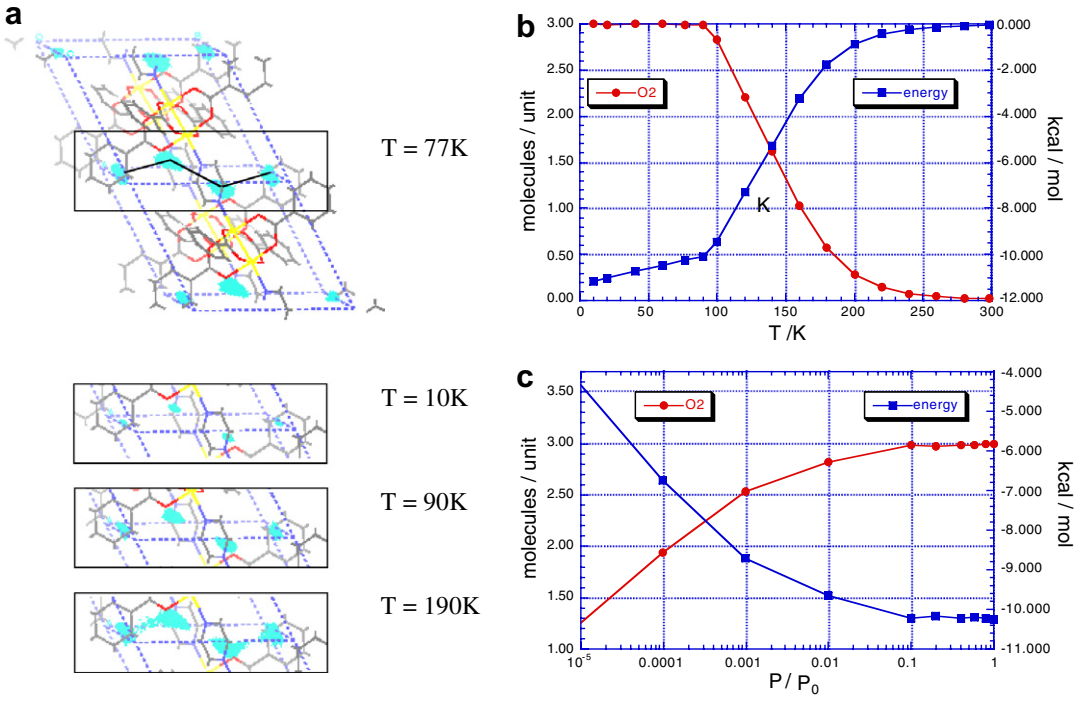


Fig. 3. The results of O_2 adsorption into crystal **2** by using MD simulation. (a) The evaluated cloud of mass densities in condition of various temperature. Dependency of number of adsorbed O_2 and stabilization energies on temperature (b) and external pressure (c).

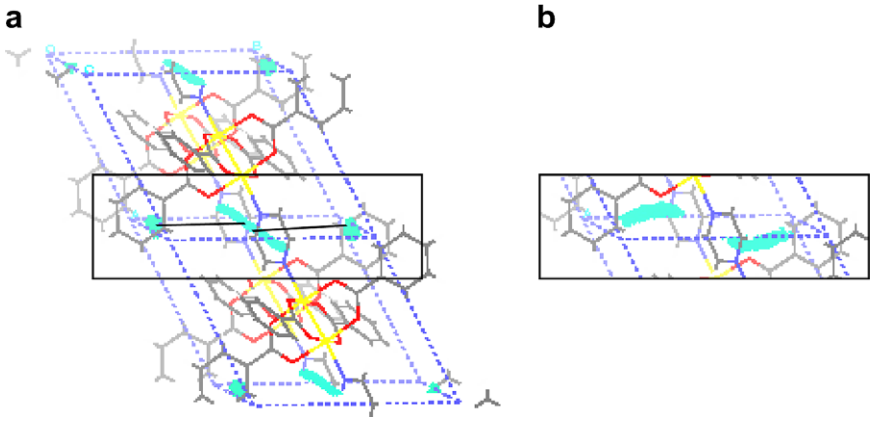


Fig. 4. The results of CO_2 adsorption into crystal **2** by using MD simulation. The evaluated cloud of mass densities by calculation with (a) and without (b) Coulomb interaction.

cules/unit) and stabilization energy (kcal/mol), respectively. The number of adsorption decreased gradually over 100 K and become to nearly zero above 240 K. The saturated value reached about 3.00 molecules of O_2 per 1 unit cell. It was equivalent to experimental reports of 3 molecules/unit at $T = 10$ K.

Table 3
Evaluated number of molecules and stabilization energies for various simulation type

Simulation type	Number of molecules	Stabilization energies
Guest = O_2		
With all interaction	2.99[a]	−10.242[b]
Without only Coulomb interaction	2.99	−10.231
Without only VDW interaction	3.00	−10.204
Guest = CO_2		
With all interaction	2.00	−14.745
Without only Coulomb interaction	1.99	−11.254

[a] Molecules/unit.
[b] kcal/mol.

The external pressure dependence of O_2 adsorption calculated by using molecular simulation was shown in Fig. 3c. In this figures, left scale indicated number of adsorption molecules per one unit cell and right one indicated stabilization energies. The plots were depicted as log-plot of P/P_0 (P: external pressure; P_0: 1 atm). The adsorption values increased and were saturated above $P/P_0 = 0.1$. The saturated values for O_2 molecules reached about 3.00 molecules per one unit cell. In the crystal number of adsorbed gas will be controlled by external pressure effectively.

Here, we tried similar simulation to a CO_2 as guest molecules. Though the O_2 molecules had no charge densities on it, the CO_2 molecules were induced charge distribution because of the structure ($O^{\delta-} - C^{\delta+} - O^{\delta-}$). The simulated results were depicted in Fig. 4a and the cloud

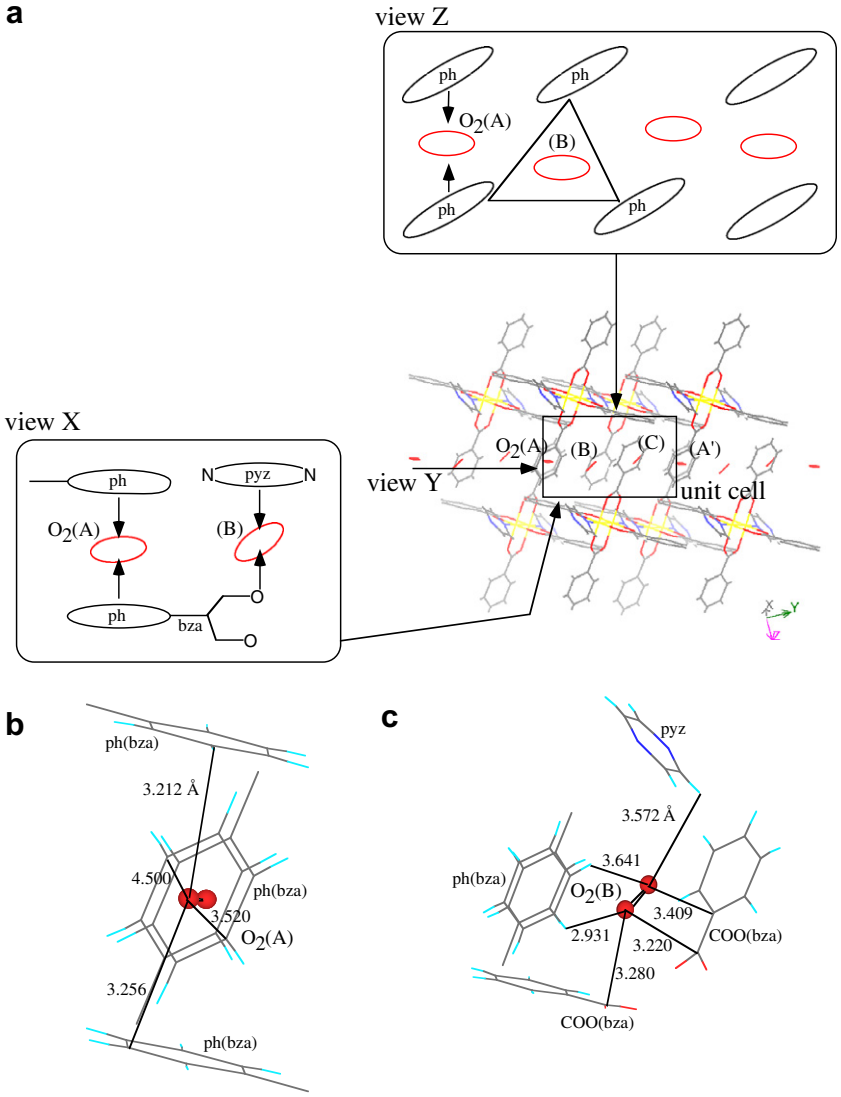


Fig. 5. Orientation of the adsorbed O_2 molecules in the cavities (a) and the detailed spatial interaction for O_2(A) (b) and O_2(B) (c).

of mass densities located in both ends and center in our squire box. The saturated values for CO_2 molecules reached about 2.00 molecules per one unit cell. When we used CO_2 molecules instead of O_2 molecules as guest gas, number of adsorbed gas were reduced. We could first assume that possibility of difference of size of each molecule. We attempted to re-calculate distribution of mass densities by controlling three interactions (hybridization between atoms; van der Waals interaction; Coulomb interaction) in MC simulation procedures. From our calculation it was found that Coulomb interaction was very important for all simulation. For example, the evaluated stabilization energies per one unit cell for CO_2 molecules were −14.745 and −11.254 kcal/mol for with and without Coulomb interaction, though number of CO_2 molecules was equal to each other (2.00 and 1.99), respectively, as summarized in Table 3. In Fig. 4a and b clouds for both simulations were given and it was easily found that style of distribution of CO_2 molecules were so different. The Coulomb interaction could control position of adsorbed molecules in cavities. The calculations of charge densities by using MO methods were essential for CO_2 molecules. However, for O_2 molecules this Coulomb interaction was negligible, since no charge densities were induced because of two same atoms. In addition, simulation for O_2 molecules with and without VDW interaction was carried out. As summarized in Table 3, 2.99 and 3.00 molecules/unit for adsorbed number and −10.242 and −10.204 kcal/mol for stabilization energies were evaluated, respectively. It was concluded that VDW interaction was not important.

5. Orientation of oxygen molecules in cavity of crystals

In the above MD simulation with the interaction parameters evaluated by MO calculations, the obtained cloud of mass densities statistically showed positions of adsorbed molecules. However, in experimental structural studies both position of orientation could be directly measured in the condition of low temperature. Here, we focus on orientation as well as potion of each adsorbed O_2 molecule.

First, we investigated local interaction between host frames and guest molecules. Fig. 5a shows how each O_2 molecule located in cavities. Simplified illustration in this view in *X*- and *Z*-axes will help us to understand spatial contact. It is found that O_2(A) and O_2(B) are suppressed by two phenyl groups and pyrazin – carboxyl groups in view *X*, respectively. In addition, in view *Z* two O_2 molecules occupy the space between two phenyl groups and among three phenyl groups, respectively. Thus, spatial pockets for each O_2 molecule are already prepared. In Fig. 5b and c, coordination distances among O_2(A) and O_2(B) are summarized. The range of these distances was about 3.0 Å.

Here, let us discuss the orientation for O_2(A) mainly. The nearly contacted phenyl groups were replaced by four benzene molecules in order to execute theoretical calculation effectively as shown in Fig. 6a. There were two pairs of two face-to-face benzene molecules and two planes (plane 1, plane 2) could be defined. With our rough estimation the O_2 molecules were suppressed in intersection of two planes, since O_2 molecules will avoid π-electrons on benzene molecules. Indeed, O_2 molecules in experimental

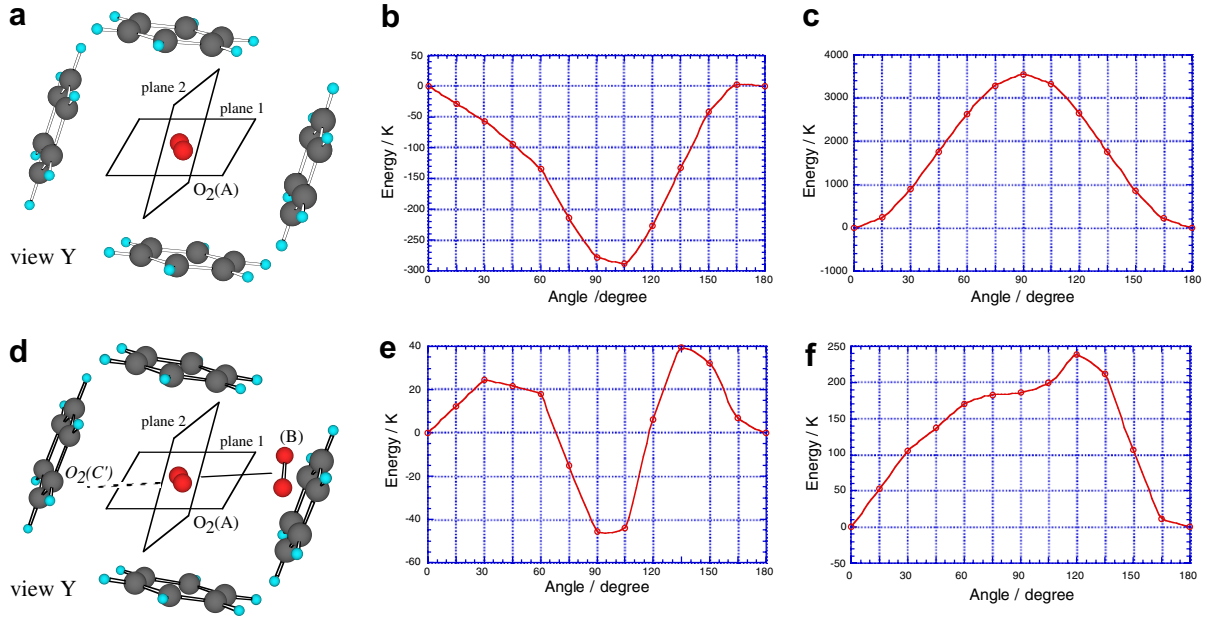


Fig. 6. Simple model for O_2(A) molecule which was surrounded by four benzene molecules (a). Variation of total energies by UB3LYP method by rotating O_2(A) molecule on plane 1 (b) and plane 2 (c). In addition, simple model for O_2(A) molecule which was surrounded by not only four benzene molecules but also the one/two next O_2 molecules (d). Variation of total energies for the systems of O_2(A)–O_2(B) (e) and O_2(C″)–O_2(A)–O_2(B) (f).

studies located in these orientation ($\theta_1 = 17,\ \theta_2 = 0$). In order to ensure this speculation several geometry was made by rotating one O_2 molecule in each plane. Energy calculations were carried out by using UB3LYP method and angle dependency was illustrated in Fig. 6b and c. Here, zero-points of energy were defined to the evaluated total energies in the conformation without rotation. Unit of energies a.u. (atomic unit) can be convert to another unit: 1 a.u. = 27.211 eV = 219470 cm^{-1} = 315771 K. The last relation (a.u. – K) was very useful in case of studying freedom of orientation to temperature. For rotation in plane 1, the most stable orientation was given in $\theta_1 = 105$, though original structure of $\theta_1 = 17$ was concluded to be very unstable. For rotation in plane 2, original structure $\theta_2 = 0$ was very stable and consistent to experimental results. These orientations were much steady, since the energy scale for plane 2 was very large than temperature range (up to room temperature). On the other hand, potential valley in plane 1 was not so large and rotation of the O_2 molecule was rather free.

In addition, let us locate another O_2(B) molecule besides the target O_2(A), which was reasonable because of existence of O_2 chains in cavities. In Fig. 6d, the rotation model with the next O_2 molecule O_2(B) was illustrated. Similar calculations carried out and transition of energies were illustrated in Fig. 6e. Judging from this curvature, orientation around $\theta_1 = 0$ become more stable and local minimum region ($\theta_1 = 0$–30, 135–180) appeared. It was natural that we expected the most stable orientation when second O_2 molecule (italic-face O_2(C″) in Fig. 6d) was also introduced in the opposite site. Fortunately, the obtained energy curvature concluded that global minimum appeared in this situation as shown in Fig. 6f. Interaction between target O_2 molecule and two the next O_2 molecules in the chain was important, though that between target O_2 molecule and four benzene molecules was not negligible. Theoretical calculations could reproduce experimental facts.

6. Concluding remark

Adsorption properties of magnetic species in nano-porous crystals were studied theoretically. The crystal **2** was one of very suitable systems for our purpose. Especially, a O_2 molecule ($S = 1$) for adsorbed magnetic radical species was treated. Weak magnetic interaction between O_2 molecules in cavities existed and two types of magnetic interaction (ferro- and antiferro-magnetic) made alignment of trimer spin structure.

In addition, this study demonstrated importance of nano-porous organometallic conjugation systems for gas adsorption by using MD simulation and MO calculations. These theoretical calculations could decide not only position but also orientation of the adsorbed O_2 molecules. For the former, cloud of mass densities of O_2 molecules by MD simulation showed stacking style in nano-pores statistically and number of adsorbed gas was estimated to be 3.00 molecules/unit. The distribution of O_2 molecules get sharper in case of lower temperature. These results could explain experimental results by Takamizawa and his coworkers. For the latter, orientation of the O_2(A), which was surrounded four phenyl groups, was stabilized by contribution of the two next O_2 molecules as well as phenyl groups. All results in this study will lead new approach to arrangement of organic spin radical sources.

Acknowledgements

This work has been supported by a Grant-in-Aid for Scientific Research on Priority Areas (Nos. 18350008 and 18205023) from Ministry of Education, Science, Sports and Culture, Japan.

References

[1] W. Mori, S. Takamizawa, J. Solid State Chem. 152 (2000) 120.
[2] W. Mori, S. Takamizawa, C.N. Kato, T. Ohmura, T. Sato, Micropor. Mesopor. Mater. 73 (2004) 31.
[3] S. Kitagawa, Chemistry & Chemical Industry 56 (2006) 020 (in Japanese).
[4] W. Mori, F. Inoue, K. Yoshida, H. Nakayama, S. Takamizawa, M. Kishita, Chem. Lett. (1997) 1219.
[5] W. Mori, S. Takamizawa, M. Fujiwara, K. Seki, Patent No. JP 09132580 (1995) and EP 0727608 (1996).
[6] W. Mori, T.C. Kobayashi, J. Kurobe, K. Amaya, Y. Narumi, T. Kumada, K. Kindo, H.A. Katori, T. Goto, N. Miura, S. Takamizawa, H. Nakayama, K. Yamaguchi, Mol. Cryst. Liq. Cryst. 306 (1997) 1.
[7] R. Kitaura, S. Kitagawa, Y. Kubota, T.C. Kobayashi, K. Kindo, Y. Mita, A. Matsuo, M. Kobayashi, H. Chang, T.C. Ozawa, M. Suzuki, M. Sakata, M. Takata, Science 298 (2002) 2358.
[8] S. Takamizawa et al., Angew. Chem., Int. Ed. 43 (2004) 1368.
[9] S. Takamizawa et al., Cryst. Eng. Comm. 6 (2004) 197.
[10] S. Takamizawa, E. Nakata, T. Akutsuka, Andew. Chem., Int. Ed. 45 (2006) 2216.
[11] T. Kawakami, S. Takamizawa, Y. Kitagawa, F. Matsuoka, T. Maruta, W. Mori, K. Yamaguchi, Mol. Cryst. Liq. Cryst. 343 (2000) 215.
[12] S. Takamizawa, W. Mori, Y. Yokomichi, Y. Kitagawa, T. Maruta, T. Kawakami, Y. Yoshioka, K. Yamaguchi, Mol. Cryst. Liq. Cryst. 342 (2000) 285.
[13] T. Kawakami, S. Takamizawa, Y. Kitagawa, T. Maruta, W. Mori, K. Yamaguchi, Polyhedron 20 (2001) 1197.
[14] A. Nakamura, N. Ueyama, K. Yamaguchi (Eds.), Organometallic Conjugation, Kodansha Springer, 2002.
[15] T. Kawakami, S. Takamizawa, W. Mori, K. Yamaguchi, Kotaibutsuri 41 (2006) 85 (in Japanese).
[16] T. Soda, Y. Kitagawa, T. Onishi, Y. Takano, Y. Shigeta, H. Nagao, Y. Yoshioka, K. Yamaguchi, Chem. Phys. Lett. 319 (2000) 223.
[17] M.J. Frisch et al., J.A. Pople, Gaussian, Inc.

is one of the main challenges in molecular material science in order to utilise them for information processing and information storage [8]. Furthermore, the design of spin-crossover compounds with multi-function, supramolecular structure and porous materials, has been noted because of leading specific magnetic or optical properties [9,10]. For some iron(II) spin-crossover (high-spin ($S = 2$) ↔ low-spin ($S = 0$)) compounds, light-induced low-spin → high-spin conversion can be observed by green light illumination into a d–d or MLCT (metal-to-ligand charge transfer) absorption band at temperatures well bellow the thermal transition temperature. A mechanism for this phenomenon, denoted as "light-induced excited spin state trapping" (LIESST), has been proposed [11,12]. The development of novel compounds exhibiting LIESST is one of the main challenges in this field [7,13,14]. The LIESST compounds can be used as optical switching molecular devices, and various functional materials including the optical switches can be constructed.

Here we focused on the spin-crossover iron(II) compounds in order to control liquid crystals not only by temperature but also magnetic field and photo-illumination. The spin-crossover iron(II) compounds exhibit spin conversion between diamagnetism ($S = 0$) and paramagnetism ($S = 2$), and the LIESST effect. The design of metallomesogens containing spin-crossover iron(II) center stimulates producing unexpected advanced materials by combining spin-crossover and LIESST with liquid-crystal properties [15,16].

The iron(II) compounds $[Fe(1C16\text{-}O\text{-}bzimpy)_2](BF_4)_2$ (**1**) and $[Fe(2C16\text{-}bzimpy)_2](BF_4)_2$ (**2**) were designed in order to construct a spin-crossover and LIESST material with liquid-crystal properties, where 1C16-O-bzimpy and 2C16-bzimpy are tridentate ligands (Fig. 1). Because the iron(II) compound $[Fe(bzimpy)_2](ClO_4)_2 \cdot 0.25H_2O$ exhibits spin-crossover above room temperature ($T_c\uparrow = 403$ K and $T_c\downarrow = 415$ K), the ligand bzimpy of the complex was modified as long alkyl substituent derivatives [17] (Fig. 2).

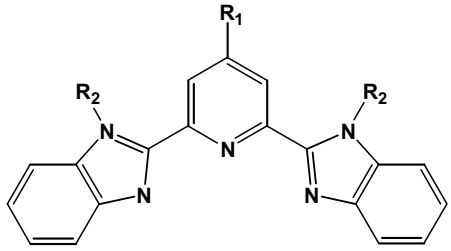


Fig. 1. Structure of the ligands.

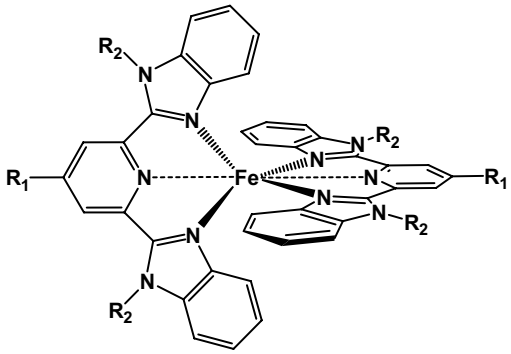


Fig. 2. Chemical structure of the compounds **1** and **2**.

2. Experimental

2.1. Preparation of the ligands [18,19]

2.1.1. Preparation of 2,6-bis(benzimidazol-2′-yl)pyridine (*bzimpy*)

2,6-Pyridinedicarboxylic acid (5.0 g, 27.5 mmol) and *o*-phenylenediamine (6.49 g, 58.7 mmol) were suspended in phosphoric acid (85%, 55 ml). The mixture was kept at 210–220 °C for 6 h with vigorous stirring. After cooling to room temperature, the mixture was poured into ice-water (400 ml), and the precipitate was filtered off and added to hot 10% aqueous Na_2CO_3 solution (340 ml). The resulting solid was filtered off and added to hot methanol saturated with Na_2CO_3. Then the solution was diluted with water (100 ml) and acidified with 15% hydrochloric acid to pH 1. The white precipitate was filtered off and extracted several times with boiling methanol. The collected extracts were evaporated until precipitation began. The colorless product was filtered and dried under vacuum; yield: 3.9 g (42%); white solid. ^{1}H NMR (DMSO): $\delta = 8.45$ (d, $J = 8.13$ Hz, 2H), 8.31 (*t*, $J = 7.53$ Hz, 1H), 7.84–7.82 (m, 4H), 7.44–7.42 (m, 4H). 2,6-Bis(benzimidazol-2′-yl)-4-hydroxypyridine (**OH-bzimpy**) was prepared in the same way as **bzimpy**; yield: 6.3 g (71%), white solid. ^{1}H NMR (DMSO): $\delta = 7.91$ (s, 2H), 7.86–7.84 (m, 4H), 7.49–7.46 (m, 4H).

2.1.2. Preparation of 2,6-bis(benzimidazol-2′-yl)-4-hexadecyloxypyridine (*1C16-O-bzimpy*)

OH-bzimpy (1.0 g, 3.06 mmol) and K_2CO_3 (0.64 g, 4.58 mmol) were mixed in DMF (35 ml). The mixture was stirred at 80 °C. After 30 min, 1-bromohexadecane (1.40 ml, 4.58 mmol) was added and stirred overnight at 80 °C. The solution was evaporated and the residue was recrystallized from $CHCl_3$; yield: 0.99 g (62%), white solid. ^{1}H NMR ($CDCl_3$): $\delta = 7.98$ (s, 2H), 7.89–7.87 (m, 2H), 7.50–7.48 (m, 2H), 7.33–7.31 (m, 4H), 4.15 (t, $J = 6.49$ Hz, 2H), 2.17–1.22 (m, 30H), 0.88 (t, $J = 6.98$ Hz, 3H).

*2.1.3. Preparation of 2,6-bis(N-hexadecylbenzimidazol-2′-yl)pyridine (**2C16-bzimpy**)*

NaH (oil dispersion, 60%: 0.51 g, 12.85 mmol) was washed with *n*-hexane and then suspended in dried DMF (20 ml) under Ar atmosphere. To this suspension was added **bzimpy** (1.0 g, 3.21 mmol), and the mixture was stirred and heated to 80 °C for 2 h. 1-Bromohexadecane (4.31 ml, 12.9 mmol) in DMF (20 ml) was added dropwise and then heated to 100 °C. After being cooled room temperature, the solution was poured into 10% aqueous NH_4Cl (100 ml), and then extracted with $CHCl_3$. The extract was washed with water and aqueous NaCl solution, and then dried by $MgSO_4$. The solution was evaporated, and the residue was purified by column chromatography on silica gel with ethyl acetate/hexane; yield: 0.61 g (50%), white solid. ^{1}H NMR ($CDCl_3$): 8.32 (d, $J = 7.93$ Hz, 2H), 8.05 (t, $J = 8.10$ Hz, 1H), 7.88–7.86 (m, 2H), 7.47–7.45 (m, 2H), 7.36–7.31 (m, 4H), 4.70 (t, $J = 7.32$ Hz, 4H), 1.75–1.00 (m, 60H) 0.88 (t, $J = 6.52$ Hz, 6H).

2.2. Preparation of the iron(II) compounds

*2.2.1. Preparation of [Fe(1C16-O-baimpy)$_2$](BF$_4$)$_2$ (**1**)*

To a solution of **1C16-O-bzimpy** (0.2 g, 0.36 mmol) $CHCl_3$/MeOH (20 cm^3) was added MeOH solution (10 cm^3) of $FeCl_2 \cdot 4H_2O$ (0.036 g, 0.18 mmol) and $NaBF_4$ (0.040 g, 0.36 mmol). The reaction mixture was stirred and refluxed for 30 min. The resulted solution was concentrated to precipitate the product. The red-purple product was collected by filtration and dried in vacuo; yield: 0.35 g (72%). *Anal*. Calc. for $C_{70}H_{90}B_2F_8FeN_{10}O_2$: C, 62.23; H, 6.86; N, 10.37. Found: C, 62.30; H, 6.90; N, 10.40%.

*2.2.2. Preparation of [Fe(2C16-bzimpy)$_2$](BF$_4$)$_2$ (**2**)*

To a solution of **2C16-bzimpy** (0.2 g, 0.40 mmol) $CHCl_3$/MeOH (20 cm^3) was added MeOH solution (10 cm^3) of $FeCl_2 \cdot 4H_2O$ (0.040 g, 0.20 mmol) and $NaBF_4$ (0.044 g, 0.40 mmol). The reaction mixture was stirred for a few minutes. The resulted solution was concentrated to precipitate the product. The red-purple product was collected by filtration and dried in vacuo; yield: 0.46 g (65%). *Anal*. Calc. for $C_{102}H_{154}B_2F_8FeN_{10}$: C, 70.01; H, 8.87; N, 8.00. Found: C, 70.00; H, 8.86; N, 8.07%.

2.3. Measurements

Elemental analyses of carbon, hydrogen, and nitrogen were carried out at The Service Center of Elemental Analyses of Kyushu University.

^{1}H NMR were measured on a Bruker AVANCE SERIES DPX 400 instrument operating at 400 MHz (using the deuterated solvent as the lock and the residual solvent or tetramethylsilane as the internal reference).

Magnetic susceptibilities of ground samples were measured on a Quantum Design MPMS-5S. Samples were put into a gelatin capsule, mounted inside the straw, and then fixed to the end of the sample transport rod. Illumination experiment was done using an Hg–Xe lamp ($\lambda = 550$ nm, 1.5 mW/cm^2) as a light source. The light passing through IR and green filters was guided via an optical fiber into the SQUID magnetometer. The sample was placed on the edge of the optical fiber.

The Mössbauer spectra (isomer shift versus metallic iron at room temperature) were measured using a Wissel MVT-1000 Mössbauer spectrometer with a ^{57}Co/Rh source in the transmission mode. All isomer shifts are given relative to α-Fe at room temperature. The measurements at low temperature were performed with a closed-cycle helium refrigerator cryostat (Iwatani Co., Ltd.)

Differential scanning calorimetry (DSC) thermal analysis was carried out on a SHIMADZU DSC50 differential scanning calorimeter.

X-Ray powder diffraction (XRD) studies were performed on a Rigaku X-ray diffractometer RAD-2A with a 2.0 kW Cu Kα X-ray.

Optical polarized microscopy was carried out on a Nippon Chemical Industrial corporation polarization microscope OPTICAL POL with a Yanagimoto factory MODEL MP-J3 micro melting point meter.

3. Results and discussion

3.1. Structure of the compounds

Single crystals of the compounds **1** could not be grown, therefore geometry optimization for the compounds were performed by computer simulation. Boča et al. reported that the iron atom is hexacoordinated by six nitrogen atoms belonging to the two tridentate ligands, which are located perpendicular to each other [17]. In consideration of the structure of the spin-crossover iron(II) compounds, that of the compound **1** has been optimized. The resulted geometry structure has been shown in Fig. 3. The long alkyl chains $C_{16}H_{33}O$ are stuck out of 4 position in the pyridine moiety, and the total is rod-like structure. On the other hand, the single crystal X-ray analysis was done for the iron(II) compound [Fe(2C10-bzimpy)$_2$](BF$_4$)$_2$ (**2′**) instead of the compound **2**, but the *R* value of the X-ray analysis did not decrease. However, we could estimate about the structure of **2** from that of **2′**. Fig. 3 shows the estimated structure of **2**. The iron atom is also hexacoordinated by six nitrogen atoms belonging to two tridentate ligands, which are located perpendicular to each other. The long alkyl chains $C_{16}H_{33}$ are stuck out of the N position in the imidazol moiety. Two long chains lengthen for one bzimpy plane up and down, and four long chains for one molecule intersect each other.

3.2. Differential scanning calorimetry (DSC)

Phase transition enthalpies were measured by carrying out DSC thermal analysis for the compounds **1** and **2**. The results of the DSC for **1** and **2** are shown in Table 1.

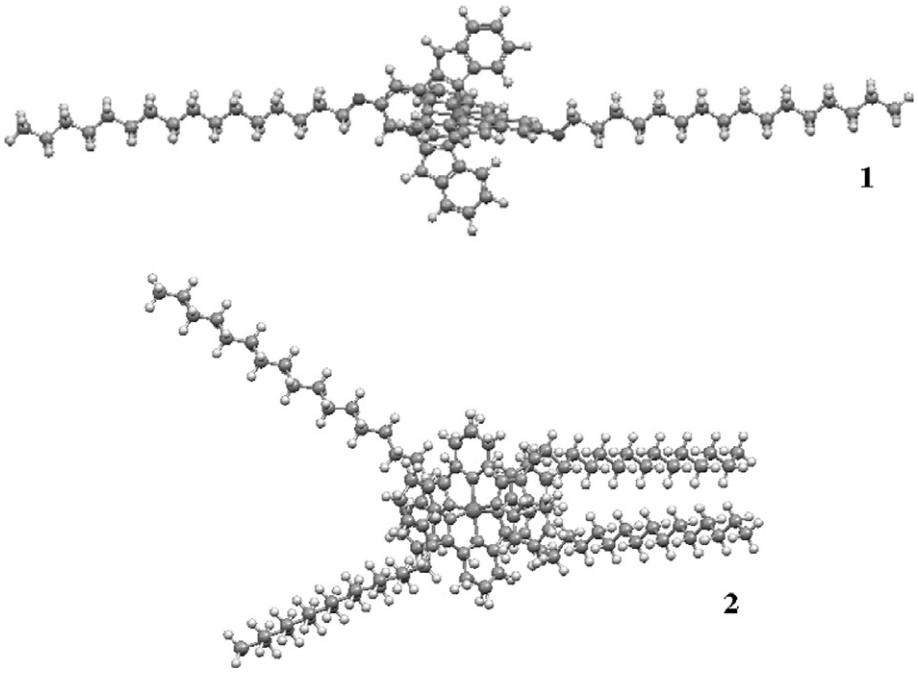


Fig. 3. Computer simulation of the molecular structure of the compounds **1** and **2**.

Table 1
Phase transition temperatures for **1** and **2**

Compound	Transition temperature (K)		SCO	*T* (LIESST)
	Cr–LQ	LQ–L		
1	547	607	225	47
2	322	525		

Cr is solid state, LQ is liquid crystal state and L is liquid state.

Two peaks were observed for **1** at 547 K and 607 K. The DSC peak at 547 K ($\Delta H = 27$ kJ mol^{-1}) corresponds to a crystal-mesophase transition, and that at 607 K is assigned to a mesophase-liquid transition. Two peaks were also observed for **2** at 322 K and 525 K. The first peak at 322 K ($\Delta H = 40$ kJ mol^{-1}) refers to a crystal-mesophase transition, and the second peak at 525 K is assigned to a mesophase-liquid transition. The compounds **1** and **2** exhibit two endothermic peaks in the heating cycles. A large peak at low temperature is assigned to the solid-mesophase transition, and a small peak at high temperature, assigned to mesophase-liquid transition. DSC were measured in the temperature range from crystal to liquid crystal on the warming and cooling mode reversibly. On cooling, the transition temperatures from mesophase to crystal for the compounds **1** and **2** are 540 K and 313 K, respectively. The free ligands, **1C16-O-bzimpy** and **2C16-baimpy**, exhibit only one peak, being assigned to solid-to-liquid transition.

3.3. Polarizing optical microscopy (POM)

The mesophase was studied by hot-stage polarized optical microscopy (POM) for **2**, and the texture of the liquid crystal state was observed by optical microscopy. The compound **2** is in the solid state at room temperature. Upon heating on the stage of the optical microscope under polarized light, the compounds exhibited mesomorphism. On heating, the compounds undergo a transition from the solid to birefringent viscous fluid, and exhibited a characteristic mosaic texture. When the compounds were cooled from the isotropic liquid to room temperature, the same mosaic texture as before heating was observed. An example of the texture under crossed polarizers for **2** is shown in Fig. 4. The identification of the phase of the liquid crystal

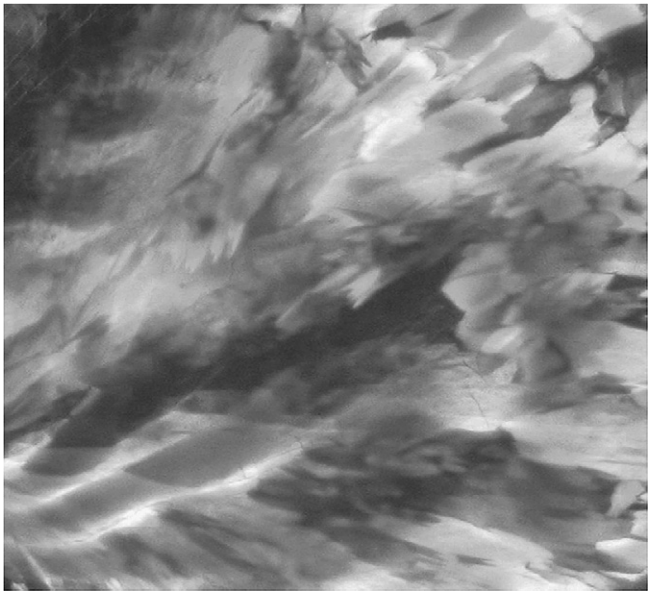


Fig. 4. Texture of the compound **2** under crossed polarizers at 330 K.

state based on the texture observed by optical microscopy was not possible.

3.4. Powder X-ray diffractions

Temperature-dependent X-ray diffraction measurements were carried out to confirm this mesophase. Fig. 5 shows the powder X-ray diffraction patterns of the crystal and the mesophase states for the compound **2** observed in the temperature range from 293 K to 328 K. A sharp reflection in the small-angle ($2\theta = 5.8°$) with *d*-spacing of 15.3 Å was detected at 293 K. This *d*-spacing may correspond to the distance between the iron atom and the long alkyl chain ($l = 16$ Å). At 328 K, the peak at $2\theta = 5.8°$ decreased and a new peak appeared at $2\theta = 2.7°$ ($d = 32.7$ Å). The peak at $2\theta = 19$–$23°$ ($d = 4.6$–3.8 Å) observed below 320 K becomes broad at the same time. The formation of the mesophase is completed at 323 K in accordance with the result observed by DSC.

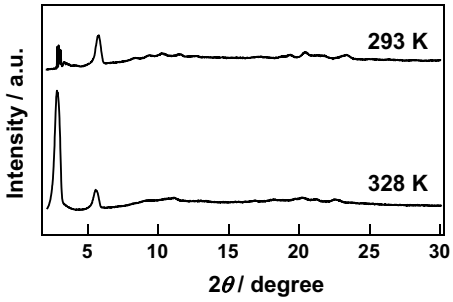


Fig. 5. Temperature dependence of powder XRD pattern of the compound **2**.

3.5. Magnetic properties

Iron(II) spin-crossover compounds with crystal-mesophase transition should be in the low-spin state at room temperature, i.e. have high T_c. We have first focused on the iron(II) compound $[Fe(bzimpy)_2](ClO_4)_2 \cdot 0.25\ H_2O$ with high T_c. Boča et al. have reported that the iron(II) compound exhibits spin-crossover above room temperature ($T_c\uparrow = 415$ K and $T_c\downarrow = 403$ K) [17]. The spin-crossover phenomenon between the high-spin and low-spin states for the compound **1** was followed by measurements of the molar magnetic susceptibility χ_m as a function of temperature. The $\chi_m T$ versus T plots for **1** are given in Fig. 6. The $\chi_m T$ value for the compound **1** is equal to 2.1 $cm^3\ K\ mol^{-1}$ at 50 K, which shows that about 64% of the iron(II) ions remain in the high-spin state.The decrease of the $\chi_m T$ value below 50 K is due to zero-field splitting. On warming, the $\chi_m T$ values were almost constant from 50 K to 100 K, then gradually increased near the spin transition temperature $T_{1/2} = 225$ K. The $\chi_m T$ value at 300 K is ca. 3.3 $cm^3\ K\ mol^{-1}$, showing that the spin transition from the low-spin to the high-spin state is induced. When the samples of the compound **1** were illuminated at 5 K for

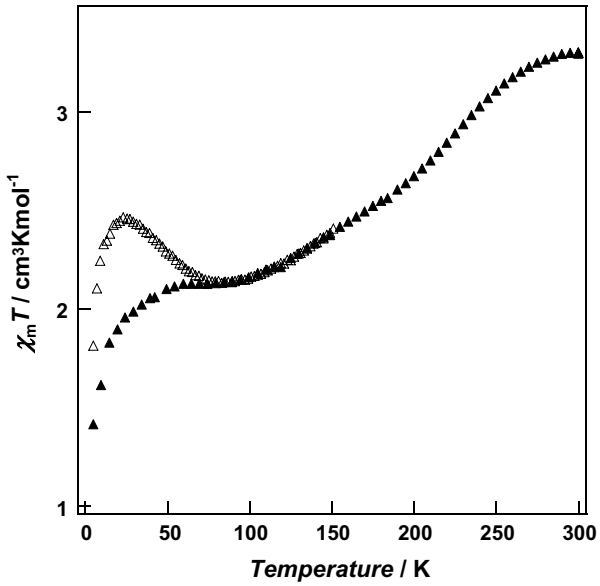


Fig. 6. $\chi_m T$ vs. T plots for the compound **1** (▲). $\chi_m T$ vs. T plots for LIESST experiment were recorded in the warming mode (△).

1 h, the $\chi_m T$ value was increased (Fig. 6). The change in the $\chi_m T$ value persisted for many hours, even after the illumination was stopped. This suggests that the transition from the low-spin state to the high-spin state can be induced by illumination. The relaxation temperature of the LIESST effect is defined as T (LIESST) [20], the temperature dependence of $\chi_m T$ after illumination shows that the $\chi_m T$ value decreases with the increase in temperature and that the thermal relaxation to the ground state occurs. The T (LIESST) is 47 K, the compound **1** can exhibit photo-switching below 47 K. About 12% of the metastable high-spin fraction were induced by illumination. The $\chi_m T$ value for **2** was 0 $cm^3\ K\ mol^{-1}$ in the temperature range of 5–400 K. Spin-crossover was not observed, and the compound **2** was in the low-spin state ($S = 0$). The Mössbauer spectra were also measured in the temperature range between 80 K and 300 K. Mössbauer spectra at 80 K and 300 K show a doublet peak with quadrupole-split doublet (quadrupole-splitting $\Delta Q = 0.42$ mm s^{-1}, isomer shift $\delta = 0.34$ mm s^{-1} at 80 K, and $\Delta Q = 0.38$ mm s^{-1}, $\delta = 0.26$ mm s^{-1} at 300 K) representing the low-spin state. The compound **2** exhibits the crystal-mesophase transition at 322 K, but the compound was in the low-spin state even above 322 K.

We are now measuring the magnetic and mesophase properties of the iron(II) compound $[Fe(3C16\text{-}O\text{-}bzimpy)_2](BF_4)_2$ (3C16-O-bzimpy = 2,6-bis(*N*-hexadecylbenzimidazol-2′-yl))-4-hexadecyloxypyridine eventually exhibiting a spin-crossover behavior induced by mesophase transition or a mesophase transition induced by LIESST.

4. Conclusion

The iron(II) compounds **1** and **2** with long alkyl chains have been synthesized, the properties of these compounds

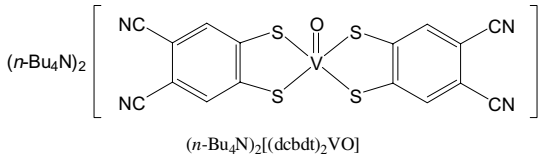
were characterized. The compounds **1** and **2** exhibited liquid-crystal properties which were confirmed by DSC, XRD diffractions, and texture under crossed polarizers. The compound **2** was in the low-spin state. The compound **1** exhibited spin-crossover and LIESST phenomena, i.e. three physical properties, spin-crossover, LIESST effect and liquid-crystal properties, can coexist in a single compound. Geometrical flexibility in the molecules is very important in order to achieve co-occurrence of various physical properties in the functional molecular-based materials. We believe that our approach, i.e., the co-occurrence of spin-crossover, LIESST and liquid-crystal properties, can be widely applied, not only in the design of LIESST compounds with liquid-crystal properties but also in the design of a variety of optically switchable molecular compounds.

Acknowledgements

This work was supported by Grant-in-Aids for Science Research (No. 17750130) from the Ministry of Education, Culture, Sports, Science and Technology of the Japanese Government, Inamori, Foundation, Kato Foundation, The Murata Science Foundation, and "Development of Molecular Devices in Ferroelectric Metallomesogens" in 2006 from New Energy and Industrial Technology Development Organization (NEDO) of Japan.

References

[1] K. Binnemans, Y.G. Galyametdinov, R.V. Deun, D.W. Bruce, S.R. Collinson, A.P. Polishchuk, I. Bikchantaev, W. Haase, A.V. Prosvirin, L. Tinchurina, I. Litvinov, A. Gubajdullin, A. Rakhmatullin, K. Uytterhoeven, L.V. Meervelt, J. Am. Chem. Soc. 122 (2000) 4335.
[2] K. Ohta, N. Yamaguchi, I. Yamamoto, J. Mater. Chem. 8 (1998) 2637.
[3] R. Werner, K. Falk, S. Ostrovsky, W. Haase, Macromol. Chem. Phys. 202 (2001) 2813.
[4] C. Piechocki, J. Simon, A. Skoulios, D. Guillon, P. Weber, J. Am. Chem. Soc. 104 (1982) 5245.
[5] A.M. Giround-Godquin, J.C. Marchon, J. Phys. Lett. 45 (1984) L681.
[6] Y. Galyametdinov, V. Ksenofontov, A. Prosvirin, I. Ovchinnikov, G. Ivanova, P. Gütlich, W. Haase, Angew. Chem., Int. Ed. Engl. 40 (2001) 4269.
[7] S. Hayami, Z. Gu, M. Shiro, Y. Einaga, A. Fujishima, O. Sato, J. Am. Chem. Soc. 122 (2000) 7126.
[8] O. Kahn, C.J. Martinez, Science 279 (1998) 44.
[9] J.A. Real, E. Andrés, M.C. Muñoz, M. Julve, T. Granier, A. Bousseksou, F. Varret, Science 268 (1995) 265.
[10] G.J. Halder, C.J. Kepert, B. Moubaraki, K.S. Murray, J.D. Cashion, Science 298 (2002) 1762.
[11] S. Decurtins, P. Gütlich, C.P. Köhler, H. Spiering, A. Hauser, Chem. Phys. Lett. 105 (1984) 1.
[12] P. Gütlich, A. Hauser, H. Spiering, Angew. Chem., Int. Ed. Engl. 33 (1994) 2024.
[13] J-F. Létard, J.A. Real, N. Moliner, A.B. Gaspar, L. Capes, O. Cador, O. Kahn, J. Am. Chem. Soc. 121 (1999) 10630.
[14] S. Hayami, Z. Gu, Y. Einaga, Y. Kobayasi, Y. Ishikawa, Y. Yamada, A. Fujishima, O. Sato, Inorg. Chem. 40 (2001) 3240.
[15] S. Hayami, K. Danjobara, K. Inoue, Y. Ogawa, N. Matsumoto, Y. Maeda, Adv. Mater. 16 (2004) 869.
[16] S. Hayami, K. Danjobara, S. Miyazaki, K. Inoue, Y. Ogawa, Y. Maeda, Polyhedron 24 (2005) 2821.
[17] R. Boča, M. Boča, L'. Dlháň, K. Falk, H. Fuess, W. Haase, R. Jaroščiak, B. Papánková, F. Renz, M. Vrbová, R. Werner, Inorg. Chem. 40 (2001) 3025.
[18] W. Linert, M. Konecny, F. REnz, J. Chem. Soc., Dalton Trans. (1994) 1523.
[19] M. Haga, H. Hong, Y. Shiozawa, Y. Kawata, H. Monjushiro, T. Fukuo, R. Arakawa, Inorg. Chem. 39 (2000) 4556.
[20] J-F. Létard, L. Capes, G. Chastanet, N. Moliner, S. Létard, J-A. Real, O. Kahn, Chem. Phys. Lett. 313 (1999) 115.



$(n\text{-}Bu_4N)_2[(dcbdt)_2VO]$

Scheme 1.

2. Experimental

$(n\text{-}Bu_4N)_2[(dcbdt)_2VO]$ was prepared in accordance with the literature [9]. Glass substrates (Matsunami, Japan) were washed with pure water, acetone and dried under UV irradiation before fabrication. Positively charged polystyrene particles (214 ± 19 nm, trimethylammonium latex, Merck) were used for absorption. Fig. 1 shows schematic fabrication process of deposition by colloidal lithography.

Ultrasonic irradiation of glass substrates in the solution of particles was performed for 5 min before immersion. Immersion time was 30 min to allow the absorption to reach saturation. Excess particles were removed during the substrate dipping in 98 °C pure water for 30 s. The substrates were then dipped in cold water and dried with clean air. Monolayered particles were obtained on the substrate (Fig. 1a). Cast process of the dithiolene metal complex solution was performed as follows. Firstly 0.13 ml of an acetonitrile solution of the metal complex (45.4 mg/l) was cast on a glass substrate in a vacuum desiccator. Under reduced pressure of 100 mm Hg, the solvent on the substrate was evaporated within 5 min. After the solvent evaporation the particles were selectively removed by an adhesive tape (Fig. 2c). Finally ring structure deposits were obtained on the substrate (Fig. 2d).

The deposits were examined with an analytic scanning electron microscope (JSM-6360LA, JEOL Ltd.), an atomic force microscope (VN-8000, Keyence Corp.) and a scanning probe microscope (SPI 3700, SII Nanotechnology Inc.).

3. Results and discussion

In fabricating the ordered domains of molecules, controllability of the adsorption of polystyrene particles is important because the adsorbed particles are used as a template of ring structures. First we examined the relationship between particle concentration and surface coverage. Surface coverage was measured as an area of particles divided by total area. Fig. 2a shows a SEM image of the substrate surface after immersion in particle concentration of 1% (by weight). Multilayered particles were observed after rinsing of excess particles in pure water. When particle concentration of 0.1% (by weight) was used for immersion, a particle monolayer film of coverage 0.30 was observed (Fig. 2b). Below this concentration, such as particle concentration of 0.01% (by weight), particles did not uniformly cover a substrate surface and only gave particles islands (Fig. 2c).

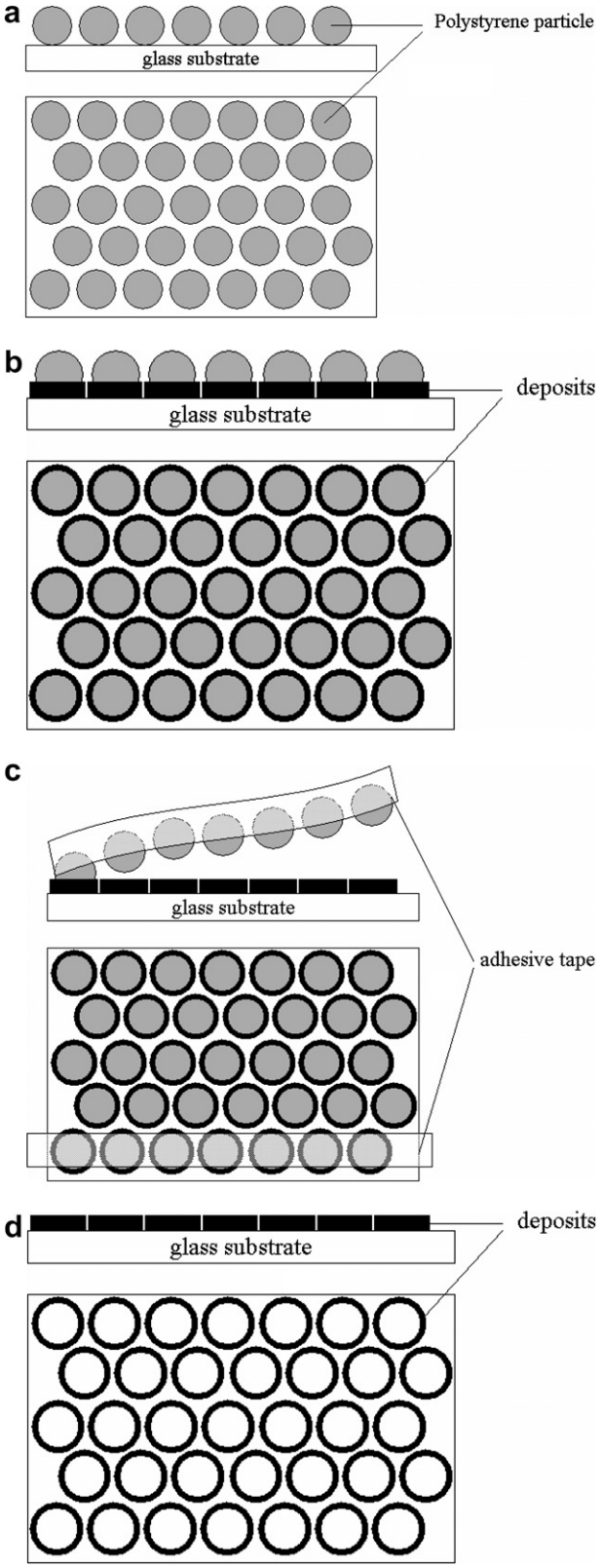


Fig. 1. Schematic side and top view illustrations of the fabrication process of nano-scale rings using colloidal lithography: (a) adsorption of polystyrene particles on a glass substrate, (b) deposition obtained by cast of the metal complex solution and rapid solvent evaporation, (c) removal of the particles by an adhesive tape and (d) deposits having regulated size and position.

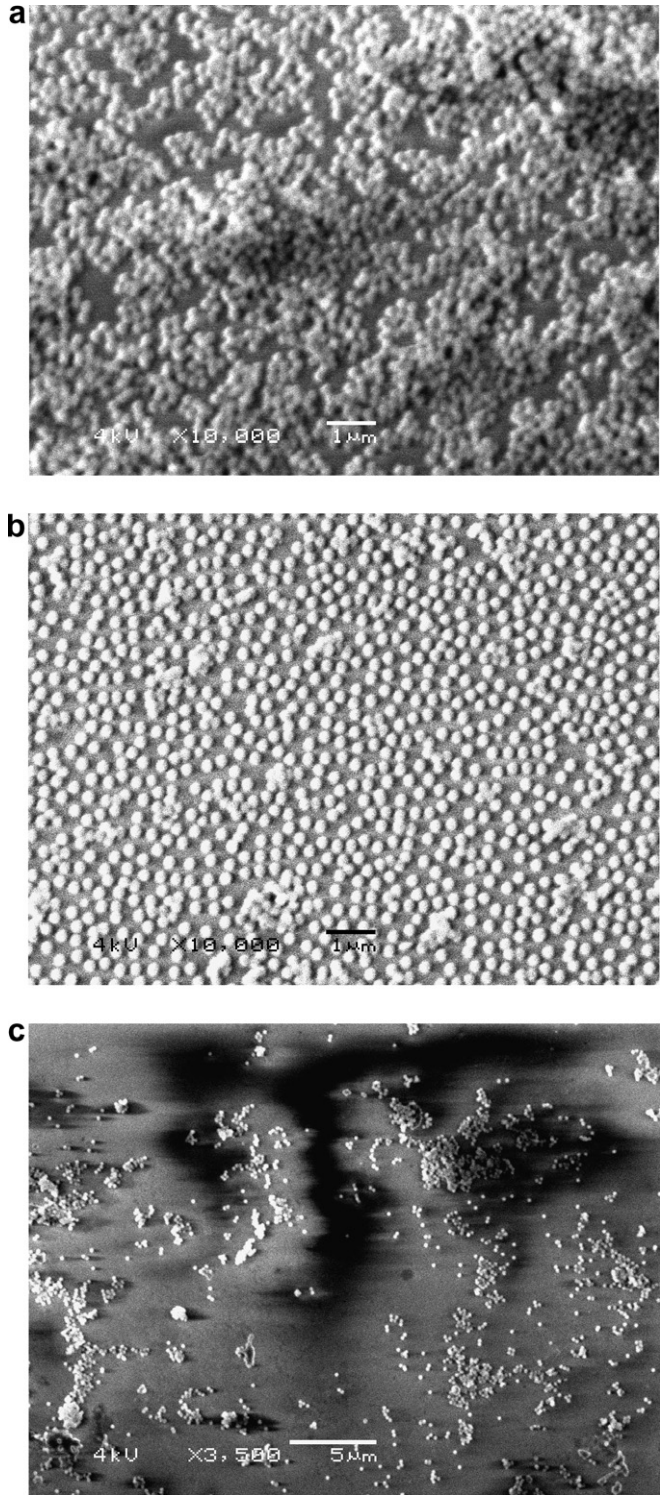


Fig. 2. Particle concentration dependence of adsorbed particles distribution: (a) 1 wt% (b) 0.1 wt% and (c) 0.01 wt% concentration, respectively.

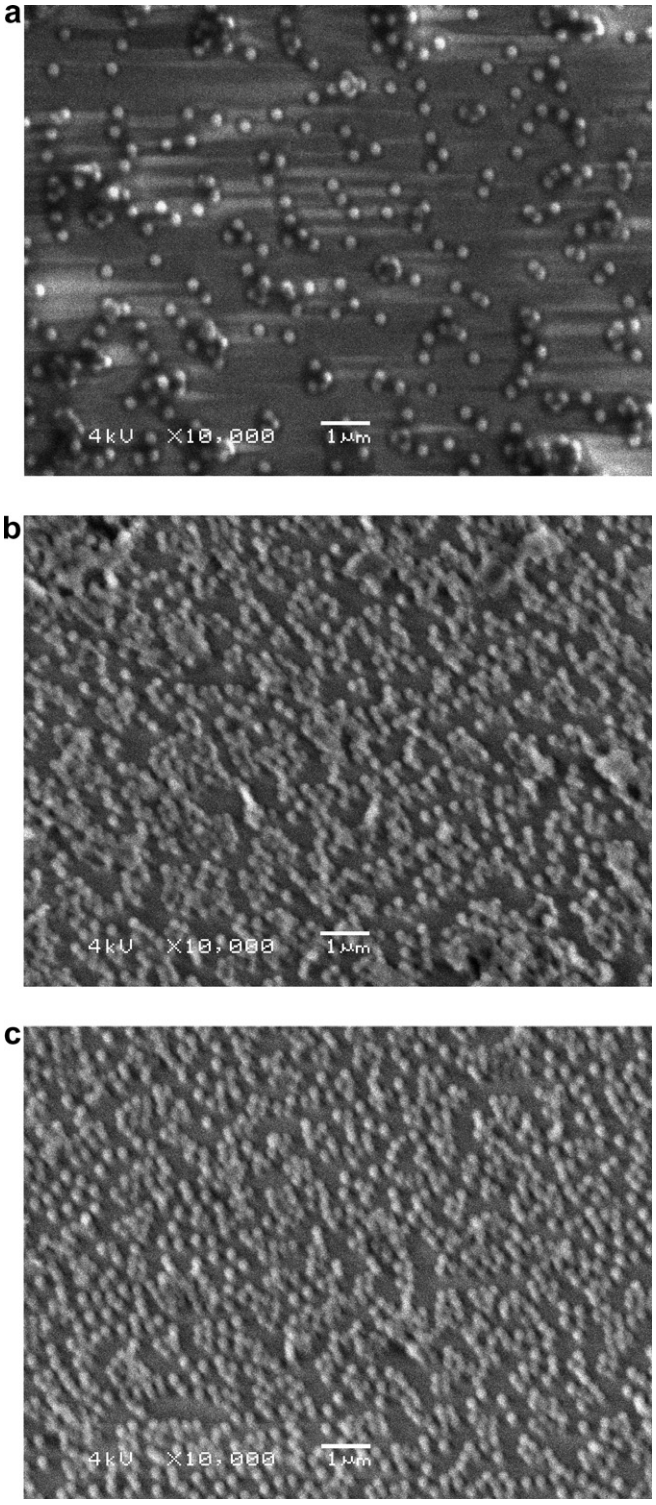


Fig. 3. Acetonitrile evaporating time dependence of adsorbed particles expansion: (a) 20 min, (b) 10 min and (c) 5 min evaporating time, respectively.

Second we examined the relationship between exposing time of particles to acetonitrile and their appearance change because polystyrene is known to adsorb commonly used organic solvents. When solvent evaporating time over 20 min under ambient pressure, 120% expansion of particles and particle aggregation was found (Fig. 3a).

This aggregation of the particles could be explained as follows. During solvent exposure the particles absorbed the solvent and changed their shape to expand their diameter. This shape change reduced the adhesive force to the substrate surface. The aggregation of particles on the sur-

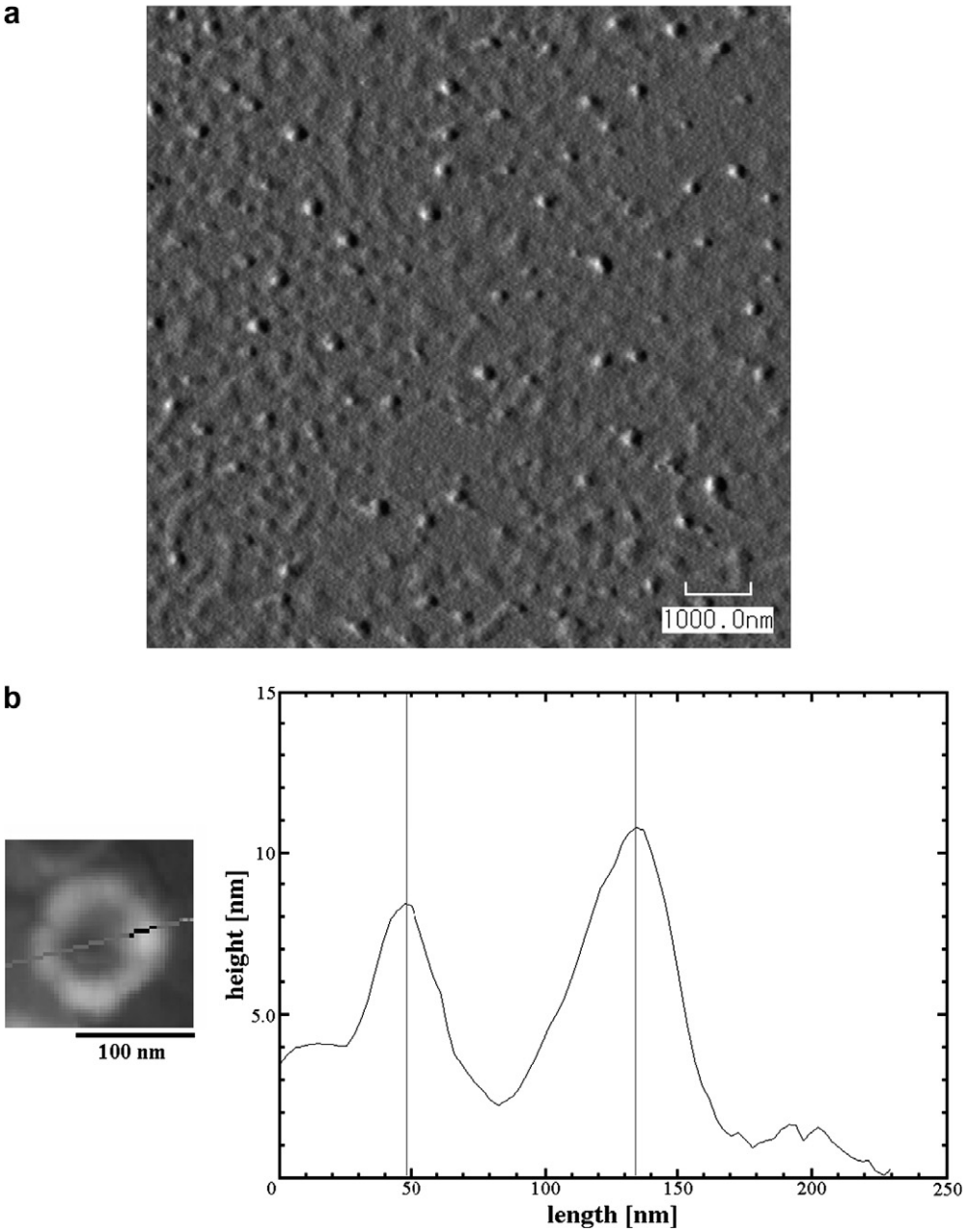


Fig. 4. A top view AFM image of the deposits (a) and a cross section diagram of the corresponding deposits (b).

face is normally ascribed to capillary forces created by the menisci between particles as the solvent evaporates [12]. So further evaporation of solvent made particles aggregate by capillary forces. To suppress the particle aggregation, evaporation of solvent should be terminated before particle shape change not to lose adhesive force to the surface. We examined more rapid evaporating condition. For 10 min at less than 250 mm Hg only 5% particle expansion was observed and there was no aggregated particles on the substrate (Fig. 3b). Further shorter evaporating time of 5 min did not show obvious improvement (Fig. 3c). We adopted the 5 min solvent evaporating as a metal complex deposition condition. An AFM image of the ring structure deposits appeared after removal of the particles by an adhesive tape revealed that average diameters of deposits are around 150 nm (Fig. 4a). Furthermore the cross section diagram of deposits showed that the ring structure deposits a ring structure of the outer diameter of 130 nm has a thickness of around 10 nm (Fig. 4b).

This result suggests that the polystyrene particle acted as a template of nano-scale ring of the complex and the ring position was regulated by the template polystyrene particle.

4. Summary

We have successfully fabricated nano-scale ring structures of paramagnetic metal complex, (n-Bu_4N)[$(dcbdt)_2$-VO], on a glass substrate using a simple and easy colloidal

lithography for the first time. Our simple and easy technique can be applicable to low cost nano-scale lithography. We are now experimentally investigating relationship between magnetic properties and size-dependence of the ring structures and the results will be reported elsewhere.

Acknowledgements

This work was partially supported by a grant-in-aid for scientific research (No. 16750114) from JSPS, Research Foundation for the Electrotechnology of Chubu and Foundation for Scientific Promotion from Shizuoka University.

References

[1] J.S. Miller, A.J. Epstein, MRS Bull. 11 (2000) 21.
[2] M. Clemente-León, H. Soyer, E. Coronado, C. Mingotaud, Angew. Chem., Int. Ed. 37 (1998) 2842.
[3] G.C. Condorelli, A. Motta, I.L. Fragala, E. Giannazzo, V. Rainieri, A. Caneschi, D. Gatteschi, Angew. Chem., Int. Ed. 43 (2004) 4081.
[4] D. Ruiz-Molina, M. Mas-Torrent, J. Gómez, A.I. Balana, N. Domingo, J. Tejada, M.T. Martínez, C. Rovira, J. Veciana, Adv. Mater. 15 (2003) 42.
[5] A. Cornia, A.C. Fabretti, M. Pacchioni, L. Zobbi, D. Bonacchi, A. Caneschi, D. Gatteschi, R. Biagi, U. Del Pennino, V. D Renzi, L. Gurevich, H.S. Van der Zant, Angew. Chem., Int. Ed. 42 (2003) 1645.
[6] M. Cavallini, F. Biscarini, J. Gómez-Segura, D. Ruinz, J. Veciana, Nano Lett. 3 (2003) 1527.
[7] M. Cavallini, J. Gomez-Segura, D. Ruiz-Molina, M. Massi, C. Albonetti, C. Rovira, J. Veciana, F. Biscarini, Angew. Chem., Int. Ed. 44 (2005) 888.
[8] K. Ueda, G. Tanaka, T. Suzuki, R. Kita, S. Kokado, Polyhedron 24 (2005) 2533.
[9] T. Suzuki, K. Ueda, R. Kita, S. Kokado, K. Harigaya, Polyhedron 24 (2005) 2492.
[10] P. Hanarp, D.S. Sutherland, J. Gold, B. Kasemo, Colloids Surf. A 214 (2003) 23.
[11] K. Fujimoto, T. Hiroi, M. Nakamura, e-J. Surf. Sci., Nanotech. 3 (2005) 327.
[12] C.A. Johnson, A.M. Lenhoff, J. Colloid Interface Sci. 179 (1996) 587.

carboxylates [11], sulfonates [12–15], glucose [16], phosphonates [17], polyoxyethylene [18], amino [19] and carboranyl groups [20] have been reported. Most of these compounds are highly aggregated in aqueous media, this phenomenon being most-easily recognized by severe broadening of the absorption bands in their optical spectra. Tetrasulfonated phthalocyanines are well known with their great theoretical and practical significance thanks to their high solubility in aqueous solution in a wide range of pH and their easy preparation [12–15]. The expanded π orbitals of condensed multicyclic aromatic compounds (e.g., naphthalocyanines) create a large oscillator strength in the Q band region and result in high quantum yields of fluorescence for photoemission studies [21]. Introduction of naphthalenyl groups with bulky electron rich units on the macrocycle core is expected to enhance photophysical or electrochemical properties of phthalocyanines in solution or film states [7a,21a,22].

We have recently reported the synthesis, electrochemical and spectroelectrochemical properties of mono metal phthalocyanines [23–25], dimeric phthalocyanine [26], double-decker phthalocyanines [27–29] and some *vic*-dioxime metal complexes [30–34] in aqueous and non-aqueous media. We report herein the synthesis and characterization of a new highly water-soluble metal-free phthalocyanine bearing naphthoxy-4-sulfonic acid sodium salt. This new compound exhibits the characteristic monomeric UV–Vis absorption of phthalocyanine in methanol and DMSO. In most applications of phthalocyanine complexes, a good understanding of the redox properties of these complexes is important. Spectroelectrochemical studies of phthalocyanines facilitate understanding of the nature of the redox processes that may take place at either the central metal atom or the phthalocyanine ring. Such processes cannot usually be distinguished by electrochemistry only [35]. Spectroelectrochemical studies of phthalocyanines are also important with regard to their possible use as electrochromic materials, where several colors are displayed depending on the potential applied to the electrode surface [23–29]. Considering these purposes in our work, the results of the electrochemical and spectroelectrochemical investigation of 2,9,16,23-tetrakis-(4-(1-naphthoxy-4-sulfonic acid sodium salt))phthalocyanine are also reported in detail in our study.

2. Experimental section

2.1. Chemicals and reagents

1-Naphthol-4-sulfonic acid sodium salt **2** (Merck, 70%) was purified by column chromatography (silica gel, MeOH–CH_2Cl_2, 5:1) before used. DMSO was dried over a molecular sieve of 4 Å. 4-Nitrophthalonitrile **1** was prepared and purified according to the methods described in the literature [36]. Electrochemical grade tetrabutylammonium perchlorate (*n*-Bu_4NClO_4, TBAP, Fluka Chemical Company) (0.1 mol dm^{-3}) was employed as the supporting electrolyte.

2.2. Instrumentation

^{1}H NMR spectra were recorded on a Bruker 250 MHz spectrometer. (FTIR) spectra were recorded on a Perkin–Elmer FTIR spectrophotometer where samples were dispersed in KBr. Elemental analyses were carried out in the Marmara Research Center. UV–Vis spectra were recorded on an Agillent Model 8453 diode array spectrophotometer. Cyclic voltammograms (CV) were carried out using CV measurements with a Princeton Applied Research Model 2263 potentiostat controlled by an external PC. A three electrode system (BASI (Bioanalytical System Incorporation) model solid cell stand) was used for CV measurements in DMSO and consisted of a 2 mm sized platinum disc electrode as a working electrode, a platinum wire counter electrode and a pseudo Ag/AgCl reference electrode. The reference electrode was separated from the bulk solution by a fritted-glass bridge filled with the solvent/supporting electrolyte mixture. The ferrocene/ferrocenium couple (Fc/Fc^+) was used as an internal standard but all potentials in the paper are referenced to the pseudo Ag/AgCl reference electrode. Solutions containing **$NhtH_2Pc$** were deoxygenated by a stream of high purity nitrogen for at least 5 min before running the experiment and the solution was protected from air by a blanket of nitrogen during the experiment. Controlled potential electrolysis (CPE) was performed with a Princeton Applied Research Model 2263 potentiostat/galvanostat. A BASI model electrolysis cell with a fritted glass to separate the cathodic and anodic portions of the cell was used for bulk electrolysis. The sample and solvent were placed in the electrolysis cell under nitrogen. UV–Vis spectroelectrochemical experiments were performed with a home-built thin-layer cell that utilized a light transparent platinum gauze working electrode [37]. A platinum wire counter electrode and a pseudo Ag/AgCl reference electrode were used for the spectroelectrochemical cell. Potentials were applied and monitored with a Princeton Applied Research Model 2263 potentiostat. Time-resolved UV–Vis spectra were recorded on an Agillent Model 8453 diode array spectrophotometer.

2.3. Synthesis of 4-(1-naphthoxy-4-sulfonic acid sodium salt)phthalonitrile (3)

4-Nitro-phthalonitrile **1** (1.00 g, 5.78 mmol) and 1-naphthol-4-sulfonic acid sodium salt **2** (1.18 g, 5.78 mmol) were stirred and dissolved in 10 ml of dry DMSO at 45 °C. Anhydrous Na_2CO_3 was added portionwise over 2 h under a nitrogen atmosphere, then the reaction mixture was stirred vigorously for a further 48 h. After reaction completed, the mixture was cooled to ambient temperature and then filtered off to remove undesired inorganic salts. The filtration that was collected was poured onto 10 ml of cold chloroform. The precipitated thus obtained was collected and filtered off, then washed with chloroform, cold ethanol and acetone, respectively. The crude product was dissolved in 15 ml of methanol and precipitated by adding 50 ml of

ethanol. It was then further purified by column chromatography (silica gel, MeOH–CH_2Cl_2, 5:1) This compound is soluble in water, methanol and in DMSO. Yield: 1.13 g (53%). *Anal.* Calc. for $C_{18}H_9NaN_2O_4S$ (M_w: 372.33): C, 58.07; H, 2.44; N, 7.52. Found: C, 57.57; H, 2.51; N, 7.21%. IR [(KBr)ν_{max}/cm^{-1}]: 3073 (Ar H), 2233 (–CN), 1593, 1564 (Ar), 1275 (Ar–O–Ar), 1190 (O–S–O), 777, 655. ^{1}H NMR ([D_4]-methanol): δ ppm = 7.20–8.90 (m, 9H, ArH). UV–Vis (MeOH): λ_{max} = 290.

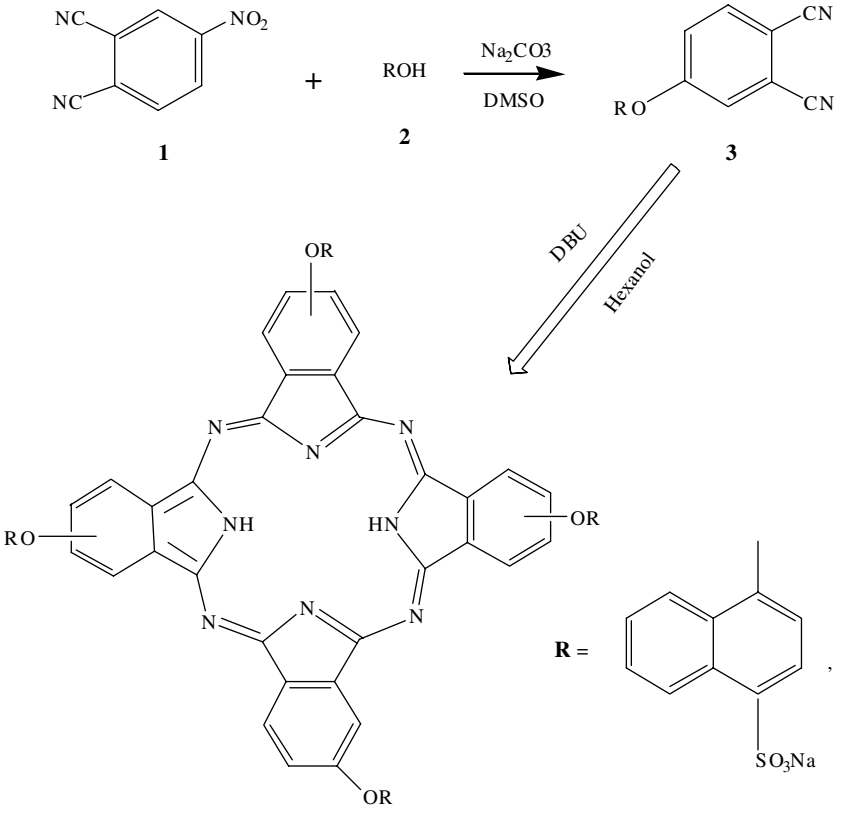
2.4. Synthesis of 2,9,16,23-tetrakis(4-(1-naphthoxy-4-sulfonic acid sodium salt))phthalocyanine (**NhtH$_2$Pc**)

4-(1-Naphthoxy-4-sulfonic acid sodium salt)phthalonitrile **3** (0.50 g, 1.2 mmol), 1-hexanol (5 ml) and 1.8-diazabicyclo[5.4.0]undec-7-ene (DBU) (0.7 ml) were mixed together. The mixture was refluxed for 30 h under a nitrogen atmosphere. After the reaction completed, the mixture was cooled to ambient temperature. Ethanol (50 ml) was added into the reaction mixture to completely precipitate the crude product, which was then filtered off and washed with ethanol and acetone. The crude product, taken into 50 ml of ethanol, was refluxed for 30 min, then the hot mixture was filtered off. The same procedure was repeated for three times. The obtained product was purified by column chromatography (silica gel, MeOH–CH_2Cl_2, 10:1). This compound is soluble in water, methanol and DMSO. Yield: 0.33 g (16%). *Anal.* Calc. for $C_{72}H_{42}Na_4N_8O_{16}S_4$ (M_w: 1495.38): C, 57.83; H, 2.83; N, 7.49. Found: C, 57.09; H, 2.61; N, 7.17%. IR [(KBr)ν_{max}/cm^{-1}]: 3383 (NH), 3073 (Ar H), 1590, 1574 (Ar), 1275 (Ar–O–Ar), 1183 (O–S–O), 763, 688. ^{1}H NMR ([D_6]-DMSO)): δ ppm = 7.01–8.90 (m, 36H, ArH). UV–Vis (MeOH): λ_{max} (log ε) = 290 (5.06), 340 (5.05), 662 (5.17), 696 (5.22).

3. Results and discussion

3.1. Synthesis

4-(1-Naphthoxy-4-sulfonic acid sodium salt)phthalonitrile **3** was prepared through the displacement reaction of 4-nitrophthalonitrile **1** with 1-naphthol-4-sulfonic acid sodium salt **2** in DMSO solution in a moderate yield. Conversion of **3** into the corresponding metal-free phthalocyanine **NhtH$_2$Pc** was accomplished in anhydrous 1-hexanol in the presence of 1,8-diazabicyclo[5.4.0]undec-7-ene (Scheme 1). Column chromatography with methanol/dichloromethane (5:1) eluent on silica gel was employed to obtain the pure product. As expected, the dark green product was soluble in water, methanol and DMSO thanks to the introduction of the naphthoxy-sulfonic acid sodium salt which has hydrophilic character on



Scheme 1. Synthetic route to metal-free phthalocyanine **NhtH$_2$Pc**.

the peripheral position of the phthalocyanine core. Elemental analysis and spectroscopic data (IR, ^{1}H NMR and UV–Vis) confirmed the assigned structure for **NhtH$_2$Pc**. Comparing the IR spectrum of **1** with that of phthalonitrile derivative **3** confirmed the proposed structure of **3** by the disappearance of the aromatic –NO$_2$ band at 1548 cm^{-1} and the appearance of new bands at 1275 (Ar–O–Ar) and 1190 cm^{-1} (O–S–O). After conversion of **3** to the metal-free phthalocyanine **NhtH$_2$Pc**, the characteristic band corresponding to the C≡N vibration at 2233 cm^{-1} disappeared. The characteristic NH stretching absorption of the inner core of the metal-free phthalocyanine was observed around 3300 cm^{-1} besides the absorption bands observed at 1275 (Ar–O–Ar), and 1183 cm^{-1} (O–S–O).

The ^{1}H NMR spectra of **3** and **NhtH$_2$Pc** are given in Fig. 1a and b. The aromatic protons of **3** and **NhtH$_2$Pc** (aromatic core on the phthalocyanine unit and naphtho groups) appeared as multiplets between at 7.01 and 8.90 ppm (m, 9H, ArH) for **3** and (m, 36H, ArH) for **NhtH$_2$Pc**. The N–H protons of the metal-free phthalocyanine were also observed as a weak–broad peak upfield ($\delta = -3.60$ ppm), probably due to its low solubility in the solution used for the ^{1}H NMR spectrum.

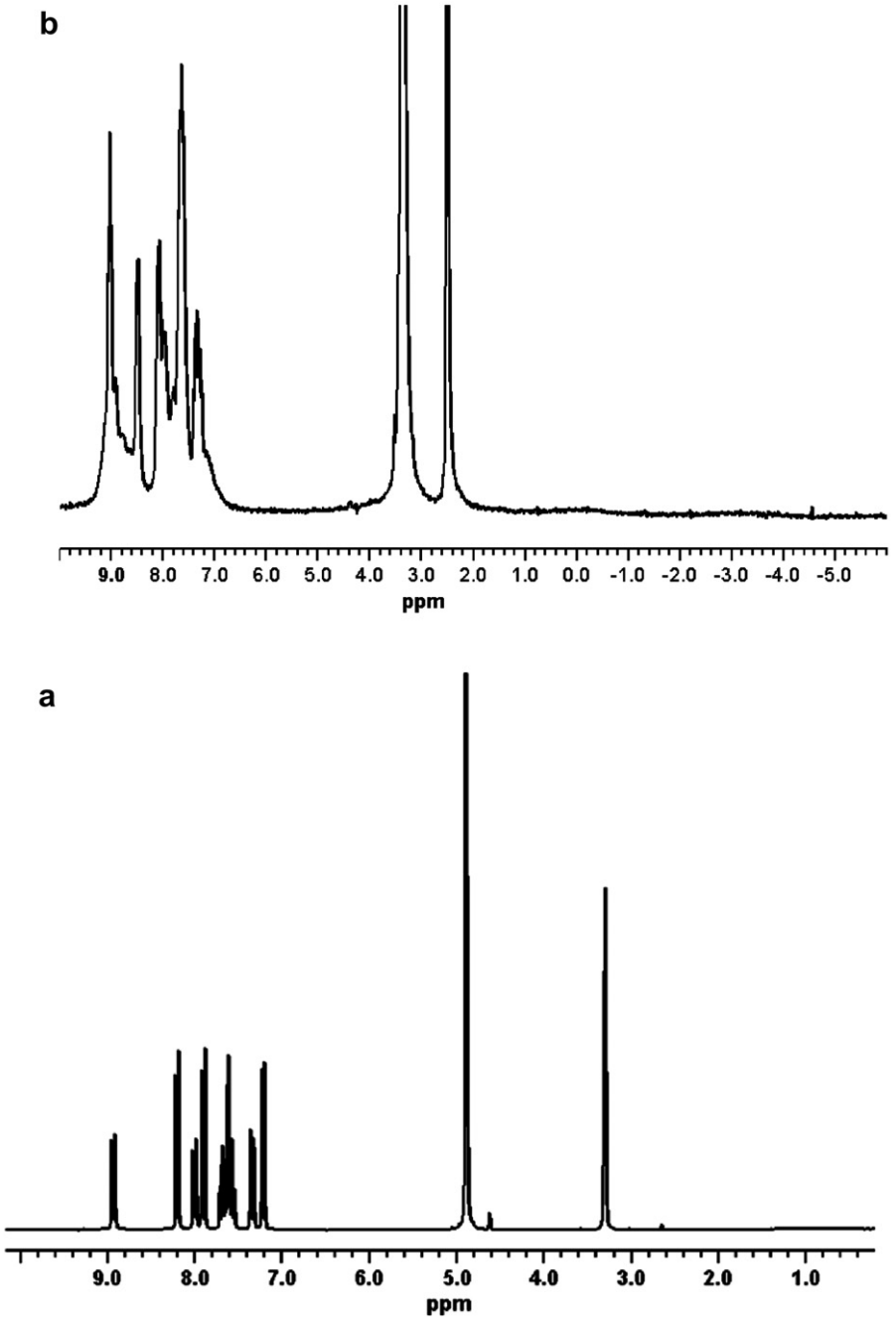


Fig. 1. ^{1}H NMR spectra of **3** (a) and **NhtH$_2$Pc** (b).

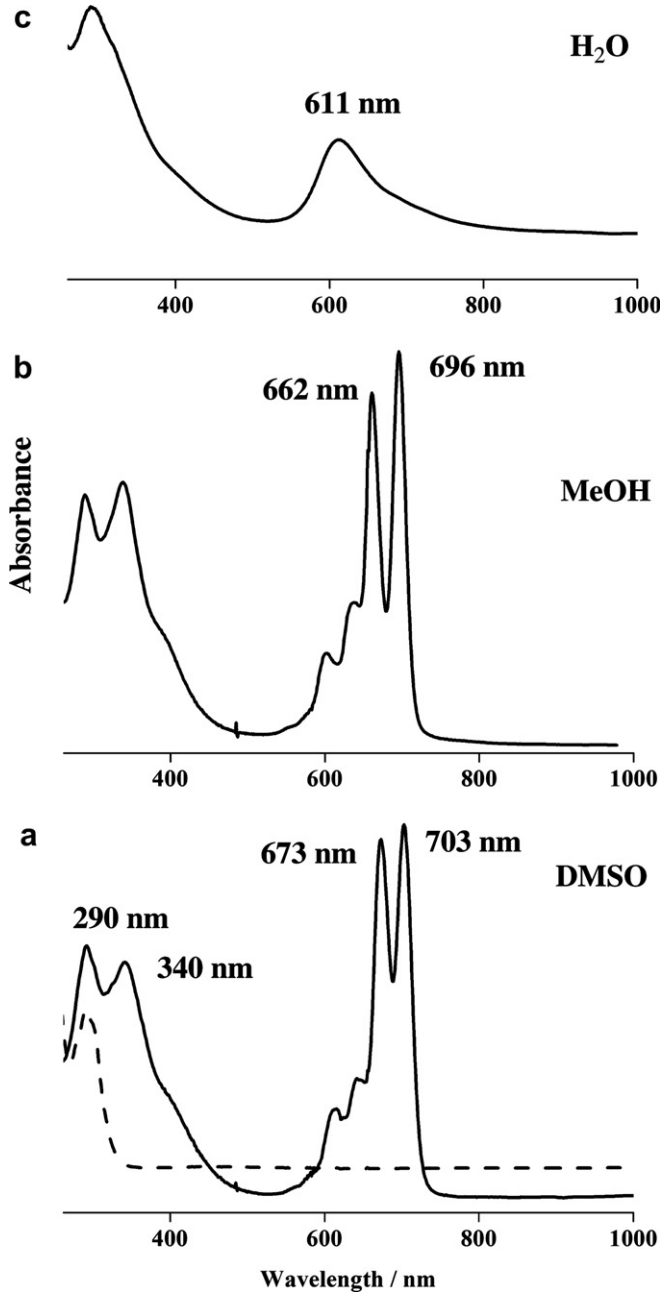


Fig. 2. UV–Vis spectra of **3** (a) (dashed line), **NhtH$_2$Pc** (a) (solid line) in DMSO; **NhtH$_2$Pc** (b) in MeOH; **NhtH$_2$Pc** (c) in H_2O.

The UV–Vis absorption spectra of **3** and **NhtH$_2$Pc** in protic and aprotic solvents are given in Fig. 2. As can be seen from Fig. 2a (the dashed line), compound **3** shows the characteristic absorption band at 290 nm corresponding to a $\pi\rightarrow\pi^*$ transition due to the existence of the naphthalenyl group on the molecule. In the case of **NhtH$_2$Pc**, two main split intense bands, (Q_1 and Q_2 bands) and B (soret bands) were observed at 703, 673 and 340 nm in DMSO, respectively (Fig. 1a, solid line). The $\pi\rightarrow\pi^*$ transitions of the naphthalenyl groups integrated on phthalocyanine core were also observed at 290 nm. It could be seen that the $\pi\rightarrow\pi^*$ transitions of the naphthalenyl groups attached on the phthalocyanine main core are not affected in spite of

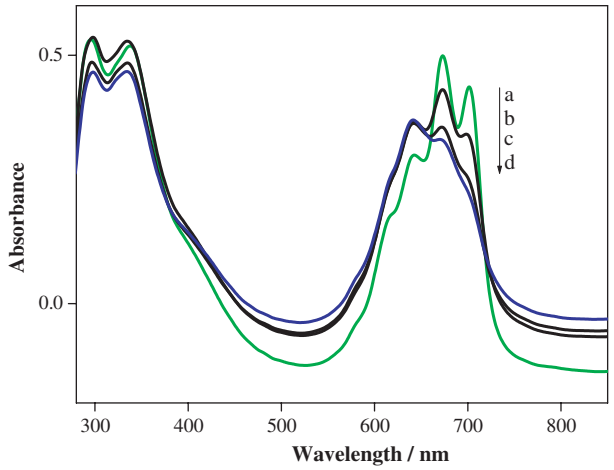


Fig. 3. UV–Vis spectral changes on aggregation of **NhtH$_2$Pc**.

integration of the π-electrons of the naphthalenyl substituent into the phthalocyanine system. Because the full conjugation of the π-systems is not changed with this integration, no large shifts toward the near IR region for the Q and B bands in the UV–Vis spectrum of **NhtH$_2$Pc** were observed compared with those of phthalocyanine fused aromatic rings (e.g., naphthalocyanines) [38]. It can also be seen from Fig. 2a and b that the Q bands in DMSO solution shift to lower energy by about 10 nm compared with those in methanol solution. Fig. 2c shows that the **NhtH$_2$Pc** molecules aggregate in water but not in methanol (Fig. 2b) and DMSO solutions (Fig. 2a, solid line). The band corresponding to the aggregated form of the molecules in water appears as broad peak at 611 nm (Fig. 2c) as expected. The aggregation study of **NhtH$_2$Pc** molecules was performed by UV–Vis spectral changes for a methanol solution where water was added step by step into the methanol solution to understand the degree of aggregation depended upon the ratio of methanol and water used in the experiment. The UV–Vis spectral changes showed at the 611 nm peak, and the 662 and 696 nm peaks in the case of the 1:1 ratio of methanol and water, which refer to both aggregated and non-aggregated mono phthalocyanine forms in the methanol–water solution (Fig. 3, blue[1] solid line).

3.2. Electrochemistry

The electrochemical behavior of **NhtH$_2$Pc** was investigated using a cyclic voltammetric (CV) technique in a DMSO solution containing 0.1 M TBAP. The data obtained in this work and some selected data from the literature are summarized in Table 1. Fig. 4 shows the CV of **NhtH$_2$Pc**, which displays three reversible one-electron reductions with the corresponding anodic waves and one irreversible oxidation without a corresponding anodic wave at a 0.100 V s^{-1} scan rate in DMSO containing the pseudo

[1] For interpretation of references in color, the reader is referred to the web version of this article.

Table 1
The electrochemical half-wave potentials of **$NhtH_2Pc$** and some selected metal-free phthalocyanines from the literature

Complexes	Solvent	Reductions			Oxidation	Ref.
		Pc^{5-}/Pc^{4-} $E_{1/2}$[a] (V)	Pc^{4-}/Pc^{3-} $E_{1/2}$[a] (V)	Pc^{3-}/Pc^{2-} $E_{1/2}$[a] (V)		
($NhtH_2Pc$)	DMSO	−1.24 (0.011)	−0.924 (0.011)	−0.510 (0.062)	0.590[b]	tw
H_2Pc	DMSO		−1.06	−0.66		[40]
$[(SO_3)_4H_2Pc]$	DMSO		−0.97	−0.53	0.90 (2e)	[40]

[a] $E_{1/2}$ (V) = $E_{pa} + E_{pc}/2$.
[b] Cathodic peak potential, values of $\Delta E_p(=E_{pa} - E_{pc})$ for complexes are given in parenthesis; tw: this work.

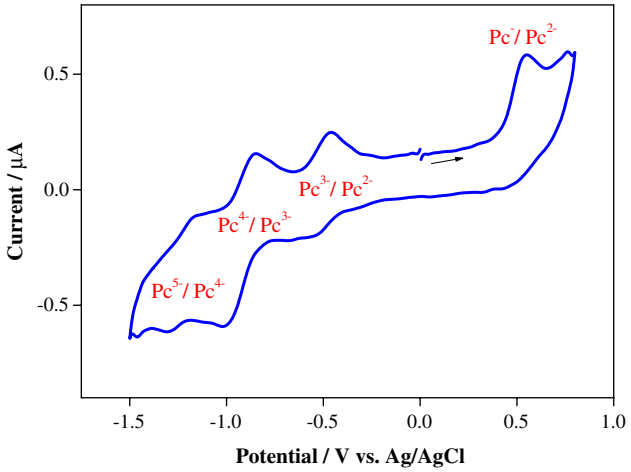
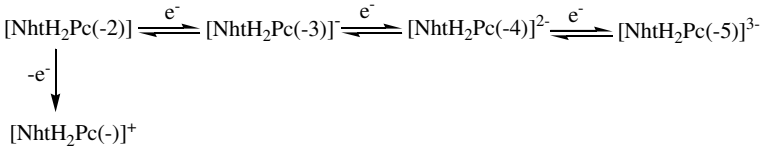


Fig. 4. Cyclic voltammogram of **$NhtH_2Pc$** in DMSO solution containing 0.1 M TBAP. Scan rate = 0.100 V s^{-1}.

Ag/AgCl electrode system. The lack of reversibility of the oxidation process is probably due to the increasing polarization effect by means of four sulfonates groups attached on the phthalocyanine ring. Similar behavior was observed for some *vic*-dioxime complexes having four carboxylate groups on the oxime moiety [39]. It is clear that the reduction waves are assigned to the macrocycle system, and these are indicated in Fig. 4 and Table 1 as Pc^{3-}/Pc^{2-}, Pc^{4-}/Pc^{3-} and Pc^{5-}/Pc^{4-} couples, respectively. Even if highly reduced states of the metal-free phthalocyanine are frequently mentioned, the reduction of the proton bound to the macrocycle has never been reported [40]. So all the reduced forms observed in this study were attributed to the macrocycle system. It can be seen from Table 1 that the electrochemical half-wave potentials of the first, second and third reduction processes are located at $E_{1/2} = -0.510$, -0.924 and -1.24 V, respectively while the anodic potential of the oxidation process displays at $E_{1/2} = 0.590$ V versus pseudo Ag/AgCl. The values of the cathodic to the anodic peak separation (0.062–0.011 V) for the reduction processes are listed in Table 1, which were assigned to reversible character for the reduced species in DMSO solution within the scan rate 0.025–0.25 V s^{-1}. The half-wave potentials of the first and second reductions for **$NhtH_2Pc$** were positively shifted by 0.150 and 0.136 V as compared to those for unsubstituted metal-free phthalocyanine (H_2Pc) [40]. These shift values are almost the same with those of $[(SO_3)_4H_2Pc]$ [40]. The results indicate that the electron-withdrawing naphthalenyl units with sulfonate groups make $NhtH_2Pc$ easier to reduce as observed in the case of $[(SO_3)_4H_2Pc]$ where four sulfonate groups are directly attached to the phthalocyanine core. The potential difference between the first and second reduction processes of **$NhtH_2Pc$** is 0.414 V, which refers to an average separation for the first and second reduction processes of metal-free phthalocyanines on the phthalocyanine ring system [40]. This potential difference is almost the same as those of H_2Pc and $[(SO_3)_4H_2Pc]$. On the other hand, oxidation potentials of electroactive molecules are expected to be positively shifted if the molecule contains electron-withdrawing substituents. However, **$NhtH_2Pc$** did not exhibit this tendency in our case. It could be attributed to interaction of the oxidized phthalocyanine species having four sulfonate groups and the counter anions of the supporting electrolyte [25,27,29], which resulted in the fixed oxidation potential of $NhtH_2Pc$. The redox processes of **$NhtH_2Pc$** were examined as a function of potential scan rate in order to ascertain the mode of mass transport. The cathodic and anodic currents for the reduction couples in DMSO each increased in direct proportion to the square root of scan rate between 0.025 and 0.25 V s^{-1}, thus suggesting the redox reactions in solution are controlled by diffusion [41]. The controlled potential coulometric (CPC) study indicated that the number of electrons transferred for the electrochemical reactions of the complex was one for each oxidation and reduction processes. The proposed electron-transfer mechanism of **$NhtH_2Pc$** on the electrode surface is given in Scheme 2.



Scheme 2. The proposed electron-transfer mechanism of **$NhtH_2Pc$**.

3.3. UV–Vis spectra of electro-oxidized and electro-reduced complexes

The spectroelectrochemical behavior of **$NhtH_2Pc$** was investigated using an in situ spectroelectrochemical technique including chronoamperometry and UV–Vis spectroscopy in a DMSO solution containing 0.2 M TBAP. The UV–Vis spectral changes for the first reduced species of **$NhtH_2Pc$** obtained in a thin layer cell with the applied potential ($E_{app} = -0.70$ V) are given in Fig. 5, where the inset figure corresponds to the CV of **$NhtH_2Pc$** in a thin-layer cell. The convenient applied potential value for the in situ spectroelectrochemical experiment was determined to be $E_{app} = -0.70$ V by taking the CV of **$NhtH_2Pc$** in a thin-layer cell (the inset figure in Fig. 5). As can be seen from Fig. 5, the main Q band almost disappeared in the course of the reduction process and new bands appeared at 573 and 445 nm. This spectral change arises from the rearrangement of the molecular orbital on addition of one electron into the present system, as expected [42]. At the beginning of the spectroelectrochemical measurements in DMSO solution, two main Q bands of the neutral state of **$NhtH_2Pc$** observed in the regular UV–Vis experiment (Fig. 2a and b) were seen as a lifted degeneracy. It is probably due to DMSO being basic, often resulting in a single Q band when studied at high concentration. The evaluation of the UV–Vis spectral changes upon the first reduction of **$NhtH_2Pc$** showed that the reduced form of **$NhtH_2Pc$** was assigned to a one-electron reduction process on the macrocycle and is accompanied with a change of color from green to blue. As can be expected, there is no change in the energy or the absorption intensity of the $\pi \rightarrow \pi^*$ transitions corresponding to the naphthalenyl groups on the phthalocyanine core due to the long-distance interaction between the naphthalenyl and macrocycle units. As can also be seen from Fig. 5, the isosbestic points of the UV–Vis spectral changes were found at 415, 613 and 571 nm, which clearly confirm the formation of the reduced species of **$NhtH_2Pc$**. The spectrum of $[NhtH_2Pc]^-$ is typical of Pc^{3-}/Pc^{2-} species, and is similar to that of the reduced mono-phthalocyanines based on the same macrocycle [25,42]. It can be deduced from monitoring the redox reaction that the electron-transfer reaction is reversible on the spectroelectrochemical timescale, and the original spectrum (and color) of the compounds is obtained upon re-oxidation. Thus, the reduced phthalocyanine remains fully stable throughout the experiment. These results obtained from the study of the in situ spectroelectrochemistry are consistent with those from the study of CV, which provide a good understanding of the reversible one-electron reaction process with long-term stability for the mono-anionic species $[NhtH_2Pc]^-$.

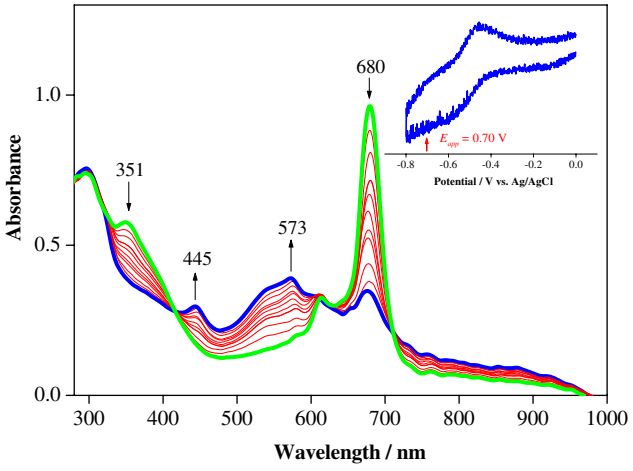


Fig. 5. Time-resolved UV–Vis spectral changes of **$NhtH_2Pc$** during the first reduction at $E_{app} = -0.70$ V in DMSO solution containing 0.2 M TBAP where the inset figure shows the cyclic voltammogram of **$NhtH_2Pc$** in DMSO solution containing 0.2 M TBAP in thin-layer cell. Scan rate = 0.100 V s^{-1}.

4. Conclusion

In this study, a new water-soluble metal-free phthalocyanine, 2,9,16,23-tetrakis(4-(1-naphthoxy-4-sulfonic acid sodium salt))phthalocyanine **$NhtH_2Pc$**, was synthesized. The aggregation study of **$NhtH_2Pc$** showed that **$NhtH_2Pc$** had both aggregated and non-aggregated mono phthalocyanine forms in the case of the 1:1 ratio of methanol and water, whilst it exhibited the characteristic UV–Vis absorption spectrum of monomeric phthalocyanine in methanol and DMSO. It is clear that this new molecule, having anionic character with naphthoxy sulfonate groups on the phthalocyanine core, may be a potential candidate molecule in the application of photodynamic therapy thanks to its enhanced fluorescence and water-solubility properties.

On the other hand, the studies of CV and in situ spectroelectrochemistry for **$NhtH_2Pc$** in DMSO solution provide useful information on the electron-transfer reactions of the reduced species on the electrode surface.

Acknowledgements

The support of the State Planning Organization (DPT, Project No. 90177) is gratefully acknowledged. This work has also been supported, in part, by the Turkish Academy of Sciences in the framework of the Young Scientist Award Program (EA-TÜBA-GEBİP/2001-1-1).

References

[1] P. Erk, H. Hengelsberg, Phthalocyanine dyes and pigments, in: K.M. Kadish, K.M. Smith, R. Guilard (Eds.), The Porphyrin Handbook, vol. 16, Academic Press, Boston, 2003, pp. 117–170.
[2] A.W. Snow, W.R. Barger, Phthalocyanine films in chemical sensors, in: C.C. Leznoff, A.B.P. Lever (Eds.), Phthalocyanines: Properties and Applications, vol. 3, VCH, Weinheim, 1993, pp. 341–392.
[3] M.M. Nicholson, Electrochromism and display devices, in: C.C. Leznoff, A.B.P. Lever (Eds.), Phthalocyanines: Properties and Applications, vol. 3, VCH, Weinheim, 1993, pp. 75–117.

[4] (a) J. Simon, P. Bassoul (Eds.), Design of Molecular Materials: Supramolecular Engineering, John Wiley & Sons, Chichester, 2000, pp. 197–291;
(b) M. Bouvet, Radical phthalocyanines and intrinsic semiconduction, in: K.M. Kadish, K.M. Smith, R. Guilard (Eds.), The Porphyrin Handbook, vol. 16, Academic Press, Boston, 2003, p. 37.
[5] (a) J. Obirai, T. Nyokong, Electrochim. Acta 50 (2005) 5427;
(b) E. Karmann, D. Schlettwein, N.I. Jaeger, J. Electroanal. Chem. 405 (1996) 149;
(c) J.H. Zagal, Coord. Chem. Rev. 119 (1992) 89.
[6] N. Kobayashi, in: C.C. Leznoff, A.B.P. Lever (Eds.), Phthalocyanines: Properties and Applications, vol. 2, VCH, Weinheim, 1993, pp. 97–161.
[7] (a) E. Ben-Hur, W.-S. Chan, Phthalocyanines in photobiology and their medical applications, in: K.M. Kadish, K.M. Smith, R. Guilard (Eds.), The Porphyrin Handbook, vol. 19, Academic Press, Boston, 2003, pp. 1–35;
(b) U. Drechsler, M. Pfaff, M. Hanack, Eur. J. Chem. (1999) 3441.
[8] Y. Pan, W. Chen, S. Lu, Y. Zhang, Dyes and Pigment 66 (2005) 115.
[9] (a) L. Howe, J.Z. Zhang, J. Phys. Chem. A 101 (1997) 3207;
(b) N. Kobayashi, R. Higashi, K. Ishii, K. Hatsusaka, K. Ohta, Bull. Chem. Soc. Jpn. 72 (1999) 1263.
[10] (a) A.W. Snow, Phthalocyanine aggregation, in: K.M. Kadish, K.M. Smith, R. Guilard (Eds.), The Porphyrin Handbook, vol. 19, Academic Press, Boston, 2003, pp. 129–176;
(b) X.Y. Li, A.C.H. Ng, D.K.P. Ng, Macromolecules 22 (2000) 2119.
[11] L.I. Solovéva, E.A. Luk'yanets, Zh. Obs. Khim. 50 (1980) 1122.
[12] S. Wei, J. Zhou, D. Huang, X. Wang, B. Zhang, J. Shen, Dyes Pigments 71 (2006) 61.
[13] Y.-C. Yang, J.R. Ward, R.P. Seiders, Inorg. Chem. 24 (1985) 1765.
[14] Z.A. Schelly, D.J. Harward, P. Hemmes, E.M. Eyring, J. Phys. Chem. 74 (1970) 3040.
[15] R.P. Linstead, F.T.J. Weiss, Chem. Soc. (1950) 2975.
[16] P. Maillard, S. Gaspard, Guerquin-Kern, Jean Luc, M. Momenteau, J. Am. Chem. Soc. 111 (1989) 9125.
[17] (a) R.W. Boyle, J.E. van Lier, Synthesis (1995) 1079;
(b) W.M. Sharman, S.V. Kudrevich, J.E. van Lier, Tetrahedron Lett. 37 (1996) 5831.
[18] G.J. Clarkson, N.B. McKeown, K.E. Treacher, J. Chem. Soc., Perkin Trans. 1 (1995) 1817.
[19] K. Kasuga, H. Hayashi, M. Handa, Chem. Lett. (1991) 1877.
[20] C. Fabris, G. Jori, F. Giunini, G. Roncucci, J. Photochem. Photobiol. B: Biol. 64 (2001) 1.
[21] (a) K. Ishii, N. Kobayashi, in: K.M. Kadish, K.M. Smith, R. Guilard (Eds.), The Photophysical Properties of Phthalocyanines and Related Compounds in the Porphyrin Handbook, vol. 19, Academic Press, Boston, 2003, pp. 1–42;
(b) K. Kameyama, M. Morisue, A. Satake, Y. Kobuke, Angew. Chem., Int. Ed. 44 (2005) 4763.
[22] V.V. Rozhkov, M. Khajehpour, S.A. Inogradov, Inorg. Chem. 42 (2003) 14.
[23] A.R. Özkaya, I. Yilmaz, Ö. Bekaroğlu, J. Porphyrins Phthalocyanines 2 (1998) 483.
[24] I. Yilmaz, O. Bekaroğlu, Chem. Ber. 129 (1996) 967.
[25] I. Yilmaz, A.G. Gurek, V. Ahsen, Polyhedron 24 (2005) 791.
[26] I. Yilmaz, M. Kocak, Polyhedron 23 (2004) 1279.
[27] K.M. Kadish, T. Nakanishi, V. Ahsen, A. Gürek, I. Yilmaz, J. Phys. Chem. B 105 (2001) 9817.
[28] I. Yilmaz, T. Nakanishi, A. Gürek, K.M. Kadish, J. Porhyrins Phthalocyanines 7 (2003) 227.
[29] T. Nakanishi, I. Yilmaz, N. Nakashima, K.M. Kadish, J. Phys. Chem. B 107 (2003) 12789.
[30] M. Kandaz, I. Yilmaz, S. Keskin, A. Koca, Polyhedron 21 (2002) 825.
[31] M. Kandaz, S.Z. Coruhlu, I. Yilmaz, A.R. Ozkaya, Transit. Metal. Chem. 27 (2002) 877.
[32] I. Yilmaz, M. Kandaz, AR. Özkaya, A. Koca, Monatshefte für Chemie 133 (2002) 609.
[33] E. Tas, M. Ulusoy, M. Guler, I. Yilmaz, Transit. Metal. Chem. 29 (2004) 180.
[34] A. Kilic, E. Tas, B. Gumgum, I. Yilmaz, Transit. Metal. Chem. 31 (2006) 645.
[35] T. Nyokong, Z. Gasyna, M.J. Stillman, Inorg. Chim. Acta 112 (1986) 11.
[36] J.G. Young, W. Onyebuagu, J. Org. Chem. 55 (1990) 2155.
[37] X.Q. Lin, K.M. Kadish, Anal. Chem. 57 (1985) 1498.
[38] N. Kobayashi, Synthesis and spectroscopic properties of phthalocyanine analogs, in: K.M. Kadish, K.M. Smith, R. Guilard (Eds.), The Porphyrin Handbook, vol. 16, Academic Press, Boston, 2003, pp. 117–170.
[39] A. Kılıc, E. Tas, B. Gumgum, I. Yilmaz, Transit. Metal. Chem. 31 (2006) 645.
[40] M. L'Her, A. Pondaven, in: K.M. Kadish, K.M. Smith, R. Guilard (Eds.), Electrochemistry of Phthalocyanines in the Porphyrin Handbook, vol. 16, Academic Press, Boston, 2003, pp. 117–170.
[41] A.J. Bard, L.R. Faulkner (Eds.), Electrochemical Methods: Fundamentals and Applications, 2nd ed., John Wiley & Sons, New York, 2001, pp. 228–234.
[42] J. Mack, M.J. Stilman, in: K.M. Kadish, K.M. Smith, R. Guilard (Eds.), Electronic Structure of Metal Phthalocyanine and Porphyrin Complexes from Analysis of the UV–Visible Absorption and Magnetic Circular Dichroism Spectra and Molecular Orbital Calculations in the Porphyrin Handbook, vol. 16, Academic Press, Boston, 2003, pp. 117–170.

of interest in metal ion therapeutics for both diagnosis and treatment [7,8]. For example Cu(II)-L-histidine [9] has been used in the treatment of Menkes disease [10,11]. Such interest has been due to the biochemical and pharmacological properties of the metal–ligand system, with extensive research carried out to determine the role of the ligand in copper uptake into cells. On the other hand many articles [12,13], indicating the effective role of various copper chelating agents in the alleviation of inflammation associated with RA have also appeared in literature, indicating the physiological importance of these agents as well as their therapeutic applications. Important in this regard is the ability of biologically essential metal ions such as Cu(II), Ca(II), Zn(II) and Ni(II) to interact with various ligand systems, particularly those containing a pseudo-peptide-mimic of the N-terminus of serum albumin [14–18].

Serum albumin (SA) is a major metal binding protein in the body, with about 40 μg of copper able to bind to the albumin contained in 1 ml of human plasma [19]. The Cu(II) transport site of serum albumin is one of the most extensively studied binding site of any protein [20]. The proposed structure (Fig. 1) of the major Cu(II) binding site in HSA involves the α-NH_2 nitrogen, two peptide nitrogens, and the imidazole nitrogen of the N-terminal Asp-Ala-His residues [12]. Recently, we have shown, using animal experiments, that Cu(II)-*N*-(2-(2-aminoethylamino)ethyl)picolinamide ([H(555)–N]), a system related to Cu(II)–HSA, is capable of surviving *in vivo* [21] with a relatively long biological half life. Encouraged by these results, we have extended our efforts to the thermodynamic and spectroscopic study of the solution equilibria of Cu(II), Ca(II), Zn(II) and Ni(II) with 2-amino-*N*-(2-oxo-2-(2-(pyridin-2-yl)ethyl amino)ethyl)acetamide ([H_2(556)–N]) (Fig. 2). The major difference between [H_2(556)–N] and HSA is the replacement of the imidazole group by a pyridyl system. Speciation modelling studies [22] have shown that ligands containing the pyridyl group have a higher Cu(II) mobilizing ability than analogous ligands with the imidazole group. Presumably this is related to metal ion specificity and hence *in vivo* competition with

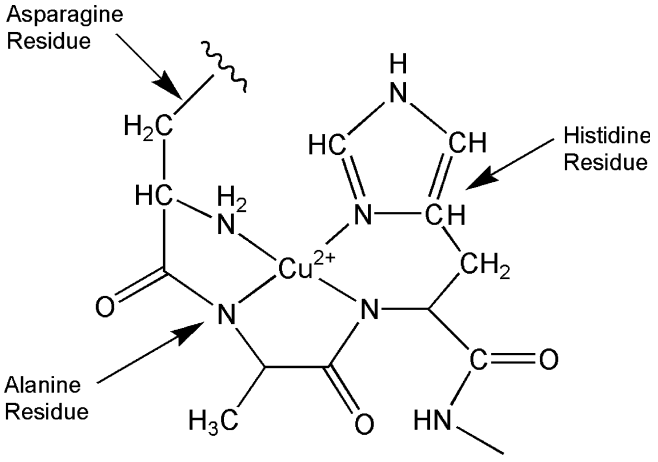
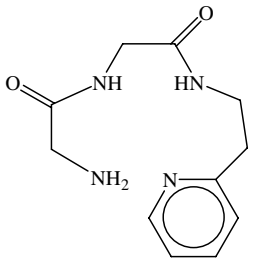


Fig. 1. Copper binding site in Human Serum Albumin (HSA).



[H_2(556)-N]

Fig. 2. Schematic structure of chelating agent.

Ca(II) and Zn(II) which are present in much higher concentration than Cu(II) in blood plasma [20,23].

2. Experimental

Formation constants were measured at 298 K and an ionic strength of 0.15 M (NaCl) using a procedure described previously [24]. The reagents used were all of analytical grade and the synthesis of the metal chelating agent was based on a method described previously [17]. The overall formation constant, β_{pqr}, refers to the equilibrium below, where p, q and r are the stoichiometric coefficients of the components in the complex

$$pM + qL + rH \rightleftharpoons M_pL_qH_r \quad (1)$$

$$\beta_{pqr} = \frac{[M_pL_qH_r]}{[M]^p[L]^q[H]^r} \quad (2)$$

The species formed in the investigated systems can be characterized by this general equilibrium process (1) where charges are omitted. The formation constants (β_{pqr}) given by (2) for the generalized reaction (1) were evaluated from the pH-potentiometric titration data using the Equilibrium Simulation for Titration Analysis (ESTA) computer program [25].

Molecular mechanics calculations were performed on a SyncMaster 1100p workstation using the Discover module of InsightII software [26]. The extensible systematic force field (esff) [27] was used for all energy calculations. All calculations were done in vacuum.

Electronic spectra in aqueous solution were recorded in 1.00-cm quarts cells using a Varian UV-Cary 100 spectrophotometer equipped with a temperature-controlled cell holder.

Water/octanol partition coefficients were measured as a function of pH using the shake flask method [28–30]. The aqueous solutions in the vials at different pH were spiked with $^{64}CuCl_2$ solution of activity 7.50–9.00 mCi, before shaking with an equal volume of water saturated octan-1-ol. An equal amount (1 ml) of each phase was counted in a Minaxi Auto gamma counter (5000 Series-Packard) using a window set at 340–540 keV [31–34].

Blood plasma modelling was carried out by incorporation of the formation constants determined in this study into the blood plasma model consisting of data for 10

metal ions and more than 5000 ligands [23]. This enlarged database was efficiently and conveniently interrogated by the Evaluation of Constituent Concentrations in Large Equilibrium System (ECCLES) computer program [20] to yield results pertaining to the influence of the chelating agents on the equilibria in terms of the plasma mobilizing index (p.m.i) of each agent. P.m.i., defined as the ability to move metal from a protein bound form to a low-molecular weight form, can be represented by the following expression:

$$\text{p.m.i.} = \frac{(\text{total concentration of low-molecular-weight metal complex species in the presence of drug})}{(\text{total concentration of low-molecular-weight metal complex species in normal plasma})}$$

The superoxide dismutase (SOD) mimetic activity of the $CuLH_{-2}$ species was determined using the nitroblue tetrazolium (NBT) assay as described by González-Álvarez et al. [35] and Auclair and Voisin [36]. The procedure and concentrations of various species were as reported by Nomkoko et al. [37].

3. Results and discussion

3.1. Protonations

The two protonation constants that were determined by ESTA optimization [25] of the potentiometric data for $[H_2(556)–N]$ are: $pK_1 = 5.18$ and $pK_2 = 7.91$. The first value (pK_1) corresponds to the protonation constant of the pyridyl ring and the second value (pK_2) to that of the amino group. The pK_2 value is close to the pK_2 value of glycylglycylhistamine, Gly-Gly-Ha (7.85) [17] and alanylglycylhistamine, Ala-Gly-Ha (7.87) [18]. However the pK_1 suggests reduced basicity in the pyridyl nitrogen of $[H_2(556)–N]$ as compared to that for 2-ethyl pyridine ($pK_{a,1} = 6.07$). This can be attributed to the electron-withdrawing properties of the two CONH-groups [38] present in the ligand, capable of drawing electrons towards themselves through inductive effects.

For Gly-Gly-Ha and Ala-Gly-Ha it is proposed that because the pK_as of the two protonation sites were so similar, that protonation occurred at both sites simultaneously. In the case of $[H_2(556)–N]$ the pK_as differ by ~3.0 log units and so such a microprotonation pathway is unlikely.

3.2. Complexation

Two functions [39–41], which are derived from the experimental data and are quantitatively related to the $\log \beta_{pqr}$'s were used to investigate the reproducibility of the experimental data and the reliability of evaluated β_{pqr} values. The complex formation function, Z_M-bar, measures the average number of ligands bound per metal ion due to complexation. This function is plotted against the negative logarithm of the free ligand concentration (pL).

On the other hand the deprotonation function, Q-bar, indicates the average number of protons released due to complexation and is plotted against the pH of the solution. Q-bar is evaluated in conjunction with the n-bar function, which measures the average number of protons that would be bound to the ligand in the absence of complexation.

These two functions serve two purposes. Firstly they give one a visual check on the experimental data and secondly their shape gives one an idea of the speciation model applicable to the system. Theoretically, the complex formation function (Z_M-bar) is only defined for simple, stepwise complexation and the curves at different metal to ligand ratios should be superimposable. If the curves are not superimposable, this indicates that polynuclear species are present. Fanning back of the Z_M-bar curves indicates the presence of hydroxo and/or mixed hydroxo species [42].

Fig. 3 shows the complexation (Z_M-bar) and deprotonation (Q-bar) function for the Cu(II)–$[H_2(556)–N]$ system at different metal to ligand ratios. Z_M-bar for different metal–ligand ratios are superimposable indicating the absence of polynuclear species. The fact that Z_M-bar is not levelling off at 1.0 suggest that simple stepwise complexation does not occur in solution thereby indicating that mononuclear species of 1:1 metal–ligand stoichiometry are not the dominant species in solution. The titration curves, obtained for ligand to metal ratios higher than 1:1, indicate that there is no formation of complexes including more than one ligand molecule per metal ion while fanning back of this function indicates the loss of the amide protons upon metal ion coordination [43].

At pH values less than 4.00 the deprotonation function, Q-bar, is zero indicating that no protons have been displaced due to complexation. The protonation function n-bar has a value of 2.0 at this pH confirming that the ligand is still protonated at low pH. For pH values above 4.00, Q-bar rapidly rises to intersect the protonation curve, n-bar, at a pH of 5.00, reaching a maximum value of about 3.3 at pH 5.60. At this pH, the difference between Q-bar and n-bar is 2 indicating that complexation has resulted in the loss of a total of four protons from the ligand. Since the protonated ligand has only two possible dissociable protons these extra protons are suggested to come from the amide groups. Above this pH the Q-bar curves run parallel to the protonation curve and then levels off at a value of 2.2, in the strongly alkaline region. Since the two curves, n-bar and Q-bar are parallel, this means that there is no change in the number of protons displaced by complexation and so no further complexation can be detected potentiometrically.

The analysis of the curves for the functions given in Fig. 3 using the ESTA suite of programs [25] resulted in

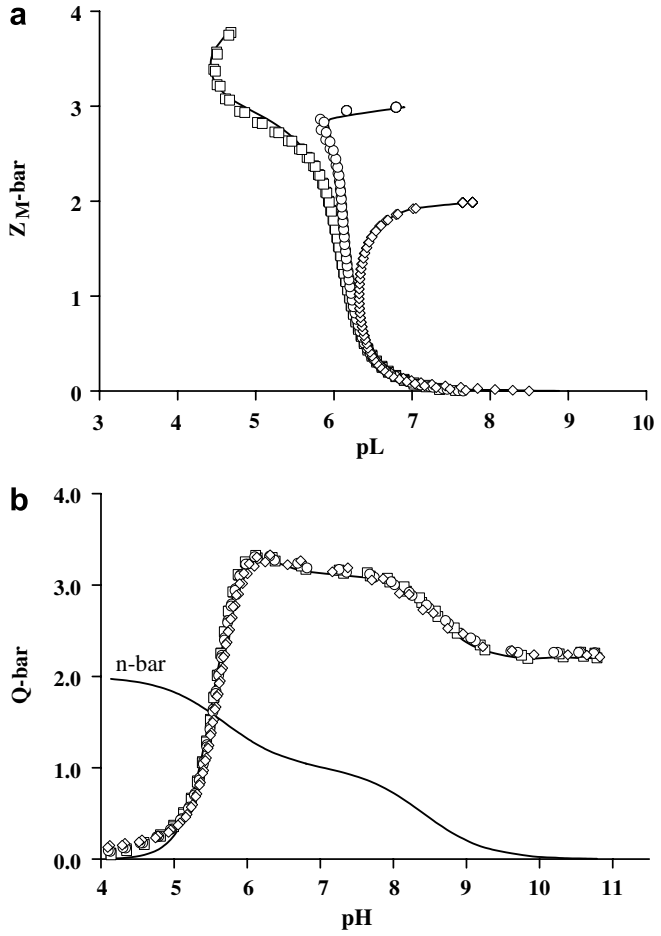


Fig. 3. (a) Formation and (b) deprotonation curves for the Cu–[H_2(556)–N] system. Experimental data are shown for titration at 1:2 (◇), 1:3 (○) and 1:4 (□) metal:ligand concentration ratios. The theoretical data (solid line) was calculated using model 4 given in Table 2.

the determination of five models (Table 1) which describe the experimental data equally well. Within these models, formation of the following Cu(II) complexes: MLH, ML MLH_{-1}, MLH_{-2} and MLH_{-3} with [H_2(556)–N] was observed. In each of these models the *R*-factor, R_f^H, which represents the 'goodness of fit' is $<R_{lim}$. R_{lim} is calculated from the random errors in the experimental data and is the minimum value of R_f^H that is statistically significant. Hence there is no difference between the 'goodness of fit' of these five models.

Table 1
Various models generated from potentiometric analysis of the Cu(II)–[H_2(556)–N] system using ESTA suite of programs

Model	*p q r*	$\log\beta_{pqr}$	(σ_{pqr})	n_P	n_T	pH range	R_f^H (R_{lim}^H)
1	1 1 1	10.97	(0.088)	678	6	3.0–11.0	0.010 (0.022)
	1 1 0	5.75	(0.005)				
	1 1 −2	−3.90	(0.024)				
2	1 1 0	5.85	(0.011)	678	6	3.0–11.0	0.014 (0.027)
	1 1 −2	−4.09	(0.004)				
3	1 1 0	5.85	(0.009)	678	6	3.0–11.0	0.011 (0.027)
	1 1 −2	−4.09	(0.004)				
	1 1 −3	−12.59	(0.028)				
4	1 1 0	5.82	(0.021)	678	6	3.0–11.0	0.013 (0.027)
	1 1 −1	−0.39	(0.026)				
	1 1 −2	−4.10	(0.006)				
5	1 1 0	5.80	(0.018)	678	6	3.0–11.0	0.011 (0.027)
	1 1 −1	−0.19	(0.135)				
	1 1 −2	−4.10	(0.028)				
	1 1 −3	−12.60	(0.028)				

This is a problem that occurs commonly in the computational analysis of potentiometric data when two or more models describe the experimental data equally well. In this situation additional information must be used to decide between the different models. Model 1 was dismissed on chemical grounds. This model has an MLH species which implies that while the pyridyl nitrogen is coordinated the amino nitrogen is still protonated. This structure is unlikely due to the chelate effect.

Models 3 and 5 can be dismissed by inspection of the theoretical *Q*-bar curves (not shown). These models have an MLH_{-3} species which is formed at high pH. However, the *Q*-bar curves level off at 2 indicating that only an MLH_{-2} species is formed at this pH. The theoretical *Q*-bar curves for these models level off at 3.

The final 2 models have the same beta values and only differ in the postulate of an intermediate MLH_{-1} species. Since complexation is likely to take place stepwise, this species is a reasonable intermediate and hence we have chosen model 4 to represent the Cu(II)–[H_2(556)–N] system. Vacca et al. [44] has also suggested that in situations like this, the choice of the chemical model(s) becomes a matter of personal judgement. A speciation plot (Fig. 6) shows the MLH_{-1} species is a minor species and this is why it does not affect the statistical error significantly.

The influence of substituents on the coordinating ability of peptides has been widely reported [17,18]. Due to the multidentate nature of [H_2(556)–N], and of all serum albumin mimicking pseudo-peptides, monomeric complexes, are formed, with the MLH_{-2} species in the Cu(II)–[H_2(556)–N] system predominating at physiological pH. The formation constants determined in this study are somewhat lower than those of analogous ligands containing an imidazole ring. For example, the following formation constants have been reported for the MLH_{-2} species: Gly-Gly-Ha [17] $\log\beta_{11-2} = -2.48$; Ala-Gly-Ha [18] $\log\beta_{11-2} = -2.86$; Gly-Gly-His [14,15] $\log\beta_{11-2} = -1.80$; Gly-Gly-His-*N*-methylamide [45] $\log\beta_{11-2} = -0.48$ and Asp-Ala-His-*N*-methylamide [46] $\log\beta_{11-2} = -0.55$. The difference in stability of these imidazole containing ligands has been attributed to the effect of the various substituents [14,15,17,18,45] present.

A noticeable feature about the two peptides Gly-Gly-Ha and Ala-Gly-Ha is the stability associated with the MLH_{-1} species which was difficult to detect in the Cu(II)–[H_2(556)–N] system, which is only seen as a minor species in both Figs. 6 and 7a. This suggests that the two amides in [H_2(556)–N] are dissociated in overlapping steps. This is not unusual as it has been reported for the Cu(II)-*N*,*N*′-diglycyltrimethylenediamine system [47] and can be

explained in terms of the pH delayed coordination of either the second amide nitrogen or both amide nitrogen donors once the terminal nitrogen donors are coordinated in the Cu(II)–[H_2(556)–N] system.

Table 2 lists the formation constants of the final Cu(II)–[H_2(556)–N] model together with those of Ni(II) and Zn(II). The formation constants all have low standard deviations and Hamilton *R*-factors, indicating that the models are good descriptions of the equilibria occurring in solution. The agreement between the theoretical and experimental formation and deprotonation functions as well as the reproducibility of the titrations at different metal:ligand ratios lends confidence to the results. Slow kinetics was observed in the Ni(II)–[H_2(556)–N] system. However, despite the known difficulty of measuring equilibrium constants under conditions of slow kinetics, excellent agreement between the experimental and theoretical complexation and deprotonation functions was obtained. The titrations, while slow, were found to be reversible and reproducible.

As expected, the two metal ions Ni(II) and Zn(II) form reasonably stable complexes with [H_2(556)–N], but their stability is much lower than that of Cu(II), particularly for the physiologically important MLH_{-2} species. A noticeable feature with these two metals is the prevalence of the MLH species. The presence of protonated MLH species in the Ni(II)–[H_2(556)–N] ($\log\beta_{111} = 10.91$) and Zn(II)–[H_2(556)–N] ($\log\beta_{111} = 11.36$) systems is an indication of the inability of these two metal ions to readily deprotonate the ligand. It is also observed that $\log\beta_{pqr}$'s for the MLH and ML species in the Zn(II)–[H_2(556)–N] system are slightly higher than those for the Ni(II)–[H_2(556)–N] system, a clear violation of the Irving–Williams series [48].

Unlike Cu(II), Ni(II) and Zn(II), Ca(II) was found to form very weak complexes with [H_2(556)–N]. Several attempts, using different metal to ligand concentrations, failed to detect any interaction between Ca(II) and the ligand [H_2(556)–N]. Similar results have been found for a majority of ligands with soft nitrogen donor atoms such as glycylglycine [49]. Generally, there are no reported constants of this metal ion with the majority of ligands containing nitrogen donor atoms [49]. This behaviour of Ca(II), which is classified as a Hard Lewis Acid (HSAB classification), is expected as this metal ion prefers ligands with hard donor atoms such as oxygen [50]. Thus failure to form any complexes with [H_2(556)–N] is therefore a result of such behaviour.

Table 2
Formation constants ($\log\beta_{pqr}$) and derived data for Cu(II), Ni(II) and Zn(II) complexes of [H_2(556)–N], $\beta_{pqr} = [M_pL_qH_r]/[M]^p[L]^q[H]^r$, $I = 0.15$ mol dm^{-3} (NaCl), $T = 298$ K

Metal	*p q r*	$\log\beta_{pqr}$ (σ_{pqr})	n_P	n_T	pH range	R_f^H (R_{lim}^H)
H^+	0 1 1	7.91 (0.004)	453	3	3.0–11.0	0.007 (0.011)
	0 1 2	13.09 (0.005)				
Cu(II)	1 1 0	5.82 (0.021)	678	6	3.0–11.0	0.013 (0.027)
	1 1 −1	−0.39 (0.026)				
	1 1 −2	−4.10 (0.006)				
Ni(II)	1 1 1	10.91 (0.02)	906	6	3.0–11.0	0.02 (0.02)
	1 1 0	4.40 (0.02)				
	1 1 −2	−10.16 (0.02)				
	1 1 −3	−18.09 (0.03)				
Zn(II)	1 1 1	11.36 (0.01)	826	6	3.0–10.0	0.02 (0.02)
	1 1 0	4.77 (0.01)				
	1 1 −2	−11.52 (0.01)				
	1 1 −3	−20.03 (0.07)				

σ_{pqr} denotes the standard deviation in $\log\beta_{pqr}$; R_f^H and R_{lim}^H is the Hamilton *R*-factor and its limit. n_T and n_P are the number of titrations and titration points. The general formula of a complex is $M_pL_pH_r$.

3.2.1. Structure of complexes

In their study of glycylglycylhistamine (Gly-Gly-Ha) and alanylglycylhistamine (Ala-Gly-Ha) Gadja et al. [17] and Gizzi et al. [18] postulated that metal ion coordination occurred simultaneously at both the imidazole nitrogen and the terminal amine. The pK_a's of these two groups were very similar and so the metal ion would not show a preference for one above the other. [H_2(556)–N] also has two basic sites but in this case the pyridyl nitrogen and the amino group have very different pK_a's. Hence the metal ion is expected to bind exclusively to the more basic amine. In this position it is also possible for the metal ion to coordinate to the adjacent amide group. Hence, the structure of the MLH species is as depicted in Fig. 4a(i) with the pyridyl nitrogen still protonated. Deprotonation of this nitrogen to form the ML species occurs with a pK_a of 5.2 ($\log\beta_{111} - \log\beta_{110}$). This is the same as p$K_1$ which has been assigned to the pyridyl group. This structure is depicted in Fig. 4b(i). The fact that the pK_a of the MLH species and pK_1 of the free ligand are so similar supports the proposed structure for both MLH and ML.

If the structure of ML is as depicted in Fig. 4b(i) then metal assisted deprotonation of the adjacent amide leads to a structure in which the carbonyl of the second amide may or may not be coordinated. Fig. 4c shows two possible structures for the MLH_{-1} complex. Finally, deprotonation of the second amide would lead to structures given in 4d as two possible structures for the MLH_{-2} species. In both these structures metal assisted deprotonation of the second amide has occurred leading to the MLH_{-2} stoichiometry. The difference between the two structures is the coordination of the pyridyl nitrogen. Considering the formation of MLH_{-1} from ML, the pK_a of this process is 6.2 ($\log\beta_{110} - \log\beta_{11-1}$). If structure 4b(i) is correct, this pK_a refers to metal assisted deprotonation of the first amide. Formation of the MLH_{-2} species from MLH_{-1} has a pK_a of 3.7 ($\log\beta_{11-2} - \log\beta_{11-1}$). Again if structure 4c(i) and d(i) are correct this refers to metal assisted deprotonation of the second amide. The fact that this second deprotonation step is so much easier than the first deprotonation suggests the coordination involvement of the pyridyl nitrogen as shown in Fig. 4d(i). This would also explain why the MLH_{-1} species is difficult to detect because it readily converts to the MLH_{-2} species (see Fig. 6, the speciation distribution curve).

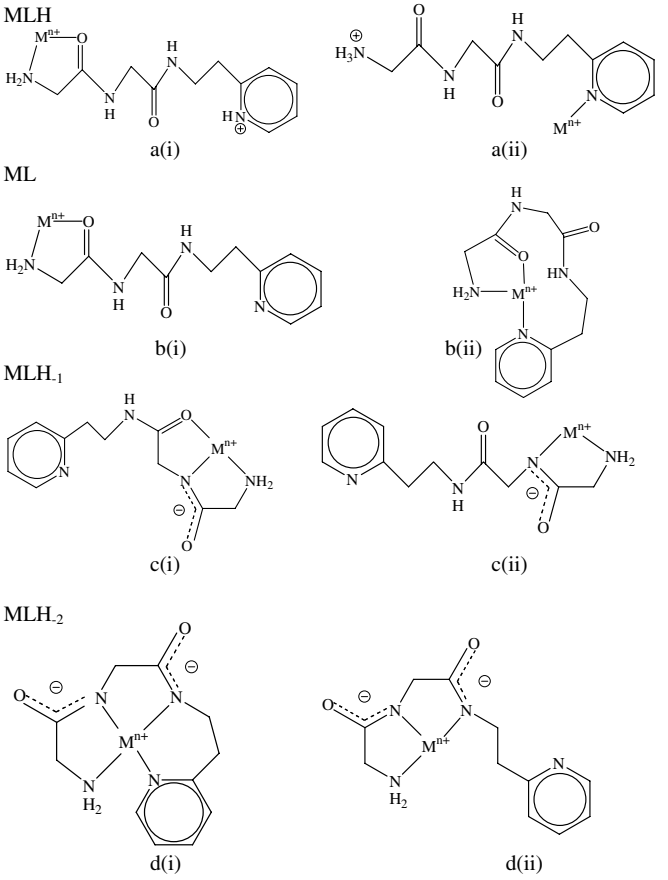


Fig. 4. Possible structures for different copper complexes showing the site of metal-ion coordination. For simplicity the axial H_2O ligands are omitted in these structures.

3.2.2. Molecular mechanics

When a ligand binds to a metal ion it loses rotational freedom and may have to adopt a less favourable conformation. This is an energy penalty that must be paid in order to form the complex. Molecular mechanics (MM) can be used to calculate this potential energy penalty. Table 3 lists the potential energy penalty associated with structures 4d(i) and d(ii) while Fig. 5 shows the energy minimised structures respectively.

Interestingly the total internal energy of 4d(i) is half that of 4d(ii) even though 4d(i) is more constrained than 4d(ii). The bond, angle and torsion angle contributions to the total internal energy are all higher. The main reason for this is shown in Fig. 5 (5,5) where the distortion of the octahedral coordinate geometry around the copper is clearly seen.

Table 3
Internal energy (kcal mol^{-1}) associated with structures Fig. 4d(i) (5,5,6) and Fig. 4d(ii) (5,5)

	5,5,6	5,5
Total	23.4	58.2
Bond	5.9	17.5
Angle	11.3	31.0
Torsion	6.0	9.1
Out-of-plane	0.1	0.6

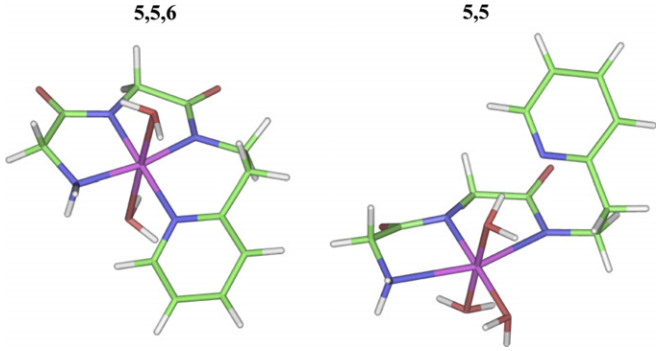


Fig. 5. Possible structures of the MLH_{-2} species for the Cu(II)–[H_2(556)–N] system calculated by InsightII.

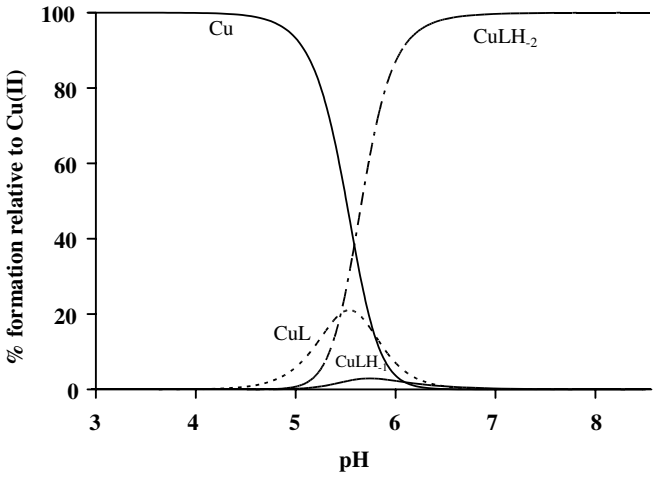


Fig. 6. Distribution diagram for the different species in the Cu(II)–[H_2(556)–N] system at 298 K as a function of pH, metal to ligand ratio is 1:4.

3.3. Spectroscopy and solution structures

The formation of the Cu(II)–[H_2(556)–N] and Ni(II)–[H_2(556)–N] complexes can be followed by UV–visible spectrophotometry because distinct colour changes occur as a result of the changing speciation of the solution with pH. By recording the spectra at different component concentrations and at different pH values, using a deconvolution algorithm, it is possible to calculate the spectrum of each individual species. The calculated aqueous UV–visible spectra for the Cu(II)–[H_2(556)–N] and Ni(II)–[H_2(556)–N] systems are shown in Fig. 7. The peaks corresponding to three species, CuL, $CuLH_{-1}$, $CuLH_{-2}$ can clearly be seen for the Cu(II)–[H_2(556)–N] system. The calculated λ_{max} and ε values for Cu(II), CuL, $CuLH_{-1}$, $CuLH_{-2}$ are: 800 nm ($\varepsilon = 29.0\ M^{-1}\ cm^{-1}$), 540 nm (20.0 $M^{-1}\ cm^{-1}$), 540 nm (2.6 $M^{-1}\ cm^{-1}$) and 530 nm (233.9) $M^{-1}\ cm^{-1}$) respectively. Pure aqua ion of Cu(II) have been reported to have an extinction coefficient value of 12 $M^{-1}\ cm^{-1}$ at a λ_{max} of 810 nm [51].

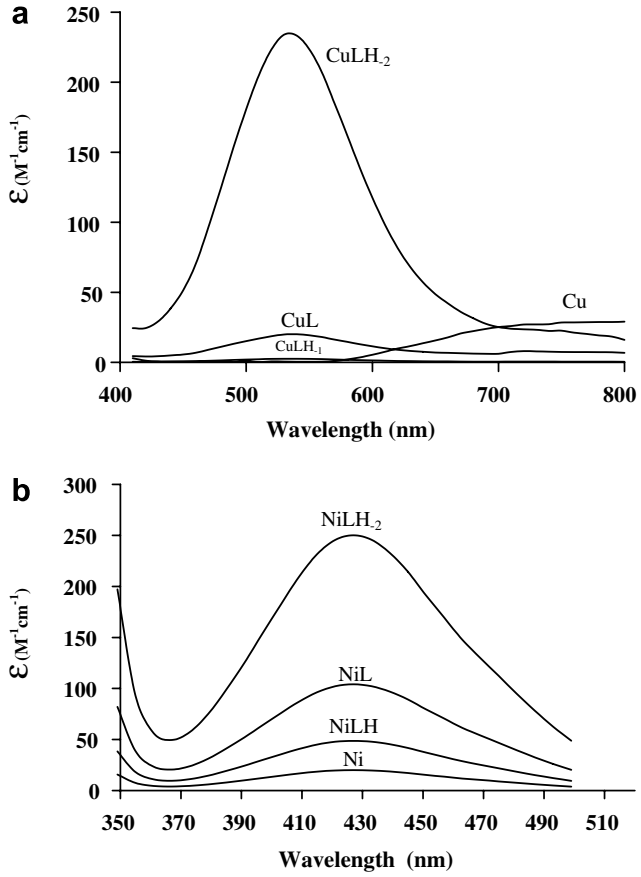


Fig. 7. Individual spectra $\varepsilon = f(\lambda)$ of the corresponding (a) Cu(II)–[H_2(556)–N] and (b) Ni(II)–[H_2(556)–N] system as a function of pH ([Cu(II)/Ni(II)] = 0.01 M:[L] = 0.04 M at 298 K).

The λ_{max} and ε values for $CuLH_{-2}$ allows us to make some conclusions to the coordination of the amino, the pyridyl and two deprotonated peptide nitrogen groups in accordance to similar reported literature data [17,18,52,53]. The λ_{max} and ε values are very close to those reported for Gly-Gly-His [17] and Ala-Gly-His [18].

Direct evidence for the amide proton dissociation on complexation has been widely reported [54–56] for Cu(II) complexes in solution. Moreover, results of X-ray crystallographic studies [57] have also shown unequivocally that the amide proton displacement takes place in the solid with the coordination of the resulting negative amide groups occurring to the metal ion. The crystallographic structures of the $CuLH_{-2}$ complexes for different, but related models have also been reported for Cu(II)-glycylglycylhistamine [17], Cu(II)-alanylglycylhistamine [18], Cu(II)-glycylglycylhistidine-*N*-methylamide [58] and Cu(II)-(α,β-didehydro-glycylglycylhistamine) [59]. The solid state structures of these related Cu(II)-peptides indicate coordination of Cu(II) by four nitrogen atoms; an amino, two peptides and imidazole-N3 nitrogen atoms forming a slightly distorted square planar arrangement. Our results also suggest the same coordination mode in the $CuLH_{-2}$ complex as shown in Fig. 4d(i).

Octahedral six coordinate Ni(II) complexes, being d^8, should give rise to three electronic $d \rightarrow d$ transitions involving three spin allowed transitions from $^3A_{2g}$ to $^3T_{2g}$, $^3T_{1g}$ and $^3T_{1g}(P)$ with intensities less than 30 M^{-1} cm^{-1} [60]. The absorption spectra of octahedral nickel hexahydrate ion, $Ni(H_2O)_6$ has been reported [60] to show three characteristic bands, one at around 400 nm and two broad bands above 600 nm. From Fig. 7b, the band at a λ_{max} of 427 nm ($\varepsilon = 20$ M^{-1} cm^{-1}) corresponds to octahedral six coordinate $Ni(H_2O)_6$. The calculated λ_{max} and ε values for NiLH, NiL and $NiLH_{-2}$ are: 427 nm ($\varepsilon = 48.7$ M^{-1} cm^{-1}), 427 nm (104.1 M^{-1} cm^{-1}) and 427 nm (250 M^{-1} cm^{-1}) respectively. This characteristic absorption band (427 nm) for the three species falling within the range 425–435 nm is assigned to $^1A_{1g} \rightarrow {}^1A_{2g}$ transition [61]. The band starts to increase above pH 7.00, reaching a maximum above pH 9.00 with a change in colour of solution from light green to yellow. A similar species for Ala-Gly-Ha, a related peptide has been reported [18] to give an absorption band at a λ_{max} value of 417 nm at pH 6.30.

It has been reported [62] that Ni(II) complexes with the tetraamine ligand, trien (1,4,7,10-tetraazadecane), has an equilibrium mixture of the yellow, diamagnetic square planar species $[Ni(trien)]^{2+}$ and of the blue, high-spin, diaqua octahedral species $[Ni(trien)(H_2O)_2]^{2+}$. Based on this assertion and the observed predominance of the yellow colour during titration, the dominant species ($NiLH_{-2}$ at pH 9.69) in the Ni(II)–[H_2(556)–N] system is suggested to be diamagnetic and square planar. Moreover, most Ni(II) complexes coordinated to amide-nitrogen atoms have been reported to be square-planar and diamagnetic [63], with the two deprotonated amide groups providing a strong ligand field leading to a singlet ground state. Like $CuLH_{-2}$, $NiLH_{-2}$ does not react with hydroxide in accordance with the planar nature of this chelate. The absorption band at 427 nm is, however, obscured by a ligand to metal charge transfer (LMCT) band centred at 301 nm. The LMCT transition originates from the carbonyl oxygen or deprotonated peptide nitrogen to the vacant $^1A_{2g}$ orbital of the metal ion. The high molar extinction coefficients of the LMCT bands for the NiLH, NiL and $NiLH_{-2}$ species in the range of 1000–5000 M^{-1} cm^{-1} in this study indicate the charge transfer character of the system.

3.4. Partition coefficients measurements

Partition coefficients measurements can be used as extra-thermodynamic reference parameters for "hydrophobic bonding" in biochemical and pharmacological systems.

Octanol/water partition coefficients were used to give an estimation of the trans-dermal transport of the Cu(II)–[H_2(556)–N] complexes. For a drug to be considered lipophilic, the $\log P_{oct/aq}$ value should be at least 0.60. The octanol/water partition coefficients results as a function of pH for the Cu(II)–[H_2(556)–N] system are given in Fig. 8. A noticeable feature about Fig. 8 is that all

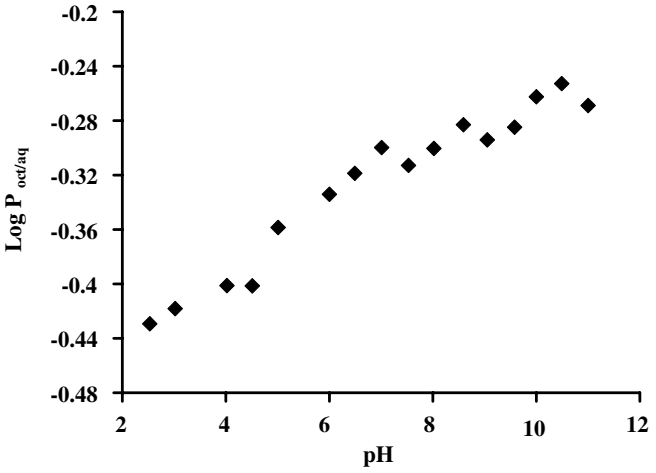


Fig. 8. Log $P_{oct/aq}$ of Cu(II)–[H_2(556)–N] complexes plotted as a function of pH.

log $P_{oct/aq}$ values are negative but increase with pH. Negative values of log $P_{oct/aq}$ suggest that these complexes are largely hydrophilic.

From Fig. 8 the log $P_{oct/aq}$ values for the two systems at physiological pH (7.40) can be estimated as −0.30, indicating a 30% extraction of copper into the octanol phase. From the species distribution curves (Fig. 6), at this pH, the $CuLH_{-2}$ species predominates and so the partition coefficient can be assigned to this species. Above pH 10.00 log-$P_{oct/aq}$ decreases.

A comparison of our partition coefficients with those reported in literature [64] for related chelating agents show an improvement factor of 6–14. To our knowledge, the ^{67}Cu(II) and ^{64}Cu(II)-labelled [*N*(2-pyridylmethyl-*N*1-(salicylaldimino)-1,3-propanediamine] and pyruvaldehyde-bis(N^4-methylthiosemi-carbazone) derivatives studied by Green and co-workers [65,66] are the only Cu(II) containing complexes to have high, positive log $P_{oct/aq}$ values ranging from 1.97 to 3.61. Using a predictive model for skin permeation rate developed by Michaels et al. [67,68] a trans-dermal flux value of 7.71×10^{-2} cm h^{-1} is determined for the Cu(II) complex of [H_2(556)–N]. This trans-dermal flux rate is encouraging enough to merit membrane crossing of the complex by passive transport.

3.5. Blood-plasma simulation studies

In order to establish the true selectivity of [H_2(556)–N] for Cu(II) over Ca(II) and Zn(II) *in vivo*, the blood-plasma mobilizing index (p.m.i.) has been calculated. This calculation takes into account competition with some 10 metal ions and more than 5000 ligands present in plasma. The index is defined as the concentration of low molecular mass Cu(II) complex species in the presence of a drug divided by their concentration in the absence of the drug [20]. The Cu(II) p.m.i. of [H_2(556)–N] was calculated by incorporating the formation constants measured in this study into a computer model of blood plasma [23]. The total ligand concentration ($[L]_T$) was varied over the range 10^{-3}–10^{-9} M and p.m.i. calculated at each point. The results are shown in Fig. 9. For comparison, results for [H(555)–N] are also shown.

From this we see that although [H(555)–N] is some three orders of magnitude better than [H_2(556)–N] at mobilizing Cu(II) *in vivo*. Both [H(555)–N] and [H_2(556)–N] are able to cause a 10-fold increase in low molecular weight (l.m.w.) Cu(II) concentration at total ligand concentration of 10^{-5} and 10^{-2} M respectively. The remarkably high mobilizing ability of [H(555)–N] by a factor of three log units compared to [H_2(556)–N] is related to the presence of two electron withdrawing CONH-group in [H_2(556)–N]. However, at the aforementioned ligand concentrations, the Zn(II) and Ca(II) p.m.i.'s are insignificant. Hence the speciation of these two essential metal ions is not disturbed. Thus, in spite of the higher concentrations of Zn(II) and Ca(II) than Cu(II) *in vivo*, their weak binding strength with the ligand make them insignificant competitors for Cu(II).

3.6. Superoxide dismutase mimetic activity of the $CuLH_{-2}$ complex

Copper–zinc superoxide dismutase is an enzyme that catalyses the dismutation of the superoxide anion radical to molecular oxygen, water and/or hydrogen peroxide [35,36,69]. Low molecular weight Cu(II) complexes are also able to catalyse the dismutation of the superoxide anion radical albeit with a much lower activity [69]. In view of this observation, we have investigated the SOD mimetic activity of the Cu(II)–[H_2(556)–N] complex.

By using the nitroblue tetrazolium (NBT) assay in the presence of ethylenediaminetetraacetic acid (edta) as an *in vitro* chelation simulator [35,36,69], the results given in Fig. 10 were obtained. From Fig. 10, an IC_{50} value of 6.25 μM was determined. Roberts and Robinson [69] have reported an IC_{50} value of 0.011 μM for the native CuZn-SOD, which is more than 500 times less. Based on this comparison, it can be concluded that the $CuLH_{-2}$ complex for the Cu(II)–[H_2(556)–N] system is a poor mimic of the

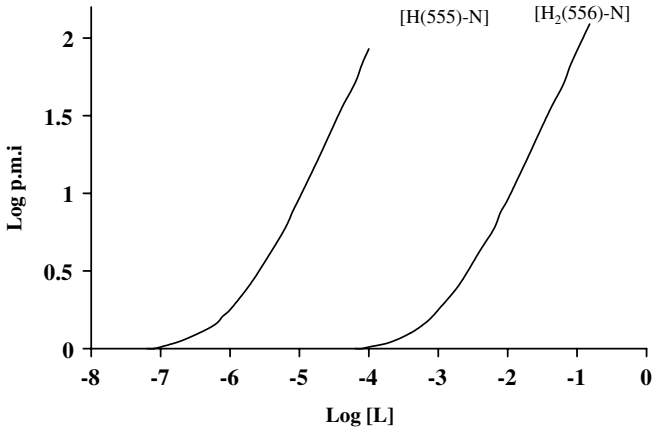


Fig. 9. Cu(II) plasma mobilizing index for [H(555)–N] and [H_2(556)–N].

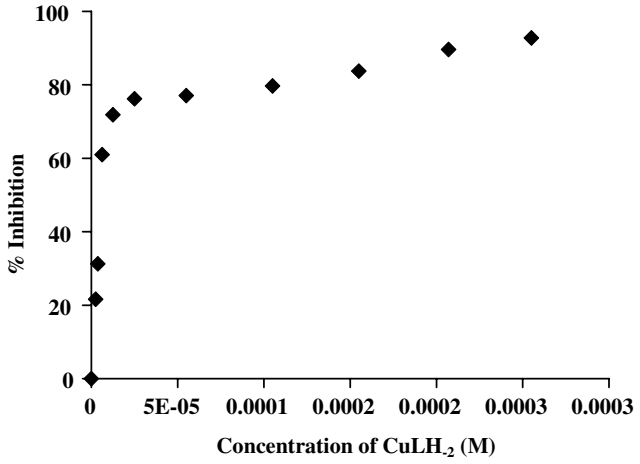


Fig. 10. % Inhibition as a function of the concentration of the $CuLH_{-2}$ species for the Cu(II)–[H_2(556)–N] system.

enzyme. This is a common observation for square planar copper complexes where the very weak axial coordination does not catalyse the dismutation of the superoxide radical.

4. Conclusion

This study has shown the computational problems associated with the design and study of copper-based therapeutics suggesting that great caution has to be exercised in model selection. However despite these limitations, the *in vitro* selectivity for Cu(II) over the *in vivo* competitors of [H_2(556)–N] is suggested based on thermodynamic investigations, molecular mechanics calculations and blood plasma simulations.

The coordination modes in the different complexes formed in solution were proposed using both potentiometric and UV–visible spectroscopic data. Although the $CuLH_{-2}$ species is a poor mimic of the native CuZnSOD enzyme, blood plasma simulations indicate that the complex is unlikely to dissociate *in vivo*. The use of percutaneous drug therapy is a promising method as incorporation of bulky groups within the chelating agents improved octanol/water partition coefficients, indicating enhanced trans-dermal absorption of the copper complexes.

Acknowledgements

The authors thank the National Research Foundation (NRF), Council for the University of Cape Town and the Beit Trust for financial support.

References

[1] H.R. Schumacher Jr., J.H. Klippel, W.J. Koopman, Primer on the Rheumatic Diseases, 10th ed., Arthritis Foundation, Atlanta, Georgia, 1993.
[2] A. Omoto, Y. Kawahito, I. Prudovsky, Y. Tobouchi, M. Kimura, H. Ishino, M. Wada, M. Yoshida, M. Kohno, R. Yoshimura, T. Yoshikawa, H. Sano, Arthritis Res. Ther. 7 (2005) R1174.
[3] M. Feldmann, F.M. Brennan, R.N. Maini, Cell 85 (1996) 307.
[4] A.E. Koch, Arthritis Rheum. 41 (1998) 951.
[5] R.W. Kinne, E.P. Kinne, F. Emmrich, Biochim. Biophys. Acta 360 (1997) 109.
[6] B. Henderson, J.C.W. Edwards, E. Pettipher, Mechanisms and Models in Rheumatoid Arthritis, Academic Press, New York, 1995.
[7] D.E. Reichert, J.S. Lewis, C.T. Anderson, Coord. Chem. Rev. 184 (1999) 3.
[8] C.W. Schwietert, J.P. McCue, Coord. Chem. Rev. 184 (1999) 67.
[9] P. Deschamps, P.P. Kulkarni, M. Gautam-Basak, B. Sarkar, Coord. Chem. Rev. 249 (2005) 895.
[10] B. Sarkar, Chem. Rev. 99 (1999) 2535.
[11] D.M. Danks, in: C.R. Scriver, A.L. Beaudet, W.M. Sly, D. Valle (Eds.), The Metabolic and Molecular Basis of Inherited Disease, 6th ed., Disorders of Copper Transport, McGraw-Hill, New York, 1995, p. 2211.
[12] J.E. Weder, C.T. Dillion, T.W. Hambley, B.J. Kennedy, P.A. Lay, J.R. Biffin, H.L. Regtop, N.M. Davies, Coord. Chem. Rev. 232 (2002) 95.
[13] C.T. Dillion, T.W. Hambley, B.J. Kennedy, P.A. Lay, Q. Zhou, N.M. Davies, J.R. Biffin, H.L. Regtop, Chem. Res. Toxicol. 16 (2003) 28.
[14] T.P.A. Kruck, B. Sarkar, Inorg. Chem. 14 (1975) 2383.
[15] S. Lau, B. Sarkar, J. Chem. Soc., Dalton Trans. (1981) 491.
[16] E. Farkas, I. Sovago, T. Kiss, A. Gergely, J. Chem. Soc., Dalton Trans. (1984) 611.
[17] T. Gadja, B. Henry, A. Aubry, J.J. Delpuech, Inorg. Chem. 35 (1996) 586.
[18] P. Gizzi, B. Henry, P. Rubini, S. Giroux, E. Wenger, J. Inorg. Biochem. 99 (2005) 1182.
[19] M.C. Linder, M. Hazegh-Azam, Am. J. Clin. Nutr. 63 (1996) 797.
[20] P.M. May, P.M. Linder, D.R. Williams, J. Chem. Soc., Dalton Trans. (1977) 588.
[21] J.N. Zvimba, G.E. Jackson, J. Inorg. Biochem. 101 (2007) 148.
[22] G.E. Jackson, M.J. Kelly, Inorg. Chim. Acta 152 (1988) 215.
[23] G.E. Jackson, P.M. May, D.R. Williams, J. Inorg. Nucl. Chem. 40 (1978) 1227.
[24] G.E. Jackson, B.S. Nakani, J. Chem. Soc., Dalton Trans. (1996) 1373.
[25] K. Murray, P.M. May, Equilibrium Simulation for Titration Analysis, 1984.
[26] InsightII, System Guide, Issued by Accelrys, Cambridge, UK, July 2005.
[27] S. Shi, L. Yan, Y. Yang, J. Fisher-Shaulsky, T. Thacher, J. Comput. Chem. 24 (9) (2003) 1059.
[28] Guidelines for Testing Chemicals, Section 1—Physical–Chemical Properties, 105 *n*-Octanol/Water Partition Coefficient, Organisation for Economic Cooperation and Development (OECD), Paris, 1981.
[29] A. Leo, C. Hansch, D. Elkins, Chem. Rev. 71 (1971) 525.
[30] T.X. Xiang, B.D. Anderson, J. Membr. Biol. 140 (1994) 111.
[31] L.J. Ackerman, D.X. West, C.J. Mathias, M.A. Green, Nucl. Med. Biol. 26 (1999) 551.
[32] J.S. Lewis, A. Srinivasan, M.A. Schmidt, C.J. Anderson, Nucl. Med. Biol. 26 (1999) 267.
[33] M. Yu, H. Qing, H. Guojian, Z. Shu, W. Wenging, He. YouFeng, J.T. Kuikka, Nucl. Med. Biol. 25 (1998) 111.
[34] L.M. Guerdoud, R. Ouellet, J.E. Van Lier, Nucl. Med. Biol. 21 (1994) 1101.
[35] M. González-Álvarez, G. Alzuet, J. Borrás, L.C. Agudo, J.M. Montejo-Bernardo, S. García-Granda, J. Biol. Inorg. Chem. 8 (2003) 112.
[36] C. Auclair, E. Voisin, in: R.A. Greenwald (Ed.), Handbook of Methods for Oxygen Radical Research, Nitroblue tetrazolium reduction, CRC Press, Inc., Boka Raton, 1985, p. 123.
[37] E.T. Nomkoko, G.E. Jackson, B.S. Nakani, K.A. Werner Louw, J.R. Zeevaart, J. Inorg. Chem. Dalton Trans. (2004) 741.
[38] J. Clark, D.D. Perrin, Quart. Rev. Chem. Soc. 18 (1964) 295.
[39] P.M. May, D.R. Williams, P.W. Linder, R.G. Torrington, Talanta 29 (1982) 249.

[40] P.M. May, K. Murray, D.R. Williams, Talanta 32 (1985) 483.
[41] P.M. May, K. Murray, D.R. Williams, Talanta 35 (1988) 825.
[42] E.T. Nomkoko, G.E. Jackson, B.S. Nakani, S.A. Bourne, J. Chem. Soc., Dalton Trans. (2004) 1789.
[43] H. Ojima, K. Nonoyama, Coord. Chem. Rev. 92 (1988) 85.
[44] A. Vacca, A. Sabatini, M.A. Gristina, Coord. Chem. Rev. 8 (1972) 45.
[45] T.P.A. Kruck, S. Lau, B. Sarkar, Can. J. Chem. 54 (1976) 1300.
[46] K.S. Iyer, S. Lau, S.H. Laurie, B. Sarkar, Biochem. J. 169 (1978) 61.
[47] A. Zuberbuehler, S. Fallab, Helv. Chim. Acta 50 (1967) 889.
[48] H. Irving, J.P.R. Williams, Nature 162 (1948) 746.
[49] A.E. Martell, R.M. Smith, Critical Stability Constants, Vol. 1, Plenum Press, New York and London, 1975.
[50] R.G. Pearson, J. Am. Chem. Soc. 107 (1985) 6801.
[51] E. Prenesti, P.G. Daniele, S. Toso, Anal. Chim. Acta 459 (2002) 323.
[52] H.H. Jaffé, M. Orchin, Theory and Applications of Ultraviolet Spectroscopy, Wiley, New York, 1962.
[53] E.J. Billo, Inorg. Nucl. Chem. Lett. 10 (1974) 613.
[54] M.K. Kim, A.E. Martell, Biochemistry 3 (8) (1964) 1169.
[55] M.K. Kim, A.E. Martell, J. Am. Chem. Soc. 88 (5) (1966) 914.
[56] M.K. Kim, A.E. Martell, J. Am. Chem. Soc. 89 (20) (1967) 5138.
[57] H.C. Freeman, J.E.W. L Smith, Acta Crystallogr. 20 (2) (1966) 153.
[58] N. Cammerman, A. Cammerman, B. Sarkar, Can. J. Chem. 54 (1976) 1309.
[59] P. de Meester, D.J. Hodgson, Inorg. Chem. 17 (1978) 440.
[60] A.P.B. Lever, Studies in Physical and Theoretical Chemistry—Inorganic Electronic Spectroscopy, Elsevier, Amsterdam, 1984.
[61] A.E. Éva, C. Hajnalka, L. István, M. Giovanni, G. Eugenio, E. Farkas, J. Chem. Soc., Dalton Trans. (2002) 2632.
[62] M. Ciampolini, L. Fabbrizzi, M. Licchelli, A. Perotti, F. Pezzini, A. Poggi, Inorg. Chem. 25 (1986) 4131.
[63] M. Nonoyama, K. Yamasaki, Inorg. Chim. Acta 5 (1971) 124.
[64] E.T. Nomkoko, G.E. Graham, S.B. Nakani, J. Inorg. Chem. Dalton Trans. (2004) 1432.
[65] M.A. Green, Nucl. Med. Biol. 14 (1987) 59.
[66] M. Sri-Aran, C.J. Mathias, J.K. Lim, M.A. Green, Nucl. Med. Biol. 25 (1998) 107.
[67] A.S. Michaels, P.S.L. Wong, R. Prather, R.M. Gale, AIChE J. 21 (1975) 1073.
[68] J.E. Shaw, M. Prevo, R. Gale, Su Yum II, in: L.A. Goldsmith (Ed.), Physiology, Biochemistry, and Molecular Biology of the Skin, Percutaneous Absorption, 2nd ed., vol. 2, Oxford University Press, Oxford, 1991, p. 1447.
[69] N.A. Roberts, P.A. Robinson, Br. J. Rheumatol. 24 (1985) 128.

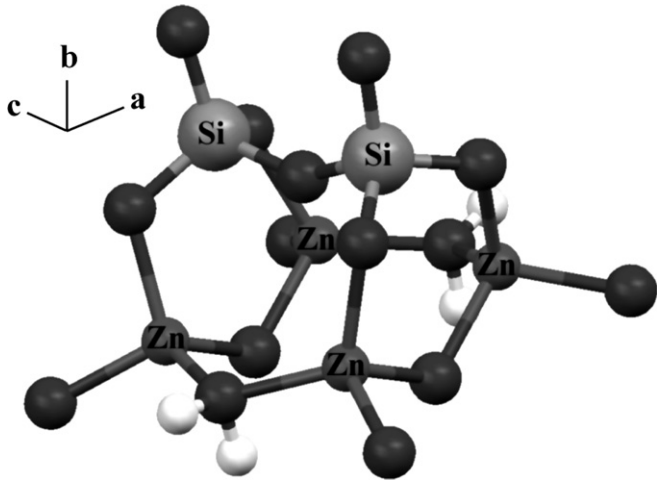


Fig. 1. Model of hemimorphite structure.

crystals are arranged in fan shaped aggregates. The other form produces a blue to blue-green botryoidal crust.

2. Experimental

2.1. Minerals

Selected hemimorphite minerals were obtained from the Mineral Research Company (http://www.minresco.com/default.htm) and other sources including Museum Victoria (Museum Victoria, Melbourne, Victoria, Australia). The samples were phase analysed by powder X-ray diffraction and for chemical composition by EDX measurements.

2.2. Raman microprobe spectroscopy

The crystals of hemimorphite were placed and oriented on the stage of an Olympus BHSM microscope, equipped with 10× and 50× objectives and part of a Renishaw 1000 Raman microscope system, which also includes a monochromator, a filter system and a Charge Coupled Device (CCD). Raman spectra were excited by a HeNe laser (633 nm) at a resolution of 2 cm^{-1} in the range between 100 and 4000 cm^{-1}. Repeated acquisition using the highest magnification was accumulated to improve the signal to noise ratio. Spectra were calibrated using the 520.5 cm^{-1} line of a silicon wafer. In order to ensure that the correct spectra are obtained, the incident excitation radiation was scrambled. Previous studies by the authors provide more details of the experimental technique. Spectra at liquid nitrogen temperature were obtained using a Linkam thermal stage (Scientific Instruments Ltd, Waterfield, Surrey, England). Details of the technique have been published by the authors [4–7].

2.3. Mid-IR spectroscopy

Infrared spectra were obtained using a Nicolet Nexus 870 FTIR spectrometer with a smart endurance single bounce diamond ATR cell. Spectra over the 4000-525 cm^{-1} range were obtained by the co-addition of 256 scans with a resolution of 4 cm^{-1} and a mirror velocity of 0.6329 cm/s. Spectra were co-added to improve the signal to noise ratio.

Spectral manipulation such as baseline adjustment, smoothing and normalisation were performed using the Spectracalc software package GRAMS (Galactic Industries Corporation, NH, USA). Band component analysis was undertaken using the Jandel 'Peakfit' software package which enabled the type of fitting function to be selected and allows specific parameters to be fixed or varied accordingly. Band fitting was done using a Lorentz–Gauss cross-product function with the minimum number of component bands used for the fitting process. The Lorentz–Gauss ratio was maintained at values greater than 0.7 and fitting was undertaken until reproducible results were obtained with squared correlations of $r^2 > 0.995$.

3. Results and discussion

3.1. Factor group analysis

The classic rules of vibrational spectroscopy show that the free SiO_4^{4-} tetrahedron of T_d symmetry has a

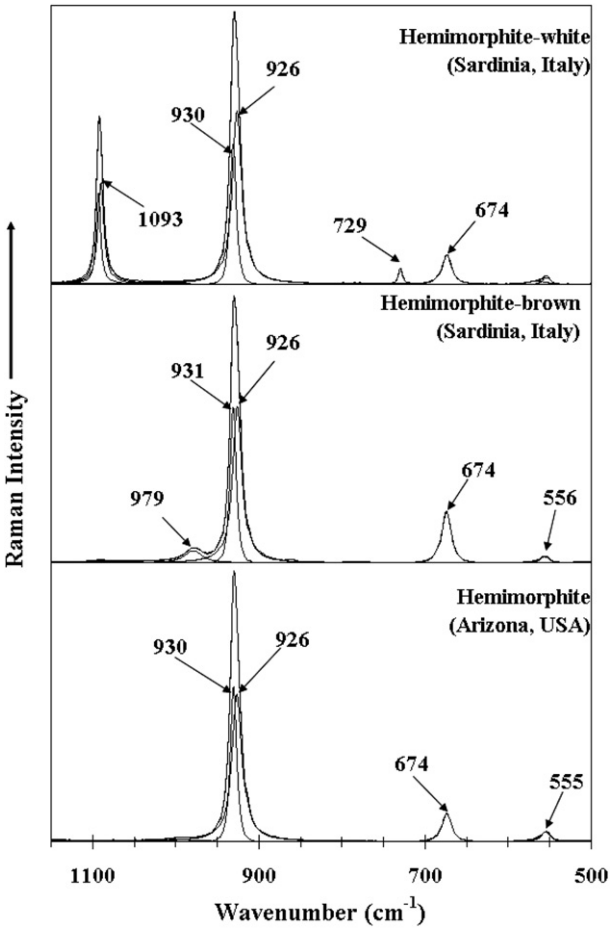


Fig. 2. Raman spectra of hemimorphite in the 500–1200 cm^{-1} range.

Table 1
Table of the results of the Raman and infrared spectroscopic analysis of hemimorphite

Hemimorphite-white (Sardinia, Italy)			Hemimorphite-brown (Sardinia, Italy)			Hemimorphite (Arizona, USA)					
Raman			Raman			Raman			Infrared		
Centre cm^{-1}	FWHM cm^{-1}	% Area	Centre cm^{-1}	FWHM cm^{-1}	% Area	Centre cm^{-1}	FWHM cm^{-1}	% Area	Centre cm^{-1}	FWHM cm^{-1}	% Area
						3565	120.5	4.65	3352	218.4	18.37
3534	157.0	11.92							3297	48.1	1.33
			3510	165.3	10.52				3234	59.6	4.94
						3455	171.3	42.75	3180	236.1	9.64
3438	130.0	15.33	3436	125.8	24.23						
			3339	121.4	6.10						
3328	98.5	6.22				3321	74.8	1.59			
3240	111.2	6.36	3235	99.8	3.56	3240	116.0	4.83			
1733	10.5	0.32									
1634	12.1	0.36	1634	12.2	0.40	1634	16.5	0.40	1633	15.6	0.25
									1588	10.8	0.14
									1548	17.4	0.57
									1514	36.7	4.86
1406	6.9	0.99							1496	43.5	11.77
			1366	27.9	0.18	1366	29.6	0.21	1386	39.6	6.29
									1357	26.9	1.61
									1336	66.9	2.46
									1335	16.5	0.60
1196	40.4	0.53	1195	50.1	0.59				1105	47.7	1.05
									1078	39.4	2.90
									1049	9.9	0.38
1093	6.4	3.56				1180	114.9	1.17	1043	15.4	0.52
1090	9.0	5.38	1084	89.7	0.86				1027	39.3	2.26
						996	45.8	0.50			
			979	25.4	1.77				974	61.7	4.89
931	9.0	5.97	931	9.0	6.47	930	9.2	6.34	933	57.3	7.69
926	14.1	14.42	926	13.7	12.44	926	15.0	12.28	894	48.4	3.40
			861	10.4	0.07				863	18.9	0.96
									836	19.1	4.28
									831	117.2	4.74
									737	17.6	0.82
729	5.9	0.45							709	8.5	0.66
674	13.6	1.91	674	13.7	3.33	674	14.2	1.69	702	15.5	0.42
									676	27.6	1.29
									609	13.8	0.39
565	23.2	0.27	556	11.8	0.32	555	11.5	0.62	597	17.2	0.52

(*continued on next page*)

Table 1 (*continued*)

Hemimorphite-white (Sardinia, Italy)			Hemimorphite-brown (Sardinia, Italy)			Hemimorphite (Arizona, USA)					
Raman			Raman			Raman			Infrared		
Centre cm^{-1}	FWHM cm^{-1}	% Area	Centre cm^{-1}	FWHM cm^{-1}	% Area	Centre cm^{-1}	FWHM cm^{-1}	% Area	Centre cm^{-1}	FWHM cm^{-1}	% Area
554	9.4	0.25									
451	12.5	4.63	451	13.9	5.97	451	12.8	3.31			
400	29.7	1.77	400	41.5	5.17	399	34.6	4.42			
329	9.3	1.48	330	10.0	2.46	330	9.8	1.91			
303	12.2	2.85									
275	19.4	0.71	282	20.1	1.33	274	19.9	0.72			
			266	22.0	0.87						
			231	51.1	2.65	230	53.3	0.69			
212	24.8	0.93	211	21.1	1.87	213	17.5	0.67			
194	9.7	1.44	194	16.9	0.34	193	11.9	0.59			
168	13.6	3.95	167	14.4	1.58	168	12.0	3.19			
152	39.2	2.29				157	34.8	2.40			
			142	35.1	3.02						
132	13.0	4.92	132	11.8	3.57	132	14.2	4.44			
111	12.5	0.77	110	13.1	0.35	111	14.8	0.61			

vibrational set $\Gamma = 1A_1 + 1E + 1F_1 + 3F_2$. By eliminating translations and rotations, the reduced representation $\Gamma' = 1A_1 + 1E + 2F_2$. Thus all in all, four vibrations with the E vibration twice degenerate and the F vibration 3 times degenerate match up with the nine vibrations under the 3N-6 rule.

The linear $Si_2O_7^{6-}$ ion of assumed symmetry $\bar{3}_m$ has a vibration set $\Gamma_2 = 3A_{1g} + 1A_{1u} + 1A_{2g} + 4A_{2u} + 4E_g + 5E_u$ and without rotations and translations $\Gamma'_2 = 3A_{1g} + 1A_{1u} + 1A_{2g} + 2A_{2u} + 3E_g + 4E_u$. So 14 vibrations with seven degenerate match up with the 21 vibrations under the 3N-6 rule. For the $Si_2O_7^{6-}$ ion of *mm*2 binary symmetry i.e., with non-linear SiOSi bridges, the irreducible representation $\Gamma_{3=}8A_1 + 5A_2 + 6B_2 + 8B_1$. This reduces to, upon elimination of the rotational and translational modes to $\Gamma_{3=}7A_1 + 4A_2 + 4B_2 + 6B_1$. Thus 21 predicted vibrations would be expected.

3.2. Raman spectroscopy

The Raman spectra of hemimorphite from three different origins are shown in Fig. 2. The results of the Raman and infrared spectroscopic analysis are reported in Table 1. Table 1 shows a comparison of the Raman spectroscopic data from three hemimorphite samples together with the infrared data from one sample. The table reports the peak position (cm^{-1}), the relative intensity of the component bands as a percentage and the width of the bands (cm^{-1}). A very sharp band is observed in each of the three spectra at 930 cm^{-1}. This band is not symmetric. This means there are two component bands making up the spectral profile. This band may be band component analysed into two components at 931 and 926 cm^{-1}. The band width as full width at half peak maximum (FWHM) is 9.0 cm^{-1} for the first peak and between 13.7 and 15.0 cm^{-1} for the second peak. These bands are attributed to the SiO stretching vibration of the Si_2O_7 units. An intense band is observed at 1093 cm^{-1} for the white hemimorphite from Sardinia. This band is not observed in the Raman spectra of the other hemimorphite samples. It is interesting that Brunel and Verne reported a band in this position to the A_{1g} vibrational mode of the $Si_2O_7^{6-}$ units [8]. In the light of these Raman spectra this assignment is open to question. This band is ascribed to the symmetric stretching vibration of a carbonate impurity. Poulet and Mathieu assigned the band at 930 cm^{-1} to the A_1 mode of the $Si_2O_7^{6-}$ units [9]. No Raman spectra were reported in their article, only the results of the spectra were reported. In the infrared spectrum of the hemimorphite from Arizona, an intense band at 933 cm^{-1} is observed (Fig. 2). Brunel and Vierne reported the infrared band at 932 cm^{-1} for a single crystal of hemimorphite and attributed the band to the B_1 vibrational mode [8]. These authors showed that the position of this band varied in position, if the hemimorphite was powdered. Farmer ([10, p. 296]) showed there was a correlation between the wavenumber of the SiO antisymmetric stretching vibration and the SiO bond length [10]. The ν_{as}

vibration is localised on the bridging oxygen. Lazarev showed that this wavenumber is determined by the OSiO bond angle.

A band common to all the three hemimorphite minerals is the band at 674 cm^{-1}. Brunel and Vierne identified an infrared band in this position and assigned the band to an A_1 vibration [8]. These workers showed that the position of this band varied according to the infrared techniques used for measurement. In the infrared spectrum, (Fig. 3) an intense band is observed at 676 cm^{-1}. Poulet and Mathieu observed a Raman band in this position and an infrared band at 677 cm^{-1} of medium intensity [9]. The band position varied according to the experimental settings of the single crystal experiment. They assigned the band to a O–Si–O bending vibration [9]. The band observed at 729 cm^{-1} for the white hemimorphite sample is ascribed to a carbonate bending mode. The band is not observed in the Raman spectra of the other two hemimorphite samples. A low intensity band is observed in all of the Raman spectra at 556 cm^{-1}. A distinct infrared band of hemimorphite is observed at 597 cm^{-1} (Fig. 3). Poulet and Mathieu observed a Raman band at 554 cm^{-1} in the Raman spectrum and at 545 cm^{-1} in the infrared spectrum [9]. Brunel and Vierne also defined a band at 563 cm^{-1} [8]. In this later work, the position of the band depended on the infrared technique used and upon the amount of sample in the KBr disc. This tends to suggest that there was an interaction between the hemimorphite and the KBr. Such a problem is avoided by using reflectance techniques as reported in this research. In the spectrum of the brown hemimorphite sample, a Raman band is observed at 979 cm^{-1}. Such a band was observed by Poulet and Mathieu [9] and was attributed to A_2(ab) vibration. The band is also observed for the hemimorphite from Arizona but is of very low intensity.

A number of infrared bands are observed at 1078, 1049, 1043 and 1027 cm^{-1} (Fig. 3). Poulet and Mathieu also observed infrared bands at 1380, 1170, 1085 and 1020 cm^{-1} and assigned these bands to δ OH vibrations. Brunel and Vierne also observed an infrared band at around 1090 cm^{-1}. However they attributed the band to E_u modes of the Si_2O_7 units. No Raman bands were observed in these positions which tends to suggest that the assignment of Poulet and Mathieu is perhaps more accurate. A number of infrared bands are observed at 1386, 1357 and 1336 cm^{-1} (Fig. 4). The probable assignment of these bands is to the δ OH deformation modes. The $\nu_{antisym}$ vibration is localised on the bridging oxygen. Lazarev showed that this wavenumber is determined by the OSiO bond angle. In the figure developed by Farmer,

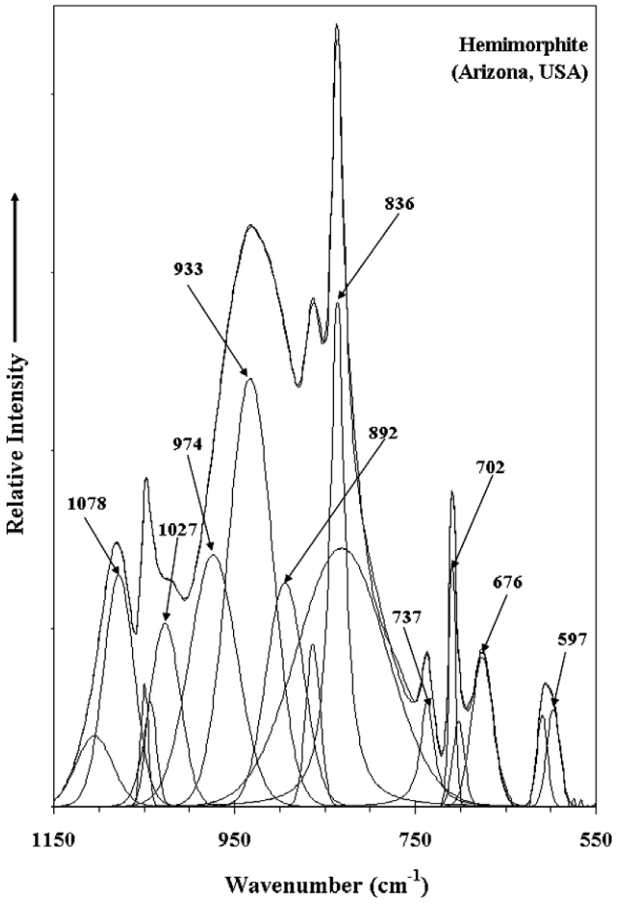


Fig. 3. Infrared spectra of hemimorphite in the 550–1150 cm^{-1} range.

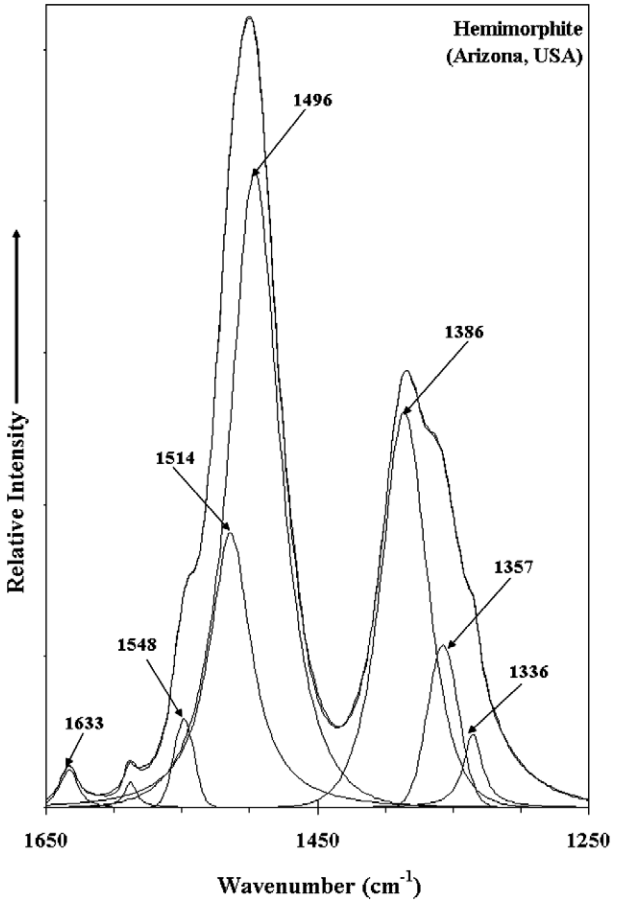


Fig. 4. Infrared spectra of hemimorphite in the 1250–1650 cm^{-1} range.

a band assigned to the antisymmetric stretching vibration at around 1110 cm^{-1} for pyromorphite is shown and is assigned to the SiO antisymmetric stretching vibration. Thus it is likely that the infrared bands observed by Poulet and Mathieu at 1170 and 1085 cm^{-1} are the infrared active Raman inactive antisymmetric stretching vibrations.

Two Raman bands are observed at 451 and 400 cm^{-1} (Fig. 5). These bands are attributed to out-of-plane bending vibrations of the Si_2O_7 units. Poulet and mathieu also observed Raman bands in these positions and described the bands as "déformations angulaires et réseau". They also observed an infrared band at 450 cm^{-1}. Bands in these positions are not able to be detected using the ATR technique with the diamond anvil cell as the cell absorbs at wavenumbers below 550 cm^{-1}. An intense Raman band is observed at 330 cm^{-1}. This band is attributed to the Zn–O stretching vibration. A second band is observed at around 280 cm^{-1}. This band may also be assigned to a ZnO stretching vibration. The band at 303 cm^{-1} for the white hemimorphite from Sardinia is considered to be due to a ZnO stretching vibration of the zinc carbonate impurity. The intense bands at 168 and 132 cm^{-1} are ascribed to the OZnO bending vibrations.

In the Raman spectra, bands of significant intensity are observed around 1634 cm^{-1} (Fig. 6). In the infrared spectrum (Fig. 4), a distinct band is observed at 1633 cm^{-1}. These bands are attributed to δ H_2O vibrations. In some ways it is unusual to observe the water bending mode in the Raman spectrum. The band is normally intense in the infrared spectrum and is of very low intensity or is not at all observed in the Raman spectrum. These results compare well with those of Brunel and Vierne and also Poulet and Mathieu [8,9]. Both previous studies showed the infrared bands of water in hemimorphite. In the structure of hemimorphite, perpendicular to the *C* axis, four, six and eight-fold tetrahedral rings are formed. The six and eight fold rings are connected along the *C* axis in wide1 channels which are occupied by water molecules. It is these water molecules which give the deformation modes at 1630 cm^{-1}. These water molecules must be in an ordered arrangement to give a water bending mode in the Raman spectrum of significant intensity.

The Raman spectra of hemimorphite from three different localities show consistently similar spectra, especially in the OH stretching region (Fig. 7). Two Raman bands are observed at around 3510–3565 and 3436–3455 cm^{-1}.

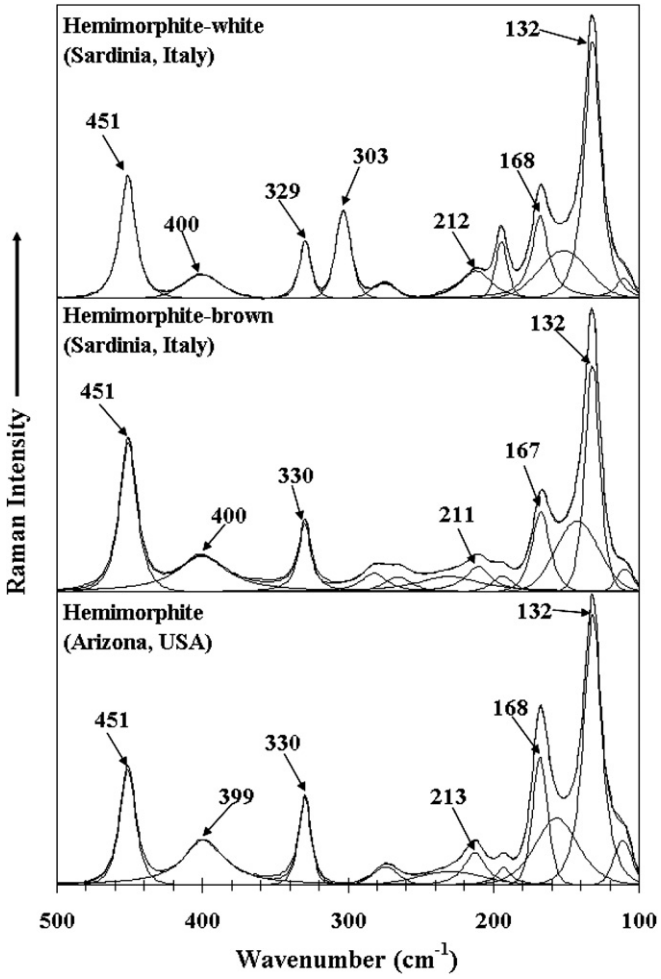


Fig. 5. Raman spectra of hemimorphite in the 100–500 cm^{-1} range.

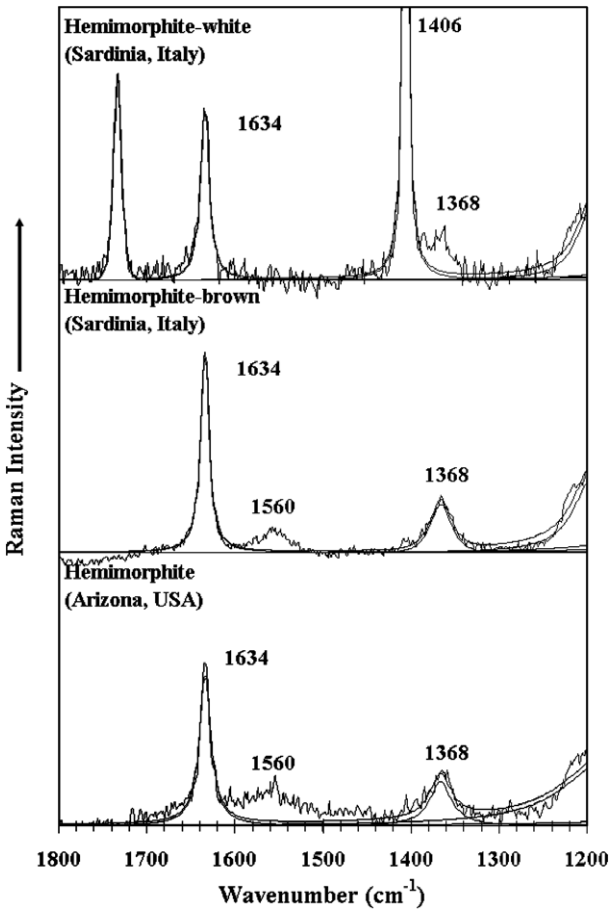


Fig. 6. Raman spectra of hemimorphite in the 1200–1800 cm^{-1} range.

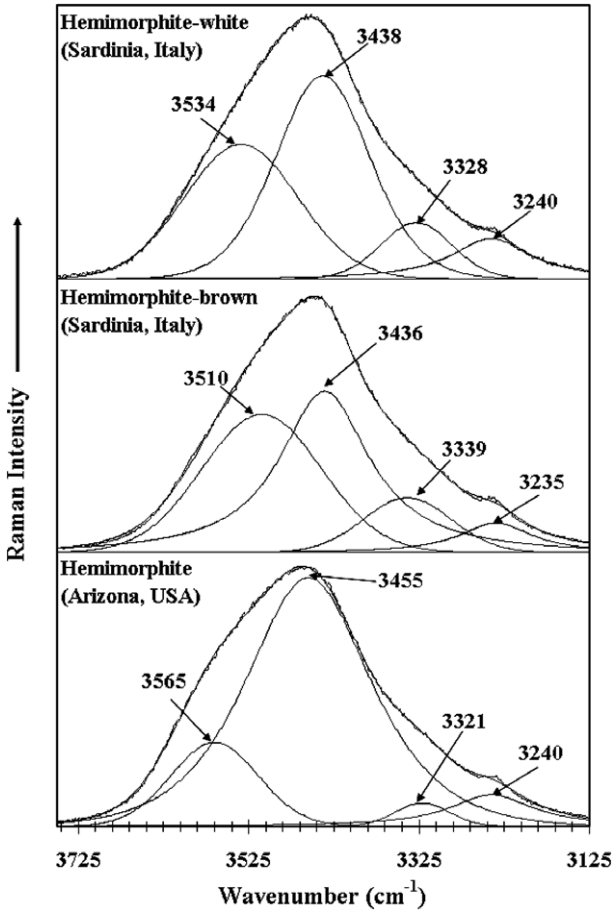


Fig. 7. Raman spectra of hemimorphite in the 3125–3725 cm^{-1} range.

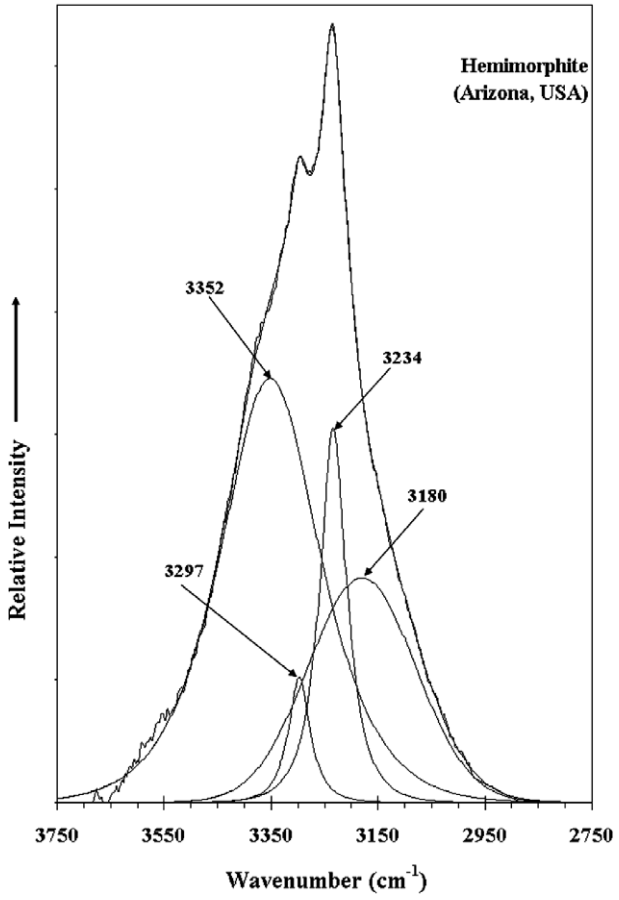


Fig. 8. Infrared spectra of hemimorphite in the 2750–3750 cm^{-1} range.

These bands are assigned to OH stretching vibrations of the mineral $Zn_4Si_2O_7(OH)_2 \cdot H_2O$. Raman bands are observed at around 3328 and 3240 cm^{-1} and are attributed to the OH stretching vibrations of the OH units. Polarized FTIR absorption spectra of oriented hemimorphite crystals have been published [11,12]. Infrared spectra of the Aizona hemimorphite in the OH stretching region are shown in Fig. 8.

Studies have shown a strong correlation between OH stretching frequencies and both O···O bond distances and H···O hydrogen bond distances [13–16]. Libowitzky (1999) showed that a regression function can be employed relating the hydroxyl stretching frequencies with regression coefficients better than 0.96 using infrared spectroscopy [17]. The function is described as: $v_1 = (3592 - 304) \times 109^{\frac{-d(O-O)}{0.1321}}$ cm^{-1}. Thus OH···O hydrogen bond distances may be calculated using the Libowitzky empirical function. The values for the OH stretching vibrations listed above provide hydrogen bond distances of 3510 cm^{-1} giving a calculated hydrogen bond distance of 0.2910 pm, 3436 cm^{-1}→ 0.2825 pm, 3739 cm^{-1}→ 0.2762 pm and 3235 cm^{-1} → 0.2716 pm. The conclusion may be drawn that the hydrogen bond distances formed from the water units are stronger than those formed from the OH units.

4. Conclusions

Hemimorphite because of its nature is most interesting to study using vibrational spectroscopic techniques. In this paper we report the study of hemimorphite minerals from three different origins and show that a carbonate impurity is found in some of the mineral samples. Raman bands observed at 3510 to 3565 and 3436 to 3455 cm^{-1} are assigned to OH stretching vibrations. Using a Libowitzky type formula, these OH bands provide hydrogen bond distances of 2.910, 2.825, 2.762 and 2.716 Å. Water bending modes are observed in the Raman spectrum at 1633 cm^{-1}. An intense Raman band at 930 cm^{-1} is attributed to SiO symmetric stretching vibration of the Si_2O_7 units.

Acknowledgements

The financial and infra-structure support of the Queensland University of Technology, Inorganic Materials Research Program is gratefully acknowledged. The Australian Research Council (ARC) is thanked for funding the instrumentation. Mr D. A. Henry of Museum Victoria (Melbourne, Australia) is thanked for the loan of the mineral samples.

References

[1] Y. Liu, J. Deng, Q.-f. Wang, Y.-h. Zhou, Crystal chemistry and color genesis of the hemimorphite from Jinding Pb–Zn deposit, Yunnan Province, Gaoxiao Dizhi Xuebao 11 (3) (2005) 434–441.

[2] R. Nakamura, K. Arikata, Y. Suginohara, T. Yanagase, Structure of silicates as studies by trimethylsilylation, Kogaku Shuho – Kyushu Daigaku 50 (5) (1977) 635–641.

[3] J.W. Anthony, R.A. Bideaux, K.W. Bladh, M.C. Nichols, Handbook of Mineralogy. Silica, Silicates (part 1), vol. 2, Mineral Data Publishing, Tuscon, Arizona, USA, 1995.

[4] R.L. Frost, D.A. Henry, K. Erickson, Raman spectroscopic detection of wyartite in the presence of rabejacite, J. Raman Spectr. 35 (4) (2004) 255–260.

[5] R.L. Frost, An infrared and Raman spectroscopic study of the uranyl micas, Spectrochim. Acta, Part A: Mol. Biomol. Spectr. 60A (7) (2004) 1469–1480.

[6] R.L. Frost, O. Carmody, K.L. Erickson, M.L. Weier, J. Cejka, Molecular structure of the uranyl mineral andersonite-a Raman spectroscopic study, J. Mol. Struct. 703 (1-3) (2004) 47–54.

[7] R.L. Frost, O. Carmody, K.L. Erickson, M.L. Weier, D.O. Henry, J. Cejka, Molecular structure of the uranyl mineral uranopilite-a Raman spectroscopic study, J. Mol. Struct. 733 (1–3) (2004) 203–210.

[8] R. Brunel, R. Vierne, Vibration spectra of hemimorphite, Bull. de la Societe Francaise de Mineral. et de Cristallogr. 100 (1) (1977) 14–20.

[9] H. Poulet, J.P. Mathieu, Vibration spectra and structure of hemimorphite, Bull. de la Soc. Francaise de Mineral. et de Cristallogr. 98 (1) (1975) 3–5.

[10] VC. Farmer, Mineralogical Society Monograph 4: The Infrared Spectra of Minerals. 1974, pp. 539.

[11] E. Libowitzky, T. Kohler, T. Armbruster, G.R. Rossman, Proton disorder in dehydrated hemimorphite. IR spectroscopy and x-ray structure refinement at low and ambient temperatures, Eur. J. Mineral. 9 (4) (1997) 803–810.

[12] E. Libowitzky, G.R. Rossman, IR spectroscopy of hemimorphite between 82 and 373 K and optical evidence for a low-temperature phase transition, Eur. J. Mineral. 9 (4) (1997) 793–802.

[13] J. Emsley, Very strong hydrogen bonding, Chem. Soc. Rev. 9 (1980) 91–124.

[14] H. Lutz, Hydroxide ions in condensed materials – correlation of spectroscopic and structural data, Struct. Bond. (Berlin, Germany) 82 (1995) 85–103.

[15] W. Mikenda, Stretching frequency versus bond distance correlation of O-D(H).Y (Y = N, O, S, Se, Cl, Br, I) hydrogen bonds in solid hydrates, J. Mol. Struct. 147 (1986) 1–15.

[16] A. Novak, Hydrogen bonding in solids. Correlation of spectroscopic and crystallographic data, Struct. Bond. (Berlin) 18 (1974) 177–216.

[17] E. Libowitsky, Correlation of the O–H stretching frequencies and the O–H···H hydrogen bond lengths in minerals, Monatschefte Für Chem. 130 (1999) 1047–1049.

dimensions <2 nm and is superparamagnetic [5]. Here, "superparamagnetic" denotes a magnetic system that has an anisotropy energy (or a zero field splitting) resulting in a fixed moment at low temperatures, and a fluctuating moment at temperatures above the corresponding anisotropy energy. Fe_8 is one of the best chemically and magnetically characterized materials. Much of the focus of the research on SMMs has been geared towards its fundamental chemical [6], EPR spectroscopic [7–12], and magnetic properties [13–15]. Potential solid-state applications of SMMs are use in high density magnetic memory, quantum computing [16], and spintronics devices such as high-frequency spin-based oscillators and signal processors [17].

Three recent studies have indicated potential applications of these materials dissolved in aqueous solution as versatile MRI contrast agents [2–4]. Rodriguez et al. published a comprehensive work comparing MRI phantoms at 64 MHz (1.5 T), and nuclear magnetic resonance (NMR) results at 400 MHz (9.4 T) for $Fe_{8(aq)}$ with Gd-DTPA (DTPA = diethylenetriamine-pentacetic acid) obtained as the commercial preparation Magnevist [2]. They found that the relaxivities of $Fe_{8(aq)}$ were about equal to that of Magnevist at 64 MHz and possibly superior at higher resonance frequencies [2]. They also examined the cytotoxicity of Fe_8 and found a lethal concentration for 50% mortality, LC_{50}, of ~1 mM [2]. Isaacman et al. also compared Fe_8 versus Magnevist using NMR relaxivity at 400 MHz [3]. They found, however, that $Fe_{8(aq)}$ was much less efficient than Magnevist for MRI contrast applications [3]. In a study of tailored iron-based imaging agents using MRI phantoms at 64 MHz, Barker et al. compared de-ionized (DI) water and DI water containing the dissolved Fe_8, and found that $Fe_{8(aq)}$ had potential as a contrast agent for both the T_1 and T_2 weighted contrast experiments [4]. Barker et al., however, did not provide any quantitative comparisons with Magnevist [4]. To resolve the conflict we undertook the current study to determine the relative merits of $Fe_{8(aq)}$ and Magnevist as a function of concentration.

The spin arrangement of the SMM Fe_8 at low temperatures can be thought of as a spin $S = 10$ particle where six $S = 5/2$ Fe^{3+} are aligned antiparallel to two $S = 5/2$ Fe^{3+} [5]. In general, this compound is modeled using a double-well potential with each well minimum corresponding to the preferred moment orientations. The depth of this well, $\Delta E/k$, (where k is the Boltzmann constant and ΔE is the anisotropy energy or barrier to reorientation) is about 24 K [18,19]. This results in Arrhenius-like thermally activated slow relaxation of the magnetization such that the magnetization fluctuation time is, $\tau = \tau_0 e^{\Delta E/kT}$, where τ_0 is the characteristic oscillation time in the energy well and T is the temperature. At temperatures of less than 1 K the dc magnetization of Fe_8 becomes constant relative to the typical measurement time of 100 s [20]; some SMMs have been shown to take months to relax [5]. This phase will be referred to as the blocked phase. Above 1 K each Fe_8 molecule fluctuates rapidly relative to this measurement time scale and the dc magnetization begins to decrease with increasing temperature, similar to a paramagnet, and due to the large moment per molecule is referred to as the superparamagnetic phase. This temperature dependent fluctuation time will lead to a frequency-dependent susceptibility. At room temperature the magnetic structure is less well known and will be more complex than an $S = 10$ macrospin particle.

The attractive qualities of Fe_8 for MRI contrast are aqueous solubility, possible ligand modification for bioconjugation, the large moment per molecule; and, unlike larger iron particles derived from solvo-thermal synthesis and top–down deposition techniques, these molecules are homogenous, identical units. The unknown quantities investigated here are the relaxivity over a range of concentrations spanning both previous studies using NMR and MRI techniques at 300 and 64 MHz, respectively, and the solution phase chemical identity using a novel ac susceptibility (χ_{ac}) study as a function of concentration. We then correlate the results from χ_{ac} with the relaxivity data to demonstrate why, in fact, both previous studies are correct at the relevant range of concentration.

2. Experimental

2.1. Synthesis

Fe_8 was synthesized in single crystal form using the original method of Weighardt [6] and summarized in earlier reports [7,9,21].

2.2. Ac susceptibility

The χ_{ac} data were obtained at zero applied dc magnetic field using a commercial 1.8–400 K susceptometer. The magnitude of the ac field was 0.65 mT and the frequency range was 200–1400 Hz . The samples consisted of differing concentrations of dissolved Fe_8 in deionized (DI) H_2O, ~100 μL measured within three hours of mixing in a sealed acrylic sample holder. The χ_{ac} of the holder with DI H_2O was negligible from 1.8 to 3 K.

2.3. NMR relaxometry

The NMR relaxation rates were obtained with a commercial 300 MHz (7 T) NMR system at room temperature within 3 h of mixing. In order to avoid radiation damping (a strong feedback between the transverse magnetization of the aqueous protons and the rf circuit) [22] the Fe_8 and Gd-DTPA (obtained as the commercial preparation Magnevist) were dissolved in a deuterated phosphate buffered saline solution (PBS). The NMR relaxivity r_1 results were obtained by a standard inversion recovery, $\pi_x - \tau - \pi/2_\phi$ – detect, sequence where the protons of the residual water in the sample are initially aligned along the applied field axis z, π_x is a pulse along axis x of such duration and power to invert the spins 180°, τ is a series of times between 0.01 and 2 s varied to obtain the relaxa-

tion along the z-axis, and a $\pi/2_{\phi}$ pulse is used to read out the remaining z-magnetization after the τ delay. A standard cyclically ordered phase sequence (ϕ) is used with the read pulse to eliminate quadrature artifacts. The T_2 relaxation of the H_2O was obtained by the Carr–Purcell–Meiboom–Gill sequence of $\pi_x/2 - (\tau - \pi_y - \tau)_n$ – detect, where multiple echoes were used over the range of 0.01–2 s to measure the spin–spin relaxation in the transverse plane prior to detection of the magnetization. A minimum of eight points were generated for each sequence; these data were processed by the internal NMR software system to generate T_1 and T_2 values for each concentration. The study in Ref. [2] was carried out in an aqueous non-dueterated PBS solution, and that in Ref. [3] in D_2O with the pH adjusted by NaOH.

2.4. MRI

Magnetic resonance images of the contrast agents were obtained with a commercial MRI operating at 64 MHz (1.5 T). Each sample tube was loaded upright in the circularly polarized extremity coil. A series of spin echo sequences were obtained with the following parameters: image matrix 256×256, pixel spacing 0.59 mm × 0.59 mm, slice thickness 5 mm, flip angle 180°, imaging frequency 63.67 MHz, magnetic field strength of 1.5 T, 1 average. The time to repetition (t_r) was 2500 ms and the time to echo (t_e) was varied over a series of 16 images starting at 22 ms and increased at 22 ms increments to 352 ms. A custom program using a simplex algorithm was used to calculate a T_2 map of each sample dilution.

3. Results and discussion

3.1. NMR relaxivity at 300 MHz

The basis of imaging in MRI is the difference in relaxation rates of the imaged aqueous protons due to the local biological environmental. The T_1 weighted image uses fast pulse repetition rates which produce brighter images for shorter T_1 times. T_2 weighted images sample the spin echo at long times weighting protons with long T_2's, which are then brighter. The concept of contrast enhancement using magnetic particles is to selectively shorten either T_1 or T_2 by placing them within proximity of structures of interest, such as lesions and tumors. This is quantified by the relation [23], $(1/T_i)_{obs} = (1/T_i)_d + r_i[M]$ $(i = 1, 2)$, where $(T_i)_{obs}$ is the observed relaxation time of the solvent in the presence of the paramagnetic contrast agent M, and $(T_i)_d$ is the observed relaxation time in the absence of M, and r_i is the relaxivity coefficient that describes the concentration dependence of M. Contrast is generally based on maximizing the difference in relaxation times; therefore a large value of r_i (conventionally in units of $s^{-1}\,mM^{-1}$) indicates large contrast potential. The slope of $(1/T_i)$ as a function of $[M]$ provides r_i.

An examination of the r_i data presented by Refs. [2,3] showed one major difference in the experiments: the concentration range investigated. Here, the relaxivity of Fe_8 is investigated over the entire range of both studies. Fig. 1 shows the inverse T_1 of Magnevist and Fe_8 as a function of concentration over the range of 0.1–3.7 mM. The Magnevist exhibits linear behavior over this range with relaxivity, $r_1 = 5.7\ s^{-1}\,mM^{-1}$, in general agreement with Ref. [3]. On the other hand, Fe_8 exhibited two distinct linear regions, one at low concentration <1.5 mM and one at higher concentrations. The r_1 value at low concentration was $5.4\ s^{-1}\,mM^{-1}$, which compares well to the value of Ref. [2] of $5.1\ s^{-1}\,mM^{-1}$ at 9.4 T. The r_1 value at concentrations above 1.5 mM was $1.1\ s^{-1}\,mM^{-1}$, which compares well with the value reported by Ref. [3] of $1.2\ s^{-1}\,mM^{-1}$, also at 9.4 T. The conflict in the literature is attributed to the concentration range that each group studied.

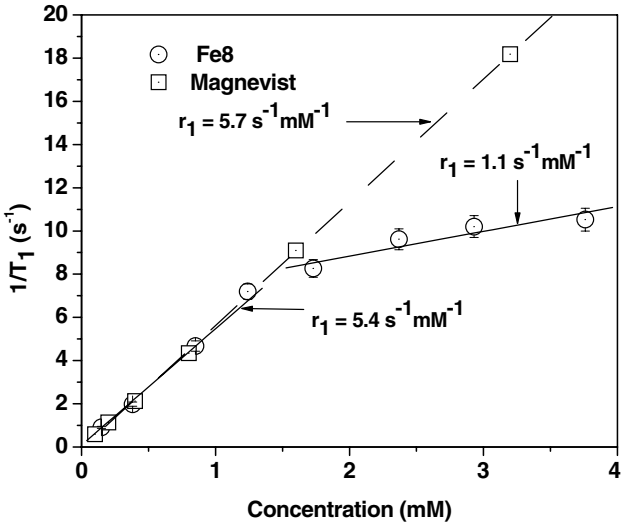


Fig. 1. The inverse proton longitudinal relaxation time T_1^{-1} of 0.1% H_2O in D_2O of Fe_8 and Magnevist solutions as functions of concentration. The Magnevist data are linear across the range investigated. The Fe_8 data, however, show two distinct linear regions above and below 1.5 mM as marked. The slope (r_1) of the low concentration region agrees with Ref. [2], and the slope of the high concentration region agrees with Ref. [3]. These data explain the discrepancy in the literature.

The behavior of T_2^{-1} as a function of contrast agent concentration is shown in Fig. 2. Gd-DTPA (Magnevist) is linear over the entire concentration range with an r_2 of $7.3\ s^{-1}\,mM^{-1}$. In contrast Fe_8 shows two distinct linear regions. Below 1.5 mM the r_2 value is $8.2\ s^{-1}\,mM^{-1}$, compared with Ref. [2] of $8.04\ s^{-1}\,mM^{-1}$. Above 1.5 mM r_2 is $3.2\ s^{-1}\,mM^{-1}$, compared with Ref. [3] of $3.1\ s^{-1}\,mM^{-1}$. Once again, the discrepancy between the two works is attributed to the concentration ranges investigated.

3.2. MRI relaxivity at 64 MHz

The behavior of Fe_8 and Magnevist was investigated using MRI phantoms in DI H_2O at 64 MHz (1.5 T). The MRI signal intensity as a function of the echo time, $S(t_e)$, is related to the transverse relaxation T_2 by [24], $S(t_e) = S_o \exp(-t_e/T_2)$, where S_o is a fit parameter related

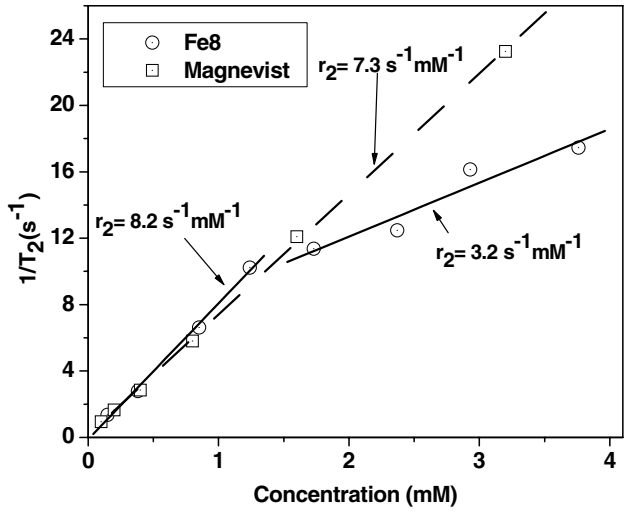


Fig. 2. The inverse transverse relaxation T_2^{-1} of Fe_8 and Magnevist as functions of concentration. In agreement with the relaxation data of Fig. 1, below 1.5 mM the data agree with Ref. [2], and above 1.5 mM the data agree with Ref. [3].

to the initial height of the free induction decay. The values of T_2^{-1} obtained this way as a function of contrast agent concentration are given in Fig. 3. The r_2 for Fe_8 below 1 mM is 4.9 s^{-1} mM^{-1} which compares well with the value in Ref. [2] of 5.01 s^{-1} mM^{-1} obtained by NMR at 1.4 T. Similar to data in Figs. 1 and 2 there is a dramatic decrease in the slope above 1 mM, although more points are needed. This indicates that the concentration dependence of the relaxivity, obtained here by NMR at 300 MHz (7 T), are valid in terms of in vitro MRI at 64 MHz (1.5 T). The relaxivity values are tabulated in Table 1. While the varying conditions and frequencies of these three studies compli-

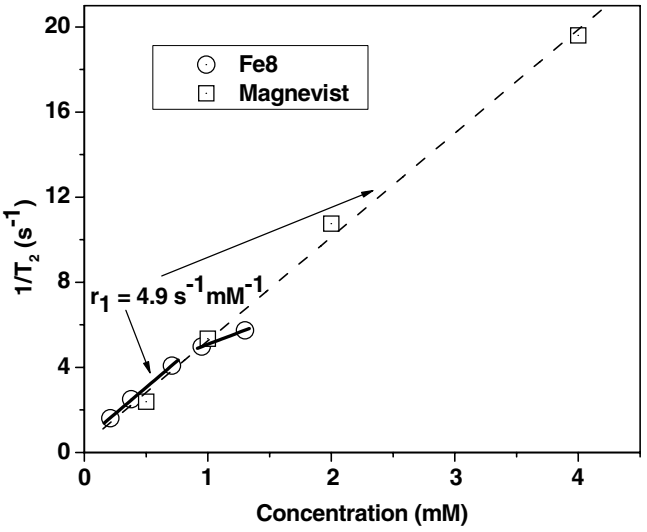


Fig. 3. The inverse transverse relaxation T_2^{-1} of Fe_8 and Magnevist as functions of concentration as obtained from MRI phantoms at 64 MHz (1.5 T). Notice that the $Fe_{8(aq)}$ shows a slope change above 1 mM. This indicates that the data in Figs. 2 and 2 are translatable to clinical in vitro MRI.

Table 1
Comparison of *r*-values

Sample	r_1 (mM^{-1} s^{-1})	r_2 (mM^{-1} s^{-1})	ν (MHz)	Ref.
Fe_8 (<1 mM)	5.10 ± 0.3	8.04 ± 0.12	400	[2]
(<1 mM)	4.76 ± 0.07	5.01 ± 0.08	64	[2]
(<1 mM)		4.9 ± 0.3	64 (MRI)	this work
(<1.5 mM)	5.4 ± 0.3	8.2 ± 0.3	300	this work
(>1 mM)	1.2	3.1	400	[3]
(>1.5 mM)	1.1 ± 0.3	3.2 ± 0.3	300	this work
Gd-DTPA	3.71 ± 0.22	4.44 ± 0.73	400	[2]
	4.29 ± 0.01	4.89 ± 0.02	64	[2]
		4.9 ± 0.3	64 (MRI)	this work
	5.7 ± 0.3	7.3 ± 0.3	300	this work
	5.5	7.0	400	[3]

cate direct *r*-value comparisons, the essential point of concentration dependent *r*-values for Fe_8 seems very clear, and should not depend on the frequency investigated. We are currently evaluating Fe_8 over a wide frequency and temperature range.

3.3. Frozen solution ac susceptibility

In order to assess the degree of stability of the Fe_8 in aqueous solution, we carried out a systematic study of its ac susceptibility using frozen solutions. $Fe_{8(solid)}$ is known to exhibit a frequency-dependent response in the out-of-phase ac susceptibility (χ'') at temperatures of 1.8–5 K [19]. The ac susceptibility of a 6 mM Fe_8 frozen solution was measured by quick insertion into the 1.8 K cryostat of a commercial SQUID magnetometer. In Fig. 4, the dependence of χ''_{ac} as a function of temperature (1.8–3.5 K) and frequency (200–1400 Hz) is shown. A series of maxima which shift to higher temperatures with higher frequencies are present. They are qualitatively similar to the known response of $Fe_{8(solid)}$ observed by Barra et al. [19],

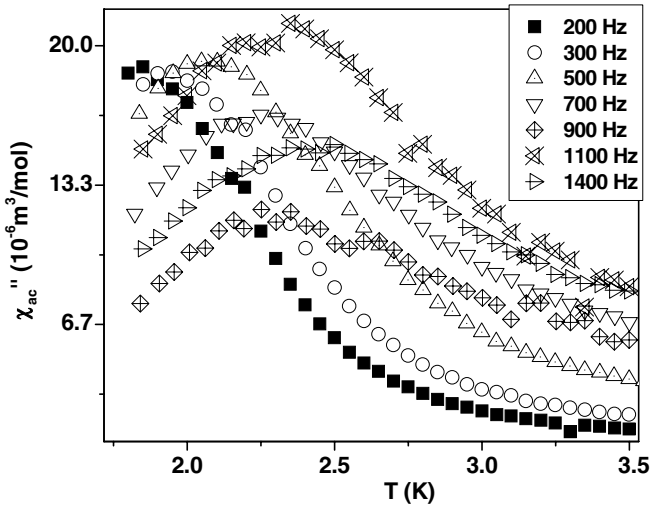


Fig. 4. The χ''_{ac} of a 6 mM frozen solution of Fe_8 in deionized H_2O at an ac field amplitude of 0.65 mT and zero applied dc field. This response is very similar to the response of Fe_8 powder, with the maxima being shifted to lower temperature.

with an overall shift to slightly lower temperature. These data show that in the frozen solution there exists species whose magnetic moment is blocked on the ac time scale at temperatures below 3 K and superparamagnetic above.

The depth of the potential well required to explain the χ'' frozen solution data is of interest for comparison with the Fe_8 solid. For each ac frequency, the temperature of the maxima, T_{max}, in χ'' is inversely related to τ such that at T_{max}, $\tau = (2\pi\upsilon_{ac})^{-1}$. In Fig. 5, the $\ln\tau$ versus the reciprocal of the temperature is plotted and a thermally activated Arrhenius behavior is present. From the slope, $\Delta E/k$ is 14 K and from the intercept $\tau_0 = 3.2\times10^{-7}$ s. The literature values of $\Delta E/k = 24.5$ K and $\tau_0 = 3.4\times10^{-8}$ s have been obtained for $Fe_{8(solid)}$ [18,19]. This approximate agreement suggests the blocked species in Fig. 4 is due to some of the Fe_8 retaining its essential magnetic identity in a frozen solution. The lower value of $\Delta E/k$ with the shift of the maxima to lower temperature implies that the barrier is particle-size and/or conformation dependent: a point that needs additional systematic investigation.

Given the concentration dependence of the relaxivity, the concentration dependence of the χ_{ac} of the Fe_8 frozen solutions was investigated. In Fig. 6. the in-phase response is given, which is sensitive to both blocked as well as paramagnetic species, of the frozen solution at 300 Hz as a function of concentration. At high concentrations, 5 mM for example, a profile characteristic of slow relaxation similar to Fe_8 solid is present, i.e. an inflection point leading to a maximum. This species is then blocked at these time scales and temperatures, and superparamagnetic at temperatures above. At 1 mM, however, a monotonic decrease with increasing temperature is observed indicative of components whose fluctuations are very rapid compared to the observation frequency, such as a paramagnet. The inset shows the molar χ' at 1.8 K as a function of concentration. There is an increase in the χ' as a function of decreasing concentration. Molar susceptibilities should be independent of concentration, this will be discussed later.

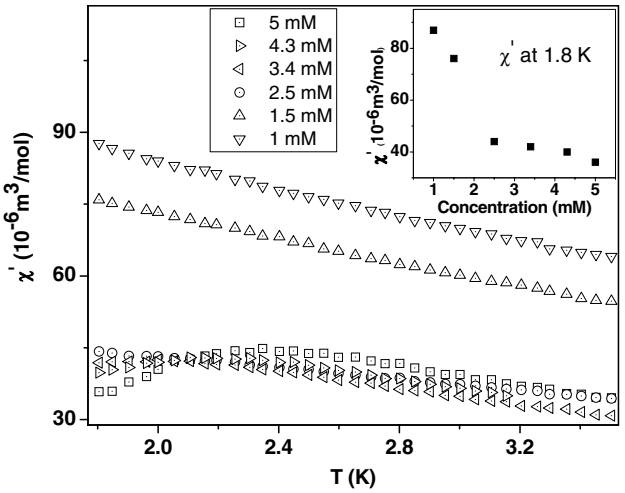


Fig. 6. The concentration dependence of the molar in-phase ac susceptibility at 300 Hz (ac field amplitude of 0.65 mT). The inset shows the χ'_{ac} at 1.8 K as a function of concentration. Note that there is an increase with χ'_{ac} with decreasing concentration.

The out-of-phase susceptibility, which is sensitive only to slow relaxation relative to the observation frequency is given in Fig. 7. At higher concentrations a strong response is observed in the χ'' indicating that the slow relaxation of the magnetic moment is present. As the concentration is lowered below 1.5 mM the maxima in χ'' is much less pronounced. The inset to Fig. 7 shows the maxima in χ'' as a function of concentration. There is a strong increase in the signal at concentrations above 1.5 mM, which roughly corresponds to the break in the $Fe_{8(aq)}$ relaxivity data at room temperature of Figs. 1 and 2.

The data for both low temperature frozen solutions and room temperature relaxivity have demonstrated non-linear

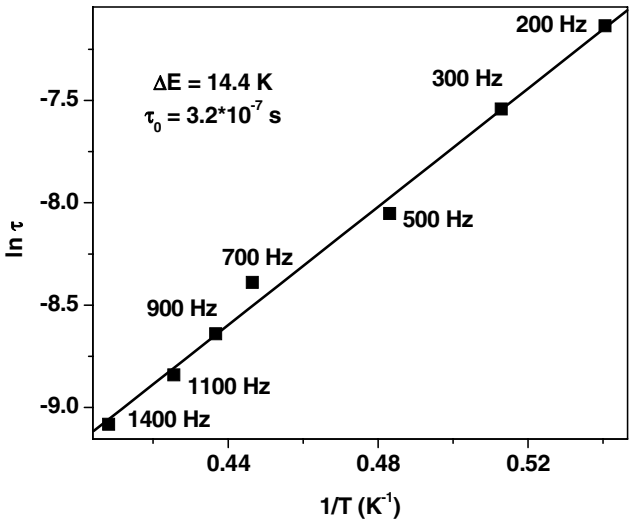


Fig. 5. An Arrhenius plot of the data from Fig. 4 that shows the natural logarithm of the relaxation time as a function of the inverse temperature.

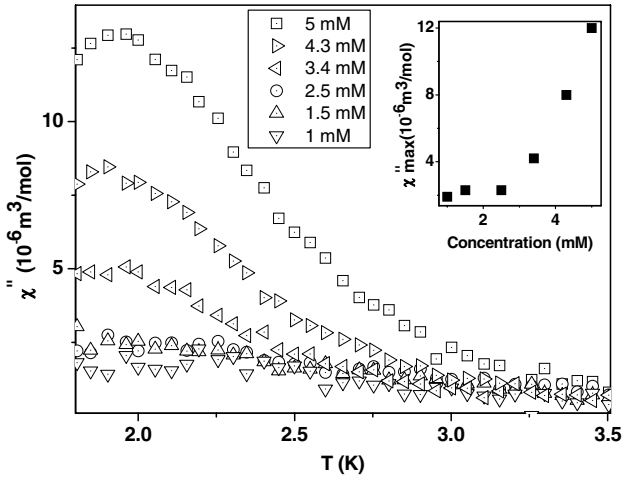


Fig. 7. The concentration dependence of the out-of-phase ac susceptibility at 300 Hz (ac field amplitude of 0.65 mT). Inset shows the maximum as a function of concentration. Notice that there is a non-linear decrease in the molar χ''_{ac} with increasing concentration.

behavior with a break point at ~1.5 mM. In works at concentrations above 1.5 mM both Refs. [3,25] demonstrated that Fe_8 is unstable in aqueous solution. Ref. [3] showed at >1 mM concentrations a partial decomposition into the precursor $Fe(tacn)Cl_3$ occurred. Ref. [25] used Mössbauer spectra of frozen solutions (similar to the conditions in Figs 4 and 5) at concentrations of 5 mM and temperatures of 4 K. Ref. [25] postulated three components; two paramagnetic representing 75% of the spectral area, and a magnetically split (blocked on the Mössbauer time scale) component comprising the remaining 25%. Our high concentration results agree with both works, i.e., that the Fe_8 is unstable in aqueous solutions, and these solutions exhibit blocked superparamagnetic behavior when frozen to low temperatures. However, the data in Fig. 7 show that the molar χ'', which is only sensitive to the blocked superparamagnetic component, seems to decrease at concentrations below 1 mM; while the molar χ' shown in Fig. 6, which is sensitive to the paramagnetic as well as superparamagnetic species, increases as the concentration decreases. In fact, at low concentrations, the molar χ' is essentially paramagnetic in nature.

These results are interpreted as the breakdown of the Fe_8 into small paramagnetic clusters and by-products at low concentrations. As the concentration is increased to around 1.5 mM a saturation of the solution begins to occur. The saturated solution has a much higher degree of relative antiferromagnetic coupling between Fe centers and therefore a lower overall moment per mol or χ'. The species in solution at high concentrations are such, that, when frozen they crystallize out as a compound which has a blocked superparamagnetic component. This component possesses a molar χ'' response similar to Fe_8 powder, but shifted to lower temperatures. This component does not appear to be significantly present at low concentrations.

Does the concentration dependence of the frozen solution data correlate with the room temperature relaxivity? In general, relaxivity scales with moment and sites available for labile water exchange [23]. At concentrations less than 1.5 mM only small paramagnetic Fe clusters or single ions are present. Little antiferromagnetic coupling is present, therefore more moment per mol is available to interact with the aqueous protons. These small clusters and single ions will have more sites available for labile water conjugation directly to the metal centers. At concentrations above 1.5 mM the solution saturates and more Fe–O–Fe interactions come into play. These interactions are antiferromagnetic which reduces the moment per mol as well as the sites available for water exchange, and therefore the relaxivity.

4. Conclusion

We have demonstrated that the discrepancy in the literature regarding the comparative enhancement of relaxation of $Fe_{8(aq)}$ versus the commercial preparation Magnevist is due to the different concentration ranges investigated by each group. Specifically, below 1.5 mM, Fe_8 appears to be competitive with Magnevist, in agreement with Ref. [2], whereas above 1.5 mM it would appear to not compare well with Magnevist, in agreement with Ref. [3]. While the exact nature of the iron particles in the solution phase is unknown, frozen solution χ'' data at concentrations above 1.5 mM strongly suggest that the Fe_8 cores survive in some fashion that contains a magnetically blocked component at low temperatures and superparamagnetic above. Below 1.5 mM the Fe_8 solutions appear to be composed of smaller units that fluctuate magnetically fast on the time scales used in this experiment. The methods here developed of sampling the χ''_{ac} of frozen solutions as a function of frequency and concentration may provide a guideline for future research into the identity and utility of aqueous magnetic species for MRI contrast.

In terms of in vivo utility three factors come to play, toxicity, non-linear relaxivity, and aqueous stability. Ref. [2] pointed out that the concentration normally employed clinically in the extracellular fluid space would be around 0.5 mM. This number is well within the toxicity value of ~1 mM given by Ref. [2]. It is also well within the linear relaxivity range shown in this work of 1 mM or less. While true understanding of the aqueous phase species is desirable, given that the relaxivity at clinical concentrations is comparable to Magnevist, linear, and well within toxicity limits, in vivo experiments would seem to be in order. Further, if the transition from low relaxivity to high relaxivity shown in Figs. 1 and 2 could be taken advantage of, as alluded to in the pH dependence experiments of Ref. [3], perhaps this system could realize a smart contrast mechanism that turns on in the presence of areas of medical interest.

Acknowledgements

We thank Ron Goldfarb of NIST for helpful discussions of aqueous magnetometry and careful reading of the manuscript, and Ruchira Garg of The Department of Pediatric Cardiology, The Childrens Hospital, Denver, CO 80218, for MRI scans, and NSF-DMR (Grant #0506946) for partial support.

References

[1] R.B. Clarkson, Top. Curr. Chem. 221 (2002) 202.
[2] E. Rodriguez, A. Roig, C. Arus, M.R. Quintero, M.E. Cabanas, S. Cerdan, P. Lopez-Larrubia, C. Sanfeliu, NMR Biomed. 18 (2005) 300.
[3] S. Isaacman, R. Kumar, E. del Barco, A.D. Kent, J.W. Canary, A. Jerschow, Polyhedron 24 (2005) 2691.
[4] A. Barker, B. Cage, S. Russek, R. Garg, R. Shandas, C. Stoldt, in: Proceedings of the ASME International Mechanical Engineering Congress and Exposition, Orlando, FL, November 05–11, 2005, IMECE2005-81503.
[5] (a) J.A.A.J. Perenboom, J.S. Brooks, S. Hill, T. Hathaway, N.S. Dalal, Phys. Rev. B 58 (1998) 330;
(b) R. Sessoli, D. Gatteschi, Angew. Chem., Int. Ed. Engl. 42 (2003) 268.

[6] K. Wieghardt, K. Pohl, I. Jibril, G. Hutner, Angew. Chem., Int. Ed. Engl. 23 (1984) 77.
[7] K. Park, M.A. Novotny, N.S. Dalal, S. Hill, P.A. Rikvold, Phys. Rev. B 65 (2002) 014426.
[8] A.L. Barra, D. Gatteschi, R. Sessoli, Chem. Eur. J. 6 (2000) 1608.
[9] D. Zipse, J.M. North, N.S. Dalal, S. Hill, R.S. Edwards, Phys. Rev. B 68 (2003) 184408.
[10] S. Hill, S. Maccagnano, K. Park, R.M. Achey, J.M. North, N.S. Dalal, Phys. Rev. B 65 (2002) 224410.
[11] B. Cage, S.E. Russek, D. Zipse, M. North, N. S Dalal, Appl. Phys. Lett. 87 (2005).
[12] B. Cage, S.E. Russek, D. Zipse, N.S. Dalal, J. Appl. Phys. 97 (2005) 10M507.
[13] S. Maccagnano, R. Achey, E. Negusse, A. Lussier, M.M. Mola, S. Hill, N.S. Dalal, Polyhedron 20 (2001) 1441.
[14] C. Delfs, D. Gatteschi, L. Pardi, R. Sessoli, K. Weighardt, D. Hanke, Inorg. Chem. 32 (1993) 3099.
[15] R. Caciuffo, G. Amoretti, A. Murani, R. Sessoli, A. Caneschi, D. Gatteschi, Phys. Rev. Lett. 81 (1998) 4744.
[16] M.N. Leuenberger, D. Loss, Nature 410 (2001) 789.
[17] W.H. Rippard, M.R. Pufall, S. Kaka, S.E. Russek, T.J. Silva, Phys. Rev. Lett. 92 (2004) 027201.
[18] C. Sangregorio, T. Ohm, C. Paulsen, R. Sessoli, D. Gatteschi, Phys. Rev. Lett. 78 (1997) 4645.
[19] A.L. Barra, P. Debrunner, D. Gatteschi, Ch. E. Schulz, R. Sessoli, Europhys. Lett. 35 (1996) 133.
[20] W. Wernsdorfer, A. Caneschi, R. Sessoli, D. Gatteschi, A. Cornia, V. Villar, C. Paulsen, Phys. Rev. Lett. 84 (2000) 2965.
[21] E. del Barco, J.M. Hernandez, J. Tejada, N. Biskup, R. Achey, N. Dalal, J. Brooks, Phys. Rev. B 62 (2000) 3018.
[22] X. Mao, J. Guo, Ch. Ye, Chem. Phys. Lett. 222 (1994) 417.
[23] R.B. Lauffer, Chem. Rev. 87 (1987) 901.
[24] D.R. McRobbie, E.A. Moore, M.J. Graves, M.R. Prince, MRI: From Picture to Proton, Cambridge University Press, Cambridge, 2004.
[25] E. Rodriguez, M. Gich, A. Roig, E. Molins, N. Nedelko, A. Slawska-Waniewska, A. Szewczyk, Polyhedron 25 (2006) 113.

on a BRUKER AM 300 spectrometer. ^{1}H NMR shifts were recorded relative to residual ^{1}H resonances of the deuterated solvent and ^{31}P{^{1}H} chemical shifts are relative to external 85% H_3PO_4 with downfield values reported as positive. Elemental analyses on a FISONS 1108 instrument.

2.1.1. IrCl(COD)(CQ) (1)

A solution of $[Ir(COD)Cl]_2$ (100 mg, 0.15 mmol) in ethanol (30 ml) was stirred until complete dissolution was achieved and then CQ (144 mg, 0.45 mmol) was added. The stirring was continued for 50 min at room temperature. The volume of the solvent was reduced under a nitrogen stream and diethyl ether was added until the solution became turbid; on cooling to −5 °C overnight the yellow product precipitated, it was isolated by filtration, washed with diethyl ether, and dried under vacuum. Yield: 63%. *Anal*. Calc. for $IrC_{26}H_{42}N_3Cl_2O_3$: C, 43.94; H, 6.20; N, 5.92. Found: C, 44.19; H, 5.44; N, 6.07%. M.p.: 290 °C. IR (cm^{-1}): *v*(N–H) 3332, *v*(C=C) 1590, *v*(C=N) 1609. ^{1}H NMR ($(CD_3)_2SO$) (ppm) 7.32 (br) NH, 8.36 (d, $J = 6.13$ Hz H2), 6.55 (d, $J = 6.13$ Hz, H3), 8.42 (d, $J = 8.54$ Hz, H5), 7.51 (d, $J = 8.54$ Hz, H6), 8.45 (s, H8), 3.33 (br, H1′), 1.22 (d, $J = 6.33$ Hz, H1″), 1.67 (m, H2′, H3′), 2.49 (m, H4′, H5′), 0.93 (t, $J = 7.14$ Hz, H6′), COD 3.76 (br, CH), 2.50 (br, 4H), 2.20 (br, 4H). ^{13}C{^{1}H} NMR (ppm) C2 151.9, C3 99.4, C4 147.9, C5 124.6, C6 125.4, C7 133.7, C8 127.2, C9 149.9, C10 117.9, C1′ 47.9, C1″ 19.8, C2′ 33.9, C3′ 31.3, C4′ 40.3, C5′ 51.8, C6′ 11.1, CH (AA′, BB′), 64.4 (d, $J_{C-Rh} = 9.43$ Hz), CH2 22.9 (s).

2.1.2. $Ir_2Cl_6(CQ)\cdot 3H_2O$ (2)

To a solution of $IrCl_3\cdot 3H_2O$ (250 mg, 0.72 mmol) in methanol (45 ml) CQ was added (463 mg, 1.45 mmol). The mixture was stirred and refluxed for 6 h. During the reaction a yellow-green solid was formed. The product was isolated by filtration, washed with water and diethyl ether and dried under vacuum. Yield: 56%. *Anal*. Calc. for $Ir_2C_{18}H_{32}N_3Cl_7O$: C, 22.24; H, 3.29; N, 4.32. Found: C, 21.80; H, 3.36; N, 4.47%. IR (cm^{-1}): *v*(N–H) 3488, *v*(C=C) 1613, *v*(C=N) 1628. ^{1}H NMR ($(CD_3)_2SO$) (ppm) 8.12 (br) NH, 8.54 (d, $J = 6.13$ Hz H2), 6.83 (d, $J = 6.13$ Hz, H3), 8.54 (d, $J = 8.54$ Hz, H5), 7.67 (d, $J = 8.54$ Hz, H6), 7.89 (s, H8), 4.02 (br, H1′), 1.28 (d, $J = 6.33$ Hz, H1″), 1.69 (m, H2′, H3′), 3.10 (m, H4′, H5′), 1.12 (t, $J = 7.14$ Hz, H6′). ^{13}C{^{1}H} NMR (ppm) C2 151.3, C3 98.9, C4 148.0, C5 124.8, C6 124.8, C7 135.0, C8 124.8, C9 151.3, C10 116.8, C1′ 47.9, C1″ 19.7, C2′ 32.6, C3′ 20.4, C4′ 48.2, C5′ 50.8, C6′ 8.6.

2.1.3. $[Ir(CQ)((CH_3)_2CO)_2]PF_6$ (3)

A solution of $[Ir(COD)Cl]_2$ (160 mg, 0.24 mmol) in ethanol (30 ml) was stirred until complete dissolution was achieved, then CQ (220 mg, 0.70 mmol) was added, the mixture was stirred for 15 min at room temperature. KPF_6 was added (220 mg, 1.44 mmol) and the reaction was continued for 4.5 h at room temperature. The solvent was removed under reduced pressure, the dry residue was redissolved in acetone and a white solid (KCl) separated. The solution was filtered through celite, the volume of the solvent was reduced under vacuum and diethyl ether was added until the solution became turbid; on cooling −5 °C overnight, the yellow product precipitated. It was isolated by filtration, washed with water and diethyl ether, and dried under vacuum. Yield: 89%. *Anal*. Calc. for $IrC_{21}H_{34}ClN_3OPF_6$: C, 34.15; H, 4.48; N, 6.66. Found: C, 34.37; H, 4.63; N, 5.73%. IR (cm^{-1}): *v*(N–H) 3220, *v*(C=C) 1588, *v*(C=N) 1616, vPF_6^- 838. ^{1}H NMR ($(CD_3)_2SO$) (ppm) 7.91 (br) NH, 8.50 (d, $J = 6.13$ Hz H2), 6.73 (d, $J = 6.13$ Hz, H3), 8.46 (d, $J = 8.54$ Hz, H5), 7.60 (d, $J = 8.54$ Hz, H6), 7.85 (s, H8), 3.94 (br, H1′), 1.27 (d, $J = 6.33$ Hz, H1″), 1.69 (m, H2′, H3′), 3.05 (m, H4′, H5′), 1.14 (t, $J = 7.14$ Hz, H6′). ^{13}C{^{1}H} NMR (ppm) C2 149.1, C3 98.9, C4 146.5, C5 124.8, C6 124.8, C7 135.0, C8 124.8, C9 151.3, C10 116.8, C1′ 47.9, C1″ 19.7, C2′ 32.3, C3′ 20.4, C4′ 46.4, C5′ 50.8, C6′ 8.61. ^{31}P{^{1}H} NMR PF_6^- 141.3 ppm (hept).

2.1.4. In vitro test for anti-malarial activity

Anti-malarial activity of the experimental compounds **1**–**3** were first assessed on short-term in vitro cultures of *P. berghei* and the further evaluation on *P. falciparum* is in progress. The working solutions of **1**–**3** were 18 mM in RPMI medium containing 0.16% (v/v) DMSO (Sigma). Chloroquine diphosphate (Sigma) was diluted in RPMI-1640 (GIBCO-BRL) medium without serum/plasma to obtain a working solution of 19.4 μM. Drug testing was performed in triplicate in 96-well, flat bottomed plates (Linbro, Flow Lab. Inc., VA) with cultures containing mostly ring stages. Short-term cultures of *P. berghei* were prepared according to the protocol described by Kamiyama and Matsubara [9]. In brief, infected blood was obtained from mice harboring low parasitemias (3–5%) for which predominant blood stages were rings and young trophozoites (one nucleus). Blood was washed with RPMI medium supplemented with HEPES (*N*-(2hydroxyethyl)piperazine-*N*′-2-ethanesulfonic acid, 2 nM L-glutamine, 18 mM sodium bicarbonate, 3.25 μM reduced glutathione and 5% (v/v) normal rat serum which had been previously inactivated at 56 °C/30 min. The same batch of rat serum gathered from animals 4–6 weeks old was used throughout the experiments. Suspensions of uninfected and infected erythrocytes in complete culture medium were mixed to obtain a working cell suspension containing 2×10^7 parasitized cells and 1.8×10^8 uninfected erythrocytes per mL. Uninfected erythrocytes (2×10^8/mL) served as controls. One hundred microliters of the cell suspension and 25 μL of the tested compound or medium alone (with or without 0.16% DMSO) were mixed in the appropriate well followed by 25 μL of the [^{3}H]hypoxanthine (Amersham International) solution (0.5 μCi) in culture medium. After a 24 h incubation period in an atmosphere of 5% CO_2, 10% O_2 and 85% N_2, the cells were collected on glass-fiber disks (934 AH, Whatman, Inc., NJ) using a cell

harvester (MASH II; Microbiological Associates, MD), counted in a liquid scintillation counter (LKB 1217 Rackbeta). Dose–response curves for each compound were generated and the IC_{50} values calculated from the corresponding regression line.

3. Results and discussion

3.1. Chemistry

CQ reacts readily with appropriate iridium salts or complexes under mild conditions to produce a variety of Ir–CQ complexes in high yields as summarized in Scheme 1. The new compounds are air stable in the solid state and in solution, a necessary condition for biological use. They were characterized by a combination of elemental analysis, IR and NMR spectroscopy, as described in Section 2. The elemental analysis of these complexes is in agreement with the molecular formulas for all of them. The IR spectra displayed peaks clearly associated with the presence of the coordinated ligands, and of the counteranions, where present. All ^1H NMR resonances could be unequivocally assigned on the basis of 1D- and 2D-correlated COSY and HETCOR experiments (for complete NMR data see Section 2; atom numbering for CQ in Scheme 1). The selected NMR data are collected in Table 1. The ^1H chemical shift variation of each signal with respect to those of the free ligand ($\Delta\delta$) was used as a parameter to deduce the mode of bonding of CQ to the metal. It has been previously shown [2,10] that the largest variations are always observed for the protons located in the vicinity of the N-atom attached to the iridium.

3.1.1. $IrCl(COD)(CQ)$ (1)

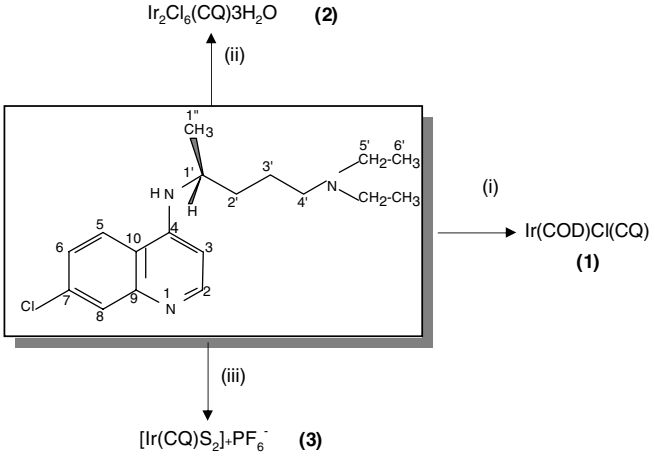
Reaction of $[IrCl(COD)]_2$ with 3 equiv. of CQ under mild conditions leads to the new complex IrCl(COD)(CQ) (**1**), which was isolated in good yields. Besides elemental analysis, and IR spectroscopy the new complex has been well characterized by NMR spectroscopy. Selected data contained in Table 1 indicates that in complex **1** CQ binds to iridium through the quinoline ring N(1) atom. Correspondingly, the largest shift with respect to the free ligand is observed for H8 ($\Delta\delta = 0.70$ ppm) located in the vicinity of N(1). All the other CQ protons shift $\angle 0.15$ ppm, except NH which moves 0.42 ppm downfield. Further support for this structural assignment came from the analysis of ^1H longitudinal relaxation times and NOESY spectra which showed the overall motion and internal flexibility of the CQ ligand in **1** were not significantly different from that of free CQ. According with these data the formulation for thus correspond to the usual 16-electron square-planar configuration for Ir (I) as show in Fig. 1, similar to the Rh analog previously reported [2].

Table 1
Selected ^1H NMR data for complexes **1**–**3**

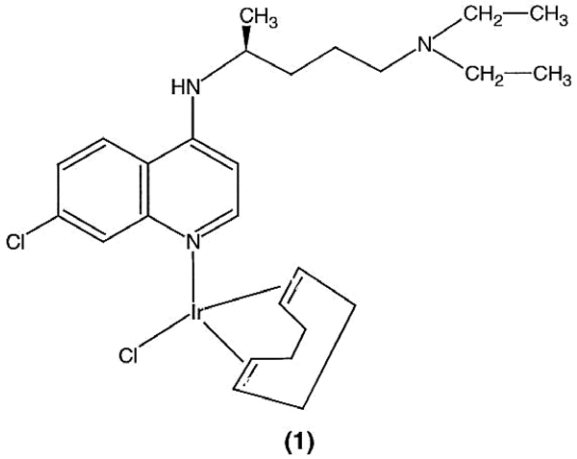
Assignment	$\Delta\delta_{H\ (ppm)}$		
	1	**2**	**3**
H2	0.03	0.19	0.15
H3	0.09	0.37	0.30
H8	0.70	0.14	0.10
NH	0.42	1.22	1.10
H4′H5′	0.15	0.76	0.71

3.1.2. $IrCl_6(CQ)\cdot 3H_2O$ (2)

The reaction of iridium chloride salts with CQ produces **2** whose proposed structure is shown in Fig. 2. The elemental analysis of the complex agreed with the molecular formula calculated for the proposed structure, the IR spectrum displays peaks associated with the presence of coordinated CQ. The NMR proton shifts indicate that CQ binds to the iridium in **2** through both N4 and N4′ atoms, since large shifts with the respect free CQ were observed for H4′H5′ ($\Delta\delta = 0.76$ ppm), NH which moves 1.22 ppm downfield, and H1′ ($\Delta\delta = 0.35$ ppm) located in the vicinity of NH. The NH signal showed an unexpected

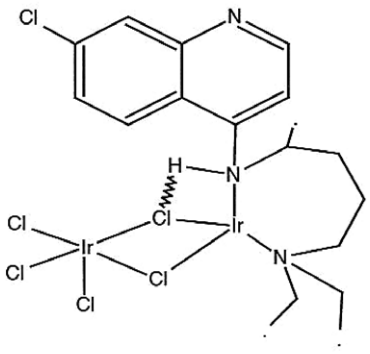


Scheme 1. Synthesis of new complexes. (i) $[Ir(COD)Cl]_2$ in MeOH, CQ for 50 min RT. (ii) $IrCl_3\cdot 3H_2O$ in MeOH, CQ reflux 6 h. (iii) $Ir(COD)Cl]_2$ in EtOH, KPF_6 4.5 h RT.



(1)

Fig. 1. Proposed structure for **1**.



(2)

Fig. 2. Proposed structure for **2**.

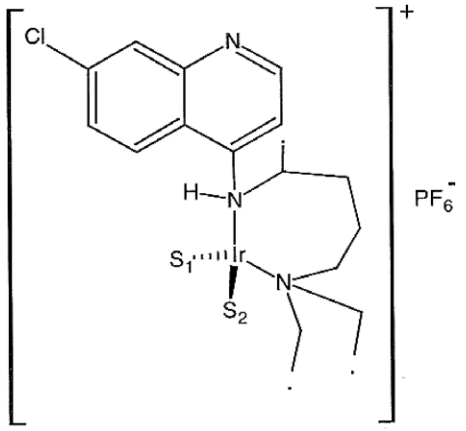
behavior on treatment with D_2O. Instead of the usual fast interchange with the deuterium, the sample had to be warmed up and after a few days the NH finally disappeared. This can be explained by the presence of a hydrogen bridge between the NH and one of the chlorine atoms directly bonded to the metallic center, as is shown in Fig. 2. The T_1 measurements (Table 2) for complex **2** indicate that the proton relaxation times are smaller than those for the free CQ, suggesting a dinuclear structure for complex **2**.

3.1.3. *[Ir(CQ)(S)$_2$]PF$_6$ (3)*

Removal of the chloride ligand of **1** by NH_4PF_6 produces complex **3** for which the proposed structure is shown in Fig. 3. The elemental analysis of the complex agreed with the molecular formula calculated for the proposed structure, the IR spectrum displays peaks associated with the presence of coordinated CQ, plus a band at 843 cm^{-1} characteristic of the PF_6 anion. The ^1H, $^{13}C\{H\}$, COSY and HETCOR NMR spectra allowed us to assign all the protons and carbons in the molecule. The variation in the chemical shifts observed for NH ($\Delta\delta = 1.10$ ppm), H1′ ($\Delta\delta = 0.31$ ppm) located in the vicinity of NH as well as for H4′–H5′ ($\Delta\delta = 0.71$ ppm) of the coordinated CQ with respect to the free ligand, indicate that the binding to the metal is through N4 and N4′. Besides, the T_1 measurements (Table 2) for complex **3** indicate that the proton relaxation times are similar to those of the free drug an evidence of a similar molecular volume that points toward a mononuclear structure.

Table 2
Measurement of the T_1 (ms) for complexes **2** and **4**

	CQ T1 (ms)	Complex **1** T_1 (ms)	Complex **2** T_1 (ms)	Complex **3** T_1 (ms)
H1″	344.5	365.1	270.9	325.1
H6′	941.1	1064.5	417.8	636.4
H3	450.6	448.3	281.6	430.4
H5	1269.1	1058.7	279.9	908.7
H6	1586.0	1931.1	869.9	1814



(3)

Fig. 3. Proposed structure for **3**.

The NOESY spectra shows dipolar couplings between the aliphatic protons H1″, H4′, H5′, H6′ and the aromatic protons, indicating the metallacycle conformation of the complex and the free rotation of the single bond between the quinoline ring and the aliphatic chain of the CQ. The ^{31}P spectrum exhibits a heptuplet at 141.3 ppm due to the PF_6 anion. The proposed geometry of **3** is square planar, corresponding to an Ir(I) d^8 of 16 electrons, typical for this metal.

3.2. Biology

Chloroquine resistance of *P. falciparum* represents today a major health care problem in malaria endemic countries [1]. Current evidence indicate that PfCRT, a member of the drug/metabolite transporter superfamily, plays a central role in the resistance of *P. falciparum* to CQ linked with polymorphisms within the *pfcrt* gene [11–14]. Since PfCRT is involved in carrier-mediated CQ efflux from resistant cells [15] it is attractive to speculate that binding of CQ to transition metals moderates its efflux from resistant cells leading to improved CQ activity.

Preliminary experiments carried out to determine the anti-malarial activities of complexes **1**–**3** were set up using short-term in vitro cultures of *P. berghei*. Inhibition of the uptake of [^{3}H]-hypoxanthine served as a measure of parasites viability. The biological tests were carried using DMSO as the solvent in which the complexes are stable. Final parasitemia and hematocrit were 2% and 1%, respectively. Parasite cultures were exposed to increasing concentrations of either parental compound or the corresponding complexes **1**–**3** for 24 h. Cells were harvested, their viability was assessed, and the concentration of drug for 50% inhibition (IC_{50}) was determined for each compound [16,17]. The effect of the assayed compounds on the development of *P. berghei* are summarized in Table 3. In three separate experiments the IC_{50} was estimated to be 72 nM for chloroquine diphos-

Table 3
Effect of CQDP and complexes **1**–**3** on the in vitro growth of *P. berghei*

Compound	IC_{50} (nM)	$IC_{50\,ratio}$CQDP
CQDP	72	
Ir(COD)(CQ)Cl (**1**)	72	1.0
$Ir_2Cl_6(CQ)\cdot 3H_2O$ (**2**)	59	1.2
$[Ir(CQ)_2(S)_2]^+PF_6^-$ (**3**)	126	0.6

phate (CQDP) whereas that for complexes **1**, **2** and **3** were 72, 59, 126 nM, respectively. The ratio of IC_{50} (parental compound)/ IC_{50} (metal complex) indicated that complex **2** is slightly better than CQ, whereas complex **1** has similar activity to that of CQDP. In contrast the ratio for complex **3** was <1. Unfortunately, no clear activity trend as a function of molecular structure or oxidation state of the iridium from the data obtained for these complexes. It was noted however, that **1** and the previously described Rh(CQD)(CQ)Cl [2] display similar structures both sharing inability to modify the parental drug anti-malarial activity. A previous study reported [18] the synthesis of Ir (II)-CQ complexes which were tested in vitro for their activity against tumor cells and African trypanosomes but anti-malarial activity was not examined.

Control cultures treated with medium containing 0.16 % (v/v) DMSO in the culture medium, equivalent to the level of DMSO in the cultures containing the complexes, did not show any inhibition of parasite growth, indicating that the observed inhibition was solely due to the presence of the drug in the medium.

In summary, three new iridium-CQ complexes were synthesized all of them showing antimalarial activity against *P. berghei* in vitro. Complex **3** was found more active than CQDP. These results further illustrate the potential of coordinating transition metals to CQ in order to improve the anti-malarial activity of this drug.

Acknowledgements

We thank Dr. Julio Urbina for help in NMR discussion, Dr. Roberto Sanchez Delgado for his useful comments and José Bolívar and Mercedes de la Rosa for technical help. This work was supported in part by CONICIT Grants RPV-0032-6, S1-2696 and S1-98000945.

References

[1] J.G. Breman, Am. J. Trop. Med. Hyg. 64 (2001) S1–S11.
[2] R.A. Sánchez-Delgado, M. Navarro, H. Pérez, J. Urbina, J. Med. Chem. 39 (1996) 1095.
[3] M. Navarro, R.A. Sánchez-Delgado, H. Pérez, J. Med. Chem. 40 (1997) 1937.
[4] M. Navarro, F. Vásquez, R.A. Sánchez-Delgado, H. Pérez, V. Sinou, J. Schrével, J. Med. Chem. 47 (2004) 5204.
[5] B. Rosenberg, in: T.G. Spiro (Ed.), Nucleic Acid–Metal Ion Interactions, Wiley, New York, 1980.
[6] N. Farrell, in: B.R. James, R. Ugo (Eds.), Transition Metal Complexes as Drugs and Chemotherapeutic Agents, in Catalysis by Metal Complexes, Kluwer, Dordrecht, 1989.
[7] M. Sun, Science 222 (1983) 145.
[8] J.L. Herde, J.C. Lambert, C.V. Senoff, Inorg. Synth. 15 (1974) 18.
[9] T. Kamiyama, J. Matsubara, Int. J. Parasitol. 22 (1992) 1137.
[10] W.I. Sundquist, D.P. Bancroft, S. Lippard, J. Am. Chem. Soc. 112 (1990) 1590.
[11] D.A. Fidock, T. Nomura, A.K. Talley, R.A. Cooper, S.M. Dzekunov, M.T. Ferdig, D. Ursos, A.B. Sidhu, B. Naude, K.W. Deitsch, X.Z. Su, J.C. Wootton, P.D. Roepe, T.E. Wellems, Mol. Cell 6 (2000) 861.
[12] T.E. Wellems, C.V. Plowe, J. Infect. Dis. 84 (2001) 770.
[13] A.B. Sidhu, D. Verdier-Pinard, D.A. Fidock, Science 298 (2002) 74.
[14] R.E. Martin, K. Kirk, Mol. Biol. Evol. 21 (2004) 1938.
[15] C.P. Sanchez, J.E. McLean, P. Rohrbach, D.A. Fidock, W.D. Stein, M. Lanzer, Biochemistry 44 (2005) 9862.
[16] R.E. Desjardins, C.J. Canfield, J.D. Haynes, J.D. Chulay, Antimicrob. Agents Chemother. 16 (1979) 710.
[17] P.H. Van Vianen, D.L. Klaiman, B. Mins, Exp. Parasitol. 70 (1990) 115.
[18] D.G. Craciunescu, C. Molina, E. Parrondo-Iglesias, M.P. Alonso, L. Lorenzo Molina, J.C. Doadrio-Villarejo, M.T. Gutierrez-Rios, M.I. De Frutos, G. de Iriarte, G. Certad Bombona, N. Ercoli, An. Real Acad. Farm. 57 (1991) 15.

organic acids have been used to diprotonate the porphyrin core [5].

In the present work, we have used a series of carboxylic acids weaker than CF_3COOH to diprotonate different porphyrins. Interestingly, we have found that even propionic acid is able to diprotonate arylporphyrins (Fig. 1) and *meso*-tetra(*n*-Pr)porphyrin, H_2t(*n*-Pr)p. Also, the effects of porphyrin core saddling, *meso*-aryl- and alkyl-substituents and electron donation to acceptors, i.e. carboxylic acids, on the UV–Vis spectra of porphyrins have been studied.

2. Results and discussion

Diprotonation of H_2t(*n*-Pr)p and arylpor with weak and strong carboxylic acids (Table 1) led to a spectral shift of the Soret and Q(0,0) bands.

2.1. H_2t(*n*-Pr)p

Interaction of H_2t(*n*-Pr)p with different carboxylic acids, including trifluoroacetic acid, chloroacetic acid, oxalic acid, formic acid, acetic acid and propionic acid, led to a red shift of the Soret band and a blue shift of the Q(0,0) band (Table 2). However, due to the weaker acid strengths of acetic acid and propionic acid with respect to the other carboxylic acids (Table 2), excess amounts (beyond 2:1 molar ratio of acid/porphyrin) of the acids have been used to complete the reaction (Fig. 2). It should be noted that due to the weak interaction of carboxylic acids such as acetic acid and propionic acid with porphyrins, their adducts may be considered as hydrogen-bonded charge-transfer complexes.

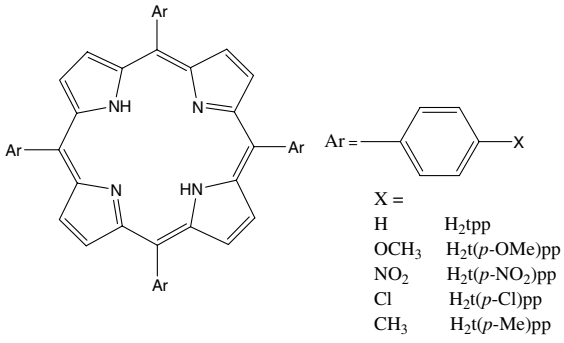


Fig. 1. *para*-Substituted *meso*-tetraphenylporphyrins used in this study.

Table 1
pK_a values for the carboxylic acids

Acids	pK_a	Acids	pK_a
CH_3COOH	4.76	$ClCH_2COOH$	2.86
CH_3CH_2COOH	4.87	$H_2C_2O_4$	1.25, 4.27
HCOOH	3.75	CF_3COOH	

2.2. The Soret band

The Soret bands of the dications are red shifted relative to that of the free base H_2t(*n*-Pr)p (Table 2). The absorption spectra of $(C_2H_5COOH)_2H_2$t(*n*-Pr)p is shown in Fig. 2. The observed red shifts are in the range 346.22–1060.50 cm^{-1}.

Diprotonation of the porphyrins leads to (i) the shift of electron density from the pyrrolenine nitrogen atoms to the central acceptors, i.e. the carboxylic acids and in the case of *meso*-tetraarylporphyrins, (ii) the saddling of the porphyrin core and (iii) enhanced coplanarity of the *meso*-aryl groups with the porphyrin core [5e,6].

Although propionic acid is the weakest acid of the series, it causes the greatest red shift of the Soret band. The observed red shift of the Soret band for H_2t(*n*-Pr)p $(CF_3COOH)_2$ is only 346.22 cm^{-1}, which is the smallest

Table 2
UV–Vis spectral data for the dications of H_2t(*n*-Pr)p with different carboxylic acids in CH_2Cl_2 at 25 °C

Porphyrin and dications	Soret band (λ/nm)	Q(0,0) band (λ/nm)	Q(0,0) band ($\lambda_{corr.}$/nm)[a]
H_2t(*n*-Pr)p	416	656.6	
H_2t(*n*-Pr)p$(CF_3COOH)_2$	422.4	631.04	664.80
$\Delta\upsilon$ (cm^{-1})[b]	−364.22	616.88	−187.85
H_2t(*n*-Pr)p$(H_2C_2O_4)_2$	428.8	634.8	668.98
$\Delta\upsilon$ (cm^{-1})	−717.57	523.02	−281.84
H_2t(*n*-Pr)p$(ClCH_2COOH)_2$	430.08	634.8	668.98
$\Delta\upsilon$ (cm^{-1})	−827.22	523.02	−281.84
H_2t(*n*-Pr)p$(HCOOH)_2$	427.5	631.04	664.80
$\Delta\upsilon$ (cm^{-1})	−646.65	616.88	−187.85
H_2t(*n*-Pr)p$(CH_3COOH)_2$	430.08	632.3	666.20
$\Delta\upsilon$ (cm^{-1})	−827.22	585.30	−219.46
H_2t(*n*-Pr)p$(CH_3CH_2COOH)_2$	435.2	641.2	676.09
$\Delta\upsilon$ (cm^{-1})	−1060.5	365.78	−439.04

[a] $\lambda_{corrected}(\lambda_{corr.})$ are calculated as follows: $10^7/\lambda_{corr.} = 10^7/\lambda_{Q(0,0)} - 804.81$ (cm^{-1}); 804.81 cm^{-1} is the minimum estimated blue shift of the Q(0,0) band caused by the diprotonation of the porphyrin core (see the text).

[b] $\Delta\upsilon$ (cm^{-1}) $= (1/\lambda_2 - 1/\lambda_1)10^7$.

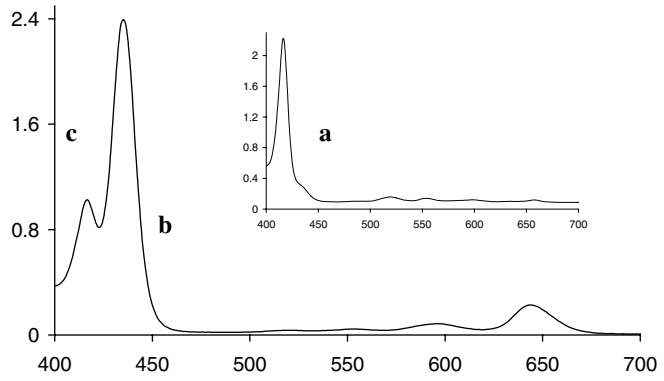


Fig. 2. UV–Vis spectra for $H_2t(n\text{-Pr})p$ (7×10^{-5} M): (a) $H_2t(n\text{-Pr})p(C_2H_5COOH)_2$, (b) in CH_2Cl_2, and in a 0.1 cm cell; (c) the Soret band of the free base porphyrin due to the partial dissociation of $(C_2H_5COOH)_2H_2t(n\text{-Pr})p$ in solution.

one of the series (Table 2). On the basis of the four orbital model of porphyrins, the Soret band is due to the a_{1u} to e_g transition. For the a_{1u} orbitals the electron densities are largest on the pyrrole carbon atoms and the methene bridges lie on nodal planes [7]. Accordingly, it is reasonable to think that the shift of non-bonding electron density from the pyrrolenine nitrogen atoms to the pure σ-acceptors by itself leads to little or no change on the energy of the a_{1u} to e_g transition. Such a suggestion is more reasonable especially in the case of $H_2t(n\text{-Pr})p(CH_3CH_2COOH)_2$ or $H_2t(n\text{-Pr})p(CH_3COOH)_2$ adducts in which the central acceptors are very weak acids. The carboxylic acid orbital involved in the adduct formation may be considered as the σ^* orbital of the O–H bond or the 1s orbital of the bare proton. But due to the contact dication-carboxylate ion pair in nearly non-coordinating solvents such as CH_2Cl_2, the former description seems to be more convenient.

It is notable that the electronic effects of the *n*-propyl groups are nearly the same in the free base porphyrin or the dications. Introduction of four *n*-propyl substituents on the *meso*-positions of porphine (H_2p) led to a 1342.25 cm^{-1} red shift of the Soret band. Also, comparison of the Soret bands for the corresponding dications shows that the Soret band of $H_2t(n\text{-Pr})p(CF_3COOH)_2$ is ca. 1263.41 cm^{-1} red shifted relative to that of the porphine dication (see Table 3).

The various red shifts of the dications in Table 2 may be properly explained on the basis of porphyrin core saddling upon diprotonation of the porphyrin macrocycle. The core protonation of porphyrins has to result in an out-of-plane tilting of the individual pyrrole rings as four hydrogen atoms do not fit into the central core of the macrocycle while maintaining a square-planar N_4-unit [5b,5c,5d,5e]. Also, it has been shown that the degree of saddling for $H_4tpp(X)_2$ ($X=F^-$, Cl^-, Br^- and I^-) increases with the increasing size of halide, suggesting that the necessity to optimize the hydrogen bond interactions between the halides and the dication is an additional factor in determining the actual degree of saddling [8]. It has been observed that in spite of the stronger X···N–H hydrogen bond for $X=F^-$ with respect to the other halides, the largest amount of core saddling has been observed for $X=Br^-$.

Accordingly, the larger red shift of the Soret band for $H_2t(n\text{-Pr})p(CH_3COOH)_2$ relative to that of $H_2t(n\text{-Pr})p(CF_3COOH)_2$, in spite of very similar sizes of counter ions, seems to be due to the enhanced $H_4t(n\text{-Pr})p$···carboxylate hydrogen bonding in the former. Due to very close acid strength of propionic and acetic acid, the hydrogen bonding in $H_2t(n\text{-Pr})p(CH_3CH_2COOH)_2$ is expected to be similar to that of $H_2t(n\text{-Pr})p(CH_3COOH)_2$. Therefore, the larger red shift of the Soret band for the former may be attributed to the larger size of propionate ion relative to the acetate ion. In the case of oxalic acid, there are two identical COO groups to form hydrogen bonding with $[H_4t(n\text{-Pr})p]^{2+}$ from every sides of the porphyrin mean plane. Also, for $CH_2ClCOOH$ the chlorine atom would be available for hydrogen bonding, as well as the carboxylate ion (Scheme 1). However, it is reasonable to accept that the observed red shifts of the $H_2t(n\text{-Pr})p$ Soret band, through adduct formation with the carboxylic acids, is mainly due to the saddling of the porphyrin core.

According to the four orbital model of porphyrins, the a_{1u} and e_g orbitals have 4 and 5 nodes, respectively (Fig. 4). The saddling of the porphyrin core that is accompanied with the alternate tilting of the pyrrole rings up and down with respect to the porphyrin mean plane is proposed to decrease the antibonding interactions between the

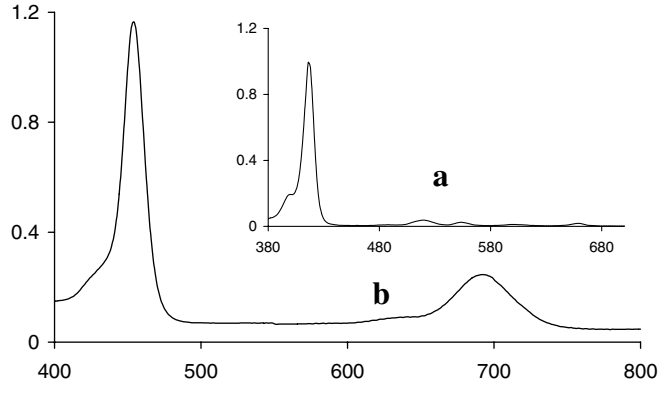
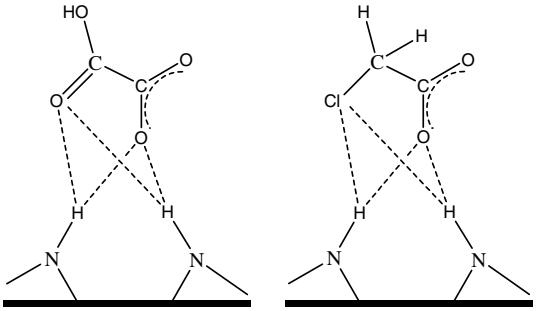


Fig. 3. UV–Vis spectra for $H_2t(p\text{-OMe})pp$ (a) and $(C_2H_5COOH)_2H_2t(p\text{-OMe})pp$ (b) in CH_2Cl_2.

Table 3
Comparison of the Soret bands of H_2p, $H_2t(n\text{-Pr})p$ and the corresponding dications with CF_3COOH

Porphyrin	Soret band (λ/nm)
Porphine [10]	394
$H_2t(n\text{-Pr})p$	416
$\Delta\upsilon$ (cm^{-1})	−1342.25
$H_2p(CF_3COOH)_2$ [10]	401
$H_2t(n\text{-Pr})p(CF_3COOH)_2$	422.4
$\Delta\upsilon$ (cm^{-1})	−1263.41



Scheme 1. Pattern of hydrogen bonding in $H_2t(n\text{-Pr})p(H_2C_2O_4)_2$ and $H_2t(n\text{-Pr})p(CH_2ClCOOH)$.

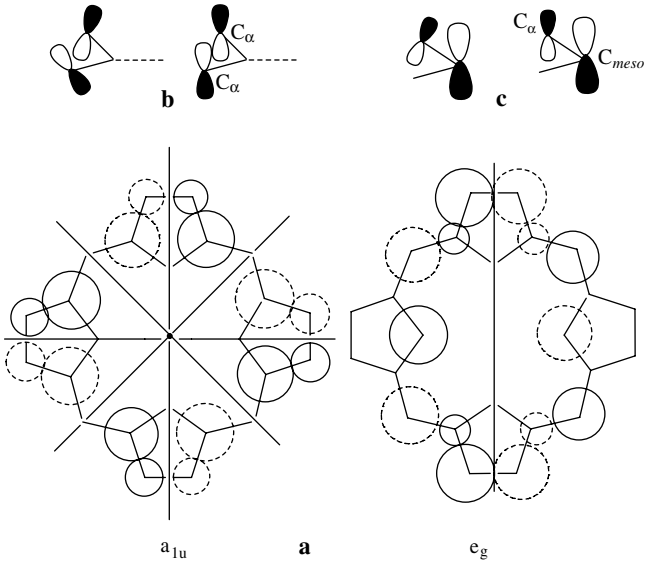
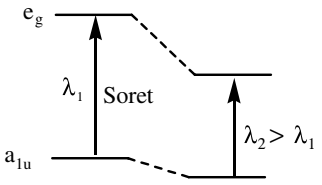


Fig. 4. The a_{1u} and one of the e_g orbitals (a) [7] and schematic demonstration of decreased antibonding interactions in the a_{1u} (b) and e_g (c) orbitals caused by the saddling of the porphyrin core.

electron densities on C_α positions with those at the alternate C_α (Fig. 4b) and adjacent C_{meso} (Fig. 4c) in a_{1u} and e_g orbitals, respectively. So the out-of-plane deformation of the porphyrin core seems to decrease the energy levels of both a_{1u} and e_g orbitals. Due to the larger distance between the alternate C_α positions relative to that between the adjacent C_α and C_{meso} atoms, it seems reasonable to assume that the saddling of the porphyrin core would lead to more stabilization of the e_g orbital with respect to the a_{1u} orbital and consequently the red shift of the Soret band (Scheme 2).



Scheme 2. Greater stabilization of the e_g orbital relative to the a_{1u} orbital upon saddling of the porphyrin core.

2.3. The Q(0, 0) band

The data in Table 2 clearly indicate that the Q(0,0) band of $H_2t(n\text{-Pr})p$ shows a substantial blue shift upon adduct formation with carboxylic acids. It can be seen that the smaller the red shift of the Soret band, the larger the blue shift of the Q(0,0) band. The observed blue shifts may be the result of saddling of the porphyrin core or/and electron donation from the porphyrin core to the σ-acceptors.

The a_{2u} to the e_g transition is responsible for the Q(0,0) band. The a_{2u} electron densities are largest on the methene carbons and pyrrole nitrogens. Therefore, the shift of electron densities from the nitrogen atoms to the central acceptors seems to affect the energy level of the a_{2u} orbital. It is noteworthy that the reaction of arylporphyrins with haloboranes in the absence of significant tilting of the porphyrin core, led to very large blue shifts of the Q(0,0) bands (40–50 nm), whereas the dihedral angles between the aryl groups and the porphyrin mean planes remained essentially unchanged with respect to those of the corresponding free base porphyrins [9].

To quantify the net effects of protonation on the shifts of Q(0,0) bands of the porphyrins upon reaction with carboxylic acids, we have used the spectral data for the protonation of porphine. This porphyrin with no substituent at the *meso* positions is convenient to this study. The porphine dication that is used in this discussion is a hypothetical dication with a saddling angle of 23.4° and its spectral data are obtained by subtracting the contributions of *n*-butyl groups from the spectral data of $H_4t(n\text{-Bu})p^{2+}$.

Comparison of the UV–Vis data for porphine and $H_2t(n\text{-Bu})p$ in the same solvents (Table 4) shows that upon substitution of four *n*-butyl groups (also any other primary alkyl groups) a red shift of 1399.89 cm^{-1} for the Soret band and 1138.71 cm^{-1} for the Q(0,0) band are observed. Accordingly, we assume that subtraction of these differences from those of $H_4t(n\text{-Bu})p^{2+}$ should give the spectral data for a porphine acid dication with a tilting angle of 23.4°, i.e. the saddling angle reported for $H_4t(n\text{-Bu})p^{2+}$

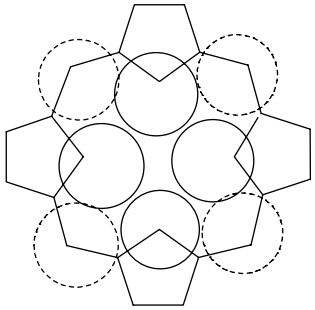
Table 4
The Q(0,0) and Soret bands for some porphyrins and their dications

Compounds	Soret (λ/nm)	$Q_I(0,0)$ (λ/nm)	Conformation	Solvent
$H_2t(n\text{-Bu})p$	417	659	planar	CH_2Cl_2
Porphine	394	613	planar	CH_2Cl_2
Δυ (cm^{-1})	1399.89	1138.71		
$H_4t(n\text{-Bu})p^{2+}$ [a]	424	630.5	sad. (23.4)[b]	CH_2Cl_2
$H_2Porphine^{2+}$ [c]	400.25	588.26	sad. (23.4)[b]	CH_2Cl_2
$H_2Porphine^{2+}$ [b]	401	~571[d]	[e]	benzene
Porphine		617.5	sad. (25)[f]	

[a] CF_3COOH has been used to prepare the dications.
[b] The values in parentheses are tilting (saddling) angles in the solid state.
[c] Estimated values (see the text).
[d] It has been observed as a shoulder and cannot be evaluated exactly [10].
[e] It has not been reported.
[f] Artificial dihedrally constrained saddle-shaped porphine.

[5c]. The results are in good agreement with the reported spectrum for the porphine acid dication in benzene solvent [10]. It should be noted that, according to the reported spectrum for the porphine dication in benzene, the long wavelength band has very low intensity and has been observed as a shoulder on the adjacent band. Also, comparison of the reported spectra for H_4tpp^{2+} in benzene [10] with the corresponding spectral data in CH_2Cl_2 (Table 7), demonstrates that although the wavelength of the Soret band is the same in the two solvents, the Q(0,0) band depends on the solvent and a red shift of about 168.5 cm^{-1} occurs upon change of the solvent to CH_2Cl_2. Thus, 168.5 cm^{-1} should be subtracted from the wavenumber of the reported Q(0,0) band of the porphine dication in benzene (ca. $10^7/571$ cm^{-1}) to obtain that of CH_2Cl_2 (i.e. 17344.6 cm^{-1} or 576.54 nm). On the other hand, the Q(0,0) bands for different dihedrally constrained saddle-shaped porphine conformers have been calculated by DiMagno [11]. We have used the calculated Q(0,0) band wavelength for a dihedral angle of 25°, which is very close to the saddling angle of 23.4°. Subtraction of the Q(0,0) band wavenumber of our hypothetical porphine dication (dihedral angle = 23.4°) from that of saddled porphine (dihedral angle = 25°) calculated by DiMagno, indicates that the contribution to the shifts of the Q(0,0) band by porphyrin core protonation is ca. 804.81 cm^{-1}, which is a considerable value. On the other hand, using 571 nm as the wavelength of the Q(0,0) band of porphine gives a value of 1318.80 cm^{-1}. Therefore, it may be concluded that diprotonation of the porphyrin core, by itself, leads to a blue shift of 804.81–1318.80 cm^{-1} in the Q(0,0) band of porphyrins.

Accordingly, adding −804.81 cm^{-1} to the observed blue shifts of the Q(0,0) band in Table 2 changes them into red shifts in the range 187.85–439.04 cm^{-1}. It may be concluded that the saddling of the porphyrin core leads to the red shift of the Q(0,0) band. The a_{2u} orbital is shown in Fig. 5. Due to the position of the nodal planes, it seems that the saddling of the porphyrin core, which decreases the antibonding interactions in the HOMOs and LUMOs of the macrocycle, stabilizes the e_g orbital more than the a_{2u} orbital and leads to the red shift of the Q(0, 0) band. The



a_{2u}

Fig. 5. The a_{2u} orbital [7].

e_g orbital has more antibonding character than the a_{1u} and e_g orbitals together, so it is reasonable to think that the decrease of antibonding interaction destabilizes the e_g orbitals more than the HOMOs of the porphyrin.

Upon diprotonation of $H_2t(n\text{-Pr})p$ with the carboxylic acids, the values of red shifts for the Soret band (364–1060.5 cm^{-1}) are about two times of those of the Q(0,0) band (187–439 cm^{-1}) which suggests that the Soret band is more affected by the saddling of the porphyrin core. X-ray crystallographic studies have shown a tilting angle of ca. 23.4–29.9° for the dications of the *meso*-tetraalkylporphyrins (primary and secondary alkyl residues = *n*-butyl, *iso*-propyl and 1-ethylpropyl) with CF_3COOH [5c]. Therefore, the observed red shifts of the Soret (364 cm^{-1}) and Q(0,0) band (187 cm^{-1}) upon diprotonation of $H_2t(n\text{-Pr})p$ with CF_3COOH results in saddling of the porphyrin core by ca. 23°. On the other hand, a comparison of the tilting angles for the dications of four alkylporphyrins (Table 5), using $H_2t(n\text{-Bu})p(CF_3COOH)_2$ as the zero level for determining red shifts, shows that a 5.1°, 6.4° and 17.3° increase in tilting angle causes 222.86 (167.27), 295.76 (386.66) and 1602.85 (1424.96) cm^{-1} red shifts in the Q(0,0) band (and the Soret bands, the data in parentheses), respectively. We have shown that a 23.4° saddling of the porphyrin core led to a red shift of only 187 cm^{-1} for the Q(0,0) and 364 cm^{-1} for the Soret band of $H_2t(n\text{-Pr})p$. It may be concluded that saddling angles larger than ca. 25° are needed to cause significant red shifts in the Q(0,0) or the Soret bands (see Table 5). Although using the other carboxylic acids may increases the observed shifts of the bands, in the following discussion we will show that the presence of aryl substituents at the *meso*-positions causes the enhanced red shifts of the Soret and Q(0,0) bands so that the observed red shifts of the Soret and Q(0,0) bands of the dications of arylpor are comparable to those of $H_2t(tert\text{-Bu})p(CF_3COOH)_2$.

2.4. Arylporphyrins

The UV–Vis spectra of $H_2t(p\text{-OMe})pp$ and the 1:2 adduct with propionic acid are presented in Fig. 3. Diprotonation of *para*-substituted *meso*-tetraarylporphyrins with carboxylic acids led to the red shifts of the Soret ($\Delta\upsilon_1$, Table 7) and Q(0,0) bands ($\Delta\upsilon_2$, Table 7) with respect to the corresponding bands of the free base porphyrins. We have shown that diprotonation of the porphyrin core, by

Table 5
The Q(0,0) bands and tilting angles for some *meso*-tetraalkylporphyrins in $CHCl_3$[5c]

Dications	Q(0,0) (λ/nm)	Soret (λ/nm)	Saddling angles
$H_2t(n\text{-Bu})p(CF_3COOH)_2$	631	422	23.4
$H_2t(iso\text{-Pr})p(CF_3COOH)_2$	640	425	28.5
$H_2t(1\text{-ethylpropyl})p(CF_3COOH)_2$	643	429	29.9
$H_2t(tert\text{-Bu})p(CF_3COOH)_2$	702	449	41.7

itself, causes a blue shift of at least 804.81 cm^{-1} of the Q(0,0) bands. Subtracting 804.81 cm^{-1} from the red shift of the Q(0,0) bands ($\Delta\upsilon_2$) gives the shifts of these bands ($\Delta\upsilon_3$) resulting from the effects of porphyrin core saddling and the enhanced coplanarity of the aryl substituents with the porphyrin mean plane. It is observed that the introduction of better π-electron donating groups such as (4-OMe)-phenyl at *meso*-positions enhances the ratio of $\Delta\upsilon_3/\Delta\upsilon_1$. It is expected that electron-donating substituents will raise the energy of the a_{2u} orbital by increasing its electron density and lead to the red shift of the Q(0,0) band [5a].

The upfield shift of the H_β signal of the porphyrin core may be attributed to the ring current decrease upon out-of-plane deformation of the macrocycle [4b]. The observed chemical shifts of this signal for the dications of H_2t(*n*-Bu)p (δ 9.27 ppm), H_2t(*iso*-Pr)p (δ 8.84 ppm), H_2t(1-ethylpropyl)p (δ 8.78 ppm) and H_2t(*tert*-Bu)p (δ 8.0 ppm) with CF_3COOH correlate well with the solid state tilting angles of the dications, i.e. 23.4°, 28.5°, 29.9° and 41.6°, respectively [5c]. The chemical shifts of H_β for H_2tpp-$(CF_3COOH)_2$, H_2t(4-OMe)p$(CF_3COOH)_2$, H_2t(4-Me)p-$(CF_3COOH)_2$ and H_2t(4-Cl)p$(CF_3COOH)_2$ are similar and are, respectively, as follows: 8.61, 8.53, 8.53 and 8.59 ppm. So, it seems reasonable to assume that the substitution of groups such as OCH_3, CH_3, Cl, NO_2 at the *para*-position of the phenyl ring have little effect on the saddling angle of the porphyrin dications; the *ortho*-positions are the most effective ones that affect the conformation of the porphyrins [12]. X-ray crystallographic studies have shown that upon diprotonation with CF_3COOH the tilting

Table 6
Some alkylporphyrin and arylporphyrin dications with CF_3COOH, the Soret and Q(0,0) bands and the saddling angles

Dications	Tilting angle	Soret (λ/nm)	Q(0,0) (λ/nm)
H_2t(*iso*-Pr)p$(CF_3COOH)_2$	28.5	425	640
H_2t(1-ethylpropyl)p$(CF_3COOH)_2$	29.9	429	643
H_2tpp$(CF_3COOH)_2$	28–33	435	648.1
H_2t(4-OCH_3)pp$(CF_3COOH)_2$		449.28	682.24

Table 7
UV–Vis spectral data for the dications of *meso*-tetraarylporphyrins with the carboxylic acids in CH_2Cl_2

Entry	Porphyrins and dications	Soret band (λ_1/nm)	$\Delta\upsilon_1$ (cm^{-1})	Q(0,0) band (λ_2/nm)	Q(0,0) band ($\lambda_{corr.}$[a]/nm)	$\Delta\upsilon_2$ (cm^{-1})	$\Delta\upsilon_3$[b] (cm^{-1})	$\Delta\upsilon_3/\Delta\upsilon_1$
1	H_2tpp	416		648				
2	H_2tpp$(CF_3COOH)_2$	435.04	−1052.07	648.1	688.92	−2.38	−916.62	0.87
3	H_2tpp$(H_2C_2O_4)_2$	439.12	−1265.64	647.76	683.39	5.71	−799.16	0.63
4	H_2tpp$(ClCH_2COOH)_2$	440.32	−1327.70	648.4	684.10	−9.52	−814.35	0.61
5	H_2tpp$(HCOOH)_2$	439.12	−1265.64	650.32	686.23	−55.05	−859.72	0.68
6	H_2tpp$(CH_3COOH)_2$	442.88	−1458.98	648.96	684.72	−22.83	−827.59	0.57
7	H_2tpp$(CH_3CH_2COOH)_2$	441.6	−1393.53	649	684.77	−23.78	−828.65	0.59
8	H_2t(4-Cl)pp	418.5		641.28				
9	H_2t(4-Cl)pp$(CF_3COOH)_2$	441.6	−1249.93	655.3	691.78	−333.63	−1138.35	0.91
10	H_2t(4-Cl)pp$(H_2C_2O_4)_2$	448	−1573.43	655.3	691.78	−333.63	−1138.35	0.72
11	H_2t(4-Cl)pp$(ClCH_2COOH)_2$	446.7	−1508.47	657.9	694.68	−393.93	−1198.69	0.79
12	H_2t(4-Cl)pp$(HCOOH)_2$	446.7	−1508.47	657.9	694.68	−393.93	−1198.69	0.79
13	H_2t(4-Cl)pp$(CH_3COOH)_2$	448	−1573.43	654.1	690.45	−305.63	−1110.50	0.70
14	H_2t(4-Cl)pp$(CH_3CH_2COOH)_2$	448	−1573.43	660.4	697.47	−451.47	−1256.28	0.80
15	H_2t(4-CH_3)pp	418.5		645.12				
16	H_2t(4-CH_3)pp$(CF_3COOH)_2$	441.6	−1249.93	663.04	700.42	−401.88	−1223.84	0.98
17	H_2t(4-CH_3)pp$(H_2C_2O_4)_2$	448	−1573.43	668.1	706.06	−533.17	−1337.89	0.85
18	H_2t(4-CH_3)pp$(ClCH_2COOH)_2$	444.1	−1377.41	661.7	698.92	−388.40	−1193.20	0.83
19	H_2t(4-CH_3)pp$(HCOOH)_2$	446.7	−1508.47	668.16	706.13	−534.52	−1339.29	0.89
20	H_2t(4-CH_3)pp$(CH_3COOH)_2$	448	−1573.43	672	710.42	−620.04	−1424.81	0.90
21	H_2t(4-CH_3)pp(CH_3CH_2COOH)	448	−1573.43	669.4	707.51	−562.24	−1366.92	0.87
22	H_2t(4-NO_2)pp	423.6		642.5				
23	H_2t(4-NO_2)pp$(CF_3COOH)_2$	442.8	−1023.62	645.1	680.42	−62.73	−867.39	0.85
24	H_2t(4-NO_2)pp$(H_2C_2O_4)_2$	454.4	−1600.13	655.3	691.78	−304.02	−1108.74	0.69
25	H_2t(4-NO_2)pp$(ClCH_2COOH)_2$	453.1	−1536.99	652.8	689.06	−245.57	−1051.68	0.68
26	H_2t(4-NO_2)pp$(HCOOH)_2$	451.8	−1473.49	652.8	688.99	−245.57	−1050.20	0.71
27	H_2t(4-NO_2)pp$(CH_3COOH)_2$	456.9	−1720.55	656.6	693.23	−334.23	−1138.97	0.66
28	H_2t(4-NO_2)pp$(CH_3CH_2COOH)_2$	456.88	−1719.59	661.68	698.90	−451.16	−1256.00	0.73
29	H_2t(4-OCH_3)pp	421.12		646.4				
30	H_2t(4-OCH_3)pp$(CF_3COOH)_2$	449.28	−1488.36	682.24	721.88	−812.70	−1617.58	1.09
31	H_2t(4-OCH_3)pp$(H_2C_2O_4)_2$	451.84	−1614.47	683.52	723.30	−840.15	−1644.77	1.02
32	H_2t(4-OCH_3)pp$(ClCH_2COOH)_2$	456.92	−1860.53	686.12	726.22	−895.59	−1700.36	0.91
33	H_2t(4-OCH_3)pp$(HCOOH)_2$	451.84	−1614.47	687.36	727.61	−921.88	−1726.67	1.07
34	H_2t(4-OCH_3)pp$(CH_3COOH)_2$	453.12	−1676.99	686.12	726.22	−895.59	−1700.36	1.01
35	H_2t(4-OCH_3)pp$(CH_3CH_2COOH)_2$	453.12	−1676.99	687.3	727.55	−920.61	−1725.54	1.03

[a] See Table 2.
[b] $\Delta\upsilon_3$ (cm^{-1}) = $\Delta\upsilon_2$ − 804.81 (see the text).

angle of *meso*-tetraalkylporphyrins (with primary and secondary alkyl residues) are very similar to that of $H_2tpp(CF_3COOH)_2$ (Table 6) [5c]. Therefore, the red shifts of the Soret (1416.41 cm^{-1}) and Q(0,0) (1189.40 cm^{-1}) bands of $H_2t(4\text{-}OCH_3)pp(CF_3COOH)_2$with respect to those of $H_2t(n\text{-}Pr)p(CF_3COOH)_2$ may reflect the π-donation of the aryl groups to the porphyrin core. Diprotonation of *meso*-tetraarylporphyrins decreases the dihedral angle between the porphyrin mean plane and the aryl group plane, which would lead to greater π-donation to the porphyrin core. Also, the red shifts of the Q(0,0) band of $H_2t(4\text{-}OCH_3)pp(CF_3COOH)_2$ relative to those of the other arylpor dications with CF_3COOH (Table 7) correlate with the order of π-donor ability of the *para*-substituents.

A comparison of the Soret bands of different *para*-substituted *meso*-tetraarylporphyrins (Table 7) shows that for a given acid, e.g. CF_3COOH, the largest red shifts of the Soret band are observed for the dications of $H_2t(4\text{-}OCH_3)pp$ and $H_2t(4\text{-}NO_2)pp$. The value of the red shifts are very similar for the adducts of $H_2t(4\text{-}OCH_3)pp$ and $H_2t(4\text{-}NO_2)pp$ (Table 7, entries 23–35). The range of red shifts, using H_2tpp as the zero level for determining red shifts, for different acids is demonstrated in Table 8. It may be assumed that in spite of the placement of nodes on *meso*-positions, a weak interaction between the proper HOMO of the aryl group (one of the e_{1g} orbitals) and the a_{1u} orbital of the porphyrin causes the observed red shifts of the Soret band (Fig. 6). Very weak basicity of $H_2t(4\text{-}NO_2)pp$ indicates that, contrary to the other arypor, *meso*-aryl groups of $H_2t(4\text{-}NO_2)pp$ are electron withdrawing with respect to the porphyrin π-system [5a]. Accordingly, the observed red shifts of the Soret band of $H_2t(4\text{-}NO_2)pp$ upon diprotonation with different carboxylic acids may be due to the stabilization of the e_g orbitals (Fig 4a) through overlap with the unoccupied π^* orbitals of the electron withdrawing aryl group, $(4\text{-}NO_2)$phenyl in the excited state, i.e. $a_{1u}^1e_g^1$ [1]. The e_g orbitals have no nodes at the *meso*-positions and so may overlap with the π-system of the aryl substitents. However, comparison of the values of red shifts of the Soret and Q(0,0) bands of the dications of different arylpor with respect to those of the corresponding free base porphyrins and also the dications of $H_2t(n\text{-}Pr)p$ clearly indicates the importance of π-resonance interactions in the observed spectral shifts of the Soret and Q(0,0) bands, so it may be concluded that in the presence of strong π-electron donating groups the red shifts of the Soret and Q(0,0) bands are predominantly due to the electronic effects of *meso*-substituents rather than the out-of-plane deformation of the porphyrin core. Also, we have shown that the large red shift of the Soret band may be observed in the presence of either strong π-electron donating, (4-OMe)phenyl, or π-electron withdrawing, $(4\text{-}NO_2)$phenyl, substituents at the *meso*-positions. But large red shifts of the Q(0,0) bands are observed only in the case of strong π-electron donating groups at the *meso*-positions.

Table 8
Range of red shifts for the acids in the presence of different porphyrins, using the bands of corresponding dication of H_2tpp as the zero-level

Acids	Range of red shifts of the Soret bands (cm^{-1})	Range of red shifts of the Q(0,0) bands (cm^{-1})
CF_3COOH	1023.62–1488.36	867.39–1617.58
$H_2C_2O_4$	1265.64–1614.47	799.16–1644.77
$ClCH_2COOH$	1327.70–1860.53	814.35–1700.36
HCOOH	1265.64–1614.47	859.72–1726.67
CH_3COOH	1458.98–1720.55	827.59–1700.36
CH_3CH_2COOH	1393.53–1720.59	828.65–1725.54

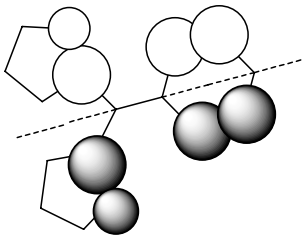


Fig. 6. Interaction between the a_{1u} orbital of the porphyrin and one of the e_{1g} orbitals of the aryl group.

3. Experimental

The free base porphyrins H_2tpp, $H_2t(4\text{-}OMe)pp$ [13], $H_2t(4\text{-}Me)pp$ [13], $H_2t(4\text{-}Cl)pp$ [13], $H_2t(4\text{-}NO_2)pp$ [14] and $H_2t(n\text{-}Pr)p$ [15] were prepared and purified by methods reported previously. Benzaldehyde, *para*-substituted benzaldehydes, butyraldehyde, trifluroacetic acid (⩾98%), glacial acetic acid, propionic acid (for synthesis) (Fluka and Merck), formic acid (⩾96%, Sigma–Aldrich) and oxalic acid (⩾97%, Fluka) were used as received. Pyrrole (Fluka, for synthesis) was distilled before use.

The dications were prepared according to the method previously described by Senge for the conversion of porphyrins to the corresponding ditrifluroacetate [5c]. Due to the relative thermal instability of the diprotonated species of the porphyrins with acetic acid, propionic acid and formic acid, with respect to the other carboxylic acids, the corresponding diprotonated porphyrins have been obtained by slow evaporation of dichloromethane and excess amounts of the corresponding carboxylic acid at room temperature. In the absence of an excess amount of the carboxylic acids, there is an equilibrium between the diprotonated species and the free base porphyrins in dichloromethane solution.

The electronic absorption spectra were recorded utilizing a Multispect-1501 Shimadzu within the wavelength 350–800 nm. ^1H NMR spectra were obtained on a Bruker Avance DPX 250 MHz spectrometer.

4. Conclusion

In summary, it may be concluded that even very weak carboxylic acids such as propionic acid are able to diprotonate the porphyrins. Saddling of the porphyrin core leads to a red shift of both the Soret and Q(0,0) bands

of H_2t(*n*-Pr)p. For a given carboxylic acid, the observed red shifts of the Soret and Q(0,0) bands of the arylpor are significantly larger than those of H_2t(*n*-Pr)p, which demonstrates the importance of the π-conjugation mediated electron coupling of the *meso*-aryl substituents to the porphyrin core. Although the saddling of the porphyrin core causes a red shift of the Soret band, the presence of strong π-electron donating groups at *meso*-positions may also lead to a red shift of this band, through stabilization of the a_{1u} orbital. On the other hand, strong π-electron accepting *para*-substituents, through the stabilization of the e_g orbitals, may also lead to a shift of the Soret band to longer wavelengths. The values of red shifts of the Q(0,0) bands are as large as those of the Soret bands. Again, strong π-electron donating *para*-substituents lead to the substantially large red shifts of the Q(0,0) bands. Also, it has been observed that in the case of the dications of arylpor, the red shifts of the Soret and Q(0,0) bands are similar to those of the severely saddled porphyrin, H_2t(*tert*-Bu)p$(CF_3COOH)_2$. Accordingly, upon diprotonation of arylpor, the Soret and Q(0,0) bands seem to be more strongly affected by the π-resonance effects of the aryl-groups than the saddling of the porphyrin core.

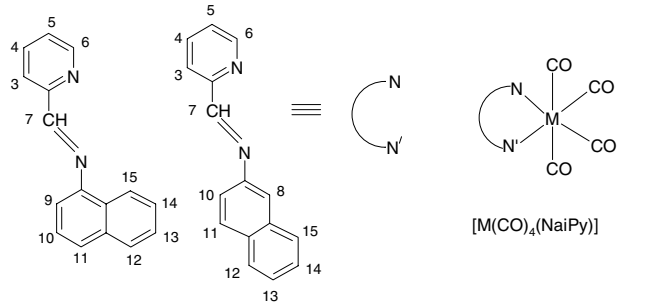
Acknowledgement

This work was supported by the Damghan University of Basic Sciences Research Council.

References

[1] (a) K.M. Barkigia, L. Chantranupong, K.M. Smith, J. Fajer, J. Am. Chem. Soc. 110 (1988) 7566;
(b) J.A. Shelnutt, X.Z. Song, J.G. Ma, S.L. Jia, W. Jentzen, C.J. Medforth, Chem. Soc. Rev. 27 (1998) 31;
(c) I. Bertini, H.B. Gray, S. Lippard, J. Valentine (Eds.), Bioinorganic Chemistry, University Science Books, 20 Edgehill Road, Mill Valley, CA, 94941, 1994 (Chapter 4).
[2] R.E. Haddad, S. Gazeau, J. Pe' caut, J.-C. Marchon, C.J. Medforth, J.A. Shelnutt, J. Am. Chem. Soc. 125 (2003) 1253.
[3] K.M. Smith, Porphyrins and Metalloporphyrins, Elsevier, Amsterdam, 1975, pp. 1–910.
[4] (a) S. Aronoff, J. Phys. Chem. 62 (1958) 428;
(b) R.I. Walter, E.C.A. Ojadi, H. Linschitzll, J. Phys. Chem. 97 (1993) 13308.
[5] (a) M. Meot-Ner, A. D Adler, J. Am. Chem. Soc. 97 (1975) 5107;
(b) A. Stone, E.B. Fleischer, J. Am. Chem. Soc. 90 (1968) 2735;
(c) M.O. Senge, Z. Naturforsch. 55b (2000) 336;
(d) E.B. Fleischer, Acc. Chem. Res. 3 (1970) 105;
(e) B. Cheng, O.Q. Munro, H.M. Marques, R. Scheidt, J. Am. Chem. Soc. 119 (1997) 10732.
[6] D. Mandon, P. Ochsenbein, J. Fischer, R. Weiss, K. Jayaraj, R.N. Austin, A. Gold, P.S. White, O. Brigaud, P. Battioni, D. Mansuy, Inorg. Chem. 31 (1992) 2044.
[7] (a) M. Gouterman, J. Chem. Phys. 30 (1959) 1139;
(b) M. Gouterman, J. Mol. Spectrosc. 6 (1961) 138.
[8] A. Rosa, G. Ricciardi, E.J. Baerends, A. Romeo, L.M. Scolaro, J. Phys. Chem. A 107 (2003) 11468.
[9] (a) W.J. Belcher, M. Breede, P.J. Brothers, C.E.F. Rickard, Angew. Chem. Int. Ed. Engl. 37 (1998) 1112;
(b) A. Weiss, H. Pritzkow, P.J. Brothers, W. Siebert, Angew. Chem. Int. Ed. Engl. 40 (2001) 4182.
[10] O. Ohno, Y. Kaizu, H. Kobayashi, J. Chem. Phys. 82 (1985) 1779.
[11] S.G. DiMagno, A.K. Wertsching, C.R. Ross, J. Am. Chem. Soc. 117 (1995) 8279.
[12] (a) D.J. Nurco, C.J. Medforth, T.P. Forsyth, M.M. Olmstead, K.M. Smith, J. Am. Chem. Soc. 118 (1996) 10918;
(b) X.Z. Song, W. Jentzen, S.J. Jia, L. Jaquinod, D.J. Nurco, C.J. Medforth, K.M. Smith, J.A. Shelnutt, J. Am. Chem. Soc. 118 (1996) 12975;
(c) M.O. Senge, T. Ema, K.M. Smith, J. Chem. Soc. Chem. Commun. (1995) 733.
[13] A.D. Adler, F.R. Longo, J.D. Finarelli, J. Goldmacher, J. Assour, L. Korsako, J. Org. Chem. 32 (1967) 476.
[14] A. Bettelheim, B.A. White, S.A. Raybuck, R.W. Murray, Inorg. Chem. 26 (1987) 1009.
[15] S. Neya, N. Funasaki, J. Heterocyclic Chem. 34 (1997) 689.

characterization, solvatochromism and luminescence properties of $M(CO)_4$\{*N*-[(2-pyridyl)methyliden]-α(or β)-aminonaphthalene (α or β-NaiPy)\}.



α-NaiPy (**a**) β-NaiPy (**b**) **1-3** (M = Cr(**1**), Mo(**2**), W (**3**))

2. Experimental

2.1. Materials and measurements

α-Naphthylamine and β-naphthylamine were purchased from Thomas Baker and Co, pyridine-2-carboxaldehyde was purchased from Lancaster Ltd., England. *N*-[(2-pyridyl)methyliden]-α (or β)-aminonaphthalene (α or β-NaiPy) were synthesized by equimolar condensation of pyridine-2-carboxaldehyde and naphthylamine in ethanol following a previously reported procedure [25,26]. $M(CO)_6$ (M = Cr, Mo) and $Me_3NO \cdot 2H_2O$ were Sigma–Aldrich reagents. Dehydrated Me_3NO was obtained by reduced pressure sublimation of the purchased compound. Reactions were carried out under extremely dry oxygen free atmosphere under Atmos bags (Sigma–Aldrich). THF and *n*-heptane were dried before use [27]. All other chemicals used were of A.R. quality and were used as received from SRL, India.

For the solution spectral studies spectroscopic grade solvents were used from Lancester, UK Microanalyses (C, H, N) were performed using a Perkin–Elmer 2400 CHN elemental analyzer. Spectroscopic measurements were carried out using the following instruments: UV–VIS spectra, Lambda 25 Perkin–Elmer; FT-IR spectra (KBr disk, 4000–450 cm^{-1}), RX-1 Perkin–Elmer; ^1H NMR and ^{13}C NMR spectra in $CDCl_3$ Bruker 300 MHz FT NMR spectrometers in the presence of TMS as an internal standard. The luminescence properties were measured using a LS-55 Perkin–Elmer fluorescence spectrophotometer at room temperature (298 K) in benzene solution with a 1 cm path length quartz cell. FAB-MS was collected from a JEOL-JMS 600. Electrochemical measurements were carried out with the use of a computer controlled EG & G PARC VersaStat model 250 Electrochemical instrument using a Pt-disk working electrode and Pt-wire auxiliary electrode under inert (dry N_2) environment in CH_2Cl_2. The solution was IR compensated and the results were collected at 298 K. The reported results were referenced to Ag/AgCl in CH_2Cl_2 and were uncorrected for junction potential, [*n*-Bu_4N][ClO_4] was used as the supporting electrolyte.

Solvatochromism was examined using at best 15 dry solvents (non-hydroxylic: hexane, heptane, benzene, toluene, dichloromethane, chloroform; hydroxylic solvents: tetrahydrofuran, methanol, 2-propanol, *tert*-butanol, 2-methoxy ethanol, nitromethane, acetonitrile, *N*,*N*-dimethylformamide, dimethylsulfoxide) and the plots of $E_T(30)$ versus E_{MLCT} were generated by Origin 6.1. The effect of solvent dipole moment and refractive indices $f(D, \eta^2)$ on the E_{MLCT} were examined [28].

The fluorescence quantum yield of the complexes was determined using Coumarin-120 laser dye as a reference with a known ϕ_R of 0.63 in MeCN. The complex and the reference dye were excited at 340 nm, maintaining nearly equal absorbance (~0.1), and the emission spectra were recorded from 350 to 600 nm. The area of the emission spectrum was integrated using the software available in the instrument and the quantum yield is calculated according to the following equation:

$$\phi_S/\phi_R = [A_S/A_R] \times [(Abs)_R/(Abs)_S] \times [\eta_S^2/\eta_R^2]$$

Here ϕ_S and ϕ_R are the fluorescence quantum yields of the sample and reference, respectively. A_S and A_R are the areas under the fluorescence spectra of the sample and the reference, respectively, $(Abs)_S$ and $(Abs)_R$ are the respective optical densities of the sample and the reference solution at the wavelength of excitation, and η_S and η_R are the values of refractive index for the respective solvent used for the sample and reference.

2.2. Preparation of $Mo(CO)_4$(α-NaiPy) (*1a*)

A representative case of $[Mo(CO)_4$(α-NaiPy)] (**2a**) is described below.

To $Mo(CO)_6$(50 mg, 0.189 mmol) dissolved in dry THF (15 cm^3), Me_3NO (30 mg, 0.40 mmol) was added and the solution was stirred for 50 min. To the resulting yellow solution α-NaiPy (43.95 mg, 0.189 mmol) was added, the solution was stirred for 4 h and the colour of the solution changed from light yellow to deep purple. Then the solvent was evaporated under low pressure and the crude product was chromatographed in a neutral Al_2O_3 column prepared in petroleum-ether (60–80° fraction). A blue-violet portion was eluted with benzene. Removal of the solvent afforded analytically pure product, $[Mo(CO)_4$(α-NaiPy)] in 65% yield.

In analogous reactions treatment of $Cr(CO)_6$, $W(CO)_6$ with two equimolar quantities of Me_3NO and an equimolar quantity of α-NaiPy, β-NaiPy afforded the complexes $[Cr(CO)_4$(α-NaiPy)] (**1a**) (yield 45%; blue), $[Cr(CO)_4$(β-NaiPy)] (**1b**) (yield 46%; blue), $[Mo(CO)_4$(β-NaiPy)] (**2b**) (yield 45%; purple), $[W(CO)_4$(α-NaiPy)] (**3a**) (yield 55%; purple), $[W(CO)_4$(β-NaiPy)] (**3b**) (yield 57%; purple).

Micro-analytical data are as follows: *Anal.* Calc. for $[Cr(CO)_4$(α-NaiPy)] (**1a**), $C_{20}H_{12}N_2O_4Cr$, C, 60.6; H, 3.03; N, 7.07. Found C, 60.0; H, 3.04; N, 7.05%. Decomposition

temperature, 72 ± 2 °C. *Anal.* Calc. for Cr(CO)$_4$(β-NaiPy)] (**1b**), $C_{20}H_{12}N_2O_4Cr$, C, 60.6; H, 3.03; N, 7.07. Found C, 60.1; H, 3.04; N, 7.08%. Decomposition temperature, 85 ± 2 °C. *Anal.* Calc. for [Mo(CO)$_4$(α-NaiPy)] (**2a**), $C_{20}H_{12}N_2O_4Mo$, C, 54.55; H, 2.73; N, 6.36. Found C, 54.50; H, 2.74; N, 6.38%. Decomposition temperature, 75 ± 1 °C. *Anal.* Calc. for [Mo(CO)$_4$(β-NaiPy)] (**2b**), $C_{20}H_{12}N_2O_4Mo$, C, 54.55; H, 2.73; N, 6.36. Found C, 54.51; H, 2.71; N, 6.34%. Decomposition temperature, 88 ± 2 °C. *Anal.* Calc. for [W(CO)$_4$(α-NaiPy)] (**3a**), $C_{20}H_{12}N_2O_4W$, C, 45.45; H, 2.27; N, 5.30. Found C, 45.42; H, 2.25; N, 5.33%. Decomposition temperature, 70 ± 1 °C. *Anal.* Calc. for [W(CO)$_4$(β-NaiPy)] (**3b**), $C_{20}H_{12}N_2O_4W$, C, 45.45; H, 2.27; N, 5.30. Found C, 45.40; H, 2.20; N, 5.36%; Decomposition temperature 80 ± 1 °C.

3. Results and discussion

3.1. Synthesis

The equimolar reaction of α/β-NaiPy and M(CO)$_6$ (M = Cr, Mo, W) under stirring conditions in dry THF in the presence of two equivalents of Me_3NO under nitrogen environment for a period of 4–6 h has synthesized blue or green complexes in 45–65% yield. The ligands, *N*-[((2-pyridyl)methyliden)-α/β-aminonaphthalene] (α-NaiPy, **a**; β-NaiPy, **b**) are a *N*,*N*′ chelating system where *N* and *N*′ refer to *N*(pyridyl) and *N*(imine) donor centres, respectively. Use of Me_3NO has reduced the reaction time to one-tenth in the absence of it and also increases the yield of product from <5% to >45%. The composition of the complexes, *cis*-[M(CO)$_4$(NaiPy)] (M = Cr **1a** for α-NaiPy and **1b** for β-NaiPy); Mo (**2a** for α-NaiPy and **2b** for β-NaiPy), W (**3a** for α-NaiPy and **3b** for β-NaiPy) has been supported by microanalytical and spectroscopic data. We have attempted to crystallize these complexes but failed to get a good quality diffracting crystals. Use of excess ligands to synthesise *cis*-[M(CO)$_2$(NaiPy)$_2$] and [M(NaiPy)$_3$] failed and in each experiment (at varied temperature and solvent) we get only an intractable brown solid.

$$M(CO)_6 + 2Me_3NO + \alpha/\beta\text{-NaiPy} \rightarrow [M(CO)_4(\alpha/\beta\text{-NaiPy})] + 2CO_2 + 2Me_3N \quad (1)$$

The complexes are soluble in polar solvents like DMF as well as non-polar solvents like heptane. Solutions of *cis*-[M(CO)$_4$(α/β-NaiPy)] in benzene are blue-violet, but in DMF they are orange-red. They are non-electrolytes and are diamagnetic.

3.2. Spectroscopic characterization

3.2.1. FT-IR and mass spectra

FT-IR spectra were taken in KBr discs and in CH_2Cl_2 solution. The carbonyl stretching frequencies of the complexes are presented in Table 1. The spectra show three or four bands three bands appear in the intensity ratio 1:2:1 (intensity is compared from the area measurement using the Origin 6.0 program) (Fig. 1). The spectra in solution (CH_2Cl_2) show *ν*(CO) at 5–30 cm^{-1} higher frequency than that of the KBr-phase data. The mean value of three or four *ν*(CO) in these cases is lower ($\Delta\nu$(CO) = 15–25 cm^{-1}) than that of [M(CO)$_4$(2-PAP)] (2-PAP = 2-(phenylazo)pyridine) [4]. This supports weaker π-acidity of naphthylazoimidazoles than that of phenylazopyridine. On comparing with the spectral pattern and frequency of CO stretches of [M(CO)$_4$(2-PAP)] [4] and [M(CO)$_4$-(RaaiR′)] [12] (RaaiR′ = 1-alkyl-2-(arylazo)imidazole), the present complexes are assigned to *cis*-tetracarbonyl complexes with octahedral coordination where the ligand α/β-NaiPy binds as a bidentate chelating agent. The *ν*(N=N) and *ν*(C=N) bands appear at 1390–1400 and 1590–1600 cm^{-1}, respectively. The mass fragmentation by FAB-MS of the complexes support the expected fragmentation pattern of M^+, $(M–CO)^+$, $(M–2CO)^+$, $(M–3CO)^+$, $(M–4CO)^+$ (Table 1). This information also helps us to identify the tetracarbonyl complexes of α/β-NaiPy.

3.2.2. UV–Vis spectra and solvatochromism

The spectra show two characteristic bands, one at lower wavelength (295, 335 nm) for an intra-ligand charge transfer transition and an intense broad band appearing at >550 nm. This longer wavelength transition is assigned to a MLCT band d(M(0)) → π* (ligand) (Table 2, Fig. 2). The energy of the MLCT transition state of the compounds follows the order Mo > W > Cr, which is similar to the previously reported [M(CO)$_4$(α-diimine)] compounds [10,16,17].

Table 1
FT-IR and mass spectral data of [M(CO)$_4$(α/β-NaiPy)] (**1–3**)

Compound	ν_{CO} (cm^{-1}) value	*m*/*z* value (% conversion)				
		M^+	$(M–CO)^+$	$(M–2CO)^+$	$(M–3CO)^+$	$(M–4CO)^+$
1a	2005, 1893, 1839 (2007, 1902, 1847)	396 (10)	368 (20)	340 (17)	312 (12)	284 (21)
1b	2006, 1907, 1883, 1815 (2008, 1908, 1843)	396 (11)	368 (22)	340 (20)	312 (14)	284 (24)
2a	2011, 1903, 1845 (2014, 1908, 1845)	442 (12)	414 (28)	386 (20)	358 (13)	330 (27)
2b	2013, 1910, 1883, 1818 (2015, 1910, 1842)	442 (20)	414 (32)	386 (35)	358 (20)	330 (33)
3a	2004, 1889, 1833 (2007, 1923, 1899, 1845)	528 (5)	500 (10)	472 (4)	444 (4)	416 (8)
3b	2002, 1886, 1831 (2008, 1898, 1839)	528 (6)	500 (12)	472 (4)	444 (3)	416 (9)

In KBr disc (values in parentheses are from CH_2Cl_2 solution).

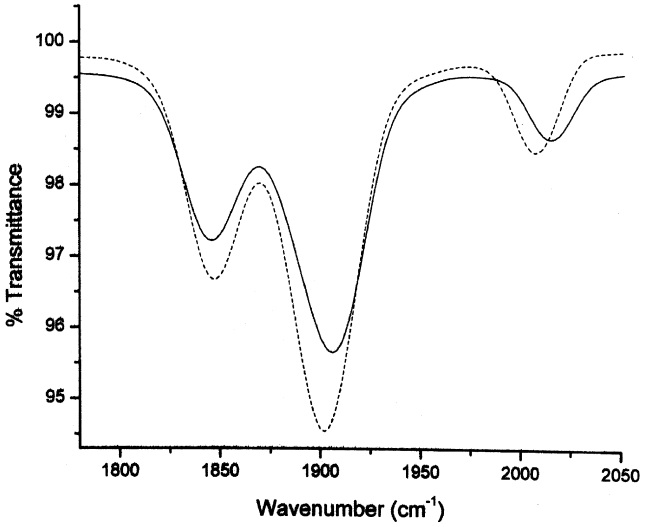


Fig. 1. Solution IR spectra of $[Mo(CO)_4(\alpha\text{-NaiPy})]$ (−), $[Cr(CO)_4(\alpha\text{-NaiPy})]$ (...) in CH_2Cl_2.

The effect of solvent polarity on this MLCT band was examined for a series of non-hydroxylic and hydroxylic solvents (Fig. 3). The plots of Reichardt's solvent parameters [28] $E_T(30)$ versus the E_{MLCT} are separately linear (Fig. 4). The effect of solvent polarity is examined by plotting E_{MLCT} versus $f(D, \eta^2)$ of the different solvents (D = dipole moment; η = refractive index) [29–31] Positive slopes of the plots (Fig. 5) support the lower dipolar property of the complexes at the excited state compared to that of the ground state (data are given as supplementary material). With increasing solvent polarity the MLCT band is blue shifted and in general the solvent effect is described negative solvatochromism. The MLCT maxima shifts 100–110 nm on changing the solvent polarity (Fig. 3). This can be attributed to superior solvation of the dipolar ground state and inferior solvation of the less dipolar excited state by polar solvent. There is a decrease in dipole moment during the electronic transition, the excited state in a solvent cage of oriented dipoles does not have the correct disposal to efficiently stabilize the excited state. Thus with increasing solvent polarity, the energy of the ground state is lowered more than that of the excited state and describes a hypsochromic effect [16,17,28]. A change in geometry by the solvation process is excluded due to hydrogen bonding as the band structure of the CT transition remains unchanged in the non-hydrogen bonded solvent. Kamlet and Taft's Π^* solvent polarity parameter [16,17,32] is also used to correlate to a high degree the metal to ligand charge transition energies. The resultant correlations are shown in Fig. 6. The high energy transitions are almost independent of solvent polarity.

3.2.3. ^1H and ^{13}C NMR spectra

The ^1H NMR spectra were assigned on comparing with the free ligand values [21]. An important observation is the downfield shifting of the pyridine protons (3- to 6-H) by

Table 2
UV–Vis,[a] fluorescence[b] spectral and cyclic voltammetric[c] data

Compound	UV–Vis data λ_{max} (nm) (10^{-3} ε/M^{-1} cm^{-1})	λ_{ex} (nm)	λ_{em} (nm)	Quantum yield (ϕ)	Cyclic voltammetric data metal oxidation[d], ligand reduction[e]	
$[Cr(CO)_4(\alpha\text{-NaiPy})]$ (**1a**)	603 (2.467), 374 (5.631), 333 (12.53), 286 (16.277)	333	395	0.42	0.908	−0.642 (180)
$[Cr(CO)_4(\beta\text{–NaiPy})]$ (**1b**)	604 (2.636), 346 (12.04), 326 (19.89), 296 (16.73)	346	388	0.39	0.809, 0.503	−0.882 (220)
$[Mo(CO)_4(\alpha\text{-NaiPy})]$ (**2a**)	568 (1.502), 334 (3.954), 293 (6.13)	334	396	0.45	1.043	−1.461[e]
$[Mo(CO)_4(\beta\text{–NaiPy})]$ (**2b**)	564 (0.572), 334 (5.251), 294 (10.342), 284 (11.519)	334	385	0.40	0.986	−1.307[e]
$[W(CO)_4(\alpha\text{-NaiPy})]$ (**3a**)	574 (1.149), 322 (17.526), 272 (7.838)	322	397	0.55	1.274	−0.773 (200)
$[W(CO)_4(\beta\text{–NaiPy})]$ (**3b**)	577 (1.071), 336 (7.963), 296 (13.074)	336	382	0.48	1.077	−1.308[e], −0.663 (200)

[a] In C_6H_6.
[b] In C_6H_6 at 298 K.
[c] Solvent, CH_2Cl_2; Pt-working electrode, Ag/AgCl, Cl^- reference, Pt-auxiliary electrode. [n-Bu_4N](ClO_4) supporting electrolyte, scan rate 50 mV/s; metal oxidation $E^1_M = 0.5\,(E_{pa} + E_{pc})$, V for $M(I)/M(0)$ couple, E^2_M for $M(II)/M(I)$ couple in units of V; $\Delta E_p = |E_{pa} - E_{pc}|$, mV.
[d] E_{pa} (anodic-peak-potential).
[e] E_{pc} (cathodic-peak-potential).

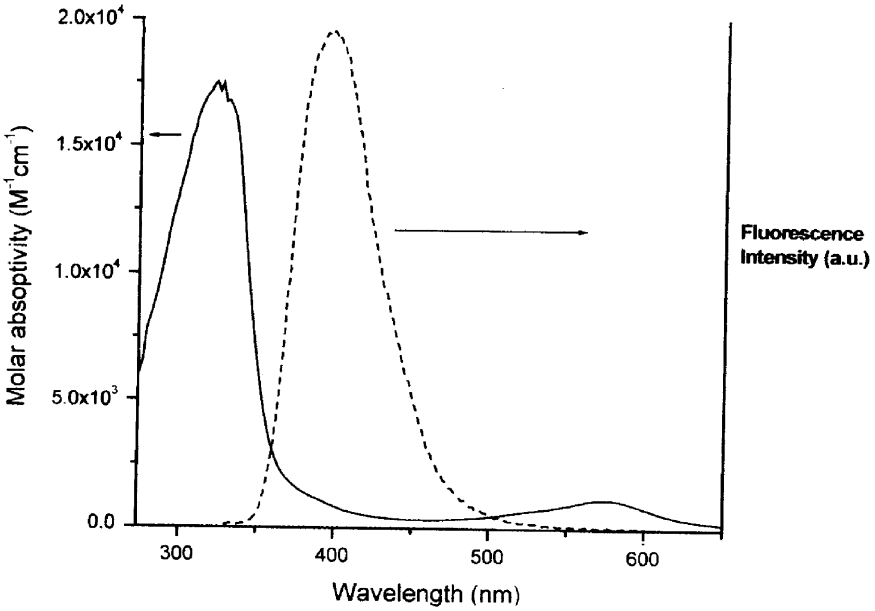


Fig. 2. UV–Vis spectrum of *cis*-[W(CO)$_4$(α-NaiPy)] (–); fluorescence spectrum of *cis*-[W(CO)$_4$(α-NaiPy)] (...) in benzene at 298 K.

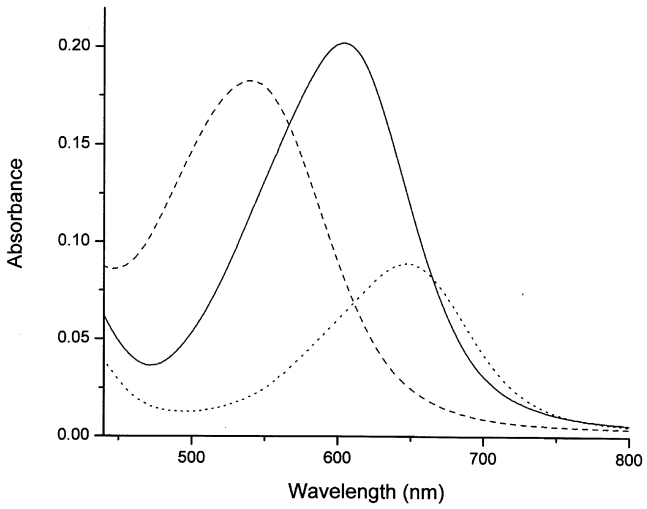


Fig. 3. Electronic spectra of [Cr(CO)$_4$(β-NaiPy)] (–) in benzene, (...) in DMF, (---) in heptane. Red shift of λ_{max} with increase in solvent polarity (DMF > benzene > heptane) suggests negative solvatochromism.

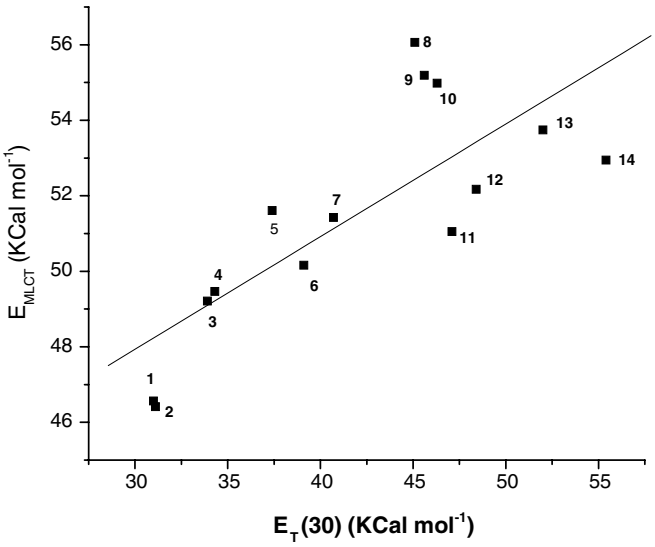


Fig. 4. Energies of the MLCT absorption (E_{MLCT}) of [W(CO)$_4$(β-NaiPy)] plotted against E_T (30) values. 1, hexane; 2, heptane; 3, toluene; 4, benzene; 5, tetrahydrofuran; 6, chloroform; 7, dichloromethane; 8, dimethylsulfoxide; 9, acetonitrile; 10, nitromethane; 11, *t*-butanol, 12, 2-propanol; 13, 2-methoxy ethanol; 14, methanol.

0.2–0.4 ppm. This supports the coordination of pyridine-N to the metal centre. Naphthyl protons (8-H to 15-H) experience a small perturbation and the chemical shift data are comparable with the free ligand data. The imine proton (–CH=N–) appears as a singlet at 8.6–8.9 ppm (data are given as supplementary material).

The ^{13}C NMR spectra are complicated due to the large number of C-centres. The assignment has been done on comparing with the spectra of the free ligands. A DEFT study has also distinguished the primary, secondary, tertiary and quaternary C-centres. Most downfield signals observed at 210–220 ppm are due to C in CO. Mo(CO)-complexes show higher chemical shift data than the Cr(CO)-system and follow the sequence Mo > Cr > W.

3.2.4. Emission spectra

The Schiff bases exhibit photoluminescence with emissions at 414 and 405 nm for α-NaiPy and β-NaiPy, respectively at room temperature in $CHCl_3$ solution upon excitation at 330 nm [24,25]. The excitation at >350 nm shows a low intense emission while [M(CO)$_4$(NaiPy)] exhibit high intense emission properties upon excitation at the

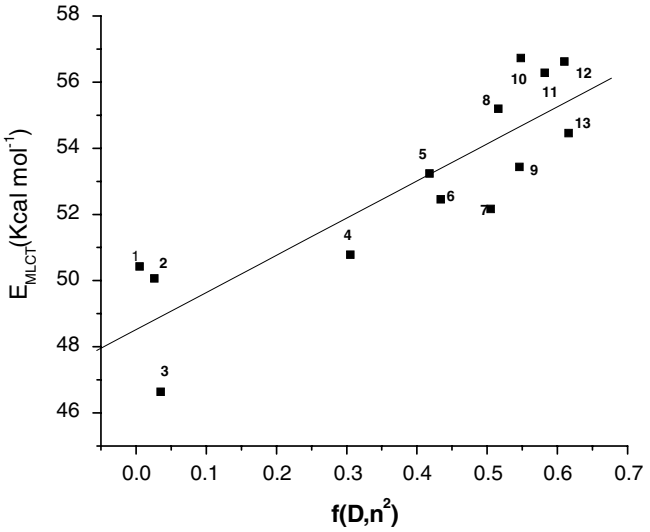


Fig. 5. Energies of the MLCT absorption (E_{MLCT}) of [Mo(CO)$_4$(β-NaiPy)] plotted against $f(D,n^2)$ values: 1, benzene; 2, toluene; 3, hexane; 4, chloroform; 5, tetrahydrofuran; 6, dichloromethane; 7, *t*-butanol; 8, 2-methoxy ethanol; 9, 2-propanol; 10, dimethylformamide; 11, nitromethane; 12, acetonitrile; 13, methanol.

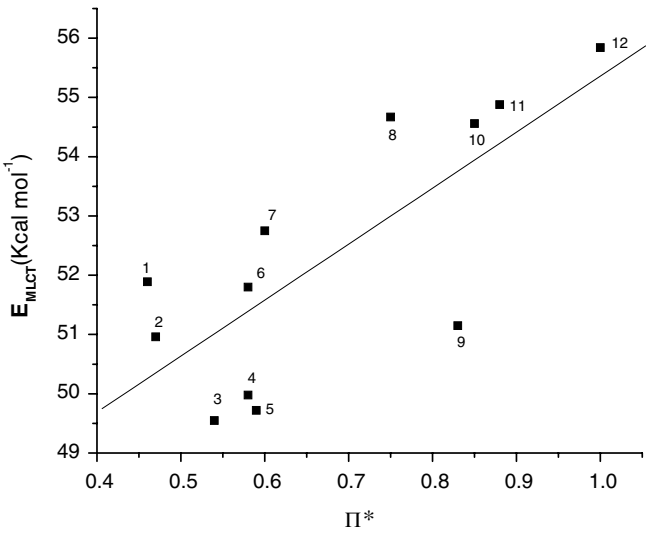


Fig. 6. Energies of MLCT absorption (E_{MLCT}) of [W(CO)$_4$(α-NaiPy)] plotted against Π^* value, 1, 2-propanol; 2, *t*-butanol; 3, toluene; 4, chloroform; 5, benzene; 6, thf; 7, methanol; 8, acetonitrile; 9, dichloromethane; 10, nitromethane; 11, dimethylformamide; 12, dimethylsulfoxide.

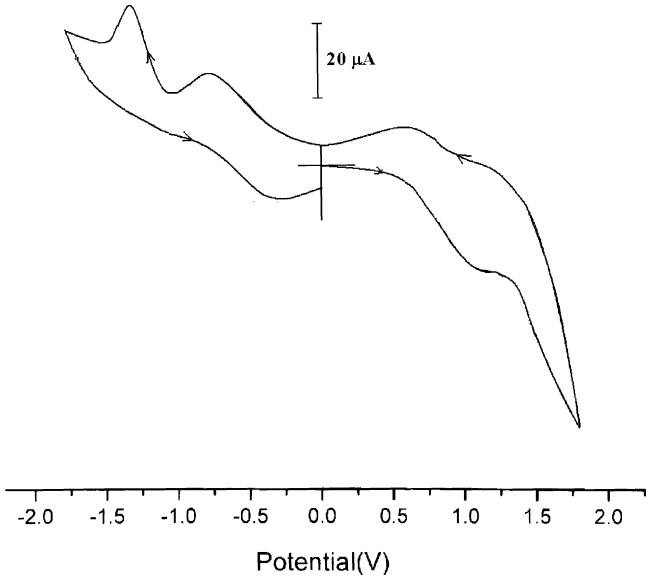


Fig. 7. Cyclic voltammogram of [W(CO)$_4$(β-NaiPy)] in CH_2Cl_2 using a Pt-disk milli electrode, Pt-wire auxiliary electrode and Ag, AgCl reference electrode.

π–π* transition wavelength (320–345 nm) (Table 2). We did not observe any emission when the complexes were excited at the MLCT wavelength (>550 nm). It has been reported that the metal ions can enhance or quench the fluorescence emission of pyridine containing compounds [32,33]. In the absence of metal ions the fluorescence of the ligand is probably quenched by the occurrence of a photoinduced electron transfer (PET) process due to the presence of a lone pair of nitrogen atoms. Such a PET process is prevented by the complexation of ligand with metal ions; due to rigidity of the chelate ring. Intersystem crossing due to spin-orbit coupling introduced by the metal centre may also influence the emission intensity. This enhances the fluorescence intensity upon coordination to the metal ion. This in fact happens to the group 6 metal carbonyl complexes of NaiPy. The intraligand charge transfer band shows a very high intensity emission, greater than the MLCT band. There are two or three bands <400 nm which are characterized as ligand centred transitions (n–π* and π–π* transitions) (Table 2). We found an identical emission pattern upon excitation at the *n*–π* and π–π* positions. We have taken the π–π* transition in the complexes to investigate the emission properties (Fig. 2). The quantum yields (ϕ) vary from 0.4 to 0.55. [M(CO)$_4$(α-NaiPy)] complexes, in general, shows higher quantum yields than [M(CO)$_4$(β-NaiPy)]. One would expect that excitation into the π–π* state would lead to rapid internal conversion to the lowest energy excited state, which is presumably the MLCT state, and that emission should occur from the MLCT state. However, it appears that the emission in these complexes is occurring from the high energy π–π* state, which has ruled out the possibility of competitive energy transfer to the MLCT state. The free ligands are considerably more fluorescent and one possible explanation is either the presence of free ligand impurity or free ligand produced as a result of photodissociation. This possibility is also ruled out by running ^{1}H NMR spectra of [M(CO)$_4$(NaiPy)] after irradiation for 5 min in $CDCl_3$ solution. The spectra of non-radiated and irradiated [M(CO)$_4$(NaiPy) are identical in all aspects.

Both the absorption and emission maxima are dependent on solvent polarity. In low polar solvents like hexane the emission maxima are almost same for all α-Naipy and β-NaiPy tetra-carbonyl compounds and the emissions occur at about 45–50 nm longer wavelength than the

excitation. Whereas in polar solvents the emission maxima occur about 100 nm longer wavelength for [M(CO)$_4$(α-NaiPy)] and about 70 nm longer wavelength for [M(CO)$_4$(β-NaiPy)]. These facts reveal that the excited state has higher stability as the polarity of the solvent increases, i.e. the excited state is more polar than the ground state. Again from the difference of the shift of emission maxima it is clear that the excited states of [M(CO)$_4$(α-NaiPy)] are more polar than those of [M(CO)$_4$(β-NaiPy)].

3.2.5. Electrochemistry

The electrochemical properties of the complexes were investigated by cyclic voltammograms (CV) in 0.1 M [*n*-Bu$_4$N][ClO$_4$] in CH_2Cl_2 solution at a scan rate of 50 mV S^{-1}. All CV data were collected under a nitrogen environment and potentials are expressed with reference to Ag/AgCl. The results are collected in Table 2. A representative voltammogram is shown in Fig. 6. All of the compounds show one oxidation and two reductions. By analogy with similar types of α-diimine complexes [1] and [M(CO)$_4$(2-PAP)] (2-PAP = 2-(phenylazo)pyridine) [4] we suggest that the oxidation is primarily a metal-centred electron extraction. In almost every case only one oxidation ($M^0 \rightarrow M^+$) is observed, it is irreversible in nature and the cathodic peak does not appear on scan reversal (Fig. 7). The second oxidation ($M^+ \rightarrow M^{2+}$) is observed only in one case. The reduction is referred to electron accommodation of the π^* MO of the chelated ligand. The first reduction in each case appears at a more positive potential than that of the free ligand, reflecting the stabilization of the π^* MO upon coordination. The reduction is referred to the accommodation of an electron in the imine based orbital.

4. Conclusion

Cis-[M(CO)$_4$(α/β-NaiPy)] (M = Cr(0), Mo(0), W(0); α/β-NaiPy = *N*-[(2-pyridyl)methyliden]-α (or β)-aminonaphthalene) are characterized by different spectroscopic tools (FT-IR, UV–Vis, Mass, ^{1}H and ^{13}C NMR). The mass fragmentation pattern shows successive removal of CO. The ligands belong to the π-acidic diimine family and stabilize efficiently the M(0) oxidation state. Cyclic voltammograms gives metal centred oxidation, M^+/M^0 and ligand centred reductions. The complexes exhibit a high efficient π–π^* emission; *cis*-[M(CO)$_4$(α-NaiPy)] emits at higher energy than *cis*-[M(CO)$_4$(β-NaiPy)].

Acknowledgements

Financial support from the Department of Science and Technology, New Delhi are gratefully acknowledged. One of us (PD) thanks the Council of Scientific and Industrial Research, New Delhi for a fellowship. Our sincere thanks are due to Prof. S. Bagchi, Department of Chemistry, Burdwan University, India for his kind help in evaluating the solvatochromism properties of the complexes.

Appendix A. Supplementary material

Supplementary data associated with this article can be found, in the online version, at doi:10.1016/j.poly.2006.12.029.

References

[1] K. Kalyansundaram, Coord. Chem. Rev. 46 (1982) 159.
[2] R.–Q. Fan, D.-S. Zhu, Y. Mu, G.–H. Li, Y.–L. Yang, Q. Su, S.–H. Feng, Eur. J. Inorg. Chem. (2004) 4891.
[3] Y.L. Pui, K.K. Cheung, J. Chem. Soc., Dalton Trans. (2000) 3658.
[4] Y. Wang, X.–M. Ouyang, Y.–Z. Li, W.–Y. Sun, Bull. Chem. Soc. Jpn. 76 (2003) 1403.
[5] H.–F. Zhu, L. Li, T. Okamura, W. Zhao, W.–Y. Sun, N. Ueyama, Bull. Chem. Soc. Jpn. 76 (2003) 761.
[6] L.A. Garcia-Escudero, D. Miguel, J.A. Turiel, J. Organomet. Chem. 691 (2006) 3434.
[7] M. Menon, A. Pramanik, A. Chakravorty, Inorg. Chem. 34 (1995) 3310.
[8] A. Mentes, Trans. Met. Chem. 24 (1999) 77.
[9] E.C. Fitzgerald, R.W. Grime, H.C. Knight, M. Helliwell, J. Raftery, M.W. Whiteley, J. Organomet. Chem. 691 (2006) 1879.
[10] A. Vlcek Jr., Coord. Chem. Rev. 230 (2002) 225, and references therein.
[11] Q. Ye, Q. Wu, H. Zhao, Y.-M. Song, X. Xue, R.-G. Xiong, S.-M. Peng, G.-H. Lee, J. Organomet. Chem. 690 (2005) 286.
[12] V.N. Nemykin, J.G. Olsen, E. Perera, P. Basu, Inorg. Chem. 45 (2006) 3557.
[13] E. Bayram, S. Ozkar, J. Organomet. Chem. 691 (2006) 3267.
[14] F. Alper, C. Kayram, S. Ozkar, J. Organomet. Chem. 691 (2006) 2734.
[15] R.W. Balk, T. Snobeck, D.J. Stufkens, A. Oskam, Inorg. Chem. 19 (1980) 3015.
[16] D.M. Manuta, A.J. Lees, Inorg. Chem. 22 (1983) 3825.
[17] D.M. Manuta, A.J. Lees, Inorg. Chem. 25 (1986) 3212.
[18] Y. Che, X. Tian, H. Chen, Z. Tang, J. Lin, New J. Chem. 30 (2006) 883.
[19] D. Zhao, Z. Hong, C. Liang, D. Zhao, X. Liu, W. Li, C.S. Lee, S.T. Lee, Thin Solid Films 363 (2000) 208.
[20] J. Slinnes, D. Bernards, P.L. Houston, H.D. Abruna, S. Bernhard, G.G. Malliaras, Chem. Commun. (2003) 2392.
[21] J. Dinda, C. Sinha, Transition Met. Chem 28 (2003) 864.
[22] J. Zhang, W. Li, W. Bu, L. Wu, L. Ye, G. Yang, Inorg. Chim Acta 358 (2005) 964.
[23] L.G. Nickolacheva, C.M. Vogels, R.A. Stefan, H.A. Warwish, S.J. Duffy, R.J. Ireland, A. Decken, R.H. Hudson, S.A. Westcott, Canadian J. Chem. 81 (2003) 269.
[24] D. Das, J. Dinda, T.K. Mondal, C. Sinha, J. Indian Chem. Soc. 83 (2006) 342.
[25] D. Das, B.G. Chand, K.K. Sarker, J. Dinda, C. Sinha, Polyhedron 25 (2006) 2333.
[26] D. Das, J. Dinda, T.K. Mondal, K.K. Sarker, C. Sinha, J. Indian Chem. Soc. 83 (2006) 861.
[27] A.I. Vogel, A Text Book of Practical Organic Chemistry, Longman, London, 1959.
[28] (a) C. Reichardt, Chem. Rev. 94 (1994) 2319;
(b) C. Reichardt, Solvents and Solvent Effects in Organic Chemistry, 2nd ed., VCH, Weinheim, 1988.
[29] Y. Marcus, Ion Solvation, Wiley, Chichester, 1985.
[30] Y.Y. Akhadov, Dielectric Properties of Binary Solutions – A Data Handbook, Pergamon Press, Oxford, 1981.
[31] B. Valeur, Modern Luminescence Spectroscopy, G. Schulman Wiley Inc., 1993.
[32] R.W. Taft, M.J. Kamlet, Inorg. Chem. 22 (1983) 250.
[33] (a) J.L. Klappa, A.A. Geers, S.J. Schmidtke, L.A. MacManus-Spencer, K. McNeill, Dalton Trans. (2004) 883;
(b) B. Valuer, Molecular Fluorescence: Principles and Applications, Wiley–VCH, Weinheim, 2001.

stable in the gas phase until deposition on the substrate. Therefore, temperature variable MS and TGA-IR spectra of the gases evolved during the decomposition processes will be described in the presented paper. Data from the latter studies will be use for elaboration of the fragmentation schemes. Moreover, the fragmentation schemes of coordinated ligands, should provide unique knowledge about the chemistry of silver(I) complexes in the gas phase. The article is also intended to describe a mechanism of carboxylates thermal decomposition, therefore VT-IR spectra were measured and discussed.

2. Experimental

2.1. Chemicals and instrumentation

$CH_3CH_2C(CH_3)_2COOH$ (97%), trimethylphosphine (PMe_3) (1 M solution in THF), triethylphosphine (PEt_3) (1 M solution in THF), triethylorthoformate (TEOF) were purchased from Aldrich, $AgNO_3$, $NaHCO_3$ and C_2H_5OH were purchased from POCh (Poland), and all compounds were used as received. Ethanol was dried by standard methods.

Thermal studies (TG, DTG, DTA) were performed on a SDT 2960 TA analyser. Decomposition processes were studied in a dynamic atmosphere of dry nitrogen flowing at 40 ml min^{-1}, heating rate 2.5 °C min^{-1}, heating range up to 400 °C and sample mass 2–5 mg. Gaseous products of thermal decomposition were detected by a FT IR Bio-Rad Excalibur spectrophotometer equipped with a thermal connector for gases evolved from a SDT 2960 TA analyser. The thermal connector was heated to 200 °C. Powder X-ray diffraction data for the thermal analysis residues were obtained with a Philips X'PERT diffractometer using Cu Kα radiation. Variable temperature mass spectra were registered using a Finnigan MAT 95 spectrometer with the EI technique (heating range 30–300 °C). ^1H and ^{13}C NMR spectra in CD_3CN or C_6D_6 were collected with a Varian Gemini 200 MHz spectrometer using TMS as the standard, and 85% H_3PO_4 for ^{31}P NMR (80.96 MHz). IR spectra were recorded using a Perkin–Elmer 2000 FT IR spectrometer in the range 4000–400 cm^{-1}, in KBr discs. Variable temperature IR (VT-IR) studies in the solid phase were carried out with a SPECAC (Perkin–Elmer) temperature variable cell. The composition of vapors formed during the thermolysis of the studied compounds was determined by VT-IR spectroscopy. Spectra of vapors transported with the carrier gas (Ar) were recorded using the equipment as reported [21]. Silver was determined argentometrically (after complex mineralization), whereas C, H, P were determined by elemental microanalysis.

2.2. Synthesis

2.2.1. $[Ag_2(CH_3CH_2C(CH_3)_2COO)_2]$ (1)

2,2-Dimethylbutyric acid (3.5 mmol) and potassium nitrate (0.43 mmol) were suspended in a water–ethanol solution (1:1), heated to 40 °C and stirred 1 h, followed by silver nitrate (3.5 mmol) addition (all manipulations were carried out in the darkness). The obtained precipitate was filtered, washed with water, ethanol and dried. *Anal.* Calc. for $C_{12}H_{22}Ag_2O_4$: C, 32.2; H, 5.0; Ag, 48.3. Found: C, 32.0; H, 5.2; Ag, 48.7%. IR: 1555, 1477, 1405, 1366, 1357, 1290 cm^{-1}; ^1H NMR (CD_3CN): 0.83 ppm (3H, t, CH_3), 1.10 ppm (6H, s, CH_3), 1.49 ppm (2H, q, CH_2); ^{13}C NMR (CD_3CN): 10.3 ppm (CH_3), 26.9 ppm $(CH_3)_2$, 35.5 ppm (CH_2), 44.7 ppm (C), 183.9 ppm (COO).

2.2.2. $[Ag_2(CH_3CH_2C(CH_3)_2COO)_2(PMe_3)_2]$ (2) and $[Ag_2(CH_3CH_2C(CH_3)_2COO)_2(PEt_3)_2]$ (3)

Complexes were synthesized, in dried argon, using Schlenk techniques, in the darkness. In a general procedure: **1** (4 mmol) in C_2H_5OH (40 cm^3) was mixed with 5 cm^3 of TEOF and PR_3 (4 mmol) (THF solution), where R = Me, Et. The mixture was stirred at room temperature for 4 h, filtered and solvents evaporated on a vacuum line. $[Ag_2(CH_3CH_2C(CH_3)_2COO)_2(PMe_3)_2]$ (**2**) was obtained as white crystals, which were recrystallized from ethanol, whereas $[Ag_2(CH_3CH_2C(CH_3)_2COO)_2(PEt_3)_2]$ (**3**) was obtained as a green–yellow oil and was analyzed directly after evaporation. *Anal.* Calc. for $C_{18}H_{40}Ag_2O_4P_2$ (**2**): C, 36.1; H, 6.7; P, 10.3; Ag, 36.1. Found: C, 36.3; H, 6.9; P, 10.2; Ag, 36.4%. IR: 1550, 1472, 1399, 1359, 1286, 960 cm^{-1}. ^1H NMR (CD_3CN, ppm): 0.81 (3H, t, CH_3), 1.03 (6H, s, CH_3), 1.34 (9H, d, PCH_3), 1.46 (2H, q, CH_2); ^{13}C NMR (CD_3CN, ppm): 9.7 (CH_3), 14.8 P(CH_3), 26.1 $(CH_3)_2$, 34.6 (CH_2), 43.0 (C), 184.4 (COO); ^{31}P NMR (CD_3CN, ppm): −35.4.

Anal. Calc. for $C_{24}H_{52}Ag_2O_4P_2$ (**3**): C, 42.2; H, 7.7; P, 9.1; Ag, 31.6. Found: C, 42.3; H, 7.4; P, 9.0; Ag, 31.1%. IR: 1549, 1458, 1405, 1364, 1045, 764 cm^{-1}. ^1H NMR (CD_3CN, ppm): 0.84 (3H, t, CH_3), 1.07 (6H, s, CH_3), 1.18 (9H, t, PEt_3), 1.47 (2H, q, CH_2), 1.69 (2H, q, PEt_3). ^{13}C NMR (CD_3CN, ppm): 9.19 (CH_3), 10.5 P(CH_2CH_3), 16.9 P(CH_2CH_3), 26.8 $(CH_3)_2$, 35.0 (CH_2), 43.6 (C), 185.8 (COO); ^{31}P NMR (CD_3CN, ppm): 28.2.

2.3. CVD experiments

The deposition experiments were carried out using horizontal *hot-wall* CVD reactor as described [11]. Silver films were deposited on Si(1 1 1) and steel substrates, under 2 mbar, and in the deposition temperature 200–280 °C. The films were characterized by X-ray diffraction (XRD). XRD data were collected with a Philips X'PERT diffractometer, in 30–80° 2Θ ranges, using CuKα irradiation and sample spinning (step size – 0.1°, program. res. slit – 0.5, measuring time – 11 s per point). The silver films' morphology were studied by a scanning electron microscopy (SEM – LEO 1460 V) and an atomic force microscopy instrument (Veeco, Multimode, Nanoscope IIIa Controler, Taping Mode AFM).

3. Results and discussion

3.1. Preparation

All silver compounds were synthesized in the darkness. Silver 2,2-dimethylbutyrate **1** was obtained by the reaction of 2,2-dimethylbutyric acid and silver nitrate in a 1:1 ratio in a water–ethanol solution. This reaction is fast and the white product can be simply isolated. Both silver 2,2-dimethylbutyrate complexes with phosphines $[Ag_2(CH_3CH_2C(CH_3)_2COO)_2(PMe_3)_2]$ (**2**) and $[Ag_2(CH_3CH_2C(CH_3)_2COO)_2(PEt_3)_2]$ (**3**) were synthesized by the direct reaction of silver carboxylate and the respective phosphine in a 1:1 ratio, using ethanol as solvent and in dried argon. **2** was obtained as white crystals, which were recrystallized from ethanol, whereas **3** was a green–yellow oil.

3.2. IR and NMR spectra

Table 1 demonstrates characteristic absorption bands in the IR spectra, which can be assigned to the stretching modes of the COO group. Carboxylates can coordinate in many modes such as: unidentate, chelating or bridging bidentate [22–24]. The carboxylate coordination can be proposed by analysis of the parameter $\Delta\nu_{COO} = \nu_{asym} - \nu_{sym}$, calculated for studied compounds and identical sodium salts. In the case of silver 2,2-dimethylbutyrate the COO bands were detected at: $\nu_{asym} = 1548\ cm^{-1}$, $\nu_{sym} = 1405\ cm^{-1}$. For complexes **2** and **3** $\Delta\nu_{COO}$ was $153\ cm^{-1}$ and $159\ cm^{-1}$, respectively, which suggest similar coordination as for **1**. The calculated Δ parameters for the discussed compounds are bigger than those for the appropriate sodium salts. This fact suggests a bridging coordination mode of the carboxylic group and a polymeric structure [9,25]. Absorption bands of phosphines derived from P–C stretching vibrations are shifted for **2** by $32\ cm^{-1}$ and for **3** by $19\ cm^{-1}$ in comparison to the free phosphines, which confirms the coordination of the ligands [26,27].

The ^{13}C and ^{31}P NMR spectral chemical shifts of **1–3** are listed in Table 2. One might expect that the ^{13}C signal of the COO carbon should give the most significant changes upon coordination. However, the ^{13}C NMR spectra of **1–3** revealed the COO carbon line at 184.0–185.8 ppm, with a coordination shift (0.9–2.7 ppm) downfield in comparison to the free acid spectra. In the case of perfluorinated silver carboxylates, this signal was observed at higher field (159.1–165.7 ppm) [32]. The observed chemical shifts suggest an opposite effect on the COO carbon due to the inductive effect imposed by the fluorine atoms. However, the coordination shifts of the COO carbon in perfluorinated carboxylates (~1 ppm) were similar to the value calculated for **1**, which reveal comparable silver–carboxylate interactions for fluorinated and non-fluorinated silver salts. In the case of complexes **2** and **3**, the carbonyl carbon exhibited weak singlets at 184.4 and 185.8 ppm, respectively. For $[Ag_2(PPh_3)_2(\mu\text{-}RCOO)_2]$, R – aliphatic chain and $[Ag(PPh_3)(RCOO)]$, R – silylated radical, COO singlets were detected in the range 180.8–187.7 ppm [28,29]. However, in the case of silver complexes with perfluorinated carboxylates $[Ag_2(PR'_3)_2(\mu\text{-}RCOO)_2]$ (R′ = Me, Et), resonances of COO were observed upfield (161.3–163.2 ppm) [30,34]. The coordination shifts for **2** of 1.3 and **3** of 2.7 ppm were close to the values calculated for the compounds $[Ag_2(PR'_3)(RCOO)]$. Therefore, the bridging mode of the silver–carboxylate linkage in $[Ag_2(PR'_3)(RCOO)]$ salts can be similar for aliphatic, silylated and perfluorinated carboxylates. Single ^{31}P resonances appeared at −35.4 **2** and 28.2 ppm **3** – Table 2. The values of chemical and coordination shifts for **2** are close to those observed for perfluorinated carboxylate complexes $[Ag_2(PMe_3)_2(\mu\text{-}RCOO)_2]$. However, for **3** only the coordination shift is similar to the value registered for $[Ag_2(PEt_3)_2(\mu\text{-}RCOO)_2]$, but the signal was detected at higher fields (13.5–13.1 ppm) [30,34].

Table 2
^{13}C, ^{31}P NMR spectral analysis data [ppm]

Compound	^{13}C		^{31}P	
	δ COO	Δ_1	δ	Δ_2
$[Ag_2(CH_3CH_2C(CH_3)_2COO)_2]$ (**1**)	184.0	0.9		
$[Ag_2(CH_3CH_2C(CH_3)_2COO)_2(PMe_3)_2]$ (**2**)	184.4	1.3	−35.4	24.9
$[Ag_2(CH_3CH_2C(CH_3)_2COO)_2(PEt_3)_2]$ (**3**)	185.8	2.7	28.2	46.3

$\Delta_1 = \delta$ COO(complex) − δ COO(acid); δ COO(acid) = 183.1 ppm.
$\Delta_2 = \delta - \delta$ PR_3; $\delta(PMe_3) = -60.3$ ppm; $\delta(PEt_3) = -18.1$ ppm.

3.3. Analysis of variable temperature IR spectra

An application of **1–3** as CVD precursors requires determination of their thermal stability and composition of the vapors formed during their thermolysis. Therefore variable temperature IR (VT-IR) studies have been carried out and the results are presented in Figs. 1–4. IR spectra of **1–3**, registered between 20 and 250 °C, revealed differences in the mechanism of their thermal decomposition (Fig. 1). In the case of **1** and **2**, the thermolysis proceeds with complete decomposition of these compounds. Bands registered at 1676, $1608\ cm^{-1}$ **1** and 1680, $1598\ cm^{-1}$ **2**, at 250 °C,

Table 1
Selected IR band (cm^{-1}) of the studied compounds

Compound	ν_{as}(COO)	ν_s(COO)	$\Delta\nu$(COO)	ν(P–C)
$[Ag_2(CH_3CH_2C(CH_3)_2COO)_2]$ (**1**)	1548	1405	143	
$[Ag_2(CH_3CH_2C(CH_3)_2COO)_2(PMe_3)_2]$ (**2**)	1549	1396	153	740
$[Ag_2(CH_3CH_2C(CH_3)_2COO)_2(PEt_3)_2]$ (**3**)	1553	1394	159	689

$\Delta\nu_{COO(sodium\ salt)} = 119\ cm^{-1}$.

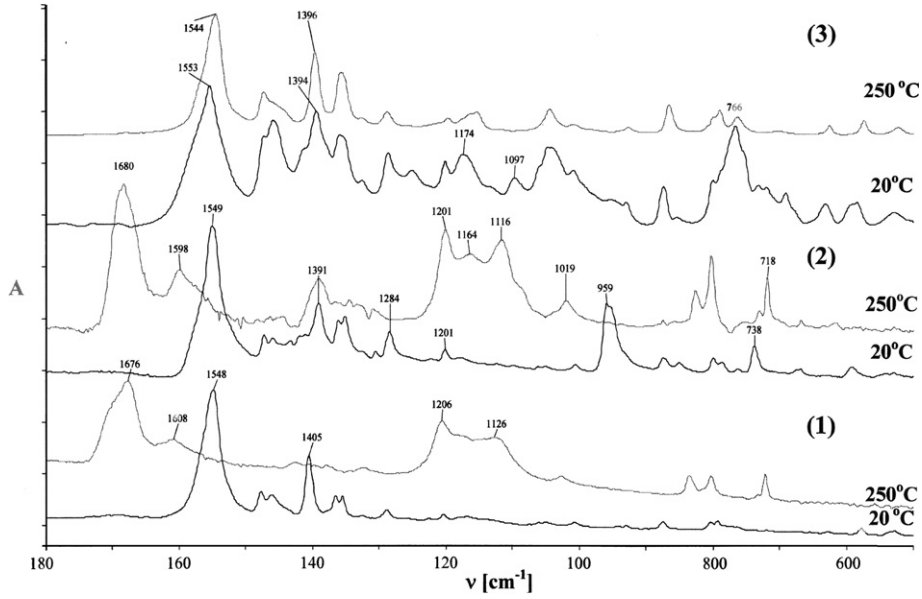


Fig. 1. Variable temperature IR spectra of **1**–**3**, registered at 20 and 250 °C.

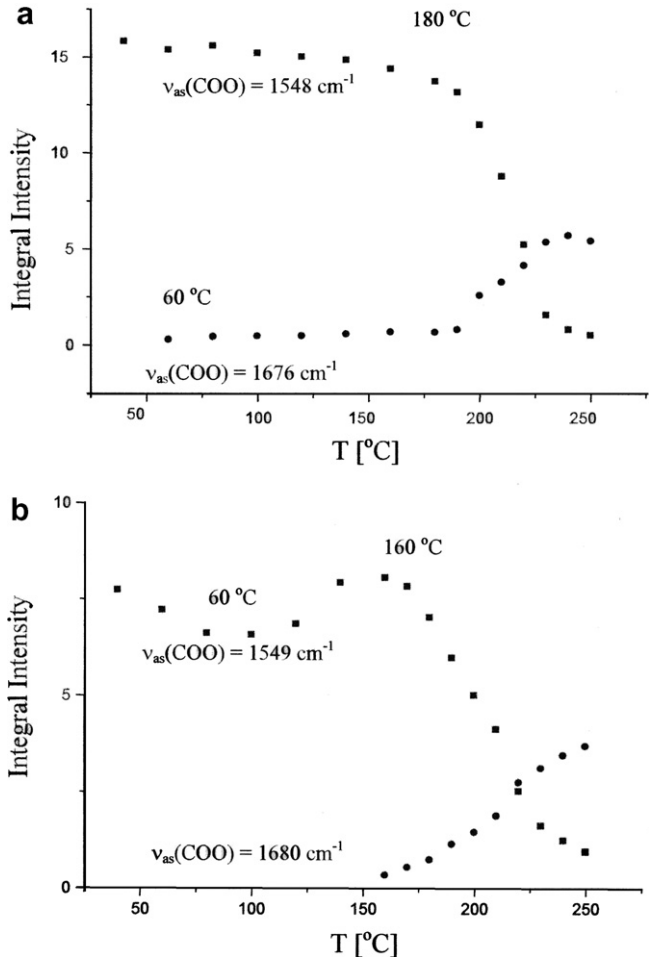


Fig. 2. Temperature dependence of the integral intensity of bands assigned to ν_{as}(COO) and ν(CO), observed between 1480 and 1800 cm^{-1}, in spectra of **1** (a) and **2** (b).

suggest formation of a different type of Ag–OOCR linkage in the solid residue than at room temperature. Calculated $\Delta\nu$ parameters exhibit the increase from 208 to 252 cm^{-1} for **1** and from 239 to 291 cm^{-1} for **2**, in comparison to spectra registered at 20 °C (Table 1). The latter suggests decomposition of the polymeric structure of **1** and **2**, where carboxylate ligands form *syn–syn* bidendate bridges, and the formation of another type of Ag(I) interaction with the carboxylate ligands [22,23].

The differences in the decomposition pathway of **1** and **2** are also observed on the plot of integral intensity of ν_{as}(COO) bands versus temperature (Fig. 2). The relatively high thermal stability of **1** can be noted between 40 and 180 °C. However, the presence of a weak band at 1676 cm^{-1} suggests decomposition process onset at 60 °C. Above 180 °C a rapid increase of this band's intensity is observed, while the ν_{as}(COO) = 1548 cm^{-1} band reveals the opposite effect. The latter can be related to complete decomposition of **1** with the evolution of carboxylic acid. Between 180 and 230 °C (Fig. 3) the main components of the gas phase of **1** are: CO_2 (2359, 667 cm^{-1}), ester species ($\nu_{C=O}$ = 1767, δ_{OCO} = 1116 cm^{-1}), and fragments containing carboxylate acid groups (ν_{OH} = 3520, $\nu_{C=O}$ = 1716 cm^{-1}). Bands that could be assigned to volatile silver–carboxylate species were not found, which confirms the postulated decomposition pathway by DTA/TGA studies. The latter is in favor of decomposition of **1** leaving silver containing species in the solid phase.

For **2**, the dependence of the integral intensity of ν_{as}-(COO) bands versus temperature changes stepwise, exhibiting the first step at 60 °C, with the second one at 160 °C (Fig. 2b). Simultaneously CH_3 librational modes (rocking and/or wagging) at 959 cm^{-1} and ν(P–C) (738 cm^{-1}) bands

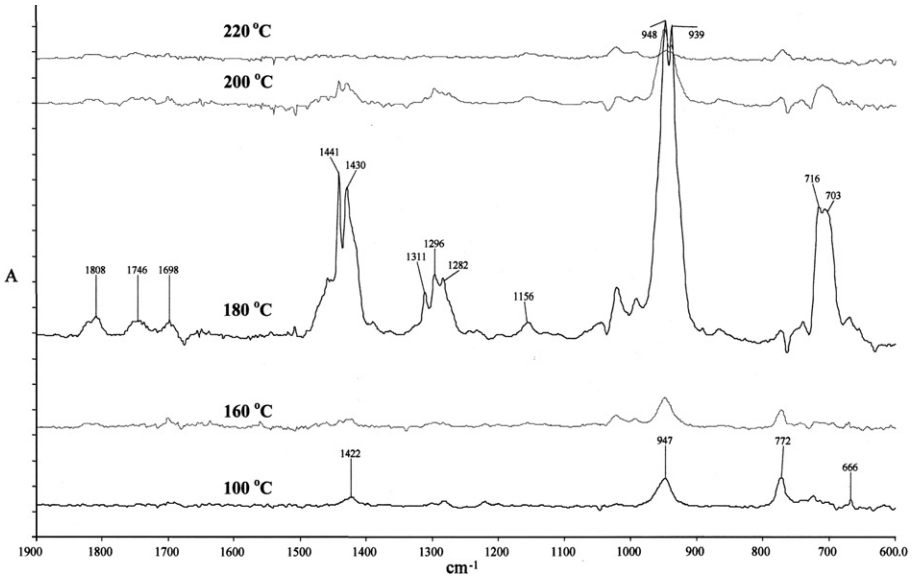


Fig. 3. VT-IR spectra of vapors formed during the thermal decomposition of **2**.

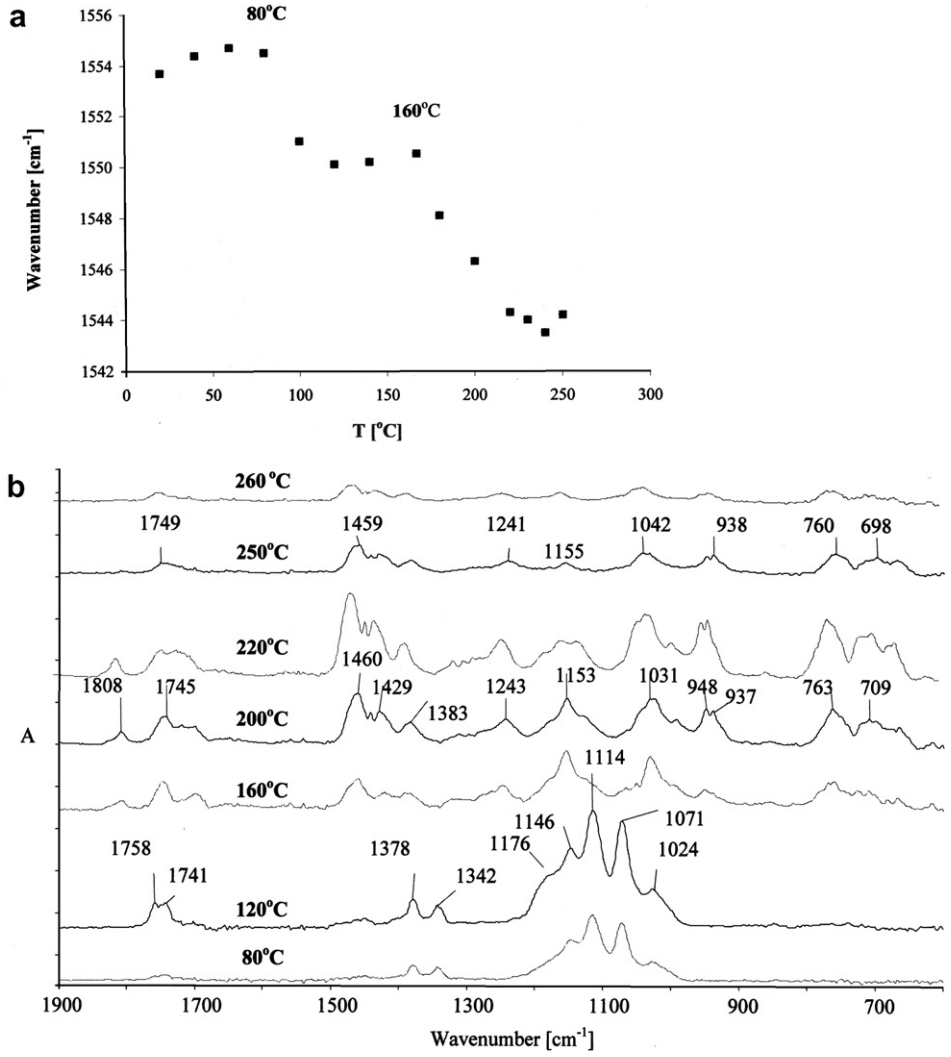


Fig. 4. The dependence of the frequency of ν_{as}(COO) motions vs. temperature (a), and changes of the vapor composition during the thermal decomposition of **3** (b).

revealed intensity decrease. Hence, the phase transition at lower temperatures can be attributed to phosphine detachment from **2**. The same as for **1**, the main decomposition product appears to be Ag(I) carboxylate intermediates. However, their complete decomposition processes was observed above 160 °C, (bands at 1680 and 1549 cm^{-1}), which indicate low thermal stability of these species.

Analysis of vapors spectra, registered in the range 160 and 200 °C, revealed phosphine bands: $\delta(CH_2)$ 1430–1441 cm^{-1}, $\delta_{sym}(CH_3)$ 1282–1311 cm^{-1}, $\delta(CH_3)$ 939–948 cm^{-1} and ν_{asym}(P–C) 703–716 cm^{-1}. The latter is in favor of phosphine species (PCH_2, PCH_3), which are predominant in the vapors of **2**. Besides that, weak bands observed in the range 1698–1808 cm^{-1}, (registered at 180 °C), can be assigned to a volatile acid anhydride (1808, 1746 cm^{-1}) and aliphatic carboxylate (1698 cm^{-1}).

Comparison VT-IR and MS data confirms the proposed decomposition mechanism of **2**. According to MS data (Table 3), the complete decomposition of **2**, proceeds between 80 and 260 °C, with volatile species formation. The main constituents are: $[PH(CH_3)]^+$, $[P(CH_3)_2]^+$ and $[P(CH_3)_3]^+$ fragments, whereas only trace quantities of $[AgP(CH_3)_3]^+$ were noticed. Carboxylate silver bonded fragments (e.g. $[Ag_2(OOCC(CH_3)_2CH_2CH_3)]^+$) were not observed in the vapors. This can be explained by the low stability of species containing the above fragments and their rapid decomposition.

In comparison to **1** and **2**, the thermolysis pathway of **3** is different (Fig. 1). The dependence between frequency of ν_{asym}(COO) bands and temperature (Fig. 4a) suggests that the decomposition pathway of **3** proceed in two stages, with the first step near 80 °C and second one at 160 °C. Moreover, significant differences in the vapors composition in the temperature ranges 60–140 °C and 160–260 °C were observed (Fig. 4b). Species containing ester groups (1741, 1758, and 1176 cm^{-1}) and aliphatic ethers (group of bands between 1024 and 1146 cm^{-1}) were the main volatile components at lower temperatures. Above 160 °C, the composition of the vapors changes and bands at 763, 1031, 1243 and 1460 cm^{-1} indicate the presence of Ag–phosphine derivatives as the main volatile decomposition products. When compared to the room-temperature spectrum of **3** the bands assigned to $Ag–PEt_3$ groups are almost identical (766, 1046, 1250 and 1459 cm^{-1}). Simultaneously, absorption bands derived from volatile species containing Ag–OOCR fragments were not observed. In the temperature range 160–260 °C, only bands from acid anhydride (1745, 1808 cm^{-1}) and ester derivatives (1153, 1720–1750 cm^{-1}) were noticed.

According to the VT-IR results it can be concluded that **1** and **2** are not suitable precursors for CVD of silver, due to their low thermal stability in the temperature range 20–250 °C. In contrast, the formation of volatile and stable silver–phosphine intermediates between 160 and 260 °C during the decomposition of **3** suggests its potential usability as a Ag CVD precursor, as was confirmed by CVD experiments (*vide infra*).

3.4. Mass spectra analysis

Variable temperature mass spectra were studied to detect the metallated species, which can be transported in the gas phase during precursor heating in a CVD process. EI-MS spectra of **1**, **2** and **3** were recorded in the range 30–300 °C and the results are listed in Table 3. The following most intensive organic ions: $[CH_3CH_2CH_2]^+$, $[CH_3CH_2C{=}CH_2]^+$ and $[CH_3CH_2C(CH_3)_2]^+$, as well as $[COO]^+$ and $[COOH]^+$, were detected in the studied tem-

Table 3
Mass spectra analysis data

Fragmentation ion	*m/z*	Compound/Temperature/Int. (%)						
		1	**2**			**3**		
		197 (°C)	86 (°C)	107 (°C)	256 (°C)	116 (°C)	182 (°C)	245 (°C)
$[CH_3CH_2CH_2]^+$	43	100	15.1	13.6	100	56.6	100	93.8
$[COO]^+$	44	23.3	21.4	14.8	40.8	12.4	24.2	22.1
$[COOH]^+$	45	7.9	71.6	46.1	9.4	17.7	16.7	5.9
$[(CH_3)HP]^+$	47	xxx	23.9	12.7		xxx	xxx	xxx
$[CH_3CH_2C{=}CH_2]^+$	55	31.0	4.8	4.2	60.0	25.4	36.8	33.2
$[CH_3CH_2CHCH_2]^+$	56	6.8	12.2	8.0	10.2	7.7	8.7	5.9
$[(CH_3)_2P]^+$	61	xxx	100	100		xxx	xxx	xxx
$[CH_3CH_2C(CH_3){=}CH_2]^+$	70	9.0	1.1	1.1	15.3	5.3	9.1	11.1
$[CH_3CH_2C(CH_3)_2]^+$	71	63.8	7.3	6.5	79.6	30.0	50.0	65.3
$[(CH_3)_3P]^+$	76	xxx	83.6	44.9		xxx	xxx	xxx
$[(C_2H_5)_2HP]^+$	90	xxx	xxx	xxx	xxx	55.6	30.5	
$[Ag]^+$	107	2.0			4.1			
$[(C_2H_5)_3P]^+$	118	xxx	xxx	xxx	xxx	27.3	14.9	
$[AgP(CH_3)_3]^+$	183	xxx	2.6	3.5		xxx	xxx	xxx
$[Ag_2]^+$	216	9.5			10.6			7.2
$[AgP(C_2H_5)_3]^+$	225	xxx	xxx	xxx	xxx	77.3	57.9	
$[(CH_3CH_2C(CH_3)_2COO)Ag_2]^+$	331	38.3			81.8	4.5		56.7

xxx, unable to observe.

perature range. Moreover, analysis of the spectra revealed the presence of certain metallated species formed in the strictly defined temperature ranges. The spectrum of **1** (at 197 °C) exhibited $[(CH_3CH_2C(CH_3)_2COO)Ag_2]^+$ (R.I. = 38%) as the most intensive signal. Similar disilver species were observed in MS spectra of perfluorinated and aliphatic non-fluorinated silver carboxylates [20,31]. The latter silver(I) salts form dimers or aggregates of these dimers in the solid phase with bridging carboxylates, and likewise the same can be suggested for **1**. The observed silver bonded species can be formed by detachment of RCOO$^{\cdot}$ at the temperature characteristic for the studied precursor (e.g. 197 °C for **1**). In the next stage, the $[(CH_3CH_2C(CH_3)_2COO)Ag_2]^+$ fragment decomposes to Ag_2^+ and organic ions, which is evident from the characteristic line pattern for Ag_2^+ [3 lines, R.I. = 1:1.860:0.865, natural isotopic abundance of ^{107}Ag (51.4%) and ^{109}Ag (48.6%)].

In the case of **2** between 30 and 120 °C the following phosphorous containing species $[(CH_3)_2P]^+$ (R.I. = 100% at 86 °C and 107 °C), $[(CH_3)_3P]^+$ (R.I. = 84% at 86 °C; R.I. = 45% at 107 °C), $[(CH_3)_2HP]^+$ (R.I. = 24% at 86 °C; R.I. = 13% at 107 °C) and $[Ag(PCH_3)]^+$ (R.I. = 2.6% at 86 °C; R.I. = 3.5% at 107 °C) were detected. These phosphorous embodied fragments are in favor of trimethylphosphine detachment and complex decomposition in the 30–120 °C range. At higher temperatures (160–240 °C), the desirable metallated ions $[(CH_3CH_2C(CH_3)_2COO)Ag_2]^+$ (R.I. = 82% at 220 °C), $[Ag_2]^+$ (R.I. = 11% at 220 °C) and $[Ag]^+$ (R.I. = 4% at 220 °C) appeared (Fig. 5). Fragments detected in the spectrum of **2** (30–300 °C) suggest detachment and fragmentation of trimethylphosphine followed by RC–COO bond dissociation (absence of RCOO and RCO ions) [31]. The latter causes silver bonded species formation, which decompose in the last stage to Ag_2^+ and Ag^+ (Fig. 5).

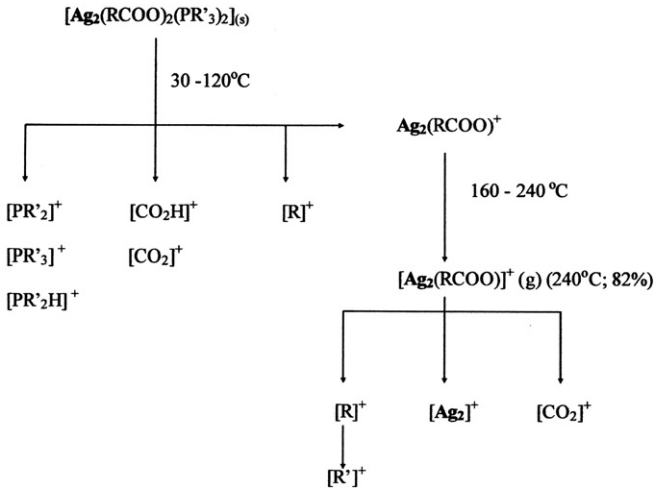


Fig. 5. Fragmentation scheme for $[Ag_2(CH_3CH_2C(CH_3)_2COO)_2(PMe_3)_2]$ (**2**).

In the case of **3**, below 200 °C, phosphorous containing metallated fragments $[AgP(C_2H_5)_3]^+$ (R.I. = 77% at 116 °C; R.I. = 15% at 182 °C) were registered, which suggest a stronger Ag–P bond in comparison to the trimethylphosphine complex **2**. Phosphine bonded fragments are less desirable in CVD of metals, due to possible increase of film contamination with P. The $[Ag_2]^+$ signals revealed similar intensity (R.I. = 10%) for both complexes, whereas $[Ag]^+$ appeared only for **2**. The above demonstrate that the most stable volatile silver coordinating fragment for **1**–**3** is the $[(CH_3CH_2C(CH_3)_2COO)Ag_2]^+$ ion.

In the case of complex **2** abundance of $[(CH_3CH_2C(CH_3)_2COO)Ag_2]^+$ ion was twofold higher than for **3**, which corresponds to the detachment of the PR_3 from **2** in the first stage. For **3** the lower relative intensity of $[(CH_3CH_2C(CH_3)_2COO)Ag_2]^+$ can be related to the presence of the stable phosphine (PEt_3) bonded silver(I) ions. The formation of $[AgP(C_2H_5)_3]^+$ and other similar ions can be explained by higher stability of the Ag–P bond, coming from the stronger σ-electron donor character of PEt_3 than PMe_3.

Above results demonstrate that compounds **1**, **2** and **3** can be used for the deposition of silver layers using the CVD method, due to formation of the volatile metallated species (e.g. $[(CH_3CH_2C(CH_3)_2COO)Ag_2]^+$, $[AgP(C_2H_5)_3]^+$).

3.5. Results of thermal analysis (TGA/DTG/DTA)

Thermal properties of the studied compounds are also important for the assessment of their future usage in CVD of silver layers. The temperature of decomposition process onset and temperature of silver formation are two factors which determine CVD procedure parameters. The results of thermal analysis are listed in Table 4 [10]. Salt **1** decomposes in one endothermic process (onset = 125 °C, maximum rate of reaction = 198 °C). The mass loss on the TG curve corresponds to detachment of carboxylate and the final residue is metallic silver formed at $T_f = 208$ °C. The observed silver formation temperature is below 250 °C, which makes **1** a promising precursor for hot-wall CVD of silver layers. When comparing **1** to perfluorinated silver(I) carboxylates it is evident that they decompose at higher temperatures (e.g. $CF_3(CF_2)_2COOAg$; $T_f = 470$ °C) [32]. The latter suggests that perfluorinated ligands revealed improved volatility, but they are more thermally stable then branched non-fluorinated carboxylates. In the case of **2** and **3** one endotherm was also observed on the DTA, with onset temperatures of 164 °C and 170 °C, respectively. The onset temperatures are almost in the range of instrument accuracy; hence one may presume that decomposition starts with the partial dissociation of the carboxylate residue, which has further evidence in the MS spectra of **1**–**3**. Analysis of the TG curves indicates mass losses which correspond to the detachment of carboxylate residue and phosphine in the same endothermic reaction. The maximum reaction rates (DTG) were detected at 205 °C and 250 °C, respectively, which confirms

Table 4
Thermal analysis results

Compound	Heat effect on DTA	Temperature (°C)			Residue (%)	
		T_{init}	T_{max}	T_f	Calc.	Found
$[Ag_2(CH_3CH_2C(CH_3)_2COO)_2]$ (**1**)	Endo	125	197	208	48.4	52.9
$[Ag_2(CH_3CH_2C(CH_3)_2COO)_2(PMe_3)_2]$(**2**)	Endo	50	205	206	36.1	35.5
$[Ag_2(CH_3CH_2C(CH_3)_2COO)_2(PEt_3)_2]$ (**3**)	Endo	60	250	290	31.6	32.8

T_{init}, initial temperature; T_{max}, maximum temperature; T_f, final temperature.

MS observations that PEt_3 forms a stronger Ag–P σ-donor, π-acceptor bond than PMe_3. A similar phenomenon was observed for $[Au(RCOO)(PR_3)]$ and $[Ag(RCOO)(PR_3)]$ complexes with the studied phosphines and perfluorinated carboxylates [30,34]. The decomposition reaction was completed at: T_f **2** = 206 °C, T_f **3** = 290 °C. In both cases, metallic silver was confirmed by TG calculations and detected by XRD studies of the residue in the crucible. The observed diffractogram lines (0.2352, 0.2026, 0.1179, 0.1444, 0.1233 nm) correspond to metallic silver (Powder Diffraction File) [33]. Temperatures of silver formation are accept for CVD purposes with the heating device working below 300 °C.

Considering decomposition mechanism of **2** and **3**, one can propose simultaneous or very close in time, consecutive carboxylate residue and phosphine detaching reactions. In comparison to the reported silver perfluorinated carboxylates complexes with PPh_3 (T_f = 219–340 °C), the studied complexes exhibited significantly lower temperatures of silver formation [34]. The latter makes them much more promising CVD precursors of metallic silver than analogues with heavier (aromatic) phosphines.

Analysis of the IR spectra of the gases evolved during the thermal decomposition of **1** suggest the presence of acid ($\nu_{(OH)} = 3577\ cm^{-1}$, C–H stretching at 2967 cm^{-1}, $\nu_{(C=O)} = 1752\ cm^{-1}$, $\nu_{(C-O)} = 1258\ cm^{-1}$, $\delta_{(O-C=O)} = 668\ cm^{-1}$) which was also detected in the gaseous products of the silver acetate thermal decomposition reaction [17].

TGA/IR studies of the gas phase from decomposition reactions of **2** and **3** revealed the characteristic absorption bands for acid anhydride ($\nu_{a(COO)} = 1816\ cm^{-1}$, $\nu_{s(COO)} = 1759\ cm^{-1}$) (Fig. 1). Moreover, bands typical for the phosphines were observed.

3.6. Results of CVD experiments

Silver films were deposited using precursor **3** and *hot-wall* CVD equipment. The substrates were Si(1 1 1) and steel plates, at a deposition temperature between 200 and 280 °C, under 2.0 mbar of the total reactor vaccum, in argon atmosphere. The vaporization temperature was fixed at 170 °C for CVD experiments resulting in an efficiency of 75–83%. The fabricated silver films revealed thickness below 50 nm, and were whitish colored and slightly matt. Variation of the deposition temperature and the amount of precursor used in the CVD experiments (100–300 mg) appeared to be the main parameters which have an impact on the thickness of the silver layers. Deposition rates of the films were calculated from the change of films weights determined on a microbalance. Tendency for rate increase between 200 and 250 °C (from 0.3 to 0.8 nm min^{-1}), was observed, whereas above 250 °C the opposite trend was noted. The changes of the deposition parameters seems to be a consequence of: (a) the significant decrease of deposition efficiency, caused by the partial decomposition of silver species transported in the vapors, (b) deposition of metallic films on other parts of the CVD reactor (not only on substrate surfaces). XRD studies exhibit characteristic peaks of polycrystalline cubic metallic silver (38.4, 44.6, 64.7, 77.9 [deg], assigned to (1 1 1), (2 0 0), (2 2 0), (3 1 1) lines) as reported by JCPDS (International Centre for Diffraction Data) without preferential orientation.

The SEM and AFM micrographs of the films produced from **3** are presented in Fig. 6. It can be noted that at vaporization temperatures below 220 °C and deposition temperatures below 250 °C, films deposited on Si(1 1 1) substrates were composed of the separated Ag grains with diameters of 30–60 nm. Further heating resulted in coalescence of silver grains and the increase of their size (diameter 60–280 nm), as well as packing density (Fig. 6a). SEM and AFM studies of Ag films, deposited from **3** on steel substrates, under similar conditions, turned out to be very thin and dispersed, with an average grain size between 50 and 90 nm (Fig. 6b).

4. Conclusions

Analysis of variable temperature MS and IR data revealed that thermolysis of **1** and **2** proceed with complete decomposition of these compounds in the temperature range 20–250 °C. However, volatile silver containing species were not detected in the gas phase during the decomposition processes, resulting in exclusion of **1** and **2** from further thermally induced CVD experiments. Formation of volatile and stable silver–phosphine intermediates during decomposition of **3** suggested its usage as a precursor in CVD methods. However, partial decomposition of a silver bonded species during transport in the gas phase of **3** seems to be the main disadvantage in the application of this complex in metallization processes. Performed CVD experiments using **3** as a precursor proved deposition of thin silver films on Si(1 1 1) and steel substrates. In general procedures, nanometric silver films (thicknesses below 50 nm), at moderate temperature (220–250 °C) can be produced from **3**.

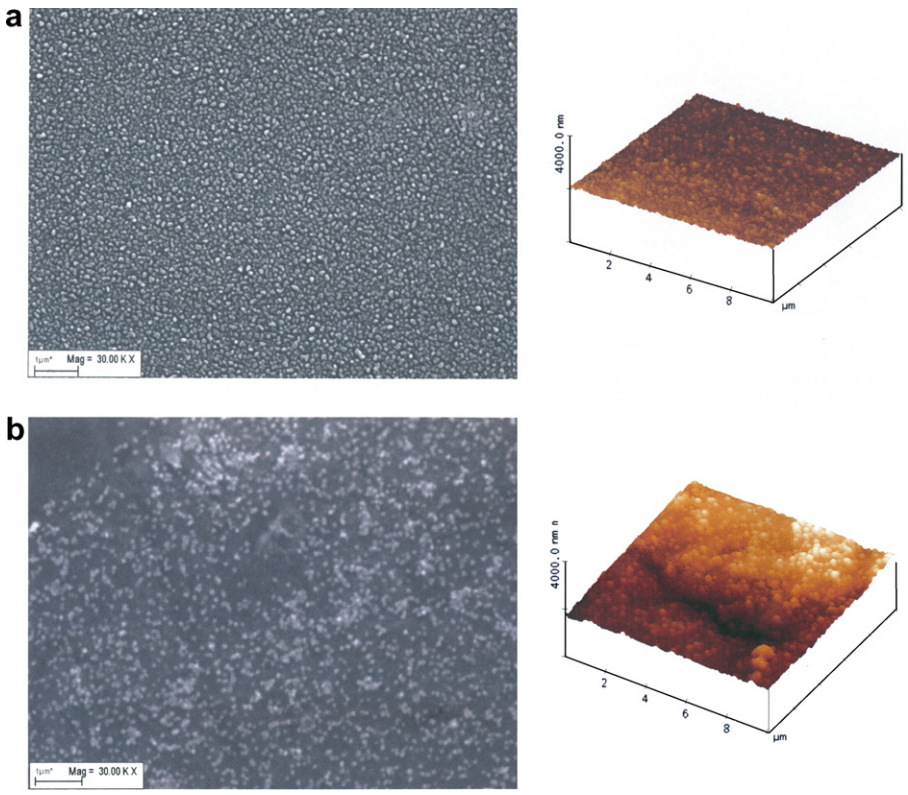


Fig. 6. SEM and AFM micrographs of silver films deposited on (a) Si(1 1 1) and (b) steel surfaces ($T_V = 170$ °C, $T_D = 240$ °C, $p = 2$ mbar, Ar).

Acknowledgement

Authors wish to thank Polish State Committee for Scientific Research for a Grants: PBZ-KBN-118/T09/2004 and N204 045 31/1142.

References

[1] M.J. Hampden-Smith, T.T. Kodas, Adv. Mater. 7 (1995) 8.
[2] T.T. Kodas, M.J. Hampden-Smith, in: The Chemistry of Metal CVD, Weinheim, 1994.
[3] N.H. Dryden, J.J. Vittal, R.J. Pudderphatt, Chem. Mater. 5 (1993) 765.
[4] H. Schmidt, Y. Shen, M. Leschke, Th. Haase, K. Kohse-Höinghaus, H. Lang, J. Organomet. Chem. 25 (2003) 669.
[5] Z. Yuan, N.H. Dryen, J.J. Vittal, R.J. Puddephatt, Chem. Mater. 7 (1995) 1696.
[6] K. Chi, K. Chen, L. Peng, G. Lee, Organometallic 15 (1996) 2575.
[7] K.-M. Chi, Y.-H. Lu, Chem. Vap. Dep. 7 (2001) 117.
[8] A. Itsuki, H. Uchida, M. Satou, K. Ogi, Nucl. Instr. Meth. Phys. Res. B 121 (1997) 116.
[9] D.A. Edwards, R.M. Haker, M.F. Mahon, K.C. Molloy, Inorg. Chim. Acta 328 (2002) 134.
[10] E. Szłyk, P. Piszczek, A. Grodzicki, M. Chaberski, A. Goliński, J. Szatkowski, T. Błaszczyk, Chem. Vap. Dep. 7 (2001) 111.
[11] E. Szłyk, P. Piszczek, I. Łakomska, A. Grodzicki, J. Szatkowski, T. Błaszczyk, Chem. Vap. Dep. 6 (2000) 105.
[12] R.G. Goel, P. Pilon, Inorg. Chem. 17 (1978) 2876.
[13] L.S. Zheng, H.H. Yang, Q.E. Zhang, J. Struct. Chem. 10 (1991) 97.
[14] P. Rombke, A. Schier, H. Schmidbaur, S. Cronje, H. Rheimer, Inorg. Chim. Acta 357 (2004) 235.
[15] N.F. Uvarov, L.P. Burleva, M.B. Mizen, D.R. Whitcomb, C. Zou, Solid State Ionic 107 (1998) 31.
[16] L.P. Butleva, V.M. Andreev, V.V. Boldyrev, J. Therm. Anal. 33 (1988) 735.
[17] M.D. Judd, B.A. Plankett, M.I. Pope, J. Therm. Anal. 6 (1974) 555.
[18] E. Szłyk, P. Piszczek, M. Chaberski, A. Goliński, Polyhedron 20 (2001) 2853.
[19] G.D. Roberts, E. White, Org. Mass Spectrom. 12 (1981) 546.
[20] S.K. Adams, D.A. Edwards, R. Richards, Inorg. Chim. Acta 12 (1975) 163.
[21] P. Piszczek, A. Grodzicki, M. Richert, A. Radtke, Mater. Sci.-Poland 23 (2005) 663.
[22] K. Nakamoto, Infrared and Raman Spectra of Inorganic and Coordination Compounds, Wiley and Sons, 1978.
[23] G.B. Deacon, R.J. Philliphs, Coord. Chem. Rev. 33 (1980) 227.
[24] G. Wilkinson, R.D. Gillard, J.A. McClaverty, Comprehensive Coordination Chemistry, vol. 2, Pergamon Press, NY, 1987, p. 437.
[25] S.E. Paramonov, N.P. Kazumina, S.I. Troyanov, Polyhedron 22 (2003) 837.
[26] L.W. Daasch, D.C. Smith, Anal. Chem. 23 (6) (1951) 853.
[27] J. Mounier, B. Mula, A. Potier, J. Organomet. Chem. 105 (1976) 289.
[28] E. Szłyk, I. Łakomska, A. Surdykowski, A. Goliński, Pol. J. Chem. 73 (1999) 1763.
[29] E. Szłyk, I. Szymańska, R. Szczęsny, Pol. J. Chem. 79 (2005) 627.
[30] I. Łakomska, E. Szłyk, A. Grodzicki, Thermochim. Acta 315 (1998) 121.
[31] G.D. Roberts, E.V. White, Org. Mass Spectrom. 16 (1981) 564.
[32] E. Szłyk, I. Łakomska, A. Grodzicki, Thermochim. Acta 223 (1993) 207.
[33] Powder Diffraction File, Sets 4-783, International Centre for Diffraction Data (JCPDS), USA, 1977.
[34] I. Łakomska, A. Grodzicki, E. Szłyk, Thermochim. Acta 303 (1997) 41.

and X-ray crystal structures of 3-*tert*-butyl-4-cyanopyrazole ($Hpz^{t\text{-}Bu,4CN}$)[1] and its complexes with cobalt(II), copper(II) and manganese(II).

2. Results and discussion

2.1. 3-*tert*-butyl-4-cyano pyrazole

A number of syntheses have been reported for pyrazoles with cyano substituents in the 4-position [4]. Many of these syntheses require the use of extreme reaction conditions or highly toxic reactants such as cyanoform or dimethyl sulfate. Tupper and Bray reported the synthesis of 4-cyano-3-phenylpyrazole ($Hpz^{Ph,4CN}$) from *t*-butylcyanoacetate [5]. Replacement of benzoyl chloride in this synthesis with trimethylacetyl chloride allows for the isolation of a new compound, 3-*tert*-butyl-4-cyanopyrazole ($Hpz^{t\text{-}Bu,4CN}$) in good yield. X-ray quality crystals of the neutral pyrazole were isolated from a toluene solution. An ORTEP drawing of the structure is shown in Fig. 1 with data collection parameters in Table 1 and selected bond distances and angles in Table 2. The pyrazole crystallizes in the monoclinic space group *C*2/*m* with the pyrazole ring, CN substituent, and one methyl group (C6) coincident with a crystallographic mirror plane. Crystal structures of neutral pyrazoles generally show some form of intermolecular hydrogen bonding. Four classes of hydrogen bonding are common: linear chains, cyclic dimers, cyclic trimers, and cyclic tetramers. $Hpz^{t\text{-}Bu,4CN}$ forms a cyclic dimer with an N(1)···N(2)′ distance of 2.859 Å and an N–H···N angle of 124.17°.

This hydrogen-bonding distance is in the range of that seen in other pyrazoles which display cyclic dimers; the average N···N distance is 2.897 Å [6] with a minimum of 2.630 Å [7] for $Hpz^{i\text{-}Pr2,4NO_2}$ and a maximum of 3.017 Å [8] for $Hpz^{Ph2,4NO_2}$. The most obvious comparison is to the structure of $Hpz^{t\text{-}Bu2}$, which has been reported eight times with N···N distances ranging from 2.856 to 2.900 Å [9]; the distance in $Hpz^{t\text{-}Bu,4CN}$ is in line with these other structures. The structure of $Hpz^{t\text{-}Bu}$ shows a cyclic tetramer, rather than a cyclic dimer [10].

2.2. Transition metal complexes

Reaction of $Hpz^{t\text{-}Bu,4CN}$ with salts of divalent transition metal ions in THF solution, followed by crystallization from toluene, results in the isolation of pink $Co(Hpz^{t\text{-}Bu,4CN})_4Cl_2$, colorless $Mn(Hpz^{t\text{-}Bu,4CN})_2(CF_3SO^3)_2(H_2O)_2$, and blue $Cu(Hpz^{t\text{-}Bu,4CN})_2Cl_2$. ORTEP drawings of these complexes are shown in Figs. 2–4, respectively, with data collection parameters in Table 1 and selected bond distances and angles in Tables 3–5. The structures of these complexes are described below.

[1] Substituted pyrazoles will be referred to as follows: 3-R^1,4-R^2-substituted pyrazoles – $Hpz^{R^1,4R^2}$; 3,5-R_2-substituted pyrazoles – Hpz^{R2}; 3-R^1,5-R^2–substituted pyrazoles – $Hpz^{3R^1,5R^2}$; 3,5-R^1_2,4-R^2-substituted pyrazoles – $Hpz^{R^12,4R^2}$.

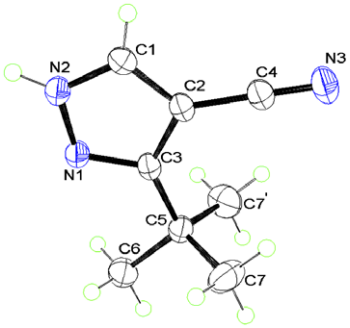


Fig. 1. ORTEP diagram of $Hpz^{t\text{-}Bu,4CN}$ showing 50% thermal ellipsoids.

The octahedral $Co(Hpz^{t\text{-}Bu,4CN})_4Cl_2$ crystallizes on an inversion center in the monoclinic space group $P2_1/n$. A disordered area of solvent is also present.[2] As is true with all 3(5)-substituted pyrazoles, the cobalt is coordinated to the N atom furthest from the substituted ring C atom. The coordination environment of the Co shows the four pyrazole N donors in a plane and two axial chlorides. The pyrazole rings are approximately perpendicular to the CoN_4 plane and are protonated at the non-coordinated ring N atom. There are two other reported structures of octahedral Co(II) complexes containing pyrazoles and halides, $Co(Hpz^{3OH,5CH_3})_4Cl_2$ [11] and $Co(Hpz^{prm})_2Cl_2(H_2O)_2$. [12] The Co–N bond distances in $Co(Hpz^{t\text{-}Bu,4CN})_4Cl_2$ are comparable to those in the other two structures.

The octahedral $Mn(Hpz^{t\text{-}Bu,4CN})_2(CF_3SO_3)_2(H_2O)_2$ crystallizes on an inversion center in the triclinic space group $P\bar{1}$. This formulation differs from the other Mn/pyrazole complexes which have been reported, all of which have the formula $Mn(Hpz)_4X_2$ ($X = H_2O$, Br, or Cl) or $Mn(Hpz)_6^{2+}$ [13]. The reaction was carried out with a Mn:Hpz stoichiometry of 1:2, so the stoichiometry of the resulting complex may simply reflect the reaction stoichiometry or it could stem from steric and electronic factors in the Mn/$Hpz^{t\text{-}Bu,4CN}$/OTf^- system. The pyrazole rings are approximately parallel to the OTf-Mn-OTf axis. A hydrogen bonding network (Fig. 3b) is built up consisting of interactions between the CN group and one of the water protons (N3···O4 2.946 Å) and between a triflate O atom and the other water proton (O1···O4 2.744 Å). An intramolecular hydrogen bond also exists between another triflate O atom and the ring N atom of a pyrazole bound to the same Mn (N2···O2 2.806 Å). This results in a linear double chain of Mn complexes running parallel to the crystallographic B face.

$Cu(Hpz^{t\text{-}Bu,4CN})_2Cl_2$ crystallizes on a general position in the triclinic space group $P\bar{1}$. The geometry of this complex is slightly distorted square-planar, with an almost linear N(1)–Cu–N(3) angle (179.3°), but a Cl(1)–Cu–Cl(2) angle of 166.1°. This structure is unique, as other crystallographically characterized Cu(II) complexes of pyrazoles are

[2] The solvent area was modeled with seven full-occupancy carbon atoms, in agreement with the toluene molecule inferred in the elemental analysis results.

Table 1
Crystal and refinement data for $Hpz^{t\text{-}Bu,4CN}$ structures

	$Hpz^{t\text{-}Bu,4CN}$	$Co(Hpz^{t\text{-}Bu,4CN})_4Cl_2 \cdot$ toluene	$Cu(Hpz^{t\text{-}Bu,4CN})_2Cl_2$	$Mn(Hpz^{t\text{-}Bu,4CN})_2(CF_3SO_3)_2(H_2O)_2$
Formula	$C_8H_{11}N_3$	$C_{39}H_{52}N_{12}CoCl_2$	$C_{16}H_{22}N_6CuCl_2$	$C_{18}H_{26}N_6O_8F_6S_2Mn$
Formula weight	149.2	818.8	432.8	687.6
Diffractometer	Nonius CAD4	Nonius CAD4	Nonius CAD4	Nonius CAD4
Temperature (K)	150	150	150	150
Crystal system	monoclinic	monoclinic	triclinic	triclinic
Space group	$C2/m$	$P2_1/n$	$P\bar{1}$	$P\bar{1}$
a (Å)	11.552(23)	10.321(17)	10.086(3)	7.916(2)
b (Å)	6.693(29)	11.773(8)	10.360(4)	9.193(2)
c (Å)	11.590(21)	19.82(3)	10.729(4)	10.406(3)
α (°)	90	90	73.88(3)	71.55(2)
β (°)	108.84(14)	98.59(13)	68.18(3)	77.18(2)
γ (°)	90	90	71.21(3)	82.14(2)
V (Å)^3	848(4)	2395(6)	969.2(6)	698.6(3)
Z	4	4	2	1
Color, habit	colorless	pink	blue	white
Crystal dimensions (mm)	$0.20 \times 0.20 \times 0.10$	$0.65 \times 0.43 \times 0.35$	$0.30 \times 0.30 \times 0.25$	$0.10 \times 0.10 \times 0.20$
D_{calc} (g cm^{-1})	1.17	1.25	1.48	1.63
μ (mm^{-1})	0.074	0.517	1.414	0.715
Unique reflections (R_{int})	900 (0.022)	4216 (0.0801)	3812	2739
Observed reflections [$I > 2\sigma(I)$]	702	2737	3108	2269
Parameters	64	300	227	195
R, R_w	0.052, 0.160	0.081, 0.214	0.030, 0.077	0.044, 0.118
Goodness-of-fit	1.026	1.066	1.025	1.059
T_{max}, T_{min}	0.987, 0.925	0.498, 0.062	0.725, 0.277	0.929, 0.712
ρ_{min}, ρ_{max} (e Å^{-3})	−0.654, 0.723	−0.766, 0.778	−0.316, 0.381	−1.158, 0.904

Table 2
Bond distances (Å) and angles (°) for $Hpz^{t\text{-}Bu,4CN}$

N(1)–N(2)	1.357(4)	C(1)–N(2)–N(1)	105.1(2)
C(4)–N(3)	1.143(4)	N(2)–N(1)–C(3)	113.5(2)
		C(2)–C(4)–N(3)	179.3(3)

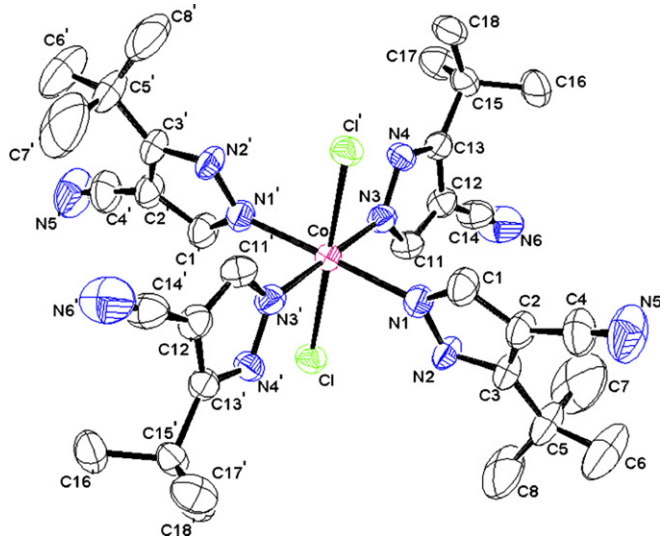


Fig. 2. ORTEP diagram of $Co(Hpz^{t\text{-}Bu,4CN})_4Cl_2$ showing 50% thermal ellipsoids, H atoms omitted for clarity.

either octahedral with four pyrazoles and two halides coordinated to the copper center [14], tetrahedral with two pyrazoles and two halides [15], or distorted square-planar with both Cl–Cu–Cl and N–Cu–N angles deviating significantly from 180° towards tetrahedral [14b,16]. The distortion in $Cu(Hpz^{t\text{-}Bu,4CN})_2Cl_2$ is caused by a short contact between Cu and a N atom (Cu···N6′ 2.81 Å) from one of the cyano groups on an inversion-related Cu complex. This creates a pseudodimer with each Cu atom displaying a slightly distorted square-pyramidal coordination geometry when the CN···Cu interaction is included. The infrared spectrum of this complex shows the expected splitting of the CN stretching frequency, with bands at 2229 and 2238 cm^{-1} representing the non-interacting and interacting CN groups. Cu–N and Cu–Cl bond lengths are similar to those seen in other Cu(II)–pyrazole complexes, including $Cu(Hpz^{t\text{-}Bu})_4Cl_2$.

3. Conclusions

Transition metal complexes of the new pyrazole ligand, 3(5)-*tert*-butyl-4-cyanopyrazole, have been synthesized and structurally characterized. Structural parameters of the coordination of this ligand to transition metals are not significantly different from those for related pyrazole ligands. The effect of the CN substituent is noticed, however, in the formation of a hydrogen-bonding network involving the coordinated water molecules in the Mn(II) structure, and in the formation of a pseudodimer by weak axial coordination of the CN group in the Cu(II) complex. This final structure exemplifies the effect that we hope to realize with these molecules and the polypyrazolylborate ligands derived therefrom, namely the ability to form coordination polymers with interesting electronic and magnetic properties.

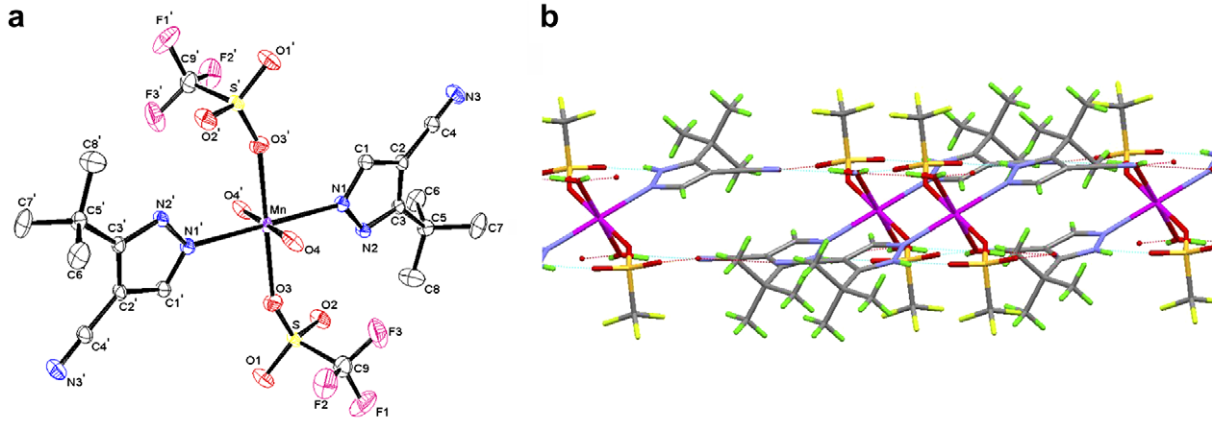


Fig. 3. (a) ORTEP diagram of $Mn(Hpz^{t\text{-}Bu,4CN})_2(CF_3SO_3)_2(H_2O)_2$ showing 50% thermal ellipsoids, H atoms omitted for clarity. (b) Mercury drawing of H-bonding network.

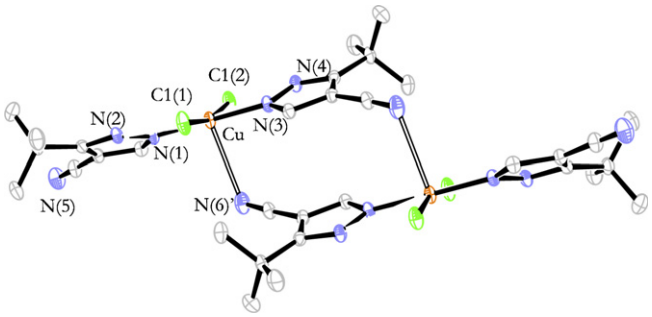


Fig. 4. ORTEP diagram of $Cu(Hpz^{t\text{-}Bu,4CN})_2Cl_2$ showing the pseudodimer with 50% thermal ellipsoids, H atoms omitted for clarity. Open bonds indicate weak axial interactions.

Table 3
Bond distances (Å) and angles (°) for $Co(Hpz^{t\text{-}Bu,4CN})_4Cl_2$

Co–N(1)	2.131(5)	N(1)–Co–N(3)	87.7(2)
Co–N(3)	2.133(5)	N(1)–Co–Cl	90.37(15)
Co–Cl	2.450(4)	N(3)–Co–Cl	88.15(17)
N(1)–N(2)	1.344(6)	C(2)–C(4)–N(5)	179.1(7)
N(3)–N(4)	1.349(6)	C(12)–C(14)–N(6)	176.5(7)
C(4)–N(5)	1.137(8)		
C(14)–N(6)	1.141(8)		

Table 4
Bond distances (Å) and angles (°) for $Mn(Hpz^{t\text{-}Bu,4CN})_2(CF_3SO_3)_2(H_2O)_2$

Mn–N(1)	2.272(2)	N(1)–Mn–O(3)	84.42(7)
Mn–O(3)	2.168(2)	N(1)–Mn–O(4)	86.08(8)
Mn–O(4)	2.150(2)	C(2)–C(4)–N(3)	177.5(3)
N(1)–N(2)	1.365(3)		
C(4)–N(3)	1.146(3)		

4. Experimental

4.1. General

Unless otherwise stated, all solvents and reagents were used as received from Aldrich, Acros, TCI, and Fisher Scientific without further purification. IR spectra were recorded on a Nicolet Avatar 360 FTIR. Electrospray mass spectra were obtained on a Finnigan LCQ DECA spectrometer. NMR spectra were obtained using either a Varian Mercury 300 MHz NMR or Varian Inova 400 MHz NMR. Elemental analyses were obtained from M-H-W Laboratories, Phoenix, AZ. When dry solvents are specified, they were prepared by distillation from sodium/benzophenone.

Table 5
Bond distances (Å) and angles (°) for $Cu(Hpz^{t\text{-}Bu,4CN})_2Cl_2$

Cu–N(1)	1.989(2)	N(1)–Cu–N(3)	179.34(8)
Cu–N(3)	1.997(2)	Cl(1)–Cu–Cl(2)	166.14(3)
Cu–Cl(1)	2.254(1)	N(1)–Cu–Cl(1)	89.95(7)
Cu–Cl(2)	2.260(1)	N(1)–Cu–Cl(2)	90.08(7)
Cu–N(6)′	2.808(2)	N(3)–Cu–Cl(1)	89.54(7)
N(1)–N(2)	1.356(3)	N(3)–Cu–Cl(2)	90.51(7)
N(3)–N(4)	1.355(3)	C(2)–C(4)–N(5)	179.6(3)
C(4)–N(5)	1.143(3)	C(12)–C(14)–N(6)	176.4(3)
C(14)–N(6)	1.143(3)		

4.2. 3-tert-Butyl-4-cyanopyrazole, $Hpz^{t\text{-}Bu,4CN}$

A suspension of sodium hydride (60% dispersion in mineral oil, 2.812 g, 70.3 mmol) in 150 mL dry toluene was put under nitrogen and cooled by means of an ice/water bath. To this suspension a solution of *tert*-butylcyanoacetate (10 mL, 70.3 mmol) in 10 mL of dry toluene was added dropwise with bubbles appearing immediately. The mixture was stirred 18 h. The solution became viscous, and to this was added, dropwise, trimethylacetyl chloride (8.65 mL, 70.3 mmol) in 10 mL of dry toluene. The solution immediately became less viscous and slightly yellow. After stirring overnight, 100 mL of aqueous 0.2 M sodium hydroxide was added and the aqueous layer was separated from the organic layer. The organic layer was extracted with two more portions (100 mL each) of 0.2 M sodium hydroxide. The yellow aqueous layers were combined and washed once with ethyl ether. The aqueous solution was acidified with 100 mL of 2 M HCl – an amount that neutralizes the NaOH used for extraction,

and provides two additional equivalents to fully protonate the product. A white precipitate came out immediately with the addition of HCl. The acidified solution with precipitate (pH ~ 1) was then extracted with three portions of ethyl ether (100 mL each), which were combined, and dried over magnesium sulfate. After filtration, the solvent was removed under reduced pressure to yield 6.69 g (29.7 mmol, 42.3%) of *tert*-butyl-2-cyano-3-oxo-4,4-dimethylpentanoate. The product was then dissolved in dry toluene (150 mL), to which was added *p*-toluenesulfonic acid (0.56 g, 2.97 mmol). This solution was heated at reflux for 18 h and then filtered to remove some insoluble material. The solvent was removed under reduced pressure to yield 3-oxo-4,4-dimethylpentanenitrile (4.70 g, 26.7 mmol, 90%), as a yellow solid. This product was redissolved in 150 mL of dry toluene and 3.90 mL (29.37 mmol) of DMF-dimethylacetal was added. The mixture was stirred for 18 h under nitrogen. The solvent was removed under reduced pressure, and the product was chromatographed using a silica gel column (100–200 mesh) with CH_2Cl_2 as the mobile phase. The desired product had a very low retention time, and almost all other products adsorbed onto the silica very strongly. Eluent from the column was evaporated under reduced pressure, yielding 2-*tert*-butyl-3-dimethylaminoacrylonitrile as a yellow solid (4.17 g, 23.2 mmol, 86.77%). This product was dissolved in 100 mL of methanol and was treated with hydrazine monohydrate (2.25 mL, 46.4 mmol). This mixture was stirred for 18 h, resulting in slightly lighter color. The solvent was removed under reduced pressure and the product was chromatographed using a silica gel column (100–200 mesh) with 50/50 ethyl acetate/hexanes to give 3-*tert*-butyl-4-cyanopyrazole (very light yellow solution) as the first fraction. The solvent was removed under reduced pressure, yielding 3-*tert*-butyl-4-cyanopyrazole as a pale yellow solid (1.95 g, 13.1 mmol, 56.41%). IR (KBr disc, cm^{-1}): 1366(m), 2226(ν_{CN}, vs), 3234(w). ^1H NMR ($CDCl_3$): 1.451(s, 9H), 7.82(s, 1H). ESI-MS (THF, negative detection): $m/z = 148.3$ $[pz^{t\text{-}Bu,4CN}]^-$. Elemental *Anal.* Calc. for $C_8H_{11}N_3$: C, 64.40; H, 7.43; N, 28.16. Found: C, 64.16; H, 7.56; N, 26.70%. X-ray quality crystals were grown by slow evaporation from the toluene solution.

4.3. Dichlorotetrakis(3-tert-butyl-4-cyanopyrazole)cobalt(II), $[Co(Hpz^{t\text{-}Bu,4CN})_4Cl_2]$

Anhydrous $CoCl_2$ (0.8 g, 6.15 mmol) and $Hpz^{t\text{-}Bu,4CN}$ (3.67 g, 24.6 mmol) were mixed in dry THF and stirred for an hour. The solvent was removed by rotary evaporation and the product was redissolved in toluene. The solution was filtered, the toluene was removed under reduced pressure and $[Co(pz^{t\text{-}Bu,4CN})_4Cl_2]$ was collected as a pink solid (3.33 g, 4.59 mmol, 74.6%). IR (KBr, cm^{-1}): 2235(ν_{CN}, s). Elemental *Anal.* Calc. for $C_{32}H_{44}N_{12}CoCl_2 \cdot H_2O \cdot$ toluene: C, 55.98; H, 6.50; N, 20.09. Found: C, 55.42; H, 5.88; N, 20.99%. X-ray quality crystals were grown by slow evaporation of the toluene solution.

4.4. Diaquabis(3-tert-butyl-4-cyanopyrazole)bis(trifluoromethylsulfonato)manganese(II), $[Mn(Hpz^{t\text{-}Bu,4CN})_2(CF_3SO_3)_2(H_2O)_2]$

A solution of $Mn(CF_3SO_3)_2 \cdot 2CH_3CN$ (0.2 g, 0.46 mmol) in 10 mL dry THF was put under nitrogen and a solution of $Hpz^{t\text{-}Bu,4CN}$ (0.14 g, 0.92 mmol) in 10 mL of dry THF was added. The mixture was stirred for an hour. The solvent was removed by evaporation and the resulting solid was redissolved in CH_2Cl_2. The solution was filtered, the CH_2Cl_2 was removed under reduced pressure and $[Mn(Hpz^{t\text{-}Bu,4CN})_2(CF_3SO_3)_2(H_2O)_2]$ was collected as a white solid (0.23 g, 0.33 mmol, 72.1%). IR (KBr, cm^{-1}): 2233(ν_{CN}, s). Elemental *Anal.* Calc. for $C_{18}H_{26}N_6O_8S_2F_6Mn$: C, 31.45; H, 3.81; N, 12.22. Found: C, 31.24; H, 3.98; N, 12.41%. X-ray quality crystals were grown by slow evaporation of the CH_2Cl_2 solution.

4.5. Dichlorobis(3-tert-butyl-4-cyanopyrazole)copper(II), $[Cu(Hpz^{t\text{-}Bu,4CN})_2Cl_2]$

To a solution of anhydrous $CuCl_2$ (0.9 g, 6.69 mmol) in 10 mL dry THF was added $Hpz^{t\text{-}Bu,4CN}$ (1.99 g, 13.4 mmol) in 10 mL of dry THF. The mixture was stirred for an hour. The solvent was removed by rotary evaporation and the resulting solid was redissolved in toluene. After filtration and removal of the toluene under reduced pressure, $[Cu(Hpz^{t\text{-}Bu,4CN})_2Cl_2]$ was collected as blue solid (2.0 g, 4.62 mmol, 69.1%). IR (KBr, cm^{-1}): 2229(ν_{CN}, s), 2238(ν_{CN}, s). Elemental *Anal.* Calc. for $C_{16}H_{22}N_6CuCl_2$: C, 44.40; H, 5.12; N, 19.42. Found: C, 44.55; H, 5.29; N, 19.35. X-ray quality crystals were grown by slow evaporation of the toluene solution.

4.6. X-ray crystallography

Data were collected using a Nonius CAD4 diffractometer (Mo Kα, $\lambda = 0.71069$ Å) equipped with an Oxford Cryosystems Cryostream 700 low-temperature apparatus. Suitable crystals were identified using a polarizing microscope, affixed to a glass fiber using Paratone-N oil (Exxon) and were immediately transferred to the cold stream of the diffractometer. The unit cells were determined from the setting angles of 24 reflections with $20° < 2\theta < 24°$. The data were processed and the structures solved and refined using the WinGX software package [17]. The data were corrected for Lorentz and polarization effects and an empirical absorption correction based on azimuthal scans of three intense reflections (Mn and unmetallated pyrazole structures) or using the DIFABS program [18] (Co and Cu structures) was applied. The structures were solved by direct methods [19] and refined by full-matrix least-squares techniques [20] with values for $\Delta f'$ and $\Delta f''$ from Creagh and McAuley [21]. All non-hydrogen atoms, except those in the disordered toluene molecule in the Co structure, were refined with anisotropic temperature factors. Hydrogen atoms were included at idealized positions, but were not

refined. The hydrogen atoms on the coordinated water molecules in the Mn structures were included at positions determined from the difference Fourier map, but not refined. Pertinent details are given in Table 1.

Acknowledgments

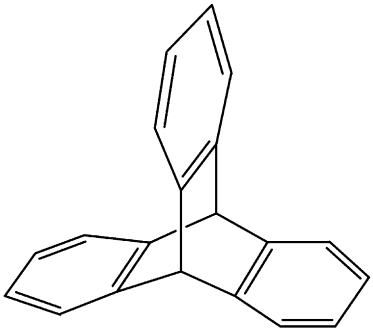
The authors thank Wichita State University for funding and Dr. Colin Thomas for synthesizing [Mn-($Hpz^{t\text{-}Bu,4CN}$)$_2$(CF_3SO_3)$_2$(H_2O)$_2$] for elemental analysis.

Appendix A. Supplementary material

CCDC 626487, 626488, 626489 and 626490 contain the supplementary crystallographic data for this paper. These data can be obtained free of charge via http://www.ccdc.cam.ac.uk/conts/retrieving.html, or from the Cambridge Crystallographic Data Centre, 12 Union Road, Cambridge CB2 1EZ, UK; fax: (+44) 1223-336-033; or e-mail: deposit@ccdc.cam.ac.uk. Supplementary data associated with this article can be found, in the online version, at doi:10.1016/j.poly.2006.12.035.

References

[1] (a) N.A. Daugherty, J.H. Swisher, Inorg. Chem. 7 (1968) 1651;
(b) J. Elguero, in: I. Shinkai (Ed.), Comprehensive Heterocyclic ChemistryII, Elsevier, Oxford, 1996, pp. 1–75;
(c) B. Stanovnik, J. Svete, Sci. Synth. 12 (2002) 15;
(d) J. Elguero, J. Mol. Struct. 319 (1994) 231.
[2] (a) F. Mani, Coord. Chem. Rev. 120 (1992) 325;
(b) F. Bonati, Chim. Ind. 62 (1980) 323;
(c) S. Trofimenko, Prog. Inorg. Chem. 34 (1986) 115;
(d) S. Trofimenko, Chem. Rev. 72 (1972) 497.
[3] (a) C.J. Siemer, N. Goswami, P.K. Kahol, M.J. Van Stipdonk, D.M. Eichhorn, Inorg. Chem. 40 (2001) 4081;
(b) C.J. Siemer, M.J. VanStipdonk, P.K. Kahol, Polyhedron 23 (2004) 235.
[4] H.G. McFadden, J.L. Huppatz, Aust. J. Chem. 44 (1991) 1263.
[5] D.E. Tupper, M.R. Bray, Synthesis (1997) 337.
[6] Cambridge Structural Database: F.H. Allen, Acta Crystallogr., Sect. B 58 (2002) 380.
[7] L.E. Ochando, J.M. Amigo, J. Rius, D. Louer, C. Fontenass, J. Elguero, J. Mol. Struct. 562 (2001) 11.
[8] A.L. Llamas-Saiz, C. Foces-Foces, F.H. Cano, P. Jimenez, J. Laynez, W. Meutermans, J. Elguero, H.-H. Limbach, F. Aquilar-Parilla, Acta Crystallogr., Sect. B 50 (1994) 746.
[9] (a) F. Aguilar-Parilla, H.-H. Limbach, C. Foces-Foces, F.H. Cano, N. Jagerovic, J. Elguero, J. Org. Chem. 60 (1995) 1965;
(b) G.B. Deacon, A. Gitlits, P.W. Roesky, M.R. Burgstein, K.C. Lim, B.W. Skelton, A.H. White, Chem. Eur. J. 7 (2001) 127;
(c) A.N. Sobollev, A.H. White, Acta Crystallogr., Sect. B 60 (2004) 621.
[10] F. Zhang, M. Magner, J.W. Bats, Acta Crystallogr., Sect. E 60 (2004) o1804.
[11] R. Winpenny, A. Dearden, S. Parsons, D. Messenger, unpublished results in Cambridge Structural database (Ref. [6]).
[12] G. Hanggi, H. Schmalle, E. Dubler, Acta Crystallogr., Sect. C 44 (1988) 1560, Hpz^{prm} refers to pyrazole(3,4)pyrimidin-6-one-N^8.
[13] (a) P. Lumme, E. Lindell, I. Mutikainen, Acta Crystallogr., Sect. C 44 (1988) 1564;
(b) P.O. Lumme, E. Lindell, I. Mutikainen, Acta Crystallogr., Sect. C 44 (1988) 967;
(c) P. Lumme, E. Lindell, J. Coord. Chem. 15 (1987) 383;
(d) J. Reedijk, B.A. Stork-Blaisse, G.C. Verschoor, Inorg. Chem. 10 (1971) 2594.
[14] (a) Y.-J. Sun, P. Cheng, S.-P. Yan, D.-Z. Liao, Z.-H. Jiang, P.-W. Shen, J. Mol. Struct. 597 (2001) 191;
(b) X. Liu, C.A. Kilner, M. Thornton-Pett, M.A. Halcrow, Acta Crystallogr., Sect. C 57 (2001) 1253;
(c) A. Mighell, A. Santoro, E. Prince, C. Reimann, Acta Crystallogr., Sect. B 31 (1975) 2479;
(d) U. Casellato, R. Ettorre, Graziani, Z. Kristallogr. – New Cryst. Struct. 21 (2000) 287;
(e) S. Bieller, A. Haghiri, M. Bolte, J.W. Bats, M. Wagner, H.-W. Lerner, Inorg. Chim. Acta 359 (2006) 1559;
(f) M. Malecka, L. Checinsak, Acta Crystallogr., Sect. C 59 (2003) m115.
[15] (a) N. Zhao, D.M. Eichhorn, Acta Crystallogr., Sect. C 61 (2005) m822;
(b) A. Hergold-Brundic, B. Kaitner, B. Kamenar, V.M. Leovac, E.Z. Iveges, N. Juranic, Inorg. Chim. Acta 188 (1991) 151.
[16] (a) A.A. Watson, D.A. House, P.J. Steel, Polyhedron 8 (1989) 1345;
(b) G. Valle, R. Ettore, V. Peruzzo, Acta Crystallogr., Sect. C 51 (1995) 1293.
[17] L.J. Farrugia, J. Appl. Crystallogr. 32 (1999) 837.
[18] N. Walker, D. Stuart, Acta Crystallogr., Sect. A 39 (1983) 158.
[19] SIR92 – A program for crystal structure solution. A. Altomare, G. Cascarano, C. Giacovazzo, A. Guagliardi, J. Appl. Crystallogr. 26 (1993) 343.
[20] G.M. Sheldrick, SHELX97 – Programs for Crystal Structure Analysis (Release 97-2), Institut für Anorganische Chemie der Universität, Göttingen, Germany, 1998.
[21] D.C. Creagh, W.J. McAuley, in: A.J.C. Wilson (Ed.), International Tables for Crystallography, Kluwer Academic Publishers, Dordrecht, 1992.



Triptycene
(tpty)
Schematic view of the ligand

2. Experimental

All manipulations were performed under an argon atmosphere using Schlenk techniques. Organic solvents were reagent grade, and were dried and distilled using standards methods before use. Triptycene, silver perchlorate and silver triflate were purchased from Aldrich, all other chemicals were purchased from Wako Pure Chemical Co., Japan, and were used as receive without further purification. IR spectra were measured as KBr disks on a JASCO FT/IR-8000 spectrometer. TG analysis was performed on a Rigaku Thermo Plus TG 8120 spectrometer at 20 °C/min and under argon. All crystallizations of the silver complexes were performed in the dark.

Safety note: Perchlorate salts with organic ligands are potentially explosive! Only small amounts of materials should be prepared and they should be handled with great care.

2.1. Synthesis

2.1.1. $[Ag(tpty)(THF)_2](ClO_4)$ (1)

A solution of $AgClO_4 \cdot H_2O$ (19.1 mg, 0.08 mmol) in 5 ml of THF was added to triptycene (10.2 mg, 0.04 mmol). After 20 min of stirring, the resultant colorless solution was filtered. The filtrate was introduced into a narrow-diameter glass tube and carefully layered with 2 ml of *n*-pentane as a diffusion solvent. The glass tube was sealed under Ar and wrapped with aluminum foil. The filtrate was allowed to stand at room temperature for two weeks, upon which colorless platelet crystals of **1** were obtained. *Anal*. Calc. for $AgClO_6C_{28}H_{30}$: C, 55.46; H, 4.95. Found: C, 55.75; H, 5.21%. Main IR bands (KBr, ν/cm^{-1}): 2969(w), 1456(s), 1144(s), 1111(s), 1086(s), 797(m), 741(s), 627(s).

2.1.2. $[Ag_6(tpty)_4(CF_3SO_3)_2(H_2O)_6](CF_3SO_3)_4$ (2)

A solution of $Ag(CF_3SO_3) \cdot H_2O$ (27.1 mg, 0.1 mmol) in toluene (5.0 ml) was added to tpty (12.7 mg, 0.05 mmol). The mixture was stirred at room temperature for 20 min, and the resultant colorless solution was filtered. The filtrate was transferred to a 7 mm diameter glass tube under argon and was layered with *n*-pentane as a diffusion solvent. The glass tube was sealed under argon and wrapped with aluminum foil. The filtrate was left standing at room temperature for two weeks. Colorless brick single crystals of **2** were obtained. *Anal*. Calc. for $Ag_6S_6F_{18}O_{24}C_{86}H_{56}$: C, 37.87; H, 2.11. Found: C, 38.17; H, 2.31%. Main IR bands (KBr, ν/cm^{-1}): 3750(m), 2966(m), 2371(s), 2353(s), 2342(s), 1458(s), 1300(s), 1235(s), 1178(s), 1042(s), 1026(s), 797(m), 741(s), 646(s), 640(s), 625(s).

2.2. Crystallography

Diffraction data for **1** were collected at a temperature of -73 ± 1 °C on a Quantum CCD area detector coupled with a Rigaku AFC8 diffractometer, and for **2** on a Rigaku AFC7 diffractometer with graphite-monochromated Mo Kα radiation ($\lambda = 0.71069$ Å) at a temperature of 23.0°. Intensity data were collected by using standard scan techniques (ω–2θ) to a maximum 2θ value of 55.2° for **1** and 55.7° for **2**. All intensity data were corrected for Lorentz and polarization effects.

The structures were solved by direct methods (SIR-88 [9] for **1** and SIR-97 [10] for **2**) and expanded using Fourier techniques [11]. All non-H atoms were refined with anisotropic thermal parameters. The final cycle of full-matrix least-squares refinements [12] for all the structures were performed on these data having $I > 2\sigma(I)$ and included anisotropic thermal parameters for non-hydrogen atoms. Reliability factors are defined as $R = \sum \| F_o| - |F_c| \| / \sum |F_o|$ and $R_w = [\sum w(F_o^2 - F_c^2)^2 / \sum w(F_o^2)^2]^{1/2}$. All crystallographic computations were performed using the teXsan

Table 1
Crystallographic data for complexes **1** and **2**

Complex	**1**	**2**
Formula	$AgClO_6C_{28}H_{30}$	$Ag_6S_6F_{18}O_{24}C_{86}H_{68}$
Formula weight	605.86	2666.98
Crystal system	orthorhombic	monoclinic
Space group	*Pbca* (no. 61)	$P2_1$ (no. 4)
a (Å)	15.168(3)	14.122(2)
b (Å)	16.2911(9)	16.180(2)
c (Å)	20.753(2)	20.037(3)
α (°)		90.00
β (°)		90.350(15)
γ (°)		90.00
V (Å^3)	5128(1)	4578.4(12)
Z	8	2
F(000)	2480.00	2632.00
T (°C)	−73.0	23.0
D_{calc} (g/cm^3)	1.569	2.006
λ (Mo Kα) (Å)	0.71069	0.71073
μ (cm^{-1})	9.30	15.65
Number of observed reflections	4824	16783
Number of variable parameters	326	1261
Residuals: R[a], R_w[b]	0.053, 0.155	0.0664, 0.1581
Goodness-of-fit	1.05	1.077

[a] $R = \sum \| F_o| - |F_c| \| / \sum |F_o|$.
[b] $R_w = [\sum w(F_o^2 - F_c^2)^2 / \sum w(F_o^2)^2]^{1/2}$.

Table 2
Selected bond distances (Å) and bond angles (°) for complexes **1** and **2**

*Complex **1***					
Bond distances (Å)					
Ag(1)–O(5)	2.357(3)	Ag(1)–O(6)	2.299(3)	Ag(1)–C(5)	2.498(4)
Ag(1)–C(17)	2.392(4)				
Bond angles (°)					
O(5)–Ag(1)–O(6)	106.2(1)	O(5)–Ag(1)–C(5)	92.7(1)	O(5)–Ag(1)–C(17)	107.6(2)
O(6)–Ag(1)–C(5)	98.1(1)	O(6)–Ag(1)–C(17)	122.0(1)	C(5)–Ag(1)–C(17)	125.5(1)
*Complex **2***					
Bond distances (Å)					
Ag(1)–O(1)	2.502(6)	Ag(1)–O(4)	2.346(5)	Ag(1)–O(5)	2.299(7)
Ag(1)–O(6)	2.481(6)	Ag(2)–C(2)	2.511(8)	Ag(2)–C(7)	2.662(9)
Ag(2)–O(6)	2.444(6)	Ag(2)–C(39)	2.437(7)	Ag(2)–C(78)	2.679(9)
Ag(2)–C(79)	2.454(9)	Ag(3)–C(19)	2.570(9)	Ag(3)–C(22)	2.500(8)
Ag(3)–C(42)	2.446(8)	Ag(3)–O(2)	2.446(6)	Ag(4)–C(58)	2.483(8)
Ag(4)–C(62)	2.445(9)	Ag(4)–C(63)	2.659(9)	Ag(4)–O(7)	2.526(6)
Ag(4)–C(32)	2.437(8)	Ag(5)–O(9)	2.473(6)	Ag(5)–O(10)	2.321(6)
Ag(5)–O(11)	2.360(6)	Ag(5)–O(12)	2.498(5)	Ag(6)–O(12)	2.436(5)
Ag(6)–C(12)	2.550 (9)	Ag(6)–C(52)	2.489(9)	Ag(6)–C(72)	2.498(9)
C(2)–C(7)	1.426(1)	C(62)–C(63)	1.355(8)	C(78)–C(79)	1.363(1)
Bond angles (°)					
O(5)–Ag(1)–O(4)	120.0(2)	O(5)–Ag(1)–O(6)	120.3(2)	O(4)–Ag(1)–O(6)	89.9(2)
O(5)–Ag(1)–O(1)	139.2(2)	O(4)–Ag(1)–O(1)	88.9(2)	O(6)–Ag(1)–O(1)	84.7(2)
C(39)–Ag(2)–O(6)	102.3(2)	C(39)–Ag(2)–C(79)	119.8(2)	O(6)–Ag(2)–C(79)	94.2(2)
C(39)–Ag(2)–C(2)	116.0(2)	O(6)–Ag(2)–C(2)	82.8(2)	C(79)–Ag(2)–C(2)	123.4(2)
C(39)–Ag(2)–C(7)	109.9(2)	O(6)–Ag(2)–C(7)	114.4(2)	C(79)–Ag(2)–C(7)	114.6(2)
C(2)–Ag(2)–C(7)	31.8(3)	C(39)–Ag(2)–C(78)	110.2(2)	O(6)–Ag(2)–C(78)	124.4(2)
C(79)–Ag(2)–C(78)	30.4(3)	C(2)–Ag(2)–C(78)	118.4(2)	C(7)–Ag(2)–C(78)	95.4(2)
C(42)–Ag(3)–O(2)	96.3(2)	C(42)–Ag(3)–C(22)	117.6(2)	O(2)–Ag(3)–C(19)	124.7(2)
C(42)–Ag(3)–C(19)	124.7(2)	O(2)–Ag(3)–C(19)	97.2(2)	C(22)–Ag(3)–C(19)	116.3(3)
C(32)–Ag(4)–C(62)	117.5(3)	C(32)–Ag(4)–C(58)	125.4(3)	C(62)–Ag(4)–C(58)	115.4(3)
C(32)–Ag(4)–O(7)	100.1(2)	C(62)–Ag(4)–O(7)	83.6(2)	C(58)–Ag(4)–O(7)	98.2(2)
C(32)–Ag(4)–C(63)	108.2(2)	C(62)–Ag(4)–C(63)	30.4(2)	C(58)–Ag(4)–C(63)	110.2(2)
O(7)–Ag(4)–C(63)	114.0(2)	O(10)–Ag(5)–O(11)	126.5(2)	O(10)–Ag(5)–O(9)	133.7(2)
O(11)–Ag(5)–O(9)	89.0(2)	O(10)–Ag(5)–O(12)	116.8(2)	O(11)–Ag(5)–O(12)	91.1(2)
O(9)–Ag(5)–O(12)	87.1(2)	O(12)–Ag(6)–C(52)	87.3(2)	O(12)–Ag(6)–C(72)	97.9(2)
O(52)–Ag(6)–C(72)	113.3(2)	O(12)–Ag(6)–C(12)	92.2(2)	C(52)–Ag(6)–C(12)	124.9(2)
C(72)–Ag(6)–C(12)	121.3(2)				

package [13]. Details of the X-ray experiments and crystal data are summarized in Table 1. Selected bond lengths and angles for the three complexes are given in Table 2.

3. Results and discussion

In order to probe the influence of the ligand stereochemical preference with different anions on the coordination of a porous complex of silver(I), the study was carried out with the ligand tpty and the perchlorate and triflate counter anions. While single crystals of **1** show a 1D chain structure using ClO_4^- anions; when $CF_3SO_3^-$ is employed as the counter anion, complex **2** gives a 3D porous structure with a cavity including guest molecules by using THF as the solvent. The IR spectra of the two complexes exhibit bands that can be readily assigned to ClO_4^- with strong bands at 1144, 1111 and 1086 cm^{-1} for **1**, and to $CF_3SO_3^-$ with strong bands at 1235, 1178 and 1042 cm^{-1} for **2**. Compared to the criteria for non-coordination of ClO_4^-, with strong non-split broad bands at 1140, 1109 and 1087 cm^{-1}, and $CF_3SO_3^-$, with strong non-split broad bands at 1256, 1179 and 1036 cm^{-1}, it indicates that ClO_4^- and $CF_3SO_3^-$ are present not as ionic species, but as coordinated ones. The two complexes exhibit a strong ν(C–C) absorption at 1456 cm^{-1} as expected for the presence of tpty.

3.1. 1D chain of $[Ag(tpty)(THF)_2](ClO_4)$ (**1**)

The crystallographic studies reveal that complex **1** consists of a one-dimensional chain of [Ag(tpty)(THF)$_2$] units, in which the crystallographically independent metal ions are bridged by triptycene. The structure of the trimeric molecular unit of the crystals is shown in Fig. 1a with the atomic numbering scheme employed. The Ag(1) ion has a tetrahedral coordination geometry, coordinated to two aromatic carbon atoms with Ag–C bond distances of 2.392(4) and 2.498(4) Å, and two THF groups at Ag–O distances of 2.357(3) and 2.299(3) Å, Table 2. One crystallographically independent ligand bridges the silver(I) atoms in a μ–η^1–η^1 mode and gives a 1D chain in which the

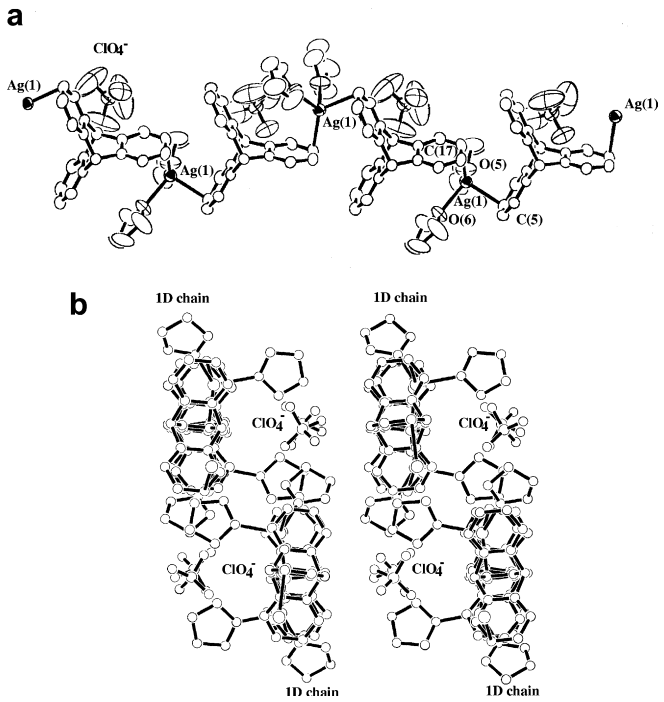


Fig. 1. (a) 1D chain structure of the complex $[Ag(tpty)(THF)_2](ClO_4)$ (**1**). (b) Molecular packing of complex **1**.

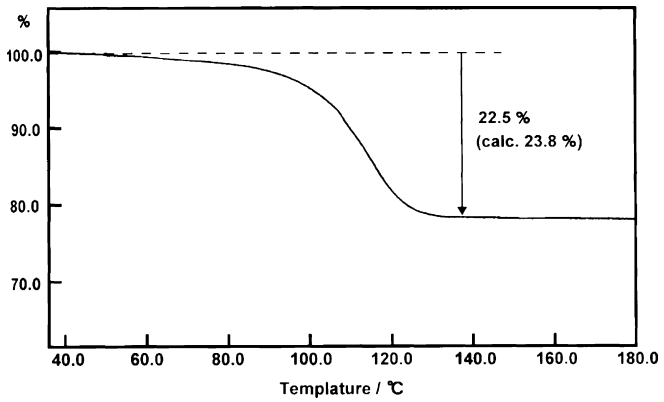


Fig. 2. TG curve of $[Ag(tpty)(THF)_2](ClO_4)$ (**1**).

perchlorate groups occupy the space between the chains, Fig. 1b. From the TG analysis results of complex **1** (Fig. 2), the weight loss of 22.5% at 70 °C indicates the severing of the two THF molecules (calculated value: 23.8%) which coordinated to Ag(I).

3.2. 3D porous structure of $[Ag_6(tpty)_4(CF_3SO_3)_2(H_2O)_6](CF_3SO_3)_4$ (2)

Complex **2** consists of a 2D sheet of $[Ag_6(tpty)_4(CF_3SO_3)_2(H_2O)_6]$ units (shown in Fig. 3), in which the six crystallographically independent metal ions are bridged by ligands and oxygen atoms. Ag(1) and Ag(5) are coordinated to three hydrate oxygen atoms and one triflate oxygen atom. Ag(2) is coordinated to three tpty moleculars in a η^2/η^1-mode and one triflate oxygen atom. Ag(3) and

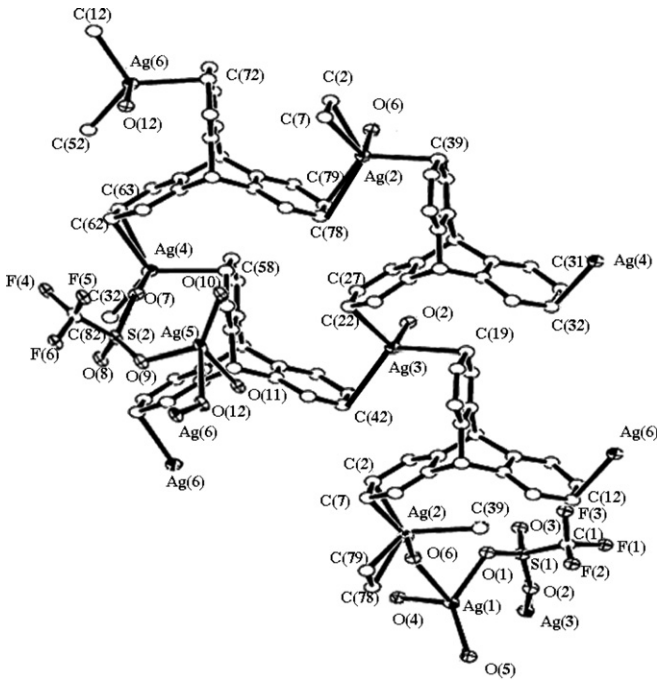


Fig. 3. Molecular structure of $[Ag_6(tpty)_4(CF_3SO_3)_2(H_2O)_6](CF_3SO_3)_4$ (**2**).

Ag(6) are coordinated to three tpty moleculars in a η^1-coordination mode and one hydrate oxygen. Interestingly, Ag(4) is coordinated to two tpty moleculars in a η^1-coordination mode, one tpty in a η^2-mode and one triflate oxygen. So the Ag(I) ions are all four-coordinated and have a tetrahedral coordination geometry. The Ag–O bond distances are from 2.249(7) to 2.502(6) Å for Ag(1), 2.444(6) Å for Ag(2), 2.446(6) Å for Ag(3), 2.526(6) Å for Ag(4), from 2.321(6) to 2.498(5) Å for Ag(5) and 2.436(5) Å for Ag(6), whereas Ag–C bond distance range from 2.437(7) to 2.679(9) Å for Ag(2), from 2.446(8) to 2.570(9) Å for Ag(3), from 2.437(8) to 2.483(8) Å for Ag(4) and from 2.489(9) to 2.550(9) Å for Ag(6), Table 2. Because of the rigid triangular molecule of tpty, the Ag–O bond distances do not show any significant variations in this complex.

The molecule also contains four crystallographically independent ligands with distinctly different coordination modes, two with a μ–η^1–η^1–η^1 fashion bridging Ag(2), Ag(3), Ag(4) and Ag(6) ions, and the other two involve μ–η^1–η^1–η^2 and μ–η^1–η^2–η^2 fashions bridging four silver centers. A 2D sheet is thus formed in which the ligands are arranged alternately such that twofold in two lines up in one direction and the next four stand in the same direction (Fig. 4a). The two adjacent sheets are connected by a bridging triflate group and one hydrate linking Ag(1) or Ag(5) with Ag(2) and Ag(3) or Ag(4) and Ag(6), leading to a 3D porous polymer (Figs. 4b and 5a) with a cavity size of 5.0×4.8 Å and 5.0×4.3 Å (Fig. 5b). In addition, cavities are occupied by triflate anions. So there are two types of triflate group: one is used as a bridging group and the other exists in a cavity. The cavity is difficult to use owing to the triflate anions, but not to neutral small solvent mol-

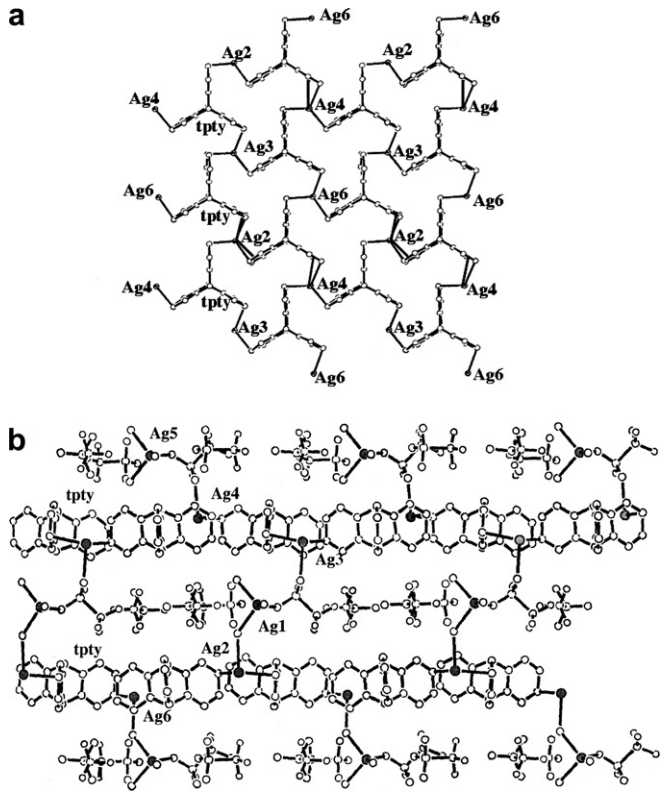


Fig. 4. (a) 2D sheet of $[Ag_6(tpty)_4(CF_3SO_3)_2(H_2O)_6](CF_3SO_3)_4$ (**2**). (b) 3D structure of $[Ag_6(tpty)_4(CF_3SO_3)_2(H_2O)_6](CF_3SO_3)_4$ (**2**).

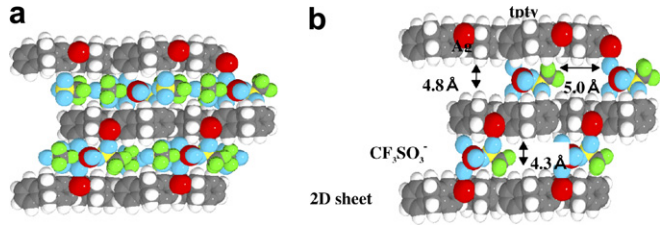


Fig. 5. (a) Space filling model of complex **2**. (b) Space filling model of $CF_3SO_3^-$ excluded from complex **2**.

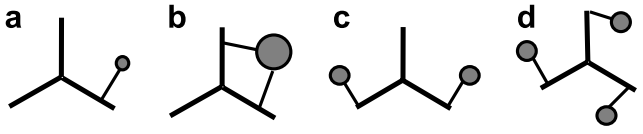


Fig. 6. Coordination modes of triptycene complexes.

ecules located at cavities in which the triflate guests desorption does not occur on heating. This is dissimilar to silver(I) coordination complexes $[Ag_3(tpty)_3(ClO_4)_3](toluene)_2$ in our previous work [7,8].

3.3. Coordination types of tpty with metal ions

The triangular molecule triptycene is a very special hydrocarbon with a relatively rigid molecular geometry, having three equivalent benzene rings mutually inclined at 120°. Prior to the present work, some X-ray crystal structures of triptycene π complexes have been reported, such as $[Cr(tpty)(CO)_3]$ [14], $[Co_4(tpty)(CO)_9]$ [14], $[SnCl(tpty)(AlCl_4)]_2$ [15], $[Cr_2(tpty)CO]_6$ [16] and $[(Cp^*Ru)_3(tpty)](CF_3SO_3)_3$ [17]. Fig. 6 cites instances of illustrations of the coordination mode from these complexes and the present complexes. For smaller metal atoms, it tends to interact with one metal atom by one arene ring in type (a) with a small widening of the inter-arene angles [14,17], such as $[Cr(tpty)(CO)_3]$, $[Co_4(tpty)(CO)_9]$ and $[(Cp^*Ru)_3(tpty)](CF_3SO_3)_3$, while with the larger metal atom tin it offers bis(arene) coordination with type (b) in $[SnCl(tpty)(AlCl_4)]_2$, sandwiching the cation, with the angle between the two arene rings contracted to 108.2° and the remaining inter-arene angles widened accordingly to 125.8° and 126.0° [15]. In addition, type (c) also exist in $[(Cp^*Ru)_3(tpty)](CF_3SO_3)_3$ with the coordination of three tpty arene rings with the metal atoms. Triptycene in these complexes exhibits only a η^6-mode by one to three benzene rings, the η^1-mode and η^2-mode are never observed. In the present Ag(I) coordination complexes with triptycene, $[Ag(tpty)(THF)_2](ClO_4)$ (**1**), $[Ag_6(tpty)_4(CF_3SO_3)_2(H_2O)_6](CF_3SO_3)_4$ (**2**) and $[Ag_3(tpty)_3(ClO_4)_3](toluene)_2$ [7], tpty exhibits an unprecedented η^1-and η^2-fashion bridging two or three Ag atoms, by (d) type in $[Ag(tpty)(THF)_2](ClO_4)$, by (c) type in $[Ag_6(tpty)_4(CF_3SO_3)_2(H_2O)_6](CF_3SO_3)_4$, and by (c) and (d) coordination type in $[Ag_3(tpty)_3(ClO_4)_3](toluene)_2$ [7], affording novel polymeric materials. Surprisingly, the tpty framework was found to involve relatively little deformation as compared to the metal-free hydrocarbon and the variation of the three inter-arene angles (115.6–124.4°) is relatively small regardless of bis- or tris(arene) coordination. Such an eased conformation of the aromatic may in part be the contributing factor for the stable three-dimensional complex network formed and the relatively similar Ag–O bond distances observed.

4. Conclusion

In this paper, two silver(I)–tpty complexes have been synthesized and characterized by single-crystal X-ray determination, IR, TG analysis and element analysis. In two silver(I)–tpty complexes, the structure of the silver(I) coordination polymer is closely related to the ligand geometry and coordination site as well as coordination direction. In addition, the anion and solvent also play an important role in the construction of the complexes. In the tpty/$AgClO_4$/THF system, silver(I) ions are bridged by tpty and give rise to a 1D chain coordination complex $[Ag(tpty)(THF)_2](ClO_4)$ (**1**). In addition, the solvent THF is coordinated to the silver(I) ions. Using a larger size anion, $CF_3SO_3^-$ instead of ClO_4^-, a 3D porous complex $[Ag_6(tpty)_4(CF_3SO_3)_2(H_2O)_6](CF_3SO_3)_4$ (**2**), with large cavities, with a size of 5.0×4.8 Å and 5.0×4.3 Å, has been obtained in toluene solvent. Although $CF_3SO_3^-$ is included

in the cavity, it is impossible to desorption and incorporate triflate molecules.

Acknowledgements

This work was partially supported by a Grants-in-Aid for Science Research [Nos. 10440201, 11874092, 12440189, 10016743 (priority area: metal-assembled complexes)] from the Ministry of Education, Science, Culture, Sports of Japan, and the Project-sponsored by SRF for ROCS from the SEM [No. 1380241005], EYT funds [No. 1380219055] from Tongji University of China.

Appendix A. Supplementary material

CCDC 220692 and 610349 contain the supplementary crystallographic data for this paper. These data can be obtained free of charge via http://www.ccdc.cam.ac.uk/conts/retrieving.html, or from the Cambridge Crystallographic Data Centre, 12 Union Road, Cambridge CB2 1EZ, UK; fax: (+44) 1223-336-033; or e-mail: deposit@ccdc.cam.ac.uk. Supplementary data associated with this article can be found, in the online version, at doi:10.1016/j.poly.2006.12.036.

References

[1] M. Munakata, L.P. Wu, G.L. Ning, Coord. Chem. Rev. 198 (2000) 171.
[2] V. Gama, R.T. Henriques, M. Almeida, L. Veiros, M.J. Calhorda, A. Meetsma, J.L. de Boer, Inorg. Chem. 32 (1993) 3705.
[3] L.P. Battaglia, C. Bellitto, M.R. Cramarossa, I.M. Vezzosi, Inorg. Chem. 35 (1996) 2390.
[4] J.C. Ma, D.A. Dougherty, Chem. Rev. 97 (1997) 1303.
[5] P.T. Corbett, L.H. Tong, J.K.M. Sanders, S. Otto, J. Am. Chem. Soc. 127 (2005) 8902.
[6] X.Z. Zhu, C.F. Chen, J. Am. Chem. Soc. 127 (2005) 13158.
[7] M. Munakata, L.P. Wu, K. Sugimoto, T. Kuroda-Sowa, M. Maekawa, Y. Suenaga, N. Maeno, M. Fujita, Inorg. Chem. 38 (1999) 5674.
[8] M. Wen, M. Munakata, Y. Suenaga, T. Kuroda-Sowa, M. Maekawa, Inorg. Chim. Acta 340 (2002) 8.
[9] M.C. Burla, M. Camalli, G. Cascarano, C. Giacovazzo, G. Polidori, R. Spagna, D. Viterbo SIR-88, J. Appl. Crystallogr. 22 (1989) 389.
[10] A. Altomare, M.C. Burla, M. Camalli, G.L. Cascarano, C. Giacovazzo, A. Guagliardi, A.G.G. Moliterni, G. Polidori, R. Spagna SIR-97, J. Appl. Crystallogr. 32 (1999) 115.
[11] P.T. Beurskens, G. Admiraal, G. Beurskens, W.P. Bosman, R. de Gelder, R. Israel, J.M.M. Smits, DIRDIF-94: The DIRDIF-94 Program System, Technical Report of the Crystallography Laboratory, University of Nijmegen, The Netherlands, 1994.
[12] G.M. Sheldrick, SHELXL-97: Program for the Refinement of Crystal Structures, University of Göettingen, Göettingen, Germany, 1997.
[13] teXsan: Crystal Structure Analysis Package, Molecular Structure Corporation, 1985 and 1999.
[14] R.A. Gancarz, J.F. Blount, K. Mislow, Organometallics 4 (1985) 2028.
[15] H. Schmidbaur, T. Probst, O. Steigelmann, Organometallics 10 (1991) 3176.
[16] S. Toyata, H. Okuhara, M. Oki, Organometallics 16 (1997) 4012.
[17] P.J. Fagan, M.D. Ward, J.C. Calabrese, J. Am. Chem. Soc. 111 (1989) 1698.

the luminescent properties of the supramolecular compounds [28,29]. The combination of organic emitting units with suitable metal ions and supramolecular interactions could fabricate a variety of luminescent materials. H_2aip is a good candidate for assembling such complexes due to its interesting structural characteristics. Compared with the ip ligand (H_2ip = isophthalic acid), the introduction of an amino group in H_2aip results in the following two effects at least: (i) a supramolecular effect, namely, providing more hydrogen-bonding donor or acceptor sites in the construction of supramolecualr packing; (ii) a coordination effect, namely, adding a new coordination site to coordinate with more metal centers. To the best of our knowledge, only a few supramolecular complexes with H_2aip have been reported so far [30–35]. Furthermore, the introduction of *N*-containing ligands [such as atz or amtz (amtz = 2-amino-5-mercapto-1,3,4-thiadiazole)] may induce new structural evolution. The atz or amtz ligand is important in maintaining the desired low dimensional coordination polymer and may provide potential supramolecular recognition sites for hydrogen bonding and π–π aromatic stacking interactions. We assumed that the H_2aip ligand could be useful in the formation of interesting supramolecular networks with some important features in the presence of atz or amtz ligand. So, we have started a systematic study on metal(II) coordination with the mixed H_2aip and atz or amtz ligands. One of the aims of this project is to analyze the influence that factors such as hydrogen bonding, rigidity and the possibility of specific attractive interactions between aromatic rings can exert on the structure and functional properties of aip containing metal(II) complexes. In the present paper, we report two novel three dimensional supramolecular coordination polymers $[Cd(Haip)_2(H_2O)_2]\cdot 2H_2O$ (**1**) and $[Zn(aip)(atz)]\cdot 3H_2O$ (**2**) based on mixed H_2aip and atz ligands. These complexes have been found to exhibit blue photoluminescence at room temperature.

2. Experimental

2.1. Materials and characterization

All reagents were purchased commercially and were used without further purification. Elemental analyses (C, H and N) were carried out on a 240C Elemental analyzer. FT-IR spectra (400–4000 cm^{-1}) were recorded from KBr pellets in a Magna 750 FT-IR spectrophotometer. Solid state emission spectra of the compounds were recorded using a 48000DSCF fluorescence spectrometer. Thermogravimetric analysis (TG) was taken on a NETZSCH STA 409 PG/PC instrument.

2.2. Synthesis

2.2.1. $[Cd(Haip)_2(H_2O)_2]\cdot 2H_2O$ (*1*)

Amtz (2-amino-5-mercapto-1,3,4-thiadiazole) (0.0258 g, 0.165 mmol) was dissolved in water (3 ml) and then an aqueous solution of $CdCl_2\cdot 2.5H_2O$ (0.0510 g, 0.165 mmol) in water–methanol (v:v = 1:1; 3 ml) was added whilst stirring. To this solution a mixture of H_2aip (0.0300 g, 0.165 mmol) and NaOH (0.0080 g, 0.200 mmol) in water–methanol (v:v = 1:1; 10 ml) was added and stirred for 10 min, and then filtered. The filtrate was kept at ambient temperature for several days and colorless crystals were formed. They were filtered and washed thoroughly with methanol and dried in a vacuum (41% based on H_2aip). *Anal*. Calc. for $C_{16}H_{20}CdN_2O_{12}$: C, 27.13; H, 2.28; N, 12.66. Found: C, 26.85; H, 2.25; N, 12.10%.

2.2.2. $[Zn(aip)(atz)]\cdot 3H_2O$ (*2*)

Atz (0.0140 g, 0.165 mmol) was dissolved in water (3 ml) and then an aqueous solution of $Zn(NO_3)_2\cdot 6H_2O$ (0.0492 g, 0.165 mmol) in water–methanol (v:v = 1:1; 3 ml) was added whilst stirring. To this solution a mixture of H_2aip (0.0300 g, 0.165 mmol) and NaOH (0.0132 g, 0.330 mmol) in water (8 ml) was added and stirred for 10 min, and then filtered. The solution was kept at ambient temperature for several days and brown crystals formed. They were filtered and washed thoroughly with methanol

Table 1
Crystallographic data and structure refinement for the title complexes

Empirical formula	$C_{10}H_{15}N_5O_7Zn$	$C_{16}H_{20}CdN_2O_{12}$
Formula weight	382.64	544.74
Temperature (K)	293(2)	293(2)
Wavelength (Å)	0.71073	0.71073
Crystal system	monoclinic,	monoclinic
Space group	$P2(1)/n$	$P2(1)/n$
a (Å)	12.0313(14)	12.7148(7)
b (Å)	8.2794(10)	11.3018(7)
c (Å)	15.5741(18)	14.6495(9)
α (°)	90	90
β (°)	111.3070(10)	114.8950(10)
γ (°)	90	90
Volume (Å^3)	1445.3(3)	1909.5(2)
Z	4	4
Calculated density (Mg/m^3)	1.758	1.895
Absorption coefficient (mm^{-1})	1.746	1.216
F(0 0 0)	784	1096
θ Range for data collection (°)	1.85–25.02	1.79–25.01
Limiting indices	$-14 \leqslant h \leqslant 14$, $-9 \leqslant k \leqslant 8$, $-18 \leqslant l \leqslant 18$	$-15 \leqslant h \leqslant 13$, $-13 \leqslant k \leqslant 11$, $-16 \leqslant l \leqslant 17$
Reflections collected/unique (R_{int})	7604/2544 (0.0178)	10108/3366 (0.0192)
Completeness to $\theta = 25.02°$	99.7%	($\theta = 25.01°$) 100%
Maximum and minimum transmission	1.00000 and 0.749005	1.00000 and 0.847411
Data/restraints/parameters	2544/9/209	3366/0/279
Goodness-of-fit on F^2	1.065	1.037
Final R indices [$I > 2\sigma(I)$]	$R_1 = 0.0211$, $wR_2 = 0.0570$	$R_1 = 0.0207$, $wR_2 = 0.0574$
R indices (all data)	$R_1 = 0.0237$, $wR_2 = 0.0580$	$R_1 = 0.0240$, $wR_2 = 0.0592$
Largest difference in peak and hole (e Å^{-3})	0.269 and −0.245	0.426 and −0.514

and dried in a vacuum (yield: 45% based on H_2aip). *Anal.* Calc. for $C_{10}H_{15}ZnN_5O_7$: C, 31.39; H, 3.95; N, 18.31. Found: C, 31.46; H, 3.75; N, 18.20%.

2.3. X-ray single-crystal structure determination

Crystallographic data for the complexes **1** and **2** were collected at 293(2) K with a Siemens SMART CCD diffractometer using graphite-monochromated (Mo Kα) radiation ($\lambda = 0.71073$ Å), ψ and ω scans mode. The structures were solved by direct methods and refined by the full-matrix least-squares on F^2 method. Intensity data were corrected for Lorenz and polarization effects and an empirical absorption correction was performed. All non-hydrogen atoms were refined anisotropically. The carbon-bound hydrogen atoms were added geometrically and allowed to ride on their respective parent atoms. The oxygen-bound hydrogen atoms were located in the difference Fourier map and kept fixed in that position. The contribution of these hydrogen atoms was included in the structure factor calculations. All calculations were carried out on a PC computer using the SHELXL-97 program [36]. Details of crystal data, collection and refinement are listed in Table 1.

3. Results and discussion

3.1. Preparation

The solvent used to synthesize the compound and the method to grow single crystals usually has great effect on the structure of the compound. Self-assembly of stoichiometric amounts of H_2aip, amtz, $CdCl_2 \cdot 2.5H_2O$ and NaOH in the mixed water–methanol solvent and slow evaporation of solution in open air provided metal-organic three-dimensional supramolecular network **1**, while the reaction of $Cd(O_2CCH_3)_2 \cdot 2H_2O$, H_2aip and H_2O under hydrothermal conditions leads to the formation of a three-dimensional (3,4)-connected network $[Cd(aip)(H_2O)] \cdot H_2O$ [30]. The title complexes are stable in the open air. The N-donor ligand (amtz) is very important for the quality of the crystal **1**. Although this ligand does not appear in complex **1**, omission of it leads to the formation of polycrystals instead of single crystals.

3.2. Structural analysis of $[Cd(Haip)_2(H_2O)_2] \cdot 2H_2O$ (1)

The self-assembly of $CdCl_2 \cdot 2.5H_2O$ with H_2aip and amtz in the presence of NaOH gives a two-dimensional framework **1** which is quite different from the reported complex $[Cd(aip)(H_2O)] \cdot H_2O$ [30]. Determination of the structure of the complex $[Cd(Haip)_2(H_2O)_2] \cdot 2H_2O$ (**1**) by X-ray crystallography reveals that the asymmetric unit consists of one Cd atom, two Haip ligands, two coordinated water molecules and two lattice water molecules, as shown in Fig. 1. The Cd atom is six-coordinated with a greatly distorted octahedral geometry (Fig. 1). The equatorial plane is occupied by two monodentate carboxylate

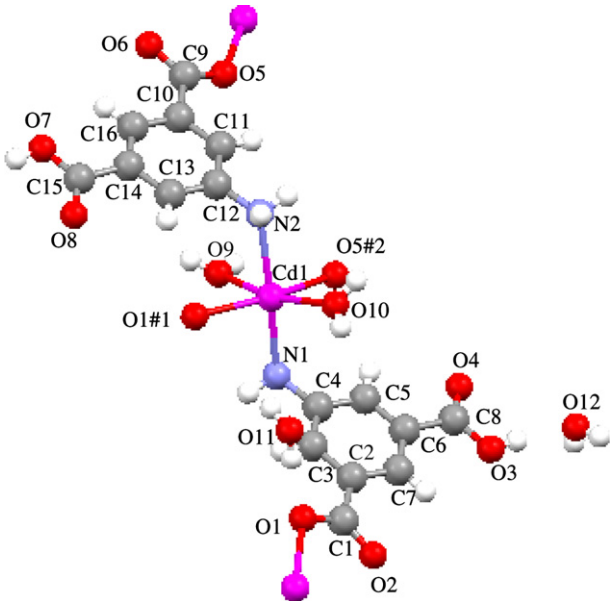


Fig. 1a. Molecular structure of complex **1** showing the coordination environment of the Cd(II) ion.

oxygen atoms from two Haip ligands [Cd(1)–O(1)#1 2.2542(15) Å; Cd(1)–O(5)#2 2.3016(15) Å] and two water oxygen atoms [Cd(1)–O(9) 2.4309(12) Å; Cd(1)–O(10) 2.2746(12) Å], while the axial sites are occupied by two nitrogen atoms of the amino groups from two Haip ligands [Cd(1)–N(1) 2.3323(18) Å; Cd(1)–N(2) 2.3810(18) Å]. The angles subtended the Cd atom ranges from 80.53(5)° to 172.97(6)°. The bond angles of O(1)#1–Cd(1)–O(10) and O(1)#1-Cd(1)–O(5)#2 in the equatorial plane are 167.95(9)° and 114.44(5)°, respectively, which deviate from linearity greatly. Selected bond distances and angles are listed in Table 2. It should be noted that the Haip ligand in complex **1** uses one of its two carboxylate groups to coordinate monodentately to one Cd(II) ion, whereas the other protonated carboxylate group does not participate in coordination to the Cd(II) center. The amino group of Haip coordinates to a second Cd(II) atom. Complex **1** is the first example where only one carboxylate group of H_2aip ligand coordinates to a metal(II) ion in a monodentate fashion, compared with the reported complexes with H_2aip ligands [30–35]. It is interesting that the dihedral angles of the carboxylate groups O(5)C(9)O(6), O(7)C(15)O(8) and the amino group $N(2)H_2$ with the corresponding benzene ring C(10)C(11)C(12)C(13)C(14)C(16) are 11.80°, 5.99° and 62.15°, respectively, while those of O(3)C(8)O(4), O(1)C(1)O(2) and the amino group $N(1)H_2$ with the benzene ring C(2)C(3)C(4)C(5)C(6)C(7) are 3.19°, 15.06° and 60.68° respectively. So, the carboxylate groups are almost in the same plane with the corresponding benzene ring, but the amino group is not. Each Haip ligand in the complex **1** acts as a bidentate ligand linking to two Cd(II) centers, while the aip ligand in the reported complex $[Cd(aip)(H_2O)] \cdot H_2O$ links to four Cd(II) centers through one amino group, one monodentate carboxylate group

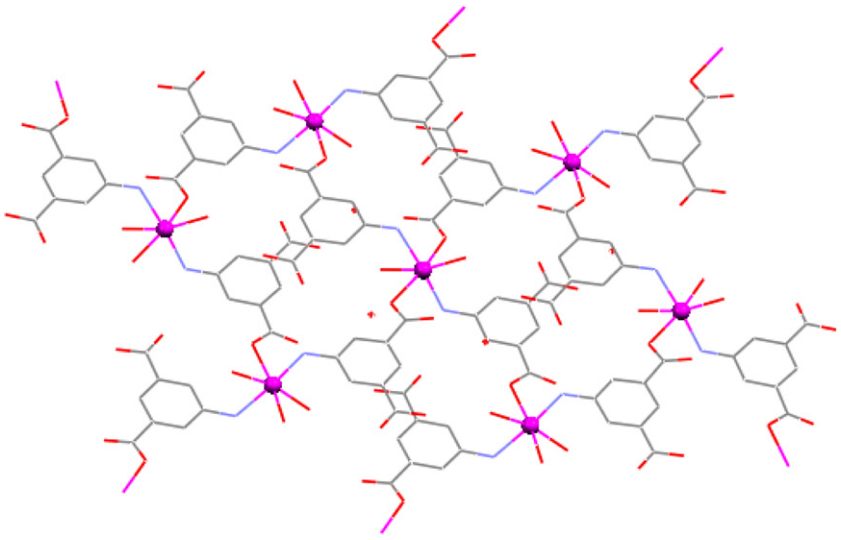


Fig. 1b. View of the layer parallel to the (0 0 1) plane, showing the 28-membered macrometalcycle in **1**.

Table 2
Selected bond lengths (Å) and angles (°) for complex **1**

Bond distances			
Cd(1)–O(1)#1	2.2542(15)	Cd(1)–O(10)	2.2746(12)
Cd(1)–O(5)#2	2.3016(15)	Cd(1)–N(1)	2.3323(18)
Cd(1)–N(2)	2.3810(18)	Cd(1)–O(9)	2.4309(12)
Bond angles			
O(1)#1–Cd(1)–O(10)			114.44(5)
O(1)#1–Cd(1)–O(5)#2			163.48(6)
O(10)–Cd(1)–O(5)#2			82.05(5)
O(1)#1–Cd(1)–N(1)			91.26(6)
O(10)–Cd(1)–N(1)			99.05(5)
O(5)#2–Cd(1)–N(1)			84.77(6)
O(1)#1–Cd(1)–N(2)			88.35(6)
O(10)–Cd(1)–N(2)			87.48(5)
O(5)#2–Cd(1)–N(2)			93.64(6)
N(1)–Cd(1)–N(2)			172.97(6)
O(1)#1–Cd(1)–O(9)			80.53(5)
O(10)–Cd(1)–O(9)			163.97(6)
O(5)#2–Cd(1)–O(9)			83.19(5)
N(1)–Cd(1)–O(9)			85.76(5)
N(2)–Cd(1)–O(9)			87.26(5)

Symmetry transformations used to generate equivalent atoms: #1 $-x+3/2,\ y+1/2,\ -z+1/2$; #2 $-x+1/2,\ y-1/2,\ -z+1/2$; #3 $-x+3/2,\ y-1/2,\ -z+1/2$; #4 $-x+1/2,\ y+1/2,\ -z+1/$.

and one chelating/bridging carboxylate group [30]. As a result, **1** forms a novel two-dimensional framework with a 28-membered macrometalcycle (Fig. 1b), while the reported complex $[Cd(aip)(H_2O)]\cdot H_2O$ exhibits a three dimensional (3,4)-connected network [30]. Interestingly, there are strong $\pi\cdots\pi$ stacking interactions between the adjacent layers. The centeroid–centeroid distance and the dihedral angles of the parallel benzene rings in the nearest adjacent layers are 3.716 Å and 3.27°, respectively (Fig. 2a). Furthermore, there are extensive hydrogen bonds between the layers. The system of hydrogen bonds, which includes carboxylate oxygen atoms [O(1), O(2), O(3), O(4), O(6), O(7) and O(8)], nitrogen atoms N(1) and N(2) from the Haip ligand, four oxygen atoms from coordinated and lattice water molecules [O(9), O(10), O(11) and O(12)] and one carbon atom C(3) from the benzene ring, is very complicated as shown in Table 3. Thus, a novel three-dimensional supramolecular network is formed as a result of strong intermolecular hydrogen bonding and $\pi\cdots\pi$ stacking interactions between the adjacent layers (Fig. 2b). Both $\pi\cdots\pi$ stacking interactions and hydrogen bonding are very important in the construction of supramolecular architectures [37]. Undoubtedly, both the hydrogen bonding and $\pi\cdots\pi\cdots\pi$ interactions play important roles in the stabilization of the supramolecular network of **1**.

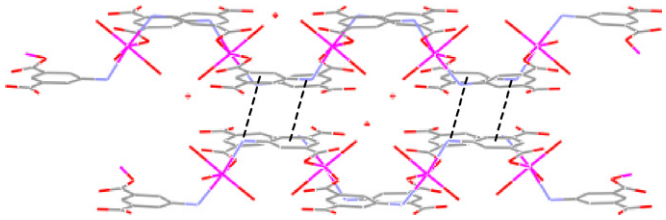


Fig. 2a. View of the strong interlayer π–π stacking interactions indicated by the black dashed lines in **1**.

3.3. Structural analysis of $[Zn(aip)(atz)]\cdot 3H_2O$ (2)

When we investigated the coordination chemistry of a Zn(II) salt with H_2aip and atz in the presence of NaOH, a 2D coordination polymer (**2**) was formed. The single crystal analysis reveals that the asymmetric unit of complex **2** consists of one Zn atom, one aip ligand, one atz ligand and three lattice water molecules, as shown in Fig. 3. The important bond distance and angles are listed in Table 4. The Zn (II) centre lies in a distorted $[ZnN_2O_2]$ tetrahedral coordination sphere, with two oxygen atoms and one nitrogen atom from three aip ligands, as well as one nitrogen atom from one atz ligand. The Zn(1)–N(1) (atz) distance [1.9978(16) Å] is

Table 3
Details of the hydrogen bonds for complex **1**

D–H···A	*d*(D–H)	*d*(H···A)	*d*(D···A)	∠DHA	Symmetry of A
N1–H1A···O8	0.9000	2.1800	3.0540	165.00	
N1–H1B···O4	0.9000	2.1800	3.0329	158.00	$-x, -y,2-z$
N2–H2A···O8	0.9000	2.1800	3.0587	166.00	$1-x, -y,2-z$
N2–H2B···O4	0.9000	2.1800	3.0768	171.00	$1+x, y,z$
O3–H3···O12	0.8200	1.8400	2.6533	176.00	$-1/2+x, 1/2-y, 1/2+z$
O7–H7···O11	0.8200	1.8200	2.6148	164.00	$-1/2+x, 1/2-y, 1/2+z$
O9–H9A···O6	0.8500	2.0400	2.6197	125.00	
O9–H9B···O3	0.8500	2.4300	2.9339	119.00	$1/2-x, -1/2+y, 3/2-z$
O10–H10A···O12	0.8500	1.9300	2.7705	168.00	$1/2+x, 1/2-y, 1/2+z$
O10–H10B···O7	0.8500	2.3200	3.1290	160.00	$x, 1+y,z$
O11–H11A···O2	0.8500	1.8600	2.6898	164.00	$1/2+x, 1/2-y, -1/2+z$
O11–H11B···O1	0.8500	1.9800	2.8201	171.00	$1-x, -y,1-z$
O12–H12A···O6	0.8500	1.8200	2.6362	161.00	$1-x, -y,1-z$
O12–H12B···O9	0.8500	2.1300	2.9091	152.00	
O12–H12B···O11	0.8500	2.5900	3.1424	124.00	$1-x, -y, 1-z$
C3–H3A···O1	0.9300	2.4500	2.7602	100.00	

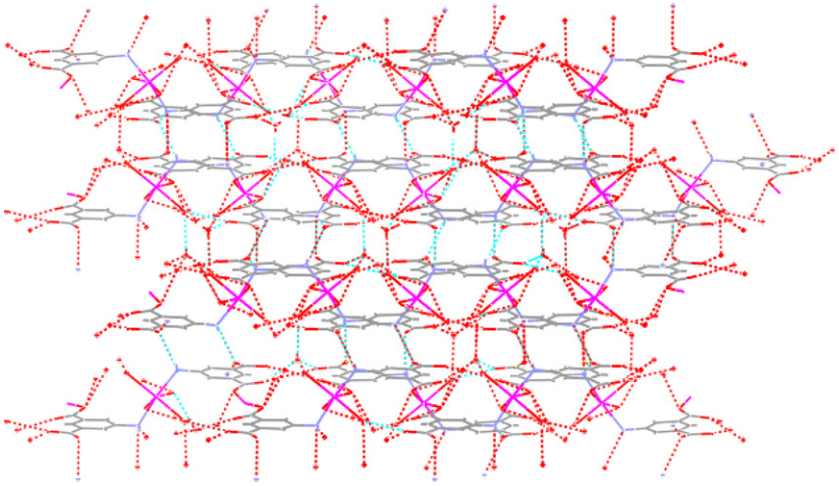


Fig. 2b. A view of the 3D supramolecular network formed by strong hydrogen bonds and π···π stacking interactions down the *a* axis, showing the "ABAB" stacking pattern of the 2D wave-like layers in **1**.

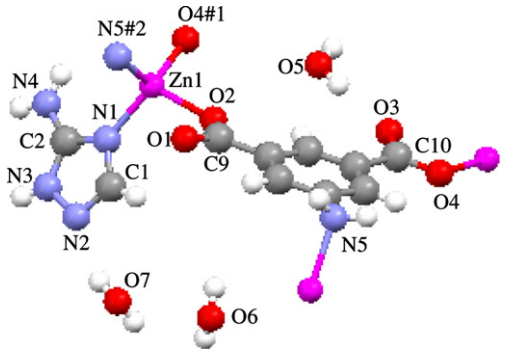


Fig. 3. Diagram of the coordination environment around the zinc center in complex **2**.

Table 4
Bond lengths [Å] and angles [°] for complex **2**

Bond distances			
Zn(1)–O(4)#1	1.9661(13)	Zn(1)–O(2)	1.9700(13)
Zn(1)–N(1)	1.9978(16)	Zn(1)–N(5)#2	2.0613(15)
Bond angles			
O(4)#1–Zn(1)–O(2)	93.74(6)		
O(4)#1–Zn(1)–N(1)	123.62(6)		
O(2)–Zn(1)–N(1)	104.50(7)		
O(4)#1–Zn(1)–N(5)#2	117.77(6)		
O(2)–Zn(1)–N(5)#2	110.46(6)		
N(1)–Zn(1)–N(5)#2	104.90(6)		

Symmetry transformations used to generate equivalent atoms:
#1 $x-1/2, -y+3/2, z-1/2$; #2 $x-1/2, -y+1/2, z-1/2$; #3 $x+1/2, -y+3/2, z+1/2$; #4 $x+1/2, -y+1/2, z+1/2$.

slightly shorter than that of Zn(1)–N(5)#1 (amino) [2.0613(15) Å]. The Zn(1)–O (carboxylate) distances are almost the same as those in the reported zinc complex [35]. The dihedral angle between the carboxylate plane and the benzene ring is 6.10°, whilst that between the amino group and the benzene ring is 60.35°, which indicates that the carboxylate groups are almost in the same plane with the benzene ring but the amino group is not. Different from the

coordination mode in complex **1**, all the carboxylate groups participate in coordination with the Zn(II) center. Each aip ligand in complex **2** employs its two monodentate carboxylate groups and one amino group to coordinate to three zinc atoms. Therefore three metal centers are linked by three ligands into a 21-membered macrometalcycle, which is further linked to six nearest-neighbour zinc centers by three independent aip ligands to give rise to a lattice plane with a cavity of 8.643 × 8.279 Å (Fig. 4). The lattice water $H_2O(5)$ lies in the cavity. It is interesting that the atz ligands are arranged at one side of the layer. The two-dimensional network layers are parallel with each other as shown in Fig. 5. The adjacent layers recognize each other through offset π–π stacking interactions of the atz ligand and the pyridyl ring in the aip ligand (the centeroid-centeroid distances of adjacent aromatic rings are 3.747 Å for pyridyl rings and 4.166 Å for atz rings).

The 2D grids are further assembled by strong hydrogen bonds, in addition to the π–π stacking interactions, leading to the formation of an extended three-dimensional supramolecular framework with dimensions of 9.278 × 7.099 $Å^2$, featuring an "ABAB" packing mode along the *b* axis, as shown in Fig. 6. Two lattice water molecules, $H_2O(6)$ and $H_2O(7)$, lay in the channel. Hydrogen bonds exist extensively in complex **2**. Details of the hydrogen bonds are listed in Table 5.

3.4. FT-IR Spectra

The FT-IR spectra of both complexes **1** and **2** show broad peaks in the range 3600–3151 cm^{-1} due to the existence of hydrogen bonding between water molecules and amino groups. IR results are commonly employed to distinguish the coordination modes of carboxylate groups. A correlation of the carboxylate coordination mode to metal ions is usually made by examining the difference $\Delta\nu(COO) = \nu_{as}(COO) - \nu_s(COO)$ of the complexes [38]. The vibrations of $\nu_{as}(COO)$ and $\nu_s(COO)$ are at 1686,

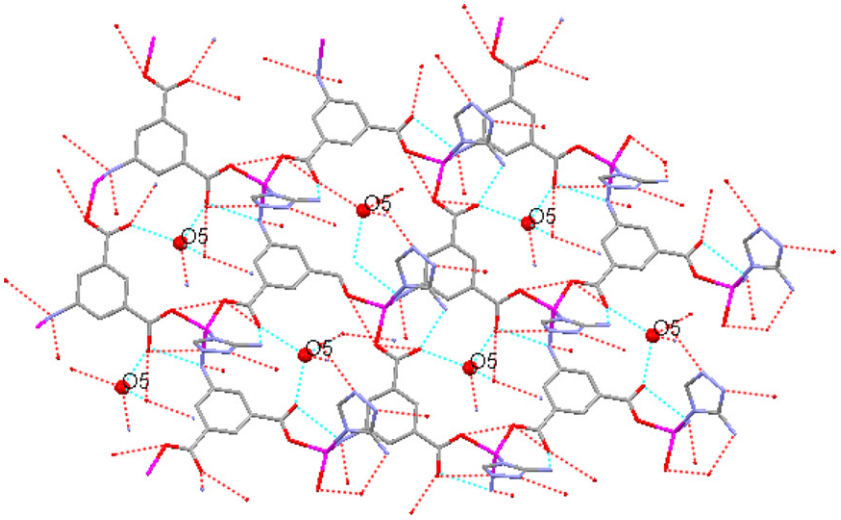


Fig. 4. View of the coordination mode of the aip ligand and the grid lamellar framework of complex **2** showing the 21-membered macrometalcycle. The lattice water $H_2O(5)$ exists in the cavity. Hydrogen atoms are omitted for clarity.

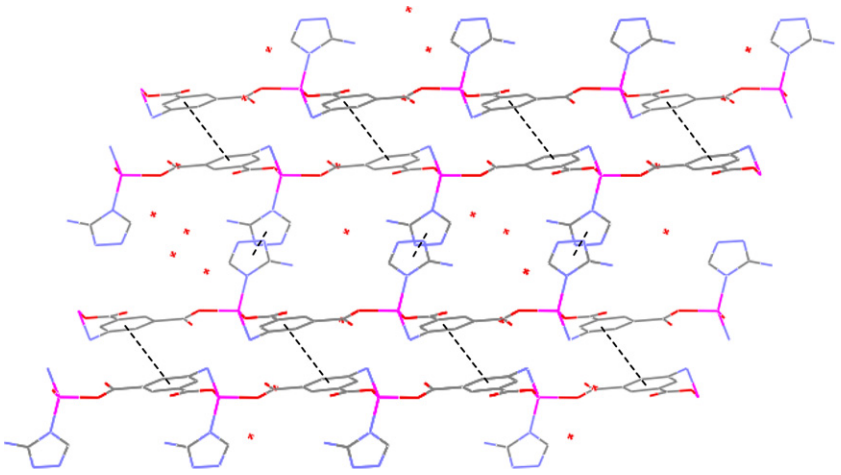


Fig. 5. The molecular packing of complex **2** showing the "ABAB" stacking pattern between the layers. The dashed lines indicate the offset π–π stacking interactions. Hydrogen bonding is omitted for clarity.

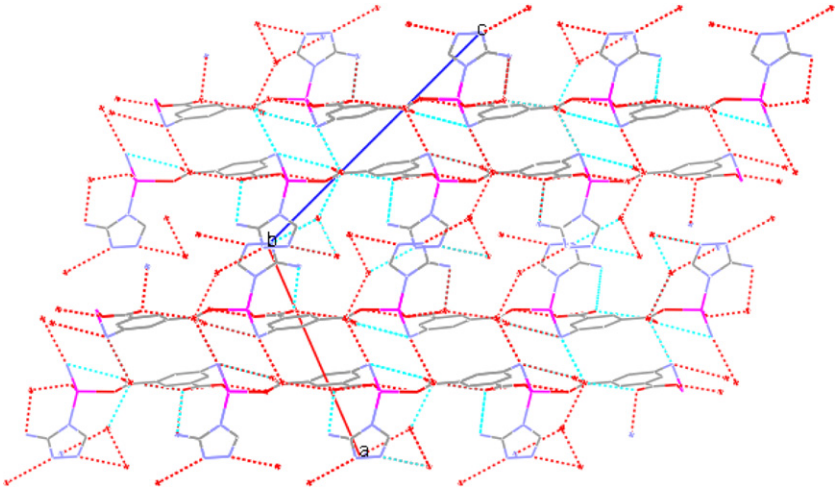


Fig. 6. View of the 3D supramolecular framework down the *b* axis constructed by π–π stacking interactions and hydrogen bonds.

Table 5
Details of the hydrogen bonds for complex **2**

D–H···A	*d*(D–H)	*d*(H ··· A)	*d*(D···A)	∠DHA	Symmetry of A
O5–H5A′···O3	0.8500	1.9400	2.7707	166.00	$1/2-x, -1/2+y, 1/2-z$
O5–H5B′···O1	0.8500	1.8000	2.6449	175.00	$1/2-x, 1/2+y, 1/2-z$
N3–H3···O6	0.8600	1.9900	2.7717	151.00	$-1/2+x, 1/2-y, -1/2+z$
N4–H4A···O6	0.8600	2.6000	3.2399	132.00	$-1/2+x, 1/2-y, -1/2+z$
N4–H4A···O7	0.8600	2.4300	3.2101	151.00	$-1/2+x, 1/2-y, -1/2+z$
N4–H4B···O3	0.8600	2.0600	2.8976	164.00	$-1/2+x, 3/2-y, -1/2+z$
N5–H5A···O5	0.9000	2.0000	2.8820	167.00	$-1/2+x, 1/2-y, 1/2+z$
N5–H5B···O4	0.9000	2.4800	3.2172	140.00	$1/2-x, -1/2+y, 3/2-z$
N5–H5B···O1	0.9000	2.3700	2.9939	127.00	$1/2+x, 1/2-y, 1/2+z$
O6–H6A···O7	0.8500	1.9800	2.8064	166.00	$1/2-x, 1/2+y, 1/2-z$
O6–H6B···O5	0.8500	2.1200	2.8679	146.00	
O7–H7A···O6	0.8500	2.3900	3.0478	135.00	
O7–H7A···O2	0.8500	2.3900	3.0737	138.00	$1/2-x, -1/2+y, 1/2-z$
O7–H7B···N2	0.8500	2.1400	2.9536	160.00	
C4–H4···O2	0.9300	2.4300	2.7470	100.00	

1629, 1569 and 1470, 1394 cm^{-1} for complex **1**. Among them, the characteristic band at 1686 cm^{-1} is attributed to the protonated carboxylate group of the Haip ligand. Compared with complex **1**, ν_{as}(COO) are at 1613, 1574 cm^{-1} and ν_s(COO) are at 1441, 1376 cm^{-1} for complex **2**. The absence of the expected characteristic bands at 1730–1680 cm^{-1}, which are attributed to the protonated carboylate group, indicate the complete deprotonation of aip in complex **2**. The IR results indicate that the carboxylate groups of the aip ligand acts n the monodentate coordination mode in these complexes. In all these cases, the results of the X-ray analysis allowed the unambiguous assignment of the binding modes of the carboxylate groups.

3.5. Thermogravimetric analysis

To study the thermal stability of the title complexes, thermogravimetric analysis (TG) was performed on polycrystalline samples under a nitrogen atmosphere in flowing N_2 with a heating rate of 10 °C min^{-1} in the temperature range 25–800 °C. The TG curve of complex **1** is divided into three stages. The first weight loss of 5.5% occurs in the temperature range 92–237 °C, which can be attributed to the loss of lattice water molecules (calculated value 6.6%). Subsequent to this, there is a distinct weight loss stage of 6.9% in the temperature range 257–307 °C, corresponding to the loss of two coordinated water molecules (calculated value 6.6%). Above 321 °C, the product begins to decompose. Free H_2aip decomposes at 303 °C [35]. This indicates that complex **1** is more stable than the free H_2aip ligand.

The thermal behavior of the coordination compound **2** has also been deduced from the TG analysis. The weight loss of 12.02% in the temperature range 42–249 °C can be attributed to the removal of three lattice H_2O molecules (calcd. 14.14%), and then the compound continues to decompose to lose its organic ligands above 272 °C and complete decomposition is not achieved until above 800 °C.

3.6. Photoluminescence properties

It is well known that metal-organic polymeric complexes with a d^{10} closed-shell electronic configuration have been found to exhibit fluorescent properties. The solid-state photoluminescence spectrum of complex **1** at room temperature is depicted in Fig. 7. H_2aip exhibits a broad fluorescent emission centered on 450 nm with an excitation maximum at 300 nm. In the case of the metal-organic coordination polymer **1**, a blue-shifted photoluminescence with the main emission at 411 nm and with a shoulder at about 587 nm ($\lambda_{ex} = 271$ nm) is observed. This emission may arise from a ligand-to-metal charge transfer (LMCT). The fluorescent properties of complex **2** and atz are also examined in the solid state at room temperature. The excitation bands of complex **2** under the emission wavelength 335 nm possess two peaks at 255 and 267 nm, and the one located at 267 nm is the main peak (see supplementary data). As shown in Fig. 8, the emission spectrum of complex **2** under the excitation wavelength 267 nm shows two intense maximum emissions at 335 nm and 450 nm, which are equal to those of the atz ligand. The excitation wavelength of the atz ligand ($\lambda_{ex} = 269$ nm) is almost the same as that of complex **2**. Therefore, the emission bands of complex **2** may be mainly ascribed to the π–π^* transition of the atz ligand. Thus, these complexes may be good candidates for highly thermally stable and solvent-resistant photoactive materials because they are almost insoluble in common polar and non-polar solvents.

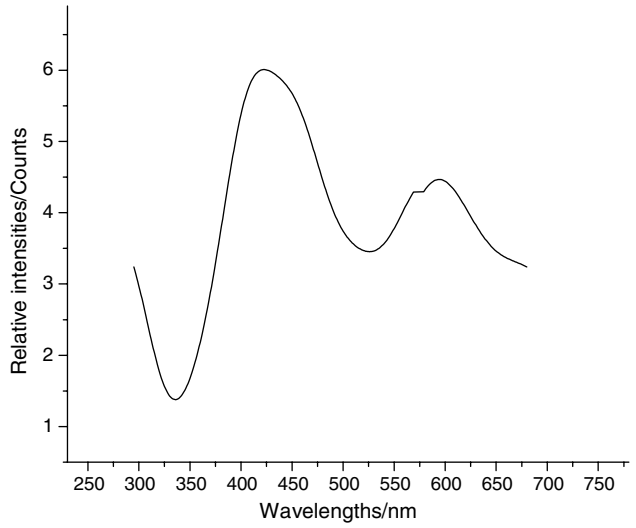


Fig. 7. The emission spectrum of **1** in the solid state at room temperature. The corresponding excitation wavelengths, λ_{ex}, is 271 nm.

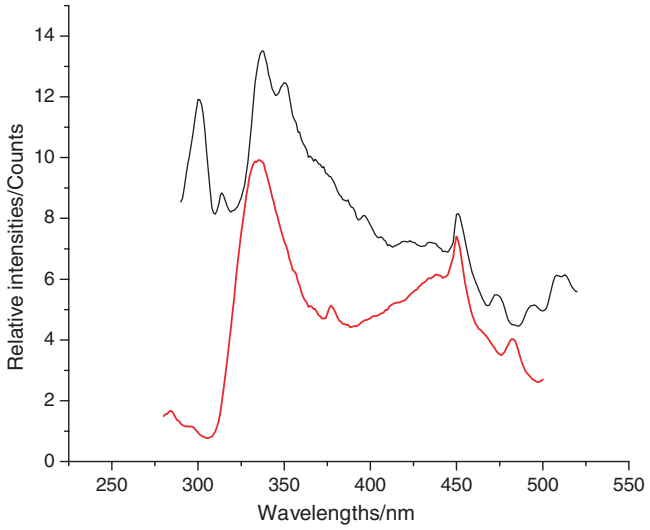


Fig. 8. The emission spectra of atz (black) and **2** (red) in the solid state at room temperature. The corresponding excitation wavelengths (λ_{ex}) are almost the same, and are 269 and 267 nm, respectively. (For interpretation of the colour representation in this figure legend the reader is referred to the web version of this article.)

4. Conclusion

In conclusion, two novel 3D supramolecular coordination polymers based on the H_2aip ligand have been obtained by self-assembly. The aip ligand exhibits different coordination modes in these complexes. There are strong interlayer π–π stacking interactions in complex **1**, which further stabilizes the whole 3D supramolecular network. Complex **2** forms a novel 3D supramolecular network due to the strong hydrogen bonds and interlayer π–π stacking interactions. The fact that their skeletons are thermally stable up to 321 and 272 °C, respectively, and their fluorescent emission of $\lambda_{em} = 411$ nm and $\lambda_{em} = 450$, 335 nm, shows they may be promising as optoelectronic devices.

Acknowledgement

We gratefully acknowledge the Foundation of Jiangsu Provincial Key Program of Physical Chemistry in Yangzhou University and the National Natural Science Foundation of China (Grant No. 50373034) for financial support of this work.

Appendix A. Supplementary material

Complete listings of bond distances and angles, hydrogen atoms coordinates and isotropic displacement parameters, non-hydrogen coordinates, anisotropic displacement parameters and least-squares planes are available either quoting the deposition number. CCDC 607816 and 620691 contain the supplementary crystallographic data for **1** and **2**. These data can be obtained free of charge via http://www.ccdc.cam.ac.uk/conts/retrieving.html, or from the Cambridge Crystallographic Data Centre, 12 Union Road, Cambridge CB2 1EZ, UK; fax: (+44) 1223-336-033; or e-mail: deposit@ccdc.cam.ac.uk. Supplementary data associated with this article can be found, in the online version, at doi:10.1016/j.poly.2006.12.047.

References

[1] F.A. Cotton, C. Lin, C.A. Murillo, Accounts Chem. Res. 34 (2001) 759.
[2] T.K. Maji, K. Uemura, H.-C. Chang, R. Matsuda, S. Kitagawa, Angew. Chem., Int. Ed. 43 (2004) 3269.
[3] S. Kawata, S. Kitagawa, H. Kumagai, C. Kudo, H. Kamesaki, T. Ishiyama, R. Suzuki, M. Kondo, M. Katada, Inorg. Chem. 35 (1996) 4445.
[4] A. Morsali, A.R. Mahjoub, Polyhedron 23 (2004) 2427.
[5] D. Dobrzyńska, T. Lis, L.B. Jerzykiewicz, Inorg. Chem. Commun. 8 (2005) 1090.
[6] O.M. Yaghi, C.E. Davis, G. Li, H. Li, J. Am. Chem. Soc. 119 (1997) 2861.
[7] J.P. García-Terán, O. Castillo, A. Laque, U. Garcia-Couceivo, P. Román, F. Lloret, Inorg. Chem. 43 (2004) 5761.
[8] A.M. Chippindale, M.R. Grimshaw, A.V. Powell, A.R. Cowley, Inorg. Chem. 44 (2005) 4121.
[9] S.J. Loeb, Chem.Commun. (2005) 1511.
[10] T.K. Maji, G. Mostafa, H.-C. Chang, S. Kitagawa, Chem. Commun. (2005) 2439.
[11] A.C. Sudik, A.P. Côté, O.M. Yaghi, Inorg. Chem. 44 (2005) 2998.
[12] O.M. Yaghi, H. Li, J. Am. Chem. Soc. 118 (1996) 295.
[13] Q. Wei, M. Nieuwenhuyzen, F. Meunier, C. Hardacre, S.L. James, J. Chem. Soc., Dalton Trans. (2004) 1807.
[14] A.R. Millward, O.M. Yaghi, J. Am. Chem. Soc. 127 (2005) 17998.
[15] B.J. Holliday, C.A. Mirkin, Angew. Chem., Int. Ed. 40 (2001) 2022.
[16] P.J. Hagraman, D. Hagrman, J. Zubieta, Angew. Chem., Int. Ed. 38 (1999) 2638.
[17] S.-I. Noro, H. Miyasaka, S. Kitagawa, T. Wada, T. Okubo, M. Yamashita, T. Mitani, Inorg. Chem. 44 (2005) 133.
[18] P. Diaz, J. Benet-Buchholz, R. Vilar, A.J.P. White, Inorg. Chem. 45 (2006) 1617.
[19] F.S. Delgado, J. Sanchiz, C. Ruiz-Pérez, F. Lloret, M. Julve, Inorg. Chem. 42 (2003) 5938.
[20] H.W. Roesky, M. Andruh, Coord. Chem. Rev. 236 (2003) 91.
[21] E. Colacio, F. Lloret, R. Kivekäs, J. Ruiz, J. Suārez-Varela, M.R. Sunberg, Chem. Commun. (2002) 592.
[22] C. Janiak, J. Chem. Soc., Dalton. Trans. (2003) 2781.
[23] X.H. Bu, W. Weng, J.R. Li, W. Chen, R.H. Zhang, Inorg. Chem. 41 (2002) 413.
[24] A. Kraft, A.C. Grimsdale, A.B. Holmes, Angew. Chem., Int. Ed. Engl. 33 (1998) 402.
[25] H.-K. Fun, S.S. Sundara Raj, R.-G. Xiong, J.-L. Zuo, Z. Yu, J. Chem. Soc., Dalton Trans. (1999) 1915.
[26] D.M. Ciurtin, N.G. Pschirer, M.D. Smith, U.H.F. Bunz, H.C. zur Loye, Chem. Mater. 13 (2001) 2743.
[27] E. Cariati, X. Bu, P.C. Ford, Chem. Mater. 12 (2000) 3385.
[28] L. Hao, M.A. Mansour, R.J. Lachicotte, H.J. Gysling, R. Eisenberg, Inorg. Chem. 39 (2000) 5520.
[29] N.W. Alock, P.R. Barker, J.M. Haider, M.J. Hannon, C.I. Painting, Z. Pikramenou, E.A. Plummer, K. Rissanen, P. Saarenketo, J. Chem. Soc., Dalton Trans. (2000) 1447.
[30] J. Tao, X. Yin, Y.-B. Jiang, R.-B. Huang, L.-S. Zheng, Inorg. Chem. Commun. 6 (9) (2003) 1171.
[31] R. Yang, N. Zheng, H. Xu, Z. Li, X. Jin, Chin. Sci. Bull. 48 (11) (2003) 1111.
[32] H. Xu, N. Zheng, X. Jin, R. Yang, Z.. Li, Chem. Lett. 11 (2002) 1144.
[33] C.-D. Wu, C.-Z. Lu, H.-H. Zhuang, J.-S. Huang, Z. Anorg, Allg. Chem. 628 (9–10) (2002) 1935.
[34] R. Yang, N. Zheng, H. Xu, Z. Li, Huaxue Tongbao 66 (7) (2003) 492.
[35] C.-D. Wu, C.-Z. Lu, W.-B. Yang, H.-H. Zhuang, J.-S. Huang, Inorg. Chem. 41 (12) (2002) 3302.
[36] G.M. Sheldrick, SHELXL 97. Programs for Crystal Structure Analysis (Release 97-2), University of Götingen, Germany, 1997.
[37] M.J. Krische, J.-M. Lehn, Struct. Bonding 96 (2000) 3.
[38] K. Nakamoto, Infrared and Raman Spectra of Inorganic and Coordination Compounds, John Wiley and Sons, New York, 1997.

clear need to synthesize and investigate novel species of this type.

Here, we present the synthesis, crystal, molecular and electronic structure of the *fac*-[Re(CO)$_3$(bpzpy)Cl] tricarbonyl with 2,6-bis(pyrazo-1-yl)-pyridine (bpzpy). The ligand shows superficial similarity to 2,2′:6′,2″-terpyridine. However, incorporation of different heterocycles into the ligand framework, with their differing basicities and π-orbital energies, may have a substantial effect on the photochemical properties of the resultant metal complexes [13].

The molecular orbital diagram of the examined complex has been calculated with the density functional theory (DFT) calculations. Currently DFT method is commonly used to examine the electronic structure of transition metal complexes. It meets with the requirements of being accurate, easy to use and fast enough to allow the study of relatively large molecules of transition metal complexes [14]. The spin-allowed singlet–singlet electronic transitions of *fac*-[Re(CO)$_3$(bpzpy)Cl] have been calculated with the time-dependent DFT method (TDDFT method), and a good assignment with the experimental spectrum has been observed.

2. Experimental

2.1. General procedure

The reaction was performed under argon atmosphere. The solvents were dried before use, using the appropriate drying reagents. Re(CO)$_5$Cl was purchased from Aldrich, and used as received. 2,6-Bis(pyrazo-1-yl)-pyridine (bpzpy) was prepared according to the literature method [13].

IR spectrum was recorded on a Nicolet Magna 560 spectrophotometer in the spectral range 4000–400 cm^{-1} with the samples in the form of KBr pellets. Electronic spectrum was measured on a spectrophotometer Lab Alliance UV–Vis 8500 in the range 1000–200 nm in dichloromethane solution. Elemental analyses (C, H, N) were performed on a Perkin–Elmer CHN-2400 analyzer.

2.2. Preparation of [Re(CO)$_3$(bpzpy)Cl]

Re(CO)$_5$Cl (0.2 g, 0.55 mmol) and bpzpy (0.13 g, 0.60 mmol) in toluene (80 cm^3) were refluxed for 6 h. The resulting reaction mixture was allowed to cool to room temperature and reduced in volume to ~1 ml. An off-yellow solid was filtered off, washed with hexane, diethyl ether, and dried; yield 85%.

Single crystals of [Re(CO)$_3$(bpzpy)Cl] were grown by the slow diffusion of diethyl ether into a solution of the complex dissolved in dichloromethane.

IR (KBr, cm^{-1}): $\nu_{CO} = 2025$, 1917 and 1897 cm^{-1}; ν_{CN} and $\nu_{C=C} = 1614$, 1568 and 1520 cm^{-1}.

Anal. Calc. $C_{14}H_9N_5O_3ClRe$: C, 32.53; H, 1.75; N, 13.55. Found: C, 32.70; H, 1.60; N, 13.40%.

2.3. Crystal structures determination and refinement

The yellow crystal of [Re(CO)$_3$(bpzpy)Cl] was mounted on a KM-4-CCD automatic diffractometer equipped with a CCD detector, and used for data collection. X-ray intensity data were collected with graphite monochromated Mo Kα radiation ($\lambda = 0.71073$ Å) at temperature of 293.0(2) K, with ω scan mode. Thirty-three seconds exposure time was used and all Ewald sphere reflections were collected up to $2\theta = 50.0°$. The unit cell parameters were determined from least-squares refinement of the setting angles of 12 165 strongest reflections respectively. Details concerning crystal data and refinement are given in Table 1. Lorentz, polarization and empirical absorption corrections [15] were applied. The structure was solved by the Patterson method and subsequently completed by the difference Fourier recycling. All the non-hydrogen atoms were refined anisotropically using full-matrix, least-squares technique. The hydrogen atoms were treated as ''riding'' on their parent carbon atoms [d(C–H) = 0.93 Å] and assigned isotropic temperature factors equal 1.2 times the value of equivalent temperature factor of the parent carbon atom. SHELXS97 [16], SHELXL97 [17] and SHELXTL [18] programs were used for all the calculations. Atomic scattering factors were those incorporated in the computer programs.

Table 1
Crystal data and structure refinement for [Re(CO)$_3$(bpzpy)Cl]

Empirical formula	$C_{14}H_9N_5O_3ClRe$
Formula weight	516.91
Temperature (K)	291.0(3)
Wavelength (Å)	0.71073
Crystal system	orthorhombic
Space group	*Pbca*
Unit cell dimensions	
a (Å)	15.1949(7)
b (Å)	12.3517(6)
c (Å)	16.8156(7)
Volume (Å^3)	3156.0(2)
Z	8
Density (calculated) (Mg/m^3)	2.176
Absorption coefficient (mm^{-1})	7.894
F(000)	1952
Crystal size (mm)	0.499 × 0.397 × 0.394
θ Range for data collection (°)	3.22–25.11
Index ranges	$-16 \leqslant h \leqslant 18$
	$-14 \leqslant k \leqslant 14$
	$-20 \leqslant l \leqslant 19$
Reflections collected	31 397
Independent reflections [R_{int}]	2804[0.0469]
Completeness to 2θ (%)	98.7
Max. and min. transmission	0.407 and 0.156
Data/restraints/parameters	2804/0/217
Goodness-of-fit on F^2	1.244
Final R indices [$I > 2\sigma(I)$]	$R_1 = 0.0261$
	$wR_2 = 0.0583$
R indices (all data)	$R1 = 0.0268$
	$wR_2 = 0.0586$
Largest difference in peak and hole (e Å^{-3})	0.798 and −0.824

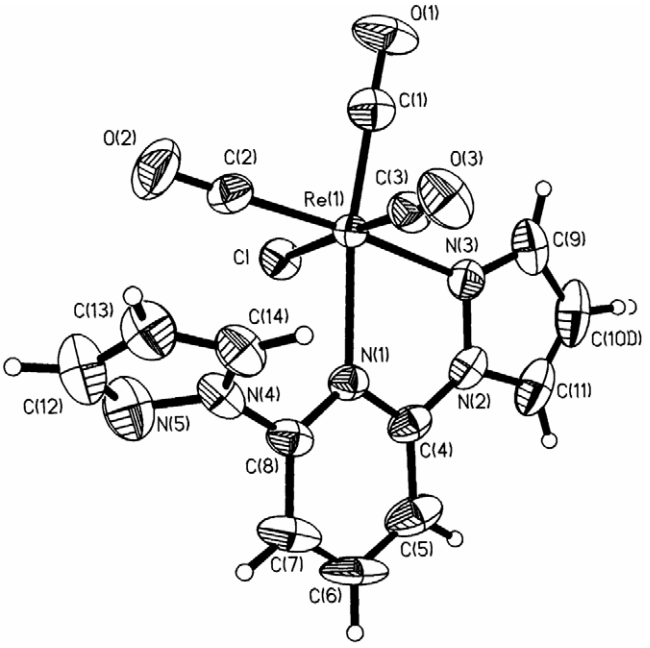


Fig. 1. Thermal ellipsoid plot of $[Re(CO)_3(bpzpy)Cl]$ showing the atom numbering scheme (50% probability ellipsoids).

2.4. Computational details

Gaussian03 program [19] was used in the calculations. The geometry optimization was carried out with the DFT method with the use of B3LYP functional [20,21]. The electronic spectrum was calculated with the TDDFT method [22]. The calculations were performed by using ECP basis set on the rhenium atom, the standard 6-31+G** basis for chlorine, oxygen, carbon and nitrogen, and 6-31G basis for hydrogen atoms. The Xe core electrons of Re were replaced by an effective core potential and DZ quality Hay and Wadt Los Alamos ECP basis set (LANL2DZ) [23] was used for the valence electrons. Additional *d* function with exponent $\alpha = 0.3811$ and *f* function with exponent $\alpha = 2.033$ on the rhenium atom were added.

3. Results and discussion

3.1. Preparation and infrared data

The $[Re(CO)_3(bpzpy)Cl]$ complex was prepared by refluxing the $[Re(CO)_5Cl]$ compound with a small excess of 2,6-bis(pyrazo-1-yl)-pyridine in toluene. The complex was isolated as air-stable, microcrystalline solid, soluble in common organic solvents. The infrared spectrum of the complex displays three bands in the carbonyl stretching region: a sharp intense band at 2025 cm^{-1} and two lower-energy bands closely spaced (1917 and 1897 cm^{-1}). This pattern corresponds to three CO units in a *fac* isomer arrangement [24]. The characteristic bands of the C=C

Table 3
Atomic charges of $[Re(CO)_3(bpzpy)Cl]$

Atom	Atomic charge
Re(1)	−0.113
Cl(1)	−0.568
N(1)	−0.499
N(2)	−0.187
N(3)	−0.287
N(4)	−0.240
N(5)	−0.296
C(1)	0.627
C(2)	0.618
C(3)	0.527
O(1)	−0.475
O(2)	−0.464
O(3)	−0.507

Table 2
The experimental and optimized bond lengths (Å) and angles (°) for $[Re(CO)_3(bpzpy)Cl]$

	Bond lengths			Bond angles	
	Experimental	Optimized		Experimental	Optimized
Re(1)–C(1)	1.881(6)	1.911	C(1)–Re(1)–C(2)	87.4(2)	88.45
Re(1)–C(2)	1.933(5)	1.937	C(1)–Re(1)–C(3)	89.4(2)	90.60
Re(1)–C(3)	1.904(5)	1.911	C(3)–Re(1)–C(2)	91.7(2)	92.56
Re(1)–Cl	2.4968(12)	2.528	C(1)–Re(1)–N(3)	95.5(2)	96.37
Re(1)–N(1)	2.237(4)	2.331	C(3)–Re(1)–N(3)	96.62(19)	93.87
Re(1)–N(3)	2.149(4)	2.173	C(1)–Re(1)–Cl	92.85(16)	92.17
C(1)–O(1)	1.175(7)	1.161	C(2)–Re(1)–N(3)	171.20(19)	171.91
C(2)–O(2)	1.138(6)	1.157	C(1)–Re(1)–N(1)	169.4(2)	166.98
C(3)–O(3)	1.158(6)	1.169	C(2)–Re(1)–Cl	88.00(16)	90.30
			C(3)–Re(1)–N(1)	92.44(17)	97.18
			C(2)–Re(1)–N(1)	102.95(19)	101.56
			C(3)–Re(1)–Cl	177.67(15)	176.07
			N(3)–Re(1)–N(1)	73.97(15)	72.78
			N(3)–Re(1)–Cl	83.55(11)	83.05
			N(1)–Re(1)–Cl	85.37(10)	79.59
			O(1)–C(1)–Re(1)	179.1(5)	177.84
			O(2)–C(2)–Re(1)	176.1(5)	178.32
			O(3)–C(3)–Re(1)	177.8(5)	179.41

and C=N stretching modes of 2,6-bis(pyrazo-1-yl)-pyridine are observed in the range 1620–1510 cm^{-1} [25].

3.2. Crystal structure

The crystallographic data for the title complex are given in Table 1. The perspective drawing of the $[Re(CO)_3(bpzpy)Cl]$ complex with atomic numbering is shown in Fig. 1. The coordination geometry at the Re atom is a distorted octahedron with the three carbonyl ligands arranged in a *facial* fashion. The deviation of the rhenium coordination sphere from an ideal octahedron is ascribed to the small bite angle of the five membered chelate ring [73.97(15)°]. The selected bond lengths and angles of $[Re(CO)_3(bpzpy)Cl]$ are given in Table 2. The Re–C and Re–N bond distances are within the range expected for such complexes [26]. A noticeable difference between Re–N(pyrazole) and Re–N(pyridine) bond lengths indicates different donor strength of these two nitrogen atoms. The pyridine ring favours π-back donation from the rhenium ion to the carbonyl in *trans* position. Hence, the Re–C(1) is shorter in comparison with the Re–C(2), whereas the C(1)–O(1) bond is longer than the C(2)–O(2).

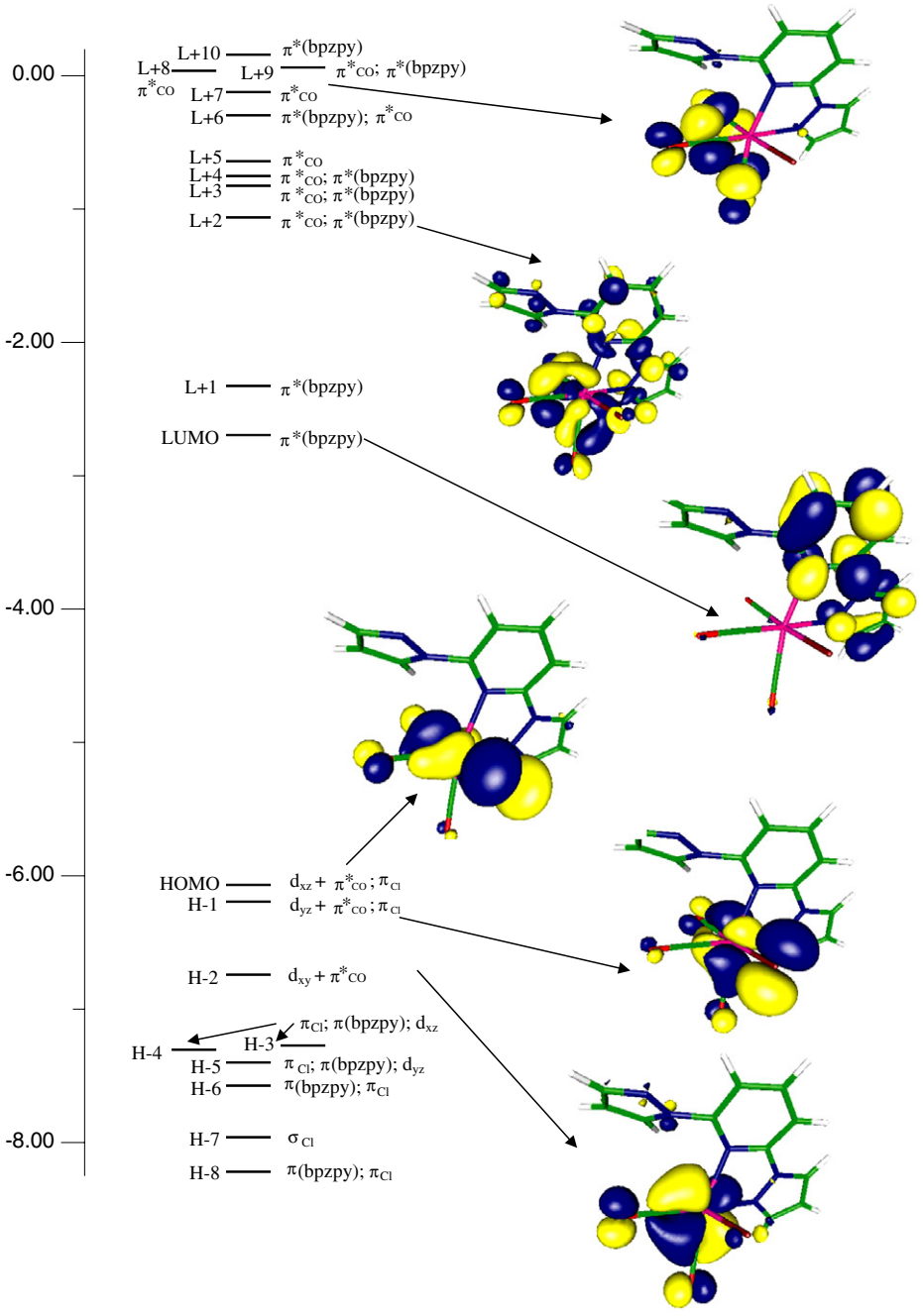


Fig. 2. The energy (eV), character and some contours of the unoccupied molecular orbitals of $[Re(CO)_3(bpzpy)Cl]$.

3.3. Optimized geometry

The geometry of $[Re(CO)_3(bpzpy)Cl]$ was optimized in a singlet state by the DFT method with the B3LYP functional. The optimized geometric parameters are gathered in Table 2. The calculated bond lengths and angles are in agreement with the values based upon the X-ray crystal structure data, and the general trends observed in the experimental data are well reproduced in the calculations.

3.4. Charge distribution

The atomic charges from the Natural Population Analysis (NPA) for $[Re(CO)_3(bpzpy)Cl]$ are shown in Table 3. The calculated charge on the rhenium atom of $[Re(CO)_3(bpzpy)Cl]$ is lower than the formal charge +1, as a result of significant charge donation from the ligands. The charges on the carbon atoms of the carbonyl ligands are positive, whereas the oxygen atoms are negatively charged. The largest positive charge is localized on the C(1) atom, whereas the least positive is carbon in the trans position to the chloride ion (π-donor ligand).

The populations of the $5d_{xy}$, $5d_{xz}$, $5d_{yz}$, $5d_{x^2-y^2}$ and $5d_{z^2}$ orbitals of the central atom in $[Re(CO)_3(bpzpy)Cl]$ are following: 1.050, 1.490, 1.380, 1.522 and 1.229. The smaller electron density on the $5d_{yz}$ in comparison with the $5d_{xz}$ rhenium orbital confirms stronger π-back donation from the rhenium ion to the carbonyl in *trans* position to the pyridine ring, and correlates well with the differences between the Re(1)–C(1) and Re(1)–C(2) bond lengths.

3.5. Electronic structure

The $[Re(CO)_3(bpzpy)Cl]$ complex is a closed-shell structure. Its molecular orbital diagram with several HOMO and LUMO contours is presented in Fig. 2. The HOMO–LUMO gap equals to 3.37 eV. The low-lying virtual orbitals correspond to π^*_{bpzpy} and π^*_{CO}, and the energy of the π^*_{bpzpy} is lower than π^*_{CO} orbitals. The three highest occupied molecular orbitals are predominately localized on the rhenium atom, corresponding to the $(5d_{xy})^2\ (5d_\pi)^4$ occupation of the central ion. They are, to a large extent, formed by Re 5d orbitals mixed with CO π^* orbitals. The HOMO and HOMO-1 orbitals contain also an admixture of chloride p_π orbitals.

3.6. Electronic spectrum

The experimental (measured in dichloromethane solution) and calculated electronic spectra of $[Re(CO)_3(bpzpy)Cl]$ are presented in Fig. 3. Each calculated transition is represented by a gaussian function $y = ce^{-bx^2}$ with the height (c) equal to the oscillator strength and b equal to 0.04 nm^{-2}.

Table 4 shows the spin-allowed singlet–singlet electronic transitions calculated with the TDDFT method for $[Re(CO)_3(bpzpy)Cl]$. For the high energy part of the spectrum, only transitions with oscillator strengths larger than 0.010 are listed in Table 4. The assignment of the calculated transitions to the experimental bands is based on the criterion of the energy and oscillator strength of the calculated transitions.

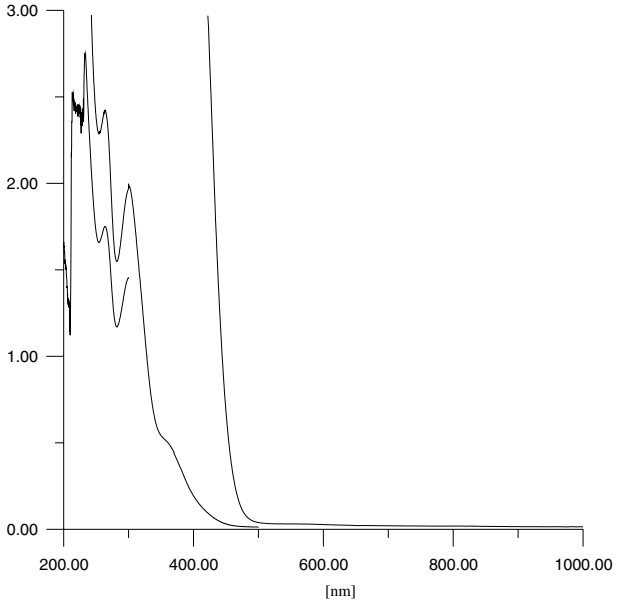


Fig. 3. The experimental (—) and calculated (---) electronic absorption spectrum of $[Re(CO)_3(bpzpy)Cl]$.

The mixed metal/chloride character of the HOMO and HOMO-1 orbitals implies that the lowest excited states have a mixed MLCT ($d \rightarrow \pi^*_{bpzpy}$) and LLCT ($\pi_{Cl} \rightarrow \pi^*_{bpzpy}$) character. The low-energy absorption band of $[Re(CO)_3(bpzpy)Cl]$ appears at 370.8 nm, and is similar to those observed for $[Re(CO)_3(bipy)Cl]$ (370 nm), $[Re(CO)_3(bipy)Br]$ (378 nm) and $[Re(CO)_3(phen)Br]$ (370 nm) [7].

The experimental absorption bands at 301.6, 264.0 and 233.6 nm result from *Metal–Ligand Charge Transfer* (occurring from the rhenium ion to the π-antibonding orbitals of the N–N ligand or π-antibonding orbitals of the carbonyl group), *Ligand–Ligand Charge Transfer* and intraligand (IL) transitions. The last excitations have a major contribution into the absorption band at 264 nm.

4. Conclusions

A novel $Re(CO)_3^+$ complex has been prepared and structurally as well as spectroscopically characterized. X-ray and IR studies confirm a *facial* geometry of the carbonyl ligands in the $[Re(CO)_3(bpzpy)Cl]$ complex. The molecular orbital diagram of the title complex has been calculated with the density functional theory (DFT) method. The HOMO, HOMO-1 and HOMO-2 orbitals are predominantly of d_{Re} orbital character corresponding to the $(5d_{xy})^2\ (5d_\pi)^4$ occupation. The low-lying virtual orbitals correspond to π^*_{bpzpy} and π^*_{CO}. The spin-allowed electronic transitions of *fac*-$[Re(CO)_3(bpzpy)Cl]$ have been calculated

Table 4
The energy and molar absorption coefficients of experimental absorption bands and the electronic transitions calculated with the TDDFT method for [$Re(CO)_3$(bpzpy)Cl]

The most important orbital excitations	Character	λ (nm)	E (eV)	f	Experimental λ (nm) (E (eV)) ε
H → L	$d/\pi_{Cl} \rightarrow \pi^*$(bpzpy)	472.4	2.62	*0.0038*	
H-1 → L	$d/\pi_{Cl} \rightarrow \pi^*$(bpzpy)	443.7	2.79	*0.0264*	
H → L + 1	$d/\pi_{Cl} \rightarrow \pi^*$(bpzpy)	405.9	3.05	*0.0052*	370.8 (3.34) 4900
H-1 → L + 1	$d/\pi_{Cl} \rightarrow \pi^*$(bpzpy)	389.8	3.18	*0.0050*	
H-2 → L	$d \rightarrow \pi^*$(bpzpy)	378.5	3.28	*0.0042*	
H-4 → L	π_{Cl}/π(bpzpy) → π^*(bpzpy)	321.9	3.85	*0.0052*	
H-5 → L	π_{Cl}/π(bpzpy)/d → π^*(bpzpy)	314.4	3.94	*0.0584*	
H → L + 2	$d/\pi_{Cl} \rightarrow \pi^*_{CO}/\pi^*$(bpzpy)	311.5	3.98	*0.0114*	301.6 (4.11) 22 600
H-5 → L	π_{Cl}/π(bpzpy)/d → π^*(bpzpy)				
H-3 → L	π(bpzpy)/$\pi_{Cl} \rightarrow \pi^*$(bpzpy)	307.6	4.03	*0.0846*	
H → L + 2	$d/\pi_{Cl} \rightarrow \pi^*_{CO}/\pi^*$(bpzpy)				
H-5 → L + 1	π_{Cl}/π(bpzpy)/d → π^*(bpzpy)	282.1	4.39	*0.0708*	
H-1 → L + 3	$d/\pi_{Cl} \rightarrow \pi^*_{CO}/\pi^*$(bpzpy)	279.1	4.44	*0.0153*	
H-4 → L + 1	π(bpzpy)/$\pi_{Cl} \rightarrow \pi^*$(bpzpy)	276.9	4.48	*0.0725*	
H-3 → L + 1					
H → L + 4	$d/\pi_{Cl} \rightarrow \pi^*_{CO}/\pi^*$(bpzpy)	272.5	4.55	*0.0123*	
H-7 → L	$\sigma_{Cl} \rightarrow \pi^*$(bpzpy)	270.6	4.58	*0.0197*	
H-2 → L + 2	$d \rightarrow \pi^*_{CO}/\pi^*$(bpzpy)	268.0	4.63	*0.0232*	
H-6 → L + 1	π(bpzpy) → π^*(bpzpy)	265.7	4.67	*0.0844*	
H-1 → L + 4	$d/\pi_{Cl} \rightarrow \pi^*_{CO}/\pi^*$(bpzpy)	263.3	4.71	*0.0130*	264.6 (4.69) 50 000
H-7 → L + 1	$\sigma_{Cl} \rightarrow \pi^*$(bpzpy)	250.7	4.95	*0.0114*	
H-8 → L	π(bpzpy)/$\pi_{Cl} \rightarrow \pi^*$(bpzpy)	249.5	4.97	*0.0812*	
H-7 → L + 1	$\sigma_{Cl} \rightarrow \pi^*$(bpzpy)				
H-1 → L + 5	$d/\pi_{Cl} \rightarrow \pi^*_{CO}$	247.7	5.01	*0.0244*	
H → L + 6	$d/\pi_{Cl} \rightarrow \pi^*$(bpzpy)/$\pi^*_{CO}$	244.1	5.08	*0.0281*	
H-8 → L + 1	π(bpzpy)/$\pi_{Cl} \rightarrow \pi^*$(bpzpy)	237.3	5.23	*0.0986*	
H-9 → L	n(bpzpy) → π^*(bpzpy)	235.1	5.27	*0.0120*	
H → L + 12	$d/\pi_{Cl} \rightarrow d/\pi^*_{CO}$	234.6	5.29	*0.0115*	
H-1 → L + 6	$d/\pi_{Cl} \rightarrow \pi^*$(bpzpy)/$\pi^*_{CO}$	231.9	5.35	*0.0196*	
H → L + 8	$d/\pi_{Cl} \rightarrow \pi^*_{CO}$				
H-4 → L + 2	π(bpzpy)/$\pi_{Cl} \rightarrow \pi^*_{CO}/\pi^*$(bpzpy)	231.3	5.36	*0.0423*	
H-1 → L + 12	$d/\pi_{Cl} \rightarrow d/\pi^*_{CO}$	229.3	5.41	*0.0114*	
H-10 → L	π(bpzpy)/$\pi_{Cl} \rightarrow \pi^*$(bpzpy)	224.7	5.52	*0.0258*	
H-2 → L + 5	$d \rightarrow \pi^*_{CO}$	224.5	5.52	*0.0104*	
H-2 → L + 6	$d \rightarrow \pi^*$(bpzpy)/π^*_{CO}	215.3	5.76	*0.0189*	233.6 (5.31) 78 300
H-1 → L + 10	$d/\pi_{Cl} \rightarrow \pi^*$(bpzpy)				
H-2 → L + 6	$d \rightarrow \pi^*$(bpzpy)/π^*_{CO}	214.0	5.79	*0.0117*	
H-3 → L + 3	π(bpzpy)/$\pi_{Cl} \rightarrow \pi^*_{CO}/\pi^*$(bpzpy)	213.2	5.81	*0.0408*	
H-4 → L + 4	π(bpzpy)/$\pi_{Cl} \rightarrow \pi^*_{CO}/\pi^*$(bpzpy)	209.2	5.93	*0.0134*	
H-10 → L	π(bpzpy)/$\pi_{Cl} \rightarrow \pi^*$(bpzpy)	208.2	5.95	*0.0217*	
H-1 → L + 15	$d/\pi_{Cl} \rightarrow d/\pi^*_{CO}$	206.8	6.00	*0.0117*	
H → L + 11	$d/\pi_{Cl} \rightarrow \pi^*_{CO}/\pi^*$(bpzpy)				
H-7 → L + 3	$\sigma_{Cl} \rightarrow \pi^*_{CO}/\pi^*$(bpzpy)	203.5	6.09	*0.0112*	
H-4 → L + 5	π(bpzpy)/$\pi_{Cl} \rightarrow \pi^*_{CO}$				
H-4 → L + 3	π(bpzpy)/$\pi_{Cl} \rightarrow \pi^*_{CO}/\pi^*$(bpzpy)	203.2	6.10	*0.0139*	
H-2 → L + 10	$d \rightarrow \pi^*$(bpzpy)	198.3	6.25	*0.0186*	
H-6 → L + 4	π(bpzpy) → π^*_{CO}/π^*(bpzpy)				
H-6 → L + 4	π(bpzpy) → π^*_{CO}/π^*(bpzpy)	198.2	6.26	*0.0192*	

with the time-dependent DFT method, and a good agreement between calculated and experimental spectra is observed.

5. Supplementary material

CCDC 623385 contains the supplementary crystallographic data for $C_{14}H_9N_5O_3ClRe$. These data can be obtained free of charge via http://www.ccdc.cam.ac.uk/conts/retrieving.html, or from the Cambridge Crystallographic Data Centre, 12 Union Road, Cambridge CB2 1EZ, UK; fax: (+44) 1223-336-033; or e-mail: deposit@ccdc.cam.ac.uk.

Acknowledgements

The Gaussian03 calculations were carried out in the Wrocław Centre for Networking and Supercomputing,

WCSS, Wrocław, Poland. Crystallographic part was financed by funds allocated by the Ministry of Science and Higher Education to the Institute of General and Ecological Chemistry, Technical University of Łódź. This work was supported by The State Committee for Scientific Research, Project No. 3 T09A 147 29.

References

[1] V. Balzani, A. Juris, M. Venturi, S. Campagna, S. Serroni, Chem. Rev. 96 (1996) 759.
[2] D.J. Stufkens, A. Vlček Jr., Coord. Chem. Rev. 177 (1998) 127.
[3] I.R. Farrell, A. Vlček Jr., Coord. Chem. Rev. 208 (2000) 87.
[4] A. Vogler, H. Kunkely, Coord. Chem. Rev. 200–202 (2000) 991.
[5] D.R. Striplin, G.A. Crosby, Coord. Chem. Rev. 211 (2001) 163.
[6] A. Vlček, M. Busby, Coord. Chem. Rev. 250 (2006) 1755.
[7] S. Ranjan, S.-Y. Li, K.-C. Hwang, W.-L. Ching, C.-S. Liu, Y.-T. Tao, C.-H. Chien, S.-M. Peng, G.-H. Lee, Inorg. Chem. 42 (2003) 1248.
[8] F. Li, G. Cheng, Y. Zhao, J. Feng, S. Liu, M. Zhang, Y. Ma, J. Shen, Appl. Phys. Lett. 83 (2003) 4716.
[9] P. Christensen, A. Hamnett, A.V.G. Muir, J.A. Timney, J. Chem. Soc., Dalton Trans. (1992) 1455.
[10] H. Hori, F.P.A. Johnson, K. Koike, K. Takeuchi, T. Ibusuki, O. Ishitani, J. Chem. Soc., Dalton Trans. (1997) 1019.
[11] S.S. Jurisson, J.D. Lydon, Chem. Rev. 99 (1999) 2205.
[12] W.A. Volkert, T.J. Hoffman, Chem. Rev. 99 (1999) 2269.
[13] M.A. Halcrow, Coord. Chem. Rev. 249 (2005) 2880.
[14] H. Chermette, Coord. Chem. Rev. 178–180 (1998) 699.
[15] STOE & Cie, X-RED. Version 1.18. STOE & Cie GmbH, Darmstadt, Germany, 1999.
[16] G.M. Sheldrick, Acta Crystallogr. A 46 (1990) 467.
[17] G.M. Sheldrick, SHELXL97, Program for the Solution and Refinement of Crystal Structures, University of Göottingen, Germany, 1997.
[18] G.M. Sheldrick, SHELXTL: release 4.1 for Siemens Crystallographic Research Systems, 1990.
[19] Gaussian 03, Revision B.03, M.J. Frisch, G.W. Trucks, H.B.Schlegel, G.E. Scuseria, M.A. Robb, J.R. Cheeseman, J.A. Montgomery, Jr., T. Vreven, K.N. Kudin, J.C. Burant, J.M. Millam, S.S. Iyengar, J. Tomasi, V. Barone, B. Mennucci, M. Cossi, G. Scalmani, N. Rega, G.A. Petersson, H. Nakatsuji, M. Hada, M. Ehara, K. Toyota, R. Fukuda, J. Hasegawa, M. Ishida, T. Nakajima, Y. Honda, O. Kitao, H. Nakai, M. Klene, X. Li, J.E. Knox, H.P. Hratchian, J.B. Cross, C. Adamo, J. Jaramillo, R. Gomperts, R.E. Stratmann, O. Yazyev, A.J. Austin, R. Cammi, C. Pomelli, J.W. Ochterski, P.Y. Ayala, K. Morokuma, G.A. Voth, P. Salvador, J.J. Dannenberg, V.G. Zakrzewski, S. Dapprich, A.D. Daniels, M.C. Strain, O. Farkas, D.K. Malick, A.D. Rabuck, K. Raghavachari, J.B. Foresman, J.V. Ortiz, Q. Cui, A.G. Baboul, S. Clifford, J. Cioslowski, B.B. Stefanov, G. Liu, A. Liashenko, P. Piskorz, I. Komaromi, R.L. Martin, D.J. Fox, T. Keith, M.A. Al-Laham, C.Y. Peng, A. Nanayakkara, M. Challacombe, P.M.W. Gill, B. Johnson, W. Chen, M.W. Wong, C. Gonzalez, J.A. Pople, Gaussian, Inc., Pittsburgh PA, 2003.
[20] A.D. Becke, J. Chem. Phys. 98 (1993) 5648.
[21] C. Lee, W. Yang, R.G. Parr, Phys. Rev. B 37 (1988) 785.
[22] M.E. Casida, in: J.M. Seminario (Ed.), Recent Developments and Applications in Modern Density Functional Theory, Theoretical and Computational Chemistry, vol. 4, Elsevier, Amsterdam, 1996.
[23] P.J. Hay, W.R. Wadt, J. Chem. Phys. 82 (1985) 299.
[24] P.J. Giordano, M.S. Wrighton, J. Am. Chem. Soc. 101 (1979) 2888.
[25] K. Nakamoto, Infrared and Raman Spectra of Inorganic and Coordination Compounds, 4th ed., Wiley Interscience, New York, 1986.
[26] Cambridge Structural Database, Version 1.8, 2005: [Re(CO)$_3${2,4,6-tris(2-pyridyl)-1,3,5-triazine}Cl]: Re–N: 2.191(7), 2.226(7); Re–C: 1.915(8), 1.903(8), 1.924(9); [Re(CO)$_3${2,4,6-tris(2-pyridyl)-1,3,5-triazine}Br]: Re–N: 2.185(6), 2.204(6); Re–C: 1.890(8), 1.910(8), 1.927(8); [Re(CO)$_3$(2,9-Me$_2$phen)(py-3-mal)]$^+$: Re–N: 2.199(7), 2.215(7), 2.219(6); Re–C: 1.90(1), 1.918(10), 1.916(9); [Re(CO)$_3$(4,4′-tBu$_2$bipy)(4-NH$_2$py)]: Re–N: 2.164(3), 2.164(3), 2.224(5); Re–C: 1.907(6), 1.916(5), 1.916(5); [Re(CO)$_3$(4,7-Me$_2$phen)(py)]$^+$: Re–N: 2.15(2), 2.13(2), 2.24(2); Re–C: 1.93(3), 1.87(3), 1.90(2).

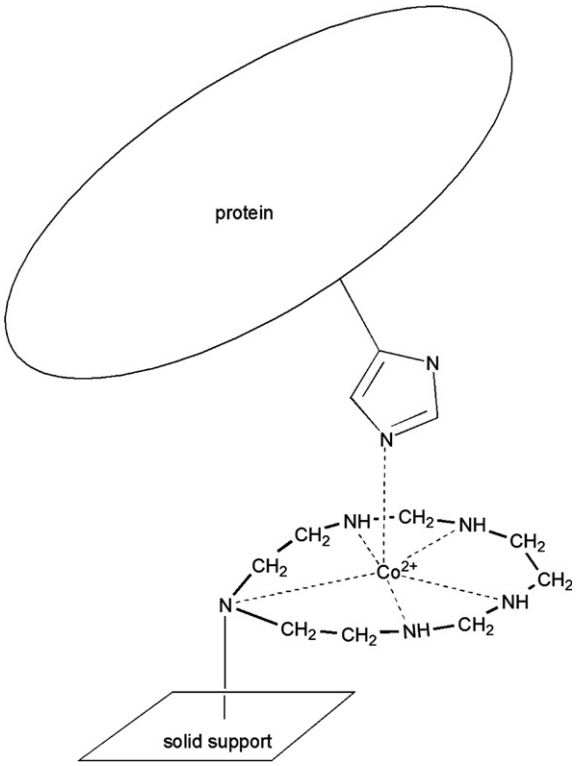


Fig. 1. Schematic illustration of a protein binding to a metal–chelator system on a surface.

and cyclotridecanes, however, make them good candidates as cobalt chelators with high affinity toward amino acids. These systems can also be prepared in a relatively easy, two-step reaction, with *N′*-(2-aminoethyl)-ethane-1,2-diamine as the starting agent (Fig. 2) [16].

In this work we present a density functional theory (DFT) study of twelve cyclododecanes and cyclotridecanes derivatives complexing cobalt and their ability to bind histidine. The obtained affinity values are compared to the results for the IDA–cobalt system commonly used in the protein purification [17,18]. The results of this work may lead to synthesis of better chelators for use as new immobilizing systems in IMAC, as well as in manufacturing of nanoscale biosensors and electronic devices.

2. Computational methods

Twelve different derivatives of cyclododecanes and cyclotridecanes: 1-pentaaza-cyclotridecane **1**, 1,3,6,8,11-pentaaza-cyclotridec-4-ene **2**, 1,3,6,8,11-pentaaza-cyclotridec-4-yne **3**, 1,3,6,8,11-pentaaza-cyclotrideca-1,7-diene **4**, 1,3,6,8,11-pentaaza-cyclotrideca-8,13-diene **5**, 1,3,6,8,11-pentaaza-cyclotrideca-9,12-diene **6**, 1,8-dimethyl-1,3,6,8,11-pentaaza-cyclotridecane **7**, 1,8-dichloro-1,3,6,8,11-pentaaza-cyclotridecane **8**, 1,4,7,10-tetraaza-cyclododecane **9**, 1,3,5,7,10-pentaaza-cyclododecane **10**, 1,3,5,7,10-pentaaza-cyclododeca-2,5-diene **11**, and [1,3,5,8]-tetrazecane **12** (Fig. 3), have been studied in this work. For each of the 12 derivatives four different molecular model systems have been considered: an empty chelator, a chelator loaded with cobalt, and a chelator loaded with cobalt and interacting with either a water molecule or an imidazole molecule (a model for histidine) (Fig. 4). To investigate the chelator–histidine interactions the following set of reactions have been considered:

$$\text{chelator–Co} + H_2O \rightarrow \text{chelator–Co–}H_2O, \quad (1)$$

$$\text{chelator–Co} + \text{imidazole} \rightarrow \text{chelator–Co–imidazole}, \quad \text{and} \quad (2)$$

$$\text{chelator–Co–}H_2O + \text{imidazole} \rightarrow \text{chelator–Co–imidazole} + H_2O. \quad (3)$$

Reaction (1) allows to evaluate the theoretical affinity of chelators loaded with cobalt toward a water molecule, whereas reaction (2) provides the theoretical affinity of the loaded chelator system toward imidazole. Reaction (3) allows to quantify the relative affinity of the chelator–Co–imidazole system with respect to the chelator–Co–water system, which is the key value for this study because it characterizes the strength of the chelator–amino acids interaction.

The geometries of the studied systems have been fully optimized at the DFT level of theory. The DFT calculations have been carried out with the three-parameter density functional B3LYP [19,20] using the standard 6-31+G* basis set. Harmonic frequency calculations have been performed for the equilibrium DFT geometries and the frequency results have been used to account for the zero-point vibrational-energy corrections. The calculations have been performed using the quantum chemistry package Gaussian 03 [21].

3. Results and discussion

Based on the previous theoretical works in this field one can point at three properties of the chelating systems that directly influence their binding abilities [12–14]. Clearly, the ability to strongly bind water or imidazole depends directly on the molecular structure of the complex. The derivatives of cyclododecanes and cyclotridecanes considered in this work are tetra- or pentadentate chelators, but they widely differ in the structural flexibility of their main molecular chains. This feature is important because it is

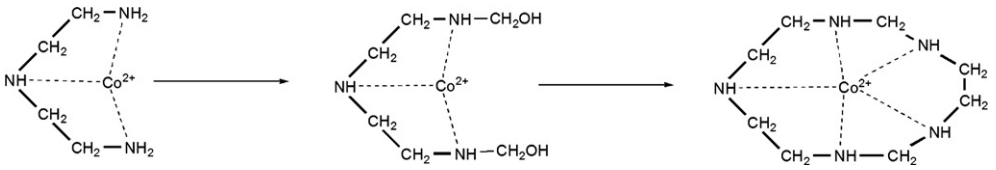


Fig. 2. Synthesis of cyclotridecane derivative loaded with Co.

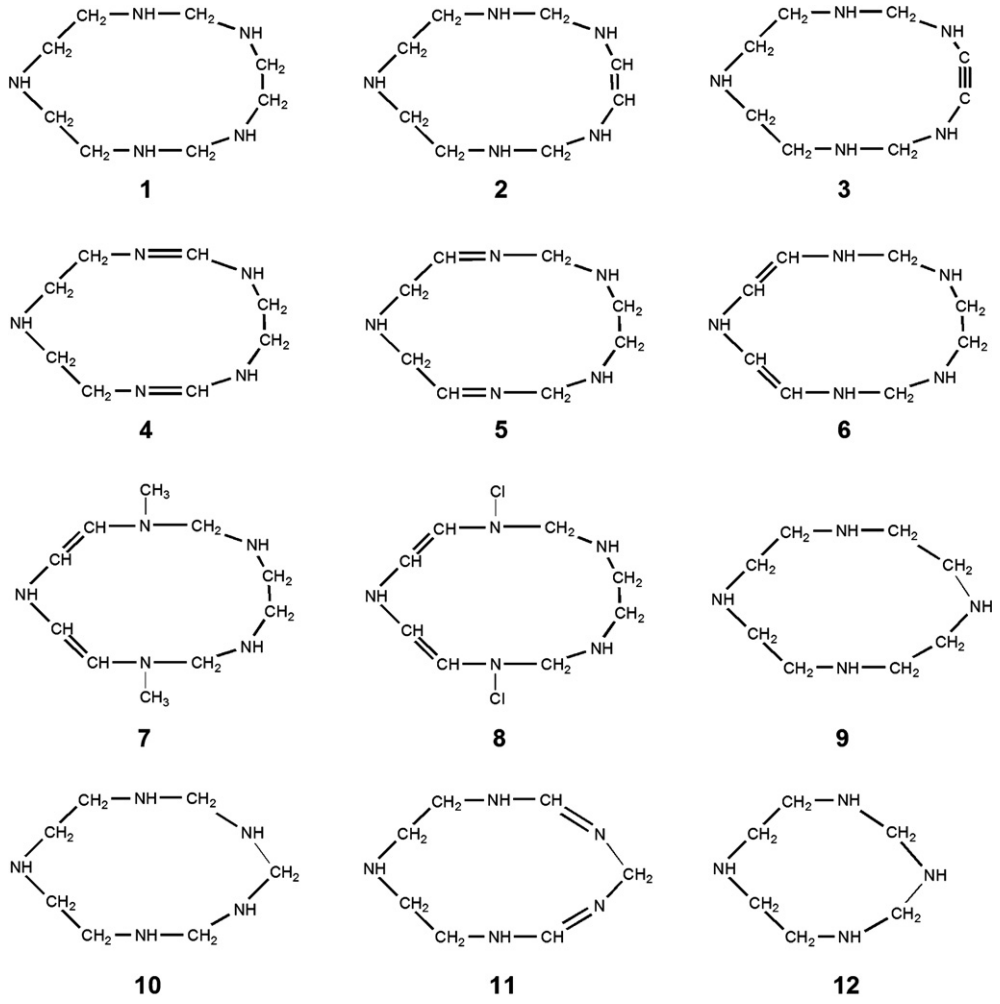


Fig. 3. Schematic representation of the twelve cyclododecanes and cyclotridecanes derivatives studied in this work.

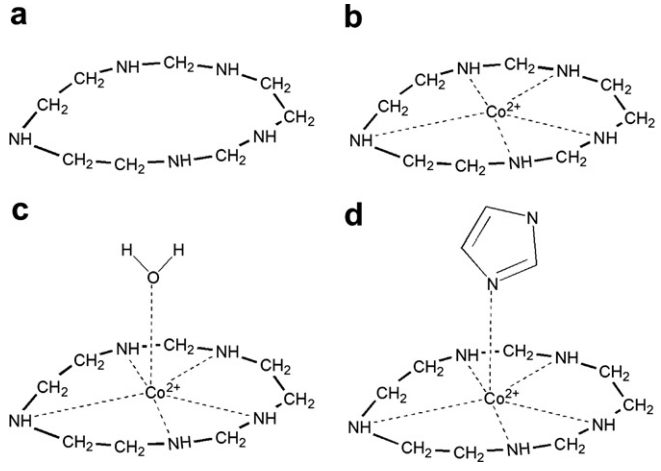


Fig. 4. Schematic representation of the systems studied in the theoretical calculations, a: an empty chelator **1**, b: system **1** chelating cobalt, c: system **1** chelating cobalt and interacting with water molecule, d: system **1** chelating cobalt and interacting with imidazole molecule.

responsible for the geometry of the complex which is formed upon the chelator binding either water or imidazole. Some systems are flexible enough to attain a geometry close to the most-energetically favorable one around the cobalt while others, which are more rigid, may have this ability significantly reduced.

The second important feature responsible for the selectivity of the interaction is the size of the bound molecule. If only the flexibility of the main chain of the chelator were determining the affinity energy, all those energies would be similar for water and imidazole. This is, however, not the case, since imidazole introduces additional steric, and possibly also chemical interactions, which may change the affinity value in either direction.

The third and the last feature determining the affinity value is the ability of the chelator and the bound molecule to donate electrons. There is a clear difference between the water and the imidazole molecules in this respect, since they include either an oxygen atom or a nitrogen atom as the electron donor. The difference in the interaction energy between the cobalt ion and the O-donor or the N-donor leads to a difference in the affinity value. The ability to donate/accept electrons can also be affected by functionalizing the chelator side of the complex by electron-withdrawing or electron-donating moieties.

The affinity of the chelator toward a certain molecule depends on the interplay of all three above-mentioned factors. The quantum chemical models used in this work allow to determine the role of each of them in the calculation of the affinity value. With that one can investigate systems that have not yet been synthesized.

In Table 1 the chelator–cobalt–water, chelator–cobalt–imidazole, and relative imidazole/water affinity values for systems studied in this work are presented. The values of ~−20–60 kcal/mol are typical for systems used in IMAC [14]. These values may also be directly compared to the values obtained for IDA–Co complexes, which are −46.5 kcal/mol (IDA–cobalt–water), −61.4 kcal/mol (IDA–cobalt–imidazole), and −14.9 kcal/mol (relative imidazole/water affinity), respectively. The results shown in Table 1 suggest that most of the new compounds considered in this work have similar molecular affinities toward imidazole as IDA. Interestingly, there are also some derivatives with higher affinities toward imidazole much above the IDA–cobalt–imidazole level.

It is interesting to note that in most cases a high affinity toward imidazole goes along with a high affinity toward water, so the relative imidazole/water affinity remains at a similar level. On the other hand, even small changes in the geometrical parameters of the chelator–cobalt–water and chelator–cobalt–imidazole systems may affect their relative affinities. This, for example, is the case for compounds **1** and **2**. The structures of these two cyclotridecanes derivatives are very similar with the only difference being a double bond connecting the carbon atoms 4 and 5 in compound **2** instead of a single bond in compound **1**. This small change in the molecular structure does not affect much the affinity of the two systems toward water, but affects the imidazole binding energy leading to a 25% rise of the relative water/imidazole affinity value.

The second interesting comparison can be made for systems **1**, **7**, and **8**. The first of these three systems is an unsubstituted 1,3,6,8,11-pentaaza-cyclotrideca-9,12-diene, while the other two are also the same dienes but with two methyl groups (compound **7**) or two chlorine atoms (compound **8**) introduced in positions 1 and 8. Those additional moieties act as electron-donating or electron-withdrawing groups leading to a change in the chelator interaction with cobalt and affecting the chelator affinity toward imidazole. The addition of the electron-donating methyl groups destabilizes the whole system lowering the affinity of the chelator toward both water and imidazole. By contrast, the addition to **1** of two chlorine moieties, which are electron-withdrawing groups, stabilizes the system, resulting in higher affinities of the chelator toward the two ligands. In both cases, however, the stabilization/destabilization is similar for both the water and imidazole complexes.

Another interesting system is derivative **12**, which does not form stable complexes with either water or imidazole. The reason for the instability of the tetrazece complex can be found in the geometry of the complex. The tight binding of the cobalt ion in this small complex leaves little space available for the interacting ligand, which results in steric hindrance and the overall instability of the system. A similar trend is observed for derivatives **5** and **6**. These compounds are larger than derivative **12**, but due to multiple double bonds they are relatively rigid and form similarly tight complexes with cobalt. The final result is the same as in the previous case, since the interaction with the ligand introduces a number of sterical hindrances leading to the instability of the whole system.

The goal of this work is to design and identify those derivatives, which have much higher molecular affinities toward imidazole than the commonly used IDA. Two compounds seem to be the good candidates for such potent chelators. The first one is 1,3,6,8,11-pentaaza-cyclotrideca-1,7-diene **4**. This system has a relatively low affinity toward the water molecule, but a high affinity toward imidazole resulting in a large value of the relative affinity. The second candidate is the 1,3,5,7,10-pentaaza-cyclododeca-2,5-diene **11**, which has high affinities toward both water and imidazole. Both of these systems have the relative imidazole/water affinities approximately two times higher than those for the IDA–cobalt system.

The two systems with the highest affinities predicted by the computational approach have common geometrical features. A detailed analysis of the geometries of these two chelators reveals an unusual geometry around the central ion. In most of the studied systems all four or five Co–N bonds are similar, with their lengths between 2.05 and 2.2 Å. This feature allows for strong cobalt bonding by the chelator. On the other hand all the studied systems are planar or mostly planar systems, forcing the non-octahedral geometry around the central ion. In the case of systems **4** and **11,** however, two of the Co–N bonds are much longer (between 3.2 and 3.3 Å), thus are much weaker (Fig. 5). This additional feature makes the Co^{2+} even more flexible and allows the whole system chelating the imidazole to acquire a more favorable geometry from the energetical point of view.

Table 1
Affinities for the chelator–Co–water and chelator–Co–water–imidazole systems, and relative imidazole–water affinities (see reactions (1)–(3)) predicted with the DFT method (in kcal/mol)

Chelator	H_2O affinity	Imidazole affinity	Relative imidazole/H_2O affinity
1	−20.2	−39.4	−19.2
2	−19.8	−43.8	−24.0
3	−25.3	−49.1	−23.8
4	−11.9	−46.7	−34.9
5	unstable	unstable	
6	unstable	unstable	
7	−18.0	−35.9	−17.8
8	−25.6	−41.9	−16.2
9	−16.8	−33.5	−16.8
10	−26.2	−50.1	−24.0
11	−36.6	−66.8	−30.2
12	unstable	unstable	
IDA	−46.5	−61.4	−14.9

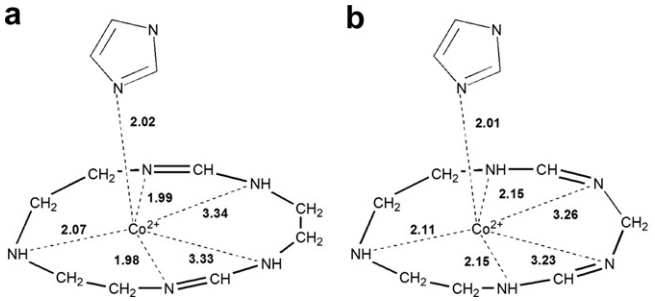


Fig. 5. The most important geometrical features of systems with the highest affinities. a: 1,3,6,8,11-pentaaza-cyclotrideca-1,7-diene **4**, b: 1,3,5,7,10-pentaaza-cyclododeca-2,5-diene **11**. Bond lengths are in Angstroms.

4. Conclusions

In this work quantum mechanical calculations have been used to demonstrate that some of the new derivatives of cyclotridecanes and cyclododecanes considered in this work are good candidates for new potent chelating compounds. The calculations performed with the density functional theory method of 12 derivatives allowed us to identify two compounds, 1,3,6,8,11-pentaaza-cyclotrideca-1,7-diene and 1,3,5,7,10-pentaaza-cyclododeca-2,5-diene, with high molecular affinity toward imidazole, which in the calculations is modeling a histidine molecule. Upon synthesis these two derivatives may become interesting alternatives to IDA for use in IMAC and other experiments relying on the immobilization of biomacromolecules.

This work is also a step toward forming LigMIP, a theoretical database of ligand–metal ion–protein interactions. Such a database with the quantitatively described interactions between ligands, metal ions, and amino acids could serve as a useful tool in selecting the best possible chelating compounds for different applications, as well as in facilitating designing of novel chelating systems.

Acknowledgement

NSF Grant #0303863 and CPU time from University of Arizona supercomputing center are gratefully acknowledged.

References

[1] J. Porath, J. Carlsson, I. Olsson, G. Belfrage, Nature 258 (1975) 598.
[2] J. Porath, Trends Anal. Chem. 7 (1988) 254.
[3] D.R. Shnek, D.W. Pack, D.Y. Sasaki, F.H. Arnold, Langmuir 10 (1994) 2382.
[4] B. Loddenkotter, B. Kammerer, K. Fischer, U. Flugge, Proc. Natl. Acad. Sci. USA 90 (1993) 2155.
[5] P.C. Jain, E.C. Lingafelter, J. Am. Chem. Soc. 89 (1967) 724.
[6] A.D. Gupta, F.S. Richardson, Inorg. Chem. 20 (1981) 2616.
[7] I. Garcia, M. Solache-Rios, P. Bosch, S. Bulbulian, Langmuir 12 (1996) 4474.
[8] R.J. Sundberg, B.B. Martin, Chem. Rev. 74 (1974) 471.
[9] E.J. Laskowski, D.N. Hendrickson, Inorg. Chem. 17 (1978) 457.
[10] E. Sinn, G. Sim, E.V. Dose, M.F. Tweedle, L.J. Wilson, J. Am. Chem. Soc. 100 (1978) 3375.
[11] P. Starynowicz, Polyhedron 22 (2003) 2761.
[12] B. Trzaskowski, A. Leś, L. Adamowicz, P.A. Deymier, R. Guzman, S.G. Stepanian, J. Comput. Theor. Nanosci. 2 (2005) 456.
[13] S.G. Stepanian, B. Trzaskowski, P.A. Deymier, R. Guzman, L. Adamowicz, J. Comput. Theor. Nanosci. 3 (2006) 78.
[14] B. Trzaskowski, S.G. Stepanian, A. Leś, R. Guzman, P.A. Deymier, L. Adamowicz, J. Comput. Theor. Nanosci. 3 (2006) 775.
[15] K.W. Chan, S. Barra, M. Botta, W.T. Wong, J. Inorg. Chem. 98 (2004) 677.
[16] R. Guzman, unpublished data.
[17] J.E. Hale, Anal. Biochem. 231 (1995) 46.
[18] E. Zatloukalova, Z. Kučerová, J. Chromatogr. B 808 (2004) 99.
[19] A.D. Becke, J. Chem. Phys. 98 (1993) 5648.
[20] C. Lee, W. Yang, R.G. Parr, Phys. Rev. B 37 (1988) 785.
[21] M.J. Frisch, G.W. Trucks, H.B. Schlegel, G.E. Scuseria, M.A. Robb, J.R. Cheeseman, J.A. Montgomery Jr., T. Vreven, K.N. Kudin, J.C. Burant, J.M. Millam, S.S. Iyengar, J. Tomasi, V. Barone, B. Mennucci, M. Cossi, G. Scalmani, N. Rega, G.A. Petersson, H. Nakatsuji, M. Hada, M. Ehara, K. Toyota, R. Fukuda, J. Hasegawa, M. Ishida, T. Nakajima, Y. Honda, O. Kitao, H. Nakai, M. Klene, X. Li, J.E. Knox, H.P. Hratchian, J.B. Cross, V. Bakken, C. Adamo, J. Jaramillo, R. Gomperts, R.E. Stratmann, O. Yazyev, A.J. Austin, R. Cammi, C. Pomelli, J.W. Ochterski, P.Y. Ayala, K. Morokuma, G.A. Voth, P. Salvador, J.J. Dannenberg, V.G. Zakrzewski, S. Dapprich, A.D. Daniels, M.C. Strain, O. Farkas, D.K. Malick, A.D. Rabuck, K. Raghavachari, J.B. Foresman, J.V. Ortiz, Q. Cui, A.G. Baboul, S. Clifford, J. Cioslowski, B.B. Stefanov, G. Liu, A. Liashenko, P. Piskorz, I. Komaromi, R.L. Martin, D.J. Fox, T. Keith, M.A. Al-Laham, C.Y. Peng, A. Nanayakkara, M. Challacombe, P.M.W. Gill, B. Johnson, W. Chen, M.W. Wong, C. Gonzalez, J.A. Pople, Gaussian 03, Revision C.02, Gaussian, Inc., Wallingford CT, 2004.

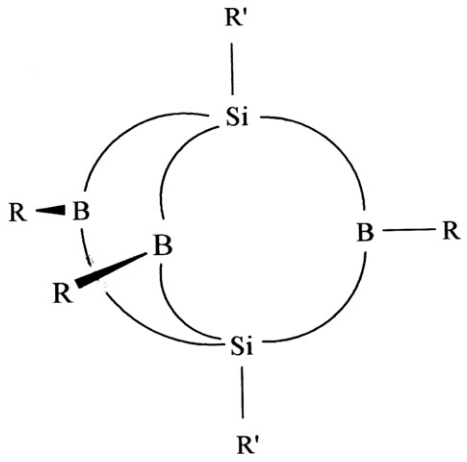


Diagram 1.

"spherical" cage borosiloxanes with the syntheses of 11 analogues of [R′Si(OBRO)$_3$SiR′] with a wide variety of R groups, Diagram 1.

The details of the structures of five of these compounds have been determined with X-ray crystallography. Additionally, we have studied the reactions between [Bu^{t}Si{O(PhB)O}$_3$SiBu^t] (**1**) and (a) pyridine or (b) *N*,*N*,*N*′,*N*′-tetramethyl-ethylenediamine and established the solid-state structure of the adduct [Bu^{t}Si{O(PhB)O}SiBu^t] · NC$_5$H$_5$ (**12**).

2. Results and discussion

2.1. Syntheses and structural studies of [R′Si(ORBO)$_3$SiR′] borosiloxanes 1 to 11

All the borosiloxane cages with the formulae [R′Si(ORBO)$_3$SiR′] were synthesised in a Dean-Stark apparatus by water elimination reactions between R′Si(OH)$_3$ (R′ = Bu^t or *cyclo*-C$_6$H$_{11}$) and boronic acids RB(OH)$_2$ in a 2:3 molar ratio in toluene solution heated at the reflux temperature, Eq. (1). In general the *tert*-butyl compounds were isolated in 30–40% higher yields than the corresponding *cyclo*hexyl derivatives with the same R groups.

$$2R'Si(OH)_3 + 3RB(OH)_2 \rightarrow [R'Si(ORBO)_3SiR'] \quad (1)$$

where R′ = Bu^t and R = Ph (**1**), 4-PhC$_6$H$_4$ (**2**), 4-Bu^{t}C$_6$H$_4$ (**3**), 3-NO$_2$C$_6$H$_4$ (**4**), 4-CH(O)C$_6$H$_4$ (**5**), CpFeC$_5$H$_4$ (**6**), 4-C(O)CH$_3$C$_6$H$_4$ (**7**), 4-ClC$_6$H$_4$ (**8**), 2,4-F$_2$C$_6$H$_3$ (**9**), and R′ = *cyclo*-C$_6$H$_{11}$ and R = C$_6$H$_5$ (**10**), and 4-BrC$_6$H$_4$ (**11**).

An alternative route via the reactions between *tert*-butyltrichlorosilane or *cyclo*hexyltrichlorosilane and boronic acids in the presence of an amine, either Et$_3$N or aniline, afforded the products **1** to **9** in 5–10% lower yields and compounds **10** and **11** in ca. 30% lower yields. Attempts to use phenyl- or tolyltrichlorosilane reagents afforded boroxines as the only characterisable products.

Initial characterisation of **1**–**11** by chemical analysis was followed by spectroscopic (FT-IR, NMR) and, in some cases, mass spectrometric analysis. For the compounds with R′ = Bu^t and R = 4-PhC$_6$H$_4$ (**2**), 4-Bu^{t}C$_6$H$_4$ (**3**), 3-NO$_2$C$_6$H$_4$ (**4**), CpFeC$_5$H$_4$ (**6**), and 2,4-F$_2$C$_6$H$_3$ (**9**), single-crystal X-ray diffraction studies were carried out. A summary of crystal data for these compounds is given in Section 4.

2.2. Crystal and molecular structures of [Bu^{t}Si{O(4-PhC$_6$H$_4$B)O}$_3$SiBu^t] (2), [Bu^{t}Si{O(4-Bu^{t}C$_6$H$_4$B)O}$_3$SiBu^t] (3), [Bu^{t}Si{O(3-NO$_2$C$_6$H$_4$B)O}$_3$SiBu^t] (4), [Bu^{t}Si{O(CpFeC$_5$H$_4$B)O}$_3$SiBu^t] (6), and [Bu^{t}Si{O(2,4-F$_2$C$_6$H$_3$B)O}$_3$SiBu^t] (9)

Comparison of the structures of compounds [Bu^{t}Si(OBRO)$_3$SiBu^t] where R = 4-PhC$_6$H$_4$ (**2**), 4-Bu^{t}C$_6$H$_4$ (**3**), 3-NO$_2$C$_6$H$_4$ (**4**), CpFeC$_5$H$_4$ (**6**) and 2,4-F$_2$C$_6$H$_3$ (**9**) reveals that the structural details of the Si$_2$O$_6$B$_3$ cages are remarkably similar, Table 1.

All five compounds contain two tetrahedral Bu^{t}SiO$_3$-units and three trigonal planar RBO$_2$-units held together by an 11-atom Si(OBO)$_3$Si framework. Figs. 1–3 show ORTEP views of molecules with R = 4-PhC$_6$H$_4$ (**2**), 4-Bu^{t}C$_6$H$_4$ (**3**) and CpFeC$_5$H$_4$ (**6**) from a general perspective.

The structures of compounds **2** and **6** are shown viewed along the axes passing through both silicon atoms in Figs. 4 and 5, respectively. The *tert*-butyl groups attached to the silicon atoms in compounds **2** and **6** are in "eclipsed" arrangements. The same structural motif is found in **3**, **4**, **6** and **9**.

The C$_6$-rings attached to the boron atoms in **2** and **3** are arranged in a "paddlewheel" formation, see Fig. 4, and are almost co-planar with the adjacent Si–O–B–O–Si bonded sequence. The same structural motif was observed in **3**, **4**, and **9**, and in the compound [Bu^{t}Si{O(4-BrC$_6$H$_4$B)O}$_3$SiBu^t] [4]. A similar situation is observed in the ferrocenyl compound [Bu^{t}Si{O(CpFeC$_5$H$_4$B)O}$_3$SiBu^t] (**6**), where the C$_5$H$_4$ ring is almost co-planar with the attached borosiloxane group, Fig. 5. The reason for the preference for co-planarity may reside in a partial overlap of the π system of the aromatic C$_6$-ring and some delocalised bonding in the Si–O–B–O–Si sequence. However, it is also possible that the co-planarity is due to "crystal packing" forces. It is interesting to note that in the case of **6** the ferrocenyl groups are not all arranged to give a pseudo-D_{3h} molecular symmetry. The reasons are unclear but may be due either to weak intramolecular H···π–C$_5$H$_5$ ring interactions or more general "crystal packing" forces.

The B–O lengths in **2**, **3**, **4**, **6** and **9** range from 1.348(5) to 1.380(4) and are at the upper end of the reported range for trigonal boron species with Si–O–B bonds i.e. 1.313(2) in (OBF)(OSiBu$^t_2$)$_2$(OSiMe$_2$) (**13**) [9] to 1.374(7) Å in [B(OSiPh$_2$SiPh$_2$O)$_3$B] (**14**) [5]. They are similar to B–O distances in the previously reported spherical cage [Bu^{t}Si{O-(4-BrC$_6$H$_4$B)O}$_3$SiBu^t] (**15**) [4], which were

Table 1
Selected bond distance (Å) and angle (°) data for [Bu^{t}Si(OBRO)$_3$SiBu^t] where R = 4-PhC$_6$H$_4$ (**2**), 4-Bu^{t}C$_6$H$_4$ (**3**), 3-NO$_2$C$_6$H$_4$ (**4**), CpFeC$_5$H$_4$ (**6**) and 2,4-F$_2$C$_6$H$_3$ (**9**)

Compound	**2**	**3**	**4**	**6**	**9**
Range of Si–O distances	1.615(2)–1.6212(19)	1.613(3)–1.624(3)	1.603(3)–1.631(3)	1.621(3)–1.637(2)	1.620(4)
Mean Si–O	1.620(2)	1.620(3)	1.620(3)	1.628(3)	1.620(4)
Range of B–O distances	1.353(4)–1.380(4)	1.348(5)–1.376(6)	1.354(5)–1.370(5)	1.359(4)–1.373(5)	1.372(6)
Mean B–O	1.365(4)	1.364(6)	1.364(5)	1.369(5)	1.372(6)
Mean B–C	1.553(4)	1.546(6)	1.559(6)	1.541(5)	1.544(12)
Mean Si–C	1.833(3)	1.841(5)	1.829(4)	1.851(4)	1.838(11)
Range of B–O–Si angles	135.3(2)–142.9(2)	135.0(3)–143.0(3)	134.0(3)–143.0(3)	133.9(2)–142.4(2)	139.4(5)
Mean B–O–Si	138.6(2)	138.7(3)	138.5(3)	137.8(2)	139.4(5)
Range of O–Si–O angles	107.53(11)–110.51(11)	107.90(17)–110.05(17)	108.12(14)–110.32(15)	107.31(13)–110.90(13)	109.14(15)
Mean O–Si–O	109.18(11)	109.19(17)	109.03(15)	109.08(13)	109.14(15)
Range of O–B–O angles	120.9(3)–121.5(3)	120.6(4)–121.4(4)	121.0(4)–122.2(4)	120.7(3)–121.1(3)	120.6(8)
Mean O–B–O	121.1(3)	121.0(4)	121.8(4)	120.9(6)	120.6(8)
Range of O–B–C angles	118.0(3)–120.4(3)	118.8(4)–120.2(4)	117.7(4)–120.1(4)	118.8(3)–120.1(3)	119.7.(4)
Mean O–B–C	119.4(3)	119.5(4)	119.0(4)	119.5 (3)	119.7.(4)

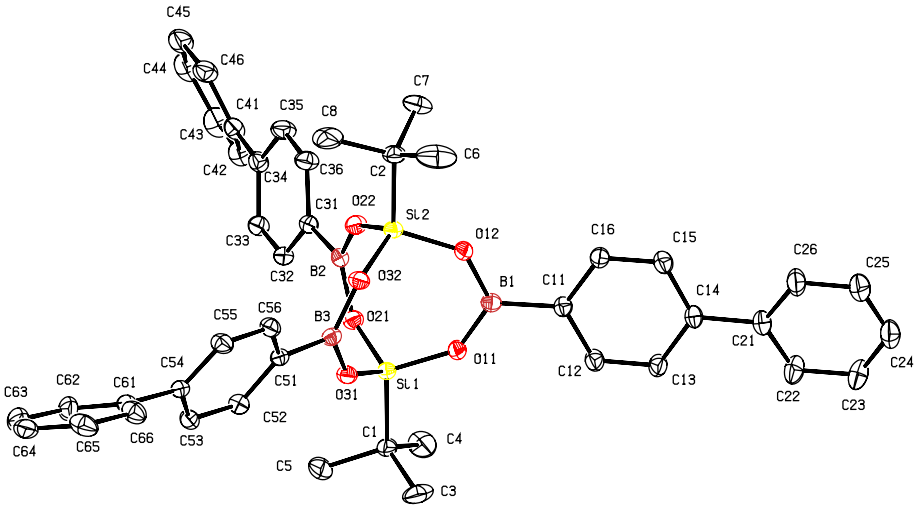


Fig. 1. An ORTEP view of [Bu^{t}Si{O(4-PhC$_6$H$_4$B)O}$_3$SiBu^t] (**2**) with atom numbering.

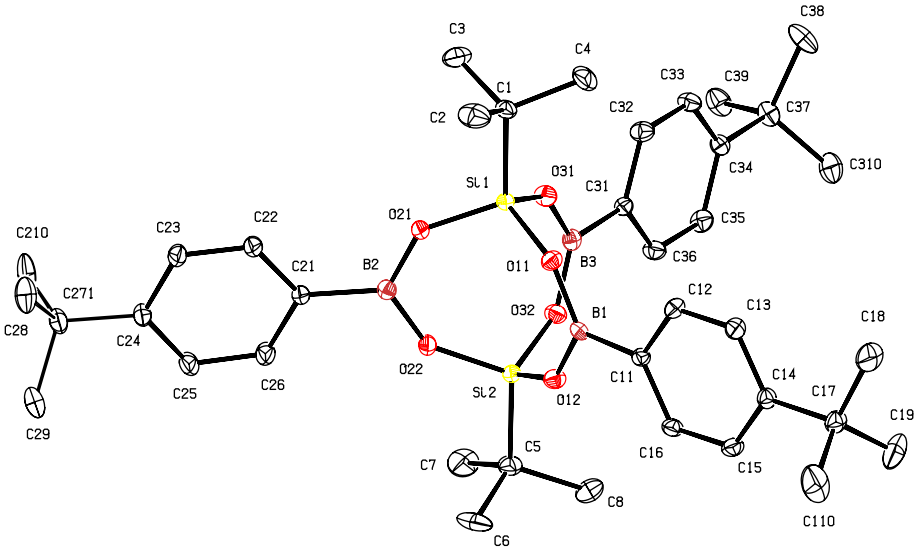


Fig. 2. An ORTEP view of [Bu^{t}Si{O(4-Bu^{t}C$_6$H$_4$B)O}$_3$SiBu^t] (**3**), with atom numbering.

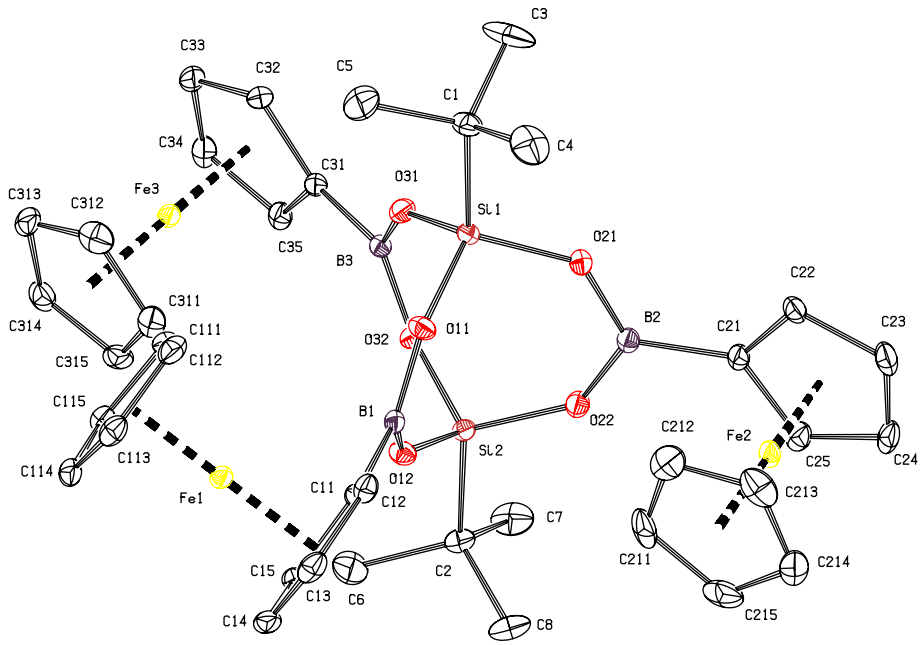


Fig. 3. An ORTEP view of [Bu^{t}Si{O(CpFeC$_5$H$_4$B)O}$_3$SiBu^t] (**6**), with atom numbering.

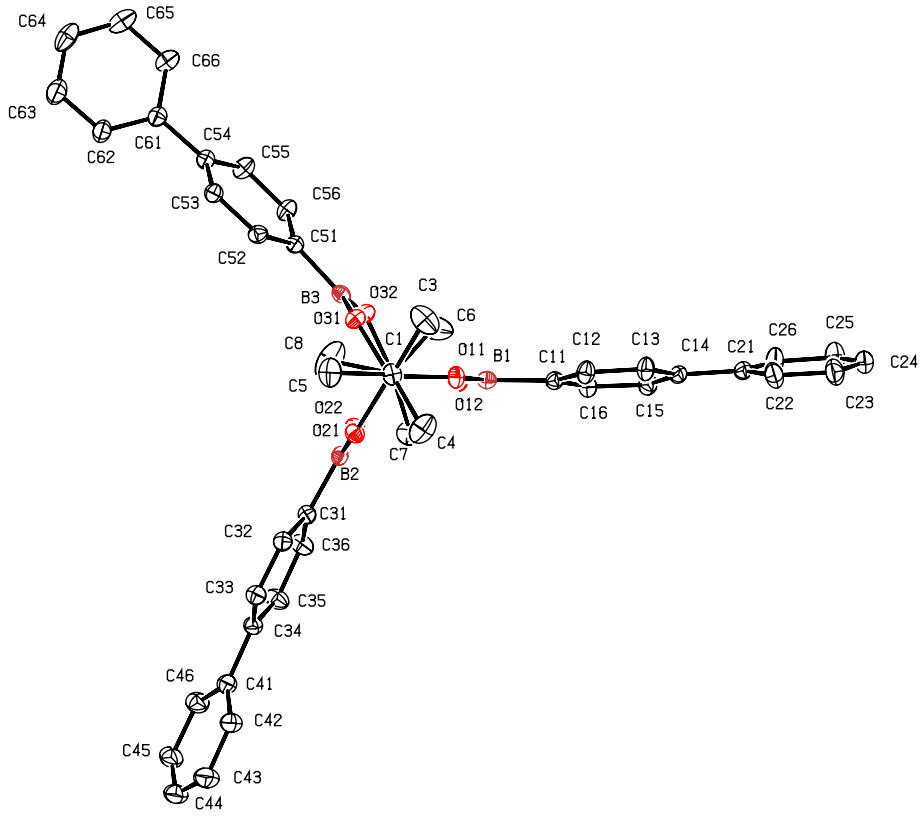


Fig. 4. ORTEP view of [Bu^{t}Si{O(4-PhC$_6$H$_4$B)O}$_3$SiBu^t] (**2**) along the Si···Si axis.

1.364(11)–1.372(10) Å and in the cube-based structure [(Bu^{t}Si)$_4$(CH$_2$=CHC$_6$H$_4$B)$_4$O$_{10}$] [6] (1.361(4)–1.369(4) Å). A mean value of 1.367 Å has been reported for B–O distances where the boron is tricoordinated [10] and the mean values of the B–O distances reported here are all the same within one s.u.

The Si–O distances in **2**, **3**, **4**, **6** and **9** vary between 1.603(3) and 1.638(3) Å, but the mean values of the six Si–O distances are remarkably similar at about 1.620 Å, Table 1. The range of previously reported Si–O distances for borosiloxanes containing trigonal boron was 1.603(2) [7] to 1.655(5) [4,11]. The mean values of Si–O distances

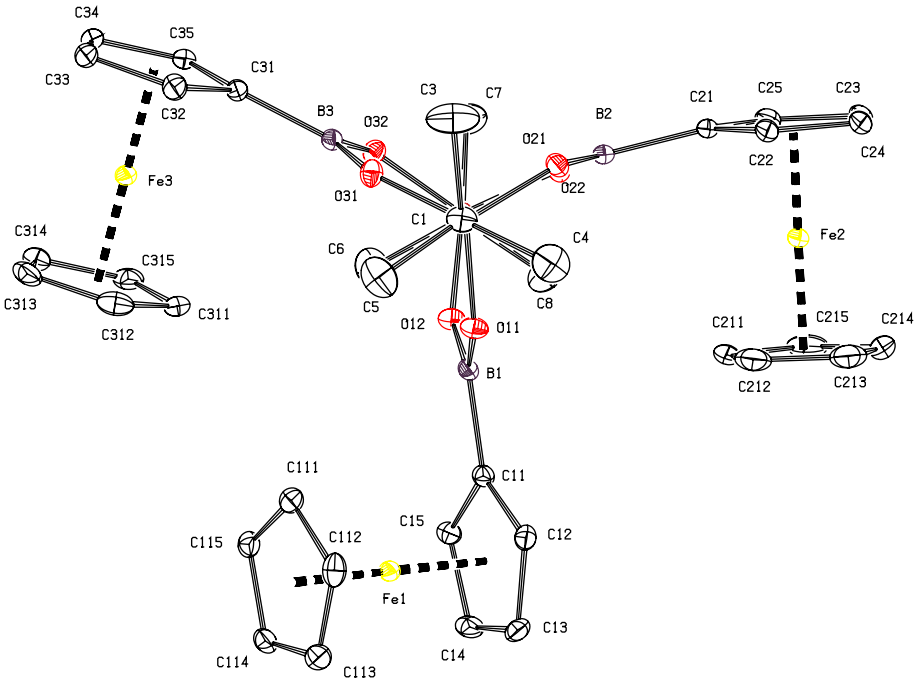


Fig. 5. ORTEP view of [Bu^{t}Si{O(CpFeC$_5$H$_4$B)O}$_3$SiBu^t] (**6**) along the Si···Si axis.

in [B(OSiPh$_2$SiPh$_2$O)$_3$B] (**14**) [5], [Bu^{t}Si{O(4-BrC$_6$H$_4$B)O}$_3$SiBu^t] (**15**) [4] and [(Bu^{t}Si)$_4$(CH$_2$=CHC$_6$H$_4$B)$_4$O$_{10}$] [6], were 1.631(2), 1.621(5) and 1.616(4) Å, respectively, and a mean value of 1.631(2) Å has been reported for Si–O distances where the silicon is four coordinated [10].

The mean B–C distances in **2**, **3**, **4**, **6** and **9** range from 1.541(5) to 1.559(6) Å. The B–C$_{Ph}$ distances in PhB(OSiPh$_3$)$_2$, **16** [12] and (PhBO)$_2$(OSiPh$_2$)$_2$ (**17**) [13], were 1.558(8) and 1.555(6) Å, respectively, and the B–C distances reported in [Bu^{t}Si{O(4-BrC$_6$H$_4$B)O}$_3$SiBu^t] (**15**) [4] ranged from 1.541(11) to 1.585(11) Å, with a mean value of 1.566 Å.

The average value of the Si–C distances in **2**, **3**, **4**, **6** and **9** were 1.833(3), 1.841(5), 1.829(4), 1.853(4) and 1.846(9) Å, respectively. A mean value of 1.863 Å has been reported for Si–C bonds, where C is sp^3-hybridised and bonded to carbon or hydrogen atoms only and the silicon atom is four coordinated [10].

B–O–Si angles at trigonal boron atoms are known to be very flexible [12] in both acyclic and cyclic compounds. Examples include the two chemically equivalent B–O–Si angles in PhB(OSiPh$_3$)$_2$ (**18**), {139.8(4)° and 157.9(3)°} [12], and in cyclic systems, 128.89(14)° in (PhBO)(Ph$_2$SiO)$_2$ (**19**) [14] and 160.9(3)° in (PhBO)$_2$(Ph$_2$SiO)$_2$ (**17**) [13]. Hence, it is noteworthy that in the compounds **2**, **3**, **4** and **6** the variation is relatively small at ca. ±4° from a mean angle of ca. 138°, Table 1. The six B–O–Si angles in **2** vary from 135.3(2)° to 142.9(2)° with a mean value of 138.6(2)° and those in **3** show an almost identical range of 135.0(3)–143.0(3)° and a mean value of 138.8(3)°. In **4** these angles vary from 134.0(3)° to 143.0(3)° with a mean value of 138.5(3)°. The B–O–Si angles in **6** range from 133.9(3)° to 142.4(3)° with a mean value of 137.8(9)°. Compound **9** has a symmetry determined single B–O–Si angle of 139.5(4)°. All B–O–Si angles for **2**, **3**, **4**, **6** and **9** are notably similar to those for [B(OSiPh$_2$SiPh$_2$O)$_3$B] (**14**) [5], and [Bu^{t}Si{O(4-BrC$_6$H$_4$B)O}$_3$SiBu^t] (**15**) [4] where the B–O–Si angles varied over the range 137.89(18)–140.03(18)° with a mean value of 138.6(18)° for **14** and 137.5(6)–140.7(6)° with a mean value of 138.6(6)° for **15**, respectively. In the more open structure of the cube-based [(Bu^{t}Si)$_4$(CH$_2$=CHC$_6$H$_4$B)$_4$O$_{10}$] [6], the B–O–Si angles vary more from 137.5(2)° to 154.4(2)°.

Like the B–O–Si angles, the O–B–O angles in **2**, **3**, **4**, **6** and **9** are notably similar and close to 121°, Table 1. The three O–B–O angles in [Bu^{t}Si{O(4-BrC$_6$H$_4$B)O}$_3$SiBu^t] (**15**) [4] varied from 119.9(8)° to 124.0(8)° the mean value being 122.2(8)° and the four O–B–O angles in [(Bu^{t}Si)$_4$(CH$_2$=CHC$_6$H$_4$B)$_4$O$_{10}$] [6], varied from 120.7(3)° to 120.9(3)° with a mean value of 120.8(3)°.

The O–Si–O and O–B–C angles in **2**, **3**, **4**, **6** and **9** are even more remarkably similar with ranges and means which are almost identical, Table 1. The range over all the compounds for O–Si–O angles is from 107.29(15)° to 110.90(15)° both of which were observed in [Bu^{t}Si{O(CpFeC$_5$H$_4$B)O}$_3$SiBu^t] (**6**). The mean value of O–Si–O angles in **2**, **3**, **4**, **6** and **9** was 109.12° which was very close to the mean value observed in [(Bu^{t}Si)$_4$(CH$_2$=CHC$_6$H$_4$B)$_4$O$_{10}$] [6]. For [B(OSiPh$_2$SiPh$_2$O)$_3$B] (**14**) [5], the three O–Si–O angles ranged from 108.78(12)° to 109.34(10)° with a mean

value of 109.12(12)°. In [Bu^{t}Si{O(4-BrC$_6$H$_4$B)O}$_3$SiBu^t] (**15**) [4] the O–Si–O angles ranged from 108.5(3)° to 109.7(3)° with a mean value of 109.2(3)°. The O–B–C angles range from 118.0(3)° to 120.4(3)° which are both found in **2**. The mean values in compounds **2**, **3**, **6** and **9** are all close to 119.5° and that in **4** is 119.1°. The O–B–C angles in compound **15** range from 116.6(9)° to 120.7(8)° with a mean of 118.9(8)°.

As with the O–Si–O angles, the O–Si–C angles are close to the tetrahedral value in all cases.

2.3. Reactions between the borosiloxane cage [Bu^{t}Si(OPhBO)$_3$SiBu^t] and pyridine or N,N,N′,N′-tetramethylethylenediamine

2.3.1. Synthesis and structural study of [Bu^{t}Si(OPhBO)$_3$SiBu^t] · NC$_5$H$_5$ (12)

The reaction between [Bu^{t}Si{O(PhB)O}$_3$SiBu^t] (**1**), and three equivalents of pyridine in ether at r.t. for 16 h followed by crystallisation of the solid product from dichloromethane–heptane (1:3) afforded [Bu^{t}Si{O(PhB)O}$_3$SiBu^t] · NC$_5$H$_5$ (**12**) in 73% yield. This compound was soluble in toluene, dichloromethane, ether and acetone at room temperature. Chemical analysis for C, H, B and N supported the formulation of **12** as a 1:1 adduct. The ^{11}B NMR spectrum of **12** showed two signals in a 2:1 ratio with one corresponding to three coordinate boron at 25.4 ppm and one associated with four coordinate boron at 0.6 ppm, respectively. Crystals of [Bu^{t}Si{O(PhB)O}$_3$SiBu^t] · NC$_5$H$_5$ (**12**) suitable for X-ray diffraction studies were grown by the slow evaporation of a dichloromethane–heptane solution of **12**. Fig. 6 is an ORTEP plot showing a general view of [Bu^{t}Si{O(PhB)O}$_3$SiBu^t] · NC$_5$H$_5$ (**12**), and the atom numbering scheme is shown in Fig. 6. Significant bond distance and bond angle data for **12** are given in Table 2. The basic Si$_2$O$_6$B$_3$ cage structure of [Bu^{t}Si{O(PhB)O}$_3$SiBu^t] · NC$_5$H$_5$ (**12**) is very similar to the Si$_2$O$_6$B$_3$ cage in the borosiloxanes **2**, **3**, **6** and **9** reported above. The structure of **12** also involves near-eclipsed arrangements of the *tert*-butyl groups at Si(1) with those at Si(21) and a "paddlewheel" arrangement of the three phenyl groups and the pyridine group is adopted as can be seen if the structure is viewed above the Si(1)···Si(21) axis.

The four B–O distances in [Bu^{t}Si{O(PhB)O}$_3$SiBu^t] · NC$_5$H$_5$ (**12**) for the tricoordinate boron atoms span a relatively wide range from 1.354(17) to 1.394(18) Å. The two B–O distances for the tetracoordinate bonded boron atom in **12** are 1.457(18) and 1.469(18) Å, Table 2. These values are similar to data from the tetrahedrally coordinated boron compounds Ph(OSiR$_2$R′)B{O(CH$_2$)$_3$N} (**20**), where the boron atom is directly bonded to two oxygen atoms, a Ph group and the nitrogen atom and R or R′ = Ph or Me. These compounds have B–O$_{Si}$ distances of 1.439(4) [15] and 1.443(6) [16] in the Ph$_2$Me and PhMe$_2$ derivatives, respectively. The increased B–O distance at the tetrahedral boron site may be associated with the removal of any B–O π-bonding component on going from trigonal to tetrahedral coordination at boron.

The Si–O distances in **2**, **3**, **4**, **6** and **9** varied between 1.603(3) and 1.638(3) Å, with a mean value of 1.621 Å and these values are comparable with the four Si–O distances in [Bu^{t}Si{O(PhB)O}$_3$SiBu^t] · NC$_5$H$_5$ (**12**) which range from 1.625(9) to 1.631(9) Å where the boron atom is tricoordinate. The average value is 1.628 Å. The two Si–O distances where the boron atom is tetracoordinate are notably shorter with values of 1.585(7) and 1.594(9) Å suggesting that electron density has increased in the Si–O bond corresponding to the decrease in B–O electron density.

The B–N distance in [Bu^{t}Si{O(PhB)O}$_3$SiBu^t] · NC$_5$H$_5$ (**12**) was 1.655(17) Å. For simple borosiloxane Ph(OSiR$_2$R′)B{O(CH$_2$)$_3$N} species, **20**, the B–N distances are 1.639(4) [15] and 1.639(6) Å [16] in the Ph$_2$Me and PhMe$_2$ derivatives, respectively. A value of 1.556 Å has been reported for B–N distances where the boron atom is tetracoordinate [10].

The two B–C distances in **12** with the boron atom tricoordinate were 1.552(19) Å and 1.594(19) Å. Similar B–C distances in **2**, **3**, **4**, **6** and **9** with mean values of 1.553(4), 1.546(6), 1.559(6), 1.541(5) and 1.544(10) Å were noted in Table 1. A mean value of 1.556 Å has been reported for B–C$_{ar}$ distances, where the boron atom is tricoordinate and the carbon atom is part of an aromatic system [10]. The B–C distance in **12** where the boron atom is tetracoordinate was 1.58(2) Å which is within 3x s.u. of the two other B–C distances. The mean Si–C distance in **12** was typical of such distances at 1.832(15) Å.

In [Bu^{t}Si{O(PhB)O}$_3$SiBu^t] · NC$_5$H$_5$ (**12**) the four B–O–Si angles in which the boron is tricoordinate range from 134.4(10)° to 140.7(9)° which is a similar range to the corresponding angles in **2**, **3**, **6** and **9**, Table 1. The two B–O–Si angles in **12** where the boron is tetracoordinate are 134.2(8)° and 138.0(9)°.

The O–B–O angles in [Bu^{t}Si{O(PhB)O}$_3$SiBu^t] · NC$_5$H$_5$ (**12**) vary from 111.6(11)° at the tetracoordinate boron atom to 121.1(13)° and 122.3(13)° at the tricoordinate boron atoms. These angles are close to the 109° and 120° expected for tetrahedral and trigonal planar geometries, respectively. Likewise the O–Si–O angles in **12** range from 108.2(5)° to 111.0(5)° with a mean value of 109.6(5)° which is normal for tetrahedral silicon and the four O–B–C angles in [Bu^{t}Si{O(PhB)O}$_3$SiBu^t] · NC$_5$H$_5$ (**12**) where the boron is trigonal planar range from 117.9(12)° to 120.1(13)°. The two O–B–C values in **12** where the boron atom is tetrahedral had values greater than 109° at 112.6(11)° and 115.5(12)°, respectively.

The six O–Si–C angles in **12** ranged from 106.4(6)° to 112.6(5)° with a mean value of 109.4(6)° but the angles where the oxygen is bonded to a tetracoordinate boron atom, mean value 112.4(6)°, appeared to be larger than the O–Si–C angles where the oxygen is bonded to a trigonal boron, mean value 107.9(6)°.

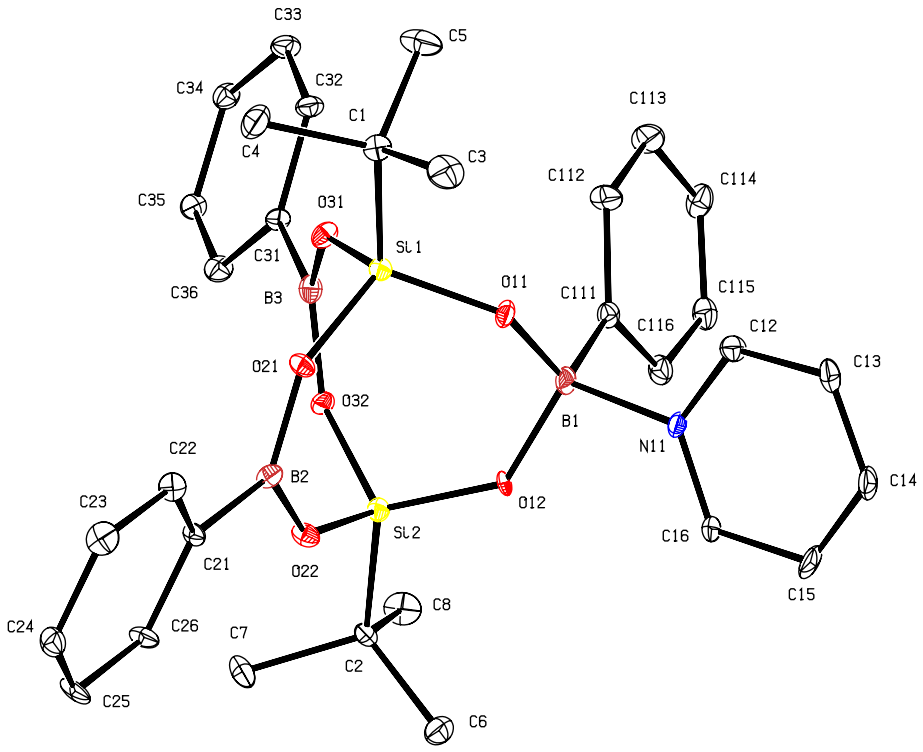


Fig. 6. An ORTEP view of $[Bu^tSi(OPhBO)_3SiBu^t]\cdot NC_5H_5$ (**12**), with atom numbering. Selected interatomic distances (Å) and angles (°): Si(1)–O(11) 1.594(9), Si(1)–O(21) 1.630(9), Si(1)–O(31) 1.631(9), Si(1)–C(1) 1.832(15), Si(2)–O(12) 1.585(7), Si(2)–O(22) 1.626(9), Si(2)–O(32) 1.625(9), Si(2)–C(2) 1.831(14), B(1)–N(11) 1.655(17), B(1)–O(11) 1.457(18), B(1)–O(12) 1.469(18), B(1)–C(111) 1.58(2), B(2)–O(21) 1.394(18), B(2)–O(22) 1.370(17), B(2)–C(21) 1.552(19), B(3)–O(31) 1.354(17), B(3)–O(32) 1.375(19), B(3)–C(31) 1.594(19); O(11)–Si(1)–O(21) 111.0(5), O(11)–Si(1)–O(31) 109.6(5), O(21)–Si(1)–O(31) 108.2(5), O(11)–Si(1)–C(1) 111.8(6), O(21)–Si(1)–C(1) 106.4(6), O(31)–Si(1)–C(1) 109.7(6), O(12)–Si(2)–O(22) 109.3(5), O(12)–Si(2)–O(32) 110.6(5), O(22)–Si(2)–O(32) 108.6(5), O(12)–Si(2)–C(2) 112.6(5), O(22)–Si(2)–C(2) 106.4(6), O(32)–Si(2)–C(2) 109.2(6), B(1)–O(11)–Si(1) 138.0(9), B(2)–O(21)–Si(1) 139.7(9), B(3)–O(31)–Si(1) 134.4(10), B(1)–O(12)–Si(2) 134.2(8), B(2)–O(21)–Si(2) 137.3(9), B(3)–O(32)–Si(2) 140.7(9), O(12)–B(1)–O(11) 111.6(11), O(11)–B(1)–C(111) 115.5(12), O(12)–B(1)–C(111) 112.6(11), O(11)–B(1)–N(11) 103.2(10), O(12)–B(1)–N(11) 104.9(11), C(111)–B(1)–N(11) 107.9(10), O(21)–B(2)–C(21) 120.1(13), O(21)–B(2)–C(22) 118.8(12), O(21)–B(2)–O(22) 121.1(13), O(31)–B(3)–O(32) 122.3(13), O(32)–B(3)–C(31) 117.9(12), O(31)–B(3)–C(31) 119.8(13).

Table 2
Summary of crystal data details for **2**, **3**, **4**, **6**, **9** and **12**

Crystal data	**2**	**3**	**4**	**6**	**9**	**12**
Empirical formula	$C_{44}H_{45}B_3O_6Si_2$	$C_{38}H_{57}B_3O_6Si_2$	$C_{29.5}H_{33.5}B_3N_3O_{12}Si_2$	$C_{38}H_{45}B_3Fe_3O_6Si_2$	$C_{26}H_{27}B_3F_6O_6Si_2$	$C_{31}H_{38}B_3NO_6Si_2$
Molar mass	758.41	698.45	710.70	853.9	638.09	609.23
Color	colourless	colourless	colourless	orange	colourless	colourless
Habit	plate	needle	block	block	cube	block
a (Å)	12.9156(17)	12.5922(16)	9.533(2)	10.4736(11)	15.6121(8)	11.030(6)
b (Å)	15.6120(9)	13.8371(18)	20.295(3)	10.9281(14)	15.6121(8)	18.227(6)
c (Å)	22.678(2)	24.674(2)	18.697(3)	19.0690(28)	15.6121(8)	16.235(5)
α (°)	90.00	90.00	90.00	97.905(11)	90.00	90.00
β (°)	103.899(9)	93.830(9)	101.775(12)	102.628(10)	90.00	94.24(3)
γ (°)	90.00	90.00	90.00	106.750(10)	90.00	90.00
V (Å^3)	4311.0(7)	4289.6(10)	3541.4(11)	1991.9(4)	3805.3(3)	3255(2)
Space group	$P2_1/c$	$P2_1/c$	$P2_1/c$	$P\bar{1}$	P_{4132}	Cc
Z	4	4	4	2	4	4
F(000)	1600	1504	1482	884	1312	1288
D_{calc} (g cm^{-1})	1.169	1.081	1.333	1.424	1.114	1.243
μ (mm^{-1})	0.127	0.122	0.164	1.182	0.153	0.152
T (K)	294(1)	294(1)	293(2)	293(2)	293(2)	150(2)
Reflections measured	8019	7964	3338	9117	657	2828
R	0.0549	0.0638	0.0739	0.0427	0.0828	0.0711
R_w	0.1085	0.1709	0.1497	0.0987	0.1391	0.1569
Goodness-of-fit	0.916	1.043	0.919	1.151	1.197	1.104

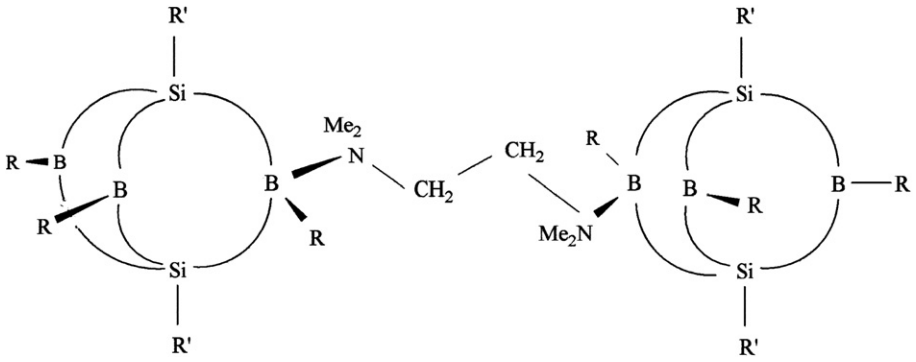


Diagram 2.

2.4. Synthesis of $[Bu^tSi\{O(PhB)O\}_3SiBu^t]_2 \cdot Me_2NCH_2CH_2NMe_2$ (13)

The reaction between $[Bu^tSi\{O(PhB)O\}_3SiBu^t]$ (**1**), and one equivalent of *N*,*N*,*N*′,*N*′-tetramethylethylenediamine in ether at r.t. for 8 h afforded $[Bu^tSi\{O(PhB)O\}_3SiBu^t]_2 \cdot Me_2NCH_2CH_2NMe_2$ (**13**) in low yield (27%) after crystallisation of the crude product from CH_2Cl_2–heptane (1:2) solution. As with compounds **1**–**12**, this compound was soluble in typical organic solvents such as toluene, dichloromethane, ether and acetone at room temperature. Chemical analysis for C, H, B and N suggested the formulation of **13** as a 2:1 adduct and FT-IR and multinuclear NMR spectroscopy supported this formulation. The ^{11}B NMR spectrum showed signals at 31.8 and 2.8 ppm in a ratio of 2:1 which correspond to three and four coordinate boron environments, respectively. On the basis of these data we suggest that the overall structure of **13** is as shown in Diagram 2.

Unfortunately, crystals suitable for an X-ray diffraction study could not be obtained even after many attempts from many different solvents.

3. Conclusions

Eleven borosiloxane $[R'Si(ORBO)_3SiR']$ cage compounds ($R' = Bu^t$ and R = Ph (**1**), 4-PhC_6H_4 (**2**), 4-$Bu^tC_6H_4$ (**3**), 3-$NO_2C_6H_4$ (**4**), 4-$CH(O)C_6H_4$ (**5**), $CpFeC_5H_4$ (**6**), 4-$C(O)CH_3C_6H_4$ (**7**), 4-ClC_6H_4 (**8**) and R = 2,4-$F_2C_6H_3$ (**9**), and R′ = *cyclo*-C_6H_{11} and R = Ph (**10**) and 4-BrC_6H_4 (**11**)) have been synthesized and characterized by spectroscopic (IR, NMR), mass spectrometric and for compounds where $R' = Bu^t$ and R = 4-PhC_6H_4 (**2**), 4-$Bu^tC_6H_4$ (**3**), 3-$NO_2C_6H_4$ (**4**), $CpFeC_5H_4$ (**6**) and 2,4-$F_2C_6H_3$ (**9**) X-ray diffraction studies. These compounds contain trigonal planar RBO_2 and tetrahedral $R'SiO_3$ units located around 11-atom "spherical" $B_3Si_2O_6$ cores. The reaction between $[Bu^tSi\{O(PhB)O\}_3SiBu^t]$, **1**, and excess pyridine yields a 1:1 adduct while the reaction between **1** and *N*,*N*,*N*′,*N*′-tetramethylethylenediamine in equimolar amounts affords a 2:1 borosiloxane:amine adduct.

It is clear from the structural analyses of 2, 3, 4, 6 and 9 that the $B_3Si_2O_6$ core structures are very similar and those in 2 and 3 being almost identical. All the structures involve near eclipsed arrangements of the *tert*-butyl groups at Si(1) and Si(2) when viewed along the Si···Si axis. The B–O–Si angles in the $B_3Si_2O_6$ cores of 2, 3, 4, 6 and 9 are found in a relatively narrow range from 134.0° to 143.0°. The structure of the pyridine adduct, 12, was determined with X-ray techniques. It had two trigonal planar RBO_2 units and one tetrahedral RBO_2N unit and a number of features in common with the unadducted compounds including a narrow range of B–O–Si angles (133.2–140.9°).

4. Experimental

All reactions were carried out under an inert atmosphere of dry nitrogen. Solvents were dried and distilled prior to use. Both *tert*-butylsilanetriol and *cyclo*-hexylsilanetriol were prepared according to the literature synthesis of $Bu^tSi(OH)_3$ [17]. All boronic acids used were obtained from either Aldrich or Lancaster Chemical Co. and used as supplied. Infrared spectra were recorded as KBr disks on a Perkin–Elmer Paragon 1000 FT-IR Spectrometer. ^1H and ^{13}C NMR spectra were recorded in $CDCl_3$ solvent on a JEOL FT NMR Spectrometer, GSX-270 Series or, for ^{11}B and ^{29}Si NMR spectra, on a Bruker AM 400. Chemical shifts δ are expressed in ppm relative to $\Xi = 100$ MHz for δ (^1H) (quoted ±0.05 ppm) (standard $SiMe_4$) and $\Xi = 32.083\,971$ MHz for δ (^{11}B) (quoted ±0.5 ppm) (nominally F_3BOEt_2 in $CDCl_3$). Mass spectra (EI, 70 eV) were recorded on a Kratos Profile GC–MS Spectrometer. Elemental analyses were carried out on a Perkin–Elmer 240C elemental analyser at the Microanalytical Laboratory, University College, Cork.

4.1. Syntheses of borosiloxane $[R^1Si(ORBO)_3SiR^1]$ cage compounds ($R^1 = Bu^t$ and R = Ph (1); 4-PhC_6H_4 (2); 4-$Bu^tC_6H_4$ (3); 3-$NO_2C_6H_4$ (4); 4-$CH(O)C_6H_4$ (5); $CpFeC_5H_4$ (6); 4-$C(O)CH_3C_6H_4$ (7); 4-ClC_6H_4 (8); 2,4-$F_2C_6H_3$ (9); and R^1 = *cyclo*-C_6H_{11} and R = Ph (10); 4-BrC_6H_4 (11))

4.1.1. Synthesis of $[Bu^tSi\{O(PhB)O\}_3SiBu^t]$ (1)

A mixture of *tert*-butylsilanetriol (0.507 g, 3.72 mmol) and phenylboronic acid (0.680 g, 5.58 mmol) in toluene

(50 ml) was heated at reflux temperature in a Dean-Stark apparatus for 10 h. After cooling, the removal of toluene on a rotary evaporator (40 °C) yielded a colourless solid. This was crystallised from hot benzene (50°C) affording [$Bu^tSi\{O(PhB)O\}_3SiBu^t$] (153, 0.943 g, 95.7%), m.p. 220–222°C. *Anal*. Calc. for $C_{26}H_{33}B_3O_6Si_2$: C, 58.9; H, 6.3; B, 6.1. Found: C, 59.05; H, 6.2; B, 6.0%. FT-IR (KBr) ν_{max}/cm^{-1}: 1305(vs), 1133(vs), 677(s). ^1H NMR ($CDCl_3$, 294 K): δ: 7.91–7.22 [m, 5H, C_6H_5]; 1.35 [s, 6H, $C(CH_3)_3$]. ^{13}C NMR ($CDCl_3$, 294 K) δ: 135.5, 133.4, 132.2, 127.9 [all C_6H_5]; 25.5 [$C(CH_3)_3$]; 16.6 [$C(CH_3)_3$]. MS, *m*/*z*: 530 $[M]^+$, 473 $[M-Bu]^+$, 453 $[M-Ph]^+$.

4.1.2. Synthesis of [$Bu^tSi\{O(4\text{-}C_6H_5C_6H_4)BO\}_3SiBu^t$ (2)

The procedure was the same as that described for **1**. The quantities used were: *tert*-butylsilanetriol (0.1536g, 1.13 mmol); 4-biphenylboronic acid (0.3254g, 1.64 mmol); toluene 50ml; reaction time 18 h. Crystallisation from CH_2Cl_2–heptane (1:3) afforded [$Bu^tSi\{O(4\text{-}C_6H_5C_6H_4)BO\}_3SiBu^t$], **2** (0.35 g, 81.1%), mp 282–284 °C. *Anal*. Calc. for $C_{44}H_{45}O_6B_3Si_2$: C, 69.7; H, 6.3. Found: C, 69.6; H, 6.3%. FT-IR (KBr) ν_{max}/cm^{-1}: 1299(vs), 1132(vs), 660(s). ^1H NMR ($CDCl_3$, 294 K): δ 8.03–7.21 [m, 3H, $C_6H_4C_6H_5$], 1.33 [s, 2H, $C(CH_3)_3$], ^{11}B NMR ($CDCl_3$, 294 K) δ 28.3, ^{13}C NMR ($CDCl_3$,294 K) δ 144.4, 141.0, 135.9, 131.0, 127.9, 126.8, 126.5 [all $C_6H_4C_6H_5$], 26.6 [$C(CH_3)_3$], 16.3 [$C(CH_3)_3$], ^{29}Si NMR ($CDCl_3$, 294 K) δ −57.5. Crystal data for **2**, see Table 1.

4.1.3. Synthesis of [$Bu^tSi\{O(4\text{-}Bu^tC_6H_4)BO\}_3SiBu^t$] (3)

The procedure was the same as that described for **1**. The quantities used were: *tert*-butylsilanetriol (0.1311 g, 0.96 mmol); *tert*-butylphenylboronic acid (0.2548 g, 1.43 mmol); toluene 50 ml; reaction time 15 h. Crystallisation from CH_2Cl_2–heptane (1:2) afforded [$Bu^tSi\{O\text{-}(4Bu^tC_6H_4)BO\}_3SiBu^t$] (**3**) (0.24 g, 74.9%). mp 253–255 °C. Found: C, 65.3; H, 8.2. *Anal*. Calc. for $C_{38}H_{57}O_6B_3Si_2$: C, 65.3; H, 8.2. Found: C, 65.3; H, 8.2. FT-IR (KBr) ν_{max}/cm^{-1}: 1302(vs), 1137(s), 660(m). MS, *m*/*z*: 698 $[M]^+$, 641 $[M-Bu]^+$, 57 $[Bu]^+$. Crystal data for **3**: see Table 1.

4.1.4. Synthesis of [$Bu^tSi\{O(3\text{-}NO_2C_6H_4)BO\}_3SiBu^t$] (4)

The procedure was the same as that described for **1**. The quantities used were: *tert*-butylsilanetriol (0.430 g, 3.16 mmol), 3-nitrophenylboronic acid (0.789 g, 4.73 mmol), toluene, 50ml; reaction time 10 h. The product, [$Bu^tSi\{OB(3\text{-}C_6H_4NO_2)O\}_3SiBu^t]\cdot(0.5C_7H_8)$, crystallised from a toluene solution at room temperature. Yield 0.913 g (87.1%) of **4**, m.p. 176–178°C. Found: C, 49.9; H, 4.9; N, 5.8; B, 4.3%. *Anal*. Calc. for $C_{29.5}H_{34}B_3N_3O_{12}Si_2$: C, 49.8; H, 4.8; N, 5.9; B, 4.6. Found: C, 49.9; H, 4.9; N, 5.8; B, 4.3%. FT-IR (KBr) ν_{max}/cm^{-1}: 1300(vs), 1143(vs), 657(m). ^1H NMR ($CDCl_3$, 294 K): δ: 8.67–7.31 [m, 2H, $C_6H_4NO_2$]; 1.43 [s, 3H, $C(CH_3)_3$]. ^{13}C NMR ($CDCl_3$, 294 K) δ: 148.4, 141.4, 134.2, 130.0, 128.7, 127.1 [all $C_6H_4NO_2$]; 25.7 [$C(CH_3)_3$]; 16.6 [$C(CH_3)_3$]. MS, *m*/*z*: 665 $[M]^+$, 619 $[M-NO_2]^+$, 608 $[M-Bu]^+$, 451 $[M-2NO_2-C_6H_4NO_2]^+$, 122 $[C_6H_4NO_2]^+$, 57 $[Bu]^+$.

4.1.5. Synthesis of [$Bu^tSi\{O(4\text{-}CHOC_6H_4)BO\}_3SiBu^t$] (5)

The procedure was the same as that described for **1**. The following quantities were used: *tert*-butylsilanetriol (0.4021 g, 2.96 mmol); 4-formylphenylboronic acid (0.6621 g, 4.41 mmol); toluene, 50 ml; reaction time 18 h. This afforded [$Bu^tSi\{O(4\text{-}CHOC_6H_4)BO\}_3SiBu^t$] (**5**) as a colourless crystalline solid (0.75 g, 82.1%), mp 194–196 °C. *Anal*. Calc. for $C_{29}H_{33}O_9B_3Si_2$: C, 56.7; H, 5.4. Found: C, 56.5; H, 5.6%. FT-IR (KBr) ν_{max}/cm^{-1}: 1298(vs), 1128(vs), 681(s). ^1H NMR ($CDCl_3$, 294 K): δ 9.98 [s, 3H, C_6H_4CHO], 8.00–7.19 [m, 4H, C_6H_4CHO], 1.27 [s, 6H, $C(CH_3)_3$], ^{13}C NMR ($CDCl_3$, 294 K): δ 192.4 [C_6H_4CHO], 138.7, 135.8, 128.9 [all C_6H_4CHO], 25.8C($CH_3)_3$], 16.2 [$C(CH_3)_3$]. MS, *m*/*z*: 614 $[M]^+$, 105 $[C_6H_4CHO]^+$, 57 $[Bu]^+$.

4.1.6. Synthesis of [$Bu^tSi\{O(CpFeC_5H_4)BO\}_3SiBu^t$] (6)

The procedure was the same as that described for **1**. The following quantities were used: *tert*-butylsilanetriol (0.1971 g, 1.45 mmol); ferrocenylboronic acid (0.5211 g, 2.25 mmol); toluene, 60 ml; reaction time 15 h. Crystallisation from CH_2Cl_2–heptane (1:3) afforded orange crystals of [$Bu^tSi(OC_5H_4FeCpBO)_3SiBu^t$] (**6**) (0.50 g, 82.2%), m.p. 244–246 °C. *Anal*. Calc. for $C_{38}H_{45}O_6B_3Fe_3Si_2$: C, 53.4; H, 5.3. Found: C, 53.4; H, 5.3%. FT-IR (KBr) ν_{max}/cm^{-1}: 1316(s), 1290(s), 621(m). MS, *m*/*z*: 854 $[M]^+$, 186 $[(C_5H_5FeC_5H_5)]^+$. Crystal data for **6**: see Table 1.

4.1.7. Synthesis of [$Bu^tSi\{O(CH_3C(O)C_6H_4B)O\}_3SiBu^t$] (7)

The procedure was the same as that described for **1**. The following quantities were used: *tert*-butylsilanetriol (0.3024 g, 2.22 mmol); 4-acetylphenylboronic acid (0.5511 g, 3.31 mmol); toluene, 50 ml; reaction time 18 h. This afforded [$Bu^tSi\{O(CH_3C(O)C_6H_4B)O\}_3SiBu^t$] (**7**) as a crystalline solid (0.54 g, 75.2%), m.p. 134–135 °C. *Anal*. Calc. for $C_{32}H_{39}O_9B_3Si_2$: C, 58.5; H, 6.0. Found: C, 58.6; H, 6.1%. FT-IR (KBr) ν_{max}/cm^{-1}: 1301(vs), 1133(s), 632(m). ^1H NMR ($CDCl_3$, 294 K): δ 8.04–7.26 [m, 4H, C_6H_4]; 2.62 [s, 3H, $C(O)CH_3$]; 1.27 [s, 6H, $C(CH_3)_3$]. ^{13}C NMR ($CDCl_3$, 294 K): δ 198.1 [$C(O)CH_3$]; 139.8, 137.2, 135.9, 134.1, 127.9 [all C_6H_4]; 27.0 [$C(O)CH_3$]; 25.5 [$C(CH_3)_3$], 16.3 [$C(CH_3)_3$]. MS, *m*/*z*: 656 $[M]^+$, 599 $[M-Bu]^+$, 57 $[Bu]^+$.

4.1.8. Synthesis of [$Bu^tSi\{O(4\text{-}ClC_6H_4)BO\}_3SiBu^t$] (8)

The procedure was the same as that described for **1**. The quantities of starting materials used were: *tert*-butylsilanetriol (0.1541 g, 1.13 mmol); 4-chlorophenylboronic acid (0.2641 g, 1.67 mmol); toluene 60 ml; reaction time 16 h. Crystallisation from a toluene–heptane (ca. 1:3) solution afforded [$Bu^tSi\{O(4\text{-}ClC_6H_4)BO\}_3SiBu^t$] (**8**) (0.29 g, 34.1%), m.p. 304–308 °C. *Anal*. Calc. for $C_{26}H_{30}O_6B_3Cl_3Si_2$: C, 49.4; H, 4.7. Found: C, 49.6; H, 4.5%.

FT-IR (KBr) ν_{max}/cm^{-1}: 1306(vs), 1130(m), 678(m). ^1H NMR ($CDCl_3$, 294 K): δ 7.81–7.20 [m, 2H, C_6H_4Cl];. 1.26 [s, 3H, $C(CH_3)_3$]. (HR-MS), *m/z*: Found 632.094. Calculated for $^{12}C_{26}{}^1H_{30}{}^{11}B_3{}^{35}Cl_3{}^6O_6{}^{28}Si_2$ 632.017.

4.1.9. Synthesis of [$Bu^tSi\{O(2,4\text{-}F_2C_6H_3)BO\}_3SiBu^t$] (9)

The procedure was the same as that described for **1**. The following quantities were used: *tert*-butylsilanetriol (0.4112 g, 3.0 mmol); 2,6 difluorophenylboronic acid (0.6821 g, 4.4 mmol); toluene, 60 ml; reaction time 15 h. Crystallisation from CH_2Cl_2–heptane (1:3) afforded [Bu^t-$Si\{O(2,4\text{-}F_2C_6H_3)BO\}_3SiBu^t$] (**9**) (0.75 g, 87.3%), m.p. 183–185°C. *Anal*. Calc. for $C_{36}H_{27}B_3F_6O_6Si_2$: C, 49.0; H, 4.3. Found: C, 50.1H, 4.4%. FT-IR (KBr), ν_{max}/cm^{-1}: 1310(s), 1130(vs), 651(m). ^1H NMR ($CDCl_3$, 294 K): δ 7.80–6.75[m, 1H, C_6H_3], 1.26[s, 2H, $C(CH_3)_3$]. ^{29}Si NMR ($CDCl_3$, 294 K) δ −58.12. Crystal data for **9**, see Table 2.

4.1.10. Synthesis of [$C_6H_{11}Si\{O(PhB)O\}_3SiC_6H_{11}$] (10)

The procedure was essentially the same as that described for **1**. The quantities used were: *cyclo*hexylsilanetriol (0.4162 g, 2.54 mmol); phenylboronic acid (0.4599 g, 3.77 mmol); toluene 50 ml; reaction time 14 h. Crystallisation from CH_2Cl_2, toluene and heptane (1:1:2) afforded [$C_6H_{11}Si\{O(PhB)O\}_3SiC_6H_{11}$] (**10**) (0.30 g, 42.2%), m.p. 192–194 °C. *Anal*. Calc. for $C_{30}H_{37}O_6B_3Si_2$: C, 61.8; H, 6.4. Found: C, 62.1; H, 6.3%. FT-IR (KBr), ν_{max}/cm^{-1}: 1306(vs), 1140(vs), 639(s). ^1H NMR ($CDCl_3$, 294 K): δ 7.53–7.17 [m, 15H, C_6H_5]; 2.12–1.12 [m, 22H, C_6H_{11}].

4.2. Synthesis of [$C_6H_{11}Si\{O(4\text{-}BrC_6H_4B)O\}_3SiC_6H_{11}$] (11)

The procedure was essentially the same as that described for **1**. The quantities of reagents were: *cyclo*hexylsilanetriol (0.3199 g, 1.97 mmol), bromophenylboronic acid (0.7011 g, 3.49 mmol); toluene 50 ml; reaction time 10 h. A benzene solution was layered with *cyclo*hexane (ca. 1:3). The microcrystalline product was [$C_6H_{11}Si\{O(4\text{-}BrC_6H_4B)O\}_3$-$SiC_6H_{11}$] (**11**) (0.44 g, 57.3%), m.p. 252–254 °C. *Anal*. Calc. for $C_{30}H_{34}O_6B_3Br_3Si_2$: C, 44.0; H, 4.2; Br, 29.3. Found: C, 44.0; H, 4.3; Br, 29.4%. FT-IR (KBr), ν_{max}/cm^{-1}: 1300(vs), 1129(vs), 636(s). ^1H NMR ($CDCl_3$, 294 K): δ 7.90–7.25[m, 6H, C_6H_4Br]; 2.17–2.13 [m, 11H, C_6H_{11}].

4.3. Reactions between [$Bu^tSi\{O(PhB)O\}_3SiBu^t$] (1) and (a) pyridine, (b) N,N,N′,N′-tetramethylethylenediamine

4.3.1. Synthesis of [$Bu^tSi\{O(PhB)O\}_3SiBu^t$] · C_5H_5N (12)

Compound **1**, [$Bu^tSi\{O(PhB)O\}_3SiBu^t$] (0.11 g, 0.275 mmol) was dissolved in ether (30 ml). While vigorously stirring, pyridine (0.05 g, 6.23 mmol) was added via micopipette. The reaction mixture was stirred for 16 h. Removal of ether on a rotary evaporator afforded a colourless product. Crystallisation from CH_2Cl_2–heptane (1:3) yielded [$Bu^tSi\{O(PhB)O\}_3SiBu^t$] · C_5H_5N (**12**) (0.046 g, 73.4%), m.p. 218–219 °C. *Anal*. Calc. for $C_{31}H_{38}O_6B_3NSi_2$: C, 61.1; H, 6.2; N, 2.3; B, 5.4. Found: C, 61.7; H, 6.3; N, 2.9; B, 5.1%. FT-IR (KBr) ν_{max}/cm^{-1}: 1327(s), 1297(s), 1194(s), 1103(s), 1051(s), 1018(s), 701(s). ^1H NMR ($CDCl_3$, 294 K): δ 8.80–7.21 [m, 10H, C_6H_5 and C_5H_5], 1.32 [s, 9H, $C(CH_3)_3$]. ^{13}C NMR ($CDCl_3$, 294 K): δ 147.3, 137.7, 134.3, 130.0, 127.4, 124.3 [all C_6H_5 and C_5H_5], 25.6 [$C(CH_3)_3$], 16.6 [$C(CH_3)_3$]. ^{11}B NMR ($CDCl_3$, 294 K): δ 25.5 OB(Ph)O, 0.6 $OPhBO(NC_5H_5)$. Crystal data for **12**: see Table 2.

4.3.2. Synthesis of [$Bu^tSi\{O(PhB)O\}_3SiBu^t]_2$ · $Me_2NCH_2CH_2NMe_2$ (13)

Compound **1** (0.251 g, 0.473 mmol) was dissolved in ether (40 ml). *N*,*N*,*N*′,*N*′-Tetramethylethylenediamine (0.055 g, 0.472 mmol) was added via micropipette and a colourless precipitate formed. With further stirring, this almost completely dissolved. After 8 h, the solution was filtered. Removal of the solvent gave a colourless powder. Crystallisation from CH_2Cl_2–heptane (1:2) afforded [Bu^t-$Si\{O(PhB)O\}_3SiBu^t]_2 \cdot Me_2NCH_2CH_2NMe_2$ (**13**) (0.151 g, 27.3%), m.p. 233–234 °C. *Anal*. Calc. for $C_{58}H_{82}O_{12}B_6N_2$-Si_4:C, 59.2; H, 7.0, N, 2.4; B, 5.6. Found: C, 58.8; H, 6.9; N, 2.2; B, 5.4%. FT-IR (KBr) ν_{max}/cm^{-1}: 1439(s), 1356(s), 1308(vs), 1165(s), 1172(s), 1085(s), 1032(s), 680(s), 652(s). ^1H NMR ($CDCl_3$, 294 K): δ 7.81–7.14 [m, 15H, C_6H_5]; 2.62 [m, 2H, $Me_2NCH_2CH_2NMe_2$], 2.21 [s, 6H, $(CH_3)_2NCH_2$-$CH_2N(CH_3)_2$], 1.34 [s, 18H, $C(CH_3)_3$], ^{13}C NMR ($CDCl_3$, 294 K): δ 135.5, 134.9, 131.2, 129.7, 127.4 [all, C_6H_5], 55.4 [$Me_2NCH_2CH_2NMe_2$], 44.9[$(CH_3)_2NCH_2$-$CH_2N(CH_3)_2$], 26.1 [$C(CH_3)_3$], 16.3 [$C(CH_3)_3$]. ^{11}B NMR ($CDCl_3$, 294 K): δ 31.8 OB(Ph)O and 2.8 $OPhBO(Me_2NCH_2)_2$.

4.3.3. Data Collection and structure refinement for compounds 2, 3, 4, 6, 9 and 12

Data for **2**, **3** and **4** were collected on an Enraf-Nonius CAD-4 diffractometer with graphite-monochromatised Mo Kα radiation ($\lambda = 0.71073$ Å). Data for **6**, **9** and **12** were collected on a Nonius MACH3 diffractometer with graphite-monochromatised Mo Kα radiation ($\lambda =$ 0.71073 Å). Data analysis for **2**, **3**, **4** [18], **6**, **9** and **12** [19] were carried out to provide 8018, 7964, 7780, 9117, 3379 and 5384 independent reflections, respectively. The structures were solved using direct methods [20]. Non-hydrogen atoms were refined with anisotropic thermal parameters. The hydrogen atoms bonded to carbon were included in geometric positions and given thermal parameters equivalent to 1.2 times those of the atom to which they were attached, although a 1.5 factor was used for the methyl groups. A Gaussian absorption correction on **2** was carried out [18]. For **9** there was disordered solvent present which could not be modelled correctly and was removed using the SQUEEZE algorithm [21].

The structures were refined on F^2 [22] to R_1 0.055, 0.064, 0.074, 0.043, 0.083 and 0.071 for 3389, 3115, 3338, 6403, 496 and 1589 reflections, respectively, with $I > 2\sigma(I)$ and

wR_2 0.127, 0.193, 0.177, 0.129, 0.155 and 0.238 for all independent reflections.

Acknowledgements

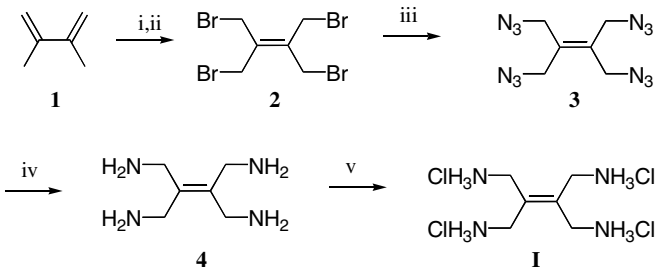
The ^{11}B and ^{29}Si NMR spectra were kindly recorded on a Bruker AM 400 instrument at the University of Leeds by Prof. J.D. Kennedy. G.F. and S.E.L. thank NSERC Canada and University College Cork for funds for diffractometers.

Appendix A. Supplementary material

CCDC 615803, 615804, 615805, 615806, 615807 and 615808 contain the supplementary crystallographic data for this paper. These data can be obtained free of charge via http://www.ccdc.cam.ac.uk/conts/retrieving.html, or from the Cambridge Crystallographic Data Centre, 12 Union Road, Cambridge CB2 1EZ, UK; fax: (+44) 1223-336-033; or e-mail: deposit@ccdc.cam.ac.uk. Supplementary data associated with this article can be found, in the online version, at doi:10.1016/j.poly.2006.12.045.

References

[1] F.J. Feher, T.A. Budzichowski, Polyhedron 14 (1995) 3239, and references therein.
[2] S.S. Kumar, H.W. Roesky, Dalton Trans. (2004) 3927, and references therein.
[3] T.R. Spalding, B. O'Leary, L. Neville, G. Ferguson, in: M. Davidson, A.K. Hughes, T.B. Marder, K. Wade (Eds.), Contemporary Boron Chemistry, Special Publication No. 253, Royal Society of Chemistry, 2000, p. 92.
[4] B.J. O'Leary, D.M. Murphy, T.R. Spalding, G.F. Ferguson, J. Organomet. Chem. 526 (1996) 195.
[5] A.T. O'Dowd, T.R. Spalding, G.F. Ferguson, J.F. Gallagher, D. Reed, J. Chem. Soc., Chem. Commun. (1993) 1816.
[6] L.A. Neville, T.R. Spalding, G. Ferguson, Angew. Chem., Int. Ed. 39 (2000) 3598.
[7] A.G. Avent, S.E. Lawrence, M.M. Meehan, T.G. Russell, T.R. Spalding, Collect. Czech. Chem. Commun. 67 (2002) 1051.
[8] F.J. Feher, T.A. Budzichowski, J.W. Ziller, Inorg. Chem. 31 (1992) 5100.
[9] O. Graalmann, U. Klingebiel, W. Clegg, M. Haase, G.M. Sheldrick, Z. Anorg. Allg. Chem. 519 (1984) 87.
[10] F.H. Allen, O. Kennard, D.G. Watson, L. Brammer, A.G. Orpen, R. Taylor, J. Chem. Soc., Perkin Trans. II (1987) S1.
[11] B.J. O'Leary, Ph.D. Thesis, University College Cork, National University of Ireland, Cork, Ireland, 1998.
[12] D. Murphy, J.P. Sheehan, T.R. Spalding, G. Ferguson, A.J. Lough, J.F. Gallagher, J. Mater. Chem. 3 (1993) 1275.
[13] B.J. Brisdon, M.F. Mahon, K.C. Molloy, P.J. Scholfield, J. Organomet. Chem. 435 (1992) 11.
[14] D.A. Foucher, A.J. Lough, I. Manners, Inorg. Chem. 31 (1992) 3034.
[15] G. Ferguson, A.J. Lough, J.P. Sheehan, T.R. Spalding, Acta Crystallogr., Sect. C 47 (1991) 379.
[16] G. Ferguson, J.F. Gallagher, D. Murphy, J.P. Sheehan, T.R. Spalding, Polyhedron 12 (1993) 859.
[17] N. Winkhofer, H.W. Roesky, M. Noltemeyer, W.T. Robinson, Angew. Chem., Int. Ed. 31 (1992) 599.
[18] E.J. Gabe, Y. Le Page, J.-P. Charland, F.L. Lee, P.S. White, J. Appl. Crystallogr. 22 (1989) 384.
[19] S. Mackay, W. Dong, C. Edwards, A. Henderson, C.J. Gilmore, N. Stewart, K. Shankland, A. Donald, maXus, University of Glasgow, Glasgow, Scotland, 1998.
[20] G.M. Sheldrick, Acta Crystallogr., Sect. A 46 (1990) 467.
[21] A.L. Spek, PLATON, University of Utrecht, Utrecht, Holland, 2002.
[22] G.M. Sheldrick, SHELXL-97, University of Göttingen, Göttingen, Germany, 1997.



Scheme 1. Reagents and conditions: (i) Br_2, CCl_4, 0 °C; (ii) NBS, 24 h, reflux, 60% (over two steps); (iii) NaN_3 (4.4 equiv.), DMF, −40 °C, 20 h; (iv) PPh_3 (4.4 equiv.), H_2O (6 equiv.), THF, −40 °C, 20 h; (v) HCl_{aq}, 80% (over three steps).

(210 mL, 4.4 equiv., 20.1 mmol), the solution was stirred for 1 h. The separated aqueous phase was washed with ethyl acetate (250 mL). The tetramine tetrachlorhydrate (**I**) was obtained after water removal as a solid (1.34 g, 80% yield, 4 mmol). ^{1}H NMR (400 MHz, D_2O), δ (ppm, DSS): 4.05 (s, 8H), 4.78 (s, 12H). ^{13}C NMR (100 MHz, D_2O): 38.0, 136.0.

2.2. Synthesis of $[H_4ten]\cdot(AlF_5)_2$ (*II*)

A microcrystalline powder of $[H_4ten]\cdot(AlF_5)_2$ was prepared from Al_2O_3, *ten* (obtained after Cl^-/OH^- exchange on an anionic resin.), HF, H_2O in 1:0.5:10:515 molar ratios by microwave heating assisted hydrothermal synthesis (Fig. 1). The solid product was washed with deionised water and dried at room temperature. XRD powder patterns indicated that the $[H_4ten]\cdot(AlF_5)_2$ (**II**) sample was contaminated with pyrochlore $(Al_2[(OH),F]_6\cdot H_2O$ [14]).

2.3. Determination of crystal structure

A single-crystal of **I**, suitable for X-ray diffraction, was selected by using an optical microscope. The crystal cell parameters were obtained from a random reflection search and X-ray diffraction data were collected on a Siemens AED2 four-circle diffractometer. Chlorine atoms were located by direct methods using the SHELXS-86 program [15]. Nitrogen and carbon atoms were found by difference Fourier maps and the positions of hydrogen atoms were geometrically constrained (HFIX option). Structure refinements were performed using the SHELXS-97 program [16]. The positions of all non-hydrogen atoms were refined anisotropically and a unique isotropic thermal motion was used for all hydrogen atoms.

The indexation of the XRD pattern of $[H_4ten]\cdot(AlF_5)_2$ was carried out with the McMaille [17] software from the 20 first lines. A monoclinic solution was found with satisfactory figures of merit ($M(20) = 47$, $F(20) = 75$ (0.0054, 48) and was confirmed at the structure factor extraction stage using the FULLPROF program [18] (Le Bail method [19]). Directs methods failed to provide structure solutions. Calculations were then performed with Espoir, a reverse Monte Carlo program with a pseudo simulated annealing code for ab initio crystal structure determination by the direct space method. The strategy consisted of the introduction of three objects, translated and rotated randomly, until a satisfying fit to a pseudo powder pattern regenerated from the extracted structure factors was obtained: one *ten* molecule (hydrogen atoms omitted), one AlF_6 octahedron and one AlF_4 square plane. The geometry of *ten* was deduced from the structure of $[H_4ten]Cl_4$. In the first stage, the structure was determined in the non-centrosymmetric *Pc* space group and a model with $(AlF_5)_\infty$ chains was obtained. This model was introduced into the Rietveld method (Fullprof) for refinement (Fig. 2). It was found that two Al atoms and the center of $[H_4ten]^{4+}$ cations were compatible with the presence of an inversion center and consequently, the final results are given in the *P*2/*c* space group.

The conditions of data collection are summarized in Table 1. Atomic coordinates and main bond lengths are given in Tables 2–5.

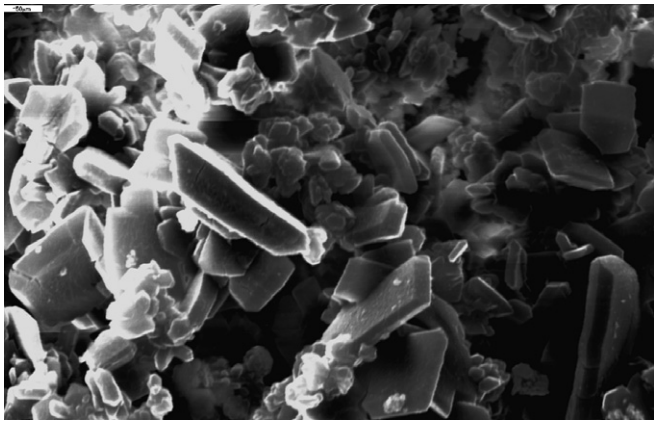


Fig. 1. Electron scanning micrograph of $[H_4ten]\cdot(AlF_5)_2$ crystals.

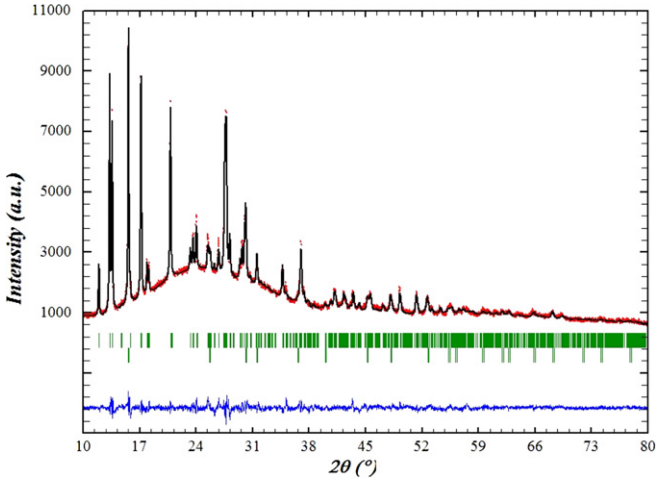


Fig. 2. Final Rietveld plot crystal structure of $[H_4ten]\cdot(AlF_5)_2$. The bottom sticks show the presence of $Al_2[(OH),F]_6\cdot H_2O$.

Table 1
X-ray crystallographic data of $[H_4ten]Cl_4$ (**I**), and $[H_4ten]\cdot(AlF_5)_2$ (**II**)

Compound	**I**	**II**
Formula	$C_6N_4H_{20}Cl_4$	$C_6N_4H_{20}Al_2F_{10}$
Formula weight	290	392
Crystal system	monoclinic	
Space group	*C*2/*m*	*P*2/*c*
a (Å)	11.651(3)	8.528(1)
b (Å)	8.159(2)	7.394(1)
c (Å)	6.847(1)	13.237(1)
β (°)	101.53(3)	128.777(2)
V (Å^3), Z	637.8(3), 2	650.7(1), 2
ρ_{calc} (g cm^{-3})	1.51	2.00
Wavelength (Å)	0.71069	1.54056
Temperature (K)	293	
2*θ* range (°)	3–55	10–80
Reflections measured/unique/ ($I > 2\sigma(I)$)	777/774/643	
Refined parameters	39	96
R/R_w	0.0475/ 0.140	
$\Delta\rho_{min}/\Delta\rho_{max}$ (e Å^{-3})	−0.52/0.57	
Number of independent reflections		2032
Number of intensity-dependent parameters		403
Distance restraints		51
R_P, R_{wp}, R_B, R_F		0.031, 0.017, 0.078, 0.146

Table 2
Atomic coordinates and equivalent isotopic displacement parameters for $[H_4ten]Cl_4$ (**I**)

Atom	Site	*x*	*y*	*z*	$U_{equiv.}$ (Å^2)
Cl(1)	4i	0.38917(8)	0	0.2790(1)	0.0483(4)
Cl(2)	4i	0.32647(7)	1/2	−0.6440(1)	0.0423(3)
N	8j	0.3987(2)	0.2458(3)	−0.2851(3)	0.0441(6)
C(1)	4h	1/2	0.5825(4)	0	0.0333(7)
C(2)	8j	0.3926(2)	0.3174(3)	−0.0860(4)	0.0401(6)

Table 3
Atomic coordinates for $[H_4ten]\cdot(AlF_5)_2$ (**II**)

Atom	Site	*x*	*y*	*z*	$U_{equiv.}$ (Å^2)
Al(1)	2c	0	1/2	1/2	0.074(3)
Al(2)	2a	0	0	1/2	0.074(3)
F(1)	4g	0.240(1)	0.478(1)	0.5360(7)	0.069(2)
F(2)	4g	0.025(1)	0.255(7)	0.4881(9)	0.069(2)
F(3)	4g	0.113(1)	0.470(1)	0.6577(6)	0.069(2)
F(4)	4g	0.021(1)	0.020(1)	0.3719(6)	0.069(2)
F(5)	4g	0.270(1)	0.022(1)	0.6176(6)	0.069(2)
C(1)	4g	0.492(1)	0.090(1)	0.5144(4)	0.136(4)
C(2)	4g	0.586(1)	0.241(1)	0.6214(9)	0.136(4)
C(3)	4g	0.344(1)	0.178(1)	0.3812(8)	0.136(4)
N(1)	4g	0.782(1)	0.281(1)	0.6499(9)	0.136(4)
N(2)	4g	0.446(1)	0.245(1)	0.3262(9)	0.136(4)

Table 4
Selected bond distances (Å) of $[H_4ten]Cl_4$ (**I**)

N(1)–C(2)	1.498(3)
C(1)–C(1)	1.347(7)
C(1)–C(2)	1.511(3)
C(1)–C(2)	1.511(3)
C(2)–C(1)	1.511(3)

Table 5
Selected bond distances (Å) of $[H_4ten]\cdot(AlF_5)_2$ (**II**)

Al(1)–F(3)	1.678(9)
Al(1)–F(1)	1.795(9)
Al(1)–F(2)	1.844(6)
Al(2)–F(5)	1.805(6)
Al(2)–F(4)	1.82(1)
Al(2)–F(2)	1.915(6)
C(1)–C(1)	1.42(1)
C(1)–C(3)	1.53(1)
C(1)–C(2)	1.57(1)
C(2)–N(1)	1.489(2)
C(3)–N(2)	1.53(2)

3. Results and discussion

The tetra(azidation-Staudinger) route we previously described for pentaerythrityl tetramine [20] was applied for the preparation of $[H_4ten]Cl_4$. However, this three step pathway from the known 2,3 di-2-bromomethyl 1,4 bromonobut-2-ene (**2**) [21] depicted in Scheme 1 proved to lead to $[H_4ten]Cl_4$ (**5**) in good purity and yield only after extensive optimization of the reaction conditions.

Indeed, conventional azidation of the tetrabromide **2**, carried out at 100 °C in DMF or DMSO, led to a mixture of the expected tetrazide **3** and its regioisomer **3′** (Table 6). The formation of **3′** is explained by a concerted [3,3]′-sigmatropic rearrangement of **3** (Fig. 3), as suggested for

Table 6
Effect of reaction conditions on the **3**/**3′** allyl azide isomerisation ratio[a]

T (°C)	DMF	DMSO
100	30/70	50/50
20	40/60	60/40
−40	100/0	

[a] Determined by ^{1}H NMR of the crude product.

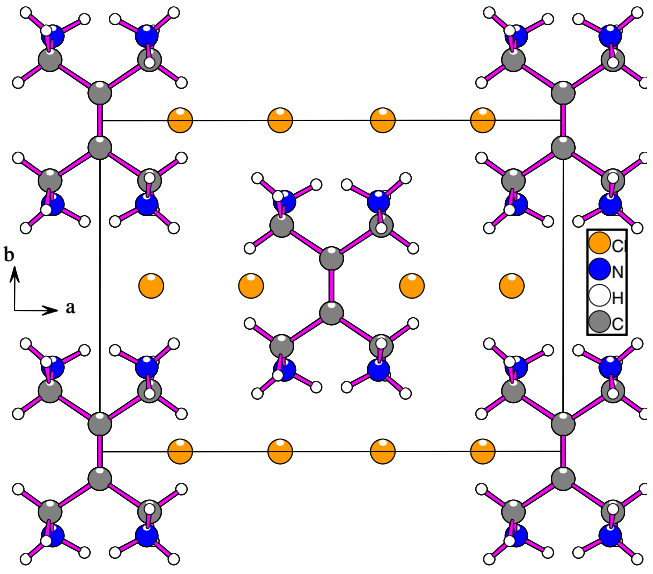


Fig. 3. Crystal structure of $[H_4ten]Cl_4$.

the interconversion of allylic azides [22]. This rearrangement occurs to a large extent even at room temperature (Table 5). In contrast, when produced at −40 °C in DMF, tetrazide **3** is stable and can be isolated in a pure isomeric form.

Unfortunately, in the next step, applying classical Staudinger conditions to pure tetraazide **3** at room temperature led to tetramine **4** contaminated by a significant amount of pre-isomerized tetramine **4′**. These results exemplify that (i) a significant [3,3]-sigmatropic equilibration process occurs under these conditions and (ii) that the formation of the primary allylamine **4** is not selective with respect to those of the tertiary one **4′**, in contrast with previous findings reported in geranyl versus linalyl series [23]. However, we disclosed that the side *in situ* isomerization process could be efficiently suppressed by performing the Staudinger reaction on **3** at −40 °C in THF. Under these conditions and after acidification, $[H_4ten]Cl_4$ (**5**) was thus obtained in 80% overall yield from **2** as a crystalline pure product. The structure of $[H_4ten]Cl_4$ was determined by single crystal X-ray diffraction (Fig. 4).

The structure of $[H_4ten]\cdot(AlF_5)_2$ is built up from [0 1 0] $(AlF_5)_\infty$ chains of corner sharing AlF_6 octahedra (Fig. 5). Charge balance is ensured by tetraprotonated $[H_4ten]^{4+}$ cations. Two crystallographically non-equivalent aluminum atoms Al(1) and Al(2) are coordinated to six fluoride anions. Aluminum to bridging fluorine distances (≈1.88 Å) are longer than aluminum to terminal fluoride distances (≈1.78 Å). Similar chains of trans-connected octahedra are encountered in $[H_4tetra]\cdot(AlF_5)_2$ [19]. Hydrogen bond interactions, established between terminal NH_3 groups of the amine cations and fluoride anions, ensure the cohesion of the structure.

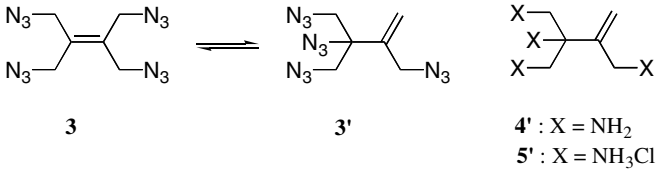


Fig. 4. Concerted [3,3]-sigmatropic rearrangement of **3** as a potential source of by-products **3′**–**5′**.

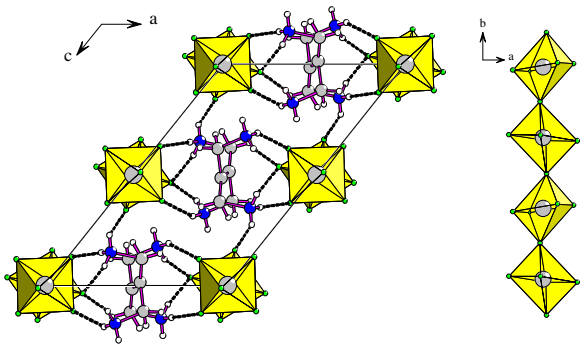


Fig. 5. Crystal structure of $[H_4ten]\cdot(AlF_5)_2$ (left), projections of trans $(AlF_5)_\infty$ chains (right).

4. Conclusion

In summary, an efficient synthesis of a new allyl tetramine, labelled *ten*, has been achieved in good overall yield. The hydrothermal synthesis of the Al_2O_3–*ten*–HF–H_2O system leads to the first *ten* fluoroaluminate. The structure is *ab initio* determined from X-ray powder data by using the geometry of $[H_4ten]^{4+}$ cations which was obtained from single-crystal analysis of $[H_4ten]Cl_4$. A broad study of the influence of the amine geometry on the template effect is currently ongoing. Both planar *ten* amine and the saturated analog (labelled *tan*) will be tested. The crystallization fields of the solids will be determined on large concentration domains of the starting materials.

Appendix A. Supplementary materials

CCDC 621905 and 621906 contain the supplementary crystallographic data for **I** and **II**. These data can be obtained free of charge via http://www.ccdc.cam.ac.uk/conts/retrieving.html, or from the Cambridge Crystallographic Data Centre, 12 Union Road, Cambridge CB2 1EZ, UK; fax: (+44) 1223-336-033; or e-mail: deposit@ccdc.cam.ac.uk. Supplementary data associated with this article can be found, in the online version, at doi:10.1016/j.poly.2006.12.041.

References

[1] D.B. Shinn, D.S. Crockett, H.M. Haendler, Inorg. Chem. 5 (1966) 11.
[2] F.J. Christoph, M.D. Elkton, G. Teufer, C. Ford, U.S. Patent 2 (1965) 178,483.
[3] U. Bentrup, M. Feist, E. Kemnitz, Prog. Solid Chem. 27 (1998) 65.
[4] (a) U. Calov, R. Seydel, K.H. Jost, R. Hedel, G. Reck, Z. Anorg. Allg. Chem. 619 (1993) 1307;
(b) G. Rother, H. Worzala, U. Bentrup, Z. Anorg. Allg. Chem. 622 (1996) 1991;
(c) G. Rother, H. Worzala, U. Bentrup, Z. Anorg. Allg. Chem. 213 (1998) 119;
(d) U. Bentrup, A. Ahmadi, H.C. Kang, W. Massa, Z. Anorg. Allg. Chem. 624 (1998) 1465;
(e) J. Touret, X. Bourdon, M. Leblanc, R. Retoux, J. Renaudin, V. Maisonneuve, J. Fluorine Chem. 110 (2001) 133.
[5] (a) B. Adamczyk, S.I. Troyanov, M. Scheinder, E. Kemnitz, Z. Anorg. Allg. Chem. 626 (2000) 2543;
(b) L.Q. Tang, M.S. Dadachov, X.D. Zou, Z. Kristallogr. – New Cryst. Struct. 216 (2001) 389;
(c) K. Adil, M. Leblanc, V. Maisonneuve, Acta Crystallogr. E60 (2004) m1379.
[6] L.Q. Tang, M.S. Dadachov, X.D. Zou, Z. Kristallogr. – New Cryst. Struct. 216 (2001) 385.
[7] K. Adil, A. Ben Ali, G. Dujardin, R. Dhal, M. Leblanc, V. Maisonneuve, J. Fluorine Chem. 125 (2004) 1709.
[8] K. Adil, M. Leblanc, V. Maisonneuve, J. Fluorine Chem. 127 (2006) 1349.
[9] E. Goreshnik, V. Maisonneuve, M. Leblanc, Z. Anorg. Allg. Chem. 628 (2002) 162.
[10] R.L. Harlow, N. Herron, Z. Li, T. Vogt, L. Solovyov, S. Kirik, Chem. Mater. 11 (1999) 2562.
[11] N. Herron, D.L. Thorn, R.L. Harlow, G.A. Jones, J.B. Parise, J.A. Fernadez-Baca, T. Vogt, Chem. Mater. 7 (1995) 75.

[12] A. Le Bail, J.L. Fourquet, U. Bentrup, J. Solid State Chem. 100 (1992) 151.
[13] ESPOIR A. Le Bail, Mater. Sci. Forum 65 (2001) 378.
[14] A. Le Bail, C. Jacoboni, M. Leblanc, R. De Pape, H. Duroy, J.L. Fourquet, J. Solid State Chem. 77 (1988) 96.
[15] G.M. Sheldrick, in: G.M. Sheldrick, C. Krüger, R. Goddard (Eds.), SHELXS86 in Crystallographic Computing, vol. 3, Oxford University Press, 1985, p. 175.
[16] G.M. Sheldrick, SHELXS97, A Program for Crystal Structure Determination (release 97-2), Göttingen University, Germany, (1998).
[17] McMaille A. Le Bail, Powder Diffr. 19 (2004) 249.
[18] FULLPROFF , J. Rodriguez-Carvajal, LLB (CEA-CNRS), 1998, v3.5d.
[19] A. Le Bail, H. Duroy, J.L. Fourquet, Mater. Res. Bull. 23 (1988) 447.
[20] K. Adil, E. Goreshnik, S. Courant, G. Dujardin, M. Leblanc, V. Maisonneuve, Solid State Sci. 6 (2004) 1229.
[21] A.C. Cope, F. Kagan, J. Am. Chem. Soc. 80 (1958) 5499.
[22] (a) J.S. Panek, M. Yang, I. Muler, J. Org. Chem. 57 (1992) 4063;
(b) A. Padwa, M.M. Sa, Tetrahedron Lett. 38 (1997) 5087;
(c) A. Padwa, M.M. Sa, J. Braz. Chem. Soc. 10 (1999) 231;
(d) K. Banert, M. Hagedorn, C. Liedtke, A. Melzer, C. Schoffler, Eur. J. Org. Chem. (2000) 257;
(e) A.K. Feldman, B. Colasson, K.B. Sharpless, V.V. Fokin, J. Am. Chem. Soc 127 (2000) 13444.
[23] S. Murahashi, Y. Taniguchi, Y. Imada, Y. Tanigawa, J. Org. Chem. 54 (1989) 3292.

have studied and described in the literature the reactivity of the ligand bdtp with different metals such as Ni(II), Co(II), Cu(I), Zn(II), Ag(I), Cd(II) and Re(I) [9], and our research group recently has reported the reactivity of the ligand bdtp with Pd(II). We have demonstrated the hemilabile properties of this ligand when coordinated to Pd(II) [7c].

In this paper, we have studied the reactivity of the ligand bdtp [7c,8] towards Pt(II), under various conditions and with several platinum starting materials.

2. Results and discussion

2.1. Synthesis and spectroscopic properties

Reaction of 1,5-bis(3,5-dimethyl-1-pyrazolyl)-3-thiapentane (bdtp) [7c,8] (Scheme 1) with several platinum starting materials, such as K_2PtCl_4, $PtCl_2$, $[PtCl_2(CH_3\text{- }CN)_2]$ [10] and $[PtCl_2(PhCN)_2]$ [11], have been developed under different conditions (Scheme 2). In general, and in contrast to the Pd(II) complexes, these reactions take a longer time and need higher temperatures to occur. This same behaviour is observed with the ligands 1,8-bis-(3,5-dimethyl-1-pyrazolyl)-3,6-dithiaoctane (bddo), 1,9-bis(3,5-dimethyl-1-pyrazolyl)-3,7-dithianonane (bddn) and 1,6-bis(3,5-dimethyl-1-pyrazolyl)-2,5-dithiahexane (bddh) [12].

The reaction did not yield pure products. Unfortunately, isolation of the different isomers by silica gel chromatography was unsuccessful. Recrystallisations of the mixture with different solvents have been carried out but pure products could not be obtained.

The resulting products of these reactions have been characterised by elemental analyses, and infrared and NMR spectra.

The ratio of NS, NSN and NN products has been calculated through ^{1}H NMR experiments (integration of C–H_{pz} signals, see Section 4) (see Fig. 1).

The different isomers were distinguished using the following criteria:

Isomer NSN: pure NSN complex (δ(C–H_{pz}) = 6.03 ppm) could be obtained when the platinum starting material is $[PtCl_2(CH_3CN)_2]$.

Isomer NS: two signals can be observed for the C–H_{pz} of the coordinated ligand in this isomer. One of them appears at the same position as the free ligand (δ(C–H_{pz}) = 5.76 ppm) and the other one at δ(C–H_{pz}) = 5.82 ppm. Integration of both peaks is identical.

Isomer NN: this is a third isomer, which was characterised by comparison to the complex $[PdCl_2(bdtp)]$ (δ(C–H_{pz}) = 5.90 ppm) [7c].

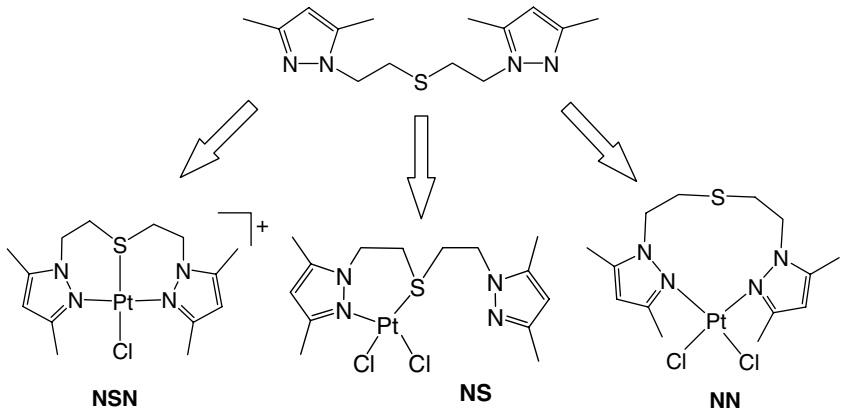
Elemental analyses are consistent with the mixtures.

The IR spectra of the complexes with bdtp show bands at 1555–1553 cm^{-1} (ν(C=C), ν(C=N))$_{ar}$, 1465–1418 cm^{-1} (δ(C=C), δ(C=N))$_{ar}$, 1100–1021 cm^{-1} δ(C–H)$_{ip}$ and 801–800 cm^{-1} δ(C–H)$_{oop}$, indicating the presence of the unaltered coordinated ligand [7c,8]. Coordination to platinum is demonstrated in the IR spectra between 500 and 100 cm^{-1} of the mixture of compounds. According to IR data, the Pt atom is coordinated to nitrogen atoms [ν(Pt–N) between 444 and 441 cm^{-1}], sulfur atoms [ν(Pt–S) between 419 and 380 cm^{-1}] and chlorine atoms [ν(Pt–Cl) between 333 and 326 cm^{-1}] [13].

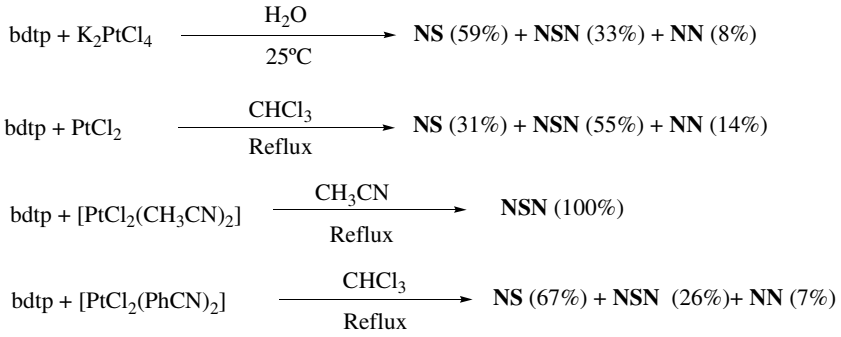
The ^{1}H NMR, ^{13}C{^{1}H} NMR, HMQC, COSY and NOESY spectra were recorded in $CDCl_3$. The NMR experiments corroborate the obtaining of mixtures and the coordination of the ligands around the metallic centre. This ligand can act as tridentate (NSN) or bidentate (NS or NN) chelates depending on the Pt(II) starting material.

In order to be able to isolate one of the isomers (NSN) from the mixture, treatment of the bdtp mixture with $NaBPh_4$ was carried out. This reaction gave a compound of the formula $[Pt(bdtp)](BPh_4)$ (**1**) as a pure products (NSN isomer).

When the complex **1** was heated under reflux in a solution of Et_4NBr in CH_2Cl_2/MeOH (1:1) for 24 h, mixtures of complexes were again obtained (NSN (55%) and NN (45%) isomers with bromides instead of chlorides bonded to the metallic centre). This proves the type III hemilability of the ligand bdtp towards Pt(II) [1a]. The elemental analysis of **1** is consistent with the formula $[PtCl(bdtp)](BPh_4)$. The positive ionisation electrospray mass spectrum of **1** gave a peak with a m/z value of 509 $[PtCl(bdtp)]^+$ (molecular peak of the cation is observed with the same isotope



Scheme 1.



The ratio of the species has been calculated through ^{1}H-NMR experiments, especially from the integration of the pyrazolic proton

Scheme 2.

distribution as the theoretical one). The conductivity measurements in DMF for **1**, show that the complex behaves as 1:1 electrolyte in solution [14].

The IR spectrum of complex **1** is similar to that of the ligand, the most characteristic bands being those attributable to the pyrazolyl group: ν(C=C), ν(C=N) at 1579, 1576 cm^{-1} and δ(C–H)$_{oop}$ at 799 cm^{-1}. The ν(B–C) band at 736 cm^{-1} is characteristic for **1** [15]. The ν(Pt–N), ν(Pt–S) and ν(Pt–Cl) bands can be attributable to the signals appearing at 442 cm^{-1}, 380 cm^{-1} and 326 cm^{-1}, respectively [13].

^{1}H and ^{13}C{^{1}H} NMR spectra of compound **1** were recorded in [D$_6$]acetone solution, and show the signals of the coordinated ligands. NMR spectroscopy data are reported in Section 4 (see Fig. 1).

The ^{1}H NMR spectrum of complex **1** shows that the two protons of each CH$_2$ moiety in the S–CH$_2$–CH$_2$–N chains are diastereotopic, thus leading to four groups of signals, which can be associated to a single hydrogen atom in each chain. This happens because of the rigid conformation of the ligand when complexed. Thus, each group of signals can be assigned as doublets of doublets of doublets (Fig. 2). The HMQC spectrum allowed us to assign the two doublets of doublets of doublets of lower δ to 7-H and the ones at higher δ to 6-H (Fig. 3). Study of the S–CH$_2$–CH$_2$–N fragment as an AA′XX′ system gave a set

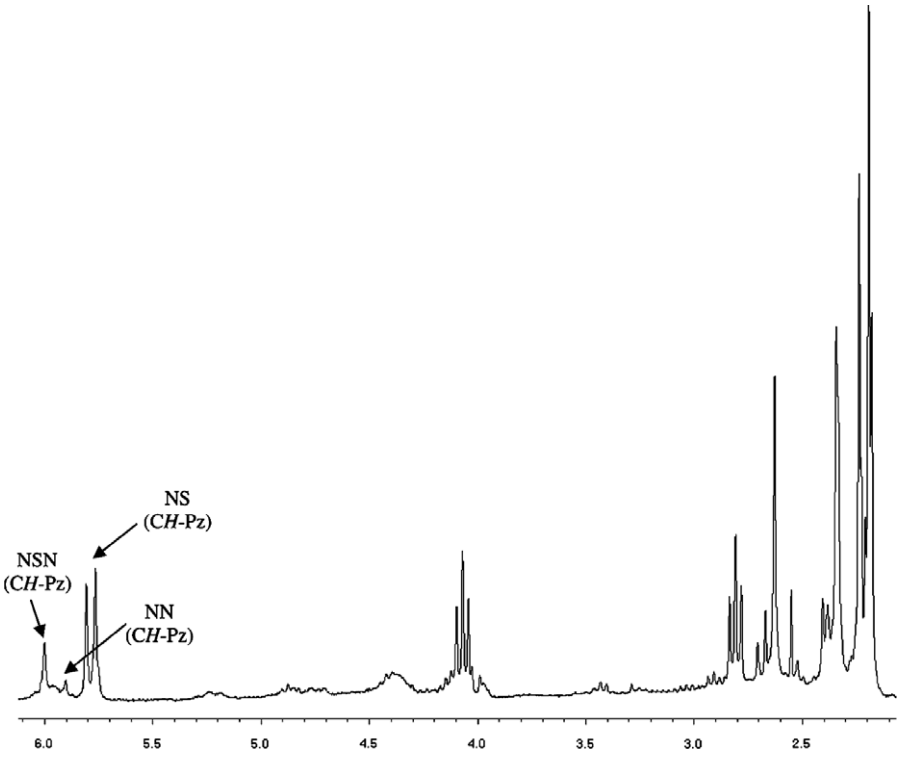


Fig. 1. ^{1}H NMR 250 MHz spectrum of the mixture bdtp + [PtCl$_2$(PhCN)$_2$].

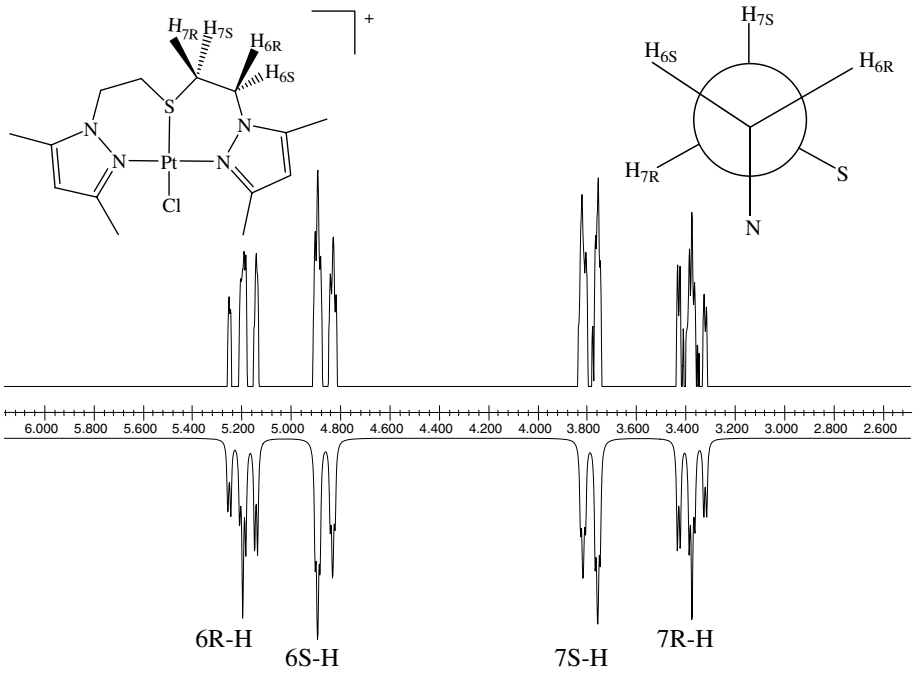


Fig. 2. The 250-MHz ^{1}H NMR and the simulated *g*NMR spectrum for the NCH_2CH_2S fragment of [PtCl(bdtp)](BPh$_4$) (**1**) including the numbering and the dihedral angles for the NCH_2CH_2S fragment.

of coupling constants (Table 1). These constants were consistent with the simulated spectra obtained with the aid of the *g*NMR program [16].

In the NOESY spectrum it can be seen that the methyl group at $\delta = 2.48$ ppm shows a NOE interaction with the doublet of doublets of doublets at $\delta = 4.87$ ppm, but not with the one at $\delta = 5.19$ ppm. From the X-ray structure of **1**, it can be observed that the nearest proton to the $CH_3(5)$ moiety is 6S-H (Figs. 2 and 4) and therefore it should be the one with the NOE interaction (2.70 Å cation **A** and 2.73 Å cation **B**). This information leads us to assign 6S-H to the doublet of doublets of doublets at $\delta = 4.87$ ppm and 6R-H to the signal at $\delta = 5.19$ ppm. The coupling constants enabled us to differentiate 7S-H

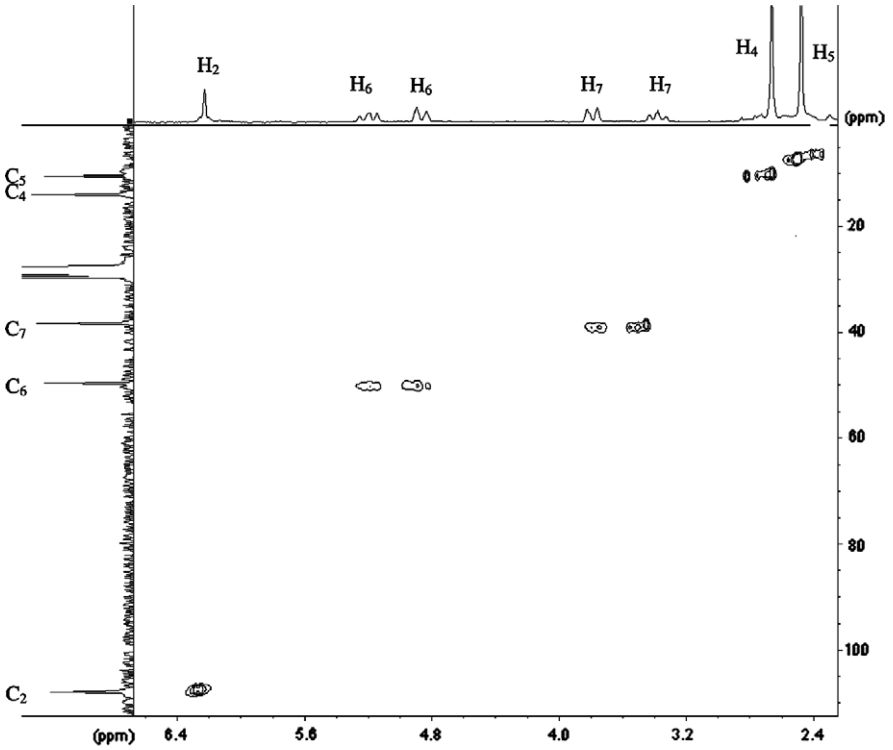


Fig. 3. The 250-MHz 2D HMQC spectrum of [PtCl(bdtp)](BPh$_4$) (**1**).

Table 1
^{1}H NMR results: chemical shifts (ppm) and ^{1}H, ^{1}H coupling constants (Hz) for **1** in [D_6]acetone

Compound	**1**
δ 6R-H	5.19
δ 6S-H	4.87
δ 7S-H	3.79
δ 7R-H	3.38
^2J(6R-H, 6S-H)	15.24
^2J(7R-H, 7S-H)	14.90
^3J(6R-H, 7R-H)	12.03
^3J(6S-H, 7S-H)	2.85
^3J(6R-H, 7S-H)	2.99
^3J(6S-H, 7R-H)	2.09

and 7R-H. These coupling constants agree with the conformation of the S–CH_2–CH_2–N chain as seen in the X-ray crystal structure (Figs. 2 and 4). Geminal ^2J and ca. 180°, ^3J coupling constants have significantly higher values than ca. 30° and ca. 60° ^3J coupling constants. Thus, 7R-H should correspond to the doublet of doublets of doublets at 3.38 ppm and 7S-H to the one at $\delta = 3.79$ ppm [15,17].

Additional ^{195}Pt{^{1}H} NMR experiments for complex **1** at 298 K revealed only one band ($\delta = -1880$ ppm). The ^{195}Pt{^{1}H} chemical shifts are downfield compared to other complexes with [PtN_2SCl] cores (−4098, −2312 ppm) [18].

2.2. Crystal structure of [PtCl(bdtp)](BPh$_4$)-CH$_3$CN

The crystal structure of **1** contains two kinds of discrete [PtCl(bdtp)]$^+$ cations (cations **A** and **B**) (Fig. 4), two BPh_4^- anions and two acetonitrile solvent molecules. Table 2 lists some selected bond distances and angles.

The cations **A** and **B** have the same structure, [PtCl(bdtp)]$^+$. In both, the cationic complex is mononuclear, and the Pt(II) is coordinated to the bdtp ligand by its three donor atoms (two nitrogen atoms of the pyrazolyl group and one sulfur atom), along with one chlorine atom, in a slightly distorted square-planar geometry. Tetrahedral distortion can be observed from the bond angles and from the largest deviation to the mean plane (0.039(4) Å cation **A** and 0.072(4) Å cation **B**) of the atoms coordinated to the Pt atom in relation to the mean plane that contains these four atoms and the Pt atom (cation **A**: N(1), N(4), S(1), Cl(1); cation **B**: N(8), N(5), S(2), Cl(2)). The dihedral angle between the planes N(1)–Pt(1)–Cl(1) and N(4)–Pt(1)–S(1); and N(5)–Pt(2)–Cl(2) and N(8)–Pt(2)–S(2) are 4.10(2)° and 5.88(2)°, respectively. The bdtp ligand acts as a tridentate chelate and forms two six-membered rings, with a boat form for Pt(1)S(1)C(8)C(9)N(3)N(4) and Pt(1)S(1)C(7)C(6)N(2)N(1) (cation **A**) and with a twist-boat form for Pt(2)S(2)C(22)C(23)N(7)N(8) and a boat conformation for Pt(2)S(2)C(21)C(20)N(6)N(5) (cation **B**).

The [PtN_2SCl] core is present in 45 complexes in the literature. Only in 13 of them is the S a thioether [19]. The Pt–Npz bond lengths [2.025(4) and 1.999(5) Å (cation **A**); 2.008(4) and 2.014(4) Å (cation **B**)], the Pt–S bond lengths [2.2616(12) Å (cation **A**); 2.2559(12) Å (cation **B**)] and the

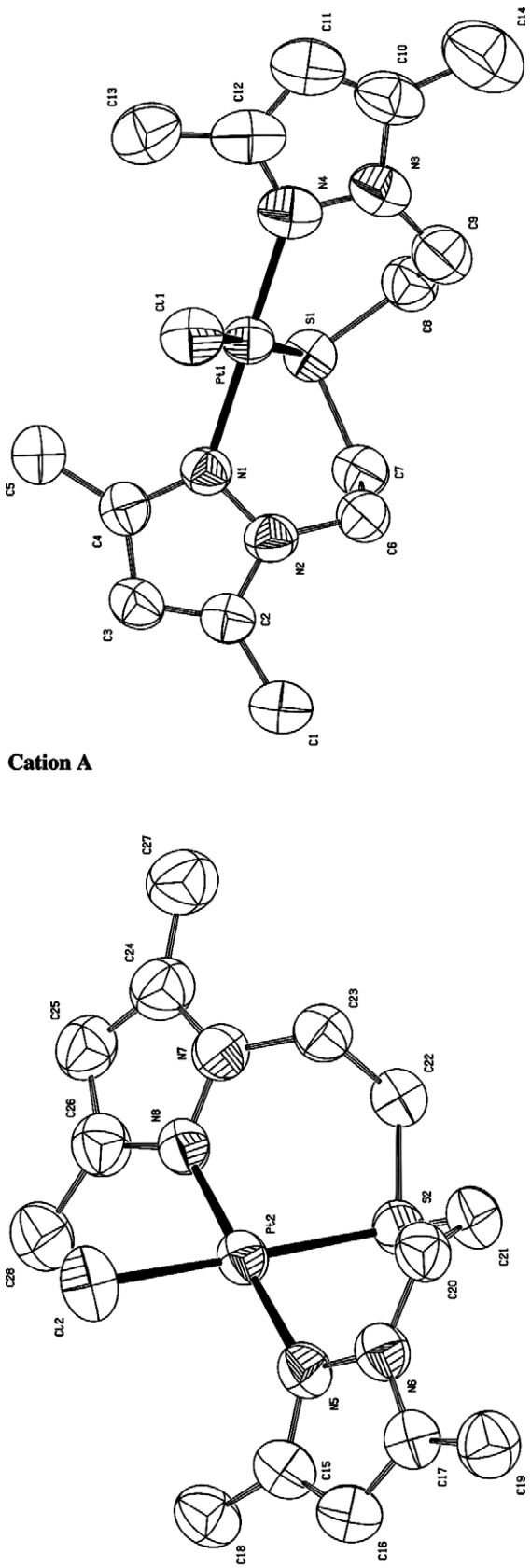


Fig. 4. ORTEP drawing of [PtCl(bdtp)]$^+$ (a: cation **A**, b: cation **B**) showing all non-hydrogen atoms and the atom numbering scheme; 50% probability amplitude displacement ellipsoids are shown.

Table 2
Selected bond lengths (Å) and bond angles (°) for $[PtCl(bdtp)](BPh_4)\cdot CH_3CN$

*Cation **A***			
Pt(1)–N(1)	2.025(4)	Pt(1)–S(1)	2.2616(12)
Pt(1)–N(4)	1.999(5)	Pt(1)–Cl(1)	2.3168(14)
N(4)–Pt(1)–N(1)	179.44(17)	N(4)–Pt(1)–S(1)	91.87(15)
N(4)–Pt(1)–Cl(1)	91.05(15)	N(1)–Pt(1)–S(1)	88.60(11)
N(1)–Pt(1)–Cl(1)	88.47(11)	S(1)–Pt(1)–Cl(1)	174.97(5)
*Cation **B***			
Pt(2)–N(8)	2.008(4)	Pt(2)–S(2)	2.2559(12)
Pt(2)–N(5)	2.014(4)	Pt(2)–Cl(2)	2.3139(14)
N(8)–Pt(2)–N(5)	177.62(15)	N(8)–Pt(2)–S(2)	91.81(11)
N(8)–Pt(2)–Cl(2)	91.06(11)	N(5)–Pt(2)–S(2)	86.42(11)
N(5)–Pt(2)–Cl(2)	90.86(12)	S(2)–Pt(2)–Cl(2)	173.63(5)

Pt–Cl bond lengths [2.3168(14) Å (cation **A**); 2.3139(15) Å (cation **B**)] can be regarded as normal compared with the distances found in the literature. For Pt–N_{pz}, the literature describes values between 1.930 and 2.021 Å [20], for Pt–S(thioether) between 2.18 and 2.46 Å [19,21], and for Pt–Cl between 2.198 and 2.381 Å [20].

The N_{pz}–Pt–S bite angles of the ligand are 91.87(15)° and 88.60(11)° (cation **A**) and 91.81(11)° and 85.42(11)° (cation **B**), and are similar to the corresponding bite angles in the complex $[PdCl(bdtp)](BF_4)$ (90.5(2)° and 88.5(2)°) [7c].

3. Conclusion

Reaction of the bdtp ligand with different Pt(II) starting materials forms different mixtures of the NN, NS and NSN isomers. A similar reaction with $[PdCl_2(CH_3CN)_2]$ as the starting material yielded the NN and NS isomers (the NSN isomer was not observed with Pd before addition of $AgBF_4$) [7c] in a dynamic equilibrium in solution at room temperature. This equilibrium is not observed for the Pt(II) mixture on the NMR timescale (under the same conditions), showing that Pt(II) forms more inert complexes with bdtp than Pd(II).

In order to isolate the NSN isomer, we performed the reaction of the bdtp mixture of isomers with $NaBPh_4$, obtaining $[Pt(bdtp)](BPh_4)$ as a pure product. In this case, the only coordination observed is NSN (similar behaviour to Pd(II)). When this product is refluxed in CH_2Cl_2/CH_3OH in the presence of Et_4NBr a new mixture of NN, NS and NSN isomers is obtained. This proves the hemilability of this ligand with Pt(II) [1a], as was observed for Pd(II).

4. Experimental

4.1. General details

The reactions were carried out under nitrogen atmosphere using vacuum line and Schlenk techniques. Solvents were dried and distilled according to standard procedures and stored under nitrogen. Elemental analyses (C, H, N, S) were carried out by the staff of the Chemical Analyses Service of the Universitat Autònoma de Barcelona on a Carlo Erba CHNS EA-1108 instrument. Conductivity measurements were performed at room temperature (r.t.) in 10^{-3} M DMF solutions, employing a CyberScan CON 500 (Euthech instrument) conductimeter. Infrared spectra were run on a Perkin–Elmer FT spectrophotometer, series 2000 cm^{-1} as KBr pellets or polyethylene films in the range 4000–100 cm^{-1}. ^1H NMR, $^{13}C\{^1H\}$ NMR, HMQC, COSY, NOESY spectra were recorded on a NMR-FT Bruker AC-250 MHz spectrometer in $CDCl_3$, and [D_6]acetone solutions at room temperature. $^{195}Pt\{^1H\}$ NMR spectra were recorded at 25 °C and 77.42 MHz on a DPX-360 Bruker spectrometer using aqueous solutions of $[PtCl_6]^{2-}$ (0 ppm) as an external reference and delay time 0.01 s. All chemical shifts values (δ) are given in ppm. Positive ion ESI-MS mass spectrometer experiments were performed by the Scientific technique Services of the Universitat de Barcelona on a ZQ (Micromass Instruments, UK). The electrospray interface (pneumatically assisted) was operated under the following conditions: the nebulizing nitrogen gas flow was 25 l h^{-1} and the drying nitrogen 250 l h^{-1}, source temperature 100 °C with a capillary voltage of 3.5 kV and cone voltage 20 V. The flow rate was 100 µl min^{-1}. Samples were dissolved in a 1:1 mixture of H_2O/CH_3CN.

Samples of $[PtCl_2(CH_3CN)_2]$ [10] and $[PtCl_2(PhCN)_2]$ [11] were prepared as described in the literature. 1,5-bis(3,5-dimethyl-1-pyrazolyl)-3,7-thiapentane (bdtp) [7c,8] was prepared according to the published methods (Scheme 1).

4.2. Reactions of bdtp with K_2PtCl_4 in H_2O

0.23 mmol (0.065 g) of the bdtp ligand dissolved in 10 ml of water was added to a solution of 0.23 mmol (0.095 g) of K_2PtCl_4 in 10 ml of water. The solution was stirred at room temperature for 24 h (until the red colour of the starting material K_2PtCl_4 had completely disappeared), and a yellow solid precipitated. It was filtered off, washed twice with 5 ml of cold water and dried in vacuum.

4.3. Reactions of bdtp with $PtCl_2$

To 0.26 mmol (0.070 g) of $PtCl_2$ in 15 ml of chloroform, 0.27 mmol (0.070 g) of the bdtp ligand dissolved in 15 ml of the same solvent was quickly added. The mixture was refluxed for 48 h. The yellowish solution was filtered to separate Pt(0) and the starting material $PtCl_2$. The solvent was evaporated to dryness leaving a white solid, which was filtered off, washed with 10 ml of CH_2Cl_2/diethyl ether (1:1) and dried in vacuum.

4.4. Reactions of bdtp with $[PtCl_2(CH_3CN)_2]$

0.24 mmol (0.067 g) of the bdtp ligand dissolved in 15 ml of acetonitrile was added to a solution of 0.24 mmol (0.085 g) $PtCl_2(CH_3CN)_2$ in 15 ml of acetonitrile. The solu-

tion was refluxed for 24 h. The solvent was evaporated to dryness leaving a yellow solid, which was filtered off, washed with 10 ml of CH_2Cl_2/diethyl ether (1:1) and dried in vacuum.

4.5. Reaction of bdtp with $[PtCl_2(PhCN)_2]$

0.20 mmol (0.055 g) of the bdtp ligand dissolved in 15 ml of chloroform was added to a solution of 0.20 mmol (0.095 g) of $[PtCl_2(PhCN)_2]$ in 15 ml of the same solvent. The mixture was refluxed 24 h. From the yellow solution the solvent was evaporated to dryness yielding a yellow solid, which was filtered off, washed with 10 ml of CH_2Cl_2/diethyl ether (1:1) and dried in vacuum.

4.5.1. bdtp + K_2PtCl_4

Yield: 93%. *Anal*. Calc. for $C_{14}H_{22}N_4SCl_2Pt$: C, 30.89; H, 4.07; N, 10.29; S, 5.89. Found: C, 31.10; H, 4.33; N, 10.40; S, 5.51%. Conductivity ($\Omega^{-1}\,cm^2\,mol^{-1}$, 1.05×10^{-3} M in DMF): 152. IR (KBr, cm^{-1}): 3159 ν(C–H)$_{ar}$, 2968, 2922 ν(C–H)$_{al}$, 1553 (ν(C=C), ν(C=N))$_{ar}$, 1461, 1421 (δ(C=C), δ(C=N))$_{ar}$, 1069, 1034 δ(C–H)$_{ip}$, 801 δ(C–H)$_{oop}$. (Polyethylene, cm^{-1}): 442 ν(Pt–N), 394 ν(Pt–S), 326 ν(Pt–Cl). ^{1}H NMR ($CDCl_3$ solution, 250 MHz) δ: NS: (59%) 5.83 [1H, s, C*H*(pz)], 5.76 [1H, s, C*H*(pz)], 5.25/4.41 [1H/1H, m, $N_{pz}CH_2CH_2S$], 4.08 [2H, t, $N_{pz}CH_2CH_2S$], 3.43/2.90 [1H/1H, m, $N_{pz}CH_2CH_2S$], 2.82 [2H, t, SCH_2CH_2S], 2.63 [3H, s, CH_3(pz)], 2.34 [3H, s, CH_3(pz)], 2.24 [3H, s, CH_3(pz)], 2.19 [3H, s, CH_3(pz)] ppm. NSN: (33%) 6.00 [1.12H, s, C*H*(pz)], 5.25/4.78 [1.12H/1.12H, m, $N_{pz}CH_2CH_2S$], 3.98 [1.12H, m, $N_{pz}CH_2CH_2S$], 2.67 [3.36H, s, CH_3(pz)], 2.40 [3.36H, s, CH_3(pz)] ppm. NN: (8%) 5.90 [0.27H, s, C*H*(pz)], 5.30 [0.55H, m, $N_{pz}CH_2CH_2S$], 2.90 [0.55H, m, $N_{pz}CH_2CH_2S$], 2.70 [0.82H, s, CH_3(pz)], 2.38 [0.82H, s, CH_3(pz)] ppm ^{13}C{^{1}H} NMR (CD_3Cl solution, 63 MHz) δ: NS + NSN + NN: 153.3–147.9 (pz-*C*), 144.4–139.3 (pz-*C*), 108.8, 108.7, 106.0, 105.1 (*C*H(pz)), 62.0–48.6 (Npz*C*H_2CH_2S), 46.3–32.4 (SCH_2CH_2S), 15.4–11.2 (CH_3(pz)) ppm.

4.5.2. bdtp + $PtCl_2$

Yield: 70%. *Anal*. Calc. for $C_{14}H_{22}N_4SCl_2Pt$: C, 30.89; H, 4.07; N, 10.29; S, 5.89. Found: C, 31.16; H, 3.98; N, 9.95; S, 5.45%. Conductivity ($\Omega^{-1}\,cm^2\,mol^{-1}$, 1.12×10^{-3} M in DMF): 46. IR (KBr, cm^{-1}): 3193 ν(C–H)$_{ar}$, 2964, 2930 ν(C–H)$_{al}$, 1555 (ν(C=C), ν(C=N))$_{ar}$, 1465, 1418 (δ(C=C), δ(C=N))$_{ar}$, 1100, 1021 δ(C–H)$_{ip}$, 800 δ(C–H)$_{oop}$. (Polyethylene, cm^{-1}): 441 ν(Pt–N), 419 ν(Pt–S), 328 ν(Pt–Cl). ^{1}H NMR ($CDCl_3$ solution, 250 MHz) δ: NS: (31%) 5.82 [0.57H, s, C*H*(pz)], 5.76 [0.57H, s, C*H*(pz)], 5.25/4.40 [0.57H/0.57H, m, $N_{pz}CH_2CH_2S$], 4.07 [1.13H, t, $N_{pz}CH_2CH_2S$], 3.50/2.83 [0.57H/0.57H, m, $N_{pz}CH_2CH_2S$], 2.81 [1.13H, t, SCH_2CH_2S], 2.63 [2.84H, s, CH_3(pz)], 2.34 [2.84H, s, CH_3(pz)], 2.23 [2.84H, s, CH_3(pz)], 2.19 [2.84H, s, CH_3(pz)] ppm. NSN: (55%) 6.01 [2H, s, C*H*(pz)], 5.25/4.76 [2H/2H, m, $N_{pz}CH_2CH_2S$], 3.98/2.90 [2H/2H, m, $N_{pz}CH_2CH_2S$], 2.67 [6H, s, CH_3(pz)], 2.40 [6H, s, CH_3(pz)] ppm. NN: (14%) 5.92 [0.53H, s, C*H*(pz)], 5.30 [1.05H, m, $N_{pz}CH_2$- CH_2S], 2.79 [1.05H, m, $N_{pz}CH_2CH_2S$], 2.52 [1.58H, s, CH_3(pz)], 2.38 [1.58H, s, CH_3(pz)] ppm. ^{13}C{^{1}H} NMR (CD_3Cl solution, 63 MHz) δ: NS + NSN + NN: 153.1–148.6 (pz-*C*), 143.6–142.2 (pz-*C*), 108.8, 107.4, 106.0, 105.1 (*C*H(pz)), 61.9–49.7 (Npz*C*H_2CH_2S), 38.6 (SCH_2CH_2S), 15.3–11.4 (CH_3(pz)) ppm.

4.5.3. bdtp + $[PtCl_2(CH_3CN)_2]$

Yield: 68%. *Anal*. Calc. for $C_{14}H_{22}N_4SCl_2Pt$: C, 30.89; H, 4.07; N, 10.29; S, 5.89. Found: C, 30.36; H, 4.38; N, 9.68; S, 5.91%. Conductivity ($\Omega^{-1}\,cm^2\,mol^{-1}$, 0.98×10^{-3} M in DMF): 65. IR (KBr, cm^{-1}): 3147 ν(C–H)$_{ar}$, 2967, 2917 ν(C–H)$_{al}$, 1553 (ν(C=C), ν(C=N))$_{ar}$, 1465, 1422 (δ(C=C), δ(C=N))$_{ar}$, 1093, 1032 δ(C–H)$_{ip}$, 801 δ(C–H)$_{oop}$. (Polyethylene, cm^{-1}): 444 ν(Pt–N), 380 ν(Pt–S), 333 ν(Pt–Cl). ^{1}H NMR ($CDCl_3$ solution, 250 MHz) δ: NSN: (100%) 6.03 [2H, s, C*H*(pz)], 5.30/4.76 [2H/2H, m, $N_{pz}CH_2CH_2S$], 3.98/2.81 [2H/2H, m, $N_{pz}CH_2CH_2S$], 2.67 [6H, s, CH_3(pz)], 2.40 [6H, s, CH_3(pz)] ppm. ^{13}C{^{1}H} NMR (CD_3Cl solution, 63 MHz) δ: NSN: 153.2 (pz-*C*), 143.9 (pz-*C*), 108.9 (*C*H(pz)), 51.5 (Npz*C*H_2CH_2S), 38.6 (SCH_2CH_2S), 15.6, 12.5 (CH_3(pz)) ppm.

4.5.4. bdtp + $[PtCl_2(PhCN)_2]$

Yield: 56%. *Anal*. Calc. for $C_{14}H_{22}N_4SCl_2Pt$: C, 30.89; H, 4.07; N, 10.29; S, 5.89. Found: C, 31.05; H, 4.40; N, 10.58; S, 5.74%. Conductivity ($\Omega^{-1}\,cm^2\,mol^{-1}$, 1.05×10^{-3} M in DMF): 20. IR (KBr, cm^{-1}): 3181 ν(C–H)$_{ar}$, 2967, 2922 ν(C–H)$_{al}$, 1553 (ν(C=C), ν(C=N))$_{ar}$, 1465, 1422 (δ(C=C), δ(C=N))$_{ar}$, 1097, 1026 δ(C–H)$_{ip}$, 800 δ(C–H)$_{oop}$. (Polyethylene, cm^{-1}): 443 ν(Pt–N), 396 ν(Pt–S), 328 ν(Pt–Cl). ^{1}H NMR ($CDCl_3$ solution, 250 MHz) δ: NS: (67%) 5.80 [1H, s, C*H*(pz)], 5.76 [1H, s, C*H*(pz)], 5.24/4.39 [1H/1H, m, $N_{pz}CH_2CH_2S$], 4.06 [2H, t, $N_{pz}CH_2CH_2S$], 3.44/2.90 [1H/1H, m, $N_{pz}CH_2CH_2S$], 2.80 [2H, t, SCH_2CH_2S], 2.62 [3H, s, CH_3(pz)], 2.34 [3H, s, CH_3(pz)], 2.23 [3H, s, CH_3(pz)], 2.19 [3H, s, CH_3(pz)] ppm. NSN: (26%) 6.00 [0.78H, s, C*H*(pz)], 5.24/4.76 [0.78H/0.78H, m, $N_{pz}CH_2CH_2S$], 3.98 [0.78H, m, $N_{pz}CH_2CH_2S$], 2.67 [2.33H, s, CH_3(pz)], 2.40 [2.33H, s, CH_3(pz)] ppm. NN: (7%) 5.90 [0.22H, s, C*H*(pz)], 2.54 [0.65H, s, CH_3(pz)], 2.38 [0.65H, s, CH_3(pz)] ppm. ^{13}C{^{1}H} NMR (CD_3Cl solution, 63 MHz) δ: NS + NSN + NN: 153.1–147.9 (pz-*C*), 143.6–139.3 (pz-*C*), 108.7, 106.0, 105.2, 105.1 (*C*H(pz)), 61.9–48.6 (Npz*C*H_2CH_2S), 46.3–29.2 (SCH_2CH_2S), 15.3–11.2 (CH_3(pz)) ppm.

4.6. Complexes $[PtCl(bdtp)](BPh_4)$ (**1**)

A solution of $NaBPh_4$ (0.14 mmol, 0.050 g) in 10 ml acetonitrile/methanol 1:1 was added dropwise with vigorous stirring to a solution of $[PtCl_2(bdtp)]$ (0.14 mmol, 0.075 g) in 10 ml of acetonitrile/methanol 1:1. The solution was stirred at room temperature for 12 h. The yellowish solution was filtered to separate NaCl. When the volume of the resultant solution had been reduced to roughly 5 ml,

diethyl ether (5 ml) was then added to induce precipitation. The resulting precipitate was then filtered and washed with 5 ml diethyl ether.

Yield: 79% (0.076 g). *Anal.* Calc. for $C_{38}H_{44}N_4SClPtB$: C, 65.82; H, 4.72; N, 5.31; S, 5.41. Found: C, 65.80; H, 4.71; N, 5.74; S, 5.39%. MS (*m*/*z*) (%) = 509 (100%) $[PtCl(bdtp)]^+$. Conductivity (Ω^{-1} cm^2 mol^{-1}, 1.06×10^{-3} M in DMF): 90. IR (KBr, cm^{-1}): 3442 ν(C–H)$_{ar}$, 2984, 2927 ν(C–H)$_{al}$, 1579, 1556 (ν(C=C), ν(C=N))$_{ar}$, 1476, 1425 (δ(C=C), δ(C=N))$_{ar}$, 1067, 1031 δ(C–H)$_{ip}$, 799 δ(C–H)$_{oop}$, 736 ν(B–C). (Polyethylene, cm^{-1}): 442 ν(Pt–N), 380 ν(Pt–S), 326 ν(Pt–Cl). ^{1}H NMR ([D$_6$]acetone solution, 250 MHz) δ: 7.31–6.78 [20H, Ph], 6.22 [2H, s, C*H*(pz)], 5.19 [2H, ddd, $N_{pz}CH_2CH_2S$], 4.87 [2H, ddd, $N_{pz}CH_2CH_2S$], 3.79 [2H, ddd, $N_{pz}CH_2$-CH_2S], 3.38 [2H, ddd, $N_{pz}CH_2CH_2S$], 2.66 [6H, s, CH_3(pz)], 2.48 [6H, s, CH_3(pz)] ppm. ^{13}C{^{1}H} NMR ([D$_6$]acetone solution, 63 MHz) δ = 165.8–122.0 (Ph), 153.1 (pz-*C*), 144.8 (pz-*C*), 108.8 (*C*H(pz)), 50.5 ($N_{pz}CH_2CH_2S$), 39.2 ($N_{pz}CH_2$-CH_2S), 14.9 (CH_3(pz)), 11.4 (CH_3(pz)) ppm. ^{195}Pt{^{1}H} NMR (CD_3CN solution, 77.42 MHz) δ = singlet at −1880 ppm.

4.7. X-ray crystal structure for compound $[PtCl(bdtp)](BPh_4)\cdot CH_3CN$

Suitable crystals for X-ray diffraction of compound *cis*-$[PtCl(bdtp)](BPh_4)\cdot CH_3CN$ were obtained through crystallisation from an acetonitrile:*n*-pentane solution. A prismatic crystal was selected and mounted on a MAR345 diffractometer with a image plate detector. Unit-cell parameters were determined from 8310 reflections ($3 < \theta < 31°$) and refined by least-squares method. Intensities were collected with graphite-monochromatised Mo Kα radiation. 39970 reflections were measured in the range $2.62° \leqslant \theta \leqslant 30.00°$, 20296 of which were non-equivalent by symmetry (R_{int}(on I) = 0.039). 19908 reflections were assumed as observed applying the condition $I > 2\sigma(I)$. Lorentz-polarisation but no absorption corrections were made.

The structure was solved by direct methods, using the SHELXS computer program [22], and refined by the full-matrix least-squares method with SHELX-97 computer programs [23] using 39970 reflections (very negative intensities were not assumed). The function minimised was $\sum w||F_o|^2 - |F_c|^2|^2$ where $w = [\sigma^2(I) + (0.0444P)^2 + 6.5332P]^{-1}$, and $P = (|F_o|^2 + 2|F_c|^2)/3$. All H atoms were computed and refined, using a riding model, with an isotropic temperature factor equal to 1.2 times the equivalent temperature factor of the atom to which they are linked. The final $R(F)$ factor and $R_w(F^2)$ values as well as the number of parameters and other details concerning the refinement of the crystal structure are gathered in Table 3.

Table 3
Crystallographic data for $[PtCl(bdtp)](BPh_4)\cdot CH_3CN$

Empircal formula	$C_{82}H_{93}B_2Cl_2N_{11}Pt_2S_2$
Formula weight	1779.49
Temperature (K)	293(2)
Crystal system	triclinic
Space group	$P\bar{1}$
Unit cell dimensions	
a (Å)	14.446(6)
b (Å)	15.306(6)
c (Å)	19.500(4)
α (°)	88.71(2)
β (°)	74.43(2)
γ (°)	76.08(2)
V (Å^3)	4027(2)
Z	2
D_{calc} (g cm^{-3})	1.467
μ (mm^{-1})	3.638
F(000)	1788
Crystal size (mm^{-1})	$0.2\times0.1\times0.1$
θ Range (°)	2.62–30.00
Index range	$-19 \leqslant h \leqslant 20$, $-19 \leqslant k \leqslant 19$, $0 \leqslant l \leqslant 27$
Reflexions collected/unique (R_{int})	39970/20296 (0.0393)
Completeness to θ (%)	86.3
Absorption correction	empirical
Data/restraints/parameters	20296/3/917
Goodness-of-fit	1.188
Final R_1, wR_2	0.0469, 0.1146
R_1 (all data), wR_2	0.0476, 0.1152
Extinction coefficient	0.00310(14)
Maximum and minimum residual electron density (e Å^{-3})	0.715 and −0.596

5. Supplementary material

CCDC 620335 contains the supplementary crystallographic data for this paper. These data can be obtained free of charge via http://www.ccdc.cam.ac.uk/conts/retrieving.html, or from the Cambridge Crystallographic Data Centre, 12 Union Road, Cambridge CB2 1EZ, UK; fax: (+44) 1223-336-033; or e-mail: deposit@ccdc.cam.ac.uk.

Acknowledgement

Support by the Spanish Ministerio de Educación y Cultura (Project BQU2003-03582) is gratefully acknowledged.

References

[1] (a) P. Braunstein, N. Naud, Angew. Chem., Int. Ed. 40 (2001) 680;
(b) C.S. Slone, D.A. Weinberger, C.A. Mirkin, Prog. Inorg. Chem. 48 (1999) 233;
(c) K.R. Dunbar, Comments Inorg. Chem. 13 (1992) 313;
(d) A. Bader, E. Lindner, Coord. Chem. Rev. 108 (1991) 27.
[2] J.C. Jeffrey, T.B. Rauchfuss, Inorg. Chem. 18 (1979) 2658.
[3] P. Braunstein, J. Organomet. Chem. (2004) 3953.
[4] (a) A. Pañella, J. Pons, J. García-Antón, X. Solans, M. Font-Bardía, J. Ros, Eur. J. Inorg. Chem. (2006) 1678;
(b) G. Aullón, G. Esquius, A. Lledós, F. Maseras, J. Pons, J. Ros, Organometallics (2004) 5530;
(c) G. Zamora, J. Pons, J. Ros, Inorg. Chim. Acta 357 (2004) 2899;
(d) R. Mathieu, G. Esquius, N. Lugan, J. Pons, J. Ros, Eur. J. Inorg. Chem. (2001) 2683.
[5] G. Esquius, J. Pons, R. Yánez, J. Ros, R. Mathieu, B. Donnadieu, N. Lugan, Eur. J. Inorg. Chem. (2002) 2999.

[6] (a) A. Boixassa, J. Pons, X. Solans, M. Font-Bardía, J. Ros, Inorg. Chim. Acta 357 (2004) 827;
(b) A. Boixassa, J. Pons, J. Ros, R. Mathieu, N. Lugan, J. Organomet. Chem. (2003) 233;
(c) A. Boixassa, J. Pons, X. Solans, M. Font-Bardía, J. Ros, Inorg. Chim. Acta 355 (2003) 254.
[7] (a) A. Rimola, M. Sodupe, J. Ros, J. Pons, Eur. J. Inorg. Chem. (2006) 447;
(b) J. García-Antón, R. Mathieu, N. Lugan, J. Pons, J. Ros, J. Organomet. Chem. (2004) 1599;
(c) J. García-Antón, J. Pons, X. Solans, M. Font-Bardía, J. Ros, Eur. J. Inorg. Chem. (2003) 3952;
(d) J. García-Antón, J. Pons, X. Solans, M. Font-Bardía, J. Ros, Eur. J. Inorg. Chem. (2002) 3319.
[8] T.N. Sorrell, M.R. Malachowski, Inorg. Chem. 22 (1983) 1883.
[9] (a) P. Ghosh, M. Wood, J.B. Bonanno, T. Hascall, G. Parkin, Polyhedron 18 (1999) 1107;
(b) (b) W.G. Haanstra, W.L. Driessen, M. van Roon, A.L.E. Stoffels, J. Reedijk, J. Chem. Soc., Dalton Trans. (1992) 481;
(c) A.L.E. Stoffels, W.G. Haanstra, W.L. Driessen, J. Reedijk, Angew. Chem., Int. Ed. 29 (1990) 1419;
(d) S. Alves, A. Paulo, J.D.G. Corrreia, A. Domingos, I. Santos, J. Chem. Soc., Dalton Trans. (2002) 4714.
[10] F.P. Fanizzi, F.P. Intini, L. Maresca, G. Natile, J. Chem. Soc., Dalton Trans. (1990) 199.
[11] D.A. White, Inorg. Synth. 13 (1972) 62.
[12] A. de León, J. Pons, J. García-Antón, X. Solans, M. Font-Bardía, J. Ros. Inorg. Chim. Acta, (in press).
[13] K. Nakamoto, Infrared and Raman Spectra of Inorganic Coordination Compounds, Wiley, New York, 1986.
[14] W.J. Geary, Coord. Chem. Rev. 7 (1971) 81.
[15] D.H. Williams, I. Fleming, Spectroscopic Methods in Organic Chemistry, McGraw-Hill, London, 1995.
[16] P.H.M. Budzelaar, *g*NMR ver. 4.0, IvorySoft, Cherwell Scientific Oxford, UK, 1997.
[17] E. Pretsh, T. Clerc, J. Seibl, W. Simon, Tables of Determination of Organic Compounds. ^{13}C NMR, ^{1}H NMR, IR, MS, UV/Vis, Chemical Laboratory Practice, Springer, Berlin, 1989.
[18] (a) J.R.L. Priqueler, F.D. Rochon, Inorg. Chim. Acta 357 (2004) 2167;
(b) E. Szlyk, I. Lakomska, J. Kobe, A. Surdykowski, T. Glowiak, J. Sitkowski, Polyhedron 21 (2002) 2001;
(c) M.S. Ali, U. Mukhopadhyay, J. Thurston, K.H. Whitmire, A.R. Khokhar, Polyhedron 21 (2002) 125;
(d) E. Bermejo, R. Carballo, A. Castiñeiras, R. Domínguez, A.E. Liberta, C. Maichle-Mössmer, M.M. Salberg, D.X. West, Eur. J. Inorg. Chem. (1999) 965;
(e) U. Bierbach, T.W. Hambley, N. Farrell, Inorg. Chem. 37 (1998) 708;
(f) F.D. Rochon, S. Boutin, Pi-Chang Kong, R. Melanson, Inorg. Chim. Acta 264 (1997) 89;
(g) E. Schuhmann, J. Altman, K. Karaghiosoff, W. Beck, Inorg. Chem. 34 (1995) 2316;
(h) R.E. Norman, J.D. Ranford, P.J. Sadler, Inorg. Chem. 31 (1992) 877.
[19] F.A. Allen, O. Kennard, Chem. Des. Autom. News 8 (1993) 31.
[20] (a) M.A. Cinellu, S. Stoccoro, G. Minghetti, A.L. Bandini, G. Banditelli, B. Bovio, J. Organomet. Chem. 372 (1989) 311;
(b) K. Sakai, Y. Tomita, T. Ue, K. Goshima, M. Ohminato, T. Tsubomura, K. Matsumoto, K. Ohmura, K. Kawakami, Inorg. Chim. Acta 297 (2000) 64;
(c) J.A. Broomhead, L.M. Rendina, M. Sterns, Inorg. Chem. 31 (1992) 1880;
(d) R.G. Raptis, J.P. Fackler Jr., Acta Crystallogr., Sect. C 47 (1991) 1180;
(e) V. Montoya, J. Pons, X. Solans, M. Font-Bardía, J. Ros, Inorg. Chim. Acta 358 (2005) 2312;
(f) V. Montoya, J. Pons, X. Solans, M. Font-Bardía, J. Ros, Inorg. Chim. Acta 358 (2005) 2763;
(g) V. Montoya, J. Pons, X. Solans, M. Font-Bardía, J. Ros, Inorg. Chim. Acta 359 (2006) 25.
[21] (a) F. Contu, F. Demartin, F.A. Devillanova, A. Garau, F. Isaia, V. Lippolis, A. Salis, G. Verani, J. Chem. Soc., Dalton Trans. (1997) 4401;
(b) G.J. Grant, K.N. Patel, M.L. Helm, L.F. Mehne, D.W. Klinger, D.G. VanDerveer, Polyhedron 23 (2004) 1361;
(c) T.W. Green, R. Lieberman, N.M.J.A. Krause Bauer, W.B. Connick, Inorg. Chem. 44 (2005) 1955;
(d) K.I. Golberg, J. Valdés-Martínez, G. Espinosa-Pérez, L.J. Ackerman, D.X. West, Polyhedron 18 (1999) 1777;
(e) F. Teixidor, P. Anglés, C. Viñas, R. Kivekas, R. Sillanpäa, Inorg. Chem. 38 (1999) 1642;
(f) C. Wilson, M.L. Scudder, T.W. Hambley, H.C. Freeman, Acta Crystallogr., Sect. C 48 (1992) 1012;
(g) J. Zhang, X. Wang, C. Tu, J. Lin, J. Ding, L. Lin, Z. Wang, C. He, C. Yan, X. You, Z. Guo, J. Med. Chem. 46 (2003) 3502;
(h) D. Kovala-Demertzi, P.N. Yadav, M.A. Demertzis, M. Coluccia, J. Inorg. Biochem. 78 (2000) 347.
[22] G.M. Sheldrick, SHELXS-97: Program for Crystal Structure Determination, University of Göttingen, Göttingen, Germany, 1997.
[23] G.M. Sheldrick, SHELXS-97: Program for Crystal Structure Refinement, University of Göttingen, Göttingen, Germany, 1997.

thermal dependence of the Stark level populations has to be implicitly taken into account. However, when the lanthanide ion is Gd(III), the magneto-structural correlations are not complicated since the f^7 system has no orbital momentum [1h]. With this advantage some magnetically coupled 3d–4f complexes containing Gd(III) have been reported and in most of the cases the magnetic studies are limited to Gd(III)–Cu(II) systems [1a,1d,10a,10b,10c,10g,10l,11c,18,19], with a few exceptions [10l][20]. The interactions between Gd(III) and Cu(II) ions are mostly ferromagnetic with a few exceptions [19a,19c,21]. The nature of the ferromagnetism is generally very weak (J values typically smaller than 10 cm^{-1} [22]) and the extent of the ferromagnetism appears not to depend on the structural details. It is of note that there are a few reports addressing the problem of analysing the magnetic interaction in Ln(III)–Cu(II) couples other than Gd(III)–Cu(II) [10c, 10l,12e,12g,12h,23].

For an assessment and a better understanding of the magnetic interactions between Ln(III)–Cu(II) couples we report here the synthesis, single crystal structure, magnetic property and thermal study of $[Cu_3(IDA)_6Ln_2]\cdot n(H_2O)$ [IDA = iminodiacetate dianion; Ln = Gd, $n = 3$ (**1**); Ln = Nd, $n = 6$ (**2**); Ln = Sm, $n = 6$ (**3**)] and of $[Cu(Cl)(NTA)Sm(H_2O)_6]\cdot(ClO_4)\cdot(H_2O)$ (**4**) [NTA = nitrilotriacetate trianion]. We used IDA and NTA anions since they are flexible and contain nitrogen and oxygen donors suitable for generating heterometallic (3d–4f) systems.

2. Experimental

2.1. Materials

High purity neodymium nitrate hexahydrate, samarium chloride hexahydrate and gadolinium nitrate hexahydrate were purchased from Aldrich Chemical Co. Inc. and were used as received. All other chemicals were of AR grade.

2.2. Physical measurements

Elemental analyses (carbon, hydrogen and nitrogen) were performed using a Perkin–Elmer 240C elemental analyzer. IR spectra were measured from KBr pellets on a Nicolet 520 FTIR spectrometer. The magnetic measurements were carried out in the ''Servei de Magnetoquímica (Universitat de Barcelona)'' on polycrystalline samples (30 mg) with a Quantum Design MPMS XL-5 SQUID susceptometer operating at a magnetic field of 0.1 T between 2 and 300 K. The diamagnetic corrections were evaluated from Pascal's constants. Thermogravimetric analyses were carried out using a Perkin–Elmer DIAMOND TG/DTA machine.

2.3. Synthesis

2.3.1. $[Cu_3(IDA)_6Gd_2]\cdot 3(H_2O)$ (*1*)

An aqueous solution (5 ml) of disodium iminodiacetate (0.177 g, 1 mmol) was added to an aqueous solution (5 ml) of copper perchlorate hexahydrate (0.185 g, 0.5 mmol), resulting in a deep blue solution. To it an aqueous-ethanol (2:1) solution (5 ml) of gadolinium nitrate hexahydrate (0.225 mg, 0.5 mmol) was added drop by drop under stirring conditions. The resultant reaction mixture was transferred into a Teflon-lined steel vessel and heated for 14 h at 140 °C. Overnight cooling of the vessel to room temperature (~27 °C) resulted in shining blue crystals (72 % yield) suitable for X-ray analysis. *Anal.* Calc. $Cu_3Gd_2C_{24}H_{36}N_6O_{27}$ (1345.71): C, 21.40; H, 2.67; N, 6.24. Found: C, 21.41; H, 2.66; N, 6.25%. The infrared spectra exhibited bands in the following regions: 3470–3020 (sbr), 2930 (s), 1627 (vs), 1575 (vs), 1495 (vw), 1453 (w), 1407 (s), 1322 (w), 1115 (w), 1074 (w), 1029 (vw), 946 (vw), 728 (s), 539 (s) cm^{-1}.

2.3.2. $[Cu_3(IDA)_6Nd_2]\cdot 6(H_2O)$ (*2*)

This was synthesized adopting the same procedure as in **1**, using neodymium nitrate hexahydrate (0.219 g, 0.5 mmol) instead of the gadolinium salt. Deep blue crystals for X-ray diffraction were obtained after overnight cooling of the reaction vessel. Yield 70%. Elemental analyses are in good agreement with the calculated values. *Anal.* Calc. $Cu_3Nd_2C_{24}H_{42}N_6O_{30}$ (1373.74): C, 20.96; H, 3.05; N, 6.11. Found: C, 20.97; H, 3.04; N, 6.11%. The infrared spectra exhibited bands in the following regions: 3480–3025 (sbr), 2931 (s), 1622 (vs), 1570 (vs), 1453 (vw), 1407 (s), 1320 (s), 1256 (vw), 1113 (w), 1073 (w), 1028 (w), 946 (w), 726 (s), 539 (s) cm^{-1}.

2.3.3. $[Cu_3(IDA)_6Sm_2]\cdot 6(H_2O)$ (*3*)

An aqueous solution (5 ml) of disodium iminodiacetate (0.177 g, 1 mmol) was added to an aqueous solution (5 ml) of copper perchlorate hexahydrate (0.185 g, 0.5 mmol) under stirring conditions. The resultant blue colored solution was mixed with an aqueous solution (10 ml) of samarium chloride hexahydrate (0.182 g, 0.5 mmol) and refluxed for 1 h and allowed to cool to ambient temperature. The resultant solution was filtered and the filtrate kept in a $CaCl_2$ desiccator. After a few weeks bright blue crystals suitable for X-ray diffraction were obtained. Yield: 68%. *Anal.* Calc. $Cu_3Sm_2C_{24}H_{42}N_6O_{30}$ (1385.96): C, 20.77; H, 3.03; N, 6.06. Found: C, 20.76; H, 3.02; N, 6.07%. The infrared spectra exhibited bands in the following regions: 3490–3015 (sbr), 2932 (s), 1621 (vs), 1571 (vs), 1484 (vw), 1452 (w), 1407 (s), 1320 (w), 1120 (w), 1074 (w), 1027 (vw), 946 (w), 726 (s), 539 (s) cm^{-1}.

2.3.4. $[Cu(Cl)(NTA)Sm(H_2O)_6]\cdot(ClO_4)\cdot(H_2O)$ (*4*)

This was synthesized following the same procedure as for **3** by using trisodium nitrilotriacetate (0.257 g, 1 mmol) instead of disodium iminodiacetate. Blue crystals suitable for X-ray analysis were obtained from the $CaCl_2$ desiccator after two weeks. Yield: 65%. *Anal.* Calc. $CuSmC_6H_{20}NO_{17}Cl_2$ (663.02): C, 10.85; H, 3.01; N, 2.11. Found: C, 10.84; H, 3.01; N, 2.12%. The infrared spectra exhibited bands in the following regions: 3435–3180 (sbr), 2931 (s), 1575 (vs), 1093 (vs), 1115 (s), 927 (w), 624 (w) cm^{-1}.

Table 1
Crystal data and details of the structure determination for complexes **1**, **2**, **3** and **4**

Complex	**1**	**2**	**3**	**4**
Formula	$Cu_3Gd_2C_{24}H_{36}N_6O_{27}$	$Cu_3Nd_2C_{24}H_{42}N_6O_{30}$	$Cu_3Sm_2C_{24}H_{42}N_6O_{30}$	$CuSmC_6H_{20}NO_{17}Cl_2$
Formula weight	1345.71	1373.74	1385.96	663.02
Wavelength (Å)	1.54178	1.54178	0.71073	0.71073
Crystal system	trigonal	trigonal	trigonal	monoclinic
Space group	*P*-3*c*1	*P*-3*c*1	*P*-3*c*1	$P2_1$
a (Å)	13.343(3)	13.414(3)	13.454(3)	8.222(3)
b (Å)				12.864(3)
c (Å)	14.515(4)	14.706(4)	14.856(4)	9.479(3)
β (°)				100.98(2)
Cell volume (Å^3)	2238.0(9)	2291.6(10)	2328.8(10)	984.2(5)
Z	2	2	2	2
D_{calc} (g cm^{-3})	1.997	1.991	1.976	2.237
μ (Mo Kα) (mm^{-1})	21.255	19.406	3.928	4.387
F(000)	1246	1350	1358	648
θ Range (°)	3.83–64.57	3.80–63.53	3.03–30.54	2.70–30.16
Reflection collected	25678	18600	29348	10783
Unique reflections	1257	1295	2384	4585
R_{int}	0.0554	0.0610	0.0334	0.0904
Data [$I > 2\sigma(I)$]	1089	849	1641	4322
Refined parameters	96	105	105	253
Goodness-of-fit (F^2)	1.134	1.077	0.976	1.087
R_1 ($I > 2\sigma(I)$)	0.0501	0.0485	0.0387	0.0446
wR_2 [a]	0.1359	0.1321	0.1209	0.1205
Flack parameters				0.07(2)
Residuals (e Å^{-3})	1.937, −1.430	0.702, −0.602	1.371, −2.486	1.356, −1.752

[a] $R_1(F_o) = \sum||F_o| - |F_c||/\sum|F_o|$, $wR_2(F_o^2) = [\sum w(F_o^2 - F_c^2)^2/\sum w(F_o^2)^2]^{1/2}$.

2.4. Crystallographic data collection and refinement

Crystal data and details of refinements for the structures reported are summarized in Table 1. The data collections of complexes **1** and **2** were carried out on a Bruker-Nonius FR591 rotating anode (Cu Kα, $\lambda = 1.54178$ Å) equipped with a Kappa CCD detector, those of complexes **3** and **4** at 293(3) K by using Mo Kα radiation ($\lambda = 0.71073$ Å) on a Nonius DIP-1030 H system. Cell refinement, indexing and scaling of the data sets were performed using the programs MOSFLM [24], Denzo and Scalepack [25]. The lattice water molecule in **4** was found to be disordered over two close positions (each with an occupancy of 0.5). In **2** and **3**, two peaks were interpreted as water oxygens with half occupancy. The H atoms of these disordered lattice water molecules were not located. All the structures were solved by direct methods and Fourier analyses and refined by the full-matrix least-squares method based on F^2 with all observed reflections [26]. The calculations were performed using the WINGX System, Ver 1.70.01 [27].

3. Results and discussion

3.1. Description of the structures

3.1.1. Complexes *1*, *2* and *3*

The X-ray diffraction analyses indicate that complexes **1**–**3** are isomorphous and show a 3D coordination framework. The copper ion, located on an inversion center, exhibits a highly distorted octahedral coordination sphere, being ligated by nitrogen and carboxylate oxygen donors from two IDA anions, as shown in Fig. 1. The equatorial Cu–O bond distances (1.954(5)–1.964(4) Å) are ca. 0.05 Å shorter in comparison to the Cu–N ones (2.011(4)–2.020(3) Å, Table 2). On the other hand, the apical Cu–O bond lengths are considerably longer (~2.39 Å). The lanthanide ion resides on a crystallographic three-fold axis and is coordinated by three unidentate carboxylate groups through O(2) and chelated by three carboxylate groups through oxygens O(3) and O(4) (Fig. 2). A selection of coordination bond lengths and angles is reported in Table 2, while the shortest intermetallic distances are shown in Table 3. The 3D crystal packing represented in Fig. 3 shows a tubular channel running parallel to the *c* axis, and Fig. 4 is a view down axis *a*. In complexes **2** and **3** these empty spaces are occupied by six lattice water molecules per formula unit, while only three water molecules were located in the crystal of **1**, the potential volume available for solvent being about 28% in these unit cells (Table 3), as calculated with the program PLATON. It is interesting to note that the water molecules do not form H-bonds with the framework atoms, but only amongst themselves: the channels appear in fact hydrophobic in character, the methylene $C(3)H_2$ groups drawing the inner channel surface. Table 4 lists the isomorphous $[Cu_3(IDA)_6M_2]\cdot nH_2O$ structures, crystallizing in the space group *P*-3*c*1, reported to date. An analysis of these data indicates that there is a linear trend of the crystal

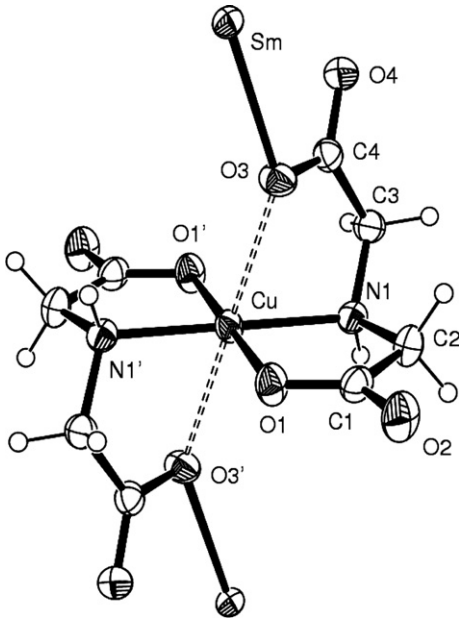


Fig. 1. Centrosymmetric coordination sphere of the copper ion in complex **3** (ORTEP drawing, 40% probability ellipsoid) [the same scheme applies also to **1** and **2**].

Table 2
Selected bond lengths (Å) and angles (°) for complexes **1**, **2** and **3**

	1	**2**	**3**
Cu–O(1) (2x)	1.964(4)	1.954(5)	1.958(2)
Cu–N(1) (2x)	2.011(4)	2.015(5)	2.020(3)
Cu–O(3) (2x)	2.398(4)	2.389(4)	2.381(3)
Sm–O(2) (3x)	2.328(4)	2.402(5)	2.419(3)
Sm–O(3) (3x)	2.394(3)	2.456(4)	2.487(2)
Sm–O(4) (3x)	2.716(5)	2.736(5)	2.766(3)
O(1)–Cu–O(1′)	180.0	180.0	180.0
N(1′)–Cu–N(1)	180.0	180.0	180.0
O(3′)–Cu–O(3)	180.0	180.0	180.0
O(1)–Cu–N(1)	85.66(16)	85.8(2)	85.66(11)
O(1)–Cu–N(1′)	94.34(16)	94.2(2)	94.34(11)
O(1)–Cu–O(3)	89.25(15)	89.17(18)	89.68(10)
O(1)–Cu–O(3′)	90.75(15)	90.83(18)	90.32(10)
N(1)–Cu–O(3)	73.43(15)	73.60(17)	73.73(10)
N(1)–Cu–O(3′)	106.57(15)	106.40(17)	106.27(10)
O(3b)–Ln–O(3) (3x)	80.63(14)	80.00(16)	79.82(10)
O(3)–Ln–O(4) (3x)	50.50(14)	49.10(17)	49.35(8)
O(3)–Ln–O(4b) (3x)	68.41(15)	68.08(16)	67.66(9)
O(3)–Ln–O(4a) (3x)	124.49(14)	122.53(16)	122.36(9)
O(4)–Ln–O(4b) (3x)	115.32(7)	114.25(10)	114.14(5)
O(2c)–Ln–O(2d) (3x)	82.72(19)	82.4(2)	82.32(13)
O(2e)–Ln–O(3) (3x)	130.17(16)	129.87(17)	130.08(10)
O(2c)–Ln–O(3) (3x)	82.24(16)	82.92(18)	83.09(11)
O(2d)–Ln–O(3) (3x)	141.17(16)	141.92(17)	141.84(10)
O(2e)–Ln–O(4) (3x)	79.69(16)	80.80(18)	80.77(10)
O(2c)–Ln–O(4) (3x)	73.77(17)	74.98(19)	75.28(10)
O(2d)–Ln–O(4) (3x)	152.13(17)	153.4(2)	153.46(11)

Symmetry codes: (a) $-y+1,\ x-y+1,\ z$; (b) $-x+y,\ -x+1,\ z$; (c) $-y+1,\ -x+1,\ z-1/2$, (d) $-x+y,\ y,\ z-1/2$; (e) $x,\ x-y+1,\ z-1/2$.

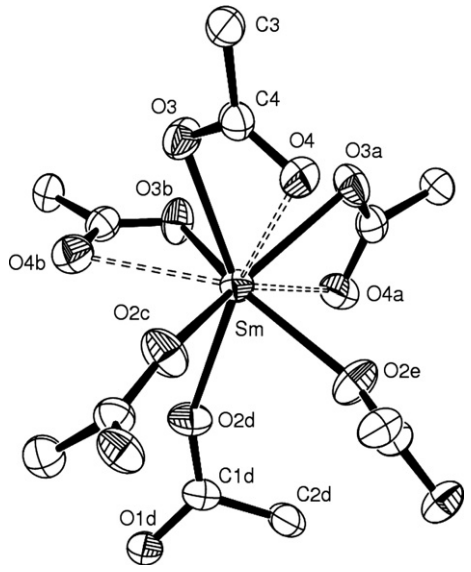


Fig. 2. Coordination sphere about the Sm ion in complex **3** [the same scheme applies also to **1** and **2**].

Table 3
Shortest intermetallic distances (Å) and potential solvent volume (%) per unit cell

	1	**2**	**3**
Cu–Cu	6.672	6.707	6.727
Cu–Ln	4.559	4.602	4.627
Ln–Ln	7.258	7.353	7.428
Volume void (Å^3)	612.1	640.9	656.4
% Cell volume	27.4	28.0	28.2

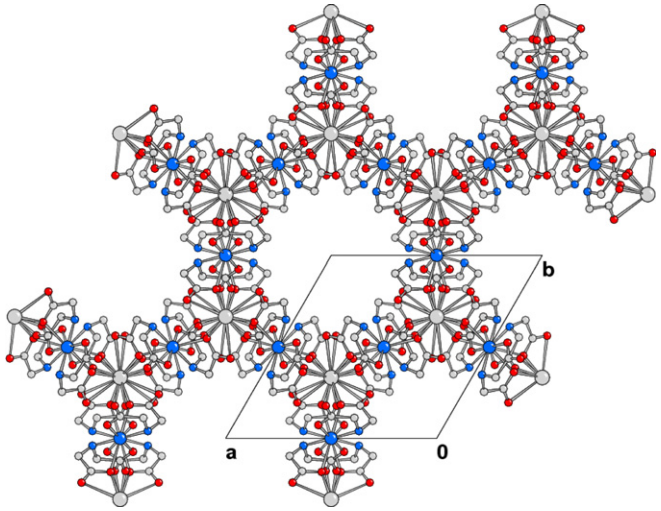


Fig. 3. Crystal packing of complex **3** showing tubular channels directed along the *c* axis.

parameters *a* and *c*, as well as of the cell volume with the atomic radius of the respective metal ion(III). The number of water molecules per unit formula of the structures (Table 4) varies between 0 and 8. This feature seems also to modulate small differences observed in the crystal structure parameters. In fact Long et al. reported a thermogravimetric studies for a series of Cu/M polymers (M = La, Eu) [28]. They observed that

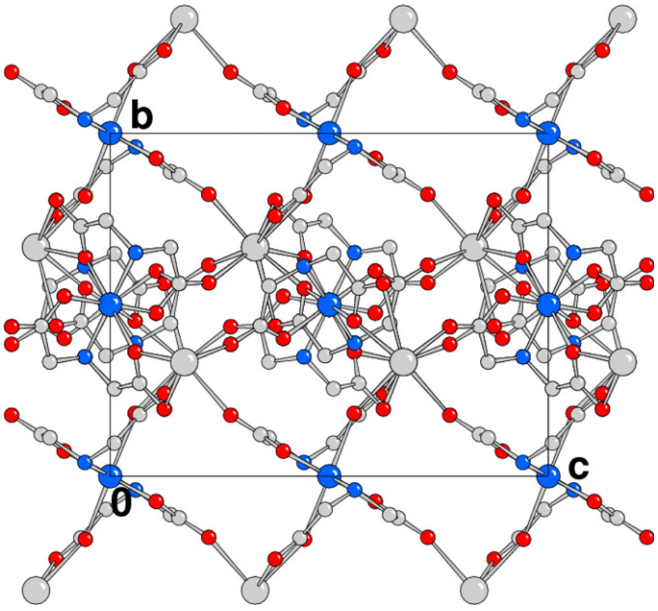


Fig. 4. View of crystal packing of complex **3** down axis *a* (water molecules not shown for clarity).

after dehydration the number of water molecules reabsorbed by the frameworks is less than the original one, i.e. five versus eight of the starting material. Moreover, the cell axes and the cell volume are slightly larger after this process (see entries of La and Eu of Table 3). This trend is confirmed in the Nd derivatives: the cell parameters of complex **2**, containing six water molecules, appear slightly larger than the values reported in the literature [28] for the structure with eight molecules. This effect is even more enhanced in Gd (complex **1**) in comparison to the structure reported [29]. The latter complex, which does not contain any lattice water molecule, retains a volume 70 $Å^3$ more.

3.1.2. Complex *4*

The structure shows a 1D polymeric chain of alternating copper and samarium ions connected by NTA (Fig. 5) in a *zig-zag* arrangement. The Cu–Sm distance is 4.687(2) Å with a Sm–Cu–Sm′ angle of 129.71(3)°. Both the Cu–Cu

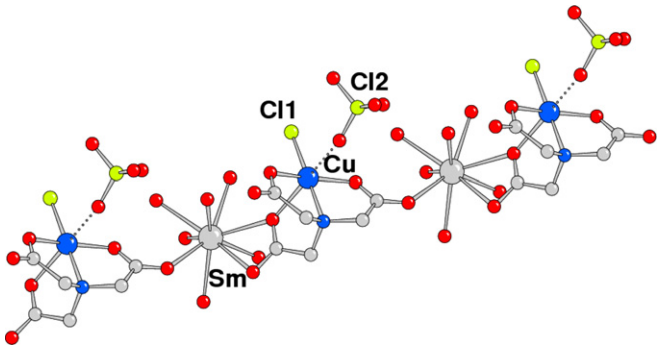


Fig. 5. 1D polymeric chain of complex **4**.

and Sm–Sm intermetallic distances along the chain are 9.479(3) Å, corresponding to the crystallographic *c* axis. The copper coordination sphere is distorted square pyramidal, being coordinated in the basal plane by two carboxylate oxygens, the nitrilotriacetate nitrogen donor and by a chloride, while the apical position is occupied by an oxygen from the third carboxylate group of the NTA ligand. The equatorial Cu–O bond lengths (Cu–O(3) 1.961(6), Cu–O(1) 1.980(6) Å) are slightly shorter than the Cu–N one (2.051(6) Å). The Cu–Cl(1) bond distance is 2.231(2) Å and the apical Cu–O(5) one is 2.269(5) Å. The geometrical parameters are as expected for this kind of complex, with bond angles that show significant deviations from the ideal values (Table 5). The atoms in the equatorial plane are coplanar to within ±0.16 Å, with the copper displaced from the mean plane by 0.12 Å towards O(5). However, it is worth noting that the copper(II) ion appears also to interact with a perchlorate oxygen at a longer distance (2.83(1) Å). The samarium(III) ion is nine coordinated by six water molecules, a chelating NTA carboxylate group, and by another oxygen O(4) from a symmetry related carboxylate of NTA (Fig. 6). The Sm–O distances fall in the range 2.451(6)–2.596(5) Å, the longest values being those relative to the chelating carboxylate, and the corresponding O(5)–Sm–O(6) bond angle is the narrowest at 50.34(17)°.

The crystal packing shows an extensive H-bonding scheme occurring between coordinated and lattice water

Table 4
Crystal data of $[Cu_3(IDA)_6M_2]\cdot nH_2O$ compounds (M = lanthanide(III) ion) reported to date together with number of water molecules per formula unit and metal radius

	a (Å)	*c* (Å)	Cell volume ($Å^3$)	*n*(H_2O)	*R* (Å)	Reference
La	13.471	14.922	2345.1	8	1.17	[28]
La	13.559	14.999	2388.1	5	1.17	[28]
Pr	13.424	14.752	2302.2	0	1.13	[30]
Er	13.317	14.297	2195.6	7	1.03	[31]
Nd	13.403	14.669	2282.1	8	1.12	[28]
Nd	13.414	14.706	2291.6	6	1.12	this work
Sm	13.454	14.856	2328.8	6	1.10	this work
Eu	13.306	14.528	2227.6	8	1.09	[28]
Eu	13.303	14.566	2232.4	5	1.09	[28]
Gd	13.343	14.515	2238.0	3	1.08	this work
Gd	13.433	14.770	2308.1	0	1.08	[29]

Table 5
Selected bond lengths (Å) and angles (°) for complex **4**

Cu–O(3)	1.961(6)	Sm–O(6w)	2.498(7)
Cu–O(1)	1.980(6)	Sm–O(4w)	2.505(7)
Cu–N(1)	2.051(6)	Sm–O(5w)	2.539(7)
Cu–Cl(1)	2.231(2)	Sm–O(4′)	2.545(6)
Cu–O(5)	2.269(5)	Sm–O(3w)	2.572(6)
Sm–O(1w)	2.451(6)	Sm–O(6)	2.583(6)
Sm–O(2w)	2.491(6)	Sm–O(5)	2.596(5)
O(3)–Cu–O(1)	158.9(2)	N(1)–Cu–Cl(1)	177.3(2)
O(3)–Cu–N(1)	83.0(2)	O(3)–Cu–O(5)	109.1(2)
O(1)–Cu–N(1)	84.7(2)	O(1)–Cu–O(5)	86.0(2)
O(3)–Cu–Cl(1)	95.85(18)	N(1)–Cu–O(5)	82.0(2)
O(1)–Cu–Cl(1)	97.12(18)	Cl(1)–Cu–O(5)	96.15(15)
O(1w)–Sm–O(2w)	68.6(2)	O(4w)–Sm–O(3w)	82.6(3)
O(1w)–Sm–O(6w)	73.6(3)	O(5w)–Sm–O(3w)	77.7(2)
O(2w)–Sm–O(6w)	115.4(2)	O(4′)–Sm–O(3w)	146.3(2)
O(1w)–Sm–O(4w)	138.1(3)	O(1w)–Sm–O(6)	142.2(2)
O(2w)–Sm–O(4w)	71.5(3)	O(2w)–Sm–O(6)	145.4(2)
O(6w)–Sm–O(4w)	137.6(3)	O(6w)–Sm–O(6)	74.4(2)
O(1w)–Sm–O(5w)	72.4(2)	O(4w)–Sm–O(6)	79.7(3)
O(2w)–Sm–O(5w)	136.7(2)	O(5w)–Sm–O(6)	77.8(2)
O(6w)–Sm–O(5w)	68.9(2)	O(4′)–Sm–O(6)	79.0(2)
O(4w)–Sm–O(5w)	136.6(2)	O(3w)–Sm–O(6)	120.5(2)
O(1w)–Sm–O(4′)	107.0(3)	O(1w)–Sm–O(5)	132.6(2)
O(2w)–Sm–O(4′)	74.9(2)	O(2w)–Sm–O(5)	128.9(2)
O(6w)–Sm–O(4′)	68.8(3)	O(6w)–Sm–O(5)	115.4(2)
O(4w)–Sm–O(4′)	73.8(3)	O(4w)–Sm–O(5)	67.8(2)
O(5w)–Sm–O(4′)	135.7(2)	O(5w)–Sm–O(5)	69.23(18)
O(1w)–Sm–O(3w)	75.2(3)	O(4′)–Sm–O(5)	119.8(2)
O(2w)–Sm–O(3w)	75.0(2)	O(3w)–Sm–O(5)	70.4(2)
O(6w)–Sm–O(3w)	139.5(3)	O(6)–Sm–O(5)	50.34(17)

Primed atom O(4′) at x, y, $z-1$.

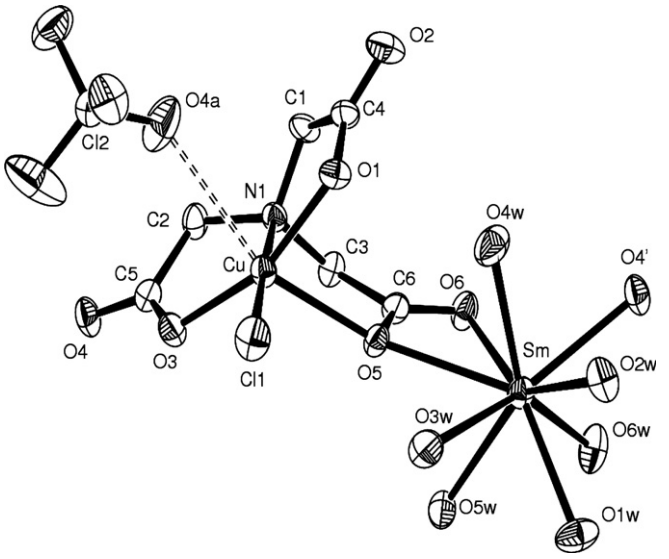


Fig. 6. Detail of the polymeric chain in complex **4** (ORTEP drawing, 40% probability ellipsoid).

molecules with carboxylate and perchlorate oxygen atoms, as reported in Table 6, leading to a 3D architecture. The cell parameters of complex **4** are longer than those measured in the isomorphous Gd complex [32], in agreement with the smaller Gd(III) ion radius. The cited paper reports other complexes of the general formula $[Cu(Cl)(NTA)Ln(H_2O)_6]\cdot(ClO_4)\cdot(H_2O)$ (Ln = La, Gd, Er), crystallizing in different space groups.

3.2. Magnetic properties

The electronic configuration, the ground and low-lying excited states, the g value of the ground state, the energy average difference between these two states and the standard $\chi_M T$ values for the four Ln(III) ions utilized in this work are given in Table 7.

3.2.1. Complex *1*

The temperature dependence of $\chi_M T$ for complex **1** is shown in Fig. 7 (χ_M being the molar magnetic susceptibility for a Cu_3Gd_2 entity). $\chi_M T$ at 300 K is 17 $cm^3\,mol^{-1}\,K$, a value that is as expected for three isolated Cu^{II} plus two Gd^{III} ions (16.87 $cm^3\,mol^{-1}\,K$ assuming $g = 2.00$). Decreasing the temperature, $\chi_M T$ values increase monotonically to 24.6 $cm^3\,mol^{-1}\,K$ at 2 K. The shape of the curve indicates weak ferromagnetic coupling, in agreement with the coupling reported for these Cu^{II}–Gd^{III} systems (vide supra). Taking into account the three-dimensional character of the net, it is impossible to fit the $\chi_M T$ values. The curve of the reduced magnetization ($M/N\beta$) versus H is shown in Fig. 7 (inset). The experimental data tend to 17 $N\beta$ (electrons), which is in perfect agreement with the number of electrons for the formula unit (Cu_3Gd_2).

Gd^{III} is an f^7 ion, with an ^8S ground state. Since the excited states are relatively high in energy, the zero-field splitting of the ground state is fairly small (less than 1 cm^{-1}) so that $S = 7/2$ is a good quantum number. Thus, the coupling of the spin momentum of gadolinium and copper can be described by the typical isotropic spin Hamiltonian $H = -J_{ij}\Sigma S_i S_j$. This is not true for any other lanthanide(III) ions. The ferromagnetic character of the interaction between Cu^{II} and Gd^{III} is rather general and was attributed to the coupling between the 4f–3d ground configuration and the excited configuration coming from the 3dCu → 5dGd electron transfer [1d,33], following a mechanism first suggested by Goodenough [34]. This electron transfer integral involves the singly occupied copper orbital and the five 5d gadolinium orbitals. Several magneto-structural studies concerning the Cu^{II}–Gd^{III} spin carriers separated by mono- or polyatomic bridges have shown the occurrence of a significant ferromagnetic interaction between these cations in di- [35], tri- [1b,10a,10b,36], tetra- [11c], penta-nuclear [12h,37], ladder-like [12a] and tube-like [12b,12c] structures. However, the hypothesis that ferromagnetism is an intrinsic property of the Cu^{II}–Gd^{III} couple, irrespective of the nuclearity and the nature of the bridging ligand, was questioned by Costes et al. who recently reported on the first magneto structurally characterized examples of discrete dinuclear [Cu^{II}–Gd^{III}] [38] and trinuclear [Cu^{II}–Gd^{III}–Cu^{II}] [10l,19a] unit species showing weak antiferromagnetism. These results point out the need of more experimental/theoretical studies

Table 6
Hydrogen bonds in complex **4** (O···O distances below 3.0 Å)

D–H	*d*(D–H)	*d*(H···A)	∠DHA	*d*(D···A)	A[a]	Symmetry code
O1w–H11	0.860	1.925	160.96	2.752	O8w	$[-x+2, y+1/2, -z+1]$
O1w–H11	0.860	1.948	140.12	2.665	O7w	$[-x+2, y+1/2, -z+1]$
O1w–H21	0.868	1.957	149.64	2.741	O6	$[-x+2, y+1/2, -z]$
O2w–H12	0.848	1.988	160.34	2.802	O2	$[-x+1, y+1/2, -z]$
O2w–H22	0.852	1.972	139.48	2.678	O3	$[x, y, z-1]$
O4w–H14	0.856	2.102	152.70	2.890	O1a	$[x, y, z-1]$
O4w–H24	0.850	1.986	179.83	2.836	O1	
O5w–H15	0.852	2.132	157.70	2.937	O1	$[x+1, y, z]$
O5w–H25	0.838	2.103	159.93	2.905	O2a	$[x+1, y, z]$
O6w–H16	0.843	1.809	174.26	2.649	O2	$[x+1, y, z]$
O6w–H26	0.837	2.105	156.45	2.892	O3a	$[x+1, y, z-1]$

[a] O7w, O8w are disordered water molecules. O1a and O2a are perchlorate oxygen atoms.

Table 7
Electronic configuration, *g* value of the ground state, ground and low-lying excited states, energy average difference between these states and standard $\chi_M T$ value (at room temperature) for the Ln(III) ions of this work [39,40]

Ln(III)	Electronic configuration	*g*	Ground state	First excited state[a]	Δ (cm^{-1})	Standard $\chi_M T$ ($cm^3\ mol^{-1}\ K$)
Gd^{3+} (**1**)	$4f^7$	2	$^8S_{7/2}$			7.9
Nd^{3+} (**2**)	$4f^3$	8/11	$^4I_{9/2}$	$^4I_{11/2}$	1900	1.64
Sm^{3+} (**3**,**4**)	$4f^5$	2/7	$^6H_{5/2}$	$^6H_{7/2}$	200	0.1

[a] Same spin multiplicity.

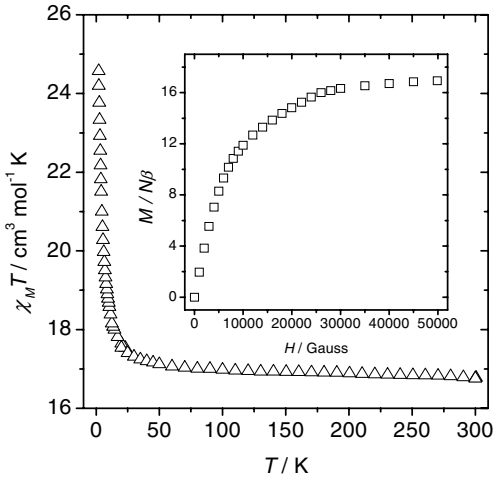


Fig. 7. Plot of $\chi_M T$ vs. *T* and the reduced magnetization ($M/N\beta$) vs. *H* curve (inset) for complex **1**.

about this heterometallic system in order to get a clear answer on the nature and pathway of the involved magnetic coupling.

3.2.2. Complex *2*

Taking into account the molecular formula of **2**, the magnetic properties have been given for a Nd_2Cu_3 unit. Thus the $\chi_M T$ and $1/\chi_M$ (inset) versus *T* plots (χ_M is the molar magnetic susceptibility for the Nd_2Cu_3 entity) are shown in Fig. 8. The value of $\chi_M T$ at 300 K is 4.08 $cm^3\ mol^{-1}$ K, which is slightly smaller than the value expected for two magnetically quasi-isolated Nd^{III} ions ($2 \times 1.64\ cm^3\ mol^{-1}$ K) [39] plus three isolated Cu^{II} ions (ca. $3 \times 0.4\ cm^3\ mol^{-1}$ K), namely 4.48 $cm^3\ mol^{-1}$ K. The value of 1.64 $cm^3\ mol^{-1}$ K for a Nd^{III} free ion ($g = 8/11$) [39] can change in a given complex, but the variation should be small, owing to the character of the f^n complexes [39]. The $\chi_M T$ values monotonically decrease from r.t. to approximately 20 K and then quickly decreases to 1.716 $cm^3\ mol^{-1}$ K at 2 K. The extrapolation of the $1/\chi_M$ curve (Fig. 8, inset) will cut the *T* axis at negative temperature. At a first approach this feature may indicate antiferromagnetic character, but as suggested by Kahn, 'it is important to point out that the deviation with respect to the Curie law may have other origins than the magnetic interactions' [39]. In particular, for elements with strong spin–orbit coupling, like Nd^{III} (f^3), the deviation from the Curie law is not necessarily an indication of ferro- or antiferromagnetic interactions.

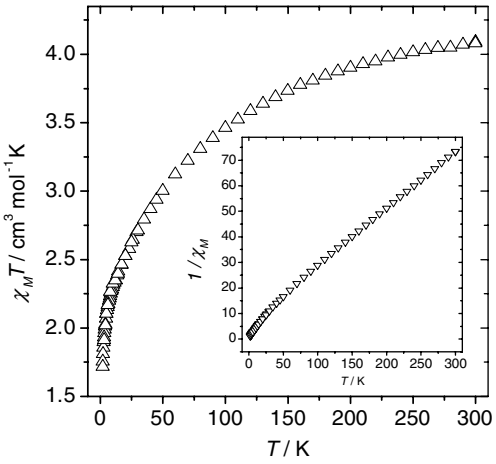


Fig. 8. Plot of $\chi_M T$ vs. *T* and $1/\chi_M$ vs. *T* (inset) for complex **2**.

3.2.3. Complexes 3 and 4

The theoretical $\chi_M T$ value for the Sm^{3+} ion would be ca. 0.1 $cm^3\ mol^{-1}\ K$ if the ground multiplet were the only populated. However the spin–orbit coupling is of the order of 200 cm^{-1}, such that the first excited state $^6H_{7/2}$ can be populated at room temperature (a gap between ground and first excited state of ca. 1000 cm^{-1}). For this reason, the average experimental $\chi_M T$ values are close to 0.3–0.4 $cm^3\ mol^{-1}\ K$ rather than 0.1 [39,40]. When the temperature approaches to 0 K, $\chi_M T$ tends to 0.09 $cm^3\ mol^{-1}\ K$ [39].

The $\chi_M T$ versus T plot for **3** (for $2Sm^{III} + 3Cu^{II}$ ions) is shown in Fig. 9. The expected (theoretical) $\chi_M T$ value at room temperature should be ca. 0.6 $(2Sm^{3+}) + 1.2$ $(3Cu^{2+}) \approx 1.8\ cm^3\ mol^{-1}\ K$, in good agreement with the experimental value (Fig. 10). The decrease of the curve from room temperature to 10 K is due to the effect of spin–orbit coupling of the Sm^{3+} ion. At very low temperature the pronounced decrease in the shape of the curve could indicate small antiferromagnetic coupling.

The $\chi_M T$ versus T plot for **4** ($1Sm^{III} + 1Cu^{II}$ ions per formula unit) is shown in Fig. 10. The expected $\chi_M T$ value at room temperature should be ca. 0.4 $(1Sm^{3+}) + 0.4$ $(1Cu^{2+}) \approx 0.8\ cm^3\ mol^{-1}\ K$, slightly smaller than the experimental value (Fig. 10) (vide infra, complex **2**). The monotonous decrease of the curve from room temperature to 2 K is due to the spin–orbit coupling effect of the Sm^{3+} ion. Thus there is no evidence of any magnetic coupling. For complexes **3** and **4**, as it occurs with all lanthanide (with the exception of Gd^{3+}) it is impossible for any calculation of the J parameter.

3.3. TGA and XRPD studies

Thermogravimetric analyses (Fig. 1S) reveal that complexes **1**–**3** lose water molecules in a single step, showing weight decreases of 4.013%, 7.862% and 7.792% corresponding to the loss of three, six and six water molecules, respectively, that corroborates the content of water molecules found in the crystal lattice. The initial (T_i) and final (T_f) temperatures of deaquation are $T_i = 50$ °C, $T_f = 75$ °C for **1**; 40, 80 °C for **2**, and 60, 100 °C for **3**, and the deaquated species of complexes **1**–**3** are stable up to 290, 340 and 320 °C, respectively. On exposure to humid atmosphere (RH ~ 90%), they revert as evidenced by IR spectra, TGA and X-ray powder diffraction (XRPD) studies (Fig. 11). However, the XRPD patterns of the initially

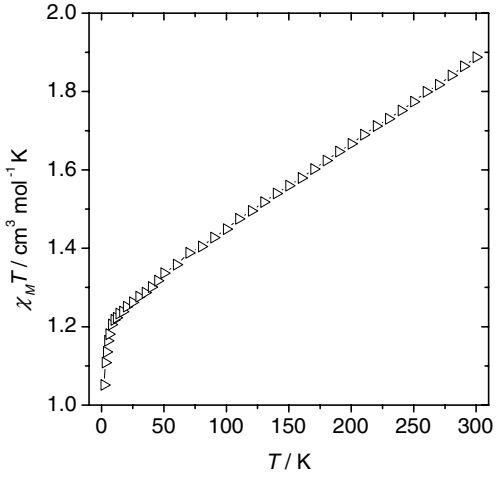


Fig. 9. Plot of $\chi_M T$ vs. T for complex **3**.

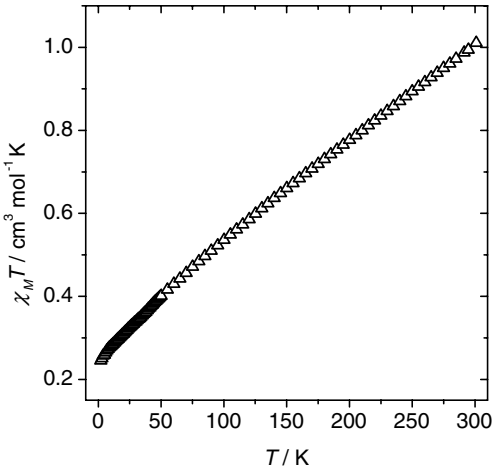


Fig. 10. Plot of $\chi_M T$ vs. T for complex **4**.

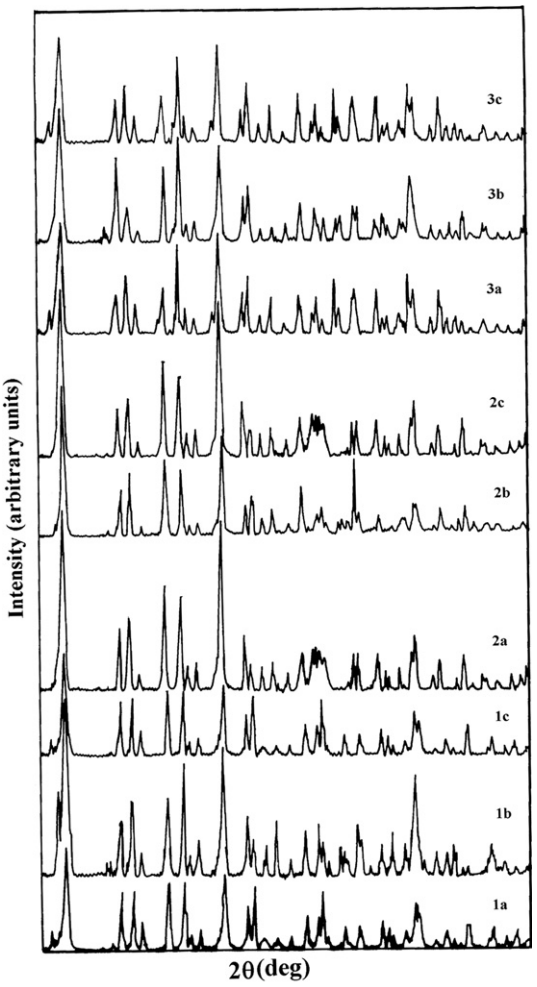


Fig. 11. XRPD patterns of complexes **1**–**3**: (a) as synthesized, (b) dehydrated, (c) rehydrated.

synthesized complexes and their corresponding deaquated species are very similar, which questions the stability of the deaquated species at ambient temperature. By carrying out the XRPD measurement at lower humidity (RH ~ 60%) the absorption of water molecules from atmosphere is avoided. The above mentioned observations suggest that the basic metal-organic frameworks are highly stable and remain practically unaffected even after removal of lattice water molecules, which have no strong interaction with the host network. Finally, the thermogravimetric analysis for complex **4** is hampered by the presence of the perchlorate anion that immediately explodes upon heating.

4. Conclusion

In summary, we have prepared and structurally characterized four heterometallic 3d–4f polymeric architectures. Complexes **1**–**3** are isomorphous, having a covalent bonded 3D polymeric network with tubular channels occupied by lattice water molecules. Complex **4** is a covalent bonded 1D chain which through H-bonding transforms into a 3D supramolecular network. Low temperature magnetic study indicates ferromagnetic behavior in the case of complex **1**. Covalent bonded networks are stable up to ~300 °C in the solid state and the deaquated networks show very similar XRPD patterns as the hydrated species, which indicates the basic metal-organic frameworks remain almost unchanged after removal of channel water molecules.

Acknowledgments

N.R.C. thanks Council of Scientific and Industrial Research, New Delhi and J.R. thanks Spanish Govt. (BQU2003/00539) for financial support.

Appendix A. Supplementary material

CCDC 617485, 617486, 617487 and 617488 contain the supplementary crystallographic data for **1**, **2**, **3** and **4**. These data can be obtained free of charge via http://www.ccdc.cam.ac.uk/conts/retrieving.html, or from the Cambridge Crystallographic Data Centre, 12 Union Road, Cambridge CB2 1EZ, UK; fax: (+44) 1223-336-033; or e-mail: deposit@ccdc.cam.ac.uk. Figures showing the TG curves of complexes **1**, **2** and **3** have also been deposited. Supplementary data associated with this article can be found, in the online version, at doi:10.1016/j.poly.2006.12.042.

References

[1] (a) T. Kido, Y. Ikuta, Y. Sunatsuki, Y. Ogawa, N. Matsumoto, Inorg. Chem. 42 (2003) 398;
(b) T. Shiga, M. Ohba, H. Ôkawa, Inorg. Chem. Commun. 6 (2003) 15;
(c) E.K. Brechin, S.G. Harris, S. Parsons, R.E.P. Winpenny, J. Chem. Soc., Dalton Trans. (1997) 1665;
(d) I. Ramade, O. Kahn, Y. Jeannin, F. Robert, Inorg. Chem. 36 (1997) 930;
(e) R.E.P. Winpenny, Chem. Soc. Rev. 27 (1998) 447;
(f) O. Kahn, Acc. Chem. Res. 33 (2000) 647;
(g) M. Sakamoto, K. Manseki, H. Okawa, Coord. Chem. Rev. 219–221 (2001) 379;
(h) C. Benelli, D. Gatteschi, Chem. Rev. 102 (2002) 2369;
(i) J.-K. Tang, Y.-Z. Li, Q.-L. Wang, E.-Q. Gao, D.-Z. Liao, Z.-H. Jiang, S.-P. Yan, P. Cheng, L.-F. Wang, G.-L. Wang, Inorg. Chem. 41 (2002) 2188.

[2] (a) C. Edder, C. Piguet, J.-C.G. Bünzli, G. Hopfgartner, Chem. Eur. J. 7 (2001) 3014;
(b) W.-K. Wong, H. Liang, W.-Y. Wong, Z. Cai, K.-F. Li, K.-W. Cheah, New J. Chem. 26 (2002) 275.

[3] O. Margeat, P.G. Lacroix, J.P. Costes, B. Donnadieu, C. Lepetit, K. Nakatani, Inorg. Chem. 43 (2004) 4743.

[4] M.A. Subhan, T. Suzuki, S. Kaizaki, J. Chem. Soc., Dalton Trans. (2002) 1416.

[5] A. Gleizes, M. Julve, N. Kuzmina, A. Alikhanyan, F. Lloret, I. Malkerova, J.L. Sanz, F. Senocq, Eur. J. Inorg. Chem. (1998) 1169.

[6] (a) B. Zhao, P. Cheng, Y. Dai, C. Cheng, D.Z. Liao, S.P. Yan, Z.H. Jiang, G.L. Wang, Angew. Chem., Int. Ed. 42 (2003) 934;
(b) B. Zhao, P. Cheng, X.Y. Chen, C. Cheng, W. Shi, D.Z. Liao, S.P. Yan, Z.H. Jiang, J. Am. Chem. Soc. 126 (2004) 3012.

[7] (a) B. Zhao, X.Y. Chen, P. Cheng, D.Z. Liao, S.P. Yan, Z.H. Jiang, J. Am. Chem. Soc. 126 (2004) 15394;
(b) G. Blasse, Mater. Chem. Phys. 31 (1992) 3;
(c) N. Sabatini, M. Guardigli, J.-L. Lehn, Coord. Rev. 123 (1993) 201.

[8] (a) H. Deng, S.G. Shore, J. Am. Chem. Soc. 113 (1991) 8538;
(b) H. Deng, S. Chun, P. Florian, P.J. Grandinetti, S.G. Sore, Inorg. Chem. 35 (1996) 3891.

[9] Z. He, C. He, E.Q. Gao, Z.M. Wang, X.F. Yang, C.S. Liao, C.H. Yan, Inorg. Chem. 42 (2003) 2206.

[10] (a) A. Bencini, C. Benelli, A. Caneschi, R.L. Carlin, A. Dei, D. Gatteschi, J. Am. Chem. Soc. 107 (1985) 8128;
(b) A. Bencini, C. Benelli, A. Caneschi, A. Dei, D. Gatteschi, Inorg. Chem. 25 (1986) 572;
(c) C. Benelli, A. Caneschi, D. Gatteschi, O. Guillou, L. Pardi, Inorg. Chem. 29 (1990) 1750;
(d) N. Matsumoto, M. Sakamoto, H. Tamaki, H. Okawa, S. Kida, Chem. Lett. (1990) 853;
(e) M. Andruh, I. Ramade, E. Codjovi, O. Guillou, O. Kahn, C. Trombe, J. Am. Chem. Soc. 115 (1993) 1822;
(f) J.P. Costes, F. Dahan, A. Dupuis, J.P. Laurent, Inorg. Chem. 35 (1996) 2400;
(g) J.P. Costes, F. Dahan, A. Dupuis, J.P. Laurent, Inorg. Chem. 36 (1997) 3429;
(h) J.P. Costes, F. Dahan, A. Dupuis, J.P. Laurent, Inorg. Chem. 36 (1997) 4284;
(i) J.P. Costes, A. Dupuis, J.P. Laurent, Eur. J. Inorg. Chem. (1998) 1543;
(j) J.P. Costes, A. Dupuis, J.P. Laurent, J. Chem. Soc., Dalton Trans. (1998) 735;
(k) J.P. Costes, F. Dahan, A. Dupuis, J.P. Laurent, New J. Chem. 22 (1998) 1525;
(l) J.P. Costes, F. Dahan, A. Dupuis, J.P. Laurent, Chem. Eur. J. 4 (1998) 1616.

[11] (a) D.M.L. Goodgame, D.J. Williams, R.E.P. Winpenny, Polyhedron 8 (1989) 1531;
(b) A.J. Blake, P.E.Y. Milne, P. Thornton, R.E.P. Winpenny, Angew. Chem., Int. Ed. Engl. 31 (1991) 1139;
(c) C. Benelli, A.J. Blake, P.E.Y. Milne, J.M. Rawson, R.E.P. Winpenny, Chem. Eur. J. 9 (1995) 614, and references therein;
(d) A.J. Blake, R.O. Gould, C.M. Grant, P.E.Y. Milne, S. Parsons, R.E.P. Winpenny, J. Chem. Soc., Dalton Trans. (1997) 485.

[12] (a) O. Guillou, P. Bergerat, O. Kahn, E. Bakalbassis, K. Boubekeur, P. Batail, M. Guillot, Inorg. Chem. 31 (1992) 110;
(b) O. Guillou, O. Kahn, R.L. Oushoorn, K. Boubekeur, P. Batail, Angew. Chem., Int. Ed. Engl. 31 (1992) 626;

(c) O. Guillou, O. Kahn, R.L. Oushoorn, K. Boubekeur, P. Batail, Inorg. Chim. Acta 198 (1992) 119;
(d) O. Kahn, O. Guillou, in: C.J. O'Connor (Ed.), New Frontiers in Magneochemistry, World Scientific, Singapore, 1993;
(e) O. Kahn, O. Guillou, R.L. Oushoorn, M. Drillon, P. Rabu, K. Boubekeur, P. Batail, New J. Chem. 19 (1995) 655;
(f) O. Kahn, Adv. Inorg. Chem. 43 (1995) 179;
(g) M.L. Kahn, C. Mathoniere, O. Kahn, Inorg. Chem. 38 (1999) 3692;
(h) J.L. Sanz, R. Ruiz, A. Gleizes, F. Lloret, J. Faus, M. Julve, J.J. Borras-Almenar, Y. Journaux, Inorg. Chem. 35 (1996) 7384.

[13] (a) W.E. Bailey, R.J. Williams, W.O. Milligan, Acta Crystallogr., Sect. B 29 (1973) 1365;
(b) D.W. Knoeppel, S.G. Shore, Inorg. Chem. 35 (1996) 5328;
(c) A. Figuerola, C. Diaz, J. Ribas, V. Tangoulis, J. Granell, F. Lloret, J. Mahaa, M. Maestro, Inorg. Chem. 42 (2003) 641.

[14] J.-P. Costes, G. Novitchi, S. Shova, F. Dahan, B. Donnadieu, J.-P. Tuchagues, Inorg. Chem. 43 (2004) 7792.

[15] (a) Y.C. Liang, R. Cao, W.P. Su, M.C. Hong, W.J. Zhang, Angew. Chem., Int. Ed. 39 (2000) 3304;
(b) Y.C. Liang, R. Cao, M.C. Hong, D.F. Sun, Y.J. Zhao, J.B. Weng, R.H. Wang, Inorg. Chem. Commun. 5 (2002) 366.

[16] (a) J.S. Miller, A.J. Epstein, Angew. Chem., Int. Ed. Engl. 33 (1994) 385;
(b) A. Caneschi, D. Gatteschi, R. Sessoli, P. Rey, Acc. Chem. Res. 22 (1989) 392;
(c) D. Gatteschi, Adv. Mater. 6 (1994) 635;
(d) J.S. Miller, A.J. Epstein, W.M. Reiff, Science 240 (1988) 40;
(e) S. Konar, P.S. Mukherjee, E. Zangrando, F. Lloret, N. Ray Chaudhuri, Angew. Chem., Int. Ed. 41 (2002) 1561;
(f) P.S. Mukherjee, T.K. Maji, G. Mostafa, J. Ribas, M.S.E. Fallah, N. Ray Chaudhuri, Inorg. Chem. 40 (2001) 928;
(g) T.K. Maji, S. Sain, G. Mostafa, T.-H. Lu, J. Ribas, M. Monfort, N. Ray Chaudhuri, Inorg Chem. 42 (2003) 709;
(h) S. Konar, P.S. Mukherjee, M.G.B. Drew, J. Ribas, N. Ray Chaudhuri, Inorg. Chem. 42 (2003) 2545;
(i) P.S. Mukherjee, S. Konar, E. Zangrando, T. Mallah, J. Ribas, N. Ray Chaudhuri, Inorg. Chem. 42 (2003) 2695.

[17] (a) A. Furrer, H.U. Güdel, E.R. Krausz, H. Blank, Phys. Rev. Lett. 64 (1990) 68, and references therein;
(b) H. Lueken, P. Hannibal, K. Handrick, J. Chem. Phys. 143 (1990) 151, and references therein;
(c) P.M. Levy, Phys. Rev. 147 (1966) 147;
(d) H. Kamimura, Y. Yamaguchi, Phys. Rev. 1 (1970) 2002.

[18] (a) For the mechanism of ferromagnetic coupling in copper(II)–gadolinium(III) complexes, see the following: J. Paulovic, F. Cimpoesu, M. Ferbinteanu, K. Hirao, J. Am. Chem. Soc. 126 (2004) 3321;
(b) J.-P. Costes, F. Dahan, A. Dupuis, J.-P. Laurent, Inorg. Chem. 36 (1997) 3429;
(c) M. Sasaki, H. Horiuchi, M. Kumagai, M. Sakamoto, H. Sakiyama, Y. Nishida, Y. Sadaoka, M. Ohba, H. Okawa, Chem. Lett. (1998) 911;
(d) J.-P. Costes, F. Dahan, A. Dupuis, Inorg. Chem. 39 (2000) 165;
(e) M. Sasaki, K. Manseki, H. Horiuchi, M. Kumagai, M. Sakamoto, H. Sakiyama, Y. Nishida, M. Sakai, Y. Sadaoka, M. Ohba, H. Okawa, J. Chem. Soc., Dalton Trans. (2000) 259;
(f) T. Kido, S. Nagasato, Y. Sunatsuki, N. Matsumoto, Chem. Commun. (2000) 2113;
(g) C. Brewer, G. Brewer, W.R. Scheidt, M. Shang, E.E. Carpenter, Inorg. Chim. Acta 313 (2001) 65.

[19] (a) J.-P. Costes, F. Dahan, A. Dupuis, Inorg. Chem. 39 (2000) 5994;
(b) T. Shiga, M. Ohba, H. Okawa, Inorg. Chem. 43 (2004) 4435;
(c) X.-M. Chen, Y.-L. Wu, Y. Y-. Yang, S.M.J. Aubin, D.N. Hendrickson, Inorg. Chem. 37 (1998) 6186;
(d) A.J. Stemmler, J.W. Kampf, M.L. Kirk, B.H. Atasi, V.L. Pecoraro, Inorg. Chem. 38 (1999) 2807;
(e) A.D. Cutland, R.G. Malkani, J.W. Kampf, V.L. Pecoraro, Angew. Chem., Int. Ed. 39 (2000) 2689;
(f) X.-M. Chen, S.M.J. Aubin, Y.-L. Wu, Y.-S. Yang, T.C.W. Mak, D.N. Hendrickson, J. Am. Chem. Soc. 117 (1995) 9600.

[20] (a) Y. Yukawa, S. Igarashi, A. Yamano, S. Sato, Chem. Commun. (1997) 711;
(b) D.M.J. Doble, C.H. Benison, A.J. Blake, D. Fenske, M.S. Jackson, R.D. Kay, W.-S. Li, Angew. Chem., Int. Ed. 38 (1999) 1915.

[21] (a) R. Baggio, M.T. Garland, Y. Moreno, O. Pena, M. Perec, E. Spodine, J. Chem. Soc., Dalton Trans. (2000) 2061;
(b) S. Gao, O. Borgmeier, H. Leuken, Acta Phys. Pol. A 90 (1996) 393;
(c) J.-P. Costes, F. Dahan, A. Dupuis, J.-P. Laurent, Inorg. Chem. 39 (2000) 169.

[22] F. Avecilla, C. Platas-Iglesias, R. Rodríguez-Cortiñas, G. Guillemot, J.-C.G. Bünzli, C.D. Brondino, C.F.G.C. Geraldes, A. de Blas, T. Rodríguez-Blas, J. Chem. Soc., Dalton Trans. (2002) 4658.

[23] Q.-D. Liu, S. Gao, J.-R. Li, Q.-Z. Zhou, K.-B. Yu, B.-Q. Ma, S.-W. Zhang, X.-X. Zhang, T.-Z. Jin, Inorg. Chem. 39 (2000) 2488.

[24] Collaborative Computational Project, Number 4. Acta Crystallogr. Sect. D 50 (1994) 760.

[25] Z. Otwinowski, W. Minor, in: C.W. CarterJr., R.M. Sweet (Eds.), Methods in Enzymology, Macromolecular Crystallography, part A, vol. 276, Academic Press, New York, 1997, pp. 307–326.

[26] G.M. Sheldrick, SHELX 97 Programs for Crystal Structure Analysis (Release 97-2), University of Göttingen, Germany, 1998.

[27] L.J. Farrugia, J. Appl. Crystallogr. 32 (1999) 837.

[28] Y.-P. Ren, L.-S. Long, B.-W. Mao, Y.-Z. Yuan, R.-B. Huang, L.-S. Zheng, Angew. Chem., Int. Ed. 42 (2003) 532.

[29] J.-G. Mao, L. Song, J.-S. Huang, J. Chem. Cryst. 28 (1998) 475.

[30] J.-G. Mao, L. Song, J.-S. Huang, J. Huaxue, Chinese J. Struct. Chem. 18 (1999) 4.

[31] M.-Y. Xu, F.-H. Liao, J.-R. Li, H.-L. Sun, Z.-S. Li, X.-Y. Wang, S. Gao, Inorg. Chem. Commun. 6 (2003) 841.

[32] Q.-D. Liu, S. Gao, J.-R. Li, B.-Q. Ma, Q.-Z. Zhou, K.-B. Yu, Polyhedron 21 (2002) 1097.

[33] M. Andruch, I. Ramade, E. Codjovi, O. Guillou, O. Kahn, J.C. Trombe, J. Am. Chem. Soc. 115 (1993) 1822.

[34] J.B. Goodenough, Magnetism and the Chemical Bond, Interscience, New York, 1963.

[35] (a) M. Ryazanov, V. Nikiforov, F. Lloret, M. Julve, N. Kuzmina, A. Gleizes, Inorg. Chem. 41 (2002) 1816;
(b) T.M. Rajendiran, R. Kannappan, R. Mahalakshmi, R. Venkatesan, P.S. Rao, L. Govindaswamy, D. Velmurugan, Transition Met. Chem. 28 (2003) 644;
(c) A.M. Atria, Y. Moreno, E. Spodine, M.T. Garland, R. Baggio, Inorg. Chim. Acta 335 (2002) 1;
(d) S. Mohanta, H.-H. Lin, C.-J. Lee, H.-H. Wei, Inorg. Chem. Commun. 5 (2002) 585.

[36] C. Benelli, A.C. Fabretti, A. Giusti, J. Chem. Soc., Dalton Trans. (1993) 409.

[37] L. Zhang, S.-B. Wang, G.-M. Yang, J.-K. Tang, D.-Z. Liao, Z.-H. Jiang, S.-P. Yan, P. Cheng, Inorg. Chem. 42 (2003) 1462.

[38] J.P. Costes, F. Dahan, A. Dupuis, Inorg. Chem. 39 (2000) 169.

[39] O. Kahn, Molecular Magnetism, VCH Publishers, Inc, New York, 1993.

[40] A.T. Casey, S. Mitra, in: E.A. Boudreaux, L.N. Mulay (Eds.), Theory and Applications of Molecular Paramagnetism, Wiley, New York, 1976, p. 271.

of *trans*-bis(ferrocenecarboxylato)(5,10,15,20-tetraphenylporphyrinato)tin(IV).

2. Experiments

2.1. Materials and measurements

Ferrocenecarboxylic acid was purchased from Aldrich, and *trans*-dihydroxo(5,10,15,20-tetraphenylporphyrinato)-tin(IV), **Sn(TPP)(OH)$_2$** was prepared by the reported procedure [11]. CH_2Cl_2 was purified by distillation over CaH_2. UV–Vis and IR spectra were recorded on a Hewlett-Packard 8453 diode array and a Jasco FTIR-460 Plus spectrophotometers, respectively. ^{1}H and ^{13}C NMR spectra were obtained on a Bruker DRX-500 spectrometer. MALDI-TOF mass spectra were recorded on a Bruker Daltonics Reflex III spectrometer. Elemental analyses were performed on a ThermoQuest EA 1110 analyzer.

2.2. Synthesis

2.2.1. trans-Bis(ferrocenecarboxylato)(5,10,15,20-tetraphenylporphyrinato)tin(IV) Sn(TPP)(FcCOO)$_2$

trans-Dihydroxo(5,10,15,20-tetraphenylporphyrinato)-tin(IV) (100 mg, 0.13 mmol) and ferrocenecarboxylic acid (59 mg, 0.26 mmol) were dissolved in anhydrous CH_2Cl_2 (20 mL). The reaction mixture was stirred at room temperature. After 24 h, the solution was filtered through a Celite pad. The solvent of the filtrate was evaporated under reduced pressure to give a crude product. It was then recrystallized from CH_2Cl_2/CH_3CN solution to afford crystalline solids of *trans*-bis(ferrocenecarboxylato)(5,10,15,20-tetraphenylporphyrinato)tin(IV) **Sn(TPP)(FcCOO)$_2$**. Yield: 100 mg (66%). ^{1}H NMR (500 MHz, $CDCl_3$): δ 9.25 (s, 8H, β-pyrrolic H, ^4J(Sn–H) = 14.3 Hz), 8.36 (d, J = 6.76 Hz, 8H, *o*-Ph), 7.81 (m, 12H, *m*-Ph + *p*-Ph), 3.19 (s, 4H, η^5-C_5H_4COO), 2.57 (s, 10H, η^5-C_5H_5), 2.13 (s, 4H, η^5-C_5H_4COO). ^{13}C NMR ($CDCl_3$): δ 166.5, 147.3, 141.3, 135.2, 133.0, 128.6, 127.2, 121.8, 74.4, 68.7, 68.5, 68.4. UV–Vis (CH_2Cl_2, nm): λ_{max} (log ε) 404(4.00), 424(5.16), 521(2.95), 560(3.68), 600(3.41). IR (KBr, cm^{-1}): ν_{CO} 1644, 1299. MS (MALDI-TOF): m/z 961.08 [(M–O_2CFc)$^+$ requires 961.13]. *Anal.* Calc. for $C_{66}H_{46}N_4O_4Fe_2Sn$: C, 66.64; H, 3.90; N, 4.71. Found: C, 66.82; H, 3.48; N, 4.91%.

2.3. X-ray crystal structure determination

Single crystals suitable for X-ray work were grown by slow diffusion of CH_3CN into a CH_2Cl_2 solution of **Sn(TPP)(FcCOO)$_2$**. A crystal covered with Paratone-N hydrocarbon oil on a glass fiber was mounted on a Bruker AXS SMART APEX II single crystal diffractometer equipped with a graphite monochromated Mo Kα (λ = 0.71073 Å) radiation source and a CCD area detector. Three sets of 20 frames of two-dimensional diffraction images were collected and processed to deduce a cell parameter and orientation matrix. Data collection was performed at 100 K. Crystal data and structure refinement for **Sn(TPP)(FcCOO)$_2$** are summarized in Table 1. The intensity data were corrected for Lorentz and polarization effects. Empirical absorption correction was also applied (SADABS) [12]. The structure was solved by the direct method and refined initially by full-matrix least-squares method (SHELXTL) [13]. All atoms were refined anisotropically for non-hydrogen atoms and isotropically for hydrogen atoms. Final block-diagonal matrix least-squares refinement on F^2 with all 6154 reflections and 349 variables converged to R_1 ($I > 2\sigma(I)$) = 0.0342, wR_2 (all data) = 0.0814, and GOF = 1.040.

2.4. Electrochemistry

Cyclic voltammetry and square wave voltammetry were performed with a Princeton Applied Research potentiostat/galvanostat 2273 multipurpose instrument interfaced to a personal computer. Anhydrous THF (Aldrich) was used as the solvent under an argon atmosphere, and 0.2 M tetrabutylammonium hexafluorophosphaste (Bu_4NPF_6) was used as the supporting electrolyte. Cyclic voltammograms were obtained from approximately 5×10^{-4} M solutions of the samples in 0.2 M Bu_4NPF_6/THF inside Faraday cage. A standard three-electrode cell was

Table 1
Crystal data and structure refinement for **Sn(TPP)(FcCOO)$_2$**

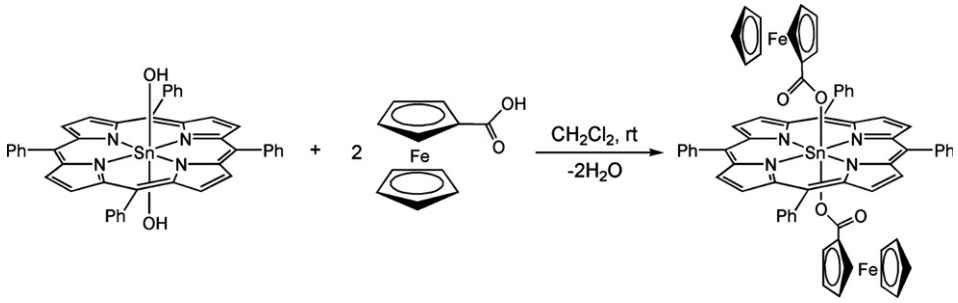
Empirical formula	$C_{66}H_{46}N_4O_4Fe_2Sn$
Formula weight	1189.48
Temperature (K)	100
Wavelength (Å)	0.71073
Crystal system	monoclinic
Space group	$P2_1/c$
Unit cell dimensions	
a (Å)	10.53990(10)
b (Å)	21.2973(3)
c (Å)	12.0952(2)
α (°)	90
β (°)	113.7050(10)
γ (°)	90
Volume (Å^3)	2485.95(6)
Z	2
D_{calc} (Mg/m^3)	1.589
Absorption coefficient (mm^{-1})	1.133
F(000)	1208
Crystal size (mm^3)	0.27 × 0.12 × 0.09
θ Range for data collection (°)	1.91–28.31
Index ranges	$-14 \leqslant h \leqslant 13$, $-28 \leqslant k \leqslant 23$, $-13 \leqslant l \leqslant 16$
Reflections collected	25417
Independent reflections [R_{int}]	6154 [0.0371]
Completeness to theta = 28.31° (%)	99.6
Absorption correction	SADABS
Refinement method	full-matrix least-squares on F^2
Data/restraints/parameters	6154/0/349
Goodness-of-fit on F^2	1.040
Final R indices [$I > 2\sigma(I)$]	R_1 = 0.0342, wR_2 = 0.0734
R indices (all data)	R_1 = 0.0565, wR_2 = 0.0814

$R_1 = \sum(|F_o| - |F_c|)/\sum|F_o|$; $wR_2 = [\sum w(F_o^2 - F_c^2)^2/\sum w(F_o^2)^2]^{0.5}$

used, with a glassy carbon working electrode (diameter: 3.0 mm), a platinum counter electrode, and a silver wire electrode as a pseudo reference electrode. All the redox potential values are reported relative to the ferrocene/ferrocenium (Fc/Fc^{+}) redox couple used as the internal standard. All solutions were deoxygenated by purging with argon gas and maintained under an inert atmosphere during the electrochemical experiments.

3. Results and discussion

Bis(ferrocenecarboxylato)tin(IV) porphyrin complex **Sn(TPP)(FcCOO)$_2$** was synthesized by the reaction of *trans*-dihydroxo(5,10,15,20-tetraphenylporphyrinato)tin(IV) complex **Sn(TPP)(OH)$_2$** with 2 equiv. of ferrocenecarboxylic acid, **FcCOOH**, as shown in Scheme 1. The complex **Sn(TPP)(FcCOO)$_2$** was fully characterized by various spectroscopic methods and elemental analysis. In the ^{1}H NMR spectrum of **Sn(TPP)(FcCOO)$_2$**, three singlet resonances attributed to the protons of the cyclopentadienyl ring in ferrocenecarboxlate moiety are significantly shifted to higher field compared to those of free **FcCOOH**, as depicted in Fig. 1. The significant upfield shifts of these resonances due to the large shielding by the porphyrin ring current strongly support that ferrocenecarboxlate moiety is linked to the tin(IV) porphyrin moiety via tin(IV)-carboxylate coordination. The IR spectrum of **Sn(TPP)- (FcCOO)$_2$** also indicates the tin(IV)-carboxylate coordination, since the absorbing frequency for the C=O stretching mode of **Sn(TPP)(FcCOO)$_2$** appears at 1644 cm^{-1} which is lower than that at 1657 cm^{-1} of free **FcCOOH**. The MALDI-TOF mass spectrum of **Sn(TPP)(FcCOO)$_2$** exhibits a



Scheme 1.

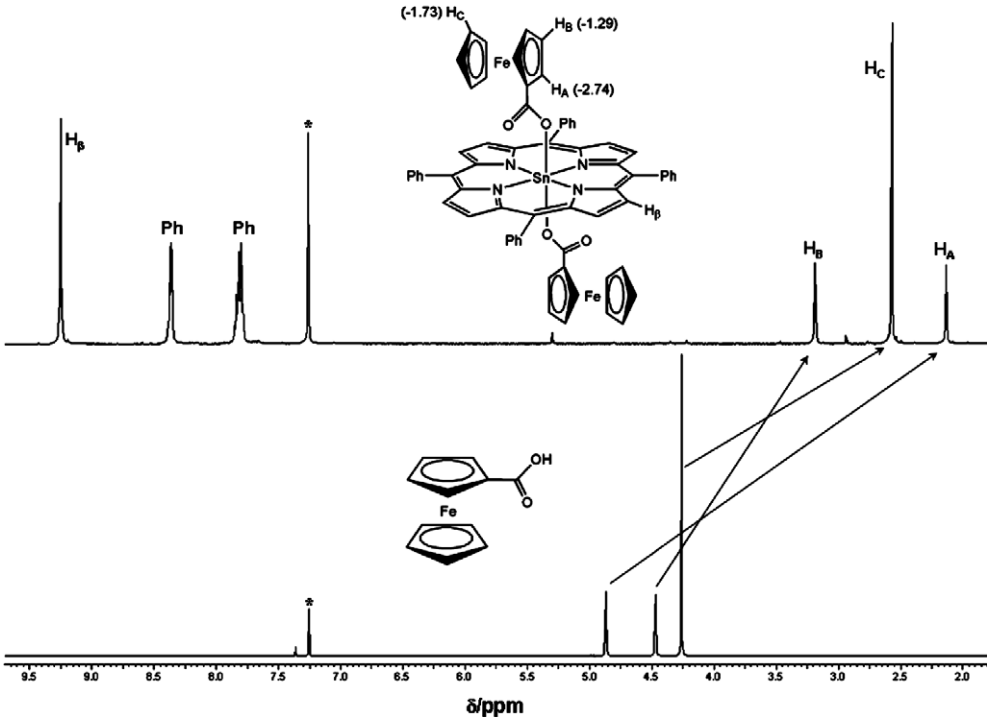


Fig. 1. ^{1}H NMR spectra of **Sn(TPP)(FcCOO)$_2$** (top) and free ferrocenecarboxylic acid (bottom). Porphyrin-induced shifts ($\Delta\delta$/ppm) are shown with the chemical structure of **Sn(TPP)(FcCOO)$_2$** in which $\Delta\delta = \delta$(complex) $- \delta$(free acid). The resonances represented by asterisk correspond to a residual $CHCl_3$ peak.

parent ion peak at $m/z = 961.08$ resulting from the loss of one ferrocenecarboxlate ligand although the molecular ion peak was not observed under our condition. Such ligand lability of tin(IV) porphyrin complexes in the mass spectrometry has been commonly observed [11].

The structure of **Sn(TPP)(FcCOO)$_2$** has been confirmed by X-ray crystallography. Single crystals of **Sn(TPP)(FcCOO)$_2$** suitable for X-ray crystallography were grown from the slow diffusion of CH_3CN into a CH_2Cl_2 solution of **Sn(TPP)(FcCOO)$_2$**. The X-ray structural analysis of **Sn(TPP)(FcCOO)$_2$** revealed the expected axially coordinated structure with 1:2 stoichiometry of the tin(IV) porphyrin and ferrocenecarboxylate moieties, as illustrated in Fig. 2. The tin center is octahedrally coordinated by the porphyrin occupying the square base and axial coordination of two ferrocenecarboxylato ligands. The tin atom lies on an inversion center, so that the two ferrocenecarboxylato ligands are exactly oriented to opposite sides with respect to each other. Such *anti* orientation of the carboxylato ligands is commonly found in other carboxylato-tin(IV) porphyrin complexes [3b,7a,14] as well as in structures where ferrocene molecules bind to metals in porphyrin rings [15].

The selected bond distances and angles for **Sn(TPP)(FcCOO)$_2$** are given in Table 2. The two Sn–N bond distances (2.094(2) and 2.093(2) Å) are almost identical to each other, and the Sn–O distance is found to be 2.0730(16) Å. Comparing these structural parameters with those found in a phthalocyaninato-silicon(IV) analogue **Si(Pc)(FcCOO)$_2$** [16], the much longer bond lengths in **Sn(TPP)(FcCOO)$_2$** than those (av. Si–N 1.906(4) and av. Si–O 1.751(3) Å) in **Si(Pc)(FcCOO)$_2$** are mainly caused by the larger ionic radius of Sn^{IV} (0.83 Å) versus Si^{IV} (0.54 Å) [17]. On the other hand, the Sn–O distance in **Sn(TPP)(FcCOO)$_2$** is longer than that (2.055(5) Å) of the corresponding benzoate complex **Sn(TPP)(PhCOO)$_2$** [14a]. Ligands of high basicity generally have short Sn–O

Table 2
Selected bond distances (Å) and angles (°) for **Sn(TPP)(FcCOO)$_2$**

Sn–N1	2.095(2)	O1–Sn–O1$^{\#1}$	180.00(16)
Sn–N2	2.093(2)	O1–Sn–N2	95.72(7)
Sn–O1	2.0730(16)	O1$^{\#1}$–Sn–N2	84.28(7)
Fe–C24	2.027(2)	N2–Sn–N2$^{\#1}$	180.00(19)
Fe–C25	2.048(3)	O1–Sn–N1$^{\#1}$	86.77(7)
Fe–C26	2.055(3)	O1$^{\#1}$–Sn–N1$^{\#1}$	93.23(7)
Fe–C27	2.053(3)	N2–Sn–N1$^{\#1}$	89.18(8)
Fe–C28	2.035(3)	N2$^{\#1}$–Sn–N1$^{\#1}$	90.82(8)
Fe–C29	2.034(3)	N1$^{\#1}$–Sn–N1	180.00(7)
Fe–C30	2.029(3)		
Fe–C31	2.040(3)		
Fe–C32	2.051(3)		
Fe–C33	2.054(3)		

Symmetry transformations used to generate equivalent atoms: #1 $-x+1$, $-y$, $-z$.

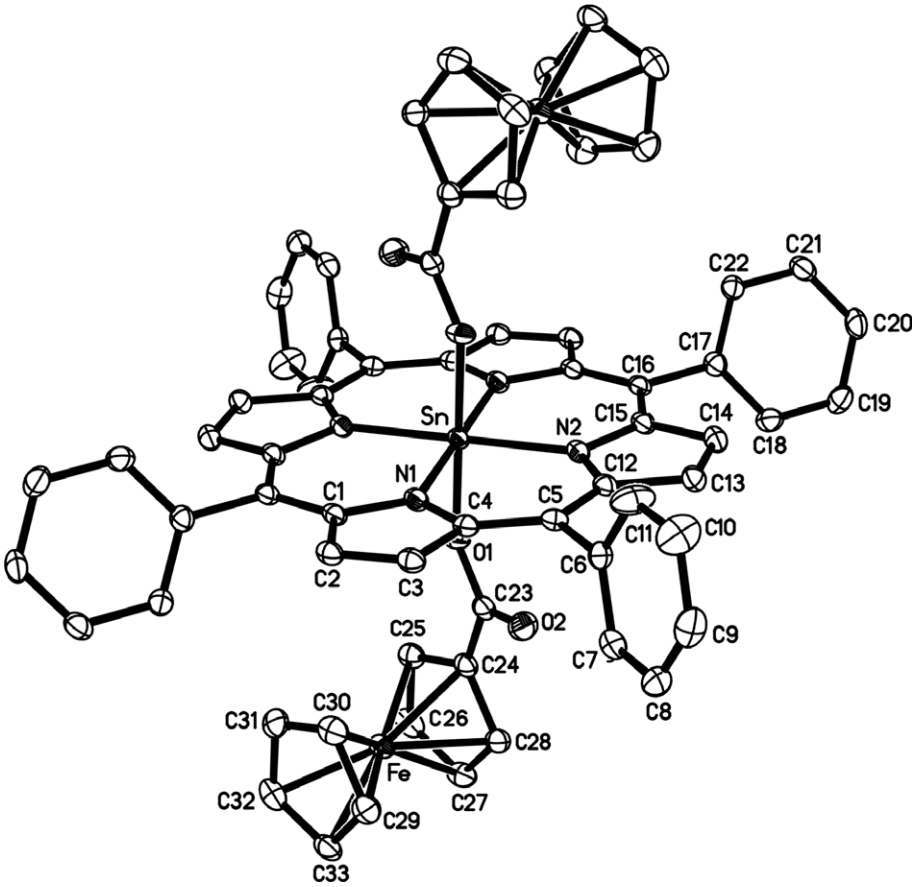


Fig. 2. An ORTEP view of the molecular structure of **Sn(TPP)(FcCOO)$_2$** drawn at 50% probability level. The hydrogen atoms are omitted for clarity.

bonds in the tin(IV) porphyrin complexes [1a]. It can be thus deduced that the basicity of the ferrocenecarboxylate ligand would be weaker than that of benzoate ligand.

The second carboxylate oxygen being 3.325 Å from the tin(IV) ion strongly suggests that the interaction of the carboxylate group with the tin(IV) ion is purely monodentate. The bond lengths for the two carbon–oxygen bonds of carboxylate unit are significantly different. The nonbonding C═O length (C23–O2; 1.228(3) Å) is much smaller than the bonding C–O length (C23–O1; 1.301(3) Å). Furthermore, the former length is even smaller than that (1.26 Å) found in ferrocenedicarboxylic acid [18] which forms hydrogen-bonded dimer in the crystal lattice, but is comparable to those found in diacetylferrocene (1.217 Å) [19]. The monodenate binding of the carboxylate groups in **Sn(TPP)(FcCOO)$_2$** revealed by X-ray crystallography further confirms the IR spectroscopic method of assigning bond type of the carboxylates in **Sn(TPP)(FcCOO)$_2$**. The frequency difference between the asymmetric (1644 cm^{-1}) and symmetric (1299 cm^{-1}) C–O vibration is 345 cm^{-1}. This is indicative of monodentate binding because the ionic bidentate carboxylates normally exhibit frequency differences less than 160 cm^{-1} [20].

The Fe(II) center of the ferrocenecarboxylato ligand lies 5.703 Å from the tin(IV) center of the porphyrin ring. The bond distances associated with the ferrocenecarboxylato ligand of **Sn(TPP)(FcCOO)$_2$** are within the usual range found in other structures containing this ligand. The carboxylate groups are approximately coplanar with the cyclopentadienyl ring to which they bond (torsion angle of O1–C23–C24–C28, 170°). The η^5-C_5H_4COO and η^5-C_5H_5 rings in each ferrocenecarboxylato ligand are coordinated the Fe(II) ion with the eclipsed conformation. But the two cyclopentadienyl rings are not perfectly parallel to each other. The η^5-C_5H_4COO ring is slightly tilted with respect to the η^5-C_5H_5 ring by about 7.6(5)°, and the bond distances of Fe–C24 (2.027(2) Å) and Fe–C30 (2.029(3) Å) are rather shorter than those between the Fe(II) ion and other carbons (2.034(3)–2.055(3) Å) in the cyclopentadienyl rings.

The electrochemical behavior of **Sn(TPP)(FcCOO)$_2$** was examined by cyclic voltammetry and square wave voltammetry. The cyclic and the square wave voltammograms of **Sn(TPP)(FcCOO)$_2$** are compared with those of **Sn(TPP)(OH)$_2$** and free **FcCOOH**, as shown in Fig. 3. Their half-wave redox potentials are also summarized in Table 3. The half-wave potentials were determined using square wave voltammetry relative to a ferrocene/ferrocenium redox potential. The half-wave potential of the ferrocenecarboxylato groups in **Sn(TPP)(FcCOO)$_2$** was found to be at 0.11 V as a single reversible oxidation wave, which implies that they apparently undergo simultaneous rather than sequential oxidation and reduction. The oxidation potential of the ligand is more negative than that of free **FcCOOH** at 0.22 V in the same solvent. It is thus easier to oxidize this moiety when it is complexed to Sn(TPP) moiety than it is uncomplexed. On the other hand, two

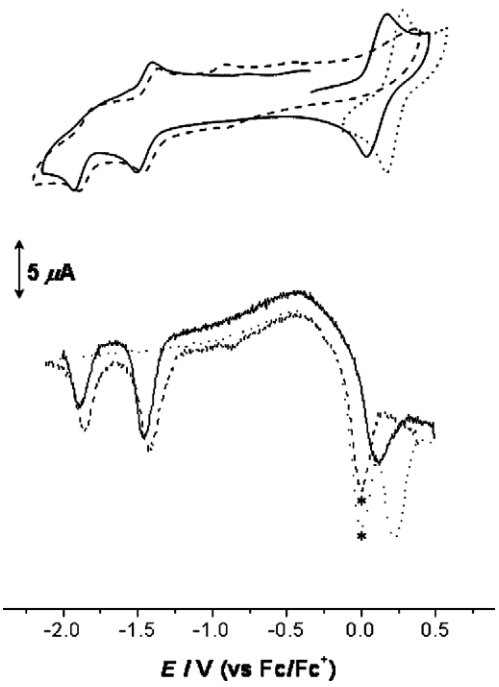


Fig. 3. Cyclic voltammograms (top) and square wave voltammograms (bottom) at scan rate 0.1 V s^{-1} of **Sn(TPP)(FcCOO)$_2$** (solid), **Sn(TPP)(OH)$_2$** (dashed), and free **FcCOOH** (dotted) in THF with 0.2 M Bu_4NPF_6 as the supporting electrolyte. The redox peaks represented by asterisk are attributed to the ferrocene/ferrocenium redox couple used as the internal standard.

Table 3
Half-wave potentials (V vs. Fc/Fc$^+$) of **Sn(TPP)(FcCOO)$_2$**, **Sn(TPP)(OH)$_2$**, and **FcCOOH** in THF, 0.2 M Bu_4NPF_6

Complex	Oxidation (ferrocene moiety)	Reduction (porphyrin ring)
Sn(TPP)(FcCOO)$_2$	0.11	−1.47, −1.89
Sn(TPP)(OH)$_2$		−1.42, −1.85
FcCOOH	0.22	

reduction waves were clearly observed at −1.47 and −1.89 V, which are caused by the reduction of the porphyrin ring in **Sn(TPP)(FcCOO)$_2$**. The first reduction wave is apparently quasi-reversible and the second one appears to be irreversible. The half-wave potentials of the both reduction for **Sn(TPP)(FcCOO)$_2$** are shifted to slightly more negative potential compared to those of **Sn(TPP)(OH)$_2$** (−1.42, −1.85 V).

4. Conclusion

We have synthesized and fully characterized *trans*-bis(ferrocenecarboxylato)(5,10,15,20-tetraphenylporphyrinato)tin(IV) complex, **Sn(TPP)(FcCOO)$_2$**. The molecular structure of **Sn(TPP)(FcCOO)$_2$** has been confirmed by X-ray crystallography, in which the tin(IV) center is octahedrally coordinated by the porphyrin occupying the square base and axial coordination of two ferrocenecarboxylato ligands in an *anti* orientation with respect to

each other. The cyclic voltammetry for **Sn(TPP)-(FcCOO)$_2$** exhibits three distinctive redox couples consisting of one oxidative wave and two reductive waves due to the ferrocenecarboxylato ligands and the porphyrin ring, respectively. We have also carried out the investigation of photophysical properties in conjunction with the process of the photoinduced electron transfer in **Sn(TPP)(FcCOO)$_2$** [21].

Acknowledgements

This work was supported by Kumoh National Institute of Technology. We thank Mr. Ilha Hwang for preliminary measurements of cyclic voltammetry.

Appendix A. Supplementary material

CCDC 630336 contains the supplementary crystallographic data for **Sn(TPP)(FcCOO)$_2$**. These data can be obtained free of charge via http://www.ccdc.cam.ac.uk/conts/retrieving.html, or from the Cambridge Crystallographic Data Centre, 12 Union Road, Cambridge CB2 1EZ, UK; fax: (+44) 1223-336-033; or e-mail: deposit@ccdc.cam.ac.uk. Supplementary data associated with this article can be found, in the online version, at doi:10.1016/j.poly.2006.12.023.

References

[1] (a) D.P. Arnold, J. Blok, Coord. Chem. Rev. 33 (2004) 299;
(b) J.K.M. Sanders, N. Bampos, Z. Clyde-Watson, S.L. Darling, J.C. Hawley, H.-J. Kim, C.C. Mak, S.J. Webb, in: K.M. Kadish, K.M. Smith, R. Guilard (Eds.), The Porphyrin Handbook, vol. 3, Academic Press, San Diego, 2000, p. 1.

[2] (a) H.-J. Kim, N. Bampos, J.K.M. Sanders, J. Am. Chem. Soc. 121 (1999) 8120;
(b) J.E. Redman, N. Feeder, S.J. Teat, J.K.M. Sanders, Inorg. Chem. 40 (2001) 2486;
(c) A.A. Kumar, L. Giribabu, D.R. Reddy, B.G. Maiya, Inorg. Chem. 40 (2001) 6757;
(d) S.J. Langford, C.P. Woodward, Collect. Czech. Chem. Commun. 69 (2004) 996;
(e) C.A. Hunter, S. Tomas, J. Am. Chem. Soc. 128 (2006) 8975.

[3] (a) G.D. Fallon, M.A.-P. Lee, S.J. Langford, P.J. Nichols, Org. Lett. 4 (2002) 1895;
(b) H.-J. Kim, H.J. Jo, J. Kim, S.-Y. Kim, D. Kim, K. Kim, CrystEngComm 7 (2005) 417.

[4] (a) M. Moghadam, S. Tangestaninejad, V. Mirkhani, R. Shaibani, Tetrahedron 60 (2004) 6105;
(b) J. Handman, A. Harriman, G. Porter, Nature 307 (1984) 534.

[5] (a) T.O. Philippova, B.N. Galkin, N.Y. Golovenko, Z.I. Zhilina, S.V. Vodzinskii, J. Porphyrins Phthalocyan. 4 (2000) 243;
(b) M.L. Embleton, S.P. Nair, B.D. Cookson, M. Wilson, J. Antimicrob. Chemother. 50 (2002) 857.

[6] (a) Y. Song, Y. Yang, C.J. Medforth, E. Pereira, A.K. Singh, H. Xu, Y. Jiang, C.J. Brinker, F. van Swol, J.A. Shelnutt, J. Am. Chem. Soc. 126 (2004) 635;
(b) Z. Wang, Y. Song, C.J. Medforth, J.A. Shelnutt, J. Am. Chem. Soc 128 (2006) 9284.

[7] (a) H.J. Kim, K.-M. Park, T.K. Ahn, S.K. Kim, K.S. Kim, D. Kim, H.-J. Kim, Chem. Commun. (2004) 2594;
(b) J.Y. Lee, S.J. Lee, H.J. Kim, H.-J. Kim, J. Phys. Chem. B 110 (2006) 5337.

[8] K.M. Kadish, Q.Y. Xu, G.B. Maiya, J.-M. Barbe, R. Guilard, J. Chem. Soc., Dalton Trans. (1989) 1531.

[9] (a) Examples for covalently linked porphyrin–ferrocene: D.T. Gryko, F. Zhao, A.A. Yasseri, K.M. Roth, D.F. Bocian, W.G. Kuhr, J.S. Lindsey, J. Org. Chem. 65 (2000) 7356, and references therein;
(b) G.B. Maiya, J.-M. Barbe, K.M. Kadish, Inorg. Chem. 28 (1989) 2524.

[10] D.-C. Lee, G.M. Morales, Y. Lee, L. Yu, Chem. Commun. (2006) 100.

[11] M.J. Crossley, P. Thordarson, R.A.-S. Wu, J. Chem. Soc., Perkin Trans. 1 (2001) 2294.

[12] Bruker, SMART, SAINT, SADABS, XPREP, SHELXTL, Bruker AXS Inc., Madison. WI, USA, 1998.

[13] G.M. Sheldrick, SHELXTL-97: Program for Crystal Structure Refinement, University of Göttingen, Göttingen, Germany, 1997.

[14] (a) G. Smith, D.P. Arnold, C.H.L. Kennard, T.C.W. Mak, Polyhedron 10 (1991) 509;
(b) I.-C. Liu, C.-C. Lin, J.-H. Chen, S.-S. Wang, Polyhedron 15 (1996) 459.

[15] (a) M. Cesario, C. Giannotti, J. Guilhem, J. Silver, J. Zakrzewski, J. Chem. Soc., Dalton Trans. (1996) 47;
(b) J. Zakrzewski, M. Cesario, J. Guilhem, C. Giannotti, J. Chem. Soc., Dalton Trans. (1992) 3059.

[16] J. Silver, J.L. Sosa-Sanchez, C.S. Frampton, Inorg. Chem. 37 (1998) 411.

[17] R.D. Shannon, Acta Crystallogr., Sect. A 32 (1976) 751.

[18] G.J. Palenik, Inorg. Chem. 8 (1969) 2744.

[19] G.J. Palenik, Inorg. Chem. 9 (1970) 2424.

[20] K. Nakamoto, Infrared and Raman Spectra of Inorganic and Coordination Compounds, Wiley, New York, 1986, p. 232.

[21] J.H. Jang, H.J. Kim, C.H. Kim, T. Joo, H.-J. Kim, M. Yoon, manuscript in preparation.

Schlenk tube under nitrogen for 12 days at −25 °C led to the deposition of colourless, needle-shaped crystals. The ^{1}H NMR spectrum of this compound showed two methylene signals at δ 3.28 and δ −1.11 in a 1:1 intensity ratio, commensurate with O-bound and Mg-bound CH_2SiMe_3, respectively, and suggested the formation of a magnesium alkyl alkoxide. The corresponding two $SiMe_3$ signals appeared at δ 0.28 and 0.11.

Crystals of sufficient quality for single-crystal X-ray diffraction were obtained from a light petroleum solution at −25 °C. The compound was identified as $[Mg(CH_2SiMe_3)(\mu^3\text{-}OCH_2SiMe_3)]_4$ (**1**). There are two independent molecules in the crystal differing principally in their orientation. The structure of one of these molecules is depicted in Fig. 1. Selected bond lengths and angles are collected in Table 1.

Each magnesium atom has essentially tetrahedral coordination and is bonded to one alkyl ligand and three bridging oxygen atoms of the cluster core. Whereas the O–Mg–O angles are acute (mean angle 85.05(12)°), the Mg–O–Mg angles are noticeably obtuse (mean 94.73(13)°). The mean Mg···Mg distance in the two molecules of **1** is 3.018(5) Å. The CH_2SiMe_3 groups are bound to the Mg and O atoms in directions that deviate slightly from the direction of the corresponding cubane space diagonals, presumably as the result of steric interactions of the bulky CH_2SiMe_3 groups; the deviations about the O atoms are significantly greater than those about the Mg atoms (Table 1). We note that there are two groups of Mg–O–C angles (denoted #1 and #2 in Table 1), one at *ca* 135° and two at *ca* 114°, at each O atom; similarly, the three C–Mg–O angles at each Mg show a wide range of values, but these are divided less clearly into three groups, with angles of *ca* 123°, 128° and 133°. We cannot identify any systematic pattern in the arrangement of $SiMe_3$ groups about the central Mg_4O_4 core. There are no noteworthy intermolecular contacts.

Table 1
Selected mean and ranges of bond lengths (Å) and angles (°) in the two molecules of **1**

	Mean length	Range of lengths
Mg···Mg	3.018(5)	2.993(2)–3.043(2)
Mg–O	2.051(2)	2.032(3)–2.067(3)
Mg–C	2.092(3)	2.080(4)–2.102(4)
(Mg)C–Si	1.841(2)	1.834(4)–1.845(4)
$(MgCH_2)Si–C_{Me}$	1.867(3)	1.843(5)–1.885(4)
O–C	1.463(3)	1.453(4)–1.473(4)
(O)C–Si	1.878(3)	1.866(4)–1.887(4)
$(OCH_2)Si–C_{Me}$	1.855(2)	1.838(5)–1.873(4)
	Mean angle	Range of angles
O–Mg–O	85.05(12)	83.79(11)–85.95(11)
C–Mg–O	128.6(9)	119.73(14)–135.29(15)
Mg–O–Mg	94.73(13)	93.82(10)–95.60(11)
Mg–O–C (#1)	135.5(11)	131.5(2)–139.9(2)
Mg–O–C (#2)	114.3(5)	111.7(2)–118.7(3)
Mg–C–Si (#1)	127.8(3)	127.1(2)–128.3(2)
Mg–C–Si (#2)	122.5(3)	122.0(2)–123.3(3)
O–C–Si	117.7(4)	116.4(2)–119.9(3)
C–Mg···O[a]	174.7(8)	171.39(13)–177.87(14)
Mg···O–C[a]	166.0(10)	161.6(2)–169.3(2)

#1 and #2 denote distinct groups of angles.
S.ds of the mean values and e.s.ds of the individual results in the ranges, are in parentheses. Values in the disordered $SiMe_3$ group were not included in the mean value calculations.
[a] Here, Mg···O denotes a cubane space diagonal.

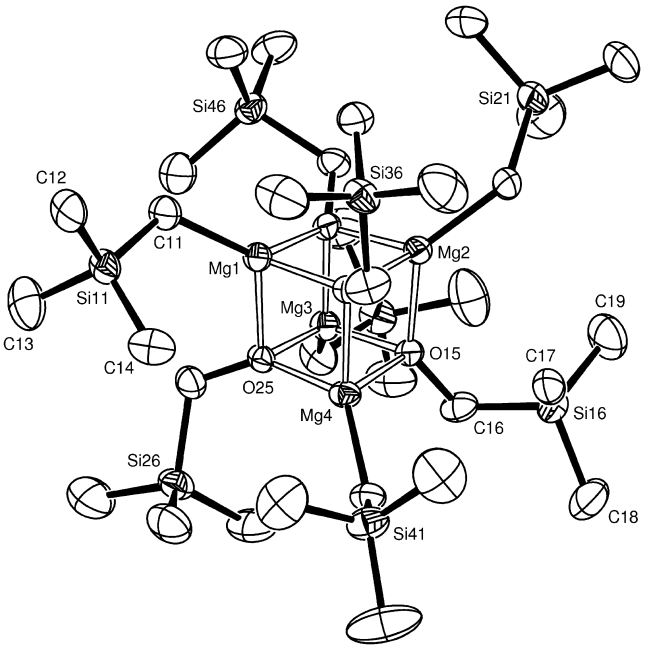
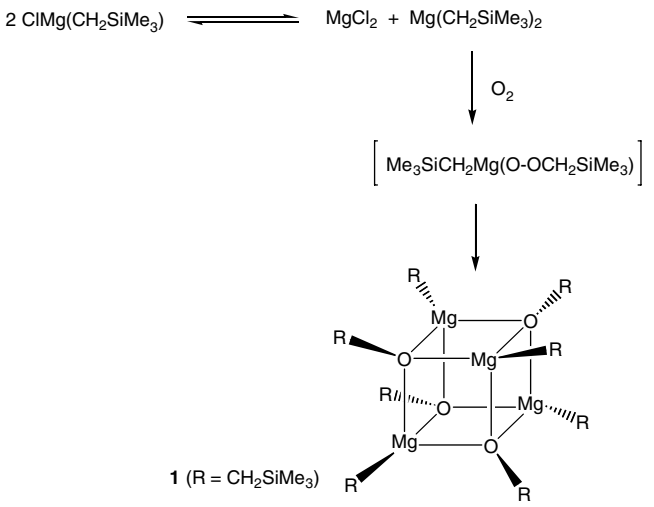


Fig. 1. View of one of the two crystallographically independent molecules of $[Mg(CH_2SiMe_3)(\mu^3\text{-}OCH_2SiMe_3)]_4$, showing the atom numbering scheme. Hydrogen atoms are omitted for clarity. Thermal ellipsoids are drawn at the 50% probability level.

Grignard reagents in solutions form a number of association and ligand exchange equilibria [14]. The most significant of those is the Schlenk equilibrium. The formation of **1** can be explained by the existence of equilibrium concentrations of magnesium dialkyl which undergoes preferential oxidation (Scheme 1). The reaction conditions leading to



Scheme 1. Postulated reaction sequence leading to the formation of **1**.

the isolation of **1** did not allow the detection of the possible alkylperoxide intermediate.

3. Experimental

All manipulations were performed under an atmosphere of dry nitrogen using standard Schlenk techniques. Light petroleum was purified by distillation under nitrogen from sodium–potassium alloy (b.p. 40–60 °C). Deuterated benzene was degassed by several freeze–thaw cycles and dried over activated 4 Å molecular sieves. NMR spectra (^{1}H, ^{13}C) were recorded on a Bruker Avance DPX-300 spectrometer. ^{1}H NMR spectra were referenced to residual solvent protons.

3.1. Synthesis and characterization of *1*

Colorless needle-shaped crystals of $[Mg(CH_2SiMe_3)(\mu^3\text{-}OCH_2SiMe_3)]_4$ (**1**) (0.6 g, 0.7 mmol, 3%) were obtained from a solution of $ClMgCH_2SiMe_3$ (3.23 g, 22 mmol) in petrol/diethyl ether (9/1) and the serendipitous introduction of oxygen, after cooling to −25 °C for a period of 12 days.

^{1}H NMR (300 MHz, 25 °C, C_6D_6): δ 3.84 (s, 8H, OCH_2-$SiMe_3$), 0.28 (s, 36H, $OCH_2Si\mathit{Me}_3$), 0.11 (s, 36H, $MgCH_2Si\mathit{Me}_3$), −1.11 (s, 8H, $MgCH_2SiMe_3$). ^{13}C NMR (75.47 MHz, 25 °C, C_6D_6): δ 52.1 (OCH_2SiMe_3), 19.3 ($MgCH_2SiMe_3$), 0.2 ($OCH_2Si\mathit{Me}_3$), −1.1 ($MgCH_2Si\mathit{Me}_3$).

3.2. Crystal structure

Crystal data: $C_{32}H_{88}Mg_4O_4Si_8$, $M = 859.0$. Triclinic, space group $P\bar{1}$ (No. 2), $a = 10.7614(8)$, $b = 21.680(2)$, $c = 24.724(2)$ Å, $\alpha = 100.854(8)$, $\beta = 89.542(7)$, $\gamma = 96.211(7)°$, $V = 5631.3(8)$ Å^3. $Z = 4$, $D_{calc} = 1.013$ g cm^{-3}, $F(000) = 1888$, $T = 180(1)$ K, μ(Mo Kα) = 2.6 cm^{-1}, λ (Mo Kα) = 0.71069 Å.

Crystals are colourless prisms. From a sample under oil, one, *ca* 0.89 × 0.32 × 0.16 mm, was mounted on a glass fibre and fixed in the cold nitrogen stream on an Oxford Diffraction Xcalibur-3 CCD diffractometer equipped with Mo Kα radiation and graphite monochromator. Intensity data were measured by thin-slice ω- and ϕ-scans. Total number of reflections recorded, to $\theta_{max} = 23.8°$, was 50073 of which 16847 were unique ($R_{int} = 0.077$); 8479 were 'observed' with $I > 2\sigma_I$. Data were processed using the CRYSALIS-CCD and -RED [15] programs. The structure was determined by the direct methods routines in the SHELXS program and refined by full-matrix least-squares methods, on F^2's, in SHELXL [16].

There are two independent molecules in the crystal. One $SiMe_3$ group was disordered in two orientations. The non-hydrogen atoms were refined with anisotropic thermal parameters. Hydrogen atoms were included in idealised positions and their U_{iso} values were set to ride on the U_{eq} values of the parent carbon atoms. At the conclusion of the refinement, $wR_2 = 0.118$ and $R_1 = 0.125$ for all 16847 reflections weighted $w = [\sigma^2(F_o^2) + (0.0566P)^2]^{-1}$ with $P = (F_o^2 + 2F_c^2)/3$; for the 'observed' data only, $R_1 = 0.051$. In the final difference map, the highest peak (*ca* 0.4 e Å^{-3}) was close to Mg(3).

Scattering factors for neutral atoms were taken from Ref. [17]. Computer programs used in this analysis have been noted above, and were run through WINGX [18] on a Dell Precision 370 PC at the University of East Anglia.

4. Supplementary material

CCDC 625225 contains the supplementary crystallographic data for $[Mg(CH_2SiMe_3)(\mu^3\text{-}OCH_2SiMe_3)]_4$. These data can be obtained free of charge via http://www.ccdc.cam.ac.uk/conts/retrieving.html, or from the Cambridge Crystallographic Data Centre, 12 Union Road, Cambridge CB2 1EZ, UK; fax: (+44) 1223-336-033; or e-mail: deposit@ccdc.cam.ac.uk.

Acknowledgements

C.A. thanks the Junta de Comunidades de Castilla-La Mancha and the Fondo Social Europeo (Grant No. 05/24) for financial support.

References

[1] K. Ziegler, E. Holzkamp, Liebigs Ann. Chem. 605 (1957) 93.
[2] E.C. Ashby, J. Nackashi, G.E. Parris, J. Am. Chem. Soc. 97 (1975) 3162.
[3] H.O. House, R.A. Latham, G.M. Whitesides, J. Org. Chem. 32 (1967) 2481.
[4] L. Bouveault, Bull. Soc. Chim. 29 (1903) 1051.
[5] M.T. Goebel, C.S. Marvel, J. Am. Chem. Soc. 55 (1933) 1693.
[6] R. Han, G. Parkin, J. Am. Chem. Soc. 114 (1992) 749.
[7] T.Y. Her, C.C. Chang, G.H. Lee, S.M. Peng, Y. Wang, Inorg. Chem. 33 (1994) 99.
[8] A.R. Kennedy, R.E. Mulvey, R.B. Rowlings, J. Am. Chem. Soc. 120 (1998) 7816.
[9] P.J. Bailey, R.A. Coxall, C.M. Dick, S. Fabre, L.C. Henderson, C. Herber, S.T. Liddle, D. Loroño-González, A. Parkin, S. Parson, Chem. Eur. J. 9 (2003) 4820.
[10] (a) H. Lehmkuhl, K. Mehler, R. Benn, A. Rufinska, C. Krüger, Chem. Ber. 119 (1986) 1054;
(b) H. Thomas, M. Epple, H. Viebrock, A. Reller, J. Mater. Chem. 5 (1995) 589;
(c) Z.A. Starikova, A.I. Yanovsky, E.P. Turevskaya, N.Ya. Turova, Polyhedron 16 (1997) 967;
(d) V.C. Arunasalam, I. Baxter, J.A. Darr, S.R. Drake, M.B. Hursthouse, K.M.A. Malik, D.M.P. Mingos, Polyhedron 17 (1998) 641;
(e) Z.A. Starikova, A.I. Yanovsky, D.E. Chebukov, E.P. Turevskaya, N.Ya. Turova, Russ. J. Inorg. Chem. 43 (1998) 1308;
(f) Z. Janas, L.B. Jeryzkiewicz, P. Sobota, J. Utko, New J. Chem. 23 (1999) 185;
(g) H.O. Davies, A.C. Jones, T.J. Leedham, M.J. Crosbie, P.J. Wright, N.M. Boag, J.R. Thompson, Chem. Vap. Depos. 6 (2000) 71;
(h) V.G. Kessler, S. Gohil, M. Kritikos, O.N. Korsak, E.E. Knyazeva, I.F. Moskovskaya, B.V. Romanovsky, Polyhedron 20 (2001) 915;

(i) M.M. Sung, C.G. Kim, J. Kim, Y. Kim, Chem. Mater. 14 (2002) 826;
(j) B.F. Abrahams, T.A. Hudson, R. Robson, J. Am. Chem. Soc. 126 (2004) 8624;
(k) G.S. Nichol, W. Clegg, Inorg. Chim. Acta 359 (2006) 3474.
[11] A. Xia, M.J. Heeg, C.H. Winter, J. Organomet. Chem. 669 (2003) 37.
[12] R.E. Mulvey, Organometallics 25 (2006) 1060.
[13] (a) B. Conway, E. Hevia, A.R. Kennedy, R.E. Mulvey, S. Weatherstone, Dalton Trans. (2005) 1532;
(b) N.D.R. Barnett, W. Clegg, A.R. Kennedy, R.E. Mulvey, S. Weatherstone, Chem. Commun. (2005) 375.
[14] E. Lindsell, in: E.W. Abel, F.G.A. Stone, G. Wilkinson (Eds.), Comprehensive Organometallic Chemistry, vol. I, Pergamon, Oxford, 1982, pp. 155–252.
[15] Programs CRYSALIS-CCD and -RED, Oxford Diffraction Ltd., Abingdon, UK, 2005.
[16] G.M. Sheldrick, SHELX-97 – Programs for (a) Crystal Structure Determination (SHELXS) and (b) Refinement (SHELXS), University of Göttingen, Germany, 1997.
[17] International Tables for X-ray Crystallography, Kluwer Academic Publishers, Dordrecht, vol. C, 1992, pp. 500, 219 and 193.
[18] L.J. Farrugia, J. Appl. Cryst. 32 (1999) 837.

exhibit thermally-induced structural phase transition [24–26] even if they are chiral compounds [27,28].

In this paper, we describe preparations, crystal structures, electronic spectra of chiral Schiff base complexes, bis(*N*-*R*-1-naphthylethyl-3,5-dichlorosalicydenaminato)nickel(II) (**1**), copper(II) (**2**), and zinc(II) (**3**) (Scheme 1). Absorption and circular dichroism (CD) spectra of **1**–**3** were recorded in *N*,*N*′-dimethylformamide (DMF), acetone, methanol, chloroform, and toluene solutions to discuss spectral shifts by structural changes. Moreover, we estimate mechanism of photoinduced conformational changes of the complexes caused by three photochromic compounds, azobenzene (**AZ**), 4-hydroxyazobenzene (**AZOH**), and 4-aminoazobenzene (**AZNH$_2$**), by comparing various conditions of experiments.

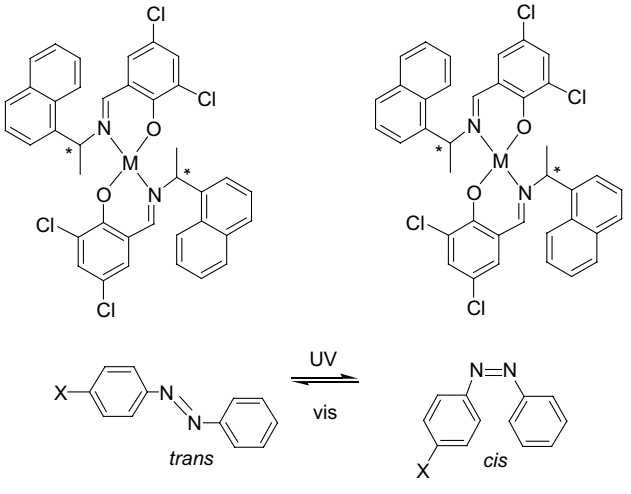
2. Experimental

2.1. Synthesis

Chemicals of the highest commercial grade available (Aldrich and Wako) were used as received without further purification.

2.1.1. Synthesis of bis(*N*-*R*-1-naphthylethyl-3,5-dichlorosalicydenaminato)nickel(II) (*1*)

To a solution of 3,5-dichlorosalicylaldehyde (0.48 g, 2.5 mmol) dissolved in methanol (50 ml), *R*-(+)-1-naphthylethylamine (0.43 g, 2.5 mmol) was added dropwise and stirred at 313 K for 2 h to give orange solution of ligand. Nickel(II) acetate tetrahydrate (0.31 g, 1.25 mmol) was added to the resulting solution to give brown precipitates. After stirring for 2 h, this crude brown compound was filtered and recrystallized from acetone to give brown prismatic single crystals suitable for X-ray analysis. Yield 0.63 g (68.5%). *Anal.* Calc. for $C_{38}H_{28}Cl_4N_2NiO_2$: C, 61.25; H, 3.79; N, 3.76. Found: C, 60.90; H, 3.84; N, 4.16%. IR (KBr, cm^{-1}): 447(w), 547(w), 780(s), 864(w), 906(w), 964(w), 1043(w), 1106(s), 1172(w), 1211(w), 1211(w), 1286(w), 1334(w), 1458(s), 1529(w), 1613(s), 2929(w), 2979(w), 3945(w), 2987(w), 3435(s). m.p. 559 K (decomposition). $\mu_{eff}/\mu_{BM} = 0$ at 298 K (diamagnetism).



M =Ni(**1**), Cu(**2**), Zn(**3**); X = H(**AZ**), OH(**AZOH**), NH_2(**AZNH$_2$**)

Scheme 1. Structures of **1**–**3** and **AZ**, **AZOH**, and **AZNH$_2$** and their photoisomerization induced by UV and visible light irradiation.

2.1.2. Synthesis of bis(*N*-*R*-1-naphthylethyl-3,5-dichlorosalicydenaminato)copper(II) (*2*)

To a solution of 3,5-dichlorosalicylaldehyde (0.48 g, 2.5 mmol) dissolved in methanol (50 ml), *R*-(+)-1-naphthylethylamine (0.43 g, 2.5 mmol) was added dropwise and stirred at 313 K for 2 h to give orange solution of ligand. Copper(II) acetate (0.23 g, 1.25 mmol) was added to the resulting solution to give brown precipitates. After stirring for 2 h, this crude compound was filtered green plate-like single crystals suitable for X-ray analysis. Yield 0.66 g (70.4%). *Anal.* Calc. for $C_{38}H_{28}Cl_4CuN_2O_2$: C, 60.85; H, 3.76; N, 3.74. Found: C, 60.70; H, 3.52; N, 4.02%. IR (KBr, cm^{-1}): 452(w), 489(w), 510(w), 552(w), 600(w), 632(w), 658(w), 779(s), 863(w), 974(w), 1028(w), 1049(w), 1107(w), 1175(w), 1207(w), 1291(w), 1324(w), 1460(s), 1518(w), 1618(s), 2870(w), 2928(w), 2975(w), 3952(w), 2086(w), 3435(s). m.p. 566 K (decomposition).

2.1.3. Synthesis of bis(*N*-*R*-1-naphthylethyl-3,5-dichlorosalicydenaminato)zinc(II) (*3*)

To a solution of 3,5-dichlorosalicylaldehyde (0.48 g, 2.5 mmol) dissolved in methanol (50 ml), *R*-(+)-1-naphthylethylamine (0.43 g, 2.5 mmol) was added dropwise and stirred at 313 K for 2 h to give orange solution of ligand. Zinc(II) acetate dihydrate (0.23 g, 1.25 mmol) and $NaHCO_3$ (0.17 g, 2.0 mmol) was added to the resulting orange solution to give yellow precipitates. After stirring for 2 h, this crude compound was filtered yellow plate-like single crystals suitable for X-ray analysis. Yield 0.68 g (72.3%). *Anal.* Calc. for $C_{38}H_{28}Cl_4N_2O_2Zn$: C, 60.71; H, 3.75; N, 3.73. Found: C, 60.70; H, 3.58; N, 4.16%. IR (KBr, cm^{-1}): 541(w), 769(w), 869(w), 980(w), 1975(w), 1112(w), 1160(s), 1212(w), 1301(w), 1413(w), 1442(s), 1518(w), 1616(s), 2934(w), 2975(w), 3054(w), 3429(s). m.p. 615 K (decomposition).

2.2. Physical measurements

Elemental analyses (C, H, N) were performed by an Elemetar Vario EL analyzer at Keio University. IR spectra were recorded as KBr pellets on a JASCO FT-IR 660 plus spectrophotometer in the range of 4000–400 cm^{-1} at 298 K. Thermal analysis was performed on a SHIMADZU DSC-60 differential scanning calorimeter (DSC), where the heating rate was 10 K min^{-1} in the range of 313–673 K. Diffuse reflectance spectra were measured on a JASCO V-560 spectrophotometer equipped with an integrating

sphere in the range of 850–220 nm at 298 K. Absorption spectra were measured on a JASCO V-560 spectrophotometer in the range of 900–200 nm at 298 K. Circular dichroism (CD) spectra were measured on a JASCO J-720WI spectropolarimeter in the range of 900–200 nm at 298 K. Magnetic susceptibility was measured with a Sherwood Scientific magnetic susceptibility balance at 298 K. Luminescence spectra (emission by $\lambda_{ex} = 27000\ cm^{-1}$) were measured on a JASCO FP-6500 spectrofluorometer at 298 K. Photoillumination were carried out using a lamp ($1.0\ mW/cm^2$) with optical filters (UV $\lambda = 200$–400 nm) leading to a sample by using optical fibers through optical filters.

2.3. X-ray crystallography

Intensity data were collected on a Rigaku AFC-7R four-circle diffractometer with graphite monochromated Mo Kα radiation ($\lambda = 0.71073$ Å). Data analysis was carried out with a teXsan program package [29]. The structure was solved by direct methods with a SIR 92 program [30] and refined by full-matrix least-squares methods based on F^2 using the program SHELXL-97 [31]. An empirical absorption correction was applied based on ψ scans. No significant decay in the intensity of three standard reflections was observed throughout the data collection. All non-hydrogen atoms were readily located and refined by anisotropic thermal parameters. All hydrogen atoms were located at geometrically expected positions and refined using riding models.

The size of crystal **2** served for measurement was relatively small (or thin), and there was large void space made by bulky organic ligands in the crystal of **2**, which was an essential problem of this compound. The intensity of diffraction was weak for the crystal of **2**, which resulted in poor result. However, the *R*-factor of 0.0800 for **2** was sufficient quality to discuss overall molecular structure except for detailed molecular geometries with large esds.

Crystal data for **1**: $C_{38}H_{28}Cl_4N_2NiO_2$, crystal dimension $0.50 \times 0.40 \times 0.40\ mm^3$, $M_w = 745.11$, orthorhombic, space group $P2_12_12_1$, $a = 12.862(5)$ Å, $b = 30.27(2)$ Å, $c = 8.682(3)$ Å, $V = 3380(3)$ Å^3, $Z = 4$, $D_{calc} = 1.464\ mg/m^3$, $F(000) = 1528$, $R_1 = 0.0396$, $R_w = 0.0953$, $S = 0.991$, Flack parameter $= -0.02(2)$.

Crystal data for **2**: $C_{38}H_{28}Cl_4CuN_2O_2$, crystal dimension $0.50 \times 0.20 \times 0.20\ mm^3$, $M_w = 749.97$, orthorhombic, space group $P2_12_12$, $a = 32.243(8)$ Å, $b = 8.758(3)$ Å, $c = 12.813(4)$ Å, $V = 3618.2(19)$ Å^3, $Z = 4$, $D_{calc} = 1.377\ mg/m^3$, $F(000) = 1532$, $R_1 = 0.0800$, $R_w = 0.2280$, $S = 1.518$, Flack parameter $= -0.03(4)$.

Crystal data for **3**: $C_{38}H_{28}Cl_4N_2O_2Zn$, crystal dimension $0.50 \times 0.20 \times 0.20\ mm^3$, $M_w = 751.81$, tetragonal, space group $I4_1$, $a = b = 22.001(4)$ Å, $c = 14.135(4)$ Å, $V = 6842(3)$ Å^3, $Z = 8$, $D_{calc} = 1.460\ mg/m^3$, $F(000) = 3072$, $R_1 = 0.0394$, $R_w = 0.0848$, $S = 0.984$, Flack parameter $= -0.013(17)$.

3. Results and discussion

3.1. Description of the structures

3.1.1. Crystal structure of *1*

The molecular structure of **1** is depicted in Fig. 1 and selected bond distances and angles are given in its caption. Complex **1** affords a square planar *trans*-[NiN_2O_2] coordination geometry with a step conformation. The molecule in the crystal examined is Δ(*R*,*R*) conformation. Coordination bonds of Ni1–O1 = 1.823(4), Ni1–O2 = 1.823(4), Ni1–N1 = 1.936(4), and Ni1–N2 = 1.935(4) Å and imine double bond distances of N1–C7 = 1.280(7) and N2–C26 = 1.283(7) Å are normal values for Schiff base Ni^{II} complexes [9,11,19]. Both naphthyl groups are almost perpendicular to six-membered rings with dihedral angles of C1–C6/C10–C19 = 86.58(16)° and C20–C25/C29–C38 = 92.85(22)° and N1–Ni1–O1/N2–Ni1–O2 = 4.91(1)°. The crystal packing is formed by weak van der Waals force mainly without both hydrogen bonds and π–π stacking interactions.

3.1.2. Crystal structure of *2*

The molecular structure of **2** is depicted in Fig. 2 and selected bond distances and angles are given in its caption. Complex **2** affords a square planar *trans*-[CuN_2O_2]

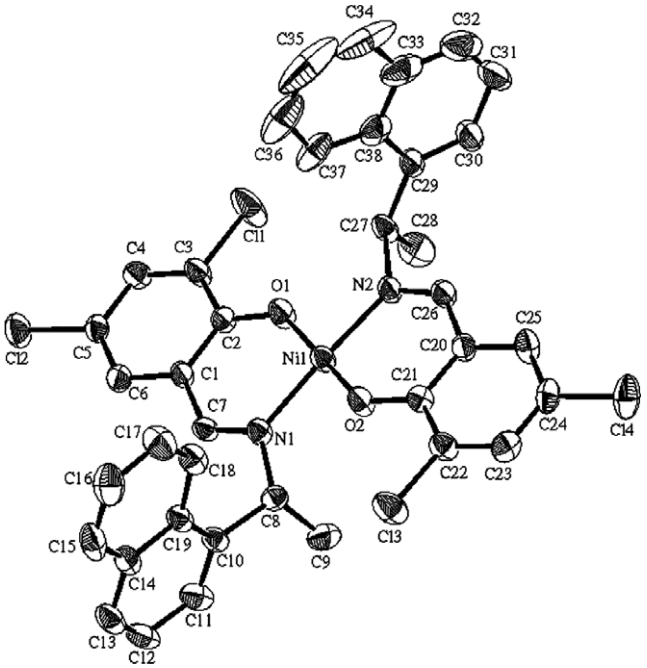


Fig. 1. The molecular structure of **1** showing the atom labeling scheme. Displacement parameters are drawn at the 30% probability level. H atoms are omitted for clarity. Selected bond lengths (Å) and angles (°): Ni1–O1 = 1.823(4), Ni1–O2 = 1.823(4), Ni1–N1 = 1.936(4), Ni1–N2 = 1.935(4), O1–C2 = 1.298(7), O2–C21 = 1.299(7), N1–C7 = 1.280(7), N1–C8 = 1.507(7), N2–C26 = 1.283(7), N2–C27 = 1.526(7), O1–Ni1–O2 = 176.8(2), O1–Ni1–N1 = 92.1(2), O1–Ni1–N2 = 88.2(2), O2–Ni1–N1 = 87.9(2), O2–Ni1–N2 = 92.0(2), N1–Ni1–N2 = 176.1(2), C7–N1–C8 = 115.8(4), C26–N2–C27 = 114.4(4).

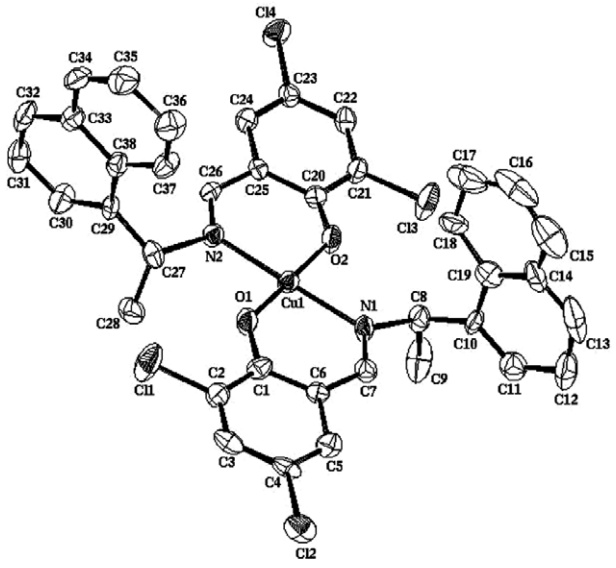


Fig. 2. The molecular structure of **2** showing the atom labeling scheme. Displacement parameters are drawn at the 30% probability level. H atoms are omitted for clarity. Selected bond lengths (Å) and angles (°): Cu1–O1 = 1.885(8), Cu1–O2 = 1.900(8), Cu1–N1 = 2.044(8), Cu1–N2 = 2.051(8), O1–C1 = 1.316(13), O2–C20 = 1.268(12), N1–C7 = 1.290(12), N1–C8 = 1.487(12), N2–C26 = 1.283(13), N2–C27 = 1.548(12), O1–Cu1–O2 = 176.6(4), O1–Cu1–N1 = 91.5(3), O1–Cu1–N2 = 89.3(3), O2–Cu1–N1 = 88.7(3), O2–Cu1–N2 = 90.5(3), N1–Cu1–N2 = 179.0(4), C7–N1–C8 = 116.7(9), C26–N2–C27 = 116.5(9).

coordination geometry with a step conformation, and overall structure of **2** is similar to that of **1**. The molecule in the crystal examined is $\Delta(R,R)$ conformation. Coordination bonds of Cu1–O1 = 1.885(8), Cu1–O2 = 1.900(8), Cu1–N1 = 2.044(8), and Cu1–N2 = 2.051(8) Å and imine double bond distances of N1–C7 = 1.290(12) and N2–C26 = 1.283(13) Å are normal values for Cu^{II} complexes having Schiff base ligands [10,11,24–28]. Elongation of coordination bond lengths of **2** than that of **1** is due to the difference of radii of Cu^{II} and Ni^{II} ions. Both naphthyl groups are almost perpendicular to six-membered rings with dihedral angles of C1–C6/C10–C19 = 95.45(31)° and C20–C25/C29–C38 = 86.25(30)° and N1–Cu1–O1/N2–Cu1–O2 = 3.47(1)°. No hydrogen bonds and π–π stacking are found in molecular crystals packed by weak van der Waals force.

3.1.3. Crystal structure of 3

The molecular structure of **3** is depicted in Fig. 3 and selected bond distances and angles are given in its caption. Complex **3** affords a distorted tetrahedral *trans*-[ZnN_2O_2] coordination geometry, and overall structure of **3** is quite different from those of **1** and **2**. The molecule in the crystal examined is $\Delta(R,R)$ conformation. Some coordination bonds among Zn1–O1 = 1.914(5), Zn1–O2 = 1.914(5), Zn1–N1 = 2.033(6), and Zn1–N2 = 2.003(6) Å are longer than the corresponding ones of **1** and **2**, which is due to both ionic radii of Zn^{II} and distortion of coordination environment. The imine double bond distances are N1–C7 = 1.274(8) and N2–C26 = 1.251(9) Å for **3**. Selected dihedral angles are as follows: N1–Zn1–O1/N2–Zn1–

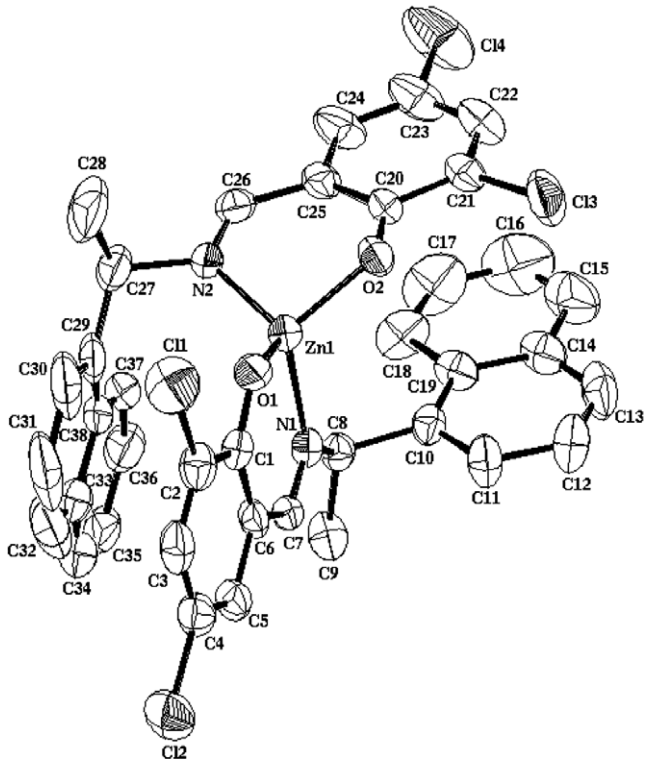


Fig. 3. The molecular structure of **3** showing the atom labeling scheme. Displacement parameters are drawn at the 30% probability level. H atoms are omitted for clarity. Selected bond lengths (Å) and angles (°): Zn1–O1 = 1.914(5), Zn1–O2 = 1.914(5), Zn1–N1 = 2.033(6), Zn1–N2 = 2.003(6), O1–C1 = 1.290(8), O2–C20 = 1.288(8), N1–C7 = 1.274(8), N1–C8 = 1.470(8), N2–C26 = 1.251(9), N2–C27 = 1.494(8), O1–Zn1–O2 = 118.0(2), O1–Zn1–N1 = 96.4(2), O1–Zn1–N2 = 119.5(2), O2–Cu1–N1 = 115.3(2), O2–Zn1–N2 = 93.9(2), N1–Zn1–N2 = 115.4(2), C7–N1–C8 = 121.4(6), C26–N2–C27 = 117.6(7).

O2 = 90.49(1)°, C1–C6/C10–C19 = 85.10(28)°, C20–C25/C29–C38 = 77.24(35)°, C1–C6/C29–C38 = 77.24(35)°, and C20–C25/C10–C19 = 5.18(29)°. In general, σ-character of Zn–N coordination bonds is stronger than that of dπ–pπ interaction [32]. In contrast to **1** and **2**, two π-conjugated moieties, naphthyl groups (C14–C16) and six-membered rings (C20–C25) of the opposite side of ligands and ring moieties (Zn1–N1–C1–C6–C7–O1/C29–C30–C31–C32–C33–C38) do not interact strongly. There are no hydrogen bonds in the crystals of **3**.

3.2. Structural phase transition

In the solid state, DSC curves on heating exhibited endothermic peaks at 521 and 547 K for **1** and **2**, respectively. It is well known that the analogous Ni^{II} and Cu^{II} complexes occur thermally-induced structural phase transition from square planar (or less distorted tetrahedral) to tetrahedral coordination environment [18]. The transition temperature was 456 K for the related Ni^{II} complex incorporating 1-phenylethylamine moieties [9], and higher temperature of **1** incorporating 1-naphthylethylamine moieties may be attributed to molecular weight mainly. Furthermore, compressed tetrahedral complex **3** also

exhibited similar endothermic peak at 523 K, which was observed for the first time among the analogous Zn^{II} complexes as far as we know. In analogy with **1** and **2**, the thermally-induced structural phase transition for **3** may be attributed to changes of the degree of distortion deviated from regular tetrahedral geometry. In this way, coordination environment was flexible for not only Ni^{II} (**1**) and Cu^{II} (**2**) complexes but also Zn^{II} complex (**3**) at least even in the solid state.

3.3. IR and electronic spectroscopy in the solid state

IR spectra exhibited characteristic peaks of imine bands at 1610, 1618, and 1616 cm^{-1} for **1**, **2**, and **3**, respectively. These values are reasonable by comparing with the analogous Ni^{II}, Cu^{II}, Zn^{II}, and other Schiff base complexes [33].

By the way, it is known that tautomers of free Schiff base ligands without coordinated metal ions exhibit photochromism as well as thermochromism in the solid state [34–36]. However, such metal complexes do not possess hydrogen atom transferring sites, and we cannot observe such phenomenon for **1**–**3** by means of IR spectroscopy in the solid state and solutions. Therefore, we can confirm that photoirradiation effects on Schiff base moieties do not concern with metal complexes.

As shown in Fig. 4, diffuse reflectance spectra showed broad d–d bands around 15300 cm^{-1} for **1** and 14000 cm^{-1} for **2**. As for **1**, the spectral features of spin-allowed $^1A_g \rightarrow {}^1B_{1g}$ and $^1A_g \rightarrow {}^1B_{3g}$ transitions and spin-forbidden $^1A_g \rightarrow {}^3B_{1g}$ transition are consistent with both diamagnetism and a square planar coordination geometry. In addition, there also appeared LMCT bands around 21000 cm^{-1} as shoulder and broad π–π^* bands around 25000 cm^{-1} for **1**–**3**.

3.4. Electronic, CD, and emission spectra in solutions

Absorption and CD spectra for **1**–**3** in various solvents are shown in Figs. 5–7, respectively. These absorption spectra are different from the corresponding diffuse reflectance spectra, which suggest drastic structural changes of **1**–**3** between solid state and solutions. The sign of CD spectra is due to $\Delta(R,R)$ absolute configuration for **1**–**3**. Physical properties of the solvents are as follows [37]: *N*,*N*′-dimethylformamide (DMF) ($\mu = 3.82$; $\varepsilon = 36.710$; $n_D^{20} = 1.428$), acetone ($\mu = 3.11$; $\varepsilon = 20.700$; $n_D^{20} = 1.356$), methanol ($\mu = 2.97$; $\varepsilon = 32.630$; $n_D^{20} = 1.326$), chloroform ($\mu = 1.11$; $\varepsilon = 4.806$; $n_D^{20} = 1.444$), and toluene ($\mu = 0.37$; $\varepsilon = 2.438$; $n_D^{20} = 1.494$). The values in parentheses denote dipole moment, μ (Debye), dielectric constant, ε, and refractive index, n_D^{20}, respectively.

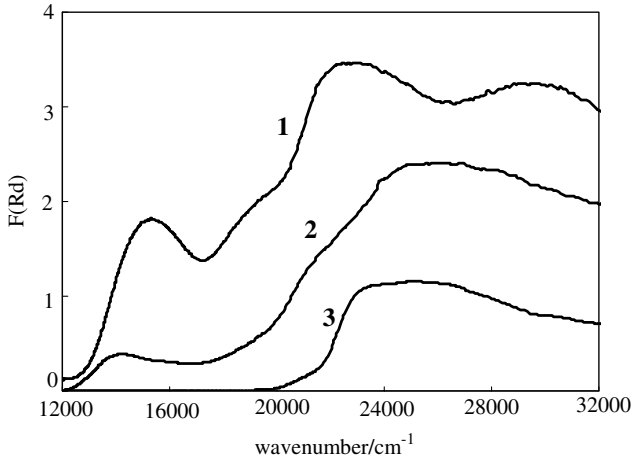


Fig. 4. Diffuse reflectance spectra for **1**–**3**.

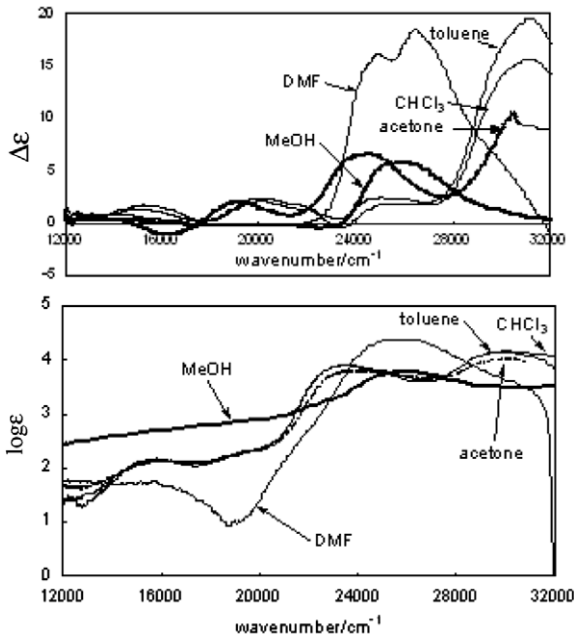


Fig. 5. Absorption and CD spectra of **1** in 0.1 mM various solvents.

In D_{2h} symmetry, absorption bands for Ni^{II} complexes can be assigned as follows [38,39]: $^1A_g \rightarrow {}^3B_{1g}$ (12000 cm^{-1}), $^1A_g \rightarrow {}^1B_{1g}$ (16000 cm^{-1}), $^1A_g \rightarrow {}^3B_{3g}$ and $^1A_g \rightarrow {}^3B_{2g}$, and LMCT (20000 cm^{-1}), $^1A_g \rightarrow {}^1B_{2g}$ (24000 cm^{-1}), $^1A_g \rightarrow {}^1B_{3u}$, $^1B_{2u}$ (28000 cm^{-1}), and $^1A_g \rightarrow {}^1B_{3u}$ (30000 cm^{-1}), and π–π^* bands (more than 30000 cm^{-1}). On the other hand, as for Cu^{II} complexes, a broad d–d band composed of $^2A_1 \rightarrow {}^2A_1$, $^2A_1 \rightarrow {}^2B_1$, and $^2A_1 \rightarrow {}^2B_2$ transitions (*ca.* 16000–20000 cm^{-1}), CT and π–π^* bands (*ca.* 24000–28000 cm^{-1}) can be expected in C_{2v} symmetry [39–41]. Since Zn^{II} complexes exhibit no d–d transition, all spectral bands in UV region in Fig. 7 are attributable to LMCT and π–π^* transitions of ligands (more than 24000 cm^{-1}) [32]. In the CD spectra for **3**, solvent dependence of intensities and wavenumbers can be observed except for toluene showing large deviation from other solvents. In particular, spectral shifts depending on solvents of Ni^{II} (**1**) complex are larger than those of Cu^{II} (**2**) and Zn^{II} (**3**) complexes regardless of concentration of solutions or types of photochromic solutes (see also 'solution paramagnetism' in later section).

In order to refer previous assignments established for the related Schiff base complexes, we employed wavenumber

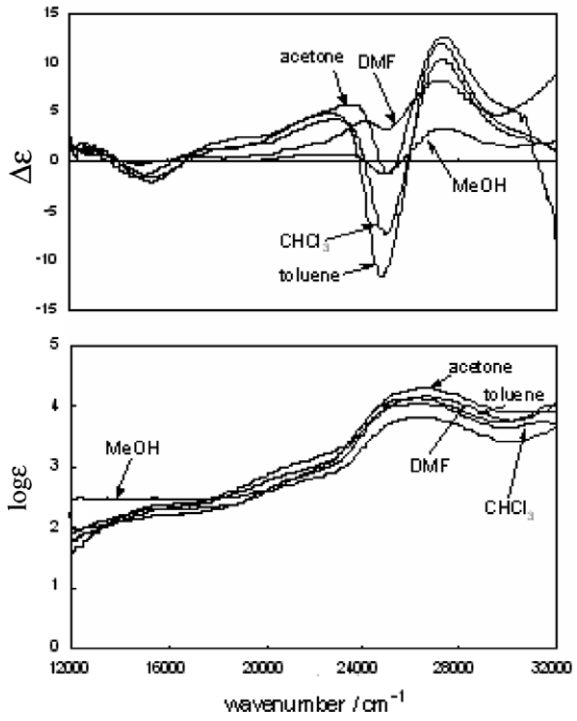


Fig. 6. Absorption and CD spectra of **2** in 0.1 mM various solvents.

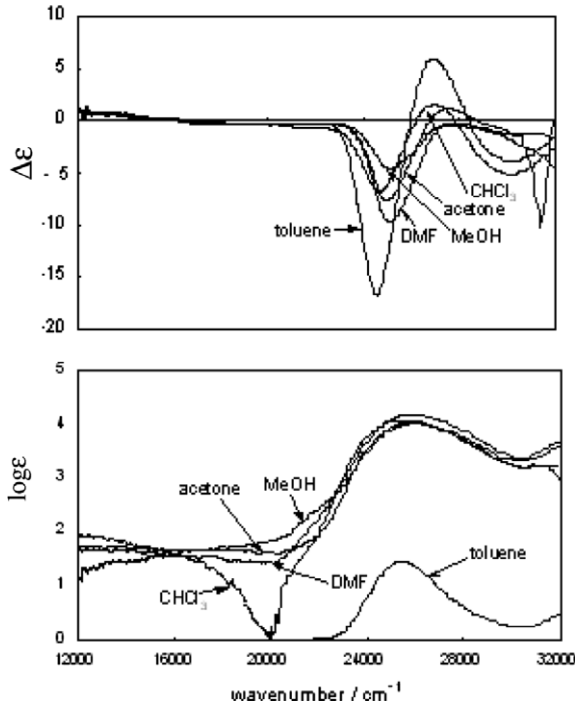


Fig. 7. Absorption and CD spectra of **3** in 0.1 mM various solvents.

scale for all spectra in this paper. On the other hand, intensity was plotted in $\log\varepsilon$ (or $\Delta\varepsilon$) scale in order for determining spectra of sole solute. While they are plotted in absorbance (or θ) scale in order for expressing the magnitude of difference observed for mixed solutions being dependent on concentration clearly. Variation with solvents was reproducible as far as we measured at the same time. However, in particular for CD spectra, unexpected artifact or noise might be observed at UV region of quite intense absorption. In addition, particle size of solutes (azobenzenes and complexes) does not show scattering for light of this wavenumber.

Emission spectra of **3** ($\lambda_{ex} = 27\,800\ cm^{-1}$) at 298 K in various solvents are shown in Fig. 8. Solvent dependence of the peaks is as follows: 21 300 cm^{-1} for toluene, chloroform, and methanol, 21 500 cm^{-1} for acetone, and 22 100 cm^{-1} for DMF. There is not distinct linear correlation between peaks (wavenumber or intensity) and polarity (dielectric constants) of the solvents. The fact suggests that electronic transitions concerned with emission occur between different molecular orbital levels, in other words, it is not solvatochromism keeping the identical molecular structures having the identical molecular orbitals [42]. In addition, large conformational changes of **3** can be expected in different solvents. Detailed molecular structures in each solution are unclear at present.

3.5. Photochromic solute induced structural changes in solutions

In order to elucidate appropriate conditions for the phenomenon, we compared several conditions of the supramolecular systems containing chiral complexes (**1**–**3**) and photochromic compounds (azobenzene (**AZ**), 4-hydroxyazobenzene (**AZOH**), and 4-aminoazobenzene ($\mathbf{AZNH_2}$)) in the five organic solvents (0.1 mM). Although we prepared both solutions of 0.1 mM and 0.01 mM, we could not prepare 1 mM solutions because of low solubility. For both concentrations, π–π^* bands in UV region were strong, while d–d bands in visible region were relatively weak. However, 0.01 mM solutions were too dilute to detect the phenomenon clearly. Thus we employed 0.1 mM solution for investigation after all. As elucidated later, weak intermolecular interactions between chiral metal complexes and photochromic azobenzenes play an

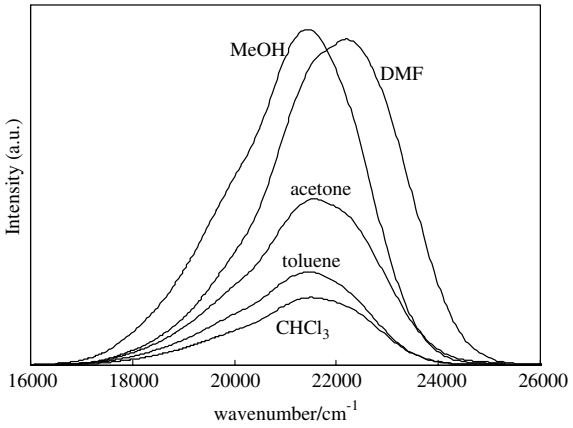


Fig. 8. Emission spectra ($\lambda_{ex} = 27\,800\ cm^{-1}$) of **3** at 298 K in 0.1 mM various solvents.

important role in the phenomenon. Serious changes must be expected for supramolecular solution systems by using different concentrations.

Firstly, we investigated appropriate solvents for the phenomenon. According to the previous study (Ni^{II} complex and **AZOH**) [9], we examined a system containing **1** and **AZOH** in chloroform and observed smooth changes of both π–π* and d–d bands (Fig. 9). As for acetone, DMF, and methanol solutions (not shown), little spectral changes could be observed in both π–π* (*ca.* 28 000 cm^{-1}) and d–d (*ca.* 22 000 cm^{-1}) bands. As for toluene solution (not shown), we could observe reversible change of π–π* bands and little change of d–d bands. Thus, we selected 0.1 mM chloroform solutions for later discussion.

Secondly, we deal with steric effects of largely extended π-conjugate chiral ligands. The CD (and absorption) spectra exhibited somewhat irreversible changes in both π–π* and d–d bands for **1** and **AZOH** (Fig. 9). In contrast, CD spectra previous system of Ni^{II} complex incorporating 1-phenylethylamine moieties and **AZOH** exhibited almost reversible changes of weak d–d and strong π–π* bands [9]. We can extract the following possibility from the comparison: (1) Incomplete reversible conformational changes of the chiral complexes indicate that bulky ligands is kept a certain conformation, in other words, weak intermolecular interactions is necessary for transferring mechanisms of the effects between azobenzenes and chiral complexes. (2) The axial coordination sites opened by the bulky ligands enable **1** to coordinate **AZOH** molecules as ligands or to exhibit so-called 'solution paramagnetism' to coordinate solvent molecules as ligands [43]. As mentioned above, only **1** may drastically convert from a square planar geometry (diamagnetic) in the solid state or in a certain solvent to a tetrahedral (paramagnetic) geometry in solutions. Moreover, it is also well known that the related four-coordinated Ni^{II} complexes (diamagnetic) can convert to six-coordinated ones (paramagnetic) by coordinating solvent molecules as ligands. Anyway, characteristic behavior of spectra for **1** may be ascribed to such equilibrium in the solutions.

Thirdly, we investigate the effects of polar (–OH and $–NH_2$) groups of azobenzene derivatives as follows: (1) Is there possibility of additional coordination to axial site(s) especially for Ni^{II} complexes (**1**) as mentioned above? (2) Is isotropic electrostatic effects of polarity (dielectric constants) of solutions induced by photoisomerization of azo groups effective or not? Difference between *cis* and *trans* forms is *ca.* 3 Debyes for non-substituted azobenzene [9,10]. In the case of **1** and **AZ** in chloroform (Fig. 10), both CD and absorption spectra exhibited almost reversible changes in both π–π* and d–d bands smoothly. This result of **AZ** reveals that polar groups are not essential to enhance spectral changes. Of course, the phenomenon with **AZ** is not in connection with axial coordination. However, the system of **1** and $\mathbf{AZNH_2}$ in chloroform (Fig. 11) showed relatively larger changes of a d–d band (20 000 cm^{-1}) in absorptions spectra than that of **1** and **AZ** (Fig. 10). In this way, $\mathbf{AZNH_2}$ and **AZOH** may coordinate to the axial sites of **1**, but **AZ** without the polar groups can also occur the phenomenon with **1**.

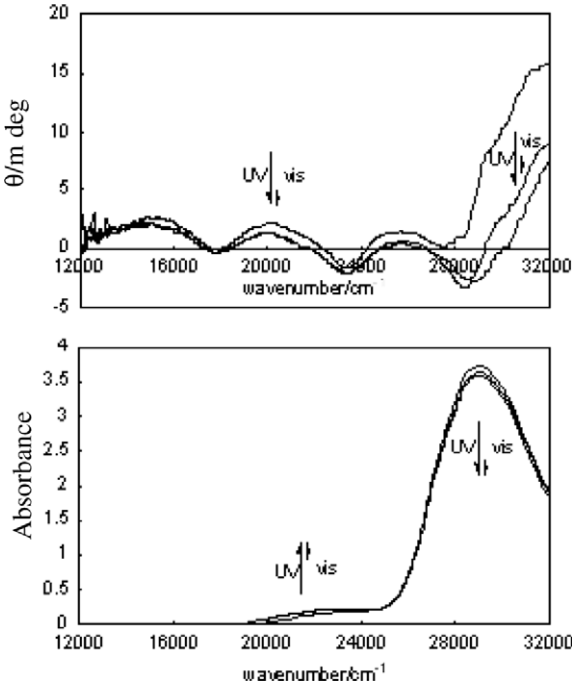


Fig. 9. Absorption and CD spectra of **1** and **AZOH** in 0.1 mM chloroform solution and before and after UV and visible light irradiation for 5 min.

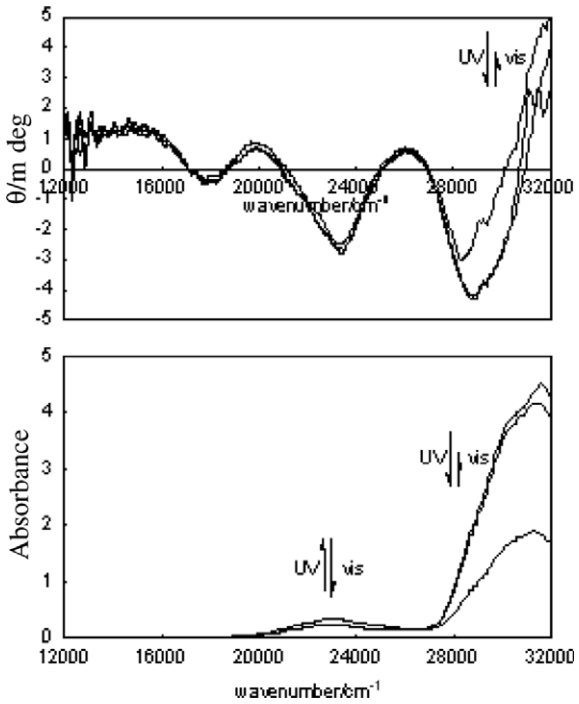


Fig. 10. Absorption and CD spectra of **1** and **AZ** in 0.1 mM chloroform solution and before and after UV and visible light irradiation for 5 min.

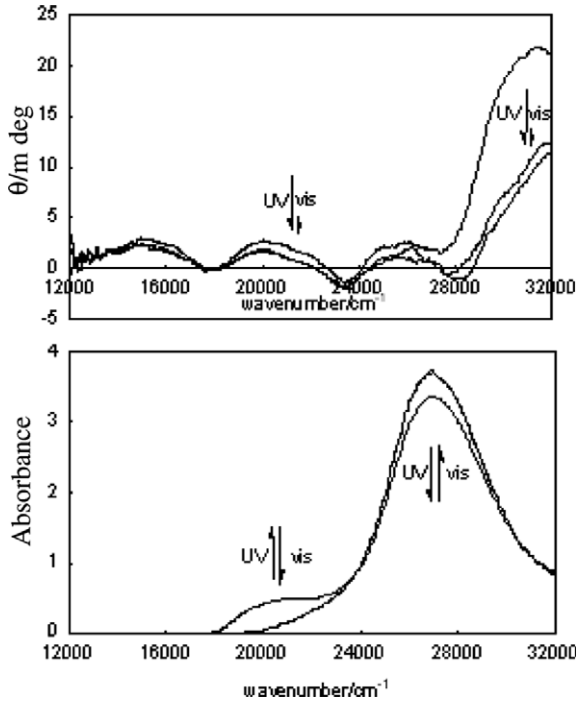


Fig. 11. Absorption and CD spectra of **1** and $\mathbf{AZNH_2}$ in 0.1 mM chloroform solution and before and after UV and visible light irradiation for 5 min.

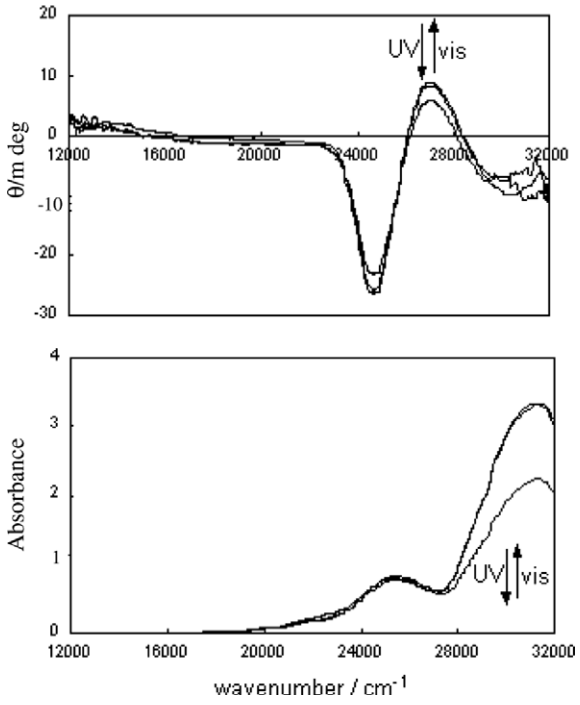


Fig. 13. Absorption and CD spectra of **3** and **AZ** in 0.1 mM chloroform solution and before and after UV and visible light irradiation for 5 min.

By the way, not all azobenzene molecules in solutions exhibit photoisomerization after UV or visible light irradiation generally. Therefore, many systems do not return to an original state after alternate irradiation of UV and visible light. In particular, the present supramolecular systems use weak intermolecular interactions to conduct the influences, namely photoisomerization of azobenzenes to chiral metal complexes. Even if photoisomerization of azobenzene can occur completely, not all molecules of complexes can convert their conformation smoothly. Thus, the fact also supports contribution of intermolecular interactions between azobenzenes and complexes.

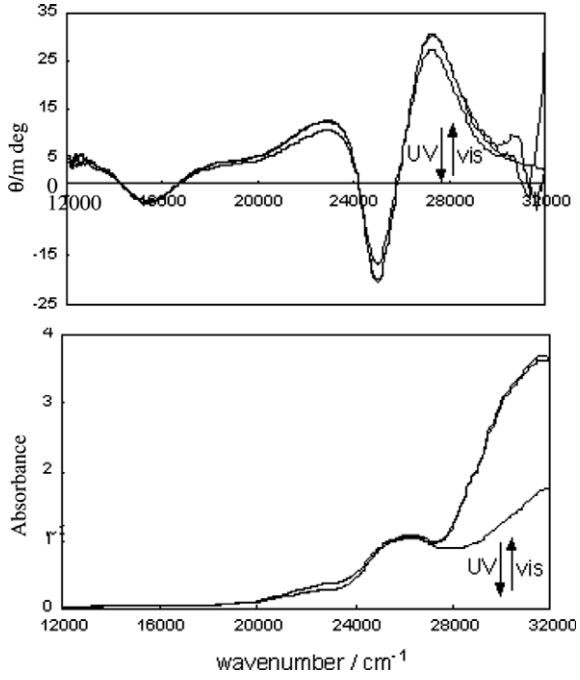


Fig. 12. Absorption and CD spectra of **2** and **AZ** in 0.1 mM chloroform solution and before and after UV and visible light irradiation for 5 min.

Finally, to confirm that the conformational changes are attributed to π-conjugated chiral ligands and/or coordination environment, we compare flexible Cu^{II} complex (**2**) and rigid Zn^{II} complex (**3**) in Figs. 12 and 13, respectively. Regardless of transition metals, both **2** and **3** exhibited reversible spectral changes mainly in π–π* region (little in d–d region). Consequently, the phenomenon is concerned with conformational changes of π-conjugated moieties of the ligands rather than coordination spheres.

To separate overlap of bands of achiral azozenzene and chiral metal complexes, we employed not only absorption spectra but also CD spectra to detect conformational changes for the present study. However, detailed conformation of the complexes in solutions is unclear at present.

4. Concluding remarks

In summary, we examined the conditions conformational changes induced by photoisomerization of azobenzenes via intermolecular interactions in solutions by comparing complexes **1**–**3**, photochromic compounds **AZ**, **AZOH**, and $\mathbf{AZNH_2}$, and five organic solvents. Chloroform is best solvent to observe the phenomenon. Among **1**–**3**, **1** exhibits conformational changes most smoothly.

That rigid **3** also exhibits the conformational changes suggests that it is due to not only π-conjugate moiety of the chiral ligands predominantly but also coordination environment. The phenomenon can be occurred by **AZ** as well as**AZOH** and **AZNH$_2$** solutes, which suggest that the phenomenon is independent of polarity or coordination of photochromic solutes. Incomplete reversible conformational changes of chiral complexes indicate that bulky ligands are kept a certain conformation. Accordingly, weak intermolecular interactions are necessary for transferring mechanisms of the effects of photoisomerization between azobenzenes and flexible chiral complexes.

Since we understand that this phenomenon can control long-range order of solutes in solutions, we will apply this methodology to various photofunctional supramolecular materials containing metal complexes, for example magnetic ionic liquids [44].

Acknowledgements

This work was supported by Grant-in-Aid for the 21st Century COE program 'KEIO Life Conjugate Chemistry' form the Ministry of Education, Culture, Sports, Science, and Technology, Japan and the Steel Industry Foundation for the Advancement of Environmental Protection Technology (05 C-31-44). The author thanks Professor Tohru Yamada and Dr. Taketo Ikeno (Keio University) for the use of the DSC apparatus, Professor Hidenari Inoue (Keio University) for the use of the CD spectrometer.

Appendix A. Supplementary material

CCDC 265920, 622668, and 622669 contain the supplementary crystallographic data for **1**, **2**, and **3**. These data can be obtained free of charge via http://www.ccdc.cam.ac.uk/conts/retrieving.html, or from the Cambridge Crystallographic Data Centre, 12 Union Road, Cambridge CB2 1EZ, UK; fax: (+44) 1223-336-033; or e-mail: deposit@ccdc.cam.ac.uk. Supplementary data associated with this article can be found, in the online version, at doi:10.1016/j.poly.2006.12.031.

References

[1] Y. Einaga, Bull. Chem. Soc. Jpn. 79 (2006) 361.
[2] Y. Einaga, O. Sato, T. Iyoda, A. Fujishima, K. Hashimoto, J. Am. Chem. Soc. 121 (1999) 3745.
[3] Y. Einaga, M. Taguchi, G. Li, T. Akitsu, T. Sugai, O. Sato, Chem. Mater. 15 (2003) 8.
[4] R. Mikami, M. Taguchi, K. Yamada, K. Suzuki, O. Sato, Y. Einaga, Angew. Chem. Int. Ed. 43 (2004) 6135.
[5] M. Taguchi, K. Yamada, K. Suzuki, O. Sato, Y. Einaga, Chem. Mater. 17 (2003) 4554.
[6] T. Yamamoto, Y. Umemura, O. Sato, Y. Einaga, J. Am. Chem. Soc. 127 (2005) 16065.
[7] T. Yamamoto, Y. Umemura, O. Sato, Y. Einaga, Chem. Mater. 16 (2004) 1195.
[8] Y. Einaga, R. Mikami, T. Akitsu, G. Li, Thin Solid Films 493 (2005) 230.
[9] T. Akitsu, Y. Einaga, Polyhedron 24 (2005) 1869.
[10] T. Akitsu, Y. Einaga, Polyhedron 24 (2005) 2933.
[11] S. Yamada, Coord. Chem. Rev. 190–192 (1999) 537.
[12] R.L. Braun, E.C. Lingagelter, Acta Crystallogr. 21 (1966) 546.
[13] K. Ravikumar, S.S. Rajan, V. Rajaram, S.K. Ramalingam, S. Natarajin, Z. Kristallogr. 175 (1986) 117.
[14] V. Manriquez, J. Vargas, J. Costamagna, H.G. von Schnering, K. Peters, Acta Crystallogr. C 46 (1990) 772.
[15] M.R. Fox, E.C. Lingafelter, P.L. Orioli, L. Sacconi, Nature 197 (1963) 1104.
[16] M.R. Fox, L. Orioli, L. Sacconi, Acta Crystallogr. 17 (1964) 1159.
[17] R.L. Braun, E.C. Lingagelter, Acta Crystallogr. 22 (1967) 780.
[18] N. Arai, M. Sorai, S. Seki, Bull. Chem. Soc. Jpn. 45 (1972) 2398.
[19] T. Ashida, S. Iwata, T. Yamane, M. Kakudo, A. Takeuchi, S. Yamada, Bull. Chem. Soc. Jpn. 49 (1976) 3502.
[20] J.B. Willis, D.P. Mellor, J. Am. Chem. Soc. 69 (1947) 1237.
[21] L. Sacconi, P. Paoletti, M. Ciampolini, J. Am. Chem. Soc. 85 (1963) 411.
[22] H. Hoss, H. Elias, Inorg. Chem. 32 (1993) 317.
[23] M.K. Saha, I. Bernal, F.R. Fronczek, Chem. Commun. (2004) 84.
[24] T. Akitsu, Y. Einaga, Acta Crystallogr. E 60 (2004) m436.
[25] T. Akitsu, Y. Einaga, Acta Crystallogr. E 60 (2004) m1552.
[26] T. Akitsu, Y. Einaga, Acta Crystallogr. E 60 (2004) m1555.
[27] T. Akitsu, Y. Einaga, Acta Crystallogr. E 60 (2004) m1602.
[28] T. Akitsu, Y. Einaga, Acta Crystallogr. C 60 (2004) m640.
[29] Molecular Structure Corporation, TEXSAN, Version 1.11, MSC, 9009 New Trails Drive, The Woodlands, TX 77381-5209, USA, 2001.
[30] A. Altomare, G. Cascarano, C. Giacovazzo, A. Guagliardi, M.C. Brurla, G. Polidori, M. Camalli, J. Appl. Cryst. 27 (1994) 435.
[31] G.M. Sheldrick, SHELXL-97, Program for the Refinement of Crystal Structures, University of Gottingen, Germany, 1997.
[32] H. Sakiyama, H. Okawa, N. Matsumoto, S. Kida, J. Chem. Soc., Dalton Trans. (1990) 2935.
[33] G. Santoni, D. Rehder, J. Inorg. Biochem. 98 (2004) 758.
[34] E. Hadjoudis, A. Rontoyianni, K. Ambroziak, T. Dziembowska, I.M. Mavridis, J. Photochem. Photobiol. A: Chem. 162 (2004) 521.
[35] T. Akitsu, Y. Takeuchi, Y. Einaga, Acta Crystallogr. C 60 (2004) o801.
[36] T. Akitsu, Y. Einaga, Acta Crystallogr. E 62 (2006) o4315.
[37] I. Veroni, A. Rontoyianni, C.A. Mitsopoulou, J. Chem. Soc., Dalton Trans. (2003) 255.
[38] B. Bosnich, J. Am. Chem. Soc. 90 (1968) 627.
[39] C. Evans, D. Luneau, J. Chem. Soc., Dalton Trans. (2002) 83.
[40] H. Okawa, M. Nakamura, S. Kida, Inorg. Chim. Acta 120 (1986) 185.
[41] Y. Nishida, S. Kida, Bull. Chem. Soc. Jpn. 43 (1970) 3814.
[42] S. Mizukami, H. Houjou, K. Sugaya, E. Koyama, H. Tokuhisa, T. Sasaki, M. Kanesato, Chem. Mater. 17 (2005) 50.
[43] R.E. Ernst, M.J. O'Connor, R.H. Holm, J. Am. Chem. Soc. 89 (1969) 6104.
[44] T. Akitsu, Y. Einaga, Inorg. Chem. Commun. 9 (2006) 1108.

and (v) triple oxygen coordination or formation of secondary building blocks, enhance the construction of novel frameworks. Malonic acid ($n = 1$, H_2mal) offers the additional advantage of the relative location of the carboxylato groups in the 1,3-positions supporting simultaneous chelating bidentate and various carboxylato-bridging coordination modes leading to multi-dimensional polymers [8]. Moreover, its combination with other chelating and/or bridging ligands affects dramatically the identity of the products leading to the formation of monomers, dimers, trimers, tetramers as well as 1D, 2D and 3D polymers [9–15]. An additional parameter, which can influence the coordination versatility of mal^{2-} and consequently the structural characteristics of the products, is the induction of steric hindrance effects due to the presence of substituents in the aliphatic carbon, which lower the conformational freedom of the carbon backbone. Within this respect we have recently started to investigate the copper(II) chemistry of substituted malonates in the presence of neutral heterocyclic N-donor ligands.

We present herein our initial work on methylmalonate ($Memal^{2-}$) i.e. the synthesis, structural, spectroscopic and magnetic characterization of 1D coordination polymers presenting the [Cu(L)(Memal)] repeating unit [L = 1,10-phen (**1**), 2,2′-bpy (**2**)].

2. Experimental

2.1. Complex preparations

All manipulations were performed under aerobic conditions using materials as received (Aldrich Co). All chemicals and solvents were of reagent grade.

2.1.1. *[Cu(phen)(Memal)]n · nMeOH (1 · nMeOH) and [Cu(bpy)(Memal)]n (2)*

Solid 1,10-phen · H_2O (0.099 g, 0.50 mmol) and $CuCl_2 \cdot 6H_2O$ (0.043 g, 0.25 mmol) for **1**, or solid 2,2′-bpy (0.078 g, 0.50 mmol) and $CuCl_2 \cdot 6H_2O$ (0.085 g, 0.50 mmol) for **2**, were added to a refluxed methanolic solution (20 mL) of H_2Memal (0.059 g, 0.50 mmol) and $LiOH \cdot H_2O$ (0.042 g, 1.0 mmol). The colour of the solution in both cases immediately turned to blue and the reflux continued for 15 min, during which time no noticeable colour change or solid precipitation was observed. Blue-turquoise crystals of **1** suitable for X-ray analysis were obtained either by slow evaporation or by vapour diffusion of Et_2O (2:1 v/v) to the blue solution after 1 week (Yield: 0.067 g, ~75%). Blue-turquoise crystals of **2** suitable for X-ray analysis were obtained by vapour diffusion of Et_2O (2:1 v/v) to the blue reaction solution after 1 week (Yield: 0.092 g, ~55%). In both cases the crystals were collected by filtration and dried in vacuo. The resulting powder of **1** was analyzed as solvent-free. *Anal.* Calc. for (**1**) ($C_{16}H_{12}CuN_2O_4$): C, 53.41; H, 3.36; N, 7.79. Found: C, 52.34; H, 3.29; N, 7.63%. *Anal.* Calc. for (**2**) ($C_{14}H_{12}CuN_2O_4$): C, 50.08; H, 3.60; N, 8.34. Found: C, 49.08; H, 3.53; N, 8.17%.

2.2. General and physical measurements

Elemental analysis for carbon, hydrogen, and nitrogen was performed on a Perkin Elmer 2400/*II* automatic analyzer. Infrared spectra were recorded as KBr pellets in the range 4000–400 cm^{-1} on a Bruker Equinox 55/S FT-IR spectrophotometer. X-band Electron Paramagnetic Resonance spectra were recorded with a Bruker ER200D spectrometer equipped with an NMR-Gaussmeter, an Anritsu microwave frequency counter, and an Oxford ESR9 cryostat. Variable temperature magnetic susceptibility measurements were carried out on polycrystalline samples of **1** and **2** in the 5–300 K temperature range using a Quantum Design MPMS SQUID susceptometer under a magnetic field of 1 T. Magnetization isotherms between 0 and 5.4 T were collected at 5 K. Diamagnetic corrections for the complexes were estimated from Pascal's constants. The error factor R is defined as $R = \sum \frac{(x_{\text{exp}} - x_{\text{calc}})^2}{N x_{\text{exp}}^2}$, where N is the number of experimental points.

2.2.1. *X-ray crystallography and solution of structures*

Blue-turquoise prismatic crystals of **1** and **2** were mounted in capillaries. Diffraction measurements were made on a Crystal Logic Dual Goniometer diffractometer using graphite monochromated Mo Kα radiation. Important crystal data and parameters for data collection are reported in Table 1. Unit cell dimensions were determined and refined by using the angular settings of 25 automatically centered reflections in the range $11° < 2\theta < 23°$. Three standard reflections monitored every 97 reflections showed less than 3% intensity fluctuation and no decay. Lorentz, polarization and psi-scan absorption corrections (for **2** only) were applied using Crystal Logic software. The structures were solved by direct methods using SHELXS-86 [16]

Table 1
Crystallographic data for **1** · *n*MeOH and **2**

	1 · *n*MeOH	**2**
Formula	$C_{17}H_{16}CuN_2O_5$	$C_{14}H_{12}CuN_2O_4$
F_w	391.86	335.80
Space group	*Pc*	$P2_1/n$
T (°C)	298	298
λ (Å)	Mo Kα (0.71073)	Mo Kα (0.71073)
a (Å)	4.889(2)	4.862(3)
b (Å)	10.925(4)	20.48(1)
c (Å)	15.478(5)	13.333(8)
β (°)	97.62(1)	95.66(2)
V (Å^3)	819.4(5)	1321.1(1)
Z	2	4
ρ_{calcd} (g cm^{-3})	1.588	1.688
μ (Mo Kα), (mm^{-1})	1.364	1.671
Goodness-of-fit on F^2	1.064	1.181
R_1/wR_2[a] ($I > 2\sigma(I)$)	0.0275/0.0693[b]	0.0448/0.1004[c]
R_1/wR_2[a] (all data)	0.0293/0.0708	0.0750/0.1329

[a] $w = 1/[\sigma^2(F_o^2) + (aP)^2 + bP]$ and $P = (\max)(F_o^2, 0) + (2F_c^2)/3$; $R_1 = \sum(|F_o| - |F_c|)/\sum(|F_o|)$ and $wR_2 = \left\{\sum[w(F^2_o - F^2_c)^2]/\sum[w(F^2_o)^2]\right\}^{1/2}$.

[b] For 2783 reflections with $I > 2\sigma(I)$.

[c] For 1777 reflections with $I > 2\sigma(I)$.

and refined by full matrix least-squares techniques on F^2 with SHELXL-97 [17]. Further experimental crystallographic details for **1**: $2\theta_{max} = 50°$, scan speed 5.0°/min; scan range $1.6 + \alpha_1\alpha_2$ separation; reflections collected/unique/used, 2884/2884 [$R_{int} = 0.0000$]/2884; 268 parameters refined; $(\Delta/\sigma)_{max} = 0.002$; $(\Delta\rho)_{max}/(\Delta\rho)_{min} = 0.662/-0.305$ e/Å^3. Hydrogen atoms of the methyl groups were introduced at calculated positions as riding on bonded atoms, the rest H-atoms were located by difference maps and were refined isotropically. All non-H atoms were refined anisotropically. Further experimental crystallographic details for **2**: $2\theta_{max} = 50°$, scan speed 1.0 °/min; scan range $1.6 + \alpha_1\alpha_2$ separation; reflections collected/unique/used, 2612/2325 [$R_{int} = 0.0506$]/2325; 227 parameters refined; $(\Delta/\sigma)_{max} = 0.004$; $(\Delta\rho)_{max}/(\Delta\rho)_{min} = 0.403/-0.590$ e/Å^3. Hydrogen atoms of the methyl group were introduced at calculated positions as riding on bonded atoms, the rest H-atoms were located by difference maps and were refined isotropically. All non-H atoms were refined anisotropically.

3. Results and discussion

3.1. Syntheses and diagnostic IR bands

The $CuCl_2/H_2Memal$/phen reaction mixture in MeOH in the 1:1:1 respective molar ratio, in the presence of stoichiometric amounts of $LiOH \cdot H_2O$ to ensure full deprotonation of the acid, yielded blue solutions which upon standing for slow evaporation, afforded blue-turquoise crystals of **1** after 1 week (Eq. (1)).

$$CuCl_2 \cdot 6H_2O + H_2Memal + \text{ phen} \cdot H_2O + 2LiOH \cdot H_2O \xrightarrow{MeOH} \underset{\mathbf{1}}{[Cu(phen)(Memal)]_n} + 2LiCl + 11\ H_2O \quad (1)$$

The initial $CuCl_2/H_2Memal$/phen stoichiometry employed is reflected in the stoichiometry of the repeating unit of the polymeric complex **1**. To further investigate the parameters affecting the identity of the products derived from the $CuCl_2/H_2Memal$/phen reaction system we employed different molar ratios and various crystallization methods. Thus, the 1:1:2, the 1.5:1:1 and the 1:2:2 respective molar ratios followed by different crystallization methods (slow evaporation, vapor diffusion or layering with Et_2O) afforded only complex **1**[1]. Therefore, compound **1** was judged to be the less soluble (and probably the most stable) product of the reaction system, albeit the presence of other species in the reaction mixture cannot be excluded.

In order to investigate to what extend the nature of the neutral heterocyclic N-donor ligand might affect the identity of the products we also studied the $CuCl_2/H_2Memal$/bpy reaction system. Thus, the 1:1:1 respective molar ratio reaction mixture in MeOH, in the presence of stoichiometric amounts of $LiOH \cdot H_2O$ to ensure full deprotonation of the acid, yielded blue solutions which afforded blue-turquoise crystals of **2** upon vapor diffusion of Et_2O after 1 week (Eq. (2)).

$$CuCl_2 \cdot 6H_2O + H_2Memal + \text{ bpy} + 2LiOH \cdot H_2O \xrightarrow{MeOH} \underset{\mathbf{2}}{[Cu(bpy)(Memal)]_n} + 2LiCl + 10H_2O \quad (2)$$

As in the case of **1**, the initially employed stoichiometry is reflected in the stoichiometry of the repeating unit of the polymeric complex **2**.

In the IR spectrum of **1** and in the 1600–1200 cm^{-1} region the ν(C⋯C) and ν(C⋯N) stretching vibrations of the phen are observed [18], which are known to shift to slightly higher frequencies upon complexation. However, some of these bands are unobserved due to overlaps with the carboxylate asymmetric and symmetric stretching vibrations. Thus, we can identify some of those bands having shifted to 1622, 1568, 1520, 1494, 1431 and 1226 cm^{-1}. The bands of the free phen in the 1050–700 cm^{-1} region are shifted to lower frequencies upon complexation, and in the spectra of **1** these bands appear at 855 and 723 cm^{-1}. The symmetric stretching vibration of the carboxylate group ν_s(COO) in the spectra of **1**, is observed in the region 1375–1340 cm^{-1}, while the ν_{as}(COO) is difficult to assigned, due to overlaps with the characteristic bands of the phen appeared in the same region. In the IR spectra of **2**, and in the region 1600–1200 cm^{-1} we identify some of the characteristic bands of the bpy attributed to the ν(C⋯C) and ν(C⋯N) stretching vibrations, having shifted to 1605, 1561, 1496, 1418 and 1225 cm^{-1} upon complexation. The asymmetric stretching vibration of the carboxylate group is difficult to be assigned due to overlaps with the above bands, while the symmetric stretching vibration ν_s(COO) is observed at 1366 cm^{-1}. The bands of the free bpy in the 1050–700 cm^{-1} region are shifted to lower frequencies upon complexation, and in the spectra of **2** these bands appear at 840 and 729 cm^{-1}.

3.2. Structural description of $[Cu(phen)(Memal)]_n \cdot nMeOH$ ($1 \cdot nMeOH$)

An ORTEP plot of **1** is given in Fig. 1. Selected bond distances and angles are listed in Table 2. The molecular structure of **1** reveals the presence of the [Cu(phen)(Memal)] repeating unit leading to 1D polymeric arrays (extended parallel to the *a*-axis) promoted by the bidentate [chelating] + unidentate coordination mode of the Memal^{2-} ligand. This type of coordination of the Memal^{2-} ligand has been also observed in the molecular structure of $\{[Co(NH_3)_6][UO_2(C_4H_4O_4)(C_5H_6O_4)]\}_2Cl_2 \cdot 6H_2O$ [19] ($C_4H_4O_4$ = the dianion of methylmalonic acid, $C_5H_6O_4$ = the dianion of dimethylmalonic acid), as well as in malonato containing complexes [20]. The closest intrachain Cu⋯Cu distance is equal to the *a* axis i.e. 4.889 Å. The coordination geometry around each Cu^{II} ion is square pyramidal ($\tau = 0.05$); the phen and the chelating oxygen atoms of the Memal^{2-} (O(1) and O(4)) occupy

[1] The identity of the products in each case was confirmed by unit cell determination.

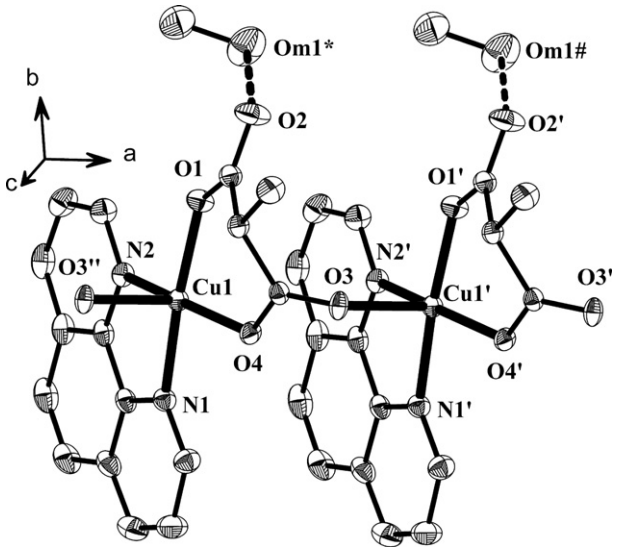


Fig. 1. Partially labelled ORTEP plot of the polymeric structure of **1** at 30% thermal probability ellipsoids (H-bonds are shown as black dashed lines). Symmetry operations to generate equivalent atoms: $' = 1 + x, y, z$, $'' = -1 + x, y, z$, $* = x, 1 - y, -0.5 + z$, $\# = 1 + x, 1 - y, -0.5 + z$.

Table 2
Selected bond distances (Å) and angles (°) in **1** · *n*MeOH and **2**

	1 · nMeOH	**2**
Distances		
Cu(1)–O(4)	1.918(3)	1.927(4)
Cu(1)–O(1)	1.925(2)	1.914(4)
Cu(1)–N(1)	2.018(3)	1.998(4)
Cu(1)–N(2)	2.022(3)	2.004(4)
Cu(1)–O(3″)	2.296(2)	2.358(4)
Angles		
O(4)–Cu(1)–O(1)	93.92(9)	94.05(15)
O(4)–Cu(1)–N(1)	90.88(10)	90.67(16)
O(1)–Cu(1)–N(1)	166.39(9)	169.88(17)
O(4)–Cu(1)–N(2)	163.16(10)	161.85(18)
O(1)–Cu(1)–N(2)	89.98(10)	92.35(16)
N(1)–Cu(1)–N(2)	81.91(11)	80.57(17)
O(4)–Cu(1)–O(3″)	97.70(10)	95.97(15)
O(1)–Cu(1)–O(3″)	93.82(9)	93.53(16)
N(1)–Cu(1)–O(3″)	98.15(9)	94.87(16)
N(2)–Cu(1)–O(3″)	98.38(10)	100.57(16)

$'' = -1 + x, y, z$ (for **1**) and $1 + x, y, z$ (for **2**).

the equatorial plane and the apical position is occupied by the unidentate oxygen of a neighbouring $Memal^{2-}$ (O(3″)) ligand. The Cu–N and Cu–O bond lengths in the equatorial plane fall in the range 1.918(3)–2.022(3) Å, the $Cu–O_{ax}$ bond distance is 2.296(2) Å. The forth oxygen atom (O(2)) of the $Memal^{2-}$ ligand is strongly hydrogen bonded to the solvate methanol (Om1···O2 (x, $1 - y$, $0.5 + z$) = 2.862 Å, HOm1···O2 = 2.095 Å, Om1–HOm1···O2 = 170.0°) thus preventing polymerization to that direction.

3.3. Structural description of [Cu(bpy)(Memal)]$_n$ (2)

An ORTEP plot of **2** is given in Fig. 2. Selected bond distances and angles are listed in Table 2. The molecular

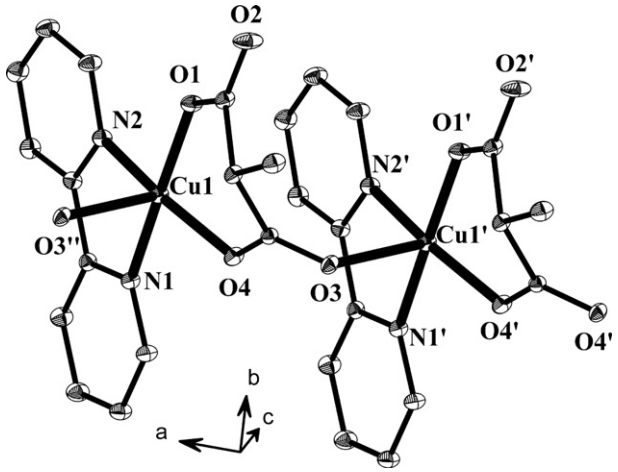


Fig. 2. Partially labelled ORTEP plot of the polymeric structure of **2** at 30% thermal probability ellipsoids. Symmetry operations to generate equivalent atoms: $' = -1 + x, y, z$, $'' = 1 + x, y, z$.

structure of **2** is analogous to that of **1** and will be discussed in less detail. The one-dimensional coordination polymer contains the [Cu(bpy)(Memal)] repeating unit, with the methylmalonato ligand adopting the bidentate [chelating] + unidentate coordination mode. The coordination geometry around the Cu^{II} ion is square pyramidal, the trigonality index τ is 0.13. The closest intrachain Cu···Cu distance is equal to the a axis, i.e. 4.862 Å. The Cu–N and Cu–O bond lengths in the equatorial plane fall in the range 1.914(4)–2.004(4) Å, the $Cu–O_{ax}$ bond distance is 2.258(4) Å.

In both compounds, the forth oxygen atom of the $Memal^{2-}$ ligand, although deprotonated, does not participate in metal coordination which would promote higher-dimensionality polymeric networks. This behaviour might be attributed either to the limited conformational freedom of the carbon backbone due to the methyl substituent, or to the blocking of two metal coordination sites by the phen or bpy ligands. The former does not seem to play any significant role, since bpy [13,21] or phen [10a]/mal^{2-} mixed-ligand complexes stabilize 1D polymeric structures through coordination or hydrogen bonds and 2D polymeric structures only through hydrogen bonding interactions, whereas higher dimensionality coordination polymers require the simultaneous presence of other bridging ligands, such as 4,4′-bpy [14]. On the other hand, the ability of both mal^{2-} [15e] and $Memal^{2-}$ [22] ligands to form 3D coordination polymers in the absence of other chelating ligands, lead us to assume that the blocking of certain metal coordination sites by phen or bpy plays the predominant role in the case of **1** and **2**.

3.4. Magnetic behaviour

The $\chi_M T$ product at 300 K is 0.41 $cm^3\,mol^{-1}\,K$ for **1** and 0.42 $cm^3\,mol^{-1}\,K$ for **2**, slightly above the value predicted for an isolated $S = 1/2$ spin with $g = 2.0$ (0.37 $cm^3\,mol^{-1}\,K$). This remains practically unchanged down to

Table 3
Indicative examples of Cu^{II} malonato 1D coordination polymers

Complex[a]	R	Cu–O_{eq}[b]	Cu–O_{ax}	J (cm^{-1})	References
$[Cu(bpym)(Phmal)]_n$	Ph	1.911	2.262	0.10	28a
$[Cu(phen)(Phmal)]_n \cdot 3nH_2O$	Ph	1.923	2.314	0.31	28a
$[Cu(Im)_2(mal)]_n$	H	1.947	2.394	1.64	28b
$[Cu(meIm)_2(mal)]_n$	H	1.967	2.270	0.39	28b
$(H_2bpe)[Cu(mal)_2]$	H	1.934	2.611	0.04	15c
1	Me	1.9215	2.296	0.24	this work
2	Me	1.9205	2.358	0.09	this work

The Malonates Bridge between the apical and basal coordination positions of the adjacent Cu^{II} ions, in the bidentate [chelating] + unidentate mode. Where possible, complexes with ligands similar to those of **1** and **2** were selected for reasons of comparison.
[a] bpym = 2,2′-bipyrimidine, Im = imidazole, meIm = 2-methylimidazole, bpe = 1,2-bis(4-pyridyl)ethylene.
[b] Mean values.

20 K for both complexes, below which temperature a slight increase is observed (Fig. 3) This is attributed to weak ferromagnetic intrachain interactions mediated by the $Memal^{2-}$ bridges. The complexes obey the Curie–Weiss law (Fig. S1) with $C = 0.42\ cm^3\ mol^{-1}\ K$ and $\Theta = +0.7\ K$ for **1** $C = 0.42\ cm^3\ mol^{-1}\ K$ and $\Theta = +0.5\ K$ for **2**, consistent with weak ferromagnetic coupling. The data were fitted with an analytical expression derived from a high-temperature series expansion, which simulates the magnetic behaviour of ferromagnetic $S = 1/2$ Heisenberg chains [23]:

$$\chi_M = \frac{Ng^2\beta^2}{4kT}\left(\frac{N}{D}\right)^{2/3} \quad (3)$$

where

$$N = 1.0 + 5.7979916y + 16.902653y^2 + 29.376885y^3 + 29.832959y^4 + 14.036918y^5,$$

$$D = 1.0 + 2.79799y + 7.0086780y^2 + 8.6538644y^3 + 4.5743114y^4$$

and $y = J/2kT$.

The fitting procedure yielded best-fit parameters $J = 0.24(4)\ cm^{-1}$, $g = 2.11(1)$ and $R = 2.4 \times 10^{-5}$ for **1** and $J = 0.09(4)\ cm^{-1}$, $g = 2.12(1)$ and $R = 1.2 \times 10^{-5}$ for **2**.

Fits considering a Curie-law behaviour along with a mean-field correction according to the Hamiltonian $\hat{H} = -2zJ\langle S_z\rangle\hat{S}_z$, to account for the exchange interactions, yielded practically identical results[2].

To verify these results, simulations on the magnetization isotherms of **1** and **2** at 5 K were carried out (i) by assuming a Brillouin behaviour for an $S = 1/2$ spin (g fixed to the best-fit value from the magnetic susceptibility data) and (ii) by approximating the chain with a Cu_{10} ring in which intramolecular J and g parameters are fixed to the best-fit values from the magnetic susceptibility data [24]. In both cases the simulations considering a Cu_{10} ring were closer to the experimental data than the Brillouin curves, thus corroborating our previous conclusions. It should be stressed that for such weak couplings, the absolute values may not be precisely determined, however, we are confident about their order of magnitude and their relative strengths.

The sign and size of the exchange couplings within **1** and **2** may be understood by examining the bridging mode of the $Memal^{2-}$ ligands. The carboxylato groups of the $Memal^{2-}$ ligands are in a *syn–anti* bridging mode, occupying a basal coordination position of one Cu atom (with the *syn*-coordinated donor atom O(4)) and the apical one of the adjacent Cu atom (with the *anti*-coordinated donor atom O(3)). The *syn–anti* bridging mode is known to minimize the overlap of the magnetic orbitals, which is inherently antiferromagnetic, thus enhancing ferromagnetism [25]. The very weak values of the exchange couplings may be viewed as a consequence of the participation of an apical coordination position to the exchange pathway

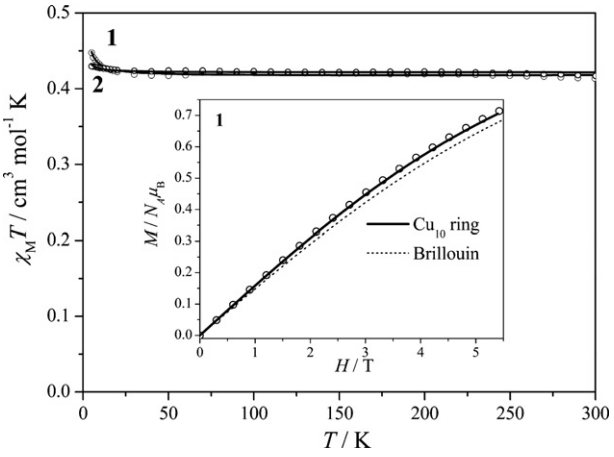


Fig. 3. $\chi_M T$ vs T experimental data for complexes **1** and **2**, and the best-fit theoretical curves based on model discussed in the text. Magnetization M vs applied magnetic field H data (○) at 5 K for complex **1** are shown in the inset. The calculated curves are based on the Cu_{10} ring model (solid line) and on an $S = 1/2$ Brillouin curve (dashed line) using the best-fit parameters from the magnetic susceptibility data. The case is similar for complex **2** (not shown).

[2] Using the expression $\chi_M = \frac{\chi_{Curie}}{1-\left(\frac{2zJ}{Ng^2\beta^2}\chi_{Curie}\right)}$, best-fit parameters were: $g = 2.107$, $zJ = 0.50\ cm^{-1}$, with $R = 2.6 \times 10^{-5}$ for **1** and $g = 2.120$, $zJ = 0.17\ cm^{-1}$, with $R = 1.2 \times 10^{-5}$ for **2**. Considering that for a 1D chain $z = 2$, then we obtain that $J = 0.25\ cm^{-1}$ for **1** and $J = 0.08\ cm^{-1}$ for **2**, in agreement with the results derived from the treatment described in the text.

(atom O(3)). This position is mainly characterized by a d_{z^2} orbital, which is not a magnetic one, and interactions are propagated due to geometrical distortions from ideal geometries, square pyramidal in our case ($\tau = 0.05$ and 0.13 for **1** and **2**, respectively). In any case these are very weak if not null.

The values of the exchange couplings in **1** and **2** fall within the range (+0.05 to +1.9 cm^{-1}) derived for other complexes containing the *syn–anti* bridging mode between a basal (or equatorial) and an apical (or axial) coordination position [26].

Indicative examples of analogous complexes with different malonato bridges are shown on Table 3. From a first survey of the data, it seems that the nature of the malonato sidegroup does not influence the magnitude of the intrachain exchange coupling.

3.5. EPR spectroscopy

X-band EPR spectra from powdered samples of **1** and **2** at 293 K are shown in Fig. 4. The spectra from both compounds are quite similar which is consistent with the almost identical stereochemistry around the Cu^{II} ions. They consist of almost axial signals with $g_{\|} > g_{\perp}$ consistent with and $d_{x^2-y^2}$ ground orbital state as it is expected for a square pyramidal symmetry [27]. The lack of hyperfine patterns especially at the $g_{\|}$ peak is attributed to narrowing effects [28] due to exchange interactions in agreement with the bulk magnetic properties of the complexes.

Both spectra are fitted [29] assuming the anisotropic $S = 1/2$ spin Hamiltonian:

$$\hat{H} = \beta \hat{\mathbf{S}} \tilde{\mathbf{g}} \mathbf{H} \quad (4)$$

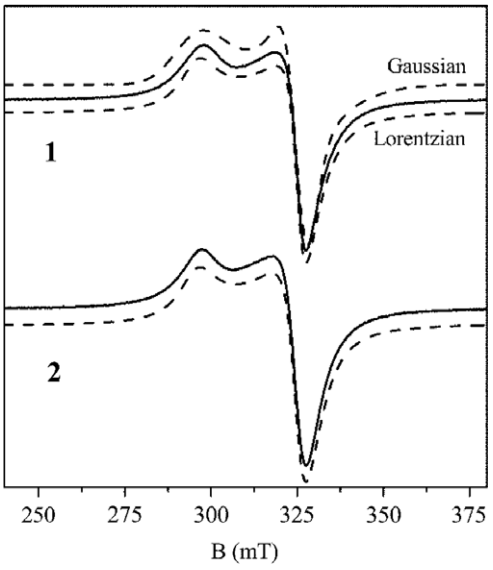


Fig. 4. X-band EPR spectra from powdered samples of **1** and **2** at 293 K. Solid lines: experimental spectra; dashed lines: theoretical curves resulting from the fitting procedure assuming either Gaussian or Lorentzian lines for **1** or Lorentzian for **2**. EPR conditions: microwave power, 2.2 mW, modulation amplitude 1.0 G_{pp}, microwave frequency 9.41 GHz.

Table 4
EPR parameters from the 293 K spectra for complexes **1** and **2**

Complex	$g_{\|}(\sigma g_{\|})$	$g_{\perp 1}(\sigma g_{\perp 1})$	$g_{\perp 2}(\sigma g_{\perp 2})$	LW(G)
1	2.274(0.04)	2.068(0.06)	2.046(0.00)	38.2
2	2.274(0.04)	2.071(0.05)	2.052(0.00)	46.0

During the fitting process we introduced a small rhombicity in the *g*-tensor by allowing for two different perpendicular components $g_{\perp 1}$ and $g_{\perp 2}$. In order to reproduce the spectra we assumed a distribution tensor, σg, for the g-tensor. For each orientation (θ, φ) of the magnetic field with respect to the *g*-tensor a linewidth of $\sigma g(\theta, \varphi)$ was computed in magnetic field units. To this an additional width, LW was added. The line at each orientation was a Gaussian or Lorentzian of width $\sigma = (\sigma g(\theta, \varphi)^2 + \mathrm{LW}^2)^{1/2}$. The spectra for both complexes were better reproduced assuming Lorentzian lineshapes; the simulations assuming Gaussian lineshapes are of lower quality (Fig. 4). The results of the fitting are listed in Table 4.

We also examined the temperature dependence of the EPR spectra for **1** in the region 4.2–293 K. The spectra are essentially the same with the room temperature one exhibiting only subtle changes in the line-shape.

4. Conclusions

The work presented herein describes our initial attempts to verify the key factors affecting the identity of the $CuCl_2$/H_2Memal/L (L = phen, bpy) reaction system. In both cases 1D coordination polymers, $[Cu(L)(Memal)]_n$ have been isolated. In the particular case of L = phen, several synthetic attempts revealed that variation of the molar ratios or crystallization methods employed do not affect the identity of the product. Employment of bpy instead of phen also led to the analogous product. It was thus concluded that (i) Use of $Memal^{2-}$ leads to a specific type of 1D coordination polymers for a wide range of reaction conditions. This may be due to its higher thermodynamic stability, or lower solubility with respect to other products that might be present in solution. (ii) The use of bpy instead of phen seems to have little or no effect to the final product. Weak ferromagnetic intrachain interactions have been confirmed both by magnetic susceptibility measurements and X-band EPR spectra of **1** and **2**, and attributed to the *syn–anti* bridging mode of the $Memal^{2-}$ ligands. The bidentate [chelating] + unidentate coordination mode of the $Memal^{2-}$ ligand in both compounds, provides possibilities for coordination of the forth carboxylato oxygen atom, a work that is currently under investigation in our group.

Acknowledgements

A. K. B. thanks the Greek State Scholarship Foundation (IKY) for support through a postdoctoral grant. We thank Prof. M. Hendrich, Department of Chemistry, Carnegie Mellon University, Pittsburgh, Pennsylvania, USA, for providing us with the EPR simulation program.

Appendix A. Supplementary material

One Figure showing the χ_M^{-1} vs T plot for **1**. CCDC 614901 and 614902 contain the supplementary crystallographic data for **1** and **2**. These data can be obtained free of charge via http://www.ccdc.ac.uk/conts/retrieving.html, or from the Cambridge Crystallographic Data Centre, 12 Union Road, Cambridge CB2 1EZ, UK; fax: (+44) 1223-336-033; or e-mail: deposit@ccdc.cam.ac.uk. Supplementary data associated with this article can be found, in the online version, at doi:10.1016/j.poly.2006.12.033.

References

[1] (a) See for example: S.O.H. Gutschke, D.J. Price, A.K. Powell, P.T. Wood, Angew. Chem. Int. Ed. 40 (2001) 1920;
(b) K. Barthelet, J. Marrot, D. Riou, G. Férey, Angew. Chem. Int. Ed. 41 (2002) 281;
(c) K. Barthelet, D. Riou, G. Férey, Chem. Commun. (2002) 1492;
(d) M. Riou-Cavellec, C. Albinet, C. Livage, N. Guillou, M. Noguès, J.M. Grenèche, G. Férey, Solid State Sci. 4 (2002) 267.

[2] (a) See for example: S. Bordiga, C. Lamberti, G. Ricchiardi, L. Regli, A. Damin, K.-P. Lillerud, M. Bjorgen, A. Zecchina, Chem. Commun. (2004) 2300;
(b) J.-M. Shi, W. Xu, Q.-Y. Liu, F.-L. Liu, Z.-J. Huang, H. Lei, W.-T. Yu, Q. Fang, Chem. Commun. (2002) 756;
(c) E. Coronado, M. Clemente-León, J.R. Galán-Mascarós, C. Giménez-Saiz, C.J. Gómez-García, E. Martínez-Ferrero, J. Chem. Soc. Dalton Trans. (2000) 3955.

[3] (a) O.R. Evans, W. Win, Chem. Mater. 13 (2001) 3009;
(b) H.-Y. Bie, J.-H. Yu, K. Zhao, J. Lu, L.-M. Duan, J.-Q. Xu, J. Mol. Struc. 741 (2005) 77.

[4] (a) See for example: M. Eddaoudi, J. Kim, N. Rosi, D. Vodak, J.B. Wachter, M. O'Keeffe, O.M. Yaghi, Science 295 (2002) 469;
(b) N.L. Rosi, M. Eddaoudi, J.Kim.M. O'Keeffe, O.M. Yaghi, Cryst. Eng. Comm. 4 (2002) 401;
(c) O.M. Yaghi, G. Li, H. Li, Nature 378 (1995) 703;
(d) M. Eddaoudi, D.B. Moler, H. Li, B. Chen, T.M. Reineke, M. O'Keeffe, O.M. Yaghi, Acc. Chem. Res. 34 (2001) 319, and references therein.

[5] For an excellent review see: C.N.R. Rao, S. Natarajan, R. Vaidhyanathan, Angew. Chem. Int. Ed. 43 (2004) 1466.

[6] A. Caneschi, D. Gatteschi, N. Lalioti, C. Sangregorio, R. Sessoli, G. Venturi, A. Vindigni, A. Rettori, M.G. Pini, M.A. Novak, Angew. Chem., Int. Ed. 40 (2001) 1760.

[7] (a) See for example: C. Coulon, R. Clérac, L. Lecren, W. Wernsdorfer, H. Miyasaka, Phys. Rev. B69 (2004) 132408;
(b) L. Bogani, A. Caneschi, D. Gatteschi, M. Massi, M.A. Novak, M.G. Pini, A. Rettori, R. Sessoli, A. Vindigni, Phys. Rev. Lett. 92 (2004) 207204.

[8] (a) Y. Rodríguez-Martín, J. Sanchiz, C. Ruiz-Pérez, F. Lloret, M. Julve, Cryst. Eng. Comm. 4 (2002) 631;
(b) C. Ruiz-Pérez, M. Hernández-Molina, J. Sanchiz, T. López, F. Lloret, M. Julve, Inorg. Chim. Acta 298 (2000) 245;
(c) D. Ghosal, T.K. Maji, T. Mallah, T.-H. Lu, G. Mostafa, N.R. Chaudhuri, Inorg. Chim. Acta 358 (2005) 1027;
(d) C. Ruiz-Pérez, J. Sanchiz, M. Hernández-Molina, F. Lloret, M. Julve, Inorg. Chim. Acta 298 (2000) 202;
(e) Y.-Q. Zheng, H.-Z. Xie, J. Coord. Chem. 57 (2004) 1537;
(f) S.F. Saadeh, K.L. Trojan, J.W. Kampf, W.E. Hatfield, V.L. Pecoraro, Inorg. Chem. 32 (1993) 3034.

[9] (a) W.-L. Kwik, K.-P. Ang, H.S.-O. Chan, V. Chebolu, S.A. Koch, J. Chem. Soc. Dalton Trans. (1986) 2519;
(b) L. Gasque, R. Moreno-Esparza, E. Mollins, J. Briansó-Penalva, L. Rutz-Ramírez, G. Medina-Dickinson, Acta Cryst. C55 (1999) 158;
(c) E. Suresh, M.M. Bhadbhade, Acta Cryst. C53 (1997) 193.

[10] (a) S. Sain, T.K. Maji, G. Mostafa, T.-H. Lu, N.R. Chaudhuri, Inorg. Chim. Acta 351 (2003) 12;
(b) Y. Rodríguez-Martín, J. Sanchiz, C. Ruiz-Pérez, F. Lloret, M. Julve, Inorg. Chim. Acta 326 (2001) 20.

[11] Q.-Z. Zhang, C.-Z. Lu, W.-B. Yang, J. Coord. Chem. 58 (2005) 1759.

[12] Y. Rodríguez-Martín, M. Hernández-Molina, F.S. Delgado, J. Pasán, C. Ruiz-Pérez, J. Sanchiz, F. Lloret, M. Julve, Cryst. Eng. Comm. 4 (2002) 440.

[13] C. Ruiz-Pérez, M. Hernández-Molina, P. Lorenzo-Luis, F. Lloret, J. Cano, M. Julve, Inorg. Chem. 39 (2000) 3845.

[14] Y. Rodríguez-Martín, C. Ruiz-Pérez, J. Sanchiz, F. Lloret, M. Julve, Inorg. Chim. Acta 318 (2001) 159.

[15] (a) H.-Y. Bie, J.-H. Yu, K. Zhao, J. Lu, L.-M. Duan, J.-Q. Xu, J. Molec. Struc. 741 (2005) 77;
(b) S. Sain, T.K. Maji, G. Mostafa, T.-H. Lu, N.R. Chaudhuri, New J. Chem. 27 (2003) 185;
(c) F.S. Delgado, J. Sanchiz, C. Ruiz-Pérez, F. Lloret, M. Julve, Inorg. Chem. 42 (2003) 5938;
(d) T.-F. Liu, H.L. Sun, S. Gao, S.-W. Zhang, T.C. Lau, Inorg. Chem. 42 (2003) 4792;
(e) X. Zhang, C. Lu, Q. Zhang, S. Lu, W. Yang, J. Liu, H. Zhuang, Eur. J. Inorg. Chem. (2003) 1181.

[16] G.M. Sheldrick, SHELXS-86: Structure Solving Program, University of Göttingen, Germany, 1986.

[17] G.M. Sheldrick, SHELXL-97: Crystal Structure Refinement, University of Göttingen, Germany, 1997.

[18] L.J. Bellamy, The Infra-red Spectra of Complex Molecules, Chapman and Hall, London, 1975.

[19] Y. Zhang, D. Collison, F.R. Livens, M. Helliwell, F. Heatley, A.K. Powell, S. Wocadlo, H. Eccles, Polyhedron 21 (2002) 81.

[20] (a) C. Ruiz-Pérez, J. Sanchiz, M. Hernández-Molina, F. Lloret, M. Julve, Inorg. Chem. 39 (2000) 1363;
(b) D. Chattopadhyay, S.K. Chattopadhyay, P.R. Lowe, C.H. Schwalde, S.K. Mazumder, A. Rana, S. Ghosh, J. Chem. Soc. Dalton Trans. (1993) 913.

[21] H.-Y. Shen, W.-M. Bu, D.-Z. Liao, Z.-H. Jiang, S.-P. Yan, G.-L. Wang, Inorg. Chem. Commun. 3 (2000) 497.

[22] M.E. Curry, D.S. Eggleston, D.J. Hodgson, J. Am. Chem. Soc. 107 (1985) 8234.

[23] G.A. Baker Jr, G.S. Rushbrooke, H.E. Gilbert, Phys. Rev. A 135 (1964) 1272.

[24] (a) The calculation of the magnetization was accomplished with use of the MAGPACK program package (ISOMAG): J.J. Borrás-Almenar, J.M. Clemente-Juan, E. Coronado, B.S. Tsukerblat, Inorg. Chem. 38 (1999) 6081;
(b) J.J. Borrás-Almenar, J.M. Clemente-Juan, E. Coronado, B.S. Tsukerblat, J. Comput. Chem. 22 (2001) 985.

[25] J. Pasán, F.S. Delgado, Y. Rodríguez-Martín, M. Hernández-Molina, C. Ruiz-Pérez, J. Sanchiz, F. Lloret, M. Julve, Polyhedron 22 (2003) 2143.

[26] (a) J. Pasán, J. Sanchiz, C. Ruiz-Pérez, F. Lloret, M. Julve, Eur. J. Inorg. Chem. (2004) 4081;
(b) J. Sanchiz, Y. Rodriguez-Martin, C. Ruiz-Perez, A. Mederos, F. Lloret, M. Julve, New. J. Chem. 26 (2002) 1624;
(c) Y. Rodriguez-Martin, M. Hernández-Molina, F.S. Delgado, J. Pasán, C. Ruiz-Perez, J. Sanchiz, F. Lloret, M. Julve, Cryst Eng Comm. 4 (2002) 522, and references therein.

[27] J. Hathaway, D.E. Billing, Coord. Chem. Rev. 5 (1970) 143.

[28] P.W. Anderson, J. Phys. Soc. Jpn. 9 (1954) 316.

[29] Fitting of the EPR spectra was done by software provided to us by Prof. M. Hendrich, Dept of Chemistry, Carnegie Mellon University, Pittsburgh, Pennsylvania, USA.

easy to use and fast enough to allow the study of relatively large molecules of transition metal complexes [15]. The spin-allowed singlet–singlet electronic transitions of *fac*-[Re(CO)$_3$(tbtmma)Cl] have been calculated with the time-dependent DFT method (TDDFT method), and a good assignment with the experimental spectrum has been observed.

2. Experimental

2.1. General procedure

The reaction was performed under argon atmosphere. The solvents were dried before use, using the appropriate drying reagents. Re(CO)$_5$Cl and 2-thienyl-*N*,*N*-bis(2-thienylmethylene)methanediamine (tbtmma) were purchased from Aldrich, and used as received.

IR spectrum was recorded on a Nicolet Magna 560 spectrophotometer in the spectral range 4000–400 cm^{-1} with the sample in the form of KBr pellet. Electronic spectrum was measured on a spectrophotometer Lab Alliance UV–VIS 8500 in the range 1000–200 nm in dichloromethane solution. Elemental analyses (CHN) were performed on a Perkin-Elmer CHN-2400 analyzer.

2.2. Preparation of [Re(CO)$_3$(tbtmma)Cl]

Re(CO)$_5$Cl (0.2 g, 0.55 mmol) and tbtmma (0.18 g, 0.58 mmol) in toluene (80 cm^3) were refluxed for 6 h. The resulting reaction mixture was allowed to cool at room temperature and reduced in volume to ~10 ml. An off-yellow solid was filtered off, washed with hexane, diethyl ether, and dried; yield: 85%.

X-ray quality crystals of complex [Re(CO)$_3$(tbtmma)Cl] were grown by the vapour diffusion of diethyl ether into a solution of the complex dissolved in dichloromethane.

IR (KBr, cm^{-1}): $\nu_{CO} = 2018$, 1910 and 1898 cm^{-1}; $\nu_{CN} = 1613$ cm^{-1}.

Anal. Calc. for $C_{19}H_{14}Cl_3N_2O_3S_3Re$ Calc.: C, 32.27; H, 2.00; N, 3.96. Found: C, 32.35; H, 2.10; N, 3.85%.

2.3. Crystal structures determination and refinement

The yellow crystal of [Re(CO)$_3$(tbtmma)Cl] was mounted on a KM-4-CCD automatic diffractometer equipped with a CCD detector, and used for data collection. X-ray intensity data were collected with graphite monochromated Mo Kα radiation ($\lambda = 0.71073$ Å) at temperature of 293(2) K. Details concerning crystal data and refinement are given in Table 1. Lorentz, polarization and empirical absorption correction using spherical harmonics implemented in SCALE3 ABSPACK scaling algorithm [16] were applied. The structure was solved by the Patterson method and subsequently completed by the difference Fourier recycling. All the non-hydrogen atoms were refined anisotropically using full-matrix, least-squares technique. The hydrogen atoms were treated as, ''riding'' on their parent carbon atoms [d(C–H) = 0.930 (phenyl) and 0.970 (methylene) Å] and assigned isotropic temperature factors equal 1.2 times the value of equivalent temperature factor of the parent carbon atom. SHELXS 97 [17], SHELXL 97 [18] and SHELXTL [19] programs were used for all the calculations. Atomic scattering factors were those incorporated in the computer programs.

Table 1
Crystal data and structure refinement for [Re(CO)$_3$(tbtmma)Cl]·CH$_2$Cl$_2$

Empirical formula	$C_{19}H_{14}Cl_3O_3N_2S_3Re$
Formula weight	707.05
Temperature (K)	293(2)
Wavelength (Å)	0.71073
Crystal system	triclinic
Space group	$P\bar{1}$
Unit cell dimensions	
a (Å)	9.8950(7)
b (Å)	10.2490(7)
c (Å)	12.8005(9)
α (°)	75.967(6)
β (°)	76.713(6)
γ (°)	86.580(5)
Volume (Å^3)	1225.68(14)
Z	2
D_{calc} (Mg/m^3)	1.916
Absorption coefficient (mm^{-1})	5.563
F(000)	680
Crystal size (mm)	0.08 × 0.20 × 0.30
θ Range for data collection (°)	2.94–25.00
Index ranges	$-10 \leqslant h \leqslant 11$, $-11 \leqslant k \leqslant 12$, $-15 \leqslant l \leqslant 13$
Reflections collected	7762
Independent reflections [R_{int}]	4189 [0.0234]
Completeness to 2θ (%)	97.2
Maximum and minimum transmission	0.644 and 0.271
Data/restraints/parameters	4189/0/280
Goodness-of-fit on F^2	1.002
Final R indices [$I > 2\sigma(I)$]	$R_1 = 0.0243$, $wR_2 = 0.0583$
R indices (all data)	$R_1 = 0.0296$, $wR_2 = 0.0592$
Largest difference in peak and hole (e Å^{-3})	1.337 and −0.737

2.4. Computational details

GAUSSIAN 03 program [20] was used in the calculations. The geometry optimization was carried out with the DFT method with the use of B3LYP functional [21,22]. The electronic spectrum was calculated with the TDDFT method [23]. The calculations were performed by using ECP basis set on the rhenium atom, the standard 6-31+g** basis for chlorine, oxygen, carbon, nitrogen and sulphur, and 6-31G basis for hydrogen atoms. The Xe core electrons of Re were replaced by an effective core potential and DZ quality Hay and Wadt Los Alamos ECP basis set (LANL2DZ) [24] was used for the valence electrons. Additional d function with exponent $\alpha = 0.3811$ and f function with exponent $\alpha = 2.033$ on the rhenium atom were added. Natural bond orbital (NBO) calculations were performed with the NBO code [25] included in GAUSSIAN 03.

3. Results and discussion

3.1. Preparation and infrared data

The $[Re(CO)_3(tbtmma)Cl]$ complex was prepared by refluxing the $[Re(CO)_5Cl]$ compound with a small excess of 2-thienyl-*N*,*N*-bis(2-thienylmethylene)methanediamine in toluene. The complex was isolated as air-stable, microcrystalline solid, soluble in common organic solvents. The infrared spectrum of the complex displays three bands in the carbonyl stretching region: a sharp intense band at 2018 cm^{-1} and two lower-energy bands closely spaced (1910 and 1898 cm^{-1}). This pattern corresponds to three CO units in a *fac* isomer arrangement [26]. The band of the C=N stretching modes of 2-thienyl-*N*,*N*-bis(2 thienylmethylene)methanediamine is observed at 1613 cm^{-1} [27].

3.2. Crystal structure

The $[Re(CO)_3(tbtmma)Cl]$ complex crystallises as the $[Re(CO)_3(tbtmma)Cl] \cdot CH_2Cl_2$ solvate in the triclinic space group $P\bar{1}$. There are no significant contacts involving the dichloromethane molecule and the tricarbonyl complex, with the possible exception of some rather weak hydrogen bonds [28,29]: C(14)–H(14)···Cl(2) $(-x, -1-y, 1-z)$ with D···A distance 3.664(4) Å and D–H···A angle 148.0°. The perspective drawing of the $[Re(CO)_3(tbtmma)Cl]$ complex with atomic numbering is shown in Fig. 1. The coordination geometry at the Re atom is a distorted octahedron with the three carbonyl ligands arranged in a *facial* fashion. Upon coordination of 2-thienyl-*N*,*N*-bis(2-thienylmethylene)methanediamine to a metal, a four-membered cycle (made by the two nitrogen atoms, the rhenium atom and the carbon atom) is formed. The small bite angle of the four-membered ring [62.31(13)°] is responsible for deviation of the rhenium coordination sphere from an ideal octahedron. The all thienyl rings are planar in the range of experimental error. The central ring makes dihedral angles of 88.51(15)° and 72.24(15)° with the side rings, and these last ones are inclined at 20.1(2)°. The C5–C4–N1–C14–N2–C9–C10 moiety torsion angles are 178.3(4)°, 164.3(3)°, −163.7(3)°, 179.0(4)°, respectively and C(15)–C(14)–N(1)–C(4), C(15)–C(14)–N(2)–C(9) torsion angles are 40.2(5)°, −39.5(5)°, thus the complex has a pseudo symmetry mirror plane going through Re(1),

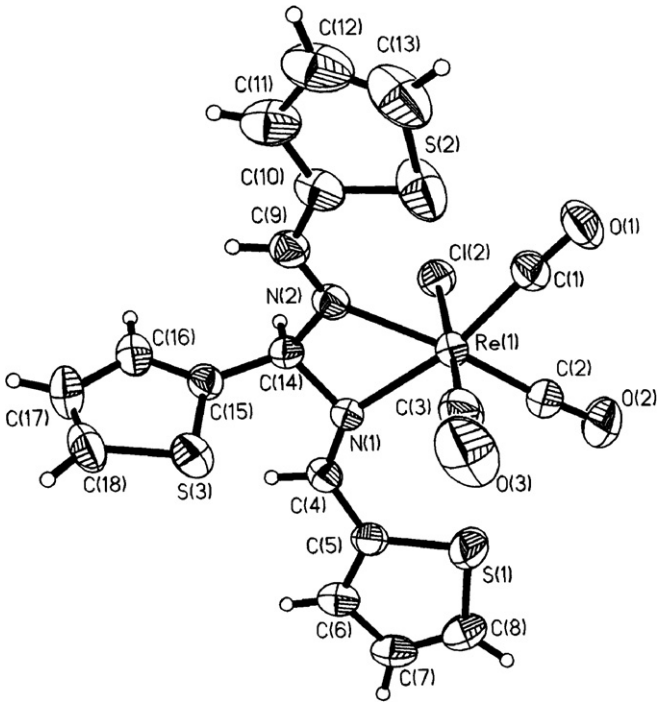


Fig. 1. Plot of $[Re(CO)_3(tbtmma)Cl]$ showing the atom numbering scheme (50% probability ellipsoids).

Table 2
The experimental and optimized bond lengths (Å) and angles (°) for $[Re(CO)_3(tbtmma)Cl]$

Bond lengths			Bond angles		
	Experimental	Optimized		Experimental	Optimized
Re(1)–C(1)	1.908(5)	1.927	C(1)–Re(1)–C(2)	82.3(2)	85.19
Re(1)–C(2)	1.905(5)	1.927	C(1)–Re(1)–C(3)	91.8(2)	92.20
Re(1)–C(3)	1.899(6)	1.917	C(3)–Re(1)–C(2)	91.4(2)	92.22
Re(1)–Cl(2)	2.4803(13)	2.547	C(1)–Re(1)–N(2)	106.51(17)	106.08
Re(1)–N(1)	2.199(3)	2.223	C(3)–Re(1)–N(2)	92.87(19)	95.61
Re(1)–N(2)	2.187(3)	2.223	C(1)–Re(1)–Cl(2)	90.56(14)	89.20
C(1)–O(1)	1.145(5)	1.160	C(2)–Re(1)–N(2)	170.05(18)	165.96
C(2)–O(2)	1.153(6)	1.160	C(1)–Re(1)–N(1)	167.56(16)	165.99
C(3)–O(3)	1.120(6)	1.166	C(2)–Re(1)–Cl(2)	88.98(17)	89.19
			C(3)–Re(1)–N(1)	94.09(17)	95.60
			C(2)–Re(1)–N(1)	108.42(17)	106.06
			C(3)–Re(1)–Cl(2)	177.61(16)	178.08
			N(2)–Re(1)–N(1)	62.31(13)	61.62
			N(2)–Re(1)–Cl(2)	86.43(9)	82.75
			N(1)–Re(1)–Cl(2)	83.56(9)	82.76
			O(1)–C(1)–Re(1)	175.5(4)	177.88
			O(2)–C(2)–Re(1)	175.3(4)	177.88
			O(3)–C(3)–Re(1)	179.6(6)	179.83

Cl(1), C(14), H(14), C(16), H(16), C(17), H(17), C(18), H(18), and S(3) atoms.

The selected bond lengths and angles of [Re(CO)$_3$(tbtmma)Cl] are given in Table 2. The Re–C and Re–N bond distances are within the range expected for such complexes [30].

3.3. Optimised geometry

The geometry of [Re(CO)$_3$(tbtmma)Cl] was optimised in a singlet state by the DFT method with the B3LYP functional. The optimised geometric parameters are gathered in Table 2. Generally, the calculated bond lengths and angles are in agreement with the values based upon the X-ray crystal structure data.

3.4. Electronic structure and NBO analysis

The [Re(CO)$_3$(tbtmma)Cl] complex is a closed-shell structure. Its molecular orbital diagram with several HOMO and LUMO contours is presented in Fig. 2. The HOMO–LUMO gap equals to 3.27 eV. The low-lying virtual orbitals correspond to $\pi^*(SC_4H_3)/\pi^*$ (N=C) orbitals of 2-thienyl-*N*,*N*-bis(2-thienylmethylene)methanediamine

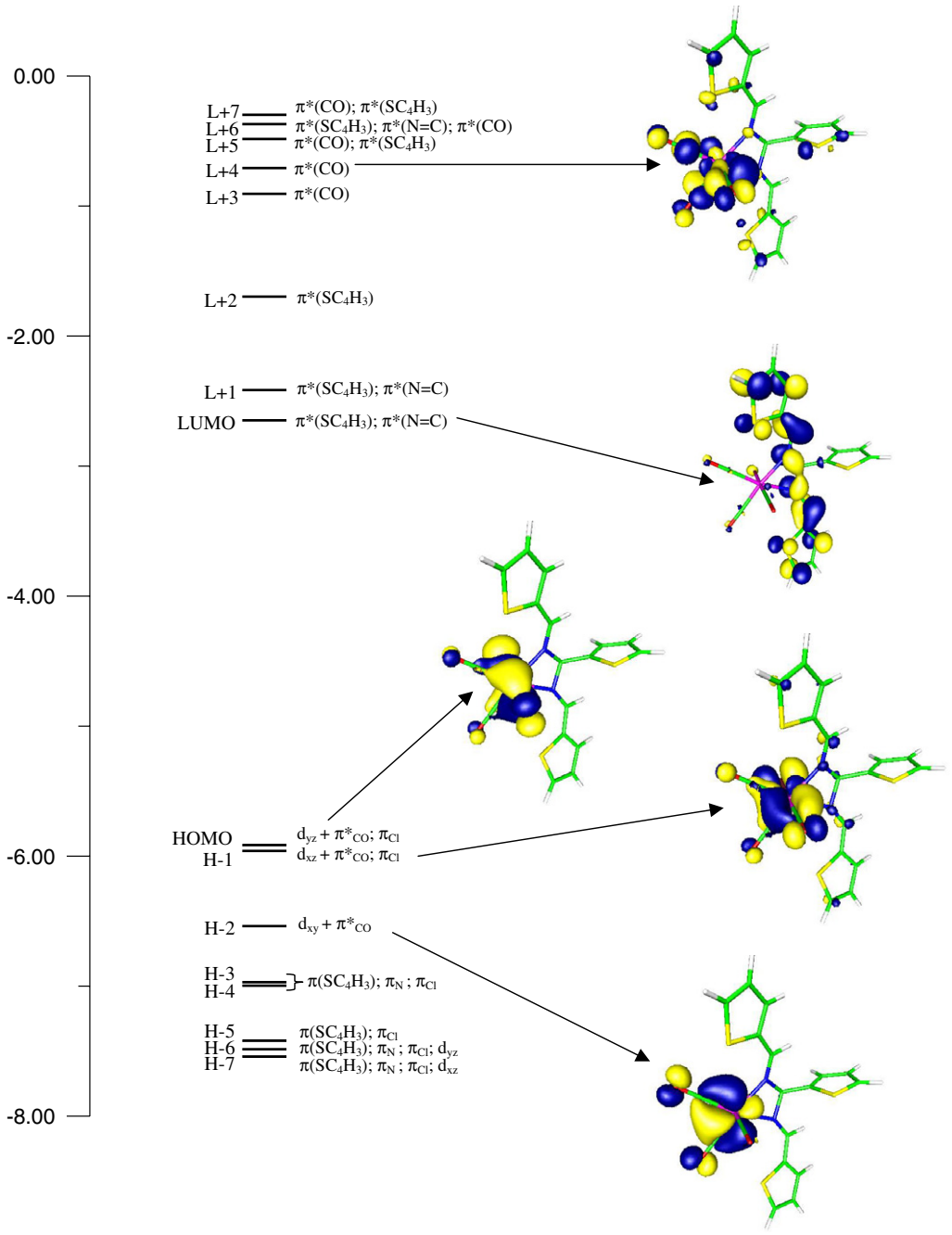


Fig. 2. The energy (eV), character and some contours of the unoccupied molecular orbitals of [Re(CO)$_3$(tbtmma)Cl].

Table 3
The occupancies and hybridization of the calculated Re–C and C–O natural bond orbitals (NBOs) for [Re(CO)$_3$(tbtmma)Cl]

BD	Occupancy	Hybridization of NBO
Re(1)–C(1)	1.975 (0.439)	$0.599(sd^{3.61})_{Re} + 0.801(sp^{0.55})_C$
Re(1)–C(2)	1.975 (0.439)	$0.599(sd^{3.61})_{Re} + 0.801(sp^{0.55})_C$
Re(1)–C(3)	1.972 (0.426)	$0.587(sd^{3.15})_{Re} + 0.810(sp^{0.55})_C$
C(1)–O(1)	1.998 (0.035)	$0.552(sp^{2.26})_C + 0.834(sp^{1.39})_O$
	1.996 (0.205)	$0.502(p)_C + 0.865(p)_O$
	1.996 (0.197)	$0.499(p)_C + 0.866(p)_O$
C(2)–O(2)	1.998 (0.035)	$0.552(sp^{2.26})_C + 0.834(sp^{1.39})_O$
	1.996 (0.205)	$0.502(p)_C + 0.865(p)_O$
	1.996 (0.197)	$0.499(p)_C + 0.866(p)_O$
C(3)–O(3)	1.999 (0.011)	$0.559(sp^{1.74})_C + 0.829(sp^{1.14})_O$
	1.997 (0.267)	$0.492(p)_C + 0.871(p)_O$
	1.996 (0.221)	$0.497(p)_C + 0.868(p)_O$

BD denotes 2-center bond.

and π^*_{CO}. The HOMO, HOMO − 1 and HOMO − 2 orbitals are predominantly of d_{Re} orbital character corresponding to the $(5d_{xy})^2(5d_\pi)^4$ occupation of the central ion.

Table 3 presents the occupancies and hybridization of the calculated Re–C and C–O natural bond orbitals (NBOs) for [Re(CO)$_3$(bpzpy)Cl].

Each natural bond orbital (NBO) σ_{AB} can be written in terms of two directed valence hybrids (HHOs) h_A i h_B on atoms A and B:

$$\sigma_{AB} = c_A h_A + c_B h_B$$

where c_A i c_B are polarization coefficients. Each valence bonding NBO must in turn be paired with a corresponding valence *anti*-bonding NBO:

$$\sigma*_{AB} = c_B h_A - c_A h_B$$

to complete the span of the valence space. The Lewis-type (donor) NBOs are thereby complemented by the non-Lewis-type (acceptor) NBOs that are formally empty in an idealized Lewis picture. The interactions between 'filled' Lewis-type NBOs and 'empty' non-Lewis NBOs lead to loss of occupancy from the localized NBOs of the idealized Lewis structure into the empty non-Lewis orbitals, and they are referred to as 'delocalization' corrections to the zeroth-order natural Lewis structure [31].

For each carbonyl group of the [Re(CO)$_3$(tbtmma)Cl] complex, three natural bond orbitals were detected for the C–O bond, and one orbital – for the Re–C bond. All the Re–C bond orbitals are polarized towards the carbon atom, and the C–O bond orbitals are polarized towards the oxygen end. Each oxygen atom of the carbonyl ligand possesses one lone pair (LP) orbital. The occupancies of the *anti*-bonding NBOs are given in round brackets.

The resonance structure $M-C\equiv O^{+}:$, which presents the best bonding between CO ligands and Re ion in [Re(CO)$_3$(tbtmma)Cl], is consistent with the values of the calculated atomic charges. The atomic charges from the Natural Population Analysis (NPA) for [Re(CO)$_3$(tbtmma)Cl] are shown in Table 4. The calculated charges on the carbon atoms of the carbonyl ligands are positive, whereas the oxygen atoms are negatively charged. The least positive is carbon in the *trans* position to the chloride ion. The calculated charge on the rhenium atom of [Re(CO)$_3$(tbtmma)Cl] is lower than the formal charge +1. The populations of the $5d_{xy}$, $5d_{xz}$, $5d_{yz}$, $5d_{x^2-y^2}$ and $5d_{z^2}$ orbitals of the central atom in [Re(CO)$_3$(tbtmma)Cl] are following: 0.951, 1.568, 1.555, 1.558 and 1.029.

Table 4
Atomic charges and spin densities of [Re(CO)$_3$(tbtmma)Cl]

Atom	Atomic charge
Re(1)	−0.105
Cl(2)	−0.481
N(1)	−0.481
N(2)	−0.481
S(1)	0.672
S(2)	0.672
S(3)	0.621
C(1)	0.609
C(2)	0.609
C(3)	0.546
O(1)	−0.477
O(2)	−0.477
O(3)	−0.501

3.5. Electronic spectrum

The experimental and calculated electronic spectra of [Re(CO)$_3$(tbtmma)Cl] are presented in Fig. 3. Each calculated transition is represented by a gaussian function $y = ce^{-bx^2}$ with the height (c) equal to the oscillator strength and b equal to 0.04 nm^{-2}.

Table 5 shows the spin-allowed singlet–singlet electronic transitions calculated with the TDDFT method for [Re(CO)$_3$(tbtmma)Cl]. For the high energy part of the

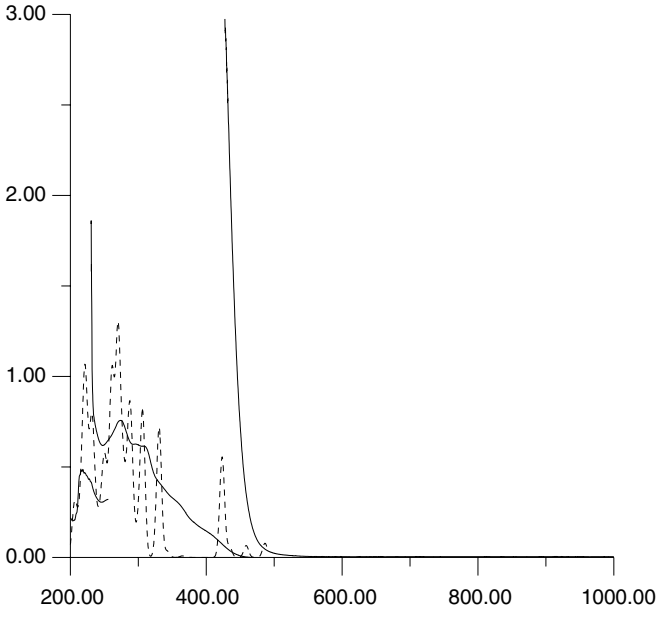


Fig. 3. The experimental (——) and calculated (----) electronic absorption spectrum of [Re(CO)$_3$(tbtmma)Cl].

Table 5
The energy and molar absorption coefficients of experimental absorption bands and the electronic transitions calculated with the TDDFT method for $[Re(CO)_3(tbtmma)Cl]$

The most important orbital excitations	Character	λ (nm)	E (eV)	f	Experimental λ (nm) (E (eV)) ε
H → L	d → $\pi^*(SC_4H_3)/\pi^*(N{=}C)$	486.4	2.55	*0.0156*	381.6 (3.25) 8400
H − 1 → L	d → $\pi^*(SC_4H_3)/\pi^*(N{=}C)$	458.7	2.70	*0.0131*	
H → L + 1	d → $\pi^*(SC_4H_3)/\pi^*(N{=}C)$	434.2	2.86	*0.0120*	
H − 1 → L + 1	d → $\pi^*(SC_4H_3)/\pi^*(N{=}C)$	423.3	2.93	*0.1109*	
H − 2 → L	d → $\pi^*(SC_4H_3)/\pi^*(N{=}C)$	364.9	3.40	*0.0017*	338.4 (3.66) 17480
H → L + 2	d → $\pi^*(SC_4H_3)/\pi^*(N{=}C)$	342.4	3.62	*0.0069*	
H − 3 → L	$\pi(SC_4H_3)/\pi_N/\pi_{Cl} \rightarrow \pi^*(SC_4H_3)/\pi^*(N{=}C)$	330.7	3.75	*0.1399*	
H − 4 → L + 1	$\pi(SC_4H_3)/\pi_N/\pi_{Cl} \rightarrow \pi^*(SC_4H_3)/\pi^*(N{=}C)$	306.3	4.05	*0.1518*	308.0 (4.03) 26500
H → L + 3	d → $\pi^*(CO)$	299.5	4.14	*0.0126*	
H → L + 4	d → $\pi^*(CO)$	299.2	4.14	*0.0131*	
H − 6 → L	$\pi(SC_4H_3)/\pi_N/\pi_{Cl} \rightarrow \pi^*(SC_4H_3)/\pi^*(N{=}C)$	290.1	4.28	*0.0612*	
H − 2 → L + 2	d → $\pi^*(SC_4H_3)/\pi^*(N{=}C)$	287.7	4.31	*0.0740*	
H − 7 → L	$\pi(SC_4H_3)/\pi_N/\pi_{Cl} \rightarrow \pi^*(SC_4H_3)/\pi^*(N{=}C)$	285.3	4.35	*0.0526*	
H − 5 → L + 1	$\pi(SC_4H_3)/\pi_{Cl} \rightarrow \pi^*(SC_4H_3)/\pi^*(N{=}C)$	282.6	4.39	*0.0188*	
H − 1 → L + 4	d → $\pi^*(CO)$	279.5	4.44	*0.0108*	274.2 (4.52) 32600
H − 8 → L	$\pi(SC_4H_3)/\pi_{Cl} \rightarrow \pi^*(SC_4H_3)/\pi^*(N{=}C)$	277.3	4.47	*0.0263*	
H − 9 → L	$\pi(SC_4H_3) \rightarrow \pi^*(SC_4H_3)/\pi^*(N{=}C)$	276.6	4.48	*0.0433*	
H − 7 → L + 1	$\pi(SC_4H_3)/\pi_{Cl} \rightarrow \pi^*(SC_4H_3)/\pi^*(N{=}C)$				
H − 10 → L	$\pi(SC_4H_3) \rightarrow \pi^*(SC_4H_3)/\pi^*(N{=}C)$	275.2	4.50	*0.0135*	
H − 7 → L + 1	$\pi(SC_4H_3)/\pi_{Cl}/d \rightarrow \pi^*(SC_4H_3)/\pi^*(N{=}C)$	270.2	4.59	*0.2083*	
H − 6 → L + 1	$\pi(SC_4H_3)/\pi_N/\pi_{Cl}/d \rightarrow \pi^*(SC_4H_3)/\pi^*(N{=}C)$	268.3	4.62	*0.0313*	
H − 11 → L	$\sigma_{Cl} \rightarrow \pi^*(SC_4H_3)/\pi^*(N{=}C)$	261.2	4.75	*0.0308*	
H − 8 → L + 1	$\pi(SC_4H_3)/\pi_{Cl} \rightarrow \pi^*(SC_4H_3)/\pi^*(N{=}C)$	261.0	4.75	*0.1434*	
H → L + 6	d → $\pi^*(SC_4H_3)/\pi^*(N{=}C)/\pi^*(CO)$	253.8	4.88	*0.0264*	230.4 (5.38) 56500
H − 11 → L + 1	$\sigma_{Cl} \rightarrow \pi^*(SC_4H_3)/\pi^*(N{=}C)$	250.8	4.94	*0.0445*	
H − 1 → L + 6	d → $\pi^*(SC_4H_3)/\pi^*(N{=}C)/\pi^*(CO)$	248.6	4.99	*0.0467*	
H → L + 7	d → $\pi^*(CO)/\pi^*(SC_4H_3)/\pi^*(N{=}C)$	245.1	5.06	*0.0124*	
H − 1 → L + 8	d → $\pi^*(CO)/\pi^*(SC_4H_3)/\pi^*(N{=}C)$	243.4	5.09	*0.0118*	
H − 6 → L + 2	$\pi(SC_4H_3)/\pi_N/\pi_{Cl}/d \rightarrow \pi^*(SC_4H_3)$	238.2	5.20	*0.0138*	
H − 3 → L + 3	$\pi(SC_4H_3)/\pi_N/\pi_{Cl} \rightarrow \pi^*(CO)$	232.0	5.34	*0.0549*	
H − 1 → L + 10	d → $\pi^*(SC_4H_3)$	231.7	5.35	*0.0506*	
H − 6 → L + 2	$\pi(SC_4H_3)/\pi_N/\pi_{Cl}/d \rightarrow \pi^*(SC_4H_3)$				
H − 4 → L + 3	$\pi(SC_4H_3)/\pi_N/\pi_{Cl} \rightarrow \pi^*(CO)$	231.5	5.36	*0.0148*	
H − 3 → L + 4	$\pi(SC_4H_3)/\pi_N/\pi_{Cl} \rightarrow \pi^*(CO)$	226.0	5.49	*0.0134*	
H − 4 → L + 4	$\pi(SC_4H_3)/\pi_N/\pi_{Cl} \rightarrow \pi^*(CO)$	222.2	5.58	*0.0282*	
H − 3 → L + 4	$\pi(SC_4H_3)/\pi_N/\pi_{Cl} \rightarrow \pi^*(CO)$	221.9	5.59	*0.0349*	
H − 1 → L + 11	d → $\pi^*(CO)/\pi^*(SC_4H_3)$				
H − 10 → L + 2	$\pi(SC_4H_3) \rightarrow \pi^*(SC_4H_3)$	221.0	5.61	*0.0908*	
H − 1 → L + 13	d → $\pi^*(CO)/\pi^*(SC_4H_3)$	220.8	5.62	*0.0115*	
H − 12 → L + 1	$N_N \rightarrow \pi^*(SC_4H_3)/\pi^*(N{=}C)$	215.0	5.77	*0.0210*	
H − 4 → L + 5	$\pi(SC_4H_3)/\pi_N/\pi_{Cl} \rightarrow \pi^*(CO)/\pi^*(SC_4H_3)$	206.0	6.02	*0.0315*	
H − 2 → L + 10	d → $\pi^*(SC_4H_3)$				
H − 5 → L + 3	$\pi(SC_4H_3)/\pi_{Cl} \rightarrow \pi^*(CO)$	205.5	6.04	*0.0120*	

spectrum, only transitions with oscillator strengths larger than 0.010 are listed in Table 5.

The assignment of the calculated transitions to the experimental bands is based on the criterion of the energy and oscillator strength of the calculated transitions. In the description of the electronic transitions only the main components of the molecular orbital are taken into consideration.

The low-energy absorption band at 381.6 nm is attributed to MLCT transitions occurring from the rhenium center to the π-antibonding orbitals of the chelating ligand. The experimental absorption band at 338.4 nm is ascribed to the d → $\pi^*(SC_4H_3)/\pi^*(N{=}C)$ transitions (calculated at 364.9 and 342.4 nm) and ligand–ligand charge transfer transition at 330.7 nm. The oscillator strength of the last one is considerable larger than f values of the MLCT transitions; it has main contribution to this band. The experimental absorption bands at 308.0, 274.2 and 230.4 nm result from metal–ligand charge transfer (occurring from the rhenium ion to the π-antibonding orbitals of the N–N ligand or π-antibonding orbitals of the carbonyl group) and ligand–ligand charge transfer transitions. The oscillator strengths of LLCT transitions are generally considerable larger than that ones of MLCT transitions.

4. Conclusions

A novel $Re(CO)_3^+$ complex has been prepared and structurally as well as spectroscopically characterized. X-ray and IR studies confirm a *facial* geometry of the carbonyl ligands in the [$Re(CO)_3$(tbtmma)Cl] complex. The molecular orbital diagram of the title complex has been calculated with the density functional theory (DFT) method. The HOMO, HOMO − 1 and HOMO − 2 orbitals are predominantly of d_{Re} orbital character corresponding to the $(5d_{xy})^2(5d_{\pi})^4$ occupation. The low-lying virtual orbitals correspond to π-antibonding orbitals of the N–N ligand or π-antibonding orbitals of the carbonyl group. The spin-allowed electronic transitions of *fac*-[$Re(CO)_3$(tbtmma)Cl] have been calculated with the time-dependent DFT method, and a good agreement between calculated and experimental spectra is observed.

Supplementary material

CCDC 626360 contains the supplementary crystallographic data for $C_{19}H_{14}Cl_3O_3N_2S_3Re$. These data can be obtained free of charge via http://www.ccdc.cam.ac.uk/conts/retrieving.html, or from the Cambridge Crystallographic Data Centre, 12 Union Road, Cambridge CB2 1EZ, UK; fax: (+44) 1223-336-033; or e-mail: deposit@ccdc.cam.ac.uk.

Acknowledgement

The GAUSSIAN 03 calculations were carried out in the Wrocław Centre for Networking and Supercomputing, WCSS, Wrocław, Poland.

References

[1] V. Balzani, A. Juris, M. Venturi, S. Campagna, S. Serroni, Chem. Rev. 96 (1996) 759.
[2] D.J. Stufkens, A. Vlček Jr., Coord. Chem. Rev. 177 (1998) 127.
[3] I.R. Farrell, A. Vlček Jr., Coord. Chem. Rev. 208 (2000) 87.
[4] A. Vogler, H. Kunkely, Coord. Chem. Rev. 200–202 (2000) 991.
[5] D.R. Striplin, G.A. Crosby, Coord. Chem. Rev. 211 (2001) 163.
[6] A. Vlček, M. Busby, Coord. Chem. Rev. 250 (2006) 1755.
[7] S. Ranjan, S.-Y. Li, K.-C. Hwang, W.-L. Ching, C.-S. Liu, Y.-T. Tao, C.-H. Chien, S.-M. Peng, G.-H. Lee, Inorg. Chem. 42 (2003) 1248.
[8] F. Li, G. Cheng, Y. Zhao, J. Feng, S. Liu, M. Zhang, Y. Ma, J. Shen, Appl. Phys. Lett. 83 (2003) 4716.
[9] P. Christensen, A. Hamnett, A.V.G. Muir, J.A. Timney, J. Chem. Soc., Dalton Trans. (1992) 1455.
[10] H. Hori, F.P.A. Johnson, K. Koike, K. Takeuchi, T. Ibusuki, O. Ishitani, J. Chem. Soc., Dalton Trans. (1997) 1019.
[11] S.S. Jurisson, J.D. Lydon, Chem. Rev. 99 (1999) 2205.
[12] W.A. Volkert, T.J. Hoffman, Chem. Rev. 99 (1999) 2269.
[13] J.R. Farrell, C. Becker, D.P. Lavoie, J.L. Shaw, Ch.J. Ziegler, J. Organomet. Chem. 689 (2004) 1122.
[14] T.L. Stott, M.O. Wolf, Coord. Chem. Rev. 246 (2003) 89.
[15] H. Chermette, Coord. Chem. Rev. 178–180 (1998) 699.
[16] CRYSALIS RED, Oxford Diffraction Ltd., Version 1.171.29.2.
[17] G.M. Sheldrick, Acta Crystallogr., Sect. A 46 (1990) 467.
[18] G.M. Sheldrick, SHELXL 97. Program for the Solution and Refinement of Crystal Structures, University of Göttingen, Germany, 1997.
[19] G.M. Sheldrick, SHELXTL: release 4.1 for Siemens Crystallographic Research Systems, 1990.
[20] M.J. Frisch, G.W. Trucks, H.B. Schlegel, G.E. Scuseria, M.A. Robb, J.R. Cheeseman, J.A. Montgomery Jr., T. Vreven, K.N. Kudin, J.C. Burant, J.M. Millam, S.S. Iyengar, J. Tomasi, V. Barone, B. Mennucci, M. Cossi, G. Scalmani, N. Rega, G.A. Petersson, H. Nakatsuji, M. Hada, M. Ehara, K. Toyota, R. Fukuda, J. Hasegawa, M. Ishida, T. Nakajima, Y. Honda, O. Kitao, H. Nakai, M. Klene, X. Li, J.E. Knox, H.P. Hratchian, J.B. Cross, C. Adamo, J. Jaramillo, R. Gomperts, R.E. Stratmann, O. Yazyev, A.J. Austin, R. Cammi, C. Pomelli, J.W. Ochterski, P.Y. Ayala, K. Morokuma, G.A. Voth, P. Salvador, J.J. Dannenberg, V.G. Zakrzewski, S. Dapprich, A.D. Daniels, M.C. Strain, O. Farkas, D.K. Malick, A.D. Rabuck, K. Raghavachari, J.B. Foresman, J.V. Ortiz, Q. Cui, A.G. Baboul, S. Clifford, J. Cioslowski, B.B. Stefanov, G. Liu, A. Liashenko, P. Piskorz, I. Komaromi, R.L. Martin, D.J. Fox, T. Keith, M.A. Al-Laham, C.Y. Peng, A. Nanayakkara, M. Challacombe, P.M.W. Gill, B. Johnson, W. Chen, M.W. Wong, C. Gonzalez, J.A. Pople, GAUSSIAN 03, Revision B.03, Gaussian, Inc., Pittsburgh, PA, 2003.
[21] A.D. Becke, J. Chem. Phys. 98 (1993) 5648.
[22] C. Lee, W. Yang, R.G. Parr, Phys. Rev. B 37 (1988) 785.
[23] M.E. Casida, in: J.M. Seminario (Ed.), Recent Developments and Applications in Modern Density Functional Theory, Theoretical and Computational Chemistry, vol. 4, Elsevier, Amsterdam, 1996.
[24] P.J. Hay, W.R. Wadt, J. Chem. Phys. 82 (1985) 299.
[25] E.D. Glendening, A.E. Reed, J.E. Carpenter, F. Weinhold, NBO (version 3.1).
[26] P.J. Giordano, M.S. Wrighton, J. Am. Chem. Soc. 101 (1979) 2888.
[27] K. Nakamoto, Infrared and Raman Spectra of Inorganic and Coordination Compounds, 4th ed., Wiley-Interscience, New York, 1986.
[28] G.A. Jeffrey, W. Saenger, Hydrogen Bonding in Biological Structures, Springer-Verlag, 1994.
[29] G.R. Desiraju, T. Steiner, The Weak Hydrogen Bond in Structural Chemistry and Biology, Oxford University Press, 1999.
[30] Cambridge Structural Database, version 1.8, 2005.
[31] A.E. Reed, L.A. Curtiss, F. Weinhold, Chem. Rev. 88 (1988) 899.

observation on isomers differing in charge distribution together under equilibrium condition giving rise to valence tautomerism [4–6].

Our interest is focused on studying mixed-valence complexes with SQ and Cat ligands and nitrogen-donor ancillary ligand. Our previous work on manganese and iron complexes with 3,6-DBBQ and pyridine ancillary ligand demonstrated complexes that exhibit valance tautomerism in the solid state [7–9]. The electronic spectra of such complexes show intense low-energy intervalence charge-transfer (IVCT) transition between catecholate and semiquinonate ligands.

In the literature there are number of complexes that contain mixed-valence quinone ligand and nitrogen-donor ancillary ligand. In almost all the cases either the *cis*- or the *trans*-isomer could be separated from the reaction medium. In the present work, we describe the synthesis and characterization of the two geometrical isomers of $Cr(py)_2$(chrySQ)(chryCat). The magneto-structural correlation has been studied. The electronic properties of the two isomeric complexes have been studied using ZINDO/S-CI routine. The electrochemical behaviors of the two complexes are described as well.

2. Experimental

The ligand 5,6-chrysenequinone, chryQ, was synthesized following a previously reported method [10]. All solvents were dried according to the standard procedures. For cyclic voltammetry measurements, acetonitrile solvent was further purified by vacuum distillation from calcium chloride and stored over molecular sieves. All other compounds were of reagent grade and were used as received.

The infrared spectra were recorded on a Thermo Nicolet Nexus 670 FTIR spectrometer with samples prepared as KBr pellets. Elemental analyses were performed using a Perkin–Elmer 2400 CHN elemental analyzer. Variable-temperature magnetic measurements were carried out on an Oxford Faraday magnetometer. The electronic absorption spectra (190–1100 nm) were recorded on a Cary 50 spectrophotometer in acetonitrile solution. Cyclic voltammograms were obtained with a model 303 HMDE in conjunction with a PAR model 173 potentiostat and PAR 175 universal programmer. A Ag/Ag^+ reference electrode was used that consisted of acetonitrile solution of $AgPF_6$ in contact with a silver wire placed in glass tubing with a Vycor frit at one end to allow ion transport. A 3.0 mm diameter glassy carbon disc was used as working electrode and a platinum wire as auxiliary electrode. Tetrabutylammonium hexafluorophosphate was used as the supporting electrolyte.

The semiempirical calculations in this study have been carried out using the HYPERCHEM 6.01 program package [11]. The Polak–Ribiere version of the conjugate gradient method was used in all energy minimization calculations with a coverage criterion less than 0.0001 kcal mol^{-1} $Å^{-1}$. First and separately chrysenesemiquinone and chrysenecatecholate ligands have been optimized and the results obtained have been applied in each calculation thereafter. The values of Cr–O and Cr–N bond lengths and angles in the literatures were used as the starting inputs [12–17]. Initial optimization of the two isomeric complexes was performed with molecular mechanics (MM+). The geometry was further refined using parameterized PM3 method. Available parameters for Cr metal were implemented in PM3 semiempirical method [18]. The parameterized PM3 was used for geometry optimization of the complexes under study. Triplet state URH spin pairing has been selected in addition to the standard SCF (with accelerated convergence). Theoretical harmonic vibrational frequencies are related to the experimental fundamentals by optimum scaling factor λ determined through a least-squares procedure giving by $\lambda = \sum_i^{all} \omega_i^{theor} \nu_i^{exp\,t} / \sum_i^{all} (\omega_i^{theo})^2$, where ω_i^{theor} and $\nu_i^{exp\,t}$ are the ith theoretical harmonic and ith experimental fundamental frequencies (in cm^{-1}) [19]. The molecular root mean square error (rms) was calculated by the square root of the sum over all the modes of Δ_{min} given in Ref. [19], where Δ_{min} is the minimized residual for each mode. The ZINDO/S-CI method parameterized to produce UV–Vis electronic transitions has been used to estimate the molecular orbital diagram of the complexes under study [20,21]. Electronic transition energies and oscillator strengths of both complexes were calculated using all valence electrons. The maximum excitation energy for configuration interaction calculations was 8.0 eV. The overlap weighing factors $f_{\sigma\sigma}$ and $f_{\pi\pi}$ were taken as 1.267 and 0.585 which had been used with good success for transition metals [22,23].

2.1. Synthesis of [Cr(py)$_2$(chrySQ)(chryCat)] complexes

2.1.1. Method 1

A mixture of chromium hexacarbonyl (0.15 g, 0.68 mmol) and chrysenequinone (0.35 g, 1.36 mmol) was dissolved in 50 mL of acetonitrile solvent under an inert atmosphere of dry nitrogen. The mixture was photolyzed with a Hg-lamp and heated at 65 °C for 3 h. To the purple solution obtained was added 0.2 mL (2.47 mmol) of pyridine and the solution is continued to heating for 12 h more. A solution color was then changed to brown. The solution was then rotary evaporated until dryness. A concentrated solution of the crude solid in acetonitrile was subjected to chromatography on neutral Al_2O_3 column. Three bands were separated by CH_2Cl_2 eluent; the red-brown and the dark-brown ones was found out to be *cis*- and the *trans*-$Cr(py)_2(ChryQ)_2$ complexes, respectively, whereas the orange band was identified by spectroscopy to be the unreacted chrysenequinone ligand. Slow evaporation of the solvent with a flow of dry nitrogen has resulted in microcrystals of the complexes. The products were obtained in 23% (*cis*-isomer) and 48% (*trans*-isomer) yields.

Anal. Calc. for $C_{46}H_{30}CrN_2O_4$ (MW = 726.76): C, 76.02; H, 4.16; N, 3.85. Found for *cis*-isomer: C, 75.85;

H, 4.24; N, 3.8%. Found for *trans*-isomer: C, 76.11; H, 4.13; N, 3.88%.

2.1.2. Method 2

The *tris*-[Cr(chrySQ)$_3$] complex was prepared as described in literature [24]. A 0.3 g (0.36 mmol) of [Cr(chrySQ)$_3$] was dissolved in 50 mL pyridine and refluxed at 100 °C. The solution turned form from purple to dark-brown over a period of 12 h. The resultant solution was then rotary evaporated until dryness. The crude solid was washed several times with petroleum ether (b.p. 40–60 °C). A concentrated solution of the crude solid in acetonitrile was subjected to chromatography on neutral Al_2O_3 as described in method 1. The products were obtained in 33% (*cis*-isomer) and 56% (*trans*-isomer) yields.

Anal. Found for *cis*-isomer: C, 75.87; H, 4.21; N, 3.82%. Found for *trans*-isomer: C, 76.08; H, 4.11; N, 3.87%.

3. Results and discussion

Irradiation of solutions containing a mixture of metal carbonyls, *o*-quinone ligand and nitrogen-donor coligand has been used as a general route for the synthesis of [M(N-base)$_n$(SQ)(Cat)] complexes, where $n = 1$ for bipyridine and $n = 2$ for pyridine ligands [7,25,26]. Photolysis of a solution containing either $Fe(CO)_5$, $Mn_2(CO)_{10}$ or $Co_2(CO)_8$ and 3,6-di-*tert*-butyl-1,2-benzoquinone in presence of *tert*-butyl-pyridine as a co-ligand had led to the formation of *trans*-isomer as the only isolated product [7,25]. Similar reactions with $Ni(CO)_4$ and $Co_2(CO)_8$ had led to the *cis*-[M(py)$_2$(phenSQ)$_2$], where phenSQ is phenanthrene-semiquinonate ligand [26].

In the present study, *cis*- and *trans*-[Cr(py)$_2$(chrySQ)-(chryCat)] complexes were synthesized by two different synthetic routes, where chrySQ and chryCat are chrysene-semiquinone and chrysenecatecholate, respectively. In the first procedure, a solution containing a mixture of chromium hexacarbonyl, chrysenequinone, chryQ and pyridine were photolyzed by a Hg-lamp. Another route for the synthesis of the complexes is by the displacement of one semiquinonate ligand in the *tris*-[Cr(chrySQ)$_3$] complex with two molecules of pyridine ligand. Isolation of chrysenequinone ligand from the reaction medium suggests that [Cr(py)$_2$(chrySQ)(chryCat)] complex might be formed as a result of one electron transfer from the displaced semiquinonate to one of the coordinated chrysenesemiquinone. In both of the synthetic procedures it was noticeable that the yield of the *cis*-isomer is lower than that of the *trans*-isomer. This may reflect the stability of the *trans*-isomer compared to the *cis*-isomer (vide infra).

The infrared spectra of the two isomeric complexes are dominated by a strong absorption near 1450 cm^{-1} due to CO stretching mode of the semiquinone ligand [27]. Characteristic bands assigned to the C–O stretching vibration and the ring stretching mode of the catecholate moiety of the complex, respectively, were observed for the *cis*-isomer at 1238 and 1485 cm^{-1} and for the *trans*-isomer at 1227 and 1486 cm^{-1} [28,29]. The IR data clearly demonstrate the ligand-based mixed-valence state of the chrysenequinone ligand in both complexes. Vibrations attributed to the coordinated pyridine were observed in the 750–630 cm^{-1} region of the spectra. There is no band observed at 605 cm^{-1} due to the C–H out-of-plane bending of the free pyridine. This is a clear indication of pyridine coordination to chromium metal ion in both complexes [29].

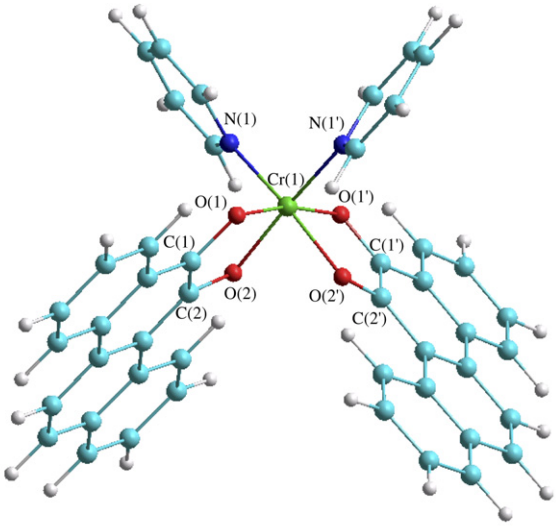
The spectroscopic techniques give no information about the geometry of the complex. Unfortunately, there is no structural data available for the two isomeric complexes due to the poor quality of the crystals obtained. Also to our knowledge there have not been crystal structures reported for chrysenequinone ligand or its complexes. Hence, it is considered worthwhile to model the two isomers using semiempirical parameterized PM3 method and calculate their vibrational frequencies.

The heat of formation calculated for *cis*- and *trans*-[Cr(py)$_2$(chrySQ)(chryCat)] using parameterized PM3 were −79.3 and −82.1 kcal/mol, respectively. This could explain the higher yield of the more stable *trans*-isomer obtained

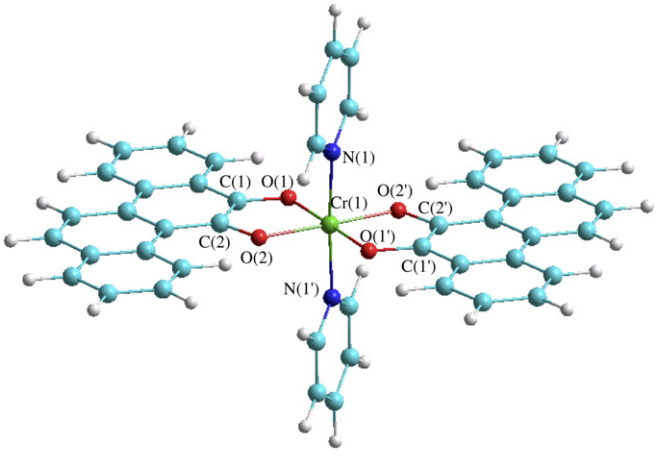
Table 1
Selected bond lengths (Å) and angles (°) for *cis*- and *trans*-[Cr(py)$_2$(chrySQ)(chryCat)] obtained from parameterized PM3 geometry optimization

	cis-Isomer	*trans*-Isomer
Bond lengths		
Semiquinonate		
Cr(1)–O(1)	1.953	1.946
Cr(1)–O(2)	1.941	1.940
O(1)–C(1)	1.319	1.299
O(2)–C(2)	1.293	1.322
C(1)–C(2)	1.441	1.436
Catecholate		
Cr(1)–O(1′)	1.931	1.926
Cr(1)–O(2′)	1.929	1.930
O(1′)–C(1′)	1.364	1.359
O(2′)–C(2′)	1.357	1.368
C(1′)–C(2′)	1.416	1.417
Pyridine		
Cr(1)–N(1)	1.987	2.031
Cr(1)–N(1′)	1.973	2.031
Bond angles		
O(1)–Cr(1)–O(2)	82.5	82.6
O(1′)–Cr(1)–O(2′)	85.6	86.1
O(1)–Cr(1)–O(1′)	169.3	178.8
O(2)–Cr(1)–O(2′)	85.8	177.7
O(1)–Cr(1)–O(2′)	88.4	95.1
O(2)–Cr(1)–O(1′)	88.0	96.2
N(1)–Cr(1)–N(1′)	96.7	176.3
O(1)–Cr(1)–N(1)	93.7	91.5
O(1)–Cr(1)–N(1′)	89.2	91.5
O(2)–Cr(1)–N(1)	88.6	91.3
O(2)–Cr(1)–N(1′)	172.8	91.3
O(1′)–Cr(1)–N(1)	94.7	88.6
O(1′)–Cr(1)–N(1′)	96.4	88.6
O(2′)–Cr(1)–N(1)	173.8	88.8
O(2′)–Cr(1)–N(1′)	89.1	88.8

from the two synthetic procedures. The calculated bond lengths and angles obtained from the semiempirical PM3 geometry optimization for the two isomers are summarized in Table 1. The optimized geometries for the *cis*- and *trans*-[Cr(py)$_2$(chrySQ)(chryCat)] are shown in Fig. 1. The chromium center is six-coordinated with four oxygen donors from the two chrysenequinone based ligands and two nitrogens atoms from the pyridine ligand. The average Cr–O bond distances calculated for the *cis*-isomer were 1.947 Å (SQ) and 1.930 Å (Cat). The values reported for *cis*-[Cr(bpy)(SQ)(Cat)] were 1.949 Å (SQ) and 1.939 Å (Cat) and those reported for [Cr(Cl$_4$SQ)$_3$] and [Cr(3,5-DBSQ)$_3$] were 1.949 Å (SQ) and 1.939 Å (SQ), respectively [13,15,30]. The average Cr–O bond distances calculated for the *trans*-isomer were 1.943 Å (SQ) and 1.928 Å (Cat) and those reported for the *trans*- [Cr(CH$_3$CN)$_2$(Cl$_4$SQ)-(Cl$_4$Cat)] were 1.935 Å and 1.929 Å [13]. The Cr–N bond distances with an average value of 2.031 Å for the *trans*-isomer, are slightly longer than the corresponding average for the *cis*-isomer (1.980 Å) and compares well with those reported for Cr–N bond distances [15,16]. While the Cr–O bond distance is an indicative of chromium oxidation state, the C–O and C–C bond distances are the evidence of oxidation state of the quinone ligand. The average C–O bond distances calculated for the *cis*- and the *trans*-isomers were 1.306 and 1.362 Å and 1.311 and 1.364 Å, respectively. The average C–O value reported for the semiquinonate and the catecholate ligands in the [Cr(bpy)(DTBSQ)-(DTBCat)] were 1.297 and 1.358 Å, respectively [31]. However, those reported for the phenenthrenesemiquinonate and phenanthrenecatecholate were 1.321 and 1.346 Å, respectively [32,33]. These structure differences imply a mixed-valence state for the two quinone based ligands. Another difference between SQ and Cat ligands can be found in the bit angle which is approximately 2° smaller in SQ than that of the Cat ligand [13]. This can be seen in the structure of the two isomers, where the calculated O(1′)–Cr(1)–O(2′) angle (Cat) for the *cis*- and *trans*-siomers were, respectively, 85.6° and 86.1° larger than the 82.5° and 82.6° of O(1)–Cr(1)–O(2) angle (SQ).



cis-[Cr(py)$_2$(chrySQ)(chryCat)]



trans-[Cr(py)$_2$(chrySQ)(chryCat)]

Fig. 1. The geometrical structures of [Cr(py)$_2$(chrySQ)(chryCat)] complexes optimized using parameterized PM3 method.

The vibrational frequencies based on the optimized geometries were calculated and compared with the observed fundamental frequencies in Table 2. The optimized scale factors determined for *cis*- and *trans*-isomers were 0.998362 and 0.996720, respectively. As can be seen in Table 2, the calculated harmonic vibrational frequencies compare well with the fundamental experimental frequencies. The calculated root mean square error (rms) per molecule is 58.5 and 47.2 cm^{-1} for *cis*- and *trans*-isomers, respectively. The rms values compare very well with those reported for vibrational frequencies calculations using HF/6-311 G(df, p) (rms = 56), MP2-fc/6-311 G(d, p) (rms = 60) and B-LYP/6-31 G(d) (rms = 45) [34].

Table 2
Characteristic calculated and observed vibrational frequencies (cm^{-1}) for *cis*- and *trans*-[Cr(py)$_2$(chrySQ)(chryCat)] complexes

cis-Isomer		*trans*-Isomer		Assignment
Calculated	Observed	Calculated	Observed	
1601	1609	1595	1600	νC=C (Cat)
1578	1594	1525	1537	νC=C (SQ)
1510	1516	1510	1513	νC=N (py)
1498	1485	1492	1486	ring deformation (Cat)
1452	1445	1443	1450	νC=O (SQ)
1335	1330	1336	1337	νC–O (SQ)
1232	1238	1230	1227	νC–O (Cat)
823	834	821	819	ν_{asymm} O–M–O (*trans*)
800	799	804	807	ν_{symm} O–M–O (*trans*)
772	774	759	757	ν_{asymm} O–M–O (*cis*)
749	752	742	733	ν_{symm} O–M–O (cis)
723	717	711	702	ν_{asymm} N–M–N
713	694			ν_{symm} N–M–N
667	662	678	678	δ O–M–O (SQ, Cat)
623	619	646	635	δ N–M–N
642	633	646	638	C–H out-of-plane bending (py)

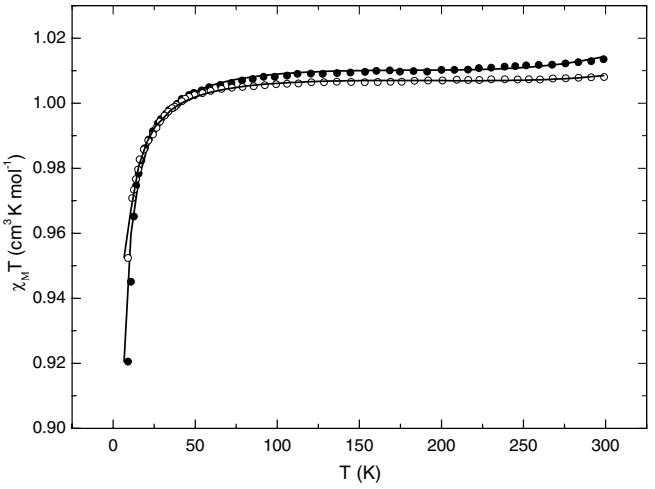


Fig. 2. Plots of the temperature dependence of $\chi_M T$ for *cis*- (•) and *trans*- (○) isomers of [Cr(py)$_2$(chrySQ)(chryCat)] complex. The solid lines represent the non-linear least-squares fits of the experimental data to theoretical equation given in text.

The temperature dependence of the magnetic susceptibility in the range 10–300 K for solid samples of the two isomeric complexes is shown in Fig. 2. At 300 K, the values are 1.013 and 1.008 cm^3 K mol^{-1} for the *cis*- and *trans*-isomers, respectively. They are close to the theoretical value of 1.00 cm^3 K mol^{-1} expected for an $S = 1$ spin ($g = 2.00$). The $S = 1$ ground state could be attributed to the intramolecular antiferromagnetic interactions between an $S = 3/2$, spin on the Cr(III) ion and an $S = 1/2$ spin on the chrySQ ligand. With these values of $\chi_M T$ and the little temperature dependence observed in the region of 53–300 K for the two complexes, it must be concluded that the coupling is strongly antiferromagnetic with a ground state $S = 1$. These results are similar to those reported for *trans*-[Cr(Cl$_4$SQ)(Cl$_4$Cat)(CH$_3$CN)$_2$] and *cis*-[Cr(Cl$_4$SQ)-(Cl$_4$Cat)(bpy)] containing the same spin components as the present complexes [15]. At temperature below ~50 K the $\chi_M T$ decreases below the spin-only value to 0.92 and 0.95 cm^3 K mol^{-1} for the *cis*- and *trans*-isomers, respectively. This decrease of $\chi_M T$ values at lower temperatures may be attributed to weak antiferromagnetic intermolecular interaction (θ) between the neighboring complexes [8,15].

The electron exchange between Cr(III) metal ion and chrySQ ligand in the two complexes can be described by the simple Heisenberg Hamiltonian, $H = -2JS_1 \cdot S_2$ ($S_1 = 3/2$, $S_2 = 1/2$), where J is the electron exchange integral that gauges the magnitude of electronic coupling between the spin centers. The exchange interaction J between chromium ion and chrySQ ligand was estimated by the non-linear least-squares fits for the magnetic susceptibilities, χ_M, given by the following equation:

$$\chi_M = (N\beta^2 g^2/k(T-\theta))[(2\exp(-4J/kT) + 10) /(3\exp(-4J/kT) + 5)] + \mathrm{TIP} \quad (1)$$

where N, β, g, k have their usual meaning. The Weiss constant (θ) is introduced in the equation to gauge intermolecular magnetic interaction at lower temperature and the temperature-independent paramagnetism (TIP) is to account for the slight positive slope observed in the data with increasing temperature [16]. The non-linear least-squares fits of the $\chi_M T$ to 52 experimental data points through the above equation yielded $J = -365 \pm 6$ cm^{-1}, $g = 2.01 \pm 0.0006$, $\theta = -0.35 \pm 0.007$ cm^{-1}, TIP $= 2 \times 10^{-5} \pm 1.07 \times 10^{-6}$ cm^3 mol^{-1} with $R = 6.3 \times 10^{-4}$ (*cis*-isomer) and $J = -395 \pm 4$ cm^{-1}, $g = 2.01 \pm 0.0003$, $\theta = -0.24 \pm 0.005$ cm^{-1}, TIP $= 2 \times 10^{-5} \pm 1.5 \times 10^{-6}$ cm^3 mol^{-1} with $R = 4.3 \times 10^{-4}$ (*trans*-isomer). The function minimized in the curve fitting was $R = (\sum(\chi_M T^{obs} - \chi_M T^{calc})^2 / \sum(\chi_M T^{obs})^2)^{1/2}$. The fits are illustrated in Fig. 2 as solid lines. The results obtained from the curve fitting agree well with those reported by Benelli et al. for [Cr(CTH)(DTBSQ)]$_2$Cl(PF$_6$)$_3$ and Wheeler and McCusker for [Cr(tren)(3,6-DTBSQ)](PF$_6$)$_2$ [16,35].

The electrochemical properties of [Cr(py)$_2$(chrySQ)-(chryCat)] complexes were studied by cyclic voltammetry in acetonitrile solvent. The results are given in Fig. 3 and Table 3. The dominant feature of the voltammograms is one-electron oxidation and reduction of the ligand moieties

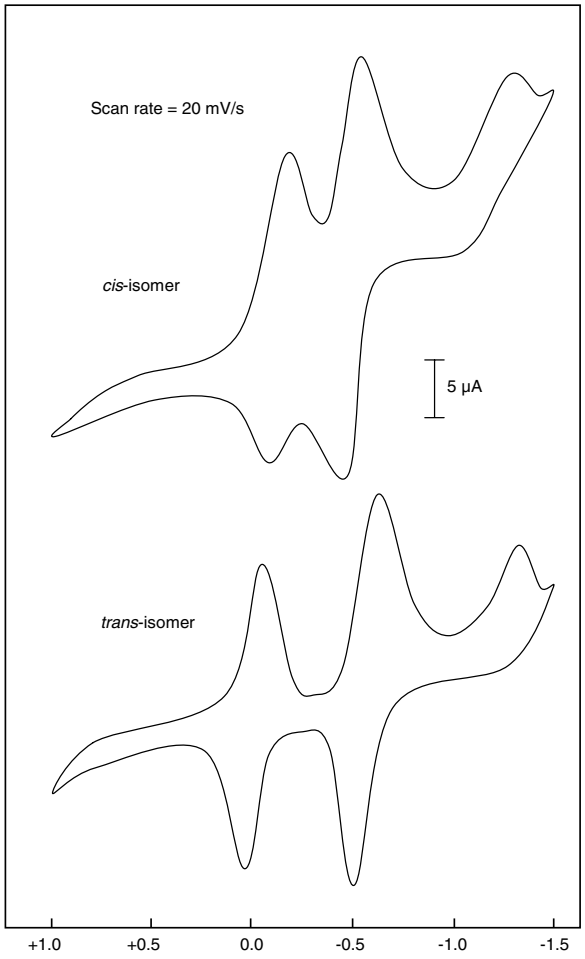


Fig. 3. Cyclic voltammograms of [Cr(py)$_2$(chrySQ)(chryCat)] complexes.

Table 3
Electrochemical data for *cis*- and *trans*-[Cr(py)$_2$(chrySQ)(chryCat)] in CH_3CN

	cis-Isomer[a,b]							*trans*-Isomer[a,b]						
	E_{red}	E_{ox}	ΔE_p	$E_{1/2}$	i_{pc}	i_{pa}	i_{pa}/i_{pc}	E_{red}	E_{ox}	ΔE_p	$E_{1/2}$	i_{pc}	i_{pa}	i_{pa}/i_{pc}
+1/0	−190	−88	102	−139	17.1	16.7	0.98	−43	24	67	−10	12.3	11.7	0.95
0/−1	−538	−452	86	−495	23.2	18.5	0.80	−620	−501	119	−561	16.7	16.5	0.99
−1/−2	−1286				8.7			−1314				7.3		

[a] Potentials in mV, current in μA.
[b] Separation between $E_{1/2}$(+1/0) and $E_{1/2}$(0/−1) is 302 mV (*cis*-isomer) and 551 mV (*trans*-isomer).

since the chromium ion retains a trivalent state in this potential region. The reduction wave was observed for the *cis*- and *trans*-isomers near −495 and −561 mV *versus* $Ag/Ag^+/CH_3CN$, respectively. Surprisingly, the oxidation wave for the *trans*-isomer was observed at more positive potential (−10 mV) compared to that for the *cis*-isomer (−139 mV). Also, the separation between the redox waves for oxidation and reduction processes was surprisingly 302 and 551 mV for the *cis*- and *trans*-isomers, respectively. This could be attributed to charge delocalization between mixed-valence ligands which is greater in the *trans*-isomer. The degree of charge delocalization can be determined by calculating the comproportionation constant, $K_c = \exp(\Delta EF/RT)$ [36,37]. As the degree of delocalization increases, ΔE and also K_c increase. The K_c values calculated for *cis*- and *trans*-isomers were 1.3×10^5 and 2.1×10^9, respectively. The calculated values indicate greater degree of delocalization between the SQ and Cat ligands in the *trans*-isomer. In agreement with these results, X-ray structural studies of *trans*- [Cr(Cl_4SQ)(Cl_4Cat)(CH_3CN)$_2$] indicated charge delocalization between the SQ and Cat ligands while for *cis*-[Cr(Cl_4SQ)(Cl_4Cat)(bpy)] the charge is localized on the ligands [15]. The two one-electron processes can be represented by Eq. (2). The one-electron reduction would provide $[Cr^{III}(py)_2(chryCat)_2]^-$ species (right) with two

$$[Cr(py)_2(chrySQ)_2]^+ \overset{+e}{\underset{-e}{\rightleftharpoons}} [Cr(py)_2(chrySQ)(chryCat)] \overset{+e}{\underset{-e}{\rightleftharpoons}} [Cr(py)_2(chryCat)_2]^- \quad (2)$$

Cat ligands, while the oxidation affords a cationic $[Cr^{III}(py)_2(SQ)_2]^+$ species (left) with two SQ ligands. Finally, both complexes showed additional irreversible one-electron reduction waves near −1300 mV. The process could be attributed to the reduction of the Cr(III) to the Cr(II) ion.

The electronic absorption spectra of the *cis*- and *trans*-isomers in acetonitrile solution in the region 350–1100 nm are shown in Figs. 4 and 5, respectively. The dominant feature of the electronic spectra of the two isomers is intense bands at 392, 443 and 566 nm, with shoulders at 486 and 517 nm for the *cis*-isomer, and 396, 445 and 566 nm, with a shoulder at 511 nm for the *trans*-isomer. Lower intensity bands were observed at 681, 786 and 968 nm for the *cis*-isomer and 732, 804 and 968 nm for the *trans*-isomer. A low-energy band of medium intensity ($\log \varepsilon = 3.35$) was observed at 1085 nm for the *cis*-isomer. Benelli et al. reported the electronic spectrum of $[Cr(CTH)(TCSQ)]^{2+}$ that revealed bands at 990 nm with shoulders at 1136 and 877 nm which were assigned as diagnostic of semiquinone ligand and were attributed to transitions to the HOMO from the second highest occupied molecular orbital [35].

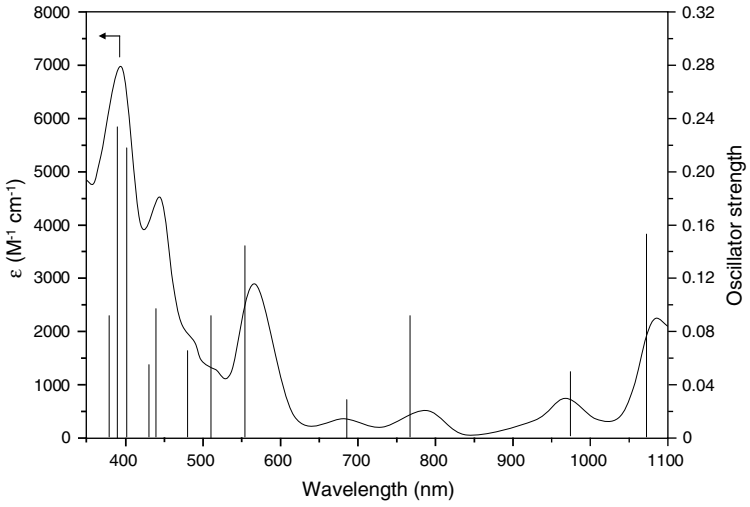


Fig. 4. The observed electronic spectrum in acetonitrile (curve) and the computed transitions resulted from ZINDO/S-CI calculations (lines) of *cis*-[Cr(py)$_2$(chrySQ)(chryCat)].

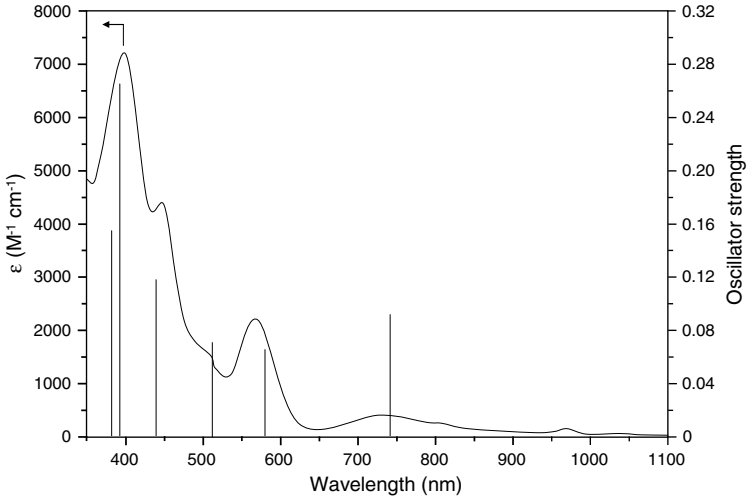


Fig. 5. The observed electronic spectrum in acetonitrile (curve) and the computed transitions resulted from ZINDO/S-CI calculations (lines) of *trans*-[Cr(py)$_2$(chrySQ)(chryCat)].

Another band was observed for the $[Cr(CTH)(TCSQ)]^{2+}$ complex near 400 nm and was attributed to internal ligand transitions. However the metal-to-ligand charge-transfer transition was observed at 498 and 458 nm. Chang et al. reported similar metal-to-ligand charge-transfer transition at 526 nm for *cis*-[Cr(bpy)(Cl_4SQ)(Cl_4Cat)] complex [15]. In addition, a transition attributed to bpy ligand was observed at 476 nm. In fact the assignment of the spectra for the *cis*- and *trans*-[Cr(py)$_2$(chrySQ)(chryCat)] is not straightforward especially with a system that shows a strong exchange coupling interaction between Cr(III) metal ion and SQ ligand. To interpret these spectra one has to include the effect of the exchange coupling on the electronic states of the complexes under study. To accomplish this goal, the ZINDO/S-CI method was used to interpret the spectra of both complexes.

The ZINDO/S method parameterized to produce the UV–Vis electronic transitions has been used to estimate the molecular orbitals of the two complexes. This method has been previously used to reproduce the spectra of several complexes of the first transition-metal series and more particularly for studying the spectroscopy of the

Table 4
Energies, percent contribution from Cr, SQ, Cat and py, and main character of some frontier orbitals obtained from the ZINDO/S calculations for *cis*- and *trans*-[Cr(py)$_2$(chrySQ)(chryCat)]

	Orbital[a]	Type[b]	Energy (eV)	%Cr	%SQ	%Cat	%py	Main character
cis-Isomer	L + 3	V	−0.267	7.0	71.6	9.2	12.1	SQ(π)
	L + 2	V	−0.349	30.8	2.5	2.5	60.9	Cr(t_{2g}), py(π)
	L + 1	V	−0.647	70.0	15.9	10.9	2.3	Cr(e_g), SQ, Cat(σ)
	L	V	−0.706	13.3	1.9	1.6	82.9	py(π)
	H	S	−3.658	60.1	11.6	10.9	17.3	Cr(t_{2g}), SQ, Cat, py(π)
	H − 1	S	−4.048	44.1	43.5	8.0	4.2	Cr(t_{2g}), SQ(π)
	H − 2	O	−6.311	13.0	1.1	83.6	1.6	Cat–O and rings(π)
	H − 3	O	−6.441	34.0	55.7	4.3	4.9	Cr(t_{2g}), SQ(π) bonding
	H − 4	O	−7.234	1.0	2.0	96.2	0.7	Cat(π) rings
	H − 5	O	−7.399	1.1	77.4	2.0	19.1	SQ(π) rings
trans-Isomer	L + 3	V	0.026	0.1	62.9	36.8	0.1	SQ-rings, Cat-rings(π)
	L + 2	V	−0.204	18.2	5.0	25.4	51.5	Cr(t_{2g}), Cat, py(π)
	L + 1	V	−0.649	69.3	4.0	11.3	14.5	Cr(e_g), Cat, py(σ)
	L	V	−0.700	16.4	0.9	4.7	77.6	Cr(t_{2g}), py(π)
	H	S	−3.914	41.9	26.9	21.6	9.4	Cr(t_{2g}), SQ, Cat, py(π)
	H − 1	S	−4.269	63.7	17.8	17.2	1.1	Cr(t_{2g}), SQ–CO, Cat–CO(π)
	H − 2	O	−6.220	2.4	50.3	46.0	0.5	SQ, Cat(π)
	H − 3	O	−6.690	18.6	33.6	44.6	2.2	Cr(t_{2g}), SQ–O, Cat–O(π)
	H − 4	O	−7.411	0.3	24.2	74.8	0.1	Cat(π)
	H − 5	O	−7.508	2.7	78.7	18.3	0.2	SQ(π)

[a] L and H represent LUMO and HOMO, respectively. L + *n* indicates the *n*th molecular orbital above the LUMO and H − *n* indicates the *n*th molecular orbital below the HOMO.

[b] V, S and O represent unoccupied (virtual), singly occupied and doubly occupied molecular orbitals, respectively.

internal d–d excitations [38]. Also, it was successful in studying the electronic spectrum of dinuclear Co(III) and Cr(III) complexes of bis(ditholene) radical [39].

Table 4 lists the results of ZINDO/S-CI energies, composition, and main character of some frontier molecular orbitals. The shape of the magnetic (HOMO and HOMO − 1) and the doubly occupied (HOMO − 2) molecular orbitals for the two isomers are pictorially shown in Fig. 6. As can been seen, the two singly occupied molecular orbitals (HOMO and HOMO − 1) are more delocalized on metal, SQ and Cat in the *trans*-isomer compared to those for the *cis*-isomer. Also, the highest doubly occupied molecular orbital (HOMO − 2) is delocalized over SQ and Cat ligands in the *trans*-isomer while is localized on the Cat ligand in the *cis*-isomer.

Results of the calculated electronic transitions for the *cis*- and *trans*-isomers are shown in Figs. 4 and 5, respectively. The assignment of the computed electronic transitions is listed in Table 5. There is a good agreement between the computed active transitions and the observed bands. As expected for complexes having the general formula [M(N-base)(SQ)(Cat)], where M is a transition metal and N-base is pyridine, bipyridine, or phenanthroline ligands, to show varieties of charge-transfer transitions [9,15,40–44]. For the complexes under studies the possible charge-transfer transitions are metal-to-ligand (MLCT) from Cr(d_π) to acceptor orbitals on SQ and py and/or ligand-to-metal (LMCT) from Cat and SQ to Cr(III),

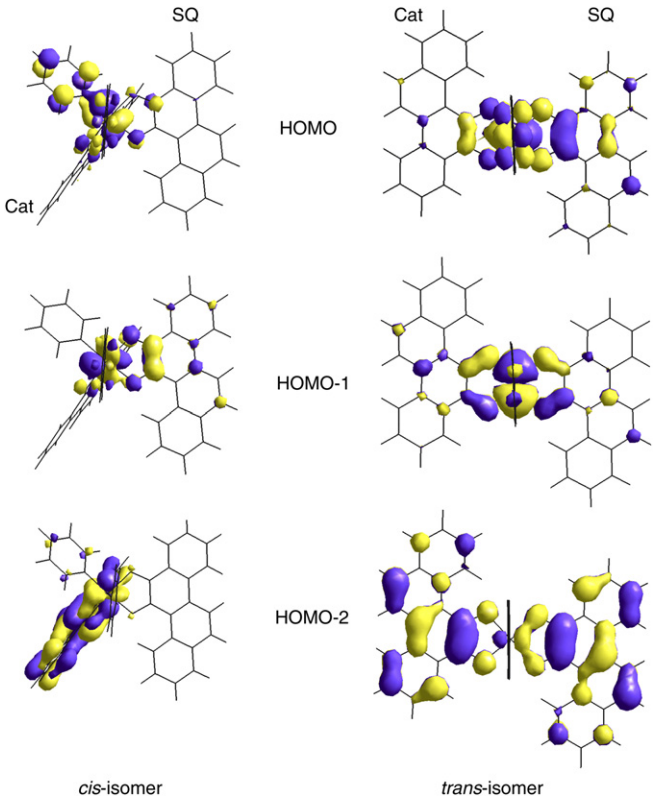


Fig. 6. The two singly occupied (HOMO and HOMO − 1) and the highest doubly occupied (HOMO − 2) molecular orbitals for *cis*- and *trans*-[Cr(py)$_2$(chrySQ)(chryCat)] complexes.

Table 5
Observed and calculated electronic absorption data for [Cr(py)$_2$(chrySQ)(chryCat)] complexes and assignment of the electronic transitions

Observed		Calculated		
λ^{obs} (nm)	log ε (M^{-1} cm^{-1})	λ^{calc} (nm)	Oscillator strength	Composition of transition
cis-Isomer				
1085	3.35	1072	0.156	0.51(H − 2 → H − 1)
968	2.88	973	0.044	0.46(H − 3 → H)
786	2.72	766	0.088	0.49(H → L + 1)
681	2.58	685	0.030	0.49(H − 1 → L + 1)
566	3.46	553	0.148	0.59(H → L + 3)
517	3.12	511	0.093	0.91(H − 2 → H)
486	3.26	479	0.068	0.76(H → L + 2)
443	3.66	438	0.099	0.75(H − 1 → L + 2)
		428	0.059	0.51(H − 3 → L)
392	3.84	400	0.219	0.55(H − 2 → L)
		389	0.238	0.5(H − 4 → L)
		378	0.093	0.51(H − 5 → L)
trans-Isomer				
968	2.26			
804	2.43			
732	2.67	739	0.093	0.51(H → L + 1)
566	3.35	572	0.088	0.5(H − 1 → L + 3)
511	3.19	511	0.072	0.99(H − 2 → H − 1)
445	3.64	438	0.120	0.76(H → L + 2)
396	3.86	393	0.268	0.47(H − 4 → L)
		382	0.157	0.48(H − 5 → L)

and interligand charge-transfer (ILCT) transitions from Cat to SQ, Cat to py and/or SQ to py.

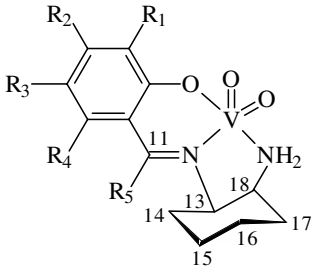
The most characteristic band in the electronic spectra of [Cr(py)$_2$(chrySQ)(chryCat)] complexes observed at 566 nm was well predicted by ZINDO/S calculations. It was assigned as Cr → SQ metal-to-ligand charge-transfer transition with major configurations 0.59(H → L + 3) and 0.5(H − 1 → L + 3) for the *cis*- and *trans*-isomers, respectively. Where the H in the *cis*-isomer has 60.1% metal character and the H− 1 in the *trans*-isomer has 63.7% metal character, whereas the L + 3 in both complexes have SQ as a major contribution to the molecular orbital. In agreement with this assignment the [Cr(DTBSQ)$_3$] complex showed a strong band at 570 nm [28]. Also, the electronic spectrum of $[Cr(CTH)(TCSQ)]^{2+}$ are dominated by a strong absorption band at 498 nm that was assigned as Cr → SQ MLCT transition [35]. Transitions of the type Cat or SQ → Cr(III) LMCT were also predicted by ZINDO/S calculations to be the bands observed for the *cis*-isomer at 986 (SQ → Cr) and 517 nm (Cat → Cr) with major configurations 0.46(H − 3 → H) and 0.91(H − 2 → H), respectively and for the *trans*-isomer at 511 nm (Cat → Cr and SQ → Cr) with major configurations 0.99(H − 2 → H − 1). Transitions involving the pyridine ligand were assigned to absorption bands at 486, 443 and 392 nm for the *cis*-isomer and at 445 and 396 for the *trans*-isomer with major configurations shown in Table 5. Interestingly, the ZINDO/S calculations indicated that the intense band observed near 445 nm is Cr → py MLCT

for the *trans*-isomer whereas for the *cis*-isomer it is composed of Cr → py and SQ → py transitions. Also, the absorption band near 392 nm has a contribution from Cat → py and SQ → py ILCT transitions with more contribution form the former for the *cis*-isomer. The most spectacle observation of the spectrum of the *cis*-isomer is a lower-energy band at 1085 nm ($\log\varepsilon = 3.35\ M^{-1}\ cm^{-1}$) which was predicted by ZINDO/S calculation as Cat → SQ intervalence charge-transfer (IVCT) transition with major configuration $0.51(H-2 \rightarrow H-1)$. This transition occurs between the highest doubly occupied and the lowest singly occupied molecular orbitals. Consistence with this assignment the electronic absorption spectrum of *cis*-[Fe(bpy)(phenSQ)(phenCat)] showed a transition that attributed to Cat → SQ intervalence charge-transfer transition at 1131 in THF solution and at 1050 nm in the solid state as KBr pellet, while these bands was not observed for $[Fe(DBSQ)_3]$ [29]. It was striking that the *trans*-isomer did not show this transition. This could be attributed to higher charge delocalization between the Cat and SQ ligands in the *trans*-isomer which might show this transition at much lower energy of the IR region of the spectrum. Finally, ligand field (LF) transitions, $Cr(t_{2g}) \rightarrow Cr(e_g)$ were well predicted for the low-intensity transitions observed at 687 and 681 nm for the *cis*-isomer and at 732 nm for the *trans*-isomer. The computed LF transitions for the *cis*-isomer were 766 and 785 nm with major configurations $0.49(H \rightarrow L+1)$ and $0.49(H-1 \rightarrow L+1)$, respectively, whereas that computed for the *trans*-isomer was 739 nm with a major configuration $0.51(H \rightarrow L+1)$. These transitions were expected to be spin-forbidden however its intensity is several hundred times compared with that observed for $[Cr(tren)(DTBCat)]^+$ and $[Cr(acac)_2(en)]^+$ [16,45]. Such enormous enhancement in the spin-forbidden transition was ascribed to the exchange coupling between Cr(III) and the SQ radical [35]. These observations agree with the results of ZINDO/S calculations which show that H in the *trans*-isomer composed of 41.9% Cr and 26.9% SQ and H − 1 in the *cis*-isomer composed of 44.1% Cr and 43.5% SQ.

References

[1] V.L. Davidson, Principle and Applications of Quinoproteins, Marcel Dekker, Inc., 1993.
[2] J.A. Duin, J.A. Jongejan, Annu. Rev. Biochem. 58 (1989) 403.
[3] D.M. Dooley, M.A. McGuiri, D.E. Brown, P.N. McIntire, Nature 349 (1991) 262.
[4] C.G. Pierpont, A.S. Attia, Collect. Czech., Chem. Commun. 66 (2001) 33.
[5] C.G. Pierpont, C.W. Lange, Prog. Inorg. Chem. 41 (1994) 331.
[6] C.G. Pierpont, Coord. Chem. Rev. 99 (2001) 216.
[7] A.S. Attia, O. Jung, C.G. Pierpont, Inorg. Chim. Acta 226 (1994) 91.
[8] A.S. Attia, C.G. Pierpont, Inorg. Chem. 34 (1995) 1172.
[9] A.S. Attia, C.G. Pierpont, Inorg. Chem. 37 (1998) 3051.
[10] V.C. Greabe, F. Honigsberger, Justus Liebigs Ann. Chem. 311 (1900) 257.
[11] HYPERCHEM 6.01, Hypercube Inc., 2000.
[12] C.G. Pierpont, R.M. Buchanan, Coord. Chem. Rev. 38 (1981) 45.
[13] S.R. Sofen, D.C. Ware, S.R. Cooper, K.N. Raymond, Inorg. Chem. 18 (1979) 234.
[14] H. Chang, K. Mochizuki, S. Kitagawa, Inorg. Chem. 40 (2001) 146.
[15] H. Chang, K. Mochizuki, S. Kitagawa, Inorg. Chem. 41 (2002) 4444.
[16] D.E. Wheeler, J.K. McCusker, Inorg. Chem. 37 (1998) 2296.
[17] R.M. Buchanan, J. Claflin, C.G. Pierpont, Inorg. Chem. 22 (1983) 2552.
[18] M. Mohr, J.P. McNamara, H. Wang, S.A. Rajeev, J. Ge, C.A. Morgado, I.H. Hillier, Faraday Discuss. 124 (2003) 413.
[19] A.P. Scott, L. Radom, J. Phys. Chem. 100 (1996) 6502.
[20] A.D. Bacon, M.C. Zerner, Theor. Chim. Acta. 32 (1973) 111.
[21] M. Kotzian, N. Roesch, M.C. Zerner, Theor. Chim. Acta. 81 (1992) 201.
[22] K.K. Stavrev, M.C. Zerner, T.J. Meyer, J. Am. Chem. Soc. 117 (1995) 8684.
[23] K.K. Stavrev, M.C. Zerner, J. Chem. Phys. 102 (1995) 34.
[24] R.M. Ramadan, W.H. Mahmoud, A.S. Attia, M.F. El-Shahat, Polyhedron 49A (1993) 117.
[25] C. Floriani, R. Henzi, F. Calderazzo, J. Chem. Soc., Dalton Trans. (1972) 2640.
[26] M.W. Lynch, R.M. Buchanan, C.G. Pierpont, D.N. Hendrickson, Inorg. Chem. 20 (1981) 1038.
[27] M.W. Lynch, M. Valentine, D.N. Hendrickson, J. Am. Chem. Soc. 104 (1982) 6982.
[28] P.A. Wicklund, D.G. Brown, Inorg. Chem. 15 (1976) 396.
[29] D.G. Brown, W.L. Johnson, Z. Naturforsch, B. Anorg, Chem. Org. Chem. 34B (1979) 712.
[30] C.G. Pierpont, H.H. Downs, J. Am. Chem. Soc. 98 (1976) 4834.
[31] R.M. Buchanan, C.G. Pierpont, J. Am. Chem. Soc. 102 (1980) 4951.
[32] C.G. Pierpont, R.M. Buchanan, J. Am. Chem. Soc. 97 (1975) 6465.
[33] C.G. Pierpont, R.M. Buchanan, J. Am. Chem. Soc. 97 (1975) 4912.
[34] A.P. Scott, L. Radom, J. Phys. Chem. 100 (1996) 16502.
[35] C. Benelli, A. Dei, D. Gatteschi, H.U. Gudel, L. Pardi, Inorg. Chem. 28 (1989) 3089.
[36] A.W. Bott, Curr. Sep. 16 (1997) 61.
[37] T. Ito, T. Hamaguchi, H. Nagino, T. Yamaguchi, H. Kido, I.S. Zavarine, T. Richmond, J. Washington, C.P. Kubiak, J. Am. Chem. Soc. 121 (1999) 4625.
[38] W.P. Anderson, W.D. Edwards, M.C. Zerner, Inorg. Chem. 25 (1986) 2728.
[39] A. Bencini, C.A. Daul, A. Dei, F. Mariotti, H. Lee, D.A. Shultz, L. Sorace, Inorg. Chem. 40 (2001) 1582.
[40] D.M. Adams, L. Noodleman, D.N. Hendrickson, Inorg. Chem. 36 (1997) 3966.
[41] A.B.P. Lever, P.R. Auburn, E.S. Dodsworth, M. Haga, W. Liu, M. Melnik, W.A. Nevin, J. Am. Chem. Soc. 110 (1988) 8076.
[42] C.G. Pierpont, Coord. Chem. Rev. 219 (2001) 415.
[43] S.R. Cooper, Y.B. Koh, K.N. Raymond, J. Am. Chem. Soc. 104 (1982) 5092.
[44] D.D. Cox, S.J. Benkovic, L.M. Bloom, F.C. Bradley, M.J. Nelson, L. Que Jr., D.E. Wallick, J. Am. Chem. Soc. 110 (1988) 2026.
[45] S. Kaizaki, Bull. Chem. Soc. Jpn. 76 (2003) 673.

as well bulk mixtures of vanadyl, aldehyde and chiral amine [24] are effective catalyst in the reaction of asymmetric oxidation of prochiral sulfides to sulfoxides. Chiral sulfoxides form an important class of compounds finding an increasing use as chiral auxiliaries in asymmetric syntheses of biologically active compounds [25]. Recently [26] we have shown that the coordination geometry of vanadium in VO_2L, where L is the deprotonated product of 1:1 condensation of 2-methyl-1,2-diaminopropane and 4,6-dimethoxysalicylaldehyde, is approximately trigonal bipyramidal and that the complex catalyses the oxidation of methyl phenyl sulfide to the methyl phenyl sulfoxide. Optically active *trans*-1,2-diaminocyclohexane singly condensed with salicylaldehyde residue attached to a resin was synthesized by Sherington et al. [27] and used as a starting material for preparation of resin-supported chiral metal–salen complexes to form a basis of immobilized catalysis. In continuation of our studies on synthesis, structure, spectroscopic and catalytic properties of vanadium complexes incorporating a product of single condensation of a diamine [26], we prepared a series of new chiral dioxovanadium(V) complexes comprising coordinated single condensation products of *RR*(−) and *SS*(+)-1,2-diaminocyclohexane with aromatic *o*-hydroxyaldehydes and *o*-hydroxyketones presented in Fig. 1. We examined their spectroscopic (^{1}H, ^{13}C, ^{51}V NMR, UV–Vis, IR) and catalytic properties in the asymmetric oxidation of methyl phenyl sulfide by cumene hydroperoxide. Crystal and molecular structure of the



	R_1	R_2	R_3	R_4	R_5
1s, 1r	H	H	H	H	H
2s, 2r	OMe	H	H	H	H
3s, 3r	H	H	OMe	H	H
4s, 4r	H	OMe	H	OMe	H
5s, 5r	H	H	Me	H	H
6s, 6r	H	H	Br	H	H
7s, 7r	H	H	NO_2	H	H
8s, 8r	H	H	-$(CH)_4$-		H
9r	-$(CH)_4$-		H	H	Me

Fig. 1. Structural formulae of dioxovanadium(V) complexes with the monocondensation products of *SS*(+) and *RR*(−)-1,2-diaminocyclohexane denoted by **s** and **r**, respectively. The azomethine and cyclohexane carbon atoms in **8r** and **9r** are labeled as shown in the drawing.

{*RR*(−)-1-amino-2-*N*-[1′-(1″-oxido-κ*O*-2″-naphthyl)ethylidene]aminocyclohexane-κ^2*N*}dioxovanadium(V) hemihydrate hemiethanol solvate is reported.

2. Experimental

2.1. Measurements

Carbon, hydrogen and nitrogen contents were determined on a Carlo Erba MOD 1106 elemental analyser. FT-IR spectra of solid samples (KBr pellets) were run on a Brucker IFS 66, and electronic spectra on the Perkin–Elmer LAMBDA 18 spectrophotometer. ^{1}H and ^{51}V spectra were obtained in DMSO-d_6 solutions at 50 °C with a Varian Mercury-400BB (400 MHz) spectrometer using TMS (^{1}H) and $VOCl_3$ (^{51}V) as reference compounds. Chromatography was carried out with a Hewlett–Packard 1050 chromatograph.

2.2. X-ray investigations

Diffraction data for **9r** were collected at 293(2) K using a Nonius Kappa CCD diffractometer with graphite monochromatized Mo Kα radiation ($\lambda = 0.71073$ Å). Details of cell data, data collection and refinement are summarized in Table 1. Compound **9r** is monoclinic, for which the space group $P2_1$ was uniquely assigned from systematic absences. The structure was solved by direct methods using SHELXS-97 [28] and refined with all data on F^2 with the aid of SHELXL-97 [29]. H atoms attached to carbon were placed in calculated positions and allowed to ride on their parent atoms with $U_{iso}(H) = 1.2U_{eq}(C)$ with the exception of methyl protons for which $U_{iso}(H) = 1.5U_{eq}(C)$ was inserted. H atoms linked with nitrogen atoms were located in the difference map and refined freely. Analysis utilizes the 2003 version of the program PLATON [30]. Selected bond lengths and angles are listed in Table 2.

2.3. Catalytic oxidation of sulfides

A DMSO solution containing a dioxovanadium(V) Schiff base complex (4×10^{-5} mol) and cumene hydroperoxide (4×10^{-3} mol) was stirred for 5 h at 20 °C. To the resulting yellow solution thermostated to 20 or 50 °C the methyl phenyl sulfide (4×10^{-4} mol) was added. The kinetics of the oxidation reaction was investigated by high performance chromatography. Samples of the reaction mixture were withdrawn at intervals and then analysed with a Hewlett–Packard 1050 chromatograph equipped with a Shimadzu C-R4A Chromatopack area peak calculator and with a Kromasil-100 C-8 column (Knauer GmBH, Germany) using acetonitrile–water (4:6 v/v) as an eluent. Chromatography was carried out with a flow rate of 1 ml min^{-1} and components were detected with a UV Detector ($\lambda = 254$ nm). The enantiomeric excesses (ee) were determined either from the specific rotation at 589 nm of the sulfoxide isolated by chromatographic elution or by measurement of intensities of ^{1}H

Table 1
Crystal data and structure refinement for **9r**

Empirical formula	$(C_{18}H_{21}N_2O_3V)_2 \cdot C_2H_6O \cdot H_2O$
Formula weight	792.70
Temperature (K)	293(2)
Wavelength (Å)	0.71073
Crystal system	monoclinic
Space group	$P2_1$
Unit cell dimensions	
a (Å)	13.9289(3)
b (Å)	8.6221(2)
c (Å)	15.6765(4)
β (°)	98.562(2)
Volume (Å^3)	1861.71(8)
Z	2
D_{calc} (g cm^{-3})	1.414
Absorption coefficient (mm^{-1})	0.559
$F(000)$	1664
Crystal size (mm)	$0.25 \times 0.05 \times 0.05$
θ Range for data collection (°)	2.99–23.18
Limiting indices	$-15 \leqslant h \leqslant 15$, $-8 \leqslant k \leqslant 9$, $-17 \leqslant l \leqslant 17$
Reflections collected/unique [R_{int}]	13 865/4921 [0.061]
Completeness to $\theta = 27.45$ (%)	99.4
Refinement method	full-matrix least-squares on F^2
Data/restraints/parameters	4921/3/484
Goodness-of-fit on F^2	1.061
Final R indices [$I > 2\sigma(I)$]	$R_1 = 0.058$, $wR_2 = 0.121$
R indices (all data)	$R_1 = 0.072$, $wR_2 = 0.128$
Absolute structure (Flack) parameter	0.00(4)
Largest difference peak and hole (e Å^{-3})	0.417 and −0.437

Table 2
Selected bond lengths (Å) and angles (°) for **9r**

V1A–O1A	1.915(5)	O1A–V1A–N1A	81.7(2)
V1A–O2A	1.604(5)	O1A–V1A–N2A	156.5(2)
V1A–O3A	1.622(5)	O2A–V1A–O3A	111.0(3)
V1A–N1A	2.135(5)	O2A–V1A–N1A	119.7(2)
V1A–N2A	2.124(6)	O2A–V1A–N2A	94.0(3)
		O3A–V1A–N1A	128.2(2)
O1A–V1A–O2A	101.9(2)	O3A–V1A–N2A	91.7(2)
O1A–V1A–O3A	98.6(2)	N1A–V1A–N2A	75.3(2)
V1B–O1B	1.902(4)	O1B–V1B–N1B	81.3(2)
V1B–O2B	1.608(5)	O1B–V1B–N2B	155.9(2)
V1B–O3B	1.638(5)	O2B–V1B–O3B	111.7(3)
V1B–N1B	2.158(5)	O2B–V1B–N1B	118.0(2)
V1B–N2B	2.122(7)	O2B–V1B–N2B	94.7(3)
		O3B–V1B–N1B	129.3(2)
O1B–V1B–O2B	101.6(2)	O3B–V1B–N2B	91.7(3)
O1B–V1B–O3B	98.6(2)	N1B–V1B–N2B	75.3(2)

NMR signals of sulfoxide in the presence of chiral shift reagent Eu(hfc)$_3$ [31]. In order to perform the latter procedure the sample (10 ml) withdrawn from of the reaction mixture was poured in the 40% aqueous solution (30 ml) of sodium bisulfite and the resulting suspension was extracted several times by methylene chloride. The collected extracts were dried over sodium sulfate, filtered and evaporated to dryness under diminished pressure. The solid product dissolved in $CDCl_3$ was analysed by ^{1}H NMR in the presence of chiral shift reagent.

2.4. Complexes

The complexes were obtained in a template/complexation reactions analogous to those described for preparation of dioxovanadium(V) complexes with monocondensation products of 1,2-diaminopropane and its derivatives [26,32]. A sample of 10 mmol of *RR*(−)-1,2-diaminocyclohexane in 10 ml of EtOH was added with stirring to a freshly filtered solution of triethyl vanadate (10 mmol) in 250 ml of absolute EtOH producing a dark suspension of an intermediate. An aromatic *o*-hydroxyaldehyde (salicylaldehyde, 3-methoxysalicylaldehyde, 5-methoxysalicylaldehyde, 4,6-dimethoxysalicylaldehyde, 5-methylsalicylaldehyde, 5-bromosalicylaldehyde, 5-nitrosalicylaldehyde, 2-hydroxy-1-naphthaldehyde) or an aromatic *o*-hydroxyketone (1-hydroxy-2-acetonaphthone) dissolved in absolute EtOH was added to the aforementioned suspension. After refluxing of the resulting mixture for 2 (aldehydes) or for 10 h (ketones) and its cooling to room temperature the separated solids were filtered off, washed several times with EtOH, recrystallized from DMSO–EtOH mixtures and dried over molecular sieves. {*RR*(−)-1-amino-2-*N*-[(2′-oxido-κ*O*-5′-nitrophenyl)methylene]aminopropane-κ^2*N*}dioxovanadium(V) (**10r**), was prepared in a similar way as described above using 5-nitrosalicylaldehyde, *R*(−)-1,2-diaminopropane and triethyl vanadate as reactants.

2.4.1. {*RR*(−)-1-amino-2-*N*-[(2′-oxido-κ*O*-phenyl)methylene]aminocyclohexane-κ^2*N*}dioxovanadium(V) (*1r*)

Yield 56%. *Anal.* Calc. for $C_{13}H_{17}N_2O_3V$: C, 52.0; H, 5.7; N, 9.3. Found: C, 52.1; H, 5.7; N, 9.2%. IR (KBr, cm^{-1}): 3261, 3211 (ν_{N-H}); 1631, 1600 $\nu_{C=N} + \nu_{C=C}$; 928, 864 ($\nu_{V=O}$). UV–Vis spectrum in DMSO [λ_{max} (nm), ε (M^{-1} cm^{-1})]: 262 (20 000), 367 (4000). CD spectrum in DMSO [λ_{max} (nm), $\Delta\varepsilon$ (M^{-1} cm^{-1})]: 264 (−7.45), 328 (−2.70), 388 (0.61). ^{1}H NMR (DMSO-d_6): 7.226 (1H, d, $^3J = 7$ Hz), 7.024 (1H, t, $^3J = 7$ Hz), 6.788 (1H, t, $^3J = 8$ Hz), 6.768 (1H, d, $^3J = 8$ Hz) (aromatic); 8.772 (1H, s) (azomethine); 5.462 (1H, d, $^2J = 9$ Hz), 4.916 (1H, t, $J = 10$ Hz) (NH_2); 3.326 (1H, t, $J = 10$ Hz), 2.606 (1H, d, $J = 10$ Hz), 2.294 (1H, q, $J = 10$ Hz), 1.992 (1H, d, $J = 10$ Hz), 1.864 (1H, d, $J = 10$ Hz), 1.690 (1H, d, $J = 10$ Hz), 1.16–1.46 (4H, m) (cyclohexane protons). ^{51}V NMR (DMSO-d_6): −551.3.

2.4.2. {*RR*(−)-1-amino-2-*N*-[(2′-oxido-κ*O*-3′-methoxyphenyl)methylene]aminocyclohexane-κ^2*N*}dioxovanadium(V) (*2r*)

Yield 88%. *Anal.* Calc. for $C_{14}H_{19}N_2O_4V$: C, 50.9; H, 5.8; N, 8.5. Found: C, 51.1; H, 5.8; N, 8.4%. IR (KBr, cm^{-1}): 3253, 3212 (ν_{N-H}); 1634 $\nu_{C=N} + \nu_{C=C}$; 927, 850 ($\nu_{V=O}$). UV–Vis spectrum in DMSO [λ_{max} (nm), ε (M^{-1} cm^{-1})]: 266 (12 800), 337 (3200). CD spectrum in DMSO [λ_{max} (nm), $\Delta\varepsilon$ (M^{-1} cm^{-1})]: 268 (−3.20), 298 (−2.84), 353 (−2.32). ^{1}H NMR (DMSO-d_6, ppm): 7.221 (1H, d, $^3J = 3$ Hz), 7.083 (1H, dd, $^3J = 8$ Hz, $^4J = 3$ Hz),

6.737 (1H, d, $^3J = 8$ Hz) (aromatic); 8.761 (1H, s) (azomethine); 5.441 (1H, d, $^2J = 9$ Hz), 4.893 (1H, t, $J = 10$ Hz) (NH_2); 3.748 (3H, s) (methoxy); 3.302 (1H, t, $J = 10$ Hz), 2.608 (1H, d, $J = 10$ Hz), 2.312 (1H, q, $J = 10$ Hz), 2.014 (1H, d, $J = 10$ Hz), 1.884 (1H, d, $J = 10$ Hz), 1.712 (1H, d, $J = 10$ Hz), 1.18–1.47 (4H, m) (cyclohexane protons). ^{51}V NMR (DMSO-d_6, ppm): −549.2.

2.4.3. {*RR*(−)-1-amino-2-N-[(2′-oxido-κO-5′-methoxyphenyl)methylene]aminocyclohexane-κ^2N} dioxovanadium(V) (**3r**)

Yield 93%. *Anal.* Calc. for $C_{14}H_{19}N_2O_4V$: C, 50.9; H, 5.8; N, 8.5. Found: C, 50.8; H, 5.8; N, 8.3%. IR (KBr, cm^{-1}): 3258, 3212 (ν_{N-H}); 1633, 1607 $\nu_{C=N} + \nu_{C=C}$; 920, 862 ($\nu_{V=O}$). UV–Vis spectrum in DMSO [λ_{max} (nm), ε ($M^{-1}\,cm^{-1}$)]: 272 (20 000), 399 (4000). CD spectrum in DMSO [λ_{max} (nm), $\Delta\varepsilon$ ($M^{-1}\,cm^{-1}$)]: 272 (−8.28), 365 (−1.77), 414 (0.42). ^{1}H NMR (DMSO-d_6, ppm): 7.227 (1H, d, $^3J = 2$ Hz), 7.085 (1H, dd, $^3J = 9$ Hz, $^4J = 2$ Hz), 6.729 (1H, d, $^3J = 9$ Hz) (aromatic); 8.765 (1H, s) (azomethine); 5.414 (1H, d, $^2J = 10$ Hz), 4.851 (1H, t, $J = 10$ Hz) (NH_2); 3.736 (3H, s) (methoxy); 3.273 (1H, t, $J = 10$ Hz), 2.402 (1H, d, $J = 10$ Hz), 2.276 (1H, q, $J = 10$ Hz), 2.015 (1H, d, $J = 10$ Hz), 1.882 (1H, d, $J = 10$ Hz), 1.713 (1H, d, $J = 10$ Hz), 1.18–1.42 (4H, m) (cyclohexane protons). ^{51}V NMR (DMSO-d_6, ppm): −549.9.

2.4.4. {*RR*(−)-1-amino-2-N-[(2′-oxido-κO-4′,6′-dimethoxyphenyl)methylene]aminocyclohexane-κ^2N} dioxovanadium(V) (**4r**)

Yield 91%. *Anal.* Calc. for $C_{15}H_{21}N_2O_5V$: C, 50.0; H, 5.9; N, 7.8. Found: C, 50.0; H, 6.0; N, 7.7%. IR (KBr, cm^{-1}): 3243, 3203 (ν_{N-H}); 1628, 1597 $\nu_{C=N} + \nu_{C=C}$; 916, 846 ($\nu_{V=O}$). UV–Vis spectrum in DMSO [λ_{max} (nm), ε ($M^{-1}\,cm^{-1}$)]: 317 (18 000). CD spectrum in DMSO [λ_{max} (nm), $\Delta\varepsilon$ ($M^{-1}\,cm^{-1}$)]: 320 (−9.09). ^{1}H NMR (DMSO-d_6, ppm): 5.973 (1H, d, $^4J = 2$ Hz), 5.938 (1H, t, $^4J = 2$ Hz) (aromatic); 8.858 (1H, s) (azomethine); 5.348 (1H, d, $^2J = 9$ Hz), 4.912 (1H, t, $J = 10$ Hz) (NH_2); 3.843 (3H, s), 3.773 (3H, s) (methoxy); 3.269 (1H, t, $J = 10$ Hz), 2.458 (1H, d, $J = 10$ Hz), 2.265 (1H, q, $J = 10$ Hz), 1.942 (1H, d, $J = 10$ Hz), 1.852 (1H, d, $J = 10$ Hz), 1.684 (1H, d, $J = 10$ Hz), 1.14–1.42 (4H, m) (cyclohexane protons). ^{51}V NMR (DMSO-d_6, ppm): −548.0.

2.4.5. {*RR*(−)-1-amino-2-N-[(2′-oxido-κO-5′-methylphenyl)methylene]aminocyclohexane-κ^2N} dioxovanadium(V) (**5r**)

Yield 73%. *Anal.* Calc. for $C_{14}H_{19}N_2O_3V$: C, 53.5; H, 6.1; N, 8.9. Found: C, 53.6; H, 6.2; N, 8.9%. IR (KBr, cm^{-1}): 3258, 3216 (ν_{N-H}); 1632, 1592 $\nu_{C=N} + \nu_{C=C}$; 926, 858 ($\nu_{V=O}$). UV–Vis spectrum in DMSO [λ_{max} (nm), ε ($M^{-1}\,cm^{-1}$)]: 272 (20 000), 379 (3700). CD spectrum in DMSO [λ_{max} (nm), $\Delta\varepsilon$ ($M^{-1}\,cm^{-1}$)]: 272 (−7.28), 345 (−1.91), 398 (0.53). ^{1}H NMR (DMSO-d_6, ppm): 7.420 (1H, s), 7.265 (1H, d, $^3J = 8$ Hz), 6.690 (1H, d, $^3J = 8$ Hz) (aromatic); 8.727 (1H, s) (azomethine); 5.475 (1H, d, $^2J = 10$ Hz), 4.913 (1H, t, $J = 10$ Hz) (NH_2); 2.249 (3H, s) (methyl); 3.307 (1H, t, $J = 10$ Hz), 2.596 (1H, d, $J = 10$ Hz), 2.286 (1H, q, $J = 10$ Hz), 1.987 (1H, d, $J = 10$ Hz), 1.860 (1H, d, $J = 10$ Hz), 1.700 (1H, d, $J = 10$ Hz), 1.22–1.42 (4H, m) (cyclohexane protons). ^{51}V NMR (DMSO-d_6, ppm): −550.2.

2.4.6. {*RR*(−)-1-amino-2-N-[(2′-oxido-κO-5′-bromophenyl)methylene]aminocyclohexane-κ^2N} dioxovanadium(V) (**6r**)

Yield 75%. *Anal.* Calc. for $C_{13}H_{16}BrN_2O_3V$: C, 41.2; H, 4.3; N, 7.4. Found: C, 41.0; H, 4.2; N, 7.3%. IR (KBr, cm^{-1}): 3263, 3216 (ν_{N-H}); 1632, 1590 $\nu_{C=N} + \nu_{C=C}$; 929, 852 ($\nu_{V=O}$). UV–Vis spectrum in DMSO [λ_{max} (nm), ε ($M^{-1}\,cm^{-1}$)]: 268 (20 000), 375 (3700). CD spectrum in DMSO [λ_{max} (nm), $\Delta\varepsilon$ ($M^{-1}\,cm^{-1}$)]: 268 (−6.45), 346 (−1.52), 396 (0.47). ^{1}H NMR (DMSO-d_6, ppm): 7.889 (1H, d, $^4J = 3$ Hz), 7.532 (1H, dd, $^3J = 9$ Hz, $^4J = 3$ Hz), 6.753 (1H, d, $^3J = 9$ Hz) (aromatic); 8.781 (1H, d, $^4J = 1.5$ Hz) (azomethine); 5.539 (1H, d, $^2J = 10$ Hz), 4.951 (1H, t, J = 11 Hz) (NH_2); 3.327 (1H, t, $J = 10$ Hz), 2.573 (1H, d, $J = 10$ Hz), 2.307 (1H, q, $J = 10$ Hz), 1.991 (1H, d, $J = 10$ Hz), 1.872 (1H, d, J = 9 Hz), 1.704 (1H, d, J = 9 Hz), 1.20–1.42 (4H, m) (cyclohexane protons). ^{51}V NMR (DMSO-d_6, ppm): −552.1.

2.4.7. {*RR*(−)-1-amino-2-N-[(2′-oxido-κO-5′-nitrophenyl)methylene]aminocyclohexane-κ^2N} dioxovanadium(V) (**7r**)

Yield 89%. *Anal.* Calc. for $C_{13}H_{16}N_3O_5V$: C, 45.2; H, 4.7; N, 12.2. Found: C, 45.5; H, 4.7; N, 12.1%. IR (KBr, cm^{-1}): 3296, 3230 (ν_{N-H}); 1648, 1602 $\nu_{C=N} + \nu_{C=C}$; 935, 836 ($\nu_{V=O}$). UV–Vis spectrum in DMSO [λ_{max} (nm), ε ($M^{-1}\,cm^{-1}$)]: 355 (20 100). CD spectrum in DMSO [λ_{max} (nm), $\Delta\varepsilon$ ($M^{-1}\,cm^{-1}$)]: 268 (−11.8), 303 (−4.07), 372 (1.27). ^{1}H NMR (DMSO-d_6, ppm): 8.768 (1H, d, $^4J = 3$ Hz), 8.239 (1H, dd, $^3J = 8$ Hz, $^4J = 3$ Hz), 6.899 (1H, d, $^3J = 8$ Hz) (aromatic); 8.968 (1H, s) (azomethine); 5.565 (1H, d, $^2J = 9$ Hz), 4.928 (1H, t, $J = 11$ Hz) (NH_2); 3.408 (1H, td, $J = 10$ Hz), 2.613 (1H, d, $J = 10$ Hz), 2.404 (1H, q, $J = 10$ Hz), 2.021 (1H, d, $J = 10$ Hz), 1.889 (1H, d, $J = 10$ Hz), 1.721 (1H, d, $J = 9$ Hz), 1.18–1.42 (4H, m) (cyclohexane protons). ^{51}V NMR (DMSO-d_6, ppm): −550.0.

2.4.8. {*RR*(−)-1-amino-2-N-[(2′-oxido-κO-1′-naphthyl)methylene]aminocyclohexane-κ^2N} dioxovanadium(V) (**8r**)

Yield 83%. *Anal.* Calc. for $C_{17}H_{19}N_2O_3V$: C, 58.3; H, 5.5; N, 8.0. Found: C, 58.0; H, 5.6; N, 7.8%. IR (KBr, cm^{-1}): 3280, 3209 (ν_{N-H}); 1625, 1593 $\nu_{C=N} + \nu_{C=C}$; 932, 842 ($\nu_{V=O}$). UV–Vis spectrum in DMSO [λ_{max} (nm), ε ($M^{-1}\,cm^{-1}$)]: 319 (11 000), 394 (6000). CD spectrum in DMSO [λ_{max} (nm), $\Delta\varepsilon$ ($M^{-1}\,cm^{-1}$)]: 284 (−4.59), 324 (−3.08), 361 (−1.21), 413 (0.33). ^{1}H NMR DMSO-d_6, ppm: 8.328 (1H, d, $^4J = 3$ Hz), 7.995 (1H, d, $^3J = 10$ Hz), 7.846 (1H, d, $^3J = 8$ Hz), 7.578 (1H, t, $^3J = 8$ Hz), 7.367 (1H, t, $^3J = 8$ Hz), 7.043 (1H, d, $^3J = 8$ Hz) (aromatic);

9.539 (1H, s) (azomethine); 5.461 (1H, d, $^2J = 8$ Hz), 5.038 (1H, t, $J = 11$ Hz) (NH_2). Assignments of the remaining protons are given in Table 4. ^{51}V NMR DMSO-d_6, ppm: −548.7.

2.4.9. {*RR*(−)-1-amino-2-N-[1′-(1″-oxido-κO-2″-naphthyl)ethylidene]aminocyclohexane-κ^2N} dioxovanadium(V) hemihydrate hemiethanol solvate (**9r**)

Yield 45%. *Anal.* Calc. for $C_{19}H_{25}N_2O_4V$: C, 57.6; H, 6.4; N, 7.1. Found: C, 57.4; H, 6.3; N, 7.1%. IR (KBr, cm^{-1}): 3451 (ν_{O-H}); 3282, 3225 (ν_{N-H}); 1616, 1587 $\nu_{C=N} + \nu_{C=C}$; 922, 845 ($\nu_{V=O}$). UV–Vis spectrum in DMSO [λ_{max} (nm), ε ($M^{-1}\,cm^{-1}$)]: 271 (13200), 326 (3600), 408 (8700). CD spectrum in DMSO [λ_{max} (nm), $\Delta\varepsilon$ ($M^{-1}\,cm^{-1}$)]: 288 (8.39), 319 (−3.02), 378 (5.21). ^{1}H NMR DMSO-d_6, ppm: 8.262 (1H, d, $^3J = 7$ Hz), 7.796 (1H, d, $^3J = 9$ Hz), 7.764 (1H, d, $^3J = 8$ Hz), 7.568 (1H, t, $^3J = 8$ Hz), 7.446 (1H, t, $J = 8$ Hz), 7.190 (1H, d, $^3J = 9$ Hz) (aromatic); 5.461 (1H, d, $^2J = 8$ Hz), 5.038 (1H, t, $J = 11$ Hz) (NH_2); 2.719 (3H, s) (methyl); 4.224 (1/2H, t), 3.455 (1H, m), 1.068 (11/2H, t) (ethanol). Assignments of the remaining protons are given in Table 4. ^{51}V NMR DMSO-d_6, ppm: −548.9.

2.4.10. {*R*(−)-2-amino-1-N-[(2′-oxido-κO-5′-nitrophenyl)methylene]aminopropane-κ^2N} dioxovanadium(V) (**10r**)

Yield 81%. *Anal.* Calc. for $C_{10}H_{12}N_3O_5V$: C, 39.4; H, 4.0; N, 13.8. Found: C, 39.5; H, 3.9; N, 13.6%. IR (KBr, cm^{-1}): 3221 (ν_{N-H}); 1639 $\nu_{C=N} + \nu_{C=C}$; 936, 834 ($\nu_{V=O}$). UV–Vis spectrum in DMSO [λ_{max} (nm), ε ($M^{-1}\,cm^{-1}$)]: 355 (19500). CD spectrum in DMSO [λ_{max} (nm), $\Delta\varepsilon$ ($M^{-1}\,cm^{-1}$)]: 273 (−2.83), 318 (−1.59), 363 (0.14). ^{1}H NMR DMSO-d_6, ppm: 8.603 (1H, d, $^4J = 3$ Hz), 8.241 (1H, dd, $^3J = 9$ Hz, $^4J = 3$ Hz), 6.910 (1H, d, $^3J = 9$ Hz) (aromatic); 9.036 (1H, s) (azomethine); 5.492 (1H, d, $^2J = 9$ Hz), 4.974 (1H, t, $J = 11$ Hz) (NH_2); 4.017 (1H, dd, $^3J = 12$ Hz, $^4J = 5$ Hz), 3.705 (1H, dd, $^3J = 10$ Hz, $^4J = 7$ Hz) (methylene); 3.124 (1H, br s) (methine); 1.207 (3H, d, $^3J = 7$ Hz) (methyl). ^{51}V NMR DMSO-d_6, ppm: −551.1.

2.4.11. {*SS*(+)-1-amino-2-N-[(2′-oxido-κO-phenyl)methylene]aminocyclohexane-κ^2N} dioxovanadium(V) (**1s**)

Yield 79%. *Anal.* Calc. for $C_{13}H_{17}N_2O_3V$: C, 52.0; H, 5.7; N, 9.3. Found: C, 51.9; H, 5.8; N, 9.2%. IR (KBr, cm^{-1}): 3262, 3214 (ν_{N-H}); 1631, 1600 $\nu_{C=N} + \nu_{C=C}$; 928, 864 ($\nu_{V=O}$). UV–Vis spectrum in DMSO [λ_{max} (nm), ε ($M^{-1}\,cm^{-1}$)]: 262 (20000), 367 (3900). CD spectrum in DMSO [λ_{max} (nm), $\Delta\varepsilon$ ($M^{-1}\,cm^{-1}$)]: 271 (7.12), 331 (2.67), 389 (−0.49).

2.4.12. {*SS*(+)-1-amino-2-N-[(2′-oxido-κO-3′-methoxyphenyl)methylene]aminocyclohexane-κ^2N} dioxovanadium(V) (**2s**)

Yield 75%. *Anal.* Calc. for $C_{14}H_{19}N_2O_4V$: C, 50.9; H, 5.8; N, 8.5. Found: C, 51.0; H, 5.9; N, 8.3%. IR (KBr, cm^{-1}): 3252, 3211 (ν_{N-H}); 1634 $\nu_{C=N} + \nu_{C=C}$; 928, 850 ($\nu_{V=O}$). UV–Vis spectrum in DMSO [λ_{max} (nm), ε ($M^{-1}\,cm^{-1}$)]: 267 (12400), 336 (3100). CD spectrum in DMSO [λ_{max} (nm), $\Delta\varepsilon$ ($M^{-1}\,cm^{-1}$)]: 266 (3.18), 298 (2.84), 352 (2.37).

2.4.13. {*SS*(+)-1-amino-2-N-[(2′-oxido-κO-5′-methoxyphenyl)methylene]aminocyclohexane-κ^2N} dioxovanadium(V) (**3s**)

Yield 85%. *Anal.* Calc. for $C_{14}H_{19}N_2O_4V$: C, 50.9; H, 5.8; N, 8.5. Found: C, 50.9; H, 6.0; N, 8.5%. IR (KBr, cm^{-1}): 3260, 3211 (ν_{N-H}); 1633, 1608 $\nu_{C=N} + \nu_{C=C}$; 920, 863 ($\nu_{V=O}$). UV–Vis spectrum in DMSO [λ_{max} (nm), ε ($M^{-1}\,cm^{-1}$)]: 272 (20000), 399 (4100). CD spectrum in DMSO [λ_{max} (nm), $\Delta\varepsilon$ ($M^{-1}\,cm^{-1}$)]: 278 (7.18), 364 (1.79), 415 (−0.38).

2.4.14. {*SS*(+)-1-amino-2-N-[(2′-oxido-κO-4′,6′-dimethoxyphenyl)methylene]aminocyclohexane-κ^2N} dioxovanadium(V) (**4s**)

Yield 74%. *Anal.* Calc. for $C_{15}H_{21}N_2O_5V$: C, 50.0; H, 5.9; N, 7.8. Found: C, 50.1; H, 6.1; N, 7.6%. IR (KBr, cm^{-1}): 3252, 3213 (ν_{N-H}); 1636, 1602 $\nu_{C=N} + \nu_{C=C}$; 924, 862 ($\nu_{V=O}$). UV–Vis spectrum in DMSO [λ_{max} (nm), ε ($M^{-1}\,cm^{-1}$)]: 317 (17900). CD spectrum in DMSO [λ_{max} (nm), $\Delta\varepsilon$ ($M^{-1}\,cm^{-1}$)]: 322 (8.72).

2.4.15. {*SS*(+)-1-amino-2-N-[(2′-oxido-κO-5′-methylphenyl)methylene]aminocyclohexane-κ^2N} dioxovanadium(V) (**5s**)

Yield 71%. *Anal.* Calc. for $C_{14}H_{19}N_2O_3V$: C, 53.5; H, 6.1; N, 8.9. Found: C, 53.5; H, 6.1; N, 8.8%. IR (KBr, cm^{-1}): 3256, 3216 (ν_{N-H}); 1633, 1591 $\nu_{C=N} + \nu_{C=C}$; 925, 859 ($\nu_{V=O}$). UV–Vis spectrum in DMSO [λ_{max} (nm), ε ($M^{-1}\,cm^{-1}$)]: 272 (20000), 379 (3800). CD spectrum in DMSO [λ_{max} (nm), $\Delta\varepsilon$ ($M^{-1}\,cm^{-1}$)]: 272 (7.89), 347 (2.54), 401 (−0.31).

2.4.16. {*SS*(+)-1-amino-2-N-[(2′-oxido-κO-5′-bromophenyl)methylene]aminocyclohexane-κ^2N} dioxovanadium(V) (**6s**)

Yield 73%. *Anal.* Calc. for $C_{13}H_{16}BrN_2O_3V$: C, 41.2; H, 4.3; N, 7.4. Found: C, 41.2; H, 4.2; N, 7.2%. IR (KBr, cm^{-1}): 3262, 3217 (ν_{N-H}); 1634, 1588 $\nu_{C=N} + \nu_{C=C}$; 928, 852 ($\nu_{V=O}$). UV–Vis spectrum in DMSO [λ_{max} (nm), ε ($M^{-1}\,cm^{-1}$)]: 268 (20000), 375 (3700). CD spectrum in DMSO [λ_{max} (nm), $\Delta\varepsilon$ ($M^{-1}\,cm^{-1}$)]: 271 (7.13), 345 (1.89), 395 (−0.31).

2.4.17. {*SS*(+)-1-amino-2-N-[(2′-oxido-κO-5′-nitrophenyl)methylene]aminocyclohexane-κ^2N} dioxovanadium(V) (**7s**)

Yield 87%. *Anal.* Calc. for $C_{13}H_{16}N_3O_5V$: C, 45.2; H, 4.7; N, 12.2. Found: C, 45.4; H, 4.7; N, 12.1%. IR (KBr, cm^{-1}): 3295, 3232 (ν_{N-H}); 1648, 1602 $\nu_{C=N} + \nu_{C=C}$; 935, 836 ($\nu_{V=O}$). UV–Vis spectrum in DMSO [λ_{max} (nm), ε ($M^{-1}\,cm^{-1}$)]: 354 (20100). CD spectrum in DMSO [λ_{max}

(nm), $\Delta\varepsilon$ ($M^{-1}\,cm^{-1}$)]: 265 (13.6), 301 (4.39), 367 (−1.36).

2.4.18. {SS(+)-1-amino-2-N-[(2′-oxido-κO-1′-naphthyl)methylene]aminocyclohexane-κ^2N} dioxovanadium(V) (**8s**)

Yield 79%. *Anal*. Calc. for $C_{17}H_{19}N_2O_3V$: C, 58.3; H, 5.5; N, 8.0. Found: C, 58.5; H, 5.7; N, 7.8%. IR (KBr, cm^{-1}): 3288, 3215 (ν_{N-H}); 1625, 1592 $\nu_{C=N} + \nu_{C=C}$; 932, 841 ($\nu_{V=O}$). UV–Vis spectrum in DMSO [λ_{max} (nm), ε ($M^{-1}\,cm^{-1}$)]: 320 (11 400), 395 (6400). CD spectrum in DMSO [λ_{max} (nm), $\Delta\varepsilon$ ($M^{-1}\,cm^{-1}$)]: 280 (5.89), 323 (3.28), 361 (1.63), 414 (−0.40).

3. Results and discussion

The complexes were not accessible by the preformed ligand strategy used by us earlier for the preparation of Ni(II) and Pd(II) complexes with monocondensed diamines [33,34], but may be obtained in a template reaction proceeding in the refluxed ethanol solution containing aromatic *o*-hydroxycarbonyl compound, enantiopure 1,2-diaminocyclohexane and triethyl vanadate in 1:1:1 ratio. All the complexes derived from hydroxyaldehydes precipitated from the reaction mixtures as yellow powders, but the **9r** complex derived from 1-hydroxy-2-acetonaphthone separated slowly yielding crystals containing solvent molecules. The template reaction proceeds as evidenced by the **9r** structure.

3.1. Crystal and molecular structure of *9r*

The asymmetric unit contains two symmetry independent complex molecules A and B, one molecule of water and one molecule of ethanol, as shown in Fig. 2. The atom numbering scheme is included. The molecules A and B are of similar structure since A can be superimposed by B with a rms value of 0.08 Å by the 61° rotation about the (pseudo)-axis [0 $\bar{1}$ 0], where bracketed numbers are direction cosines with orthogonal cell. Since B is similar in structure to A we restraint our analysis to the latter molecule. The coordination geometry about the vanadium (V1A) atom can be considered as distorted trigonal bipyramidal containing both oxo (O2A and O3A) ligands and the azomethine nitrogen (N1A) in the equatorial plane but the phenolic oxygen (O1A) and the primary amino nitrogen (N2A) in apical position. The extent of the distortion, quantified by the distance between trigonal bipyramid and square pyramid along the Berry pseudorotation coordinate [35–37], is 39.4%. The metal deviates from the equatorial trigonal plane by 0.11 Å towards O1. The five-membered ring containing V1A, N1A, C13A, C18A, N2A atoms adopts an envelope conformation on N2A in contrast to the carbon centered folding of five-membered chelate rings in the [*N*-(3-methyl-6-*tert*-butylsalicylidene)-*N*′-methylethylenediaminato]dioxovanadium(V) [38] and 2-(4-amino-4-methyl-2-aza-1-penten-1-yl-κ^2N)-3,5-dimethoxyphenolato-κ*O*-dioxovanadium(V) [12] complexes possessing a distorted trigonal bipyramidal arrangement around the vanadium. The much smaller angle of N1A–V1A–N2A [75.3(2)°] than other angles in the five-membered chelate ring (104.9–115.0°) seems to arise from the equatorial positions of both nitrogen atoms in the cyclohexane-1,2-diamine fragment which restrict the N1A···N2A distance so that the bite angle formed by V1A–N1A and V1A–N2A bonds has a limited range. The six-membered chelate ring formed by O1A, N1A, C1A, C1OA, C11A, V1A atoms assumes an envelope (sofa) conformation with vanadium (V1A) atom deviating by 0.880(5) Å from the least squares plane through the remaining atoms. The Cremer and Pople puckering parameters [39] of $Q = 0.607(8)$ Å, $\Theta = 8.4(4)°$ and $\sigma = 335(4)°$ for the cyclohexane ring compared with the map of cyclohexane conformations reported by Boeyens [40] indicate that the cyclohexane ring is almost in a chair conformation with a very small distortion towards half-chair and envelope forms. The hydrogen atoms linked to the secondary carbon atoms (C13 and C18) occupy axial positions. The distances 1.604(5) and 1.622(5) Å for V=O2A and V=O3A respectively are typical of non-hydrogen or weak hydrogen bonded V=O bond lengths [41,42]. The V1A–N1A, V1A–N2A distances are ca 0.05 Å longer than the averaged values of V–N(amine) bond lengths (2.090 Å), but the V1A–O1A distance agrees within 0.01 Å with the averaged V–O(phenolic oxygen) bond lengths (1.917 Å) reported by Orpen et al. [43]. Crystal structure of **9r** is stabilized by hydrogen bonds linking complex and solvent molecules in rings and chains as shown in Fig. 3. Parameters of hydrogen bonding geometry are given in Table 3. Short intramolecular contact between C12 and C14 (shown in Table 3) indicates steric strains in the ethylidene part of the molecule.

3.2. Spectroscopic properties of complexes

The IR spectra of solid complexes display two bands in the range of 3200–3300 cm^{-1} corresponding to the asymmetric ν_{as} and symmetric ν_{sym} N–H stretching modes of the complexed primary amino group. In addition the **9r** complex shows a broad absorption at ca. 3450 cm^{-1} derived from ν(O–H) of solvated water and ethanol molecules. The ν(C=N) observed below 1634 cm^{-1} is characteristic of N-bound complexes [44]. In the spectrum of **r** and **s** **1**–**7** complexes two intense bands are observed, one sharp in the 936–916 cm^{-1} region, and the other broadened in 864–834 cm^{-1} range which can be assigned to the ν_{as} and ν_s vibration of the *cis*-VO_2 group [22].

Section 2 lists electronic spectral data of complexes in DMSO. The low energy band $\varepsilon_{max} = (3000–6000)$ $dm^3\,mol^{-1}\,cm^{-1}$ between 354 and 405 nm may be assigned as a ligand-to-metal charge transfer (LMCT) transition originating from the p_π orbital on the phenolate oxygen to the empty d orbitals of the metal [42]. A more intense, $\varepsilon_{max} = (11\,000–20\,000)$ $dm^3\,mol^{-1}\,cm^{-1}$, band with λ_{max} between 262 and 272 nm is considered to arise from π to π*

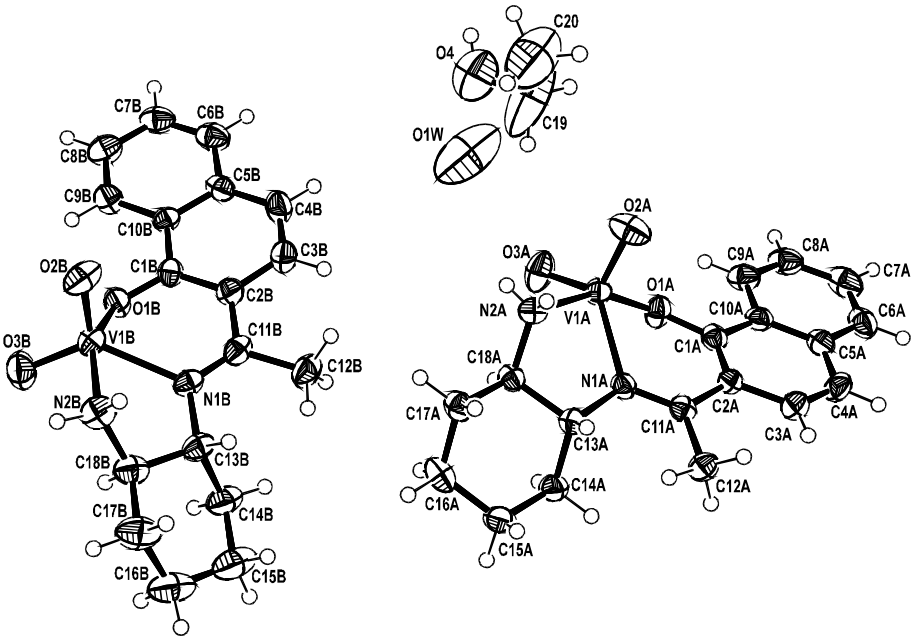


Fig. 2. An ORTEP drawing of **9r** complex molecule (A), its crystallographically independent form (B) together with molecules of water and ethanol, showing atom-labelling system. Displacement ellipsoids are drawn at the 30% probability level.

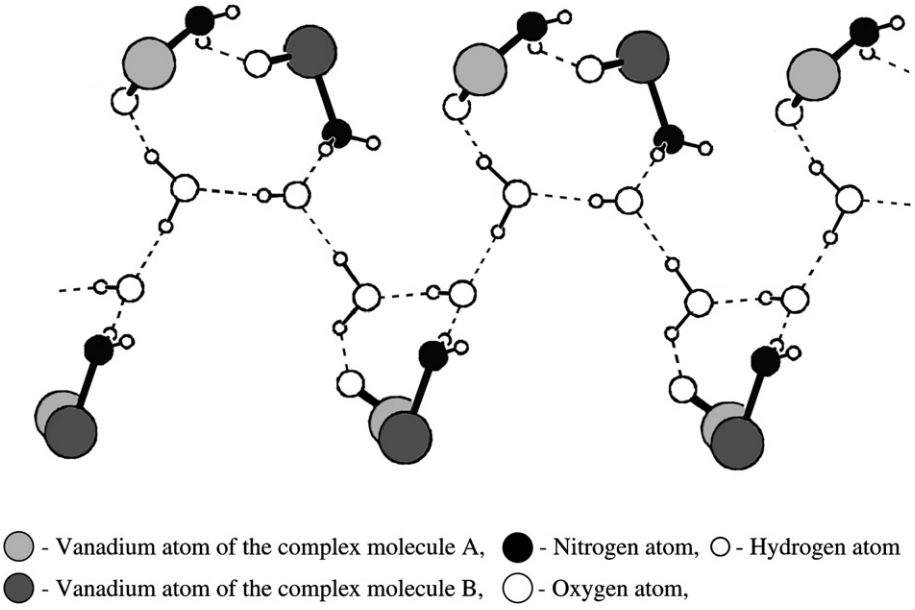


Fig. 3. A fragment of the crystal structure of **9r** showing the arrangement of complex and solvent molecules in rings and chains generated by hydrogen bonding interactions. For the sake of clarity atoms which are not involved in the structure build from hydrogen bonds were omitted. Hydrogen bonds are depicted as dashed lines.

transitions in the aromatic ring. The circular dichroism measurements revealed an additional absorption in the 290–350 nm range, which by comparison with the CD spectra of Cu(sal)$_2$(*RR*(−)chxn) [45], VO(sal)$_2$(*RR*(−)chxn) [46] and Zn(sal)$_2$pn [47] chelates, may be assigned to π–π^* transitions encompassing the azomethine chromophore. Fig. 4 shows CD spectra of **7r**, **7s** and **10r** complexes, the latter included for comparison. The spectra of **7r** and **10r** do not bear a mirror image relationship noticed for the CD spectra of V(V), V(IV), Cu(II) and Ni(II) complexes comprising double condensation products of chiral 1,2-diaminocyclohexane when they are compared with the spectra of their counterparts derived from 1,2-diaminopropane in the same absolute configuration [8,45,46,48]. Since the sign of the Cotton effect of a given transition reflects the conformation of the central chelate ring [45], they revealed identical signs of Cotton effects in the spectra of **7r** and **10r** suggest the same predominant conformational helicity of

Table 3
Hydrogen bonding geometry and a close contact (Å, °) for **9r**. The letter d is the interatomic distance

DH···A	d(D–H)	d(H···A)	d(D···A)	<(D–H···A)
N2A–H2A2···O3B^{i}	0.65(7)	2.50(7)	3.091(7)	152(9)
N2B–H2B1···O4^{ii}	0.76(8)	2.26(8)	3.02(1)	172(9)
O4–H4···O1W			2.89(2)	
O1W–H1WA···O4^{iii}			3.01(2)	
O1W–H1WB···O3A			2.98(1)	
C12A–H12C···O2^{iii}			3.227(7)	
C12B–H12F···O2B^{i}			3.219(7)	
C14A–H14A···Cg^{iii}			2.556(9)	

Atoms which are separated considerably less than the sum of van their der Waals radii.

d(C12A···C14A)	2.953(8)

Symmetry code: (i) $-x+1, y+1/2, -z+1$; (ii) $-x+1, y-1/2, -z+1$; (iii) $-x, y-1/2, -z+1$.
Cg refers to the gravity center of the C1–C2–C3–C4–C5–C10 ring.

five-membered chelate rings of these compounds in DMSO solution.

^{1}H, ^{13}C and ^{51}V NMR spectra of complexes were obtained in DMSO-d_6. Since the ^{1}H NMR spectra of complexes derived from *RR*(−) and *SS*(+)-1,2-diaminocyclohexane are superimposable, Section 2 list NMR data only for the former complexes. ^{1}H NMR signals were assigned on the basis of intensity, spin–spin coupling pattern, chemical shifts, deuteration experiment, ^{1}H, ^{1}H COSY, and double resonance techniques. In addition the HSQC experiment was included to achieve a clear differentiation of the geminal AB system of individual CH_2 groups. Chemical shifts and coupling constants of aromatic protons do not differ distinctly from those which were reported recently [26] for dioxovanadium complexes with monocondensation products derived from the same aromatic hydroxycarbonyl compounds but from different diamines. The amine protons, which were identified by deuteration experiment, are magnetically inequivalent. The resonance in the 5.348–5.565 ppm range is a doublet and the resonance in the 4.851–5.038 ppm range is a triplet, the multiplicity of the latter signal is recognized as due to geminal and vicinal (Ha18) coupling. Signals of the protons on carbon atoms as the N atoms (Ha13, Ha18) are shifted downfield on account of the electron withdrawing effect of N-atoms and can be readily recognized. It is more difficult to assign the resonances of (**1**–**7**)**r** complexes in the 1.5–1.6 ppm range because of signal overcrowding. On the other hand the signals of **8r** and **9r** complexes appear as separate two one-proton quartets and one two-proton multiplet in the above range, and could be easily analysed on the basis of homonuclear (COSY, double resonances) and heteronuclear (HSQC) shift correlations. The most deshielded azomethine proton, H11, and the Ha13 proton of the cyclohexane fragment in **8r** are involved in a long range coupling apparently analogous to the allylic like coupling observed in systems where one of the intervening carbon atoms has been replaced by nitrogen [49]. Positioning of Ha13 was the starting point for the assignment of all remaining protons of the cyclohexane moiety. Table 4 lists assignments of ^{1}H and ^{13}C resonances of the cyclohexane fragments of the **8r** and **9r** complexes read from the gHSQC plots and confirmed by the 1D spectra. It is seen (Table 4) that axial protons of CH_2 groups (1.2–1.5 ppm) are more shielded than their equatorial coupling partners on the same C atom as a result of anisotropic effects; they show pseudoquartets because of the geminal and diaxial coupling It can also be seen that the methyl group in **9r** results in a shift of C13A resonance to more shielded but of Ha13 to less shielded positions relative to the corresponding resonances in **8r**. These spectroscopic changes may be a result of strong intramolecular steric interactions reflected by short contact shown in Table 3. Steric crowding of proton bearing carbon atoms C13A and C12A being in γ disposition results in their shielding as expected from the γ effect observed in the ^{13}C NMR spectroscopy [50]. Steric perturbation of C13A–Ha13 bond results in the electrons moving away from hydrogen atom towards the carbon atom thus resulting in C13A being shielded and Ha13 deshielded. The deshielding of the He14 proton in **8r**, respectively to that in **9r** might be substantially attributed to the van der Waals effect that arises by strong H11, He14 steric interaction presumed on the basis of a short C12A···C14A contact (Table 3) in **9r** and on the position of H11 in **8r** which like C12 in **9r** is joined to the methine carbon atom, C11, of the ═C11═N2 ═C13═C14═He14 structural fragment. According to the ring current model and the additivity of contributions of individual aromatic rings to the chemical shift [51] the decrease in shielding of the azomethine proton by going from (**1**–**7**)**r** ($\delta = 8.81 \pm 0.07$) to **8r** ($\delta = 9.539$ ppm) equal on average to $\Delta\sigma = -0.73$ ppm indicates that in **8r** that proton, H11, is located in plane of, close and exterior to two aromatic rings and that the ring current effect originating in the C5–C10 ring of naphthalene moiety contributes significantly to the decrease of its shielding. The contribution of the C5–C10 ring to the shielding of H11 in **8r**, $\Delta\sigma'$, equal to −0.508 ppm was calculated with the help of equation $\Delta\sigma'$ [ppm] $= -0.0276R^{-3}$ [51] and with $R = 0.379$ nm where R in this formula stands for the

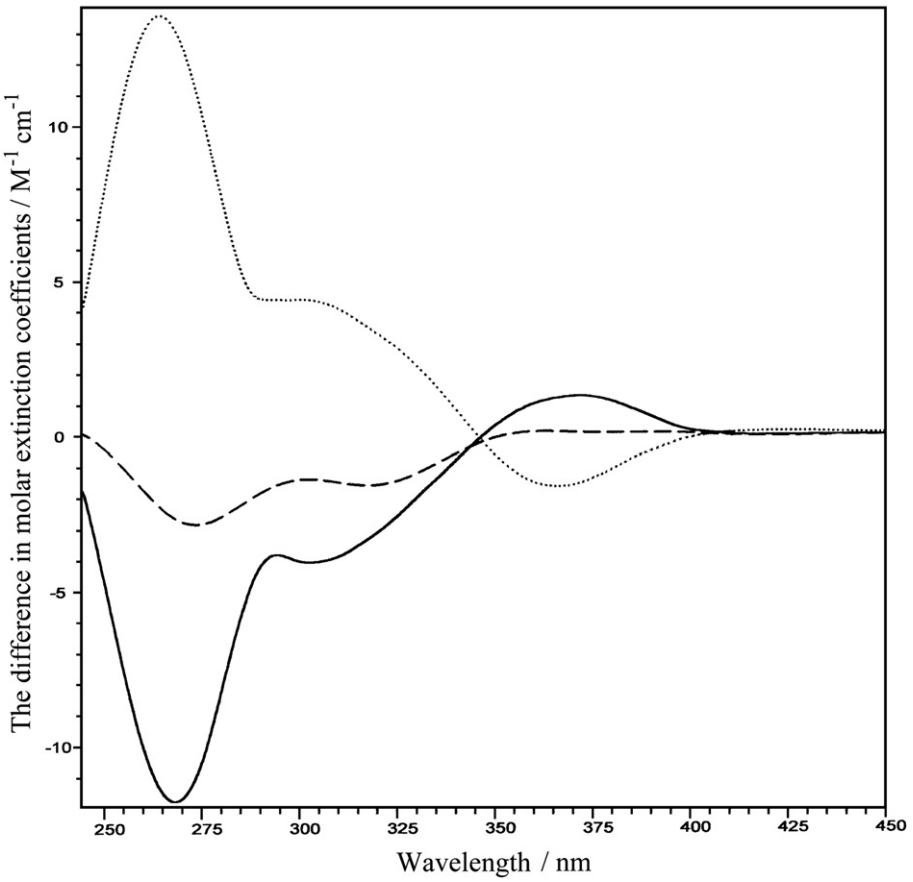


Fig. 4. CD spectra of **7r** (—), **7s** (···) and **10r** (---) complexes, containing *RR*(−)-1,2-diaminocyclohexane, *SS*(+)-1,2-diaminocyclohexane and *R*(−)-1,2-diaminopropane singly condensed with 5-nitrosalicylaldehyde respectively, in DMSO solution.

Table 4
^{13}C and ^{1}H chemical shifts for the substituted cyclohexane rings in **8r** and **9r**

Atoms	Chemical shifts and gHSQC			
	8r		**9r**	
	δ_H (ppm)	δ_C (ppm)	δ_H (ppm)	δ_C (ppm)
CH				
13	3.560 td	69.42	3.769 td	66.02
18	2.431 q	57.80	2.992 q	57.61
CH_2				
14	ax 1.486 q	30.42	ax 1.274 q	31.21
	eq 2.786 d		eq 2.173 d	
15	ax|^{i} 1.31 m		ax|^{i} 1.38 m	23.88
16	ax|		ax|	
15	eq 1.914 d	24.80	eq|^{i} 1.74 d	
16	eq 1.750 d	24.62	eq|	
17	ax 1.412 q	33.21	ax 1.485 q	31.91
	eq 2.026 d			31.98

s, singlet; d, doublet; t, triplet; q, quartet; m, multiplet; td, triplet of doublets; i, superimposed.

calculated separation of H11 to the center of the C5–C10 aromatic ring. A considerably high deshielding of Ha18 proton in **9r** may be due to its specific solvation by water and/or ethanol molecules present in the solution of hemihydrated and hemiethanol solvated compound. All the complexes exhibit a single ^{51}V resonance in the −548.0 to −552.1 ppm range, which is close to the reported (−553) to (−556) ppm [32] and (−547.8) to (−552.0) ppm [26] ^{51}V chemical shift ranges for diovanadium(V) complexes comprising single condensation products of aromatic hydroxyaldehydes with 1,2-diaminopropane and 2-methyl-1,2-diaminopropane respectively.

3.3. Catalytic oxidation of methyl phenyl sulfide (thioanisole)

Complexes **2r**, **3r** which incorporate singly condensed products of *RR*(−)-1,2-diaminocyclohexane with 3- or 5-methoxysalicylaldehyde as well as their analogues derived from *SS*(+)-1,2-diaminocyclohexane **2s** and **3s** act as catalyst to the oxidation of thioanisole by cumene hydroxyperoxide. Changes in sulfide and sulfoxide concentrations indicated that oxidations carried out in conditions of a large excess of cumene hydroperoxide at 20° and also at 50° proceed as reactions of first order. Yields of the conversion of thioanisole to the corresponding sulfoxide after 24 h in 20° and after 4 h at 50° exceed 96%. Complexes **2r**, **2s**, **3r** and **3s** exhibit also an asymmetric induction. The *S*-configurated sulfoxide was obtained in the reaction at 20° with 21% enantiomeric excess (ee) when **2r** or **3r** were used, and *R* was obtained with 19% and 23% ee using **2s**

and **3s** respectively. The influence of the OCH_3 substituent in 3 or 5 position of the aryl group (but not in positions 2 and 4) on the catalytic activity and asymmetric induction indicated the importance of electronic factors on enantioselective catalysis in sulfide oxidation. Enantiomeric excesses of sulfoxidation products are higher than those obtained in the reaction catalysed by VO(V) complexes incorporating double condensation product of *trans-RR*-1,2-diaminocyclohexane with 3-methoxysalicylaldehyde and chloride (11% ee) or perchlorate (0% ee) as counterions [23].

Acknowledgements

The research was supported by the University Grants: BW/8000-5-0277-5, BW/8000-5-0308-6, DS/8210-4-0086-6 and DS/8210-4-0086-7.

Appendix A. Supplementary material

CCDC 625078 contains the supplementary crystallographic data for this paper. These data can be obtained free of charge via http://www.ccdc.cam.ac.uk/conts/retrieving.html, or from the Cambridge Crystallographic Data Centre, 12 Union Road, Cambridge CB2 1EZ, UK; fax: (+44) 1223-336-033; or e-mail: deposit@ccdc.cam.ac.uk. Supplementary data associated with this article can be found, in the online version, at doi:10.1016/j.poly.2006.12.032.

References

[1] E.N. Jacobsen, in: I. Ojima (Ed.), Catalytic Asymmetric Synthesis, VCH, Weinheim, 1993, p. 159.
[2] T. Katsuki, Coord. Chem. Rev. 140 (1995) 189.
[3] E.N. Jacobsen, in: E.W. Abel, F.G.A. Stone, E. Willinson (Eds.), Comprehesive Organometallic Chemistry II, vol. 12, Pergamon, New York, 1995, p. 1097.
[4] G. Hoshina, M. Tsuchimoto, S. Ohba, K. Nakajima, Inorg. Chem. 37 (1998) 142.
[5] L. Canali, D.C. Sherington, Chem. Soc. Rev. 28 (1999) 85.
[6] J.C. Pessoa, I. Cavaco, I. Correia, M.T. Duarte, R.D. Gillard, R.T. Henriques, F.I. Higes, C. Madeira, I. Tomaz, Inorg. Chim. Acta 293 (1999) 1.
[7] A. Gama, L.Z. Flores-Lopez, G. Aguirre, M. Parra-Hake, R. Somanathan, P.J. Walsch, Tetrahedron Asymmetry 13 (2002) 149.
[8] M. Kojima, H. Taguchi, M. Tsuchimoto, K. Nakajima, Coord. Chem. Rev. 237 (2003) 183.
[9] K.I. Smith, L.L. Borer, M.M. Olmstead, Inorg. Chem. 42 (2003) 7410.
[10] B.S. Lane, K. Burgess, Chem. Rev. 103 (2003) 2457.
[11] D. Rehder, Coord. Chem. Rev. 237 (2003) 57.
[12] A.G.J. Ligtenbarg, R. Hage, B.L. Ferringa, Coord. Chem. Rev. 237 (2003) 89.
[13] H.B. Zhu, Z.Y. Doi, W. Huang, K. Cui, S.H. Gou, C.J. Zhu, Polyhedron 23 (2004) 1131.
[14] R. Ando, H. Inden, M. Sugino, H. Ono, D. Sakaeda, T. Yagyu, M. Maeda, Inorg. Chim. Acta 357 (2004) 1337.
[15] Y.C. Jeong, S. Choi, Y.D. Hwang, K.H. Ahn, Tetrahedron Lett. 45 (2004) 9249.
[16] N.S. Venkataramanan, G. Kuppuraj, S. Rajagopal, Coord. Chem. Rev. 249 (2005) 1249.
[17] L. Dyers Jr., S.Y. Que, D. Van Derver, X.R. Bu, Inorg. Chim. Acta 359 (2006) 197.
[18] M. De Rosa, M. Lamberti, C. Pellechia, A. Scettri, R. Villano, A. Soriente, Tetrahedron Lett. 47 (2006) 7233.
[19] T. Katsuki, J. Mol. Catal. A 113 (1996) 87.
[20] C. Bousquet, D.G. Gilheany, Tetrahedron Lett. 36 (1995) 7739.
[21] J. Fernandez, J.R. Pedro, R. Salud, Tetrahedron 52 (1996) 12031.
[22] K. Nakajima, M. Kojima, J. Fujita, Chem. Lett. (1986) 1483.
[23] K. Nakajima, K. Kojima, M. Kojima, J. Fujita, Bull. Chem. Soc. Jpn. 63 (1990) 2620.
[24] C. Bolm, F. Bienewald, Angew. Chem., Int. Ed. Engl. 34 (1995) 2640.
[25] M.C. Carreno, Chem. Rev. 95 (1995) 1717.
[26] E. Kwiatkowski, G. Romanowski, W. Nowicki, M. Kwiatkowski, K. Suwińska, Polyhedron 22 (2003) 1009.
[27] L. Canali, E. Covan, H. Deleuze, C.L. Gibson, D.C. Sherington, J. Chem. Soc., Perkin Trans. 1 (2000) 2055.
[28] G.M. Sheldrick, SHELXS-97, Program for Crystal Structure Solution, University of Göttingen, Germany.
[29] G.M. Sheldrick, SHELXL-97, Program for Structure Refinement, University of Göttingen, Germany.
[30] A.L. Spek, J. Appl. Crystallogr. 36 (2003) 7.
[31] M.E. Cucciolito, R. Del Litto, G. Roviello, F. Ruffo, J. Mol. Catal. A 36 (2005) 176.
[32] C.A. Root, J.D. Hoeschele, C.R. Cornman, J.W. Kampf, V.L. Pecoraro, Inorg. Chem. 32 (1993) 3855.
[33] E. Kwiatkowski, M. Klein, G. Romanowski, Inorg. Chim. Acta 293 (1999) 115.
[34] E. Kwiatkowski, G. Romanowski, K. Suwińska, Polyhedron 21 (2002) 2071.
[35] R.S. Berry, J. Chem. Phys. 32 (1960) 933.
[36] E.L. Muetterties, L.J. Guggenberger, J. Am. Chem. Soc. 96 (1974) 1748.
[37] R.R. Holmes, Prog. Inorg. Chem. 32 (1984) 119.
[38] L.M. Mokry, C.J. Carrano, Inorg. Chem. 32 (1993) 6119.
[39] D. Cremer, J.A. Pople, J. Am. Chem. Soc. 97 (1975) 1354.
[40] J.C.A. Boeyens, J. Cryst. Mol. Struct. 8 (1978) 317.
[41] C.J. Carrano, C.M. Nunn, R. Quan, J.A. Bonadies, V.L. Pecoraro, Inorg. Chem. 29 (1990) 944.
[42] G. Asgedom, A. Sreedhara, J. Kivikoski, E. Kolehmainen, C.P. Rao, J. Chem. Soc., Dalton Trans. (1996) 93.
[43] G. Orpen, L. Brammer, F.H. Allen, O. Kennard, D.G. Watson, R. Taylor, J. Chem. Soc. (1989) S1.
[44] G. Asgedom, A. Sreedhara, J. Kivikoski, R. Valkonen, C.P. Rao, J. Chem. Soc., Dalton Trans. 2459 (1995).
[45] R.S. Downing, F.L. Urbach, J. Am. Chem. Soc. 91 (1969) 5977.
[46] R.L. Farmer, F.L. Urbach, Inorg. Chem. 9 (1970) 2652.
[47] B. Bosnich, J. Am. Chem. Soc. 90 (1968) 627.
[48] R.S. Downing, F.L. Urbach, J. Am. Chem. Soc. 90 (1968) 5344.
[49] L.M. Jackman, S. Sternhell, Applications of Nuclear Magnetic Resonance Spectroscopy in Organic Chemistry, 2nd ed., Pergamon Press, Oxford, 1969, p. 386.
[50] H. Günther, 2nd ed., NMR Spectroscopy. Basic Principles, Concepts and Application in Chemistry, Wiley, New York, 1995, p. 503.
[51] H. Günther, 2nd ed., NMR Spectroscopy. Basic Principles, Concepts and Application in Chemistry, Wiley, New York, 1995, p. 87.

ligands containing variable neutral middle chain, characterization of these complexes by $^{31}P\{^{1}H\}$ NMR and by IR spectroscopy, and mainly the molecular structures of these compounds.

2. Results and discussion

The complexes **1** to **5** were prepared by the reaction of 4-methoxyphenyltellurium trichloride with the respective ligand in dichloromethane. The formation of product was indicated by the change of color from pale yellow to darker shades or even orange. The crystalline products were then obtained by the diffusion of hexane into concentrated mixtures. Most compounds were reasonably stable with the exception of **4**, which rapidly decomposed on air. Therefore, the characterization of the latter is mainly limited to the X-ray diffraction experiment on its single crystals. The complexes are characterized by singlets in their ^{31}P NMR spectra as expected from identically coordinated P═S ligand endings. In IR spectra, the P═S stretching frequencies are lowered by ca. 40 cm^{-1} in comparison to the uncoordinated ligands.

All binuclear compounds are centrosymmetric, thus the asymmetric part of the unit cell contains only one half of the complex. The exception is the compound with $dpphS_2$ (**2**), having two crystallographically independent halves of the complex in the unit cell. The tellurium atoms in all present compounds have pseudo-octahedral coordination with the aryl and the lone electron pair in axial positions relative to the $TeCl_3S$ equatorial plane. The attempts to fit tellurium, sulfur and chlorines into the best common plane provide the r.m.s. deviations varying from 0.038 to 0.100 Å. When least squares planes are calculated through sulfur and three chlorine atoms, the Te atoms all deviate outwards the aryl group, within 0.047(1) and 0.112(1) Å. Because of the strong disorder affecting the coordination polyhedra in **2**, the values for them were excluded from the above comparison.

As pointed out in Section 1, there are two types of five-coordinate complexes known, resulting from the interaction of 4-methoxyphenyltellurium trichloride with diphosphine disulfides. With negatively charged ligands of the $[R_2P(S)\text{-}N\text{-}P(S)R_2]^-$ general formula, one of the chloride anions was displaced from the coordination sphere of the tellurium, and chelates of the $4\text{-}MeOC_6H_4TeCl_2\{R_2P(S)\text{-}N\text{-}P(S)R_2\}$ type were formed [5]. Another class of complexes are binuclear compounds with neutral diphosphine disulfides, like those described here [6,7]. No six-coordinate complexes with $4\text{-}MeOC_6H_4TeCl_3$ are known, while the octahedral complex resulting from $TeCl_4$ was prepared and crystallographically characterized [8]. We were interested whether the tendency of 4-methoxyphenyltellurium trichloride to form pseudo-octahedral complexes is given by the presence of the aryl, or there is some restriction arising from the structure of the bidentate ligand which is not capable of closing the chelate ring using its another donor. We have therefore performed the reaction between $4\text{-}MeOC_6H_4TeCl_3$ and the simple monodentate ligand Ph_3PS, triphenylphosphine sulfide, in 1:1 and 1:2 molar ratios. Although the formation of $[(4\text{-}MeOC_6H_4\text{-}TeCl_3)Ph_3P(S)]$ (**5**) was predictable in a 1:1 ratio, no other complexes were isolated even in the presence of excess ligand. It is therefore legitimate to infer that the formation of five-coordinate complexes **1** to **5** is entirely the consequence of nature of the parent tellurium compound.

In the crystal structure of **1**, we find intermolecular Te···Cl contacts, almost collinear with the Te–C bonds. Comparing their length of 3.614(2) Å to the sum of the respective van der Waals radii (3.81 Å) [9], we may consider them very weak. As a result of these secondary bonding interactions, the molecules are knit together into chains, extending in the crystallographic *a* direction. The secondary bonding within tellurium complexes is rather common, as illustrated by reviews in this area [4,10]. In our report, however, **1** is the only compound with intermolecular Te···Cl contacts, other complexes do not show secondary bonding in crystals. The presence of secondary bonds is closely related to the stereochemical role of the Te(IV) lone pair. In the absence of additional intermolecular contacts in **2** to **5** the stereochemistry of the coordination polyhedron can be understood using the VSEPR model, with lone pair of electrons being stereochemically active and pointing opposite to the Te–C bond. In the distorted octahedral arrangement involving the weak secondary Te···Cl bond in **1**, the lone pair should not lie in the direction of that bond in accordance with the rules proposed by Alcock [11]. Either the lone pair is somewhat deflected from the direction of the secondary Te···Cl bond as previously suggested by Husebye and Maartmann-Moe [12], or simply the Alcock's rules are not always followed [11].

The selected bond lengths and angles for binuclear complexes **1** to **4** and complex with triphenylphosphine sulfide **5** are listed in Table 2 which also includes two previously reported binuclear compounds with diphosphine disulfides for comparison. The P═S bond lengths agree well with the values for other coordinated phosphine sulfides found in the Cambridge Structural Database (CSD) [13]. In all listed compounds there are two distinct sets of chloride ligands. The first includes Cl atoms positioned *trans* to the sulfur donors. As apparent from the table, their distances from tellurium centres are shorter than for Cl atoms *trans*-positioned to each other. This is a reflection of weak donating properties of sulfur donors, and hence ability of opposite chlorides to get closer to tellurium. Accordingly the bonding distances Te–S are relatively long. Using CSD we have selected partly the homoleptic coordination compounds with Te–S bonds, partly the heteroleptic complexes in which the opposite coordination sites are occupied by identical S-donor ligands. Moreover, the complexes in which the coordination sphere might be distorted by geometrical reasons were excluded. Therefore, the complexes with either monodentate or sufficiently large bidentate ligands were present in the final hit list. The analysis of obtained parameters showed that the maximum number of Te–S

Table 1
Crystal data and structure refinement parameters

Compound	1	2	3	4	5
Empirical formula	$C_{42}H_{42}Cl_6O_2P_2S_2Te_2$	$C_{45}H_{48}Cl_8O_2P_2S_2Te_2$	$C_{51}H_{44}Cl_8O_2P_2S_2Te_2$	$C_{44}H_{40}Cl_6N_2O_2P_2S_2Te_2$	$C_{25}H_{22}Cl_3OPSTe$
Formula weight	1172.72	1285.69	1353.72	1222.74	635.41
Crystal system	triclinic	triclinic	triclinic	monoclinic	monoclinic
Space group	$P\bar{1}$	$P\bar{1}$	$P\bar{1}$	$P2_1/n$	$P2_1/n$
a (Å)	9.405(1)	13.270(3)	9.205(1)	8.200(1)	10.7542(1)
b (Å)	11.356(1)	13.811(3)	10.922(2)	13.763(2)	9.2637(1)
c (Å)	12.806(1)	16.535(3)	14.217(2)	21.298(2)	26.350(1)
α (°)	74.46(1)	111.78(3)	80.42(1)	90	90
β (°)	74.91(1)	92.80(3)	82.58(1)	100.37(1)	96.90(1)
γ (°)	65.88(1)	102.24(3)	88.57(1)	90	90
Volume (Å^3)	1184.9(2)	2722.8(10)	1397.6(4)	2364.4(5)	2606.1(1)
Z	1	2	1	2	4
ρ (Mg/m^3)	1.644	1.568	1.608	1.717	1.619
μ (mm^{-1})	1.759	1.634	1.596	1.768	1.607
Reflections collected/unique	13135/4137	26794/9581	11791/4895	17818/4167	30089/4572
Data/parameters	4137/253	9581/702	4895/307	4167/271	4572/289
Final R indices	0.0576/0.1483	0.0417/0.1001	0.0426/0.0932	0.0301/0.0569	0.0294/0.0754
R indices (all data)	0.0755/0.1567	0.0699/0.1104	0.0717/0.0970	0.0603/0.0608	0.0401/0.0783
$\Delta\rho_{max}/\Delta\rho_{min}$ (e Å^{-3})	2.104/−1.861	0.968/−0.802	0.866/−1.345	0.714/−0.385	0.793/−0.397

Table 2
Selected bond lengths (Å) and angles (°) for prepared compounds and the literature values for [(4-$MeOC_6H_4TeCl_3$)$_2${μ-$Ph_2P(S)(CH_2)_2P(S)Ph_2$}] (**6**) [6] and [(4-$MeOC_6H_4TeCl_3$)$_2${μ-$^iPr_2P(S)(C_5H_5)Fe(C_5H_5)P(S)^iPr_2$}] (**7**) [7]

Compound	1	2	3	4	5	6	7
Te(1)–S(1)	2.772(2)	2.787	2.785(2)	2.753(1)	2.752(1)	2.775(1)	2.756(2)
						2.820(5)	2.691(1)
Te(1)–Cl(1)	2.461(2)	2.474	2.435(2)	2.455(1)	2.434(1)	2.440(1)	2.422(2)
						2.425(1)	2.418(1)
Te(1)–Cl(2)	2.509(2)	2.526	2.515(2)	2.529(1)	2.512(1)	2.534(1)	2.500(1)
						2.492(1)	2.546(2)
Te(1)–Cl(3)	2.544(2)	2.554	2.528(2)	2.499(1)	2.510(1)	2.474(1)	2.486(1)
						2.531(1)	2.452(2)
Te(1)–C(1D)	2.171(6)	2.152	2.123(5)	2.124(3)	2.124(3)	2.126(2)	2.109(4)
						2.135(2)	2.112(4)
P(1)–S(1)	2.012(2)	2.058	1.999(2)	2.008(1)	2.008(1)	1.998(1)	2.006(2)
						2.003(1)	1.999(2)
Te(1)–S(1)–P(1)	110.27(9)	101.1	103.16(7)	105.29(5)	102.78(4)	102.96(3)	105.69(6)
						108.29(2)	111.69(6)
Cl(1)–Te(1)–S(1)	167.05(6)	170.3	171.49(5)	174.19(3)	170.31(3)	171.95(2)	173.57(4)
						168.80(2)	169.14(4)
Cl(2)–Te(1)–Cl(3)	178.09(6)	177.8	178.67(5)	179.16(4)	178.99(3)	177.71(2)	177.72(4)
						173.25(2)	177.00(5)

Cl(1) is *trans* to S, Cl(2) is *trans* to Cl(3). In compounds **1**, **3** and **4**, the two halves of the binuclear complex are related by symmetry, thus only one value is given. For **6** and **7** values for both crystallographically independent molecular fragments are listed. The crystal structure of **2** was subject to a considerable disorder and only the average parameters from all corresponding disordered parts were calculated.

bond distances lies at ca. 2.7 Å. When compared to the values in Table 2, the sulfur atoms in our complexes are rather strongly expelled by the *trans* influence of opposite Cl atoms.

To conclude, we have prepared four complexes of 4-$MeOC_6H_4TeCl_3$ with ligands of diphosphine disulfide type. Consistently with previous data, we have observed that the coordination sphere of tellurium in 4-methoxyphenyltellurium trichloride is not capable of extending the coordination number above 5 (neglecting secondary bonding) and forming chelates with these ligands similarly to $TeCl_4$. The bidentate ligands are then coordinated toward tellurium using only one sulfur atom, and form binuclear addition complexes regardless of the length and flexibility of their central moieties.

3. Experimental

3.1. General and instrumental

The $^{31}P\{^1H\}$ NMR were recorded in dichloromethane on a Bruker Avance DRX 300 instrument using 85% H_3PO_4 as external standard. IR spectra (KBr pellets, 4000–400 cm^{-1}) were recorded using an EQUINOX 55/S/

NIR FTIR spectrometer. Microanalyses were performed on a Thermo Finnigan CHN Analyzer Flash EA 1112, and melting points were measured on a Boëtius melting-point apparatus. $Ph_2PNH(C_6H_4)NHPPh_2$ was prepared similarly to $[Ph_2PN(Me)]_2CO$ [14], using Ph_2PCl and *p*-diaminobenzene as starting materials and Et_3N as a base to remove HCl. $Ph_2P(C_6H_4)_2PPh_2$ was synthesized according to the literature [15], using Ph_2PCl and dilithiated biphenyl salt. $Ph_3P(S)$ and $Ph_2P(S)(CH_2)_nP(S)Ph_2$ ($n = 2$, 4) were prepared by heating commercially available Ph_3P and $Ph_2P(CH_2)_nPPh_2$ with sulfur in toluene. $Ph_2P(S)(C_6H_4)_2P(S)Ph_2$ and $Ph_2P(S)NH(C_6H_4)NHP(S)Ph_2$ were prepared from $Ph_2PNH(C_6H_4)NHPPh_2$ and $Ph_2P(C_6H_4)_2PPh_2$ using the same method. $4\text{-}MeOC_6H_4TeCl_3$ was synthesized according to the literature [16].

The complexes were prepared by the following general procedure. A mixture of $MeOC_6H_4TeCl_3$ and the respective ligand in dichloromethane (20–25 ml) was stirred for 30 min at ambient temperature and subsequently the volume was reduced by 30–50% under the vacuum. Then the solution was overlayered by hexane and the crystals were formed within the period of 5–24 h.

3.2. *[(4-MeOC$_6$H$_4$TeCl$_3$)$_2${μ-Ph$_2$P(S)(CH$_2$)$_4$P(S)Ph$_2$}] (**1**)*

$Ph_2P(S)(CH_2)_4P(S)Ph_2$ (0.100 g, 0.204 mmol) and $4\text{-}MeOC_6H_4TeCl_3$ (0.139 g, 0.408 mmol). Yield: 0.125 g (52%). M.p.: 140 °C. *Anal.* Calc. for **1**: C, 43.0; H, 3.6. Found: C, 42.8; H, 3.5%. $^{31}P\{^1H\}$ NMR: δ 51 ppm. IR: ν(PS) 609vs (see Fig. 1).

3.3. *[(4-MeOC$_6$H$_4$TeCl$_3$)$_2${μ-Ph$_2$P(S)(CH$_2$)$_6$P(S)Ph$_2$}] (**2**)*

$Ph_2(S)P(CH_2)_6P(S)Ph_2$ (0.100 g, 0.193 mmol) and $4\text{-}MeOC_6H_4TeCl_3$ (0.132 g, 0.387 mmol). Yield: 0.120 g (52%). M.p.: 146 °C. *Anal.* Calc. for **2** (including solvent): C, 44.0 (42.0); H, 3.9 (3.8). Found: C, 41.7; H, 3.8%. $^{31}P\{^1H\}$ NMR: δ 53 ppm. IR: ν(PS) 579vs.

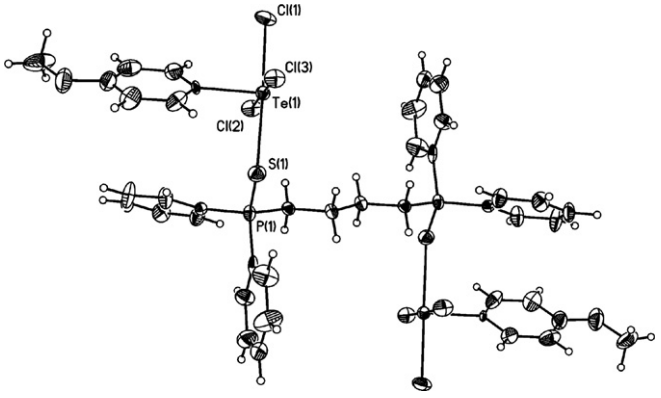


Fig. 1. The molecular structure of $[(4\text{-}MeOC_6H_4TeCl_3)_2\{\mu\text{-}Ph_2P(S)(CH_2)_4P(S)Ph_2\}]$ (**1**).

3.4. *[(4-MeOC$_6$H$_4$TeCl$_3$)$_2${μ-Ph$_2$P(S)(C$_6$H$_4$)$_2$P(S)Ph$_2$}] (**3**)*

$Ph_2P(S)(C_6H_4)_2P(S)Ph_2$ (0.100 g, 0.170 mmol) and $4\text{-}MeOC_6H_4TeCl_3$ (0.116 g, 0.340 mmol). Yield: 0.128 g (59%), M.p.: 156 °C. *Anal.* Calc. for **3** (including solvent): C, 47.3 (45.2); H, 3.3 (3.3). Found: C, 47.6; H, 3.2%. $^{31}P\{^1H\}$ NMR: δ 43 ppm. IR: ν(PS) 599vs (see Fig. 2).

3.5. *[(4-MeOC$_6$H$_4$TeCl$_3$)$_2${μ-Ph$_2$P(S)NH(C$_6$H$_4$)HNP(S)Ph$_2$}] (**4**)*

$Ph_2P(S)NH(C_6H_4)NHP(S)Ph_2$ (0.100 g, 0.185 mmol) and $4\text{-}MeOC_6H_4TeCl_3$ (0.126 g, 0.369 mmol). Yield: 0.130 g (57%), M.p.: 165 °C.$^{31}P\{^1H\}$ NMR: δ 55 ppm (see Fig. 3).

3.6. *[(4-MeOC$_6$H$_4$TeCl$_3$)Ph$_3$P(S)] (**5**)*

$Ph_3P(S)$ (0.100 g, 0.340 mmol) and $4\text{-}MeOC_6H_4TeCl_3$ (0.116 g, 0.340 mmol). Yield: 0.115 g (53%), M.p.: 135 °C. *Anal.* Calc. for **4**: C, 47.3; H, 3.5. Found: C, 46.9; H, 3.3%. $^{31}P\{^1H\}$ NMR: δ 43 ppm. IR: ν(PS) 596vs (see Fig. 4).

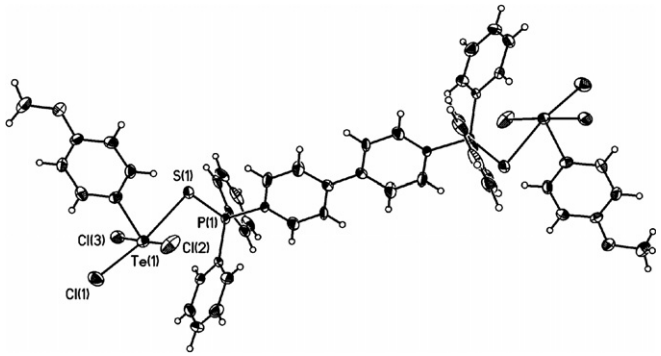


Fig. 2. The molecular structure of $[(4\text{-}MeOC_6H_4TeCl_3)_2\{\mu\text{-}Ph_2P(S)(C_6H_4)_2P(S)Ph_2\}]$ (**3**).

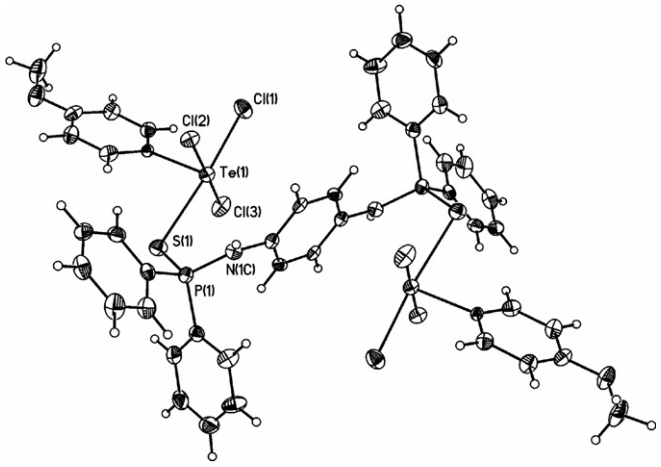


Fig. 3. The molecular structure of $[(4\text{-}MeOC_6H_4TeCl_3)_2\{\mu\text{-}Ph_2P(S)\text{-}NH\text{-}C_6H_4\text{-}NH\text{-}P(S)Ph_2\}]$ (**4**).

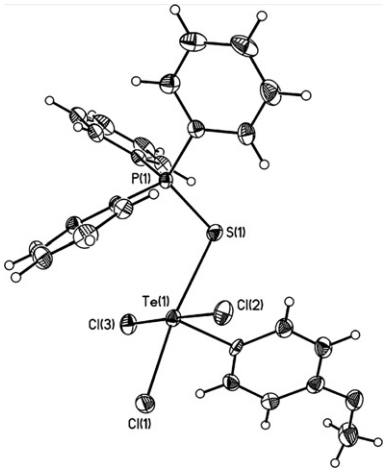


Fig. 4. The molecular structure of [(4-$MeOC_6H_4TeCl_3$)$Ph_3P(S)$] (**5**).

3.7. Crystallography

Diffraction data were collected on a KUMA KM-4 κ-axis diffractometer equipped with a CCD detector with Mo Kα radiation ($\lambda = 0.71073$ Å). The temperature during data collection was 120(2) K. The structures were solved by direct methods and refined by full-matrix least-squares methods. The software packages used were: Xcalibur CCD system for the data collection/reduction [17], and SHELXTL for the structure solution, refinement, and drawing preparation [18]. The thermal ellipsoids in figures were drawn at the 50% probability level. Details of the data collection and structure refinement are listed in Table 1.

Acknowledgments

This work was supported by the Grant Agency of the Czech Republic (203/07/1657). We thank Professor Zdenek Travnicek, Palacky University, Olomouc, for elemental analyses.

Appendix A. Supplementary material

CCDC 621468, 621469, 621470, 621471 and 621472 contain the supplementary crystallographic data for this paper. These data can be obtained free of charge via http://www.ccdc.cam.ac.uk/conts/retrieving.html, or from the Cambridge Crystallographic Data Centre, 12 Union Road, Cambridge CB2 1EZ, UK; fax: (+44) 1223-336-033; or e-mail: deposit@ccdc.cam.ac.uk. Supplementary data associated with this article can be found, in the online version, at doi:10.1016/j.poly.2007.01.001.

References

[1] K.L. Nash, C. Lavallette, M. Borkowski, R.T. Paine, X. Gan, Inorg. Chem. 41 (2002) 5849.
[2] M. Goyal, J. Novosad, M. Necas, H. Ishii, R. Nagahata, J. Sugiyama, M. Asai, M. Ueda, K. Takeuchi, Appl. Organomet. Chem. 14 (2000) 629.
[3] F. Caruso, M. Rossi, J. Tanski, C. Pettinari, F. Marchetti, J. Med. Chem. 46 (2003) 1737.
[4] S. Husebye, Phosphorus Sulfur Silicon Relat. Elem. 136 (1998) 377.
[5] D.J. Birdsall, J. Novosad, A.M.Z. Slawin, D. Woollins, J. Chem. Soc., Dalton Trans. (2000) 435.
[6] J. Novosad, K.W. Törnroos, M. Necas, A.M.Z. Slawin, J.D. Woollins, S. Husebye, Polyhedron 18 (1999) 2861.
[7] M. Necas, J. Novosad, S. Husebye, J. Organomet. Chem. 623 (2001) 124.
[8] C.J. Carmalt, N.C. Norman, L.J. Farrugia, Polyhedron 14 (1995) 1405.
[9] A. Bondi, J. Phys. Chem. 68 (1964) 441.
[10] I. Haiduc, R.B. King, M.G. Newton, Chem. Rev. 94 (1994) 301.
[11] G.A. Landrum, R. Hoffmann, Angew. Chem., Int. Ed. 37 (1998) 1887.
[12] S. Husebye, K. Maartmann-Moe, Acta Chem. Scand. 49 (1995) 834.
[13] F.H. Allen, Acta Crystallogr., Sect. B 58 (2002) 380.
[14] A.M.Z. Slawin, M. Wainwright, J.D. Woollins, J. Chem. Soc., Dalton Trans. (2001) 2724.
[15] R.A. Baldwin, M.T. Cheng, J. Org. Chem. 32 (1967) 1572.
[16] G.T. Morgan, R.E. Kellet, J. Chem. Soc. (1926) 1080.
[17] Oxford Diffraction Ltd., Xcalibur CCD System, CrysAlis Software System, Version 1.171. Oxford, UK, 2004.
[18] SHELXTL, Version 5.10, Bruker AXS Inc., Madison, WI, 1997.

ligands [7]. Also, it may be noted that in most of the reported mononuclear metal complexes all the coordination positions are satisfied by the same ligand and ternary complexes have not been reported. Recently we have reported a tridentate phenolate ligand having N_1O_2 donor sites [11]. We thought to explore the ligation capability of the ligand towards copper. Our aim was to synthesize ternary complexes of copper using the tridentate ligands along with a monodentate co-ligand. Herein we report the synthesis, characterization and structure of the copper complex, $[CuL^1(H_2O)(Pyz)]$ (**1**) [L^1H_2 = {(3,5-di-*tert*-butyl-2–hydroxybenzyl)amino}acetic acid; Pyz = pyrazole]. Also, reported herein is the synthesis and characterization of a new optically active tridentate ligand, *S*(−)2-(3,5-di-*tert*-butyl-2-hydroxy-benzylamino)-3-methyl-butyric acid (L^2H_2), derived form L-valine, and its copper complex, $[CuL^2(H_2O)(Pyz)]$ (**2**).

2. Experimental

2.1. General remarks

All the chemicals used were reagent grade products. The ligand, {(3,5-di-*tert*-butyl-2-hydroxybenzyl)amino}acetic acid (L^1H_2) was prepared by the reported procedure [11]. ^1H NMR spectra were recorded on a Bruker AC 200, 200 MHz NMR spectrometer in $CDCl_3$ solutions at room temperature. EPR spectra were recorded on a Bruker EMX X-band spectrometer. IR spectra were recorded on a Thermo Nicklet Model 870 FT IR spectrometer. The UV–visible spectra were recorded on a Shimadzu UV 600 spectrophotometer. CD spectral measurements were done in methanol using a JASCO CD polarimeter, model J-810. Specific rotations were measured in methanolic solutions of the compound using a JASCO P1020 polarimeter. Cyclic voltammetry experiments were performed using a fully automated CH Instruments electrochemical analyzer (Model 620a) and a three-electrode set-up consisting of a glassy carbon working electrode, a platinum wire counter electrode and an Ag/AgCl reference electrode. All experiments were performed in dry CH_3CN containing tetra-*N*-butylammonium perchlorate (0.2 mol dm^{-3}) as the background electrolyte. The magnetic measurements were done using the Gouy method. The C, H and N contents were estimated using microanalyses on a Perkin Elmer microanalyser, 2400. For the mass spectral measurements a 1:1 methanol/water solution of the compounds was taken and the mass spectra were recorded on a Waters LCT mass spectrometer using the electrospray ionization (ES^- mode) technique.

2.2. Synthesis of the mono sodium salt of S-(−)2-(3,5-di-tert-butyl-2-hydroxy-benzylamino)-3-methyl-butyric acid (L^1H_2)

L-Valine (1.17 g; 10 mmol) was dissolved in an aqueous solution (20 cm^3) of NaOH (0.450 g; 11.25 mmol). To this was added 40% aqueous formaldehyde (8 cm^3; 100 mmol) and the solution was heated for 20 min on a water bath. To the reaction solution was added an ethanolic solution (40 cm^3) of 2,4-di-*tert*-butyl phenol (2.06 g; 10 mmol) dropwise. The reaction mixture was then heated for 5 h on an oil bath at 50 °C. The reaction solution was cooled to room temperature and allowed to stand overnight. The precipitated mono sodium salt of the ligand 2-(3,6-di-*tert*-butyl-2-hydroxy-benzylamino)-3-methyl-butyric acid (L^2H_2) was filtered washed with water and hexane and finally dried in vaccuo. Yield: 3.08 g; 86.5%. *Anal.* Calc. for $C_{20}H_{32}NO_3Na$ (357.46): C, 67.20; H, 9.02; N, 3.92. Found (%): C, 67.18; H, 8.89; N, 3.88. IR (KBr pellet, ν [cm^{-1}]): 3434, 2959, 2361, 1585, 1476, 1226, 1122. UV–visible [λ_{max} (nm) (ε)]: 279 (2205), 227 (3056). ^1H ($CDCl_3$) (ppm): 1.00 (br, m, 6H), 1.26 (s, 9H), 1.45 (s, 9H), 2.21 (br, 1H), 3.35 (d, $J = 4$ Hz), 3.89 (d, $J = 14$ Hz, 1H), 4.36 (d, $J = 14$ Hz 1H), 6.95 (d, $J = 1$ Hz, 1H), 7.30 (d, $J = 1$ Hz, 1H). Mass (significant peak and its assignment): m/z 334.2212 [$C_{20}H_{32}NO_3^-$, M^-].

2.3. Syntheses of $[CuL^1(H_2O)(Pyz)]$ (1) and $[CuL^2(H_2O)(Pyz)]$ (2)

Compounds **1** and **2** were prepared by a similar procedure and the general procedure is given below. The ligand (1 mmol) was dissolved in methanol (25 cm^3) in a beaker. To this was added solid NaOH (0.08 g; 2 mmol) followed by addition of water (5 cm^3) (Solution A). Pyrazole (1 mmol) was added to a methanolic solution (10 cm^3) of $Cu(ClO_4)_2 \cdot 6H_2O$ (1 mmol) in another beaker (Solution B). To this solution (Solution B) was then added the solution of sodium salt of the ligand (Solution A) and the reaction solution was stirred for an hour. The reaction solution on standing overnight afforded crystalline **1** or **2**. The compound was filtered, washed with water, and finally recrystallized from acetonitrile. Recrystallization of **1** from acetonitrile afforded crystals suitable for X-ray diffraction. Yield: 0.335 g; 76% (**1**), 0.338 g; 70% (**2**). *Anal.* Calc. for $C_{20}H_{31}CuN_3O_4$ (**1**) (441.02): C, 54.47; H, 7.08; N, 9.53. Found: C, 54.40; H, 7.02; N, 9.47%. *Anal.* Calc. for $C_{23}H_{37}CuN_3O_4$ (483.1) **2**: C, 57.18; H, 7.72; N, 8.70. Found: C, 57.08; H, 7.67; N, 8.61%. IR (KBr pellet, ν [cm^{-1}]) (**1**): 3436, 2956, 1631, 1057, 1140, 1111, 939, 758. IR (KBr pellet, ν [cm^{-1}]) (**2**): 3439, 2958, 1629, 1471, 1384, 1087, 1140, 1114, 759. UV–visible [λ_{max} (nm) (ε)] (**1**): 630 (80), 380 (420), 237 (3887), 278 (1890); [λ_{max} (nm) (ε)] (**2**): 635 (145), 431 (463), 245 (3945), 293 (3247).

2.4. X-ray crystallographic study

Suitable crystals of $[CuL^1(H_2O)(DMPZ)]$ (**1**) were grown from a dilute acetonitrile solution at room temperature over a period of 5–6 days. The single crystal data was collected on a Nonius Kappa CCD X-ray diffractometer using graphite monochromated Mo Kα radiation ($\lambda = 0.71073$ Å) by the Φ scan and ω-scan methods. The

structure was solved using the program SIR-97 [12]. The refinement and all further calculations were carried out using SHELXL-97 [13]. The H-atoms were refined isotropically except those involved in disordered moieties which were included in calculated positions and treated as riding atoms using SHELXL default parameters. The non-H atoms were refined anisotropically using weighted full-matrix least-squares on F^2. The three methyl groups of the *tert*-butyl linked to the C8 atom and the $C3H_2$–N1H moiety were found to be disordered and were refined over two positions with occupancies of 0.656(9) and 0.344(9), respectively. An empirical absorption correction was applied using the SORTAV routine [14]; transmission factors: $T_{min}/T_{max} = 0.856/0.949$. Crystal data: Empirical formula: $C_{20}H_{31}CuN_3O_4$, MW = 441.02, monoclinic, space group $P2_1/a$, $a = 10.6217(2)$ Å, $b = 10.1645(2)$ Å, $c = 19.4909(5)$ Å, $\beta = 90.7729(9)°$, $V = 2104.13(8)$ Å^3, $Z = 4$, d (calcd.) = 1.392 Mg/m^3, $F(000) = 932$, $T = 150$ K, $\mu = 1.068$ mm^{-1}, crystal size = $0.36 \times 0.15 \times 0.05$ mm^3, data collection range $2.96 \leqslant \theta \leqslant 27.00°$, $-13 \leqslant h \leqslant 13$, $-12 \leqslant k \leqslant 12$, $-24 \leqslant l \leqslant 24$. Reflections measured: 23 131, 4566 unique ($R_{int} = 0.0680$, $R_\sigma = 0.0517$), $R_1 = 0.0527$, $wR_2 = 0.1203$ for 3457 reflections with $I > 2\sigma(I)$ and $R_1 = 0.0760$, $wR_2 = 0.1303$ for all data.

3. Results and discussion

3.1. Synthesis and characterization of the mono sodium salt of L^2H_2

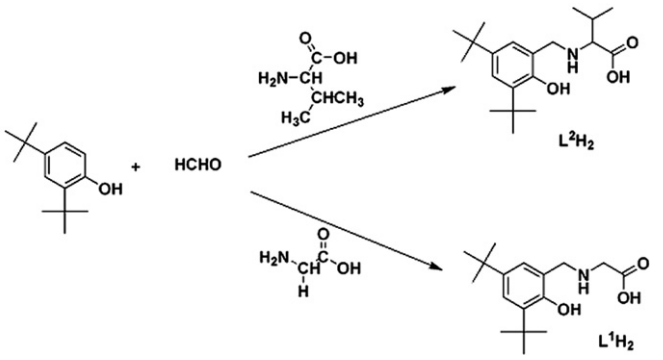
This ligand has been synthesized from a one pot Manich reaction of L-valine with 2, 4-di-*tert*-butyl phenol and formaldehyde in aqueous ethanol under basic conditions (Scheme 1). The ligand has been characterized by elemental analyses, mass spectrometry, IR, UV–visible, circular dichroism (CD) and ^{1}H NMR spectroscopy. The elemental analyses agree well with the composition. The high resolution mass spectrum (HRMS) of the monosodium salt of the compound shows a molecular ion peak at m/z 334.2212 due to $M^-(CH_{32}NO_3^-)$. The IR spectrum of the compound shows –COO^- stretches at 1585 and 1476 cm^{-1} along with other characteristic bands. The ^{1}H NMR spectrum of the ligand shows signals at δ 1.00 ppm (br m, 6H) due to –CH_3 protons of the *iso*-propyl group, δ 1.26 ppm (s, 9H) and δ 1.45 ppm (s, 9H) due to the –CH_3 protons of the *tert*-butyl groups. The signal due to the –CH proton of the *iso*-propyl group appears as a broad signal at δ 2.21 ppm (1H) and the –CH proton (αH) adjacent to the –COOH group appears at δ 3.35 ppm (d, $J = 4$ Hz, 1H). The assignment of the –CH protons and the methyl protons of the *iso*-propyl group and the –CH proton (αH) adjacent to the –COOH group was further confirmed from proton decoupling experiments. The methylene protons of the –$HNCH_2$ group appear at δ 3.89 ppm (d, $J = 14$ Hz, 1H) and δ 4.36 ppm (d, $J = 14$ Hz, 1H). The aromatic protons appear at δ 6.95 ppm (d, $J = 1$ Hz, 1H) and δ 7.30 ppm (d, $J = 1$ Hz, 1H).

The UV–visible spectrum of the compound shows bands at 279 nm ($\varepsilon = 2205$) and 227 nm ($\varepsilon = 3056$) due to aromatic π–π^* transitions. The circular dichroism spectrum (CD) spectrum (Fig. 1) of the ligand shows a signal with a positive Cotton effect at 211 nm and one signal with a negative Cotton effect at 276 nm due to π–π^* transitions.The specific rotation of the ligand was found to be $-15.89°$ $\{[\alpha]_D^{24.5}\}$. Thus, the spectral measurements agree well with the formulation and structure of the ligand.

3.2. Synthesis and characterization of 1 and 2

The compounds **1** and **2** have been synthesized from the reaction of the sodium salt of the corresponding ligand with preformed pyrazole complex of copper, which was prepared from a reaction of pyrazole with $Cu(ClO_4)_2 \cdot 6H_2O$ in aqueous methanol.

Compounds **1** and **2** have been characterized by elemental analyses, IR, UV–visible and EPR spectral studies, and also by electrochemical and magnetic susceptibility measurements. Compound **2** was further characterized by CD spectroscopy. The elemental analyses agree well with the formulations of the compounds. The IR spectra of the compounds show a band at *ca.* 1620 cm^{-1} due to a



Scheme 1.

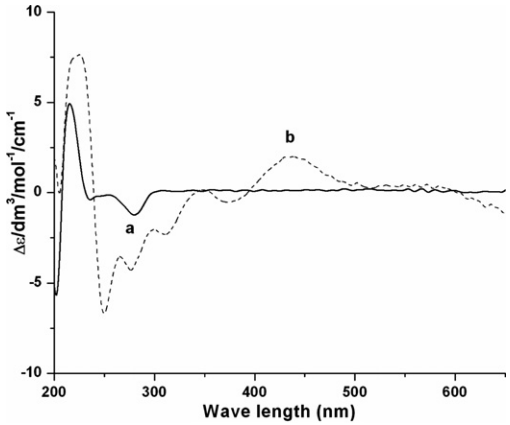


Fig. 1. Circular dichroism spectra of solutions of the monosodium salt of L^2H_2 (—) in methanol (10^{-3} M) (a) and its copper complex **1** (- - -) (b) in methanol (10^{-3} M).

carboxylate stretch. The marked shift of the carboxylate stretch from those of the ligand clearly shows that the ligand is bonded to the metal center through the carboxylate oxygen. The room temperature magnetic moment of compounds **1** and **2**, measured by the Gouy method, was found to be *ca.* 1.81 BM, which is typical for Cu(II) mononuclear complexes.

The electronic spectrum of **1** shows a band due to d–d transitions at 640 nm ($\varepsilon = 207$). Apart form the d–d transition, compound **1** shows a band at 440 nm (sh) ($\varepsilon = 380$). This may be assigned to a ligand to metal charge transfer (LMCT) transition. In **1** the ligand internal π–π^* transitions appear at 250 nm ($\varepsilon = 3570$) and 280 nm (sh) ($\varepsilon = 3430$). In **2** the d–d transition appears at 630 nm ($\varepsilon = 201$) and the LMCT transitions appear at 450 nm ($\varepsilon = 420$) and 390 nm ($\varepsilon = 530$). The ligand internal π–π^* transitions appear at 260 nm ($\varepsilon = 3740$) and 300 nm (sh) ($\varepsilon = 3460$). The marked shift of the ligand internal π–π^* transition as well as appearance of the LMCT band clearly show that the ligand is bonded to the metal center.

The CD spectrum of **2** (Fig. 1) shows a band with a positive Cotton effect at 224 nm and a band with a negative Cotton effect at 276 nm. A comparison with the ligand CD spectrum indicates that these signals are due to intra-ligand π–π^* transitions. In addition to the intra-ligand transitions, two bands with negative Cotton effect appear at 310 and 373 nm and a band with positive Cotton effect appears at 440 nm. These may originate from LMCT transitions. The specific rotation of **2** was found to be −214.85 $\{[\alpha]_D^{24.5}\}$.

The EPR spectra of frozen solutions of **1** and **2** at 77 K shows an anisotropic $S = 1/2$ signal at $g = <2$ (Figs. 2a and 3a, respectively) ($A_{\parallel} = 161 \times 10^{-4}\ cm^{-1}$). The observed g values ($g_{\parallel} = 2.28$ and $g_{\perp} = 2.01$ for **1** and $g_{\parallel} = 2.29$ and $g_{\perp} = 2.04$ for **2**), that is $g_{\parallel} > g_{\perp} > 2$, indicate that the ground state is $d_{x^2-y^2}$ in both complexes.

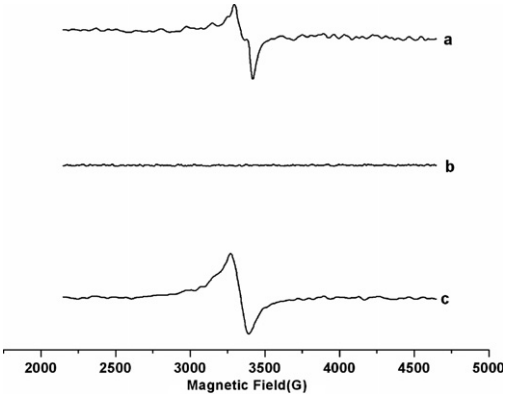


Fig. 2. X-band EPR spectra of **1**. (a) Frozen solution (acetonitrile) spectrum of **1**. (b) (a) + $(NH_4)_2Ce(NO_3)_6$ [1:1]. (c) (a) + $(NH_4)_2Ce(NO_3)_6$ [1:2]. General conditions: temperature = 77 K, microwave frequency = 9.57 GHz, microwave power = 1.00 mW, modulation frequency = 50 kHz, modulation amplitude = 5 G, receiver gain = 2.52×10^5. Sweep width = 2500 G. Time constant = 655.36 ms. Conversion time = 162.84 ms; $g_{dpph} = 2.0032$.

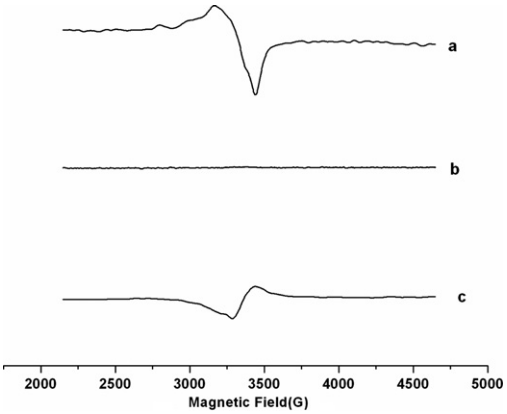


Fig. 3. X-band EPR spectra of **2**. (a) Frozen solution (acetonitrile) spectrum of **2**. (b) (a) + $(NH_4)_2Ce(NO_3)_6$ [1:1]. (c) (a) + $(NH_4)_2Ce(NO_3)_6$ [1:2]. General conditions: temperature = 77 K, microwave frequency = 9.59 GHz, microwave power = 1.00 mW, modulation frequency = 50 kHz, modulation amplitude = 5 G, receiver gain = 2.52×10^5. Sweep width = 2500 G. Time constant = 655.36 ms. Conversion time = 162.84 ms; $g_{dpph} = 2.0032$.

The room temperature solution (acetonitrile) EPR spectra (Fig. 4a and b) of **1** and **2** are isotropic in nature, with four equally spaced lines due to the coupling of the electron with the $I = 1/2$ nuclear spin on both ^{63}Cu and ^{65}Cu isotopes ($g_{iso} = 2.12$ and $A_{iso} = 83\ 4 \times 10^{-4}\ cm^{-1}$).

3.3. Structure of *1*

Compound **1** was characterized by single crystal X-ray crystallography. The compound crystallizes as green plates in the space group $P2_1/a$ from acetonitrile. The X-ray analysis reveals that the asymmetric unit contains one molecule of **1** (Fig. 5).

The ligand L^1 binds the copper center in a tridentate fashion and is bonded to Cu(II) through a phenolate oxygen {Cu1···O3 = 1.870(3) Å}, one carboxylate oxygen

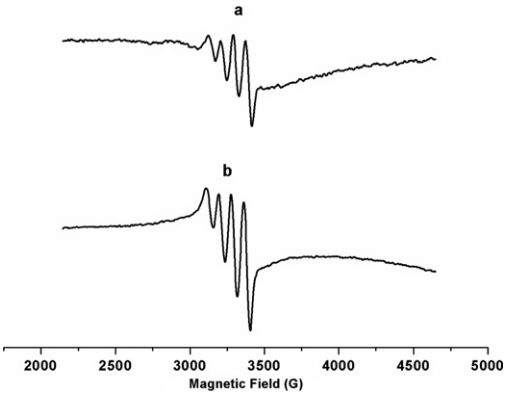


Fig. 4. Room temperature solution (acetonitrile) X-band EPR spectra of **1** (a) and **2** (b). General conditions: temperature = 298 K, microwave frequency = 9.64 GHz, microwave power = 1.00 mW, modulation frequency = 50 kHz, modulation amplitude = 5 G, receiver gain = 2.52×10^5. Sweep width = 2500 G. Time constant = 655.36 ms. Conversion time = 162.84 ms; $g_{dpph} = 2.0032$.

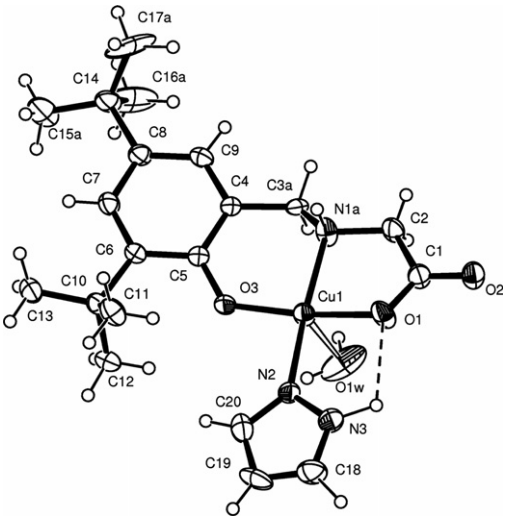


Fig. 5. ORTEP drawing of **1** (thermal ellipsoids at 30% probability). The disorder in the methyl carbons (C15, C16, C17) of the *tert*-butyl group, methylene (C3) and nitrogen (N1) have not been shown.

{Cu1···O1 = 1.966(3) Å} and a nitrogen (N1). In addition the copper center is bonded to one pyrazole nitrogen {Cu1···N2 = 1.989(3) Å} and a water molecule {Cu1···O1W = 2.374(3) Å}. Thus, the copper center is in a distorted square pyramidal environment.

The equatorial positions are occupied by the two oxygens (O1 and O3) (∠O1Cu1O3 = 169.07(13)°) and one nitrogen (N1) of the ligand L^1, and the fourth position is occupied by the pyrazole nitrogen (N2) (∠O1Cu1N2 = 88.28(9)°). The oxygen atoms, O1 and O3, lie in the equatorial plane. The two nitrogen atoms, N1B and N2, and the copper atom lie slightly above the plane by 0.156, 0.150 and 0.019 Å, respectively. The axial position is occupied by the water molecule (O1W) (∠O1Cu1O1W = 90.24(13)°; ∠O1WCu1O3 = 100.52(13)°; ∠O1WCu1N2 = 90.00(12)°). The compound shows crystallographic disorder. In one of the *tert*-butyl groups of the ligand, the carbon atom (C14) is surround by six methyl carbons of 0.656 (9) and 0.344 (9) occupancy each. In addition, the methylene carbon C3 and the nitrogen N1 of the ligand also show disorder. Due to the disorder in N1, the Cu1···N1 distance is not reliable {Cu1···N1A = 1.987(4) Å, Cu1···1N1B = 1.957(7) Å}. Similarly, the bond angles are also not reliable. The pyrazole ring lies roughly on the Cu1 coordination plane owing to the intramolecular hydrogen bond interaction between N3–H and O1 of the carboxylate group {N3···O1 = 2.767(4) Å}. Some important bond distances and bond angles are given in Table 1.

Table 1
Selected bond lengths (Å) and bond angles (°) of **1**

Bond distances (Å)		Bond angles (°)	
Cu1–O1	1.965(2)	O1–Cu1–O1W	90.24(13)
Cu1–O1W	2.374(4)	O1–Cu1–O3	169.07(13)
Cu1–O3	1.870(3)	O1–Cu1–N1A	82.82(17)
Cu1-N1A	1.987(4)	O1–Cu1–N2	88.28(9)
Cu1–N2	1.990(2)	O1–Cu1–N1B	85.7(3)
Cu1–N1B	1.958(7)	O1W–Cu1–O3	100.52(13)
		O1W–Cu1–N1A	98.50(19)
		O1W–Cu1–N2	90.00(12)
		O1W–Cu1–N1B	81.7(3)

3.4. Cyclic voltammetry and chemical and electrochemical oxidation of *1* and *2*, and generation of phenoxyl radical

Cyclic voltammetry of **1** (Fig. 6a) shows two quasi-reversible oxidative peaks at half-wave potentials ($E_{1/2}$) of 0.775 V ($\Delta E_P = 138$ mV) and 1.09 V ($\Delta E_P = 134$ mV) versus Ag/AgCl. These oxidative responses are attributed to the following oxidation process. The first is due to the ligand based oxidation, which is phenoxide to phenoxyl radical oxidation, (Eq. (1)) and the second is due to Cu(II) to Cu(III) oxidation (Eq. (2)) (*vide infra*).

Similarly, compound **2** (Fig. 6b) shows quasi-reversible oxidative responses at $E_{1/2} = 0.813$ V ($\Delta E_P = 150$ mV) and $E_{1/2} = 1.157$ V ($\Delta E_P = 153$ mV). In this case the oxidative responses are assigned to Cu(II) to Cu(III) oxidation and phenoxide to phenoxyl radical oxidation respectively (Eqs. (3) and (4)) (*vide infra*). Along with these peaks, unlike compound **1**, compound **2** shows an irreversible peak at 0.505 V. This may be due to oxidative decarboxylation.

$$[Cu^{II}L^1(Pyz)(H_2O)] \underset{+e}{\overset{-e}{\rightleftharpoons}} [Cu^{II}L^1(Pyz)(H_2O)]^{\cdot+} \quad (1)$$

$$[Cu^{II}L^1(Pyz)(H_2O)] \underset{+e}{\overset{-e}{\rightleftharpoons}} [Cu^{III}L^1(Pyz)(H_2O)]^{\cdot 2+} \quad (2)$$

$$[Cu^{II}L^1(Pyz)(H_2O)] \underset{+e}{\overset{-e}{\rightleftharpoons}} [Cu^{III}L^1(Pyz)(H_2O)]^{+} \quad (3)$$

$$[Cu^{III}L^1(Pyz)(H_2O)] \underset{+e}{\overset{-e}{\rightleftharpoons}} [Cu^{III}L^1(Pyz)(H_2O)]^{\cdot 2+} \quad (4)$$

The results of the electrochemical measurements lead us to investigate further the formation of the copper coordinated phenoxyl radical. The compounds were oxidized electrochemically. The spectral changes observed upon one

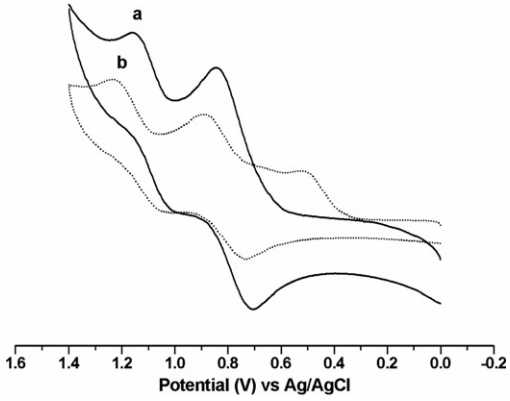


Fig. 6. Cyclic voltammogram of compound **1** (a, —) and compound **2** (b, ···) with an Ag/AgCl reference electrode, glassy carbon working electrode and a platinum wire auxiliary electrode. Scan rate = 0.2 V/s.

electron and two electron oxidation of **1** are shown in Fig. 7. After one electron oxidation of **1** the observed d–d transition at 640 nm is shifted to 600 nm ($\varepsilon = 240$) with an increase in intensity. The shoulder at 450 nm in **1** completely disappears and a new band appears at 380 nm ($\varepsilon = 1810$). This may be assigned to the LMCT transition phenolate – Cu(II). Thus, appearance of the 380 nm band shows that the first oxidative response is due to the phenoxide to phenoxyl radical generation [1–7,15–17]. Upon two electron oxidation, the d–d transition shifts to 670 nm ($\varepsilon = 68$). In the case of **2**, upon one electron oxidation the d–d band shifts to 675 nm ($\varepsilon = 41$) and the bands at 350 and 490 disappear. Unlike that observed in **1**, no band could be observed in the region of 380–410 nm in **2**. This clearly shows that, the first oxidative response is due to metal based oxidation. Upon two electron oxidation, a new high intensity band appears at 390 nm ($\varepsilon = 2500$) (Fig. 8). This clearly shows that the second oxidative response is due to phenoxide to phenoxyl radical oxidation.

The oxidation process was further investigated by in situ EPR spectral measurements. The EPR spectral changes observed at 77 K during the chemical oxidation of **1** and **2** have been shown in Figs. 2 and 3. Upon addition of Ce(IV) to the acetonitrile solution of **1** and **2** in a 1:1 ratio, the EPR signal disappears (Figs. 2b and 3b). In the case of **1** the diamagnetic nature of the intermediate may be explained in terms of antiferromagnetic coupling between the unpaired electrons on the Cu(II) center and the ligand [14]. This is in commensurate with the observed UV–visible spectral studies. When another equivalent of Ce(IV) is added to this solution a new isotropic signal appears at $g = 2.04$ (Figs. 2c and 3c). This signal may be attributed to the generation of Cu(III), a diamagnetic d^8 system, coordinated phenoxyl radical. In the case of **2**, the disappearance of the EPR signal can be attributed to the generation of Cu(III), a d^8 system. Upon second oxidation the generation of a phenoxyl radical is responsible for the appearance of the EPR signal. The observed higher g values of the radical species as well as the broad nature of the signals suggest that the unpaired electron is in a delocalized orbital which has a substantial amount of metal character [18].

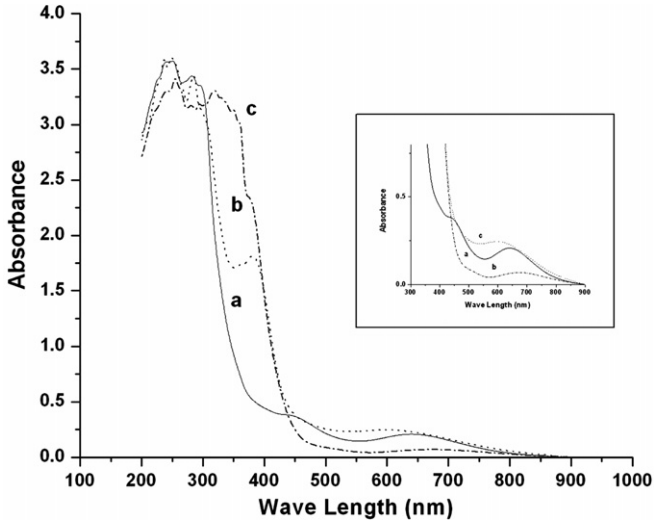


Fig. 7. UV–visible spectra of **1**. (a) Spectrum of the original compound (—). (b) One electron oxidized species (···). (c) Two electron oxidized species. Inset: enhanced spectra of (a), (b) and (c) in the region 300–900 nm.

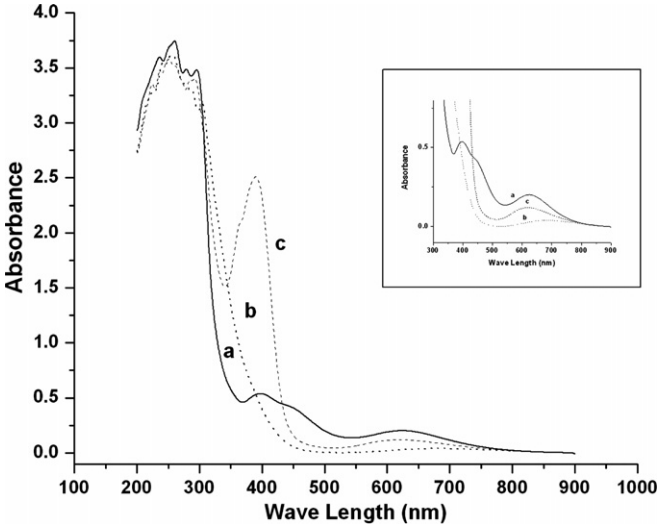


Fig. 8. UV–visible spectra of **2**. (a) Spectrum of the original compound (—). (b) One electron oxidized species (···). (c) Two electron oxidized species. Inset: enhanced spectra of (a), (b) and (c) in the region 300–900 nm.

4. Conclusion

In conclusion, it has been shown that using multidentate ligands containing phenoxide, carboxylate and nitrogen donor sites, a stable copper (III) coordinated phenoxyl radical can be generated. The parent complexes have been fully characterized using various spectroscopic techniques and one of the compounds has been characterized by single crystal X-ray structure determination. Radical species have been characterized by UV–visible and EPR spectroscopy.

Acknowledgements

We thank the Department of Science and Technology, Government of India, New Delhi for a FIST grant for the single crystal X-ray facility. S.D. thanks the University Grants Commission, Government of India, New Delhi for the award of an individual fellowship. The authors thank Professor Amit Basak, Department of Chemistry, IIT, Kharagpur for helpful discussions and the reviewers for their helpful comments.

Appendix A. Supplementary material

CCDC 607768 contains the supplementary crystallographic data for the structure reported in this paper. These data can be obtained free of charge via http://www.ccdc.

cam.ac.uk/conts/retrieving.html, or from the Cambridge Crystallographic Data Centre, 12 Union Road, Cambridge CB2 1EZ, UK; fax: (+44) 1223-336-033; or e-mail: deposit@ccdc.cam.ac.uk. Supplementary data associated with this article can be found, in the online version, at doi:10.1016/j.poly.2007.01.011.

References

[1] L. Benisvy, A.J. Blake, D. Collison, E.S. Davies, C.D. Garner, E.J.L. McInnes, J. McMaster, G. Whittaker, C. Wilson, Chem. Commun. (2001) 1824.

[2] L. Benisvy, A.J. Blake, D. Collison, E.S. Davies, C.D. Garner, E.J.L. McInnes, J. McMaster, G. Whittaker, C. Wilson, J. Chem. Soc., Dalton Trans. (2003) 1975.

[3] L. Benisvy, E. Bill, A.J. Blake, D. Collison, E.S. Davies, C.D. Garner, C.I. Guindy, E.J.L. McInnes, G. McArdle, J. McMaster, C. Wilson, J. Wolowska, J. Chem. Soc., Dalton Trans. (2004) 3647.

[4] L. Benisvy, E. Bill, A.J. Blake, D. Collison, E.S. Davies, C.D. Garner, G. McArdle, E.J.L. McInnes, J. McMaster, S.H.K. Ross, C. Wilson, J. Chem. Soc., Dalton Trans. (2006) 258.

[5] Y. Shimazaki, S. Huth, A. Odani, O. Yamauchi, Angew. Chem., Int. Ed. Engl. 39 (2000) 1666.

[6] S. Itho, M. Taki, S. Fukuzumi, Coord. Chem. Rev. 198 (2000) 3.

[7] E. Bill, J. Muller, T. Weyhermulle, K. Weighardt, Inorg. Chem. 38 (1999) 5795.

[8] (a) J.W. Whittaker, in: H. Sigel, A. Sigel (Eds.), Metalloenzymes Involving Amino Acid Residue and Related Radicals, vol. 30, Marcel Dekker, New York, 1994, p. 315;
(b) P.F. Knowles, N. Ito, Perspectives in Bio-inorganic Chemistry, vol. 2, Jai Press Ltd., London, 1994, pp. 207–244.

[9] P. Chaudhuri, M. Hess, U. Florke, K. Wieghardt, Angew. Chem., Int. Ed. 37 (1998) 2217.

[10] P. Chaudhuri, M. Hess, J. Mu1ller, K. Hildenbrand, E. Bill, T. Weyhermu1ller, K. Wieghardt, J. Am. Chem. Soc. 121 (1999) 9599.

[11] S. Khatua, S. Dasgupta, K. Biradha, M. Bhattacharjee, Eur. J. Inorg. Chem. (2005) 5005.

[12] A. Altomare, G. Cascarano, C. Giocovazzo, A. Gualardi, J. Appl. Crystallogr. 26 (1993) 343.

[13] G. Sheldrick, SHELXL-97, Universität Göttingen, Göttingen, Germany, 1999.

[14] R.H. Blessing, Acta Crystallogr. Sect. A 51 (1995) 33.

[15] A.K. Nairn, S.J. Archibald, R. Bhalla, B.C. Gilbert, E.J. MacLean, S.J. Tea, P.H. Walton, J. Chem. Soc., Dalton Trans. (2006) 172.

[16] A. Philibert, F. Thomas, C. Philouze, S. Hamman, E. Saint-Aman, J.L. Pierre, Chem. Eur. J. 9 (2003) 3803.

[17] A. Sokolowski, H. Leutbecher, T. Weyhermüller, R. Schnepf, E. Bothe, E. Bill, P. Hildebrandt, K. Wieghardt, J. Biol. Inorg. Chem. 2 (1997) 444.

[18] V.T. Kasumov, F. Koḱsal, A. Sezer, Polyhedron 24 (2005) 1203.

In this report we focus on the examinations of the reactions of $[ReOCl_3(OAsPh_3)(AsPh_3)]$ and $[ReOCl_3(PPh_3)_2]$ with bis(pyrazol-1-yl)methane (bpzm) and present the synthesis, spectroscopic data, crystal, molecular, and electronic structures of $[ReOCl_3(bpzm)]$. Contrary to phenanthroline, the course of the reaction does not depend on the starting oxocomplex. In the both reactions only formation of $[ReOCl_3(bpzm)]$ has been observed.

The electronic structure of $[ReOCl_3(bpzm)]$ has been determined on the basis of the density functional theory (DFT) calculations, and additional information about binding has been obtained by NBO analysis. Currently density functional theory (DFT) is commonly used to examine the electronic structure of transition metal complexes. It meets with the requirements of being accurate, easy to use and fast enough to allow the study of relatively large molecules of transition metal complexes [8]. The spin-allowed electronic transitions of the $[ReOCl_3(bpzm)]$ complex have been calculated with the time-dependent DFT method (TDDFT), and the UV–Vis spectrum of the title compound has been discussed on this basis. The recent calculations with TD-DFT method for open- and closed-shell of 5d-metal complexes (including rhenium complexes) have supported the TD-DFT method to be applicable for such systems giving good assignment of experimental spectra [9,10].

2. Experimental

2.1. General procedure

All the reagents used to the syntheses were commercially available and were used without further purification. The $[ReOCl_3(AsPh_3)(OAsPh_3)]$ [11], $[ReOCl_3(PPh_3)_2]$ [12], and bis(pyrazol-1-yl)methane [13] were prepared according to the literature methods.

IR spectrum was recorded on a Nicolet Magna 560 spectrophotometer in the spectral range 4000–400 cm^{-1} with the samples in the form of KBr pellets. Electronic spectrum was measured on a spectrophotometer Lab Alliance UV–Vis 8500 in the range 1000–200 nm in dichloromethane solution. Elemental analyses (C H N) were performed on a Perkin–Elmer CHN-2400 analyzer.

2.2. Preparation of $[ReOCl_3(bpzm)]$ (*1*)

Method A. A mixture of $[ReOCl_3(AsPh_3)(OAsPh_3)]$ (0.5 g, 0.53 mmol), bpzm (0.1 g, 0.67 mmol), and acetone (50 ml) was stirred for 12 h. A turquoise powder was precipitated from the reaction mixture. It was filtered off, washed with diethyl ether and dried. Yield 80%.

Method B. A similar procedure with $[ReOCl_3(PPh_3)_2]$ (0.5 g, 0.60 mmol) and bpzm (0.11 g, 0.74 mmol) in acetone was used.

IR (KBr): 3121 (m) and 3022 (m) ν_{C-H}; 1520 (m) ν_{CN} and $\nu_{C=C}$; 978 (s) $\nu_{Re=O}$.

Anal. Calc. for $C_7H_8N_4Cl_3ORe$: C, 18.41; H, 1.77; N, 12.27. Found: C, 18.55; H, 1.75; N, 12.35%.

2.3. X-ray diffraction studies

A blue crystal of $[ReOCl_3(bpzm)]$ was mounted on a KM-4-CCD automatic diffractometer equipped with a CCD detector, and used for data collection. X-ray intensity data were collected with graphite monochromated Mo Kα radiation ($\lambda = 0.71073$ Å) at temperature of 293(2) K. Details concerning crystal data and refinement are given in Table 1. Lorentz, polarization and empirical absorption correction using spherical harmonics implemented in SCALE3 ABSPACK scaling algorithm [14] were applied. The structure was solved by the Patterson method and subsequently completed by the difference Fourier recycling. All the non-hydrogen atoms were refined anisotropically using full-matrix, least-squares technique. The hydrogen atoms were treated as ''riding'' on their parent carbon atoms and assigned isotropic temperature factors equal 1.2 times the value of equivalent temperature factor of the parent atom. SHELXS97 [15], SHELXL97 [16], and SHELXTL [17] programs were used for all the calculations. Atomic scattering factors were those incorporated in the computer programs. At the end of refinement on the difference Fourier synthesis maximum peak/hole are located 0.7 Å from rhenium atom. The next peaks/holes are distinctly smaller (<1 e $Å^{-3}$).

3. Computational details

Gaussian03 program [18] was used in the calculations. The geometry optimization of the $[ReOCl_3(bpzm)]$ complex was carried out with the DFT method with the use of B3LYP functional [19,20]. The electronic spectrum of the $[ReOCl_3(bpzm)]$ complex was calculated with the TDDFT method [21]. The solvent effect was simulated using the polarizable continuum model (PCM). The calculations were performed by using ECP basis set on the rhenium atom, the standard 6-31+g** basis for chlorine, oxygen, and nitrogen, 6-31g* basis for carbon and 6–31G basis for hydrogen atoms. The Xe core electrons of Re were replaced by an effective core potential and DZ quality Hay and Wadt Los Alamos ECP basis set (LANL2DZ) [22] was used for the valence electrons. Additional d function with exponent $\alpha = 0.3811$ and f function with exponent $\alpha = 2.033$ on the rhenium atom were added. Natural bond orbital (NBO) calculations were performed with the NBO code [23] included in Gaussian03.

4. Results and discussion

4.1. Preparation

The reactions of the $[ReOCl_3(AsPh_3)(OAsPh_3)]$ or $[ReOCl_3(PPh_3)_2]$ oxocompounds with a small excess of bis(pyrazol-1-yl)methane in acetone at ambient temperature lead to the formation of $[ReOCl_3(bpzm)]$ in high yield.

Table 1
Crystal data and structure refinement for [$ReOCl_3$(bpzm)]

Empirical formula	$C_7H_8N_4Cl_3ORe$
Formula weight	456.72
Temperature (K)	293(2)
Wavelength (Å)	0.71073
Crystal system	triclinic
Space group	$P\bar{1}$
Unit cell dimensions	
a (Å)	6.9082(4)
b (Å)	7.4912(5)
c (Å)	12.3760(8)
α (°)	103.548(5)
β (°)	98.418(5) (6)
γ (°)	102.086(5)
Volume (Å^3)	595.84(7)
Z	2
D_{calc} (Mg/m^3)	2.546
Absorption coefficient (mm^{-1})	10.852
$F(000)$	424
Crystal size (mm)	$0.08 \times 0.12 \times 0.22$
θ Range for data collection (°)	2.89–32.74
Index ranges	$-10 \leqslant h \leqslant 9$
	$-8 \leqslant k \leqslant 11$
	$-18 \leqslant l \leqslant 17$
Reflections collected	5977
Independent reflections (R_{int})	3777 (0.0156)
Completeness to $2\theta = 25.00°$ (%)	98.7
Maximum and minimum transmission	0.424 and 0.223
Data/restraints/parameters	3777/0/145
Goodness-of-fit on F^2	1.108
Final R indices [$I > 2\sigma(I)$]	$R_1 = 0.0236$, $wR_2 = 0.0583$
R indices (all data)	$R_1 = 0.0282$, $wR_2 = 0.0593$
Largest difference in peak and hole (e Å^{-3})	3.468 and −1.844

The complex is slightly soluble in most polar solvents, and it has been recrystallized from acetonitrile.

4.2. Infrared data

The IR spectrum of [$ReOCl_3$(bpzm)] exhibits strong band at 978 cm^{-1} assignable to ν(Re=O) mode. This value compares well with those reported for monooxo rhenium(V) complexes with chelating ligands: [$ReOBr_3$(dppen)] (dppen = *cis*-$Ph_2PCH{=}CHPPh_2$) – 984 cm^{-1}, [$ReOBr_3$(dppm)] (dppm = $Ph_2PCH_2PPh_2$) – 980 cm^{-1}, and [$ReOBr_3$(dppe)] (dppe = $Ph_2PCH_2CH_2PPh_2$) – 982 cm^{-1} [24]. The characteristic band corresponding to the ν(CN), ν(C=C) mode of the bpzm ligand appears at 1520 cm^{-1} [25].

4.3. Crystal structure

The [$ReOCl_3$(bpzm)] complex crystallises in $P\bar{1}$ space group. The molecules are linked *via* weak intermolecular hydrogen bonds [26,27]: C(4)–H(4A)···Cl(1) $(x, y-1, z)$ with D···A distance 3.400(4) Å and D–H···A angle 119.1°; C(4)–H(4A)···Cl(2) $(x, y-1, z)$ with D···A distance 3.647(4) Å and D–H···A angle 163.7° and C(4)–H(4A)···Cl(3) $(x, y-1, z)$ with DA distance 3.405(4) Å and D–H···A angle 119.0°. The intramolecular hydrogen bond linking C(4)–H(4B)···O(1) (D···A distance 3.131 (5) Å and D–H···A angle 118.5°) provides additional stabilization of *fac* geometry of the [$ReOCl_3$(bpzm)] molecule. It can not exist in *mer*-configuration of [$ReOCl_3$(bpzm)].

The molecular structure of [$ReOCl_3$(bpzm)] is given in Fig. 1. The pseudooctahedral environment of Re center in [$ReOCl_3$(bpzm)] shows clear distortions, induced by the multiple bonding ligand (oxo). The high concentration of electronic density along the Re–O axis strongly influences the positions of the adjacent chlorine and nitrogen atoms, which are pushed away. The chloride ions are arranged in a *facial* fashion, and the oxo ligand occupies the *trans* position to the Cl(2) ion. The *fac* geometry of the ReX_3 fragment has been found for some other oxo-rhenium(V) complexes, but it is definitely rarer observed than *mer* arrangement. Presumably, π-acceptor capability of bis(pyrazol-1-yl)methane sustains the *fac* geometry in the title complex. The *cis*-location of π-acid ligands in relation to the oxo group seems to be dominated by electronic influence of the multiply bonded ligand, which forces the metal nonbonding d electrons to lie in the plane perpendicular to the M–O bond axis. This general rule appears to hold for isonitrile, carbonyl, olefin, acetylene, thioether and often phosphine ligands [28–30].

Upon coordination of bis(pyrazol-1-yl)methane to the rhenium, a six-membered cycle (made by the four nitrogen atoms, the rhenium atom and the carbon atom) is formed. This six-membered ring shows a *boat* arrangement, with the rhenium and the carbon atoms off the plane defined by the four nitrogen atoms.

The most important bond lengths and angles for [$ReOCl_3$(bpzm)] are reported in Table 2. The Re–O bond in [$ReOCl_3$(bpzm)] is a typical example of reported terminal multiple Re–O_{oxo} distances in mononuclear $[ReO]^{3+}$ compounds and indicates the presence of a triple bond Re≡O [31]. The Re(1)–Cl(2) distance, affected by *trans* influence of the oxo ligand, is significantly longer than the Re(1)–Cl(1) and Re(1)–Cl(3) bond lengths.

4.4. Geometry optimization

The geometry of [$ReOCl_3$(bpzm)] was optimized in a singlet state by the DFT method with the B3LYP functional. The optimized geometric parameters are gathered in Table 2. The calculated bond lengths and angles are in agreement with the values based upon the X-ray crystal structure data, and the general trends observed in the experimental data are well reproduced in the calculations.

4.5. Charge distribution

Table 3 presents the atomic charges from the natural population analysis (NPA) for [$ReOCl_3$(bpzm)]. The calculated charge on the rhenium atom is considerable lower than the formal charge 5+. The populations of the $5d_{xy}$, $5d_{xz}$, $5d_{yz}$, $5d_{x^2-y^2}$ and $5d_z^2$ orbitals of the central atom in [$ReOCl_3$(bpzm)] are following: 0.920, 0.867, 0.851, 1.938 and 0.917. This is a result of significant charge donation from the ligands; the charges on the chloride and oxo ligands are significantly smaller than −1 and −2, respectively. The

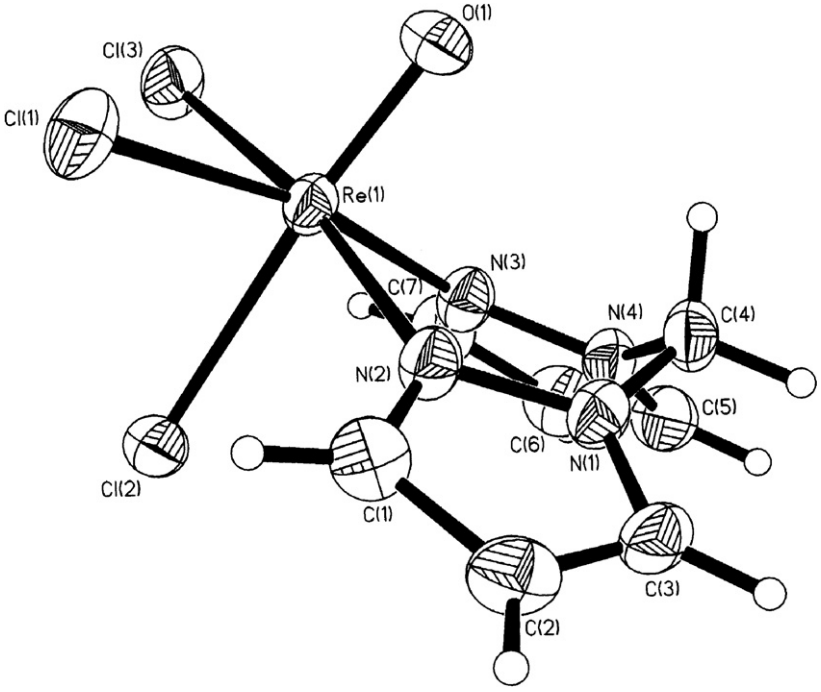


Fig. 1. The molecular structure of [$ReOCl_3$(bpzm)].

Table 2
The experimental and optimized bond lengths (Å) and angles (°) for [$ReOCl_3$(bpzm)]

Bond lengths	Experimental	Optimized	Bond angles	Experimental	Optimized
Re(1)–O(1)	1.679(3)	1.678	O(1)–Re(1)–N(2)	92.18(13)	88.56
Re(1)–N(2)	2.102(3)	2.158	O(1)–Re(1)–N(3)	93.82(14)	88.54
Re(1)–N(3)	2.098(3)	2.158	N(3)–Re(1)–N(2)	87.73(12)	89.02
Re(1)–Cl(1)	2.3623(10)	2.390	O(1)–Re(1)–Cl(1)	96.99(11)	101.10
Re(1)–Cl(2)	2.4502(9)	2.485	O(1)–Re(1)–Cl(2)	174.94(10)	163.30
Re(1)–Cl(3)	2.3653(9)	2.390	O(1)–Re(1)–Cl(3)	96.65(10)	101.08
			Cl(1)–Re(1)–Cl(2)	86.55(4)	90.68
			Cl(1)–Re(1)–Cl(3)	90.36(4)	89.67
			Cl(3)–Re(1)–Cl(2)	86.92(3)	90.68
			N(2)–Re(1)–Cl(1)	89.83(9)	89.83
			N(2)–Re(1)–Cl(3)	171.08(9)	170.26
			N(2)–Re(1)–Cl(2)	84.19(9)	79.60
			N(3)–Re(1)–Cl(1)	169.00(9)	170.26
			N(3)–Re(1)–Cl(2)	82.54(9)	79.59
			N(3)–Re(1)–Cl(3)	90.40(8)	89.83

Table 3
Atomic charges from the natural population analysis (NPA) for [$ReOCl_3$(bpzm)]

Atom	Charge
Re(1)	1.060
O(1)	−0.432
Cl(1)	−0.351
Cl(2)	−0.444
Cl(3)	−0.351
N(1)	−0.221
N(2)	−0.314
N(3)	−0.314
N(4)	−0.221

considerable differences in values of charges are observed for the chloride ligands – less negative are chloride ions in the *cis* position to the terminal oxo ligand. It indicates the higher electron density delocalization from these ligands towards the rhenium center and corresponds to differences in the Re–Cl bonds lengths.

4.6. NBO analysis

Table 4 presents the occupancy and hybridization of the calculated Re–O_t natural bond orbitals (NBOs) for [$ReOCl_3$(bpzm)].

Table 4
The occupancies and hybridization of the calculated natural bond orbitals (NBOs) between the rhenium and the oxo ligand for [$ReOCl_3$(bpzm)]

BD	Occupancy	Hybridization of NBO	BD[a]	Occupancy
Re–O	1.964	$0.493(sd^{3.78})_{Re} + 0.870(sp^{2.23})_O$	$0.870(sd^{3.78})_{Re} - 0.493(sp^{2.23})_O$	0.358
Re–O	1.985	$0.573(d)_{Re} + 0.820(p)_O$	$0.820(d)_{Re} - 0.573(p)_O$	0.288
Re–O	1.981	$0.566(d)_{Re} + 0.824(p)_O$	$0.824(d)_{Re} - 0.566(p)_O$	0.313

BD denotes 2-center bond.
[a] Denotes antibond NBO.

Each natural bond orbital (NBO) σ_{AB} can be written in terms of two directed valence hybrids (HHOs) h_A and h_B on atoms A and B:

$$\sigma_{AB} = c_A h_A + c_B h_B$$

where c_A and c_B are polarization coefficients. Each valence bonding NBO must in turn be paired with a corresponding valence *anti*-bonding NBO:

$$\sigma^*_{AB} = c_B h_A - c_A h_B$$

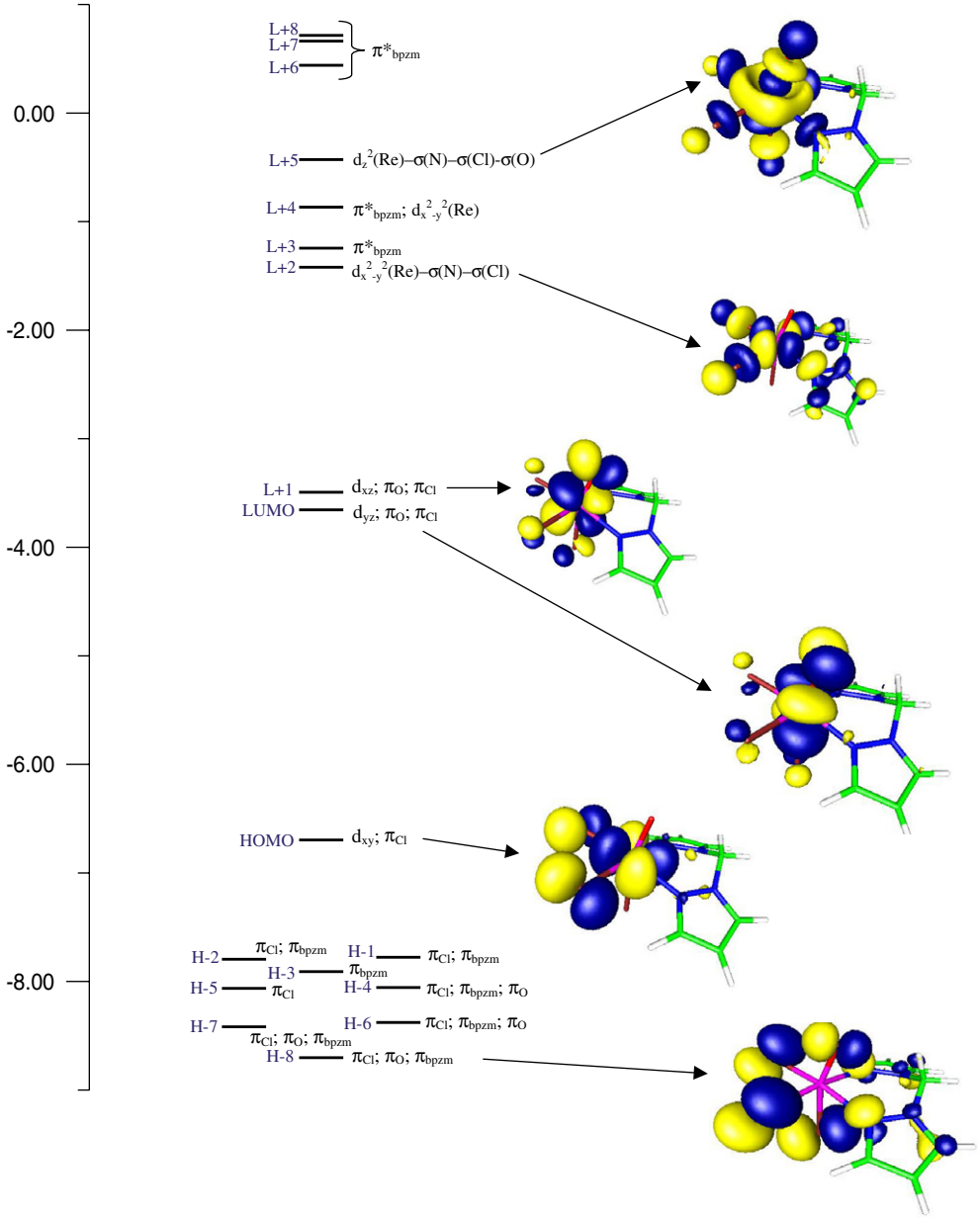


Fig. 2. The energy (eV), character, and some contours of the unoccupied and occupied molecular orbitals of [$ReOCl_3$(bpzm)].

to complete the span of the valence space. The Lewis-type (donor) NBOs are thereby complemented by the non-Lewis-type (acceptor) NBOs that are formally empty in an idealized Lewis picture. The interactions between 'filled' Lewis-type NBOs and 'empty' non-Lewis NBOs lead to loss of occupancy from the localized NBOs of the idealized Lewis structure into the empty non-Lewis orbitals, and they are referred to as 'delocalization' corrections to the zeroth-order natural Lewis structure [32].

For $[ReOCl_3(bpzm)]$ complex, three natural bond orbitals were detected. The s and p oxygen orbitals and s and d rhenium orbitals take part in the σ_{Re-Ot} bond formation, whereas the π_{Re-Ot} bond orbitals result from overlapping of the empty d_{xz} and d_{yz} rhenium orbitals with the occupied p_x and p_y orbitals of the terminal oxygen ligands. Both the σ and π Re–O bonds are clearly polarized towards the oxygen end.

4.7. Electronic structure

The energies, characters and contours of several lowest unoccupied molecular orbitals (LUMO or L) and highest

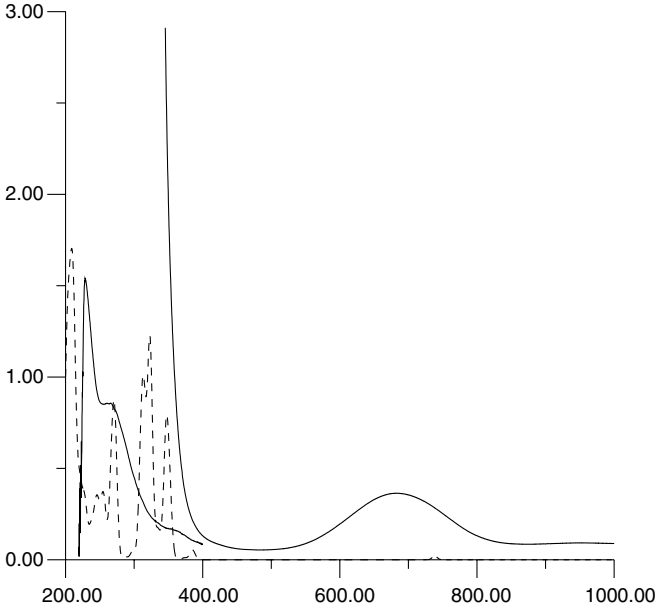


Fig. 3. The experimental (—) and calculated (- - -) electronic absorption spectrum of $[ReOCl_3(bpzm)]$.

Table 5
The energy and molar absorption coefficients of experimental absorption bands and the electronic transitions calculated with the TDDFT method for $[ReOCl_3(bpzm)]$

The most important orbital excitations	Character	λ (nm)	E (eV)	f	Experimental Λ (nm) (E (eV)) ε
H → L + 1	d → d	738.4	1.68	0.0014	692.4 (1.79) 60
H-2 → L	π(Cl)/π(bpzm) → d	387.6	3.20	0.0010	370.0 (3.35) 320
H-1 → L	π(Cl)/π(bpzm) → d	384.2	3.23	0.0029	
H-3 → L	π(bpzm) → d	352.0	3.52	0.0129	
H-5 → L + 1	π(Cl) → d	352.0	3.52	0.0062	
H-3 → L	π(bpzm) → d				
H-2 → L + 1	π(Cl)/π(bpzm) → d	347.0	3.57	0.0321	
H-5 → L + 1	π(Cl) → d	346.0	3.58	0.0134	
H-4 → L	π(Cl)/π(O)/π(bpzm) → d				
H-4 → L + 1	π(Cl)/π(O)/π(bpzm) → d	333.8	3.71	0.0089	
H-7 → L	π(Cl)/π(O)/π(bpzm) → d	325.3	3.81	0.0088	
H-6 → L	π(Cl)/π(O)/π(bpzm) → d	322.9	3.84	0.0711	
H-8 → L	π(Cl)/π(O)/π(bpzm) → d	315.4	3.93	0.0300	
H-6 → L + 1	π(Cl)/π(O)/π(bpzm) → d	312.1	3.97	0.0336	
H-7 → L + 1	π(Cl)/π(O)/π(bpzm) → d	309.2	4.01	0.0173	
H-9 → L	π(Cl)/π(O)/π(bpzm) → d	271.6	4.56	0.0473	266.0 (4.66) 1360
H-8 → L + 1					
H → L + 3	d → π*(bpzm)	266.9	4.64	0.0194	
H-10 → L	π(Cl)/σ(Cl)/σ(O) → d	265.4	4.67	0.0052	
H-10 → L + 1	π(Cl)/σ(Cl)/σ(O) → d	255.5	4.85	0.0170	
H → L + 4	d → π*(bpzm)	251.6	4.93	0.0060	
H-11 → L + 1	π(Cl) → d	244.9	5.06	0.0181	
H-12 → L	σ(Cl)/n(bpzm) → d	238.5	5.20	0.0072	
H-1 → L + 2	π(Cl)/π(bpzm) → d	228.5	5.43	0.0139	228.4 (5.43) 23 340
H-2 → L + 2	π(Cl)/π(bpzm) → d	226.6	5.47	0.0072	
H-5 → L + 2	π(Cl) → d	220.0	5.64	0.0228	
H-1 → L + 3	π(Cl)/π(bpzm) → π*(bpzm)	212.3	5.84	0.0298	
H-2 → L + 3	π(Cl)/π(bpzm) → π*(bpzm)	211.1	5.87	0.0456	
H-6 → L + 2	π(Cl)/π(O)/π(bpzm) → d	207.4	5.98	0.0341	
H-3 → L + 3	π(bpzm) → π*(bpzm)	207.2	5.98	0.0128	
H-7 → L + 2	π(Cl)/π(O)/π(bpzm) → d	204.0	6.08	0.0278	
H-4 → L + 3	π(Cl)/π(O)/π(bpzm) → π*(bpzm)	201.4	6.16	0.0356	
H-2 → L + 4	π(Cl)/π(bpzm) → π*(bpzm)	200.5	6.18	0.0064	

ε – molar absorption coefficient [$dm^3\ mol^{-1}\ cm^{-1}$], f – oscillator strength, H – highest occupied molecular orbital, L – lowest unoccupied molecular orbital.

occupied molecular orbitals (HOMO or H) of [$ReOCl_3$(bpzm)] are presented in Fig. 2. The HOMO–LUMO gap is 3.04 eV. The highest occupied MO of [$ReOCl_3$(bpzm)] is of d_{xy} type with an antibonding contributions from p_π chlorine orbitals. The remaining four d-type orbitals of rhenium are found among unoccupied MOs. The LUMO and LUMO+1 are closely spaced in energy and they can be ascribed as π-antibonding rhenium–oxygen molecular orbitals.

The rhenium atom uses six valence orbitals, $5d_{x^2-y^2}$, $5dz^2$, 6s, $6p_x$, $6p_y$ and $6p_z$ to form σ-bonds with the six ligands, the occupied $5d_{xy}$ orbital of the Re ion remains nonbonding, and empty $5d_{yz}$ and $5d_{xz}$ orbitals interact with the filled $2p_y$ and $2p_x$ orbitals of the terminal oxo ligand to give two π-bonding and two π-antibonding molecular orbitals.

4.8. Electronic spectrum

The experimental and calculated electronic spectra of [$ReOCl_3$(bpzm)] are presented in Fig. 3. Each calculated transition is represented by a Gaussian function $y = ce^{-bx^2}$ with the height (c) equal to the oscillator strength and b equal to 0.04 nm^{-2}.

Table 5 shows the spin-allowed singlet–singlet electronic transitions calculated with the TDDFT method for [$ReOCl_3$(bpzm)]. For the high energy part of the spectrum, only transitions with oscillator strengths larger than 0.0050 are listed in Table 5.

The UV–Vis spectrum of [$ReOCl_3$(bpzm)] exhibits a few intense absorption bands in the range 400–200 nm and a weak absorption in the low energy range – at 692.4 nm.

The longest wavelength experimental band of [$ReOCl_3$(bpzm)] is attributed to the transition of d → d character with small oscillator strengths calculated at 738.4 nm.

The absorption band at 370 nm is assigned to the electronic transitions calculated in the range 390–309 nm. They have *LMCT* (*Ligand–Metal Charge Transfer*) character and originate from the chlorine, oxo and bpzm ligands to the d_{Re} orbitals.

The experimental bands below 300 nm result mainly from *Ligand–Metal Charge Transfer*: π(Cl)/π(O)/π(bpzm) → d, *Ligand–Ligand Charge Transfer*: π(Cl)/π(O) → π*(bpzm) transitions and intraligand (IL) transitions: π(bpzm) → π*(bpzm).

5. Supplementary material

CCDC 625233 contains the supplementary crystallographic data for $C_7H_8N_4Cl_3ORe$. These data can be obtained free of charge via http://www.ccdc.cam.ac.uk/conts/retrieving.html, or from the Cambridge Crystallographic Data Centre, 12 Union Road, Cambridge CB2 1EZ, UK; fax: (+44) 1223-336-033; or e-mail: deposit@ccdc.cam.ac.uk.

Acknowledgement

The Gaussian03 calculations were carried out in the Wrocław Centre for Networking and Supercomputing, WCSS, Wrocław, Poland.

References

[1] R.H. Holm, Chem. Rev. 87 (1987) 1401.
[2] C.C. Romão, F.E. Kühn, W.A. Hermann, Chem. Rev. 97 (1997) 3197.
[3] S. Das, A. Chakravorty, Eur. J. Inorg. Chem. (2006) 2285.
[4] W. Volkert, W.F. Goeckeler, G.J. Ehrhardt, A.R. Ketring, J. Nucl. Med 32 (1991) 174.
[5] E.A. Deutsch, K. Libson, J.L. Vanderheyden, Technetium and Rhenium in Chemistry and Nuclear Medicine, Raven Press, New York, 1990.
[6] C. Pettinari, R. Pettinari, Coord. Chem. Rev. 249 (2005) 663.
[7] M. Machura, R. Kruszynski, M. Jaworska, J. Klak, J. Mroziński, Polyhedron 25 (2006) 2537.
[8] H. Chermette, Coord. Chem. Rev. 178–180 (1998) 699.
[9] M.C. Aragoni, M. Arca, T. Cassano, C. Denotti, F.A. Devillanova, F. Isaia, V. Lippolis, D. Natali, L. Nitti, M. Sampietro, R. Tommasi, G. Verani, Inorg. Chem. Commun. 5 (2002) 869.
[10] P. Romaniello, F. Lelj, Chem. Phys. Lett. 372 (2003) 51.
[11] T.J. Bartczak, W. Czurak, J.O. Dzięgielewski, B. Machura, A. Jankowska, J. Kusz, J. Warczewski, J. Coord. Chem. 52 (2001) 361.
[12] G. Rouschias, G. Wilkinson, J. Chem. Soc. A (1966) 465.
[13] S. Julia, P. Sala, J. del Mazo, M. Sancho, C. Ochoa, J. Elguero, J.P. Fayet, M.C. Vertut, J. Heterocycl. Chem. 19 (1982) 1141.
[14] CrysAlis RED, Oxford Diffraction Ltd., Version 1.171.29.2.
[15] G.M. Sheldrick, Acta Crystallogr., A 46 (1990) 467.
[16] G.M. Sheldrick, SHELXL97. Program for Refinement of Crystal Structures, University of Göottingen, Germany, 1997.
[17] G.M. Sheldrick, SHELXTL: Release 4.1 for Siemens Crystallographic Research Systems, 1990.
[18] M.J. Frisch, G.W. Trucks, H.B. Schlegel, G.E. Scuseria, M.A. Robb, J.R. Cheeseman, J.A. Montgomery Jr., T. Vreven, K.N. Kudin, J.C. Burant, J.M. Millam, S.S. Iyengar, J. Tomasi, V. Barone, B. Mennucci, M. Cossi, G. Scalmani, N. Rega, G.A. Petersson, H. Nakatsuji, M. Hada, M. Ehara, K. Toyota, R. Fukuda, J. Hasegawa, M. Ishida, T. Nakajima, Y. Honda, O. Kitao, H. Nakai, M. Klene, X. Li, J.E. Knox, H.P. Hratchian, J.B. Cross, C. Adamo, J. Jaramillo, R. Gomperts, R.E. Stratmann, O. Yazyev, A.J. Austin, R. Cammi, C. Pomelli, J.W. Ochterski, P.Y. Ayala, K. Morokuma, G.A. Voth, P. Salvador, J.J. Dannenberg, V.G. Zakrzewski, S. Dapprich, A.D. Daniels, M.C. Strain, O. Farkas, D.K. Malick, A.D. Rabuck, K. Raghavachari, J.B. Foresman, J.V. Ortiz, Q. Cui, A.G. Baboul, S. Clifford, J. Cioslowski, B.B. Stefanov, G. Liu, A. Liashenko, P. Piskorz, I. Komaromi, R.L. Martin, D.J. Fox, T. Keith, M.A. Al-Laham, C.Y. Peng, A. Nanayakkara, M. Challacombe, P.M.W. Gill, B. Johnson, W. Chen, M.W. Wong, C. Gonzalez, J.A. Pople, Gaussian 03, Revision B.03, Gaussian, Inc., Pittsburgh, PA, 2003.
[19] A.D. Becke, J. Chem. Phys. 98 (1993) 5648.
[20] C. Lee, W. Yang, R.G. Parr, Phys. Rev. B 37 (1988) 785.
[21] M.E. Casida, in: J.M. Seminario (Ed.), Recent Developments and Applications in Modern Density Functional Theory, Theoretical and Computational Chemistry, vol. 4, Elsevier, Amsterdam, 1996.
[22] P.J. Hay, W.R. Wadt, J. Chem. Phys. 82 (1985) 299.
[23] E.D. Glendening, A.E. Reed, J.E. Carpenter, F. Weinhold, NBO (version 3.1).
[24] X.L.R. Fontaine, E.H. Fowles, T.P. Layzell, B.L. Shaw, M. Thornton-Pett, J. Chem. Soc., Dalton Trans. (1991) 1519.
[25] K. Nakamoto, Infrared and Raman Spectra of Inorganic and Coordination Compounds, fourth ed., Wiley-Interscience, New York, 1986.

[26] G.A. Jeffrey, W. Saenger, Hydrogen Bonding in Biological Structures, Springer-Verlag, 1994.
[27] G.R. Desiraju, T. Steiner, The Weak Hydrogen Bond in Structural Chemistry and Biology, Oxford University Press, 1999.
[28] D.C. Bradley, M.B. Hursthouse, K.M.A. Malik, A.J. Nielson, R.L. Short, J. Chem. Soc., Dalton Trans. (1983) 2651.
[29] V.S. Sergienko, M.A. Porai-Koshits, V.E. Mistryukov, K.V. Kotegov, Koord. Khim. 8 (1982) 230.
[30] J.M. Mayer, D.L. Thorn, T.H. Tulip, J. Am. Chem. Soc. 107 (1985) 7454.
[31] J.M. Mayer, Inorg. Chem. 27 (1988) 3899.
[32] A.E. Reed, L.A. Curtiss, F. Weinhold, Chem. Rev. 88 (1988) 899.

evaluated and its metal complexes, especially with copper(II), showed an enhanced biological activity with respect to the free ligand. One of these copper *N*-aroyl-*N*′-thioaroylhydrazines derivatives was able to inhibit cell proliferation and induce apoptosis [15]. Copper(II) complexes of α-ketoglutaric acid thiosemicarbazone also inhibited cell proliferation through the apoptosis mechanism [16]. Copper(II) complexes of thiosemicarbazones derived from acyl diazines showed cytotoxic activity against colon adenocarcinoma HT-29 cells and large and small lung carcinoma cells. They inhibit the enzyme ribonucleoside diphosphate reductase and affect the synthesis of DNA. One of these complexes is a potent inducer of apoptosis in Burkitt's lymphoma cells [17].

Cu(II) complexes of thioaroylhydrazines derivatives show significant inhibition of ^{3}H-thymidine and ^{3}H-uridine incorporation into DNA and RNA in P-815 and L-929 tumor cells and have an effect on DNA synthesis. They inhibit tumor growth and that process is associated with induction of apoptosis in lymphocytes, but the detailed mechanism of inhibition is still unclear. The inhibition in tumor cell blastogenesis could be a direct result of the interaction of the metal complexes with DNA, thus interfering with the normal process of its replication. The inhibition of uridine incorporation suggests their influence on the activity of enzymes involved in DNA replication, especially DNA endonucleases causing DNA fragmentation [18].

Over recent years, increasing attention has been paid to pyrazoles, pyrimidines and related N-containing heterocyclic derivatives, which play an important role in many biological processes due to their coordinating ability for metal ions [19]. The studies have been stimulated by promising pharmacological [20], analytical [21] and agrochemical [22] applications. Pyrazoles and their complexes with metals, besides having antitumor activity, are analgesic and antiinflammatory agents, such as the pyrimidinopyrazole derivative – mepirizole [19]. Some mixed chelate copper-based drugs have exhibited greater antineoplastic potency than cisplatin in in vitro and in vivo studies of a variety of tumor cell lines [23]. Pyrazol-thioketone derivatives have antimicrobial activity. They inhibit growth of *Staphylococcus aureus*, *Staphylococcus typhii*, *Candida albicans* and *Mycobacterium tuberculosis* [24]. *O*-Hydroxyphenylopyrazoles are used as UV stabilizers, analytical reagents in the complexation of metal ions, analgesic agents and platelet aggregation inhibitors [21]. Diarylopyrazoloquinolinones have affinity for the benzodiazepine receptor and their activity is similar to that of diazepam [25].

Here we present the synthesis of the new chelating ligands 5-(2-hydroxybenzoyl)-3-methyl-1-(2-pyridinyl)pyrazol-4-carboxylic acid methyl ester (**2**) and 3-methyl-1 -(2-pyridinyl)-1*H*-chromene[4,3-*c*]pyrazol-4-on (**3**), as well as their solid pyrazole complexes with Cu(II). Physical and the protolytic properties of the ligands as well as their interaction with Cu(II) in solution are also shown.

2. Experimental

2.1. Materials

All substances were used without further purification. Chloroform-D solvent for NMR spectroscopy was obtained from Dr. Glaser AG Basel. Solvents for synthesis (toluene, methanol, dimethylformamide, acetone) were reagent grade or better and were dried according to standard methods. The melting points were determined using an Electrothermal 1A9100 apparatus and they are uncorrected. The IR spectra were recorded on a Pye-Unicam 200G Spectrophotometer in KBr and CsI. The ^{1}H NMR spectra were registered at 300 MHz on a Varian Mercury spectrometer. The MS data were obtained on a LKB 2091 mass spectrometer (70 eV ionization energy). The MS-FAB data were determined on Finnigan Matt 95 mass spectrometer (NBA, Cs^{+} gun operating at 13 keV). For the new compounds satisfactory elemental analyses (±0.3% of the calculated values) were obtained using a Perkin–Elmer PE 2400 CHNS analyzer.

2.2. Synthesis of the ligands

2.2.1. Synthesis of 5-(2-hydroxybenzoyl)-3-methyl-1-(2-pyridinyl)pyrazol-4-carboxylic acid methyl ester (2)

2-Hydrazinopyridin (5 mmol) in EtOH (5 mL) was added at room temperature to a solution of 2-methyl-4-oxo-4*H*-chromene-3-carboxylic acid methyl ester (**1**) (5 mmol) in EtOH (10 mL). The mixture was refluxed for 1 h. The solid crude product, which precipitated after 24 h, was filtered off, dried and crystallized from ethanol. The pure compound was obtained as a white solid.

Yield: 942 mg (61%), mp: 158.5–159.9 °C. IR: ν_{max}/cm^{-1} 3190 (OH); 1705 (C=O); 1613 (C=N) cm^{-1}. ^{1}H NMR ($CDCl_3$): $\delta = 2.57$ (s, 3H, C–CH_3); 3.62 (s, 3H, O–CH_3); 6.83–8.34 (m, 8H, aromat) ppm. ^{13}C NMR ($CDCl_3$): $\delta = 14.55$ (C–CH_3); 51.53 (O–CH_3); 164.46 (C=O) ppm. MS *m*/*z*: 309.0. *Anal*. found: C, 65.97; H, 4.67; N, 13.30. Calc. for $C_{17}H_{13}N_3O_3$ (309.311): C, 66.01; H, 4.89; N, 13.59.

2.2.2. Synthesis of 3-methyl-1-(2-pyridinyl)-1H-chromene[4,3-c]pyrazol-4-on (3)

N-Methylhydrazin (0.5 mmol) was added at room temperature to a solution of 5-(2-hydroxybenzoyl)-3-methyl-1-(2-pyridin)pyrazol-4-carboxylic acid methyl ester (**2**) (0.5 mmol) in MeOH (10 mL). The mixture was refluxed for 1 h. The solid product, which precipitated after 1 h, was filtered off, dried and crystallized from ethyl acetate. The pure compound was obtained as a white crystal solid.

Yield: 88 mg (63%), mp: 202.8–205.1 °C. IR: ν_{max}/cm^{-1} 1742 (C=O); 1615 (C=N) cm^{-1}. ^{1}H NMR ($CDCl_3$): $\delta = 2.71$ (s, 3H, CH_3); 7.41–8.76 (m, 8H, aromat) ppm. ^{13}C NMR ($CDCl_3$): $\delta = 13.32$ (C–CH_3); 158.12 (C=O) ppm. MS *m*/*z*: 278.0. *Anal*. found: C, 68.91; H, 3.51; N,

15.17. Calc. for $C_{16}H_{11}N_3O_2$ (277.269): C, 69.30; H, 4.0; N, 15.16.

2.3. Synthesis of copper(II) complexes 4 and 5

2.3.1. Synthesis of complex 4

Copper(II) chloride (0.1 mmol) in MeOH (2 mL) was slowly added at room temperature to a solution of 5-(2-hydroxybenzoyl)-3-methyl-1-(2-pyridinyl)pyrazol-4-carboxylic acid methyl ester (**2**) (0.1 mmol) in MeOH (10 mL). The mixture was left at room temperature for 24 h. The yellow solid product which precipitated was filtered off and crystallized from acetonitryl. The pure compound was obtained as a yellow crystal solid.

Yield: 36 mg (81%), mp: 197.4–199.1 °C. IR: ν_{max}/cm^{-1} 3221 (OH); 1717 (C=O); 455 (Cu–N); 295 (Cu–Cl) cm^{-1}. FAB-MS *m/z*: 443.0. *Anal* found: C, 46.01; H, 3.32; N, 9.41. Calc. for $C_{17}H_{15}N_3O_3CuCl_2$ (443.35): C, 46.05; H, 3.41; N, 9.48.

2.3.2. Synthesis of complex 5

Copper(II) chloride (0.1 mmol) in ethyl acetate (3 mL) was slowly added at room temperature to a solution of 3-methyl-1-(-2-pyridinyl)-1*H*-chromene[4,3-c]pyrazol-4-on (**3**) (0.1 mmol) in ethyl acetate (10 mL). The green solid precipitated after a few minutes. The product was filtered off. The pure compound was obtained as a green crystal solid.

Yield: 22 mg (53%), mp: 297–298 °C. IR: ν_{max}/cm^{-1} 1749 (C=O); 457 (Cu–N); 302 (Cu–Cl) cm^{-1}. FAB-MS *m/z* 412.0. *Anal*. found: C, 46.41; H, 2.62; N, 10.21. Calc. for $C_{16}H_{11}N_3O_2CuCl_2$ (411.619): C, 46.68; H, 2.69; N, 10.21.

2.4. Potentiometric studies

The protonation constants of ligands **2** and **3** were determined by pH-metric titration of 4 cm^3 samples, at 25 ± 0.1 °C. The total concentration of ligand **2** in each sample ranged within $3.75–6.25 \times 10^{-4}$ mol dm^{-3}. For ligand **3** the concentration range amounted to $3.75–6.25 \times 10^{-4}$ mol dm^{-3}. Owing to the very low solubility in pure water, the mixed 5% v/v 1,4-dioxane–water solvent was used for ligands **2** and **3**, respectively. The titrations were carried out with carbonate-free NaOH solution of known concentration (0.1 mol dm^{-3}). The value of $pK_w = 13.77$ resulted from our acid–base calibrations in the same solvent. The hydrolysis constants of the aquo-ion were determined under the same conditions as in the titrations in the presence of ligand.

The metal–ligand interaction was studied by pH-metric titration of the same volume, medium and temperature as described for the ligand alone. The ligand was in excess – the L:M molar ratio amounted to 4:1, 5:1 and 6:1 at a total metal concentration within $1.1–5.0 \times 10^{-4}$ mol dm^{-3}. $Cu(NO_3)_2$ purum p.a. of Fluka AG was used. The standard solution was titrated with the disodium salt of EDTA in the presence of murexide.

The pH was measured with a Molspin Ltd. (Newcastle upon Tyne, England) automatic titration set and combined OSH 10-10 electrode (Metron, Poland). The total volume of the Hamilton microsyringe in the autoburette was 250 µl, the volume increments amounted to 0.0025 ml. The experiments were performed using MOLSPIN.EXE software.

The electrode was calibrated in the $-\log[H^+]$ scale by titration of 0.005 M HNO_3 (in 5% dioxane) with 0.1 M NaOH, temperature 25 °C. Then concentration overall protonation constants $\beta_{lh} = [L_lH_h]/[L]^l[H]^h$ were calculated by the SUPERQUAD computer program [26].

2.5. X-ray measurements

The light white single crystal of ligand **2** was used for measurement on an AFC5S Rigaku diffractometer [27]. X-ray intensities were collected using graphite monochromated Mo Kα radiation and the ω scan technique. After each group of 150 reflections three standard reflections were monitored and insignificant (<2%) intensity fluctuation was observed. All data were corrected for Lorentz and polarization effect [28].

The structure of ligand **2** was solved by direct methods (SHELXS97 [29]) and refined on F^2 by the full-matrix least-squares technique (SHELXL97 [27]). All non-hydrogen atoms were refined anisotropically. During the refinement the atoms of the C13–C17 pyridyl ring were found to be disordered. Two components of the disorder were modelled, using rigid planar hexagons for the phenyl rings. Refinement of the site-occupation factors of the disordered atoms indicated that the two conformations were approximately equally occupied. Finally, the occupancies of the disordered atoms were fixed at 0.5 and similar restraints were applied to the atomic displacement parameters of those disordered atoms. The distances between atom pairs N2/C13A and N2/C13B were restrained to be equal, with an effective s.u. of 0.003 Å.

Carbon-bonded H-atoms were included in calculated positions (C–H = 0.93–0.98 Å) and constrained to ride on their parent atoms with isotropic displacement parameters equal to $1.2U_{eq}$(C) (or $1.5U_{eq}$ for methyl C atoms). The oxygen-bonded H-atoms (H3 and H41, H42 in the water molecule) were located from the difference map and refined isotropically.

Selected crystal data and details of the structure refinement are collected in Table 2. Geometrical calculations and drawings were performed with PLATON [30].

Table 1
Selected IR bands for ligands **2**, **3** and complexes **4**, **5**

ν (cm^{-1})	OH	–C=O	C=C	C=N	M–N–	M–Cl
2	3190	1705	1613	1543		
3		1742	1615	1542		
4	3221	1717	1615	1554	455	295
5		1749	1612	1580	457	302

Table 2
Crystallographic data, data collection and refinement for ligand **2**

	Ligand **2**
Crystal data	
Chemical formula	$C_{17}H_{15}N_3O_3 \times H_2O$
M_r	327.34
Cell setting, space group	monoclinic, $P2_1/c$
a (Å)	13.945(3)
b (Å)	12.536(3)
c (Å)	16.497(5)
β (°)	144.87(2)
V (Å^3)	1659.5(11)
Z	4
D_x (Mg m^{-3})	1.310
Radiation type	Mo K_α ($\lambda = 0.7107$ Å)
Number of reflections for cell parameters	20
θ Range (°)	20.03–24.89
μ (mm^{-1})	0.095
Temperature (K)	293(2)
Crystal form, colour	prism, white
Crystal size (mm)	$0.50 \times 0.35 \times 0.25$
Data collection	
Diffractometer	AFC-5S Rigaku
Number of measured reflections	4038
Number of independent reflections	3814
Number of observed reflections	1703
Criterion for observed reflections	$I > 2\sigma(I)$
θ_{max} (°)	27.51
Range of h, k, l	$-18 \Rightarrow h \Rightarrow 18$ $0 \Rightarrow k \Rightarrow 16$ $-18 \Rightarrow l \Rightarrow 21$
Refinement	
Refinement on	F^2
R [$F^2 > 2\sigma(F^2)$]	0.0584
wR (F^2)	0.1889
S	0.873
Number of reflections	3814
Number of parameters	258
$(\Delta/\sigma)_{max}$	0.000
$\Delta\rho_{max}$ (e Å^{-3})	0.661
$\Delta\rho_{min}$ (e Å^{-3})	−0.470

3. Results and discussion

3.1. Preparation of the ligands and their complexes

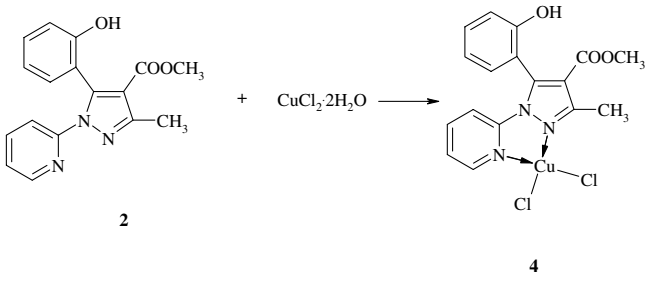
It has been reported that certain copper(II) complexes catalyze radical formation while others seem to have antioxidant properties [31]. Their actual behavior depends upon the chemical environment and the nature of chelating agents. In the reaction of 2-methyl-4-oxo-4*H*-chromene-3-carboxylic acid methyl ester (**1**) and 2-hydrazinepyridin (1:1) in boiling methanol we have obtained 5-(2-hydroxybenzoyl)-3-methyl-1-(2-pyridin)pyrazol-4-carboxylic acid methyl ester (**2**) with a good yield (61%). This compound easily cyclizes under basic conditions to form 3-methyl-1-(2-pyridinyl)-1*H*-chromene[4,3-*c*]pyrazol-4-on (**3**) (see Scheme 1).

The physical data are given in Section 2.

3.2. Synthesis of the complexes

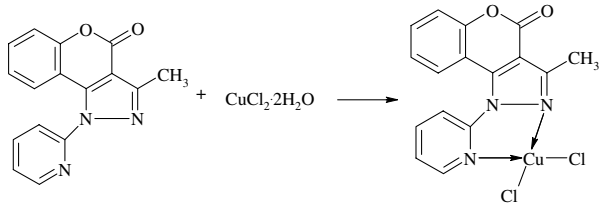
Complex **4**, of the formula $Cu(L)Cl_2$, was obtained by treatment of the corresponding ligand **2** with $CuCl_2 \cdot 2H_2O$ (in a 1:1 molar ratio) in methanol. Complex **5** was not formed in methanolic solution, most likely due to methanolysis (see Schemes 2 and 3) as we have isolated the free ligand **3**. We have obtained complex **5** in the reaction of **3** and $CuCl_2 \cdot 2H_2O$ in ethyl acetate. Under this condition methanolysis or hydrolysis is not possible and the complex is formed.

The IR spectra of the complexes are similar to those of the free ligands (see Table 1). The most characteristic bands are those at 1612 and 1580 cm^{-1}, attributable to the pyraz-



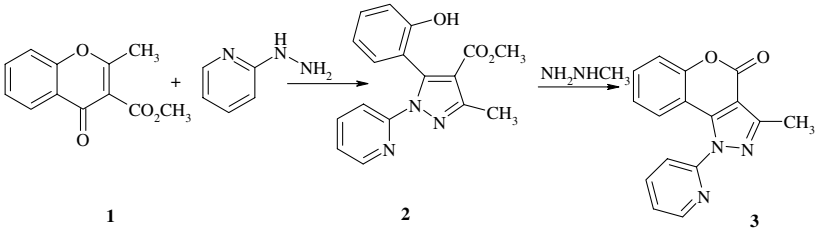
2 4

Scheme 2. Synthesis of complex **4**.



3 5

Scheme 3. Synthesis of complex **5**.



1 2 3

Scheme 1. The synthesis of ligands **2** and **3**.

olyl ν(C=C) and ν(C=N) groups. The band at 3200 cm^{-1} is characteristic of the OH group in ligand **2** and its complex **4**.

The IR spectra of the Cu complexes in the region 500–100 cm^{-1} were also recorded and show well-defined bands corresponding to ν(Cu–Cl) at 295 and 303 cm^{-1}. Bands attributable to ν(Cu–N) at 455 and 457 cm^{-1} are also present.

The $\nu_{C=N}$ band observed for compound **2** at 1543 cm^{-1} is shifted towards higher frequencies (to 1554 cm^{-1}) for complex **4**. This observation can be explained by participation of the nitrogen atom in the coordination with the metal ions in the complex [32].

3.3. Crystal and molecular structure of ligand 2

The molecular structure of ligand **2** is shown in Fig. 1. The molecule consists of four fragments: pyridyl and phenolic rings, methyl and carboxylate groups substituted on the pyrazole ring. The pyridyl rings have been found to be disordered (see Section 2.5). Both components of the disordered pyridyl rings are refined to be planar, the dihedral angle between their planes is 30(1)°. The pyrazole and benzene rings are also planar with a dihedral angle equal to 66(1)°. The bond lengths and angles listed in Table 3 are within the normal ranges, hence no detailed discussion is needed. The principal structural interest lies in the molecular interactions. Hydrogen-bonding geometries are listed in Table 4. The molecules of structure **2** are linked into two-dimensional layers by a combination of O–H···O and O–H···N hydrogen bonds. These layers are stacked along the [0 1 0] direction. Fig. 2 presents the hydrogen-bonding network projected on the *ac* plane. There are only weak C–H···O contacts between neighboring layers and no specific interactions are observed; in particular, aromatic π–π stacking interactions are absent from the structure of **2**.

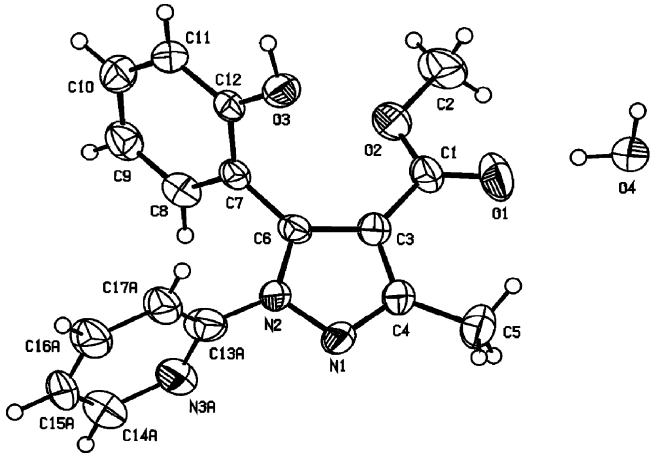


Fig. 1. The molecular structure of ligand **2** with the atom numbering scheme. The second component of the disordered pyridyl ring (C13*B*–C17*B*) has been omitted for clarity. Displacement ellipsoids are drawn at the 40% probability level and H atoms are shown as small spheres of arbitrary radii.

Table 3
Selected geometric parameters for ligand **2**

Bond lengths (Å)			
N1–N2	1.375(3)	O3–C12	1.355(3)
N1–C4	1.324(7)	C4–C5	1.495(9)
C3–C4	1.411(4)	C1–C3	1.468(4)
C3–C6	1.378(7)	C1–O1	1.211(8)
N2–C6	1.358(3)	C1–O2	1.329(4)
C6–C7	1.479(4)	O2–C2	1.454(4)
Bond angles (°)			
N2–N1–C4	105.1(2)	C6–N2–N1	112.3(2)
N1–C4–C3	110.5(2)	C3–C1–O1	124.0(3)
C4–C3–C6	106.6(2)	C3–C1–O2	114.1(5)
C3–C6–N2	105.5(2)	C1–O2–C2	115.4(2)

Table 4
Hydrogen-bonding geometry for ligand **2**

	D–H (Å)	H···A (Å)	D···A (Å)	D–H···A (°)
O3–H3···O4^{i}	0.98(3)	1.73(3)	2.696(3)	169(6)
O4–H41···N1^{ii}	0.92(3)	2.04(4)	2.923(4)	161(6)
O4–H42···O1	0.91(7)	1.98(8)	2.880(7)	170(4)
C9–H9···O3^{iii}	0.93	2.56	3.302(4)	137

Symmetry codes: (i) x, $1/2 - y$, $z - 1/2$; (ii) $x - 1$, $1/2 - y$, $z - 1/2$; (iii) $1 - x$, $1/2 + y$, $1/2 - z$.

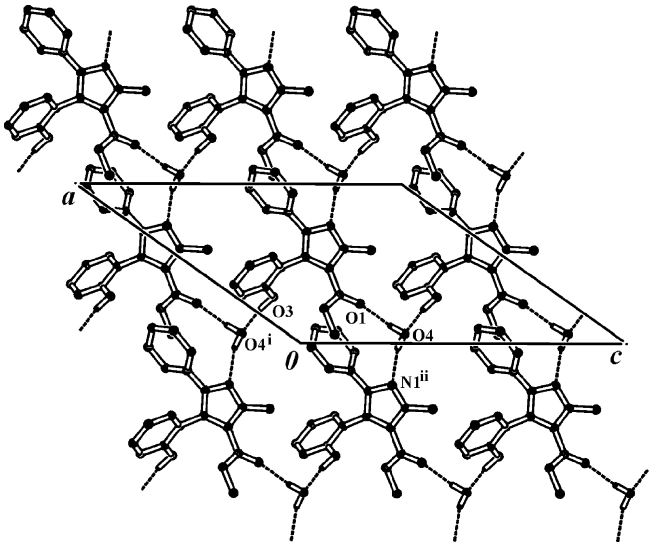


Fig. 2. The hydrogen-bonding layer in **2** projected on the *ac* plane. The *B* component of the disordered atoms and H-atoms not participating in the hydrogen-bonding have been omitted for clarity. [Symmetry codes: (i) x, $1/2 - y$, $z - 1/2$; (ii) $x - 1$, $1/2 - y$, $z - 1/2$].

3.4. Determination of protonation constants

As a result of the protonation constants, it follows that ligand **2** behaves as a triprotonated molecule, whereas ligand **3** is indicative of two functional groups. The stepwise protonation constants $\log K$ reported here (Table 5) may be compared with the corresponding values of relatively simple heterocyclic compounds – corresponding to the groups found in ligands **2** and **3**.

Table 5
Experimental conditions of potentiometric titrations and values of overall protonation constants of **2** and **3** at 25 °C

	Ligand **2**		Ligand **3**
Number of titrations	3		2
Range of $-\log[H^+]$	3.1–11.0		3.0–5.5
$\log\beta_{11}$	9.31(2)[a]		3.99(1)[d]
$\log\beta_{12}$	13.36(2)[b]		7.33(1)[e]
$\log\beta_{13}$	16.78(3)[c]		
σ	3.36		0.31
χ^2	2.57		7.20
$\log K$ (OH, phenol)	9.31		
		9.79 [33]	
$\log K$ (N, pyridine)	4.04		3.99
		5.22[34]	
$\log K$ (N, Me-pyrazole)	3.42		3.34
		3.58 [35]	

Solvent: 5% v/v 1,4-dioxane–H_2O. Standard deviations in parentheses. The literature data correspond to the same temperature.
L^- in the case of ligand **2** denotes the form with deprotonated phenol OH.
[a] Equilibrium: $L^- + H^+ \rightleftharpoons LH$.
[b] Equilibrium: $L^- + 2H^+ \rightleftharpoons LH_2^+$.
[c] Equilibrium: $L^- + 3H^+ \rightleftharpoons LH_3^{2+}$.
[d] Equilibrium: $L + H^+ \rightleftharpoons LH^+$.
[e] Equilibrium: $L + 2H^+ \rightleftharpoons LH_2^{2+}$.

3.5. Determination of stability constants (ligand **2**)

In the case of ligand **2** with a deprotonated phenol ring (L^-), the metal renders accessible six coordination sites (Table 6). The three consecutive equilibria are accepted in the refinements although none of the assumed bridged dimeric species has been found suitable in the model. *N*-Pyridine and *N*-pyrazole are the most probable electron pair donors, giving rise to highly favourable five-membered chelate rings. At lower pH, however, when the OH group is undissociated, only a complex with a L:M ratio of 2:1 could be confirmed (Fig. 3).

Table 6
Experimental conditions of potentiometric titrations and values of overall stability constants of ligand **2** at 25 °C

	Ligand **2**
Number of titrations	5
Range of $-\log[H^+]$	3.8–10.1
$\log\beta_{10-1}$	−7.22(6)[a]
$\log\beta_{10-2}$	−13.36(2)[b]
$\log\beta_{110}$	7.31(4)[c]
$\log\beta_{120}$	12.27(2)[d]
$\log\beta_{130}$	15.72(3)[e]
$\log\beta_{122}$	26.05(3)[f]
σ	1.06
χ^2	5.64

Solvent: 5% v/v 1,4-dioxane–H_2O. Standard deviations in parentheses.
[a] Equilibrium: $Cu^{2+} \rightleftharpoons CuH_{-1}^{+} + H^+$.
[b] Equilibrium: $Cu^{2+} \rightleftharpoons CuH_{-2} + 2H^+$.
[c] Equilibrium: $L^- + Cu^{2+} \rightleftharpoons CuL^+$.
[d] Equilibrium: $2L^- + Cu^{2+} \rightleftharpoons CuL_2$.
[e] Equilibrium: $3L^- + Cu^{2+} \rightleftharpoons CuL_3^-$.
[f] Equilibrium: $2L^- + 2H^+ + Cu^{2+} \rightleftharpoons CuL_2H_2^{2+}$.

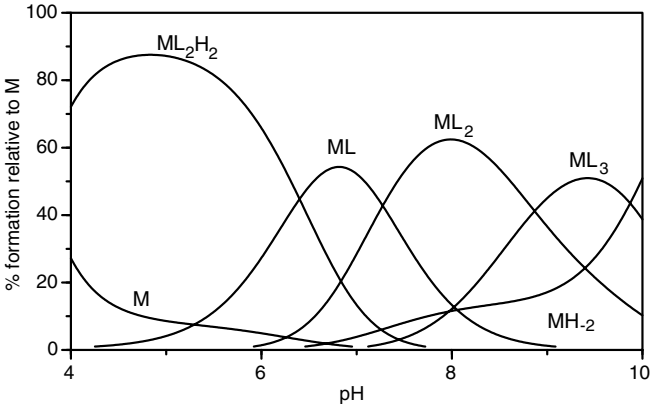


Fig. 3. Species distribution in a solution containing M = Cu from $Cu(NO_3)_2$ and L = ligand **2** at a 1:4 molar ratio. Solv. 5% v/v 1,4-dioxane–water. $C_{Cu} = 3.4 \times 10^{-4}$ mol dm^{-3}. Temperature 25 °C.

The interaction of **3** with copper(II) during the titration was very weak in spite of the protolytic properties of the nitrogen functions being quite similar to **2** (Table 5). This resulted in a visible precipitation already at pH ~ 5.

As can be seen in Fig. 3 the MH_{-1} monohydroxo complex is completely overhelmed by a dihydroxo MH_{-2} complex and the formation of significant amounts of the MH_{-2} complex occurs essentially at pH > 8.5.

4. Spectrophotometric studies of the Cu(II)–ligand interaction

With a L:M molar ratio of 4:1, due to high concentrations of the metal (1.25×10^{-3} mol dm^{-3}), the experiments needed for this method were made in 1,4-dioxane–water solutions (10% v/v). The basicity of the solution was enhanced by adding small portions of 0.1 M NaOH of known density (20–40 μl) to a sample with an initial volume of 2.4 cm^3. The accurate number of millimoles was evaluated by weighing the cell after each addition.

As can be seen in Fig. 4, a rise in absorbance occurred already at pH ~ 4. With alkalization the solution became more and more yellow (up to dark-yellow) until pH = 8.63 when the precipitation disturbed further absorption measurements.

As it is well known for hexacoordinate Cu(II) compounds [36,37] in a tetrahedral environment, the crystal field splitting leads to three transitions (both for a tetragonal bipyramid elongated along the *z*-axis – ground state $^2B_{1g}$ and for the shortened bipyramid – ground state $^2A_{1g}$). Accordingly, in our spectra we may propose to assign the broad maximum at ~700 nm (shifting from 730 to 707 nm) as the lowest energy band. The second band, initially only an inflection, becomes visible at higher pH, at ca. 430–440 nm, together with the rising complex formation, whereas the third band is probably masked by the highly intensive tail below 400 nm (Fig. 4). The very high intensity (ε exceeding 10^4) indicates the tail of a strong charge transfer band. Moreover, the rise of absorbance within the observed tail makes it impossible to observe

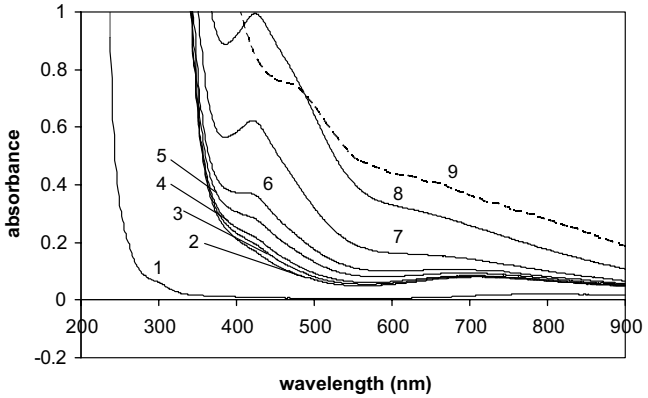


Fig. 4. Absorption spectra in a solution containing $Cu(NO_3)_2$ and ligand **2** at a 1:4 molar ratio (starting from the aquo-ion; curve 1). Solv. 10% v/v 1,4-dioxane–water $C_{Cu} = 1.25 \times 10^{-3}$ mol dm^{-3}. Curves 2–9 denote the spectra scanned after adding a consecutive portion of acid. pH: 2 – 4.07; 3 – 4.32; 4 – 4.68; 5 – 5.26; 6 – 6.92; 7 – 7.94; 8 – 8.63. Curve 9 – precipitation.

the blue shift of the much weaker d–d band near 430 nm – the shift is slightly towards longer wavelengths.

5. Conclusions

In this paper, we have shown a simple and convenient route for the synthesis of new chelating ligands and their copper(II) complexes. The newly synthesized ligands **2** and **3** create neutral complexes of the general type $MLCl_2$. The molecular structure of ligand **2**, which crystallizes as a monohydrate, has been confirmed by X-ray analysis. The crystal packing of **2** consists of two-dimensional layers generated by hydrogen bonds. Between these layers weak C–H···O contacts are observed.

The complexing properties of **2** with Cu(II) in solution could be related to the phenol 2-hydroxy group. In alkali medium, the ionization of this group, introducing an additional negative charge, enhances the donor properties of the potential nitrogen functions (pyridine and Me-pyrazole) by an inductive effect. As a result the refinements confirm the presence of three consecutive complexes (ML, ML_2 and ML_3) where the chelate rings use up to all six coordination sites. On contrary, in more acidic medium (pH 4–6) only one of the potential coordination modes was accepted: the ML_2H_2 species with undissociated OH.

The lack of inductive effects in the case of **3** leads to a very weak interaction with the metal in solution, which in connection with the low first hydrolysis constant of $Cu(II)_{aq.}$ (as follows from Table 6: $\log K_{OH} = -\log \beta_{10-1} = 7.22$) results in precipitation at relatively low pH.

Studies on the biological activity (cytotoxicity) of the synthesized compounds are in progress.

6. Supplementary material

CCDC 621681 contains the supplementary crystallographic data for the compound referred in this paper. These data can be obtained free of charge via http://www.ccdc.cam.ac.uk/conts/retrieving.html, or from the Cambridge Crystallographic Data Centre, 12 Union Road, Cambridge CB2 1EZ, UK; fax: +(44) 1223-336-033; or e-mail: deposit@ccdc.cam.ac.uk.

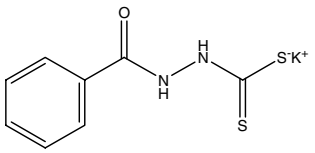
Acknowledgements

Financial support from the Medical University of Łódź: Grant No. 503-3066-2 to E. Budzisz and 503-3014-2 to the Laboratory of Physical and Biocoordination Chemistry is gratefully acknowledged.

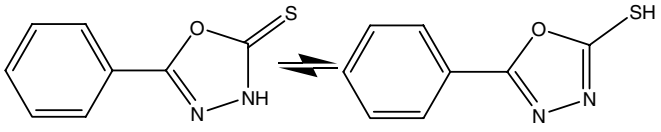
References

[1] M.C. Linder, Biochemistry of Copper, Plenum Press, New York, 1991.
[2] I.A. Koval, K. van der Schilden, A.M. Schuitema, P. Gamez, C. Belle, J.-L. Pierre, M. Lueken, B. Krebs, O. Roubeau, J. Reedijk, Inorg. Chem. 44 (2006) 4372.
[3] T. Wang, Z. Guo, Curr. Med. Chem. 13 (2006) 525.
[4] T.A. Bayer, S. Schafer, H. Breyhan, O. Wirths, C. Treiber, G. Multhaup, Clin. Neuropathol. 25 (2006) 163.
[5] Y.H. Sung, C. Rospigliosi, D. Eliezer, Biochim. Biophys. Acta 1764 (2006) 5.
[6] H. Hayashi, M. Yano, Y. Fujita, S. Wakusawa, Med. Mol. Morphol. 39 (2006) 121.
[7] M.L. Schlief, T. West, A.M. Craig, D.M. Holtzman, J.D. Gitlin, Proc. Natl. Acad. Sci. U.S.A. 103 (2006) 14919.
[8] T. Fujimori, S. Yamada, H. Yasui, H. Sakurai, Y. In, T. Ishida, J. Biol. Inorg. Chem. 10 (2005) 831.
[9] Y. Zheng, Y. Yi, Y. Wang, W. Zhang, M. Du, Bioorg. Med. Chem. Lett. 16 (2006) 4127.
[10] B. Rosenberg, L.V. Camp, J.E. Trosko, V.H. Mansour, Nature 223 (1969) 385.
[11] G. Zhao, H. Lin, Cur. Med. Chem. 5 (2005) 137.
[12] I. Garcia-Mora, L. Ruiz-Ramirez, C. Gomez-Ruiz, M. Tinco-Mendez, A. Marquez-Quinones, L. Romero de Lira, A. Marin-Hernandez, L. Macias-Rosales, M.E. Bravo-Gomez, Metal-Based Drugs 8 (2001) 19.
[13] T.S. Lobana, R. Rekha, R.J. Butcher, A. Castineiras, E. Bermejo, P.V. Bharatam, Inorg. Chem. 45 (2006) 1535.
[14] M. Belicchi-Ferrari, F. Bisceglie, G. Pelosi, M. Sassi, P. Tarasconi, M. Dornia, S. Capacchi, R. Albertini, S. Pinelli, J. Inorg. Biochem. 90 (2002) 113.
[15] M. Baldini, M. Belicchi-Ferrari, F. Bisceglie, G. Pelosi, S. Pinelli, P. Tarasconi, Inorg. Chem. 42 (2003) 2049.
[16] M. Baldini, M. Belicchi-Ferrari, F. Bisceglie, P.P. Dall'Aglio, G. Pelosi, S. Pinelli, P. Tarasconi, Inorg. Chem 43 (2004) 7170.
[17] J. Easmon, G. Purstinger, G. Heinisch, T. Roth, H.H. Fiebig, W. Holzer, W. Jager, M. Jenny, J. Hofmann, J. Med. Chem. 44 (2001) 2164.
[18] N.K. Singh, S.T. Singh, N. Singh, A. Shriviastav, BioMetals 16 (2003) 471.
[19] G.B. Onoa, V. Moreno, M. Font-Bardia, X. Solans, J.M. Perez, C. Alonso, J. Inorg. Biochem. 75 (1999) 205.
[20] G. Menozzi, P. Schenone, L. Mosti, J. Heterocycl. Chem. 30 (1993) 997.
[21] D.C.G.A. Pinto, A.M.S. Silva, J.A.S. Cavaleiro, C. Foces-Foces, A.L. Llamas-Saiz, N. Jagerovic, J. Elguero, Tetrahedron 55 (1999) 10187.
[22] A. Cameron Church, M.U. Koller, S.A. O'Grady, C.F. Beam, Synth. Commun. 26 (1996) 2603.
[23] A. Marin-Hernandez, I. Gracia-Mora, L. Ruiz-Ramirez, R. Moreno-Sanchez, Biochem. Pharmacol. 65 (2003) 1979.

[24] M.S. Chande, N.V. Thakkar, D.V. Patil, Drug Res. 56 (1999) 207.
[25] G. Pallazino, L. Cecchi, F. Melani, V. Collota, G. Filacchioni, C. Martini, A. Lucacchini, J. Med. Chem. 30 (1987) 1737.
[26] A. Sabatini, A. Vacca, P. Gans, Coord. Chem. Rev. 120 (1992) 389.
[27] Molecular Structure Corporation, MSC/AFC Diffractometer Control Software. MSC, 3200 Research Forest Drive, The Woodlands, TX 77381, USA, 1989.
[28] Rigaku/MSC, Crystal Structure. Version 3.10. Rigaku/MSC, 9009 New Trails Drive, The Woodlands, TX 77381-5209, USA, 2002.
[29] G.M. Sheldrick, SHELXS97 and SHELXL97, University of Göttingen, Germany, 1997.
[30] A.L. Spek, PLATON, University of Utrecht, The Netherlands, 2001.
[31] M.C. Linder, M. Hazegh-Azam, Am. J. Clin. Nutr. 63 (1996) 797.
[32] J. Kuduk-Jaworska, A. Puszko, M. Kubiak, M. Pelczynska, J. Inorg. Biochem. 98 (2004) 1447.
[33] G. Crisponi, M. Casu, V. Nurchi, T. Pivetta, Talanta 56 (2002) 441.
[34] S. Espinosa, E. Bosch, M. Roses, Anal. Chim. Acta 454 (2002) 157.
[35] B. Barszcz, B. Lenarcik, Pol. J. Chem. 63 (1989) 371.
[36] S.F.A. Kettle, Physical Inorganic Chemistry, A Coordination Chemistry Approach, Pol. Ed., PWN Warsaw, 1999, p. 218.
[37] B.P. Lever, E.I. Solomon, Ligand field theory and the properties of transition metal complexes, in: E.I. Solomon, A.B.P. Lever (Eds.), Inorganic Electronic Structure and Spectroscopy, Vol. 1, Wiley-Interscience, Hoboken, NJ, 2006, p. 70.



(I) H_2L



(II) = 5-phenyl,1,3,4-oxadiazole-2-thiol (pot)

2. Experimental

2.1. Synthesis

Commercial reagents were used without purification and all experiments were carried out in open atmosphere. Addition of carbondisulfide to benzoic acid hydrazide using the literature procedure [15] afforded *N*-benzoyldithiocarbazate (H_2L) in reasonably good yield. The transition metal complexes were obtained as a precipitate by reacting H_2L with the respective metal acetate in a 1:2 molar ratio. These were isolated and suspended in $CHCl_3$–MeOH mixture to which an excess of en was added. The mixture was refluxed at 60 °C for 30 min, until total dissolution of complex or permanent colour change was observed. The resulting clear solution of **1** was filtered off. On keeping this solution of the Cu(II) complex for 3–4 days, purple crystals of **1** suitable for an X-ray crystallographic study were obtained. Other complexes were obtained as precipitates which were filtered off, washed with ethanol and finally dried *in vacuo*.

$[Cu(en)_2](pot)_2$ (**1**): purple crystals. *Anal* Calc. for $C_{20}H_{26}N_8O_2S_2Cu$: C, 44.64; H, 5.95; N, 20.82; Cu, 11.81. Found: C, 44.64; H, 5.55; N, 20.22; Cu, 11.81%. $\mu_B = 1.74$ BM. M.p. 150 °C (dec.). IR data (KBr, cm^{-1}): ν(NH) 3280 m; ν(C=N) 1594 s; (C–O–C), 1282 w; ν(NN), 1045 s; ν(CS) 851 m; ν(CuN) 466w. UV–Vis spectrum [λ_{max} DMF, cm^{-1}]: 16130, 23270, 30770. The compound is soluble in MeOH/EtOH but sparingly soluble in other common organic solvents and is stable in air for periods of months.

$[Ni(en)_2(pot)_2]$ (**2**): Red pink. *Anal* Calc. for $C_{20}H_{26}N_8O_2S_2Ni$ C: 45.05; H, 5.90; N, 21.01; Ni, 11.01. Found: C, 44.74; H, 5.75; N, 21.22; Ni, 10.81%. $\mu_B = 2.90$ BM. M.p. 180 °C (dec.). IR data (KBr, cm^{-1}): ν(NH) 3215 m; ν(C=N) 1602s; (C–O–C) 1250 w; ν(N–N) 1024 s; ν(C–S) 869 m; ν(Ni–N) 468w. UV–Vis spectrum [λ_{max} in DMF, cm^{-1}]: 15030, 22320, 32050.

$[Mn(en)_2(pot)_2]$ (**3**): Pink. *Anal* Calc. for $C_{20}H_{26}N_8O_2S_2Mn$: C, 45.36; H, 5.90; N, 21.16; Mn, 10.37. Found: C, 45.13; H, 5.75; N, 21.00; Mn, 10.01%. $\mu_B = 5.90$ BM. M.p. 192 °C (dec.). IR data (KBr, cm^{-1}): ν(NH) 3229 m; ν(C=N) 1593 s; (C–O–C) 1250 w; ν(NN) 1016 s; ν(CS) 869 m; ν(MnN) 470 w. UV–Vis spectrum [λ_{max} in DMF, cm^{-1}]: 19530, 32200.

$[Zn(en)(pot)_2]$ (**4**): Pink. *Anal* Calc. for $C_{18}H_{18}N_6O_2S_2Zn$: C, 45.05; H, 3.78; N, 17.51; O, 6.67; S,13.36; Zn, 13.63. Found: C, 44.87; H, 3.75; N, 17.79; Zn, 13.11%. μ_B = diamagnetic. M.p. 230 °C (dec.). IR data (KBr, cm^{-1}): ν(NH) 3237 m; ν(C=N) 1620 s; (C–O–C), 1250 w; ν(NN) 1022 s; ν(CS) 877 m; ν(ZnN) 474 w. UV–Vis spectrum [λ_{max} DMSO, cm^{-1}]: 23260–30770. ^1H NMR(DMSO-d_6, δ, ppm): 4.53 (m, 2 H, NH_2), 7.83 (m, 5 H, C_6H_5) ^{13}C NMR (DMSO-d_6, δ, ppm): C(9) 166.71, C(10) 156.6, C(3) and C(6) 46.3, Phenyl ring carbons 128.6–131.2.

2.2. Physical measurements

The complexes were analyzed for their metal content, after decomposition with a mixture of conc. HNO_3 and HCl, followed by conc. H_2SO_4. Carbon, hydrogen and nitrogen contents were estimated on a Carlo Erba 1108 model microanalyser. Magnetic susceptibility measurements were performed at room temperature on a Cahn Faraday balance using $Hg[Co(NCS)_4]$ as the calibrant. Electronic spectra were recorded on a CARY 100 Varian EL01055314 UV–Vis spectrophotometer in MeOH, DMF or DMSO. IR spectra were recorded in the 4000–400 cm^{-1} region as KBr pellets on a JASCO FT-IR-5300 spectrophotometer. ^1H and ^{13}C NMR spectra were recorded in DMSO-d_6 on a JEOL AL300 FT NMR spectrometer using TMS as an internal reference.

3. Crystal structure determination

Data for the structure were collected on a Bruker three-circle diffractometer equipped with a SMART 6000 CCD detector and with a mirror-system-monochromated Cu Kα source. Intensity measurements were performed on a rapidly cooled crystal. The structure was solved by direct methods (SHELXS-97) and refined against all data by full-matrix least-squares on F^2 using anisotropic displacement parameters (Table 1) for all non-hydrogen atoms. All hydrogen atoms were included in the refinement at geometrically ideal positions and refined with a riding model [16,17]. The DIAMOND [18] and MERCURY [19] packages were used for molecular graphics.

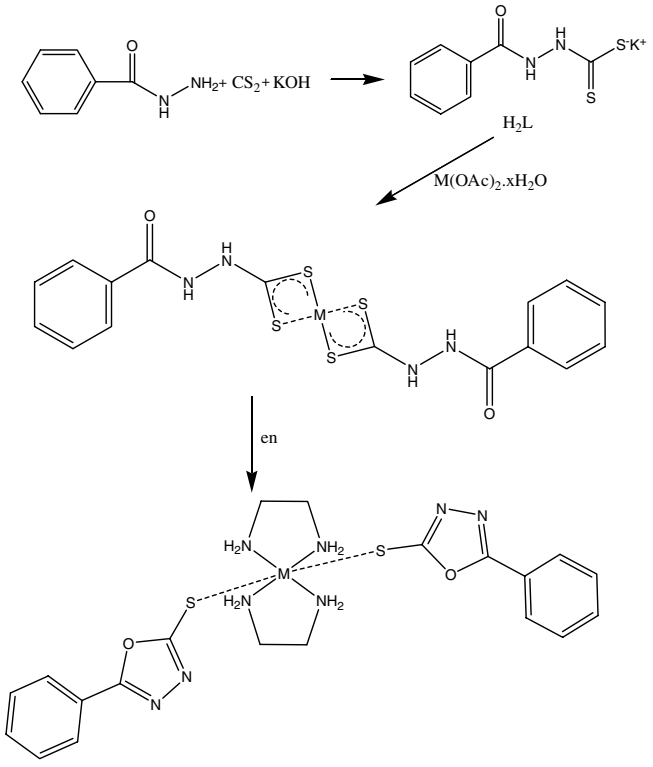
4. Results and discussion

The potassium salt of *N*-benzoyldithiocarbazate (H_2L) generates 5-phenyl,1,3,4-oxadiazole-2-thiol(pot^-) in an alkaline medium by an internal ring closure reaction *via* desulfurization [20]. In view of this, the work described here is quite unusual and interesting because the above reaction has been found to take place with the complexes of H_2L in the presence of an excess en. Compounds **1–4**

Table 1
Crystal refinement parameters of $[Cu(en)_2](pot)_2$

Formula	$C_{20}H_{26}CuN_8O_2S_2$
F_w	538.15
Crystal system	triclinic
Space group	$P\bar{1}$
T, K	99(2)
λ, Cu K_α (Å)	1.54178
a (Å)	6.938(10)
b (Å)	7.266(10)
c (Å)	12.831(10)
α (°)	84.64(10)
β (°)	81.53(10)
γ (°)	64.26(10)
V (Å^3)	575.98
Z	1
ρ_{calcd} (Mg/m^3)	1.551
μ (mm^{-1})	3.336
$F(000)$	279
Crystal size (mm)	$0.10 \times 0.10 \times 0.20$
θ Range for data collection (°)	3.48–58.65
Index range	$-7 \leqslant h \leqslant 7$
	$-8 \leqslant k \leqslant 8$
	$-13 \leqslant l \leqslant 14$
Number of reflections collected	5762
Number of indent reflections (R_{int})	1606
Number of data/restraints/parameters	1606/6/167
Goodness-of-fit on F^2	1.101
R_1[a], wR_2[b] ($I > 2\sigma(I)$)	0.0213, 0.550
R_1[a], wR_2[b] (all data)	0.0220, 0.0556
Largest difference in peak/hole (e Å^{-3})	0.179 and −0.261

[a] $R_1 = \sum \|F_o| - |F_c\| / \sum |F_o|$.
[b] $R_2 = [\sum w(|F_o^2| - |F_c^2|)^2 / \sum w|F_o^2|^2]^{1/2}$.



Scheme 1.

were obtained by refluxing $[M(HL)_2]$ with an excess of ethylenediamine in chloroform–methanol medium. The elemental analyses and physical measurements indicated towards very surprising results, where signals due to hydrazinic C(O)NHNHC(S) protons were found to be absent and one sulfur atom was missing. These observations suggest that H_2L underwent cyclisation to give 1,3,4-oxadizole derivatives. The preparation of complexes **1–4** is depicted in Scheme 1.

The infrared spectra of the complexes have been interpreted in the light of earlier investigations. The absorptions in the region of 3300–3200 cm^{-1} are due to the N–H stretching vibrations of en which are shifted to lower frequency than those encountered in the free en [21]. These shifts and the appearance of a new band near 490(±30) cm^{-1} suggest formation of a chelate. On the other hand, IR spectra of the complexes are observed to be devoid of any peak due to ν(NH) hydrazine (3108 cm^{-1}), which was present in metal–ligand precursor complexes. Additionally, ν(C=O) (1665 cm^{-1}), ν(C=S) (1145 cm^{-1}) and ν(C–S) (940 cm^{-1}) disappeared and new peaks appeared in the region of 1610–1590 (due to the endocyclic C=N bond), 1280–1260 (C–O–C) and 855–840 (C–S) cm^{-1} suggesing cyclisation of the acyclic dithiocarbazate moiety. The IR data are thus consistent with the presence of a 1,3,4-oxadiazole moiety in the compounds [10].

In addition to the IR spectral measurement, magnetic moments and electronic spectral data were used to determine the geometry of the isolated solid complexes. $[Cu(en)_2](pot)_2$ shows a magnetic moment of 1.74 BM, which corresponds to the presence of one unpaired electron. The presence of a broad band around 16130 cm^{-1} assigned to the envelope of $^2B_{1g} \rightarrow {}^2A_{1g}$, $^2B_{2g}$, ^2E_g transitions suggest a square planar geometry for the molecule. $[Mn(en)_2(pot)_2]$ exhibits a magnetic moment of 5.90 BM showing the presence of five unpaired electrons and the band at 19530 cm^{-1} due to the $^6A_{1g} \rightarrow T_{1g}$ transition suggests a high-spin octahedral geometry for the complex. $[Ni(en)_2(pot)_2]$ exhibits a magnetic moment of 2.9 BM and shows two bands at 15040 and 22320 cm^{-1}, which are considered to arise from the $^3A_{2g} \rightarrow {}^3T_{1g}$ (F) (ν_2) and $^3T_{1g}$ (P) (ν_3) transitions, respectively, in the distorted octahedral geometry around nickel(II). The high energy band at 28570 cm^{-1} in the ligand and in the region of 23260–30770 cm^{-1} in the diamagnetic complexes may be due to intraligand and/or charge transfer transitions [23].

The ^{1}H and ^{13}C NMR spectra of $[Zn(en)(pot)_2]$ in DMSO-d_6 were interpreted by comparing the spectra of 5-phenyl-1,3,4-oxadiazole-2-thione synthesized in the laboratory. The ^{1}H NMR spectrum of $[Zn(en)(pot)_2]$ shows a signal at 4.53 ppm due to NH_2 protons. The signals due to the phenyl ring protons, appearing at 7.83 ppm (m, 5 H) in the ligand, remain practically unchanged. The ^{13}C NMR spectral data of the compound was very informative. The peak due to the C9 carbon appears at 166.71 ppm as

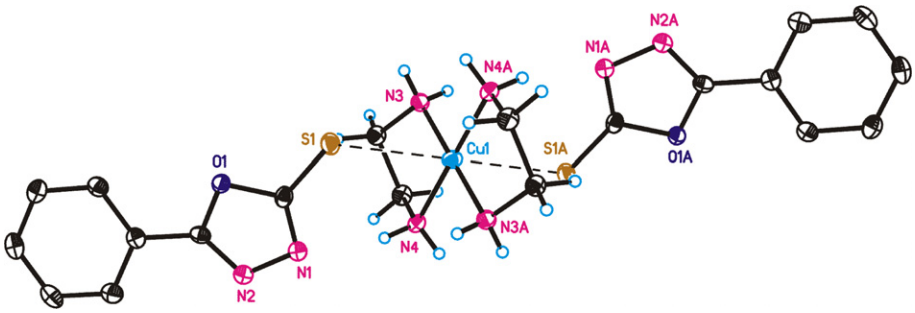


Fig. 1. Molecular structure of $[Cu(en)_2](pot)_2$ with the atom labelling, showing weak Cu···S interactions.

compared to 176.74 ppm in the oxadiazole, which suggests bonding through sulfur.

The X-ray crystal structure analysis of **1** shows that the Cu(II) compound has a composition, $[Cu(en)_2](pot)_2$ with an extended H-bonded structure (Fig. 1). The crystallographic asymmetric unit consists of the complex cation $[Cu(en)_2]^{2+}$ and the 1,3,4-oxadiazole thiol(pot^-) anions. The complex cation consists of two ethylenediamine molecules which chelate Cu(II) in equatorial positions and two 1,3,4-oxadiazole-2-thiol anions occupy apical positions. The Cu–N distances are in the range 2.01(15)–2.02(15) Å which is normal for Cu–N amine coordination. The bite angles for the CuN_4 five membered rings are 95.95(6)° and 85.05(6)°, indicating a substantial distortion in the molecule. Similar geometrical parameters for the coordination sphere have been reported for other diaquabis(ethylenediamine)Cu(II) salts [23,24]. In the complex under study Cu(II) resides in the plane formed by the nitrogen atoms of two en ligands arranged equitorially and the thiol S from two pot anions occupying the apical positions in a *trans* manner. Each $[Cu(en)_2]^{2+}$ forms a pair of weak intermolecular Cu···S bond interactions (3.02 Å). This distance is well within the distance of 3.2 Å for the sum of van der Waal radii of Cu and S [25]. The observed Cu···S distance suggests a comparatively strong interaction (Table 2). The propensity towards such an interaction is probably due to the tendency of Cu(II) to increase its coordination number.

The Cu atom in C_{2h} symmetry is bonded to four N atoms of two en molecules which offer interesting hydrogen bonding to the packing. The elements of the structure are joined to each other in the crystal packing (Figs. 2a, 2b and 3) by means of an extended system of H-bonds where the protons belonging to the NH_2 group are participating in the structure. The hydrogen bonding parameters are listed in Table 3. The N4 atom of the symmetrical half unit forms an intermolecular hydrogen bond with N1 of pot^- [N4–H4″···N1 2.17(2) Å], holding two pot anions on diagonally opposite ends. Whereas, N3–H3′ shows an interaction with N2 of the neighbouring anionic unit [N3–H3′···N2 2.19(18) Å]. Few other hydrogen bonding interactions viz N4–H4′···N1 2.36 (19) and C3–H3A···O1 2.53 Å help to propagate the bonded units along the *b* axis. Adjacent chains arrayed in a parallel mode are further linked by weak CH–π interactions to form a 2-dimensional planar network. In the solid state, the molecules are self-assembled *via* N–H···S and N–H···N intermolecular hydrogen bonding and π–π weak interactions (Figs. 2a, 2b and 3). Crystal packing in the complex $[Cu(en)_2](pot)_2$ is stabilised through C–H···π interactions and face to face π–π stacking (π–π distances = 3.666 Å) between ring centroids. The arrangement of $[Cu(en)_2]^{2+}$ at a dihedral angle of 49.43° to pot^- provides a network of intermingled chains that lead to a π–π stacked 3-dimensional framework.

Table 2
Interatomic distances (Å) and angles (°) for $[Cu(en)_2](pot)_2$

Copper coordination sphere			
Cu(1)–N(3)	2.0142(15)	N(3)–Cu(1)–N(3)#1	180.0
Cu(1)–N(3)#1	2.0142(15)	N(3)–Cu(1)–N(4)#1	94.95(6)
Cu(1)–N(4)#1	2.0169(15)	N(3)#1–Cu(1)–N(4)#1	85.05(6)
Cu(1)–N(4)	2.0169(15)	N(3)–Cu(1)–N(4)	85.05(6)
		N(3)#1–Cu(1)–N(4)	94.95(6)
		N(4)#1–Cu(1)–N(4)	180.0
Ethylenediamine			
C(3)–N(3)	1.480(2)	N(4)–C(6)–C(3)	106.99(14)
C(3)–C(6)	1.515(2)	N(3)–C(3)–C(6)	107.26(14)
N(4)–C(6)	1.480(2)	C(3)–N(3)–Cu(1)	107.22(11)
		C(6)–N(4)–Cu(1)	108.21(11)
Oxadiazole ring			
Cu(1)–S(1)	3.0031(6)	N(3)–Cu(1)–S(1)	88.81(4)
Cu(1)–N(3)	2.0142(15)	N(3)#1–Cu(1)–S(1)	91.19(4)
O(1)–C(10)	136.9(2)	N(4)#1–Cu(1)–S(1)	87.67(4)
O(1)–C(9)	139.5(2)	N(4)–Cu(1)–S(1)	92.32(4)
N(1)–C(9)	131.4(2)	C(10)–O(1)–C(9)	103.92(12)
N(1)–N(2)	141.0(2)	C(9)–N(1)–N(2)	107.53(13)
S(1)–C(9)	1.6947(18)	C(4)–C(1)–C(5)	120.50(17)
N(2)–C(10)	129.1(2)	C(9)–S(1)–Cu(1)	103.13(6)

In conclusion, to the best of our knowledge we report here for the first time metal-assisted transformation of N–benzoyldithiocarbazate to its 1,3,4-oxadiazole derivative in the presence of ethylenediamine, involving desulfurisation followed by cyclisation. This strategy offers an easy and facile route to complex the unstable 1,3,4-oxadiazole as its stable metal complexes. Moreover, we anticipate that this procedure would allow a rational synthetic protocol to biologically active molecules.

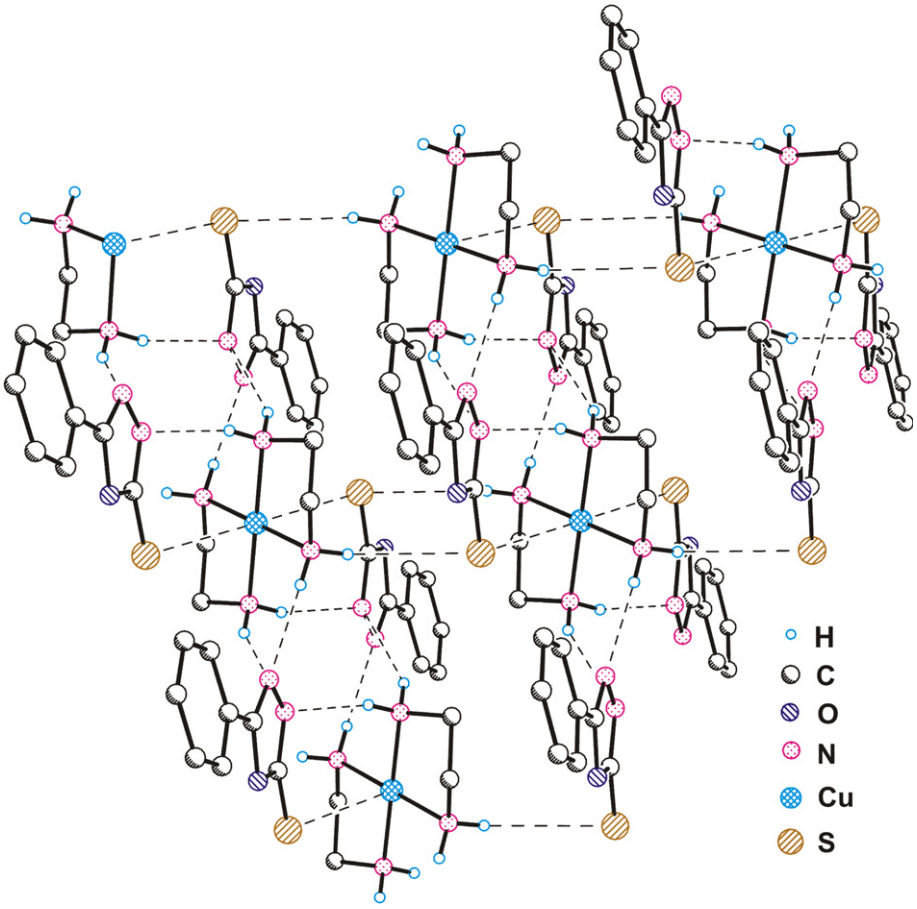


Fig. 2a. Perspective view of the crystal packing of $[Cu(en)_2](pot)_2$ showing N–H···S and N–H···N intermolecular H-bonding.

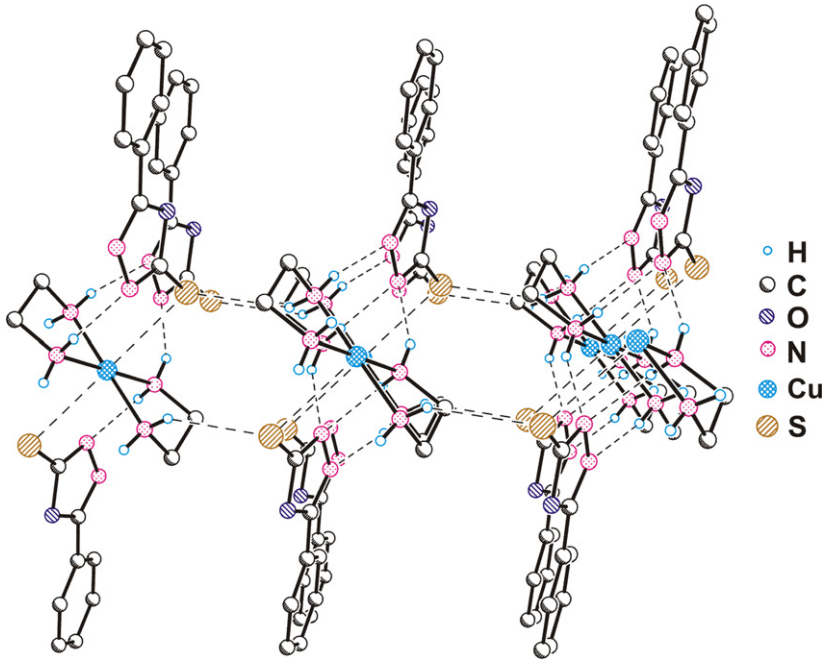


Fig. 2b. Perspective view of the crystal packing of $[Cu(en)_2](pot)_2$ growing through N–H···S, N–H···N intermolecular H-bonding and Cu···S interactions.

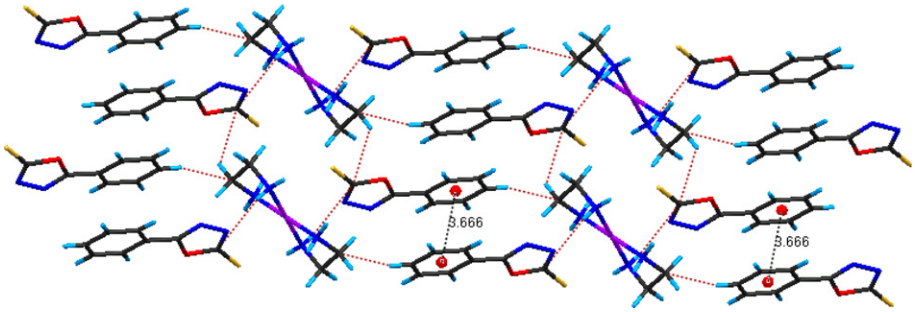


Fig. 3. Mercury view of the crystal packing of $[Cu(en)_2](pot)_2$ showing face to face π–π and C–H···π interactions.

Table 3
Hydrogen bonds for $[Cu(en)_2](pot)_2$ (Å and °)

D–H···A	*d*(D–H)	*d*(H...A)	*d*(D...A)	∠(DHA)	Symmetry coordinate
N3–H3″···S1	0.86	2.95	3.71	149	$x, -1+y, z$
N4–H4″···N1	0.86	2.17	3.00	165	x, y, z
N3–H3′···N2	0.85	2.19	3.03	167	$-1+x, y, z$
N4–H4···N1	0.85	2.36	3.13	150	$1-x, 1-y, 1-z$
C3–H3A···O1	0.99	2.53	3.47	160	$x, -1+y, z$

Appendix A. Supplementary material

CCDC 626364 contains the supplementary crystallographic data for **1**. These data can be obtained free of charge *via* http://www.ccdc.cam.ac.uk/conts/retrieving.html, or from the Cambridge Crystallographic Data Centre, 12 Union Road, Cambridge CB2 1EZ, UK; fax: (+44) 1223-336-033; or e-mail: deposit@ccdc.cam.ac.uk. Supplementary data associated with this article can be found, in the online version, at doi:10.1016/j.poly.2006.12.046.

References

[1] M. Das, S.E. Livingstone, Inorg. Chim. Acta 19 (1976) 5.
[2] L. Marchi, L. Uccelli, R. Marvelli, M. Rossi, V. Giganti, Bertolasi, V. Ferretti, J. Chem. Soc., Dalton Trans. (1996) 3105.
[3] A.I. El-Said, Trans. Met. Chem. 28 (2003) 749.
[4] A. Hetzheim, K. Möckel, Adv. Heterocycl. Chem. 7 (1966) 183.
[5] B.L. Sharma, S.K. Tandon, Pharmazie 39 (H-12) (1984) 858.
[6] M. Du, X.-J. Zhao, J. Mol. Struct. 694 (2004) 235.
[7] M. Du, X.-J. Zhao, J.H. Guo, Inorg. Chem. Commun. 8 (2005) 1.
[8] A. Jedlovska, J. Lesko, Synth Commun. 24 (1994) 1879.
[9] S.P. Hiremath, V.N. Sonar, K. Raja Sekhar, M.G. Purohit, Indian J. Chem. 28B (1989) 626.
[10] G.-S. Patricia, G.-T. Javier, A.M. Miguel, J. Arnaiz Francisco, R. Teófilo, Inorg. Chem. 41 (2002) 1345.
[11] R.W. Young, K.H. Wood, J. Am. Chem. Soc. 77 (1955) 400.
[12] J.R. Reid, N.D. Heindel, J. Heterocycl. Chem. 13 (1976) 925.
[13] H. Foks, J. Mieczkowska, M. Janowiec, Z. Zwolska, Z. Andrzejczyk, Chem. Heterocycl. Comp. 38 (2002) 810.
[14] E. Hoggarth, J. Chem. Soc. (1952) 4811.
[15] M. Busch, M. Starke, J. Prakt. Chem. 93 (1916) 49.
[16] G.M. Sheldrick, Acta Cryst. Sec. A 46 (1990) 467.
[17] G.M. Sheldrick, SHELXL-97, Program for Crystal Structure Refinement, University of Göttingen, Göttingen, Germany, 1997.
[18] K. Brandenburg, H. Putz, DIAMOND Version 3.0, University of Bonn, Germany, 2004.
[19] I.J. Bruno, J.C. Cole, P.R. Edgington, M. Kessler, C.F. Macrae, P. McCabe, J. Pearson, R. Taylor, Acta Cryst. B58 (2002) 389.
[20] K.S. Siddiqi, F. Rafat, S.H. Kar, Synth. React. Inorg. Metal-Org. Chem. 34 (2004) 93.
[21] P. Molina, A. Tarraga, A. Espinosa, Synthesis (1988) 690.
[23] A.B.P. Lever, Inorganic Electronic Spectroscopy, second ed., Elsevier, Amsterdam, 1984.
[23] J. Emsely, M. Arif, P.A. Bates, M.H. Hursthouse, Chem. Commun. (1998) 1387.
[24] P. Gomez-Romero, G.B. Jameson, J.J. Borras-Almenar, E. Escriva, E. Coronado, D. Beltran, J. Chem. Soc., Dalton Trans. (1988) 274.
[25] A.J. Bondi, Phys. Chem. 68 (1964) 441.

of the presence of metal–sulfur and metal–nitrogen bonds at the active sites of several oxidoreductases such as hydrogenase, xanthine-oxidase and nitrogenase [21,22] have stimulated interest in pyrimidine chemistry [23–28] with mixed sulfur and nitrogen donor atoms. Synthesis, characterization, structure and reactivity studies of such complexes with N, S and N, N, S donor ligands lead to valuable information toward understanding the functions of different enzymes at the molecular level [21]. Nucleic acids, vitamins and coenzymes containing the pyrimidine ring systems provide potential binding sites for metal ions. A variety of nitrogen and sulfur donors have been investigated involving both five and six membered heterocyclic thiosemicarbazones and dithiocarbazates [29–33]. Most of such studies have largely been concentrated on various pyridine-derived ligands [34–36]. However, the higher π-acidity and presence of more than one hetero atom in pyrimidine play an important role in its coordination chemistry compared to that of pyridine bases and serve as better models in biological systems [37–40]. Comparatively less research has centered on the transition metal chemistry with the Schiff base ligands having pyrimidine as the heterocyclic part. This has inspired us to explore the chemistry of pyrimidine based dithiocarbazate ligands with different metal ions. We report here for the first time, the syntheses and ligational behaviour of two pyrimidine derived dithiocarbazate ligands HL_1 and HL_2 towards Ni(II), Co(III) and Fe(III) metal ions. The crystal and molecular structures, magnetism and electronic spectra of $[Ni(HL_1)(L_1)]ClO_4$, $[Co(L_2)_2]ClO_4$ and $[Fe(L_2)_2]ClO_4$ complexes have been investigated.

2. Experimental

2.1. Materials

Ethyldiethoxyacetate and d_6-DMSO were purchased from Aldrich Chemical Company, USA and were used as received. All other solvents and reagents were obtained from commercial sources and purified by standard procedures [41]. *S*-Methyl dithiocarbazate was synthesized following the literature method [42]. *S*-Benzyl dithiocarbazate was prepared by an analogous method using benzyl chloride instead of methyl iodide. 2-*S*-Methylmercapto-6-methylpyrimidine-4-carbaldehyde was synthesized following the established method [43].

Caution! Although we have not encountered any problems, it should be kept in mind that perchlorate compounds of metal ions are potentially explosive especially in the presence of organic ligands. Only a small amount of the material should be prepared and it should be handled with care.

2.2. Physical measurement

Elemental analyses (carbon, hydrogen, nitrogen and sulfur) of the ligands HL_1 and HL_2 and the metal complexes were determined with a Perkin–Elmer CHNS/O analyzer 2400 at the Indian Association for the Cultivation of Science, Kolkata. The molar conductance values of the complexes were measured in purified CH_3OH solution with a Systronic model 304 digital conductivity meter. The electronic spectra of the complexes in purified CH_3OH solution and the diffuse reflectance spectra of the complexes were recorded on a Hitachi model U-3501 spectrophotometer. IR spectra (KBr pellet, 4000–400 cm^{-1}) were recorded on a Perkin–Elmer model 883 infrared spectrophotometer. ^1H NMR spectra of the ligands were recorded in d_6-DMSO with a Bruker AM 300L (300 MHz) superconducting FTNMR. Mass spectra of the ligands were done at the Indian Institute for Chemical Biology, Kolkata with a JEOLJMS-AX 500 mass spectrometer. Room temperature magnetic susceptibilities were measured with a PAR 155 vibrating sample magnetometer.

2.3. Preparation and characterization of the ligands

2-*S*-Methylmercapto-6-methylpyrimidine-4-carbaldehyde was condensed with the respective dithiocarbazate in a 1:1 molar ratio (Scheme 1). Details are described below.

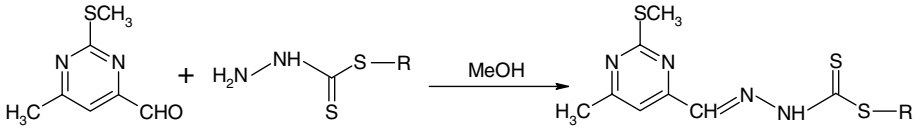
The two ligands HL_1 and HL_2 were synthesized in a similar way by refluxing a methanolic solution (10 cm^3) of 2-*S*-methylmercapto-6-methylpyrimidine-4-carbaldehyde (0.168 g, 1 mmol) with *S*-methyl dithiocarbazate (0.122 g, 1 mmol) and *S*-benzyl dithiocarbazate (0.198 g, 1 mmol) respectively, also taken in methanol (10 cm^3). Reflux was continued for ca. 2 h at water bath temperature during which a solid microcrystalline compound separated. It was filtered off, washed several times with cold methanol and dried in vacuo over fused $CaCl_2$. Single crystals of HL_2, suitable for X-ray diffraction were obtained by slow evaporation of a methanolic solution of the ligand.

HL_1: pale yellow; yield, 0.217 g (80%); m.p. (°C) 186, *m*/*z* 272 (M^+, 100%). *Anal.* Calc. for $C_9H_{12}N_4S_3$: C, 39.70; H, 4.41; N, 20.58; S, 35.29. Found: C, 39.83; H, 4.72; N, 20.52; S, 35.23%.

HL_2: yellow; yield, 0.278 g (80%); m.p. (°C) 175, *m*/*z* 348 (M^+, 100%). *Anal.* Calc. for $C_{15}H_{16}N_4S_3$: C, 51.72; H, 4.59; N, 16.09; S, 27.05. Found: C, 51.84; H, 4.89; N, 16.01; S, 27.51%.

The elemental analyses (C, H, N and S) and IR spectral data [characteristic bands (cm^{-1})] at 2940 (ν_{NH}); 1511 ($\nu_{CH=N}$); 1570 ($\nu_{C=Npym}$); 774 ($\nu_{C=S}$) in HL_1 and 2945 (ν_{NH}); 1523 ($\nu_{CH=N}$); 1570 ($\nu_{C=Npym}$); 776 ($\nu_{C=S}$) in HL_2 are in good agreement with the structure in Scheme 1. The absence of any band in the 2600–2200 cm^{-1} region of the IR spectra of the free ligands suggest that the ligands exist in the thione form in the solid state. In solution spectra, the ligands exhibit intraligand CT bands at ca. 380 nm, ca. 370 nm and ca. 355 nm.

The ^1H NMR spectra (δ_H ppm) in d_6-DMSO at 300 MHz of the ligands HL_1 and HL_2 give a singlet at δ 2.50(3H) for HL_1 and at δ 2.44(3H) for HL_2, which are assignable to C_2–SCH_3 (ring pym). Similarly singlets at δ



HL_1 ; R = -CH_3

HL_2 ; R = -$CH_2C_6H_5$

Scheme 1.

2.52(3H) HL_1 and at δ 2.49(3H) for HL_2 are due to C_6–CH_3 (ring pym). The C_5–H (ring pym) appears as a singlet at δ 8.06 for HL_1 and HL_2. A singlet at δ 7.40 for HL_1 and a slightly broad singlet at δ 7.34 for HL_2 are ascribed to HC=N. The terminal S–CH_3 signal is observed as a singlet at δ 2.50 for HL_1. Similarly, a singlet at δ 4.51 for HL_2 is ascribed to S–CH_2–C_6H_5. A narrow split multiplet at δ 7.44, 7.32 and 7.29 for HL_2 are ascribed to the *o*-, *p*- and *m*- hydrogen atoms (benzene ring) respectively. Singlets at δ 13.63 for HL_1 and at δ 13.67 for HL_2 confirm the presence of thioimine NH in the two ligands.

2.4. Preparation of the complexes

2.4.1. $[Ni(L_1)(HL_1)]ClO_4$ (1)

A methanolic solution (5 cm^3) of $Ni(ClO_4)_2 \cdot 6H_2O$ (0.0915 g, 0.25 mmol) was added dropwise to a solution of HL_1 (0.136 g, 0.5 mmol) in the same solvent (15 cm^3) with constant stirring. The resulting light green solution was further stirred for ca. 15 min and then refluxed at water bath temperature for ca. 2 h. The solution was cooled to room temperature and filtered. The filtrate was kept for slow evaporation. After two days, X-ray quality crystals of **1** were isolated. Yield, 0.49 g (70%). *Anal.* Calc. for $C_{18}H_{23}ClN_8NiO_4S_6$ (**1**): C, 30.77; H, 3.27; N, 15.95; S, 27.35. Found: C, 30.95; H, 3.59; N, 15.97; S, 27.39%. IR: ν (cm^{-1}) 2923 (ν_{NH}); 1579 ($\nu_{C=Npym}$); 1500 ($\nu_{CH=N}$); 1313, 1271 ($\nu_{C=S}$); 1086 (ν_{N-N}); 762 [$\nu_{C=S(protonated)}$]; 714 [$\nu_{C=S(deprotonated)}$]. UV–Vis, λ_{max}: 451, 836 nm. DRS: 378, 454, 833 nm. λ_M (MeOH, $ohm^{-1}\,cm^2\,mol^{-1}$): 92. μ_{eff} (at 298 K): 2.96 B.M.

2.4.2. $[Co(L_2)_2]ClO_4$ (2)

$Co(ClO_4)_2 \cdot 6H_2O$ (0.061 g, 0.16 mmol) was dissolved in methanol (20 cm^3). Solid HL_2 (0.116 g, 0.33 mmol) was added to the above methanolic solution with constant stirring using a magnetic stirrer. The resulting pink coloured solution was stirred for an additional 15 min and was refluxed at water bath temperature for ca. 3 h. The solution was cooled to room temperature, filtered and the filtrate was kept for slow evaporation. After three days, single crystals, suitable for X-ray diffraction were separated. Yield, 0.17 g (60%). *Anal.* Calc. for $C_{30}H_{30}ClN_8CoO_4S_6$ (**2**): C, 42.18; H, 3.51; N, 13.12; S, 22.49. Found: C, 42.29; H, 3.57; N, 13.13; S, 22.51%. IR: ν (cm^{-1}) 2928 (ν_{NH}); 1582 ($\nu_{C=Npym}$); 1510 ($\nu_{CH=N}$); 1267, 1198 ($\nu_{C=S}$); 1077 (ν_{N-N}); 719 ($\nu_{C=S}$). UV–Vis, λ_{max}: 411, 711 nm. DRS: 433, 483, 685 nm. λ_M (MeOH, $ohm^{-1}\,cm^2\,mol^{-1}$): 95. μ_{eff} (at 298 K): 0.00 B.M.

2.4.3. $[Fe(L_2)_2]ClO_4$ (3)

Complex **3** was prepared using the same procedure and reaction stoichiometry as for **1**. The colour of the resulting reaction mixture was dark red. Yield, 0.17 g (60%). *Anal.* Calc. for $C_{30}H_{30}ClN_8FeO_4S_6$ (**3**): C, 42.34; H, 3.52; N, 13.17; S, 22.58. Found: C, 42.46; H, 3.58; N, 13.15; S, 22.60%. IR: ν (cm^{-1}) 2924 (ν_{NH}); 1577 ($\nu_{C=Npym}$); 1500 ($\nu_{CH=N}$); 1349, 1265 ($\nu_{C=S}$); 1061 (ν_{N-N}); 725 ($\nu_{C=S}$). UV–Vis, λ_{max}: 351, 607, 701 nm. DRS: 412, 514, 741 nm. λ_M (MeOH, $ohm^{-1}\,cm^2\,mol^{-1}$): 86. μ_{eff} (at 298 K): 1.83 B.M.

2.5. Single crystal X-ray crystallography

Relevant crystallographic data are summarized in Table 1. The intensity data for complexes **1**, **2** and **3** were collected on a Bruker SMART 1K CCD diffractometer, using graphite monochromated Mo Kα radiation ($\lambda = 0.71073$ Å) in the ω–2θ scan mode at 103(2) K. Those of ligand HL_2 were collected on a Bruker SMART APEX CCD diffractometer, using graphite monochromated Mo Kα radiation ($\lambda = 0.71073$ Å) in the ω scan mode at 100(2) K. Accurate unit cell parameters and orientation matrices for data collection were obtained from least-squares refinement using the programs SMART and SAINT [44] and the data were corrected for absorption using SADABS [44]. All structures were solved using SHELXTL and the SHELX-97 packages of programs [44] i.e. SHELXS-97 for the solution of the structure and refined by full-matrix least-squares technique based on F^2 (SHELXL-97). Positions of H-atoms were treated as riding on their parent atoms with an isotropic thermal parameter varying as 1.2 or 1.5 times the U_{eq} of the parent atoms.

3. Results and discussion

3.1. Syntheses

Two new tridentate monoanionic ligands HL_1 and HL_2 both having an NNS donor atom set were synthesized by the 1:1 condensation reaction of the precursor 2-*S*-methylmercapto-6-methylpyrimidine-4-carbaldehyde with *S*-methyl/*S*-benzyl dithiocarbazates in purified methanol. Some complexation reactions of these ligands were investigated. All the complexes (**1**–**3**) of these ligands were obtained from

Table 1
Experimental data for crystallographic analysis

Compound	HL_2	**1**	**2**	**3**
Empirical formula	$C_{15}H_{16}N_4S_3$	$C_{18}H_{23}ClN_8NiO_4S_6$	$C_{30}H_{30}ClCoN_8O_4S_6$	$C_{30}H_{30}ClFeN_8O_4S_6$
Formula weight	348.50	701.96	853.36	850.28
Temperature (K)	100(2)	103(2)	103(2)	103(2)
Wavelength (Å)	0.71073	0.71073	0.71073	0.71073
Crystal system	monoclinic	triclinic	monoclinic	monoclinic
Space group	$P2_1$	$P\bar{1}$	$P2_1/c$	$P2_1/c$
Unit cell dimensions				
a (Å)	8.5463(9)	9.9874(17)	9.7984(8)	9.7490(12)
b (Å)	7.6046(8)	11.796(2)	15.8407(12)	15.872(2)
c (Å)	13.2512(14)	13.693(2)	24.0658(19)	24.071(3)
α (°)		69.440(2)		
β (°)	104.208(2)	85.173(2)	99.7730(10)	100.639(2)
γ (°)		65.795(2)		
Volume (Å^3)	834.87(15)	1374.3(4)	3681.1(5)	3660.6(8)
z	2	2	4	4
Density$_{calc}$ (Mg m^{-3})	1.386	1.696	1.540	1.543
Absorption coefficient (mm^{-1})	0.445	1.302	0.927	0.875
$F(000)$	364	720	1752	1748
Crystal size (mm^3)	$0.66 \times 0.24 \times 0.12$	$0.40 \times 0.27 \times 0.09$	$0.46 \times 0.13 \times 0.08$	$0.48 \times 0.17 \times 0.11$
θ Range (°) for data collection	1.59–30.54	1.59–28.22	1.55–30.84	1.54–29.65
Index ranges	$-12 \leqslant h \leqslant 10$, $-10 \leqslant k \leqslant 10$, $-18 \leqslant l \leqslant 18$	$-10 \leqslant h \leqslant 13$, $-15 \leqslant k \leqslant 15$, $-18 \leqslant l \leqslant 18$	$-13 \leqslant h \leqslant 13$, $-17 \leqslant k \leqslant 22$, $-33 \leqslant l \leqslant 32$	$-13 \leqslant h \leqslant 13$, $-22 \leqslant k \leqslant 17$, $-33 \leqslant l \leqslant 33$
Goodness-of-fit on F^2	1.049	1.032	1.016	1.001
Completeness to theta = 25.00°	99.4%	99.1%	99.6%	99.8%
Independent reflections [R_{int}]	4397 [0.0352]	6703 [0.0188]	10741 [0.0187]	10221 [0.0960]
Absorption correction	multi-scan	multi-scan	multi-scan	multi-scan
Maximum and minimum transmission	0.948 and 0.880	0.8940 and 0.6239	0.9337 and 0.6751	0.9099 and 0.6787
Refinement method	full-matrix least-squares on F^2	full-matrix least-squares on F^2	full-matrix least-squares on F^2	full-matrix least-squares on F^2
Data/restraints/parameters	4397/1/201	6703/0/343	10741/0/455	10221/0/455
Reflections collected	9522	13974	41459	40687
Final R indices [$I > 2\sigma(I)$]	$R_1 = 0.0495$, $wR_2 = 0.1283$	$R_1 = 0.0311$, $wR_2 = 0.0787$	$R_1 = 0.0284$, $wR_2 = 0.0716$	$R_1 = 0.0515$, $wR_2 = 0.0904$
R indices (all data)	$R_1 = 0.0526$, $wR_2 = 0.1298$	$R_1 = 0.0395$, $wR_2 = 0.0837$	$R_1 = 0.0341$, $wR_2 = 0.0752$	$R_1 = 0.1100$, $wR_2 = 0.1077$
Largest difference peak and hole (e Å^{-3})	0.541 and −0.532	0.882 and −0.536	0.825 and −0.496	0.502 and −0.475

a refluxing mixture of the respective ligand and the corresponding hydrated metal salts, taken in a 2:1 molar proportion in methanol. X-ray quality crystals of these ligands were obtained upon slow evaporation of the respective reaction mixture at room temperature. All the three complexes were characterized by elemental analyses, solution electrical conductivity, magnetic susceptibility, IR, UV–Vis and ^{1}H NMR spectroscopy (for **2**). The results are consistent with the proposed mononuclear formulation. The complexes were found to be fairly soluble in most common organic solvents. Molar conductivities of all the three complexes are in accord with 1:1 electrolyte behavior.

3.2. Description of crystal structures

Perspective views of the ligand HL_2 and those of the complexes **1**, **2** and **3** with atom numbering schemes are shown in Figs. 1–4 respectively. Selected metrical parameters are listed in Table 2. The unit cell of HL_2 and **1** comprises of two molecules and those for **2** and **3** comprise of four molecules.

The ligand HL_2 crystallizes in the space group $P2_1$. It is non-centrosymmetric and the absolute structure parameter for HL_2 is 0.09(9). The structure of HL_2 (Fig. 1) shows that the pyrimidyl nitrogen atom N(1a), azomethine nitrogen atom N(2a) and the thione sulfur atom S(1a) are *trans* oriented to each other. Upon chelation of the ligand, the above donor atoms are arranged in a *cis*-fashion toward the metal center. The *cis* conformation of the ligand is necessary for its participation as a tridentate NNS chelate ligand. The

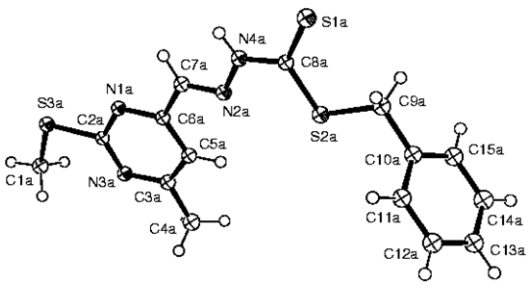


Fig. 1. ORTEP diagram of the ligand HL_2 (50% thermal ellipsoids).

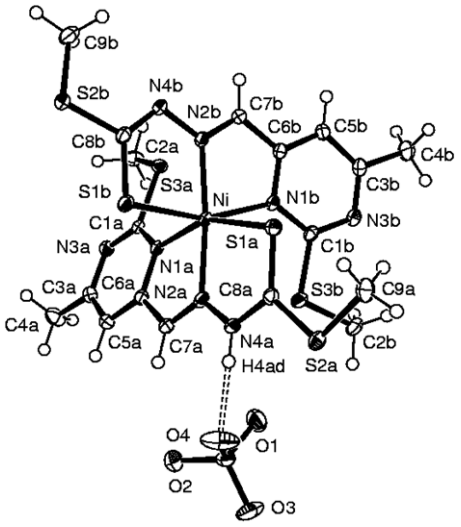


Fig. 2. Molecular structure and atom numbering scheme of complex **1** (50% thermal ellipsoids). The H-bond is shown as dotted line.

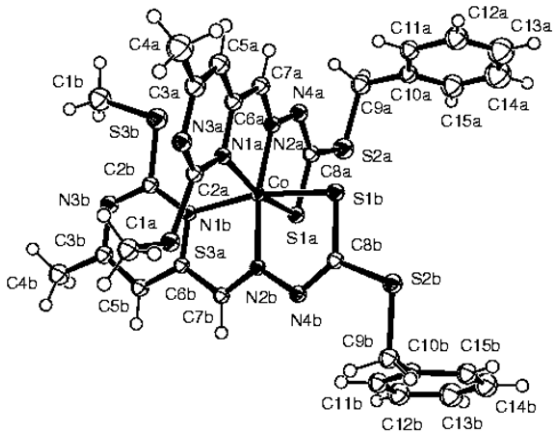


Fig. 3. ORTEP diagram and atom numbering scheme of the cationic part of complex **2** (50% thermal ellipsoids).

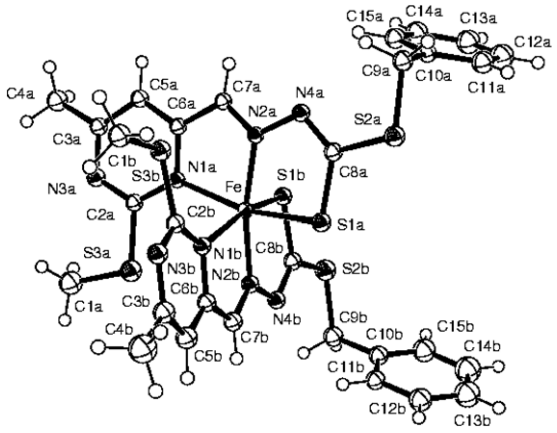


Fig. 4. ORTEP diagram and atom numbering scheme of the cationic part of complex **3** (50% thermal ellipsoids).

Table 2
Selected bond distances (Å) and angles (°) involving HL_2, **1**, **2** and **3**

	HL_2	**1**	**2**	**3**
Bond distances (Å)				
C(8a)–S(1a)	1.656(3)	1.667(2)	1.7277(14)	1.740(3)
C(8b)–S(1b)		1.719(2)	1.7308(14)	1.745(3)
C(8a)–N(4a)	1.350(4)	1.346(3)	1.3088(18)	1.302(3)
C(8b)–N(4b)		1.312(3)	1.3025(17)	1.297(4)
C(7a)–N(2a)	1.281(4)	1.283(3)	1.2960(17)	1.298(3)
C(7b)–N(2b)		1.287(3)	1.2915(16)	1.293(4)
M–N(2b)		2.0115(17)	1.8997(11)	1.916(2)
M–N(2a)		2.0323(17)	1.8982(11)	1.921(2)
M–N(1b)		2.1380(17)	2.0249(10)	2.038(2)
M–N(1a)		2.2178(18)	2.0223(11)	2.038(2)
M–S(1b)		2.3825(6)	2.2245(4)	2.2213(9)
M–S(1a)		2.4668(7)	2.2291(4)	2.2255(9)
	1	**2**	**3**	
Bond angles (°)				
N(2b)–M–N(2a)	173.33(7)	168.62(5)	168.11(10)	
N(2b)–M–N(1b)	78.12(7)	81.28(4)	79.75(10)	
N(2a)–M–N(1b)	108.56(7)	107.22(5)	108.54(10)	
N(2b)–M–N(1a)	103.78(7)	106.19(5)	109.28(10)	
N(2a)–M–N(1a)	76.06(7)	81.46(5)	79.80(9)	
N(1b)–M–N(1a)	95.23(6)	92.16(4)	89.77(9)	
N(2b)–M–S(1b)	81.78(5)	85.01(3)	84.70(8)	
N(2a)–M–S(1b)	91.55(5)	86.78(3)	87.71(7)	
N(1b)–M–S(1b)	159.78(5)	165.94(3)	163.44(7)	
N(1a)–M–S(1b)	91.67(5)	88.66(3)	90.00(7)	
N(2b)–M–S(1a)	100.36(5)	87.12(3)	87.52(7)	
N(2a)–M–S(1a)	80.57(5)	85.28(4)	84.35(7)	
N(1b)–M–S(1a)	84.63(5)	90.53(3)	87.96(7)	
N(1a)–M–S(1a)	155.29(5)	166.67(3)	162.36(7)	
S(1b)–M–S(1a)	96.89(2)	91.895(14)	97.09(3)	

Here M stands for the corresponding metal ion.

C(8)–S(1) [a and b] bond distances [except S(1a)–C(8a) in **1**] in **1**, **2** and **3** appear to be longer (Table 2) than those reported for free thiosemicarbazones, such as 1.678(2) Å in 4-formylpyridinethiosemicarbazone [45] and 1.684(4) Å in 2-keto-3-ethoxybutyraldehyde-bis(thiosemicarbazone) [46]. In all the complexes the C(8)–N(4) and C(7)–N(2) [b only in **1** and a, b for **2**, **3**] bond distances show partial double bond character due to delocalization of π-electrons throughout the whole molecule [47] [except in the ligand moiety 'a' in **1**] where the ligand molecules exist in the deprotonated thiol form. However, in **1**, the C(8a)–N(4a) bond distance, being comparable to that in HL_2 and also being longer than the corresponding C(8b)–N(4b) bond (Table 2), suggests that the ligand moiety 'a' utilizes its thione sulfur in its 'thione' form for coordination where C(8a)–N(4a) is perfectly of double bond character. Likewise, the double bond character in C(7a)–N(2a) is quite obvious from the comparison of this length with that in the free ligand (Table 2).

The ligand HL_2 is stabilized through a network of hydrogen bonding (Fig. 5). It shows that there is a weak H-bond interaction through the H(4b) and N(1a) atoms between the two parallel lying HL_2 molecules. This results in formation of an infinite 2D straight chain throughout the crystal. The geometrical details of the hydrogen bonds are given in Table 3.

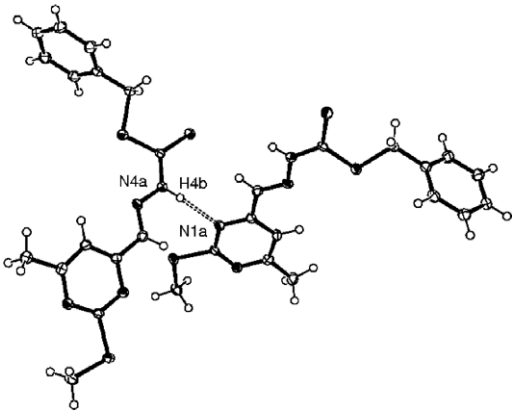


Fig. 5. Intermolecular H-bonding in HL_2 shown as a dotted line (50% thermal ellipsoids).

The complex **1** contains a $[Ni(L_1)(HL_1)]^+$ cation and a ClO_4^- anion, while complexes **2** and **3** contain $[M(L_2)_2]^+$ cations and ClO_4^- anions (M = Co for **2** and Fe for **3**). It is interesting to note that in **1**, one ligand molecule acts as a uninegative one and the other acts as a neutral molecule, whereas in **2** and **3**, each ligand molecule acts as a uninegative tridentate. In the structures of **1**, **2** and **3** the sulfur and pyrimidyl nitrogen atoms are positioned *cis* to each other while the azomethine nitrogen atoms are *trans* oriented to each other i.e. the ligands coordinate the metal in a meridional fashion. The meridional configuration of the NNS tridentate thiosemicarbazone ligands around the metal ion have been found in other similar bis-ligated metal chelates [48,49]. The coordination polyhedron around the metal centers is best described as a distorted octahedral geometry with an N_4S_2 chromophore. The equatorial positions are occupied by the two pyrimidyl nitrogen atoms [N(1a) and N(1b)] and the two thiolato sulfur atoms [S(1a) and S(1b)] (in **1**, one is thiolato sulfur and other is thione sulfur). In all the complexes, the atoms defining the equatorial plane lie 0.453, 0.425, −0.486 and −0.391 Å in **1**; 0.266, 0.237, −0.262 and −0.242 Å in **2** and 0.327, 0.284, −0.333 and −0.279 Å in **3**, respectively, out of the least-squares plane through them. The axial positions are occupied by the two remaining azomethine nitrogen atoms [N(2a) and N(2b)] which is evident from the N(2a)–Ni–N(2b) angles (173.32° in **1**, 168.62° in **2** and 168.11° in **3**).

The equatorial M–S bond distances in **2** and **3** are nearly same, ranging from 2.212 to 2.229 Å, but for **1** [Ni–S(1a) 2.467 Å. Ni–S(1b) 2.383 Å], they show a significant variation because of the different coordination modes of the S atoms in the two ligand molecules toward the Ni center. The axial M–N bond in **1** is significantly larger (average distance 2.021 Å) than that in **2** (average distance 1.899 Å) and **3** (average distance 1.918 Å). These values compare well with those of other six-coordinate Ni(II) complexes of related NNS ligands [50,51]. The N–M–N, N–M–S and S–M–S angular distributions indicate that the coordination polyhedron is distorted in each complex. This distortion of the metal ion coordinated polyhedron results from the steric interactions and asymmetric nature of the ligand molecules (HL_1 and HL_2). The maximum distortions from the ideal octahedral geometry occur for N(1a)–Ni–N(2a) (76.06°), N(2a)–Ni–S(1a) (80.57°) and N(2a)–Ni–N(1b) (108.55°) angles in **1**; N(1a)–Co–N(2a) (81.45°) and N(2a)–Co–N(1b) (107.22°) angles in **2** and N(1a)–Fe–N(2a) (79.82°) and N(2a)–Fe–N(1b) (108.53°) angles in **3**. Similar distortions have been reported previously in the literature [52]. Encapsulation of the metal ions by the coordination of six donor atoms results in the formation of four five membered chelate rings [M, N(1), C(6), C(7), N(2) (Ia,Ib)]; [M, N(2), N(4), C(8), S(1) (IIa, IIb)] in **1**, **2** and **3**, where M stands for the corresponding metal ion. The analysis of torsion angles Table 4 and a puckering analysis [53] Table 5 of the five membered chelate rings reveals that they are basically planar with none of the weighted average torsion angles being larger than 12.69° [for the ring Ni–N(1a)–C(6a)–C(7a)–N(2a)]. For each of the complexes, each set of two chelate rings have weighted average torsion angles above 5°. The maximum puckering amplitude, again measured for Ni–N(1a)–C(6a)–C(7a)–N(2a), is 0.195(2) Å. In both ligands HL_1 and HL_2, the chelate rings and the pyrimidine ring lie nearly in the same plane and the angles between the planes are 6.64(10)° and 87.83(9)° for **1**, 7.53(6)° and 5.77(6)° for **2**, and 6.03(13)° and 8.63(13)° for **3**. The pyrimidine ring thus makes an extended coplanar system with the two chelate rings. These extended coplanar ring systems of the two ligands approach each other orthogonally. This is evident from the analysis of their bond angles Table 2.

In **1**, a weak hydrogen bond interaction involving the perchlorate oxygen O(4) atom and hydrogen H(4ad) of

Table 4
Selected torsion angles (°) involving HL_2, **1**, **2** and **3**

	Torsion angles (°)			
	HL_2	**1**	**2**	**3**
N(1a)–C(6a)–C(7a)–N(2a)	174.0(3)	1.4(3)	−2.16(17)	−0.4(4)
N(2a)–N(4a)–C(8a)–S(1a)	−179.5(2)	11.2(3)	1.30(17)	1.7(4)
N(1b)–C(6b)–C(7b)–N(2b)		4.4(3)	1.18(16)	3.3(4)
N(2b)–N(4b)–C(8b)–S(1b)		4.2(3)	−2.17(16)	−1.7(4)

Table 3
Details of hydrogen bond distances (Å) and angles (°)

Compound	D–H ... A	*d*(D–H)	*d*(H ... A)	*d*(D ... A)	∠(DHA)
HL_2	N(4a)–H(4b) ... N(1a)#1	0.88	2.13	3.006(3)	174.8
1	N(4a)–H(4ad) ... O(4)	0.88	1.94	2.806(2)	165.7

Table 5
Puckering analysis for **1–3** for all chelate rings with weighted average torsion angles above 5°

	Ni–S(1b)–C(8b)–N(4b)–N(2b)	Ni–N(1a)–C(6a)–C(7a)–N(2a)	Co–N(1a)–C(6a)–C(7a)–N(2a)	Co–N(1b)–C(6b)–C(7b)–N(2b)	Fe–S(1b)–C(8b)–N(4b)–N(2b)	Fe–N(1a)–C(6a)–C(7a)–N(2a)	Fe–N(1b)–C(6b)–C(7b)–N(2b)
Weighted average torsion angle	6.14	12.69	6.11	7.75	5.94	9.32	7.28
Puckering amplitude Q	0.104(1)	0.195(2)	0.089(1)	0.116(1)	0.097(2)	0.136(2)	0.106(2)
Puckering phase Φ	196.3(11)	183.6(7)	11.0(9)	356.6(6)	8.3(16)	179.6(12)	194.0(16)
Closest puckering descriptor	twisted on Ni–S(1b)	envelope on Ni	twisted on Co–N(1a)	envelope on Co	envelope on Fe	envelope on Fe	twisted on Fe–N(1b)

the thioimine nitrogen atom is present (Fig. 2) . The details of hydrogen bonding parameters are presented in Table 3.

4. Characterization of the complex species

All the three complexes gave satisfactory C, H, N and S analyses. Spectral properties of these complexes are described below in details.

4.1. IR spectra of the complexes

A comparative study of the IR spectral data of the reported complexes with those of the uncomplexed ligand gives meaningful information regarding bonding sites of the ligand molecules. All the Schiff bases contain a proton adjacent to the thiocarbonyl group and consequently can exhibit thione–thiol tautomerism. The IR spectra of the ligands, however, display no band at ca. 2600 cm^{-1} corresponding to ν_{S-H} [54], indicating that the ligands remain as a thione tautomer. The ligand (HL_2) when dissolved in methanol in the presence of Co(II) salts quickly converts to the corresponding 'thiol' form with the concomitant formation of cobalt(III) complexes of the deprotonated mercaptide form of the ligand. Thus oxidation to Co(III) occurs during preparation of the complex. Although the mechanism of this oxidation is not proven we can safely assume that the starting cobalt(II) salt presumably undergoes aerial oxidation in presence of the ligand in methanolic solution.

Some characteristic and recognizable spectral changes have been noticed in the IR spectra of the complexes as compared to that of the free ligands and the data can be successfully utilized for an additional support of the bonding mode. A red shift of $\nu_{(C=N)}$ from 1511 cm^{-1} (in HL_1) and 1523 cm^{-1} (in HL_2) to 1500 cm^{-1} (in **1** and **3**), 1510 cm^{-1} (in **2**) is consistent with coordination of the azomethine nitrogen [55]. The presence of a band at ca. 550 cm^{-1} is also assignable to $\nu_{(M-N)}$. A blue shift of $\nu_{(C=Npym)}$ from 1570 cm^{-1} in the uncomplexed ligand towards 1580 cm^{-1} in all the complexes is also consistent with coordination of the pyrimidine nitrogen [55]. For all the complexes, the thioamide band at ca. 775 cm^{-1} in the free ligand due to $\nu_{(C=S)}$ undergoes a red-shift by ca. 50–60 cm^{-1}, pointing to the sulfur atom of thiol as a possible coordination site [55]. The additional peak at 762 cm^{-1} in **1** indicates the protonated 'thione' sulfur as a possible coordination site from one ligand molecule.

4.2. UV–Vis and DRS of the complexes

The diffuse reflectance spectra of **1** is characterized by three main bands at 833, 454 and 378 nm which may be assigned as $^3A_{2g}$ (F) → $^3T_{2g}$ (F) (ν_1), $^3A_{2g}$ (F) → $^3T_{1g}$ (F) (ν_2) and $^3A_{2g}$ (F) → $^3T_{1g}$ (P) (ν_3) transitions respectively in an Oh symmetry. The calculated value of the ligand field parameters Dq = 1200 cm^{-1}, $B = 831$ and $\beta = 0.78$ furnish reasonable support for the octahedral geometry from a

comparison with similar N_4S_2 chromophores [48]. The electronic spectral data of the above nickel(II) complex in methanol indicate no gross deviation in electronic or geometric environment on dissolution in the same solvent. The solution spectrum is also characterized by two bands in the same region as in the solid state. The third band may be obscured by the intense LMCT band. The complex shows an intense band at 355 nm. This is an intraligand CT band as obvious from the UV-spectrum of the corresponding ligand.

The DRS of **2** exhibits a broad band at ca. 433 nm with two distinct shoulders at the low energy side (at ca. 483 and ca. 685 nm). The broad band is due to the S → Co(III) charge transfer transition as is also evident from the solution spectral study. The other two bands may be assigned as $^1A_{1g} \rightarrow {}^1T_{1g}$ and $^1A_{1g} \rightarrow {}^3T_{2g}$ transitions, respectively [56]. In methanolic solution, it displays a S → Co(III) charge transfer transition (LMCT) at 411 nm with one d–d band at 711 nm. The intense band at ca. 350 nm is due to the intraligand CT band.

The DRS of **3** shows a band at 412 nm which may be due to a S → Fe(III) transition. Two other bands at 514 and 741 nm are assigned as d–d transitions for the spin paired d^5 iron(III) ions [57]. The methanolic solution exhibits one strong absorption band at 351 nm with a shoulder at 403 nm. This band is assigned to a LMCT transition. Two comparatively low intense bands at 607 and 701 nm are due to d–d transitions [58]. Likewise to **2**, the intense band at 351 nm is assigned as the intraligand CT band.

4.3. ^1H NMR spectrum of 2

Table 6 gives a listing of the ^1H NMR assignments of the cobalt complex as compared with those of the corresponding free ligand. The peak at ca. δ 13.67 ppm due to the azomethine NH in the free ligand disappears after complexation. This indicates that during complexation the ligand in its thiol form undergoes deprotonation followed by coordination to the Co(III) ion through the thiolato sulfur atom. The S–CH_2 peak at δ 4.51 ppm, showing a slight downfield (δ 4.61 ppm) shift, is ascribed to coordination of the thiol sulfur. An upfield shift occurs with the C_5–H (ring pym) proton, appearing at δ 7.35 ppm in the complex compared to δ 8.06 ppm in the uncomplexed ligand. This is due to coordination of the pyrimidine nitrogen atom to the central Co(III) ion. The ^1H NMR spectrum also gives an additional support for the bonding characteristics of the ligands in forming complexes with Co(III) through the pyrimidine ring nitrogen (tertiary), azomethine nitrogen and thiolato sulfur atoms.

Table 6
^1H NMR spectral data (d_6-DMSO, δ in ppm) of HL_2 and the cobalt(III) complex relative to TMS

Compound	NH	C_5–*H* (ring)	C_6–CH_3 (ring)	Azomethine *CH*	Pyrimidine S–CH_3	Terminal S–CH_2–C_5H_5
HL_2	13.67	8.06	2.49	7.34	2.44	4.51
2		7.35	2.51	7.61	2.45	4.61

5. Conclusion

We have prepared a Ni(II) complex of HL_1 and Co(III), Fe(III) complexes of HL_2 where HL_1 and HL_2 are similar pyrimidine derived Schiff base ligands. In case of the Ni-complex, one ligand molecule in its deprotonated thiol form functions as a mononegative tridentate and another ligand in its thione form acts as neutral tridentate, whereas for the Co(III) and Fe(III) complexes, each of the ligand molecules in its deprotonated thiol form functions as a uninegative tridentate.

Acknowledgements

Financial support [01(1916)/04/EMR-II] from Council of Scientific and Industrial Research (CSIR), New Delhi, India, is gratefully acknowledged. The Smart Apex diffractometer was funded by NSF Grant 0087210, by the Ohio Board of Regents Grant CAP-491 and by YSU.

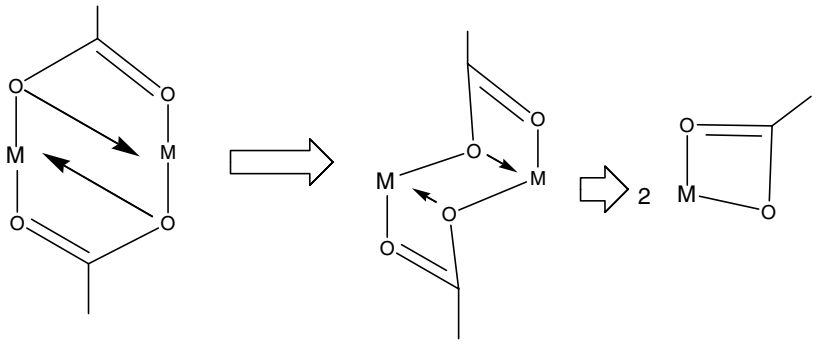
Appendix A. Supplementary material

CCDC 622192, 622193, 622194 and 622195 contains the supplementary crystallographic data for HL_2, **1**, **2** and **3**. These data can be obtained free of charge via http://www.ccdc.cam.ac.uk/conts/retrieving.html, or from the Cambridge Crystallographic Data Centre, 12 Union Road, Cambridge CB2 1EZ, UK; fax: (+44) 1223-336-033; or e-mail: deposit@ccdc.cam.ac.uk. Supplementary data associated with this article can be found, in the online version, at doi:10.1016/j.poly.2007.01.006.

References

[1] F.A. French, E.J. Blanz Jr., D.O. Amaral Jr., D.A. French, J. Med. Chem. 13 (1970) 1117.
[2] Jh. Cory, A.E. Fleischeher, Cancer Res. 39 (1979) 4600.
[3] A.C. Sartorelli, K.C. Agarwal, A.S. Tsiftsoglou, E.C. Moore, Adv. Enzyme Regul. 15 (1977) 117.
[4] W.G. Rice, C.A. Schaeffer, L. Graham, D. Clanton, R.W. Buckheit Jr., D. Zaharevitz, M.F. Summers, A. Wallqvist, D.G. Covell, J. Med. Chem. 39 (1996) 3606.
[5] M. Otsuka, M. Fujita, Y. Sugiura, J. Med. Chem. 37 (1994) 4267.
[6] T. Hitoshi, N. Tamao, A. Hideykki, F. Manabu, M. Takayuki, Polyhedron 16 (1997) 3787.
[7] E.S. Roper, Coord. Chem. Rev. 61 (1985) 115.
[8] J.S. Casas, E.E. Castellans, M.D. Louce, J. Ellena, A. Sanchez, J. Sordo, C. Taboada, J. Inorg. Biochem. 11 (2006) 1858.
[9] M.J. Campbell, Coord. Chem. Rev. 15 (1975) 297.
[10] D.X. West, S.B. Padhye, P.B. Sonawane, Struct. Bond (Berlin) 76 (1991) 4.
[11] Y.P. Tian, C.Y. Duan, Z.L. Lu, X.Z. You, H.K. Fun, S. Kandasamy, Polyhedron 15 (1996) 2263.
[12] S.K. Jain, B.S. Garg, Y.K. Boon, J.P. Scovill, D.L. Klayman, Spectrochim. Acta 24 (1985) 407.
[13] S.B. Padhye, G.B. Kanffman, Coord. Chem. Rev. 63 (1985) 127.

[14] D.X. West, A.E. Liberta, S.B. Padhye, R.C. Chilate, P.B. Sonawane, A.S. Kumbhar, R.G. Yerande, Coord. Chem. Rev. 123 (1993) 49.
[15] T.S. Lobana, P.K. Bhatia, J. Sci. Ind. Res. 48 (1989) 394.
[16] M.C. Rodriguez-Arguelles, S.J. Pinelli, J. Inorg. Biochem. 58 (1995) 157.
[17] J.S. Casas, M.S. Garcia-Tasende, C. Maichel-Mossmer, M.C. Rodriguez- Arguelles, A. Sanchez, J. Sordo, A. Vazquez-Lopez, S. Pinelli, P. Lunghi, R. Albertini, J. Inorg. Biochem. 62 (1996) 41.
[18] M.B. Ferrari, G.G. Fava, G. Tarasconi, R. Albertini, S. Pinelli, R. Starcich, J. Inorg. Biochem. 53 (1994) 13.
[19] T. Lobana, Proc. Indian Acad. Sci. (Chem. Sci.) 112 (2000) 323.
[20] U. Koch, B. Attenni, S. Malancona, S. Colarusso, I. Conte, M.D. Filippo, S. Harper, B. Pacini, C. Giomini, S. Thomas, I. Incitti, L. Tomei, R.D. Francesco, S. Altamura, V.G. Matassa, F. Narjes, J. Med. Chem. 49 (2006) 1693.
[21] A. Mullar, B. Krebs (Eds.), Sulfur, its Significance for Chemistry, for the Geo- and Cosmosphere and Technology, Studies in Inorganic Chemistry, vol. 5, Elsevier Sciences Publishers, Amsterdam, 1984.
[22] S.D. Conradsson, B.K. Burgess, W.W. Newton, K.O. Hodgson, J.W. Mcdonald, J.F. Robinson, S.F. Gheller, L.E. Mortenson, M.W.W. Adams, P.K. Mascharak, W.A. Armstrong, R.H. Holm, J. Am. Chem. Soc. 107 (1985) 7935.
[23] E.C. Constable, Coord. Chem. Rev. 93 (1989) 205.
[24] T. Yamamoto, Z. Zhou, T. Kanbara, M. Shimura, K. Kizu, T. Maruyama, Y. Nakamura, T. Fukuda, B. Lee, N. Ooba, S. Tomaru, T. Kurihara, T. Kaino, K. Kubota, S. Sasaki, J. Am. Chem. Soc. 118 (1996) 10389.
[25] F. Lloret, G. De Munno, M. Julve, J. Cano, R. Ruiz, A. Caneschi, Angew. Chem., Int. Ed. 37 (1998) 135.
[26] R. Cortes, M.K. Urtiaga, L. Lezama, J.L. Pizarro, M.I. Arriortua, T. Rojo, Inorg. Chem. 36 (1997) 5016.
[27] S.W. Keller, Angew. Chem., Int. Ed. 36 (1997) 247.
[28] B. Neuman, T. Hegmann, R. Wolf, C. Tschierske, Chem. Commun. (1998) 105.
[29] M. Hossian, S.K. Chattopadhyay, S. Ghosh, Polyhedron 16 (1997) 143.
[30] D.K. Demertzi, A. Domopoulou, A.P. Demertzis, D.X. West, Polyhedron 16 (1997) 3625.
[31] L.M. Fostiak, I. Garcia, J.K. Swearingen, E. Bermejo, A. Castineiras, D.X. West, Polyhedron 22 (2003) 83.
[32] D.X. West, H. Gebremedhin, R.J. Butcher, J.P. Jasinski, A.E. Liberta, Polyhedron 12 (1993) 2489.
[33] E.S. Roper, Coord. Chem. Rev. 153 (1996) 199.
[34] J.G. Tojal, B. Donnadieu, J.P. Costes, J.L. Serra, L. Lezama, T. Rojo, Inorg. Chim. Acta 333 (2002) 132.
[35] P.F. Rapheal, E. Manoj, M.R.P. Kurup, E. Suresh, Polyhedron 3 (2007) 607.
[36] K.A. Ketcham, J.K. Swearingen, A. Castineiras, I. Garcia, E. Bermejo, D.X. West, Polyhedron 20 (2001) 3265.
[37] F. Zamora, M. Kunsman, M. Sabat, B. Lippart, Inorg. Chem. 36 (1997) 1583.
[38] M. Louloudi, Y. Deligiannakis, J.P. Tuchagues, B. Donnadien, N. Nadjiliadis, Inorg. Chem. 36 (1997) 6335.
[39] F. Jolibois, J. Cadet, A. Grand, R. Subra, N. Raga, V. Barone, J. Am. Chem. Soc. 120 (1998) 1864.
[40] A.R. Katritzky, C.W. Pees, A.J. Boulton, C. Mckillop, J. Heterocycl. Chem. 3 (1984) 57.
[41] D.D. Perrin, W.L.F. Armarigo, D.R. Perrin, Purification of Laboratory Chemicals, 2nd ed., Pergamon Press, Oxford, 1980.
[42] (a) M.A. Ali, S.E. Livingstone, D.J. Phillips, Inorg. Chim. Acta 7 (1973) 179;
(b) R. Bose, M.A. Ali, J. Inorg. Nucl. Chem. 39 (1977) 265.
[43] H. Bredereck, R. Sell, F. Effenberger, Chem. Ber. 97 (1964) 3406.
[44] (a) Bruker, XPREP v2005/4, Bruker AXS Inc., Madison, WI, USA, 2005;
(b) Bruker, SMART v5.631, Bruker AXS Inc., Madison, WI, USA, 2001;
(c) Bruker, SAINT v7.34A, Bruker AXS Inc., Madison, WI, USA, 2005;
(d) Bruker, SHELXTL v6.12, Bruker AXS Inc., Madison, WI, USA, 2000;
(e) Bruker, SADABS v2004/1, Bruker AXS Inc., Madison, WI, USA, 2004;
(f) G.M. Sheldrick, Acta Crystallogr., Sect. A 46 (1990) 467.
[45] E.J. Gabe, M.R. Taylor, J.P. Pickworth Glusker, J. Minkin, A.L. Patterson, Acta Cryst., Sect. B 25 (1969) 1620.
[46] N.F. Curtis, in: G.A. Melson (Ed.), Coordination Chemistry of Macrocyclic (24 of c) Compounds, Plenum, New York, 1979.
[47] A. Mitra, T. Banerjee, P. Roychowdhury, S. Chaudhuri, P. Bera, N. Saha, Polyhedron 16 (1997) 3735.
[48] A.K. Barik, S. Paul, S.K. Kar, R.J. Butcher, J.C. Bryan, Polyhedron 18 (1999) 571.
[49] M.A. Ali, S.M.M. Majumder, R.J. Butcher, J.P. Jasinski, J.M. Jasinski, Polyhedron 16 (1997) 2749.
[50] R.J. Restivo, G.J. Palenik, Acta Crystallogr., Sect. B 26 (1970) 1397.
[51] N.F. Curtis, in: G.A. Melson (Ed.), Coordination Chemistry of Macrocyclic Compounds, Plenum, New York, 1979.
[52] S. Seth, Acta Cryst., Sect. C 50 (1994) 1196.
[53] A.L. Spek, Acta Crystallogr., Sect. A 46 (1990) C34, PLATON-A.
[54] M.M. Mostafa, A. Hammid, A.M. Shallaby, A.A. El-Asmy, Trans. Met. Chem. 6 (1981) 303.
[55] S.K. Chattopadhyay, D. Chattopadhyay, T. Banerjee, R. Kuroda, S. Ghosh, Polyhedron 6 (1997) 1925.
[56] A. Castineiras, D.X. West, H. Gebremedhin, T.J. Romack, Inorg. Chim. Acta 216 (1994) 229.
[57] D.X. West, J.K. Swearingen, J.V. Martinez, S.H. Ortega, A.K. El-Sawaf, F.V. Meurs, A. Castineiras, I. Garcia, E. Bermejo, Polyhedron 18 (1999) 2919.
[58] W.O. Koch, V. Schunemann, M. Gerdan, A.X. Trautwein, H.J. Kruger, Chem. Eur. J. 4 (1998) 1255.



Scheme 1. Limiting condition of paddle-wheel structure going to mononuclear structure.

we pursued reactions of cadmium(II)acetate with aromatic carboxylic acids followed by reaction with nitrogen donor ligands such as 3,5-dimethylpyrazoles or pyridine and the results are presented in this article.

2. Experimental

The X-ray diffraction data were collected at room temperature [296(2) K] on a Bruker 3-circle diffractometer (Bruker Nonius SMART APEX 2) equipped with CCD area detectors, and using graphite-monochromated Mo Kα radiation ($\lambda = 0.71073$ Å) from 60W microfocus Siemens Microsource with glass polycapillary optics. X-ray diffraction data for all the crystals were collected using Bruker SMART software. This software was also used for indexing and determining unit cell parameters. The structures were solved by direct methods and refined by full-matrix least squares against F^2 for all data using SHELXTL software. All non-H atoms were refined by full-matrix least squares in the anisotropic approximation and the hydrogen atoms attached to these atoms the hydrogen atoms have been located on the difference Fourier maps. In all cases the hydrogen atoms attached to polar atoms such as O and N were located on the difference Fourier maps and refined in the final structure in isotropic approximation. Experimental absorption correction method is none in all cases. The crystal data are given in Table 1. The proton NMR spectra were recorded in a Varian 400 MHz spectrophotometer at room temperature while the FT-IR spectra were recorded in NICOLET IMPACT-410 spectrometer using OMNIC software.

3. Experimental procedure for preparation of the complexes 1–9

To a well-stirred solution of benzoic acid/substituted benzoic acid (2 mmol) in methanol (10 ml) a solution of cadmium acetate dihydrate (0.266 g, 1 mmol) in methanol (5 ml) was added. The resulting homogeneous solution was stirred at room temperature for 4 h. To this homogeneous solution 3,5-dimethylpyrazole (2 mmol) or pyridine (2 mmol) was added and the colorless mixture was further stirred for 2 h. The solution was filtered and the filtrate on standing led to crystallization of the product.

4. Crystalline yield and spectroscopic data of the compounds

Complex **1**: Crystalline yield 61%, ^{1}H NMR (DMSO-d_6) 7.98–7.96(m, 2H), 7.47–7.39(m, 3H), 5.76(s 1H), 2.13 (s, 6H). IR(KBr, cm^{-1}) 3434(bs), 1596(s), 1538(s), 1404(s), 1279(s), 1166(m), 1147(m), 1040(m), 1024(m), 855(m), 803(m), 723(s). Elemental *Anal.* Calc. for $C_{24}H_{26}CdN_4O_4$: C, 52.66; H, 4.75. Found: C, 52.60; H, 4.74%. Complex **2**: Crystalline yield 30%, ^{1}H NMR (DMSO-d_6) 7.69(md, $J = 8$ Hz, 1H), 7.49–7.30(m, 3H), 5.74(s, 1H), 2.12(s, 6H). IR(KBr, cm^{-1}) 3445(bm), 3199(s), 3146(s), 1577(s), 1550(s), 1396(s), 1299(m), 1169(w), 1149(w), 1050(m), 860(m), 792(m), 755(s). Elemental *Anal.* Calc. for $C_{24}H_{24}CdN_4O_4Cl_2$: C, 46.77; H, 3.90. Found: C, 46.82; H, 3.92%. Complex **3**: Crystalline yield 15%, ^{1}H NMR (DMSO-d_6) 12.00(s, 1H), 7.79–7.78(m, 1H), 7.31–7.27(m, 1H), 6.78–6.71(m, 2H), 5.73(s, 1H), 2.10(s, 6H). IR(KBr, cm^{-1}) 3198(s), 3144(s), 3044(s), 2984(s), 1623(s), 1590(s), 1540(s), 1483(s), 1452(s), 1396(s), 1352(s), 1292(m), 1251(s), 1143(w), 1044(w), 875(w), 760(s). Complex **4**: Crystalline yield 34%, ^{1}H NMR (DMSO-d_6) 9.80(bs, 1H), 7.81(d, 8 Hz, 2H), 6.75(d, 8 Hz, 2H), 5.75(s,1H), 2.12(s, 6H). IR(KBr, cm^{-1}) 3420(bs), 3193(s), 3146(s), 1600(s), 1532(s), 1395(s), 1280(s), 1238(s), 1160(w), 1034(w), 825(m), 780(m). Complex **5**: Crystalline yield 51%, ^{1}H NMR (DMSO-d_6) 7.84(dd, 4, 8 Hz, 2H), 7.75(dd, $J = 4$, 8 Hz, 2H), 7.67–7.56(m, 4H), 5.75(m, 1H), 2.12(s, 6H). IR(KBr, cm^{-1}) 3445(bs), 1592(s), 1573(s), 1393(s),1356(s), 1153(w), 783(w), 741(w). Complex **6**: Crystalline yield 51%, ^{1}H NMR (DMSO-d_6) 8.27–8.25(m, 4H), 8.18–8.16(m, 4H), 5.74(s, 1H), 2.12(s, 6H). IR(KBr, cm^{-1}) 3422(bs), 3199(s), 3136(s), 2931(s), 2875(s), 1572(s), 1388(s), 1339(s), 1031(m), 815(s), 727(m). Elemental *Anal.* Calc. for $C_{19}H_{16}CdN_4O_8$: C, 42.16; H, 2.96. Found: C, 42.20; H, 2.99%. Complex **7**: Crystalline yield 26%, ^{1}H NMR (DMSO-d_6) 7.96–7.93(m, 4H), 7.47–7.45(4H), 5.74(s, 1H), 2.12(s, 6H). IR (KBr, cm^{-1}) 3269(bs), 1590(s), 1500(s), 1411(s), 1284(w), 1096(w), 858(m), 776(m). Complex **8**: Crystalline yield 24%, ^{1}H NMR (DMSO-d_6) 8.58 (s, 2H), 8.04(t, $J = 8$ Hz, 4H), 7.92(t, $J = 8$ Hz , 4H),

Table 1
Crystal data and refinement parameters for **1–9**

	1	**2**	**3**	**4**	**5**
Formulae	$C_{24}H_{26}CdN_4O_4$	$C_{24}H_{24}CdN_4O_4Cl_2$	$C_{24}H_{26}CdN_4O_6$	$C_{24}H_{26}CdN_4O_6$	$C_{76}H_{72}CdN_{16}O_{36}$
Molecular weight	546.89	615.77	578.89	578.89	2235.10
Crystal system	monoclinic	monoclinic	monoclinic	monoclinic	triclinic
Space group	$P2_1/n$	$C2/c$	$P2_1/n$	$P2_1/c$	$P\bar{1}$
a (Å)	12.6043(5)	23.7361(15)	13.1139(3)	10.0548(5)	14.0437(8)
b (Å)	13.9558(6)	11.2097(6)	13.0501(3)	21.1953(12)	14.1965(9)
c (Å)	14.2804(6)	10.6339(12)	14.7963(4)	12.0152(7)	14.6448(10)
α (°)	90.00	90.00	90.00	90.00	63.324(4)
β (°)	93.250(2)	115.578(5)	94.2690(10)	109.5650(10)	62.683(3)
γ (°)	90.00	90.00	90.00	90.00	64.211(3)
V (Å^3)	2507.03(18)	2552.1(4)	2525.18(11)	2412.8(11)	2219.5(2)
Z	4	4	4	4	1
Density (g cm^{-3})	1.448	1.603	1.523	1.594	1.672
Absorption coefficient (mm^{-1})	0.906	1.103	0.910	0.953	1.042
F(000)	1112	1240	1176	1176	1120
Total number of reflections	9137	16001	25494	12211	24479
Reflections $I > 2\sigma(I)$	5097	2703	4609	4351	9028
Maximum 2θ (°)	28.40	28.21	28.37	28.38	28.38
Ranges (h,k,l)	$-16 \leqslant h \leqslant 16$, $-18 \leqslant k \leqslant 18$, $-19 \leqslant l \leqslant 19$	$-29 \leqslant h \leqslant 31$, $-14 \leqslant k \leqslant 14$, $-14 \leqslant l \leqslant 13$	$-17 \leqslant h \leqslant 17$, $-17 \leqslant k \leqslant 17$, $-19 \leqslant l \leqslant 19$	$-13 \leqslant h \leqslant 13$, $-25 \leqslant k \leqslant 15$, $-16 \leqslant l \leqslant 13$	$-18 \leqslant h \leqslant 18$, $-18 \leqslant k \leqslant 18$, $-19 \leqslant l \leqslant 18$
Complete to 2θ (%)	99.1	96.4	99.2	89.1	97.8
Data/restraints/parameters	6235/0/310	3044/0/161	6270/0/336	5394/0/336	10849/0/623
Goodness of fit (F^2)	1.019	1.050	1.012	0.995	1.017
R indices [$I > 2\sigma(I)$]	0.0252	0.0292	0.0289	0.0260	0.0243
R indices (all data)	0.0689	0.0785	0.0683	0.0628	0.0615

	6	**7**	**8**	**9**
Formulae	$C_{19}H_{16}CdN_4O_8$	$C_{19}H_{16}CdN_2O_4Cl_2$	$C_{27}H_{22}CdN_2O_4$	$C_{32}H_{26}CdN_2O_5$
Molecular weight	540.76	519.64	550.87	630.95
Crystal system	triclinic	triclinic	monoclinic	monoclinic
Space group	$P\bar{1}$	$P\bar{1}$	$P2_1/c$	$P2_1/n$
a (Å)	7.8825(6)	7.8546(4)	7.9424(9)	15.7113(15)
b (Å)	11.4426(10)	10.8632(7)	29.076(4)	6.0304(5)
c (Å)	12.2286(10)	13.3295(8)	10.5680(12)	29.197(3)
α (°)	85.004(5)	111.717(3)	90.00	90.00
β (°)	72.214(5)	91.225(3)	97.118(7)	92.195(6)
γ (°)	82.499(5)	97.744(2)	90.00	90.00
V (Å^3)	1039.97(15)	1043.85(11)	2421.3(5)	2764.3(4)
Z	2	2	4	4
Density (g cm^{-3})	1.727	1.653	1.511	1.516
Absorption coefficient (mm^{-1})	1.105	1.328	0.973	0.834
F(000)	540	516	1112	1280
Total number of reflections	8297	13329	30720	23494
Reflections ($I > 2\sigma(I)$)	3342	4609	3591	5021
Maximum 2θ (°)	26.00	28.33	28.33	28.34
Ranges (h,k,l)	$-9 \leqslant h \leqslant 9$, $-13 \leqslant k \leqslant 13$, $-15 \leqslant l \leqslant 15$	$-10 \leqslant h \leqslant 10$, $-14 \leqslant k \leqslant 14$, $-17 \leqslant l \leqslant 17$	$-10 \leqslant h \leqslant 10$, $-38 \leqslant k \leqslant 38$, $-13 \leqslant l \leqslant 14$	$-20 \leqslant h \leqslant 20$, $-7 \leqslant k \leqslant 8$, $-37 \leqslant l \leqslant 39$
Complete to 2θ (%)	88.3	97.5	99.3	98.3
Data/restraints/parameters	3609/0/195	5087/0/260	5994/0/313	6766/0/369
Goodness-of-fit (F^2)	1.077	1.031	1.041	1.012
R indices [$I > 2\sigma(I)$]	0.0202	0.0243	0.0531	0.0325
R indices (all data)	0.0527	0.0643	0.1410	0.0675

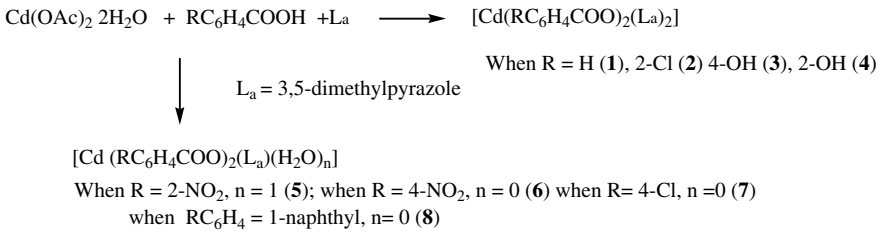
7.60–7.55(m, 4H), 5.73(s, 1H), 2.12(s,6H). IR(KBr, cm^{-1}) 3392(bs), 3056(w), 2923(w), 1547(s), 1396(s), 792(s). Complex **9**: Crystalline yield 23%, ^{1}H NMR (DMSO-d_6) 8.59(s, 1H), 8.09–8.04(m, 2H), 7.94(t, $J = 8$ Hz , 2H), 7.78(mt, $J = 8$ Hz, 2H), 7.61–7.54(m,2H), 7.41–7.38(m, 3H). IR(KBr, cm^{-1}) 3444(bs), 2925(m), 1631(s), 1602(s), 1537(s), 1504(m), 1046(m), 1400(s), 1281(w), 1035(m), 790(s).

5. Results and discussion

The reaction of cadmium acetate with aromatic carboxylic acid followed by treatment with 3,5-dimethylpyrazole (L_a) led to mixed ligand cadmium complexes. The number of (L_a) ligand/s in cadmium carboxylate complexes varies with the aromatic carboxylic acid from which it is

prepared. Either two nitrogen donor ligands or one nitrogen donor ligand per cadmium ion are observed depending on the substituents present in the aromatic carboxylate. For example, the reaction of cadmium acetate dihydrate with aromatic carboxylic acids such as benzoic acid, 2-chlorobenzoic acid, 2-hydroxybenzoic acid or 4-hydroxybenzoic acid in the presence of (L_a) led to the formation of corresponding benzoate complexes having two benzoate groups and two (L_a) ligands. The 2-nitro-, 4-nitro-, 4-chloro-benzoic acids and 1-naphthoic acid led to complex having one (L_a) and two carboxylate ligands per cadmium. However, the 2-nitrobenzoate complex of cadmium contains an additional aqua ligand; which is absent in the case of 4-nitrobenzoate complex. The results are depicted Scheme 2.

The crystal structure of each of these complexes is determined and the structures of the complexes **1**–**4** are shown in Fig. 1. Trigonal prismatic geometry with six co-ordination around cadmium ions are observed in the cases of the complexes **1**–**4**. The bond angles and bond distances of the complexes are listed in Table 2 and structures of the complexes are shown in Fig. 1. It may be mentioned that in the case of **1** two types of cadmium ligand bonds in terms of bond length are observed. There are four cadmium–ligand bonds of similar length and two other are slightly longer. It has been already reported [3a] that in cadmium complexes outer and inner co-ordination spheres are possible and the outer Cd–N bond lengths are in the range of 2.5–2.7 Å whereas inner ones are less by about 0.3 Å from the outer ones. In our system also the bond distances of the four Cd–N and Cd–O bonds are comparable and makes a pseudo tetrahedral inner structure comprising of Cd–O3, Cd–O4, Cd–N1 and Cd–N4 bonds. The other two Cd–O1 and



Scheme 2.

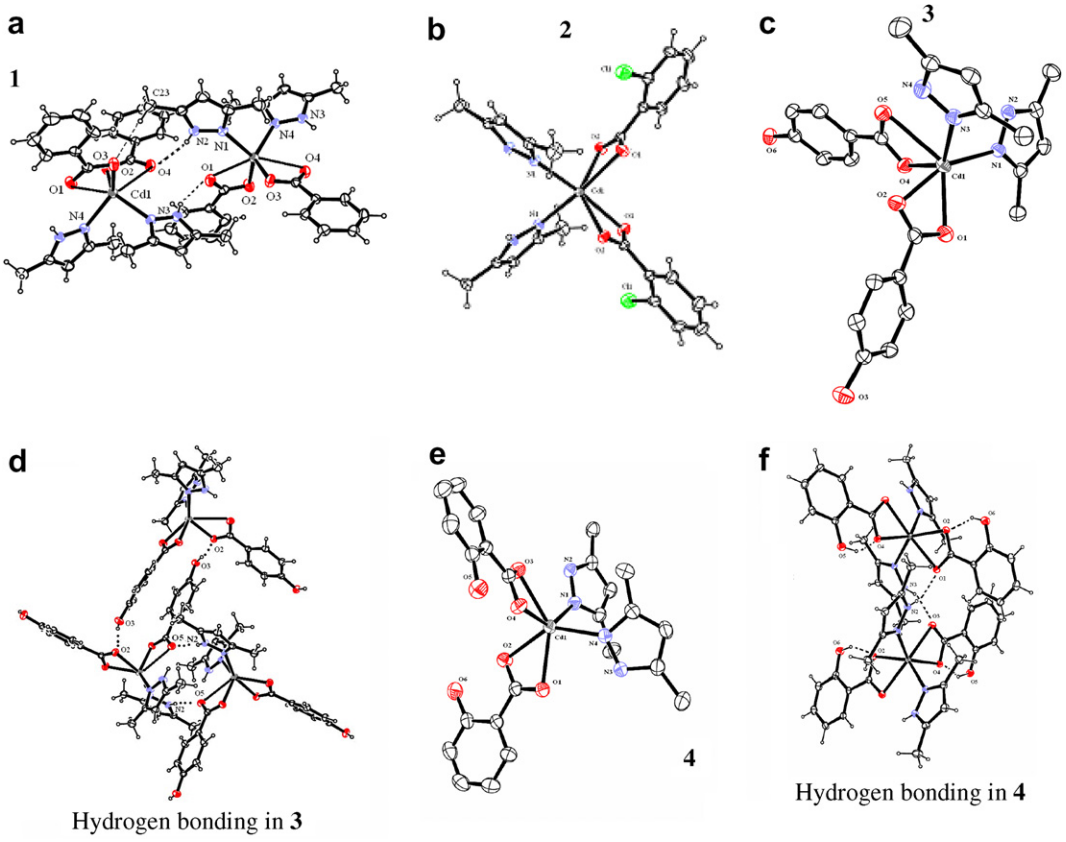


Fig. 1. Structures of cadmium benzoate complexes **1**–**4** and their hydrogen bonded assembly [ORTEP are drawn with 20% thermal ellipsoid, in cases of (c) and (e) hydrogen atoms are omitted for clarity].

Table 2
Cadmium–ligand bond geometry (distances and angles) in complexes **1**–**4**

Cd–L	Co–L (Å)	L–Cd···L	∠L–Cd···L (°)	Cd–L	Co–L (Å)	L–Cd···L	∠L–Cd···L (°)
*For **1***				*For **2***			
Cd–O1	2.561	O4–Cd–N4	80.96	Cd–O1	2.371	O1–Cd–N1	114.56
Cd–O2	2.234	O4–Cd–N1	125.52	Cd–O2	2.358	N1–Cd–N2	87.34
Cd–O3	2.276	O3–Cd–O1	95.16	Cd–O1	2.371	O2–Cd–N1	92.27
Cd–O4	2.480	O4–Cd–O2	107.04	Cd–O2	2.358	O1–Cd–O2	92.77
Cd–N4	2.254	O3–Cd–N1	93.87	Cd–N1	2.272	O2–Cd–O2	89.89
Cd–N1	2.278	O3–Cd–N4	132.13	Cd–N1	2.272	O1–Cd–O1	136.88
*For **3***				*For **4***			
Cd–O1	2.288	N1–Cd–O4	95.64	Cd–O1	2.365	O1–Cd–N4	85.03
Cd–O2	2.400	O2–Cd–O5	90.98	Cd–O2	2.379	O3–Cd–O2	97.98
Cd–O5	2.779	O1–Cd–O4	96.84	Cd–O3	2.422	O1–Cd–O4	100.11
Cd–O4	2.222	O1–Cd–N1	105.56	Cd–O4	2.302	O3–Cd–N1	85.20
Cd–N1	2.259	O2–Cd–N3	90.74	Cd–N1	2.251	O2–Cd–N4	139.05
Cd–N3	2.779	N3–Cd–N1	94.27	Cd–N4	2.276	O2–Cd–N1	100.64

Cd–O4 bonds have bond length 2.561 and 2.480 Å and with bond angles O1–Cd–O4 137.62°, respectively. This suggests that under suitable condition these two atoms would serve as bridging group if another metal atom can approach. However, in this case presence of two 3,5-dimethylpyrazole ligands prevents further approach oxygen to the cadmium ion to form co-ordination polymer. The 2-chlorobenzoate complex **2** has a more symmetric trigonal prismatic structure. Both the compounds **1** and **2** have similar hydrogen bonding interactions and they remain as hydrogen bonded self-assemblies. In these two complexes the N–H bond of 3,5-dimethylpyrazole interacts with the carbonyl group of co-ordinated carboxylate ligand of another molecule to form self-assemblies. Such assemblies are further held by C23–H···O2 interaction between C–H of a methyl group with an oxygen atom of carboxylate group of another molecule (Fig. 1a). The important bond angles and distances for compound **1** are listed in Table 2. Cadmium complex of 4-amino-carboxylic acid adopts two dimensional polymeric hydrogen bonded structure [7]. The structure of the complexes **3** and **4** are shown in Fig. 1c and e respectively. Both these complexes have six co-ordinations with distorted trigonal prismatic geometry and in the solid state they form H-bonded self-assembly. The complex **3** has a one dimensional layer structure held by N–H···O interactions between the N–H of 3,5-dimethylpyrazole un-coordinated nitrogen atoms with carbonyl oxygen of 2-hydroxybenzoate. There is also intra-molecular hydrogen bonding (O6–H···O2) between the hydroxy groups with the carbonyl oxygen of the benzoate (Table 3). In the 4-hydroxybenzoate complex **4**, hydrogen bonding between hydroxy groups and the carbonyl oxygen of another molecule adjacent to it takes place. In addition to this, the opposite side of the molecule is associated with N–H···O interactions with another neighboring molecule as illustrated in Fig. 3f. These interactions result in the formation of three-dimensional hydrogen bonded network. It is already reported that the picolinic acid forms six-coordinated polymeric network. Our results also support that N1O5 environment around cadmium [1n,2] can lead to co-ordination polymer in one-dimension.

The nitro-substituent on the aromatic carboxylic acid affects the structure as well as the co-ordination environment of cadmium complexes. The complex **5** has an aqua-ligand and it is a tetra nuclear complex as shown in Fig. 2a. The formation of such tetra nuclear complex is attributed to the variation in composition due to the steric effect of nitro-group at *ortho*-position leading to a thermodynamically stable product. The complex **5** has eight co-ordination around two central cadmium ion and the other two cadmium ions at both the ends of the tetra nuclear complex have six co-ordination geometry. Polymeric cadmium complexes having seven co-ordination is common in co-ordination chemistry of cadmium [1a], however the complex **5** is a rare example of tetra nuclear complex having eight co-ordination. It is interesting to note that each of the tetra nuclear complex possesses aqua-ligand at the end cadmium atoms; each and these aqua ligands interacts with

Table 3
Hydrogen bonding geometry (distances and angles) in complexes **1**–**4**

D–H···A	$d_{D–H}$ (Å)	$d_{H···A}$ (Å)	$d_{D···A}$ (Å)	∠D–H···A (°)
*For **1***				
C23–H···O2	0.960	2.470	3.412	187.02
O4–H···N2	0.926	2.242	2.990	158.24
N6–H···O2	0.817	1.935	2.737	166.98
*For **2***				
N2–H···O1	0.880	1.961	2.821	165.57
*For **3***				
O3–H...O2	0.730	1.963	2.683	168.42
O6–H...O4	0.803	1.933	2.729	171.25
N2–H... O5	0.854	2.062	2.864	156.08
*For **4***				
O6–H···O2 (intramolecular)	0.889	1.788	2.589	148.63
N2–H···O1	0.832	2.280	3.041	152.41
N3–H···O3	0.832	2.188	2.954	153.05

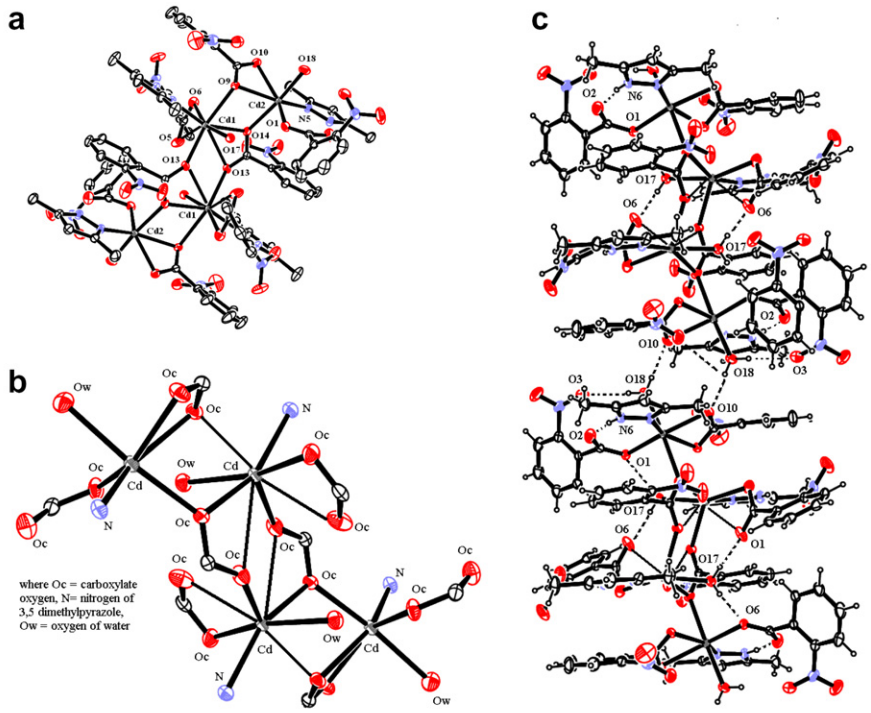


Fig. 2. (a) Structure of tetra nuclear complex **5** (hydrogen atoms are omitted for clarity). (b) The arrangement of ligands around the cadmium in the tetra nuclear complex. (c) Hydrogen bonding interactions in the self assembled structure (drawn with 20% thermal ellipsoids).

the carbonyl group of another tetra-nuclear complex making an one dimensional self-assembled polymeric structure. Some of the important hydrogen bonding interactions present in the hydrogen bonded assembly is listed in Table 4. This structure is also important from another point of view is that it is an exception to the structure that is observed as mononuclear complex from 2-chlorobenzoic acid and 2-hydroxybenzoic acid which are *ortho*-substituted aromatic carboxylates. However, it is observed that the solid phases reaction of 2-nitrobenzoic acid with cadmium acetate with (L_a) results in the formation of mononuclear hexa-coordinated species namely tetra (3,5-dimethylpyrazole) cadmium(II) (2-nitrobenzoate). In the case of solid phase reaction we did not observe tetra nuclear species rather observed a mononuclear species; this suggests that tetra nuclear species may be a kinetic control product. In fact tetra-nuclear complex on heating transforms to mononuclear hexa-coordinated complex.

Table 4
Hydrogen bonding geometry (distances and angles) in complex **5**

D–H···A	d_{D-H} (Å)	$d_{H\cdots A}$ (Å)	$d_{D\cdots A}$ (Å)	∠D–H···A (°)
N6–H···O2	0.817	1.935	2.737	166.98
O1–H···O17	0.748	2.092	2.831	169.24
O6–H···O17 (2−*x*, 1−*y*, *z*)	0.781	1.998	2.766	167.41
O3–H···O18	0.784	2.274	3.035	160.76

The complex **6** has a polymeric structure with the carboxylate oxygen atoms as bridging atoms to the cadmium ions. The structure of the complex **6** is shown in Fig. 3a. The 4-nitrobenzoate complex **6** does not have aqua ligand as compared to that of **5**. Thus, it may be said that the position of water molecule is occupied up by bridging oxygen atom of a carboxylate group leading to co-ordination polymer. In the one-dimensional polymer all the cadmium are in seven co-ordination environment. The metal–ligand bond geometries are listed in Table 5. Similar structures are obtained in the case of 4-chlorobenzoate complex **7** as well as in the 1-naphthoate complex **8**. Important bond distances are listed in Table 5. In these two cases the metal–ligand composition of the complex is identical to that of **6**. A similar reason may be put forward in these cases for explaining polymer formation. The attack of one nitrogen donor ligand is favored in these three complexes due to steric reasons and this makes approach of another molecule to form bridging carboxylate bonds between two discrete units. Careful analysis of the structure shows (Fig. 3b) that every carboxylate can be a bridging as well as chelating in the polymeric system. Such system can be constructed from the dinuclear building blocks as depicted in Fig. 3f. Support to this fact arises from the fact that there are two different Cd–Cd distances in each of these complexes in alternating manner. For example the Cd–Cd distances in 4-nitrobenzoate, 4-chlorobenzoate and 1-naphthoate complexes are 4.138 Å, 3.748 Å; 4.119 Å, 3.745 Å and 4.152 Å, 3.801 Å respectively. The observation of long and short separation clearly indicates that there is a part of the poly-

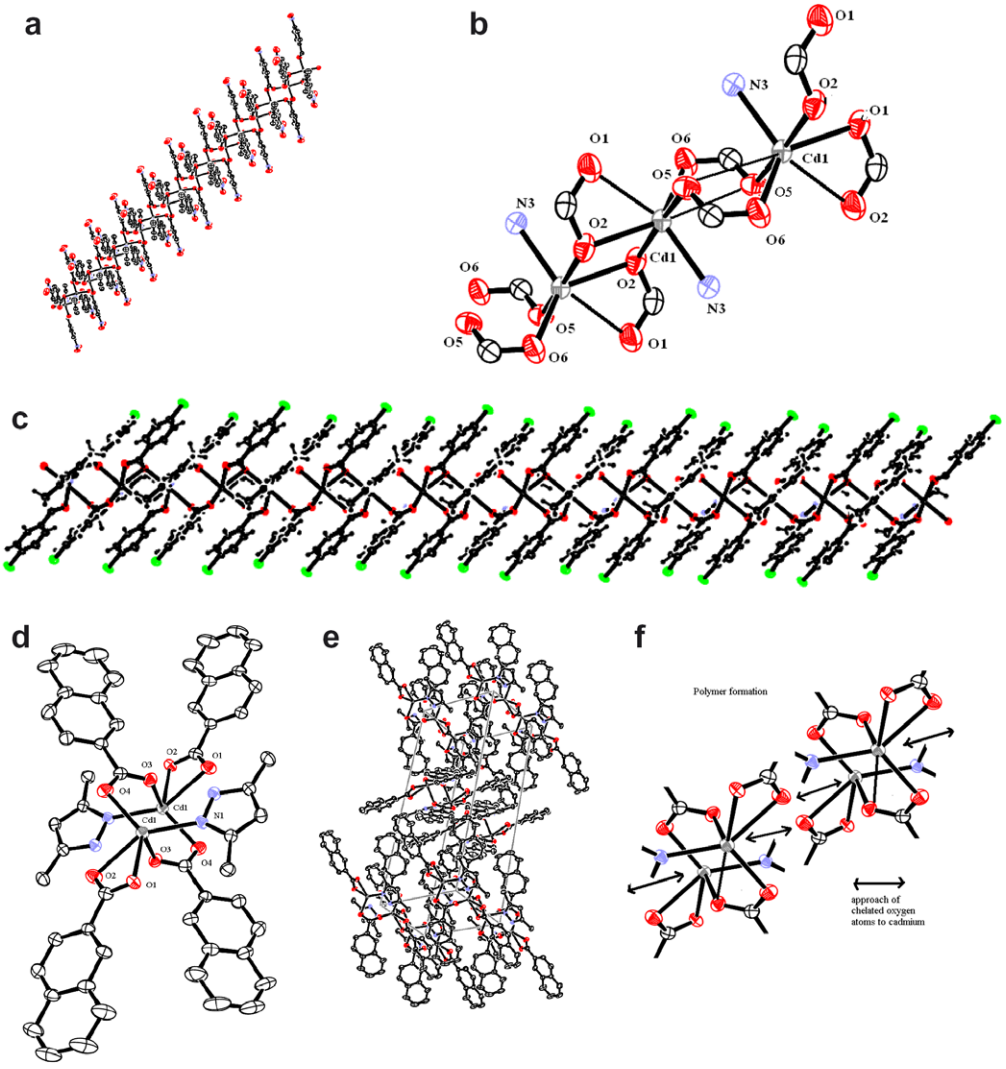


Fig. 3. The structure of (a) **6** (b) ligand environment in the co-ordination polymer of **6**, (c) the structure of **7** (d) the repeated units in the co-ordination polymer **8** (e) unit cell of **8** (f) representation showing a route for formation of co-ordination polymers in **6**–**8**.

mer having paddlewheel type structure and another unit has features of mononuclear structure and combination of which is leading to the co-ordination polymers. Thus, formation of mononuclear complexes may be imagined to be from cleavage of such polymeric species. It may be proposed that that the polymeric units are having mononuclear and dinuclear paddlewheel structure and each paddlewheel can be squeezed to give mononuclear species if the diagonal bridging atoms can be connected to the cadmium atom. Such distortion in paddlewheel would preferentially take the system to a mononuclear species. This is illustrated in Scheme 1, where arrows are indicating the approach of an oxygen atom to cause distortion to a limiting case and beyond which distortion would make two mononuclear chelate from one parent bridged binuclear system. We have observed in the case of copper [6a] and cobalt [6e] and in nickel [6b,6c] that similar reactions are highly sensitive to the reaction conditions. However, the present study is designed such a way that all the reactions are carried out under identical molar ratios and identical condition. The driving force in the case of cadmium complexes to have polymeric form thus arises from the competition between the steric factor and attack of a bridging ligand to form co-ordination polymer. The (4-chloro-2-methylphenoxy) acetate complex of cadmium(II) complex has polymeric structures having six coordination number of cadmium [8]. In this complex, two water molecules and a carboxylate group serves as bridging ligand [8]. All the complexes presented in this manuscript are also characterized by recording their proton-NMR. The integration of protons confirmed that they have the same composition in solution and solid state. However, it is found that for complex **5** and **9** in DMSO the water signals of the complexes are merged with the water signal from dissolved water in the solvent. Each of the complexes has characteristic N–H stretching frequency from the 3,5-dimethylpyrazole ring however, at a different position. For example, complex **1** has absorption at 3434 cm^{-1} for N–H stretching whereas the 3,5-dimethyl pyrazole has absorption at 3201 cm^{-1}. The compound has absorption frequencies that have

Table 5
Cadmium–ligand bonding geometry (distances and angles) in complex **6**, **7**, **8** and **9**

Cd–L	Co–L (Å)	L–Cd···L	∠L–Cd···L (°)	Cd–L	Co–L (Å)	L–Cd···L	∠L– Cd···L (°)
For ***6***				*For 7*			
Cd–O1	2.219	O6–Cd–O1	87.71	Cd–O1	2.293	O1–Cd–O2	101.99
Cd–O2	2.767	O5–Cd–N3	87.65	Cd–O3	2.479	O4–Cd–O3	97.75
Cd–O5	2.291	O5–Cd–O5′	75.37	Cd–O2	2.383	O1–Cd–N1	104.08
Cd–O6	2.524	O2–Cd–N3	77.78	Cd–O4	2.209	O2–Cd–N1	78.11
Cd–N3	2.279	O6–Cd–N3	148.02	Cd–N1	2.271	O2–Cd–O3	77.78
				For ***9***			
				Cd–O1	2.430	O4–Cd–N2	97.23
For ***8***				Cd–O2	2.384	O4–Cd–N2	91.47
Cd–O2	2.302	O1–Cd–O3	77.52	Cd–O3	2.484	O4–Cd–N1	85.40
Cd–O1	2.461	O2–Cd–O2′	75.44	Cd–O4	2.363	O3–Cd–O2	84.51
Cd–O3	2.402	O3–Cd–N1	77.85	Cd–N1	2.358	O4–Cd–O5(aq)	81.35
Cd–O4	2.212	O1–Cd–O4	89.25	Cd–N2	2.356	O5–Cd–N2(aq)	88.37
Cd–N1	2.253	O2–Cd–N1	104.59	Cd–O5(aq)	2.328	O5–Cd–N1(aq)	95.21

characteristic features of bi-dentate carboxylate ligand [9]. For example the complex **1** has absorption at 1538(ν_{as}) and 1404(ν_s) cm^{-1} due to the bidentate carboxylic acid group. The parent benzoic acid has absorptions at 1682 and 1421 cm^{-1}. The other mono-nuclear complexes also have similar trends in absorptions over the parent carboxylic acid, confirming bi-dentate nature of the carboxylate groups. The complexes **6**, **7**, **8** have both bidentate and bridging carboxylates from crystallographic study. Although, in these cases clear distinction could not be made between the two type of binding mode from the IR-absorptions but some inference can be made; for example in the case of **7**, the absorptions from carboxylate groups occurs at 1590, 1500, 1411 and 1390 cm^{-1} in contrast to the parent carboxylic acid namely 4-chlorobenzoic acid, which has absorptions at 1683, 1592, 1424 cm^{-1}.

Since we have obtained a polymeric structure for the 1-naphthoate complex **8**, we extended our study to the reaction of cadmium acetate with 1-naphthoic acid and pyridine

$$Cd(OAc)_2 2H_2O + 1\text{-}C_{10}H_7COOH + L_b \rightarrow \underset{\mathbf{9}}{[Cd(C_{10}H_7COO)_2(L_b)_2(H_2O)]} \quad (1)$$

where Lb = pyridine

This reaction led to complex having composition $[M(L)_2(L_b)_2(H_2O)]$ (**9**) where L is 1-naphthoate and L_b is pyridine. As expected from the trend from the composition that in this class of compound there is no polymeric structure, we have found it to be so for the complex. It is found that the complex has a distorted pentagonal bipyramidal seven co-ordination geometry as shown in Fig. 4a. Four oxygen atoms from naphthoate groups and oxygen atom of the aqua ligand form the basal plane. The axial positions are taken up by two pyridine ligands. The complex in solid state has extensive hydrogen bonded structure through the interaction of the aqua

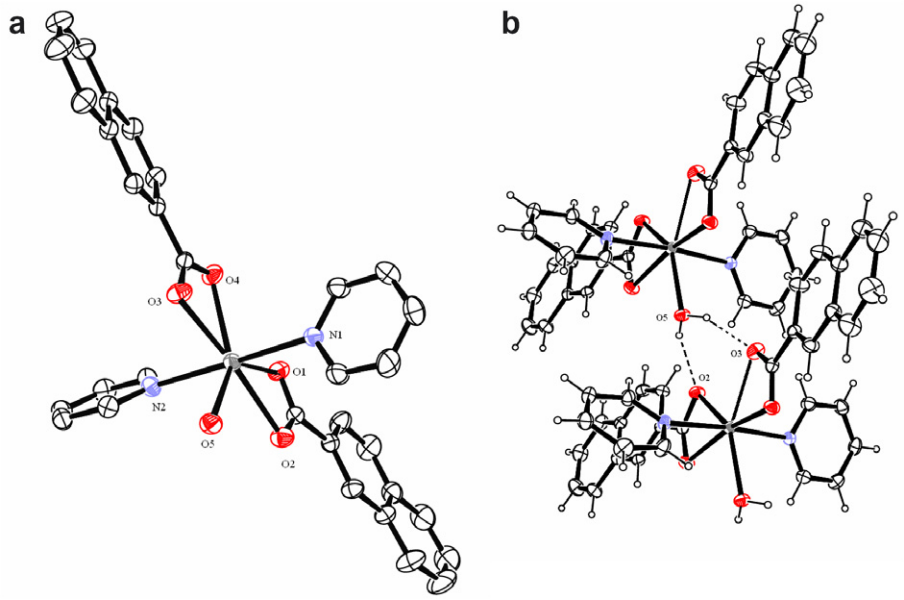


Fig. 4. (a) The structure of **9** (hydrogen atoms are omitted for clarity). (b) The hydrogen bond interactions between two molecules of **9** (drawn with 20% thermal ellipsoid).

ligand with the oxygen of carboxylate groups. The hydrogen bonded chain like structures are formed from O5–H···O3 with 0.901 (d_{D-H}), 1.934 ($d_{H\cdots A}$), 2.766 ($d_{D\cdots A}$), 152.759 (∠D–H···A/°) and O5–H···O2 with 0.809 (d_{D-H}), 1.995 ($d_{H\cdots A}$), 2.727 ($d_{D\cdots A}$) 150.18 (∠D–H···A/°). The hydrogen bonding between two molecules of **9** is shown in Fig. 4b.

In conclusion it has been possible to rationalize the relation between composition and structure in 3,5-dimethypyrazole containing cadmium carboxylates. The cadmium carboxylate complex having composition $[Cd(L)_2(L_a)_2]$ leads to mononuclear structure and the composition $[Cd(L)_2(L_a)]$ leads to polynuclear co-ordination polymers, whereas the complex having the composition $[Cd(L)_2(L_a)(H_2O)]$ leads to tetranuclear complex. It is also observed that the compositions are more important than the substituent at the *ortho* or *para*-position of the aromatic carboxylate ligands, however, to a great extent the composition of L_a containing cadmium carboxylates are decided by the substituents; keeping a close correlation between the steric factor with thermodynamic control of synthesis. The overall structure in solid state is stabilized by various weak interactions. The cadmium complex having the composition $[M(L)_2(L_b)_2(H_2O)]$ leads to mononuclear pentagonal bipyramid structure.

Acknowledgements

The authors thank Department of Science and Technology, New-Delhi for financial assistance. The author thanks Dr. R.J. Sarma for helping in the work.

Appendix A. Supplementary material

CCDC 626304, 626305, 626306, 626307, 626308, 626309, 6263010, 6263011 and 626312 contain the supplementary crystallographic data for this paper. These data can be obtained free of charge via http://www.ccdc.cam.ac.uk/conts/retrieving.html, or from the Cambridge Crystallographic Data Centre, 12 Union Road, Cambridge CB2 1EZ, UK; fax: (+44) 1223-336-033; or e-mail: deposit@ccdc.cam.ac.uk. Supplementary data associated with this article can be found, in the online version, at doi:10.1016/j.poly.2007.01.005.

References

[1] (a) F.A. Cotton, C. Lin, C.A. Murillo, Acc. Chem. Res. 34 (2001) 759;
(b) M. Eddaoudi, D.B. Moler, H. Li, B. Chen, T.M. Reineke, M. Keeffe, O.M. Yaghi, Acc. Chem. Res. 34 (2001) 319;
(c) B. Moulton, M.J. Zaworotko, Chem. Rev. 101 (2001) 1629;
(d) S.L. James, Chem. Soc. Rev. 32 (2003) 276;
(e) R. Murugavel, M.G. Walawalkar, M. Dan, H.W. Roesky, C.N.R. Rao, Acc. Chem. Res. 37 (2004) 763;
(f) K.S. Gavrilenko, S.V. Punin, O. Cador, S. Golhen, L. Ouahab, V.V. Pavlishchuk, J. Am. Chem. Soc. 127 (2005) 12247;
(g) M. Eddaoudi, D.B. Moler, H. Li, B. Chen, T.M. Reineke, M. O'Keeffe, O.M. Yaghi, Acc. Chem. Res. 34 (2001) 319;
(h) M. Casarin, C. Corvaja, C.D. Nicola, D. Falcomer, L. Franco, M. Monari, L. Pandolfo, C. Pettinari, F. Piccinelli, Inorg. Chem. 44 (2005) 6265;
(i) M. Eddaoudi, H. Li, O.M. Yaghi, J. Am. Chem. Soc. 127 (2005) 7110;
(j) E. Tynan, P. Jensen, A.C. Lees, B. Moubaraki, K.S. Murray, P.E. Kruger, CrysEngComm 7 (2005) 90;
(k) Z. Wang, V.C. Kravtsov, M.J. Zaworotko, Angew Chem., Int. Ed. Eng. 44 (2005) 2877;
(l) D. Sun, D.J. Collins, Y. Ke, J.-L. Zuo, H.-C. Zhou, Chem. Eur. J. 12 (2006) 3768;
(m) S.N. Wang, H. Xing, Y.Z. Li, J.F. Bai, J.F. Bai, Y. Pan, M. Scheer, X.Z. You, Eur. J. Inorg. Chem. (2006) 3041;
(n) O.R. Evans, W.B. Lin, Inorg. Chem. 39 (2000) 2189.
[2] O.R. Evans, W.B. Lin, Acc. Chem. Res. 35 (2002) 511.
[3] (a) A. Michaelides, C.D. Papadimitriou, J.C. Plakatouras, S. Skoulika, P.G. Veltsistas, Polyhedron 23 (2004) 25873;
(b) B. Barszcz, S. Hodorowicz, A. Jablonska-Wawrzycka, K. Stadnicka, J. Coord. Chem. 58 (2005) 203;
(c) Z.-F. Chen, R.-G. Xiong, B.F. Abrahams, X.-Z. You, C.-M. Che, J. Chem. Soc., Dalton Trans. (2001) 2453;
(d) H. Strasdeit, S. Pohl, Zeitschrift fuer Naturforschung, B: Chem. Sci. 43 (1988) 1579;
(e) X.-L. Wang, C. Qin, E.-B. Wang, Z.-M. Su, Chem. Eur. J. 12 (2006) 2680;
(f) H.C. LopezSadovel, N. Barbabehrens, S. Bernes, N. FarfanGarcia, H. Hoplf, J. Chem. Soc., Dalton Trans. (1997) 3415;
(g) S. Sen, M.K. Saha, P. Kundu, S. Mitra, C. Kruger, J. Bruckmann, Inorg. Chim. Acta 288 (1999) 118.
[4] T.C. Stamatatos, E. Katsoulakou, V. Nastopoulos, C.P. Raptopoulou, E. Manessi-Zoupa, S.P. Perlepes, Zeitschrift fuer Naturforschung, B: Chem. Sci. 58 (2003) 1045.
[5] C. Balarew, R. Stefanova, Cryst. Res. Tech. 31 (1996) 99.
[6] (a) A. Karmakar, R.J. Sarma, J.B. Baruah, Inorg. Chem. Commun. 9 (2006) 931;
(b) A. Karmakar, K. Deka, R.J. Sarma, J.B. Baruah, Inorg. Chem. Commun. 9 (2006) 2942;
(c) A. Karmakar, R.J. Sarma, J.B. Baruah, Eur. J. Inorg. Chem. (2006) 4673;
(d) A. Karmakar, R.J. Sarma, J.B. Baruah, Polyhedron (2006), in press, doi:10.1016/j.poly.2006.11.001.;
(e) A. Karmakar, R.J. Sarma, J.B. Baruah, Inorg. Chem. Commun. 9 (2006) 1169.
[7] R.H. Wang, M.C. Hong, J.H. Cao, Q. Shi, J.B. Weng, Eur. J. Inorg. Chem. (2002) 2904.
[8] R. Kruszynski, A. Turek, J. Coord. Chem. 57 (2004) 1089.
[9] K. Nakamoto, fifth ed., Infrared and Raman Spectra of Inorganic and Coordination Compounds, Part B: Applications in Coordination, Organometallic, and Bioinorganic Chemistry, Wiley, New York, 1997.

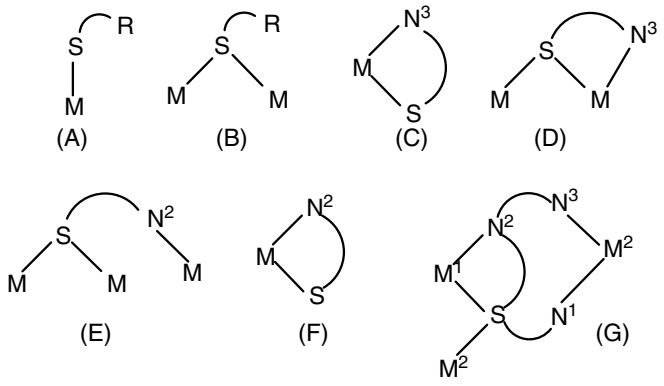
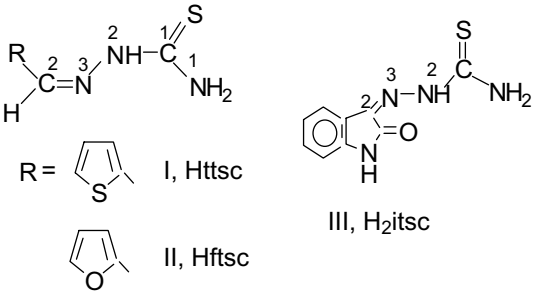


Chart 1.

mode G are also present. Mode G involves N^2, S-chelation to one metal, and N^1, N^3-chelation to second metal with sulfur also bridging another metal center [23].

The coordination chemistry of thiophene-2-carbaldehyde thiosemicarbazone (I, Httsc) and furanaldehyde thiosemicarbazones (II, Hftsc) is limited [24–26], and likewise only a few complexes of isatin-3-thiosemicarbazone (III, H_2itsc) are known [9a]. We have been interested in the study of the interaction of d^{10} metal ions (Cu, Ag) with thiosemicarbazones by changing the R groups at the C^2 carbon and the halogen bonded to the M^I center [10]. Reaction of thiophene-2-carbaldehyde thiosemicarbazone (Httsc) and furanaldehyde thiosemicarbazones (Hftsc) with copper(I) iodide formed iodo-bridged dimers and with copper(I) bromide formed sulfur bridged dimers [10a], while isatin-3-thiosemicarbazone (H_2itsc) formed monomers for X = Br, I [9a]. In this paper, we report the reactions of copper(I) chloride with Httsc, Hftsc and H_2itsc, and the products are characterized using elemental analysis, spectroscopy and X-ray crystallography (**1**, **3**).



2. Experimental

2.1. Materials and techniques

Copper(I) chloride was prepared by the reduction of $CuSO_4 \cdot 5H_2O$ using SO_2 in the presence of NaCl in distilled water [2]. Ph_3P was procured from Aldrich Sigma Ltd. C, H, N analysis were obtained with a Carbo-Ebra 1108 instrument. IR spectra were recorded using KBr pellets on a Nicolet 320 FTIR spectrophotometer in the 4000-200 cm^{-1} range. ^1H NMR spectra were recorded on a JEOL AL300 FT spectrometer at 300 MHz in $CDCl_3$ with TMS as the internal reference. ^{31}P NMR spectra were recorded at 121.5 MHz with TMP $\{(CH_3O)_3P\}$ as the external reference taken as zero position.

2.2. Preparation of the ligands (Httsc, Hftsc, H_2itsc)

Thiophene-2-carbaldehyde thiosemicarbazone, furanaldehyde thiosemicarbazone and isatin-3-thiosemicarbazone were prepared by condensation of thiophene-2-carbaldehyde, furan-2-carbaldehyde and isatin with thiosemicarbazide in a 1:1 molar ratio in methanol using a procedure similar to that given in the literature [27].

2.3. Synthesis of the complexes

2.3.1. Synthesis of $[Cu_2Cl_2(\mu\text{-}S\text{-}Httsc)_2(PPh_3)_2] \cdot 2\,H_2O$ (**1**)

To a stirred solution of copper(I) chloride (0.025 g, 0.252 mmol) in acetonitrile (20 mL) was added solid Httsc (0.046 g, 0.252 mmol) and the contents were stirred for 4 h. This was followed by the addition of solid Ph_3P (0.066 g, 0.252 mmol), and stirring was continued for a further period of 1 h. The clear solution formed was filtered, allowed to evaporate at room temperature and a yellow colored crystalline product was formed (yield: 0.087 g, 59%; m.p.: 136–138 °C). The complex is highly soluble in $CHCl_3$ and CH_2Cl_2 and warm CH_3CN. *Anal.* Calc. for $C_{48}H_{48}Cu_2Cl_2N_6O_4P_2S_4$: C, 51.1; H, 4.28; N, 7.44. Found: C, 50.8; H, 4.12; N, 7.38%. Main IR peaks (KBr, cm^{-1}): ν(O–H) 3553s; ν(N–H) 3450m, 3410m, 3331m; ν(–NH–) 3162m; ν(C–H) 3051m, 2949m, 2822m; $\delta(NH_2) + \nu(C{=}N) + \nu(C{-}C)$ 1591s, 1556s; ν(C=S) 820s (thioamide moiety); $\nu(P{-}C_{Ph})$ 1095s. ^1H NMR data (δ, ppm; J, Hz, $CDCl_3$): 12.78 (s, N^2H), 8.36 (s, C^2H), 6.97 (s, N^1H_2), 7.49 (d, C^6H), 7.43 (d, C^4H), 7.06 (dd, C^5H), 7.29–7.42 (m, 30H, Ph); ^{13}C NMR data (δ, ppm; *J*, Hz, $CDCl_3$): 173.8 (C^1), 142.2 (C^2), 137.6 (C^3), 129.3 (C^4), 127.9 (C^5), 132.8 (*i*-C, J_{P-C}, 30.9 PhP), 133.9 (*o*-C, J_{P-C}, 14.3, PhP), 128.6 (*m*-C, J_{P-C}, 9.2, PhP), 129.8 (*p*-C, PhP). ^{31}P NMR data (δ, ppm; *J*, Hz, $CDCl_3$): −111.03, ($\Delta\delta = \delta_{complex} - \delta_{ligand}$) 2.12. ^{31}P NMR of PPh_3 $\delta = -113.15$ ppm. The crystals were grown and stored in CH_3CN for X-ray structure determination as in the absence of solvent they turn opaque.

2.3.2. Synthesis of $[Cu_2Cl_2(Hftsc)_2(PPh_3)_2] \cdot 2H_2O$ (**2**)

Complex **2** was prepared similarly. (Color: orange, yield: 0.074 g, 54%; m.p.: 117–119 °C.) The complex is poorly soluble in $CHCl_3$ and CH_2Cl_2, but highly soluble in dmso-d_6 and warm CH_3CN. *Anal.* Calc. for $C_{48}H_{48}Cu_2Cl_2N_6O_4P_2S_2$: C, 52.6; H, 4.41; N, 7.66. Found: C, 52.5; H, 4.13; N, 7.23%. Main IR peaks (KBr, cm^{-1}): ν(O–H) 3560s; ν(N–H) 3450m, 3310m; ν(–NH–) 3162m; ν(C–H) 3100m; $\delta(NH_2) + \nu(C{=}N) + \nu(C{-}C)$ 1596s, 1550s, 1529s; ν(C=S) 832s (thioamide moiety); $\nu(P{-}C_{Ph})$, 1094s. ^1H

NMR data (δ, ppm; J, Hz, $CDCl_3$): 12.32 (s, N^2H), 8.12 (s, C^2H), 7.53 (d, C^6H), 6.79 (d, C^4H), 6.51 (dd, C^5H), 7.38–7.46 (m, 30H, Ph + N^1H_2); ^{31}P NMR data (δ, ppm; *J*, Hz, $CDCl_3$): −110.0, ($\Delta\delta = \delta_{complex} - \delta_{ligand}$) 3.15.

2.3.3. [CuCl(H$_2$itsc)(Ph$_3$P)$_2$] · 2CH$_3$CN (3)

Complex **3** was also prepared similarly except that two moles of Ph_3P were used. (colour: orange; yield: 0.14 g, 62%; m.p.: 210–212 °C). *Anal.* Calc. for $C_{49}H_{44}CuClN_6OP_2S$: C, 64.3; H, 4.7; N, 7.0. Found: C, 63.8; H, 4.55; N, 6.58%. Main IR peaks (KBr, cm^{-1}): ν(N–H) 3421m, 3325m; ν(–NH–) 3153m; (NH, pyrrole) 3075m; ν(C–H) 2920m; ν(C=O) 1691s; $\delta(NH_2) + \nu$(C=N) + ν(C–C) 1612 ms, 1593s; ν(C=S) 850s (thioamide moiety); ν(P–C_{Ph}) 1099s.

2.4. Crystallography

Yellow prismatic crystals of compound **1** and orange prismatic crystals of **3** were mounted on glass fibres and used for data collection. Crystal data were collected at 100(2) K for **1** and 103(2) K for **3** using a Bruker SMART CCD 1000 diffractometer. Graphite monochromated Mo Kα radiation ($\lambda = 0.71073$ Å) was used throughout. The data were processed with SAINT [28] and corrected for absorption using SADABS [29]. The structure was solved by direct methods using the program SHELXS [30], and refined by full-matrix least squares techniques against F^2 using SHELXL-97 [31]. Positional and anisotropic atomic displacement parameters were refined for all non-hydrogen atoms. Hydrogen atoms were placed geometrically and positional parameters were refined using a riding model. The crystal data are given in Table 1.

Table 1
Crystallographic data for complexes **1** and **3**

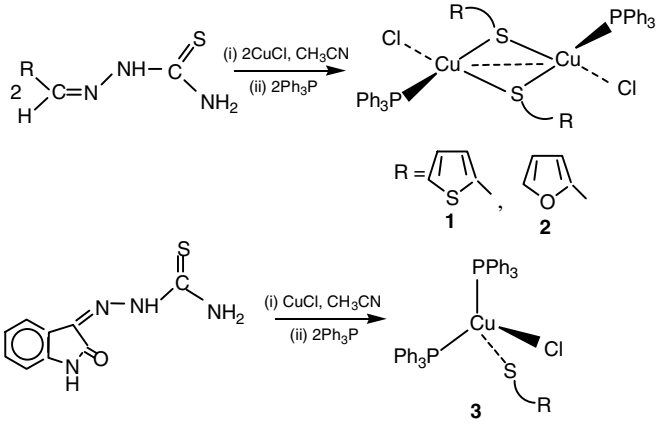
Parameters	1	3
Empirical formula	$C_{26}H_{25}ClCuN_4PS$	$C_{49}H_{44}ClCuN_6OP_2S$
M	587.58	925.89
T (K)	100(2)	103(2)
Crystal system	triclinic	triclinic
Space group	$P\bar{1}$	$P\bar{1}$
a (Å)	9.2407(15)	12.294(2)
b (Å)	11.1336(17)	12.800(2)
c (Å)	14.125(2)	16.502(3)
α (°)	74.720(9)	101.593(3)
β (°)	71.123(9)	102.280(3)
γ (°)	78.615(9)	112.447(3)
V, Å ^{3}	1316.4(3)	2227.8(6)
Z	1	2
D_{calcd} (g cm^{-3})	1.482	1.380
μ (mm^{-1})	1.174	0.714
Reflections collected	7556	16460
Unique reflections (R_{int})	8016(0.0314)	10600(0.0225)
Reflections with $[I > 2\sigma(I)]$	6812	8607
R indices	$R = 0.0363$, $wR = 0.0719$	$R = 0.0331$, $wR = 0.0782$

3. Results and discussion

3.1. Synthesis and infrared spectroscopy

Reaction of copper(I) chloride with thiophene-2-carbaldehyde thiosemicarbazone (Httsc) and furan-2-carbaldehyde thiosemicarbazone (Hftsc) in the presence of Ph_3P formed complexes of formulas $[CuCl(Httsc)(Ph_3P)]_2 \cdot 2CH_3CN$ (**1**) and $[CuCl(Hftsc)(Ph_3P)]_2 \cdot 2H_2O$ (**2**), respectively. The reaction of copper(I) chloride with isatin-3-thiosemicarbazone and Ph_3P yielded a monomer complex, $[CuCl(H_2itsc)(Ph_3P)_2] \cdot 2CH_3CN$ (**3**) (Scheme 1). In order to establish the bonding and structures, single crystal X-ray crystallography of **1** and **3** has been carried out. The crystals were stored in CH_3CN, as they get opaque in its absence. Complex **1** is soluble in chloroform, while complexes **2** and **3** are partially soluble in this solvent; all three are soluble in warm acetonitrile.

The IR spectra of complexes **1**, **2** and **3** show a set of two bands at 3450m, 3331m (**1**), 3450, 3310 cm^{-1} (**2**) and 3421m, 3325m cm^{-1} (**3**), due to ν(N–H) of the NH_2 group, and one band at 3162 cm^{-1} in (**1**, **2**) and 3153m cm^{-1} (**3**), due to ν(–NH–). The presence of these bands suggest that the thiosemicarbazone ligands are coordinating to the copper center in the neutral form. The ν(O–H) band in complexes **1** and **2** appeared at 3553 and 3560 cm^{-1}, respectively, which supports the presence of water molecules as the solvent of crystallization. The $\delta(NH_2)$, ν(C=N) and ν(C=C), vibrational modes appear at 1591s,1556s cm^{-1} in **1**, in the range 1596–1529 cm^{-1} in **2**, and at 1612m cm^{-1} in **3**, while the characteristic thioamide bands, ν(C=S), appear in the range 820–850 cm^{-1} in the complexes (ν(C=S) 837s Httsc; 830s Hftsc; 852s H_2itsc). The ν(C=O) band in complex **3** appears at 1691 cm^{-1}, and shows a lower energy shift as compared with the free carbonyl group due to its involvement in strong intra-molecular hydrogen bonding with the imino (N^2H) hydrogen of the thiosemicarbazone. The appearance of characteristic ν(P–C_{Ph}) bands at 1095 cm^{-1} in **1**, 1094 cm^{-1} in **2** and at 1099 cm^{-1} in **3** indicates the presence



Scheme 1.

of Ph_3P in the complexes, similar to the literature trend [10].

3.2. Crystal structures of the complexes

3.2.1. Dimer

The atom numbering scheme for complex **1** is given in Fig. 1, and selected bond lengths and bond angles are given in Table 2 (also includes data for **3**). In complex **1**, the Cu is bonded to one Cl atom, one P atom of Ph_3P and one S atom, forming a three coordinate unit, {$CuCl(Ph_3P)$-(Httsc)}, and two such units dimerize via the bonded S atoms to yield a sulfur-bridged dimer $[Cu_2Cl_2(\mu\text{-S-Httsc})_2(PPh_3)_2]\cdot 2CH_3CN$ (**1**) (Fig. 1). The central Cu_2S_2 core forms a parallelogram with two unequal Cu–S bond distances, {2.3626(5), 2.4298(5) Å}, which are longer than the terminal Cu–S distance, 2.3505(9) Å in the iodide bridged dimer, $[Cu_2(\mu\text{-I})_2(\eta^1\text{-S-Httsc})_2(Ph_3P)_2]$ (**4**). Further, each Cu atom is bonded to one PPh_3 with a Cu–P bond distance of 2.2402(5) Å, and one Cl atom with a Cu–Cl distance of 2.3392(5) Å, and these distances are similar to 2.2309(6) and 2.3280(6) Å, respectively, as observed in the analogous S-bridged dimer, $[Cu_2Cl_2(\mu\text{-S-Hbtsc})_2(Ph_3P)_2]$ (**5**) (Hbtsc = benzaldehyde thiosemicarbazone) [10a]. Compound **2** has two water molecules per dimer and is isostoichiometric with compound **1**, and is thus believed to have a similar structure.

Table 2
Bond lengths (Å) and angles (°) for complexes **1** and **3**

*Compound **1***			
Cu(1)–Cl(1)	2.3392(5)	C(16)–N(13)	1.3250(17)
Cu(1)–S(1)	2.3626(5)	C(16)–N(12)	1.3287(17)
$Cu(1)^{\#1}$–S (1)	2.4298(5)	N(11)–N(12)	1.3829(16)
Cu(1)–P(1)	2.2402(5)	C(15)–C(14)	1.444(2)
$Cu(1)–Cu(1)^{\#1}$	2.7719(5)	P(1)–C(21)	1.8227(14)
C(16)–S(2)	1.7257(15)		
$Cu(1)–S(2)–Cu(1)^{\#1}$	70.661(15)	Cu(1)–S(2)–C(16)	110.52(5)
$S(2)–Cu(1)–S(2)^{\#1}$	109.339(15)	S(2)–C(16)–N(12)	120.44(10)
Cl(1)–Cu(1)–P(1)	110.135(17)	S(2)–C(16)–N(13)	121.00(11)
P(1)–Cu(1)–S(2)	107.688(15)	N(13)–C(16)–N(12)	118.55(13)
Cl(1)–Cu(1)–S(2)	101.078(16)	C(16)–N(12)–N(11)	119.50(11)
*Compound **3***			
Cu–Cl	2.3892(6)	C(1)–N(2)	1.348(2)
Cu–P(1)	2.2621(5)	N(2)–N(3)	1.352(2)
Cu–P(2)	2.2773(6)	N(3)–C(2)	1.283(2)
Cu–S	2.3323(5)	P(1)–C(21A)	1.8120(18)
S–C(1)	1.6811(18)	P(2)–C(31B)	1.8112(18)
C(1)–N(1)	1.309(2)		
P(2)–Cu–Cl	104.815(18)	Cu–S–C(1)	112.14(6)
P(2)–Cu–P(1)	121.763(19)	S–C(1)–N(1)	125.07(13)
P(1)–Cu–S	105.04(2)	S–C(1)–N(2)	116.75(13)
S–Cu–Cl	108.222(17)	N(1)–C(1)–N(2)	118.17(16)
P(2)–Cu–S	109.61(2)	C(1)–N(2)–N(3)	119.35(15)
P(1)–Cu–Cl	106.818(19)	N(2)–N(3)–C(2)	115.65(15)

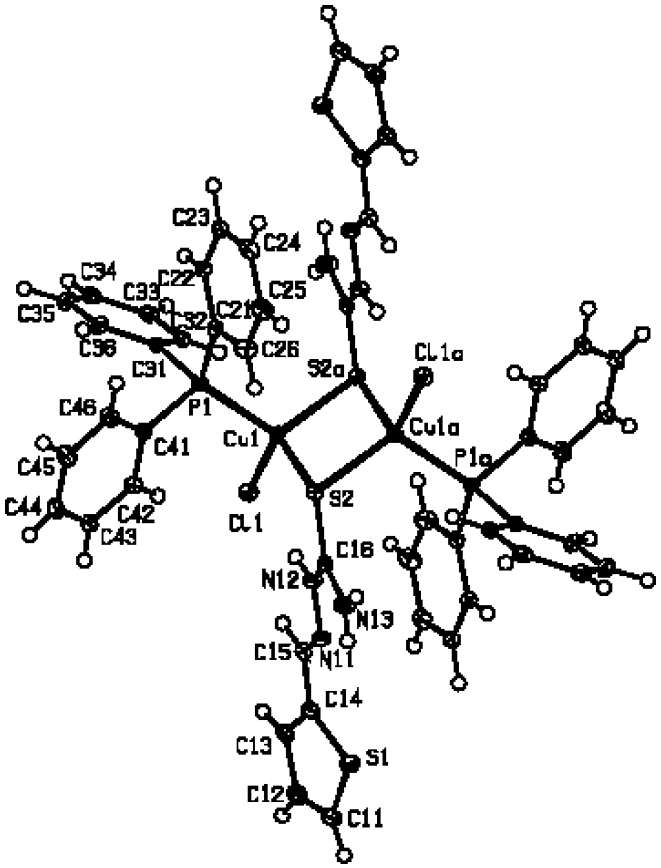


Fig. 1. Structure of complex **1** with the numbering scheme.

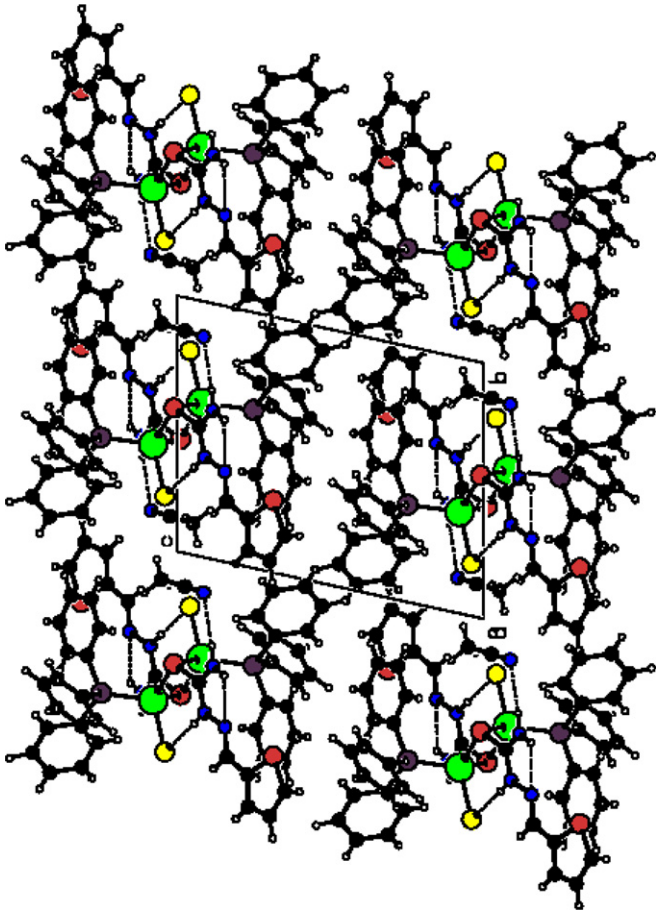


Fig. 2. Packing diagram of complex **1**.

From the packing diagram of **1** (Fig. 2), it can be seen that the amino group forms H-bonds, one intramolecular with N^3 of the thiosemicarbazone ($H^1NH\cdots N^3$) and a second intermolecular one with nitrogen of a CH_3CN molecule, viz., $H^1NH\cdots NCCH_3$ (Table 3). Further, two methyl hydrogens of acetonitrile are H-bonded to the same chlorine atom, {$NCCHH_2\cdots Cl$, 2.62, 2.79 Å}, a similar intermolecular interaction with chlorine was observed in the analogous sulfur-bridged dimer, $[Cu_2Cl_2(\mu\text{-S-Hbtsc})_2(Ph_3P)_2]\cdot 2CH_3CN$ (**5**) [10a]. Thus there is no inter-dimer interaction in compound **1**, while in the latter complex dimer-dimer interactions led to the formation of a linear chain polymer via acetonitrile hydrogen bonds, as just mentioned.

Table 3
Hydrogen bonds of compounds **1** and **3**

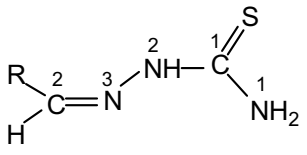
D–H···A	*d*(D–H)	*d*(H···A)	*d*(D···A)	<(DHA)
*Compound **1***				
N(12)–H(12A)···Cl(1)	0.82	2.28	3.0966(13)	176.0
N(13)–H(13A)···N(1)	0.86	2.33	3.188(2)	176.1
N(13)–H(13B)···N(11)	0.91	2.27	2.6435(18)	104.2
C(3)–H(3A)···Cl(1)	0.90	2.79	3.6270(16)	154.6
C(3)–H(3B)···Cl(1)	0.97	2.62	3.5874(16)	173.9
*Compound **3***				
N(1)–H(1A)···Cl$^{\#1}$	0.88	2.83	3.5122(17)	135.8
N(1)–H(1B)···Cl	0.88	2.27	3.1274(16)	165.1
N(2)–H(2A)···O	0.88	2.01	2.7114(19)	135.5
N(4)–H(4B)···N(1S)$^{\#2}$	0.88	2.19	2.960(2)	146.3

Symmetry transformations used to generate equivalent atoms: $^{\#1}$ $-x+1$, $-y+1$, $-z$; $^{\#2}$ $x-1$, y, z.

Table 4 shows S–Cu–S and Cu–S–Cu angles within the Cu_2S_2 core in **1** and other analogous dimeric complexes, **8**–**10** (the Table also includes iodide-bridged dimers **4**, **6** and **7** for comparison). In Httsc compounds, **1** (Cl)·$2CH_3CN$ and **9** (Br)·$2H_2O$, Cu–S–Cu angles are 70.66° and 84.88° respectively, while in Hptsc compounds **8**(Br)·$2H_2O$ and **10**(Cl)·$2H_2O$, the same Cu–S–Cu angles are 77.99° and 77.40° respectively. Likewise, compounds **1**(Cl)·$2CH_3CN$ and **5**(Cl)·$2CH_3CN$ have Cu–S–Cu angles of 70.66° and 72.16° respectively. The S–Cu–S angles at Cu, vary in a complementary manner vis-à-vis the Cu–S–Cu angles. It is also observed that a change in the bridging atom from sulfur to iodine in **4**, **6** and **7** leads

Table 4
Bond parameters (bond lengths (Å), angles (°)) of various dimeric complexes

Complex	Ring at C^2 carbon	Cu–S–Cu	S–Cu–S	Cu···Cu	References
$[CuCl(Httsc)(Ph_3P)]_2\cdot 2CH_3CN$ (**1**)		70.661	109.339	2.7719	This work
$[CuCl(Hbtsc)(Ph_3P)]_2\cdot 2CH_3CN$ (**5**)		72.16	107.83	2.8131	[10a]
$[CuBr(Hptsc)(Ph_3P)]_2\cdot 2H_2O$ (**8**)		77.99	102.00	3.008	[10a]
$[CuBr(Httsc)(Ph_3P)]_2\cdot 2H_2O$ (**9**)		84.88	95.12	3.232	[10a]
$[CuCl(Hptsc)(Ph_3P)]_2\cdot 2H_2O$ (**10**)		77.40	102.60	2.99	[10a]
		Cu–I–Cu	I–Cu–I		
$[CuI(Hftsc)(Ph_3P)]_2$ (**6**)		67.99	112.00	2.980	[10a]
$[CuI(Hptsc)(Ph_3P)]_2$ (**7**)		70.72	109.28	3.097	[10b]
$[CuI(Httsc)(Ph_3P)]_2$ (**4**)		75.58	104.41	3.224	[10a]



to higher I–Cu–I angles (104.47–112.00°) and smaller Cu–I–Cu angles (67.99–75.58°). From the above it can be concluded that the Cu–S–Cu angles appear to (i) be independent of the nature of the halogen, (ii) depend upon the nature of the ring at the C^2 carbon, and (iii) depend upon the presence of solvent, notably acetonitrile (different hydrogen patterns). In contrast, the Cu–I–Cu angles depend upon the nature of the ring at the C^2 carbon. The angles at iodine vary with the change in the substituent at the C^2 carbon of the thiosemicarbazone in the order: **4** > **7** > **6**. Finally, the Cu···Cu separation is smallest in compound **1** (2.7719 Å), next in order is compound **5** (2.8131 Å), while all other compounds, as listed in Table 4, show this separation in the range: 2.98 –3.232 Å. A smaller angle at S or iodine brings two Cu atoms closer Fig. 3.

3.2.2. Monomer

In complex **3**, the copper is coordinated via the thione sulfur, chloride atom and two P atoms from two Ph_3P ligands to complete its tetra-coordination. The angles around Cu, in the range, 104.8–121.8°, suggest a distorted tetrahedral geometry. The Cu–S bond distance of 2.3323(5) Å is smaller than in the analogous complexes with bromide {2.3566(10) Å} and iodide {2.399(2) Å} [9a]. This Cu-S bond distance increases in the order Cl < Br < I with the decrease in electronegativity of the halogen atom. The Cu–Cl bond distance, 2.3892(6) Å, is comparable with 2.4097 Å in a similar type of complex of copper(I) chloride with pyridine-2-carbaldehyde thiosemicarbazone [10a]. The Cu–Cl bond distances are much less than the sum of the ionic radii of Cu^+ and Cl^- ions, (2.58 Å) [2]. The Cu–P bond distances, {2.2621(5), 2.2773(6) Å} are close to other monomeric complexes with two Ph_3P ligands in the literature [9a,10a]. Further, amino ($-HN^1H-$) and imino ($-N^2H-$) hydrogens are engaged in intramolecular hydrogen bonding with chlorine ($-HN^1H\cdots Cl$) and with the oxygen atom of the isatin ring ($-N^2H\cdots O_{(isatin)}$) (Fig. 4, Table 3).

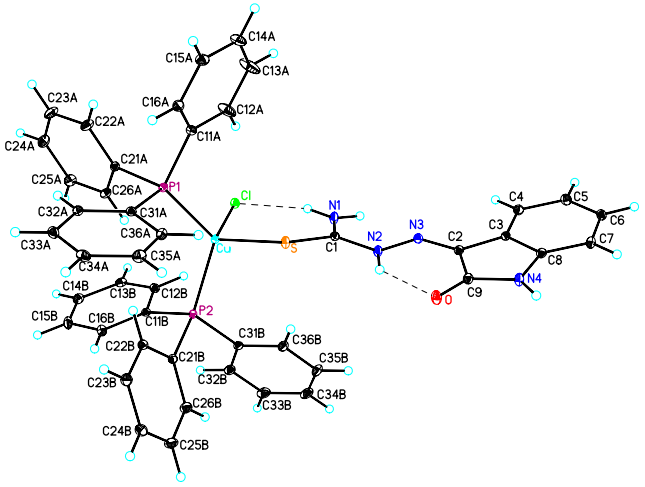


Fig. 3. Structure of complex **3** showing the atomic numbering scheme.

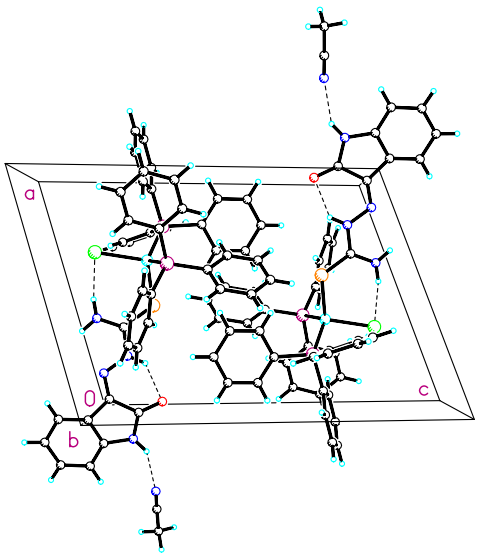


Fig. 4. Packing diagram of complex **3**.

It may be pointed out here that the analytical data of **1** showed two water molecules per dimer, and the crystal structure showed the presence of two acetonitrile molecules per dimer unit. Thus water, as shown by elemental analysis, was replaced by acetonitrile when stored in this solvent and vice versa. Theoretical calculations on dimeric copper(I) complexes with a model thisemicarbazone {H_2C=N–NH–C(=S)–NH_2} and PH_3 predicted that only the halogen bridging is stable [10a], and that the presence of water of crystallization (or some solvent such as CH_3CN) is necessary for stability of sulfur-bridged dimers, in which case the halogens formed hydrogen bonds with the solvents mentioned. Examples **1**, **2**, **5**, **8**–**10** provide testimony to this fact, but it may be pointed out that it was generally true for more electronegative halogens (Cl, Br), and not for iodide, which formed iodo-bridged dimers (**4**, **6**, **7**) (Table 4). Weaker hydrogen bonding with iodide and a tendency of softer iodide for bridging probably explain iodo-bridging in **4**, **6** and **7**, and no acetonitrile was found in these complexes.

In complex **3**, hydrogen bonding of acetonitrile is different from that in complex **1**. A strong H-bond is formed between the nitrogen of acetonitrile and NH of the pyrrole group of isatin, ($NH_{(pyr)}\cdot NCCH_3$, 2.19 Å) (Fig. 4), and thus methyl hydrogens orient away from the chlorine atom. It may be pertinent to bring to notice that in the isatin complex **3**, a 1:1:1 molar ratio formed an insoluble product and addition of a further one mole of PPh_3 was needed to form a clear solution, and product was established as monomer **3**. The lack of formation of a dimer by isatin thiosemicarbazone with copper(I) chloride may be due to a different pattern of hydrogen bonding as discussed above. Alternatively, the difference could be due to the nature of the substituents at the C^2 carbon, more flexible groups such as thiophen etc. provide more structure and bonding possibilities versus a rigid isatin group which only forms tetrahedral monomers as in the present case and in the literature

[9a]. Further, the presence of two Ph rings at the C^2 carbon was found to favor only monomeric complexes [32].

It is added here that theoretical calculations favored only monomers or dimers and no other geometry tested was found to be stable [10a].

3.3. Solution phase behavior

The N^2H proton signals appear at low field positions, 12.28 and 12.3 ppm in complexes **1** and **2** respectively, compared to the free ligands {δ 9.45 (sb) ppm, Httsc, δ11.4 (sb) ppm Hftsc} [27c], and it confirms the coordination of the neutral thiosemicarbazone ligands via S-donor atoms. Only one NH_2 signal of **1** appeared, at δ 6.97 ppm, with the second signal obscured by the signals due to Ph_3P in the range δ 7.26–7.53 ppm. The C^2H proton showed a slight downfield shift at δ 8.36 ppm (free Httsc, 8.01 ppm) in **1** and δ 8.11 ppm in **2** (free Hftsc, δ 7.78) [27c]. Ring protons peaks are given in the experimental section and show slight upfield shifts with respect to the free ligands [27c].

The ^{13}C NMR signal due to the C^1 carbon appears at δ 173.8 ppm in complex **1** which is upfield relative to the free ligand [27c], whereas the C^2 carbon at δ 142.2 ppm is shifted downfield on complexation; other ring carbons appeared at δ 137.6 (C^3), 129.3 (C^4), 127.9 (C^5) ppm. The ortho, para and meta carbons of the triphenyl phosphine ligands are clearly resolved vis-à-vis the free ligand. The ^{31}P NMR spectra showed a coordination shift ($\Delta\delta = \delta_{complex} - \delta_{ligand}$) of 2.12 ppm in **1** and 3.1 ppm in **2**, similar to the literature trends [32].

It is concluded that for R = thiophene, furan and pyrrole at the C^2 carbon with X = Cl or Br, sulfur bridging is favored as stabilized by the solvent, and X = I favors only iodide bridging. Further, the presence of acetonitrile as a solvent of crystallization can have diverse influence on the nature of the compounds. While in some cases it is bonded to the ring of the ligand (e.g. **3**), in other cases it is bonded to the halogen via the methyl hydrogen (e.g. **1**, **5**) and still in other cases such as, $[CuCl(Hpytsc)(PPh_3)_2]\cdot CH_3CN$ (Hpytsc = pyridine-2-carbaldehyde thiosemicarbazone) [10a], it is lying as non-bonded in the lattice.

Acknowledgement

Financial assistance from the University Grants Commission New Delhi is gratefully acknowledged.

Appendix A. Supplementary material

CCDC 622855 and 608172 contain the supplementary crystallographic data for **1** and **3**. These data can be obtained free of charge via http://www.ccdc.cam.ac.uk/conts/retrieving.html, or from the Cambridge Crystallographic Data Centre, 12 Union Road, Cambridge CB2 1EZ, UK; fax: (+44) 1223-336-033; or e-mail: deposit@ccdc.cam.ac.uk. Supplementary data associated with this article can be found, in the online version, at doi:10.1016/j.poly.2006.12.044.

References

[1] (a) B.-J. Liaw, T.S. Lobana, Y.-W. Lin, J.-C. Wang, C.W. Liu, Inorg. Chem. 44 (2005) 9921;
(b) A. Sundararaman, L.N. Zakharov, A.L. Rheingold, F. Jaekle, Chem. Commun. (2005) 1708;
(c) J.-P. Zhang, Y.-B. Wang, X.-C. Huang, Y.-Y. Lin, X.-M. Chen, Chem. Eur. J. 11 (2005) 552;
(d) W.-F. Fu, X. Gan, C.-M. Che, Q.-Y. Cao, Z.-Y. Zhou, N.-Y. Zhu, Chem.sEur. J. 10 (2004) 2228.

[2] J.E. Huheey, E.A. Keiter, R.L. Keiter, Inorganic Chemistry: Principals of structure and Reactivity, 4th ed., Harper Collins College Publishers, New York, 1993.

[3] (a) L.R. Hanton, C. Richardson, W.T. Robinson, J.M. Turnbull, Chem. Commun. (2000) 2465;
(b) Q.-F. Zhang, W.-H. Leung, X.Q. Xin, H.K. Fun, Inorg. Chem. 39 (2000) 417;
(c) R. Ahlrichs, J. Besinger, A. Eichhoefer, D. Fenske, A. Gbureck, Angew. Chem., Int. Ed. 39 (2000) 3929;
(d) J. Zhang, R.G. Xiong, J.L. Zuo, X.Z. You, Chem. Commun. (2000) 1495;
(e) J. Zhang, R.G. Xiong, J.L. Zuo, C.M. Che, X.Z. You, J. Chem. Soc., Dalton Trans. (2000) 2898;
(f) C.B. Aakeroy, A.M. Beatty, K.R. Lorimer, J. Chem. Soc., Dalton Trans. (2000) 3869;
(g) P.M. Graham, R.D. Pike, M. Sabat, R.D. Bailey, W.T. Pennington, Inorg. Chem. 39 (2000) 5121.

[4] Y.-Q. Tian, H.-J. Xu, L.-H. Weng, Z.-X. Chen, D.-Y. Zhao, X.-Z. You, Eur. J. Inorg. Chem 1813 (2004).

[5] W.-F. Fu, X. Gan, C.-M. Che, Q.-Y. Cao, Z.-Y. Zhou, N.N.-Y. Zhu, Chem. Eur. J. 10 (2004) 2228.

[6] K. Fujisawa, K. Fujita, T. Takahashi, N. Kitagima, Y. Moro-Oka, Y. Miyashita, K. Okamoto, Inorg. Chem. Commun. 7 (2004) 1188.

[7] (a) M. Karppinen, H. Yamauchi, Y. Morita, M. Kitabatake, T. Motohashi, R.S. Liu, J.M. Lee, J.M. Chen, J. Solid State Chem. 177 (2004) 1037;
(b) O.G. Mancheno, R.G. Arrayas, J.C. Carretero, J. Am. Chem. Soc. 126 (2004) 456.

[8] (a) M.J.M. Campbell, Coord. Chem. Rev. 15 (1975) 279;
(b) S.B. Padhye, G. Kauffman, Coord. Chem. Rev. 63 (1985) 127;
(c) D.X. West, S.B. Padhye, Sonawane, P.B. Struct. Bonding, Berlin, Ger. 76 (1991) 4;
(d) D.X. West, A.E. Liberta, S.B. Padhye, R.C. Chikate, P.B. Sonawane, A.S. Kumbhar, R.G. Yerande, Coord. Chem. Rev. 123 (1993) 49;
(e) J.S. Casas, M.S. Garcia-Tasende, J. Sordo, Coord. Chem. Rev. 209 (2000) 197.

[9] (a) T.S. Lobana, Rekha, B.S. Sidhu, A. Castineiras, E. Bermejo, T. Nishioka, J. Coord. Chem. 58 (2005) 803, and references therein;
(b) P. Pen, T. Liu, J. Qin, C. Chen, J. Coord. Chem. 56 (2003) 125;
(c) Y.-P. Tian, J.-Y. Wu, F.-X. Xie, S.S.S. Raj, P. Yang, H.-K. Fun, Acta Crystallogr. Sect. C: Cryst. Struct. Commun. 55 (1999) 1641;
(d) J.S. Casas, E.E. Castellano, J. Elena, M.S.G. Tasende, A. Sanchez, J. Sordo, M.J. Vidarte, Inorg. Chem. 42 (2003) 2684.

[10] (a) T.S. Lobana, Rekha, R.J. Butcher, A. Castineiras, E. Bermejo, P.V. Bharatam, Inorg. Chem. 45 (2006) 1535;
(b) T.S. Lobana, Rekha, R.J. Butcher, Trans. Met. Chem. 29 (2004) 91.

[11] (a) S. Lhuachan, S. Siripaisarnpipat, N. Chaichat, Eur. J. Inorg. Chem. (2003) 263;
(b) J. Valdes-Martinez, R.A. Toscano, M. Sorino-Garcia, M. Rubio, J. Gomez-Lara, Polyhedron 8 (1989) 27;

(c) R. Carbello, J.S. Casas, E. Garcia-Martinez, G. Perrieras-Gabian, A. Sanchez, J. Sordo, E.M. Vazquez-Lopez, J.C. Garcia-Monisaguelo, U. Abram, J. Organomet. Chem. 656 (2002) 1.
[12] J.-M. Yang, W.-B. Ma, B.-H. Chen, G.-S. Huang, Y.-X. Ma, Acta Crystallogr. Sect. E: Struct. Rep. Online 60 (2004) m852.
[13] D. Kovala-Demertzi, M.A. Demertzis, J.R. Miller, C.S. Prampton, J.P. Jasinski, D.X. West, J. Inorg. Biochem. 92 (2002) 137.
[14] T.S. Lobana, A. Sanchez, J.S. Casas, A. Castineiras, J. Sordo, M.S. Garcia-Tasende, Polyhedron 17 (1998) 3701.
[15] J.S. Casas, E.E. Castellano, M.C. Rodriguez-Arguelles, A. Sanchez, J. Sordo, J. Zukerman-Schpector, Inorg. Chim. Acta 260 (1997) 183.
[16] P.N. Yadav, M.A. Demertzis, D. Kovala-Demertzi, S. Skoulika, D.X. West, Inorg. Chim. Acta 349 (2003) 30.
[17] G.F. de Sousa, V.M. Deflon, E. Niquet, J. Mol. Struct. 587 (2004) 17.
[18] R. Carballo, A. Castineiras, T. Perez, Z. Naturforsch. B. Chem. Sci. 56 (2001) 881.
[19] R. Carballo, J.S. Casas, E. Garcia-Martinez, G.P. Gabian, A. Sanchez, J. Sordo, E.M. Vazquez-Lopez, J.C. Garcia-Monteagudo, U. Abram, J. Organomet. Chem. 658 (2002) 1.
[20] J.S. Casas, M.V. Castano, A. Sanchez, J. Sordo, Polyhedron 21 (2002) 1651.
[21] F. Basuli, S.-M. Peng, S. Bhattacharya, Inorg. Chem. 39 (2000) 1120.
[22] L.A. Ashfield, A.R. Cowley, J.R. Dilworth, P.S. Donnely, Inorg. Chem. 43 (2004) 4121.
[23] I. Paul, F. Basuli, T.C.W. Mak, S. Bhattacharya, Angew. Chem., Int. Ed. 40 (2001) 2923.
[24] (a) J. Garcia-Tojal, A. Garcia-Orad, J.L. Serra, J.L. Pizarro, L. Lezama, M.I. Arriortua, T. Rojo, J. Inorg. Biochem. 75 (1999) 45;
(b) T.S. Lobana, A. Sanchez, J.S. Casas, A. Castineiras, J. Sordo, M.S. Garcia-Tasende, Main Group Met. Chem. 24 (2001) 61;
(c) C.G. Suresh, A. Deshpande, S.S. Tavale, P. Umapathy, J. Crystallogr. Spectrosc. Res. 21 (1991) 17;
(d) S.-G. Teoh, S.-H. Ang, H.-K. Fun, C.-W. Ong, J. Organomet. Chem. 580 (1999) 17.
[25] (a) V.G. Puranik, S.S. Tavale, T.N.G. Row, P. Umpathy, A.P. Budhkar, Acta Crytallogr. Sect. C: Cryst. Struct. Commun. 43 (1987) 2303;
(b) Y. Kang, N. Yang, S.D. Kang, J. Ko, C.-H. Lee, Y.-H. Lee, Organometallics 16 (1997) 5522.
[26] E.M. Jouad, G. Larcher, M. Allian, A. Riou, G.M. Bouet, M.A. Khan, X.D. Thanh, J. Inorg. Biochem. 86 (2001) 565.
[27] (a) F.E. Anderson, C.J. Duca, J.V. Scudi, J. Am. Chem. Soc. 73 (1951) 4967;
(b) N.T. Akinchan, R. Akinchan, P.M. Drozdewski, Y.H. Yang, T.L. Klein, D.X. West, Synth. React. Inorg. Met. 26 (1996) 1735;
(c) T.S. Lobana, A. Sanchez, J.S. Casas, A. Castineiras, J. Sordo, M.S. Garcia-Tasende, E.M. Vazquez-Lopez, J. Chem. Soc., Dalton Trans. 4289 (1997).
[28] Bruker, SMART, SAINT and XPREP. Area detector control and data integration and reduction software. Bruker Analytical X-ray Instruments Inc., Madison, Wisconsin, USA, 1995.
[29] G.M. Sheldrick, SADABS, Program for Empirical Absorption Correction of Area Detector data; University of Gottingen; Gottingen, Germany, 1997.
[30] G.M. Sheldrick, Acta Crystallogr. A46 (1990) 467.
[31] G.M. Sheldrick, SHELXL-97, Program for the Refinement of Crystal Structures; University of Gottingen; Gottingen, Germany, 1997.
[32] T.S. Lobana, Sonia Khanna, R.J. Butcher, A.D. Hunter, M. Zeller Polyhedron 25 (2006) 2755.

2. Results and discussion

2.1. Synthesis and characterization of complexes 2a–d

The synthetic route for the novel NHC adducts of cyclopalladated ferrocenylimines is shown in Scheme 1. These new compounds were characterized by IR, ^{1}H NMR, MS and high-resolution mass spectrometry. They are air- and moisture-stable and can be recrystallized in dichloromethane/petroleum ether.

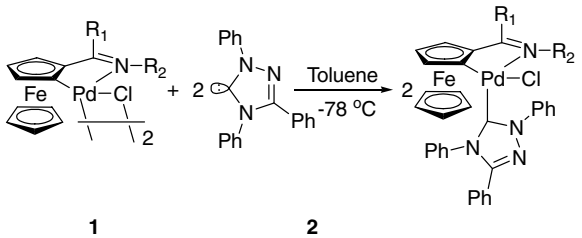
The IR spectra of the free ferrocenylimines show an intense sharp band in the range 1620–1640 cm^{-1}. However for the new complexes **2a**–**d**, this band shifted to lower energy (1562–1594 cm^{-1}), indicating that the nitrogen atom of the ferrocenylimines is coordinated with palladium through its lone pair [13]. The strong absorptions at *ca.* 765 and 694 cm^{-1} observed in these compounds, a feature of a mono-substituted benzene ring, are assigned to the δ (CH) of the carbene's phenyl rings.

The ^{1}H NMR spectra indicate that **2a**–**d** exist as a mixture of two isomers. The molar ratios are 3.28:1, 3.51:1, 3.88:1 and 17.46:1 for **2a**, **2b**, **2c** and **2d** respectively. Attempts to separate the two isomers by column chromatography and fractional recrystallization were unsuccessful. It is, therefore, difficult unequivocally to define the structures of the isomers. Even so, it is our belief that this isomerism must be in relation to the carbene group, and it is likely that there is steric hindrance of the three phenyl rings in the carbene group which influences the free rotation of the Pd–C (carbene) bond, consequently resulting in two isomers.

2.2. Structural characterization of complexes 2a–d

The single-crystal structures of **2a**–**d** were determined by single-crystal X-ray analysis. These molecular structures are shown in Figs. 1–4. Crystallographic and data collection parameters are summarized in Table 1. Selected bond lengths and angles are listed in Table 2.

The Pd atom in each complex is in a slightly distorted square-planar environment bonded to the carbon atom of the carbene, the chlorine atom, the nitrogen atom and the carbon atom of the ferrocenyl moiety. In all cases the plane of Pd is defined by N, C (Cp ring), Cl, C (carbene) atoms with a deviation of Pd1 of 0.1087 Å, 0.1140 Å, 0.1146 Å and 0.0239 Å for **2a**, **2b**, **2c** and **2d**, respectively. The plane of the carbene is approximately orthogonal to the square plane (95.9°, 95.8°, 95.8° and 94.1° for **2a**, **2b**, **2c** and **2d**, respectively). The bicyclic system formed by the palladacycle and the C_5H_3 moiety is approximately coplanar (dihedral angle 3.3°, 3.4°, 3.3° and 3.6° for **2a**, **2b**, **2c** and **2d**, respectively), and the dihedral angles between the two Cp rings in **2a**, **2b**, **2c** and **2d** are 3.2°, 3.4°, 4.2° and 0.6°. The Pd–C (carbene) bond lengths (1.965–1.977 Å) are shorter than those of the related carbene complexes (1.992–2.123 Å) [4a,4d,11], and Pd–C (Cp) bond lengths (1.945–1.974 Å) are also shorter than those of the related PCy_3, PPh_3 adducts (2.019, 2.006 and 1.998 Å) [7f,14].



1 2

2a $R_1 = CH_3$, $R_2 = p\text{-}CH_3C_6H_4$
2b $R_1 = CH_3$, $R_2 = p\text{-}BrC_6H_4$
2c $R_1 = CH_3$, $R_2 = p\text{-}NO_2C_6H_4$
2d $R_1 = H$, $R_2 = Cy$

Scheme 1. Synthesis of complexes **2a**–**d**.

2.3. Suzuki–Miyaura cross-coupling reaction

Initially, we performed a brief investigation on the reactivity of catalyst **2a** in the presence of different bases and solvents. The cross-coupling reaction of 4-bromoanisole with phenylboronic acid was used as the test system without the protection of an inert gas (Table 3). It can be seen from Table 3 that the reaction proceeded smoothly in toluene and more than 99% isolated yield was obtained after only 45 min with $K_3PO_4 \cdot 7H_2O$ as a base and 0.01 mol% catalyst loading (Table 3, entry 8).

To test the catalytic activities of these new catalysts, we used them in comparison with the cyclopalladated ferrocenylimine (**1a**). We chose the cross-coupling between 4-bromoanisole with phenylboronic acid as a model, under the optimized conditions with a catalyst loading of 0.01 mol%. As shown in Table 4, carbene adducts **2a**, **2b** and **2d** showed high activity towards this reaction, while the carbene adduct **2c**, with a strong electron-withdrawing group, only gave 75% isolated yield (Table 4, entry 4), which implied that the substituent in the N-phenyl ring of the ferrocenylimine could influence the catalytic activity of the cyclopalladated complex.

Under the optimized conditions, a wide array of aryl bromides (including *ortho*-substituted and electronically deactivated substrates) could react with phenylboronic acid to provide the cross-coupling products in excellent yields by using **2a** as catalyst (Table 5). However, when the catalyst loading was reduced to 0.001 mol%, only 47% isolated yield was obtained, even after 8 h for 4-bromoanisole which has a strongly electron-donating group (Table 5, entry 2). As to the electron-deficient aryl bromides, the coupling reaction just need 0.5 h, using 0.01 mol% of Pd to give high yields (Table 5, entries 11, 12 and 14), when the catalyst loading was reduced to 0.001 mol%. These reactions also gave excellent yields by prolonging the reaction time to 8 h (Table 5, entries 13 and 15). *ortho*-Substituents were also tolerated and even the very sterically hindered 2-bromo-*m*-xylene provided the biaryl product

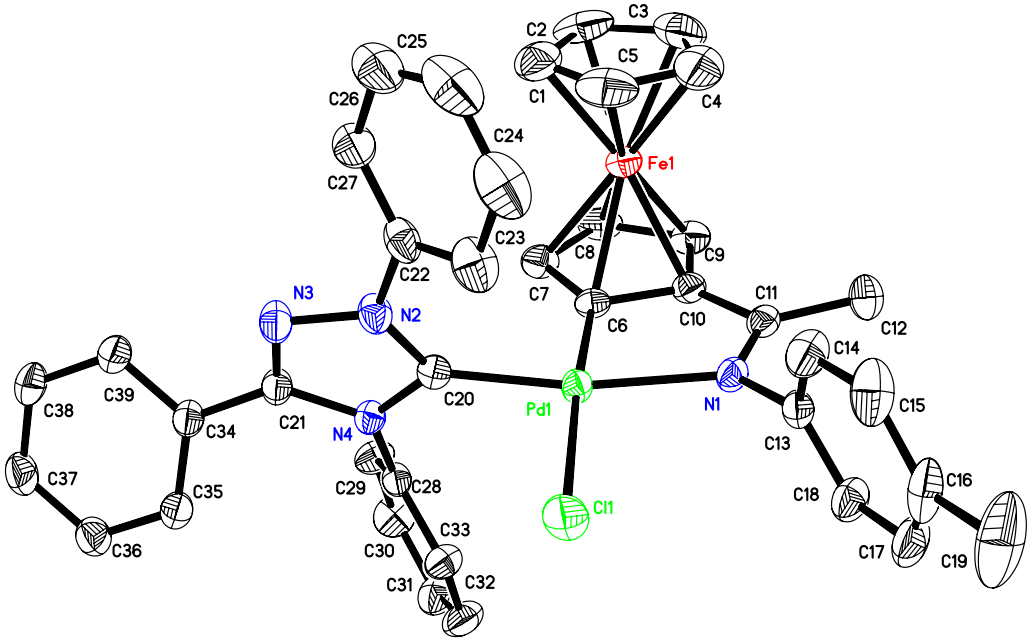


Fig. 1. Molecular structure of complex **2a**.

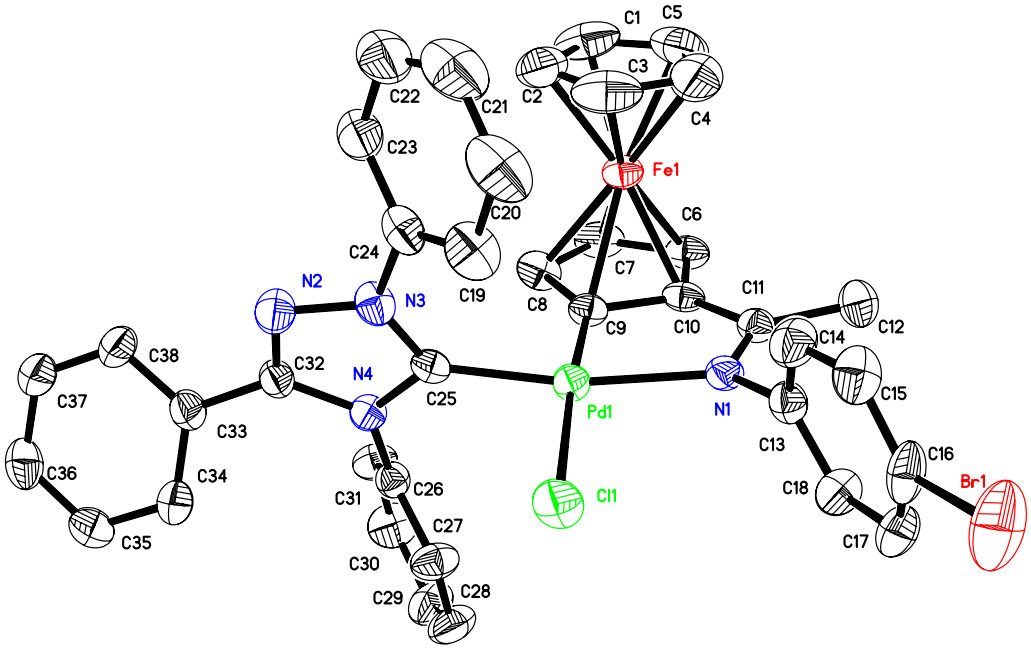


Fig. 2. Molecular structure of complex **2b**.

in 88% isolated yield by using 0.01 mol% of **2a** (Table 5, entry 6).

3. Conclusion

In summary, we have prepared a series of novel, air-stable *N*-heterocyclic carbene adducts of cyclopalladated ferrocenylimines and obtained the crystal structures of these compounds. These new complexes were found to be effective for the Suzuki–Miyaura reaction.

4. Experimental

4.1. General comments

Melting points were measured on a WC-1 microscopic apparatus and are uncorrected. IR spectra were recorded on a Bruker VECTOR22 spectrophotometer. ^{1}H NMR spectra were recorded on a Bruker DPX-400 spectrometer in $CDCl_3$ with TMS as an internal standard. Mass spectra were measured on a LC-MSD-Trap-XCT instrument.

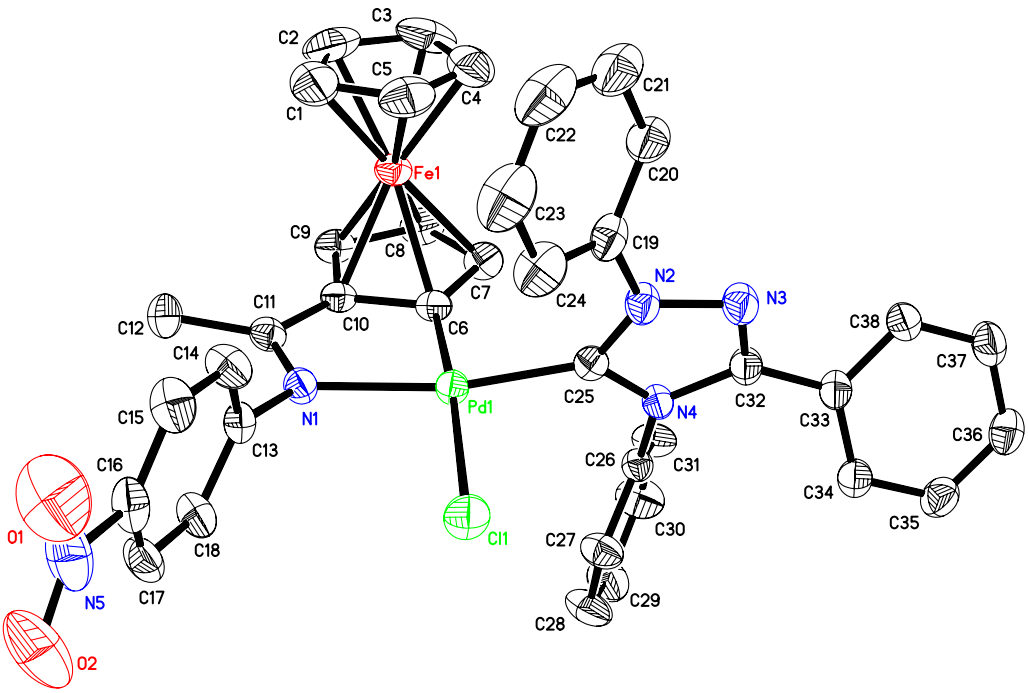


Fig. 3. Molecular structure of complex **2c**.

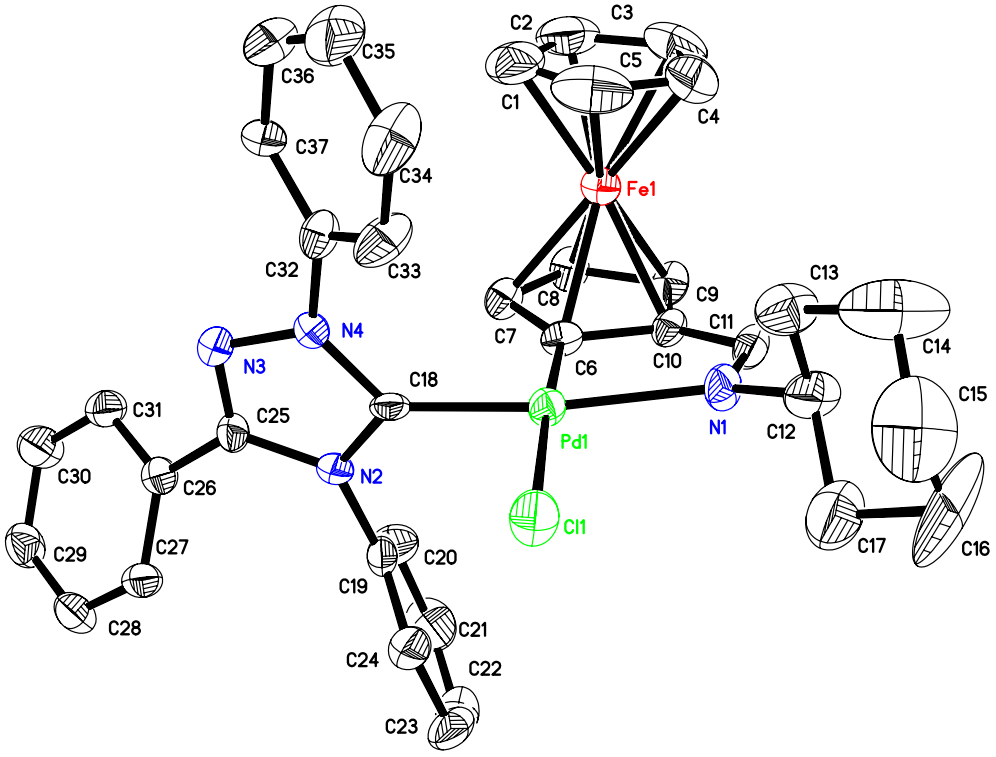


Fig. 4. Molecular structure of complex **2d**.

High-resolution mass spectra were measured on a Waters Q-T of Micro spectrometer.

All the solvents were purified by standard methods. The chloride-bridged palladacyclic dimers [13,15] and *N*-heterocyclic carbene [16] were prepared according to the published procedures. The phenylboronic acid was prepared according to the literature [17]. The aryl bromides for the Suzuki–Miyaura reaction were obtained from commercial sources and were used without purification.

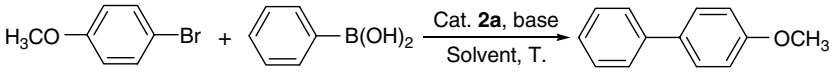
Table 1
Crystallographic and data collection parameters for complexes **2a**–**d**

Compound	**2a**	**2b**	**2c**	**2d**
Empirical formula	$C_{39}H_{33}ClFeN_4Pd$	$C_{38}H_{30}BrClFeN_4Pd$	$C_{38}H_{30}ClFeN_5O_2Pd$	$C_{37}H_{35}ClFeN_4Pd$
Formula weight	755.39	820.27	786.37	733.39
Temperature (K)	291(2)	291(2)	291(2)	291(2)
Crystal system	orthorhombic	orthorhombic	orthorhombic	triclinic
Space group	*Pbcn*	*Pbcn*	*Pbcn*	$P\bar{1}$
a (Å)	29.627(6)	29.668(6)	29.493(6)	11.443(2)
b (Å)	10.134(2)	10.137(2)	10.185(2)	17.449(4)
c (Å)	22.685(5)	22.686(5)	22.702(5)	17.584(4)
α (°)	90	90	90	82.40(3)
β (°)	90	90	90	86.93(3)
γ (°)	90	90	90	71.37(3)
Volume (Å^3)	6811(2)	6823(2)	6820(2)	3297.7(11)
D_{calc} (g cm^{-3})	1.473	1.597	1.532	1.477
Z	8	8	8	4
Absorption coefficient (mm^{-1})	1.066	2.235	1.073	1.098
$F(000)$	3072	3280	3184	1496
Crystal size (mm)	$0.20 \times 0.18 \times 0.17$	$0.20 \times 0.18 \times 0.17$	$0.20 \times 0.18 \times 0.17$	$0.20 \times 0.18 \times 0.17$
Data/restraints/parameters	5873/0/416	5486/0/416	6616/0/434	11 088/0/794
Goodness-of-fit on F^2	1.081	1.093	1.096	1.090
Final R indices [$I > 2\sigma(I)$]	$R_1 = 0.0448$, $wR_2 = 0.0781$	$R_1 = 0.0707$, $wR_2 = 0.1365$	$R_1 = 0.0587$, $wR_2 = 0.1368$	$R_1 = 0.0441$, $wR_2 = 0.0981$
R indices (all data)	$R_1 = 0.0787$, $wR_2 = 0.0859$	$R_1 = 0.1474$, $wR_2 = 0.1613$	$R_1 = 0.0762$, $wR_2 = 0.1461$	$R_1 = 0.0599$, $wR_2 = 0.1046$

Table 2
Selected bond lengths (Å) and angles (°) for complexes **2a**–**d**

Compound	**2a**	**2b**	**2c**	**2d**
Pd–C(carbene)	1.965(3)	1.970(7)	1.971(4)	1.977(4)
Pd–C(Cp ring)	1.972(3)	1.945(7)	1.971(5)	1.974(4)
Pd–N	2.123(3)	2.122(5)	2.118(4)	2.116(3)
Pd–Cl	2.408(1)	2.412(2)	2.412(1)	2.418(1)
C(carbene)–Pd–C(Cp ring)	92.7(1)	92.5(3)	92.7(2)	89.9(1)
C(carbene)–Pd–Cl	90.9(1)	91.1(2)	91.7(1)	93.7(1)
C(carbene)–Pd–N	170.1(1)	169.8(3)	169.6(2)	170.7(1)
C(Cp ring)–Pd–N	80.3(1)	80.6(3)	80.3(2)	81.1(1)
C(Cp ring)–Pd–Cl	171.4(1)	171.0(2)	170.8(1)	174.5(1)
N–Pd–Cl	97.1(8)	96.9(1)	96.4(1)	95.2(1)

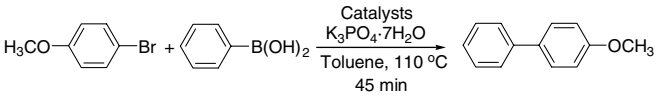
Table 3
Investigation of the Suzuki–Miyaura reaction conditions



Entry[a]	Base	Yield[b] (%)		
		DMF (140 °C)	Dioxane (100 °C)	Toluene (110 °C)
1	Na_2CO_3	49	25	5
2	K_2CO_3	41	90	68
3	Cs_2CO_3	52	59	70
4	NaOH	36	79	86
5	NaO^{t}Bu	25	16	80
6	$KF \cdot 2H_2O$	36	75	62
7	K_3PO_4	89	84	54
8	$K_3PO_4 \cdot 7H_2O$	16	76	>99[c]

[a] Reaction conditions: 4-bromoanisole 0.5 mmol, $PhB(OH)_2$ 0.6 mmol, base 1.0 mmol, solvent 2.5 ml, 5.0×10^{-5} mmol of Pd of catalyst **2a**. Reaction time is 8 h.
[b] Isolated yields based on 4-bromoanisole in two runs.
[c] Reaction time is 45 min.

Table 4
Suzuki–Miyaura reaction: catalyst study



Entry[a]	Catalyst	Yield[b] (%)
1	**1a**	89
2	**2a**	>99
3	**2b**	>99
4	**2c**	75
5	**2d**	>99

[a] Reaction conditions: 4-bromoanisole 0.5 mmol, $PhB(OH)_2$ 0.6 mmol, $K_3PO_4 \cdot 7H_2O$ 1.0 mmol, toluene 2.5 ml, 110 °C.
[b] Isolated yields.

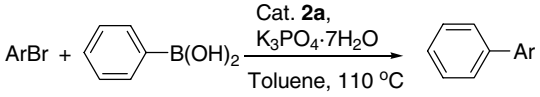
4.2. General procedure for the preparation of catalysts **2a–d**

The free carbene 1,3,4-triphenyl-4,5-dihydro-1*H*-1,2,4-triazolin-5-ylidene (0.5 mmol) and the cyclopalladated ferrocenylimines (0.2 mmol) were dissolved in dry toluene and cooled to −78 °C, respectively. The carbene solution was slowly added via a syringe to the dimers under the protection of N_2, then slowly warmed to room temperature and stirred for 2.5 h. The solvent was then removed in vacuo, and the remaining solid was dissolved in a small amount of CH_2Cl_2. The product was separated by flash chromatography column using $CHCl_3$ as eluent. Recrystallization from dichloromethane and petroleum ether afforded the corresponding catalysts with 63–77 % yields.

4.2.1. Characterization data for **2a–d**

Compound **2a**: mp 256 °C (dec.). IR (KBr pellet): 3447, 3052, 1565, 1495, 1462, 1389, 1331, 1228, 1105, 1024, 765, 694 cm^{-1}. ^1H NMR (400 MHz, 300 K, $CDCl_3$): δ 8.74 (2H, d, $J = 7.6$ Hz), 7.67 (3H, m), 7.50–7.31 (10H, m), 7.21 (2H, m), 6.80 (2H, d, $J = 7.4$ Hz), 4.29 (1H, m, C_5H_3), 4.19 (1H, m, C_5H_3), 3.69 (6H, m, C_5H_3 and

Table 5
Suzuki coupling of aryl bromides with phenylboronic acid catalyzed by complex **2a**



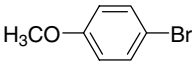
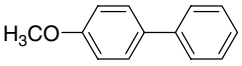
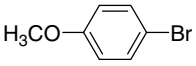
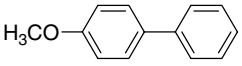
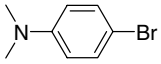
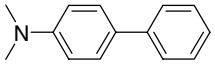
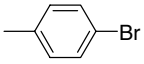
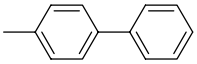
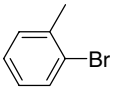
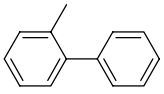
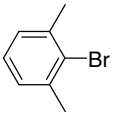
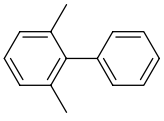
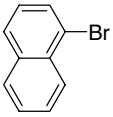
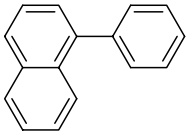
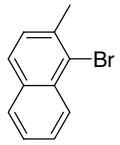
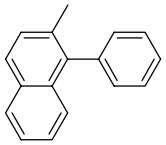
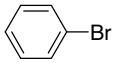
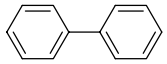
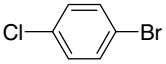
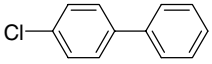
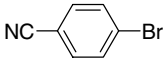
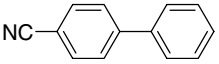
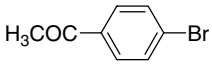
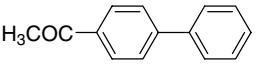
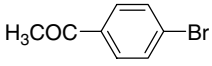
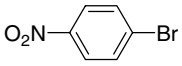
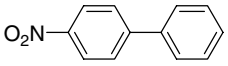
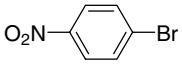
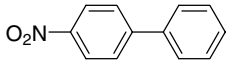
Entry[a]	ArBr	mol% of Pd	*T*	Product	Yield[b] (%)
1		0.01	45 min		>99
2		0.001	8 h		47
3		0.01	45 min		95
4		0.01	45 min		>99
5		0.01	45 min		89
6		0.01	45 min		88
7		0.01	45 min		>99

Table 5 (*continued*)

Entry[a]	ArBr	mol% of Pd	*T*	Product	Yield[b] (%)
8		0.01	45 min		86
9		0.01	45 min		95
10		0.01	45 min		>99
11		0.01	30 min		93
12		0.01	30 min		91
13		0.001	8 h		97
14		0.01	30 min		97
15		0.001	8 h		>99

[a] Reaction conditions: aryl bromides 0.5 mmol, $PhB(OH)_2$ 0.6 mmol, $K_3PO_4 \cdot 7H_2O$ 1.0 mmol, toluene 2.5 ml, 110 °C.
[b] Isolated yields. The purified products were identified by ^1H NMR spectra and comparison of the melting points with the literature data [18].

C_5H_5), 2.35 (3H, s, CH_3), 1.89 (3H, s, CH_3). MS (FAB) *m/z* (%): 1474 ($2M^+-Cl^-$), 719.2 (M^+-Cl^-). HRMS (positive ESI) calc. for $C_{39}H_{33}ClFeN_4Pd$: 719.1089, found: 719.1066.

Compound **2b**: mp 262 °C (dec.). IR (KBr pellet): 3448, 3060, 1562, 1494, 1463, 1391, 1328, 1230, 1104, 1070, 1004, 765, 694 cm^{-1}. ^1H NMR (400 MHz, 300 K, $CDCl_3$): δ 8.76 (2H, d, $J = 6.7$ Hz), 7.68 (3H, m), 7.56–7.39 (10H, m), 7.30 (2H, m), 6.80 (2H, d, $J = 7.7$ Hz), 4.35 (1H, m, C_5H_3), 4.28 (1H, m, C_5H_3), 3.72 (6H, m, C_5H_3 and C_5H_5), 1.89 (3H, s, CH_3). MS (FAB) *m/z* (%): 1603 ($2M^+-Cl^-$), 784.9 (M^++2-Cl^-). HRMS (positive ESI) calc. for $C_{38}H_{30}BrClFeN_4Pd$: 783.0038, found: 783.0016.

Compound **2c**: mp >280 °C. IR (KBr pellet): 3446, 3065, 1594, 1559, 1515, 1340, 1234, 1107, 1003, 765, 693 cm^{-1}. ^1H NMR (400 MHz, 300 K, $CDCl_3$): δ 8.74 (2H, d, $J = 7.0$ Hz), 8.30 (2H, m), 7.68-7.30 (11H, m), 7.30 (2H, m), 7.01 (2H, d, $J = 7.7$ Hz), 4.39 (2H, m, C_5H_3), 3.74 (6H, m, C_5H_3 and C_5H_5), 1.92 (3H, s, CH_3). MS (FAB) *m/z* (%): 1535 ($2M^+-Cl^-$), 750.0 (M^+-Cl^-). HRMS (positive ESI) calc. for $C_{38}H_{30}ClFeN_5O_2Pd$: 750.0784, found: 750.0777.

Compound **2d**: mp 252 °C (dec.). IR (KBr pellet): 3449, 3054, 2927, 2852, 1592, 1494, 1450, 1390, 1330, 1105, 1071, 765, 693 cm^{-1}. ^1H NMR (400 MHz, 292 K, $CDCl_3$): δ 8.83 (2H, d, $J = 7.8$ Hz), 7.80 (1H, s), 7.66 (2H, t, $J = 7.7$ Hz), 7.60–7.56 (2H, m), 7.47 (1H, t, $J = 7.3$ Hz), 7.42–7.38 (3H, m), 7.34–7.30 (5H, m), 4.22 (1H, s, C_5H_3), 4.08 (1H, s, C_5H_3), 3.81–3.79 (1H, m), 3.61–3.54 (6H, m, C_5H_3 and C_5H_5), 2.27 (1H, d, $J = 11.2$ Hz), 1.86–1.78 (3H, m), 1.70 (1H, d, $J = 12.6$ Hz), 1.51–1.35 (3H, m), 1.23–1.14 (2H, m). MS (FAB) *m/z* (%): 1429 ($2M^+-Cl^-$), 697 (M^+-Cl^-). HRMS (positive ESI) calc. for $C_{37}H_{35}ClFeN_4Pd$: 697.1246, found: 697.1226.

4.3. General procedure for the Suzuki–Miyaura reaction

A 5 ml round-bottom flask was charged with the aryl bromides (0.5 mmol), phenyl boronic acid (0.6 mmol) and base (1.0 mmol). The catalyst was introduced as a toluene solution (0.01 mmol/ml) via syringe, and additional toluene was added to obtain a total volume of 2.5 ml. The reaction mixture was stirred at reflux temperature (110 °C) in air. After the completion of the reaction, the mixture was quenched by 5 ml water and then extracted with ethyl acetate (3×10 ml). The combined organic layer was dried over $MgSO_4$. After removal of the solvent in vacuo, the product was obtained by preparative TLC, eluting with ethyl acetate/petroleum ether and the yield was calculated based on the aryl bromides (the purified products were identified by ^1H NMR spectra and comparison of the melting points with the literature data [18]).

4.4. Crystal structure determination

Intensity data of **2a**–**d** were measured on a Rigaku-Raxis-IV X-ray diffractometer using graphite monochromated Mo Kα radiation ($\lambda = 0.71073$ Å), The data were corrected for Lorentz and polarization factors. The structures were solved by direct methods [19] and expanded using Fourier techniques and refined by full-matrix least-squares methods. All calculations were performed using the TEXSAN [20] crystallographic software package of the Molecular Structure corporation.

Acknowledgements

We are grateful to the National Natural Science Foundation of China (Project 20472074) and the Innovation Found for Outstanding Scholar of Henan Province (Project 0621001100) for the financial support of this research.

Appendix A. Supplementary material

CCDC 611599, 611600, 625911 and 611598 contain the supplementary crystallographic data for **2a**, **2b**, **2c** and **2d**. These data can be obtained free of charge via http://www.ccdc.cam.ac.uk/conts/retrieving.html, or from the Cambridge Crystallographic Data Centre, 12 Union Road, Cambridge CB2 1EZ, UK; fax: (+44) 1223-336-033; or e-mail: deposit@ccdc.cam.ac.uk. Supplementary data associated with this article can be found, in the online version, at doi:10.1016/j.poly.2007.01.031.

References

[1] (a) J. Tsuji, Palladium Reagents and Catalysts: Innovations in Organic Synthesis, John Wiley & Sons Ltd, Chichester, 1995;
(b) E. Negishi, Handbook of Organopalladium Chemistry for Organic Synthesis, John Wiley & Sons Inc, New York, 2002;
(c) J. Tsuji, Palladium Reagents and Catalysts: New Perspectives for 21st Century, John Wiley & Sons Ltd, Chichester, 2004.

[2] (a) A.F. Littke, G.C. Fu, Angew. Chem., Int. Ed. 41 (2002) 4176;
(b) R.B. Bedford, C.S.J. Cazin, D. Holder, Coord. Chem. Rev. 248 (2004) 2283;
(c) U. Christmann, R. Vialr, Angew. Chem., Int. Ed. 44 (2005) 366;
(d) A. Zapf, M. Beller, Chem. Commun. (2005) 431;
(e) N.T.S. Phan, M.V.D. Sluys, C.W. Jones, Adv. Synth. Catal. 348 (2006) 609.

[3] (a) T.E. Barder, S.D. Walder, J.R. Martinelli, S.L. Buchwald, J. Am. Chem. Soc. 127 (2005) 4685;
(b) A.V. Vorogushin, X. Huang, S.L. Buchwald, J. Am. Chem. Soc. 127 (2005) 8146;
(c) L. Wu, J.F. Hartwig, J. Am. Chem. Soc. 127 (2005) 15824;
(d) K.W. Anderson, S.L. Buchwald, Angew. Chem., Int. Ed. 44 (2005) 6173;
(e) N. Kudo, M. Perseghini, G.C. Fu, Angew. Chem., Int. Ed. 45 (2006) 1282;
(f) K.L. Billingsley, K.W. Anderson, S.L. Buchwald, Angew. Chem., Int. Ed. 45 (2006) 3484;
(g) C.H. Burgos, T.E. Barder, X. Huang, S.L. Buchwald, Angew. Chem., Int. Ed. 45 (2006) 4321;
(h) A.M. Johns, M. Utsunomiya, C.D. Incarvito, J.F. Hartwig, J. Am. Chem. Soc. 128 (2006) 1828;
(i) M.A. Fernández-Rodríguez, Q. Shen, J.F. Hartwig, J. Am. Chem. Soc. 128 (2006) 2180;
(j) T. Hama, D.A. Culkin, J.F. Hartwig, J. Am. Chem. Soc. 128 (2006) 4976.

[4] (a) M.S. Viciu, R.A. Kelly III, E.D. Stevens, F. Naud, M. Studer, S.P. Nolan, Org. Lett. 5 (2003) 1479;
(b) A.K.K. Lewis, S. Caddick, F.G.N. Cloke, N.C. Billingham, P.B. Hitchcock, J. Leonard, J. Am. Chem. Soc. 125 (2003) 10066;
(c) E. Peris, R.H. Crabtree, Coord. Chem. Rev. 248 (2004) 2239;
(d) G.D. Frey, J. Schütz, E. Herdtweck, W.A. Herrmann, Organometallics 24 (2005) 4416.

[5] (a) W.A. Herrmann, Angew. Chem., Int. Ed. 41 (2002) 1290;
(b) A. Hillier, G.A. Grasa, M.S. Viciu, H.M. Lee, C. Yang, S.P. Nolan, J. Organomet. Chem. 653 (2002) 69;
(c) M.C. Perry, K. Burgess, Tetrahedron: Asymmetry 14 (2003) 951.

[6] (a) J. Dupont, C.S. Consorti, J. Spencer, Chem. Rev. 105 (2005) 2527;
(b) R.B. Bedford, Chem. Commun. (2003) 1787;
(c) J.P. Beletskaya, A.V. Cheprakov, J. Organomet. Chem. 689 (2004) 4055.

[7] (a) R.B. Bedford, C.S.J. Cazin, Chem. Commun. (2001) 1540;
(b) A. Schnyder, A.F. Indolese, M. Studer, H. Blaser, Angew. Chem., Int. Ed. 41 (2002) 3668;
(c) R.B. Bedford, C.S.J. Cazin, Organometallics 22 (2003) 98717;
(d) R.B. Bedford, S.J. Coles, M.B. Hursthouse, V.J.M. Scordia, J. Chem. Soc., Dalton Trans. (2005) 991;
(e) C.L. Chen, Y.H. Liu, S.M. Peng, S.T. Liu, Organometallics 24 (2005) 1075;
(f) J.F. Gong, G.Y. Liu, C.X. Du, Y. Zhu, Y.J. Wu, J. Organomet. Chem. 690 (2005) 3963.

[8] (a) O. Navarro, R.A. Kelly III, S.L. Nolan, J. Am. Chem. Soc. 125 (2003) 16194;
(b) O. Navarro, N. Marion, Y. Oonishi, R.A. Kelly III, S.L. Nolan, J. Org. Chem. 71 (2006) 685.

[9] G.D. Frey, J. Schütz, W.A. Herrmann, J. Organomet. Chem. 691 (2006) 2403.

[10] (a) S. Iyer, A. Jayathi, Synlett 8 (2003) 1125;
(b) S. Iyer, G.M. Kulkarni, C. Ramesh, Tetrahedron 60 (2004) 2163.

[11] R.B. Bedford, M. Betham, M.E. Blake, R.M. Frost, P.N. Horton, M.B. Hursthouse, R. López-Nicolás, Dalton Trans. (2005) 2774.

[12] Y.J. Wu, S.Q. Huo, J.F. Gong, X.L. Cui, L. Ding, K.L. Ding, C.X. Du, Y.H. Liu, M.P. Song, J. Organomet. Chem. 637–639 (2001) 27.

[13] Y.J. Wu, Y.H. Liu, X.L. Cui, Polyhedron 15 (1996) 3315.

[14] (a) C. Xu, J.F. Gong, Y.H. Zhang, Y. Zhu, C.X. Du, Y.J. Wu, Inorg. Chem. Commun. 9 (2006) 456;

(b) C. López, R. Bosque, X. Solans, M. Font-Bardia, New J. Chem. (1998) 977.
[15] (a) S.Q. Huo, Y.J. Wu, C.X. Du, Y. Zhu, H.Z. Yuan, X.A. Mao, J. Organomet. Chem. 483 (1994) 139;
(b) V. Kovač, A. Višnjevac, V. Rapić, B.K. Prodić, J. Mol. Struct. 687 (2004) 107.
[16] D. Enders, K. Breuer, U. Kallfass, T. Balensiefer, Synthesis 8 (2003) 1292.
[17] S.L. Chen, C.G. Xu, K.Q. Zhao, P. Hu, J. Sichuan Normal Univ. (Nature Science) 23 (2000) 511.
[18] Dictionary of Organic Compounds, 5th ed., Chapman and Hall, New York, 1982.
[19] A. Altomare, M.C. Burla, M. Camali, M. Cascarano, C. Giacovazzo, A. Guagliardi, G. Polidori, J. Appl. Crystallogr. 27 (1994) 435.
[20] Crystal Structure Analysis Package, Molecular Structure Corporation, 1985 and 1992.

2. Experimental

2.1. Synthesis

IR spectra were recorded on a Shimadzu FTIR-8300 Fourier Transform Infrared spectrophotometer using KBr pellets, UV–VIS spectra on a Shimadzu UV-1601 UV–Vis spectrophotometer, and ^{1}H and ^{13}C NMR spectra on a Varian UNITY INOVA 500 MHz spectrometer. Elemental analysis were performed by the Instrumental Analysis Laboratory of the TUBITAK Marmara Research Centre. Mass spectra were recorded on a Varian 711 spectrometer. 4-Nitrophthalonitrile was synthesized according to the reported procedure [14] and 4-hydroxyphenylacetic acid was purchased from Fluka Chemical Company, and was used as purchased. All reagents and solvents were of reagent-grade quality obtained from commercial suppliers. All solvents were dried and purified. The solvents were stored over molecular sieves (4 Å). The homogeneity of the products were tested in each step by TLC (SiO_2).

2.1.1. p-(3,4-Dicyanophenoxy)phenylacetic acid (**1**)

4-Hydroxyphenylacetic acid (0.88 g, 5.78 mmol) and 4-nitrophthalonitrile (1.0 g, 5.78 mmol) were dissolved in dry DMF (100 ml) under nitrogen and anhyd. K_2CO_3 (1.60 g, 11.56 mmol) was added. After stirring for 24 h at 50–60 °C, the reaction mixture was treated with diluted HCl under ice cooling. The pure precipitate was filtered, washed with water to neutralize, and dried. Yield: 0.812 g (50.73%). M.p. 177–180 °C. FT-IR (KBr), $\nu_{max}/(cm^{-1})$: 3500 (carboxylic acid OH), 3067–3050 (Ar–CH), 2930–2918 (aliphatic CH), 2231 (C≡N), 1703 (C=O), 1588–1488 (Ar C=C), 1246 (Ar–O–Ar), 1205, 1161, 1079, 942, 842, 801, 664 and 523. ^{1}H NMR (*d*-DMSO 500 MHz, δ ppm): 12.36 (s, 1H, COOH), 8.09 (d, 1H, Ar–H), 7.77 (d, 1H, Ar–H), 7.39 (d, 1H, Ar–H), 7.35 (dd, 2H, Ar–H), 7.15 (dd, 2H, Ar–H), 3.63 (s, 2H, CH_2). ^{13}C NMR (*d*-DMSO 500 MHz, δ ppm): 173.20 (acid C=O), 161.83 (Ar–C), 153.17 (Ar–C), 137.02 (Ar–C), 133.38 (Ar–C), 132.28 (Ar–C), 123.38 (Ar–C), 122.58 (Ar–C), 120.81 (Ar–C), 117.40 (Ar–C), 116.61 (C≡N), 116.09 (C≡N), 108.80 (Ar–C). MS (LC–MS, Scan ES$^+$) *m*/*z*: 278 [M$^+$]. UV–Vis λ_{max} (nm) ($\log\varepsilon$) in $CHCl_3$: 306 (3.73).

2.1.2. 2,9,16,23-Tetrakis(4-phenyloxyacetic acid)phthalocyanine (**2**)

Compound **1** (0.5 g, 1.80 mmol) and lithium metal (0.2 g, 28.6 mmol) were heated and stirred at 170 °C for 3 h under nitrogen in a mixture of 1,2-dichlorobenzene (4 ml) and pentanol (4 ml). After cooling to room temperature, acetonitrile was added in order to precipitate the product. The green precipitate was filtered and then washed with water and acetonitrile. It was dissolved in a small amount of methanol and precipitated by diluted HCl. In this mixture, the Li_2pcs formed was converted into H_2pcs. The green precipitate was filtered and washed with water, hot acetonitrile, hot methanol, chloroform and diethyl ether, and dried. It is soluble in DMF, DMSO and pyridine. Yield: 0.255 g (51%). M.p. >300 °C. *Anal*. Calc. for $C_{64}H_{42}N_8O_{12}$: C, 68.94; H, 3.77; N, 10.05. Found: C, 68.89; H, 3.68; N, 10.11%. FT-IR (KBr), $\nu_{max}/(cm^{-1})$: 3410 (carboxylic acid OH), 3290 (NH), 3037 (Ar–CH), 2955–2866 (aliphatic CH), 1715 (C=O), 1603–1474 (Ar C=C), 1232 (Ar–O–Ar), 1165, 1090, 1013, 932, 831, 745, 644 and 608. ^{1}H NMR (*d*-DMSO 500 MHz, δ ppm): 12.40 (br s, 4H, COOH), 7.24–6.02 (m, 28H, Ar–H), 3.97 (s, 8H, CH_2), −7.22 (br s, 2H, NH). MS (LC-MS, Scan ES$^+$) *m*/*z*: 1114 [M$^+$]. UV–Vis λ_{max} (nm) ($\log\varepsilon$) in DMF: 287 (4.82), 340 (4.87), 638 (4.74), 667 (4.79), 699 (4.69).

2.1.3. General procedure for the 2,9,16,23-tetrakis (4-phenyloxyacetic acid)phthalocyaninatometal derivatives (**2a–d**)

A mixture of compound **2** (0.05 g, 0.045 mmol) and 0.45 mmol metal salts [$CoCl_2\cdot 6H_2O$ 0.11 g, $Zn(AcO)_2\cdot 2H_2O$ 0.10 g, $NiCl_2\cdot 6H_2O$ 0.11 g or $CuCl_2$ 0.06 g] in dry DMF (1.5 ml) was heated and stirred at 155 °C for 24 h under N_2 in a sealed glass tube. After cooling to room temperature, the reaction mixture was treated with diluted HCl. After that, the precipitated green-blue solid was filtered off. The product was washed with water, hot methanol, hot acetonitrile and diethyl ether, and dried.

*2.1.3.1. 2,9,16,23-Tetrakis(4-phenyloxyacetic acid)phthalocyaninatocobalt (II) (**2a**).* This is soluble in THF, DMF, DMSO and pyridine. Yield: 0.029 g (55%). M.p. >300 °C. *Anal*. Calc. for $C_{64}H_{40}N_8O_{12}Co$: C, 65.58; H, 3.42; N, 9.56. Found: C, 65.86; H, 3.39; N, 9.73%. FT-IR (KBr), $\nu_{max}/(cm^{-1})$: 3396 (carboxylic acid OH), 3045 (Ar–CH), 2925–2866 (aliphatic CH), 1728 (C=O), 1603–1474 (Ar C=C), 1232 (Ar–O–Ar), 1161, 1094, 1057, 1016, 953, 880, 824, 745, 671 and 579. MS (LC-MS, Scan ES$^+$) *m*/*z*: 1171 [M$^+$]. UV–Vis λ_{max} (nm) ($\log\varepsilon$) in DMF: 328 (4.90), 662 (5.03).

*2.1.3.2. 2,9,16,23-Tetrakis(4-phenyloxyacetic acid)phthalocyaninatozinc (II) (**2b**).* This is soluble in THF, DMF, DMSO and pyridine. Yield: 0.038 g (72%). M.p. >300 °C. *Anal*. Calc. for $C_{64}H_{40}N_8O_{12}Zn$: C, 65.25; H, 3.40; N, 9.53. Found: C, 65.16; H, 3.47; N, 9.65%. FT-IR (KBr), $\nu_{max}/(cm^{-1})$: 3402 (carboxylic acid OH), 3067–3030 (Ar–CH), 2925–2866 (aliphatic CH), 1728 (C=O), 1603–1470 (Ar C=C), 1232 (Ar–O–Ar), 1161, 1090, 1045, 1016, 941, 889,864, 824, 745 and 664. ^{1}H NMR (*d*-DMSO 500 MHz, δ ppm): 12.40 (br s, 4H, COOH), 8.00–7.20 (b, 28H, Ar–H), 3.31 (s, 8H, CH_2). MS (LC-MS, Scan ES$^+$) *m*/*z*: 1177 [M$^+$]. UV–Vis λ_{max} (nm) ($\log\varepsilon$) in DMF: 356 (4.77), 612 (4.44), 679 (5.13).

*2.1.3.3. 2,9,16,23-Tetrakis(4-phenyloxyacetic acid)phthalocyaninatonickel (II) (**2c**).* This is soluble in THF, DMF, DMSO and pyridine. Yield: 0.045 g (85.6%). M.p. >300 °C. *Anal*. Calc. for $C_{64}H_{40}N_8O_{12}Ni$: C, 65.58; H,

3.42; N, 9.56. Found: C, 65.06; H, 3.37; N, 9.45%. FT-IR (KBr), ν_{max}/ (cm^{-1}): 3425 (carboxylic acid OH), 3067–3038 (Ar–CH), 2926–2918 (aliphatic CH), 1722 (C=O), 1599–1410 (Ar C=C), 1234 (Ar–O–Ar), 1161, 1121, 1086, 1057, 953, 883, 824, 748, 671 and 644. ^{1}H NMR (*d*-DMSO 500 MHz, δ ppm): 12.80 (br s, 4H, COOH), 7.74–7.23 (b, 28H, Ar–H), 3.24 (s, 8H, CH_2). UV–Vis λ_{max} (nm) ($\log\varepsilon$) in DMF: 333 (4.48), 609 (4.58), 672 (4.40).

*2.1.3.4. 2,9,16,23-Tetrakis(4-phenyloxyacetic acid)phthalocyaninatocopper (II) (**2d**).* This is soluble in THF, DMF, DMSO and pyridine. Yield: 0.029 g (55%). M.p. >300 °C. *Anal.* Calc. for $C_{64}H_{40}N_8O_{12}Cu$: C, 65.33; H, 3.40; N, 9.53. Found: C, 65.63; H, 3.36; N, 9.85%. FT-IR (KBr), ν_{max}/(cm^{-1}): 3410 (carboxylic acid OH), 3074–3030 (Ar–CH), 2918-2850 (aliphatic CH), 1715 (C=O), 1603–1466 (Ar C=C), 1232 (Ar–O–Ar), 1165, 1094, 1049, 1016, 953, 872, 824, 741, 671 and 648. UV–Vis λ_{max} (nm) ($\log\varepsilon$) in DMF: 342 (4.63), 626 (4.56), 678 (4.71).

*2.1.4. General procedure for the N-benzylamide derivatives of phthalocyanine (**3**, **3a**–**d**)*

The phthalocyanine derivatives (**2**, **2a**–**d**) (0.02 g) were refluxed for 4 h in thionylchloride (2 ml). At the end of the reaction, thionylchloride was removed under reduced pressure. The resulting solid was dissolved in dry THF (1 ml). Dry benzylamine (0.5 ml, 4.58 mmol) was dissolved in dry THF (1 ml) and dropped into the acid chloride at 10 °C. The mixture was stirred at room temperature for 15–16 h. After the reaction, THF was removed under reduced pressure. The reaction mixture was treated with water to precipitate the product, and filtered. The products were washed with water, methanol, acetonitrile and diethyl ether, and dried.

*2.1.4.1. 2,9,16,23-Tetrakis(N-benzyl-4-phenyloxyacetamide) phthalocyanine (**3**).* This is soluble in DMF, DMSO and pyridine. Yield: 0.014 g (53.4%). M.p. >300 °C. *Anal.* Calc. for $C_{92}H_{70}N_{12}O_8$: C, 75.10; H, 4.76; N, 11.43. Found: C, 75.16; H, 4.47; N, 11.12%. FT-IR (KBr), ν_{max}/(cm^{-1}): 3290 (NH), 3059–3030 (Ar–CH), 2918–2850 (aliphatic CH), 1728 (C=O), 1655 (amide NH), 1603–1462 (Ar C=C), 1250 (Ar–O–Ar), 1165, 1132, 1094, 1028, 949, 827, 745, 696, 599 and 507. ^{1}H NMR (*d*-DMSO 500 MHz, δ ppm): 8.65 (s, 4H, –CONH), 7.63–7.11 (b, 48H, Ar–H), 4.31 (d, 8H, –NH$\underline{CH_2}$Ar), −8.00 (br s, 2H, NH). MS (LC-MS, Scan ES^+) *m*/*z*: 1470 [M^+]. UV–Vis λ_{max} (nm) ($\log\varepsilon$) in DMSO: 302 (4.28), 330 (4.28), 646 (4.17), 682 (4.36), 704 (4.30).

*2.1.4.2. 2,9,16,23-Tetrakis(N-benzyl-4-phenyloxyacetamide) phthalocyaninatocobalt (II) (**3a**).* This is soluble in THF, DMF, DMSO and pyridine. Yield: 0.022 g (84.3%). M.p. >300 °C. *Anal.* Calc. for $C_{92}H_{68}N_{12}O_8Co$: C, 72.29; H, 4.45; N, 11.00. Found: C, 72.34; H, 4.62; N, 11.12%. FT-IR (KBr), ν_{max}/(cm^{-1}): 3290 (NH), 3074–3030 (Ar–CH), 2926–2858 (aliphatic CH), 1726 (C=O), 1651 (amide NH), 1603–1462 (Ar C=C), 1254 (Ar–O–Ar), 1198,1161, 1117, 1020, 984,916, 824, 748, 696, 604 and 503. MS (LC-MS, Scan ES^+) *m*/*z*: 1527 [M^+]. UV–Vis λ_{max} (nm) ($\log\varepsilon$) in DMF: 330 (4.79), 667 (4.75).

*2.1.4.3. 2,9,16,23-Tetrakis(N-benzyl-4-phenyloxyacetamide) phthalocyaninatozinc (II) (**3b**).* This is soluble in THF, DMF, DMSO and pyridine. Yield: 0.016 g (60.2%). M.p. >300 °C. *Anal.* Calc. for $C_{92}H_{68}N_{12}O_8Zn$: C, 72.02; H, 4.44; N, 10.96. Found: C, 72.16; H, 4.62; N, 10.72%. FT-IR (KBr), ν_{max}/(cm^{-1}): 3290 (NH), 3067–3022 (Ar–CH), 2918–2858 (aliphatic CH), 1728 (C=O), 1651 (amide NH), 1603–1462 (Ar C=C), 1250 (Ar–O–Ar), 1161, 1094, 1016, 976,897, 831, 764, 696, 596 and 507. ^{1}H NMR (*d*-DMSO 500 MHz, δ ppm): 8.70 (s, 4H, –CONH), 7.78–7.01 (b, 48H, Ar–H), 4.42 (d, 8H, –NH$\underline{CH_2}$Ar),. UV–Vis λ_{max} (nm) ($\log\varepsilon$) in DMF: 360 (4.77), 614 (4.49), 683 (5.15).

*2.1.4.4. 2,9,16,23-Tetrakis(N-benzyl-4-phenyloxyacetamide) phthalocyaninatonickel (II) (**3c**).* This is soluble in DMF, DMSO and pyridine. Yield: 0.017 g (66%). M.p. >300 °C. *Anal.* Calc. for $C_{92}H_{68}N_{12}O_8Ni$: C, 72.29; H, 4.45; N, 11.00. Found: C, 72.56; H, 4.28; N, 10.84%. FT-IR (KBr), ν_{max}/(cm^{-1}): 3388 (NH), 3059–3030 (Ar–CH), 2934–2851 (aliphatic CH), 1736 (C=O), 1647 (amide NH), 1595–1458 (Ar C=C), 1254 (Ar–O–Ar), 1202, 1165, 1109, 1016, 989, 920, 839, 745, 692, 596 and 511. ^{1}H NMR (*d*-DMSO 500 MHz, δ ppm): 8.67 (s, 4H, –CONH), 7.68–7.11 (b, 48H, Ar–H), 4.45 (d, 8H, –NH$\underline{CH_2}$Ar). UV–Vis λ_{max} (nm) ($\log\varepsilon$) in DMSO: 287 (4.47), 621 (4.01), 672 (3.79).

*2.1.4.5. 2,9,16,23-Tetrakis(N-benzyl-4-phenyloxyacetamide) phthalocyaninatocopper (II) (**3d**).* This is soluble in DMF, DMSO and pyridine. Yield: 0.018 g (71%). M.p. >300 °C. *Anal.* Calc. for $C_{92}H_{68}N_{12}O_8Cu$: C, 72.09; H, 4.44; N, 10.97. Found: C, 72.27; H, 4.18; N, 10.62%. FT-IR (KBr), ν_{max}/(cm^{-1}): 3396 (NH), 3067–3022 (Ar–CH), 2926–2858 (aliphatic CH), 1740 (C=O), 1647 (amide NH), 1595–1462 (Ar C=C), 1246 (Ar–O–Ar), 1161, 1109, 1016, 984, 905, 841, 745, 700, 599 and 515. (LC-MS, Scan ES^+) *m*/*z*: 1531 [M^+]. UV–Vis λ_{max} (nm) ($\log\varepsilon$) in DMSO: 344 (4.48), 627 (4.42), 679 (4.44).

*2.1.5. General procedure for the synthesis of octylacetate derivatives of phthalocyanine (**4**, **4a**–**d**)*

A mixture of the phthalocyanine derivatives (**2**, **2a**–**d**) (0.02 g) and thionylchloride (2 ml) were refluxed for 4 h. At the end of the reaction, thionylchloride was removed under reduced pressure. The resulting solid was dissolved in dry pyridine (0.5 ml, 3.17 mmol). Dry octanol (0.5 ml) was dissolved in dry pyridine (0.5 ml) and dropped into acid chloride at 0 °C. The mixture was stirred at 50–60 °C for 30 min at room temperature for 15–16 h, and poured into cold diluted HCl. The oily product was treated with diethyl ether to precipitate the ester. The crude

product washed with water and dried , purified on silica gel column chromatography with chloroform as the eluent.

*2.1.5.1. 2,9,16,23-Tetrakis(octyl 4-phenyloxyacetate)phthalocyanine (**4**).* This is soluble in THF, $CHCl_3$, CH_2Cl_2, DMF, DMSO and pyridine. Yield: 0.016 g (57.8%). M.p. >300 °C. *Anal.* Calc. for $C_{96}H_{106}N_8O_{12}$: C, 73.75; H, 6.79; N, 7.17. Found: C, 73.13; H, 6.53; N, 7.42%. FT-IR (KBr), $\nu_{max}/(cm^{-1})$: 3290 (NH), 3074 (Ar–CH), 2926–2858 (aliphatic CH), 1732 (C=O), 1595–1466 (Ar C=C), 1250 (Ar–O–Ar), 1165 (ester C–O), 1024, 941, 835, 748, 627 and 519. ^{1}H NMR (*d*-DMSO 500 MHz, δ ppm): 8.21–6.75 (b, 28H, Ar–H), 4.11 (t, 8H, $COOCH_2R$), 1.72–1.08 (m, 48H, $COOCH_2(\underline{CH_2})_6CH_3$), 0.89 (t, 12H, CH_3), −7.8 (br s, 2H, NH). MS (LC-MS, Scan ES^+) *m*/*z*: 1562 [M^+]. UV–Vis λ_{max}(nm) ($\log\varepsilon$) in DMF: 320 (4.19), 619 (3.94), 644 (3.94), 681 (4.27).

*2.1.5.2. 2,9,16,23-Tetrakis(octyl 4-phenyloxyacetate)phthalocyaninatocobalt (II) (**4a**).* This is soluble in THF, $CHCl_3$, CH_2Cl_2, DMF, DMSO and pyridine. Yield: 0.012 g (43%). M.p. >300 °C. *Anal.* Calc. for $C_{96}H_{104}N_8O_{12}Co$: C, 71.15; H, 6.42; N, 6.92. Found: C, 71.85; H, 6.69; N, 6.56%. FT-IR (KBr), $\nu_{max}/(cm^{-1})$: 3056 (Ar–CH), 2926–2858 (aliphatic CH), 1736 (C=O), 1595–1458 (Ar C=C), 1246 (Ar–O–Ar), 1157-1101 (ester C–O), 1020, 916, 835, 748, 667, 627 and 519. MS (LC-MS, Scan ES^+) *m*/*z*: 1619 [M^+]. UV–Vis λ_{max} (nm) ($\log\varepsilon$) in DMF: 303 (4.83), 324 (4.82), 663 (4.75).

*2.1.5.3. 2,9,16,23-Tetrakis(octyl 4-phenyloxyacetate)phthalocyaninatozinc (II) (**4b**).* This is soluble in THF, $CHCl_3$, CH_2Cl_2, DMF, DMSO and pyridine. Yield: 0.015 g (53%). M.p. >300 °C. *Anal.* Calc. for $C_{96}H_{104}N_8O_{12}Zn$: C, 70.89; H, 6.40; N, 6.89. Found: C, 71.21; H, 6.54; N, 6.42%. FT-IR (KBr), $\nu_{max}/(cm^{-1})$: 3067 (Ar–CH), 2926–2851 (aliphatic CH), 1728 (C=O), 1595–1462 (Ar C=C), 1250 (Ar–O–Ar), 1161–1101 (ester C–O), 1020, 972, 901, 839, 745, 683, 623 and 519. ^{1}H NMR (*d*-DMSO 500 MHz, δ ppm): 8.31–6.62 (b, 28H, Ar–H), 4.17 (t, 8H, $COOCH_2R$), 1.76–1.03 (m, 48H, $COOCH_2(\underline{CH_2})_6CH_3$), 0.86 (t, 12H, CH_3). MS (LC-MS, Scan ES^+) *m*/*z*: 1625 [M^+]. UV–Vis λ_{max} (nm) ($\log\varepsilon$) in DMF: 353 (4.70), 638 (4.59), 680 (4.92).

*2.1.5.4. 2,9,16,23-Tetrakis(octyl 4-phenyloxyacetate)phthalocyaninatonickel (II) (**4c**).* This is soluble in THF, $CHCl_3$, CH_2Cl_2, DMF, DMSO and pyridine. Yield: 0.023 g (84%). M.p. >300 °C. *Anal.* Calc. for $C_{96}H_{104}N_8O_{12}Ni$: C, 71.15; H, 6.42; N, 6.92. Found: C, 71.68; H, 6.27; N, 7.11%. FT-IR (KBr), $\nu_{max}/(cm^{-1})$: 3074 (Ar–CH), 2926–2858 (aliphatic CH), 1732 (C=O), 1595–1462 (Ar C=C), 1250 (Ar–O–Ar), 1165–1113 (ester C–O), 1020, 988, 916, 845, 787, 748, 683, 627 and 527. ^{1}H NMR (*d*-DMSO 500 MHz, δ ppm): 8.12–6.73 (b, 28H, Ar–H), 4.19 (t, 8H, $COOCH_2R$), 1.72–1.05 (m, 48H, $COOCH_2(\underline{CH_2})_6CH_3$), 0.84 (t, 12H, CH_3). UV–Vis λ_{max} (nm) ($\log\varepsilon$) in DMSO: 287 (4.75), 339 (4.39), 617 (4.49), 664 (4.25).

*2.1.5.5. 2,9,16,23-Tetrakis(octyl 4-phenyloxyacetate)phthalocyaninatocopper (II) (**4d**).* This is soluble in THF, $CHCl_3$, CH_2Cl_2, DMF, DMSO and pyridine. Yield: 0.020 g (74%). M.p. >300 °C. *Anal.* Calc. for $C_{96}H_{104}N_8O_{12}Cu$: C, 70.96; H, 6.41; N, 6.90. Found: C, 70.62; H, 6.52; N, 7.04%. FT-IR (KBr), $\nu_{max}/(cm^{-1})$: 3067 (Ar–CH), 2926–2858 (aliphatic CH), 1732 (C=O), 1591–1462 (Ar C=C), 1246 (Ar–O–Ar), 1165–1101 (ester C–O), 1020, 980, 908, 841, 741, 619 and 519. UV–Vis λ_{max} (nm) ($\log\varepsilon$) in DMSO: 346 (4.20), 630 (4.17), 641 (4.12), 679 (4.21).

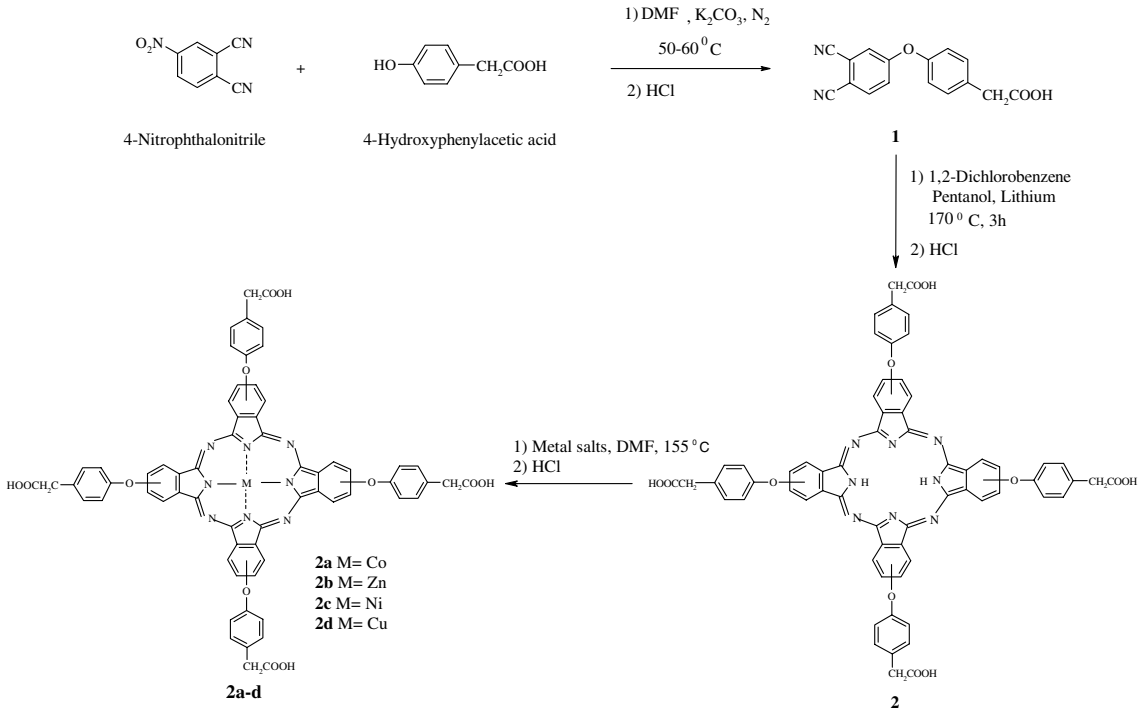
2.2. Electrochemistry

The cyclic voltammetry, differential pulse voltammetry and controlled potential chronocoulometry measurements were carried out with a Princeton Applied Research Model Versostat II potentiostat/galvanostat controlled by an external PC and utilizing a three-electrode configuration at 25 °C. The working electrode was a Pt plate with a surface area of 0.10 cm^2. The surface of the working electrode was polished with a H_2O suspension of Al_2O_3 before each run. The last polishing was done with a particle size of 50 nm. A Pt wire served as the counter electrode. A saturated calomel electrode (SCE) was employed as the reference electrode and separated from the bulk of the solution by a double bridge. Ferrocene was used as an internal reference. Electrochemical grade tetrabutylammonium perchlorate (TBAP) in extra pure dimethylsulfoxide (DMSO) was employed as the supporting electrolyte at a concentration of 0.10 mol dm^{-3}. High purity N_2 was used for deoxygenating the solution for at least 20 min prior to each run and to maintain a nitrogen blanket during the measurements. For CPC studies, a Pt gauze working electrode (10.5 cm^2 surface area), Pt wire counter electrode separated by a glass bridge and a SCE as a reference electrode were used.

3. Results and discussion

3.1. Synthesis and characterization

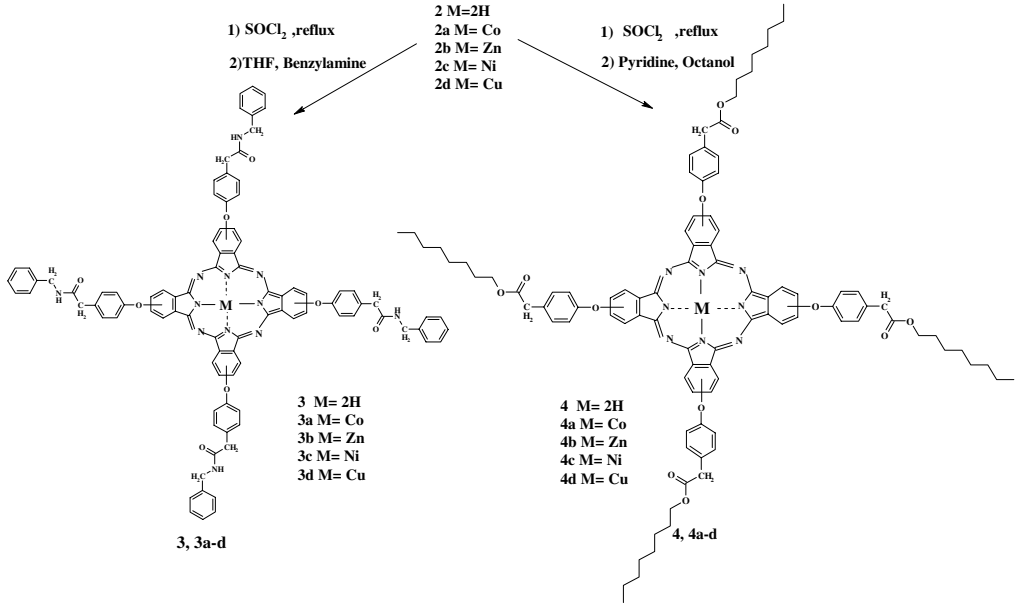
p-(3,4-Dicyanophenoxy)phenylacetic acid (**1**) was obtained by the base-catalyzed nucleophilic aromatic nitro displacement of 4-nitrophthalonitrile with 4-hydroxyphenylacetic acid (Scheme 1) [15,16]. The reaction was carried out in a single-step synthesis using K_2CO_3 as the nitro-displacing base at 50–60 °C in dry DMF under a N_2 atmosphere. Conversion of **1** into the metal-free phthalocyanine (**2**) is accomplished in a mixture of 1,2-dichlorobenzene and pentanol in the presence of lithium [17]. Dilithium Pcs can be labile towards water and acid, and can easily be converted to the metal-free phthalocyanine (**2**). The metallophthalocyanines (**2a**–**d**) [M = Co(II),



Scheme 1. *p*-(3,4-Dicyanophenoxy)phenylacetic acid (**1**) and phthalocyanines derived from it.

Zn(II), Ni(II) and Cu(II)] were prepared from compound **2** and the corresponding metal salts [$CoCl_2 \cdot 6H_2O$, $Zn(AcO)_2 \cdot 2H_2O$, $NiCl_2 \cdot 6H_2O$ and $CuCl_2$] in dimethylformamide [17]. Further reactions of these phthalocyanines (**2**, **2a**–**d**) with thionylchloride and benzylamine in tetrahydrofuran, and octanol in pyridine gave amide (**3**, **3a**–**d**) and ester (**4**, **4a**–**d**) derivatives, respectively (Scheme 2) [18]. Formation of the amides and esters from the phenyloxyacetic acid groups of the phthalocyanine derivatives (**2**, **2a**–**d**) was carried out in order to show the reactivity of these side groups.

The four polar peripheral substituents conferred upon these macromolecules (**2**, **2a**–**d**, **3**, **3a**–**d**) good solubility in polar solvents such as pyridine, DMF and DMSO. The products (**2**, **2a**–**d**, **3**, **3a**–**d**) were obtained in sufficient purity after successive washing with different solvents. The ester derivatives (**4**, **4a**–**d**) show good solubility in organic solvents such as $CHCl_3$, THF and CH_2Cl_2. The products



Scheme 2. Phthalocyanines bearing *N*-benzyl-4-phenyloxyacetamide and octyl 4-phenyloxyacetate moieties.

(**4**, **4a–d**) were purified by silica gel column chromatography with chloroform as the eluent.

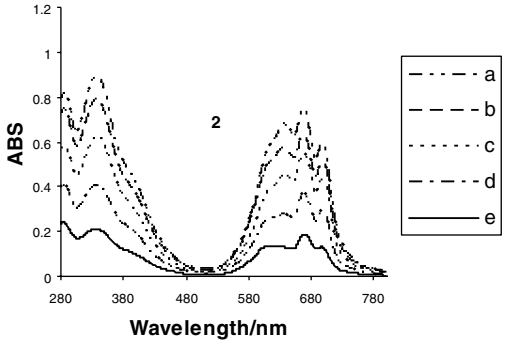
Characterization of the products involved a combination of methods including elemental analysis, FT-IR, UV–Vis, mass and ^{1}H NMR spectroscopy. The spectroscopic data of the new compounds were in accordance with the structures.

When the IR spectrum of 4-nitrophthalonitrile is compared with that of **1**, a distinct difference is the disappearance of the aromatic –NO_2 band at 1548 cm^{-1} and the appearance of a new absorption at 1246 cm^{-1}, attributable to aromatic (C–O–C). In the IR spectrum of **1** the presence of C≡N and C=O groups is indicated by intense stretching bands at 2231 cm^{-1} and 1703 cm^{-1}, respectively. The ^{1}H NMR spectrum of **1** in deuterated DMSO gave a singlet at δ 12.36 ppm (COOH), a singlet at δ 3.63 ppm (CH_2) and the doublets at δ 8.09–7.15 ppm correspond to aromatic protons. The ^{13}C NMR spectrum of **1** indicated nitrile carbons at δ 116.61 and 116.09 ppm as expected. Protonated aromatic and unsaturated carbon atoms appeared in the range δ 161.83–108.80 ppm. Also the carbon atom of carboxylic acid was observed at the lowest field value at δ 173.20 ppm.

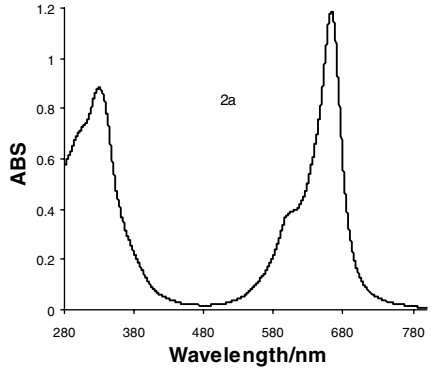
Cyclotetramerization of the dinitrile (**1**) into the phthalocyanine (**2**) was confirmed by the disappearance of the sharp C≡N vibration at 2231 cm^{-1}. The IR band characteristic of the metal-free phthalocyanine ring is an N–H stretching at 3290 cm^{-1}. The IR spectra of the metal-free (**2**) and metallo (**2a–d**) phthalocyanines are very similar, except the ν(NH) vibrations of the inner phthalocyanine core in the metal-free molecule. These protons are also very well characterized by the ^{1}H NMR spectra which show a peak at δ −7.22 ppm, −8.0 ppm and −7.80 ppm for **2**, **3** and **4**, respectively, and the signals disappeared after the addition of D_2O. The ^{1}H NMR spectrum of **2** indicates carboxylic acid protons (COOH) at δ 12.40 ppm as a singlet, aromatic protons at δ 7.24–6.02 ppm as a broad peak and aliphatic protons (CH_2) δ 3.97 ppm as a singlet. ^{1}H NMR measurements were precluded owing to the paramagnetic nature of the cobalt (II) phthalocyanines (**2a**, **3a** and **4a**) and copper (II) phthalocyanines (**2d**, **3d** and **4d**). The only difference between the ^{1}H NMR spectra of the metal-free phthalocyanines (**2**, **3** and **4**) and the metallo derivatives (**2b**, **2c**, **3b**, **3c**, **4b** and **4c**) is the lack of broad chemical shifts of the inner core NH protons. The ^{1}H NMR spectra of the phthalocyanines are rather broad, owing probably to the aggregation of the phthalocyanines which is frequently encountered at the concentrations used for NMR spectroscopy [2].

Comparison of the IR spectral data indicated the formation of compounds **3**, **3a–d** by the disappearance of the COOH band of compounds **2**, **2a–d** at 3400–3500 cm^{-1}, and the appearance of amide NH bands at 3290 and 1655 cm^{-1}. In the ^{1}H NMR analysis of **3** in deuterated DMSO, the aromatic protons appear as a broad peak at δ 7.63–7.11, the amide NH protons as a singlet at δ 8.65 and the NH$\underline{CH_2}$Ar protons as a doublet at δ 4.31 ppm. The phthalocyanines containing octyl 4-phenyloxyacetate moieties (**4**, **4a–d**) were confirmed by the disappearance of the COOH band of **2**, **2a–d** at 3400–3500 cm^{-1}, and the appearance of ester C–O bands at 1157–1101 cm^{-1} and more intense aliphatic CH_2 bands at 2926–2858 cm^{-1}. The ^{1}H NMR spectrum of **4** showed the aromatic protons as a broad peak at δ 8.21–6.75 and the COOCH_2R protons as a triplet at δ 4.11 ppm. The –CCH_2C– protons in the long aliphatic chain appear at δ 1.72–1.08 and the CH_3 at the end of the chain as a triplet at δ 0.89 ppm.

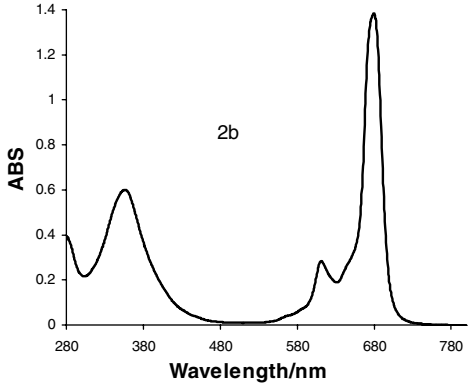
The phthalocyanines **2**, **2a–d**, **3**, **3a–d**, **4** and **4a–d** show typical electronic spectra with two strong absorption regions, one of them in the UV region at about 300–350 nm (B band) and the other in the visible part of the spectrum around 600–700 nm (Q band) [19]. The Q band of all the compounds was attributed to the $\pi \rightarrow \pi^*$ transition from the highest occupied molecular orbital (HOMO) to the lowest unoccupied molecular orbital (LUMO) of the phthalocyanine (−2) ring [20,21]. The B band of all the phthalocyanines arise from the deeper π levels → LUMO transitions [20–22]. The electronic absorption spectrum of the metal-free phthalocyanine **2** exhibits a partly split Q band absorption at 699 and 667 nm, that of **3** at 704 and 682 nm and **4** at 681 and 644 nm. There is a shoulder at the slightly higher energy side for each phthalocyanine (**2**, **3** and **4**) at 638 nm, 646 nm and 619 nm, respectively. The B band of these pcs appeared in the UV region at 340 nm, 330 nm and 320 nm, respectively. The metallo derivatives (**2a–d**, **3a–d** and **4a–d**) show only an intense single Q band absorption for the $\pi \rightarrow \pi^*$ transitions at around 660–680 nm with weaker absorptions at around 609–620 nm. Weaker absorptions on the higher energy side of the Q bands are generally observed in the case of metallophthalocyanines, indicating the presence of aggregated species together with the monomeric ones which are essentially responsible for the intense absorption occurring in the main Q bands [2]. When the electronic spectra of the metal-free phthalocyanine (**2**), nickel and copper phthalocyanines (**2c–d**, **3c–d** and **4c–d**) were carefully examined, a clear difference from the usual phthalocyanines could be easily observed. The Q band of **2** was split into three peaks. The Q band of the nickel and copper phthalocyanines was split into two peaks (Fig. 1). At higher concentrations, the intensity of the higher energy peak corresponding to aggregated species increased while that of the monomeric ones at lower energy decreased. At lower concentrations, the intensity of the peak corresponding to monomeric species increased. ZnPc (unsubstituted) dye is characterized by a band with a maximum at 673 nm as observed in the literature for ZnPc [23]. The zinc metallophthalocyanines (**2b**, **3b**, and **4b**) showed a bathochromic shift of 6 nm, 10 nm, 7 nm, respectively. The B band absorptions of these pcs were observed at 356 nm, 360 nm and 353 nm, respectively (Fig. 2).



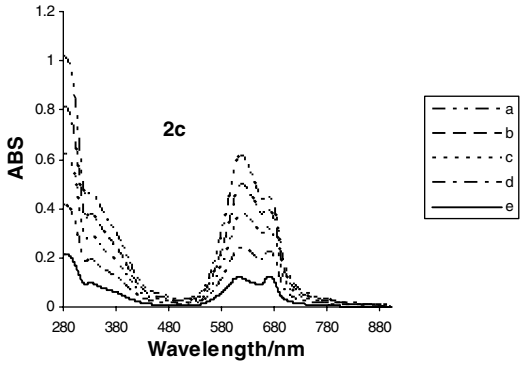
(a =1.62; b =1.44; c =1.08; d =0.72; e =0.36)×10^{-5} M in DMF.



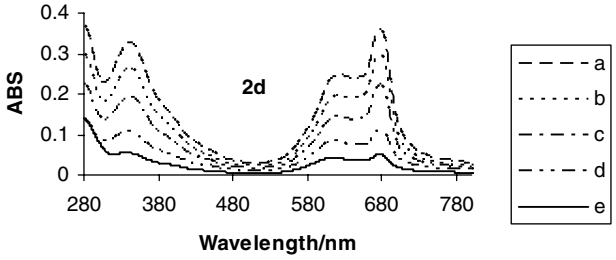
1.11×10^{-5} M in DMF.



1.02×10^{-5} M in DMF.



(a =1.71; b =1.37; c =1.03; d =0.68; e =0.34)×10^{-5} M in DMF.



(a =1.70; b =1.36; c =1.02; d =0.68; e =0.34)×10^{-5} M in DMF.

Fig. 1. Changes in the electronic spectra of **2**, **2a**–**d** with different concentrations.

3.2. Electrochemistry

The solution redox properties of ligand **2** and its metal complexes (**2a**–**d**) were studied using cyclic voltammetry, differential pulse voltammetry and controlled potential chronocoulometry in DMSO on a platinum electrode. Voltammetric data and the assignment of the redox couples recorded for the ligand and its complexes are listed in Table 1.

Fig. 3 shows the cyclic voltammogram of the metal-free phthalocyanine **2** in DMSO containing TBAP. It gives three one-electron reduction processes labelled as R_1 at −0.65 V, R_2 at −0.96 V and R_3 at −1.78 V, and a one-electron oxidation process labelled as O_1 at 0.83 V vs. SCE at 0.100 V s^{-1} scan rate. Reduction and oxidation redox processes, usually associated with the transfer of one electron and thus the formation of anionic and cationic radicals, occur only at the ligand in metal-free phthalocyanines and in some metallophthalocyanines involving a redox-inactive metal center, while they occur both at the metal center and at the phthalocyanine ring in those with redox-active metal centers [6,24–30]. Thus, all the couples of **2** are assigned undoubtedly to the phthalocyanine ring. The ratio of the anodic to cathodic peak currents for these couples are usually close to unity, suggesting reversible redox processes. Anodic to cathodic peak separations

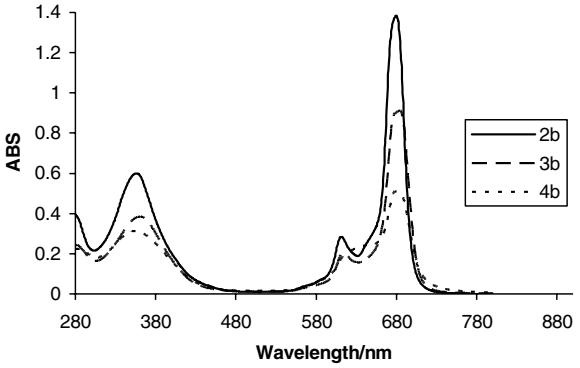


Fig. 2. Electronic spectra of **2b**, **3b** and **4b** in DMF.

(ΔE_p) changed from 0.050 to 0.160 V within the scan rates from 0.010 to 0.500 V s^{-1} (ΔE_p changed from 0.060 to 0.140 V for ferrocene), providing additional support for a reversible electron transfer. The peak currents increased linearly with the square root of the scan rates for scan rates ranging from 0.010 to 0.500 V s^{-1}, indicating purely diffusion-controlled behavior [31].

Voltammetric studies revealed that the redox behaviour of metallophthalocyanines **2b**, **2c** and **2d** is very similar to that of the metal-free phthalocyanine **2** (Table 1). The inset in Fig. 3 exemplifies a typical cyclic voltammogram of **2c**. This similarity suggests that all the one-electron redox processes of **2b**, **2c** and **2d** are phthalocyanine ring based. However, the redox potentials of these metallophthalocyanines occur usually at potentials slightly more negative as compared to **2**. The shift in the potentials can be attributed to the polarizing effect of the M(II) ions. When we compare the redox potentials of the phthalocyanines bearing four 4-phenyloxyacetic acid moieties with those of the relevant unsubstituted phthalocyanines in the literature [24] it is clear that the redox potentials of **2**, **2a**, **2b**, **2c** and **2d** shift to relatively more positive potentials, probably due to the electron withdrawing effect of the phenyloxyacetic acid substituents (Table 1). Reduction of the phthalocyanine ligand is associated with the position of the LUMO, whereas oxidation of the ligand is associated with the position of the HOMO. Thus, the difference between the potentials of the first oxidation and the first reduction processes ($\Delta E_{1/2}$) reflects the HOMO–LUMO gap for the metal free Pcs and it is closely related with the HOMO–LUMO gap in MPc species involving the redox inactive metal center. The $\Delta E_{1/2}$ values recorded for **2**, **2b**, **2c** and **2d** in this study are in agreement with the values reported previously for the relevant phthalocyanines [24].

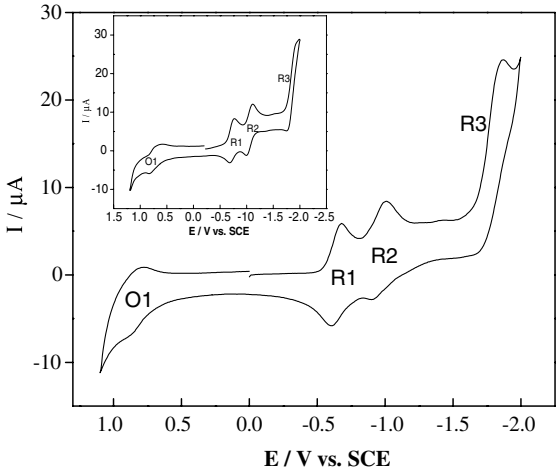


Fig. 3. Cyclic voltammogram of **2** and **2c** (inset) at 0.100 V s^{-1} in TBAP/DMSO.

Table 1
The electrochemical data of **2**, **2a**, **2b**, **2c** and **2d**

Complex	Redox processes	$E_{1/2}$ (V vs. SCE)[a]	ΔE_p (mV)[b]	I_{pa}/I_{pc}[c]	$\Delta E_{1/2}$ (V)[d]
2	R1	−0.65	0.070	0.96	1.48
	R2	−0.96	0.080	0.98	
	R3	−1.78	0.160	[e]	
	O1	0.83	0.060	[e]	
2a	R1	−0.37	0.100	1.00	0.82
	R2	−1.28	0.080	0.95	
	O1	0.45	0.100	0.94	
2b	R1	−0.73	0.080	0.96	1.44
	R2	−1.06	0.080	0.98	
	R3	−1.84	0.100	[e]	
	O1	0.71	0.120	1.00	
2c	R1	−0.72	0.080	0.94	1.45
	R2	−1.05	0.090	1.00	
	R3	−1.84	0.120	[e]	
	O1	0.73	0.140	0.98	
2d	R1	−0.71	0.090	0.94	1.45
	R2	−1.06	0.080	1.00	
	R3	−1.82	0.100	[e]	
	O1	0.74	0.150	0.98	

[a] $E_{1/2} = (E_{pa} + E_{pc})/2$ at 0.100 V s^{-1}.
[b] $\Delta E_p = E_{pa} - E_{pc}$ at 0.100 V s^{-1}.
[c] I_{pa}/I_{pc} for reduction, I_{pc}/I_{pa} for oxidation processes at 0.100 V s^{-1}.
[d] $\Delta E_{1/2} = E_{1/2}$(first oxidation) − $E_{1/2}$ (first reduction). This value reflects the HOMO–LUMO gap for the ligand and its complexes, except **2a**.
[e] ΔE_p could not be determined due to an ill-defined redox wave.

The redox potential of **2a** is considerably different as compared with that of **2**, **2b**, **2c** and **2d**. Fig. 4 shows the cyclic and differential pulse voltammograms of **2a** in DMSO containing TBAP. Within the electrochemical window of TBAP/DMSO, compound **2a** undergoes a quasi-reversible one-electron oxidation and two quasi-reversible one-electron reductions at 0.45, −0.37 and −1.28 versus SCE at 0.100 V s^{-1} scan rate, respectively. The difference in the voltammetric behaviour of **2a** is due to the fact that metallophthalocyanines such as MnPc, CoPc and FePc, having a metal that possesses energy levels lying between the HOMO and the LUMO of the phthalocyanine ligand, in general exhibit redox processes centered on the metal [24–26,28,29]. For CoPc complexes, the first oxidation and first reduction processes occur on the metal center in polar solvents such as DMF and DMSO, however the first oxidation process occurs on the Pc ring in non-polar solvents such as DCM and THF. Therefore, the first reduction and the first oxidation processes of **2a** could be

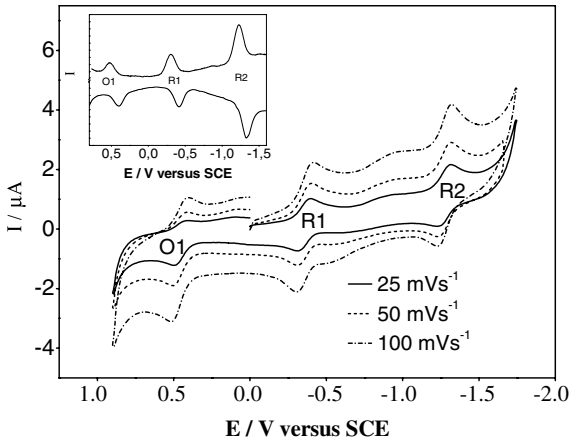


Fig. 4. Cyclic and differential pulse voltammograms of **2a** in TBAP/DMSO.

assigned easily to the $[Co(II)Pc(-2)]/[Co(I)Pc(-2)]^{1-}$ and $[Co(II)Pc(-2)]/[Co(III)Pc(-2)]^{+}$ redox couples and the second reduction process to the phthalocyanine ring as $[Co(I)Pc(-2)]^{-}/[Co(I)Pc(-3)]^{2-}$. The separation between the first oxidation and the first reduction potentials of the metal center (~0.82 V) is comparable with the relevant values in the literature [24–26,28,29], and does not reflect the HOMO–LUMO gap.

In conclusion, we have described the synthesis and spectral characterization of some new phthalocyanines with 4-phenyloxyacetic acid, *N*-benzyl-4-phenyloxyacetamide and octyl 4-phenyloxyacetate substituents on the periphery. Cyclic voltammetry of these compounds is also presented. Esterification of carboxy groups brings forward more soluble products in less polar solvents such as chloroform, THF and dichloromethane.

Acknowledgements

The support of State Planning of Organization (DPT), Project No: 2003K 120810 is gratefully acknowledged. We are also thankful to the Research Fund of Marmara University, Commission of Scientific Research Project under grant FEN-055/070403, 2005.

References

[1] J. Sleven, C. Görller-Walrand, K. Binnemas, Mater. Sci. Eng. C 18 (2001) 229.
[2] C.C. Leznoff, A.B.P. Lever, Phthalocyanines Properties and Applications, VCH, Weinheim, 1989.
[3] N. Kobayashi, Curr. Opin. Solid State Mater. Sci. 4 (1999) 345.
[4] Ş. Abdurrahmanoğlu, A. Altındal, A.R. Özkaya, M. Bulut, Ö. Bekaroğlu, Chem. Commun. (2004) 2029.
[5] Ş. Abdurrahmanoğlu, A.R. Özkaya, M. Bulut, Ö. Bekaroğlu, J. Chem. Soc., Dalton Trans. (2004) 4022.
[6] M. Özer, A. Altındal, A.R. Özkaya, M. Bulut, Ö. Bekaroğlu, Synth. Met. 155 (2005) 222.
[7] M. Kandaz, H.S. Çetin, A. Koca, A.R: Özkaya, Dyes Pigm, doi:10.1016/j.dyepig.2006.02.008, in press (2006).
[8] Ü. Salan, A. Altındal, M. Bulut, Ö. Bekaroğlu, Tetrahedron Lett. 46 (2005) 6057.
[9] R. Zhou, F. Josse, W. Göpel, Z.Z. Öztürk, Ö. Bekaroğlu, Appl. Organomet. Chem. 10 (1996) 557.
[10] M. Liu, A. Hu, C. Tai, M. Sain, F. Chou, J. Photochem. Photobiol. A: Chem. (2004) 1.
[11] L. Xi-you, K.P.Ng. Dennis, Tetrahedron Lett. 42 (2001) 305.
[12] Ö. Bekaroğlu, Appl. Organomet. Chem. 10 (1996) 605.
[13] M. Kandaz, İ. Yılmaz, Ö. Bekaroğlu, Polyhedron 19 (2000) 115.
[14] J.G. Young, W. Onyebuagu, J. Org. Chem. 55 (1990) 2155.
[15] A.W. Snow, J.R. Griffith, N.P. Marullo, Macromolecules 17 (1984) 1614.
[16] D. Wöhrle, M. Eskes, K. Shigehara, A. Yamada, Synthesis (1993) 194.
[17] P. Zimcik, M. Miletin, M. Kostka, Z. Fiedler, J. Photochem. Photobiol. A: Chem. 155 (2003) 127.
[18] M.A. Dekeyser, R.A. Davis, J. Agric. Food Chem. 46 (1998) 2827.
[19] E. Hamuryudan, S. Merey, Z.A. Bayır, Dyes Pigm. 59 (2003) 263.
[20] S. Dabak, G. Gümüş, A. Gül, Ö. Bekaroğlu, J. Coord. Chem. 8 (1996) 287.
[21] J. Simon, P. Bassoul, Design of Molecular Materials, Wiley, New York, 2000, pp. 196–296 (Chapter 6).
[22] S. Gürsoy, A. Cihan, M.B. Koçak, Ö. Bekaroğlu, Monatsh für Chem. 32 (2001) 813.
[23] D. Wrobel, A. Boguta, J. Photochem. Photobiol. A: Chem. 150 (2002) 67.
[24] A.B.P. Lever, E.R. Milaeva, G. Speier, in: C.C. Leznoff, A.B.P. Lever (Eds.), Phthalocyanines: Properties and Applications, vol. 3, VCH Publishers, New York, 1993, pp. 1–63.
[25] M. Özer, A. Altindal, A.R. Özkaya, M. Bulut, Ö. Bekaroglu, Polyhedron 25 (2006) 3593.
[26] A.R. Özkaya, E. Hamuryudan, Z.A. Bayır, Ö. Bekaroglu, J. Porphyrin Phthalocy. 4 (2000) 689.
[27] A.R. Özkaya, A.İ. Okur, A. Gül, Ö. Bekaroglu, J. Coord. Chem. 33 (1994) 311.
[28] M. Kandaz, A.R. Özkaya, Ö. Bekaroğlu, Monats Chem. 132 (2001) 1013.
[29] A. Koca, H.A. Dinçer, H. Çerlek, A. Gül, M.B. Koçak, Electrochim. Acta 52 (2006) 1199.
[30] A. Koca, H.A. Dinçer, M.B. Koçak, A. Gül, Russ. J. Electrochem. 42 (2006) 31.
[31] A.J. Bard, L.R. Faulkner, Electrochemical Methods: Fundamentals and Applications, 2nd ed., Wiley, New York, 2001.

we report the syntheses, crystal structures, intra-and intermolecular second-sphere hydrogen-bonded interactions of five coordination compounds with mixed ligands of 4,4′-bipy and arenesulfonates, namely $[Zn_2(N,N'\text{-}4,4'\text{-bipy})(N\text{-}4,4'\text{-bipy})_2(H_2O)_8](bpds)_2 \cdot 5H_2O$ (**1**), $[Ag_2(N,N'\text{-}4,4'\text{-bipy})_2(bpds)]$ (**2**), $[Cd(N,N'\text{-}4,4'\text{-bipy})(H_2O)_4]_2(4\text{-abs})_4 \cdot 5H_2O$ (**3**), $[Cu(N,N'\text{-}4,4'\text{-bipy})(O\text{-bs})_2(H_2O)_2] \cdot 4H_2O$ (**4**), and $[Zn(N,N'\text{-}4,4'\text{-bipy})_2(H_2O)_2](4,4'\text{-bipy})(bs)_2 \cdot 4H_2O$ (**5**) (bpds = 4,4′-biphenyldisulfonate, 4-abs = 4-aminobenzenesulfonate, bs = benzenesulfonate).

2. Experimental

2.1. Materials and methods

All materials were commercially available and used as received. Elemental analyses were carried out with a Vario EL elemental analyzer. FTIR spectra were obtained on a Bruker EQUINOX 55 FTIR spectrometer with KBr pellets. TGA was performed using a Netzsch TG 209 analyzer in flowing nitrogen.

2.2. Syntheses and characterization

2.2.1. $[Zn_2(N,N'\text{-}4,4'\text{-bipy})(N\text{-}4,4'\text{-bipy})_2(H_2O)_8](bpds)_2 \cdot 5H_2O$ (1)

The aqueous solution of $Zn(CH_3COO)_2 \cdot 2H_2O$ (0.11 g, 0.5 mmol), 4,4′-bipy (0.10 g, 0.5 mmol) and Na_2(bpds) (0.18 g, 0.5 mmol) was stirred for 20 min at 50 °C. After filtration, a clear solution was obtained and allowed to stand at room temperature. Colorless crystals of **1** were collected after 6 days (yield: 66% based on Zn). *Anal*. Calc. for $C_{54}H_{66}N_6O_{25}S_4Zn_2$ (**1**): C, 44.48; H, 4.56; N, 5.71. Found: C, 44.31; H, 4.62; N, 5.79%. IR (cm^{-1}, KBr): 3363(s), 3055(w), 1636(s), 1603(s), 1501(m), 1490(m), 1414(s), 1297(m), 1200(s), 1124(s), 1074(s), 1032(s),1007(s), 833(m), 807(m), 700(s), 700(s), 629(s) 566(m).

2.2.2. $[Ag_2(N,N'\text{-}4,4'\text{-bipy})_2(bpds)]$ (2)

$AgNO_3$ (0.085 g, 0.5 mmol), Na_2(bpds) (0.18 g, 0.5 mmol), and 4,4′-bipy (0.10 g, 0.5 mmol) were dissolved in 10 mL of distilled water, and stirred for 30 min. The resulting solution was sealed in a Teflon-lined stainless autoclave and heated at 150 °C for 3 days under autogenous pressure, then cooled to room temperature. Purple crystals of **2** were collected in 40% yield (based on Ag). *Anal*. Calc. for $C_{16}H_{12}AgN_2O_3S$ (**2**): C, 45.73; H, 2.88; N, 6.67. Found: C, 45.65; H, 2.79; N, 6.59%. IR (cm^{-1}, KBr): 3468(s), 3041(w), 1598(s), 1551(m), 1510(m), 1411(s), 1384(s), 1208(s), 1131(s), 1041(s), 1028(s), 1012(m), 997(s), 806(s), 726(s), 712(m), 613(s), 568(s), 544(w).

2.2.3. $[Cd(N,N'\text{-}4,4'\text{-bipy})(H_2O)_4]_2(4\text{-abs})_4 \cdot 5H_2O$ (3)

$Cd(CH_3COO)_2 \cdot 2H_2O$ (0.133 g, 0.5 mmol), 4-abs (0.17 g, 1 mmol), and 4,4′-bipy (0.10 g, 0.5 mmol) were dissolved in a mixed solvent of distilled water and CH_3CN (V:V = 1:1), and stirred for 30 min. The pH of the resulting solution was adjusted to 7.0 by NaOH (0.1 M). After filtration, a clear solution was obtained and allowed to stand at room temperature. Purple crystals of **3** were collected in 55% yield (based on Cd). *Anal*. Calc. for $Cd_2C_{44}H_{66}N_8$- $O_{25}S_4$ (**3**): C, 36.19; H, 4.56; N, 7.67. Found: C, 36.28; H, 4.61; N, 7.62%. IR (cm^{-1}, KBr): 3406(s), 1611(s), 1698(s), 1535(s), 1498(s), 1414(s), 1208(s), 1131(s), 1070(s), 1040(s), 1015(s), 998(s), 823(m), 809(s), 725(s), 642(m), 616(s), 570(s).

2.2.4. $[Cu(N,N'\text{-}4,4'\text{-bipy})(O\text{-bs})_2(H_2O)_2] \cdot 4H_2O$ (4)

The procedure used to synthesize compounds **4** and **5** was the same as that of compound **2**. The yield was 30% based on Cu. *Anal*. Calc. for $CuC_{22}H_{30}N_2O_{12}S_2$ (**4**): C, 41.15; H, 4.71; N, 4.36. Found: C, 41.20; H, 4.78; N,

Table 1
Crystal data for compound **1**–**5**

Compound	1	2	3	4	5
Empirical formula	$C_{54}H_{66}N_6O_{25}S_4Zn_2$	$C_{16}H_{12}AgN_2O_3S$	$Cd_2C_{44}H_{66}N_8O_{25}S_4$	$CuC_{22}H_{30}N_2O_{12}S_2$	$ZnC_{42}H_{46}N_6O_{12}S_2$
Formula weight	1458.11	420.21	1460.09	642.14	956.34
Crystal system	triclinic	monoclinic	monoclinic	monoclinic	monoclinic
Space group	$P\bar{1}$	$C2/c$	$P2_1$	$P2_1/n$	$C2/c$
a (Å)	9.909(3)	19.057(14)	15.880(2)	11.146(7)	17.586(9)
b (Å)	13.333(6)	11.417(5)	7.9988(12)	7.753(5)	11.487(6)
c (Å)	14.138(8)	14.578(10)	23.300(3)	16.572(10)	22.752(11)
α (°)	68.080(10)	90	90	90	90
β (°)	71.43	108.87(2)	90.149(3)	106.630(10)	106.878(9)
γ (°)	84.36(2)	90	90	90	90
V (Å^3)	1642.2(13)	3001(3)	2959.5(8) 3	1372.2(15)	4398(4)
Z	1	8	2	2	4
D_{calc} (g cm^{-3})	1.474	1.860	1.638	1.554	1.444
Absorption coefficient (mm^{-1})	0.940	1.498	0.946	1.012	0.722
Reflections collected	7055	3382	17142	7751	12872
Independent reflections	6617	3285	12135	2980	4773
Reflections observed ($I > 2\sigma(I)$)	4130	2000	10442	2583	4030
Data/restraints/parameters	6617/0/410	3285/0/209	12135/1/749	2980/0/185	4773/0/293
Goodness-of-fit	1.032	1.004	1.050	1.101	1.055
$R(F)$, $R_w(F)$ [$I > 2\sigma(I)$]	0.0711, 0.1967	0.0444, 0.0902	0.0389, 0.1046	0.0303, 0.0830	0.0380, 0.0982

4.29%. IR (cm^{-1}, KBr): 3429(s), 1609(s), 1564(m), 1488(m), 1415(s), 1219(s), 1210(s), 1125(s), 1084(m), 1051(m), 1011(m), 813(s), 728(s), 641(s), 617(s).

2.2.5. $[Zn(N,N'\text{-}4,4'\text{-}bipy)_2(H_2O)_2](4,4'bipy)(bs)_2 \cdot 4H_2O$ (**5**)

The yield was 46% based on Zn. *Anal*. Calc. for $ZnC_{42}H_{46}N_6O_{12}S_2$ (**5**): C, 52.7; H, 4.85; N, 8.79. Found: C, 52.59; H, 4.72; N, 8.75%. IR (cm^{-1}, KBr): 3350(m), 1611(s), 1535(m), 1490(s), 1416(s), 1219(s), 1071(s), 1046(s), 1012(s), 809(s), 727(m), 642(s), 634(s), 497(m).

2.3. X-ray crystallography

Single crystals were mounted on a Bruker Smart CCD using Mo Kα radiation and a graphite monochromator at room temperature for compounds **1**, **2**, **4** and **5**, and at 173 K for compound **3**. Absorption corrections were performed by using the SADABS program [12]. All the structures were solved by direct methods and refined by full-matrix least-squares fitting on F^2 by SHEXLS [13,14]. All of the non-hydrogen atoms were refined anisotropically. Hydrogen atoms attached to C atoms and N atoms were located at geometrically calculated positions and refined with isotropic thermal parameters. Hydrogen atoms of water molecules in the structures of **4** and **5** were located from the difference Fourier map at the final state of refinement, and refined as riding atoms with coordinates riding on the oxygen atoms to which they are attached. The hydrogen atoms of water molecules in the structures of **1** and **3** could not be located from the difference Fourier map. The crystallographic data are given in Table 1. Selected bond distances and angles are shown in Table 2.

3. Results and discussion

3.1. Thermal analyses

The TGA of compound **1** shows a successive weight loss of the lattice water molecules and the coordinated water

Table 2
Selected bond distance (Å) and angles (°) for compound **1**–**5**

$[Zn_2(N,N'\text{-}4,4'\text{-}bipy)(N\text{-}4,4'\text{-}bipy)_2(H_2O)_8](bpds)_2 \cdot 5H_2O$ (**1**)					
Zn(1)–O(1W)	2.117(5)	Zn(1)–O(4W)	2.119(4)	Zn(1)–O(2W)	2.162(4)
Zn(1)–O(3W)	2.174(4)	Zn(1)–N(1)	2.199(5)	Zn(1)–N(3)	2.224(5)
O(1W)–Zn(1)–O(4W)	90.75(17)	O(1W)–Zn(1)–O(2W)	87.71(18)	O(4W)–Zn(1)–O(2W)	177.62(16)
O(1W)–Zn(1)–O(3W)	176.56(17)	O(4W)–Zn(1)–O(3W)	92.16(17)	O(2W)–Zn(1)–O(3W)	89.32(17)
O(1W)–Zn(1)–N(1)	94.68(19)	O(4W)–Zn(1)–N(1)	89.86(17)	O(2W)–Zn(1)–N(1)	92.06(18)
O(3W)–Zn(1)–N(1)	87.17(17)	O(1W)–Zn(1)–N(3)	91.18(19)	O(4W)–Zn(1)–N(3)	86.69(18)
O(2W)–Zn(1)–N(3)	91.53(18)	O(3W)–Zn(1)–N(3)	87.15(17)	N(1)–Zn(1)–N(3)	173.24(18)
$[Ag_2(N,N'\text{-}4,4'\text{-}bipy)_2(bpds)]$ (**2**)					
Ag(1)–N(2)^{2a}	2.170(4)	Ag(1)–N(1)	2.180(4)		
N(2)–Ag(1)–N(1)^{2a}	168.60(14)	C(5)–N(1)–Ag(1)	121.2(3)	C(1)–N(1)–Ag(1)	121.0(3)
C(6)–N(2)–Ag(1)^{2b}	122.0(3)	C(10)–N(2)–Ag(1)^{2b}	120.7(3)		
$[Cd(N,N'\text{-}4,4'\text{-}bipy)(H_2O)_4]_2(4\text{-}abs)_4 \cdot 5H_2O$ (**3**)					
Cd(1)–OW1	2.247(4)	Cd(1)–OW3	2.352(4)	Cd(1)–OW2	2.312(4)
Cd(1)–OW4	2.288(4)	Cd(1)–N(3)	2.327(3)	Cd(1)–N(1)	2.316(3)
Cd(2)–OW5	2.313(4)	Cd(2)–OW7	2.289(4)	Cd(2)–OW6	2.352(4)
Cd(2)–OW8	2.291(4)	Cd(2)–N(2)^{3a}	2.319(4)	Cd(2)–N(4)	2.312(3)
OW1–Cd(1)–OW4	91.19(17)	OW1–Cd(1)–OW2	89.38(15)	OW4–Cd(1)–OW2	175.96(14)
OW1–Cd(1)–N(1)	99.61(14)	OW4–Cd(1)–N(1)	91.31(17)	OW2–Cd(1)–N(1)	84.66(17)
OW1–Cd(1)–N(3)	90.01(14)	OW4–Cd(1)–N(3)	85.11(18)	OW2–Cd(1)–N(3)	98.89(17)
N(1)–Cd(1)–N(3)	169.82(13)	OW1–Cd(1)–OW3	173.02(14)	OW4–Cd(1)–OW3	91.18(16)
OW2–Cd(1)–OW3	88.73(14)	N(1)–Cd(1)–OW3	86.91(13)	N(3)–Cd(1)–OW3	83.65(12)
OW7–Cd(2)–OW8	83.48(17)	OW7–Cd(2)–N(4)	92.79(14)	OW8–Cd(2)–N(4)	96.85(16)
OW7–Cd(2)–OW5	175.74(13)	OW8–Cd(2)–OW5	94.46(15)	N(4)–Cd(2)–OW5	91.16(14)
OW7–Cd(2)–N(2)^{3a}	95.49(15)				
$[Cu(N,N'\text{-}4,4'\text{-}bipy)(O\text{-}bs)_2(H_2O)_2] \cdot 4H_2O$ (**4**)					
Cu(1)–OW1	1.9802(17)	Cu(1)–N(1)	2.027(2)	Cu(1)–O(1)	2.3817(19)
OW1–Cu(1)–O(1)	84.00(7)	OW1–Cu(1)–N(1)^{4a}	88.65(6)	N(1)–Cu(1)–O(1)^{4a}	90.72(6)
N(1)–Cu(1)–O(1)	89.28(6)				
$[Zn(N,N'\text{-}4,4'\text{-}bipy)_2(H_2O)_2](4,4'\text{-}bipy)(bs)_2 \cdot 4H_2O$ (**5**)					
Zn(1)–OW1	2.1330(19)	Zn(1)–N(1)	2.1470(19)	Zn(1)–N(2)	2.192(2)
Zn(1)–N(3)	2.211(3)				
OW1–Zn(1)–OW1^{5a}	176.67(8)	OW1–Zn(1)–N(1)^{5a}	90.28(7)	OW1–Zn(1)–N(1)	89.76(7)
OW1–Zn(1)–N(2)	88.34(4)	N(1)–Zn(1)–N(2)	90.62(5)	N(1)–Zn(1)–N(1)^{5a}	178.76(9)
N(1)–Zn(1)–N(2)^{5a}	90.62(5)	OW1–Zn(1)–N(3)	91.66(4)	N(1)–Zn(1)–N(3)	89.38(5)
N(2)–Zn(1)–N(3)	180.0				

Symmetry code: (2a) $x, y-1, z$; (2b) $x, y+1, z$; (3a) $x, y, z+1$; (4a) $-x+1, -y+1, -z$; (5a) $-x+1, y, -z+1/2$.

molecules in the temperature range of 114–216 °C (Calc: 6.1%, 9.9%, Found: 6.2%, 5.7%), and another weight loss of 26.2% (Calc: 32.1%) at 331 °C, contributed by the release of 4,4′-bipy. TGA result of compound **2** reveals that it is stable until 320 °C. There is a successive weight loss of 37.4% (Calc: 37.1%) in the range of 320–386 °C, and another weight loss of 24.4% (Calc: 33.3%) at 552 °C, contributed by the release of 4,4′-bipy and decomposition of bpds, respectively. Compound **3** releases the lattice water molecules and the coordinated water molecules in multiple steps in the temperature range of 68–180 °C (Found: 16.2%, Calc: 15.9%), with the second batch of release followed by the loss of 4,4′-bipy (Found: 21.3%, Calc: 21.4%), and decomposition of 4-abs at 309 °C and 524 °C, respectively. TGA curve of compound **4** shows a successive weight loss in the range of 69–700 °C, where compound **4** releases the lattice water molecules and the coordinated water molecules in 69–173 °C (Found: 16.8%, Calc: 16.9%), and losses 4,4′-bipy in multiple steps in the range of 190–270 °C (Found: 27.1%, Calc: 24.3%). Compound **5** releases the lattice water molecules and the coordinated water molecules in multiple steps in the range of 90–180 °C (Found: 9.9%, Calc: 11.3%), and losses the 4,4′-bipy molecules in multiple steps in the range of 250–600 °C (Found: 49.9%, Calc: 44.7%) with the decomposition of the framework.

After the removal of the clathrate water molecules, PXRD patterns show that compounds **1**, **3**, **4** and **5** lose their identity as a network.

3.2. Description of the structures

The structure of $[Zn_2(N,N'\text{-}4,4'\text{-bipy})(N\text{-}4,4'\text{-bipy})_2(H_2O)_8](bpds)_2 \cdot 5H_2O$ (**1**) is shown in Fig. 1a. It is a binuclear octahedral metal complex constructed by two Zn centers linked by one μ_2 4,4′-bipy bridging ligand (Zn–N3 = 2.224 Å). Each Zn center is further coordinated by one monodentate 4,4′-bipy ligand (Zn–N1 = 2.199 Å) and four aqua molecules (Zn–O = 2.117–2.174 Å). The angles of *cis* O–Zn–O are in the range of 87.71–92.16°, indicating that the octahedral geometry is distorted slightly. The pyridine ring of the bridging 4,4′-bipy ligand is coplanar, while the monodentate 4,4′-bipy ligand is twisted by 22.79°. Bpds exists as a counter anion with the aryl rings twisted by 38.07°. The $[Zn_2(N,N'\text{-}4,4'\text{-bipy})(N\text{-}4,4'\text{-bipy})_2(H_2O)_8]$ complex units are linked by the lattice water molecules via hydrogen bonds formed between the coordinated water molecules and the lattice water molecules (Ow1···Ow6 = 2.731 Å, Ow2···Ow7 = 2.720 Å), between the lattice water molecules (Ow7···Ow6 = 3.192 Å), and between the lattice water molecules and N atoms from the 4,4′-bipy ligands (N2···Ow6 = 2.811 Å), resulting in 2D cationic sheets as shown in Fig. 1b. The bpds anions are located between the hydrogen-bonded sheets, and connect the sheets via hydrogen bonds formed between the sulfonate oxygen atoms and the coordinated water molecules [O3···Ow3 = 2.891 Å, Ow4···O6 = 2.841 Å, O6···Ow3 = 2.772 Å], and between the sulfonate oxygen atoms and the lattice water molecules [O3…Ow7 = 2.879 Å, O4···Ow5 = 2.892 Å, O1···Ow6 = 2.999 Å], finally generating 3D hydrogen bonding networks.

Compound $[Ag_2(N,N'\text{-}4,4'\text{-bipy})_2(bpds)]$ (**2**) forms 1D chains as shown in Fig. 2a. The 4,4′-bipy ligands bridge the Ag centres with Ag1–N1 = 2.180 Å and Ag1–N2 = 2.170 Å to form 1D Ag-bipy chains similar to those reported previously [15]. There are weak coordination interactions between Ag and the sulfonate oxygen atoms (Ag1–O1 = 2.832 Å, Ag1A–O2 = 2.856 Å, Fig. 2a). The pyridyl rings of the 4,4′-bipy ligand are twisted by 29.38°. The aryl rings of bpds anion are coplanar, which is different from that observed in compound **1**. The most interesting features of this structure are that Ag–Ag interactions are formed between the 1D chains which are generated by inversion centers (Ag–Ag = 3.398 Å), resulting in 1D ribbons. As shown in Fig. 2b, these ribbons are connected by bpds via weak coordination interactions between Ag and the sulfonate groups, generating a 2D layered structure. π···π interactions between layers, formed by the bipy ligands with distance of 3.46 Å, are also observed.

The asymmetric unit of $[Cd(N,N'\text{-}4,4'\text{-bipy})(H_2O)_4]_2(4\text{-abs})_4 \cdot 5H_2O$ (**3**) is shown in Fig. 3a. There are four independent 4-abs anions in the asymmetric unit. The Cd centre is coordinated by four water molecules and two N atoms from two different bipy ligands, resulting in infinite chains

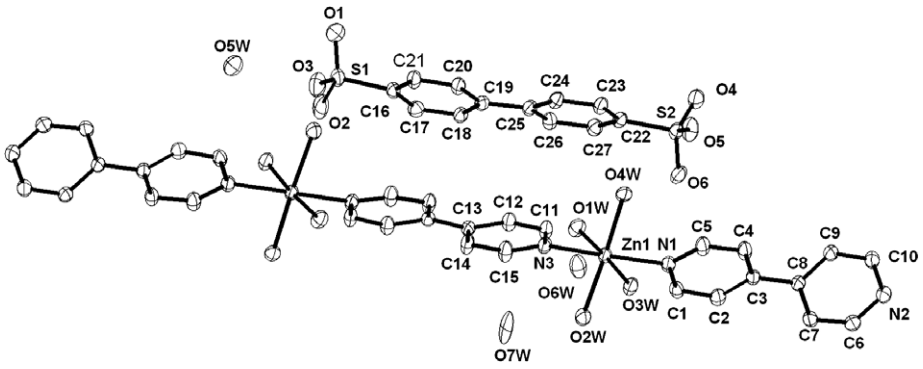


Fig. 1a. Ortep drawing of compound **1** with thermal ellipsoids at 20% probability. H atoms are omitted for clarity.

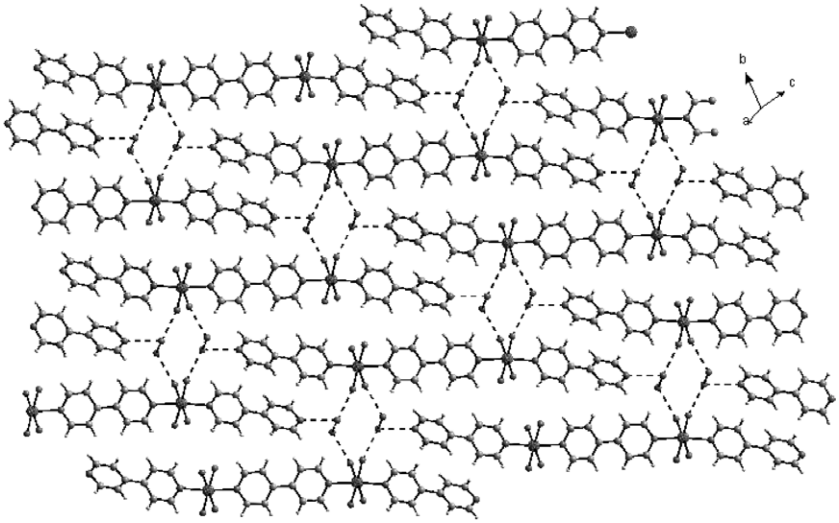


Fig. 1b. Two-dimensional extended network of compound **1**. Hydrogen bonds are represented as broken lines.

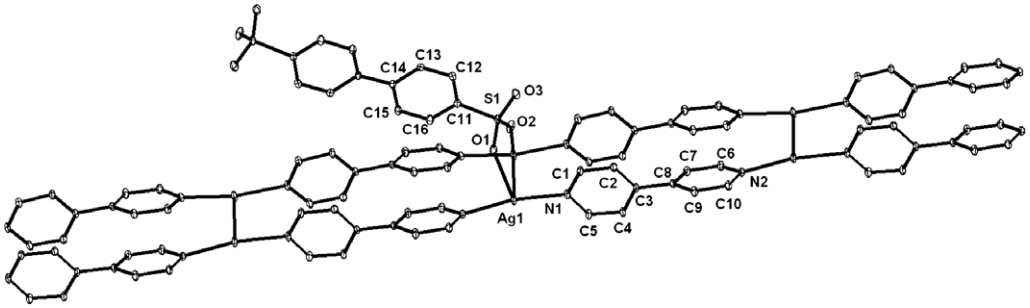


Fig. 2a. Ortep drawing of compound **2** with thermal ellipsoids at 10% probability. H atoms are omitted for clarity.

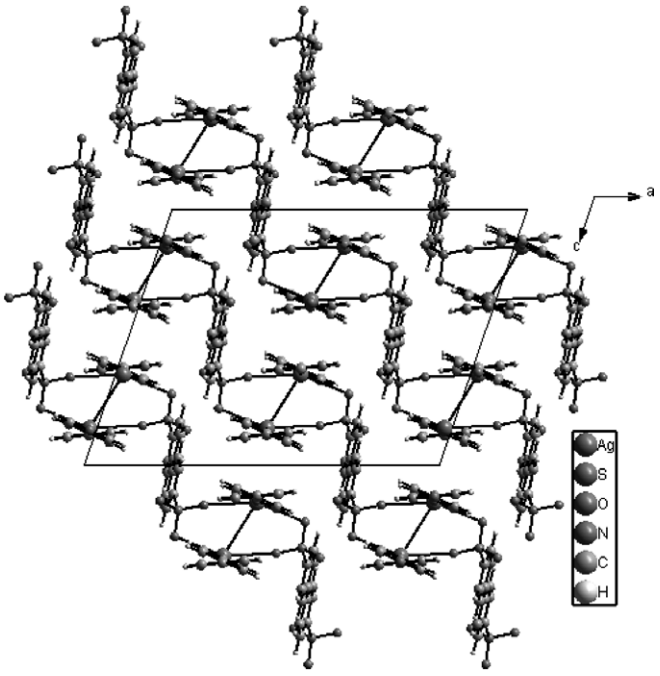


Fig. 2b. Packing structure of compound **2** along *b* axis.

packing alone the crystallographic *c* axis. The Cd–N bond lengths are in the range of 2.312–2.327 Å. The Cd–Ow bond lengths are in the range of 2.247–2.352 Å. The angles of *cis* O–Cd–O are in the range of 83.48–94.46°. The pyridyl rings of 4,4′-bipy are twisted with dihedral angles of 10.96° and 10.00°, respectively. Six 4-abs anions arranged in head-to-tail fashion are held together via hydrogen-bonding interactions between N atoms and the sulfonate oxygen atoms of 4-abs [N5···O11 = 3.009 Å, N6···O8 = 3.059 Å, N7···O6 = 3.225 Å, N7···O10 = 3.238 Å, N8···O3 = 3.094 Å], between the lattice water molecules and N atoms of 4-abs [N5···Ow9 = 3.037 Å, N7···Ow13 = 3.109 Å, N8···Ow11 = 2.946 Å], and between the sulfonate oxygen atoms and the lattice water molecules (O···Ow = 2.760 Å), to produce hexameric aggregates. These hexameric aggregates are furthered connected via hydrogen bonds to formed 1D columns running along crystallographic *c* axis. The [Cd(4,4′-bipy)$_2$(H$_2$O)$_4$] chains are located inside the hexameric channels formed by the 4-abs anions and water molecules, as shown in Fig. 3b.

The structure of [Cu(*N*,*N*′-4,4′-bipy)(*O*-bs)$_2$(H$_2$O)$_2$]·4H$_2$O (**4**) is shown in Fig. 4a. The Cu atom is coordinated by two water molecules (Cu–O = 1.980 Å), two sulfonate groups of the bs ligands (Cu–O = 2.382 Å), and two nitrogen atoms from two bridging 4,4′-bipy ligands (Cu–N = 2.027 Å), and form a 1D polymeric structure. The pyridyl rings of 4,4′-bipy are coplanar, which is different from that observed in compound **3**. The bs ligands are located between the chains in head to head fashion and connect

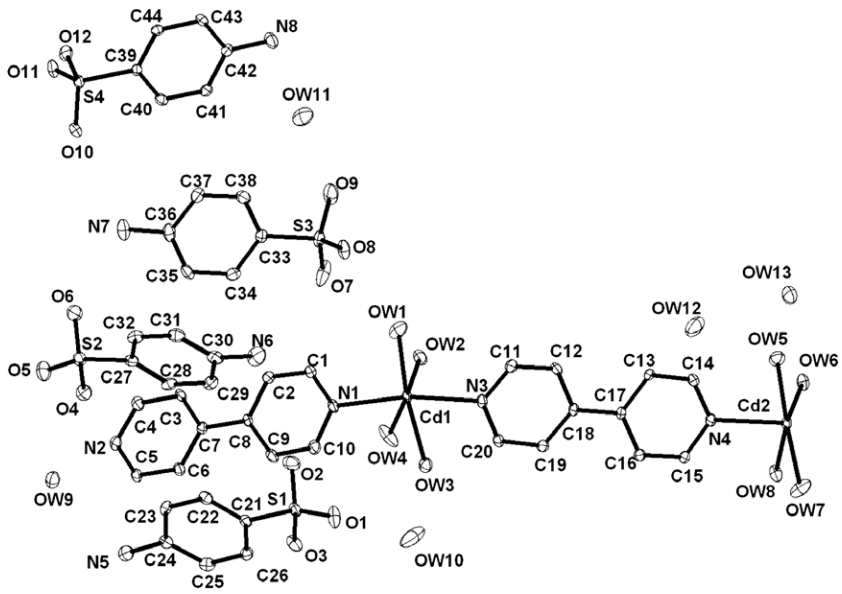


Fig. 3a. Ortep drawing of compound **3** with thermal ellipsoids at 20% probability. H atoms are omitted for clarity.

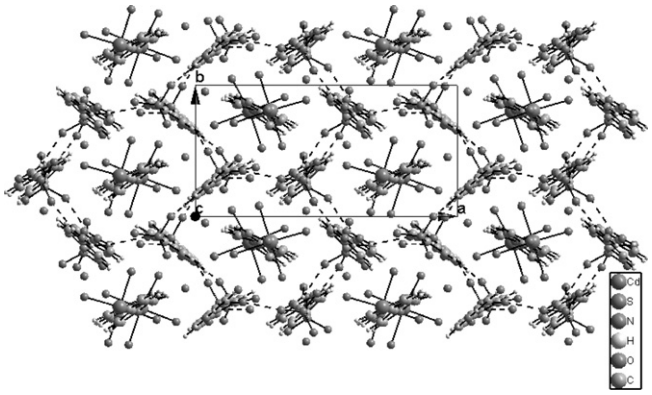


Fig. 3b. Three-dimensional extended network of compound **3**. Hydrogen bonds are represented as broken lines.

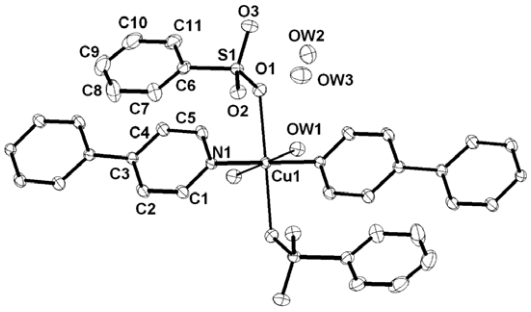


Fig. 4a. Ortep drawing of compound **4** with thermal ellipsoids at 30% probability. H atoms are omitted for clarity.

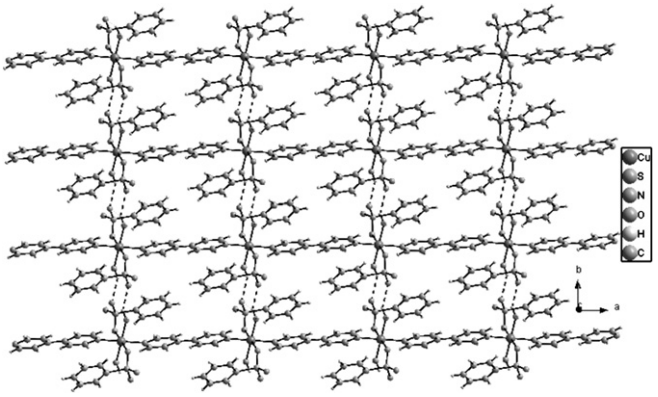


Fig. 4b. Two-dimensional extended network of compound **4**. Hydrogen bonds are represented as broken lines.

the chains through hydrogen bonds between the uncoordinated sulfonate oxygen atoms and the coordinated water molecules [O2···O1w = 2.893 Å, O1w···O2 = 2.859 Å] to form 2D hydrogen-bonded square grids as shown in Fig. 4b. The square cavity has dimensions of 11.487 × 7.75 Å which hosts a pair of phenyl rings from the bs ligands. The lattice water molecules are located between hydrogen-bonded layers, which are anchored by extensive hydrogen bonds formed with the sulfonate groups and coordinated water molecules.

Compounds [Zn(*N*,*N*′-4,4′-bipy)$_2$(H$_2$O)$_2$](4,4′-bipy)(bs)$_2$ · 4H$_2$O (**5**) and [Cu(*N*,*N*′-4,4′-bipy)(*O*-bs)$_2$(H$_2$O)$_2$] · 4H$_2$O (**4**) have the same ligand components and synthesized via similar procedures. Interestingly, a total different structural topology is adopted in compound **5** and the structure is shown in Fig. 5a. The Zn centre is six-coordinated by two aqua ligands (Zn–O = 2.133 Å) and four nitrogen atoms from four different bipy bridging ligands (Zn–N = 2.147–2.211 Å), resulting in a 2D grid structure as shown in Fig. 5b. The grid structure is similar to those reported by Chen [16,17]. The square cavity has dimensions of 11.146 × 11.383 Å and accommodates a pair of centrosymmetrically-orientated bs anions with the hydrophobic groups embedded in the cavity. The separation of the two aryl groups is 3.518 Å, indicating that there is weak aromatic interaction between these bs anions. Aside from the aromatic interactions, the bs anions also make contact with the host

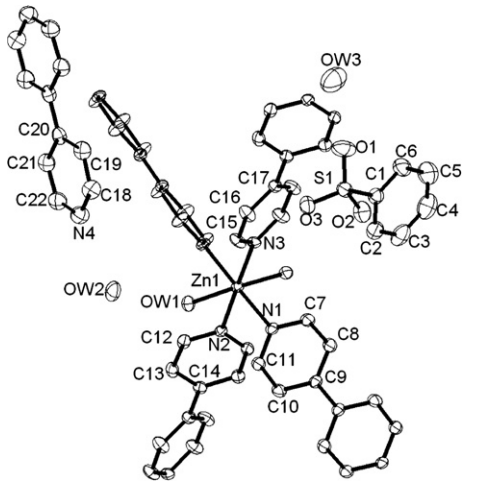


Fig. 5a. Ortep drawing of compound **5** with thermal ellipsoids at 30% probability. H atoms are omitted for clarity.

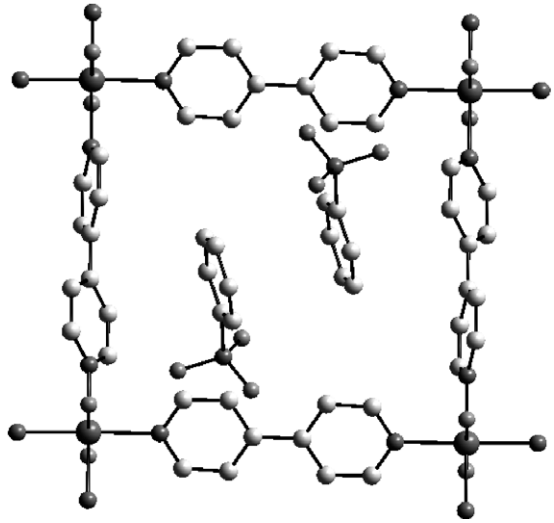


Fig. 5b. View of the square unit of compound **5**.

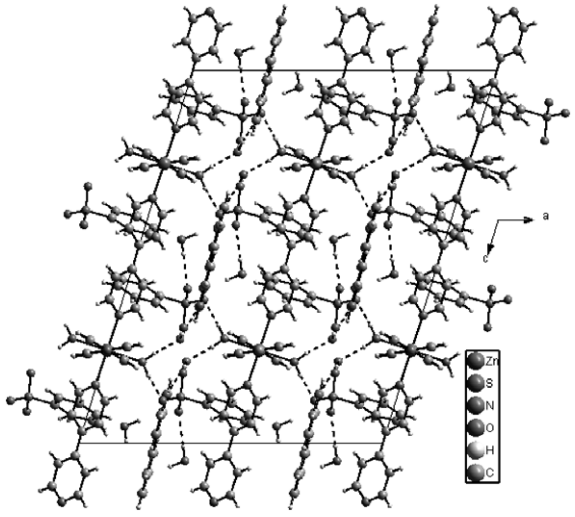


Fig. 5c. Three-dimensional extended network of compound **5**. Hydrogen bonds are represented as broken lines.

grids through C–H···π interactions, and form hydrogen bonds with the lattice water molecules. The uncoordinated bipy ligands are located between the coordination layers and anchored by hydrogen bonds formed with the lattice water molecules (Ow2···N4 = 2.891 Å), as shown in Fig. 5c.

4. Conclusions

Compounds **1**–**5** show structural varieties to a great extend and there are three different coordination modes adopted by both the 4,4′-bipy ligand and the sulfonate molecules. The 4,4′-bipy molecule presents both as a monodentate and μ_2 bridging ligand in compound **1**, solely as a μ_2 bridging ligand in compounds **2**–**4**, and a μ_2 bridging ligand and an intercalated molecule in compound **5**. The sulfonate molecules do not have any direct interactions with the metal centers in compounds **1**, **3** and **5**. In compound **2**, both of the sulfonate groups of the bpds ligand form weak coordination interactions in η_2 fashion to Ag. While in compound **3**, the sulfonate group of the bs ligand coordinates monodentately to Cu.

4,4′-Bipy is a well-studied rigid ligand with μ_2 bridging as the most commonly observed coordination mode. In comparison, sulfonates are soft ligands with flexible coordination behaviors. Our results demonstrate that by adopting rigid and soft ligands, coordination complexes with diversified structural frameworks could be produced; and the presence of sulfonates, either as counter anions or soft ligands, can diversify the extended structures formed by the strong transition metal-bipy interactions. For instance, in compound **1**, a discrete binuclear complex is formed in which the bipy ligand shows two different coordination modes to Zn(II). In compounds **2**–**4**, conventional 1D chains are formed by the μ_2 bridging 4,4′-bipy ligands, and further extended into 3D structures via Ag–Ag and Ag–sulfonate interactions in compound **2**. While in **5**, a unique 2D grid layered structure is constructed by two bridging 4,-4′-bipy ligands, and free 4,4′-bipy molecules are intercalated between the layers.

Finally, it is interesting to note that, even in the presence of strong and dominant ligands such as water molecules and 4,4′-bipy, the bulky arenesulfonate can still form coordination interactions with transition metals such as in compounds **2** and **4**, and adjusting the formation of the extended framework via strong hydrogen bonds.

Acknowledgements

The authors thank the National Natural Science Foundation of China for their financial support.

Appendix A. Supplementary material

CCDC 617352, 617353, 617354, 617355 and 617356 contain the supplementary crystallographic data for **1**, **2**, **3**, **4** and **5**. These data can be obtained free of charge via http://www.ccdc.cam.ac.uk/conts/retrieving.html, or from

the Cambridge Crystallographic Data Centre, 12 Union Road, Cambridge CB2 1EZ, UK; fax: (+44) 1223-336-033; or e-mail: deposit@ccdc.cam.ac.uk. Supplementary data associated with this article can be found, in the online version, at doi:10.1016/j.poly.2007.01.002.

References

[1] (a) O.M. Yaghi, H. Li, C. Davis, D. Richardson, T.L. Groy, Acc. Chem. Res 31 (1998) 474;
(b) G.R. Desiraju, Nature. 412 (2001) 397;
(c) J.S. Seo, D. Whang, H. Lee, S. Jun, J. Ok, Y. Jin, K. Kim, Nature 404 (2000) 982;
(d) D. Bradshaw, J.B. Claridge, E.J. Cussen, T.J. Prior, M.J. Rosseinsky, Acc. Chem. Res. 38 (2005) 273;
(e) B. Kesanli, W.B. Lin, Coord. Chem. Rev. 246 (2003) 305;
(f) R.G. Xiong, X.Z. You, B.F. Abrahams, Z. Xue, C.M. Che, Angew. Chem., Int. Ed. 40 (2001) 4422.

[2] (a) B.F. Abrahams, J.S. Egan, R.J. Richard, Am. Chem. Soc. 121 (1999) 3535;
(b) A.J. Black, N.R. Champness, A.N. Kholbystov, S. Parsons, M. Schroder, Angew. Chem., Int. Ed 39 (2000) 2317;
(c) Z.-F. Chen, R.-G. Xiong, J. Zhang, J-L. Zuo, X.-Z. You, J. Chem. Soc., Dalton Trans. (2000) 4010;
(d) Y. Qiong, Y.-H. Li, Q. Wu, Y.-M. Song, J.-X. Wang, H. Zhao, R.-G. Xiong, Z.-L. Xue, Chem. Eur. J. 11 (2005) 988;
(e) R. Kitaura, G. Onoyama, H. Sakamoto, R. Matsuda, S.I. Noro, S. Kitagawa, Angew. Chem., Int. Ed. 43 (2004) 2684.

[3] (a) Kumar Biradha, CrystEngComm 5 (2003) 374;
(b) G.K.H. Shimizu, J. Solid State Chem. 178 (2005) 2519.

[4] (a) E.J. Cussen, J.B. Claridge, M.J. Rosseinsky, C.J. Kepert, J. Am. Chem. Soc. 124 (2002) 9574;
(b) L. Carlucci, G. Ciani, M.P. Davide, S. Angelo, Chem. Commun. (1994) 2755;
(c) S. Subramnian, Michael J. Zaworotko, Angew. Chem., Int. Ed. Engl. 34 (1995) 2127;
(d) J.B. Alexander, N.R. Champness, S.M. Simon Chung, W.-S. Li, M. Schroder, Chem. Commun. (1997) 1005.

[5] (a) Danil N. Dybtsev, H. Chun, K. Kim, Angew. Chem., Int. Ed. Engl. 43 (2004) 5033;
(b) D.B. Andrew, C. Kevin, M.W. Richard Friend, F.M. Mary, S.P. Rigby, E.W. John, CrystEngComm. 7 (2005) 548;
(c) S.S.-Y. Chui, S.M.-F. Lo, J.P.H. Charmant, A.G. Orpen, I.D. Williams, Science 283 (1999) 1148;
(d) L. Pan, K.M. Adams, H.E. Hernaandez, X. Wang, C. Zheng, Y. Hattori, K. Kaneko, J. Am. Soc. 125 (2003) 3062.

[6] (a) H. Chun, D.N. Dybtsev, H. Kim, K. Kim, Chem. Eur. J. 11 (2005) 3521;
(b) X.-M. Zhang, M.-L. Tong, M.-L. Gong, X.-M. Chem, Eur. J. Inorg. Chem. (2003) 138;
(c) L. Pan, H.-M. Liu, X. Lei, X.-Y. Huang, D.H. Olson, N.J. Turro, L. Li, Angew. Chem., Int. Ed. Engl. 42 (2003) 542;
(d) J. Tao, M.-L. Tong, X.-M. Chen, J. Chem. Soc., Dalton Trans. (2000) 3669;
(e) B.Q. Ma, K.L. Mulfort, J.T. Hupp, Inorg. Chem. 44 (2005) 1942.

[7] (a) A.J. Blake, S.J. Hill, P. Hubberstey, W.-S.J. Li, Chem. Soc., Dalton Trans. (1997) 913;
(b) Y.-H. Wang, L.-Y. Feng, Y.-G. Li, C.-W. Hu, E.-B. Wang, N.-H. Hu, H.-Q. Jia, Inorg. Chem. 41 (2002) 6351;
(c) S.-I. Noro, S. Kitagawa, M. Kondo, K. Seki, Angew. Chem., Int. Ed. Engl. 39 (2000) 2082;
(d) L. Carlucci, G. Ciani, D. Proserpio, A. Sironi, J. Chem. Soc., Dalton Trans. (1997) 1801;
(e) X.-M. Chen, M.-L. Tong, Y.-J. Luo, Y.-D. Chen, Aust. J. Chem. 49 (1996) 835;
(f) B.-Q. Ma, S. Gao, H.-L. Sun, G.-X. Xu, J. Chem. Soc., Dalton Trans. (2001) 30.

[8] (a) J. Cai, Coord. Chem. Rev. 248 (2004) 1061;
(b) J. Cai, C.H. Chen, C.Z. Liao, X.L. Feng, C.M. Chen, Acta Crystallogr., Sect. B 57 (2001) 520;
(c) J. Cai, C.-H. Chen, C.-Z. Liao, J.-H. Yao, X.-P. Hu, X.-M. Chen, J. Chem. Soc., Dalton Trans. (2001) 1137;
(d) J. Cai, C.-H. Chen, X.-L. Feng, C.-Z. Liao, C.-M. Chen, J. Chem. Soc., Dalton Trans. (2001) 2370;
(e) C.-H. Chen, J.-W. Cai, C.-Z Liao, X.-L. Feng, C.-M. Chen, S.-W. Ng, Inorg. Chem. 41 (2002) 4967;
(f) J.-W. Cai, C.-H. Chen, J.-S. Zhou, Chin. J. Inorg. Chem. 19 (2003) 81;
(g) J.-W. Cai, J.-S. Zhou, M.-L. Lin, J. Mater. Chem. 13 (2003) 1906;
(h) J.-S. Zhou, J. Cai, L. Wang, J. Chem. Soc., Dalton Trans. (2004) 1493.

[9] (a) G.K.H. Shimizu, G.D. Enright, C.I. Ratcliffe, G.S. Rego, J.L . Reid, J.A. Ripmeester, Chem. Mater. 10 (1998) 3282;
(b) G.K.H. Shimizu, G.D. Enright, C.I. Ratcliffe, K.F. Preston, J.L. Reid, J.A. Ripmeester, Chem. Commun. (1999) 1485;
(c) A.P. Côté, G.K.H. Shimizu, Chem. Commun (2001) 251;
(d) J.O. Yu, A.P. Côté, G.D. Enright, G.K.H. Shimizu, Inorg. Chem. 40 (2001) 582;
(e) S.K. Mäkinen, N.J. Melcer, M. Parvez, G.K.H. Shimizu, Chem. Eur. J. 7 (2001) 5176;
(f) A.P. Côté, M.J. Ferguson, K.A. Khan, G.D. Enright, A.D. Kulynych, S.A. Dalrymple, G.K.H. Shimizu, Inorg. Chem. 41 (2002) 287;
(g) D.S. Reddy, S. Duncan, G.K.H. Shimizu, Angew. Chem., Int. Ed. Engl. 42 (2003) 1360;
(h) S.A. Dalrymple, M. Parvez, G.K.H. Shimizu, Chem. Commun. (2001) 2672;
(i) S.A. Dalrymple, M. Parvez, G.K.H. Shimizu, Inorg. Chem. 41 (2002) 6986;
(j) S.A. Dalrymple, G.K.H. Shimizu, Chem. Eur. J. 8 (2002) 3010;
(k) D.J. Hoffart, A.P. Côté, G.K.H. Shimizu, Inorg. Chem. 42 (2003) 8603;
(l) S.A. Dalrymple, G.K.H. Shimizu, Chem. Commun. (2002) 2224;
(m) B.D. Chandler, A.P. Côté, D.T. Cramb, J.M. Hill, G.K.H. Shimizu, Chem. Commun. (2002) 1900;
(n) A.P. Côté, G.K.H. Shimizu, Inorg. Chem. 43 (2004) 6663;
(o) A.P. Côté, G.K.H. Shimizu, Chem. Eur. J. 9 (2003) 5361;
(p) A.P. Côté, G.K.H. Shimizu, Coord. Chem. Rev. 245 (2003) 49–64.

[10] (a) K.T. Holman, A.M. Pivovar, J. A Swift, M.D. Ward, Acc. Chem. Res. 34 (2001) 107;
(b) J.A. Swift, M.D. Ward, Chem. Mater. 12 (2001) 1501;
(c) M.J. Horner, K.T. Holman, M.D. Ward, Angew. Chem., Int. Ed. Engl. 40 (2001) 4045;
(d) R. Custelcean, M.D. Ward, Angew. Chem., Int. Ed. Engl. 41 (2002) 1724.

[11] X.-L. Zhang, B.-H. Ye, X.-M. Chen, Cryst. Growth Des. 5 (2005) 1609.

[12] R. Blessing, Acta Crystallogr., Sect. A 51 (1995) 33.

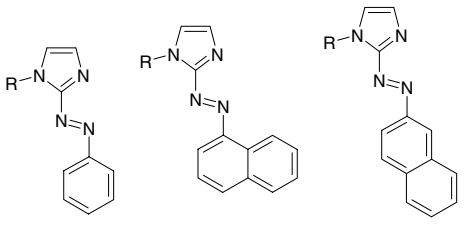
[13] Bruker AXS, SHELXTL, Version 5.1, Bruker AXS, Madison, WI, USA, 1999.

[14] G.M. Sheldrick, SHELX 97, Program for X-ray Crystal Structure Solution and Refinement, Göttingen University, Germany, 1997.

[15] D.-S. Sun, R. Cao, Y.-Q. Sun, W.-H. Bi, X.-J. Li, Y.-Q. Wang, Q. Shi, X. Li, Inorg. Chem. 23 (2003) 7512.

[16] (a) M.-L. Tong, X.-M. Chen, X.-L. Yu, T.C W. Mak, J. Chem. Soc., Dalton Trans. (1998) 5;
(b) X.-M. Chen, M.-L. Tong, Y.-J. Luo, Z.-N. Chen, Aust. J. Chem. 51 (1998) 637;
(c) M.-L. Tong, H.K. Lee, X.-M. Chen, R.-B. Huang, T.C.W. Mak, J. Chem. Soc., Dalton Trans. (1999) 3657.

[17] (a) M.-L. Tong, X.-M. Chen, CrystEngCommun. (2000) 1;
(b) M.-L. Tong, H.-J. Chen, X.-M. Chen, Inorg. Chem. 39 (2000) 2235;
(c) M.-L. Tong, S.-L. Zheng, X.-M. Chen, Polyhedron. 19 (2000) 1809;
(d) M.-L. Tong, X.-M. Chen, S.W. Ng, Inorg. Chem. Commun. 3 (2000) 436.



Phenylazoimidazole (**i**) Naphthylazoimidazole (**ii**)

2. Experimental

2.1. Reagents/materials

The complexes were prepared by a reported procedure [19,20]. 8-Quinolinol (SRL, Mumbai) was purified by recrystallization from a hot ethanol solution. Acetonitrile (MeCN) was purified by a known procedure [21,22]. All kinetic and spectroscopic measurements were recorded on an Agilent 8453E UV–visible Spectroscopy System. Quartz cells (1.0 cm path length) from Hellma were used. IR spectra (KBr pellet) were recorded on a FT-IR spectrophotometer Spectrum RX1, Perkin–Elmer. ^{1}H NMR spectra were drawn from a 300 MHz Bruker NMR instrument in CD_3CN using TMS as an internal standard. Microanalyses were carried out on a Perkin–Elmer 2400 CHN elemental analyzer. The specific conductance was measured on a JENCONS 4010 Conductivity Meter. The pH was measured on a SYSTRONICS 361 Digital pH meter. Rate constants and standard deviations were calculated by linear regression using a PC-based program, Microcal-origin version Origin-6.1.

2.1.1. Kinetic measurements

For kinetic measurements, stock solutions of the complexes (*ca.* 10^{-3} mol dm^{-3}) and of 8-quinolinol (HQ) (*ca.* 10^{-2} mol dm^{-3}) were prepared in dry MeCN. Solutions of different concentrations were prepared by quantitative dilution of stock solutions using dry MeCN. All experiments were performed at 298 K (unless otherwise mentioned) by mixing required volumes of the thermostated reactants and transferring the mixture to the absorption cell (1.0 cm length). On addition of 8-quinolinol (HQ) to the solution of Pd(NaiR)Cl_2 in MeCN, the orange solution changed to yellow-orange. The influence of the addition of 8-quinolinol on the spectra of Pd(α-NaiR)Cl_2 is shown in the Fig. 1. The change proceeds through a single isobestic point at *ca.* 472 nm. The decrease in absorbance of the reaction mixture was recorded automatically at *ca.* 500 nm as a function of time (s). A_∞ was measured after ~24 h of mixing, when the absorbance became constant. In all experiments, the initial molar concentration of HQ, $[HQ]_0$, was kept at least ten times in excess so as to maintain a pseudo-first-order kinetic condition. Pseudo-first-order rate constants, k_{obs}, were obtained from the plots of $(A_t - A_\infty)$ versus time (s) (Fig. 2) where A_t = absorbance of the reaction mixture at time t (s) after mixing of the HQ solution and A_∞ = absorbance of same reaction mixture after completion of the reaction.

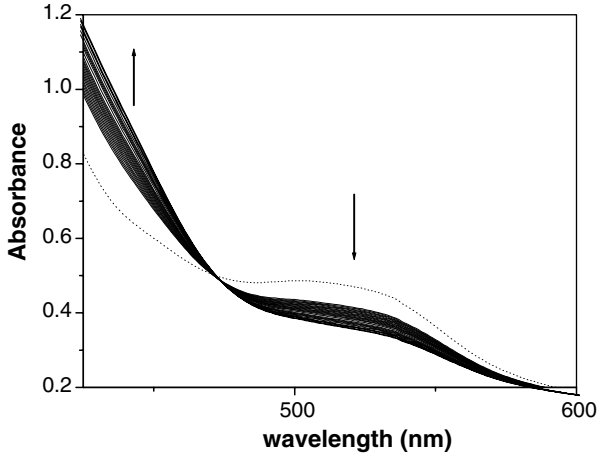


Fig. 1. Spectra of Pd(α-NaiMe)Cl_2in MeCN and a reaction mixture of Pd(α-NaiMe)Cl_2 and HQ in MeCN solution at 298 K. The arrows indicate the decrease and increase of band intensities as the reaction proceeds.

2.2. Synthesis of [Pd(α-/β-NaiR)(Q)](ClO$_4$) (α-NaiR, **3**; β-NaiR, **4**)

A representative synthesis of [Pd(α-NaiMe)(Q)](ClO_4) (**3a**) is given below.

To a MeCN solution of the complex Pd(α-NaiMe)Cl_2 (0.025 g, 6.05×10^{-2} mmol), HQ (0.026 g, 18.15×10^{-2} mmol) was added and the orange colored solution was stirred for about 24 h. It was filtered and allowed to evaporate to dryness at room temperature. The mass was then dissolved in MeOH, and $NaClO_4$ (aq) (1 g) was added to it. The brown precipitate that formed was filtered and washed

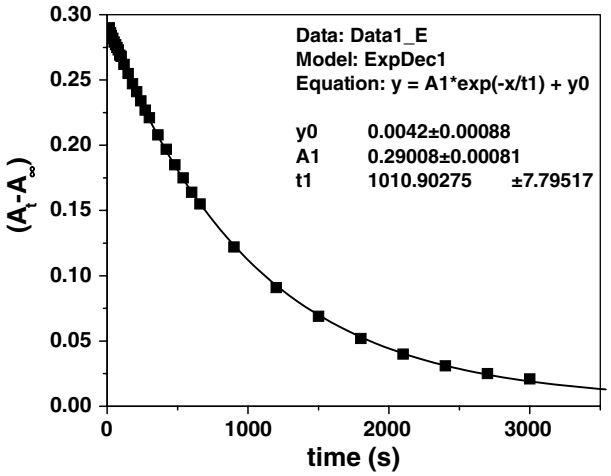


Fig. 2. Plot of $(A_t - A_\infty)$ vs. time (s) for the reaction: [Pd(α-NaiMe)Cl_2]$_0 = 1.09 \times 10^{-4}$ mol dm^{-3}, $[HQ]_0 = 3 \times 10^{-3}$ mol dm^{-3} and temperature = 298 K.

with water. The dried product was then chromatographed over silica gel and MeCN eluted an orange band. Yield: 0.023 g (64.7%).

All other complexes were prepared by the same procedure and the yields varied within 60–70%.

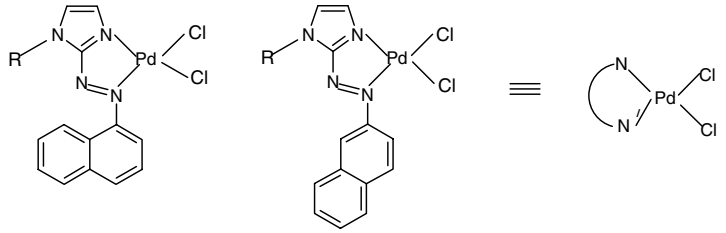
Microanalytical data of the complexes are as follows: For [Pd(α-NaiMe)(Q)][ClO_4) (**3a**): *Anal.* Found: C, 47.00; H, 3.02; N, 11.79%. Calc. for $C_{23}H_{18}O_5N_5PdCl$: C, 47.10; H, 3.07; N, 11.95. For [Pd(α-NaiEt)(Q)][ClO_4) (**3b**) *Anal.* Found: C, 48.08; H, 3.30; N,11.71%. Calc. for $C_{24}H_{20}O_5N_5PdCl$: C, 48.00; H, 3.33; N, 11.67. For [Pd(α-NaiBz)(Q)][ClO_4)(**3c**) *Anal.* Found: C, 52.72; H, 3.35; N, 11.11%. Calc. for $C_{29}H_{22}O_5N_5PdCl$: C, 52.58; H, 3.32; N, 11.04. For [Pd(β-NaiMe)(Q)][ClO_4) (**4a**) *Anal.* Found: C, 47.18; H, 3.12; N, 11.66%. Calc. for $C_{23}H_{18}O_5N_5PdCl$: C, 47.10; H, 3.07; N, 11.95. For [Pd(β-NaiEt)(Q)][ClO_4) (**4b**) *Anal.* Found: C, 47.88; H, 3.28; N, 11.78%. Calc. for $C_{24}H_{20}O_5N_5PdCl$: C, 48.00; H, 3.33; N, 11.67. For [Pd(β-NaiBz)(Q)][ClO_4) (**4c**) *Anal.* Found: C, 52.50; H, 3.27; N, 10.86%. Calc. for $C_{29}H_{22}O_5N_5PdCl$: C, 52.58; H, 3.32; N, 10.58.

3. Results and discussion

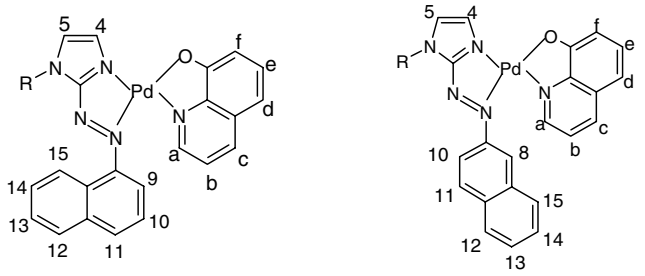
3.1. Kinetics and mechanism

Two classes of naphthylazoimidazole complexes of palladium(II) have been used in this work. They are Pd(α-NaiR)Cl_2 (**1**) (α-NaiR = 1-alkyl-2-(naphthyl-α-azo)-imidazole) and Pd(β-NaiR)Cl_2 (**2**) (β-NaiR = 1-alkyl-2-(naphthyl-β-azo)imidazole) [where R = Me (**a**)/Et (**b**)/Bz (**c**)]. The ligands belong to the unsymmetric bidentate *N*,*N*′-donor type and form dichloropalladium(II) complexes, here after we abbreviate the complexes as Pd(*N*,*N*′)Cl_2 (Scheme 1). The reaction kinetics between Pd(*N*,*N*′)Cl_2 and 8-quinolinol (HQ) was examined spectrophotometrically. The reaction is first order in Pd(II) complex as k_{obs}-values are almost constant when all variants are constant except the complex concentration. The k_{obs}-values (Table 1) and the linear plots for the k_{obs} versus $[HQ]_0$ (Figs. 3 and 4) indicate the reaction is first order in HQ. The slope of the plot is the second order rate constant (k_2) of the reaction. The presence of a defined intercept (k_0) indicates the existence of a minor solvent assisted path to the overall reaction products (MeCN is a coordinating solvent).

The rate increases with a rise in temperature, as expected from the Eyring equation. Activation parameters, standard enthalpy of activation ($\Delta^{\ddagger}H^{\circ}$) and standard entropy of activation ($\Delta^{\ddagger}S^{\circ}$) were calculated from Eyring plots (Figs. 5 and 6) and are recorded in Table 2. The $\Delta^{\ddagger}H^{\circ}$ value is actually the sum of the $\Delta^{\ddagger}H^{\circ}$ value for the reaction (for the pre-equilibrium step) and the $\Delta^{\ddagger}H^{\circ}$ value for the second Cl^- displacement. The same is true for the $\Delta^{\ddagger}S^{\circ}$ value also. The activation parameter values corroborate with the experimental k_2-values. The order for $\Delta^{\ddagger}H^{\circ}$ and $\Delta^{\ddagger}S^{\circ}$ are: Pd(NaiEt)Cl_2 > Pd(NaiMe)Cl_2 > Pd(NaiBz)Cl_2 and Pd-(α-NaiR) > Pd(β-NaiR). The iso-kinetic plot (Fig. 7) supports an identical mechanism for the reaction of Pd(*N*,*N*′)Cl_2 with HQ. Kinetic studies in the presence of



Pd(α-NaiR)Cl_2 (**1**) Pd(β-NaiR)Cl_2 (**2**) Pd(N,N′)Cl_2



R = Me (**a**), Et (**b**), CH_2Ph (**c**)

[Pd(α-NaiR)(Q)][ClO_4) (**3**) [Pd(β- NaiR)(Q)][ClO_4) (**4**)

Scheme 1.

Table 1
Pseudo-first-order rate constants (k_{obs}) for reactions of 8-quinolinol with Pd(R′aiR)Cl_2 in MeCN at 298 K

Pd(R′aiR)Cl_2	10^3 [HQ]$_0$ (mol dm^{-3})	10^3 k_{obs} (s^{-1})	10 k_2 (dm^3 mol^{-1} s^{-1})	10^3 k_0 (s^{-1})
Pd(α-NaiMe)Cl_2 (**1a**)	1.0	0.51	2.30	0.29
	3.0	0.99		
	5.0	1.45		
	7.0	1.90		
	10.0	2.59		
Pd(α-NaiEt)Cl_2 (**1b**)	1.0	0.48	1.94	0.28
	3.0	0.86		
	5.0	1.25		
	7.0	1.64		
	10.0	2.22		
Pd(α-NaiBz)Cl_2 (**1c**)	1.0	0.57	3.45	0.23
	3.0	1.27		
	5.0	1.97		
	7.0	2.67		
	10.0	3.70		
Pd(β-NaiMe)Cl_2 (**2a**)	1.0	0.62	4.27	0.19
	3.0	1.46		
	5.0	2.32		
	7.0	3.20		
	10.0	4.45		
Pd(β-NaiEt)Cl_2 (**2b**)	1.0	0.58	3.91	0.18
	3.0	1.36		
	5.0	2.12		
	7.0	2.92		
	10.0	4.10		
Pd(β-NaiBz)Cl_2 (**2c**)	1.0	0.67	5.22	0.14
	3.0	1.71		
	5.0	2.73		
	7.0	3.80		
	10.0	5.37		

[Pd(R′aiR)Cl_2]$_0$ = 1.00×10^{-4} mol dm^{-3}.

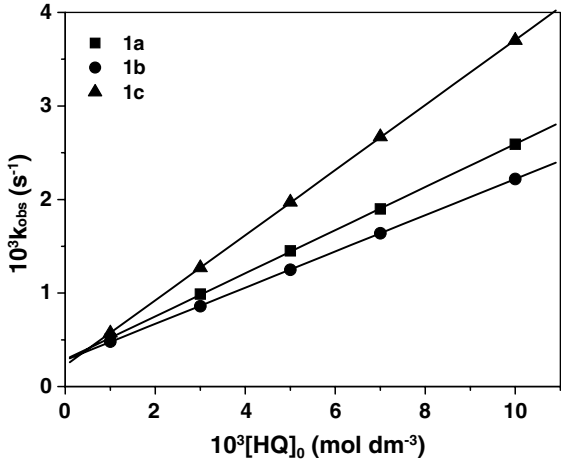


Fig. 3. Plots of k_{obs} vs. [HQ]$_0$ for the reactions: Pd(α-NaiR)Cl_2 + HQ in MeCN. [Pd(α-NaiR)Cl_2]$_0$ = 1.00×10^{-4} mol dm^{-3} at 298 K.

externally added Cl^-(LiCl) reveal that the rate as well as k_{obs} decreases inversely with [Cl^-]$_0$ (Table 3), which supports the mechanism given in Scheme 2. The dissociation

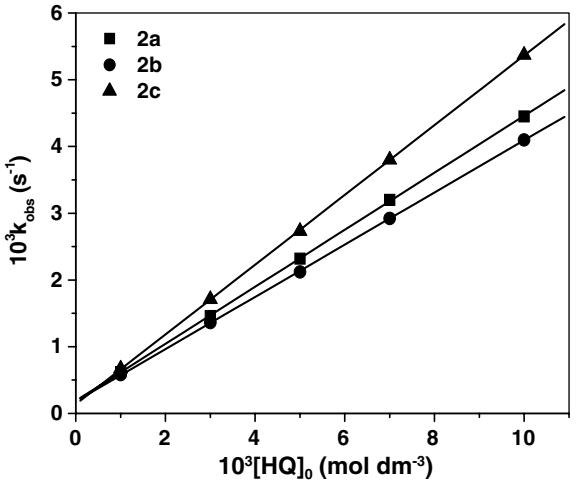


Fig. 4. Plots of k_{obs} vs. [HQ]$_0$ for the reactions: Pd(β-NaiR)Cl_2 + HQ in MeCN. [Pd(β-NaiR)Cl_2]$_0$ = 1.00×10^{-4} mol dm^{-3} at 298 K.

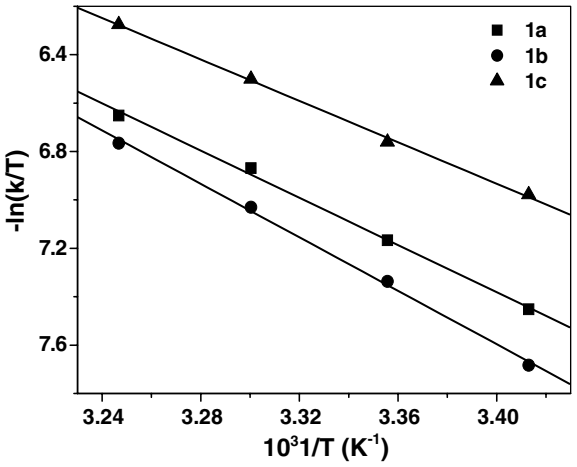


Fig. 5. Plots of ln(k/T) vs. ($1/T$) for the reactions: Pd(α-NaiR)Cl_2 + HQ in MeCN.

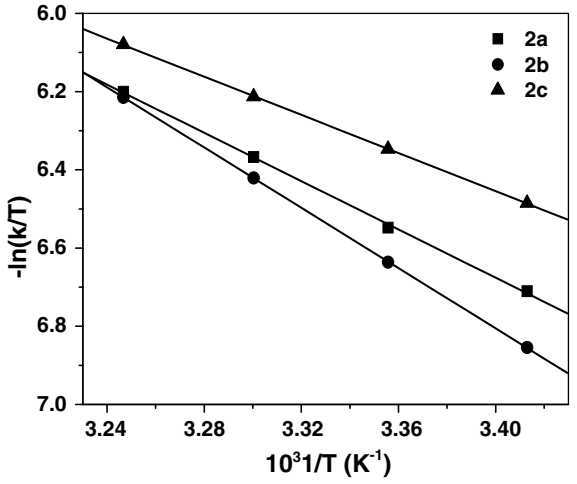
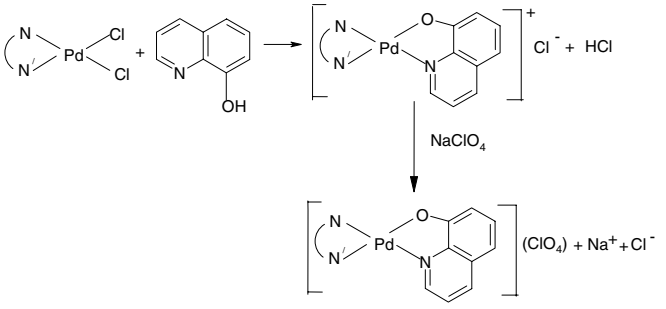


Fig. 6. Plots of ln(k/T) vs. ($1/T$) for the reactions: Pd(β-NaiR)Cl_2 + HQ in MeCN.

Table 2
Second order rate constants (k_2) at different temperatures and activation parameters of the reactions

Pd(R′aiR)Cl_2	Temperature (K)	$10 \times k$ ($dm^3\ mol^{-1}\ s^{-1}$)	$\Delta^{\ddagger}H^{\circ}$ (kJ mol^{-1})	$\Delta^{\ddagger}S^{\circ}$ (J K^{-1} mol^{-1})
Pd(α-NaiMe)Cl_2 (**1a**)	293	1.70	41(±5)	−121(±23)
	298	2.30		
	303	3.15		
	308	3.98		
Pd(α-NaiEt)Cl_2 (**1b**)	293	1.35	46(±5)	−105(±21)
	298	1.42		
	303	2.68		
	308	3.55		
Pd(α-NaiBz)Cl_2 (**1c**)	293	2.73	36(±3)	−134(±15)
	298	3.58		
	303	4.55		
	308	5.80		
Pd(β-NaiMe)Cl_2 (**2a**)	293	3.57	26(±2)	−166(±8)
	298	4.37		
	303	5.20		
	308	6.25		
Pd(β-NaiEt)Cl_2 (**2b**)	293	3.42	32(±3)	−145(±12)
	298	3.95		
	303	5.47		
	308	6.01		
Pd(β-NaiBz)Cl_2 (**2c**)	293	3.71	20(±2)	−182(±15)
	298	5.26		
	303	6.12		
	308	7.05		

of the second Pd–Cl bond is the rate controlling process and the dissociation of the first Pd–Cl bond is affected by externally added Cl^- ion. The product was isolated and characterized as [Pd(*N*,*N*′)(Q)]ClO_4. The nucleophilic substitution process involves direct displacement of 2 Cl^- ions by 8-quinolinol (Eq. (1)). In the acetonitrile medium, HQ will exist largely in the undissociated form [23].



(1)

The observed rate is

$$\text{Rate} = \{k_0 + k_2[\text{HQ}]_0\}[\text{Pd(R′aiR)Cl}_2] = k_{\text{obs}}[\text{Pd(R′aiR)Cl}_2]$$

(where $k_2 = \frac{kK1}{[\text{Cl}^-]_0}$ = constant at constant $[\text{Cl}^-]_0$ and $k_{\text{obs}} = k_0 + k_2[\text{HQ}]_0$). The k_0 and k_2 are the intercept and the slope of the plot of k_{obs} versus $[\text{HQ}]_0$ respectively. The nucleophile is a undissociated N,OH donor ligand. It is probable that the highly negative O donor will coordinate first with the positively charged metal center, with fast dissociation

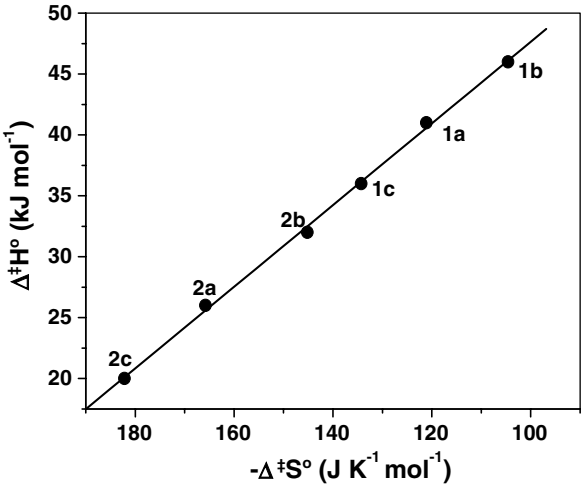
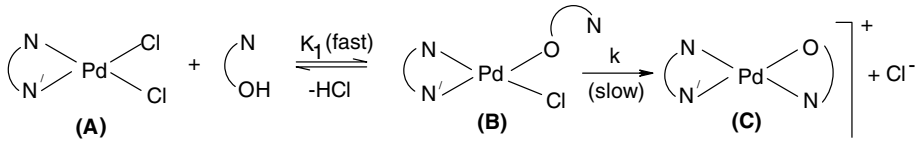


Fig. 7. Plot of $\Delta^{\ddagger}H^{\circ}$ vs. $\Delta^{\ddagger}S^{\circ}$ i.e. iso-kinetic plot for the reactions: Pd(R′aiR)Cl_2 + HQ in MeCN.

Table 3
Effect of externally added LiCl on the pseudo-first-order rate constants (k_{obs}) for reactions of 8-quinolinol with Pd(R′aiR)Cl_2 in MeCN at 298 K

Pd(R′aiR)Cl_2	10^3 $[\text{LiCl}]_0$ (mol dm^{-3})	$10^3 \times k_{\text{obs}}$ (s^{-1})
Pd(α-NaiMe)Cl_2 (**1a**)	0.2	1.38
	0.4	0.75
	0.6	0.53
	0.8	0.42
	1.0	0.34
Pd(α-NaiEt)Cl_2 (**1b**)	0.2	1.19
	0.4	0.67
	0.6	0.50
	0.8	0.41
	1.0	0.35
Pd(α-NaiBz)Cl_2 (**1c**)	0.2	1.89
	0.4	0.88
	0.6	0.60
	0.8	0.43
	1.0	0.33
Pd(β-NaiMe)Cl_2 (**2a**)	0.2	2.22
	0.4	1.09
	0.6	0.72
	0.8	0.52
	1.0	0.39
Pd(β-NaiEt)Cl_2 (**2b**)	0.2	2.03
	0.4	0.93
	0.6	0.62
	0.8	0.40
	1.0	0.27
Pd(β-NaiBz)Cl_2 (**2c**)	0.2	2.62
	0.4	1.17
	0.6	0.73
	0.8	0.44
	1.0	0.21

$[\text{Pd(R′aiR)Cl}_2]_0 = 1.00 \times 10^{-4}$ mol dm^{-3}, $[\text{HQ}]_0 = 5.00 \times 10^{-3}$ mol dm^{-3}.



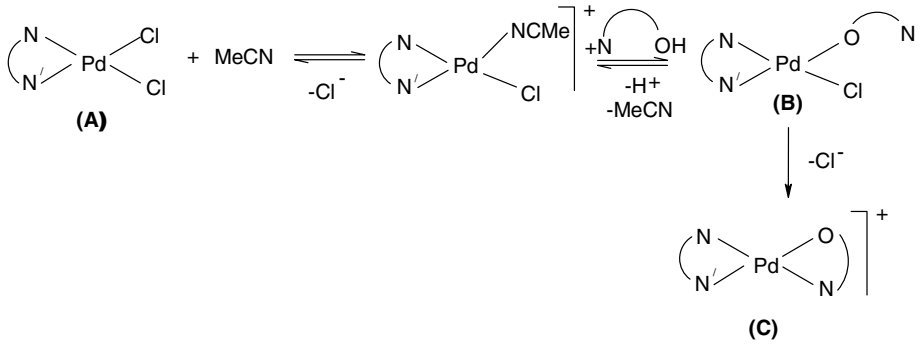
Scheme 2.

of the first Pd–Cl bond, and finally forms a stable four coordinated square planar intermediate complex (**B**). Then quinoline-N (which remains free in **B**) slowly coordinates with Pd(II) as a compulsion of chelate stability. Obviously the latter rate is slower than the former rate. Therefore the second Pd–Cl bond cleavage is the rate-determining step. This is also supported by the effect of externally added Cl^- ions (LiCl). A plausible mechanism is given in Scheme 2. There are two parallel pathways: one is the existence of a minor solvent assisted path where MeCN substitutes Cl^- initially, then MeCN is displaced by HQ and finally forms the reaction product (**C**) (Scheme 3). Although the steric crowding of the α-/β-naphthyl group in the N,N' chelating ligand is significant, its electron withdrawing property, due to conjugation, stabilizes the Pd(N,N') chelated species in preference to de-chelation.

The kinetic data in Table 1 reveal that the magnitude of k increases in the order Pd(α-NaiEt)Cl_2 < Pd(α-NaiMe)Cl_2 < Pd(α-NaiBz)Cl_2. This is because the electron withdrawing tendency of the Bz group is greater than Me, which in turn is slightly greater than Et.

3.2. Product characterization

To a MeCN solution of the complex Pd(N,N')Cl_2, HQ was added and the orange colored solution was stirred for about 24 h. It was filtered and allowed to evaporate almost to dryness at room temperature. The mass so produced was then dissolved in MeOH and $NaClO_4$ (aq) was added. A brown precipitate formed which was filtered and then washed with water and cold MeCN. The dried product was chromatographed over silica gel and MeCN eluted an orange-red band. Finally the dried product was characterized by micro-analytical data (experimental section), UV–Vis, IR. (Table 4) and ^{1}H NMR (Table 5) spectral data. The molar conductance data in MeCN solution (Λ_M = 75–90 S cm^2 mol^{-1}) show a 1:1 electrolytic nature of the complexes. The IR spectra of the complexes display a sharp stretch at 1360–1375 cm^{-1} which corresponds to ν(N=N) and is red shifted by 5–10 cm^{-1} from that of Pd(NaiR)Cl_2 [24]. This may be attributed to the charge delocalization from coordinated Q^- to the chelated NaiR motif. The binding is indirectly established by the disap-



Scheme 3.

Table 4
Spectral data (FT-IR and UV–Vis) of [Pd(α/β-NaiR)(Q)](ClO$_4$)

Compounds	IR spectral data[a] (cm^{-1})			UV–Vis spectral data[b] λ_{max}, nm (ε, dm^3 mol^{-1} cm^{-1})
	ν(N=N)	ν(C=N)	ν(Pd–O)	
[Pd(α-NaiMe)(Q)](ClO$_4$) (**3a**)	1560	1651	465	393 (18730), 482 (9498)
[Pd(β-NaiMe)(Q)](ClO$_4$) (**4a**)	1558	1651	472	394(18724), 481 (9495)
[Pd(α-NaiEt)(Q)](ClO$_4$) (**3b**)	1560	1651	468	395 (18720), 485 (9500)
[Pd(β-NaiEt)(Q)](ClO$_4$) (**4b**)	1558	1651	470	394 (18718), 486 (9499)
[Pd(α-NaiBz)(Q)](ClO$_4$) (**3c**)	1559	1652	466	395 (18726), 483 (9489)
[Pd(β-NaiBz)(Q)](ClO$_4$) (**4c**)	1559	1652	469	391 (18728), 483 (9488)

[a] KBr disk.
[b] In MeCN solution.

Table 5
^{1}H NMR spectral data of [Pd(α/β-NaiR)(Q)](ClO$_4$) in CD$_3$CN

Compound	δ, ppm (J, Hz)													
	4-H[i]	5-H[i]	8-H[i]	9-H[j]	10-H[k]	11- 13-H[k]	14-H[k]	15-H[k]	a-H[j]	b-H[k]	c-H[k]	d-H[k]	e-H[k]	f-H[j]
[Pd(α-NaiMe)(Q)](ClO$_4$) (**3a**)	7.02	6.88		7.67 (8.0)	7.52	7.40	7.35	7.46	9.65 (8.0)	9.08	8.54	8.22	8.00	8.28 (8.0)
[Pd(α-NaiEt)(Q)](ClO$_4$) (**3b**)	7.00	6.85		7.65 (8.0)	7.50	7.40	7.33	7.45	9.60 (8.0)	9.00	8.58	8.20	8.00	8.30 (8.0)
[Pd(α-NaiBz)(Q)](ClO$_4$) (**3c**)	7.10	6.95		7.72 (8.0)	7.55	7.42	7.38	7.50	9.68 (8.0)	9.10	8.60	8.25	8.05	8.34 (8.0)
[Pd(β-NaiMe)(Q)](ClO$_4$) (**4a**)	7.07	6.90	7.76		7.96	7.60	7.50	7.40	9.45 (8.0)	8.80	8.53	8.10	8.00	8.27 (8.0)
[Pd(β-NaiEt)(Q)](ClO$_4$) (**4b**)	7.04	6.85	7.80		8.00	7.58	7.50	7.45	9.40 (8.0)	8.80	8.50	8.20	8.00	8.30 (8.0)
[Pd(β-NaiBz)(Q)](ClO$_4$) (**4c**)	7.10	6.90	7.86		8.05	7.64	7.50	7.45	9.50 (8.0)	8.85	8.55	8.22	8.05	8.35 (8.0)

[i] Broad singlet.
[j] Doublet.
[k] Multiplet.

pearance of two *ν*(Pd–Cl) bands corresponding to the *cis*-$PdCl_2$ configuration [24–26] and the appearance of new bands at 1560–1570 and 480–500 cm^{-1} due to *ν*(C–O) and *ν*(Pd–O), respectively. All the complexes exhibit a structureless band at 1090–1100 cm^{-1} corresponding to *ν*(ClO_4), suggesting the lack of any significant interaction in the solid state [27].

The solution electronic spectra of the complexes were recorded in the range 900–200 nm in MeCN. The absorptions below 400 nm are due to intramolecular charge transfer and are not considered further. Two absorptions at 475–485 and 515–525 nm (Fig. 8), absent in the free ligands, may represent charge transfer transitions localized on the metallated fragment [28].

The ^{1}H NMR spectra of the complexes were recorded in CD_3CN and the data are collected in Table 5. The proton numbering pattern is shown in Scheme 1. The data reveal that the signals in the spectra of the complexes are shifted downfield relative to the free ligand values [18]. This supports the coordination of the ligand to Pd(II). An important feature of the spectra is the shifting of the imidazole protons 4-H and 5-H to lower *δ*-values, in general, relative to the naphthyl protons (6-H–13-H). The imidazole protons suffer downfield shifting by 0.1-0.2 ppm compared to the free ligand positions. This supports the strong preference of imidazole-N binding to Pd(II). The naphthyl protons appear as multiplets, except a broad singlet for 6-H and doublet for 8-H in [Pd(β-NaiR)(Q)](ClO$_4$) and a

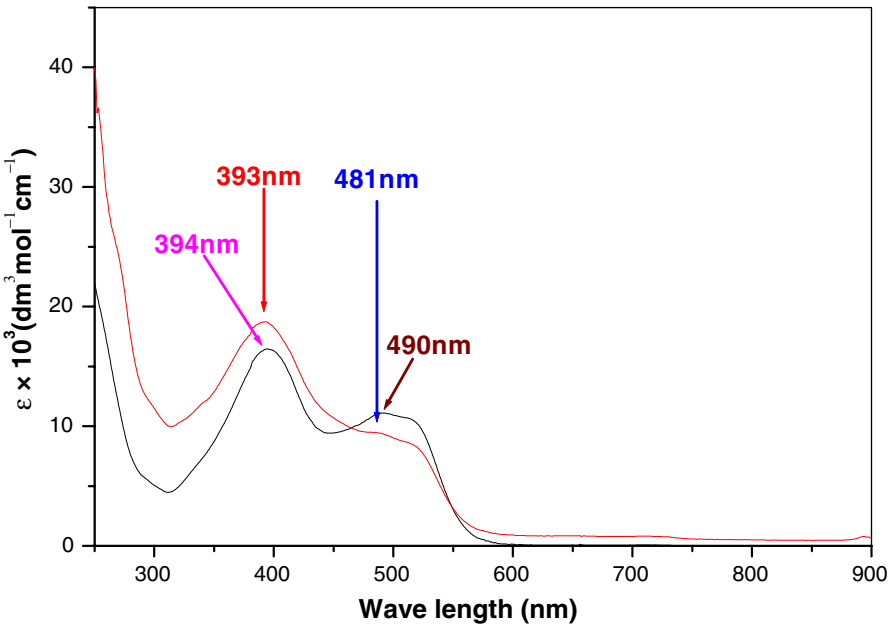


Fig. 8. UV–Vis spectra of [Pd(β-NaiMe)Cl$_2$] (black line) and [Pd(β-NaiMe)(Q)](ClO$_4$) (red line) in MeCN solution. (For interpretation of the references in color in this figure legend, the reader is referred to the web version of this article.)

doublet for 15-H in all the complexes. The 1-alkyl group appears as a singlet for 1-Me in [Pd(α/β-NaiMe)(Q)](ClO$_4$), a quartet for –N–CH$_2$– and a triplet for the –CH$_3$ group in [Pd(α/β-NaiEt)(Q)](ClO$_4$) and a singlet for –CH$_2$– and benzyl protons in the [Pd(α/β-NaiCH$_2$Ph)(Q)](ClO$_4$) complexes.

4. Conclusion

The kinetics of the reactions between Pd(*N*,*N*′)Cl$_2$ and 8-quinolinol (HQ) were examined spectrophotometrically at 500 nm under pseudo-first-order conditions in MeCN. The reactions are first order with respect to the complex and HQ. The rate of the reaction is largely influenced by the π-acidity of the chelating ligand; substitution in the naphthylazoimidazole backbone influences the rate of the substitution process significantly. Activation parameters $\Delta^{\ddagger}H^{\circ}$ and $\Delta^{\ddagger}S^{\circ}$ of the reactions were measured, which corroborates the kinetic rate data. The products isolated from the reaction between Pd(NaiR)Cl$_2$ and HQ in MeCN have been characterized by spectral data and support the composition [Pd(NaiR)(Q)](ClO$_4$).

Acknowledgements

Financial help from Jadavpur University is gratefully acknowledged. We thank Dr. C. Sinha, Professor of Chemistry, Jadavpur University for his helpful discussions.

References

[1] H. Chen, J.A. Parkinson, S. Parsons, R.A. Coxall, R.O. Gould, P.J. Sadler, J. Am. Chem. Soc. 124 (2002) 3064.
[2] A.H. Velders, H. Kooijman, A.L. Spek, J.G. Haasnoot, D. de Vos, J. Reedijk, Inorg. Chem. 39 (2000) 2966.
[3] P. Banerjee, Coord. Chem. Rev. 19 (1999) 190.
[4] B. Lippert, Coord. Chem. Rev. 18 (1999) 263.
[5] M. Kato, J. Takahashi, Y. Sugimoto, C. Kosuge, S. Kishi, S. Yano, J. Chem. Soc., Dalton Trans. (2001) 747.
[6] J. Li, L.M. Zheng, I. King, T.W. Doyle, S.H. Chan, Curr. Med. Chem. 8 (2001) 121.
[7] S.J. Lippard, in: I. Bertini, H.B. Gray, S.J. Lippard, J.S. Valentine (Eds.), Bioinorganic Chemistry, University Science Books, Mill Valley, CA, 1994, p. 505.
[8] P.D. Beer, Acc. Chem. Res. 31 (1998) 71.
[9] Y.S. Yoo, Y.S. Sohn, Y.K. Do, J. Inorg. Biochem. 73 (1999) 187.
[10] F.A. Cotton, G. Wilkinson, Advanced Inorganic Chemistry, 5th ed., John Wiley, New York, 1988.
[11] D. Das, M.K. Nayak, C. Sinha, Transition Met. Chem. 22 (1997) 172.
[12] S. Dey, M. Ray, P. Banerjee, Inorg. React. Mech. 2 (2000) 267.
[13] S. Saha, P.K. Ghosh, A. Mahapatra, Transition Met. Chem. 30 (6) (2005) 706.
[14] S. Saha, T. Majumdar, A. Mahapatra, Inorg. React. Mech. 6 (2006) 19.
[15] S. Saha, T. Majumdar, A. Mahapatra, Transition Met. Chem. 31 (2006) 1017.
[16] S. Saha, T. Majumdar, A. Mahapatra, Indian J. Chem. A 45 (2006) 877.
[17] S. Saha, P.K. Sarkar, A. Mahapatra, Transition Met. Chem. 31 (3) (2006) 389.
[18] S. Saha, A. Mahapatra, Inorg. React. Mech. 6 (2006) 71.
[19] J. Dinda, P.K. Santra, C. Sinha, L.R. Falvello, J. Organomet. Chem. 629 (2001) 28.
[20] S. Pal, D. Das, P. Chattopadhyay, C. Sinha, K. Panneerselvam, T.H. Lu, Polyhedron 19 (2000) 1263.
[21] R. Roy, T.K. Misra, C. Sinha, A. Mahapatra, A. Sanyal, Transition Met. Chem. 22 (1997) 453.
[22] R. Roy, D. Das, M. Banerjee, A. Mahapatra, Transition Met. Chem. 26 (2001) 205.
[23] T. Suganuma, A. Tanada, H. Tomizawa, M. Tanaka, E. Miki, Inorg. Chim. Acta 320 (2001) 22.
[24] J. Dinda, P.K. Santra, C. Sinha, L.R. Falvello, J. Organomet. Chem. 629 (2001) 28.
[25] C.K. Pal, S. Chattopadhyay, C. Sinha, D. Bandyopadhyay, A. Chakravorty, Polyhedron 13 (1994) 999.
[26] D. Das, M.K. Nayak, C. Sinha, Transition Met. Chem. 22 (1997) 172.
[27] S. Goswami, W. Kharmawphlang, A.K. Deb, S.M. Peng, Polyhedron 15 (1996) 3635.
[28] Y. Wakatsuki, M. Yamazaki, P.A. Grutasch, M. Santhanam, A.C. Ku, J. Am. Chem. Soc. 107 (1985) 8153.

has an axial ligand such as chlorine, or by introducing bulky peripheral substituents. Bulky peripheral groups prevent an effective π–π interaction between the phthalocyanine subunits [19]. In light of this, (chloro)gallium(III) phthalocyanine derivatives with chlorine atoms at axial positions and bulky peripheral substituents should show no aggregation in solution. The syntheses, photophysical and photochemical studies on some new (chloro)gallium phthalocyanine derivatives are hereby presented.

2. Experimental

2.1. Materials

2.1.1. Syntheses

Acetic anhydride (Ac_2O), acetone, ammonia solution (NH_4OH), methanol (MeOH), 1-chloronaphthalene, hexane and deuterated chloroform ($CDCl_3$) were obtained commercially and dried before use; formamide ($HCONH_2$), potassium carbonate (K_2CO_3), phthalonitrile, thionyl chloride ($SOCl_2$), phenol and 4-*tert*-butylphenol were purchased from Aldrich and used as received. 4,5-Dichloro-1,2-dicyanobenzene [20] and unsubstituted (chloro)gallium(III)phthalocyanine [21] were synthesized and purified according to the literature procedures.

2.1.2. Photophysics and photochemistry

Zinc(II) phthalocyanine (ZnPc), chlorophyll *a* and 1,3-diphenylisobenzofuran (DPBF) were obtained from Aldrich. Chloroform ($CHCl_3$) dimethylsulfoxide (DMSO), *N*,*N*′-dimethylformamide (DMF, freshly distilled), tetrahydrofuran (THF) and toluene were purchased from SAARCHEM, and dried in alumina before use.

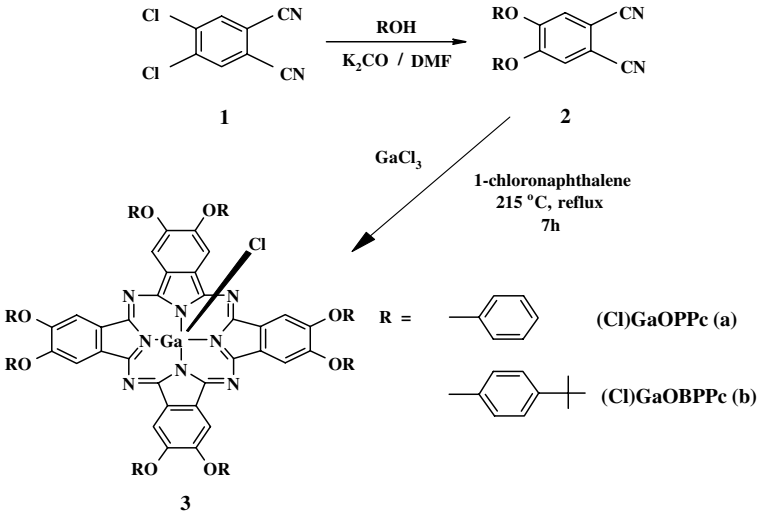
2.2. Equipment

Column chromatography was performed on silica gel 60 (0.04–0.063 mm) and preparative thin layer chromatography was performed on silica gel 60 P F_{254}. Ground state electronic absorption spectra were performed on a Varian Cary 500 UV–Vis–NIR spectrophotometer; infra-red spectra (KBr pellets) on Perkin–Elmer Spectrum 2000 FT-IR spectrometer and ^1H NMR on a Bruker EMX 400 NMR spectrometer. Fluorescence excitation and emission spectra were recorded on a Varian Cary Eclipse Fluorescence spectrophotometer. Photo-irradiations were done using a General electric Quartz line lamp (300 W). A 600 nm glass cut off filter (Schott) and a water filter were used to filter off ultraviolet and infrared radiations, respectively. An interference filter (Intor, 670 nm with a band width of 40 nm) was additionally placed in the light path before the sample. Light intensities were measured with a POWER MAX 5100 (Molelectron detector incorporated) power meter. Triplet absorption and decay kinetics were recorded on a laser flash photolysis system. The excitation pulses were produced by a Nd:YAG laser (Quanta-Ray, 1.5 J/90 ns)-pumped tunable dye laser (Lambda Physic FL 3002, Pyridine 1 dye in methanol). The analyzing beam source was from a Thermo Oriel xenon arc lamp, and a photomultiplier tube (PMT) was used as the detector. Signals were recorded with a Tektronix TDS 360 two-channel digital real-time oscilloscope. Triplet lifetimes were determined by exponential fitting of the kinetic curves using OriginPro 7.5 software.

2.3. Syntheses

2.3.1. Synthesis of 4,5-bis(phenoxy)-1,2-dicyanobenzene (*2a*) (Scheme 1)

4,5-Bis(phenoxy)-1,2-dicyanobenzene (**2a**) was synthesized from 4,5-dichloro-1,2-dicyanobenzene (**1**) and phenol in dried DMSO as reported before [20]. The amounts of the reagents employed were: 4,5-dichloro-1,2-dicyanobenzene (4.01 g, 20 mmol), phenol (3.76 g, 40 mmol), K_2CO_3 (13.8 g, 100 mmol) and dried DMSO (40 ml). Yield: 3.24 g (52%); IR (KBr): ν_{max}/cm^{-1}; 3040–3051 (Ar-H),



Scheme 1. Synthetic pathway to octa-substituted phenoxy and *tert*-butylphenoxy phthalocyaninato gallium chloride.

2237 (C≡N), 1209 (C–O–C); ^{1}H NMR: (DMSO-d_6) δ, ppm; 7.7 (2H, s, Ar-H), 7.4 (4H, t, Ar-H), 7.2 (2H, t, Ar-H), 7.1 (4H, d, Ar-H).

2.3.2. Synthesis of 4,5-bis(4-tert-butylphenoxy)-1,2-dicyanobenzene (**2b**) (Scheme 1)

4,5-Bis(4-*tert*-butylphenoxy)-1,2-dicyanobenzene (**2b**) was synthesized from 4,5-dichloro-1,2-dicyanobenzene (**1**) and 4-*tert*-butylphenol as reported before [20]. The amounts of the reagents employed were: 4,5-dichloro-1,2-dicyanobenzene (**1**) (4.01 g, 20 mmol), 4-*tert*-butylphenol (6.00 g, 40 mmol), K_2CO_3 (13.8 g, 100 mmol) and dried DMSO (40 ml). Yield: 4.07 g (48%); IR (KBr): ν_{max}/cm^{-1}; 3041–3051 (Ar-H), 2213 (C≡N), 1219 (C–O–C); ^{1}H NMR: (DMSO-d_6) δ, ppm; 9.1 (2H, s, Ar-H), 7.1 (4H, d, Ar-H), 6.6 (4H, d, Ar-H), 1.2 (s, 18H, CH_3).

2.3.3. Synthesis of octaphenoxyphthalacyaninato gallium chloride (**3a**, **(Cl)GaOPPc**) (Scheme 1) [22]

A mixture of 4,5-bis(phenoxy)-1,2-dicyanobenzene (**2a**) (3.12 g, 10 mmol), anhydrous $GaCl_3$ (0.88 g, 5 mmol) and 1-chloronaphthalene (4 ml) were placed in a preheated oil bath (215 °C). The reaction mixture was stirred at this temperature for 7 h under a dry nitrogen atmosphere. After cooling the green product was placed in a silica gel column, washed with hexane to remove the brownish layer of 1-chloronaphthalene. THF was then used to elute the green product from the column. THF was then removed by evaporation. Preparative thin layer chromatography (TLC) silica gel plates were used for further purification with chloroform as the eluting solvent. The impurities (brown layers) were then cut from the plates leaving the pure green product. The silica gel/green product was placed in a beaker of chloroform to dissolve the product. The mixture was then filtered, and the solvent was removed by evaporation. Yield: 1.59 g (47%); UV–Vis (DMSO): λ_{max} (log ε); 687 (5.10), 616 (4.56), 370 (4.90); IR (KBr): ν_{max}/cm^{-1}; 3034, 3052 (Ar-H), 1588 (C=C), 1460, 1452, 1407, 1339, 1275, 1201(C–O–C), 1162, 1089, 1089, 1037, 1003, 860; ^{1}H NMR: ($CDCl_3$) δ ppm; 8.6 (d, 8H, Pc-H), 7.4 (t, 16H, phenyl-H), 7.3 (t, 16H, phenyl-H), 7.2 (m, 8H, phenyl-H). Calc. for $C_{80}H_{48}N_8O_8GaCl$: C, 69.10; H, 3.47; N, 8.06. Found: C, 68.14; H, 3.59; N, 7.34. MALDI-TOF-MS *m*/*z*: calc. 1354.34; found, 1352.00 $[M-2]^+$.

2.3.4. Synthesis of octakis(4-tert-butylphenoxy)phthalocyaninato gallium chloride (**3b**, **(Cl)PGaOTBPPc**) (Scheme 1) [22]

Synthesis and purification of compound **3b** was as explained for compound **3a**. However, instead of using **2a**, compound **2b** was used. The amounts of the reagents employed were: **2b** (3.16 g, 7,44 mmol), anhydrous $GaCl_3$ (0.65 g, 3.72 mmol) and 1-chloronaphthalene (4 ml). Yield: 1.11 g (35%); UV–Vis (DMSO): λ_{max} (log ε); 690 (5.31), 620 (3.82), 347 (4.15); IR (KBr): ν_{max}/cm^{-1}; 3034–3052 (Ar-H), 2952–2866 (C–H), 1589 (C=C), 1506, 1489, 1454, 1411, 1338, 1274, 1205 (C–O–C), 1098, 1037, 891, 861, 741; ^{1}H NMR: ($CDCl_3$) δ ppm; 8.6 (broad s, 8H, Pc-H), 7.0–7.4 (m, 32H, phenyl-H), 1.3–1.4 (m, 72H, CH_3). *Anal.* Calc. for $C_{112}H_{112}N_8O_8GaCl$: C, 74.60; H, 6.26; N, 6.21. Found: C, 73.03; H, 5.71; N, 6.03%. MALDI-TOF-MS *m*/*z*: calc. 1803.20; found $[M-Cl]^+$ 1765.53.

2.4. Photophysical and photochemical studies

2.4.1. Fluorescence quantum yields and lifetimes

Fluorescence quantum yields (Φ_F) were determined by the comparative method [23,24] (Eq. (1)):

$$\Phi_F = \Phi_F(\mathrm{Std})\frac{F \cdot A_{\mathrm{Std}} \cdot \eta^2}{F_{\mathrm{Std}} \cdot A \cdot \eta^2_{\mathrm{Std}}} \quad (1)$$

where F and F_{Std} are the areas under the fluorescence curves of the (Cl)GaPc derivatives and the standard, respectively. A and A_{Std} are the respective absorbances of the sample and standard at the excitation wavelengths ($A = 0.05$ in all solvents used), and η and η_{Std} are the refractive indices of the solvents used for the sample and standard, respectively. Chlorophyll *a* in ether ($\Phi_F = 0.32$) [25] was employed as the standard. Both the sample and standard were excited at the same wavelength (630 nm).

Natural radiative lifetimes (τ_0) were determined using the program PhotochemCAD [26]. This determination is based on the method proposed by Strickler and Berg [27], which uses parameters derived from spectral (absorption and emission) data of the fluorescing material. From τ_0 values, fluorescence lifetimes (τ_F) were determined using the following equation:

$$\Phi_F = \frac{\tau_F}{\tau_0}. \quad (2)$$

2.4.2. Triplet quantum yields and lifetimes

The solutions for triplet quantum yields and lifetimes were introduced into a 1 cm pathlength UV–Vis spectrophotometric cell, deaerated using nitrogen and irradiated at the Q band maxima. Triplet state quantum yields (Φ_T) of the (Cl)GaPc derivatives were determined by the triplet absorption method. A comparative method [28] using zinc phthalocyanine as a standard was employed for the calculations, Eq. (3):

$$\Phi_T = \Phi_T^{\mathrm{Std}} \cdot \frac{\Delta A_T \cdot \varepsilon_T^{\mathrm{Std}}}{\Delta A_T^{\mathrm{Std}} \cdot \varepsilon_T} \quad (3)$$

where ΔA_T and ΔA_T^{Std} are the changes in the triplet state absorbances of the (Cl)GaPc derivatives and the standard, respectively. ε_T and ε_T^{Std} are the triplet state molar exctinction coefficients for the (Cl)GaPc derivative and the standard, respectively. Φ_T^{Std} is the triplet quantum yield for the standard, ZnPc ($\Phi_T = 0.65$ in DMSO [29], 0.58 in DMF [30] and 0.65 in toluene [31]). ε_T and ε_T^{Std} were determined from the molar extinction coefficients of their respective ground singlet state (ε_S and ε_S^{Std}), the changes in absorbances of the ground singlet states (ΔA_S

and ΔA_S^{Std}) and changes in the triplet state absorptions (ΔA_T and ΔA_T^{Std}) according to the following equations:

$$\varepsilon_T = \varepsilon_S \frac{\Delta A_T}{\Delta A_S} \quad (4a)$$

$$\varepsilon_T^{Std} = \varepsilon_S^{Std} \frac{\Delta A_T^{Std}}{\Delta A_S^{Std}} \quad (4b)$$

Quantum yields of internal conversion (Φ_{IC}) were obtained from Eq. (5), which assumes that only three processes (fluorescence, intersystem crossing and internal conversion) jointly deactivate the excited singlet state of a (Cl)GaPc molecule

$$\Phi_{IC} = 1 - (\Phi_F + \Phi_T). \quad (5)$$

2.4.3. Singlet oxygen quantum yields

Quantum yields of singlet oxygen were determined in air (no oxygen bubbled) using the relative method with ZnPc as a reference and DPBF as a chemical quencher for singlet oxygen, using the following equation:

$$\Phi_\Delta = \Phi_\Delta^{Std} \cdot \frac{R_{DPBF} I_{abs}^{Std}}{R_{DPBF}^{Std} I_{abs}} \quad (6)$$

where Φ_Δ^{Std} is the singlet oxygen quantum yield for the standard, ZnPc ($\Phi_\Delta = 0.67$ in DMSO [32], 0.56 in DMF [33], 0.58 in toluene [34] and 0.53 in THF [35]). R_{DPBF} and R_{DPBF}^{Std} are the DPBF photobleaching rates in the presence of the (Cl)GaPc derivative under investigation and the standard, respectively. I_{abs} and I_{abs}^{Std} are the rates of light absorption by the (Cl)GaPc derivatives and the standard, respectively. To avoid chain reactions induced by DPBF in the presence of singlet oxygen [33], the concentration of DPBF was lowered to $\sim 3 \times 10^{-5}$ mol dm^{-3}. Solutions of sensitizer (absorbance = 0.2 at the irradiation wavelength) containing DPBF were prepared in the dark and irradiated in the Q band region using the setup described above. DPBF degradation at 417 nm was monitored. The light intensity for singlet oxygen studies was 6×10^{15} photons s^{-1} cm^{-2}. The error in the determination of Φ_Δ was ~10% (determined from several Φ_Δ values).

2.4.4. Photodegradation quantum yields

For determination of photodegradation quantum yields, the usual equation (7) was employed:

$$\Phi_{Pd} = \frac{(C_0 - C_t) V N_A}{I_{abs} S t} \quad (7)$$

where C_0 and C_t (mol dm^{-3}) are the (Cl)GaPc derivative's concentrations before and after irradiation, respectively; V is the reaction volume; S, the irradiated cell area (2.0 cm^2); t, the irradiation time; N_A, the Avogadro's number and I_{abs}, the overlap integral of the radiation source intensity and the absorption of the Pc (the action spectrum) in the region of the interference filter transmittance. The light intensity for photodegradation studies was 7×10^{16} photons s^{-1} cm^{-2}.

3. Results and discussion

3.1. Syntheses and characterization

Scheme 1 gives the synthetic pathways used to synthesize the compounds used in this work. 1,2-Dicyanobenzene was used [20] to prepare 4,5-disubstituted phthalonitrile derivatives through base-catalysed nucleophilic aromatic displacement. The same route was applied to prepare phenoxy and 4,5-bis(*tert*-butylphenoxy) substituted 1,2-dicyanobenzene (**2a** and **2b**) from phenol and 4-*tert*-butylphenol, respectively (Scheme 1). The reactions were carried out in DMSO at room temperature and gave yields of 52% for **2a** and 48% for **2b**.

The preparation of the phthalocyanine derivatives from aromatic 1,2-dicyanobenzenes occur under different reaction conditions. The syntheses of MPc complexes (**(Cl)GaOPPc** and **(Cl)GaOTBPPc**) were achieved by treatment of 1,2-dicyanobenzenes **2a** and **2b** with gallium (III) chloride in 1-chloronaphthalene (Scheme 1). Because gallium is a large atom, high energy is required to insert the metal ion into the phthalocyanine ring, thus a high-boiling solvent such as 1-chloronaphthalene is used to achieve this purpose. Complex **3a** is octaphenoxy substituted and complex **3b** is octa-*tert*-butylphenoxy substituted. Column and preparative thin layer chromatography with silica gel were employed to obtain the pure products from the reaction mixtures.

Generally, phthalocyanine complexes are insoluble in most organic solvents, however, introduction of phenoxy and 4-*tert*-butyl phenoxy substituents on the ring increases the solubility. Unsubstituted phthalocyanines are known to have poor solubility in most organic solvents. They dissolve mostly in coordinating solvents such as pyridine. **(Cl)GaPc** behaves likewise; it dissolves in polar and coordinating solvents such as DMSO, DMF and THF. Both new substituted complexes (**(Cl)GaOPPc** and **(Cl)GaOTBPPc**) exhibit excellent solubility in organic solvents such as dichloromethane, chloroform, THF, toluene, acetone and DMSO. The new compounds were characterized by UV–Vis, IR and NMR spectroscopies, MALDI-TOF mass spectra and elemental analysis. The analyses are consistent with the predicted structures as shown in Section 2. After conversion into gallium phthalocyanines, the characteristic C≡N stretch at 2237 and 2213 cm^{-1} of 1,2-dicyanobenzenes **2a** and **2b** disappeared, indicative of metallophthalocyanine formation. The characteristic vibrations corresponding to ether groups (C–O–C) were observed at 1209 and 1219 cm^{-1} for the dinitrile compounds, 1201 and 1205 cm^{-1} for the phthalocyanine complexes. Aromatic CH stretchings were observed at 3034–3052 cm^{-1}.

^{1}H NMR investigations of 1,2-dicyanobenzene compounds **2a** and **2b** provide the characteristic chemical shifts for the structures as expected. The ^{1}H NMR spectrum for compound **2a** shows a singlet peak at δ 7.7 ppm, a triplet at δ 7.4 ppm, a triplet at δ 7.2 ppm and a doublet at δ 7.1 ppm for the aromatic protons, integrating to 2, 4, 2, 4 protons

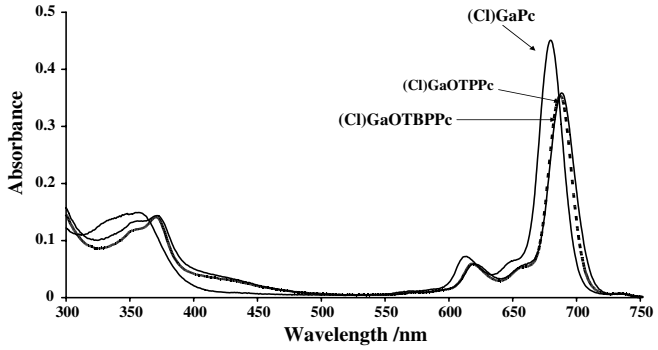


Fig. 1. Ground state electronic absorption spectra of **(Cl)GaPc**, **(Cl)GaOPPc** and **(Cl)GaOTBPPc** in DMSO. Concentration: $\sim 1.5 \times 10^{-6}$ mol dm^{-3}.

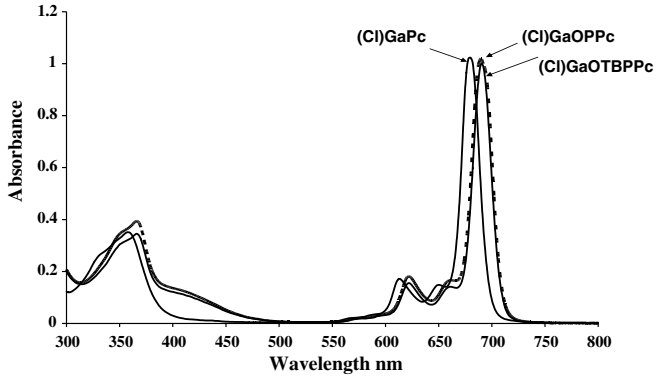


Fig. 2. Ground state electronic absorption spectra of **(Cl)GaPc**,**(Cl)GaOPPc** and **(Cl)GaOTBPPc** in THF. Concentration: $\sim 1.8 \times 10^{-6}$ mol dm^{-3}.

each, respectively, making a total of 12 protons as expected. Compound **2b** shows a singlet peak at δ 9.1 ppm, a doublet at δ 7.1 ppm and a doublet at δ 6.6 ppm for the aromatic protons, integrating to 2, 4, 4 protons each, respectively, making a total of 10 protons as expected, and methyl protons appear as a singlet peak at ca. δ 1.2 ppm, integrating to 18 protons.

The ^{1}H NMR spectrum of the unsubstituted gallium(III) phthalocyanine (**(Cl)GaPc**) shows ring protons as two singlet peaks at δ 9.65 and 8.47 ppm, integrating to 8 protons each. The substituted gallium(III) phthalocyanine complexes were found to be pure by ^{1}H NMR, with all the substituents and ring protons observed in their respective regions. The phenoxy substituted complex **3a** showed the resonances belonging to the ring protons as a doublet at δ 8.6 ppm, a triplet at δ 7.4 ppm, a triplet at δ 7.3 ppm and a multiplet at δ 7.2 ppm, integrating to 8, 16, 16, 8 protons each, making a total of 48 protons as expected. The *tert*-butylphenoxy substituted complex (**(Cl)GaOTBPPc**) showed the resonances belonging to the ring protons as a singlet at δ 8.6 ppm and a multiplet between δ 7.0 and 7.4 ppm for aromatic protons, integrating to 8 and 32 protons each, respectively, making a total of 40 protons as expected. The methyl protons appear as multiplets between δ 1.3 and 1.4 ppm, integrating to 72 protons.

3.2. Ground state electronic absorption and fluorescence spectra

The ground state electronic absorption spectra of **(Cl)GaPc**, **(Cl)GaOPPc** and **(Cl)GaOTBPPc** show sharp single Q bands (Figs. 1 and 2, Table 1), which depict the monomeric nature of these complexes in all solvents studied. The non-aggregated nature of these complexes is not unconnected with their possession of chlorine atoms at axial positions to the central metal atoms. Atoms or groups on MPc axial positions are known to prevent aggregation

Table 1
Spectral, photophysical and photochemical parameters of GaPc derivatives in various solvents

Solvent	MPc	λ_{max}		Φ_F	Φ_T[a]	Φ_{IC}[a]	S_Δ[a,b]	Φ_Δ	Φ_{Pd} (10^5)	τ_T (μs)
		Q_{abs} (nm)	Q_{ems} (nm)							
DMSO	**(Cl)GaPc**	680	692	0.21	0.69	0.10	0.59	0.41	1.84	200
	(Cl)GaOPPc	687	699	0.19	0.66	0.15	0.80	0.53	1.23	370
	(Cl)GaOTBPPc	690	701	0.22	0.67	0.11	0.84	0.56	1.77	290
DMF	**(Cl)GaPc**	678	687	0.12	0.78	0.10	0.64	0.50	1.96	10
	(Cl)GaOPPc	689	702	0.19	0.79	0.02	0.84	0.66	0.42	20
	(Cl)GaOTBPPc	688	702	0.15	0.74	0.11	1.00	0.74	1.52	76
Toluene	**(Cl)GaOPPc**	697	709	0.14	0.65	0.21	1.04	0.68	2.91	79
	(Cl)GaOTBPPc	697	706	0.17	0.75	0.08	0.87	0.65	2.84	10
THF	**(Cl)GaPc**	677	691	0.19				0.41	1.49	2.1
	(Cl)GaOPPc	688	700	0.14				0.51	3.44	3.4
	(Cl)GaOTBPPc	689	700	0.18				0.56	3.93	4.4
$CHCl_3$[c]	**(Cl)GaOPPc**	700	708	0.12				0.41	5.89	2.9
	(Cl)GaOTBPPc	701	709	0.12				0.42	4.66	3.4

[a] Values not obtained in THF and $CHCl_3$ due to lack of reference standards.
[b] $S_\Delta = \Phi_\Delta/\Phi_T$.
[c] **(Cl)GaPc** is not soluble in $CHCl_3$.

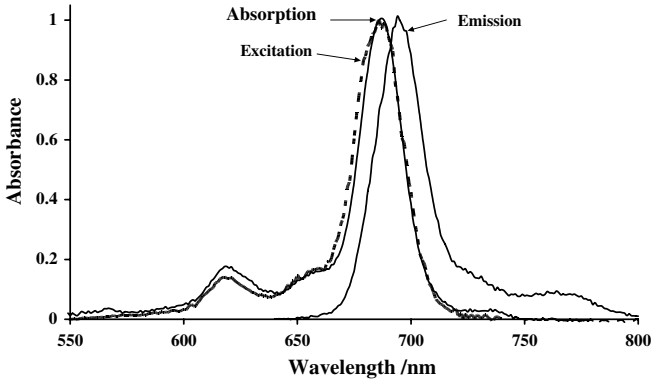


Fig. 3. Absorption, fluorescence excitation and fluorescence emission spectra of **(Cl)GaOPPc** in DMSO.

by restraining the overlap of two MPc units in solution [36]. The positions of the Q band in **(Cl)GaOPPc** and **(Cl)GaOTBPPc** are red-shifted relative to that in **(Cl)GaPc**. The presence of an electron donating phenoxy substituent on the phthalocyanine ring leads to a red-shift of the Q band. For a particular MPc in different solvents, it can be observed that the longest Q absorption wavelengths are obtained in chloroform while the shortest are obtained in THF. This observation could partly be explained by considering the refractive indices of the solvents. It is known that red-shifting of absorption spectra is a function of the solvent's refractive index [34]. In all the solvents studied, **(Cl)GaPc**, **(Cl)GaOPPc** and **(Cl)GaOTBPPc** showed monomeric behaviour up to $\sim 1 \times 10^{-5}$ mol dm^{-3}. For the substituted derivatives, **(Cl)GaOPPc** and **(Cl)GaOTBPPc**, new absorption bands are observed at ~430 nm in both coordinating (Fig. 1) and non-coordinating (Fig. 2) solvents. Since these are observed only for the substituted derivatives, they must be due to charge transfer transitions involving the substituents.

The fluorescence behaviours of the three MPc complexes are similar. Fig. 3 shows the fluorescence excitation and emission spectra for **(Cl)GaOPPc** in DMSO. The excitation spectra are similar to absorption spectra and both are mirror images of the fluorescence spectra.

3.3. Photophysical studies

3.3.1. Fluorescence quantum yields and lifetimes

The fluorescence quantum yield (Φ_F) is the fraction of molecules in the excited singlet state that are deactivated radiatively. Factors like temperature, molecular structure and solvent parameters (polarity, viscosity, refractive index and the presence of heavy atoms in the solvent molecule) are widely known to influence the values of Φ_F. Table 1 shows that the Φ_F values do not vary much among the three MPcs studied; for example in DMSO, the Φ_F values for **(Cl)GaPc**, **(Cl)GaOPPc** and **(Cl)GaOTBPPc** are 0.21, 0.19 and 0.22, respectively. These values are similar (within experimental error limits) hence we conclude that the substituent effect on Φ_F values is not significant among **(Cl)GaPc**, **(Cl)GaOPPc** and **(Cl)GaOTBPPc**. Considering solvent effects on Φ_F values, chloroform gave the lowest values. The low values in chloroform could be attributed to the presence of heavy atoms (chlorine) in chloroform, which could induce spin–orbit coupling, and consequently reduce the number of fluorescing molecules. However, the values of Φ_F listed in Table 1 for **(Cl)GaPc** are lower than the value reported for this complex in chloronaphthalene ($\Phi_F = 0.31$) [37], thus showing it is not only the heavy atom effect that affects these values. The differences in Φ_F values for the remaining complexes were insignificant with the exception of high values obtained for **(Cl)GaPc** and **(Cl)GaOTBPPc** in DMSO compared to DMF, toluene and THF. The relatively high Φ_F values in DMSO for some complexes could to some extent be attributed to solvation by the solvent. Solvation by DMSO makes the fluorescing MPc more rigid and therefore more fluorescent. The coordinating strength of a solvent is a function of its donor ability. DMSO has a higher donor ability (1.24) than DMF (0.72) [38], which is in turn more donating than THF and

Table 2
Rate constants for the excited singlet state deactivation processes

Solvent	MPc	τ_F (ns)	k_F (10^{-7} s^{-1})[a]	k_{ISC} (10^{-8} s^{-1})[a]	k_{IC} (10^{-7} s^{-1})[a]
DMSO	**(Cl)GaPc**	3.8	5.6	1.8	2.7
	(Cl)GaOPPc	2.3	8.3	2.9	6.5
	(Cl)GaOTBPPc	2.1	10.	3.2	6.1
DMF	**(Cl)GaPc**	1.9	6.2	4.0	5.2
	(Cl)GaOPPc	1.3	14	5.9	1.5
	(Cl)GaOTBPPc	4.0	3.6	1.9	2.8
Toluene	**(Cl)GaOPPc**	1.5	9.4	4.4	14
	(Cl)GaOTBPPc	3.8	4.5	2.0	2.1
THF	**(Cl)GaPc**	7.8	2.4		
	(Cl)GaOPPc	1.5	9.1		
	(Cl)GaOTBPPc	1.3	14		
$CHCl_3$	**(Cl)GaOPPc**	1.0	13		
	(Cl)GaOTBPPc	2.0	6.0		

[a] $k_F = \frac{\Phi_F}{\tau_F}$; $k_{ISC} = \frac{\Phi_T}{\tau_F}$ and $k_{IC} = \frac{\Phi_{IC}}{\tau_F}$.

toluene. This partly explains why the MPcs are more fluorescent in DMSO than in the other solvents.

Fluorescence lifetimes τ_F are listed in Table 2. The values do not conform to any particular trend; hence it is difficult to draw any conclusion from them. Comparing the τ_F values with those reported in the literature [39] for other substituted GaPc complexes, shows close similarities. The τ_F values are useful for the calculation of the rate constants for intrinsic processes (fluorescence, intersystem crossing and internal conversion), which jointly deactivate the excited singlet state.

3.3.2. Triplet quantum yields and lifetimes

Fig. 4 shows the triplet decay curve for **(Cl)GaOPPc** in DMSO. The triplet quantum yield (Φ_T) is a measure of the fraction of absorbing molecules that undergo intersystem crossing to the metastable triplet excited state. Since intersystem crossing and fluorescence are two competing deactivating processes for the excited singlet state, their values for a particular species are expected to be complementary. As discussed above, the Φ_F values do not vary much with the introduction of phenoxy and *tert*-butylphenoxy substituents onto the **(Cl)GaPc** ring. This trend is also manifested in the Φ_T values (Table 1), which do not change much with the presence of the substituents. Solvent effects on Φ_T values are opposite to what was obtained in the case of Φ_F; Φ_T values are lower in DMSO than in DMF and toluene. The effect of the phenoxy and *tert*-butylphenoxy substituents on triplet quantum yields is minimal, with Φ_T values ranging between 0.66 and 0.69 in DMSO, and between 0.74 and 0.79 in DMF. The difference in Φ_T values is larger in toluene (0.65 for **(Cl)GaOPPc** and 0.75 for **(Cl)GaOTBPPc**). These values are much higher than the values reported [37] for octabutoxy substituted GaPc in benzene, with $\Phi_T = 0.35$, again showing that the values are highly dependent on the solvent. Sulfonated GaPc derivatives containing different number of sulfonates also gave a low Φ_T value of 0.36 [40] in methanol.

The triplet lifetimes of the complexes are conspicuously higher in DMSO than in all other solvents used in this work. The longer lifetimes in DMSO are attributed to the higher viscosity of this solvent than the other solvents. Molecular movements that lead to the deactivation of the excited state are impeded in viscous solvents, resulting in longer excited state lifetimes. The presence of ring substituents also lengthened the triplet lifetimes in this work (Table 1). The triplet lifetimes are very low in the low viscocity solvents $CHCl_3$ and THF. The triplet lifetime was also found [37] to be low ($\tau_T = 67$ μs) for octabutoxy substituted GaPc in benzene, which is comparable to the values obtained in this work in DMF and toluene. However, τ_T values ranging from 2.1 to 667 μs in toluene were reported for a series of substituted GaPc complexes [39]. The values (2.1 and 71 μs) on the low side were [39] attributed to strong intramolecular interactions existing in the excited state for dimeric complexes. The τ_T values for sulfonated GaPc derivatives containing different number of sulfonates ranged between 300 and 450 μs [40]. Thus some of the values reported here in DMSO are within this range.

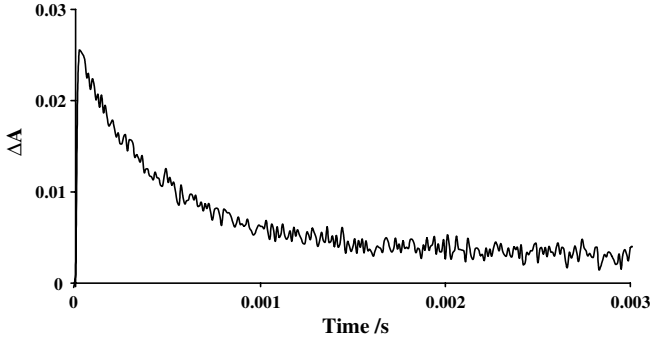


Fig. 4. Triplet decay curve for **(Cl)GaOPPc** in DMSO.

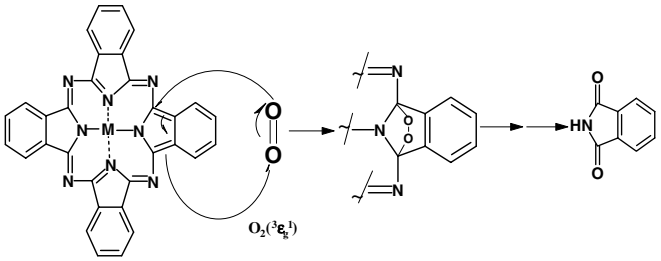
Quantum yields of internal conversion (Φ_{IC}) were calculated according to Eq. (5). Internal conversion is the radiationless transition between energy states of the same spin state (compare with fluorescence, a radiative process). The values of Φ_{IC} indicate the extent to which the excited molecules can de-excite by increasing the thermal energy of their surroundings. However, as can be seen in Table 1, the values of Φ_{IC} do not conform to any particular pattern.

Rate constants for the intrinsic processes (processes that deactivate the excited singlet state) are given in Table 2. The values of these rate constants are a reflection of the efficiency of the respective processes, and should conform to the same trends as the corresponding quantum yields. Calculated k_F, k_{ISC} and k_{IC} values for **(Cl)GaPc**, **(Cl)GaOPPc** and **(Cl)GaOTBPPc** in all solvents were found to be within the excepted range for MPc complexes. k_F values in DMSO and THF increased in the presence of substituents, while k_{ISC} increased in all solvents (DMSO, DMF, toluene) suggesting that substituents encourage intersystem crossing.

3.4. Photochemical studies

3.4.1. Singlet oxygen quantum yields

Singlet oxygen is formed via interaction (energy transfer) between the triplet state of a photosensitizer and ground state molecular (triplet) oxygen. As a result, the efficiency of singlet oxygen generation (quantified as singlet oxygen quantum yield, Φ_Δ) should depend on (i) the triplet state quantum yield, (ii) triplet state lifetime, (iii) efficiency of energy transfer, which depends on the energy of the triplet state, amongst other factors. On the basis of increased triplet lifetimes, the introduction of ring substituents should increase Φ_Δ values, and this is the case in Table 1. Solvent effects on Φ_Δ values are subtle, as seen in Table 1. The values are somewhat smaller in DMSO than in DMF and toluene, which is the same trend observed for Φ_T values. S_Δ is a measure of the efficiency of excitation energy transfer from the triplet photosensitizer molecule to ground state (triplet) molecular oxygen, $O_2(^3\Sigma_g^-)$. Sulfonated GaPc complexes showed much lower Φ_Δ values



Scheme 2. [4+2] cycloaddition reaction of MPc with singlet oxygen.

($\Phi_\Delta \sim 0.4$) in methanol [40], these values were thus comparable to the values shown in Table 1 for chloroform solutions. In Table 1, S_Δ values reveal that energy transfer to $O_2(^3\Sigma_g^-)$ is more efficient (with values closer to unity) with the substituted (Cl)GaPc derivatives than with unsubstituted **(Cl)GaPc**. It is possible that the substituents lower the energy of the triplet states to a level where energy transfer to $O_2(^3\Sigma_g^-)$ is easily achieved.

3.4.2. Photodegradation quantum yields

Photodegradation is brought about by the oxidative attack on the MPc excited triplet state by singlet oxygen. The ability of singlet oxygen to react with macrocyclic metal complexes is well documented [41,42]. Singlet oxygen reacts with tetra-azaporphyrin derivatives in a Diels–Alder [4+2]-cycloaddition, with the MPc ring acting as a diene and singlet oxygen as the dienophile. For MPcs, phthalimide was found to be the photo-oxidation product [42] (Scheme 2). The excited singlet state is deemed not to be a target for singlet oxygen because of its short lifetime ($\sim 10^{-9}$ s), which considerably reduces the state's probability of participating in photochemical reactions; hence the excited triplet state is being considered to be the main target for singlet oxygen. The interaction of the excited triplet state with singlet oxygen can be represented by the following equation:

$$^3\mathrm{MPc}^{\cdot} + O_2(^1\Delta_g) \xrightarrow{k_{Pd}} \text{phthalimide} \quad (8)$$

Therefore, the rate of photodegradation, according to the law of mass action is:

$$R = k_{Pd}[^3\mathrm{MPc}^*][O_2(^1\Delta_g)] \quad (9)$$

where R is the rate of photodegradation; k_{Pd}, the photodegradation rate constant (a bimolecular rate constant); $[^3\mathrm{MPc}^*]$, the concentration of the MPc excited triplet state; and $[O_2(^1\Delta_g)]$, the concentration of singlet oxygen. Therefore from Eq. (8), it could be inferred that the rate of photodegradation is directly proportional to the triplet quantum yield as well as singlet oxygen quantum yield. However, in this study, there is no clear correlation between Φ_{Pd} values and those of Φ_T or Φ_Δ, for the complexes. Considering solvent effects on photodegradation, Φ_{Pd} values for **(Cl)GaOPPc** and **(Cl)GaOTBPPc** are lower in DMSO and DMF (coordinating and highly solvating) than in non-coordinating solvents like toluene and chloroform (Table 1); which implies that these complexes are more photostable in coordinating solvents than in non-coordinating solvents. This observation could be explained in terms of singlet oxygen interaction with the MPc central metal to form a complex (for non-coordinating solvents) [43]. Solvent coordination to the metal centre partly shields the MPc molecule against interaction with singlet oxygen, leading to a decrease in the rate of photodegradation.

4. Conclusion

This work has demonstrated that gallium(III) phthalocyanine derivatives are well-suited for applications that require metastable excited states. The photophysical and photochemical parameters of the complexes reveal that the complexes would find use as photosensitizers in PDT and other applications. We have reported the photochemical and photophysical parameters of **(Cl)GaPc**, **(Cl)GaOPPc** and **(Cl)GaOTBPPc** in different solvents. It was concluded that fluorescence quantum yields vary in different environments. It was also found that substituents do not have a major effect on the results. The triplet and singlet oxygen quantum yields for the new complexes are higher than reported in the literature for other GaPc complexes, making these complexes excellent candidates for use as photosensitizers in, for example, PDT. The Φ_T values range from 0.66 to 0.79 in DMSO and DMF and the Φ_Δ values range from 0.41 to 0.74 in the same solvents.

Acknowledgements

This work has been supported by the National Research Foundation (NRF GUN = 2053657) of South Africa as well as Rhodes University.

References

[1] R. Rella, A. Serra, P. Siciliano, A. Talli, A. Zocco, Langmuir 13 (1997) 6562.
[2] C.J. Liu, C.H. Peng, Y.H. Ju, J.C. Hsieh, Sensors Actuators B 52 (1998) 264.
[3] T.A. Temofonte, K.F. Schoch, J. Appl. Phys. 65 (1989) 1350.
[4] Y. Wang, K. Deng, L. Gui, Y. Tang, J. Zhou, L. Cai, J. Qiu, D. Ren, J. Colloid Interface Sci. 213 (1999) 270.
[5] I.A. Levitsky, W.B. Euler, N. Tokranova, B. Xu, J. Castracene, Appl. Phys. Lett. 85 (2004) 6245.
[6] W. Hu, M. Matsumura, J. Phys. D 37 (2004) 1434.
[7] Z. Rong-Yi, Q. Xue-Qiong, Y. Chen, Q. Shi-Xiong, Chin. Phys. Lett. 23 (2006) 622.
[8] A. Gonzalez-Cabello, C.G. Claessens, G. Martin-Fuch, I. Ledoux-Rack, P. Vazquez, J. Zyss, F. Agullo-Lopez, T. Torres, Synth. Met. 137 (2003) 1487.
[9] L.R. Milgrom, in: Colours of Life, Oxford University Press, Oxford, 1997.
[10] A. Ogunsipe, T. Nyokong, J. Porphyr. Phthalocya. 9 (2005) 121.
[11] A. Ogunsipe, T. Nyokong, J. Photochem. Photobiol. A 173 (2005) 211.
[12] A. Ogunsipe, T. Nyokong, Photochem. Photobiol. Sci. 4 (2005) 510.
[13] S. Dhami, D. Phillips, J. Photochem. Photobiol. A 100 (1996) 77.
[14] M.T. Choi, P.P. Li, D.K. Ng, Tetrahedron 56 (2000) 3881.

[15] A. Ferencz, D. Neher, M. Schulze, G. Wegner, L. Viaene, F.C. Achryver, Chem. Phys. Lett. 23 (1995) 245.
[16] Y. Yang, J.R. Ward, R. Seiders, Inorg. Chem. 24 (1985) 1765.
[17] X. Zhang, H.J. Xu, J. Chem. Soc., Faraday Trans. 89 (1993) 3347.
[18] J.E. Van Lier, J.D. Spikes, in: G.S. Bock, S. Harnett (Eds.), Photosensitizinig Compounds: Their Chemistry Biology and Clinical Use, Wiley, Chichester, 1989, pp. 17–32.
[19] A. Sastre, A. Gouloumis, P. Va'zquez, T. Torres, V. Doan, B.J. Schwartz, F. Wudl, L. Echegoyen, J. Rivera, Org. Lett. 1 (1999) 1807.
[20] D. Wo̎hrle, M. Eskes, K. Shigehara, A. Yamada, Synthesis (1993) 194.
[21] J.P. Linsky, T.R. Paul, R.S. Nohr, M.E. Kenney, Inorg. Chem. 19 (1980) 3131.
[22] S. Vagin, M. Hanack, Eur. J. Org. Chem. (2004) 600.
[23] S. Fery-Forgues, D. Lavabre, J. Chem. Educ. 76 (1999) 1260.
[24] J. Fu, X.Y. Li, D.K.P. Ng, C. Wu, Langmuir 18 (2002) 3843.
[25] A. Montalban, H. Meunier, R. Ostler, A. Barrett, B. Hoffman, G. Rumbles, J. Phys. Chem. A 103 (1999) 4352.
[26] H. Du, R.-C.A. Fuh, J. Li, L.A. Corkan, J.S. Lindsey, Photochem. Photobiol. 68 (1998) 141.
[27] S.J. Strickler, R.A. Berg, J. Chem. Phys. 37 (1962) 814.
[28] P. Kubát, J. Mosinger, J. Photochem. Photobiol. A 96 (1996) 93.
[29] T.H. Tran-Thi, C. Desforge, C. Thiec, J. Phys. Chem. 93 (1989) 1226.
[30] J. Kossanyi, D. Chahraoui, Int. J. Photoenergy 2 (2000) 9.
[31] S.M. Bishop, A. Beeby, A.W. Parker, M.S.C. Foley, D. Phillips, J. Photochem. Photobiol. A 90 (1995) 39.
[32] N. Kuznetsova, N. Gretsova, E. Kalmykova, E. Makarova, S. Dashkevich, V. Negrimovskii, O. Kaliya, E. Luk'yanets, Russ. J. Gen. Chem. 70 (2000) 133.
[33] W. Spiller, H. Kliesch, D. Wöhrle, S. Hackbarth, B. Roder, G. Schnurpfeil, J. Porphyr. Phthalocya. 2 (1998) 145.
[34] A. Ogunsipe, D. Maree, T. Nyokong, J. Mol. Struct. 650 (2003) 131.
[35] L. Kaestner, M. Cesson, K. Kassab, T. Christensen, P.D. Edminson, M.J. Cook, I. Chambrier, G. Jori, Photochem. Photobiol. Sci. 2 (2003) 660.
[36] M. Barthel, D. Dini, S. Vagin, M. Hanack, Eur. J. Org. Chem. 22 (2002) 3756.
[37] K. Ishii, N. Kobayashi, in: K.M. Kadish, K.M. Smith, R. Guilard (Eds.), The Porphyrin Handbook, vol. 16, Elsevier, Amsterdam, 2003 (Chapter 1).
[38] M. Munakata, S. Kitagawa, M. Miyazima, Inorg. Chem. 24 (1985) 1638.
[39] Y. Chen, Y. Araki, M. Hanack, M. Fujitsuka, O. Ito, Eur. J. Inorg. Chem. (2005) 4655.
[40] T. Nyokong, Coord. Chem. Rev. (2006), doi:10.1016/j.ccr.2006.11.011.
[41] G. Schnurpfeil, A.K. Sobbi, W. Spiller, H. Kliesch, D. Wöhrle, J. Porphyr. Phthalocya. 1 (1997) 159.
[42] A.K. Sobbi, D. Wöhrle, D. Schlettwein, J. Chem. Soc., Perkin Trans. 2 (1993) 481.
[43] N.A. Kuznetsova, V.V. Okunchikov, V.M. Derkacheva, O.L. Kaliya, E.A. Lukyanets, J. Porphyr. Phthalocya. 9 (2005) 9 393.

The continuation of our interest in various dithiophosphate ligands led us to work on the reactions of aryl dithiophosphate nickel complexes with nitrogen donor moieties to examine how the aromatic moiety influences coordination with the metal. Thus, we report the syntheses of nickel (II) adducts of the general type $Ni[S_2P(OR)_2]_2 \cdot nL$ (where R = *o*-, *m*-, *p*-C_6H_4Me; $n = 2$, L = C_5H_5N; $n = 1$, L = $C_{10}H_8N_2$, $C_{14}H_{12}N_2$) and their characterization by various spectroscopic techniques. We also report the molecular structures of $Ni[S_2P(OC_6H_4Me\text{-}p)_2]_2 \cdot C_{10}H_8N_2$ and $Ni[S_2P(OC_6H_4Me\text{-}o)_2]_2 \cdot C_{14}H_{12}N_2 \cdot C_6H_6$.

2. Results and discussion

Reactions of bis (*O*,*O*′-ditolyldithiophosphato)nickel(II) complexes were carried out with pyridine or 2,2′-bipyridyl or 2,9-dimethyl-1,10-phenanthroline in benzene

$$Ni[S_2P(OR)_2]_2 + nL \rightarrow Ni[S_2P(OR)_2]_2 \cdot nL \quad (1)$$

(R = *o*-, *m*-, *p*-C_6H_4Me; $n = 2$, L = C_5H_5N; $n = 1$, L = $C_{10}H_8N_2$, $C_{14}H_{12}N_2$)

The purple colour changed on addition of nitrogen base to give a consistent green colour on addition of a slight excess of base. In each case a green powder (yield, 67–78%), soluble in organic solvents, was obtained.

2.1. IR spectra

The IR spectra of the nitrogen base adducts of bis(*O*,*O*′-ditolyl dithiophosphato)nickel(II) were measured over the range of 4000–200 cm^{-1}. The assignments of the relevant IR bands (Table 1) were made by comparisons with the spectra of the corresponding nickel(II) *O*,*O*′-ditolyldithiophosphate complexes [28]. The two strong intensity bands present in the 1168–1123 and 841–790 cm^{-1} regions are assigned to ν[(P)–O–C] and ν[P–O–(C)] stretching vibrations, respectively. Bands due to $\nu(P–S)_{asym}$ and $\nu(P–S)_{sym}$ observed at 693–656 and 568–516 cm^{-1} in adducts 1–9, indicate a slight change in the bonding patterns of the dithiophosphate moieties upon adduct formation. However, in case of dmphen adducts, 7–9 additional bands corresponding to $\nu(P–S)_{asym}$ and $\nu(P–S)_{sym}$ are also observed suggesting the *S*-mondentate and *S*,*S*-chelating nature of the ligands. The presence of medium to weak bands in the regions 380–362 and 344–324 cm^{-1} have been assigned to ν(Ni–S) vibrations consistent with the metal sulfur bonding. One or two peaks due to ν(C–N) vibrations appears in the region 1604–1579 cm^{-1} suggests the formation of adducts.

2.2. UV–visible spectra

The spectra of the adducts of bis(*O*,*O*′-ditolyl dithiophosphato)nickel(II) recorded in CH_2Cl_2 (Table 2) show three absorption bands corresponding to $^3A_2g \rightarrow {}^3T_2g$, $^3A_2g \rightarrow {}^3T_1g(F)$, $^3A_2g \rightarrow {}^3T_1g(P)$ transitions expected for octahedral nickel species [16,18]. The first band corresponding to $^3A_2g \rightarrow {}^3T_2g$ transition is obtained in the range of 1102–1130 nm. The second absorption $^3A_2g \rightarrow {}^3T_1g(F)$ is observed in the range 727–735, 654–658 for pyridine and bipyridyl adducts, respectively but split in two absorptions in the range 676–686 and 866–886 nm for 2,9-dimethyl-1,10-phenanthroline adducts. This split is probably due to spin-orbit coupling of $^1E(D)$ with ^3T_1g. The third band, $^3A_2g \rightarrow {}^3T_1g$ is seen in the range of 447–451, 416–422 and 423–441 nm for pyridine, bipyridyl and 2,9-dimethyl-1,10-phenanthroline adducts, respectively.

2.3. Magnetic moments measurements

The magnetic measurements (Table 2) for nitrogen base adducts of bis(*O*,*O*′-ditolyldithiophosphato)nickel(II) obtained in the range of 3.20–3.26 BM at 298 K indicate the presence of two unpaired electrons. Similar values are found in the literature for a number of other bis(*O*,*O*′-ditolyldithiophosphato)nickel(II) adducts [16].

2.4. Molecular structures of $Ni[S_2P(OC_6H_4Me\text{-}p)_2]_2 \cdot C_{10}H_8N_2$ (6) and $Ni[S_2P(OC_6H_4Me\text{-}o)_2]_2 \cdot C_{14}H_{12}N_2 \cdot C_6H_6$ (7)

$Ni[S_2P(OC_6H_4Me\text{-}p)_2]_2 \cdot C_{10}H_8N_2$ (**6**) and $Ni[S_2P(OC_6H_4Me\text{-}o)_2]_2 \cdot C_{14}H_{12}N_2 \cdot C_6H_6$ (**7**), crystallize as triclinic and monoclinic in space groups $P\bar{1}$ and $P2_1/c$, respectively. The ORTEP diagrams in Figs. 1 and 2 illustrate that in **6** the nickel atom lies at the centre of a

Table 1
IR spectral data (cm^{-1}) for the nitrogen base adducts of bis(*O*,*O*′-ditolyldithiophosphate)nickel(II) complexes[a]

No.	Compound	ν(C–N)	ν[(P)–O–C]	ν[P–O–(C)]	$\nu(P–S)_{asym.}$	$\nu(P–S)_{sym}$	ν(Ni–S)
1	$Ni[S_2P(OC_6H_4Me\text{-}o)_2]_2(C_5H_5N)_2$	1585 m	1142 s	820 s	682 s	555 m	370 w, 324 w
2	$Ni[S_2P(OC_6H_4Me\text{-}m)_2]_2(C_5H_5N)_2$	1584 s	1123 s	824 s	687 s	568 m	365 w, 325 w
3	$Ni[S_2P(OC_6H_4Me\text{-}p)_2]_2(C_5H_5N)_2$	1598 m	1162 m	822 s	693 m	535 s	370 w, 333 w
4	$Ni[S_2P(OC_6H_4Me\text{-}o)_2]_2 \cdot N_2C_{10}H_8$	1581, 1603 m	1130 s	831 s	681 s	565 m	367 w, 344w
5	$Ni[S_2P(OC_6H_4Me\text{-}m)_2]_2 \cdot N_2C_{10}H_8$	1590 m	1130 s	831 s	685 s	564 m	362 w, 327w
6	$Ni[S_2P(OC_6H_4Me\text{-}p)_2]_2 \cdot N_2C_{10}H_8$	1595, 1604 m	1153 m	812 m	680 s	556 m	377 w, 328 w
7	$Ni[S_2P(OC_6H_4Me\text{-}o)_2]_2 \cdot N_2C_{14}H_{12}$	1579 m	1167 s	790 m 674 m,	657 m	549 sh	380 m, 330 m
8	$Ni[S_2P(OC_6H_4Me\text{-}m)_2]_2 \cdot N_2C_{14}H_{12}$	1590 m	1139 m	841 m 680 m,	665 m	560 sh	377 w, 328 w
9	$Ni[S_2P(OC_6H_4Me\text{-}p)_2]_2 \cdot N_2C_{14}H_{12}$	1580, 1592 m	1168 s	790 s	672 s, 656,m	550 m, 516 m	378 w, 325 w

[a] Key: s = strong, m = medium, w = weak, sh = shoulder.

Table 2
Electronic spectra and magnetic moments for the nitrogen base adducts of bis(*O*,*O*′-ditolyldithiophosphate)nickel(II) complexes

S. no.	Compound	Λ_{max} (nm)	μ_{eff} (BM)
1	$Ni[S_2P(OC_6H_4Me\text{-}o)_2]_2(C_5H_5N)_2$	1120, 735, 451	3.20
2	$Ni[S_2P(OC_6H_4Me\text{-}m)_2]_2(C_5H_5N)_2$	1110, 727, 447	3.19
3	$Ni[S_2P(OC_6H_4Me\text{-}p)_2]_2(C_5H_5N)_2$	1130, 734, 449	3.22
4	$Ni[S_2P(OC_6H_4CH_3\text{-}o)_2]_2 \cdot N_2C_{10}H_8$	1130, 658, 418	3.23
5	$Ni[S_2P(OC_6H_4CH_3\text{-}m)_2]_2 \cdot N_2C_{10}H_8$	1114, 656, 416	3.21
6	$Ni[S_2P(OC_6H_4CH_3\text{-}p)_2]_2 \cdot N_2C_{10}H_8$	1102, 654, 422	3.23
7	$Ni[S_2P(OC_6H_4CH_3\text{-}o)_2]_2 \cdot N_2C_{14}H_{12}$	1105, 676, 430	3.25
8	$Ni[S_2P(OC_6H_4CH_3\text{-}m)_2]_2 \cdot N_2C_{14}H_{12}$	1125, 676, 441	3.23
9	$Ni[S_2P(OC_6H_4CH_3\text{-}p)_2]_2 \cdot N_2C_{14}H_{12}$	1110, 686, 423	3.24

distorted octahedral, NiN_2S_4, chromophore whereas in **7** the geometry around nickel is that of a distorted trigonal bipyramidal, NiN_2S_3 chromophore. Solvent benzene molecules are also incorporated into the crystal of the latter. In **6** the square planar structure of $Ni[S_2P(OC_6H_4Me\text{-}p)_2]_2$ [29] has readily accommodated the introduction of bipy while maintaining the integrity of the two bidentate $S_2P(OC_6H_4Me\text{-}p)_2$ ligands, as was also found for $Ni[S_2P(OC_6H_4Me\text{-}p)_2]_2$(phen) [27]. By contrast, in **7** the analogous distorted square planar structure of $Ni[S_2P(OC_6H_4Me\text{-}o)_2]_2$ [28] with two bidentate ligands is not maintained in the presence of dmphen because the cleavage of one Ni–S bond results in the formation of a monodentate ligand. The presence of methyl groups in **7** on the nitrogen base, dmph increases the crowding near Ni atom resulting the cleavage of one Ni–S bond. Hence one of the ligand is rendered as monodentate and other as bidentate. The *cis* orientation of the nitrogen donor atoms is also responsible for this cleavage.

In $Ni[S_2P(OC_6H_4Me\text{-}p)_2]_2(C_{10}H_8\ N_2)$ (**6**), all four Ni–S bond lengths are fairly similar (2.4757(7) to 2.5096(6) Å) in the two bidentate dithiophosphate ligands and in the range of other analogous six-coordinated compounds, $Ni[S_2P(OBu^n)_2]_2$(bipy) (2.463(2)–2.524(2) Å) [25], $Ni[S_2P(OMe)_2]_2$(phen) (2.47(1)–2.52(1) Å) [24] and $Ni[S_2P(OC_6H_4Me\text{-}p)_2]_2$(phen) (2.486(1)–2.532(1) Å) [27]. The distances are significantly larger and cover a larger range than in the four-coordinate precursors $Ni[S_2P(OC_6H_4Me\text{-}p)_2]_2$ (average 2.332(2) Å) [29] and $Ni[S_2P(OC_6H_4Me\text{-}o)_2]_2$ (average 2.233(8) Å) [28]. By contrast, in $Ni[S_2P(OC_6H_4Me\text{-}o)_2]_2 \cdot (C_{14}H_{12}N_2) \cdot C_6H_6$ (**7**), the bidentate dithiophosphate ligand, with Ni–S bond lengths of 2.352(1) and 2.539(1) Å, might more accurately be defined as anisobidentate, while the second dithiophosphate ligand is clearly monodentate with Ni(1)–S(3) at 2.386(1) Å and Ni(1)–S(4) at 5.462(2) Å. The closest approach of this pendant S atom to the Ni atom of the nearest adjacent molecule is 7.208(2) Å. Similar behavior is seen in the analogous five-coordinate complexes, $Ni[S_2P(OMe)_2]_2$(dmphen) [24] and $Ni[S_2P(OCMe_2CMe_2O)_2]_2$(dmphen) [26], with the monodentate Ni–S bonds 2.42(1) and 2.398(3) Å, respectively, and the (aniso)bidentate ligands having Ni–S distances ranging from 2.30(1) to 2.58(1) Å. The Ni–N bond lengths are similar in **6** (2.060(1) and 2.079(1) Å) and **7** (2.010(1) and 2.009(1) Å) which is in good agreement with the distances found in the six-coordinate analogues, $Ni[S_2P(OBu^n)_2]_2$(bipy) (2.088(4) and 2.089(4) Å) [25], $Ni[S_2P(OMe)_2]_2$(phen) (2.08(1) and 2.09(1) Å) [24] and $Ni[S_2P(OC_6H_4Me\text{-}p)_2]_2$(phen) (2.082(3) and 2.086(3) Å) [27] as well as in the five-coordinate analogues $Ni[S_2P(OMe)_2]_2$(dmphen) (1.97(1) and 2.03(1) Å) [24] and $Ni[S_2P(OCMe_2CMe_2O)_2]_2$(dmphen) (2.005(8) and 2.015(7) Å) [26]. Although the differences are small, the trend of slightly shorter Ni–N bonds in the five coordinate complexes is clear and suggestive of slightly stronger bonding

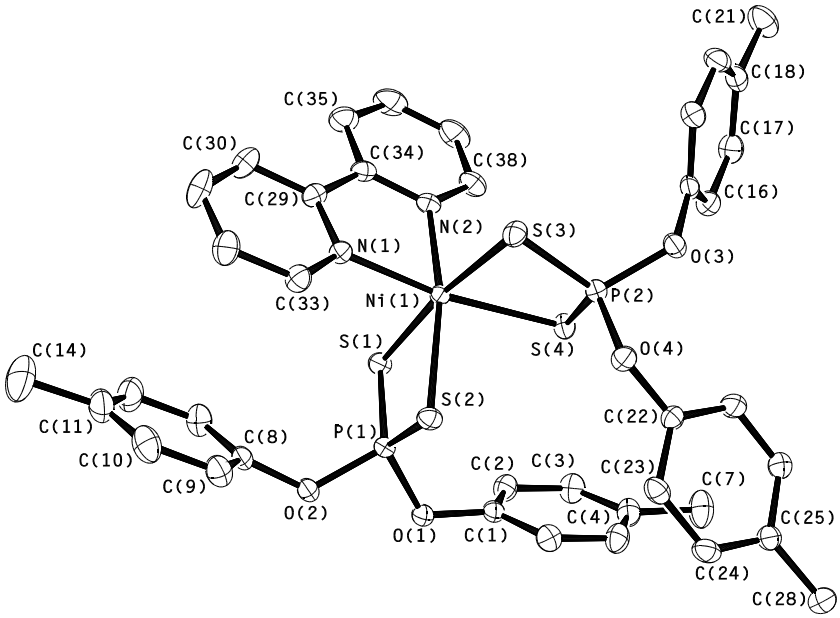


Fig. 1. ORTEP plot of the molecule $Ni[S_2P(OC_6H_4Me\text{-}p)_2]_2 \cdot C_{10}H_8N_2$. The non-hydrogen atoms are drawn with 50% probability ellipsoids.

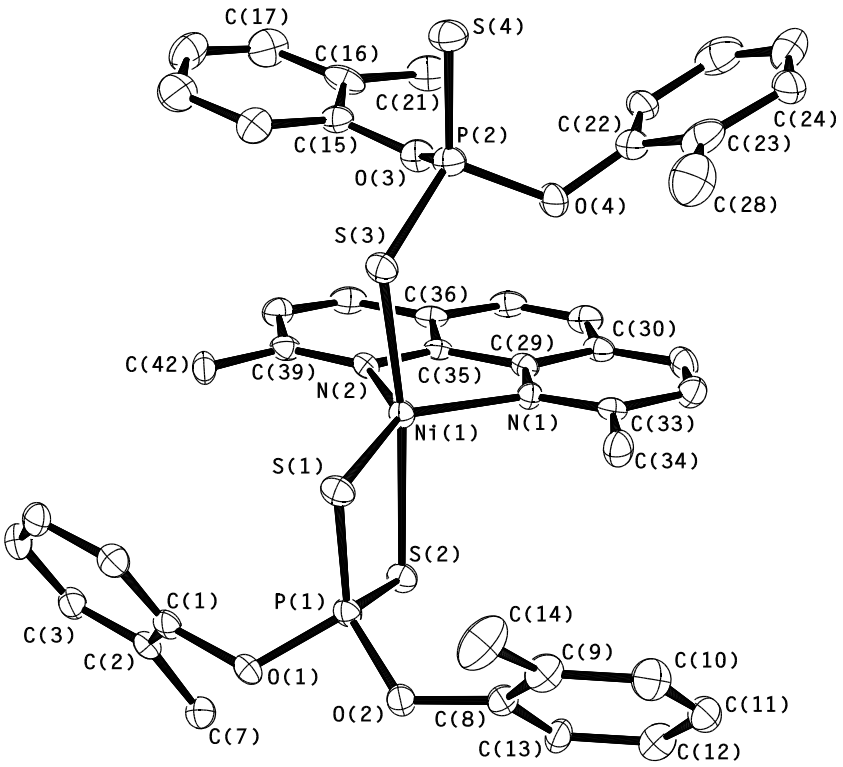


Fig. 2. ORTEP plot of $Ni[S_2P(OC_6H_4Me\text{-}o)_2]_2 \cdot C_{14}H_{12}N_2 \cdot C_6H_6$. The non-hydrogen atoms are drawn with 25% probability ellipsoids and the benzene molecule is omitted for clarity.

when accommodation has been made to incorporate the bulkier nitrogen ligand by the cleavage of an Ni–S bond and reorientation of the resulting monodentate sulfur ligand. The average lengths of the four P–S bonds in **6** are the same as in $Ni[S_2P(OC_6H_4Me\text{-}p)_2]_2$ (average 1.973(6) Å) which suggests that the competitive chelation of sulfur and nitrogen donor atoms has no significant influence on the partial double bond character of these P–S bonds. In **7**, the P(2)–S(4) bond of the pendant, non-interacting sulfur atom is by far the shortest (1.941(2) Å), with the P(1)–S(2) bond associated with the much longer Ni(1)–S(2) bond in the anisobidentate ligand being somewhat longer (1.969(2) Å). The P(1)–S(1) associated with the shorter Ni(1)–S(1) anisobidentate bond and the P(1)–S(3) associated with the monodentate Ni(1)–S(3) bond are longer and essentially the same, 1.997(2) and 1.995(2) Å, respectively.

In $Ni[S_2P(OC_6H_4Me\text{-}p)_2]_2(C_{10}H_8\ N_2)$ (**6**), the S–Ni–S ligand bite angles of 81.33(2) and 81.99(2)° are similar to the values observed in $Ni[S_2P(OBu^n)_2]_2$(bipy) (81.40(7) and 81.63(7)°) [25], $Ni[S_2P(OMe)_2]_2$(phen) (81.3(2)° and 81.6(2)°) [24] and $Ni[S_2P(OC_6H_4Me\text{-}p)_2]_2$(phen) (81.13 and 81.57(2)°) [27]. The bite angle of the chelating ligand in $Ni[S_2P(OC_6H_4Me\text{-}o)_2]_2 \cdot C_{14}H_{12}N_2 \cdot C_6H_6$ (**7**) is similar (82.05(4)°) and comparable to that in $Ni[S_2P(OMe)_2]_2 \cdot$ dmphen (81.7(1)° [24] and $Ni[S_2POCMe_2CMe_2O)_2]_2 \cdot$ dmphen (82.1(1)°) [26]. The N–Ni–N bite angles of 79.10(5)° in **6** and 82.6(2)° in **7**, are typical of the values found in the corresponding six-coordinate, $Ni[S_2P(OBu^n)_2]_2 \cdot$ bipy, $Ni[S_2P(OMe)_2]_2 \cdot$ phen and $Ni[S_2P(OC_6H_4Me\text{-}p)_2]_2 \cdot$ phen (average 79.4(3)°) and five coordinate analogues $Ni[S_2P(OCMe_2CMe_2O)_2]_2 \cdot$ dmphen and $Ni[S_2P(OMe)_2]_2 \cdot$ dmphen (average 82.5(0.3)°), respectively. In **6**, the least deviation from 180° involves the two shorter (stronger) Ni–S bonds in the bidentate ligands (S(1)–N(1)–S(4) (173.09(2)°), while those involving the donor and the longer Ni–S bonds are slightly more deviated with N–Ni–S angles of 171.63(4)° and 168.03(4)°. The three cis S–Ni–S angles, other than the ligand bite angles, cover the range 91.33–93.53°, whereas the six involving S–Ni–N angles range from 88.41(4)° to 97.18(4)°. In **7**, the axial positions of the distorted trigonal bipyramid are occupied by the Ni–S bond of the monodentate ligand and the longer Ni–S bond of the (aniso)bidentate ligand (S(2)–Ni(1)–S(3) 167.05(5)°). The sum of the three angles in the trigonal plane (S(1)–Ni(1)–N(1) 134.3(1)°, S(1)–Ni(1)–N(2) 142.1(1)° and N(1)–Ni(1)–N(2) 82.6(2)°) is 359.1°. The dmphen group is also essentially in the equatorial plane. Similar corresponding angles have been reported for $Ni[S_2POCMe_2CMe_2O)_2]_2 \cdot$ dmphen (axial S–Ni–S 169.1(1)°; equatorial S–Ni–N 131.1(3)°, S–Ni–N 144.3(2)° and N1–Ni–N 82.5(3)°) [26] and $Ni[S_2P(OMe)_2]_2 \cdot$ dmphen (axial S–Ni–S 165.8(1)°; equatorial S–Ni–N 130.2(3)°, S–Ni–N 145.7(2)° and N1–Ni–N 82.4(43)°) [24].

In **6** the S–P–S bond angles for the bidentate ligands are 110.34(2)° and 112.53(3)° as was reported for the six-coordinate analogues $Ni[S_2P(OC_6H_4Me\text{-}p)_2]_2 \cdot$ phen (110.37(6)–112.81(5)°) [27] and $Ni[S_2P(OMe)_2]_2 \cdot$ phen

(110.8(2)–111.6(2)°) [24]. In **7**, the two angles differ considerably with the S–P–S bond angle of 116.1(1)° for the monodentate ligand being considerably larger than that of the (aniso)bidentate ligand (108.27(8)°). These values are similar to those found in the analogous five-coordinated complexes, $Ni[S_2P(OMe)_2]_2 \cdot dmphen$ (116.9(2)° and 111.1(2)°) [24] and $Ni[S_2P(OCMe_2CMe_2O)_2]_2 \cdot dmphen$ (117.2(2)° and 108.0(2)°) [26].

3. Experimental

Solvents (benzene, dichloromethane, *n*-hexane, diethyl ether) were dried by standard methods before use. All reactions were carried out in pre-dried glassware under anhydrous conditions. Literature methods were used for the preparation of bis(*O*,*O*′-ditolyldithiophosphato)nickel(II) [28] and ammonium salts of *O*,*O*-ditolyldithiophosphoric acids [30,31].

3.1. Preparations

3.1.1. $Ni[S_2P(OC_6H_4Me\text{-}o)_2]_2 \cdot 2C_5H_5N$ (**1**)

$Ni[S_2P(OC_6H_4Me\text{-}o)_2]_2$ (0.489 g, 0.723 mmol) was dissolved in dry benzene (20 ml). Pyridine was added until the purple colour of the solution changed to green. The solution was concentrated under vacuo. Diethylether was added to the concentrated solution to obtain a green precipitate. The adduct was recrystallized using a dichloromethane/ether mixture (1:2 v/v). Yield: 0.328 g, 67%. *Anal.* Calc. for $C_{38}H_{38}O_4N_2S_4P_2Ni$: Ni, 7.02; S, 15.35. Found: Ni, 6.83; S, 15.17%.

3.1.2. $Ni[S_2P(OC_6H_4Me\text{-}m)_2]_2 \cdot 2C_5H_5N$ (**2**)

Method as above gave a green powdery solid. Yield: 0.401 g, 73%. *Anal.* Calc. for $C_{38}H_{38}O_4N_2S_4P_2Ni$: Ni, 7.02; S, 15.35. Found: Ni, 6.94; S, 15.48%.

3.1.3. $Ni[S_2P(OC_6H_4Me\text{-}p)_2]_2 \cdot 2C_5H_5N$ (**3**)

Yield: 0.205 g, 69%. *Anal.* Calc. for $C_{38}H_{38}O_4N_2S_4P_2Ni$: Ni, 7.02; S, 15.35. Found: Ni, 7.10; S, 15.51%.

3.1.4. $Ni[S_2P(OC_6H_4Me\text{-}o)_2]_2 \cdot C_{10}H_8N_2$ (**4**)

Yield: 0.263 g, 78.2%. *Anal.* Calc. for $C_{38}H_{36}O_4N_2S_4P_2Ni$: Ni, 7.04; S, 15.39. Found: Ni, 7.25; S, 15.52%.

3.1.5. $Ni[S_2P(OC_6H_4Me\text{-}m)_2]_2 \cdot C_{10}H_8N_2$ (**5**)

Yield: 0.349 g, 74%. *Anal.* Calc. for $C_{38}H_{36}O_4N_2S_4P_2Ni$: Ni, 7.04; S, 15.39. Found: Ni, 7.25; S, 15.72%.

3.1.6. $Ni[S_2P(OC_6H_4Me\text{-}p)_2]_2 \cdot C_{10}H_8N_2$ (**6**)

Yield: 0.357 g, 77.5%. *Anal.* Calc. for $C_{38}H_{36}O_4N_2S_4P_2Ni$: Ni, 7.04; S, 15.39. Found: Ni, 7.11; S, 15.48%.

3.1.7. $Ni[S_2P(OC_6H_4Me\text{-}o)_2]2 \cdot C_{14}H_{12}N_2$ (**7**)

Yield: 0.288 g, 69.7%. *Anal.* Calc. for $C_{42}H_{40}O_4N_2S_4P_2Ni$: Ni, 6.84; S, 14.96. Found: Ni, 6.75; S, 14.72%.

3.1.8. $Ni[S_2P(OC_6H_4Me\text{-}m)_2]_2 \cdot C_{14}H_{12}N_2$ (**8**)

Yield: 0.321 g, 71.9%. *Anal.* Calc. for $C_{42}H_{40}O_4N_2S_4P_2Ni$: Ni, 6.84; S, 14.96. Found: Ni, 6.81; S, 14.90%.

3.1.9. $Ni[S_2P(OC_6H_4Me\text{-}p)_2]_2 \cdot C_{14}H_{12}N_2$ (**9**)

Yield: 0.426 g, 73.4%. *Anal.* Calc. for $C_{42}H_{40}O_4N_2S_4P_2Ni$: Ni, 6.84; S, 14.96. Found: Ni, 6.79; S, 14.87%.

3.2. Physical measurements

Sulfur was estimated gravimetrically as barium sulfate (Messengers method) and nickel as dimethylglyoximate. IR spectra were recorded in the range 4000–200 cm^{-1} on a Perkin–Elmer 983G spectrophotometer (Nujol mull). Electronic spectra in the range 200–1200 nm were recorded on a Perkin Elmer UV/VIS/NIR spectrometer-Lambda 19 in CH_2Cl_2. The magnetic measurements at 298 K were determined using the Evans NMR method [32].

Table 3
Crystal data and structure refinements for $Ni[S_2P(OC_6H_4Me\text{-}p)_2]_2 \cdot C_{10}H_8N_2$ and $Ni[S_2P(OC_6H_4Me\text{-}o)_2]_2 \cdot C_{14}H_{12}N_2 \cdot C_6H_6$

Empirical formula	$C_{38}H_{36}O_4N_2P_2S_4Ni$	$C_{48}H_{46}O_4N_2P_2S_4Ni$
Formula weight	833.58	963.76
Temperature (*K*)	120(2)	120(2)
Wavelength (Å)	0.71073	0.71073
Crystal system	triclinic	monoclinic
Space group	$P\bar{1}$	$P2_1/c$
a (Å)	10.8219(7)	13.950(1)
b (Å)	12.035(3)	22.697(2)
c (Å)	16.737(3)	14.4965(7)
α (°)	70.73(1)	
β (°)	75.004(9)	90.050(6)
γ (°)	70.752(8)	
Volume ($Å^3$)	1915.1(5)	4589.8(5)
Z	2	4
Density (calculated) (g/cm^3)	1.446	1.395
Absorption coefficient (mm^{-1})	0.851	0.721
F(000)	864	2008
Crystal size (mm^3)	$0.20 \times 0.10 \times 0.10$	$0.20 \times 0.14 \times 0.07$
θ Range for data collection (°)	3.30–27.55	3.06–25.08
Index ranges	$-14 \leqslant h \leqslant 13$, $-15 \leqslant k \leqslant 15$, $-21 \leqslant l \leqslant 21$	$-16 \leqslant h \leqslant 16$, $-26 \leqslant k \leqslant 27$, $-17 \leqslant l \leqslant 15$
Reflections collected	40 064	41 699
Independent reflections [R_{int}]	8756 [0.0289]	8062 [0.1040]
Max. and min. transmission	0.9197 and 0.8483	0.9513 and 0.8693
Refinement method	Full-matrix least-squares on F^2	Full-matrix least-squares on F^2
Data/restraints/parameters	8756/0/461	8062/0/551
Goodness-of-fit on F^2	1.037	1.019
Final *R* indices [$F^2 > 4\sigma(F^2)$]	$R_1 = 0.0277$, $wR_2 = 0.0703$	$R_1 = 0.0590$, $wR_2 = 0.1083$
R indices (all data)	$R_1 = 0.0328$, $wR_2 = 0.0730$	$R_1 = 0.1097$, $wR_2 = 0.1260$
Extinction coefficient	0.0029(5)	
Largest difference in peak and hole (e $Å^{-3}$)	0.489 and −0.390	0.738 and −0.564

3.3. Crystal structure determination

A translucent green, block crystal of $Ni[S_2P(OC_6H_4Me\text{-}p)_2]_2 \cdot C_{10}H_8N_2$ (**6**) and a green prism crystal of $Ni[S_2P(OC_6H_4Me\text{-}o)_2] \cdot C_{14}H_{12}N_2 \cdot C_6H_6$ (**7**) were mounted on a glass fibre. Data were collected on a Bruker-Nonius Kappa CCD area detector diffractometer, with ϕ and ω scans chosen to give a complete asymmetric unit. Cell refinement [33] gave cell constants corresponding to a triclinic cell for **6** and a monoclinic cell for **7** whose dimensions are given in Table 3 along with other experimental parameters. The crystal of **7** was a monoclinic pseudo merohedral twin with beta approximately 90° emulating orthorhombic. An absorption correction was applied [34].

The structures were solved by direct methods [35] and refined using the WinGX version [36] of SHELX-97 [37]. All of the non-hydrogen atoms were treated anisotropically. Hydrogen atoms were included in idealized positions with isotropic thermal parameters set at 1.2 times that of the carbon atom to which they were attached. The final cycle of full-matrix least-squares refinement was based on 8756 observed reflections (7822 for $F^2 > 4\sigma(F^2)$) and 461 variable parameters for **6** and 8062 observed reflections (5543 for $F^2 > 4\sigma(F^2)$); and 551 variable parameters for **7** and converged (largest parameter shift was 0.001 times its esd).

Selected distances and bond angles are given in Tables 4 and 5 for molecules **6** and **7**, respectively and the molecules are displayed as ORTEP diagrams in Figs. 1 and 2.

Table 4
Bond lengths (Å) and angles (°) for $Ni[S_2P(OC_6H_4Me\text{-}p)_2]_2 \cdot C_{10}H_8N_2$

Ni(1)–S(1)	2.4757(7)	Ni(1)–S(3)	2.4814(7)
Ni(1)–S(2)	2.5049(4)	Ni(1)–S(4)	2.5096(6)
Ni(1)–N(1)	2.060(1)	Ni(1)–N(2)	2.079(1)
S(1)–P(1)	1.9788(5)	S(3)–P(2)	1.9727(6)
S(2)–P(1)	1.9751(6)	S(4)–P(2)	1.9645(6)
P(1)–O(1)	1.602(1)	P(2)–O(3)	1.609(1)
P(1)–O(2)	1.604(1)	P(2)–O(4)	1.605(1)
O(1)–C(1)	1.406(2)	O(3)–C(15)	1.404(2)
O(2)–C(8)	1.406(2)	O(4)–C(22)	1.401(2)
N(1)–C(29)	1.352(2)	N(2)–C(34)	1.351(2)
N(1)–C(33)	1.340(2)	N(2)–C(38)	1.339(2)
S(1)–Ni(1)–S(2)	81.33(2)	S(3)–Ni(1)–S(4)	81.99(2)
S(1)–Ni(1)–S(3)	173.09(2)	S(1)–Ni(1)–S(4)	93.46(2)
S(2)–Ni(1)–S(3)	93.53(2)	S(2)–Ni(1)–S(4)	91.33(2)
N(1)–Ni(1)–N(2)	79.10(5)		
N(1)–Ni(1)–S(1)	92.73(4)	N(2)–Ni(1)–S(1)	88.41(4)
N(1)–Ni(1)–S(2)	95.17(4)	N(2)–Ni(1)–S(2)	168.03(4)
N(1)–Ni(1)–S(3)	92.33(4)	N(2)–Ni(1)–S(3)	97.18(4)
N(1)–Ni(1)–S(4)	171.63(4)	N(2)–Ni(1)–S(4)	95.45(4)
P(1)–S(1)–Ni(1)	84.50(2)	P(2)–S(3)–Ni(1)	81.71(2)
P(1)–S(2)–Ni(1)	83.79(2)	P(2)–S(4)–Ni(1)	81.13(2)
C(33)–N(1)–Ni(1)	126.2(1)	C(38)–N(2)–Ni(1)	126.6(1)
C(29)–N(1)–Ni(1)	115.1(1)	C(34)–N(2)–Ni(1)	114.1(1)
O(1)–P(1)–O(2)	92.19(6)	O(3)–P(2)–O(4)	97.02(6)
S(1)–P(1)–S(2)	110.34(2)	S(3)–P(2)–S(4)	112.53(3)
O(1)–P(1)–S(1)	112.77(5)	O(3)–P(2)–S(3)	112.20(5)
O(1)–P(1)–S(2)	113.46(5)	O(3)–P(2)–S(4)	114.10(5)
O(2)–P(1)–S(1)	113.25(5)	O(4)–P(2)–S(3)	107.01(4)
O(2)–P(1)–S(2)	113.84(5)	O(4)–P(2)–S(4)	112.81(5)
C(1)–O(1)–P(1)	121.48(9)	C(15)–O(3)–P(2)	125.33(9)
C(8)–O(2)–P(1)	123.38(9)	C(22)–O(4)–P(2)	125.19(9)
C(6)–C(1)–O(1)	118.7(1)	C(20)–C(15)–O(3)	118.0(4)
C(2)–C(1)–O(1)	119.5(1)	C(16)–C(15)–O(3)	119.9(1)
C(13)–C(8)–O(2)	119.4(1)	C(27)–C(22)–O(4)	123.1(1)
C(9)–C(8)–O(2)	119.0(1)	C(23)–C(22)–O(4)	116.0(1)
C(33)–N(1)–C(29)	118.7(1)	C(38)–N(2)–C(34)	118.4(1)
N(1)–C(29)–C(30)	121.5(1)	N(2)–C(34)–C(35)	121.9(2)
N(1)–C(29)–C(34)	115.1(1)	N(2)–C(34)–C(29)	115.4(1)
N(1)–C(33)–C(32)	122.7(2)	N(2)–C(38)–C(37)	122.5(2)

Table 5
Bond lengths (Å) and angles (°) for $Ni[S_2P(OC_6H_4Me\text{-}o)_2]_2 \cdot C_{14}H_{12}N_2 \cdot C_6H_6$

Ni(1)–S(1)	2.352(1)	Ni(1)–S(3)	2.386(1)
Ni(1)–S(2)	2.539(1)	Ni(1)···S(4)	5.462(2)
Ni(1)–N(1)	2.010(4)	Ni(1)–N(2)	2.009(5)
S(1)–P(1)	1.997(2)	S(3)–P(2)	1.995(2)
S(2)–P(1)	1.969(2)	S(4)–P(2)	1.941(2)
P(1)–O(1)	1.604(4)	P(2)–O(3)	1.607(4)
P(1)–O(2)	1.596(4)	P(2)–O(4)	1.610(4)
O(1)–C(1)	1.437(7)	O(3)–C(15)	1.411(8)
O(2)–C(8)	1.401(7)	O(4)–C(22)	1.385(8)
N(1)–C(29)	1.363(7)	N(2)–C(35)	1.366(7)
N(1)–C(33)	1.325(7)	N(2)–C(41)	1.330(7)
S(1)–Ni(1)–S(2)	82.05(4)	N(1)–Ni(1)–N(2)	82.6(2)
N(1)–Ni(1)–S(1)	134.3(1)	S(1)–Ni(1)–S(3)	85.17(5)
N(2)–Ni(1)–S(1)	142.1(1)	S(2)–Ni(1)–S(3)	167.05(5)
N(1)–Ni(1)–S(2)	89.9(1)	N(1)–Ni(1)–S(3)	100.6(1)
N(2)–Ni(1)–S(2)	91.6(1)	N(2)–Ni(1)–S(3)	97.3(1)
P(1)–S(1)–Ni(1)	87.06(6)	P(2)–S(3)–Ni(1)	113.28(7)
P(1)–S(2)–Ni(1)	82.60(6)		
S(1)–P(1)–S(2)	108.27(8)	S(3)–P(2)–S(4)	116.1(1)
O(1)–P(1)–S(1)	113.0(2)	O(3)–P(2)–S(3)	111.0(2)
O(2)–P(1)–S(1)	112.7(2)	O(4)–P(2)–S(3)	105.2(2)
O(1)–P(1)–S(2)	114.2(2)	O(3)–P(2)–S(4)	112.8(2)
O(2)–P(1)–S(2)	114.8(2)	O(4)–P(2)–S(4)	113.2(2)
O(1)–P(1)–O(2)	93.6(2)	O(3)–P(2)–O(4)	96.5(2)
C(1)–O(1)–P(1)	120.9(3)	C(15)–O(3)–P(2)	127.6(4)
C(8)–O(2)–P(1)	122.4(3)	C(22)–O(4)–P(2)	125.0(4)
C(2)–C(1)–O(1)	119.9(6)	C(16)–C(15)–O(3)	116.8(6)
C(6)–C(1)–O(1)	116.4(5)	C(20)–C(15)–O(3)	119.5(6)
C(9)–C(8)–O(2)	119.8(6)	C(23)–C(22)–O(4)	120.9(7)
C(29)–N(1)–Ni(1)	112.2(4)	C(35)–N(2)–Ni(1)	112.0(4)
C(33)–N(1)–Ni(1)	128.1(4)	C(41)–N(2)–Ni(1)	129.2(4)
C(29)–N(1)–C(31)	119.7(5)	C(35)–N(2)–C(41)	118.9(5)
N(1)–C(29)–C(35)	116.4(5)	N(2)–C(35)–C(29)	116.8(5)
N(1)–C(29)–C(30)	122.6(6)	N(2)–C(35)–C(36)	123.8(5)
N(1)–C(33)–C(32)	120.4(5)	N(2)–C(41)–C(40)	120.6(6)
N(1)–C(33)–C(34)	118.6(5)	N(2)–C(41)–C(42)	117.1(5)

4. Concluding comments

We have successfully prepared and characterized the following complexes, $Ni[S_2P(OR)_2]_2 \cdot nL$ ((R = *o*-, *m*-, *p*-C_6H_4Me; $n = 2$, $L = C_5H_5N$; $n = 1$, $L = C_{10}H_8N_2$, $C_{14}H_{12}N_2$). The IR, UV–visible and magnetic measurements of all of these nickel adducts and molecular structures of two representative complexes, $Ni[S_2P(OC_6H_4Me\text{-}p)_2]_2 \cdot C_{10}H_8N_2$ and $Ni[S_2P(OC_6H_4Me\text{-}o)_2]_2 \cdot C_{14}H_{12}N_2 \cdot C_6H_6$ suggest the distorted octahedral for complexes **1**–**6** and distorted trigonal bipyramidal environ-

ments around nickel for complexes **7**–**9** and are consistent with the proposed structures for the analogous complexes $Ni[S_2P(OMe)_2]_2 \cdot phen$, $Ni[S_2P(OMe)_2]_2 \cdot dmphen$ and $Ni[S_2POCMe_2CMe_2O)_2]_2 \cdot dmphen$.

Acknowledgements

One of us (M.N.) is grateful to CSIR, New Delhi for financial support and Department of Chemistry, University of Southampton for spectroscopic facilities. M.B.H. thanks EPSRC for support of the X-ray facilities at Southampton University. J.E.D. wishes to thank the University of Windsor for financial support.

Appendix A. Supplementary material

CCDC 630576 and 630577 contain the supplementary crystallographic data for $Ni[S_2P(OC_6H_4Me\text{-}p)_2]_2 \cdot C_{10}H_8N_2$ and $Ni[S_2P(OC_6H_4Me\text{-}o)_2]_2 \cdot C_{14}H_{12}N_2 \cdot C_6H_6$. These data can be obtained free of charge via http://www.ccdc.cam.ac.uk/conts/retrieving.html, or from the Cambridge Crystallographic Data Centre, 12 Union Road, Cambridge CB2 1EZ, UK; fax: (+44) 1223-336-033; or e-mail: deposit @ccdc.cam.ac.uk. Supplementary data associated with this article can be found, in the online version, at doi:10.1016/j.poly.2007.01.003.

References

[1] R. Micu-Semeniuc, L. Silaghi-Dumitreschu, I. Haiduc, Inorg. Chim. Acta 33 (1979) 281.
[2] Y. Yamada, M. Shimoi, A. Ouchi, Chem. Lett. (8) (1978) 867.
[3] W. Szczepaniak, A.S. Plaziak, Pol. J. Chem. 63 (4-12) (1989) 323.
[4] A.S.A. Zidan, Phosphorus, Sulfur Silicon Relat. Elem. 178 (3) (2003) 567.
[5] Y.P. Singh, R.C. Mehrotra, Polyhedron 5 (4) (1986) 967.
[6] R. Visalakshi, V.K. Jain, Trans. Met. Chem. 15 (4) (1990) 278.
[7] U.N. Tripathi, M.S. Singh, J. Indian Chem. Soc. 76 (7) (1999) 360.
[8] C.P. Bhasin, G. Srivastava, R.C. Mehrotra, Indian J. Chem. 26A (10) (1987) 834.
[9] C.P. Bhasin, G. Srivastava, R.C. Mehrotra, Inorg. Chim. Acta 128 (1) (1987) 69.
[10] C.P. Bhasin, R.C. Mehrotra, J. Indian Chem. Soc. 79 (4) (2002) 336.
[11] C.P. Bhasin, G. Srivastava, R.C. Mehrotra, Inorg. Chim. Acta 131 (2) (1987) 195.
[12] C.P. Bhasin, G. Srivastava, R.C. Mehrotra, Inorg. Chim. Acta 144 (2) (1988) 157.
[13] J.A. McCleverty, S. Gill, R.S.J. Kowalski, N.A. Bailey, H. Adams, K.W. Lumbard, M.A. Murphy, J. Chem. Soc., Dalton Trans. (1982) 493.
[14] A.K.S. Gupta, R.C. Srivastava, S.S. Parma, Can. J. Chem. 45 (1967) 2293.
[15] A. Sgamellotti, C. Furlani, F. Magrini, J. Inorg. Nucl. Chem. 30 (1968) 2655.
[16] S.E. Livingstone, A.E. Mihkelson, Inorg. Chem. 9 (11) (1970) 2545.
[17] C.P. Bhasin, R. Bohra, G. Srivastava, R.C. Mehrotra, Inorg. Chim. Acta 77 (1983) L131.
[18] R. Micu-Semeniuc, L. Silaghi-Dumitreschu, I. Haiduc, Inorg. Chim. Acta 17 (1976) 5.
[19] M.J. Hynes, P.F. Brannick, J. Chem. Soc., Chem. Comm. (1977) 642.
[20] V. Machala, Z. Travnicek, Z. Sindelar, L. Kvitek, Trans. Met. Chem. 25 (2000) 715.
[21] S. Ooi, Q. Fernando, Inorg. Chem. 6 (1967) 1558.
[22] F. Jian, H. Xiao, Y. Li, K. Jiao, J. Chem. Cryst. 33 (9) (2003) 705.
[23] Q. Hao, F. Jian, X. Wang, I.A. Razak, S.S.S. Raj, H.K. Fun, Acta Cryst. Commun. C57 (2001) 160.
[24] P.S. Shetty, Q. Fernando, J. Am. Chem. Soc. (1970) 3964.
[25] X.Z. You, Z. Xu, Y.P. Yu, S.X. Liu, C.C. Lin, J. Struct. Chem. 5 (1986) 154.
[26] C.P. Bhasin, R. Bohra, G. Srivastava, R.C. Mehrotra, P.B. Hitchcock, Inorg. Chim. Acta 164 (1989) 11.
[27] Q. Hao, H.K. Fun, S. Chantrapromma, I.A. Razak, F. Jian, X. Yang, L. Lu, X. Wang, Acta Crystallogr. 57 (2001) 717.
[28] A.L. Bingham, J.E. Drake, M.E. Light, M. Nirwan, R. Ratnani, Polyhedron 25 (2006) 945.
[29] S.S. Zhang, B. Yang, Y-F. Wang, X-M. Li, K. Jiao, M.B. Kassim, B.M. Yamin, Acta. Crystallogr. E 60 (2004) m485.
[30] R. Ratnani, J.E. Drake, C.L.B. Macdonald, A. Kumar, S.K. Pandey, J. Chem. Crystallogr. 35 (6) (2005) 447.
[31] R. Ratnani, A.L. Bingham, J.E. Drake, C. Gurnani, M.B. Hursthouse, M.E. Light, M. Nirwan, J. Chem. Crystallogr. 36 (10) (2006) 627.
[32] D.F. Evans, J. Chem. Soc. (1959) 2003.
[33] A.J.M. Duisenberg, J. Appl. Crystallogr. 25 (1992) 92.
[34] G.M. Sheldrick, SADABS V2.10, 2003.
[35] G.M. Sheldrick, Acta Crystallogr. A46 (1990) 467.
[36] L.J. Farrugia, J. Appl. Crystallogr. 32 (1999) 837.
[37] G.M. Sheldrick, SHELXL97, University of Gottingen, Germany, 1997.

is expected to disturb the HOMO and LUMO of the metal complexes, and afford a subtle color tuning via substituting either pyrazolate, tetrazolate or acetylacetonate sites.

2. Experimental

2.1. General information and materials

All materials including the *N*-phenylpyrazole ligands were obtained from Aldrich, Acros or TCI and were used without further purification. 5-(2′-Pyridyl)tetrazole is a known compound and can be prepared easily in one step from commercially available 2-cyanopyridine and sodium azide [16]. Scheme 1 outlines how the iridium dimers were synthesized by the method reported by Nonoyama and were utilized for preparing a series of $(C^N)_2Ir(O^O)$ or $(C^N)_2Ir(N^N)$ complexes [17,15]. All synthetic procedures and manipulations involving $IrCl_3 \cdot H_2O$ and other Ir(III) species were carried out under N_2.

Column chromatography was carried out using 70–230 mesh silica gel. ^1H NMR and ^{13}C NMR spectra were recorded in CD_2Cl_2 solution on Bruker Avance-300 (300 MHz) or AMX-400 (400 MHz) NMR spectrometers with tetramethylsilane (TMS) as the internal standard; all chemical shifts were reported in ppm from TMS. Elemental analyses were performed on a Heraeus CHN-RAPID elemental analyzer and Elementar vario EL III analyzer. The EI-Mass spectra were recorded on Bruker APEX II and VG 70-250S spectrometers. HRMS spectra were obtained using a MAT-95XL high resolution mass spectrometer. The UV–Vis spectra were measured in a 1.0×10^{-5} M CH_2Cl_2 solution on an Agilent 8453 spectrophotometer, and the photoluminescence spectra were recorded in a 1.0×10^{-5} M CH_2Cl_2 solution with a HITACHI model F-2500 fluorescence spectrophotometer.

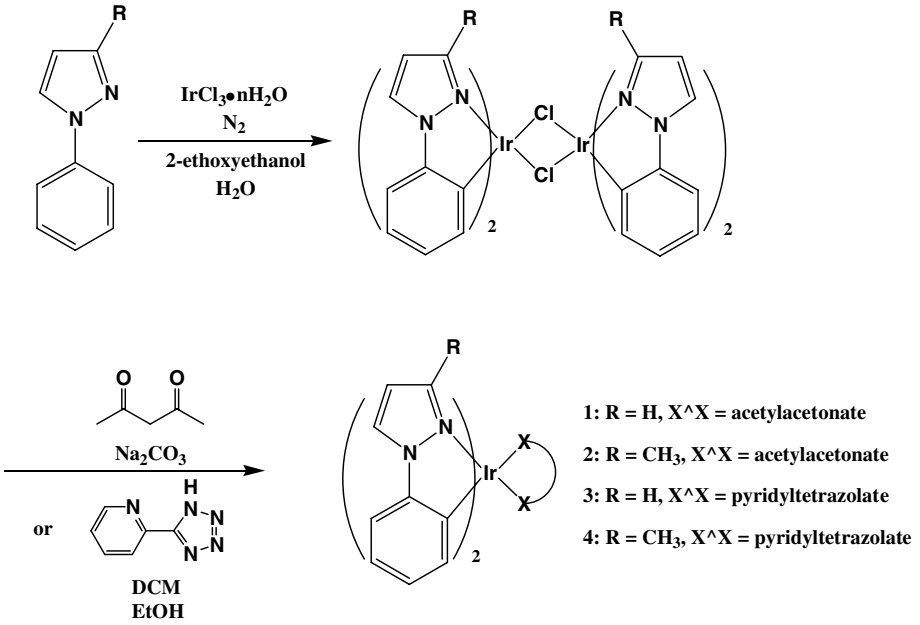
2.2. General information for the preparation of the iridium complexes

Scheme 1 outlines the synthetic process for an example of the iridium complexes $(C^N)_2Ir(O^O)$ or $(C^N)_2Ir(N^N)$. Detailed procedures of the preparation, the ^1H NMR spectra and chemical analysis data of the iridium complexes are given afterwards.

2.3. Synthesis of bis(1-phenylpyrazolato-*N*,$C^{2'}$)iridium(III)(acetylacetonate) (**1**)

The dimer $[(C^N)_2IrCl]_2$ was synthesized according to a previous report [17]. 1-Phenylpyrazole (1.22 g, 8.38 mmol) and iridium trichloride ($IrCl_3 \cdot nH_2O$, 1.0 g, 3.34 mmol) were dissolved in a 1:3 mixture of water and 2-ethoxyethanol. The mixture was refluxed at 110 °C for 24 h under a nitrogen atmosphere and then cooled to room temperature. After cooling, the product was isolated by filtration and washed with several portions of distilled water and then vacuum dried. The solid was collected by filtration and pumped to dry to give crude $[(1\text{-ppz})_2IrCl]_2$, 1.16 g (67.8%).

After cyclometallated Ir(III) μ-chloro-bridged dimers were obtained, 1.16 g of the dimer was dispersed in 2-ethoxyethanol in a flask, followed by addition of acetylacetone (0.56 g, 6.78 mmol) and sodium carbonate (1.32 g, 12.43 mmol), and the mixture was stirred under nitrogen for 15 min. After that, the mixture was refluxed at 126 °C for 15 h and then cooled to room temperature. The crude product was isolated by filtration and washed with distilled water, *n*-hexane and ether. (77% crude product yield) The crude product was chromatographed using ethyl acetate/*n*-hexane (1:1) to yield a yellow green powder, **1**. ^1H NMR (CD_2Cl_2, 400 MHz) δ 8.19 (s, 2H), 7.61 (s, 2H), 7.23 (d, $J = 7.7$ Hz, 2H), 6.92 (dd, $J = 7.7$, 7.5 Hz, 2H),



Scheme 1. Synthesis of the iridium(III) complexes.

6.73 (t, $J = 7.4$ Hz, 4H), 6.30 (d, $J = 7.5$ Hz, 2H), 5.28 (s, 1H), 1.85 (s, 6H); ^{13}C NMR (CD_2Cl_2, 100 MHz) δ 175.3, 134.8, 128.0, 124.9, 118.5, 116.2, 115.2, 111.6, 100.7, 96.9, 90.1, 18.0; FABMS: m/z 578, $[M+H]^+$; HRFABMS calcd for $C_{23}H_{22}O_2N_4Ir$, 578.1295, found 578.1291. *Anal*. Calc for $C_{23}H_{21}O_2N_4Ir \cdot 1/6n$-hexane: C, 48.28; N, 9.39; H, 3.91. Found: C, 48.13; N, 9.12; H, 4.19%.

2.4. Synthesis of bis(3-methyl-1-phenylpyrazolato-$N,C^{2'}$)iridium(III)(acetylacetonate) (2)

Yield: 65%; yellow green powder; ^{1}H NMR (CD_2Cl_2, 400 MHz) δ 7.91 (d, $J = 2.5$ Hz, 2H), 7.05 (d, $J = 7.6$ Hz), 6.76 (dd, $J = 7.6$, 7.4 Hz, 2H), 6.61 (t, $J = 7.3$ Hz, 2H), 6.30 (d, $J = 2.5$ Hz), 5.28 (s, 1H), 2.35 (s, 6H), 1.70 (s, 6H); ^{13}C NMR (CD_2Cl_2, 100 MHz) δ 175.6, 140.8, 135.0, 124.9, 117.5, 116.5, 114.7, 111.6, 100.0, 97.3, 91.3, 17.9, 1.9; FABMS: m/z 606, $[M+H]^+$; HRFABMS calc. for $C_{25}H_{26}O_2N_4Ir$, 606.1608, found 606.1603. *Anal*. Calc. for $C_{25}H_{25}O_2N_4Ir$: C, 49.57; N, 9.25; H, 4.13. Found: C, 49.38; N, 9.11; H, 4.27%.

2.5. Synthesis of bis(1-phenylpyrazolato-$N,C^{2'}$)iridium(III)[5-(2′-pyridyl)tetrazolate] (3)

Crude dimer $[(C\hat{}N)_2IrCl]_2$ (0.35 g, 0.34 mmol), 5-(2′-pyridyl)tetrazole (0.13 g, 0.85 mmol), dichloromethane and ethanol were added to a flask. The mixture was stirred at room temperature for 4–6 h. After drying in a vacuum the solid was washed with distilled water, *n*-hexane and ether. The crude product was chromatographed using chloroform/acetone (1:1) to yield a yellow powder, **3**. (58%) ^{1}H NMR (CD_2Cl_2, 500 MHz) δ 8.38 (d, $J = 7.9$ Hz, 1H), 8.10–8.07 (m, 2H), 8.00 (d, $J = 5.6$ Hz, 1H), 7.95 (td, $J = 7.9$, 1.4 Hz, 1H), 7.30 (dd, $J = 7.2$, 6.8 Hz, 2H), 7.22 (ddd,$J = 7.4$, 5.6, 1.4 Hz, 1H), 7.11–6.89 (m, 2H), 6.83–6.81 (m, 4H), 6.48–6.44 (m, 2H), 6.41 (dd, $J = 7.4$, 1.0 Hz, 1H), 6.32 (dd, $J = 7.4$, 1.0 Hz, 1H); ^{13}C NMR (CD_2Cl_2, 125 MHz) δ 154.5, 140.6, 140.4, 133.8, 133.3, 129.1, 129.0, 127.6, 123.9, 123.8, 119.2, 116.6, 116.5, 116.4, 116.0, 115.4, 112.9, 112.6, 112.5, 101.5, 101.3, 97.9, 97.6, 19.9; FABMS: m/z 626, $[M+H]^+$; HRESIMS calcd for $C_{24}H_{19}N_9Ir$, 626.1393, found 626.1396.

2.6. Synthesis of bis(3-methyl-1-phenylpyrazolato-$N,C^{2'}$)iridium(III)[5-(2′-pyridyl)tetrazolate] (4)

Yield: 65%; yellow green powder; ^{1}H NMR (CD_2Cl_2, 300 MHz) δ 8.37 (d, $J = 7.8$ Hz, 1H), 7.96 (d, $J = 6.7$ Hz, 2H), 7.91 (d, $J = 7.5$ Hz, 2H), 7.27–7.18 (m, 3H), 7.06–7.00 (m, 2H), 6.97–6.76 (m, 2H), 6.45 (d,$J = 7.4$ Hz, 1H), 6.33 (d, $J = 7.5$ Hz, 1H), 6.00 (s, 2H), 1.65 (s, 3H), 1.53 (s, 3H); ^{13}C NMR (CD_2Cl_2, 75 MHz) δ 154.3, 141.5, 140.5, 134.0, 133.7, 128.9, 124.0, 123.8, 123.1, 120.0, 117.9, 116.9, 116.7, 116.0, 115.6, 115.5, 112.9, 112.6, 104.8, 100.9, 100.6, 98.0, 97.8, 85.1; FABMS: m/z 606, $[M+H]^+$; HRESIMS calc. for $C_{26}H_{23}N_9Ir$, 654.1706, found 654.1707. *Anal*. Calc. for $C_{25}H_{25}O_2N_4Ir \cdot CH_2Cl_2$: C, 43.96; N, 17.09; H, 3.26. Found: C, 44.13; N, 17.03; H, 3.45%.

3. Electrochemistry

Cyclic voltammograms (CV) were performed with a Voltammetric Analyzer (Bioanalytical Model CV-50W). All CV measurements were carried out in CH_2Cl_2 containing 0.1 M tetrabutylammonium perchlorate (n-Bu_4NClO_4) as the supporting electrolyte. A Pt disk electrode was used as the working electrode, a Pt wire as the counter electrode, and $Ag/AgNO_3$as the reference electrode. The ferrocenium/ferrocene redox couple in CH_2Cl_2/n-Bu_4NClO_4 occurs at $E^{\circ\prime} = +0.35$ V versus $Ag/AgNO_3$. The oxidation potential of the Ir complexes is reported versus the ferrocenium/ferrocene redox couple.

4. X-ray crystallographic analyses

Crystals of **1**, **2** and **4** were obtained from solutions of CH_2Cl_2-Ether. The crystal data were selected for indexing and intensity data collection on a Siemens SMART CCD diffractometer equipped with a normal focus, 3-kW sealed tube X-ray source at 21–23 °C. No significant decay was observed for all samples during the data collection. Data were processed on a PC using the Bruker AXS SHELXTL NT software package. Neutral atom scattering factors were taken from Cromer and Waber. The crystals of **1** and **2** belong to the orthorhombic space group *Pca*2(1) and *Pbca*, respectively. The crystal of **4** belongs to the Prism space group *P*2(1)*cn*. All the structures were solved by direct methods. All non-hydrogen atoms were refined anisotropically. The positions for all hydrogen atoms were either calculated or located directly from difference Fourier maps and their contributions to structural factor calculations were included. The crystallographic data of **1**, **2** and **4** are given in Table 1, and selected bond lengths and angles are summarized in Table 2.

5. Results and discussion

5.1. Synthesis and characterization

The ligands 1-phenylpyrazole and 3-methyl-1-phenylpyrazole were purchased from Aldrich and were used without further purification. According to the procedure in the literature [16], 5-(2′-pyridyl)tetrazole could be synthesized by the cyclization of 2-cyanopyridine and sodium azide. The iridium complexes, $(C\hat{}N)_2Ir(O\hat{}O)$, were prepared from the phenylpyrazole ligands and iridium trichloride hydrate to form a dimer, $[(C\hat{}N)_2IrCl]_2$, followed by the reaction with acetylacetone in the presence of sodium carbonate. On the other hand, the iridium complexes, $(C\hat{}N)_2Ir(N\hat{}N)$, were prepared by reacting the dimer with 5-(2′-pyridyl)tetrazole in the presence of dichloromethane and methanol [15]. All procedures involving Ir(III) species were carried out under a nitrogen gas atmosphere. All these materials

Table 1
Crystallographic data of **1**, **2** and **4**

	1	**2**	**4**
Formula	$C_{23}H_{21}IrN_4O_2$	$C_{25}H_{25}IrN_4O_2$	$C_{26}H_{22}IrN_9$
FW	577.64	605.69	652.73
Crystal system	orthorhombic	orthorhombic	prism
Space group	*Pca*2(1)	*Pbca*	*P*2(1)*cn*
a (Å)	28.802(2)	15.4982(6)	10.3170(5)
b (Å)	8.8039(7)	16.8619(6)	15.2370(7)
c (Å)	8.1204(6)	17.7218(7)	15.5510(9)
α (°)	90	90	90
β (°)	90	90	90
γ (°)	90	90	90
Volume (Å^3)	2059.1(3)	4631.2(3)	2444.6(2)
Z	4	8	4
Density (Mg/m^3)	1.863	1.737	1.773
Absorption coefficient (mm^{-1})	6.512	5.795	5.496
F(000)	1120	2368	1272
Reflections collected	14 524	32 745	9573
Independent reflections [$R_{(int)}$]	5066 [0.0484]	5773 [0.0457]	4125 [0.0608]
Number of parameters	271	289	326
Final *R* indices [$I > 2\sigma(I)$]	$R_1 = 0.0306$, $wR_2 = 0.0609$	$R_1 = 0.0269$, $wR_2 = 0.0592$	$R_1 = 0.0663$, $wR_2 = 0.1733$
Goodness-of-fit on F^2	0.897	0.895	1.091

[a] $R_1 = \sum|F_o| - |F_c|/\sum|F_o|$. [b] $wR_2 = [\sum w[(F_o^2 - F_c^2)^2]/\sum[w(F_o^2)^2]]^{1/2}$. [c] $w = 1/\sigma^2(F_o^2) + (0.075P)^2]$, where $P = [\mathrm{Max}(F_o^2, 0) + 2F_c^2]/3$.

Table 2
Bond lengths (Å) and bond angles (°) for **1**, **2** and **4**

Complex **1**			
Ir(1)–C(18)	2.003(6)	Ir(1)–C(9)	2.004(6)
Ir(1)–N(1)	2.011(5)	Ir(1)–N(3)	2.019(5)
Ir(1)–O(1)	2.169(4)	Ir(1)–O(2)	2.134(4)
N(1)–C(1)	1.333(8)	N(2)–C(3)	1.360(7)
N(2)–C(4)	1.424(7)	N(3)–C(10)	1.327(7)
C(18)–Ir(1)–C(9)	85.3(2)	C(9)–Ir(1)–N(1)	80.4(2)
C(18)–Ir(1)–N(3)	80.2(2)	C(18)–Ir(1)–N(1)	95.7(2)
C(9)–Ir(1)–N(3)	98.9(2)	N(1)–Ir(1)–N(3)	175.9(2)
Complex **2**			
Ir(1)–C(1)	1.998(4)	Ir(1)–C(11)	1.991(4)
Ir(1)–N(3)	2.036(3)	Ir(1)–N(1)	2.037(3)
Ir(1)–O(1)	2.146(2)	Ir(1)–O(2)	2.150(2)
N(1)–C(9)	1.342(5)	N(3)–C(19)	1.338(5)
N(2)–C(7)	1.348(5)	N(2)–C(6)	1.416(5)
C(11)–Ir(1)–C(1)	88.9(2)	C(1)–Ir(1)–N(3)	92.9(1)
C(11)–Ir(1)–N(1)	93.8(1)	C(11)–Ir(1)–N(3)	80.7(2)
C(1)–Ir(1)–N(1)	80.3(1)	N(3)–Ir(1)–N(1)	171.5(1)
Complex **4**			
Ir(1)–C(16)	2.030(2)	Ir(1)–C(26)	2.012(1)
Ir(1)–N(6)	2.014(2)	Ir(1)–N(8)	2.065(2)
Ir(1)–N(1)	2.171(2)	Ir(1)–N(5)	2.173(2)
C(1)–C(2)	1.490(4)	N(7)–C(11)	1.430(2)
N(9)–C(21)	1.440(3)	N(1)–C(1)	1.310(3)
C(16)–Ir(1)–C(26)	93.7(1)	C(16)–Ir(1)–N(6)	79.4(7)
C(16)–Ir(1)–N(8)	97.6(8)	C(26)–Ir(1)–N(8)	77.4(1)
C(26)–Ir(1)–N(6)	95.0(1)	N(1)–Ir(1)–N(5)	76.2(8)

were characterized by elemental analysis, ^{1}H and ^{13}C NMR, and mass spectrometry. Whereas **1**, **2** and **4** were further identified using single-crystal X-ray analysis to establish their three-dimensional structures, complex **3** is a yellow powder, and we could not get reliable elemental analysis data for this complex. The HRESIMS, ^{1}H and ^{13}C NMR spectra of **3** are given in the Supplementary material.

The single-crystal structures of complexes **1**, **2** and **4** are presented with an ORTEP diagram in Fig. 1. They were obtained from solutions of dichloromethane–ether. As shown in Fig. 1, complexes **1** and **2** reveal a distorted octahedral geometry around the iridium atom with two cyclometallated phenylpyrazole (C^N) ligands and one anionic acetylacetone (O^O) ligand. Complex **4** also shows a distorted octahedral geometry around the iridium atom but with two cyclometallated phenylpyrazole (C^N) ligands and one anionic pyridyltetrazole (N^N) ligand. These three complexes crystallized in different space groups, complexes **1**, **2** and **4** belong to the orthorhombic space group *Pca*2(1), the orthorhombic space group *Pbca* and the *Prism* space group *P*2(1)*cn*, respectively. The diversity of the space groups of these complexes suggests that the packing of these complexes is very sensitive to the different substituents of the ligands. The phenylpyrazole ligands mutually adopt an eclipsed configuration with the nitrogen atoms residing in trans locations, and the Ir–N distances lie between 2.011(5) and 2.019(5) Å for **1**, 2.037(3) and 2.035(3) Å for **2**, and 2.014(2) and 2.065(2) Å for **4**. The longer Ir–N distance is believed to be caused by the 3-methyl substituent of the phenylpyrazole. The cyclometallated carbon atoms are mutually cis on the iridium and show similar distances between 1.991(4) to 2.030(2) Å. The overall structural arrangement is similar to several previously reported examples [11,12,14].

Interestingly, the third small acetylacetone ligand shows big bite angles of 87.54°(2) for **1** and 88.11°(2) for **2**, and the phenylpyrazole ligands show big bite angles of

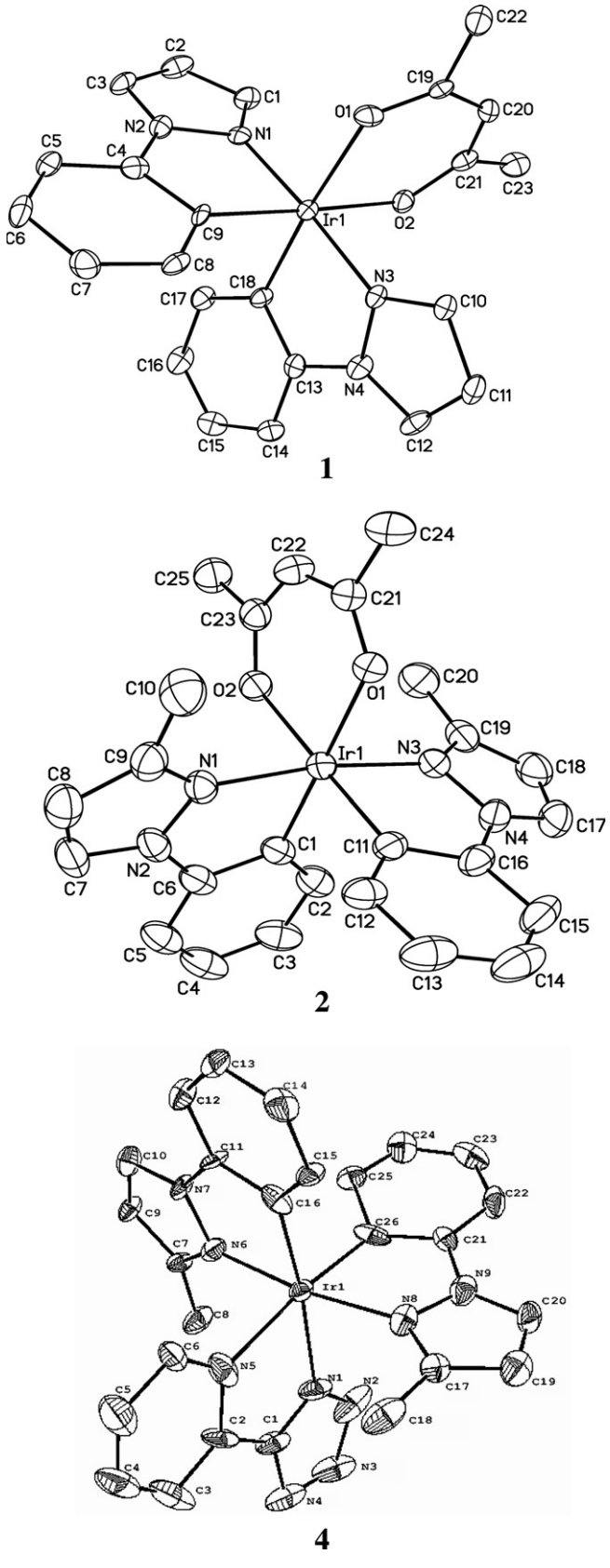


Fig. 1. ORTEP diagrams of **1**, **2** and **4**.

80.2°(2) to 80.74°(2). With the introduction of the third big pyridyltetrazole ligand to replace acetylacetone, the bite angle is small (76.2°(8)) and the phenylpyrazole ligands show smaller bite angles of 77.4°(10) to 79.4°(7). This result can be ascribed to the big molecular structure of the pyridyltetrazole ligand. Moreover, X-ray data show that the dihedral angles between the two planes for **4** (1.199° to 5.184°) and **2** (1.923° to 3.619°) are much larger than **1** (1.133° to 2.032°). This result suggests that the methyl group on the C-3 site of pyrazole creates the largest steric hindrance amongst the complexes.

6. Photophysical data

Figs. 2 and 3 show the UV–Vis absorption and emission spectra of complexes **1**–**4** at 298 K. The data of all the iridium(III) complexes are summarized in Table 3. In general, the dominant absorption band in the spectra region of 250–270 nm is attributed to the local $^1\pi\pi^*$ transition of the phenylpyrazole ligands. The structureless bands at 280–350 nm can be assigned to a combination of intra-ligand

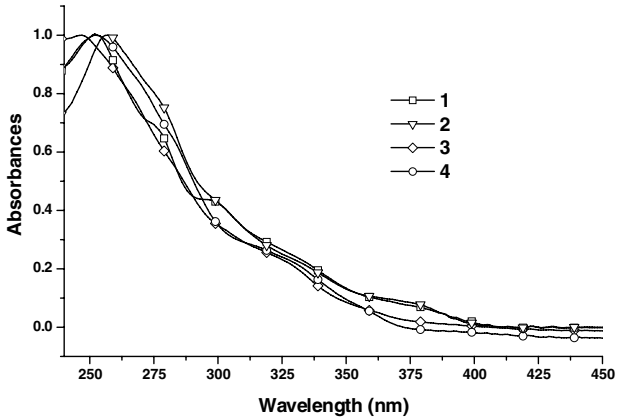


Fig. 2. Normalized UV–Vis spectra of the iridium complexes in CH_2Cl_2.

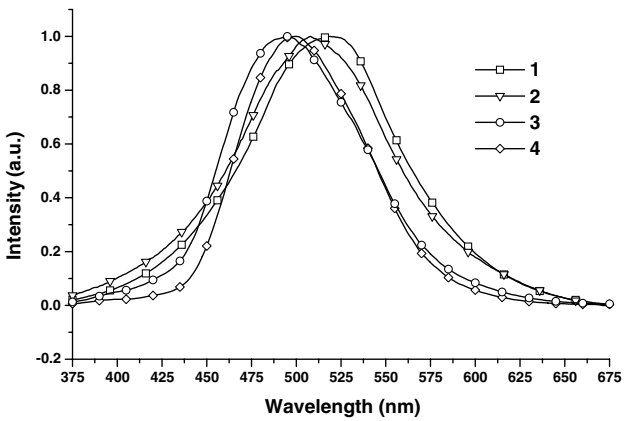


Fig. 3. Normalized photoluminescence spectra of the iridium complexes in CH_2Cl_2.

charge transfer (ILCT) and metal to ligand charge transfer (MLCT) in the singlet manifold. The lower lying band that is located at 350–400 nm can be assigned to the mixing of ^{3}MLCT and $^3\pi\pi^*$ transition character bands. Complexes **3** and **4** exhibit ~5–10 nm blue shift in comparison with **1** and **2**. This result is predictable because the stronger electron-withdrawing ligand 5-(2′-pyridyl)tetrazole is introduced for the N^N site coordination.

As depicted in Table 3 and Fig. 3, all of the iridium complexes exhibit a bluish green emission at 495–520 nm in CH_2Cl_2. Complexes **3** and **4** exhibit blue shift (about 8–25 nm) in comparison to complexes **1** and **2**. Accordingly, the third ligand (O^O or N^N) contributes to the lowest T_1–S_0 transition. Interestingly, the 3-methyl substituent at phenylpyrazole shows different effects in the (O^O) and (N^N) coordination complexes. Complex **2** is blue shift but complex **4** is red shift. The electron-donating group (methyl group) plays only a part in the contribution. After introducing the third different ligands, the degree of perturbation in the iridium center and ligands is different and causes different lowest T_1–S_0 transitions.

The emission intensities of complexes **1** and **2** were found to be relatively weak by using FIrN4 (iridium(III)bis(4,6-difluorophenylpyridinato)-5-(pyridine-2-yl)-1*H*-tetrazolate) as a reference in degassed CH_2Cl_2 [8]. This result agreed with reports about phenylpyrazolate iridium complexes. Surprisingly, complexes **3** and **4** exhibit stronger quantum efficiency. After introducing pyridyltetrazole ligand as the third ligand for N^N coordination, the photophysical properties of the iridium complexes are changed. Evidently, the radiative constant (k_r) of complexes **3** and **4** is faster than the non-radiative constant (k_{nr}), and this changes the temperature-dependent characteristics of phenylpyrazolate iridium complexes.

Table 3
λ_{max} of UV–Vis and photoluminescence data of the iridium(III) complexes

Complex	Absorbance[a] λ_{max} (nm) (log ε)	FWHM (nm)	Emission[a] λ_{max} (nm)	$\Phi_{degassed}$[b]
1	255(4.71), 302(4.30), 331(4.07)	99	520	0.02
2	260(4.96), 305(4.54), 338(4.23)	98	508	0.005
3	250(4.51), 330(3.82)	90	495	0.18
4	256(4.36), 327(3.72)	81	500	0.13

[a] All data were obtained in CH_2Cl_2 solution (concentration = 10^{-5} M). The unit of ε is M^{-1} cm^{-1}.

[b] The quantum yields (Φ, relative emission intensities) in degassed CH_2Cl_2 solution were measured at 298 K and used $FIrN_4$ ($\Phi = 1$) as a standard.

7. Redox chemistry

Cyclic voltammetry was conducted at a Pt disk electrode (BAS Co.) in CH_2Cl_2 solutions containing 0.001 M of the iridium complexes and 0.1 M tetra-*n*-butylammonium perchlorate as the supporting electrolyte. The voltammograms of the iridium complexes are shown in Fig. 4 together with the voltammogram of ferrocene. The electrochemical data of these compounds are collected in Table 4. It shows that complexes **1** and **2** undergo a reversible one-electron oxidation (peak potential separation ~60 mV) with no reduction process observed within the solvent cathodic potential limit. Complexes **3** and **4** undergo a quasi-reversible oxidation because of the instability of the oxidative intermediates. The energy level of the LUMO was evaluated from the long-wavelength absorption edge using the theory reported by Burrows et al. [18,19]. The summarized $E_{1/2}$, HOMO, LUMO and energy gap data of complexes **1** and **2**, shown in Table 4, are very close to each other. This

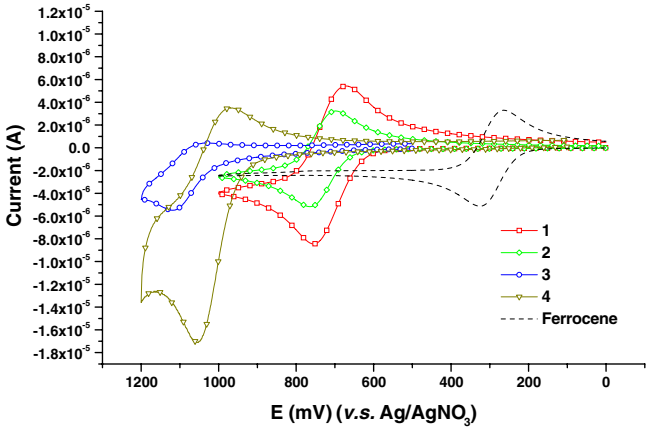


Fig. 4. Cyclic voltammograms of the iridium complexes. CV data were measured in CH_2Cl_2 solution with Pt disk electrode, $Ag/AgNO_3$ electrode and Pt electrode as working, reference and counter electrode, respectively. The scan rate was 100 mV/s, using ferrocene as a reference.

Table 4
Electrochemical data, HOMO, LUMO and energy gap of the iridium(III) complexes

Complex	$E^a_{p(ox)}$ (mV)	$E^c_{p(ox)}$ (mV)	$E_{1/2(ox)}$[a] (mV)	HOMO[c] (eV)	Energy gap[d] (eV)	LUMO[e] (eV)
1	756	670	713 [420][b]	−5.22	2.98	−2.24
2	766	696	713 [420][b]	−5.22	2.98	−2.24
3	1118	1036	1077 [340][b]	−5.54	3.22	−2.32
4	1060	964	1012 [340][b]	−5.47	3.33	−2.14

[a] Data were collected in CH_2Cl_2 solution.

[b] $E_{1/2(ox)}$ vs ferrocene/ferrocenium.

[c] Data were collected in CH_2Cl_2 solution containing 0.001 M of the iridium(III) complexes by cyclic voltammetry.

[d] Data were collected in CH_2Cl_2 solution by UV–Vis spectrophotometry.

[e] Data were calculated from the HOMO + energy gap.

result implies that the contribution of the methyl group in $(ppz)_2Ir(O\hat{}O)$ complexes is small and does not affect the photo- and electrochemical properties. After replacing the acetylacetone with pyridyltetrazole, the $E_{1/2(ox)}$ of **3** and **4** shifts to 1077 and 1012 mV in comparison to **1** and **2**. This result indicates that the effect of introducing the strong electron-withdrawing pyridyltetrazole is stronger than for acetylacetone. This effect also shows the same shift in the HOMO and energy gap. The electron-donating effect in $(ppz)_2Ir(N\hat{}N)$ complexes is apparent, **4** is oxidized more easily than **3** because of the electron-donating character of the methyl group. The methyl substituent in pyrazole donates electron density and makes oxidation of the iridium center occur more easily.

8. Conclusion

This work reports the detailed synthesis and electrochemical and photophysical properties of phenylpyrazolate iridium(III) complexes. Among these iridium(III) complexes, **3** and **4** show excellent quantum yields because the electron density is perturbed by introducing the pyridyltetrazole ligand and makes $k_r > k_{nr}$. This concept is helpful for ligand design in the future.

Acknowledgment

This work was supported by the National Science Council of Republic of China, Taiwan (NSC 94-2113-M-006-017).

Appendix A. Supplementary material

CCDC 261556, 261557 and 601712 contain the supplementary crystallographic data for **1**, **2** and **4**. These data can be obtained free of charge via http://www.ccdc.cam.ac.uk/conts/retrieving.html, or from the Cambridge Crystallographic Data Centre, 12 Union Road, Cambridge CB2 1EZ, UK; fax: (+44) 1223-336-033; or e-mail: deposit @ccdc.cam.ac.uk. Supplementary data associated with this article can be found, in the online version, at doi:10.1016/j.poly.2007.01.030.

References

[1] Y.T. Huang, T.H. Chuang, Y.L. Shu, Y.C. Kuo, P.L. Wu, C.H. Yang, I.W. Sun, Organometallics 24 (2005) 6230.
[2] K.H. Fang, L.L. Wu, Y.T. Huang, C.H. Yang, I.W. Sun, Inorg. Chim. Acta 359 (2006) 441.
[3] C.H. Yang, K.H. Fang, W.L. Su, S.P. Wang, S.K. Su, I.W. Sun, J. Organomet. Chem. 691 (2006) 2767.
[4] T. Sajoto, P.I. Djurovich, A. Tamayo, M. Yousufuddin, R. Bau, M.E. Thompson, R.J. Holmes, S.R. Forrest, Inorg. Chem. 44 (2005) 7992.
[5] K.R.J. Thomas, M. Velusamy, J.T. Lin, C.H. Chien, Y.T. Tao, Y.S. Wen, Y.H. Hu, P.T. Chou, Inorg. Chem. 44 (2005) 5677.
[6] C.H. Yang, C.C. Tai, I.W. Sun, J. Mater. Chem. 14 (2004) 947.
[7] C.H. Yang, K.H. Fang, C.H. Chen, I.W. Sun, Chem. Commun. (2004) 2232.
[8] S.J. Yeh, M.F. Wu, C.T. Chen, Y.H. Song, Y. Chi, M.H. Ho, S.F. Hsu, C.H. Chen, Adv. Mater. 17 (2005) 285.
[9] H.C. Li, P.T. Chou, Y.H. Hu, Y.M. Cheng, R.S. Liu, Organometallics 24 (2005) 1329.
[10] V. Adamovich, J. Brooks, A. Tamayo, A.M. Alexander, P.I. Djurovich, B.W. D'Andrade, C. Adachi, S.R. Forrest, M.E. Thompson, New. J. Chem. 26 (2002) 1171.
[11] A.B. Tamayo, B.D. Alleyne, P.I. Djurovich, S. Lamansky, I. Tsyba, N.N. Ho, R. Bau, M.E. Thompson, J. Am. Chem. Soc. 125 (2003) 7377.
[12] T. Sajoto, P.I. Djurovich, A. Tamayo, M. Yousufuddin, R. Bau, M.E. Thompson, Inorg. Chem. 44 (2005) 7992.
[13] K. Dedeian, J. Shi, N. Shepherd, E. Forsythe, D.C. Morton, Inorg. Chem. 44 (2005) 4445.
[14] C.H. Yang, S.W. Li, Y. Chi, Y.M. Cheng, Y.S. Yeh, P.T. Chou, G.H. Lee, C.H. Wang, C.F. Shu, Inorg. Chem. 44 (2005) 7770.
[15] P. Coppo, E.A. Plummer, L.D. Cola, Chem. Commun. (2004) 1774.
[16] J.M. McManus, R.M. Herbst, J. Org. Chem. 24 (1959) 1462.
[17] M. Nonoyama, Bull. Chem. Soc. Jpn. 47 (1974) 767.
[18] P.E. Burrows, Z. Shen, V. Bulovic, D.M. McCarty, S.R. Forrest, J. Appl. Phys. 79 (1996) 7991.
[19] H.M. Koepp, H. Wendt, H. Strehlow, Z. Electrochem. 64 (1960) 483.

2.1. Synthesis of [RuCl(CO)(PPh$_3$)$_2$(C$_5$H$_4$ NCOO)] (1)

A suspension of [RuHCl(CO)(PPh$_3$)$_3$] (0.95 g; 1×10^{-3} mol) and 2-benzoylpyridine (0.36 g; 2×10^{-3} mol) in dimethoxyethane (100 cm^{-3}) was refluxed until the solid dissolved, then the solution was cooled and filtered. Brown crystals suitable for X-ray crystal analysis were obtained by slow evaporation of the reaction mixture. Yield 72%.

Anal. Calc. for $C_{90}H_{82}Cl_2N_2O_{10}P_4Ru_2$: C, 61.82; H, 4.73; Cl, 4.06; N, 1.60; O, 9.15; P, 7.09; Ru, 11.56. Found: C, 62.01; H, 4.63; N, 1.66%.

IR (KBr, cm^{-1}): 3566 ν_{OH}; 3058 ν_{CH}; 2897 $\nu_{CH-phenyl}$; 1946 $\nu_{C\equiv O}$; 1647 ν_{CN}; 1568 asν_{COO}; 1482 $\delta_{(C-CH\ in\ plane)}$; 1433 $\nu_{Ph(P-Ph)}$; 1344 sν_{COO}; 1094 $\delta_{(C-CH\ in\ plane)}$; 997 $\delta_{(C-C\ out\ of\ plane)}$; 748 $\delta_{(C-C\ out\ of\ plane)}$; 692 $\delta_{(C-C\ in\ plane)}$; 598 ν_{P-Ph}.

^{1}H NMR (δ, CDCl$_3$): 7.24–7.82 (m, PPh$_3$/pyridine), 8.54 (s 1H pyridine ring).

^{31}P NMR (δ, CDCl$_3$): 31.61 (s, PPh$_3$).

UV–Vis [nm] in CH_2Cl_2 (log ε): 370.0 (2.24); 264.2 (3.93); 216.0 (4.37).

2.2. Synthesis of [RuCl$_2$(C$_{12}$H$_9$NO)$_2$] (2)

A suspension of $[(C_6H_6)RuCl_2]_2$ (0.25 g; 5×10^{-4} mol) and 2-benzoylpyridine (0.18 g; 1×10^{-3} mol) in dimethoxyethane (100 cm^{-3}) was refluxed until the solid dissolved, then the solution was cooled and filtered. The dark blue crystals suitable for X-ray crystal analysis were obtained by slow evaporation of the reaction mixture. Yield 68%.

Anal. Calc. for $C_{24}H_{18}Cl_2N_2O_2Ru$: C, 53.54; H, 3.37; Cl, 13.17; N, 5.20; O, 5.94; Ru, 18.77. Found: C, 53.01; H, 3.23; N, 5.16%.

IR (KBr, cm^{-1}): 3056 ν_{CH}; 2918 $\nu_{CH-phenyl}$; 1663 ν_{CN}; 1594 $\nu_{C=O}$; 1449 $\nu_{C=C}$; 1335 $\nu_{C=O}$; 1155 δ_{CH}; 1011 δ_{CH}; 696 δ_{ring}.

^{1}H NMR (δ, CDCl$_3$): 7.51, 7.53, 8.08 (Ph), 8.75, 7.93, 7.81 (pyridine ring hydrogens).

UV–Vis [nm] in CH_2Cl_2 (log ε): 737.6 (2.39); 600.0 (2.06); 462.0 (sh); 370.4 (1.96); 266.0 (3.28); 218.2 (4.12).

2.3. Physical measurements

Infrared spectra were recorded on a Nicolet Magna 560 spectrophotometer in the spectral range 4000–400 cm^{-1} with the sample in the form of a KBr pellet. Electronic spectra were measured on a Lab Alliance UV–Vis 8500 spectrophotometer in the range 800–200 nm in dichloromethane solution. Elemental analyses (C, H, N) were performed on a Perkin–Elmer CHN-2400 analyzer. The ^{1}H NMR spectra were obtained at room temperature in $CDCl_3$ using a INOVA 300 spectrometer.

Table 1
Crystal data and structure refinement details of 2[RuCl(CO)(PPh$_3$)$_2$(C$_5$H$_4$NCOO)] · DME · 2H$_2$O (**1**) and [RuCl$_2$(C$_{12}$H$_9$NO)$_2$] (**2**)

	1	**2**
Empirical formula	$C_{90}H_{82}Cl_2N_2O_{10}P_4Ru_2$	$C_{24}H_{18}Cl_2N_2O_2Ru$
Formula weight	1748.50	538.37
Temperature (K)	291.0(3)	291.0(3)
Crystal system	triclinic	monoclinic
Space group	$P\bar{1}$	Cc
Unit cell dimensions		
a (Å)	10.3915(5)	11.6644(10)
b (Å)	13.0075(9)	16.0329(12)
c (Å)	16.9007(10)	13.1440(16)
α (°)	108.670(6)	90.00
β (°)	104.746(5)	110.099(9)
γ (°)	93.552(5)	90.00
Volume (Å^3)	2067.1(2)	2308.4(4)
Z	1	4
Calculated density (Mg/m^3)	1.405	1.549
Absorption coefficient (mm^{-1})	0.567	0.934
F(000)	898	1080
Crystal dimensions (mm)	$0.367 \times 0.366 \times 0.360$	$0.489 \times 0.091 \times 0.073$
θ Range for data collection (°)	3.14–25.60	3.15–25.10
Index ranges	$-12 \leqslant h \leqslant 12$	$-13 \leqslant h \leqslant 13$
	$-15 \leqslant k \leqslant 13$	$-19 \leqslant k \leqslant 19$
	$-20 \leqslant l \leqslant 20$	$-15 \leqslant l \leqslant 13$
Reflections collected	21768	12174
Independent reflections [$R_{(int)}$]	7697 [0.0260]	3604 [0.0324]
Data/restraints/parameters	7697/0/497	3604/2/280
Goodness-of-fit on F^2	1.051	0.916
Final R indices [$I > 2\sigma(I)$]	$R_1 = 0.0352$	$R_1 = 0.0291$
	$wR_2 = 0.0886$	$wR_2 = 0.0375$
R indices (all data)	$R_1 = 0.0393$	$R_1 = 0.0408$
	$wR_2 = 0.0912$	$wR_2 = 0.0399$
Largest difference in peak and hole (e Å^{-3})	0.664 and −0.642	0.245 and −0.220

2.4. DFT calculations

The GAUSSIAN-03 program [10] was used in the calculations. The geometry optimisation was carried out with the DFT method with the use of the B3LYP functional [11,12]. The electronic transitions were calculated with the PCM model [13] in dichloromethane as the solvent. The calculation was performed using the DZVP basis set [14] with *f* functions with exponents 1.94722036 and 0.748930908 on the ruthenium atom, and polarization functions to all other atoms: 6-31g(2d,p) – chlorine, 6-31g** – carbon, nitrogen, oxygen and 6-31g(d,p) on hydrogen atoms. Natural bond orbital (NBO) calculations were performed with the NBO code [15] included in GAUSSIAN-03.

2.5. Crystal structure determination and refinement

A brown prism of complex **1** and dark-blue needle of **2** were mounted in turn on a KM-4-CCD automatic diffractometer equipped with a CCD detector, and were used for data collection. X-ray intensity data were collected with graphite monochromated Mo Kα radiation ($\lambda = 0.71073$ Å) at a temperature of 291.0(3) K, with the ω scan mode. The full Ewald sphere reflections were collected up to $2\theta = 51.2°$ for complex **1** and $2\theta = 50.2°$ for **2**. The unit cell parameters were determined from least-squares refinement of the setting angles of 7697 and 3604 strongest reflections for complexes **1** and **2**, respectively. Details concerning crystal data and refinement are gathered in Table 1. The reference frames monitored every 40 measurement frames show 1.01% decay for the crystal of compound **1** and none for the crystal of compound **2**. During the data reduction above, the decay correction coefficient was taken into account. Lorentz, polarization and numerical absorption [16] corrections were applied. The structures were solved using the Patterson method combined with a partial structure expansion procedure. All the non-hydrogen atoms were refined anisotropically using full-matrix, least-squares techniques on F^2. The hydrogen atoms were found from difference Fourier synthesis after four cycles of anisotropic refinement, and refined as "riding" on the adjacent atom with individual isotropic temperature factors equal to 1.2 times the value of the equivalent temperature factor of the parent atom. SHELXS97 [17,18] and SHELXTL [19] programs were used for all the calculations. Atomic scattering factors were those incorporated in the computer programs.

3. Results and discussion

The reactions of $[RuHCl(CO)(PPh_3)_3]$ and $[(C_6H_6)RuCl_2]_2$ with 2-benzoylpyridine have been examined in the same solvent and under the same conditions, as may be seen in Fig. 3. In the first case, the oxidation of 2-benzoylpyridine was observed. As the two reactions have been made in air under the same conditions, we consider the hydrido ligand or the hydrido ruthenium complex plays the role in this oxidation rather than the molecular oxygen.

The reaction between $[RuHCl(CO)(PPh_3)_3]$ and 2-benzoylpyridine in dimethoxyethane solution, under atmospheric conditions, yielded the mononuclear ruthenium(II) compound $[RuCl(CO)(PPh_3)_2(C_5H_4NCOO)]$ with a 2-pyridinecarboxylate ligand as a brown, air-stable, crystalline solid. The infrared spectrum of the complex exhibits characteristic bands of the COO stretching mode: an asymmetric vibration at 1568 cm^{-1} and a symmetric vibration at 1344 cm^{-1}. The C=N stretching modes are visible at 1647 cm^{-1}. The $\nu_{Ph(P-Ph)}$ absorption band is visible at 1433 cm^1. The strong band at 1946 cm^{-1} is assigned to the ν_{CO} stretching of the carbonyl bonded to the ruthenium centre.

The pyridinecarboxylato and triphenylphosphine ligands give signals at 8.54 ppm (position six of the 2-pyridinecarboxylate ring) and in the 7.24–7.82 ppm region, respectively. The singlet at 31.61 ppm in the ^{31}P NMR spectrum indicates the coordinated triphenylphosphine ligands.

The reaction of $[(C_6H_6)RuCl_2]_2$ with 2-benzoylpyridine in the same solvent gave the ruthenium(II) chloride complex with coordinated benzoylpyridine ligands. In this reaction, the 2-benzoylpyridine is not oxidized to 2-pyridylocarboxylate.

The infrared spectrum of the complex exhibits characteristic bands of the C=N stretching modes, visible at 1663 cm^{-1}. The bands at 1594 and 1335 cm^{-1} are assigned to ν_{CO} stretching of the carbonyl bonded to the ruthenium centre. In the ^1H NMR spectrum, the sets of signals characteristic of the 2-benzoylpyridine ligand are visible.

3.1. Crystal structures

Complex **1** crystallizes as the solvate $\mathbf{1} \cdot DME \cdot 2H_2O$ (where DME = 1,2-dimethoxyethane). The crystal data of the complexes $\mathbf{1} \cdot DME \cdot 2H_2O$ and **2** are given in Table 1. The molecular structures of **1** and **2** are presented in Figs. 1 and 2, respectively. The complexes crystallize respectively in the triclinic $P\bar{1}$ and monoclinic *Cc* space group. The most important angles and bond lengths for **1** and **2**are reported in Tables 2 and 3, respectively. The weak intra- and intermolecular hydrogen bonds [20,21] of $\mathbf{1} \cdot DME \cdot 2H_2O$ are presented in Table 4.

The ruthenium atom in the complex $[RuCl(CO)(PPh_3)_2(C_5H_4NCOO)]$ (**1**) has a distorted octahedral environment with *trans* triphenylphosphine ligands (P(1)–Ru(1)–P(2) 174.50(2)°). The carbonyl ligand is in a *trans* position to the pyridine N donor atom (C(43)–Ru(1)–N(1) 176.60(9)°) and the chloride ion lies *trans* to the coordinated oxygen from the COO group at an angle of 169.98(5)°. All Ru-ligand distances, such as Ru–Cl 2.4037(7) Å, Ru–P 2.3942(7), 2.3961(7) Å, Ru–N

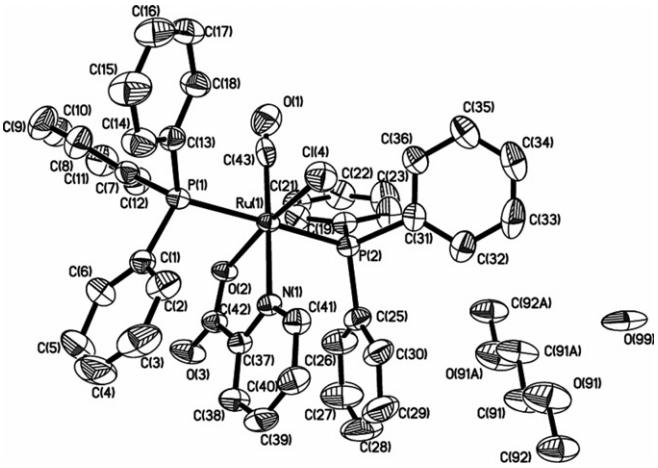


Fig. 1. ORTEP drawing of $[RuCl(CO)(PPh_3)_2(C_5H_4NCOO)]$ with 50% probability thermal ellipsoids. The hydrogen atoms are omitted for clarity.

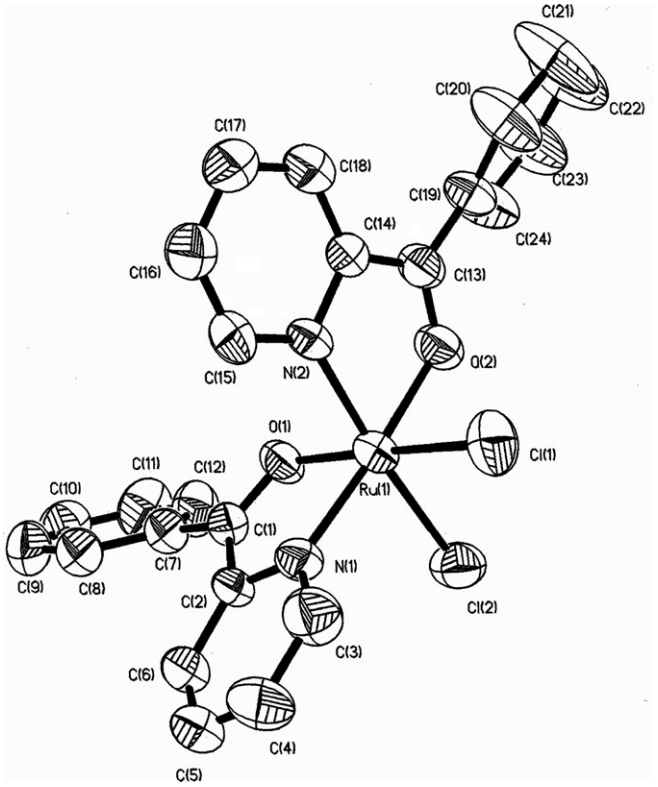


Fig. 2. ORTEP drawing of $[RuCl_2(C_{12}H_9NO)_2]$ with 50% probability thermal ellipsoids. The hydrogen atoms are omitted for clarity.

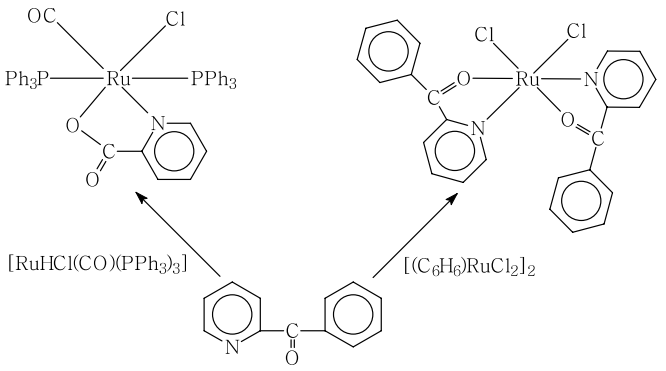


Fig. 3. The scheme of the reactions between 2-benzoylpyridine and $[RuHCl(CO)(PPh_3)_3]$ and $[(C_6H_6)RuCl_2]_2$ complexes.

Table 2
Selected bond lengths (Å) and angles (°) for $[RuCl(CO)(PPh_3)_2(C_5H_4NCOO)]$

	Experimental	Calculated
Bond lengths (Å)		
Ru(1)–C(43)	1.978(4)	1.872
Ru(1)–O(2)	2.1195(16)	2.129
Ru(1)–N(1)	2.1439(19)	2.196
Ru(1)–P(1)	2.3942(7)	2.474
Ru(1)–P(2)	2.3961(7)	2.474
Ru(1)–Cl(4)	2.4037(7)	2.451
C(42)–O(2)	1.300(3)	1.306
C(42)–O(3)	1.228(3)	1.226
C(43)–O(1)	0.922(4)	1.159
Bond angles (°)		
C(43)–Ru(1)–O(2)	99.29(9)	99.19
C(43)–Ru(1)–N(1)	176.60(9)	175.71
O(2)–Ru(1)–N(1)	77.41(7)	76.51
C(43)–Ru(1)–P(1)	89.09(8)	87.58
O(2)–Ru(1)–P(1)	87.98(5)	88.21
N(1)–Ru(1)–P(1)	91.59(6)	92.24
C(43)–Ru(1)–P(2)	89.04(8)	87.58
O(2)–Ru(1)–P(2)	87.22(5)	88.21
N(1)–Ru(1)–P(2)	89.98(6)	92.25
P(1)–Ru(1)–P(2)	174.50(2)	173.46
C(43)–Ru(1)–Cl(4)	90.61(8)	94.09
O(2)–Ru(1)–Cl(4)	169.98(5)	166.71
N(1)–Ru(1)–Cl(4)	92.71(5)	90.20
P(1)–Ru(1)–Cl(4)	90.71(3)	92.37
P(2)–Ru(1)–Cl(4)	94.48(3)	92.37

2.1439(19) Å Ru–C 1.978(4) Å and Ru–O 2.1195(16) Å, are normal and are comparable with the distances in other ruthenium complexes containing heterocyclic ligands [22–24]. The conformation of the molecule is stabilised by three weak intramolecular hydrogen bonds, two between phenyl CH and O(2) (COO) (the D···A distance varies from 3.112(3) to 3.250(3) Å and the D–H···A angle varies from 141.9° to 143.5°) and one linking the pyridine C(41)–H(41) and Cl(4) (D···A distance 3.354(3) Å and D–H···A angle 123.1°). The fourth intermolecular hydrogen bond is formed between water and dimethoxyethane molecules – O(99)–H(99)···O(91) (D···A distance 2.842(6); D–H···A angle 135.0).

The $[RuCl_2(C_{12}H_9NO)_2]$ (**2**) complex possesses chlorine ligands in a *cis* arrangement. The distortions from the ideal octahedral geometry are particularly distinct in the angles between O(1)–Ru(1)–N(1) – 79.03(12)°, N(2)–Ru(1)–O(2) – 78.55(12)° and N(1)–Ru(1)–N(2) – 100.96(13)°. The Ru-ligand distances are normal. No unusual short intermolecular contacts can be found in the structure.

Table 3
Selected bond lengths (Å) and angles (°) for $[RuCl_2(C_{12}H_9NO)_2]$

	Experimental	Calculated
Bond lengths (Å)		
Ru(1)–Cl(1)	2.3893(11)	2.3952
Ru(1)–Cl(2)	2.3981(11)	2.4066
Ru(1)–N(1)	2.019(3)	2.0488
Ru(1)–N(2)	2.025(3)	2.0818
Ru(1)–O(1)	2.013(2)	2.0762
Ru(1)–O(2)	2.048(3)	2.0768
C(1)–O(1)	1.254(4)	1.2546
C(13)–O(2)	1.276(4)	1.2607
Bond angles (°)		
O(1)–Ru(1)–N(1)	79.03(12)	76.80
O(1)–Ru(1)–N(2)	91.21(11)	94.37
N(1)–Ru(1)–N(2)	100.96(13)	102.89
O(1)–Ru(1)–O(2)	94.34(11)	99.15
N(1)–Ru(1)–O(2)	173.35(15)	176.65
N(2)–Ru(1)–O(2)	78.55(12)	77.53
O(1)–Ru(1)–Cl(1)	176.93(8)	173.44
N(1)–Ru(1)–Cl(1)	98.15(10)	96.07
N(2)–Ru(1)–Cl(1)	88.11(9)	86.64
O(2)–Ru(1)–Cl(1)	88.47(8)	87.24
O(1)–Ru(1)–Cl(2)	88.06(8)	85.58
N(1)–Ru(1)–Cl(2)	85.85(10)	85.94
N(2)–Ru(1)–Cl(2)	172.88(9)	171.13
O(2)–Ru(1)–Cl(2)	94.45(8)	94.34
Cl(1)–Ru(1)–Cl(2)	92.99(4)	94.43

Table 4
Hydrogen bonds for $[RuCl(CO)(PPh_3)_2(C_5H_4NCOO)]\cdot DME\cdot 2H_2O$ (Å and °)

D–H···A	*d*(D–H)	*d*(H···A)	*d*(D···A)	∠(DHA)
C(12)–H(12)···O(2)	0.93	2.33	3.112(3)	141.9
C(20)–H(20)···O(2)	0.93	2.45	3.250(3)	143.5
C(41)–H(41)···Cl(4)	0.93	2.75	3.354(3)	123.1
O(99)–H(99)···O(91)	0.96	2.09	2.842(6)	135.0

3.2. Geometry optimisation

The geometries of **1** and **2** were optimised by the DFT method with the B3LYP functional. The optimised geometry parameters for the studied complexes are gathered in Tables 2 and 3. In general, the predicted bond lengths and angles are in good agreement with the values based upon the X-ray crystal structure data, and the general trends observed in the experimental data are well reproduced in the calculations. The calculated bond lengths and angles for $[RuCl(CO)(PPh_3)_2(C_5H_4NCOO)]$ (**1**) agree with the experimental results; the largest difference is found for the Ru(1)–C(43) bond (~0.1 Å). The maximum difference between the calculated and experimental angles is visible for O(2)–Ru(1)–Cl(4) and it is close to 3.3°.

The largest differences for complex $[RuCl_2(C_{12}H_9NO)_2]$ (**2**) between the experimental and calculated geometry are visible in the Ru(1)–O(1) distance (~0.06 Å) and O(1)–Ru(1)–O(2) angle – 4.81°.

3.3. Charge distribution and NBO analysis

The calculated charge on the ruthenium atom in the complex $[RuCl(CO)(PPh_3)_2(C_5H_4NCOO)]$ (**1**) is considerable lower than the formal +2 charge, and it is close to 0.3. This is a result of significant charge donation from the ligands. The charges on the P atoms are positive and close to 1.15; the charge on the chloride ligand is significantly smaller than −1 (−0.57), the charge on the pyridinecarboxylate ligand is close to −0.544. Three natural bond orbitals were detected for the C≡O bond in the complex, and one for the Ru–C bond.

The Ru–C bond orbitals are polarized towards the carbon atom, and the C–O bond orbitals are polarized towards the oxygen end. The oxygen atom of the carbonyl ligand has one lone pair (LP) orbital. The occupancies and hybridization of the CO and Ru–C bonds are given in Table 5 (*anti*-bonding NBOs are given in round brackets). The occupancies of the ruthenium d orbitals, obtained from NBO analysis, are as follows: d_{xy} – 1.76; d_{xz} – 1.93; d_{yz} – 1.39; $d_{x^2-y^2}$ – 1.13; d_{z^2} – 1.13.

The central ruthenium ion in complex **2** has a formal charge of +2. Its natural charge from Natural Populations Analysis is close to 1.01. The charges on the chloride ligands are −0.565 and −0.564; the O and N donors have −0.540, −0.520 and −0.424, −0.428 charges, respectively. The Re–Cl, Ru–N and Ru–O natural bonds were not detected in the complex, indicating predominant Coulomb-type interactions between the central ion and the chloride and 2-benzoylpyridine ligands. The occupancies of the ruthenium d orbitals, obtained from NBO analysis, are as follows: d_{xy} – 0.84; d_{xz} – 1.40; d_{yz} – 1.74; $d_{x^2-y^2}$ – 1.69; d_{z^2} – 1.02.

3.4. Electronic structure

The energies and characters of several highest occupied and lowest unoccupied molecular orbitals of the studied complexes are presented in Table 6. The percent shares of the atomic orbitals in the HOMO and LUMO orbitals are given in round brackets. The HOMO–LUMO gaps for complexes **1** and **2** are 4.19 and 2.43 eV, respectively. In both cases, the ruthenium atom possesses a d^6 configuration, the highest MO is of d_{xz} type with antibonding contributions from p_π chlorine and p_π oxygen orbitals for complex **1** and p_π chlorine ligands for **2**. The remaining four d-type orbitals of ruthenium are found in HOMO − 1,

Table 5
The occupancies and hybridization of the calculated Ru–C and C–O natural bond orbitals (NBOs) for $[RuCl(CO)(PPh_3)_2(C_5H_4NCOO)]$

BD (2-center bond)	Occupancy	Hybridization of NBO
Ru(1)–C(43)	1.935 (0.322)	$0.550(sd^{5.08})_{Ru} + 0.835(sp^{0.54})_C$
C(43)–O(1)	1.997 (0.204)	$0.553(spd^{1.97})_C + 0.833(spd^{1.36})_O$
	1.997 (0.012)	$0.496(p)_C + 0.868(p)_O$
	1.994 (0.076)	$0.554(sp^{1.85})_C + 0.833(sp^{1.14})_O$

Table 6
The energy and character of selected molecular orbitals for complexes **1** and **2**

	[RuCl(CO)(PPh_3)$_2$(C_5H_4NCOO)] (**1**)		[$RuCl_2(C_{12}H_9NO)_2$] (**2**)	
	E (eV)	Character	*E* (eV)	Character
HOMO − 20	−8.107	d_{Ru}(31.9); π_{Cl}(34.2)	−9.613	π_{Ph}
HOMO − 19	−8.064	d_{Ru}(28.2); π_{Cl}(23.5); π_{O}(20.1)	−9.517	π_{Ph}
HOMO − 18	−7.519	π_{Cl}(50.8); π_{O}(17.5)	−9.027	$\pi_{pyridine}$(33.1); π_{O}(25.9)
HOMO − 17	−7.504	$\pi_{pyridine}$	−8.839	$\pi_{pyridine}$
HOMO − 16	−7.338	$\pi_{pyridine}$	−8.753	$\pi_{pyridine}$
HOMO − 15	−7.162	π_{Ph}	−8.525	$\pi_{pyridine}$(46.7); π_{O}(36.4)
HOMO − 14	−7.045	π_{O}(62.8); $\pi_{pyridine}$(16.8)	−8.108	π_{Cl}
HOMO − 13	−7.035	π_{Ph}	−7.984	π_{Cl}(34.9); $\pi_{pyridine}$(38.5)
HOMO − 12	−7.033	π_{Ph}	−7.942	π_{Cl}(26.2); $\pi_{pyridine}$(46.4)
HOMO − 11	−6.995	π_{Ph}(32.4); d_{xz}(23.8)	−7.823	π_{Cl}(34.7); $\pi_{pyridine}$(36.8)
HOMO − 10	−6.958	π_{Ph}	−7.570	π_{Cl}
HOMO − 9	−6.917	π_{Ph}	−7.423	π_{Cl}
HOMO − 8	−6.880	π_{Ph}	−7.244	π_{Ph}
HOMO − 7	−6.825	π_{Ph} (31.4); d_{l}(27.7)	−7.186	π_{Ph}
HOMO − 6	−6.821	π_{Ph}	−7.164	π_{Ph}
HOMO − 5	−6.806	π_{Ph}(34.8); d(22.5)	−7.1143	π_{Ph}
HOMO − 4	−6.801	π_{Ph}	−7.064	π_{Cl}
HOMO − 3	−6.704	π_{Ph}(32.0); d(22.3)	−6.664	π_{Cl}
HOMO − 2	−6.129	π_{Ph}(21.1); d(21.2); n_{P}(27.5)	−5.477	d(69.2); π_{Cl}(15.8)
HOMO − 1	−6.044	d(53.9); π_{Cl}(25.9)	−5.403	d(70.2); π_{Cl}(11.8)
HOMO	−5.708	d(64.3); π_{Cl}(22.2)	−5.186	d(72.6); π_{Cl}(17.9)
LUMO	−1.522	$\pi^*_{pyridine}$	−2.759	d(14.2); π^*_{O}(15.8); $\pi^*_{pyridine}$ (24.7)
LUMO + 1	−1.319	d(44.3)–σ_{P}(18.9)	−2.719	d(12.5); π^*_{Cl}(16.6); $\pi^*_{pyridine}$ (25.9)
LUMO + 2	−0.946	$\pi^*_{pyridine}$	−1.253	$\pi^*_{pyridine}$
LUMO + 3	−0.855	d(30.3)–σ_{P}(23.8)	−1.201	$\pi^*_{pyridine}$
LUMO + 4	−0.706	d(25.3)–σ_{P}(26.5)	−0.790	d(12.1); $\pi^*_{pyridine}$ (35.8); π^*_{Ph} (42.7)
LUMO + 5	−0.699	π^*_{Ph}	−0.739	$\pi^*_{pyridine}$ (40.6); π^*_{Ph} (52.1)
LUMO + 6	−0.534	π^*_{Ph}	−0.425	d(42.4); π^*_{Ph} (24.3); π^*_{Cl} (14.1)
LUMO + 7	−0.526	π^*_{Ph}	−0.348	π^*_{Ph}
LUMO + 8	−0.377	π^*_{Ph}	−0.316	π^*_{Ph}
LUMO + 9	−0.316	π^*_{Ph}	−0.041	d(55.6); $\pi^*_{pyridine}$ (10.5)
LUMO + 10	−0.222	π_{CO}	0.906	π^*_{Ph}(33.0); $\pi^*_{pyridine}$(35.8)
LUMO + 11	−0.219	π^*_{Ph}	0.981	π^*_{Ph}(33.2); $\pi^*_{pyridine}$(34.4)
LUMO + 12	−0.037	π^*_{Ph}	1.563	$\pi^*_{pyridine}$
LUMO + 13	−0.003	π^*_{Ph}	2.625	π^*_{Ph}

HOMO − 2 and unoccupied LUMO and LUMO + 1 molecular orbitals.

3.5. Electronic spectrum

The experimental and calculated allowed singlet transitions, with the TDDFT method, electronic spectra of complexes **1** and **2** are presented in Figs. 4 and 5. With the use of this method, 100 electronic transitions were calculated for the studied complexes using the DZVP with *f* functions basis set on the ruthenium atom.

The first experimental band at 370.0 nm in [RuCl(CO)(PPh_3)$_2$(C_5H_4NCOO)] (**1**) consists of d → d (LF – ligand field) and d → $\pi^*_{pyridine}$ (MLCT – metal–ligand charge transfer) transitions. The second one was calculated as a LLCT (ligand–ligand charge transfer). The transitions are interligand type between $\pi_{phosphine}$ and $\pi^*_{pyridine}$ orbitals with contribution of MLCT – excitation between ruthenium d and $\pi^*_{phosphine}$ orbitals.

The UV–Vis spectrum was calculated to ~226 nm, so the shortest wavelength experimental bands cannot be assigned to calculated transitions. However, considering that the solution spectra of PPh_3 and pyridenecarboxylic acid exhibit intense absorption bands in the 260–200 nm region, some additional intraligand and interligand transitions are expected to be found at higher energies in the calculations.

In the case of [$RuCl_2(C_{12}H_9NO)_2$] (**2**), the low energy unsymmetrical experimental band with a maximum at 737.6 nm was assigned to the transition from HOMO, HOMO − 1 and HOMO − 2 to LUMO and LUMO + 1 molecular orbitals. As the LUMO and LUMO + 1 orbitals are composed of ruthenium d and π^* orbitals of 2-benzoylpyridine, the transitions are LF (ligand field) ones with a contribution of MLCT type. The next maximum in the experimental spectrum at 600.0 nm results from the excitation between d-type HOMO orbitals to LUMO + 1, LUMO + 2 and LUMO + 7 MOs. The excitations are also of LF and MLCT type.

The band with a maximum at 3760.4 nm is composed mainly from the excitation from π_{Cl} to LUMO MOs composed of ruthenium d and $\pi^*_{2\text{-benzoylpyridine}}$ orbitals. This is a

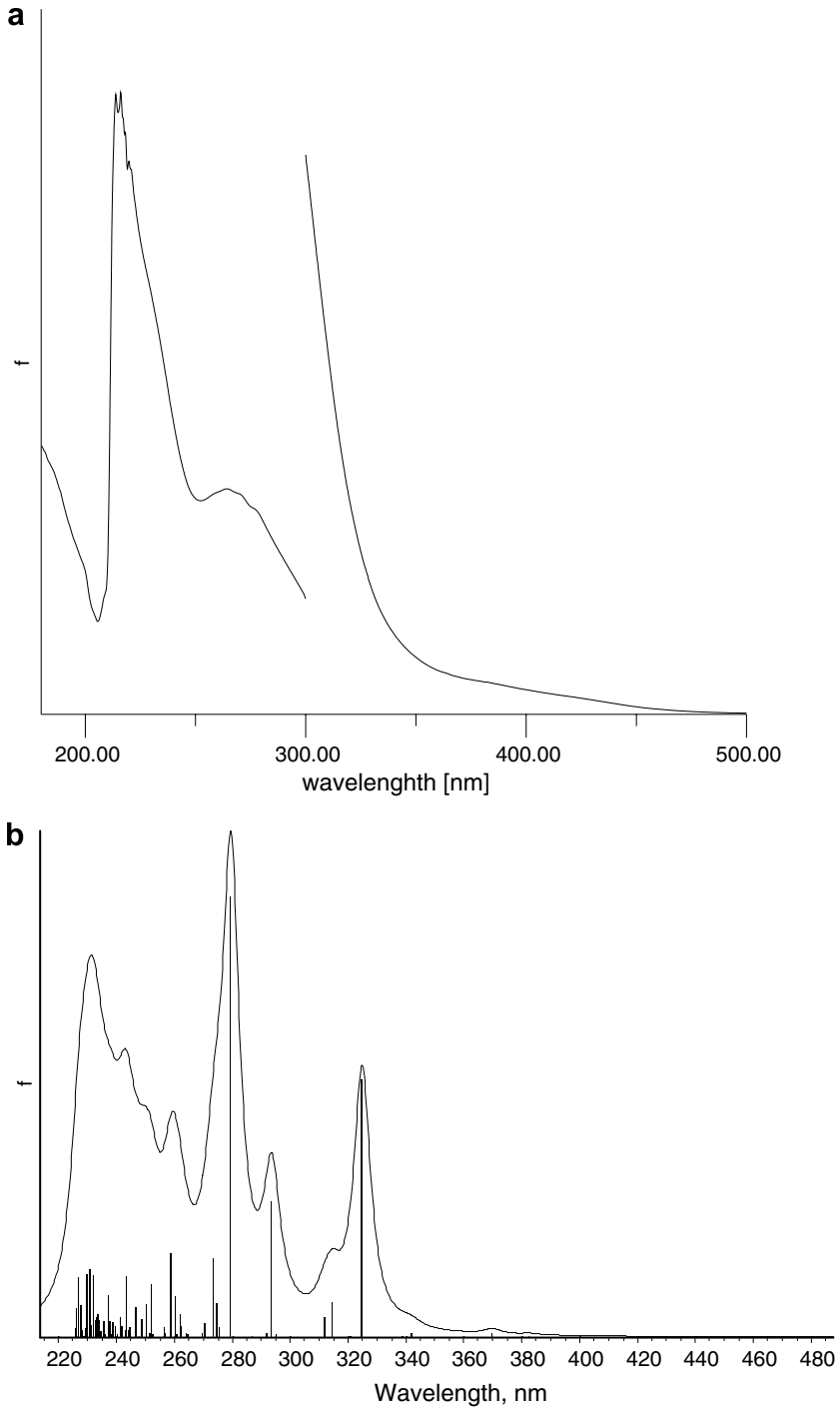


Fig. 4. The UV–Vis spectra of $[RuCl(CO)(PPh_3)_2(C_5H_4NCOO)]$ (a) experimental; (b) calculated.

LMCT type. The LLCT transitions play a role in the high energy experimental bands with maxima at 266.0 and 218.2 nm. The first band is mainly composed of interligand transitions ($\pi_{phosphine} \rightarrow \pi^*_{pyridine}$; $\pi_{Cl} \rightarrow \pi^*_{pyridine}$) with contribution of MLCT transitions ($d \rightarrow \pi^*_{pyridine}$). In the highest energy band (maximum at 218.2 nm), mainly the intra- and interligand transitions are observed ($\pi_{phosphine} \rightarrow \pi^*_{pyridine}$; $\pi_{pyridine} \rightarrow \pi^*_{pyridine}$; $\pi_{Cl} \rightarrow \pi^*_{pyridine}$).

4. Supplementary material

CCDC 626007 and 626449 contain the supplementary crystallographic data for **1** and **2**. The data can be obtained free of charge via htpp://www.ccdc.cam.ac.uk/conts/retrieving.html, or from the Cambridge Crystallographic Data Centre, 12 Union Road, Cambridge CB2 1EZ, UK; fax: (+44) 1223-336-033; or e-mail: deposit@ccdc.cam.ac.uk.

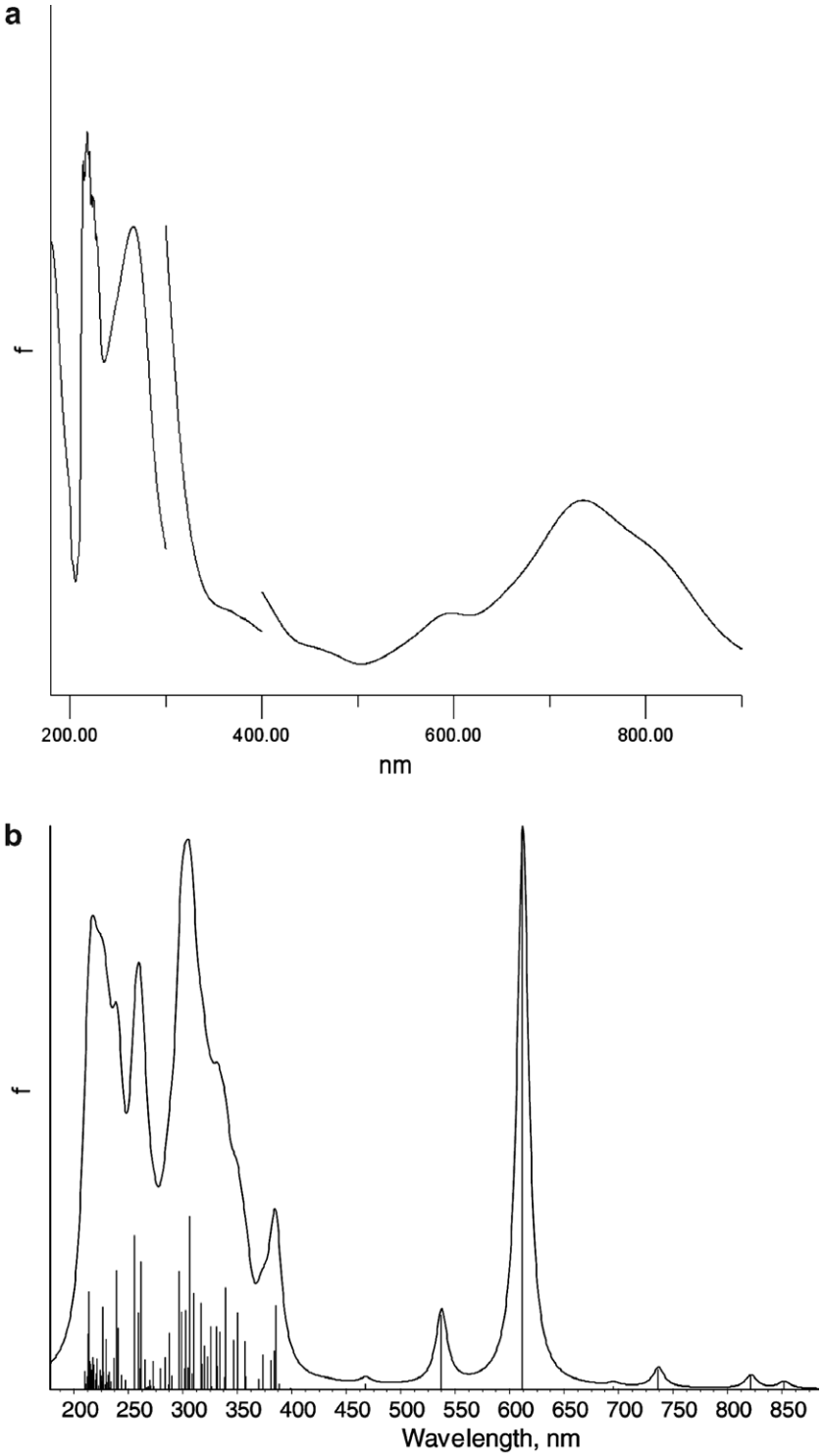


Fig. 5. The UV–Vis spectra of $[RuCl_2(C_{12}H_9NO)_2]$ (a) experimental; (b) calculated.

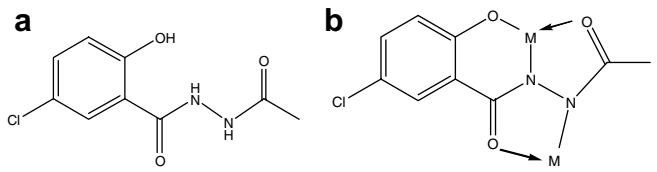
Acknowledgements

The crystallographic part was financed by funds allocated by the Ministry of Science and Higher Education to the Department of X-ray Crystallography and Crystal Chemistry, Institute of General and Ecological Chemistry, Technical University of Łódź.

References

[1] C. Pettinari, F. Accorroni, A. Cingolani, F. Marchetti, A. Cassetta, L. Barba, J. Organomet. Chem. 566 (1998) 187.
[2] M.A.M. Abu-Youssef, A. Escuer, D. Gatteschi, M.A.S. Goher, F.A. Mautner, R. Vicente, Inorg. Chem. 38 (1999) 5716.
[3] C. Sudbrake, H. Vahrenkamp, Inorg. Chim. Acta 318 (2001) 23.

[4] D.L. Reger, J.R. Gardinier, M.D. Smith, P.J. Pellechia, Inorg. Chem. 42 (2003) 482.
[5] C.J. Milios, T.C. Stamatatos, P. Kyritsis, A. Terzis, C.P. Raptopoulou, R. Vicente, A. Escuer, S.P. Perlepes, Eur. J. Inorg. Chem. (2004) 2885.
[6] I. Aiello, A. Crispini, M. Ghedini, M.L. Deda, F. Barigelletti, Inorg. Chim. Acta 308 (2000) 121.
[7] Y. Fuchita, H. Ieda, Y. Tsunemune, J. Kinoshita-Nagaoka, H. Kawano, J. Chem. Soc., Dalton Trans. (1998) 791.
[8] H. Brunner, in: B. Cornils, W.A. Herrmann (Eds.), Applied Homogeneous Catalysis with Organometallic Compounds, vol. 2, VCH, Weinheim, 1996, p. 201.
[9] N. Ahmad, J.J. Levinson, S.D. Robinson, M.F. Uttely, Inorg. Synth. 15 (1974) 48.
[10] M.J. Frisch, G.W. Trucks, H.B. Schlegel, G.E. Scuseria, M.A. Robb, J.R. Cheeseman, J.A. Montgomery Jr., T. Vreven, K.N. Kudin, J.C. Burant, J.M. Millam, S.S. Iyengar, J. Tomasi, V. Barone, B. Mennucci, M. Cossi, G. Scalmani, N. Rega, G.A. Petersson, H. Nakatsuji, M. Hada, M. Ehara, K. Toyota, R. Fukuda, J. Hasegawa, M. Ishida, T. Nakajima, Y. Honda, O. Kitao, H. Nakai, M. Klene, X. Li, J.E. Knox, H.P. Hratchian, J.B. Cross, C. Adamo, J. Jaramillo, R. Gomperts, R.E. Stratmann, O. Yazyev, A.J. Austin, R. Cammi, C. Pomelli, J.W. Ochterski, P.Y. Ayala, K. Morokuma, G.A. Voth, P. Salvador, J.J. Dannenberg, V.G. Zakrzewski, S. Dapprich, A.D. Daniels, M.C. Strain, O. Farkas, D.K. Malick, A.D. Rabuck, K. Raghavachari, J.B. Foresman, J.V. Ortiz, Q. Cui, A.G. Baboul, S. Clifford, J. Cioslowski, B.B. Stefanov, G. Liu, A. Liashenko, P. Piskorz, I. Komaromi, R.L. Martin, D.J. Fox, T. Keith, M.A. Al-Laham, C.Y. Peng, A. Nanayakkara, M. Challacombe, P.M.W. Gill, B. Johnson, W. Chen, M.W. Wong, C. Gonzalez, J.A. Pople, Gaussian 03, Revision B.03, Gaussian, Inc., Pittsburgh PA, 2003.
[11] A.D. Becke, J. Chem. Phys. 98 (1993) 5648.
[12] C. Lee, W. Yang, R.G. Parr, Phys. Rev. B 37 (1988) 785.
[13] B. Mennucci, J. Tomasi, J. Chem. Phys. 106 (1997) 5151.
[14] K. Eichkorn, F. Weigend, O. Treutler, R. Ahlrichs, Theor. Chim. Acc. 97 (1997) 119.
[15] E.D. Glendening, A.E. Reed, J.E. Carpenter, F. Weinhold, NBO (version 3.1).
[16] A.D. Becke, J. Chem. Phys. 98 (1993) 5648.
[17] G.M. Sheldrick, Acta Cryst. A46 (1990) 467.
[18] SHELXL97 G.M. Sheldrick, SHELXL97. Program for the Solution and Refinement of Crystal Structures, University of Göottingen, Germany, 1997.
[19] G.M. Sheldrick, SHELXTL: release 4.1 for Siemens Crystallographic Research Systems, 1990.
[20] G.A. Jeffrey, W. Saenger, Hydrogen Bonding in Biological Structures, Springer-Verlag, 1994.
[21] G.R. Desiraju, T. Steiner, The Weak Hydrogen Bond in Structural Chemistry and Biology, Oxford University Press, 1999.
[22] R. Mukherjee, Coord. Chem. Rev. 203 (2000) 151.
[23] I.D. Brown, Acta Cryst. B53 (1997) 381.
[24] T. Hirano, M. Kuroda, N. Takeda, M. Hayashi, M. Mukaida, T. Oi, H. Nagao, J. Chem. Soc., Dalton Trans. (2002) 2158.



Scheme 1. Ligand H_3acshz (a) and the basic bonding sites of H_3acshz in compounds (b).

diethyl ketipinate [16], 3-hydroxy-2-pyridone [17] or 3-thione-1,2-dithione-4,5-dithiolato [18] also been used for metallacrown preparation. Metallacrowns can be molecular building blocks, forming one, two and three dimensional network structures by facial interactions and anion bridging [19–22], and stacking metallacrowns [23,16], a variety of dimers as well as fused metallacrowns [4b,8,24] have been found.

To examine the mode of binding and possible antagonistic or synergetic effects, much research has been carried out. Antibacterial screening data showed that 15-$MC_{Mn(III)N(shi)}$-5 and 12-$MC_{Mn(III)N(shi)}$-4 metallacrowns are more active than the simple manganese herbicide or carboxylate complexes, and the number of chlorides in the second ligand is likely to affect the efficiency of the compounds [25]. Whereas all the metallacrowns relative to the studies are of the hydroxamic acid type, our interests are focused on salicylhydrazide derivatives. Another important reason is that these ligands are not only propitious for the preparation of metallacrowns but they also have biological activities [11,12,26].

In this paper, we report a new potential pentadentate ligand H_3acshz, *N*-acetyl-5-chlorosalicylhydrazide, and two novel metal(III) 18-metallacrown-6 complexes, $[Mn_6(acshz)_6(H_2O)_6]\cdot 18H_2O$ (**1**) and $[Fe_6(acshz)_6(CH_3OH)_6]\cdot 6CH_3OH\cdot 6H_2O$ (**2**). The triply deprotonated $acshz^{3-}$ of the compounds may bridge the neighboring metal ions through its hydrazide N–N group as shown in Scheme 1. Minimum inhibitory concentrations (MIC) of the metallacrown complexes against four different bacteria species were also measured.

2. Experimental

2.1. Materials

All reactions were carried out in air. The following solvents were used as received with no further purification: methanol and *N*,*N*-dimethylformamide (DMF). 5-Chlorosalicylic acid, sulfuric acid, hydrazine hydrate, acetic anhydride, tetrabutylammonium perchlorate (tbap), $Mn(OAc)_2\cdot 4H_2O$ and $Fe(NO_3)_3\cdot 9H_2O$ were purchased from China Sinopharm Group Chemical Reagent Co., Ltd. All chemicals and solvents were reagent grade. *Staphylococcus aureus* (*S. aureus*), *Escherichia coli* (*E. coli*), *Bacillus subtilis* and *Proteus vulgaris* (*P. vulgaris*) were purchased from the China Center for Type Culture Collection.

2.2. Physical measurements

^1H and ^{13}C NMR spectra were recorded on a Varian Inova 600 MHz NMR spectrometer at 25 °C. Chemical shifts were referenced to the residual solvent peak. IR spectra were recorded on AVATAR 360 FT-IR spectrophotometer. UV–Vis spectra were recorded on a Shimadzu-UV-2501 spectrophotometer. Melting points were obtained with a digital melting-point apparatus, TP Micro Printer S-X6. Elemental analyses were performed on a Perkin–Elmer 2400 CHN elemental analytical instrument for C, H, N and Perkin–Elmer OPTIMA 2000 DV Optical Emission Spectrometer for Mn and Fe. Positive and negative electrospray ionization mass spectra (ESI(±)-MS) were performed on API-2000 LC/MS/MS system for the metallacrown **1** dissolved in methanol and DMF. Cyclic voltammetry (CV) studies were performed on Eco Chemie Autolab Eletrochemical analyzer. The experiments were carried out in a three-electrode cell with a platinum electrode, a glass–carbon electrode as the working electrode and a Ag/AgCl electrode saturated with KCl as the reference electrode. The supporting electrolyte was tetrabutylammonium perchlorate (tbap) recrystallized twice from ethanol and dried under vacuum. Pure nitrogen was insufflated in the solution of the compounds to remove the oxygen. All electrochemical measurements were carried out at room temperature.

2.3. Synthesis of the ligand H_3acshz

5-Chlorosalicyhyrazide was synthesized according to the literature procedure [27]. Acetic anhydride (6.8 g, 66.8 mmol) and 5-chlorosalicylhydrazide (11.0 g, 56.0 mmol) were added to 120 mL of chloroform with an external ice-water bath. The reaction mixture was slowly warmed to room temperature and stirred for 8 h. After leaving overnight in a refrigerator, the resulting white precipitate was filtered and rinsed with chloroform and diethyl ether. Yield: 12.2 g, 95.3%. Melting point: 209–210 °C. *Anal.* Calc. for $C_9H_9N_2O_3Cl$: C, 47.24; H, 3.96; N, 12.26. Found: C, 47.18; H, 3.98; N, 12.19%. IR (KBr pellet, cm^{-1}): 3446 m; 3190 vs, broad; 2710 w; 1650 m; 1625 s; 1605 vs; 1572 m; 1488 m; 1405 m; 1220 w; 1178 w; 817 m; ^1H NMR (600 MHz, DMSO-d_6, 25 °C), δ ppm: 11.94 (s, 1H, Ar–OH); 10.54 (s, 1H, Ar–CO–NH–); 10.31 (s, 1H, Me–CO–NH–); 7.90 (s, 1H, *o*-Ar–H); 7.49 (1H, *p*-Ar–H); 7.01 (1H, *p*-Ar–H); 1.94 (s, 3H, –CH_3). ^{13}C NMR (150.9 MHz, DMSO-d_6, 25 °C), δ ppm: 168.35 (Me–CO–); 165.38 (Ar–CO–); 157.82 (ArC–OH); 134.11 (*p*-ArC); 128.70 (*o*-ArC); 123.43 (ArC–); 119.85 (*m*-ArC); 117.37 (*m*-ArC–Cl); 21.08 (–CH_3).

2.4. Preparation of the compounds

$[Mn_6(acshz)_6(H_2O)_6]\cdot 18H_2O$ (**1**). H_3acshz (0.11 g, 0.50 mmol) was dissolved in 40 mL of 20:1 methanol + DMF, and 0.13 g (0.50 mmol) of $Mn(OAc)_2\cdot 4H_2O$ was

dissolved in 5 mL methanol. The two solutions were mixed and stirred for 2 h with the color of the mixture changing to dark brown, then the mixture was filtered. After slow evaporation of the mother liquor over 2 weeks, dark brown block crystals suitable for X-ray diffraction were obtained. Yield: 85.2%. *Anal.* Calc. for $C_{54}H_{84}Cl_6Mn_6N_{12}O_{42}$: C, 30.65; H, 4.00; N, 7.94; Mn, 15.58. Found: C, 30.94; H, 3.89; N, 8.01; Mn, 15.96%. IR (KBr pellet, cm^{-1}): 3437 m, broad; 1656 m; 1607 ms; 1561 m; 1512 s; 1398 vs; 1317 w; 1275 w; 640 w; 562 w. UV–Vis (CH_3OH, nm) [$\lambda_{max}(\varepsilon)$, L mol^{-1} cm^{-1}]: 234 (137840), 297 (51040), 374 (19430), 472 (3580).

$[Fe_6(acshz)_6(CH_3OH)_6] \cdot 6CH_3OH \cdot 6H_2O$ (**2**). This compound was prepared in a manner analogous to the manganese metallacrown above, without DMF in the solvent mixture. Three equivalents of anhydrous sodium acetate were added to adjust the pH of the solvent. After a few days some black block crystals were obtained. Yield: 88.6%. *Anal.* Calc. for $C_{66}H_{96}Cl_6Fe_6N_{12}O_{36}$: C, 36.34; H, 4.43; N, 7.71; Fe, 15.36. Found: C, 36.18; H, 4.28; N, 8.01; Fe, 15.64%. IR (KBr pellet, cm^{-1}): 3441 m, broad; 1657 m; 1608 ms; 1562 m; 1508 vs; 1405 vs; 1318 m; 1274 w; 633 w; 564 w. UV–Vis (CH_3OH, nm) [$\lambda_{max}(\varepsilon)$, L mol^{-1} cm^{-1}]: 224 (140284), 276 (82606), 318 (51313), 506 (5648).

2.5. Crystallographic data collection and refinement of the structures

Suitable crystals of the compounds **1** and **2** were mounted in glass capillaries with the mother liquor to prevent the loss of the structural solvent molecules during X-ray diffraction data collection. Intensity data were collected with graphite monochromatic Mo Kα radiation ($\lambda = 0.71073$ Å) at 292(2) K on a Bruker Smart APEX diffractometer. For **1**, from a total of 47540 reflections corrected by SADABS [28,29] in the $1.96 \leqslant \theta \leqslant 25.50°$ range, 3211 were independent with $R_{int} = 0.0613$, of which 2533 observed reflections with $I > 2\sigma(I)$ were used in the structural analysis. For **2,** from a total of 21265 reflections corrected in the $1.76° \leqslant \theta \leqslant 25.00°$ range, 8471 were independent with $R_{int} = 0.1076$, of which 5277 observed reflections with $I > 2\sigma(I)$ were used in the structural analysis. The structures were solved by direct methods and all non-hydrogen atoms were refined with anisotropic thermal parameters. All hydrogen atoms were located in calculated positions and/or in the positions from difference Fourier map. The positions and anisotropy from differences of non-hydrogen atoms were refined on F^2 by full-matrix least-squares techniques with the SHELXTL program package [29,30]. The crystallographic data are given in Table 4.

From the structure analysis, compound **1** consists of a Mn6 cluster and 18 water molecules of crystallization. Parts of the latter molecules were disordered and could not be modelled properly, thus the SQUEEZE subroutine of the PLATON program suite [31,32] was used to calculate the solvent disorder area and to remove its contribution to the overall intensity data.

Similarly, compound **2** consists of a Fe6 cluster, six methanol and six water molecules of crystallization. Difference electron density maps revealed the presence of the six disordered lattice water molecules which were ultimately modelled by use of SQUEEZE, and the atom C30 in the coordinated methanol (C30 H30A H30B H30C O12 H12) showed some disorder with a large U_{eq}. So the carbon atom and oxygen atom in this methanol molecule were refined anisotropically with splitting over two sites. The atoms H30A, H30B and H30C attached to the C30 atom were fixed geometrically and constrained to ride on the parent atom, C30.

2.6. Biological activity

The antimicrobial activity of the complexes was assessed by their ability to inhibit the growth of *S. aureus*, *E. Coli*, *B. subtilis* and *P. vulgaris* in Mueller–Hinton broth medium. The minimum inhibitory concentration in μg/mL against the four bacteria species was measured. The bacteria concentration was 500–800 cfu/mL and concentrations of 1600, 800, 400, 200, 100, 50 and 25 μg/mL of the complexes in methanol and DMF were tested. The solvents showed no antimicrobial action.

3. Results and discussion

3.1. Synthesis and characterization

One of the most important considerations is to have readily accessible or, at least, easily prepared building blocks when designing metal–cluster macrocyclic assemblies. From the first reported metallacrown compound, metallacrowns are typically prepared from hydroxamic acids and/or ketonoximic acids as the constructing ligand. In our report, the metallacrowns were synthesized by the reaction of another suitable ligand with transitional metal salts in an open system.

In the synthesis of compound **1**, dioxygen acts as the oxidant in the following reaction :

$$6H_3acshz + 6Mn(OAc)_2 + 18H_2O + 3O_2 \xrightarrow{\downarrow CH_3OH \text{ and DMF}} (\mathbf{1}) + 12HOAc \quad (1)$$

$$6H_3acshz + 6Fe(NO)_3 + 18NaOAc + 6H_2O + 12CH_3OH \xrightarrow{\downarrow CH_3OH} (\mathbf{2}) + 18HOAc \quad (2)$$

In the synthesis of compound **2**, there is no oxidation in the reaction (Eq. (2)). NaOAc was added to regulate the pH of the mother liquid.

In the ligand IR spectrum, there is a medium intensity band at 3446 cm^{-1} and strong intensity band at 3190 cm^{-1}, assigned to $\nu(OH)_{phenolic}$ and $\nu(NH)$ stretching vibrations, respectively. A strong intensity band at

1605 cm^{-1} and a medium intensity band at 1572 cm^{-1} are assigned to ν(C=O) and ν(N–C=O) vibrations of the salicyhydrazide ligand [33]. The frequency of $\delta(C–H)_{acetyl}$ at 1405 cm^{-1} differs from the δ-bending of the normal methyl in alkyls. Weak bands at 1220 and 1178 cm^{-1} should be assigned to ν(N–C) and δ(NH), respectively. In the compounds' IR spectra, the absence of the ν(N–H) band and the weakness of the ν(C=O) stretching vibration bands are consistent with the deprotonation of the CONH groups and coordination to the Mn(III) or Fe(III) ion. The deprotonation and coordination is also confirmed by the bands at 640 or 633 cm^{-1}, attributed to M–O linkages (phenolic and enolic oxygen), and the bands at 562 or 564 cm^{-1} assigned to M–N linkages [34,11b]. The medium intensity broad band at 3437 cm^{-1} in **1** and 3441 cm^{-1} in **2** are reasonably assigned to coordinated H_2O and crystal water molecules [35]. The N–C=O framework can be seen at 1572 cm^{-1} in the ligand and this band is shifted to 1561 and 1562 cm^{-1} on coordination to Mn and Fe atoms, and its relative intensity decreased. The disappearance of the bands at 3190 and 2710 cm^{-1} and the appearance of bands at 1317 and 1275 cm^{-1} support the involvement of the phenolic oxygen in coordination through deprotonation.

The electronic spectra were recorded in methanol for the ligand and the compounds. The spectrum of the ligand displayed absorption peaks at 244 nm (ε, 29 550) and 312 nm (ε, 22 898). The spectrum of compound **1** displayed absorption peaks at 234, 297, 374 and 472 nm. The bands at 234 nm can be attributed to internal ligand $\pi \rightarrow \pi^*$ or $n \rightarrow \pi^*$ transitions of the benzene rings, the substituted group of acetylhydrazide and π conjugation. The absorption maxima at 374 nm can be assigned to metal to ligand $M(d\pi) \rightarrow O(\pi)$ charge transfer (MLCT) transitions and the absorption maxima at 472 nm is assigned to a d–d transition of the transitional metal ions. The spectrum of compound **2** in methanol shown absorption peaks at 224, 276, 318 and 506 nm. Their assignments are analogous to the ones in compound **1**.

Cyclic voltammetry suggested that the metallacrowns **1** and **2** are electrochemical inactive in DMF in the range +1.5 to −1.5 V, which is consistent with the conjecture and conclusions in the earlier literature [7,25,36]. The absence of any redox activity of metallacrowns indicates that the metallacrown rings are redox stable. Notably, this ligand can stabilize three valent manganese ions in DMF.

3.2. Description of the structures of *1* and *2*

A perspective of the complete Mn6 cluster molecule of $[Mn_6(acshz)_6(H_2O)_6] \cdot 18H_2O$ is provided in Fig. 1. Compound **1** crystallizes in the rhombohedral system and space group $R\bar{3}c$. Important bond distances and bond angles are presented in Table 1.

The structure of compound **1** exhibits a hexanuclear ring of manganese atoms linked by six hydrazide N-N groups. The deprotonated ligand $acshz^{3-}$ acts as a trianionic pentadentate ligand, one phenolate oxygen, one carbonyl oxygen and one hydrazine nitrogen in the ligand are bound to one Mn^{3+} cation, and the other carbonyl oxygen plus the other hydrazide nitrogen in the same ligand are chelated to an adjacent Mn^{3+} cation. The ligand forces all Mn^{3+} cations into a propeller configuration with alternating Λ/Δ stereochemistry as $\Lambda\Delta\Lambda$ forms. Three water groups coordinated at the metal centers with Λ configuration are found on one face of the metallacrown, and the three remaining water groups coordinated to the other metal centers with

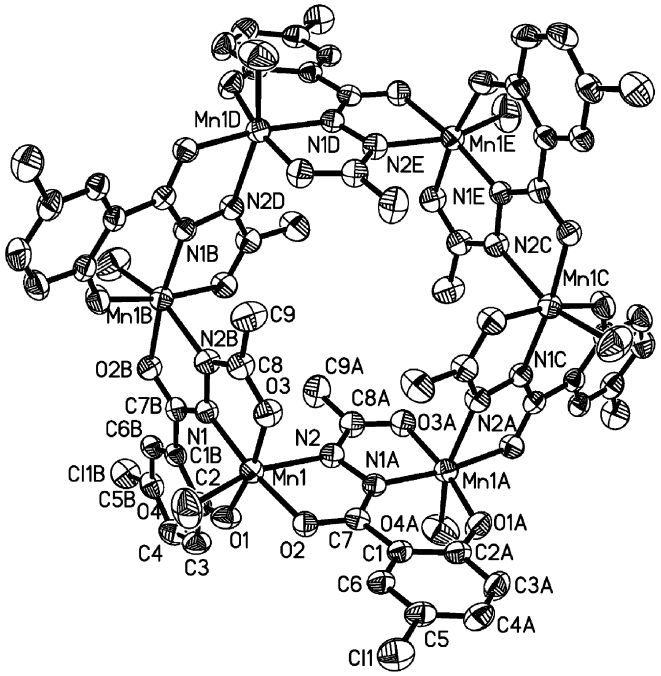


Fig. 1. Perspective view of compound **1**, solvent molecules and all hydrogen atoms have been omitted for clarity.

Table 1
Selected bond distances (Å) and angles (°) for compound **1**

Mn1–O1 1.8651(2)	Mn1–O2 1.9677(2)	Mn1–O3 1.9170(2)	Mn1–O4 2.236(3)
Mn1–N1 1.941(2)	Mn1–N2 2.252(2)	N1–N2 1.408(3)	
O1–Mn1–O3 170.03(8)	O1–Mn1–N1 90.74(8)	O3–Mn1–N1 79.89(8)	O1–Mn1–O2 97.60(8)
O3–Mn1–O2 91.91(7)	N1–Mn1–O2 171.34(8)	O1–Mn1–O4 88.99(1)	O3–Mn1–O4 88.77(1)
N1–Mn1–O4 96.91(1)	O2–Mn1–O4 85.61(1)	O1–Mn1–N2 94.17(9)	O3–Mn1–N2 91.19(8)
N1–Mn1–N2 102.42(8)	O2–Mn1–N2 74.77(7)	O4–Mn1–N2 160.36(1)	

Δ configuration are found on the other face of the metallacrown. The two faces of the hexanuclear ring have opposite chiralities to each other. This organization results in an 18-membered hexanuclear core ring system with a [Mn–N–N] repeat unit. The approximate dimensions of the oval-shaped cavity are estimated by SHELXTL, to be about 6.97 Å in diameter at the entrance and about 9.53 Å at its largest diameter at the center of the cavity. It is also observed that all the atoms in the ligand are almost coplanar and the metal ion 6-membered ring is in a chair conformation. All manganese ions in compound **1** are in an octahedral MnN_2O_4 environment with a very distinct Jahn–Teller extension. The average neighboring Mn···Mn separation is 4.874 Å. There are no solvent molecules in the 'host' cavity of the metallacrown. In the packing diagram, the molecules translated one unit cell along the *a*-axis are stacked with minimum short contacts for $O3\cdots C7^{i}$ (3.36 Å) and $O3\cdots O2^{i}$ (2.79 Å) symmetry code (i): $[x-y, x, -z]$. The crystal packing may also be stabilized by intermolecular Cl–O interactions for each Cl atom in the structure, with an unusually short distance of 3.21 Å.

A perspective view of the complete Fe6 cluster molecule of $[Fe_6(acshz)_6(CH_3OH)_6]\cdot 6CH_3OH\cdot 6H_2O$ is provided in Fig. 2. This compound crystallizes in the triclinic system and space group $P\bar{1}$. Important bond distances and bond angles are presented in Table 2.

The metallacrown containing Fe6 cluster is analogous to **1**. It has the same backbone ligand and chelating mode of the central metal ion, except for the sixth coordinating atom from methanol. Although the chiralities of the metal

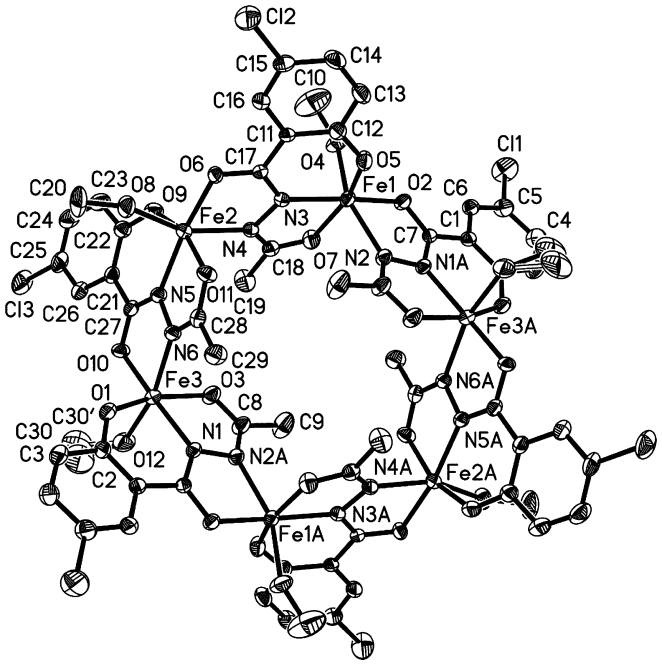


Fig. 2. Perspective view of compound **2**, solvent molecules and all hydrogen atoms have been omitted for clarity.

centers in complex **2** are between the Δ and Λ forms, it linked as a ΔΛΔ turn. The alternation of the chiralities force the cyclic ring system of **2** to form as the following train: –Fe1–N3–N4–Fe2–N5–N6–Fe3–N1–N2A–Fe1A–N3A–N4A–Fe2A–N5A–N6A–Fe3A–N1A–N2–. The cavity sizes of the **1** and **2** are different. The approximate

Table 2
Selected bond distances (Å) and angles (°) for compound **2**

Fe1–O2 2.009(3)	Fe1–O4 2.082(3)	Fe1–O5 1.936(3)	Fe1–O7 2.045(3)
Fe1–N2 2.111(3)	Fe1–N3 2.045(3)	N1–N2 1.410(4)	
O5–Fe1–O2 106.79(1)	O5–Fe1–N3 85.49(1)	O2–Fe1–N3 166.89(1)	O5–Fe1–O7 160.29(1)
O2–Fe1–O7 2.84(1)	N3–Fe1–O7 75.11(1)	O5–Fe1–O4 93.55(1)	O2–Fe1–O4 79.58(1)
N3–Fe1–4 95.40(1)	O7–Fe1–O4 91.77(1)	O5–Fe1–N2 92.73(1)	O2–Fe1–N2 76.26(1)
N3–Fe1–N2 108.35(1)	O7–Fe1–N2 90.12(1)	O4–Fe1–N2 155.83(1)	

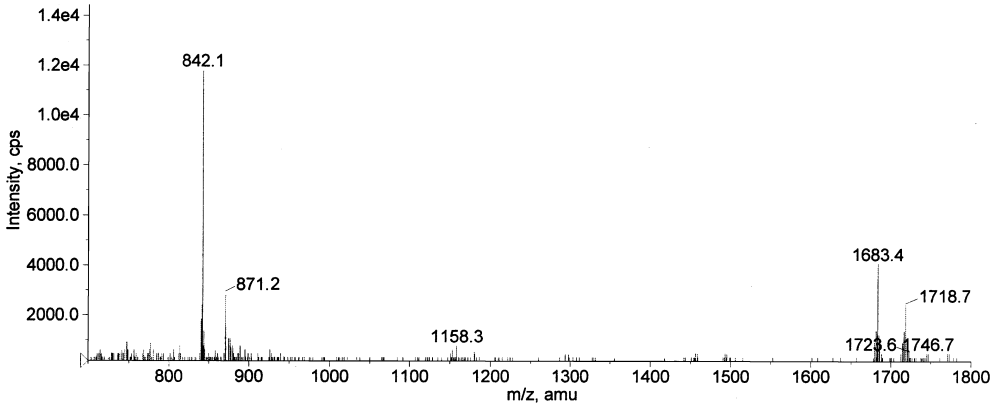


Fig. 3. The positive electrospray ionization mass spectra of **1** in methanol.

dimensions of the oval-shaped cavity are about 7.94 Å in diameter at the entrance and about 10.24 Å at its largest diameter at the center of the cavity in compound **2**. The change of the cavity size is probably caused by the metal ions themselves. There are some hydrogen bonds in the compound and their bond distances range from 2.616 to 2.888 Å. In particular, the phenolate–methanol (solvent)–methanol (coordinated) linkages formed by hydrogen bonds maybe are partly responsible for the difference in cavity shapes between the two complexes. The shortest distance of two neighboring iron(III) ions is 4.882 Å, which is longer than the distance of the two neighboring Mn(III) ions in **1**. The longest distance is 4.909 Å between Fe1 and Fe2 in **2**.

Comparing the above structures to $[Co_6(ashz)_6(CH_3OH)_6]\cdot 6CH_3OH$[11b], the chelating mode and coordination environment of the metal ions is similar. The M···M distances of the compounds in this paper are longer than those of the latter compound (Co···Co, 4.477 Å), and there are some distinct differences in the diameter of cavities (about 4.75 Å diameter at the entrance and 6.45 Å at its widest point in the latter compound). The cause of these differences maybe is from the little discriminating ligands and different metal ion arranged in the rings.

3.3. Structural integrity and stability in methanol

Electrospray ionization (ESI) mass spectroscopy, a soft ionization technique, has been proved useful in providing solution molecular weights of formally neutral metallacrown salt complexes [37]. The methanol solution of the Mn-containing cluster gave some peaks at *m*/*z* 1718.7, 1683.4 and 842.1 in ESI(+)-MS. These peaks correspond to the hexanuclear cluster ions $[Mn_6(acshz)_6(H_2O)_2+H]^+$, $[Mn_6(acshz)_6+H]^+$ and $[Mn_6(acshz)_6+2H]^{2+}$, respectively (Fig. 3). To explore the solution stability of the complexes in methanol solution, the concentration-dependent absorbance was measures at 374 and 506 nm for compounds **1** and **2**, respectively (Figs. 4 and 5). For **1**, the absorbance increases linearly with the concentration in the range between 3.1 and 100 μM [38], while for **2**, the concentration is between 3.8 and 75 μM. No change was observed for the absorption of the two solutions after two weeks. The results indicate that complexes **1** and **2** retain the integrity of the rings and are stable at least in these concentration ranges in methanol.

3.4. Antimicrobial activity

Minimum inhibitory concentrations of the ligand and compounds **1** and **2** against *S. aureus*, *E. coli*, *B. subtilis* and *P. vulgaris* are listed in Table 3. As can be clearly seen from the table, none of the compounds have strong antimicrobial activity against most of the tested microorganisms, except that compound **2** may restrain the propagation of *B. subtilis* effectively. Moreover, in this study,

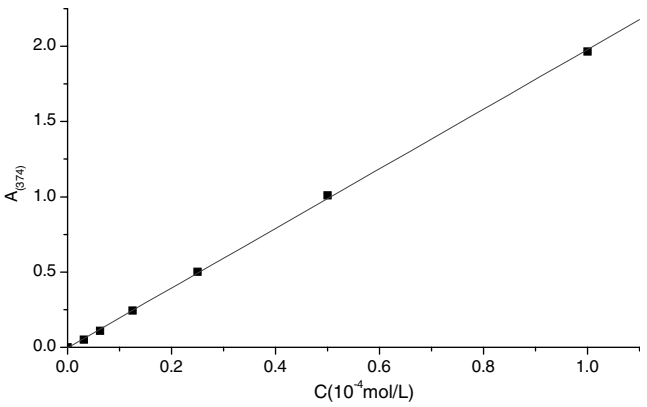


Fig. 4. The concentration dependent absorbance of complex **1** in methanol was measured at 374 nm.

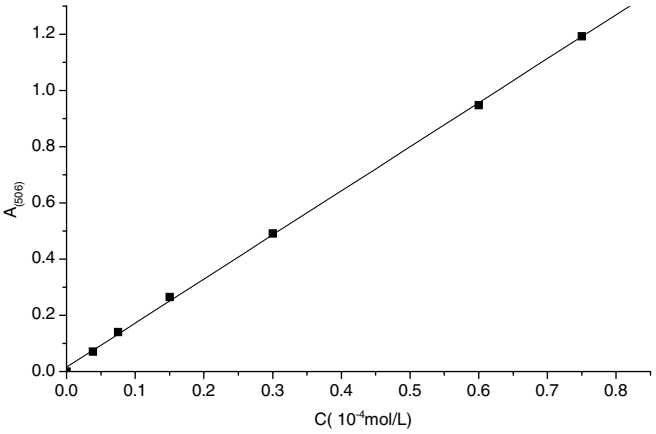


Fig. 5. The concentration dependent absorbance of complex **2** in methanol was measured at 506 nm.

Table 3
Minimum inhibitory concentration (MIC) of the ligand *N*-acetyl-5-chlorosalicylhdrazide and compounds **1** and **2** in μg/mL

Microorganisms	Complexes		
	Ligand	**1**	**2**
S. aureus (Gram+)	100	1600	200
E. coli (Gram−)	400	1600	200
B. subtilis (Gram+)	400	400	25
P. vulgaris (Gram−)	300	1600	200

the results do not indicate specificity against Gram-positive or Gram-negative bacteria although it is generally expected that a much greater number would be active against Gram-positive than Gram-negative bacteria [39]. In terms of the ligand H_3acshz, its antimicrobial activities are stronger than those in the foregoing literature [40]. Antibacterial screening data indicated that metallacrown **1** has an antagonistic effect to the ligand H_3acshz, resulting in the huge reduction of the antimicrobial activity, while metallacrown **2** has stronger antimicrobial activity against *B. subtilis*. One of reasons for it maybe is the difference of the bond capability of the Mn ion and the Fe

Table 4
The crystallographic data for compounds **1** and **2**

	1	**2**
Empirical formula	$C_{54}H_{84}Cl_6Mn_6N_{12}O_{42}$	$C_{66}H_{96}Cl_6Fe_6N_{12}O_{36}$
Fw (amu)	2115.67	2181.35
T (K)	292(2)	292(2)
Crystal system, space group	rhombohedral, $R\bar{3}c$	triclinic, $P\bar{1}$
a (Å)	17.0019(1)	12.210(1)
b (Å)	17.0019(1)	14.864(1)
c (Å)	62.241(1)	14.913(1)
α (°)	90.00	70.628(1)
β (°)	90.00	78.092(1)
γ (°)	120.00	72.678(1)
V (Å^3)	15581(4)	2420(4)
Z, D_{calc} (g cm^{-3})	6, 1.353	1, 1.497
μ (mm^{-1})	0.942	1.125
F(000)	6480	1122
Crystal size (mm^3)	0.40 × 0.40 × 0.30	0.20 × 0.10 × 0.10
Number of data/restraints/parameters	3211/3/166	8471/4/562
Number of reflections [$I > 2\sigma(I)$]	2533	5277
Goodness-of-fit on F^2	1.003	0.896
Final *R* indices [$I > 2\sigma(I)$]	R_1[a] = 0.0452	R_1[a] = 0.0544
R Indices (all data)	wR_2[b] = 0.1377	wR_2[b] = 0.1245

[a] $R_1(F) = \sum ||F_o| - |F_c|| / \sum |F_o|$.
[b] $wR_2(F2) = [\sum w(F_o^2 - F_c^2)^2 / \sum w(F_o^2)^2]^{1/2}, w = 1/[\sigma^2(F_o^2) + (0.1005P)^2 + 0.0000P]$ for **1** and $w = 1/[\sigma^2(F_o^2) + (0.0574P)^2 + 0.0000P]$ for **2**, $P = ((F_o^2 + 2F_c^2)/3)$.

ion to the ligand. The different coordinated solvent molecules are likely to affect the antimicrobial activity of these compounds.

4. Conclusion

Compounds **1** and **2** are the first examples of 18-metallacrown-6 compounds containing Mn^{3+} and Fe^{3+} as ring ions with the ligand *N*-acetyl-5-chlorosalicylhdrazide. Due to the meridional coordination of the ligand to the Mn^{3+} and Fe^{3+} ions, the ligand enforces the stereochemistry of the Mn^{3+} and Fe^{3+} ions as a propeller configuration with alternating Λ/Δ or Δ/Λ forms, respectively. The other important structural feature in $[Mn_6(acshz)_6(H_2O)_6]\cdot 12H_2O$ and $[Fe_6(acshz)_6(CH_3OH)_6]\cdot 6CH_3OH\cdot 6H_2O$ is that there is not only a vacant cavity in the center of the 18-metallacrown-6 core ring, but also opposite chiralities on the two faces of the metallacrown ring system. Although the two metallacrown compounds are constructed with the same ligand, there are great differences between them in terms of antimicrobial activity. Antibacterial screening data showed that metallacrown **1** has an antagonistic effect to the ligand H_3acshz resulting in a huge reduction of the antimicrobial activity, while metallacrown **2** has stronger antimicrobial activity against *B. subtilis*.

Acknowledgement

This work was supported by the National Natural Science Foundation of China (Grant No. 20171035).

Appendix A. Supplementary material

CCDC 614745 and 614744 contain the supplementary crystallographic data for **1** and **2**. These data can be obtained free of charge via http://www.ccdc.cam.ac.uk/conts/retrieving.html, or from the Cambridge Crystallographic Data Centre, 12 Union Road, Cambridge CB2 1EZ, UK; fax: (+44) 1223-336-033; or e-mail: deposit@ccdc.cam.ac.uk. Supplementary data associated with this article can be found, in the online version, at doi:10.1016/j.poly.2007.01.020.

References

[1] (a) B. Olenyuk, J.A. Whiteford, P.J. Stang, J. Am. Chem. Soc. 118 (1996) 8221;
(b) P.J. Stang, B. Olenyuk, J. Fan, A.M. Arif, Organometallics 15 (1996) 904;
(c) L.G. Abbati, A. Cornia, A. Caneschi, A.C. Fabretti, C. Mortalo, Inorg. Chem. 43 (2004) 4540;
(d) Z.P. Zheng, C.B. Knobler, M.D. Mortimer, G. Kong, M.F. Hawthorne, Inorg. Chem. 35 (1996) 1235;
(e) J.A.R. Navarro, M.B.L. Janik, E. Freisinger, B. Lippert, Inorg. Chem. 38 (1999) 426.
[2] (a) V.L. Pecoraro, Inorg. Chim. Acta 155 (1989) 171;
(b) M.S. Lah, V.L. Pecoraro, J. Am. Chem. Soc. 111 (1989) 7258;
(c) M.S. Lah, M.L. Kirk, W. Hatfield, V.L. Pecoraro, J. Chem. Soc., Chem. Commun. (1989) 1606.
[3] (a) J.J. Bodwin, A.D. Cutland, R.G. Malkani, V.L. Pecoraro, Coord. Chem. Rev. 216–217 (2001) 489;
(b) C.M. Zaleski, E.C. Depperman, C. Dendrinou-Samara, M. Alexiou, J.W. Kampf, D.P. Kessissoglou, M.L. Kirk, V.L. Pecoraro, J. Am. Chem. Soc. 127 (2005) 12862.
[4] (a) M.S. Lah, V.L. Pecoraro, Inorg. Chem. 30 (1991) 878;
(b) M.S. Lah, B.R. Gibney, D.L. Tierney, J.E. Penner-Hahn, V.L. Pemraro, J. Am. Chem. Soc. 115 (1993) 5857;
(c) C. Dendrinou-Samara, G. Psomas, L. Iordanidis, V. Tangoulis, D.P. Kessissoglou, Chem. Eur. J. 7 (2001) 5041;
(d) A.D.C-V. Noord, J.W. Kampf, V.L. Pecoraro, Angew. Chem. 114 (2002) 4861.
[5] (a) B. Kwak, H. Rhee, S. Park, M.S. Lah, Inorg. Chem. 37 (1998) 3599;
(b) S.X. Liu, S. Lin, B.Z. Lin, C.C. Lin, J.Q. Huang, Angew. Chem., Int. Ed. 40 (2001) 1084.
[6] B.R. Gibney, D.P. Kessissoglou, J.W. Kampf, V.L. Pecoraro, Inorg. Chem. 33 (1994) 4840.
[7] A.J. Stemmler, J.W. Kampf, V.L. Pecoraro, Inorg. Chem. 34 (1995) 2271.
[8] G. Psomas, C. Dendrinou-Samara, M. Alexiou, A. Tsohos, C.P. Raptopoulou, A. Terzis, D.P. Kessissoglou, Inorg. Chem. 37 (1998) 6556.
[9] D.P. Kessissoglou, J. Kampf, V.L. Pecoraro, Polyhedron 13 (1994) 1379.
[10] (a) A.J. Stemmler, A. Barwinski, M.J. Baldwin, V. Young, V.L. Pecoraro, J. Am. Chem. Soc. 118 (1996) 11962;
(b) A.J. Stemmler, J.W. Kampf, M.L. Kirk, B.H. Atasi, V.L. Pecoraro, Inorg. Chem. 38 (1999) 2807.
[11] (a) I. Kim, B. Kwak, M.S. Lah, Inorg. Chim. Acta 317 (2001) 12;
(b) S. Lin, S.X. Liu, J.Q. Huang, C.C. Lin, J. Chem. Soc., Dalton Trans. (2002) 1595.
[12] S. Lin, S.X. Liu, Z. Chen, B.Z. Lin, S. Gao, Inorg. Chem. 43 (2004) 2222.
[13] C. Dendrinou-Samara, C.M. Zaleski, A. Evagorou, J.W. Kampf, V.L. Pecoraro, D.P. Kessissoglou, Chem. Commun. (2003) 2668.
[14] P.J. Rohith, K. Lee, M.S. Lah, Chem. Commun. (2004) 2660.

[15] Y. Bai, D.D. Dang, C.Y. Duan, Y. Song, Q. J. Meng. Inorg. Chem. 44 (2005) 5972.
[16] R.W. Saalfrank, N. Low, S. Kareth, V. Seitz, F. Hampel, D. Stalke, M. Teichert, Angew. Chem., Int. Ed. 37 (1998) 172.
[17] H. Piotrowski, G. Hilt, A. Schulz, P. Mayer, K. Polborn, K. Severin, Chem. Eur. J. 7 (2001) 3197.
[18] A.E. Pullen, J. Piotraschke, K.A. Abboud, J.R. Reynolds, Inorg. Chem. 35 (1996) 793.
[19] A.D. Cutland, J.A. Halfen, J.W. Kampf, V.L. Pecoraro, J. Am. Chem. Soc. 123 (2001) 6211.
[20] A.C. Cutland-Van Noord, J.W. Kampf, V.L. Pecoraro, Angew. Chem., Int. Ed. 41 (2002) 4668.
[21] J.J. Bodwin, V.L. Pecoraro, Inorg. Chem. 39 (2000) 3434.
[22] M. Moon, I. Kim, M.S. Lah, Inorg. Chem. 39 (2000) 2710.
[23] R.W. Saalfrank, I. Bernt, E. Uller, F. Hampe, Angew. Chem., Int. Ed. 36 (1997) 2482.
[24] G. Psomas, A.J. Stemmler, C. Dendrinou-Samara, J. Bodwin, M. Schneider, M. Alexiou, J.W. Kampf, D.P. Kessissoglou, V.L. Pecoraro, Inorg. Chem. 40 (2001) 1562.
[25] C. Dendrinou-Samara, L. Alevizopoulou, L. Iordanidis, E. Samaras, D.P. Kessissoglou, J. Inorg. Biochem. 89 (2002) 89.
[26] (a) H. Zhao, N. Neamati, S. Sunder, H. Hong, S. Wang, G.W.A. Milne, Y. Pommier, T.R. Burke Jr., J. Med. Chem. 40 (1997) 937; (b) H. Rutner, N. Lewin, E.C. Woodbury, T.J. McBride, K.V. Rao, Cancer Chemother. Reports, Part 1 58 (1974) 803.
[27] S. Lin, S.X. Liu, B.Z. Lin, Inorg. Chim. Acta 328 (2002) 69.
[28] G.M. Sheldrick, SADABS, University of Gottingen, Germany, 1996.
[29] Bruker AXS Inc. SMART APEX (Version5.628), SAINT^{+} (Version 6.45) and SHELXTL-NT (Version 6.12), Bruker AXS Inc., Madison, WI, USA, 2001.
[30] G.M. Sheldrick, SHELXS97 and SHELXL97, University of Gottingen, Germany, 1997.
[31] P.V.D. Sluis, A.L. Spek, Acta. Crystallogr. A. 46 (1990) 194.
[32] L.J.J. Farrugia, Appl. Cryst. 32 (1999) 837.
[33] E. Pretsch, P. Buhmann, C. Affloter, Structure Determination of Organic Compounds Tables of Spectral Data (transitions), East China University of Science and Technology, Shanghai, China, 2002.
[34] K. Nakamoto, Infrared and Raman Spectra of Inorganic and Coordination Compounds, 4th ed., John Wiley & Sons, New York, 1986.
[35] S. Ziming, K.G. Peter, N.H. David, Polyhedron 17 (1998) 1511.
[36] M.S. Lah, Comments Inorg. Chem. 11 (1990) 59.
[37] A.J. Stemmler, J.W. Kampf, M.L. Kirk, B.H. Atasi, V.L. Pecoraro, Inorg. Chem. 38 (1999) 2807.
[38] The figures that show the concentration-dependent absorbance of compound **1** at 374 nm and compound **2** at 506 nm is in Supplementary material.
[39] A.R. Mc-Cutheon, S.M. Ellis, R.E.W. Hancock, G.H.N. Towers, J. Ethnopharmacol. 37 (1992) 213.
[40] C. Dendrinou-Samara, A. Lito, L. Iordanidis, E. Samaras, D.P. Kessissogloua, J. Inorg. Biochem. 89 (2002) 89.